60th Anniversary Symposium of the International Association for Shell and Spatial Structures

IASS Symposium 2019

9th International Conference on Textile Composites and Inflatable Structures

Structural Membranes 2019

FORM and FORCE

7-10 October 2019, Barcelona, Spain

Carlos Lázaro, Kai-Uwe Bletzinger and Eugenio Oñate (Eds.)



IASS Symposium 2019

60th Anniversary Symposium of the International Association for Shell and Spatial Structures

Structural Membranes 2019

9th International Conference on Textile Composites and Inflatable Structures

FORM and FORCE

Barcelona, Spain
October 7 - 10, 2019

A publication of:

International Centre for Numerical Methods in Engineering (CIMNE)
Barcelona, Spain

ISBN: 978-84-121101-0-4

Printed by: Artes Gráficas Torres S.L., Huelva 9, 08940 Cornellà de Llobregat, Spain

TABLE OF CONTENTS

Preface 7

Acknowledgements 9

Summary 11

Contents 13

Papers 43

Authors Index 2966

PREFACE

This volume contains the full papers presented at the international conference **Form and Force**, incorporating the 60th Anniversary Symposium of the International Association for Shell and Spatial structures (**IASS Symposium 2019**) and the 9th International Conference on Textile Composites and Inflatable Structures (**Structural Membranes 2019**) in Barcelona

This year marks the celebration of the IASS 60th Anniversary and is therefore a very special occasion for the IASS community. It is also an important landmark for the Structural Membranes series of conferences, which are being held since 2003. Having Barcelona as the venue of this international event fulfils several goals: it honours the tradition of celebrating the IASS Symposium every ten years in Spain, where the association was founded by Eduardo Torroja; Barcelona was also the venue of the first Structural Membranes conference in 2003; since then, it has been held bi-annually alternating between Barcelona, Stuttgart and Munich. Most importantly, **Form and Force** offers the opportunity to merge two communities that have converging scientific, technological and professional interests: advancing the knowledge in the design, production and building of structures, as well as devising best ways to do it to benefit society and environment.

The title of the conference, Form and Force, reflects a shared idea of all those concerned with innovation in structures: the interplay between structural form and physical forces is key to understanding behaviour, improving design, achieving beauty, increasing efficiency and reducing carbon footprint. Tension and membrane structures, shells and spatial structures show, better than any other structural type, that shape and stress, form and force, are deeply interrelated. This relationship reaches well beyond purely static aspects and has an impact on performance, design, environment and aesthetics of structures in multiple fields of application.

The topics of **Form and Force** encompass all aspects of design, analysis, construction, manufacturing, maintenance and environmental compatibility of lightweight, shell and spatial structures, with emphasis in the field of tension, membrane and inflatable structures and in the creative integration of structural engineering and architecture.

- Structural systems (shell structures, tension and membrane structures, inflatable structures, tensegrity systems, origami and folded systems, elastic gridshells and bending-active systems, deployable and adaptive systems);
- Material-based structures (metal spatial structures, timber and bio-based structures, glass structures);
- Design projects and realizations;
- Computation, form-finding and optimization;
- Historical structures and memorial contributions (on David P. Billington and Mike Barnes);
- Environmental compatibility and lifecycle of structures;
- Teaching of spatial structures;
- Advanced manufacturing and non-conventional materials

We do not want to conclude this preface without honouring the memory of two persons who recently passed away and have been most prominent figures of our communities:

Prof. Bernd Kröplin, co-chair and founder of the Structural Membranes conferences series, a brilliant mind who proposed and developed ideas ahead of his time, and Prof. Mamoru Kawaguchi, former President of the IASS and one of the most prominent structural designers of the 20th century. Prof Kawaguchi had a very special relationship with Barcelona as the structural designer of the 'Palau Sant Jordi' stadium for the 1992 Olympics.
The collection of full papers includes contributions sent directly from the authors and the editors cannot accept responsibility for any inaccuracies, comments and opinions contained in the text.
The organizers would like to take this opportunity to thank all authors for submitting their contributions.

Barcelona, 7 October 2019

Carlos Lázaro, Universitat Politècnica de València (UPV), València, Spain
Kai-Uwe Bletzinger, Technische Universität München (TUM), Munich, Germany
Eugenio Oñate, Universitat Politècnica de Catalunya (UPC), Barcelona, Spain

ACKNOWLEDGEMENTS

The conference organizers acknowledge the support of the following organizations:

International Association for Shell and Spatial Structures (IASS)

European Community on Computational Methods in Applied Sciences (ECCOMAS)

International Association for Computational Mechanics (IACM)

Asociación Española de Ingeniería Estructural

Universitat Politècnica de Catalunya (UPC)

International Centre for Numerical Methods in Engineering (CIMNE), Spain

E.T.S. Ingeniería de Caminos, C. y P. (UPV)

SUMMARY

INVITED SESSIONS

IS - Actual Structural Behavior of Thin Shells (IASS WG 5) 45

IS - Adaptive Lightweight Structures 68

IS - Additive Manufacturing of Architectural Components..... 87

IS - Analysis and Design of Adaptive Structures.....121

IS - Bio-inspiration for Structural Forms + Fractal and Form 129

IS - Celebrating the Work of Mike Barnes.....145

IS - Constructive Geometry for Structural Design (IASS WG 15).....175

IS - Contemporary Tensile Structures of Europe (IASS WG 6).....229

IS - Contributions in Memory of David P. Billington 237

IS - Design and Analysis of Bending-active Structures (IASS WG 15) 320

IS - Detailing - Case Studies - Installation Process.....344

IS - Embracing Inter-/crossdisciplinarity Through New Roles, Methods and Tools for Design and Fabrication of Spatial Structures (IASS WG 20) 394

IS - Form and Force Expo Pavillions (IASS WG 21) 447

IS - Form and Force in Bio-based Structures and Architecture (IASS WG 12) 614

IS - Form-finding/Force-finding of Tension Structures Using Novel Computational Methods (IASS WG 13) 653

IS - Graphic Statics / Reciprocal Diagrams (IASS WG 15) 677

IS - Gridshells: Computational Methods and Case Studies 712

IS - Improving and Assessing the Life Cycle of Structures (IASS WG 18) 744

IS - Numerical Methods and Modeling for Lightweight Structures.....769

IS - Optimization Driven Architectural Design of Structures 828

IS - Preservation and Reuse of Reinforced Concrete Shells (IASS WG5 - IASS WG 17) ..850

IS - Pressurized Membrane Structures: Analysis and Applications 882

IS - Reliability Analysis of Membrane Structure (IASS WG 6).....907

IS - Stability and Dynamics of Metal Gridshell Structures (IASS WG 8) 930

IS - Structural Origami (IASS WG 15) 1047

IS - Textile and Foil Synergies and Advances in Shell and Membrane Structures 1088

IS - The Next Generation of Parametric Design 1096

IS - Transformable Structures (IASS WG 15)..... 1171

IS - Wind Engineering and Fluid-structure Interaction..... 1179

CONTRIBUTED SESSIONS

CS - Advanced Manufacturing - 3D Printing 1239
CS - Advanced Manufacturing - General 1310
CS - Advanced Manufacturing - Ice 1341
CS - Advanced Manufacturing - Robotics 1366
CS - Analysis and Design 1389
CS - Analytical Methods 1465
CS - Case Studies 1513
CS - Computational Methods 1547
CS - Conceptual Design 1684
CS - Deployable and Adaptive Systems 1720
CS - Design Projects 1820
CS - Elastic Gridshells and Bending Active Systems 1878
CS - Environmental Compatibility and Life-Cycle of Structures 1940
CS - Form-finding and Optimization 1992
CS - Form-finding with Graphic Statics 2155
CS - Glass Structures 2180
CS - Historical Structures 2217
CS - Inflatable Structures 2257
CS - Membrane Materials 2297
CS - Membrane Structures 2363
CS - Metal Spatial Structures 2384
CS - Non-conventional Materials 2480
CS - Origami and Folded Systems 2511
CS - Realizations 2535
CS - Shell Structures 2627
CS - Structural Morphology 2685
CS - Teaching and Education 2772
CS - Tensegrity Systems 2798
CS - Timber and Bio-based Structures 2854

HANGAI PRIZE LECTURE

Hangai Prize Lecture 2933

CONTENTS

INVITED SESSIONS

IS - Actual Structural Behavior of Thin Shells (IASS WG 5)

About the funicularity of Velaroidal Shells - KEYNOTE 45
S. Gabriele, F. Marmo and V. Varano

Bioinspired design of shell structures: a lesson from echinoids 53
F. Marmo, V. Perricone, C. Langella, G. Pontillo and L. Rosati

Design and Analysis of Freeform Shell Structures Composed of Doubly Curved Sheet Metal Panels 60
A. Seiter, T. Pofahl, M. Trautz, L.-M. Reitmaier and G. Hirt

IS - Adaptive Lightweight Structures

Dynamic Space Truss-Textile Membrane Assemblies 68
K Tracy, S. Gupta and D. Jayashankar

Retractable Roof Tecklenburg..... 76
G. Schmid

IS - Additive Manufacturing of Architectural Components

Additive Formwork for Concrete Shell Constructions 87
R. Naboni and L. Breseghello

Challenges of 3d printed architectural ceramic components structures: controlling the shrinkage and preventing the cracking 95
B. Figueiredo, P J S Cruz, J. Carvalho and J. Moreira

From rapid prototyping to real building: methodologies for upscaling additive manufacturing prototypes to functional architectural components.....103
P. Cruz, B. Figueiredo, J. Carvalho and J. Ribeiro

Terramia: Drone-Aided Construction for a Sustainable Biobased Housing Prototype.....113
S Chaltiel, D Veenendaal and F Verzura

IS - Analysis and Design of Adaptive Structures

Analysis of an adaptive tensegrity module.....121
S. Kmet, V. Urban, M. Tomko and R. Soltys

IS - Bio-inspiration for Structural Forms + Fractal and Form

A Bio-Informed Topology Optimization Algorithm Based on Leaf Venation Structures.....129
N. Frangos, D. Reynolds, G. Fagerström and N. Richardson

A generation of frame structure based on Koch curve and an application to spatial frame 137
T. Mae and I.Md. Rian

IS - Celebrating the Work of Mike Barnes

Architecture and Engineering - a double degree educational program at Chalmers University of Technology.....145
K.-G. Olsson

Isogeometric Analysis and formfinding for thin elastic shells 153
J Hilmersson, F. Larsson, J. Olsson and M. Ander

Mike Barnes's legacy: the emergence of form finding and analysis approaches for bending active and elastic grid shell structures.....161
S. Adriaenssens

Unloaded prestressed shell formed from a closed surface unattached to any supports.....167
A. Sehlstöm and C. Williams

IS - Constructive Geometry for Structural Design (IASS WG 15)

A digital design process for shell structures 175
M. Contestabile and O. Iuorio

Computational morphogenesis and digital simulation of the construction process of masonry domes built without centrings.....183
L. Esposito, G. Boccia, A. Luporino and S. Pone

Design and optimization of grid shell structured using Christoffel duality.....193
Z. Tošić, S. Krasic and D. Kostic

STEREODOME I: design, production and installation of a Styrofoam masonry vault 201
R. M. Avelino, P. H.P. Torres, A. v.L. Carvalho, B. Montelato, B. Teixeira, B. T. Vasconcelos, M. Oliveri, M. S. O. Soto and R.M. Pauletti

Structural efficiency of segmental shells, depending on segment geometries and connection properties.....209
C. Dijoux, F. Schmidt-Kleespies and A. Stahr

Study Case: Design & Construction Of A Spherical Actively-Bent Chebychev Net Triangular Gridshell Covered By A Stretchable Membrane 218
A. Rynne, N. Rodriguez, J. Rodriguez, M. Fabré, M. Sais, C. Dimitri, G. Bertomeu, P. Tornabell and E. Soriano

IS - Contemporary Tensile Structures of Europe (IASS WG 6)

Contemporary Membrane Structures in Europe (2010-2018).....229
J. Llorens

IS - Contributions in Memory of David P. Billington

Connecting technical rigor and visual creativity.....237
G Herning

Current Realities and New Opportunities for Efficiency, Economy, and Elegance in Bridge Design.....245
P. Gauvreau

Exploring the ideals and character of structural art. 253
C. Huntington

Lateral load resisting facades 261
M. Lopez, J. Blanchfield, P. Murray, D. Kazibwe, C. Bai and R. Gilsanz

Making His Story of Structures My Own 269
E. Salikis

Quintessentially Billington: The Evolution of Structural Art Teaching at Princeton.....275
M. Garlock, S. Adriaenssens and B. Glisic

Simplified closed-form expressions for horizontal reactions in linear elastic arches under self-weight 282
B. Glisic

Structural Art and Conceptual Design in Engineering Education: a Perfect Marriage 290
I. Paya-Zaforteza

Structural Art, the 4th Dimension, and Metaphors for Teaching Design 298
J. Matteo

The art of collaborative structural design: Structural art in the age of cross-disciplinary collaboration.....305
C Herr

Travel and the Structural Engineer 312
P. Draper and E.M. Segal

IS - Design and Analysis of Bending-active Structures (IASS WG 15)

Bending active structures with a variable cross-section boundary 320
M. Redoutey, S. Ahlquist, J. Shaw and E. Filipov

Longterm Behaviour of graded CNC knitted Bending Active Textile Hybrids under real world conditions 328
M. Tamke, M. Ramsgaard Thomsen, Y. Sinke, R. De La Manga, J. Lienhard and M. Hazzard

Strip-Based Double-Layered Lightweight Timber Structure 336
D. Stanojevic and K. Takahashi

IS - Detailing - Case Studies - Installation Process

A new generation of coated belts for structural membranes 344
H. Poeppinghaus

Airport City Belgrade Membrane Structure : design, production and installation process 351
A.P. Vucur and G.H. Filz

Detailing masts 359
J. Llorens

Fixation Details and Membrane Assembly 367
M. Cardenas Pantoja

Most Common Connections Details in ETFE Constructions 372
J. Salo

On the static calculation of biogas containers with radial and parallel cutting patterns 380
D. Ströbel and J. Holl

Switchable ETFE cushion: designing and building a model for experimental testing 388
J.-F. Flor, Y. Sun, P. Beccarelli, Y. Wu and J. Chilton

IS - Embracing Inter-/crossdisciplinarity Through New Roles, Methods and Tools for Design and Fabrication of Spatial Structures (IASS WG 20)

An academic experiment on the design of spatial truss models and teamwork 394
L. Meneghetti, R. Pauletti and L. Bitencourt Jr

Interlocking spaces: A structural prototype inspired by Kigumi Architecture 401
L. Allner, P. Reinsberg and J. Sato

Reinventing the truss: A collaborative pedestrian bridge design project...408
C. Herr, W. Hou, S. Li, H. Zhang and D. Lombardi

The (changed) roles of physical models in building design practice and education 416
O. Popovic Larsen

The Working Model: A cross-disciplinary collaborative tool.....424
V Petrova and O. Popovic Larsen

Towards the classroom of the future: new ideas and proposals 433
I. Paya-Zaforteza, N. Matarredona-Desantes, T. Pellicer-Armiñana and P. Fuentes-Durá

Tutorials for Tutorials: Guidelines for Creating Video Tutorials on Teaching Structural Morphology to Architecture Students. 439
A. Khodadadi and N. Emami

IS - Form and Force Expo Pavillions (IASS WG 21)

A Method for Flat-pack Origami Construction of Spatial Structures.....447
Y. Ishida, T. Lewis, K. Kane, R. Gupta and A. Heang

An Adaptive Pretension Structure......459
J. Rieth, L. Kastner, C. Holzinger and A. Trummer

Common Multiple, an active-bent lightweight structure......467
M. Bukovec, V. Schabbon, K. Scharler, C. Holzinger and A. Trummer

Deployable bamboo dome.....475
N. Torres, E. Cortes-Paez, S. Sastre, X. Gimferrer, F. Intrieri and I. González

Design and Construction of an Innovative Pavilion Using Topological Optimization and Robotic Fabrication.....485
D.W. Bao, X. Yan, R. Snooks and Y.M. Xie

Design of Discretized Acrylic Shells with Heat-Induced Form-Finding.....493
L. Ramsburg, A. Chao, E.M. Segal and P. Draper

Digital Tessellation and Fabrication of the ECHO shell 501
O. Iuorio, E Korkis and M Contestabile

FlexMaps Pavilion: a twisted arc made of mesostructured flat flexible panels 509
F. Laccone, L. Malomo, J. Perez, N. Pietroni, F. Ponchio, B. Bickel and P. Cignoni

Hybridating vertex and face normals to design torsion-free gridshells: application to the X-Mesh pavilion.....516
X. Tellier, C. Douthe, N. Leduc, S. Zerhouni, G. Jami, A. Le Pavec, T. Lenart, M. Lerouge, L. Hauswirth and O. Baverel

Inventory Constrained Funicular Modelling.....524
K. Baber, J. Burry, C. Chen, J. Gattas and A. Bukauskas

Knit Tensegrity Shell Structures 534
K. Tracy, S. Gupta, Y Tan, P Chia, C Pambudi and C Yogiaman

Lightweight Cellular Structure: A Formless Fiberglass Buildup Utilize Bending-Active 543
B.S. Liu, T. Faisal, C. Saft, J. Heath, S. Jaber, Q.M. Dang, C. Reaux, O. Welty and S. Nguyen

Lightweight Rigidly Foldable Canopy using Composite Materials.....548
K. Ando, B. Izumi, M. Shigematsu, H. Tamai, J. Matsuo, Y. Mizuta, T. Miyata, J. Sadanobu, K. Suto and T. Tachi

Minimal surface tensegrity networks: The case of an enneper surface pavilion structure.....558
K. Liapi, A. Papantoniou, C. Nousias and A. Ioannidi

Prefabricated Component Structure made of corn starch flips 563
T. Ludwig, H. Melzer, A. Trummer and C. Holzinger

Quipustructure 568
M. Espinoza, L. Pacheco, K. Torres, H. Caedro and A. Apumayta

Reviving a Craft through Architecture: Computational Making of a lightweight pavilion based on wire-bending techniques.....574
V. A. A. Noel

Self-deploying Tensegrity Structures with Inflatable Struts.....582
J. Dessi-Olive, M. Koliner, J. Case and V. Teja Meda

The excellence of construction timber details throughout a Tectonic methodology 590
L. Catala Bustos and P.H. Kirkegaard

Tribute to Kenneth Snelson 598
F. Brusciotti, I. Giannetti, A. Micheletti, S. Nwokoye, D. Ruggeri and G. Ruscica

X-Shell Pavilion: A Deployable Elastic Rod Structure.....606
F. Isvoranu , J. Panetta, E. Bouleau, T CHEN and M. Pauly

IS - Form and Force in Bio-based Structures and Architecture (IASS WG 12)

Eco-friendly Mid-rise Apartments Using CLT Panels 614
A. Khodadadi

Finnish Fins: a novel approach to short-span bridges by the use of stiffening fins 622
J. M. García-Guerrero, G. Fink and G.H. Filz

Relationship between bending performance and chip size of strand board made from reed 629
T. Nagai

Space truss built with wastes from the sawmill industry 637
O. Baverel, T Le Borgne, F Zaninetti and G Hivin

Sustainable design concepts for short span, timber-only structures 645
G. Fink, G. Ruan and G.H. Filz

IS - Form-finding/Force-finding of Tension Structures Using Novel Computational Methods (IASS WG 13)

Form-finding and structural modification of a hybrid cable-strut system.....653
R. Asghari, K. Abadi and M.R Chenaghlou

Optimization of initial prestress for cable-strut systems with multiple symmetric self-stress modes 661
P. Zhang

Optimization of tensegrity lattice with truncated octahedral units.....669
M. Ohsaki, J. Y. Zhang, K. Kogiso and J. J. Rimoli

IS - Graphic Statics / Reciprocal Diagrams (IASS WG 15)

A geometrical approach to assess levels of structural robustness in statically indeterminate concrete elements.....677
A. Deschuyteneer, D. Zastavni and J.-F. Remacle

Form-finding method of cable-net structures using Grassmann algebra and mass-points. 685
M. Banicek, K. Fresl, M. Uros and T. Kostric

From Polyhedral to Minimal Surface Funicular Spatial Structures 693
M. Akbari, M. Bolhassani and M. Akbarzadeh

Geometric approach to form finding of a spoke wheel system: Mathematical explanations.....703
H. Tamai

IS - Gridshells: Computational Methods and Case Studies

An equivalent continuum of gridshell model 712
M.L. Regalo, S. Gabriele, G. Salerno and V. Varano

Applications of Timber Gridshells for Humanitarian Assistance and Disaster Relief Efforts 720
T. Imhoff and S. Malek

Fabrication-aware design of architectural envelopes using surfaces with planar curvature lines 728
X. Tellier, C. Douthe, L. Hauswirth and O. Baverel

The design, analysis, fabrication and assembly of an asymptotic plywood gridshell 736
E. Adiels, C Brandt-Olsen, J Isaksson, K.-G. Olsson, I Näslund, E. Poulsen and C. Williams

IS - Improving and Assessing the Life Cycle of Structures (IASS WG 18)

ADOBE BRICKS FOR SUSTAINABLE BUILDING 744
C. Mircea, G. Calatan and A. Mircea

Parametric design and LCA for temporary structures: structural material options and optimization of multiple installation cycles using genetic algorithm 751
C. Mazzola, S. Viscuso, C. Monticelli and A. Zanelli

Towards Methodology of Life Cycle Analysis for Structural Reuse 759
K. Kuzmenko, C. Douthe, A. Feraille and O. Baverel

IS - Numerical Methods and Modeling for Lightweight Structures

A unified approach for shell analysis on explicitly and implicitly defined surfaces 769
D. Schoellhammer and T.P. Fries

Application of a Computer Aided Design Program for Shells with Aluminum Alloy Gusset Jointsâ--Case Study 777
S. Zong, X. Guo, S. Zhu, Q. Zeng and Y. Chen

Biaxial tensile analysis in a high tenacity polyester fabric 784
C. Suzin, M. Coelho and P. Gosling

Geometric and structural analysis of existing vaults using parametric surfaces. 791
J. Tutsch, C. Reihl and R. Barthel

Isogeometric Analysis in the Design Process of Lightweight Structures 799
A. M. Bauer, R. Wüchner and K.-U. Bletzinger

Large torsion on elastic lamella grid structures 807
J. Schikore, A. M. Bauer, R. Barthel and K.-U. Bletzinger

Numerically inflating air domes 815
J. Bellmann and A. von Breymann

The new German standard DIN 18204-1:
Design of tents and halls with PVC-coated polyester fabrics. 820
N. Stranghöner and J. Uhlemann

IS - Optimization Driven Architectural Design of Structures

A review on environmental and economic potential of robotic construction in actual scale driven by structural optimization 828
O Kontovourkis, G. Tryfonos and P Konatzii

An Automated Reconfiguration Sequence Process of a Bar-Linkage Structure 836
M. Matheou, I. Chamseddine, M. Kokkolaras and M.C. Phocas

Structural Optimization of Tubular Steel Wind Turbine Towers with Respect to Buckling 842
K.G Koulatsou, K.-A. Chondrogiannis and C.J. Gantes

IS - Preservation and Reuse of Reinforced Concrete Shells (IASS WG5 - IASS WG 17)

How to gain from loss - Heinz Isler's Haba project and its testing under critical load.....850
G. Boller and M. Beckh

Preservation and reuse of reinforced concrete hyperbolic paraboloid shells in the UK 858
M Mendoza and J Chilton

Preservation and reuse of reinforced concrete shells in Guatemala 866
V. D. Pozuelos Polanco, S. Castillo Gallusser, M. Sosa and G. Meléndez Fuentes

Strengthening of the Hypar Shell in Magdeburg with Carbon Reinforced Concrete - Design and Calculations 874
A. Schumann, M. Hentschel, R. Zobel and M. Curbach

IS - Pressurized Membrane Structures: Analysis and Applications

A parametrized design space for pneumatic flood barriers.....882
A. Niewiarowski, S. Adriaenssens and R.M. Pauletti

Inflated cushions under uniformly distributed loading......890
S. Gellin and R. Tarczewski

Some improvements on the static analysis a large pneumatic envelope ..898
R. Pauletti, K. Rocha and P. Bolelli

IS - Reliability Analysis of Membrane Structure (IASS WG 6)

Do we need technical specifications for membrane structures´ 907
B. Stimpfle

Strength values of ETFE-foils correlated to limited residual strains 913
N. Stranghöner, F. Surholt and J. Uhlemann

The calibration of the partial factors to be used in the design of membrane structures 922
E. De Smedt, M. Mollaert and L. Pyl

IS - Stability and Dynamics of Metal Gridshell Structures (IASS WG 8)

A Showroom with a Mesh Structure in Roppongi, Tokyo: Design and Construction.....930
Y. Saito, R. Watada, T. Oshima, T. Kinoshita and I. Hanaoka

A showroom with a mesh structure in roppongi, tokyo: topology design of bracing. 938
R. Watada, Y. Saito, T. Kinoshita and T. Oshima

Ariake Arena - Seismically-isolated Large-Space Roof Structure -.....946
Y. Hamada, M. Hoshino, M. Sakata, S. Yoneda, M. Tabei, H. Ito and M. Kawai

Buckling strength of timber grid-shell roof with steel connections considering rotational stiffness.....954
S Nakajima, Y Terazawa, T. Takeuchi, T. Ogawa, Y. Yamazaki and H Saakata

Calculation and Classification Method of Member Importance of Spatial Latticed Structure in Service.....962
YS. Li, YF. Luo and Q. Nie

Configuration based on meshes derived from Crystallographic concepts and study of System stability of domes.....970
R. Kolakkattil and A. Jayachandran S.

Damage evaluation index of long-span spatial grid structure 978
X. Zhang, J. Cai and J. Feng

Influence of length tolerances in space frames' resistance.....984
G. Ruiz, M. Monasterio, S. Gonzalez, J. Goni, R. Rosenkranz, G. Blanco and J.M. Rico

Load factor to be applied to buckling design of cylindrical lattice shells under asymmetric snow loads 991
Y. Niho, S. Kato and S. Nakazawa

Proposal of new roof support considering seismic performance......999
Y Mukaiyama, S. Kato and S. Nakazawa

Seismic Response Evaluation of Long-span Domes Supported by Multi-storey Substructures Incorporating Spine Frames 1007
D. Nair, Y. Terazawa, B. Sitler and T. Takeuchi

Shell-like and member buckling of latticed shells made of H-shaped steel 1015
T. Yamashita and K. Kageyama

Structural Design of "Steel Pavilion" 1023
M Uchiyama, H Nozawa, M. Ohno and T. Kobayashi

Study on Equivalent Static Seismic Force of Free-Form Reticulated Shell Roofs Supported by Substructures..... 1031
S. Nakazawa, T. Iwata, Y. Takiuchi and S. Kato

The roof structural design of Fukui Prefectural Gymnasium located in heavy snow fall region..... 1039
S. Yamazaki, C. Okuno and H. Yoda

IS - Structural Origami (IASS WG 15)

Curved-crease paperfolding shell 1047
D. Koschitz

Design of Novel Origami Shell Structures 1055
Z. He and S. D. Guest

Exploration of Compliant Hinges in Origami-based Structures 1063
Y. Klett, P. Middendorf, F. Muhs, W. Sobek, S. Weidner and W. Haase

Folding a dome. 1071
F. Tuczek

Frame model for analysis and form generation of rigid origami for deployable roof structure...... 1080
K. Hayakawa and M. Ohsaki

IS - Textile and Foil Synergies and Advances in Shell and Membrane Structures

Fabrication of three-dimensional curved surface using ETFE film by stretching drape strips considering friction contact conditions 1088
Q.H. Bui and M. Kawabata

IS - The Next Generation of Parametric Design

Application of parametric design tools for the roof of the C3 tech demonstration house - CUBE. 1096
I. Vakaliuk, M. Frenzel and M. Curbach

Design space exploration for high-performance greenhouse design 1104
D. Fang, A. Arsano, N. Brown, C. Reinhart and C. Mueller

DigitalTWIN to improve future gridshell installations 1114
F. Schmid, P. Kopriwa and M. Teich

Novel Parametric Knowledge Modelling approach applied to Viaducts 1127
M. Gkioka, J Coenders, R Nijsse, S. van Nederveen, S. Pasterkamp and A. Rutgers

Parametric design of Built Structures - State of the Art 1135
S. Somanath, V. Reed, R. Carpenter, S. Davidson, J. Wu and P. Beccarelli

Proposal of design method of natural and rational tree-structure based on computational hanging upside-down simulation 1147
C. Eguchi, N. Sugiura and H. Tagawa

Seeing Numbers: Considering the Effect of Presentation of Engineering Data in Design..... 1155
S Joyce, B. Dy, G Gou, N. Ibrahim and A. Poorthuis

The combination of SQL database queries and stochastic search methods used to explore generative design solutions 1163
P. von Buelow

IS - Transformable Structures (IASS WG 15)

Multi-objective optimization of reciprocal timber panels from reused stock elements..... 1171
D. Parigi and L. Damkilde

IS - Wind Engineering and Fluid-structure Interaction

Buckling behavior of open-top stocky flat bottom tanks subject to wind load 1179
A. Jäger-Cañás and P. Knödel

Calculation of static deformation of membrane structures under the load of ponding water..... 1187
N. Kodunthirappully Narayanan, R. Wüchner and J. Degroote

Efficient aeroelastic analysis of wind loads on inflatable hangars 1195
R. Flores and E. Ortega

Experiment Study on Wind Resistant Performance of Standing Seam Roof System with Anti-wind Clip 1203
T. Wu, Y. Sun, W. Liu and Z. Cao

First Code of Practice for Rubber Gates in Germany..... 1209
R. Gurt and M. Deutscher

High performance computing of wind-induced pressures on various domes under real conditions 1216
T. Tamura, Y. Cao, Y. Nagao, H. Kawai, K. Nishiguchi and M. Tsubokura

Numerical simulation of an inflated structure for an aircraft hangar 1224
J.M. Gonzalez, J. Marcipar, C. Estruch, E. Cuartero and E. Oñate

Wind analysis of an air-inflated membrane structure 1232
K. Hincz, S. J. Pool Blanco and M. Gamboa Marrufo

CONTRIBUTED SESSIONS

CS - Advanced Manufacturing - 3D Printing

3D-Printed Formwork for Integrated Funicular Concrete Slabs 1239
A. Jipa, C. Calvo-Barentin, G. Lydon, M. Rippmann, G. Chousou, M. Lomaglio, A. Schluter, P. Block and B. Dillenburger

Additive Manufacturing of cantilever - from masonry to concrete 3d printing 1247
P. Carneau, R. Mesnil, N. Roussel and O. Baverel

Design and Manufacturing of The First Freeform 3D-Printed House 1256
P. Boyd, D. Goodloe, M. Rees and B. Hilbert

Fabrication of Topology Optimized Concrete Components Utilizing 3D Printed Clay Mould 1263
S. Wang, K. Huang, Z. Huang, M. Sodano, W. Xu and F. Raspall

High-Performance Corrugated Concrete Shell Construction on Bending-actuated Robotically 3D-printed Formworks 1270
K. M. M. Tam, X. Wang, D. Földesi, H. Lee, J.I. Seo, A. Vasileiou, Y. Luo, C.P. So, X. Zhang, Z. Karsan, G.T-C. Kao, L. Zhang, H. Chai and P.F. Yuan

Optimized Internal Structure for 3D-Printed Sandwich Elements. 1278
H. Kwon and B. Dillenburger

Potentials of 3D Printing Technique in Optimum Design of Reinforced-Concrete Elements 1286
A. Baghdadi, C. Mueller and H. Kloft

Study on Static and Dynamic Behavior of Roof Structures Consisting of Radially Arranged Cables under Strong Winds 1294
Akira OSHIUMI, Akira OKADA, Naoya MIYASATO, Shuzo HIROISHI and Takuto YAGASAKI

Tile Vault Construction on Bending-actuated Robotically 3D-printed Formworks 1302
K.M.M. Tam, X. Wang, A. Beaudouin-Mackay, B. Hoyle, M. Mason, Z. Guo, W. Gao, C. Li, W. Zhu, Z. Karsan, G.T-C. Kao, L. Zhang, H. Chai and P.F. Yuan

CS - Advanced Manufacturing - General

Digital Fabrication of a Timber Bridge 1310
L. Koning and S. Joosten

Into lightness: Furniture as Proxies for radical experimental Structural Design using Advanced Manufacturing 1317
C. Banon, F. Raspall and H.P. Toh

Metal-reinforced Membranes - Electroplating high-strain membranes into metal shells 1325
F Forestiero and B Knychalla

Selective cement activation - new possibilities for additive manufacturing in construction 1333
D. Talke, K. Henke and D. Weger

CS - Advanced Manufacturing - Ice

3D-Printed Grid Shell in Ice Composite 1341
A. Pronk, I. Bouw, T. Ezendam, N. Hierden, J. Vleeshouwers and D. Weijden vd

The World's first Sprayed Net Hyperboloid Ice Structure 1349
C. Millar, J. Orr, Q. Li, A. Yeung, A. Chan, M. Sheasby, M. Giménez Fernández, M. Baxter Chinery, M. Qu and S. Wai

TW-ICE: A Freestanding Ice Shell Pavilion 1357
R. Liu and M. Mistur

CS - Advanced Manufacturing - Robotics

Adaptable Meshes: A Dynamic Approach to the Construction of Membranes 1366
J. Costa, F. Kraemer, C. Bader, J. Disset and N. Oxman

Graded Textile Shaping: Manufacture of Curved Cladding Panels using Multi-material Knitted Preforms 1373
Y.Y. Tan and Y.H. Quek

Structural optimization of coreless filament wound components connection system through orientation of anchor points in the winding frames 1381
M. Gil Perez, N. Dambrosio, B. Rongen, A. Menges and J. Knippers

CS - Analysis and Design

A vaulted multi-storey concrete floor system without external ties - a structural analysis 1389
F. Omloo

Dynamic experiment of integrated ceiling system used in large span office buildings 1397
S. Ishiguro and T. Yamashita

Experimental Research on the Reinforcement of Cylindrical Concrete Shell with Opening 1405
N. Goroumaru and T. Hara

Field Test for a Prefabricated External Prestressed Concrete Wind Turbine Tower 1413
Y. Cao, R. Ma, H. Liu and F. Liang

Model Fidelity between Automated Simplified Model and Full FEA Model as Compared in SAP2000 1420
A Kemp

Reinforcements of the Cylindrical Panel with Opening 1428
T. Hara

Structural Analysis and Design of a Sectored Cylindrical Vertical Tank ... 1436
C. Ferrer, J. Ferrán, M. Redón, J. B. Torregrosa and F. Sánchez

Structural stability analysis of stadium roof 1444
A. Cresnar, M. Uros and P. Gidak

Studying the shape of a helical ramp 1451
M. Rynkovskaya

The Finite Element Analysis of Welding Effect on Curtain Wall Joints of Shenzhen Ping An Financial Center 1457
Lei Gu, X. Lu, J. Chen and F. Wu

CS - Analytical Methods

A building of unlimited height 1465
M. Ander, J. Olsson, P. Shepherd, R Stuart-Smith and C. Williams

Determination of Mixing Principles of Precast Reinforced Concrete Structures with Hybrid Connections Based on Elastic Displacement Control of Small Earthquake 1473
G. Li, Bin Du, Z. He, G. Huang and F. Pan

Elastic buckling behavior of anisotropic latticed shells 1481
T. Matsuda and T. Yamashita

Geometry of the crack-free spherical masonry dome 1489
I. Sajtos, O. Gáspár and A. Sipos

Ordinary analysis of concrete porticoes: a modification of Cholesky's method for graphically solving their equation systems 1497

A.G. Lacort

SEMI ANALYTICAL SOLUTION FOR MATERIAL AND GEOMETRIC NONLINEARITY ON 2D TRUSSES 1505
P. Cunha, P. Ribeiro, R. Durand and T. Oliveira

CS - Case Studies

Before, At the height, After the Tsunami and Now of Ogatsu Inkstone Museum: a case study in the seashore area of Ishinomaki 1513
K. Ito, J. Matsumoto, N. Kowatari and M. Onuma

Constructing Form Versus Constructing Architecture ---- A Comparison Of Two Modular Buildings Using Irregular Prefabricated Panels 1517
Y. Zhai, J.X. Zhu, R. Diedering and H. C. Lau

Exploring Folded Plate Design in Realized Works of Varied Scale and Materials 1523
A. Topbas, A. Demir, K. Jozaghi and B. Kaplan

Structural Design for a Wide Span Roof Structure made from small to medium cross sectional structural wood components 1531
N. Yamada

Structural Design of Gridshells aiming at Lightweight Design and Rapid Assembly 1539
F. Yuan, J. Jin, L. Han and H. Chai

CS - Computational Methods

Application of continuous column concept to morphogenesis of super-high-rise building and large spatial stadium 1547
M. Okada, H. Tagawa, S. Fujiwara and N. Sugiura

DEM modelling of masonry vaults: influence of brick pattern and infill on stability during supports displacements 1555
C. Boni, D. Ferretti, E. Lenticchia and A. Tasora

Dry Self-balanced vaulting 1563
V. Paris, A. Pizzigoni, G. Ruscica, M. Panzeri, A. Locatelli, M. Pievani, J. Gherardi, M. Caseri, F. Lombardoni and G. Marchetti

Dual Boundary Element Method applied in aircraft fuselage fatigue analysis 1571
T. Oliveira

Element Force Equation Using Multiple Non-stressed Length for Tensegrity Form-finding 1579
C. K. Soe, H. Obiya, K. Ijima and M. N.b Zakaria

Field tests, laboratory evaluation and modelling of slip joints 1587
J. Brodniansky, T. Klas, J. Brodniansky, M. Magura, J. Reckí and M. Tilinger

Finding Membrane Shells Subjected to Horizontal Body Forces with Radial Basis Functions 1595
Y.-C. Chiang, A. Borgart and Q. Li

Force Field Typological Design Strategies - A Data Centric Approach to Design 1603
R. Otani, E. Poulsen and S. Pigach

Limit state approach for structurally informed design of shells composed of interlocking blocks. 1610
E. Mousavian and C. Casapulla

Maintenance procedures and modelling of gas pipeline components 1618
J. Brodniansky, M. Magura and J. Brodniansky

Numerical modelling of barrel and cross masonry vaults with different brick pattern 1626
M Alforno, C. Calderini, A Monaco and F Venuti

Numerical simulation and application of unloading clearance element method for temporary bracing of long-span orthogonal space truss structures 1634
R. Yuan, A. Chen and H. Wan

OBSERVATIONS ON BRIDGES DYNAMIC BEHAVIOUR 1645
J. Obrebski

Stability analysis for an arch supported membrane roof 1653
D. Hegyi

Stress evaluation of real shape seashell by image-based finite element analysis 1661
M. Ogoshi, M Teranishi, K. Ishikawa and D Matsubara

Study of dynamic behavior in cylindrical shell coupled with fluid 1669
D. de Oliveira Franca Junior and L. Jose Pedroso

The role of rotational collapse mode and catenary-type thrust lines in the limit state analysis of masonry arches. 1676
O. Gaspar, A. A. Sipos and I. Sajtos

CS - Conceptual Design

A new approach to free form wooden shell structures using helical cut 1684
M. Calvarese and P. Haller

Architectural ceramics influenced by structured materials. 1696
D. Saez, J. Musto and M. Trautz

Creative rational design of free form buildings and their constructions roofed with transformed corrugated steel sheeting 1704
J. Abramczyk and A. Prokopska

Study on Scheme of Annular Crossed Cable-truss Structure - Membrane Roof Structure 1712
S. Xue, J. Lu, X. Li and R. Liu

CS - Deployable and Adaptive Systems

A study on shape determination method and operation experiment of inspection guide frame to avoid obstacles in tunnel 1720
F Inoue, S Kwon, M Terata, S. Nakamura and Y. Yanagihar

Comparative Structural Evaluation and Analysis of Modular Deployable Structures of Expandable Frames. 1728
M Soto-Rubio and C. Jew

Design requirements for maximum compactness in Deployable Structures 1736
C. Ramos-Jaime and J. Sánchez-Sáncheza

Distributed Pneu Elements for Surface Kinetics 1748
V. Parlac

Energy-efficient actuator placement for a convertible bending active structure 1756
P. Marker, L. Stammen and A. Bleicher

Expandable origami for architectural applications: layers of ORIGAMI-SCISSOR hinged deployable structures 1764
E. Rivas-Adrover

Experimental and analytical investigation of the Spin-Valence kirigami space frame 1772
J. Sahuc, G Herning and E. Baker

Load and Constructional Experiments on Beam-shape String Crescent Structure with Pretension Cables fitted to the neutral surface 1780
A. Tanaka

Our world in a line: Deploying the reality 1788
C.J. Garcia - Mora and J. Sanchez - Sanchez

Structural finite-element analysis of steel kirigami space frame to characterize global behavior 1796
N. Sherrow-Groves and E. Baker

Structural optimisation of a bistable deployable scissor module 1804
L.I.W. Arnouts, T.J. Massart, N. De Temmerman and P.Z. Berke

The Development of Space Flexible Deployable Structure Technology 1811
H. Wei

CS - Design Projects

A Prefabricated UHPC Shell Pedestrian Bridge 1820
A. Topbas, F. O. Tulen, M. Marasli and B. Kohen

Design of a free-form single-layer lattice shell connecting ten building 1828
J. Zhou, Y.P LI, H.J Wang, Y.K Zhang, B.W Jiang, X.T. Yang and J.C CUI

Kinetic umbrellas for coastal defense applications 1836
S. Wang, M. Garlock and B. Glisic

Multi-Objective Optimization of a Concrete Shell 1843
V Henriksson, S. Lomax and J Richardson

Structural design of the new Sørlandets Kunstmuseum 1851
A. Clemente, A. Ordinana, G. Mo, M. Rando and M. Sanchez-Solis

Structural optimisation and rationalisation of the BUGA fibre composite dome 1859
B. Rongen, V. Koslowski, M. Gil Perez and J. Knippers

Subaru Nursery School with the 3D curved roof structurally optimized by sensitivity analysis 1867
E. Mitsuda and K. Ebata

The Large Scale Wooden Structure Composed with the Replaceable Small Units 1873
I. Hanaoka, N. Asou, A. Hanai and K. Hotta

CS - Elastic Gridshells and Bending Active Systems

Design, analysis and construction of a bending-active tensile hybrid structure 1878
E. L. M. Slabbinck, S. Suzuki, A. Mader, F. A. Jonas and J. Knippers

Experimental investigation of beams under coupled bending and torsion 1886
N. Montagne, C. Douthe, O. Baverel and C. Fivet

G-shells: Flat collapsible geodesic mechanisms for gridshells 1894
E. Soriano, R. Sastre and D. Boixader

Lightweight curved surface structures composed of bending-active plate units 1902
Y. Tu, T.-Y. Kuo and C.-C. Li

MOBIUS Pavilion: A Double-Layer Grid Shell Combined with Ice Based on Bending-active Weaving Structure 1910
W. Huang, Y. Sun, J. Zhou and H. Pan

Numerical Analysis of a Hybrid Bending-Active Gridshell 1916
I. Anastasiadou and M.C. Phocas

Point load Actuated, Adaptive Elastic Gridshells: Methods for initial design and modeling 1924
E. Bonavia, Sabine Vecvagare, A. Koerner, D. Wood and J. Knippers

X-Shell, a new spatial deployable lattice compared to traditional reticulated shells 1932
E. Bouleau, F. Isvoranu, J. Panetta and M. Pauly

CS - Environmental Compatibility and Life-Cycle of Structures

From Utilizing Material to Listening to What ”Material Speaks” 1940
N. Imagawa

Next Generation Residential High-Rise: Evaluating and Comparing the Global Warming Potential of Different Structural Systems and Materials 1946
M. Budig, O. Heckmann, M. Hudert and A. Ng

On the Ecology of Climate and Structures 1954
J. Christ, H. Koss, J. Fernandoy-Bak and J. Fiebig

Optimized structure for Ice Stupa - Architecture that supports nature to resist climate change 1964
S. Maheshwary, F. Raspall and Simant Verma

Performative shading structures for public spaces applied in San Andres Cholula, Mexico. 1972
E. Gonzalez, D. A. Chi, E. Gutierrez and R. Valdivia

The ideal ETFE fenestration: The influence of material properties on thermal performance. 1980
J. Cremers, H. Liebhart, D. Mirbach, H. Marx and O. Hajek

CS - Form-finding and Optimization

A comparative study on the optimisation-based form-finding of tensile membrane structures 1992
A. L. Marbaniang, S Dutta and S Ghosh

A new form-finding method for shell structures based on BESO algorithm 2000
X. Yan, D.W. Bao, K. Cai, Y.F. Zhou and Y.M. Xie

An Extended Linear Procedure for Constrained Form Finding 2008
E. Samec, K. Fresl and P. Gidak

Comparison between branch-and-cut method and meta-heuristic approach for topology optimization formulated as MISOCP. 2016
S. Fujita

How to obtain diverse and efficient structural designs through topological optimization 2024
Y.M. Xie, K. Yang, Y. He, Z.-L. Zhao and K. Cai

Hybrid connection distribution optimization of precast concrete frames using GA-based method 2032
B. Jiang, X. Lai, B. Du, Z. He, G. Huang and F. Pan

Layout optimization of elasto-plastic dampers for perimeter steel braced frames based on Generalized Response Spectrum Analysis 2040
Y. Terazawa and T. Takeuchi

Machine Hallucinations 2048
M del Campo, S. Manninger, A Carlson, M. Sanche and L Wang

Multi-objective optimization of non-rigid stratospheric airship 2060
T-E. Li, X-Y. Sun and Y. Wu

Numerical and practical experiments for maximally stiff structure under tensile loading based on the topology optimization theory and the FEM 2068
T. Kurahashi, K. Yoshihara and M. Kobayashi

Optimization of grid patterns for single-layer latticed domes 2073
M. Teranishi, S. An and K. Ishikawa

Prediction of minimum weight design of 3D steel frame structure from decomposition into 2D frames 2081
Y. Asakawa and M. Yamakawa

Rationalization of layout optimization result by updating discretization of the design domain 2089
Q. Li, P. Shepherd, M. Gilbert and L. He

Rule-based topology finding of patterns towards multi-objective structural design 2097
R. Oval, R. Mesnil, M. Rippmann, T. Van Mele, P. Block and O. Baverel

Shape optimization of braced frames for tall timber buildings 2105
K. Mam, C. Douthe, R. Le Roy and F. Consigny

Structural Optimization of frames or lattices with beam elements 2115
I. Tsiptsis and K.-U. Bletzinger

Tendon Geometry Optimization Using Path Integrals 2123
J. Lehrecke, J. P. Osman-Letelier and M. Schlaich

Topology Optimization in Architectural Spaces: From Logical to Rational Design Domains 2131
S. Al-Azri, I. Paoletti and J. Noulin

Topology Optimization of Free Formed Shells using Improved ESO 2139
K Otani, K. Kamimura, S Matsumoto and D Fujii

Unified treatment of some different fabrication-cost functions in truss topology optimization 2147
Y. Kanno, M. Ohsaki and J.K. Guest

CS - Form-finding with Graphic Statics

Continuum form and force diagrams in NURBS-based shell form-finding 2155
M. Miki, T. Mitchell and W.F. Baker

Superposed functions as Airy stress functions for form-finding of funicular shell structures 2163
A. F. Devin, M Miki, D. Fang, J Baranowski, J Wang and W. F. Baker

Ultimate Force Boundary of Trusses 2172
C. Jiang

CS - Glass Structures

Concept and cable-tensioning optimization of post-tensioned shells made of structural glass 2180
F. Laccone, L. Malomo, M. Froli, P. Cignoni and N. Pietroni

Exploratory numerical investigation on Aluminum reinforced PVB-laminated glass beam 2188
D-J Zhang and S-W Chen

Thin glass in membrane-like structures - applications, modelling and testing. 2196
T. Peters, S. Jaschke and J. Schneider

Ultra-Thin Glass Connections 2204
S. Pennetier and J. Stoddard

CS - Historical Structures

Foam-born concrete shells - the peculiar first free-form shells of Heinz Isler 2217
M. Beckh and G. Boller

Interaction between architecture and structures designed by Waclaw Zalewski 2223
Sabina Kuc and W. Bober

PIONEERS CANTILEVER CONCRETE SHELLS 2231
P. Cassinello

Revisiting the M Stadium Project by Luigi Moretti: A Forgotten Model of Parametric Architecture 2239
P. Caponi, F. Cutroni and L. Rhode-Barbarigos

The concrete shell of the Engineers Center in the state of Zulia, Maracaibo, Venezuela, analyzed with parametric tools 2249
E. Gonzalez, A. Petzold, F. Mustieles and G. Di Marco

CS - Inflatable Structures

Design and fabrication of a mesh reinfored membrane inflatable deployable reflector and its shape stability 2257
Q. Tao, C.G. Wang and H.F. Tan

Development of comprehensive health monitoring system for a new air-supported membrane structure hall 2264
W. Chen, Y. Yin, J. Hu and B. Zhao

Pedestrian evacuation model of an air-supported membrane structure under emergency 2272
J. Gao, Q. Qing and G.Z. Qiu

PNEULASTICS, pneumatically activated differentiated stretchable membranes 2280
A. Rizou, E. Soriano and R. Sastre

Structural behavior and design criterion of air-cushion considering change of internal pressure and plasticity of film. 2289
M. Kawabata

CS - Membrane Materials

Deformation Analysis and Processing Stability Assessment for Fabric Specimens with Local Defects or Seams Based on Inflatable Bulging Test. 2297
Y. Z. Shen, T. Ma, G. C. Lin and H.F. Tan

Experiment of bi-axial creep of fabric membranes under cyclic temperature and its formulation of constitutive equation based on Fabric Lattice Model 2305
S. Kato and T. Yoshino

Experimental studies on tear failure of PVC coated fabric 2313
Han Bao, M. Wu, X. Zhang and F. Guan

Study on mechanical properties of coated biaxial warp knitted fabrics 2321
B. Yang and Z. Yu

Using a nonlinear thermo-viscoelastic constitutive model for the design and analysis of ETFE structures 2328
A. Cabello and A. C. Bown

Viscous characteristics near the initial yield stress of ETFE film sheet under biaxial tension and temperature change 2346
T. Yoshino and S. Kato

Weathering influence on the mechanical properties of PVC-coated polyester fabrics with special emphasis on irradiance control 2354
H. Asadi, J. Uhlemann and N. Stranghöner

CS - Membrane Structures

Architecture from textiles in motion 2363
E. Hörteborn, M Zboinska, D. Dumitrescu, C. Williams and B Felbrich

Smart Wraps: adaptive textile faÃ§ades for old and new buildings 2371
K. Bernert

CS - Metal Spatial Structures

An enhanced modal pushover analysis procedure for seismic evaluation of single-layer latticed shell structures 2384
Y. Qu, Y.F. Luo, Q.L. Huang and Z.C. Zhu

Analysis of anti-collapse performance of the multi-scale model of terminal building under blast loads 2392
Z. MU, Y. Yang and Yali Chen

Compression-Flexion for sleeveless space frame connections 2400
J. Goñi, R. Fernandez, M. Monasterio, A. Garcia and Z. Kostura

Damping characteristics of aluminum alloy cylindrical latticed shell 2408
S. Gao, X. Guo, X. Luo and J. Zhang

Effects of geometrical factors on the buckling behaviour of free-edge single-layer gridshells 2416
F. Venuti

Experimental study on mechanical properties of three-dimensional composite uplift isolation bearing 2424
X. Li, S. Liang and S. Xue

Free vibration characteristic of single-layer spherical aluminium alloy latticed shells 2432
L. Wang, X. Guo, S. Gao and Q. Zeng

Linear buckling analysis considering no-compression property of metal grid shells stiffened by tension braces 2440
K. Yamamoto and Hayato Utebi

Manufacturing constraints for structural aluminium nodes in free form reticulated structures 2448
Steinar H. Dyvik, B. Manum and M. Luczkowski

Shaking table test on the failure of OLF1000 by considering the dynamic coupling effect of transmission lines 2456
J. Gong, X. D. Zhi and F. Fan

Spatial System Sampling Method for Calculating Joint Positions of Existing Spatial Structures 2464
X. Yang, YF. Luo and J. Liu

Stability analysis of super-large steel hyperbolic cooling towers 2472
X. Zhao

CS - Non-conventional Materials

Compression-Only Structures with Irregular Rock and 3D Printed Connectors 2480
B. Wibranek and O. Tessmann

Natural Form(s): case study of a spatial framework composed of naturally grown forked branches 2488
L. Allner, D. Kroehnert, A. Rossi and M. Tam

Structural Behavior of Ice Composite for 3D Printing 2495
A. Pronk, D. Jansen, K. Kara, J. Laar v. and H. Willems

Structural Multi-Material Printing of Biocomposite Membranes 2503
R. E. Weber, N.A. Lee, J.H. Kennedy, J. J. Van Zak, J. Duro-Royo and N. Oxman

CS - Origami and Folded Systems

Buckling resistance of a Miura origami-based tube 2511
Y.Q. Liu, J.G. Cai and J. Feng

Folding laminar cover and water collector - Prototype 2519
J. Simon and C. Moscoso

Form finding of stress adapted folding as a lightweight structure under different load cases 2527
J. Musto, M. Lyon, M. Trautz and K. Leif

CS - Realizations

40 Years After -Development and Possibility of Beam String Structures 2535
M. Saitoh

Al Wasl Plaza Trellis of Dubai Expo 2020 2543
J. Tobolski, R. Sinn and J. Peronto

Asymmetric suspension footbridge in the town Písek 2551
V. Janata, J. Včelák, J. Beran and D. Gregor

Changi Jewel: Pushing the limits on shell design 2559
C. Schwitter and C. Correa

Complex Structure Combined with Timber BSS and Cantilever Trusses 2567
K. Kume, M. Saitoh, Y. Esaka, T. Nishiya, H. Tanaka, M. Yamashita and K. Murakami

Construction of the Roof of the New National Stadium of Japan Considering Efficiency and Structural Capacity 2575
S. Matsudo, O. Hosozawa, I. Nakakawaji, T. Mizutani, S. Kawamoto, M. Murase and T. Kanno

Design and Construction of Wheel-shaped String Beam Roof with U-turn on the Bottom Chord Cables..... 2583
T. Yoshihara, Y. Nakamura, H. Tabata, R. Hirabayashi, H. Matsuda and M. Saitoh

Kuwait International Airport Terminal 2: Detailed Design and Fabrication of a Large-Span Composite Shell 2591
G. Nieri, L. Blandini and W. Sobek

Strengthening of the transfer floor of Berlin's Steglitzer Kreisel 2601
D. Apellaniz, C. Groth, H. Alpermann and C. Gengnagel

Structural Design for Arch-shaped Cantilever Beams..... 2609
Y. Shimizu, M. Onuma and K. Ito

The Enfolding Form for the Bereaved Families and the Souls of Victims on the Seashore of Ishinomaki City - Oshika Ring of Hope 2613
M. Onuma, Y. Shimizu and K. Ito

The Railway Station Stuttgart 21: Computational Design and Digital Fabrication of Freeform Concrete Shells 2619
F. Waimer, T. Noack, A. Schmid and R. Bechmann

CS - Shell Structures

Bending-driven Dynamic Corrugation for a Funnel Shell Design..... 2627
J. Christie, J. Solly, S. Bechert and J. Knippers

Collaborative Design of composite Ice Shell between Architecture and Structure 2635
P. Luo, R.N. Zhang, DM. Liu and XM. Liu

Computational Workflow for Segmented Shell Structures: an ANN Approach for Fabrication Efficiency. 2645
E. Giannopoulou, P. Baquero, A. Warang and A.T. Estevez

Craft and Manufacture of Modular Thin-Tile Shells..... 2653
M. W. Al Asali and M. H. Ramage

Lightweight segmented timber shell for the Bundesgartenschau 2019 in Heilbronn..... 2661
D. Sonntag, L. Aldinger, S. Bechert and J. Knippers

Structural Optimization of Prestressed Concrete Shells with Ruled Surface Geometry 2669
J. P. Osman-Letelier, J. Lehrecke and M. Schlaich

Sustainable lightweight structures constructed with bamboos, paperboard, bricks, nylon and a textile membrane of jute fibers...... 2677
J.G. Oliva, M. Trujillo and H. Guerrero

CS - Structural Morphology

Catalogue of equilibrium forms of structures 2685
H. Tamai, K. Takahashi, M. Shigematsu, K. Ando and B. Izumi

Designing strategies for Topological Interlocking Assemblies in architecture. Flat Vaults 2693
K. Moreno Gata, C. Mueller and E. Echeverria Valiente

Digital Tool for Reciprocal Frame 2701
A. Palumbo, D. Lancia and S. Pone

Geometry generation of reciprocal systems made of non-uniform elements - A case study of bamboo culms 2709
M. Godina, R. Lorenzo and G. Van Der Heijden

Multi-Modal marine permeable sponge shell structures: Serving as breakwaters and building land-substitute platforms 2717
M. Burt and Y. Rosenfeld

Non-Linear Technique for Spherical Coverings and Application to Forms 2725
C Kitrick

SPACEPLATES Building System 2733
A. Romme, A. Bagger and I. Sørvin

Structural bending system. A constructive possibility for geodesic domes. 2741
H. de Matos, N. Torres and M. Nascimento

Textile Informed Structures: How to braid a roof 2748
L. Wallander, M. Borgny, E. Hörteborn, D. Dumitrescu and M. Ander

The Timber Reciprocal Frame Designer: Free Form Design to Production 2756
T. Godthelp, J. Jorissen, A. Habraken and R. Roelofs

Three ways to stabilize polyhedra according to Chinese thought, Wester's work review 2764
S. Monnot

CS - Teaching and Education

A Project-based Learning on Tension Membrane Structures in Architectural Education 2772
J. Miloševic

Teaching creativity in structural design - approaches and problems in Germany 2780
E. Moeller and H. Nungesser

Teaching Design Sensitivity 2788
S. Rutzinger, K. Schinegger, R. Maleczek and J.-O. Klingemann

CS - Tensegrity Systems

A new T4 configuration for a deployable tensegrity pavilion 2798
A. Pizzigoni, A. Micheletti, G. Ruscica, V. Paris, S. Bertino, M. Mariani, V. Trianni and S. Madaschi

Deformation of the tensegrity units 2804
H. Liu, F. Meng and A. Luo

Geometric features and parameter sensitivity analysis for the prestressed state of the innovative honeycomb multi-post cable dome structures 2812
Y. Tu and S.L. Dong

Influence of random loads on the optimal design of tensegrity footbridges 2820
J. Feron, I. Bouckaert, P. Mengeot, J. Van Steirteghem and P. Latteur

On the creation of infinitesimal mechanisms through cellular morphogenesis 2828
O. Aloui, D. Orden and L. Rhode-Barbarigos

Proposal of Plate Structures Consisting of Intersecting Tensegrity Truss Units and Grasp of Structural Characteristics of the Plates 2838
J. Lee, A. Okada, N. Miyasato, S. Hiroishi and K. Fukuda

Static properties of a new class of planar tensegrity truss 2846
S. LI and X. Xu

CS - Timber and Bio-based Structures

BioMat Pavilion 2018: Development, Fabrication and Erection of a Double Curved Segmented Shell from Biocomposite Elements 2854
H. Dahy, J. Petrs, D.H. Bos, P. Baszynski, A.P.H.W. Habraken and P.M. Teuffel

Composite Glulam Timber and Concrete for the Performing Arts 2864
D Foxe

Damping reinforcement for traditional wooden house using CLT bearing panel connected with damper 2871
Yu Kihara and T. Nagai

Design and Fabrication of a Timber Tower Structure through the reinterpretation of Interlocking Joints 2879
H. Chai, D. Marino, E. So and P. Yuan

Experimental study of truss using CLT (Cross Laminated Timber) for lower chord 2887
S. Tada

Finansparken Bjergsted, Stavanger: an innovative timber-framed office building 2895
P. Tarin, K. Overton, M. Rando, M. Sanchez-Solis and F. Ibanez

Modern timber design approaches for traditional Japanese architecture: analytical, experimental, and numerical approaches for the Nuki joint ... 2903
D. Fang, J. Moradei, J. Brütting, A. Fischer, D. K. Landez, B. Shao, N. Sherrow-Groves, C. Fivet and C. Mueller

Performance Assessment of Double-Layered Timber Plate Shells using Alternative Structural Systems 2911
A. C. Nguyen, B. Himmer, P. Vestartas and Y. Weinand

Segmented Spiral Using Inter-Connected Timber Elements 2919
P. Vestartas, L. Pelletier, M. Nakad, A. Rezaei Rad and Y. Weinand

Spanning 9m with various combinations of small and short lumber - Structural Design of Kindergarten in Date City 2927
R. Murata

HANGAI PRIZE LECTURE

Hangai Prize Lecture

Form follows availability - Designing structures through reuse 2933
J. Brütting, G. Senatore and C. Fivet

Hangai Prize - CAD-integrated Parametric Design Cycle for Structural Membranes 2941
A-K. Goldbach and K.-U. Bletzinger

Parametrization, integration and buildability: Design and construction of a 50m span freeform roof in Bangkok 2949
C. Poirriez, M. Franceschi and Y. Bouzida

Path Planning for Rolling Locomotion of Polyhedral Tensegrity Robots 2957
Y. Lu, X. Xu and Y. Luo

PAPERS

Proceedings of the IASS Annual Symposium 2019 - Structural Membranes 2019
Form and Force
7-10 October 2019, Barcelona, Spain
C. Lázaro, K.-U. Bletzinger, E. Oñate (eds.)

About the funicularity of Velaroidal Shells

Stefano GABRIELE[*a], **Francesco MARMO**[b], **Valerio VARANO**[a]

[*a] Dept. of Architecture, LIMeS, Appl. Math. & Struct. Mechanics Lab., University Roma Tre
Via della Madonna dei Monti, 40, Rome, Italy
stefano.gabriele@uniroma3.it

[b] Dept. of Structures for Engineering and Architecture, University of Naples Federico II, Napoli, Italy

Abstract

We present some preliminary results of a funicularity analysis of the so called Velaroidal surfaces, a class of analytical forms widely used between the '50s and the '70s to define de shape of thin reinforced concrete shells. After recalling the membrane theory of shells, we illustrate how mentioned analytical forms can be obtained as an approximate solution of the membrane equation. Additionally, the same equation is used to form find a shell by the finite difference scheme. The velaroidal surface and the finite difference solution are then compared by evaluating the generalized eccenticity in order to estimate the R-funicularity of the two solutions.

Keywords: funicular shells, membrane theory, velaroid

1 Introduction

One of the advantages of using thin double-curved shells for covering large areas is connected to their ability to carry applied loads mainly by membrane actions. However, this property is governed by the structural form, the actual configuration of applied loads and the boundary conditions represented by the presence and effectiveness of shell supports.
Infinitely many shell forms can be obtained numerically, either by solving the equilibrium equation associated to the membrane theory of shells or by alternative numerical approaches such as the Force Density Method or the Thrust Network Analysis [1]. Among these shapes, the so called velaroidal surface has the useful property of being provided by an analytical expression. The idea of employing this form to design compressed concrete shells dates to 1961, when Ramaswamy [2] used the analytical solution to the differential equation associated to an uniformly stressed membrane subjected to constant transversal load [3]. Within the same paper Ramaswamy named these forms *funicular shell* due to their ability to carry applied load by compressive membrane actions only, equal in both directions and without shear stresses.
We discuss on the actual fulfilment of the funicularity condition for velaroidal shells. This is done by employing both analytical and numerical tools. In particular, the membrane theory of shells is used to compute membrane actions associated to shells whose mid surface is defined by the velaroidal surface. A numerical solution to such a differential equation is then used to obtain a funicular shape generated by the same loading and boundary conditions. Obtained shape is compared with the analytical one to discuss about similarities and differences. Finally, both the analytical shape and the numerical solution are implemented within a finite element code

Copyright © 2019 by S: GABRIELE, F. MARMO, V. VARANO
Published by the International Association for Shell and Spatial Structures (IASS) with permission.

in order to verify their R-funicularity [4] by computing the generalized eccentricity as already used in a real case study [5].

2 Velaroidal surfaces

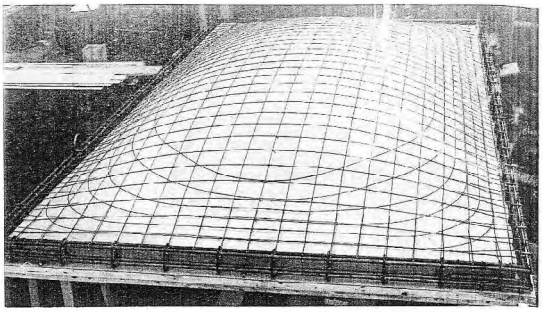
The mathematical definition of a Velaroid is that of a translational surface. Translational surfaces are named *velaroidal* [6] when they are defined on a rectangular plan and drawn by the parallel translation of a generatrix curve along a directrix curve, the former changing its curvature during such translation. The engineering interest for such surfaces is due to their stability and rigidity, associated to the double curvature. Additionally, their capability of carrying loads mainly by membrane actions has attracted the interests of designers between the '50s and '70s to build thin reinforced concrete shells (Figure 1a).
Among three different types of velaroidal surfaces [6], the parabolic Velaroid is the one that better reproduces mentioned structures. It is defined by means of the following equation

$$z = f(x, y) = c\left(\frac{x^2}{a^2} - 1\right)\left(\frac{y^2}{b^2} - 1\right), \tag{1}$$

corresponding to the surface in Figure 2, where the geometric parameters a, b and c are clearly depicted.



(a) Velaroidal shallow reinforced concrete shell of Nekrasov Market in St. Petersburg, 1960 [6]



(b) Lab model of Velaroidal shell - Membrane reinforcements [7]

Figure 1: Examples of velaroidal shells: realized (a) and lab model for testing (b)

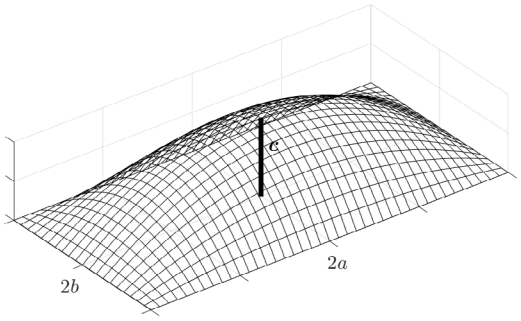


Figure 2: A parabolic velaroidal surface

2.1 The membrane theory of shells: a summary

In a Cartesian reference frame of axis x, y and z, the shell mid-surface is described by the function $z = f(x, y)$, see, e.g., Figure 3a. At any point P of this surface, a reference frame of axis $\boldsymbol{\xi} = (1,\, 0,\, f_{,x})$, $\boldsymbol{\eta} = (0,\, 1,\, f_{,y})$, $\boldsymbol{\zeta} = \boldsymbol{\xi} \times \boldsymbol{\eta} = (-f_{,x},\, f_{,y},\, 1)$ is considered.
An infinitesimal quadrilateral neighbourhood of P, having sides parallel to $\boldsymbol{\xi}$ and $\boldsymbol{\eta}$, has area

$$dA = |d\boldsymbol{\xi} \times d\boldsymbol{\eta}| = \sqrt{f_{,x}^2 + f_{,y}^2 + 1}\, dxdy \tag{2}$$

Accordingly, loads applied to the shell mid surface are modelled as forces per unit area and are indicated as $\mathbf{p} = (p_x,\, p_y,\, p_z)$. The resultant of $\mathbf{p}$ over the infinitesimal element dA is

$$\mathbf{p}dA = \mathbf{p}\sqrt{f_{,x}^2 + f_{,y}^2 + 1}\, dxdy = \mathbf{q}\, dxdy \tag{3}$$

where $\mathbf{q}$ takes the meaning of a force per unit projected area.
The membrane stress tensor $\mathbf{N}$, defined in the $\xi - \eta$ plane, can be projected on the $x - y$ plane as

$$N_x = \frac{\sqrt{1 + f_{,y}^2}}{\sqrt{1 + f_{,x}^2}} N_\xi, \qquad N_y = \frac{\sqrt{1 + f_{,x}^2}}{\sqrt{1 + f_{,y}^2}} N_\eta \qquad \text{and} \qquad N_{xy} = N_{yx} = N_{\xi\eta} = N_{\eta\xi}. \tag{4}$$

Considering (3) and (4) the equilibrium of dA along the three axes of the Cartesian reference frame reads

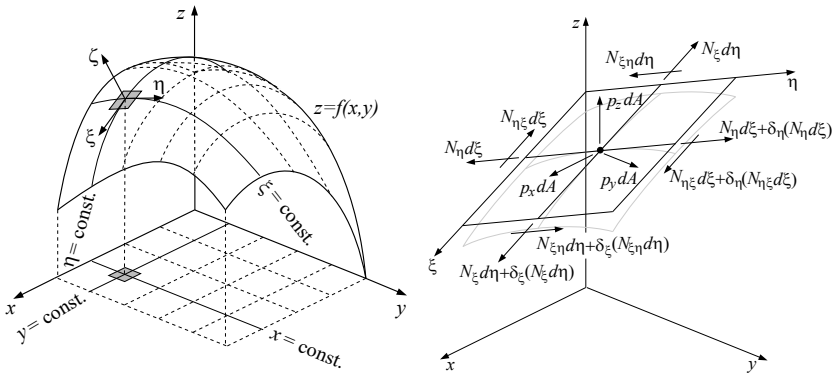
$$\begin{aligned} &N_{x,x} + N_{yx,x} + q_x = 0\,, \qquad N_{y,y} + N_{xy,x} + q_y = 0\,, \\ &N_{x,x} f_{,x} + N_x f_{,xx} + N_{xy,x} f_{,y} + N_{xy} f_{,yx} + N_{y,y} f_{,y} + N_y f_{,yy} + N_{yx,y} f_{,x} + N_{yx} f_{,xy} + q_z = 0 \end{aligned} \tag{5}$$

The first two equations of (5) give

$$N_{yx,y} = -N_{x,y} - q_x \qquad N_{xy,x} = -N_{y,x} - q_y \tag{6}$$

which are substituted into the third one, obtaining

$$N_x f_{,xx} + 2N_{xy} f_{,xy} + N_y f_{,yy} = q_x f_{,x} + q_y f_{,y} - q_z \tag{7}$$



(a) Curvilinear coordinate lines (b) Load and membrane stress resultants

Figure 3: Shell mid-surface and its infinitesimal element.

Equation (7) represents the definitive equilibrium condition that a curved membrane has to fulfil. It relates the projected components of the membrane stress tensor, N_x, N_y and N_{xy}, with the projected components of the applied loads, q_x, q_y and q_z, and the shape of the membrane f. Although not explicitly indicated, all these quantities are a function of x and y.

2.2 Funicular shells

Assuming $\mathbf{N}$ and $\mathbf{q}$ be given, equation (7) can be solved for f. This approach is the basis for finding the form of shells working in pure membrane actions. Within this context, a significant simplification of (7) can be obtained by assuming that the projected stress tensor is spherical and constant, i.e. $N_x = N_y = S$ and $N_{xy} = 0$, and the load is vertical and constant, i.e. $q_x = q_y = 0$ and $q_z = q$, $\forall(x, y)$. Under these assumptions equation (7) becomes

$$f_{,xx} + f_{,yy} = -\frac{q}{S} \tag{8}$$

A useful employment of (8) is that of finding the form of a shell that covers a rectangular area R of size $2a \times 2b$. The entire perimeter of the shell is assumed to be at the same height. Without loss of generality we can assume $f(\pm a, y) = 0$, $|y| \leq b$, and $f(x, \pm b) = 0$, $|x| \leq a$.
Equation (8) can be solved numerically by employing Ritz method, which transforms such a differential equation into a set of linear algebraic equations. This is done by rewriting (8) into an integral form in which the unknown function f is expressed as a linear combination of binomials of the kind $x^h y^k$, being h, $k \in \mathcal{N}_0$, multiplied by $(x^2 - a^2)(y^2 - b^2)$, which is null on the perimeter of the rectangle:

$$f = (x^2 - a^2)(y^2 - b^2) \sum_{k=0}^{K} \sum_{h=0}^{H} a_{hk} x^h y^k \tag{9}$$

where a_{hk} are $D = (H + 1) \times (K + 1)$ unknown scalar parameters which can be computed by solving a system of D linear equations.
The simplest case is that of having just one algebraic equation of unknown a_{00} corresponding to the assumption $H = K = 0$. This gives

$$f = \frac{5q}{8S(a^2 + b^2)}(x^2 - a^2)(y^2 - b^2) = \frac{5q}{8S} \frac{a^2 b^2}{(a^2 + b^2)} \left(\frac{x^2}{a^2} - 1\right) \left(\frac{y^2}{b^2} - 1\right) \tag{10}$$

that is a velaroidal surface having

$$c = \frac{5q}{8S} \frac{a^2 b^2}{(a^2 + b^2)} \tag{11}$$

see, e.g., formula (1). Notice that the maximum height of the surface, attained at the point $x = y = 0$, is equal to c and depends on the ratio between the projected load and the projected membrane stress, a property similar to that of catenary curves.
.
An alternative solution of equation (8) can be found numerically, by employing the Finite Difference Method. In this case the differential form is transformed into a set of algebraic equations, whose generic item is

$$f^{(i-1,j)} + f^{(i+1,j)} + f^{(i,j-1)} + f^{(i,j+1)} - 4f^{(i,j)} = \Delta^2 \frac{q^{(i,j)}}{S^{(i,j)}} \tag{12}$$

holding for the nodes of indices i, j of a grid of spacing Δ, defined on the $x-y$ plane. Here, the unknowns are the values of f at the nodes of this grid, namely the values $f^{(i,j)}$. Introduction of Dirichlet boundary conditions at the perimeter of a rectangular region is straightforward. It is sufficient to set to zero the corresponding values of $f^{(i,j)}$ and consider the equations associated to the internal nodes only.

2.3 R-Funicularity

A shell can be considered perfectly funicular when, for assigned boundary conditions, it is able to carry a given load by exploiting only membrane actions. It has been shown in [4] that this statement is practically unfeasible, since the assumption underlying the pure membrane solution is that of neglecting the shell thickness. In practical applications, the non zero thickness of the shell adds bending stiffness and produces bending actions.
For this reason, the term *funicular* has been reconsidered in [4] in a relaxed way, where the concept of *relaxed funicularity* (R-Funicularity) has been defined in order to quantify the funicular behaviour of form found shells. In order to define an admissible limit for bending actions within real shells having non null thickness, the so called *generalized eccentricity* has been used. It is defined by the ratio

$$e(\alpha) = \frac{M(\alpha)}{N(\alpha)} \tag{13}$$

being α the angle between a generic direction $\mathbf{u}$ and the local basis orientation at the considered point of the shell. Indicating by $\mathbf{N}$ and $\mathbf{M}$ the membrane and bending tensors evaluated with respect to the local basis, then $M(\alpha) = \mathbf{u}^T\mathbf{M}\mathbf{u}$ and $N(\alpha) = \mathbf{u}^T\mathbf{N}\mathbf{u}$ are defined. The generalized eccentricity has the graphical representation given in Figure 4 which is an ellipsis on the $N(\alpha) - -M(\alpha)$ plane. The two tangents from the origin to the ellipse have slopes that represent the minimum and maximum eccentricity, $e_{\min}$ and $e_{\max}$ respectively. The two red lines depicted represent the eccentricity limits that define the R-Funicularity limits $[-\lambda t, \lambda t]$, being λ the ratio between the eccentricity limit and the thickness t of the shell. For example, if the shell chord is required to be fully compressed, it is set $\lambda = 1/6$. The figure shows two different ellipses that can be associated to two different points of the shell. The ellipse that lies all inside the

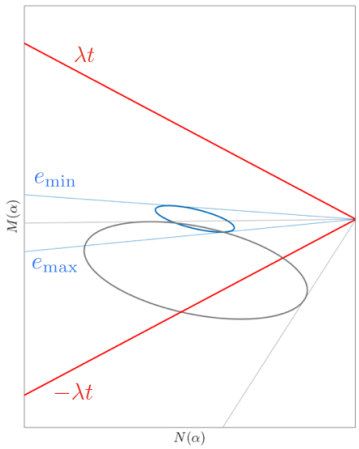


Figure 4: Graphical depiction of the R-Funicularity.

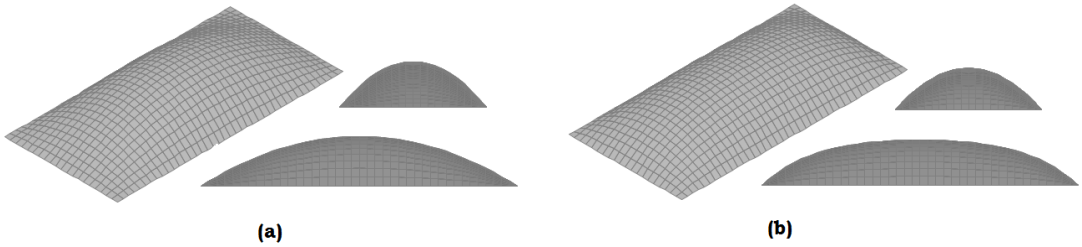
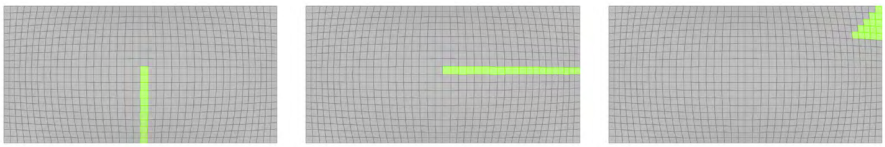


Figure 5: Form found shells: (a) Velaroidal surface, (b) Finite difference solution



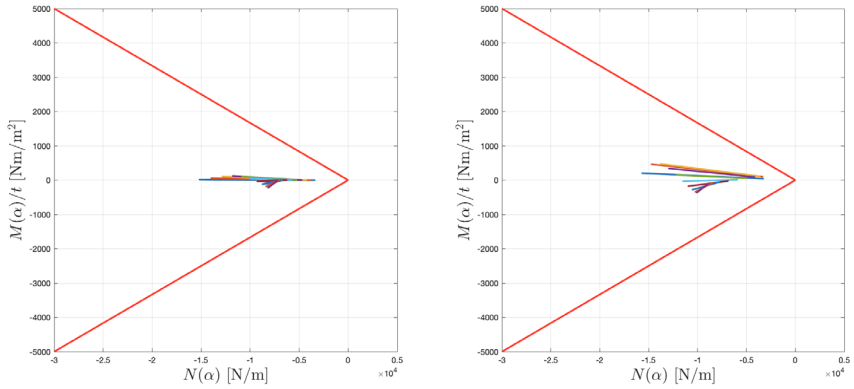
(a) Elements group G1 (b) Elements group G2 (c) Elements group G3

Figure 6: Groups of elements selected for verification of the R-Funicularity.

given limits defines a R-Funicular point of the shell, while the ellipse that is outside, or partially outside, defines a not R-Funicular point.

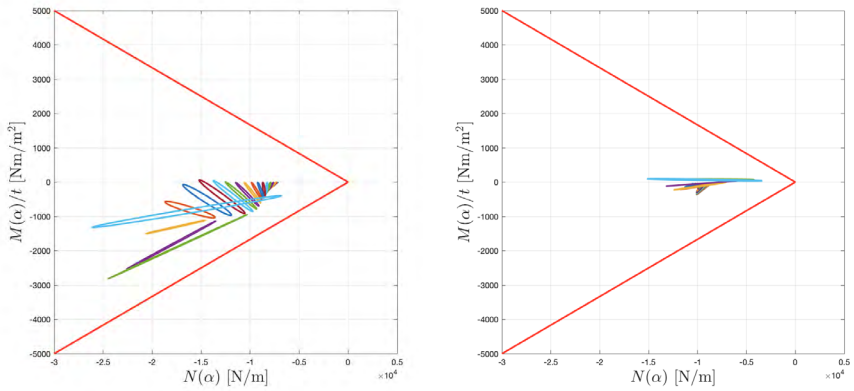
3 Results and conclusions

In this section we present results about the evaluation of the R-Funicularity for two velaroidal shells. The former is obtained by simply applying the approximate solution of the membrane theory of shells as given in equation (10). This solution is indeed the one that defines the velaroidal surface in a strict sense, in particular a parabolic velaroid. The second shape is obtained by applying the form finding procedure based on the finite difference scheme above described. These two velaroidal shapes will be referred to as *Velaroidal surface* and *Finite difference solution*, respectively. In both cases it is assumed a constant projected load $q = 2500$ Pa, a constant membrane traction $S = 10$ N/m, with $a = 10$ m and $b = 5$ m.
The form found geometries are depicted in Figure 5, where three different views of the surfaces are shown in order to highlights the small but existing geometrical differences. The more evident one is the different height, that is 3.125 m for the *Velaroidal surface*, Figure 5(a), versus 2.845 m for the *Finite difference solution*, Figure 5(b). Both shapes are then implemented in a Finite Element code by employing a mesh of quadrilateral shell elements so as to verify the role played by the shell thickness $t = 0.1$ m on the actual distribution of internal forces.
Figures 7–9 depict the results of the R-Funicularity of the analyzed shells, in the selected Groups of elements G1, G2 and G3 shown in Figure 6. According to Figure 4, the results are given in terms of ellipses of eccentricity. In the presented results each ellipse is calculated in the mid point of the shell elements pertaining to each of the considered groups. The results show that for the elements of G1 both models result to be equally R-Funicular, since all ellipses lie within the eccentricity limit cone. Notice that ellipses associated to the elements of G1 collapse to straight segments, meaning that the principal directions of $\mathbf{N}$ and $\mathbf{M}$ are parallel one each other, i.e. see reference [4]. Moreover, many of the ellipses are flattened onto the $N(\alpha)$ axis, what indicates



(a) Velaroidal Surface (b) Finite difference solution

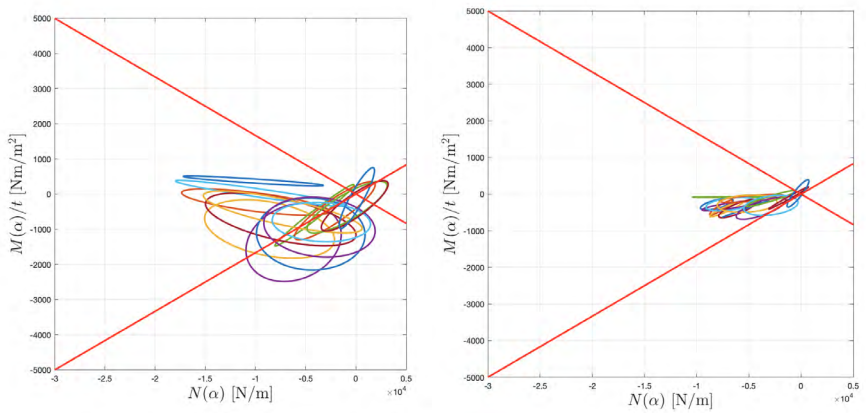
Figure 7: R-Funicularity.



(a) Velaroidal Surface (b) Finite difference solution

Figure 8: R-Funicularity.

that the computed values of $M(\alpha)$ keeps low for every direction.
A more different behavior between the two shells is shown in Figure 8, where it is clear that the *Finite difference solution* is more R-Funicular than the *Velaroidal surface*. Actually, ellipses of the former show both lower values of eccentricity and lower variability of $M(\alpha)$. An interesting observation can be made observing that the longitudinal section of the two shells depicted in Figure 5, is different. In particular, the *Finite difference solution* is more flat in the central region and more curved toward the boundaries. This larger curvature gives lowers the bending actions near the boudaries of the shell, as demonstrated by the R-Funicularity analysis.
For both models, the edge effect results in a loss of R-Funicularity as it is clear from the plots regarding the elements of G3 (see Figure 9). Actually, some ellipses exceed the eccentricity limits. However, it is worth noticing that the *Finite difference solution* has evident lower moments and can be considered a better form found solution.
In conclusion it is possible to assert that the *Finite difference solution* is more R-Funicular than



(a) Velaroidal Surface (b) Finite difference solution

Figure 9: R-Funicularity.

the *Velaroidal surface*. This result is expected and the R-Funicularity validate this expectation. The R-Funicularity method is proved to be an effective tool to test the quality of a form-finding outcome; to select between different shapes obtained from different form-finding methods or applying different form-finding constraints. It also proves that the interest towards velaroidal types of surface is worth to be investigated for real case applications and design, as they have an optimized mechanical behavior with respect to bending moments. This work also proves that proper numerical strategies for solving the equilibrium equations of the membrane theory of shells can be used as form finding tools.

References

[1] S. Adriaenssens, P. Block, D. Veenendaal, C. Williams, *Shell structures for architecture: form finding and optimization*. New York: Routledge, 2014.

[2] G. S. Ramaswamy, "Design and construction of a new shell of double curvature," *Proceedings of the Symposium on Shell Research*, Delft, 1961, North Holland Publishing Co. Amsterdam pp 102-115.

[3] S. Timoshenko, J. N. Goodier, *Theory of Elasticity*. (2^{nd} ed.). New York: McGrow-Hill, 1951.

[4] S. Gabriele, V. Varano, G. Tomasello, D. Alfonsi, "R-Funicularity of form found shell structures," *Engineering Structures*, vol. 157, pp. 157-169, 2018.

[5] F. Marmo, C. Demartino, G. Candela, C. Sulpizio, B. Briseghella, R. Spagnuolo, Y. Xiao, I. Vanzi, L. Rosati, "On the form of the Musmeci's bridge over the Basento river," *Engineering Structures*, vol. 191, pp. 658-673, 2019.

[6] S. N. Krivoshapko, V. N. Ivanov, *Encyclopedia of analytical surfaces*. New York: Springer, 2015.

[7] A. Chronowicz, A. C. Dennison, "Parabolic velaroidal shells," *Magazine of Concrete Research*, vol. 20(63), pp. 103-110, 1968.

Proceedings of the IASS Annual Symposium 2019 - Structural Membranes 2019
Form and Force
7-10 October 2019, Barcelona, Spain
C. Lázaro, K.-U. Bletzinger, E. Oñate (eds.)

Bioinspired design of shell structures: a lesson from echinoids

Francesco MARMO*[a], Valentina PERRICONE[b], Carla LANGELLA[c], Gabriele PONTILLO[b], Luciano ROSATI[a]

*[a] Dept. of Structures for Engineering and Architecture, University of Naples Federico II
via Claudio 21, 80124, Napoli, Italy
f.marmo@unina.it

[b] Dept. of Engineering, University of Campania Luigi Vanvitelli, Aversa, Italy
[c] Dept. of Architecture and Industrial Design, University of Campania Luigi Vanvitelli, Aversa, Italy

Abstract

Echinoids are a class of marine organisms that includes sea urchins and sand dollars. They underwent an incredible adaptive radiation, and specialized in variable forms and life styles to live in different marine environments. In particular, the geometry and structure of their calcitic test has evolved to efficiently withstand biotic and abiotic actions. Such an optimization process, conducted by natural selection and evolution, serves as an inspi-ration for designing light and efficient shell structures capable to bear a large variety of loading conditions mainly by membrane actions and limited bending stresses. We examine the feasibil-ity of developing a bio-inspired design process that combines classical form-finding algorithms with the introduction of flexible connections inspired by those developed by echinoids to reduce bending actions within their endoskeletons.

Keywords: echinoids, biomimetics, conceptual design, shells, bio-inspired.

1 Introduction

Internal forces in shell structures can be modelled as a combination of membrane and shear-bending actions. While the former corresponds to a uniform distribution of stresses along the shell thickness, thus resulting in an optimal employment of material, the latter is characterized by uneven distribution of both normal and shear stresses. As a consequence, a structural solution that minimizes bending-shear actions in favour of the membrane ones is desirable when material employment needs to be optimized.
With this aim, the design approaches based on the form-finding of shell structures is that of determining the geometry of the shell mid-surface in such a way that applied loads can be equilibrated mainly by membrane actions. Several tools have been developed with this goal; however an optimal configuration of the structure can be found for a specific load case and it is unlikely adaptable to all load conditions which a real structure is expected to undergo [2, 7].
On the other hand, a limitless diversity of optimized shell structures, designed to effectively bear a vast variety of loading conditions, can be found in nature. Many living organisms employ

Copyright © 2019 by F. MARMO, V. PERRICONE, C. LANGELLA, G. PONTILLO, L. ROSATI
Published by the International Association for Shell and Spatial Structures (IASS) with permission.

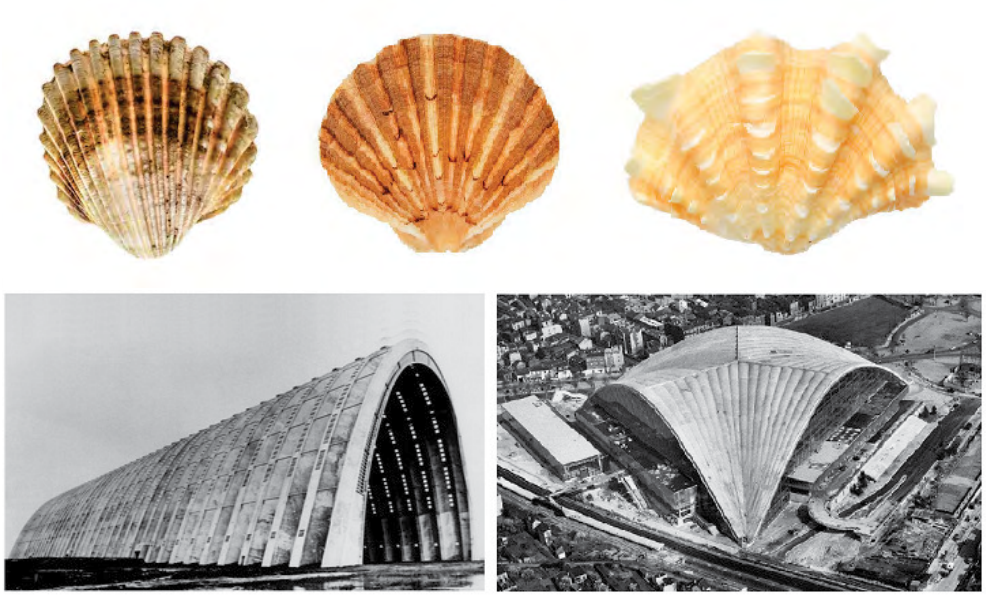


Figure 1: Corrugation in sea shells (Acanthocardia, Pecten and Tridacna) and in architecture (Hangar in Orly, CNIT in Paris).

protective shells against predators or ambient loadings, and some of them, such as Acanthocardia, Pecten or Tridacna sea shells, see, *e.g.*, Fig. 1 (top), use corrugation as a strategy to optimize structural performance of their shells. The efficiency of shell corrugation has been well employed in structural engineering, see, *e.g.*, Fig. 1 (bottom), to increase shell stiffness and strength against any variation of loading conditions with a limited increase of structural thickness and weight [8].
A completely different solution can be observed in other living organisms such as sand dollars,

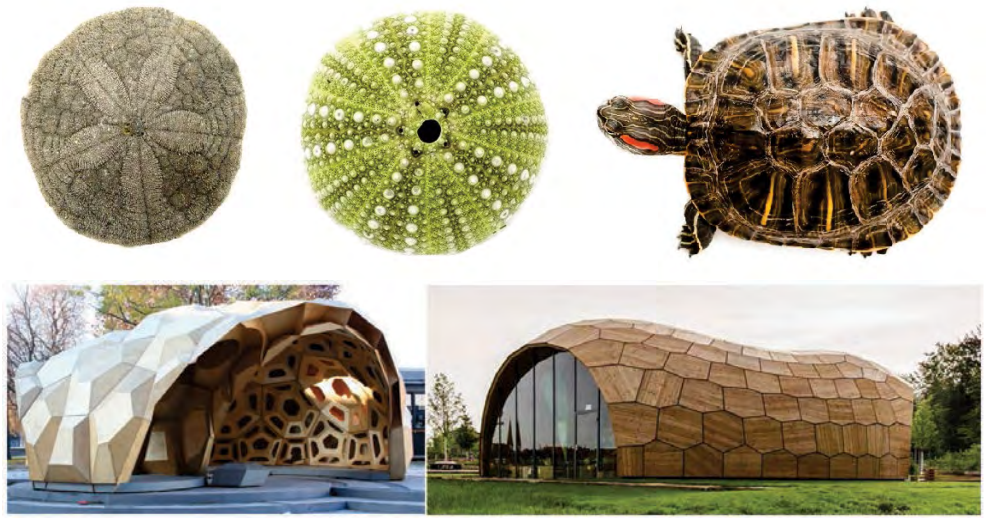


Figure 2: Shell segmentation in nature (sand dollars, sea urchins and turtles) and in architecture (ICD/ITKE Research Pavilion [5], Landesgartenschau Exhibition Hall [6]).

sea urchins and turtles (Fig. 2 top). Evolution has worked on their skeletal systems by finding an optimized configuration characterized by shell segmentation. It has been mimicked in architecture only in the last decade [5, 6] by taking inspiration of the beneficial effect associated with the presence of collagenous sutural ligaments that join the plates of echinoids tests [1].

2 Echinoids and their skeletal structure

Due to their interesting structural features, echinoid's test has always attracted the attention of both biologists and engineers, who began to apply engineering notions and material science to understand the structural behaviour of these organisms [10]. These tools allow scholars to understand the functional meanings of morphological and structural components, which are extremely useful for biological, ecological and evolutional researches and also for the biomimetic field where they can be considered for the creation of new technical bioinspired solutions [5].
Echinoid's test is a complex shell, a light-weight structure characterized by a porous arrangement (stereom), highly variable in density and architecture, composed of a high-magnesium calcium carbonate material filled with cells and dermal fibers (stroma). In regular echinoids, see, *e.g.* Fig. 3, the skeleton is differentiated into pseudo-hexagonal skeletal plates arranged into five ambulacral and five interambulacral areas, each consisting of two column of plates, for a total of 20 meridian alignments. Plates are linked together by interlocking calcareous protrusions and flexible collagenous ligaments. Rounded tubercles are on top of each plate and serve as an articulation of spines connected by ball and socket joints.
Using different mechanical experiments (crushing, three-point bending and tensile tests), Ellers and coworkers [1] demonstrated how the structural strengthening of sea urchin skeletons are improved by collagenous sutural ligaments. In order to better understand the role played by the flexible connection between the rigid hexagonal plates that compose these natural shells, we performed a Finite Element (FE) analysis of the test of *Paracentrotus lividus* (Lamarck, 1816), a species of regular echinoids living in the Mediterranean sea. The geometry of the skeletal structure has been obtained by means of a photogrammetric survey. The surveyed geometry has been regularized by employing a parameterized description and then partitioned into plates and sutures in order to separate the regions having different structural behaviour (Fig. 4). Both geometric entities have been modelled by a mesh of quadrilateral finite elements so as to obtain the geometric basis of a FE model.

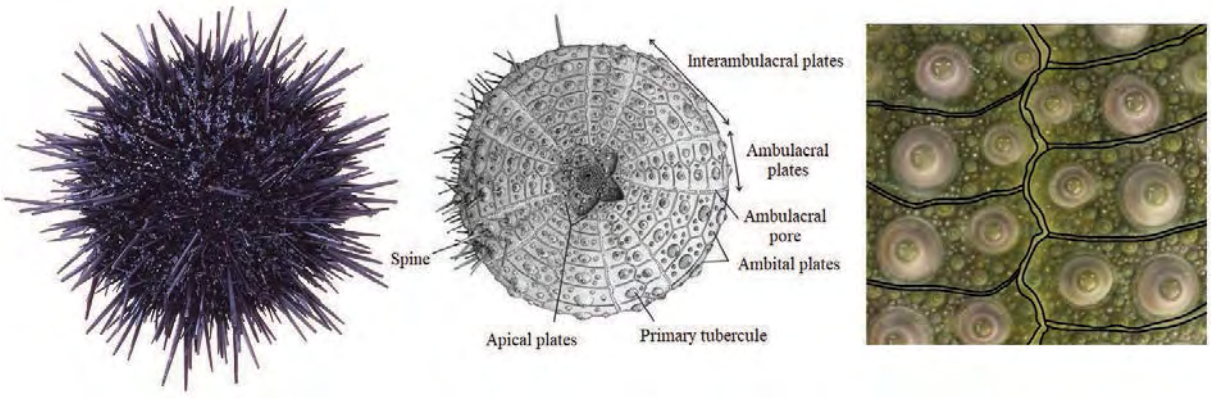


Figure 3: Aboral view of the echinoid test (the schematic drawing is adapted from Trousset [9]).

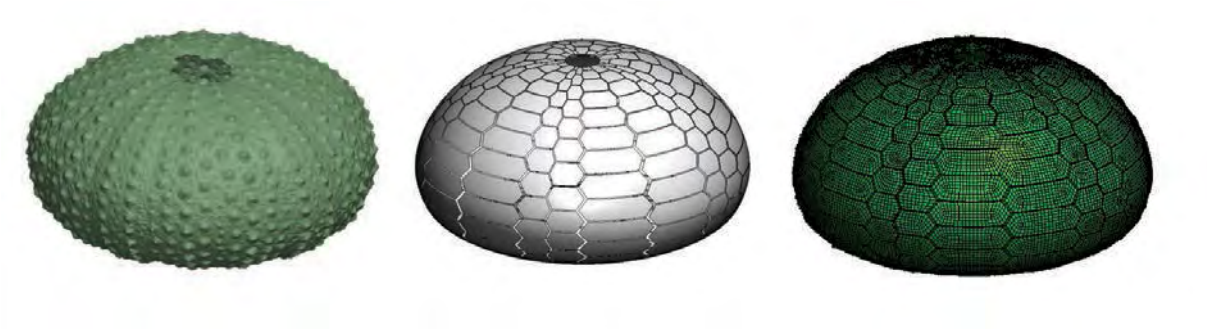


Figure 4: The test of a *Paracentrotus Lividus*: photogrammetric reconstruction, parametrized geometry with plates and sutures, FE mesh

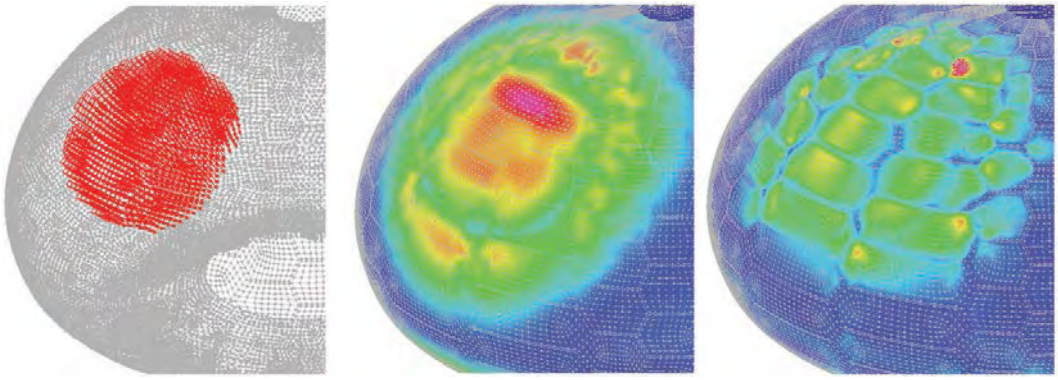


Figure 5: The test of *Paracentrotus lividus*: Loading condition and bending stresses computed for the monolithic and the segmented shells

Starting from this unique geometry, two different models have been obtained. They differentiate each other for the way sutures are modelled. In particular, the *monolithic* model has been obtained by assigning the same material properties to both elements pertaining to plates and sutures, while the *segmented* model is characterized by reduced flexural stiffness of the elements corresponding to collagenous sutures.
Several analyses have been conducted on both the monolithic and the segmented models by considering different loading conditions corresponding to normal and tangential loads applied to a portion of the test shell of different size. In all the cases analysed, bending and membrane actions computed for both models have been compared, showing the beneficial effect of flexible sutures in mitigating the magnitude of bending stresses within the structure.
As a representative example, we report in Fig. 5 the contour-plots of the bending stresses generated by a normal load applied to an approximatively circular portion of the structure. As it is clearly visible from these solutions, the segmented model exhibits a significant reduction of bending actions with respect to the monolithic one. This confirms the experimental observation by Ellers et al. [1] on the strengthening effect generated by the flexible sutural ligaments.

3 Bio-inspired design of segmented shells

The behaviour of the echinoid test has served as an inspiration for designing shell structures composed of rigid plates with flexible joints [5, 6]. Hereafter we report the results of our in-

vestigation on the efficiency of this idea when applied to both generic and form-found shell structures.

The first example regards a concrete arch shell obtained by slicing a spherical dome of radius $5\,m$ by means of parallel planes placed at distance $\pm 1.3\,m$ from the centre. The structure has thickness $0.3\,m$ and is subjected to gravity loads and to seismic actions determined by means of a modal analysis with response spectra, which is a common practice in many building engineering

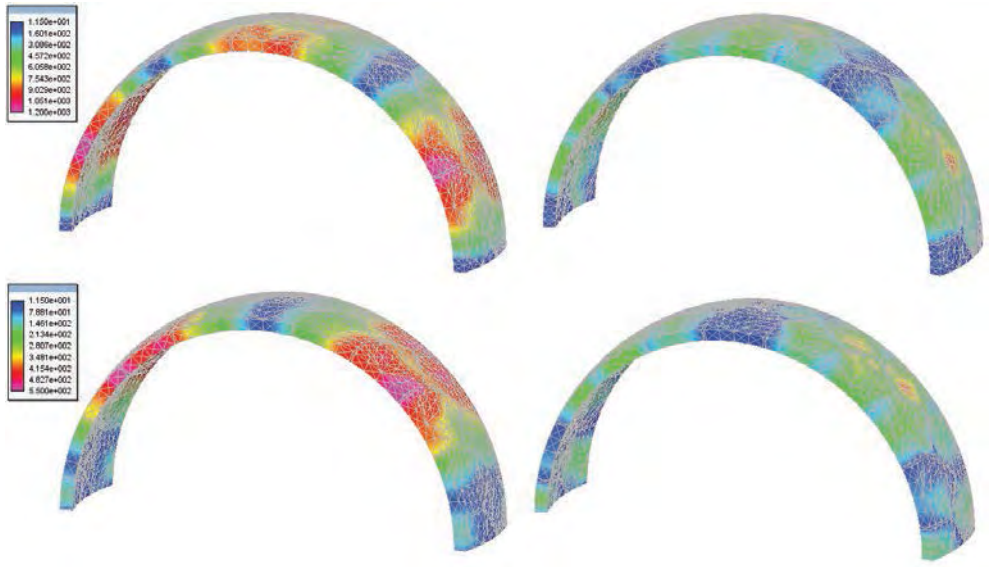


Figure 6: Bending stresses in a concrete arch shell: monolithic (left) vs. segmented (right); effect of gravity (top) and seismic (bottom) loads.

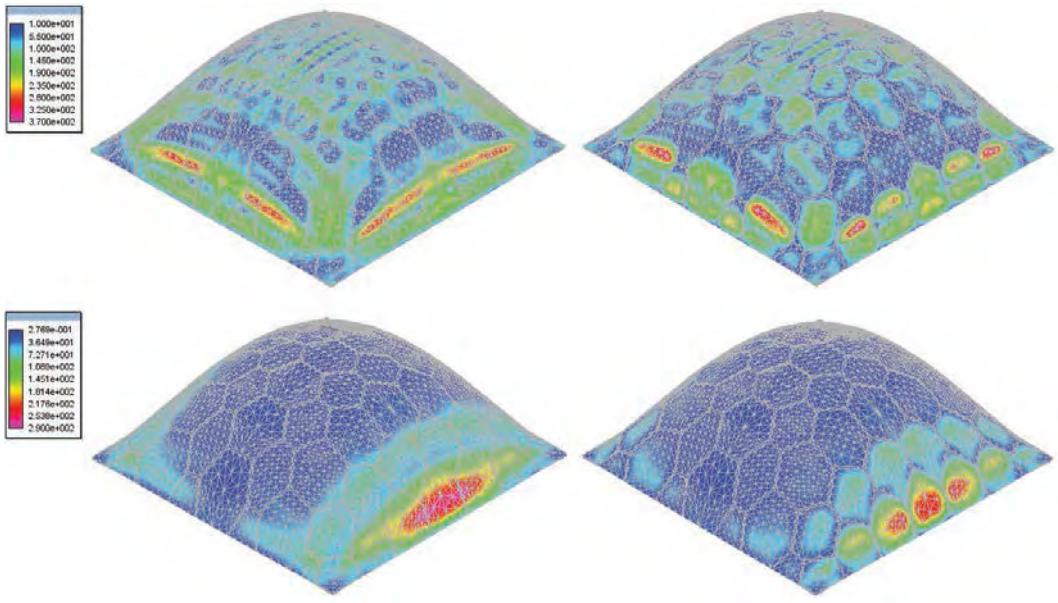


Figure 7: Bending stresses in funicular concrete shell: monolithic (left) vs. segmented (right); effect of gravity (top) and seismic (bottom) loads.

applications.
Fig. 6 shows the comparison between the bending stresses computed for the monolithic (left) and segmented (right) cases, subjected to gravity (top) and seismic (bottom) loads. It is clearly visible the beneficial effect of flexible joints between the plates, which reduces the magnitude of bending stresses by a factor of about 2.
The second example regards a $10\,m$ high funicular concrete shell roof that covers a square area of $30\,m \times 30\,m$ with a thickness of $0.3\,m$. Similarly to the previous case, the structure has been loaded by gravity loads and seismic force; results relevant to a monolithic and a segmented model have been compared. In particular, Fig. 7 shows the bending stresses computed for the monolithic (left) and segmented (right) cases, subjected to gravity (top) and seismic (bottom) loads. From these figures it is clear that the presence of flexible joints produces negligible effects on the maximum value of the bending stresses.

4 Conclusions

Based on numerical comparisons relevant to the test of *Paracentrotus lividus*, some experimental observations regarding the beneficial effect associated with the presence of collagenous sutures has been verified. The effects of flexible joints between rigid plates has been associated with the lowering of bending stresses within the shell skeleton of echinoids.
This structural behaviour has been mimicked in building engineering in the context of concrete shell structures. Numerical comparisons regarding both generic and funicular shells have shown that the effect of flexible joints in segmented shells is more relevant when the shell has a form that is not optimized to reduce bending stresses, while this effect is practically negligible for funicular shells.

References

[1] O. Ellers, A. S. Johnson, P. E. Moberg, "Structural Strengthening of Urchin Skeletons by Collagenous Sutural Ligaments," *Biological Bulletin*, vol. 195, pp. 136-144, 1998.

[2] S. Gabriele, V. Varano, G. Tommasiello, D. Alfonsi, "R-Funicolarity of form found shell structures," *Engineering Structures*, vol. 157, pp. 157-169, 2018.

[3] P. Guidetti, M. Mori, "Morpho-functional defences of Mediterranean sea urchins, *Paracentrotus lividus* and *Arbacia lixula*, against fish predators," *Marine Biology*, vol 147(3), pp 797-802, 2005.

[4] J. Knippers, A. Menges, M. Gabler, R. La Magna, F. Waimer, S. Reichert, T. Schwinn, "From nature to fabrication: biomimetic design principles for the production of complex spatial structures," *Advances in architectural geometry 2012*. Springer, Wien, pp. 107-122, 2013.

[5] J. Knippers, K. G. Nickel, T. Speck, *Biomimetic Research for Architecture and Building Construction*. Switzerland: Springer International Publishing, 2016.

[6] O. D. Krieg, T. Schwinn, A. Menges, J. Li, J. Knippers, A. Schmitt, V. Schwieger, "Biomimetic lightweight timber plate shells: computational integration of robotic fabrication, architectural geometry and structural design," *Advances in architectural geometry 2014*. Springer, Cham, pp. 109-125, 2015.

[7] F. Marmo and L. Rosati, "Reformulation and extension of the thrust network analysis," *Computers and Structures*, vol. 182, pp. 104-118, 2017.

[8] T. Michiels, S. Adriaenssens, M. Dejong, "Form finding of corrugated shell structures for seismic design and validation using non-linear pushover analysis," *Engineering Structures*, vol. 181, pp. 362-373, 2019.

[9] J. Trousset, *Nouveau dictionnaire encyclopedique universel illustre: repertoire des connaissances humaines*, vol. 4, p. 372, 1885.

[10] S. A. Wainwright, W. D. Biggs, J. D. Currey, J. M. Gosline, *Mechanical design in organism.* London, UK: Edward Arnold Publishers, 1976.

Proceedings of the IASS Annual Symposium 2019 — Structural Membranes 2019
Form and Force
7—10 October 2019, Barcelona, Spain
C. Lázaro, K.-U. Bletzinger, E. Oñate (eds.)

Design and Analysis of Freeform Shell Structures Composed of Doubly Curved Sheet Metal Panels

Alex SEITER[a], Thorsten POFAHL[a], Martin TRAUTZ[a]
Lisa-Marie REITMAIER[b], Gerhard HIRT[b]

[a] Chair of Structures and Structural Design, RWTH Aachen University
Schinkelstraße 1, 52062 Aachen, Germany
seiter@trako.arch.rwth-aachen.de
[b] Institute of Metal Forming, RWTH Aachen University
Intzestraße 10, 52056 Aachen, Germany

Abstract

Our current research deals with innovative structures made up of doubly-curved sheet metal panels for realization of wide-spanning, lightweight freeform structures. We introduce the design and geometrical optimization of a prototype shell structure consisting of two thin layers of sheet metal. Thin sheet metal construction poses various design challenges: Global and local buckling effects and local stress phenomena such as shear and hole bearing forces. The main focus is structural analysis of the shell structure with an in depth discussion on the challenging modelization of multilayered, ultra-thin sheet metal components.

Keywords: Individual Freeform Panels, Sheet Metal, Incremental Sheet Forming, Stretch Forming, Self Supporting Structures

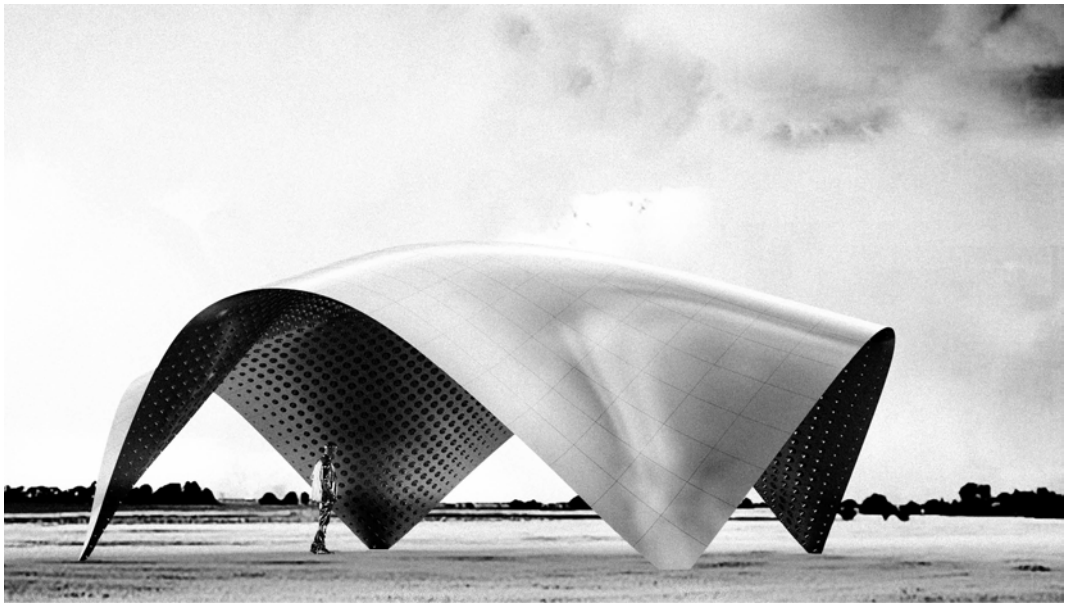


Figure 1: Demonstrator design

Copyright ©2019 by the authors as listed above
Published by the International Association for Shell and Spatial Structures (IASS) with permission.

1 Introduction

The concept for self-supporting panels made out of doubly curved layers of thin metal sheets is developed under simultaneous consideration of structural performance and manufacturing routines. The concept is derived from the principle of sandwich constructions, which are, up to now, limited to planar or single-curved elements. Our approach aims to extend the principle to wide-spanning shell geometries with individual panels of positive as well as negative Gaussian curvature. The panels are exclusively composed of layered metal sheets, which are formed separately and assembled in a subsequent step. An offset among the sheets is maintained through conical embossments, which are directly impressed in one of the layers. The panels are formed using an innovative combination of Stretchforming (SF) and Incremental Sheet Forming (ISF).

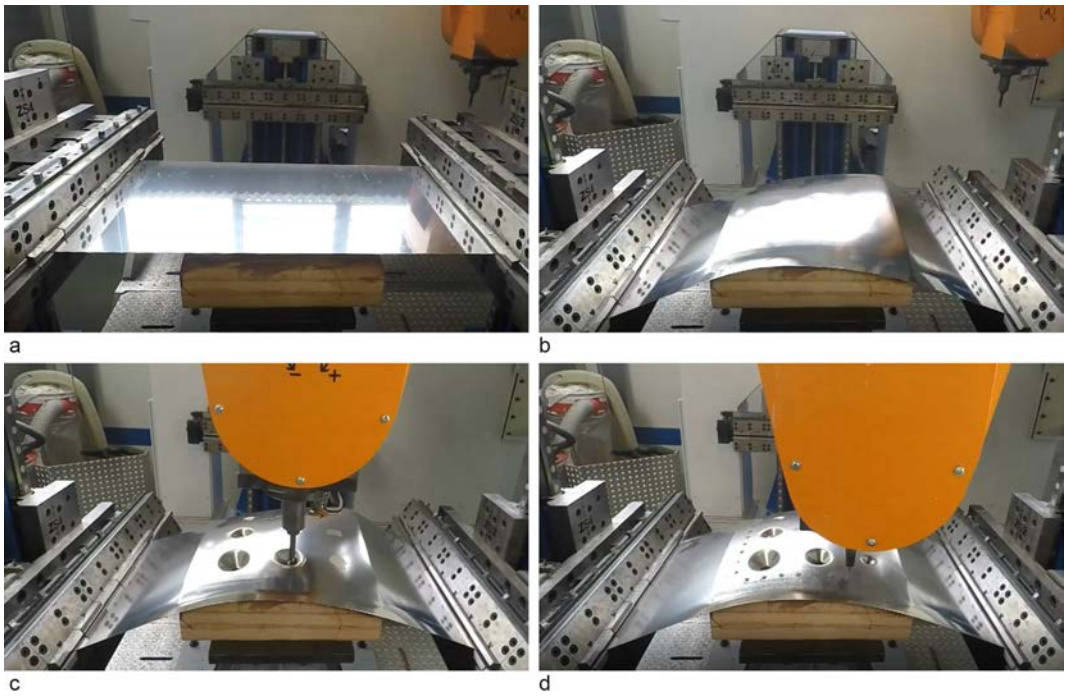


Figure 2: Single steps of metal forming

In a first step, the basic curvature of the panel is generated using SF. Here, only basic, positive or anticlastic curvatures can be directly manufactured (Figure 2a+b). For more complex curvatures, a intermediate form is produced, which is then postprocessed by ISF. The cones are manufactured using ISF in a subsequent step (Figure 2c). Due to the low forming forces in SF and ISF, the use of cheap tooling material is possible. This way a bonded block of Medium Density Fiberboard (MDF) is foreseen for milling of the customized dies. Thickness and dimensions of the sheets are determined by the process forces and corresponding machine design. Panels up to 4 meters in width and even longer dimensions in length can be formed by state of the art SF machinery. With ISF, sheets with a thickness of up to 4mm can be processed. The machine used in this project is capable of forming stainless steel (1.4404) with a width of 0.4m and a thickness of 8mm. A detailed description of the process can be found under [1] and [2].

A case study pavilion is forseen to exploit the abilities of the principle. A freeform shell spans over four foundation points disposed in plan at the corner of a 8,15m by 8,15m square basis, with a maximal height at the apex of 4,80 m. The thickness of the shell evenly decreases towards its rims, creating the illusion of a paper-thin membrane. This way, the actual thickness of the shell can be set for optimal structural performance, without mayor concequences for its estetics.

2 Parametric Study

In principle, sheet metal has a high degree of formability and can be formed into individual, high complex parts with acceptable tolerances. However, the minimal thickness of the material increases susceptibility to failure of such structures caused by even small geometrical imperfections and springback effects. Therefore, accurate modelization on a very detailed scale is essential to identify and react to structural discontinuities. Such models may easily extend computational restrictions of state of the art FEA Environments.

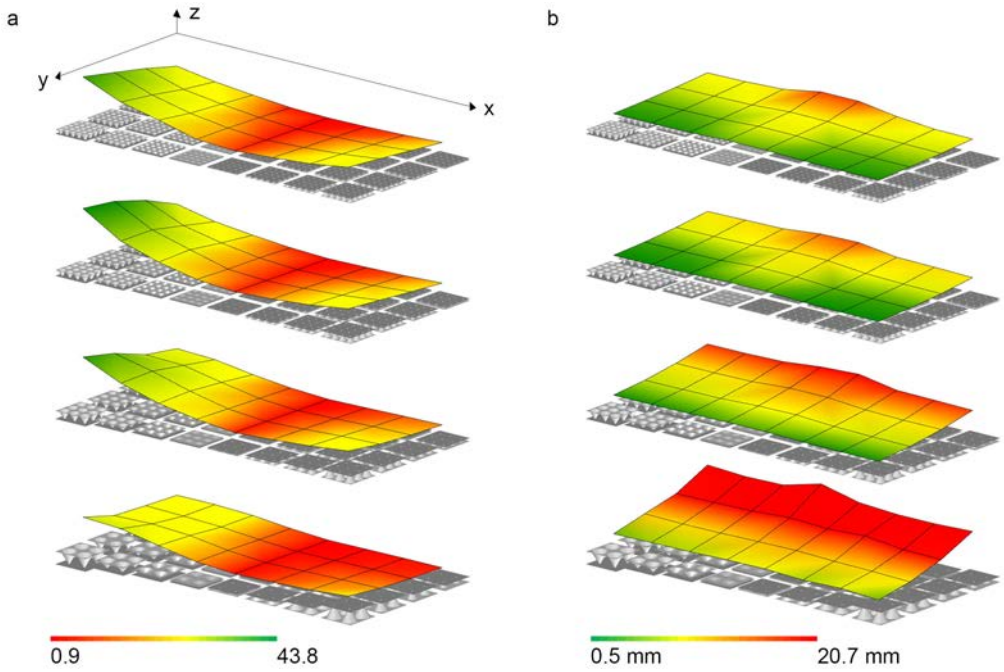


Figure 3: Results of the parametric study a) buckling factor b) averaged von mises equivalent stress

The aim of structural optimization is to provide a statement on alternating effects and influence of the individual geometry parameters with regard to a high load-bearing capacity of the panels or the overall structure with the lowest possible forming and material costs.
Based on the developed workflow, calculations with different parameter combinations were carried out: Number of cones per panel, folding angle of cones as well as the ratio of cone base area to panel base area were examined as parameters. The calculation is based on a linear analysis. A non-linear analysis was not suitable at this point, as the interactions of the individual parameters and not the absolute load-bearing capacity of the examined panels were in focus. In addition to their own weight, the panels were loaded with 1kN/m^2 perpendicular to the panel surface, which corresponds to the direction of wind loads. For the results relevant for the evalu-

ation of the parameter study the average Mises equivalent stress and the average displacement in z-direction of all elements of a panel as well as the buckling factor of the structure are used. The study with 127 panel variations shows the complex interactions of the parameters. First recommendations for the general design of the panels could be derived from the study: A low number of cones maximizes the static height of the panel, whereas a high number of cones reduces the relevance of buckling phenomena. A high wall angle has a positive effect on the structural height and thus on the load-bearing capacity of the panel. The positioning of the cones in the pressure-loaded position is to be preferred. A increase in the ratio of cones to panels leads to a reduction in buckling phenomena and enables larger static heights of a panel.

3 Application of the Results to the Design

For the prototype, two variants were derived from the parameter study. Both variants have a steep wall angle of the cones of 60 degrees. Variant 1 populates each panel of approx. 800mm by 800mm with 3 by 3 cones. This results in a maximum structural height of the panels of 120mm. Variant 2 occupies the same panel with 2 on 2 cones each. This increases the structural height of the panels to 190mm. However, the widths of unsupported areas within the panels increase and buckling is expected to be more relevant to the overall performance of the structure.

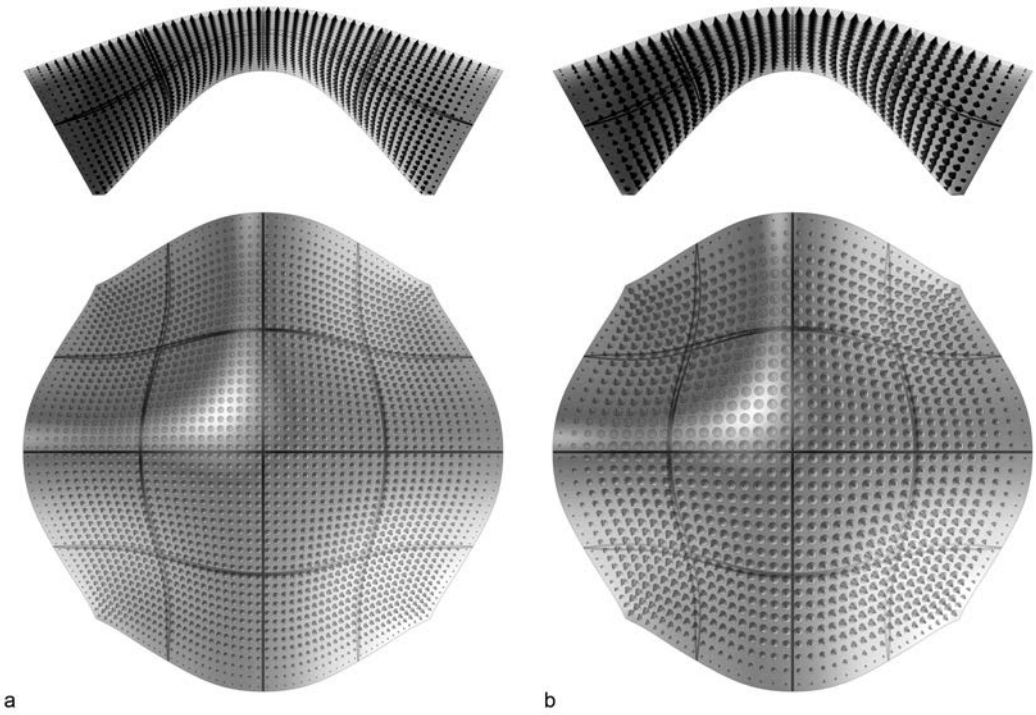


Figure 4: Geometries of the demonstrator with different static heights and amount of cones

4 Structural Model

Our approach uses a custom interface of parametric CAD Modeller Rhino GH with the robust and scalable FEA Environment Ansys, shifting the entire modelling and the implementation of finite elements, loads, supports and joints to GH.

All meshing operations are carried out in Grasshopper. This way, a direct workflow from manufacturing- to simulation geometry can be achieved. A custom interface translates the Rhinoceros mesh model into the command representation of Ansys parametric design language (APDL). This approach enables definition of the structural model by directly implementing the finite elements themselves including all their properties such as element type, material properties, material thickness and load over previously defined coordinate vertices. A detour via surface generation which then have to be meshed in Ansys is not necessary. This is a significant advantage, especially for freeform models, as the mesh of the structural model is fully customizable and can be extensivly adjusted. Only this way, mesh with sufficient accuracy and facecounts within aceptable bounds can be achieved.

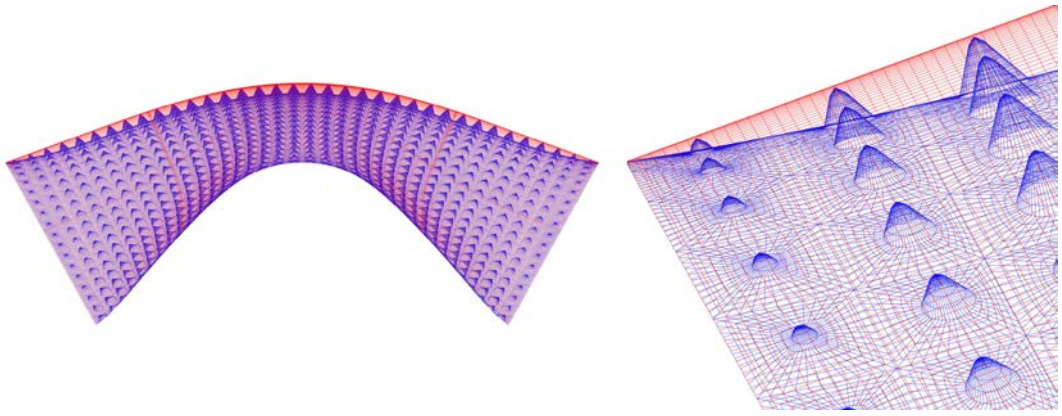


Figure 5: Meshing with individual strategies for flat (red) and embossed sheets (blue)

The meshes of the unstructured sheets are generated using the most simple approach by a grid of square facets. A balanced approximation of the embosed sheets was achieved by subdividing the geometry and a individual meshig of each conical detail point. Here, none of the standard meshing algorithms was abble to deliver a evenly distributed, suitable quad mesh. Hence, a custom tool based on facade paneling strategies was developed. 2 million facets was used as a rule of thumb guideline. This figure has proven to be a useful compromise between accuracy and computational effort. Every sheet is implemented as a individual analysis component , results cantherefre be viewed and interpreted separately for each panel. This e.g. enables for easy adjustment of sheet thicknesses of individual panels according to structural performance.

4.1 Joints

The structural layer and the top layer of the panels as well as the panels must be joined together in the model. The connections of the panels or individual panel layers are modelled in different ways based on a case study and the results are evaluated regarding a local stress distribution. Two different types of connections are investigated. Type 1 is a node-to-node joining. Each joint is defined by a set of coupled degrees of freedom. Type 2 is a surface-to-surface joining. This approach considers the effects of the fastener radius. The strength of the fastener connection isn't underestimated when the radius of the fastener is the same or lesser order of magnitude than the mesh size. A force-distribution in the connection region is achieved. A joint with this approach can be easily defined by specifying two surfaces to be connected and a single node called the spot weld node near the surfaces. The spot weld node determines the location of the

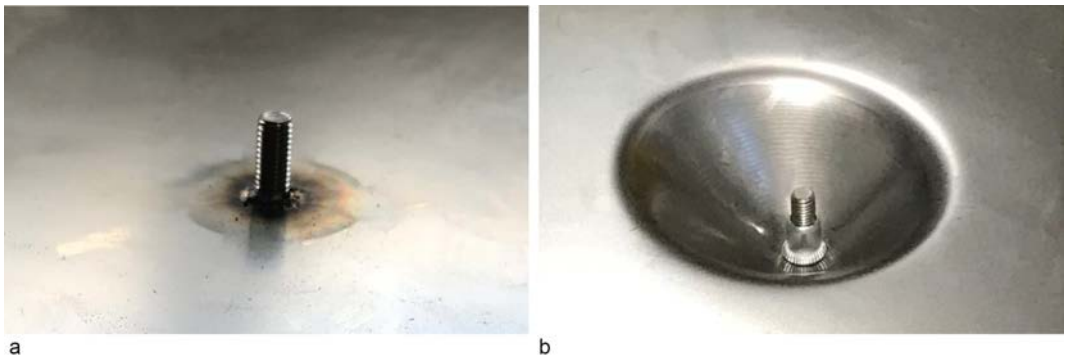


Figure 6: Cones are screwed onto studs, which are welded onto the flat layers

spot weld [3]. Parts can be meshed independently with this approach, which is a great advantage for complex geometry. In the overall model of the shells shown above, there are up to 15000 connections. A substitute model is used to test which of the two connection types is to be used for the structural model. The reference is the resistance of a single-section connection which is determined according to Eurocode 3. Two rectangular flat plates with a thickness of 2mm are joint. The bolt is set to a M6. One of the two sheets is held at the vertical edge facing away from the fastener. The other of the two plates is loaded at the vertical edge facing away from the fastener. The fastener is thus subjected to shear forces. The resistance of the connection of 8.94 kN according to Eurocode 3 is determined by the minimum strength of the hole embrasure or shear.
The connection with the CP approach fails at a force of approx. 6.2 kN. In Figure 7 the failure is shown by the displacement of the loaded sheet as a whole. In the load deformation diagram (Figure 9), the maximum deformation in the x-direction at load step 7 (approx. 6.2 kN) becomes infinitely large. The connection is overloaded from this load step on. The plastic strain range (red area in Figure 8c) shows the failure mechanism at the failure load step. The connection with the spot weld approach is still intact with a force of 8.94 kN. The spot weld approach is thus well suited for the structural model. Up to load step 20 (approx. 10 kN), there is neither a noticeable deformation of the loaded sheet metal nor a large range of plastic strains (see figure Figure 7b, 8d and 9).

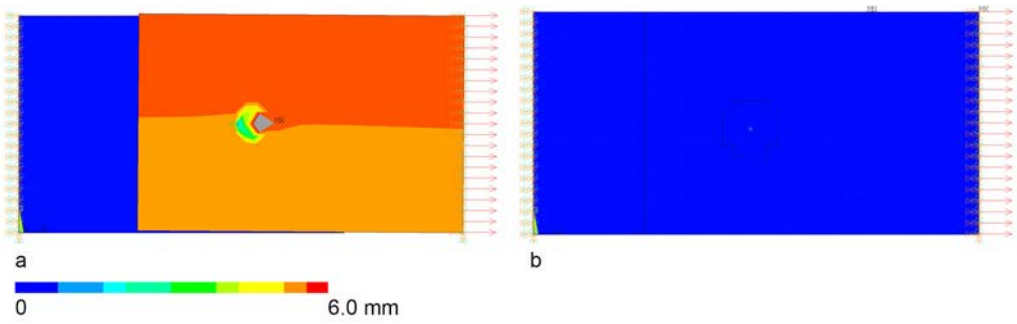


Figure 7: Dicplacement in x-direction of a) CP approach b) Spotweld approach at load step 14 (approx. 6,2 kN)

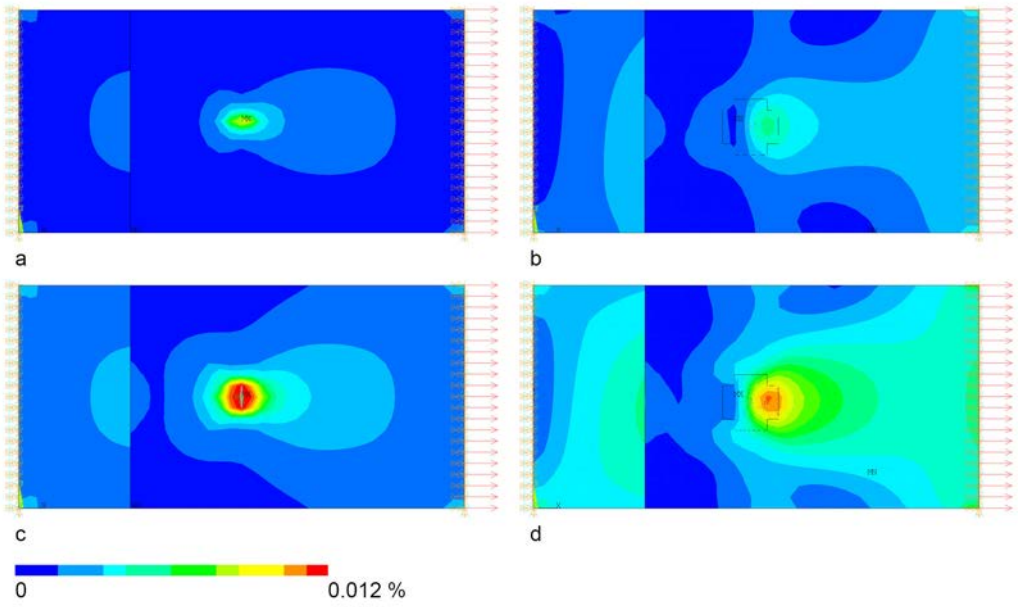


Figure 8: Dicplacement in x-direction of a) CP approach b) Spotweld approach at load step 14 (approx. 6,2 kN)

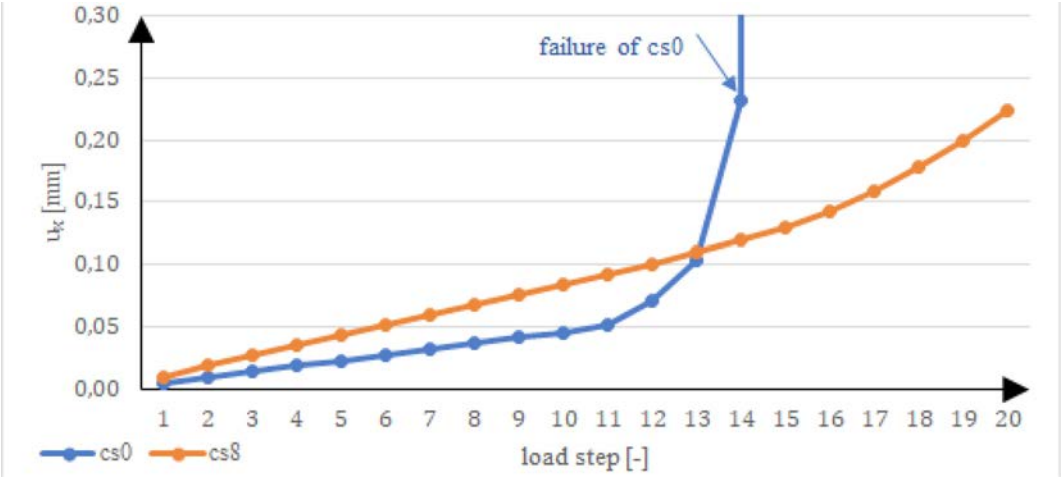


Figure 9: Deformation in x-direction of CP approach (cs0) and spotweld approach (cs8)

Modeling the fasteners (bolts) itself is not possible. Too many additional elements are generated. Modeling the holes in the sheets is also ruled out. The size of the holes in relation to the overall geometry is too small to generate an appropriate mesh. Preliminary investigations also showed no added value.

5 Application of the Approach

A linear buckling analysis and a material non-linear static analysis are performed on each of the two different geometries of the shell construction. Since the structural performance of the

two geometries serves a qualitative comparison, this is sufficient. It should be noted that imperfections, especially their amplitude, have a significant influence on the load-bearing behavior of such constructions. As soon as the amplitudes of the imperfections become known from the production process of the panels and the shell is to be analyzed quantitatively, imperfections will be applied. The linear buckling analysis shows a reliable guide value for the buckling susceptibility of the structure. The material non-linear static analysis determines the deformation behavior and visualizes areas of plastic strain. The shells are loaded with an even surface load of 1 kN/m^2. The four corner points are supports. Since a reinforcement of the construction is necessary in the support areas, several element nodes are used as bearing supports.
According to the deformation plot (see Figure 10), shell a shows on average greater deformations than shell b. The buckling factor of shell a with a value of 2.42 is however approx. 30 percent higher than that of shell b with a value of 1.85. The correlation of the parameters to the structural performance, which was recognized in the parameter study, is transferable to the overall model.

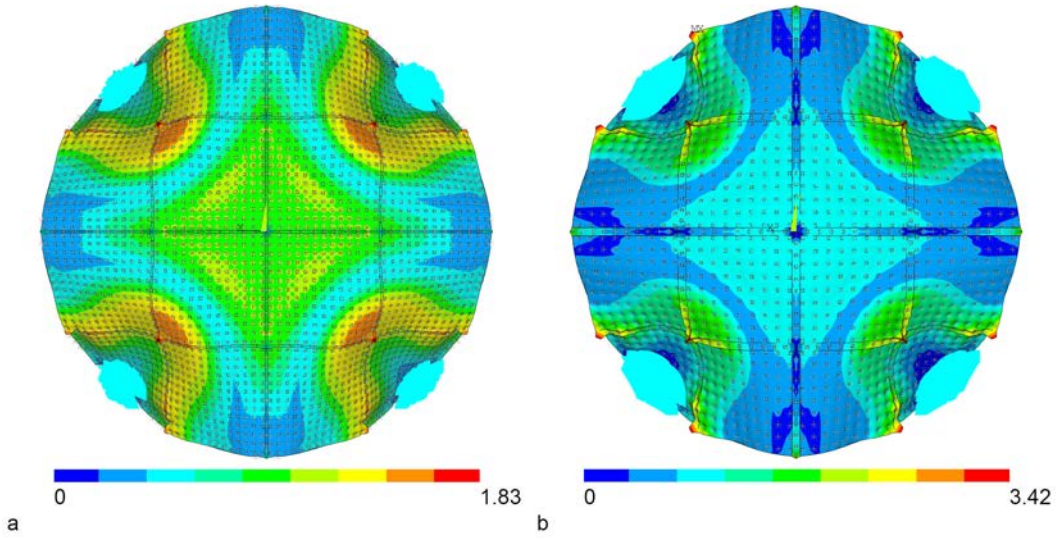


Figure 10: Displacement of sheel a and b

References

[1] T. Pofahl, G. Della Puppa, M. Trautz, D. Bailly, R. Schmitz, G. HIRT, *Self-Supporting Free-Form Structures Made of Individual Sheet Metal Panels*, Proceedings of the IASS Annual Symposium 2017, September 25 - 28th, 2017, Hamburg, Germany.

[2] T. Pofahl, G. Della Puppa, M. Trautz, D. Bailly, G. HIRT, *A new concept for freeform shell structures composed of doublycurvedmultilayered panels*, Proceedings of the IASS Annual Symposium 2014, September 15 - 19th, 2014, Brasilia.

[3] *ANSYS® Academic Research Mechanical, Release 17.2, Help System, Command Reference, ANSYS, Inc.*

Proceedings of the IASS Annual Symposium 2019 – Structural Membranes 2019
Form and Force
7 – 10 October 2019, Barcelona, Spain
C. Lázaro, K.-U. Bletzinger, E. Oñate (eds.)

Dynamic Space Truss-Textile Membrane Assemblies

Sachin Sean GUPTA, Dhileep Kumar JAYASHANKAR, Kenneth J. TRACY*

*SUTD Digital Manufacturing and Design Centre
Singapore University of Technology and Design
8 Somapah Road, Singapore 487372
kenneth_tracy@sutd.edu.sg

Abstract

In this paper, we present the design and fabrication of a dynamic composite assembly consisting of two key structural components that simultaneously behave as actuators: hygroscopic space trusses and a textile membrane. By designing cantilevering trusses with bio-composite chitosan films as critical tension members, a water-responsive structure with a large-scale shape change was conceived. The textile membrane spanning between the trusses also actuates the structure through its internal prestress. The reciprocity between the trusses and the membrane enables a performative mediation between structural rigidity and flexible motion. A digital simulation tool was created to predict the shape change of the assembly considering the hygro-mechanical properties of the chitosan films, the depth profile of the trusses, and the tensile properties of the membrane. As demonstrative examples, we present physical prototypes of this new composite structural system with tailored shape changes.

Keywords: Hygroscopic, space truss, textile membrane, chitosan

1. Introduction

Structural systems composed of complementary material components can achieve new calibers of performance. As a classic example, reinforced concrete synthesizes the high tensile strength of steel rebar with the compressive properties of concrete, offering a superb mixture of properties that provoked widespread adoption of this composite system in the construction industry [1]. While this represents a simplified case of attaining both tensile and compressive properties for load-bearing scenarios, one can imagine alternative material relationships that induce high degrees of functionality for different requirements. One interesting notion is the cultivation of material reciprocities for dynamic structures, which have the capacity to change form over time in response to environmental stimuli. State-of-the-art shape-changing structures in architecture are still hampered by limitations in scale and response time [2], and so uncovering and developing these complementary material relationships can potentially improve upon these parameters.

In light of these compelling concepts, the present work investigates novel, passively-actuated dynamic structural assemblies composed of water-activated cantilevering space trusses and a textile membrane. The movement of the structure is enabled by the inclusion of hygroscopic chitosan films as critical tensile members in the cantilevers, whose structural integrity vary with water content in the film (Figure 1). When the films become saturated with water, the trusses weaken, allowing the membrane prestress to pull them downwards into one premeditated configuration which we have termed the "wet state". As the chitosan films naturally dry, they regain their initial stiffness and strength so that they are able to lift the lightweight trusses into a curled "dry state". Therefore, two actuating material components – the hygroscopic chitosan films and the textile membrane – are used in conjunction to create the full actuation range of the structure. The shape changes are designed in the context of using such structures for outdoor canopies that can transition in between one profile that increases the amount of sheltered area under the

Copyright © 2019 by S. S. Gupta, D. K. Jayashankar, K. J. Tracy
Published by the International Association for Shell and Spatial Structures (IASS) with permission.

trusses at sharp angles of rain (wet state) and one that emulates an airfoil to encourage wind to move beneath (dry state). We have simulated and prototyped such structures using a combination of digital design and custom fabrication methods and tested them for actuation.

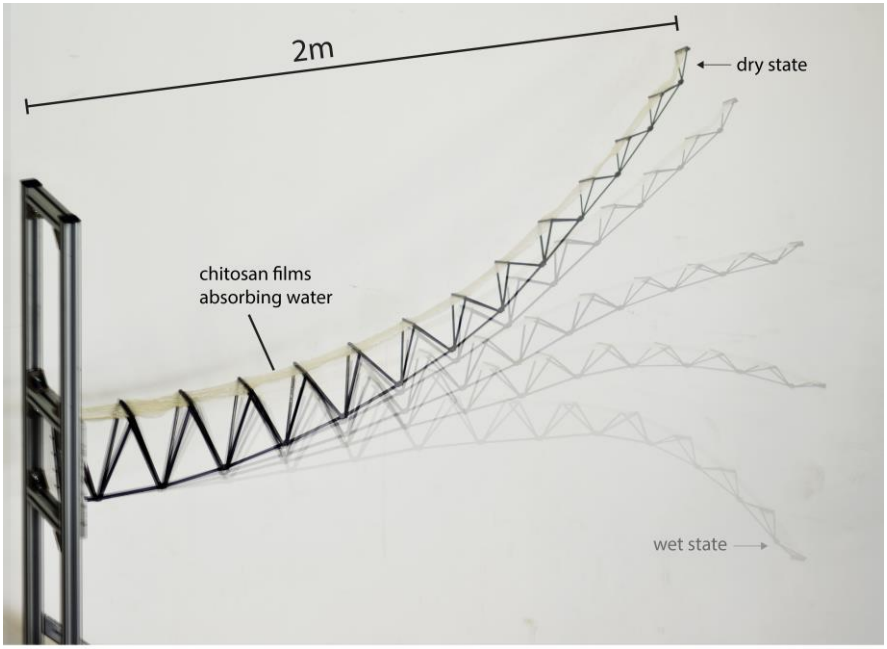


Figure 1: Dynamic space truss moving in between dry and wet states due to absorption of water by chitosan film

2. Background

Research of hygroscopically actuated structures have primarily showcased the potential of hygroscopic materials to create dynamic apertures for building skins to respond to fluctuations in ambient humidity [3] [4]. However, a few recent projects have started to diverge from this surface typology and create spatial structures, such as space frames, that experience fundamental and transformative shape changes [5]. While these projects serve as key works demonstrating successful material programming and fabrication developments, the main drawbacks that have been identified are the load-bearing ability and response time of these experimental structures. These limitations stem from a preference for material compositions of entirely wood bilayers or wood fiber-synthetic polymer composites, which depend on minimized thickness for increased actuation time (at least several hours).

The synthesis of textiles with responsive materials has primarily been embodied as the field of smart textiles, which achieve functionality through the use of a stimuli-responsive material in the form of a yarn [6]. However, smart textiles do not usually leverage the intrinsic tensile capacity of the materials as an actuation mechanism. This lies in contrast to the realm of architectural design research, where the use of textile membrane prestress to actuate the programmed deformation of a structure is an active area of research. This has been applied in the context of forming the membrane or the slender elements to which the membrane is attached in a specific manner. The former can be seen in the self-formation of membranes with embedded rigid members such as membrane tensegrity structures [7] and membrane-actuated stiffness gradient composites [8], while the latter characterizes the development of bending-active textile hybrids [9]. The present work differentiates itself by combining hygroscopic and membrane actuation in order to achieve large-scale, quick-acting, environmentally-responsive shape changes. In order for this to happen, the design of each material component, as well as their relation to one another, had to be understood and resolved.

3. Materials and Fabrication

3.1. Space Truss

The dynamic space trusses are discretized as a kit-of-parts consisting of chitosan films, joints, strut and tie members, and precision components. By designing the structures with specific tolerances according to Design for Assembly/Manufacturing (DFA/DFM) principles, a fluid assembly process is possible. The chitosan films serve as the top chords of the cantilevering trusses and are therefore critical tensile members that determine the overall deformation of the structure. The chitosan films are produced through a custom production method that has already been reported in another work [10]. In summary, the chitosan is prepared as a 3wt% solution that is cast into an acrylic mold lined with cotton fiber, and upon drying, creates a fiber-reinforced bio-composite of 0.3mm thickness. The chitosan films are laser cut to shape and size with metric standard size holes to secure the films to the trusses with metal fasteners.

The joints of the space trusses are the key components enabling their movement. The joints are designed for hinge rotation and are composed of male and female halves centered around a pin and ball bearings. The joints are also retrofit with a membrane connection detail materialized as a countersunk-radii joint in which sections of membrane can be inserted, capped, and fastened (Figure 2). To permit the actuated movement, each joint is designed with an extruded cut that provides a specific rotation angle. By designing the cumulative rotation about all the joints, the shape change of the assembly can be directly programmed. Because each joint must have a unique extruded cut and interface with the various diameters and angles of the truss members, the joint geometries were computationally generated and then fabricated with 3D-printing using fused deposition modeling (FDM) technology. Furthermore, because the joints were predicted to serve as focal points of load transfer during the shape change, a continuous fiber fabrication (CFF)-FDM method to reinforce the joints was selected. The Mark Two Markforged printer allows insertion of long carbon fibers in a layer-by-layer fashion into a nylon-based matrix, which enabled high-strength, low-weight customization of each joint in consideration of the anticipated forces. This was critical for our application. Similarly, the strut and ties of the truss were rationalized as carbon-fiber-reinforced epoxy tubes that were bought as stock material and cut to size.

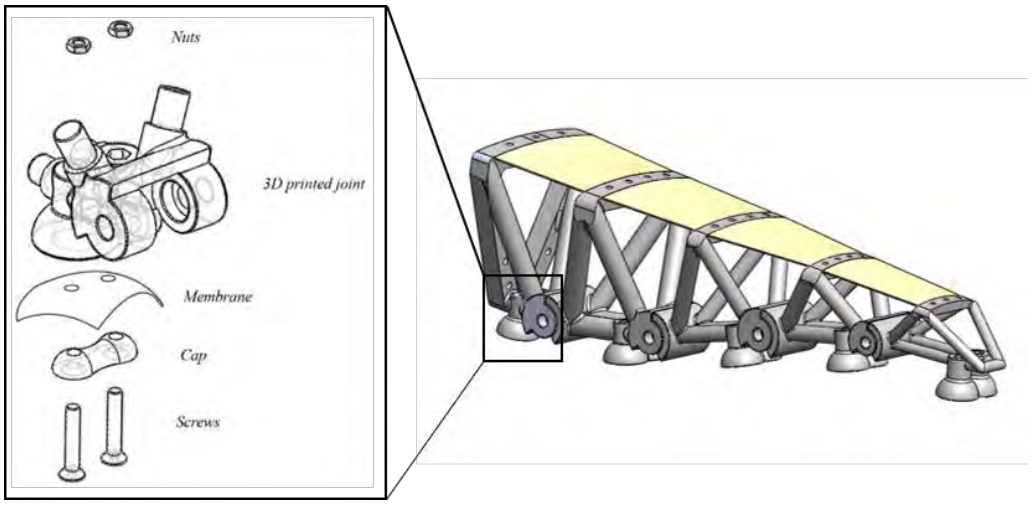


Figure 2: (Left) Exploded view of membrane connection detail and (right) space truss model

3.2. Textile Membrane

The primary design aspect for the textile membrane was the choice of material. Most structural textiles offer very little elastic strain, but for our case, the membrane needed to accommodate the truss movement and actuate the structure in its wet state with sufficient prestress. Thus, an elastic material

that offered a satisfactory degree of stretchability was required. Bedouinflex®, a readily-available polyester-based material used for outdoor canvases, was selected, offering at least 25% strain in its first linear elastic region in warp, weft, and bias directions. The canvas material was cut by hand to desired size in its bias direction and attached to the truss using the custom joint detail. The amount of stretch between consecutive joints was experimented with, as too much prestress in the membrane would disallow the movement of the trusses into their dry curled upwards conformation, and too little prestress would be insufficient for the actuation of the structure towards its wet form.

4. Digital Simulation

To predict the motion of the assembly, a simulation tool was developed in Rhinoceros using the Kangaroo physics engine. The goal of this tool was to provide the user with the ability to vary different parameters to determine the effect on the shape change. The material properties of the various components were abstracted as Kangaroo goals that undergo live position-based dynamics to converge upon resultant geometries.

The trusses were drawn as collection of lines which were represented as linear springs, with the springs modeling the chitosan films given the ability to change their length depending on if the simulation was determining the wet condition (allowable expansion in length) or dry condition (specific reduction in length). The maximum possible length change (12.8%) between wet and dry states was determined by testing of the films' swelling properties. The other springs representing the struts and ties of the truss were instructed to maintain their length. The membrane was modeled by lofting between the bottom chords of the trusses to create a surface which was then meshed. The mesh edges of this model were similarly represented as springs and given the ability to shrink to induce prestress in the membrane, as well as general flexibility in their length to mirror the compliance of the physical counterpart. The entire model was fixed with anchor points on one end to create a cantilevering structure. An ideal case was assumed in which the joints were stiff enough to resist lateral motion of the trusses due to the membrane prestress.

The simulation of the wet condition initiates when the mesh edges of the membrane model are given pretension and the chitosan film are allowed to expand. Because the rest of the truss members wish to maintain their length, simulated energetic frustration between the inert truss members and the activated materials results in changes in truss curvature in a concave downward manner (Figure 3). To simulate the dry condition, the chitosan films are provided a targeted length that reflects their shrinkage and the membrane is permitted to adjust its length. This results in a transition in assembly curvature from concave downward to concave upward. These shape changes were explored in an iterative fashion, with the parameters of truss geometry, chitosan expansion/shrinkage, and membrane pretension varied. Furthermore, this simulation tool directly output the joint rotation angles required to achieve a specific shape change, which were input into the computational generation of the joint design. Several shape-changing prototypes were designed using this simulation tool and fabricated using the methods described above.

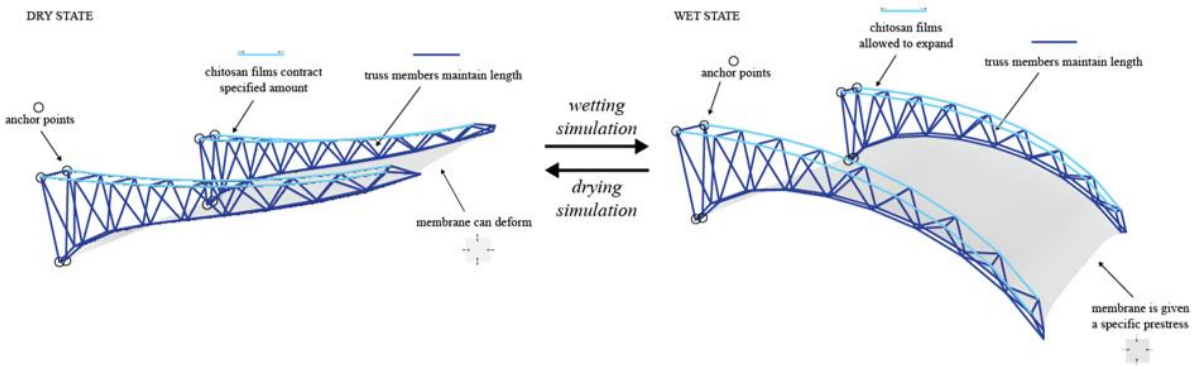


Figure 3: Explanation of shape change simulation tool

5. Experimentation

Prototypes of this class of structure were built in an experimental, iterative process, resolving issues such as friction between the joint's parts, film production parameters, and lateral torsion. Here we showcase two built prototypes that were used to test the actuation of the dynamic assembly as well as to validate the simulation tool. Criteria such as actuation time and general mechanical performance of the material components were observed and noted. Finally, the ability of the structure to respond to the actuators was investigated with different wetting and drying conditions.

5.1. Prototype 1

Prototype 1 consisted of a single truss to test the ability of the chitosan film to lift the truss in opposition to a rubber band that acted as a prototypical tensile actuating element for the structure. Different amounts of extension in the rubber band were experimented to determine how much pretension was sufficient in achieving the wet state condition without hindering the chitosan's actuation to the dry state. A test setup was built to mount the truss and interchangeably apply a shower of water or streams of dry air to the structure. In the simulation for this prototype, a prestressed cable element was modeled in lieu of the membrane, as only one truss was being tested.

5.1. Prototype 1

Prototype 2 consisted of two trusses with the integrated membrane. In this prototype, the truss-membrane connection detail described in Section 3.1 was tested. The trusses measured 450mm in length and were each composed of four chitosan films. The membrane was cut to a 450mm x450mm square size and attached to the trusses after mounting them on an acrylic plate. The test was applied outdoors, with water being applied by soaking with spray bottles and drying occurring through a heat gun. The trusses were then brought inwards for documentation.

6. Results

6.1. Prototype 1

The experimentation with Prototype 1 led to a calibration of 10mm extension with the rubber band in order to allow the structure to lift back into the dry state conformation. In this case, actuation time was average of 5.3 minutes for the wet state and 29.8 minutes for the dry state. This test proved that the combination of actuation from a prestressed tensile element and the chitosan film could be successfully resolved. Figure 4 shows a comparison of the simulated shape change with the actual change, lending a degree of confirmation to the simulation tool.

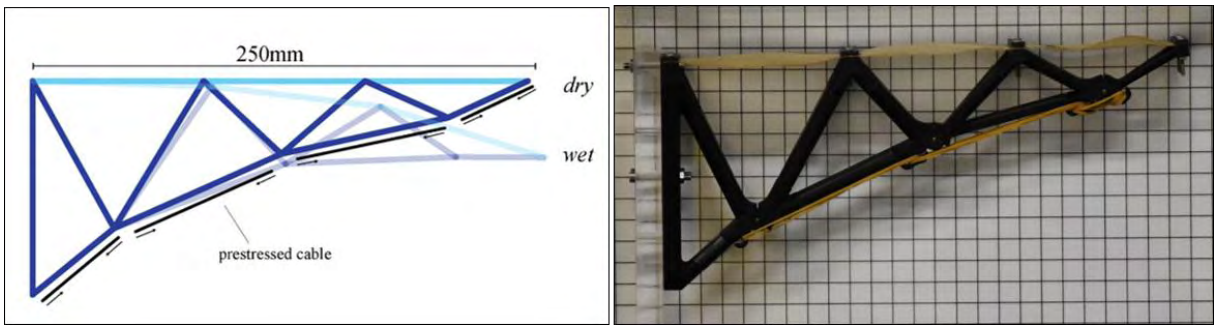


Figure 4: Comparison between simulation (left) and physical experiment (right) of Prototype 1

6.2. Prototype 2

The truss-membrane connection detail performed well, securing the membrane during all phases of actuation (Figure 5). The 10mm stretching of the membrane between consecutive joints permitted the shape change of the structure in both directions. In this case, actuation time was average of 6.0 minutes for the wet state and 22.0 minutes for the dry state. The higher actuation time for the dry state was most likely due to the use of the heat gun as opposed to the air streams as used in the testing of Prototype 1. Figure 6 shows a comparison of the simulated shape change with the actual change. While the physical object expresses some slight deviations from the digital model, the transformation at the cantilevering ends showed appreciable fidelity.



Figure 5: The membrane truss connection via 3D-printed joint was validated in these experiments

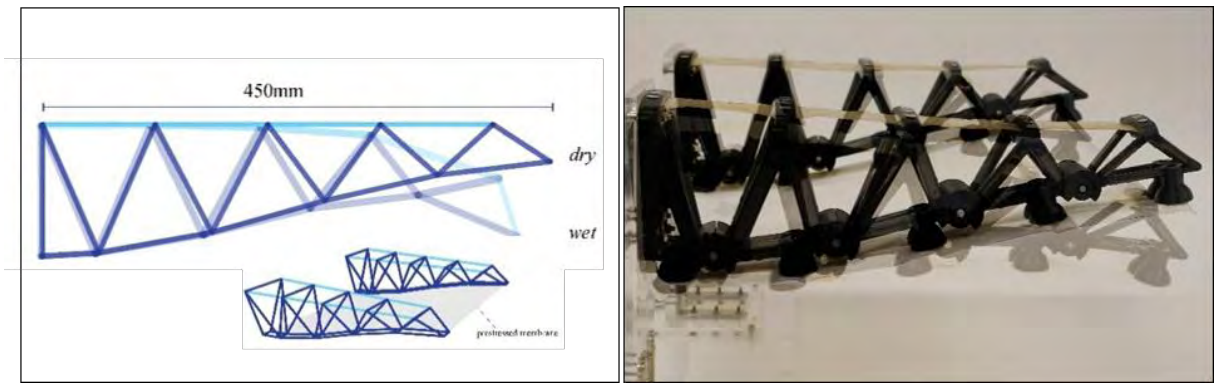


Figure 6: Comparison between simulation (left) and physical experiment (right) of Prototype 2

7. Discussion

The experiments shown above demonstrate that the chitosan films and membrane successfully actuate the structural assembly. The chitosan films exhibit resurgence in strength required to lift the entire structure during drying, while the membrane's pretension catalyzes the curling downwards motion when the films weaken. This proves the ability of two underexplored actuators to perform in a synergistic manner to instigate functional shape changes. The general fidelity between the simulation and the physical experiment makes sense considering that the joint design, which ultimately determines the motion of the structures, is directly fed from the simulation data.

So far to our knowledge, no other hygroscopic structural application has shown the response time that our system has achieved. Furthermore, the custom fabrication methods of the high-strength material components and the use of digital simulation to explore an infinite number of shape changes attest to the increased feasibility of designing dynamic structures that is enabled by new technologies. This points to the birth of novel classes of passively actuated building structures that can respond to the environment for increased thermal or climatic performance.

8. Further Work

The next steps for this work are spread across different research paths. A more quantifiable means of measuring the shape changes of the structure is necessary to test for repeatability. The application of 3D scanning can help digitize the shape changes for closer comparison to the predicted result. In terms of the physical aspects, in order to scale up this structure, the mechanical properties of the films would have to be enhanced, as the increased weight of the trusses and membrane would induce larger forces on the films. The 3D-printed joints would similarly have to be substantiated to counter these increased forces or could even by replaced by high-strength compliant mechanisms. The custom fabrication of the membrane through large-scale additive manufacturing processes like CNC knitting could allow tailored properties to decrease weight and grade stiffness in accordance to stress concentrations at the joint-membrane interface. Once scaled, this structure could be tested outdoors in a real-case scenario testing if its profile changes achieve the desired sheltering effect from rain and the air flow redirection for its inhabitants (Figure 7).

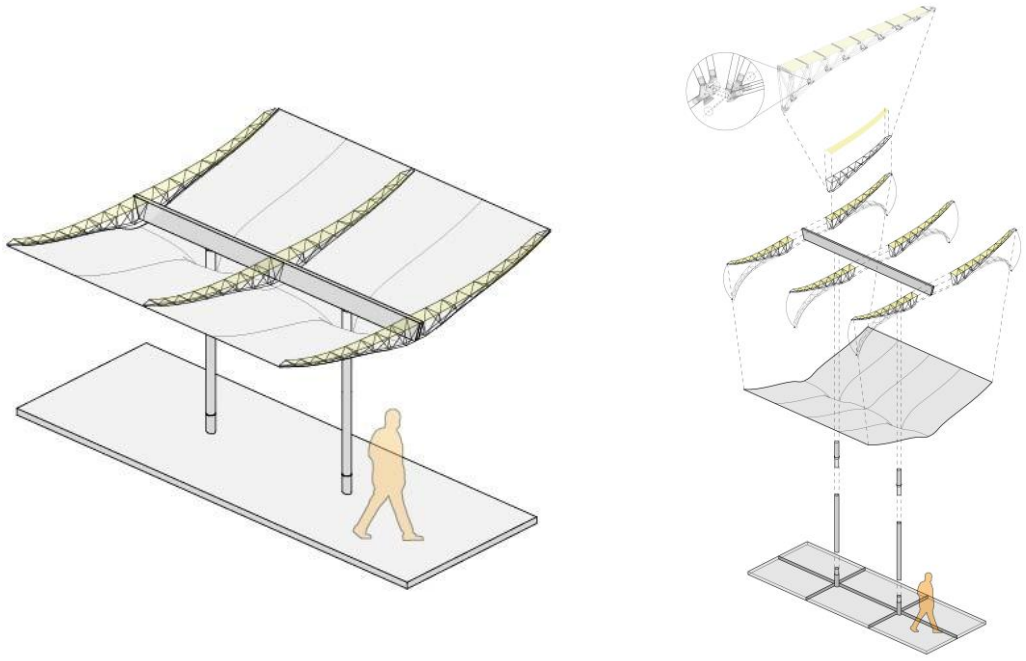


Figure 7: Schematic of future research direction for dynamic space truss-textile membrane assemblies

Acknowledgements

We would like to thank SUTD's Digital Manufacturing and Design Centre and the National Research Foundation for their support for this research project. We would also like to thank Pei Zhi Chia, Zenon Tan, Christyasto Pambudi, Julius Ang, and Lance Yu for their assistance.

References

[1] W. H. Dilger, "Reinforced concrete: mechanics and design," *Canadian Journal of Civil Engineering*, 2000.

[2] S. Tibbits, "4D printing: Multi-material shape change," *Architectural Design*, vol. 84, no. 1, pp. 116–121, 2014.

[3] S. Reichert, A. Menges, and D. Correa, "Meteorosensitive architecture: Biomimetic building skins based on materially embedded and hygroscopically enabled responsiveness," *Computational Design*, vol. 60, pp. 50–69, Mar. 2015.

[4] D. Correa, A. Papadopoulou, C. Guberan, N. Jhaveri, S. Reichert, A. Menges, and S. Tibbits, "3D-Printed Wood: Programming Hygroscopic Material Transformations," *3D Printing and Additive Manufacturing.*, vol. 2, no. 3, pp. 106–116, Sep. 2015.

[5] F. Forestiero, N. Xenos, D. Wood, and E. Baharlou, "Low-tech Shape-Shifting Space Frames," in *Proceedings of the IASS 2018, Boston, USA.*

[6] J. Scott, "Hierarchy in Knitted Forms: Environmentally Responsive Textiles for Architecture," in *Acadia 2013 Adaptive Architecture*, pp. 361–366, 2013.

[7] M. Shigematsu, M. Tanaka and H. Noguchi, "Form finding analysis of tensegrity membrane structures based on variational method," in *Advances in the Optimization and Form-finding of Tensegrity Structures: Proceedings of the 6th International Conference on Computation of Shell and Spatial Structures IASS-IACM 2008, Ithaca, USA, May 28-31, 2008.*

[8] L. Aldinger, G. Margariti, A. Körner, S. Suzuki, and J. Knippers, "Tailoring Self-Formation fabrication and simulation of membrane-actuated stiffness gradient composites," in *Proceedings of the IASS 2018, Boston, USA.*

[9] S. Suzuki and J. Knippers, "ElasticSpace: A computational framework for interactive form-finding of textile hybrid structures through evolving topology networks," *International Journal of Parallel, Emergent, and Distributed Systems*, vol. 32, pp. S4–S14, 2017.

[10] S. Gupta, D. Jayashankar, N. Sanandiya, J. Fernandez, K. Tracy, "Prototyping of Chitosan-Based Shape-Changing structures," in *Intelligent & Informed, Proceedings of the 24th International Conference of the Association for Computer-Aided Architectural Design Research in Asia (CAADRIA) 2019.*

Proceedings of the IASS Annual Symposium 2019 – Structural Membranes 2019
Form and Force
7 – 10 October 2019, Barcelona, Spain
C. Lázaro, K.-U. Bletzinger, E. Oñate (eds.)

Retractable Roof Tecklenburg

Gerd SCHMID*

* formTL ingenieure für tragwerk und leichtbau gmbh
güttinger straße 37, 78315 radolfzell
gerd.schmid@form-TLde

Abstract

Membrane structures are often used as an interim measure and rarely survive for more than 20 years. In particular, textile constructions are characterized in this context by their special aesthetics, and by the demolition are often lost real engineering artworks. An exception is the roof of the open-air theatre in Tecklenburg – it is a fine example of how durable lightweight constructions can be and what their potentials are. formTL, which emerged from IPL in 2004, was involved in inspections of the roof and supported Cenotec in its 2017 modernization. This paper presents previously unknown original design ideas from our IPL archive. Based on original 3D CAD data and photos of the inspections, the original design is shown and explained, with a focus on the special nature of the reface. Emphasis will be put on the "weak spots", the aging of which necessitated an exchange of the membrane envelope and our corrections and "soft" optimizations for the next period of use.

Keywords: reface, membrane structures, retractable roof

1. History of Tecklenburg

26 years ago, the open-air stage in Tecklenburg got a mobile weather protection roof and since then not only offers the ambience of an open-air grandstand, but also, if required, sun and rain protection.

The 1200 square meter canopy protects 2000 spectators - stage and actors were not covered, which remained so today.

We have found first ideas of Carl Nolte and IPL in 1987 for the operator Freilichtbühne Tecklenburg e.V.

1992 was planned, 1993 manufactured and mounted.

Copyright © 2019 by Gerd Schmid
Published by the International Association for Shell and Spatial Structures (IASS) with permission.

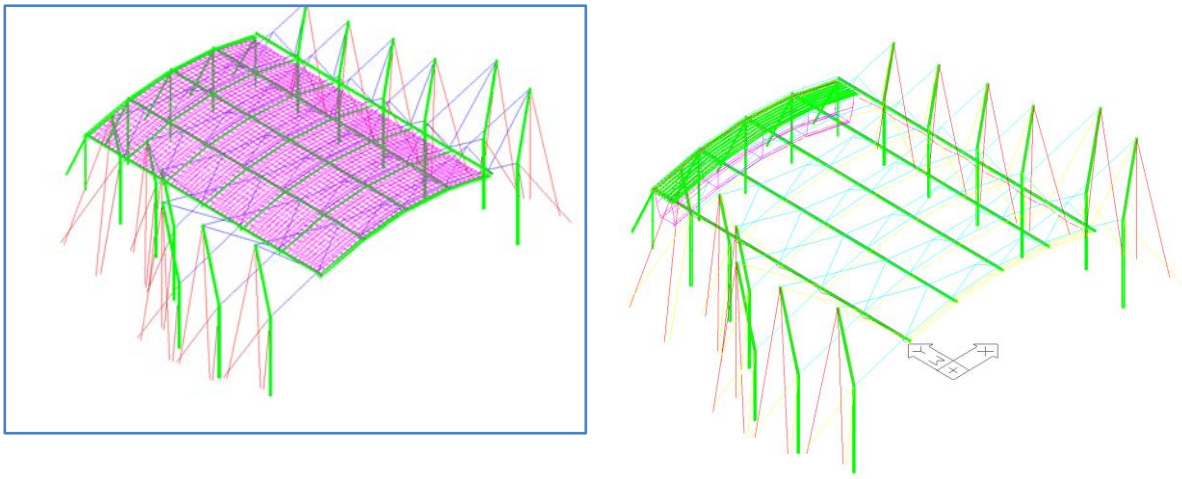


Figure 1+2: 3D model of 1992 with both opening states [formTL archive]

The last review in 2010 triggered the renewal of the roof skin, which was affected by the many driving and reefing operations. The roof skin was dismantled at the end of 2015, the new membrane planned in early 2016, assembled in summer and mounted in autumn.

2. Building types in comparison

Mobile roofs, super sized convertible roofs are often fascinating and unique. There are rigid roofs and even entire halls that run on rails, such as the Magrodome halls of DSD and the Tournesol baths in France from the 1970s, the open air roofs from the 1980s or the Zeitbäder since the 2010s. Particularly attractive organically shaped membrane roofs, which are centrally reefed, as in the Abbey Ruins Bad Hersfeld (since 1968, membrane renewal 1993 and 2019) or the Allwetterbad Flingern (1977-2012) and since the millennium retractable roofs over the playing fields of modern stadiums. If you like it more robust, it is advantageous to reef the membrane only parallel, such as the Athens Heart in Piraeus (since 2009) or the open air theater Tecklenburg (since 1993).

3. Structure, drive

The load-bearing structure of Tecklenburg adapts sensitively and organically to the irregularly wide terrain and the different slopes, while fulfilling the geometric and static requirements that a membrane can be moved along.

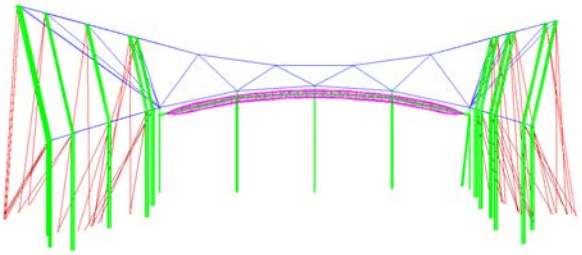


Figure 3: Elevation with all cable binders [formTL archive]

The supporting structure consists of 6 cable girders of different heights, inclined and guyed supports. Under the rope hang 5 steel profiles, which are at the same time rails on which to move the membrane cushions with the help of wheel carriages.

Unique are chains trapped in the rails. The gears of the 5 DC motors reach into the chains. Only this bow carries the drives. The remaining bows and their membrane cushions are pulled or pushed back only in the airless state.

For storage, the membrane cushions hang at the end of the grandstand reefed under the arches.

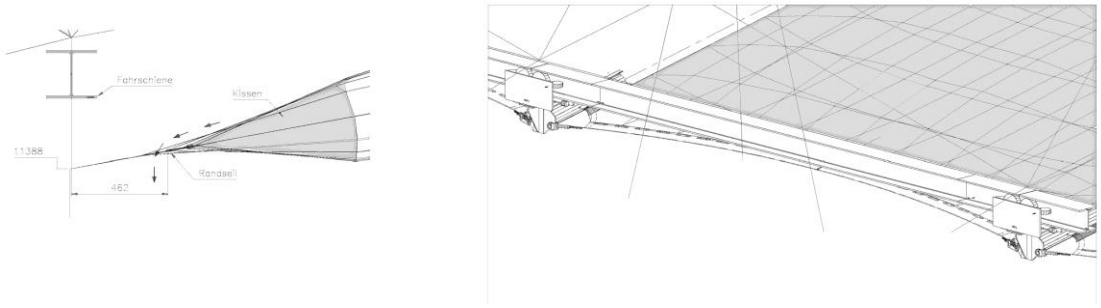


Figure 4: suspended steel profile which has the function of a rail for the wheel carriages of the membrane cushions [formTL archive]



Figure 5: Wheel carriage the in steel profile [formTL archive]

4. Exkursus membrane materials

For non-convertible textile covers in the outdoor area, a variety of films, coated and uncoated fabrics are suitable. They just have to be strong enough and naturally weather-resistant.

Removable and retractable membrane covers experience additional stress due to handling during assembly, disassembly or reefing. Only flexible membranes can be reefed without cracks into narrow folds. Thus, PTFE-coated glass fabrics are unsuitable because their fibers are stiffened by the "hard" Teflon coating and break their fibers upon bending.

Suitable are PVC-coated polyester fabrics and silicone-coated glass fabrics, whose coating softly embeds the fibers and allows the tightest bending radii. Both materials are ideal for 1-axis reefing, as they occur in Tecklenburg. Even more flexibal are wooven fabrics made of polyester fibers, which are only a few years sun resistant, and fabrics made of Teflon fibers, which are very expensive but particularly resistant to kinking and aging. Both fabrics are resistent to cross-folds which occurs in centrally reefed membranes.

There are good experiences with the 1-axial reefing of PVC films and fluor films for tents. Since ETFE films are very unsusceptible to kinking, it is only a matter of time before convertible building envelopes, which are reefed radially or in parallel, are made of ETFE.

5. Aging in comparison

Membranes age at different speeds: Solid constructions usually have a service life of 15 to 30 years. Movable structures are said to last from 10 to 15 years, as movement stresses the coating and fibers. The strength of the fabric decreases faster. Especially for the renewal we selected a membrane which allows 100.000 foldings.

6. The new membrane

The new membrane 669 Polyplan Architecture Type II is from Low & Bonar, formerly Mehler-Texnologie. It has a breaking strength of 4200/4000 N / 5cm, that is 8 t per meter. It is utilised under 300 Pascal internal pressure only to 7% and with an additional 0.27 kN / m² wind suction to 18%. The membrane meets the usual fire protection requirements B-S2, d0 according to DIN 13501.

7. Analysis

The roof is designed for summer operation with a wind speed of up to 75 km/h. On without performance days, the membrane should be vented and parked under a canopy. In winter, a cover protects from storms.

8. Condition of the primary structure

In contrast to the now exemplary renewed membrane, the primary structure has remained unchanged. The partially slack cables of the cable girders and the suspension cables were not tensioned. An elaborate job that is important for the stability, the function of the driving mechanics and the future life span of the entire roof.



Figure 6: 2017 Slack cables [R. Borgmann]

9. Scope of renovation 2016

The membrane cushions were renewed, the supporting air system became more efficient, the air hoses made of aluminum spiral pipe were replaced by permanently elastic plastic hoses with inserted spiral. The drainage points have been revised. More cable pockets were attached. The primary steel and the ropes were cleaned and repaired. The secondary steel was removed and reinstalled with new screws. The cable pockets are now a bit bigger.



Figure 7: Dismantling [CenoTec]

The compensation of the membrane was adapted, as each membrane expands differently under load. For this purpose, a biaxial load profile was defined to which the cushion membrane is exposed during its start-up phase. The test results show us how much this membrane stretches permanently in the two main bearing directions. This stretch is applied as compensation in the cushions.

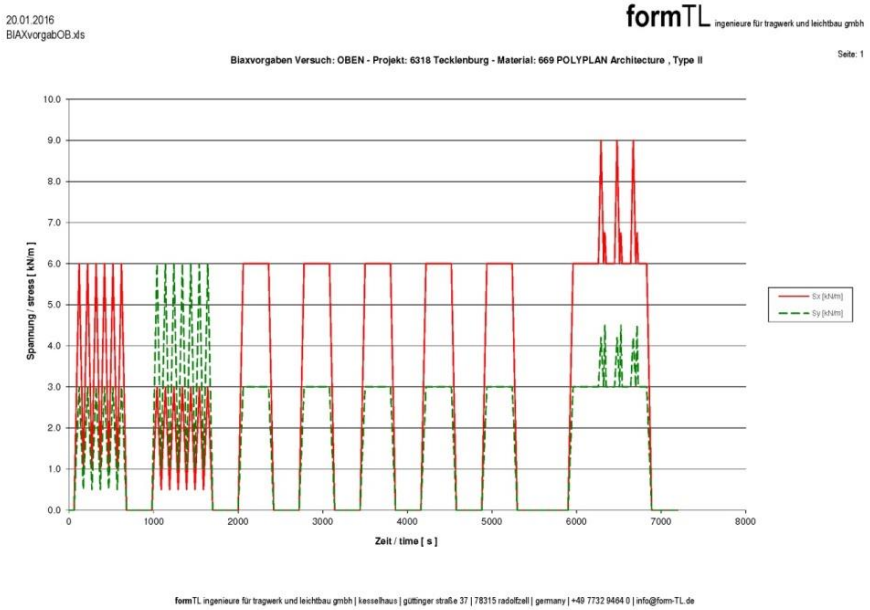


Figure 8: Biaxial test profile [formTL archive]

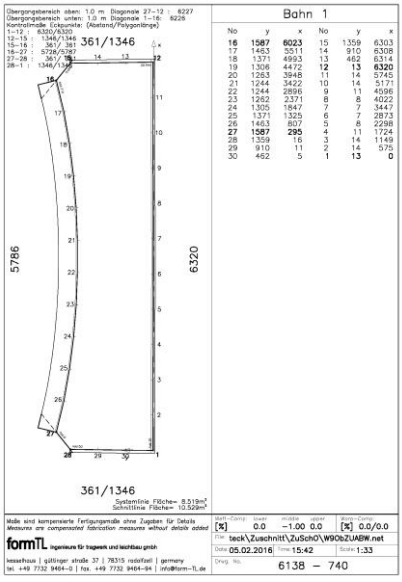


Figure 9: strip from the lower cushion panel [formTL archive]

This ensures that the membrane cushions, after multiple wind suction and wind pressure, take the defined shape. An interesting phenomenon therefore occurs at the beginning of the freshly installed roof cushions, when the lower cushion membrane is even shorter and therefore the roof can not be completely closed. Only after several inflation, the lower cushion membrane is stretched so that the roof closes completely.

10. What has not changed and why?

To keep the Z.i.E. valid, the connection details were carried out with a "Kombinaht", which is sewn first and then welded with a here 40 mm wide HF seam.

Today such complex connections are unusual, since the needles puncture load carrying fibers and weaken the fabric, and air can exit through the pinholes.

11. What has been changed and why?

Today, the seams are a wider. The original seam layout with seams in the longitudinal direction without cross seams and the web width of 143 cm were repeated.

12. What do we learn in the evaluation of the old membrane?

In the area of the lower pillow membrane repair patches accumulated in the area of the pillow crease. Although the roof is reefed only parallel, here are cross folds, which have stressed the membrane heavily. This will also happen with the new membrane. Ideally, therefore, a parallel reefed membrane is attached to a flat profile rather than to an arch.

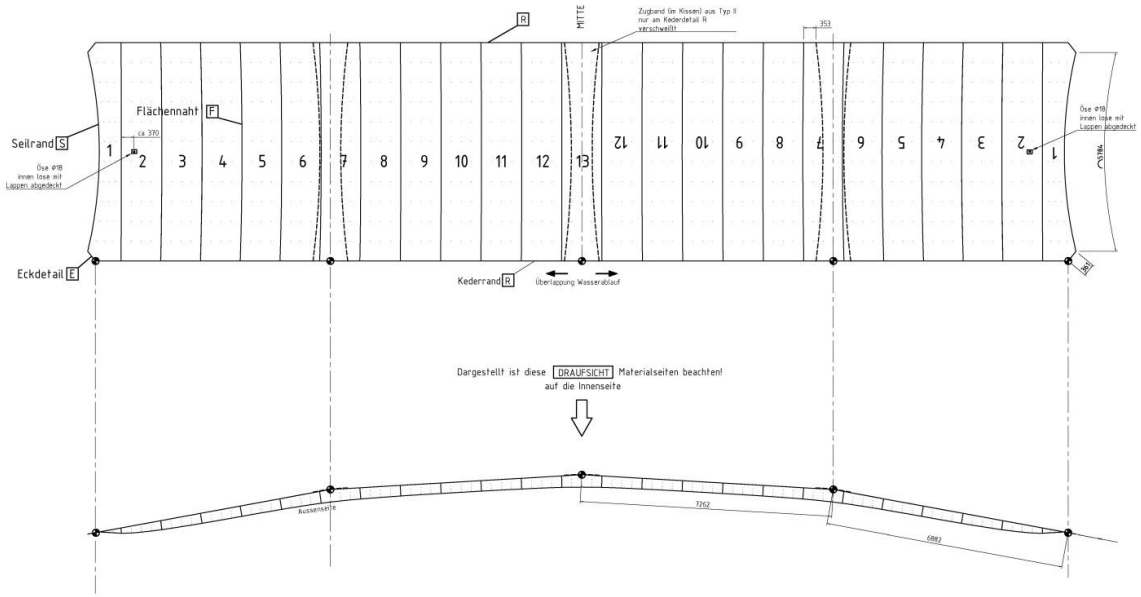


Figure 10: Membrane layout 2017 [formTL 2017]

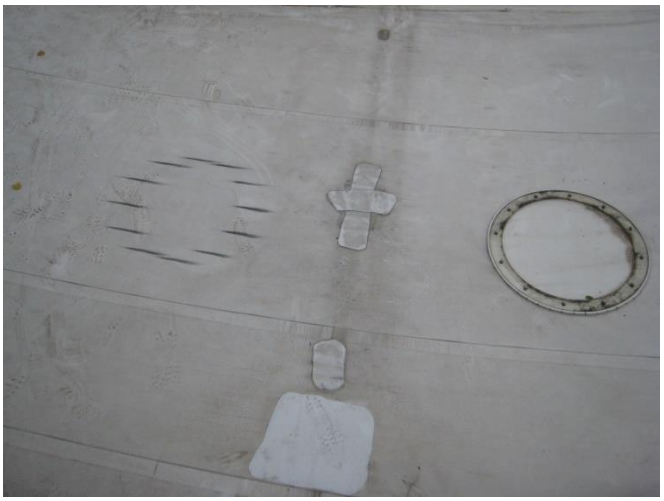


Figure 11: Patch in the area of the cross folds [CenoTec]

13. Too young for monument protection

Convertible textile structures are often used as interim structures and therefore rarely reach the age of 20 years or more. Especially textile constructions are characterized by a special aesthetics and with the demolition, as in the case of the all-weather bath in Flingern, often engineering artworks are lost. An exception are the roofs of the open-air stages in Tecklenburg and Bad Hersfeld - they show examples how durable textile constructions can be and what potential these structures have.

14. 3D planning and digital archive

IPL planned 1993 already digitally and in 3D. Since Autocad's DXF exchange format has been used at IPL times as well as today at formTL, the old geometry data is still legible today and an ideal basis for cost-effective renovations. The well-stocked digital archive, which we acquired from IPL in 2004, contains correspondence, statics, digital design files, detail design and workshop drawings, and even the drawings of the drive mechanics developed by IPL and realized by the company Dornieden in Tecklenburg. Thus, at the Tecklenburg project, only the customization of the removed membranes and fittings with the old drawings was necessary. Since there were only a few discrepancies, it was possible to deliver the cutting pattern adapted to the new membrane material within one month.

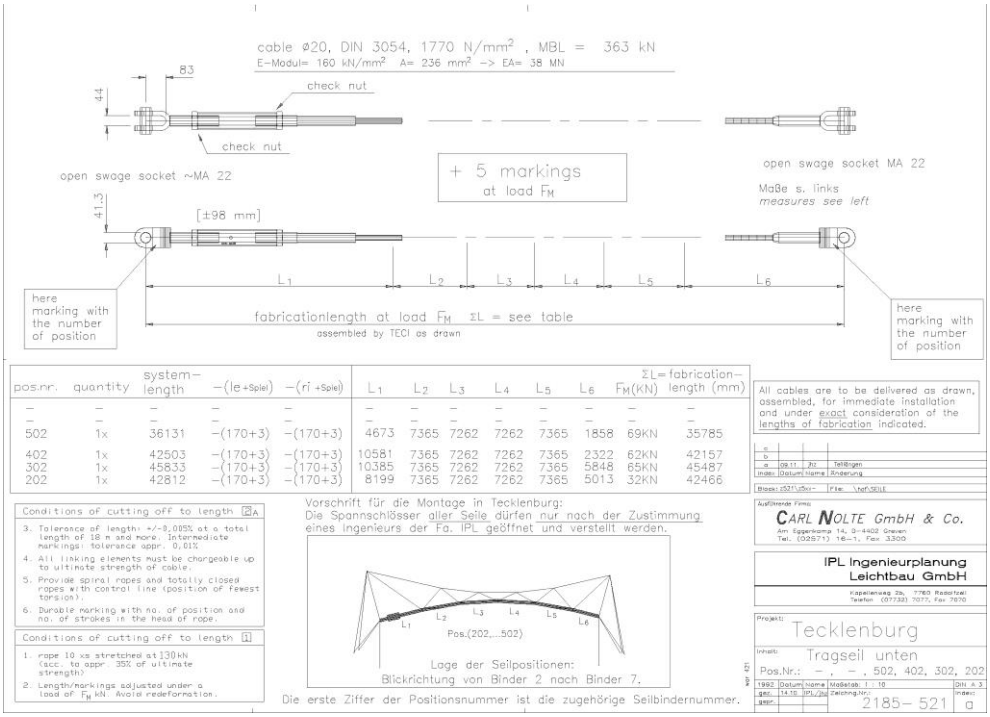


Figure 12: Cable drawing 1992 [formTL archive]

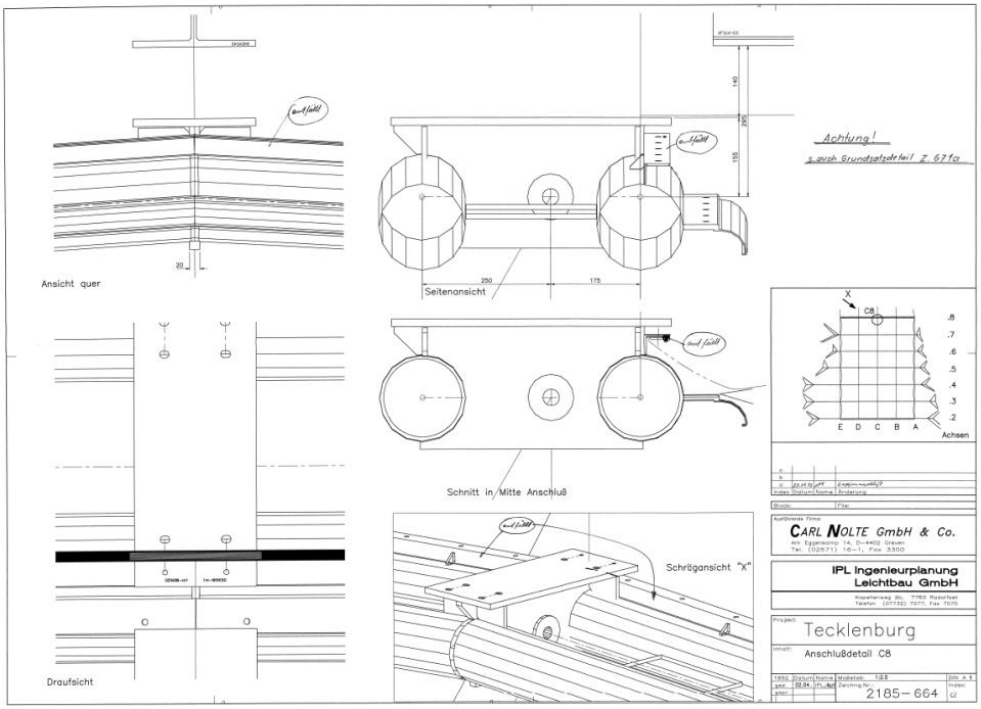


Figure 13: Membrane arch with carriage connection 1992 [formTL archive]

15. Conclusion

The Tecklenburg open-air stage is a remarkable example of a special and robust textile construction that makes it easy for the operator to replace heavily used components such as the membrane cushions.

The basis is a high-quality corrosion protection, in this case hot-dip galvanizing, which is still largely intact 25 years later.

The bolted connections known from textile structures are ideal if replacement should be fast and economical.

In anticipation of BIM: The centrally stored information and digital geometry data in one place corresponds to the principle of modern BIM planning.

The refurbishment of old IPL and future formTL projects will benefit from our data maintenance carried out since 1974.



Figure 14: 2017 robust textile construction Tecklenburg [R. Borgmann]

Client		Freilichtbühne Tecklenburg e.V.
Design		IPL Ingenieurplanung Leichtbau GmbH, Radolfzell/DE
General Contractor Roof		Carl Nolte, Greven
Manufacturer mechanics		Dornieden
Renewal engineering		formTL ingenieure für tragwerk und leichtbau gmbh, Radolfzell/DE, www.form-TL.de
Contractor Membrane Roof		CENO Membrane Technology GmbH, Greven/DE

References

[1] Gerd Schmid, "*Festspiele unter neuem Gewand, Sanierung der Freilichtbühne in Tecklenburg"* in Umrisse 2017/04. pp. 22-29

[2] Rudorf Witrin Techtextil-Symposium 1993 Vortrag Nr. 426 "*Neue Wege: Textilarchitektur bei der Freilichtbühne Tecklenburg*", 8 pages.

[3] "*Aufblasbare Regenhaut*" in green building 9/10-2017 pp.54-57

[4] "*Long live the membrane*" in Tensinews 35/2018 pp. 12-13

Proceedings of the IASS Annual Symposium 2019 – Structural Membranes 2019
Form and Force
7 – 10 October 2019, Barcelona, Spain
C. Lázaro, K.-U. Bletzinger, E. Oñate (eds.)

Additive Formwork for Concrete Shell Constructions

Roberto NABONI*, Luca BRESEGHELLO*

*CREATE Group, University of Southern Denmark (SDU) - Unit of Civil and Architectural Engineering
Odense, DK-5230, Denmark
ron@iti.sdu.dk

Abstract

Additive Manufacturing is rapidly developing in the area of concrete constructions. However, to date, several challenges still exist in terms of material and structural performance, which require further studies. In order to avoid such limitations, we research in the use of additive technologies to produce formwork for concrete construction elements to be applied in freeform shell structure. Specifically, this paper discusses early experiments conducted in the use of Fused Deposition Modelling to make shell components with unlimited curvature variation, high resolution and precision. Through design-driven experiments, we illustrate a viable workflow for the computational design of custom concrete panels, discuss material choices, and present a new manufacturing. In parallel with technical developments, discussion tectonic advancements enabled by this approach.

Keywords: Additive Manufacturing, digital fabrication, formwork, digital concrete

1. Introduction

With 4.1 billion cubic meters of material used per year to build structures of any type, concrete is the most used material in the realm of constructions after water [1]. Still today, making concrete structures is strictly constrained to our capacity to build formworks in order to give shape, provide functional requirements and ensure building precision. Despite the large impact of digital fabrication, the construction industry still relies on archaic methods for producing formworks: very limited in terms of automation, demanding a large quantity of labour-force, constrained geometrically, mostly made of temporary timber or steel structures that are hard to customize, with little precision [2]. In the contemporary context, these methods are becoming more and more inefficient, and impacting about half the cost of construction in a conventional structure, and more than two thirds in a non-standard doubly curved structure (Fig. 1).

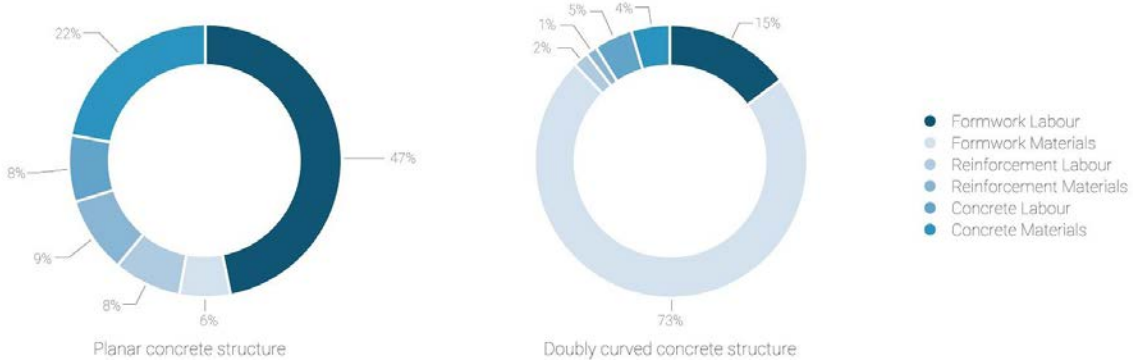


Figure 1: Cost of concrete works in planar and non-standard doubly curved constructions [3]

Copyright © 2019 by Roberto Naboni, Luca Breseghello
Published by the International Association for Shell and Spatial Structures (IASS) with permission.

Starting from the simple principle that concrete in its liquid state can fit almost any container, unexplored potential can be found in shell design based on non-standard high-performance geometries [4]. The rapid development of digital design tools is currently supporting modelling and analysis of complex architectural shapes, which are currently limited in use by the existing gap between the digital environment and the modes of production mentioned above [5]. In our research, we focus on developing an approach where Additive Manufacturing (AM) is tested for sustainable realization of complex and highly detailed construction elements to be used in freeform shell structures.

1.1 Existing approaches to additively manufactured formworks

In the field of AM for constructions, the current research focus is on improving extrusion techniques and material mixes to directly 3D print with concrete [6]. In alternative to this, a relatively unexplored area is focusing on the use of AM techniques to manufacture the formworks where concrete is poured and formed into [7]. A worthwhile advantage of this approach is that concrete casting process is a well-established procedure with very few uncertainties in terms of structural assessment and mechanical behaviour of the actual construction components produce with it. In this paper, we illustrate the use of large scale Fused Deposition Modelling (FDM) for the additive prefabrication of concrete shell elements, where a new level of shape control and complexity is enabled, in a cost-effective manner.

2 Methodology

Building upon the state-of-the-art research [8,9], we present a feasible pipeline of design and manufacturing that optimizes the use of FDM for the production of formworks to be employed for concrete elements at the building scale. In this way, we aim at combining the advantages of high-precision 3D Printing at the large scale, while avoiding existing material limitations of direct 3D printing. Coupled with thermoplastic formworks, we use of high-performing concrete mixture that is currently applied in constructions, complemented with fiber additions (Fig. 2).

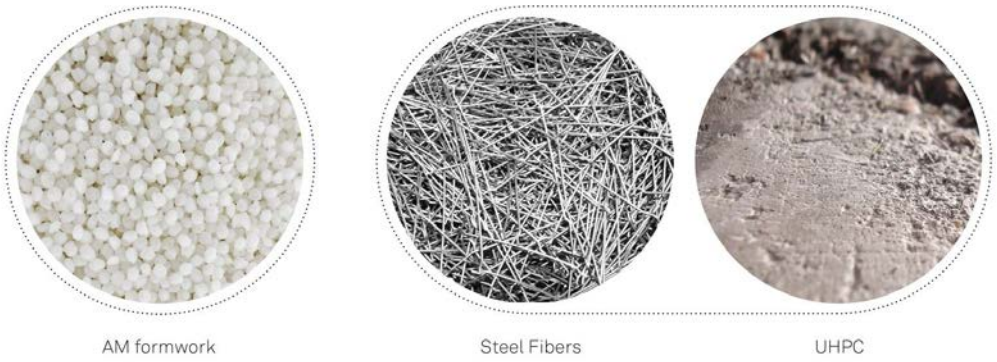


Figure 2: The three main materials for the presented research: ABS for the AM-manufactured formwork, UHPC with the addition of short 15 mm steel fibres for the final panel

Computational and fabrication developments are applied to the design and manufacturing of a set of concrete shell elements characterized by extreme control in curvature, sectional features and surface detailing. Following initial investigations on the material and manufacturing system, the work is here presented in a linear workflow, from design to fabrication, which includes three main phases: *Experimental Shell Design*: where the design is conceived and optimised through feedback from fabrication and performance-related attributes; *Formwork Fabrication*: where volumetric design is

transformed into machining code and manufactured by an FDM large scale 3D printer; *Concrete Casting*: the fluid mix of UHPFRC is poured into the formwork and then demoulded.

2.1 Experimental design of concrete shell components

In the XX century concrete shells have been commonly conceived, with few exceptions, as continuous cast-in-place monolithic constructions, while discrete assemblies with connections have been mostly disregarded given the challenge of ensuring a continuous load transfer [10]. However, recent advancements in computational design, simulation and digital fabrication offer opportunities to challenge this condition, and to conceive component-based shells. The experimental design strategy presented in this paper relies on discrete concrete elements to be assembled in-situ, focusing on the development of a computational workflow and the exploitation of emerging tectonic features. Exploiting the unique features of additive manufacturing, our design seeks to expand the performative capabilities of typical shell elements. Specifically, we utilize volumetric modelling strategies to achieve morphological integration between distinct performative elements. The exploration includes the development and fabrication of two distinct prototype (Fig.6):

- In prototype P1 (400 by 300 by 800 mm) we look into the articulation of a single shell element, which blends with a ribbing geometry, experimenting with variations in the freeform curvature, thickness between ranging from 20 to 170 mm, and high-resolution surface detailing (Fig. 6);
- In prototype P2 (950 by 850 by 1100 mm), we scale up the findings to a more massive and complex design, where we experiment a model of double shell connected by an internal web, and external skin with local reinforcements, variation in thickness between 35 to 140 mm combined with surface detailing (Fig. 7).

2.2 Design for Manufacturing

Despite its versatility, FDM has crucial manufacturing constraints that have to be taken into account during the design process. Considering the printing bed as the reference plane, printing parts shall generally be oriented vertically when it comes to mould production. Geometries that exceed an inclination of 60° are challenging to be produced without extra-supports since the plastic deposited by the printer's nozzle does not have sufficient supporting material to lay onto. Therefore, a set of algorithmic tools have been developed to provide real-time feedback. In particular a tool developed through C# in Grasshopper provide a feedback on the angle analysis with a highlight of the critical areas (Fig. 3). The model is then translated into a machining toolpath (.gcode) through a custom C# code in Grasshopper, where the tool movement, its speed, acceleration and material feed are calculated and optimised. Given the scale of fabrication, it is crucial to avoid non-essential movements during the printing process. To improve the adhesion of the formwork parts and their stability during the printing process, a wider base is automatically generated and added to the toolpath, and to counteract the hydrostatic pressure of the fluid concrete during the casting process, extra layers with an increased flow are added in the bottom third of the formwork. Final formworks have a layer height of 1 mm and an average width of 5 mm.

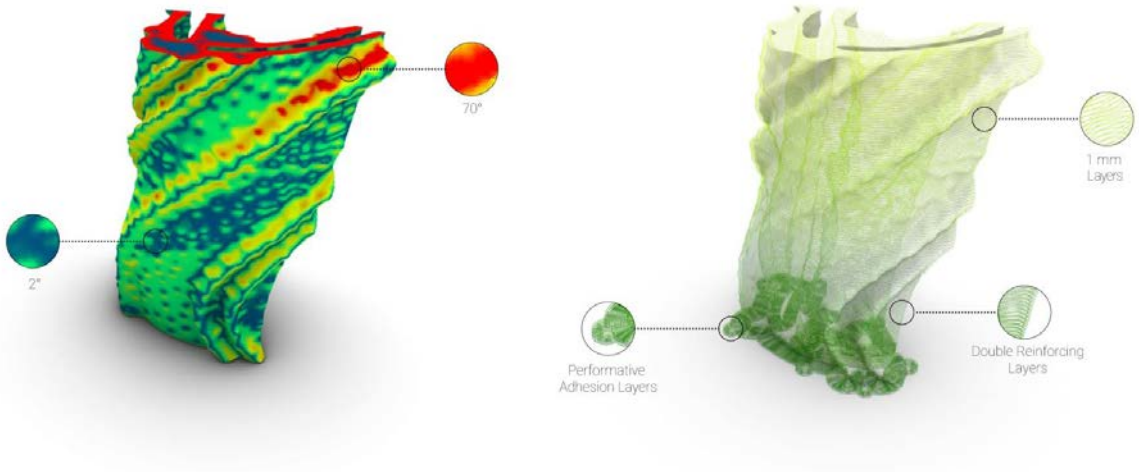


Figure 3: Left, analysis of printing angles giving a real-time feedback on potential criticalities during the printing process; right, toolpath optimisation to limit unnecessary movements and have local control over each variable, i.e. speed, material flow, layer height, layer width

2.3 3D Printing system and Formwork Fabrication

The manufacturing process of the concrete elements consists of two phases: the production of the formwork and the operation of casting. The formwork is produced using a large size Delta 3D Printer, which bases its movement on three vertical axes, with a total printing volume of 1200 by 1200 by 1000 mm and is equipped with a pellet extruder which allows a printing speed of more than 80 mm/s (Fig. 4) and a shell thickness up to 6 mm. Although scalable, the printer setup is currently considered in this work the main bounding condition to the dimensions of the concrete elements that can be produced.

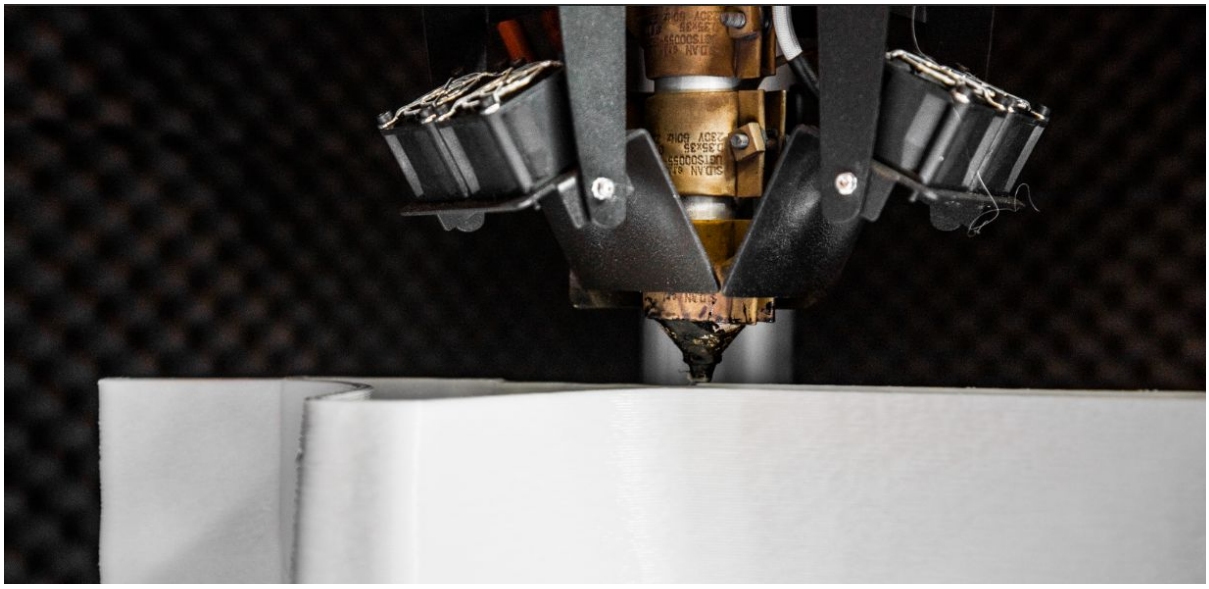


Figure 4: The custom-made formwork is produced by a WASP 3MT large scale 3D printer following a toolpath generated from a digital model and a computational design routine

For the formwork fabrication, printing with pellet has allowed the testing of a number of materials to be employed in the process, different typologies of PLA, PP, ABS. After several tests, one specific

type of the later one has been chosen because of its mechanical strength to withstand the hydraulic pressure of poured concrete, relative flexibility to favour the detachment from the concrete, and its resistance to high temperatures, with a glass transition at about 105°C, avoiding potential distortion from the heat produced during the curing process. For a clean demoulding process and the subsequent reuse the moulds, starting from the 3D model of the panel an disassemblable formwork is developed such that once the concrete has hardened, the plastic parts can be removed without any invasive labour or any stress applied to the concrete. External joinery surfaces are used to connect and disconnect quickly the different parts of the formwork by bolts (Fig.5).



Figure 5: The ABS formwork for the first prototype, a panel with a high-resolution pattern

2.4 Concrete Casting

Given the formal complexity of the mould and its reduced thickness, together with the need for a performative and relatively light material, Ultra-High Performance Fibre-Reinforced Concrete (UHPFRC) is used for the final prototypes, given its capacity to adapt to narrow geometries, and self-compacting. Compared to ordinary concrete, this retains a higher mechanical performance, mostly due to its mix having a different amount of binder, the size of the aggregate and the extensive presence of steel fibres. These are added to UHPC to enhance the ductility of the material, the tensile and flexural strength. The use of steel fibres is due to its favourable properties: high modulus of elasticity, high strength, high ductility and durability in the alkaline environment of the concrete. The compressive strength measured on cubes on the selected material used in the experimental phase of this research is around 150 MPa. The production of such material brings higher initial costs and energy consumption, but its use guarantees higher mechanical properties, hence the need of less material, the longer life cycle of the structure and lower maintenance. The mechanical properties of UHPFRC allow for a 50% reduction in material usage compared to conventional concrete, thus offering opportunities to create lightweight and dimensionally efficient structures [11]. After testing various mixes, ideal proportions in the mix of the different constituents of the UHPFRC were obtained using 1 part of cement and aggregate mix, 0.1 parts of fibres and 0.1 of water. After curing for 32 hours, the sides of the formwork are removed applying pressure on the external surfaces where bolt and nuts are inserted.

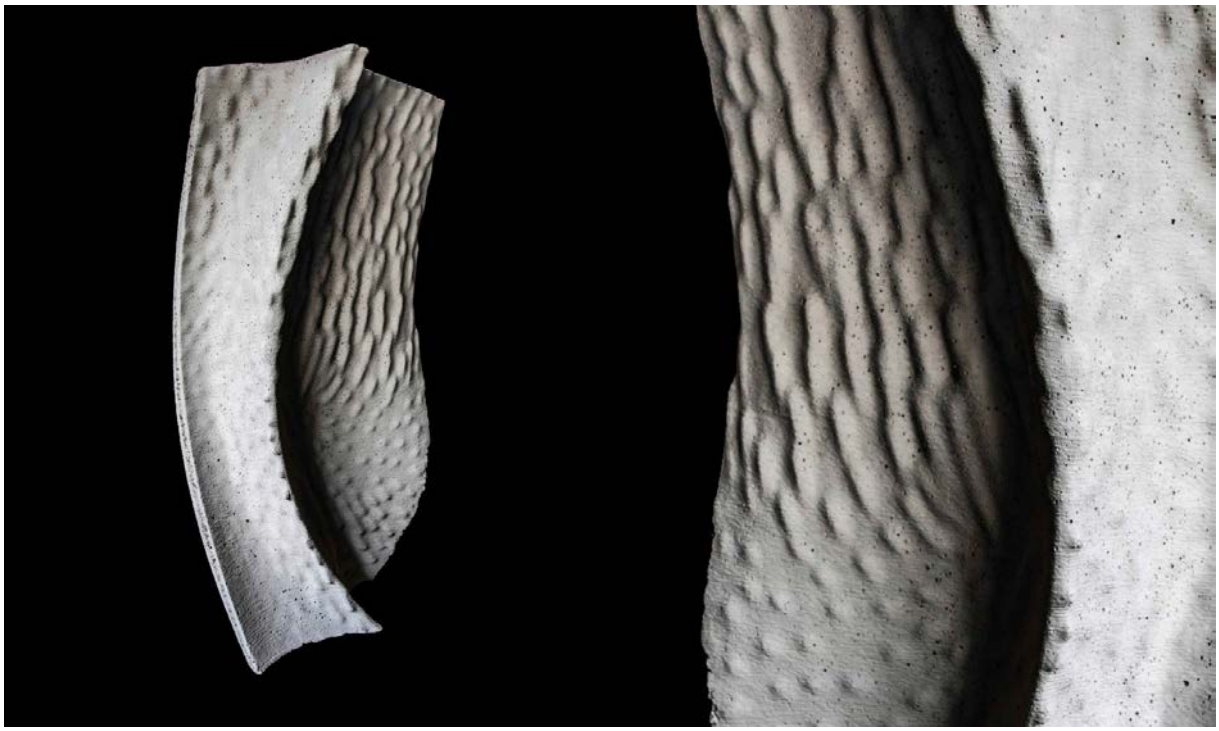


Figure 6: left, P1 showcasing extreme curvature and variation in thickness; right, detail of the high-resolution pattern of P1



Figure 7: prototype P2 is characterised by a double-shell design and features a high geometrical intricancy

3 Results

The proposed method speculates over a very well defined area of architectural constructions, which is that of non-standard precast concrete building components. The successful completion of building scale prototypes highlight the effectivity of using FDM to prefabricate doubly curved panels with extreme curvature, high resolution detailing and reduced thickness. This combination of features allow the exploration of unseen tectonic and performative features (Fig. 8). Precision and flexibility are achievable without any increase in the cost of production or in the operational complexity.



Figure 8: The double shell system of the prototype P2 features and internal reinforcing and connecting system driven by structural analysis

4. Discussion

Learning from the series of experiments carried out and described, the following aspects are foreseen for the development of the current research:

- *Precision feedback:* an assessment of tolerances, deviations and errors has to be addressed by means of photogrammetry, laser scanning and detailed measuring, before, during and after every step of the fabrication process, to integrate and compensate the design workflow;
- *Connections design:* a crucial aspect in the making of structural shell panels is that of connections. Further work will focus on the formwork integration of connection elements;
- *Tensile reinforcements:* steel fibres have an outstanding impact on the performance of UHPFRC concrete, however, in the case of freeform shell structures, reinforcing elements to

resist tensile stress are still needed. Further research will investigate the integration of post-tensioning elements.

Acknowledgements

This work was carried out at the CREATE Lab, a research infrastructure for digital fabrication at the University of Southern Denmark - Unit of Civil and Architectural Engineering, in cooperation with WASP Hub Denmark. The authors wish to thank Henrik Brøner Jørgensen for his inputs in concrete technology and for contributing to initial material testing; Hi-Con for in-kind support of concrete material, Eni-Versalis for in-kind support of 3D printing material.

References

[1] USGS, *Mineral Commodity Summary 2018*, https://www.usgs.gov, 2018

[2] B. G. De Soto, I. Agustí-juan, J. Hunhevicz, G. Habert and B. Adey, *The Potential of Digital Fabrication to Improve Productivity in Construction: Cost and Time Analysis of a Robotically Fabricated Concrete Wall*, Automation in Constructions (92), 2018

[3] Lab, R., *Think Formwork - Reduce Costs*, Struct. Mag., no. April, pp. 14–16, 2007

[4] Wangler, T., Lloret, E., Reiter, L., Hack, N., Gramazio, F., Kohler, M., et al., *Digital Concrete: Opportunities and Challenges.* RILEM Technical Letters (1, 67-75), 2016

[5] Lloret, E. F., Shahab, A. R., Linus, M., Flatt, R.J., Gramazio, F., Kohler, M., Langenberg, S., *Complex concrete structures*. Computer Aided Design, (60C, 40-49), 2015

[6] Khoshnevis, B., *Additive Fabrication Apparatus and Method,* US Patent 5529471, 1996

[7] Aghaei-Meibodi, M., Mathias Bernhard, Andrei Jipa, and Benjamin Dillenburger, *The Smart Takes from the Strong.* In Fabricate, edited by B. Sheil, A. Menges, R. Glynn, S. Marilena, (210, 17), 2017

[8] Jipa, A., Bernhard, M., Dillenburger, B., *skelETHon Formwork 3D Printed Plastic Formwork for Load-Bearing Concrete Structures*, in XXI Congreso Internacional de la Sociedad Iberoamericana de Gráfica Digital, (3), 2017

[9] Naboni R., Breseghello L., *Fused Deposition Modelling Formworks for Complex Concrete Constructions.* XXII Congresso Internacional da Sociedade Ibero-americana de Gráfica Digital, Blucher Design Proceedings, (5, 700-707), 2018

[10] Lowenthal, M. L., *Fabrication Of Concrete Modular Surfaces for Architecture,* The University of Texas at Arlington, 2010

[11] Habert, G., Denarié, E., Šajna, A., Rossi, P., *Lowering the global warming impact of bridge rehabilitations by using Ultra High Performance Fibre Reinforced Concretes.* In Cement & Concrete Composites, (38, 1-11) 2013

Proceedings of the IASS Annual Symposium 2019 – Structural Membranes 2019
Form and Force
7 – 10 October 2019, Barcelona, Spain
C. Lázaro, K.-U. Bletzinger, E. Oñate (eds.)

Challenges of 3d printed architectural ceramic components structures: controlling the shrinkage and preventing the cracking

Bruno FIGUEIREDO*, Paulo J. S. CRUZ, João CARVALHO, João MOREIRA

*Lab2PT, School of Architecture, University of Minho
4800-058 Guimarães, Portugal
bfigueiredo@arquitetura.uminho.pt

Abstract

The use of ceramic materials in the additive manufacturing (AM) of architectural components has more and more examples and undeniably shows the potential of its application. However, one of the main characteristics inherent to this material, which happens in drying and firing phases, is the shrinkage of the material, which causes deformations and cracks in the surface of the produced elements. Thus, the shrinkage of the ceramic material may constitute an obstacle to the regular use of this material in the AM of architectural components. In this sense, it is important to study and point out ways and strategies to mitigate this drawback, making possible the correspondence between the final produced models and the digital ones in which they are based. This paper presents the main challenges and outcomes of several projects that use Liquid Deposition Modelling (LDM) of clay-paste as construction methodology.

Keywords: Ceramic 3D printing, additive manufacturing, ceramic retraction, parametric design, computational models, shrinkage, ceramic paste, Liquid Deposition Modelling.

1. Introduction

Digital manufacturing processes allows for a faster and more precise production of complex architectural components, expanding the role of possibilities of how and what is possible to build. The merge of digital design tools and AM technologies enable the execution of entirely customized systems, developed with a specific target, responding to the problem issues with balance and adapted solutions.

Features such as hardness, density, durability and the possibility of having a vast number of shapes and finishes provide the application of this material in buildings all over the world for centuries [1].

The combination of the use of additive manufacturing technologies and ceramic materials can result in a compromise between a high performance material and the execution of complex geometries, impossible to obtain by any other production process, or by traditional methods.

The material used by the printer for the production of prototypes is a ceramic paste, a mixture of sandstone and water. Depending on the amount of water present in the mixture we obtain different types of paste that serve different purposes.

One of the negative aspects of using ceramic pastes for the execution of architectural elements is the difficulty to control the natural retraction of the material when it loses the water present in the mixture, namely the behaviour that this effect will have on complex or irregular geometries. Simultaneously and as a consequence of this characteristic, and others, there may be room for breaks or cracks that result in the reduction of the response to the load requests on the produced element.

According to K. Khalili [2] the dehydration process is the major source of defects in most ceramic products, ranging from aesthetical to mechanical properties, such as strength or elastic modulus. Susang

Copyright © 2019 by Bruno FIGUEIREDO, Paulo J. S. CRUZ, João CARVALHO, João MOREIRA
Published by the International Association for Shell and Spatial Structures (IASS) with permission.

Costa [3] refers that the evaporation of water from the surface gives rise to restrained shrinkage generating tensile stress leading to shrinkage cracks when stress forces reach the material strength. Ana Anton and Ahmed Abdelmahgoub [4] affirm that by the shapeless contraction of the material, caused by the loss of water, there may be breaks along and between the extruded layers, resulting in loss of structural capacity due to the failure of the material around these breaks. Therefore it is important to understand the behaviour of these forces and how they cause delamination of the extruded layers.

There are several projects that use this technology to develop architectural components such as the work developed by the groups Emerging Objects [6] and Building Bytes [7], both specialized in three-dimensional printing, however there seems to be always acceptance of this feature, never solving the effects of retraction.

In this sense, and based on a set of researches developed in the last 3 years, we consider that it is important to point out ways to control the behavior of the ceramic material during the production of architectural components that use the LDM methodology, and finally, to model considering the retraction of material.

2. Context

The above subject, in particular the problems related to the shrinkage of the ceramic material during the drying and firing phases, is evident in a series of investigations carried out by Advanced Ceramics R&D Lab in recent years, having the aim of mitigate or at least understand them, allowing greater control and knowledge of the material behaviour during the various stages of the production process.

As the most representative projects that testify this problem that affects formal agreement and structural integrity, we have the example of (a) Wave Wall, a wall system for building envelopes based on the traditional format of a ceramic block, (b) Hexashade, a domed shading system which is constructed from hexagonal blocks in which its internal structure varies in function of its position and the space-time ratio we want to shade, (c) Ficus, a system of structurally optimized biomorphic columns constituted by several stacked elements, and (d) Hive Wall, a honeycomb wall constructed from the stacking of blocks in predefined spaces.

After careful analysis of successive formal and structural failures, we formalized a set of methods and practices that can help control the behavior of the ceramic paste during the various production phases, taking better advantage of this material. To this end, a set of measures has been put in practice to overcome these issues, making the final physical object approximate the geometry of the initial digital model on which it is based.

3. Deformation by friction

The LDM deformation by friction occurs as soon as the material is extruded, at which point the water present in the ceramic paste begins to evaporate, leading to a decrease in the size of the printed part. Friction occurs between the printing bed, where the production of the part is made, and the base layer of the object. The high roughness of the printing bed which at an early stage assists in adhesion of the base layer to the printer surface, later becomes a destabilizing element and causes severe constraints on the material and on the final product in that it prevents that the material has a natural and balanced behavior. When the ceramic material loses its incorporated water its volume decreases by a percentage relative to the initial amount of water present in the paste. However, due to the constraint caused by the base, the volume reduction is not uniform in the object and results in non-correspondence between the top and bottom retraction values. The effects described above are evident in Figure 1. The left image shows the first printing tests of the Ficus column in segments, where it is noticeable that the base of each of the elements of the set has a scale significantly superior to the top of the previous piece and with which it should be coincident, resulting from the high friction that exists between the plate and the base layers of the part and that does not exist at the top of the element.

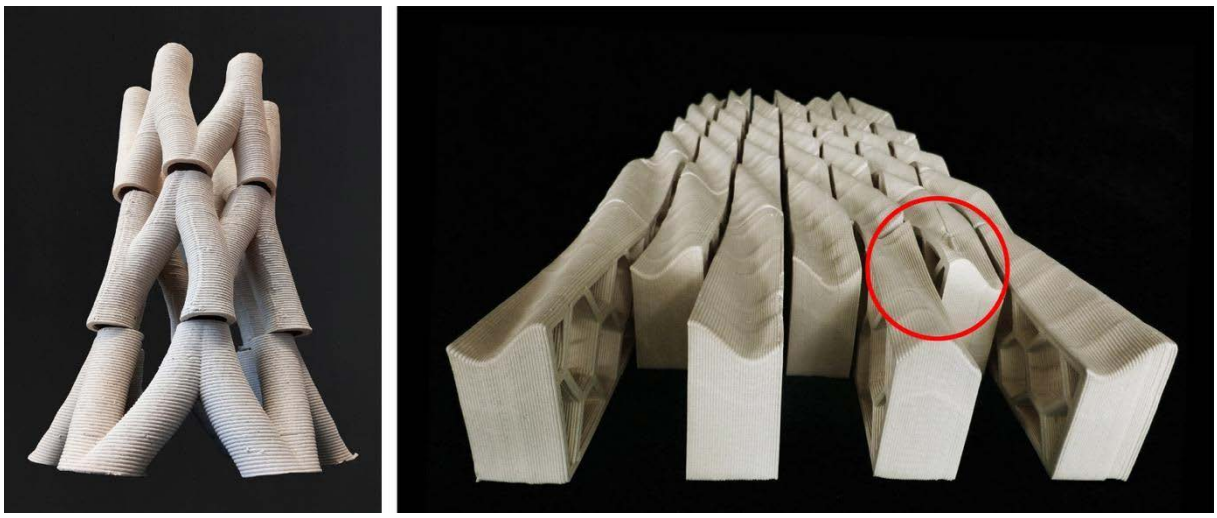


Figure 1. Segmented Ficus column – Initial test. Wave Wall – Effects of friction in retraction.

In the image on the right (red circle) it is observed that the wavy form of the top of the blocks surfers a large deformation in the base of the block, again caused by the resistance offered by the printing bed. In this case as a result we obtain a clear offset in the curvature of the corrugated surface that forms the front face of the wall.

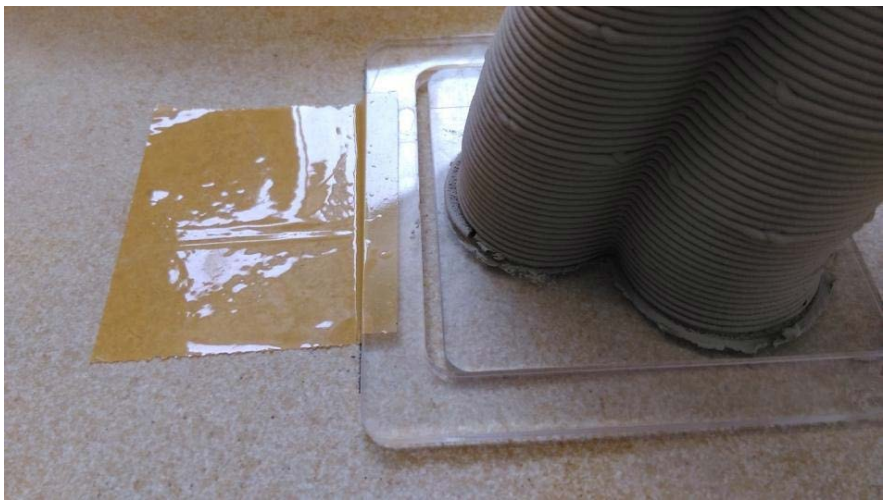


Figure 2.Example of free base with restricted movement.

To solve the problem manifested by the friction between the printing bed and the element produced, two solutions that can work in different contexts were thought. In a first phase, in order to solve situations similar to those evidenced in the Ficus column, where the base of the piece is constituted by several separate elements, we propose the introduction of a base that allows the freedom of movement of each one of the parts that touches the base after finishing of the production process. First, freely, leaving all directions freely, and second, restrictively, limiting freedom in the desired directions. Figure 2 shows an example of how to introduce a restrictive base that limits movement in a single direction and relieves structural stress on the object, allowing it to move naturally. In the image is also observable the effects of retraction by the distance that exists between the guide and the base plate.

Complementarily, in situations where it is not possible or feasible to use the previous method, we propose the implementation of a computational model that analyzes the geometry of the element to be produced and makes the necessary formal modifications, so that, in the end, taking into account the characteristics of the material, previously designated, the final model is an exact physical representation of the digital model that gives rise to it. The shape changes introduced by the computational model encompass three moments, the base shape control polygon (modification of the X and Y axes), the top shape control polygon (modification of the X and Y axes), and the distance between the two previous polygons (shape change with respect to the Z axis).



Figure 3. Result of the application of the computational model.

4. Deformation by non-uniform mass distribution

Besides the differentiated retraction being caused by the difference in the freedom of movement of the ceramic material during the post-production phase, there is still another factor that conditions the retraction and that causes the appearance of deformations on the surface that make the correspondence between the digital models and the parts produced. This factor is characterized by the non-uniform distribution of mass in the extension of the object, which later will cause instability in the retraction in the different moments that punctuate it. In areas where there is more material concentration, more mass, retraction values tends to be smaller than in areas where there is less material. Consequently, the part will suffer abnormal deformations during the drying phase.

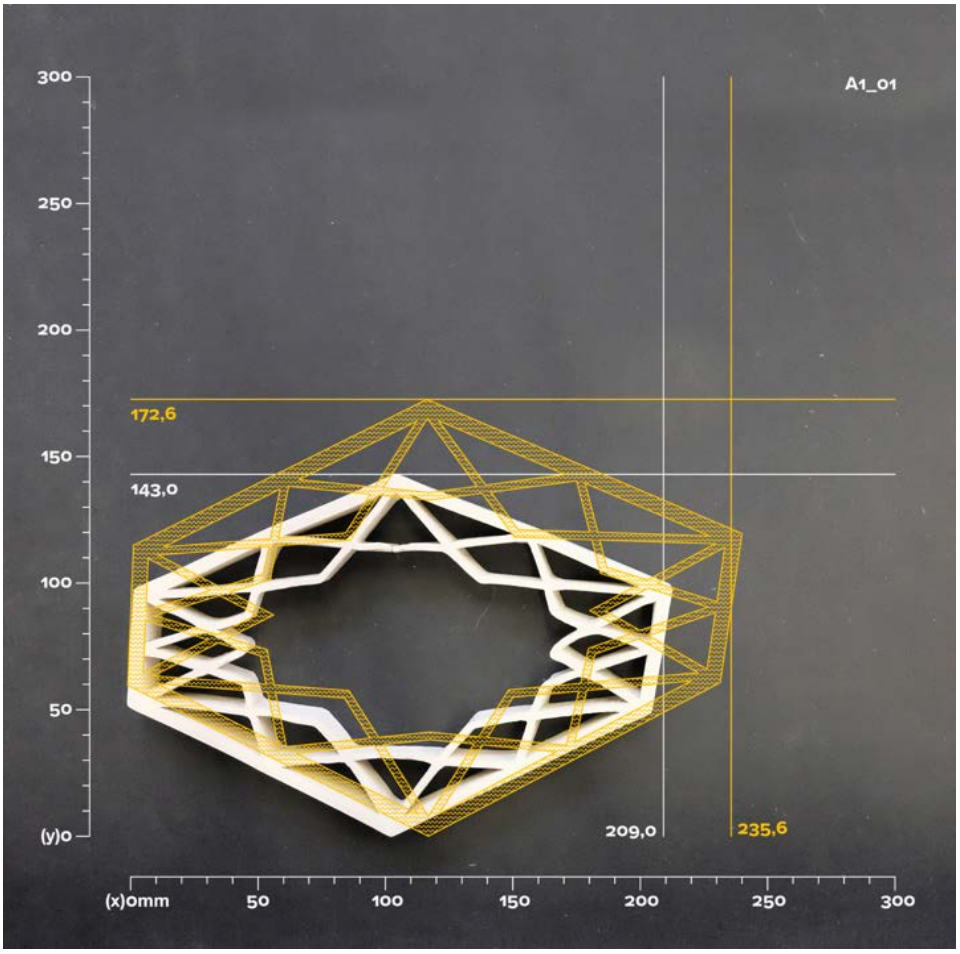


Figure 4. Hexashade, test arch 1 – piece 1 – retraction analysis.

Figure 4 expresses the discrepancy that exists between the retraction values of the two opposite directions (X and Y) only distinguished by the amount of material in each one of them. It is possible to observe that the smaller the extension of the piece in a certain direction, causing that the quantity of material is also smaller, there will be place to sharper values of retraction, since the resistance of the material to the efforts provoked by the dehydration will be smaller, leading to the retraction value being higher.

5. Wall breaks and cracks

The wall breaks of the produced elements also appear as a consequence of the previously exposed deformation. They are manifested mainly when there are large variations in the mass distribution in the three-dimensional object, resulting in axial tensions of varying intensity, which when they exceed the resistance limit of the ceramic material cause breaks in the wall of the element, reducing the resistance to mechanical requests.

We consider that there are two types of breaks. These are a direct consequence of the geometry of the piece, as is the case of the mass distorted distribution that causes differentiated tensions in the part, leading initially to deformations and, in more extreme cases, to partial or total rupture of the wall of the element. The second type of break is manifested when the friction between the printing base and the object exceeds the force the material can handle. This type of break occurs mainly when the amount of material in a particular direction is reduced in comparison with its extension, that is, when a linear

element of short extension has few layers (little material in height) or is very thin (little transverse material) is expected to occur during dehydration of the material.

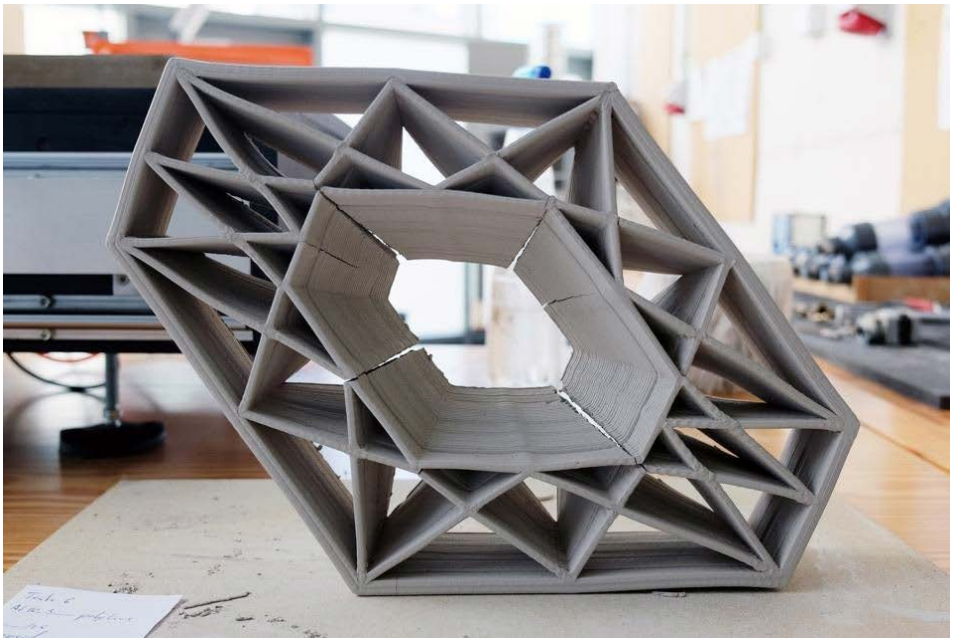


Figure 5. Hexashade, test arch 1 – real scale – interior wall break.

The issue of surface breaks is not limited to the material's normal behavior and behavior over time and is more difficult to prevent or avoid. The superficial breaks occur, as already mentioned, at particular moments, where the tensional stress in the material surpasses the maximum resistance of the same, leading to the collapse of the connections. In order to avoid cracking, the inclusion of additives in the composition of the ceramic paste, namely glass fiber, sawdust and cellulose was tested, giving the pulp greater resistance to tensile stresses during dehydration.

The inclusion of additives in the ceramic paste, while providing the blend with more tensile strength at the moment it is retracting, lowering the water levels, also has implications for the final performance of the element, insofar as it changes its composition compared to an element solely formed by ceramic. In addition to changing the chemical properties of the material and consequent its response to stress forces, the addition of some types of material to the ceramic paste, such as glass fiber (Figure 6), considerably changes the workpiece finish, giving it a rough final appearance and with many irregularities.



Figure 6: Tests of ceramic paste with fiberglass (5%).

6. Deficient joints

As a consequence of all previous defects, the deficient association of ceramic elements is a problem that can prevent the execution of some projects in which, as is the case of Hexashade, its structural integrity is dependent on the formal correspondence between the juxtaposed faces of the elements that make up the whole set. Here the effect of non-uniform retraction causes slight deformations of the side walls of the pieces which, when assembled, make impossible the correct positioning of each element, making the assembly of the aggregation unstable and without self-supporting capacity.

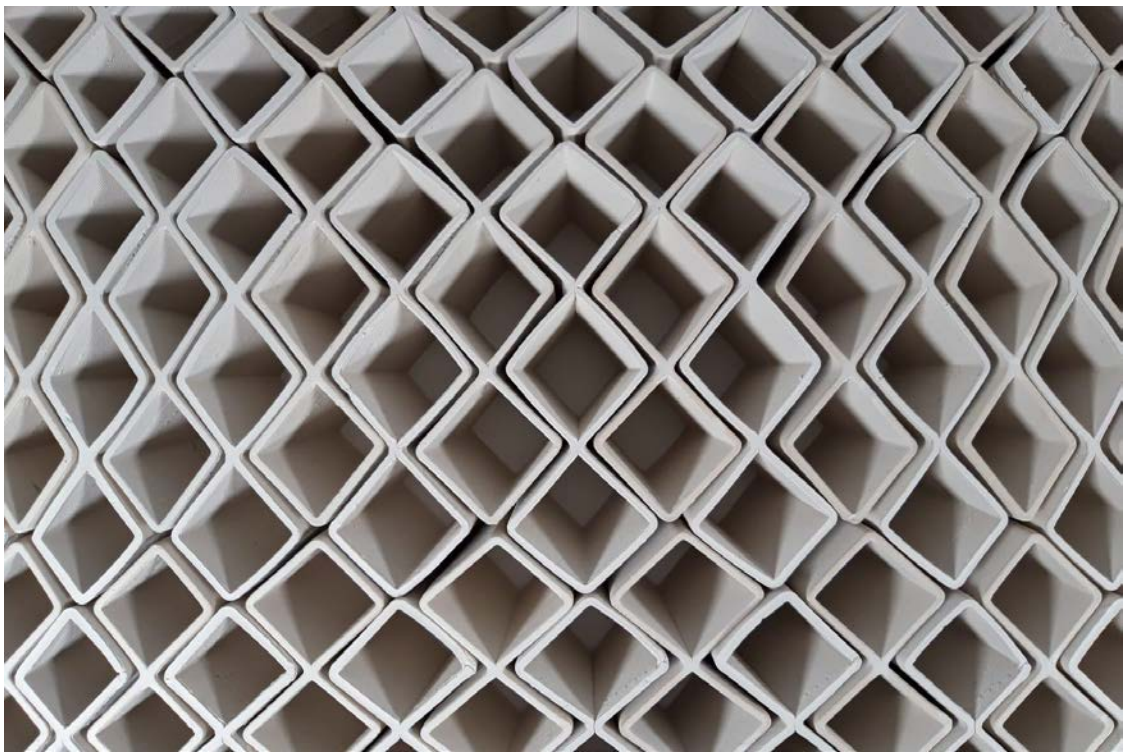


Figure 7. Hive wall - Deficient joins between pieces.

Figure 7, where the example of the Hive Wall is shown, illustrates the problem set out above by clearly showing the differences that exist between the joints connecting the pieces. The differentiated deformations result in joints with different dimensions that make impossible the correct assembly of the parts, compromising the structural and formal integrity of the wall, leading to the need of external support systems.

In this example, where the objective was to construct the wall only from the stacking of the pieces, it was necessary to include another material in order to fill the joints between parts and to reverse the effects of the deformation, giving the support and union needed between the various parts of the assembly.

7. Discussion

The methods presented above represent a set of actions that we consider as possibilities to help the correspondence between the digital model developed in a digital environment and its material formalization produced in ceramic through the LDM technology.

As a result of the methods implemented in order to control the behavior of the ceramic paste during the moments after the production, predicting and counteracting the deformations that it could suffer, we

consider that, in the end, although there is no total correspondence between the final product and the model in which it is based, the methodologies presented constitute a positive starting point for mitigating the problems identified at the beginning of this article.

Assuming this as a continuous work that requires further in-depth studies we point to the future the introduction of additives (superplasticizers) that help control the plasticity of the ceramic paste while the amount of water present in the mixture is reduced.

Acknowledgements

This work has the financial support of the Project Lab2PT – Landscapes, Heritage and Territory laboratory – AUR/04509 and FCT through national founds and when applicable of the FEDER cofinancing, in the aim of the new partnership agreement PT2020 and COMPETE2020 – POCI 01 0145FEDER 007528.

We are also grateful to the Institute of Design of Guimarães for hosting and supporting the activities of the Advanced Ceramics R&D Lab on the use of their facilities and equipment, and all the assistance from the technician Samuel Ribeiro.

References

[1] Barbosa, I., & Figueiredo, B. (2017). Optimized Brick – Print Optimization. In Chanllenges For Technology Innovation - An Agenda for the Future: Proceedings of the International Conference on Sustainable SmartManufacturing (S2M 2016): The International Conference on SustainableSmart Manufacturing (S2M), Lisboa, Portugal, 207-210. Leiden, Portugal: CRCPress.

[1] Khalili, K. et al. (2014). Numerical simulation of drying ceramic using finite element machine vision. Procedia Technology 12. 388-393.

[2] Susanga Costa, Jayantha Kodikara. Modelling of desiccation crack development in clay soils. International Association for Computer Methods and Advanced in Geomechanices (IAMCMAG). 2008; 1099-1107

[3] Anton, A., Abdelmahgoub, A. (2018). Ceramic Components – Computational Design for Bespoke Robotic 3D Printing on Curved Support. Computing for a better tomorrow, Volume 2, eCAADe 2018 36th Annual Conference. 71-78

[4] Cruz, P. J. S., Knaack, U., Figueiredo, B., & Witte, D. De. (2017). Ceramic 3D printing – The future of brick architecture, Proceedings of the IASS Annual Symposium 2017. A. Crisfield, *Non-linear Finite Element Analysis of Solids and Structures. Volume 2: Advanced Topics*. (2nd ed.). New York: Wiley, 1997.

[5] Emerging Objects. Web page URL - http://www.emergingobjects.com/

[6] Building Bytes. Web page URL - http://www.buildingbytes.info/

FORM and FORCE

Proceedings of the IASS Annual Symposium 2019 – Structural Membranes 2019
Form and Force
7 – 10 October 2019, Barcelona, Spain
C. Lázaro, K.-U. Bletzinger, E. Oñate (eds.)

From rapid prototyping to building in real scale: methodologies for upscaling additive manufacturing in architecture

Paulo J. S. CRUZ*, Bruno FIGUEIREDO, João CARVALHO, João RIBEIRO

*Lab2PT, School of Architecture, University of Minho
4800-058 Guimarães, Portugal
pcruz@arquitetura.uminho.pt

Abstract

The manufacture of architectural components mediated by computer-controlled Additive Manufacturing (AM) technologies has highlighted several positive aspects of their application, namely by enabling customised design solutions and high-performance complex geometries. Taking into account the experience of the Advanced Ceramics R&D Lab, in the production of small- / medium- scale prototypes, this paper explores the main variables and constraints of the production of real-scale architectural components. This information points to a set of procedures that should be avoided and others that should be privileged, allowing to anticipate how AM can contribute for the achievement of high performance components on a large scale.

Keywords: 3D printing, additive manufacturing, material extrusion, LDM, parametric design, computational models.

1. Introduction

From the 1960s onwards, a set of Additive Manufacturing (AM) technologies were applied in the most diverse industrial areas, from aeronautics to aerospace, from automotive to naval, etc. On the one hand, in these sectors, these practices demonstrated versatility, and when combined with processes of Digital Fabrication (DF), a remarkable capacity for improve and optimize the technical capacities that the industries already had, on the other hand, only in the transition to the XXI century those processes started been applied in the architectural and construction industry, sectors that are traditionally more conservative in the integration of innovative technologies.

It is widely recognized that the introduction of digital tools in architectural design allowed an evolutionary change in design and construction methodologies. This reformulation in which architects master digital techniques and technologies, represents a paradigm shift that is often manifested in the emergence of new formal solutions, controlled through the use of computational and parametric design principles. In parallel, principles of mass customisation fostered over the last decades by the use of DF covers not only preliminary design phases, but also seeks its adequacy in the construction itself. In this field, computer-controlled AM is one of the most auspicious production methods.

2. Context

One of the first references to the potential of AM in construction arise in the mid-1990s by Mitchell and McCullough (1997) under the term "Incremental Forming". Often referred as 3D printing, these processes allow an "object" to be obtained from the successive addition of layered material, revealing a sustainable and a very cost effective method due to the fact that material it will be placed exclusively at

Copyright © 2019 by Paulo J. S. CRUZ, Bruno FIGUEIREDO, João CARVALHO, João RIBEIRO
Published by the International Association for Shell and Spatial Structures (IASS) with permission.

the places required, by opposition to subtractive processes or traditional techniques of extrusion on mould which, in addition to revealing a high degree of waste of raw material, do not allow customisation.

Currently, AM technologies are readily available for the production of small components, on the 'desktop' scale, however they still not represent an effective solution for the scale of the building. In recent years there has been an increasing number of entities – academic institutions, researchers, builders, architects, engineers, software and hardware companies – that have been concentrating efforts on the application of AM techniques in architecture. This investment resulted in a wide range of prototypes and experiences, as well as in the proposal and development of new manufacturing methods. Each of them introduces new possibilities, new materials or changes in the production process, resulting in the advancement of technology and what can be achieved with it. Yet, despite the recognition of sustained experimentation and knowledge, there are still difficulties in shifting scale and its application to common constructive contexts. It is therefore necessary to understand the implications of these changes and develop solutions that meet the sustainability of their use.

3. Methodology

Considering the paper objectives, an analysis of the most relevant experiences was carried out in order to map the different approaches that are being taken and to frame the potentials and limits of these methods for, finally, better understanding how they can be successfully integrated into architecture.

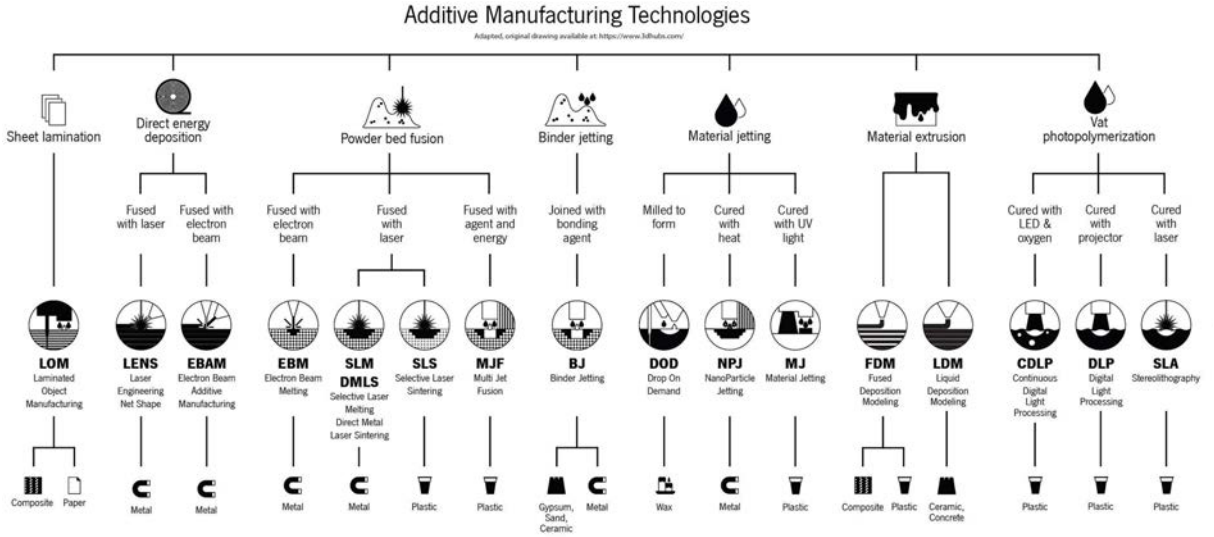


Figure 1: Additive Manufacturing Technologies [Adapted, original drawing available at: www.3dhubs.com]

Although all AM processes follow the same generative principle - three-dimensional geometry is obtained by successively layered material overlapping - it is possible to detect substantial differences in the way this is done. For this registration and the knowledge of several possible approaches, it was adopted the hierarchy used by 3dhubs.com, an online portal specialized in AM [2]. The next scheme synthesizes all the seven techniques (Figure 1).

Given the context of our research being the Advanced Ceramics R&D Lab (ACLab), a research laboratory dedicated to the use of AM extrusion technologies in architecture [3], this paper focuses essentially in those processes which can be divided into two topics, "The scale of production" addressing the issue of the scale of manufacture, the support and the size of the objects fabricated, and the "Control of the manufacturing process" seeking to understand how to improve the quality of the object produced as well as develop ways to exponentiate the limits of the technology.

4. Material Extrusion

Material extrusion is the most widespread process of AM due to its ease of use, cost and maintenance. The most common are desktop printers with Fused Deposition Modelling (FDM), also called Fused Filament Fabrication (FFF) prepared to extrude thermoplastics filaments or grain.

Liquid Deposition Modelling (LDM) technique, which was added to the original scheme (Figure 1), reveals a very similar manufacturing process. This nomenclature, proposed by Rosenthal et al. (2018) for the extrusion of paste-like suspensions made from ground beech sawdust and methylcellulose dissolved, was adopted at ACLab to denominate the process of ceramic paste extrusion due to the fact of the feedstock is not heated but successively extruded into layers in the form of a paste having a controlled degree of plasticity.

Contrary to the prior technique where the extrude polymer solidifies instantly due to the temperature drop down, viscous materials such as ceramic and concrete continues to react and the fabricated object undergoes a curing/drying phase (in the air or in a greenhouse). This is a major constraint, however, being a suitable process for almost all types of materials, as long as they make extrusion possible, the ease of use of traditional materials – cement mortars, ceramics or other composite materials – makes it particularly appealing for the construction industry. Thus, most of the experiments carried out with large-scale 3D printing, which will be analysed next, use extrusion techniques of the raw material in the "liquid" state.

5. The scale of production

The ability of transposing AM techniques at the scale of the building represents a major issue for its application to the construction industry. In this sense, the dimensions and mechanisms of the extrusion apparatus and the reaction of the material are the main constraints. The principle of depositing the layered material assumes that the manufactured object fits within the working area of the 3D printer. For this there are two approaches that can be taken: (1) Continuous deposition manufacturing – Scaling the printing apparatus; (2) Manufacture of discrete elements – Scaling the components to the available print area.

5.1. Continuous deposition manufacturing

Continuous deposition manufacturing aim the direct transposition of techniques of prototyping of small objects to the scale of the construction. This method assumes that the printer's work area is equal to or greater than the building area (of a single element). In this case two approaches have been identified: (1) to increase the size or (2) to enlarge the coverage of the printing apparatus. Both types have already been tested in some exploratory projects.

The work of Behrokh Khoshnevis, creator of the Contour Crafting (CC) process and founder of a company with the same name, is directly associated with the first experiences on the use of large gantry structures that support and move a concrete extrusion system. Khoshnevis demonstrated the possibility of applying AM to a single house or colonies of buildings, may be automatically constructed as whole structures, embedding in each building all the infrastructures during de process [4]. More recently, the printer manufacturer WASP, in the Shamballa Technological Village project, developed a manufacturing system through a Delta-type printer installed on a 12 meter high hexagonal structure [5]. There are many other strategies, however all of them despite valid experiences, these are strongly conditioned by the size of the machinery. The need for a static larger printer machine than the intended object, from certain dimensions, proves to be an unbearable strategy.

Therefore, the approach taken by a research group of the Institute of Advanced Architecture of Catalonia, under the guidance of Sasa Jokic and Petr Novikov, sought to overcome this dichotomy increasing the reach of robots. The apparent need for larger machines than the construction itself was

solved with the use of *"minibuilders",* a small-scale, locomotive robot family that can work simultaneously on the same object. According to the authors, with this method of continuous and coordinated deposition between the different machines, it becomes possible to manufacture objects much larger than the machines [6].

5.2. Manufacture of discrete elements

Most research groups or corporations interested in testing AM technologies in construction end up following a line of thinking that is based on discrete elements. In this approach, instead of requiring a machine that provides a larger work area than the building to be built, it is proposed to adjust the size of the different parts according to the physical characteristics of the machinery (the 3D printer work area, the size of the kiln if necessary, etc.). In this way, there is an approximation to traditional building systems based on three moments: (1) the various constituent components of the building are prefabricated with smaller dimensions; (2) transportation to the work site; (3) Assembly in their positions, creating larger structures.

In relation to the component manufacturing, the boundaries of the machinery or the printer's work area must inform the design. When the aim is discretization, a previous research should be done on the implications of the division into elements, aesthetically and structurally, as well as a study of stereotomies and effective methods of linking between elements, in a system thought from the whole and not as a simple form of post-rationalisation [7].

These pre-fabrication principles were applied by some laboratories and corporations that sought to quickly follow the evolution of technology. The Chinese company Winsun3D, for the creation of low-cost and fast-build housing solutions, has resorted to the pre-fabrication of large-scale components. For this purpose, they developed their own extrusion AM system for the production of structural components where, during the manufacturing process, they add metallic rebar to give structural strength to the concrete [8]. However, despite the development of the custom extrusion machine, so far, they have not yet extrapolated on the impact of technology on architectural forms, not drawing much of their potential.

Otherwise, there are projects that take advantage of discretization to explore the potential of AM. One of the most paradigmatic examples is Smart Slab, the prototype of a slab developed by ETH Zürich's Laboratory, Digital Building Technologies [9]. The slab design resulted from the structural optimization of the areas of greater and smaller load, introducing concave shapes in the latter and allowing to obtain a slab 70% lighter than if it were obtained by conventional methods, and more sustainable, since it uses less material. For the production of the lost formwork of the final prototype it was used a Binder Jetting technology (powder and a selectively deposited binder). The size of each of its 8 segments was limited by the printer workspace. After the formwork was obtained, it was filled with reinforced concrete with fibers, for later transport and assembly in the place through post tensioned connections.

Another interesting approach is the biomorphic-inspired column developed by the XtreeE for a school in Aix-en-Provence, France [11]. The 4 segments of the column formwork were manufactured trough customised concrete extruder supported by an industrial robotic arm. Then, the joining between parts by chemical glue and filling with high performance concrete resulted in a system that combines a complex geometric design with a high structural capacity.

6. Control of the manufacturing process

In addition to the size constraints referred to in the previous section, issues of strength and durability of materials, quality and manufacturing time are still major obstacles to the integration of these technologies in construction. In a field of experimentation that is still under development and is very focused on prototyping, it is essential the coordination between four factors: (1) environment, (2) material(s), (3) manufacturing process and (4) production time.

6.1. The production environment

The control over the manufacturing conditions has practical repercussions in the performance of the extrusion technique and also in the material behaviour at that specific context.

As far as the manufacturing site is concerned, there are two methods that have been adopted: the manufacture of components directly in the workplace (*in-situ*) and the production of components in a laboratory environment, followed by transportation and assembly at the construction site. Each method reveals its own conditioning factors.

Upscaling techniques based on continuous large-scale printing, referred to initially, naturally lead to in-situ manufacturing logics. This method forces the transportation of delicate and large-scale computer-controlled technology to the construction site, as proposed by the Contour Crafting Corp, or the Shamballa Technological Village project or the IAAC experiences with *"minibuilders"*. Although the potentiality of a single machine (or a machine system) is feasible and attractive, allowing to produce an entire architectural structure in a single run and minimizing the human workforce, the truth is that all the logistics needed for the machinery transportation and assembly or even on-site weather conditions are more difficult to control and potentially less productive.

In contrast, upscaling based on pre-fabrication processes in the laboratory, which is usually accompanied by discretization processes, allows greater control over the production conditions of the elements. However, this forces the transportation and assembly of parts on the job, increasing the need for post-production labour, resulting in the object constructed of an intelligent combination of the work of man and machine. Moreover, although the material extrusion methods, in principle, do not require closed-chamber printing like other AM technologies, in order to obtain high performances, control of the environment, techniques and production conditions is essential. The deposition process, with very high or very low temperatures, changes the behaviour of the materials and does not allow to strictly control the level of workability of the extruded pulp. Thus, laboratory production is not subject to variables such as meteorological/environmental conditions, for example, allows a greater dominance of the temperature and the whole manufacturing process and to explore optimal conditions for the deposition of the material.

6.2. The materials

Although in practical terms it is possible to exploit AM using materials already tested and commercialized, the research and adaptation of its properties should be considered. Factors such as plasticity, flexibility, hydration, texture or the paste own friction have a direct influence on the extrusion process.

In addition to the reaction and resistance of the materials during the deposition process, it is essential to realize their behaviour after printing – the time and temperature of the curing and firing for the ceramic, the study of the transition process from liquid to solid in concrete or temperature and heating and cooling time for polymers, etc. – are important issues regarding rigorous 1/1 scale results.

Diverse stakeholders on this field of research, realizing these needs, paved the way for the exploration of new materials and composite materials that result from the addition fibres to improve the structural strength, or superplasticizers to control viscosity maintaining the moisture content of the mixture, etc..

Each experiment represents an evolution of the raw materials. CyBe Industries, a company focused in AM in concrete, has developed an optimized mortar, which acquires consistency in a few minutes achieving structural strength in just one hour, dramatically reducing the time of construction [12]. Also the XtreeE, together with the cement manufacturer LafargeHolcim, developed a series of concrete mixtures specifically adapted to 3D printing. From another point of view, the WASP printer manufacturer, in the Shamballa Technological Village project, has successfully tested a mixture of soil, straw and water.

Lastly, on the context of ACLab, a study on the properties of ceramic paste was conducted in order to improve its extrusion behaviour and ensure a good performance during the dehydration process. A set of tests were conducted using the Pfefferkorn method to infer an optimal relation between the paste hydration and viscosity [14]. The firing process was also analysed, different temperature curves were revealed different levels resistance and shrinkage. In addition, experiments of composite materials of stoneware paste and small percentages of powdered cellulose resulted in an interesting reduction of cracks after the curing and firing processes and decrease of the pieces final weight [15].

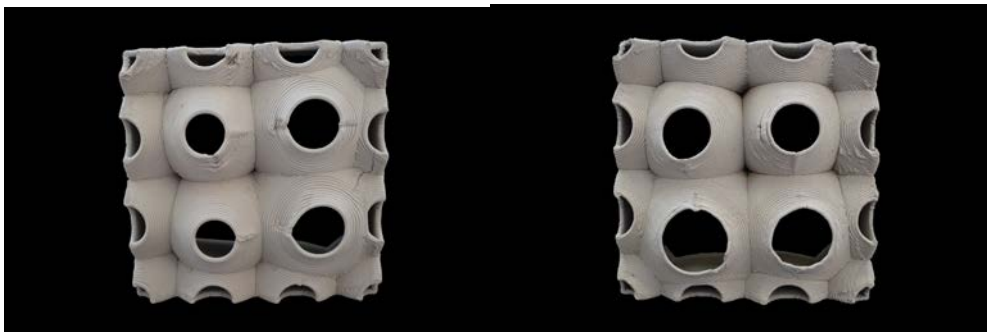


Figure 4: Same block produced with stoneware paste (left) and a mix of stoneware paste and cellulose (right).

6.3. The process

In addition to material studies, information on machine operation and extrusion processes – such as air pressure, extrusion flow, speed and kinematics of the printer, the nozzle diameter and their relation with the number of layers and thickness, inclinations and radii of curvature of the fabricated geometries, etc. – should be considered and integrated in the design, being adapted to each case [16].

Although many of these parameters are essential to control the extrusion process they represent constraints that are not always transposable to the digital model or their effect is not predictable for some models. This paper analyses two of the major issues: geometric constraints (during the printing process) and deformations in the manufactured object.

6.3.1. Geometric constraints

One of the most limiting factors in the processes of AM by extrusion is the production of inclined surfaces. If, with the polymeric extrusion, one can easily obtain inclinations of 60° without the need for additional supports, in the case of the LDM technique such values cannot be obtained.

As a reference for the reduced scale, in the context of AM in ceramic paste, a set of sequential tests were carried out in the ACLab [14] revealed that inclinations with angles greater than 30° resulted either in noticeable deformations or in the abatement of the surfaces. From another point of view, there are two methods already developed to exponentiate these values: (1) controlling the movement of the printer head or (2) using auxiliary structures.

The former is deeply connected with the control of the movement of the extruder tip. The XtreeE proposed a system that, according to their own, improves the AM process on a large scale. By using a 6-axis robot, instead of the deposition following a constant layer height and a vertical extrusion, it is performed tangentially to the inclination of the object and with height variation between layers, achieving a larger and more uniform area of contact between layers [17]. A similar system is possible using a 3-axis printer. Although not being able of rotating the extruder nozzle, height variations between layers can be customised in order to increase the adhesion between the layers and, of course, to allow greater inclinations and superior strength.

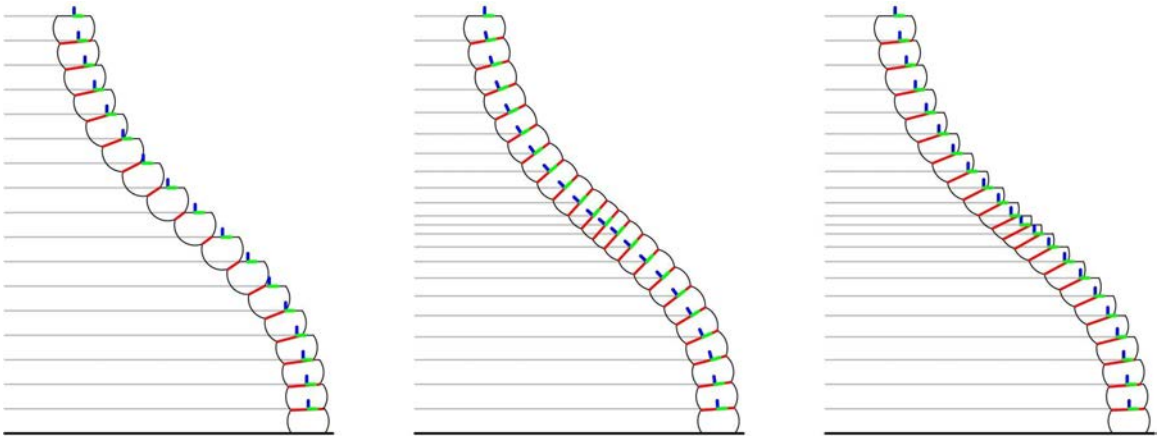


Figure 5: Schematic cut using the vertical extrusion system with equal height between layers (left), tangential continuity method proposed by XtreeE (centre) and vertical extrusion system with variation of height between layers appropriate for any 3-axis machines (right).

Other method is concerned with the creation of support structures. When the top layer exceeds the contours of the former making the structure unstable, it is very common in FFF to use a thinner structure or a soluble material in order to allow a continuous deposition of the material and its removal in post-production. LDM is substantially different as the material continues to react during and after the extrusion process. Some tests were performed in the ACLab considering reduction of the area of contact between the desired model and the supporting structure to the minimum necessary, namely by printing the support structure in a direction opposite to the direction of the part produced, it became possible to create protrusions or the ceramic deposition at an angle of 45°, being conceivable in the curing/firing phase to separate the models.

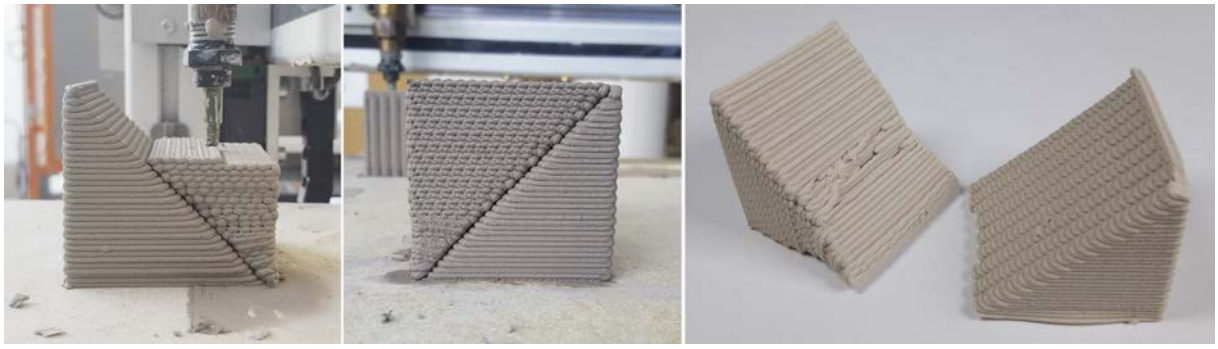


Figure 6: Ceramic deposition on support structure - Printing process (left, centre) and after firing (right).

Another supported extrusion solution is presented by Amalgamma, a group of master's students from the Bartlett School of Architecture. This method looks for references in the powder impression and combines it with the concrete extrusion process. Thus, while the concrete is extruded on a platform, layer-by-layer, a bed of granular material that supports the following layers, is deposited, making possible the printing of objects with various suspended parts [18].

6.3.2. Geometric deformations

Although AM by extrusion is able of producing objects with margin of error of tenths of a millimetre, it is practically impossible to produce objects with exactly the same shape and physical characteristics.

The printed object, although similar to the computational model, is always subject to deformation, both during the manufacturing phase and the curing or drying phase.

The shrinkage due to the dehydration of the material is perhaps the main cause of geometric changes, mainly in ceramic materials, whose loss of volume of the printed objects difficult the agreement between the scales of the digital and physical models. In addition, the shrinkage effect is not uniform. During the drying or firing process, the object is subjected to a set of forces (friction caused by the base plate, its own weight, etc.) that directly influence its final geometry, further distancing the physical model of the digital model. As an example, the Ficus Column prototype developed in the ACLab at 1/5 scale, had a mean shrinkage of 21% in height, 7% in the base and 15% in the top (Figure 7). In this case, after being analysed, these data allowed to generate compensations in the digital model making it possible to create links between the printed elements.

However, these parameters are deeply dependent on the scale of printing. Recent tests carried out at 1/2 scale allow to foresee a whole new associated problem. For constraints related to the limits of the printer's work area, to increase the scale, it was necessary to subdivide the column into more parts which caused the ribs to be undone (the geometry does not stay connected at the top and bottom). This circumstance, together with the reaction of the material during dehydration caused the abatement of the ribs and the subsequent rotation of the upper connecting surfaces made it difficult to articulate with the other parts. A solution to avoid these constraints is shown in the previously mentioned biomorphic inspiration column for Aix-en-Provence. In it, XtreeE solved this problem through the joint printing of an auxiliary structure which limits their degree of freedom and increases the resistance of the whole, namely, to resist the deposition of concrete. Afterwards this auxiliary geometry had to be cut off after being assured that the structure is self-supporting.



Figure 7: Ficus column system manufactured in ACLab at 1/5 and 1/2 scale

6.4. Manufacturing time

Manufacturing time is an essential factor to realize the potential of AM at the construction scale, but its control is essential to enable parts with high levels of quality. A balance between the speed of manufacture and the extruder path must be sought in LDM technique. Increasing the scale of the object is usually associated with an increase in the thickness of the layer, change in the section of the extruder tip or even increase the speed of movement. These are controllable parameters that alter the resolution

of the produced models, as such, must be tested according to the desired geometry and finishing. In addition, very high layer heights, sharp radii of curvature are likely to generate conflicts with the kinematics of the machinery, which can, by excessive vibration, generate unstable structures and, in the limit, lead to the collapse of the fabricated part.

The solution to accelerate the process should not fall into processes that increase the fragility of the object obtained, but often only increase the number of printers working simultaneously. For example, at Trabeculae Pavilion, Roberto Naboni in collaboration with WASP used a 3D printer's farm installed in the laboratories of ABC's Department of Politecnico di Milano, consisting of 5 Delta-type printers working continuously for 4352 hours to produce the 352 components that conform the pavilion [13]. In this sense, the printing process must be optimized but it should not force the limits of technology, nor reduce the quality of the part produced.

7. Conclusions

AM techniques are an asset to traditional building systems. Its application allows to obtain more sustainable solutions and a greater freedom of design - manufacture of non-standard elements, addition of multifunctional properties, autonomous construction systems, more rigorous forecasting of delivery times, etc. However, its application still has many obstacles that need to be overcome.

The issues discussed throughout the paper outline the potentialities and constraints of the adequacy of AM systems on real-scale. It was tried, with a wide set of examples, to discuss topics that directly or indirectly have repercussions in the solutions of project and the results obtained. To this end, questions were raised regarding the manufacturing scale and quality control of the manufacturing, building on the different approaches, possible methodologies for the adequacy of these rapid prototyping systems, to the needs revealed by an increase of scale. In each project/experience there is a meaningful learning.

Regarding the size of the manufacturing, solutions were considered that deal with the suitability of the machine to the scale of production or suitability of the different components of this machine to the size of the machine. In terms of quality control, a number of variables have been addressed that affect extrusion methods. In this sense, issues related to the production environment, materials, suitability of the extrusion process and manufacturing time are essential to obtain unique results.

These results are deeply dependent on the scale of manufacture. Thus, the production of reduced-scale prototypes can help dispel doubts about suitable functional or extrusion techniques, but should not negate the occurrence of full-scale tests where the behaviour of the materials, the extrusion system, and the manufacturing will be differentiated.

In addition to the research and development on the AM technologies by extrusion, which this article focuses on, it is essential that these be adapted to project development. The production of components should not be an issue at the end of the process, but should be put in place from the outset. In this sense, the manufacturing constraints, recognized by experimentation, must be integrated in the computational models from the design phase, in order not to require changes that are crucial for their manufacture.

Some of the prototypes referred revealed viable solutions, but there are still additional improvements in terms of speed and cost associated with higher performances. There is a wide field of research to explore until the AM is able to respond adequately to all the needs of the construction industry.

Acknowledgements

This work has the financial support of the Project Lab2PT – Landscapes, Heritage and Territory laboratory – AUR/04509 and FCT through national founds and when applicable of the FEDER cofinancing, in the aim of the new partnership agreement PT2020 and COMPETE2020 – POCI 01 0145FEDER 007528.

We are also grateful to the Institute of Design of Guimarães for hosting and supporting the activities of the Advanced Ceramics R&D Lab on the use of their facilities and equipment, and all the assistance from the technician Samuel Ribeiro.

References

[1] Mitchell, W., Mccullough, M. (1997). Digital Design Media. New York: John Wiley & Sons, Inc.

[2] 3DHubs: https://www.3dhubs.com/ in 21/05/2019

[3] Advanced Ceramics R&D Lab: https://www.aclab-idegui.org

[4] Khoshnevis, B. (2004). Automated construction by contour crafting-related robotics and information technologies.

[5] Big Delta WASP: https://www.3dwasp.com/en/bigdelta-experimental-field/ in 18/05/2019

[6] Minibuilders IAAC: https://robots.iaac.net/ in 18/05/2019

[7] Jimenez Garcia, M., Retsin, G. (2015). Design Methods for Large Scale Printing. ECAADE Conference, At Vienna, Austria, Volume: Real Time - Proceedings of the 33rd eCAADe Conference - Volume 2.

[8] Winsun 3D: http://www.winsun3d.com/ in 10/05/2019

[9] The Smart Slab project: http://dbt.arch.ethz.ch/project/smart-slab/ in 19/05/2019

[10] de Laubier, R., Wunder, M., Witthöft, S., Rothballer, C. (2018). Will 3D Printing Remodel the Construction Industry. Article available in: https://www.bcg.com/publications/2018/will-3d-printing-remodel-construction-industry.aspx?fbclid=IwAR2Lf58VYKuX5LsCaANaFuWIz-y5FNvtHldMPYJktB1wRRY6_nh8COpcguw&redir=true in 21/05/2019

[11] Post in Aix-en-Provence: http://www.xtreee.eu/post-in-aix-en-provence/ in 19/05/2019

[12] CyBe Industries site: https://www.cybe.eu/ in 10/05/2019

[13] Naboni, R., Breseghello, L., Kunic, A. (2019). Multi-scale Design and Fabrication of the Trabeculae Pavilion. Additive Manufacturing. Volume 27. p 305-317.

[14] Cruz, P. J. S., Knaack, U., Figueiredo, B., & Witte, D. De. (2017). Ceramic 3D printing – The future of brick architecture, Proceedings of the IASS Annual Symposium 2017. A. Crisfield, *Non-linear Finite Element Analysis of Solids and Structures. Volume 2: Advanced Topics*. (2nd ed.). New York: Wiley, 1997.

[15] Campos, T. (2019). Exploração da utilização da pasta de papel na fabricação aditiva em arquitetura. Master's Dissertation in Architecture defended at the School of Architecture of the University of Minho.

[16] Barbosa, I., & Figueiredo, B. (2017). Optimized Brick – Print Optimization. In Chanllenges For Technology Innovation - An Agenda for the Future: :Proceedings of the International Conference on Sustainable SmartManufacturing (S2M 2016): The International Conference on SustainableSmart Manufacturing (S2M), Lisboa, Portugal, 207-210. Leiden, Portugal: CRCPress.

[17] Gosselin, C., Duballet, R., Roux, Ph., Gaudillière N., Dirrenberger, J., Morel, Ph. (2016). Large-scale 3D printing of ultra-high performance concrete – a new processing route for architects and builders in (2016) Materials and Design 100. p.102–109.

[18] Amalgamma site: https://www.amalgamma.org/

[19] Ahmed, Z. Y., Bos, F.P., Wolfs, R.J.M., Salet, T.A.M. (2016). Design Considerations Due to Scale Effects in 3D Concrete Printing. Parametricism Vs. Materialism: Evolution of Digital Technologies for Development [8th ASCAAD Conference Proceedings ISBN 978-0-9955691-0-2] London (United Kingdom) 7-8 November 2016, p. 115-124

Proceedings of the IASS Annual Symposium 2019 – Structural Membranes 2019
Form and Force
7 – 10 October 2019, Barcelona, Spain
C. Lázaro, K.-U. Bletzinger, E. Oñate (eds.)

Terramia: Drone-Aided Construction for a Sustainable Biobased Housing Prototype

Stephanie CHALTIEL*, Diederik VEENENDAAL[a], Francesco VERZURA[a]

*MuDD Architects
Ave Diagonal 645 Barcelona
stephaniechaltiel@gmail.com

[a] Summum Engineering, Rotterdam, Netherlands

Abstract

Terramia is a group of sustainable housing prototypes built during the 2019 Milan Design Week using drones fitted with a spraying pump to deposit different layers of natural mortars onto lightweight formworks. This built project is the largest and most challenging to date - in terms of engineering and on-site fabrication of large elements - compared to previous pavilion-size structures using the same drone architecture referred to as 'bioshotcrete'. The Terramia project consists of three different shells, each built with lightweight lost formworks involving clusters of bamboo rods and textiles, subsequently drone-sprayed, thus offering variations in terms of techniques and results. Different non-cementitious mortars composed of clay, sand, fibers and water are carefully formulated to match the capabilities of the drone spray apparatus while still achieving homogeneous layers and good adhesion. The mortars are sprayed following a precise sequence specific to the mix type, proportions and corresponding drying time. The design and engineering of the shells were tailored to the concept of using actively bent bamboo as falsework to create natural mortar, compression-only structures. The project also provided the opportunity to map the drone spraying trajectory in real-time and to identify optimum values for parameters such as distance to the surface, angles and speed. These new processes, developed by a multidisciplinary team, could open up a new page in the shotcrete industry and allow earthen architecture to be used in large urban contexts. In addition, it could result in increased affordability of architectural freeform envelopes.

Keywords: light formwork, bamboo structure, drone spray architecture, drones in architecture, earthen architecture

1. Introduction

A series of pavilion-scale prototypes were developed as part of a four-year research period on digital fabrication using natural materials [1-9]. For the construction of these prototypes, drones fitted with spraying hoses were used to deposit different layers of carefully formulated earthen mortars onto different kinds of light formworks following a precise phasing. The technique called 'bioshotcrete', lies at the intersection between shotcrete and wattle and daub. The Terramia project is the latest iteration of the bioshotcrete projects. In all these projects, the deposition of biomortars by drones aimed at allowing large constructions to happen without the need for labour-intensive, bespoke

Copyright © 2019 by Stephanie Chaltiel, Diederik Veenendaal, Francesco Verzura
Published by the International Association for Shell and Spatial Structures (IASS) with permission.

scaffolding or cranes on site amongst other improvements compared to the current shotcrete construction.

Earlier bioshotcrete pavilions included the Mud Shells for Domaine de Boisbuchet [9] and the London Design Festival, both in 2018 (Figure 1). In these series of small scale prototypes (4 m domes) built in five days, the formwork consisted of a timber geodesic dome fitted with jute bags filled with straw for insulation. Mortar was sprayed by drones in five layers, supplied as ready-mix bags from Claytec.



Figure 1: Top view of the finished Terramia pavilions during the 2019 Milan Design Week Photos. @ NAARO.

The dry matter had to be prefabricated, which was labour-intensive and could only be appropriate for larger scale buildings where the manufacturing would be automated. For these reasons, a new strategy was adopted for Terramia, consisting of alternating drone spraying of wet, viscous mortar with drone blowing of the dry fibers alone. Furthermore, Claytec could not be used for Terramia, as one objective was to source local ingredients, combined on site for spraying.

In addition, alternative strategies for the geodesic and jute bag formworks were also explored based literature. There is a long history in the application of mortar, either sprayed or rendered, to a wide range of lightweight fabric or mesh formworks [10]. During the initial stages of the present study, using air-inflated formworks, bending-active vaults or gridshells or a combination of both, as well as hanging fabrics were considered:

- Air inflated formworks have been used since the 1940s, Karl Billner, Wallace Neff, Dante Bine and many others up to the present day to construct concrete domes [10]. A deployable gridshell as formwork is a more obscure concept, developed in the 1960s [10], and gaining more recent traction [11-12]. The combination of both ideas, using air-inflation to deploy a gridshell, is new [13-14], and the authors suggest it could serve as formwork as well.
- Bent rods, such as reed, as formwork for vaults dates back to Roman times [10], and has been used more recently by CanyaViva from Spain for more freeform vaults [15].
- Several hundreds of concrete vaults were made by hanging fabric between falsework arches in the 1940s and 50s, referred to as the ‘Ctesiphon’ system, developed by James Waller [10].

For Terramia, the final design combined bioshotcrete drone-spraying and the 'Ctesiphon' system of parallel arches with fabric, with bending-active bamboo arches made by CanyaViva using their techniques (see Section 4). A tailored, bespoke fabric was applied as shuttering, before applying mortar by drone-spraying.

2. Project description

The three Terramia pavilions - highlighting innovative, fast and affordable housing systems - were showcased during the 2019 Milan Design Week in the public, covered courtyard space of Regione Lombardia. The larger pavilion is roughly 7.8×6.7 m in plan, and 5.1 m high, while the other smaller ones are 5.3×4.7 m in plan, and 4 m high.

The pavilions are made using a lost falsework of bamboo rods, better known as culms. The culms form series of five arches. The arches were connected by secondary culms, referred to as "nerves", as well a rope. At the base, the arches were tied by rope, and positioned along a horizontal bamboo culm, itself also tied by rope and weighed down with ballast. This system of bamboo and rope was then covered by jute fabric, which serves as lost formwork for multiple coatings of alternating wet and dry mixes, sprayed by drones in public.

3. Engineering

The main structural system consisted of bamboo, as falsework for the jute and mortar. The main arches, consisting of multiple bamboo culms, were bent into their form. The culms were analysed as hollow-tube structures [16]. Sectional properties can be determined from the culm's mean diameter and thickness, according to ISO 22156. However, since our structure strongly relies on active bending, a more accurate tapering diameter and thickness was modelled. The arches have 10–20 times higher bending stiffness than their individual culms do, suggesting composite action exists [15].

The species of bamboo used was assumed to be *p.(phyllostachys) edulis*, also known as *p. pubescens* or moso bamboo. This species is a likely candidate, as it both appears in the wild, and is commercially grown, in Italy. The diameter was estimated by the contractor to be around 5 mm at the tip, and 90–120 mm around the 8 m mark, the length at which they were cut for transportation. The wall thickness was estimated to be 10 % of the diameter.

The material is assumed to behave linearly elastic, according to ISO 22156. Properties for Italian grown *p. edulis* were taken from test data above the fibre saturation point (FSP) [17], and converted to design values at 12 % moisture content (MC) [16]. The moisture content factor C_{mois} = 1.3 instead of 1.2, based on how *p. edulis* develops in strength at 12% MC relative to an MC above the FSP [18]. The shear strength and Poisson's ratio were taken from general values for bamboo [16,19]. The bamboo was checked following recommendations [20] (Figure 2). The modulus of elasticity E_0 for 4-year old *p. edulis* in green condition [21] was used to calculate initial bending stresses.

Permanent loads consisted of self-weight, and prestress from the fabric, applied at the outer two arches (Figure 3). The outdoor extreme wind pressure is 0.42 kN/m^2. Uniform wind suction and pressure were applied with internal coefficients C_{pi} = +0.2/ − 0.3, and asymmetric wind pressures were applied, by assuming the pavilions are equivalent to a dome, with 30% of the outdoor wind pressure to approximate the level of sheltering inside (Figure 3). In addition, the outdoor wind pressures were monitored online for the duration of the Milan Design Week.

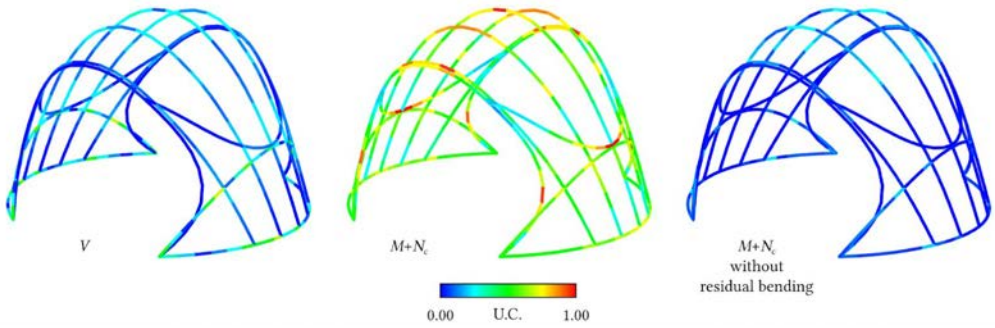


Figure 2: Checks on strength [20] for shear (left) and combined bending and compression, with (center) or without residual bending stress (right).

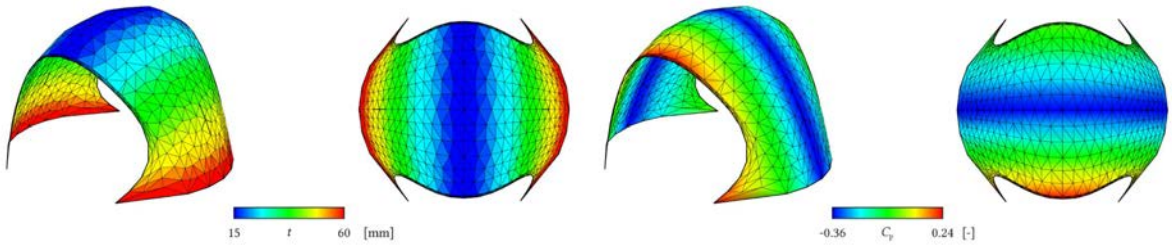


Figure 3: Assumed mortar thickness distribution (left) and asymmetric wind load (right)

Due to the active bending of the fresh bamboos, an additional residual bending stress was added to the results of the finite element calculation (Figure 2). This is a conservative, as for active bending stresses are typically assumed to creep away [22], or the bending strength is reduced [23-24]. This bending stress σ_b was assumed to be no greater than that caused by pure bending determined from the initial stiffness of the green bamboo, E_0, the deformation factor due to instantaneous creep k_{def}, the local radius of curvature R, and the local radius of the culm r, $\sigma_b = E_0/ (1 + k_{def,0}) * r/ R$, where $k_{def,0}$ was assumed to be 2.00, used for green timber which is expected to dry (NTC-2018), as no deformation factor was known for bamboo.

In the ultimate limit state, vertical reactions were checked such that they did not exceed the capacity of the courtyard of 20 kN/m^2. The four corners of the pavilions had to be weighted down by ballast of 67 or 41 kg, for the larger and smaller pavilions respectively.

4. Light formwork construction

Bamboo construction followed the CanyaViva method [15,25]. This method is based on building thick bamboo arches (25 cm diameter) with months to build on site, while in our case, the arches had to be mounted in a public space in the city center in only three days. This created an opportunity for the team to work on uniquely optimized geometries with thin arches and braces, which could be arranged without the need for ladders or scaffolding.

The bamboo, freshly harvested in Dormelletto, was classified in terms of their diameter, and arranged to obtain arches with constant diameters. These clusters of 6 to 10 culms were pre-mounted half arches of up to 8 m, joined by ropes every meter, before transportation to Milan. The full arches and bracing nerves were then mounted on site. The three shells follow a diagonal line in plan, spaced min. 5 m

apart for the drone spraying to be performed in between. The arches and braces are manually bent by about four people steadily moving towards the middle, to avoid cracks until reaching their desired geometries.

The jute fabric was cut by an industrial CNC machine for textiles at Endutex in Spain, and double stitched by hand. The fabric patterns were geometrically unrolled from the latest geometries, based on a 2m roll width. Circular PVC plastic, fitted with long strings, were fixed along their perimeter with tape, to protect the windows during drone spraying. They were removed - without damaging the windows - by pulling the strings when the sprayed coating was still wet.

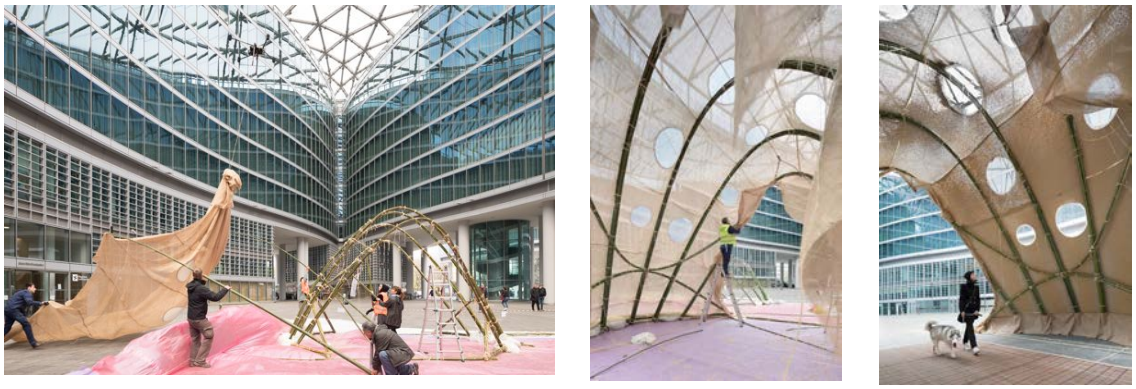


Figure 4: (left) Drone lifting together with the team (center); tailored fabric is stretched by hand after drop on the other side of the arches by the drone; and, (right) tallest shell after opening to the public. Photos @ NAARO

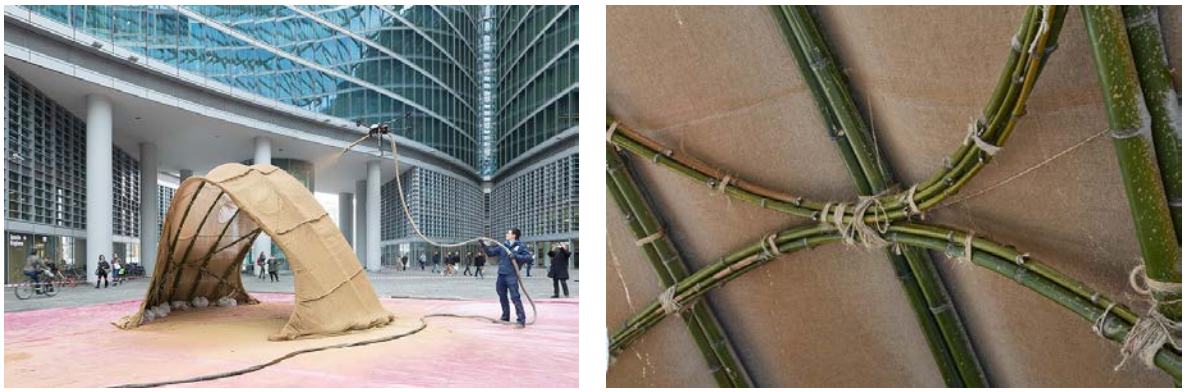


Figure 5. Left Drone spraying of the viscous mix. Public demonstration. Area protected by cordon. Photo @ NAARO Right Bamboo arches and horizontal braces are attached together with ropes manually Photo @IsolaDesignDistrict

5. Drone Actions

For the 5 m tall shell, the drone was fitted with a magnet system [26], allowing the drone pilot to activate to lift and drop the fabric on the other side of the arches, working simultaneously with the team on site (Figure 4). The 2 m wide drone, manufactured by RC Take Off and developed by UC Louvain, is fitted with 50 cm high legs for safe landing when tools are attached to it. Furthermore, it has an autonomy of 20 minutes on average, depending on the weight it is carrying (max. load is 30 kg). The two Euromair pump machines were equipped with 20 m long hoses fitted underneath the

drone. The drone applied multiple coatings of alternating wet and dry mixes (Figure 5). The dry mix consists solely of 1cm rice husks; an agricultural byproduct. The wet, viscous mix is a mortar of sand, clay, rice husks and water, adjusted in terms of mix proportions (1:1:1:2), stirring time and water content.

Table 1: Drone spraying, drone blowing and drone lifting characteristics

	unit	**drone spraying**	**drone blowing**	**drone lifting 150 kgs fabric**
speed	cm/s	80	50	5
trajectory type		spiral from bottom to top	lines from bottom to top	continuous ascension until reaching the other side of the arches
distance to surface	cm	20-80	50 cm	N/A
matter flow		12 l/min (grain size 5mm)	1 bag/min (30 kg/bag)	N/A
drone tilting angle	°	5-10 degrees	0-35	0
machine specs.		Project CP 35 E.W:I Verison, with black nozzle ref: 10048	Turbisol 112 ref. 30394, with 63mm hose diameter	

Table 1 identifies the main parameters that need to be kept within certain ranges, for the drone actions to be suitable in future bioshotcrete construction. The distance to the surface appeared to allow dramatic variations in values without affecting the performance, while the ideal speed of 80 cm/s of the drone spray was found to be crucial for an optimum result. The drone spraying allows much higher values for the deposition speed of the mortar than if it was performed by hand, which could result in significant savings in future shotcrete constructions.

6. Conclusions

The Terramia project is the most recent iteration and largest of the bioshotcrete projects, which combine digital fabrication and natural materials for construction. The project used a novel combination of actively bent bamboo arches covered by tailored jute fabric, as formwork for a drone-sprayed mortar of clay and rice husks. Aerial drones were not only used for mortar spraying, but also for lifting and releasing of the fabric, meaning no scaffolding was needed.

The mortar's raw materials were locally sourced, meaning mix proportions, stirring time and water content had to be calibrated on site, based on the drone-spraying apparatus, adding a significant amount of construction time. On the other hand, separation of wet from dry raw materials prevented blockage of the pumps, and allowed for a high matter deposition rate, resulting in greater efficiency and time savings, compared previously adopted strategies [27].

The calibration of the mortar, along with identifying the drone's optimum speed, trajectory, and distance to the formwork surface, ultimately led to proper adhesion of the mortar layers, resulting in homogeneous and stable earthen shell structures.

The Terramia project highlights that drone spraying of very thin layers of mortar at high speed is beneficial to fit a tight construction timeframe, and could result in material savings if applied to the wider shotcrete industry.

Acknowledgements

The authors would like to thank: Regione Lombardia; Isola Design District; Minerali Industriali; Jonathan Cory-Wright of CanyaViva; Michaël Daris of RC Take Off; Sebastien Goessens of UC Louvain; Gavin Sayers, Edoardo Tibuzzi and Hanif Kara of AKT II; and, Wilfredo Carazas of CRAterre for their contributions to the Terramia project. A special thanks to our construction volunteers: Nadia Avezzano, Alessandra Benigno, Miriam Ceravolo, Michele Francia, Giulia Rosa and Mark Witte.

References

[1] Bravo, M. and Chaltiel, S., 'Paste Matter 3D printing in monolithic shells fabrication methods', in Proceedings of Kine[SIS]tem International Conference, Joao de Oliveira, M. and Crespo, F. (eds.), Lisbon, Portugal, June 2017, 10-18.

[2] Chaltiel, S., Bravo, M. and Chronis, A. 'Digital fabrication with Virtual and Augmented Reality for Monolithic Shells', in Proceedings of the 35th eCAADe Conference, Rome, Italy, July, 2017, 2(35): 211-218.

[3] Chaltiel, S. & Bravo, M., ' Digital fabrication phasing for monolithic shells', in Proceedings of the IASS Annual Symposium, Hamburg, Germany, September, 2017.

[4] Chaltiel, S., Bravo, M., 'Monolithic earthen shells robotic fabrication' in Proceedings of the ACADIA conference, Boston, November, 2017

[5] Chaltiel, S., Bravo, M., Goessens, S., Latteur, P., Mansouri, M. and Ahmad I., 'Dry and Liquid clay mix drone spraying for Bioshotcrete' in Proceedings of the IASS Symposium, Boston, July, 2018.

[6] Bravo, M. and Chaltiel, S. 'Monolithic Earthen Shells Digital Fabrication: Hybrid Workflow', in Proceedings of the Design Modelling Symposium 2017, De Rycke, K., et al. (eds), 2018, 509-521.

[7] Bravo, M., Chaltiel, S. and Carazas, W., 'Matter – Robotic Calibration for Bioshotcrete', Temes de disseny, 34:80-91, 2018.

[8] Chaltiel, S., Bravo, M. and Abdullah, I. 'Adaptive Strategies for Mud Shell Robotic Fabrication', International Journal on Environmental Science and Sustainable Development, 2019, 3(2):64-74.

[9] Šamec, E., Srivastava, A. and Chaltiel, S. 'Light Formwork for Earthen Monolithic Shells', in Proceedings of the International Symposium on Sustainable Materials, Systems and Structures, Rovinj, Croatia, March 2019.

[10] Veenendaal, D., "Design and form finding of flexibly formed concrete shell structures". PhD thesis, ETH Zurich, 2017.

[11] Tang, G. (2012), Deployable gridshells and their application as temporary, reuseable and flexible concrete formwork, in J. Orr et al., eds, 'Proceedings of the 2nd international conference on flexible formwork', Bath, UK, pp. 324-333.

[12] Cuvilliers, P., Douthe, C., du Peloux, L. & Le Roy, R. (2017), 'Hybrid structural skin: Prototype of a GFRP elastic gridshell braced by a ber-reinforced concrete envelope', Journal of the International Association for Shell and Spatial Structures 58(1), 65-78.

[13] Quinn, G. & Gengnagel, C. (2018). Full scale prototype for the pneumatic erection of elastic gridshells, in Mueller, C. & Adriaenssens, S., eds., 'Proceedings of the IASS Symposium 2018', Boston, USA.

[14] Liuti, A., Colabella, S. & Pugnale, A. (2017). Airshell prototype: a timber gridshell erected through a pneumatic formwork, in Bögle, A. & Grohmann, M., eds., 'Proceedings of the IASS Annual Symposium 2017', Hamburg, Germany.

[15] Andújar Moreno, R., Fando Morell, M., Palou Julián, O., Peris Renngli, B. and Maristany Carreras, J. (2013), 'Estudi del comportament mecànic d'arcs de canya arundo donax', Quaderns d'estructures (46), 38–52.

[16] Kaminski, S., Lawrence, A., Trujillo, D., Feltham, I. and López, L. F. (2016), 'Structural use of bamboo. Part 3: Design values', The Structural Engineer 94(12), 42–45.

[17] Fabiani, M. (2015), Physical and mechanical properties of italian bamboo culms, in 'Proceedings of the 10th World Bamboo Congress', Korea.

[18] Janssen, J. (1981), Bamboo in building structures, PhD thesis, Eindhoven University of Technology, Netherlands.

[19] Kaminski, S., Lawrence, A., Trujillo, D., Feltham, I. and López, L. F. (2017), 'Structural use of bamboo. Part 4: Element design equations', The Structural Engineer 95(3), 24–27.

[20] Ota, M. (1953), 'Studies on the properties of bamboo stem (part 9). On the relation between compressive strength parallel to grain and moisture content of bamboo splint', Bulletin of the Kyushu University Forestry 22(9), 87–108.

[21] Kiryu, T., Miyoshi, Y. and Furuta, Y. (2016), 'The mechanism of improvement of physical properties of moso bamboo (Phyllostachys pubescens) with increasing age I. Relationship between modulus of elasticity in bending and cell wall thickness and/or percentage of cell walls', Mokuzai Gakkaishi 62(3), 61–66.

[22] Happold, E. and Liddell, W. (1975), 'Timber lattice roof for the Mannheim Bundesgartenschau', The Structural Engineer 53(3), 99–135.

[23] Toussaint, M. (2007), A design tool for timber gridshells. The development of a grid generation tool, Master's thesis, Delft University of Technology, Netherlands.

[24] D'Amico, B., Kerman, A., Zhang, H., Pugnale, A., Colabella, S. and Pone, S. (2015), 'Timber gridshells: Numerical simulation, design and construction of a full scale structure', Structures 3, 227–235.

[25] Ecohabitar, Canya Viva en Green Utopia, 2015. http://www.ecohabitar.org/22201/ Accessed 14/04/2019

[26] Sébastien Goessens, Caitlin Mueller, Pierre Latteur Feasibility study for drone-based masonry construction of real-scale structures Automation in Construction Volume 94, October 2018, Pages 458-480, ELSEVIER

[27] HUBS: Geodesic domes made simple. https://buildwithhubs.co.uk/Accessed 14/04/2019

Proceedings of the IASS Annual Symposium 2019 – Structural Membranes 2019
Form and Force
7 – 10 October 2019, Barcelona, Spain
C. Lázaro, K.-U. Bletzinger, E. Oñate (eds.)

Analysis of an adaptive tensegrity module

Stanislav KMET*, Viktor URBAN, Michal TOMKO, Robert SOLTYS

*Technical University of Kosice, Faculty of Civil Engineering, Institute of Structural Engineering
Vysokoskolska 4, 042 00 Kosice, Slovak Republic
stanislav.kmet@tuke.sk

Abstract

This paper describes a newly developed adaptive tensegrity module which has the ability to alter its geometrical form and pre-stress properties in order to adapt its behaviour to current loading conditions. The novel adaptive structure and its connections create a new aspect presented in the paper. This system contains sensors that sense forces from the environment and actuators that adjust its shape accordingly, depending upon the load applied. The structure, in the form of an octahedral cell, consists of twelve pre-stressed cables and four compressed struts which are designed to function as actuators. Tests confirmed the functionality of the developed adaptive system and the applicability of the proposed equipment, software, computational models and control commands. Responses of the structure obtained numerically are compared with experimental results. A 3D discrete geometrically nonlinear analysis of the adaptive tensegrity module is based on the application of the nonlinear finite element method. The results demonstrate that the behaviour of the adaptive active tensegrity system obtained by tests can in general be closely theoretically predicted. Results confirmed a physical relevance and mathematical correctness of the applied theoretical approaches.

Keywords: tensegrity structures, adaptive tensegrity module, characteristics, structural members, experimental analysis, nonlinear FE analysis, simulation, models verification, behaviour and response research.

1. Introduction

Lightweight self-stressed tensegrity systems, composed of tensioned cables and compressed struts, offer an economical and efficient alternative to many classical civil-engineering and aerospace structures [1, 2]. Their implementation is very promising in projects that require active or deployable systems [3-6]. Tensegrity structures have been intensively studied since first appearing in the fifties and their applications have been extended from art and architecture to other areas that include aerospace structures, robotics and cell mechanics.

Active tensegrity systems equipped with sensors and actuators provide shape-control potential that adapts to changing loads and environmental conditions. Structural control is carried out by modifying the self-stress state of the tensegrity structure in order to satisfy prescribed reliability criteria due to ultimate and mainly serviceability limit states.

Tensegrity system geometry and initial pre-stresses applied to members of the tensegrity system at its self-equilibrium state, significantly influence the behaviour of a loaded structure and greatly contribute to its stiffness and stability. In general, stiffness depends upon geometry and pre-stress, but rational choices of geometry play a dominant role.

Many regular and also non-regular tensegrity systems have been developed in recent years and considerable research related to their geometry, form-finding, static analysis and architecture has since been conducted [7-11]. Developed concepts based on motions, forces or energy approaches provide a mathematical framework to design the appropriate form and initial stiffness of tensegrity structures

Copyright © 2019 by Stanislav Kmet.
Published by the International Association for Shell and Spatial Structures (IASS) with permission.

and to analyze their behaviour and stability properties. However, research of tensegrity structures concentrates mainly on theoretical studies of non-adaptive systems. Tests on full-scale adaptive models (prototypes), as presented in the papers [12-14], are rare.

The development of adaptive tensegrity structures has been a subject of research since the end of last century. This area is studied systematically at the Institute of Structural Engineering of the Faculty of Civil Engineering of the Technical University of Kosice where full-scale prototypes of active double layer tensegrity systems have been built and tested [12-14]. Finding a good set of control commands for the nonlinear systems is a complex problem, because often there is no closed-form solution for these structures. Multi-objective search is used to select control commands. An appropriate tool for the optimization of the control process is an application of genetic algorithms. The Multi-Objective Genetic Algorithm (MOGA) used in Goal Driven Optimization (GDO) as a hybrid variant of the popular Non-dominated Sorted Genetic Algorithm-II (NSGA-II) based on controlled elitism concepts are used in these studies. Initial population, necessary to run the MOGA algorithm, consists of the movements (elongations or contractions) of the active structural members. The methodology for multi-objective control is based on Pareto filtering and hierarchical selections. This approach was successfully applied for a control of an adaptive cable dome of the Levy type with seven action members as is shown in Figure 1.

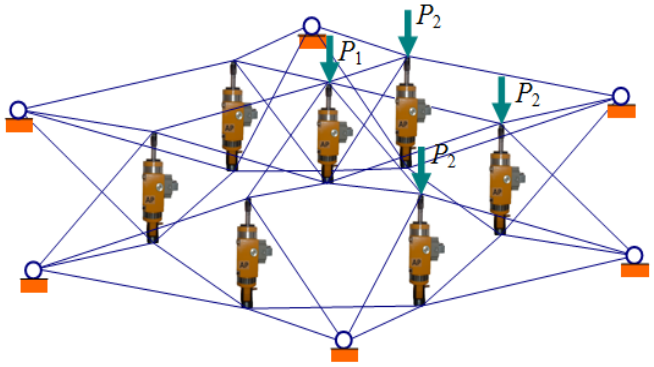


Figure 1: An adaptive cable dome of the Levy type with seven action members

In order to speed up this approach and improve the prediction of the structural behaviour for each possible action more advanced methods were proposed. The process that finds the control commands for adaptive structures can be combined with artificial neural networks applications because relationships between inputs and outputs are available for numerical analyses.

2. Adaptive tensegrity module

A full-scale prototype of an adaptive tensegrity module was designed and built in the Laboratory of Structural Engineering at the Technical University of Kosice's, Faculty of Civil Engineering.

2.1 Characteristics of the adaptive tensegrity module

The elementary shape of the developed adaptive tensegrity structure in the form of a truncated pyramid (a quadruplex module) is shown in Figure 2. The adaptive bearing system consists of four action struts held together in space by twelve cables.

Theoretical dimensions of the lower square base are 2000x2000 *mm*, the upper square base are 1414x1414 *mm* and a height of the truncated pyramid is 1500 *mm*. The upper and lower base are rotated 30 degrees each other. This basic structural bearing system consists of four compression members (struts S4) and twelve tension members (cables C12). All members are mutually connected

at the nodes by hinge joints. All the four compressed members of the tensegrity module are designed as actuators (active struts AS4). These active telescopic struts are used to modify the geometry and self-stress of the tensegrity system. So the marking of the tensegirty module is S4-AS4-C12. The basic members and geometry of the tensegrity module are shown in Figure 2.

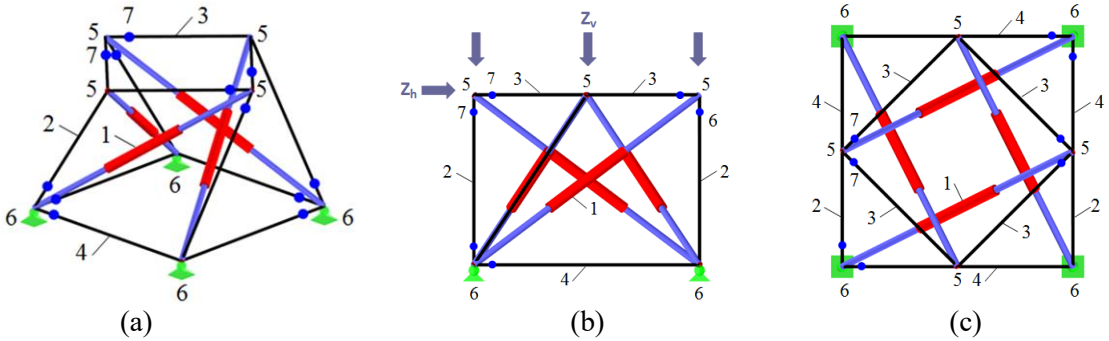


Figure 2: An adaptive tensegrity module consisting of the action members (1), diagonal cables (2), cables of the upper base (3), cables of the lower base (4), nodes (5), supports (6) and sensors (7): (a) an axonometric view, (b) a side view and (c) a top view

Schemes of the experimental setup with the adaptive tensegrity module consisting of four action members with the control electronics, computer system and a device for governing the movement of the action members are shown in Figure 3.

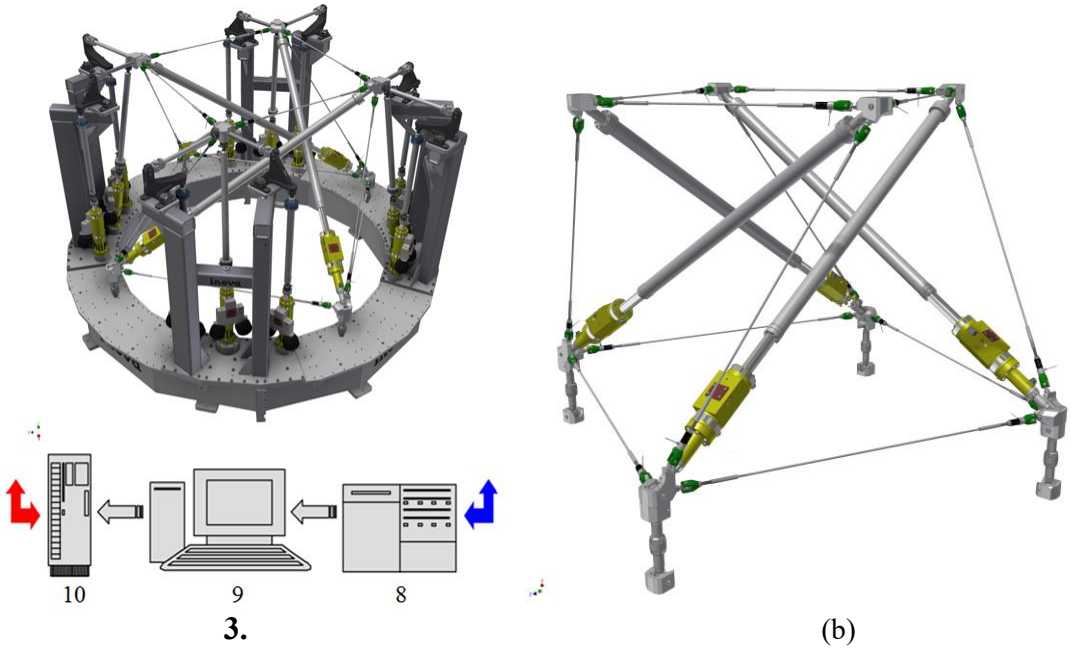


Figure 3: Schemes of the experimental setup with the adaptive tensegrity module: (a) an axonometric view with the control electronics (8), computer system (9) and a device for governing the movement of the action members (10) and (b) a detail axonometric view on the adaptive tensegrity module with the four action members

General view on a prototype of the adaptive tensegrity system is shown in Figure 4.



Figure 4: General view on a prototype of the adaptive S4-AS4-C12 tensegrity system

Four active struts of the tensegrity system are created as circular hollow sections of 76/3,5 *mm* (external diameter/web thickness) and are made from steel S235. The nominal values of the yield strength f_y and the ultimate strength f_u are f_y = 235 Nmm^{-2} and f_u = 360 Nmm^{-2}, respectively. The cross-sectional area of the tubular struts is A_s=797,0 mm^2 and Young's modulus of elasticity is E_s = 210000 Nmm^{-2}. The theoretical length of the struts is L_s=2693,0 *mm*.

Spiral strand ropes consisting of 1x19 constructions (1 core wire, 6 inner wires and 12 outer wires) with a nominal diameter of d = 6,0 *mm*, with a rope grade which is equal to the tensile strength grades of wires R_r = 1570 Nmm^{-2} were used for tensile cables. Cables were made from stainless austenitic steel with an increased resistance to corrosion. The metallic cross-sectional area of the all cables is A_c= 21,49 mm^2 and Young's modulus of elasticity is E_c = 150000 Nmm^{-2}. The tension members in the described tensegrity system can be divided into several groups in terms of their geometry and position in the structure. In the first group are the cables of the upper base (number 1 to 4). The second group consists of diagonal cables (number 5 to 8) and in the third group are cables of the lower base (number 9 to 12). Cables are terminated with swaged fittings with threads. The characteristic value of the breaking force of the tension components is F_{uk} = 26705 *N*.

2.2 Characteristics of structural properties of the active struts and active system

Basic geometrical and structural properties of the active struts are as follows. The hydraulic actuator is a part of the tensegrity system's compressed struts. The actuators consist of rectilinear hydraulic motors with inductive position sensors embedded in the piston rods. These sensors enable the current forces F_{AM} in the action struts to be recorded together with the corresponding current positions Δ_{AM} (the current state of the movement). External dimensions of the hydraulic motor are 95x95x442 *mm*, and its weight is 16 *kg*. The maximum lift of the hydraulic motor is 100 *mm*. Servo valves are used for force and movement control of the action struts. If the action struts extend, tensile forces in the cable members increase and inversely, decrease when the action members retract. The actuators are connected to a hydraulic machine set. Since oils are nearly incompressible, a hydraulic actuator can provide controlled precise linear displacement of the piston. However, pressured oil has disadvantages with respect to electro-mechanical or electro-magnetical actuators for some applications whilst force control may raise problems compared with displacement control in certain situations. These choices should be justified for specific practical applications.

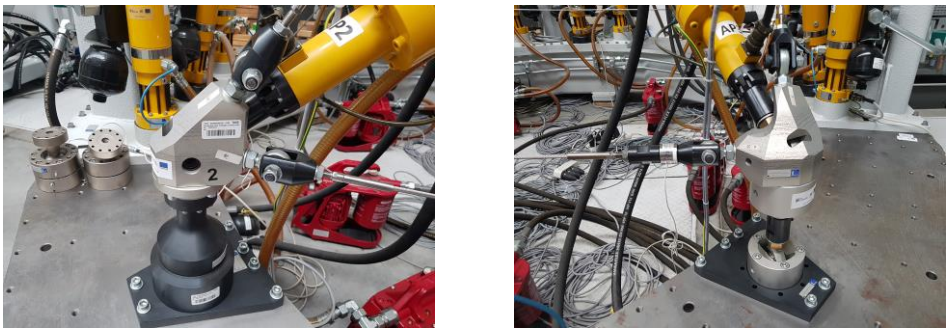
Considerable attention has been given to the design and implementation of joints and connections details of the adaptive tensegrity system's forming structural members. The aim was to achieve a perfect hinge interconnection between individual members, cables and struts and thus precisely capture the principles of action for tensegrity structures. Cable members terminated by moulded terminals with adjustable parts are attached to the top and bottom ends of the compressed struts by spherical pins. Consequently, these connections create total hinges (the possibility of rotation in all directions). Connections of cable members with embedded force transducers require the special arrangements of details. Characteristic details are shown in Figure 5.



Figure 5: Characteristic details

2.3 Characteristics of the boundary conditions

The tensegrity structure is supported at all four bottom nodes by two fixed hinges which are located in opposite sides (all displacements in x, y and z directions of coordinate axes are constrained and rotations in all directions are free) and two movable hinges in opposite sides (displacements in z directions of coordinate axes are constrained, displacements in x and y directions of coordinate axes are free and also rotations in all directions are free). Supports of the adaptive tensegrity system are shown in Figure 6. All the foundation constraints of the tensegrity module are eight, which create the statically indeterminate system. The module has eight components of the reaction forces from which four are in the z direction, two in the x and two in the y direction. The described supporting system was deliberately chosen to allow the bottom cables to be deformed (shortening and elongation).



(a) (b)

Figure 6: Supports of the tensegrity system: (a) an unmovable hinge support (prevents displacement in the directions of the x, y and z coordinate axes, allowing for rotation in all three directions) and (b) a movable hinge support (prevents vertical displacement in the direction of the z coordinate axis and allows rotation in all three directions)

2.3 Characteristics of external loads

External loads can be applied in all four top nodes of the tensegrity module (blue, green and red bars in Figure 6). In each node the loading vector in the directions of x, y and z coordinate axes can be introduced. According to the combination of these directions, numerous various symmetric or asymmetric loading states can be defined.

3. Tests and FEM analysis of the adaptive tensegrity module

A finite element method was used to study the behaviour of the adaptive tensegrity system and to compare the calculated simulated response with experimental values obtained from the individual tests. The method is also employed to assess the results obtained through developed closed-form solutions. The nonlinear analyses were conducted by using the ANSYS 12 Classic finite-element software package [15]. Resultant experimentally and theoretically (Analysis = a finite element method application) obtained courses of forces in the action members and in the upper cables of the tensegrity module subjected to the individual elongations of the action members are shown in Figure 7.

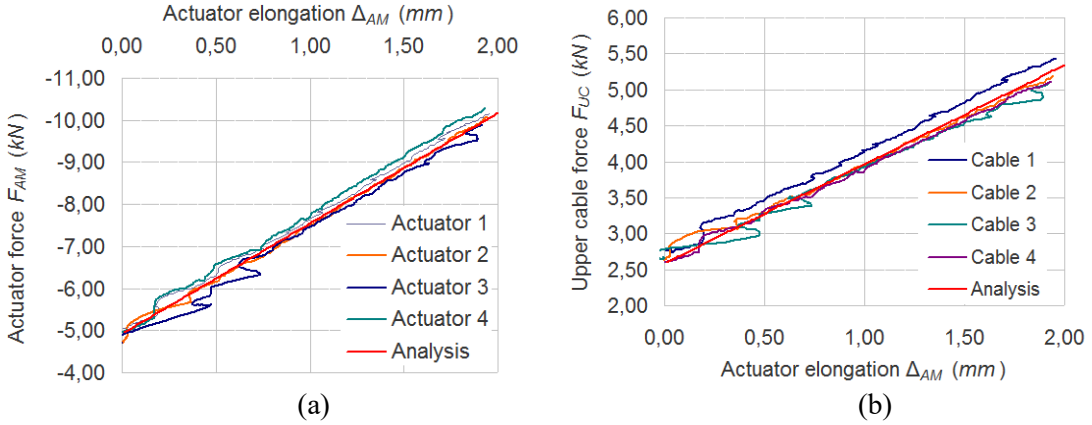


Figure 7: Resultant experimentally and theoretically (Analysis) obtained courses of (a) forces in the action members and (b) forces in the upper cables of the tensegrity module subjected to the individual elongations of the action members

Tests were aimed at investigating the behaviour of the initially pre-stressed tensegrity system subjected to a gradual increase of load. Required values of the initial pre-stress in the cables of the tensegrity system were attained by extending the action members with the corresponding axial force of approximately F_{AM} =10 kN.

Resultant experimentally obtained courses of vertical nodal displacements, forces in the action members, forces in the upper cables, diagonal cables and forces in the lower cables of the tensegrity module subjected to vertical loading forces of P_z = 2 kN at all of the four upper nodes and a finite element model of the system are shown in Figure 8.

Tests confirmed the required functionality of the developed adaptive tensegrity system and the applicability of the proposed electronic equipment and software.

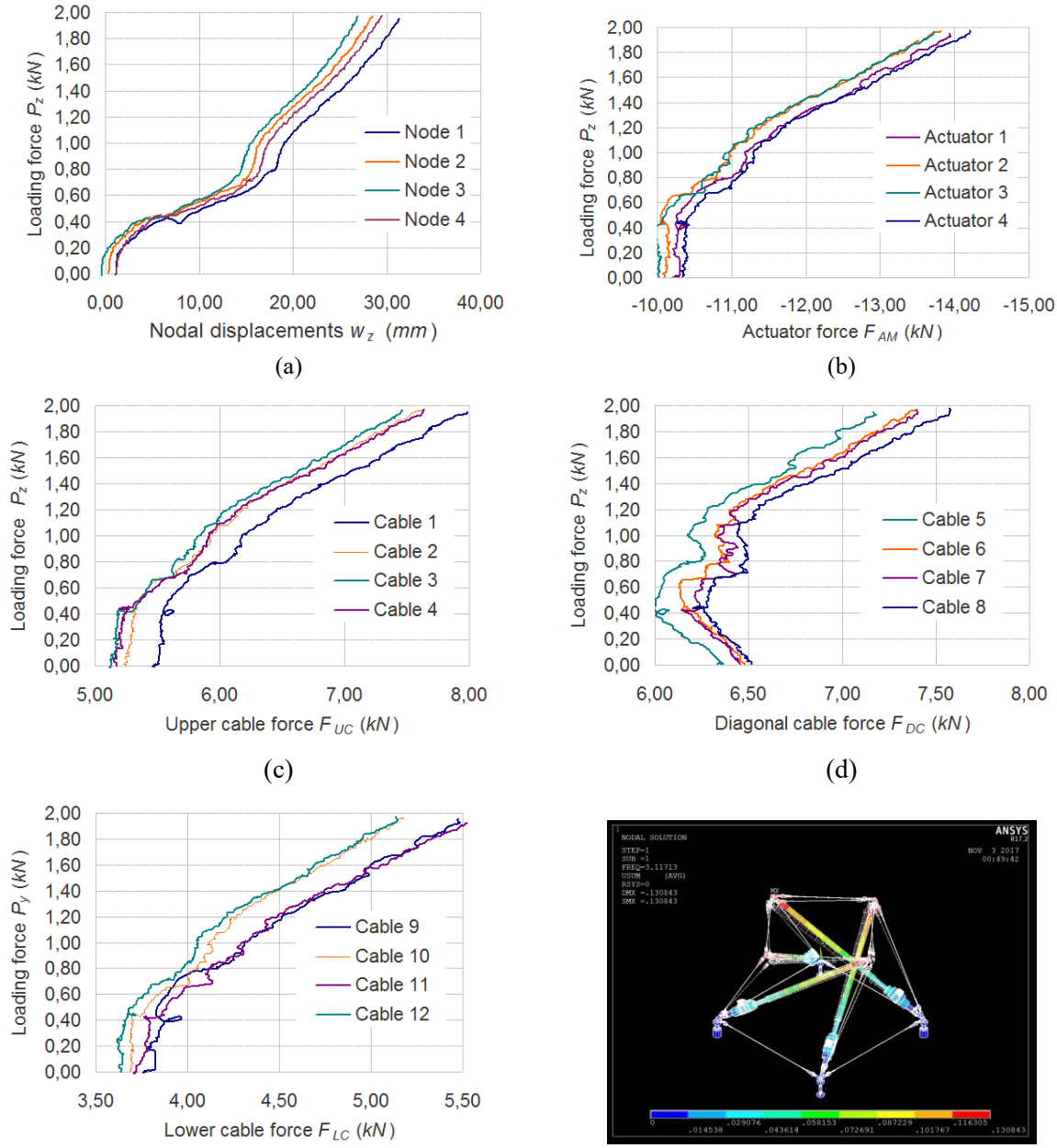


Figure 8: Resultant experimentally obtained courses of (a) vertical nodal displacements, (b) forces in the action members, (c) forces in the upper cables, (d) forces in the diagonal cables and (e) forces in the lower cables of the tensegrity module subjected to vertical loading forces of $P_z = 2$ *kN* at all of the four upper nodes and (f) a finite element model

4. Conclusions

A newly developed adaptive tensegrity system which has the ability to alter its geometrical form and stress properties in order to adapt its behaviour in response to current loading conditions was presented in the paper. This tensegrity module contains the active members and sensors that sense forces from the system and adjust its shape and stress state, making the structure more rigid or flexible depending upon the actual load. The active adaptation process is based on control and automatic actuation.

Tests confirmed the required functionality of the developed adaptive active tensegrity system and the applicability of the proposed electronic equipment and software. The functionality of the active tensegrity system was demonstrated.

Results demonstrated that the behavior of the adaptive active tensegrity system obtained by tests can, generally be closely predicted theoretically (numerically). This approach is deemed useful due to its pragmatic ability to increase the reliability and enhance the performance of tensegrity structures. It is believed that the presented adaptive active tensegrity system will create a basis for innovative technology for a variety of civil engineering applications.

Acknowledgements

This work is part of Research Project No. 1/0302/16, partially founded by the Scientific Grant Agency of the Ministry of Education, Science, Research and Sport of the Slovak Republic and the Slovak Academy of Sciences.

References

[1] R. Motro, *Tensegrity: Structural systems for the future*. United Kingdom: Hermes, ed., Penton Science, 2003.

[2] R. E. Skelton and M. C. de Oliveira, *Tensegrity systems*. New York: Springer Science and Business Media, 2009.

[3] E. Fest, K. Shea and I. F. C. Smith, "Active tensegrity structure," *Journal of Structural Engineering - ASCE*, vol. 130(10), pp. 1454-1465, 2004.

[4] W. Sobek and P. Teuffel, "Adapative lightweight structures," *Newsletter no. 12 of IASS Working group on Structural morphology*, 12, pp. 3-12, 2003.

[5] B. Adam and I. F. C. Smith, "Active tensegrity: A control framework for an adaptive civil-engineering structure," *Computers and Structures*, vol. 86(23-24), pp. 2215-2223, 2008.

[6] N. Veuve, A. C. Sychterz and I. F. C. Smith, "Adaptive control of a deployable tensegrity structure," *Engineering Structures*, vol. 152, pp. 14-23, 2017.

[7] L. Zhang, B. Maurin and R. Motro, „Form-finding of nonregular tensegrity systems," *Journal of Structural Engineering - ASCE*, vol. 132(9), pp. 1435-1440, 2006.

[8] J. F. Dubé, N. Angellier and B. Crosnier, "Comparison between experimental tests and numerical simulations carried out on a tensegrity minigrid," *Engineering Structures*, vol. 30(7), pp. 1905-1912, 2008.

[9] B. S. Gan, J. Zhang, D. K. Nguyen and E. Nouchi, "Node-based genetic-finding of irregular tensegrity structures," *Computers and Structures*, vol. 159, pp. 61-73, 2015.

[10] X. Feng, "The optimal initial self-stress design for tensegrity grid structures," *Computers and Structures*, vol. 193, pp. 21-30, 2017.

[11] G. Senatore, P. Duffour and P. Winslow, "Exploring the application domain of adaptive structures," *Engineering Structures*, vol. 167, pp. 608-628, 2018.

[12] S. Kmet and P. Platko, "Adaptive tensegrity module. Part 1: Closed-form and finite-element analyses," *Journal of Structural Engineering - ASCE*, vol. 140(9), pp. 14055-14055, Sept. 2014.

[13] S. Kmet and P. Platko, "Adaptive tensegrity module. Part 2: Tests and comparison of results," *Journal of Structural Engineering - ASCE*, vol. 140(9), pp. 14056-14056, Sept. 2014.

[14] S. Kmet and M. Mojdis, "Adaptive cable dome," *Journal of Structural Engineering - ASCE*, vol. 141(9): Article Number: 04014225, Sept. 2015.

[15] ANSYS, Inc. *Release documentation of Ansys 11.0*, Southpointe, 275 Technology Drive, Canonsburg, 2005.

Proceedings of the IASS Annual Symposium 2019 – Structural Membranes 2019
Form and Force
7 – 10 October 2019, Barcelona, Spain
C. Lázaro, K.-U. Bletzinger, E. Oñate (eds.)

A Bio-Informed Topology Optimization Algorithm Based on Leaf Venation Structures

Naomi FRANGOS*, Daniel REYNOLDS[a], Gustav FAGERSTRÖM[b], Norman RICHARDSON[c]

College of Architecture, Art, and Planning, Cornell University
139 Sibley Hall, Ithaca, NY 14853
nfrangos@nfarchitect.com

[a, b, c] Walter P. Moore, New York, NY

Abstract

Current trends in biomimicry show an interest in the simulation of generative branching systems found in plants to inform structural design of dendritic forms. Instead, this paper considers a leaf's less studied and mysteriously flat venation system as a lightweight ramifying surface structure. While leaf venation patterns grow through self-organizing systems centered around mechanical and structural efficiency, relationships between topology, geometry and venation density have mostly been studied for their mechanical properties. Recent research on venation-based algorithms describes a process for generating venation patterns based on performance criteria using the distribution of auxin hormone sources. This paper studies the effects of leaf venation patterning to leaf stress and stiffness to develop a novel topology optimization algorithm. The algorithm implements a structural example to illustrate a full workflow for testing structurally efficient branching patterns for a variety of shapes, support conditions, and applied loads.

Keywords: algorithmic botany, leaf morphology, venation algorithm, venation patterns, topology optimization, morphogenesis.

1. Introduction

Nature as a model for architectural forms has been mimicked as imagery since the first archetypal building, and now, natural biological systems are reaching a heightened interest in emerging trans-disciplinary fields rooted in technology that combine architecture, structure, science. J.W. Von Goethe's treatise on botany from 1790, *The Metamorphosis of Plants*, [1] followed by biologist D.W. Thompson's book, *Growth and Form*, [2] more than a century after, began the scientific understanding of "dynamic organisms" focused on transformation and evolution rather than fixed forms and species. Since living organisms in nature change their form as they grow, they have been most regarded in computational design applications concerned with evolutive or variable forms. These biomimetic approaches are often resolved through simulation of generative growth patterns in search of optimizing various solutions. However, forms inspired by branching systems seem to place an emphasis on global morphologies often overlooking the potential of systemic world of micro-structures found in nature. In the plant world, leaf venation plays a crucial role in transporting essential resources to the leaf surface while simultaneously enhancing the mechanical properties of the leaf [3]. The surface to volume ratio is thus maximized to increase surface area as efficiently as possible. Yet, the natural formation of hierarchical vein distribution and density also attributes to a leaf's structural stability. The seemingly random arrangement and proportion of primary, secondary and tertiary micro-structures can be observed through microscopy and high-resolution photography. These visualization techniques we performed prompted us to investigate venation growth patterns that most efficiently act as "structural forces" and still maintain a leaf's overall shape. Rather than trying to decode nature's way of organizing itself by replication, the

Copyright © 2019 by Naomi Frangos, Dan Reynolds, Gustav Fagerström, Norman Richardson
Published by the International Association for Shell and Spatial Structures (IASS) with permission.

study of its behavior inspires a bio-informed algorithmic approach to generate optimal structural patterns.

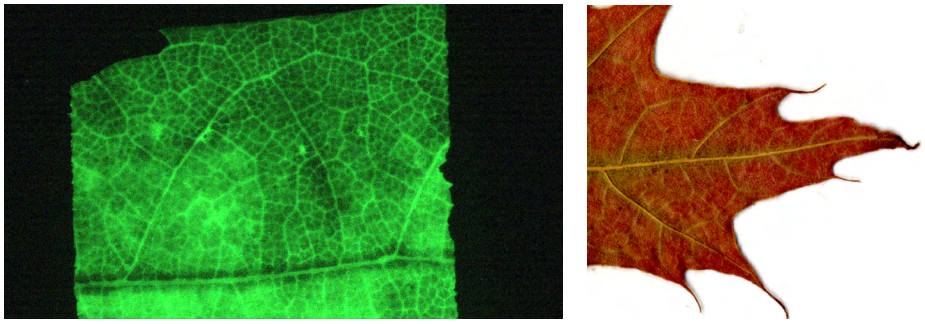


Figure 1: Leaf scan microscopy (left, and high-resolution photometry (right), showing venation patterns.

2. Background - Algorithmic Botany

Algorithmic botany as a design tool is relatively recent yet finds roots in a few key literary sources over the last thirty years. Sack and Scoffini [4] instigated the study of plant performance through a network of its structural systems, vein plasticity, length and width as affected by environmental adaptation and cross-sectional proportions, mass and volume. This was previously explored by KJ. Niklas [5] with the aim of future applications in design and technology. Early interest in generative botany and simulation of geometric computation and modeling informed by biological structures was based on L-systems for computer graphics applications focused on creating believable growth of plant species for placement in virtual scenes, such as the work by Prusinkiewicz and Lindenmayer [6]. The idea that computed stages of growth could be visualized as fixed forms was already novel for that time. More recent approaches of growth simulation are inspired by biologically motivated theories of how branching morphology is achieved in nature. Runions' et al. [7] algorithms aim to mimic the natural diversity of the leaf's morphogenesis generated from the interrelationships that occur between leaf growth, placement of auxin sources and vein development. Algorithmic modifications were based on distance between venation nodes, auxin sources, vein widths and kill distances in the leaf's growth patterns.

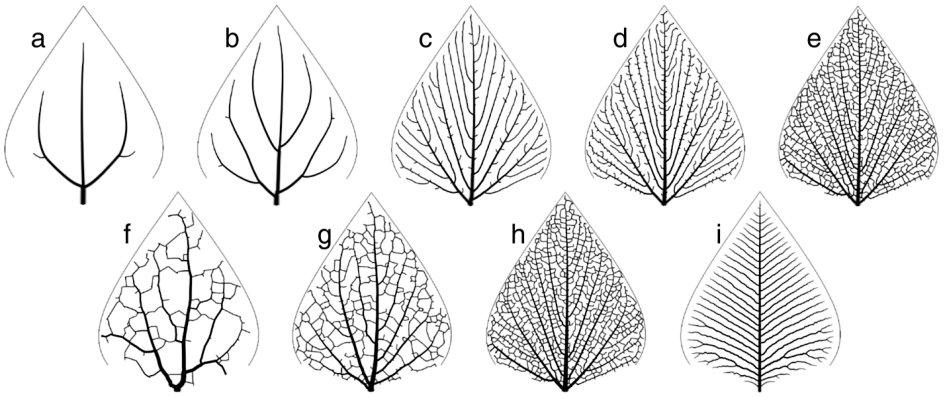


Figure 2: Venation patterns based on varying "kill distance" from Runions et al. [7]

Other approaches generate venation patterns based on perceived geometric rules to capture fundamental morphological characteristics, such as the algorithms by Klemmt and Bollinger [8]. Perhaps the most progressive version of algorithmic botany as an architectural application is by Gokmen [9] who describes a process for generating venation patterns based on performance criteria using the distribution

of auxin sources. The algorithm studies enlarged surface patterns for façade panels that can wrap around a form at an architectural scale. While this research has begun to explore the possibilities of algorithmic botany for design applications, the criteria used to generate the algorithm is non-structural. This reveals a gap in the study and application of systemic networks that provide multiple functions. This paper builds upon the various precedent research that combines biology, computation, structure and architecture to yield an optimization algorithm based on structural morphologies.

Method

In this paper, we adapt Runions et al. [7] approach and augmented the method to produce venation patterns that are influenced by the stress field. Runions et al. describe a process of creating auxin points on the domain. We reproduce this; however, we replace the "dart-throwing algorithm" with a non-uniform random generation. We choose to use a random number generation that samples from the stress field distribution. The steps are as follows:

3.1 Generate the stress field distribution

Using a shell model of the structure a stress distribution is generated for the shell. One of the stress fields is chosen (at the designer's discretion) to form the basis for the sampling distribution for the auxin point generation.

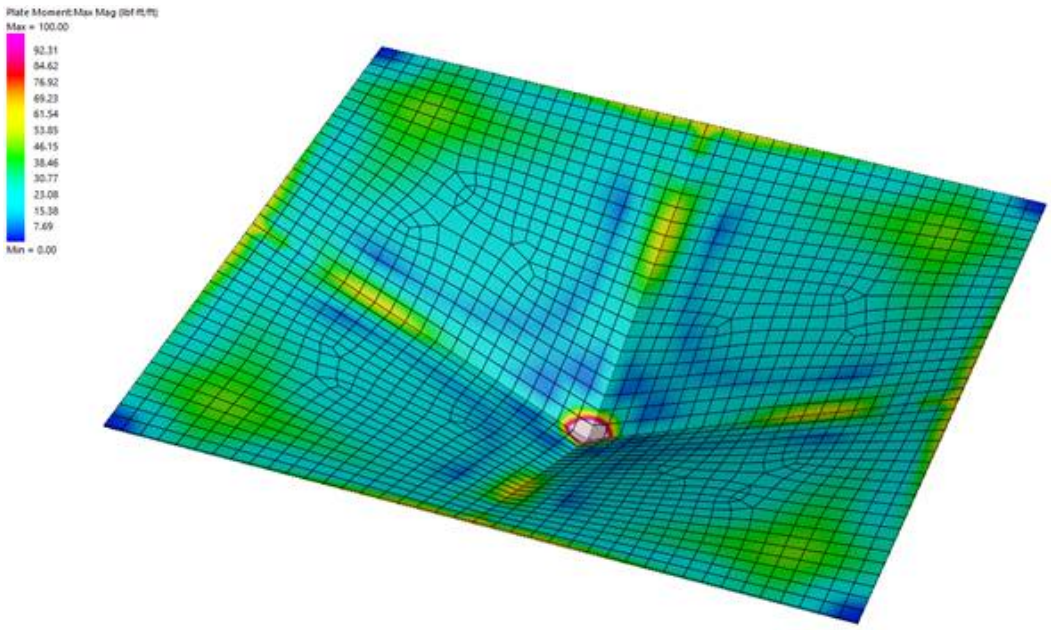


Figure 3: Stress plot from analysis use the max principal moment

3.2 Generate the auxin points

The stress distribution is used as a sampling distribution of pseudo random numbers. This process is well documented, see for example the rejection method in Numerical recipes in C [10]. Using this technique more auxin points are generated at the points of high stress and fewer are generated at points with lower stress. N equals the number of points.

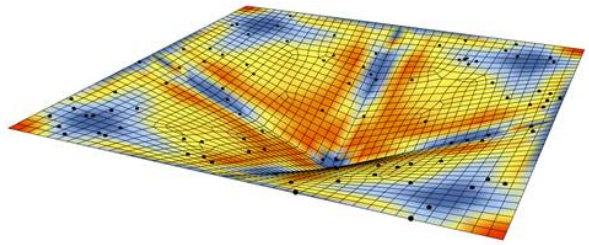


Figure 4: N=100

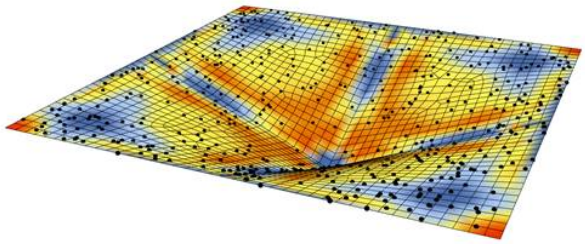


Figure 5: N=500

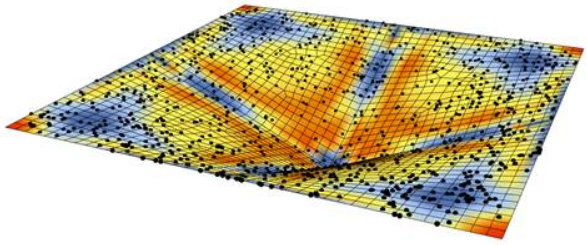


Figure 6: N=1,000

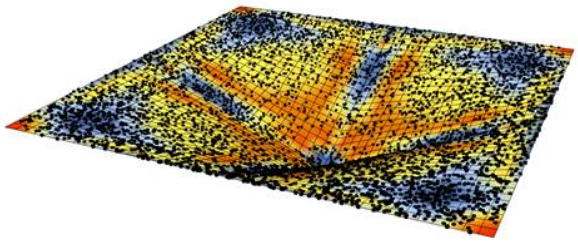


Figure 7: N=5,000

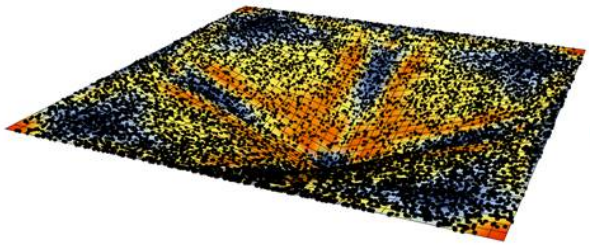


Figure 8: N=10,000

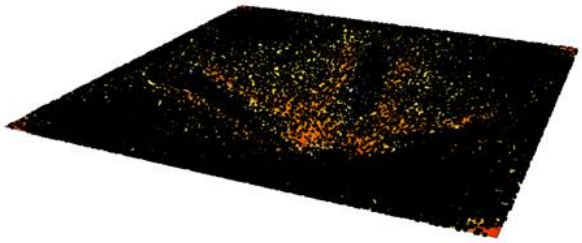


Figure 9 : N=50,000

3.3 Grow the vein network

Based on the auxin points a venation pattern can be generated. This is done by generating vein nodes in an iterative process. To initialize the iterative process one or more "root" nodes are chosen. Then, a grouping process occurs on the auxin points to determine which subset of auxin point belongs to each vein node. If a vein node has a subset of auxin points group to it, it then generates additional vein nodes in the direction of the subset:

$$v' = v + D\frac{\vec{n}}{|\vec{n}|}, \qquad \text{where } \vec{n} = \sum_{s \in S(v)} \frac{s-v}{|s-v|}$$

Once a vein point is within a step size D of an auxin point, this point is deactivated and no longer participates in the grouping process. The algorithm iteratively generates vein points until all auxin points have been deactivated.

There are several nuances to be considered in the vein network growth algorithm. Different behaviors can be generated by:

1. Changing the grouping definition
2. Generating additional auxin points at each iteration of the vein growth
3. Varying the number of iterations, the auxin points stays active after it is reached by a vein point.

For the sake of simplicity an "open" venation algorithm was chosen. Meaning that the simplest variation of 1-3 were chosen:

1. The nearest neighbors were used to determine the grouping
2. No additional auxin points were generated at each iteration of the vein growth
3. Auxin points were deactivated immediately

3.4 Experiments

For the sake of comparison, a constant auxin point cloud was generated, and several root node/s placements were explored. The generated auxin point cloud as described in section 3.1 and 3.2:

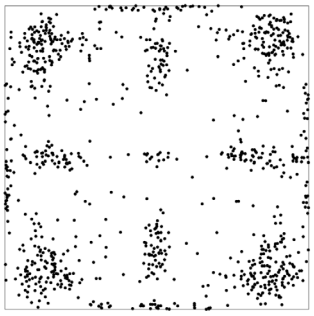


Figure 10: Point cloud for testing experiments

For reference, we will label the domain of the point cloud as α and β.

Experiment 1: Four root nodes are placed at $(1/4\alpha, 1/2\beta)$, $(3/4\alpha, 1/2\beta)$, $(1/2\alpha, 1/4\beta)$, and $(1/2\alpha, 3/4\beta)$.

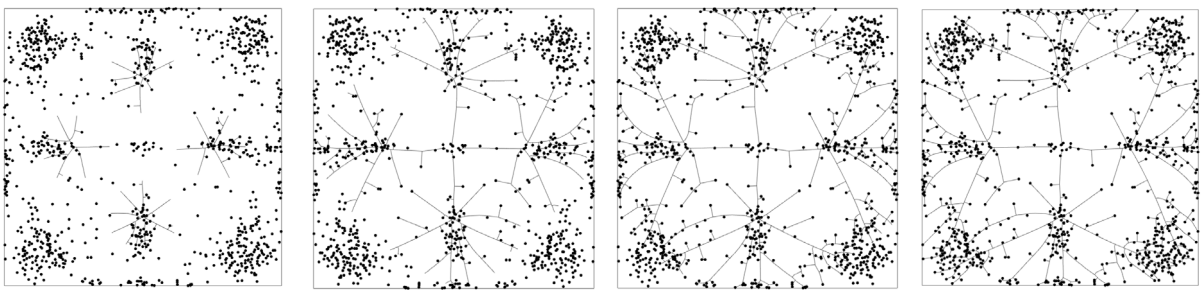


Figure 11: Experiment 1, N = 25%, 50%, 75%, 100% (from left to right)

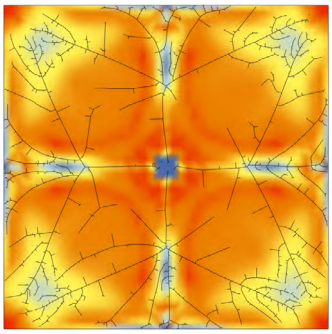


Figure 12: Overlaying the stress plot with the venation pattern

Experiment 2: A single root node is placed in the center of the point cloud $(1/2\alpha, 1/2\beta)$.

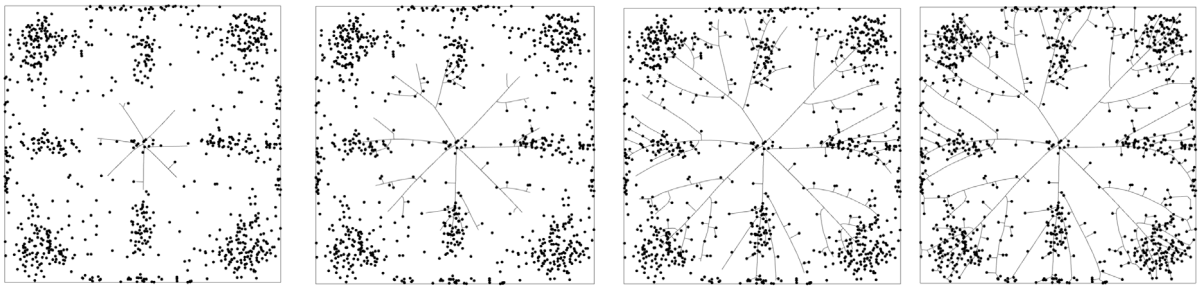


Figure 13: Experiment 2, N = 25%, 50%, 75%, 100% (from left to right)

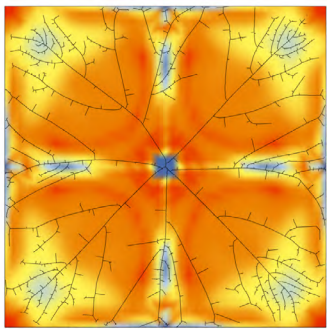


Figure 14: Overlaying the stress plot with the venation pattern

Experiment 3: Four root nodes are placed at $(0,1/2\beta)$, $(\alpha, 1/2\beta)$, $(1/2\alpha, 0)$, and $(1/2\alpha, \beta)$.

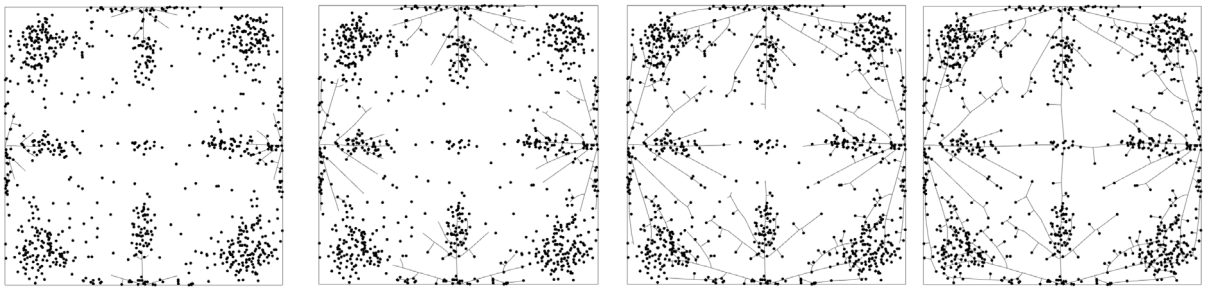


Figure 15: Experiment 3, N = 25%, 50%, 75%, 100% (from left to right)

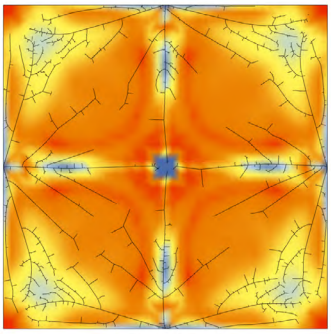


Figure 16: Overlaying the stress plot with the venation pattern

The three experiments show that the venation pattern varies significantly depending on the root location/s. In each case the algorithms show some similarities. Each experiment develops veins down the line $1/2\alpha$ and $1/2\beta$. Each experiment has densest branching near the corners $(0,0)$, (α,β), $(\alpha,0)$, and $(0,\beta)$. Each experiment has primary veins or dense branching around the perimeter. Only in the case of experiment 2 do the primary veins extend out radially.

4. Conclusions and Future Work

The results show that the generated venation patterns can vary depending on the chosen root point, which suggests that there is a range of optimal venation patterns. The experiments do show some similarities and promising structural behavior. Although not all the experiments show a strong tendency to follow the principle stress lines, there are favorable signs that this kind of behavior could be amplified.

From the perspective of the venation algorithm, future work will focus on:

1. quantifying the structural benefits
2. modify the venation algorithm such that additional auxin points are generated at each venation iteration
3. developing a "closed cell" venation algorithm. The authors see opportunity in using the "closed cell" algorithm in grid shell applications.

Further development and applications of this work is manifold. Observation of various leaf species and their vein hierarchy densities using microscopy, with both open and closed venation, would allow for a comparative analysis of different micro-structure patterns existing in nature with those generated by the algorithm. This could be used to inform and modify the algorithm. As an application towards architectural form, this work shows the potential for both surface structures and three-dimensional forms. Rather than presuppose a specific scale of application, this research aims to establish a robust work-flow allowing for inter-scalar approaches in design that may emerge from modifying the growth algorithm. This could range from small-scale prototypical joints in architectural assemblies, to overall structural topology optimization layouts, with the possibility of generating a taxonomy of variable forms illustrative of structural efficiency.

Acknowledgements

The authors wish to thank Aleksandr Vasilyev, Ph.D., Assistant Professor of Biomedical Sciences at New York Institute of Technology for assistance with initial leaf scanning as a point of inquiry, inspiration, and first-hand visualization.

References

[1] J.W. Von Goethe. *The Metamorphosis of Plants*. Cambridge: MIT Press, 2009.

[2] D. W. Thompson. *On Growth and Form*. Cambridge: University Press, 1917.

[3] A. Roth-Nebelsick, D. Uhl, V. Mosbrugger, H. Kerp. "Evolution and Function of Leaf Venation Architecture: A Review," in *Annals of Botany Company, vol. 87*, 2001, pp. 553-566. doi:10.1006/anbo.2001.1391

[4] L. Sack and C. Scoffoni, "Leaf venation: structure, function, development, evolution, ecology and applications in the past, present and future," in *New Phytologist*, vol. 198, pp. 983–1000, 2013. doi: 10.1111/nph.12253.

[5] KJ. Niklas, "A Mechanical Perspective on Foliage Leaf Form and Function," in *New Phytologist*, vol. 143, pp. 19-31, 1999.

[6] P. Prusinkiewicz and A. Lindenmayer, *The Algorithmic Beauty of Plants*. New York: Springer-Verlag, 1990.

[7] A. Runions, M. Fuhrer, B. Lane, P. Federl, A. Rolland-Lagan, P. Prusinkiewicz, "Modeling and Visualization of Leaf Venation Patterns," *ACM Transactions on Graphics*, 24(3), pp. 702–711, 2012.

[8] C. Klemmt and K. Bollinger. "Cell-Based Venation Systems," in *Generative Design – Biological,* vol. 2, eCAADe 33, pp. 573-580, 2015.

[9] S. Gokmen, "*A Morphogenetic Approach for Performative Building Envelope Systems Using Leaf Venatian Patterns*," eCAADe 31, pp. 497-506, 2013.

[10] W. Press, S. Teukolsky, W. Vetterling, B. Flannery, *Numerical Recipes in C: The Art of Scientific Computing*. (3rd ed.), Cambridge: University Press, 2007.

Proceedings of the IASS Annual Symposium 2019 – Structural Membranes 2019
Form and Force
7 – 10 October 2019, Barcelona, Spain
C. Lázaro, K.-U. Bletzinger, E. Oñate (eds.)

A generation of frame structure based on Koch curve and an application to spatial frame

Toshifumi MAE *, Iasef Md RIAN[a]

* Department of Civil and Environmental Engineering, National Institute of Technology, Oita College
1666 Maki, Oita 8700152, Japan
mae@oita-ct.ac.jp

[a] Xi'an Jiaotong-Liverpool University, Suzhou, China

Abstract

The authors have been engaging to apply self-similar forms in nature to architectural form. The self-similarity is one of the characters of fractal. Mandelbrot set, Sierpinski gasket, the Koch curve, and so on are famous as the fractal geometric forms. It seems difficult to apply Koch curve to architectural form because they are complicated in shape. But we can treat numerically because they are composed of a combination of original figures and its self-similar mappings. So, new self-similar frames are generated by adding an angle as a parameter to Koch curve. Here, a parameter is given at the base angle of the equilateral triangles and given at the angle for the line of divided both sides. Though angle 1 varies 0~15 degree and angle 2 does 0~60 degree. However, if angles are raised, the shape is larger obviously and fractal dimension is higher, which varies from 1.00 to 1.28. On a static mechanical characteristic against to vertical load, if both angles are larger, bending moment and displacement are less in a whole. Also, bending moment and vertical displacement are suppressed by increasing of inclination in angle1 or decreasing of angle2 and shapes will be similar to an arch structure. As a result of frame analysis, it was shown that some new Koch curve was superior to a general Koch curve. In addition, some structural examples are shown extending the Koch curve to spatial structures that maintain complexity and self-similarity followed by the fractal characters of Koch curve.

Keywords: fractal, self-similarity, fractal dimension, frame analysis.

1. Introduction

Some shapes like a tree, cloud and topography in nature are quite complex. It seems that they have fractal geometric form. They have some rationality in their own, because they keep withstanding their own weight and external forces. Fractal geometry has self-similarity and non-integer dimension as characteristics of the form, and it seems that fractal contributes to the rationality of things in nature.

The authors have been engaging to apply self-similar forms in nature to architectural form(T. MAE and S. ASAYAMA [1], S. ASAYAMA and T. MAE [2], [3], I. M. Rian and M. Sassone [4]). Mandelbrot set, Sierpinski gasket, the Koch curve, and so on are famous as the fractal geometric forms.

There are few studies of application of complex figure like Koch curve (N. KISHIMOTO and M. C. NATORI [5]) to an architectural structure. For example, it is easy to apply Sierpinski gasket to a building structure, because it is composed of self-similar set based on triangle. On the other hand, it is difficult to apply Koch curve to a structure, because it has large irregularities and the angle at the node of the connected segments is large. But fractal figure is composed of original figure and its self-similar mapping, and we thought that it was possible to apply it to structural form by adding another parameter to Koch curve. Therefore, the aim of this study is to show Koch curve that varies with

Copyright © 2019 by Toshifumi MAE and Iasef Md RIAN
Published by the International Association for Shell and Spatial Structures (IASS) with permission.

angular change by newly setting the angle of it.

2. Generation of Koch curve

At first, one line is divided into three lines and four mappings which is contracted to 1/3 length is placed. Koch curve is drawn by repeating the above operation as shown in Figure 1 (a). Fractal dimension D_F is obtained by calculating equation (1) and it is 1.26.

$$\sum \lambda_i{}^{D_F} = 1 \tag{1}$$

, where contractive of mapping is 1/3 and number of mappings is four and the dimension is 1.26.

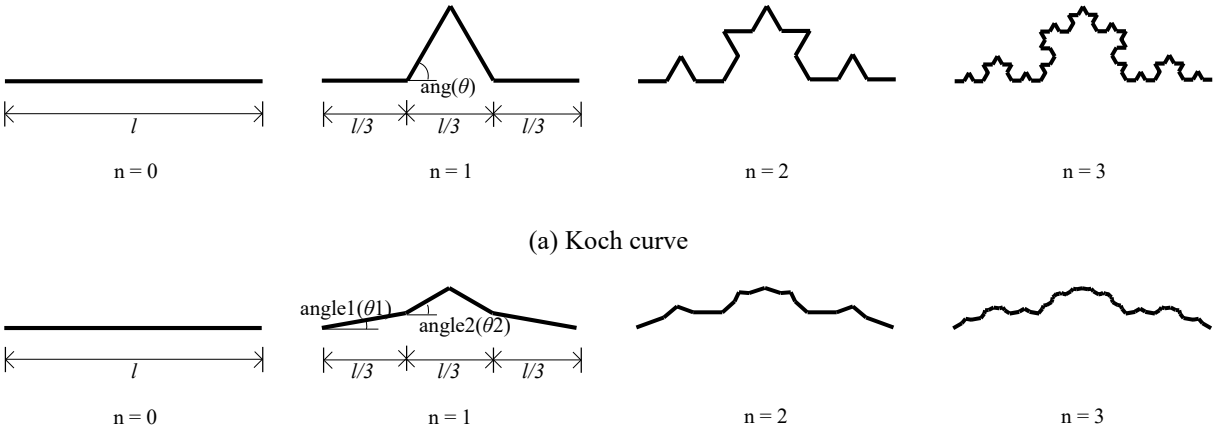
Here, for an application of more suitable Koch curve to architectural form, angle 1 which is a parameter is given at the base angle of the equilateral triangles and angle 2 given at the angle for the line of divided both sides as shown in Figure 1 (b). In this study, there are two contractive and two types of mappings, because parameters of angles are added. Therefore fractal dimension D_F is obtained by equation (2).

$$\sum \lambda 1_i{}^{D_F} + \sum \lambda 2_i{}^{D_F} = 1. \tag{2}$$

The equation of Iterated Function System for drawing Koch curves is shown as

$$W\begin{Bmatrix} x \\ y \end{Bmatrix} = \begin{bmatrix} \alpha_{11} & \alpha_{12} \\ \alpha_{21} & \alpha_{22} \end{bmatrix} \begin{Bmatrix} x \\ y \end{Bmatrix} + \begin{Bmatrix} a \\ b \end{Bmatrix} \tag{3}$$

, where α_{11}, α_{12}, α_{21}, α_{22}, a and b are IFS codes for it as shown in Table 1. Angle 1 varies by 5 degree from 0 degree to 15 degree. And angle 2 varies by 15 degree from 0 degree to 60 degree. Figure 2 shows Koch curves that has two parameters which angle 1 and angle 2 are combined in Figure 2.



(a) Koch curve

(b) New Koch curve with 2 parameters

Figure 1: Convergent sequence of Koch curves

Table 1: IFS code for Koch curve

	α_{11}	α_{12}	α_{21}	α_{22}	a	b
W1	λ1cos(angle1)	-λ1sin(angle1)	λ1sin(angle1)	λ1cos(angle1)	0	0
W2	λ2cos(angle2)	-λ2sin(angle2)	λ2sin(angle2)	λ2cos(angle2)	*l*/3	l/3*tan(angle1)
W3	λ2cos(-angle2)	-λ2sin(-angle2)	λ2sin(-angle2)	λ2cos(-angle2)	*l*/2	l/3*tan(angle1)+l/6*tan(angle2)
W4	λ1cos(-angle1)	-λ1sin(-angle1)	λ1sin(-angle1)	λ1cos(-angle1)	2*l*/3	l/3*tan(angle1)

As a matter of course, Koch curve becomes convex expanded with inclination of the angles and becomes flat shape with decreasing of angles as a whole. In particular, when the angle 2 is small such as 0 degree, the Koch curve becomes closer to the arc geometry as the angle 1 increases. Fractal dimension becomes large with increase of angles and it varies from 1.00 to 1.28.

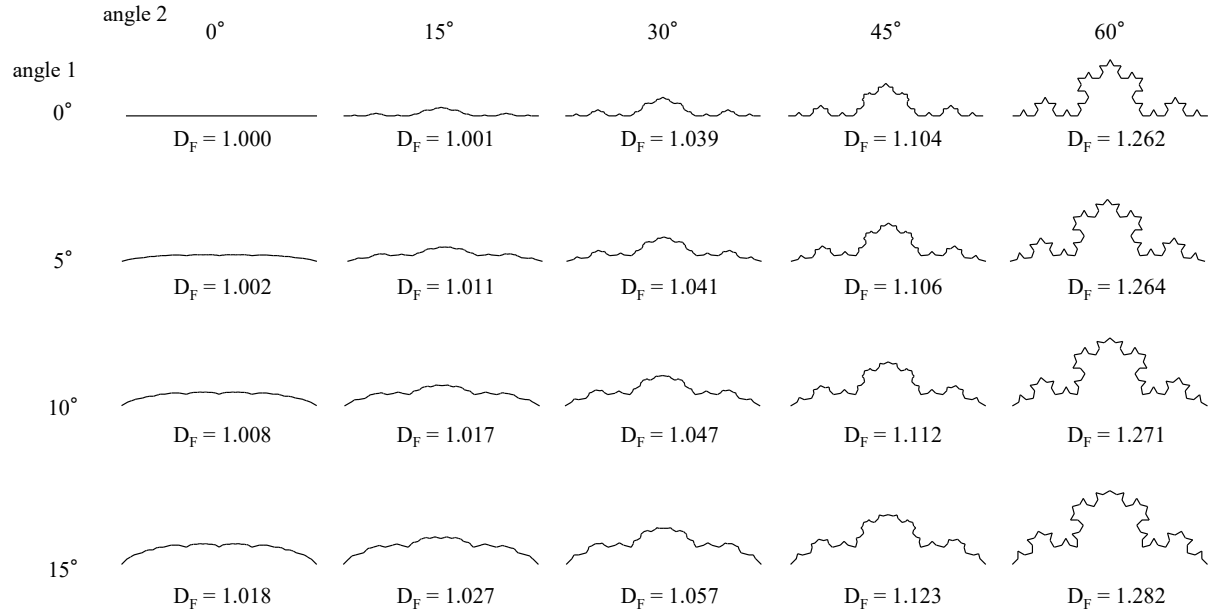


Figure 2: Forms and fractal dimension of Koch curves

3. Two-dimensional structural analysis of Koch curve

3.1. Setting condition for frame analysis

Here, condition for frame analysis of two-dimensional structure based on Koch curve is set. The Both end of supporting point of structure is fixed and other nodal points are rigid. Cross sections are 5cmx5cm square of steel in this frame analysis. The span of supporting points is 6.000m. As the mechanical characteristics against external loading, the vertical loadings are imposed to each nodal point except supporting points of structure so that the total load amount is 1 kN. Young's modulus is 205 kN/mm^2, the rigidity is 80.88 kN/mm^2, and Poisson's ratio is 0.3.

3.2. Result of frame analysis

The relationship between angles and the maximum displacement is shown in Figure 3. With the exception of the Koch curves which angle 2 is 0 degree, the maximum displacement of structures will increase as the inclination of the angle 2 become large. Also, as the inclination of the angle 1 become large, the maximum displacement of them will decrease. Maximum displacement is seen at the central node or at the node near the connected segments of structure in first iteration.

Next, for the model with an angle 1 of 0 degree, the maximum bending moment had an almost constant value of 0.45 kN*m regardless of the increase in angle 2 as shown in Figure 4. As well as maximum displacement, in the case of a model in which the angle 1 is not 0 degree, the maximum bending moment will increase as the inclination of the angle 2 becomes larger. And, as the angle 1 increases, the maximum bending moment will decrease. The maximum bending moment is seen at any of the supporting point, the central node and at the node of the connected segments of structure in first iteration.

The structures with the best mechanical characteristics and normal Koch curve are shown in Figure 5 and 6. The former's both angles are 15 and the latter's angle1 is 0 degree and angle2 is 60 degree. The maximum displacement of the best structure is 0.070 cm and the maximum bending moment is 0.215 kN*m. On the other hand, as a structure based on Koch curve generally known, maximum displacement is 0.629 cm and the maximum bending moment is 0.456 kN*m. The nodal points which have maximum values are shown by blue circle in both Figures. The values of superior structure are less than half that of the model based on Koch curve generally known in comparison of two structures.

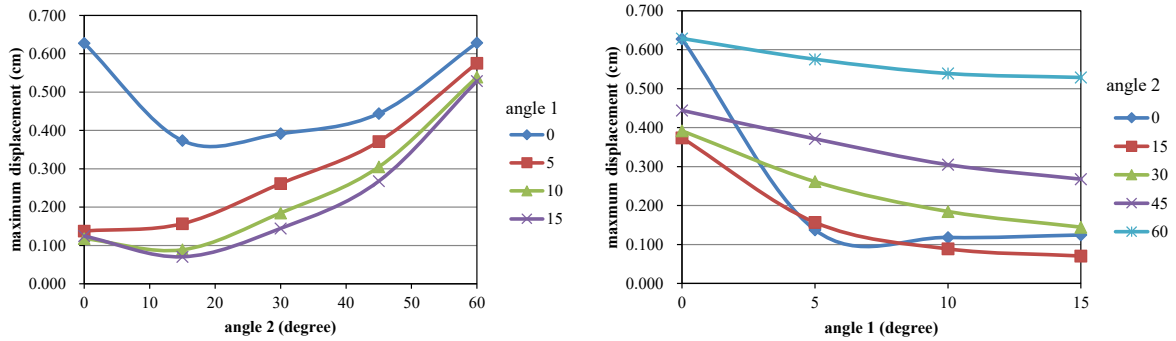


Figure 3: Maximum displacement

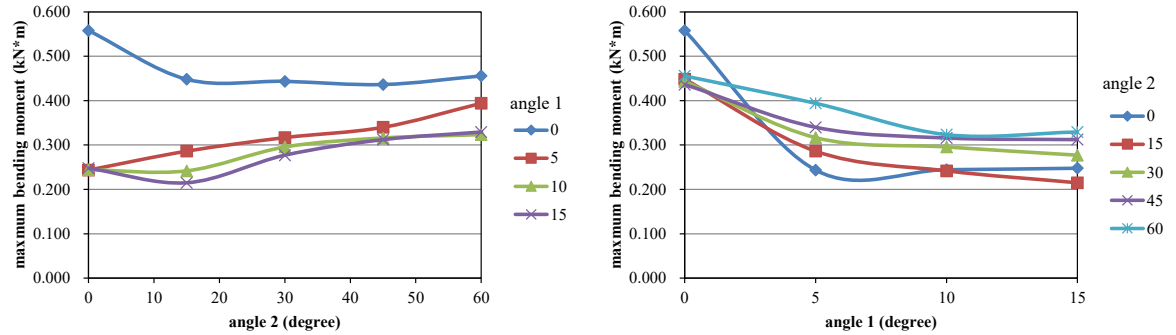
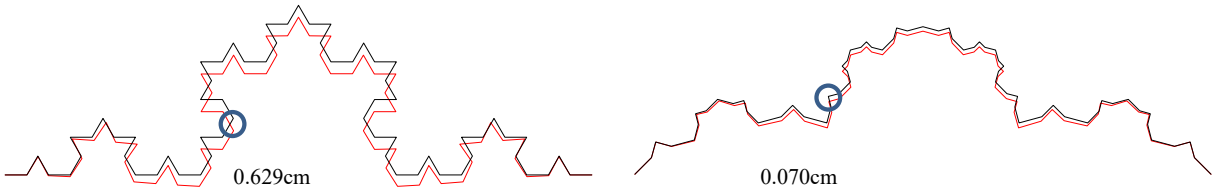
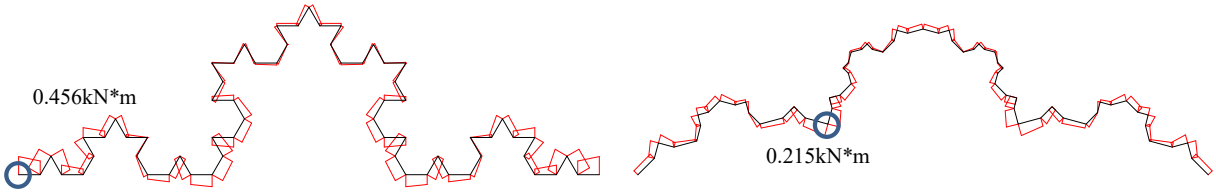


Figure 4: Maximum bending moment



(a) angle 1 = 0 degree, angle 2 = 60 degree (b) angle 1 = angle 2 = 15 degree

Figure 5: Deflection of structures



(a) angle 1 = 0 degree, angle 2 = 60 degree (b) angle 1 = angle 2 = 15 degree

Figure 6: Diagram of bending moment

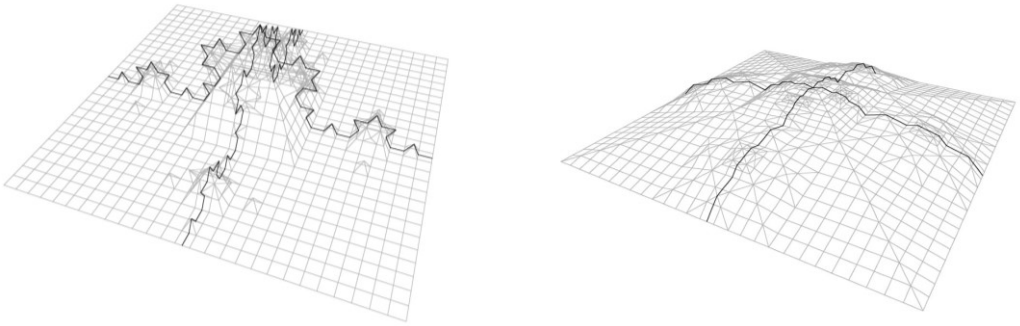
4. Application of Koch curve to 3D models

4.1 Application to spatial frame using Koch curve in cross section

It is described that two-dimensional frames of Koch curve are applied to spatial frames. Here, the Koch curves analyzed in Chapter 3 are used for the cross section of the 3D shape in two directions and two examples are shown in Figure 7. One of them is Koch curve generally known model in which the angle 1 is 0 degree and the angle 2 is 60 degree. Another one is the model which the maximum of displacement and bending moment are least and both angles are 15 degree. It is clear that the model applied using Koch curve generally known is more complex than another model because difference between the angles is large. On the other hand, the form of superior model looks like seems to be a gentle slope as a whole because both angles are same and not so high.

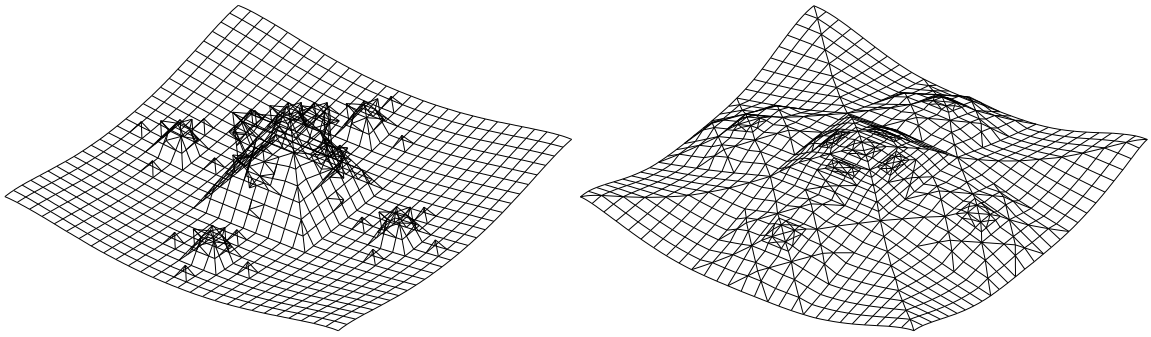
Then the structures are analyzed in the case of acted by dead load and vertical load which is 0.1 kN on each nodal point as a unit force. A space of 9 x 9 m^2 is covered with the structure. The cross section of member is 165.2 mm x 3.8 mm of steel pipe. The supporting points at the corner of the structure are fixed and other nodal points are rigid.

Next, analytical result is discussed. The deflection of spatial frame is shown in Figure 8. The center of structure is moved to down by vertical loading obviously. In spite of same total length approximately, the difference of vertical displacement is very large. The maximum displacement of the model applied using Koch curve generally known is 3.959 cm and another model is 0.434 cm. The diagram of bending moment is shown in Figure 9. As well as displacement, a maximum bending moment of the former is bigger than the latter and it is 25.755 kN*m. On the other hand, a maximum bending moment of the latter is 9.141 kN*m.



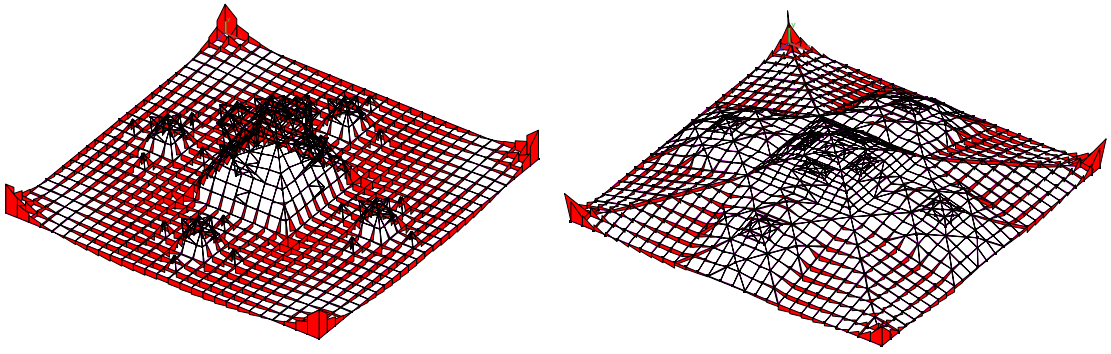
(a) angle 1 = 0 degree, angle 2 = 60 degree (b) angle 1 = angle 2 = 15 degree

Figure 7: Examples of Koch curve applied to spatial frame



(a) angle 1 = 0 degree, angle 2 = 60 degree (b) angle 1 = angle 2 = 15 degree

Figure 8: Deflection of spatial frame based on Koch curve



(a) angle 1 = 0 degree, angle 2 = 60 degree (b) angle 1 = angle 2 = 15 degree

Figure 9: Moment diagram of spatial frame based on Koch curve

4.2 Koch Lattice

The structural application of the Koch curve, which lies in the two-dimensional space, is limited to design planar-only frame structures. However, the Koch curve can be transformed into its three-dimensional counterpart which is named as Koch lattice, and therefore, it can be applied for developing a new type of spatial structure. With this idea, we modeled a Koch lattice from an equilateral triangle by transforming each side of the triangle into a Koch curve followed by the same fractal process. The plane of the Koch curves of all sides of each new iterated triangle is inclined such a way that they converge into the same point which lies above the centroid of their own triangle.

Figure 10 clarifies the modeling of Koch lattice that is generated by vector-based IFS (Iterated Function System) method which follows two stages. The first stage is the affine transformation of the triangle and the second stage is the continuous repetitions of the same transformation on newly resulted triangles. Three vectors as vertices v_1, v_2, and v_3 define the equilateral triangle T_0 whose centroid is c_0. Starting with affine transformation, each side of the triangle is divided into three segments which generate m_1 and m_2 internal points such a way that the distances of m_1 and m_2 from v1 are (a/2 - a/10) and (a/2 + a/10) respectively where a is the length of each side of the triangle. Similarly, m_3, m_4, m_5, and m_6 were also obtained. Meanwhile, the centroid c_0 is elevated vertically by h unit along the local Z-axis with respect to the plane of the equilateral triangle T_0, whereas $h = a \cdot \sqrt{3}/2$. All the internal points are then connected to c by straight lines which create six new smaller equilateral triangles T_1, T_2, ….., T_6 (shown as shaded), thus completing the first stage. In the second stage, the same process is repeated on each new-born triangle considering that all the vertices of each new triangle are again v_1, v_2, and v_3. Figure X shows three generations of the Koch lattice. The Koch lattice has the advantage of having self-similar geometric character which is potentially useful if applied in designing a unique modular spatial structure.

Similarly, the structural analysis against dead load and 0.1 kN to each nodal point is discussed. An equilateral triangle with the side length of 10 m is covered with Koch lattice. The cross section of member is 165.2 mm x 3.8 mm of steel pipe. The supporting points at the corner of the structure are fixed and other nodal points are rigid.

Next, analytical result is discussed. The deflection and diagram of bending moment are shown in Figure 11. The maximum displacement is very small and it is 0.437 cm. It is significant that a maximum bending moment is very small and it is 3.761 kN*m. It seems that a member connected to mappings is a role of tie beam. Also, the amount of members is smaller than that of the above spatial frame, and is about half. That is to say, it is shown that Koch lattice has rationality in the shape as a structure.

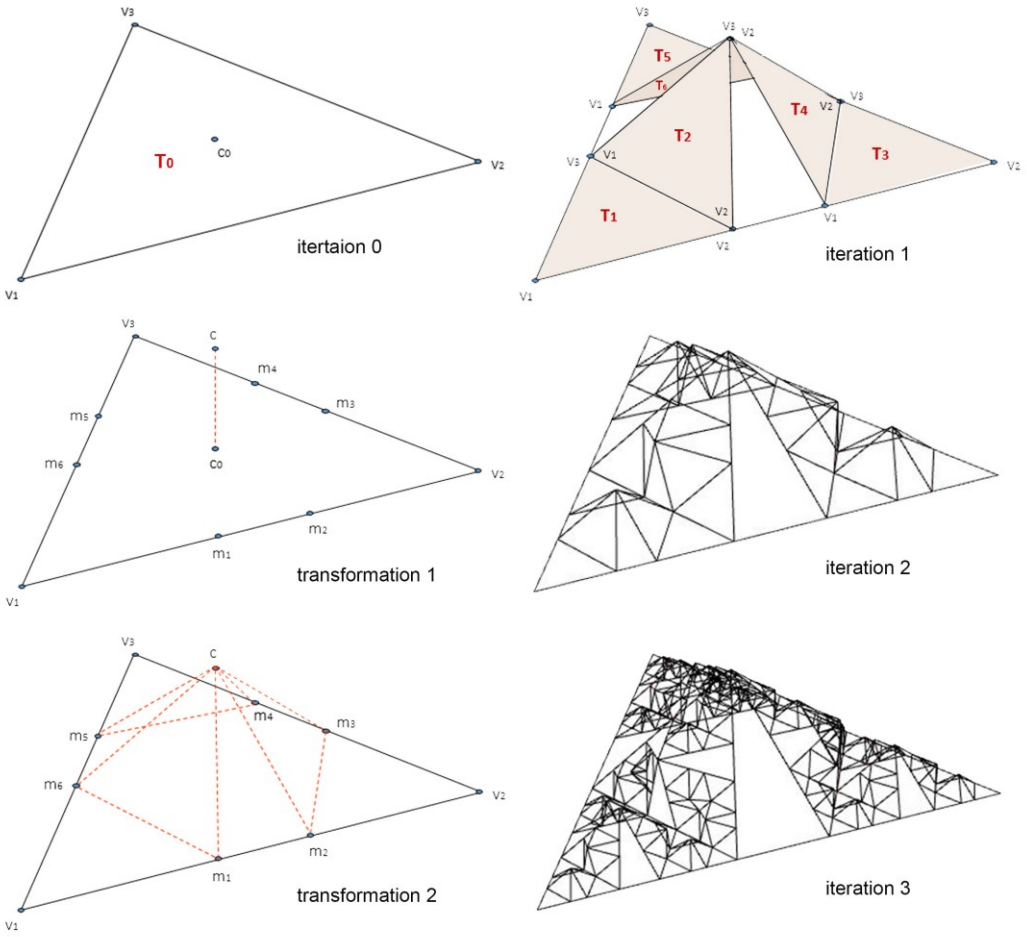
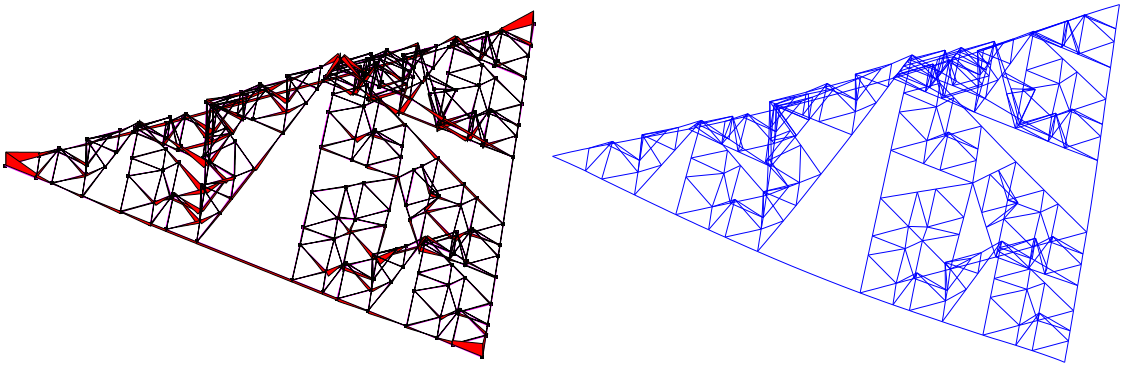


Figure 10: Modeling of Koch lattice on three-dimensional space. Left – Affine transformation, Right – Iterations.



(a) Diagram of bending moment (b) Deflection of structure

Figure 11: Analytical result of Koch lattice

5. Conclusion

In this study, it was examined that the possibility of treating a complex shape that is difficult to apply to architecture based on the Koch curve as an architectural framework. Here, by adding parameters to the Koch curve, it was possible to show a new Koch curve that kept self-similarity while changing the

angles. The variation of shapes and the relationship between fractal dimension and the parameter were cleared, and the basic mechanical characteristics were shown through frame analysis. Although remarkable complexity was lost, shallow ordinary arches with self-similarity were expressed and it was cleared that displacement and bending moment of them were less than other models. In addition, new structural examples were shown extending the Koch curve to spatial frame that had complexity and self-similarity as fractal characteristics.

References

[1] T. MAE and S. ASAYAMA, *Architectural Design and Structure of Computer-generated Arch with Fractal Geometric Form*, *Proceeding of ICCCBE-VIII*, 2000; vol. 1; pp.748-755.

[2] S. ASAYAMA and T. MAE, *Fractal Truss Structure and Automatic Form Generation Using Iterated Function System*, *Proceeding of ICCCBE-X*, Weimar, Germany, 2004.

[3] S. ASAYAMA, and T. MAE, *Geometrical basis and Mechanical characteristics of fractal hexagon dome*, *Proceedings of the IASS Annual Symposium 2016*, 2016.

[4] I. M. Rian and M. Sassone, *Fractal-Based Generative Design of Structural Trusses Using Iterated Function System*, *Engineering Computation*, International Journal of Space Structures 29(4) · February 2015.

[5] N. KISHIMOTO and M. C. NATORI, *Basic Consideration of Structures with Fractal Propertiesand Their Mechanical Characteristics*, Forma 15, pp.113-119, 2000.

Proceedings of the IASS Annual Symposium 2019 – Structural Membranes 2019
Form and Force
7 – 10 October 2019, Barcelona, Spain
C. Lázaro, K.-U. Bletzinger, E. Oñate (eds.)

Architecture and Engineering – education of Form and Force

Karl-Gunnar OLSSON*, Ulf JANSON*, Magnus PERSSON*, Claes CALDENBY*, Jana MADJAROVA*, Morten LUND*, Peter CHRISTENSSON*, Kajsa CRONA*, Paula WAHLGREN*, Mats ANDER*, Chris WILLIAMS*

* Department of Architecture and Civil Engineering
Chalmers University of Technology
412 58 Gothenburg, Sweden
kgo@chalmers.se

Abstract

Inspired by the work and attitudes of architects and engineers like Jörg Schlaich, Renzo Piano, Piero Luigi Nervi, Sverre Fehn, Ted Happold, and environments like ILEK in Stuttgart and ETH in Zürich, a vision of a new kind of architects and engineers arose at Chalmers University of Technology in the early 2000. With support from the university and the branch, a double degree Architecture and Engineering programme was developed. Since the programme started in 2006 it has been a very popular programme, and among all Swedish MSc in Engineering and Master of Architecture programmes it has almost every year been the most difficult programme to get admitted to. The concept of the programme is a 180 ects (European Credit Transfer and Accumulation System) bachelor's degree, where the fundamentals from the engineering science: mathematics, mechanics, physics and materials, is combined with history of architecture and engineering, artistic explorative courses, and the fundamentals of the architectural design process. After three years the students can choose to continue for a Master of Science in Engineering with different possible directions, from mathematics and data science to industrial ecology, acoustics, management, structural engineering, and building technology, or to continue for a Master of Architecture. For the latter they need 150 etcs minimum in pure architectural design projects. In this paper the basic concepts of the programme, the culture developed around it and the strengths we can experience in the examined students will be discussed and reflected. Today students from the programme can be found at architecture and engineering companies all over the world and are appreciated for their ability to address complex architectural and engineering design issues with attitudes, insights and skills from the both professions.

Keywords: Architecture, Engineering, Master of Architecture, Master of Science in Engineering, dual degree, education, mathematical sketching, form, force.

1. Introduction

Architects and engineers represent two strong professional cultures with a common history. Since the renaissance and the subsequent emergence of the modern engineering science, they have evolved in different directions to form different roles in the design, construction, and management of the built environment. The educations of the two professions have followed this development, and a comparison of the criteria for the professional degrees Master of Architecture and Master of Science in Engineering shows today great differences in what knowledge and skills are expected for each of the professions. With inspiration from the Structural Engineering and Architecture dual honours degree programme at the University of Sheffield in the UK [1], and influence from the joint Department of Architecture & Civil Engineering at Bath University, a double degree Architecture and Engineering

Copyright © 2019 by the authors.
Published by the International Association for Shell and Spatial Structures (IASS) with permission.

programme started to be shaped at Chalmers. The Bath course is not a joint degree, but there is a close interweaving of the courses, particularly in the design projects and Mike Barnes took over as Professor of Civil Engineering after Ted Happold retired. In the Swedish context Chalmers University of Technology have a governmental assignment to educate students for Master of Architecture and Master of Science in Engineering. There were at Chalmers many directions in engineering but just one in architecture. In dialog with different stakeholders, among them the Swedish Association of Architects, the new direction in architecture took shape. In the fall of 2006, the new programme welcomed its first class of students. Since the very first class it has been a popular programme, and among all Swedish MSc in Engineering and Master of Architecture programmes it has almost every year been the most difficult programme to get admitted to.

The basic idea is that the programme gives the students the opportunity to reach both a Master of Architecture (MArch) and a Master of Science in Engineering (MScEng), and, that regardless of their degree, they acquire knowledge, tools and approaches from the two cultures. The emphasis is placed on general methods, tools and attitudes, and that a culture is formed around the programme that challenges and arouses desire for individual pathways also in the outlands of a traditional architecture or engineering education. So, a new group of architects and engineers can be formed to contribute to the future challenges for a sustainable built environment.

2. Composition of the programme

The concept of the programme is a 180 ects bachelor's degree, where the fundamentals from the engineering science: mathematics, mechanics, physics and materials, is combined with history of architecture and engineering, artistic explorative courses, and the fundamentals of the architectural design process. After three years the students earn a BSc in Architecture and Engineering and can then choose to continue for either a Master of Science in Engineering (MScEng) or for a Master of Architecture (MArch). By completing two master's programmes, a student can meet the requirements for both a professional architecture and engineering master's degree.

For a MScEng there are several possible directions, from mathematics and data science to industrial ecology, acoustics, management, structural engineering, and building technology. Currently the following MSc programmes are offered at Chalmers:

MPCAS	Complex Adaptive Systems
MPDCF	Design and Construction Project Management
MPDSC	Data Science
MPENM	Engineering Mathematics and Computational Science
MPLOL	Learning and Leadership
MPSEB	Structural Engineering and Building Technology
MPSOV	Sound and Vibration
MPTSE	Industrial Ecology

For a Master of Architecture, a master programme in Architecture is required together with a minimum of 150 etcs in pure architectural design projects. Currently the following MSc programmes are offered at Chalmers:

MPARC	Architecture and Urban Design
MPDSD	Architecture and Planning Beyond Sustainability

Engineering courses, architectural courses and architectural projects

The bachelor's level consists of three types of courses: Engineering courses, architectural courses and architectural design projects. The engineering courses provide basic knowledge and skills in mathematics, applied mechanics, structures, indoor climate design, and materials science. The architectural courses provide basic knowledge and skills in architecture and engineering history,

communication and digital tools and in an artistic approach. In parallel with courses, a series of architectural projects are running with gradually increasing complexity. The architecture design projects are characterized by iterative processes where alternative designs are tested against formulated programmes, qualities sought and set criteria, and where the ability to be able to reflect upon, evaluate and motivate design choices made, is continuously developed.

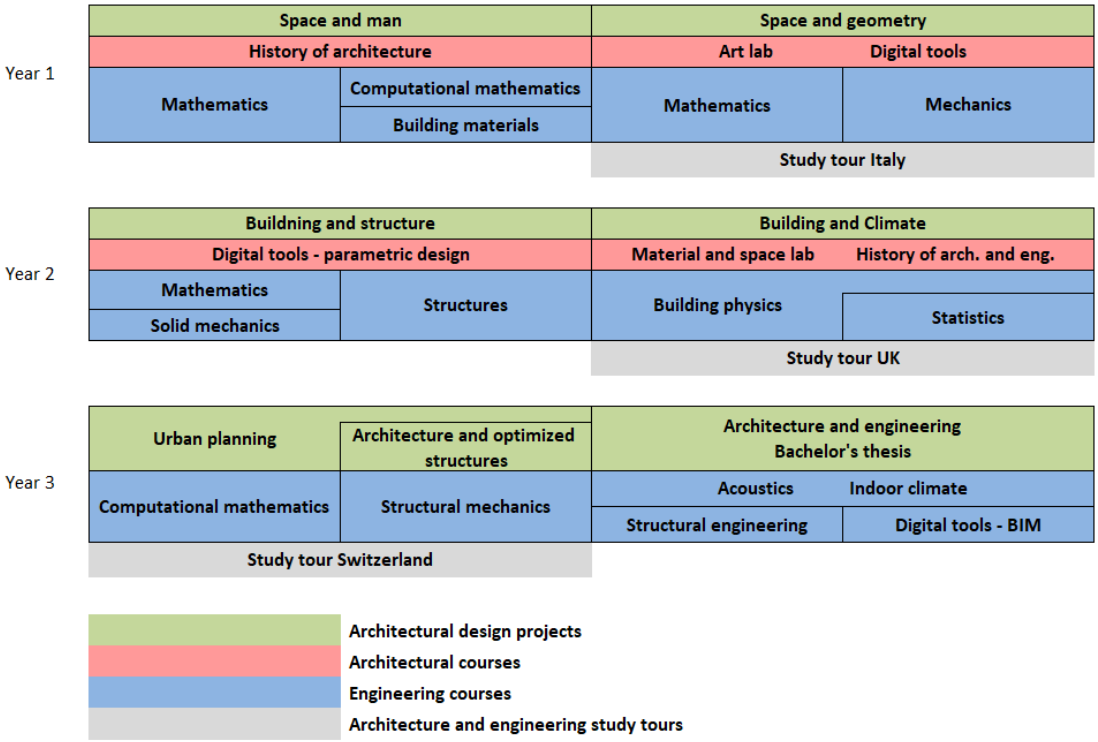


Figure 1: Architecture and Engineering year 1-3 (Bachelor's level)

Border areas that both enrich and secure the independence of the two knowledge cultures

The programme plan is designed in such a way that there are prepared interfaces between architectural projects and parallel running architectural and engineering courses. Programme management and concerned teachers continuously develop these border areas and specific learning outcomes are formulated. The theories and questions of the courses seek applications in architecture design project tasks which in return offers a focus on these issues within the framework of the respective projects. The outcome of the course exercises are results of requested investigations for the architectural design project and given space in presentation of the project. In the planning and implementation of these interfaces, teachers from different knowledge cultures learn about each other's goals and methods. Autonomy around goals, methods and values of the own knowledge culture is respected, while the wider context the other culture offers enriches in both directions.

Voluntary Courses

The programme plan also includes eight voluntary courses. These stimulate students to develop their skills in physical and digital design and production tools, to broaden their reference frameworks around the field of architecture and engineering, and to meet the two professions. Through the format of the voluntary courses, these relatively simple can be adapted to rapid changes of knowledge and tools. Several of them have developed in an international direction by forming formal frameworks around study tours, international workshops and internships.

3. Educational culture and attitudes

Mathematics and Mathematical Sketching

Mathematics is the fundamental language and tool of engineering. The Architecture and Engineering programme therefore follows almost the same mathematics as other engineering programmes at Chalmers and in joint courses if possible. Many of the buildings of architectural history have, both for their production and design, relied on geometric knowledge. To be able to read these works today, get inspiration from them, and possess tools that in new design can explore the possibilities of geometry, there are elements of geometry inlaid in the curriculum and learning objectives. Knowledge and skills in geometry can open the eyes to proper functionality, efficient production and good architectural design. As an analogy to the architect's exploratory sketching, the concept of "mathematical sketching" has been coined for the programme. This emphasizes the presence of mathematics in an exploratory design process and the strength of using mathematical algorithms to carry out rapid investigations. To the architect's design process has been added a traditional engineering tool, but here often for other issues and for other purposes. The courses in computational mathematics and learning outcomes concerning training in the use of mathematical software form a basis for this approach to mathematics. The optional course Virtual Tools in a Material Culture and recurring guest lectures, workshops and conferences contribute to strengthening the approach and desire for mathematics.

Architectural design projects

The architecture design projects are a sequence of courses that most clearly distinguishes the programme from other engineering programmes. Seven architectural projects run continuously through the education's bachelor level. The projects examine the students process and how this interact with the presented and communicated results. During the initial projects the process is highlighted. It is only in the bachelor’s thesis that the result is a more significant part of the examination. Examiners in design projects are mainly teachers who have been recruited from the profession. The examination takes place in two steps. First, a critique of the proposed design proposal, how it is communicated and how it responds to the challenges and issues of the task. This is followed by a so-called portfolio critique where the student explains an reflect upon their design process, which explorations that have been made, how these have influenced design choices and then final results, what are good and what could be developed or made differently. In consultation with the supervisor, the examiner makes a comprehensive assessment of the process, presentation, results and ability to self-reflection. At the bachelor’s level there is no grading. This is because design ability is an individual and nonlinear maturing process where different students final level is impossible to assess in the early projects.

Each year of the bachelor's level of the Architecture and Engineering programme has a theme, a topic, that describes focus and increasing complexity of the architectural design projects. During the first year the theme is *space*. Here the concept of space and the ability of the senses to perceive the different shades of space and matter are trained. The second year has the theme *building*. Rooms are organized into functional spatial connections and buildings into technical systems. An overall approach is empathy: being able to think into different people's circumstances and needs. The theme of the third year is *architecture* and contains two key elements: context and concept. Based in the first two years of study tours and in the courses in Architecture and History of Technology, a more systematic approach to these concepts and their application in architectural projects is being developed.

Communication and scientific writing

The Architecture and Engineering programme has to do with expected skills and abilities from the both professions. Here, the education draws a conscious advantage of the students being trained in both professions' forms of communication and have the ambition to expand and develop them both in

parallel. This in knowledge that an engineer who masters the architectural profession's formats and tools for communication becomes a better engineer and vice versa.

Communication in the form of a reflective dialogue is fundamental for the development of an architectural design project. This is trained during the different phases of the project: in concept studies where different ideas are tested and developed, in the sketch phase where these ideas are shaped and connected to contexts and more precise preconditions for the project, and further in a processing phase where chosen concepts guide the development and materialization of the project. In the early architectural projects, it is primarily the student's internal dialogue and dialogue between student and supervisor (experienced architect and engineer) who is trained. Through some of the projects, this reflective dialogue is also developed between students within a student group. During the bachelor's thesis, the groups are composed of two architecture and engineering students and one engineering student from the master programme Sound and Vibration. Thus, the dialogue is developed to include students with different knowledge backgrounds, all of which are needed for the project. When a general architectural design project is presented, a proposal is communicated with a specific target group. Each design project in the programme ends with a critique where the student orally and with the support of posters and physical models communicates and discuss the proposal. Often the critique group includes representatives from the profession and sometimes also stakeholders. During the critique, the student should be able to communicate and defend the project's intentions and underlying values, how it handles its contexts, how it could be experienced by its users, how it works as a technical system, etc. The presentation format is usually a poster in A1 or A2 size with drawings, perspectives, model photos, diagrams and texts that together organize a narrative of the project. The students are also encouraged to add physical models that further explains the project. This communication involves the knowledge and expectations of a specific recipient being able to be read by the student. With an oral rhetoric supported by prepared posters, the student should be able to convince recipients with different backgrounds about their project's qualities. This ability to communicate is gradually built up through the architectural design projects and by the composition of critic groups.

Within the engineering culture there is a similar form of communication, but which is aimed at an anonymous reader who can be a general audience or a defined professional target group, such as the scientific community. It can be an essay around a chosen theme, a design programme for a building, a technical report, or a scientific article. It may also be a competition submission that is to be assessed by an unknown jury. A characteristic of this form of communication is that it takes its departure in a format and that the education is about understanding the frames and possibilities of this format. Examples of different types of communication that are trained during the bachelor level are: Poetical texts that capture and express impressions and feelings – Exploring Material and Space course. Written essay with notes and references – History of Architecture and Technology course. Technical report – Building Physics course. Environmental programme for the bachelor thesis project – Indoor Environment and Climate Systems course. Communication of design proposals and the reflections in the portfolios – all architectural design projects.

Ethics and responsibility

Questions regarding ethics and responsibility are deeply enshrined in the architecture profession. One of the most important driving forces for an architect is the awareness of how the different design choices will influence both people's everyday lives and the global sustainability. Ethics and responsibility are then obvious starting points and inextricably linked with the design process. The maturity of the students happens through the increasing complexity of the architectural design projects: in the capacity of reading the material, social, cultural and economic contexts, and through the growing awareness of which values they through design choices prioritizes in their proposals, and as an ethical analysis, which ethical foundation there is behind. In the different architectural design

projects, this reflective capacity is gradually built up, requested in the learning outcomes, and examined in reflective so-called Portfolio critics. Other ethical dilemmas present in the educational culture but not explicitly examined are the relations with professional colleagues linked to the artistic creation and the copyright that follows, and the relation to a client – about the loyalty for the assignment.

The study tours



Figure 2: Valtschielbach Bridge, Switzerland, Maillart - acoustical experiment

Studies of buildings and bridges in their real environments are and have throughout history been a central part of the education and formation of the architect. Experiencing architecture in its full and complex context can in-depth raise questions about the architecture's site-specific conditions and how the building and spaces has created different values – economic, social, cultural and ecological. The Architecture and Engineering programme have three main study tours in its curricula; Turin, London/UK and Switzerland. During these study tours, especially the industrial and technological development and the history of new materials interplay with architecture and engineering. The study tours are also tools for creating and developing connections to exemplary international architectural and engineering offices as well as education and research environments. In London, the students regularly are welcomed at Foster + Partners and Buro Happold, leading international architects and engineering offices. Former students and current interns from the programme then use to show up. The tours in year one and year three are shared by a course and a project, partly to be able to contribute to the interfaces described above, and partly to keep the cost of travel at a reasonable level for each course. The integration of study tours into the education is described in the prefaces of the

diaries published every year after the London/UK trip, and in the 10th Anniversary Book of Architecture and Technology [2], where the study tours have been given a large space.

International profile

The Architecture and engineering programme have a high ambition for a strong and clear international profile. The programme includes three elements that each contribute together: International guest lectures and workshops. Study tours with visits to international architects and engineering offices and in educational and research environments. International internship of at least six months in qualified environments. Within the programme, and not least through the voluntary courses, structures have been created which support and encourage this.



Figure 3: International workshop in the atelier with parallel physical and digital modelling

4. Learning Environments

In connection with the rebuilding of the Architecture and Civil Engineering buildings at Chalmers, completed in autumn 2017, a special focus was placed on the common learning environments for the entire field Built Environment. This resulted in joint lecture halls, training rooms, computer labs, libraries with reading places, workshops, and ateliers. In parallel the Architecture and Engineering programme also created a local learning environment for the specific needs of the programme. Important concepts for this environment was: The microlab aimed to be the programme's hub with a simple kitchen, space for hanging, a common bookshelf, recycling boxes for model materials, resistant disks and hand tools for physical model building. The Architecture and Engineering corridor, filled with boards for work sketches, project proposals, and inspiring exhibitions. The drawing spaces where mixed classes from different years allowed for crosstalk and informal support between the classes, with space for storage to all but a limited number of desks to prioritize teacher time before room costs and to create a tightness that requires cooperation and compromises.

5. Conclusions

Since the Architecture and Engineering programme started in 2006 around 150 students have reached a Master of Architecture and/or a MSc in Engineering degree, and among them around 30 percent a double degree. They are today appreciated employees at both architecture and engineering offices, national and international. Several master's theses have reached a level that qualified them for presentation at international conferences. Students from the programme have taken key roles in the organizing of international workshops and conferences at Chalmers, Smartgeometry 2016 and Advances in Architectural Geometry 2018. With their bachelor's thesis projects, they have participated in the international Student Design Competition organized by Acoustical Society of America (ASA) together with students from the Sound and vibration programme at Chalmers. So far, they have won the competition seven times. The concept of letting students grow in an environment characterized by both the fundamentals from the engineering science and the fundamentals of the architectural design process has shown to be successful.

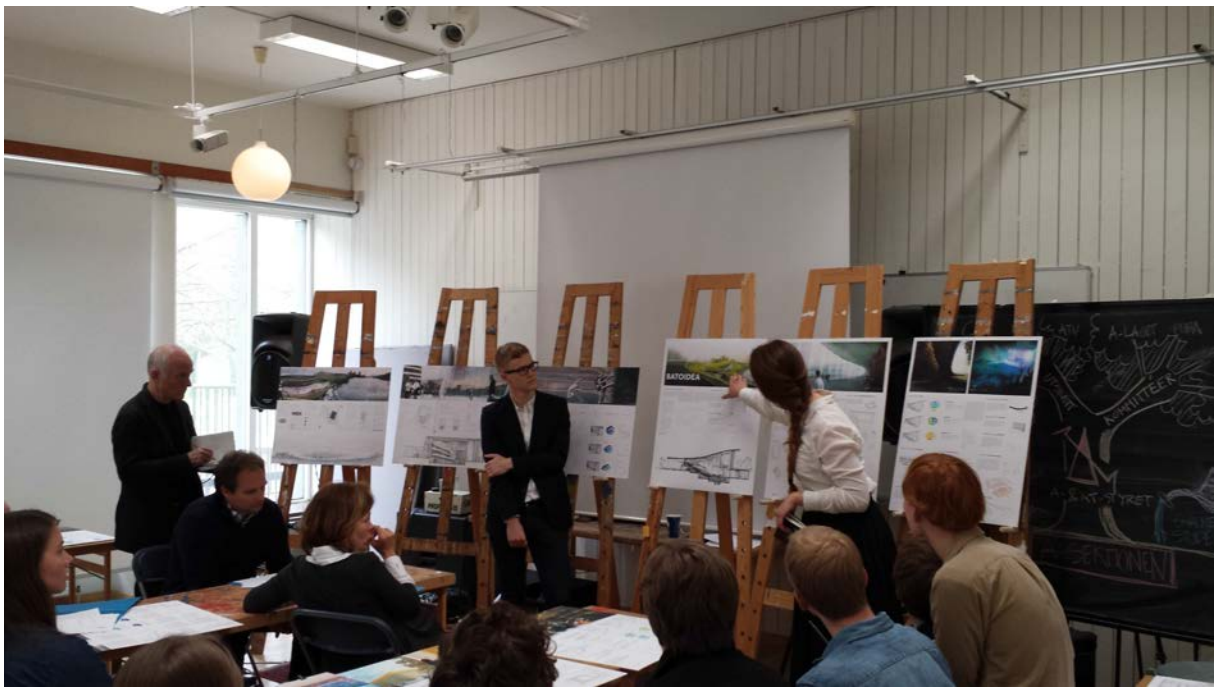


Figure 4: Winning project in the Acoustical Society of America Student Design Competition

References

[1] O. Popovic, J.B. Davison and A. Tyas. Architecture and Engineering – A Joint Education at Sheffield University, *International Journal of Space Structures – Special Edition on Teaching of Space Structures*, ed. J.Chilton, July, 2002.

[2] C. Caldenby, O. Borgström**,** K.-G. Olsson**,** U. Janson**,** M. Lund**,** J. Dahlberg and Johanna Isaksson, *Architecture and Engineering - 10 Years Anniversary Book*, Chalmers, 2016.

Proceedings of the IASS Annual Symposium 2019 - Structural Membranes 2019
Form and Force
7-10 October 2019, Barcelona, Spain
C. Lázaro, K.-U. Bletzinger, E. Oñate (eds.)

Isogeometric analysis and form finding for thin elastic shells

Joel Hilmersson*, Jens Olsson[b], Mats Ander[a,b], Fredrik Larsson[a]

* Chalmers University of Technology
SE-412 96 Gothenburg, SWEDEN
Joelhi@student.chalmers.se

[a] Chalmers University of Technology, Department of Industrial and Materials Science
[b] Chalmers University of Technology, Department of Architecture and Civil Engineering

Abstract

Recent developments within the design of shells have seen an increased interest in utilizing active bending as form giving procedure [1]. This enables complex structures to be built from simple off-the-shelf materials. However, forming bending-active structures is highly dependent on the material properties, which makes the design process reliant on either physical testing or digital simulations. An associated problem with the simulation of this behavior is the lack of integration between modeling and analysis in conventional simulation techniques, a crucial concern since the final design is always an equilibrium shape with requirements on both structural and spatial integrity. IsoGeometric analysis (IGA) is a method that aims to bridge precisely that gap between analysis and design, making it a suitable method for bending active structural design. This paper suggests an approach to the modeling and digital design of actively bent shells using the implementation of nonlinear IGA. Further on, two different ways of controlling the geometry, either by tracing the process *forwards* or *backwards* during the construction procedure are proposed. Tracing the process forwards returns an implicitly controlled shell geometry through stepwise displacement of the boundaries of a flat sheet. However, as a design approach, one is often interested in explicitly controlling the final geometry by a *backwards* tracing. This allows the designer to start from a desired outcome and instead tailor the material to approximate this desired form. The procedure is tested in a case study where a combination of both *forwards* and *backwards* tracing is included. Both processes apply the Kirchhoff-Love shell theory [6] and uses the total Lagrangian formulation for the nonlinear computations.

Keywords: Isogeometric analysis, form finding, active bending, shell design

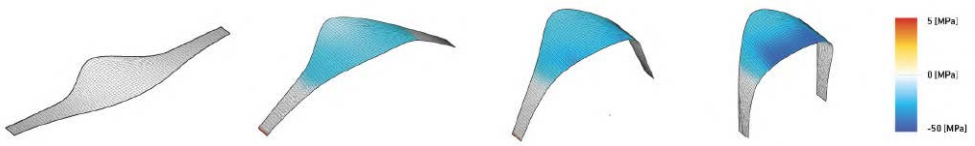


Figure 1: Process of forming a flat sheet (l) into a predefined form (r) showing stress in the bottom fibre.

Copyright © 2019 by Joel Hilmersson
Published by the International Association for Shell and Spatial Structures (IASS) with permission.

1 Introduction

The initiative behind this paper lies in an interest to continue exploring the integration of structural design and architectural geometry, and furthermore the application of elastic bending deformation as a form giving procedure. Isogeometric analysis (IGA) is the main technique applied including a non-linear Total Lagrangian (TL) -formulation. The main body of the work can be found in this master thesis project[4]. The first part of the paper gives a short introduction to IGA and the concept of active bending including the specific numerical methods applied. The second part describes the implementation of two different techniques for how to integrate IGA based active bending in a design context to assist in the search for efficient shell structures. The modes of controlling the outcome of nonlinear elastically deformed shell geometries are illustrated by a test case. Finally a discussion on the potential of these methods, how they can be combined, what limitations have been identified and a recommendation of further work is presented.

1.1 Isogeometric Analysis

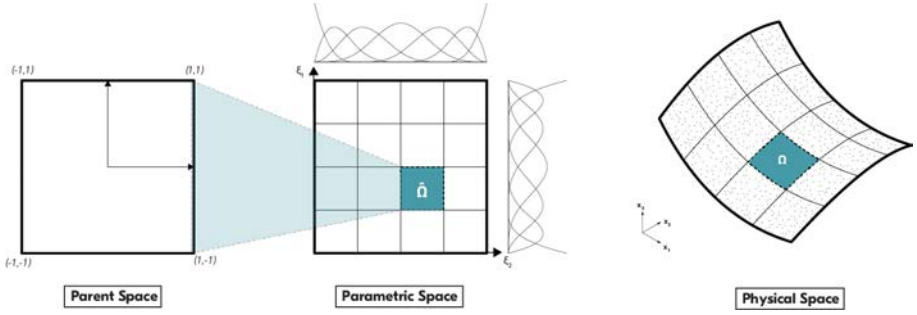


Figure 2: Illustration of the three spaces for a 2D surface that are essential to the IGA configuration.

In Isogeometric Analysis the shape function that describe the distribution of the unknown field variable for the analysis is chosen as the same shape functions that determine the geometry of the object. The most common implementation takes the shape functions of NURBS as point of departure. Isogeometric Analysis was introduced by Huges et. al in 2004 and has since gained a lot of attention [11]. Some implementations into the field of structural design and architecture can be found in [10], [6], [1]. The basic equation behind the shape functions used for NURBS modelling reads,

$$N_{i,p}(\xi) = \frac{\xi - \xi_i}{\xi_{i+p} - \xi_i} N_{i,p-1}(\xi) + \frac{\xi_{i+p+1} - \xi}{\xi_{i+p+1} - \xi_{i+1}} N_{i+1,p-1}(\xi), \tag{1}$$

and is solved using a recursive algorithm, such as Cox-De Boor [8]. For the application of IGA on 2D-surfaces these shape functions are applied in the two parameter direction, each associated with a control point, with the description for the surface S being obtained by a multiplication of the two such that,

$$S(\xi_1, \xi_2) = \sum_{i=1}^{n} \sum_{j=1}^{m} N_{i,p}(\xi_1) M_{j,q}(\xi_2) P_{i,j} \tag{2}$$

where n, m are the number of control points in direction 1 and 2, N, M are the shape functions in the two directions and $P_{i,j}$ is the bidirectional control point net. Figure 2 shows the 3 spaces

used for the Isogeometric formulation. Compared to the standard FE-formulations the main difference with IGA is in the inter-continuity of elements in the parametric space as the shape functions are defined on clusters of elements, referred to as patches. This paper will however only cover the application of single patches.

1.2 Active Bending

The term *Bending active* was coined by Julian Lienhardt [7] and refers to free form structures which get their shape from the deformation of initially planar elements, as shown in Figure 3. It is an attractive approach because of its possibilities to create complex shapes from relatively simple and cheap materials. Similar principles have been used in the design of the Mannheim Multihalle gridshell, the Japaneese Pavillion and the Downland gridshell, where the final shape is achieved by pushing the boundaries together, starting from a flat initial position [9]. However, these examples are multilayered structures where the joints are lose during erection and tightened when the final position is reached allowing for the layers to shear relative to each other as the curvature is increased. The bending active principle can be applied in component level, solar shading blindes etc. [5], [7], [3] and for full scale building such as the examples mentioned.

The construction procedure makes bending active structures difficult to design. The final geometry is a result of large deformations, tying the form, material and construction closely together. The final shape also need to be found as an equilibrium shape, based on the initially planar member. The topic has been subject to much research recently [3] including two workshops at the Advances in Architectural Geometry conference, AAG 2018.

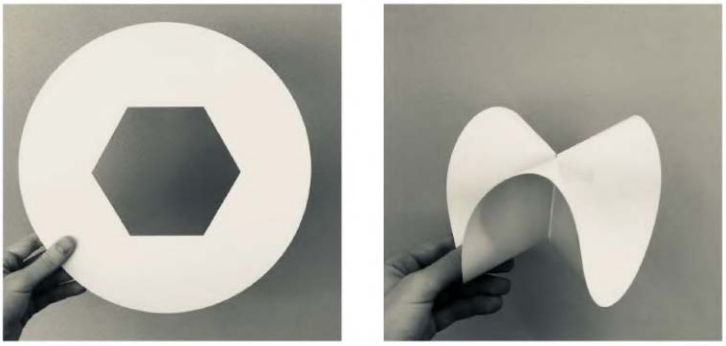


Figure 3: Example of deforming a simple flat cut out into a complex 3-dimensional shape

2 Numerical strategy

Given the large displacements inherent to the design process of bending active structures, a geometrically nonlinear formulation is needed, and since the ambition is to model behaviour of thin shells, Kirchhoff-love theory is regarded a suitable element formulation. The material is assumed to behave elastically, the strains are assumed being small. The total Lagrange formulation, with the second Piola Kirchoff stress tensor and associated Green-Lagrange strain tensor, is used to reference the geometry at time t back to it's initial state at t_0. (As opposed to the updated Lagrangian process which relates the strains back to the previous step) [2]. At any time t, the deformation is traced back to an initial time 0, cf. Figure 4. The state at time $\boldsymbol{0}$ is

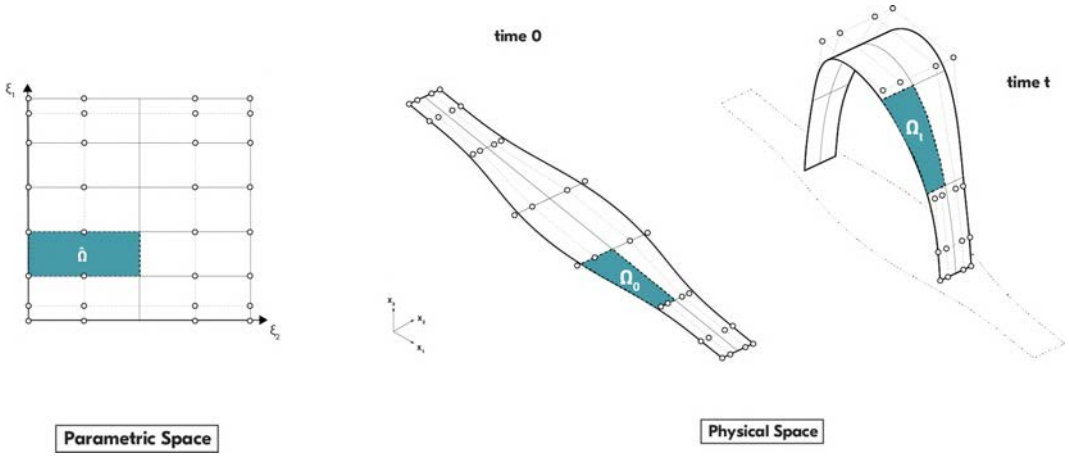
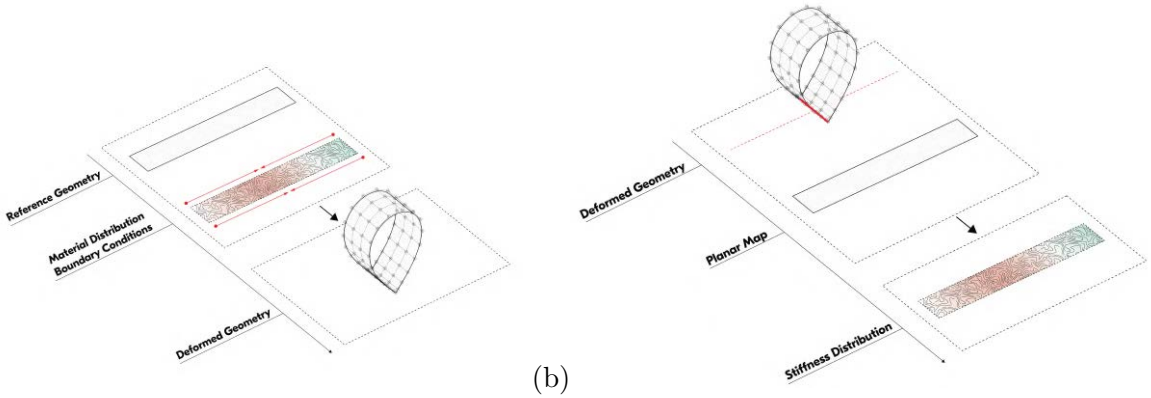


Figure 4: States of Nonlinear analysis

referred to as the reference configuration and is assumed to be represented by the geometry in its undeformed state. The state at time $\boldsymbol{t}$, denotes an arbitrary known step, from which the next and unknown step $(\boldsymbol{t} + \Delta\boldsymbol{t})$ can be computed using the displacement controlled Newton-Rapson (NR) method. For further details the reader is referred to [2] and [4].

Using the total Lagrangian formulation allows for the strains and subsequent internal forces to be computed on any geometry at time t, independent of history. The analysis can therefore be started from any position at any time $\boldsymbol{t}$, given the existence of a undeformed reference geometry.

3 Proposed Design Method



(a) (b)

Figure 5: Diagrams showing input/output for (a) *forwards* vs. (b) *backwards* tracing.

To use the nonlinear formulation as a basis for the design method, one needs to manipulate between the undeformed and deformed geometry. The deformed geometry represents the final design, however, whether this is explictly controlled or an implicit result of the process lies in how the process is traced. If the process is traced in a timewise *forwards* manner the deformed geometry will follow from the reference geometry and the material. Numerically the process can, however, also be traced backwards, instead starting from the desired outcome as an input which enables an explicit control of the outcome. The control of the relationship between

deformed and undeformed will lie in the application of a custom thickness distribution for the flat sheet, defined in the parametric space of the formulation, described as an independent NURBS parameterisation.

Forwards Tracing
In the *forwards* tracing the process, the reference geometry (time $\boldsymbol{0}$) and analysis setup (material map and boundary conditions) serve as the starting point, which is illustrated in Figure 5(a). By tracing the progression in a time-wise forwards process, the form finding will follow the same steps as a potential construction procedure, where an undeformed geometry is deformed into a new configuration. This implicitly controlled form will therefore have a clear physical interpretation. This process follows that of a conventional displacement controlled, nonlinear solution procedure and is shown in Figure 6

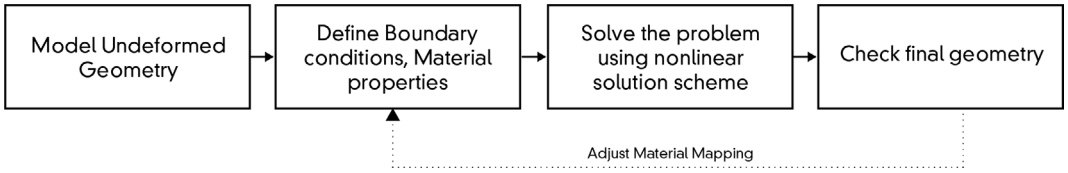


Figure 6: Flowchart for tracing the process *forwards*

Backwards Tracing
Tracing the geometry *forwards* gives an insight to the physical process of construction, but as a design exercise, however, one might want to steer the process towards a desired outcome. Thus, instead of tracing the process *forwards*, one can instead use a modeled reference form at a time $\boldsymbol{t}$ and trace the process *backwards*, by putting the desired geometry in equilibrium using the stiffness. By starting from time t, the designer gains a level of explicit control of the final geometry, instead using the material distribution as the unknown. The process can be broken down in the steps illustrated in in Figure 7:

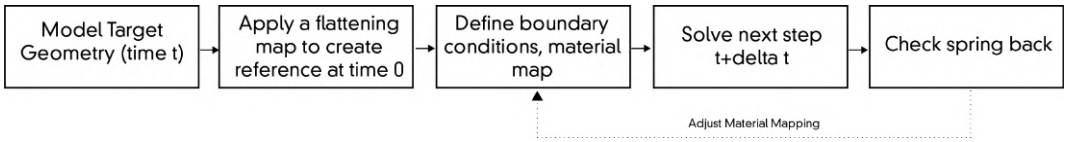


Figure 7: Flowchart for tracing the process *backwards*

3.1 Case Study (Example)

A practical modeling exercise using the aforementioned processes is illustrated in the following case study. It will recreate a modeled design geometry as a physically informed object, thus, embedding stresses and material as part of the design. The process will start from a target form and trace that backwards into a material map, which will further be used to simulate the construction and check correspondance with the desired form. A reference geometry is designed using NURBS, which can be seen in Figure 8.

The process is structured as follows:

1. Model target geometry.
2. Apply flattening map to create a reference configuration.
3. Create a material parameterisation, (in this case NURBS parameterisation).
4. Solve from step t to $t + \Delta t$.
5. minimize "spring back" through adjusting material mapping (in this case done using genetic algorithms).
6. Use the adjusted material map and flat geometry to find an approximation of target geometry.

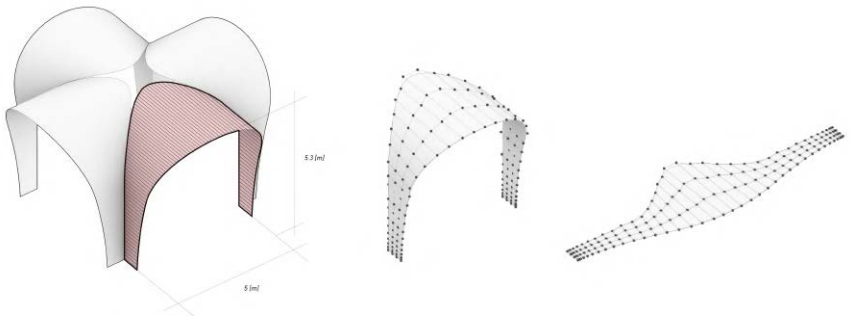


Figure 8: Modeled Design Geometry for the case application (left), Segment (middle), Flattening map (right)

Backwards Step

Going backwards, the process starts with the unrolling of the target geometry into a flat representation. From that, a material distribution is used to minimize the spring back, thus, putting the design geometry in equilibrium. The shell sheet material is parameterized using 2nd degree NURBS polynomials with a domain of thickness 2cm - 14cm, and the minimization is carried out by adjusting the control points of the thickness map using a genetic algorithm. The final material map can be seen in Figure 10. A negotiation is present here between the complexity of the material parameterisation and the final deviation.

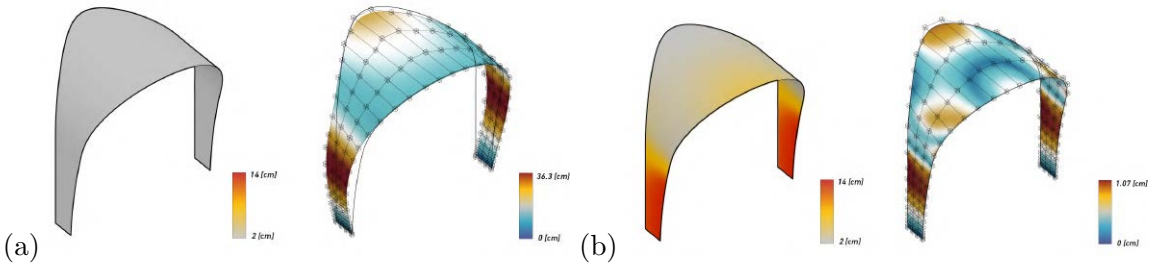


Figure 9: a)Constant thickness distribution (left) Springback (right) b) Adjusted thickness distribution (left) Springback (right)

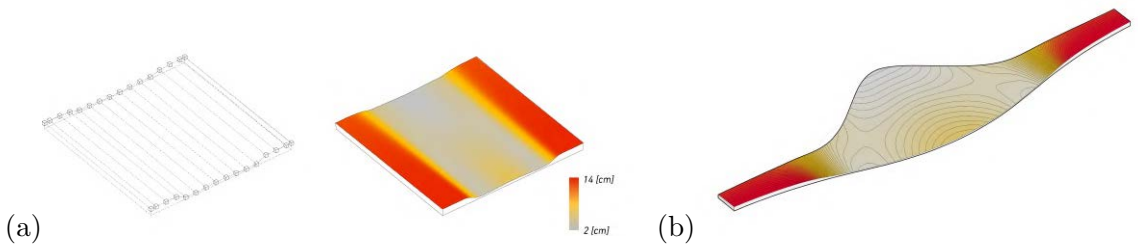


Figure 10: a) Thickness Map b) Distribution on Reference Geometry

Forwards Step

With the acquired material map, the simulation can now be performed in a forwards fashion, which should simulate the construction process and give an indication on how close to the intended geometry the design will come. Further this checks that the desired equilibrium is the one, reached, in the case of multiple possible equilibrium states. The form finding is accomplished by displacing the both ends and pushing them together, without any additional constraints. Some intermediate steps can be seen in Figure 11 a) with the final form of a segment illustrated in Figure 11 b). The final design and stresses are further shown in Figure 12 .

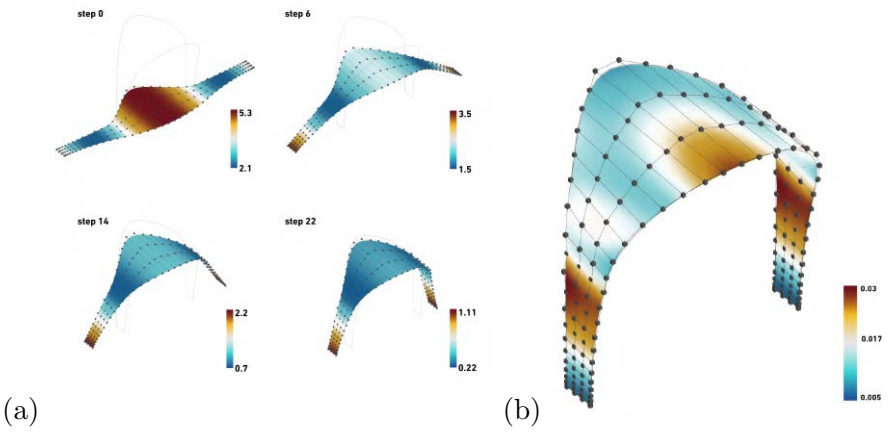


Figure 11: Form finding process / final design. Colors show deviation from target geometry in meters.

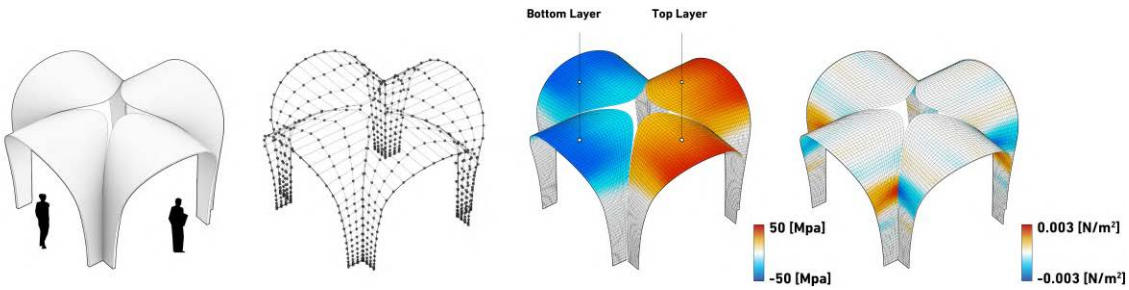


Figure 12: (from left to right) Final form, Final control polygon, Normal stress, Torsion moment

4 Conclusions and Further Work

In contrast to what is mainly associated with the term *form finding*, which is the generation of a form w.r.t a specific load case (e.g gravity) the process presented here instead targets the "load case" of the construction process, and how actively bent geometries can be controlled through the relations between *undeformed geometry*, *boundary conditions and material* and the *final design* as a mix of explicit geometric steering of the nonlinear process. The application of isogeometric analysis opens for new ways of treating the integration between digital modeling and analysis and the paper has shown one application of the integration of physical behaviour and material properties in a modeling context, but there's more potential. The process targets segmented shells and is therefore limited to the use of single patch analysis and further work is needed for multipatch models. As the material map is simply computed using genetic algorithms, the process of acquiring a suitable material distribution for a specific outcome could also be subject to further work.

References

[1] Vedad Alic and Kent Persson. Nurbs based form finding of efficient shapes for shells. In *Proceedings of 29th Nordic Seminar on Computational Mechanics NSCM29*, 2016.

[2] Klaus Jurgen Bathe. *Finite Element Procedures*. 2006.

[3] Julian Lienhard, Christoph Gengnagel. Recent developments in bending-active structures. In *Conference: Creativity in Structural Design, annual Symposium of the IASS International Association for Shell and Spatial Structures, Boston 2018*, 2018.

[4] Joel Hilmersson. Isogeometric analysis and form finding. Master's thesis, Chalmers University of Technology, 2019.

[5] Jan Knippers, Florian Schieble, Matthias Oppe, Hauke Jungjohann. Bio-inspired kinetic gfrp-faade for the thematic pavilion of the expo 2012 in yeosu. In *Proceedings of IASS-APCS Symposium 2012: From Spatial Structures to Space Structures*, 2012.

[6] Josef M. Kiendl. *Isogeometric Analysis and Shape Optimal Design of Shells Structures*. PhD thesis, The Technical University of Munich, 2011.

[7] Julian Lienhard. *Bending Active Structures*. PhD thesis, University of Stuttgart, 2014.

[8] Les Piegl and Wayne Tiller. *The NURBS Book*. Springer-Verlag, New York, NY, USA, second edition, 1996.

[9] Dragos Naicu, Richard Harris, Chris Williams. Timber gridshells: Design methods and their application to a temporary pavilion. World Conference of Timber Engineering, 2014.

[10] J. Kiendl, K.-U. Bletzinger, J. Lienhard, R. Wuchner. Isogeometric shell analysis with kirchhoff-love elements. *Computer Methods in Applied Mechanics and EngineeringSeptember*, 2009.

[11] J.Cottrell, T.Hughes, Y.Bazilevs. *Isogeometric Analysis - Toward Integration of CAD and FEA*. Wiley, 2009.

Proceedings of the IASS Annual Symposium 2019 – Structural Membranes 2019
Form and Force
7 – 10 October 2019, Barcelona, Spain
C. Lázaro, K.-U. Bletzinger, E. Oñate (eds.)

Mike Barnes's legacy: the emergence of form finding and analysis approaches for bending active and elastic gridshell structures

Sigrid ADRIAENSSENS*[a]

*[a]Department of Civil and Environmental Engineering, Princeton University
Engineering Quadrangle, E332, Princeton 08544 NJ, USA
sadriaen@princeton.edu

Abstract

In the late 90's, Michael Barnes was the Head of the Department of Architecture and Civil Engineering at Bath University and my Ph.D. advisor. He worked with Chris. J.K. Williams and me on the development of the first three-degree-of-freedom a beam (and later torsion) element, that could be incorporated in non-linear finite difference methods such as dynamic relaxation. This work enabled the form finding and analysis of a new type of structural system, namely active bending structures. Using examples, I demonstrate how this work had and continues to have an impact on 1) research, 2) practice, 3) the design community and 4) teaching. Examples, where Mike's algorithms are at work, include the form finding and analysis of tensegrity bending active arches restrained by membranes, prestressed hooped footbridges (research), the steel/glass gridshell over the courtyard of the Dutch Marine Museum (practice), the initial plug-in Kangaroo for the parametric modeling software Rhinoceros (design community) and student design entries for the IASS 2016 Competition for the Young Generation (teaching). The examples I discuss, show the importance of the questions that Mike asked and solved as well as the impact his findings had on the construction industry, the development of new research domains and design thinking of new generations of architects and engineers.

Keywords: lightweight structures, grid shell, bending active, dynamic relaxationMichael Barnes

1. Introduction

Michael (Mike) Barnes was the Head of the Department of Architecture and Civil Engineering at Bath University (UK) in the late 90's. During that period, he was my Ph.D. advisor and I was his last PhD student. In 1994, the National Lottery offered billions of quasi-public funds for Millenium projects to be designed and constructed and in doing so, revived the interest in lightweight structures. Lightweight projects included the Millenium Dome, a large tensile roof (London, UK) and the Eden Project, a gridshell with inflated Teflon cushion (Cornwall, UK). The United Kingdom and the construction industry were filled with optimism about cultural redevelopment and building activity. This context made Mike's research interests and expertise of high societal relevance.

Together with Mike and dr. Chris. J. K. Williams, my other PhD advisor, we developed and validated an algorithm for a beam element that could be incorporated in a dynamic relaxation process, a method that allows for the form finding and analysis of non-linear lightweight structures. This method has been extensively adopted by the contruction industry for the design of membrane and net structures. With the addition of the beam element, the morphogenesis of a whole new series of structures, namely elastic gridshells and even more global "bending active" structures was enabled. I would like to demonstrate the legacy of my work with Mike and Chris on academia (research), industry (practice), design community (service and dissemination) and teaching.

Copyright © 2019 by Sigrid Adriaenssens
Published by the International Association for Shell and Spatial Structures (IASS) with permission.

2. Research: First approaches to Form Finding and Analysis of Bending and Torsion Active structures

First, my PhD thesis resulted in a journal paper "Tensegrity spline beam and grid shell structures", co-authored by Mike and myself [1]. In this paper we presented a numerical analysis based on the Dynamic Relaxation (DR) method which caters specifically for the form-finding and load analysis for structures made of continuous tubular rods forming curved splines. A particular feature of the analysis is that bending components are treated in a finite difference form with three degrees of freedom per node rather than six. This paper lay the basis for further developments of beam and beam/torsion elements for non-linear structures as laid out by Lazaro et al. [2]. The paper also demonstrated the beneficial strain hardening effect in spline or what would now be called "bending active" structures. We also demonstrated the feasibility of the first membrane restrained bending active systems (see figure 1) [3]. Bending active structures has now become a new, large and exciting research domain, also within the IASS Working Group (WG) 15 Structural Morphology. Today, 18 years after that initial paper, the WG15 Active Bending group's mission is to "to support a focused exchange for engineering researchers and practitioners that share exploiting elastic bending as a means to generate curved geometries from initially straight or planar building elements."

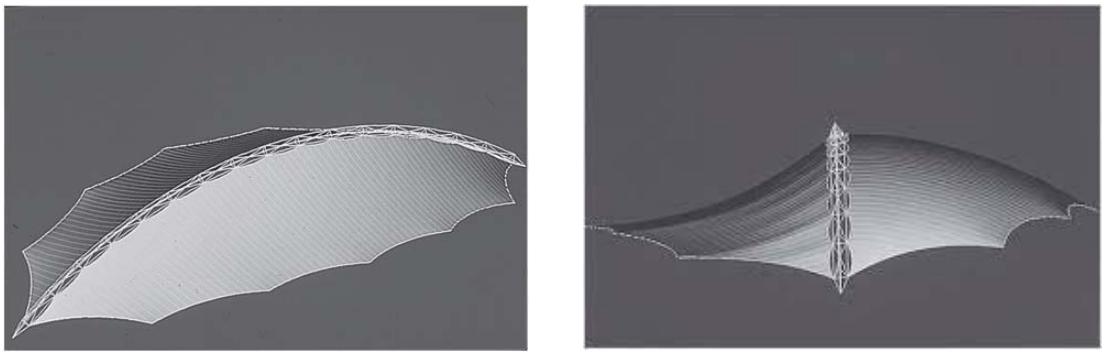


Figure 1: Tensegrity bending active arch restrained by a prestressed membrane perspective (left) and under asymmetric wind loading (right).

Much later, when I was an assistant professor at Princeton University, Mike and I and a grad student published a follow-up paper "A novel torsion/bending element for dynamic relaxation modeling' [4]. This paper proposes and validates a three degrees of freedom element formulation that accounts for torsion and transverse bending of three-dimensional curved elements in explicit numerical analyses methods (such as DR). Using finite difference modeling, in-plane distortions and moments, the increment of twist (and hence torsion) and out-of-plane bending deformations are determined. This new algorithm allowed us to form find and analyse the engineering feasibility one of Mike's original design for a cable-stressed hooped footbridge (See Figures 2, 3 and 4). He had proposed this design in his graduate thesis and we were now able to numerically form find and design it.

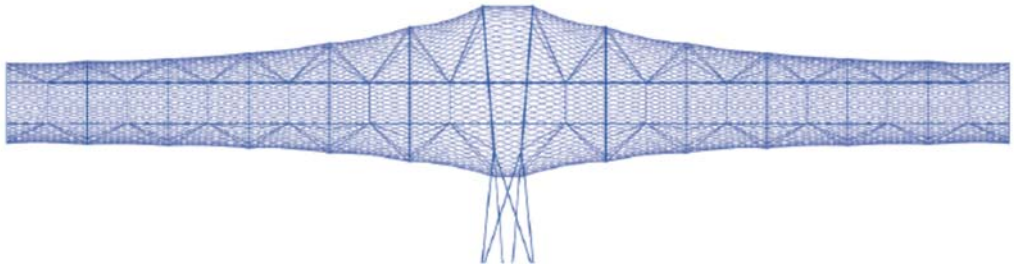


Figure 2: Elevation of structural model of prestressed hooped footbridge.

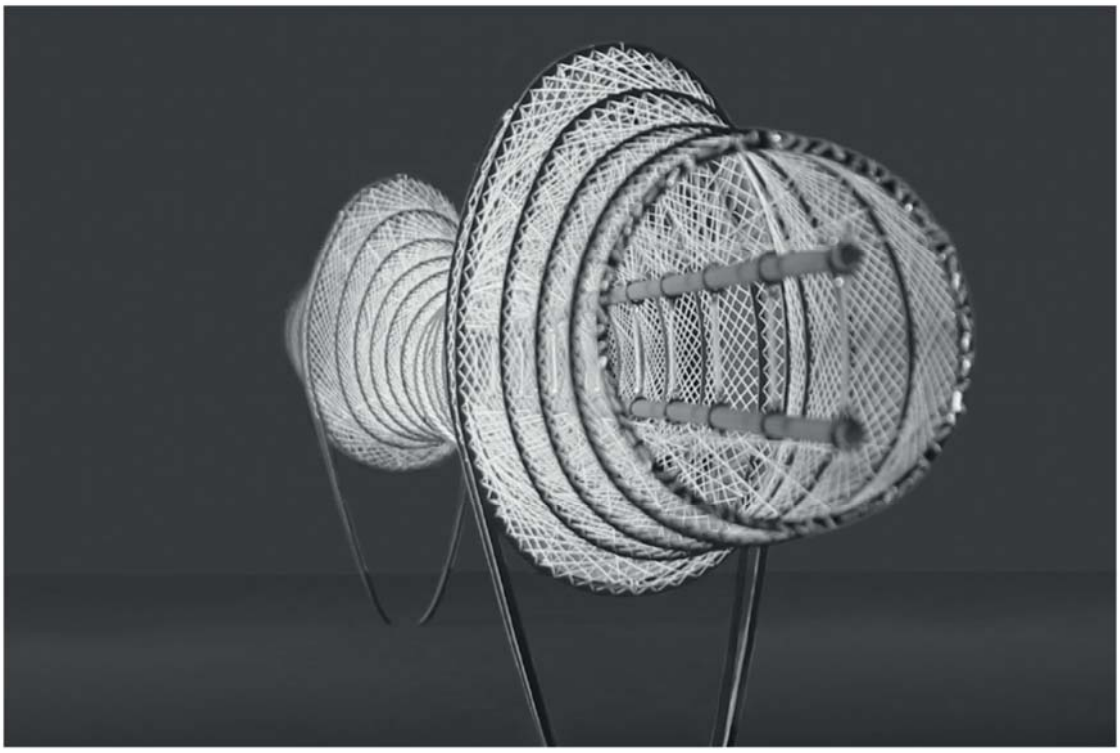


Figure 3: Perspective of physical model

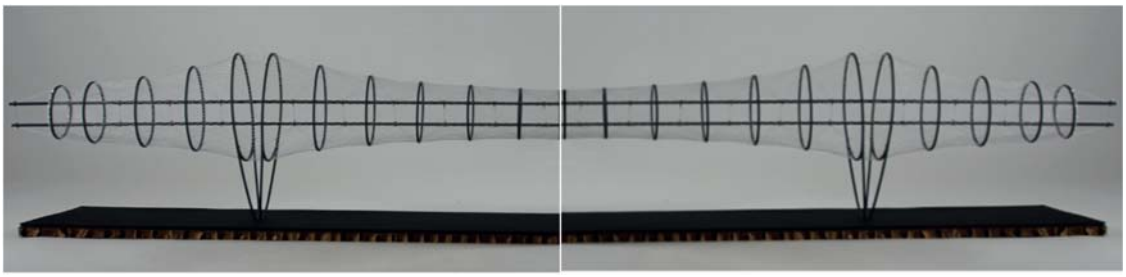


Figure 4: Elevation of physical model

3. Practice: Form Finding of the award-winning Dutch Marine Museum gridshell cupola

The research algorithms I had developed with Mike and Chris, were key to form finding of the realized gridshell cupola over Dutch Marine Museum courtyard (Amsterdam, Netherlands) (See Figure 5). This faceted steel/glass shell resulted from a design competition won by the engineering design firm Ney and Partners and further consulted by Chris Williams. The topology of the shell lattice is based a 17th century loxidrome map, the form of the lattice shell is generated using hanging chain model combined with beam elements to achieve a very efficient form based on a poetic geometric idea [5]. We adopted a construction-driven design methodology that slightly adapts the numerical form found catenary shape with the objective of achieving planarity in all the triangulated, four-sided and five-sided mesh faces. The challenge of facet planarity was gracefully solved by an analytical origami approach which can be compared with finding the Maxwell reciprocal network diagram. The final faceted shape shows elegance and structural efficiency. The grid shell won a number of architectural awards and was lauded for its extreme slenderness, an attribute that could only be achieved through the research algorithms in whose development Mike was key.

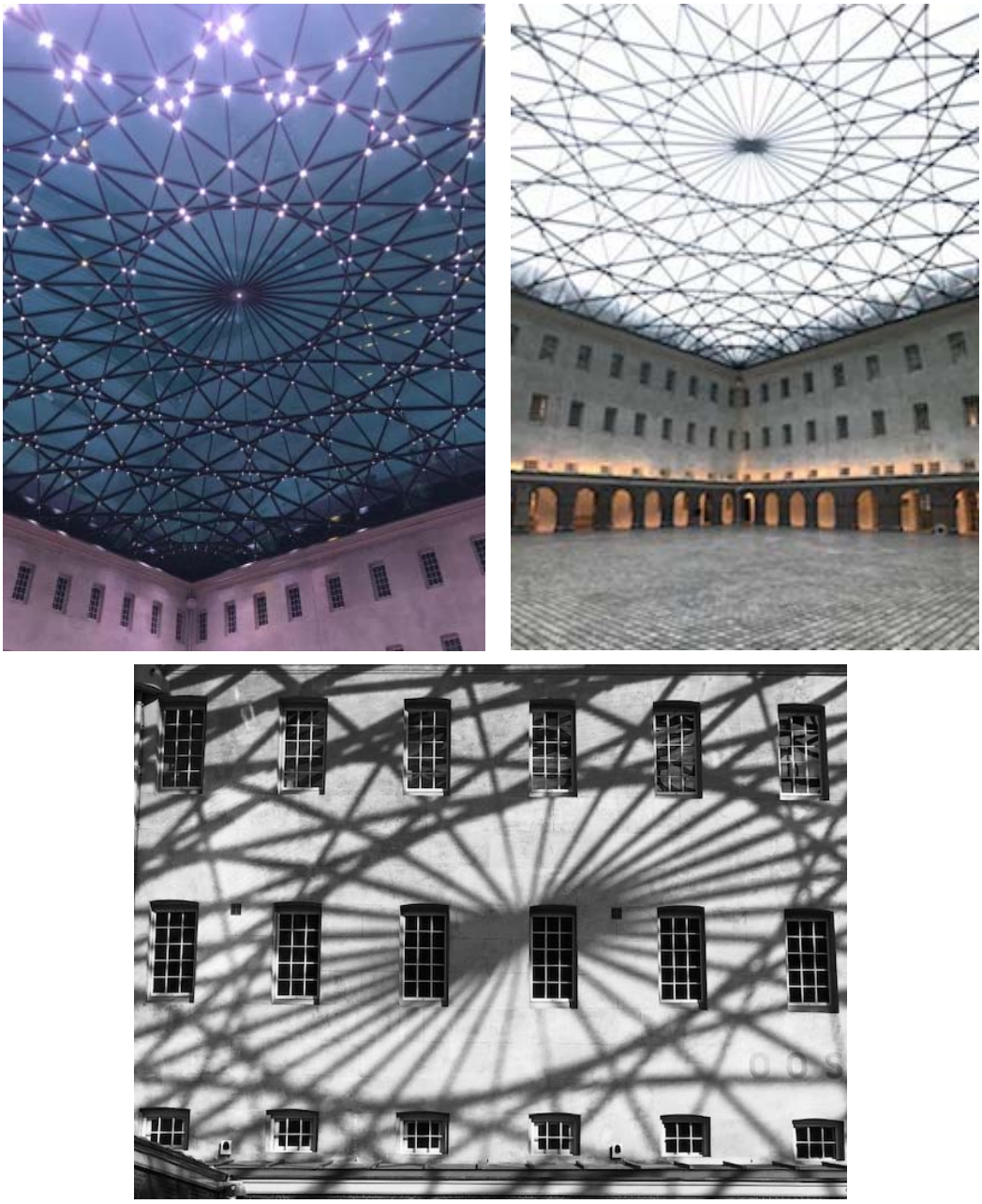


Figure 5: Interior perspective of gridshell cupola over courtyard of Dutch Marine Museum at night (top left) and during the day (top right). Shadow of grid cast ono interior façade (bottom).

4. On-line parametric community: first versions of bending active Kangaroo plug-in in

Finally, the initial paper [1] was picked up by the parametric design community and converted by Daniel Piker into the Kangaroo plugin for Grasshopper. Kangaroo is a Live Physics engine for interactive simulation, form-finding, optimization and constraint solving and has been downloaded more than 350 000 times This large number indicates the tremendous impact, beyond number of citations, the work Mike did, continues to have on the on-line design community. One user, Marten

Nettelbladt, writes on his blog “Never before have I been able to recreate bending geometry so accurately in an "artificial way"” [6]. Kangaroo is taught in many Digital Design Courses in Architecture Schools worldwide.

5. Teaching: Form Finding Courses and Student Design Competitions (1 page)

For example, these algorithms are also being explored in my graduate course “Form Finding of Structural Surfaces” [7], a course offered at Princeton University and inspired by the teaching of Mike and Chris’s “Lightweight Structures” course in Bath. The first part of my course introduces the topic of structural surfaces, tracing the ancient relationship between innovative design and construction technology with the evolution of surface structures. The second part familiarizes the student with tensile membranes. It covers the different types of membrane systems, related physical and numerical form finding methods, materials and construction techniques. The third and fourth parts focus on rigid surfaces and provide a deeper understanding of how form finding techniques can be realized in a contemporary context. To highlight the relationship between the course and practice, a number of guest speakers from the industry have enriched the lecture content by discussing their own realized force-modeled designs with the students. After gaining basic knowledge about surface structures and developing form finding skills in lectures and lab sessions, the final design project is oriented towards the application of that knowledge and skills (while continuing to deepen the knowledge) in a team project. In 2015 the students were asked to design a surface structure roof to cover the grandstands of the Tokyo Olympic Stadium. The form finding algorithms, were tools to develop a wide variety of design solutions. We entered the “Mountainous Gridshell” design of students Mauricio Loyola and Alexander (Olek) Niewiarowski into 2016 IASS Design Competition for Young Generation for the Tokyo Olympic Stadium (See Figure 6). The competition called for a “21st century spatial structure” on the site of the former National Olympic Stadium by Mitsuo Katayama. The competition jury, consisting of professor emeritus Hiroshi Ohmori (Nagoya University), architect Hiroshi Naito, engineer Knut Stockhusen (sbp), professor Ken’ichi Kawaguchi (University of Tokyo, Chair of the IASS2016), and engineer Bill Baker (SOM), considered the innovativeness of the concept system and the soundness of the structure and selected our student team as one of the winners. The impact of Kangaroo (and hence the algorithms) on the parametric design community is difficult to measure but I hypnotize that those algorithms have and will continue to shape contemporary architectural engineering teaching and practice.

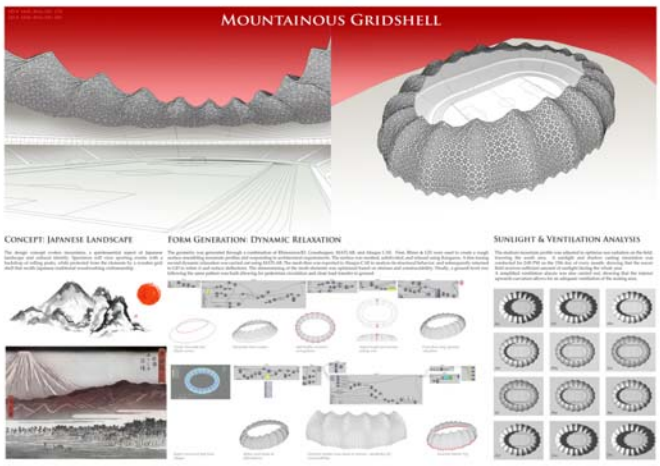


Figure 6: Presentation IASS Competition for Young Generation – Mountainous Gridshell by Mauricio Loyola and Alexander (Olek) Niewiarowski.

6. Conclusion and Impact

The examples I have discussed, show the importance of the questions that Mike asked and solved as well as the impact his findings had on the construction industry, the development of new research domains and design thinking of new generations of architects and engineers. I have shown this legacy only for the algorithms he worked on with me and with Chris, this leaves us to reflect upon the even larger legacy of his entire scholarship.

Acknowledgements

I am very grateful that I had the opportunity to learn from Mike how to be rigorous in research and go in depth of the matter at heart. I miss his jolly conversations.

References

[1] S. Adriaenssens and M. Barnes, "Tensegrity spline beam and grid shell structures", *Engineering Structures,* vol. 23, no. 1, pp. 29-36, 2001. doi.org/10.1016/S0141-0296(00)00019-5

[2] C. Lazaro, S. Monleon, J. Bessini, J. Casanova 'A review of geomtreically exact models for very flexible rods, in *IASS 2018: Creativity in Structural Design, Massachusetts, 2018.*

[3] S. Adriaenssens, 'Feasibility Study of Medium Span Spliced Spline Stressed Membranes', *International Journal of Space Structures*, vol. 23, no. 4, pp. 243-251, 2008.

[4] M. Barnes, S. Adriaenssens and M. Krupka, "A novel torsion/bending element for dynamic relaxation modeling", *Computers & Structures*, vol. 119, pp. 60-67, 2013. doi:10.1016/j.compstruc.2012.12.027.

[5] S. Adriaenssens, L. Ney, E. Bodarwe and C. Williams, 'Finding the form of an irregular meshed steel and glass shell based on construction constraints', Journal of Architectural Engineering, vol. 18, no. 3, pp. 206-213, 2012.doi.org/10.1061/(ASCE)AE.1943-5568.0000074.

[6] M. Nettelbladt, *The geometry of bending.* http://thegeometryofbending.blogspot.com/2011/02/daniel-pikers-kangaroo.html (accessed 5/30/2019)

[7] S. Adriaenssens, R. Pauletti, K. Stockhusen, S. Gabriele, P. Magrone, V. Varano and I. Lochner-Aldinger 'A project-based approach to learning Form Finding of Structural Surfaces', *International Journal of Space Structures*, vol.30, pp. 297-305, no. 3-4, 2015.

Proceedings of the IASS Annual Symposium 2019 - Structural Membranes 2019
Form and Force
7-10 October 2019, Barcelona, Spain
C. Lázaro, K.-U. Bletzinger, E. Oñate (eds.)

Unloaded prestressed shell formed from a closed surface unattached to any supports

Alexander SEHLSTÖM* **and Chris J. K. WILLIAMS**

* Department of Architecture and Civil Engineering
Chalmers University of Technology
412 58 Göteborg, Sweden
alexander.sehlstrom@chalmers.se

Abstract

In this paper we attempt to begin to answer the question, 'under what conditions can an unloaded shell formed of a closed surface unattached to any supports contain a state of membrane stress which can be induced by prestressing?'. We show that a sphere cannot be prestressed, but a torus can be.

Keywords: Unloaded prestressed shell, torus, force surface, moment surface.

1 Introduction

Shells carry loads through a combination of membrane and bending action [1], and both are required to resist buckling. However membrane action is much more efficient than bending action and so membrane action predominates if the shape of the shell and its supports permit it.

Inextensional deformation of a surface is deformation in which the surface is bent, but lengths on the surface do not change, and membrane action alone cannot resist inextensional deformation if the shape of the shell and its supports permit it.

The topic in differential geometry entitled the *rigidity of surfaces* [2, 3] is concerned with surfaces which can, at least in theory, carry loads by membrane action alone and inextensional deformation is not possible. If inextensional deformation is not possible then membrane action is possible for any load case and vice versa. Note that even if inextensional deformation is possible, then membrane action can still apply as long as the load does not 'activate' the mechanism. The form finding of masonry shells relies very much on this principal.

2 Static – kinematic analogy

The static – kinematic analogy or the static – geometric analogy [1] relates the equations of static equilibrium involving loads and stresses to the kinematic equations relating velocities to

Copyright © 2019 by Sehlström and Williams
Published by the International Association for Shell and Spatial Structures (IASS) with permission.

strain rates. Here we will limit ourselves to inextensional deformation and membrane action in an unloaded shells.

It may seem odd that we should be concerned with membrane action in an unloaded shell, but imagine that we have a model of an unloaded shell and we poke it with a finger. Ideally it will resist the poke by membrane action wherever we poke it and whatever the direction. The shell is unloaded, except under our finger and therefore what happens in an unloaded shell is of fundamental importance in resisting the load and transferring the force to the supports.

Table 1 lists the kinematic and static variables, and eqs. (1) to (8) give the two sets of analogous equations with kinematic quantities on the left and static quantities on the right. The equations apply to a surface $\mathbf{r} = \mathbf{r}\left(\theta^1, \theta^2\right)$ in which θ^1 and θ^2 are parameters or surface coordinates replacing the u and v which are often used in order to use the tensor notation for geometric, kinematic and static quantities [4]. The vector $\mathbf{n} = \mathbf{r}_{,1} \times \mathbf{r}_{,2} / ||\mathbf{r}_{,1} \times \mathbf{r}_{,2}||$ is the standard unit normal of the surface in which the subscript $,\alpha$ means $\partial / \partial\theta^\alpha$.

Table 1: Kinematic and static quantities

Kinematic quantity	**Static quantity**
angular velocity, $\mathbf{w}$	force, $\mathbf{f}$
velocity, $\mathbf{v}$	complementary moment, $\mathbf{h}$
complementary velocity, $\mathbf{y}$	moment, $\mathbf{m}$
rate of bending tensor, $\mathbf{B}$	membrane stress tensor, $\mathbf{S}$

$$\mathbf{v} - \mathbf{y} = \mathbf{w} \times \mathbf{r} \qquad \mathbf{h} - \mathbf{m} = \mathbf{f} \times \mathbf{r} \tag{1}$$

$$d\mathbf{v} = \mathbf{w} \times d\mathbf{r} \qquad d\mathbf{q} = \mathbf{f} \times d\mathbf{r} \tag{2}$$

$$d\mathbf{y} = \mathbf{r} \times d\mathbf{w} \qquad d\mathbf{m} = \mathbf{r} \times d\mathbf{f} \tag{3}$$

$$\delta\mathbf{w} \times d\mathbf{r} = d\mathbf{w} \times \delta\mathbf{r} \qquad \delta\mathbf{f} \times d\mathbf{r} = d\mathbf{f} \times \delta\mathbf{r} \tag{4}$$

$$d\mathbf{w} = (d\mathbf{r} \times \mathbf{n}) \cdot \mathbf{B} \qquad d\mathbf{f} = (d\mathbf{r} \times \mathbf{n}) \cdot \mathbf{S} \tag{5}$$

$$\mathbf{B} = \mathbf{B}^{\mathrm{T}} \qquad \mathbf{S} = \mathbf{S}^{\mathrm{T}} \tag{6}$$

$$\mathbf{b} \cdot \cdot \mathbf{B} = 0 \qquad \mathbf{b} \cdot \cdot \mathbf{S} = 0 \tag{7}$$

$$(d\mathbf{r} \times \mathbf{n}) \cdot \delta\mathbf{B} = (\delta\mathbf{r} \times \mathbf{n}) \cdot d\mathbf{B} \qquad (d\mathbf{r} \times \mathbf{n}) \cdot \delta\mathbf{S} = (\delta\mathbf{r} \times \mathbf{n}) \cdot d\mathbf{S} \tag{8}$$

Thus we have a total of six additional surfaces, $\mathbf{w}$, $\mathbf{v}$, $\mathbf{y}$, $\mathbf{f}$, $\mathbf{h}$ and $\mathbf{m}$ parameterised by θ^1 and θ^2 and two surface tensors, $\mathbf{B}$ and $\mathbf{S}$ which arise because the unit normals to $\mathbf{w}$ and $\mathbf{f}$ are equal to $\mathbf{n}$.

We shall now explain how the equations arise, beginning withe the kinematic relationships.

2.1 Kinematic relationships

Imagine two adjacent points on a moving surface. At a given instant of time $d\mathbf{r}$ is the vector from one point to the other and $d\mathbf{v}$ is the difference in velocities between the two points. If the surface is inextensional then the rate of membrane strain is zero then

$$d\mathbf{v} \cdot d\mathbf{r} = 0 \tag{9}$$

everywhere on the surface, regardless of the direction of $d\mathbf{r}$. Therefore the the difference in velocities must be due solely to an angular velocity $d\mathbf{w}$, leading to the left hand eq. (2), which automatically satisfies eq. (9).

All the other equations follow from this. For example writing the left hand eq. (2) as

$$\mathbf{v}_{,\alpha} = \mathbf{w} \times \mathbf{r}_{,\alpha}, \tag{10}$$

we have

$$\mathbf{v}_{,\alpha\beta} = \mathbf{w}_{,\beta} \times \mathbf{r}_{,\alpha} + \mathbf{w} \times \mathbf{r}_{,\alpha\beta}, \tag{11}$$

so that

$$\mathbf{w}_{,\beta} \times \mathbf{r}_{,\alpha} = \mathbf{w}_{,\alpha} \times \mathbf{r}_{,\beta}. \tag{12}$$

Thus we arrive at the left hand eq. (4) in which $\delta\mathbf{r}$ is the vector from our first point to a third adjacent point.

The left hand eq. (7) is of interest since it tells us that the Gaussian curvature remains constant during in extensional deformation, which of course follows from Gauss' *Theorema Egregium*.

2.2 Static relationships

If an unloaded shell is in static equilibrium, then the total force and total moment about a fixed point must be zero for any region of the surface, see fig. 1. This applies even if there are bending moments in the surface. This gives rise to the surfaces $\mathbf{f}$ and $\mathbf{m}$ in which $d\mathbf{f}$ and $d\mathbf{m}$ are the force and moment crossing $d\mathbf{r}$. In the membrane theory we have the right hand eq. (3), which leads to all the other equations.

The right hand eqs. (7) and (8) are the equilibrium equations in the normal and tangential directions.

2.3 Solution of equations

There are many known solutions to the above equations, particularly for surfaces of revolution, hyperbolic paraboloids and minimal surfaces. However the general case is fraught with difficulties and in the following sections we will consider some approaches.

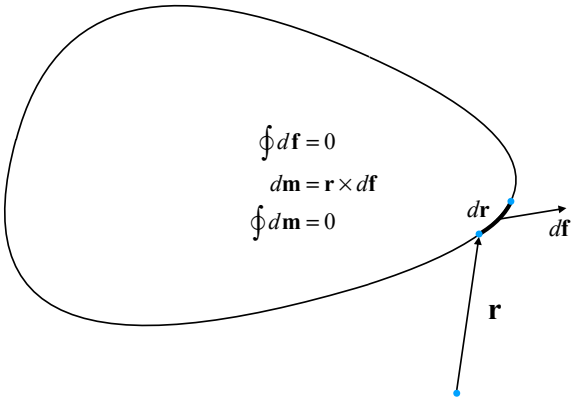


Figure 1: Portion of unloaded shell

3 Pin jointed frames

Imagine a triangulated grid shell with a fine grid. It will behave very much in the same way as a continuous shell and in the membrane theory the bars can be pin jointed, although bending stiffness is of course required to resist buckling [5].

An icosahedron has 20 triangular faces, 30 edges and 12 vertices. Thus, if we construct a pin-jointed frame in the form of an icosahedron, the number of bars, $b = 30$, and the number of joints, $j = 12$. Thus $b = 3j - 6$, satisfying Maxwell's rule [6] for a statically determinate structure. The 3 in $3j$ is because we have 3 equations of equilibrium at each node and the -6 is because we need 6 restraints to stop an object moving or rotating in 3D. The rule clearly also applies to a tetrahedron for which $b = 6$ and $j = 4$.

If $b < 3j - 6$ we have a mechanism and if $b > 3j - 6$ we have a statically indeterminate structure which can be prestressed by shortening one of the bars.

Thus an icosahedron made from pin-jointed bars which is unloaded and not attached to supports is a rigid structure which cannot be prestressed. The same applies to one of Buckminster Fuller's geodesic domes in which the triangles are subdivided and projected onto a sphere using gnomonic projection since the subdivision adds 3 times as many bars as joints. Thus we would expect a sphere to be rigid and cannot be prestressed which is confirmed by the discussion in section 4.

Now let us apply the same reasoning to a torus. We can cover a torus with a triangular grid with no poles or other extraordinary points in which every joint is connected to 6 bars. Each bar is shared by 2 joints and therefore $b = 3j$. Thus we would expect a closed torus made from pin-jointed bars which is unloaded and not attached to supports to be a rigid structure which can be prestressed in 6 possible ways. However, now let us imagine that the axis of the torus

is vertical and that our triangulation is such that we have two circles of horizontal triangles on the top and bottom of the torus, then our structure is a mechanism since there is no way to transmit a vertical force from the inside of the torus to the outside. Thus we have a mechanism, which using the logic in Calladine's classic paper [6], can be prestressed in more than 6 ways.

4 The rigidity of surfaces and the Cohn-Vossen theorem

A fully triangulated gridshell with a fine grid is very much like a continuous shell and as such the tensions or compressions in the bars are essentially the same as membrane stresses.

The Cohn-Vossen theorem [7, 8] tells us that a closed convex surface, that is a surface with positive Gaussian curvature, is rigid. Our argument about horizontal rings in the previous section tells us that a closed torus is not rigid. A torus has positive Gaussian curvature on the outside and negative Gaussian curvature inside. A hyperboloid of one sheet attached to a foundation, like a cooling tower, is a rigid surface in which loads can be transmitted to the ground along the straight line generators. A sphere with a dimple has both positive and negative Gaussian curvature and is not rigid for the same reason as for a torus. However it is not immediately clear whether an hourglass is rigid or not.

It follows that if a sphere or any closed convex surface is unloaded, then there can be no membrane stress in the surface and it cannot be prestressed.

5 Surface of revolution subject to torque about the axis

A general surface of revolution with the z-axis as rotation axis and the profile curve described in the xz-plane can be written

$$\mathbf{r} = r\mathbf{p} + z\hat{\mathbf{k}} \tag{13}$$

$$r = r\left(\theta^2\right) \tag{14}$$

$$z = z\left(\theta^2\right) \tag{15}$$

$$\mathbf{p} = \cos\theta^1\hat{\mathbf{i}} + \sin\theta^1\hat{\mathbf{j}} \tag{16}$$

in which $\hat{\mathbf{i}}$, $\hat{\mathbf{j}}$ and $\hat{\mathbf{k}}$ are unit vectors in the direction of the Cartesian axes. Writing

$$\mathbf{q} = \frac{d\mathbf{p}}{d\theta^1} = -\sin\theta^1\hat{\mathbf{i}} + \cos\theta^1\hat{\mathbf{j}} \tag{17}$$

we have

$$\mathbf{r}_{,1} = r\mathbf{q} \tag{18}$$

$$\mathbf{r}_{,2} = r'\mathbf{p} + z'\hat{\mathbf{k}}. \tag{19}$$

The simplest state of stress in an unloaded surface of revolution is that corresponding to a pure torque of value T about the axis, in which case there is a membrane shear stress equal to $\dfrac{T}{2\pi r^2}$ because the circumference is $2\pi r$ and the lever arm is r. Clearly the stress tends to infinity at the axis, but for a torus the stress is finite.

The corresponding membrane stress tensor is

$$\mathbf{S} = \frac{(\mathbf{r}_{,1}\mathbf{r}_{,2} + \mathbf{r}_{,2}\mathbf{r}_{,1})}{||\mathbf{r}_{,1}||\,||\mathbf{r}_{,2}||}\frac{T}{2\pi r^2} \tag{20}$$

and so using the equations in section 2,

$$\mathbf{f}_{,1} = -\frac{||\mathbf{r}_{,1}||\,\mathbf{r}_{,2}}{||\mathbf{r}_{,2}||}\cdot\mathbf{S} = -\frac{T}{2\pi r^2}\mathbf{r}_{,1} = -\frac{T}{2\pi r}\mathbf{q} \tag{21}$$

$$\mathbf{f}_{,2} = \frac{||\mathbf{r}_{,2}||\,\mathbf{r}_{,1}}{||\mathbf{r}_{,1}||}\cdot\mathbf{S} = \frac{T}{2\pi r^2}\mathbf{r}_{,2} = \frac{T}{2\pi r^2}\left(r'\mathbf{p} + z'\hat{\mathbf{k}}\right) \tag{22}$$

$$\mathbf{f} = \frac{T}{2\pi}\left(\frac{\mathbf{p}}{r} + \int\frac{z'}{r^2}d\theta^2\hat{\mathbf{k}}\right) \tag{23}$$

$$\mathbf{m}_{,1} = \mathbf{r}\times\mathbf{f}_{,1} = -\frac{T}{2\pi r}\left(r\mathbf{p} + z\hat{\mathbf{k}}\right)\times\mathbf{q} = -\frac{T}{2\pi r}\left(r\hat{\mathbf{k}} - z\mathbf{p}\right) \tag{24}$$

$$\mathbf{m}_{,2} = \mathbf{r}\times\mathbf{f}_{,2} = \frac{T}{2\pi r^2}\left(r\mathbf{p} + z\hat{\mathbf{k}}\right)\times\left(r'\mathbf{p} + z'\hat{\mathbf{k}}\right) = \frac{T}{2\pi r^2}\left(zr' - rz'\right)\mathbf{q} \tag{25}$$

$$\mathbf{m} = -\frac{T}{2\pi}\left(\frac{z}{r}\mathbf{q} + \theta^1\hat{\mathbf{k}}\right). \tag{26}$$

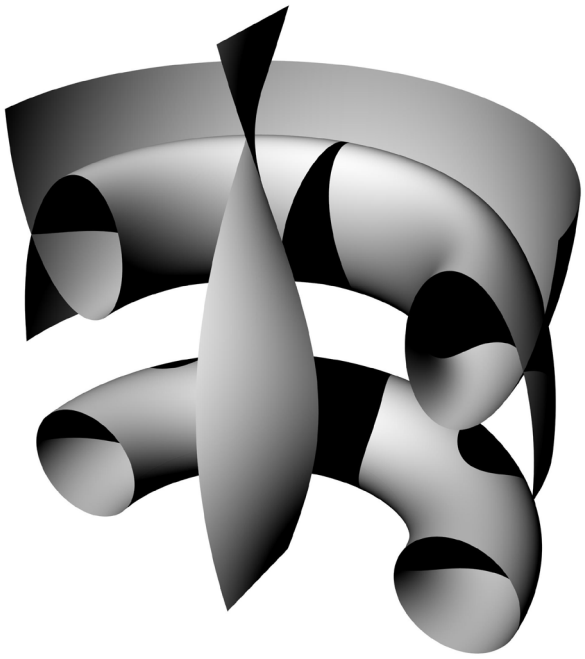


Figure 2: Half of complete torus (bottom) with the $\mathbf{f}$ (top) and $\mathbf{m}$ (down the middle) surfaces

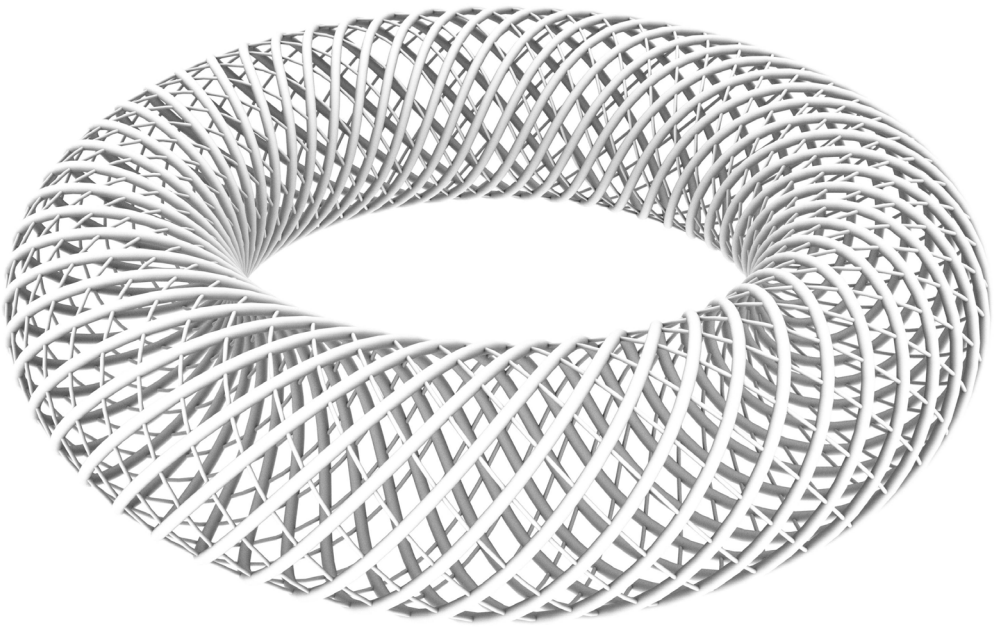


Figure 3: Prestressed torus with the thicker bars in compression and the thinner in tension

5.1 Torus

A torus is described by

$$r = A + B\cos\theta^2 \tag{27}$$

$$z = B\sin\theta^2 \tag{28}$$

in which A and B are constants. The integral

$$\begin{aligned}\int \frac{z'}{r^2}d\theta^2 &= \int \frac{B\cos\theta^2}{\left(A + B\cos\theta^2\right)^2}d\theta^2 \\ &= \frac{1}{B}\frac{\left(C^2-1\right)^2}{2C^3}\left(\left(1-C^2\right)\beta + \left(1+C^2\right)\cos\beta\sin\beta\right).\end{aligned} \tag{29}$$

The torus together with the **f** and **m** surfaces are plotted in fig. 2. The shear stress can be produced by a combination of tension and compression elements as shown in fig. 3.

Note that if a cut is made through the torus there is a resultant force acting along the axis, very much like in a coil spring, and this explains why the **f** and **m** surfaces are not closed. Of course if we cut the torus in half with 2 cuts, as in fig. 2, there is no resultant force on each half.

6 Conclusion

The starting point for this research was to examine unloaded closed surfaces unattached to any supports which can be prestressed. A sphere cannot be prestressed but a torus can be and we have examined one particular stress state. However there must almost certainly be more, and this is the topic of further research.

References

[1] Calladine, C. (1983). *Theory of Shell Structures.* Cambridge: Cambridge University Press. doi:10.1017/CBO9780511624278

[2] Minagawa, T.; Rado, T. On the infinitesimal rigidity of surfaces. *Osaka Math. J.* 4 (1952), no. 2, 241–285. https://projecteuclid.org/euclid.ojm/1200687817

[3] Gluck H. (1975) Almost all simply connected closed surfaces are rigid. In: Glaser L.C., Rushing T.B. (eds) *Geometric Topology. Lecture Notes in Mathematics*, vol 438. Springer, Berlin, Heidelberg

[4] A. E. Green and W. Zerna (1968). *Theoretical Elasticity*, 2nd edition, Oxford University Press

[5] Wright, D. T. (1965). Membrane forces and buckling in reticulated shells. *American Society of Civil Engineers Proceedings, Journal of the Structural Division,* 91:173-201.

[6] C.R. Calladine, Buckminster Fuller's Tensegrity structures and Clerk Maxwell's rules for the construction of stiff frames, *International Journal of Solids and Structures*, Volume 14, Issue 2, 1978, Pages 161-172, ISSN 0020-7683, https://doi.org/10.1016/0020-7683(78)90052-5.

[7] S. Cohn-Vossen, Zwei Sätze über die Starrheit der Einflächen, *Nachr. Ges. Wiss Gottingen Math.-Phys.* Ki. (1927) pp. 125-134.

[8] Hsü, Chin-Shui. Generalization of Cohn-Vossen's Theorem. *Proceedings of the American Mathematical Society* 11, no. 5 (1960): 845-46. doi:10.2307/2034571.

Proceedings of the IASS Annual Symposium 2019 – Structural Membranes 2019
Form and Force
7 – 10 October 2019, Barcelona, Spain
C. Lázaro, K.-U. Bletzinger, E. Oñate (eds.)

A digital design process for shell structures

Marinella CONTESTABILE*, Ornella IUORIO[a]

*School of Civil Engineering, University of Leeds
LS2 9JT, Leeds (UK)
cnmc@leeds.ac.uk

Abstract

Over the last few decades, the design of freeform structures has undergone a radical change: powerful computational tools within parametric environment associated with digital fabrication techniques are pushing the boundaries of architecture towards bold solutions. The present work proposes a digital workflow for a shell in compression. The design process starts with the form-finding phase, which generates a hanging model. Through the interoperability of digital tools within parametric environment, optimization of the shape and structural analysis were carried out in order to investigate its behavior. The resulting surface is subject to tessellation, planarization of its cells that take into account fabrication constrains, and the 3D generation of panels composing the thickness of the structure. In order to accomplish an easier assembly process a hypothesis of a puzzle-like connection system was developed. The whole process provides a guidance for the design of freeform shell by the creation of a "customized" digital workflow implemented by digital fabrication techniques for the realization phase.

Keywords: fabrication, hexagonal tessellation, parametric modelling, planarization, shell design, structural analysis.

1. Introduction

By definition, a shell structure is a system represented by a curved surface, in which one dimension is smaller than the other two. Its structural efficiency is mainly due to its geometrical features and its capacity to carry membrane stresses throughout the structure "passively" [1]. In the contemporary scenario, architects and engineers are promoting a radical change in the techniques used for the design of shell structures. Shell design has a very long tradition: the great masters of the past paved the way of obtaining efficient structures, providing powerful techniques. This remarkable legacy combined with the translation of these techniques in innovative digital tools is allowing an increased knowledge and interest in their use even from designers that never used such techniques before. The investigation of innovative methods may give a strong contribution in the architecture scenario as well as encouraging new architects to follow this direction, providing more efficient solutions.

This work presents a two-stage optimization process: in the first stage, the form-finding is used to obtain a compressed shell defined on the basis of given boundary conditions; tessellation and planarization are applied to "optimize" the shape through the definition of panels that can be easily fabricated and joint together. In the following sections, the process is discussed starting with the development of shell having a rectangular plan.

2. Design process

This paper addresses the design process applied on a shell working mainly in compression. The process phases include: form finding and planarization process, a preliminary structural analysis and the elaboration of a connection system. The brief required for this case is a rectangular plane (13.3 x 9.1 m)

Copyright © 2019 by Marinella CONTESTABILE, Ornella IUORIO
Published by the International Association for Shell and Spatial Structures (IASS) with permission.

(the dimensions are not integers since they take into account of the hexagonal discretization provided at the beginning of the process). The geometrical parameters include 4 point supports and 4 openings. This approach takes into consideration geometrical parameters together with structural and fabrication constraints that will be justified in the next sections. The process is implemented by parametric modelling, relying on Grasshopper® functions and its plugins. Thanks to their interoperability, it is possible to work on the whole design process in a unique working field, with a greater control of the outcomes regarding each aspect of the process. Working simultaneously from different perspectives gives the possibility to fulfill a wider range of requirements by acting on the parameters involved in the design.

Grasshopper® is a visual editor for algorithms. One of the main peculiarities of this tool is the possibility to create a custom work field by adding plug-ins for specific tasks, enriching its potentialities. Most of this plug-ins are open source like Grasshopper® itself enabling to work with a high degree of freedom in a wide range of applications, such as Finite Elements analysis (FEA), optimization, environmental analysis, mesh subdivision and rationalization, among others.

2.1. Form-finding-hexagonal subdivision and planarization

Form-finding is the earliest phase in the design process. It allows the definition of shape taking into account geometrical constraints and allows to develop shapes which are efficient for a specific set of forces [2]. Historically, graphic statics and hanging chains were used to define geometries and nowadays those methodologies have been translated in digital tools [3].

Such project makes use of an intuitive technique for form finding, which is Particle-Spring Systems (PSS). PSS was originally used for animation and was based on dynamic simulations and nowadays it represents an efficient methodology for the generation of 3D geometries [4]. In a general context, the starting surface is subject to a discretization process composed of particles and springs: the particles have a position and velocity and forces represented by vectors are applied to them, while the springs are the connection between the particles, and the interaction between them is governed by Hooke's law [5].

The hanging model is generated based on:

- Initial geometry, which represents the input for the generation of the 3D shape;
- Load cases, in this case gravity load is considered;
- Supports that represent anchor points.

This methodology is applied in the digital workflow through Kangaroo2 plug-in [6].

Starting from a rectangular plan and after defining the point supports the geometry is defined through a process carried out with Kangaroo2. The subdivision is a constraint applied in the process of form-finding to control deformation due to the planarization. Therefore, a subdivision composed of hexagonal cells is produced before to run the simulation. Fig. 1 shows the initial subdivision and the starting geometry. The form- finding is performed and at this stage the geometry is not planar yet, hence a further refinement which allows to planarise the cells, incorporated in this Grasshopper definition, is carried out. Fig. 2 shows the non-planar geometry, which is the result of the simulation.

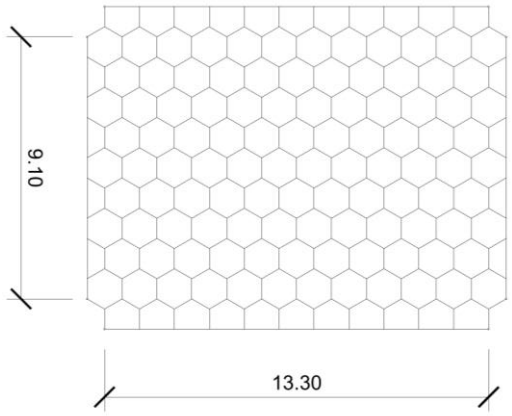


Figure 1: Starting plan with the hexagonal subdivision

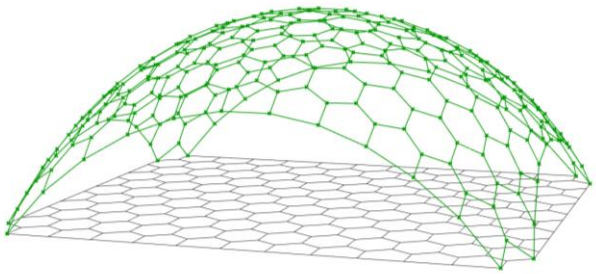


Figure 2: 3D shape after form-finding before planarization

Shell structures are double curvature surfaces and the evaluation of the curvature is an important parameter in the planarization process. This work deals with a shell with positive curvature. Positive curvatures allow the planarization to achieve good results, while in the case of negative curvature where the panels are concave some issues such as severe geometrical deformations and self-intersections could occur. When form-finding is generated and the planarization is an operation applied afterwards, then some deformations can occur in critical areas of the shell, such as at the supports. With the proposed approach, these deformations can be avoided although the resulting shape is affected. This is motivated by the presence of more constraints during the form-finding process that, indeed, controls the planarization in a more rigid way.

Therefore, the planarization process is incorporated in the form-finding process providing control during the simulation and avoiding severe deformations of the cells. By constraining vertices of a polygon in the same plane, the design process provides more optimized shapes that translate into a more efficient fabrication and potential low manufacturing costs.

This project refers to a specific work done by Muller [7], which addresses the thematic of conformal hexagons. A hexagon $(z_0,\ldots,z_5)$ is called *conformal* if both $\mathrm{cr}(z_0; z_1; z_2; z_3) = -1/2$ and $\mathrm{cr}(z_0; z_5; z_4; z_3) = -1/2$

Cr is cross-ratio and for 4 complex numbers $(z_0; z_1; z_2; z_3)$ it is given by:

$$cr = \frac{(z_0 - z_1)(z_2 - z_3)}{(z_1 - z_2)(z_3 - z_0)} \tag{1}$$

As Muller stated, in a conformal hexagon both quadrilaterals $z_0; z_1; z_2; z_3$ and $z_0; z_5; z_4; z_3$ are circular since their cross-ratios are real and all vertices of a circular polygon are contained in a sphere or plane (Fig. 3).

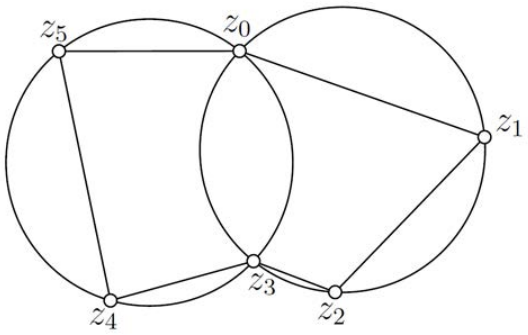


Figure 3: Conformal hexagon in two circles [Muller, 2011]

The simulation with Kangaroo2 allows to translate these properties by constraining the vertices of the hexagons in circles by using a specific component called "CoCircular". This constraint allows to control the transformations of the cells during the form-finding process and the planarization, whose successful outcome depends on another component from Kangaroo2, which is "CoPlanar". It is the principal force acting in order to run planarization allowing to "pull" a collection of point within their best fit plane. A best-fit plane is found generally by minimizing the sum of quadratic distances (perpendicular to the plane) between the plane and points. Fig. 4 shows the planar geometry proving how the use of the initial subdivision as constraint minimized the deformation of the planar cells.

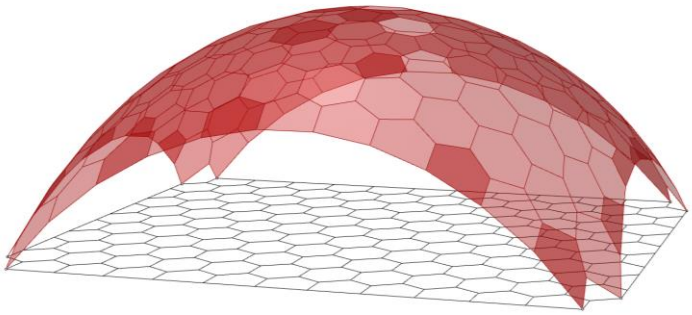


Figure 4: 3D shape after planarization

2.2. Preliminary structural analysis

The preliminary structural analysis has been performed by FEA within the Grasshopper® platform [8, 9]. A continuous surface was considered as input geometry, to perform a simplified preliminary analysis. A further structural analysis involving the discretized elements will be carried out in the future work.

The macromodel was analysed by taking into account the following conditions:

- Four point supports;
- Material properties are related to a material working mainly in compression as Table 1 displays; Material properties refer to Concrete C30/37 since such values represent a good approximation of a structure working mainly in compression. The values are taken from Eurocode 2 [10].
- A defined cross section;
- A load condition, to investigate the structural behavior in a series of context (Table 2).

Table 1: Material properties used for FEA [Eurocode]

Density	1900 kg/m3
Elastic Modulus	3300 N/mm^2
Compressive Strength Tensile strength	30 N/mm^2 2.9 N/mm^2
Shear Modulus (G)	1375 N/mm^2
Poison's ratio (V)	0.2

Table 2: Load combination

Dead load + wind load	5.7 + 0.8 (lateral wind) + 0.5 (up-lift wind)

The load combination (Table 2) consisted of dead loading acting with a horizontal wind load applied on the windward face of the structure with a vertical uplift wind load to create the maximum tensile stresses in the structure.

In order to contain tension stresses generated throughout the structure a thickness of 20 cm was considered appropriate. The results are showed in Table 3 where maximum compression stress, maximum tension stress and displacement proved a good insight of the shell's behavior. Fig. 5 and Fig. 6 show the results of the finite element analysis in terms of stress distribution and deformation.

At this stage, the results were considered acceptable according to material properties.

Table 3: Results extracted from Karamba

Max comp. stress N/mm^2	0.25
Max tensile stress N/mm^2	0.25
Max Displacement (mm)	0.65

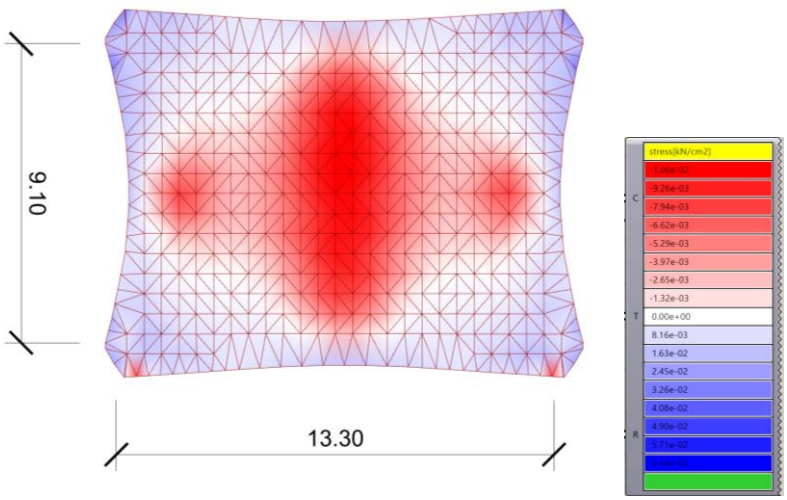


Figure 5: Stress distribution (blue-tension, red-compression)

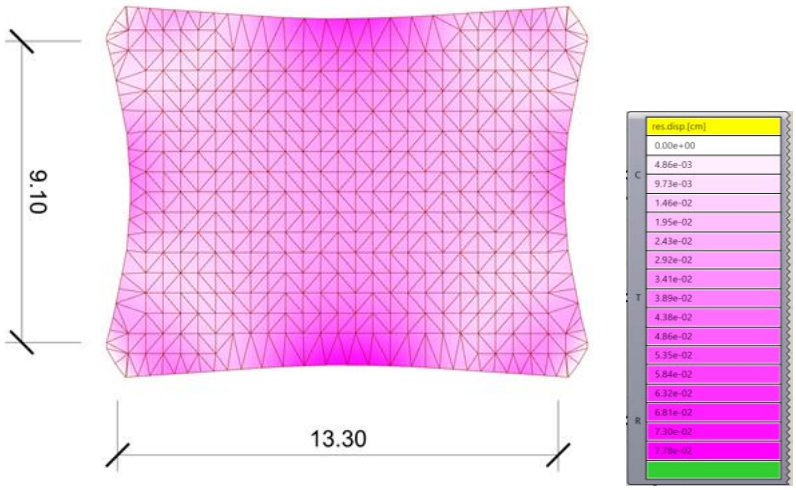


Figure 6: Displacement values

2.3. 3D generation

The 3D generation of the panels is a crucial part of the design process. It is based on the extrusion of the intradoses and the generation of the side faces. Research by Rippmann and Block [11, 12], have given important assumptions for designing shell structure. Such assumptions have provided guidelines for the next steps in this work, especially regarding structural requirements, explained as follows:

- Suitable thickness to assure safety of the structure;
- In order to avoid sliding the extrusion must follow the normal vectors of the surface.

Starting from these conditions a geometrical process has been carried out in order to generate 3D hexagonal elements. The first step was to retrieve normal vectors belonging to the continuous surface that represents the shell geometry. Fig. 7 depicts the normal vectors of the surface providing the direction of the extrusion of the hexagonal panels.

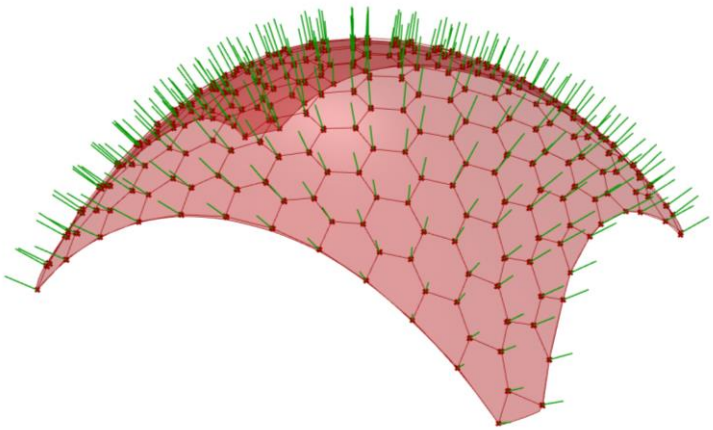


Figure 7: Normal vectors generation on the surface

The extradoses are generated, guaranteeing parallelism between corresponding faces. It is important to check the planarity of the external faces since it is not ensured for all the faces, this means that in case

of non-planar extradoses a further refinement is necessary to planarise the faces. Finally, the side contacts faces are generated by a loft operation according to the shell thickness, thus common sides are provided between the 3D panels. The whole process for a piece of the shell is described in Fig. 8.

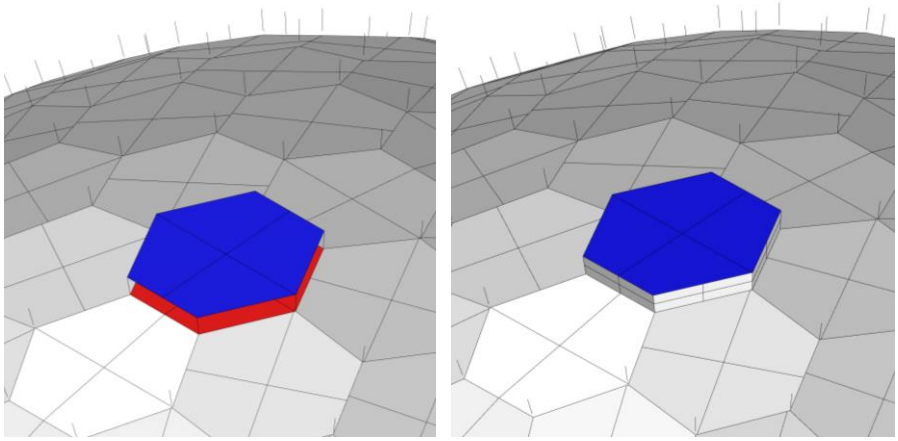


Figure 8: Generation of the extrados (on the left) and contact faces (on the right)

2.5. Connection system

A parametric definition has been developed to create connection for each panel. Although shell structures do not require connection system to ensure stability according to the assumptions described in the previous section and due to the compression stresses, an interlocking system has been elaborated mainly finalized to the realization phase. Starting from a typical puzzle layout, the system has been refined by generating a circular tapered section in order to assure interlocking during assembly test. The circular sections have been extruded by loft operation and successively Boolean operations have been carried out for addition or subtraction of the elements to the panels. The planarity was an essential requirement in order to retrieve semi-circle sections on the top and bottom part of the hexagonal panels, since they are contained in the same planes of the extrados and intrados faces. Fig. 9 summarizes the process including the application to a portion of the shell.

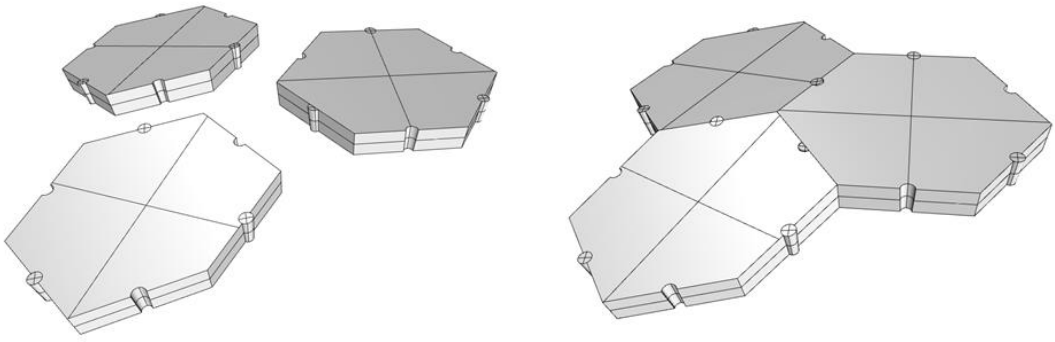


Figure 9: Connection system of the hexagonal panels

3. Conclusion

A digital process applied on a shell structure has been presented, generated within parametric modelling, through Grasshopper® functionalities. The aim of this work was to present a process for the design of a shell, which enables to optimize the realization phase by carrying out planarization and designing a connection system, which was designed for simplifying the final assembling. Firstly, a form-finding

technique was used to generate a form-found shell and it was based on a preliminary hexagonal subdivision, and then the planarization process was embedded within this simulation to have a better control of potential geometrical deformations. Its structural efficiency was evaluated through Finite Element Analysis with particular focus on the material properties, concerning a material working mainly in compression. Finally, a tessellation process consisting of 3D generation of the hexagonal panels and the elaboration of a puzzle-like connection system was developed meeting specific structural and fabrication requirements.

References

[1] S. Adriaenssens, P. Block, D. Veenendaal and C.Williams, *Shell Structures for architecture: Form Finding and Optimization*. New York: Routledge, 2014.

[2] E. Allen, Edwars and W. Zalewski, *Form and Forces: Designing Efficient, Expressive Structures*. New York: John Wiley & Sons, 2009.

[3] M. Contestabile, O. Iuorio and S. W. Garrity, "An Investigation Of Alternative Form-Finding Methods For Free-Form Masonry Shells" in *Proceedings of the10th International Masonry Conference, Milan, Italy, July 9-11, 2018.*

[4] A. Kilian and J. Ochsendorf, "Particle-Spring Systems for Structural Form Finding", *Journal of the International Association for Shell and Spatial Structures*, vol. 46(148), pp. 77-84, 2005.

[5] A. Tedeschi, AAD_Algorithms Aided Design. Parametric Strategies Using Grasshopper. Brienza: Le Penseur, 2014.

[6] D. Piker, "Kangaroo: Form Finding with Computational Physics", *Architectural Design*. vol. 83, (2), pp. 136-137, 2013.

[7] C. Müller, "Conformal Hexagonal Meshes", *Geometriae Dedicata*. DOI: 10.1007/s10711-010-9566-8, 2011.

[8] C. Preisinger, "Linking Structure and Parametric Geometry", *Archit Design*. vol. 83, pp. 110-113, 2013.

[9] C.Preisinger, "Karamba. User Manual for version 1.2.2", 2016.

[10] EN 1992-1-1 (2005). Eurocode 2- Design of concrete structures. Part 1-1: General rules and rules for buildings.

[11] M.Rippmann, and P. Block, "Rethinking structural masonry: Unreinforced, stone-cut shells", in *Proceedings of the ICE - Construction Materials*. DOI: 166. 378-389. 10.1680/coma.12.00033, 2013.

[12] M. Rippmann, "Funicular Shell Design: Geometric approaches to form finding and fabrication of discrete funicular structures", PhD Thesis, ETH Zurich, Zurich (CH), 2016.

Proceedings of the IASS Annual Symposium 2019 – Structural Membranes 2019
Form and Force
7 – 10 October 2019, Barcelona, Spain
C. Lázaro, K.-U. Bletzinger, E. Oñate (eds.)

Computational morphogenesis and digital simulation of the construction process of masonry domes built without centrings

Lorenzo ESPOSITO*, Gaetano B. Boccia[a], Alessandro LUPORINO[a], Sergio PONE[a],

* DiARC – Dipartimento di Architettura – Università di Napoli Federico II
Via Toledo 402, 80134, Napoli, Italia
espositolorenzo92@gmail.com

[a]DiARC – Dipartimento di Architettura – Università di Napoli Federico II

Abstract

The study investigates the design and construction processes of masonry domes built without the use of centrings. In particular, it focuses on those built using a 'compass', i.e. an erection device that simplifies the construction process, and guarantees the bricklaying accuracy. The foundation of this research project can be found in the work of Fabrizio Carola (1931-2019) who used an erection method for masonry domes inspired by the 'Nubian vault technique'. The design and construction processes used by Carola have been analyzed with the aim of identifying a sequence of operations, which were then simulated in a digital environment by means of recursive algorithms. Finally, the study moved to the implementation of two bespoke designed contraptions for the design of non-spherical domes. The result of this study is a computational tool which can be used to design different typologies of centring-less masonry domes and simulate their construction process.

Keywords: masonry domes, centring-less domes, computational morphogenesis, recursive algorithms.

1. Introduction

The construction of domes or vaults without the aid of centrings has been a recurring, yet uncommon, practice in architectural history. The first example dates back to 1200 BC and is represented by the barns of Thebes. This is followed by the Taq-I Kisra in Iraq (540 AD), the Brunelleschi's dome in Florence (1421), and the dome of San Gaudenzio in Novara (1844). Around 1960, the architect Hassan Fathy, engaged in the construction of the village of New Gourna, proposed the adoption of the ancient technique of the Nubian vault built without centrings and using a rudimentary string compass [1]. The same technique was taken up by the Neapolitan architect Fabrizio Carola, who performed a complete review and a richer articulation. The testing ground for this technique is the construction of the Hospital of Kaédi (a town located in southern Mauritania), which was built between 1981 and 1984[2]. Following this experience, Carola developed several geometric variants of domes, all based on the intersection of spherical segments.



Figure 1: (a) Taq-I Kisra, Iraq; (b) Nubian constructors using "Nubian vault technique"; (c) New Gourna, Egypt.

Copyright © 2019 by Lorenzo ESPOSITO, Gaetano BOCCIA, Alessandro LUPORINO, Sergio PONE
Published by the International Association for Shell and Spatial Structures (IASS) with permission.



Figure 2: (a) Compass used in San Gaudenzio dome construction, Italy; (b) Kaédi Hospital, Mauritania.

1.1 Background

Recent research on masonry vaults has been focusing on the development of digital tools for form-finding which allowed designers to experiment with this construction technology. Nevertheless, construction costs are usually neglected, as testified by the complex construction procedures specifically devised for the assembly of even more complex CNC-produced modules. Conversely, our research work stems from the low-tech paradigm. Therefore, our objective is to harness the power of digital tools while fullfilling a compromise between construction costs and achievements. The choice of using ordinary bricks as construction material follows a different direction compared to research works focused on the stereotomy of stone vaults [3], or those on the use of CNC milling machine to produce custom pieces for dry-masonry vaults [4]. Our motivation hinges on a specific interest in applying this technology in those areas where low funds are available. It follows that the use of low-tech construction systems can ensure a wider participation of people in the construction process [5], expanding the relevance of this research outside the semantic area of architecture. About Fabrizio Carola's provision to the masonry vault theme, it was studied by Prof. Luigi Alini and Studio Aion [6], that experience was fundamental for us to start the research, although their purpose was different by us one.

1.2 Practical issues

The issues related to the construction of domes without centrings are mainly two:

- the highly asymmetrical loads the structure has to bear during the construction phase before reaching equilibrium;
- the lack of a laying surface (coinciding with the centring) that guides the operator during the construction.

In this study we focus on the second one; it is a purely geometric issue; it was initially solved with the aid of one or more measuring ropes that allowed the identification of the exact point and plane for the laying of the brick. These were replaced by a wooden device named 'compass' which was firstly adopted by Alessandro Antonelli in 1844, followed by Fabrizio Carola in 1981.

According to the authors, Carola's work is the most suitable for a detailed study whose scope is the identification of a precise workflow, which can be then digitized in order to simulate the entire construction process. Once the computational tool has been tested on a case study, we developed several variations of the original compass. This let us explore a wide range of formal possibilities with the use of the same simple construction device.

2. Case study: Fabrizio Carola's works

Owing to Fabrizio Carola, the use of ropes as construction aid was dismissed in favor of a fully-fledged technological device (the compass), which is resistant, affordable, and easily reproducible even in the far-flung areas of the planet. The first compasses were made of wooden planks arranged to form a rigid

structure constrained to the ground at a point, - the center of rotation - and equipped with an arm that moves in the vertical plane. Carola adopted instead compasses made of metal rods. These were lighter and with lower tolerances compared with those in wood.



Figure 3: (a) Wooden compass used by F. Carola in the first domes [Courtesy of Luigi Di Pietro]; (b) Metal compass [Courtesy of Luigi Di Pietro], (c) detail of the head of a metal compass.

The compass is comprised by the following elements:

1. the head, which guarantees the correct laying of each brick;
2. a rotation pin connected to the ground;
3. the arm, which determines the width of the dome;
4. a wooden or metallic carpentry that determines height and eccentricity of the arm's center of rotation. It performs the same function of the formerly used rods.

The compass' kinematics is defined by:

1. a full rotation on the horizontal plane;
2. a partial rotation of the arm in the vertical plane.

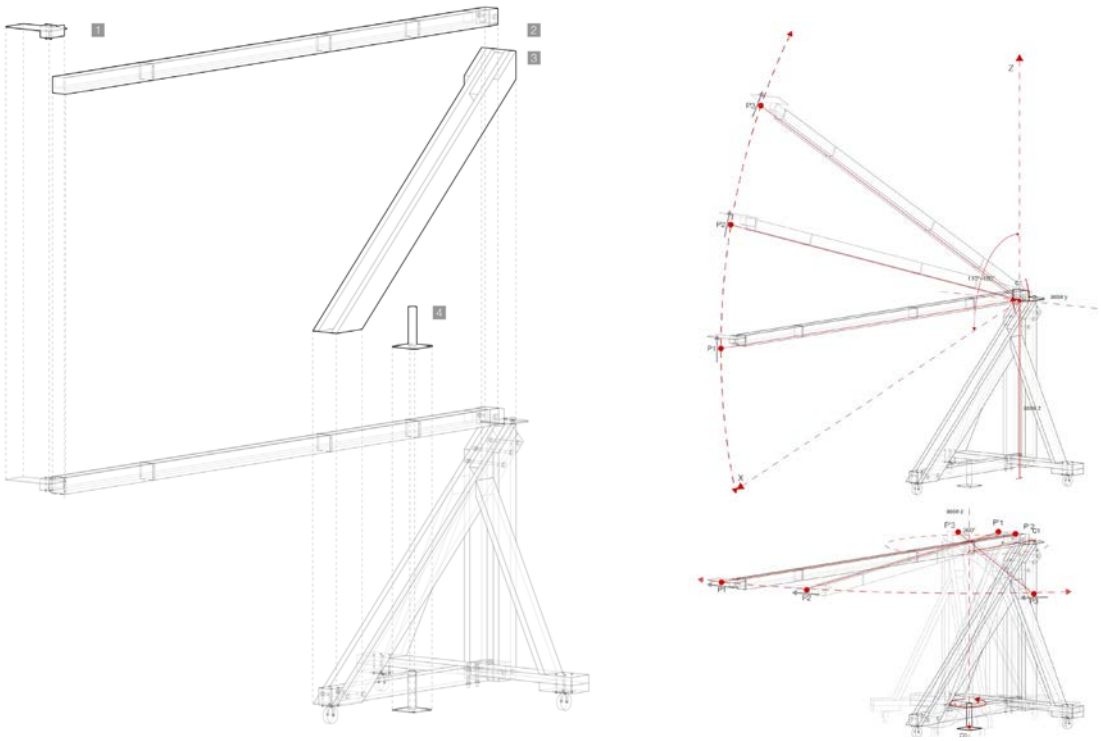


Figure 4: (a) Exploded axonometric of the compass: 1- head, 2- arm, 3- rod, 4- pin; (b) compass kinematics, vertical and horizontal plane.

2.1 Digital translation

The digital translation began choosing the most simple kind of dome, among Fabrizio Carola's family of domes: the ogive dome turned out to be the best case study for the development of the digital tool and its use for the generation of different shapes. To translate the construction process into a digital environment it was necessary to divide the entire process into the following phases:

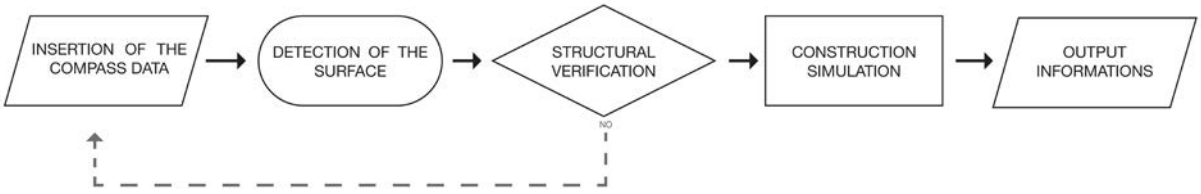


Figure 5: workflow of the digital tool

- Insertion of the compass data, creation of the compass
- Detection of the surface generated by the compass
- Graphic structural verification of the surface
- Construction simulation
- Return of the data

Input data consists of dimensional values that characterize the dome to be designed. In detail:

1. Height of the center of rotation compared to the ground. This affects the height of the intersection between the sphere and the ground plane.
2. Eccentricity of the center of rotation of the arm. This affects the "ogiveness" (I can't find "sesto" in english) of the dome.
3. Length of the arm. This affects then the diameter of the dome.

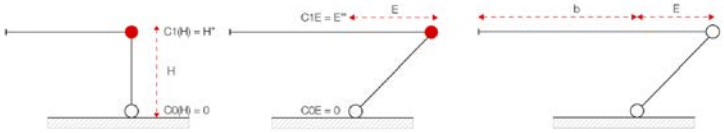


Figure 6: (a) Height; (b) Eccentricity; (c) Length of the arm

The second phase concerns the identification of the geometric surface, which the compass returns with the previously entered data (first phase). The compass can build an infinite series of surfaces belonging to the same family; the insertion of the dimensional data fixes one shape among the design spaces possibilities. This surface represents the only surface that can be made by the compass designed before.

The third phase - structural verification – consists of two preliminary checks about the constructability of the dome resulting from the previous phase is performed in two steps: (1) The check of the eccentricity of the dome, and (2) the check of the thickness of an arch inside the dome. These checks are carried out using the principles of graphic static, faithful to Carola's design process. If these checks are not passed, the digital tool returns to first phase in order to change the dimensional values. At the end of this phase, the digital tool selects, from the design space of surfaces generated by the compass, only the solutions that can be built.

The fourth phase - construction - is the one that ensures the reliability of the digital model. To precisely model the real-world construction process, all the manual movements of the operator (observed during a workshop in the south of Italy in August 2017 organized by Fabrizio Carola's team, where the authors

attended as students) have been translated into logical-mathematical processes. This was implemented using a recursive algorithm, capable to choose, like the real operator, what kind of brick to lay and how. The process was managed in a Rhinoceros/Grasshopper environment using the Anemone plugin, developed by Mateusz Zwierzycki [7]. The starting data of the digital tool are:

1. Bricks dimensions: the basic size of the brick used is 25x12.5x5 cm. Two pairs of bricks have been created. Each pair consists of a main and a secondary brick;
2. Laying curves, obtained from the intersection of the dome surface with a series of horizontal planes placed at a fixed distance equal to the height of brick summed with the mortar's height;
3. Limit value of the distance of the centre of the brick compared to the centre of the closest two bricks in the underneath course; to avoid the alignment of the mortar courses, the algorithm will use the secondary brick instead of the main one.
4. Limit length of the course, whereby the algorithm decides between the first pair and the second pair of bricks to discretize the surface evenly as the length of the courses decreases.

The process involves two nested loops: the first manages the selection of the single courses from the general list up to the completion of the dome; the second manages the laying of the bricks inside each course up to the completion of each bricks of the courses.

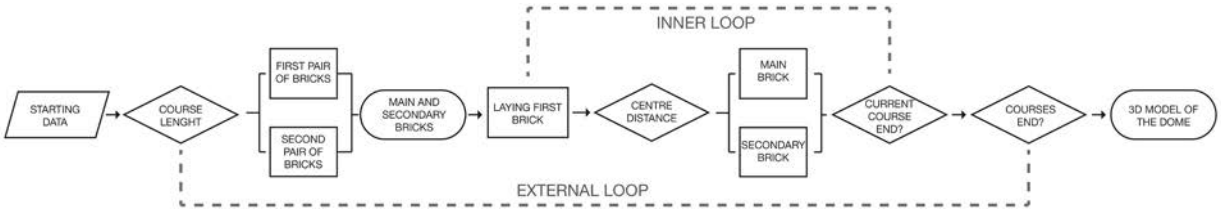


Figure 7: workflow of construction phase

The steps are the following:

a) With the first loop the digital tool measures the length of the course and then chooses the right pair of bricks to use;
b) Once the laying of the bricks is decided, the internal loop calculates the distance between the centre of the current brick and the nearest two of the courses below. If the distance is below the assigned one, the algorithm chooses the secondary brick, or lays the primary and switch to the next brick;
c) Once the course is over, the tool returns to the external loop to select the next curve and start another course. Then, once the limit length of the course is reached, the second combination of bricks is chosen;
d) Once the last brick of the last curve in the list has been placed, the exit condition is satisfied and the process ends.

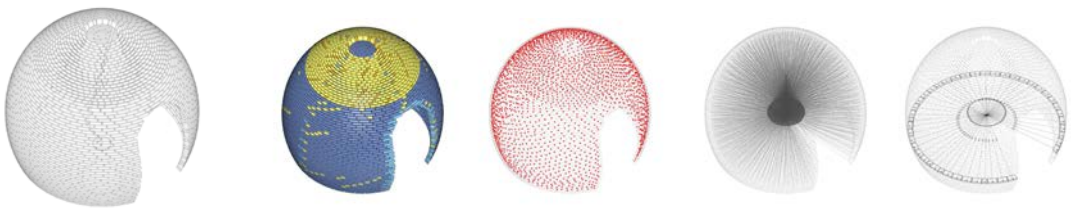


Figure 8: (a) 3d model of the dome; (b) number and classification of the bricks; (c) coordinates of centres of the bricks; (d) arm movements; (e) head angles.

The fifth phase (output) returns qualitative and quantitative information on construction process and geometric data of the compass: angles for the laying of each brick in the horizontal and vertical planes, coordinates of each brick, number of bricks and classification by their type.

3. Advancements

The studied compasses is governed by a spherical geometry, therefore its movements in plan and in section draw circumferences or portions of circumference; once the tool was able to simulate the construction process in a digital environment, the study went towards the modification of the compass to produce new shapes.

3.1 First update

The first step was the introduction of a movement different from the circumference in plan, while the vertical movement was maintained: the proposed device is a compass that, unlike its predecessor, moves along a track. The intuition draws from the study of the dome of Santa Maria del Fiore, where Brunelleschi, not being able to count on a centring to find the laying surface of each single brick, used a rope system, which allowed him to describe the intrados (Figure 7) of the sector under construction from the opposite octagonal sector [8].

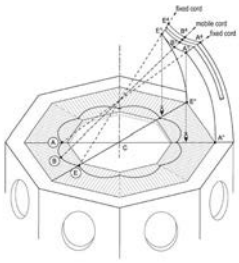


Figure 9: Reconstruction of Brunelleschi system of ropes to describe Santa Maria del Fiore intrados surface [8].

The new compass is characterized by the presence of a track, which becomes the geometric generator of the dome, as it determines its shape. In the absence of a circular plan the identity between the normal to the surface and the direction of the arm of the compass is not verified, thus forcing to free the rotation of the head positioned at the end of the arm whereby the brick is laid. On the construction site this problem may be simplified by either using a template for the first course and by relying on the skill of the operator for the next ones or by adjusting the plate position each time by using the information provided by the digital tool.

The introduction of the track changes the design process of the dome's geometry, offering two ways to obtain the surface:

- By designing a track, which, added to the initial geometric data of the compass (height, length and eccentricity), allows to obtain a surface;
- By drawing the plan at the maximum radius and from this build the corresponding track, with a reverse geometric process.

In this case the verification step present in the original workflow is accompanied by two geometric checks:

1. The non-interpenetration between track and surface or between compass and surface;
2. The adequacy of the geometry of the track to the sliding of the trolley carrying the compass, the minimum curvature radii of the track are adjusted according to the characteristic curvature radius of the trolley.

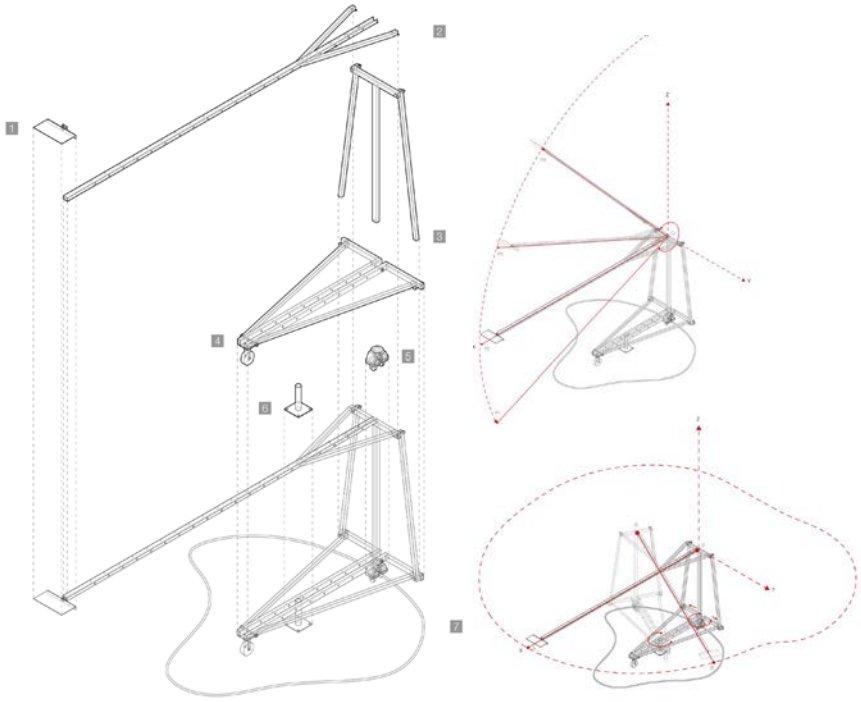


Figure 10: (a) Exploded axonometric of the first update of the compass: 1- head, 2- arm, 3- rod, 4- auxiliary track, 5- trolley, 6- pin, 7- main track; (b) compass kinematics in vertical and horizontal plane.

Once these conditions are verified, we move on to the construction phase which is identical to the previous case.

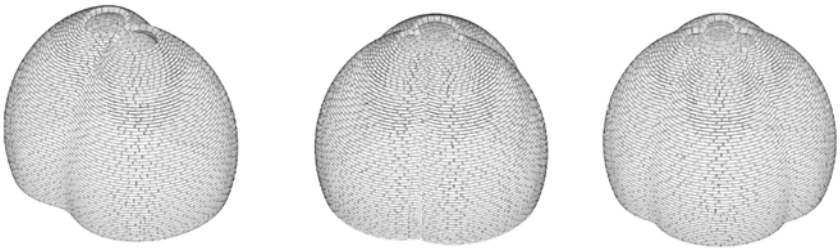


Figure 11: 3d model of the shapes capable by the first update of the compass.

3.2 Second update

The second step of progress consists in a further freeing of the compass kinetics from a spherical geometry. This is addressed by designing another compass constrained to a center of rotation, and equipped with an extendable arm and a head capable of rotating in the horizontal and vertical plane. By unlocking these three movements, the brick can be laid anywhere in the space; the surfaces that can be made with this tool are free-form, their plan or section are not related to a circumference, within obvious structural limits. For this compass the project foresees a mechanical movement managed through a mini-controller, like arduino, in order to divide the kinematic mechanisms into two categories: manual and automated. Whereas the operator will manage the general movement of the compass, the computer will calibrate each time the length of the arm and the rotations of the plate to lay a certain brick in the right place and in the right plane. A manual handling of these three values can also be provided by selectors. This choice remains faithful to the spirit of the case study. While expanding the formal vocabulary of

the compass, two general principles are preserved: the inexpensiveness of the tool and the participation of man in the construction process.

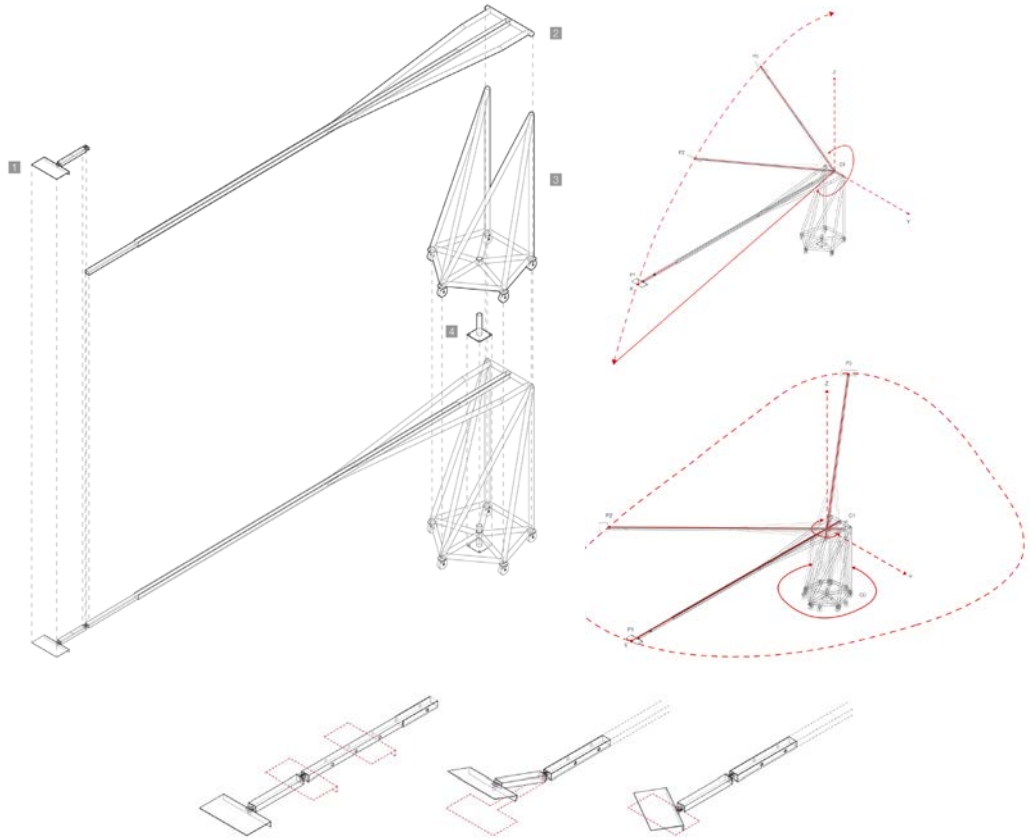


Figure 12: (a) Exploded axonometric of the second update of the compass: 1- head, 2- arm, 3- rod, 4-pin; (b) compass kinematiscs in vertical and horizontal plane; (c) details of the extensible arm and the rotating head.

The general workflow, in this last case, is simplified: the first two phases are summarized in the insertion of a geometry (sought through structural form-finding), while the verification phase becomes a finite element analysis of the inserted geometry. Here the masonry is simulated as a single material which combines the mechanical properties of brick and mortar. FEM analysis is performed in Karamba 3d [9] to guarantees that the whole process can be carried out within the same work environment. The output data, this time, represents the necessary means for the material realization of the digital process. Each brick becomes a string that summarizes all of its features e.g.: type of brick, course, position with respect to the relative course, spatial coordinate, extension of the arm, rotation of the plate in XY and YZ planes.



Figure 13: 3d model of the shapes capable by the second update of the compass.

Conclusions

The case study of Fabrizio Carola's domes and their possible variations represents a paradigm for the use of computational design, and in particular for the application of the recursive algorithms, in order to simulate some repetitive actions as they are in real life. The research first created a software capable of faithfully reproducing the operation of the compass to quickly discover that, despite the greater computing power allowed by digital technology, there were no technical solutions unkwown to the Neapolitan architect. From the simulation of the case study it was, with few and simple variations, to realize the second compass and the third one that finally allowed to prefigure different and more complex geometries. Ultimately the research exalts Carola's original intuition that allegedly was the first to establish and test a dual systematic relationship between a given construction tool and a given repertoire of shapes. This has demonstrated to be greatly widened by the introduction of digital tools. This paper presents the outcome of the Master Thesis of G. Boccia, L. Esposito, and A. Luporino developed under the supervision of Prof. Sergio Pone and discussed at the Università degli Studi di Napoli Federico II in February 2018.



Figure 14: Renders of three shapes made by the three respective compasses.

Acknowledgements

The authors are grateful to Fabrizio Carola and his team, especially to Luigi Di Pietro for his essential support during the research development, he let us to meet by close the objects of our research. We thank Gabriele Mirra for his huge contribute during the reviewing of this paper.

References

[1] H. Fathy, *Architecture for the poor: an experiment on rural Egypt*, The University of Chicago Ed., Chicago, 1973.

[2] L. Alini, *Fabrizio Carola Opere e Progetti 1954-2016*, Clean Edizioni, Napoli, 2016.

[3] Fallacara, Giuseppe. (2009). *Toward a Stereotomic Design: Experimental Constructions and Didactic Experiences.*

[4] Rippmann, Matthias & Mele T., Van & Popescu, Mariana & E, Augustynowicz & Echenagucia, Tomás & Calvo Barentin, Cristián & Frick, Ursula & P, Block. (2016). *The Armadillo Vault: Computational design and digital fabrication of a freeform stone shell*.

[5] Block, Philippe & Dejong, Matthew & Davis, Lara & Ochsendorf, John. (2010). *Tile vaulted systems for low-cost construction in Africa. Journal of the African Technology Development Forum (ATDF)* – Special Issue on Architecture for Development.

[6] A. Jaeschke, "Morfogenesi e prestazione" in *Cupole per abitare Un omaggio a Fabrizio Carola* by L. Alini, Libellula Edizioni, Tricase, 2012.

[7] https://www.food4rhino.com/app/anemone

[8] M. Ricci (2014), *Il genio di Filippo Brunelleschi e la costruzione della cupola di Santa Maria del Fiore*. Sillabe, Livorno

[9] https://www.karamba3d.com

Proceedings of the IASS Annual Symposium 2019 – Structural Membranes 2019
Form and Force
7 – 10 October 2019, Barcelona, Spain
C. Lázaro, K.-U. Bletzinger, E. Oñate (eds.)

Design and optimization of grid shell structures using Christoffel duality

PhD Candidate Zlata TOŠIĆ*, Associate Prof. Sonja KRASIĆ*, Associate Prof. Dragan[a] KOSTIĆ

*University of Niš, Faculty of Civil Engineering and Architecture, Department of Visual Communications
Bulevar Nemanjića 78/25

18000 Niš, SERBIA
zlata10@live.com
[a] University of Niš, Faculty of Civil Engineering and Architecture, Department of Structures and Construction Systems

Abstract

In the paper, the authors deal with design and optimization of grid shell, by using geometry methods, which were not often used for shell structures. They include designing, discretization and modification of the meshes (size and edge's direction) with the help of the circle geometry patterns [1]. Methods that are used all came from circle geometry that enables a lot of transformations and defines different mesh offsets. Moreover, the edges of modified meshes in the surface are known for defining the direction of principal curvatures and therefore represent fundamental shape characteristics. The authors use the curvature's direction as an input for iterative procedure of sphere mapping and projective transformation on the mesh division of the designed surface and create new, circular mesh. With changed geometry, the structural properties are changing as well. The goal is to explore the combination of this methods and optimize the free-form shell both geometrically and structurally.

Keywords: grid shell, geometry optimization, circle pattern, Christoffel duality, circular mesh surface.

1. Introduction

Nowadays, free-form grid shell structures are a big part of contemporary architecture. Nevertheless, their geometry and construction properties can be rather unfitting when overlooking other aspects of the production and static performance, and therefore must be optimized. There are a lot of techniques for making the optimal performance of spatial grid elements, depending on the different construction and design goals. The major aim is to obtain equilibrium between the rod elements, as well as the desired shape. The authors use the principal curvature for directing the surface division, which represents the discrete versions of principal curvature lines of surfaces, to optimize the structural properties *(maximum deformation and stress)* of the initial, designed shell structure. They are suitable for manufacturing because of planarity in mesh division. Their drive to orthogonal conjugate net construct nodes with lowered geometric torsion. Nevertheless, the principle curvature directions can be rather unfitting, regarding high variations in the number and size of elements, when it comes to free-form geometry. The authors mean to solve this problem by using these geometry characteristics to make balance in number and size of elements but also increase the axial force, which uses the cross-section of higher capacity making the construction more stable. The goal is to provide the computational tool for usage of the geometry methods for free-form surface transformation into more suitable one for filling these conditions.

Copyright © 2019 by Zlata TOŠIĆ, Sonja KRASIĆ, Dragan KOSTIĆ
Published by the International Association for Shell and Spatial Structures (IASS) with permission.

A significant step in mesh optimization for equilibrium comes from thrust network analysis, presented by Block and Ochsendorf [2]. Vouga *et al.* [3] provide a differential geometric understanding of this approach and use it for the design of planar quad meshes in equilibrium with graphical static. The PQ mesh optimization for equilibrium and face planarity is provided by Tang *et al.* [4], where the success of this method is dependent on the initial mesh connections. Schiftner and Balzer [5] propose a method for planar quad-remeshing of given surfaces, staring by principal stress lines. A first attempt to directly design principal meshes in equilibrium was by Sun [6], by firstly fixing the mesh combinatorics. The design of principal meshes in equilibrium is addressed in [7], thanks to the alignment of principal curvature and stress directions and a subsequent quad-remeshing. On the other hand, this method is restricted to height field shapes. Pellis and Pottmann succeeded to design principle meshes in equilibrium by aligning membrane surface stress and curvature, although not all shapes are aesthetically appropriate given the variation in element's size and number [8]. For an introduction to principal meshes in architecture, we refer to [9].

The principal curvature lines and have been realized as particularly suited for freeform structures in architecture, since they allow for a supporting beam layout with optimal node properties. Their usage and results are illustrated by discrete isotropic minimal surfaces and meshes computed by a combination of optimization and subdivision, which is successfully introduced by Pottmann and Liu [10]. Their way of designing such meshes is to alternate between subdivision and optimization. It should be noted that this optimization procedure does not convert any mesh, and there are some restrictions to the initial design. Probably the most important research task towards the implementation of freeform geometry in architecture is to find new ways of approximating a given freeform shape by meshes with properties that are desirable for architecture [10]. Moreover, the precise geometric results and relations offered by discrete differential geometry are of high importance in architectural design [11, 12, 13, 14, 15, and 16], because their mesh representation (i) is seen and greatly influences the aesthetics and (ii) is the basis for the actual construction [10].

The contributions of the present paper are the following ones:

1. Meshes which discretize the network of free-form surface design

2. Mesh edges with planar faces

3. Optimization algorithms for their design and computation, which are elaborated in C#.

4. Structural analysis for grid shell structures for the initial and optimized shape, comparison of the results and recommendations for the optimization process

2. Definition of the used methods in discrete differential geometry

2.1. Mesh offsets

In order to implement techniques, firstly we must explore some parts of discrete differential geometry, related with mesh offsets, which are closely related. Planar quad (PQ) mesh are one of the possibilities for subdivision of surfaces. They can be easily defined within the translation or rotational surfaces, but not with free-form geometry. Having this in mind, the authors explore mesh offsets, in order to use this techniques for subdivision process. *"An offset mesh M^d of a PQ mesh M is a parallel to M and lies at constant distance d to M."*[9] There are three way to measure value of *d* and it defines the three types of offset meshes: **vertex offset** *(the distance of corresponding vertices has a constant value d, which does not depend on the vertex),* **edge offset** *(the distance of corresponding parallel edges does not depend on the edge and equals d)* and **face offset** *(the distance of corresponding faces is independent of the face and equals d*).

The important fact to know about these cases is that it is not possible to prescribe an arbitrary PQ mesh and construct any of these offset types [9]. In order to pressure Christoffel duality, the authors have

chosen to implement conditions for vertex offset mesh, as they demand the circular mesh system. Firstly, let us define the vertex offset and set the conditions and methods for mesh transformation. Figure 1 illustrates the fact that the Gaussian image mesh S is parallel to M and M^d and that distance properties between M and M^d are also reflected in distances between S and the origin. Gaussian image S must have distance 1 to the origin in the same sense. This means that M^d is a vertex offset of M if and only if the vertices of the Gaussian image mesh S are contained in the unit sphere S*. In that manner, mesh M has to be a circular mesh *(each face has to have circum-circle).* Hence, each face of S is planar, the plane of that face intersects sphere in a circle and therefore S is a circular mesh.

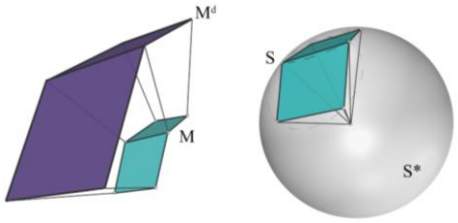


Figure 1: Two parallel meshes M and M^d with vertex offset mesh and their scaled difference S on the sphere S*

2.2. Christiffel duality method

The Christoffel duality *(also called as: static equilibrium of diagonal meshes)* [9] is usually implemented and mentioned within the *edge offset mesh*, where the edges of the mesh have to represent the tangents of the sphere S*. These meshes are parallel to Koebe mesh *(edge offset mesh on sphere)* where: (i) each face has an inscribed circle, and (ii) per edge there is only one point of tangency with the inscribed circles of the adjacent faces. As in the Euclidean case, these meshes are not suitable for approximating arbitrary surfaces [10]. The method is also closely related with polyhedral surfaces and man Gauss curvature in mathematics, which will be mentioned but are not the focus of this research so we refer to the literature [17, 18, 19, 20, and 21]. Ones we have that mesh, it is possible to transform it and make discrete minimal surface. A quad Q* in a Koebe mesh S and the corresponding parallel quad Q in the mesh M have reverse orientation and parallel diagonals: 13 || 2*4* and 24 || 1*3* (fig. 2b)). It can be also seen in the figure that if a starting quad Q* has an inscribed circle, during this transformation quad Q keeps it as well.

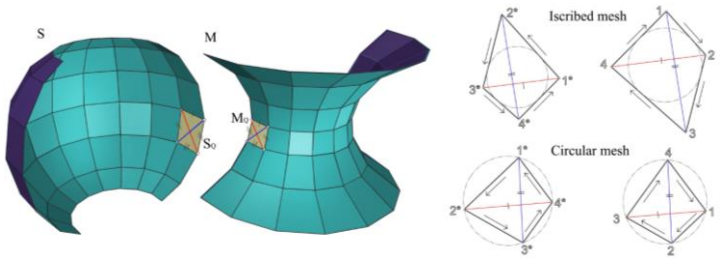


Figure 2: a) Koebe mesh (left) with its discrete minimal surface (right) b) Two parallel quads with reverse diagonals and vertex directions

Applying this procedure to designed mesh S we yield the mesh M, where we can call M the Christoffel dual of S. Such meshes are called *reciprocal parallel* and arise as *reciprocal force diagrams in graphical statics.* If external forces are applied in the vertices of the mesh S_1 *(joints in grid shell)*, the internal forces that will establish static equilibrium represent forces in M_1. If we use the same procedure for S, we will get M, which means that Christoffel duality is a symmetric relation. This process cannot be applied on arbitrary PQ mesh, as it is not possible to obtain the transformation duality. That can be explained on the example of four quad mesh. If we follow the procedure and try to create diagonal quad one by one, the fourth quad will fail to close the connection of lines (fig. 3).

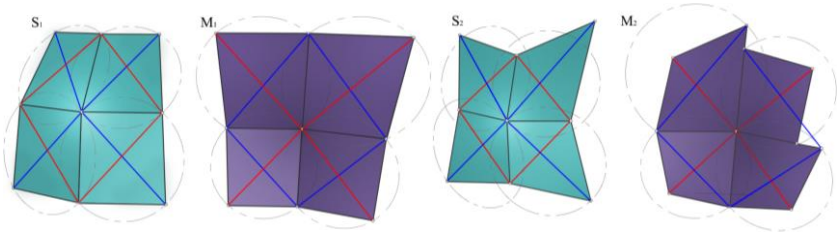


Figure 3: a) Circular mesh S_1 with its diagonal dual mesh M_1 b) Arbitrary mesh S_2 with failed dual mesh M_2

This means that the designed mesh has to satisfy a certain criteria in order to transform diagonal mesh. The authors have chosen to solve this problem by transforming the designed mesh to the circular one, as showed in the figure 3. As an inscribed one, the circum-scribed circle is preserved in dual mesh as well. Although, Christoffel duality is more used within edge offset mesh, for the implementation the authors use of the circular mesh system in order to have better manipulation of the vertices *(which will drive the edge directions)* during the implementation of the duality method. The used techniques are going to be explained in the next section.

3. Workflow

After the extensive explanation of the geometry methods which lead to Christoffel duality, in this section it will be shown how the methods are used. The task states: *Starting from the free-form surface design, optimize the shape for grid shell structure, so that the structural properties are improved and at the same time staying close to the initial design.* The overviewed parameters for optimization are direction, size and number of the elements in grid shell construction. The workflow is going to be presented in characteristic steps:

1. Taking the initial free-form surface design S* and make a mesh division guided by the direction of the principle curvature.
2. Analyzing if the designed surface has symmetry and at what cross-section has the biggest Gaussian curvature.
3. Start the process of optimization for S* with iterative procedure *"quad by quad"* making the mesh circular and planar S with some deviations. The process is starting from the chosen cross-section *(from the second step)* and depend on the chosen direction *(form the first step).*
4. To ensure the circularity of the meshes and implementation of the best edge directions of the new quads through entire mesh, the authors use Christoffel duality for the 4 quad rule *(explained in the second section)*.
5. Compare both the initial shell surface S* and the new one S and conclude the percentage of the optimized structural properties.

4. Implementation

In this section one case study is explored, with the implementation of the methods. Starting from the initial shape, we are going to analyze: the principle curvature directions and the biggest Gaussian curvature cross-section. The first is going to help with the positioning the initial directions of the grid shell rods and the second is defining the starting line of the *"quad by quad"* optimization. At this time it is important to take care of the number and size of the elements depending of the span and boundary conditions of the construction. In this case the support is located on the boundary nodes of the shell and rotation and translation in the all direction is disabled. This shell is treated with rigid connections in elements and loads are located in the nodes. Material that is used is steel S355 with tube cross-sections, which are dimensioned by FEM method.

"Quad by quad" optimization is an iterative process where we start from the one quad mesh, mapping it into a sphere, performing projective transformations, so that the final circular and planar mesh quad is as close as possible to the vertices of the initial quad. The deviation from the circle can be maximum

2% from the average length of the quad diagonals. This enabled the optimized shape to come as close as possible to the initial one, as well as to cover the shell with glass panels. The process continues through the line of the chosen cross-section *(in this case the middle)* to the ends of the mesh, quad by quad, going row by row (fig. 4 a)). Through the process there are four types of quads depending on the number and position of the fixed vertices in quad: free quad *(no fixed vertices),* quad-one *(one fixed vertex),* quad-two *(two fixed vertices)* and quad-three *(three fixed vertices)* (fig. 4 b)). The number of fixed vertices depend of the quad position in mesh. Fixed vertices are the ones that optimized quads have determined and where the procedure continues. From the figure 4a) it can be seen that most of the quads are type 3, as they have three fixed vertices from the previous iteration step. This means that the final shape result depends a lot of the start position of this phase. That is why the authors took the cross section with a biggest Gaussian curvature as a start point, to minimize the deviation from the initial shape. The process is computed in C# and implemented for geometry in Rhino 6.

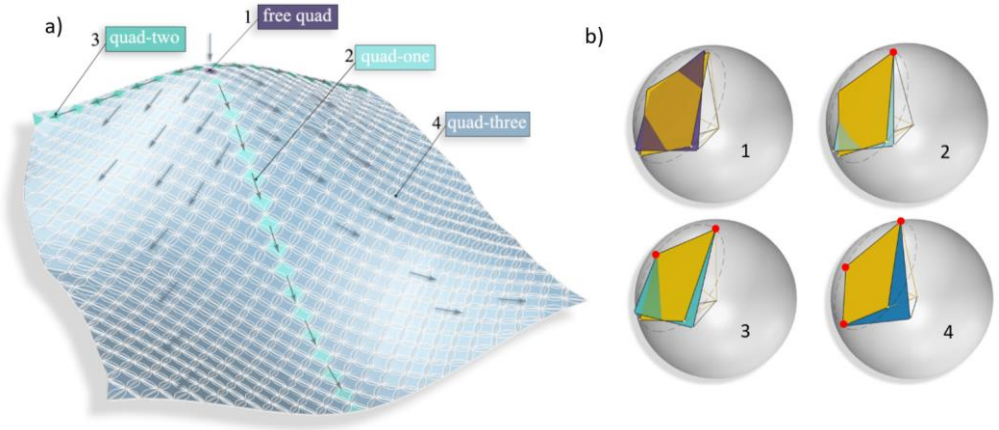


Figure 4: a) The display of the *"quad by quad"* system with all four types of quads in optimization process b) All four types of quads with their transformation into circular one and number of fixed (red) vertices

After defining the circular mesh S, with the help of Christoffel duality, it is enabled to guide direction of the mesh edges to the optimal one and prevent the quads to make zigzag while getting circular. This process is made for every four quad mesh one by one (fig. 5).

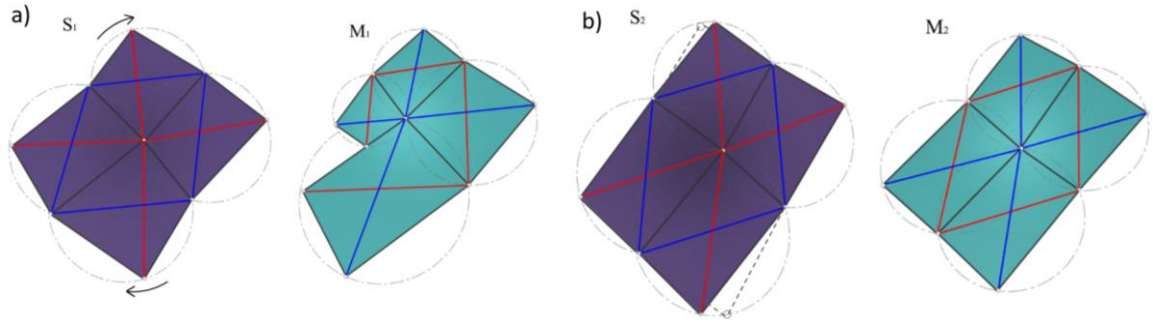


Figure 5 a) A circular mesh S_1 with no duality M_1 b) By transforming the quads the mesh S_2 gets dual mesh M_2

The transformation is done in grasshopper and it guides the fourth quad in gravitating to establish Christiffel duality. This is a part where the circularity of the quad helps in guiding the vertices into proper dual quad, as it has a defined path *(circle)* to move. As a consequence, this represents in plane transformation and not spatial one. Moreover, the final mesh does not deviate a lot from the initial shape, number and length of the elements. On the other hand, it is not possible to reach the complete duality for the entire mesh. That is why the mesh is not in complete equilibrium and the entire dual quad is not connected in each vertex. The steps are implemented in the example of the free-form shape displayed in the figure 6.

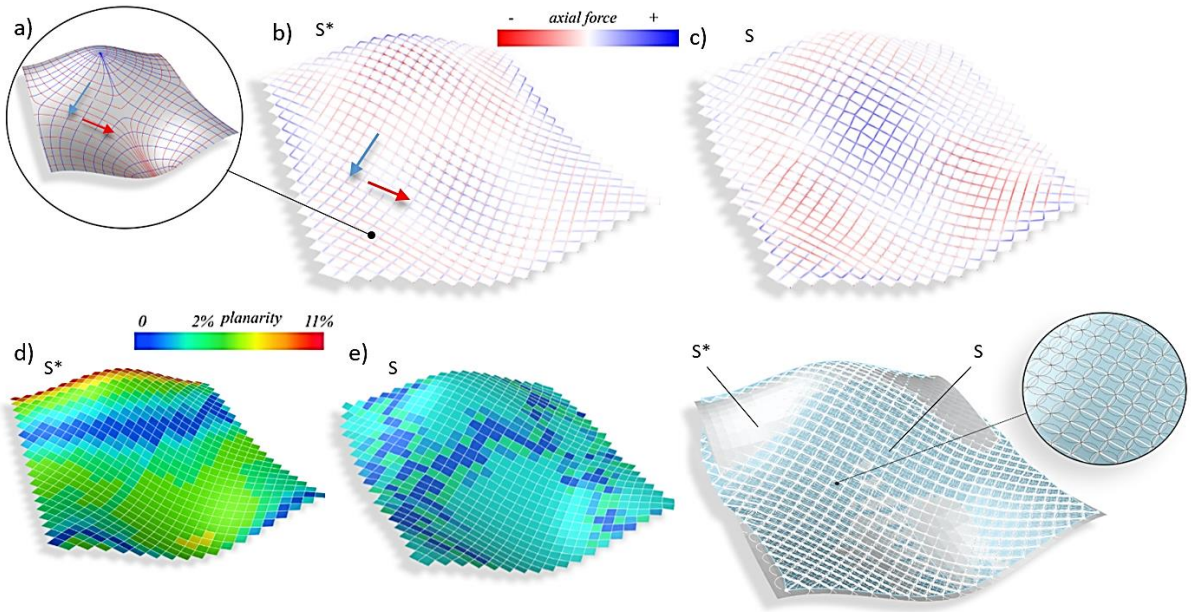


Figure 6: Design workflow a) An initial shape is given with the principle curvature lines b) The initial grid shell division with the directions followed by the shape's curvature c) After our optimization we reach the circular mesh system with better structural characteristics d) Display of the planarization of the mesh panels in initial shape S* and e) optimized S f) Overlapped S* with the new gird shell S and overview of circular mesh on the right

6. Results and discussion

In this section the authors want to show the results of the used methods and discuss the disadvantages and possible improvements. After forming the initial and optimized grid shell the calculation of the structural properties is made in Karamba. The comparison between the two is shown in the table 1.

Table 1: The representation of the structural properties of the initial and final grid structure

Structure properties	Initial grid shell S*	Final grid shell S	Difference in percentage
Mass (kg)	37 636 kg	38 800 kg	+ 3%
u = $Deformation_{max}$	18.00 cm	13.65 cm	- 24%
N_{max} (kN)	36.64 kN	39.92 kN	+ 8 %
Mx_{max} (torsion) (kNm)	4.83 kNm	4.11 kNm	- 16 %
My_{max} (kNm)	11.40 kNm	9.94 kNm	- 13 %
Mz_{max} (kNm)	9.88 kNm	9.51 kNm	- 4 %
u (from N in %)	1.3 %	3.0 %	+ 1.7 %
u (from Mx in %)	11.0 %	8.4 %	- 2.6 %
u (from My in %)	48.0 %	37.8 %	- 10.2 %
u (from Mz in %)	40.0 %	50.8 %	+ 10.8 %

Construction: The same cross-section, material and boundary conditions are given to both structures. In the table are shown the maximum values of properties. It can be seen that the most impact optimization process had on the deformation in construction. As the span of the construction is around 40m, the limit for maximum deformation that was taken is L/300, which is around 0.13m. The axial force is increased

for 8%, and one of the greatest impacts is on torsion, which is very important for the connections in grid shell. In order to have better overview of the results the authors wanted to analyze the ratio of contribution of all forces in deformation. The last four values in table 1 represent the impact of each force *(axial, torsion, moments around y and z axis)* in maximum displacement *(u)* in both constructions, shown in percentage. The impact of axial force (N) is increased for 1.7% and impact of torsion (Mx) is lowered for 2.6% in the final grid shell.

Geometry: When it comes to geometry optimization, one of the goals was to keep the directions, minimize the variation of length and concentration of the elements in one node. That will keep the concept of design but still optimize the construction. The implementation of this shell in architecture is shown in the figure 7. Number of elements are close: ***2592*** *for initial and* ***2584*** *for final grid* and length varies: *from* ***1.50m-1.70m*** *for initial grid and* ***1.0m-2.40m*** *for final grid*. The planarization was *increased from* ***11% to 2%,*** which enables the grid to be covered with glass panels. The most important is that the shape is changed with small deviation *(**d_{max} =1.40m**, only 12 nodes go over 1m, **d_{avrg} = 0.53m**)*. The downside can be the change in the initial boundary shape, which can be seen in the figure 6.



Figure 7: Implementation of final grid shell design in architecture

6. Conclusion

We have introduced a method for the design of circular meshes system on free-form shape which, combined with Christoffel duality, helps in optimizing both geometry and structural properties of the grid shell system. The structural properties that are problematic, such as deformation, torsion in elements and moments are lowered, with keeping geometry of elements: number and length of elements, establishing planarity, while staying in the area of designed shape. Limitations of this methods are that in some cases the final shape cannot be so close to the initial one. Moreover, the starting principle curvatures of the designed shape are can be very chaotic in order to establish only two directions, such as in presented example. The future work will focus on improving the methods and achieving equilibrium of meshes without moments and maximum exploration of axial force in construction. Moreover this and future methods will be presented not only on roof-type constructions such as this one, but also self-supporting shells that include entire standing structure.

References

[1] A.I. Bobenko, “Surfaces from Circles”, in *Discrete Differential Geometry,* Bobenko A.I., Sullivan J.M., Schröder P., Ziegler G.M., 2008, pp 3-35.

[2] Block, P. and J. Ochsendorf, “Thrust network analysis: A new methodology for three-dimensional equilibrium”, *Journal of International Association for Shell and Spatial Structures* 48(3), pp. 167–173, 2007.

[3] Vouga, E., M. Höbinger, J. Wallner, and H. Pottmann, “Design of selfsupporting surfaces”, *ACM Transactions on Graphics* 31(4), pp. 1–11, 2012.

[4] Tang, C., X. Sun, A. Gomes, J. Wallner, and H. Pottmann, "Form-finding with polyhedral meshes made simple", *ACM Transactions on Graphics* 33(4), pp. 1–9, 2014.

[5] Schiftner, A. and J. Balzer, "Statics-sensitive layout of planar quadrilateral meshes" *In C. Ceccato et al. (Eds.), Advances in Architectural Geometry, Springer,* pp. 221–236, 2010.

[6] Sun, X. *Discrete Curvature Theories and Applications*. Ph.D. thesis, King Abdullah University of Science and Technology, Thuwal, 2016.

[7] Kilian, M., D. Pellis, J. Wallner, and H. Pottmann, "Material-minimizing forms and structures", *ACM Transactions on Graphics,* Proc. SIGGRAPH Asia. 36(6), pp 1–12, 2017.

[8] D. Pellis, H. Pottmann, "Aligning principal stress and curvature directions", *Advances in Architectural Geometry, Chalmers University of Technology, Gothenburg, Sweden,* pp. 22-25 September 2018;

[9] H. Pottmann, D. Bentley (eds.), *Architectural Geometry*, Exton : Bentley Institute Press, 2012.

[10] H. Pottmann, Y. Liu, "Discrete Surfaces in Isotropic Geometry", Berlin; New York : *Springer-Verlag, Lecture notes in computer science*. no. 4647, (2007): pp. 341-363.

[11] S. Brell-Cokcan and H. Pottmann, *Tragstruktur f¨ur Freiformfl¨achen in Bauwerken*. Patent No. A1049/ 2006.

[12] B. Cutler and E. Whiting, "Constrained planar remeshing for architecture", *In Symp. Geom. Processing* 2006, poster.

[13] J. Glymph et al., "A parametric strategy for freeform glass structures using quadrilateral planar facets", In Acadia, pp. 303–321. ACM, 2002.

[14] Y. Liu, H. Pottmann, J. Wallner, Y.L. Yang and W. Wang, "Geometric modeling with conical meshes and developable surfaces", *ACM Trans. Graphics*, 25(3): pp. 681–689, 2006.

[15] H. Pottmann, S. Brell-Cokcan and J. Wallner, "Discrete surfaces for architectural design. In Curve and Surface Design: Avignon", *Nashboro Press*, pp. 213–234, 2006.

[16] H. Pottmann, Y. Liu, J. Wallner, A. Bobenko and W. Wang: "Geometry of multi-layer freeform structures for architecture", *ACM Trans. Graphics*, 26(3), 2007.

[17] A. I. Bobenko, H. Pottmann, J. Wallner, "A curvature theory for discrete surfaces based on mesh parallelity", *Mathematische Annalen,* v348 n1 (2010): pp 1-24.

[18] Alexander I. Bobenko, T. Hoffmann, and B. Springborn." Minimal surfaces from circle patterns: Geometry from combinatorics" *Ann. of Math*., 2006, 164: pp 231–264.

[19] Alexander I. Bobenko and Y. Suris, *Discrete differential geometry: integrable structure*, Providence, R.I. : American Mathematical Society, ©2008.

[20] Alexander I. Bobenko and Yuri Suris. *Discrete Koenigs nets and discrete isothermic surfaces*. International mathematics research notices: IMRN. 2009.

[21] W. K. Schief. "On a maximum principle for minimal surfaces and their integrable discrete counterparts" *J. Geom. Physics*, 56: pp. 1484–1495, 2006.

Proceedings of the IASS Annual Symposium 2019 – Structural Membranes 2019
Form and Force
7 – 10 October 2019, Barcelona, Spain
C. Lázaro, K.-U. Bletzinger, E. Oñate (eds.)

Stereodome I: design, fabrication and installation of a Styrofoam masonry vault

Ricardo M. AVELINO*, Pedro H.P. TORRES, Arina v.L. CARVALHO, Beatriz MONTELATO, Bianca TEIXEIRA, Bruno T. VASCONCELOS, Michele OLIVIERI, Murilo S. O. SOTO, Ruy M.O. PAULETTI[a]

*Student at Polytechnic School, University of São Paulo (USP)
Av. Prof. Luciano Gualberto, 380, São Paulo, Brasil
ricardo.avelino@usp.br

[a] Associate Professor, Department of Structural and Geotechnical Engineering, Polytechnic School, USP

Abstract

This paper presents the steps of design, fabrication and installation of a Styrofoam masonry vault, produced in 2018 at the Polytechnic School at the University of São Paulo (POLI-USP), in the context of a graduate course on Light Structures. The challenge of the project was to design and deliver an innovative structural prototype, in a relevant scale. The project selected by the students was a funicular, three-legged masonry vault laying within a 3.0m diameter circle. The structure was form-found using graphic statics. Then it was discretized into 45 irregular bricks cut out from 10cm thick Styrofoam bulk blocks, with the aid of a CNC hot wire router machine. An efficient stereotomy technique was applied to ensure that adjacent bricks could be fabricated with minimum waste of material and high precision in the final shape. The structure was nicknamed 'Stereodome I' and resulted in an eye-catching curved complex surface that was exhibited for months at the Civil Engineering Building of POLI-USP.

Keywords: Structural design, Constructive geometry, Shell structures, Temporary structure, Education.

1. Introduction

Funicular shell structures have called the attention of designers and builders in the last decades [1,2]. They are defined here as structures transferring loads only my means of compression instead of bending. For these structures, shape is intrinsically associated with the forces in the system, increasing the relationship between architectural and structural form [3]. Historically this type of structures flourished in the gothic architecture [4]. They can be designed and verified by means of graphic statics. This technique was developed in the second half of the 19th century [5], and it proves the equilibrium of 2D structures by a pair of two reciprocal diagrams: a form diagram representing the geometry of the pin-jointed frame, and a force diagram, representing the equilibrium of the internal and external forces of the structure. The extension of graphic statics to 3D problems was first studied by O'Dywer [6] and later by Block [7] in the Thrust Network Analysis (TNA), allowing an extension to 3D considering vertical loads only. New computational tools [1] made possible interactive design based on graphic statics resulting in non-standard and efficient shell shapes. Even if the analysis of such non-standard structures became possible, their shapes challenge fabricators and builders making these structures non-affordable or hard to build [8]. In this paper, interactive design and analysis method are used to conceive a funicular prototype having its manufacturing method addressed to reduce waste of material and to simplicity of construction. The fabrication technique is based on stackable elements, created by Enrique [9, 10] and applied to Styrofoam material creating a vaulted prototype built by students.

Copyright © 2019 by Ricardo M. AVELINO, Pedro H.P. TORRES, Arina v.L. CARVALHO, Beatriz MONTELATO, Bianca TEIXEIRA, Bruno T. VASCONCELOS, Michele OLIVIERI, Murilo S. O. SOTO, Ruy M.O. PAULETTI
Published by the International Association for Shell and Spatial Structures (IASS) with permission.

2. Form-finding

The funicular prototype was idealized to fit inside a circle with a diameter of 3.0m supported only by three legs touching the ground. The boundary of the structure is split in three symmetrical parts and in each of them a cutting circle with a diameter of 2.25m define three points that are used to create a parabolic profile that cut the initial circle (Figure 1a). An oculus of 0.30m is also cut-out of the initial circle and the final silhouette of the structure is defined (Figure 1b).

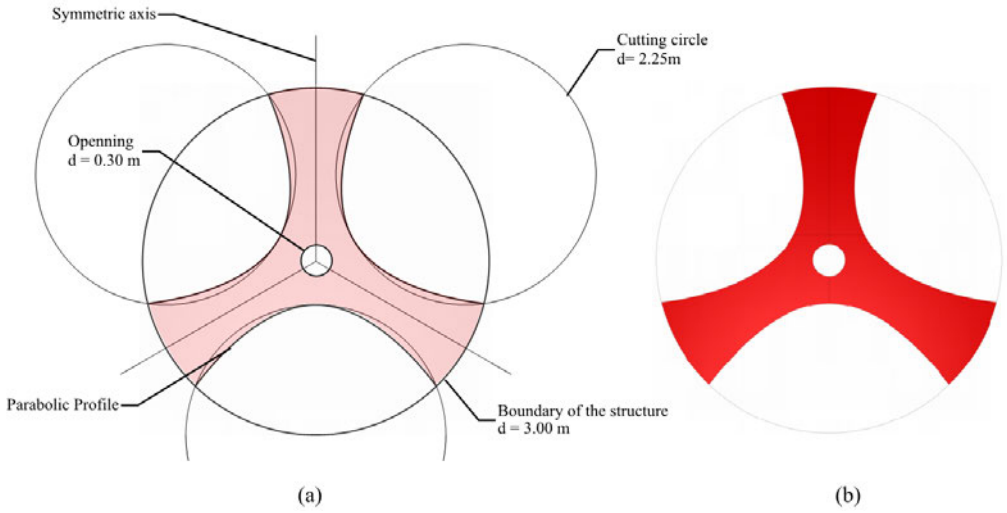


Figure 1. Geometrical definition of the structure. (a) Geometrical elements (b) Silhouette of the structure.

Based on the silhouette of Figure 1b, a form-diagram was created using the plug-in developed by Oval [11] which creates quad-meshes with singularities respecting boundaries and openings of the form. The form-diagram (Γ) created is shown in Figure 2. It has three singularities, one in each leg aligned with the symmetric axis of the structure and near the center of the bounding circle. With such a diagram the form-finding of the structure was conducted with RhinoVault [1]. The loads are applied only in the nodes of the form-diagram proportionally to their tributary area. With the aid of RhinoVault a reciprocal diagram is generated and by means of linear-optimization the force diagram (Γ*) is modified to be in equilibrium with the applied loads. In this stage, the Γ* looks like the diagram depicted in Figure 2. According to the notation of [3], each node in Γ is represented by a close polygon in Γ*; each edge e in Γ has a corresponding edge e^*, parallel to edge e, in Γ*; and the length of an edge e^* in Γ* is, proportional to the magnitude of the axial force in edge e in Γ. The final three-dimensional structure is also depicted in the thrust network (G) that shows the complexity of the non-standard shape designed.

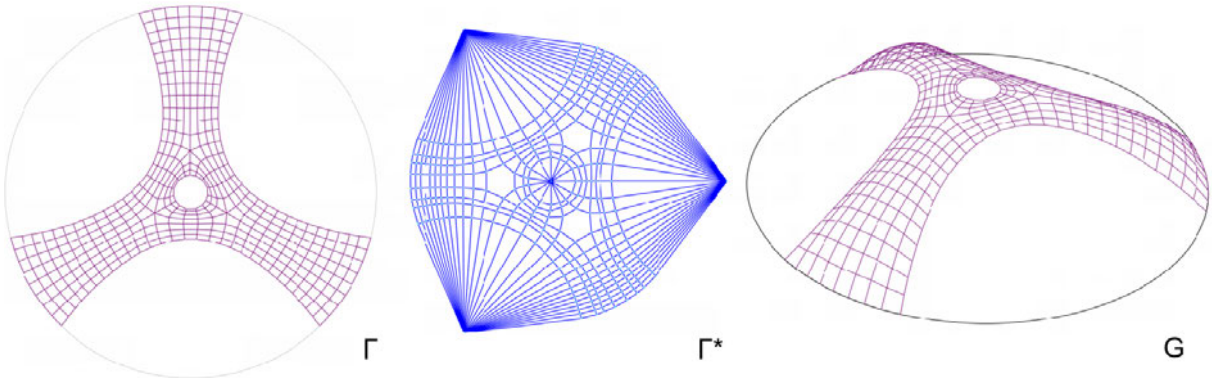


Figure 2. Form-diagram (Γ) showing the struts, force-diagram (Γ*) defining the magnitude of the forces and thrust-network (G) with the 3D.

3. Constructive geometry

From the Thrust Network (G) of Figure 2, a smooth surface was created to materialize the structure (Figure 3). The fabrication of complex surfaces has been studied by several authors [8,9,10] showing that the constructive strategy can dramatically reduce waste and simplify installation.

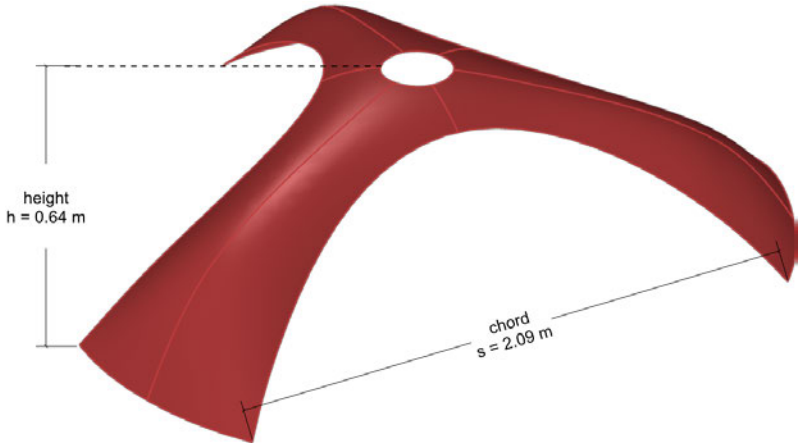


Figure 3. Smooth surface generated from the Thrust Network (G).

Many strategies could have been adopted to discretize the structure into smaller elements for fabrication and assembling. One could have it approximated by planar elements as in [2], this would, however, require a scaffolding system and would generate excessive waste for cutting the elements one-by-one. The strategy adopted in this work was based on the CASTonCAST methodology developed by Enrique [9, 10]. It consists on stackable elements that can be assembled horizontally but also be stacked in a pile. The challenge becomes: how to pass from a complex 3D surface to a pile of stackable voussoirs?

To achieve this, the surface of Figure 3 was first split in three segments, taking part of the symmetry of the structure. The one leg surface (Ω) is, then, replicated and moved 10 cm horizontally and 5 cm vertically (always towards the exterior of the structure, as in Figure 4). A volume (ϒ) is generated after this displacement. This volume will correspond to the volume of each leg in the materialized structure. To guarantee the assembling of the three legs, the contact surface between the legs is parallel to *z*.

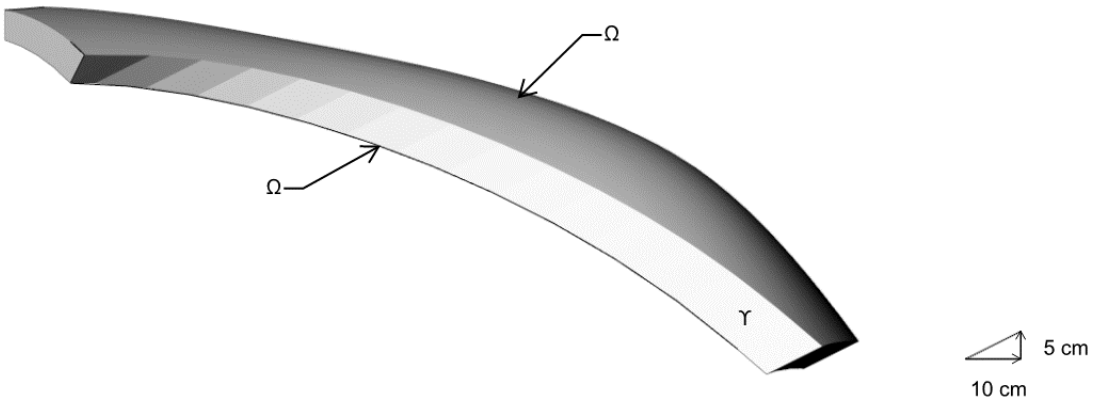


Figure 4. Replicating one leg surface to 10 cm horizontally and 5 cm vertically as shown in the triangle.

When the original surface is copied and moved horizontally by 10 cm, if we slice it in parts (*i*) of 10 cm, the superior face of one element *i* will be the same as the inferior face of the next element *i+1*. By this way, the volume ϒ is cut in 15 elements as depicted in Figure 5. Note that now the elements from 1 to 15 can be stacked in a pile as well as joined horizontally to form the same volume (Figure 6).

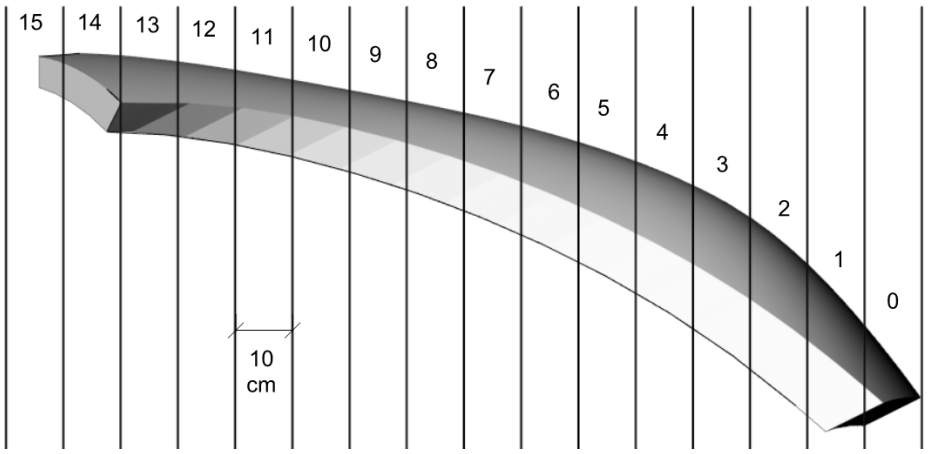


Figure 5. Cut of the one leg volume to generate the 15 stackable elements needed to build one of the legs.

The final three elements numbered 13,14 and 15 are extended to reach the end of the previous voussoirs. They require then a perpendicular cut to provide the smooth connection between the three legs. The pile of voussoirs and the constructed position of them is presented in Figure 6. The height of the blocks is variable, since the initial surface (Ω) was very irregular. It varies from around 12 cm in the base to around 6 cm close to the oculus. Several advantages can be extracted from the stackable elements [9, 10], such as a reduction on the waste of material to build the complex shaped voussoirs since the upper surface of an element is similar to the lower surface of its neighbor and also the construction can be completed by simply moving the pieces from the pile-configuration to the final structure. This will be essential to the fabrication and installation processes as presented in the following section.

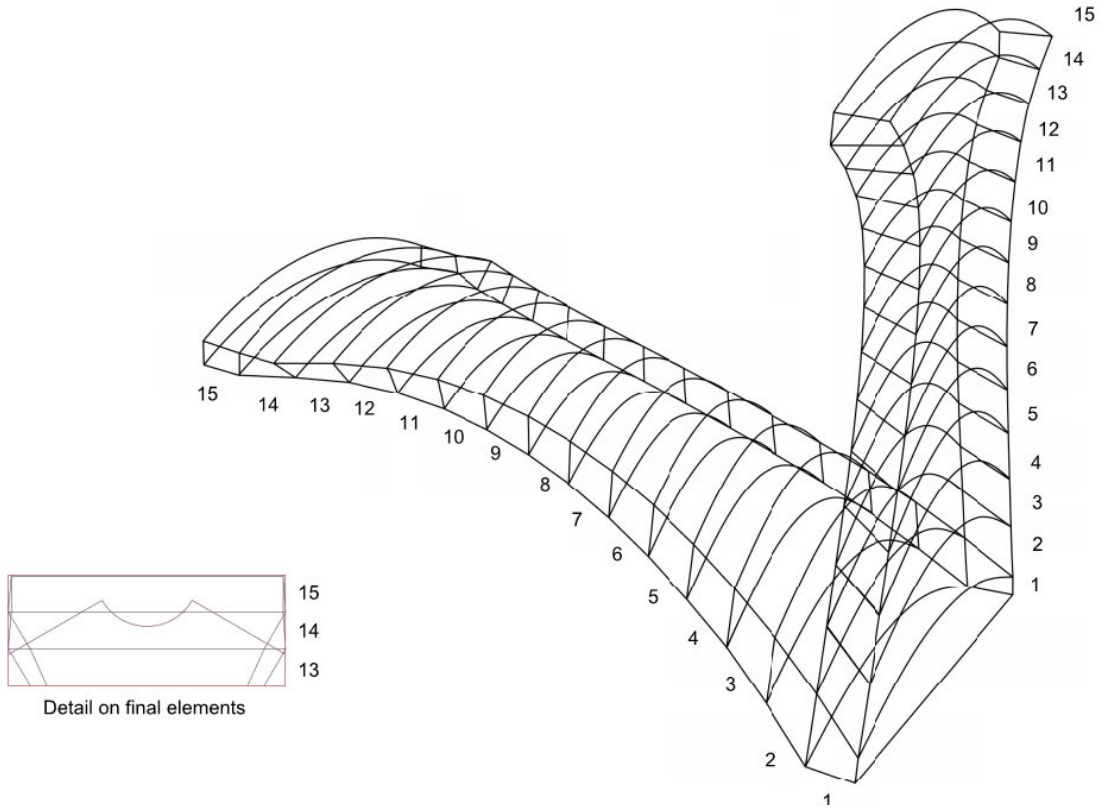


Figure 6. 15 elements in a pile and after the installation of the structure and detail of 3 last elements.

4. Fabrication

The fabrication of the voussoirs was performed using a CNC cutting machine. The CNC cutting machine is composed of two parallel frames each of them controlling independently one of the extremities of a hot-wire that cuts the blocks of Styrofoam positioned between the frames. With such configuration any developable surface can be cut. The definition of a voussoir is made in the software *devFoam 1.05* and it depends upon two cutting surfaces one in each side of the block called right (R) and left (L) plus the distance between these surfaces, corresponding to the thickness of the voussoir (10 cm). With such surfaces drawn, the sync points are defined in the vertices of the figures, so the hot-wire will align in these points. The R and L surfaces and the sync points of voussoir #4 are shown in Figure 7.

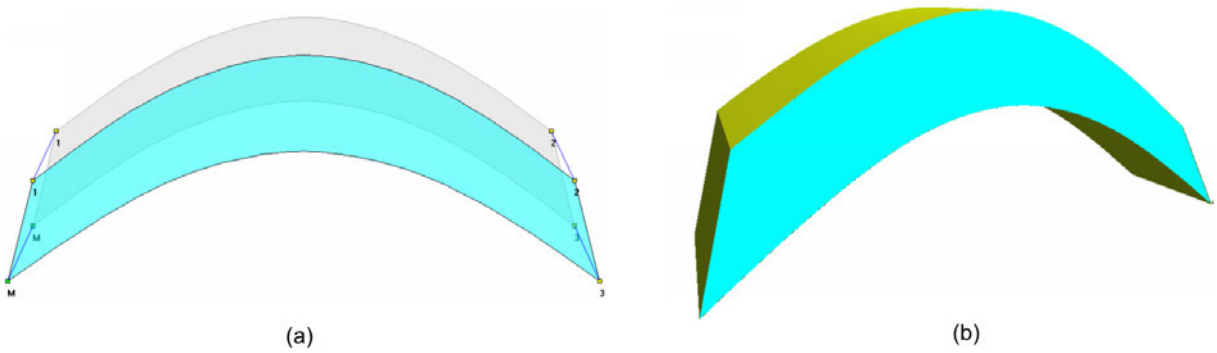


Figure 7. Voussoir #4. (a) Parallel faces - R and L - and sync points on corners (b) Rendering of cut piece.

After defining 15 irregular voussoirs the cutting simulation was performed to calculate the individual trajectory of the ends of the hot-wire. To calculate these trajectories the distance between the frames is set as 60 cm and the foam block is positioned in the middle of the frames. Figure 8 shows this simulation step-by-step for voussoir #4, from the initial position of the hot-wire, following the cut of the piece and the return to the initial position. The individual trajectories for each frame are also shown in red.

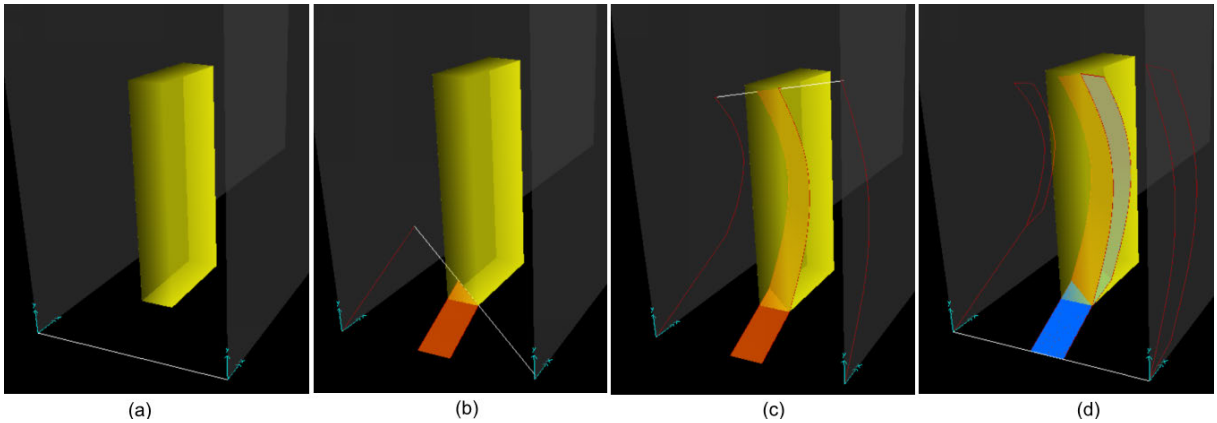


Figure 8. Cut process. (a) Initial position with bulk block in yellow between two movable frames. (b) Start of cutting, hot wire touches the Styrofoam block following the calculated trajectory (c) Cut of voussoir's lower surface (d) End of cutting process the element, wire returns to initial position.

To take part of the stackable elements, the pile of voussoirs was cut from bulk blocks. 13 elements could be cut from the same block having dimensions 1.00x1.25x0.10m. Since the frames could reach further in the horizontal directions, the pieces were cut rotated of 90deg (Figure 8). Figure 9a shows the original block and the 13 pieces that were cut from each of them (Figure 9b). Such a fabrication method reduced waste of material, the number of cut sections and ensured high precision in the tessellation of the final shape. It was observed that the alternative of cutting planar panels would have produced far more waste.

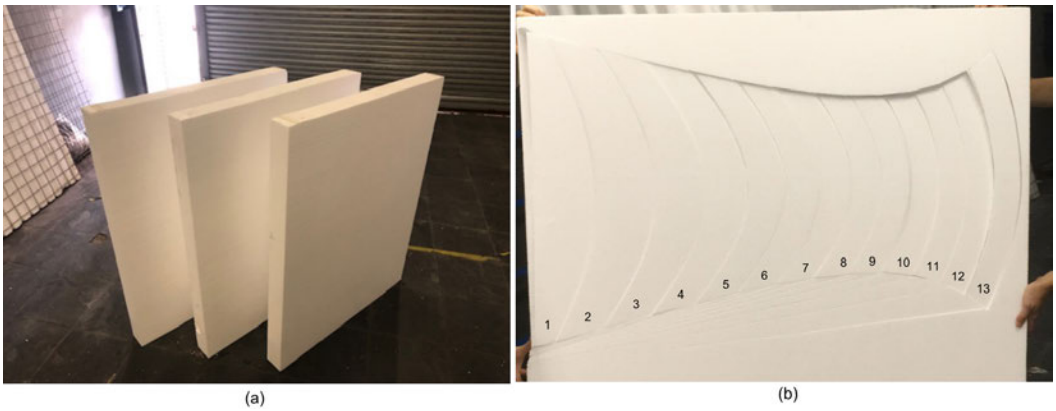


Figure 9. Fabrication of voussoirs. (a) bulk blocks used to cut the pieces; (b) 13 voussoirs cut from one block.

5. Installation

The 45 voussoirs were cut and transported to University of São Paulo to assembly. They were colored in alternate colors to emphasize the curves of the structure. Two twines sets were applied allowing the assembling of the structure. The first set was composed by three continuous twines that go through the voussoirs (Figure 10a). The second set runs underneath the structure, taking the thrust reaction of the funicular shape directing it to a central connection (Figure 10b).

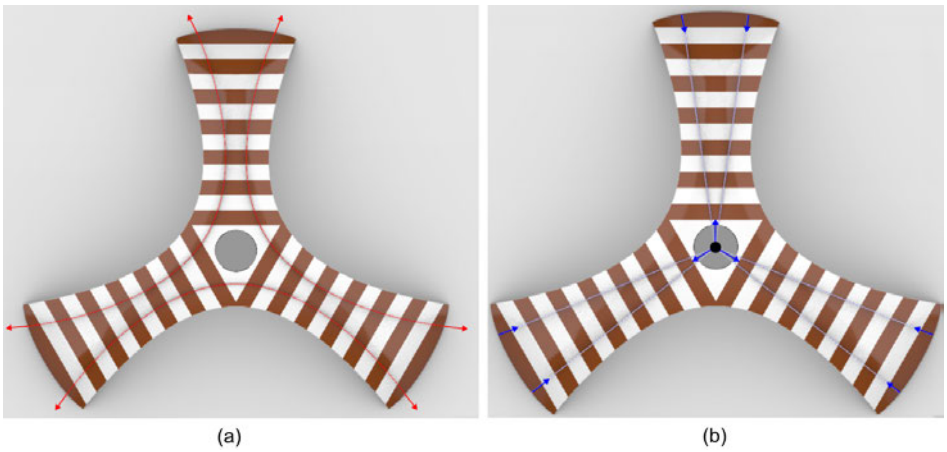


Figure 10. Scheme of the twines on the structure (a) Internal twines; (b) Ties system.

The assembling of the structure was completed in one day. The voussoirs were identified and positioned with the connecting twines joining them (Figure 11a). The erection process was proceeded manually by lifting the oculus and connecting the ties system. The internal twines were post-tensioned to augment the forces in the interfaces of the voussoirs. It was observed that only post-tensioning the twines was not enough to avoid the sliding between voussoirs (Figure 11b). In fact, since the vault legs are split by vertical planes, rather that principal planes (i.e., planes with zero shear resultant), the shear stresses between voussoirs should be taken either by friction or by shear toggles. Since the Styrofoam material had a limited strength and could be damaged at the twines' anchorages, the solution was the addition of wooden sticks between each pair of voussoirs, functioning as shear toggles. After the introduction of the toggles and the post-tensioning of the internal twines the elements were aligned. The twines were post-tensioned and anchored in the last element of the structure using a plastic anchor (Figure 11c). The ties system was composed by a ring and three variable length screw, running in the level of the floor and are attached to the base of element #1. The thrust forces could be equilibrated by adjusting the length of this screw (Figure 11d). The final structure is presented (Figure 11e).



Figure 11. Assembling of the structure (a) 45 voussoirs aligned by the internal twines; (b) erection of the structure before adding shear locks; (c) detail of the anchorage for the internal twines; (d) precision revealed by the connection in the oculus and variable-length screw of the ties system running on the ground (e) completed structure exhibited.

The match of pieces in the oculus of the structure revealed the precision of the fabrication and installation processes (Figure 11d). The height of the structure was measured as 64.7 cm against 63.9 cm in the model (1.3% error). The chord length between the legs of the structure designed to reach 209 cm (Figure 3) was measured as 215 cm (2.9% error). The structure was than exhibited in the Civil Engineering building of Escola Politécnica da Universidade de São Paulo during the Spring Semester.

4. Conclusion

This paper presented a project developed in the context of a graduate course on lightweight structures. Students successfully constructed a complex vault built from 45 Styrofoam blocks. The shape was form-found using TNA with the aid of RhinoVault and the plugin developed by Oval [11] to generate the skeleton of the structure.

The stereotomy technique adopted was inspired the methodology developed by Enrique [9, 10] in which the voussoirs were cut sequentially from a single block and then assembled horizontally in the final structure. Since the upper face of one voussoir corresponds to the lower face of another, it was possible to reduce the number of sections performed by the hot wire. This technique enabled not only to save a considerable amount of production time, but also a large amount of material when compared to cutting individual planar parallelepiped pieces. In addition, cutting them together minimized setup errors of the CNC machine, such as the positioning of the blocks at the machine's reference points, which was fundamental to achieve the great precision observed in Figure 11e.

For the structure to comply as designed, shear locks were added in the contact between two elements. These contacts were vertical planes not perpendicular to the compression flow, so they resulted in shear forces. The authors point to the need of further development of the concept, by integrating the analysis of inclination of the cutting planes between voussoirs into the stereotomy model, to eliminate the need for shear locks, or to an effective dimensioning of these elements.

Acknowledgements

The students thank Mr. Bruno Bonizolli for kindly offering his workshop with a CNC cutting machine as well as supplying the material. We also thank Prof. Dr. Ruy Pauletti for inspiring us during the course.

References

[1] Rippmann, M., Funicular Shell Design: *Geometric approaches to form finding and fabrication of discrete funicular structures*, Thesis (Doctor of Sciences) – ETH Zurich, Zurich, 2016.

[2] Rippmann, M; Van Mele, T.; Popescu, M.; Augustynowicz, E.; Echenagucia, T. M.; Barentin, C. C.; Frick, U; Block, P., The Armadillo Vault, *Advances in Architectural Geometry*, 2016.

[3] Rippmann, M., Lachauer, L., & Block, P., Interactive Vault Design. *International Journal of Space Structures*, 27(4), 219–230, 2012. https://doi.org/10.1260/0266-3511.27.4.219.

[4] Heyman, J., The stone skeleton. *International Journal of Solids and Structures*, 2(2), 249–279, 1966. https://doi.org/10.1016/0020-7683(66)90018-7.

[5] Culmann, C., *Die graphische Statik*, Meyer & Zeller, Zurich, 1864.

[6] O'Dwyer, D. (1999). Funicular analysis of masonry vaults. *Computers and Structures*, 73(1–5), 187–197. https://doi.org/10.1016/S0045-7949(98)00279-X.

[7] Block, P., Ochsendorf, J., Thrust network analysis: a new methodology for three dimensional equilibrium, *Journal of the International Association for Shell and Spatial Structures*, v. 48, 2007.

[8] Mesnil, R., *Structural explorations of fabrication-aware design spaces for non-standard architecture*, Université Paris-Est, 2017. https://hal-enpc.archives-ouvertes.fr/tel-01510053.

[9] Enrique, L., Schwartz, J., CASTonCAST Shell Structures. *Advances in Architectural Geometry*, 2016.

[10] Enrique, L. et al. CASTonCAST: Architectural freeform shapes from precast stackable components VLC arquitectura. *Research Journal*, [S.l.], v. 3, n. 1, p. 85-102, apr. 2016. ISSN 2341-2747.

[11] Oval, R.; Rippmann, M.; Van Mele, T.; Baverel, O.; Block, P., Patterns for Masonry Vault Design. *Proceedings of the IASS Annual Symposium 2017*, Hamburg, Germany, 2017.

Proceedings of the IASS Annual Symposium 2019 - Structural Membranes 2019
Form and Force
7-10 October 2019, Barcelona, Spain
C. Lázaro, K.-U. Bletzinger, E. Oñate (eds.)

Structural efficiency of segmental shells, depending on segment geometries and connection properties

Cristoph DIJOUX* , **Felix SCHMIDT-KLEESPIES, Alexander STAHR**

* Leipzig University of Applied Sciences (HTWK Leipzig)
Karl-Liebknecht-Straße 132
cristoph.dijoux@htwk-leipzig.de

Abstract

Segmenting shell structures can simplify their fabrication and erection, as the segments are produced in a controlled workshop environment and only mounted on site. Various examples show, that it is possible to build such structures with simple connections – using suited segment geometries, even hinged connections are possible without the introduction of folds. The entities planning these structures usually studied different connection properties on their specific example. Anyhow, the few built examples are usually realized with connections, that are as stiff as possible, to improve the structure's overall robustness and stiffness. In the following paper these considerations' impacts on overall stiffness and therefore material-efficiency of shell structures in a more general frame is to be studied. Two shell geometries, with positive and negative Gaussian Curvature, are to be evaluated and compared with various segmental versions of themselves. Different doubly curved, planarized and developable seg-ment geometries, tessellations, grid rotations and connection properties are to be examined and ranked according to their impact on structural efficiency. For the purpose of examining these interconnected parameters, an approach based on an analysis of 13722 specimen and intuitive visualization of the found data, is to be used.

Keywords: segmental shells, optimisation, planarisation, timber, data visualization

1 Introduction

Under the growing availability of modern timber board materials, various groups in the field of architectural/structural design research have come to the conclusion, that segmenting shells is an especially feasible method for shell construction with timber products. Some examples are:

- the Kobra, see Bogensperger and Wiltsche [1]
- the Landesgartenschau Pavillon Schwäbisch Gmünd, see Krieg et al. [2] and Li [3]
- the Timberdome, see Robeller and Viezens [4]

Compared to other methods, e.g. Lattice-Shells or Reciprocal Grid-Shells, they can reduce the amount of manual labour, as the segments can be fabricated in automatic processes. Also, the notoriously difficult covering of doubly curved shells for permanent use is obsolete, as the

Copyright © 2019 by Cristoph Dijoux
Published by the International Association for Shell and Spatial Structures (IASS) with permission.

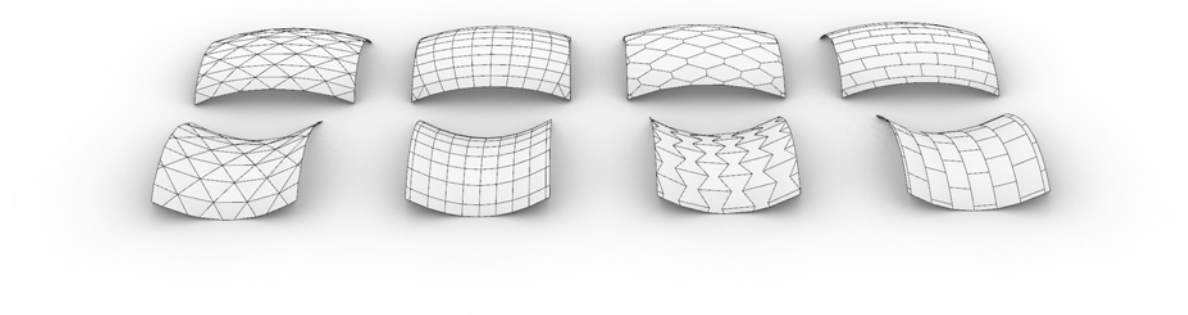


Figure 1: Triangular, quadrangular and hexagonal tesselations on a synclastic and anticlastic surface in their planarised form – except the striped solution on the right, as the segments are inherently curved.

segments are closed by themselves. Therefore, from a practical point of view, segmental shells can greatly simplify the fabrication of shells in timber construction.
The main motivation to build shells, apart from aesthetic or scientific reasons, is their inherently efficient load-bearing behaviour and therefore high material-efficiency. If a continuously curved shell surface is segmented in either planar or curved segments, the internal flow of forces is altered. This disturbance can vary greatly, depending on the segment geometries, their orientation and connection properties. These effects have been examined for specific solutions e.g. by Li and Knippers [5], but the authors are not aware of a broader, holistic comparison of different segment geometries. A qualitative insight on the resulting loss of efficiency of shell structures by segmenting them is pursued in this paper.

2 Geometries

To cover a large quantity of possible variants, a parametric approach to generate the segment geometries is used. As varying behaviour for synclastic and anticlastic surfaces is expected, both will be examined.

2.1 Shell Surfaces

The shell-surfaces are cut-outs of a torus. That way, they are easily reproducible and can be defined with only a few parameters.
The diameter of the torus centre-circle is $40m$ and the tube's diameter is 16 m. The shell surfaces are defined by a projection of a $10 * 15$ m^2 rectangle as illustrated in Figure 2.

2.2 Tessellations

A parametric approach has been used to generate the segment geometries. Four typical tessellations are implemented. Each with hindsight of delivering geometries affine for planarization. That is, three-, four- and six-sided, curved segment geometries, and so called stripes with only a curvature in one direction are implemented. These geometries, with special importance for the six-sided grids, are well planarizable by Dynamic Relaxation. That approach is inspired by Vaxman and Ben-Chen [6]. The actual implementation is of a lower, but sufficient complexity. As an exceptional case, singular curved quad-panels, or "stripes", are implemented as well. Obviously, they are not being planarized. Triangular planar tessellations are not suspected to be stable (Harding et al. [7]), besides kinks are introduced, as done by Grohmann et al. [8].

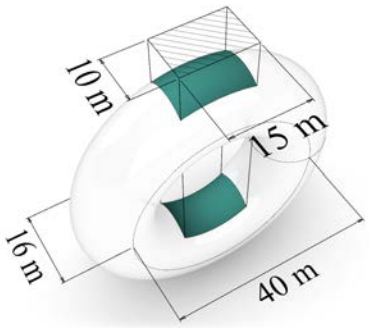


Figure 2: Definition of the shell surfaces, used as the basis for further examinations.

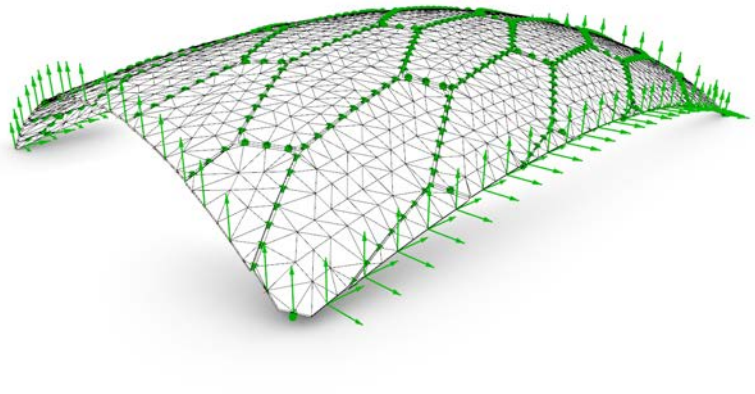


Figure 3: FE-Mesh, springs and supports

Nevertheless, it will be evaluated, as it can give an idea about the robustness of the approach. The grid-generators work with four-sided base surfaces and allow the manipulation of the grid's density by U and V division Parameters. The grid generators control the grid orientation on the surface, estimate an ideal grid rotation based on a curvature analysis and pre-shape gird-cells for an simplified planarization process where necessary. That is, the Parameters are U, V and rotation, while an estimation of ideal rotation is optional.

3 Structural Model

A directly implementable software package, based on the Finite Element Method, is used for structural analysis [9]. The segment geometries are therefore discretized with triangles, offset and connected with spring elements in between all referring vertices on their naked edges. The spring-modelling approach is inspired by the work of Li and Knippers [5].
Connection properties from freely rotatable to stiff are possible. The local coordinates of the springs are oriented on the base surfaces' normals and the springs' axes. Hinged connections are simulated by a 6-DoF definition of each spring element. The directional stiffness is set to a very high value of $10e5\ kN/m$ and the rotational stiffness is not zero either, but set to an insignificantly low number of $10e-4\ kN/rad$ for better convergence. As a second rotational stiffness, a value causing a 50% cut on deformations on an average quadrangular variant, equalling $3.5\ kN/m^2$ will be introduced to all variants. Fully stiff connections are not being examined, as it is extremely difficult to achieve rigid connections between timber plates (see Roche [10]).
A purely linear calculation of the deflections is not sufficient, as the shells are prone to non-linear effects, such as buckling. Therefore, an iterative algorithm, that considers these effects for small deflections, is being used.
The material formulation reflects an idealized, relatively soft construction of two OSB-layers, rotated by 90° with a total thickness of 4 cm. The representative values are a modulus of elasticity of 300 kN/m^2, moduli of in and out of plane shear of 108 kN/m^2 and 5 kN/m^2, and a specific weight of 5.5 kN/m^3. That choice is arbitrary, but considered reasonable, as buckling phenomena get more important the stiffer the material and therefore thinner the shell construction is.
Three design load-cases are defined (LC0, LC1, LC2). They consist of the structure's dead-load and a vertically projected area load of 2 kN/m^2. The area load effects either the full surface

(LC0), one eave-sided half (LC1) or one gable-sided half (LC2) of the surface. The different load situations deliver a robust answer about the stiffness of the structure and help to avoid singular corner-cases.
There are freely rotatable supports on all sides of the surface. While the eave-sided are locked in all translations (3-DoF) and the gable-sided ones are only locked for transformations in vertical direction (1-DoF). The decision to define supports at the gables is driven by the fact, that in real-world examples, usually arches and/or struts are applied in similar situations.

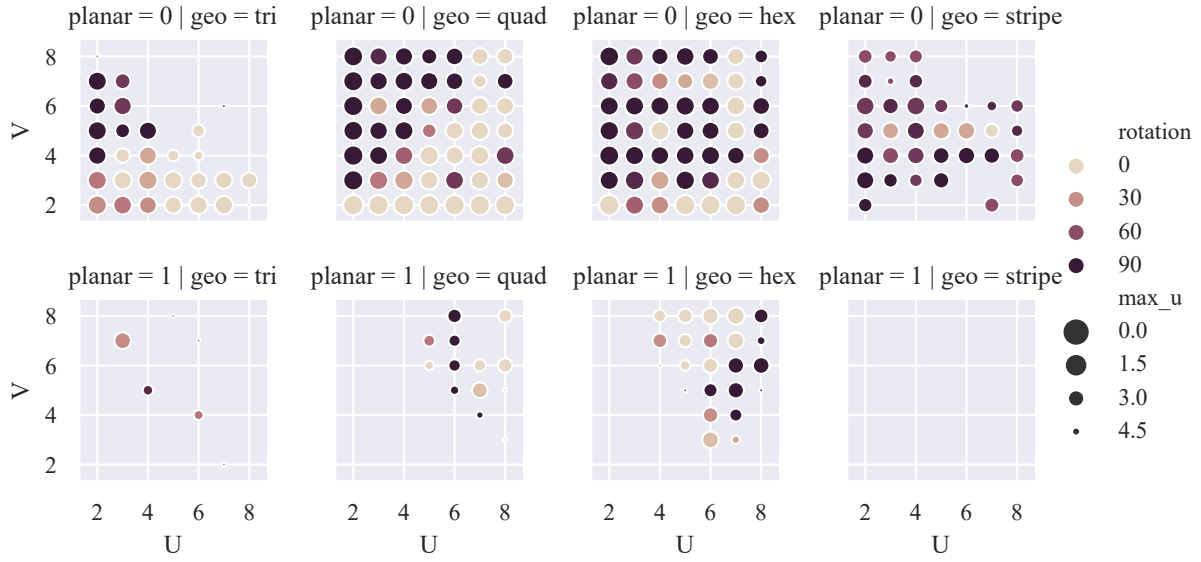


Figure 4: Parameter space for freely rotatable connections and positive Gaussian Curvature of the base surface.

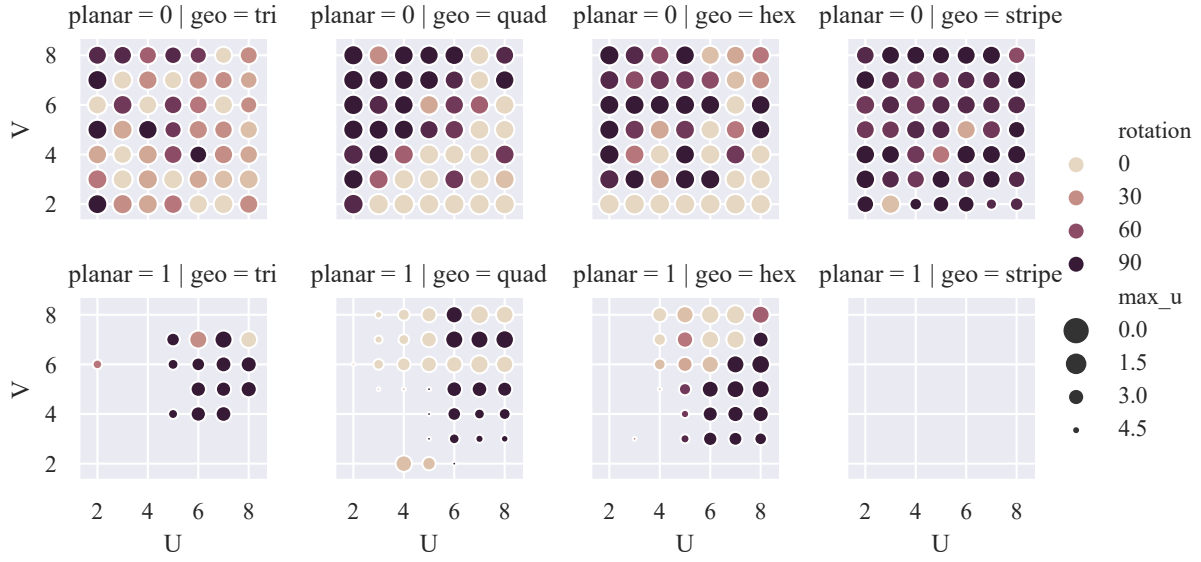


Figure 5: As Figure 4, but with semi-rigid connections.

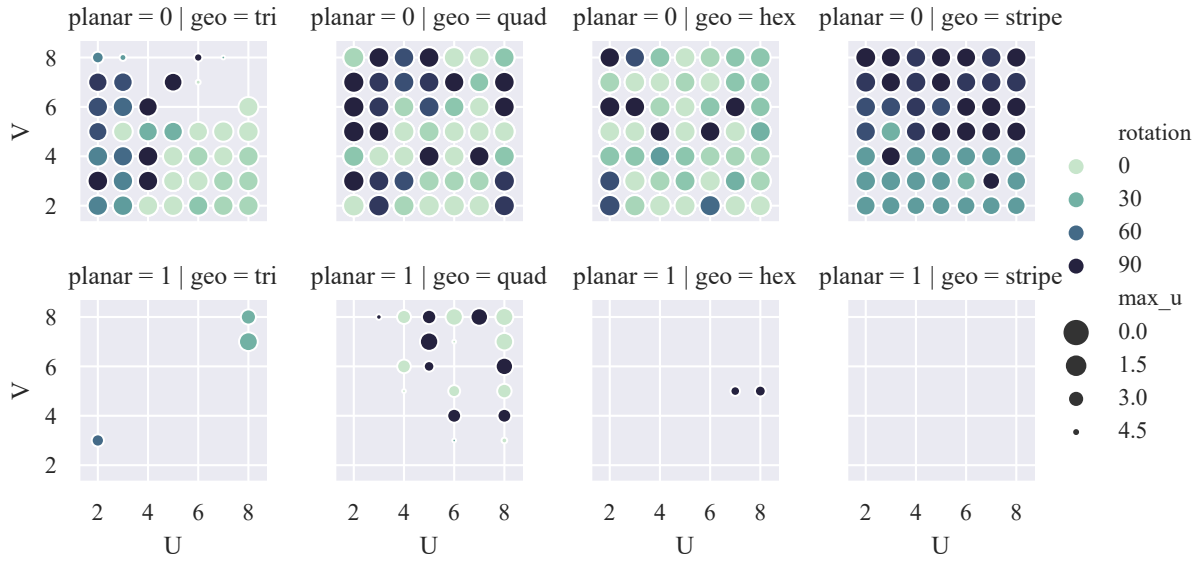


Figure 6: Parameter space for freely rotatable connections and negative Gaussian Curvature of the base surface.

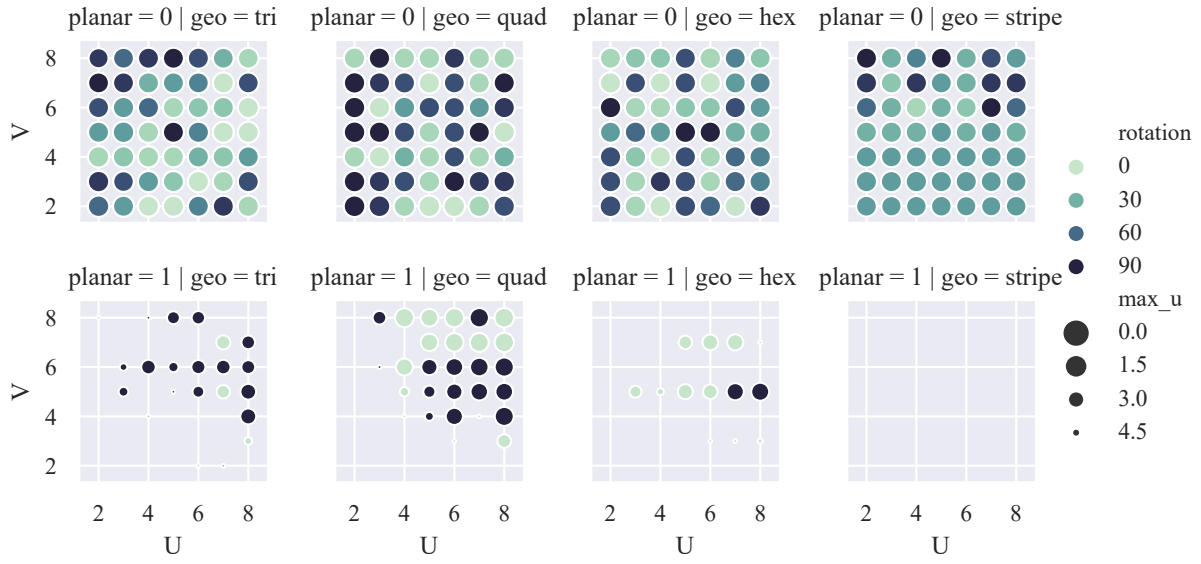


Figure 7: As Figure 6, but with semi-rigid connections.

4 Evaluation

The number of possible parameter variations for each variant depends on the domains of U and V values, as well as the step-size of the rotations. The rotation's domain is limited to 90°, due to the symmetry of the underlying surfaces. A reasonable minimum for U and V is 2 as tessellations without any connections between the supports are not related to the topic of this paper. A maximum value of 8 is chosen, to inhibit elements smaller than 1.25 m.
It is assumed, that it is accurate enough to analyse the rotations in steps of 10°. The total number

of possible parameter combinations is therefore 490, which allows a complete calculation of the parameter space. Each is used further on. Besides the continuous base surfaces, 7 tessellation-types on 2 different surfaces with 2 connection properties are evaluated. Hence, the sum of variants is 13722.
The data is used to generate intuitive graphs, that allow a deeper insight into the structures' properties. The best performing variant of each UV-combination is documented in the Figures 4 to 7.

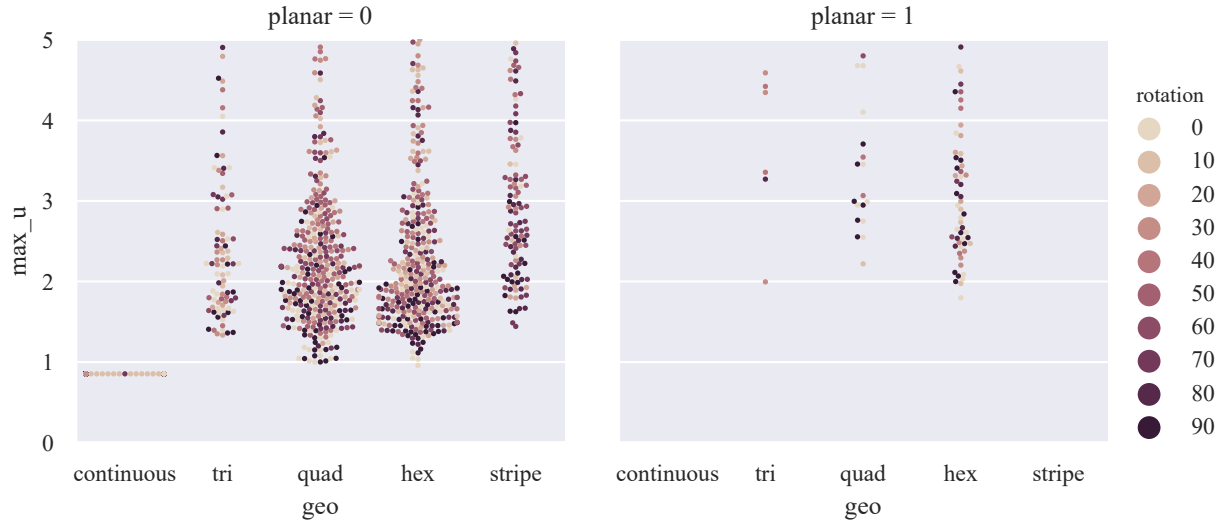


Figure 8: All freely rotatable variants on the positive surface with deformations < 5 cm, grouped by category, coloured by rotation and positioned by deformation.

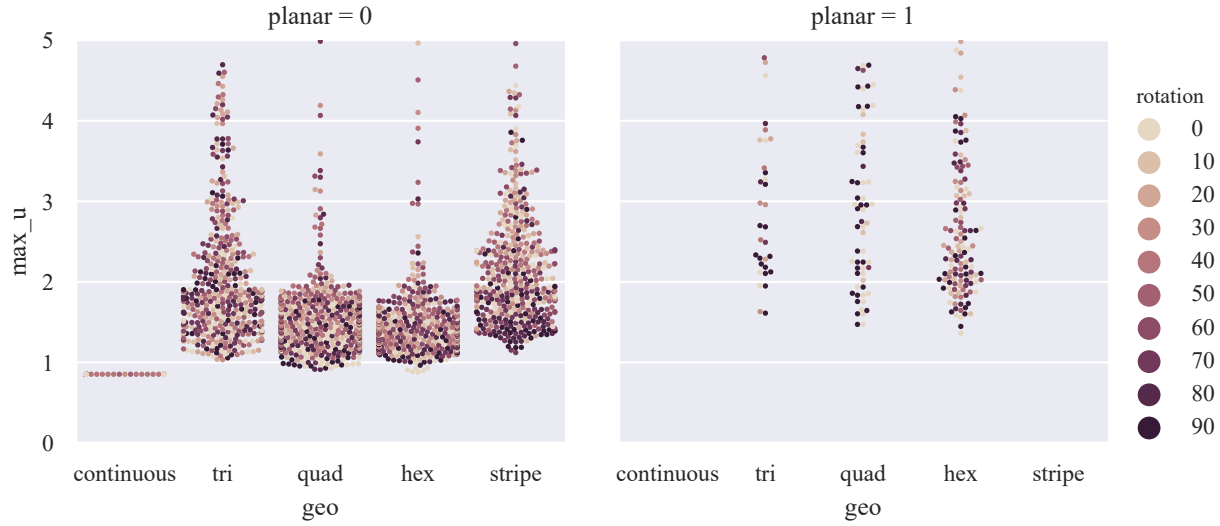


Figure 9: As Figure 8, but with a spring stiffness of 3.5 kN/rad.

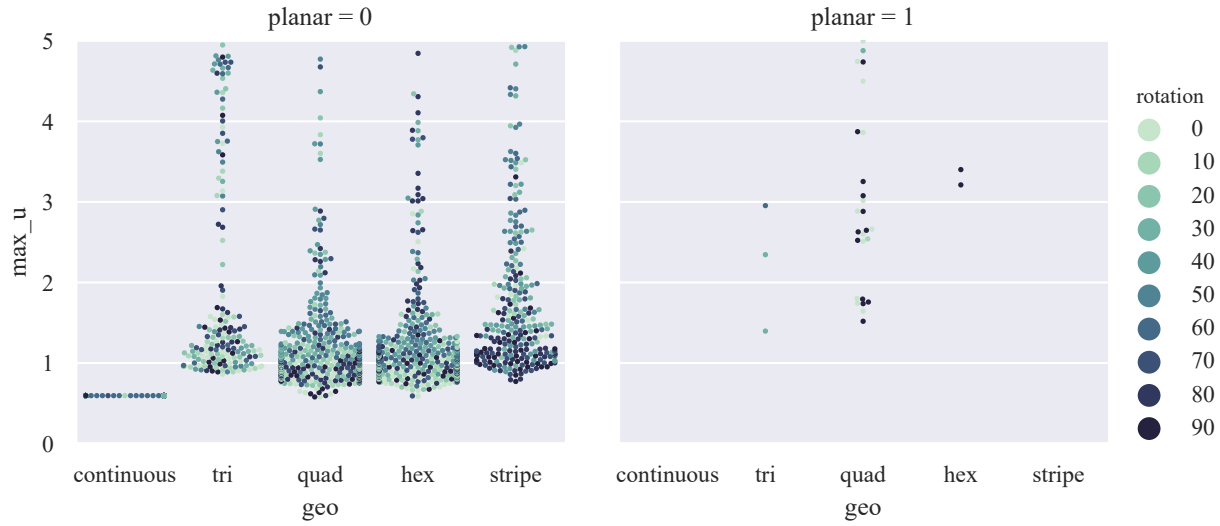


Figure 10: All freely rotatable variants on the negative surface with deformations < 5 *cm*, grouped by category, coloured by rotation and positioned by deformation.

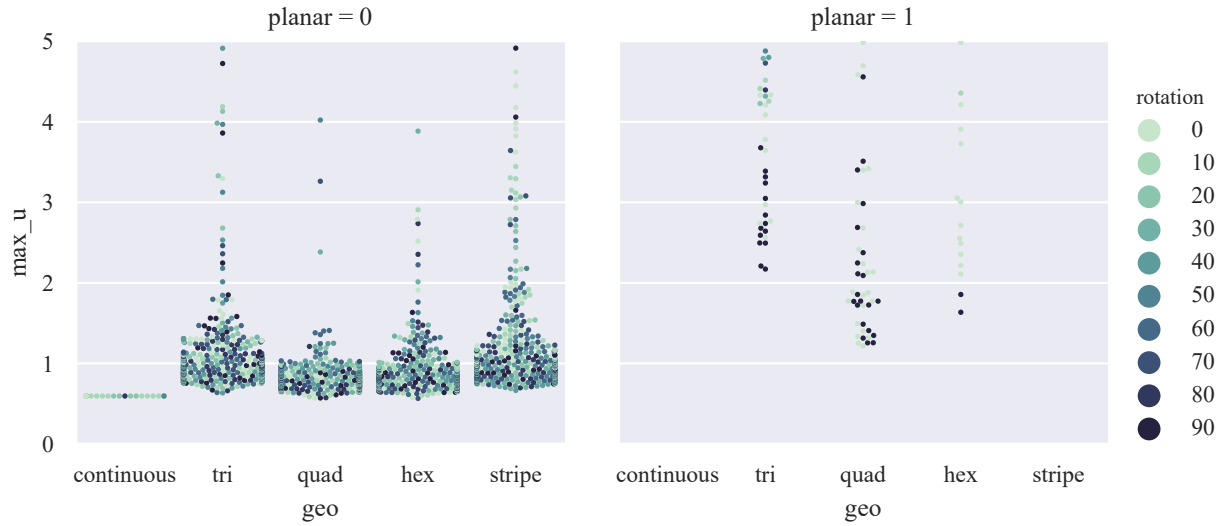


Figure 11: As Figure 10, but with a spring stiffness of 3.5 kN/rad.

5 Results

Only variants with deformations smaller than 5 *cm*, are being used for further examination. That approximately equals $l/200$ and therefore reflects a commonly accepted limit for tolerable deformations.

Variants missing in the parameter space diagrams either exceed that threshold, or have not been planarisable due to geometric constraints, e.g. polygonal segments due to cut edges. Figures 8 to 11 show the performance of every variant. As maximum, average or median deformation values do not deliver an intuitive understanding of the behaviour in an architectural context, that approach is being used.

6 Conclusions

It is possible to use different planar shapes as a discretization of doubly curved shell surfaces. The following paragraphs try to discuss the relation of deformation and discretization of the shells in general first and the influence of the segments' geometries afterwards. It has to be noted, that the isolation of these relations is only possible in a simplified manner, wherefore the plots with all results are included in this paper.

6.1 Continous, segmented and planar discertised shell

Even hinged connections between the elements are possible. The sole introduction of freely rotatable joints, without planarization of the segments, causes a significant reduction in performance. While it is possible to meet the efficiency of a continuous shell with rare variants, a fair number of the variants lies in a margin of 100% higher deformations for the anticlastic, respective 50% for synclastic shell surface. The introduction of springs between the segments shifts the majority of variants into that margin.
A planarization of the segments heavily reduces the number of possible configurations (see Figures 8 to 11), as it is causing another loss of stiffness, especially when freely rotatable joins are being assumed. Anyhow, it is possible to find variants lying within the margins stated above.

6.2 Segment geometries and connections

Performance and robustness heavily depend on the element geometries: Curved segments are performing better than planar segments, quadrangular and hexagonal variants better than triangular ones.
If freely rotatable connections are assumed, quad and hex tessellations are on par in their curved states. In accordance to theory [11], planarized hex-tessellations are more efficient than planar quads on the synclastic surface. But on anticlastic surfaces, hexagonal tesselation had a worse performance than quadrangular planar segmentations, due to the bow-tie shaped segments, needed to planarize a hexagonal grid under these constraints. As suspected, there have been only relatively few sufficiently performing planar triangular variants, as no folds have been introduced.
Regarding planarized segments, the introduction of a rotational resistance in the connections leads to a similar performance of quad and hex tessellations on the synclastic surface, while retaining the advantage of quads on the anticlastic surface.
Single curved stripes are remarkably stiff on both surfaces, rather comparable to the double curved than planar types.

6.3 Summary

It is possible to find equally well performing segmentations with hexagonal and quadrangular planar segmentations, but the former are much easier to handle geometrically. Quads were better performing on the anticlastic surface, and on par on the synclastic surface, if the connections are not freely rotatable. Therefore, it is not possible to generally advise one over the other.
An excellent alternative are single curved segments, as they are relatively easy to fabricate, but were performinng much better, than any planarized tesselation.

7 Acknowledgements

Prof. Dr.-Ing. Peer Haller of Technische Universität Dresden nurtured this study by honest discussions concerning shells in timber construction and FLEX.Professional.Research Team at Leipzig University of Applied Sciences (HTWK) delivered the vibrant environment this study was developed in.

References

[1] T. Bogensperger and A. Wiltsche. "Freie Formen Mit Brettsperrholz". In: *Bauen mit Holz: Fachzeitschrift für Konstrukteure und Entscheider* 11 (2012), pp. 34–39.

[2] O. D. Krieg et al. "Biomimetic Lightweight Timber Plate Shells: Computational Integration of Robotic Fabrication, Architectural Geometry and Structural Design". In: *Advances in Architectural Geometry 2014*. Cham: Springer International Publishing, 2015, pp. 109–125.

[3] J.-M. Li. *Timber Shell Structures : Form-Finding and Structural Analysis of Actively Bent Grid Shells and Segmental Plate Shells*. Stuttgart : Institut für Tragkonstruktionen und Konstruktives Entwerfen, Universität Stuttgart, 2017.

[4] C. Robeller and V. Viezens. "Timberdome: Construction System for CLT-Segmental Plate Shells without Screws". In: *Proceedings of the 24th International Timber Construction Forum*. 24. International Timber Construction Forum (IHF). Garmisch-Partenkirchen: Forum Holzbau, Dec. 5–7, 2018.

[5] J.-M. Li and J. Knippers. "Pattern and Form - Their Influence on Segmental Plate Shells". In: *Proceedings of the IASS Symposium 2015*. Future Visions. Vol. 2015. Amsterdam: International Association for Shell and Spatial Structures (IASS), 2015, pp. 1–12.

[6] A. Vaxman and M. Ben-Chen. *Dupin Meshing: A Parameterization Approach to Planar Hex-Dominant Meshing*. Technical Report CS-2015-01. Technion, 2015, p. 10.

[7] J. Harding and H. Lewis. "The TRADA Pavilion – A Timber Plate Funicular Shell". In: *Proceedings of the IASS Symposium 2013*. Beyond the Limits of Man. Wroclaw: International Association for Shell and Spatial Structures (IASS), 2013, pp. 1–5.

[8] M. Grohmann et al. "Hinged Folded Festival Pavilion – Membrane Bearing in Lightweight Dismountable Structures". In: *Proceedings of the IASS Symposium 2016*. Spatial Structures in the 21st Century. Tokyo: International Association for Shell and Spatial Structures (IASS), Sept. 30, 2016.

[9] C. Preisinger. *Karamba3D Parametric Engineering User Manual (Version 1.3.1)*. Aug. 9, 2018.

[10] S. N. Roche. "Semi-Rigid Moment-Resisting Behavior of Multiple Tab-and-Slot Joint for Freeform Timber Plate Structures". Dissertation. Lausanne: IIC, 2017.

[11] R. La Magna, F. Waimer, and J. Knippers. "Nature-Inspired Generation Scheme for Shell Structures". In: May 22, 2012, p. 7.

Proceedings of the IASS Annual Symposium 2019 — Structural Membranes 2019
Form and Force
7—10 October 2019, Barcelona, Spain
C. Lázaro, K.-U. Bletzinger, E. Oñate (eds.)

Study Case: Design of a spherical actively-bent chebychev net triangular gridshell covered by a stretchable membrane

Alan RYNNE*, Martina FABRÉ, Noelia RODRÍGUEZ, Jatziri RODRÍGUEZ, Marti SAIS, Christian DIMITRI, Pep TORNABELL, Gerard BERTOMEU, Enrique SORIANO,

*MPDA-UPC Barcelona Tech
Pere Serra S/N, Sant Cugat del Vallés

Abstract

The aim of this study is to design and build a spherical elastic gridshell, 6m in diameter and covered by a stretchable membrane; using the previously published work in Chebychev Net gridshells [8] and the introduction of singularity points [3], analyzing the behavior on different configurations and focusing specially on the area where a patch meets another. We exploit the special case when, introducing a single valence 3 singularity on the center of the chebychev net, leads to the assumption that structure and bracing could effectively be the same element. A number of new constructive problems arise when trying to erect the structure, wich are solved by allowing some of the joints to slide freely until the gridshell has been fully erected. Finally, using a recently developed stretchable architectural membrane, a cover for the structure was designed. Different load tests were performed on the phsysical model and compared to the analytical model to verify the structure and the reliability of the tools used.

1 Introduction

Gridshells can be defined as lightweight structures built with long slender profiles that get their strength from its double curvature shell while extracting extra material, leaving a reticulated shell. The initial mesh can be completely flat or can present topological singularities to approximate this mesh to the final surface.

These structures can be made of any kind of material -steel, aluminum, wood, composite materials, etc. Most of the gridshell structures have been made of wood because it is the only traditional building material that can be elastically bent without breaking. This flexibility generates curved shapes which generates structural stiffness. However looking at other industrial fields, it can be notices that every time high strength and high deformability are required, composite materials is replacing wood. In the case of gridshells, the optimal material should have *high elastic limit strain* and *high young modulus* in order to get a curved shape and to confer its final stiffness.

The most valuable alternative to wood is fibre reinforced polymers (GFRP). They have higher *elastic limit strain* (1.5% at best for GFRP and 0.5% for wood) and *young modulus* (25-30GPa against 10GPa for wood), allowing for greater freedom of form.

Copyright ©2018 by MPDA'18 UPC

Published by the International Association for Shell and Spatial Structures (IASS) with permission.

2 State of the Art

2.1 Chebyshev nets & compass method

The selected method for finding the grid was the compass method. This method, described in IL10 Gittershalen [9], allows the construction of a network of regular quadrangles on any given surface, plane or not. The task consists in constructing a grid using only a compass: First, a n number of curves is selected to be intersected on one point of the surface to mesh. Then, a mesh size is chosen and serves as the compass radius. The spacing of the grid is marked along each axis, from the point of intersection of the axes. The knots are determined by the intersection of two circles as shown in Fig. 1. Gradually, new points are determined.

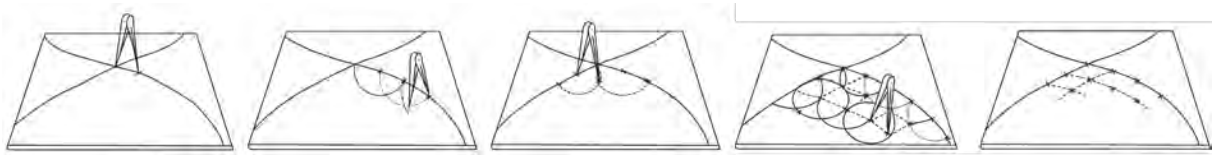


Figure 1: Construction of the grid using the compass method [9]

An infinite amount of meshes can be obtained by modifying any of the parameters (grid size, initial point, angle between axis curves, etc....), although many may fail to cover the surface correctly or present self intersections Fig. 2. In our particular case study, it is in fact impossible to cover more than half a sphere with the traditional method, skew angle between structural members becomes too small and eventually self intersects. It is important to note that this method is only a geometric approach with no structural implications whatsoever. The real shape of the gridshell is obtained later when mechanical properties are considered.

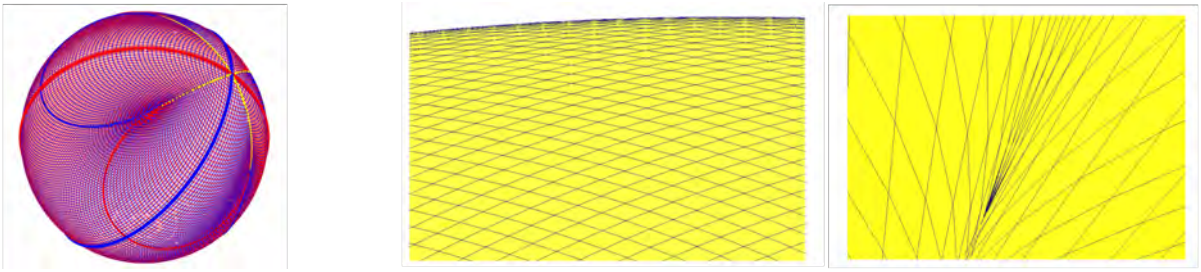


Figure 2: Chebychev Net on the sphere (left), and singularities due to curvature: fold (centre) & cusp (right) [8]

2.2 Construction process of a gridshell

The construction process of an elastic gridshell differs from other classes of gridshells. Their members are usually straight continuous profiles, arranged in superposed layers, which are progressively bent into their final shape. In our case, due to the regularity of our mesh, which is built from a deployable grid: during the erection process it can be bent starting from a flat position.
The use of straight profiles allows multiple advantages during the manufacture, transport and assembly of elastic gridshells contrary to other comparable constructions. Nevertheless, the

stresses induced in the profiles during the erection process and usually are much higher than those resulting under external loading.
Not necessary?

2.3 Limitations of chebyshev nets and singularity introduction

As stated in the introduction, new methods are being developed in order to introduce nodes with a higher or lower valance in the mesh [8], effectively dividing the surface in *'patches'*. This project implements these findings, analyzing the constructability issues of modeling singularities in elastic regular gridshells. In order to generate such regular meshes with singularities, a parametric tool was developed for Grasshopper to facilitate a fast iteration between models for comparison.

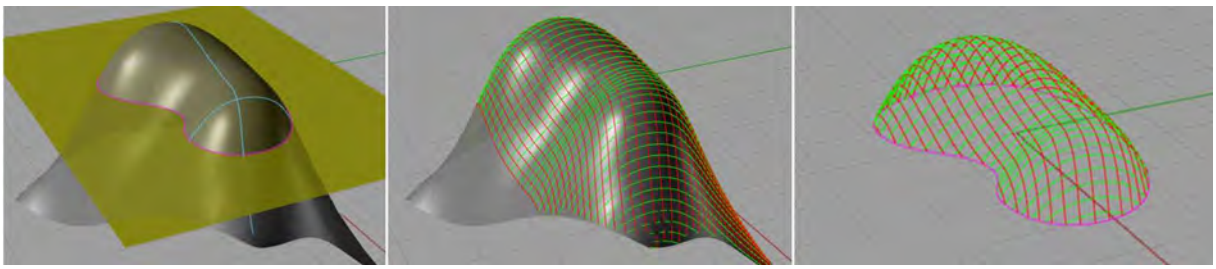


Figure 3: Construction a chebychev net for the solidays festival [4]

The final result is a 3-direction 3-layer grid Fig. 4 composed of individual chebychev patches. The model is designed with ø20mm GFRP rods, 1m spacing and an acceptable ratio between material needed for the structure, the structural behavior in the analytical models and its fairness to the reference surface.

3 Modelling Process

The challenge was constrained to a particular given surface: a 3m-radius half-sphere. The design had to include a stretchable membrane to cover the structure, and both the structure and the membrane needed to resemble the original surface as close as possible.

3.1 Structure design

3.1.1 Bracing

Bracing of the resulting structure had to be taken into account, as it would greatly improve the structural behavior of our structure and reduce considerably the boundary ring stresses. During structural explorations it was discovered that the bracing elements could also be interpreted as a continuation of the structural elements of each neighboring patch and, as such, every element in each patch would also be acting as bracing in it's contiguous patches. This has some assembly and erection implications that would be later addressed in XXXXX

3.1.2 Grid size

Different grid spacing configurations for the grid were explored in order to analyze required amount of GRFP rods, number of swivel joints and fairness to the reference surface in order to



Figure 4: Left to right: 3 chebyshev patches on a sphere; extending each rod to it's neighbour patches and the final set of patches individually.

achieve the optimal ratio between them. As can be seen in Fig. 5 the selected optimal model had a 1m spacing.

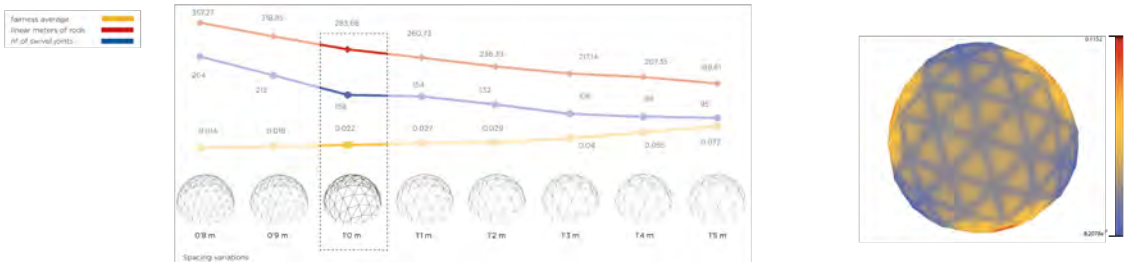


Figure 5: Left to right: analysis of different configurations of the triangular chebychev dome; surface fairness of the selected model

3.2 Membrane design

Two patterning options were evaluated in order to decide the best strategy to follow. The first strategy was done following one of the rod directions in the structure, which resulted in flat curved pieces that would generate too much cut-off material in order during fabrication.

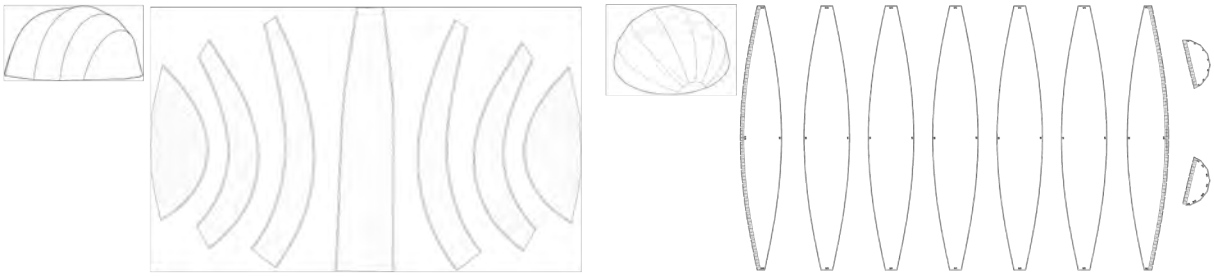


Figure 6: Comparison between the two patterning alternatives.

The second solution involved extracting the pattern out of an exact sphere of the desired radius (3m). The sphere was cut using great circles in order to generate straight membrane patterns that would reduce material waste. These straight membrane patterns were then scaled down to 95% in order to account for membrane pre-stressing, and also the fact that the elastic material chosen would accomodate for any imprecisions during design and fabrication.

All necessary 2D detailing of the membrane was done in a parametric software environment that allowed for a great amount of changes and corrections in a short period of time.
Regarding the membrane keddar, it was decided that a ø10mm GFRP rod would be placed inside a pocket with 64 openings that would be used to fix the membrane to the boundary, but also to adjust it's tension gradually.

4 Constructive Details

4.1 Swivel Joints

Several swivel joint solutions where explored for this project (see Fig. 7): metallic zip-tie joints, ø20mm pipe-hanger joint, *custom made swivel joint*, ø20mm aluminum swivel couplers and a custom pipe-hanger joint.



(a) (b) (c)

Figure 7: Aluminum swivel coupler(a), metallic zipies (b) & custom made swivel joint (c)

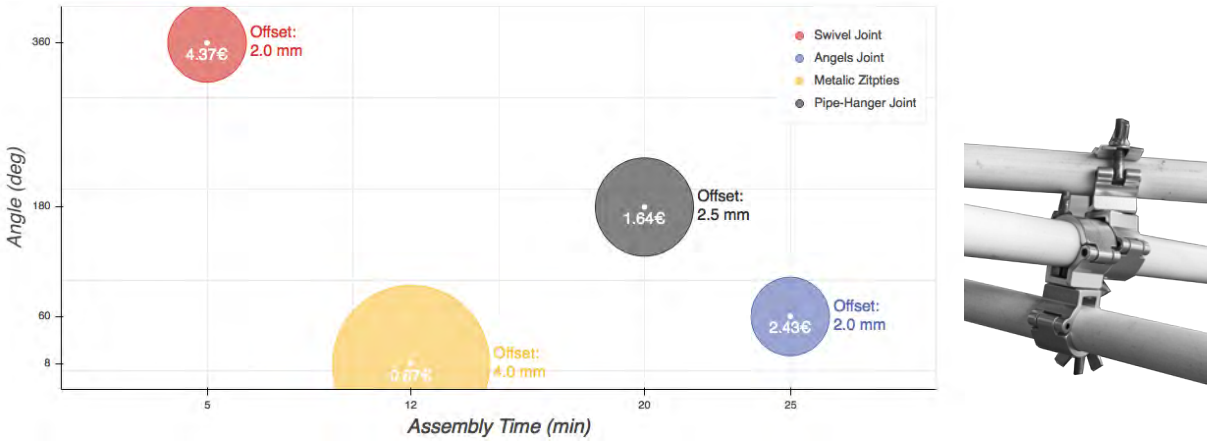
All of the options were evaluated according to their ease of assembly, cost, maximum angle deviation allowed by the joint & offset distance that each joint introduced between structural members; results can be seen on Fig. 8. Finally selecting an aluminum swivel joint as the best fitting solution for this particular case.

4.2 Linear Joints

Given that our structure had some members of length 9.35m, and the maximum length of rod we were supplied with was 6m, an optimization process was developed to evaluate the best location and ammounts of linear joints that we should introduce in the structure. The length, diameter and material was chosen for best curvature continuity results in the rods, while also taking into account structural integrity of the joint and it's ease of assembly on site. Finally, a 160mm stainless steel ø25mm (1,5mm thick) tube was selected. Since linear joints at the boundary are under tension, they were locked in place bolts.

4.3 Membrane tension straps

For the connection between the membrane and the boundary ring, the team opted for a ø10mm GFRP rod placed as kedar and tied to the boundary using 30mm wide black nylon straps and buckles, which allowed for gradual tensioning of the membrane (see Fig. 10).



(a) (b)

Figure 8: Swivel Joint Comparison (left) & selected joint (right)



(a) (b)

Figure 9: Linear joint solution (left) & solution with lock pins for boundary ring (right)



(a) (b) (c)

Figure 10: Membrane tension straps

5 Assembly Process

5.1 Flat assembly

Assembly started as a flat configuration of the 3 different patches with their continuations as seen in Fig. 11

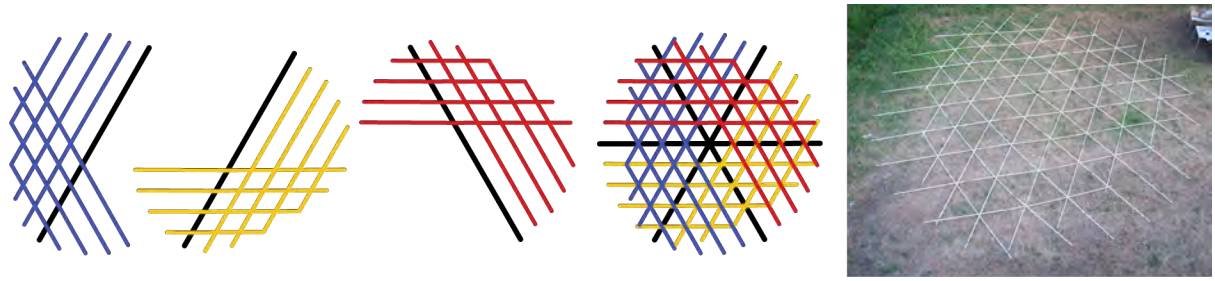


Figure 11: Diagram of the three chebychev patches (left) and picture of the flat assembled structure (right)

5.2 Erection process

After finishing the flat assembly, the first step in the erection process is to raise the central point of the structure to at least 1.75m in order relax the grid and help it to get in shape, as well as releasing tension on the ends of each rod, further facilitating erection.
After the grid was raised, the team proceeded to pull the ends of each of the grid's main diagonals to their boundary positions using only 3 nylon ratchet straps. This was a gradual process that was done advancing 50 cms at a time on each diagonal until the desired position was reached. At every step, the team made sure that the sliding joints for the bracing where moving as expected, gradually helping it to position where needed. This process lasted 10 hours.
Once the main diagonals where in place, the team proceeded to fix the rest of rods to their respective boundary positions, and finally tightening the joints that were left to slide freely, effectively bracing the structure.



Figure 12: Erection Process

5.3 Membrane unfolding

Membrane was delivered packed from the manufacturer, but needed to be extended flat and packed according to specifications Fig. 13. Once packed, it was raised to the top of the structure and unfolded in place. Once the membrane & keddar where in positioned, the membrane was gradually tensioned until bottom.



Figure 13: Membrane unrolling process

6 Structural Analysis

Further analysis was carried out using K2 engineering; a dynamic relaxation solver for structural analysis [10]. For the purpose of avoiding wrinkles in the membrane, several quality measures were taken into account while selecting the final pattern.
The aim of this chapter is to investigate the restraint effects on the nodes, the rods and the membrane. The offset between the rods were respected according to specific measure of the chosen nodes. Once the form was found, the rods and the swivels were analyzed without external loads while the anchor points were left free to move in the X and Y directions.

6.1 Structure Behavior

The behavior of the rods and their stresses (Axial Force, Axial Stress and Bending Moment) were analyzed only with their self-weight. Then we applied a load test at the highest point and we also analyzed the maximum displacement and the minimal bending radius given as a factor of the element t at 60% tensile strength (sufficient remaining lifting capacity).
The minimum bending radius of a ø20 mm GFRP rod is 1.56m and in our case we reach this value with a point load of 355kg placed in the highest point. Giving as a result a Max. Axial Force of 3.728 kN in compression, Max. Axial Stress of 11.867 MPa in compression, Max. Bending Stress of 265.001 MPa, Max Bending Moment of 0.208 kNm and a Max. displacement of 72.017mm.

6.2 Wind effect analysis

A 50kN/m2 wind load was introduced in the simulation, giving a maximum deflection of 10mm. As the membrane was pre-stressed, the mesh wind load is translated directly onto the structure without considerable deflection.

7 Conclusion and further works

After comparing the measurements between the physical & analytical models, the results [Fig. 20, Results] show a very similar behavior between both.

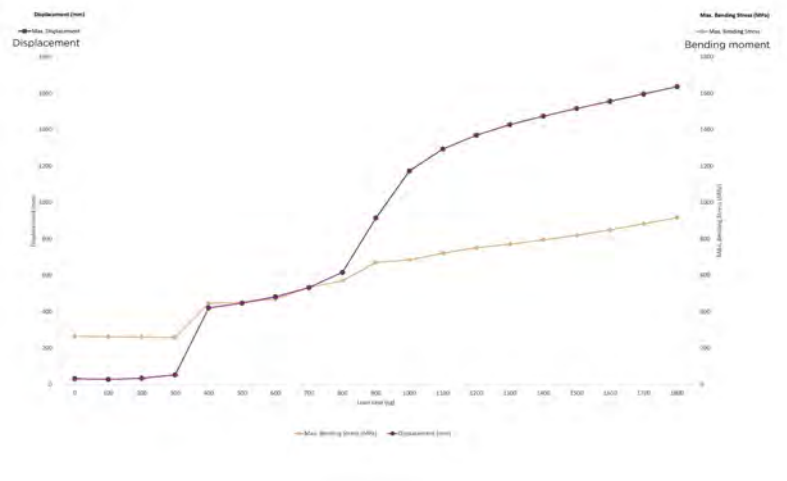


Figure 14: Relation between load case-bending moment-displacement

The selected joints for this structure were one of the main concerns during the fabrication and assembly. The erection was design to reduce the tension in the joints as much as possible; preventing damage or breakage, but also preventing from moving or twisting out of it's position. A Triangular flat configuration Fig. 11 provides a continuity to the Chebychev patches and eliminates the excess of the forces in the main diagonals while also providing a bracing concept that can be assembled along with the structure in its flat configuration. It is important to note that while the dome was successfully erected using only a team of 6 people and with no mechanical equipments nor cranes Fig. 12; the erection of vaults and domes with larger spans using this technique would need to take into account the forces acting on the structure to assess the auxialiary means that might be required on site.
The boundary ring's linear joints have been changed to allow the tension introduced by the structure. Two lock 3mm lock pins were added to the four boundary linear joints to prevent the join from sliding out.
Regarding the membrane, the keddar distance from the boundary ring should have been 15cm while, in the physical model, the distance couldn't be reduced from a range between 20-24cm without the risk of damaging the membrane. This 7cm average difference could have been caused by an incorrect calculation of the membrane scaling factor, an accumulation of errors during construction, un-even tensioning or any combination of the latter.

7.1 Further works

Further studies in this direction might include identifying the errors in the membrane patterning mentioned in the conclusion; developing better cost effective swivel joint solutions or studying the application of this method to irregular double curved surfaces among other topics.



Figure 15: Left to right: Rendered analytical model; final physical 6m dome

7.2 Acknowledgments

Special thanks to main sponsor SIOEN; manufacturer sponsorships TP Arquitectura, VISA, Tecnipul & Nioglas; and analysis software partners Kiwi3D, K2Engineering & Wintess for making this possible.

References

[1] Adriaenssens, S. et al. 2014. *Shell structures for architecture: Form finding and optimization.* Routledge.
[2] Baek, C. et al. 2018. Form finding in elastic gridshells. *Proceedings of the National Academy of Sciences.* 115, 1 (2018), 75–80.
[3] Baverel, O. et al. 2012. Gridshells in composite materials: Construction of a 300 m2 forum for the solidays' festival in paris. *Structural engineering international.* 22, 3 (2012), 408–414.
[4] Du Peloux, L. et al. 2016. Construction of a large composite gridshell structure: A lightweight structure made with pultruded glass fibre reinforced polymer tubes. *Structural Engineering International.* 26, 2 (2016), 160–167.
[5] Hernández, E.L. et al. 2013. On the design and construction of elastic gridshells with irregular meshes. *International Journal of Space Structures.* 28, 3-4 (2013), 161–174.
[6] Hernández, E.L. and Gengnagel, C. 2014. A new hybrid: Elastic gridshells braced by membranes. *WIT Transactions on the Built Environment.* 136, (2014), 157k169.
[7] Lefevre, B. et al. 2015. Buckling of elastic gridshells. *Journal of the International Association for shell and spatial structures.* 56, 3 (2015), 153–171.
[8] Masson, Y. 2017. *Existence and construction of chebyshev nets and application to gridshells.* Université Paris-Est.
[9] Otto, F. and Kenso, T. 1974. Grid shells (il-10). *Institute for Lightweight Structures, University of Stuttgart, Stuttgart.* (1974).
[10] Quinn, G. et al. 2016. Calibrated and interactive modelling of form-active hybrid structures. *Proceedings of iass annual symposia* (2016), 1–9.

Appendix

A Software Development

During the design and construction of the gridshell, several tools were developed in C# in order to facilitate the team workflow and eliminate repetitive tasks. All the code has been released under an open source license.

Chebyshev net grasshopper plugin

A plugin for Grasshopper has developed to compute a chebychev net on any given surface given a start point, a specified number of axis and a grid size. The full code and latest release of this tool can be found at

`https://github.com/AlanRynne/ChevyshevNet-GH`

Cutting stock plugin for 1-dimensional material optimization

In order to reduce waste when cutting the rods, a simple but effective 1 dimensional cutting stock algorithm was implemented. Given some input lengths to cut and a list of the available stock material lengths, the algorithm will output the lengths grouped by cut order, and the index of every rod, allowing to automatically find a configuration that will reduce the waste to an acceptable limit. The full code and latest release of this tool can be found at

`https://github.com/AlanRynne/CuttingStockProblem-GH`

B Finished gridshell pictures

Proceedings of the IASS Annual Symposium 2019 – Structural Membranes 2019
Form and Force
7 – 10 October 2019, Barcelona, Spain
C. Lázaro, K.-U. Bletzinger, E. Oñate (eds.)

Contemporary Membrane Structures in Europe (2010-2018)

Josep LLORENS

Barcelona School of Architecture (ETSAB), Universitat Politècnica de Catalunya
Diagonal, 649 - 1er, 02028 Barcelona, Spain
E-mail address: *ignasi.llorens@upc.edu*
web page: *https://wwwgat.webs.upc.edu/portada.html*

Abstract

A selection of significant examples illustrate the future trends of membrane structures that point towards the diversification of applications, the increase of the structural efficiency and the improvement of the environmental behaviour.

Keywords: membrane structures, cable structures, tension structures, tensegrities, hybrid structures

1. Introduction

To explore trends in application of membrane structures in Europe during the second decade of the 21st century, 156 case studies from 22 countries have been selected (fig.1) drawn from the documentation kindly provided by the authors, including visits to the sites and literature [1,2]. The most significant examples are presented below.

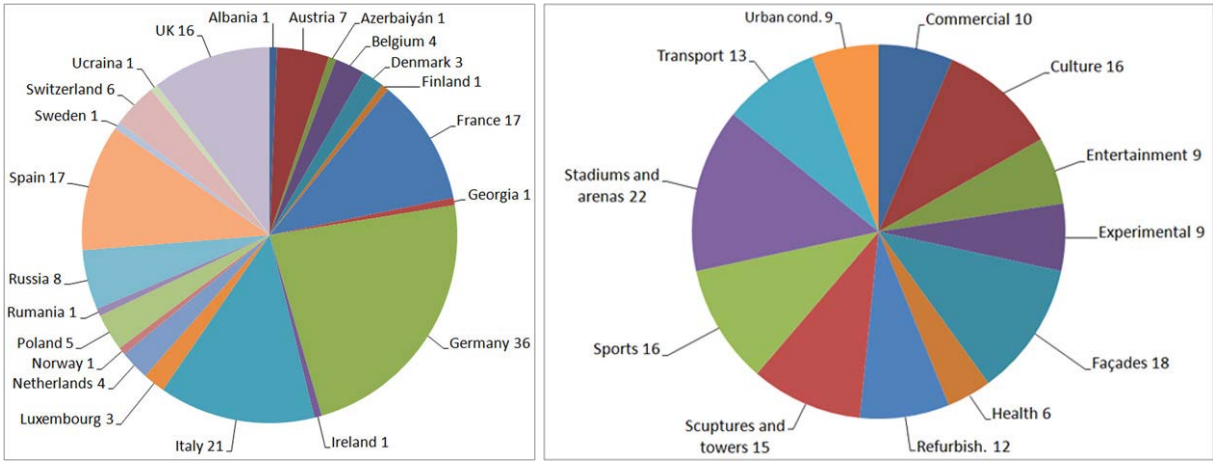


Figure 1: Distribution by country (left) and application (right) of selected cases

2. Conventional applications

During the 2nd decade of the 21st century membrane structures are characterized by the diversification of applications together with new developments. The current range of conventional applications encompasses small to large-scale structures for sports, transport, culture (education, museums, botanical gardens), fairs, exhibitions, markets, retailing, health, tourism and entertainment.

They can be illustrated with the Restaurant "Les Cols", by Aranda, Pigem & Vilalta, Architects with IASO (fig.2). A space with a special atmosphere, thanks to the combination

Copyright © 2019 by Josep LLORENS
Published by the International Association for Shell and Spatial Structures (IASS) with permission.

of shadows, lights and trees that emerge above the transparent double-layered pre-stressed ETFE roof that provides thermal insulation.




Figure 2: "Les Cols" Restaurant, Olot, 2010 [3]. Figure 3: sbp, 2011: Milk market, Limerick [4]

In Limerick a membrane canopy has been designed for the historic milk market courtyard as part of the refurbishment efforts in order to enable the local farmers market to take place independently from environmental influences but still achieve an outdoor ambience. To optimize the usability of the 1400 m2 covered area, the membrane is supported by just one eccentrically aligned mast and is suspended to the four corners of the courtyard without touching any of the preserved structures.




Figure 4: CEPSA Fuel Station, 2015 [5]. Figure 5: Steel ETFE grid shell Mitoseum, Bautzen, 2016 [6]

L.Malka Architect with IASO, designed and built respectively the Cepsa Fuel Station in Andanero (fig.4) with 18 ETFE cushions in different sizes and printed movable intermediate layers to control the solar radiation and lighting. ETFE cushions as enclosure for a steel structure were also applied to the Mitoseum, Bautzen designed by Rimpf Architekten with str.ucture (fig.5).




Figure 6: Entertainment area ArmadiLLOW, 2017 [7]. Figure 7: Cavalia Show Tent, 2011 [8]

Temporary roofing of large areas for entertainment is still a usual application of membrane structures, initiated by the traveling circus tent during the 19th century or even before. The Lowlands Festival (Mojo Concerts with H.vam Halem and Tentech, Biddinghuizen 2017, fig, 6) and the Cavalia Show Tent (Asteo-France with Canobbio 2011, fig.7) are two prominent examples.



Figure 8: J.Selas & L.Cano, Architects with BOMA and Fhecor, 2013-2017: Auditorium and Congress Centre, Plasencia [9]. Figure 9: A2 Studio Architetti with Canobbio, 2017: Auditorium 1919 Sacmi, Imola [10]. Figures 10, 11: Pape+Pape Architekten with str.ucture, 2017: Energy storage façade, Hildesheim [11].

3. New or intensified uses

Other new or intensified uses that deserve special mention are façades (figs.8 to 11), refurbishment (the fastest growing area of the building industry in Europe, figs.12 to 15) including atriums and courtyards, urban conditioning (figs.16 to 18), climate protection and improvement of public space, towers (figs.19, 20), sculptures (figs.21, 22), experimental prototypes (figs.23 to 25) and worship (figs.26 to 28). Textile shelters for archaeological areas are specially appropriate because they overcome the limitations of traditional covering systems for compatibility, reversibility, protection, flexibility, feasibility, low maintenance, ease of disassembly, and reusability.

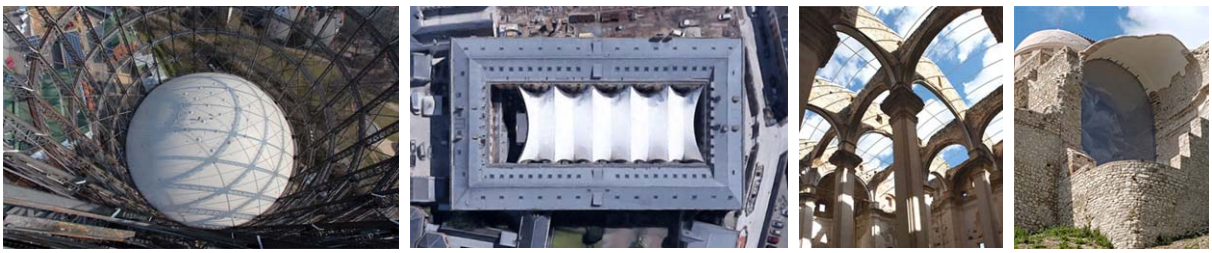


Figure 12: Textilbau GmbH and 3dtex, 2011: Roofing for the Gasometer, Schoeneberg [12]. Figure 13: AGWA Architect with Tentech, 2014: Carré des Arts, Mons [13]. Figure 14: F.Vizoso & N.Bordas with IASO, 2011: Sant Pere de Corbera Church [14]. Figure 15: Canobbio, 2016: San Michele Arcangelo, San Pietro Infine [15].



Figure 16: Vehovar & Jauslin, Architektur with form-TL, 2014: Aarau Bus Station [16]. Figure 17: Kugel Architekten with str.ucture, 2014: Convertible roof, Buchs [17]. Figure 18: Tensile Evolution with str.ucture, 2015: Temporary Membrane Roof, Velden am Vörtersee [18].



Figure 19: KKW Architekten with form TL, 2015: Phänomenta Tower, Lüdenscheid [19]. Figure 20: W.Sobek & H.Jahn, 2017: Thyssen Krupp Test Tower, Rottweil [20]. Figure 21: S.Ahlquist & J.Lienhard with Esmery Caron, 2012: Textile Hybrid M1, Monthoiron [21]. Figure 22: A.Sinz-Beerstecher & L.Meeβ-Olsohn, 2014: Weisse Salons, Swabian Gmünd [22].



Figure 23: J.Sánchez, F.Escrig & M.T.Rodríguez-León, 2011: Nature Interpretation Centre, Melilla [23]. Figure 24: Center for Information Technology and Architecture with str.ucture, 2018: Danish Pavilion, Venice Biennale [24]. Figure 25: Institute for Computational Design and Construction, Stuttgart 2018: (Re)configurable architectural system [25].



Figure 26: ATIC Architectes with AIA Ingénierie, 2012: The mobile roof of the central patio at the Great Mosque, Paris, is a mobile device divided into two parts: the first part is parked at the north side of the patio, the second part at the south side. Each part is made of a motorized arch, able to pull the current following arches. When the two motorized arches are in contact, at the centre of the patio, the cover is closed. [26]. Figure 27: J.Desablens Architecte, with Ney & Partners, 2014: Chapel of Rest, Tournai [27]. Figure 28: Groupe A Architects with Tentech, 2016: Crematorium, Zorgvlied. "The upper skylight and the upward direction of the surface strengthen the feeling of the rising departure". [28].

4. Design, materials and technology

Noticeable advances have occurred in design, materials and technology. Updates of commercial software include non-linearity, dynamic behaviour, hybrid systems, wind-structure interaction, gas law and parametric form optimization. They contribute to bring the computer models closer to reality and to clarify the misunderstandings of the so-called free-forms. The forms of membrane structures are sometimes qualified as free, but they are not at all arbitrary nor free because they have to be in equilibrium following the load paths, that is, they have to be funicular (fig.29). It was pointed out by Dr. Pauletti in SM 2915 highlighting the paradox between the formal stiffness required by flexible structures and the wide range of shapes permitted by stiff structures (figs.30, 31) [29].



Figure 29: Textile roofs are not free forms. They work only in tension. Double curvature and pretension are needed. Top: Some computer programs, like AutoCad, build surfaces from closed perimeters. Middle: Equilibrium and feasibility are not checked. Bottom: The surface created inside the same closed perimeter is in equilibrium. Figure 30: The form of flexible structures is neither arbitrary nor free. It is funicular. Rimpf Architekten with 3dtex, 2014: Harbour Point, Eckernförde. Figure 31: The shapes of rigid structures can be arbitrary. (F.Gehry, 2014: Louis Vuitton Foundation, Paris).

The materials improve constantly extending their longevity and incorporating new features including photovoltaic cells, sensors, LEDs, acoustic absorption capability, transparency or translucency. And the use of ETFE foil is being extended and consolidated because it compares favourably with glass and steel sheets, improving safety and attenuating environmental impact (figs.2, 4, 5, 9, 14, 15, 16). Its lightness reduces the structural load, and its flexibility increases the allowable deformability, so the supporting structure can be considerably reduced in size.



Figure 32: Ackerman & Partner with Taiyo Europe, 2011: Carport, Munich. Three layered ETFE film cushions with integrated flexible photovoltaic cells [30]. Figure 33: Synthesis Design & Architecture, 2013: the Volvo pure tension portable pavilion recharges a fully depleted car in 12 hours under optimum sun conditions and can be flat-packed to fit in the car boot [31]. Figure 34: Canobbio Textile Engineering 2016: Double membrane air supported structure for energy saving, Helsinki [32].

5. Environmental performance

The low level of environmental control has so far been a severe limitation to the use of membranes in cold climates. However, remarkable progress is taking place introducing translucent insulating materials such as aerogels, printing capabilities, (which increase solar absorption and reduce solar transmission), low emissivity coatings, and multi-layer, sandwiched and composite membranes, including inflated cushions, analogous to double glazing, to improve thermal, acoustic and energy

performances. In addition, new environmentally friendly applications such as environment protection and energy harvesting have emerged (figs 32 to 34).

6. Structural efficiency and appropriateness

Progress is also being made in the understanding of the appropriateness of membrane structures, led by lightweight large-scale sport stadium roofs, started in 80 AD in Rome and resumed in 1990 (Rome) and 1993 (Stuttgart). They expand all over the world imposing the tensile bicycle wheel (figs.35, 36) as a much more efficient structure than bending solutions based on trusses and cantilevers.



Figures 35, 36: gmp Architects & Pl Arena with Maffeis Engineering, 2018: Volgograd Arena [33]

Bending is expensive as it was already clear in the 50s pioneering experiences of Frei Otto and his team. But many designs do not take it into account to the point that membrane structures frequently end up being conventional steel structures (figs.37 to 39). Some recent realizations are not yet rid of this drawback but others have assumed it to the point of improving the behaviour of the structure even more. It is not only the case of the aforementioned spoked-wheels), but also of the Tensairity system (figs.40 to 42), cable-beams (figs.43, 44), active-bending or flying masts, among others.



Figures 37, 38, 39: Membrane structures frequently end up being conventional steel structures because they repeatedly resort to bending.



Figure 40: G.Stowell, Architect with form TL and Canobbio, 2010: The sports canopy for the National Tennis Centre, London is a wide-span membrane which consists of five Tensairity beams with membrane panels in between [34]. Figure 41: Maco Technology, 2014: The Ducati hospitality tent is also based on Tensairity beams which span 12 m [35]. Figure 42: S. Dubuisson, Architect with Tentech, 2014: Inno-wave-tion exhibition pavilion, a combination of a tensile compression ring with Tensairity [36]

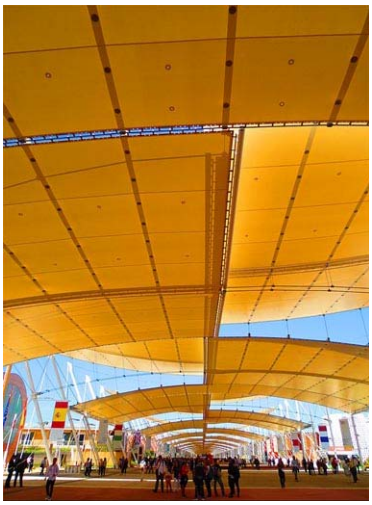



Figure 43: M.Majowiecki with Maffeis Engineering Spa and Taiyo Europe: Decumano and Cardo at Expo Milano 2015 [37]. Figure 44: Garcia German Architects with Lastra & Zorrilla, 2017: Desert city greenhouse, San Sebastian de los Reyes [38].

7 Conclusion

Looking at what has been done during the last decade, it becomes clear that the development of membrane structures moves on. Current trends point towards the increase and diversification of applications, particularly envelopes, refurbishment, large-span roofing of existing buildings, urban conditioning and research. Customized designs, including large-scale sport halls and stadium roofs fixed or retractable, will coexist with modular solutions such as pneumatic double-layered structures and ETFE cushions. Improvements are also expected in the mechanical and environmental characteristics of the materials, software and appropriate design based on the lightness and the ability to follow the load paths, provided they have the right combination of curvature and depth.

8. References

[1] *https://www.tensinet.com/index.php/tensinet-publications/tensinews* (visited 26/04/2019).

[2] *https://www.textile-roofs.com/cities* (visited 26/04/2019).

[3] *https://www.iasoglobal.com/es-ES/proyecto/restaurante-les-cols* (visited 27/04/2019).

[4] *https://www.sbp.de/en/media/publication/membranueberdachung-fuer-den-historischen-milk-market-in-limerick-irland/* (visited 28/04/2019).

[5] *https://www.iasoglobal.com/es-ES/proyecto/estacion-de-servicio-cepsa* (visited 29/04/2019).

[6] *http://www.str-ucture.com/en/what/construction-projects/reference/mitoseum-saurierpark-bautzen-2016/* (visited 29/04/2019).

[7] *https://tentech.nl/en/festivals-and-events/armadillow/* (visited 29/04/2019).

[8] *https://www.canobbio.com/cgi-bin/progetti/51/scheda-cavalia-2.pdf* (visited 29/04/2019).

[9] *https://www.plataformaarquitectura.cl/cl/910493/palacio-de-congresos-y-auditorio-de-plasencia-selgas-cano* (visited 30/04/2019)

[10] *https://www.canobbio.com/auditorium-1919-sacmi-eng* (visited 30/04/2019)

[11] *http://www.str-ucture.com/en/what/construction-projects/reference/energy-storage-facade-hildesheim-2017/* (visited 30/04/2019)

[12] *https://www.3dtex.de/gasometer-eng?lightbox=dataItem-jfv6mbl04* (visited 30/04/2019)

[13] *https://tentech.nl/en/textile-architecture/carre-des-arts/* (visited 30/04/2019)

[14] *https://www.iasoglobal.com/en-ES/pdf1* (visited 30/04/2019)

[15] *https://www.canobbio.com/coedi* (visited 30/04/2019)

[16] *https://www.form-tl.de/projects/bauwerke/busterminal-aarau/?L=1* (visited 30/04/2019)

[17] *http://www.kugel-architekten.com/content.php?n=1&d=31* (visited 30/04/2019)

[18] *https://www.german-architects.com/en/str-ucture-stuttgart/project/temporares-membrandach* (visited 30/04/2019)

[19] *https://www.form-tl.de/projects/bauwerke/phaenomenta/?L=1* (visited 30/04/2019)

[20] *https://www.wernersobek.de/en/projects/focus-en/structures/thyssenkrupp-test-tower/* (visited 30/04/2019)

[21] *https://icd.uni-stuttgart.de/?p=7799* (visited 30/04/2019)

[22] *https://www.mehler-texnologies.com/mta/Casestudies/Cases-/Weisse-Salons/weisse-salons.php* (visited 30/04/2019)

[23] *https://link.springer.com/article/10.1007%2Fs00004-014-0182-z* (visited 30/04/2019)

[24] *http://www.str-ucture.com/en/what/construction-projects/reference/isoropia-biennale-venice-danish-pavilion-2018/* (visited 30/04/2019)

[25] *https://icd.uni-stuttgart.de/?p=23178* (visited 30/04/2019)

[26] *https://www.tensinet.com/index.php/projects-database/companies?view=project&id=4534* (visited 01/05/2019)

[27] *https://www.ney.partners/project/chapel-of-rest.html* (visited 01/05/2019)

[28] *https://tentech.nl/en/textile-architecture/crematorion/* (visited 01/05/2019)

[29] *https://www.tensinet.com/files/TensiNet_Publications/Tensinews%2030%20-%20spring%202016%20LR-1.pdf* (visited 01/05/2019)

[30] *https://www.tensinet.com/files/TensiNet_Publications/Tensinews%2027%20september%201-24.pdf* (visited 01/05/2019)

[31] *https://archello.com/project/volvo-pure-tension-pavilion#stories* (visited 01/05/2019)

[32] *https://www.canobbio.com/cover-for-football-field-helsingin-jalkapalloklub-eng* (visited 01/05/2019)

[33] *https://www.mehler-texnologies.com/mta-wAssets/docs/Case-Studies/Volgograd-Stadium.pdf* (visited 01/05/2019)

[34] *https://www.form-tl.de/projects/bauwerke/tennis-centre-london/?L=1* (visited 01/05/2019)

[35] *https://www.macotechnology.com/portfolio/hospitality-with-semi-trailers-ducati-sbk/* (visited 01/05/2019)

[36] *https://www.tensinet.com/index.php/component/tensinet/?view=project&id=4633* (visited 01/05/2019)

[37] *https://www.mehler-texnologies.com/mta-wAssets/docs/Case-Studies/Expo-Milano-2015.pdf* (visited 01/05/2019)

[38] *http://www.arquitextil.net/portfolio/desert-city/* (visited 01/05/2019)

Proceedings of the IASS Annual Symposium 2019 – Structural Membranes 2019
Form and Force
7 – 10 October 2019, Barcelona, Spain
C. Lázaro, K.-U. Bletzinger, E. Oñate (eds.)

Connecting Engineering Rigor and Visual Creativity

Gordana M. HERNING*

*MIT, 77 Massachusetts Avenue, Cambridge, MA, 02139, USA
gherning@mit.edu

Abstract

This paper describes a studio-style project-based graduate course that introduces classic and computational approaches to creating design options for long span structures and tall buildings. The course aims to convey how an iterative design process serves to refine solutions that can be conceptually anticipated using methods such as Graphic Statics or the Maxwell Theorem, and validated through numerical analyses. While student teams employ engineering principles to explore relationships between form, geometry, and performance of structural systems, they also reconcile questions about the environmental impact, constructability, and visual strength of the designs. Learning from the best examples of built structures develops sensitivity to proportion and elegant structural solutions that merit architectural expression and convey economy of the design through thoughtful use of materials. In addition to structural engineering, students in the course have had a background in architecture, façade engineering, or mechanical engineering; therefore, designs reflect a variety of interests and require effective communication of ideas across disciplines. During field visits and guest lectures students gain additional insight into the engineering rigor and creativity in the real-world structures. Regular interactions and project reviews with practicing engineers emphasize critical analysis and optimizing load paths, structural systems, and connection details. A common thread in all class activities, inspired by David Billington's scholarship and teaching, is to understand the cultural and economic meaning of efficient forms that can be achieved through creative and disciplined structural design.

Keywords: conceptual design, form finding, optimization, spatial structures, tall buildings

1. Introduction

Among the most creative and challenging aspects of design is achieving technical and visual strength of structures that fulfill the goals of utility and value for users, while conserving public and natural resources consistent with the knowledge and tools that are available to designers. The notion that the highest achievements in design encompass appropriate social (costs and utility), scientific (form and materials), and symbolic (appearance and meaning) responses within the constraints of time and site conditions (among others), thus upholding the tradition of "S*tructural Art*", was defined through critical analysis of exemplary designs across the ages by David Billington (Billington [1]).

Engineers who holistically integrate elegant shaping with efficient material use and economy in construction, by employing inventive forms to span large distances and reach new building heights, have developed their artistry through experiential knowledge, rigorous application of engineering principles, and sensitivity to the human experience of structures – their aesthetics. Learning about the designers of exemplary structures reveals strivers dedicated to purposeful discovery and development of skill through refinements of design until simplified, essential solutions are found, which may be more challenging to achieve than a complex response that also satisfies design requirements.

This paper presents the activities in which students engage in the graduate course "Structural Design Project" to explore design strategies within the context of two projects, namely (1) a long-span roof, and (2) a tall building. The course is offered to seniors and graduate students studying at the intersection of

Copyright © 2019 by Gordana M. Herning
Published by the International Association for Shell and Spatial Structures (IASS) with permission.

engineering and architecture at MIT, and in particular, to the students in the Master of Engineering program focusing on Structural Mechanics and Design in the Department of Civil and Environmental Engineering. The students bring their interests in structural, mechanical, or geotechnical engineering, architecture, computational design, and experience from internships, research, or design practice to a dialogue that seeks to distill the complex design process into simple, clear concepts relating the form and behavior of a structure. Study of actual buildings that illustrate relationship between form and element forces, intuitive analytical and graphical techniques, and numerical modeling approaches are introduced with an aim to build upon the various students' experiences and create stepping stones toward their practical application in a new design.

A central course objective is to motivate student-driven learning about structural behavior as a result of geometry and materials, and to encourage students to convey their ideas in a concrete and clear manner to their peers and engineering professionals. Classic approaches to analysis, hand calculations and drawings, assigned readings, and advanced computational methods are used to illustrate possible paths from complexity to the simplified and clear solutions that can help students appraise design alternatives before they engage in a detailed design of a structure. Among the questions being asked in the course are: What lessons about creative design solutions can successful engineering works of the past offer? What does it mean to construct an optimal structure? How can complementary disciplines work together to improve the design of structures in the future? What are the engineers' and architects' roles in consideration of resilience, sustainability, and embodied energy of structures? How can we measure success of a design?

2. Overview of the course objectives and activities

The course aims to integrate educational approaches from the engineering and architecture curricula, to combine practical design and research, and to couple the academic learning with insights and expertise shared by highly regarded practicing designers through guest lectures and reviews of students' projects. Another central idea is to empower the students to work both independently and as part of a team on responding to open-ended questions that range from qualitative analyses of the form and load paths in precedent structures to the comparison of stiffness gains resulting from structural system selection in their own designs.

Throughout the two course projects (with each completed in one semester) the students should become:

- Conversant with technical terminology associated with long-span and tall structural systems
- Aware of the design legacy related to historic and modern-day spatial structures and tall buildings, including major engineering works, and analysis and construction methods employed by designers who influenced the profession
- Adept at generating design options and communicating the relationship between their form and structural action
- Proficient in simplified and numerical methods of analysis for systems resisting static and dynamic loads

2.1. Course topics

Class discussions follow the course topics through lectures, student presentations, assignments, engineering seminars, and class project reviews. For the project in which students design a roof structure to enclose an existing courtyard on the MIT campus the topics include: Study of Precedents and Art in Engineering, Introduction to Graphic Statics and Maxwell's Theorem, Form and Behavior of Spatial Structures, Structural Materials and Systems, Numerical Methods of Structural Analysis, Fabrication and Construction, Connections and Cladding, and Environmental Impacts of Design.

Students begin the project work by visiting the prospective building site on the campus to explore the existing structure and surrounding buildings in order to understand the functional requirements of the new space (for example, location for quiet study and reflection or a dynamic environment for

collaboration and gathering), the style, materials, and load bearing capacity of the existing buildings that could dictate the form of the new roof and ensuing loads that may (or may not) be supported at particular locations. The students obtain as-built structural and architectural drawings that guide their subsequent site visits and learning about actual conditions (such as laboratory or library space adjacent to and below the courtyard, foundations and soil properties, and access limitations for the construction equipment), which may define design constraints requiring specific solutions. Students also obtain information about the city and campus zoning, regional climate and hazard data to be incorporated in resilient design concepts, and identify the governing building standards.

2.2. Design exploration

Classical methods for finding optimal structural shapes based on specified material strength, element forces, support reactions, or deflections are introduced through class exercises that demonstrate the use of Graphic Statics and the Maxwell Theorem of optimal load paths in realistic examples drawn from built structures (Zalewski and Allen [2], Baker [3]). These are followed by workshops, led by advanced graduate students in architecture, that focus on computational tools for parametric study of design options including Grasshopper (for Rhinoceros by McNeil and Associates), Karamba, and Kangaroo (Grasshopper analysis and form-finding tools).

In a questionnaire at the start of the term students relate their interests and prior areas of study (e.g., structures, architecture, construction, preservation of historic buildings, geotechnical engineering, and building systems) as well as modeling experience (finite element software for classical analysis, form finding, optimization, physical models, and drawing or sculpting). While approximately one half of the students in the class have had some experience with numerical parametric tools, the classic methods are usually new and surprising to most students for their visual and direct feedback loop between a geometric arrangement in a structure and the resulting forces or deformation.

These examples of parametric analyses lead to the study of precedents, for which the students are asked to have an eye on the flow of forces and connection details when assessing how the overall form and structural action relate to the visual appearance of a built structure. The study of precedents aims to connect the theoretical concepts learned through idealized images of structural elements with the composition and behavior of a whole structure in the context of the site, materials, design decisions, and construction. For example, parallels are drawn between the theoretical analyses of an idealized arch and a built vault or a dome, in order to illustrate potential instabilities due to permanent and variable loads, interactions between systems in a structure (e.g., forces exerted by a vault on the supporting structure), and placement of stabilizing elements, such as tension ties or rings to control horizontal thrust at supports.

Student teams develop three options for their concept design, create hand drawn sketches, and include images of selected precedents for each option along with written reflections on these structures. They are asked to describe the characteristics of each concept design: “What will it look like? How would the structure support the loads? Which materials will be used? How will the roof impact the courtyard?”

In parallel with potential concept designs, teams brainstorm how they would construct a physical model using digital fabrication techniques to represent the overall form of the roof structure and convey design intentions including force paths, connection details, stability, and support conditions. Following team discussions, instructor’s feedback, and creating physical model schematics, student teams narrow down their selection to one concept design as the basis for their project. Appropriate structural systems are investigated in an iterative process of assessing potential roof support locations, spans, spatial forms, and by anticipating design and construction impacts of selected geometric arrangements.

Initial iterations based on hand sketches and simplified calculations are followed by the form-finding process using Graphic Statics or numerical tools. Design is guided by students’ decisions “to make the structure more efficient by minimizing bending”, “selecting shapes with double curvature instead of

single curvature," and "connection mechanisms that allow prefabrication," as stated in the final project reports. Students develop solutions for connection details in the main elements of the structure and as part of the cladding design. Based on final material weights the embodied carbon of the structure is calculated and compared to similar buildings to evaluate the environmental impact of the design. In a final oral presentation of the project to the Engineering and Architecture faculty, practicing engineers, and peers, students address questions and critique about their designs (Figure 1).

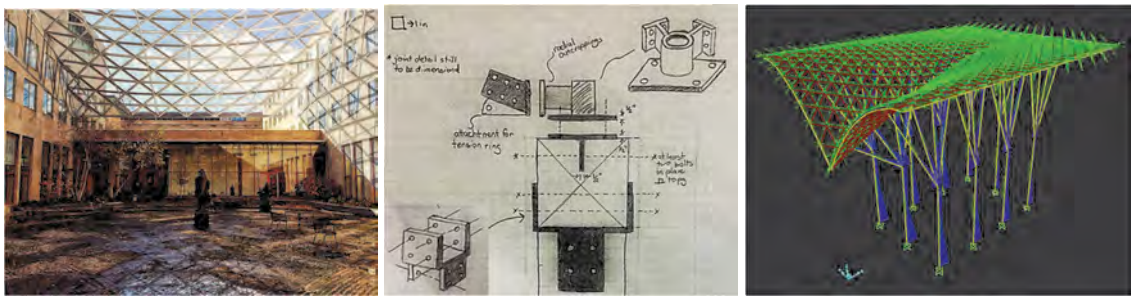


Figure 1: Rendering of a roof design, connection detail drawing, and image from a numerical analysis.

The second project responds to realistic design requirements for a mixed-use tall building situated in New York City. The students are asked to design structural solutions based on considerations of resilience, sustainability, socio-economic and environmental impacts, aesthetics, and cost. Through lectures, assigned readings, presentations and reviews of the project deliverables, individual and team assignments, the student-driven study explores class topics that include: Classifying Tall Building Forms and Structural Systems, Approaches to Conceptual Design, Load Distribution in Precedent Structures, Defining Structural Stiffness, Identifying Optimal Layouts of Lateral Force Resisting Systems, Anatomy of a Tall Building, Connecting Structural Systems, and Structural Performance. Students develop the project from concept to a detailed design, and complete five Design Studies, which are assignments that align with the course topics, and include portions that are submitted individually and by the teams of three or four students. While the team assignments aim to foster collaboration, the individual assignments challenge the students to generate diverse solutions, enrich the discussion, and in some cases, to step out of their comfort areas defined by prior experience.

More than to other aspects of design in the early conceptual stage, attention is given to the shape of a tall building, as one of the key determinants of structural efficiency. Study of historic examples, optimal structural systems for a given range of height, and building typologies driven by socio-economic factors (e.g., flexibility of floor plates to accommodate shorter lease terms in the U.S., versus the required proximity to natural light that motivates designs in Europe) takes place in parallel with generation of initial concept designs. Structural concepts including the framed, braced, and modular tube, outrigger structure, diagrid and exo-skeletal systems are considered in view of the building scale, economy, and appearance. Design begins with sketches and simplified calculations, on paper and chalkboard. Numerical simulations are used to validate static and dynamic structural behavior in the detailed phases of design. Students' proposals are inspired by their research interests, class discussion, and guest lectures. For example, Katia Bertoldi's presentation of the work by Overvelde et al. [4] inspired a student team to explore building forms based on octagonal origami shapes, as seen in Figure 2.

Distinguished engineers often reflect upon the ways in which collaboration and integration of goals across disciplines contribute to the success of projects. Writings on this topic by Ove Arup, Peter Rice, Jörg Schlaich, Leslie Robertson, and Bill Baker are among the class readings that the students explore as they embark upon their own collaborative design effort. An optional peer review questionnaire, outlined early on in the term, was completed by all students in the form of Google sheets upon finalizing

the project. Among the merits that the students evaluated were peer reliability (how confidently they could depend on a person to complete his/her task), creativity (how inspiring and original were the solutions offered for the project-related questions), and effort (initiative and interest in research and development of project decisions). Students' comments additionally characterized collaborative qualities:

> *"Creative thinker, problem solver, […] is both an open-minded and pragmatic structural engineer, and her approach is highly suitable to designing innovative systems that are feasible and reasonable."*
>
> *"None of the design decisions were made "because this is the only thing I know how to design", […] was always willing to discuss different options, list pros and cons, always looking for supportive research materials and solutions."*
>
> *"Negotiated with architecture to push and pull between form and function. This requires great problem solving."*
>
> *"Sometimes during group meetings he would solo by himself rather than contributing to the discussion."*

In a studio class that aims to motivate creative thinking rooted in disciplined application of engineering fundamentals, it may be instructive to engage the students in defining the criteria by which collaboration can intrinsically enhance the quality of a design.

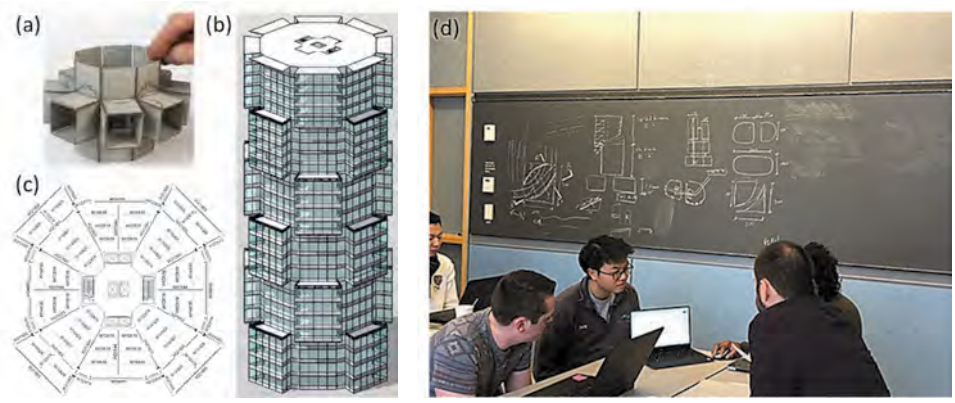


Figure 2: Tall building design: (a) origami inspiration (image reproduced from Overvelde et al. [4]), (b) building shape, (c) building floor plan, (d) project review with Paul Richardson from BuroHappold.

2.3. Design legacy

The course is conceived as a design studio that builds upon the scholarship in the theory of structures with a study of engineering heritage to enable development of practical design strategies that are applicable in the modern day interdisciplinary design environment. To explore the legacy of structural design is to recognize the evolution of form, and also to see how the greatest designers understood *and* conveyed their ideas both conceptually and practically. Using the self-study model, students select an eminent structural engineer whose brief biography they write and present to the class. They document the engineer's formative years in life, education, and career, major accomplishments, and influences by (and on) other engineering works, architecture, art, and people. Biographies also include anecdotes telling of a personal outlook or experience and inspiring quotes such as these:

> *"There is nothing more noble and elegant from an intellectual viewpoint than this – resistance through form."* (Eladio Dieste)

> *"As structural engineers, we have a responsibility to delight clients and the public, not just ensure that structures do not fall down."* (Jane Wernick)
>
> *"It is today necessary to achieve a more efficient collaboration between architectural design, statical study, and the contribution of a knowing competence in construction."* (Pier Luigi Nervi)

Images or hand drawn sketches by the students show designs or innovative concepts that the designers developed (Figure 3). Over the course of a year, students learn from their peers about more than twenty prominent engineers, and co-author a booklet in a series created by the students in the prior years of the program. These biographies affirm the significance of role models and mentors, and uncover various, sometimes winding, paths that have led to exceptional works of engineering. They are the result of talent, enthusiasm, and dedicated development of skill over time through rigorous application of mechanics and loyalty to the aesthetic ideals. They prove the adage that "Rome was not built in a day," and that design education should be grounded in the study of exemplary structures from the past.

Numerical tools for systematic generation of options and analysis of forms based on specified quantitative objectives provide powerful methods for assessing efficiency of a particular distribution of material in a structure. However, they may obscure some of the parallel relationships between performance goals, construction, and the behavior of built systems. To cultivate the "feel" for practical aspects of constructing and controlling load paths through structural elements and connections, students in the most recent class on spatial structures began their study by creating a physical model, as shown in Figure 3. While the architecture students were more comfortable than some engineers with the process of rapidly generating options to fabricate the form, the challenge for all was to authentically model the structural concepts, including joint restraint, membrane action, or system stiffness. Especially relevant for the design of lightweight spatial structures, whose presence in practice has significantly increased in recent decades, modeling (and testing) the complex structural action remains a goal for future classes.

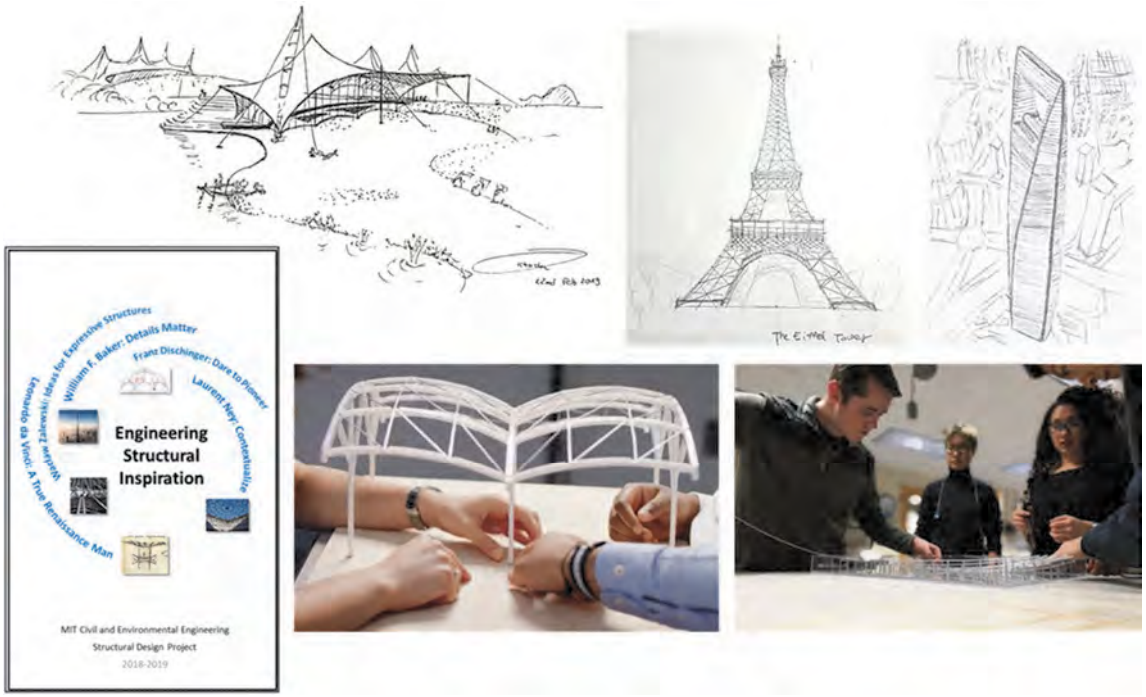


Figure 3: *Top row*: students' drawings of the Olympic Stadium in Munich, The Eiffel Tower, and Shanghai World Trade Center; *Bottom row*: booklet of eminent engineers' biographies (left), and physical model building.

2.4. Conversation with design practitioners

When presenting project ideas to the leading practitioners, students can observe *how* they assess a proposed concept and offer suggestions. Some engineers use simple calculations and hand drawn sketches while engaging in playful conversation through a rapid succession of "why" and "what if" questions. Exceptional skills in generating creative design options seem to surpass the sum of talent, practice, and time – but this sum can certainly engender creativity. Various engineers may offer similar or entirely different critiques of a particular design, and when a challenge resonates with the students' vision, the ensuing exchange of ideas may even spark questions worth exploring further, outside of the scope of a class project.

In addition to interacting with students through project reviews, the invited engineers present lectures that reflect their expertise and the state of the art in built designs that the course addresses. This academic year Laurent Ney delivered the Edward and Mary Allen Lecture in Structural Design entitled *Are Bridges Designed*?, Tim Elliassen from TriPyramid presented *Glass as a Structural Material*, Ramon Gilsanz from GMS explored *Design Options and Decision-Making for Long-Span Roofs*, Yasmin Rehmanjee from BuroHappold introduced *Detroit Hudson's Rising*, Joseph Provenza from WSP discussed *Computational Design for Complex & High-Rise Structures*, Wolf Mangelsdorf from BuroHappold described designing the *Morpheus Hotel*, Angie Neefus from Eckersley O'Callaghan spoke about *Looking Through Glass at the Principles of Structural Engineering,* and Zoe Temco from Arup presented *Data, Datums, and 3D Models*. In recent years, among the invited lecturers were Bill Baker and Georgi Petrov from SOM, Leslie Robertson of LERA, Eli Gottlieb and Hi Sun Choi from Thornton Tomasetti, Paul Richardson from BuroHappold, Powel Draper from Schlaich Bergermann Partner, and Marc Steyer from Tipping Structural Engineers.

2.5. Visiting structures and design offices

In conversations with practicing engineers one learns about examples that underscore the importance of understanding the economy of the construction process and the constraints imposed by the site. The engineers point out personal experiences, including successful partnerships with architects and construction professionals, as well as instances when problematic details required development of alternative solutions during construction, some of which impacted the cost, quality, or schedule of a project.

Visits to structures and design offices are organized during the fall or spring term and the Independent Activities Period in January, when classes are not in session (Figure 4). Conversations during these visits are very informative and timely, as the students learn about remarkable projects from engineers at different stages in their careers. While considering their own post-graduation paths, students also recognize the variety of possibilities for learning and growth within major international firms and smaller specialized design offices.



Figure 4: (left to right) Visit to the Moynihan Station in New York with Alexandra Cheng from Schlaich Bergermann Partner, Manhattan West site in New York with Georgi Petrov from SOM, TriPyramid Structures in Westford, MA, with Tim Eliassen, and Rockefeller University River Campus with Turner Construction.

3. Conclusion

The use of classic engineering and graphical methods that transparently relate geometry, equilibrium of forces, and deformation of a structure engenders an intuitive understanding of form and frees the exploration of possible and rational options in the conceptual design phase. Iterative refinement of form that occurs through a combination of efforts, including critical study of built structures, analyses performed by sketching and simplified calculations, and physical modeling and testing, enables the designer to calibrate numerical simulation of structural behavior and validate the analyses in the detailed phases of design. When the search for new, efficient, and beautiful structural patterns, forms, and systems is energized by insights from actual best works and realistic constraints on resources (both natural and monetary), designs that are respectful of nature and human culture can emerge.

Acknowledgements

The author gratefully acknowledges the inspiring experience of teaching this course with John Ochsendorf during her first year as its instructor in 2016. Special thanks are extended to all invited lecturers and our hosts at the engineering offices and construction sites for enriching conversations and examples of outstanding design. Finally, sincere thanks go to the students and colleagues for their enthusiasm, collaboration, encouraging feedback, and suggestions on how to improve the course.

References

[1] D. Billington, *The Tower and the Bridge: The New Art of Structural Engineering*. Princeton: Princeton University Press, 1985.

[2] W. Zalewski and E. Allen, *Shaping Structures: Statics*. New York: John Wiley & Sons, Inc., 1998.

[3] W. Baker, "Structural innovation: combining classic theories with new technologies," AISC T.R. Higgins Lectureship Award, 2013.

[4] J. Overvelde, J. Weaver, C. Hoberman, and K. Bertoldi, "Rational design of reconfigurable prismatic architected materials," *Nature*, vol. 541, pp. 347-352, Jan. 2017.

FORM and FORCE

Proceedings of the IASS Annual Symposium 2019 –- Structural Membranes 2019
Form and Force
7–-10 October 2019, Barcelona, Spain
C. Lázaro, K.-U. Bletzinger, E. Oñate (eds.)

Current Realities and New Opportunities for Efficiency, Economy, and Elegance in Bridge Design

Paul GAUVREAU*

* Professor, University of Toronto
35 St. George Street, Toronto, Ontario M5S 1A4, Canada
pg@ecf.utoronto.ca

Abstract

This article examines the relations that link efficiency, economy, and elegance in bridges. The relation between efficiency and economy depends on the ratio of the cost of labour to the cost of materials. When this ratio is low, as it was prior to World War II, efficiency and economy can be embodied in the same structure. When this ratio is high, as it has been since the 1960s, they cannot. In the future, it is likely that the use of robots in bridge construction will lower the ratio of the cost of production to the cost of materials, thus restoring efficiency to its previous role as an enabler of economy. Although it is possible for bridges to be endowed with both economy and elegance in the absence of efficiency, the range of choices available for the design of this type of bridge is tightly constrained. The ability of designers to utilize this limited scope for creative decisions is the primary factor in determining the aesthetic significance of this type of bridge.

Keywords: Bridges, aesthetics, efficiency, economy, elegance

1 Introduction

The central message of David P. Billington's scholarship is that the greatest works of structural engineering are distinguished by three primary qualities: efficiency (minimum materials), economy (minimum cost), and elegance (maximum aesthetic expression) [1]. The standard of excellence Billington thus defined acknowledges the important fact that works of structural engineering have a dual essence. First and foremost, they are works that perform a practical function, and like all practical objects, they are generally expected to perform their function at a reasonable cost. Structures are also visible, and like all visible objects they create an impression in the people who look at them. Because structures are highly prominent and relatively permanent features in the visible environment, the visual impression they create is particularly important. At their best, structures can take on rich aesthetic significance by virtue of their visible characteristics. Billington demonstrated that the practical and the visual natures of structures are intimately related. Through his detailed studies of the bridges of Swiss engineer Robert Maillart, Billington showed conclusively that aesthetic significance is not something that must be added onto a purely functional structure, but rather is a quality that can originate from the visual expression of the way it performs its practical function.

The realities of current bridge design practice, however, have caused engineers to question whether or not the ideals defined by Billington can actually be achieved. This proposition

Copyright © 2019 by Paul Gauvreau
Published by the International Association for Shell and Spatial Structures (IASS) with permission.

is examined in reference to the bridge shown in Figure 1, a single-span overpass consisting of parallel precast pre-tensioned concrete I-girders and a cast-in-place concrete deck slab.



Figure 1: Estaire Road over Highway 69, Ontario, Canada

This is not an elegant bridge. Its superstructure is deep and looks heavy. The visible impression it creates is at best mediocre.

Although it is difficult to make a definitive statement regarding the efficiency of this bridge on the basis of a single photograph, there is certainly no visible expression of efficiency. Simply supported spans are intrinsically less efficient than spans that can develop negative moments at their ends, which could have been done had the span been made continous with the abutment walls. The constant cross-section is not consistent with the variable distribution of bending and shear demand along the span, which implies that the bridge contains excess material that could have been eliminated.

This bridge was, however, the least expensive means of performing the required function of this crossing and thus embodies Billington's ideal of economy. By the time this bridge was designed, precast pre-tensioned concrete I-girders with cast-in-place concrete deck slab had already been established as the most cost-effective structural system for this type of crossing. This determination was made by many designers and owners independently, on the basis of actual cost data from a large number of similar bridges built throughout Canada.

The fact that the Estaire Road bridge is economical, of at best dubious efficiency, and not elegant is not particularly significant in itself. There are many bridges with these attributes. Of far greater significance is the fact that for this type of crossing in Canada, it is actually difficult to improve on efficiency and elegance without compromising economy.

This article seeks to determine whether or not this apparent incompatibility of Billington's three ideals in certain common design situations is the result of real impediments that are out of the control of designer and owner. To accomplish this, it will examine the relations that link each pair of these three ideals: efficiency and economy, efficiency and elegance, and economy and elegance.

2 Efficiency and Economy

2.1 Basic Relations

The relation between efficiency (minimum materials) and economy (minimum cost) can be described using a simple mathematical model of construction cost. In this model, total cost C

of a given bridge is expressed as the sum of the cost of materials M and the cost of labour L. The cost of materials is defined as the product of the total quantity of materials Q and the unit cost of materials c_m. (For convenience, it is assumed that the given bridge is built of a single material.) In a similar manner, the cost of labour is defined as the product of the total quantity of labour T and the unit cost of labour c_l. This yields the following equation:

$$C = Qc_m + Tc_l \tag{1}$$

This equation can be used to study the effect of a change in Q on total construction cost for a set of alternative designs, all of which perform an indentical function at the same site, by expressing T as a function of Q. In his analysis of construction costs of concrete bridges built in Switzerland in the 1950s and 1960s, Menn observed that a decrease in T required an increase in Q [2]. This makes sense, since quantities Q and T are related by the geometrical complexity of structural systems and components. An increase in geometrical complexity can produce a reduction in material quantity and will almost always increase the quantity of labour. Conversely, a decrease in geometrical complexity can reduce T but will almost always increase Q.

Gauvreau proposed the following simple formulation of the relation between T and Q for a given set of alternative designs that satisfy the same functional requirements for the same site [3]:

$$T = \frac{1}{\alpha(Q - \beta)} \tag{2}$$

Parameter α is a constant that is related to productivity, i.e., the quantity of labour required to install a given quantity of materials. Parameter β can be regarded as a theoretical lower limit for the quantity of materials. The practical lower limit for the quantity of materials, Q_{Mmin}, corresponds to a design that satisfies all applicable requirements and will be greater than β.

Substituting Equation 2 into Equation 1, taking the first derivative of C with respect to Q, and setting this expression to zero yields an expression for the quantity of materials that minimizes total construction cost, Q_{Cmin}:

$$Q_{Cmin} = \beta + \sqrt{\frac{c_l}{\alpha c_m}} \tag{3}$$

According to this simple model, therefore, the most economical design within the set of alternatives will have quantity of materials Q_{Cmin} as defined in Equation 3. The value of Q_{Cmin} varies with the ratio c_l/c_m.

For a given set of alternative designs, the quantity of materials corresponding to minimum cost, Q_{Cmin}, will always be greater than or equal to the minimum practical quantity of materials Q_{Mmin}. Although this simple model of construction cost does not provide an explicit expression for Q_{Min}, it is evident that it will be a constant for a given set of alternative designs and hence independent of unit costs c_l and c_m. As the ratio c_l/c_m decreases, quantity Q_{Cmin} will move closer to Q_{Mmin}, i.e., the prevailing economic conditions become more conducive to the creation of designs that combine the ideals of efficiency and economy. Under these circumstances, efficiency acts as an enabler of economy. As the ratio c_l/c_m increases, quantity Q_{Cmin} will move

away from Q_{Mmin}, which makes it more difficult to create a design that combines that the ideals of efficiency and economy.

2.2 Historical Evolution of the Relation Between Efficiency and Economy

Prior to World War II, the ratio c_l/c_m was generally low and hence so was Q_{Cmin}. As a result, efficiency was a strong enabler of economy. This made it possible for Maillart to design bridges that embodied both efficiency and economy.

After World War II, the ratio c_l/c_m increased rapidly in industrialized countries due to a sharp increase in wages c_l. According to Equation 3, this would be expected to produce an increase in Q_{Cmin}, i.e., a increase in material quantities. This prediction is corroborated by Menn [2], who observed that designers sought to limit the increase in total construction cost C due to the increase in c_l by reducing the total cost of labour $L = Tc_l$. This was accomplished by means of designs that reduced the total quantity of labour T, which mainly involved reducing the use of falsework and re-using formwork through the use of constant cross-sections, constant span lengths, and large precast concrete components. These measures generally required a greater quantity of materials than would otherwise have been necessary, and thus decreased efficiency. Under these economic conditions, it is thus difficult to create designs that embody both efficiency and economy.

Economic conditions have not changed significantly since the 1960s, insofar as the ratio c_l/c_m has remained high. For most short span bridges, the savings in labour arising from the use of large standardized prefabricated components outweigh the additional materials that correspond to the use of constant cross-sections. Efficiency and economy are generally incompatible for most bridges other than very long-span structures.

It is likely that the current economic situation will soon undergo significant change. Robots have already transformed manufacturing by lowering the cost of production compared to the use of human labour. They are poised to bring about a similar transformation in heavy construction.

To study the effect of this transformation on the relation between efficiency and economy, it will be assumed that robots will perform tasks that are essentially identical to those performed in the construction of current structural systems. (Robots that assemble reinforcing steel cages for concrete structural components are one example of this type of system that is currently under development [4].) This will make possible a more direct comparison of the cost structure of bridges built by human labour and those built by robots.

Robots will be used in bridge construction if and only if they lower the cost of production $L = Tc_l$ relative to the use of entirely human labour. The effect of a decrease in L can be estimated using the expressions developed previously. Using the expression for T from Equation 2, total cost of production L is expressed as follows:

$$L = \frac{c_l}{\alpha} \frac{1}{(Q - \beta)} \tag{4}$$

Parameter β is a property of the design requirements of the specific crossing and thus is not affected by the method of construction. For a given quantity of materials Q, therefore, a reduction in the cost of production will occur if and only if there is a reduction in the ratio c_l/α. This

requires a reduction in the unit cost of production c_l, an increase in productivity α, or both. It can be seen from Equation 3 that reducing the ratio c_l/α will reduce the quantity of materials Q_{Cmin} that corresponds to the minimum cost design, thus moving it closer to the minimum practical quantity of materials Q_{Mmin}. This implies that use of robots will make it economically worthwhile to design bridges that consume less material, i.e., bridges with efficient structural systems.

Just as designers responded to the challenge of controlling total construction cost in an era of increasing labour rates by producing structural systems that consumed less labour, there is little doubt that they will respond to the opportunity presented by lower overall cost of production made possible with robotic construction by designing structural systems of greater efficiency. By restoring efficiency to its previous role as an enabler of economy, robots will make it possible once again for efficiency and economy to be embodied in the same bridge.

3 Efficiency and Elegance

Minimizing materials requires structural components to be shaped such that capacity is close to demand at as many locations as possible. Since demand generally varies throughout a given structure, an efficient structural geometry will vary correspondingly. The visible form of the structure thus determined by the flow of forces will reflect the underlying state of equilibrium. Efficiency thus makes the flow of forces visible and in so doing can be an important source of aesthetic significance.



Figure 2: Royston Road Underpass, British Columbia, Canada

The effect of efficiency on the visual impression created by a given bridge can be seen by comparing the bridge shown in Figure 2 to the Estaire Road bridge of Figure 1. The two bridges perform essentially the same function, yet they create very different visual impressions. Instead of the deep, heavy looking constant-depth girder of Estaire Road, Royston Road has a variable-depth girder that is remarkably thin at midspan. The girder at Royston Road is not simply supported as at Estaire Road but rather is made continuous with the abutment walls, which enables the girder to develop negative moment at its ends. These measures were designed into Royston Road to minimize materials, i.e., to make it efficient. They also are the primary elements that not only define its visual impression, but also enable this visual impression to be superior to the one conveyed by Estaire Road.

As stated in Section 2, efficiency and economy are compatible only when the cost of labour is low relative to the cost of materials. This was the case when Maillart designed his bridges and his works derive a significant portion of their aesthetic significance from the visual expression of

efficiency. This has not been the case, however, since the 1960s in the industrialized world [2]. This implies that economical bridges cannot currently rely on efficiency as a source of aesthetic significance. As long as the cost of production remains high relative to the cost of materials, using efficiency as a source of aesthetic significance will require paying a premium over and above the most economical design.

4 Economy and Elegance

Bridges can embody economy and elegance in the absence of efficiency. The Bridge over the Rhine at Bad Ragaz (Fig. 3), which was designed by Christian Menn and built in 1962, is an example of a strikingly handsome bridge that does not project a strong visual impression of efficiency. The constant depth girder gives no indication of the distribution of forces within the structure. This is an economical bridge that derives its economy to a large extent from its use of constant cross-sections and repetition of other details to minimize labour, rather than a strict minimization of materials. It nonetheless creates a strong and positive visual impression.



Figure 3: Bridge over the Rhine at Bad Ragaz, Switzerland [5]

For bridges that must be economical but, due to a high ratio of the cost of labour to the cost of materials, cannot also be efficient, the possible sources of aesthetic significance are limited. For his design of the Bad Ragaz bridge, Menn drew on two important sources: (1) shaping of structural components and (2) the visual expression of practical innovation.

Shaping of structural components is understood here to mean the visible relations among the most important structural dimensions, which include span length, girder depth, pier width, and pier thickness. The visual impression created by the Bad Ragaz bridge is due in large part to the shaping of these components, which was informed by Menn's impeccable sense of proportion. The bridge looks right in every regard and it is difficult to imagine how it could be improved by changing any dimension. The shape of every structural component is functional and minimalistic; Menn made no attempt to embellish them in any way. He chose the dimensions of these components in the knowledge that for many of them, small changes can have a significant effect on the overall visual impression but will have a negligible effect on cost. This is where Menn excelled, since he embodied the rare combination of a strong aesthetic sensibility, which

enabled him to choose dimensions that made the structure look good, and an unparalleled understanding of structural behaviour, which enabled him to be sure that his aesthetic choices could be made without having a negative effect on economy.

The visual expression of practical innovation was identified by Gauvreau [6] as an important source of aesthetic significance. Solving practical problems better than they have previously been solved is the primary motivator of engineering innovation. The new ideas incorporated into the solution of these problems can be associated with new visible forms that could not otherwise have been conceived. At their best, these forms can take on aesthetic significance that is tightly bound to their underlying utility yet also transcends it. For the Bad Ragaz bridge, the problem was to design an economical bridge that was curved in plan (1000 m radius) and which required sharply skewed supports (average skew angle of 40°). Menn's solution was unprecedented at the time of its construction: a continuous single-cell box girder with main span of 82 m and a relatively slender span to depth ratio of 25.2. To demonstrate the validity of his design at a time when digital computers were not used by bridge designers, Menn developed a simple and rational method of calculating the forces present in curved box girders on sharply skewed supports [7], an important innovation in itself and a key component of the design process for this bridge. The visual impression created by the structure that arose from this act of innovation is bold and strong, and the creative spirit that guided its design is still evident in its visible form, even though this bridge was built over fifty years ago.

Unlike efficiency and economy, which can be compatible or incompatible depending on the ratio of the cost of labour to the cost of materials, there do not appear to be any factors outside the control of the designer that prevent economy and elegance from being embodied in the same bridge, even when economy is incompatible with efficiency. In such cases, drawing from the primary sources of aesthetic significance (shaping of structural components and the visual expression of practical innovation) generally requires that designers be highly competent and creative. The challenges of designing bridges that are economical and elegant when they are prevented from being efficient also depend to a large extent on the range of feasible options available to designers. This range is determined by the complexity and the uniqueness of the design situation.

Compared to the Estaire Road Bridge (Fig. 1), the Bridge over the Rhine at Bad Ragaz (Fig. 3) was a complex design situation. Bad Ragaz is a relatively long bridge (total length 198 m) on a horizontal curve that spans a fast-moving river and flood plain, and requires sharply skewed supports. Estaire Road, in contrast, requires a single span of about 45 m and square supports. Greater complexity of the design situation can make the design process more difficult, but it also offers a greater range of feasible solutions and hence greater scope for creative decision making.

The bridge at Bad Ragaz is also a relatively unique design situation. The site-specific requirements and constraints are unlikely to have been duplicated at other bridges. Estaire Road, in contrast, is a very common design situation. There are many overpasses that have practically identical span, width, and geotechnical conditions. This implies that there would have existed an extensive body of knowledge of previously completed similar bridges, from which the best solution could have been readily determined. This would have significantly narrowed the scope of creative work required of the designer. At Bad Ragaz, in contrast, there was no similar "optimal" solution that was known in advance of the design. This required that the designer engage in a more extensive creative process to determine the most suitable solution.

5 Conclusions

Based on this examination of the relations linking efficiency, economy, and elegance in bridge design, it is possible to answer the question of whether or not all three of these ideals can be embodied in common types of bridge such as Estaire Road (Fig. 1).

The question of whether or not efficiency and economy can co-exist in the same structure depends on prevailing economic conditions, i.e., the ratio of the cost of labour to the cost of materials. This is out of the control of designers and owners. Currently, this ratio is high, which means that, except for long-span bridges, the most economical solution will require a quantity of materials that is greater than the most efficient solution.

The current incompatibility of efficiency and economy implies that bridges that must be economical cannot derive their aesthetic significance from the visual expression of efficiency. Although it is possible for a given bridge to embody economy and elegance in the absence of efficiency, the available sources of aesthetic significance are limited and drawing on these sources requires highly competent and creative designers. For design situations that are relatively simple and common, such as Estaire Road, the optimal solutions will have in many cases already been established, which further limits the scope available for shaping of structural components and the visual expression of practical innovation.

It is expected that autonomous robots will eventually replace human labour as the primary means of production in bridge construction. This will reduce the ratio of the cost of production to the cost of materials, and is thus likely to restore efficiency to its role as an enabler of economy. This will enable efficiency and economy to be embodied in the same bridge, and thus will make it possible for common types of bridge such as Estaire Road to derive aesthetic significance from the visual expression of efficiency.

References

[1] D.P. Billington, *The Tower and the Bridge: The New Art of Structural Engineering*. New York: Basic Books, 1983.

[2] C. Menn, “Der Einfluß der Preisbildung auf die Entwicklung im Massivbrückenbau in der Schweiz”, *IABSE Publications*, vol. 26, pp. 313–325, 1966.

[3] P. Gauvreau, “Robotics in Construction and the New Era of Efficient Concrete Bridges”, in *The Evolving Metropolis: Proceedings of the 2019 IABSE Congress, New York*, 2019.

[4] B. Garcia et al., “Productivity of digital fabrication in construction: Cost and time analysis of a robotically built wall”, *Automation in Construction*, vol. 92, pp. 297-311, May 2018.

[5] C. Menn, “Rhine-Bridge Bad Ragaz”. [Online]. Available: http://christian-menn.com/english/projekte_e/badragaz_e.htm. [Accessed: 31 May 2019].

[6] P. Gauvreau, “Economy and Elegance in Bridge Design: The Beauty of Practical Objects that Do Their Job Well”, in *The Evolving Metropolis: Proceedings of the IABSE Spring Conference, Kuala Lumpur*, 2018.

[7] C. Menn, *Prestressed Concrete Bridges*. P. Gauvreau transl. and ed. Basel Boston Berlin: Birkhäuser Verlag, 1990.

Proceedings of the IASS Annual Symposium 2019 – Structural Membranes 2019
Form and Force
7 – 10 October 2019, Barcelona, Spain
C. Lázaro, K.-U. Bletzinger, E. Oñate (eds.)

Exploring the Ideals and Character of Structural Elegance

Craig G. HUNTINGTON

Huntington Design Associates, Inc.
6768 Thornhill Drive
Oakland, CA 94611 USA
craig@huntingtondesign.com

Abstract

Strength is common to all structures, but high performance requires that strength be provided efficiently, as demonstrated by minimal material use. Through form optimization, prestressing and other strategies, performance is made efficient, and the structure has the potential for visual elegance. Material economy is also the source of "leanness", an absence of superfluous mass that is key to structural beauty. Visual transparency is corollary to leanness, and structural beauty demands that non-structural elements not obscure the structural form. When a subjectively chosen structural concept is refined through analysis and judgment into an elegant final form, a unique design may appear the predestined solution to its load-bearing problem. The paper explores structures in nature, including the musculoskeletal system of the human body, as models for understanding structural beauty.

Keywords: High performance structures, gothic cathedrals, concrete shells, architecture, lightweight construction, form resistance, adaptive form resistance, internal resistance, liechtbau, human form.

1. Introduction

The Tower and the Bridge [1] and other publications by David Billington have informed and inspired the author and others who share Billington's passionate interest in structural aesthetics. The book describes "structural art" as the product of three ideas: efficiency (minimum materials), economy (construction simplicity, ease of maintenance, and integrated form), and engineering elegance. Efficiency and economy are readily defined - efficiency measurable as the ratio of weight/area, and economy as the ratio of cost/area. In defining elegance, though, Billington faced the imposible task of defining artistic merit itself, and with limited success. He lists contrast and affinity with the structure's context as elements of elegance, but these are only two of many ways we might define elegance (and beauty itself). This author can define elegance no more definitively than Billington. However, routine experience of the structures of nature and of our own bodies have strong parallels to our appreciation of beautiful structures that provides clues to the sources and character of structural elegance.

2. The High Performance Ambition

An expertly performed high jump (Figure 1) is one of sport's most beautiful and iconic movements. In the contemporary technique, brought to prominence by the American Dick Fosbury, the athlete bounds towards the bar and springs from the ground to lift his center of gravity, at the same time rotating his torso until his back faces the bar. He snakes his body over it – head first, then shoulders, hips, and legs, before dropping to his back in the landing pit. Fosbury parlayed the unconventional technique to a gold medal at the 1968 Mexico City Olympics, after which it became known as the Fosbury Flop.

The name belies the beauty of a well-executed flop and its advantage over the previous standard – the straddle. A straddler clears the bar facing down, with his body parallel to the bar, so that head, torso,

Copyright © 2019 by Craig G. Huntington
Published by the International Association for Shell and Spatial Structures (IASS) with permission.

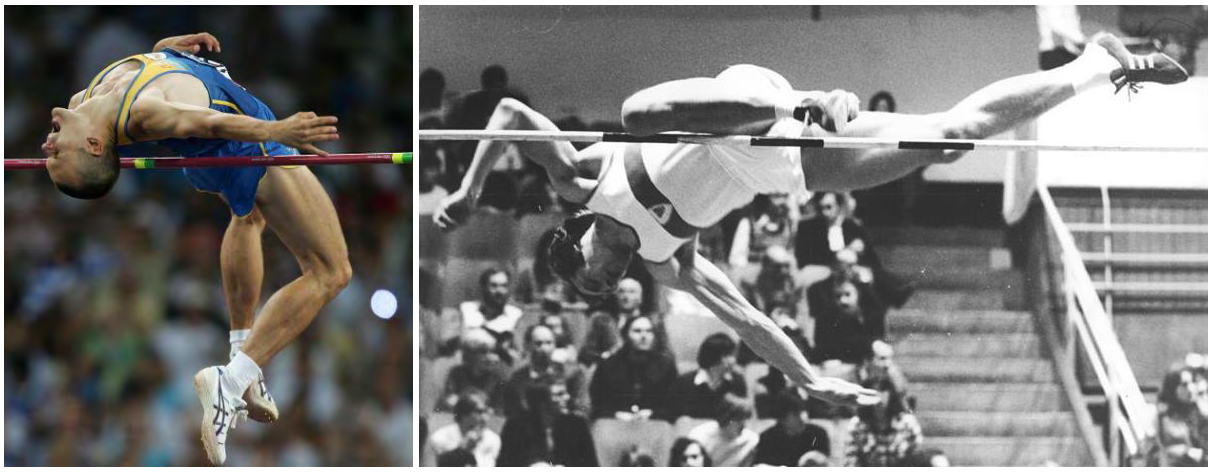


Figure 1. Well-executed flop (left) and straddle (right) high jumps. (Right image Bundesarchiv,Bild 183-S0305-0030/CC-BY-SA 3.0)

and legs pass over it nearly simultaneously. To clear the bar, the straddler must lift his center of gravity about 10-20 cm above the bar. In contrast, the backwards, serpentine movement of the flopper allows him to pass cleanly over the bar while keeping his center of gravity critical centimeters *below* it. If the jumper imparts the same upward thrust as he springs from the ground using either technique, the flop allows him to clear a higher bar. Fosbury's gold medal jump was ungainly next to the well-honed movements of the best straddlers, but jumpers that followed him gradually refined the technique. Their skill, combined with the flop's growing familiarity, make its best practitioners appear natural and graceful as they clear bars placed at heights well above their heads.

The photo captures a well-executed flop as the jumper passes over the bar. The power of the image reflects both the physical beauty of the athlete and the elegance of his technique. He has optimized the form of his body to its task, with the backward flex in his neck and torso and precise positioning relative to the bar conveying the efficiency of his movement. His body is hard-muscled, stripped of excess, and his entire being - from outstretched arm to gaping mouth - conveys singularity of purpose in maximizing his height of clearance. He has relaxed muscular tension that does not aid in clearing the bar, and the legs that have done their work in springing from the ground stream fluidly behind him. Experts might parse his motion into dozens of discrete elements, but it is performed with a fluidity that makes it appear irreducibly simple. The aspiration of the athlete inspires us. The aspiration of structures that span great distances with minimal mass inspires us as well, and is an essential part of their beauty.

3. Leichtbau

All good jumpers are strong, but strength gets them only part way to competitive success. They must also perfect their form and technique, so that this strength is efficiently deployed to clear the bar. Unlike a competitive gymnast, the jumper gains no points for style. He is rewarded only for his performance in achieving a measurable goal, and his technique is directed towards this alone.

High performance structures, similarly, are those whose form and detailing are targeted to supporting their own weight and imposed loads efficiently. Frei Otto is best known for his work on the Munich Olympic Stadium and other tensión structures, but his academic work focused on developing the principles of "leichtbau", or lightweight construction. In Otto's formulation, the work capacity of a structure is defined by its "tra": the load that it carries multiplied by the distance over which that force is transmitted to the support. Otto defined the structure's "effectiveness" as tra/structural mass. His

simple formula cannot be used by itself to evaluate the relative merits of two structures, as geometry, materials, and other variables make the demands of each design problem unique. (Supporting a load at the top of a cantilevered 10m tall mast in compression clearly requires a more massive structure than hanging the same load from a 10m long cable in tension, though both structures have the same tra.) However, Otto provides a simple expression for the goal of every high performance structure: to use the least structural mass to support a load over the required height or span.

The engineer Robert Le Ricolais, an important contributor to architect Louis Kahn's best work, aligned himself with the principle of leichtbau in his poetic evocation of the ideal "zero weight, infinite span". Le Ricolais' goal is unattainable, but in their quest to achieve it, designers sometimes create structures that satisfy unprecedented structural demands with the slightest of mass. In doing so, they may create the visceral excitement and particular beauty of high performance structures.

Engineers employ various means to create light and effective structures. The thin shells and arch bridges that are the focus of Billington's aesthetic studies are "form-resistant", or shaped to follow the most efficient load path to the support. The members of form-resistant structures are characteristically sloped, curved, or tapered to carry loads using a minimum of material. Structures as organic and exciting as Nervi's Small Sports Palace (Figure 2) may result.



Figure 2. Nervi's Small Sports Palace displays the leanness and transparency of a high-performance beauty

Variants of form resistant structures are those which change shape under the influence of an applied load in order to carry it with maximum efficiency. This strategy, "adaptive form-resistance", is demonstrated by the trampoline. Wherever the user steps, the trampoline surface deflects downward into the shape of an inverted cone with its ápex at the load point, and the tensioned, sloping surface surrounding the load pulling upward to equilibrate it. The genius of the trampoline, and of adaptive form-resistance, lies in the structure's ability to shape itself to most effectively support the load wherever it is placed on the surface. Employed frequently with flexible structures like the fabric roof used on Bigo (Figure 3) and on cable-supported glass walls, adaptive form resistance provides even greater efficiencies than are possible with its "static" form-resistant cousins built of stone or concrete.

Lightness is also achieved through "internal resistance". Rather than adjusting their shape to achieve efficiency, internally-resistant structures use prestressing to manipulate the stresses in the elements of a structure so that materials are used efficiently. Internal resistance is employed in prestressed concrete, but it is also characteristic of membrane structures and many steel applications.

Contemporary engineers are taking the pursuit of lightness a step further, using a final strategy called "load dissipation", in which the structure dampens or diverts loads, rather than supporting or resisting them. It is seen in bridge decks that are shaped for aerodynamic stability, and in skyscrapers whose stiffness is "tuned" to be out of phase with earthquake ground motions.

Light construction stategies are not unique to modern high-performance structures. Arches and shells are simple expressions of form resistance that are pervasive both in nature and in the stone construction of gothic cathedrals. Leichtbau, though, represents the systematic use of these strategies for structural efficiency, based on the analytical evaluation of internal stresses and the targeted and creative use of one or more high-performance design strategies. It creates a virtuous circle, in which structural efficiencies lead to lighter construction, with the reduced load decreasing the demand on the structure and facilitating further mass reduction. Leichtbau does not by itself assure elegance, but when a light structure is detailed to provide clear expression of the load path, and where non-structural elements do not visually conflict with this expression, the opportunity for beauty arises.

Light structures (and beautiful structures) are not necessarily economical structures, as high strength and durable materials, refinements in the shaping of members, the use of prestressing, and the introduction of curving structural forms bring added expense in fabrication and complications in the erection process. In addition, in the contemporary construction environment of the developed world, labor costs predomínate over material costs, and the material savings associated with leichtbau are often overridden by the added labor required to achieve its refinements. When designers push the techniques of leichtbau to their limits, though, there arises the potential for a special beauty that mirrors the beauty of the strongest and most technically proficient athletes.

4. The Lean & Organic Beauty of High Performance Structures

If we compare two jumpers with identical mechanics and the same ability to generate upward thrust, but with different weight, we expect the lighter jumper to clear a higher bar. A successful jumper must be lean, as well as strong, and the best have a compact but powerful musculature that can generate explosive force, and minimal body fat to hinder their ascent. A high-performance structure must also be lean, and it becomes so through the use of strong materials positioned exactly where required, and the absence of superfluous mass that might increase the tra of the structure. If the engineer employs form resistance or another of the high performance strategies to reduce dead load, the structure can be less strong (and less massive) and still reach the required span or height.

The forms of high-performance structures often curve to conform to the path that their loads take to the ground, and the cross sections of members sometimes vary along their length to reflect variations in internal forces. The forms of high-performance structures are typically derived from objective efforts to achieve lightness and efficiency, more than they are shaped by the conscious effort to create beauty. Horst Berger's Denver Airport Terminal roof (Figure 3) provides an example. Cables spanning from side to side in the fabric valleys are prestressed, pulling downward on the fabric to pretensión it. Both cables and fabric are shaped to provide equilibrium under the required design prestress. While high performance mandated curvature in cables and fabric, the masts themselves are straight and plumb, to deliver the downward pull of fabric and cables to grade by the most direct path.

Just as leanness alters a building's structural performance, it profoundly changes its visual character. Again, the athlete provides a useful metaphor. The leanness of an athlete's body draws his skin tight to the muscle and bone beneath in a way that exposes the mass and geometry of his own biological structure. Leanness also reveals the athlete's actions, telegraphing the tension or relaxation in each muscle and the articulation of joints in motion. In a lean structure, similarly, the delineation of form gives clues as to the path that forces take through the structure, and the bulk and shape of the beams and columns that compose a structure suggest the forces they resist. The layman may be unable to articulate the way that an athlete or a structure carries and responds to load. Each of us, though, through long familiarity with the action of our own bodies and observation of the trees and shells and other structures that comprise our world, can intuit with pleasure the way that a structure supports a load when leanness allows it to.



Figure 3. The Denver Airport Terminal's roof design pursued lightness and efficiency, with beauty the result.

Leanness can't be appreciated if obscured by non-structural elements like ceilings or partitions, or if structural members compete visually with mechanical ducting or other building services. A comparison of Nervi's two Rome Sports Palaces illustrates the point. The dome form of the Small Palace is clearly articulated on both exterior and interior (Figure 2). From either viewpoint, it is easy to visualize the weight of the roof thrusting downward and outward against the sloping buttresses, which distribute the roof weight to the ground at their feet. The Large Palace roof has similar form, but a tall curving wall encloses support spaces around the building perimeter, and hides the view of the dome on the exterior (Figure 4). We can admire the sculptural geometries of the Large Palace form, but its façade masks expression of the roof's load-bearing behavior. The effect is as if Fosbury had made his gold medal jump while wearing a bathrobe. The mechanics and height of the jump might be the same, but we would not appreciate its lovely efficiency. Arguments may be made for the architectural merit of either Nervi structure, yet it terms of their structural expression, the Small Palace elegantly reveals the behavior of its high performance roof, while the Large Palace does not.



Figure 4. The elegance of Nervi's Large Sports Palace roof is obscured by competing elements on its exterior.

Revealing or obscuring a structure's connections and other details also changes its visual impact. In designing Bigo, a waterfront canopy in Genoa, Italy (Figure 5), engineer Ove Arup (in collaboration with architect Renzo Piano) sought economy and ease of construction. Their design had another ambition, though - the athletic expressiveness derived from clearly articulating the structure's load path. All structural members are exposed on Bigo, and detailed in a manner that makes it easy to follow loads from roof to grade. This begins with the pretensioned fabric roof, whose weight and pretension join with wind and other applied loads to pull downward on the four arches that span over the fabric. The arches are in turn held up by the arrays of suspension cables that attach to them and rise to the tops of the two tall tapered masts. In the close up on the right of the figure, the suspension

cables (to the right of the mast) attach to steel gathering plates, which are linked in turn to the mast top. The overturning effect of the suspension cables is equilibrated by the counteracting pull from the stabilizing cables (to the left of the mast.) The tensions in both the suspension and stabilizing cables pull down on the mast, which carries this compressive load to grade.



Figure 5. Bigo's structural elements are all exposed, and clearly display the load path.

Bigo's details reinforce the clear expression of the load path, at the same time embodying all of the leanness of a fine high performance structure. The photos show a subtle increase in the diameter of the masts towards the center of their length, as required to prevent buckling, while at the same time minimizing the bulk at the mast ends. A further refinement is seen in the gathering plates which collect the suspension cables at the mast top, where the large circular cutout in the middle reduces both the the visual and actual mass of the plates.

The forces in the members of a structure vary constantly along their length, and designers of high-performance structures select carefully articulated forms and details that express the load path. They may vary the cross-sections of members along their length, in the way that an animal bone varies in stoutness from one end to the other in response to the varying forces that the leg of the living animal needed to resist along its length. This places these designers at odds with colleagues designing more conventional structures, who employ uniform cross sections and repetitive detailing to reduce the cost of construction labor (and their own design costs.)

Structures of the natural world are nearly infinite in variety, and respond in ingenious ways to the widely varying loads imposed by natural life. The diversity and cleverness of natural structures make them frequent models for engineered structures. Those who design vertical columns that split into sloping branches may describe them as "trees", while the curving roof forms pioneered by Candela and others are called "shells", in recognition of the sea shells and egg shells they suggest. Designers of curving glass walls stabilized by steel cable nets draw inspiration from spider webs.

The familiarity that all of us have with both these natural structures and the musculoskeletal structures of our own bodies provides a means for non-professionals to appreciate the behavior and beauty of high-performance structures. It also provided the means for designers of an earlier era (who lacked contemporary analytical tools) to understand and explain their work. They frequently turned to the human body as a model of how their structures carried load. When completed in 1890, the Firth of Forth railroad bridge (Figure 6) was the first long span bridge built entirely of steel. To demonstrate to the public how the bridge spanned the large chasm, the engineers used three men as props to create the iconic photograph seen on the right. The torsos of the men seated to either side of center represent the cross-braced supporting towers of the bridge displayed on the wall behind them. Each of these

"supporting" men extends one arm (braced by a sloping strut) towards the center of the bridge to support the "suspended" man seated between them. In order that the weight of the suspended man not topple the supporting men, the latter extend their outside arms (again braced by sloping struts) to ropes which are lashed to stacks of bricks. The bodies of the supporting men are balanced symmetrically between the suspended man in the center and the bricks to either side, so that they can bear their load comfortably. Their arms are straight, suggesting the tension tugging at their elbows and shoulders, but we can imagine that the muscles in their arms are relaxed. Their spines are straight and relaxed, as well, and their faces bear no strain. The ease with which they support their load provides a vivid representation of the high performance structural behavior of the Firth of Forth bridge itself.

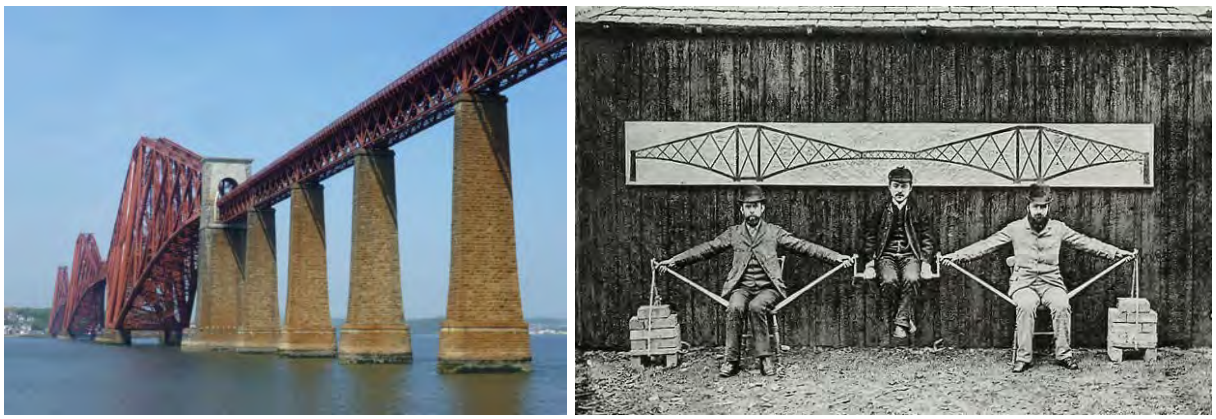


Figure 6. Human "members" were used go model the load-bearing action of the Firth of Forth railroad bridge.

5. The Pursuit of Perfection

In *The Tower and the Bridge*, Billington makes a powerful case for the subjective nature of the design choices of the select group of engineers he crowned "structural artists", and for the elements of personal style with which they worked. Billington is not incorrect, but the principles of high performance design suggest an aesthetic that relies equally on a search for "ideal" form. The architectural critic Ada Louise Huxtable eloquently captured this quality in her 1960 Nervi monograph [3]. "It is possible even for the layman to feel tension and compression, the direction of forces, and the inevitable, *correct* relationship of structure to shape", she wrote. "The fusion of structural function and abstract form creates a kind of building that is so fundamentally *right* that most other architecture seems superficial beside it." Her terms "correct" and "right" (emphasized by the present author) suggest that structures of exceptional beauty are as much the outcome of the designer's search for the ideal solution to a particular problem of loading and span as they are products of personal expression.

Rationalizing the special nature of any mode of beauty is impossible, but Nietzche's yearning "to see as beautiful what is necessary in things" provides a further clue to the aesthetic appeal of beautiful structures. Structure is the most necessary element of architecture, providing support for a building's plumbing and mechanical "organs" at the same time that it gives shape to its roofing and façade "skin".

The forms of both gothic stone cathedrals and concrete shells are founded in the simple goal of efficient load bearing – an objective more fundamental and enduring than the complex artistic and programmatic forces that drive most architectural design. Architectural critics may argue incessantly about the relative merits of particular schools of architectural practice and particular works, but there seems an unalterable quality to the structural forms of the engineering masters. How might the arch of the Salginatobel Bridge (Figure 7) be improved? Most of us prefer unblemished admiration.

Structural designers who have created work of enduring beauty have done so through a commitment to perfecting form similar to that demonstrated by elite athletes. The principal is demonstrated most

clearly in the slender forms of gothic cathedrals. Cathedral designers lacked the means to provide tensile reinforcement across the joints between the stones that formed their structural skeleton, so, in order to avoid explosive failure, they were compelled to shape structural members so that the load path always fell within the member cross section.



Figure 7. Robert Maillart's contrasting concrete arches at Salginatobel (left) and Schwandbach (right).

In examining most structures, an observant structural engineer will consider the design possibilities not chosen, perhaps imagining the supporting arches with steeper or shallower slope than its designer selected, or suggesting that the arch itself be replaced by a beam or a truss. To engineers and other critical observers, the examination of most structures is an intellectually and creatively active process. The experience of examining a masterful high performance structure, though, is less one of critical engagement than of serenity in the presence of something much like perfection. An engineer might surmise the presence of a great work by the absence of his usual desire to tinker with or change it. Speaking of his contemporary Robert Maillart, shell architect Felix Candela said, "he did possess that rare quality of being able to challenge the conventional wisdom and come up with the obvious solution, one, nevertheless, which nobody could think of before" [4].

This paradox - challenging conventional wisdom to arrive at a perfect and obvious solution – is amply illustratedby Maillart's Schwandbach Bridge near Hinterfultigen, Switzerland (Figure 7), where the bridge deck, straight in elevation but curved in plan to align with the roadway approaches, is supported by an arch which is straight in plan but curved in elevation. This design, bold and unlikely in conception, appears so perfect in its finished reality that it is difficult to imagine a change to the design, or at least one that would not be a defacement of its well-integrated beauty. The nature of structural elegance, in combination with the genius of Maillart, led to a design that is unique in conception, but executed with such skill and elegance that it appears to be the inevitable solution to the design problem.

References

[1] D.P. Billington, *The Tower and the Bridge,* Basic Books, 1983.

[2] F. Otto, *Basics,* Institut für Leichte Flächentragwerke, 1979

[3] A.L. Huxtable, *Pier Luigi Nervi,* George Brazillier, 1960, pp. 9, 10.

[4] F. Candela, letter to Anton Tedesko dated December 5, 1963. Printed in *Felix Candela Engineer, Builder, Structural Artist.* Princeton, New Jersey: Princeton University Art Museum, 1963, pp. 176.

Proceedings of the IASS Annual Symposium 2019 – Structural Membranes 2019
Form and Force
7 – 10 October 2019, Barcelona, Spain
C. Lázaro, K.-U. Bletzinger, E. Oñate (eds.)

Lateral load resisting facades

Miguel LOPEZ, Joseph BLANCHFIELD, Philip MURRAY, David KAZIBWE, Carolyn BAI, Ramon GILSANZ*

*Gilsanz Murray Steficek
129 West 27th Street, 5th Floor, New York, NY 10001, USA
ramon.gilsanz@gmsllp.com

Abstract

Simple modifications to traditional curtain wall slab anchors allow designers to incorporate a structure's building envelope system into its lateral system, leading not only to improved structural performance, but a reduction in the building construction's carbon footprint. This approach of integrating architecture with structural design to optimize building performance and construction embodies the principles of efficiency, economy, and elegance championed by David Billington. In this paper, the potential benefits of utilizing façade members to contribute to the building stiffness is studied by reanalyzing 510 Madison Avenue, a 2012 Class-A steel high rise office building in Manhattan. The building's lateral system is comprised of moment and braced frames. The building's façade is a unitized aluminum curtain wall system that utilizes traditional curtain wall anchors designed to prevent the transfer of loads between the façade and the structure. If the curtain wall slab anchor is redesigned to allow some fixity of the vertical mullions, then the curtain wall can partly carry out-of-plane loads. The results of the study indicate that a unitized hybrid curtain wall system, consisting of a shallow aluminum extrusion with a steel back-up member, can reduce the sway of the building at the upper floors and reduce the overall building CO^2 footprint for some anchor and installation layouts. The shallow aluminum extrusion provides the exterior finish, glazing cavity, thermal break, and air/water tightness system and the steel back-up member provides the structural capacity. For this case study, based on the spacing and depth of the members the curtain wall may reduce the inter story displacement by 2% to 6%.

Keywords: envelope performance, energy analysis, lateral resisting system, parametric performance modeling, carbon footprint.

1. Introduction

Current curtain wall anchors are designed to prevent the transfer of loads between the façade and structure, keeping a structure's building envelope system independent from its lateral system. However, mullions in curtain wall systems have a capacity to carry some out-of-plane loads. By integrating curtain wall design with the structural design, a building can potentially improve a building's behavior while also reducing the environmental impact of its construction. This approach of incorporating architectural elements into a building's structural system to optimize building construction and performance embodies the principles of efficiency, economy, and elegance championed by David Billington.

Exploring solutions to minimizing the "embodied energy" of the building's systems (i.e. energy used prior to a building's operational phase measured in equivalent emission of kg CO^2 per kg of material) has become increasingly important from an environmental standpoint as one considers how the performance of envelope enclosures is increasing (thereby reducing energy consumed during the operational life of a building), and the overall life expectancy of buildings is decreasing [1]. As the red

Copyright © 2019 by Miguel Lopez, Joseph Blanchfield, Philip Murray, Carolyn Bai, Ramon Gilsanz
Published by the International Association for Shell and Spatial Structures (IASS) with permission.

trend line in Figure 1 illustrates, the impact of the energy used prior to a building's operational phase (embodied energy) is increasing.

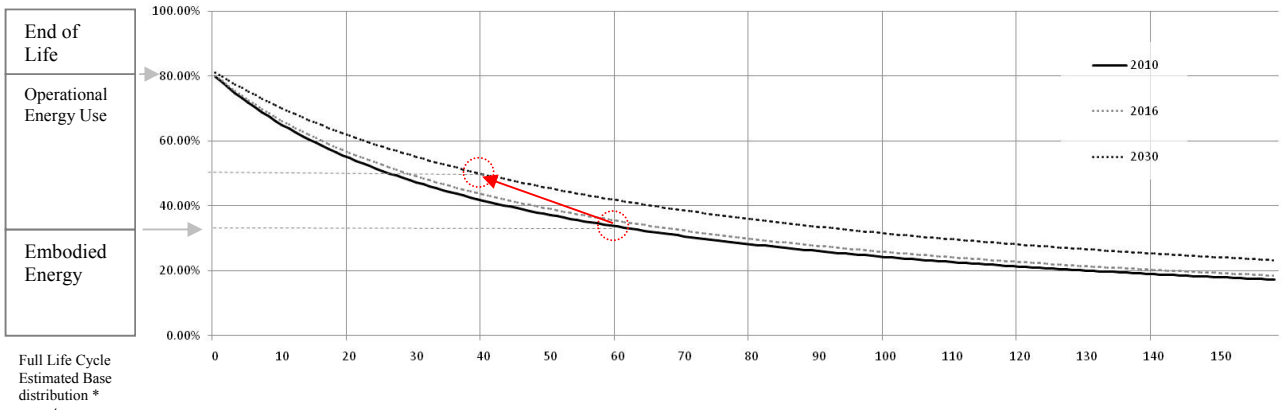


Figure 1: Embodied Energy/ Total Energy * percentage distribution over life of building.
* Total Energy to Date = (Embodied + Operational (t) + End of Life).

2. Building envelope

Current commercial buildings enclosures are dominated by lightweight unitized curtain wall facades [2]. In the last five years, these facades are estimated to make up approximately 70% of the total envelope surface area of new office buildings and they are having an increasing presence in high-end high-rise residential buildings (circa 15% increase). Of the total of curtain wall surface area erected in this period approximately 64% are unitized systems, of which 92% are extruded aluminum systems.

2.1. Current curtain wall design

The curtain wall (CW) is a non-load bearing exterior skin that does not contribute stiffness to the building structure. Current curtain wall construction technologies are optimized to perform two tasks: providing the envelope enclosure and resisting the tributary cladding wind load. Hence, mullion anchors are designed to intentionally allow rotation at the points of support.

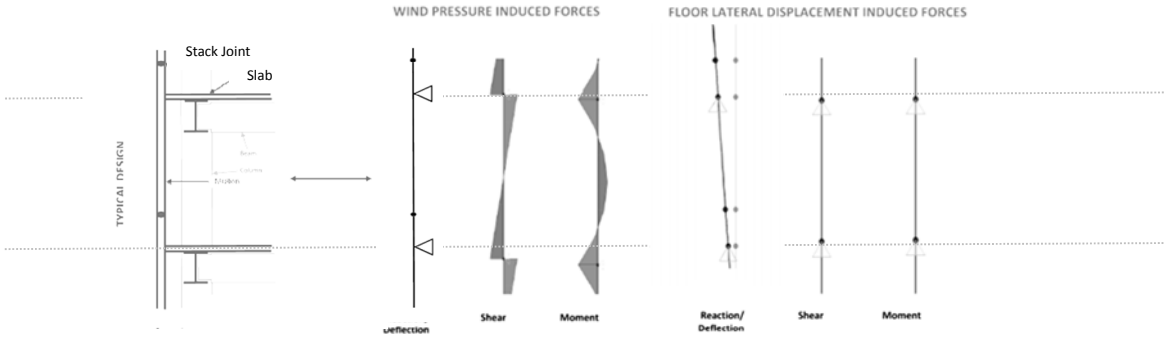


Figure 2: Existing curtain wall design load distribution diagram

Traditionally, typical mullions are made of aluminum. For high cladding wind loads or inter-story heights the mullions are reinforced with steel sections to limit the depth of the mullion and the reduce impact on the floor area ratio.

Newer façade designs are employing heavier materials than glass (e.g. terracotta, stone, or photovoltaic rain screens), hence the curtain wall is evolving from a "barrier" system to a "barrier + carrier" system

[3]. In addition, tighter thermal performance requirements have increased the minimum size of glass panels for glass curtain wall façades. The result is an increasing demand for stiffer curtain wall frames capable of withstanding higher loads.

In a unitized CW the main stresses occur at: the vertical mullions in the out-of-plane direction due to wind suction, and at the vent transom connections due to the torsion produced by the in-plane gravity load of the glass and the wind suction. The capacity of these component limits the spans and dimensions of the CW units [4].

2.2. Mullion material

In order to select the optimal mullion materials, several factors need to be considered including: structural capacity, stiffness, weight, and environmental impact. Figure 3 compares the Young modulus, the "nominal" material density, and the environmental impact or "adjusted material density" (as measured by the weight of CO^2 emissions required to produce and discard 1 m^3) of various typical CW framing member materials. As Figure 3 highlights, while steel weighs more than aluminum, it is both stiffer than aluminum and has a smaller carbon footprint depending on the type of steel and aluminum being considered.

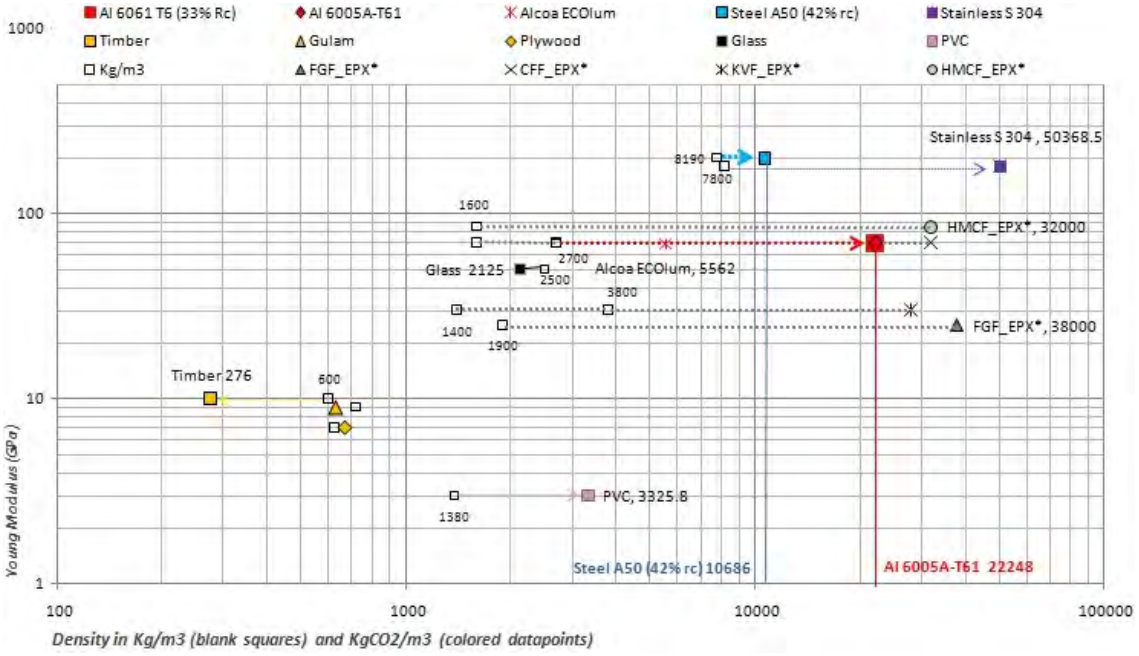


Figure 3: Typical CW framing member material* comparison. Young modulus vs. "nominal" material density (kg/m^3) vs. environmental impact or "adjusted density" ($kgCO^2/m^3$).
* FGF=fiber glass fabric, CFF=carbon fiber fabric, KVF=Kevlar fabric, HMCF=high modulus carbon fiber fabric. [Fibers @ 45° (UD), 0° (fabric) to loading axis, dry, room temperature, Vf = 60% (UD), 50% (fabric)].

Though some specialty aluminum products (e.g. Alcoa ECOlum 5562 $kgCO^2/kg$) can potentially have a lower carbon footprint per kg than typical structural steel (10686 $kgCO^2/kg$), it is unclear if this offset can compensate for their different structural capacities.

It is important to note that the carbon footprint of each material can vary considerably depending on how it is sourced and produced (e.g. raw materials versus recycled materials). For our case study, we used the current industry standards for percentages of recycled content per ingot (33% for aluminum and 42% to 47% for steel).

We can plot the ratio between the densities of a material and its Young modulus to verify if the offset between different materials can, in this application (bending), compensate for the difference in stiffness. As observed in Figure 4, the "nominal density" ratio is approximately constant between aluminum and steel. However, steel appears substantially more efficient if we consider the "adjusted density" of the materials even when compared to 100% recycled aluminum.

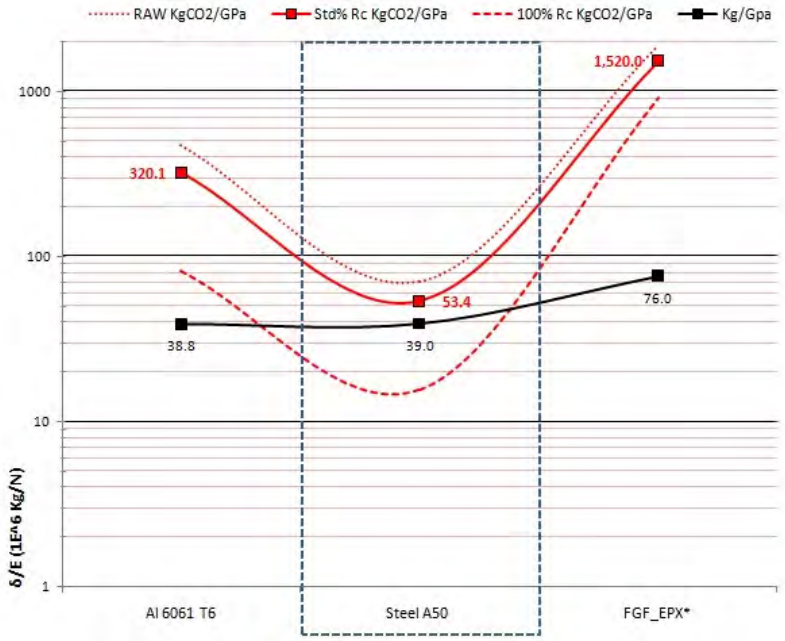


Figure 4: Proposed framing materials "nominal" (black) and "adjusted" (red) density over Young modulus ratio.

3. Proposed mullion design changes

Two proposed mullion design changes can potentially help address the design challenges discussed in this paper. First, increasing the number of CW anchors from one connection at each floor to two connections. Two connections generate fixity against rotation. The mullion then resists its tributary cladding wind load *and* contributes to the stiffness of the building's lateral resisting system.

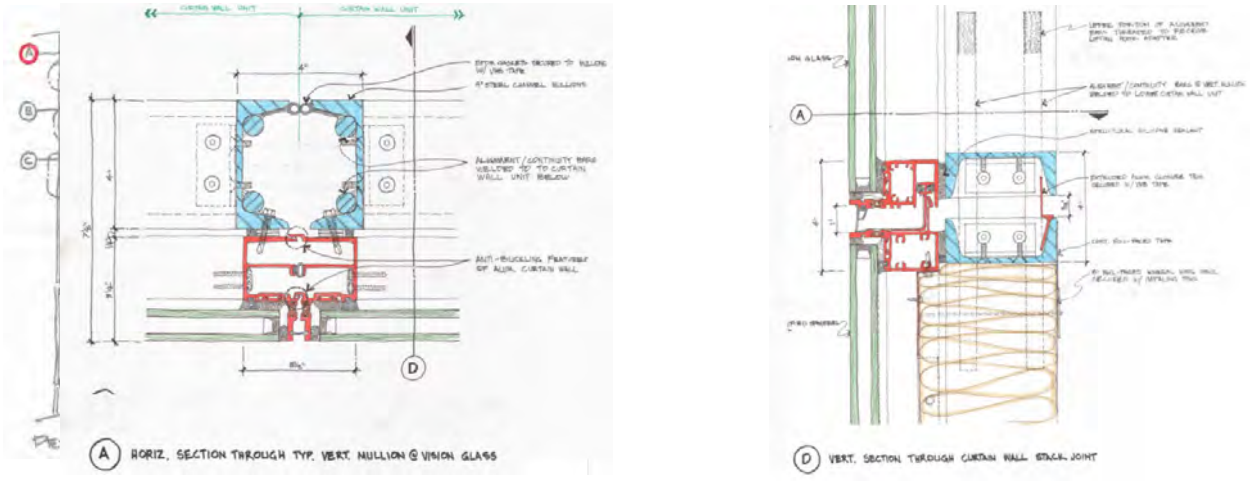


Figure 5: Proposed system typical details A & D. Hybrid (Al+steel) unitized curtain wall (HUCW)

Second, changing the single aluminum mullion to a combined aluminum plus steel mullion. The additional stiffness and strength of steel versus aluminum and the support fixity makes the new system stiffer and stronger than a CW system of the same depth.

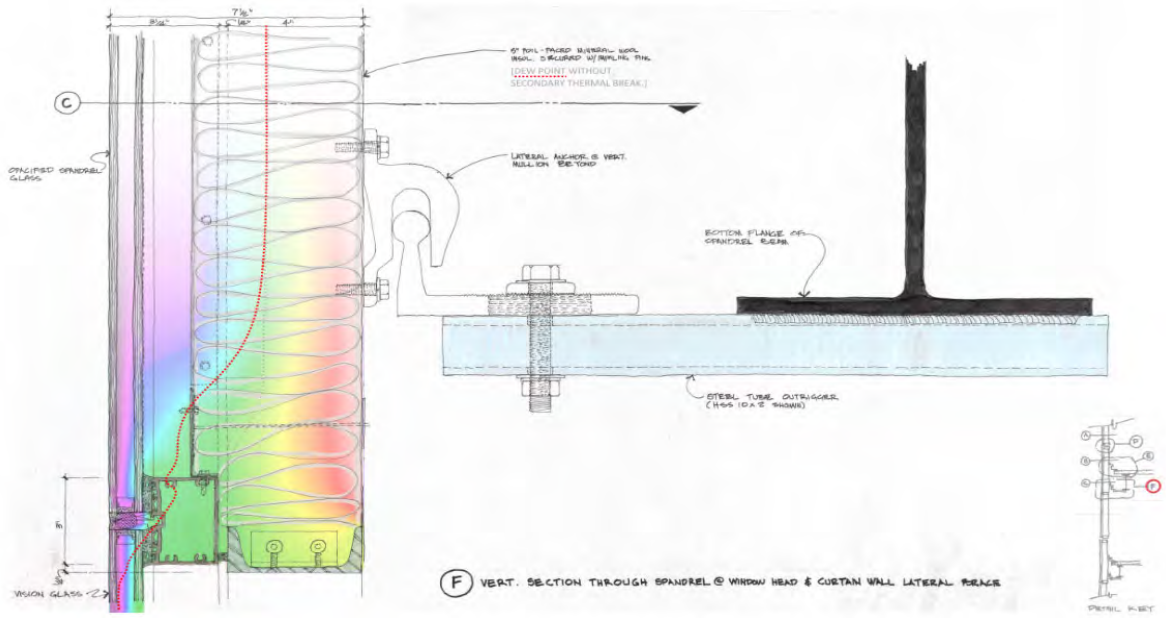


Figure 6: Proposed system typical detail F. Anchor at bottom of spandrel beam.

4. Case study

An existing Class A office building located on Madison Avenue in Manhattan, New York was used as a baseline. The base building, completed in 2012, is 30 stories high and has a gross floor area of approximately 31,500 m^2 with a floor plate form factor of 1.75**.**

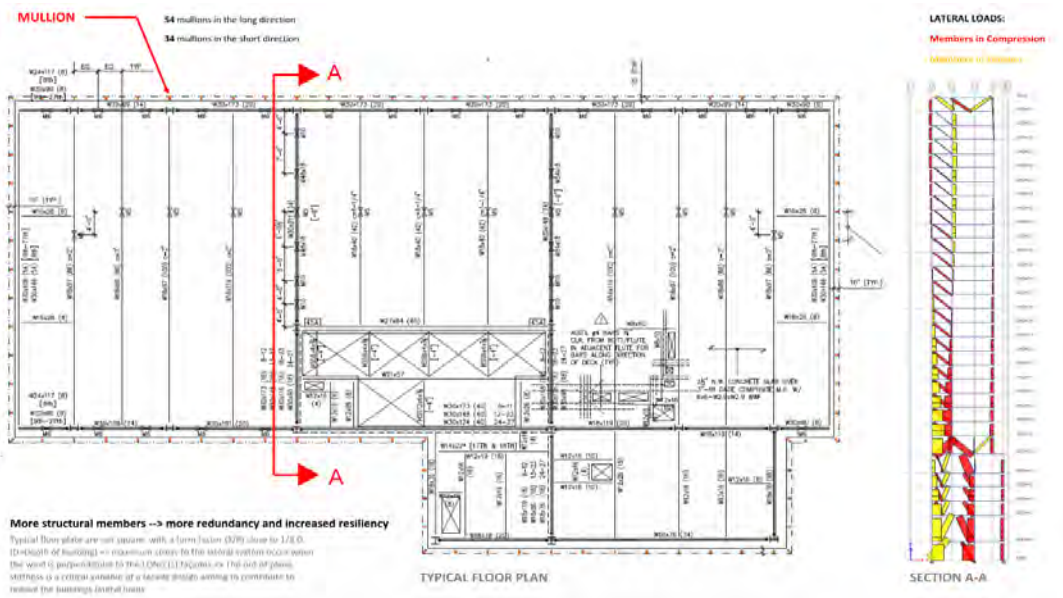


Figure 7: Typical floor framing plan

4.1. Mullion FEM modeling:

The mullion for the hybrid system was modeled with a finite element program. The support restraints were placed according to Figure 8. The stack joint connection is represented by a rotational "end release" that avoids the transmission of the bending moment between the two beams and a translational "end release" that allows the translation along the mullions axis.

The top anchor was modeled as a pin with the rotation released. The bottom anchor of the proposed hybrid system was model as a spring to account for the bracket deformation.

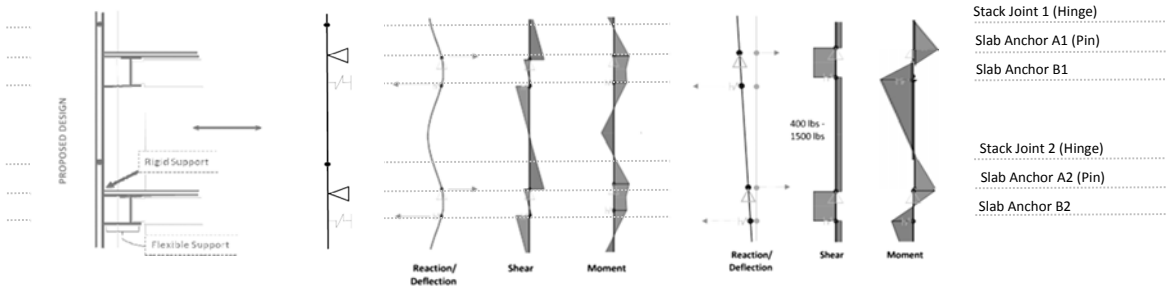


Figure 8: Proposed hybrid system load distribution diagram

4.2. Building

The building and the hybrid façade were modeled by a finite element program (SAP 2000).

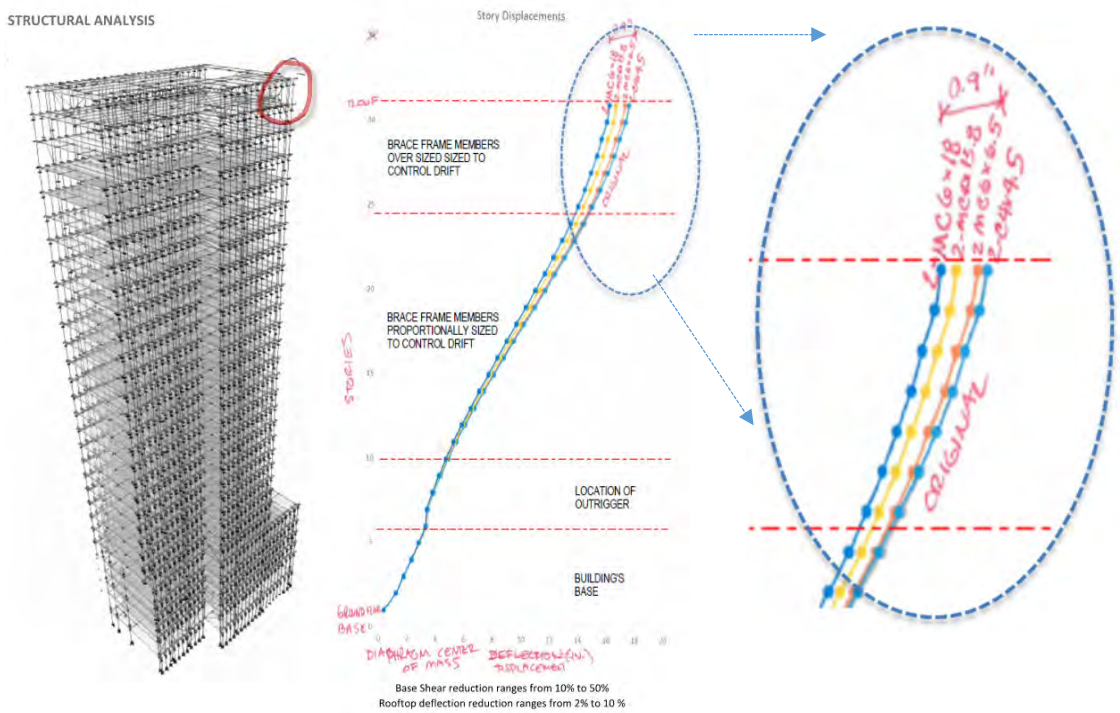


Figure 9: Building FEM 3D model and deflection curves for base and Alts 1 – 3 designs.

For the baseline building, the façade mullions were not modeled and only their tributary loads were included in the wire model as point loads as the façade transfers the wind loads to the floor diaphragm.

For the proposed hybrid system, the mullions were modeled as continuous beams with a rotational and axial release at the stack joint. The beam was connected to the diaphragm at the slab level. An elastic diagonal element connected the mullion at the bottom of the spandrel beam to the diaphragm (see Figures 8 and 9) simulating the bracket connection to the spandrel´s flange and perpendicular beams.

5. Results

A target for this study was to identify the type of trade off relationship that may exist between heavier sections, structural performance, and environmental costs. An analysis of the selected set of steel shapes identified a limited range where there was a potential reduction of the overall carbon footprint of the building's structural and envelope framing components. Figure 10 plots the environmental costs of each component against its contribution to reducing the displacement of the rooftop center of mass (CoM).

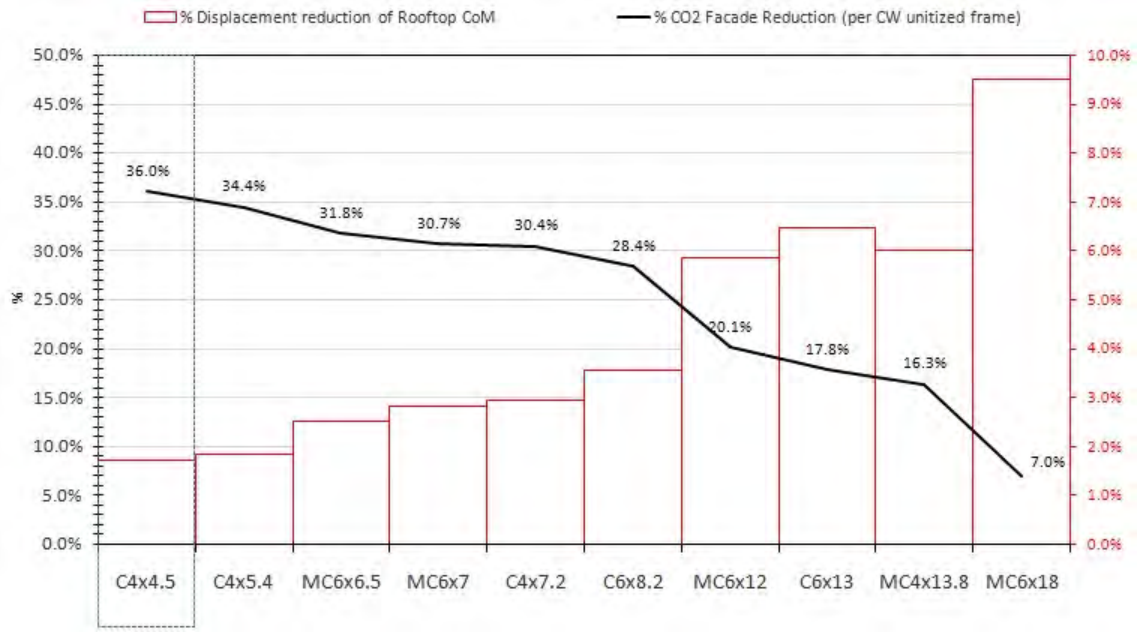
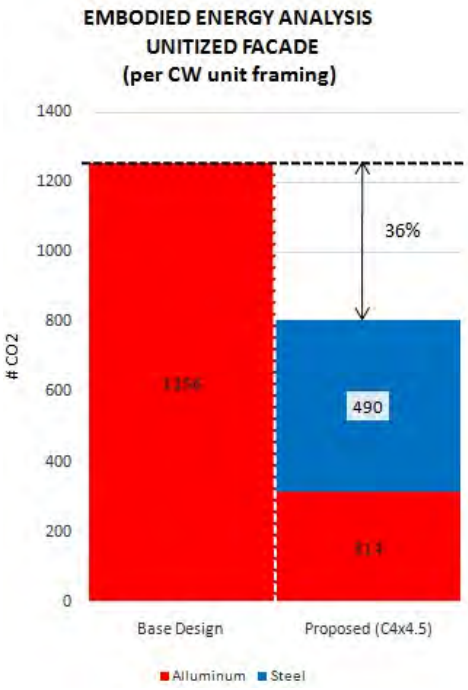


Figure 10: Proposed steel member analysis @ CW framing back-up | Braced with L/400 (wind 60 psf)

5.1. Re. Structural and thermal performance

The added stiffness of the steel backup components reduced the sway or lateral displacement of the building's rooftop center of mass by 2% to 6%. The replacement of the back-up area of the aluminum extrusion by a steel member reduced the embodied carbon tonnage of the façade components (excluding the glass) by a maximum of 36% depending on how the aluminum and the steel were produced. The total maximum reduction in the embodied carbon tonnage of the building façade and structural components is approximately 7%.

The thermal performance of the hybrid system is comparable to the baseline system. The thermal operational energy consumption was assumed as constant for the study.



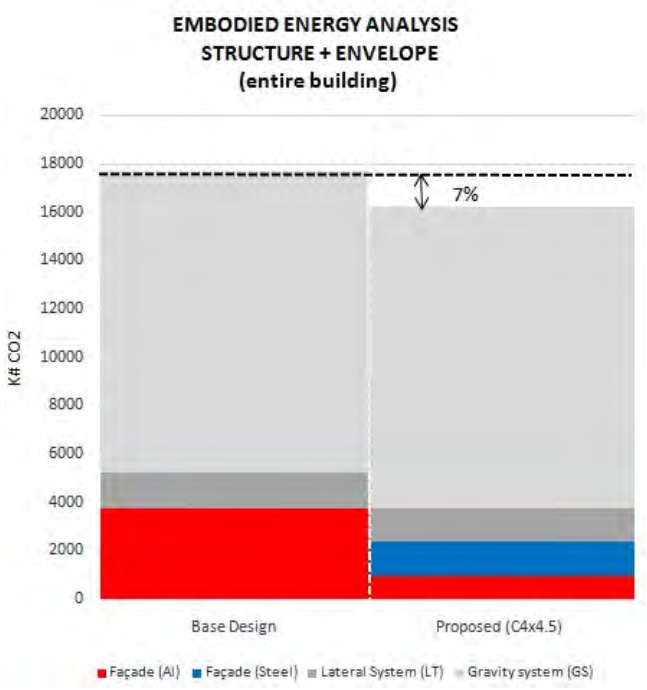


Figure 11 (left): Embodied energy analysis (EEA) per curtain wall unit (framing).

Figure 12 (right): Embodied energy analysis of above grade structural and envelope framing systems

6. Acknowledgements

The insight, editing and support of Connie Yang is greatly appreciated.

7. Conclusion

While the overall weight of the façade increases, the offset between the embodied energy of aluminum and steel, and the potential reduction of the building frame lateral system, provide a net reduction of CO^2 emissions. By replacing the back section of the aluminum extrusion with a steel member, you reduce sway and reduce the carbon footprint of a building based on industry accepted mean coefficients. These conclusions apply to the example modeled and depend on the production costs, availability of resources, and the impact on the erection.

References

[1] The Getty Conservation Institute, Conserving Modern Architecture Initiative, 2017 Workshop. http://www.getty.edu/conservation/our_projects/field_ projects/cmai/cmai_colloquium.html

[2] Grand View Research, "Aluminum Curtain Wall Market Analysis By Type (Stick-built, Semi-unitized, Unitized), By Application (Commercial, Residential), By Region, And Segment Forecasts, 2018 – 2025," 2017.

[3] B. Blasdel, "Glass and terra-cotta rise at One Vanderbilt." *The Architect's Newspaper*, July 7, 2017. https://archpaper.com/2017/07/can-see-grand-central-house/#gallery-0-slide-0

[4] Frances Loeb Library, GSD Materials Collection, Material Science Library. Harvard, 2017.

Proceedings of the IASS Annual Symposium 2019 – Structural Membranes 2019
Form and Force
7 – 10 October 2019, Barcelona, Spain
C. Lázaro, K.-U. Bletzinger, E. Oñate (eds.)

Making His Story of Structures My Own

Edmond SALIKLIS*

*California Polytechnic State University
Department of Architectural Engineering
1 Grand Avenue
San Luis Obispo, CA 93407, USA
esalikli@calpoly.edu

Abstract

The challenge of re-inventing a classic is fraught with many difficulties. A useful analogy is the performance of a cover of a well known song, most often the re-created cover is not as good as the original. Yet once in a while, a cover is remarkable because it clearly is the same as the original, yet it is still unique, it is marked by the personality of the cover artist. The strategy employed by the author in the making of a "cover" of Billington's course was to take the following three steps: (1) Take the best of the original version, namely the premise of scientific, social and symbolic critiques as well as The Pantheon of Heroes; (2) Remove the parts that need adjustment (antipathy towards architects); and (3) Make it my own, with my own style and color.

Keywords: History, Structural Art, General Education

1.Introduction

Each year from 2013 to 2019 the course History of Structures has been offered as a General Education course at California Polytechnic. It is designated as an "Arts and Humanities" course and within that category it fulfills the "Fine and Performing Arts" requirement. The initial offering had quite a humble beginning, with only 20 students. The latest offering hosted 138 students.

The Course Description in the University Catalogue is as follows:

Social, symbolic, and technical importance of landmark structures. Analysis of breakthrough ideas that led to major advances in building design. Contextualization of these advances. Tools by which to assess and critique structural art as a separate and distinct art form. No prerequisites.

The fact that History of Structures fulfills certain University General Education requirements adds one large layer of complexity, namely that this is Writing Course, which means that "a significant portion of the grade arises from written papers". One technique for addressing this complexity has been adopted.

The course philosophy has always been to celebrate and promote the best works of structural engineering completed during the last two hundred and fifty years. Some of the works studied in History of Structures rise to the level of "structural art" and the rich tradition of such masterworks, independent of the tradition of architectural history, is important to all students interested in building design and construction. The critical tools used throughout the course appeal to all students interested in the broader topic of design and art criticism. History of Structures fulfills a need because it addresses the "affective response" that many people have to large scale structures. This affective response is sometimes referred to as the emotive power of structure, and this course provides tools to assess and critique built works that

Copyright © 2019 by Edmond Saliklis
Published by the International Association for Shell and Spatial Structures (IASS) with permission.

enrich the public life of modern industrial, urbanized society through language that is precise and rigorous, language that is formed through the prism of the engineer's imagination. Such language is best utilized during the contrast of three dimensional works created by the engineer, the architect and the sculptor. Three dimensional forms created by the engineer are governed by more technical and economic concerns than are the forms of the sculptor, who typically does not have to worry about life safety issues. Yet all three forms seek to maximize aesthetic expression and sometimes reach the level of having great symbolic impact.

2. Course format

Nineteen separate lessons are currently presented. Each lesson focuses on either one person (for example Peter Rice) or one idea (for example The Spanish Tradition of Thin Shell Roof Vaults). A personal fun touch is that prior to the start of each class, as the hundred or so students are gathering, a musical video that is somehow paired to the day's lesson is playing on the large screen and filling the auditorium with music. The Gypsy Kings might be playing during the Spanish Tradition lecture, or Kurt Weill during the German Tradition lecture. Other small links to the period being studied are interspersed, these typically are either art or music, as both are considered specialties of the author. The language and critiques of structural form are meant to be consistent within each and every lesson, they begin with rudimentary scientific analyses of the structures being studied, primarily investigating load flow, tension and compression. Then a small social critique is performed such as "how was the structure used?", "how long or expensive was the construction process?". The final and most important critique however is the symbolic analysis. This is what makes the course a general education course that can be enjoyed by first year students or graduating seniors.

Attendance currently constitutes 50% of the grade. This is so because each lesson is packed with 70 or 80 slides containing almost no text. Detailed written-out narratives, mapping each slide to a specific spot in the text have been created by the author for each lesson. Yet the students do not receive this text. Rather, they receive two identical single sided sheets of paper. On these sheets are listed 10 to 12 short questions. Some are merely descriptive (Name the chief designers of the John Hancock Building in Chicago), others are more open ended (could Felix Candela be presented as a role model to high school Latino youth considering a career in engineering). Students answer a few of those questions during class and had in one copy of the sheet as their "attendance ticket". Students retain the other sheet to prepare for exams. The exams are solely made up of these 150 or so questions that have an unambiguous answer. Students know that the open-ended questions will not appear on an exam. Thus, the students have the questions as well as the answers to each and every exam!

Perhaps it is heresy to state that the required textbook for the course is not The Tower and the Bridge [1], but rather Building: 3000 Years of Design, Engineering and Construction, by Bill Addis [2]. The reason is that the Addis text is more breadth-oriented, rather like an encyclopedia, making it suitable for a first course in structural history. Ideas and language from The Tower and the Bridge are used for almost all of the topics, but specific helpful resources were very valuable in creating the story behind other topics. These other resources are cited in the following list of topics.

Topics:

- The Washington Monument and The Eiffel Tower, Symbolic and Social Critique
- Technical Critique of the Eiffel Tower
- Robert Maillart and the Origins of Reinforced Concrete [3]
- Form and Forces, an Overview of Technical and Aesthetic Ideas [4]
- Catalan Vaulting [5]
- The German Tradition of Thin Shell Concrete Roofs [6], [7]

- Max Berg and the Centennial Hall in Poland [8]
- Felix Candela and the Hyperbolic Paraboloid [9], [10], [11]
- The Italian Tradition of Thin Shell Concrete Roofs [12]
- The Spanish Tradition and some Swiss Ideas
- Skyscrapers with a focus on Chicago
- Myron Goldsmith and the Diagonally Braced Tube [13]
- Lakepoint Tower [14] ….. Poly Canyon
- Fazlur Khan and Tall Buildings [15], [16], [17]
- Bill Baker and Tall Buildings [18]
- Tange, Tsuboi and Kawaguchi, The Japanese Engineer-gods [19]
- Frei Otto and Lightweight Structures
- Peter Rice, Le Traice de la Main [20]
- Jorge Schlaich, The Ethics of Engineering Design [21]

Successes:

The course is very popular. Students from every possible major have said that it is one of their favorite courses. A common observation is that students "have never really thought of buildings in that way before", i.e. they never considered the technical and aesthetic challenges surrounding major buildings, nor were they aware of any of the members of the Pantheon of Heroes. For architectural engineering students, this course often inspires them to find a Senior Project to study in depth that was based on something they saw in class (Catalan Vault, thin concrete shell, grid shell, solar chimney). Even first year students have attempted to create structures that are based on what they saw in class (Eiffel Tower, Farnsworth House). There is one Model Making Exercise, done by teams of students as a homework assignment. They create either an Isler-type of hanging cloth structure, or a Gaudi-type of hanging chain structure. They solidify the form, invert it and photograph it with scale factors. How nervous and excited are some of the students during this exercise! For many, it was their first time ever constructing a physical model.

Challenges:

As the course grew in popularity several challenges have developed. One is that personal rapport with the students is very limited. It is simply impossible to interact, by name, with over 100 students. Another is that multiple choice questions must be used for exam. As previously stated, the students know the questions beforehand, and if they attend the lectures they know the answers as well, thus the multiple choice format has not been a source of complaints. A larger challenge is that papers must be graded by teaching assistants. The teaching students are exclusively made up of architectural engineering students who have previously taken the course. This is necessary to address the small, but significant, scientific critiques of buildings done in the papers.

The prompt for the first paper follows: Details about the process of handing in copies for peer review may be helpful to anyone who wants to manage a large number of student papers.

Learning Objectives:

- Appraise and critique key buildings using the language and criteria of the theory of structural art
- Contextualize seminal buildings by linking them to specific people (designers), cultures, and times

Use the given form to provide constructive criticism. Hand back your peer review to the authors on Monday 2/11 but PREFERABLY SOONER VIA EMAIL OR TEXT OR …

Hand in your revised assignment to the instructor on Wednesday 2/13 and hand in your peer review forms at that time also. Do not hand in the original draft.

Details:

This is the first of two larger writing assignments in this course. The purpose of this exercise is to create a "museum exhibition" didactic panel. Choose one structure that is pictured in your textbook. Include one or two images of your chosen structure, either from the textbook itself or from other sources such as the internet or the library. Images are to be printed separately, not in the writing assignment itself.

Use the tools that we have been exploring in class to analyze and critique the structure. The first level of the critique will be a technical or scientific one. How does the structure perform? How are the loads flowing? What relevant technical facts can be established about this structure (examples include, dates, location, cost, weight, name of designer, length of construction, you may or may not be able to provide all of these). Since this is your first exploration of such technical matters you will have to rely on the explanations of the book, or use the technical explanations found in other sources. Be sure to cite things properly to avoid plagiarism. Citations means using more than one reference (Wikipedia is ok if you trust it) and linking the citations to specific spots in the text using superscript numbers1, 2, etc. Don't make this technical critique too lengthy.

Next, analyze and critique the social aspect of the structure. How did people use it, how did people perceive it? Did it play a prominent role in the community? This social portion will probably be a brief critique, that is fine. There may be some citations to reference here.

Finally, create a symbolic analysis of the structure. By placing it in a broader historical context, find some larger meaning to this structure. Has it risen to the level of icon? Has it become a source of civic pride? Is it an embarrassment or a folly? Here there will almost certainly be no citations since these should be your wholly original thoughts.

Submit one or more images of your building and then printed separately approximately one and a half pages of text that would act as didactic panels in our exhibit. I will not be counting words, we are interested in content and in style. The audience is the average museum attendee who is very interested in buildings, but is not an architect or structural engineer by trade.

Use the following examples of didactic materials taken from actual museum catalogues as a possible model of writing. Feel free to search for other examples in our library, on the internet or at our local art museum in downtown SLO called SLOMA.

The prompt emphasizes Contextualization as well as Scientific, Social and Symbolic critiques. This is in alignment with the course philosophy.

3. Issues to discuss

Issues which we all should discuss at this Symposium and in the near future:

- Intellectual property, online versions, ownership
- Disseminating each other's course notes in a somewhat public manner

The first question is a bit thorny. Whose course is it? Clearly it is David Billington's creation, but what if we wanted to make it more public today? Could it be presented in an online format? Where would any royalties, if there were some, go to?

The second question is less problematic. The efforts of Princeton University and the Seminars they have conducted are greatly appreciated and are a valuable repository of important archival material. From that core group, a loose affiliation called INSA has been active via email links, but we rarely get into the fine details of how a re-invented version of David's course might work. Do we have any desire to film lessons and share them within a members-only group? Do we have special resources that we would be willing to share within the group? A good example would be the Kawaguchi lecture on the history of trusses. This lesson could be expanded and Kawaguchi has permitted the author to take steps to re-create it. But the effort has stalled. Similarly, the work of lesser known masters (Richard Bradshaw's Shells, Myron Goldsmith's structural studies, Castiglioni's Plates and Arches) could be rapidly documented if we pooled our resources together.

Acknowledgements

David Billington was my hero. He had faith in my research abilities and he nurtured my growth as a professor. I will always be grateful for this.

References

[1] D. Billington, *The Tower and the Bridge*, Princeton University Press; New Ed edition, 1985.

[2] B. Addis, Building: *3000 Years of Design Engineering and Construction*, Phaidon Press; Reprint edition 2015.

[3] D. Billington, *Robert Maillart: Builder, Designer and Artist*, Cambridge University Press 2009.

[4] E. Allen and W. Zalewski, *Form and Forces: Designing Efficient and Expressive Structures*, John Wiley and Sons; 2009.

[5] J. Ochsendorf, *Guastavino Vaulting: The Art of Structural Tile*, Princeton Architectural Press; 2013.

[6] Saliklis, E. and Billington D. "The Hershey Arena: Anton Tedesko's Pioneering Form*", ASCE Journal of Structural Engineering*, vol. 129, no. 3, pp. 278-285, 2003.

[7] Saliklis, E., Billington, D. and Carmalt, A. "The Refinement of an Idea: Tedesko's Philadelphia Skating Arena" *ASCE Journal of Architectural Engineering*, vol. 13, no. 2, pp.72-77, 2007.

[8] Die Jahrhunderthalle Und Das Ausstellungsgelände in Breslau - Das Werk Max Bergs (Schriften Des Bundesinstituts Für Kultur Und Geschichte Der) (German Edition) (German) Hardcover – May 12, 2006.

[9] M. Garlock and D. Billington, *Felix Can Félix Candela: Engineer, Builder, Structural Artist*, Princeton University Art Museum Series, 2008.

[10] C. Faber, *Candela The Shell Builder*, Reinhold Pub. Corp; First Edition edition, 1963.

[11] T. Toto, *Felix Candela*, Toto; 1st edition, 1995.

[12] B. Bergdoli et al. *Pier Luigi Nervi: Architecture as Challen*ge, Silvana Editoriale; y First edition edition 2011.

[13] Neveu, M. and Saliklis, E. "Myron Goldsmith and the Development of the Diagonally Braced Tube", *Proceedings of the International Conference on Structures and Architecture*, Guimaraes, Portugal. 2010.

[14] E. Windhorst, *Lake Point Tower: A Design History*, Chicago Architecture Foundation, 2009.

[15] Saliklis, E., Billington, D. and Bauer, M. "Scale Simplicity and Surprise: Evaluating Structural Form", *ASCE Journal of Architectural Engineering*, vol. 14, no. 1, pp. 25-29, 2008.

[16] Y. Khan, *Engineering Architecture: The Vision of Fazlur R.Khan*, W.H. Norton & Co., 2004.

[17] M. Ali, *Art of the Skyscraper: the Genius of Fazlur Khan*, Rizzoli Press, 2001.

[18] C. Schittich, *Detail Engineering 4: SOM*, Detail Engineering Press, 2015.

[19] A. Domingo and C. Lazaro, *Mamoru Kawaguchi – Structural Engineer: Innovation and Tradition in Structural Design*, Catalog for the Exposcio de l'obra I els models de Mamoru Kawaguchi, Universitat Politecnica de Valencia, 2009.

[20] P. Rice, *An Engineer Imagines*, Batsford Press re-issue, 2017.

[21] J.Schlaich et al. *Leicht Weit / Light Structures*, Prestel Publishers, 2004.

Proceedings of the IASS Annual Symposium 2019 – Structural Membranes 2019
Form and Force
7 – 10 October 2019, Barcelona, Spain
C. Lázaro, K.-U. Bletzinger, E. Oñate (eds.)

Quintessentially Billington: The Evolution of Structural Art Teaching at Princeton

Maria E. Moreyra GARLOCK*, Sigrid ADRIAENSSENS, Branko GLISIC

*Princeton University
Department of Civil and Environmental Engineering
mgarlock@princeton.edu

Abstract

One of the most classic courses at Princeton University (*CEE262, Structures in the Urban Environment*) was founded by Professor David Billington (1927-2018) in 1974. The course, based on his scholarship, argues that the best designed structures (bridges, buildings, and shells) are a work of art – structural art. The course integrates humanities with engineering through studies of cultures, people, and art as reflected in works of engineering. Professor Billington used alliterations to reinforce learning: The measures of structural art are efficiency, economy, and elegance; and the structural artist's designs evolve from imitation, to innovation, to inspiration. The authors are Princeton University faculty in who have continued teaching Billington's classic courses (*imitation*), enhanced it with modern pedagogical approaches (*innovation*), and created new classes and scholarship inspired by it (*inspiration*). This paper, in essence, illustrates the many ways that David Billington's legacy and scholarship continue to thrive in creative approaches that one can say are quintessentially Billington.

Keywords: Structures, Engineer, Art, Princeton University, Billington, Pedagogy

1. Introduction

The Industrial Revolution brought about new materials for construction, which, in turn, brought about new forms for structures such as bridges, buildings, and vaults (long spanning roofs). It is in this context that the art of the structural engineer was born, "structural art", as defined by David Billington [1]. Structural art encompasses three ideals: *efficiency* is the true ethos of engineering, namely, to conserve natural resources by minimizing materials; *economy* is the ethic of engineering, to reduce cost by intimately connecting design to construction; and *elegance* is the aesthetic of engineering, to create beautiful forms through structural honesty of the form. "Structural artists" are designers who seek and achieve these three ideals in their completed works. These designers seek to integrate elegance and efficiency rather than superimpose one on the other. They illustrate how the best technical design leaves room for ethical and aesthetic choice.

The teaching of structural art and structural artists began with Billington's course, (*CEE262, Structures in the Urban Environment*). The course was first taught in 1974, followed by the publication of *The Tower and the Bridge* [1]– a seminal book that defined a new field and inspired generations. This course is still taught today by the first author, with an enrollment of over 200 students. The course is accessible to students of all majors and all years. For the students of engineering, the course provides important historical context of their profession as well as a language and means for making aesthetic judgment on engineered designs – topics rarely taught at other institutions. For the non-engineering students, the course satisfies a general education requirement and educates them about importance of their built environment. The authors created new courses,

Copyright © 2019 by Maria E. Moreyra GARLOCK, Sigrid ADRIAENSSENS, and Branko GLISIC
Published by the International Association for Shell and Spatial Structures (IASS) with permission.

which were inspired by CEE262 and Billington's passion for integrating engineering, humanities, and art. These courses are discussed next.

2. A Classic Course Reinvented

CEE262 has evolved to include modern design and modern pedagogical methods that are now possible with new technologies. The course has also inspired other courses as will be described in the sections to follow.

2.1. CEE262: Imitation and Innovation

Forty-five years later, many of the lecture themes in CEE262 remain as they were in 1974 – but not all. Over the last 10 years, CEE262 lectures have integrated new scholarship such as that of Felix Candela [2], Laurent Ney [3], and other research developed by the authors. In addition, lectures devoted to wind design, earthquake engineering, and ethics have been added. This has necessitated the difficult challenge of combining or removing some of Professor Billington's original lectures. The 'core' lectures remain however, as does the objective and spirit of the course – the message of engineering as a *creative* discipline. In addition, the lectures include active-learning approaches, as will be explained next.

CEE262 current innovations include modern 'active-learning' activities embedded in the lectures such as internet polling and short physical experiments conducted by the students during lectures. An active learning based approach has been shown to reduce the achievement gap and benefit underrepresented minorities in STEM. Since 2013, the first author has gradually incorporated active-learning pedagogy into the lectures, and currently approximately 100% of CEE262 lectures utilize active-learning pedagogy, including demonstrations, hands-on activities, and discussion questions. Classroom response systems have been shown to be effective in raising the level of student engagement in college courses. In this course, we made use of *Poll Everywhere*, a classroom response system in which students submit answers to questions via text message or internet connected devices. We used this technology to help motivate a topic, to elicit discussion, to assess understanding, and to encourage experiential learning [4, 5, 6, 7]. An example of active learning is given in Figure 1.

The active learning enhancement, as well as dissemination of the course to other institutions, was made possible by a federal grant through the National Science Foundation. A website describing the outcomes of this grant, contains resources to teach the course [8].

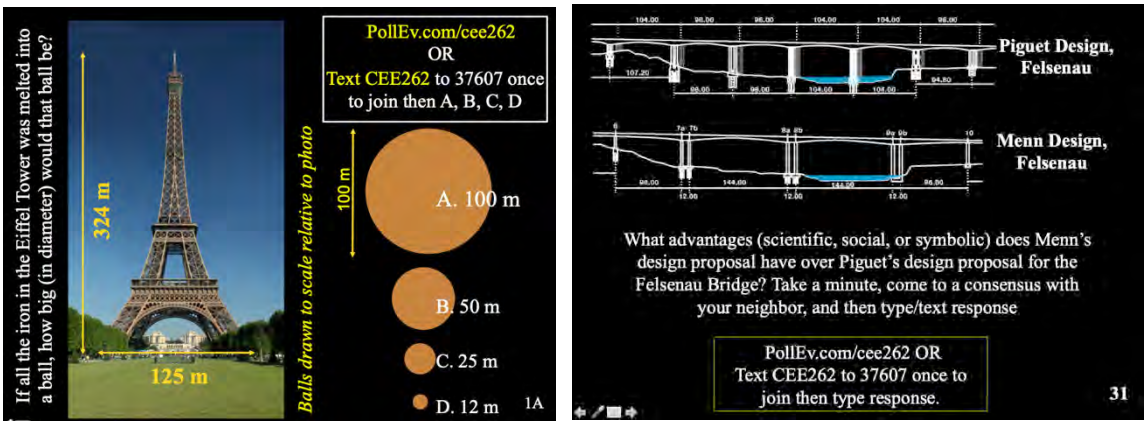


Figure 1. Example of CEE262 active-learning slides: (left) motivating learning of the Eiffel Tower (correct answer = D); (right). eliciting discussion through the works of Christian Menn.

2.2. CEE463: An Inspirational Derivative of CEE262

An inspirational derivative of CEE262 is intended for more advanced students studying structural engineering: *CEE463 (A Social and Multi-dimensional exploration of Structures*). *CEE463* has been taught biannually by the authors since 2010 and it develops the student's skills in drawing, model making, aesthetic considerations, and advanced engineering analysis. It also emphasizes the humanities aspect of our built environment through a study of the social and economic context of the built work. The theme of the course changes every time it is taught, where the themes have been Fazlur Khan: Structural Artist of Urban Building Forms (2010), Evolution of German Shells (2012), The art of Spanish Bridge Design (2014), Creativity in Cuban Thin Shell Structures (2016), and Two Millennia of Structural Architecture in Italy (2019).

The course includes: site visits, a study of historical data (both socio-political and engineering), structural analysis, building of scaled prototype models, and creation of websites, movies, essays, and an exhibition (see Figure 2). The course has several impacts: (1) students' perception of the structural engineering profession is significantly broadened and put into a global context; (2) their motivation and self-confidence to exercise structural engineering as profession is energized, and (3) their communication skills are significantly improved. Our pedagogical approach was based on the idea that the students will learn the best by teaching themselves through solving challenging open-ended assignments. Some pedagogical objectives include:

1. Start to develop a sense for implicit knowing by studying precedents;
2. Learn how to communicate complex technical issues with peers and laymen;
3. Develop spoken, written, pictorial, analytical and numerical proficiency;
4. Reflect critically upon social, political and historic influences of past successful structural designs.

Figure 2 shows students using hand drawn sketches and calculations, computer modeling, and physical models for their study of a horizontal cantilever structure in Havana, Cuba. Outcomes of this course can be observed though the course websites [9] and some more detail is given in [10].

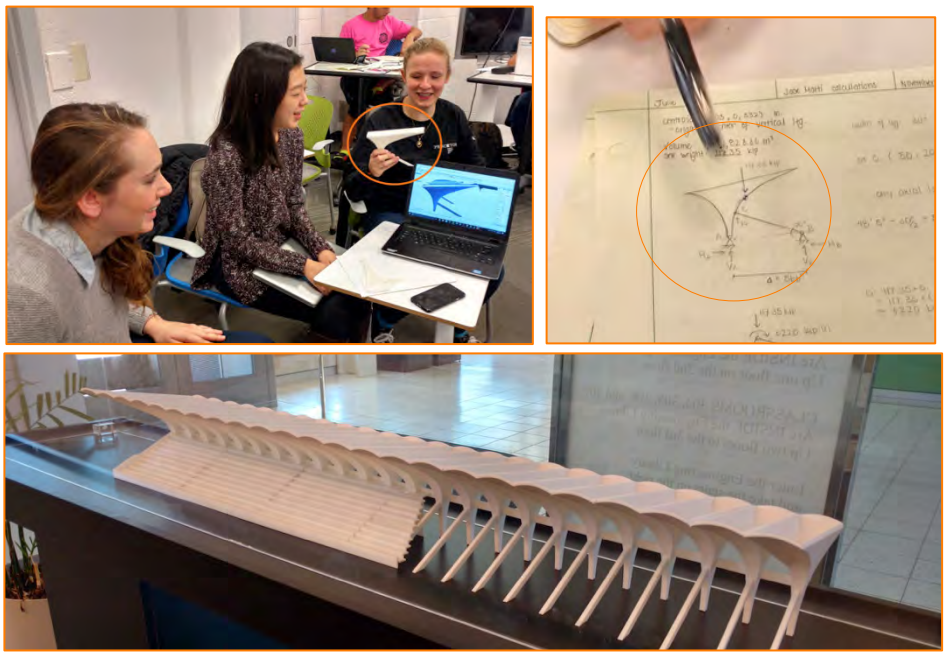


Figure 2. CEE463 students using hand drawn sketches and calculations, computer modeling, and physical models for their study of a horizontal cantilever structure in Havana, Cuba.

3. Inspiring Derivatives in the Humanities

Other inspirational derivatives of Billington's teaching and scholarship are represented in three more courses that are more heavily invested in the humanities as discussed in this section.

3.1. CEE 538 – Holistic Analysis of Heritage Structures

CEE 538 (Holistic Analysis of Heritage Structures) is held bi-annually and connects the Departments of Civil & Environmental Engineering (CEE) and Art & Archaeology (ART). Taught by the third author, the course enrolls students from CEE, ART, and the School of Architecture, and it introduces engineering students to the humanities aspects of structural reconstruction and the analysis of heritage structures, as well as introducing humanities students to the scientific and engineering rules to consider in artistic reconstruction. Graphic statics is used to help students visualize the flow of forces, but also as a simple tool for initial structural analysis. Example of slides from the course that explain flow of forces in lintel arch is given in Figure 3.

Heritage structures – such as residential, public and sacred buildings, bridges, and monuments – constitute invaluable cultural legacy. Still standing, or partially or completely collapsed, heritage structures are witnesses of the cultural, engineering, economic, scientific, and political development of humans, which engraved an everlasting impression on societies. Besides their cultural, aesthetic, and societal impact, still-standing heritage structures demonstrated an extraordinary capacity to face natural and man-made hazards, which greatly contributed to the resilience of societies they have been serving.

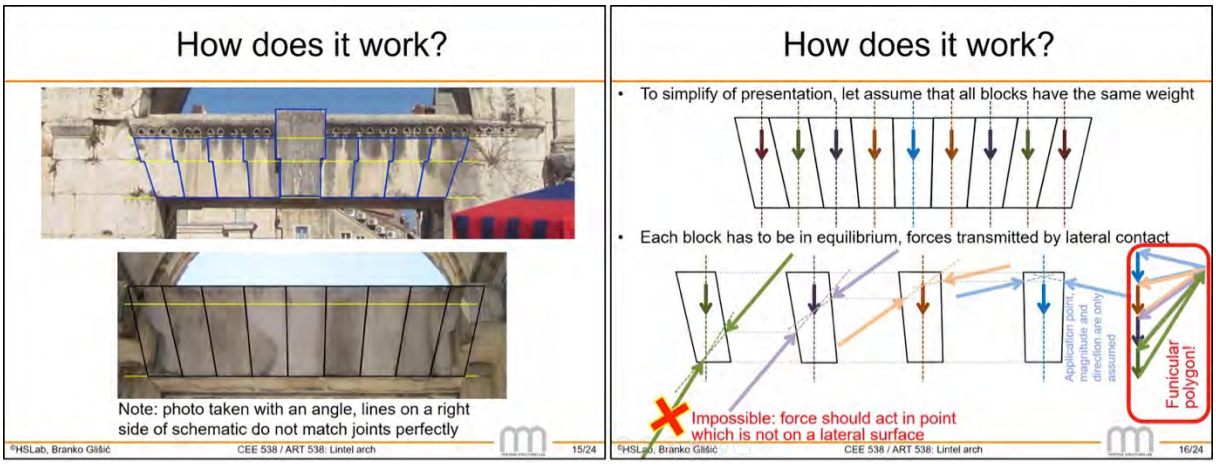


Figure 3. Example of slides from CEE 538 presenting graphic-statics analysis of lintel arch.

3.2. CEE 418 – Extraordinary Processes

Over the past 100 years, artists around the world have become increasingly interested in the aesthetic value of everyday life. Pablo Picasso's *Still Life With Chair Caning*, Virginia Woolf's *Mrs. Dalloway*, Andy Warhol's *Soup Cans*, and El Anatsui's mosaics are all examples of ordinary objects becoming extraordinary works of art. As a hands-on studio class, *CEE418 (Extraordinary Processes)* investigates the creative processes and technical skills that made these transformations possible. The course specifically focuses on the extraordinary (structural and aesthetic) potential of ash wood, currently a beetle-infested waste material in USA. The course is taught by the second author and Visual Arts Faculty [11].

Processes is a material- and studio-driven course taking place in three locations: testing labs in the department of Civil and Environmental Engineering;a sculpture studio in the Lewis Center (Figure 4) ; and field work in the natural habitat.The focus of the course is to: research the circumstances of infested ash trees; develop a thorough understanding of the wood's material properties; and ultimately

design, make, and analyze novel experiments made of infested local ash wood. Overall, the course is a hands-on learning environment in which engineering and art can intersect and inform each other in a team-taught studio setting.

The overall educational objectives of the course for both undergraduate students are: to

1. Develop an understanding of the interrelationships between material properties, forms, and forces through lab testing and simple analysis;
2. Conceive and make prototypes for a number of artworks and value added products that exploit the properties of infested ash wood, based on this analysis; 3
3. Test and evaluate these artworks/designs; and (iv) to communicate the social, economic, and aesthetic aspects of these artworks/designs in final presentation and exhibition to a group of laymen.

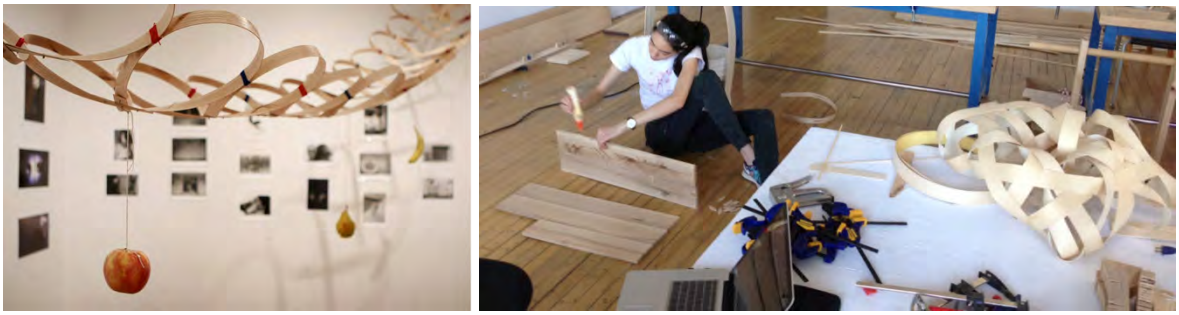


Figure 4. In CEE 418 the students cut thin strips of ash wood, using steam to soften and bend them. As a final project, the students built a wood bridge to span a gallery. The bridge was required to support 16 pounds and also portray motion (deform and spring back) when the weights were added and removed. Photo by Frank Wojciechowski for the Office of Engineering Communications

3.3. CST 209 – Transformations in Engineering and the Arts

Faculty from various engineering and humanities departments have come together to teach *CST 209 (Transformations in Engineering and the Arts)* [12]. First taught in the Spring 2016, this course explores the parallels and intersections of design and composition in engineering and the arts, emphasizing a merging of artistry and systematic thinking. Students use what they learn to create as engineer-artists and artist-engineers. The course is organized around four modules: visuals, sound, structure and movement. It is led by faculty from computer science, music, civil engineering, and mechanical engineering, with faculty from the Lewis Center for the Arts. 'Transformations' unifies the modules by engaging the different disciplines and allowing the course to serve as an introductory experience for students with diverse academic backgrounds. At the end of the four modules, students are placed in teams for a final project design. One group, inspired by the desire to help broaden boundaries for vision-impaired people, created an armband device that allows a wearer without the ability to see to interpret color (Figure 5).



Figure 5. Small group project in STC209 - armband device that allows a wearer without the ability to see to interpret color. Photo by David Kelly Crow for the Office of Engineering Communications

4. Conclusions

David Billington's influence has extended beyond teaching; it has set the foundation for and stimulated an *Engineering and the Arts* initiative on Princeton's campus. This initiative has inspired a Symposium, internal funding from an alumnus, and gathered an enthusiastic group of faculty from various engineering departments and the arts/humanities who are finding innovations and inspirations in their research by collaborating at the intersection of engineering and art.

What began as one course at Princeton in 1974 (CEE262) has inspired many more – only some were discussed here. Other notable courses include *CEE102 – Engineering in the Modern World*, which centers on the transformation of American society by the four traditional branches of engineering – civil, mechanical, electrical, and chemical. Like CEE262, the course is intended for a general audience of all majors and continues to have a large enrollment.

The paper demonstrated how Billington's classic courses (e.g. CEE262) continue to be taught (*imitation*), but they have been enhanced with modern pedagogical approaches (*innovation*). Examples of new classes inspired by Billington's structural art concept and humanities approach to teaching were given (*inspiration*).

It is concluded that Billington's legacy at Princeton is not only alive, it is thriving.

Acknowledgements

The CEE262 innovation discussion is based upon work supported by the National Science Foundation under Grant no.: 1432426. Any opinions, findings, and conclusions or recommendations expressed in this material are those of the author(s) and do not necessarily reflect the views of the National Science Foundation. CEE463 was financially supported by various institutions of Princeton University as noted in the websites [9]. CEE 418 and CEE 538 were financially and pedagogically supported by the Council for Science and Technology at Princeton University. Their support is gratefully acknowledged.

References

[1] Billington, David P. *The Tower and the Bridge: The New Art of Structural Engineering*. Princeton University Press, 1985.

[2] Garlock, Maria E. Moreyra, and David P. Billington. *Félix Candela: Engineer, Builder, Structural Artist*. Yale University Press, 2008.

[3] Adriaenssens, Sigrid, Block Philippe, Veenendaal Diederik and Williams Chris , Shell structures for architecture: form finding and optimisation, 1st ed. London: Routledge, 2014.

[4] Garlock, Maria E. Moreyra, Aatish Bhatia, and Negar Elhami-Khorasani. "Introducing Modern Teaching into a Classic Course on Structural Art." *IABSE Symposium Report*, 105:1–2. International Association for Bridge and Structural Engineering, 2015.

[5] Laffey, Evelyn H., Maria E. M. Garlock, and Aatish Bhatia. "Enhancing Student Cognition and Affect through the Creative Art of Structural and Civil Engineering" ASEE Annual Conference and Exposition, 2016.

[6] Garlock, M.E.M., Bhatia, A. Laffey, E. "Effective Approaches for Teaching Stem-Literacy for All Majors: The Example of Resonance", Proceedings of The 2017 Asee Annual Conference, Columbus, OH, June 25-28, 2017.

[7] Garlock, M.E.M., Bhatia, A. Laffey, E. "Modernizing and Disseminating The 'Structural Art' Teaching of David Billington," Proceedings of the Structural Engineers World Congress, Istanbul, Turkey, April 24-26, 2019.

[8] https://casce.princeton.edu

[9] https://garlock.princeton.edu/teaching/studio-based-teaching-cee463/

[10] Glisic, B., Garlock, M., Adriaenssens, S. "Innovative education in engineering: a social and multi-dimensional exploration of structures", *Proceedings of the ASCE Structures Congress*, ASCE, Boston, April, 2014.

[11] https://www.princeton.edu/news/2016/02/08/extraordinary-processes-course-links-art-and-engineering

[12] https://www.princeton.edu/news/2016/07/18/transformations-students-find-creativity-intersection-art-and-engineering?section=featured

Proceedings of the IASS Annual Symposium 2019 – Structural Membranes 2019
Form and Force
7 – 10 October 2019, Barcelona, Spain
C. Lázaro, K.-U. Bletzinger, E. Oñate (eds.)

Simplified closed-form expressions for horizontal reactions in linear elastic arches under self-weight

Branko GLISIC*

* Princeton University, Department of Civil and Environmental Engineering
Princeton University E330 EQuad, Princeton, NJ 08544, USA
bglisic@princeton.edu

Abstract

Finite and/or discrete element modeling are typical modern tools for determining reactions and internal forces in arches. However, while these tools are excellent in performing detailed analysis, they might be less suitable for conceptual design and "back-of-the-envelope calculation" due to their complexity of application. Simplified closed-form formulae for reactions and internal forces might be more appropriate as they enable fast solutions and easy development of parametric studies. Hence, the aim of this paper is to present novel simplified closed-form expressions for determination of horizontal reactions in segmental, catenary, and parabolic arches under self-weight. Three typical structural systems for symmetric linear-elastic arches with constant cross-section and various rise-to-span ratios were considered: three-hinged, two-hinged, and hingeless. It was found that the horizontal reactions, to large extent, do not depend on arch shape or number of hinges, but only on linear weight, span, and equivalent angle of embrace. Surprisingly, with few exceptions, single formula presented in this paper provides almost universal solution for all shapes of arches, rise-to-span ratios, and boundary conditions. In addition, linear relationship between horizontal reactions of the three structural systems (hingeless, three-hinged, and two-hinged) was discovered, which is valid for any shape (segmental, parabolic, and catenary) and any rise-to-span ratio.

Keywords: Segmental, parabolic and catenary shape, Symmetric linear-elastic arch, Closed-form equations, Horizontal reaction, Three-hinged, two-hinged and hingeless arch

1. Introduction

Creation of large-scale infrastructure in antiquity started by mastering arch structural system. First experimentation and small-scale arch structures were created by Sumerians; however, Etruscans enabled widespread methodical use of arches in IV century Before Common Era (BCE) [1]. During the next 2500 years the arch has been omnipresent in wide range of structures. In ancient and medieval times, the shape of an arch was mostly semi-circular, although some rare exceptions are identified [2]. Engineering mechanics and resulting analytical techniques that were developed in XVII-XIX century enabled analysis and understating of arch structural system [3]. Consequently, the shape of arch shifted from segmental to other forms such as elliptic, catenary, parabolic, etc., and it was optimized based on project-specific design constraints.

Leonardo da Vinci was among the first engineers who provided hints on structural behavior of arches (1508?): "An arch is nothing other than a strength caused by two weaknesses; for the arch in buildings is made up of two segments of a circle, and each of these segments being in itself very weak desires to fall, and as the one withstands the downfall of the other the two weaknesses are converted into a single strength" [4]. Robert Hooke understood that segmental shape is not ideal for an arch under self-weight

Copyright © 2019 by Branko Glisic
Published by the International Association for Shell and Spatial Structures (IASS) with permission.

and stated in 1676 in an anagram that ideal shape under self-weight is catenary [3,5]. Since then, an enormous body of knowledge regarding arches was developed (e.g., [1], [3-14], etc.).

However, to the best of author's knowledge, current literature does not present simple closed-form equations for reactions and internal forces of arches. The aim of this paper is to address that challenge. Due to restriction in paper length, the scope is limited to presenting simplified closed-form equations for horizontal reactions of segmental, parabolic, and catenary arches under self-weight and to evaluate relationships between horizontal reactions of three different structural systems – three-hinged, two-hinged, and hingeless arch. It was assumed that the arch behavior is linear-elastic. While this assumption restricts to certain extent the applicability of equations, they still have very broad applicability. Due to limited space, the paper focus is on horizontal reactions under self-weight, only; more detailed study, including internal forces, as well as other load cases can be found in [15].

2. Differential equations of segmental arch

Typical symmetric segmental arches are given in Figure 1. Let us denote the radius of arch centerline with R, span with L, rise with D, and angle of embrace with β. To simplify presentation of figures, these parameters are only shown in Figure 1c. To simplify presentation of formulas, β is substituted with 2α, where α is half-angle of embrace ($\beta=2\alpha$ i.e., $\alpha=\beta/2$).

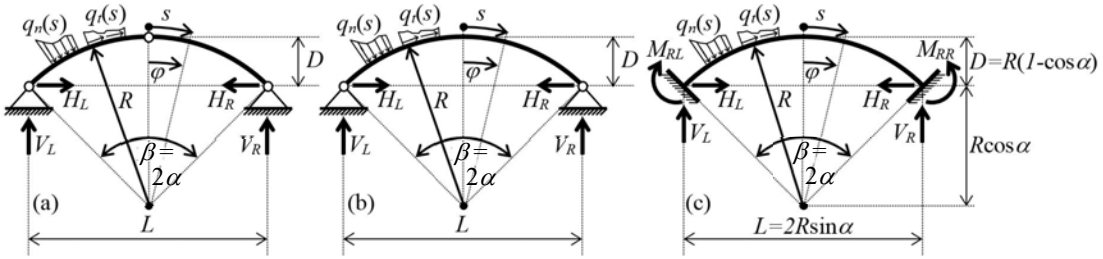


Figure 1: Typical segmental arches: a) three-hinged, b) two-hinged, and c) hingeless arch [15]

The origin of natural (curvilinear) coordinate system is set at the apex of the arch, and the natural coordinate s is positive in clockwise direction. The ratio s/R represents the angle φ (in radian) between the vertical line passing through the origin and the line connecting the center of circle defining the arch and point with coordinate s. Component of load perpendicular to the arch centerline is denoted with $q_n(s)$, while the tangential component of load is denoted with $q_t(s)$. If positive sign of load is as shown in Figure 1, differential equations of segmental arch have the appearance as given in Equations 1a-c [13].

$$\frac{\mathrm{d}N(s)}{\mathrm{d}s}-\frac{S(s)}{R}+q_t(s)=0 \tag{1a}$$

$$\frac{\mathrm{d}S(s)}{\mathrm{d}s}+\frac{N(s)}{R}+q_n(s)=0 \tag{1b}$$

$$\frac{\mathrm{d}M(s)}{\mathrm{d}s}-S(s)=0 \tag{1c}$$

where: $N(s)$, $S(s)$, and $M(s)$ are the normal force, shear force, and bending moment, respectively.

For an arch with constant cross-section loaded only by self-weight $g(s)=g$=constant, g has only vertical component and thus, the normal and tangential components of load (see Figure 1) are determined using Equations 2.

$$q_n(s) = g\cos\frac{s}{R} \tag{2a}$$

$$q_t(s) = g\sin\frac{s}{R} \tag{2b}$$

Equations 1a, 1b, 2a and 2b can be combined into a single differential equation of the second order on S(s) (by deriving Equation 1b and substituting derivative of $N(s)$ from Equation 1a, and normal and tangential components of loads from Equations 2a and 2b). This differential equation can be solved over $S(s)$, but final solution require determination of two constants of integration from boundary conditions. Once $S(s)$ is determined, Equation 1c can used to determine $M(s)$, which also require determination of one more (third) constant of integration from boundary conditions. In parallel, $N(s)$ can be determined using Equation 1b.

However, the solution proposed in previous paragraph is not easy to derive for two-hinged and hingeless arch, as their boundary conditions do not contain three known internal forces; in addition, the solution for three-hinged arch using this approach would be tiresome. Hence, alternative approaches are taken: three-hinged arch is solved from equations of equilibrium, while two-hinged and hingeless arch are solved using force method. For two latter structural systems the Equations 1 and 2 are used in the process on calculating internal forces and reactions on primary structures, see details in [15].

3. Horizontal reactions in segmental arches

To emphasize that equations presented in this text are related to load due to self-weight, superscript g is used in all equations that are presented subsequently. Given that both, the load g and the shape of the arch, are symmetric with respect to vertical axis at the arch apex, the reactions are also symmetric with respect to the same axis regardless of structural system of the arch (three-hinged, two-hinged or hingeless) i.e., $V_L^g = V_R^g = V^g$, $H_L^g = H_R^g = H^g$, and $M_{RL}^g = M_{RR}^g = M_R^g$ (see Figure 1). Hence, for simplification of presentation, index denoting left and right side reaction is omitted, i.e., only the terms V^g, H^g, and M_R^g will be used. In addition, for all three typical structural systems vertical reactions are equal half-weight of the arch, i.e.:

$$V^g = gR\alpha \tag{3}$$

3.1. Horizontal reactions in three-hinged segmental arch

In further text subscript "*3h*" is used to denote forces in three-hinged structure. Since the three-hinged arch is statically determinate structure, its reactions can be calculated from equations of equilibrium. Due to symmetry and given that the vertical reactions are known (Equation 3), the horizontal reactions H_{3h}^g are determined from the sum of moments about apex hinge G acting on one side of the hinge, and presented in Equation 4 [15]. All active and reactive forces, as well as resultant of self-weight load acting on one side of the structure are presented in Figure 2.

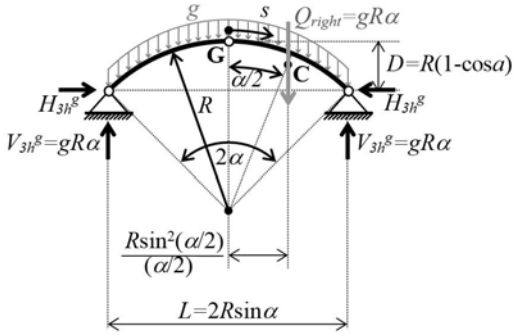


Figure 2: Active and reactive forces, and geometrical properties of three-hinged arch loaded by self-weight [15]

$$H_{3h}^{g} = gR\left(\alpha\cot\frac{\alpha}{2}-1\right)=\frac{1}{4}gL\csc\frac{\alpha}{2}\left(\alpha\csc\frac{\alpha}{2}-\sec\frac{\alpha}{2}\right) \tag{4}$$

3.2. Horizontal reactions in two-hinged segmental arch

In further text subscript "*2h*" is used to denote forces in two-hinged structure. Being indeterminate to degree one, two-hinged arch was analyzed using force method. Figure 3 shows the primary structure and all external and internal forces acting on it. Note that unknown force X_1 acting on primary structure is equal to horizontal reaction H_{2h}^{g} in the original structure. Coefficients of flexibility are calculated using Equations 5 and horizontal force is determined in Equation 6. Influence of normal and shear forces on deformation was neglected when calculating flexibility coefficients. Note that the vertical reaction is determined from symmetry in Equation 3.

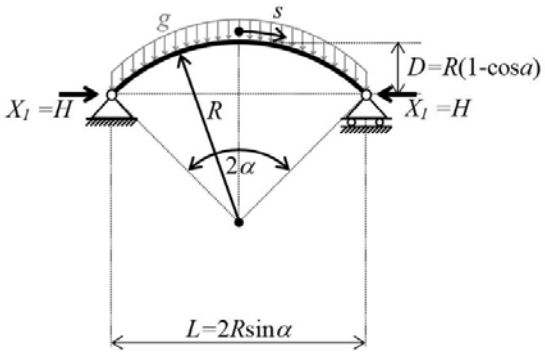


Figure 3: Primary structure of two-hinged arch [15]

$$EI\delta_{11}=\int_{-R\alpha}^{R\alpha}M_1^2(s)\mathrm{d}s=R^3\left(\alpha-3\sin\alpha\cos\alpha+2\alpha\cos^2\alpha\right) \tag{5a}$$

$$EI\delta_{10}^{g}=\int_{-R\alpha}^{R\alpha}M_1(s)M_0(s)\mathrm{d}s=-gR^4\left(\frac{1}{2}\alpha+\frac{9}{2}\sin\alpha\cos\alpha-5\alpha\cos^2\alpha-2\alpha^2\sin\alpha\cos\alpha\right) \tag{5b}$$

$$H_{2h}^{g}=-\frac{\delta_{10}^{Mg}}{\delta_{11}}=\frac{1}{2}gR\frac{\alpha+9\sin\alpha\cos\alpha-10\alpha\cos^2\alpha-4\alpha^2\sin\alpha\cos\alpha}{\alpha-3\sin\alpha\cos\alpha+2\alpha\cos^2\alpha} \tag{6}$$

where $M_1(s)$ denotes bending moment distribution along the primary structure due to X_1=1, $M_0(s)$ denotes bending moment distribution along the primary structure due to load q, δ_{11} and δ_{10} are flexibility coefficients and EI is bending stiffness of the arch (modulus of elasticity E multiplied with moment of inertia I).

3.3. Horizontal reactions in hingeless segmental arch

In further text subscript "*0h*" is used to denote forces in hingeless structure. Hingeless structure is indeterminate to the degree three, and thus, similar to the approach used in two-hinged structure, force method is used to determine the reactions. To simplify the analysis by eliminating "mixed" (non-diagonal) flexibility coefficients (i.e., if i≠j then δ_{ij}=0), the method of elastic center was used [13]. This reduces a system of three equations with three unknowns to three simple linear equations with one unknown. The primary structure, geometry and unknown forces X_1(=V_{0h}^{g}), X_2(=H_{0h}^{g}), and X_3 (no particular meaning) are shown in Figure 4. Flexibility coefficients are calculated using Equations 7 and reactions using Equation 8 [15]. Note that flexibility coefficients δ_{10} and δ_{11} are not needed as the vertical reaction is determined from symmetry in Equation 3.

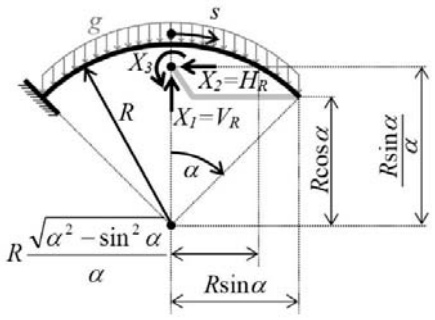


Figure 4: Primary structure of hingeless arch [15]

$$EI\delta_{22} = \int_{-R\alpha}^{R\alpha} M_2^2(s)ds = \int_{-R\alpha}^{R\alpha} R^2\left(\cos\frac{s}{R} - \frac{\sin\alpha}{\alpha}\right)^2 ds = R^3\left(\alpha + \sin\alpha\cos\alpha - 2\frac{\sin^2\alpha}{\alpha}\right) \tag{7a}$$

$$EI\delta_{33} = \int_{-R\alpha}^{R\alpha} M_3^2(s)ds = \int_{-R\alpha}^{R\alpha} 1^2 ds = 2R\alpha \tag{7b}$$

$$EI\delta_{20}^g = gR^4\left(\frac{\alpha}{2} + \frac{1}{2}\sin\alpha\cos\alpha - \frac{\sin^2\alpha}{\alpha} + 3\sin\alpha\cos\alpha + \alpha\sin^2\alpha - 3\frac{\sin^2\alpha}{\alpha}\right) \tag{7c}$$

$$EI\delta_{30}^g = 4gR^3\left(\alpha\cos\alpha - \sin\alpha\right) \tag{7d}$$

$$H_{0h}^g = -\frac{\delta_{20}^{Mg}}{\delta_{22}} = -gR\left(\frac{1}{2} + \frac{\alpha\sin^2\alpha + 3\sin\alpha\cos\alpha - 3\dfrac{\sin^2\alpha}{\alpha}}{\alpha + \sin\alpha\cos\alpha - 2\dfrac{\sin^2\alpha}{\alpha}}\right) \tag{8a}$$

$$M_{R,0h}^g = -gR^2\left(\left(\frac{3}{2} - \frac{\alpha\sin^2\alpha + 3\sin\alpha\cos\alpha - 3\dfrac{\sin^2\alpha}{\alpha}}{\alpha + \sin\alpha\cos\alpha - 2\dfrac{\sin^2\alpha}{\alpha}}\right)\left(\cos\alpha - \frac{\sin\alpha}{\alpha}\right) + \alpha\sin\alpha\right) \tag{8b}$$

Reactive moment $M^g{}_{R,0h}$ is calculated by moving generalized forces $X_1(=V_{0h}^g)$, $X_2(=H_{0h}^g)$, and X_3 to the free end of primary structure ($s=R\alpha$; forces $X_1(=V_{0h}^g)$ and $X_2(=H_{0h}^g)$ are resolved into force-couples and the resulting couples are combined with $X_3 = -\delta_{30}/\delta_{33}$).

3.4. Simplified equation for horizontal reaction in hingeless segmental arch

Equation 4, expressing horizontal reaction in three-hinged arch, is relatively simple, and to some extent intuitive. However, Equations 6 and 8a, expressing horizontal reactions in two-hinged and hingeless arch are less simple and intuitive, and their simplification would be helpful for parametric studies and back-of-the-envelope calculations. Figure 5 shows relationship between the half-angle of embrace and normalized horizontal reaction of hingeless arch. The horizontal reaction is normalized with product gL. In addition, approximation of this relationship based on the power function is also presented. The figure establishes the following simplified relationship between the horizontal reaction and angle of embrace:

$$H_{0h}^g \approx \frac{gR\sin\alpha}{\alpha} = \frac{gL}{2\alpha} = \frac{gL}{\beta} \tag{9}$$

Direct comparison demonstrates that Equation 9 underestimates Equation 8a for a fraction smaller than

than 2%. Equation 9 can be interpreted as follows: horizontal reaction of hingeless arch is proportional to product of arch span and its linear self-weight (which is not total weight of the arch), and inversely proportional to the angle of embrace. This equation has very simple form, it is easy to memorize and apply, and provides results with relative error smaller than -2%.

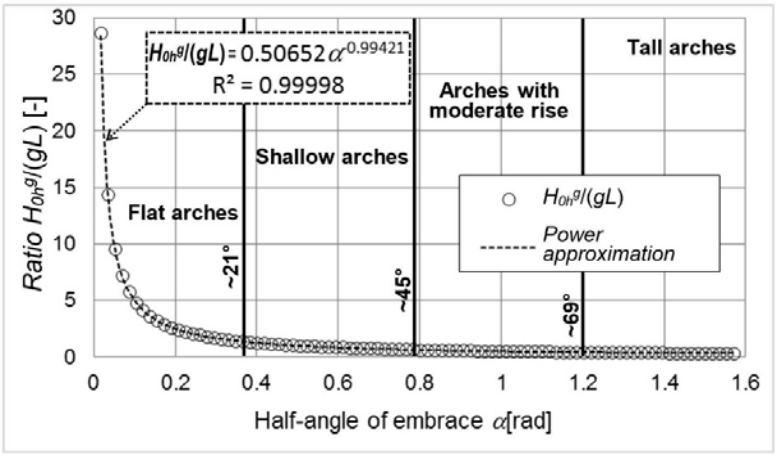


Figure 5: Relationship between normalized horizontal reaction of hingeless arch and half-angle of embrace [15]

Based on Equation 9, the following unformal classification of arches is made in Figure 5: flat arches ($0° < \alpha \leq 21°$), shallow arches ($21° < \alpha \leq 45°$), arches with moderate rise (moderate arches, $45° < \alpha \leq 69°$), and tall arches ($69° < \alpha \leq 90°$). Limit for flat arches of 21° (0.37 rad) is chosen because for larger half-angles of embrace the change in normalized horizontal force is only 5%. Upper limit for shallow arches is set to 45° (0.79 rad) as the normalized horizontal force for that angle (H_{0h}^g=0.644) is approximately two times smaller than the one for 21° (H_{0h}^g=1.368) and two times bigger than the normalized horizontal force for 90° (H_{0h}^g=0.320). Finally, upper limit of 69° (1.20 rad) is set for moderate arches as for that angle the difference between exact and approximate equations, 8a and 9 respectively, is maximal (value of normalized horizontal reaction is H_{0h}^g=0.423).

3.5. Relationship between horizontal reactions in typical segmental arches

The relationship between the horizontal reactions of the three-hinged, two-hinged and hingeless arch is explored in Figure 6, which presents the ratio between horizontal reactions of former two with respect to latter.

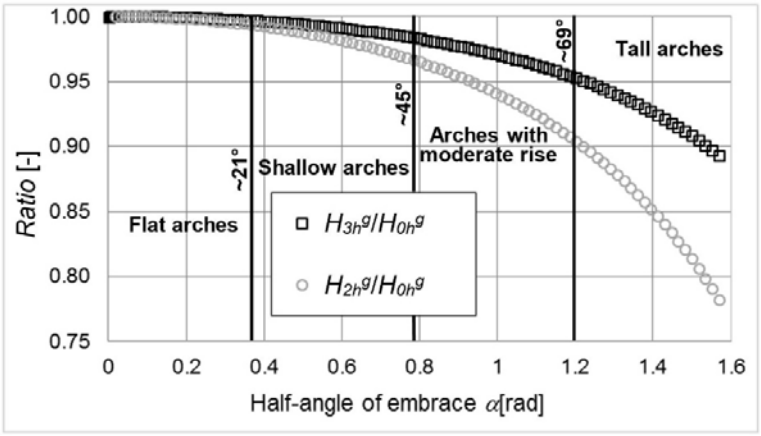


Figure 6: Ratios between horizontal reactions of the three- and two-hinged arch over hingeless arch [15]

Figure 6 shows that Equation 9 can be extended with high degree of accuracy to flat and shallow there- and two-hinged arches, with acceptable degree of accuracy to arches with moderate rise, and with simple modification (correction) even to tall arches. In addition, Figure 6 reveals an interesting relationship between horizontal reactions of the three structural systems, as shown in Equation 10.

$$H_{3h}^{g} \approx \frac{1}{2}\left(H_{0h}^{g} + H_{2h}^{g}\right) \tag{10}$$

Equation 10 states that the horizontal reaction in three-hinged arch is approximately equal to average value between horizontal reactions of two-hinged and hingeless arch.

3.6. Extension to parabolic and catenary arches

As opposed to antique arches, which mostly have had segmental shape, modern arches are frequently made in form of parabola. In addition, it is well known that the perfect (moment free) shape of the arch under self-weight is catenary. Hence, the validity of Equations 9 and 10 was examined for these two shapes of the arch. Given that both shapes are non-circular, an equivalent angle of embrace for these shapes is calculated as the angle of embrace of segmental arch that has the same rise D as observed (parabolic or catenary) arch. This equivalent angle of embrace is given in Equation 11.

$$\beta_{equivalent} = 2\alpha_{equivalent} = 4\arctan\left(2\frac{D}{L}\right) \tag{11}$$

For hingeless catenary arch, relative difference between horizontal reaction determined using Equation 9 and the exact solution is 0.01%, 0.20%, 1.04% and 2.89% for equivalent half-angles of embrace of 21°, 45°, 69°, and 90°, respectively, which confirms high accuracy of approximation. In addition, given that catenary arch is moment free regardless boundary conditions, Equation 9 extends to three- and two hinged catenary arches with the same level of accuracy. For the same reason (moment free), Equation 10 also applies for catenary arches (actually, symbol "≈" transforms into "=" in the equation).

Similar analysis shows that Equation 9 is also applicable to parabolic arches of all three types. For hingeless arches the relative difference from exact solution is 0.15%, 0.70%, 1.55% and 2.43% for equivalent half-angles of embrace of 21°, 45°, 69°, and 90°, respectively; for three hinged arches it is 0.005%, 0.09%, 0.41% and 0.96%, and for two hinged arches it is -0.16%, -0.66%, -1.42%, and -2.31%. Consequently, Equation 10 also applies.

4. Conclusion

This paper presents simplified closed-form equations for horizontal reactions of linear-elastic segmental, catenary, and parabolic arches under self-weight.

Simplified equation for determination of the horizontal reactions (thrust) of the hingeless segmental arch (Equation 9), states that the reaction is approximately equal to the product of arch span and linear weight, divided with the angle of embrace (expressed in radians). This formula is simple to memorize and apply, it is valid for full range of angles of embrace (from 0° to 180°), and it underestimates the true analytical value for less than 2%. In addition, it was found that the same formula can be applied with high accuracy to flat and shallow segmental three- and two-hinged arches, with acceptable degree of accuracy to moderate arches, and with some corrections to tall segmental three- and two-hinged arches, too. Finally, the simplified equation is applicable with high degree of accuracy to parabolic and catenary arches, regardless the arch rise or boundary conditions. For parabolic and catenary arches an equivalent angle of embrace is used in the equation.

Another important equation that was derived in this paper (Equation 10) shows the relationship between horizontal reactions in three-hinged, two-hinged and hingeless arch, i.e., states that the former is approximately equal to average value of the latter two.

In overall, the paper presents two new equations that are versatile yet simple, and that enable back-of-the-envelope determination of horizontal reactions in typical (three-hinged, two-hinge and hingeless) segmental, catenary and parabolic arched under self-weight.

Acknowledgements

This paper was enthused by the work and the vision of Prof. David P. Billington (1927-2018), Prof. Nicos Makris, Prof. Milutin Milanković (1879-1958), and Leonardo da Vinci (1452-1519).

References

[1] M. Como, *Statics of Historic Masonry Constructions*. (2nd Ed.). Springer International Publishing Switzerland, 2016.

[2] C. O'Connor, *Roman Bridges*. Cambridge, UK: Cambridge University Press, 1993.

[3] J. Heyman, *Structural Analysis, A Historical Approach*. Cambridge, UK: Cambridge University Press, 1998.

[4] E. MacCurdy, *The Notebooks of Leonardo Da Vinci*. New York: Reynal & Hitchcock, 1939 (Notebooks writing started in 1508).

[5] R. Hooke, *A description of helioscopes, and some other instruments made by Robert Hooke, Fellow of the Royal Society*. London: T. R. (for John Martyn Printer to the Royal Society), 1676 (accessed at https://quod.lib.umich.edu/e/eebo/A44317.0001.001?rgn=main;view=fulltext on June 13, 2018).

[6] J.A.C. Bresse, *Recherches analytiques sur la flexion et la résistance des pièces courbées, accompagnées des tables numériques pour calculer la poussée des arcs chargés des poids d'un manière quelconque et leur pression maximum sous une charge uniformément repartie*. Paris: Mallet-Bachelier, 1854.

[7] E. Winkler, "Formänderung und Festigkeit gekrümmter Körper, insbesondere der Ringe," *Civilingenieur*, vol. 4, pp.232-246, 1858.

[8] C.B. McCullough, E.S. Thayer, *Elastic arch bridges*. New York: John Wiley & Sons, Inc., 1931.

[9] J. Heyman, "The safety of masonry arches," *International Journal of Mechanical Sciences*, vol. 11, pp. 363-385, 1969.

[10] J. Ochsendorf, "The masonry arch on spreading supports," *The Structural Engineer*, vol. 84, pp. 29-34, 2006.

[11] H. Alexakis, N. Makris, "Limit equilibrium analysis of masonry arches," *Archive of Applied Mechanics*, vol. 85, pp. 1363-1381, 2015.

[12] K.-E. Kurrer, *The history of the theory of structures*, New York: Ernst & Sohn (A Wiley Company), 2008..

[13] M. Đurić, O. Đurić-Perić, *Statika Konstrukcija (Statics of Structures)*. (4th Ed.). Belgrade, Serbia: Građevinska Knjiga, 1990.

[14] R.C. Hibbeler, *Structural Analysis*. (7th Ed.). Upper Saddle River (NJ): Prentice Hall, Inc., 2008.

[15] B. Glisic, "New in old: simplified closed-form equations for linear-elastic segmental, catenary and parabolic arches, and some new discoveries regarding their structural behaviors," *Acta Mechanica*.

Proceedings of the IASS Annual Symposium 2019 – Structural Membranes 2019
Form and Force
7 – 10 October 2019, Barcelona, Spain
C. Lázaro, K.-U. Bletzinger, E. Oñate (eds.)

Structual Art and Conceptual Design in Engineering Education: a Perfect Marriage

Ignacio PAYA-ZAFORTEZA*

*Universitat Politècnica de València
Camino de Vera S/N, 46023 Valencia, Spain
igpaza@cst.upv.es

Abstract

Despite being a very important discipline, Structural Art is rarely taught as a full course at the schools of civil engineering. Therefore, strategies to introduce the main ideas of Structural Art in general courses on structural design, bridge engineering or building structures are needed. Within this context, this contribution will detail how the main ideas of Structural Art are introduced on a general course on conceptual design that is compulsory for all the students (around 70 per year) doing the Master in Civil Engineering at the School of Civil Engineering of Valencia (Spain). The contribution presents: (1) the contents of the course with a special focus on the Structural Art component, (2) the practical activities developed (e.g. structured debates to foster critical thinking and activities where the students create their "Decalogue of the outstanding structure"), (3) the methodologies followed to measure the students' performance and (4) measures of the success of the approach.

Keywords: conceptual design, engineering education, Structural Art, David P. Billington.

1. Introduction

The Spanish engineer Eduardo Torroja defined in the middle of the 20th century the main idea behind the words "conceptual design" when, in the first page of his book "Philosophy of Structures" [1], he wrote*: "(...) Before and above all structural analysis there is the idea. This idea shapes the material in a resisting form that enables it to fulfil its mission (...)"*. After Torroja, other authors have also pointed out the importance of simplified analysis methods and conceptual design in engineering education and practice. For example, the shell designer Félix Candela wrote *"(...) all calculations, no matter how sophisticated and complex, cannot be more than rough approximations of the natural phenomenon they try to represent (...)"* [2]. On the other hand, Princeton University professor, David P. Billington published in 1983 the book "The Tower and the Bridge: the New Art of Structural Engineering" [3] where he analyzed the best examples (to his opinion) of structural engineering built from the late 18th century until the late 20th century and coined the term "Structural Art". This term referred to works that excelled for their economy, efficiency and elegance. The work by Billington was very inspiring for engineers and non-engineers world-wide and provided a framework to develop structural critique and to connect structures to architecture and society.

The "idea" Torroja was referring to was very important in the 1950s when the book [1] was written, but it is even more important today when computers make the detailed structural analysis of almost any building form possible. However, modern engineering curricula tend to focus more on the details of the analysis than on the "idea" behind it. The philosophy of Structural Art is also very important today, since current engineering curricula do not usually explore the connection of engineering works with society, architecture, history and art. As a result, the future engineer can be deprived of the creative facet and risks to become a "mere calculator" and one can see public money wasted,

Copyright © 2019 by Ignacio Paya-Zaforteza
Published by the International Association for Shell and Spatial Structures (IASS) with permission.

especially in times of economic boom (see e.g. reference [4] for some examples related to Spain). Many authors have explored the paths opened by Torroja and Billington. For example, Mike Schlaich [5] has explained in detail the role of conceptual and structural design in the education of the engineer and other authors have explained how creativity can be a part of the engineers' education (Bögle [6], Garlock and Jorquera-Lucerga [7]) or how case studies can be used to develop structural criticism and structural intuition (Payá-Zaforteza [8]).

Within this context, this paper explains how the ideas of Structural Art are included in a course on the conceptual design of singular structures offered at the Universitat Politècnica de València (UPV henceforth), in Valencia, Spain.

2. Overview of the course "Conceptual Design of Singular Structures"

The course "Conceptual Design of Singular Structures" is taught at the second year of the studies the Master in Civil Engineering offered by the UPV. The course is compulsory for all the students and the course enrollment is close to 70 students per year. The number of teaching hours is 45 (25 of theory, 12 of practical classroom activities and 8 of activities at the computer lab). Given the location of the course in the engineering curricula, the students enrolled have an important structural background.

The main goal of the course is to introduce the students to the main principles that guide the design of singular structures, where the term "singular" refers to uncommon materials, structural systems, construction procedures and/or general dimensions (i.e., span lengths, dimensions of surfaces covered or building heights). This general goal can be split up in the following specific objectives:

- To develop historical perspective.
- To understand the relationship between form and forces in a structure.
- To learn how to perform simple calculations of apparently complex structures.
- To study the links among structural engineering, architecture and society.
- To introduce the students to bibliographic search tools.
- To develop critical thinking and communication skills.
- To practice the use of scientific English.
- To show the students how structural engineering can be a very appealing topic.

To reach these goals, the course covers the topics shown in Table 1.

Table 1: Contents of the course "Conceptual Design of Singular Structures"

Teaching unit	Main contents
Previous concepts about linear structural elements	Review of the main structural systems based on linear elements: the arch, the cable and the beam.
Vaults, domes and shell structures	Typology, structural behavior and design of: classical and modern vaults and domes; continuous shells (folded plates, cylindrical shells, revolution shells, hyperbolic paraboloids, other geometries); and grid shells.
Light structures for roofs with singular typologies	Typology, structural behavior and design of light structures for roofs: cable networks; prestressed membranes; pneumatic structures; tensegrities; tensegrities; branching structures; deployable structures; and bending-active structures.
Structural design of tall buildings	Structural types used to resist horizontal loads. State-of-the-art in the construction of tall buildings. Horizontal actions: wind and earthquakes.
Practical application of the ideas of Structural Art	Engineers and architects. Origins and ideals of Structural Art. The three dimensions of the structure. Critical analysis of structures. Importance of Structural Art today.

A detailed description of the course objectives, contents and teaching methodologies can be found in Paya-Zaforteza et al. [9] and therefore is not given here. In addition, the course aims also to make the students develop two transversal competences: (1) Innovation, creativity and entrepreneurship and (2) Design.

3. Introducing "Structural Art" in the course "Conceptual Design of Singular Structures"

3.1 Detailed description of the approach

The Structural Art component is taught at the end of the course during four sessions with the content and activities described next.

3.1.1 Session 1 (2 hours). Defining the Decalogue of the Outstanding Structure.

In a traditional approach, the students would be passive actors of the teaching-learning process who would get the main ideas of Structural Art directly from the professor. Here, a different approach is taken. Following Confucius quote ("Tell me and I will forget, show me and I may remember, involve me and I will understand"), the students are pushed to reflect on the attributes of outstanding structures by creating a "Decalogue of the Outstanding Structure". This activity serves as an introduction to the topic of Structural Art.

The Decalogue is defined by the class as a whole using a variant of the 635 brainstorming technique [10] according to the following process:

1. The students are grouped in teams of four. Each student is given a template (see Fig. 1) to write three attributes of an outstanding structure. After 5 minutes, the templates are exchanged within the group and each student should write three new attributes, a process that is repeated three times in total. Therefore, each student has to write 4 x 3 = 12 different attributes and the total number of attributes proposed by the group should be 12 x 4 = 48 (see Figs. 2a and 2b).
2. Each group selects their top ten attributes among the 48 attributes generated.
3. The top ten attributes of each group are shared with the class, grouped –since many of them might be very similar – and written in the blackboard.
4. Each student votes for the five attributes he/she considers to be the most important qualities in an outstanding structure. The 10 most voted qualities define the "Decalogue of the outstanding structure". To vote, each student is given five stickers to place close to his/her favorite idea in the blackboard (see Figs. 2c and 2d).

Name of the student	Idea 1	Idea 2	Idea 3

Figure 1: Template used as a basis for the development of the activity "The Decalogue of the Outstanding Structure"



Figure 2: Development of the activity "The Decalogue of the Outstanding Structure"

The top ten attributes of the outstanding structure in the academic year 2018-19 were:

1. Safety and functionality
2. Durability.
3. Economy.
4. Stability.
5. Efficiency.
6. The structure must be necessary.
7. Aesthetics.
8. The structure must be "comfortable" (absence of vibrations…).
9. Integration in the environment.
10. Sustainability.

This activity is also used to partly evaluate the transversal competence "Innovation, creativity and entrepreneurship". The grade of each student depends on the number of attributes proposed.

3.1.2. Session 2 (2 hours). Learning the basics of Structural Art.

Once the students have thought about the qualities a structure should have, they are ready to start developing structural critique based on the ideas of Structural Art. This is done in a lecture where first some examples of structures are shown and the students are questioned about their quality. At the end of this first part the students are asked if structures can be works of art and the main objectives of the Structural Art teaching unit are presented. This also serves to make a short debate about the type of

constructions where the contributions of the structural engineer are more relevant.

Then different models of relationships between engineers and architects are presented. The evolution of this relationship through time is shown through many examples and the current situation, where almost everything is possible, is also explained.

After this introduction, the students learn the three ideals of Structural Art (Economy, Efficiency and Elegance) and the three dimensions of the structure (scientific, social and symbolic) by examining many examples from the past and from the present. A special focus is given to the symbolic dimension to show how structures are more than utilitarian elements and can become symbols of power, of a specific area, of a country, of a continent and even of humankind. The social dimension also receives special attention to make the students become aware than most of our constructions are paid with the taxpayers money and therefore should be designed and built with especial attention to their cost.

3.1.3. Session 3 (1 hour). Debate.

After learning the basics of Structural Art, the students are ready to practice their skills in a debate-style activity. The debate is a role-playing game where the students become members of the jury of a design competition that must take a decision about who is going to design a hypothetical new singular structure in Valencia (Spain), one of the competitors being the Valencian architect Santiago Calatrava.

To do this activity, the class is divided into smaller groups of maximum 12 students. The students of each group are divided into three teams. A first team must support the choice of Calatrava as the designer of the new structure, a second group must defend another choice, and the third group acts as judges and as such conduct the discussion and take a motivated final decision (see Fig. 3). Every student must submit a report showing his/her main points for the discussion before attending the debate. Extra points in the evaluation are given to the students that show proofs of having visited the location of the analysed structure.



Figure 3: Debate about a singular structure.

The debate is organised according to some established guidelines that are given to students prior to the debate and is based on aesthetic, social and technical arguments. Details on this activity can be found in Huyhn and Payá-Zaforteza [11] and are not repeated here. In the past the debate has been related to the construction of a new bridge over the Turia river bed in Valencia and to the construction of a new high rise building hosting a hotel in a protected environment near Valencia beach (see Fig. 4).



Figure 4: Debate activity. (a) Hotel as proposed in the urban planning, source: www.lasprovincias.es (b) Turning Torso by S. Calatrava, (c) Hangzhou Wangchao Center by SOM, source: SOM. The object of the debate was to decide if the design of the new hotel had to be awarded to S. Calatrava or to SOM based on their previous works and their design philosophies.

3.1.4. Session 4 (2 hours). Structural Art today.

In the third part, the students learn how the ideas of Structural Art can be used to understand the value a specific work (Eduardo Torroja's San Nicolas Church in Gandia, Valencia [12]), to make comparative and critical analyses and to study the interaction between politics, engineering and art in a period of the history of a country (Spain). Due to the lack of time, the latter topic is only mentioned and the students are told that, if they are interested, they should watch the chapter "The Politics and Art of Spanish Bridge Design" prepared by Prof. M. Garlock and the author of this paper as part of the MOOC "The Art of Structural Engineering: Bridges".

Finally the students learn why the ideas of Structural Art are important today, even for small scale projects, and as a conclusion of the course, they discover: (1) the common attributes to some of the best structural engineers of the world, (2) how these attributes are common to the best professionals in any profession and, therefore, (3) how the great engineers and their work can be a source of inspiration for them.

It must be noted that all the lectures are very visual and interactive. The students are constantly requested to give their opinions about the displayed structures and some interviews of engineers from the Princeton course "The Art of Spanish Bridge Design" [13, 14] are shown to illustrate many of the points discussed during the lectures. The students are also told that Structural Art is a framework that they can use, not a dogma, and that they should feel free to question this framework and use a different one: the important point is to promote informed and motivated discussions and a critical citizenship, not the framework.

Finally, different non-compulsory activities to complement the course contents are offered to the students every year. For example, in the academic year 2016-17 the students could attend inspiring lectures given at the UPV in the context of the "Workshop on Bridge Design" organized by the Spanish Group of the International Association for Bridge and Structural Engineering and in the academic year 2018-19 the students could participate in a field trip to Barcelona and its surroundings that included a guided tour to the *Sagrada Familia* and meetings with eminent engineers from the firms Pedelta, Enginyeria Reventós and members of the engineering design magazine Dobooku.

3.2 Evaluation of the students

The knowledge gained by the students on the topic of Structural Art is assessed based on:

(1) The reports submitted by the students prior to the debate-style activity and their attitude and

contributions during the debate.

(2) A specific question on Structural Art asked in the course exam. In this question the students should show the knowledge they have gained by giving their opinion about the quality of a specific structure or by carrying out a comparative and critical analysis of two structures.

3.3 Success of the approach

The approach is being very successful as shown by the participation and involvement of the students in the different activities, by the high percentage of the students that pass the course and by the feedback given by the students through the course evaluation polls.

This success is due to the fact that through the lectures and activities the students wrap up all the previous knowledge they had about structures while at the same time they get a new holistic view where structures have technical, social and aesthetic values. This approach is not very common among civil engineering courses and the author thinks it should be much more spread out. The author's experience is that it is not easy to introduce changes in the existing curricula so the changes are more likely to be successful if they are introduced little by little. In fact, the author started by introducing a two hours session describing the main ideas of Structural Art and non-compulsory Structural Art tours in a general course on building structural analysis in 2008 and the success of the approach made it possible years later the birth of new courses on "Structural Systems" (Paya-Zaforteza and Lazaro [15]), "Conceptual design" [9] and "History and aesthetics of structural concrete".

4. Conclusions

Conceptual design and Structural Art are important topics that should be part of the core education of the civil/structural engineer. This paper shows the methodology developed at the School of Civil Engineering of the Universitat Politècnica de València (Spain) to integrate the main ideas of Structural Art in the syllabus of a course on the conceptual design of singular structures. The methodology has been very successful from the students' and professor's point of view and integrates activities to develop creativity and critical thinking, debates and participative lectures.

Acknowledgements

The author would like to thank Prof. David P. Billington and Prof. Maria Garlock from Princeton University, Prof. Mike Schlaich from TU Berlin and Prof. Annette Bögle from Hafencity University Hamburg for his friendship and mentorship. The contact with them was crucial for stimulating the author's curiosity and appreciation of structures as elements going well beyond the strictly technical.

References

[1] E. Torroja. *Razón y ser de los tipos estructurales*, Madrid: Instituto Eduardo Torroja, 1957.

[2] F. Candela, "New Architecture", in *Maillart Papers*, Department of Civil and Environmental Engineering, Princeton University, Princeton, NJ, 1972.

[3] D.P. Billington, *The Tower and the Bridge: the New Art of Structural Engineering,* Philadelphia: Basic Books, 1983.

[4] Diario El Mundo, *La España del Despilfarro. The overspending Spain*. See e.g. the chapter Un Puente a ningún sitio. A bridge to nowhere. https://www.elmundo.es/espana/2014/09/28/542706e6e2704ec7158b4589.html . Accessed on May 30th, 2019.

[5] M. Schlaich, "Challenges in education – Conceptual and structural design" in *Responding to Tomorrow's Challenges in Structural Engineering: Proceedings of the 15th IABSE Symposium*, Budapest, Hungary, September 2006, pp. 20-26.

[6] A. Bögle, "Creative designing – Teaching the impossible?" *Proceedings of the 17th IABSE Congress*, Chicago, IL, September 2008, pp. 330-331.

[7] M. Garlock, J.J. Jorquera-Lucerga "Innovation in teaching conceptual design of structures" Structural Engineering Education Without Borders. *Proceedings of the IV International Conference on Structural Engineering Education*, Madrid, Spain, June 2018, pp. 562-569.

[8] I. Payá-Zaforteza, "On the development of structural criticism through case studies. *Proceedings of the 19th IABSE Symposium*, Venice, Italy, September 2010, pp. 16-23.

[9] I. Payá-Zaforteza, C. Sánchez-Carratalá, J.M. Adam "Thinking beyond the conventional… Introducing a new course on the conceptual design of singular structures" Structural Engineering Education Without Borders. *Proceedings of the IV International Conference on Structural Engineering Education*, Madrid, Spain, June 2018, pp. 590-597.

[10] B. Rohrbach, "Kreativ nach Regeln – Methode 635, eine neue Technik zum Lösen von Problemen". (Creative by rules - Method 635, a new technique for solving problems)". *Absatzwirtschaft. 12: 73–75, 1969.*

[11] T. Huynh, I. Payá-Zaforteza, "Thinking critically about structural engineering through role-playing games". Challenges in Design and Construction of an Innovative and Sustainable Built Environment: *Proceedings of the 19th IABSE Congress*, Stockholm, Sweden, September 2016, pp. 732-738.

[12] G. Núñez Collado, J. Garzón Roca, I. Paya-Zaforteza, J.M. Adam Martínez, "The San Nicolas Church in Gandia (Spain) or how Eduardo Torroja devised a new, innovative and sustainable structural system for long-span roofs", *Engineering Structures* 56:1893-1904, 2013. doi:10.1016/j.engstruct.2013.08.003

[13] http://spanishbridges.princeton.edu/ Website of the course "The Art of Spanish Bridge Design". Accessed on May 30th, 2019.

[14] I. Paya-Zaforteza, M.E.M. Garlock, S. Adriaenssens, B. Glisic, Branko. "The Art of Spanish Bridge Design", a New Course Promoting the Holistic Learning of Structural Engineering. Assessment, Upgrading and Refurbishment of Infrastructures. Structural Engineering: Providing Solutions to Global Challenges: *Proceedings of the IABSE Conference 2015*, Geneva, Switzarland, 2015, pp: 315 - 316.

[15] I. Payá-Zaforteza, C. Lázaro-Fernández "Structural engineering is much more than formulas: Introducing a new course on philosophy of structures". Engineering for Progress, Nature and People: *Proceedings of the IABSE Symposium, Madrid*, Spain, September 2014, pp. 945-952.

Proceedings of the IASS Annual Symposium 2019 – Structural Membranes 2019
Form and Force
7 – 10 October 2019, Barcelona, Spain
C. Lázaro, K.-U. Bletzinger, E. Oñate (eds.)

Structural Art, the 4th Dimension, and Metaphors for Teaching Design

John A. MATTEO*

*1200 Architectural Engineers, PLLC
210 N. Lee Street, Suite 210, Alexandria, VA 22314
jmatteo@1200ae.com

Abstract

The potential for a work of structural engineering to extend beyond the literal and inspire our aesthetic sensibility – to be structural art – is to see in a physical work signs of the creative human spirit that are fundamental to design. We understand that structural art is possible from the great achievements of the past, upon which we build both technically and artistically, to design for the present and the future. This indeed was part of the spirit of David Billington's teaching at Princeton University – to abstract principles from the great works and artists of the past to fuel our design creativity. This paper elaborates upon this dual perspective as fundamental to teaching design. Also presented as laudable figures in the lineage of design education, Eugene Emanuel Viollet-le-Duc and Hardy Cross have offered an enriched perspective on time and change in structural engineering.

Keywords: conceptual design, historic structures, pedagogy, load path, relative stiffness, Robert Maillart

1. Introduction

The potential for a work of structural engineering to extend beyond utility and inspire our aesthetic sensibility – to be structural art – is to see in a physical work signs of the creative human spirit that are fundamental to design. In observing the work of art, we may imagine the artist and find inspiration in his or her achievement. We understand that structural art is possible from the great achievements of the past, upon which we build both technically and artistically, to design for the present and the future. Teachers, in various forms, document and disseminate a breadth of such valuable information and help distill its meanings and merits. This indeed was part of the spirit of David Billington's teaching at Princeton University – to abstract principles from the great works and artists of the past to fuel our design creativity. And like the works and artists themselves, the best teachers can inspire us to see more deeply. David Billington was indeed an inspiration for both students and colleagues, as he launched many of us into the world of design, with a versatility of perspective from past to future, and a sense of wonder for the potential of structural art.

As part of a collection of writings in honor of Billington's life work and profound influence, this paper elaborates upon this dual perspective in time, or the 4th Dimension, as fundamental to design and the teaching of design. It also celebrates the role of inspiration and metaphor, that may be found in works of the past and, very often, within the fabric and mechanisms of the natural world that surrounds us. As a personal note, I first became familiar with David Billington through his book, *The Tower and Bridge* [1], as an undergraduate studying Civil Engineering and Art & Architectural History at Tufts University. I also had the privilege of working with him as a Masters Student under his mentorship at Princeton University. Between those degrees I spent a year in Switzerland at the Ecole Polytechnique Federale de Lausanne studying reinforced concrete and bridge design, with regularly scheduled trips to visit the bridges of Robert Maillart. I took the photos included in this article during the academic

Copyright © 2019 by John A. MATTEO
Published by the International Association for Shell and Spatial Structures (IASS) with permission.

year from 1989-1990, which are lasting images of the life-changing inspiration a scholar and teacher such as David Billington can have.

2. Learning from the Past

We live in the built environment and envision its growth or change for the future. Part of our mission as designers and teachers is to preserve the values and lessons of the past, most poignantly demonstrated in the works themselves. In many ways, the education of structural engineers lost sight of this during its progression in the 20th century, with the earlier emphasis on precedent and "rules of thumb" being replaced by scientifically derived theory expressed mathematically (Matteo, pp. 96-97, [4]). However, a change in sensibility began to re-emerge where the value of history was seen as a key component to good design. This transition can be observed in the second edition of David Billington's first book, *Thin Shell Concrete Structures*, which was originally published in 1965. By the time the second edition was published in 1982, he rewrote the first chapter to include a historical perspective and to focus on more qualitative physical behavior, which would in later chapters be developed more comprehensively mathematically. Undoubtedly influenced by his research and 1979 publication of *Robert Maillart's Bridges: the Art of Engineering*, Billington articulates this broadened perspective on page one:

> The two types of knowledge that inform all of the best structural designs are scientific and historical. ... Scientific knowledge as defined in this text means knowing how to define structural behavior, expressed in displacements and forces, to the end of discovering how a given form carries loads safely with a minimum of materials, i.e., discovering how to design an efficient structure…But science, by which we mean primarily classical physics, seeks only to understand how given forms behave, whereas engineering design must first choose a form and it is for that activity that historical knowledge is required. Billington, p.1 [2].

Billington also alludes to his research on aesthetics, which he refrained from elaborating upon in this second edition, but which would very soon be introduced in the landmark publication of *The Tower and the Bridge*, one year later in 1983. Limited scholarship and publication on the history and aesthetic potential of structural engineering preceded this work. One example was certainly Sigfried Giedion's notable *Space, Time and Architecture*, which was first published in 1941. Giedion's work included a developed section on the work of Robert Maillart and it precipitated the 1947 exhibition of Maillart's work at the Museum of Modern Art. However, this was all primarily from an architectural history and aesthetic viewpoint that was not able to integrate the technical perspective of the structural engineer. *The Tower and the Bridge* not only infused a more technical perspective to the appreciation of Maillart and many other structural engineers of the late 19th and early-to-mid 20th centuries, but defined the aesthetic parameters of a new art form – structural art.

In articulating the values of structural art, Billington also offered a roadmap to diverse achievements, technically and aesthetically, in structural design, and began to coalesce a canon of great works that would serve as models for future engineers.

The Salginatobel Bridge, depicted in Figure 1, became somewhat of a pilgrimage site for a growing group of structural engineers and design-minded individuals who were being newly educated about the history of the profession. This paradigmatic work of structural engineering, and



Figure 1: The Salginatobel Bridge, near Schiers, Switzerland, built in 1930

numerous others, could now be appreciated within the framework of Billington's engineering aesthetic. Billington's work told engineers that there was great value in looking to the past for a broad range of creative solutions to new technical challenges.

And yet this perspective that embraced the history of structural design, perhaps akin to what architectural history is to architecture, in some significant ways remains distinct from understanding the nature of structural behavior and material condition over a continuum of time – to understand the structural history in the "life" of a structure.

Standing before a work of structural art, what we witness in our time and place is inevitably somewhat different from what was conceived during its design and seen immediately following its construction. We witness the effects of time, which may be seen in the gradual signs of environmental exposure, or from responses to loads imposed by nature, or from changes imposed by human use or intervention, all through the lens of current thinking. If we value the work, we then may ask how to best perpetuate its physical longevity and/or lessons for the future. This is what I will refer to as a conservatorial perspective.



Figure 2: The Schwandbach Bridge, near Hinterfultigen, Switzerland, built in 1933

During my year in Switzerland I traveled by train from Lausanne to Bern, then a small bus to a small town, and then a nice long hike down country roads to reach what is perhaps my favorite work of Robert Maillart, the Schwandbach Bridge (Figure 2). Frost covered every surface of the natural and man-made landscape. The thinness of the arch, despite reading about it in Billington's books, was surprising and beautiful. The bridge form artfully engages the landscape, with uniformly curving deck over an arch width that encapsulates the full plan profile, mediated by trapezoidal cross walls that are both simple and striking (Figure 3).



Figure 3: The Schwandbach Bridge, trapezoidal vertical cross walls

I spent several hours on and around the Schwandbach Bridge. Clambering underneath (perhaps somewhat ill-advised), I was rewarded with a more visceral understanding of the construction (Figure 4). Here, the imprint of the form boards in the cast concrete remained sharp and intelligible. Also apparent was one sign of an ongoing deterioration mechanism – an area of reduced concrete cover that resulted in some localized rusting of reinforcement and spalling of concrete. Though appearing in remarkably good condition, the nearly 60-year old bridge, at the time, showed some signs of its age and of its physical material history.



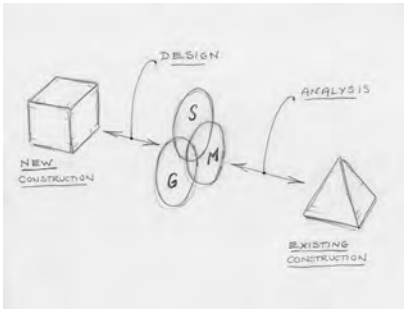
Figure 4: The Schwandbach Bridge, beneath the deck

A conservatorial perspective of the effects of time on the built environment, with the versatility to apply these ideas to new work, will help cultivate creative and enduring structures. Eugene-Emanuel Viollet-le-Duc was a 19th-century French architect and theorist who, perhaps more than any other, espoused a conservatorial perspective in understanding the mechanisms of environmental exposure on a structure over time. In his fictional, yet pedagogical, work *How to Build a House*, Viollet-le-Duc expresses the value of not only seeing the paradigms and precedents of architecture in the world around him, but also of understanding the mechanisms of time and Nature to which all structures are subjected.

> Seeing that all this would not put me in a speedy way to master my profession, and being so fortunate as to have a few hundred pounds left me, I resolved to travel—to study architecture in actual buildings, and no longer in those shown me on paper. I set myself to observe, to compare, to see practical men at work, to examine buildings that were crumbling to pieces, that I might discover *in anima vili* the causes of their ruin.
>
> Viollet-le-Duc pp. 82-83 [3]

3. Communicating in the Present

We design and communicate about the built, or envisioned to be built, environment within the framework of three main languages – Speech, Graphics and Mathematics (Matteo [4]). This idea helps students develop the breadth of communication skills needed in the profession, but also acknowledge that each language offers strengths and weaknesses in representing the physical world. Figure 5 provides a visual representation of the central role of these three languages in communicating about structures, whether looking back to analyze what exists or envisioning a new design for the future. The sketch to the right uses the analogy of driving while keeping an eye on the rear-view mirror; we inevitably design for the future but remain mindful of the lessons from the past.



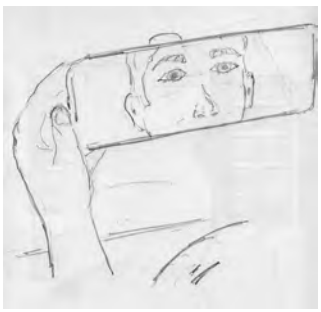


Figure 5: Analysis and Design – Past, Present and Future
(these sketches by Matteo first appeared in reference [4])

The figure may also remind us that there is a discernible space between the objects of our communication and the nature of the communication itself. The languages we use to describe a structure, however poignant, precise, or poetic, are always approximations of the physical reality.

Hardy Cross, professor of Civil Engineering perhaps known best to structural engineers for the moment distribution method which converges toward equilibrium through a series of successive approximations, possessed a healthy relationship to the limits of theory and language in the face of actual physical behavior. In subsequent published questions and responses to his first article on moment distribution, he notes the following:

> The quest of the absolute is a beautiful thing; but he who seeks in engineering analysis a precision that cannot be ultimately translated into such units as pounds of steel and yards of concrete is misled. Structures are analyzed so that they may be designed; not for the pleasure or practice of analyzing them. As Professor Findley well states, "between the analysis of a given structure, which is essentially mathematics, and the design of a required structure, which is essentially art, lie many difficulties." Cross p. 28 [5]

4. Inspiring Design for the Future

Metaphor in language is akin to design thinking itself. From the literal or prosaic, we extend our thinking beyond what is, and envision what could be. Viollet-le-Duc climbed and surveyed Mont Blanc and witnessed nature's effects on the earth's surface as analogous to the effects of time and environment on architecture. Hardy Cross, though primarily focused upon education for structural analysis and structural design, also applied his methods to the flow of water in a network of conduits or conductors (Cross [6]).

For a system of pipes, the total flow at a given junction is distributed to the pipes connecting at the junction in inverse proportion to their resistances (Cross, p. 253 [6]):

$$R = n\, r\, Q^{(n-1)} \qquad (1)$$

This is exactly the opposite of the flow of force in an indeterminate structure. In Cross's moment distribution method, forces at a given structural joint are distributed in proportion with the relative stiffness of the members connecting into that joint. Though opposite in nature, the nature of their respective flows can be determined using this very same methodology.

As one might visualize the flow of water following a path of least resistance down a mountain, the flow of force in a complex structure will follow the path of greatest resistance. And these paths, subject to the forces of environment and human interventions over time, may indeed change over time.

Figure 6 depicts a photo from 1990 of Maillart's Weissensteinstrasse Bridge and a drawing from the associated calculations created by his design office in 1938. The artful curves connecting beam and column seem expressive of this very process of fluid sharing and distribution of forces.

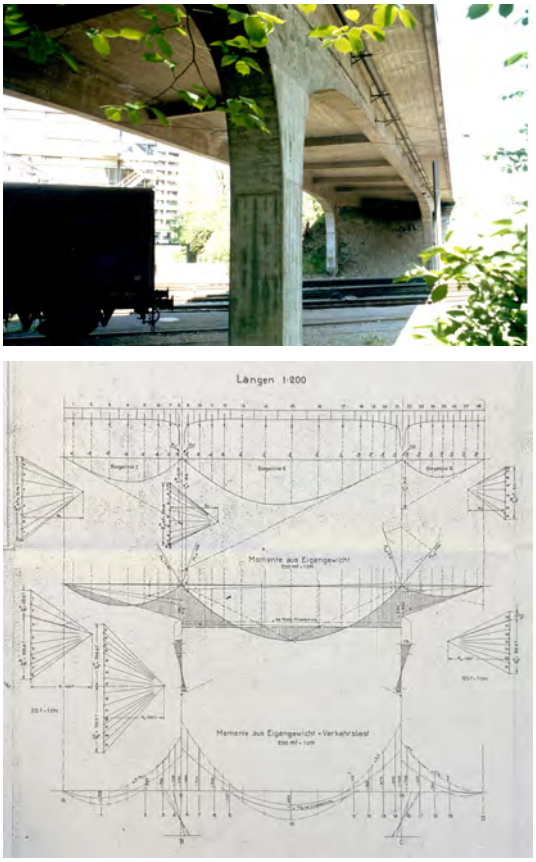


Figure 6: Weissensteinstrasse Bridge and design calculation from 1938 [7]

Rather than a moment distribution approach, the graphical statics of Maillart's calculations represents another means of correlating relative weight and stiffness to the distribution of force in the structure.

The flow of water, cascading down a mountain along the path of least resistance, serves as a compelling metaphor for design or analysis. Viollet-le-Duc also came upon this analogy as a by-product of his project to develop a topographical survey of Mont Blanc. The mountain is like a building, each must sustain and adapt to the forces of nature. Each will change over time and it is up to the observant student to read these signs to best recreate the structural history, or envision a future history of behavior. In many ways, this is the challenge of the engineer seeking to understand a structure – to understand the load path which may be singular or shared, intended by design or incidental by nature. Viollet-le-Duc describes it like this:

> Our globe is, in fact, only a great edifice, all whose parts are capable of rational explanation; its surface assumes forms dictated by imperious laws, following a logical order. To analyze carefully a group of mountains, the manner in which they were formed, and the causes of their ruin; to discover the order in which the phenomena of upheaval occurred, the conditions in virtue of which they have resisted or endured the action of atmospheric agents, to note the chronology of their history, is to devote oneself to a work of methodical analysis which is, on a grander scale, analogous to that which the practical architect and the archaeologist applies himself when drawing conclusions from the study of buildings. […]
>
> I write, however, for the general public, and this I have always kept in view; nor do I aim at anything higher, in publishing this resume of my observations, than imbuing the many with an ardent desire to study Nature, our common mother, whose teachings are always the healthiest and most profitable for the mind. Viollet-le-Duc pp. 12-13 [8]

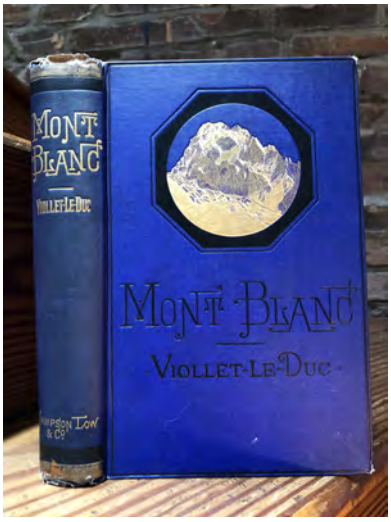


Figure 7: *Mont Blanc: A Treatise on its Geodesical and Geological Constitution; its Transformations; and the Ancient and Recent State of its Glaciers*,

Viollet-le-Duc, 1877

The forces of nature provide the "imperious laws" that ultimately guide our analysis of existing structures or our designs for the future – a common ground for structures old and new. The flow of force from structure to ground needs only one successful path, even if there are multiple paths to choose from. For an existing structure that has stood the test of time, it is common to find multiple possible load paths that may currently, or during its lifetime, offer a route to stability. Finding a successful path inevitably will induce some movement (discernable or not) or may cause a crack in part of the structure or connecting finishes. These are the signs that may inform the analyst or designer about a structure's history. Many existing structures employ materials or structural systems that predate much of the theoretical development in engineering of the 19th and 20th centuries, or predate many of the ever-changing code procedures and standards. This presents a challenge perhaps similar to the designer seeking to innovate, and is a good reminder for all students who may rely too heavily on the many tools and procedural standards we have today. Inevitably we will be faced with a challenge that pushes us off the paths most traveled, but the way to good structural design must always be rooted in the first principles of mechanics, in obeiance of the laws of nature.

5. Conclusion:

Viollet-le-Duc and Hardy Cross, both theorists and educators of the built environment, found ways to distill widely applicable principles of structural behavior from a broadened perspective in nature. Similarly, David Billington saw art in the best examples of structural engineering and articulated the parameters of a complex, layered meaning that translate to cultural value (Figure 8). To conclude this paper, the beauty and fundamental social value of structural art, and the joy experienced by engineer-artist and observer alike, are perhaps best summarized by Billington himself at the conclusion of *The Tower and the Bridge,* as he describes the role of play in design:

> But to serve the public best, these structural artists had to be playful – not denying discipline but expressing surprise and joy. … They studied long and hard to learn the rules (of nature); they tried continually to play fair (with society); and in creating order they surprised others with the beauty of their works. At the heart of technology, they found their own individuality; they created personal styles without denying any of the rigor of engineering. Billington pp. 273-274 [1].

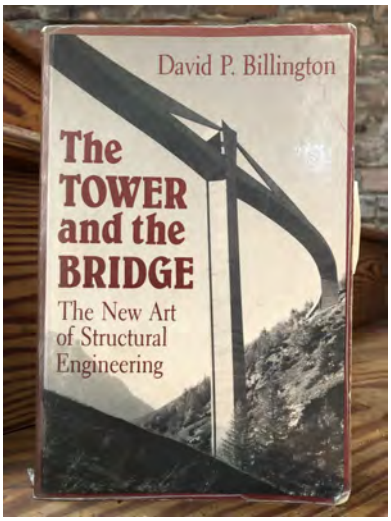


Figure 8: *The Tower and the Bridge: The New Art of Structural Engineering*

Acknowledgements

This paper is written in honor of the Professor David P. Billington who, as a scholar, teacher and mentor, has profoundly and positively influenced me, and so many others.

References

[1] D. P. Billington, *The Tower and the Bridge: The New Art of Structural Engineering*, New York, Basic Books, 1983.

[2] D. P. Billington, *Thin Shell Concrete Structures, 2nd Edition*, New York, McGraw-Hill Publishing Company, 1989.

[3] E. E. Viollet-le-Duc, *How to Build a House: An Architectural Novelette*, translated by B. Bucknall, London, Sampson Low, Maston, Searle & Rivington, 1874.

[4] J. Matteo, "Preservation Engineering: Framing a New Curriculum," in *Preservation Education and Research, Volume Four, 2011,* pp. 93-106.

[5] H. Cross, "Analysis of Continuous Frames by Distributing Fixed-End Moments," *Arches, Continuous Frames, Columns, and Conduits: Selected Papers of Hardy Cross.* Urbana: University of Illinois Press, 1963. (paper cited in this collection was first published in 1930)

[6] H. Cross, "Analysis of Flow in Networks of Conduits or Conductors," *Arches, Continuous Frames, Columns, and Conduits: Selected Papers of Hardy Cross.* Urbana: University of Illinois Press, 1963. (paper cited in this collection was first published in 1936)

[7] R. Maillart, "Statische Berechnung, Ueberfuhrung der Weissensteinstrasse," Bern, Switzerland, January 28, 1938, drawing no. 532/6/5.

[8] E. E. Viollet-le-Duc, *Mont Blanc: A Treatise on its Geodesical and Geological Constitution; its Transformations; and the Ancient and Recent State of its Glaciers*, translated by B. Bucknall, London, Sampson Low, Maston, Searle & Rivington, 1877.

Proceedings of the IASS Annual Symposium 2019 – Structural Membranes 2019
Form and Force
7 – 10 October 2019, Barcelona, Spain
C. Lázaro, K.-U. Bletzinger, E. Oñate (eds.)

The art of collaborative structural design: Structural art in the age of cross-disciplinary collaboration

Christiane M. HERR*

*Xi'an Jiaotong-Liverpool University
111 Ren'ai Road, Suzhou Industrial Park, Jiangsu, PR China
Christiane.Herr@ xjtlu.edu.cn

Abstract

While laying the foundations for an understanding of structural design as a potentially higher form of achievement, this paper argues that Billington's conception of structural art also established it as the work of a heroic creative genius driven solely by engineering values. By clearly distinguishing structural art from the domain of architectural achievement, the concept contributes to a separation of the two disciplines, and offers little support to those seeking to establish cross-disciplinary collaborative approaches to structural designing. With the criteria defining works of structural art primarily employed to describe completed works of art retrospectively, new questions to be considered may be what kind of design processes will lead to structural art? Do desirable types of design processes necessarily exclude other disciplines? This paper argues that responding to these contemporary challenges may bring about new interpretations of structural art and draw more attention to efforts directed at bridging diverging values already early on in discipline specific education.

Keywords: structural art, David Billington, collaborative design, cross-disciplinary design, design process, design values.

1. Introduction

Billington's concept of *structural art* [1] established structural engineering as a discipline with the potential for higher forms of achievement, transcending the mere accomplishment of compliance with requirements. To distinguish engineering art from other works of engineering, Billington [1] defined three primary criteria: efficiency, economy and elegance. Simultaneously, however, he also explicitly discarded collaborative design between structural engineers and architects as potentially resulting in structural artworks: "Almost without exception it seems that the best works of structural art would have been compromised had there been architectural collaboration in the design of the forms" [1, p. xvi]. Yet, many structural artists have extended histories of collaborating with architects, as outlined by Rappaport [2]. Structural art has also been identified in works of architecture, where engineering ingenuity in response to and in conjunction with architectural design intentions created works of exceptional coherence and innovation [3].

This paper questions the narrow understanding of the concept of structural art as restricted to works accomplished solely by structural engineers in the age of increasingly collaborative design processes and argues that it can also be employed to describe and guide works of collaborative structural design. The paper makes this point based on several cases well documented in existing literature and traces in what ways works of collaborative structural art can extend and enrich an engineering-centric definition of structural art. From this analysis, architectural aspects of structural art are identified and described in more detail, such as the skillful definition of boundary conditions and a refined understanding of the aspect of engineering art described as aesthetics or elegance. By mapping several differences in

Copyright © 2019 by Christiane M. HERR
Published by the International Association for Shell and Spatial Structures (IASS) with permission.

understanding seemingly shared vocabulary, differences in disciplinary values are identified as key drivers or obstacles for cross-disciplinary structural artworks.

The paper aims to extend the discourse started by Billington's work, continuing and developing it for the changing contexts, design processes, toolsets and workflows the profession(s) face in the 21st century. Drawing on existing literature, the paper finally emphasises the relevance of education in establishing design values allowing exchanges across disciplinary boundaries and discusses experiences made over several years of promoting shared values in cross-disciplinary structural design education.

2. Defining and identifying structural art

Throughout his extensive body of work, Billington established the concept of structural art through careful tracing and analysis of historic precedents. These examples and associated stories continue to provide an inspiring context to illustrate structural artworks and learn about structural artists and their accomplishments. In their comprehensive overview paper on the discourse relating to structural art, Hu et al [4] have however pointed out that most research work related to structural art has focused on either a single case study or a particular structural artist and his works: "as a result, it creates the misconception that a work of structural art can be only created by those great structural engineers." [p. 408] This is somewhat compounded by Billington's insistence that structural art is typically the work of one strong engineering personality rather than teams [1, p. 91].

The criteria for defining and identifying structural art seem deceptively simple: efficiency, economy and elegance. With efficiency and economy well known and quantifiable aspects of engineering design, elegance emerges as a central criterion of structural art, setting it apart from conventional engineering solutions. In addition, the three criteria are used loosely in descriptions of structural artworks. In particular in the case of elegance, the term remains surprisingly vague and is typically described in specific examples rather than defined explicitly. Yet, its abstract nature also lends itself to rich associations, which has generated a wide variety of interpretations.

Elegance as a key criterion of structural art seems to be understood as relating to modernist aesthetics of geometric simplicity and a preference for functional forms illustrating their purpose and structural behaviour. Discussions of elegance in structural art also tend to extend to other terms, in particular to aesthetics, which is also understood in similarly vague yet inspiring and evocative terms. Discussions of aesthetics in structural art mostly skirt around clear definitions and instead describe aesthetics contextually and related to specific cases – avoiding the historical, cultural and subjective nature of the classical discourse. Ironically, architectural discourse has abandoned discussions of aesthetics in terms of beauty for decades and instead tends to focus on compositional and contextual aspects such as conceptual clarity or coherence. An equivalent to this side-stepping of classical notions of aesthetics and a re-direction towards the engineering perspective can be found in Hines' [5, p. 124] emphasis of *conceptual transparency*. Similarly, Saliklis et al. [6] propose an engineering-centred view on aesthetics in structural design based on the analysis of Khan's seminal work in terms of the key characteristics of *simplicity*, *scale* and *surprise*. In particular the third aspect is of interest as it relates to the involvement of the viewer and her spontaneous intuitive judgement in recognising structural art. While subjective effects on users are often the focus of architectural design, there seems to be comparatively little recognition of the experiencing human being in structural engineering. In this aspect, a cross-disciplinary exchange could perhaps offer valuable insights into notions of aesthetics compared to a strict separation of structural art and its related discourse from architectural involvement?

While Hu et al. [4] provide a comprehensive overview of structural art related discourse, they are also careful to exclude the work of the current generation of structural artists: "one must be very careful in using the word ''structural artists'' in the modern multidisciplinary climate and increased complexity of new infrastructure. Only time will tell whether their work will be recognized or not." [p. 413]. With the discourse evolving, confirming contemporary structural artworks, or even predicting structural art seems a risky move when workflows and tools are changing quickly. Can structural artworks be created in this

new climate of complex design processes involving multiple disciplines? Maintaining a mostly historical approach to attributing structural art may become a strong limitation for a field that explicitly seeks to share the valuing of structural art to inspire future structural artists.

3. Cross-disciplinary collaborative structural artwork

Despite Billington's [1] warning that the involvement of architects tends to make structural artworks impossible, many structural artists have long histories of collaborating with architects. Rapaport [2] describes these collaborations as long-term dialogues between strong individual designers who are experts in their respective fields, yet share a respectful mutual understanding of each other's design intentions. It may be argued that any structure that involves direct contact with experiencing human users will benefit from an architectural collaborator in its design process, including not only buildings across all scales, but also bridges of small to medium scale. The discarding of potential architectural contributions to structural art seems to be grounded in a particular perspective on the architectural discipline, distorting its key focus on human spatial experience and reinterpreting it as a preoccupation with the visual. This is made explicit in Hu et al.'s [4] summary statement: "Efficiency concerns using the minimum amount of material consistent with adequate performance and safety; economy refers to achieving a competitive construction cost consistent with minimal maintenance requirements; and elegance is defined as emphasizing aesthetics to the greatest degree consistent with efficiency and economy. Consequently, structural art is quite distinct from the visual maxims of architecture because structural artists seek elegance without compromising safety, serviceability, and economy." [4, p. 408] Can structural art really be reduced to a cheap and efficient structure that is relatively elegant? Are structural artworks necessarily more economical than other options? Is it indeed possible to satisfy all criteria without compromising, for all cases of structural art? Could this feat even be ascertained beyond doubt?

Saliklis et al. [6] describe Fazluhr Khan's contributions to high rise building development as structural artworks, even though buildings are often excluded from the category of structural art due to architectural form potentially involving decorative or sculptural aspects: "Structural form is neither decorative nor sculptural because it arises from a melding of creativity coupled with mathematical rigor and economic restraints." [6, p. 25] Yet, Khan's high rise building structures, worked out in close collaboration with architect Bruce Graham, are excluded from this general dismissal. Perhaps the notion of *collaborative structural art* would be more fitting in such cases? Recent research has also identified structural art in a church designed collaboratively between Edoardo Torroja, the architect Echegaray-Comba and a further engineer, Nadal [3]. Hines [5] points out that Joerg Schlaich's works have consistently "demonstrated that it is possible to create structural art as an engineering consultant in collaboration with architects. For this reason, Schlaich's work offers insight into process that is consistent with contemporary culture." [p. 125] From the other side of the disciplinary divide, architects have long endeavoured to productively integrate structure into architectural design, as Andrew Charleson's book "Structure as architecture" [7] and many similar others illustrate. These structurally-oriented approaches to architectural design are driven by the ambition to create built space with a quality that transcends diverging disciplinary viewpoints and values. Those collaborating across disciplines are usually well aware that there may not be an optimised solution to multiple, interlinked and often contradictory design challenges, and design proposals may be difficult to evaluate on simple scales – gains in economy may lead to losses in efficiency or elegance, and vice versa. Yet, outcomes of collaborative design processes can demonstrate innovative ways of employing available resources, conceptual clarity and surprising ingenuity. It may be argued that both collaboratively designed works of structural art as well as classic works of structural art necessarily involve project-specific assessment as well as considerable degrees of subjective judgement.

This paper proposes that collaborative structural art is not only possible, but a desirable and contemporary development of structural art already implicit in much recent structural art discourse. Collaborative structural art results from the balancing of engineering values with architectural values in

a manner that benefits both disciplines. Beyond the classic engineering-focused criteria for structural art described by Billington, a human- and context- focused architectural perspective offers increased relevance of structural design proposals. On the other hand, the values inherent in structural art as an aspiration can provide improved conceptual coherence, feasibility and sustainability for architectural design proposals. A fruitful exchange between the values and perspectives of both disciplines can for example be observed in recent pedestrian bridge design competitions – where collaborative and human–focused design approaches are increasingly successful. Other examples of collaborative structural artworks may include works such as Balmond and Koolhaas' collaboration on the Villa Bordeaux [8], or Sasaki and Ito's collaboration on the Sendai Mediatheque [9].

4. Creating (collaborative) structural artworks

Even though the concept of structural art was conceived based mainly on analytical reflections of past works, its proponents have consistently argued that structural art can also be an aspiration for current and future applied design work. For this reason, structural art should probably be separated more clearly from the individual personalities of structural artists – to avoid the perception that only recognised past masters could achieve such design quality. How, then, can structural art be created? What kind of design process leads to structural art, and how is it different from design processes leading to collaborative structural art? While innovation and creativity are impossible to predict, it is possible to create conditions for them to thrive.

A key aspect to increase the likeliness of structural artworks is a general sensitivity for and appreciation of structural art in those who practice structural as well as architectural design: without an analytical and critical approach to assessing one's environment, the refinement required for structural artworks is unlikely to appear. Billington's descriptive criteria of efficiency, economy and elegance are outcomes of his detailed knowledge and critical analysis of engineering history, which allowed him to develop the concept of structural art and to make it explicit. While awareness of historic works of both architectural and engineering disciplines is common in architects, engineers tend to be less familiar with the history of their own discipline. Moreover, structural art combines quantitative and qualitative assessment, which positions it at the fringe of the conventional engineering canon and attracts little attention from those aiming for efficiency and economy only. The perception and appreciation of the qualities of structural art typically require prior study: Complex notions such as Hine's [5] conceptual transparency are not readily understood without a broad background context, let alone integrated into applied design work. There are parallels to a similar architectural discourse on the relationship of built form, material, structure and architectural expression revolving around the notion of *tectonics* – a discipline specific term that requires prior study and awareness of an ongoing debate in order to be properly employed in applied designing. Awareness of and critical reflection on works created by others, including historical and contemporary case studies, is identified as a key aspect for educating future engineers by Boegle [10], Gauvreau [11] as well as Hu et al. [4], who all argue that learning about case studies is essential for being able to judge quality in design.

A discussion of the criteria defining structural artworks typically leads to a discussion of creativity and innovation in the design process. Hines [5, p. 123] describes creativity as a necessity for high quality engineering design and characterises it as a process cycling through the stages of *imagination*, *expression* and *judgement*. Typically referring to the creation of the new and the surprising [5, 6], creativity is not easily defined or operationalised, as current discourse in various design-related disciplines demonstrates. There is however a broad agreement that creativity can be supported by various techniques and skills, which are at least partly teachable [12]. In the context of structural art, the question arises how design processes can aim for structural art in general, and for its criteria more specifically? According to more recent design theory, designing is not a linear process leading to a predefined outcome – this is only possible for routine design that is based on the adaptation of known structural and architectural types to new sites. Much engineering creativity revolves around routine design, as the invention of genuinely new structural types is rare. The works of sbp (schlaich bergermann

partner) illustrate this process, with many of their structural proposals reusing and adapting well known structural typologies for new contexts and site conditions. Design processes can be approached in a way that encourages creativity, by allowing them to unfold in a dialogical and recursive manner. Characteristic for more artistic disciplines, this type of design process is open to risk and uncertainties and different from the more prescriptive linear and directed design process models typically employed in engineering contexts. The latter may suffice if the aim is the adaptation of known structural types to new contexts. If the aspiration of structural art however requires transcending of existing structural types and theory in favour of creating new types and theory to fit them, then the former type of process is more appropriate. There seems to be little room for routine design in the works of a structural artist however: "Creating unique solutions to recurring structural dilemmas is a hallmark of a structural artist." [6, p. 26]

Despite a general agreement that creativity is important for both education and practice leading to structural artworks, descriptions of creativity relating to the concept of structural art are mostly based on personal experience. To date, there seems to be no shared theory of creativity or the process of creative designing in the structural art discourse. In this context, a design cybernetic [13] perspective on design may be useful, as it emphasises a trans-disciplinary vocabulary and offers strategies to navigate the creative process. Such a perspective may help to establish shared vocabulary for key terms often used in cross-disciplinary exchange, such as design, design concept and design process.

4. Education for appreciation of values across disciplinary divides

Given students' early adoption of disciplinary values in their formative years of their undergraduate studies, education emerges as a key aspect of cultivating the basis of structural art. One of the main interests of proponents of structural art has been to continue Billington's method of teaching through detailed discussion of historical case studies of both structural artists and structural artworks, with the work of Garlock and Adriaenssens providing very visible and accessible examples. From the perspective of architecture, new additions to the engineering curriculum in this context, such as case study analysis, model making and site visits, seem very familiar and resemble aspects of architectural studio education. Studio education thus offers not only an educational context to teach applied designing, but also a platform for encouraging collaborative design work between architects and engineers [14, 15].

Beyond offering increased opportunities to practice applied designing and to learn about the respective other discipline, the design studio provides a complex learning environment in which students are given opportunities to engage in design processes that involve unknown territory, risk and often uncertain criteria for success. Gauvreau [12, p. 120] posits that in order to serve society by creating value, future engineers "must be given the knowledge, skills, and values they need to rise to this challenge. For this to happen, universities need to shift their focus from the creation of innovations to the education of innovators." [p. 120] This recommendation implies a shift from learning about structural art to learning to practice, working towards structural art – a shift towards applied design in engineering. In the context of collaborative structural art, shared design studios are not the only possible approach: I have found that engineering students – particularly in their undergraduate studies – often have difficulties to adjust to the ambiguous and dynamic nature of creative design processes. For this reason, joint projects with architecture students tend to require significant preparation and more structuring of design tasks on the part of the engineering students [16].

The most substantial part of this preparation for cross-disciplinary collaborative designing in my own teaching practice is directed towards the teaching of a shared vocabulary – and an appreciation of the respective other side's interpretations of this vocabulary. Important shared language relates to the nature of the design process, conceptual design, making explicit disciplinary values and identifying areas for potential agreement or compromise, and thinking in terms of and generating options based on evaluation [14]. Only when such language is shared or mutually understood can values of the other discipline be recognised as such and integrated into the design process. This exchange is made easier if shared

overarching goals can be agreed and defined, such as a shared understanding of what constitutes quality in the built environment, a particular interest to develop a specific structural type or a vision of a sustainable future. In cross-disciplinary collaborative design practice as well as education, early discussion on the particular conceptual design approach chosen for a project often determines the quality of the design process to follow. The more experienced designers are, the better they can set boundaries that serve as constraints rather than as fixed limitations, leaving sufficient space yet also offering sufficient interesting challenges for the design collaborator to address and "own". Different personalities may be expressed in this process – some preferring to drive or help realise the other's ideas and some preferring to treat the design process as a creative conversation on eye level. In both cases, it is important to note that all these scenarios may lead to collaborative structural artworks as described above.

5. Conclusion: Towards a Collaborative Approach to Structural Art

While the concept of structural art in its original form focuses on the creativity and competence of the structural engineer working in isolation, more recent discourse has acknowledged the role of cross-disciplinary collaborations in creating works of structural art. New workflows and closer cross-disciplinary exchanges supported by new digital tools are changing the context for structural art, raising the question of how Billington's celebration of higher achievements of individual engineers can be translated into contemporary professional contexts [17]. Based on an examination of the structural art concept, this paper proposes an extension and opening of structural art to include the work of cross-disciplinary teams involving architects and structural engineers. Arguing that structural art, distinguished from conventional engineering as a domain of creative designing, has much in common with architectural designing, this paper identifies several precedents for collaborative structural art already acknowledged in previous structural art discourse. Calling for an extension of structural art discourse and education beyond references to historical precedents, the paper discusses the question of how structural art may be generated, and how disciplinary education for future engineers and architects may support future structural artists. In the words of Hu and Dai [18], "no matter how much differences between architectural art and structural art still exist, at least one thing is certain - that the ultimate goal for man-made structures is the manifestation of human spirit." Finding a shared spirit through shared aims as well as shared values across the disciplines of engineering and architecture emerges as a key concern for collaborative structural art.

References

[1] C. Olsen and S. MacNamara, *Collaborations in architecture and engineering*, Routledge, 2014.

[2] N. Rappaport, *Support and Resist: Structural Engineers and Design Innovation*, Monacelli, 2007.

[3] G. Nunez-Collado, J. Garzon-Roca, I. Paya-Zaforteza and J.M. Adam, "The San Nicolas Church in Gandia (Spain) or how Eduardo Torroja devised a new, innovative and sustainable structural system for long-span roofs," *Engineering Structures* vol. 56, pp. 1893-1904, 2013.

[4] N. Hu, P. Feng and G.L. Dai, "Structural art: Past, present and future," *Engineering Structures* vol. 79, pp. 407–416, 2014.

[5] E. Hines, "Understanding Creativity," in E. Hines, S. Buonopane, M. Garlock and D. Billington (eds.), *Festschrift Billington 2012: Essays in Honor of David P. Billington*, International Network for Structural Art, pp.122-155, 2012.

[6] E. Saliklis, M. Bauer and D. Billington, "Simplicity, scale, and surprise: evaluating structural form," *Journal of Architectural Engineering*, vol. 14, pp. 25-29, 2008.

[7] A.W. Charleson, *Structure as architecture. A source book for architects and structural engineers*, Elsevier, 2015.

[8] C. Balmond, *Informal*, Prestel, 20007.

[9] M. Sasaki, "Sendai Mediatheque, Japan," *Structural Engineering International*, Vol. 12, No. 3, pp. 146-148, 2002.

[10] A. Boegle, "Next generation structural design: Challenges and chances," in E. Hines, S. Buonopane, M. Garlock and D. Billington (eds.), *Festschrift Billington 2012: Essays in Honor of David P. Billington*, International Network for Structural Art, pp. 26-36, 2012.

[11] P. Gauvreau, "Sustainable education for bridge engineers," *Journal of Traffic and Transportation Engineering* (English Edition), vol. 5 no. 6, pp. 510-519, 2018.

[12] P. Gauvreau, "Design education for the 21st century," in E. Hines, S. Buonopane, M. Garlock and D. Billington (eds.), *Festschrift Billington 2012: Essays in Honor of David P. Billington*, International Network for Structural Art, pp. 92-121, 2012.

[13] T. Fischer and C. M. Herr (eds.), *Design cybernetics: Navigating the new*, Springer Nature, 2019.

[14] C. M. Herr, "Creativity Between Architecture and Structural Engineering: Educating Collaborative Practitioners of the Future," in *Proceedings of The VI International Conference on Engineering Education without Borders*, Madrid, pp. 30-38, 2018.

[15] S. MacNamara, "Pedestrian Bridges: Structural Design by Masters of Architecture Students", 2011, paper presented at *ASEE Annual Conference & Exposition*, Vancouver, 2011. Available from: https://peer.asee.org/18349 <accessed March 15 2019>

[16] C. M. Herr, "Teaching Architects to Design Pedestrian Bridges," *Proceedings of Footbridge 2017 Berlin – Tell A Story*, 6-8.9.2017, Technische Universität Berlin.

[17] M. Llunji, *Towards a New Engineering*, MSPROJECT, 2018.

[18] N. Hu and G.L. Dai, "From separate to combine—the ever-changing borderline between architectural art and structural art," in X. Cruz (ed.), *Structures and Architecture*, Taylor & Francis, pp. 551-552, 2010.

Proceedings of the IASS Annual Symposium 2019 – Structural Membranes 2019
Form and Force
7 – 10 October 2019, Barcelona, Spain
C. Lázaro, K.-U. Bletzinger, E. Oñate (eds.)

Travel and the Structural Engineer

Powell DRAPER*, Edward M. SEGAL[a]

* schlaich bergermann partner
555 8th Avenue, New York, NY, USA 10018
p.draper@sbp.de

[a] Hofstra University

Abstract

Travel facilitates the exchange of ideas and can lead to creative new designs for the built environment. By traveling, structural engineers can visit notable structures, designers, studios, laboratories, and cultures, as well as engage in dialogues. These opportunities, while celebrated in other creative disciplines such as architecture, have perhaps not been as appreciated in structural engineering. The goal of this paper is to demonstrate the influence that travel has had on specific structural engineers and the practice of structural engineering more generally. Documented examples of prominent engineers traveling and having it affect their work include Othmar Ammann, Peter Rice, Jörg Schlaich, and David Billington. This study ultimately seeks to understand the range of ways that travel impacts the profession.

Keywords: travel, structural design, creativity, historic analysis

1. Introduction

Travel provides opportunities to learn about the built environment firsthand. Architects have frequently traveled as a way to expand their perspective on design and building. Le Corbusier [1] is perhaps one of the best known of many prominent architects that have documented their own trips and its impact on their work. But architectural travel is not limited to just a few individuals. Schools of architecture frequently include travel or study abroad programs in their curriculum. Trips consist of not only observation, but also documentation in a range of forms: drawings, paintings, photographs, videos, etc. The observation and documentation skills that they develop in their formal education can then be utilized during future travel. Post-graduation there are a number of architecture travel fellowships available from professional organizations such as the American Institute for Architects [2, 3] and the Royal Institute of British Architects [4]. There are also many other fellowships including the Wheelwright Prize [5], the H. Allen Brooks Travelling Fellowship [6], and a series of awards provided by the SOM Foundation [7]. Recently, scholarly research has examined the impact of travel on the practice of architecture [8, 9, 10].

In contrast, the effect of travel on structural engineers has not been explored as deeply. The authors have previously begun investigating how opportunities for travel (academic travel, volunteer projects, and travel fellowships) can affect structural engineering education [11]. The goal of this study is to demonstrate how travel has impacted the structural engineering profession by examining the influence of travel on the four prominent engineers: Othmar Ammann, Peter Rice, Jörg Schlaich, and David Billington.

Copyright © 2019 by Powell Draper and Edward M. Segal
Published by the International Association for Shell and Spatial Structures (IASS) with permission.

2. Travel by prominent engineers

In structural engineering, like architecture, prominent individuals have traveled to inform their thoughts on the built environment (although it perhaps has not been as celebrated or as encouraged). This paper focuses on the travel of four individual engineers.

2.1. Othmar Ammann

Othmar Ammann, educated in the deep tradition of Swiss structural design, decided as a young individual to travel to the United States to study American bridge building and to establish himself there to find opportunities. He was no doubt influenced by his professors at the Swiss Federal Institute of Technology (locally known as the Eidgenössische Technische Hochschule, or ETH), particularly Wilhelm Ritter, who spent time studying bridges in America, lectured on them back at the ETH, and published his findings as *Der Brückenbau in den Vereinigten Staaten Amerikas*, and Karl Emil Hilgard, who had worked for a while as a bridge engineer in America [12]. Ammann not only traveled to the U.S., but moved there and established himself in bridge design positions of increasing responsibility, until ultimately, he became the great bridge designer we know today. Ammann's travel to the U.S. and immersion in the engineering and political culture there ultimately enabled him to design transformative bridges at a range of scales [13]. These include the colossal and celebrated George Washington Bridge (Figure 1) to the subtle and less well known Wards Island Bridge (Figure 2)



Figure 1: The George Washington Bridge (New York, USA)



Figure 2: The Wards Island Bridge (New York, USA) [credit: Jag9889, licensed under CC BY-SA 4.0, https://creativecommons.org/licenses/by-sa/4.0/deed.en]

2.2. Peter Rice

Peter Rice was, like Ammann, an engineer who created innovative and important works of structural engineering primarily outside of his home country (in Rice's case, Ireland). These works include the Sydney Opera House (Figure 3) with Jørn Utzon and Arup and the Pompidou Centre (Figure 4) with Renzo Piano and Richard Rogers. Rice travelled extensively for these and other projects. His travels often influenced his work, in ways both subtle and overt. An example was his travelling to Japan while he was working on the Pompidou Centre:

> Shortly after we had won the competition I made a trip to Japan to deliver a paper at a conference on tension structures. As part of that conference, trips were organized to Osaka to see the surviving structures of the 1970 World Fair. One of these structures was a giant space frame designed by Kenzo Tange and Professor Tsuboi, the eminent Japanese engineer. There I saw large cast-steel nodes… An idea was born. [14]

Thus Rice's travel to Japan, documenting the cast steel nodes there led to his celebrated "Gerberettes" in the Pompidou Centre. This open-minded approach to design, especially by traveling to and working in other countries and cultures, seems to have informed Rice's career.



Figure 3: The Sydney Opera House (Sydney, Australia) [credit: Enoch Lau, licensed under CC BY-SA 3.0, https://creativecommons.org/licenses/by-sa/3.0/deed.en]



Figure 4: The Pompidou Centre (Paris, France)

2.3. Jörg Schlaich

Jörg Schlaich, the eminent German engineer, has designed structures all over the world. In his Gold Medal address to the Institution of Structural Engineers, Schlaich told the story of his travels and the influence it had on the work of him, his family, and his colleagues:

> In 1976 the whole of my family followed the 'British Trail' in a VW van: Europe, Turkey, Persia, Afghanistan, Pakistan and all the way through India, to Calcutta, because we were doing in the true sense a 'Design for the developing world', the Second Hooghly Bridge, at that time the largest cable-stayed bridge in the world with a main span of 457m and 35m wide. It was designed towards a completely indigenous manufacture and erection. [15]

Schlaich goes on to explain how that trip to India and his and his colleagues' immersion in the local culture there influenced the design and construction of the bridge (Figure 5). This influence included the material the bridge was to be made of, since steel was produced locally, as well as the connections and means of construction (the bridge was to be riveted to take advantage of local labor traditions).

Schlaich expands this to also advocate for engineers to become more connected with the world and its needs. Travel is one way for engineers to do so.



Figure 5: The Second Hooghly Bridge (Kolkata, India) [credit: Abhijit Kar Gupta, licensed under CC BY 2.0, https://creativecommons.org/licenses/by/2.0/]

2.4. David Billington

David Billington was one of the foremost chroniclers of individual structural engineers. Beginning with his study of Robert Maillart, which Billington famously became aware of from his students of architecture, Professor Billington wrote the pioneering *The Tower and the Bridge*, which included the stories of a number of great structural engineers and their structures [16]. Billington thought of his work not as a static history, but as a living philosophy, the idea of "structural art," that should be expanded to continue learning about innovative, creative approaches to structural design. To do so, one should travel to see great structures and to document them. Billington's lectures were filled with photographs of him and his family, in front of beautiful structures. Unlike many professors of architecture, who prefer photographs of buildings devoid of any human occupation, Billington wanted his images of structures to include "scale factors," which also served to give a human face to the serious study of these works.

There are precedents for Billington's use of travel as a scholarly tool that he documented in the *Art of Structural Design: A Swiss Legacy* [17]. Billington described how Carl Culmann, prior to taking an appointment at the Federal Institute of Technology in Zürich (ETH Zürich) traveled for two years through Britain and the United States to study bridge and railway construction and published a report on his findings. Billington provided a more in-depth examination of Wilhem Ritter and his travel to the United States to see the Chicago's World's Fair and American bridges. While traveling, Ritter documented his work through writing and drawing. In addition to publishing a report on his trip Ritter also incorporated his experiences into his lectures.

In a similar manner, Professor Billington encouraged and sponsored many of his students (including the authors) to travel and document their travel [18, 19] as part of their development as structural engineers.

3. Conclusions

This paper describes how travel has influenced four prominent engineers, Othmar Ammann, Peter Rice, Jörg Schlaich, and David Billington. Ammann, influenced no doubt by some of his professors, traveled (moved, really) to the U.S. to study the bridges there and find opportunities to design them. Rice traveled extensively to other countries to learn from the works there and potentially influence his work in other countries. Schlaich traveled to create structures that responded to local cultures and their particular needs and wants. Billington utilized travel as a scholarly tool to understand the designs of others and to inspire others to do the same. All of them saw the benefits of travel for structural engineers, albeit in differing ways.

The four examples presented here show that travel can be a positive influence on the practice of structural engineering. All four of these great structural engineers believed in travel as a tool to better their practice, and that seems to be demonstrated by their work. We think the practice of structural engineering, would likewise benefit by structural engineers visiting structures in other places, considering them, documenting them, and sharing and discussing. This study is only a preliminary investigation, though. We believe that further study could show many more historic examples of travel influencing the work of structural engineers, and this might make the story fuller and more representative of the diversity within structural engineers and their work. We also hope that this study might encourage more practicing engineers and academics to share their own stories of travel and how it has influenced their work, as well.

Acknowledgements

This paper is dedicated to the memory of Professor David Billington and seeks to celebrate one of the pioneering aspects of his life and work, among many.

References

[1] Le Corbusier, *Journey to the East*. Žaknić, I., translator. Cambridge, MA: MIT Press, 2007.

[2] AIA New York, "Stewardson Keefe LeBrun Travel Grant," 2019, Available: https://www.aiany.org/architecture/competitions-grants/stewardson-keefe-lebrun-travel-grant/ [Accessed 18 June 2019].

[3] AIA, "The Delano and Aldrich/Emerson Fellowship," 2019, Available: http://new.aia.org/pages/18491-the-delano-and-aldrichemerson-fellowship [Accessed 18 June 2019].

[4] RIBA, "Scholarships and Bursaries," 2019, Available: https://www.architecture.com/education-cpd-and-careers/studying-architecture/advice-on-funding-your-architectural-studies/funding-opportunities-for-students-of-architecture [Accessed 18 June 2019].

[5] Harvard University Graduate School of Design, "Wheelwright Prize," Available: http://wheelwrightprize.org/ [Accessed 18 June 2019].

[6] Society of Architectural Historians, "H. Allen Brooks Travelling Fellowship," 2019, Available: https://www.sah.org/jobs-and-careers/sah-fellowships-and-grants/h-allen-brooks-travelling-fellowship [Accessed 18 June 2019].

[7] SOM Foundation, 2019, Available: https://somfoundation.som.com/ [Accessed 18 June 2019].

[8] Traganou, J., Mitrašinović, M., editors. *Travel, Space, Architecture*. Surrey, UK: Ashgate Publishing; 2009.

[9] Buckley, C., Rhee, P., editors. *Architects' Journeys: Building, Traveling, Thinking*. New York: GSAPP; 2011.

[10] Brillhart, J. *Voyage Le Corbusier: Drawing on the Road*. New York: W.W. Norton & Company; 2016.

[11] Segal, E.M., Draper, P. "Travel and the Education of the Structural Engineer," in *Proceedings of the International Conference on Structural Engineering Education without Borders*, Madrid, June 20-22, 2018.

[12] Petroski, Henry. *Engineers of Dreams: Great Bridge Builders and the Spanning of America*. New York: Vintage Books, 1995

[13] Rastorder, Darl. *Six Bridges: The Legacy of Othmar H. Ammann*. New Haven: Yale University Press.

[14] Rice, Peter. *An Engineer Imagines*. London: ellipsis, 1994, p. 29.

[15] Schlaich, Jörg. "Design for the developing world." *Structural Engineering: History and development*. Edited by R.J.W. Milne. London: E & FN Spon, 1997. pp. 91-107.

[16] Billington, David P. *The Tower and the Bridge*. Princeton: Princeton University Press/Basic Books, 1983.

[17] Billington, David P. *The Art of Structural Design: A Swiss Legacy*. Princeton: Princeton University Art Museum, 2003.

[18] Halsey, Sarah M. "Appendix 3," in *Félix Candela: Engineer, Builder, and Structural Artist*. M. E. M. Garlock and D. P. Billington, Princeton: Princeton University Art Museum, 2008. pp. 181-183.

[19] Segal, Edward M. "The Thin Concrete Shells of Jack Christiansen," Master of Science in Engineering Thesis, Princeton University, Princeton, 2008.

Proceedings of the IASS Annual Symposium 2019 - Structural Membranes 2019
Form and Force
7-10 October 2019, Barcelona, Spain
C. Lázaro, K.-U. Bletzinger, E. Oñate (eds.)

Bending-active structures with a variable cross-section boundary

Maria REDOUTEY*, Sean AHLQUIST[a], John SHAW[b], Evgueni FILIPOV*

* Department of Civil and Environmental Engineering, University of Michigan
2350 Hayward St., Ann Arbor, MI 48109
mariared@umich.edu, filipov@umich.edu

[a] Taubman College of Architecture and Urban Planning, University of Michigan
[b] Department of Aerospace Engineering, University of Michigan

Abstract

Bending-active textile hybrid structures are designed using form-finding to establish a state of equilibrium between a textile in tension and a boundary system in flexure [1]. We explore a new method for designing the boundary system, where rather than bundling rods closely together, we connect them using brackets to create a spatial beam. The bracket size and spacing changes along the beam in order to achieve the desired boundary stiffness. The brackets lock the rods into place as the beam is curved during assembly, leading to a system that can be more easily assembled and disassembled. We use finite element simulations to explore how the bracket spacing and the beam aspect ratio influence the overall stiffness of the bracketed beams, and use the results to propose a design methodology. This paper presents a new method for boundary design which can be integrated with computational tools to realistically model the boundary shape and behavior. This boundary design method will allow designers to accurately simulate the final design and identify potential construction issues ahead of time.

Keywords: textile-hybrid structures, bracketed beams, glass-fiber reinforced polymer

1 Introduction

Bending-active structures are curved structures whose geometry is formed by the elastic deformation of initially straight members [2]. Bending-active textile hybrid structures combine a textile in tension with a bending-active boundary system. Bending-active structures can improve the load-bearing capacity and assist with the deployment of origami structures [3], serve as interactive playscapes for children with autism [4], and create bio-mimetic architecture [5]. Conventional bending-active structures require a strong, stiff boundary system to withstand internal tensile loads from the stretched textile. The boundary system described in this paper focuses on providing redundancy and withstanding dynamic external loads. Typically, the shape of these boundary systems is designed using form-finding [6].

A previous method used to construct the bending-active boundary system bundled multiple glass fiber reinforced polymer (GFRP) rods closely together to create a stronger laminate beam [7]. Such a design for the bending-active boundary allowed its curvature to vary dramatically

Copyright © 2019 by M. Redoutey, S. Ahlquist, J. Shaw, E. Filipov
Published by the International Association for Shell and Spatial Structures (IASS) with permission.

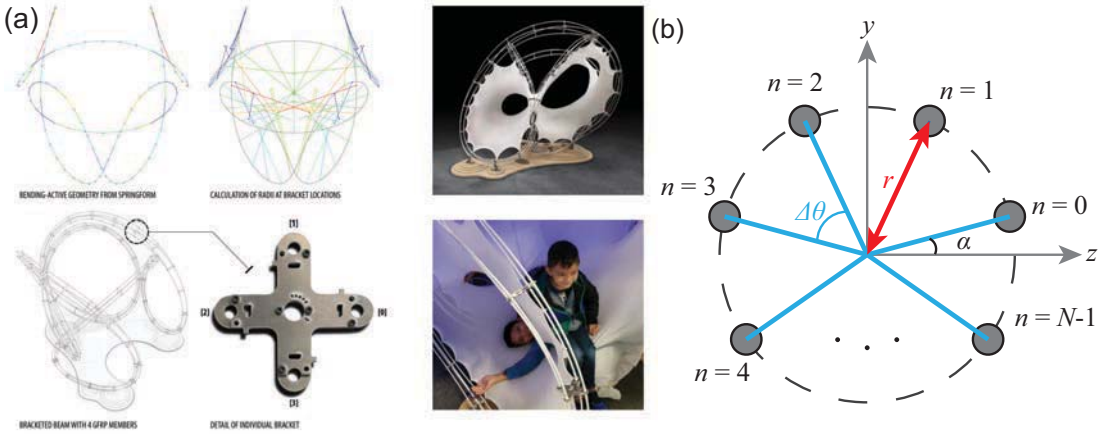


Figure 1: (a) The shape of a bending-active boundary, designed using springFORM, a form-finding software. The bending radius of the boundary can be extracted along the curve. The bracketed boundary system can be modeled using computational tools and physical prototypes. (b) Sample cross-section of a bracketed beam made of N equally spaced circular rods. The orientation angle, α, defines how the cross-section is oriented with respect to the applied moment.

by changing the number of bundled rods. While this technique provides greater stiffness than a single rod boundary, the structure is noticeably more flexible at points where the radius of curvature of the boundary is large. Thus, significant secondary bracing is needed such that the boundary system can deliver consistent stiffness at all points, regardless of the curvature. Additionally, it would be beneficial for these structures to be more easily transported, assembled, and disassembled.

In this paper, we introduce a new type of boundary system where GFRP rods are separated using bracket plates to create a *bracketed beam*. The bracket size and bracket spacing can be designed to provide adequate stiffness along the entire boundary curve. The inclusion of brackets also facilitates easy assembly. We first discuss the properties of the cross-section that determine the beam stiffness. Then, we investigate the relationship between the beam geometry, bracket spacing, and stiffness. The result of this paper is a design process that can be used to design an efficient bracketed boundary system.

2 Design Considerations

The design of bending-active structures must have sufficient strength and stiffness. These two considerations lead to a mechanical analysis that must both keep the maximum stress within allowable limits to avoid material damage or failure, and provide sufficient structural stiffness to avoid excessive deflections under load. The bending-active boundary considered here is mostly subjected to bending deformation, but may also involve some shear and twisting (which will be addressed in future work).

2.1 Allowable stress

According to Euler-Bernoulli beam theory, the maximum bending strain ϵ is related to the radius of curvature ρ by $\epsilon = c/\rho$, where c is the perpendicular distance from the neutral plane to the farthest material point on the cross-section of the beam. The stress σ is related to the strain by the elastic modulus E ($\sigma = E\epsilon$). Therefore, the maximum stress is $\sigma_{max} = E/\overline{\rho}_{min}$, where $\overline{\rho}(x) = \rho(x)/\mathrm{c}(x)$ is the dimensionless radius of curvature which varies along the boundary curve x. Keeping the stress within an allowable value σ_a, which can include a safety factor to yielding or ultimate failure, leads to the criterion

$$\overline{\rho}_{min}(x) < \frac{E}{\sigma_a}. \tag{1}$$

Note that for a fiber-reinforced composite rod (such as GFRP), σ_a will often be different in tension versus compression, so the more conservative value can be used. Knowing the desired shape of the bending-active boundary, and therefore the radius of curvature distribution $\rho(x)$, one can choose the size of the cross-section $\mathrm{c}(x)$ to satisfy Equation (1).

2.2 Bending Stiffness

The cross-section of the bracketed beam consists of N rods in an equally spaced circular arrangement, as shown in Figure 1(b). Since the layout always has at least one plane of symmetry, the product of inertia is zero ($I_{yz} = \int_A yzdA = 0$) and an uncoupled (symmetric) bending theory can be used. The moment (M) - curvature (κ) relation is then $M_z = EI_z\kappa_z$, where the axis of M_z and κ_z (here taken as the z-axis without loss of generality) corresponds to the neutral plane and $I_z = \int y^2 dA$ is the corresponding area moment of inertia of the cross-section. The bending moment of inertia for a solid circular rod of diameter d about its own centroid is $I_0 = \pi d^4/64$. Using the parallel axis theorem, the total moment of inertia is

$$I_z = \sum_{n=0}^{N-1}[I_0 + A_0 y_n^2] = NI_0 + A_0 r^2 \sum_{n=0}^{N-1} \sin^2(\alpha + n\Delta\theta), \tag{2}$$

where $A_0 = \pi d^2/4$ is the cross-section area of each rod, α is the orientation angle of the cross-section, r is the cross-section radius, and $\Delta\theta = 2\pi/N$ is the angular spacing of the rods.

For any number of rods greater than two ($N \geq 3$), the resulting I_z is independent of the orientation of the cross-section (α). The proof, which we have been unable to find elsewhere in the literature, is provided here. The summation in Equation (2) can be rewritten as

$$\sum_{n=0}^{N-1} \sin^2(\alpha + \frac{2\pi n}{N}) = \frac{1}{2}[N - \sum_{n=0}^{N-1} \cos(2\alpha + \frac{4\pi n}{N})]. \tag{3}$$

Using Euler's theorem that $\cos(\phi) = (e^{i\phi} + e^{-i\phi})/2$ with $i = \sqrt{-1}$, the sum on the right hand side becomes

$$\sum_{n=0}^{N-1} \cos(2\alpha + \frac{4\pi n}{N}) = \frac{1}{2}e^{2\alpha i} \sum_{n=0}^{N-1} (e^{4\pi i/N})^n + \frac{1}{2}e^{-2\alpha i} \sum_{n=0}^{N-1} (e^{-4\pi i/N})^n. \tag{4}$$

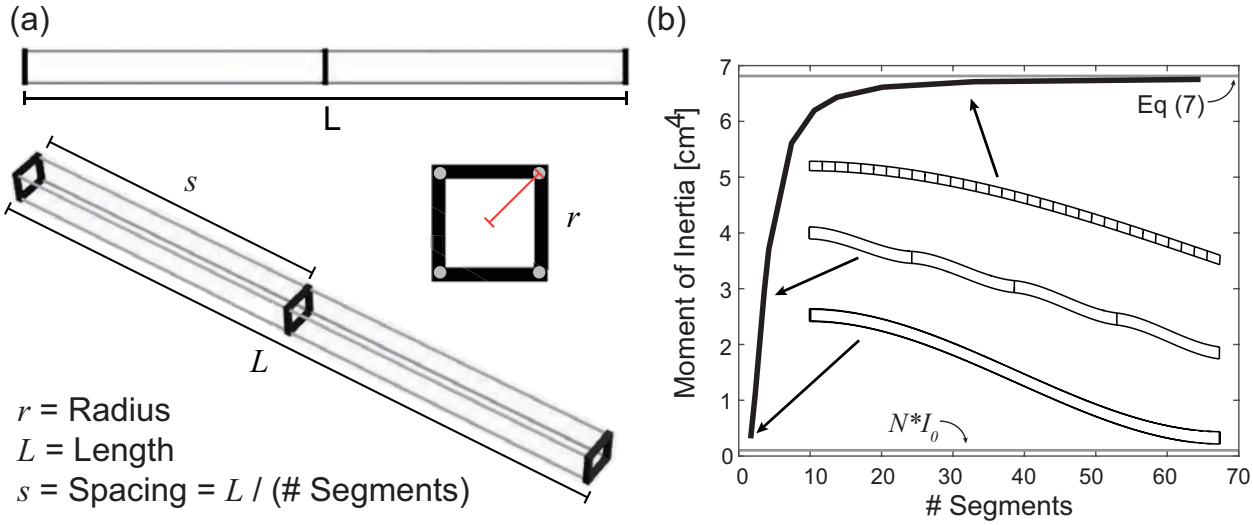


Figure 2: (a) Dimensions of a bracketed beam. (b) Adding brackets to a beam increases its stiffness. The stiffness of all real bracketed beams falls between two theoretical bounds, shown as gray lines.

Each sum on the right hand side of Equation (4) can be expressed as the geometric series $\sum_{n=0}^{N-1} a^n$, which has the known result

$$\sum_{n=0}^{N-1} a^n = \frac{1-a^n}{1-a}, \text{ if } a \neq 1. \tag{5}$$

Taking $a = e^{4\pi i/N}$ (and similarly for $a = e^{-4\pi i/N}$):

$$\sum_{n=0}^{N-1} (e^{4\pi i/N})^n = \frac{1-e^{4\pi i}}{1-e^{4\pi i/N}} = 0, \text{ if } N > 2. \tag{6}$$

Thus, the cosine term sums to zero in Equation (3), and the total area moment of inertia is

$$I = N[I_0 + \frac{1}{2} A_0 r^2] \tag{7}$$

with no dependence on α. Thus, the orientation of the cross-section does not need to be controlled during construction. For a required flexural stiffness EI, Equation (7) can be used to determine the cross-section size (using the radius r) for a given number and diameter of rods.

3 Beam Dimensions and Bracket Spacing

Finite Element (FE) analysis was used to investigate the relationship between the stiffness of a bracketed beam and its bracket spacing. Cantilever bracketed breams were modeled using the FE software Abaqus [8]. All analyses were displacement-controlled and linear. Various combinations of beam radii and length are included in the results presented. The results presented in this paper are for bracketed beams made of 4 GFRP rods ($\approx$ 0.8 cm (5/16") diameter). However, the same trends were also observed for beams made of 6 rods, and can reasonably be assumed for any number of rods.

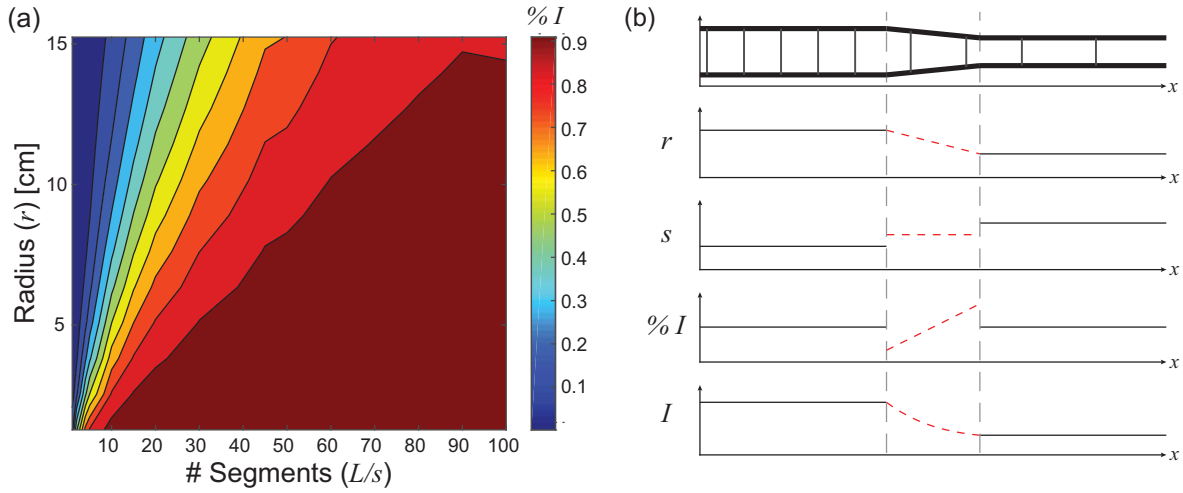


Figure 3: (a) The relationship between % maximum stiffness and bracket spacing is determined by the beam radius *(r)* and the number of segments *(L/s)*. A beam with a smaller radius requires less segments (larger spacing between brackets) to achieve a given stiffness level than a beam with a larger radius. (b) Relationship between beam radius, bracket spacing, and percent maximum I and actual I, shown along x for a region with a transitioning radius.

In this paper, bracketed beams are described by their length (L), cross-section radius (r), and bracket spacing (s). These parameters are illustrated in Figure 2 (a) and result in the dimensionless parameters of aspect ratio (r/L) and number of segments in the beam (L/s).

All models and calculations used material properties for Glass Fiber Reinforced Polymer (GFRP) rods. Axial tension, compression, and bending tests were completed to verify the mechanical properties of GFRP listed by the manufacturer (elastic modulus $E \approx 41$ GPa (6000 ksi), yield stress $\sigma_y \approx 830$ MPa (120 ksi), compressive strength ≈ 480 MPa (70 ksi)) [9]. In the finite element models, brackets were assumed to have a flexural stiffness an order of magnitude higher than GFRP ($E \approx 410$ GPa).

In general, adding brackets increases the stiffness of the boundary system. With few brackets, a cantilever beam exhibits double curvature, where individual rods in the beam essentially behave independently between the brackets. With more brackets, the deflected shape approaches single curvature as the rods begin acting together. Adding brackets creates a similar effect to an outrigger and belt truss system, used to prevent lateral displacements in tall buildings [10] [11].

The true stiffness of a bracketed beam falls between two theoretical bounds. The lower bound is the stiffness of a system of rods, not connected by any brackets, each providing stiffness independently ($N * I_0$). The upper bound is described by Equation (7) from Section 2.2, where all rods act together as a beam. The lower bound is determined by the rod diameter, while the upper bound depends on both the rod diameter and beam radius. These bounds are shown in Figure 2(b) for a sample beam with a radius of 2.5 cm (1"). When designing a boundary system, we need to decide where between these bounds the stiffness should fall. The motivation of this work is to create a boundary with sufficient stiffness (near the upper bound) while also

maintaining an aesthetically pleasing design (avoiding a solid beam of brackets). Therefore, we choose a "percent maximum stiffness" (%I), which indicates the fraction of the upper stiffness bound that the structure will be designed to achieve.

The relationship between bracket spacing (s) and stiffness depends on the radius (r) of the beam. Figure 3(a) shows the results of the Finite Element models, and can be used as a design chart to determine the appropriate bracket spacing for the desired radius and percent stiffness. Beams with large radii (deep beams) require a greater number of segments than beams with small radii (shallow beams) to achieve the same percent maximum stiffness (%I). In other words, shallow beams must have larger spacing between brackets in order to approach the high stiffness of a beam where the rods act together with stiffness described by Equation (7).

The radius of curvature $\rho(x)$ changes continuously along the boundary curve of a real bending-active structure. Using the relationships discussed in Section 2, we find that a continuous $\rho(x)$ leads to a continuous $r(x)$ as well. For practicality, the designer must discretize the boundary curve into sections where a constant r can be assumed. After the curve is divided into i sections, each with length L_i and beam radius r_i, Figure 3(a) can be used to determine a bracket spacing s_i for each section.

Figure 3(b) shows the relationships between r, s, $\%I$, and I in a transition zone between discretized regions, each with constant radius. Between regions, r will transition linearly, and an average s is used. At the start of the transition zone, this average spacing will be larger than what is needed to maintain the selected %I. As the radius approaches that of the second region, the spacing will become smaller than what is needed. This change in radius results in a $\%I$ that is at first smaller than the selected value, and then larger. The actual moment of inertia I is dependent on r^2, and will change smoothly from one region to the next.

4 Design Process

The design process begins by treating the boundary as a continuous curve with distributed parameters. The first step is to extract the radius of curvature $\rho(x)$ along the boundary curve, as shown in Figure 1. Then, using Equation (1), find the required cross-section height along the boundary curve, $2c(x)$. Next, determine the corresponding moment of inertia $I(x)$ using the equation $I(x) = \pi c(x)^4/64$. This $I(x)$ value is representative of a hypothetical single-rod system that will provide the required stiffness for the radius of curvature $\rho(x)$. At this point, we can choose to compensate for the decrease in stiffness that results from selecting a $\%I$. Dividing $I(x)$ by $\%I$ will result in a larger $r(x)$, providing extra stiffness; the stiffness will then be decreased when the $\%I$ is applied when using Figure 3(a). This is one method of integrating a second safety factor into the design and is left to the discretion of the designer. Once $I(x)$ is known, use Equation (7) to find the cross-section radius $r(x)$ along the curve.

The next step is to discretize the curve into regions that will have the same beam radius. Now, the curve is divided into i regions, each with length L_i and beam radius r_i. Use Figure 3(a) along with the selected %I to determine the spacing s_i for each region. The final step is a design check to ensure that the bending stress in each rod is less than the allowable stress σ_a.

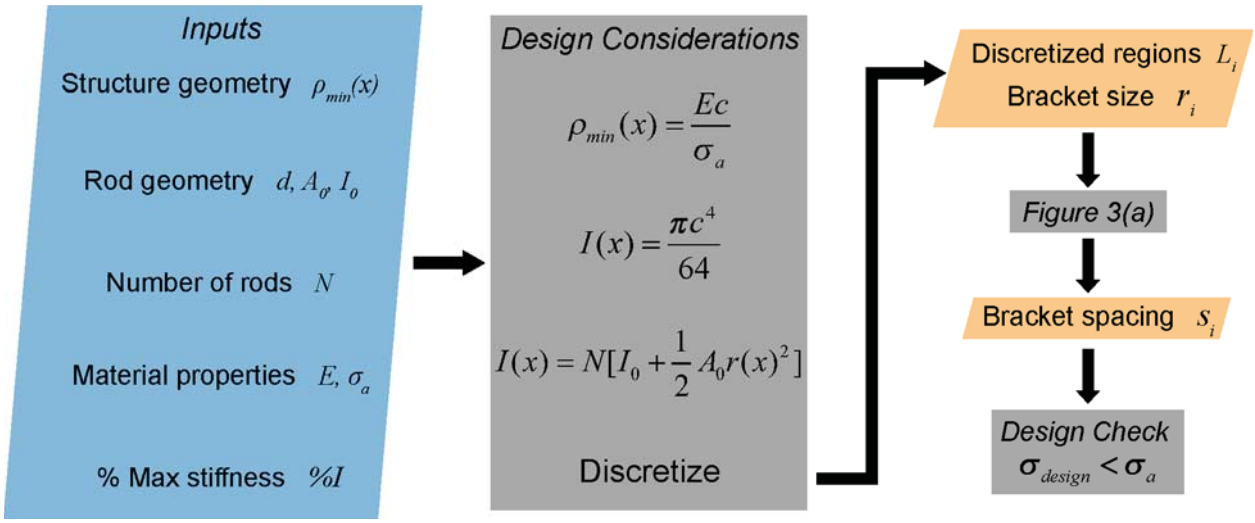


Figure 4: Design process for a bracketed boundary system.

The flowchart shown in Figure 4 outlines the process used to design a bracketed boundary system with variable cross-section size and bracket spacing.

5 Conclusion and Future Work

A new type of boundary system for bending-active textile hybrid structures was introduced where Glass Fiber Reinforced Polymer rods are connected in a bracketed beam. By adjusting the size and spacing of the brackets along the boundary, we can ensure that the desired stiffness is achieved at every point. The bracket size is determined by the radius of curvature of the boundary. When the GFRP rods are bent to their minimum bending radius, they are at their maximum capacity, determined by an allowable stress. We show that when three or more equally spaced rods are used for the bracketed beam, the orientation of the cross-section does not affect the bending stiffness of the beam.

Through the use of finite element models, the relationships between bracket size, bracket spacing, and stiffness were explored and used to create a design chart for bracketed beams. The bracketed beams exhibit lower stiffness than the value predicted by the geometry of the cross-section using the parallel axis theorem. As more brackets are added, the stiffness approaches that idealized limit. Overall, the deeper a beam is, the more brackets are needed to achieve the same fraction of the idealized maximum stiffness. All together, we present a new methodology for the design of a bracketed boundary system.

This new boundary system can be used to construct bending-active textile-hybrid structures with enough stiffness to withstand external loads just as conventional structures do. Bracketed bending-active structures with sufficient strength and stiffness have potential to create efficient structures that are modular, transportable, and deployable.

This work only considered the bending of bracketed beams, and future work will include shear

and twisting deformations as well. Additionally, this paper focused on the mechanics of straight bracketed beams, but the curved geometry of bending-active structures is expected to have a significant influence on the global behavior. Future work includes mechanical testing of straight and curved bracketed beams and applying the design methodology to a physical prototype.

Acknowledgements

This work began as part of the Master of Science in Architecture program during the Fall 2018 semester.

The authors acknowledge support from the University of Michigan MCubed Program.

References

[1] S. Ahlquist, J. Lienhard, J. Knippers, and A. Menges, "Physical and numerical prototyping for integrated bending and form-active textile hybrid structures," in *Rethinking Prototyping: Proceeding of the Design Modelling Symposium, Berlin*, pp. 1–14, 2013.

[2] J. Lienhard and J. Knippers, "Considerations on the scaling of bending-active structures," *International Journal of Space Structures*, vol. 28, no. 3-4, pp. 137–148, 2013.

[3] S. Brancart, L. De Laet, and N. De Temmerman, "Deployable textile hybrid structures: design and modelling of kinetic membrane-restrained bending-active structures," *Procedia Engineering*, vol. 155, pp. 195–204, 2016.

[4] S. Ahlquist, "Sensory material architectures: Concepts and methodologies for spatial tectonics and tactile responsivity in knitted textile hybrid structures," *International Journal of Architectural Computing*, vol. 14, no. 1, pp. 63–82, 2016.

[5] J. Lienhard, S. Schleicher, S. Poppinga, T. Masselter, M. Milwich, T. Speck, and J. Knippers, "Flectofin: a hingeless flapping mechanism inspired by nature," *Bioinspiration & biomimetics*, vol. 6, no. 4, p. 045001, 2011.

[6] J. Lienhard and J. Knippers, "Bending-active textile hybrids," *Journal of the International Association for Shell and Spatial Structures*, vol. 56, no. 1, pp. 37–48, 2015.

[7] S. Ahlquist and J. Lienhard, "Extending geometric and structural capacities for textile hybrid structures with laminated gfrp beams and cnc knitting," in *Proceedings of IASS Annual Symposia*, vol. 2016, pp. 1–10, International Association for Shell and Spatial Structures (IASS), 2016.

[8] ABAQUS, "Abaqus 2018 version documentation," 2018.

[9] "Technical material specifications," *Goodwinds Composites. https://goodwinds.com/technical-material-specifications.*

[10] P. S. Kian, "The use of outrigger and belt truss system for high-rise concrete buildings," *Civil Engineering Dimension*, vol. 3, no. 1, pp. 36–41, 2004.

[11] A. Rutenberg and D. Tal, "Lateral load response of belted tall building structures," *Engineering Structures*, vol. 9, no. 1, pp. 53–67, 1987.

Proceedings of the IASS Annual Symposium 2019 – Structural Membranes 2019
Form and Force
7 – 10 October 2019, Barcelona, Spain
C. Lázaro, K.-U. Bletzinger, E. Oñate (eds.)

Longterm Behaviour and Geometrical Precision of Graded CNC Knitted Bending Active Textile Hybrids Under Real World Conditions

Martin TAMKE*, Mette RAMSGAARD THOMSEN*, Yuliya SINKE*, Sebastian GATZ*, Riccardo LA MAGNA[a], Julian LIENHARD[a], Mark HAZZARD[b]

*CITA / KADK, Copenhagen, Denmark, martin.tamke@kadk.dk
a str.ucture GmbH, Stuttgart / Germany
b DSM, Geleen / Netherlands

Abstract

CNC knitted membranes provide a promising alternative to the traditionally woven materials in textile architectures, as they allow for bespoke material performance, sustainable and efficient production, and integration of functionality in the material itself. However there is a lack of knowledge in terms of the geometrical precision, which can be achieved with the material and its long term behaviour under stress and outdoor conditions. We use the installation Isoropia from the 2018 Venice Biennale, to evaluate the precision and behaviour of a custom made knit structure over a period of 8 months. Our investigation takes into account the multiscalar relations within knitted structures. In order to do so we develop a 3D scan based method to establish ground truth and determine the precision of bending active textile hybrids and link this with the investigations on fibre level. The analysis of the structure and material behaviour confirms the material model for the CNC knit and the structural capacity and longevity of CNC knit with Dyneema® high performance yarns. We furthermore characterise the mechanical properties of the material when used on architectural scale and make suggestions for future projects with knitted membranes.

Keywords: Membrane structures, CNC knit, Computational Knit, Simulation, Longterm Behavior, Monitoring of structures, 3d Scanning, Behaviour of Fibres

1. Introduction

CNC Knit on architectural scale is met with increasing interest as it allows for digitalisation of textile design and manufacturing processes. This is performed through direct interfacing of fabrication with the design and simulation tools that allow for customisation of behaviour and geometrical properties on all scales from fibre, yarn, and structure. [1,2,3]. The introduction of high performance yarns in CNC knit extends the spectrum of application of CNC knit into structures with higher forces [4]. In comparison to CNC knitted structures, which use lower modulus fibres [4], the use of hardly elongating fibres, such as Dyneema®, should provide a better control of the textile geometry as they inhibit stretch on the yarn level and minimise possible deformation to loop level only. This increase in precision makes mass customisation of shapes and membrane properties possible, opening up avenues for design and production of complex textile spaces that were previously unavailable [5]. As knit extends under load - is stretchable, this behaviour is strategically used in order to create 3d shapes on macro scale out of 2d knit.

As the use of CNC knit on architectural scale is still in its infancy, there is a lack of knowledge to which extent design specified geometries are actually achieved. As most CNC knit structures are indoor prototypes there is also a lack of knowledge regarding the long term behaviour of CNC knit in an external environment. Here, an investigation is performed to understand the change in geometry of the knit with exposure to outdoor conditions and it's the effect on the intrinsic material performance.

Copyright © 2019 by Martin TAMKE, Mette RAMSGAARD THOMSEN, Yuliya SINKE, Sebastian GATZ, Riccardo LA MAGNA, Julian LIENHARD, Mark HAZZARD
Published by the International Association for Shell and Spatial Structures (IASS) with permission.

2. Isoropia - investigating long term behaviour of an architectural CNC knit

This paper uses the large scale CNC knitted installation Isoropia at the 2018 Venice Biennale to investigate the precision of the build structure and its longterm behaviour in outdoor conditions. Isoropia is a Form active hybrid structure, in which bend GFRP rods are constrained by fabric patches. The installation morphs between three distinct structural systems from an indoor vault-like system to an outdoor bowlike system (Fig.1). In order to allow for this transformation all 41 textile patches are fully customised. The membrane is a twodimensional knit, the final 3d shape and Structural equilibrium is achieved through stretch in the tension points ofthe membrane (Noses). The knit is graded in order to provide for more stretch in the material around the noses, which results in larger height in the bow geometry, increasing the structural performance.

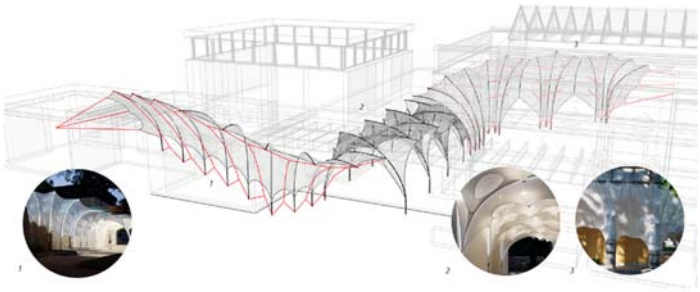


Fig.1 : Isoropia with the three distinct structural systems in front - Bows – Vault – Fans

A multiscalar approach in design and development was key to Isoropia. We use a set of digital models for design, simulation and specification of all parts including the CNC knit. The models are coupled in a digital chain [6]. Extensive prototyping from patch to 1:1 scale allowed for rapid development and in-process verification in only 4.5 months duration from commissioning of the project to assembly on site. The design and fabrication of all elements in Isoropia is based on a precise 3d model derived from a 3d laserscan of the site. Before setup the textile patches and rods were controlled for correct dimensions. During installation the geometry, and in particular, the height of the bend beams, were checked against that from the simulated model. The final tensioning of the installation focused however on an even prestress of the membranes and perceived overall appearance.

Scope of investigation

In comparison to state of the art membrane architectures, Isoropia is small scale, characterised by many patches of textiles (max 1,8x9m) which have a high degree of detailing and bespoke material properties. The intended overall shape can therefore only be achieved, when the geometries of the produced patches and the material behaviour match the specification from the underlying geometrical and material models. Our investigation will therefore focus on initial geometrical precision and the detection of increasing deviations across scales and through the time of the installation

An investigation of the mechanical forces which actually occurred in the structure through prestress and external forces would have been of great interest in order to verify the simulation of dynamic effects and the stretch of the fabric, but were not in scope of this project at the Biennale with 150.000 visitors.

Measuring longterm effects on textile architecture

The investigation on longterm effects in current membrane architecture is undertaken on element and material level according to the ruling standards. However there exists no related standards yet for building materials with large extension such as CNC knit [7]. Post-ante investigations on build membrane structures are undertaken in order verify their simulated behaviour under wind loads against the built [8,9,10] using photogrammetric methods [11]. 3D scanning is commonly used for control of geometry in the building sector [12]. However, 3D scanning of architectural structures from CNC Knit

has so far been limited [13]. A special challenge in this area is still the mapping of an unstructured point cloud of millions of points to a reference geometry with relatively few reference points, typically the vertices of a mesh. A related question of dispute are methods to qualify changes in a building scale structure over time based on point clouds alone, as these hardly qualify as ground truth [14].

From a material perspective, mechanical characterisation can be carried out at several length scales, starting from the knit itself, the yarn, and finally the filament. As the aim of this investigation was to focus on the intrinsic material response, the filament level was selected for mechanical investigation. This avoids complications with yarn testing, which can be dependent on twist and equal loading of filaments, and knits, which can be dependent on edge conditions as well geometrical change following loading in the application. Testing of Dyneema®, which has an extremely high tenacity and low coefficient of friction, can make testing difficult. This work will highlight the effects from direct application in all weather conditions experienced by Isoropia.

Long term behaviour of Isoropia across scales

Our investigation takes place on the scale of the overall structure, the individual textile element and the fibre level. The datasets for the first two scales are obtained from the simulation models and two 3D scanning sessions, executed with a FARO Focus Laserscanner 3 weeks after installation (April 2019) and 7 months after installation. This date is after the summer period and the structure went through the strongest period of UV exposure in Venice. The data for the fibre analysis is obtained at the labs of DSM on two identical patches (one used in the structure and one, which was an untouched spare).

Macro Level

The aim of the investigation on macro level is to establish knowledge on how precise the structure was built in comparison to the digital model and building on these insights, where and how much it deformed afterwards. As the shape of the membrane is determined by the GFRP beams and tips of the membranes (Noses) we use the latter two as reference geometry to track on macro scale.

On beam level we analyse the beams from the design model with the beams extracted from the pointcloud scan. This analysis shows that a deviation occurs at the tips of the beams with one support only. Characteristic for the deviation of the beams in the front, a shift occurs in the plane of the patches (up to 136cm, 27%) and that the beams bend less than intended in the back (upwards deformation up to 120 cm, 28%).

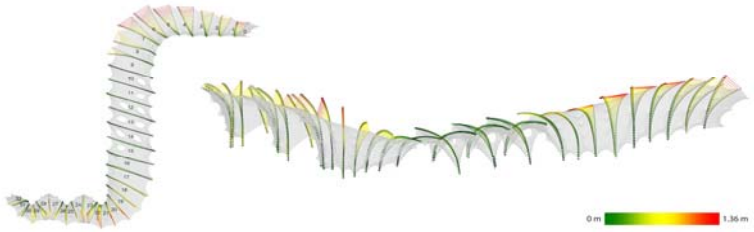


Fig. 4: Beam deviation between ground truth and April 2018 point cloud.(Top l, perspective view R)

Additionally, we compare the protrusion of the noses between K2 and 3D scan considering the shift of their absolute positions (Fig. 5) The analysis shows shorter noses around the columns in the back, shorter noses in the center area of the front part of the structure and longer noses in the areas where the front and the back part of the structure transitions into the middle part of the structure.

We conclude that the knitted material is stiffer than assumed in the simulations. The lack of extension in the knit prevents the rods on the back from spreading to a sufficient degree at their tips and the noses to protrude sufficiently for the cable net to pull the GFRP rods into shape.



Fig. 5. Deviation in the absolute protrusion of the noses between ground truth and April 2018 3D scan. Yellow: noses, which are longer than the simulated (max +20cm). Green: areas with -5 to 5 cm deviation. Red: noses, which are shorter than simulated with a deviation of (max -40)

Longterm deformation from April and October

An visual comparison of the scans indicates that the internal structure shows little to no deformation over the exhibition period while the free edges of the outer structure moved slightly out of their original position (Fig. 6).

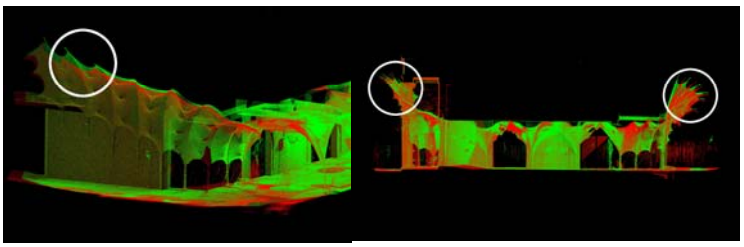


Fig. 6. Combined point cloud scans May 2018 (red) and October 2018 (green)

In order to analysis the quantitative change over time, we determine the deviation of the mesh vertices of the ground truth towards the two point clouds and calculate thereafter the absolute change of these two distances. The May deviation is between 0 and 1.10 cm different to the intended design, the October deviation 0 to 1.25 cm. Using this data we calculated the absolute change in position between May and October (Fig. 7): While the inner part and most of the front and the back part of the structure stayed in position (green) we find deviations in the tips and the front end of the structure of up to 40 cm (red).

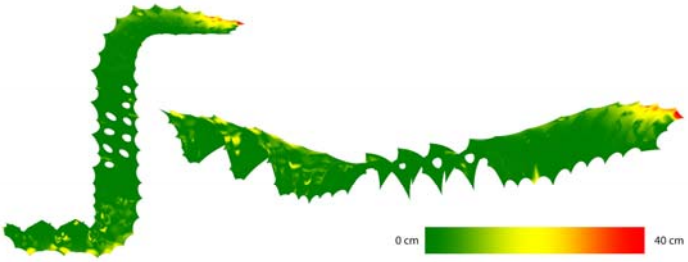


Fig. 7: Absolute change of the membrane between May and October

Meso scale

During the installation of the form-active membrane structure Isoropia a deformation of the membrane shape and knit structure was expected and observed in the noses – the areas of highest stress per patch. It is however unclear whether the process of knit deformation continued after installation.

In order to investigate meso-scale deformations over time we analyse patch 7, which is characteristic for the Isoropia system and less affected by the large deformations macro scale, which take place due to the free edges in the structure.

Method

As a point cloud consist of unstructured and inhomogeneously distributed points we develop a method for comparison of ground truth and built, which does not rely on the point cloud itself (Fig. 8).

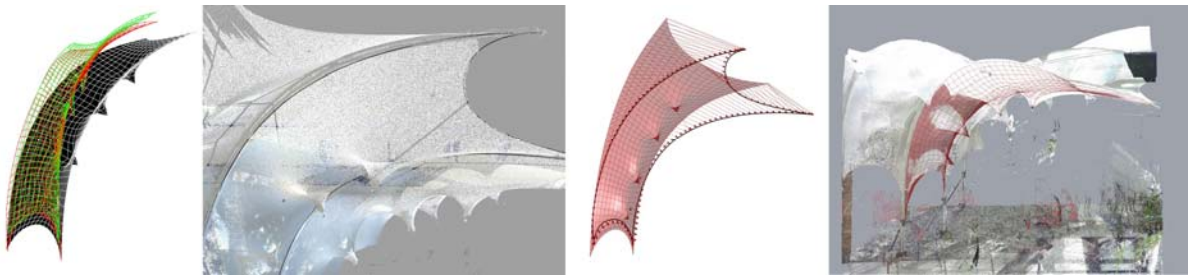


Fig. 8: a) We automatically create meshes with same topology from the scans (red: April, green: October) and ground truth (black). b) Identify patch edges (black curve) and points of rope attachment (grey spheres). c) Displacement vectors for physics simulation. d) the relaxed mesh from the original design mesh follows the shape of the scanend patch shape, but keeps the original topology

The analysis shows that the patch deformed between May and October 2018 in areas up to 10cm - (Fig. 10). The measurements show that the rope attachment points did hardly move while most of the deformation happened in the right side of the patch and bottom part of the textile. As the rope of the cablenet is made from 6mm Dyneema® we expect no elongation in the ropes between the noses. Possible reasons for the observed shift are therefore a further elongation in the textile or the slippage of the cable net.

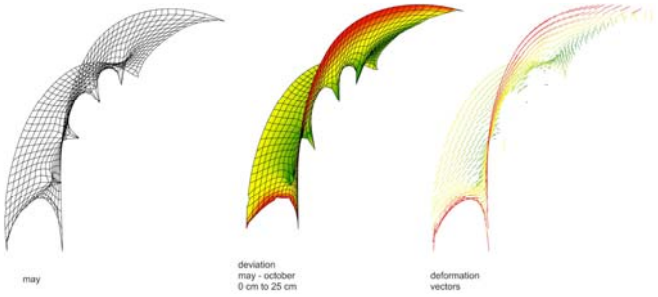


Fig. 10: Deformation of patch between May and October

Our scans show, that the whole patch slid upwards on the rods. This might have happened, as the tension cables are solely fixed by Clamcleat® Line-Loks®, which work by friction only. When these give in, the cablenet is shifting, the tension and therefore the shape of the rods and membrane changes in the observed way. We conclude that the shift in cablelength is the probable reason for the deformation and that the process of knit deformation most probably stopped after the initial resettling during the tensioning of the membrane.

Micro Scale - Fibre level

Visual examination, optical microscopy, and mechanical tests at filament level were performed on the two identical knit samples to see the effect of longterm use. Images of the knit structures can be seen in Fig.11 with the area extracted through hand cutting with Robuso proton® shears.

Following longterm use in Isoporia in the external environment the structure changes colour to an increasingly off-white color. Testing at the filament level was selected to compare the intrinsic difference in material response, rather than incorporate effects that can be observed due to the knit geometry and yarn structure. A yarn was first extracted by hand from the cut patch, followed by isolation of an individual filament. Tensile tests were performed on Textechno's Favimat single filament tester which has exchangeable grips, vibroscopic capability to determine linear density, a load cell (1200 cN) and a moving cross head.

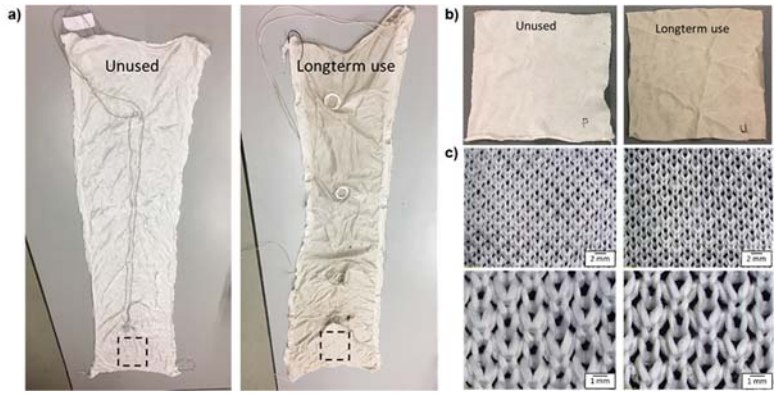


Fig. 11: a) The unused knit and the knit after longterm use in Isoropia. Dashed lines indicate area of sample. b) sample cut for microscopy and mechanical testing. c) Optical microscopy of knit structures

Results

Optical microscopy of the knit structures shows that following use all yarns and filaments appear to be intact (Fig.11c). An increasing amount of dirt and dust can be observed following long term use which will be a contributing factor to the change in color, whilst the knit geometry has been altered through longterm loading of the membrane. Each patch of the material was weighed which showed that the unused and longterm use knit had areal densities of 0.239 kg/m2 and 0.232 kg/m2 respectively. The lowest AD following use could be an indicator of the change in geometry, however this is also within the range of error of the measurement method.

The filament test from the unused knit shows the performance expected of a virgin. This suggests that no damage has been induced by the knitting process, and the high tenacity yarns of Dyneema® are damage resistant in the process (*Fig.12*). The slope of the stress strain curve, and hence the modulus, varies through the test due to the different phenomena occurring. The specific strength of the material has reduced by an average of 45%, whilst stiffness is initially maintained, followed by a reduction after approximately 0.5% elongational strain (*Fig.12*).

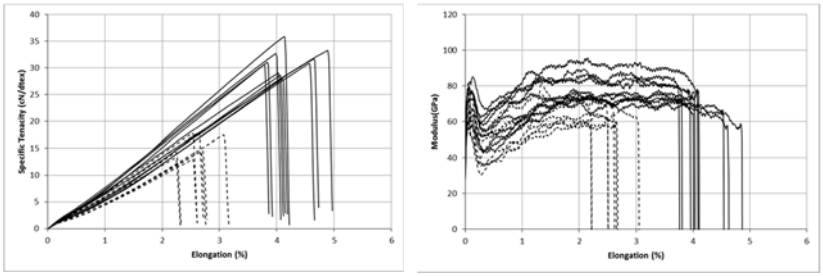


Fig. 12: Specific strength of Dyneema® filaments and modulus from prototype knit and following longterm use in Isoporia.

The drop in mechanical performance is thought to be dominated by UV degradation of the material, which is common for uncoated polymeric fibers [16]. For this application location, Italy receives on average 150 kLy/yr, which for an 8 month exposure of Isoporia, translates to an exposure of approximately 100kLy/yr. This is locally dependent on the weather and on the degree of shade so can only be used as an approximation. Accelerated aging in UV chambers with a Xenon Arc tester with an exposure of 35 W/m^2 for 1562.5 hours provides a comparable set of parameters for controlled accelerated UV testing [16]. For uncoated yarns of a similar size (where larger yarns are expected to have improved performance), this amount of exposure can result in approximately 50% reduction in strength [17]. The mechanisms behind degradation are dependent on the type of polymeric fiber, with the rate of degradation dependent on degree of exposure, wavelength, moisture, and temperature.

Dyneema® fibers have been shown to have lower rates of degradation than other uncoated polymeric fibers whilst it is also independent of moisture due to the low polarity of ultra high molecular weight polyethylene [18]. The dominating mechanism for loss in tenacity from UV exposure has been demonstrated to be chain scission in the presence of oxygen, which may contribute to some of the yellowing of the fiber which can be observed visually.

Overall Evaluation

The collected data allows an assessment of Isoropia in terms of precision and long term behaviour. We find that large deviations between the designed and built structure can only be observed in the tips of the little constrained winglike parts (absolute 136 cm, 28%), while the overall deviation of the rods is 8% on average (absolute 36 cm). The Eurocode EN 1090-2 Functional erection tolerances in buildings, describes the allowed Class1 deviation for steel beams in buildings with +-1cm. Isoropia is definitely off by these standards. The reasons for the deviation might be rooted in the lack of monitoring of the built structure where tensioned membranes and overall appearance where finally the most important parameters during construction and in the fact, that the knitted membrane had finally a lower stiffness than anticipated in the design and simulation.

In terms of the longterm behaviour we observe little geometrical change on meso and macro scale. A larger change in geometry is only observed in the tips of the wings of the structure. On a meso scale we observe a smaller change, which is most probably caused by the slippage of the cable net rather than a continuing elongation of the CNC knit structure. This observation is underpinned by the investigation on the fibre level, where no mechanical damage or stretch is detected. The change in structural shape is therefore thought to be largely driven by reorientation of the knit structure rather than the intrinsic material response. The creep from a material perspective is thought to be negligible, combining the maximum environmental temperature of 40°C with the low loading of the Dyneema®. The structural calculation from the building application of Isoropia [19] suggests max force per unit width is in Nyy direction of 7.54 kN/m, which translates to a maximum stress of 31.56MPa (Table. 1).

Nyy (kN/m)	AD Fabric (kg/m2)	Density (kg/m3)	Equivalent t (mm)	Stress (MPa)
7.54	0.23175	970	0.239	31.56

Table. 1: Calculation of the maximum stress in the Isorpia membranes (Stress = (Force/unitwidth)/(ArealDensity/(Dyneema Density))

In terms of longterm behaviour of the material we observe a drop in structural strength by 45% due to exposure of the uncoated polymer to UV radiation. However, taking into account the low utilisation of the maximum stress for Dyneema® compared with their potential (3200 MPa), this suggests that even following degradation there is significant lifetime in the material left.

Conclusion and further work

Form active structures, such as Isoropia, are by nature able to extend and are designed to react to external forces. As such, the evaluations conducted in this paper are misleading, when understood simply in terms of tolerance between the designed and built on element scale. What our evaluation of Isorpia proves, is that CNC knit can be a building material, which has the capacity to withstand external forces without significant geometrical changes over time. The contactless 3D laser scan based method used here, introduces a quick method to analyse the geometrical fit and structural behaviour of a membrane over time.

We provide further insights into the use of CNC knit in architectural application. Here we find, that the use of Dyneema® provides a capability to gain overall geometrical precision in complex graded knit structures. We see a degradation of the structural capacity of the fibre over time, as can be expected from a polymeric fibre with the intensity of UV exposure that was accumulated in application. The remaining structural capacity on yarn level is however still a magnitude of 50 times higher than the

calculated maximum stress on the structure. This showcases in an impressive way the structural potential of Dyneema®. The UV resistance of the material could in future applications be established through coating of the fibre and/or the CNC knit. While Isoropia managed to almost stay within the allowed building tolerances, we find a need to improve methods and tools to design, simulate, specify and measure the structural performance of CNC knit, especially when it is graded.

References

[1] Thomsen, M.R. et al., 2016. Knit as bespoke material practice for architecture. In Del Campo et. Al. ed. *Proceedings of the 36th Annual Conference of the Association for Computer Aided Design in Architecture (acadia), 2016.*
[2] Sabin, J.E., 2013. myThread Pavilion: Generative Fabrication in Knitting Processes.
[3] Ahlquist, S. & Menges, A., 2013. Frameworks for Computational Design of Textile Micro-Architectures and Material Behavior in Forming Complex Force-Active Structures.
[4] Thomsen, M.R. et al., 2015. Hybrid Tower, Designing Soft Structures. In Thomsen, M.R., Tamke, M., Gengnagel, C., Faircloth, B., Scheurer, F., ed. *Modelling Behaviour*. Design Modelling Symposium 2015.Springer
[5] Thomsen, M.R. et al., 2019. Systems for transformative textile structures in CNC knitted fabrics – Isoropia. In Zanelli et al. ed. *Proceedings of the TensiNet Symposium 2019*
[6] La Magna, R. et al., 2018. Isoropia: an Encompassing Approach for the Design, Analysis and Form-Finding of Bending-Active Textile Hybrids. Proceedings of the IASS Symposium 2018, Boston, Massachusett.
[7] Tamke, M. et al., 2015. Designing CNC Knit for Hybrid Membrane And Bending Active Structures. In E. Oñate, K. -U. Bletzinger, & B. Kröplin, eds. VI International Conference on Textile Composites and Inflatable Structures – Structural Membranes 2015.
[8] Kaiser, U., 2004. *Windwirkung auf schwach vorgespannte Membranstrukturen am Beispiel eines 30m-Membranschirmes*. PhD. University of Stuttgart.
[9] Michalski, A. et al., 2011. Validation of the computational fluid–structure interaction simulation at real-scale tests of a flexible 29m umbrella in natural wind flow. *Journal of Wind Engineering and Industrial Aerodynamics*, 99(4), pp.400–413.
[10] Kawamura, S. & Kiuchi, T., 1986. An experimental study of one-membrane type pneumatic structure — wind load response. *Journal of Wind Engineering and Industrial Aerodynamics*, (23).
[11] H. Wang, C. et al., 2010. Monitoring the testing, construction and as-built condition of membrane structures by close range photogrammetry. , 38, pp.592–596.
[12] Tamke, M., Myrup, M. & Evers, H.L., 2014. *Current state of 3D object processing in architectural research and practice - DURAARK Deliverable*, KADK (CITA).
[13] Thomsen, M.R. et al., 2017. Simulation in Complex Modelling. SIMAUD 2017.
[14] Tamke, M. et al., 2016. Tracking Changes in Buildings over Time-Fully Automated Reconstruction and Difference Detection of 3d Scan and BIM files. In Herneoja et al. ed. *Proceedings of the 34th eCAADe Conference - Volume 2*
[15] Zwierzycki et al., 2016. Parametric Architectural Design with Point-clouds - Volvox. In Herneoja et al. ed. *Complexity & Simplicity - Proceedings of the 34th eCAADe Conference - Volume 2*. . University of Oulu.
[16] Vlasblom & Smeets, 2014. UV-performance of UHMWPE fiber in its applications. InnoZug conference.
[17] Vlasblom, M., 2018. The manufacture, properties, and applications of high-strength, high-modulus polyethylene fibers. In A. R. Bunsell, ed. *Handbook of Properties of Textile and Technical Fibres*. Woodhead Publishing.
[18] DSM, 2016. Ultra-violet exposure of UHMWPE fiber from DSM Dyneema - After sustained UV-exposure, UHMWPE fibers show high residual strength.
[19] La Magna, R., 2019. (1729) Venice Biennale Danish pavilion, Venice, I - Structural analysis report. Available at: http://dx.doi.org/10.5281/ZENODO.3247413.

Proceedings of the IASS Annual Symposium 2019 – Structural Membranes 2019
Form and Force
7 – 10 October 2019, Barcelona, Spain
C. Lázaro, K.-U. Bletzinger, E. Oñate (eds.)

Strip-Based Double-Layered Lightweight Timber Structure

Djordje STANOJEVIC*, Kenryo TAKAHASHI[a]

*Centro de Estudios Superiores de Diseño de Monterrey CEDIM
Antiguo Camino a la Huasteca 360, Mirador de la Huasteca, 66354 Santa Catarina, N.L. México
djordjes@cedim.edu.mx

[a] Ney & Partners Brussels, Belgium
Chaussée de la Hulpe 181 /Ter Hulpsesteenweg 181, 1170 Brussels, Belgium
kta@ney.be

Abstract

In the current paper, the authors present the Bending Bridges project as part of an ongoing academic research on active bending structures with strip-based geometries and their applications for lightweight timber constructions carried during the last three years. This project builds upon previous works such as Woven Wood, Synthesis of Strip Pattern and the Laminate Pavilion, developed by the authors with various collaborators and institutes. The focus of this project is to examine load bearing capabilities through an active bending wooden double layer system. The final demonstrator is a pedestrian bridge showcasing those properties, designed and built by a group of undergraduate architecture students from the Centro de Estudios Superiores de Diseño de Monterrey CEDIM, over the entire academic year 2018.

Keywords: strip discretization, active bending, lightweight, double layer, load bearing, large span, wooden structure.

1. Introduction

Within the architectural context of double-layered shells, lightweight structures and active bending principle, designed through computational form finding methods and materialized with digital fabrication strategies, there are relevant researches developed over the last decade at various institutions, such as the Institute for Computational Design and Construction (ICD) and the Institute of Building Structures and Structural Design (ITKE) in Germany, the Laboratory for Timber Construction (IBOIS) from EPFL in Switzerland, and the Centre for Information Technology and Architecture (CITA), just to mention a few. In contemporary architecture, since the ICD/ITKE Research Pavilion 2010 [1], it has been demonstrated that the principle of active bending, brings structural advantages in designing through material internal stress forces and allows assembling three-dimensional complex curved geometries without formwork while minimizing material waste. In the following years active bending structures became a field of study, pioneering the research towards bending-active plates with projects such as Bend9 by Riccardo La Magna [2], exploring induction of curvature through the means of elastic bending of plate-based structures. The most promising project based on the treated topics was in 2016 the Robot Made: Double-Layered Elastic Bending for Large Scale Folded Plate Structures, which has notable capacity for load bearing properties, but it has not been validated as the design was applied to a wall topology. Followed by more recent investigations, the research expanded by industrially sewing thin plywood on the ICD/ITKE Research Pavilion 2015/16 [3], and later with the Sewn Timber Shell 2017 [4] sewn with a triple-layered construction system showcasing the potential of industrial sewing techniques to join geometrically complex bent components. The project A Bridge Too Far by CITA in 2016 [5], which explored processes of robotic

Copyright © 2019 by Djordje STANOJEVIC, Kenryo TAKAHASHI
Published by the International Association for Shell and Spatial Structures (IASS) with permission.

incremental sheet metal forming with a double layered bridge prototype, demonstrated an alternative way to increase strength through material manipulation. Another inspiring project from 2014 is the Duck-Work, a pavilion designed by Christina Nguyen and Sean Gaffney: a full-scale prototype with a wood double layer system exhibited the potential for load bearing large-scale structure. Relevant work with double layer timber structure has been developed at the IBOIS in Lausanne, which has been later in 2017 applied to building scale such as the Timber Pavilion of the Vidy-Lausanne Theatre [6]. The authors previous projects Woven Wood, Synthesis of Strip Pattern and the Laminate Pavilion [7] demonstrated the potential of strip-based active bending techniques for wood construction through interlocking strips, ring topologies, and lamination preparing the ground for the presented research. Although the exceptional development on active-bending and double-layer principles, these systems have not been yet applied together on a large span with high load bearing capacity. On these pages the authors present the achievements of the Bending Bridges project as shown in the figure 1, focused on the developing of a double layered wooden construction system that takes advantage of active bending for load bearing, lightweight and large span structures.



Figure 1: Side view of the Bending Bridges project

2. Design

2.1. Design development and strip pattern discretization

The bridge design explores geometrically complex curved forms that fulfils both architectural and structural constraints. The global shape of the structure is designed through a computational modelling tool, such that the structure behaves as an arch while satisfying required geometric criteria. The design of the arch has been driven by a spline-like curve, which allows to have an optimal distribution of forces, while keeping minimum bridge inclinations taking in account the needs for pedestrians crossing. The global curvature of the bridge surface has been determined by lofting three main sections placed along the arch, two of them located at the points where the structure touches the ground, and the third at the middle of the structure. The two at the bottom are wide arches designed to add stability to the bridge ground connections. The one at the top of the bridge has higher curvature to protect pedestrians from falling. The larger the curvature variation is, the higher the global double curvature is, where higher surface curvature contributes to the shell stiffness. Each arch is designed from a polyline made of three straight lines with variable fillet. This allowed to generate variable curvature while keeping a relatively flat central area facilitating the pedestrians crossing. The maximum curvature of the arches was defined through a series of prototypes in scale 1:1, built through

a steaming method developed at the institute. The global geometry was discretized by a strip pattern, generating series of unique curvy-linear developable segments with variable width between 16 to 20 cm. The segmentation strategy adopted is intrinsically connected to the assembly sequence of the bridge, which is built section by section from two sides towards the centre. Each strip neighbour is overlapping the next one along the edge with a constant offset of 3 cm, similar to the clinker built boat building technique. Each section locates a pair of plywood plates that connect the sub-strips in a shifted manner, avoiding creating a continuous weak point over the structure. The final demonstrator of the research has a constant cross section of 9 cm, a span of 12 m and a maximum height of 2.5m.

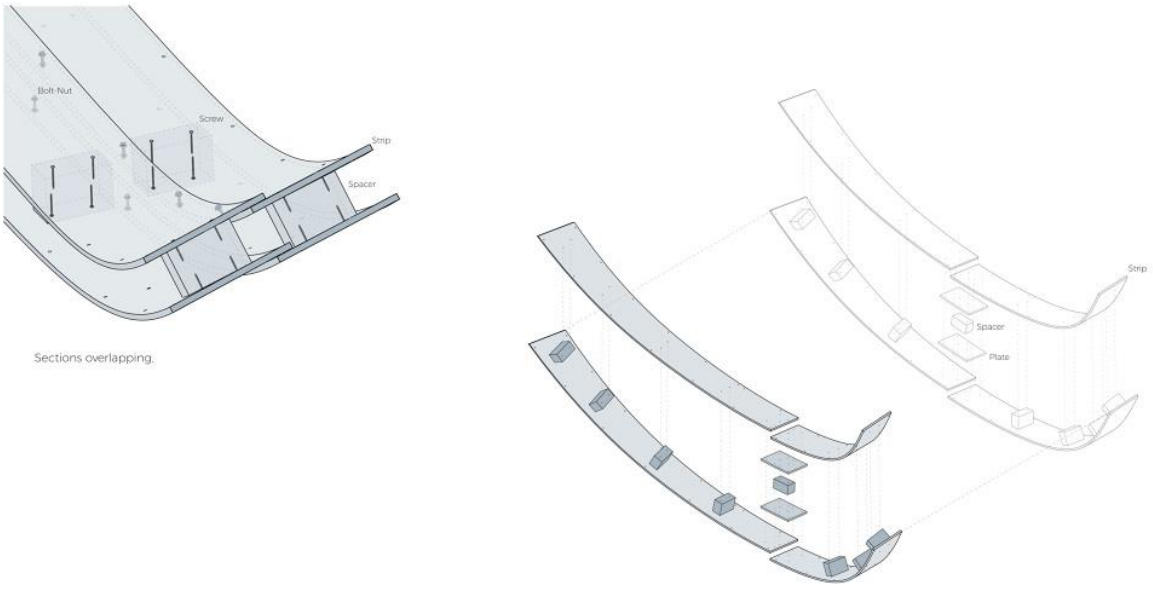


Figure 2: Double layer construction system with sub-strips, connecting plates and solid spacers

2.2. Double Layer System

The project focuses on the development of a double-layer construction system for a freestanding load bearing lightweight wooden structure. The double-layer system, integrated in the structure through 83 U-shaped unique components, allows to fix in place the curvature of each section without springback. The local load transfer between the segments is secured by shear bolt connections, while globally, structural analyses have been made with accurate detailed model to estimate the structural displacement with a pre-defined load, and to foresee the lateral buckling due to excessive additional weight. Taking advantage of bending to assemble the components allowed to build a great variety of unique curved three-dimensional objects from planar elements. The two layers of the structure are designed with the same direction in order to simplify the component system and to allow for a progressive assembly section by section. In the figure 2 it's shown how each section is made out of four plywood sub-strips, two plywood plates to connect them and a series of solid wood spacers (5.8x10.16x7 cm) assembled with screws. Each section connects to the next with bolts and nuts allowing to adjust and correct the geometry on site when necessary. The distance between the spacers affects the stiffness and the curvature of the components, while the amount of them increases considerably the weight of the structure. Therefore, a design negotiation was needed, with less spacers to reduce weight, but enough to reach the required stiffness. The entire bridge is made of 332 sub-strips, 166 plates and 704 spacers, connected with 2140 bolts/nuts and 4144 screws.

3. Structure

3.1. Conceptual design

The geometry of the structure is defined based on catenary arch, known to be an optimal shape to transfer loads. The structural height of the arch is chosen to be 1.8m for the arch span of 13.7m, which gives the span ratio of 7.6. The structural behavior of a slender shell structure depends largely on the stiffness of the open edges and the surface curvature. The cross section of the arch is defined such that the surface curvature in the transverse direction stiffens the structural behavior in the longitudinal direction (figure 3 - left). The realization of such variation of the curvature along the span length is made effortless thanks to the double layer fabrication method.

Furthermore, a simple parametric study is made to evaluate the arch shape. The figure 3 – right illustrates the first three eigenfrequencies of four different arch cross-sections from flatter to more vertical shape. The chosen cross-section (figure 3 - left) exhibits the highest eigenfrequencies, indicating about 50% stiffer than the second stiffest section.

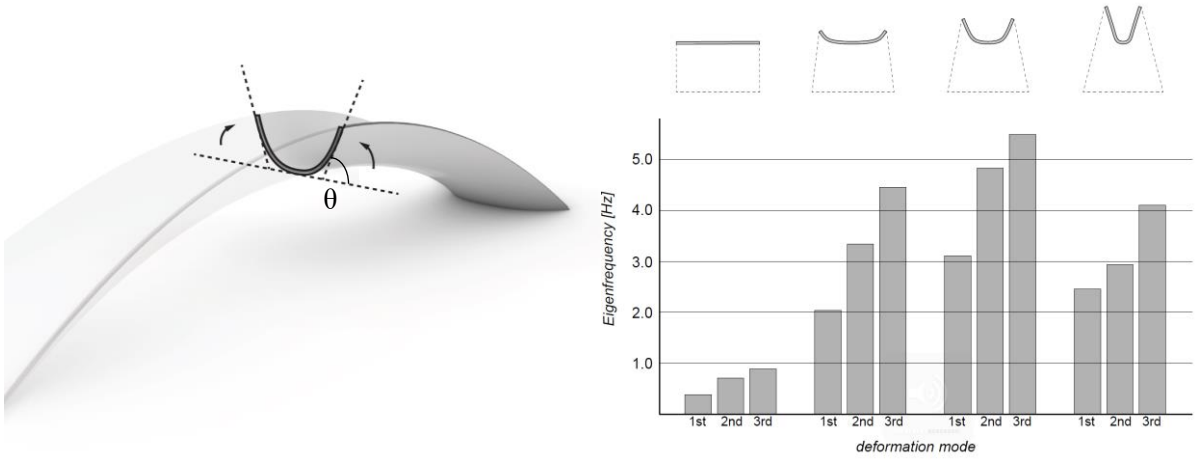


Figure 3: Parametric study on the arch shape – visualized cross section of the arch (left) / eigenfrequencies of different arch shapes (right)

3.2. Load transfer between segments

The structure is an assembly of discrete components. The joint is developed to ensure the longitudinal continuity of the structure. The figure 4 illustrates a typical longitudinal section of the joint. An analogy to Vierendeel truss can be made to understand the structural behavior of the joints under shear loading. The bolts between the joints are subject to only shear and minor tensile forces but not to bending. The nails onto spacers in solid timber ensure the shear transfer between upper and lower plates in plywood.

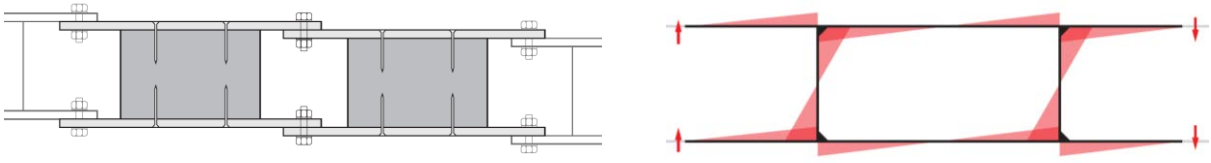


Figure 4: Longitudinal section of a joint between two components (left) / distribution of bending moment by analogy to the Vierendeel truss (right)

3.3. FE model

The structure is modelled with FE package *Sofistik*®. illustrated in the figure 5. The two layers are connected through spring elements that transfer local forces and moments. Setting individual springs for those connections allows for the effect of local connection stiffness on a global structural behavior. The springs are oriented in the local coordinate bridge longitudinal direction (x-dir), the surface normal direction (z-dir) and perpendicular to x and z (ydir).

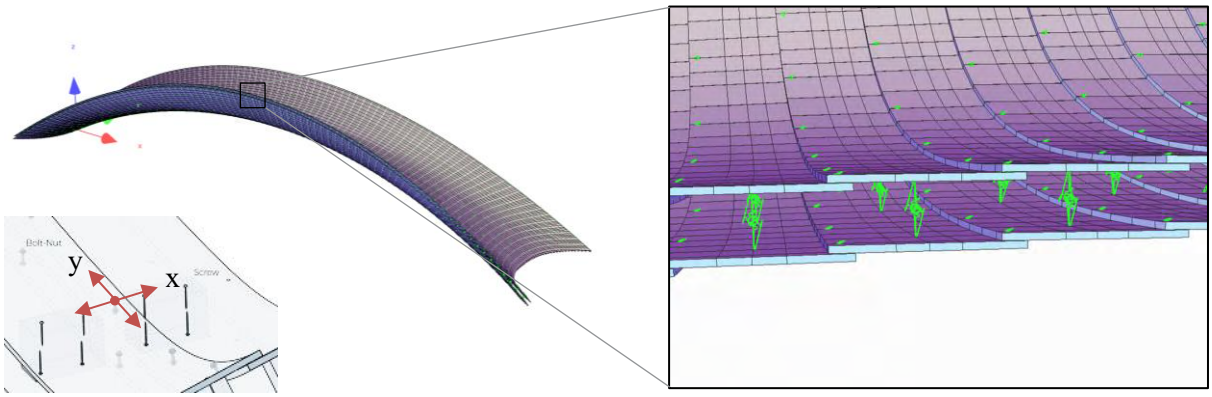


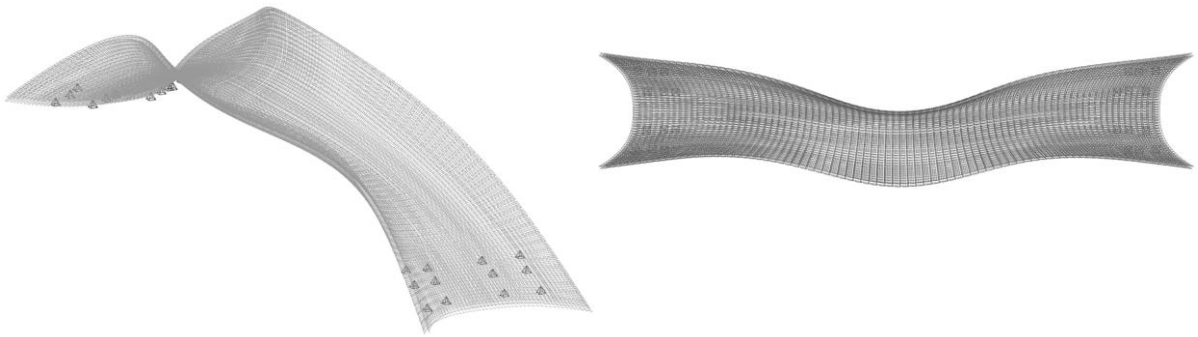
Figure 5: FE model for structural analysis – perspective view of the model (left) / close look of the spring elements (right) / definition of local coordinate (left bottom)

3.4. Sensitivity to instability

Generally, the dimensioning of an arch structure is governed by the restrain of the lateral buckling. The authors expected that the double-layered cross section with curvature would be stiff enough to remain stable under vertical loading. As it is described in the next chapter, however, the bridge suffered from lateral buckling when vertically loaded.

As the bridge has bolt connections between segments, lateral stability should be evaluated in function of shear stiffness of the connection in the transverse direction. One of the difficulties in designing timber structures is the evaluation of connection stiffnesses. Due to the lack of experiment data on the joints, a simple parametric study has been carried out in order to examine the stability of the bridge.

Buckling analysis has been performed using the FE model. A uniform vertical load of 1.0kN/m is considered. The figure 6 illustrates the deformation mode of the lateral buckling. The graph shows the buckling factors for spring stiffnesses of different orders that represent the bolt connection. The most flexible model gives the buckling factor of 0.25 and the stiffest case 9.16. From the simple comparison of the result, it can be concluded that the stability of the bridge is sensitive to the stiffness of the bolt connections.



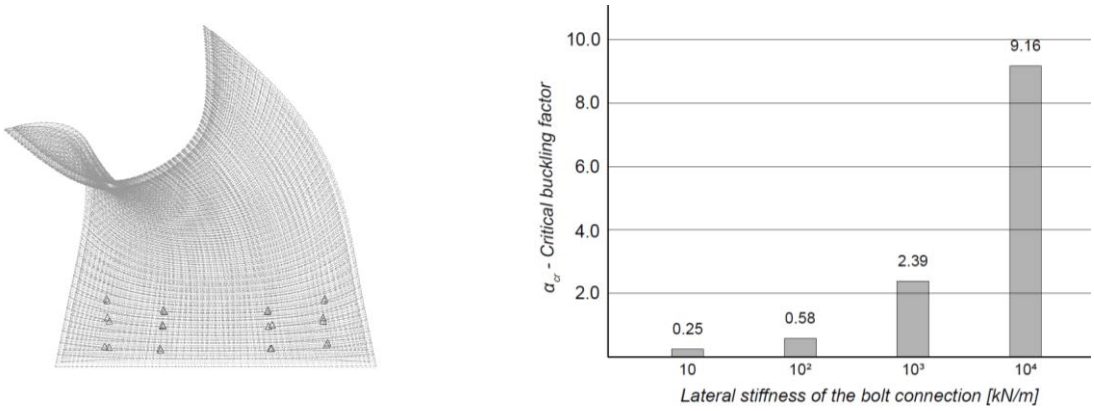


Figure 6: Buckling analysis: perspective view, top view and section view of the deformation mode (from top left, top right, bottom left) and the critical buckling factors for different connection stiffnesses

4. Realisation

4.1. Foundation

The flat foundation in concrete has been designed to transfer the horizontal reaction force to the ground. First the vertical (1.2 kN) and horizontal (15.34 kN) forces have been calculated according to the bridge span, height, weight, and additional load cases. These were then used to define the foundations volume, 2.2 m^3 each foundation. The bridge connects to the foundation through four wooden plates per side (5.4 cm thick), each one seats on a reinforced concrete beam of 15x15 cm (strip foundation) aligned with the bridge, where all the beams are connected by an additional concrete frame (2x4m). The wooden plates are connected to the concrete beams through metal custom L-shaped plates (9.52 mm thickness) with cast-in-situ anchors. The upper part of the foundation is a 8 cm concrete slab to create the platform.

4.2. Bridge

The bridge construction system explores active bending with a double layered locking method to assemble U-shaped components. The material treatment technique expands the elastic bending limits of standard thin plywood through the enhancement of its hygroscopic properties. All the bridge members and connections are unique, digitally fabricated with CNC machines, computationally designed in the 3D model and then cut through CNC milling codes. The design to construction process is structured over three main stages: 1. computational design, 2. digital fabrication, 3. enhanced material assembly. Alongside with the design process, for the digital fabrication stage, nesting algorithms of the discretized unrollable elements were used to automate the CAD to CAM process, minimizing material waste and giving the user the information about the amount of plywood boards necessary for the entire project before starting any fabrication. Once the final design has been defined, the CNC milling of the strips began. A total of 82 boards were planned for the entire structure, where each took about 40 minutes to be CNC cut. The fabrication stage considered three operations: 2.1 hole perforation for the strip to strip connections, 2.2 marking of the spacers positions, 2.3 cutting of the strips. The enhanced material assembly stage was based on three phases: 3.1 steaming, 3.2 component assembly, 3.3 bridge assembly. The three phases were crucial for time coordination as the they had to happen on the same day for each component. Once the wood has been steamed, there is a time span of two hours to assembly the component before it turns dry and loses its flexibility. The component then, having still a bit of flexibility allows for good manipulation for the bridge assembly. The entire construction process programmed fabrication and assembly stages to run in parallel. Although the development of the construction system took almost a year, the project's fabrication and construction phases took only four weeks.

5. Conclusion

The realized construction proved relevant load bearing capabilities through the active bending wooden double layer system (figure 8). The construction method it's shown to be highly efficient, it opens up geometrically complex design possibilities by accomplishing structural requirements to carry weight on large span shell structures. The buckling analysis is carried out to evaluate the behaviour of a structure with a complex assembly.

Although the bridge has been designed with a double layered system to withstand the load cases mentioned in the previous chapter, there are some shortcomings of the construction system that need to be mentioned. A physical test was designed to verify the structural behaviour of the bridge, weights of 65 Kg (average weight of a person) were iteratively placed on equal distance over the structure. With 15 weights, with a total of 650 Kg, the displacement at the centre of the bridge lowered by approximately 25 cm, passing the acceptable displacement limit. In addition to the vertical displacement, a slight torsion force began to act on the bridge. Even with a precise alignment of the foundations, and a well mounted scaffolding to support and guide the bridge assembly, once the project was completed a torsion force began to imperceptibly twist the tip of the structure. The principle cause of the twisting can be directed to the imprecise placement of the first bridge components to the foundation. As the bridge was assembled from two sides, the locking key had to pull the sides towards the centre which generated internal opposite forces. Due to the lack of a precise alignment strategy, the mistake angle of 1.7 degrees on one side and 0.9 degree on the other, made the two bridge sides mismatch at the locking component by approximately 42 cm. The flexibility of the construction system allowed to bend the structure and to secure the two parts connected, without impacting the final appearance of the bridge, but leaving internal stress issues. The construction process surely has to be improved, with a better calibration and alignment, opening up proposal for lasers and augmented reality applications. Nevertheless, not less important is the flexibility of the one directional double layer construction system, which allowed good manipulation during assembly, but also left some freedom for twisting accentuated by excess loading. For future design opportunities, in order to avoid twisting, it would be preferable to program the two layers in the longitudinal directions, or to integrate an internal substructure such ribs or a grid to achieve higher rigidity. Furthermore, due to excessive load, the bolts connecting the U-shaped components became loose, facilitated the structure movement. Once the testing weights were removed, the bridge maintained the deformed shape and only with its self-weight continued twisting slowly day by day, reaching in a week a stable position. After testing its load bearing limits, the structure never reached fracture, featuring ductility on global level (figure 7).



Figure 7: Buckling of the built structure



Figure 8: Large span load bearing capabilities

Acknowledgements

The authors are grateful to the Centro de Estudios Superiores de Diseño de Monterrey CEDIM and the director from the Architecture department David Duran for supporting the research over the last two years. A special thank you goes to the foundation advisor Jorge A. Jiménez, to Riccardo La Magna for feedbacks on the design development and to the students who designed and realized the project.

References

[1] J. Lienhard, S. Schleicher, and J. Knippers, "Bending-active Structures – Research Pavilion ICD/ITKE", *Proceedings of the International Symposium of the IABSE-IASS Symposium*, 2011.

[2] R. La Magna, S. Schleicher, J. Knippers, "Bending Active Plates", *In: Advances in architectural geometry 2016, vdf Hochschulverlag AG an der ETH, Zürich, p 174*, 2016.

[3] S. Bechert, J. Knippers, O. Krieg, A. Menges, T. Schwinn, and D. Sonntag, "Textile Fabrication Techniques for Timber Shells: Elastic Bending of Custom-Laminated Veneer for Segmented Shell Construction Systems", *in Adriaenssens, S., Gramazio, F., Kohler, M., Menges, A., and Pauly, M. (Eds.), Advances in Architectural Geometry 2016, vdf Hochschulverlag AG ETH Zurich, Zurich, pp. 154-169,* 2016.

[4] A. Martín, E. Martinez, E. Baharlou, O. Krieg, T. Schwinn, L. Vasey, C. Hua, A. Menges, P. F. Yuan, "Tailored Structures, Robotic Sewing of Wooden Shells", *on Researchgate,* 2019.

[5] P. Nicholas, M. Zwierzycki, D. Stasiuk, M. Thomsen, Concepts and Methodologies for Multi-scale Modelling: a Mesh-based Approach for Bi-directional Information Flows. *In proceedings of Association for Computer Aided Design in Architecture ACADIA 2016, University of Michigan Taubman College, Ann Arbor, Michigan, pp. 308-317,* 2016.

[6] C. Robeller, J. Gamerro, Y. Weinand, "Théâtre Vidy Lausanne - A Double-Layered Timber Folded Plate Structure". *Journal of the International Association for Shell and Spatial Structures. 58. 295-314,* 2017.

[7] A. Quartara, D. Stanojevic, "Computational and Manufacturing Strategies: Experimental Expressions of Wood Capabilities", *Part of the SpringerBriefs in Architectural Design and Technology, Springer Singapore, Singapore,* 2019.

Proceedings of the IASS Annual Symposium 2019 – Structural Membranes 2019
Form and Force
7 – 10 October 2019, Barcelona, Spain
C. Lázaro, K.-U. Bletzinger, E. Oñate (eds.)

A new generation of coated belts for structural membranes

Hubertus PÖPPINGHAUS

IF_Group, Ingenieure für Flächentragwerke GmbH
Am Dachsberg 3, 78479 Reichenau-Waldsiedlung, Germany
e-mail: hubertus@arqintegral.com, web page: http://www.if-group.de

Abstract

Belts have always been an important part of textile light weight structures. They can be folded together with the membrane and as a two-dimensional element they are capable of transmitting forces into the flat textile materials. Most of the belts in textile constructions are used as flat curved elements in order to reinforce the border of the membranes. They function against the logic of a straight lifting belt: the inner part of the curved belt is compressed and the outer part stretched. The typical off-centered fixation on either side of the membrane leads to a torque and introduces a twist into the components. By means of introducing a high security factor of 3 the engineers try to cope with all these imponderables. To overcome the above mentioned shortcomings, the objectives of this research project were to develop a straight and curved, UV-resistant belt with an equal or lower elongation than that of the textile membrane base, an equal or even higher stiffness, and a joining process that allows a continuity in the introduction of tension. A new coated Dyneema®-stem-thread-belt was developed, that should transmit the tensions directly through the straight, high-strength fibers. Four 3x3m hp-sails were fabricated with different belt solutions for the testing at the University of Konstanz. The ease of welding of the curved belt in comparison to the traditional stitching method was also tested as well as the influence of pre-tensioning combined with vaporization fixation techniques of different straight belts.

Keywords: straight belt, curved belt, weldable belt, stem-thread-belt, vaporization fixation, retractable membranes, foldable tents, small tents

1. Introduction

Today belts are only used in textile architecture when there appears to be no alternative for the specified function. This is the case in the transmission of tangential forces parallel to the edge cable, the field of retractable membranes and in general the field of temporary (seasonal) tents that need to be easily erected and dismantled. Belts are usually fixed to the textile membrane and do not have to be separated like cables or ropes. This raises the question why don´t we find a much broader market for a product that seems to belong to the world of textile membranes. The first answer lies in the complexity of knitting a belt. Because of the lateral union of the upper and lower fabric, belts are usually not even symmetric. Furthermore, important parameters such as pre-tensioning and fixation techniques that influence its static behavior are not well known even to engineers in the field of textile architecture. On top of this, there is the range of techniques that can be used for welding and stitching. How to define and reach the appropriate stiffness of the fixed belt thus becomes a complicated issue. Our engineering firm, If_group, is specialized in large scale retractable textile roofs where the use of belts is mandatory. Being aware of the present limitations of belts we initiated a co-financed German federal project in order to expand knowledge and develop new products together with one of the oldest German belt making companies, Vom Baur GmbH, and counting on the expertise in tent making of the well-known CenoTec-Sattler group. At the start of our investigation we compared four different products in each of the categories for

Copyright © 2019 by Hubertus Pöppinghaus
Published by the International Association for Shell and Spatial Structures (IASS) with permission.

their breaking load (50kN, 90kN and 120kN) and were astonished at the differences in the results. As a consequence we to start our research with an understanding of the fabrication process.

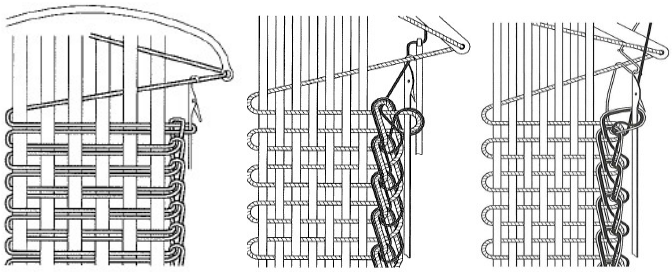


Figure 1: Different definitions of the edge of a belt [Source: J.H. vom Baur GmbH&Co.Kg]

2. Level of requirements of new coated belts for structural membranes

Straight lifting belts on the market have a stiffness below the value of a typical PVC/PES standard membrane. The desired belt should have an initial elongation similar to the membrane but be definitely stiffer than the textile material from the pre-stress level onwards. Only in that combination can the belt effectively transport the forces to the fixed points. Otherwise the adjacent membrane material will bear the load.

The new belt should be coated and thus protected against UV radiation and should permit direct welding to the structural membrane. Last but not least, a slight curvature (e.g. an average radius of 5m) would make welding much easier and avoid the typical compression of the inner part of the belt that leads to wrinkles.

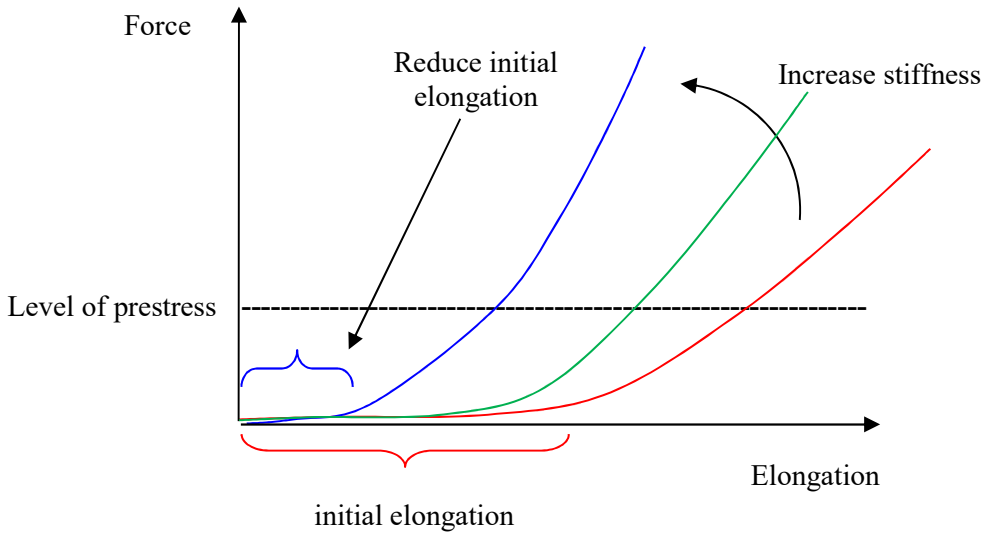


Figure 2: Force/Elongation-Diagram of a standard belt (red line) compared to the desired belt (blue line) and the membrane stiffness (green curve) [Source: Ingenierbüro Mager, English version author´s own elaboration]

3. Development of a new coated belt

Vom Baur GmbH developed a new coated Dyneema®-Stängelfadengurt (Dyneema®-stem-thread-belt) that was manufactured in both straight and curved versions.

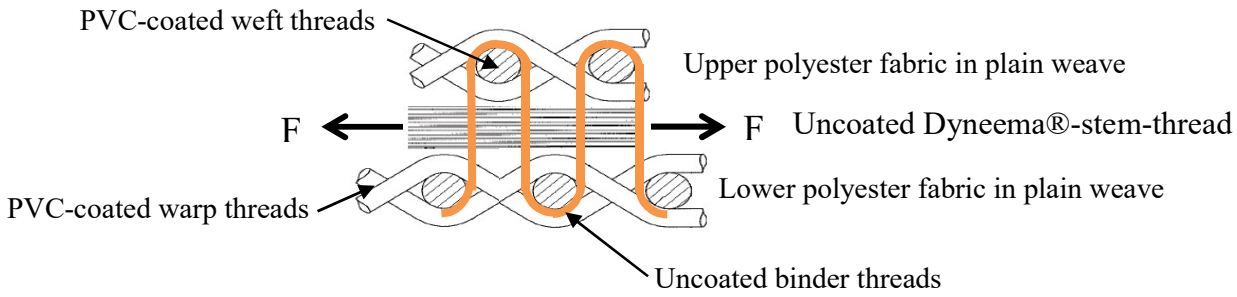


Figure 3: New Dyneema®-stem-thread-belt protected by PVC coated fabric in plain wave
[Source: J.H. vom Baur GmbH&Co.Kg, English version author´s own elaboration]

The following improvements were made:

- The belt is weldable and protected by the PVC coating of the polyester threads of the upper and lower fabric.
- Straight Dyneema®-stem-threads should carry the forces directly through the belt avoiding ondulation. The material is a high modulus polyethylene (HMPE) with extremely long chains and a very high molecular mass. As a result the threads have the highest specific strength in their category. This compensates the loss of polyester threads that occurs because of the coating of the upper and lower fabric.
- A curved belt with a radius of 5m was manufactured, which made the process of welding much easier. However, the curvature made it impossible to pre-stress the belt, which is normally done in order reduce the first extension under prestress (Figure 2).

4. Tests conducted

The testing was carried out together with a student group from the University of Applied Science of Konstanz under the guidance of Professor Francke, head of the Laboratory for Structural Dynamics. Curved and straight belt variants were investigated and compared to standard belts. For the research, four test sails were installed in a specially designed steel rig and their behavior under load was analyzed.

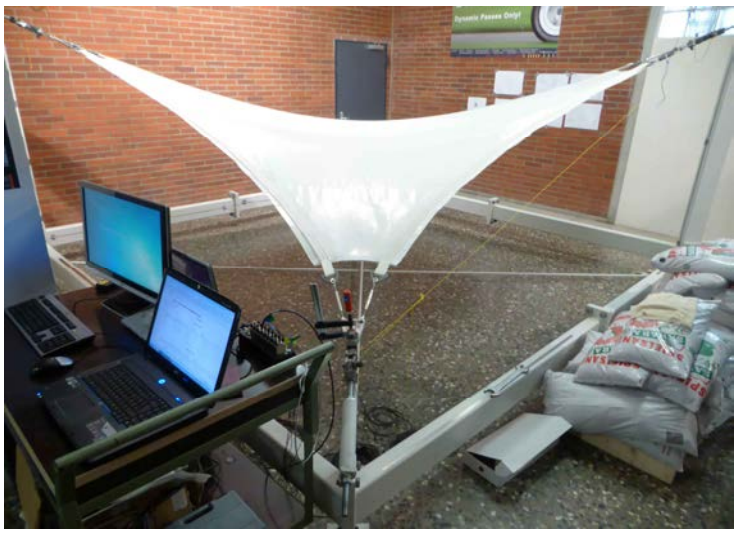


Figure 4: four point sail pretensioned in the testing rig in Konstanz [Source: Photo by the author]

The deformation was measured by the students and the forces were continuously captured by the help of six load sensors mounted according to the different versions of the test sails. In addition to the overall load at the high and low points, the focus was put particularly on the tangential and normal forces of the curved edges. Finally a ridge belt was examined leading from high point to high point. The three-stage load applied simulates a snow load hanging between the high points. At each step eight 25kg sandbags resulted in a total load of 200kg per step (8x25kg =200kg) and were applied in the flat central part of the membrane

.

4. Tests evaluated

The belts were fixed on top of the border of the membrane in order to facilitate the geometric measurements. The four-point sail was symmetrically divided in two parts in order to compare a standard pretensioned Polyester belt to the Dyneema®-stem-thread-belt. As the load was increased at each step, wrinkles appeared on both sides. The evaluation of the load sensors (figure 5) showed that during the pre-tensioning the force flowing through the belt was slightly higher than that of the standard belt. However, from the very first 200kg step, the standard belt carried considerably more load (more than 20%) than the stem-thread-belt. The sag of the standard belt passed from 12,0% to 12,1%, but that of the less stiff Dyneema®-stem-thread-belt passed from 12,3% to 12,8%. There appeared to be only one explanation for these results. The supposedly straight Dyneema®-threads were ondulated by the force of the binder threads (figure 3). A closer observation of the belt confirmed that this was the case.

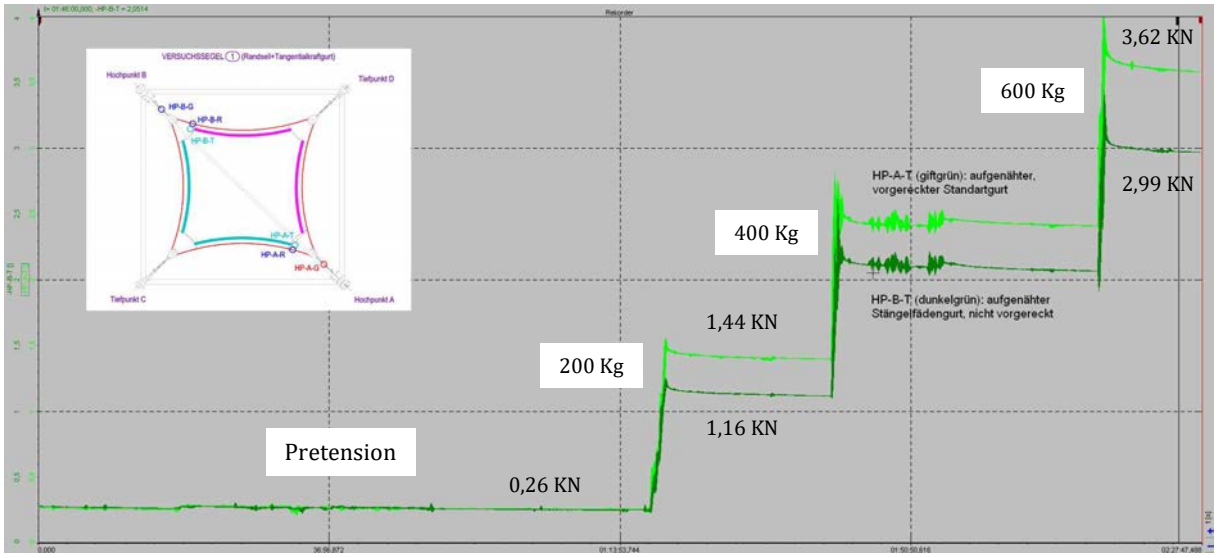


Figure 5: Comparison of standard pretensioned belt (light green) with Dyneema®-stem-thread-belt (dark green) [Source: author´s own elaboration]

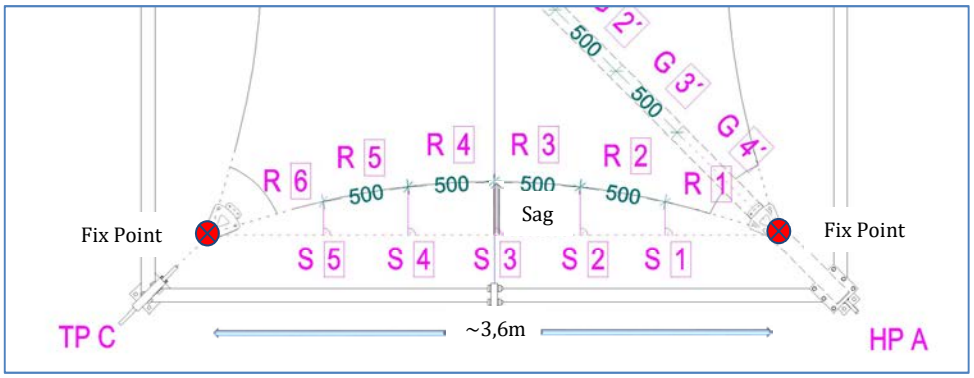


Figure 6: Picking up the geometry at fixed measuring points [Source: author´s own elaboration]

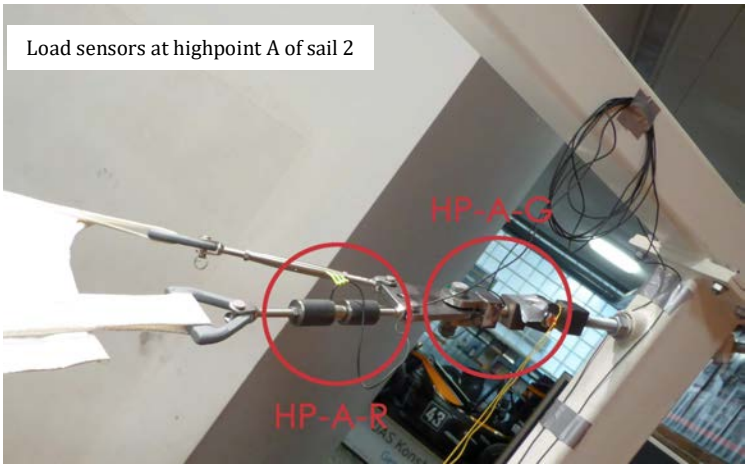


Figure 7: Load sensors to determine the tensile forces in the high points [Source: author´s own elaboration]

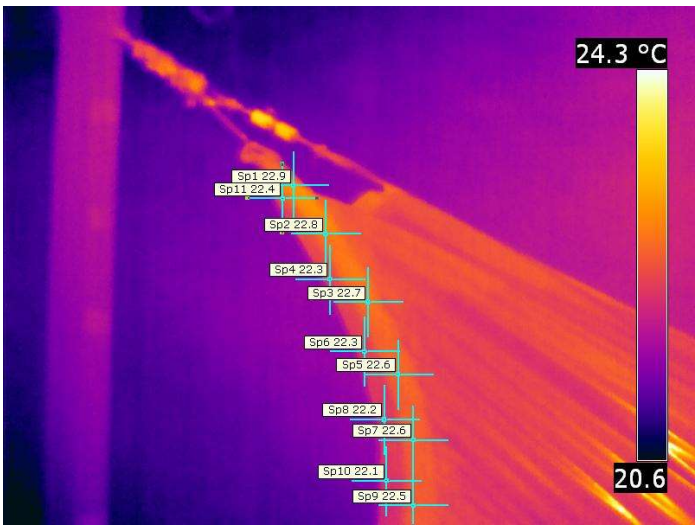


Figure 8: Thermographic image of. The growing temperature of the belt from 22,5°C to 22,9°C shows the accumulating tensile forces converted into heat on the way to the high points [Source: author´s own elaboration]

The underlying problem was that belts were ondulated by the process of weaving and are straightened only with increasing force. The problem of initial slack persisted even with the Dyneema®-stem-thread-

belt because of the necessary binder threads. As an effective means of reducing the initial slack, the insertion of monofilament spacer threads and a change of the weaving method were considered and tested. It was possible to increase the stiffness in pure polyester belts from 300-400kN to about 700kN. However, this value still failed to meet the initial requirement for the stiffness to surpass that of a standard PVC/PES membrane of about 1000-2000kN.

5. Pre-tensioning combined with steam fixation techniques applied to straight belts

In order to find a solution for the desired increase in stiffness and shortening of the initial slack, pre-tensioning combined with steam fixation techniques were investigated. This required abandoning both the application of a UV-protection and the proposed curvature to ease the fixation on top of the curved membrane borders. Standard uncoated belts are usually five times pretensioned with about 30% of their breaking load before being sewn immediately afterwards. If the belts are sewn only a few hours later, their forced length will have already begun shrinking. A process of thermal steam fixation of the pre-tensioned belt was successfully implemented in an autoclave pressure chamber in order to preserve the increased rigidity over several days.

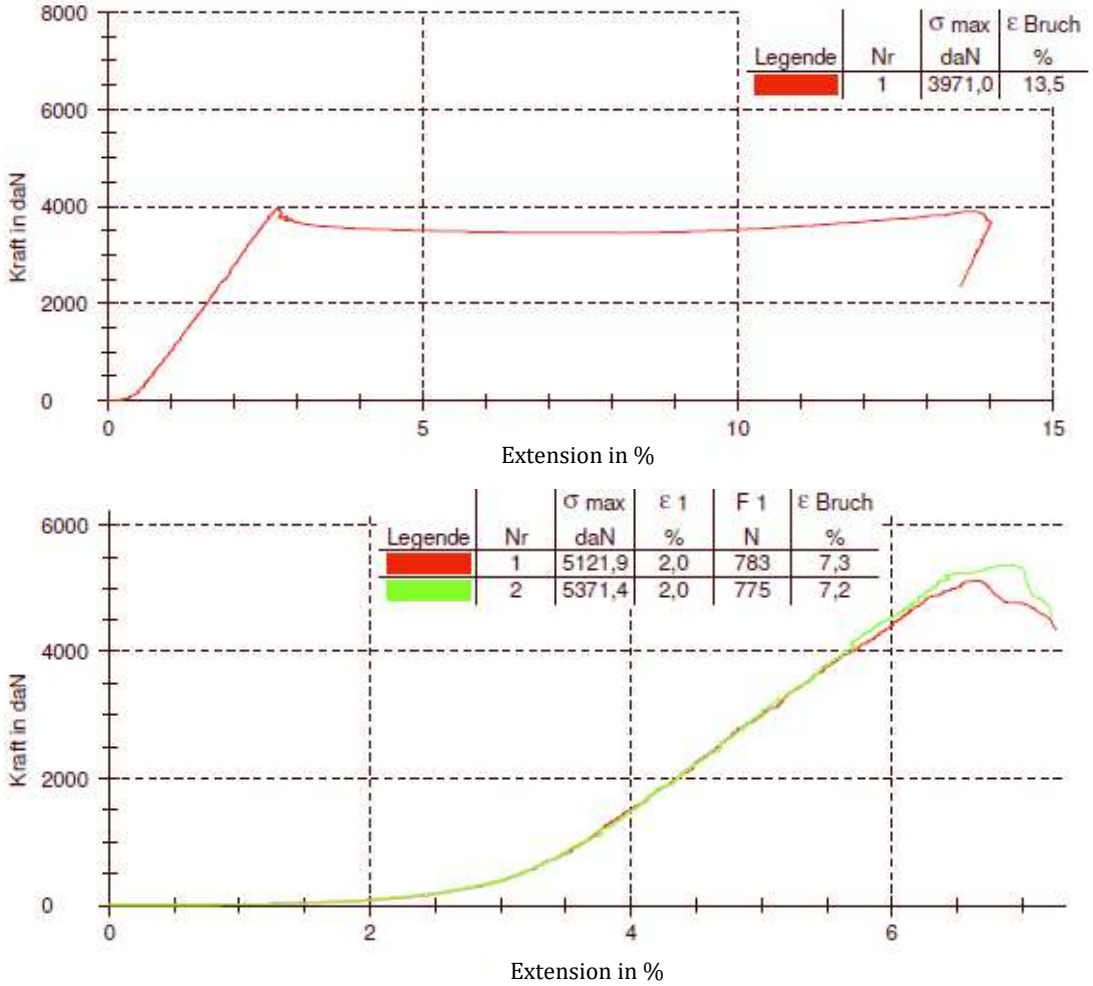


Figure 9 and 10: Force-extension diagrams of the steam-fixed Dyneema®-stem-thread-belt with (first diagram one sample: red) and without pretension (second diagram two samples: green and red)
[Source: J.H. vom Baur GmbH&Co.Kg]

A maximum rigidity of 1,800 kN could be reached by combining the two processes. But the resulting belt was considerably stiffer than a standard belt and could not be easily rolled up. Furthermore, it would be difficult to commercialize a belt whose maximum stiffness only lasts a certain amount of time before decreasing.

6. Conclusions

The sector of pre-tensioned membranes used for architectural purposes is very small relative to other applications of technical textiles. It requires considerable effort to bring together the expertise of different partners and firms in the field in order to advance knowledge. Our investigation to develop a new belt was based on goals which were in part contradictory: for instance, a curved belt is easier in its handling but cannot be pre-tensioned. Different methods to fix the pre-tensioning process need to be further investigated as they include highly specialist knowledge in the fields of weaving techniques, physics and chemistry. Structural engineers only can test the final product but know little about the effect for instance of steam fixing on the molecular structure of a specific belt. Our interdisciplinary investigation expanded knowledge in the field but still did not yet lead to a viable product for the market.

References

[1] Rosemarie Wagner (KIT Karlsruhe), ITV Denkendorf, Güth&Wolf, Walter Krause GmbH “Belts in textile Architecture” *Tensinews*, vol. 22, pp. 12-13, April. 2012.

[2] Rosemarie Wagner, Florian Weininger, Kai Hainlein (KIT Karlsruhe): “Vorlesung: Gurte im Membranbau” Fachgebiet Bautechnologie, Fakultät für Architektur

Proceedings of the IASS Annual Symposium 2019 – Structural Membranes 2019
Form and Force
7 – 10 October 2019, Barcelona, Spain
C. Lázaro, K.-U. Bletzinger, E. Oñate (eds.)

Airport City Belgrade Membrane Structure : design, production and installation process

Aleksandar P. VUČUR*, Günther H. FILZ[a]

* ArTech inžinjering d.o.o
V. Popovica 30, 11070 Belgrade, Serbia
a.vucur@artech.rs

[a] Aalto University, Finland

Abstract

In 2018, the Airport City office park in Belgrade, Serbia has commissioned an unusual membrane structure. The project has been designed, produced and installed by ArTech inženjering, Belgrade, Serbia. This paper presents the comprehensive process and workflow from the design phase to the structural analysis, to the production and to the installation of the membrane tensile structure. A membrane structure in hypar shape has been proposed. The cover spans about 28 meters and covers a footprint of about 487 m². As materials, PVC-PES membrane of type III and steel for other structural members has been selected. The project contains several unusual points, challenging for design, detailing, analysis and installation. Therefore, it serves as a good example and case study for future developments in this field of lightweight structures. The structure is located in between existing office buildings in order to cover and protect a pedestrian area and to create a plaza. The overall layout and shape of the structure has been inspired by client's logo. Even though, the conventional shape of the hypar served as the basic geometry in the design phase, novel solutions have been developed and realized e.g. for corner details and boundary edges. Simultaneously, their unusual shapes asked for new advanced solutions. As an innovative approach and visually most striking feature a novel, curved truss girder solution has been developed, which is using principles of bending active structures. The installation process turned out to be of a great challenge. Different kinds of site-specific limitations and conditions required specific planning and logistics. So, this project serves as unique case study, highlighting the interdependence of design, limitations, requirement for novel detailing and installation-processes. By the comprehensive monitoring and observation of this membrane structure a whole quantity of information has been documented since its completion.

Keywords: membrane structures, architecture, conceptual design, detailing, case study, installation process.



Figure 1: The unusual membrane structure at the Airport City office park, by ArTech inženjering, 2018.

Copyright © 2019 by Aleksandar P. VUČUR, Günther H. FILZ
Published by the International Association for Shell and Spatial Structures (IASS) with permission.

1. Introduction

In 2018, the Airport City in Belgrade, Serbia [1] has commissioned an unusual membrane structure in the office park. The project has been designed, produced and installed by ArTech inženjering, Belgrade, Serbia. (Fig.1) The structure is located in between existing office buildings in purpose to cover and protect a pedestrian area and to create a plaza for stay. The overall layout and shape of the structure has been inspired by client's logo and was facing a set of challenges and restrictions, from existing buildings to safety issues to architectural and structural requirements. So, this project serves as unique case study, highlighting the interdependence of design, limitations, requirement for novel detailing and installation-processes. This paper presents the comprehensive process and workflow from the design phase to the structural analysis, to the production and to the installation of the membrane tensile structure.

2. Design concept and design parameters

This project has been realized in city of Belgrade, in the area of New Belgrade, which is recognized as business center within Serbia. The "Airport City Office Park" [1] is an acclaimed complex of office buildings, and headquarter for a great number of large international corporations. (Fig.2) The "Airport City" is operated by an international real estate investment company, which is also investor in this case. The main project description and outline was defined by the investor and their client Telenor, a mobile network operator company.

2.1. Site specific design parameters

Telenor is located in two office towers facing each other. Their requirement has been to cover area between the two buildings. A dry and protected connection between the buildings should be provided by covering the predefined space.

Furthermore, the asked structure had to fit in-between predefined, existing architecture of contemporary office buildings, with curtain wall glass facades, paralleled to highly frequented pedestrian sidewalks. All structures are very cubic, and the guiding array of the office park is dominantly orthogonal.



Figure 2: Impressions of the site at the "Airport City Office Park" before installation of the membrane cover

As a consequence, the design has been asked to meet two contradicting requirements: firstly the requirement of the investor, who insisted in a solution that will not have any negative impact on existing constellations and existing architecture, respectively a solution with as little intervention as possible, and secondly the clients` request for functionality, and a new, attractive landmark for their headquarters offices. Analyzing the target area other, mostly technical restrictions have been discovered. The design process was facing potential obstacles, such as an existing fountain, trees, underground installations, sensitive facade material and so on.

In addition, safety during installation and later on during operation turned out to be a design driving issue. Very busy and intensive pedestrian traffic of 6.000 employees, who are working in office park, and daily 10.000 to 15.000 passages in that relatively small corridor, have been assumed. So every possible situation that might endanger the pedestrians had to be considered.

Since the climatic conditions in the respective region significantly differ during the seasons, ranging from heavy snow in winter, long rainy days in fall and spring, to the very hot sunny weather in summer time, the cover should consider protection against the main atmospheric impacts, such as snow, rain and strong sun-radiation. Overall, the applied structure has to permanently sustain to all of those conditions.

2.2. CI - design parameters and preliminary design

According to above-mentioned design parameters and restrictions, preliminary design was the most sensitive point of this project, and a significant challenge in order to find a solution that would fulfill all defined requirements.

In the very beginning, the client insisted on the development of several proposals in order to have the choice. Even though this isn´t an unusual request, the search and looking for different solutions was actually supportive for the process of analysis. That process was a filter for solutions that generated the one “winning” concept. So, many sketches led to that one proposal that merged all requirements into balance.

A hidden idea, to emphasize the corporate identity (Fig.3) and importance of the main user, was to apply the shape that will be easy to read as similarity of the client´s logo - curved spatial lines. Therefore, the hypar, one of the most basic shapes in membrane architecture, has been selected as a shape to start with – a simple, "clean" shape that mediates between the orthogonal, straight-lined design of the office buildings, and spatial curves that are perfectly suitable for membrane structures. So, shape and volume were sensitive questions, and the proposal an answer, which could be “accepted” by the authorities and the client.

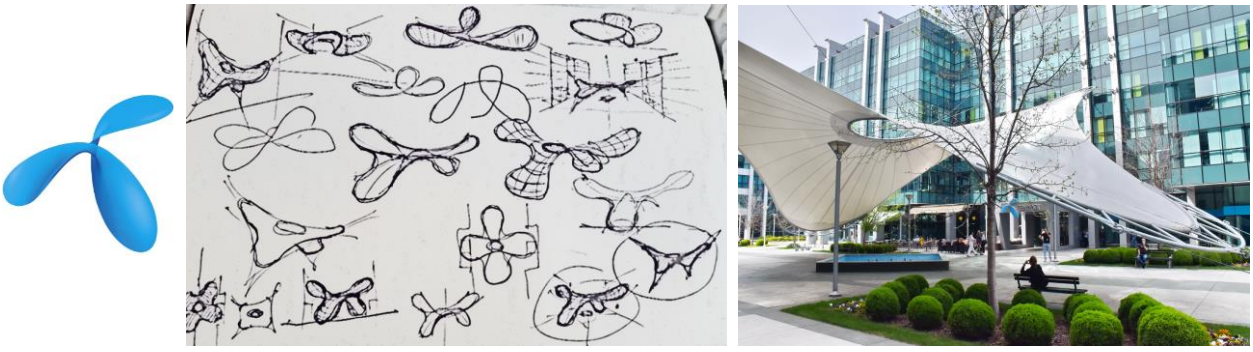


Figure 3: The client´s logo as CI design parameter, preliminary design sketches and the final structure

Considered as a permanent structure on just four supporting points, the quite significant span of 28m, and approximately 487 m^2 of covered surface, withstanding all internal and external, called for special attention. The question, if the existing building construction would be able to absorb the additional forces from the membrane structure, has been a crucial issue, as the hypar-shaped membrane has been positioned centrally over the squared piazza, two high points were thought to be attached to the office buildings and two low points to be attached directly to the ground. For the positioning of the low points it has been important to maintain the main walking directions free from obstacles for circulation of pedestrians, as well as the transversal direction that connects the two building entrances. The

existing glass facade surfaces, did not allow for much flexibility in where and how to connect the hypar´s two high points with the office buildings.

The final design proposal offered a solution that rotated the structure, around its center by 45 degrees, providing a symmetric, hypar-like figure, diagonally positioned to the main axis of the building complex. Architecturally and spatially, this position provides the visitor with an overall view of the structure, and recognizing its complex geometry. At same time the structure´s "twist" deranges the perfectly orthogonal matrix, by creating an unexpected visual dynamics.

The character of the location is defined by strict urbanism. Since the position of structure is in the heart of the building complex, it is visible and provocative from almost all angles. Its position even more emphasizes importance and significance of structure. So, the structure´s preliminary shape needed to be checked also regarding its appearance and architectural contribution. As mentioned, the structure is positioned in the central, main axis of the complex, and in front, respectively between the client´s office buildings. Therefore, there are multiple views on and impressions from the structure - spotted from far away, approaching it, passing right below it, leaving it in same direction – a complete performance and sequence of different impressions.

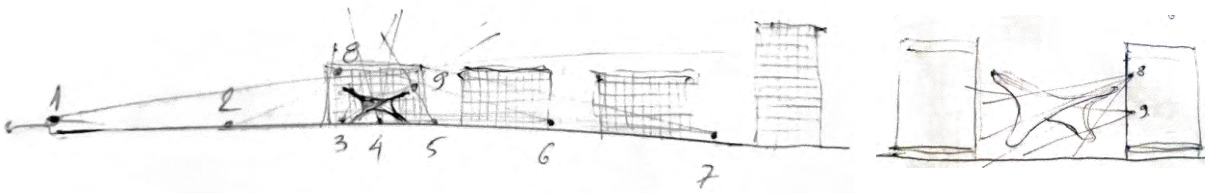


Figure 4: Viewpoints 1-9 of design observation

The provided sketches show the main points of observation (Fig.4). The most important street, Omladinskih Brigada, is orthogonally oriented to the main axis of the complex, and with several hundred meters of distance (point 1) the farest point from where the structure can be seen. Recognizable from drive by only, the first impression has to be intriguing, because it`s lasting very short time and therefore has to be very clear as a concept. Earlier a "canyon" between huge glass cubes of office buildings, now a surprising lightweight membrane connects the two sides, and clearly defines the center of the cubic building masses. At viewpoint 2, the structure can be seen in reasonable detail as a cover between buildings, but with distance from the walls and from the ground. It gives the impression of levitating among other structures and the ground, highlighting the idea of lightweight. Despite its symmetry, the 45 degree angle to our walking route, the membrane cover enfolds its dynamic shape, where nothing of the structure stays hidden – all connection points, details as well as the overall geometry can constantly be seen. Simultaneously, the curved shape defines a tunnel-like passage, and uncompromised view to the very end of the complex. Position 3 is where the visitor enters the space below the membrane. By blocking the view on significant parts of glass facades, the white roof and its details become more dominant. The ground level and the vertical axis are free, due to the detailing and circular opening in the very center of the membrane. Below the circular opening, the visitor will find a square fountain (position 4.). The visitor are lead around the fountain, while the circular opening provides views to the sky and facades of the client´s buildings. The visitor has entered the center of the business complex, after having passed the membrane structure like a big gate-like entrance, having recognized a sloping surface (position 5) that leads the view to the horizon where we see in distance the end of the building complex, where the cover opens to the build environment and where we exit the covered ambient towards position 6. Looking back from the other end of complex axis at position 7, the membrane structure is again in far distance, and centrally positioned. The view is comparable to position 2, but more framed by buildings, forming a U-shapes ensemble. Other important design aspects are the views from the offices at position 8 and 9. Due to the distance

and the detailing, the membrane seems detached from facades elements. For its double curvature, the membrane provides view to spaces above and below the structure. So, the membrane as a new element zones the space in horizontal as well as in vertical way, it improves the ambient, provides quality space below and around it, in different scales and grades of detailing.

2.3. Natural light, artificial light and sound considerations

Visual sensations, which can be achieved by natural light and artificial light have been subject of considerations. These include brightness and light effects such as day-, night-, cloudy or shiny weather- conditions as well as artificial light effects thru illumination. The chosen membrane material provides characteristic light transmission in the range of 7%. This allows for sufficient shading during sunny days, and for still providing enough natural day light in cloudy weather. (Fig.1,3) The smooth monochrome, white surface of the membrane serves as a fantastic "playground" for lighting effects. White artificial light has been chosen to underline the slenderness of the membrane`s architecture. Lights are located at the lower supporting points, spotting upwards, spreading light on the membrane surface and using the membrane as a reflector and diffusor at the same time. As expected, as a luminous body the structure becomes a prominent landmark of this complex during the night. The membrane cover also influences the perception of noise and sound. Below the surface the traffic noise is partly blocked and partly overlaid by the relaxing splatter of the fountain, which is reflected and amplified, respectively focused by the sound reflection on the membrane.

3. Final design and detailing

After approval of the design concept, the following aspects may be highlighted, firstly the supporting points, secondly the shape and function of the bending active steel trusses at the corners, thirdly the central opening of the membrane, and fourthly safety issues.

Due to four supporting points only and a relatively big span and covered space, high reaction forces have been expected. This level of forces required sufficient structural elements at existing buildings (high points), as well as heavy foundations for the low points. Since the applied forces in one point would have exceeded the load bearing capacity of the concrete structure (pillars) of the existing buildings, the resultant force has been subdivided into 2 forces, which have been distributed over 4 spots each with 2 supports. (Fig.3) To counteract the reactions in low points, foundations in concrete of about 12 m3 would have been sufficient, if the underground space wasn´t very occupied with installation, such as optical cables, electricity cables, water and sewerage pipes, and ground watering pipes. A sophisticated technological solution has been found to protect all installations, while placing reinforcement steel and pouring concrete.

The most striking and unusual detail is the corner shape of the membrane. (Fig.3) Seemingly simple, but quite complex the shape of corner follows a spatial curve from convex to concave and to convex. In addition to its geometry this was problematic, because the edge cable cannot provide the needed tension in the membrane in convex areas. As a solution a steel frame as curved plane truss has been designed, starting from the exact point where the membrane-edge changes its shape from concave to convex. As a result, the membrane´s boundary is more rigid towards the endpoints, due to the curved steel truss, and flexible in-between, due to edge-cables. Tensioning of the cables, controlled at the ends of the cable is a standard procedure but how to apply tension at rigid edges? And how to design the connection of the two as a continuous edge.

A first option of applying secondary elements for tensioning the membrane to the stiff truss has been given up to the massive use of material, its costs and visual effects. By analyzing the stiffness problem, for a completely novel approach has been discovered. In distance of 8m span a considerable deformation in plane of truss in the area of elastic deformation has been noticed, which could be used for tensioning membrane in the desired direction. Inspired by the principles of bending active structures [2,3], the required prestress in the membrane is thought to be equalized by forces that will

not exceed the elastic deformation of the curved steel truss, which has later on been designed accordingly.

Another significant detail is the central opening of the membrane, a circular shape with a diameter of 5m. (Fig.3) The central opening has visual reasons as well as it reduces considered snow loads. In order to prevent unwanted deformations a double ring at the opening perimeter was proposed, a first rigid one made from steel pipes to keep the shape, and a second flexible one from steel cables capable to balance uneven forces in the structure due to loads. As mentioned above, this combination was proven as a right decision and good solution later.

Special attention has been paid to safety measures, mostly in sense of progressive collapse. A comprehensive safety concept is defined in 3 separate levels, firstly, the safety provided by the membrane including edge cables, and steel trusses; secondly, safety by two centrally crossing cables hidden in membrane, to ensure controlled behavior of the structure in case of unexpected wind or snow loads; and thirdly, safety by four high cables that are connected to the buildings at four different corners, and which are supporting the central ring. Even in case of collapse of first two systems, the central ring stays in its position.

4. Formfinding and structural analysis

Formfinding and structural analysis were performed by means of the following software, namely Mpanel FEA for membrane formfinding, and TOWER for analysis of steel and concrete elements. 100kg/m2 for snow load and 100 km/h of wind as well as service load have been applied and analyzed in several combined, symmetric and asymmetric load cases for dimensioning membrane, cables and connection elements. However, the most challenging issue was the question of how to define the appropriate prestress for the membrane in area of steel arched truss allowing for elastic deformation only. The most relevant parameters have been the applied force that causes bending, and the resulting deformation, whereas the deformation for the steel truss is different from the membrane material, which can be defined as linear-proportional. Several iteration have been checked to meet the complex final behavior. Finally, a force of 1000 kgf has been introduced for truss deformation, causing uneven force distribution in truss elements, but guaranteeing the whole system to be in the range of elastic deformation. The applied prestress resulted in 6.37 cm deformation on each end of the truss. This distance has been used for prestressing the membrane. For this reason an additional compensation in this direction is not possible – the membrane possibly could not have been attached to the steel truss later - this deformation would correlate to 1.5% compensation in this (warp) direction. As a result, we face the risk of possible wrinkling in the dominant, warp direction, due to geometry-, and stiffness-dependent decrease of steel truss – to membrane induced prestress, when comparing the ends and the mid of the curved steel trusses.

5. Production process

For the familiar overall geometry, the production process has been the easiest part in this project, realized in parallel production of membrane, steel works, cables and connection elements.

Extra attention has been paid to steel works of hot galvanized trusses and anchor plates, which are supposed to be exposed to tension forces, but cables and connection elements, have been standard catalogue products. Only the tensioning U-shaped rod represents a bespoke element, as a tensioning length of 1m was needed.

The confectioning was standard procedure and done with standard technology. But since significant external loads are expected a PVC/PES type III has been chosen as material. Before high frequency welding some preliminary welding tests were made for seams, base material, and edges. The whole membrane was assembled into one piece, which asked for considerations of the packing process.

5. Installation process

The installation process usually is defined by recognizing problems, finding solutions and merging them into one smooth process. So, planning the installation process is part of the main draft. Here some parameters may be mentioned.

As an investor´s request, daily business in the office park must not be disturbed, which resulted in very limited time at site, especially when it comes to drilling, using heavy machinery, pumps and cranes. Simultaneously, working at late afternoon or during nights means lack of daylight, work under artificial light, and significantly lower temperatures including temperatures below 0° C.

The existing pavement is designed and dimensioned for pedestrian traffic, which represented the limitation for usable machinery, also with respect to surface quality.

The given time frame for installation, which did not allow for changes, was contractually defined with 60 days. Usually doable for this size of project, the short days, low temperatures, snow and rainfall, windy and very unstable weather conditions made the process quite challenging. In addition, safety issues, considering very busy area (6.000 every day users), coupled with the Airport City`s very strict rules regarding safety, have been biggest challenges for the installation process.

The process of installation including transport of elements, protection of existing facilities, and installation has been accomplished in two main parts, namely the preparation of supporting points, and the erection of membrane and belonging steel elements.

In addition to above-mentioned issues for support points, safety and timeframe, its preparation faced issues like inaccessibility of foundation for trucks and mixers. So, the concrete was pumped from 60m distance thru a horizontal pipe line. Again special machinery and equipment – strong and far-reaching enough for the works and as light as possible for the pavement - had to be found in order to mount steel elements, and connection plates, which are supposed to be attached to the existing buildings at 14m and 17m height. Additionally, this kind of ultra-light, high point machinery has significant, uncontrolled movements of the working basket, which makes highly precise work difficult and slow, plus highly dangerous during wet, icy or windy weather.

The erection process as the final step of installation considered the significant one-piece-membrane-surface, regarding its self-weight and regarding its uncontrollable, sail-like behavior in wind during installation. To minimize this kind of danger, the complete action was done in as short time as possible. The installation plan defines each step in detail, and very bad, unstable weather conditions (December) for the erection process were expected. No rain or snow fall, temperature of min.-5°C and a max. of 3m/s of wind are limits that must be fulfilled, and that stopped works for two weeks, waiting for acceptable weather. After building-fence positioning, the existing fountain had to be protected by a special platform. The above-described, curved steel trusses arches were attached to the membrane on site, and their shape released and introduced its prestress to a membrane surface. [3,4] In same time, the central ring was installed and the membrane was lifted and connected to upper supporting points. After the central ring was lifted to its final position and it was stabilize with high cables (safety cables). In a second step the two low points and curved steel trusses were placed in their predicted position. For this, two coordinated hoisting platforms were used. In this position the membrane was freely floating but not safely connected. So, the upper edge trusses were lifted by the use of hand winch tools to their supporting points. The cable terminals were joined in height. In a final step, all connection cables have been simultaneously prestressed. So, the structure was safe, and ready for adjusting and fine-tuning of details.

6. Retrospective and Maintenance

In addition to 24/7 service, and periodic inspection and maintenance a permanent monitoring of this structure has been part of the contract with the client and is seen as added value. So far, we have gathered data from 18month of monitoring. Immediate results can be summed up as follows: Overall,

the structure including geometry, prestress and material behavior has performed as planned. Even the most crucial areas have stayed without significant wrinkles in warp direction. Besides the technical, an extraordinary good acceptance has been achieved by permanent users and numerous visitors. After one year, the structure went thru and has been monitored under significant snow load, strong wind and strong sun, conditions, which were considered during design phase and cross-checked with reality. The structure´s behavior under snow load has been as predicted but the reality check has shown some insights with regards to snow gliding, ice forming, and specific oscillation under snow load. Strong wind caused much less deflection compared to the calculated. Strong sun can negatively affect HF-welding of seams, but so far, the applied material, and welded seams proved sufficient quality without visible defects. No problems have been detected for the steel elements, with the exception of the central steel ring. Here some micro cracks in the galvanized layer were noticed, indicating extreme tension and possible changes in the structure of the material. The spotted deformation is not of high importance, but very informative about action of tensile forces, and justifies the above-described double ring. Over time, maintenance becomes more and more important. In this regard, 18 months is a rather short time but so far this membrane structure has been absolutely maintenance friendly. In case, the accessibility of all elements is quite easy, which has been an important factor for the client.

7. Conclusion

The Airport City Belgrade Membrane Structure, Serbia is a project that has been designed, produced and installed by ArTech inženjering, and which simultaneously serves as an example for reflecting on design driving parameters, and as a showcase of problem driven innovation. We have explained the design guiding facts, like site specific design parameters, the client´s requirements and wishes, presented as CI - design parameters, and our architectural approach for the preliminary design phase. In addition, natural light, artificial light and sound considerations, as well as formfinding and structural analysis have been influencing decisions for the final design. Aspects such as the design and selection of the supporting points, the shape and function of the bending active steel trusses at the corners, the central opening of the membrane with its double center ring solution, and safety issues have been discussed in more depth, as they have been highly influencing the detailing of the project. The installation has been presented as a two-step process of preparatory works and erection. A retrospective reflects on 18 month of monitoring and gives information about maintenance. Even though, the conventional shape of the hypar served as the basic geometry in the design phase, the project contains several unusual points, challenging for design, detailing, analysis and installation. So, it serves as a good case study for future developments in this field of lightweight structures.

References

[1] Airport City Belgrade, Business Park, http://www.airportcitybelgrade.com/business-park/ accessed 31 May 2019.

[2] G. H. Filz, S. Shahzad and J. Niiranen, “Pringle : equitangential bending active frame and minimal surface robe-net,” in *Creativity in Structural Design: Proceedings of the Annual Symposium of the International Association for Shell and Spatial Structures 2018, MIT, Massachusetts Institute of Technology, Boston, USA,* S. Adriaenssens & C. Mueller (eds), 2018. pp. 164.

[3] W. Klasz, G. H. Filz, “A Cloud for Fresh Snow - Research Lab – a hybrid solution of minimal surface prestressed by bending active boundary conditions forming a spherical tetrahedron,” in *IASS Symposium 2015 "Future Visions" Amsterdam, The Nederlands,* 2015.

[4] G. H. Filz, “Low-tech or High-tech? " cut.enoid.tower " - three times two facets of irregularity,” in *VI International Conference on Textile Composites and Inflatable Structures: Proceedings Structural Membranes 2013*, Barcelona, Spain, 2013.

Proceedings of the IASS Annual Symposium 2019 – Structural Membranes 2019
Form and Force
7 – 10 October 2019, Barcelona, Spain
C. Lázaro, K.-U. Bletzinger, E. Oñate (eds.)

Detailing masts

Josep LLORENS

Barcelona School of Architecture (ETSAB), Universitat Politècnica de Catalunya
Diagonal, 649 - 1er, 02028 Barcelona, Spain
E-mail address: *ignasi.llorens@upc.edu*
web page: *https://wwwgat.webs.upc.edu/portada.html*

Abstract

As the efficiency and appropriateness of the structural membranes depends to a large extent on the supports, a research has been launched on the current design and the possibilities of optimizing the sections and the detailing are presented according to the typology established by the European Design Guide [1].

Keywords: masts, membrane structures, detailing

1. Introduction

Structural membranes need to be supported and tensioned by structural elements that condition the form and behaviour, affect the supposed lightweight appearance, and, in many cases, end up costing more than the membrane itself. As the most used supporting structural element is the mast, a research has been launched on its typology and detailing to improve efficiency and compatibility.

An extensive analysis of existing masts has been conducted to establish a typology, starting from the one mentioned on the "European design guide for tensile surface structures" [1], together with the formulation of strategies aimed at optimizing the design. Both concepts are profusely illustrated with selected examples drawn from the own experience and the documentation kindly provided by the authors, including visits to the sites and literature.

2. Antecedents

Masts were not new when tensile structures were significantly developed starting from the middle of the twenty century. Many other applications such as sailboats (fig.1 to 4), suspended and cable-stayed bridges, tents, cable suspended roofs and antennas had used and developed them considerably.



Figures 1,2: Running rigging on square sails [2]. Figures 3,4: Pilot's boat "Santa Eulàlia", Barcelona.

Copyright © 2019 by Josep LLORENS
Published by the International Association for Shell and Spatial Structures (IASS) with permission.

3. Typology

A typology based on the position related to the membrane includes:

a) boundary masts that support the edges at corner points. They are usually inclined to follow the resultant direction of the forces coming from the edge cables and going to the anchor ties. They can also be cantilevered when interferences coming from anchor ties are not permitted (fig.5).

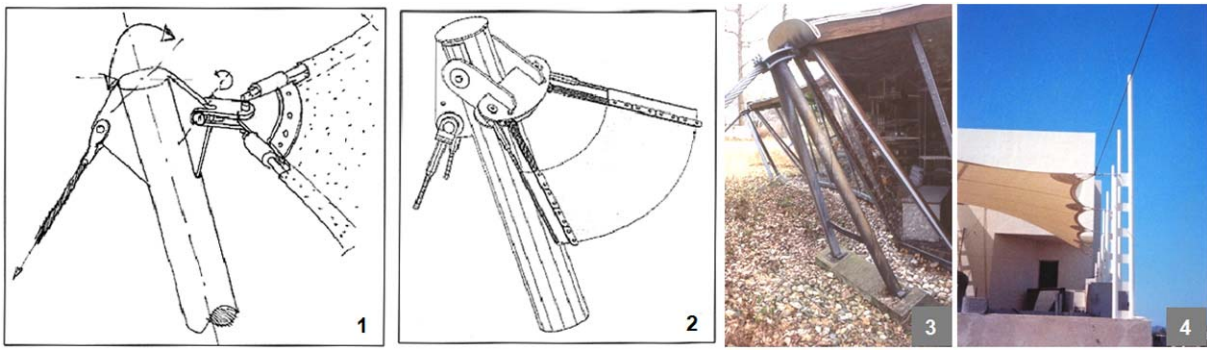


Figure 5: *Supported high points by external masts*. **1, 2** The connection with the peripheral masts can rotate around the horizontal, vertical axis or both. It is usually used for pre-tensionning. **3** A-shaped perimeter mast hinged at the base (IL Institute, Stuttgart). **4** Self supported perimeter mast. Stay ropes are not required.

b) internal masts surrounded by the membrane and resting directly on a base plate (fig.6) or floating/flying on steel cables that push them upwards (fig.7).

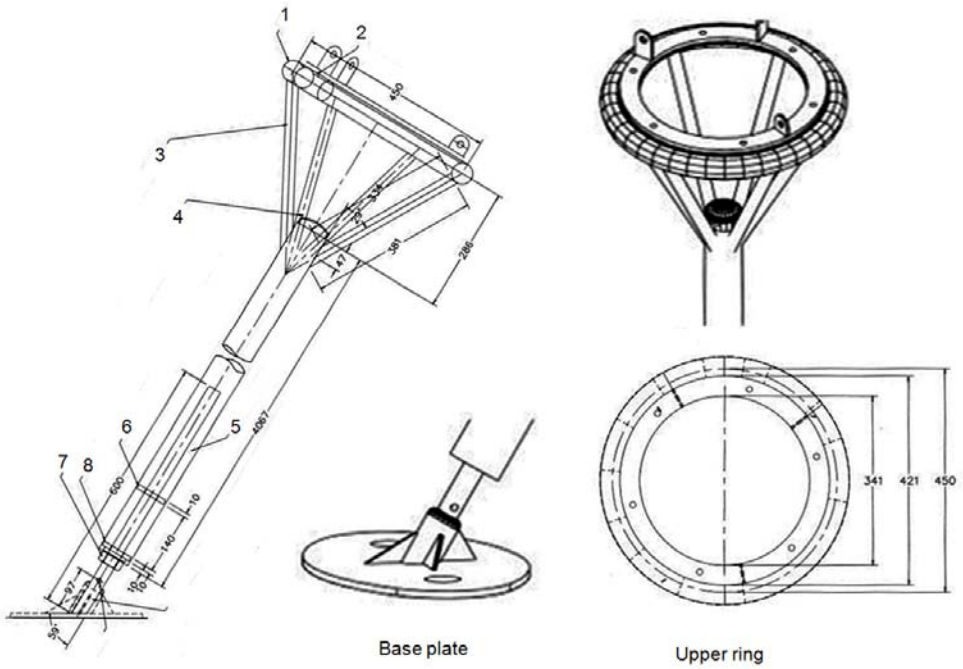


Figure 6: Central supporting mast of the Parc Astérix Dolphinarium, Plailly. It is achieved by a ring on top stabilised by guy cables and (semi)hinged at the base to relieve bending moments. A threaded assembly of the base allows for adjustment of the height and introduce prestress. The membrane is secured to the top of the mast by bolting between the ring and a circular plate. Notice the ring made of a Ø48,3 x 2,9 CHS to avoid sharp edges that could damage the membrane. The tension is introduced by adjustment of the mast length together with the tensioning devices of corners and edges [3].

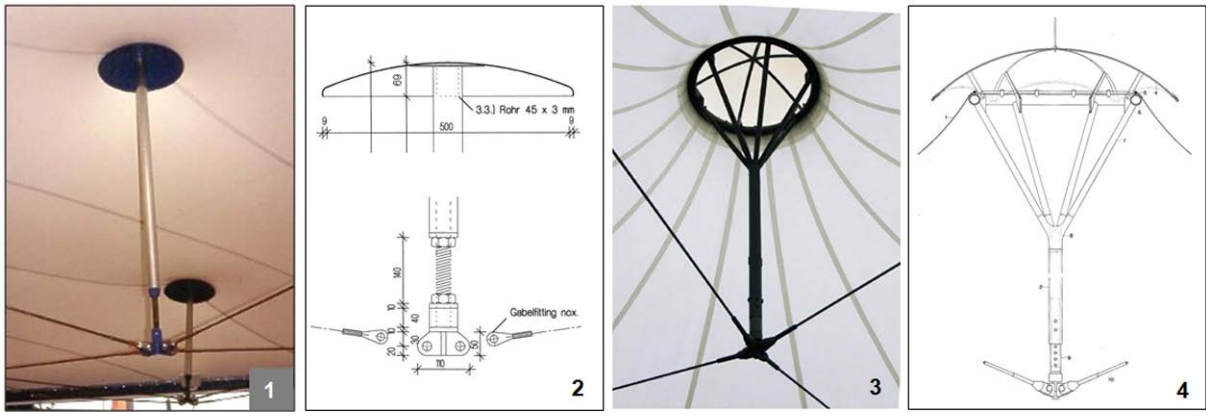


Figure 7: *Flying masts*. **1, 2** Flying masts supported on a cable net push up the membrane. They keep the covered space free of structural supports. A softening plate on the top of the flying mast enlarges the area of load distribution. Notice at the bottom the hinged fork cable-ends and adjustability of the length of the mast. **3**,**4** "A different approach to the connection between the flying mast and the membrane. The downward external loads applied to the structure are transmitted by bearing contact of the membrane on to the ring rather than by shear transfer through clamp bolts" [4].

c) external masts located outside the enclosure, from which the membrane is suspended (figs.8,9).

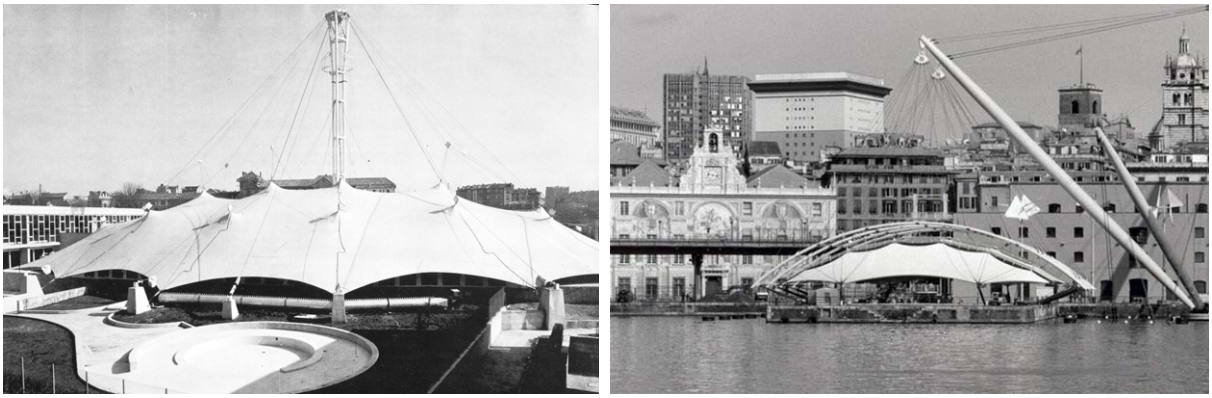


Figure 8 (left): R.Taillibert, 1966: Boulevard Carnot Swimming Pool, Paris. Figure 9 (right): R.Piano, 1991: Il Grande Bigo, Genova

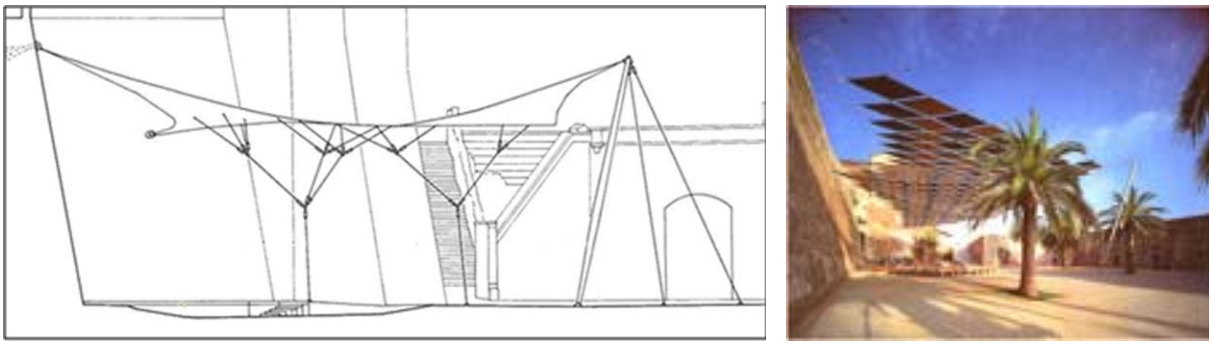


Figure 10: The tapered masts prevent from looking oversized compared to the whole structure and the site. J.A.Martínez & E.Torres with Llorens & Soldevila, Architects, 1991: Es Baluart, Palma de Mallorca

4 Shaft

The three types of mast accept different strategies to cope with over-dimensioning imposed by buckling on such long elements. They include the use of circular hollow steel sections (because of their efficiency in compression and torsion, minimal surface area to be protected, minimal wind resistance and availability) improved by tapering (fig.10), trussing (fig.11), tying (fig.12) or coupling (fig.13 to 15).

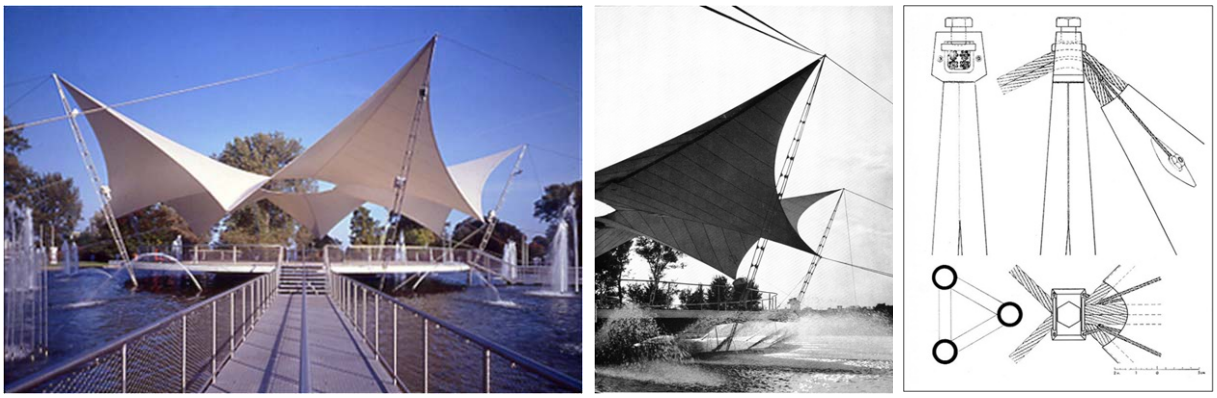


Figure 11: F.Otto & H.Spandow,1957: Dance Pavilion, Federal Garden Exhibition, Cologne. The masts are constructed very light and slender and, in addition, there are no gussets on the upper part of the masts, which means that the tops are not big-headed.

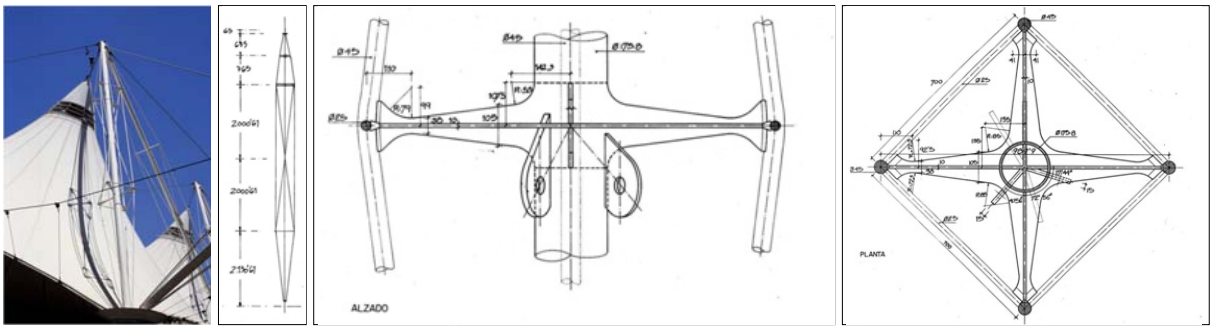


Figure 12: J.M.de Prada, 1992: "Palenque", Sevilla Expo. Cross-trees 10 mm thick and ties Ø 25 mm lighten the mast by reducing the buckling length from 7,60 m to 4 m so that a CHS of 115 x 7 mm is enough.



Figures 13, 14, 15: Coupling or clustering the masts make them thinner. Slim tubes look more elegant than a single bulky cylinder. Figure 10: M.Hopkins 1985, Schlumberger Research Laboratory, Cambridge. Figure 11: Ph.Cox 1988: Darling Harbour Exhibition Centre, Sydney. Figure12: A.Brookes 1992, East Croydon Station, London [5].

5 Mast ends

Apart from the section of the shaft, its ends also have a considerable impact on cost, appearance and ease of installation.

5.1 High points

Upper ends can be in the form of circular rings, humps, loops or scalloped cables (figs. 16 to 20).

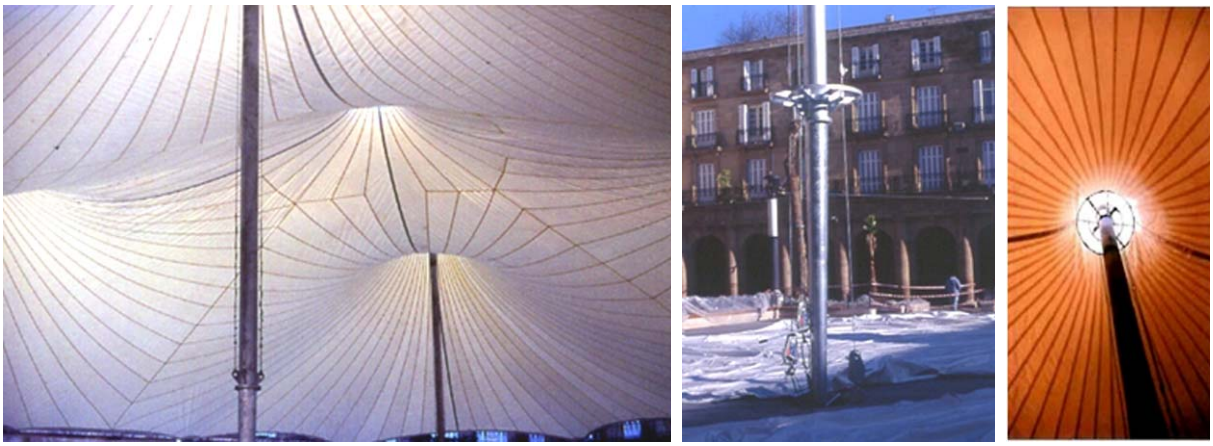


Figure 16: Llorens & Soldevila, Architects with IASO, 1990: Plaza Nueva, Bilbao. The membrane is raised along the mast by a circular ring driven by pulleys from the ground. The ring provides the perimeter length of material required to support the load not exceeding the breaking strength. The connection between the membrane and the ring can be considered a rigid edge, bearing in mind that a rigid connection is hardly compatible with the flexibility of the membrane. Here, the membrane can be prestressed from outside the ring and through the ring itself via its adjustable diameter and the pulleys [6].



Figure 17: "Jaima", the humped tent of the Berber tribes, Atlas Mountains. It is a single-family shelter including cattle, modular in construction, limited in size to the carrying capacity of the family camel (which, with the family goats, provides the hair from which the tent is woven), measuring around 20 by 40 feet and weighing about 360 lbs. The supporting hump-like high points are formed by poles topped by mushroom-shaped heads. The woven fabric acquires an anticlastic curvature except in the areas above the supporting humps [7].

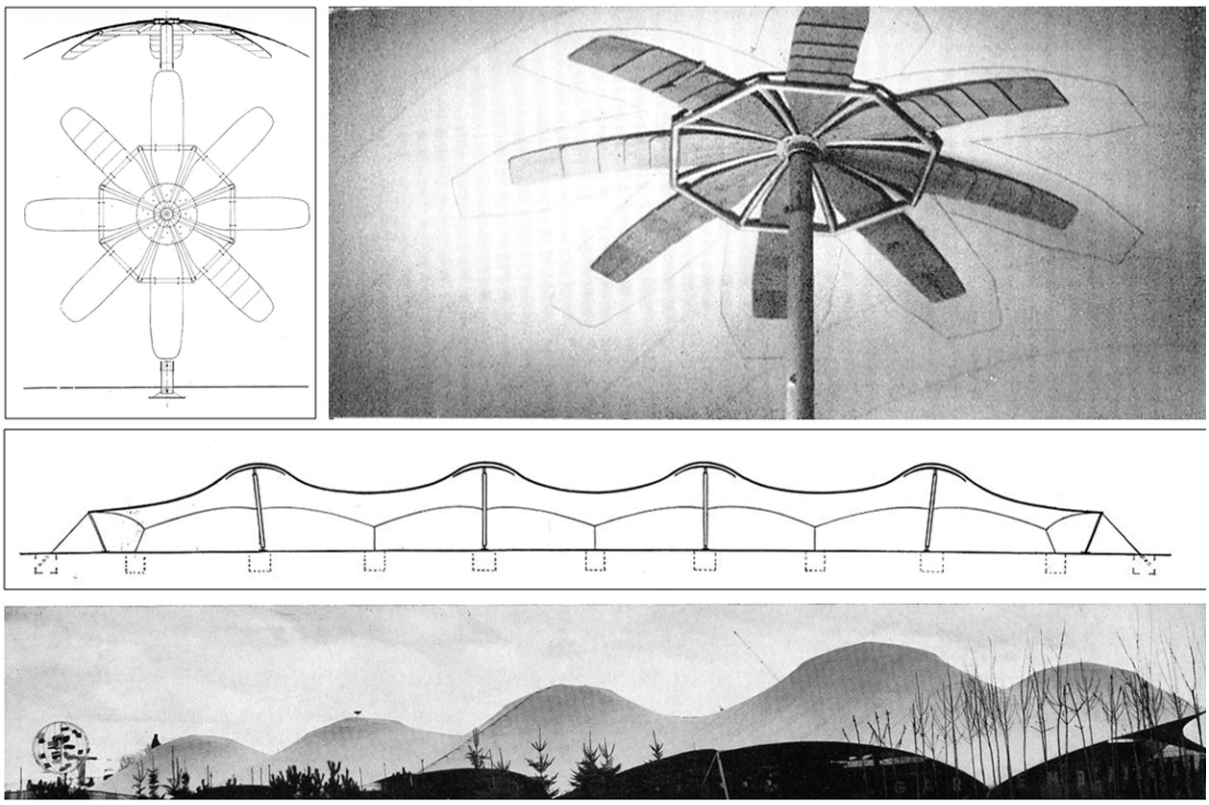


Figure 18: The hump-like high points of the tent at Hamburg International Garden Exhibition are formed by masts which have heads with flexible lamellae across which the membrane is stretched. The resilient head of each mast is 4 m in diameter and consists of radially disposed plywood blades which function as springs and are supported by a CHS with tubular spokes. A welded-on dished steel plate over the blades serves as an abutment for the latter. Each spring blade consists of five glued 8 mm thick layers of wood. Plywood is more suitable for the purpose than ordinary wood because its elasticity is more uniform. An important feature is that the deflections at the ends of the blades are very large in order to achieve smooth and uniform transmission of the force of the membrane.

The tubular poles have a total length of 5,5 m and are 180 mm in diameter. At the top and bottom they are provided with short telescopic tubular sections for adjustment springs. The latter are so designed that they transmit a prestressing force of 2,5 T to the membrane and also prevent the poles being subjected to excessively large compressive forces. The springs also compensate for the continual variations in length of the roof membrane which are caused by variations in humidity. The membrane stresses are thus kept approximately constant [8].

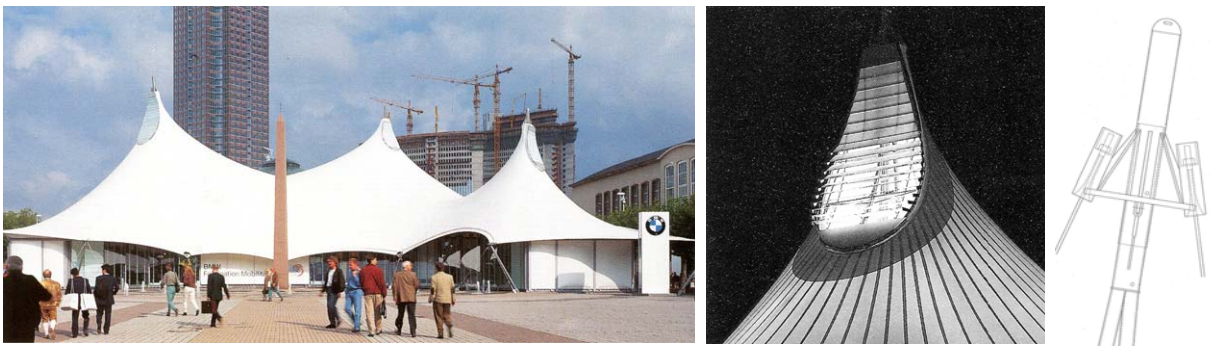


Figure 19: Frei Otto's favourite type of high point. Looped connection of membrane to masthead. Exhibition pavilion in Frankfurt, 1995 (Sobek und Rieger, Sttutgart with D.Wakefield, Bath) [9].

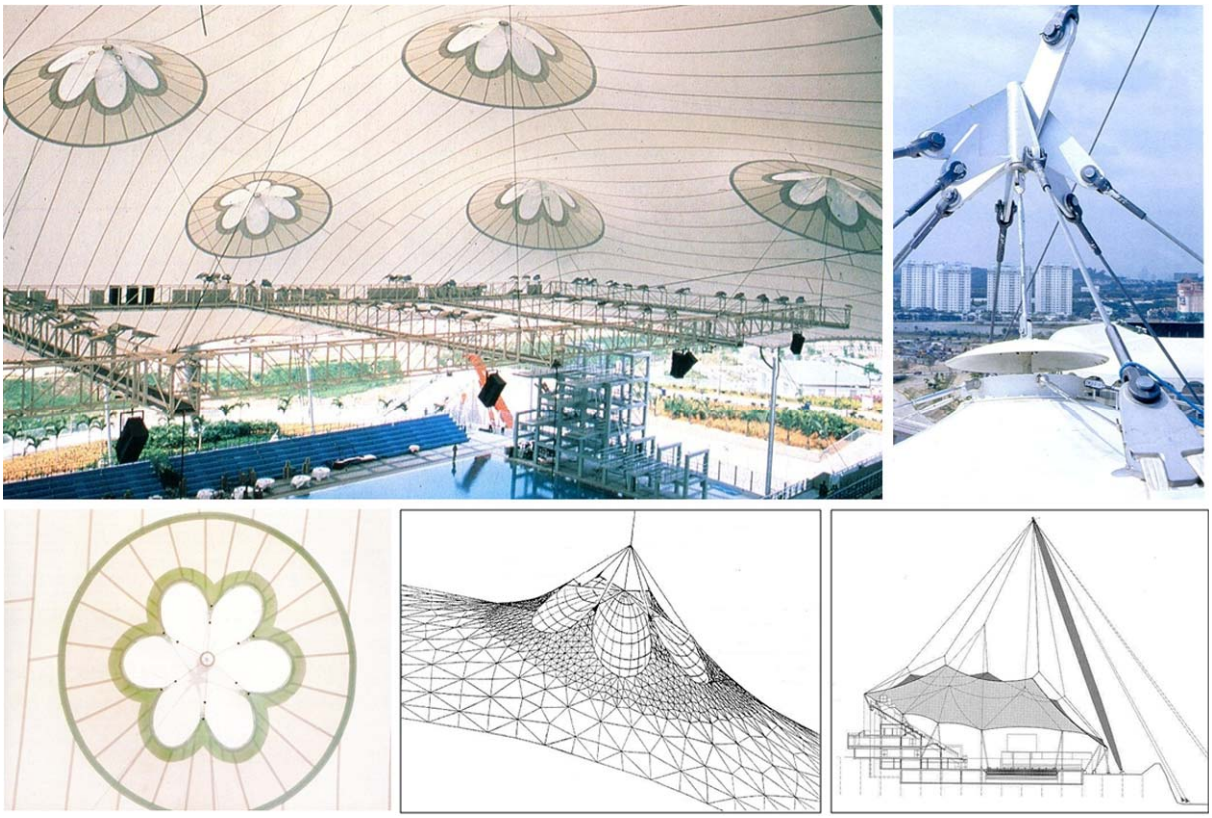


Figure 20: Widleplan Consulting with sbp, 1998: Commonwealth Games Swimming Pool, Kuala Lumpur. Scalloped high points. The cusp points of the belt are suspended from above by six straight cables and the central hole is closed over with a warped membrane panel [4].

5.2 Mast-base plates

Mast-base plates transmit compression (and shear) forces. They have to be designed carefully because they can easily result in a bulky element standing in the centre of the main visual field of the users. Mast-base plates transmit compression forces. They usually stand in the centre of the main visual field of the users. People regard them as being a main part of the structure. They are fixed or pinned about one or two axes.



Figure 21: The base of the mast is pinned about two axes (Courtesy of N.Goldsmith). Figure 22: Spherical base plate (Courtesy of S.Bertino). Figure 23: Spherical base plate. Toll gate, Manresa motorway.

Fixed bases allow for stability without guying cables, but they are not suitable if lateral loads result in bending which require an increase in the size. Pinning about one axis is typical for masts located at the perimeter which are tied by cables anchored to the foundation. If rotation may occur about two axes, two-degree of freedom bases, such as spherical connections, are used (figs.21 to 23).

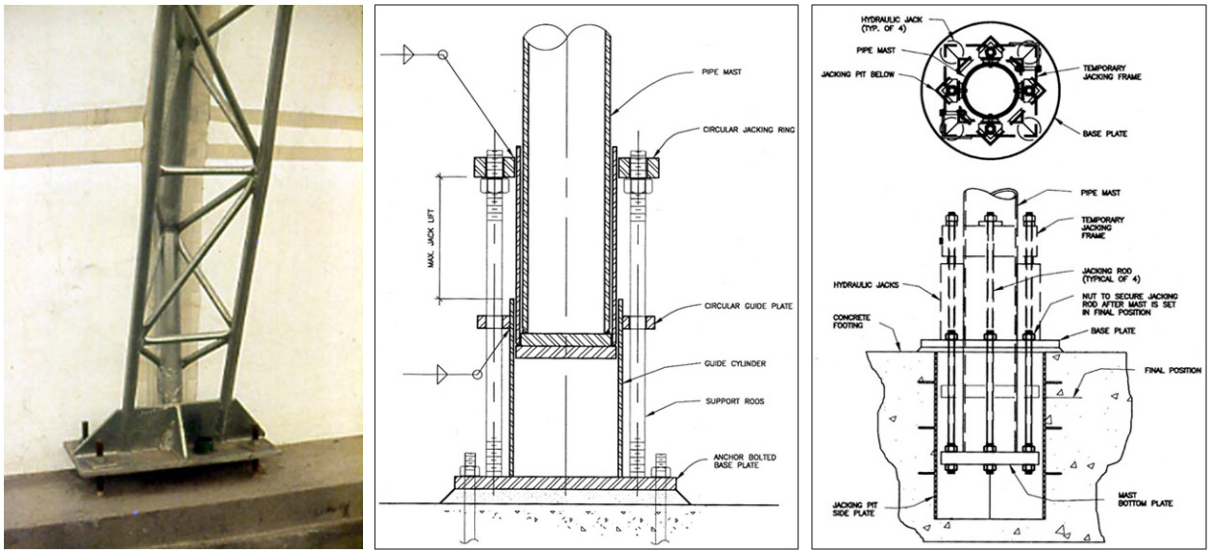


Figure 24: Base plates introduce pretension (Courtesy of M.Majowiecki). Figures 25, 26: Masts raised into position with portable hydraulic jacks [10]

7 Conclusion

Structural membranes, if not designed as such, require an imposing steel structure. As far as the masts are concerned, it is possible to achieve more efficient solutions optimizing sections, combining appropriate types, sections and profiles resorting, for example, to tapering, trussing, tying or coupling. Care has also to be taken in detailing to attend to the requirements of design and installation, avoiding bulky bases and big-headed tops.

8. References

[1] B.Forster & M.Mollaert, 2004: "European design guide for tensile surface structures". TensiNet, Brussels.

[2] H:A:Underhill, 1946: "Masting and rigging". Nautical Press, Glasgow.

[3] R.Motro (ed.), 2013: "Flexible Composite Materials". Birkhäuser, Basel.

[4] B.Fortser in K.M.Koch, 2004: "Membrane Structures". Prestel, Munich.

[5] J.B.Harris & K.Pui-K Li, 1996: "Masted structures". Butterworth Architecture, Oxford.

[6] J.Llorens, 2015: “Detailing for fabric architectural structures” in “Fabric structures in architecture”. Woodhead Publishing Limited in association with The Textile Institute, Cambridge.

[7] Shelter Publications, 1973: "Shelter". Bolinas.

[8] C.Roland, 1970: "Frei Otto: Tension Structures". Praeger Publishers Inc. New York.

[9] W.Sobek, 1995: "Exhibition Pavilion in Frankfurt"- DETAIL 8/1996, p.1240-1244.

[10] C.G.Huntington, 2004: "The tensioned fabric roof". ASCE Press, Reston.

Proceedings of the IASS Annual Symposium 2019 – Structural Membranes 2019
Form and Force
7 – 10 October 2019, Barcelona, Spain
C. Lázaro, K.-U. Bletzinger, E. Oñate (eds.)

Fixation details and membrane assembly

Miguel M. CARDENAS PANTOJA

CIDELSA S.A
Av Pedro Miotta 910, Lima 15801, Perú / https://www.cidelsa.com
E-mail: mcparquitecto@gmail.com

Abstract

Develop tensile structures projects implies from the conception of design to define the possible general solutions for any architectural approach without having to reach a final detail in an initial stage of proposals. In order to consider the most efficient installation and assembly process in this case, two important points must be considered; use the least amount of structural elements and the highest use of membrane pointing to the basic concept of lightweight coverage. Also within these 2 points consider the optimization of manufacturing and processes. In the case of the membrane achieve the least amount of repetitive modules and in the case of the structure look for the most modular and efficient geometry possible that can be adapted to any regular space or irregular.

Key words: initial geometry, optimization, assembly process

1. Introduction

The project "Polideportivo" I.E Republic of Argentina located in the city of Chimbote - Peru, is a project executed by the company COMERCIAL INDUSTRIAL DELTA S.A (CIDELSA) conceived in 2015 by the Arch. Aurora Pérez, head of the architecture area. The development begins in 2017, the design consists of a geometry of successive arcs rotated in its plane one after the other which define 2 main spaces joined through a central coverage.

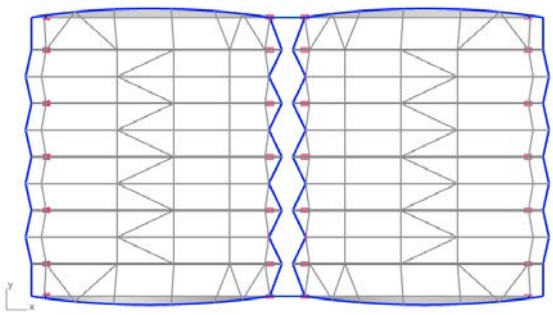


Figure 1: Design plant

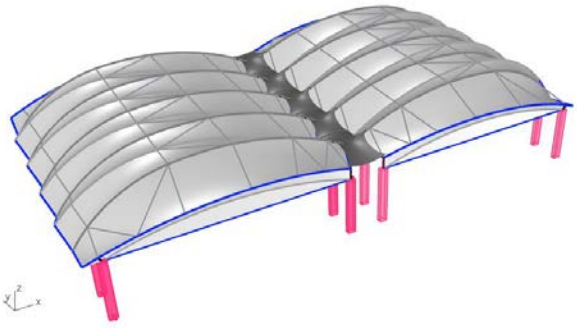


Figure 2: Isometry

Copyright © 2019 by Miguel Cardenas Pantoja
Published by the International Association for Shell and Spatial Structures (IASS) with permission.

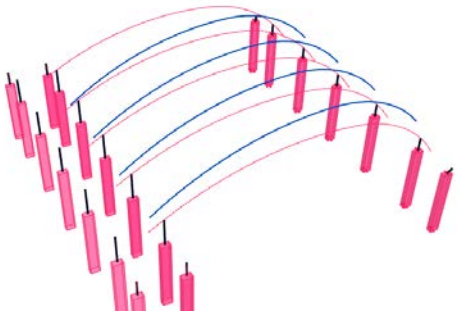


Figure 3: Main arches

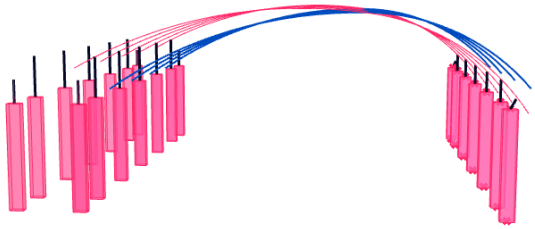


Figure 4: Rotation axis of intercalated arcs

The membranes were defined in typical sub modules that allowed to organize the elaboration of the larger blankets more quickly considering also a tentative assembly.

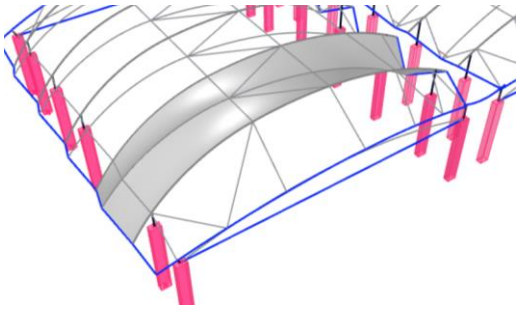


Figure 5: Typical module A with intermediate central cable

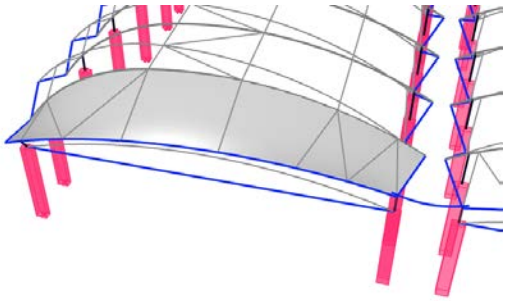


Figure 6: Typical lateral module B

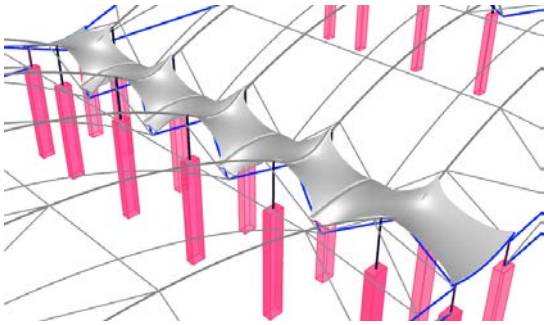


Figure 7: Central module C

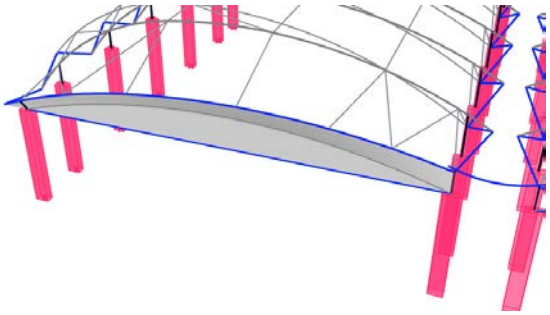


Figure 8: Typical lateral module D (vertical enclosure)

When passing to a stage of development, the possibilities of fixing the membrane are evaluated, being able to be above the structure or below. The engineering area, considering the proposed initial geometry, works in conjunction with the architectural area for the most suitable types of connection of the structure as well as the possibilities of assembly of the membrane. In this stage the final structure is defined where some additional structural elements may appear as well as the system for fixing the membrane in the structure.

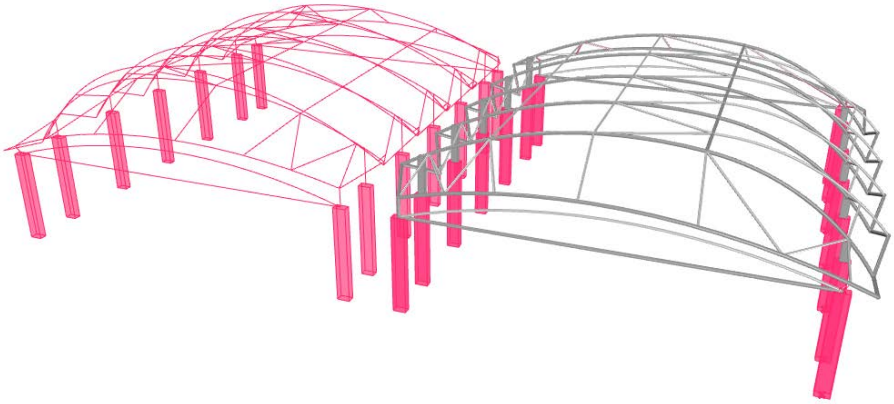


Figure 9: Engineering about geometric approach - dimensioning of pieces

For the membrane manufacturing stage it was defined to cover the entire area with 3 blankets, 2 of approximately 1500m2, a 200m2 central blanket and other vertical side enclosures.

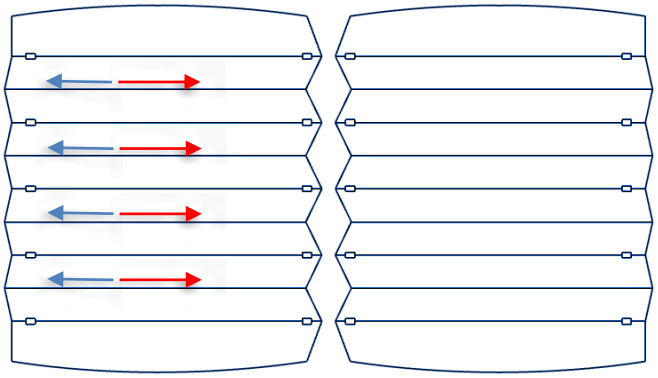


Figure 10: Main blankets of 1500 m2 c/u blue arrow and red arrow: different details

2. Fixation Details

The type of fixation of the membrane was considered according to the type of arrival at the edges, as well as the waterproofing at the edges and the opening points of the membrane to adjust the structure.



Figure 11,12,13,14: Fixation Details of membrane

2.1. Assembly process

The membranes come packaged very carefully from the factory, numbered and with a guide stuck on each corner that indicates the axis of location of each end. An assembly diagram is delivered in drawings where all the accessories and blankets are encoded, this is to have an efficient assembly process. A prior meeting with the installers and the person in charge at work is very important to clear up doubts.

For the assembly process, a membrane was first placed on the ground, which allowed protect it in the installation process and also to avoid damage with pieces that could tear the membrane. It was considered a pulley system that allowed to raise the membrane from the central tabs towards the arches more high after having fixed the entire perimeter.

For this membrane it was considered 4 cables with pressed terminals at the both ends for the fixation of the membrane, these cables are adjusted to have the other fixed edges. The membrane is raised with the cables already placed in their corresponding holsters.

In the central arches first the fixation is waterproofed by overlapping flaps that then are sealed in the place. In the perimeter of the coverage the flaps of that edge is fixed to a rectangular edge welded in the structure by means of a metal clamp that allows to create a kind of gutter of cloth that serves to orient the flow of water to the water evacuation points.



Figure 15,16,17: Membrane lifting process

The central and lateral zones are less complex, simply by means of metal elements and accessories the membrane is fixed at its high and low points, in the curved zone Fig.18, it was not necessary to put a cable in an edge holster, it was only considered in the manufacturing process make a thicker ends to define the curve of that ends well.



Figure 18,19,20: Installation of central module C and side module D

Finally there is another set of membranes to be placed between the columns of the extreme axes, these membranes are of another type of material where the perimeter fixation is basically with eyelet and halyard, having only a different detail. The upper end of these blankets is fixed by metal accessories to the main membranes solving the fixation without problems.



Figure 21,22: Installation of interior enclosures

3. Conclusions

Having a project that can apparently be solved at a general level, there will always be details that will define the final solution of a system for fixing a tensile structure. The dialogue between the specialties in this case architecture and engineering is very important to establish concrete solutions depending on the magnitude of the project.

The membrane details fulfill a special role for each case, which allows us to continue exploring different options of metal fixings, parts and accessories. The membrane with the sealing system has many benefits, which allows us to create prototypes at real scales by testing ideas we can have when developing a project.

For the assembly process, establishing a step-by-step installation process, coding parts and making a step diagram is important. For large projects, it is even more so since it can involve damaging a well-fabricated membrane. The climatic factor is also an important factor a blanket of more than 1200 m2 with the wind could be spoiled according to its lifting procedure.

References

[1] Arq. Roberto Santomauro (2008) “TENSILE STRUCTURES”. Montevideo – Uruguay.

Proceedings of the IASS Annual Symposium 2019 – Structural Membranes 2019
Form and Force
7 – 10 October 2019, Barcelona, Spain
C. Lázaro, K.-U. Bletzinger, E. Oñate (eds.)

Most common connections details in ETFE constructions

J. SALÓ*

E25006 Lleida. Spain
jaume.salo@hotmail.com

Abstract

In recent years, ETFE solutions have become more and more frequent in building technology. The most common place to find an ETFE solution is the exterior skin of a building. Sometimes as a canopy, sometimes as a roof or façade, or even as a complete envelope. Also, these construction solutions can be applied to many types of buildings with very different purposes: office buildings, airports, sports facilities, shopping malls, etc. On the other hand, this new construction technology is not as well-known as other building technologies, such as glass or polycarbonate. Thus, ETFE systems must present the same demanding features and high-level quality as the more traditional building systems do in order to compete and be successful in the construction market. One point to take into account for designers and architects is how to integrate an ETFE solution into a building. This paper plans to focus on the detailing and connections between ETFE systems and the other parts of the building, essential for fulfilling the watertightness, airtightness, and thermal insulation requirements of construction. The objective of this paper is to explain the main concepts and typical connection details and illustrate how to apply them to the design process. The construction of ETFE details must be based on a good overall understanding of the system, good detailing design, and a well-developed execution plan. This could be the best approach to avoid future problems and costly maintenance.

Keywords: membrane structures, air supported structures, ETFE, cushions, connections, details, detailing,

1. Introduction

As a cladding solution, ETFE foil can be applied as a single layer (tensioned membrane structure) or as a cushion system (air supported structure).

This paper will study the most common connections in ETFE specifically for cushion structures that enclose a volume. That means that not only watertightness is needed, but also airtightness and thermal insulation as well.

In the market there are several cushion systems available. Every specialist contractor tends to have their own aluminum profile design. Even though there can be differences between the systems, this paper will try to show the main principles to achieve a good design.

We can also learn from other building technologies such as glass, polycarbonate and façade or roofing systems. This could also help us to understand the main concepts. Actually, the problems to solve are quite the same. We cannot forget that a roof is one of the most difficult parts in a building when it comes to preventing rainwater leaks.

To go into depth on the subject, this paper will introduce the principle of the most common ETFE systems available in the market, in terms of waterproofing and internal drainage. Second, a general approach as to how an ETFE surface is incorporated into a building will be presented, to let us identify the most common links. For the third point, the most common connections between an ETFE roof and the other parts of the building (gutters, walls, roof ventilation devices and standard waterproof roofs) will be discussed.

Copyright © 2019 by Jaime Saló
Published by the International Association for Shell and Spatial Structures (IASS) with permission.

2. Principle of most common ETFE systems

An ETFE system is composed of several parts. Perhaps one of the most important, in terms of detailing, is the aluminum profile system.

Internally the total roof surface is divided following the modulation design. This pattern establishes the layout of the aluminum frame.

In general, this layout is a continuous line and it is often followed by the main structure underneath or outside.

Along the perimeter of the surface, the cushion is clamped to the profile on one side and the flashing plates on the other. This is the boundary of the skylight.

Profiles act as gutters, so they can collect some raindrops and have to evacuate to somewhere outside the building through a drainage hole. Since the system must be totally waterproof, it is advisable to have more than one barrier to avoid rain leakage inside the building.

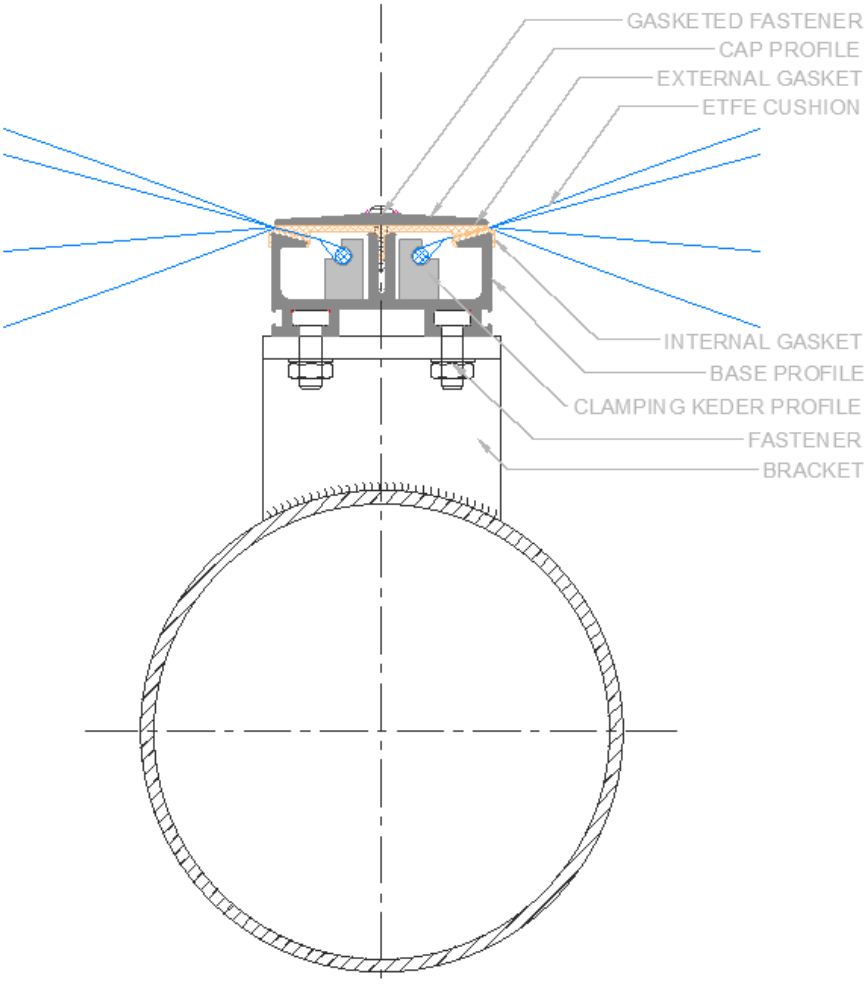


Figure 1: Schematic section of an aluminum profile system for ETFE cushions

The external gasket acts as a first barrier. The base profile acts as a second barrier and as a gutter, which collects any drops of water that make it through the first barrier or internal condensation.

This water penetration must be taken out by drainage in the low parts of the roof. A number of drainage openings in the base profile will allow the water to evacuate to the exterior.

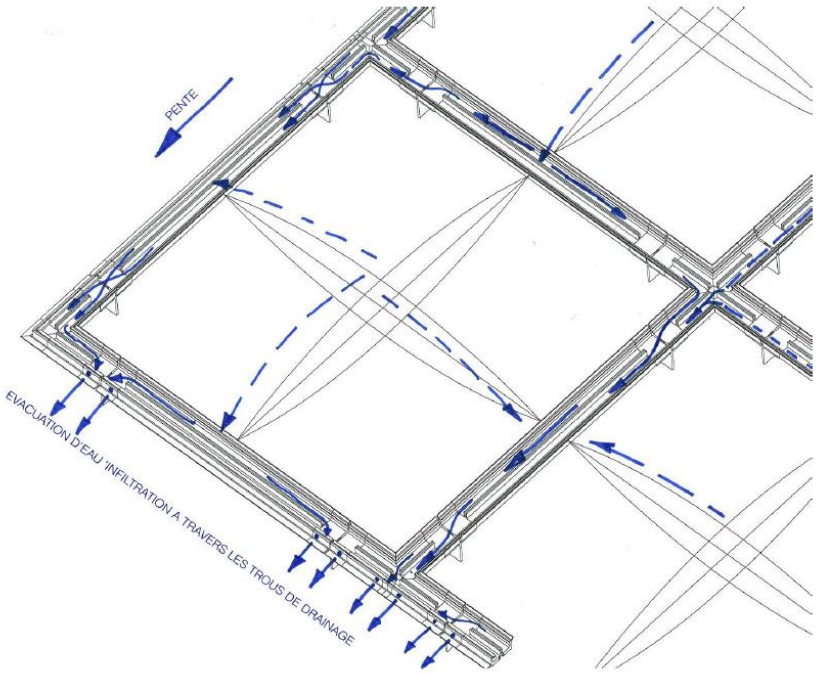


Figure 2: System drainage scheme [2]

3. How an ETFE surface belongs as part of a building

An ETFE transparent or translucent surface can be found in different parts of a building. Typical examples are roofs and facades, also complete envelopes or double skins. As we said before, the design of the connection details has to satisfy the watertightness, airtightness and thermal insulation requirements of the construction.

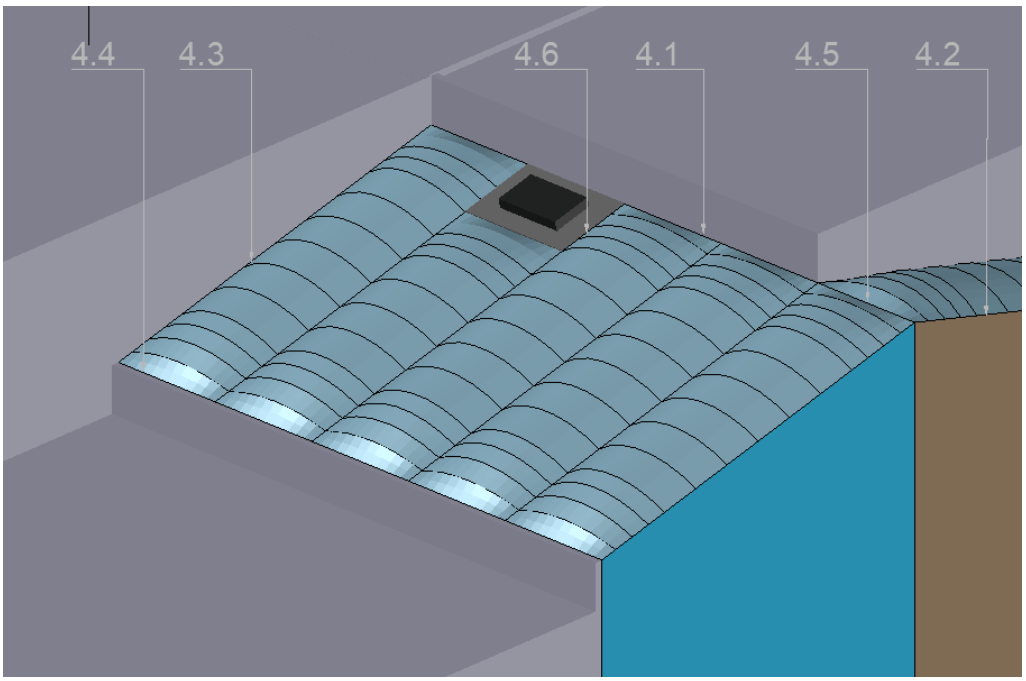


Figure 3: Axonometric view to identify most common details

4. Most common links between an ETFE cushion roof and the other parts of the building

4.1. Detail ETFE cushion roof-Wall

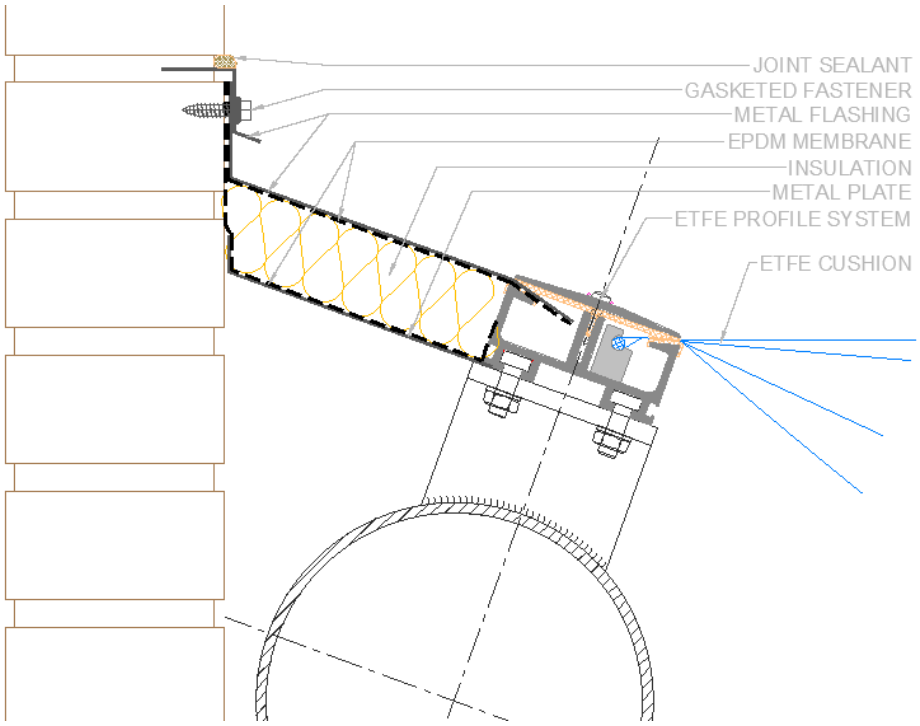


Figure 4: Detail ETFE cushion roof-Wall

4.2. Detail ETFE cushion roof- Sandwich panel

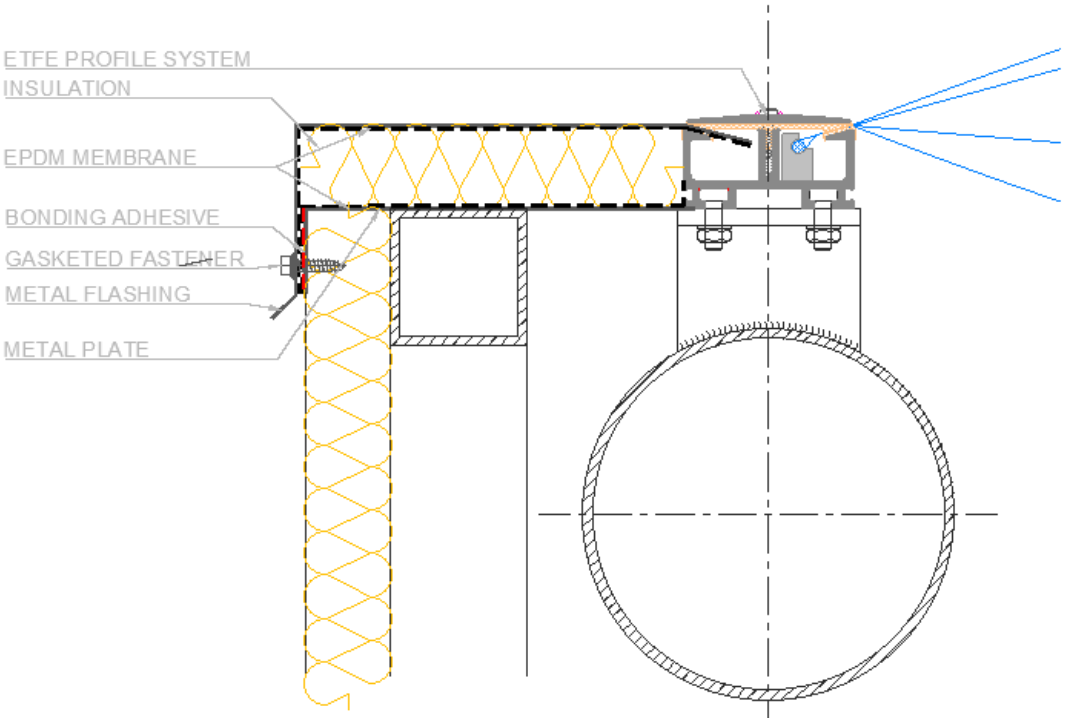


Figure 5: Detail ETFE cushion roof- Sandwich panel

4.3. Detail ETFE cushion roof- Lateral wall

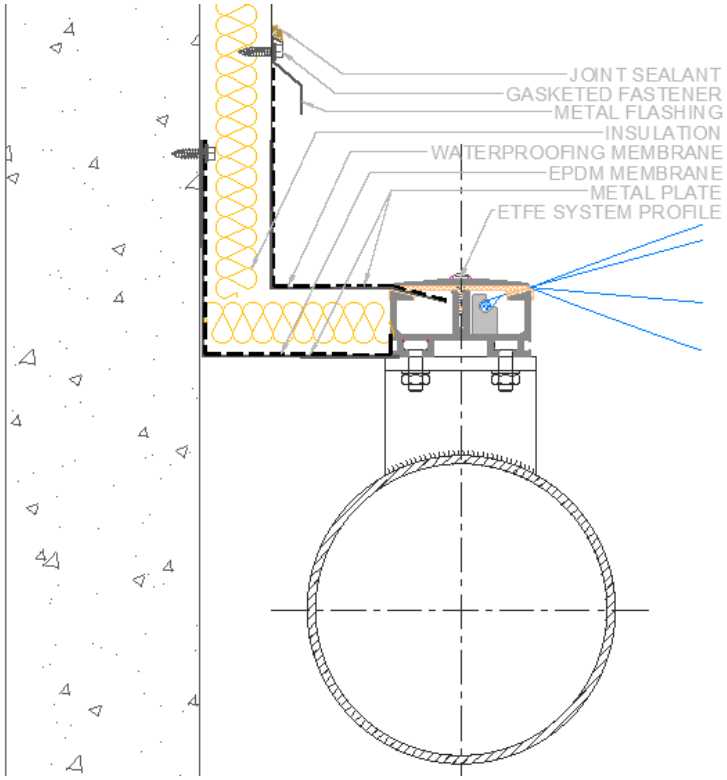


Figure 6: Detail ETFE cushion roof- Lateral wall

4.4. Detail ETFE cushion roof- Gutter

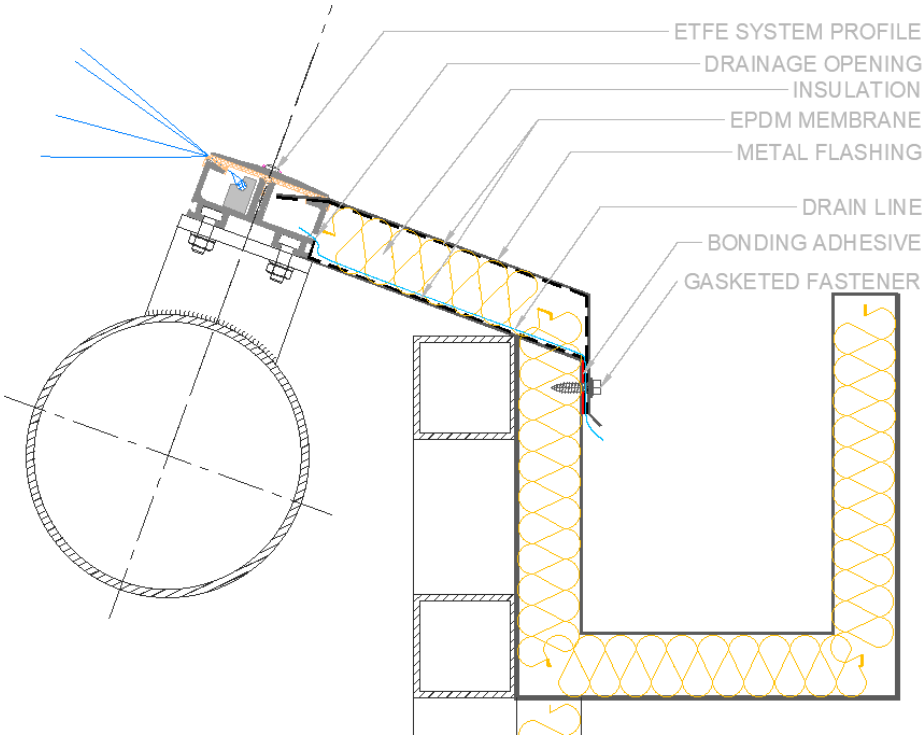


Figure 7: Detail ETFE cushion roof- Gutter

4.5. Detail ETFE cushion roof- Ridge

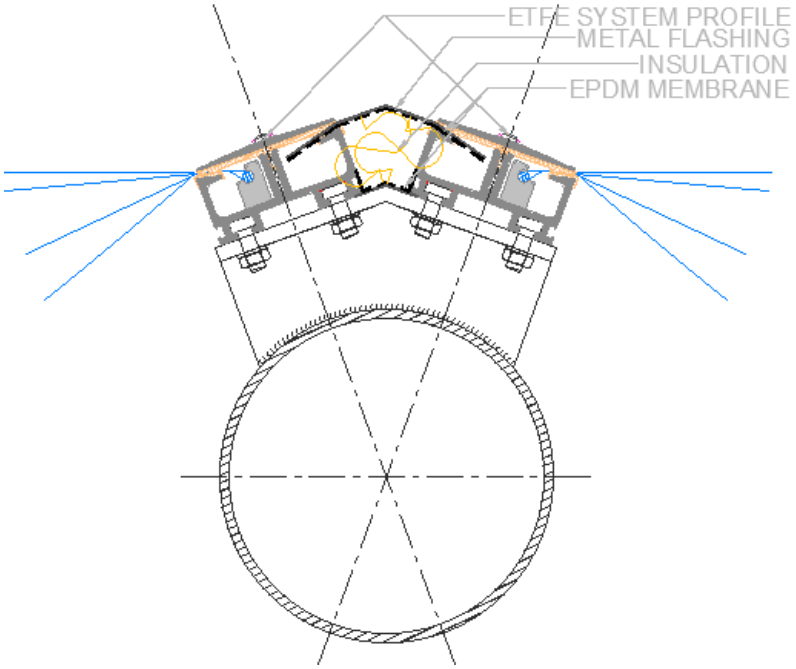


Figure 8: Detail ETFE cushion roof- Ridge

4.6. Detail ETFE cushion roof-Roof ventilation devices

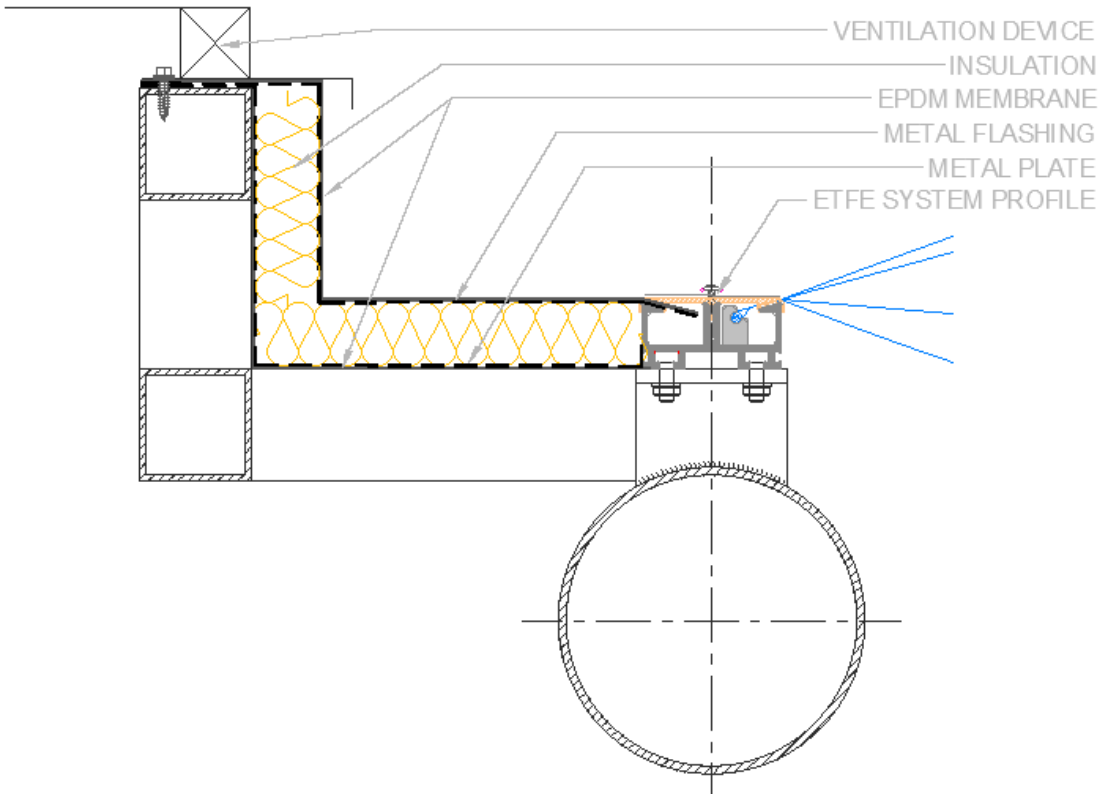


Figure 9: Detail ETFE cushion roof-Roof ventilation devices

4.7. Detail ETFE cushion roof- Dilatation joint

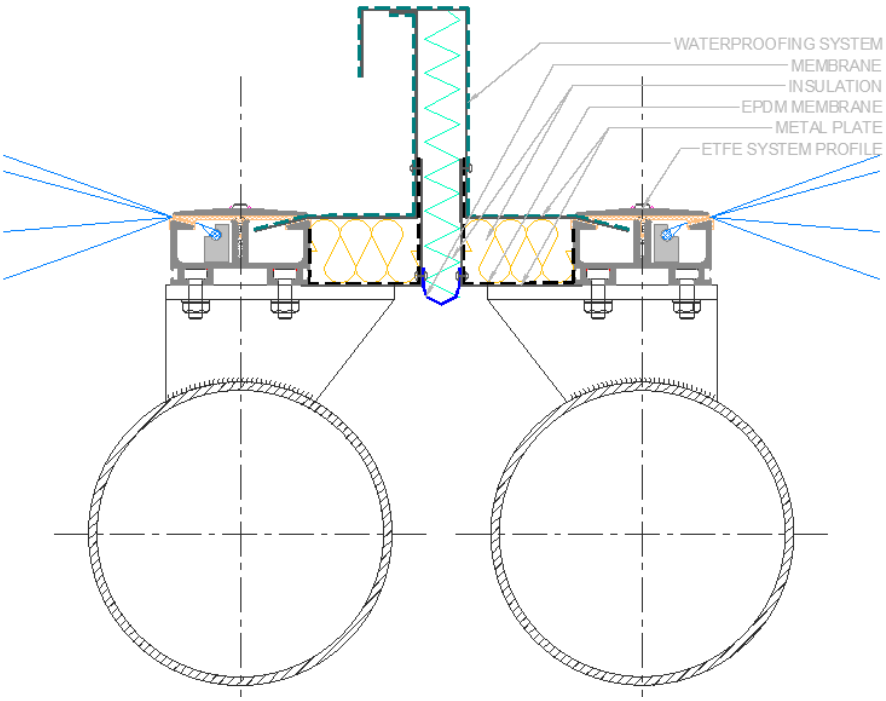


Figure 10: Detail ETFE cushion roof- Dilatation joint

4.8. Detail ETFE cushion roof-Roof pipe penetration

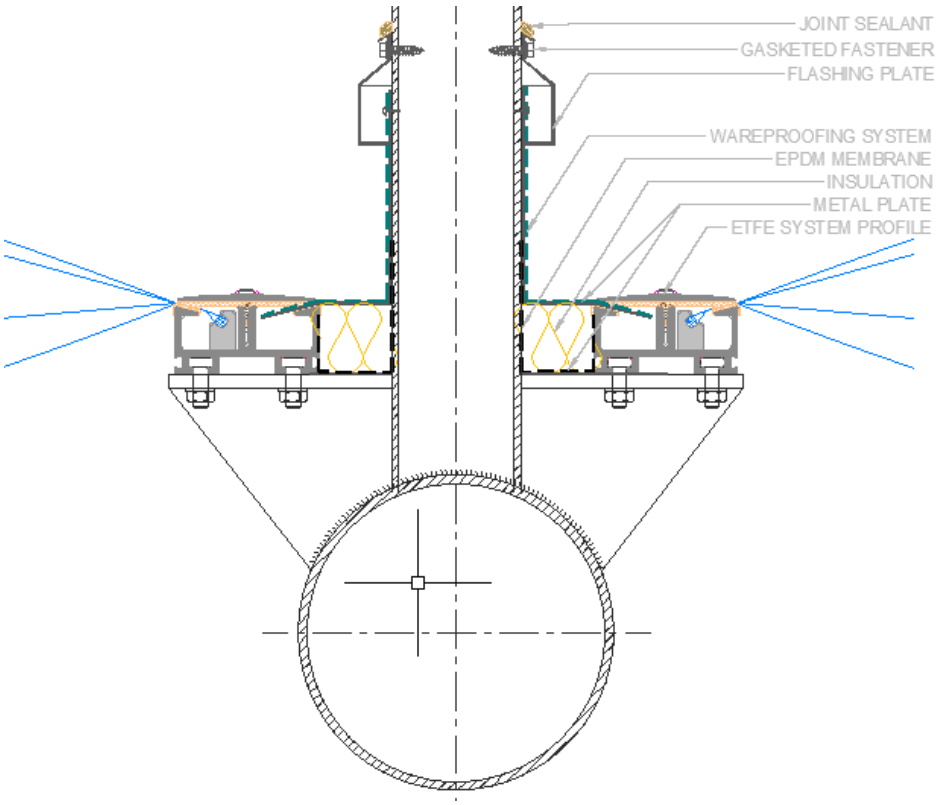


Figure 11: Detail ETFE cushion roof-Roof pipe penetration

4. Conclusion:

Due to the growing use of ETFE constructions and the demanding features of this building technology, designers and architects have to pay attention to how to integrate these solutions with the rest of the building. Designing the right connection details is key to achieving the best construction performance.

Acknowledgements

I would like to express my very great appreciation to Professor Josep Llorens. Since the beginning of my professional career, he has contributed to my education (and knowledge,) and let me discover my vocation for Textile Architecture. He encouraged me to submit this paper and he has supervised my work.

My special thanks are extended to my colleagues, engineers, architects, etc without whom these connections details would never have existed. I have learned so much from all the different projects I have worked on over the years.

I am particularly grateful for the assistance given by Ms. Hannah Allaben to help me writing this document.

References

[1] Iaso France SASU, "Système IASO de coussins gonflables en film ETFE", *Avis Technique 2/16-1726*V1*. December 2016.

[2] Vector Foiltec France, SARL, "Texlon® Verrière gonflable en film ETFE", *Avis Technique 2.1/13-1536_V2*. November 2017.

[3] Seele France, SAS, " Coussins à membranes ETFE", *Avis Technique 2/16-1760*. March 2017.

Proceedings of the IASS Annual Symposium 2019 – Structural Membranes 2019
Form and Force
7 – 10 October 2019, Barcelona, Spain
C. Lázaro, K.-U. Bletzinger, E. Oñate (eds.)

On the static calculation of biogas containers with radial and parallel cutting patterns

Dieter STRÖBEL*, Jürgen HOLL[a]

* Dieter Ströbel, Pestalozzistraße 8, Stuttgart 70563, Germany, dieter.stroebel@technet-gmbh.com
[a] Jürgen Holl, Pestalozzistraße 8, Stuttgart 70563, Germany, juergen.holl@technet-gmbh.com

Abstract

Nowadays, radial cutting patterns are common for biogas tanks above a certain construction height. The radial cutting patterns are a production challenge, especially at the polar caps. In order to avoid production difficulties, it is desirable to build plants with parallel cutting patterns. In our paper the results of a radial cutting pattern are compared and discussed with the results of a parallel cutting pattern. Our model deals with the two membrane envelopes of a double membrane system. Together with the inner membrane (gas membrane), an outer membrane forms a chamber, the so-called air support space. Together with the silo walls and the surface of the substrate, the gas membrane forms a second chamber, the so-called gas space. Different scenarios, e.g. the situation under internal operating pressure and the situation under a gust of wind were simulated. In the case of 'fast' loads (wind), the gas law applies. In the case of rapidly occurring loads, it must be investigated whether the outer shell and the gas membrane touch each other. The contact problem can be considered in our calculation model. We have applied the internal pressure perpendicular to the surface for each deformed state. We also carried the wind loads with the deformations in the iterations. The material properties are defined by warp-, weft stiffness and the so-called transverse and shear stiffness in order to simulate a realistic behavior in the radial or parallel directions.

Keywords: Pneumatic structures, Biogas plants, Lightweight structures, Formfinding, Statics, Patterning, Gas law, Contact problem, Hybrid structures, Membranes, Foils, Force density, Optimization

1 Introduction

The relationships to the calculation of spheres under internal pressure from isotropic material have been known for a long time. The stress s in the surface is the same in all points and depends in a simple way on the internal pressure p and radius R (s=p*R). A sphere is therefore a regular surface that can be formed pneumatically (such as a cylinder or torus). This simple fact is made considerably more difficult by the fact that textile fabrics do not have isotropic but orthotropic material behavior and are subject not only to internal pressure loads but also, for example, to snow and wind loads. Furthermore, in the simplest case, the structures to be investigated are not spheres, but parts of spheres (spherical calottes), or no regular surfaces anymore, if one does not have a circular, but a polygonal edge. The membrane design is simple in the case of the circular boundary. One simply takes a sphere section. In the case of the polygonal boundary, however, the geometry must be determined in a form-finding process. The result must have a geometry that represents an equilibrium figure under internal pressure loads. These facts are relevant for the determination of the cutting patterns. As with any other surface, any cutting variants and thus different material directions are possible. Static calculations

Copyright © 2019 by D. Ströbel, J. Holl
Published by the International Association for Shell and Spatial Structures (IASS) with permission.

must ensure that the maximum membrane stresses are not exceeded. In the case of the general spherical shape, which was determined by a form-finding process, the material directions must be considered in the form-finding process as the above-mentioned simple relationship s=p*R is not anymore valid in case of orthotropic material. It follows a short description of 'usual' biogas storage systems, so that the formation of computer models becomes understandable.

2 Schematic sketch

Biogas storage systems generally have 2 membrane covers. The outer shell and the so-called gas membrane. The air volume between the outer and inner shell is called the air support space. It is always under pressure. The volume under the gas membrane forms the so-called gas space. There are different pressure situations in the gas space. If the pressure in the gas space is 0, the gas membrane lies on the belts that run from a central point to the silo edges. If the gas pressure is maximum, the volume of the gas space is maximum, and the air support space is minimum.

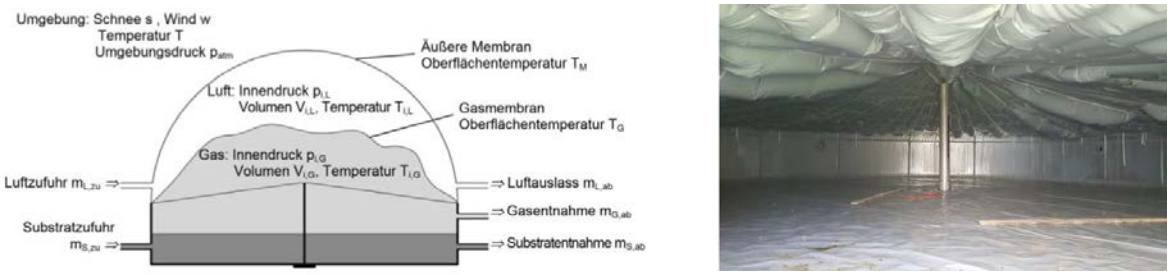


Figure 1: Schematic sketch of a biogas storage system (left), No gas pressure in the biogas-silo, gas membrane lies on the belts (right)

In the static calculation, the external loads must be safely transferred regardless of the situation in the gas and air support space.

Before we come to the calculation results for different variants of cutting patterns, we want to deepen the background of Formfinding and Statics of chambered membranes.

3 Formfinding

The theory of the Formfinding of pneumatic chambers has its basics in the well-known Force-Density Method ([1], [2] and [3]). The Force-Density Method creates a linear system of equations for the form-finding procedure by defining the ratio between Force S and stressed length l to be known. Hereby the nonlinear equations of the equilibrium change to a linear system.

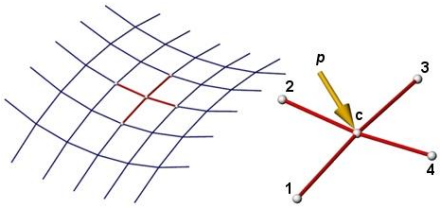


Figure 2: Four cables in point C

In order to clarify these facts *Fig. 1* shows a point *C* which is connected by cables to 4 points (*1*,*2*,*3*,*4*). The nonlinear equations of the equilibrium in the point *C* are as follows, where the external load vector can be expressed $\boldsymbol{p}^t = (p_x \quad p_y \quad p_z)$.

$$\begin{array}{llll} (x_c - x_1)\frac{S_1}{l_1} + & (x_c - x_2)\frac{S_2}{l_2} + & (x_c - x_3)\frac{S_3}{l_3} + & (x_c - x_4)\frac{S_4}{l_4} = p_x \\ (y_c - y_1)\frac{S_1}{l_1} + & (y_c - y_2)\frac{S_2}{l_2} + & (y_c - y_3)\frac{S_3}{l_3} + & (y_c - y_4)\frac{S_4}{l_4} = p_y \\ (z_c - z_1)\frac{S_1}{l_1} + & (z_c - z_2)\frac{S_2}{l_2} + & (z_c - z_3)\frac{S_3}{l_3} + & (z_c - z_4)\frac{S_4}{l_4} = p_z \end{array} \quad (1)$$

These equations become linear by assuming known force-densities, e.g. $q_1 = \frac{S_1}{l_1}$, and analogue for q_2, q_3 and q_4. The force-density equations are as follows:

$$\begin{array}{llll} (x_c - x_1)q_1 + & (x_c - x_2)q_2 + & (x_c - x_3)q_3 + & (x_c - x_4)q_4 = p_x \\ (y_c - y_1)q_1 + & (y_c - y_2)q_2 + & (y_c - y_3)q_3 + & (y_c - y_4)q_4 = p_y \\ (z_c - z_1)q_1 + & (z_c - z_2)q_2 + & (z_c - z_3)q_3 + & (z_c - z_4)q_4 = p_z \end{array} \quad (2)$$

The coordinates of the point *C* are the solution of these linear equations. In the following step we want to write the system above by considering m neighbors in the point *C*:

$$\begin{array}{ll} \sum_{i=1}^{m}(x_i - x_c)q_i - p_x = 0 \\ \sum_{i=1}^{m}(y_i - y_c)q_i - p_y = 0 \\ \sum_{i=1}^{m}(z_i - z_c)q_i - p_z = 0 \end{array} \quad (3)$$

The energy which belongs to the system (1) can be written as (see also [4], [5], [6]).

$$\prod = \frac{1}{2}\boldsymbol{v}^t\boldsymbol{R}\boldsymbol{v} - p_x(x - x_0) - p_y(y - y_0) - p_z(z - z_0) \Rightarrow stat. \quad (4)$$

The internal energy is the expression $\frac{1}{2}\boldsymbol{v}^t\boldsymbol{R}\boldsymbol{v}$. The vector $\boldsymbol{v}^t = (v_x \quad v_y \quad v_z)$ and the matrix $\boldsymbol{R} = diag(q_i \quad q_i \quad q_i)$ show this energy with respect to a single line element i .We can write the inner energy as $\frac{1}{2}q_i(v_x^2 + v_y^2 + v_z^2)$, precisely:

$$\begin{array}{lll} v_x = x_i - x_c \\ v_y = y_i - y_c \\ v_z = z_i - z_c \end{array} \qquad \boldsymbol{R} = \begin{bmatrix} q_i & 0 & 0 \\ & q_i & 0 \\ sym. & & q_i \end{bmatrix} \quad (5)$$

The chamber of a pneumatic structure has a volume *V*, which is made by an internal pressure p_i. The product from internal pressure and volume is a part of the total energy Π : a given volume V_0 leads directly to a specific internal pressure p_i : hence the total energy for the Formfinding of a pneumatic chamber is $\prod = \frac{1}{2}\boldsymbol{v}^t\boldsymbol{R}\boldsymbol{v} - p_x(x - x_0) - p_y(y - y_0) - p_z(z - z_0) - p_i(V - V_0) \Rightarrow stat.$ The derivation of the total energy to the unknown coordinates and to the unknown internal pressure ends up with

$$\begin{aligned}
\frac{\partial \prod}{\partial x} &= \sum_{i=1}^{m}(x_i - x_c)q_i - p_x - p_i\frac{\partial V}{\partial x} &= 0 \\
\frac{\partial \prod}{\partial y} &= \sum_{i=1}^{m}(y_i - y_c)q_i - p_y - p_i\frac{\partial V}{\partial y} &= 0 \\
\frac{\partial \prod}{\partial z} &= \sum_{i=1}^{m}(z_i - z_c)q_i - p_z - p_i\frac{\partial V}{\partial z} &= 0 \\
\frac{\partial \prod}{\partial p_i} &= V - V_0 &= 0
\end{aligned} \tag{6}$$

In the system (6) the internal pressure p_i can be seen as a so-called Lagrange multiplier. The fourth column in (6) shows, that our boundary condition $V = V_0$ is obtained by the derivation of the energy to this Lagrange multiplier. The vector $(\frac{\partial V}{\partial x} \quad \frac{\partial V}{\partial y} \quad \frac{\partial V}{\partial z})$ describes the normal direction in the point *(x, y, z)* and the size is the according area. By a set of given force-densities for all elements and also a given volume V_0 we end up with a pre-stressed and of course balanced pneumatic system with a volume V_0 and an internal pressure p_i.

4 Statics

A static calculation for membranes is geometrically nonlinear. We need material properties for all elements and its nondeformed geometry. The nondeformed geometry of a cable element for instance is the unstressed length of this cable. Next, we need the external loads and the internal pressure or volume information. After the Formfinding-procedure a geometry is available, and Statics can be performed.

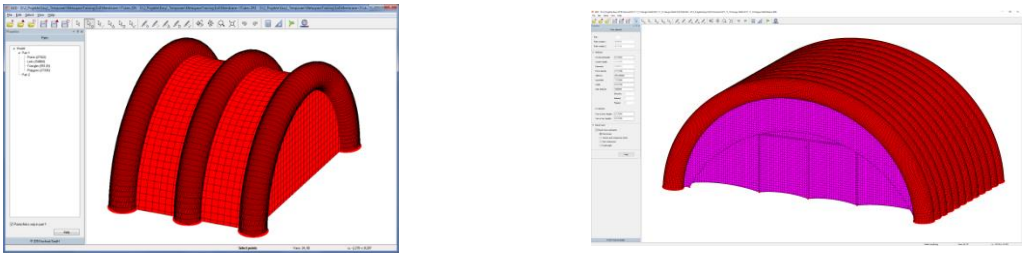


Figure 3: Pneumatic tube systems combined with mechanically stressed membranes

4.1 Statics with Formfinding models

When a usual Formfinding procedure was made also prestress values for all elements exist. We can define material properties for the membranes and then we can calculate the unstressed 'lengths' (= non-deformed geometry) of all elements as we have prestress values from the Formfinding result. Usually the first load-case in statics to be calculated should be 'internal operation pressure'. The result of this calculation must be identical with the Formfinding result as we 'shortened' the membrane elements in this way.

4.2 Statics with geometrically defined models

When a geometrical Formfinding was made, prestress values are usually not available or at least these values do not balance the structure in general. Here we recommend the following procedure:

Define the material properties. The unstressed geometry cannot be calculated by prestress values; therefore, we simply set the stressed lengths to be the unstressed lengths. Now after the load case 'internal operation pressure' we end up with a different geometry. The geometrical differences should

be small in this case. If the geometrically defined form was 'pneumatic feasible' the differences are only caused by the elastic deformations in the 'load case' prestress.

4.3 Theoretical background

We extend the form-finding theory by introducing the constitutive equations for the membrane elements to the system (1). Now the force-densities q from the form-finding are unknowns and they belong to the material equations.

$$\begin{bmatrix}\sigma_u\\ \sigma_u\\ \tau\end{bmatrix} = \begin{bmatrix} m_{11} & m_{12} & 0\\ & m_{22} & 0\\ sym. & & m_{33}\end{bmatrix}\begin{bmatrix}\varepsilon_u\\ \varepsilon_v\\ \Delta\gamma\end{bmatrix} \tag{7}$$

We must consider, that the membrane axial-stress in *u*- or *v*- direction can be expressed as $\sigma_u = \frac{S_u}{b_u}$ and $\sigma_v = \frac{S_v}{b_v}$. b_u and b_v are the widths of the *u*- and *v*-lines. The force-densities q can be introduced now as: $S_u = q_u l_u$ and $S_v = q_v l_v$. The strains in *u*- and *v*-direction can be written as follows:

$\varepsilon_u = \frac{l_u - l_{u0}}{l_{u0}}$ and $\varepsilon_v = \frac{l_v - l_{v0}}{l_{v0}}$. The angle difference $\Delta\gamma = \gamma - \gamma_0$ is needed for the shear-stress calculation. γ is the angle between *u* and *v*-direction; $\gamma_0$refers to the 'non-deformed start-situation' without any shear-stress.

The geometrical compatibility has to be considered as follows:

$l_i == \sqrt{(x_i - x_c)^2 + (y_i - y_c)^2 + (z_i - z_c)^2}$ and $\gamma = arccos(\frac{l_u * l_v}{l_u l_v})$, in which $(l_u * l_v)$ means the inner (scalar-) product between *u* and *v*-direction.

The shear-stress calculation is guaranteed also for a continuous membrane by the fact that the shear angle is between the non-deformed *u*- and *v*-direction of the material [4].

For static calculations we recommend 4 calculation modes:

1. Given internal pressure p (snow)
2. Given volume V (water)
3. Given product $p{\cdot}V$ (Boyle-Mariotte, for example wind)
4. Given product $\frac{p{\cdot}V}{T}$ (General gas equation, consideration of temperature)

$$\begin{aligned}
\frac{\partial \Pi}{\partial x} &= \frac{1}{2}\frac{\partial (v^t R v)}{\partial x} - p_x - \frac{\partial V}{\partial x} p_i &&= 0\\
\frac{\partial \Pi}{\partial y} &= \frac{1}{2}\frac{\partial (v^t R v)}{\partial y} - p_y - \frac{\partial V}{\partial y} p_i &&= 0\\
\frac{\partial \Pi}{\partial z} &= \frac{1}{2}\frac{\partial (v^t R v)}{\partial z} - p_z - \frac{\partial V}{\partial z} p_i &&= 0\\
\frac{\partial \Pi}{\partial p_i} &= V - V_0 &&= 0
\end{aligned} \tag{8}$$

Mode 1: The internal pressure p_i is no unknown. It is only adapted to the right direction and size during the iterations in the nonlinear calculation.

Mode 2 is standard case for liquid filled membranes. Here we assume that a given Volume V_0 is valid as fluids are assumed to be incompressible.

Mode 3 and Mode 4 (consideration of gas-laws) enables the realistic behavior of the internal pressure. This mode is important in case of e.g. fast wind gusts. Here the pump systems cannot update the inner pressure in the short time. We can see it as a closed system and by considering the

temperature as constant we get the gas law of Boyle and Mariotte $p \cdot V = const$ in this case. Only if the gas law is fulfilled the membrane stresses get the correct size. Equation (8) refers to mode 3, here the constant value $(p_{abs} \cdot V)_0$ is the given product and row 4 of (8) has to be fulfilled in iterations where the unknown internal pressure pi is adapted.

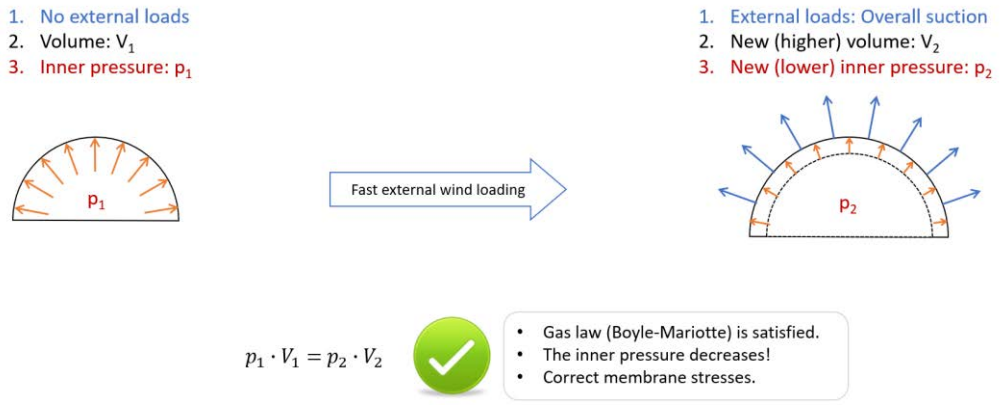


Figure 4: The physical principles of the gas law (mode 3)

On the left-hand side of Figure 4 we see an air hall with an absolute inner pressure p_1 and a volume V_1. The absolute inner pressure is the sum of the over pressure in the air hall and the atmospheric pressure. On the right-hand side, the structure is loaded by an overall wind suction. By considering the Boyle-Mariotte gas law we end up in this case with a higher volume and a lower inner pressure.

Mode 4 considers also the temperature, the principle itself is the same as mode 3 with minor modifications.

By using these modes most cases are covered. The modes can be used e.g. as follow:

1. An air hall under snow-loading (a specific internal pressure is set to resist the snow-loads).
2. A membrane filled with an incompressible fluid (water-bag).
3. A pneumatic cushion loaded by a fast wind-gust; here, the gas law ($p \cdot V = const$) is valid.
4. A pneumatic cushion loaded by a fast wind-gust; here, the gas law ($\frac{p \cdot V}{T} = const$) is valid.

It is to mention that the internal pressure effect is always perpendicular to the deformed geometry. These loads are called non-conservative as all wind loads. In order to get correct results software packages should consider these effects.

5 Investigation of modelling approaches

Nowadays, radial cutting patterns are common for biogas tanks above a certain construction height. The radial cutting patterns are a production challenge, especially at the polar caps.



Figure 5: Radial (left) and parallel (right) cutting patterns

In order to avoid production difficulties, it is desirable to build plants with parallel cutting patterns. The polar caps are now side caps, but only with the half side. Those side caps are usually made also from membrane material with 'rotated' material directions.'

5.1 Computer model

The implementation of the biogas storage systems in our software system is described below. In the case of radial cutting patterns (as shown in Figure Figure 5 (left)), the outer shell is modelled with a radial net. The same applies to the gas membrane. In our computer model 2 chambers (gas space and air support space) are generated by surface elements (triangles) and can be controlled individually. In the case of parallel cutting patterns, regular networks can be used. The following picture shows our model with radial meshes.

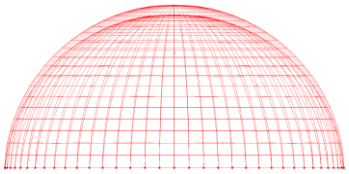


Figure 6: Double Chamber with warp- and weft directions of the textile fabric

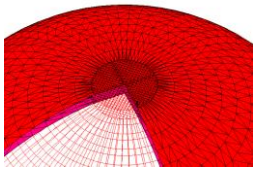


Figure 7: 2 chambers are described by triangular surface elements

5.2 Results of static calculations for radial and parallel cutting patterns

In our calculation we used non-conservative wind loads. We have applied the material properties as follows. It should be noted that the material values at the polar and side caps are doubled.

E_{1000}	E_{2000}	E_{Crimp}	E_{Shear}
800	500	200	50
1600	1000	400	100

Table 1: Membrane material properties



Figure 8: Figure 9: Parallel patterns (warp and weft directions) (gas and outer membrane) with 2 side caps

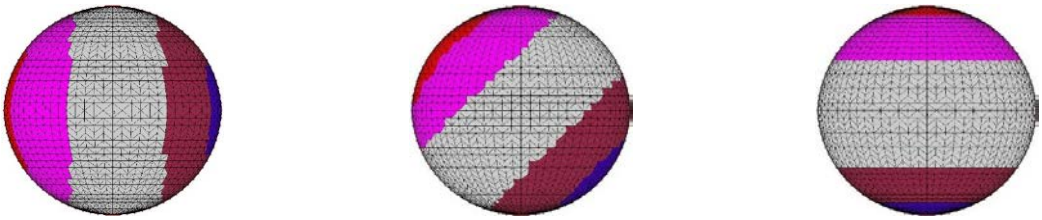


Figure 10: Wind load zone under 3 different wind directions (0°, 45° und 90°).

We have essentially calculated 6 different load cases for different situations. Different filling levels of the gas space were assumed. The 6 load cases were as follows:

- Self-weight and internal pressure.
- Self-weight and increased internal pressure.
- Self-weight, internal pressure and wind 0°.
- Self-weight, internal pressure and wind 45°.
- Self-weight, internal pressure and wind 90°.
- Self-weight, internal pressure and snow.

6 Contact

Contact between outer and inner membrane was considered in case of wind loads; contact happens especially when the gas-membrane is fully stressed with maximum gas volume. The calculation considering contact is important for the right size of the volumes of the air- and gas-space volume and so for the internal pressures in case of gas-law calculations.

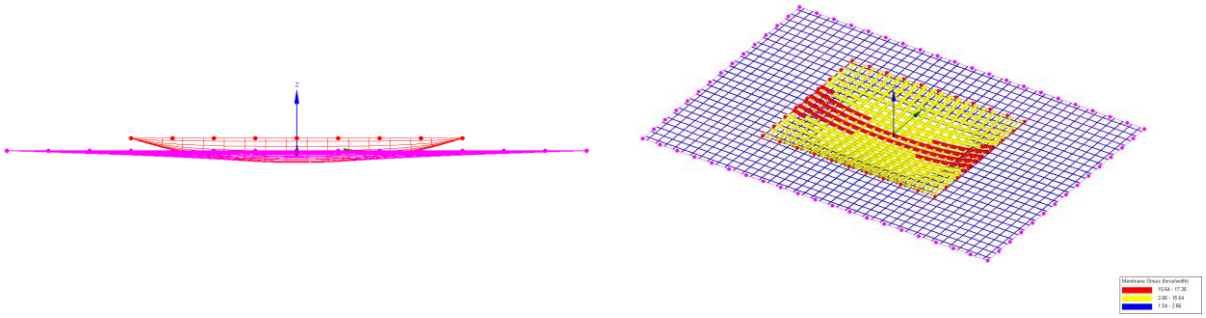


Figure 11: 2 membrane surfaces in contact. Side view (Left), perspective view (right)

7 Conclusion

The differences between the radial and parallel cutting patterns in relation to the size of the maximum membrane stresses were very small. This means that the parallel cutting patterns, which are much easier to produce, can be used in the future.

8 References

[1] Ströbel, D., Singer, P., Holl, J. „Analytical Formfinding", International Journal of Space Structures, Volume: 31 issue: 1, page(s): 52-61, March 1, 2016

[2] Holl, J., Ströbel, D., Singer, P. "Formfinding and Statical Analysis of Cable Nets with flexible covers", *VI International Conference on Textile Composites and Inflatable Structures STRUCTURAL MEMBRANES 2013*, Munich, Germany.

[3] Singer, P. (1995), „Die Berechnung von Minimalflächen, Seifenblasen, Membrane und Pneus aus geodätischer Sicht", *Dissertationsschrift*, *DGK Reihe C*, Nr. 448, 1995.

[4] Ströbel, D. (1997), „Die Anwendung der Ausgleichungsrechnung auf elastomechanische Systeme", *Dissertationsschrift*, *DGK, Reihe C*, Nr. 478.

[5] Ströbel, D. Singer, P, Holl, J: Holistic Calculation of (Multi)-Chambered ETFE-Cushions, *Tensinet, TensiNet Istanbul,* 2013.

Proceedings of the IASS Annual Symposium 2019 – Structural Membranes 2019
Form and Force
7 – 10 October 2019, Barcelona, Spain
C. Lázaro, K.-U. Bletzinger, E. Oñate (eds.)

Switchable ETFE cushion: designing and building a model for experimental testing

Jan-Frederik FLOR*, Yanyi SUN, Paolo BECCARELLI, Yupeng WU, John CHILTON

* The University of Nottingham
Department of Architecture & Built Environment, University Park, Nottingham NG7 2RD, United Kingdom
jan.flor@nottingham.ac.uk , janflor@gmx.de

Abstract

Adaptive façade systems have the potential for saving energy and enhancing comfort conditions in buildings. Creating working models with materials, components and functions which embody the design idea of a responsive building envelope is an important part of the design process of these systems, because it allows the performance to be demonstrated and tested under realistic conditions and for difficulties to be detected in advance. This paper reports on the process of building and programming a functional model of a switchable ETFE cushion for preliminary performance tests. Different techniques of reverse engineering and prototyping were explored on a range of scales to build the membrane structure and its pneumatic control system. The study showcases the inter-link of advanced manufacturing techniques and parametric design software, the application of microcontrollers, actuators and sensors in combination with the building envelope. The paper further documents and theorizes the process from design to making and testing, outlining a practical workflow for the development and prototyping of adaptive building envelopes for energy efficient buildings.

Keywords: ETFE, Adaptive Building Envelope, Prototyping, Testing

1. Introduction: responsive control mechanisms for switchable ETFE cushions

Adaptive Architecture is thought of to perform beyond formal aesthetic and functional considerations and respond in an intelligent way to the changing conditions of the environment, improving the energy efficiency of buildings [1]. ETFE foil has been used as a building material for a variety of building typologies implementing adaptive design features [2]. Reflective frit prints, multilayer constructions and adaptive systems, which switch from one state to the other, have been developed to enhance the energy and lighting performance of buildings covered with inflated ETFE cushions [3]. The specific function of the switching mechanisms presented here is to control the light transmission of a triple layer ETFE foil cushion, allowing it to respond to variations of solar radiation, using sensors and actuators that interact following the logic of an algorithm, which defines the responsive behavior and automates the shading mechanism of the foil construction (Fig. 1). While performance of static ETFE foil construction has been investigated thoroughly, information about switchable systems is currently lacking. One reason for this is that the system has been implemented only in relatively few buildings in recent years (Adelaide University Learning Hub, Adelaide, 2011; St. Bartholomew's Hospital, London, 2013; IIT Innovation Center, Illinois, 2018) and post-occupancy data is not publicly available yet. Another reason relates to the challenging and costly computational task of conducting whole building simulations with switchable systems. Therefore, the resulting aim of this research was to build a physical model, which could deliver quick feedback under realistic conditions, with the purpose of validating numerical models and improving the system performance through experimentation. However, the information presented here is limited solely to the designing and building of the testing models.

Copyright © 2019 by Jan-Frederik Flor, Yanyi Sun, Paolo Beccarelli, Yupeng Wu, John Chilton
Published by the International Association for Shell and Spatial Structures (IASS) with permission.

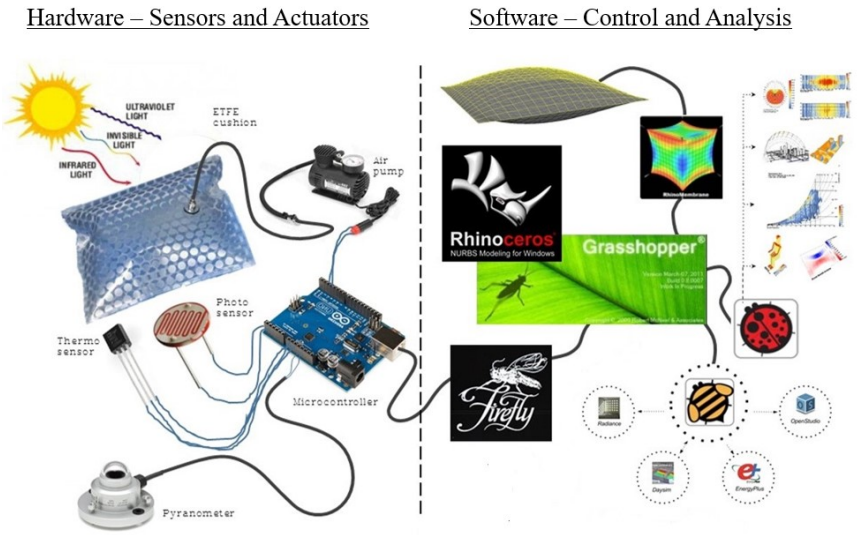


Figure 1: Conceptual image showing the elements and relationship of hard- and software switchable cushion control mechanism

2. Build-up and mechanism of the switchable ETFE cushion

The model assembly comprises three foil layers, inner-, middle- and outer -layer (IL, ML, OL), which are welded air-tight and clamped to a structural frame on the perimeter edge, forming the shape of a rectangular cushion, when fully inflated with air. The cushion becomes a pre-tensioned structural system through the air pressure inside the cushion, able to carry external loads. The middle layer divides the cushion into two air chambers, C1 (between the ML and OL) and C2 (between the ML and IL), with individual air-valves. All three layers have the same, but symmetrically mirrored, three-dimensional synclastic geometry. The position of the middle layer within the boundaries of the cushion can be changed by inflating one chamber and deflating the other. The middle layer overlaps geometrically either on the inside of the inner or the outer layer. The middle layer and the outer layer are printed with a reflective frit ink. The pattern of the frit is a geometry which covers approximately 50% of the surface area of the middle and outer layer. The pattern is shifted in a way that when the foils overlap, the unprinted areas of the inner foil are covered with the printed areas of the outer foil and vice versa, arriving at a 100% covered or "closed" position. When chamber C1 is inflated, while C2 is deflated, the middle layer changes its position and moves from the geometric position of the outer layer to the inner layer. While it does so, the geometry of the middle layer flips over from a convex to a concave shape. When the external air chamber C1 arrives at the maximum pressure and all air is evacuated from the inner chamber C2 the middle layer is geometrically overlapping with the inner layer and has arrived at the "open" position. An increased fraction of incident light is transmitted now through the unprinted areas of the outer- and middle-layer foil. The percentage of transmitted light in the open position may vary according to the orientation of the cushion and the direction of the irradiance incidence vector, as well as the chosen printing pattern [4]. The steps of the switching mechanism are summarized in Fig. 2. The details of the control system of the mechanism will be described in the following sections.

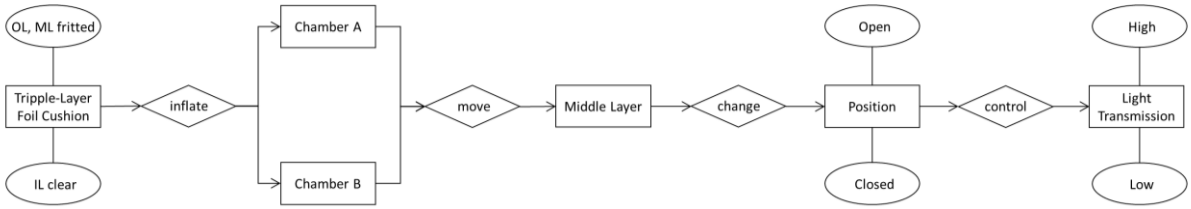


Figure 2: Function flow chart of pneumatic switchable triple layer foil cushion

3. Testing model: from design concept to manufacturing

Following the aim of the study to develop a fully functional model that could be used for indoor and outdoor environmental performance tests, several steps of design and manufacturing had to be accomplished, which are outlined in the relevant literature [5, 6, 7]. Since switchable ETFE cushion façades are already commercially available, advice from industry was sought about materials, details and operation, which facilitated the design and manufacturing of the purpose-built testing unit. The system was divided into three sub-systems as follows: foil cushion, air-supply, and control system.

3.1 Foil cushion

Initially the scale of the model had to be determined finding a compromise between a reasonably sized foil cushion, that could be representative of a unit used in commercial building applications, and limitations resulting from the test facilities, like, for example, dimensions of a climate chamber and a moveable testing rig for outdoor tests (Fig.3). The geometry was determined using form-finding software, RhinoMembrane V2.0 [8] in combination with Grasshopper [9], generative modelling plug-in for Rhinoceros, 3D modelling program. Several scale models of smaller dimensions were built, based on the digital model, until arriving at a full-size model with cushion dimensions of 1 x 1m and an external supporting frame of 1.2 x 1.2m (Fig.4). The rise/sag of the cushion was a typical 10%, leading to a maximum section width of 0.2 m. While the small-scale models served only for early stage exploration and lacked realistic detailing, the full-size model was entirely fabricated with standard materials (extruded ETFE foil, fritted and clear, 200µm thickness) and typical aluminum clamping details. Due to the reduced dimensions of the model any welding seams in the field of testing of the sample were avoided, to reduce the influence on any testing of thermal or lighting performance. The shape of the cushion was achieved through a flat patterning and a slightly higher pressure (ca. 700 Pa).

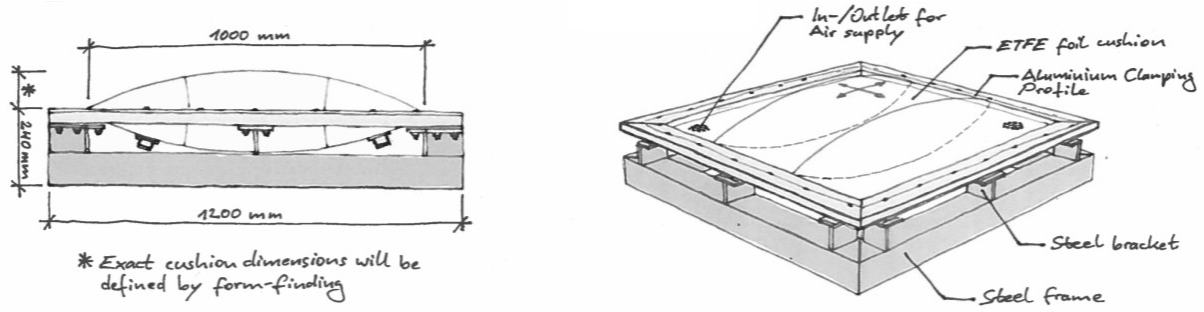


Figure 3: Front (left) and perspective (right) view of the full-size model of the ETFE cushion with structural frame and clamping profile



180 x 180 mm 330 x 330 mm 1200 x 1200 mm

Figure 4: Models of pneumatic switchable triple layer cushion at different scales, showing overall frame dimensions

3.2 Air-supply

The light transmittance of the foil cushion changes when the fritted middle layer is moved from one position (open/closed) to the other. This movement is achieved by redirecting the air supply and changing the internal pressure of chamber C1 and C2. The air supply for the foil cushion is generated by an air blower which connects to valves at chamber C1 and C2 of the foil cushion. The air blower has a maximum air volume capacity of 420 litres per minute, but air flow rate can be regulated and measured with a combined valve and flow meter. Two different schemes for the airflow control of the shading mechanism of triple layer ETFE cushions were identified and explored. Based on a case study building application (Fig.5 A), an alternative system design (Fig.5 B) with adjustments and simplifications was developed, to facilitate the manipulation of all parameters of the ETFE cushion during performance testing in external or controlled laboratory environments.

3.2.1 Type A

Type A continuously supplies air to both chambers while a second hose connects one chamber to the other with an intermediate air pump. The air pump operates bi-directionally, pumping air from one chamber to the other and moving the middle layer to an open or closed position depending on the signal from the light sensor.

3.2.2 Type B

Type B is based on the principle of a piston operated by a solenoid valve. The airflow path is controlled with two sets of solenoid valves (one for each chamber) which regulate the air inflow and outflow to the cushion chambers. The valves are normally in a closed position and are controlled by an electrical signal to open and inflate one chamber and deflate the other in order to change the position of the middle layer foil. The signal from the light sensor is evaluated in a microcontroller. If the threshold for light intensity is exceeded the solenoid valves are operated opening the exhaust valve of chamber C1 and the inflow valve of chamber C2. The pump starts blowing air into chamber C2 and moving the middle layer into a closed position. When the values from the light sensor are below the threshold the process is reversed moving the middle layer to an open position.

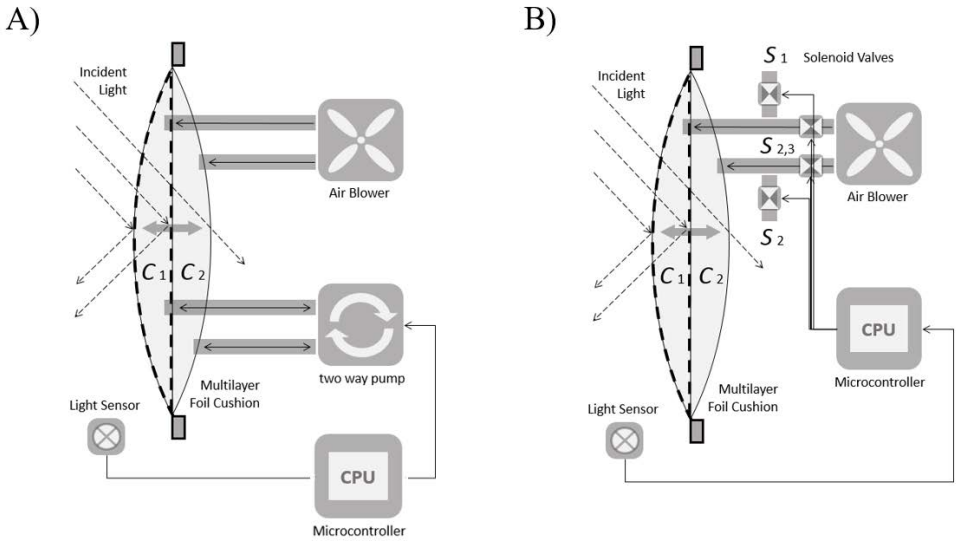


Figure 5: Diagrams showing the two investigated control schemes for the switching mechanism of the pneumatic foil cushion: A) case study building and B) proposed alternative design

3.3 Control system

The electric signal to operate the air blower and the valves is controlled with a combined system of hard- and software which is responsive to the environment by means of a set of sensors. An Arduino UNO micro-controller is the connector between software, running on a PC, actuators and sensors. The system operates on a 5V power supply. All operating devices which have a higher power demand, like the air blower and solenoid valves, are connected to a 240V supply, with specific transformers, and are digitally controlled with a relays board that connects to the digital output channels of the microcontroller. The sensors, photocells and atmospheric pressure sensors, are connected directly to the analogue input channels of the micro-controller. The air blower and the solenoid valves will be triggered by a signal from the control system which receives measurement data about the light intensity from the internal and external sensors, updated and evaluated in real time. Built in feedback loops and additional control sensors, which measure the internal pressure of the chamber, inform the decision-making algorithm of the control system. The data is exchanged with Grasshopper via the plugin Firefly [10] which communicates with the microcontroller reading the sensor signals. The data is evaluated by the software algorithm within the Grasshopper graphical programming environment (Fig.6). When a pre-set threshold for the lighting is passed the system decides whether to increase or decrease the cushions light transmittance and operates automatically the position of the middle layer. The internal sensor then feeds back a control measurement of the internal lighting levels to the system. The measurement of the pressure of the cushions chambers allows an ideal pressure level to be maintained for structural reasons but also acts as a control mechanism for the movement of the middle layer, providing feedback information about the system. In figure 7 an overview of the switchable cushion model with the control system set-up can be seen.

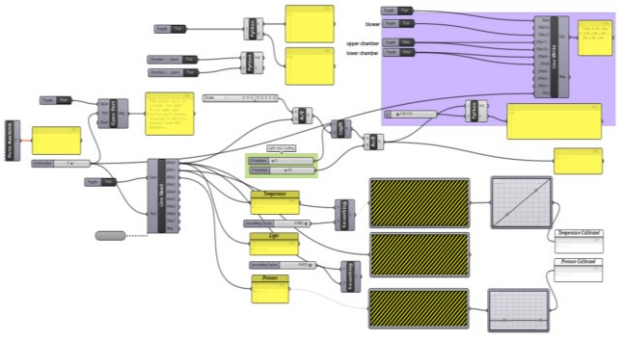


Figure 6: Screenshot of the Grasshopper / Firefly definition for the control mechanism.

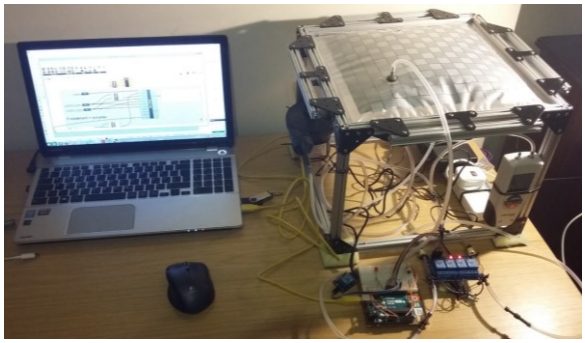


Figure 7: Model of the switchable cushion with sensor, microcontroller, valves and air supply devices.

4. Real time testing of the parametric control mechanisms

The control system was initially tested on a small-scale cushion model which facilitates easy manipulation and quick trouble shooting. The developed control algorithm was adjusted and calibrated while the system was running and collecting live data. This allowed adjustment and fine-tuning in real time of the parameters and thresholds for light and pressure thresholds and observation of the changes made. The system is able to run in two modes, manually, by switching the valves via the Grasshopper interface or automatic, where the system responds autonomously to changes in the environment. In both modes the system can be overridden at any time. These two operation modes will allow system modes and environmental conditions to be investigated individually during the performance tests, at a point in time, or in the automatic mode, where the response of the system over time is measured. It is expected that this will provide valuable data for building applications and reveal, in combination with simulation data, indications of how to further improve the control mechanism and algorithm for a better response rate to changes of solar radiation. For the testing of the real size model the control system was simply plugged in from the smaller to the bigger cushion. However, the air pump had to be upgraded to a higher

capacity (680 lpm) to compensate for the air volume of the bigger cushion (90ltr). The switching process was thus reduced to 10 minutes from open to closed mode. However, it must be stated clearly that this system was developed for testing purposes only. For building façade applications which have much bigger cushion sizes/volumes this system might not be feasible, even though cost effective, easy to manipulate and manhandle. Bigger pipe diameters as well as a different air supply set-up and operating system, like that presented in figure 5A, might be the more effective option to achieve a quick response of the system on a building scale.

5. Conclusion

In this paper the process of designing, manufacturing and operative testing of a switchable ETFE cushion was reported. Due to the final purpose of testing the energy and lighting performance of the model, different design considerations and constraints had to be taken into account in comparison to the normal design process of a typical ETFE foil construction for application in building envelopes. Reproducibility of large-scale energy and light effects on a small scale, as well as considerations about realistic representation of a full facade with a scaled model, challenged the decision making during design and construction. As much as possible standard construction details were used without compromising the practicality during testing procedures in a laboratory environment. The interconnectivity and graphical feedback interface of the chosen software plug-ins, used for programming and controlling the microprocessor, proved of much advantage during the process. Not only cost-effective and easy to learn, but fully compatible with microcontrollers and sensors, it might be of consideration as an open platform for further developments to facilitate the coding for responsive building envelopes on a prototyping scale.

Acknowledgements

This work was supported by the Faculty of Engineering at the University of Nottingham through a PhD studentship awarded to Jan-Frederik Flor. The ETFE material and the manufacturing of the real size cushion model and frame was generously provided by Architen Landrell.

References

[1] M. Hensel, *Performance-oriented Architecture: Rethinking Architectural Design and the Built Environment*. Chichester, 2013.

[2] D. M. Addington, D. L. Schodek, *Smart Materials and New Technologies for the Architecture and Design Professions*. Oxford, 2005.

[3] M. & J. Burry, *Prototyping for Architects*. London, 2016.

[4] J.-F. Flor et al., Optical aspects and energy performance of switchable ethylene-tetrafluoroethylene (ETFE) foil cushions. *Applied Energy*, 2018. 229: p. 335-351.

[5] Biloria, N. and V. Sumini, Performative Building Skin Systems: A morphogenomic approach towards developing real-time adaptive building skin systems. *International journal of architectural computing*, 2009. 07(04): p. 643 - 675.

[6] Sheil, Bob. *Manufacturing the Bespoke: Making and Prototyping Architecture*. Chichester, 2012.

[7] G. Ruairi and B. Sheil, *Fabricate: Making Digital Architecture*. Toronto, 2011.

[8] RhinoMembrane V2.0 - Minimal surfaces & mesh based Form-Finding, plugin for Rhinoceros, http://www.ixray-ltd.com/ (Accessed 13.06.2019)

[9] Grasshopper® graphical algorithm editor, plugin for Rhinoceros, https://www.grasshopper3d.com/ (Accessed 13.06.2019)

[10] A. Payne, *Interactive Prototyping An introduction to electronics using Arduino, Grasshopper, and Firefly*. 2016.

Proceedings of the IASS Annual Symposium 2019 – Structural Membranes 2019
Form and Force
7 – 10 October 2019, Barcelona, Spain
C. Lázaro, K.-U. Bletzinger, E. Oñate (eds.)

An academic experiment on the design of spatial truss models and teamwork

Leila C. MENEGHETTI*, Ruy M.O. PAULETTI, Luís A. G. BITENCOURT Jr.

* Department of Structural and Geotechnical Engineering, Polytechnic School, University of São Paulo
e-mail: lmeneghetti@usp.br

Abstract

This paper describes a 'learning by doing' experience conducted during an undergraduate course on Structural Systems at the Faculty of Architecture at the University of São Paulo. The experience was inspired on the educational project 'Design, Assemble and Dismantle (DAD Project)' devised by S.A. Behnejad at the Department of Civil and Environmental Engineering at the University of Surrey. Like DAD Project, the experiment aimed to foster students' skills in design, teamwork, communication, and problem solving, in a scheme were the design of one group of students is passed through documentation to another group, in charge of construction. However, contrary to DAD (which is based on full-scale models, with a relatively reduced number of members), our experiment considered tabletop-size models, produced from simple materials, but with many hundreds of members, to allow greater geometric freedom. The produced models were surprisingly light and robust. Overall, they showed high quality of making and dimensional precision. Students reported that by making these models they gained understanding on how forces flow within in a spatial truss.

Keywords: learning by doing, spatial truss, educational project, architecture students, structural systems.

1. Introduction

Teaching structural concepts to architecture students is a task usually delegated to civil engineers. Not an easy task, because the engineering thought is remarkably different from the architectural one. Mario Salvadori [1] believed that this was the first great difficult in the process of learning structures. During one of his lectures, more than 50 years ago, he said *Architects and engineers do not have a common language*. Alas, this is true until today, and it has a great consequence when a civil engineer accepts to enter a School of Architecture to teach structures. Making distinction between soft and hard knowledge about structures, Emami and Buelow [2] state that the role of the engineer teaching at an Architecture School is to find an approach where the hard knowledge about structures is facilitated through soft methods of teaching.

Structural issues are typically approached by engineers within an analytical procedure, with a solid base of mathematics, statics and strength of materials. Not at all, many architecture students shade away from mathematics, even knowing that math is the tool that provides deeper structural insight. Moreover, the classical sequence of presenting the structural issues may represent the most logical knowledge construct, but is usually divorced from the design processes, not supporting the basic principles of architectural creation [3].

As pointed by Ilkovic *et al.* [4], structural concepts should provide the student of architecture with information about the beauty of construction, how the construction lives and how it supports gravity or other loads. Besides, an architect should feel what is going on in a structure without needing to count exactly. That of course is valuable also when teaching structures to civil engineering students, *ça va*

Copyright © 2019 by Leila C. MENEGHETTI, Ruy M. O. PAULETTI, Luís A. G. BITENCOURT JR
Published by the International Association for Shell and Spatial Structures (IASS) with permission.

sans dire. In different areas of knowledge, many educators believe that theoretical classes should be complemented by other activities.

Among other strategies, we focus our current teaching research on *Learning by Doing*, defined by Tony Bates [5] as a teaching method that *enables students to test hypotheses or to see how well concepts, theories, procedures actually work.* In architecture education, Vrontissi [6] expresses that physical model in particular, *has a significant place in the student´s toolset, not only as a means of (re)presentation, but as an indispensable medium capable to perform a dual role: resuming and reflective (analysis) or generating and productive (synthesis)*. In addition, when the students can make a physical model, the observation of the effects of loading is immediate, helping to develop the perception of the structural behavior.

In fact, learning by doing is a well-established strategy in Architecture arts, but usually not as much favored by instructors of structural classes. In our local context, the strategy has been occasionally used by the authors in graduate and undergraduate courses of civil engineering and architecture at University of São Paulo. Reports on some predecessors to our current experiment are provided on references [7] to [10]. Presently, this type of hands-on activities has been more explicitly adopted as a teaching methodology by the authors, after establishment of GISE, a group focused on researching structural systems innovation.

Until recently, the ancillary activities chosen by the authors to exercise concepts on classical structural systems like truss, cable, arch and frames were mostly computer-based simulations. Typical structures examples were chosen by the teachers and the analysis was guided in the way that students could understand the structural behavior under different assumptions about material, cross-sections, loads and support conditions. One limitation associated with this practice is that architectural students sometimes need to spend a lot of time, first to learn the syntax of the selected computer programs and later to analyze the results, frequently missing to correlate the output of the numerical models with the theorical basis they are supposed to exemplify. The problem has become more noticeable in the last few years, perhaps due the arrival of a new generation of students, endowed with new ways of reasoning, to which the instructors find themselves uneasy to adjust. A clear perception that new architecture students were missing their motivation towards our classes on structural systems thus motivated us to refresh our classes with new activities, that could arouse again the interest on the study of structural systems.

In this paper, we report on an academic experience based on the design of spatial trusses and on collaborative work, which was developed during an undergraduate course of Structural Systems at the Faculty of Architecture at University of São Paulo, in the second semester of 2018. The experience comprised the design and production of physical models, of tabletop dimensions, their exhibition at the Faculty of Architecture at USP, and the construction of a larger-scale prototype of one specific model, chosen on basis of its good structural performance and the straightforwardness of it design.

2. Spatial trusses

Spatial trusses are light structural systems, employed to cover large spans. Traditionally, regular geometries were used to reduce costs, by using members of standard length, as well as standard connections. Nowadays, with the advent of parametric design tools, BIM, CNC routers and robots, spatial trusses are receiving renewed attention, since variation of bar length and customized connections allow to produce complex, free-format, double-curvature geometries without forbidding additional costs. Such is the case of the spatial truss used to structure the highly curved, smooth liner of the Heydar Aliyev Center (2013), designed by Architects Zaha Hadid and Patrick Schumacher (Figure 1). Nevertheless, connections remain as costly components of spatial trusses. A cheap connection system is provided by simply kneading the ends of the metallic tubes, which are then connected by bolts. The method significantly reduces the overall strength and stability of the structure, if compared to other types of connections, but the implied extra material costs may be compensated by

reduced production and workmanship costs. Therefore, precarious as it may be for real structures, the system enables easy production of models and prototypes, such as the ones envisaged in the current experiment.

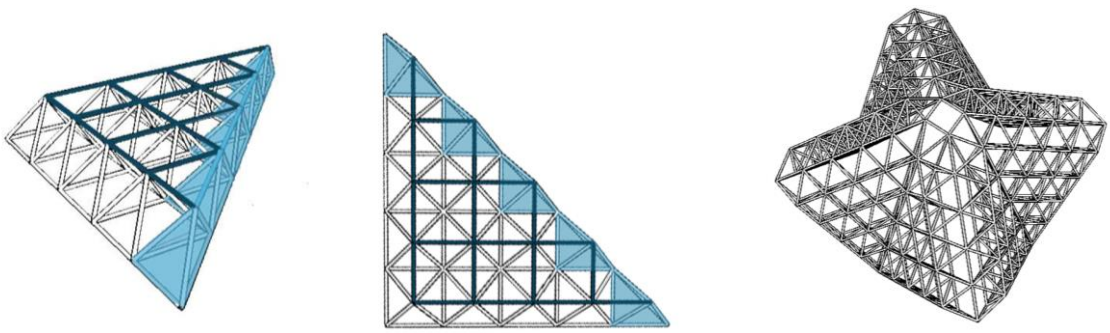


Figure 1: Heydar Aliyev Center [credits: (a) Iwan Baan, by Dezeen ; (b) available on bwncy.com].

3. The hands-on spatial truss activity

3.1. Design phase

The activity was divided in two phases: (1) a *design phase* and (2) a *construction phase*. During the design phase, students were asked to research about typical spatial trusses and relevant architectonic references and design some appealing structure, as an answer to a freely chosen architectonic plan. The dimensions of the real structures were also free, but the system should comprise a lattice with about 100 modules (for instance, a 10x10 square grid), thus requiring several hundreds of members. The design should consider a model produced with paper straws, with length members of about 10cm (obtained by cutting a typical paper straw in halves). Thus, overall models would be about 1m wide. The class of about 180 students was divided into 19 groups. The groups were encouraged to produce geometries presenting single or double curvature, having in mind that a more complex geometry requires more variability of the lengths of the bars, and the greater assembling complexity. At the end of the design phase the groups delivered a design report, as well as a printed poster, to be displayed for peer evaluation. These documents were evaluated considering their correctness, clarity and logical structure, as well as their formal qualities. It was initially considered that evaluation of the reports would be performed by the instructors, and that the posters would receive one grade from the instructors and another by peer-reviewing from the whole class. However, some students argued that they did not want to compete among themselves and finally the class voted to cancel the peer-reviewing process, with grading done exclusively by the instructors.



Axonometric projection Top view 3D view

Figure 2: Spatial truss designed by group 2

The students of group 6 took the advantage of this activity to learn parametric modelling using the Grasshopper component of Rhino. The first shape studied is shown in Figure 3. The spatial shape configuration was designed searching for symmetry in the middle of the structure. According to the student description, the proposal encloses two architectonic spaces that launch themselves into the surrounding landscape. Building up on the idea, the spatial truss was composed by a rectangular grid with constant height and members of different lengths.

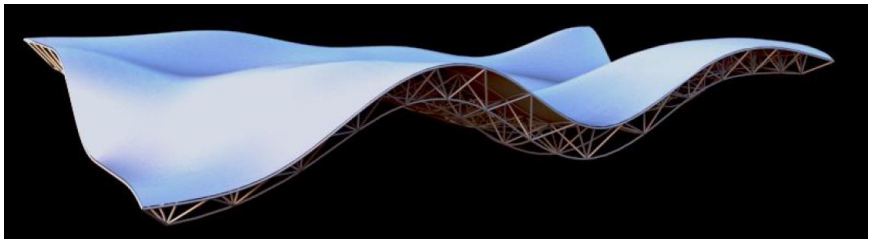


Figure 3: First shape studied by group 6

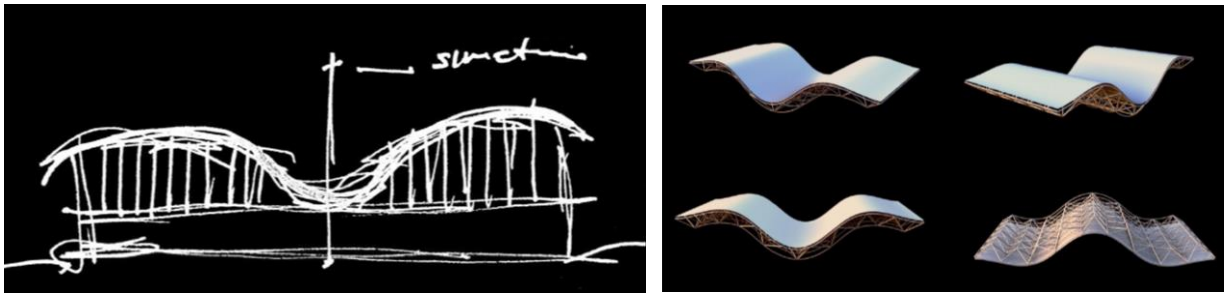


Figure 4: Spatial truss designed by group 6

Another simple but structurally efficient spatial truss was designed by group 15. The structure was globally composed by circular upper and lower chords connected by diagonals arranged as regular square pyramids as well as by longitudinal braces, with segments of same size as the diagonals and the upper chord segments. The group reported that they chose this modular shape due to the repeatability of the elements and a distinguished architectonic aesthetics.

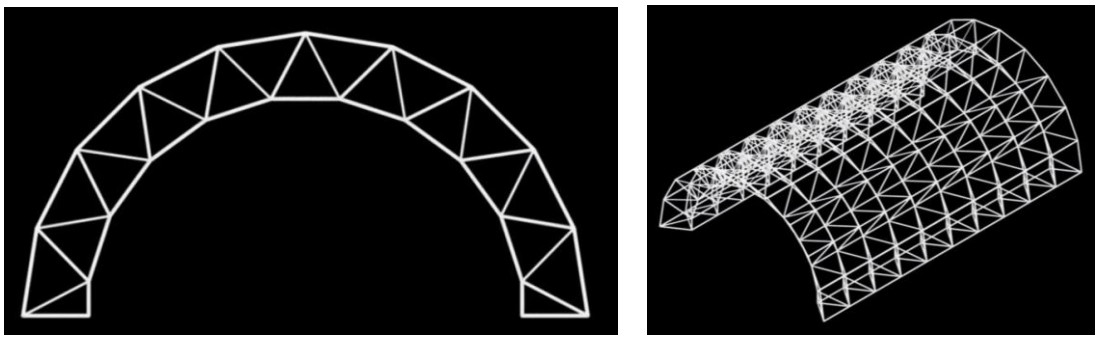


Figure 5: 2D and 3D views of spatial truss designed by group 15

3.1. Construction phase

During the *construction phase,* each group produced a physical model, according to one of the designs proposed by the other groups. Therefore, each group acted both as a *contractor*, to build a design of a third party, and a *client*, whose designs was built by some other contractor. The selection of designs

started with a group appointed by the instructors, followed then by the group which design was chosen. On one occasion this sequence closed, and another group was appointed to restart it. The groups should execute the chosen design according to its written specifications, sometimes proposing modifications, that should be approved by the designer. The instructors arbitrated a few disagreements between designers and producers. In some cases, designs were simplified by the authors, at the request of the constructors. One group failed to assemble its model and concluded that the original design was too complicated and structurally unstable. Instructors conceded extra time for designer and contractor to review the project, and finally a satisfactory model was achieved.

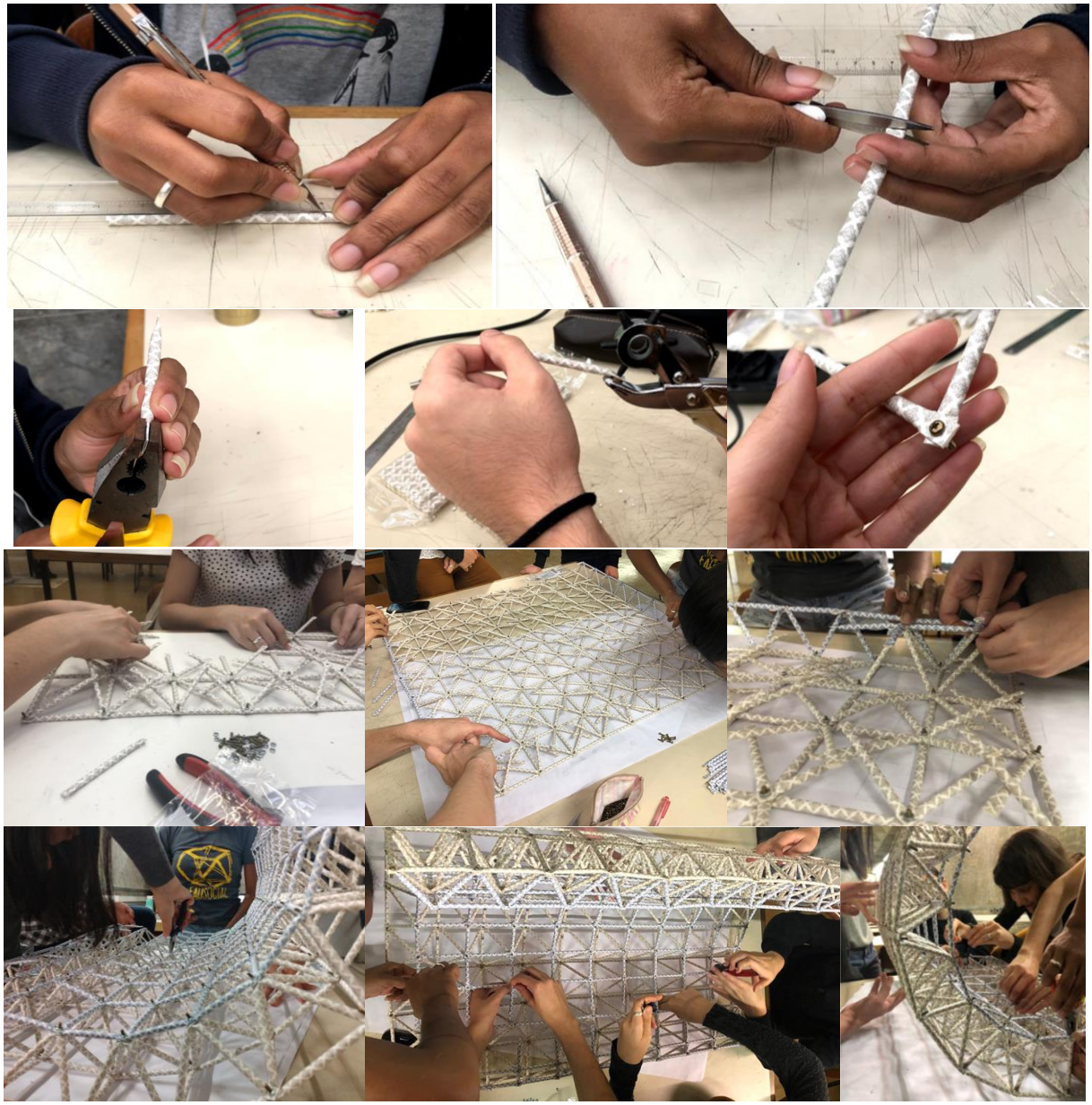


Figure 6: Sequence of construction of physical model.

The required material (paper straws, bolts and nuts and eyelet hole makers) was provided by the Department of Building Technology of the Faculty of Architecture at USP. In a few instances, some

additional material was required (such as strings or brass eyelets), and they were procured by students themselves.

Figure 6 shows the production of group 15 design by group 8. Similar processes were carried out for production of most of the models. First the paper straws were cut according to specific dimensions. Then, the ends of paper straws elements were kneaded and punched, and the bars were connected. It is worth to remark that a typical model displayed about 800 truss members and 220 nodes. At first, many students were refractory to undertake such a painstaking task, but most students felt rewarded with the outcomes. Figure 7 shows some of physical models and groups of students during the delivery day.



Figure 7: Some constructor groups and their physical models during the delivery day.

4. Exhibition and concluding remarks

As recognition of the achieved outcomes, to raise awareness about structural systems and to invite new students to the structural systems classes, this year's students have organized an exhibition of their physical models at the atrium of the Faculty of Architecture (Figure 8).



Figure 8: Exhibition at Main Hall of the Faculty of Architecture

We concluded this experiment with strong evidences that effective teaching requires creativity and innovation. We have found no strict rule to follow, but some strategies might help instructors to foster critical thinking and proactivity. Physical modelling proves to be a tool for materializing thoughts and an instrument to transform elementary tasks in problem-solving learning. We believe the class came out of the experiment with larger confidence and readiness to study more complex issues such as stability and dynamics.

As a sequel of this experiment, during the current academic semester, students are involved on building a larger prototype based on group 15 model, which was selected because of its stiffness and geometrical simplicity. The prototype will be constructed by the end of June 2019 and a report will be presented during IASS 2019 Symposium as well as on forthcoming papers.

Acknowledgements

The authors are indebted to the 180 students of PEF2602 and PEF2603 classes on Structural Systems, –effective co-authors of this paper– and acknowledge also the essential support of the Department of Building Technology at the Faculty of Architecture and the Department of Structural and Geotechnical Engineering at the Polytechnic School, University of São Paulo.

References

[1] M. Salvadori, "Teaching structures to Architects," *Journal of Architectural Education*, vol. 13, pp. 5-8, 1958.

[2] N. Emami, P. Buelow, "Teaching structures to architecture students through hands-on activities," in *Canadian International Conference on Advances in Education, Teaching & Technology: Proceedings of the EduTeach Annual Symposium 2016, Toronto, Canada, July 16-17, 2016.*

[3] Quoted by M. Chiuni, "Less is more: a design-oriented approach to teaching structures in Architecture," in *Building Technology Educators' Symposium: Proceedings, Maryland, USA, August 2006.*

[4] J. Ilkovic, L. Ilkivicová and R. Spacek, "To think in architecture, to feel in structure: Teaching Structural Design in the Faculty of Architecture," *Global Journal of Engineering Education,* vol. 16, pp. 59-65, 2014.

[5] A.W.(Tony). Bates. *Teaching in a Digital Age: guidelines for designing teaching and learning*. Creative Commons Attribution – Non Comercial Internation License, 2015.

[6] M. Vrontissi, "The physical model in structural studies within architecture education: paradigms of an analytic rationale?," in *Future Visions: Proceedings of the IASS Annual Symposium 2015, Amsterdan, The Netherlands, August 17-20, 2015.*

[7] R.M.O. Pauletti, J.Y. Chi, "Modelling and construction of the 'Dodecoid', an inflated, double-skin dodecahedron*", IASS 2004 Symposium - Shell and Spatial Structures: from Models to Realization, Montpellier, 2004*.

[8] S.L.M.C. Titotto, R. M. O. Pauletti and T. E.C. Deifeld, 'The Monument to the Futile Form II: Conception, Simulation and Realization of a Tensegrity-Membrane Structure', in *II Simposio Latinoamericano de Tensoestructuras, Caracas - Venezuela, May 4-5, 2005*.

[9] R.M.O. Pauletti, S. Adriaenssens, A. Niewiarowski, V. Charpentier, M. Coar, T. Huynh, X. Li, "A Minimal Surface Membrane Sculpture", in *Proceedings of the IASS Annual Symposium – 'Interfaces: architecture. engineering. science', Sept. 25 - 28th, 2017, Hamburg, Germany*.

[10] P.M. Bolelli, K.B. Rocha, I.M. Oliveira, W.B. Mello, A.H. Haydamus, L.C. Boechat, R.M.O. Pauletti, V. F. Arcaro, "Design and construction of a membrane-tensegrity sculpture," in *IASS Symposium 2018 - Creativity in Structural Design, July 16-20, 2018, MIT, Boston, USA.*

Proceedings of the IASS Annual Symposium 2019 – Structural Membranes 2019
Form and Force
7 – 10 October 2019, Barcelona, Spain
C. Lázaro, K.-U. Bletzinger, E. Oñate (eds.)

Interlocking spaces: A structural prototype inspired by Kigumi Architecture

Lukas ALLNER*, Philipp REINSBERG[a], Jun SATO[b]

*University of Applied Arts Vienna
Vordere Zollamtsstraße 7, 1030 Vienna
lukas.allner@uni-ak.ac.at

[a]University of Applied Arts Vienna
[b]University of Tokyo

Abstract

The presented project in this paper is based on the results of a student workshop led by structural designer Prof. Jun Sato from Tokyo University together with a team of researchers based in Vienna. It represents an experimental investigation of spatial wooden structures that are based on the concept of Kigumi, the carpentry craft of interlocking joints in traditional Japanese Architecture. The resulting full scale demonstrator was first presented at the World Wood Day festival in March 2019 in Stübing, Austria (fig.1), before being showcased in the main atrium at the University of Applied Arts (fig.2) and in the Museum of Applied Arts in Vienna (MAK), Austria in May and June 2019 respectively.



Figure 1: Interlocking Spaces Set up during World Wood Days at Austrian Open-Air Museum Stübing/Styria/AT March 2019 [Photo by Philipp Reinsberg (1), Leonard Kern (2,3)]

Irregular architectural structures with varying densities that are characterized by a high level of geometrical and spatial complexity can be perceived as "natural" and thus represent comfortable environments (Sato [1]). Furthermore wood as a solid material offers the potential of structures composed of crafted members joined without additional fasteners resulting in homogeneous simplistic yet spatially complex esthetics. Students worked on two scales simultaneously, analyzing and designing wooden joint details with two, three and four members meeting in one node as well as developing an overall aggregation of linear profiles. The highly irregular model resulting from the student workshop was translated into a structural system of reciprocal interlocking timbers in a follow-up process. Besides studying the space defining qualities and structural performance of the Kigumi

Copyright © 2019 by Lukas Allner, Philipp Reinsberg and Jun Sato
Published by the International Association for Shell and Spatial Structures (IASS) with permission.

system, the investigation within the realization process also allowed to test the potentials of digital tools and CNC manufacturing as means of contemporary joinery that is inspired by traditional techniques. The presented comprehensive workflow is an initial case study for the design and fabrication of an inhabitable structural system from standard timber elements for applications as primary building structure.

Keywords: complex timber structures, joinery, Kigumi, form finding, cnc fabrication, space frame structures



Figure 2: Interlocking Spaces presentation with Performative Artist Daniel Aschwanden at University of Applied Arts Vienna/AT [Photos by Philipp Reinsberg]

1. Introduction

"In traditional timber construction the principle of joinery emerges in a mutual relationship between material, craft and result. For the attentive observer, the wooden joints reveal the thoughtful consideration of the person building it within the given scope." (Zwerger [2])

With computer aided design and manufacturing processes complex, non-standard joinery can be considered and applied to complex geometrical configurations in contemporary and future timber construction. This allows to simulate and integrate all geometric features necessary for structural integrity into the member itself, resulting in a low tech assembly of interlocking members directly joined. This produces not only visually simple, almost invisible details, but also an efficient and quick assembly and dismantling process allowing flexible, temporary configurations. Additionally the deliberate choice of solid wood, unlike laminated wood with big cross section for long spans, introduces constrained dimensions of members in length and cross section, promoting structures that can be reassembled and easily transported.

The presented system relates to reciprocal frameworks (Pugnale and Sassone [3]) in its property as a non-hierarchical structure with mutually supporting members but is based on inherently 3-dimensional principles articulating a fully spatial formation of linear elements.

The presented project employs analog as well as digital tools and techniques in the design and fabrication process. The demonstrator is composed of 45 wooden beams of spruce with 5x5cm square section and 2,2m in length.

2. Design and process

In the initial workshop at the University of Applied Arts Vienna in October 2018 students of different departments (industrial design, architecture and art in education) worked in mixed teams with physical models as well as in digital studies (fig.3). Joining principles as well as an overall aggregation were developed, following intuitive decisions based on structural performance, negotiating irregularity, systematics and order. For the intended realization timber elements of spruce of a constant dimension of 5x5x220cm were set as a design constraint.



Figure 3: Kigumi Workshop with Jun Sato at University of Applied Arts Vienna/AT [Photos by Lukas Allner (1, 3), Daniela Kröhnert (2)]

3. Rationalization and optimization

The resulting model was digitized via 3d-scanning and translated into an axis model. In an iterative process the model was rationalized towards optimized manufacturing and assembly whilst balancing a recognizable systematic and the irregular complexity of the formation.

In a digital 3D model members were grouped and aligned into interlocking grid planes (fig.4). Additionally, the configuration was optimized to include a maximum of three members connected in one structural node (at one point) to simplify the joint detail.

In order to perform a computational simulation aiming to find a structurally optimized global form this typological layout was translated into a constraint based model in Kangaroo, a dynamic solver environment on Grasshopper for Rhinoceros developed by Senatore and Piker [4].

Centerlines representing the timber elements are split at the intersection nodes. Line segments are defined as springs with a target length set to the respective original length. A gravitational force is applied to all node points, while the bottom endpoints are constrained to stay on the ground plane.

Springs associated with one timber element are constrained to stay co-linear, and adjacent springs sharing endpoints stay connected to maintain the global typology. The flexibility in spring length allows for deformation and adjustment of the global form. The converged state after simulation shows a straightened model with all members aligned more vertically in average. Deviations in the members length in the final model are compensated by adjusting overlaps at the ends to retain the initially set constraint of 2.2m.

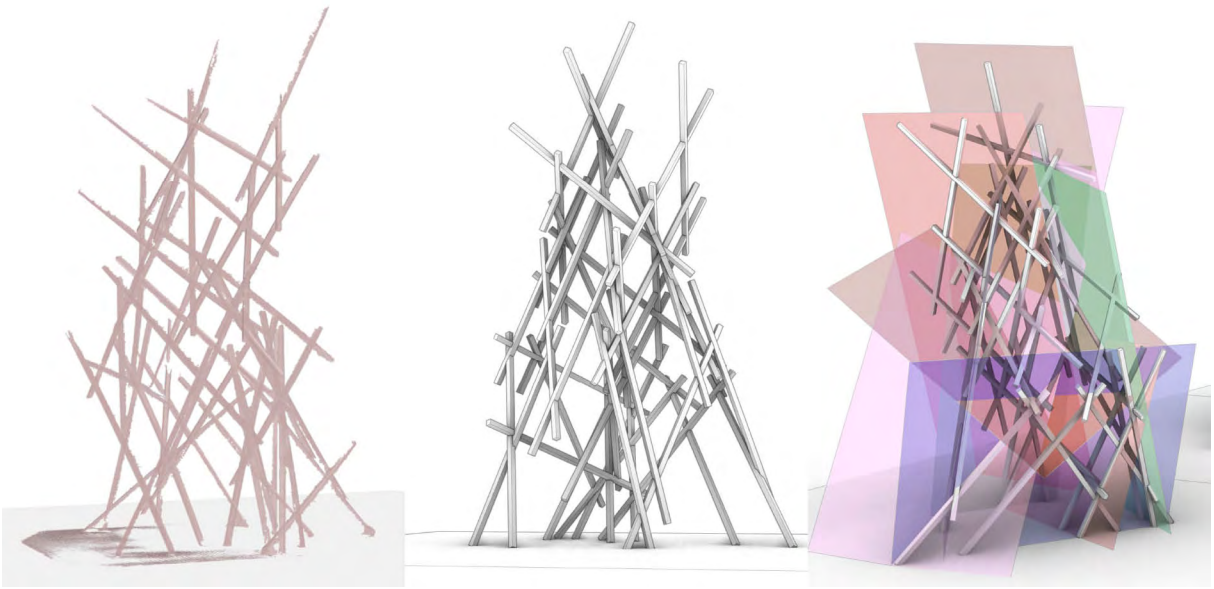


Figure 4: 3D Scan of Physical model, redesigned axial model, model with highlighted grid planes [Conceptual Joining]

The separation of member axes into sub-axes also allows to include a simultaneous structural analysis using Karamba3D a plugin developed by Preisinger *et al.* [5] rendering instant feedback about the improved performance.

The simplified structural analysis shows some reduction in local utilization in the relaxed model, nevertheless the global improvement turns out to be less significant than expected (fig.5). In the resulting aggregation the variation of angles was optimized to be limited to a finite spectrum of angles for further simplification and in search of an expandable systematic.

For this project the principle of half lap joints as the simplest form of interlocking joints was chosen to put an emphasis on spatial complexity over complex geometry in the detail. The simple joint type allows for a large range of variation and geometric freedom for the aggregation of parts. With only a few constraints in the joint geometry the necessary modifications of the basic principle are possible to accommodate spatial complexity as well as a simple assembly mechanism.

The simplicity of joints requires a high level of spatial complexity of the formation for complementary interlocking in order to accomplish overall structural integrity. In comparison, more complex joint geometries with multidirectional performance would require a more strict system of order (eg. an orthogonal grid) and a more rigid spatial system.

The mutual relationship of detail and spatial configuration, the interlocking principle active on both the scale of notched joints as well as the reciprocal positioning of members results in a system in which the architectural definition of spaces is deeply and inseparably intertwined with structural logic. This allows speculations on the architectural logic and aesthetics emerging from the nature of joinery as a reflection about the relationship between material and space. In this context spatial structures not only serve the functional purpose of statics sometimes hidden behind “design” surfaces but become fundamental for architectural organization and articulation. In a structural system with interlocking members local eccentricity can be avoided however notches also represent a local weakening of cross sections. To compensate this disadvantage an optimization methodology is proposed to locally vary depth of notches. Structural analysis informed a refined configuration of lap joints adjusting the local profile overlap to minimize weakening of cross sections in joints with higher bending moments.

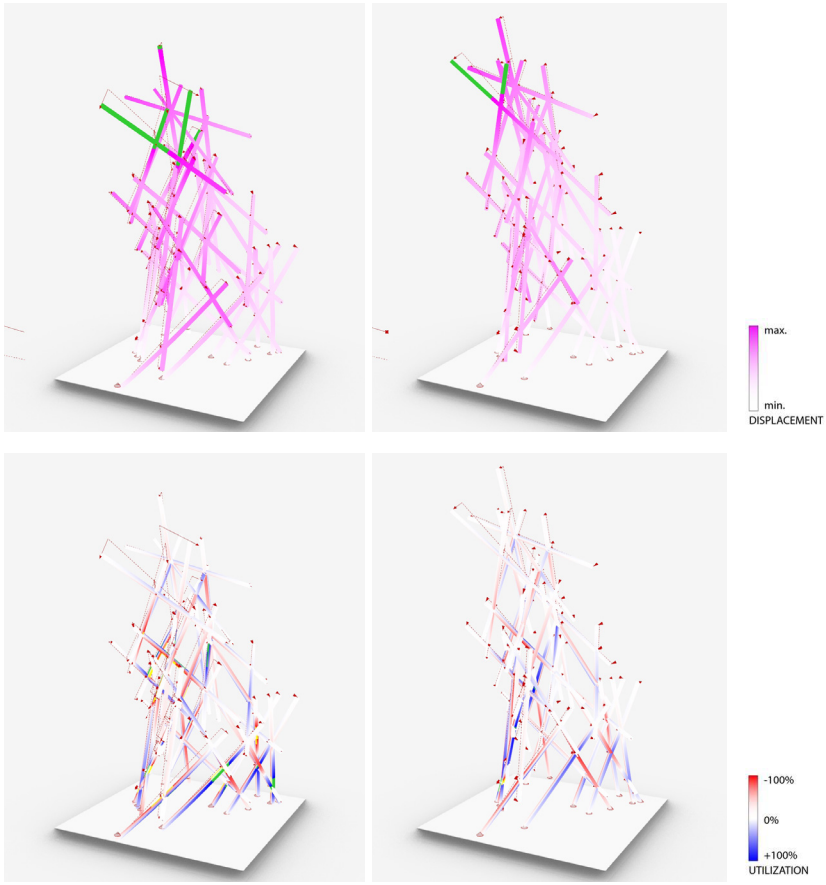


Figure 5: Before and after - spring model optimization [Diagrams by Adam Orlinski]

4. Fabrication and installation

Eventually the digital workflow was directed towards high precision manufacturing with an industrial CNC truss cutting machine. We cooperated for this with the carpentry department of the vocational training school in Murau, Austria. The school teaches young carpentry trainees the theoretical and practical background during their apprenticeship. Besides manual and traditional joining techniques students also learn how to program and operate CNC machines. The vocational training center owns a Hundegger Robot Solo [6], which is a special CNC pre-cut machine for beams with one 5-axis milling aggregate and an automatic tool changer. Hundegger is a German machine producer with a focus on CNC systems for the wood-housing industry. This machine is mainly used for pre-fab timber parts to be used as trusses and in frame constructions.

One challenge for the production process was to design a digital workflow for the programming of the machine. The overall structure has 48 joints with notches on either member, whereas in 27 joints one member is only marked for joint positioning.
Hundegger's own Software Cambium is used to accessing the CNC machine. Within the software there are many predefined parametric macros that require information for e.g. position, orientation and rotation in relation to the local coordinate system of each beam. For the demonstrator only four different operations are relevant : Saw Cut, lap joint, Marking and Text output.
The NURBS-Geometry of each beam was analyzed and processed in Rhinoceros and Grasshopper converting geometry data into xml format to be fed into Cambium for controlling the machining job. CNC processing, including labeling, took about 7 minutes in average. After machining each beam was chamfered manually along its edges before it was ready for assembly.

The design took into account that the structure should be erected without any additional support members. A specially created Augmented Reality app for android mobile devices helped to order, orient and position the numbered beams while assembling. The digital model got displayed and overlaid with the physical structure. With the help of the App, users were able to select beams in groups and show them on the display. By simple tapping and selecting the beam the ID appeared. This process helped the assembly team to intuitively use the app as the exclusive guide, no printed plans were used. The installation of the 45 beam aggregation took 90 minutes when assembled for the first time.



Figure 6: Fabrication and installation process [Photos by Leonard Kern (1,2,4,5), Philipp Reinsberg (3,6)]

5. Outlook and conclusion

The preliminary results of the ongoing research show potentials for complex timber construction defined by an esthetics of craft, characterized by material homogeneity.
The proposed method and workflow are intended as groundwork for further research on self interlocking timber structures, stabilized without metal fasteners.
The machined workpieces showed a high accuracy allowing to consider more complex joints in subsequent test iterations.

The emergent form shows potential for modularity and thus systematic scalability which will be examined in further research. The intended goal is to develop structural models for architectural applications in different scales, integrating complementary elements such as envelopes and usable surfaces.

Acknowledgements

This project is part of the arts-based research project Conceptual Joining (AR 395-G24), located at the University of Applied Arts Vienna and funded by the Austrian Science Fund (FWF), within the PEEK-program. Christoph Kaltenbrunner and our fellow team members contributed with feedback and support.

Additionally the authors would like to express their gratitude to:
Adam Orlinski, Clemes Preisinger (Bollinger Grohmann Ingenieure and Karamba 3D), Florian Fend (Technical University Graz); the participating students from the University of Applied Arts Vienna:

Julian Gamper, Milena Heussler, Catherine Hu, Ben James, Yi Jiang, Leonard Kern, Konstantin Kim, Cornelia Kolmann, Jan Kovaricek, Jakob Niemann, Constantin Rainer, Alex Rodriguez, Philomena Strack; the Carpentry Department of Landesberufsschule Murau: Wolfgang Forstner (Dean) and Johann Wallinger (Instructor), Martin Fließer, Sebastian Gollowitsch, Jürgen Kölly, René Schrei, Bernhard Töglhofer, Simon Weiner and Alexander Schön.

References

1. J. Sato, *Transparent Structures as well as Environmental Filters*, Lecture Handout Vol.15, 2017
2. K. Zwerger, *Wood and Wood Joints - Building Traditions in Europe, Japan and China*, Birkhäuser, 2012
3. A. Pugnale, M. Sassone, “Structural reciprocity: critical overview and promising research/ design,”Nexus Network Journal, vol. 16, no. 1, 2014.
4. G. Senatore and D. Piker, "Interactive real-time physics: an intuitive approach to form-finding and structural analysis for design and education," Computer-Aided Design, vol. 61, 2015
5. C. Preisinger, „Linking Structure and parametric Geometry“, *Architectural Design, 83: 110-113, doi: 10.1002/ad.1564,* 2013.
6. Hans Hundegger AG, “BVX Specification: Documentation Specification of BVX1-Format,” Hans Hundegger AG Hawangen Germany, 2014

Proceedings of the IASS Annual Symposium 2019 – Structural Membranes 2019
Form and Force
7 – 10 October 2019, Barcelona, Spain
C. Lázaro, K.-U. Bletzinger, E. Oñate (eds.)

Reinventing the truss: A collaborative pedestrian bridge design project

Christiane M. HERR, Wenyu HOU*, Shuqi LI, Haoning ZHANG, Davide LOMBARDI

*Xi'an Jiaotong-Liverpool University
111 Ren'ai Road, Suzhou Industrial Park, Jiangsu, PR China
Wenyu.Hou16@student.xjtlu.edu.cn

Abstract

In a rapidly urbanising as well as globalising world, small scale urban infrastructure such as pedestrian bridges across waterways and roads have become integral parts of urban environments. Due to their short spans, human relatable scale and urban role, the design of successful pedestrian bridges involves both architectural as well as structural aspects. Ideally, these design processes involve both architecture and engineering disciplines in creative dialogue, which requires mutual understanding and an appreciation of the respective other discipline's values and design approaches. This paper discusses the conceptual design of several short span pedestrian truss bridges by teams of architecture students in collaboration with civil engineering students and with consultant advice from an external experienced bridge design practitioner. Examining several aspects of the design process, the paper offers insights into discipline specific values driving the design process as well as key differences between the disciplines that create challenges for cross-disciplinary collaborations.

Keywords: conceptual design, truss bridge, pedestrian bridge, architectural design, collaborative design, cross-disciplinary design.

1. Introduction

The increasing specialisation of the professions of the structural engineer and the architect over the past decades has progressed alongside a differentiation of professional tools, workflows and values. Yet, collaborative design work remains a key aspect in projects that successfully address not only technical efficiency but also human experience. Cross-disciplinary collaboration requires both consciousness of professional values motivating contributions from the respective other discipline - structural engineering or architecture - and a shared language that allows exchanges across disciplinary boundaries [1, p. 7]. Without these, an engineer's focus on safety may be misunderstood as narrow-mindedness and an architect's focus on conceptual coherence may be misunderstood as ignorance. Preconceptions regarding the respective other discipline are established early on in students' discipline specific education and become very difficult to change at a later point – to the detriment of productive collaborative work [2, p. 2]. Among such preconceptions is the idea that architects are primarily interested in the aesthetics or the exterior of buildings, or that the role of structural engineers is merely to solve problems in design proposals authored by others.

This paper discusses the design process of a short-span pedestrian truss bridge in several teams of architecture students, with consultant advice from civil engineering students, teaching staff and an external structural engineering practitioner. With a particular focus on the collaborative exchanges among and across disciplinary boundaries, the paper examines the bridge design process based on the accounts of three students representing three student teams of 6 or 7 students as well as the perspective of the module tutors, observations of the exchanges students had with civil engineering student consultants and feedback from an external expert bridge design professional. Based on this overarching

Copyright © 2019 by Christiane M. HERR, Wenyu HOU, Shuqi LI, Haoning ZHANG, Davide LOMBARDI
Published by the International Association for Shell and Spatial Structures (IASS) with permission.

perspective, the paper shows how disciplinary values are established implicitly very early on, and aims to support productive discourse in future cross-disciplinary exchanges can be supported through the extension of disciplinary values, building of relevant skillsets and a general openness to mutual learning.

The pedestrian bridges discussed in this paper were designed over the course of 7 weeks as part of the third year module "ARC202 Structural Design" in the BEng Architecture programme at Xi'an Jiaotong-Liverpool University (XJTLU), Suzhou, China. The module was taught in collaboration with sbp Shanghai, with lectures and tutorials offered by Associate Director David Sommer who acted as experienced external bridge design consultant. The work of three teams was selected from among the overall 11 teams to be examined in detail in the following. One member of each team contributed to this paper as a co-author.

2. Rethinking the pedestrian truss bridge

While China, especially the Southern regions of Jiangsu and Anhui, have a rich history of short span pedestrian bridges crossing waterways, their bridge types have remained unchanged for centuries. Using local stone, these pedestrian bridges have provided structural support primarily through their mass, and have been shaped based on simple geometric shapes such as circle and triangle. While remaining bound to established bridge typologies and limited material variation, these bridges also established the pedestrian crossing as lively public and cultural spaces, attracting commercial activity as well as hosting various forms of public life until today. Only with the opening of China to the West and the start of industrialization in the very late Qing Dynasty (at the end of the 19th century) has the structural type of the truss entered the repertoires of Chinese architects, engineers and bridge designers. In the rapid social and economic changes that followed in the 20th century, Chinese engineers employed the truss in many ground-breaking achievements that are celebrated as national icons, such as the "first domestically designed and built" [3] bridge over the Yangtse river in Nanjing, completed in 1968. Today, China is home to some of the world's largest trussed arch bridges that combine historical references with contemporary engineering superlatives [4].

The pedestrian bridge proposals discussed in this paper were intentionally limited to truss types for educational purposes. On the one hand, this provided a more manageable design space for architecture students who had never designed a pedestrian bridge previously. On the other hand, architecture students are capable of creatively transforming any design task limitation, such that this typological constraint served not only as a reminder to integrate structural function but also as a creative challenge to think "out of the box" based on a constrained repertoire. On starting the project, students reported no particular preconceptions of truss bridges except for recalling historical examples such as the Yangtse River Bridge discussed above. From an architectural viewpoint, students initially perceived trusses as utilitarian and "boring", describing them as almost opposite to architectural design ideas typically aiming for "light" and "organic" approaches.

The particular design task given to students was to connect the XJTLU North and South Campus, which are separated by a road and an adjacent canal of 27m width, with the bridge spanning the canal only. Starting out from the structural type of the truss, students developed their bridge proposals in teams of 6-7 students, through an explicit negotiation of architectural and engineering considerations. This process, analysed and summarised in the following, illustrates a range of key considerations guiding the architectural design teams and their interaction with civil engineering consultants. On several occasions throughout the 7 week project, students could exchange ideas and present their work to civil engineering students (BEng Civil Engineering, year 4), civil engineering academic staff and an experienced bridge designer, David Sommer of sbp Shanghai.

3. Architectural approaches to pedestrian bridge design

Design decisions had to be taken jointly and through a discussion of the relative merits of ideas among the team. Teamworking thus encouraged students to make their design rationale explicit, which helped

to consolidate design approaches, but also enabled the explicit negotiation and consolidation of design values shared among the team. All three teams examined in detail for this paper approached the design task first from an urban context perspective, seeking to acknowledge the site and to accommodate a variety of functions on the bridge. Most teams started with the detailed analysis of case studies of similar size and scale, almost all of them recent European examples. Collected, examined and discussed among the team, the case studies provided an initial range of structural as well as architectural concepts that students subsequently transformed and recombined to derive their own ideas.

Each team however followed a different approach to create shared ownership. One group reported first agreeing on a set of abstract requirements to enable a later selection process from ideas generated among the group members through voting. Another team reported starting directly from a promising structural concept and transforming it gradually through challenging it with qualitative architectural requirements. Yet another method reported by students was to simply agree on a diagrammatic idea presented by an individual, then joining forces in further developing it. In that case, students explained that it was helpful if this initial idea was still relatively abstract, so that it could provide other team members with sufficient creative space to flesh out the idea further, i.e. creating shared ownership.

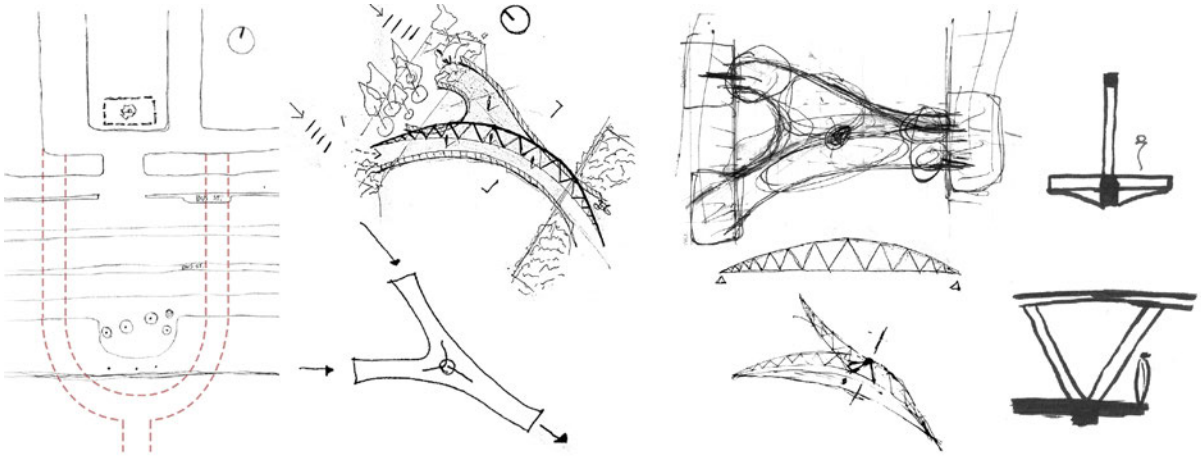


Figure 1: Design process sketches from the team of Shuqi Li

All students started out from a general concept that was strongly based in architectural values and perspectives: A shared aim among most teams was to design bridges as spaces to be experienced by human occupants. All other considerations – structure, materials and details – were supplementary to this overarching goal. This is shown in figure 1, which shows key stages of the team's design process proceeding from left to right. No tutorials encouraging this particular approach were given by the teaching team during this crucial phase of idea development, demonstrating the key role of architectural values guiding even undergraduate students' design processes. A key observation of students' design processes was that most teams initially proceeded to add a broad variety of functions and possibilities, while the second part of the conceptual design process was focused on gradually reducing these again in response to structural and material requirements. This can be characterised as an ongoing circular dialogue between architectural idea – structural response – architectural response to new structural ideas, and so on. In students' final reports, however, the subtleties of this process are mostly simplified to straightforward narratives that can be easily presented in diagrammatic descriptions.

4. Feedback: discussions with civil engineering students

To create a collaborative cross-disciplinary exchange, a meeting was arranged around week 5 of the project with undergraduate civil engineering students of Year 4, who were working on a parallel capstone design project, also consisting of a pedestrian bridge design in an almost identical location. From the tutors' perspective the exchange was seen as an opportunity for a first encounter with another

discipline in an applied design setting – preparing students for future cross-disciplinary encounters in practice. While all involved students were still undergraduate students, and none had ever designed a pedestrian bridge before, the encounter demonstrated pronounced differences between the two groups of students. Architecture students commented that engineering students were initially confused when seeing the proposals presented by the architecture students. Partly this confusion arose from the engineering students' unfamiliarity with reading scale architectural drawings. Another aspect of the confusion derived from engineering students' unfamiliarity with the types of structures presented by the architecture students, which in almost all cases diverged from textbook engineering structures. Conversations among teams mostly consisted of verbal discussion using the physical models of the architecture students, as shown in figure 2.



Figure 2: Cross-disciplinary discussion meeting between architecture and civil engineering students

Conversations often revolved around questions regarding the foundations of the bridge, as this was an area the engineering students felt significantly more confident. Architecture students appreciated the feedback but also complained later about the engineering students' inability to answer questions immediately – most reacted to questions by offering to compile a more detailed analysis later. The biggest challenge for the engineering students seemed to be to engage in the exchange by providing alternative proposals. Instead, their responses were mostly diagnostic, pointing out problems but stopping short of giving suggesting as to what could be done about them. Architecture students observed that any divergence from simple and straightforward proposals known from textbooks "may cause problems", with engineering teaching staff giving very similar comments to their students. Only few architecture students followed up with engineering students at later stages of the design process. Similarly, engineering students did not seek architecture students' feedback for their own bridge design processes, likely due to the perception that involving another discipline's suggestions would generate more questions and more difficulties.

5. Feedback: discussions with expert bridge designer

In addition to the exchanges with the civil engineering department, we were lucky to be able to collaborate with David Sommer of sbp Shanghai. Two meetings and one lecture were held to give students opportunities to receive feedback on their design proposals at different stages of the design process. An important aspect of this encounter with an experienced bridge design practitioner was David's ability to make explicit and to illustrate the values driving the design of sbp's structures across all scales. While not completely congruent with the values embraced by the architecture students, this making explicit of design values embraced in the firm supported a dialogue in which both sides could adapt to each other's language. Conversations focused on possibilities and options rather than problems.



Figure 3: Conceptual design development through sketching with expert David Sommer, sbp

Drawing on his experience of previous cross-disciplinary encounters, David Sommer easily understood and interpreted architecture students' design intentions, and used sketching to illustrate his ideas (figure 3). Engineering design values reiterated in feedback given to students often revolved around simplicity, a reduction of material and resources used as well as overall coherence. Architecture students appreciated a more detailed discussion of drainage and foundation design, and their impact on the overall bridge configuration. An important aspect of these conversations was that despite explicitly disagreeing with several of the architectural design propositions, David Sommer was still able to propose ways in which these proposals could be improved in accordance with their architectural concepts. His comments were taken by the architecture students both as direct input as well as a critical challenge to further refine and clarify their design proposals. David Sommer meanwhile conceded that despite taking different approaches to his own, a variety of ideas were generated that hold promise for translation into applied practice.

6. Bridge proposals

Despite all starting from the basic type of the truss, the conceptual bridge proposals resulting from this project vary considerably between teams. Among the more straightforward proposals is the one by Haoning Zhang's team, which can be clearly separated into a structural part and an architectural part, each fulfilling a dedicated role.

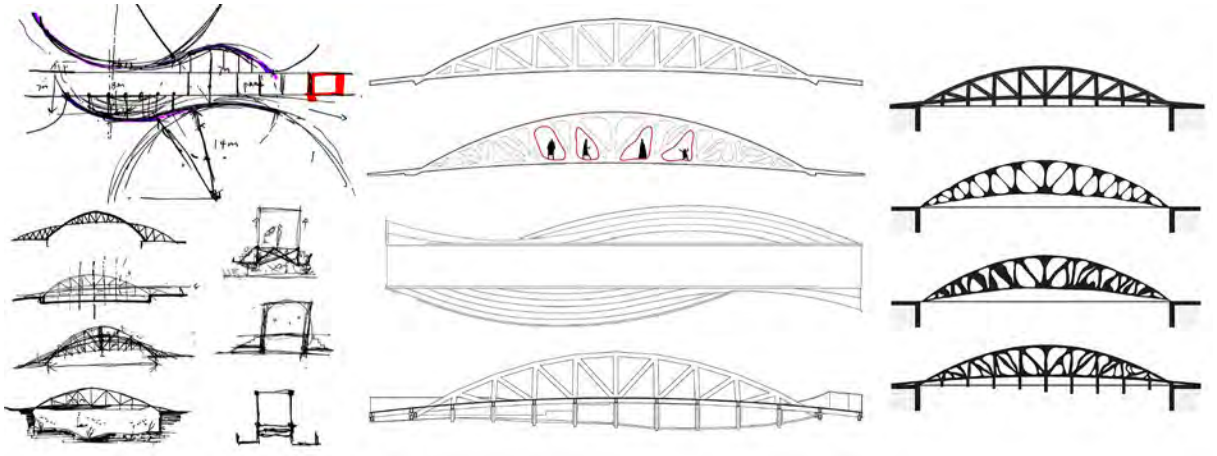


Figure 4: Truss transformation process to integrate architectural functions in the team of Haoning Zhang

Figure 4 illustrates the design process of the pedestrian bridge as a transformation of the truss in response to the team's design aim to integrate structural performance with a broader architectural programme. While this renders the bridge clearly legible and the recognisable arched truss inspires a sense of trust, it also retains a slightly uneasy match between both parts. In retrospect the proposal is still very close to one of the team's case studies, the Dawn Bridge, proposed for Shanghai by architecture firm MVRDV in 2018 [5]. While structurally less balanced, the bridge proposed by MVRDV presents a more convincing architectural integration of viewing platform and truss. With the focus in this module on structural design, it seems that the proposal was pushed towards structural efficiency and symmetry, to the disadvantage of architectural function.

The bridge proposal of Shuqi Li's team (figure 5) came out of a more contextual approach, focusing on connecting the main destinations and access pathways already existing on the bridge site. Extending and connecting these resulted in a triangular plan bridge, which generates a wider plaza-type area at its center. Placed in the middle of the bridge throughout the main span, the supporting trussed arch divides the bridge into two lanes that suggest directional movement. To allow for easy crossing between the two sides of the bridge, a Warren truss was chosen (figure 5, right). The bridge received favourable comments from both architects and engineering reviewers due to its simplicity, conceptual coherence and relative structural efficiency.

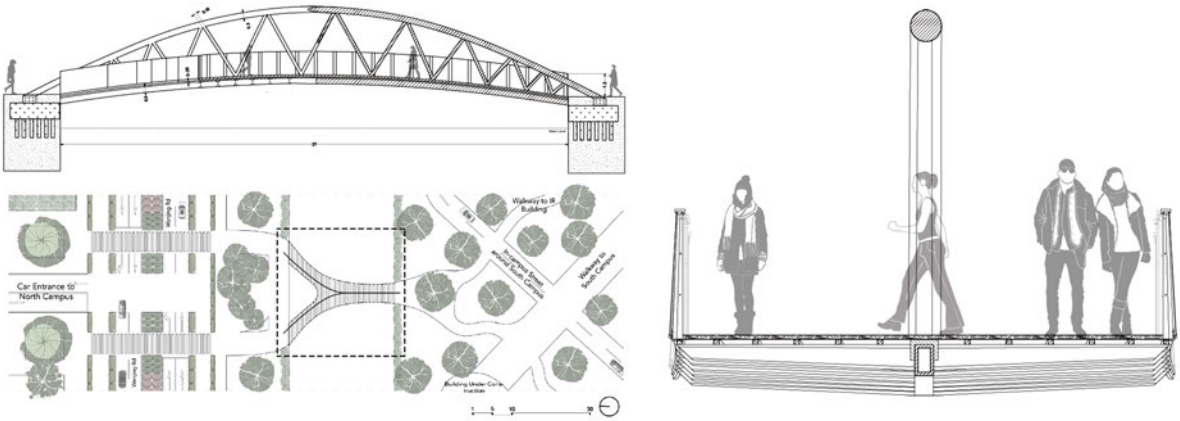


Figure 5: Truss transformation into a spatial configuration in the team of Shuqi Li

The team of Wenyu Hou employed a more abstract design approach, starting from simple conceptual diagrams that allowed the team to discuss and agree on ideas before consolidating form and material of a specific proposal, as shown on le left of Figure 7.

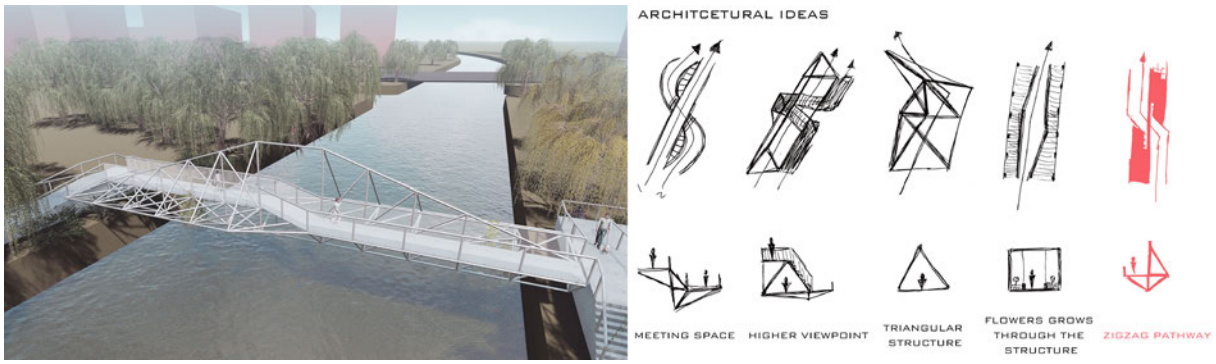


Figure 6: Diagram-focused design development of a truss bridge in the team of Wenyu Hou

The team then proposed different interpretations of this diagram, testing out a variety of ideas for both

structural as well as architectural implementation (figure 6, right). This process allowed all team members to participate in developing the idea while establishing agreement at a more abstract level from the beginning. The team furthermore used parametric modelling in Rhino Grasshopper to understand the generated geometries and to test variations of the idea for their structural properties, as shown in Figure 7, right.

7. Cross-disciplinary learning and teaching: towards shared designing

Stretching across two disciplines, and seeking to establish common ground for exchanges between architects and structural engineers, this project is not only relevant to students' learning about bridges. The module was designed to integrate human experience-focused approaches common in architectural education with technical challenges as they are common in engineering education [6]. By involving students and teaching staff from both disciplines, the module aims to create awareness of the quality of well-integrated design proposals, whether a building or a bridge. Contemporary Chinese cities suffer from a widespread lack of integration of architecture and engineering, which can be traced not only to cultural preferences in structuring design processes, but also to a lack of these values in each discipline's educational approaches [7]. This message was brought home clearly in David Sommer's presentations of the successful practice work of sbp, where design values are made explicit and serve to support exchanges with other disciplines. Aside from approaching cross-disciplinary encounters with an open mind and learning a common language, such encounters also require a set of core skills. Engineering education rarely discusses creativity and conceptual design [8, 9], resulting in engineering students' tendency to focus on problems and a limited ability to propose options, which was confirmed in this module. Similar to Hines [8], we recommend a shared set of cross-over skills such as case study research, conceptual sketching for idea development and simplified fast structural assessment to enable cross-disciplinary exchanges, and to achieve increased quality of future built environments.

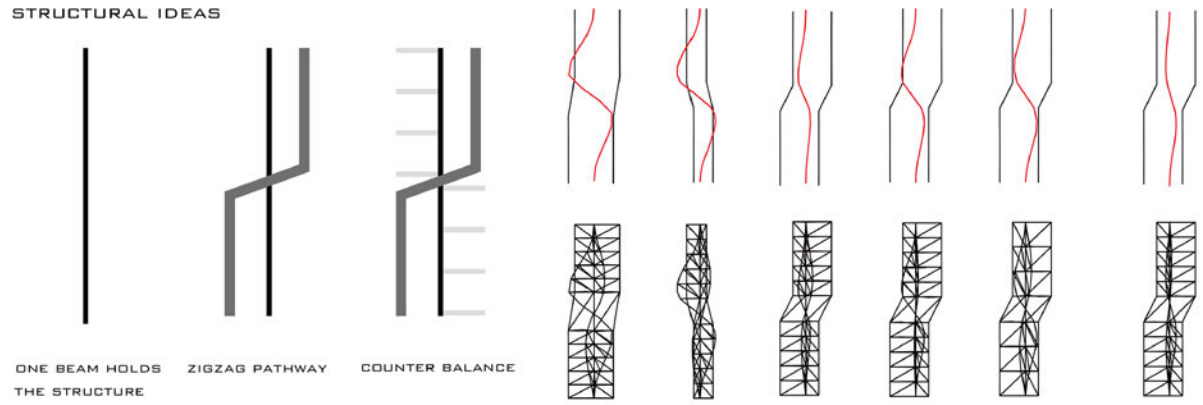


Figure 7: Conceptual bridge design tools: abstract diagrams, sketching, digital parametric models

A variety of tools were found to have a positive impact on students' bridge design processes, with analog sketching and abstract diagrams the most widely used. Students also relied heavily on physical models at various scales to understand the three-dimensional geometry, spatial quality and load-bearing capacity of their proposals. In particular in exchanges with the civil engineering students, physical models played a key part of the project. In addition, students were taught to produce digital parametric models in Rhino and Grasshopper. Several teams used the variety-generating capacity of the parametric model to test proposals and to find agreement within the team (figure 7, right). Students were furthermore shown how to model their bridges in the finite element Rhino plug-in *Karamba*, allowing them to examine the bridge proposals through the simulation of loads and stresses. Results for the digital structural testing were mixed, with some teams embracing the approach, others preferring to only use parametric variations.

Students were deterred mostly by the process of setting up the structural model, which entails a simplification from the geometry-focused design approach preferred by most architecture students.

8. Conclusion

Discussing the conceptual design process of several short span pedestrian truss bridges by teams of architecture students in collaboration with civil engineering students and with consultant advice from an external experienced bridge design practitioner, this paper illustrates typical challenges in cross-disciplinary collaborative design work. Examining the collaborative design process, the paper offers insights into discipline specific values driving it as well as key value and skill differences between architecture and structural engineering that create challenges for cross-disciplinary collaborations. The project discussed in this paper demonstrates the need for increased attention to making disciplinary values explicit already in students' undergraduate education, and to teach a shared skill set to both disciplines in order to enable successful cross-disciplinary exchanges. A shared basis also allows for productive disagreements and shared development of new options that transcend the boundaries of either discipline, where ideals of structural engineering art are complemented with architectural design values.

Acknowledgements

We thank Gisela Loehlein, Head of Department of the XJTLU Department of Architecture for her generous support of this project. We are also grateful to our colleagues from the Department of Civil Engineering for participating in this project. We very much appreciate the time dedicated to this inspiring exchange by David Sommer of sbp Shanghai. Finally, thanks to all students of ARC202 for the enthusiasm, energy and creativity contributed to this project!

References

[1] N. Rappaport, *Support and Resist: Structural engineers and design innovation*. New York: The Monacelli Press, 2007.

[2] C. Olsen and S. MacNamara, *Collaborations*. New York, London: Routledge, 2014.

[3] W. Cang, "Yangtze Bridge stands the test of time," China Daily April 17th 2019. http://www.chinadaily.com.cn/a/201904/17/WS5cb665a6a3104842260b6917.html, accessed May 30 2019.

[4] F. Hoi, J. Geyao, R. Xiao and Z. Yang, *Bridges in China (2003-2013)*, 1st ed. Beijing: People's Communications Press, 2013. (in Chinese)

[5] J. Neira, "MVRDV's dawn bridge provides viewing platform for pedestrians near Shanghai," *designboom*, February 2 2018. <https://www.designboom.com/architecture/mvrdv-dawn-bridge-shanghai-02-08-2018/>, accessed May 30 2018.

[6] C.M. Herr, "Teaching Architects to Design Pedestrian Bridges," in *Proceedings of Footbridge 2017 Berlin - Tell A Story, Berlin, Germany, September 6-8, 2017*, Technische Universität Berlin, 2017.

[7] C.M. Herr, "Creativity in Cross-disciplinary Collaborations between Architects and Structural Engineers in China," in *Proceedings of the 2018 Conference of the International Association for Spatial and Shell Structures (IASS), Boston, USA, July 16-20, 2018,* Boston: MIT, 2018.

[8] E. Hines, "Understanding Creativity," in E. Hines, S. Buonopane, M. Garlock and D. Billington (eds.), *Festschrift Billington 2012: Essays in Honor of David P. Billington*, International Network for Structural Art, 2012.

[9] P. Gauvreau, "Sustainable education for bridge engineers," *Journal of Traffic and Transportation Engineering* (English Edition), vol. 5 no. 6, pp. 510-519, 2018.

FORM and FORCE

Proceedings of the IASS Annual Symposium 2019 – Structural Membranes 2019
Form and Force
7 – 10 October 2019, Barcelona, Spain
C. Lázaro, K.-U. Bletzinger, E. Oñate (eds.)

The (changed) roles of physical models in building design practice and education

Olga POPOPOVIC LARSEN*,

*The Royal Danish Academy of Fine Arts Schools of Architecture, Design and Conservation (KADK)
Phillip de Langes Alle 10, 1435 Copenhagen K, Denmark
olga.larsen@kadk.dk

Abstract

Already used in antient history physical models have been known as an important design practice tool. Although their role has changed, models currently still aid design decisions as form, geometry and detailing; help determine and verify material/structural behavior; visualize and communicate different stages of design projects to different stake-holders. Digital platforms have completely taken over analogue approaches in building practice, yet physical models remain an important design practice tool that, used in conjunction with digital work flows still offers irreplaceable input. In both engineering and architectural education– physical models are utilized more than ever. The paper presents a study of the current status and presents the (changed) role of physical models in building design practice and education. Through examples of different types of models, case studies of working practices, as well as educational workshops in architecture and engineering, the paper puts forward the hypothesis that physical models are still a very powerful, important and current design tool. The paper concludes with current trends, opportunities and limitations of the physical model, as a tool within a digitalized design and educational practice.

Keywords: physical models, digital work flows, conceptual design, building design practice, educational practice, innovative structural form, visualization, form-finding tool.

1. Introduction

In the context of this paper a physical model should be understood as a scaled down three-dimensional representation of an object, building already constructed, or an unbuilt design. A physical model shows the vision of the designer, architect or engineer, about how they envisage the project to be - when built. Physical models allow us *to see*. They, however are not only a visualization tool; physical models allow for *explorations* with materials, forms and structures, but also *testing* of concepts and structural behavior. They enable us to *understand* specific design aspects, as well as offering us a tool that can *guide a sequence* of events, as for example the construction of a building. Models, depending on their role, can be constructed in different scales and precisions. They can be crude- dirty models in the early design phases, or fine and finished- as a visualization and presention of a design phase that communicates the project. Physical models can be small in scale or can be full-scale prototypes and anything in-between depending on the role they have been assigned in the project. Regardless of all these differences, all physical models have one very important feature in common: *they are three-dimensional.*

Whilst design discipline professionals (designers, architects and engineers) are trained to have a spatial understanding, lay people do not always have the skill to read 2D drawings and appreciate the spatial meaning these drawings may have. So, if a drawing has been done in 2D, it is not everyone that can understand it in 3D. Building designers however, often draw in 2D, yet their drawings represent a 3D object – that is realized as a structure or building that when constructed – always has three dimensions.

Copyright © 2019 by Olga Popovic Larsen
Published by the International Association for Shell and Spatial Structures (IASS) with permission.

Models are therefore a very powerful communication tool that enables exchange of ideas beyond the design team. They allow for discussions not only with design professionals, but also with others: as the general public, investors and clients. This characteristic of physical models is very important. Combined with other opportunities that arise from working with models is why, throughout history of human creation, physical models have had important roles, some of them very relevant still today.



Figure 1: Working with physical models © KADK

2. Roles of physical models in design practice

Physical models have different roles in design practice, especially currently when an alternative is possible: using digital tools. One can argue that digital tools have opened up huge opportunities for building design – especially when dealing with high complexity. However, digital tools together with physical models have opened up for enhanced possibilities, where both the physical and the digital are important but in different ways. But before going into current day projects, it is important to look back into history and how models have been utilized in building design throughout time.

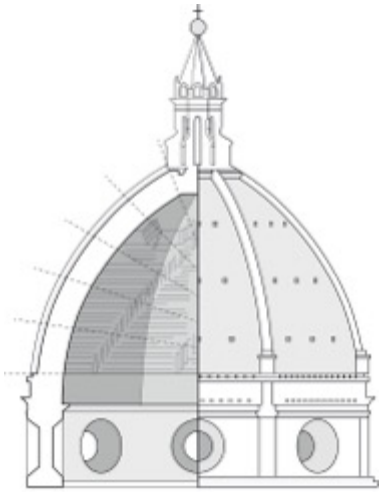
2.1. Historic models

It is difficult to know when physical models were used for the first time. The Antient Greeks and Egyptians, worked mainly in full-scale when they needed a way to define parts of their buildings. Large-scale prototypes were therefore a good way forward. As for whole buildings and the design of them, physical models were not used much, as these were designed and built respecting known and accepted sacred proportions. These were followed as main governing design principles. [1]

During the middle ages, physical models, typically made out of wood, were often used to help estimate costs, especially of important buildings.

The Renaissance was an important time for the history of physical models, with a great revival for models that were used in a number of different ways: as a concept design tool, an exploration tool, a tool for the architect to convey the tactile qualities and materiality of the design by creation of the so-called *"kleinarkitektur*" (micro architecture); as well as a tool describing the sequence and guiding the construction process. *"Kleinarkitektur*" was a way for the architects to keep the closeness to the *"making",* many of whom started as artists and sculptors, before moving into architecture. Drawings did not allow for that. In many cases physical models were more important than drawings – and often were used as a tool to *"lock"* the design, i.e if the model was seen to convey a design stage as fully developed, the design (as seen through the model) could be accepted as *"final"*. In such a context, it is not surprising that great architects, polymaths and thinkers – worked through physical models.

Filippo Brunelleschi (1377-1446), for example, worked with physical models extensively. His main contribution to building design remains resolving the complex problem of the construction of the roof of Florence cathedral. It is a project that Brunelleschi fully resolved with the use of physical models. Using wooden models, he explored different options and in 1418 he instructed four masons on how to construct a masonry model that had no reinforcement, for which, the masons needed 90 days to build. It was a model in large- scale (1:12) model. The masons used forty-nine horse loads of quicklime making the cement needed for the model. The significance of this model was, not only that it provided the vision of how the dome should look when finished, but also, because it had all the important information on how the dome should be constructed. Brunelleschi wrote a detailed description about the construction process and referred to the physical model that was an illustration of the process he had designed. The model was both a design, communication as well as a model that guided the process of construction. [2]. The model encapsulated the dome construction – possible without scaffolding due to the bricks laid in a herringbone pattern, that transferred the loads to the vertical ribs that Brunelleschi built of the octagonal base, while the mortar was drying. The ribs had slits to which wooden planks were attached supporting the small platforms, from where the construction workers could build without the need of scaffolding. It was an ingenious solution that could be executed while the cathedral was in use. And much of the work was developed through models. It was a huge achievement, and as Felix Escrig describes it: "*During three years there was a continuous debate on the way how to close that gigantic crater located at the top of the church. His (Brunelleschi's) ability was demonstrated by being able to show with his model that it could be constructed without a wooden cradle. Never before had a building of these dimensions been constructed in that way."* [3].



Figures 2: Brunaleschi's dome ©V. Petrova

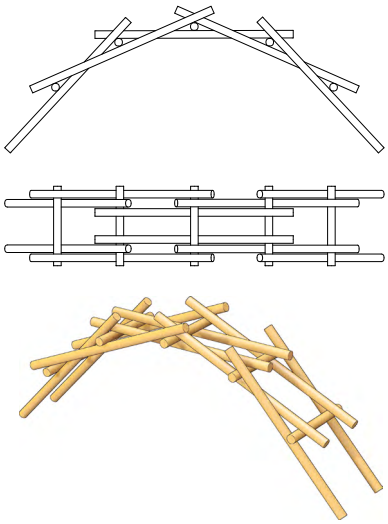


Figure 3: Leonardo's temporary bridges ©V. Petrova

Another important renaissance figure is Leonardo da Vinci (1452-1519), who used physical models for developing, exploring, testing and for refining his designs. One can easily write books about Leonardo's engineering inventions, many of them ahead of his time. The invention of the parachute, hydraulic irrigating systems, temporary bridges, war machines, testing tools (the tensile strength measuring tool and others), were original in more than one way. Leonardo understood friction, centrifugal and centripetal forces, load-carrying principles and how to combine them into his clever inventions, constructions and machines. For example, he came up with an interlocking principle for temporary timber bridges, fully based on creating connections in friction with beams that had no cuts nor carved joints and without any fabrication involved. It is likely, that these temporary bridges, used structural principles similar to the Reciprocal Frame principles understood and described much later (20th C) [4].

Michelangelo di Lodovico Buonarroti Simoni (1475-1564), known for his drawings, paintings and sculptures was another genius of the renaissance. To show how his design would look, he made a scaled model of the St. Peter's Basilica in Rome that he showed to the Pope. The famous painting by Domenico Cresti, depicting this event, presents an important moment in the history of physical models, used as a communication tool between the designer - Michelangelo and the client – the Pope [5]. Today, more than 400 years later, architects still use physical models to show clients their design. Physical models have clearly not lost their visualization and representation potential.

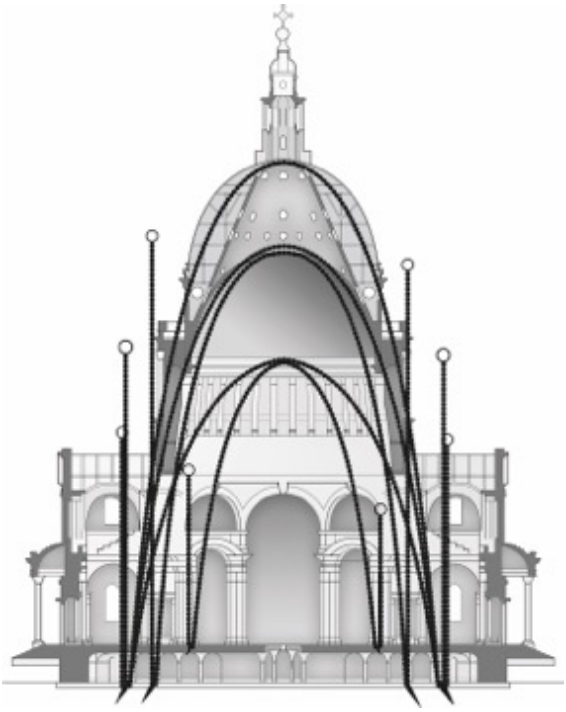


Figure 4: Hooke's work with hanging chains for St. Paul's cathedral ©V. Petrova

One can easily continue with architects and engineers who developed their designs through physical models, as Domenico Fontana – who devised the solution of moving the Roman obelisk, Cristopher Wren – the designer of St. Paul's Cathedral, Sir Isaac Newton – the scientist who defined gravitation, Robert Hooke – developed form-finding through the use of hanging chains, John Smeaton – the first to develop concrete that could be used for building under water, Sir Benjamin Baker – the designer of the Firth of Forth, and many others to follow as architect Anthony Gaudi, Lightweight structures designer Frei Otto, Heinz Ishler, Felix Candela and Eduardo Torojja – the pioneers of thin concrete shells.

There is something that connects all these designers – and that is that perhaps they had no other choice but to use physical models. Their pioneering work was done before digital tools, or for some of them, when digital tools were at their infancy.

2.2. Current roles of physical models

Currently we live in a digital world with digital tools being fully ingrained in our everyday life. It is unimaginable to think life and design, without computers. Even the smallest of design practices, with a sole practitioner currently uses digital tools. One can question the role of physical models in our present practice: *Are they still in use, or a well forgotten historic tool – obsolete as the dinosaurs?*

To find an answer to the question required looking at current design projects, developed at a time when digital tools are readily available. The main question was to find out if designers still would use physical models – or if they have been fully replaced by digital tools.



Figure 5: Vandununsten's Re-beauty cladding solutions © Kristine Autzen

Several contemporary building design practices, including UK based Architect studio dRMM, Danish Architectural Practice Vandkunsten, Engineering company Søren Jensen Engineers, Atelier One Engineers, BIG (Bjarke Ingels Group) and others were studied. For all of them, without an exception it was typical that physical models were used together with digital tools.

Vandkunsten, for example used 1:1 prototypes in their recent project Re-beauty, that investigated the potential of re-using materials with an intention of upcycling them, instead of downcycling them – as is the common practice. To achieve that, Vandkunsten developed a new distinct aesthetic, different to the one of the material's first life. Second-hand wood was used for partition walls in new houses, the flattened ventilation pipes became part of new cladding systems and the reclaimed pre-fabricated concrete elements, became new walls. Although, the re-working required time and thus the cost was not low, it has created a niche market of interested clients who believe in sustainability through re-use. Søren Nielsen, partner at Vandkunsten states: *"There is no sustainability without beauty"*. In this statement, his message is that the aesthetic is very important to get clients and users interested in a new way of thinking. Only then one can discuss performance. All this work has been developed through physical models.

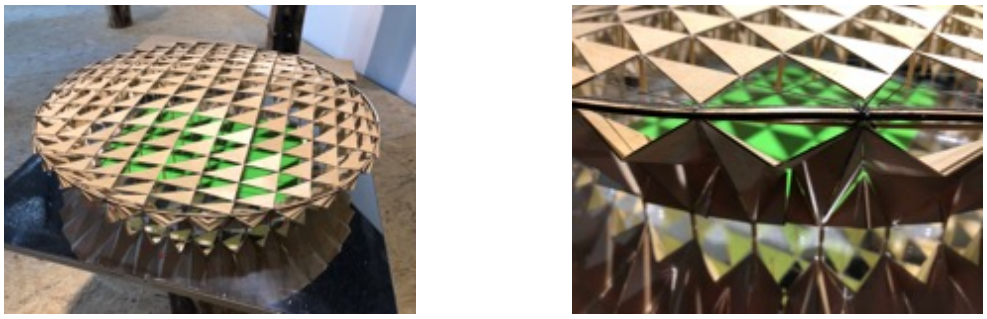


Figure 6 and 7: dRMM's Timber stadium physical model and close-up © Olga Popovic Larsen

dRMM is a London-based, international studio of architects and designers founded in 1995. It is well-known for its inventiveness and creativity in creating socially responsible architecture and higher values for all. dRMM are at the forefront of innovation in timber architecture where through research and design, they lead in engineered-timber applications in architecture. dRMM advocate for better and more sustainable construction, equality, and the creation of higher social values in society through good architecture.

At a recent dRMM exhibition *"Forest of Fabrication"* in London, where their work is presented through drawings, digital and physical models, dRMM founding partner Alex de Rijke stated: *"We use models to test ideas, structural principles and to try out materials. We use samples…The models instruct us, we*

learn from the models – they tell us things. Sometimes, the model is a representation of the building and sometimes, the building is a representation of the model because the design of the model influences the building".





Figure 8 and 9: dRMM's Timber tower physical model and close-up © Olga Popovic Larsen

When confronted about the role of physical models currently, Alex de Rijke states: *"Although we live in a digital world, we will always continue to build physical models because they are such a powerful exploration tool for architects to develop their designs. People who have not been drawing are not trained to understand drawings. We find that in meetings, when we are presenting our designs to the client or to ordinary people and we show drawings, as soon as we put a model on the table, no one looks any more at the drawings. A physical model can be understood by everyone: by children and ordinary people. And to read drawings you need to be trained. Models will never disappear because they offer a universal language, understood by all."*

This was a very powerful message, but *what about engineering practice?* Currently engineers design practice relies heavily on digital work-flows. Powerful software can model, describe and present structural behavior, *so why use physical models?*





Figure 10 and 11: Søren Jensen's digitally fabricated physical models © Olga Popovic Larsen

When looking at the work of contemporary Danish engineering consultancy Søren Jensen (SJ) Engineers, it is the high end of digital tools that are in use in their projects. The company presents itself as an engineering practice that, not only will take part in the creative process, but *"has the courage to*

lead the creative processes and create artful engineering" [6]. Covering a broad area of engineering skills, SJ are renowned for their ability to collaborate with the other project partners at an early stage of the design process. They strive to achieve highest quality through collaborative working, but also by embracing cutting-edge digital tools and using them to the benefit of the process. They are in favor of integrated design and support innovation. The company's research and development are imbedded in the working of the practice where through testing of new structural theories and materials, SJ develops new knowledge and skills to lead the field.

In this context, it is interesting that SJ's offices are full of physical models. Nearly all of them are digitally printed and looking very precise, but are physical! They are proud to inform me that at SJ, they use physical models more than ever because it is easy and fast to make them, using the already developed digital models – it is fast and easy to print a physical model in no time. At SJ the physical models are used in design development, in discussion with clients and the other design partners. In addition, large scale prototypes are being made to verify different aspects of the design. This was a very powerful message: the digital and the physical design tools can happily coexist, not only that – they complement each other and support the design in different ways.

3. Building design education through physical and digital tools

It is not surprising that physical models are used in education still. They are a very powerful educational tool when teaching structural behavior, when exploring innovative structural forms, but also in the creation of new architectural concepts, urban scale projects, design objects or explorations with new materials. There is nothing so powerful as experiencing a specific performance, a texture, a form or spatiality. All of these can be explored, understood, tested, verified, visualized and experienced through the analogue approach of the physical model. In addition to this, the readily available digital tools as CNC cutters, digital printers and robotic arms in a new way support the physical models. The new generation of physical models are faster to make, have high precision and allow for creating a link between the digital and physical work-flows.




Figure 12 and 13: Exploring casting through vacuum-formed formwork © Olga Popovic Larsen

The fast and easy to produce new generation physical models have created opportunities for all design fields, but especially for the engineering disciplines. Physical models are no longer present in artistic educations only, but also are part of the technical disciplines creating a link between the different design fields offering a new age discussion and collaboration platform.

4. Conclusion

The paper investigated the (changed) role of physical models in current design and educational practice. It presented how models have been used through history and also currently, when digital design tools are readily available. The investigations through examples of current design and educational practice suggest that physical models are used currently more than ever. The ability of connecting the physical and digital environments offers great opportunities both for practice, as well as for education.

Acknowledgements

This work is part of the research conducted for the upcoming book *Physical Modelling for Architecture and Building Design*, to be published by ICE, London. The author is grateful for the invitation to work on this interesting project and the opportunity to write the upcoming book.

Thank you to all designers Architects and Engineers for sharing your design practice and approaches in connection to physical and digital tools.

Many of the images, both drawings and photographs has been produced by Veronika Petrova. I am grateful for the help.

References

[1] Moriarity J, Dissertation: Think by Making. *A thesis submitted in partial fulfillment of the requirements for the degree of Master of Architecture*, University of Washington, 2015

[2] Prager F.D, and Scaglia G, *Brunelleschi: Studies of His Technology and Inventions*. Dover Publications, Mineola, NY, 2004

[3] Escrig F. *The Great Structures in Architecture: From Antiquity to Baroque. Advances in Architecture, Vol. 22*. WIT Press, Southampton, UK. p. 99, 2006.

[4] Popovic Larsen O, *Reciprocal Frame Architecture,* Architectural Press, Oxford, UK, 2008.

[5] Smith A.C, *Architectural Model As Machine: A New View of Models from Antiquity to the Present Day*. Jordan Hill: Routledge, Oxford, UK, 2007.

[6] Søren Jensen *Projekter*. [ONLINE] Available at: www.sj.dk [Accessed 16 January 2019].

Proceedings of the IASS Annual Symposium 2019 – Structural Membranes 2019
Form and Force
7 – 10 October 2019, Barcelona, Spain
C. Lázaro, K.-U. Bletzinger, E. Oñate (eds.)

The Working Model: A cross-disciplinary collaborative tool

Veronika PETROVA*, Olga POPOVIC LARSEN[a],

*/ a Royal Danish Academy of Fine Arts School of Architecture (KADK)
Phillip de Langes Alle 10, 1435 Copenhagen-K, Denmark
vpet@kadk.dk

Abstract

In the broad field of design, and in the context of physical representation, the working model is essential. Working with or through a physical model is still common practice as it is a highly effective and engaging way of developing conceptual ideas and achieving design objectives. Better collaboration is needed to produce good building design that can only be achieved through open dialogue, yet the working model remains an exclusive experiment within each discipline. The working model is a powerful decision-making tool to progress design and it is used in different ways to inform specific aspects of the design, depending on the user's discipline and inquiries. Architectural scale models offer architects an understandable way to develop their concepts through scale-modelling, used to aid or even guide the design process to achieve a desired goal. On the other hand, an engineer's mock-up is also a working model used to understand structural behavior by load-testing, for example. Both of these are working models in different forms, according to design intensions and specification. Thus, as a decision-making tool, it can offer an opportunity to designers to collaborate sooner. When the working model aim to respond to a broader set of questions, different disciplines can engage earlier and thus better inform the decisions. To inform a better understanding of the working model as a term and its power in design development, this paper defines the working model's purpose within each design discipline (architecture, structural, light design, etc.) providing an understanding of how it is used as a decision-making tool. This paper will identify the multi-purpose form of the working model, with the objective of interlinking disciplines to offer architects an insight to build models which study aspects through a cross-disciplinary perspective. This may lead to working models becoming more interdisciplinary, offering opportunity for a stronger, more informed design process, collaboration and thus better building design.

Keywords: working model, model making, physical modelling, decision making, interdisciplinarity, design,

1. Introduction

"The number of specialisms has increased enormously to cope with the complexity of the design/construct problem and the technologies available to provide the solution. Innovation has led to reductionism, whereby smaller parts of the problem can be sub-optimized. This innovation is now seen to have led to fragmentation and in many cases an adversarial position between the team members." (Brandon [1] p.38). Better design team collaboration is needed in order to improve project performance in terms of process, delivery, participant understanding and time frame. To achieve the 'growing array' of a project's technical requirements, understanding between collaborators is needed throughout a project. Spence [2] writes: *"Better collaboration is needed simply to produce good architecture.. achieved as a result of an intense and open dialogue between all members of the design team."* (p.3). Used by different design disciplines, the working model is a powerful decision-making tool, an aid for investigating and anticipating formal and spatial problems of a building design [3]. The model that this paper builds its arguments upon is the physical model that is used to work with in developing design, to help make decision or further exploration when the basic idea is there but not yet set in stone. The term

Copyright © 2019 by Veronika Petrova, Olga Popovic Larsen
Published by the International Association for Shell and Spatial Structures (IASS) with permission.

'working model' has different definitions and classifications. Through different building fields the 'working model' is not all that clear – architects mean simple models, engineers mean working machines. It is the aim of this paper to build an understanding of the working model, to reveal the spectrum of its purpose and coined definitions in the hope of forming a clarity and opportunity for its cross-disciplinarily - the 'working model' which could offer more interdisciplinary collaborative working during design development.

2. The Working Model – an ambiguous architectural tool

For architects, a working model is essentially a three-dimensional sketch which designers use to work out or work with. It is a phase in each design process, a development and a decision-making tool. Working models can be considered multi-purposeful and hybrid; How one works with them varies, but it always aids in problem solving and thus decision making. What is true about the working model is that it is a model *for* architecture as opposed to the model *of* architecture as outlined by Cannaerts [4]. In other words, it is not a fine representation seeking "to provide a holistic view of the finished architecture" ([3] p.78), nor a scale rendition of a finished design. Instead, working models "affect the design process" (Jančič [5] p.70).

Different scholars have attempted to classify models in categories of their refinement, use, data outputs (qualitative or quantitative), their materiality, their structure and so on, where the 'working model' or 'study model' typology is an undefined one. Referred to as study models, maquettes, mock-ups etc, working models are *ambiguous* as the way they are used is also very different from discipline to discipline: They may be worked with, tested, studied, evaluated, dismantled etc. so classifying them is not easy - they can be divided by many criteria: Stavrić [6] has placed working models within the 'study scale models' category, refined by their use, amidst white-styles models and conceptual scale models; Schilling [7] categorizes architectural models by their role in design - concept model (an idea in model form), working models (three-dimensional sketches at an adequate model scale), and presentation models (ideational and mature), writing *"working models are indispensable companions in the complete design. Whether it is at the level of urban design or the architectural formulation of the design up to the detailing, working models supply crucial information and stimulation."* (p.109). Schilling also states *"the function of the model changes during the course of the design.. In the subsequent working up of the design, representation and communication through the model moves into the spotlight."* (p109). Knoll and Hechinger [8] organize models into three groups: topographic models, volumetric models, and specialty models of what they depict. Here, working models are classified within design development beside 'design drawings', at the integral stage between preliminary design, conceptual models, and final project models. Smith [9] offers a different view, calling architectural models machines due to their *"varying uses as a thinking and defining mechanism for understanding and demonstrating architectural concepts."* To clarify the 'ambiguity' of the model, he proposes that architectural models fall within two categories: 'architectural reference standard models' (understood as playing parts of a kit), and 'architectural scale model machines' where a model machine *"serves as a device on which to project thoughts in an attempt to develop the perfect design.. by which [the maker] can test and re-examine their ideas."* (p.21). Associating the working model within Smith's view, one could call it the 'architectural scale model machine' as it is studied and ideas are tested using it. Smith also writes that *"architectural scale models offer architects an understandable way with which to develop and define their concepts"* and he proposes that *"architectural scale models are typically used as thinking mechanisms for defining"* (p.7), assisting informed decision making. The working model Morrison and Ostwald [10] believe, is considered a device equally as important as the drawings and presentation model that in building design, writing: *"the working model is used by the designer to test and refine their ideas in three dimensions"*(p.142) so, these 'rough' models, though ambiguous, play a critical role in design decisions, shaping constructions. Janke [11] discussed his experimental model which at time he calls it the working model: *"Experimental models are used for spatial studies of the possibility of joining, assembling and planning individual components"* where the *"assembly process*

can often be more thoroughly explained on a model,.. modified by adding or subtracting components" (p.62). He also writes that *"each building entails the mastery of a spatial problem.. in choosing an appropriate construction system.. and in creating form order and architectural expression."(* p.53) As tools, they are key to design development. Porter and Neale [12] express *"design development models are among the most important and exciting of all the model types.. like their conceptual predecessors from which they are spawned, they are constructed in an unselfconscious manner, their prime aim being to trial feasibility of a consolidating or challenging architectural form"* (p.24). They outline their idea of 'supermodels', *"tools for engaging disputed aspects of design.. that have impact on the outcome of our future environment"* (p.vi) describing them as 'role models' categorized by their role in the design process. Thus, the common thread amongst definitions of the working models is their use in design development.

3. Working Models in Architecture

In Architecture, process models can be made to decide on many aspects such as zoning, massing, to study elevation, structure and materials, where design principles are initially worked out on a small-model scale. They are the intermediate stage, considered *"the most important medium of contemplation in the design process"* (Gerkan *et al.* [13] p.23-24). This 'dimensional model' *"checks a design idea"* [13]. Some architects build models for idea generation, study and evaluation where 'working models' and 'presentation models' are the two different ways of modelling: If working models are when ideas are thrown together and decisions are made, presentation models show those decisions visually to the client or layperson; Working models are more abstractive: They are informative for decision making but aesthetically, they're unattractive and appear 'out dated' once the initial design is finalized. Their finish is unimportant but they embody their own authenticity, visually preserving alternatives, thought and work [13].

3.1. Interior design working models

Interior design models can be split into primary models and secondary models. Primary models focus on explorations, design evolution and tend to be more abstract whereas secondary models, usually included the exterior, structural frame, specific components and generally more detail. Much like a building itself, approaching the design of interior spaces, a designer would typically employ various means to allow visual access to internal space, worthy of the same consideration as architects give to exterior form. In these interior working models, spatial borders are defined and are constructed to study interior design, spaces and furnishings, often in parts. They can be built as corner sections or vignette models, rendered with detail and texture to visualize ideas for surfaces in relation, for example. Knock-down or flip-up models tend to also be popular interior working models, created as flat planes interchangeable to quickly flip between elevations to make decisions. If designers choose to, they may construct openable models where the roof or floors can be removed, to review spatial relationships where colour and furnishing elements play a larger role than in the so-called architect's working model. Janke [11] writes *"[the interior model] enables the future room to be experienced."* He classifies them as either simple interior models all about the inside room at a scale no smaller than 1:50, and the 'building model' with designed interiors where *"the interpenetration of the inside and the outside can be examined"* (p.78). He explains that as a building model, they can demonstrate interrelationships of spaces and flow of crowds. With more detailed interior models, the architectural orientation and context is already decided and the 'exploration' lies in the 'sculptural' assembly of actual material samples and colours [12]. Mills [14] considers all of these model types as study models, even presentation models, stating that *"study model implies that they are always open to investigation"* and *"their purpose is to generate design ideas and serve as vehicles for refinement"* (p.11).

3.2. Lighting design working models

Interior designers and lighting specialists often work together to arrive at more informed lighting design proposals. Light design can also be approached from industrial design either employing artificial light sources or daylight. Working models in industrial design for desk lamps, for example, focus on the concept as a product (its ergonomics, use and aesthetics etc.), are built from foam or card. Lighting designers work with atmosphere: Lighting design for churches, theatres and architectural spaces, tends to begin with collages which move into mock-ups in a light lab, where testing with artificial and natural light can be carried out with simple models using different light transmitting materials; they then decide based on the atmospheric conditions created by their concept.

Unlike the typical interior model focused on texture and tones, lighting models are more specialized, built *"to predict and measure the effect of natural and simulated electric illumination"* [12] (p.31). Usually constructed for research into light-sensitive environments such as art galleries and museums, they must be detailed in finish [12] with particular focus on colour. An interior model could act as both a working model for interior design and for light studies, but to simulate atmosphere as accurately as possible, it is important to mask out the additional light sources from the working environment to bring the model to life solely with the anticipated real lighting conditions. Usually an endoscope is used through a hole cut in the model to study the inner spaces [11]. Simple box interior models can be taken outside on a sunny day to visualize light distribution – different 'filters' can be interchanged to affect the internal atmosphere quickly. The role of lighting design is *"to create a suitable ratio of diffused light to directed light to meet the requirements of each individual situation"* [15] (p.78). If interior models can also be used for lighting tests, to measure light intensity [11] the crossover between interior and light designers can lead to design decision of broader understanding, not only photographs of light's natural phenomena.

Olafur Eliasson's studio in Berlin, is a mixture of artists, architects and technicians, experimenting together as in a laboratory. *"Here, installations are tested, ... prototypes hung on walls and scrutinized, and reflections of light studied"* [16] (p.10). A customized white room at the studio is the space where optical effects are tested and design objects are perceived under different lighting conditions. On his working models, Olafur states that *"their primary role is to make the connection between production and perception, acts and decisions, trial and error"* (p.11) which suggests that they are powerful developmental models.

3.3. Sculpture working models

In sculpture *"the first plastic, sketchy preparatory design for a sculpture"* (Cole [17] p.124) is commonly referred to as the 'maquette' or the 'bozzetto', - a scaled version which derives from a sketch and worked out by hand using wax, clay, or terracotta etc. These working models are prerequisites for last decisions for the final piece. They *"can also be full-sized which might serve as a guide for executing the final work in stone, or for judging the appearance and effect of the work in situ"* (p124) however, this is more common in smaller sculptures. The stone carvers' working model is considered set-in-stone: They 'mechanically measure' all shapes and features of their working model to carve (and replicate) it into the building. *Their* working model is rarely full size, as they work on scaffolds and large works are difficult to handle [18]. Slobodkin [18] writes that *"sculptor's working models are reproduced, enlarged, or reduced into cold lifeless replicas with factual accuracy.. using compasses or a pantograph system"* (p.184). This is true because as pieces of art, they're upscale is imitation. Defined very accurately at smaller scale, worked by fingers, it is not what one understands as a study model/maquette in architecture. Here, they are fine art.

3.4. Modelmaker's working models

In Janke [11], the working model is a model-maker's tool, following an 'architect's drawings'. Here, this 'Arbeitsmodelle' is a solid produced to enable production drawings for consequent and more

detailed models: *"At this stage in the design process it is important.. to examine any points of doubt.. to formulate the results of all previous studies. Ideally the building model should be able to give a sufficiently precise answer to all questions relating to the design"* (p54). Moon [19] writes: *"modelmaking is editing.. but it is also more"* (p.137). Sagrada Familia is a good example of a model-maker's role in the project process. In Sagrada Familia, modelling is without the architect or the drawings. The geometry of the cathedral is very particular in its form, construction, purpose and interaction with light – it must be understood. By scanning remnants of Gaudi's plaster models and using software to piece together these original works digitally, modelmakers are working with engineers in translating his ideas into new scale models to be used in the reconstruction of the cathedral. These models are refined further by architects and engineers to create full-size mock-ups [20]. *"This trade requires technique"* states Albert Portoles, the head of the model makers' workshop at Sagrada [20]. Modelmakers must have full understanding of the architectural design, be equipped with terminology and principles and produce work to high precision because a modelmaker problem solves. Mike Fairbass states: *"show a good modelmaker a drawing and he will show you the design problems. He questions everything because he is forced to answer everything."* (Moon [19] p.139). Janke [11] explains that *"Often it is difficult for the model-maker to interpret correctly what the design expresses and.. to embody this in the abstract form of a model"* (p.52). As the model-maker's working model is about its constructability at small-scale, these solitary models are rich in decisions about materiality, connectivity and construction joints. Perhaps this aspect of models is an opportunity lost and could well be a cross-disciplinary collaboration.

3.5. Landscape Architecture working models

Landscape architects develop changes in places and landscapes, continuously aiming to improve environment design to meet ecological requirements better. When sustainable planning ideas are generated they must be presented visually. Models are an essential part of landscape architects' design process as *"landscape design is first and foremost a problem-solving strategy.. with the aim to convey concrete planning intentions or possible consequences of developments."* (Mertens [21] p.8). Forms and ideas can emerge through model-making and materiality plays a meaningful role in this field; Landscape architects aim to work ecologically and economically, often building their working models from recyclable materials with sustainability in mind. For Louis Kahn, clay had meaning in his landscape modelling and terrain sculpting: He found it the most effective material tool to transmit his landscaping ideas [22]. Clay also had significance to the culture of the site he modelled – India. Collaborating with the sculptor Isamu Noguchi on the Levy Memorial Playground in the early 60s, they made landscapes in plaster, and later in bronze. Kahn's working models in clay allowed him to visualise the integration of his architecture to landscape, modelled openly and creatively [22].

The 2012 Olympic Park (intended to become a catalyst for the regeneration of East London, to manage flood risk amongst the ecologically rich area of wetland and meadows), was also developed and finalised on a working model. Made especially for decision making when the project began, only using card, foam and pin trees, this working model *"later became an invaluable tool for client meetings and discussions with stakeholders, community groups and planners"* and their *"largest and most informative model"* (Entwistle [23] p.74). Entwistle [23] writes *"It highlights the strong visual impact of the earthworks and landscape corridor and its relationship with architectural elements"* (p.74). In these examples, landscape working models were essential to make concrete decisions. Although they are crafted using clay or mesh for example, the contouring process gives a modeller more focus and awareness of context. The choice of material is important here to signify a meaning to the landscape.

3.6. Planning working models

Working models in planning are rough test pieces often out of card, constructed to determine the amount of material that a scale model of that size requires, although, the planning model itself, is a working model: the new is represented against the existing. Knoll and Hechinger [8] write *"working models of*

urban design projects show existing buildings, fixed and in presentation quality, while allowing for changes and playful experimentation with the portions being designed.. Alternative schemes can be made as model inserts" (p.19) It is the model inserts that are being tested and decided on in the planning model. However, looking back, Janke [11] wrote about the 'survey model', *"an instrument for documentation"* where site models were built little by little following a site survey, forming a coordinate system, where trees are pinned along the way. These models were then photographed in top view as a survey plan for decision meetings as *"compact information is useful for boardroom decisions"* (p.49). This engagement of modelling the site as it is discovered is what a working model is about in a broader way but a lot has changed since then. In town planning, site data can be collected almost instantly with the use of digital technology. Although large urban master plan models are still built, they are limited to how much data they can engage and portray. In a time-consuming way, altitude, street elevations, and landscape details can be represented – aesthetic, overcasting, circulation and altitude can be discussed – however, invisible data such as noise or air pollution, climate and density are more difficult to engage and present physically.

3.7. Civil and structural engineering working models

Engineers use models that verify their assumptions following a series of calculations, usually once comprehensive detail about the project is known and ready to be tested. For example, experiments *"carried out with models in a wind tunnel.. establish the resulting forces of suction and pressure in the individual construction member of a building"* ([11] p.88). Janke explains that *"the information gained on the deformation in turbulence and the resulting negative pressures give important conclusions for the construction of the external skin and the building form."* As these are aspects of the design decision, we can classify these models as working models too, although they achieve a quantitative output as well as qualitative [9]. *"Qualitative models would include a scale model of a highrise exposed to smoke streamers as a means of visualizing potential wind vortex patterns or a cardboard model of a frame structure created to help assess its reaction under a load"* (Smith [9] p.20). Perceiving these phenomena in nature is very valuable in decision making: *"There is nothing that will reveal better the structural behaviour of a cantilever or a truss to a layperson than a simple small-scale model made out of a simple materials such as cardboard or balsa wood loaded to destruction"* (Popovic Larsen [24] p.61). Building paper bridges can offer quick intuition about stability, buckling and other advanced systems that would otherwise be difficult to understand and explain. Simple models can especially help to resolve joints.

In engineering, a working model is commonly known as a 'machine able to work as expected on a small scale' a typology of 'model' that can be misleading in cross-disciplinary collaboration. Mock-ups and prototypes, usually built to 1:1 scale, demonstrate important parameters which help to refine important elements before the preparation of final drawings; Built carefully, they mirror the real thing [25]. At the beginning of the design process, it is beneficial to test in small-scale: *"In a hands-on, almost playful, way, things that at times seem only comprehensible to the mathematically gifted ones, become obvious to everyone. The challenge of designing a structure translates into sketching, exploring with physical models and trying new things to make these small model assemblies stand up"* [24] (p.62).

ARUP have been working to complete Sagrada Familia for 2026. It is a highly interdisciplinary project where physical working models, prototypes and digital tools have been crucial for its continuation and construction. These models help to come to agreements about aesthetics, geometry, structure and construction method. One good example of a builder's working model is the 1:1 model the contractor built with simple materials to check if a construction bolt could be done up by hand on site during assembly [26]. This shows how verification is important, and perhaps without the contractor's input, this experiment would not have been made.

Engineers Atelier One, won a competition in 2002 for their design of 'Windvane', a rotating wind shelter on the seafront at Blackpool in collaboration with architect Ian McChesney, who had developed working models of a twisted vane. The shape of the vane had to be resolved at early stages in the design to enable

the structure to rotate in the wind. In order to decide on the shape of the structure, they built a small-scale model to check model behavior (Thomas and Chadwick [27]). *"Using a desk fan we created the wind flow across our model. We used a dish of water with Blu-Tack and pins to allow the foam board base to rotate with changing wind direction"* (p.214). To demonstrate wind flows across the blades, showing any local areas of turbulent flow and to uncover if the overall form was unstable, they tied red string to the top of a pencil and moved it next to the vane in the wind flow. Later in the process, a full-scale prototype was tested for a year, but without this hands-on desk study wind test, fundamental decisions would not have been made as quickly, increasing costs.

3.8. Seismic engineering working models

Earthquake engineers translate the design concept into a working detailed design, test building mock-ups and run simulations to test the integrity of buildings in special laboratories. As a discipline, they intersect with the architectural design process much later than the 'working model phase' of the architect. This is usually when designs and building functions are more developed and number of stories is known, because the verification of seismic performance of structures such as shaking table tests, are expensive to run and mock-ups tend to be larger than 1:40, adding to the costs [25]. Meymand [28] describes the way a small-scale mock-up was constructed from simple 'hardware store' parts intended for demonstration for his project to begin with, tested on a small shaking table to be evaluated and to refine the design. Then, over a course of five months, this mock-up was improved and tested every month for further refinement. Perhaps it is the simpler, if the first draft mock-up that can be called an earthquake engineer's study/working model.

3.9. Acoustics engineering working models

"The field of architectural acoustics is another area in which model testing is still an essential part of the process of designing large theaters and concert halls" and *"despite the sophistication of today's computerized measuring techniques, simple technologies still have a place"* (Addis [25] p.563). For Sydney Opera House, Jørn Utzon designed two theatres which were to be installed under the roof. *"Utzon's vision was to isolate the auditoriums from the external skin for symbolic and acoustic reasons. His intention was to suspend the halls from the roof structure"* (Szalapaj [29] p.28). Inspired by waveform, a model of the hall's inner-space acoustic void, able to be sectioned and viewed as single slides, was made to show the final proposal for the large concert hall. Having left the project before this, the interior was finished without using Utzon's design.

Questioning the acoustics of a space through working models, may enable architects to learn more about the opportunities and consequences of their design decisions. *"The quickest way to measure the all-important volume of a model auditorium, for example, is to fill it with small polystyrene balls, decant them into a rectangular wooden box, and then measure their volume*" [25] (p.563).

4. The working model as a cross-disciplinary collaboration tool

"Architecture is a team effort, and model building promotes collaboration. A study model is easily modified by several designers during its development" (Jerry Griffin in [30] p.25). In designing construction drones, architect and robotics specialist, Teodor Petrov, works with 3D printing and engineering companies to develop autonomous construction robots. These new innovations target to cross architecture with robotics to generate a series of construction robot prototypes that aim to show the potentials of autonomous additive manufacturing in construction. In order to program the logic for the drone, he constructed a working model (fig.1) to map out and communicate his ideas to a drone engineer. Not only to aid his own working, but to work with the drone engineer using this model, he 3D printed small-scale model drones to show their movement and reposition, assisting in problem solving. In addition, this model targets a wider audience: Quick Response (QR) codes (detectable by Virtual Reality (VR) goggles) were attached to various foam model blocks on the model, which demonstrate the QR codes that would instigate an action in the drone's activity; A drone may detect the QR code on

the labelled block as an obstruction and fly towards a specified coordinate; QR codes detected by VR goggles, can translate the label into a 3D model of a building, for example. Thus, to the viewer, the context of the model becomes clearer, becoming an interactive development model to communicate with. The cross-disciplinary nature of this working model is powerful through the digital tools of today: Moving the physical blocks on the model will appear as though moving one of the robots in virtual reality.



Figure 1: Architecture vs Robotics cross-disciplinary working model [Teodor Petrov]

It should be the aim of an architect to collaborate with different fields sooner, so that the project still at a conceptual phase can foresee implications of the design earlier, leading to beneficial questions arising sooner and thus design decisions can be better informed for example: If an architect builds an interior model and addresses the question of materiality sooner, the structure of their design may need to change, so it is important to ask questions about 'the interior' earlier in the design process. On another hand, starting at the site model, working models take on a collaborative role instantly - for contextual decision making when the site is there. Collaboration is essential for better building design because a broader series of inquires enable more holistic decisions. Working models are powerful tools to develop design but also, they are a platform for learning. Multi-purpose working models can aid in the process of learning, refining and defining and by interlinking different fields through a physical entity, allow for real and open dialogue, as opposed to the current interdisciplinary digital model, BIM: *"Digital three-dimensional visualization is a powerful tool, but a solitary endeavor that limits design interaction and is not easily modified until it is substantially complete"* [30] (p.25).

Cross-disciplinary working models do not need to be complex. They are not about gathering all stakeholders into one room to discuss and decide – this can be problematic: *"if one person has difficulty knowing when problem has been solved, then how much more difficult is it for a team to agree? Hence, there is a desire for hierarchies in design decision-making.. distributed intelligence may.. make it considerably more difficult"* (Brandon [1] p.37). The working model can become more cross-disciplinary for every model builder - to ask new questions, to start working with new collaborators and disciplines, to outline the architectural program, to refine the design etc. *"The challenge for research and technology is to get us close to.. one person or team thinking clearly and acting together as one.. without the downside of a potential loss of creative thinking which can bring the 'joy of the new' to the design solution.. The overhead of understanding each other's point of view, getting it agreed and acting on it would disappear and efficiency and effectiveness would increase."* (Brandon [1] p.38). It is aimed that this paper inspires a new trend in working models that question their working materials and consider constructability, lighting, texture, location, aesthetic impact, stability etc.

5. Conclusion

The identity of the working model is ambiguous. In this paper, the working models of different disciplines were outlined, and different definitions for the working model reviewed and clarified. How different scholars classify models was evaluated and it was established that the common thread between working models from each discipline is a tool supporting decision making through design development. As a critical decision-making tool, the working model has potential to improve learning, understanding and collaboration: It is the cheapest and quickest way to make holistic decisions at the earliest opportunity.

References

[1] Kocatürk T, Medjdoub B (eds) (2011) Distributed Intelligence in Design. John Wiley & Sons, Chichester, UK.

[2] Spence R, Macmillan S, Kirby P (eds) (2001) Interdisciplinary design in practice. Thomas Telford, London, UK.

[3] Dunn, N (2007) The Ecology of the Architectural Model. Peter Lang, Bern, CH.

[4] Cannaerts, C (2009) Models of/ Models for Architecture. eCAADe 27, p781-786. Istanbul, TR.

[5] Jančič, L (2013) The Impact of Layered Technologies on Architectural Model Production and Use. AR 1, p66-75. Ljubljana, SI.

[6] Stavrić M, Šiđanin P, Tepavčević B (eds) (2011) Architectural Scale Models in the Digital Age. Springer, Vienna, AT.

[7] Schilling A (2018) Architecture and Model Building. Birkhäuser, Basel, CH.

[8] Knoll W, Hechinger M (2008) Architectural Models: Construction Techniques (2nd edn). J.Ross Publishing, Munich, DE.

[9] Smith A.C (2007) Architectural Model As Machine: A New View of Models from Antiquity to the Present Day. Routledge, Oxford, UK.

[10] Burry M, Ostwald M, Downto P, et al. (eds) (2007) Homo Faber: Modelling Architecture. Archadia Press, Sydney, AU.

[11] Janke R (1978) Architekturmodelle. Verlag Gerd Hatje, Stuttgart, DE.

[12] Porter T, Neale J (2000) Architectural Supermodels. Architectural Press, Oxford, UK.

[13] Gerkan v.M, Volkwin M (1994) Idea and Model. Ernst & Sohn, Berlin, DE.

[14] Mills C.B (2011) Designing with Models (3rd edn). John Wiley & Sons, Hoboken, NJ.

[15] Ganslandt R, Hofmann H (2002) Handbook of Lighting Design. [ONLINE] www.erco.com/download/content/4-media/2-handbook/erco-handbook-of-lighting-design-en.pdf

[16] Ursprung P (2012) Studio Olafur Eliasson: An Encyclopedia. Taschen, Cologne, DE.

[17] Levy E, Mangone C (eds) (2016) Material Bernini. Routledge, Abingdon, UK.

[18] Slobodkin L (1973) Sculpture: Principles and Practice. Dover Publications, Toronto, CA.

[19] Moon K (2005) Modeling Messages: The Architect and The Model. Monacelli Press, New York, NY.

[20] Blog Sagrada Familia (2018) Model makers, essential for testing and correction. Available at: blog.sagradafamilia.org/en/the-trades/model-makers [Accessed 30 May 2019].

[21] Mertens E (2009) Visualizing Landscape Architecture. Birkhäuser, Basel, CH.

[22] Sandoval M.J.J (2016) Louis I. Kahn, The Telluric Landscape and Clay Models. Proyecto Progreso Arquitectura, Vol 15, p84-99. Seville, ES.

[23] Entwistle T, Knighton E (2013) Visual Communication for Landscape Architecture. AVA Publishing, London, UK.

[24] Popovic Larsen O (2016) Conceptual Structural Design: Bridging the gap between architects and engineers (2nd edn). Thomas Telford, London, UK.

[25] Addis B (2007) Building: 3000 years of design engineering and construction. Phaidon, London, UK.

[26] The Building Centre (2018) Completing La Sagrada Familia, a talk by Tristram Carfrae [ONLINE] Available at: www.youtube.com/watch?v=b0WqWrnrMGA [Accessed 30 May 2019].

[27] Thomas N, Chadwick A (2019) Liquid Threshold: Atelier One. Actar Publishers, Barcelona, ES.

[28] Meymand P.J (1998) Shaking Table Scale Model Tests of Nonlinear Soil-Pile-Superstructure Interaction In Soft Clay. Dissertation submission. University of California.

[29] Szalapaj P (2005) Contemporary Architecture and the Digital Design Process. Architectural Press, Oxford, UK.

[30] Werner M (2011) Model Making. Princeton Architectural Press, New York, NY.

Proceedings of the IASS Annual Symposium 2019 – Structural Membranes 2019
Form and Force
7 – 10 October 2019, Barcelona, Spain
C. Lázaro, K.-U. Bletzinger, E. Oñate (eds.)

Towards the classroom of the future: new ideas and proposals

Ignacio PAYA-ZAFORTEZA*, Nuria MATARREDONA-DESANTES,
Teresa PELLICER-ARMIÑANA, Pedro FUENTES-DURÁ

*Universitat Politècnica de València
Camino de Vera S/N, 46023 Valencia, Spain
igpaza@cst.upv.es

Abstract

The Bologna process and the development of the European Space of Higher Education (ESHE) have provoked an important change in the teaching-learning process. The traditional teacher centered approach has been replaced by a student-centered approach. In this approach, the students must be actively involved in their learning process and both transversal skills and technical knowledge are considered crucial goals of the education. New teaching approaches and new skills require new learning spaces. However, the physical space where the learning process takes place has not experienced any significant change. Within this context, this paper presents the results of an experience carried out at the School of Civil Engineering of the Universitat Politècnica de València in Spain, where a traditional classroom is being transformed into a new inspiring space result of a bottom to top process involving students, professors, furniture manufacturers, and university staff from different areas (maintenance, health and safety and pedagogical improvement). This paper details the main features that the classroom of the future should have according to this process as well as the conceptual design of a prototype classroom currently under construction.

Keywords: education, teaching space, transversal skills, Bologna process.

1. Introduction

The Bologna process [1] and the development of the European Space of Higher Education (ESHE) provoked an important change in the teaching-learning process. The traditional teacher centered approach changed to a student-centered approach able to empower the student with lifelong learning skills. Building the ESHE has been a big challenge and has motivated the implementation of new teaching methodologies able to develop –in addition to specific professional skills- transversal competences (e.g. leadership, teambuilding), which were not considered in traditional higher education.

Logically, new teaching approaches and new competences require new learning spaces. However, the classroom, which is the space where most of the teaching-learning process happens, has not experienced any significant change.

Aware of both, this paradigm shift and the need for new spaces, a multidisciplinary team of professors of the Universitat Politècnica de València (UPV henceforth) and the Universitat de València (UV henceforth) from different areas (architecture, civil engineering, industrial design, marketing, ergonomics) is working to transform a traditional classroom from the School of Civil Engineering into a new and inspiring learning space. This space is based on the background of all the team members, but fundamentally springs from a particular experience developed at Princeton University, US

Copyright © 2019 by Ignacio Paya-Zaforteza, Nuria Matarredona-Desantes, Teresa Pellicer-Armiñana and Pedro Fuentes-Durá.
Published by the International Association for Shell and Spatial Structures (IASS) with permission.

(Garlock and Paya-Zaforteza, [2]) where a classroom was transformed into a colorful space inspired by the classrooms of kindergartens and nursery schools. The space was decorated with the participation of the students and the experience was very successful, but a survey revealed that some enhancements of the furniture were required to make the space reach its full potential.

This new classroom created at the UPV is named *"el aula del futuro"* ("the classroom of the future"). and was inspired by the Princeton experience but included a participative process to incorporate the views from both the users (students, professors) and other people related to the topic (such as UPV staff and furniture manufacturers). Section 2 describes the participative process followed to propose a specific classroom design. This design is presented in Section 4. Finally, Section 5 contains the main conclusions of this work.

2. Methodology followed to propose a design

Three workshops were held with different people related to the project to get their views. The first two workshops were designed to define the main general requirements of the classroom. The third workshop was aimed also to produce a reduced scale prototype of the classroom of the future.

2.1 Definition of the classroom requirements

The first workshop related to the general requirements of the classroom involved civil engineering students from a fourth year course called "Structural Systems". The second one involved professors, university staff from different areas (building maintenance, health and safety, pedagogy) and school furniture manufacturers.

The concept mapping (CM) tool was used in both workshops to identify the main attributes of the classroom clustered into categories. The workshops also enabled to identify key skills and competences that had to be developed in the classrooms.

CM is a general method that can be used to help to describe ideas about some issues in a pictorial form. CM is a structured process, focused on a critical issue of interest, involving input from one or more participants, that produces an interpretable pictorial view (called concept map) of their ideas and how these are interrelated [3]. Fig. 1 shows an image of one of the workshops. Details on how this methodology was applied are given in Paya-Zaforteza et al [4] and are not repeated here. Table 1 shows the most important attributes of the classroom of the future according to each group of workshop participants.



Figure 1. Workshop with professors, university staff and furniture manufacturers.

Table 1: Major attributes in classroom design according to each focus group. The order in which they appear is not relevant.

	Students	**Professors, University staff and furniture manufacturers**
1	Images & colors	Good ventilation
2	Interaction	Cleaning
3	Outdoor	Thermal comfort
4	Material resources	Furniture
5	Air conditioning	Flexible space
6	High ceilings	Acoustics
7	Acoustics	Connectivity
8	Rest Zone	Material resources
9	Furniture	Ambiance
10	Room distribution	Proper lighting
11	Craft & Boards	
12	Illumination	

2.2 Classroom reduced-scale prototypes

The third workshop was hold at the place that had to be transformed to become the classroom of the future. Students from different UPV degrees attended the workshop which consisted in two sessions of four hours per session. The goal of the first session was to create a "Decalogue of the classroom of the future". The goal of the second session was to build a reduced-scale prototype of a classroom considering the principles previously established in the Decalogue.

In the first session, the students were divided in two teams. To help the groups come up with a Decalogue, some icebreaking activities as well as some creative techniques (6-3-5, scenario design, POV, customer journey map) were used. Several professors assisted the students during the process and also gave short talks on important topics for classroom design such as ergonomics, accessibility, usability and inclusion. Details on the creative techniques used and the talks content can be found in Fuentes-Durá et al. [5]. The Decalogue proposed by each team is presented in Table 2.

Table 2: Classroom of the future Decalogue

	Team 1	**Team 2**
1	Easily moveable furniture that supports quick changeovers and varying instructional practices	Differentiated spaces for different type of activities.
2	Visual and interactive learning	Freedom of action.
3	Make the most of natural light	Music.
4	Flexible space to allow individual/group tasks	Aromatherapy and color therapy.
5	Direct or indirect interaction with natural world	Variated furniture. Different seats and adjustable height.
6	Direct or indirect interaction with external world	Comfort. Adjustable temperature and ventilation.
7	Spatial hierarchy attending to function	Leisure area.
8	Storage space	User defined.
9	Ergonomic furniture	Technology.
10	Accessibility	Accessibility.

In the second session, the principles of the Decalogue were used as a foundation to build a classroom prototype. Freedom was given to the students to choose the material and scale of the prototype. Team 1 created a foam core based model whereas Team 2 used mainly building blocks toys (see Fig. 2). The prototypes depart from the traditional classroom structure and share important points features:

- Movable furniture is used to create a flexible space.
- Walls are panelled with cork so information can be shared with colleagues and reviewed by professors publicly.
- A leisure zone at the end of the classroom is created to help the relaxation of students thanks to natural elements such plants so as to create a direct connection with the external world.
- Shelves are included to enable the storage of backpacks, skates or any other item the students might bring to the classroom.
- No class platform is allowed in the classroom.

The session also pointed out to the key role of connectivity in current classrooms. The students were very concerned about having good Wi-Fi connection and plugs for their devices. Plug placing in a very flexible space can be very challenging since there is no possibility to place the required wires on the floor of the classroom where the project is being implemented. Plugs there should be hanging from the ceiling, which negatively affects to the aesthetics of the place.



Figure 2. Models of the ideal layout of the classroom of the future. Team 1 foam core based model (left) and Team 2 building blocks toys based model (right).

3. Proposed design

Finally, and having in mind the input from all the workshops as well as the economic constraints of the project, a proposal for the new classroom was developed. This proposal includes shelves at the entrance, movable furniture, painted-wall blackboards instead of traditional blackboards, walls panelled with cork, a small leisure zone and foldable tables. Fig. 3 shows a plan view of the classroom with its main elements as well as two different possibilities for furniture distribution.

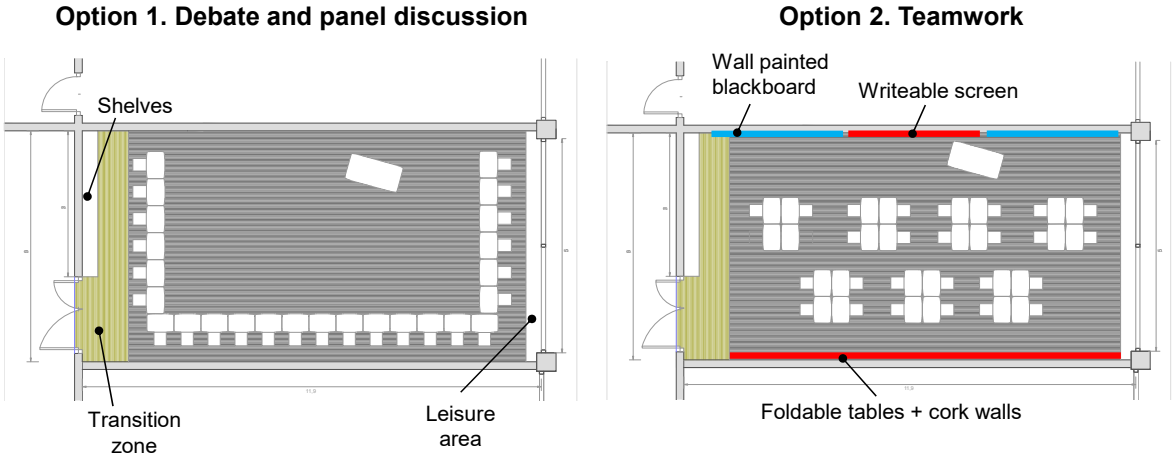


Figure 3. Plan views of the classroom showing its main elements as well as two possibilities for furniture distribution.

4. Conclusions

This paper shows the process followed to create a new learning space at the School of Civil Engineering of the Universitat Politècnica de València in Spain. The principles guiding the proposed design were established using a bottom to top multidisciplinary approach. The new design is now under implementation and should be ready for use during the academic year 2019-2020.

Acknowledgements

The authors express their gratitude to *Instituto de Ciencias de la Educación* (Institute for Education Sciences) and the School of Civil Engineering of the UPV for all the support received. Authors also want to thank the contribution of all the workshop participants.

References

[1] European Commission. The Bologna Process and the European Higher Education Area. . https://ec.europa.eu/education/policies/higher-education/bologna-process-and-european-higher-education-area_en . Accessed on 28/05/2019.

[2] M.E.M. Garlock, I. Paya-Zaforteza. "The structural playground, a new environment where to enjoy learning structural engineering" *Proceedings of the IABSE Conference, Geneva 2015: Structural Engineering: Providing Solutions to Global Challenges, Geneva, Switzerland, September 2015*, pp. 336-339.

[3] M. Kane and W.M.K. Trochim. *Applied social research methods series. Concept mapping for planning and evaluation*. Thousand Oaks, CA, US: Sage Publications, Inc., 2007.

[4] I. Paya-Zaforteza, I. Kuster Boluda, N.M. Vila López and P. Fuentes-Durá, "Further development of learning spaces through concept mapping" in *Proceedings of the 11th annual International Conference of Education, Research and Innovation*, Seville, Spain, 2018, pp. 5119-5128.

[5] P. Fuentes-Durá, N. Matarredona-Desantes, T.M. Pellicer Armiñana, S. Asensio Cuesta, and I. Payá Zaforteza, "Creating the classroom of the future through co-creation" in *Proceedings of the 11th annual International Conference of Education, Research and Innovation*, Seville, Spain, 2018, pp. 5129-5135.

Proceedings of the IASS Annual Symposium 2019 – Structural Membranes 2019
Form and Force
7 – 10 October 2019, Barcelona, Spain
C. Lázaro, K.-U. Bletzinger, E. Oñate (eds.)

Tutorials for Tutorials: Guidelines for Creating Video Tutorials on Teaching Structural Morphology to Architecture Students

Anahita KHODADADI*, Niloufar EMAMI[a]

* Portland State University
Portland, OR
anahitak@umich.edu

[a] Louisiana State University

Abstract

In several fields of studies, audio-visual tutorials have been employed to convey teaching materials to students. Video tutorials significantly contribute to demonstration-based training where the student acquires the knowledge, skills, and attitudes by observing some easy-to-follow examples of performing a task. Although video tutorials are widely used and disseminated nowadays, still little is known about the effectiveness of the produced videos as well as the design characteristics of an effective tutorial. This paper aims to provide guidelines for the creation of software training tutorials. Specific needs and backgrounds of architecture students are considered in preparation of the guidelines. This study begins with describing the theoretical research on the measures that can support students' attention, retention, production, and motivation within a demonstration-based training. Then, three series of open-access, well-known, high-quality instructional videos are selected for evaluation using the measures. These case studies include tutorials for Rhinoceros which is a NURBS modeling CAD software, the tutorials for the DIVA 4.0 plugin for Grasshopper which is used for daylighting analysis, and tutorials on Karamba3D plugin for Grasshopper respectively. The main objective of the evaluations is to highlight the potentials for improvement of these tutorial series and production of similar instructional videos to serve architecture students better. In the end, a series of video tutorials on configuration processing of spatial structures using Grasshopper is introduced.

Keywords: Video tutorial, software training, computational design, architecture education, demonstration-based training, configuration processing, spatial structures

1. Introduction

In Cambridge dictionary, a "tutorial" refers to a period of study with a tutor when an individual or a small group of students receive instructions in a certain area. Nowadays, a "tutorial" implies a computer-based medium that is to assist users within a learning process. The first research paper on the creation and development of an audio-visual tutorial program was published in 1969. The paper represents a multi-faceted and multi-sensory approach to teach Principles of Biology [1]. During the 1970s and the 1980s, application of videos in vocational training and professional development have been studied through several empirical studies [2]. In the 2000s, multimedia tools and animations have been employed to add values to video tutorials and improve students' learning process. The "do it yourself" approach among today's young generation [3, 4] in addition to extensive development of video streaming websites such as YouTube and Vimeo have made video tutorials a popular educational tool. Video tutorials are used for a variety of educational purposes. The primary aim is to demonstrate a

Copyright © 2019 by Anahita KHODADADI, Niloufar EMAMI
Published by the International Association for Shell and Spatial Structures (IASS) with permission.

procedure. For example, software companies are offering video tutorials on their websites on how to use their software systems. Besides, videos of a live class can be recorded as a backup learning material for students who miss some sessions of the class or need to review the presented materials at their own pace. Furthermore, instructional videos are useful when a lecture is offered for in-class and online courses at the same time. Social media, professional associations, and online learning centers such as LinkedIn Learning, Coursera, Education @USGBC provide online courses using instructional videos. In the recent years, teachers who employ an active learning approach [5, 6] in their classes seem to have a significant tendency to require students to make videos themselves as a leaning output [7].

Although computer-based tutorials are widely used and disseminated, still little is known about the design characteristics of an effective tutorial. Computer-based tutorials can be classified into video tutorials, interactive tutorials, and webinars. The scope of this study includes only the first category, and this paper is to represent a critical review of the application of video tutorials and guidelines for creating effective instructional videos for training architecture students to apply some software systems.

2. Application of video tutorials, benefits, and challenges

Video tutorials can assist students in acquiring knowledge, skills, and attitudes by observing some easy-to-follow examples of performing a task [8]. Studies on the effectiveness of video tutorials indicate that providing students with online instructions is always better than no instruction [9]. Multiple means of representation, engagement, and expression through video tutorials provide students with various ways to collect information and interact with [10, 11]. However, visual or auditory learners benefit more. Students who value learning at their own pace prefer hands-on or interactive tutorials [12, 13].

In an architecture program, there are some courses on computer-aided design, structural analysis, and environmental design where students learn to apply some software systems. Instructors can benefit from video tutorials to show not only the application of a certain software system but also their thought process. The way a professional thinks, analyzes a problem, and implements a solution may be dramatically different from novices' approach. The instructional videos allow instructors to dedicate more class time for active learning practices and critical thinking while , providing instructions on using the required software through video tutorial before or after class time

Video tutorials have other advantages. Screencasts can be accessed repeatedly anywhere on a PC or a mobile device. Additionally, video tutorials can provide students with the congruence between the screen-capture and real-life task execution. Hence, students may find it easier following a screencast coupled with narration rather than referring to the user manual of software or the class handouts to accomplish the given task. Some students may use video tutorials only to learn about performing a certain task. When they successfully solve the problem, a considerable part of what they have learned may be quickly forgotten.

Although the immediate positive effect of video tutorials on the learning process has been verified in several studies, still, their long-term efficacy has not been proved [13, 14]. The next section reviews the characteristics of effective video tutorials in the short term and in the long run.

3. Characteristics of effective video tutorials

An appropriate framework for designing video tutorials is a demonstration-based training (DBT) process [8, 15]. Within a demonstration-based training approach, students observe a dynamic model of performance and follow the simultaneous instructions to complete a certain task. The DBT is founded on four main interrelated components: attention, retention, production, and motivation [14, 15, 16]. Attention is the mechanism that determines what information reaches the processing stage. Retention

indicates that the incoming information needs to be transformed into a mental model or symbolic codes that can be stored in long-term memory. Production refers to the use of the created mental models as a guide or standard for carrying out similar tasks to the one that has been demonstrated during the training process. Motivation is the foundational component that acts as a driving force behind the other three. Attention, retention, and production may never take place without enough motivation. Motivation stems from the mental effort to seek a learning goal and the commitment to accomplish a learning process.

Some teachers believe that short and clear visual instruction is always useful regardless of its specific format [17]. However, there are some measures that can be considered to support attention, retention, production, and motivation within a DBT process. The effectiveness of each measure has been studied separately through several empirical and theoretical studies, and their significant effects on enhancing the learning procedure have been proved [14].

In the following section, a series of measures are introduced for creating video tutorials with specific consideration of architecture students' needs and backgrounds. These measures stem from the techniques that can support the four main components of a DBT process. The measures address the three major principles in designing any instructional video: the configuration of the whole body of the video, presentation techniques, and considerations regarding the interaction with the users.

3.1 Configuration of an effective video tutorial

Regarding the configuration of the video tutorials' content, the following measures can be considered:

- **Previewing** informs the students about the goal, jargons, and the main ideas in the video and assists students to remain focused on task-relevant information. Creating a table of content allows students not only to get a first impression of the whole content but also to navigate between different sections and sub-sections of the series of the videos [18].
- **Splitting (segmentation)** a continuous instruction into meaningful and short sections help students to understand the demonstration as discrete items and learn the content better [14, 18] Short videos with a length of 3 to 5 minutes make the learning goals in the students' minds more accessible.
- **A simple-to-complex task sequence** enhances the students' commitment to accomplish the learning process. The complexity of the tasks described in the video should be increased gradually and not sharply to keep them assured of being able to carry out the task and, at the same time, confront them with a new attainable challenge and make the whole process interesting [19, 20].
- **Anchoring the instructions within the task domain** allows the students to instantly recognize the value and relevance of the learning material to their daily professional life. This will keep them motivated to proceed through the whole series of instructional videos [21, 14].
- **Reviewing** the taught material in each or every few sections can recap the main information [22]. Videos are considered as visual references, and students require to assess and adapt their progress periodically. Studies indicate that usually 20% of each video tutorial is reviewed by the students to make sure that they have understood the main content [19].
- **Practicing** stimulates students to construct meaning, consolidates learning, and bring omissions or misunderstanding to attention. The instructions may be processed superficially or remain passive in students' minds. Practicing can prevent such malfunction and stabilize learning by reviewing the created mental model in students' minds [18]. *Appropriate arrangement of practices* depends on the main goal of watching the video tutorials as well as students' prior knowledge. For job-aiding purposes, immediate practice after each video section is recommended [23]. Besides, if the students have a high prior-knowledge, they may benefit more from trying to carry out a task before watching the video [16]. Such a challenge makes them motivated to follow the video and connects their known and new information. If no pre-assessment of students' prior knowledge is available, practicing after given instruction is recommended [16].

3.2 Presentation skills in an effective video tutorial

Regarding the presentation of materials, the following measures should be taken into account:

- **Determining the appropriate speed or pace** of instructions highly depends on the students' characteristics. But, in general, fast instruction may overload the students, and a slow one may make them bored [19]. Opting for a moderate pace seems a conservative decision.
- **Cueing or signaling** allows emphasizing on a structure, location, or object and makes them stand out. The signals may be provided verbally, such as changing the intonation of narration or scripting the screencast using some keywords and statements, or visually by applying attractive colors, creating animations with sudden appearance or movement [18].
- **Using conversational style** to narrate the demonstration makes the students feel comfortable to follow the instructions. Using personal pronouns and self-revealing comments of the instructor can be helpful in this regard [19, 24].
- **Maintaining the audio quality** and preventing the background noise can support the students' concentration on learning materials.
- **Supplying ready-to-use practice files** prevents students from distractions and allows them to focus only on learning materials [19].

3.3 User interaction and control in an effective video tutorial

User control is an important aspect that needs to be addressed.

- It is highly recommended to allow the user to manually control the learning process. The transient nature of the video tutorials may hinder students from digesting the incoming information and connecting it with what already is known. Giving the students a brief respite as they need by applying pause, stop, and play helps to control the pace of information intake and mental analysis [18].
- **Providing students with a space for giving feedback** on the content and design of the videos, allows sharing their personal experiences or even uploading examples of their accomplished task. This space can be available on the course webpage, social media, or video streaming websites. Studies have shown that practices accompanied by feedback can help students to adjust and correct the procedural knowledge that they are acquiring [25, 26].

Although there are some measures to create an effective video tutorial, there are some other features in designing video tutorials that don't improve or are not associated with learning. These features include the gender of the instructor, presence of the instructor's face on the screen, pauses within the video determined by the video creator instead of the user [27]. Table 1 briefly summarizes the characteristics of effective video tutorials.

Table 1: Four components of a DBT process, namely attention, retention, production, and motivation are mapped onto three major principle of designing a video tutorial, namely the configuration of the whole body of the video, presentation techniques, and considerations regarding the interaction with the users.

DBT Learning component		Design consideration of video tutorial	Measures and implementation techniques
Attention		Configuration of video tutorials	Previewing
Retention	Motivation	Configuration of video tutorials	Segmentation
Motivation		Configuration of video tutorials	A simple-to-complex task sequence
Motivation		Configuration of video tutorials	Instructions within the task domain
Retention		Configuration of video tutorials	Reviewing
Production		Configuration of video tutorials	Practicing
Attention	Retention	Presentation of video tutorials/ user control	Suitable speed or pace
Attention		Presentation of video tutorials	Cueing or signaling
Motivation		Presentation of video tutorials	Conversational style
Attention		Presentation of video tutorials	Audio quality
Production		Presentation of video tutorials	Ready-to-use practice files
Retention		User control of video tutorials	Manual user control
Production	Motivation	User control of video tutorials	Feedback and discussion

4. Evaluation of three series of video tutorials in the field of architecture

Three series of video tutorials for software training in the field of architecture are evaluated using the described measures. These series include tutorials for Rhinoceros [28], DIVA 4.0 plugin for Grasshopper [29], and Karamba 3D plugin for Grasshopper [30, 31]. It should be noted that all of these series of instructional videos are high-quality and reliable references for learning the corresponding software systems. The main objective of conducting evaluations in this study is to highlight the strong aspects of each series, and to identify the future improvement for producing similar instructional videos with the goal of better serving architecture students.

Rhino tutorials are produced by the Robert McNeel & Associates Company and present topics on this NURBS modeling CAD software. Some of the videos are open-access, and some of them require registration and payment. A general overview of the software along with the basic instructions are presented in a few separate videos, and the advanced instructions are presented throughout a series of modeling examples. Some of the examples are within the architectural design domain, and some of them concentrate on modeling the non-architectural products. The tutorials for DIVA 4.0 are produced by the Solemma Company, and all the videos are open-access. The videos are almost the only available reference for training for daylight and thermal analyses of buildings using DIVA. In contrast, the website of Karamba3D represents a list of open-access and high-quality video tutorials produced by different individuals. The list of videos includes different examples of structural analysis and is sorted by the type of structure that is studied versus the level of simplicity of the instructed topic. Table 2, presents the result of the evaluation of the three series of video tutorials using the described measures.

Table 2: Evaluation of Rhino, DIVA 4.0, and Karamba3D tutorials using the measures described in Section 3

Measures	Rhino	DIVA 4.0	Karamba3D
Previewing	No preview	A brief description of the whole video in 3 to 4 sentences	Keywords are provided. Some of the tutorials include an overview of the parametric model at the beginning. Some static slides are added to the screencast to include some supplemental materials [31].
Segmentation	Each topic is presented in a single 1-hour-long video	Each topic is presented in a single 12 to 27-minute video	Each topic is divided and presented in a series of 2 to 9-minute video
The task sequence	Videos are sorted regarding their topic and not their level of complexity	Videos are sorted based on their level of complexity	Videos are sorted regarding their topic and not their level of simplicity
Instructions domain	Knowing the wide application of Rhino, only a few architecture-specific tutorials are available	Instructions within the task domain	Instructions within the task domain
Reviewing	No review is included	No review	The video includes reviewing part
Practicing	No practice file	Practice examples are available	Practice examples are available
Speed or pace	Users can control the pace	Users can control the pace	Users can control the pace
Cueing or signaling	Only minor intonation change	Only minor intonation change	Only minor intonation change
Narration style	Conversational	Conversational	Conversational
Audio quality	Acceptable	Acceptable	Some of the tutorials have background noise [30]
User control	Manual user control	Manual user control	Manual user control
Feedback and discussion	Possible for each video on Vimeo	Possible for each video on Vimeo, YouTube, and diva4rhino.com	Possible for each video on Vimeo, YouTube, and [32]

5. Implementation in a video tutorials series on configurational processing of spatial structures

The result of the evaluation of the well-known references for software training in the field of architecture supports the provided guidelines for producing a series of video tutorials on configuration processing of spatial structures in Grasshopper. These video tutorials are available at [33]. Each video tutorial includes a table of content that allows students to choose the topic for learning (figure 1). Each topic starts with an overview of the steps for making the parametric model, where the outcome of each step is demonstrated (figure 2). The topics are arranged from simple to complex. In all the videos, first, different approaches for configuration processing of a certain type of spatial structures are analyzed; then, implementation of the suitable approach through the Grasshopper feature is demonstrated. The screencast is combined with the narration and scripting using some keywords and statements. Students can review the materials by moving forward or backward throughout the video. Some ready-to-use practice files are available for download. Furthermore, students are encouraged to share their ideas of configuration processing via the comment tab.

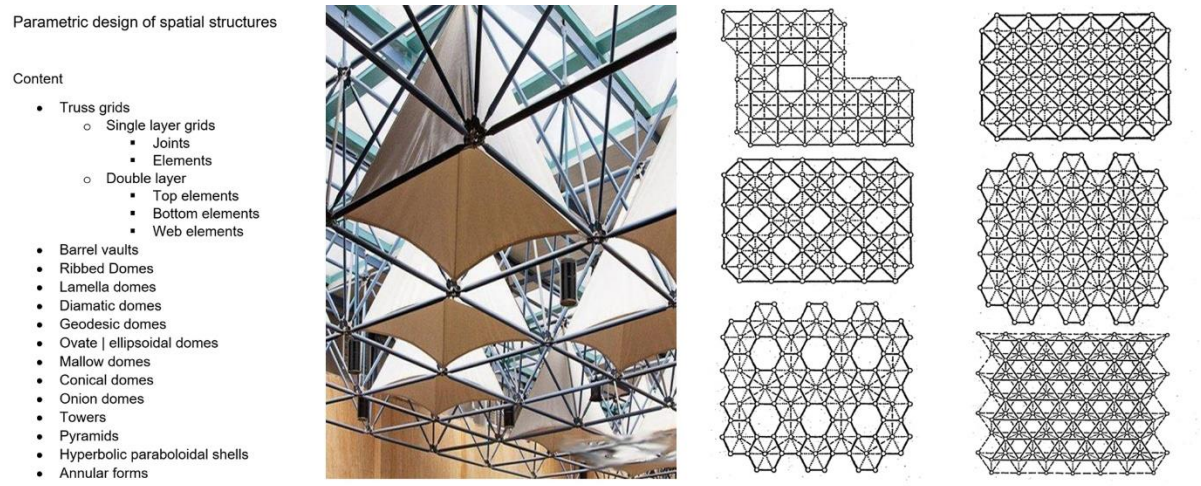


Figure 1: The table of content that allows student to choose the topic for learning

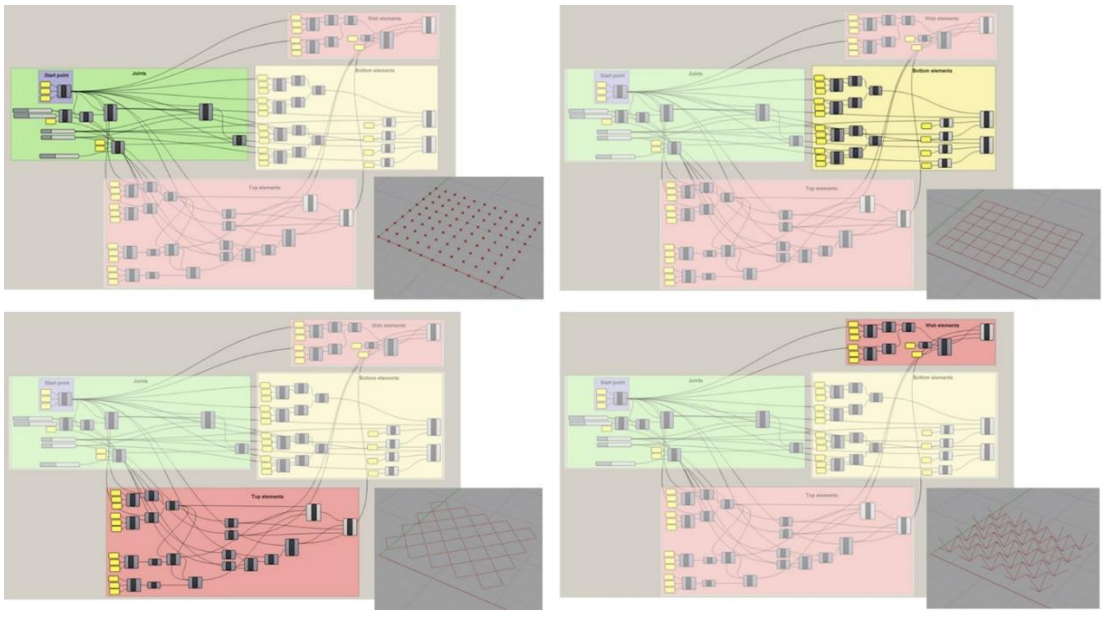


Figure 2: An overview of the steps of the parametric model

6. Conclusion

In this study, a number of measures are derived from the existent theoretical and empirical studies to support four pillars of learning, including attention, retention, production, and motivation, within a software training process using instructional videos. The described measures address the three aspects of creating a video tutorial, including the configuration of the whole body of the video, presentation techniques, and considerations regarding the interaction with the users. Next, three series of video tutorials for architecture students are evaluated using the introduced measures. Afterward, a work in progress was introduced where a series of video tutorials are being created on the configuration processing of spatial structures. In a time where computer software systems are widely used by professionals, and where many instructors create video tutorials for teaching, it is important to know the features of effective video tutorials and how they can be improved. This paper can be helpful to educators for making educational resources.

References

[1] B. J. Syrocki, C. S. Thomas and G. C. Fairchild, "The Audio-Video Tutorial Program," *The American Biology Teacher,* vol. 31, no. 2, pp. 91-96, 1969.

[2] M. Bétrancourt and K. Benetos, "Why and when does instructional video facilitate learning? A commentary to the special issue “developments and trends in learning with instructional video”," *Computers in Human Behavior,* vol. 89, pp. 471-475, 2018.

[3] M. Morain and J. Swarts, "YouTutorial: A Framework for Assessing Instructional Online Video," *Technical Communication Quarterly,* vol. 21, no. 1, pp. 6-24, 2012.

[4] P. ten Hove and H. van der Meij, "Like it or not. What characterizes YouTube's more popular instructional videos?," *Technical Communication,* vol. 62, no. 1, p. 48–62., 2015.

[5] A. Khodadadi, "Active Learning Approach in Teaching Structural Concepts to Architecture Students," in *International Association of Shells and Spatial Structures Annual Symposium (IASS)*, Amsterdam, 2015.

[6] N. Emami and P. von Buelow, "Teaching structures to architecture students through hands-on activities," in *Canadian International Conference on Advances in Education, Teaching & Technology*, Toronto, 2016.

[7] C. Zahn, N. Schaeffeler, K. E. Giel, D. Wessel, A. Thiel, S. Zipfel and F. W. Hesse, "Video clips for YouTube: Collaborative video creation as an educational concept for knowledge acquisition and attitude change related to obesity stigmatization," *Education and Information Technologies,* vol. 19, no. 3, pp. 603-621, 2014.

[8] M. A. Rosen, E. Salas, D. Pavlas, R. Jensen, D. Fu and D. Lampton, "Demonstration-Based Training: A Review of Instructional Features," *The Journal of the Human Factors and Ergonomics Society,* vol. 52, no. 5, pp. 596-609, 2010.

[9] Y. Mery, E. DeFrain, E. Kline and L. Sult, "Evaluating the Effectiveness of Tools for Online database instruction," *Communications in Information Literacy,* vol. 8, no. 1, p. 70–81, 2014.

[10] T. E. Hall, A. Meyer and D. H. Rose, Universal design for learning in the classroom, New York: Guilford Press, 2012.

[11] K. K. Webb and J. Hoover, "Universal design for learning (UDL) in the academic library: A methodology for mapping multiple means of representation in library tutorials," *College & Research Libraries,* vol. 76, no. 4, p. 537–553, 2015.

[12] S. Mikkelsen and E. McMunn-Tetangco, "Guide on the side: Testing the tool and the tutorials," *Internet Reference Services Quarterly,* vol. 19, no. 3, p. 271–282, 2014.

[13] C. Lantz, G. M. Insua, A. Armstrong, D. Dror and T. Wood, "“I'm a Visual Learner so I like this”: Investigating Student and Faculty Tutorial Preferences," *Internet Reference Services Quarterly,* vol. 22, no. 4, pp. 181-192, 2017.

[14] H. van der Meij and J. van der Meij, "Demonstration-based Training (DBT) in the Design of a Video Tutorial for Software Training," *Instructional Science,* vol. 44, no. 6, p. 527–542, 2016.

[15] A. Bandura, Social foundations of thought and actions: A social cognitive theory, Englewood Cliffs, NJ: Prentice Hall., 1986.

[16] H. van der Meij, l. Rensink and J. van der Meij, "Effects of practice with videos for software training," *Computers in Human Behavior,* vol. 89, pp. 439-445, 2018.

[17] S. Yang, "Information literacy online tutorials: An introduction to rationale and technological logical tools in tutorial creation," *The Electronic Library,* vol. 27, no. 4, pp. 684-693, 2009.

[18] H. van der Meij and J. van der Meij, "A comparison of paper-based and video tutorials for software learning," *Computers & Education,* vol. 78, pp. 150-159, 2014.

[19] J. Brar and H. van der Meij, "Complex software training: Harnessing and optimizing video instruction," *Computers in Human Behavior,* vol. 70, pp. 475-485, 2017.

[20] T. Clarke, P. Ayres and J. Sweller, "The impact of sequencing and prior knowledge on learning mathematics through spreadsheet applications," *Educational Technology Research and Development,* vol. 53, no. 3, pp. 15-24, 2005.

[21] H. van der Meij and J. M. Carroll, "Instruction, Principles and Heuristics for Designing Minimalist," *Technical Communication,* vol. 42, no. 2, pp. 243-261, 1995.

[22] H. van der Meij, "Reviews in instructional video," *Computers & Education,* vol. 114, pp. 164-174, 2017.

[23] A. Helsdingen, T. van Gog and J. van Merriënboer, "The effects of practice schedule and critical thinking prompts on learning and transfer of a complex judgment task," *Journal of Educational Psychology,* vol. 103, no. 2, pp. 383-398, 2011.

[24] P. Ginns, A. J. Martin and H. W. Marsh, "Designing Instructional Text in a Conversational Style: A Meta-analysis," *Designing Instructional Text in a Conversational Style: A Meta-analysis,* vol. 25, no. 4, p. 445–472, 2013.

[25] C. I. Johnson and H. A. Priest, "The feedback principle in multimedia learning," in *Cambridge handbook of multimedia learning*, 2nd ed., R. E. Mayer, Ed., New York, Cambridge University Press, 2014, pp. 413-432.

[26] J. Hattie, M. Gan and C. Brooks, "Instruction based on feedback," in *Handbook of research on learning and instruction*, R. E. Mayer and P. A. Alexander, Eds., New York, Routledge, 2014, pp. 290-324.

[27] L. Fiorella and R. E. Mayer, "What works and doesn't work with instructional video," *Computers in Human Behavior,* vol. 89, pp. 465-470, 2018.

[28] R. McNeel, "Learning to use Rhino," Rhinoceros, [Online]. Available: https://www.rhino3d.com/tutorials. [Accessed 16 May 2019].

[29] Solemma, "Grasshopper Training," Solemma LLC, [Online]. Available: http://solemma.net/TrainingGH.html. [Accessed 16 May 2019].

[30] J. Ripple, "Tutorials," Karamba3D, [Online]. Available: https://www.karamba3d.com/tutorials/. [Accessed 16 May 2019].

[31] A. Pugnale, S. Roudavski, A. Liuti and L. Gadd, "Tutorials," Karamba3D, [Online]. Available: https://www.karamba3d.com/tutorials/gridshell-design-analysis/. [Accessed 2016 May 2019].

[32] "Karamba3D Discussions," Grasshopper Algorithmic Modeling for Rhino, [Online]. Available: https://www.grasshopper3d.com/group/karamba3d/forum. [Accessed 16 May 2019].

[33] A. Khodadadi, "Anahita Khodadadi," [Online]. Available: https://www.anahitak.com/configuration-processing-of-spatial-structures. [Accessed 2019].

Proceedings of the IASS Annual Symposium 2019 – Structural Membranes 2019
Form and Force
7 – 10 October 2019, Barcelona, Spain
C. Lázaro, K.-U. Bletzinger, E. Oñate (eds.)

A Method for Flat-pack Origami Construction of Spatial Structures

Yasushi ISHIDA*, Trevor Stephen LEWIS[a],
Kevin KANE[b], Ravi GUPTA[b], Alex HEANG[b]

* California State Polytechnic University, Pomona, California, USA
yishida@cpp.edu
[a] BIMception INC.
[b] Arktura LLC.

Abstract
This project investigates origami as a means to construct 3-dimensional spatial structures in situ from pre-cut and pre-scribed flat sheet material composed of Aluminum. The approach relies on rationalizing a structure to origami node connectors connecting origami members. The method is intended to allow for efficient prefabricated construction of light-weight spatial structures. This paper discusses the ongoing design development, analysis and prototyping workflows that are emerging through an interdisciplinary collaboration between designers, engineers and fabricators.

Keywords form finding, origami, branching structures, aluminium, digital fabrication, prototyping, flat pack

1. Introduction
This project's objective was to design a canopy structure which is made out of flat sheet materials, transported flat packed, folded and assembled in-situ with limited use of tools and hardware. The structure is self-supporting, and the strength and stiffness of the canopy was verified in a Finite Element Model (FEM). The thickness of all material used is 1.524mm, the total weight of the canopy is approximately 70kg, the overall material used to construct fits inside one box of 1000 mm x 750 mm x 650 mm.

2. Geometry and Form-Finding
The pavilion consists of a canopy and a tree structure that supports it. The form of the structure is organized around the triangular grid and the geometry is rotationally symmetric (Figure 1). The structure fits within the envelope of 4000 mm x 4000 mm x 2300 mm (Figure 2).

Copyright © 2019 by Yasushi ISHIDA, Trevor Stephen LEWIS, Kevin KANE, Ravi GUPTA, Alex HEANG
Published by the International Association for Shell and Spatial Structures (IASS) with permission.

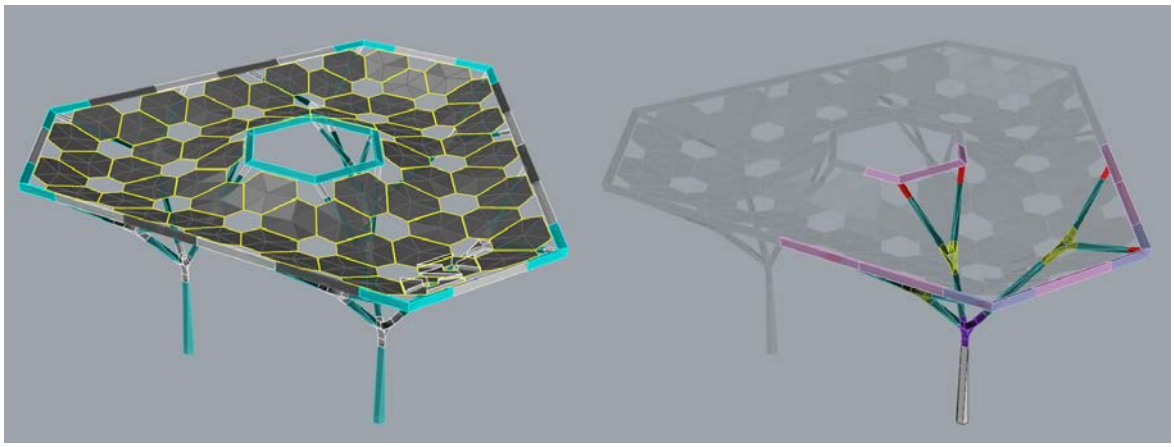


Figure 1: Left: Current overall geometry; Right: Overall geometry with a tree module highlighted.

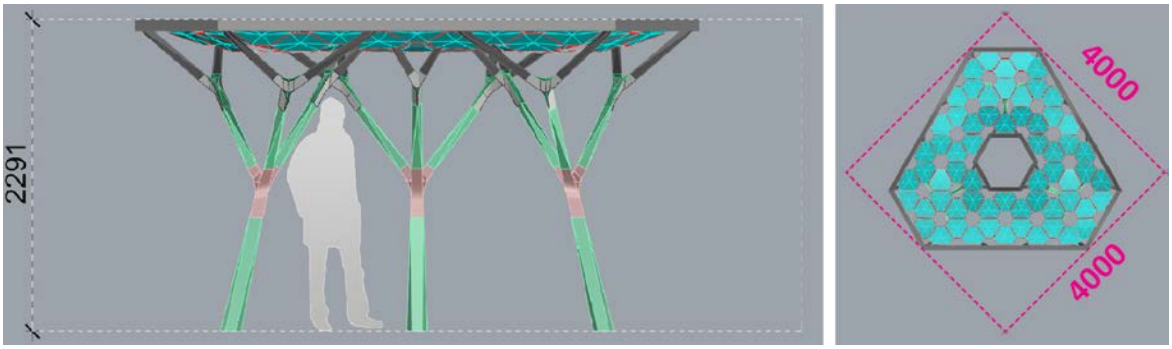


Figure 2: Orthogonal views showing the dimensions of the structure (not to scale).

2.1. Tree Geometry

Form-finding for the wire-frame geometry of the tree was done using the Kangaroo plug-in for Rhinoceros. From the root point, the wire-frame branches twice. At the first node, it branches into three lines. Each of the three lines then branches into two lines. The end points of the wire-frame is attached to the hexagonal center-lines of the canopy frame, while the root points of the wire-frame is attached to the ground plane. (Figure 3)

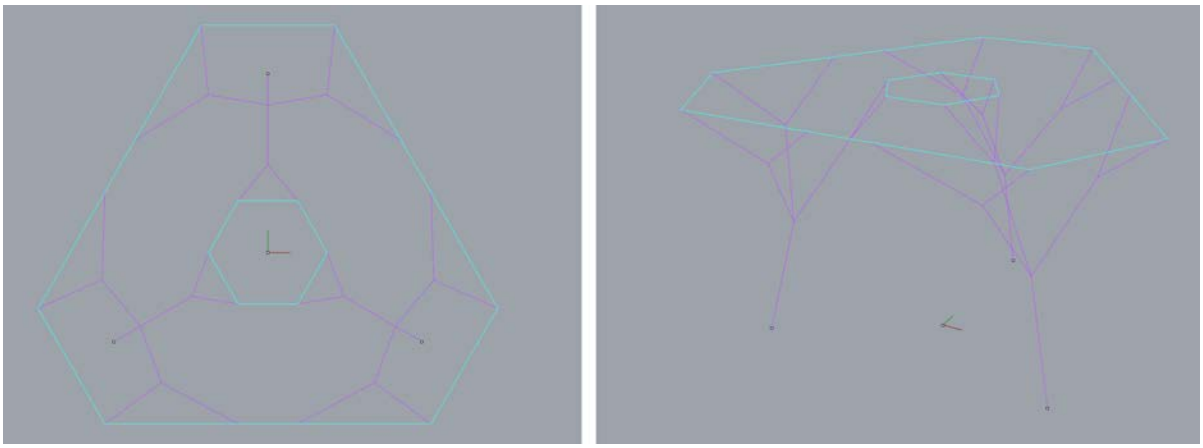


Figure 3: Wire-frame geometry of the tree.

As shown in Figure 4, each of the tree modules consists of 10 straight members (1 'trunk' and 9 'stems') and 4 branching nodes (1 'tri-branch node' and 3 'Y-shaped nodes').

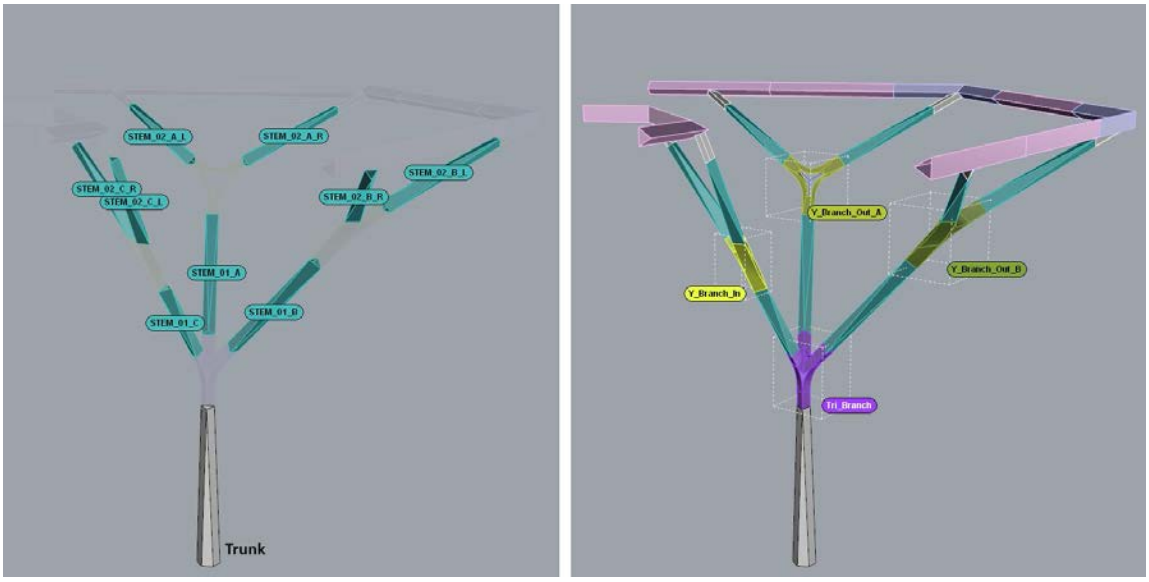


Figure 4: Components in a tree module.

2.1.1. Straight Members

All straight members can be unrolled into one surface with five folding lines. A 'trunk' member consists of flat surfaces made by connecting vertices between the hexagonal bottom and the triangular top. A 'stem' member consists of flat surfaces made by connecting vertices of top and bottom triangles that are rotated 180° from each other. The top and the bottom polygons are placed so that they are perpendicular to the wire-frame that goes through their centroids. These elements are described below in Figure 5.

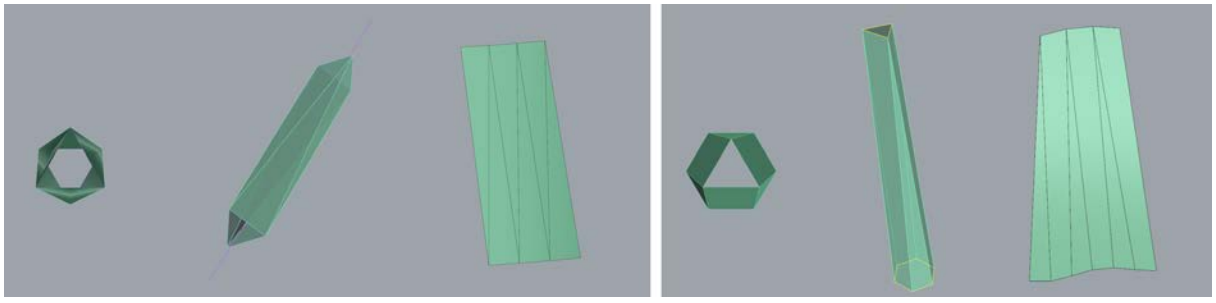


Figure 5: Straight members; Left: Typical 'stem' member; Right: 'Trunk' member.

2.1.2. Branching Nodes

As shown in Figure 6, a Y-shaped node consists of 4 flat sheets connected at the edges, and a tri-branch node consists of 6 flat sheets connected at the edges. Each of the flat sheets are either folded or rolled to shape the 3-dimensional nodes.

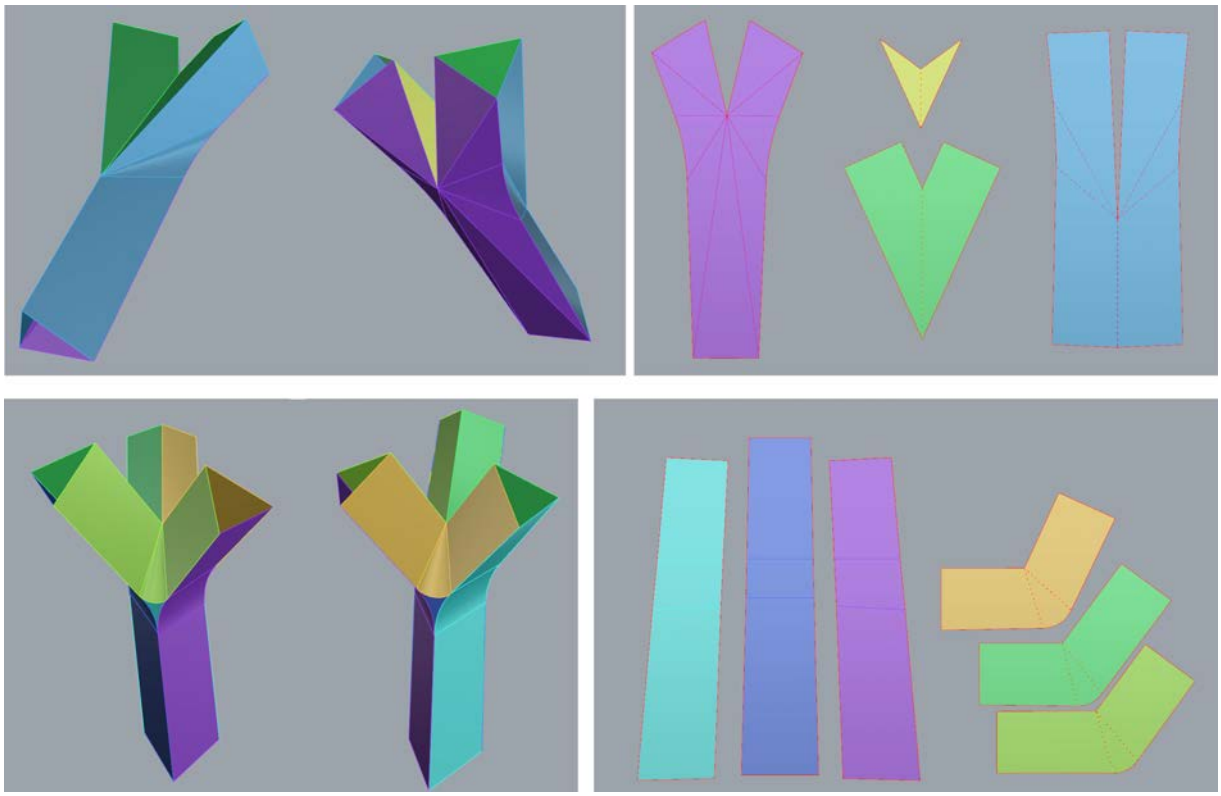


Figure 6: Above Left: Y-shaped node ; Above Right: Y-shaped node unfolded; Below Left: Tri-branch node; Below Right: Tri-branch node unfolded.

2.2. Canopy Geometry

The canopy consists of two hexagonal frames and 63 perforated panels that hang from the frames (Figure 7).

2.2.1. Perimeter Frames Geometry

Both the inner and outer perimeter frames are hexagonal in plan and consist of 6 closed triangular tubes. The cross section of the tube is an equilateral triangle whose side is 76.2mm (Figure 7). The frame carries the in plane tensile forces of the panels through flexure. The branches below then carry the gravity loads.

2.1.2. Panel Geometry

A flat canopy would need to resist its own self-weight, and accidental imposed load, through flexure. Flexure requires depth of material that would mean having to use much thicker and heavier panels that would not meet the construction/folding requirements and the restrictions on weight. Instead, a relaxed form-found geometry (Figure 8 and Figure 9) was defined as a structure hanging in equilibrium under its own weight. This allowed the panels to resist their own weight predominantly in-plane membrane tension action instead of flexure. Form-finding was done using the Kangaroo plug-in in Rhionceros 3D. The process of form-finding involved "rigidizing" each hexagonal plate by using fictitious links of high stiffness/rigidity and then connect the vertices of all the panels (Figure 10).

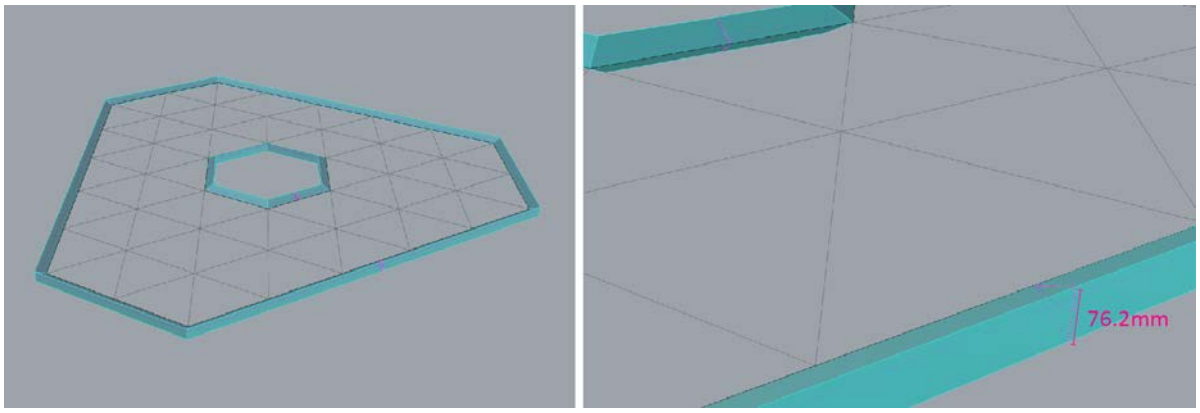


Figure 7: Geometry of inner and outer perimeter frames.

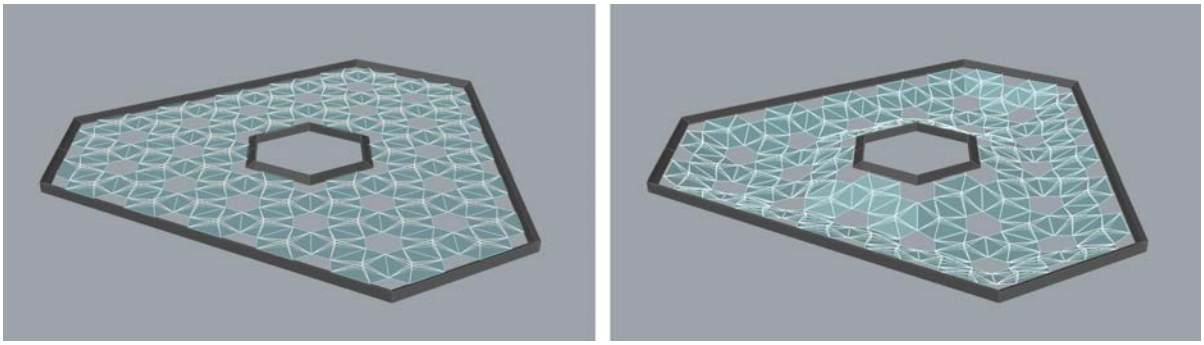


Figure 8: Left: Semi-rigid panels at the initial state; Right: Form-found semi-rigid panels.

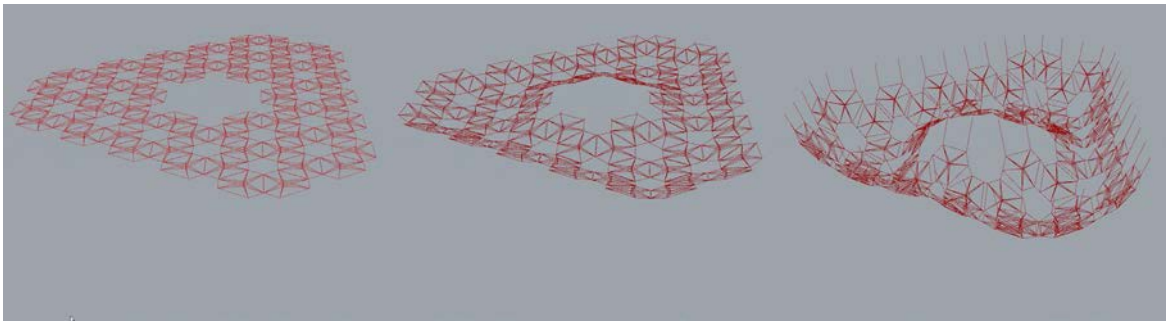


Figure 9: Left: Initial state; Middle: Found form used for design; Right: Exaggerated state.

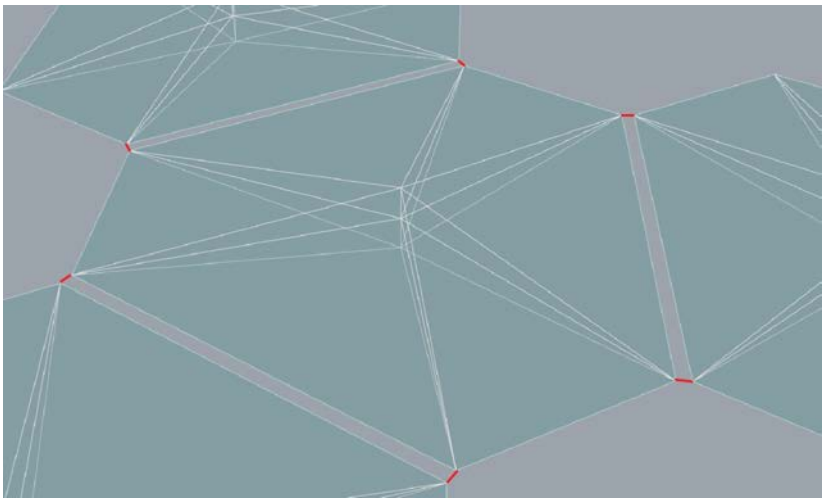


Figure 10: Rigid skeleton for the panel (white) and elastic links (red).

3. Finite Element Model (FEM)

Using grasshopper, a rationalized geometric model – pre-analysis model - suitable for pre-processing in the finite element analysis (FEA) program was created from the three-dimensional design model. The design model represents the geometrical objects of surfaces for the folded plate. The pre-analysis model is also a pure geometric model but here the surfaces have been split and trimmed to ensure vertex connectivity between the branches, nodes and edge beams. In addition, linear curves – links - are added between the vertices of the panel nodes representing intended connectivity, and a further point of intersection of connectivity between the link and edge beam surface also generated (Figure 11 and Figure 12)

Once the pre-analysis model is complete the model is meshed within the FEA program using the geometric surfaces as a reference. It is very important here that a suitably dense mesh is obtained with coincidence between vertices of all faces of the mesh where connectivity is required. The mesh model represents the three-dimensional analysis model.



Figure 11: Analysis model used by the FEA program

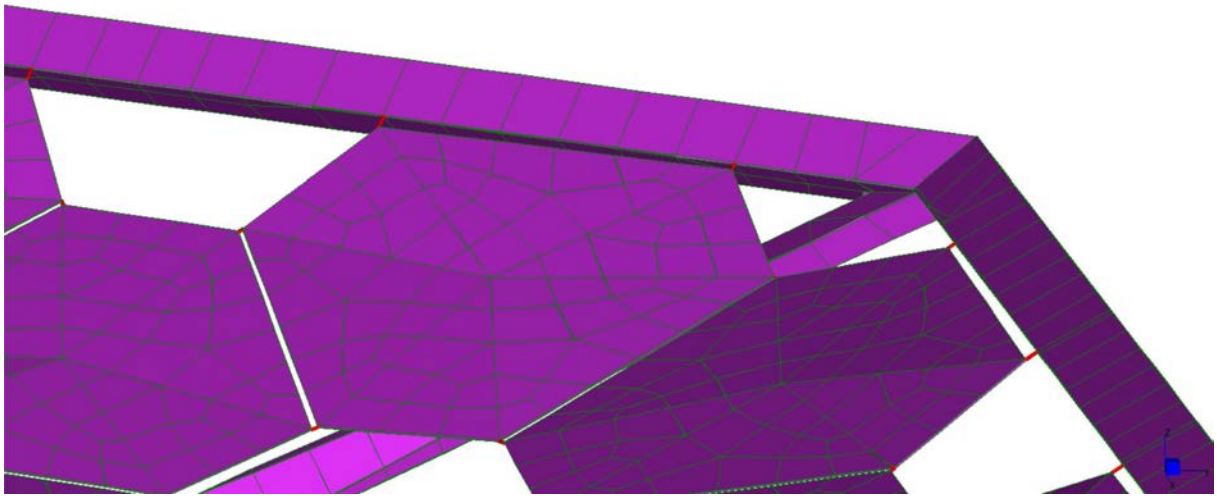


Figure 12: Analysis model fidelity with link and surface vertex coincidence for connectivity requirements

To test the mesh model two simple sensitivity analyses are run. First is with a uniform load applied downward to the panels and second is frequency analysis of the model using the self-weight of the structure. If the deflections are too high and/or frequency is very low < 1Hz, the analysis model is studied to see if there are errors of vertex connectivity. Once the analysis model passes these two tests it is deemed accurate to begin a full analysis.

The full analysis is used to 1) ensure the stresses in the folded plate under imposed loads of gravity and a uniform upward and downward load of 0.5 kPa do not exceed the allowable stress of the aluminum 2) overall stability of structure under loading is not compromised and a perception of structural safety from the observer is maintained.

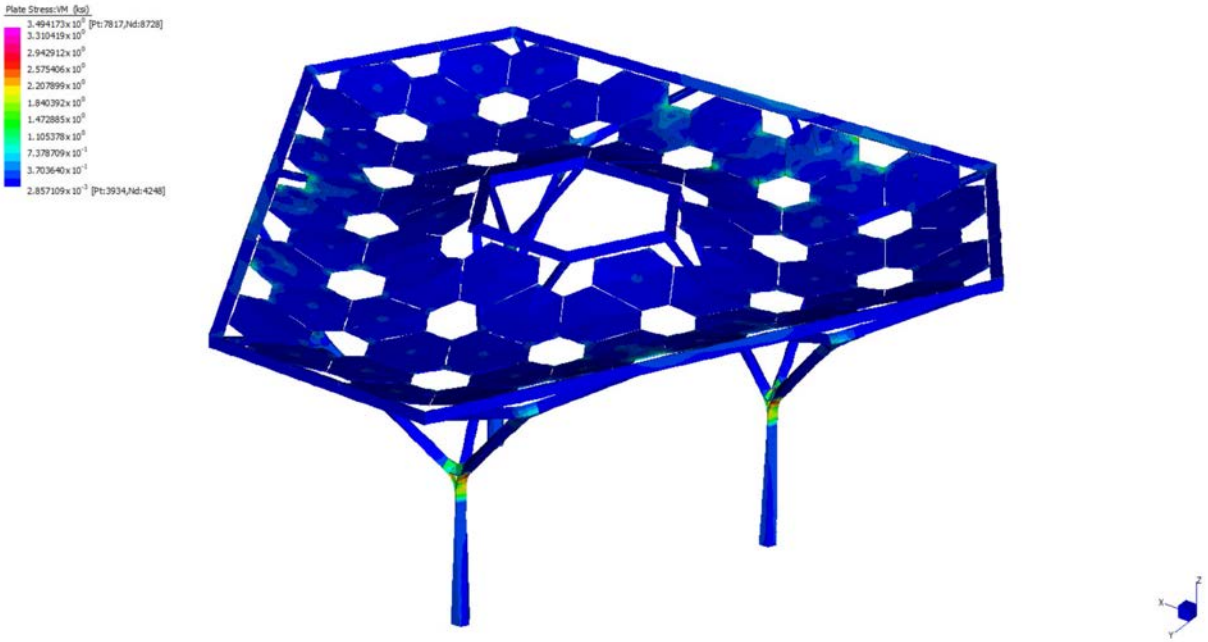


Figure 13: Envelope of stress, maximum of 3 ksi (21 MPa) at the nodes

The FEM (Figure 13) indicates that as expected the point of weakness and highest stress is where material is less, and force is significant. This occurs at the node connection between the branch. The dominate lateral frequency of the structure is good being at 5 Hz where at least 10% of the mass is participating in the mode shape (Figure 14).

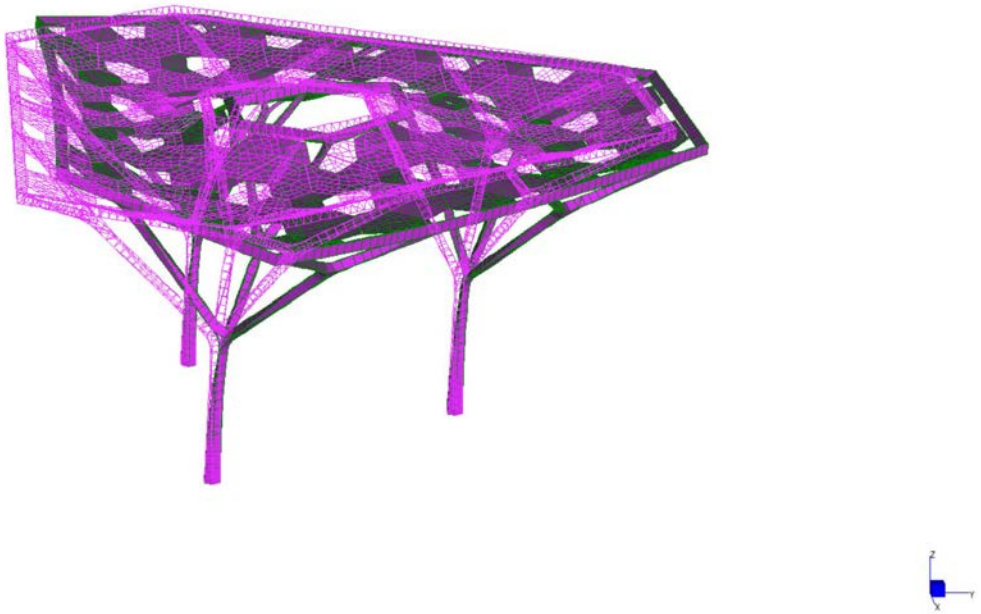


Figure 14: Dynamic Analysis showing a dominant first mode of 5 Hz

4. Prototyping Process

A series of prototypes are developed as part of the design process to study a variety of issues such as geometry, connection details, material-specific fabrication techniques and construction sequence.

4.1. Aluminium Fold Prototype

In order to make the 1.524 mm thick aluminium sheets easily foldable by hand, a cut pattern shown in Figure 15 was developed with aluminium prototypes. The folding line detail consists of a series of U-shaped through-cuts, with 1.52mm wide material left between each cut, allowing it to act as a hinge. The detail to close or stitch the edge in order to create a closed tube is currently being studied.

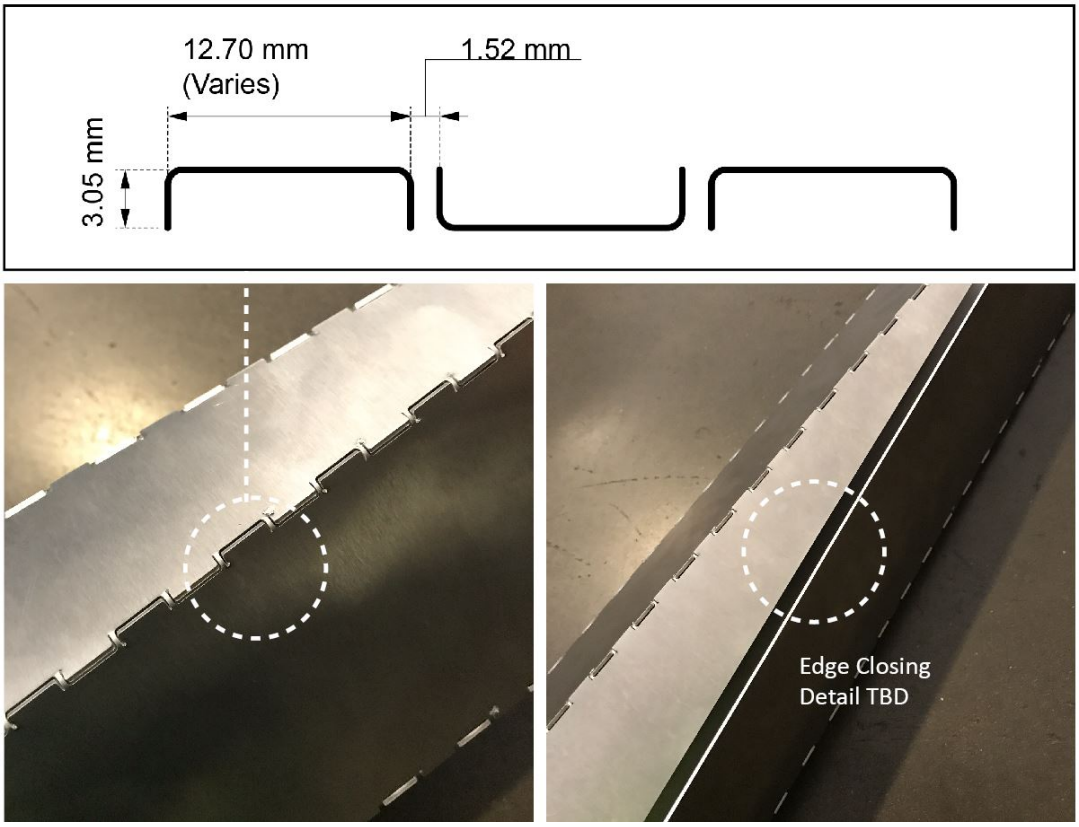


Figure 15: Aluminium prototype of a trunk showing a folded edge and an open edge.

4.2. Node Prototypes in Paper and Aluminium

The initial FEM analysis revealed that the stress concentrates on the branching nodes. Additionally, the geometry of the branching nodes containing joinery between multiple folded or curved sheets presents a series of fabrication issues. Multiple generations of prototypes were produced using sheets of paper, in order to visualize and study these issues (Figure16). A variety of detailing schemes including adding a kind of flange element as shown in Figure 16 are currently being studied.



Figure 16: Various paper prototypes of a tri-branch node.

In order to facilitate the rolling of the surface in aluminium, a technique similar to kerfing, typically used to bend plywood sheets was studied using a prototype shown in Figure 18.

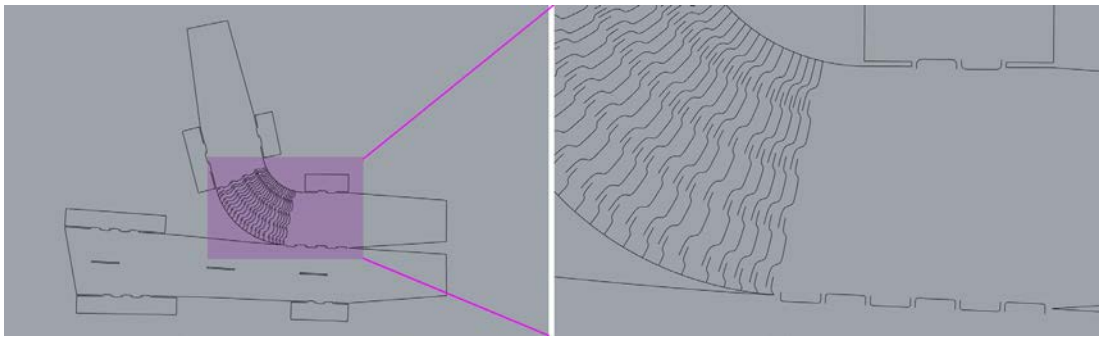


Figure 17: Cut file for an aluminium mock-up piece with cut patterns for folding and bending.

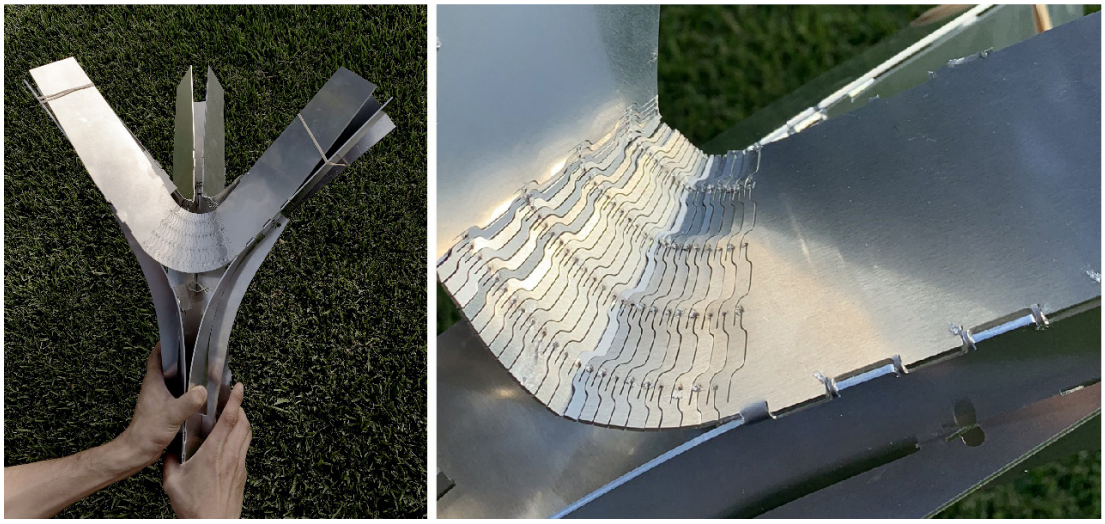


Figure 18: Aluminium mockup of a tri-branch node. Left: Assembled node; Right: Details of different cut patterns for folding and bending.

4.3. Full Scale Prototype in Paper

While the joinery details for the aluminium pieces are still being studied, a full-scale paper prototype was developed primarily to study an erection sequence and logistics (Figure 19 and Figure 20). All pieces were made from laser-cut sheets of cardboard paper, put together using adhesive tapes.

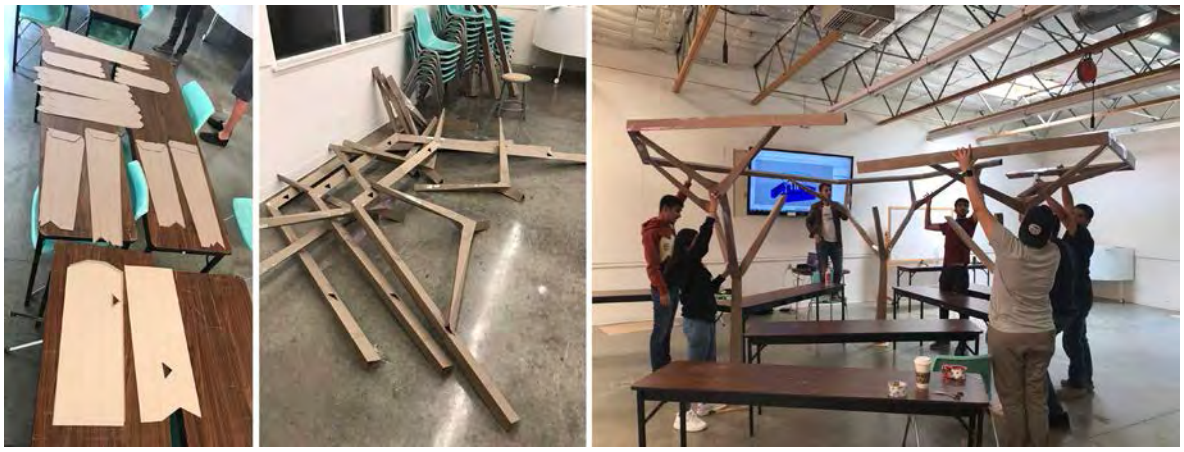


Figure 19: Assembly sequence study using a full-scale paper prototype.



Figure 20: Full-scale prototype in paper.

5. Conclusion

The design process of this project was driven by an interdisciplinary team of designers, engineers and fabricators from the initial phase of the project. By allowing multiple modes of studies using 3D

modeling, FEM analysis and physical prototyping to occur simultaneously, we were able to create a rapid feedback loop among different parties and iterate through design options quickly. The pavilion is to be realized in October 2019 at the IASS Annual Symposium 2019 in Barcelona.

Acknowledgements

This project was made possible by the generous support by Arktura LLC. The author would like to thank Kevin Kane, Ravi Gupta and Alex Heang for their kind support.

Proceedings of the IASS Annual Symposium 2019 – Structural Membranes 2019
Form and Force
7 – 10 October 2019, Barcelona, Spain
C. Lázaro, K.-U. Bletzinger, E. Oñate (eds.)

An Adaptive Pretension Structure

Jana M. RIETH*, Lorenz KASTNER, Christoph HOLZINGER, Andreas TRUMMER

*Institute of Structural Design at Technical University of Graz
Technikerstraße 4 / IV, 8010 Graz
tragwerksentwurf@tugraz.at

Abstract

An adaptive structure was chosen for the pavilion design due to its ability to react to variable conditions while increasing the material effectivity, which in turn leads to a weight reduction. The nineteen aligned arches are consisting of fifteen prefabricated modules, which are connected by a pretension cable. The adjustable modules generate the appropriate shape for the internal and external influences. According to the pretension in the cable, the shape, density and rigidity of the modules is adaptable. Each unit consists of two vertical plates, connected by a specially designed joint. The vertical elastic elements act as springs. They are made out of a deformable material with a highly elastic behavior and an adequate reset force. The material properties and dimensions are individualized to the required rigidity. Although the research of adaptive systems is widespread, the application is still minimal. In this research, it has been shown that it is possible to design and develop a practical solution with relatively limited resources, which is lightweight and contains an intelligent, adaptable load-bearing system.

Keywords: conceptual design, form finding, optimization, arch, pretension, adaptive, prototype, spring, actuators, permeability, geometry, deformable, joint, rigidity

1. Introduction

The goal is, therefore, to develop a self-supporting system, in which a deliberate change in the internal tension can create a visible structural and geometrical change.

Consistent application of lightweight design principles as well as the material selection and construction influence the material usage. As written by Sobek W., Haase W. and Teuffel P. [1] the priority of active adaptive systems is the structural change to the reduction or extinction of the load impact. In combination with appropriate sensors, these systems can react to changing influences and as a result, improve the overall building performance. The tension-based adaptive structure system can be used in a variety of fields [2]. For example, the volume of space can be varied, and the degree of opening (exposure and ventilation) of facades can be changed.

The design of an adaptive load-bearing structure combined with the requirements of being lightweight poses various challenges to the design to be developed. Additionally, the optimization of the component thicknesses, the designed joints and the development of an efficient overall structure are essential for the realization of a prototype.

Copyright © 2019 by Jana M. RIETH, Lorenz KASTNER, Christoph HOLZINGER, Andreas TRUMMER
Published by the International Association for Shell and Spatial Structures (IASS) with permission.

2. General Aspects

Adaptive systems can be divided into two basic categories.
The first system addresses adaptivity dependent on the external influences, such as sun, wind or other imposed conditions. These systems are often used as facade structures to regulate illumination or ventilation. Most of these applications apply to secondary structures and not the load bearing elements. These adaptive systems are generally based on the property of variable media transmission. As an example, in the pavilion expo Yeosu [4] by SOMA and Knippers Helbig Engineers the louvers in the facade are made of glass-fibre reinforced polymer (GFRP). The chosen material property is simultaneously strong and flexible. They have one stiff and one thin edge, actuators located at the top and bottom to provide the capability of asymmetrical bending. As a result, light radiate in and out of the building, as well as optical relations could be created.

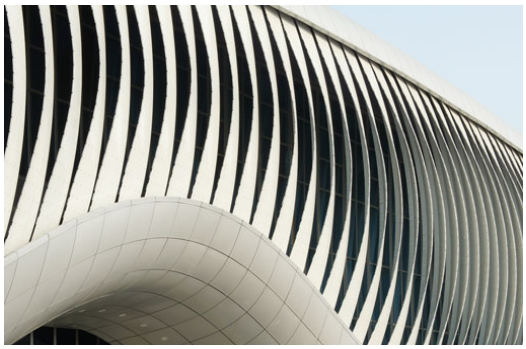


Figure 2: Adaptive facade of the theme pavilion expo yeosu [4]



Figure 1: Rendering of the Smartshell (University of Stuttgart) [5]

The second type of adaptive system includes systems where the adaptivity is barely noticeable. The sensors notice when there is a change in the loads and adapts the geometry on the structure accordingly. One example is the adaptive wooden shell from the University of Stuttgart [2]. The adaptive wooden shell prototype can adjust its internal stress levels by changing the position and direction of its supports. This reaction leads to a reduction of the peak stresses. This efficient material usage leads to a reduction in the amount of material used, and therefore, a weight reduction can be achieved. One of the advantages of these systems is the material which they save. The changeability of the systems makes it possible for the system to react to different load cases. Unlike the first type of systems mentioned, these adaptive structures are also supporting structures.

The developed system presented in this paper combines the advantages of both of the types mentioned above into one integrated adaptive system. The focus is the geometrical changes within the structure depending on the internal forces that occur.

3. Methods

The decision to create a research pavilion resulted from the research into adaptive structure systems, which change their geometry depending on the external influences.

The first step was to define the general concept. This was done using several scaled prototypes. Here the additional requirements for the structure were defined, which included not only being lightweight for the competition but also accessibility and adaptivity. The accessibility set the dimensions of the structure; the minimum height is 1.90 m and width 1.50 m. The adaptivity was defined as a change in the structure's geometry, which results in variable permeability.

Further steps focused strongly on the development of a global structure. Both the element geometry, as well as the global geometry, focused on creating one integral system.

During the development phase, prototypes of individual modules, single arches, up to a section of the final structure were produced in the scales of 1:10 to 1:1. These were necessary to understand and demonstrate the mechanical behavior of the global structure.

In the detailing phase, the elements were considered individually and optimized in terms of functionality and overall weight. Due to the advanced understanding of the operation mode, the components could be reduced to their primary functions again, and the individual geometries optimized. The optimization of the overall weight was achieved by reducing the thickness of the components down to the bare minimum.

Meeting the competition guidelines for the exhibition of innovative lightweight structures organized by the Working Group 21 “Advanced manufacturing and materials” in close cooperation with the IASS Symposium 2019 and the Structural Membranes 2019 Conference in Barcelona, the prototype was packaged and set up in a workshop under competitive conditions. The relevant competition conditions refer to the transport in six boxes, which may have maximum dimensions of 1.00 x 0.75 x 0.65 m and the maximum weight of 192 kg.

4. Results

The methods mentioned above resulted in a research pavilion, which is optimized and implemented on a scale of 1:1.

The pavilion is an arch structure. The connection of the individual modular units to formations resulted from the consideration of the force courses in combination with the self-selected requirement of the accessibility of the tunnel formed by rowing arches. The requirements of the individual arches and the units are above all in the load transfer of the overall weight and of course in the adaptivity of the module geometry.

The specified base area is limited by 4.00 x 4.00 m. The prototype of the arch was produced with a maximum clearance of 2.39 m and a width of 1.95 m. These dimensions were adapted later due to the limitations in the curvature of the module units to 1.50m and 1.95 m. To be able to represent the desired architectural image, a total of 19 arches were built in series, with a depth of 0.20 m.

The number of different modules in the prototype was minimized by changing the geometry of the upper part of the arch from a parabola to a circular arc and in the lower part to straight modules. Numerous model experiments have shown, that increasing the pretension forces results in a geometric adjustment in the direction of the parabolic shape.

The peculiarity of the module unit is the requirement of adaptability. Therefore, the modular units are both the load-bearing and variable component of the pavilion at the same time.

Principle of the structure

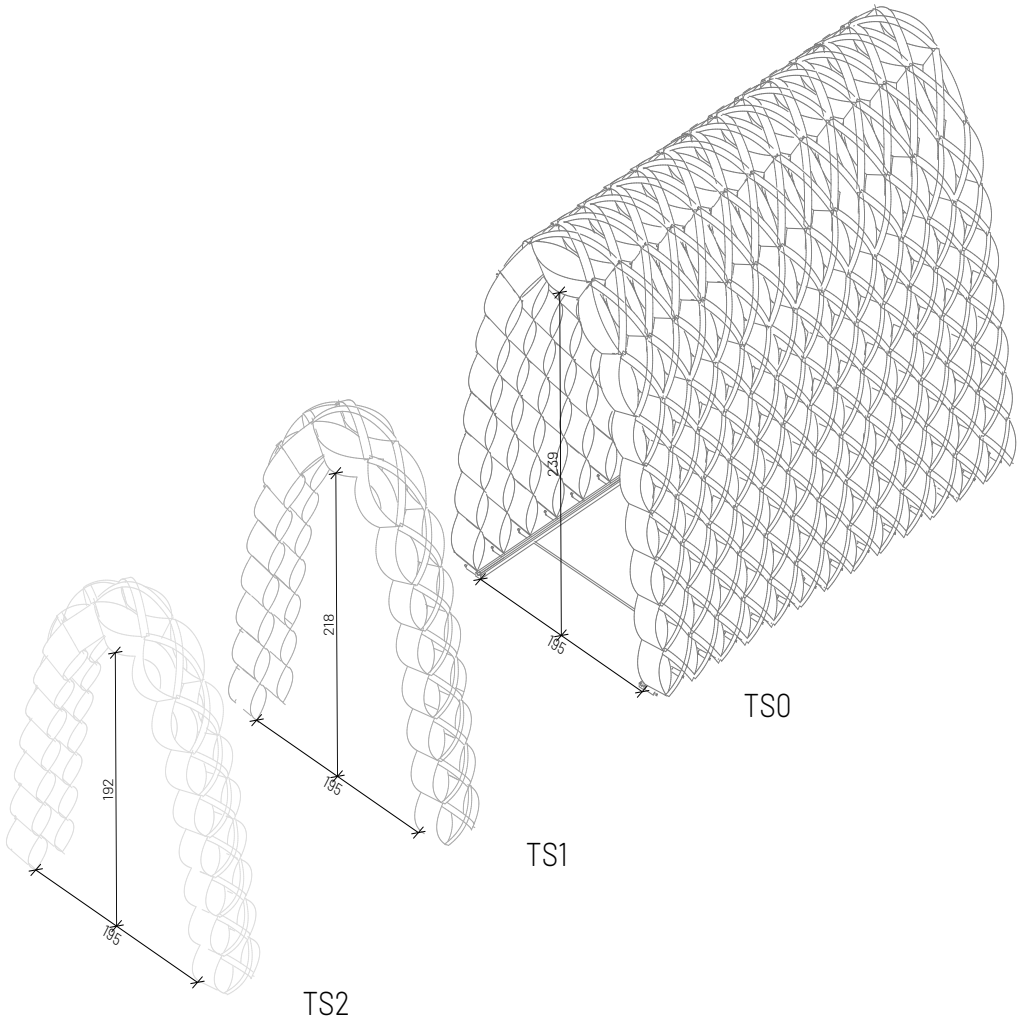


Figure 1: System in the three essencial tension states (TS0, TS1, TS2)

The 19 individual arches are connected via the bracing on the outer surface. Due to these bracings, when the tension in one of the arches tension cables is changed, it affects the adjacent arches too. This results in a wave-like impression.

Three cable tension states needed to be defined. During assembly of the structure, it is in the tension state 0 (TS0). At this point, there is no tension in the cable. For the initial situation, a defined pretension is required in the cable; this is the tension state 1 (TS1). The third state is the tension state 2 (TS2), in which about 90 % of the maximum applicable tension is reached. During usage, the maximum state of tension should not be reached. The reason is that at approx. 95 % of the maximum tension, the module geometry is fully deformed and, the adjacent modules touch each other and restrict further deformation.

Principle of a single arc

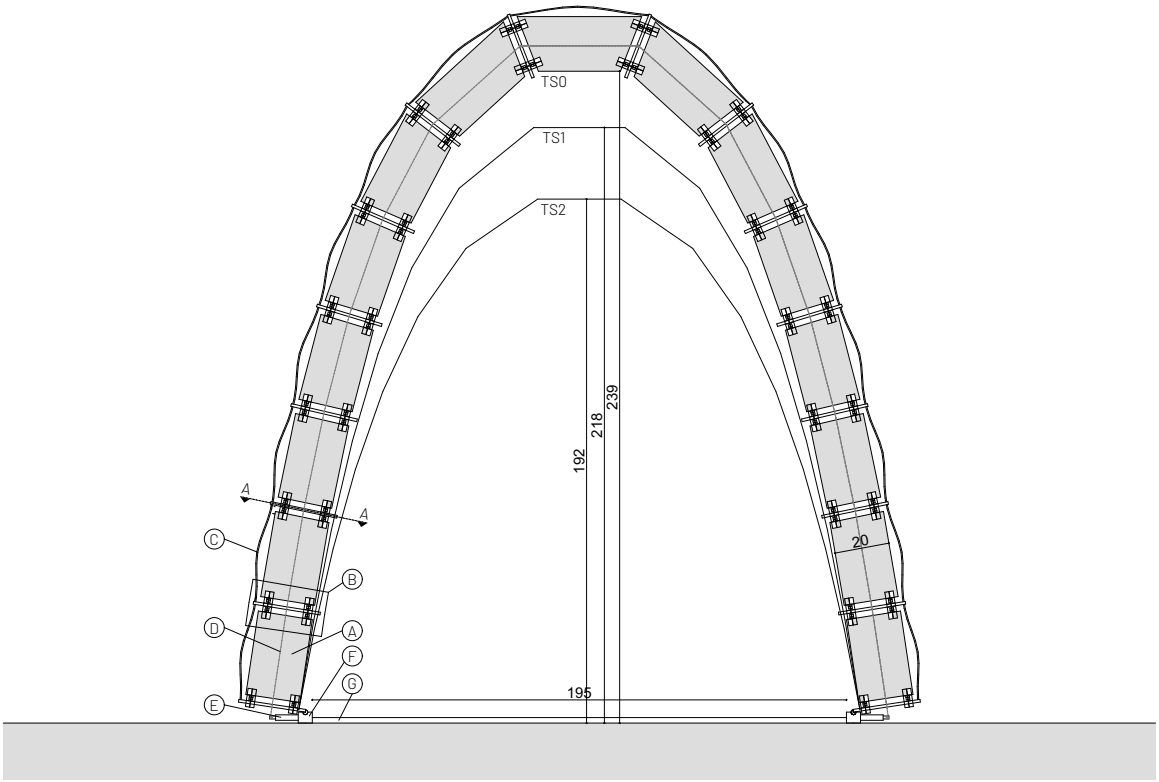


Figure 2: system section through an arch

Each of the arches consists of 15 module units (Figure 4). Each unit consists of two vertical plates (A), which are connected on both ends by a specially designed joint (B). The bracings (C) are mounted on the outer surface between the joints. The modules are held together using two tensioning cables (D) which are both fixed to the joint at the apex of the arches. The other end is coiled in the motor unit (E). This motor is controlled by one optical sensor, which is situated in the base (F). The width of the arch is fixed (G). Based on the given by the sensors, the motors change the tension within the appropriate cable.

Geometry change of the individual modules

The adaptivity of the overall structure is dependent on the geometry changes of the individual modules. The goal is to change the interior lighting conditions. The height of the modules in TS1 and TS2 were compared. The height of the modules can be reduced by 40 %, and the bulging is enlarged by a factor of 2.5 (Figure 5).

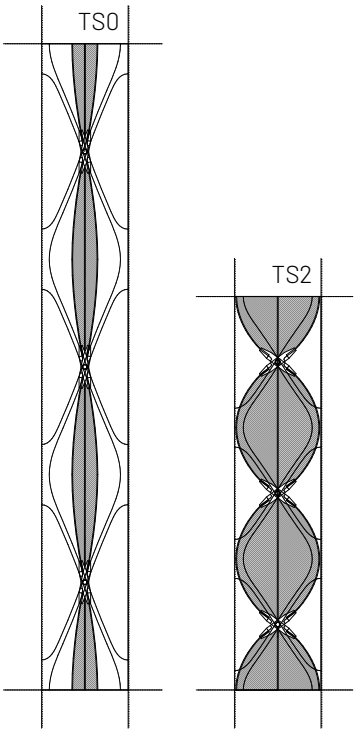


Figure 5: Elevation of the geometrical change within the system

The individual components are described in detail here.

(A) Vertical plates / Spring elements

The vertically plates act within the individual arches as spring elements. Two plates, which bulge in the opposite directions, are placed between the joints (Figure 6). Depending on the position in the arch, the plates are adapted in size and thickness. The further down the arch, the smaller the plate size, and consequently the stiffness of the plates increases. Since this is the stiffness of a buckling bar, instead of the changed buckling length of the individual plates, also a change in the plate thickness could be considered. Another option to reduce the stiffness would be a specific subtraction, e.g. a pointed perforation of the plates.

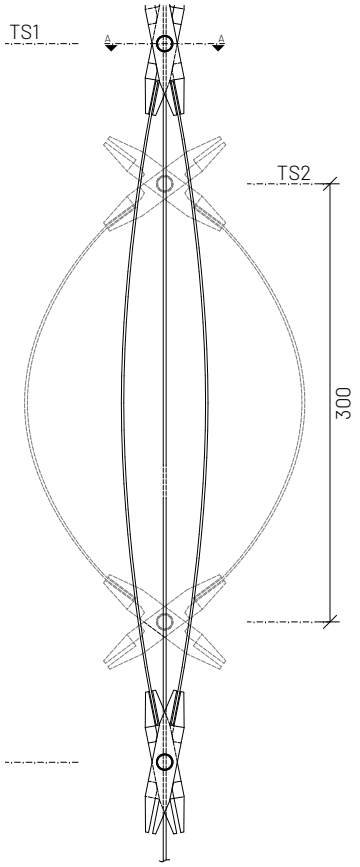


Figure 6: Detailed vertical section B-B of the tension states

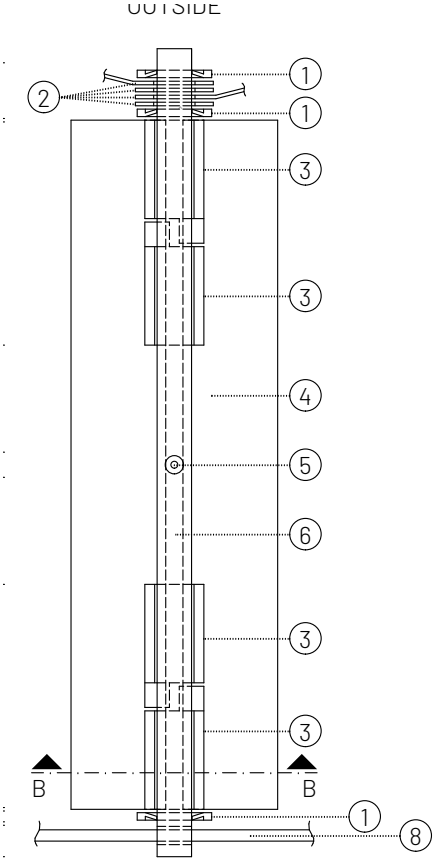


Figure 7: Systematical horizontal section A-A through the joint

(B) Joint between the vertical plates

The joint consists of a round hollow profile (6). Attached are four specially designed double clamps (3). These double clamps can rotate around the hollow profile but fixed in position by cuttings in the vertical plates (4). By linking the diagonal plates with one clamp, the buckling is transferred through the joint. Based on this mechanism a uniform deformation is guaranteed. The laterally protruding moldings prevent unintentional buckling in the wrong direction while limiting also the maximum deflection. Thus, they prevent the plates against plastic deformation. In the middle part of the hollow profile, a hole for the implementation of the tensioning cable (5) is positioned. Furthermore, four incoming arms of the horizontal bracings (2) are attached to the outer part of the hollow profile and then fixed with retaining washers (1). The inner parts of the hollow profiles are connected with each other by the horizontally conducted solid profiles (7).

(C) Horizontal bracings

The horizontal bracings are pre-curved x-shaped elements (2). Due to the changes in the horizontal distances between the four parallel axes connected by the bracings, they had to participate in the deformation orthogonal to the axis but simultaneously bear the horizontal forces.

(D) Tension cable

The internal tension cable ((5) in Figure 6) is centered, which guarantees optimum force transmission. There are two tension cables per arch to reduce the maximum clamping force. Both cables are connected to the uppermost joint of the arch and connected to all the modules down to the module at the bottom of the arch. At this point, the tension cable is wounded onto the coin, which is directly connected to the motor unit. This unit can selectively control the total length of the tensioning cable as a result of an electronic device.

(E) Engine unit and control technology

An essential component of all adaptive systems is the control technology, as well as the actuators. Two electric motor units are mounted to the base of each arch, one on each side. Both are controlled via the same sensory unit to generate a uniform deformation of the arch. An electromechanical adjusting device, which shortens or lengthens the tensioning cable result in an increasing/decrease in tension inside the tension cable.

(F) Base and sensor

The bottoms of the arches are connected horizontally to a bar. This bar is hinged to the solid rectangular base. The optical sensor is positioned within the base element. This sensor aligned to the opposite part of the arch, to sense the attendance of the user.

(G) Truss

A truss is placed in between the two solid bases to withstand the horizontal arch forces and prevent the bases from slipping apart.

Optimization of stiffness

Due to the mechanics of the system, which consists mainly of tension cables and the spring elements, the overall stability of the pavilion is achieved by the rigidity of the individual modules. At the same time, the elements should not be too stiff, to minimize the degree of adaptivity. According to that, an optimal rigidity of the individual elements is required. Looking at an entire arch, the location of the individual elements is crucial. By comparing the minimum required stiffness of the spring elements in the lower area of the arch, with the requirements in the middle and upper part of the arch, a stiffer element is needed in the lower area due to the higher loads. At the same time, a reduced rigidity of the elements in the upper regions of the arch can lead to a considerable reduction in the overall weight. Thus, the interaction between dead weight and rigidity and consequently, the consideration of the overall stability in the further development of the system was one of the main factors in further development.

5. Conclusion and discussion

Within the field of adaptive structures, the question of relevance in practice arises. Although a few projects have already been implemented, a significant increase is to be expected due to the increasing digitization in future buildings. The idea of resource conservation has become increasingly important in recent years. Aspects such as minimal use of materials, upgrading old buildings rather than building new ones by adding energy-efficient facade systems are becoming increasingly more important. The system described in this paper can improve an existing building without exerting more forces on the existing load-bearing system. Also, due to the modularity of the system, it can be made larger/smaller (longer/shorter, higher/lower) if necessary.

The appropriate system geometry can be achieved in response to an environmental condition change. The tension in the cables is changed appropriately, and the geometry changes automatically. This allows the shape, the permeability of the pavilion, as well as the resistance to the external load, to be controlled. The permeability in the implemented prototypes prioritizes the visual connection. As a further step, it would be conceivable to add controls to the modules for light transmission, wind permeability and weather protection.

Due to the focus of the research on working basic structure, as well as the development of the joint between the vertical elements and the stiffness of the overall structure, further research must focus on the following points:

Sensor technology and control technology

Due to the low financial resources available during this research project, there is still much need for development, especially in the area of sensor technology and electrical control. This would make it possible to control each of the individual arches too. The overall control of the components could be even more precise, and it would be possible to respond not only to the users' commands, but also other stimuli, such as weather conditions or specific load cases. Furthermore, it would also be possible to set the control of the motors independently to achieve even more uniform changes in the appearance of the overall structure.

Consideration of further load cases

The modules themselves are the load-bearing elements but are only designed to withstand self-weight. Other loads should also be incorporated into the design process such as wind, snow and expansion loads. The prototypes are only designed to withstand the self-weight and pretension loads.

Change in media permeability

As described in the geometry change of the individual modules, there is a considerable enlargement of the opening between the vertical plates. A targeted closure of the intermediate spaces between the module units, for example by a membrane, leads to a restriction of the view in the tension state TS1. By reducing the distance between the vertical elements, as a result of increased tension in the cable, the permeability of the overall structure can be significantly increased.

Although the research of adaptive systems is widespread, the application is still minimal. Here it has been shown that it is possible to design and develop a practical solution with relatively limited resources, which is lightweight and contains an intelligent, adaptable load-bearing system.

References

[1] W. Sobek, W. Haase, P. Teuffel, *Adaptive Systeme.* Stahlbau vol. 69, pp. 544-555, 2010.

[2] Teuffel, P., Entwerfen Adaptiver Strukturen, University of Stuttgart: Institut for Lightweight Structures and Conceptual Design. (Diss. PhD-thesis), Stuttgart, 2004.

[3] Neuhäuser, S., et al., Adaptive Tragwerke – Aktuelle Forschungen im Ultraleichtbau, Stahlbau vol. 82.6, pp. 428-437, 2013.

[4] https://knippershelbig.com/en/projects/thematic-pavilion-expo-2012 (14.6.2019)

[5] Stuttgart SmartShell, http://smartshell-stuttgart.de/?page_id=19&lang=de (23.5.2019)

Proceedings of the IASS Annual Symposium 2019 – Structural Membranes 2019
Form and Force
7 – 10 October 2019, Barcelona, Spain
C. Lázaro, K.-U. Bletzinger, E. Oñate (eds.)

Common Multiple

Katharina SCHARLER*, Mitja BUKOVEC, Vera SCHABBON,
Christoph HOLZINGER, Andreas TRUMMER

*Technical University of Graz – Institute for Structural Design
Affiliation of Corresponding Author
Technikerstraße 4 / IV
k.scharler@student.tugraz.at

Abstract

This paper documents the approach to a new hybrid building structure. Due to climate change, people are becoming more conscious of the importance of using locally available resources and other goals such as erecting structures without a crane. The aim was to develop a visually appealing, low tech, earthquake resistant, lightweight structure. The structure focuses on using wooden stripes with minimal cross-sections and a textile membrane to stabilise its shape. A series of case studies resulted in maximum utilisation of material properties to minimise material thickness and the cross-sections. The structure is adaptable to a variety of materials - as long as they fulfil specific requirements, the system can be built with the resources available locally. The pavilion described in this paper uses wooden veneer, fabric and greyboard. The minimal material thickness and the simple push-fit system simplifies the assembly process of the lightweight structure. It is location-independent and easy for users to assemble and dismantle without any crane. As long as the strict triangular pattern is adhered to, the outline can be defined as desired. By defining a few parameters in an algorithmic model, the user can quickly adapt the structure. The result is a list of necessary building parts including their dimension and tailoring as well as the position of the joints on the tension membrane.

Keywords: lightweight, bending-active, low-tech, dissipative, wood, minimal cross-section, membrane structure, digitally fabricated, algorithmic model, available materials, sustainable materials, sustainable use, earthquake design.

1. Introduction

Given the ever rapidly changing society, engineers and architects are pushing the limits in search of innovation. Advantages in computational design and analysis, digital fabrication and material processing open door for further development. These make it possible to create temporary and mobile structures to meet different needs quickly, and short-term structures for different conditions with a reusable and low-impact. [1] Modern lightweight structures that use the principle of bending active elements remind us of ancient tent structures and make us question conventional solutions. [2]

The workflow of the research documented in the following pages was mainly dominated by building models and 1:1 mock-ups. The result, a double-layered structure, a lightweight pavilion, consists of three parts: flat strips, a membrane and joints. The strips are active-bent, three-dimensional structural elements, creating a flexible frame - a triangular pattern of domed shapes. A membrane ensures the bending and stabilises the shape. The length and the material of the preformed strips can vary,

Copyright © 2019 by Katharina Scharler, Mitja Bukovec, Vera Schabbon, Christph Holzinger, Andreas Trummer
Published by the International Association for Shell and Spatial Structures (IASS) with permission.

depending on several factors including the demands of transport, construction, and the span widths. It is imperative to note that it should stay in a range of elastic deformation, i.e., after the force is removed, it returns to its original shape. The elastic deformation also facilitates fabrication and transportation. Membrane materials can vary depending on tensile requirements and the intended usage of the structure. It needs to carry loads in three directions. Similar to ordinary woven fabric, it has a weft and warp direction, that means that there are only two load carrying directions which can be activated in tension. It was necessary to manipulate the two axial woven fabrics. Either tailored: cut and sewn, or reinforced with tailored-fibre-placement. Digitally fabricated joints connect the wooden strips to the membrane. The second set of sliding joints help to define and stabilise the shape.

Three materials were chosen for the proposal of the pavilion at the exhibition: beech wood, a natural fibre, and greyboard. The team also tackled challenges regarding material characteristic attributes, for example, the brittleness of a variety of timber types as well as the optimal length and cross-section. By change of internal moisture, it was possible to bend the timber without it breaking. It was necessary to adjust the interdependency of the single elements within the system. As described above, it was crucial to adjust the fabric to our needs so that it could bear the tensile loads in three different directions. Case studies showed that the greyboard was capable of carrying loads in all directions, was strong enough to keep the strips in place solely through friction and compensate small differences in material thickness through its plasticity. While this paper focuses on the design and material aspects, further in-depth research will investigate the realisation and optimisation of structural performance.

2. Research Method

2.1 Experiment

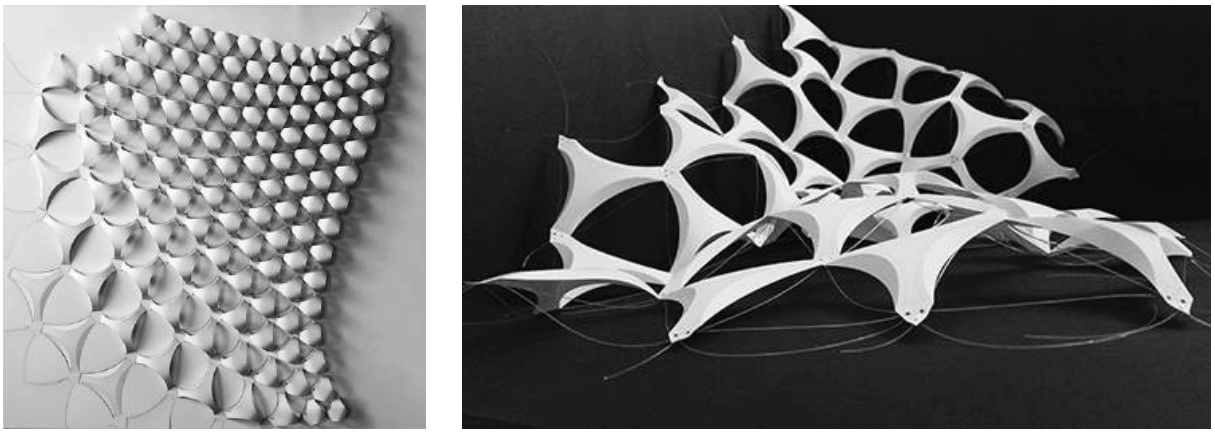


Figure 1 - 2: Paper bending fixed to cardboard – Cut out and threaded with tension threads as guidelines.

It all started with a paper-model using the principle of cutting a plane surface and moving the base points of the remaining triangles closer together with a string. The paper bends and moves vertically. The triangular structure benefits from the elasticity of the material and the minimal material thickness. The joints of the triangles are threaded on the guideline. The distance between the corners is tightened together along the axis to push up the planes. The frictional resistance of the paper allowed the incised and scribed pattern of an A4 paper to bulge without any aids other than the guiding thread. [Figure1-2]

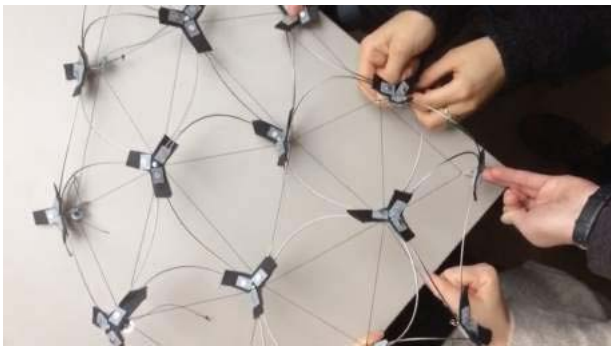


Figure 3: Bike brake cable guided along a string

To see if the bending triangles system could be translated to a larger scale, a second larger model was made using bicycle brake wires. A star-shaped leather knot with three arms held the rods in position and made the rotation possible by acting as a hinge. In the first model, a common thread was used again along which the joints were pulled closer together. All the wires buckled sideways. Because of their round cross-section, there was no guided direction for their bending. [Figure 3]

A metal eyelet connected the thread to the joint. This eyelet allowed almost frictionless movement of the thread. This resulted in a random uncontrolled pattern which needed to be readjusted by hand. Every joint had to be repositioned by hand to obtain the uniform bending pattern. The next attempt utilised straws threaded onto the thread. The length of the straws defined the final distance between the joints accurately defined the distances between the joints. Pulling the thread caused the elements to bend one by one, and the system locked and stabilised as soon as the straw elements were under pressure. [Figure 3]

2.2 Adapting Material

The previous models showed the importance of having a weak-axis in the cross-section of the bending elements. The available materials were wooden veneer, tape and string. The veneer was used for the active bending elements, the tape and string to join the modules that were arranged in a triangular pattern [Figure 5]. The tape was then replaced by laser-cut greyboard [Figure 6]. This meant that the bent active elements, at the beginning and end, is parallel to the neighbouring element. The digital fabrication ensures high precision and predefines the direction of the twisting and bending of the stripes. Three domes meet at one joint. Slots were cut for each of the veneer stripes that meet at the joint. The joints are also connected to the tension component, which stabilises the bending-active elements. The minimal deviations in material thickness, bending and torsion of the veneer stripes, makes it possible for these joints to stay in place due to friction without the need for additional fixing methods (e.g. glue, screws). Replacing the thread with fabric could enable the structure to both, span like an ornament between supports as well as serve as a shading element. [Figure 7-8]

Experiments with 1:1 models resulted in a double-layered lightweight structure consisting of 2,5 mm flat beech wooden strips, a membrane from natural fibres and greyboard joints. The strips are active-bent to shape a three-dimensional structural element, creating the structure's flexible frame. These modules are joined together in a triangular pattern of domed shapes. The membrane ensures their bending stays active and stabilises the position compared to the position of the knots. [Figure 4]

Digitally fabricated joints connect the wooden strips to the membrane. The second set of sliding joints help to define and stabilise the shape. By moving the joints, the spans are increased/reduced, and the elements are pulled closer together/pushed further apart. This movement causes the structure to rise and take its final shape. [Figure 9]



Figure 4: Principle of the plugin system, bending into modules and attaching the fabric to stabilise





Figure 5 - 6: Bending a rectangular cross-section with tape and string – a module: veneer, greyboard and string





Figure 7 – 8: Triangular pattern, every second triangle is a module; the next row is offset. – side view, before the structure was turned “upside down” to use the tension membrane on the exterior like regular domes but also as a cover

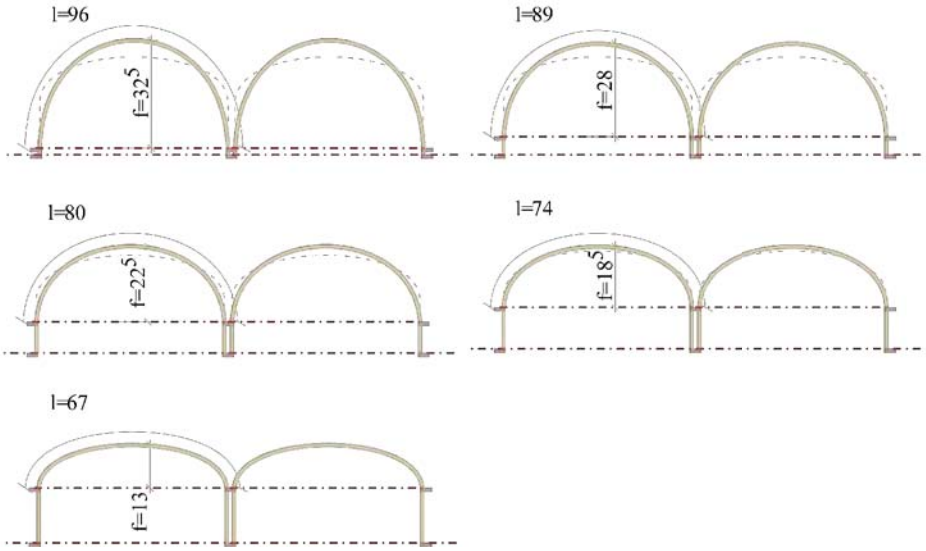


Figure 9: The position of sliding joints defining bending of the arch

3. Pavilion

The pavilion was designed to meet the competition guidelines for the exhibition of innovative lightweight structures organised"Advanced manufacturing and materials" by the Working Group 21 in close cooperation with the IASS Symposium 2019 and the Structural Membranes 2019 Conference in Barcelona. The pavilion had to be packed into six imaginary boxes that could be transported by aeroplane (1,0 x 0,75 x 0,65 m with 32 kg per Box). It should not exceed a weight of 192 kg. The structure also had to stand on the ground with the maximum floor area of 4m x 4m x 4m. [3]

3.1 Shape

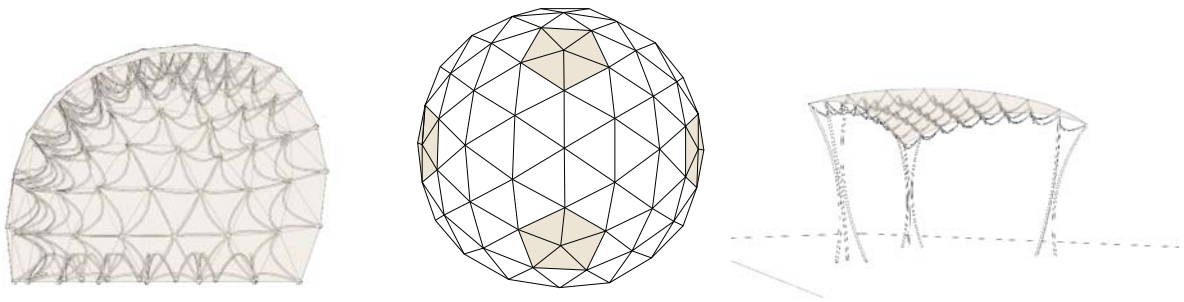


Figure 10 – 12 : the proposed pavilion structure for the competition entry // the geometrical problem of a geodesic tessellation // an option of the design adaptation

The original idea was to use the spherical triangulation of a geodesic dome. This could not be carried out as the tessellation will always have pentagons within its pattern. The geodesic dome was derived from an icosahedron, and an almost regular triangulation is achieved. Five triangular faces meet at the corners.

The construction pattern means that every triangle creates one domed module. As the two different boundary conditions mentioned above were not achieved (weight, floor area), the final outline and shape had to be adjusted. It is essential that the outline of the structure work with a "regular" triangular pattern. For the dimensional stability, the outline of the structure needs to end with bending active elements — the pavilion which has been built acts as an example of one of the many possible shapes.

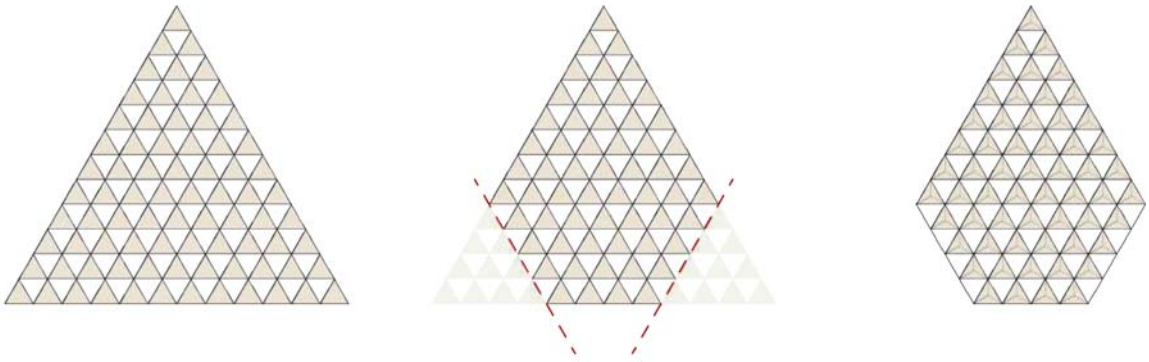


Figure 13: the basic pattern used to extract the final geometry

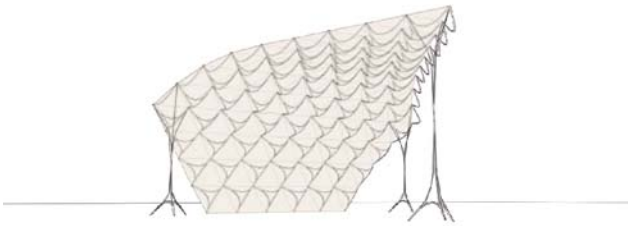


Figure 14: final proposal for the pavilions shape

3.2 Manufacturing of Elements

The objective was to use materials that are available locally, beechwood was used as it is a very common native wood. The thickness of the stripes elements was 2.5 mm. The sheets were cut using a simple table saw to obtain the required cross-section. All stripes were one metre long and 17mm wide. The beechwood stripes of the columns have the same cross-section, but due to the construction method, they vary in length. Challenges occurring due to the material characteristic attributes of a variety of timber as well as the change of internal moisture had to be tackled.

The joints were successfully created using layered cardboard. Many advantages of cardboard were utilised. It is made out of low waste paper, a mixture of various packaging papers and carton types as well as waste paper. [4] The fibres of the pressed boards are arbitrary; therefore, the load-bearing properties are the same in each direction. The 2,5 mm thick material is cut according to the slot for the veneer stripes and the necessary thickness to ensure its stability to transfer the occurring loads.

Due to minimal deviations in material thickness, bending and torsion, the veneer stripes do not need any additional glue or mechanical joining elements, they stay in place solely by friction.

As the process of development was not finalised, the extensive search for a suitable membrane was not completed yet. Woven membranes with artificial components and intensive treatment would withstand the required tensile stress. As the aim was to create a sustainable structure, the process now focuses on the optimisation of a woven fabric with natural fibres. Possibilities for the fabricating the fabric include cutting, sewing, or reinforcing with tailored-fibre-placement.

3.3 Mock UP at a scale 1:1



Figure 15 - 17: The column carries the lightweight structure – the tripod base – a segment of the pavilion

A long-term study to test different external conditions of humidity and self-weight in different positions.

5. Conclusion

Developing a visually appealing but low-tech, earthquake resistant, lightweight structure with a versatile design that can be built on different construction sites with different uses and conditions resulted in a double-layered structure. The pavilion is made out of easily tailorable materials, uses a user-friendly construction method and sustainable building materials. It is realised by the maximising the utilisation of the material properties.

The experiments on analogue models have been paramount for testing the design and detailing. Digital modelling techniques were an essential part in the elaboration of the geometry, the calculation of the required elements and the fabrication of the membrane. This paper shows that sustainability can be an integral part of the design, both in the choice of materials, the construction and the consideration of the life cycle. Especially in the field of implementing the system in everyday life, the vast potential remains in further research to explore design possibilities with alternative materials and new applications.

6. Acknowledgements

The authors would like to thank Hechenblaickner and the Institute of Timber Engineering and Wood Technology for sponsoring wooden veneer und proHolz for their financial contribution to the project. Further more we would like to mention the TU Graz with a special thank to the members of the Institute of Structural Design for their support in all aspects.

All Figures are produced by Mitja Bukovec, Vera Schabbon and Katharina Scharler

References

[1] S. Brancart, L. de Laet, N. de Temmerman, "Transformable bending-active structures: Manipulating elastic deformation in kinetic and rapidly assembled structures," in Structures and Architecture – Cruz (Ed), Taylor & Francis Group, London, 2016.

[2] Universität Stuttgart, https://www.architektur.uni-stuttgart.de/nc/portfolio/ausgewaehlte-arbeiten/archiv/sommer-2015/sommer- 2015/?details=1085&cHash=98236539a30a7aeece2dcb12de401713, Stuttgart, retrieved on the 28.05.2019.

[3] A. Pronk, Working Group 21, advanced manufacturing and materials, http://www.manufacturingmaterials.org/competition.html, Netherlands, retrieved on the 11.03.19

[4] Material Archiv, "http://www.materialarchiv.ch/app-tablet/#detail/527/graukarton", Zürich, retrieved on the 25.05.2019.

[5] J. Lienhard, "Bending-Active Structures, Form-finding strategies using elastic deformation in static and kinematic systems and the structural potentials therein" Institut für Tragkonstruktionen und Konstruktives Entwerfen, Universität Stuttgart, 2014.

[6] C. Gengnagel, H. Alpermann, E. Lafuente Hernández, "Active Bending in Hybrid Structures", Departement of Structural Design and Technology, University of Arts Berlin, 2016.

[7] J. Lienhard, C. Gengnagel, " Recent developments in bending-active structures", in Creativity in Structural Design: Proceedings of the IASS Annual Symposium 2018, Boston, July 2018, C. Mueller, S. Adriaenssens (eds.).

Proceedings of the IASS Annual Symposium 2019 – Structural Membranes 2019
Form and Force
7 – 10 October 2019, Barcelona, Spain
C. Lázaro, K.-U. Bletzinger, E. Oñate (eds.)

Deployable Bamboo Dome

Natalia TORRES *, Eliana CORTES-PAEZ*, Ramon SASTRE[a], Xavier GIMFERRER[b], Francisco INTRIERI[c], Isaac GONZÁLEZ[d]

*PhD Candidate. Polytechnic University of Catalonia. Barcelona Tech.
Vallès School of Architecture. ETSAV. Pere Serra, 1-15. 08173 Sant Cugat del Vallès.
natalia.paola.torres@upc.edu
*PhD Candidate. Department of Architecture and Civil Engineering, University of Bath
Claverton Down, Bath, BA2 7AY, United Kingdom
eccp20@bath.ac.uk

[a - b] PhD. Prof. Polytechnic University of Catalonia. Barcelona Tech
[c - d] Bambusa.es. Design and installation bamboo structures.
[c] Research group. LITA. Laboratory of Innovation and Technology in Architecture
Structural Morphology in Architecture SMIA

Abstract

This article describes the process of design, analysis, and manufacture of a modular, adaptable and lightweight folding dome. The structure is composed of six flat semi-arches, that fold through the scissor-type system reducing the size of the dome to facilitate is transport. Bamboo bars with a circular section are used as a main material for the structural arches. This research has been contextualized in the development and the form-finding process of curved surfaces with articulated bars. Félix Escrig's projects have been utilized as the main reference, in particular, his method based on the regular polyhedron's geometry, which allows obtaining the largest number of similar pieces. For this case study, a new approach to the regular polygon method is applied in the design process. The new methodology allows easy definition of the main characteristics of the bars: length and position of the joints; as well as achieving equal and modular pieces. The case study incorporates analysis and simulation graphics in two dimensions of the semi-arch type elements on its final stage of deployment. This graphical method of analysis allows finding the adequate deformation based on the self-weight of the structure and in this way to define the ideal position for the opening of the semi-arch that matches the initial geometry established to form a stable arc. The fabrication process explains the design strategies employed to select the connection mechanisms between the bamboo bars that will ensure correct structural behavior and functionality of the dome. The resulting prototype aims to demonstrate the potential of bamboo bars within deployable structures to generate innovative and sustainable solutions for temporary buildings.

Keywords: Deployable structure, scissors system, bamboo, form finding, domes, lightweight construction, bamboo connections, 3D printing.

1. Introduction

The construction industry is one of the economic sectors which carry out the most high-impact activities against the natural environment. Over the last decade, proposals to decrease this problem have been tackled in most of the ongoing research within the faculties of architecture and civil engineering. For academics and researches, this challenge has been understood as an opportunity to put in the mainstream alternative structural systems and non-conventional methods of construction that could offer more sustainable architectural solutions. The present research is part of this academic field, aiming to

Copyright © 2019 by Natalia TORRES, Eliana CORTES-PAEZ, Ramon SASTRE, Xavier GIMFERRER, Francisco INTRIERI, Isaac GONZÁLEZ, Structural Morphology in Architecture SMIA
Published by the International Association for Shell and Spatial Structures (IASS) with permission.

demonstrate through the construction of a deployable bamboo dome structure that temporary architecture can be made sustainable by using low-impact materials.

Bamboo is a natural renewable material with a low-carbon production footprint for building construction. For centuries its potential was hidden within the vernacular constructions of different cultures around the world [1]. Nonetheless, the ongoing search of sustainable materials has unveiled the amazing mechanical behaviour of most of the species belonging to this subfamily of grasses. On their work on bamboo, Dunkelberq, et al. [2] state that with '*regard to its mechanical/technological properties bamboo is superior to constructional timber (softwood) and also to constructional steel in terms of the ratio liveload /deadweight*'. This ratio is a relevant advantage when selecting a material for lightweight structures such as a deployable scissor system.

Additionally, despite misconceptions, it is a durable material when treated under an appropriated method of preservation and proper maintenance to extend its lifespan. Aesthetically, bamboo bars have unique features compared with other timber species, making the use of entire rods, the preferred profile for architectural solutions where the structure will be visually exposed. Most of the challenges imposed by using bamboo bars stem from the connections and joints between elements which still represent a labour-intensive work of craftsmanship. However, recent research applying new technologies of fabrication such as 3D printing has allowed improval of the methods of elaboration, bringing bamboo construction into a more industrialised process of manufacture with high-quality standards.

Previous research has studied bamboo as a material for temporary deployable structures [3], concluding that the implementation of functional connections represents a challenge of structural behaviour and requiring of further study. With the construction of this prototype of a deployable bamboo dome using a scissor-type system within arches, the aim is to study three types of joints proposed which can facilitate the loadbearing behaviour of the structure on its final deployable stage. Also, the performance of the structure accomplishing a function as a temporary exhibition pavilion will be analysed.

2. Form finding

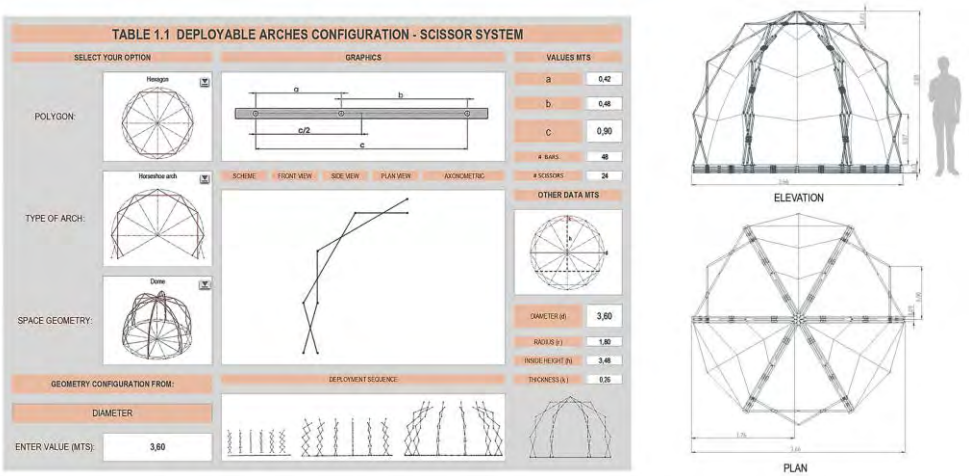


Figure 1: Diagram of the software proposed by Torres-Londoño and Peña-Villamil [4] to form-finding the geometry for the deployable dome structure using scissor type components.

The form-finding approach applied in the design of this deployable double-curved structure using articulated bars -commonly denominated scissor- has been the geometry of regular star polygons. This geometrical method proposed by one of the authors allows an easy definition of the most important construction features of the scissor-type elements: length of the bars and precise position of the articulations. As seen in Fig. 1, by introducing the diameter or the length of the bar as a parameter,

modular bars of the same length can be obtained, facilitating fabrication of the dome structure. The method also offers different geometrical alternatives of arches and its correspondingly volumetric configurations between domes and vaults. The dimensional parameters to design this structure were the 4 x 4 x 4 meter set up for the exhibition pavilion contest in the IASS-Expo 2019. Therefore, it was selected as geometrical plant for the dome, one based on a regular hexagonal geometry with a combination of three horseshoe arches in the section. It gives as a result, a dome with 3.60 m diameter as shown in Fig. 2.

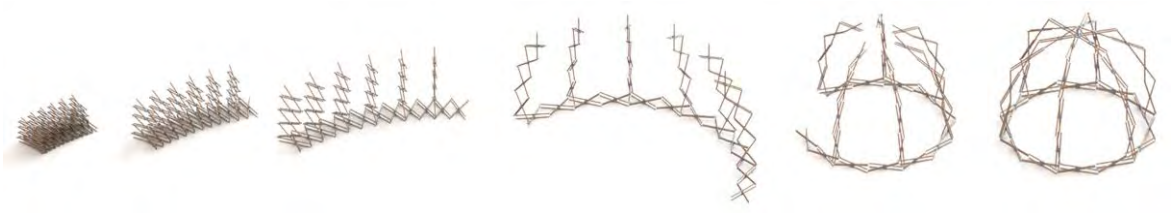


Figure 2: Axonometric, plan and section views showing its correspondent process of deployment of the bamboo dome.

The deployable system consists of six semi-arches assembled over the hexagonal ring, which functions as a guide mechanism to unfold these six elements simultaneously. The stability of the half-arches is attained by increasing the cross-sectional area of them. Therefore, it was added a bar parallel to one of its lineal elements (Fig. 3 a-b). The same action is repeated in all the lineal elements on the ring basement structure. Once it has reached its final deployed position according to with the geometry, the half-arched elements are connected into a central node, aligning them into three structural axes. The central articulation accomplishes the same function as a keystone within an arch, helping to gain the structural stability required by the entire system.

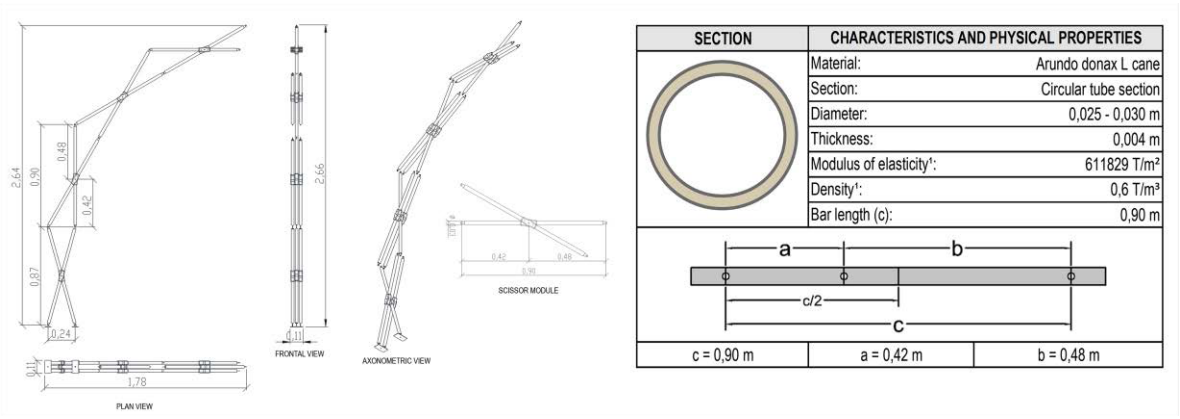


Figure 3: a-b. semi-arch details in section and isometric view. c. Chart of mechanical properties bamboo bars

3. Analysis

Structurally, the deployable dome has been designed with a half horseshoe arch as the main module, composed of four scissor-type elements as illustrated in Fig. 3. Perez Valcarcel [5] presents a wide and complex methodology of analysis for this type of deployable structures by applying matrix calculus. After this mathematical analysis, he summarises that:

'Basically, the bars work under tension-compression stresses, although the central articulation produces non-symmetric bending stress of relevant affectation within the overall behaviour of the structure. Moreover, this behaviour is generated on the weaker segment of the bar, which coincides with the position of the security bolt. For that reason, the profiles with the best performance are those of circular, tubular (hollow-circular) or rectangular geometry'

By understanding the mechanical behaviour expected from the scissor-type arch, the focus of the structural analysis will be on verifying that the deformations and displacements are the minimal allowed when the structure reaches the final position of stability. An analysis of elastic deformations and stresses resultant on the bamboo bars when the arch is deployed to its final stage was carried out by using WinEve v8. It is necessary to input within the software the physical and mechanical properties of the bamboo bars to obtain accurate results from the loadbearing simulation (Fig. 3). The material selection was done based on ongoing research carried out by Cortes-Paez at the University of Bath. On her work, she has studied the mechanical behaviour of bamboo Phyllostachys aurea and a giant reed known as Arundo donax L as construction materials for active-bending structures. One of the advantages of Around donax L. or wild cane is being a local resource and free of cost, commonly used on vernacular Spanish architecture. The cane grows in massive extensions along the Llobregat bank river in Barcelona and is considered an invasive species. Mechanical and physical analysis of specimens taken from the area [6] shown that wild cane bars had an adequate resistance and modulus elasticity for this deployable dome structure.

3.1. Semi-arch discretisation. WinEva (v. 8)

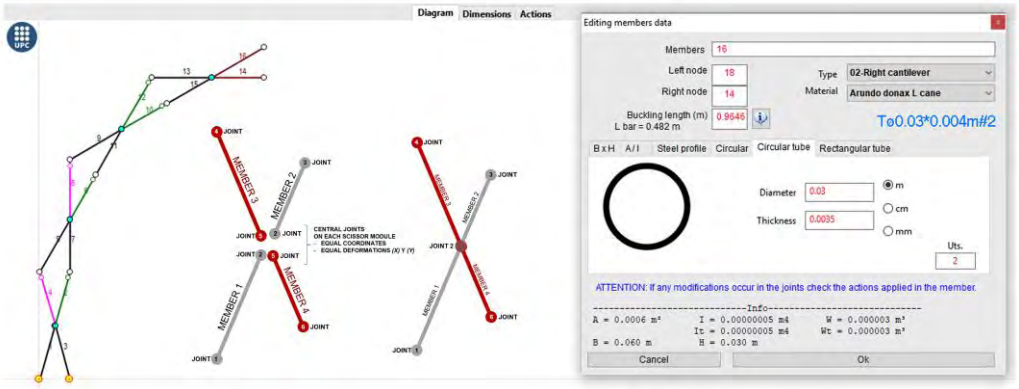


Figure 4: Visual sequence explaining the definition and position of the central nodes

Discretising this semi-arch structure on WinEva [7] requires deconstructing the scissor-type element into its two main components:

- The bars; where two collinear bars configure a single lineal element.

- Nodes; which correspond to the two ends of each bar and to the central articulation that attach two overlapping bars.

Fundamentally, the structural model of the deployable semi-arch consists of a line drawing of the geometry in any CAD software. This file is imported to WinEva, where the lower node of the external bar is positioned on the 0.0 coordinates. Finally, the physical and mechanical properties of the bamboo material and diameter of the cross-section are input on the software as illustrated in Fig. 4.

To analyse a scissor deployable arch structure on WinEva we need to specify that each module is configured by four bars interacting by the central node. This specification helps the software to identify that two linear elements integrate each scissor module, as shown in Fig. 4. Obtaining an accurate simulation of the mechanical behaviour of the scissor module in its final stage of deployment on WinEva, requires an additional step: a central node with equal deformations within the axis (x) and (y) must be inserted. Both nodes must coincide with the same position where the central node is located on each scissor module. To assure a precise location we need to input the same coordinates for each node as exemplified in Fig. 4. The the ending nodes on each bar are defined, verifying a correct collinear relationship of the two bars that compose the scissor module. This process is repeated within each scissor module that configures the deployable semi-arch.

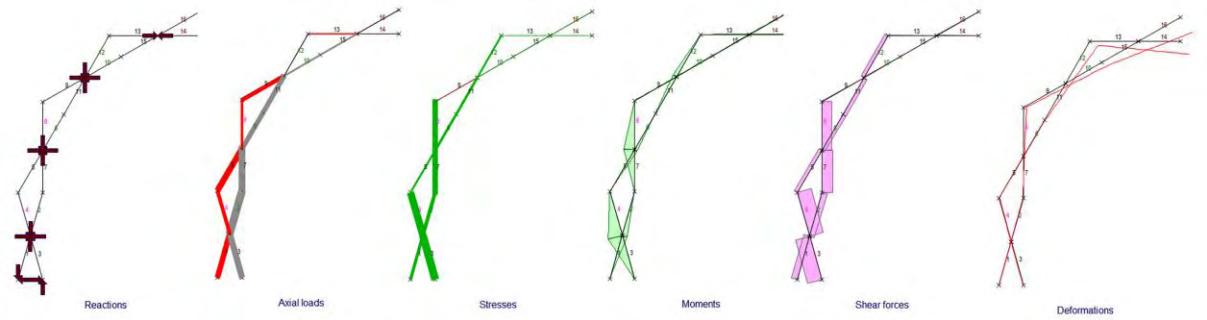


Figure 5: Sequence of diagrams plotted from WinEva simulation analysis of the semi-arch in its final stage of deployment.

Having defined the physical features and design parameters of the semi-arc, the next step is to carry out the structural analysis. For this analysis, the primary load supported by the dome is its own weight, which acts as a uniformly distributed load along the bamboo bars. Once the simulation is done, the software plots different diagrams correspondingly with the reactions, axials and tensional stresses, ultimate moments, shear and deformations (Fig. 5). The deformations diagram is crucial in finding the ideal position before the final deployable stage, on which the semi-arch will coincide with the geometry selected. The own weight of the structure attains this position while the semi-arch scissor is in movement.

3.2. Analysis of deformation within the dome structure

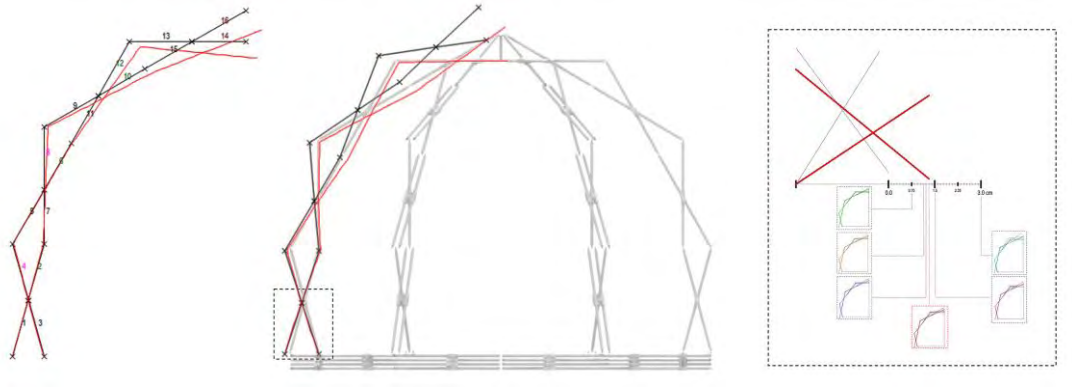


Figure 6: Method to find the ideal position of deployment to assure correct assembly of the central joint.

One of the most significant challenges designing this type of deployable dome is assuring that when each of the six semi-arches is deployed to its final stage, they will be in the right place to be assembled with the central joint and simultaneously correspond to the final design geometry. The methodology proposed by Torres-Londoño and Peñ -Villamil [4] uses the deformation's diagram and outcoming data from the simulation done with WinEva to calculate this position. In her research, she uses a combination of two parameters, such as the own weight of the arch and the deployment position of the scissors to sit all the semi-arches in place by means only of displacement forces. As illustrated in Fig. 6, on the top-ending scissor, the distance of nodes 1 and 2 must correspond with the height of the central joint piece but also reach the geometry of design of the semi-arch. It will facilitate the assembly of both components when the entire structure reaches the final stage of deployment. On this scissor-type semi-ach, the movement of the top-ending scissor element is controlled by the displacement of the bottom-ending scissor. If we run a series of pondered simulations where @ is a numerical value assigned to the distant between axis of deployment (Fig.6), it is possible to find the ideal position for the nodes 1 and 2 that simultaneously agrees with the geometry of the design proposed for the half-arch.

4. Fabrication and assembly of the dome

As has been demonstrated previously, the utilisation of computational models to determine the structural behaviour in deployable scissor-type structures has facilitated their design and calculation. However, physical models are fundamental to a realistic perspective on the challenges involved in its construction, due to the complexity involved within the deployment and functionality of the hinged connections. As this type of structures is less conventional than other systems, there is a limited supply in the construction industry of suitable hinged joints to build a medium or large span structure. In the case of this deployable dome, before the elaboration of a full-scale prototype a 1:2 scale model was built with two objectives. First, to verify the geometrical and mechanical simulations obtained from WinEva to identify possible structural failures. Working with a physical model enables the improvement of the computational model, providing a more accurate structural analysis (Fig. 8 and 9).



Figure 7: Diagram of the deployable dome and its corresponding scissor modules.

The second objective was to explore different hinged connections using a variety of mechanical pieces available in the industrial market. The major challenge was finding pieces compatible with the dimensions of the bamboo bars selected. Bamboo is a material that is not as precise and homogeneous in dimensions as man-made materials such as steel or aluminium, so it adds more complexity to the construction process. Nonetheless, the availability of new technologies such as 3D printing makes it possible to fabricate bespoke pieces at a low cost. In this section is detailed the design and functionality of the mechanical joints created for this deployable dome structure.

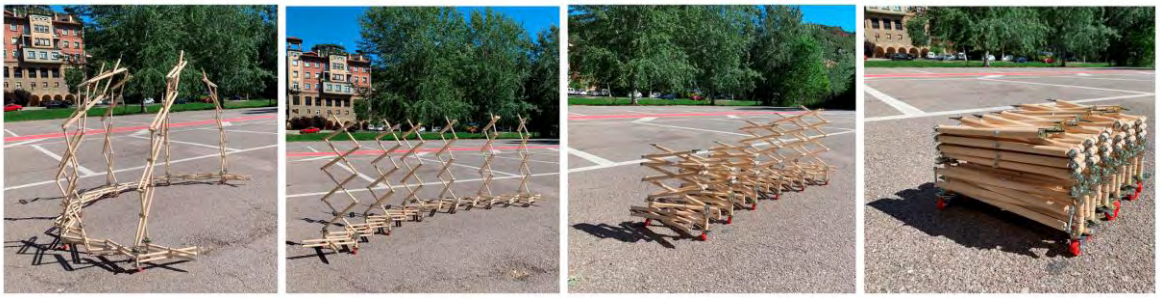


Figure 8: a. Physical model 1:2 deployed showing a single horseshoe arch and the hexagonal support ring.

4.1. Single-hinged and pinned connection on the support ring

This piece plays the role of transmitting the loads from the semi-arches to the ground as illustrated on Fig. 10. Due to it, the joint has restricted movement in the (y) axis while it allows rotation in the (x) axis. Overall the hexagonal ring has 12 of this type of hinged joints, two per each semi-arch. This connection allows the simultaneous deployment of the support ring and the six semi-arches. Against the ground has been installed a roller system to facilitate the radial movement of deployment and folding carried out by the hexagonal ring as seen in Fig. 9 and 10. This joint was designed using fittings available from the timber furniture sector, however, an alternative connection using 3D printing technology has been proposed to reduce the number of components.

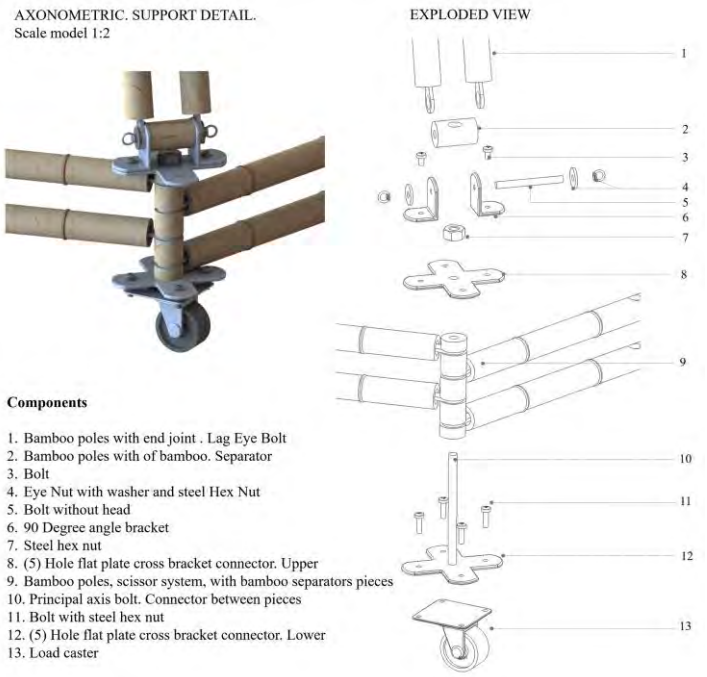


Figure 9: Photo of the single-hinged and pinned connection on the support ring in the scale model. b. Detail of the 3D design of the piece in Solidworks

4.2. Double-Hinged axial joint

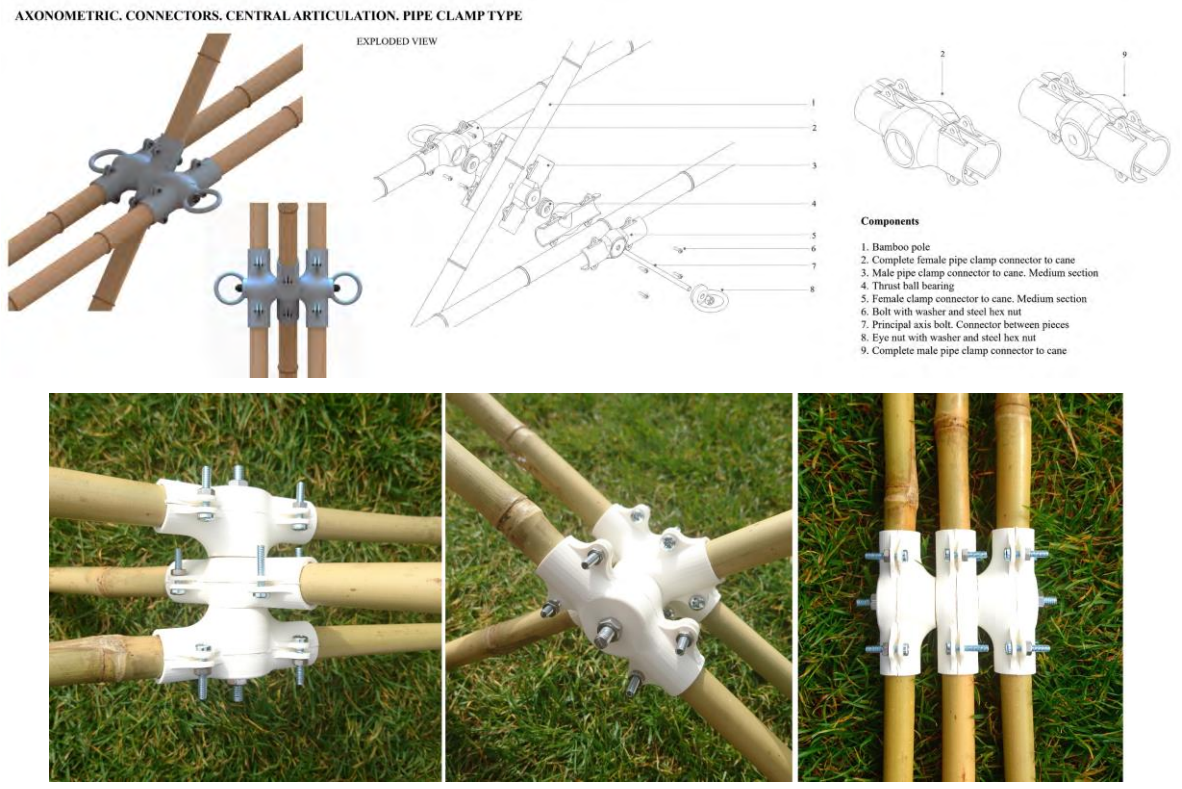


Figure 10: a. Detail of the components of the type 1 double-hinged axial joint designed in solidworks. b. Photos of the 3D printed joint using wild cane bars on real scale.

This connection is essential to allow the axial movement of the bamboo bar elements that integrated the deployable scissor modules within the semi-arch. The connection must enable a rotational movement with a minimal friction resistance in the vertical axis of the scissors. For this prototype has been developed two types of hinged axial joints. One illustrated in Fig 10. which would be located in the central node of the scissor module. This joint has been designed to allow the insertion of an entire bar assuring continuity of the load transfer within the arch. The mechanism of this piece joints simultaneously three hinged bars by a system of male-female connectors

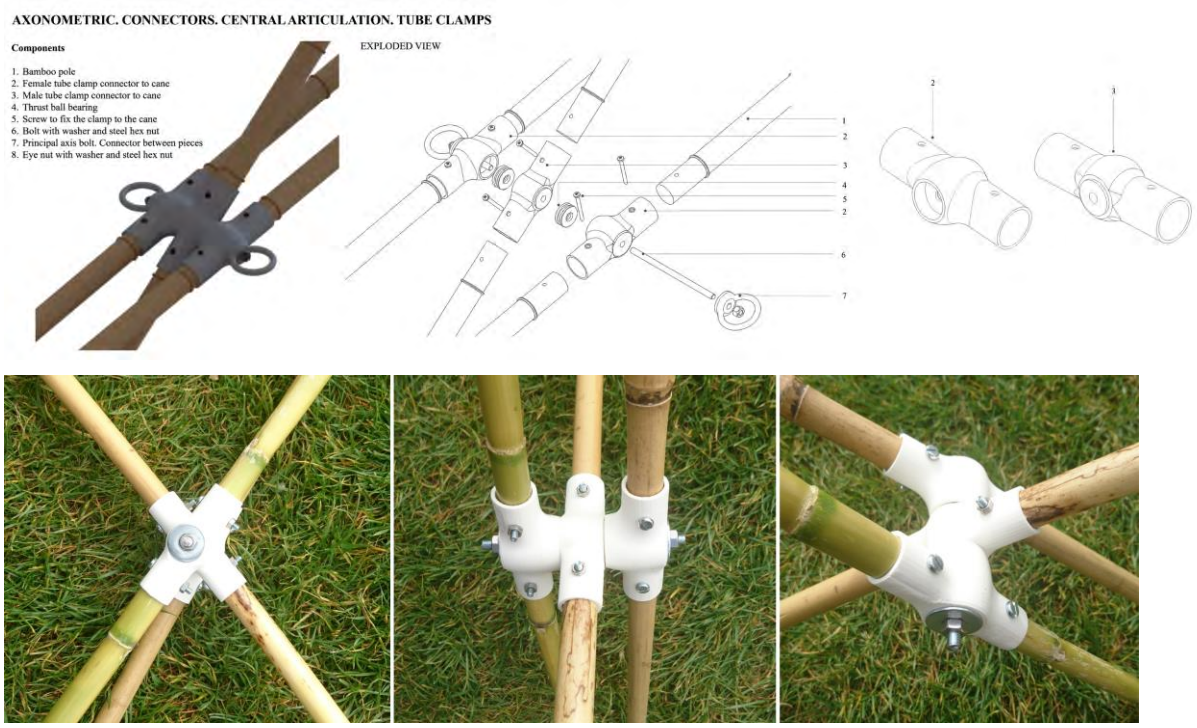


Figure 11: a. a. Detail of the components of the type 2 double-hinged axial joint designed in solidworks. b. Photos of the 3D printed joint using wild cane bars on real scale.

The second type of double-hinged joint is shown in Fig 11. This connection has been designed to interconnect deployable scissor modules. Consisting of a hollow tubular section were the endings of the parallel bars are fitted by pressure and secured with a bolt. This joint has been designed to assuring continuity and alignment of the collinear bars in the same plane. The mechanism of this piece joints simultaneously three hinged bars by a system of male-female connectors.

4.3. Central top fixed joint

This joint is crucial on giving the stability and stiffness required as it functions similarly as the keystone within a traditional dome structure. The design of this joint includes two components. One is a conical nucleus with six jointing plates which are aligned configuring the three geometrical axes of the structure. These joining plates will be connected to a tapered hollow fitting inserted at the ends of the two bamboo bars of the top-ending scissor. When all the semi-arches reach the position of deployment calculated, both joining plates are assembly using a bolt to create a rigid pinned joint as seen in Fig. 15. The height of the central piece has been defined based on the geometry assigned to the deployable arch as it was explained in § 3.4. The diameter and size of the fitting at the end of the bamboo bars has been set up based on an average dimension from the bamboo bars selected.

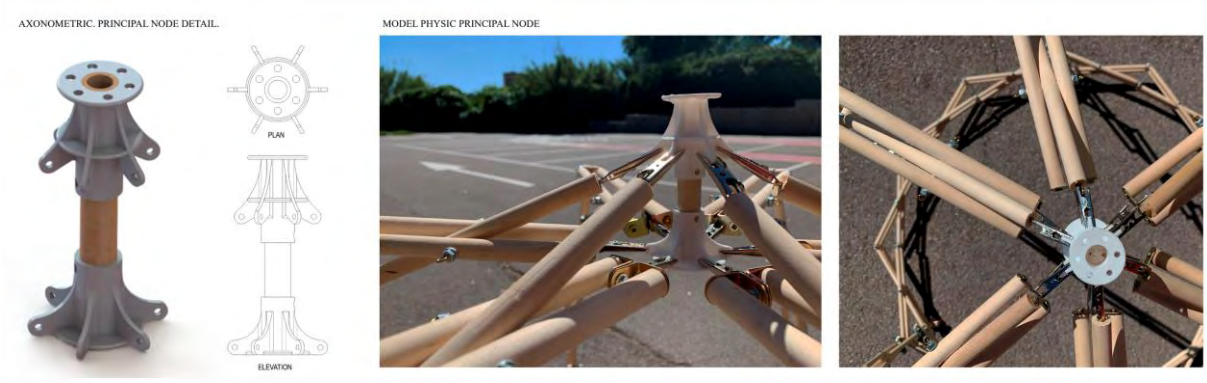


Figure 12: a. Detail of the central top fixed joint designed in Solidworks. b. Photo of the 3D printed joint installed in the 1:2 scale model.

5. Results

In one hand, the results obtained from the process of design and manufacture of this pavilion contributes to extend the knowledge regarding the potential of bamboo and cane bars within the construction of deployable scissor structures. This first approach to the material through the building of a physical scale model enables the visualisation of the challenges faced concerning the functionality and constructability. However, the fabrication of the real prototype has been postponed while are carry out additional mechanical testing an improvement on the three types of joints proposed. New possibilities of using other species of bamboo bars have emerged linked to funding granted by a local sponsor. Bambusa Estudio, which is a bamboo supplier in the city of Valencia, Spain, has offered to sponsor the construction of this pavilion using part of their products. Results obtained from building the scale 1:1 bamboo dome will be published in upcoming papers.

6. Conclusions

This prototype validates the methodology proposed by Torres based on the use of regular polygons to design and calculate deployable scissor-type domes assisted by WinEva software. The novel contribution of this paper has been the implementation of bamboo bars as the primary material for the construction of the scissor modules. Bamboo is a natural material with a low-carbon footprint when compared with aluminium, PVC or GFRP bars commonly used in the construction of this typology of lightweight structures. By using bamboo as the main material for this deployable dome, we are not only considering the advantageous mechanical properties inherent to it. The use of bamboo on this proposal includes an implicit consideration about the life-cycle of this temporary structure, aiming to reduce the waste produced during manufacture and the possibilities of being recycled after accomplishing its purpose, a feature that must be a requirement for most of the temporary and ephemeral structures.

Overall, bamboo is a low-cost material which is available around the world in different diameters and thickness. It does not require complicated methods to produce it. However, the heterogeneity of the bars involves additional complexity on the construction process of the dome structure regarding the type of hinged joints and fixings required to assure the proper functionality of the system. Therefore, the development of these pieces has centred most of the design proposal created for this semi-arched deployable dome. Designing the fittings and connections for a scissor-type structure implies a deep understanding of the stress and deformations on each joint, seeking to reduce the friction produced by the rotational movement of the bars. Also, it is important to continue expanding the different alternatives available to fabricate this type of mechanism. This paper demonstrated that by using a new method of fabrication such as 3D printing, which produces affordable bespoke solutions enabling the construction of this scissor semi-arched deployable dome.

Acknowledgements

The authors of this paper want to acknowledge the contributions and support given by Bambusa Estudio, who was willing to sponsor the construction of this pavilion during the contest exhibition. Also wants to thanks to the technicians at the timber and CAD-CAM workshop at the University of Bath.

References

[1] B. Sharma, K. A. Harries, D. Trujillo, and L. D. Lopez, "Bamboo material characterisation " in *Nonconventional and Vernacular Construction Materials - Characterisation, Properties and Applications*, ed: Elsevier, 2016, pp. 17-22.

[2] K. Dunkelberq, J. Fritz, F. Otto, S. Gass, and J. Arcillo-Lozada, *Bamboo : bamboo as a building material : building with vegetal rods* 2nd ed. vol. 31. Stuttgart: Stuttgart : Karl Kra¨ er, 1992., 1992.

[3] A. Maurina and B. Prastyatama, "Bamboo Deployable Structural Systems: An Exploration Study in Responding to Rapid Alteration Challenges," in *Proceedings of the 18th International Conference on Sustainable Environment and Architecture (SENVAR 2018)*, Indonesia 2018.

[4] N. P. Torres-Londoño and D. M. Peñ -Villamil, "Deployable Arches Based on Regular Polygon Geometry," 2017.

[5] F. Candela, *Arquitectura transformable*. Sevilla: Universidad de Sevilla, 1993.

[6] R. Andújar M. , M. Fando M. , O. Palou J., B. Peris R. , and J. Maristany C. , "Estudi del comportament mecànic d'arcs de canya Arundo Donax.," *Quaderns d'estructures,* vol. 46, pp. 38-52, April 2013.

[7] R. Sastre, "WinEva," 8, Ed., v.8 ed. Barcelona, Spain: E.T.S. Higher Technical School of Architecture of Vallès, Sant Cugat del Vallès, UPC. Polytechnic University of Catalonia,, 2018.

Proceedings of the IASS Annual Symposium 2019 – Structural Membranes 2019
Form and Force
7 – 10 October 2019, Barcelona, Spain
C. Lázaro, K.-U. Bletzinger, E. Oñate (eds.)

Design and Construction of an Innovative Pavilion Using Topological Optimization and Robotic Fabrication

Ding Wen BAO[a,b], Xin YAN[a,c], Roland SNOOKS[b], Yi Min XIE[a,d,*]

[a,*] Centre for Innovative Structures and Materials, School of Engineering, RMIT University,
Melbourne, 3001, Australia
mike.xie@rmit.edu.au

[b] School of Architecture and Urban Design, RMIT University,
Melbourne, 3001, Australia
[c] Centre of Architecture Research and Design, University of Chinese Academy of Sciences,
Beijing, 100190, China
[d] XIE Archi-Structure Design, Shanghai, 200092, China

Abstract

This research explores innovations in structural design and construction through the generative design technique BESO (Bi-directional Evolutionary Structural Optimization) [1] and the application of robotic fabrication to produce efficient and elegant spatial structures. The innovative pavilion discussed in this paper demonstrates a design and fabrication process and the collaboration between architecture and engineering research groups through a series of small-scale test models and a full-scale model of topologically optimized spatial structures. The focus of this work is the use of a modified BESO technique to optimize the structure which features branches of various sizes, inspired by Gaudi's Sagrada Familia Bacilica, and the introduction of large-scale robotic 3D printing developed at RMIT University. The advantages of the new design and construction process are efficient material usage and elegant structural forms.

Keywords: topological optimization, multi-agent, robotic fabrication, prefabricated building, pavilion, mass customization

1. Introduction

Throughout the history of architecture, the expression of building form has been limited by traditional building method, in which even slightly irregular forms can significantly change the time and cost needed for construction [2]. However, Since the introduction of computational aided design technology into the architectural design at the end of the 20th century, the topic of form-finding based on structural performance has gained new momentum [3]. The development of architectural technology is closely related to the evolution of structural morphology, from barrel arches and domes in the period of Greece and Rome to pendentives and flying buttresses in the period of Byzantium and Gothic; from physical models used by Antonio Gaudi and Frey Otto to the application of topological optimization technology to architectural designs, architectural morphology and structural optimization have always been reinforcing each other.

The Bi-directional Evolutionary Structural Optimization (BESO) method [1] is one of the most popular techniques for topology optimization. With the further enhancement of the BESO technique by Mike Xie and his team, more and more architects will have opportunities to use a new intelligent method to work with the computer interactively, to create innovative, efficient and organic architectural forms and facilitate the realization of mass customization in the construction industry through the introduction of

Copyright © 2019 by Ding Wen BAO, Xin YAN, Roland SNOOKS and Yi Min XIE
Published by the International Association for Shell and Spatial Structures (IASS) with permission.

advanced 3D printing technologies, such as large robotic 3D printing and some hybrid fabrication strategies developed by Roland Snook and his research team in RMIT Architectural Robotic Lab. The concept of topological optimization and the inspiration of Gaudi's Sagrada Familia Basilica will be reflected through the pavilion form-finding and its optimization. The new approach of generative architectural design and fabrication will be introduced in this project, which explores the architectural implications of topological optimization design through robotic 3D fabrication.

2. Morphological conditioned design based BESO method

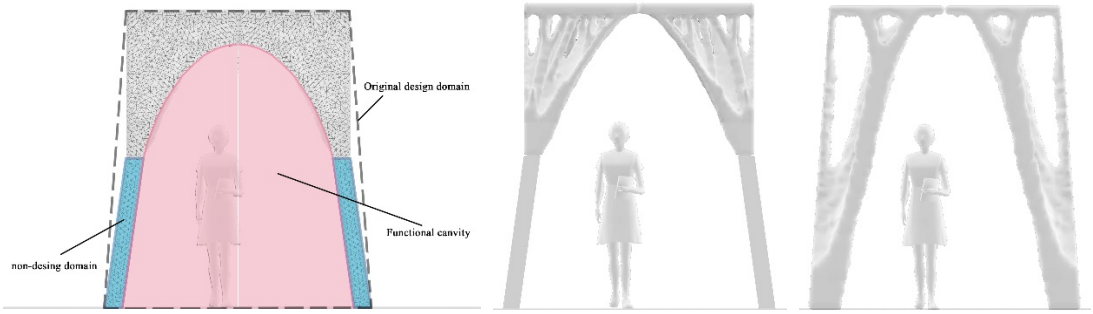
Using the BESO method, architects and engineers can generate many elegant and organic forms with high structural performance. However, there are always inevitable constraints besides structure behavior, such as functional requirements, construction limitations and aesthetic preference. As a result, it is necessary to add some controlling methods into BESO process to obtain a form which can meet composite demand. In this work, three main morphological conditioned design methods are introduced.

2.1. Geometrical restriction

In many practical projects, the geometrical restriction method is the most convenient and effective way for designers to modify BESO results with some functional requirements manually and explicitly. For functional cavities, like corridors and windows, they should be dug out of the geometries before generating the calculating meshes and functional solids can be also reserved in BESO process by setting them as the non-design domain. For example, the original design domain showed in Figure 1(a) without any modification generates the form in Figure 1(c). However, with setting the functional cavity and non-design domain into the model before calculation, the final design can be partly manipulated by designers intently Figure 1(b) [4].

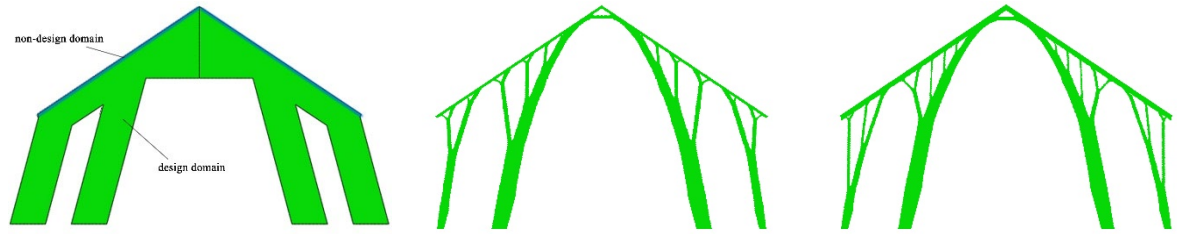
2.2. Properties influence

Another way to indirectly influence the BESO result is to set the material properties and evolutionary parameters. With the different relative material Young's modulus, the distribution density of BESO structures between the two materials can be designed purposefully [5]. For example, Figure 2(a) shows a façade model with the bottom boundaries fixed in all displacements and pressure acted on the top boundaries. And the optimized structures vary significantly with the different material properties of the top boundaries (blue areas in Figure 2).



(a) (b) (c)

Figure1: The geometrical restriction in BESO method



(a) (b) (c)

Figure 2: Façade optimized structure with different relative material properties:
(a) the load conditions; (b) the BESO result with solid material in non-design domain; (c) the BESO result with soft material in non-design domain

2.3. Prototype inspiration

Gaudi's understanding of 'structural optimization' in natural form and his strategy of physical structural modeling are very conceptually close to the principle of BESO and BESO's logic of form finding [6] (Figure 3). As an evolutionary algorithm BESO can not only generate forms independently, but also collaborate with other prototyping techniques in optimization process. The well-known Sagrada Familia in Barcelona is designed based on anti-hanging physical models by Anthony Gaudi. As a result, using a new topology optimization tool Ameba [7], this work integrates BESO method with Gaudi's prototyping strategy to obtain innovative structure/ pavilion (Figure 4)



Figure 3: The similarities between Sagrada Familia Basilica and pavilion's top and columns by BESO method



Figure 4: The process of Sagrada Familia inspired pavilion design by BESO topological optimization method

3. Large advanced automated robotic arm 3D printing process

3.1. Application of KUKA Robotic Fabrication

The Advanced Manufacturing Precinct at RMIT University hosts a range of 3D printers for metallic and polymeric materials and in the Architectural Robotics Lab there are several Kuka robots with various functions (Figure 5)



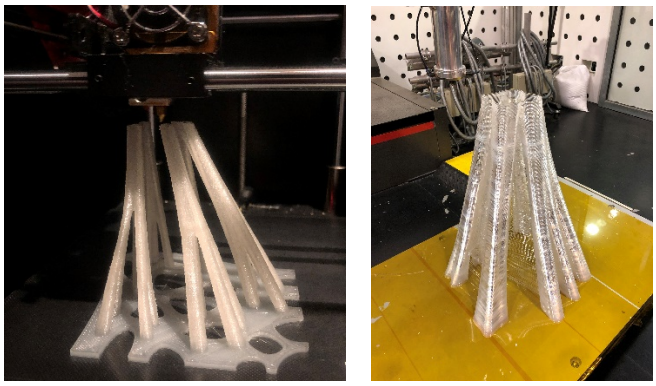
Figure 5: RMIT Architectural Robotic Lab

These new techniques for 3D printing fireproof polymer developed by Roland Snooks and his team at RMIT architecture, are now being used to build structures that can meet building code, which is used in the National Gallery of Victoria (NGV) interior pavilion panels and partition wall of Monash University SensiLab (Figure 6).



Figure 6: Monash SensiLab and NGV Floe pavilion

It is an innovative technology combination of KUKA 6 axis robot fitted with a plastic extruder that designed for building scale prefabricated architectural components, compared with the significant limitations of traditional small-scale plastic 3D printing (Figure.7).



(a) (b)

Figure 7(a): Small Scale Desktop 3D printer (printing area: 200mm x 200mm x 300mm)
Figure 7(b): Large Robotic 3D printer (printing area: 800mm x 1000mm x 1800mm)

3.2. Code development for printing fractal-like geometries

The whole tree branches system of the pavilion columns comprises four main translucent tree branches-like polymer columns printed by a desktop printer first (Figure 8) then by a large robotic printer.



Figure 8: 3D printing model testing by small scale desktop 3D printer

The updated code of printing path helps robotic to achieve the aim of printing fractal-like geometries rather than non-stop and one-curve printing path through introduction “start-stop” script into the original printing C# code (Figures 9 and 10).

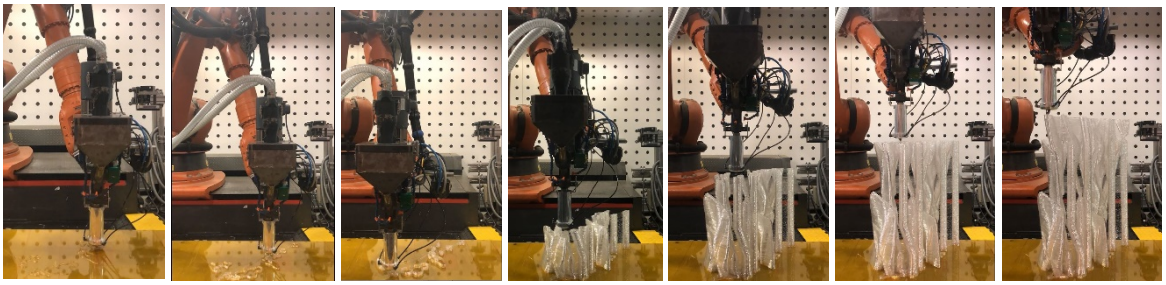


Figure 9: The process of robotic large 3D printing, using the updated code for project exhibited in Hong Kong

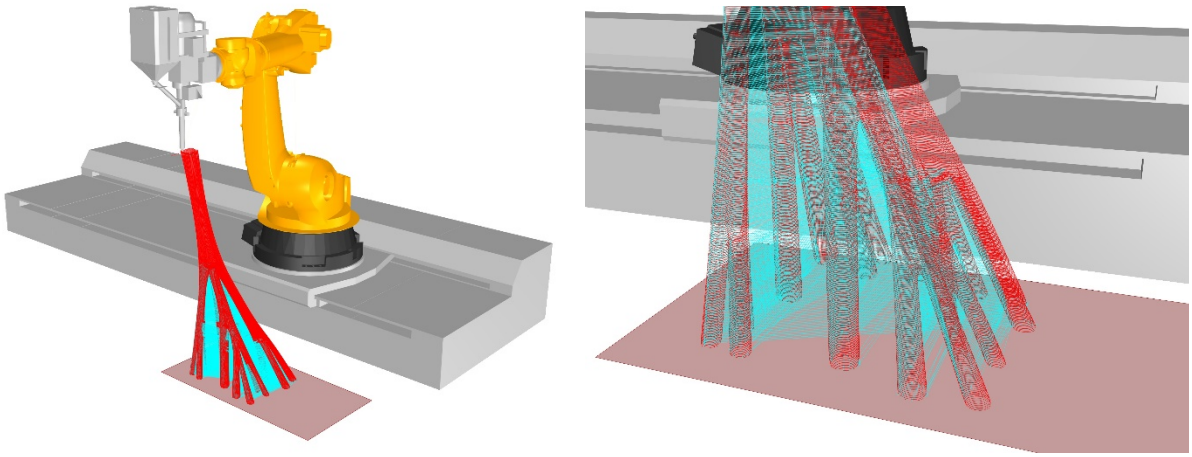


Figure 10: Grasshopper simulation of robotic printing path
(red ones are extruded path & blue ones are non-extruded path)

3.3. Testing of polymer materials for 3D printing quality

Material behavior in printing process is another issue that is hard to control. In this work, the relationship between printing parameters and material stiffness is explored with a series of trials of fractal-like geometries (Figure 11). From table 1, stability of printing will be significantly influenced by printing speed once it is more than 200 mm/s; the Z height impacts the stability and speed of printing; and bead size will cause the thickness of extrusion; one of the most influent parameters is extrude temperature, it significantly effects the transparency of printing result. Thus, the most successful result is with the 60 mm/s, 2.8 mm Z-height, 4.2 bead size and 210 degree extrude temperature.

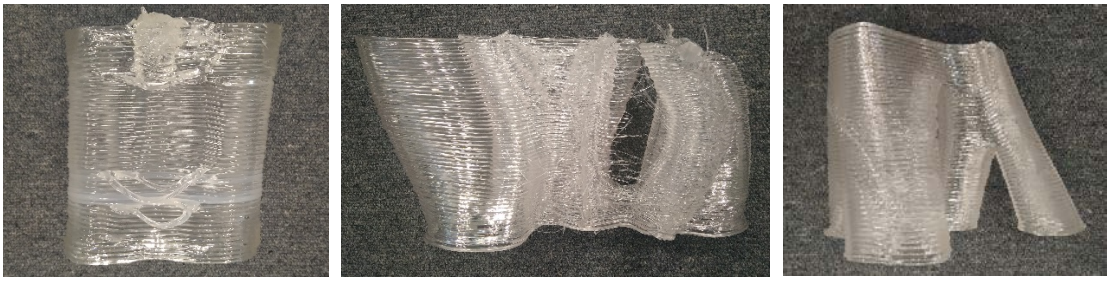


Figure 11: Printing example with various qualities (from left to right: bad to good printing qualities)

Table 1: Testing results of polymer materials with various parameters

	Speed (mm/s)	Z-Height (mm)	Bead Size	Bead Size	Extruder Temp	Mass (kg)	Height (mm)	Time
			Programmed	Actual				
1	60	3	5	3.2-4.2	210	2.6	110	60
2	70	3	5	3.8-4.8	210	1	48	24
3	70	3	6	4.5-5.5	210	3.6	115	60
4	70	2.6	6	5-6.5	205	5	150	90
5	70	2.6	7	5-10	205	4.3	90	70
6	60	3	7		200			
7	200	3	6.7		200	3.5	120	70
8	400	3	6.5	FAIL	190	FAIL	FAIL	40
9	200	3	6.5		205	3.6	95	65
10								

3.4. Printing Constraints

Current technique has some printing limitation by the issue of large overhang angles without any supporting material (Figure 12).Therefore a new BESO algorithm is currently being developed to resolve this issue in the near future.

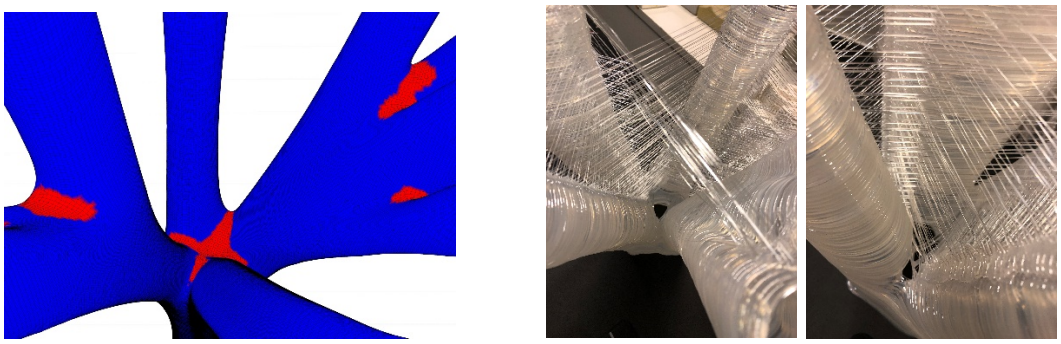


Figure 12: The result of overhang angles issue in digital and printed models: red part in digital model (left) is over 32-degree overhang angles that fail to print showing in physical models (right)

4. Conclusion

This innovative pavilion is a demonstration of the combination of new design and construction techniques, explaining the design and construct process of the pavilion through exploration of emerging technologies in both digital design and advanced manufacturing, which are respectively topology optimization-based form-finding and large-scale robotic 3D printing.

The testing results from a series of prototypes clearly illustrate that the optimized structures may play a useful role in architectural form exploration or provide inspirations for it. The Bi-directional Evolutionary Structural Optimization (BESO) method provides many possibilities in the process of creating innovative and efficient forms. Each geometrical restriction, different material properties and algorithmic parameter may result in different forms, meeting various requirements set by the user.

Also, compared with the traditional small-scale fused deposition modeling (FDM) 3D printing, robotic 3D printing has much greater potential to serve the building industry due to its capability of producing large-scale printed architectural components with high structural performance.

However, major barriers to the implementation of these technologies in the building industry include a lack of compression and strength test, UV degradation of the printed polymer components as well as the significant issue of printing overhang angle, even though some of such printed structures have passed the fire testing and building codes in Australia as well as partially been put into use. In this present study, some of the advantages and insufficiencies of the new techniques have been examined. Much more research and improvement are required in the future. Once the aforementioned issues are resolved, these new technologies could be widely applied to the mass customized design and manufacturing in the building industry.

Acknowledgements

The authors would like to thank several colleagues whose support helped fulfill the research project described in this paper:

- Mr. Charlie Boman and Mr. Hesam Mohamed (Snooks Research Lab, RMIT)
- Mr. Yulin Xiong (Centre for Innovative Structures and Materials, RMIT)

References

[1] X. Huang, Y. M. Xie, *Evolutionary Topology Optimization of Continuum Structures: Methods and Applications.* Chichester: Wiley, 2010

[2] K. G. Lee and J. S. Sun, "Clay Robotics," *Robotic Futures*, Tongji University Press, pp. 113-117, 2015

[3] Y. M. Xie, Z. H. Zuo, X. Huang, T. Black and P. Felicetti, "Application of Topological Optimization Technology to Bridge Design," *Structural Engineering International*, vol. 24, pp. 185-191, 2014.

[4] K. Yang, Z.-L. Zhao, Y. He, S. Zhou, Q. Zhou, W. Huang and Y. M. Xie, "Simple and effective strategies for achieving diverse and competitive structural designs," *Extreme Mechanics Letters*, vol. 30, 100481, 2019.

[5] Z. L. Zhao, S. Zhou, X. Q. Feng and Y. M. Xie, "On the internal architecture of emergent plants," *Journal of the Mechanics and Physics of Solids,*vol. 119, pp. 224–239, 2018.

[6] J. Burry, P. Felicetti, J. Tang, M. Burry and Y. M. Xie, "Dynamical structural modelling: a collaborative design exploration," *International Journal of Architectural Computing*, vol. 3, pp. 27-42, 2005

[7] http://ameba.xieym.com

[8] X. Huang, Y. M. Xie and M. C. Burry, "A new algorithm for bi-directional evolutionary structural optimization," *International Journal of the Japan Society of Mechanical Engineers*, vol. C49, pp. 1091-1099, 2004.

[9] P. F. Yuan, H. Chai and Y. M. Xie, "Towards a structural performance-based architectural design in digital age," *Architectural Journal*, vol. 11, pp. 1-8, 2017.

[10] S. Bialkowski, "Structural optimization methods as a new tool for architects', *Design Tools Explorations*, vol.2, eCAADe, pp. 255-264, 2016

Proceedings of the IASS Annual Symposium 2019 – Structural Membranes 2019
Form and Force
7 – 10 October 2019, Barcelona, Spain
C. Lázaro, K.-U. Bletzinger, E. Oñate (eds.)

Design of discretized acrylic shells with heat-induced form-finding

Lisa RAMSBURG*, Albert CHAO[a], Edward M. SEGAL[b], Powell DRAPER[c]

*schlaich bergermann partner
555 8th avenue, suite 2402, New York, NY 10018
lkramsburg@gmail.com

[a] Architect
[b] Hofstra University
[c] schlaich bergermann partner

Abstract

Two Blue Shells is a pavilion built for an exhibition of innovative lightweight structures at the 2019 *IASS Annual Symposium* in Barcelona. This paper presents the ongoing research process for the proposed design. The pavilion consists of two discretized acrylic plastic shell structures that utilize the response of materials exposed to heat as a generator of form. Adding to the ongoing discourse surrounding the challenge of plastic in the waste stream, *Two Blue Shells* proposes a novel way to reuse small flat sheets of acrylic scrap to create large doubly-curved shell structures without complex molds or fabrication technology. Digital simulations are informed by small-scale prototypes and are used for analysis and iteration of the full-scale form. Technical considerations include connection design, overall strength and stability, and the influence of discretization on global and local curvature. The frame used to hang the acrylic in the oven is an integral aspect of the project. While the frame must respond to limitations based on available oven sizes, it also provides opportunities to influence the final form through manipulation of the boundary conditions. The design of *Two Blue Shells* integrates a contemporary material with an acknowledgement of past forms like tiled roofs and shell structures found in and around Barcelona. The methodology presented looks to the past as well as the future to seek design solutions to current environmental challenges.

Keywords: Form-finding, shell structure, plastic, acrylic, pavilion, discretized shell

1. Introduction

The advent of synthetic plastic in the 20th century led to the creation of a vast array of products, from specialized medical equipment to ubiquitous packaging of everyday goods. Plastic is a unique and versatile material as it is light, strong, and can be molded into complex forms. Despite a multitude of advances and widespread use, plastic today has a complex relationship to the environment; its overall product life cycle is currently being re-evaluated for its role in the larger ecosystem. *Two Blue Shells* contributes to this dialogue by proposing an adaptive reuse of acrylic plastic by diverting it from the waste stream and repurposing it as a structural material.

1.1 History of plastic in architecture

Synthetic plastics were developed at the beginning of the 20th century as an alternative to natural rubber [1]. World War II saw the development of many types of plastic for applications in military technology. Following the war, the use of plastic in architecture surged as designers sought to harness the potential of a material that could be manipulated and shaped freely to generate non-orthogonal forms. Exhibitions like the IKA (International Plastic Housing Exhibition) introduced futuristic plastic houses that

Copyright © 2019 by Lisa Ramsburg, Albert Chao, Edward M. Segal, and Powell Draper
Published by the International Association for Shell and Spatial Structures (IASS) with permission.

designers intended for mass production [2]. Such formal and material explorations embodied cultural trends; as expendable products like food wrappers and ball-point pens became a familiar part of society, attitudes began to shift surrounding the acceptable lifespan of products. In 1963, the experimental architecture group Archigram touted this acceptance as "a healthy and altogether positive sign" and the "product of a sophisticated consumer society." They encouraged the acceptance of expendability beyond products to architecture and the built-environment [3]. Despite the call to action, plastic houses never achieved mass production, but plastic did become an integral material in the building industry.

Today, the attitude toward plastic has shifted significantly; rather than being considered a symbol of modern society, throw-away culture and the uncontrolled use of non-renewable resources are scorned as unsustainable elements of a society that is irreparably harming the planet. The amount of plastic in the waste stream is a challenge and an opportunity that has brought forth a new call to action for designers to imagine a more sustainable future. To contribute to this ongoing discourse, *Two Blue Shells* proposes a novel way to reuse acrylic plastic in the built environment.

1.2 Acrylic

Acrylic (Poly methyl methacrylate, or PMMA) was introduced under the trade name Plexiglas in Germany in 1933. Distinguished from other plastics by greater light transmittance and resistance to UV and weather damage, acrylic became a popular alternative to glass during World War II [1].

Though acrylic can be easily formed into shapes with complex curvature, it is commonly used in the building industry as a flat sheet for applications like signs, screens, and windows. Acrylic can be recycled by extracting and using the MMA monomer to create new acrylic. The process requires heavy oil and electricity for depolymerization, recovery, and purification, but overall has a lower environmental impact in terms of life cycle greenhouse gas emissions and fossil resource consumption than extracting fresh MMA from petroleum [4]. The demand for acrylic recycling depends on the availability of raw material. Liquid crystal display (LCD) products (television sets, laptops, and monitors) have the potential to offer a consistent source of recycled material [5], but this supply could change as technology develops and entertainment trends continue to shift. Reuse rather than recycling is a way to create a closed material loop without expensive and complicated recycling processes. *Two Blue Shells* reuses small, readily available pieces of acrylic scrap by connecting them together to form an aggregated sheet that is deformed when exposed to heat to create an efficient shape.

1.3 Form-finding of shell structures

Physical form-finding using hanging fabric [6] or chains [7] is a well-documented method for finding optimal shapes for shell structures. In these experiments, materials with little to no bending stiffness deform under their own weight into tension-only forms which can be hardened and directly inverted into compression-only forms or scaled for the development of larger structures.

Heat-induced form-finding is a less common method in which a material is heated and its stiffness decreases until it acts like a tension-only sheet when deforming under its own self-weight. When cooled, the deformed sheet hardens and retains the funicular form. Newell and McGee have applied this technique to manipulate glass into double-curved forms using custom slumping equipment, digital tooling, and computational modeling techniques [8].

With a glass transition temperature of around 105°C, acrylic can be manipulated at temperatures below those of glass [9]. Acrylic can also be cut by hand with a utility knife or precision cut with a laser cutter. Therefore, small-scale prototypes can be easily and quickly tested in a small-scale oven. Bellés et al. have used heat-induced form-finding of acrylic to create small-scale design models of structural shells that are compared to virtual simulations generated with finite element software [10]. Bradley and Gohnert also used small-scale acrylic models to analyze the extensive cracking of the shells of the

Mapungubwe Interpretation Center [11]. *Two Blue Shells* expands on and takes a new direction from this work by investigating the use of heat-induced form-finding to directly create a full-scale structure.

2. Approach

The approach to preparing for full-scale fabrication begins with small-scale design models to better understand material properties and subsequent forms that can be generated. Digital simulations informed by the physical prototypes enable structural analysis and design iteration. Once fine-tuned, the knowledge gained from the small-scale models can be applied to larger scale simulations to analyze aspects of the design like discretization, connections, material thickness, span, and fabrication methods.

2.1. Manipulation of form

When heated beyond its glass transition temperature, acrylic loses appreciable flexural stiffness due to a significant reduction in its elastic modulus and begins to act like a tension-only sheet. At this point, the shape is influenced by three factors: the initial shape and boundary conditions, an uneven distribution of thickness, and material elongations. The first factor is assumed to have a greater influence on the form than the other two factors and is the focus of this study.

Boundary conditions that were designed to shift during heating were tested to enhance and influence the final form. Altering the boundary conditions is frequently done while form-finding with fabric. When impregnated with water or wet concrete, fabric develops a funicular form. The points from which the fabric is hung can be moved closer together to further accentuate the curvature of the form. This process of adjusting the supports is more difficult with acrylic; opening the oven to alter the boundary conditions may not be straightforward and could create fluctuations in temperature. A system with mechanical, moveable parts such as ball bearings or wheels can also be challenging as the connections can potentially become ensnared or dislodged.

Instead, a simple shifting boundary condition was developed that is controlled during setup and requires no intervention during heating. The acrylic sheet is connected with strings to the corners of a flat rectangular frame which is smaller in plan than the acrylic sheet. When the acrylic is heated and the stiffness decreases, the strings rotate inward and create a funicular form (Figure 1). The length of the strings and the size difference between the acrylic and the frame can be altered to control the final form. Strings of different lengths can create asymmetries that allow for design exploration.

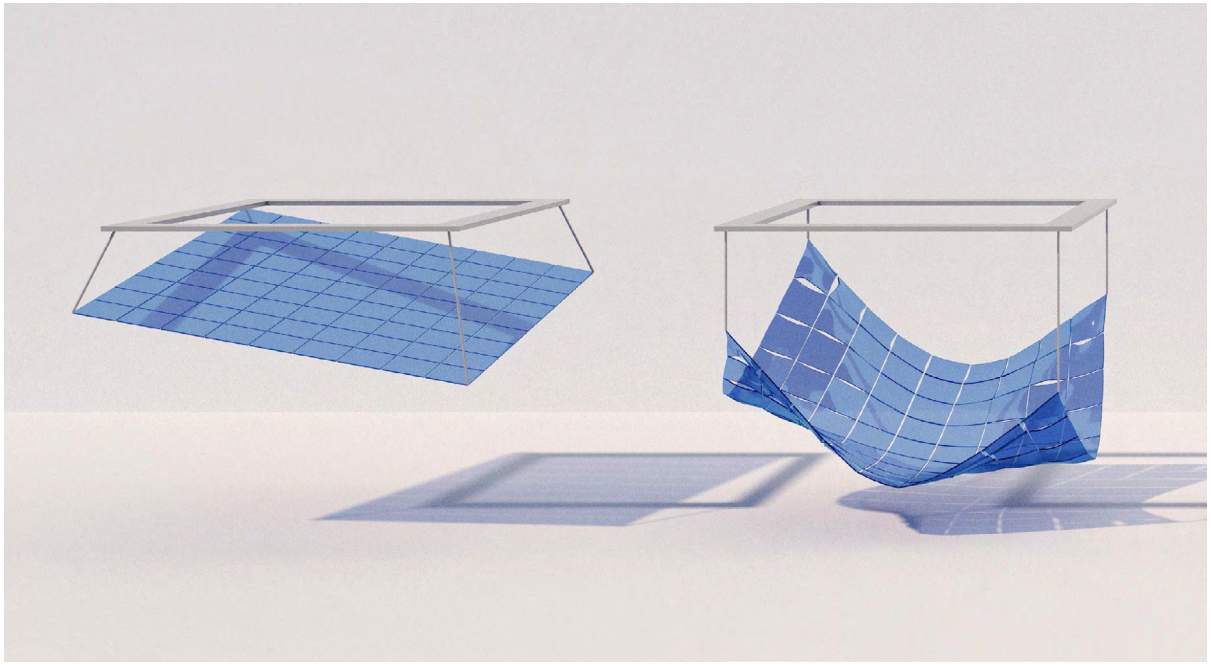


Figure 1: Digital simulation of the shifting boundary conditions

2.2. Proof of concept prototype

A small-scale prototype (0.4 m x 0.4 m) was developed as proof of concept for the process (Figures 2-4). Laser cut acrylic pieces (0.1 m x 0.1 m) were assembled into a 4 x 4 grid and mechanically connected at each corner. The connection plates were also made of acrylic and were able to slump along with the larger pieces. Washers between the layers of acrylic ensured that the shell could be disassembled and reassembled after heating and cooling.



Figure 2: Prototype in the oven before and after heating

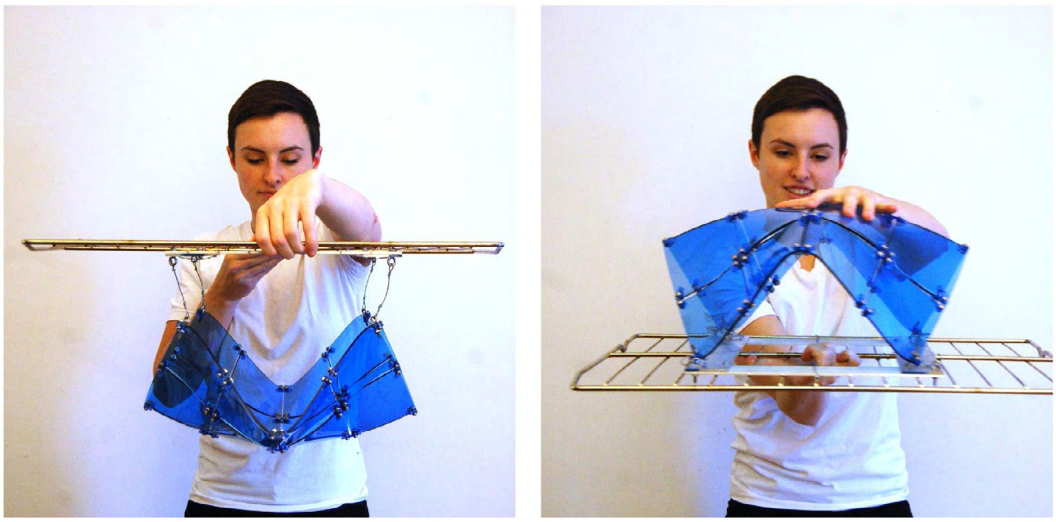


Figure 3: After cooling and hardening, the prototype is flipped

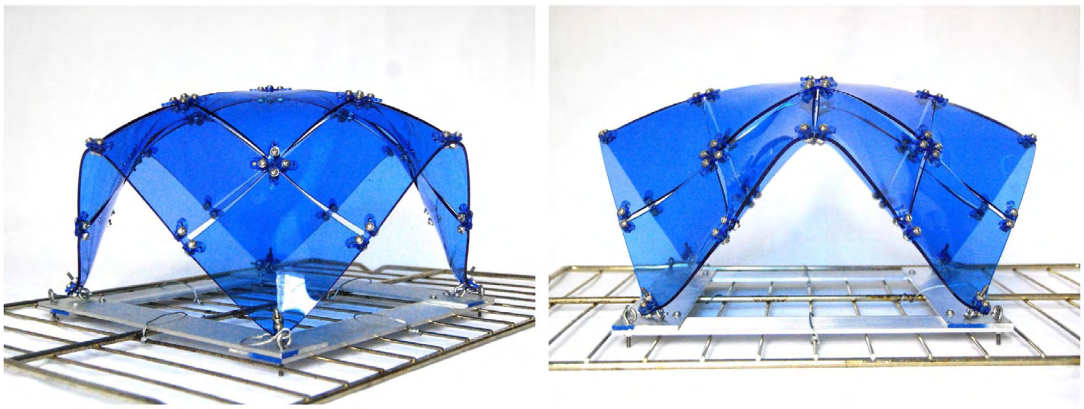


Figure 4: Views of the prototype in its final configuration

2.3. Empirical research and digital simulations

Small-scale physical models were also used to empirically verify the results of digital simulations created using Kangaroo Physics [12], a live physics engine used within Grasshopper [13], a plug-in for McNeel's Rhinoceros 3D modeling software [14]. Additional simulations are currently being conducted using finite element software and are not included in this study. The digital simulations can be used as a tool for analysis, fast-paced iteration, and design decision-making.

The tests were designed to determine and confirm the approximate stiffness parameters of the acrylic at a specific temperature (in this case 120°C) and involved small-scale monolithic sheets of acrylic with various initial geometries and boundary conditions. Once the sheets had been heated, deformed, and cooled, the dimensions were measured and documented. Digital simulations were set up which matched the conditions of the physical tests. The stiffness parameters in the digital models were then adjusted and fine-tuned until the resulting form of the simulation closely matched that of the physical test.

The first test was conducted on a 0.3 m x 0.3 m x 3 mm monolithic piece of acrylic that was directly connected to the frame at each of the corner points. Due to this support configuration the acrylic's deformation was due only to material elongation (Figure 5).

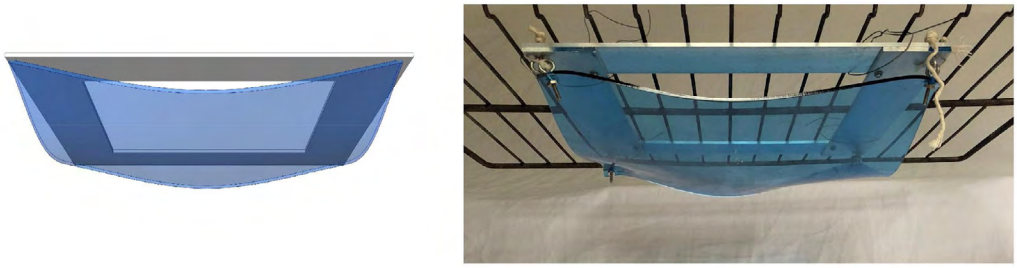


Figure 5: Comparison of digital simulation with Kangaroo Physics (left) with a physical test (right)

The second test was conducted on a 0.4 m x 0.4 m x 3 mm monolithic piece of acrylic that was connected to a 0.3 m x 0.3 m frame via strings at the corners. The shifting boundary conditions enabled significantly more deformation than from material elongation alone (Figure 6).

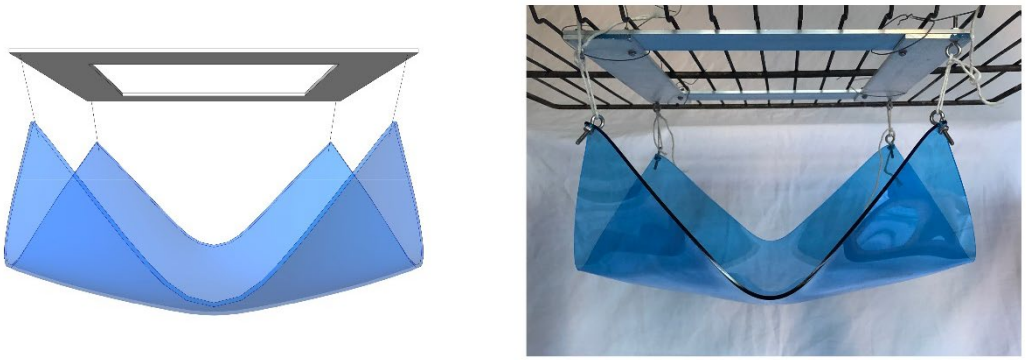


Figure 6: Comparison of digital simulation with Kangaroo Physics (left) with a physical test (right)

In both tests described above, the same stiffness parameters used in the simulations provided agreement between the form generated in the digital and physical models. Thus, the stiffness parameters applied in the digital simulation is assumed to represent the approximate stiffness of acrylic at 120°C. This stiffness can be applied to larger monolithic and aggregated models to better understand and alleviate the challenges in scaling the process for full-scale fabrication and heating. Some technical considerations that have been identified for further study include the relationship between deformation due to self-weight and that due to heat, the overall behavior of a discretized shell structure, and the geometry and configuration of the connections. Full-scale simulations also allow for an iterative design process which seeks to understand the experiential impact of the amount of overall deformation, the size of the discretized panels, and the appearance of the connections.

2.4. *Two Blue Shells* Pavilion

The current design proposal for *Two Blue Shells* consists of two 2.0 m x 2.0 m structural shells which are each made of forty-nine 0.3 m x 0.3 m pieces of flat acrylic arranged in a grid (Figures 7 and 8). The corners of the acrylic pieces are connected to create one large aggregated sheet. The overall sheet is hung from its corners and heated in a large-scale oven until it deforms under its own weight into a

tension-only shape. As analysis and fabrication progress, the design will continue to evolve and respond to new information and results.

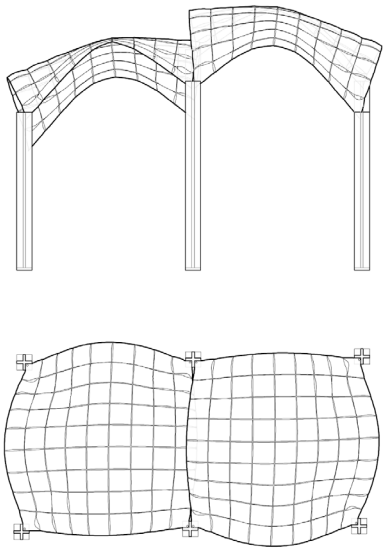


Figure 8: Elevation (top) and plan (bottom) of the proposed design

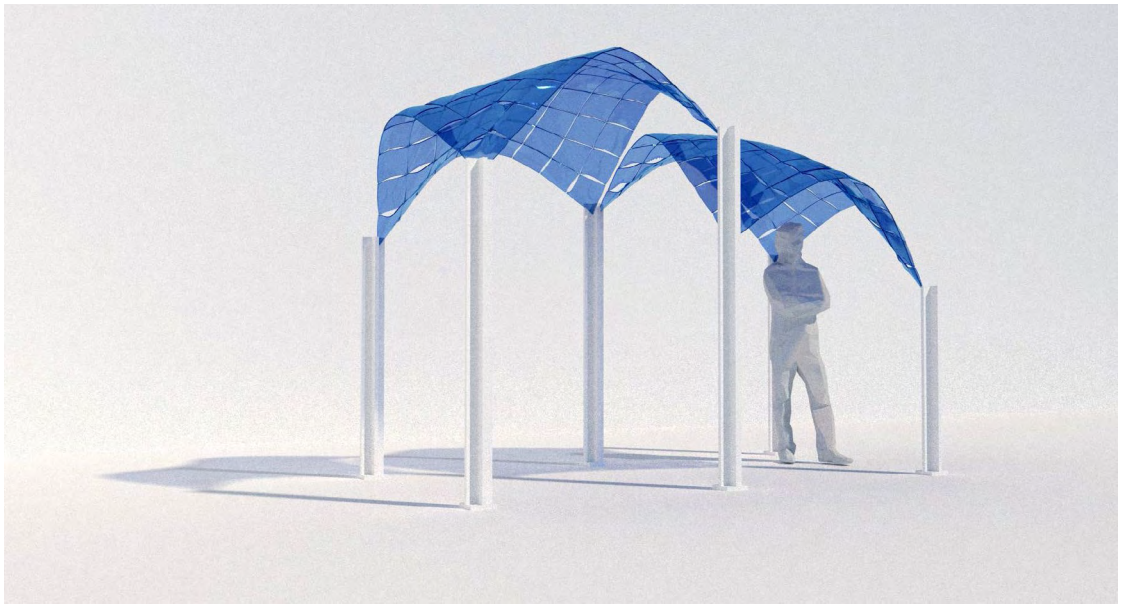


Figure 8: Rendering of the proposed design

3. Conclusion

Two Blue Shells highlights a new potential method to reuse acrylic scrap to create unique funicular shells. The process explores the natural behavior of acrylic when exposed to heat to directly fabricate full-scale doubly-curved structures. The discretized acrylic shells are architecturally evocative of vernacular tile rooftops around Barcelona as they also begin with self-similar parts. However, when heated, each repetitive panel deforms and becomes a highly individualized element as the overall

funicular form takes shape. The design process integrates feedback loops between material properties, digital simulations, and construction considerations to generate and fabricate complex geometries.

Acknowledgements

The authors would like to thank Michael Herrick of schlaich bergermann partner for contributing to the structural analysis of the small-scale models and the full-scale pavilion.

References

[1] S. Engelsmann, V. Spalding and S. Peters, *Plastics: in Architecture and Construction*. (1st ed.). Basel: Birkhauser, 2010.

[2] A. Davidson, "Moulding the future," *C20 – The Magazine of the Twentieth Century Society*, vol. 3, pp. 26-37, Dec. 2016.

[3] ARCHIGRAM and P. Taylor, "Expendability: Towards Throwaway Architecture", *Archigram magazine*, vol. 3, pp. 1-9, 1963

[4] Y. Kikuchi, M. Hirao, T. Ookubo and A. Sasaki, "Design of recycling system for poly (methyl methacrylate) (PMMA). Part 1: recycling scenario analysis," *International Journal of Life Cycle Assessment*, vol. 19, Issue 1, pp. 120-129, Jan. 2014.

[5] Y. Kikuchi, M. Hirao, H. Sugiyama, S. Papadokonstantakis, K. Hungerbühler, T. Ookubo and A. Sasaki, "Design of recycling system for poly (methyl methacrylate) (PMMA). Part 2: Process hazards and material flow analysis," *International Journal of Life Cycle Assessment*, vol. 19, Issue 2 pp. 307-319, Feb. 2014.

[6] H. Isler, "New Shapes for Shells." *Bulletin of the International Association for Shell Structures,* no. 8, pp. 123-130, 1961.

[7] S, Huerta, "Structural Design in the Work of Gaudí." *Architectural Science Review*, vol. 49.4, pp. 324-339, 2006.

[8] W. McGee, C. Newell, and A. Willette, "Glass Cast: A reconfigurable tooling system for free-form glass manufacturing," in *ACADIA 2012: synthetic digital ecologies: proceedings of the 32nd annual conference of the Association for Computer Aided Design in Architecture (ACADIA), San Francisco, USA, 2012, Oct. 18-21, 2012*, pp. 286-294.

[9] L. W. Mckeen, *The Effect of Temperature and Other Factors on Plastics and Elastomers.* (2nd ed.). Norwich, NY, USA: William Andrew Inc., 2008.

[10] P. Bellés, N. Ortega, M. Rosales, and O. Andrés, "Shell form-finding: Physical and numerical design tools", *Engineering Structures*, vol. 3, pp. 2656-2666, Jul. 2009.

[11] R. A. Bradley, M. Gohnert, "Three lessons from the Mapungubwe shells," *Journal of the South African Institution of Civil Engineering*, vol. 58, no. 3, pp. 2-12, Sept. 2016.

[12] D. Piker, Kangaroo Physics, version 2.42, Oct. 2017.

[13] Grasshopper, build 1.0.0007, Apr. 2019, © 2009 Robert McNeel & Associates.

[14] Rhinoceros 3D, version 6.0, May 2019, © 2019 Robert McNeel & Associates.

Proceedings of the IASS Annual Symposium 2019 – Structural Membranes 2019
Form and Force
7 – 10 October 2019, Barcelona, Spain
C. Lázaro, K.-U. Bletzinger, E. Oñate (eds.)

Digital Tessellation and Fabrication of the ECHO shell

Ornella IUORIO*, Emil KORKIS[a], Marinella CONTESTABILE[a]

*[a] University of Leeds,
School of Civil Engineering, LS2 9JT, Leeds
o.iuorio@leeds.ac.uk

Abstract

Complex forms, that in history have always been challenges for architects are now becoming familiar to people working at the edge between architecture and structural design. This is, in particular, true for free form shells design. Free form shells are today undergoing a wider adoption for both permanent structures as well as temporary structures [1]. These last are of particular interest, when they are conceived according to a logic of design for deconstruction, since they can respond to circular economy requirements [2]. This work explores the digital process from design to manufacturing of a shell that has the shape of sounds waves replicating like in an Echo. The structure is made of a sequence of wooden arches and a compact thin shell. The shell combines free form generation with planarization and tessellation processes, using hexagonal discretization. The hexagonal panels are CNC fabricated from 6 mm plywood and are connected together by ad hoc 3D printed joints. The arches follow the hexagonal shell patterns and are conceived as slices of shell continuity and replication. The overall structure is demountable, easy to transport and capable to be reassembled in short time, responding to the principle of design for deconstruction. The result is a neat clean space adapt to any exposition space.

Keywords: additive manufacturing, digital design, form finding, parametric modeling, tessellation

1. Introduction

In the contemporary scenario complex and freeform shapes represent a large portion of architectural solutions [3]. Impressive projects throughout the world carried out by important architects and engineers are evidence of a new way of designing. New technologies regarding the design and the fabrication are providing significant changes in architecture and total freedom in artistic expression [4]. This rising presence is due to multiple factors but firstly one of the key factors lies undoubtedly in the development of innovative methodologies associated with straightforward digital tools that affect each aspect of the design process, from the concept to the fabrication. Through the use of innovative techniques in the design first and then in the fabrication, it is possible to generate an optimized workflow that meets specific requirements in each design phase. Parametric modelling is involving all the aspects of the design creating a strong connection within the process. The interoperability with digital fabrication techniques is another demonstration of the countless potentialities that this new approach presents [5].

This paper presents a parametric approach to define an efficient shell structure, which will be digitally fabricated. In the following sections, the digital design is described in detail, from the form finding to the tessellation and planarization, up to fabrication of main components. All the digital design is carried out within Grasshopper® functionalities together with its powerful plugins. One of the key part of the all described process is the tessellation since it allows to discretize the original surface into flat panels, that will be CNC fabricated and assembled together by neat connection

Copyright © 2019 by Ornella IUORIO, Emil KORKIS, Marinella CONTESTABILE
Published by the International Association for Shell and Spatial Structures (IASS) with permission.

2. Concept and overall methodology

The ECHO shell has been developed in answering the brief set by the international context within the IASS 2019 conference, which requires to develop a shell that is included in a volume 4x4x4m, that is lightweight and follows a logic of design for disassembly and can be carried around in 6 boxes. Our aim was to develop a space that has the shape of echo soundwaves, in which the portion having single curvature is made of a continue shell, while the double curvature is obtained through a sequence of arches (Figure 1).

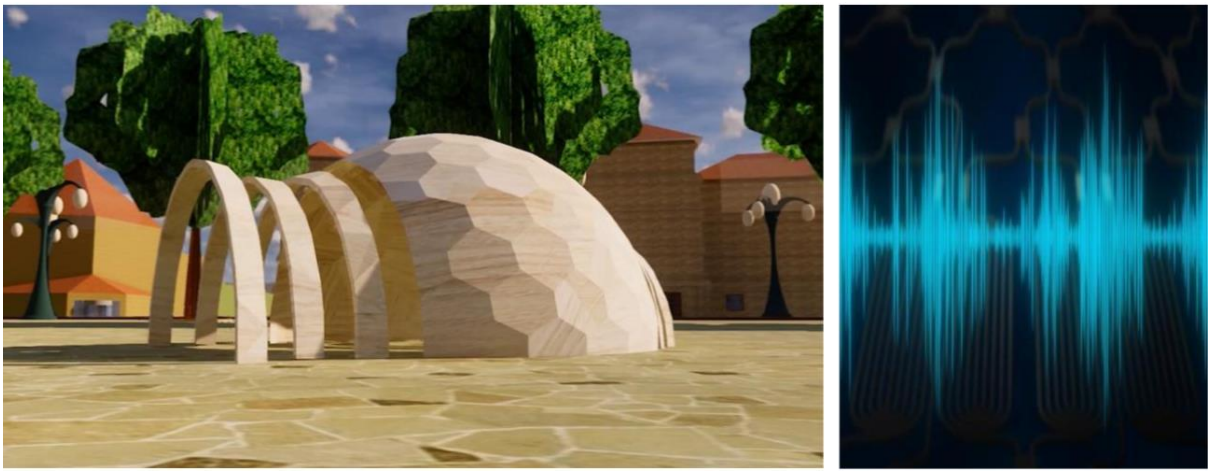


Figure 1: ECHO, 3D generated concept of the shell and an echoing soundwave

Figure 2 shows the basic design process this research follows. The first input in the design process is the initial shape. The required output of this process was a shell, which by definition has one dimension very small compared to the other two dimensions. The initial shape chosen was a three-dimensional surface, with a constant curvature. The surface was created using Rhinoceros® (Figure 3) and referenced into Grasshopper to be used directly in the tessellation process.

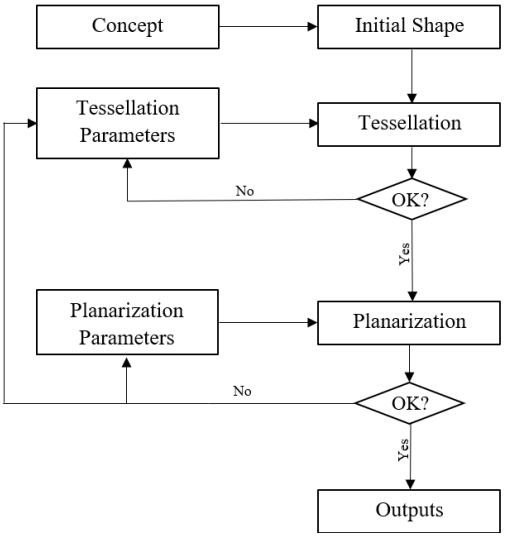


Figure 2: Basic process of a parametric shell design

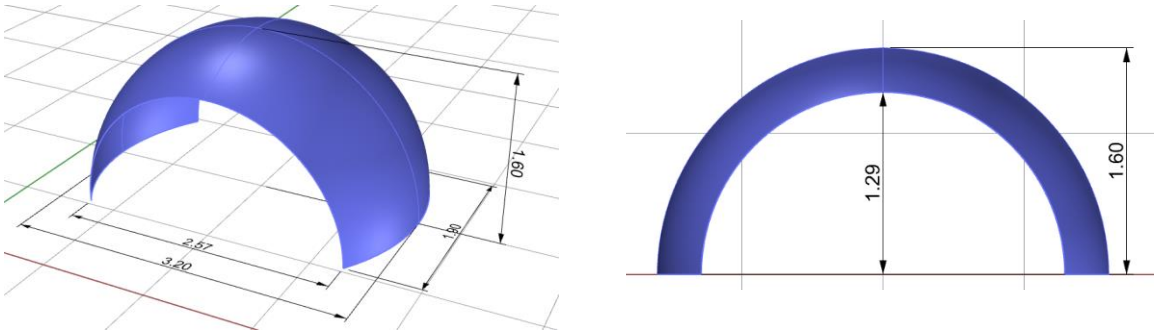


Figure 3: The surface created using Rhinoceros®

2.1 Parametric Design and Modelling

Parametric design is an algorithm-based process, that uses parameters to define the relationship between a set of inputs to derive a required result. The outputs of this process remain tightly related to these parameters. Changing a parameter at any stage of the process affects the end results directly. However, this effect and its magnitude, depends entirely on the implementation of the parameter in the system being designed. This methodology has been applied to the shell surface created previously to provide the boundary conditions for the planarization process and to form the hexagons in the tessellation process.

2.2 Tessellation of Surfaces

Tessellation is the process of dividing a surface using geometric shapes. The tessellation process has been mainly used for planar surfaces with regular repeating patterns of one or more geometries. This is referred to as tiling. Mathematically, the tiling process can be expanded into tessellation of free-form 3D surfaces. Using different algorithms, this process can be applied to any surface. Computer generated tiles using tessellation algorithms usually result in non-planar tiles that follow the shape of the tessellated surface exactly. This was the case of the ECHO project, for which planarization was then later applied to allow the fabrication by using planar sheets of plywood.

A plugin called LunchBox was used for the tessellation process. LunchBox has different components for different types of tiling. The operation is called “panelling” as it divides the surface into multiple panels of the chosen pattern. A series of different patterns were investigated, and among them hexagonal pattern was chosen because it will minimize the number of connections required between the panels while increasing the possibility of a successful planarization process. Therefore, “Hexagon Cells” or “Hex” component was used (Figure 4). This component requires three inputs and a fourth optional one. The first being the surface, the second and the third are the number of panels in two perpendicular direction U and V which were set to 10 and 16 respectively. The directions U and V are a local coordinates system applied to the surface by the “Hex” component. The fourth input is a parameter that defines the angle of the generated hexagons, which for this application was left at a default value of 0.25. Figure 5 shows the output of the tessellation process.

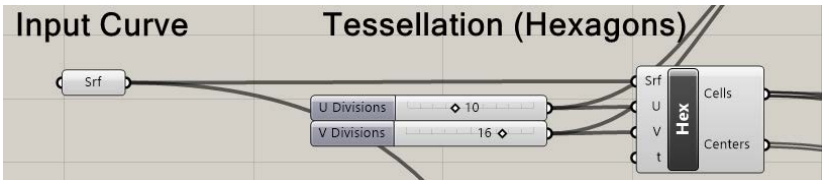


Figure 4: Hexagon Panels component of LunchBox plugin

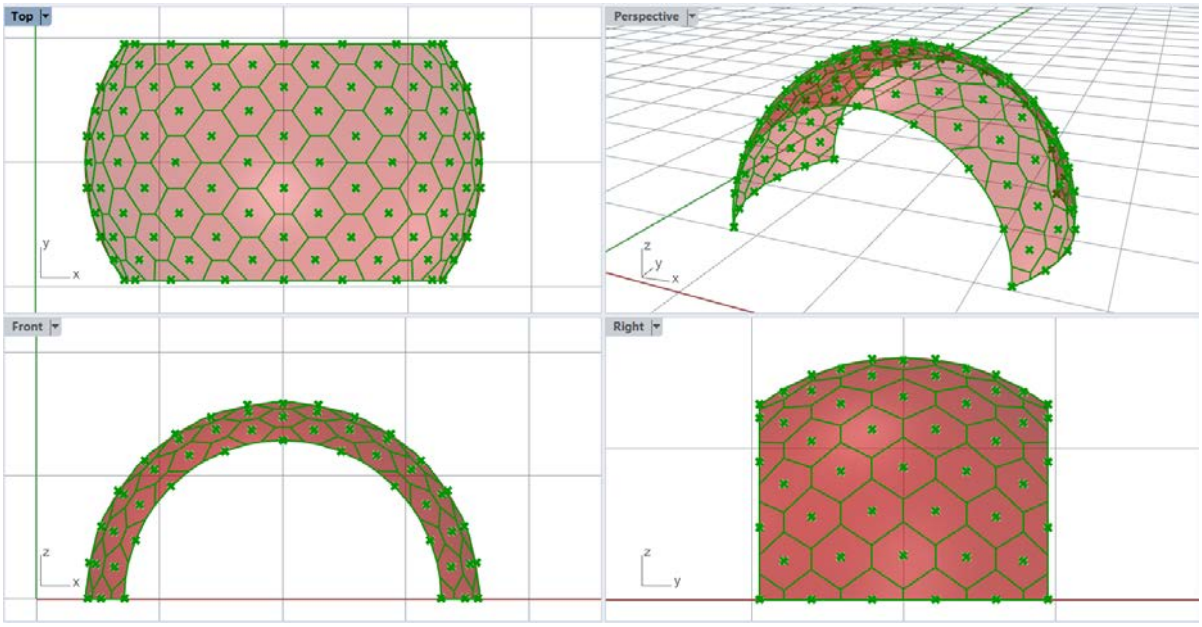


Figure 5: Hexagon panels generated by "Hex" component

2.3 Planarization

The planarization allows to increase the flatness of a surface or make it planar. This process involves applying several forces to different points on the surface to force them into planarity. The plugin Kangaroo2 is a physics engine that uses algorithms and logic to solve the provided inputs [6, 7].

Kangaroo2 provides a large set of constraints and forces that can be applied to points, curves, angles and surfaces. In addition to a set of utilities and physics solvers. The solvers accept curves, points or surfaces as an input. Then it applies the forces and constraints to these inputs. The same process is repeated for several iterations until the solver converges on a solution. The ECHO shell is made of planar plywood sheets. In order to get planar panels that are as much close as possible to the hexagons created by the tessellation, some conditions were applied; a boundary condition, a length constraint on the sides of each hexagon panel to preserve their shape, and planarization forces. The boundary conditions in the required shell is the outer curve of the shell. This is the same as the three curves used to create the shell. The requirement is for any edge vertex of a hexagon that belongs to these boundary curves should be anchored. That is because the outer boundary is the curve that gives the shell its shape. This list of vertices was extracted as shown in (Figure 6) and inserted as input into the Anchor Component of Kangaroo2 (shown in green in Figure 6). This component provides a force that resists the movement of the inputs with a strength that was set to a default high number equal to 10000.

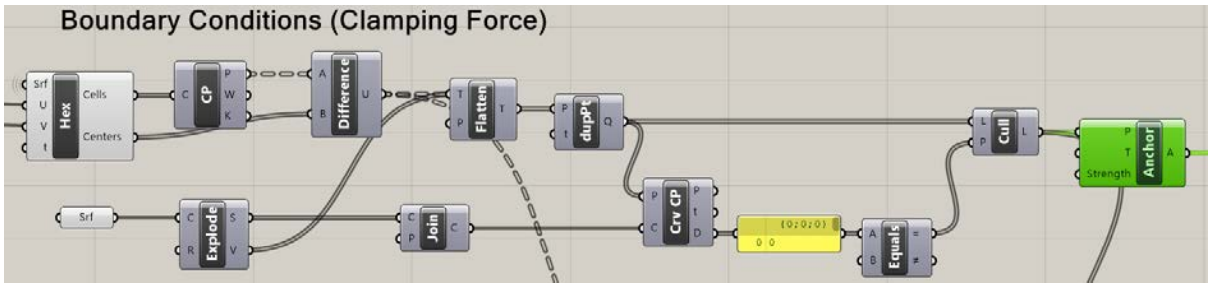


Figure 6: The process of providing boundary conditions as point anchors

The length constraint is a condition that was applied to the hexagons' edges to prevent them from deforming in an undesirable way. The length constrain component receives an input of lines to clamp their length. The lower limit and upper limit are the minimum and maximum lengths for these lines respectively. The input lines are the output of an Explode component applied to the Hex process. The strength of this clamping is a parameter that can be changed at any stage of the design process. Lowering the clamping strength resulted in more deformation in the shape of the hexagons than desirable. After few iterations, the strength was set to 1 (Figure 7).

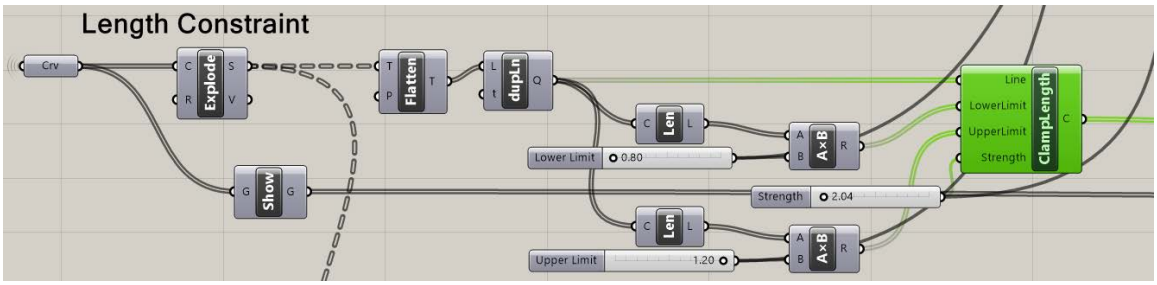


Figure 7: Length Constrain process

In this project, these lines are the edges of dissimilar hexagons. There are no known upper or lower limits. The limits were set as a multiplication of each line length by a number. The lower length for any line was set to its actual length times 0.8. The upper limit was set to the line's actual length multiplied by 1.2. This translates into a clamping force that prevents the lines from deforming by more than 20% in either lengthening or shortening. The planarization forces in Kangaroo2 can be applied to points in order to force them to occupy the same plane. The hexagons that were extracted from the Hex operation were exploded and the control points of the hexagons (edge points) were used as input for the CoPlanar command. It accepts points as input and a strength value that determines the strength of the planarization force. The default for the strength value is 1. However, it was found that a small force can sometimes result in non-planar panels. The reason for this is that the other forces acting on the panels' vertices are high enough for the solver to not converge on an answer. Since the most important goal is for the panels to be planar, this force was set to a strength value of 1000 (Figure 8). Kangaroo2 Bouncy solver is a physics engine solver that uses algorithms to achieve the goals assigned as inputs (Figure 9). The goal objects of the bouncy solver were set to the previously discussed components. The ClmapLength component that includes the hexagons' edges and prevents them from changing in length outside of the set limits, a CoPlanar command that applies a force on the vertices, and an Anchor component that fixes the input points in space.

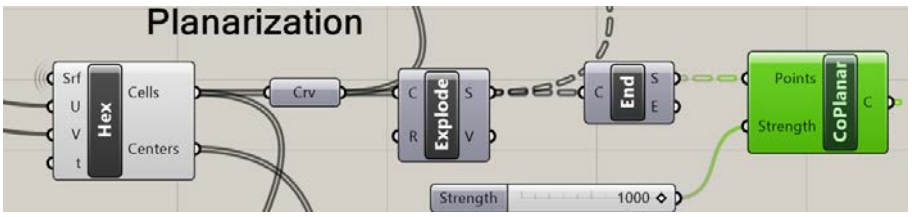


Figure 8: Planarization process and the CoPlanar component

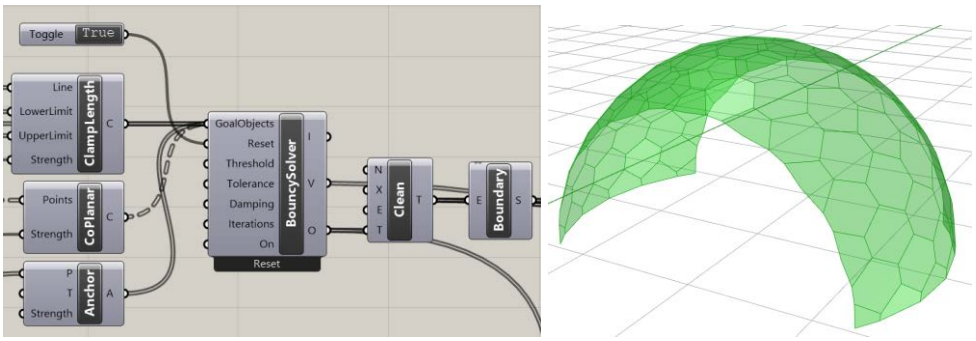


Figure 9: Kangaroo2 Bouncy Solver and the resulting planarized shell

3. Connections

An idealistic shell structure should carry all loads in membrane forces only. This is true only after the shell is completely constructed. Depending on the design, a shell that is still in construction is very unstable. For this reason, any type of connection between tessellated structure cells, should be able to carry a moment for the entire period of construction. This is especially true for shells that are constructed with minimal formwork. ECHO shell connections were designed assuming the formwork will carry most of the load, but the connections will be subjected to a bending moment at the construction stage. The shell consists of thin plywood panels. Since the panels were only 6mm thick, a connection that would interfere with the sheets axially was ruled out.

Multiple connection systems were developed using Autodesk® Fusion360. The final design shown in Figure 10 was 3D printed as 2 parts that will envelope the panels at the connection vertices (where three panels meet). The connection measures 30mm from the centre to the farthest point of the connection and has a thickness of 4mm for each part. The lower part of the connection has three blocks that fit into slots cut into the panels.

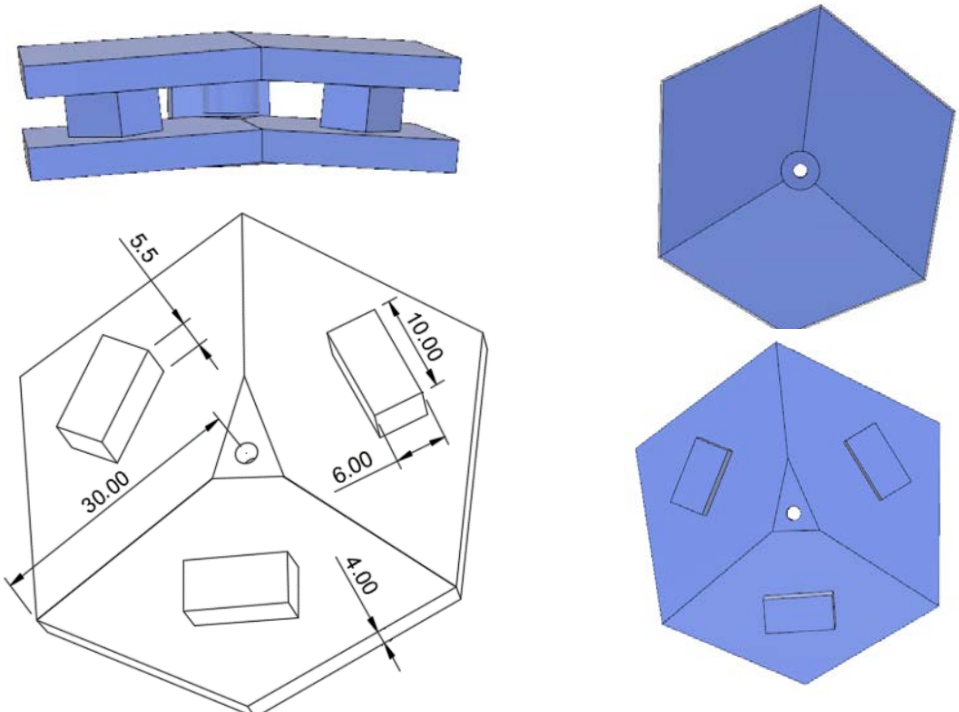


Figure 10: Final design of the connection. All dimensions shown are in mm

This design would depend on friction between the connection's blocks and the panels for stability, and to a lower degree on the clamping force provided between the two parts of the connection. It was possible to add a relief of 0.1-0.3 mm to the interface between the connection and the panels slots and still conserve the rigidity of the connection system. The ECHO shell consists of 94 planar panels connected using 144 connection of this design. Despite the symmetry of the shell, designing a large number of connections individually is time consuming, less efficient and more prone to errors. Developing the connections through parametric design is crucial to avoid these problems.

To create a parametric design of the connections, it is required to pick starting points. These points are already listed as output from the Kangaroo2 Solver. The connection is joining three panels, so three construction planes are needed. The construction planes are created from the surfaces of the panels and they intersect in one point only. This point is always the same as the solver's output. Figure 11 shows the procedure from the starting point to the final connection. Finger joints were added to the panels to provide stability and simplify the assembly. Figure 12 shows the final configuration of connections on the shell.

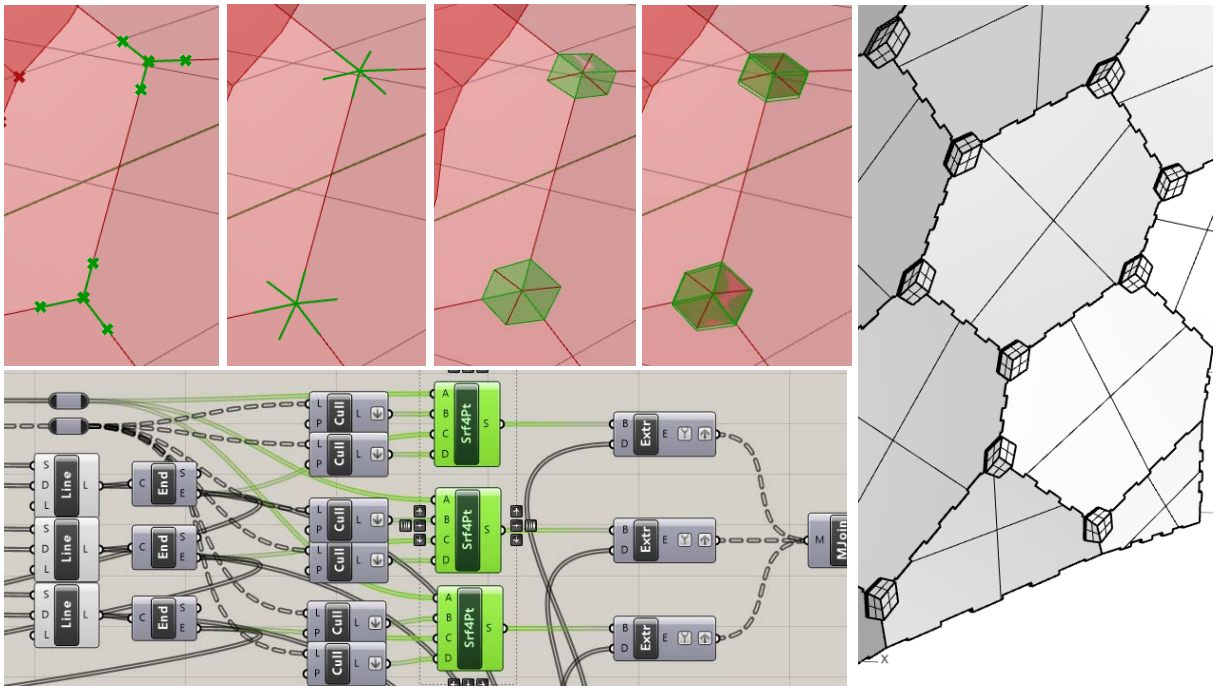


Figure 11: Connection design stages and final result

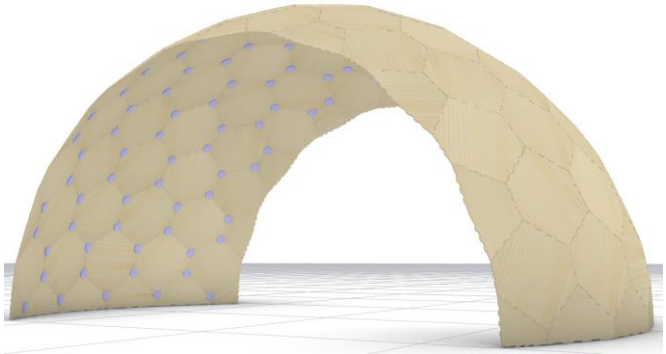


Figure 12: The ECHO Shell showing panels and connections

4. Fabrication

Three panels were fabricated as test by laser cutting 6mm plywood sheets and connected through a 3D printed connection. The connection was designed to retain the panels by friction forces only, without the need for screws or bolts that would have increased the time needed to fabricate an entire shell dramatically. The connections were tested, and proved to be able to hold the panels in place and retain the angle between them to a very good degree of accuracy. Figure 13 shows one connection resisting the bending moment caused by the weight of two panels while being supported at the farthest end of the third panel. The second part of the connection helps in retaining the angle between the panels, and can be joint to the first part by a self-tapping screw or a small metal pin.



Figure 13: Fabricated panels in place with the first connection

5. Conclusion

This paper presents the design of a lightweight wooden shell, that is made of 94 CNC hexagonal panels connected together by ad-hoc 3D printed friction joints. The work focuses on the development of the digital design, explaining tessellation and planarization of the surface, and the conceptual development of the connection system. This last has been designed to allow easy assembly and disassembly. The fabrication of a first portion demonstrates the capacity of the system, and a full prototype will be developed to analyse full feasibility and limitations.

References

[1] P. Block, T. Van Mele, A. Liew, M. DeJong, D. Escobedo, J. Ochsendorf, "Structural design, fabrication and construction of the Armadillo vault", *Structural Engineer*, Volume 96, Issue 5, 1 May 2018, Pages 10-20.
[2] C. Lemmens, C. Luebkeman, *Circular economy in the built environment*, Arup 2016.
[3] O. Iuorio, "BIM, free form shells and digital fabrication". *In: The Changing Architect*, Russo Ermolli S ed., Maggioli Editore, pp. 103-110, 2018.
[4] O. Iuorio, H. S. Matharou, "Inflatables Structures and Digital Fabrication", *ICSA2019 The 4th International Conference on Structures and Architecture*, Lisbon, 24 -26 July 2019.
[5] N. Dunn, *Digital Fabrication in Architecture*. London: Laurence King, 2012.
[6] D. Piker, "Kangaroo: Form Finding with Computational Physics". *Architectural Design*. 83, (2),136-137, 2013.
[7] A. Tedeschi, *AAD_Algorithms Aided Design. Parametric Strategies Using Grasshopper*, Le Penseur: Brienza, 2014.

Proceedings of the IASS Annual Symposium 2019 — Structural Membranes 2019
Form and Force
7—10 October 2019, Barcelona, Spain
C. Lázaro, K.-U. Bletzinger, E. Oñate (eds.)

FlexMaps Pavilion: a twisted arc made of mesostructured flat flexible panels

Francesco LACCONE*, Luigi MALOMO[a], Jesús PÉREZ[b], Nico PIETRONI[c,a], Federico PONCHIO[a], Bernd BICKEL[b], Paolo CIGNONI[a]

* ISTI - CNR and DESTEC - University of Pisa; via Giuseppe Moruzzi 1, 56124 Pisa, Italy
francesco.laccone@isti.cnr.it; francesco.laccone@destec.unipi.it
[a] ISTI - CNR
[b] IST Austria
[c] University of Technology Sidney

Abstract

Bending-active structures are able to efficiently produce complex curved shapes starting from flat panels. The desired deformation of the panels derives from the proper selection of their elastic properties. Optimized panels, called FlexMaps, are designed such that, once they are bent and assembled, the resulting static equilibrium configuration matches a desired input 3D shape. The FlexMaps elastic properties are controlled by locally varying spiraling geometric mesostructures, which are optimized in size and shape to match the global curvature (i.e., bending requests) of the target shape. The design pipeline starts from a quad mesh representing the input 3D shape, which defines the edge size and the total amount of spirals: every quad will embed one spiral. Then, an optimization algorithm tunes the geometry of the spirals by using a simplified pre-computed rod model. This rod model is derived from a non-linear regression algorithm which approximates the non-linear behavior of solid FEM spiral models subject to hundreds of load combinations. This innovative pipeline has been applied to the project of a lightweight plywood pavilion named *FlexMaps Pavilion*, which is a single-layer piecewise twisted arc that fits a bounding box of 3.90x3.96x3.25 meters.

Keywords: bending-active, form-finding, simulation, twisting, plywood CNC, spiral, piecewise



Figure 1: Overall view of the assembled plywood FlexMaps Pavilion made of bent flat panels.

Copyright © 2019 by Francesco LACCONE, Luigi MALOMO, Jesús PÉREZ, Nico PIETRONI, Federico PONCHIO, Bernd BICKEL, Paolo CIGNONI
Published by the International Association for Shell and Spatial Structures (IASS) with permission.

1 Introduction

Bending-active structures produce efficiently complex curved shapes made of flat or straight elements [1]. In the past, such structural systems were based on empiric techniques to produce curved geometry efficiently and cost-effectively. Nowadays, the availability of simulation techniques gives control of form-finding and verification processes of such lightweight and efficient structures [2]. If in the past the main advantage was to have a cheap technology to build even doubly curved surfaces, now the main reason to adopt this technique lies in the reduced weight and the economy of producing flat panes regardless of their curvature.
The bending-active technology characterizes different structural types such as plate shells [3], hybrids composed of membranes with elastically bent battens [4], and various types of adaptive and elastic kinetic structures [2].
The workflow adopted for the FlexMaps Pavilion uses a fully integrated approach [1] for the definition and the control of the mesostructures (base geometry) and consequently of the material behavior. However, the main innovation of the present approach is that the shape obtained by numerical form-finding results as close as possible to a predefined target geometry. This is a step towards a designer/artist-oriented tool.
Another novelty lies in the assembly. In post-restrained structures (where the components are bent and fixed to the ground), a common approach is to post-tension of the overall shape that initially lies in the flat position. Conversely, the FlexMaps approach is based on bending and assemble the single mesostructured element, which lays flat in the rest configuration. Its final shape results from internal elastic forces that arise when connecting progressively the spiralling elements. Thus, only a minimal amount of bending energy is required because of such a step-by-step construction sequence. If an easy fabrication is obtained by producing a flat segmented array of panels, a further cost-saving characteristic of the FlexMaps Pavilion may be found in its assembly procedures.
The main issue of bending-active structures is that the elastic bending causes initial stress. This lowers the stress reserves that the structure may attain due to external loading. The spiral geometry, which is the main idea behind the present project, tackles this point. First, having a spiral path instead of a linear path brings to minor bending stress for the same curvature. Second, the spiralling geometry can be modified to obtain bespoke FlexMaps panels in order to accommodate local curvature demands, consequently varying the bending stiffness and preserving a uniform initial stress on the panes. This approach corresponds to design custom mechanical properties without changing the material but only by acting on the geometric parameters of spirals [5].

2 FlexMaps concept

The technique presented in [5] is designed to physically approximate an input 3D shape by interlocking a set of fabricated flat panels which are coupled solely by snapping together connectors on their boundaries. Following Flexmaps [5], a generic input shape is flattened on a 2D space, and then it is split into multiple panels. Each panel is made flexible by carving out long thin spiral-shaped structures. The pattern has to be relatively dense and regular enough to be aesthetically pleasing once they are assembled to complete the final shape.
Inspired by the beauty of geometric tilings, Flexmaps uses a quadrilateral arrangement of spatially-varying, four-arm spiralling shapes. The spirals have sufficient degrees of freedom that they can be continuously shaped into multiple configurations by varying three primary parameters: scale, twist, and width. Some settings of the spiral are shown in Figure 2. As

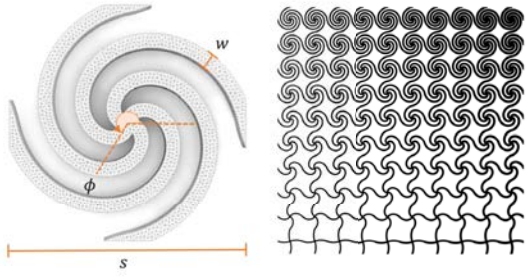


Figure 2: Left: descriptors determining the geometry of our spiral-shaped microstructrures. Right: assemblies made out of spirals can smoothly variate the twist (vertical axis) and width (horizontal axis) of the spirals.

it is possible to observe, the shape can undergo a significant change of forms, and every form corresponds to a particular set of mechanical properties.
This strategy follows a new philosophy of mechanical design of elastic properties that have been recently pursued by several optimization techniques [6]. Fabrication specific small-scale structures can control a large variety of mechanical properties. Distributing different microstructures within surfaces of areas makes it possible to manufacture deformable objects with continuously varying mechanical properties.
In the case of Flexmaps the mechanical properties are optimized such that, once the structure is assembled, its static equilibrium configuration matches as much as possible the desired 3D shape. However, the final shape mainly dependents on two main factors:

Primitive Distribution The panel subdivision and the distribution of the quads that embed the spiral has a great influence on the global equilibrium position of the entire Flexmap.

Shape of the Spirals The mechanical properties of the Flexmap can be controlled on a local basis by the varying shape of the spirals. While the underlying quad tessellation fixes the scale, twist and width can be adapted to match the desired flexibility.

The central core of the optimization process is a data-driven model that can predict the resulting deformed shape in 3D at interactive rates. The mechanical model is based on the rod coupling formulation in [7] and allows to approximates the range of spiral deformations with sufficient accuracy at an interactive rate.
The panel layout is initially derived using a state of the art algorithm [8], and then it is iteratively optimized by merging adjacent panels. This iterative optimization process tries to minimize the difference between the target shape and the predicted equilibrium shape computed by the physical model.
FlexMaps allow to design elastic surfaces with heterogeneous material properties, then the parameters of the spirals can be optimized to match the target shape at the equilibrium configuration. Intuitively, regions of high curvature of the mesh should be populated with characteristically compliant spirals. However, the equilibrium configuration is the global results of all the mechanical properties of the spirals and the boundary conditions they must satisfy. The optimization of this objective is a complex iterative process that minimizes non-linear energies and that matches a set of linear constraints to ensure the shape to be in equilibrium (details of this process are in [5]). An overview of the entire processing pipeline is shown in figure 3.

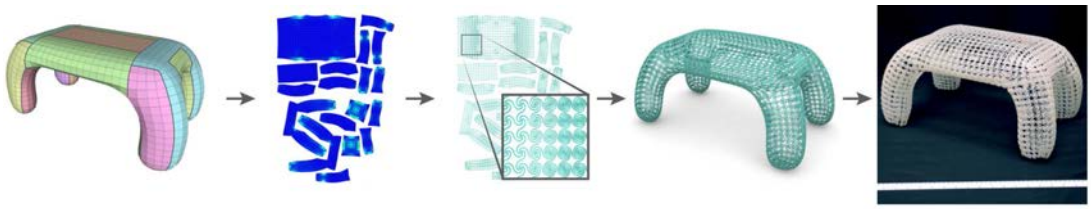


Figure 3: An overview of Flexmap modelling pipeline: An input mesh is split into multiple patches composed by quads; The patches are mapped on a 2D domain; A special spiral-shaped microstructures is embedded on each quad; The parameters defining the shape of spiral microstructures are optimized to improve accuracy in the final representation.

3 Design of the FlexMaps Pavilion

The flexmap Pavillon is a twisted lattice surface that is anchored on the ground. Base sections are inward-bent arches. The shape has been selected to be a challenge in both geometric and architectural terms. Moreover, the shape delimits a space but also allows people to walk through it. There is a sufficiently-wide curvature range and no symmetry. The dimension of the bounding box are 3.90x3.96x3.25 meters.

3.1 Form finding and segmentation

The twisted shape has been modelled manually. Then, it has been re-meshed with a quadrilateral meshing following the approach based on global parametrization proposed in [9]. The initial quad meshing is an essential step in the overall modelling pipeline since it defines the dimension of the spiral. In fact, each quad is used to embed exactly one spiral. The initial cross-field that drive the parametrization is aligned with the boundaries and smoothed in the shape interior. Then, the shape of each quad is further optimized using the approach proposed in [10]. This optimization step is fundamental to ensure each spiral to be embedded in a regular quad. In case this is not verified, significant non-rigid deformations might introduce an unexpected mechanical behavior in the embedded spiral.
Due to fabrication constraints, target quad edges of $0.25m$ have been selected. Moreover, for aesthetic reasons a constant width of 15 mm and a twist range of $100-250°$ are chosen as input parameters. The upper twist limit has a further aim to avoid too dense spirals, which may result too close with respect to the milling tolerance.
FlexMaps panels segmentation is user-defined since the earliest design phases and guided by the constraints of fitting six boxes each with a maximum external size of 1x0.75x0.65m and maximum weight of 32kg. Finally, a total amount of 75 panels are generated, each grouping two up to six spirals.

3.2 Materialization

The 2D FlexMaps panels are laser cut from Okumé plywood panels. The material has been selected according to the indications given by [11] and [1]. Particular attention has been dedicated to the recommended limitation $\sigma_{M,Rd}/E > 2.5\ MPa/GPa$ for actively-bent structures, which in this case equals $46/4.41 = 10.43\ MPa/GPa$. The ground edges are clamped in a CNC cut plywood profile; moreover, they are mutually connected and tied down. The naked edges that form two crossed arches are out-of-plane stiffened using a segmented laser cut plywood plate. The role of these arches is to provide additional restraint to the panels snapping in the assembly

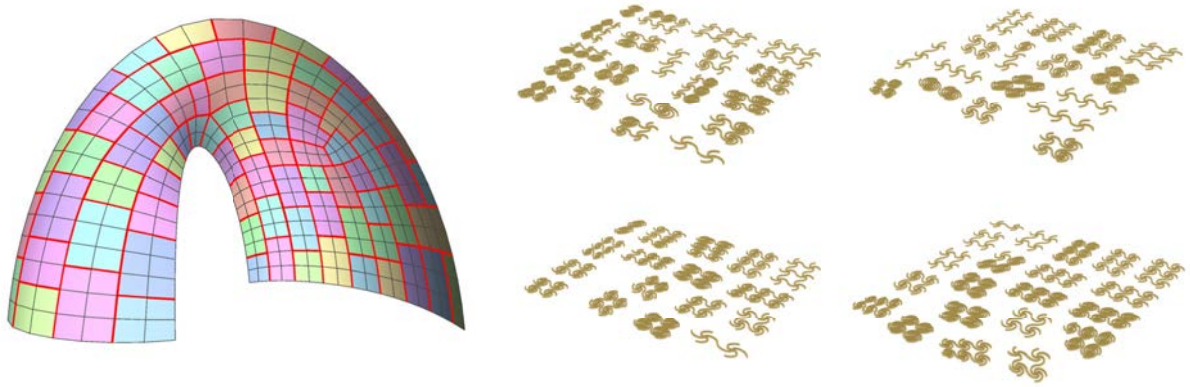


Figure 4: Pavilion patches: schematic view of the Pavilion highlighting the seams and the initial quad mesh; flat spiralling FlexMaps panels

phase.
To connect FlexMaps together connectors are encoded within the computational framework and are made of interlocking shapes, additionally secured by screws.

Table 1: Okumé plywood material properties (technical data from the manufacturer)

Nominal thickness (mm)	Num. Strata	Density ρ (kg/m^3)	Young's modulus E (N/mm^2)	Bending strength f_k (N/mm^2)
15	7	500	4410	46

4 FE Simulation

For the detailed deformation and stress verification of the Pavilion a fully nonlinear solid model has been built and anlyzed in the ANSYS package [12]. The verification consists of two phases: the first one to model the individual assembly of the panels and their initial stress; the second one to model the overall behaviour under external loading, such as gravity. Linear isotropic material properties according to Table 1 are used. In the first phase, each flat panel is rigidly moved in a position that is as closest as possible to its deformed shape. This placement aims at improving the convergence of the analysis. The deformed shape is deduced from the form-finding phase. Then, a displacement is imposed at the extremes of the spirals' free arms to bring them in their deformed position. Consequently the FlexMaps panel assumes its pre-stressed configuration.
The individually deformed (pre-stressed) panels and the accompanying stress fields are exported in a second environment in which the panels extremes are coupled, and boundary conditions are applied. In this setup, the structure is released and gravity and other external loading are applied.

5 Fabrication and assembly

The FlexMaps panels are CNC cut in the shop by means of double precision mill to accommodate tolerances of the interlocking shapes of connectors. The connectors have been previously tested in a four point bending setup to obtain a quantitative estimation of the stiffness reduction caused by the connection.

The Pavilion is assembled section by section going from one support to the other, sequentially bending and fastening each FlexMaps pane. Moreover, these patches are spliced in a staggered configuration to minimize the bending energy that is required to keep the Pavilion section in place. To this purpose, the crossed arches play a fundamental role in providing a restrain also during the assembly. Vertical supports and cross-section springs provide additional help in this phase.

6 Conclusion

The FlexMaps Pavilion proves that it is possible to effectively use mesostructured panes to build lightweight bending-active structures in which the initial stress is very low. The major advantage of the form-finding approach provided by the FlexMaps algorithm is to match the curvature demands of the target shape by varying the geometrical parameters of the spirals. Thus, even complex shapes such as the twisted arch pavilion becomes feasible. The FlexMaps approach can be applied for the design of a complex pavilion, which results a feasible structure.

References

[1] J. Lienhard, H. Alpermann, C. Gengnagel, and J. Knippers, "Active bending, a review on structures where bending is used as a self-formation process," *International Journal of Space Structures*, 28(3-4), pp.187-196, 2013.

[2] J. Lienhard, *Bending-Active Structures: Form-finding strategies using elastic deformation in static and kinematic systems and the structural potentials therein*, PhD thesis, Institut für Tragkonstruktionen und Konstruktives Entwerfen (ITKE), Universität Stuttgart, 36, 2014.

[3] R. La Magna, *Bending-active plates: strategies for the induction of curvature through the means of elastic bending of plate-based structures*, PhD thesis, Institut für Tragkonstruktionen und Konstruktives Entwerfen (ITKE), Universität Stuttgart, 43, 2017.

[4] R. La Magna, V. Fragkia, P. Längst, J. Lienhard, R. Noël, Y. Šinke Baranovskaya, M. Tamke, M. Ramsgaard Thomsen, "Isoropia: an Encompassing Approach for the Design, Analysis and Form-Finding of Bending-Active Textile Hybrids," *Proceedings of IASS Annual Symposia*, vol. 2018, No. 15, pp. 1-8, International Association for Shell and Spatial Structures (IASS), 2018.

[5] L. Malomo, J. Pérez, E. Iarussi, N. Pietroni, E. Miguel, P. Cignoni, and B. Bickel, "FlexMaps: computational design of flat flexible shells for shaping 3D objects," *ACM Trans. Graph.* 37, 6, Article 241, 2018. doi: 10.1145/3272127.3275076

[6] J. Panetta, Q. Zhou, L. Malomo, N. Pietroni, P. Cignoni, D. Zorin, "Elastic textures for additive fabrication" *ACM Trans. Graph.* 34(4): 135:1-135:12, 2015.

[7] J. Pérez, B. Thomaszewski, S. Coros, B. Bickel, J. A. Canabal, R. W. Sumner, M. A. Otaduy, "Design and fabrication of flexible rod meshes" *ACM Trans. Graph.* 34(4): 138:1-138:12, 2015.

[8] N. Pietroni, E. Puppo, G. Marcias, R. Scopigno, P. Cignoni,"Tracing Field-Coherent Quad Layouts" *Computer Graphics Forum (Proceedings of Pacific Graphics 2016)*, 2016, vol. 25, num 7, 2016.

[9] D. Bommes, H. Zimmer, L. Kobbelt "Mixed-integer quadrangulation" *ACM Trans. Graph.* 28(3): 77, 2009.

[10] N. Pietroni, D. Tonelli, E. Puppo, M. Froli, R. Scopigno, P. Cignoni, "Statics Aware Grid Shells" *Comput. Graph. Forum* 34(2): 627-641, 2015.

[11] N. Kotelnikova-Weiler, C. Douthe, E. L. Hernandez, O. Baverel, C. Gengnagel, and J. F. Caron, "Materials for actively-bent structures," *International Journal of Space Structures*, 28(3-4), pp. 229-240, 2013.

[12] ANSYS®. Academic Research Mechanical Release 18.0.

Proceedings of the IASS Annual Symposium 2019 – Structural Membranes 2019
Form and Force
7 – 10 October 2019, Barcelona, Spain
C. Lázaro, K.-U. Bletzinger, E. Oñate (eds.)

Hybridizing vertex and face normals to design torsion free structures: application to the X-mesh pavilion

Xavier TELLIER [a b], Sonia ZERHOUNI [c] *, Guillaume JAMI [c], Alexandre LE PAVEC [c], Thibault LENART [c], Mathieu LEROUGE [a], Nicolas LEDUC [a c], Cyril DOUTHE[a], Laurent HAUSWIRTH [b], Olivier BAVEREL[a d]

* [c] ENS Architecture Paris Malaquais
sonia.zerhouni@paris-malaquais.archi.fr

[a] Laboratoire Navier UMR8205, Ecole des Ponts, IFSTTAR, CNRS
[b] Université Paris-Est, Laboratoire d'Analyse et de Mathématiques Appliquées
[d] GSA / ENS Architecture Grenoble

Abstract

The fabrication of a freeform structural envelope is usually a highly complex task. The costliest aspect is often the connections between the constitutive parts. X-Mesh is a pavilion that demonstrates a new rationalization strategy. Its structure, composed of a hexagonal grid of beams and cladding panels, is based on a geometry that rationalizes connections at two levels: firstly, nodes are repetitive, only two types of nodes are used. Secondly, panels can easily be connected to the support beams as they are orthogonal to each other. We prove that the proposed geometrical configuration can be asymptotically built on a smooth surface. We generate the meshes by numerical optimization from a smooth target surface, with an initialization derived from the asymptotic case. This pavilion shows another way of rationalizing a gridshell beyond the popular planar-quad meshes and circular/conical meshes. It also demonstrates a way to generate hexagonal gridshells which are not necessarily synclastic, this limitation being typically imposed to achieve planarity of cladding panels.

Keywords: Architectural geometry, gridshell, hexagonal mesh, free-form surface, rationalization, pavilion

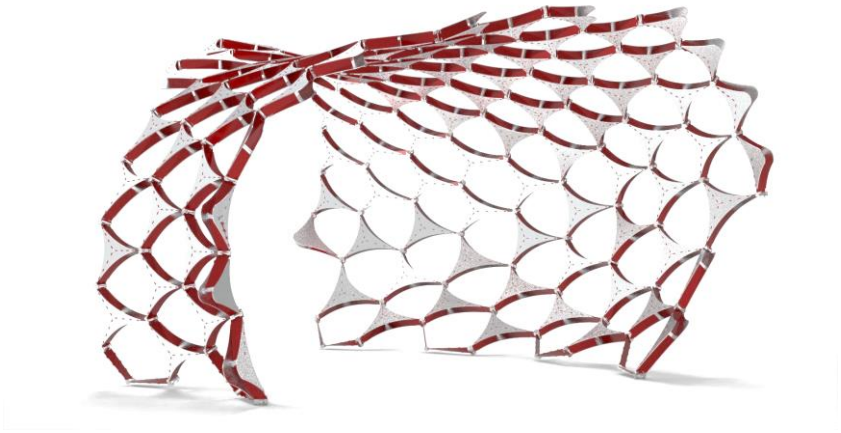


Figure 1: Rendering of the X-Mesh pavilion

Copyright © 2019 by Xavier TELLIER, Sonia ZERHOUNI, Cyril DOUTHE, Nicolas LEDUC, Guillaume JAMI, Alexandre LE PAVEC, Thibault LENART, Mathieu LEROUGE, Laurent HAUSWIRTH, Olivier BAVEREL
Published by the International Association for Shell and Spatial Structures (IASS) with permission.

1. Introduction

Free-form architectural structural envelopes have become increasingly popular in the past decades. The cost of these projects is usually strongly impacted by the fabrication of the nodes, which often need to be all unique. The connection between beams and panels is also problematic, as the kink angles between adjacent panels often vary significantly.

Two main geometrical strategies have been studied and used to simplify node fabrications in order to reduce their cost. The first one is to use a geometry that allows for torsion-free nodes. In such nodes, all the median planes of the incoming beams meet on a common axis. For example, the nodes shown in Figure 2 are torsion-free. This property can be achieved by having all beams in a vertical plane or by using circular or conical meshes ([1], [2]). Planar hexagonal meshes also have torsion-free nodes, but the hexagons are necessarily non-convex (shaped like a bow-tie) in anti-clastic surfaces [3].

The second one is node repetition. As detailed by Eike Schling in [4], node repetition can be achieved by two means. The first one is to have the exact same geometry for each node, or for some groups of nodes. For example, this can be achieved with meshes of revolution, or with isogonal molding surfaces [5]. The second one is to use construction tolerances or adjustable nodes to allow one or more degrees of angle variation with a same physical connector. This last option was for example used in the Neckarsulm swimming pool dome [6].

Regarding the beam-panel connection, the variation of the kink angle between the panel and the top surface of the beams renders impossible to make the connection structural, and thus to use the cladding system as a structural element. Furthermore, complex joining systems are needed if the king angle is too high. Solutions were studied in [7].

In this article, we propose a new geometric configuration, based on a hexagonal mesh, that solves both of these problems. In section 2, we detail this geometric structure, discuss its potential applications, and prove its existence. A generation method is then presented in section 3. Finally, in section 4, we present how this process has been applied to design and rationalize the X-Mesh pavilion.

2. A new torsion free geometrical configuration

The proposed geometrical configuration is a continuation of the work presented in [7], and is shown in Figure 2. The configuration is based on a hexagonal mesh with non-planar faces. Each of its nodes is assigned with an axis. The configuration satisfies the following properties:

(a) The axes of two adjacent nodes are coplanar and their common plane corresponds to the median plane of the beam;
(b) Every other node is flat: the incoming edges are coplanar. These nodes are referred to as 2D nodes, the other nodes are named 3D nodes;
(c) For 2D nodes, the axis is perpendicular to the plane of the node;
(d) For 3D nodes, the beam planes intersect at 120°.

This mesh can be used to design a hexagonal gridshell covered by tri-folded hexagonal panels. In that case, the properties that we just described can significantly simplify the fabrication, in particular with respect to the connections between the structural elements, as shown in Figure 3. Firstly, the contact between panels and beams top surface is perfect and the angle between beam webs and panels is 90°. Thanks to these properties, standard low-cost connections can be used to structurally connect beams to panels. Secondly each node is torsion-free: medial axes of beams meet on a common axis. As a result, structural depth can easily be given to the grid. Thirdly, one half of the nodes are planar, and for the other half, beam planes intersect at 120°, thus allowing a standardization of all beam connections.

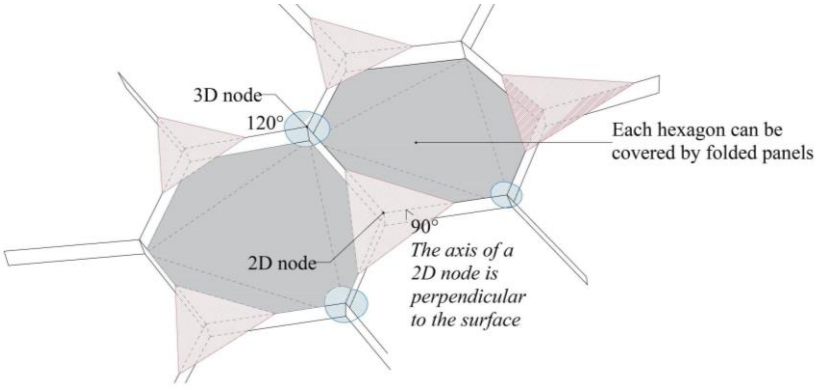


Figure 2: Geometrical configuration

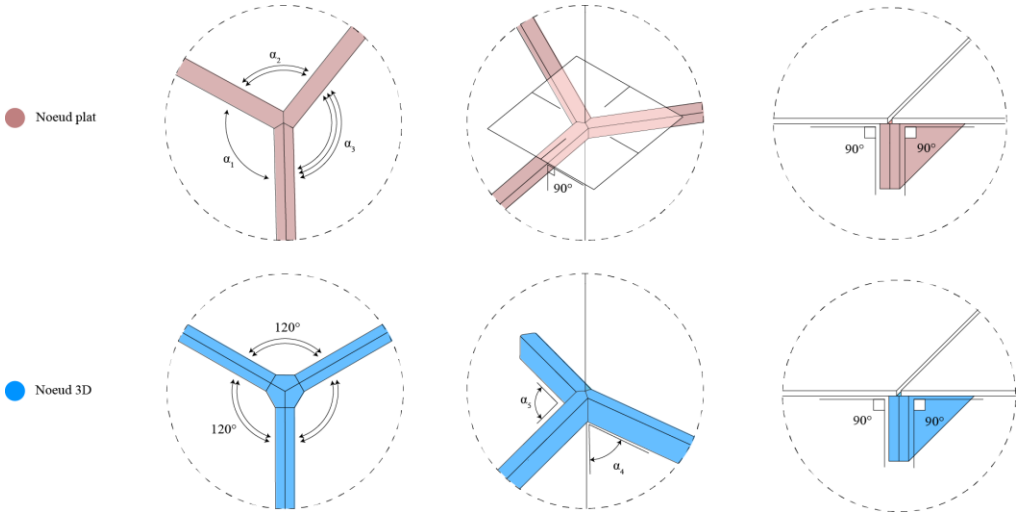


Figure 3: Geometry of connections structural elements

The thus formed gridshell is a cladded honeycomb structure. We note that Jiang *et al.* [8] proposed a method to design this type of structure without torsion on an arbitrary target surface. However, they do not constrain the node axes to be normal to the surface. This is major difference with our configuration, which is therefore much more constrained geometrically.

The proposed properties (a), (b) and (c) form a new type of geometrical structure, based on a mesh in which face normals and vertex normals are coplanar. The proposed application is based on a hexagonal pattern, but many other types of patterns and structural applications are possible [7]. For clarity, we propose to name this type of mesh a *Caravel mesh*, an acronym standing for *meshes with CoplanAR fAce and VErtex normaLs*.

3. Smooth surface approximation

In this part, we prove by construction the existence of the geometric structure described in the previous sections in the asymptotic case, i.e. in the case where a mesh approximates a surface with smaller and smaller face size. In this case, properties can then be described in the setting of smooth differential geometry. We will show that it is asymptotically possible to construct our geometry from a planar hexagonal mesh approximating a smooth surface S without umbilics and such that one family of hexagon edges is aligned with curvature directions.

Let us start by introducing a classical local approximation model of a surface. A surface *S* can be locally approximated at any point P at the second order by a paraboloid. This paraboloid is elliptic if the Gaussian

curvature K is positive (i.e. the surface is synclastic), cylindrical if K=0, and hyperbolic if K<0 (i.e. the surface is anticlastic). The equation of this paraboloid is, in the tangent plane at P:

$$z = \frac{1}{2}(k_1 x^2 + k_2 y^2)$$

Where k_1 and k_2 are the principal curvatures. The unit normal of the paraboloid at a point (x,y,z) neighboring P is given by :

$$\vec{n}(x,y) = n(x,y)(-k_1 x\ ;\ -k_2 y\ ;\ 1\ )$$

The application $(x,y) \mapsto \vec{n}(x,y)$ is referred to as the surface Gauss map. The value of the real factor $n(x,y)$will not be important here. Considering a neighborhood such that $|x| \ll 1/k_1$ and $|y| \ll 1/k_2$, $\vec{n}(x,y)$ belongs at the first order to a horizontal plane, and is then an orthotropic dilatation in the directions x and y. The ratios of the dilatation in the x and y directions are k_1 and k_2, up to an homothety (the scaling of the Gauss map is not important in our construction).

After this preliminary considerations, we are now going to construct a mesh and its vertex normals satisfying the properties described in the previous sections. We will use a capital N to describe the mesh normals, as they often differ from the surface normals n.

Let us first consider a series of planar hexagonal meshes with decreasing faces sizes approximating S, and with one family of edges aligned with a principal curvature direction. As mesh size tends towards zero, each hexagon tends to have central symmetry and to be inscribed in a homothetic copy of the Dupin indicatrix, as explained in [9] – the Dupin indicatrix being the conic resulting from the intersection between the paraboloid and the plane z=1. As shown in Figure 3 (left), the surface Gauss map of the Dupin indicatrix is also a conic, with equation $\frac{x^2}{k_1} + \frac{y^2}{k_2} = 1$ (up to a homothety).

Let us pick three vertices on an hexagon ABCDEF to form a triangle ACE. We build the Fermat center P of ACE, i.e. the point such that $(\overrightarrow{PA}, \overrightarrow{PC}) = (\overrightarrow{PC}, \overrightarrow{PE}) = (\overrightarrow{PE}, \overrightarrow{PA}) = 120°$. P will be a flat node of the mesh, and A,C and E will be 3D nodes. This construction yields properties (b) and (d).

In order to fulfill property (b), the mesh normal at P, N_P, must be the normal of triangle ABC. This normal is, in the space of normals, the center of the Gauss map of the Dupin indicatrix. As we want no torsion along PA, PB and PC (property (a)), the mesh normal at A, N_A, must lie on a line l_A parallel to (AP) passing through N_P. In the general case, this line does not include the surface Gauss map at A, therefore $N_A \neq n_a$(this is a second order difference, as the normals are equal at the limit).

Now, considering adjacent hexagons Figure 3 (middle), we observe that the lines previously built intersect on one point with the same lines from the neighboring hexagons if and only if edges AB and DE are aligned with a principal direction (i.e. parallel to an axis of the conic). These intersections points N_{Q1},N_{Q2}… are the normals of the 3D nodes.

The hexagonal network (in red) along with the attached normals described by the hexagonal mesh on the Gauss map (also in red) verify all the geometrical properties described in the previous sections.

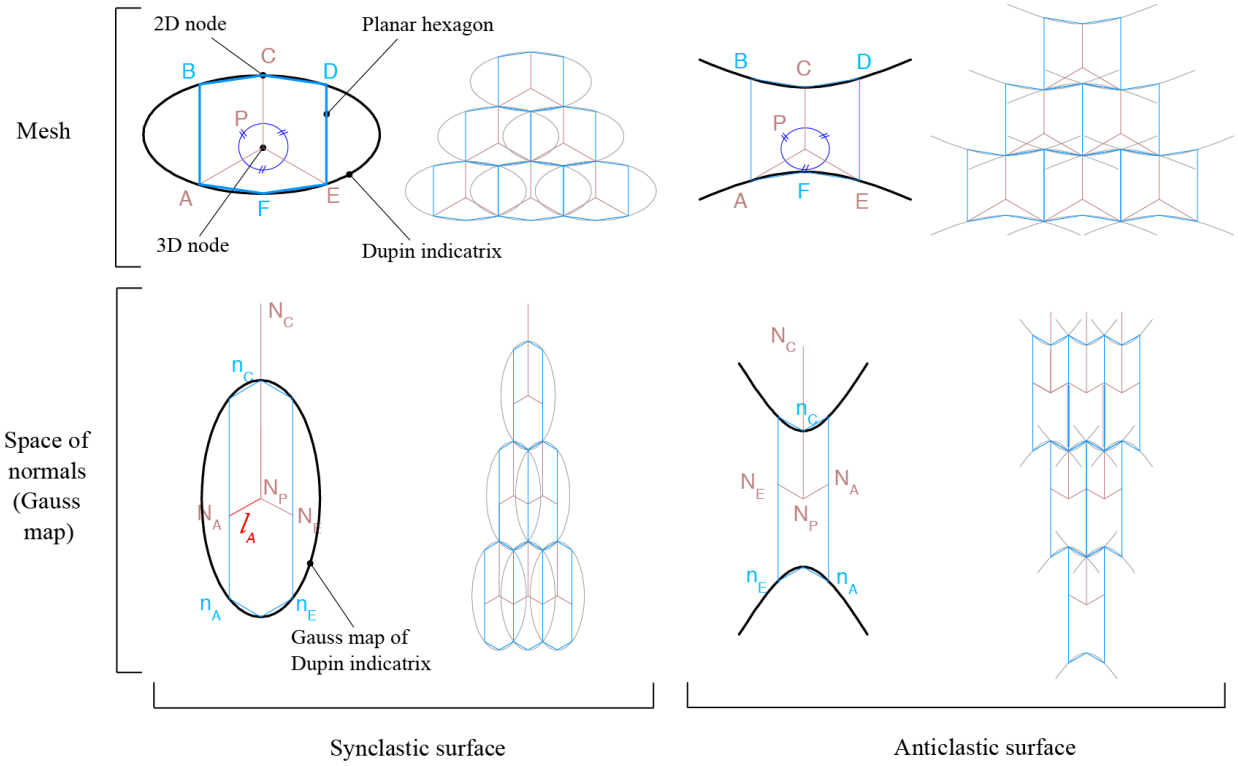


Figure 3: Asymptotic construction

3. Generation method

We now give a method to generate the geometrical configuration described in section 2. In a first step, we compute an initial mesh close to this configuration. In a second step, we optimize node position and normals orientation such that properties (a) to (d) are satisfied within given tolerances.

The initial mesh is constituted of hexagons where all edges are aligned with principal curvature directions. Each hexagon has two 180° corners, so the mesh looks like a brick wall. Wang *et al.* showed in [9] that this type of mesh can converge efficiently towards a planar-hexagons mesh. Since we showed in section 2 that our geometric configuration can be built on a planar-hexagons mesh, this initialization is also effective for our geometry.

The mesh resulting from the initialization is then used as the input of a non-linear optimization defined within the framework of Rhinoceros™'s plugin Kangaroo2. The optimization problem is made of multiple geometrical criteria. Each criterion is expressed as a projection. Every node is assigned with a normal. A first criterion forces every node of valence three to be torsion-free (property (a)), by requiring the normals of the three neighboring nodes to be such that the median planes of the beams coming to the node meet on a common line corresponding to its normal. A second criterion makes the 2D nodes and their respective neighboring nodes coplanar (property (b)). A third one constraints the normals of the 2D nodes to be respectively aligned with the normals of the planes defined by their three neighboring nodes (property (c)). Finally, a fourth one forces 3D nodes to be, when projected on the triangles defined by their three neighboring nodes, the Fermat points of these triangles (property (d)). Complementary criteria are also set for smoothing purposes, such as proximity to the target surface, and to treat the boundaries.
This optimization problem is highly non-linear and non-convex. Hence, there is no theoretical guarantee that the mesh obtained after iterations of the optimization algorithm perfectly meet all the criteria or reach a global minimum of the problem. However, empirically, the resulting mesh tends to satisfy all the

geometrical properties within very low tolerances as shown in Figure 4. Thus, this two-step method allows in practice to generate a geometrical configuration as described in section 2 within acceptable tolerances.

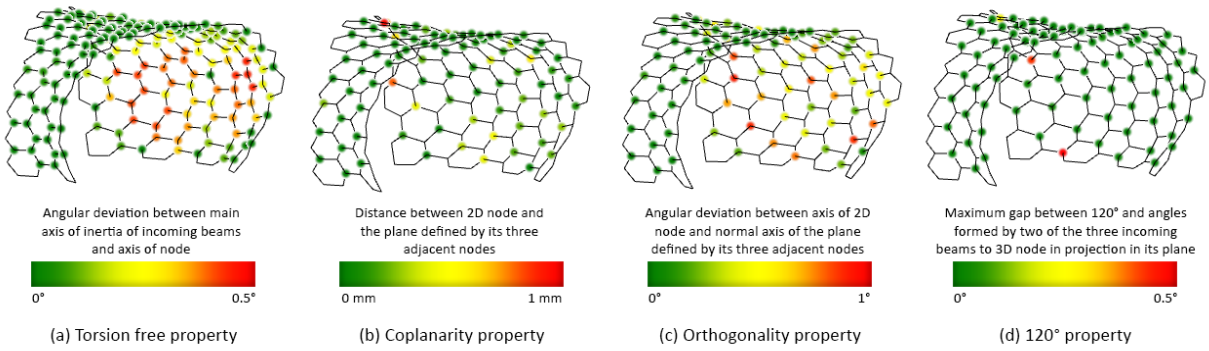


Figure 4: Convergence of algorithm regarding properties (a) to (d)

4. The X-Mesh pavilion

In order to demonstrate the innovation and the adaptability of the workflow hereby presented, it was applied to the design and realization of a pavilion for the IASS 2019 Pavilion contest.

4.1. Design

The shape of the pavilion is a doubly curved envelope, of which transversal sections are horseshoe arches. The shape has both synclastic and anticlastic portions, and demonstrates the ability of our method to generate structures on a broad class of forms. The pavilion is high enough to walk under, so it is possible to enjoy the view from the inside as well as from the outside.

The starting point of the design is a surface, which was discretized by a hexagonal mesh aligned with curvature lines. There are two ways to align a hexagonal mesh with curvature directions. The alignment with the horizontal curvature lines is chosen in order to create the graphic impression of an ascending movement, as the triangular panels are pointing upwards diagonally.

The concept of this pavilion focuses on highlighting the geometrical properties through the architectural treatment of the elements, especially the connections. The conception of each type of node is entirely based on the geometrical rationalization that simplifies its fabrication. We took advantage of each geometrical strategy to define the technology of the pavilion.

The pavilion is made of laser-cut aluminum plates. There are two main components: beams and cladding panels, as shown in Figure 6.

4.2. Structure

The torsion free nodes allowed us to conceive the main hexagonal grid as a beam structure. Indeed, since adjacent node axes are coplanar, their common plane defines the median planes of beams. This allowed us to build all of our elements out of sheet materials.

We took advantage of the node repetition to design two standards types of connections, one for each type of geometrical node (2D and 3D). These nodes are showed in Figure 6. 2D nodes offered us the possibility to create a structural connection through the common plane of the three incoming beams. This connection was realized by two aluminum panels on the superior and inferior edge of the three beams.

Structurally, the height of the beams can be adjusted to have sufficient vertical inertia. The horizontal inertia is guaranteed by the cladding panels. Panels are fixed to the edges of the three beams thanks to

locking tabs in which the carved panels are pushed into. As beams are orthogonal to panels, all the cuts are orthogonal to the sheet planes, and can thus be realized by 2D laser cutting.

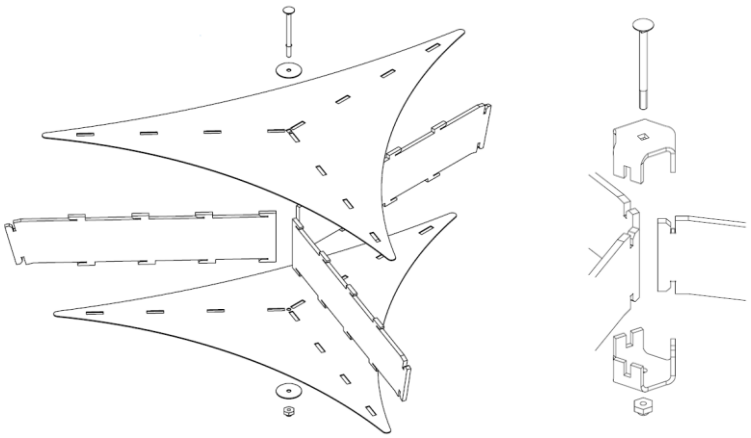


Figure 6: Technological solution for the 2D and 3D nodes

The technological treatment of the 3D nodes is based on the existence of an axis assigned to each node and on the fact that beam planes always intersect at 120°. For 3D nodes, a hinged connection is build from two pieces, cut out from thicker aluminum sheets and swagged in a stamping press. These formed parts are all identical and guaranty the 120° angle between each beam plane of the 3D node. They are maintained in place thanks to a single screw, materializing the direction of the normal axis of the node.

The two types of junctions are adapted on the free edges of the pavilion; thus it is unnecessary to develop an entirely different solution for the nodes on the boundary. Only two beams are joined on 3D nodes on naked edges, so in order to keep the same technological solution, we add a short stub that closes the node. 2D nodes with only two beams can work the same way on naked edges than on interior edges, as long as the panel is designed accordingly. This degree of freedom offers the opportunity to adapt the general design of the edge.

4.3. Mesh alignment with ground level

For aesthetic and fabrication reasons, it was desirable to align the mesh with the the ground. Since the mesh follows curvature directions, we modified the target surface so that its bottom boundaries (verifying $z=0$) are curvature lines. By the Joachimsthal theorem, this property is achieved if the surface has a constant slope along the lines $z=0$. As our target surface is a B-spline, the slope at the ground boundary is given by the bottom two rows of control points. We therefore optimized the position of these control points so that the slope of the surface is constant at the ground level.

4.4. Structural check

To ensure the safety and structural behavior of the pavilion, we implemented a finite element model of the structure and verified its behaviour under dead load and accidental load. Stress concentrations around the cuts were verified by local models using 2D plate elements.

5. Conclusion

In this article, we demonstrated the potential of the so-called Caravel meshes for structural applications by designing a full scale pavilion which is to be exhibited at the 60th IASS Symposium in October 2019. The geometry is further rationalized so that only two types of nodes are used throughout the whole structure.

Acknowledgements

Pavilion costs were covered by the I-Site Impulsion grant "Games". We thank Viry for providing steel cladding panels, and ENSA Paris Malaquais for its financial support. The first author is financially supported by LABEX MMCD (http://mmcd.univ-paris-est.fr/). We would like to thank Eike Schling and Daniel Piker for fruitful discussions.

References

[1] Y. Liu, H. Pottmann, J. Wallner, Y.-L. Yang, and W. Wang, "Geometric modeling with conical meshes and developable surfaces," *ACM Trans. Graph.*, vol. 25, no. 3, p. 681, 2006.

[2] H. Pottmann and J. Wallner, "The focal geometry of circular and conical meshes," *Adv. Comput. Math.*, vol. 29, no. 3, pp. 249–268, 2008.

[3] W. Wang, "Hexagonal Meshes with Planar Faces," no. January, 2008.

[4] E. Schling, "Repetitive Structures," TUM, 2018.

[5] R. Mesnil, C. Douthe, O. Baverel, B. Léger, and J. F. Caron, "Isogonal moulding surfaces: A family of shapes for high node congruence in free-form structures," *Autom. Constr.*, vol. 59, pp. 38–47, 2015.

[6] Schalich Bergermann und Partners, "Freizeitbad aquatoll neckarsulm." [Online]. Available: https://www.sbp.de/projekt/freizeitbad-aquatoll-neckarsulm/. [Accessed: 13-May-2019].

[7] X. Tellier, O. Baverel, C. Douthe, and L. Hauswirth, "Gridshells without kink angle between beams and cladding panels," *Proc. IASS Symp. 2018 Creat. Struct. Des. Boston, USA*, 2018.

[8] C. Jiang, J. Wang, J. Wallner, and H. Pottmann, "Freeform honeycomb structures," in *Computer Graphics Forum*, 2014, vol. 33, no. 5, pp. 185–194.

[9] W. Wang and Y. Liu, "A Note on Planar Hexagonal Meshes," in *Nonlinear Computational Geometry*, Springer,., 2009, pp. 221–233.

Proceedings of the IASS Annual Symposium 2019 – Structural Membranes 2019
Form and Force
7 – 10 October 2019, Barcelona, Spain
C. Lázaro, K.-U. Bletzinger, E. Oñate (eds.)

Inventory Constrained Funicular Modelling

Kim R. BABER*, Jane R. BURRY[a], Canhui CHEN[a] , Joseph M GATTAS[b], Aurimas BUKAUSKAS[c]

*School of Architecture, University of Queensland
St Lucia, QLD 4067, Australia
k.baber@uq.edu.au
[a] School of Design, Swinburne University of Technology
Hawthorne, VIC 3122, Australia
[b] School of Civil Engineering, University of Queensland
St Lucia, QLD 4067, Australia
[c] BRE Centre for Innovative Construction Materials, University of Bath,
Bath BA2 7AY, United Kingdom

Abstract

This paper investigates the development of a digital form finding model that combines the generation of **funicular geometry** with a material **inventory constraint**. The model provides a flexible design tool that facilitates exploration of structural form whilst simultaneously satisfying two rationalizing criteria. It maintains an equilibrated structure derived from funicular geometry; and optimally assigns an inventory of parts with natural dimensional variation to this funicular geometry. The combined goal for the design outcome is to achieve material efficiency through both structurally rational form, and minimization of material waste. The material chosen for the inventory is below-grade sawn timber1, being lightweight but with high levels of naturally occurring structural variability. Sawn timber boards that are rejected for structural application due to their frequent structural defects (knots, checks, splits etc.) can readily yield usable short length structural members, once the defects are removed. In doing so, this provides a unique inventory of random short members. These short members are well suited to articulated structures, which, by employing an inverted funicular geometry, only incur axial stresses and can employ simple non-moment timber connections. This research has been undertaken for the design of the pavilion for the "Working Group 21 – Advanced Manufacturing and Materials" exhibition at the IASS Symposium 2019.

Keywords: inventory-constrained design, form finding, funicular modelling, timber structures

1. Introduction

Antoni Gaudí's funicular or 'hanging chain' model was a sophisticated form finding tool for rationalizing structural geometry and optimizing material utilization. Gaudí's use of the tool in the design of the Colònia Güell church, was particularly innovative, in that it involved a complex three-dimensional network of interconnected structural force vectors. Previous versions of hanging chain models, such as those carried out by Heinrich Hübsch were limited to discrete, two-dimensional studies of an arch structure in a single plane [1]. Gaudí's hanging model proved to be highly effective in

[1] Timber sourced is Australian plantation grown softwood, *below-grade* refers specifically to timber members that do not meet structural grading standard requirements due to the presence of frequent structural defects.

Copyright © 2019 by Kim R. BABER, Jane R. BURRY, Canhui CHEN, Joseph M GATTAS, Aurimas BUKAUSKAS
Published by the International Association for Shell and Spatial Structures (IASS) with permission.

resolving complex geometric configurations of interconnecting structural elements into a state of equilibrium, in 'real time'.

As Block points out, physical hanging chain models, as used by Gaudí, are "excellent design explorers since they address both structural and formal considerations and present the designer at all times with a status of the design that reflects the cumulative changes applied to the model" [2]. They can be, however, incredibly time consuming and complex to build, and he states "the effect of removing, adding or adjusting the lengths of strings is not straightforward at all"[2]. This was experienced first hand by Jos Tomlow and his team when they reconstructed Gaudí's hanging chain model in 1989 [1].

Interactive computational hanging chain models, such as the CADenary model pioneered as a design tool by Axel Kilian, utilized particle spring systems in a virtual hanging chain model, allowing interaction with the model geometry in real time, providing immediate adjustment of string lengths as equilibrium is resolved [3]. The virtual model reacts in real time to changes, and "the novelty of [Kilian's] implementation is to combine the dynamic simulation and interactive environment to find equilibrium and to allow the user to playfully explore these constantly evolving structures"[2].

Particle spring systems combined with a dynamic relaxation solver have been developed in the Rhinoceros 3D and Kangaroo software environments, and provide readily available virtual hanging chain and hanging net models. In these virtual models, the particle springs provide a mechanism allowing automatic adjustment of the string lengths, as the strings collectively resolve a state of global equilibrium. For the solver, the criterion for the targeted string length is solely the virtual equilibrated state. This investigation seeks to provide an *additional criterion* into a computational procedure, that constrains the target string lengths to a prescribed range of possible lengths, based on a material inventory from which the final structure is to be constructed. In this case, it is based on naturally occurring short lengths of timber- the resultant material available from boards with frequent defects.

The aim is to introduce this additional criterion to a virtual form finding model, but ensure that the model operates with a similar level of interactive responsiveness, providing immediate spatial feedback: a design tool that facilitates exploration of form within the bounds of both structural *and* material constraints.

2. Short Length Timber as an Inventory Constraint

Every tree that is harvested and sawn into structural timber members, is subject to natural variation in its properties. Considerable variation can exist between specimens, and within the tree itself. The resultant distribution of defects within sawn timber can be unpredictable, and as a result, substantial amounts of sawn timber is rendered uncertifiable for structural use. Sawn timber containing too many structural defects will not be certified for structural use, and instead sold for non-structural applications, woodchipped to make particle based products, or burnt as fuel to power other operations on the sawmill plant. As a result, only about 50% of the volume of timber harvested will end up being certified for use as structural grade timber [4].

For those timber members containing frequent defects such as knots, checks, splits, wane, if those defects are cut out, the resultant lengths of timber may be certified as structural grade but are relatively short and also inconsistent in length. For most commercial framing applications this variability provides too much unpredictability, and such a random inventory of elements is deemed too inconvenient and time consuming for contractors to work with. This computational model aims to introduce an automated part assignment algorithm to overcome such inconveniences and time inefficiencies.

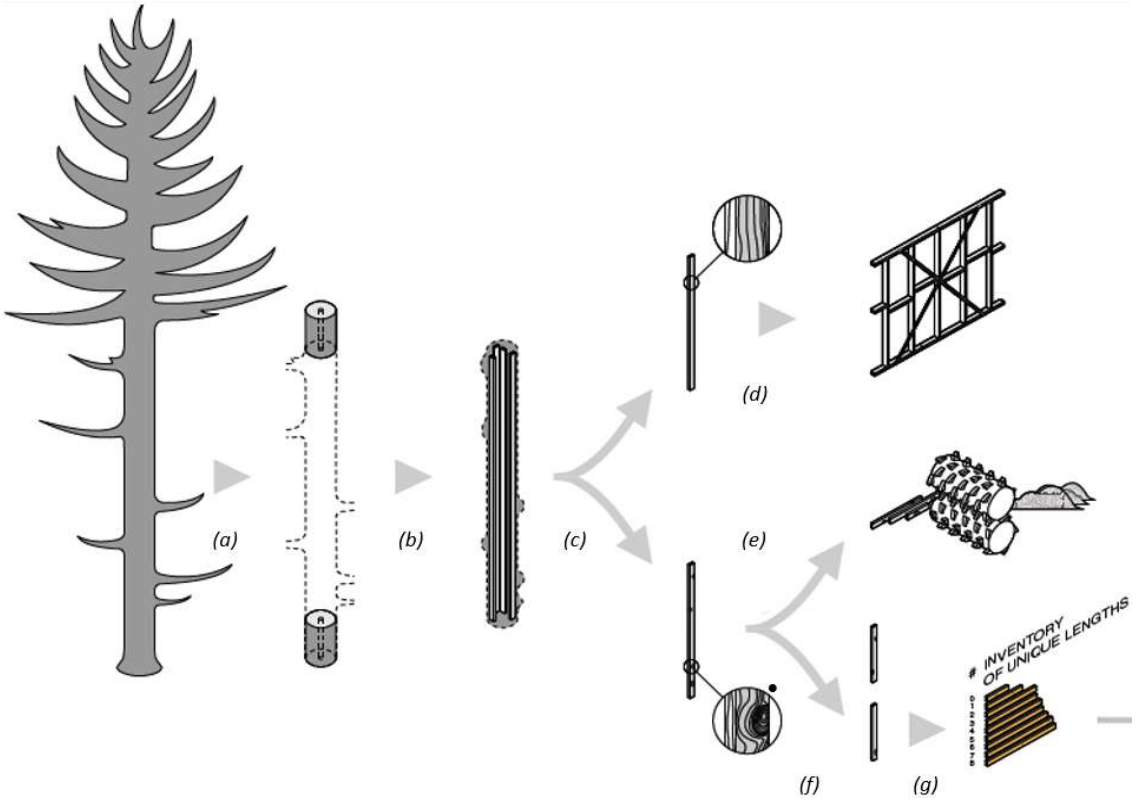


Figure 1: A typical sawmilling process: *(a)* The tree is harvested and docked into transportable lengths (approx. 6 metres) with varying branch distribution according to: silvicultural practice ,climate, soil, planting density etc.; *(b)*each log is sawn into usable framing members and is subject to the naturally occurring structural defects; *(c)*sawn members are sorted into those without, and with defects; *(d)* members free from defects are certified for use in structural applications; *(e)* members with defects are used in non-structural application or woodchipped; *(f)* defects are removed resulting in short lengths, which provide: *(g)* an inventory of short, unique lengths.

The preparation of an inventory of short timber lengths is attainable through sawmill scan data analysis, without physically removing the defects first. During the sawmilling processing, scans are taken of each board, and for a given unique pack of timber dispatched, a unique dataset for each member's material properties locates every defect in each board. From this, a digital inventory can be generated, plotting resultant short lengths of timber that would be available after the defects are removed.

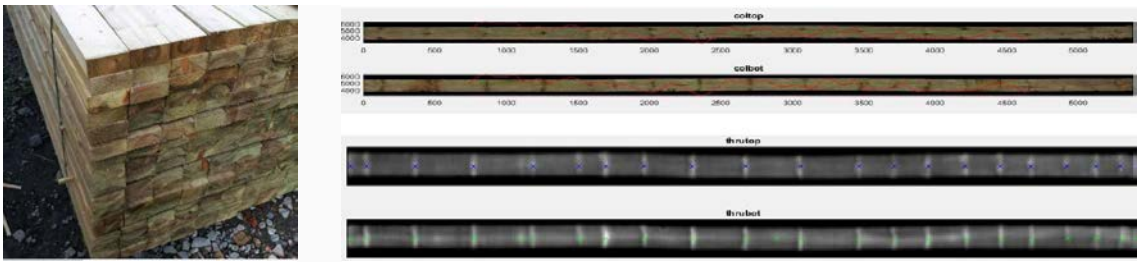


Figure 2: A pack of below-grade studs containing structural defects (left), and examples of sawmill scan data showing image capture of defects (top right) and x-ray scan of density (bottom right)

3. Funicular Form Finding

A funicular model was developed in response to the design criterion of the Working Group 21 – Advanced Manufacturing and Materials" exhibition, such as volume and height. Given the design area, a network of lines was generated and used as the initial geometry input. While the endpoints of each line were set as anchors to define the boundaries, lines within the network were further segmented to individual members required for the hanging chain model simulation. In this initial stage, the number of segmentation was set to fulfil two primary criteria:

1. To ensure that the relaxed hanging chain model was set with a height limitation of 4 metres and to provide internal head height clearance for circulation when it reaches the equilibrium.

2. To ensure that the number of segments is sufficient for the chain to form beams with smooth curvature.

At this stage, the number of segmentations does not correlate with the given inventory of short length timbers.

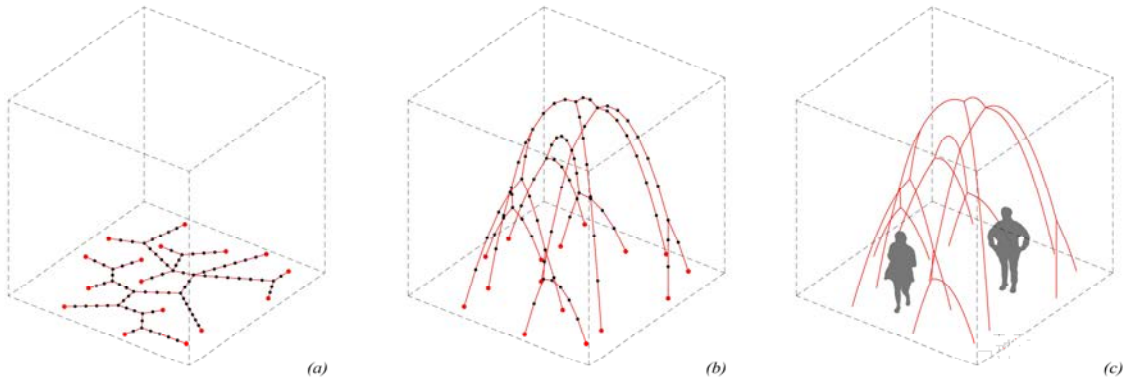


Figure 3: Generation of hanging chain model: (a) base geometry (b) relaxed chain with equal segmentation subdivisions and (c) intended pavilion design with smooth arches.

4. Part Assignment

4.1. Part Assignment Heuristic

There has been rapid recent development in computational approaches for problems where a designer must employ a constrained inventory of parts. Such constraint arises for example with use of deconstructed building components [5] or use of natural material with high variation in sectional size or length [6]. Early methods assigned parts based on the geometric correspondence between an inventory of parts and a target form, for example the Tree Fork Truss, which assigned forked trees into a Vierendeel truss using an evolutionary algorithmic approach [7]. State-of-the-art approaches use optimisation formulations that can assign parts based on a wide variety of possible fitness criteria, including structural form or topology, structural performance, minimisation of material waste, or minimisation of reprocessing expense [5, 6, 8].

Assignment algorithms for curved inventory pieces have only been explored for the Biomass Boiler House [9], which used naturally curved trees to populate a long, curved building wall. This paper investigated two approaches for part assignment: a best-fit heuristic based on tangent difference between inventory parts; and a generative assembly model that enforces G1 (curve end tangent)

continuity between sequential inventory parts. For the present work, a curved inventory assignment algorithm is proposed with three new components: curved part generation; all-targets best-fit assignment; and performative funicular form regeneration.

First, a strategy to machine curved inventory segments from straight stock material was adapted based on the technique utilized by the authors in [10]. With reference to figure 4a, the sagitta distance is used as a control parameter to nest a maximally-sized curved inventory part inside the initially-straight timber length. When a uniform sagitta is applied to straight segments of varying length, a new inventory is established with parts of varying radii of curvatures, with shorter lengths generating tighter curvatures.

Second, a Best-Fit heuristic approach was selected as appropriate for part assignment in the present context, as their relatively high speed enables rapid designer feedback as to the amount of inventory use and the quality of assignment [6]. With reference to Figure 4b,'best' was defined as the smallest *tangent difference,* measured as the angle between the end tangent of an inventory element and a tangent evaluated at a point on the target curve at a matching arc length. The tangent difference was evaluated between all inventory parts and all targets, and part assignment proceeded in order of inventory elements with the smallest tangent difference. After each iteration, the best-fit inventory element was removed from available parts, the best-fit target curve was truncated at assignment length, and the remaining target curve was updated in the list of targets with tangent difference re-evaluated. The assignment algorithm terminated when all inventory parts were used, or when all remaining inventory parts were longer than all the remaining length of the target elements

Third, inventory parts were reassembled into an approximation of the target funicular curve. If inventory parts are assembled assuming end points aligned to the target curve, the assembly has G0 (curve end position) continuity. Alternately, inventory parts can be considered as piecewise arcs and assembled with aligned end tangents and enforced G1 continuity. Both strategies are shown in Figure 4c, with the G1 continuous curve constructed using the grammar proposed in [11]. Good fidelity is seen in both cases, where fidelity is measured as the cumulative nearest point distance between the assembled inventory and target curves. Preliminary benchmark testing of part-assignment for a single funicular cable showed that the G1 assembler had better fidelity when selecting from a large inventory of parts, and worse fidelity when selecting from a constrained (minimum number required) inventory of parts.

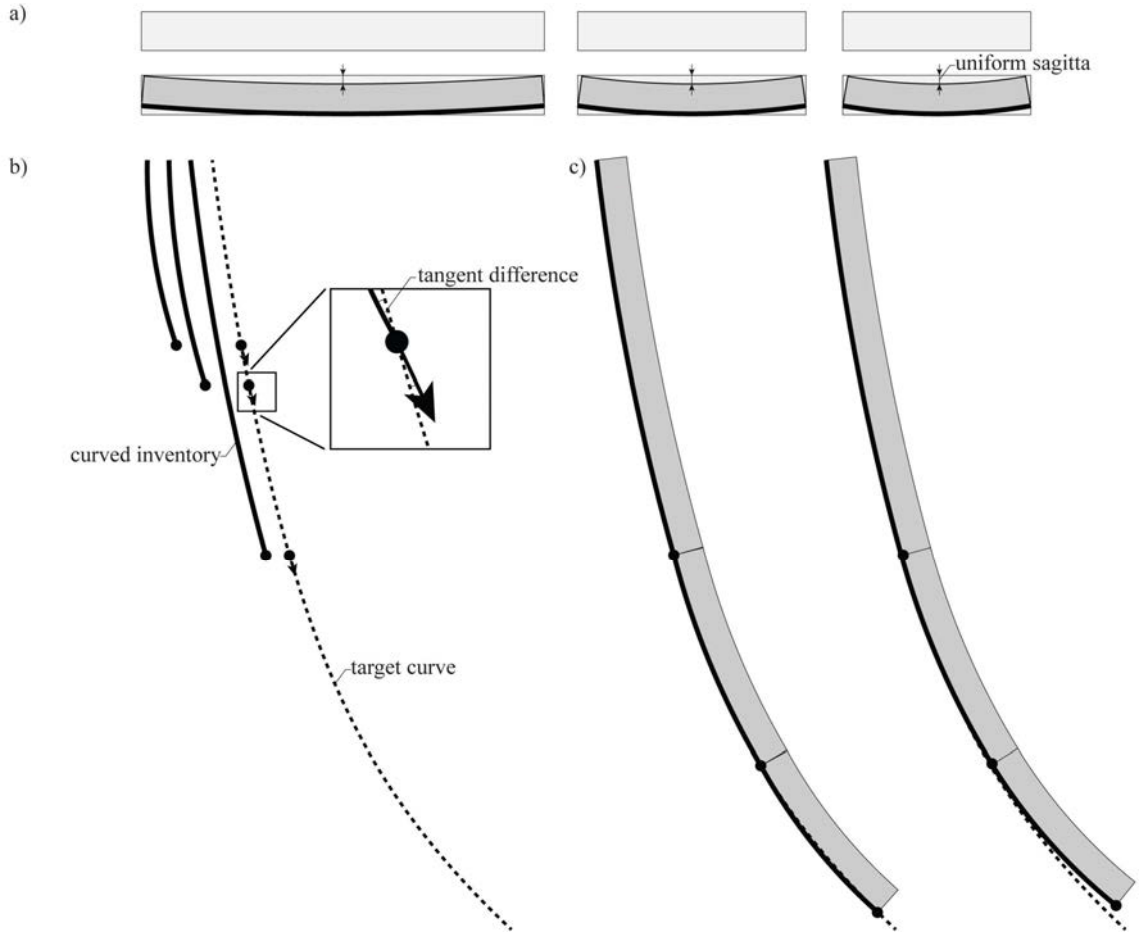


Figure 4: Curved inventory generation and assignment. a) Straight stock to curved inventory conversion. b) Best-Fit heuristic with evaluation of tangent difference between inventory and target curves. c) Inventory parts assembled with G0 (left) or G1 (right) continuity.

4.2. Evaluation and Re-Relaxation

The part assignment heuristic was tested on the funicular form described in Section 3 and from 182 inventory pieces with lengths varying from 105mm to 1200mm. Figure 5 shows the part assignments at 5, 20, and 81 iterations, mapped onto the 27 target curves comprising the funicular model. The algorithm completed in a fast 3.5s (Intel i7-4790 3.6GHz CPU, 16Gb RAM, SSD) at 81 inventory assignments, with termination due to no remaining shorter-length inventory. Observation of assignment ordering shows that longer and less-curved parts are assigned early and are well matched with the initial, low-curvature regions of the funicular cables. Shorter and more tightly curved parts are preserved for later iterations, which again suits the increasing funicular curvature and decreasing remaining target lengths. The use of minimum tangent difference ordering criteria is concluded to be a rational choice of pre-sorting criterion and results in good quality solutions for this problem.

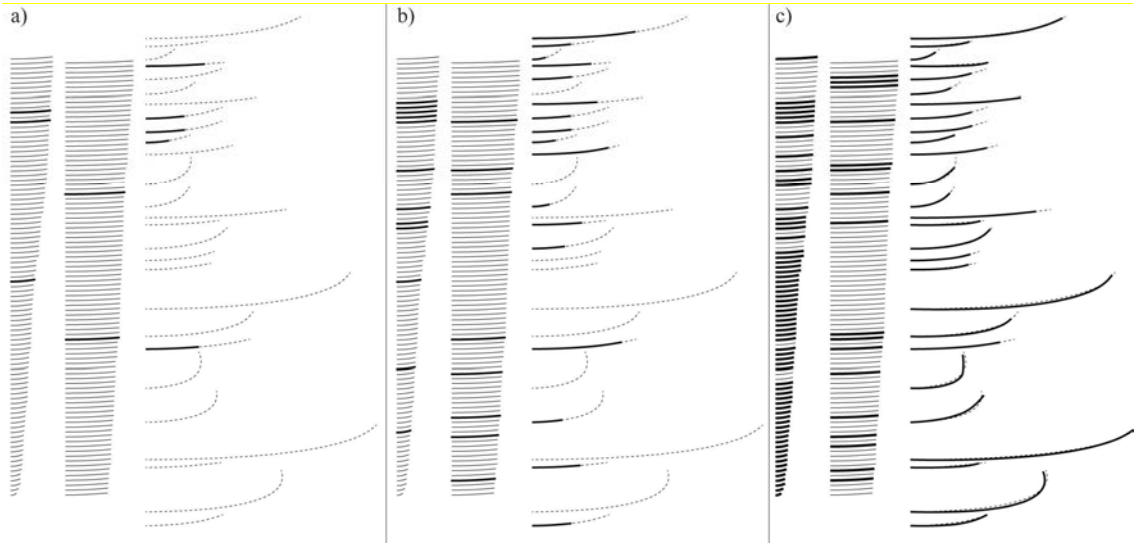


Figure 5: Part assignment results with a) 5, b) 20, and c) 81 (final) parts. Target curves shown as dashed lines, unassigned inventory parts shown as thin lines, assigned inventory parts shown as thick lines.

Based on the results of the part assignment heuristic, the selected inventory items are assembled with G1 continuity described in section 4 to form the segments of the targeted initial funicular form. The reconstructed segments are then mapped to their original locations and a comparison is made between the re-assembled model and the initial form. As figure 6 demonstrates, despite the difference between the length offered by the available inventory and the length of the targeted cable in the initial hanging chain model, the fidelity between the two models is within a reasonable range.

A second stage relaxation was also set up to update the initial funicular form with the additional information acquired through the part assignment heuristic. As figure 6(d) depicts, each segment in the original funicular form is segmented again into individual members for the new hanging chain simulation. The number of segments is set in response to the number of inventory items used in the assignment tasks. In this round of re-relaxation, the target length of each individual segment used in the funicular form-finding procedure is set to match the length of its corresponding inventory item. In addition, the target length criterion is given the utmost priority compared to other input simulation forces such as the gravitational load in the second-round simulation.

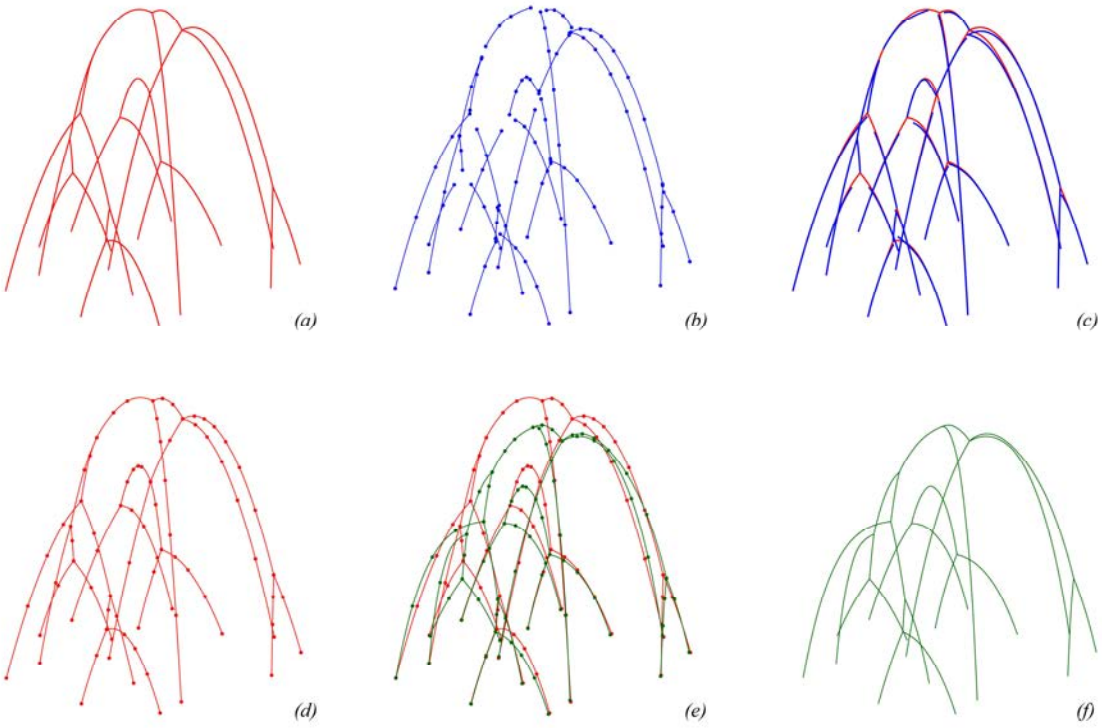


Figure 6: Second round relaxation result (a) initial design; (b) arch segments re-assembled base on part assignment results; (c) overlay and comparison between (a) and (b); (d) second round subdivision of segments of the initial design based on the number of inventory parts resulted in the heuristic;(e); re-relaxation of the initial hanging chain; (f) result from second round relaxation

While figures 6(e),(f) and 7 illustrate the result of the second-round simulation, it's evident that, to adjust the chain segments of the original funicular form to the targeted length of the selected inventory parts while maintaining the anchor points and boundary condition of the initial design, the simulation has made considerable adjustment to the original form (figure6(e), figure 7(a)). Moreover, figure 7 (b) illustrates the comparisons between the segments from the part assignment results and their corresponding parts in the final simulation. In general, the segments extracted from the final geometry matches the selected inventory items and the level of difference is within a range which could be mitigated in detail design during the later fabrication stages. Although there are cases when an arch is assembled within a limited number of inventory parts, two, for instance, and when it experiences a larger amount of shifting, the distortion could be exacerbated. However, the distortion could be solved effectively by allowing a limited range of adjustment to the ground anchors in the second round relaxation.

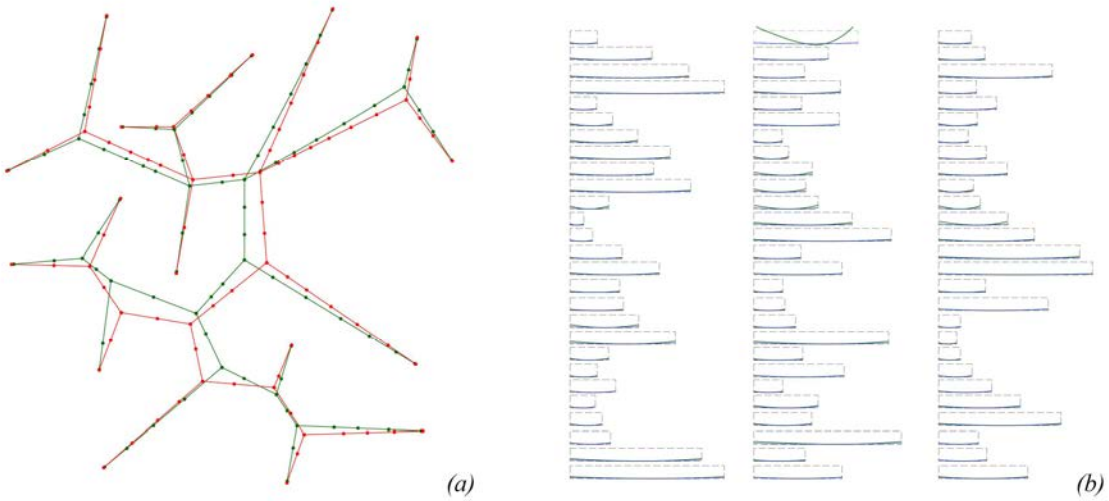


Figure 7: Result comparison: (a) original design shown in red, final result shown in green; (b) inventory parts shown in blue, final segments shown in green.

5. Conclusion

Through its development and testing, this novel form finding model has been shown to be capable of combining the dual constraints of an enforced static equilibrium through funicular geometry, in conjunction with an optimal assignment of an inventory of parts. Running the dynamic relaxation solver, the parts assignment algorithm, and the second-round relaxation in rapid succession, enabled the model to provide the user with an immediacy of spatial feedback that renders it an effective design tool. It allowed free exploration of form whilst ensuring a rational configuration of structure and deployment of material.

A key factor in achieving this rapid processing was the definition of the parts assignment as a best-fit heuristic, providing an assignment solution that is achieved very quickly even if potentially sub-optimal. A goal of a perfect fit inventory was 'traded-off' in favor of immediacy in user feedback. In addition, it was found that the funicular geometry provided a latent geometric characteristic that is particularly well aligned to a parts assignment based on curvature criteria. When starting assignment from its base anchor, the funicular curve will inherently progress from shallow to tighter curvature, correlating to an ever diminishing part length, enabling part sorting to have a predictable and efficient sequence.

Finally, it was particularly promising to see the model operate with a high level of spatial responsiveness when the adjustment of individual string lengths resulted in a global change of form. In this way it can be seen to behave like the physical hanging chain, providing interaction between spatial, structural and material determinants, but also allowing faster, iterative adjustment of string length based on the inventory constraint.

This model has been used to design the pavilion for the "Working Group 21 – Advanced Manufacturing and Materials" exhibition at the IASS Symposium 2019, and the timber pavilion resulting from this research will be on display for the duration of the symposium.

Acknowledgements

This project was funded by the Australian Research Council ARC Future Timber Hub "Industrial Transformation Hub to Transform Tall Timber Buildings." The following people have not been authors of this paper, but been involved in the preparation of the of the submission for the "Working Group 21 – Advanced Manufacturing and Materials" exhibition submission, and have contributed to preliminary research into the parts assignment algorithms, and timber fabrication techniques: Daniel Foote, Harry McCullough, Fatemeh Raouf and Nicholas Russel.

References

[1] J. Tomlow and A. Gaudí, *Das Modell*. Institut fur Leichte Flachentragwerke, 1989.

[2] P. P. C. V. Block, "Thrust network analysis: exploring three-dimensional equilibrium," Massachusetts Institute of Technology, 2009.

[3] A. Kilian and J. Ochsendorf, "Particle-spring systems for structural form finding," *Journal of the international association for shell and spatial structures,* vol. 46, no. 2, pp. 77-84, 2005.

[4] M. H. Ramage *et al.*, "The wood from the trees: The use of timber in construction," *Renewable and Sustainable Energy Reviews,* vol. 68, pp. 333-359, 2017.

[5] J. Brütting, J. Desruelle, G. Senatore, and C. Fivet, "Design of Truss Structures Through Reuse," in *Structures*, 2019, vol. 18: Elsevier, pp. 128-137.

[6] A. Bukauskas, P. Shepherd, P. Walker, B. Sharma, and J. Bregulla, "Form-Fitting strategies for diversity-tolerant design," in *Proceedings of IASS Annual Symposia*, 2017, vol. 2017, no. 17: International Association for Shell and Spatial Structures (IASS), pp. 1-10.

[7] Z. Mollica and M. Self, "Tree Fork Truss," *Advances in architectural geometry,* vol. 2016, pp. 138-153, 2016.

[8] A. Bukauskas, P. Shepherd, P. Walker, B. Sharma, and J. Bregulla, "Inventory-Constrained Structural Design: New Objectives and Optimization Techniques," in *Proceedings of IASS Annual Symposia*, 2018, vol. 2018, no. 11: International Association for Shell and Spatial Structures (IASS), pp. 1-8.

[9] Y. Wang, "Hooke park biomass boiler house," in *Advancing wood architecture: A computational approach*, A. Menges, T. Schwinn, and O. D. Krieg, Eds.: Routledge, 2016.

[10] K. B. Plasencia Alava, L. K. McCann, G. Hodge, K. Baber, and J. M. Gattas, "Computational Design and Experimental Behaviour of Deployable Mass Timber Arches," *Journal of the International Association for Shell and Spatial Structures,* vol. 60, no. 1, pp. 90-100, 2019.

[11] J. Gattas, "A Generative Shape Grammar for Piecewise Cylindrical Surfaces and Curved-Crease Origami," in *Origami^7*, vol. 3: Engineering One, R. J. Lang, Bolitho, M., You, Z., Ed.: Tarquin Group, 2018, pp. 921-934.

Proceedings of the IASS Annual Symposium 2019 – Structural Membranes 2019
Form and Force
7 – 10 October 2019, Barcelona, Spain
C. Lázaro, K.-U. Bletzinger, E. Oñate (eds.)

Knit Tensegrity Shell

Sachin Sean GUPTA, Ying Yi TAN, Pei Zhi CHIA, Christyasto P. PAMBUDI, Christine YOGIAMAN, Kenneth J. TRACY*

*SUTD Digital Manufacturing and Design Centre
Singapore University of Technology and Design
8 Somapah Road, Singapore 487372
kenneth_tracy@sutd.edu.sg

Abstract

This paper describes the design-to-fabrication workflow of the Knit Tensegrity Shell project which will be exhibited at the IASS Symposium 2019. The workflow involves a) a digital framework of design, simulation, and analysis of the tensegrity shell, b) generation of CNC knitting machine instructions for membrane fabrication, and c) production of a kit-of-parts assembly. Through multiple iterations of form-finding and FEA simulations, a shell design consisting of compressive carbon fibre struts tensioning a knitted textile membrane was materialised. This membrane element was customised using CNC knitting to feature: (i) designated regions of yarn materials of varying stiffness as informed by stress concentrations; (ii) integrated pockets to hold the compressive struts; (iii) net-shaped textile based on an input design. Finally, construction details were rationalized in order to insert the struts in an efficient manner and secure the novel structure.

Keywords: Membrane tensegrity, form finding, CNC knitting, material design

1. Introduction

This research investigates knit membrane tensegrity shells - a new class of membrane tensegrity structures. By coupling the structural efficiency of tensegrity systems with the high degree of customizability offered by CNC knitting technology, a new opportunity to create custom-tailored lightweight structures emerges. This paper outlines the design-to-fabrication workflow of the Knit Tensegrity Shell project which will be exhibited at the IASS Symposium 2019. The workflow starts from a framework of design, simulation, and analysis of the tensegrity shell, to generation of machine instructions for membrane fabrication, and finally the creation of a kit-of-parts assembly (Figure 1).

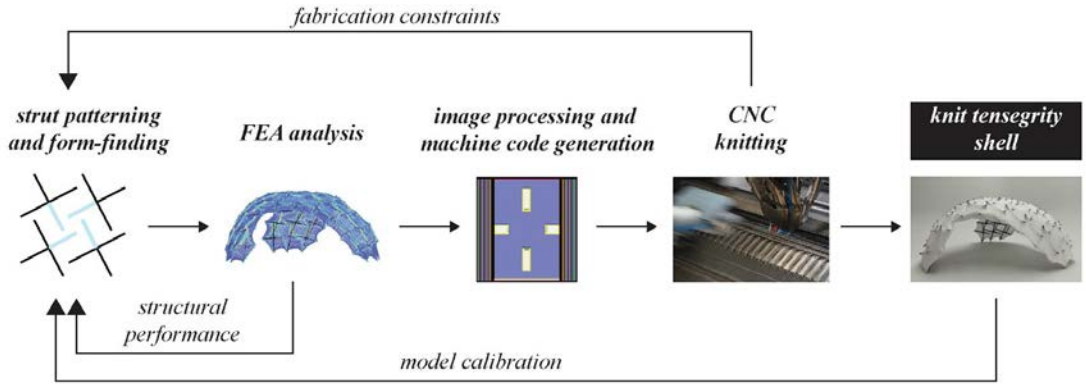


Figure 1: Workflow of the Knit Tensegrity Shell project.

Copyright © 2019 by S. S. Gupta, Y. Y. Yan, P. Z. Chia, C. P. Pambudi, C. Yogiaman, K. J. Tracy
Published by the International Association for Shell and Spatial Structures (IASS) with permission.

Knit membrane tensegrity shells consist of an elastic CNC-knitted membrane that is tensioned by the insertion of multiple rigid struts. The stretched textile's natural tendency to shrink to its original size is opposed by the compressive struts, resulting in a reaction force exerted by the membrane to cause the assembly to form a curved 3D geometry. This tensioning of the membrane also increases its stiffness, which can be manipulated into creating a structurally stable shell geometry by strategically distributing the struts. By using redundant, reciprocally patterned strut configurations, a wide variety of shells that feature large openings can be generated. This is unlike typical membrane tensegrity structures that tend to have closed forms.

The application of CNC knitting enables material and geometric variations within the manufactured textile to make it suitable as the primary structural element of the system. For the Knit Tensegrity Shell, the knitted membrane is functionally graded to optimise its stiffness based on regions of stress concentration as a result of the strut patterning. This provides enhanced structural performance that enables the expansion of the design space for such structures.

2. Literature review

Although tensegrity structures originated in the 1960s [1], membrane tensegrity shells have more recent beginnings from the past decade. One prominent case study is the MOOM pavilion which had its design and assembly supervised by Kojima & Sato. This lightweight temporary structure comprised of a thin polyester textile mesh that was tensioned uniaxially by a series of alternating aluminium tubes, creating a tunnel-like pavilion that spanned a total area of 8m (width) x 26m (length) [2]. Other proponents in this field include Shigematsu, Tanaka & Noguchi, whose work involved the fabrication of scaled prototypes with varying geometries to analyse the geometric behaviour of tensegrity membrane structures in relation to strut configuration [3].

Furthermore, customising textile membranes to influence geometric forms was of interest to our research team. Such strategies can be found in the domain of CNC knitted membrane installations, as seen in the Hybrid Tower and Isoropia by the Centre for Information Technology and Architecture (CITA). In these examples, fabric membranes were designed with zonal regions of varied elasticity through changes in the stitch pattern. This enabled the textile to accommodate or integrate external elements to facilitate the assembly of these installations [4,5]. This manipulation of geometry through varied elasticity was particularly compelling for us.

3. Form finding and FEM Analysis

To explore membrane tensegrity shells, a means of digitally modelling this structural typology had to be conceived. However, membrane tensegrity structures are form-active structures characterized by high degrees of deformation and the 3D form is a result of material interactions with nonlinear behaviour. This means that traditional top-down approaches of sculpting membrane forms to adhere to an intended geometry would be inaccurate. Instead, a form-finding approach in Rhinoceros and Grasshopper premised on position-based dynamics using the Kangaroo live physics engine was selected. The aim of this form-finding tool was to uncover a strut pattern that would achieve a dome-like shell with minimal variation in curvature (i.e. standard deviation of Gaussian curvature at mesh vertices is as close as possible to 0) and have openings of an appreciable height for people to walk through (at least 1.75m) within a $16m^2$ bounding area. The resultant pattern would also have to avoid contact between crossing strut units, which causes the assembly to perform less like a tensegrity system and more like a frame structure.

The modelling process started with a 2D pattern of struts that would compose one flattened "petal" of the structure which is to become a lateral arch in 3D. Strut patterns were parametrically designed with consideration of their lengths, spacing, angle and quantity within the bounding area of each petal. This was explored in reciprocal configurations, as previous physical prototypes demonstrated good curvature

and stiffness output with a reciprocal strut layout. It was further developed as an arrayed design with three petals. A Delaunay mesh was generated using the endpoints of each of the lines to model the membrane, with the interconnected mesh edges representing internal pathways of tensile forces that occur between neighbouring strut ends. In Kangaroo, the mesh edges were assigned the goal to shrink in length by a specified amount, mirroring the physical reality of the struts stretching the membrane to induce pretension. The strut lines were instructed to maintain their lengths, akin to the rigidity of the physical struts. With this simulated energetic frustration due to the interaction between the shrinking mesh and stiff struts in place, the system was given an upward momentum to ensure that the structure found its 3D form above the designated ground plane. Once simulated, the three arrayed petals created three interconnected lateral arches that composed the full structure.

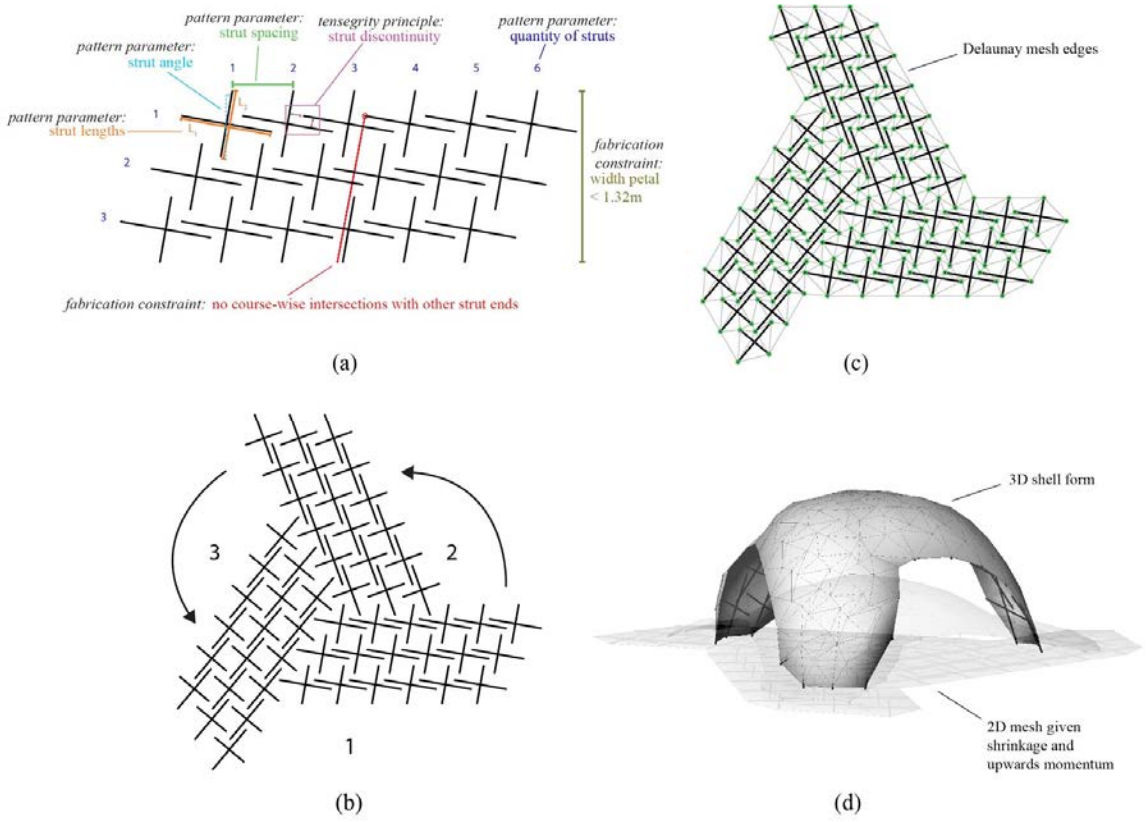


Figure 2: Strut pattern search and form-finding tool. (a) Strut pattern for one petal was designed according to a variety of parameters such as strut length, angle, spacing, and quantity, in addition to fabrication constraints. (b) The strut pattern for one petal is then arrayed 360° to create the full pattern. (c) A Delaunay mesh was generated using the endpoints of each of the struts as mesh vertices. (d) The mesh was then instructed to shrink by a predefined amount while the struts remained rigid, and this coupled with upward 'momentum' allowed the configuration to converge upon a 3D form.

However, there were two major fabrication constraints that had to be factored in this pattern search. The first was attributed to the knitting direction being aligned with the width of the leg, which was limited by the total number of needles in the machine bed. Factoring the shrinkage from the elastic yarn, this amounted to a width constraint of 1.32m for each petal. Moreover, no more than two strut end pockets could be aligned along the transverse axis (course-wise) of each petal, as this would exceed the number of available yarn carriers in our machine. Thus, the Opossum plugin [6] was used as an optimisation algorithm to search for strut placement patterns that met our desired geometric and fabrication criteria.

Being a single-objective optimisation solver, the objective value was defined as the sum of the standard deviation in positive Gaussian curvature of the form-found mesh and the number of course-wise intersections in the pattern. Furthermore, various strut pattern parameter ranges were manually constrained to ensure that the width of the leg was under 1.32m and that the parameter space search was not too broad. After a small number of 300 iterations, the solver successfully found strut patterns and shell forms that fit the fabrication and geometric requirements, from which a final design was selected (Figure 3a).

To verify and calibrate the form-finding approach, several 1:20 and 1:10 prototypes of strut units and petals were knitted on the CNC knitting machine, with additional post-processing using overlocking/sewing machines to join the petals to form complete shells (Figure 3b). These prototypes gave quick feedback on the real-world validity of simulation results and whether the strut configuration resulted in collisions between struts.

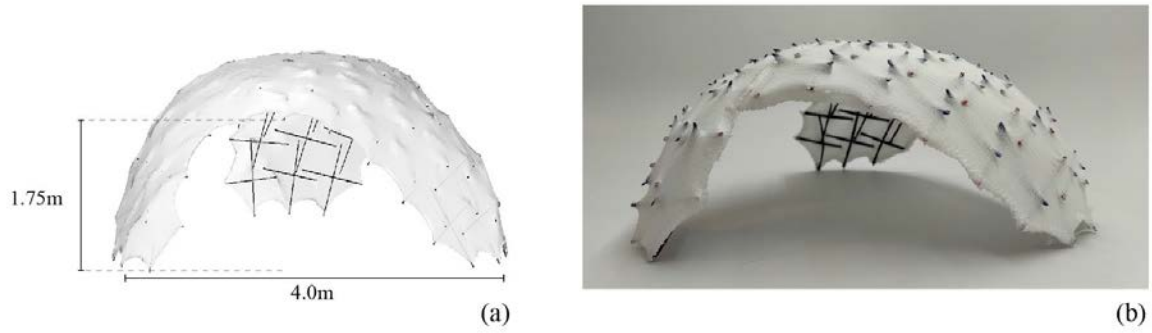


Figure 3: (a) Digital model and (b) physical knitted 1:20 prototype of our final design.

The main limitation encountered with the small-scale prototypes was the non-linear scaling of the membrane. While the membrane's length and width could be scaled proportionally, the stitch size and thickness remained constant throughout the prototypes regardless of scale. This was further complicated by the non-linear relationship between pretension extent to output curvature, limiting the usefulness of the feedback from scaled models. Future work can be undertaken to understand this non-trivial relationship.

The selected membrane tensegrity structure was analysed using the K2Engineering finite element analysis (FEA) solver plugin, which is able to analyse form-active cable and membrane-based systems [7]. The mesh was subdivided to generate a higher face count to provide higher resolution. The membrane edges were designated as cables and assigned with material and cross section properties provided by tensile test results for a piquet lacoste textile knitted from 550D Spandex-polyester yarn (450D Spandex, 100D polyester). Although knitted textiles are classified as orthotropic materials, the cable element was assumed to be an isotropic material with the properties of the textile's weaker wale-wise direction assigned. The nonlinear elastic deformation of the knit was also excluded given that the expected loads (i.e. stretch from the strut and self-weight) would not surpass its linear elastic range. Prestress was instilled in each cable by comparing its initial length to its form-found length and proportionally assigning it with the tensile force at the end of the elastic region. The struts were assumed to be carbon fibre tubes and assigned properties provided by the material supplier. A summary of the assigned properties can be found in Table 1. Nine points were selected as fixed support conditions and self-weight was the only load case.

Table 1: Material and geometrical properties for FEM analysis using K2Engineering

Knitted textile 550D Spandex-polyester yarn with piquet lacoste stitch type				Carbon fibre tube		
E-modulus (MPa)	Cross-section (mm^2)*	Density (kg/m^3)	Max pretension (N)	E-modulus (MPa)**	Cross-section (mm^2)	Density (kg/m^3)
2.39	81.7	650	30	35000	40.8	1485

*Calculated based on mesh density. **Provided by material supplier.

Figure 4 shows the axial stress results of the FEA, which were used to visualize and map the distribution of prestress in the membrane. Blue indicates lower tensile stress while yellow indicates higher tensile stress. The highest concentrations of stress existed at the strut ends and the lines of high pretension followed the Delaunay mesh edges as expected.

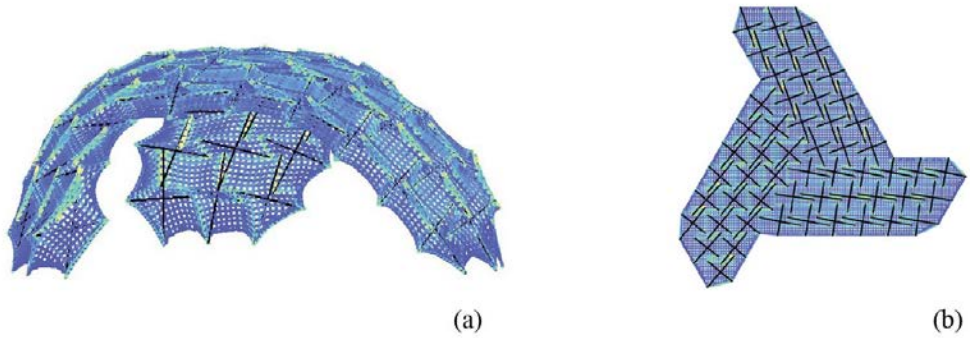


Figure 4: FEA results in the (a) 3D state and (b) remapped back to 2D state.

4. Fabrication and prototyping

4.1 CNC-knitted membrane

CNC knitting was chosen because it can produce inherently elastic knitted textiles which can be customised by the stitch-by-stitch control afforded by this fabrication technique [8]. Knitted textiles are formed by interlocking loops of yarn, resulting in an inherent elasticity that arises from the deformation of the loops. Thus, a knitted tensegrity membrane can stretch to accommodate the compressive struts and achieve the required curvature. Furthermore, CNC knitting software allows users to design the knitted product with multiple yarns types, multiple stitch types, and complex manipulation of stitches. This allows for the variation of material properties and microstructures within a single textile, making it viable to knit a textile with internal variations of mechanical properties (as informed by the FEA), integrated pockets to hold the compressive struts, and customised shaping to accommodate the form-found strut configuration.

The knitted membrane was fabricated on a Shima Seiki MACH2®XS computerized, 15-gauge WHOLEGARMENT weft-knitting machine. To grade the mechanical and functional properties of the membrane, the FEA axial stress results were translated into a bitmap image to generate machine code that dictates the yarn and stitch type at every point of the knitted membrane. Regions of high stress concentration were knitted using a 540D UHMWPE-Spandex yarn (400D ultra-high molecular weight polyethylene, 140D Spandex) to avoid material failure particularly during insertion of the struts.

UHMWPE filament was used due to its high breaking tenacity of 25.5cN/dtex (information provided by the material supplier) and significant resistance to abrasion. Since these regions coincided with the strut ends, the UHMWPE-Spandex yarn was knitted using two stitch types - single jersey and tubular single jersey - to form pockets to accommodate the strut ends (Figure 5).



Figure 5: Left - Pocket in contrast black-and-white yarn, with carbon fibre strut inserted into pocket. Right - Knit notation for piquet lacoste (main body) and tubular jersey (pockets).

To maximize the material performance and fabrication efficiency of the membrane, the regions of the membrane that would experience lower tensile stresses was knitted from 550D Spandex-polyester yarn using the geometry of piquet lacoste stitch type. The highly elastic Spandex-polyester yarn allowed the knitted textile to stretch to more than twice its original size. To minimise the weight of the membrane, single needle bed stitch types (v.s. double needle bed stitch types) were chosen. Piquet lacoste stitch type, which is formed by alternating between knit only rows and knit-tuck rows [4] (Figure 5), was chosen because the presence of tucks (as opposed to knit stitches or miss stitches) reduced the horizontal shrinkage after knitting, resulting in a wider piece of fabric compared to other single bed patterns (e.g. single jersey, rib).

To minimise the amount of cutting and sewing required for the membrane to form its final shape before strut insertion, the membrane was shaped during the knitting process using two methods. The first method was to add and/or remove stitches so that selected parts of the fabric would become wider, narrower, or skewed. The second method used water soluble yarn and sacrificial waste yarn that is removed after knitting to form the final shape of the membrane.

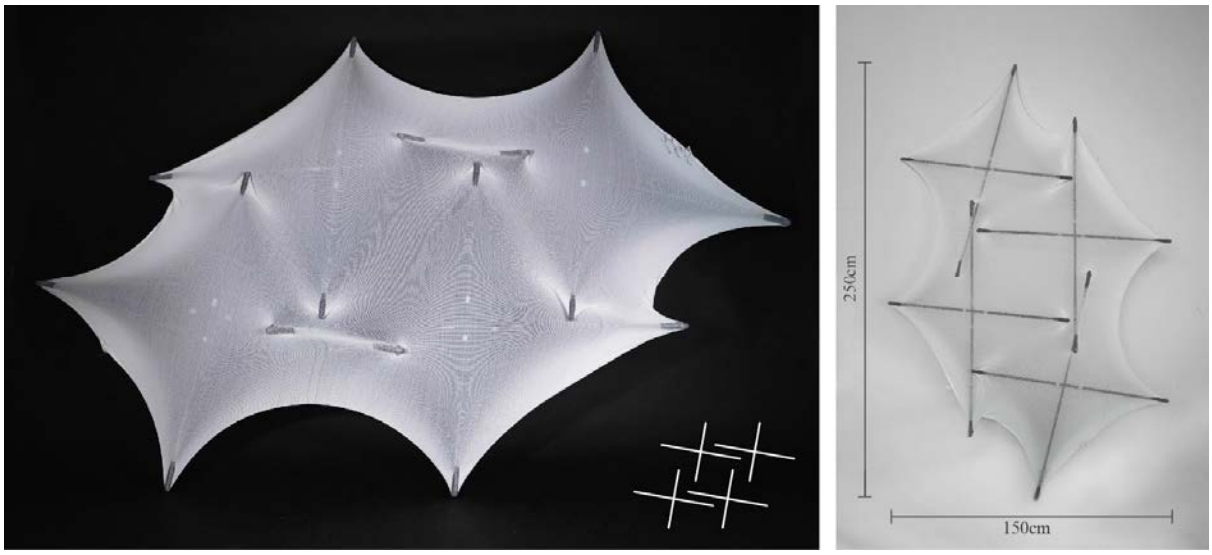


Figure 6: Documentation of 1:1 physical prototype consisting of four reciprocally patterned strut units.

4.2 Assembly

Finally, the assembly details of the structural system had to be designed. In the 1:1 prototype, the struts were 14mm diameter carbon fibre tubes that were cut into two segments to ease the insertion of the tubes into the pockets without an initial stretch of the membrane (Figure 7). The membrane was then stretched, and the strut segments were slotted together as guided by an inner sleeve joint. 3D-printed end caps were added to both ends of the carbon fibre tubes to create an even contact surface between the end of the tubes and the knitted pockets. Lastly, the entire installation was anchored to the ground at nine strut ends by 3-D printed conical base footings. These bases are further weighted down to secure the structure and resist accidental lateral forces on the pavilion.

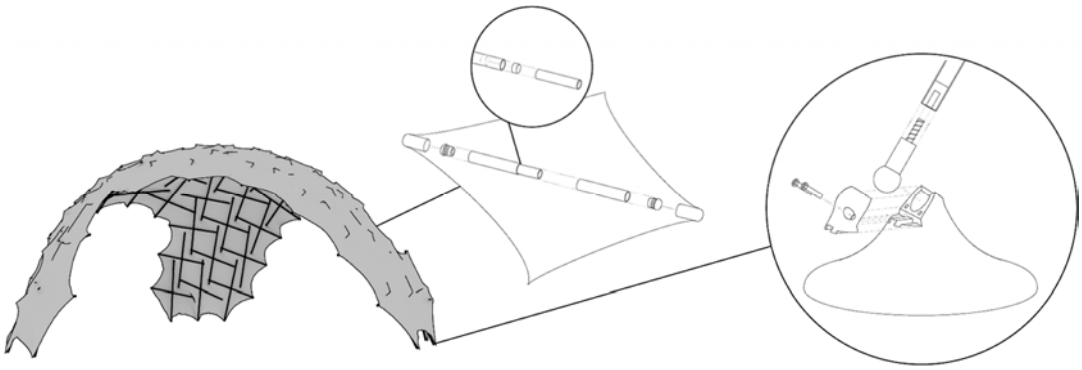


Figure 7: Sleeve joint and base.

5.0 Conclusion

This paper investigated the design and fabrication of a new class of lightweight structures of knit membrane tensegrity shells. Our workflow first involved digital form-finding, optimisation and finite element analysis to design and assess the tensegrity shell. Secondly, strut placement and FEM analysis data informed the design of the textile which was converted to CNC-knitting instructions to fabricate the customised membrane. Finally, connecting elements of sleeves joints and base footings were made to complement the main elements of carbon fibre struts and knit membrane in the creation of our tensegrity pavilion.

Building upon this research can take several directions. Innovations in CNC technology will enable a greater and more flexible array of knit types, materials, and gradation capabilities that can be explored to improve the load-bearing capacity and weather-resistance of the tensegrity membrane. Due to the highly nonlinear material properties of knitted textiles, the simulation tools can be upgraded to a more rigorous computational mechanics modelling approach to achieve a fine-grained understanding of the role of knit deformation, even at the scale of individual loops, in the shaping of the membrane [8]. In terms of macroscopic design, the performance criteria for membrane tensegrity shells can be expanded to include environmental considerations such as wind flow to control the size, arrangement, and nature of openings in the shell. Particularly compelling is the notion of leveraging both the compliance of the knit and inherent flexibility of tensegrity systems to accommodate dynamic variations in lengths of the struts, potentially enabling the formation of environmentally-responsive, shape-changing knit structures.

Acknowledgements

We would like to thank the students from the 2018 SUTD ASD options studio for their contribution to the tensegrity used in this project: Carla Tjandra, Chee Su June, Denise Nicole Lime Jeay Yee, Heng Jia Wen, Lee Jia En, Natasha Yeo Min, Pang Yun Jie, Phoon Ruyi Natalie, Sng Ei Jia, Sofia Foo Xin Di, Soh Jia Ying, Tiffany Christy, Wang Xueting.

The authors would like to thank the Architecture & Sustainable Design Pillar, the Digital Manufacturing and Design Centre, the SUTD Fabrication Laboratory, Web Structures for their institutional Support.

We would like to thank Thomas Wortman and Robert Bamford for their contribution to the modelling and form-finding workflow during and after the 2018 design studio.

We would like to thank the SUTD's Digital Manufacturing and Design Centre and the National Research Foundation for their financial support for this research project.

References

[1] R. Motro, *Tensegrity: Structural Systems for the Future.* United States: Kogan Page Science, 2003.

[2] N. Ratschke, A. Bogle, J. Lindenberg, "Parametric Analysis of Tensegrity-Membrane-Structures", in *Proceedings of the IASS Annual Symposium 2017, Hamburg, Germany.*

[3] M. Shigematsu, M. Tanaka and H. Noguchi, "Form finding analysis of tensegrity membrane structures based on variational method," in *Advances in the Optimization and Form-finding of Tensegrity Structures: Proceedings of the 6th International Conference on Computation of Shell and Spatial Structures IASS-IACM 2008, Ithaca, USA, May 28-31, 2008.*

[4] M. Tamke, A. Deleuran, C. Gengnagel, M. Schmeck, R. Cavalho, R. Fangueiro, F. Monteiro, N. Stranghoner, J. Uhlemann, T. H. Homm and M. Ramsgaard Thomsen, "Designing CNC Knit for Hybrid Membrane and Bending Active Structures," in *Structural Membranes 2015, Barcelona, Spain.*

[5] T. Wortmann, "Opossum: Introducing and Evaluating a Model-based Optimization Tool for Grasshopper," in *CAADRIA 2017, Hong Kong, China*.

[6] "K2Engineering", Format Engineers, https://formatengineers.com/research/k2-engineering.html (accessed December 10, 2018).

[7] R. La Magna, V. Fragkia, P. Langst, J. Lienhard, R. Noel, Y. Sinke Baranovskaya, M. Tamke and M. Ramsgaard Thomsen, "Isoropia: an Encompassing Approach for the Design, Analysis and Form-Finding of Bending-Active Textile Hybrids," in *Proceedings of the IASS 2018, Boston, USA.*

[8] O. Weeger, A. H. Sakhaei, Y. Y. Tan, Y. H. Quek, T. L. Lee, S. K. Yeung, S. Kaijima and M. L. Dunn, "Nonlinear multi-scale modelling, simulation and validation of 3D knitted textiles," *Applied Composite Materials*, vol. 25, pp.797-810, May 2018.

Proceedings of the IASS Annual Symposium 2019 – Structural Membranes 2019
Form and Force
7 – 10 October 2019, Barcelona, Spain
C. Lázaro, K.-U. Bletzinger, E. Oñate (eds.)

Lightweight Cellular Structure: A Formless Fiberglass Buildup Utilize Bending-Active

BoSheng LIU*, Tanvir FAISAL[a], Corey L SAFT[b], Jesse HEATH, Sami A JABER, Quoc DANG, Catherine REAUX, Olivia WELTY, Son NGUYEN

* [b] University of Louisiana at Lafayette
School of Architecture and Design
421 East Lewis Street, Lafayette, LA 70503
bosheng.liu@kent.edu
First co-authors
cls0670@louisiana.edu

[a] University of Louisiana at Lafayette
Department of Mechanical Engineering
First co-authors
tanvir.faisal@louisiana.edu

Abstract

In this work, the authors aim to contribute to the exploration of the rolling assembly method in lightweight bending-active structures by investigating the design strategy based on a biomimetic investigation of the natural cellular structures, using engineered fiberglass sheet material in mass customization of components. The anatomy and cellular morphology of radiolaria were studied, and the morphological attributes were implemented within the design loop process. Furthermore, the designed lightweight fiberglass structure required no formwork or molding through the employment of the bending-active method. This research utilized a sophisticated, holistic design process integrating digital fabrication capability with formative feedback from structural analysis using finite element analysis (FEA). As a consequence, catenary form strategies were deployed to generate the whole structural surfaces for the bending-active cellular modules, with a particular focus on the computational programming of the cellular distribution in parts of the structure where high stress is evident. The final evaluation of the design and system were validated through the material performance as well as a partial full-scale architectural prototype was constructed.

Keywords: bending-active, elastic bending, fiberglass, sheet material, catenary form, linear analysis, biometric, cellular structure.

1. Introduction

In the field of bending-active structures, researchers have investigated various bending methods [1], systems of self-formation structure [2] and engineered materials [3]. It is possible to create lightweight structures utilizing pre-stress bending/rolling sheet material or twisted rod complimented with a pre-stressed joining mechanism. The general principle of bending-active is taking advantage of a material's elastic behavior and given energy to pre-stress the material to an optimal structural disposition that linked to the adjacent bending-active units forming a self-supporting, and possible load bearing structure. Bending-active design and assembly methodologies contrast with conventional

Copyright © 2019 by BoSheng LIU, Tanvir FAISAL, Corey L SAFT, Jesse HEATH, Sami A JABER, Quoc DANG, Catherine REAUX, Olivia WELTY, Son NGUYEN
Published by the International Association for Shell and Spatial Structures (IASS) with permission.

build-up method in which an approach of minimum scaffolding and molding is required to create and build complex geometries. Therefore, it is possible to reduce the cost of construction materials and the time of fabrication and assembly process. In the past, teams of multidisciplinary researchers from architecture, engineering, and material science investigated and implemented bending-active methods to create contemporary architectural installations. Among those notable researchers, the work by Al-haddad[4], Schleicher [5], and Magna [5, 6] have influenced the adopted holistic (i.e., structural analysis and form-making/form-finding inform each other to define the aesthetic and optimal solution) approach on the study and design of the lightweight structure.

1.1 Aims of the Research

The objective of the research project utilized one of the bending-active methodologies of the researchers above, the rolling sheet material method integrated with a biomimicry design approach to create a lightweight self-supporting cellular pavilion. The pavilion design mimicked the structural character of radiolaria (Figure 1) due to its resiliency facing internal and external forces; consequently, the structure is called Radiolaria Pavilion. More importantly, the cellular pattern of the pavilion adjusted to the structural load distribution on the structure surfaces. Meanwhile, the project design team endeavored to engineer the elastic behavior of the sheet of fiberglass without compromise to its essential tensile strength. A holistic approach was deployed to generate the cellular structure formation via computational design loops, which responded to the analytical feedback throughout the design process.

2. Generative Geometry to Material

Radiolaria is a micro exoskeleton marine organism. The cellular structure of radiolaria is typically constructed with an inner endoplasm and an outer ectoplasm with a hollow organic bar in the center [7]. Each cell aggregated and aligned with its neighbor to form an irregular web of column-like structural elements. This structure typology allows the design composition to occupy maximum volume yet still maintain minimum weight. Hence, the canopy cellular structure strived to mimic the capsule structure of radiolaria [8, 9].

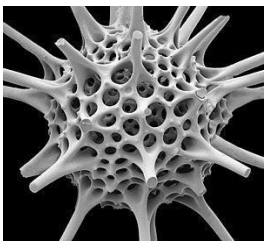


Figure 1: Radiolaria Photograph by Steve Gschmeissne.

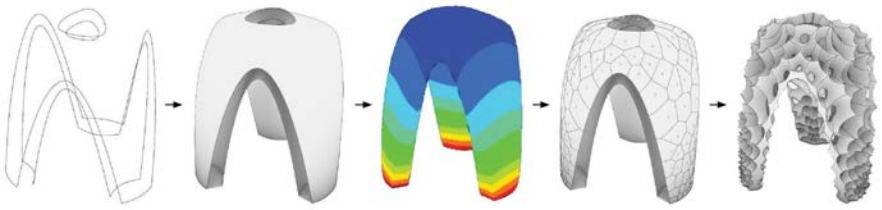


Figure 2: Radiolaria Pavilion form generated from catenary arches to cellular tessellation.

The design of the Radiolaria Pavilion geometry started with a computational catenary deformation of a 1.3 m (4'-3") radius circle with three anchors 120° apart. These catenary arches generated dome-shaped canopy surfaces which were analyzed for their internal forces to further adjust the form to a mutually reinforcing relationship between design and structure. Ultimately, the pavilion design was finalized based on the analysis of the stress distribution due to structural load (self-weight). As a result, the process created a lightweight, occupiable compression structure. Cellular tessellation [7]

was applied to the canopy surfaces, which created a web of convex polygons and thereby formed the cellular response structure (Figure 2).

2.1 Engineered Material

A material investigation transpired during the design investigation, including the study of plastic sheet material, ultra-thin willow glass, and fiberglass sheet material. Ultimately, the fiberglass sheet material was selected for its tensile strength performance while the material is in an elastic state. To determine the optimum sheet material thickness with tensile strength, a series of rupture tests (Figure 3) took place with varying thicknesses of the sheet material and considering two distinct types of raw fiber pattern, Chopped Strand Mat (CSM) sheet and Woven Roving (WR) sheet. As a result, 1.57 mm thick CSM fiberglass sheet was selected for its unbiased tensile strength performance while bending.

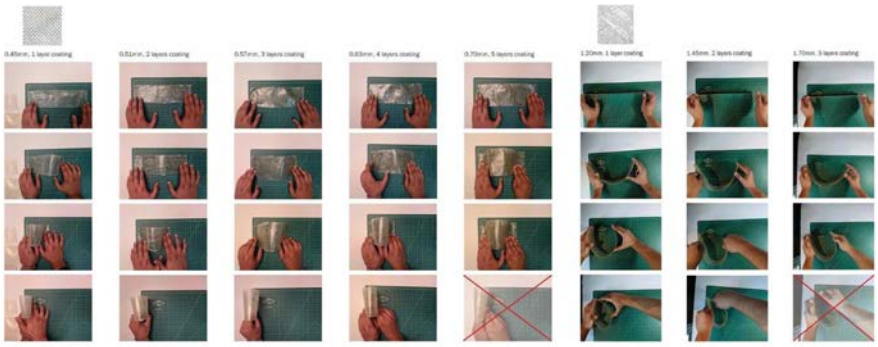


Figure 3: Fiberglass rupture tests on the two types of fiber cloth (CSM, left side & WR right side), and various thickness of resin coating.

2.2 Load Analysis Informed Cell Distribution

The primary purpose of load analysis is to determine the distribution of stress generated on the structure due to its self-weight using FEA so that an informed cellular distribution can be implemented in the design phase. Hence, a solid mesh model has been primarily considered for the FE static analysis. The CAD model (Figure 2) of the pavilion (without any cell structuring) was imported to ABAQUS 6.14 as an STL format and meshed with solid C3D10, a 10-node tetrahedron element. In this analysis, we considered only gravity load due to the self-weight of the pavilion, which acted along the z-direction (downward). Three legs were ultimately constrained (boundary condition) at the bottom (Figure 4a).

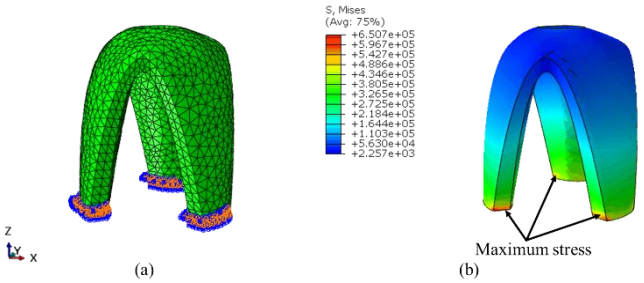


Figure 4: Meshed model with applied boundary condition (a) and von Mises stress (Pa) distribution (b).

Figure 4b shows the von Mises stress distribution. It is evident from the results that maximum stress occurs at the bottom region of the pavilion compared with stress at the top region. The stress distribution dictates the cellular distribution of the CAD model at the design phase. Since the stress is maximum at the bottom region, a graded cell distribution has been considered and implemented in the final design, where larger cells have been populated at the top, and smaller cells have been populated at the bottom. Therefore, more cells have been accommodated at the bottom region to strengthen the structure. The increasing density of cells at the base of the allowed the forces to be resolved with the tessellating nature of the cellular structure.

3. Fabrication to Cell Assembly

The Radiolaria Pavilion fabrication has two major segments, the first part is fiberglass sheet fabrication, and the second part is the cell fabrication using the subtractive manufacturing technique. Each fiberglass material ingredient was weighted base on the area of the sheet (Figure 5). As a result, the thickness of each sheet was tightly controlled, which ensures consistent elastic properties. The cell fabrication process used a CUTonCUT system which allows three sheets of fiberglass material clamped together during the waterjet cutting process. Each cell was labeled, assembled by a roll-up, and connected through an interlocking pocket (Figure 6). High-performance cable ties were used to link each cell to its neighboring cells at 100 mm (~4") apart. Once a cell was connected to its adjacent cells, a stable structure was formed.



Figure 5: Fiberglass sheet material construction.



Figure 6: Assembly process and the full-size prototype.

4. Conclusion

This paper provides a general introduction to the method of bending-active sheet material and a corresponding approach to link with the design process and structure performance. The presented Radiolaria Pavilion investigation provides the first impression of a holistic design approach that mutually benefits architectural design, structural design, project fabrication, and assembly. An additional investigation will take place to examine the structural load distribution on the cells of Radiolaria Pavilion and its response to lateral load. Future work should focus on computational design optimization integrated with material print paths in additive manufacturing, load distribution & optimization of its connection details.

Acknowledgments

This research was primarily sponsored by the University of Louisiana, Office of Provost, Office of Research, and College of the Arts. These research ideas, methods, procedures, and techniques are developed to continue and support other ongoing research projects.

References

[1] J. Lienhard, "Bending-Active Structures: form-finding strategies using elastic deformation in static and kinematic systems and the structural potentials therein", *ITKE Universität Stuttgart Forschungsberichte*, pp.56-66,2014.

[2] J. Lienhard, H. Alpermann, C. Gengnagel, and J. Knippers, "Active Bending, A Review on Structures where Bending is used as a Self-Formation Process", *International Journal of Space Structures* 28(3-4), pp.187-196, 2013.

[3] D. Sonntag, S. Bechert, and J. Knippers, "Biomimetic timber shells made of bending-active segments", *International Journal of Space Structures* 32(3-4), pp.149-159, 2017

[4] L. Iwamoto, "A Change of State" Digital Fabrications: *Architectural and Material Techniques. Princeton Architectural Press*, 2009: 28-29.

[5] S. Schleicher, and R. Magna, "Bending-Active Plates: Form-Finding and Form-Conversion" Association for Computer Aided Design in Architecture, pp.260-269, 2016.

[6] R. Magna, "Bending-Active Plates: Strategies for the Induction of Curvature through the Means of Elastic Bending of Plate-based Structures", ITKE Universität Stuttgart Forschungsberichte, 2017.

[7] University College London, "Radiolaria: Biology" [Online] https://www.ucl.ac.uk/GeolSci/micropal/radiolaria.html

[8] A. Okabe, B. Boots, K. Sugihara, and S. N. Chiu, "Spatial tessellations: concepts and applications of Voronoi diagrams." *John Wiley & Sons*, 2009.

[9] T. Yoshino, et al., "Pores in Spherical Radiolarian Skeletons Directly Determined from Three-Dimensional Data," Forma,29, pp. 21–27, 2014

Proceedings of the IASS Annual Symposium 2019 – Structural Membranes 2019
Form and Force
7 – 10 October 2019, Barcelona, Spain
C. Lázaro, K.-U. Bletzinger, E. Oñate (eds.)

Lightweight Rigidly Foldable Canopy using Composite Materials

Kensuke ANDO[a], Bunji IZUMI[a], Mizuki SHIGEMATSU[a], Hiroki TAMAI[a], Jun MATSUO[b], Yuki MIZUTA[b], Takeshi MIYATA[c], Jiro SADANOBU[d], Kai SUTO, Tomohiro TACHI*

*The University of Tokyo
3-8-1 Komaba, Meguro-Ku, Tokyo, Japan
tachi@idea.c.u-toyo.ac.jp
[a] NIKKEN SEKKEI Ltd.
[b] TEIJIN Ltd.
[c] GH CRAFT Ltd.
[d] Sadanobu Science & Technology Office

Abstract

This paper presents the design process of a novel portable deployable origami canopy system using fiber reinforced plastics. We developed a modular 1-DOF rigidly foldable and flat-foldable structure composed of multiple developable strips. Each strip is composed of rigid panels, and elastic hinges are produced in a planar configuration based on the patterning of prepreg composite sheets and multi-step curing. We performed multi-objective optimization to identify Pareto optimal design parameters of the origami pattern to maximize functionality whilst considering manufacturing constraints. We also applied geometric nonlinear analyses to assess the buckling behavior of the structure in its deployed state, and also in the process of nonlinear folding coupled with bending of the panels. The analyses indicated the necessity of tension elements for additional stability, which were then realized by triangular foldable fins on the backside of the structure. The structure has a total mass of 27 kg and can be carried and deployed by two or three persons within a minute.

Keywords: rigid origami, deployable structure, composite materials

1. Introduction

Portable deployable structures are ideal solutions for temporary buildings such as shelters for disaster relief or pavilions for various events. They are: (1) rapidly erectable and retractable to satisfy urgent demands; and, (2) reusable multiple times for a variety of purposes (each of which may happen rarely). As such, they consume fewer resources and produce fewer waste. We observed that the following properties would further maximize the effectiveness of the structures in these aspects, respectively.

1. The structure has easily controllable deployment and folding motion. The structural module is lightweight, requiring no additional equipment for erection or elements for finishing.
2. The structure is modular such that separate pieces can fit together to form various shapes and could be used in several states during deployment.

Major approaches for creating deployable structures include pneumatic structures, deployable frames, e.g., scissors mechanisms, and foldable folded plate, i.e., origami structures. Regarding property 1, the former two have an advantage in terms of their lightness. However, both require surface finishing that is usually composed of thin membranes. The folding behavior of the attached finishing is less controllable. This leads to less efficiency in the folding stage. Origami systems, in contrast, offer reversible folding and deployment functions with watertight rigid surface panels, provided that the kinematics of the rigid origami is carefully examined. This makes the system potentially more reliable

Copyright © 2019 by Kensuke ANDO, Bunji IZUMI, Mizuki SHIGEMATSU, Hiroki TAMAI, Jun Matsuo, Yuki MIZUTA, Takeshi MIYATA, Jiro SADANOBU, Kai SUTO, and Tomohiro TACHI
Published by the International Association for Shell and Spatial Structures (IASS) with permission.

in the process of folding it down into its compact stowed state. The potential downside of the origami is that the structure can be heavy when conventional plate materials and mechanical hinges are used.

In this paper, we present a modular origami-based deployable structure using carbon fiber reinforced composite (CFRP) plates with compliant hinges. As a demonstration pavilion, we created a portable origami canopy by assembling multiple modules. The average thickness of the material is about 1 mm, and the total mass of the structure is 27 kg. We chose the geometry of the module so that the structure after assembly is always flat-foldable and rigid-foldable with exactly one degree of freedom (DOF); this allows the structure to continuously fold down to a stowed state with a simple actuation control. Together with its lightness, the canopy structure we created can be carried and deployed by two persons within a minute (Figure 1).

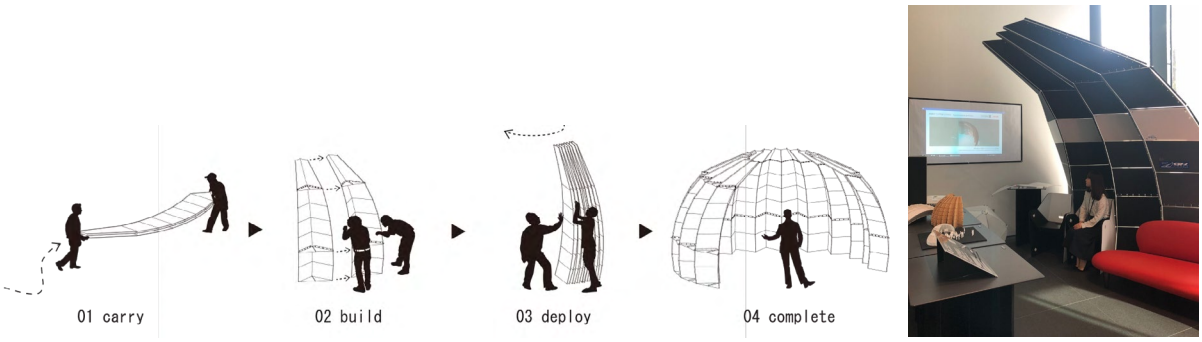


Figure 1. Deployable origami canopy.

In general, a critical issue of using composite material is their manufacturing cost, particularly the cost of creating a mold, and the cost for the manual labor; especially since the textile has to be manually laid out on to the mold in order to create a 3D surface. However, our approach is to make each module out of a developable strip, so that it can be fabricated in a simple flat state.

The design and fabrication of functional, transformable structures requires simultaneous considerations of the geometry, the function of the space, kinematics, stability, materials, and fabrication. To tackle this multi-modal design process, we formed a team comprising of structural engineers and architectural designers (from first to the fourth authors, NIKKEN), specialists in composite materials (fifth, sixth, and eighth authors, TEIJIN, Sadanobu Science & Technology Office), engineers of composite material fabrication (seventh author, GH Craft,) and scientists in origami geometry (last two authors). This paper provides an overview of the multi-modal design process and construction realized through interdisciplinary collaboration.

First, in Section 2, we show the geometric family of modular structure, where the assembly of a single type of module can create various configurations of rigidly and flatly foldable origami structures, including a fully closed structure, corridor, and open canopy. We demonstrate the application of this modular system to create a canopy that can act as an acoustic reflector and diffuser. Section 3 performs multi-objective optimization to determine the parameters of the module so that it maximizes the functional properties and stiffness under the constraints from the required dimension and material size. The geometric model assumes that the structure has exactly 1-DOF based on the assumption that the panels are rigid. However, in reality the material is super-thin (1:1000 thickness to width ratio) and so we need to consider folding-and-bending-coupled behavior of the structure. Section 4 performs such nonlinear quasi-static analyses to identify buckling mode under vertical load and to explore the folding motion control. Section 5 shows the manufacturing process of each module using composite origami materials, use of built-in compliant hinges with soft matrix, and assembly of the modules by special tie methods. Finally, Section 6 shows our future vision of origami-based composite deployable systems.

2. Origami Geometry

We introduce a modular system that creates a family of flat-foldable and rigid-foldable surface with exactly 1-DOF rigid-folding motion. The geometry of our modular system is based on a part of a big torus which, by its assembly, creates various forms e.g. a covered corridor (Figure 2). To create those geometries, we use the shape of rigidly foldable origami tubes [3]. In general, origami tubes composed of quadrilateral panels are over-constrained, so they need to have intrinsic symmetry to be a mechanism. Five steps are needed to construct a rigid-foldable and flat-foldable origami torus. In particular, the second and third steps guarantee that these characteristics can be achieved.

1. We construct the torus defined by radiuses of smaller and bigger circles, defined as r and R, respectively. We set XYZ axes such that the bigger circle lies on XY plane, the smaller circle lies on XZ plane, and the origin lies on the center of torus.
2. Construct a section polyline P on the small circle. A parallelogram strip is formed by extruding P along direction $\mathbf{d}$ on XY plane. The angle between $\mathbf{d}$ and $-$X axis is denoted by α. The choice of α is important for the stiffness of the structure. For more detailed discussion, see Section 4.
3. The strip obtained by step 2 is trimmed by a *trimming plane*, defined as the rotation of XZ plane around Z axis by angle $\theta/2$.
4. Mirror copy the trimmed parallel trapezoidal strip with respect to trimming plane.
5. Concatenate n rotated copies of the strip constructed in steps 3 and 4 around the Z axis.

(Design parameters are $r, R, \theta, \alpha, n, P$.)

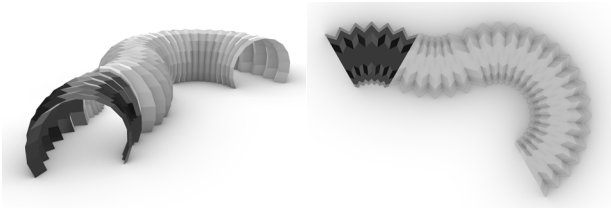


Figure 2. Flat-foldable and rigid foldable covered corridor. Each module approximates part of a torus.

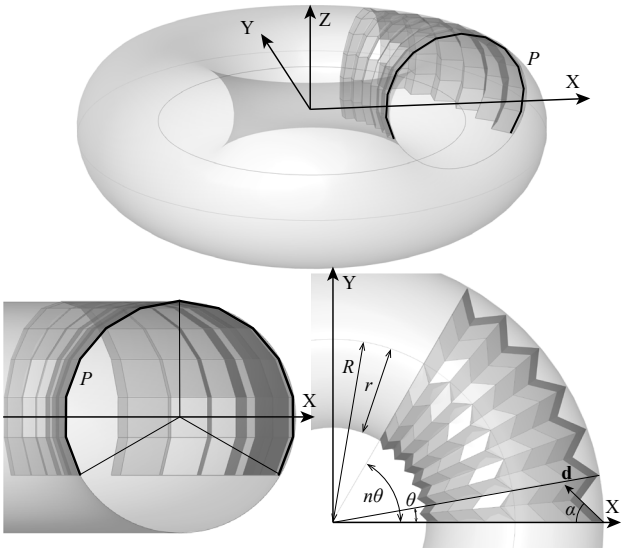


Figure 3. Geometric parameters defining the shape

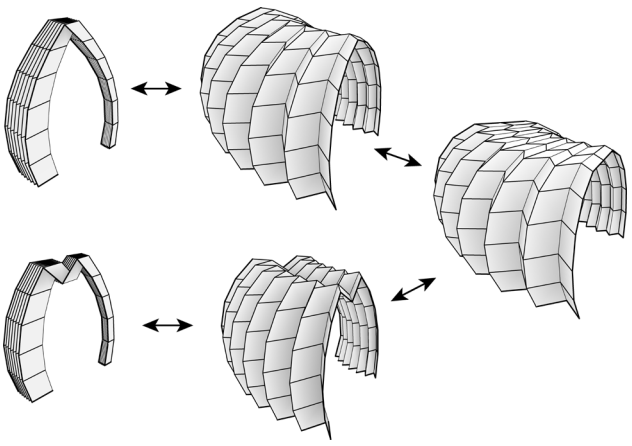


Figure 4. Folding motion of a module. The top part gets reversed at the critical folded state in the right.

The torus surface constructed as above has 1-DOF rigid folding motion. This folds flat because of mirror symmetry in step 4. Another valuable property is that all horizontal lines of parallelograms are always parallel to the XY plane during the folding motion.

If P is mirror-symmetric with respect to an axis parallel to the z axis, (i.e., arch shape), the legs are always on the ground. This leads to stability while folding. Also, the structure serves as a pavilion at any interval of the deployment motion. Since each extruded strip is developable, this forms the module of manufacturing.

Figure 4 shows the rigid folding motion. The top part of the structure gets expanded until it becomes flat, at which point, the mountain and valley of the creases get reversed. At this critical point, the angle θ projected to the XY plane hits its maximum. Additional measures are required to avoid this flipping behavior. Refer to Section 4 in details.

3. Multi-Objective Optimization (MOO)

The canopy has multiple functions: 1) a sound reflector to surround the speaker on the stage; and, 2) a solar energy collector. The solar energy collected by Photovoltaic (PV) panels attached to the canopy can be used as a supplementary electric source for outdoor use such as an outdoor stage or a temporary shelter for refugees in the event of natural disaster.

The design parameters are determined to maximize the overall performance measured in terms of 1) structural stiffness; 2) homogeneity of reflection of speaker's voice; and, 3) reception of the solar radiation by the exterior side of the panels. Multi-objective optimization (MOO) is used to evaluate the best balance of these different performance measurements. We used *Rhino/Grasshopper* as the platform for parametric design, analyses, and optimization. *Octopus*[4] was used to find the Pareto optimal solutions.

3.1. Design parameters and constraints

The design parameters r, R, θ, α, n, as defined in Section 2 are used. For the polyline section P, we focused on a cantilever shape, considering the usage as a sound reflector, so P was set to equally divide an arc of the small circle defined by two angles (angles 1 and 2 in Figure 5). The design parameters are constrained by the maximum size of each developable strip allowed for in fabrication, and the required minimum size of the enclosing space.

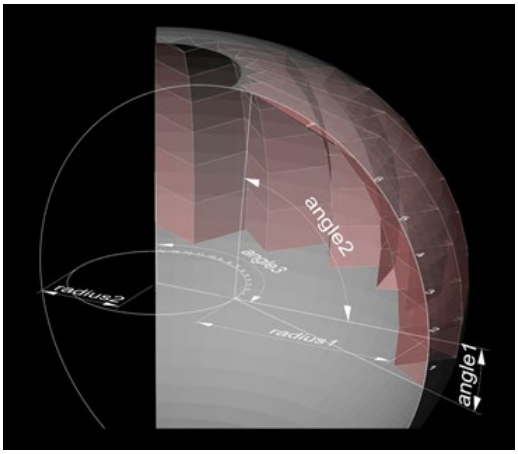


Figure 5. Design parameters of canopy.

3.2. Objective Functions

3.2.1. Stiffness of structure

We maximized the stiffness of the structure by minimizing the maximum displacement under vertical load. Linear static structural analyses were undertaken assuming that every folded hinge is continuous. Structural engineering tool *Karamba*[6] was employed.

3.2.2. Homogeneity of voice distribution

The homogeneity evaluates how the sound will be reflected on the panel and conveyed to the audience if a person speaks in front of the structure. Since the structure is composed of many panels with different angles, quantities analysis was required to evaluate the acoustic performances. Acoustics were simulated through ray tracing method. Figure 6 shows the overall set-up for the simulation. A point sound source was placed in front of the structure at about the height of a human head. Rays representing sound travel were released non-directionally. The first and second reflections are used to calculate where the sound will arrive in the area of the audience, represented by the inclined rectangular surface. The surface was

divided into sub-areas, and the number of hits were counted to measure the density of the power level. The variance of such distribution was minimized. The code was written in the Grasshopper software environment by the authors.

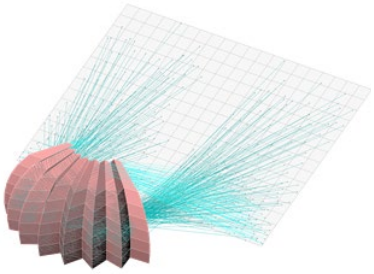


Figure 6. Acoustic simulation based on ray tracing.

3.2.3. Maximizing reception of solar radiation

The last objective is to maximize the reception of solar radiation onto the structure. At the same time, with the same objective function the shape can maximize the solar shielding effect combined with heat shielding paint. Unfortunately, these functions associated with solar radiation were not implemented to the real-scale model. But the study did demonstrate the potential benefit of applying multi-objective design approach by MOO. *Ladybug* [5] was used to carry out solar radiation simulation.

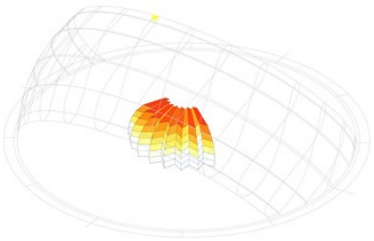


Figure 7. Solar radiation simulation

3.3 Finding a rational design

The objective functions mentioned in the previous sections tend to trade each other off. For instance, a shape with sharper folding angles (smaller α) has better structural performance because stiffness increases with the folded plate effect, while it has less reception of the solar radiation because the incident angles of the sun ray become shallow for some panels. Therefore, it was required to find the best-compromised option where values of the three objectives were within accepted ranges.

Figure 8 shows the instances on the Pareto-front surface. X, Y, Z axes correspond to the simultaneous minimization of "Structural displacement", (inverse of) "Thermal gain" and "Acoustic variance", respectively. Each instance on the surface has the property that it is not inferior to the others when all

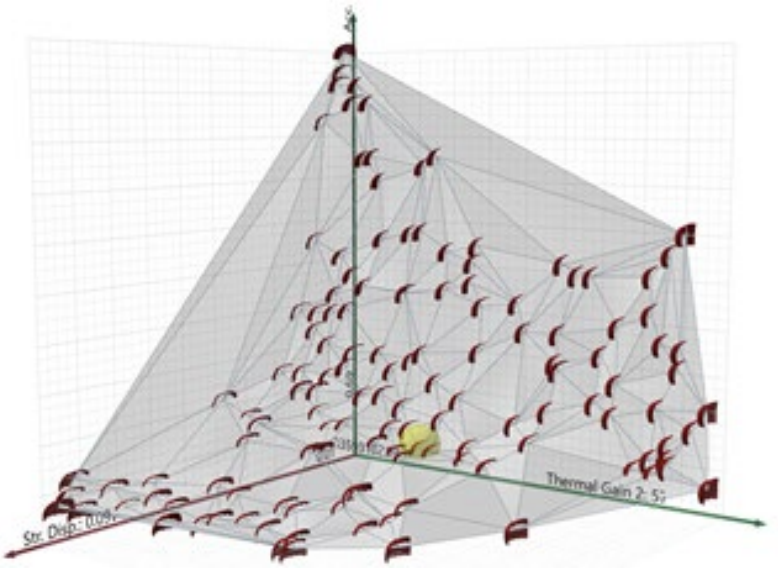


Figure 8. Instances on Pareto-front surface

the objective functions are considered. The instance highlighted in yellow in Figure 8 was selected for further nonlinear structural analyses and fabrication-aware design.

4. Structural Analysis

Although the rigid folding transformation was assumed in the conceptual design phase, the panels are, in reality, very thin and elastic. Thus the stability of the canopy with the panel bending behavior needs to be examined. Static and dynamic behaviors under gravity loading and material properties were investigated by utilizing geometrically nonlinear analysis. The structural investigations include the stability of the articulated thin-panel structure, the loose property of "*watoji*" joints (discussed in Section 5) and the transformation under a single actuator.

4.1. Description of structure

The stability relies totally on the shape of the structure because the panel's thickness ratio (ratio of length to thickness) is extremely large. The ratio is in the order of 1000 for some panels, and it could be even larger with respect to the overall stability. The shape of the structure can be seen as a part of a dome, but it is clear that the shell effects of the dome shape cannot be expected unless it is fully closed. Rather, the folded plate effects contribute to the stiffness of the stand-alone cantilever, while the angles at the articulations contribute to the local stability of the thin panels by shell-like effects.

4.2. Static analysis for stability

The geometric nonlinear calculation with thin shell elements was performed using a commercial structural analysis program, SOFiSTiK, in order to evaluate the structural behavior of the canopy. The panels linked with spring elements simulate the bending stiffness of the "*watoji*" joints and looseness due to fabrication tolerances.

The analysis results showed that the structure was very flexible due to the high thickness ratio. Some panels at the lower portion, in fact, were locally buckled, and underwent post buckling behavior based on the panel's elastic properties (Figure 9 left).

It also showed that the structure tends to lose the stiffening effects of the shape when it deforms due to its own weight. The panels at the bottom edges were found to be critical. They are stressed in compression under the cantilever action of the canopy. The out-of-plane deformations, which can be seen as local buckling, tend to squash the ridges and valleys. They effectively flatten the folded plate system and increase the deformation further. This indicates that the single DOF does not contribute to the stability of the system if elastic deformation of the thin plate is overwhelming.

In order to mitigate instability and prevent such progressive deformation, web elements were introduced between valleys on the exterior side of the canopy (Figure 9 center). The analysis shows that they can stabilize the structure significantly. They are attached in such a way that they are folded in during transformation and get taut when they are in use in the final position, keeping the folded plate system from flattening (Figure 9 right).

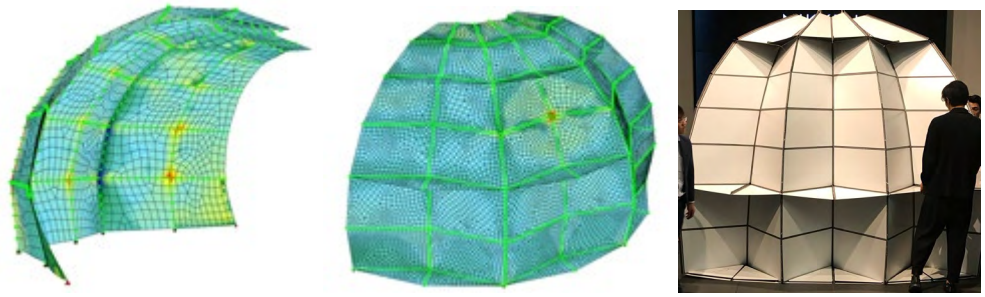


Figure 9. Local instability at bottom edges (left); FEM model reinforced with webs (center); Actual application of stiffening webs (right)

4.3. Dynamic simulation of rigid origami with an actuator element

4.3.1. Simplified dynamic model with wireframe Octahedra

In the concept phase, the transformation of the rigid origami canopy was simulated to see how it could actually fold and unfold depending on how the supports are constrained during operation, and which points are actuated. Each rigid panel was modeled with twelve bars constituting a squashed octahedron. The articulation between the panels was assumed to be linear hinge and modeled simply by sharing an edge of adjacent squashed octahedra (Figure 10). The actuator is modeled with a bar element that can be shortened and elongated in each time step. Direct integrated time history analysis is applied. With this modeling, it was possible to quickly investigate the transformation process by an actuator without resorting to sophisticated and time-consuming structural analyses. This study made us notice that the overhang facets could present bifurcation of configuration, which would make the control of the transformation more difficult. Although this behavior seems contradicts to single-DOF, this observation is due to a transformation by a single actuator. In fact, DOF analysis by finding the null-space of the Jacobean matrix of the equations for rigid bar lengths can confirm that the DOF remains only one, even though the transformation mode is at a singular point.

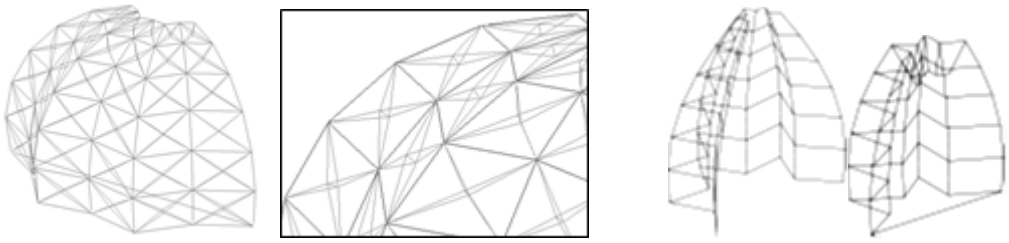


Figure 10 Wireframe dynamic model and enlarged (left); DOF Bifurcation in transformation (right)

4.3.2. Detailed quasi-static model with thin shell elements and spring joints

Finally, quasi-static sequential simulation was performed with the detailed model that considered elastic behavior of the thin panels and very flexible line connections between the panels. Due to difficulties in numeric procedure associated with structural instability, this model could not complete dynamic simulation in one shot. However, the part of the analysis results could provide useful information on the structural stability at intermediate positions in the transformation.

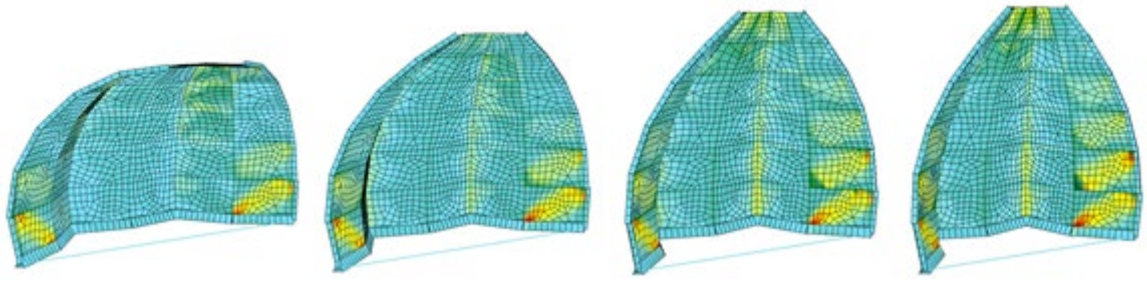


Figure 11. Geometric nonlinear quasi-static sequential analysis

5. Materials and Fabrication

This section describes the fabrication of the canopy with a focus on the FRP hinge, the cutting pattern, module making, and the connection detail for on-site assembly. Figure 12 shows a perspective view and drawings of the fabricated canopy.

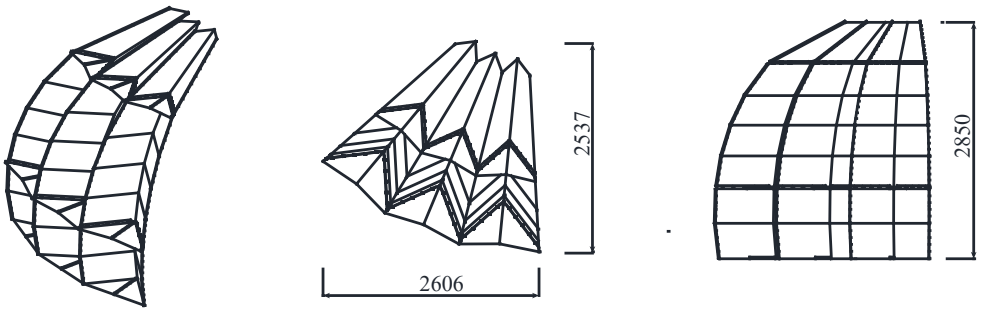


Figure 12: Perspective, top, and front views of the fabricated canopy.

5.1. FRP hinge

Our origami structure is formed by using foldable Carbon Fiber Reinforced Composite (CFRP). The foldable CFRP consists of rigid main body parts and FRP hinge parts. Here the FRP hinge is defined as a foldable line, in which matrix resin is selectively replaced by a flexible rubber in composite structures. FRP hinges have already been investigated by some researchers [1][2]. The reinforced fiber is continuous throughout the composite structure including the foldable line, which ensures the excellence in the mechanical reliability of the FRP hinge.

When FRP hinge behaves as an elastic body, its contour shape at an arbitrary bending is described by "Elastica" and formulated by using the elliptic integral of the first order with the breadth of the hinge as a parameter (Figure 13). In reality, for the actual FRP hinge, the bending force is lower in a deferent order of magnitude compared to the theoretical value. The attainable curvature also exceeds the expected level from the elongation of the break of the reinforced fiber, although the apparent contour profile is very similar to the theoretical one, The phenomena are explained by micro-buckling which is attributable to shear deformation of the rubber component under compression. The micro-buckling had no significant effects on the folding endurance of the FRP hinge in this case.

In the Origami structure using thick rigid panels, the spatial interference between adjacent panels could hamper desired folding motion. For FRP hinges, the problem can be overcome by suitable choice of the hinge breadths.

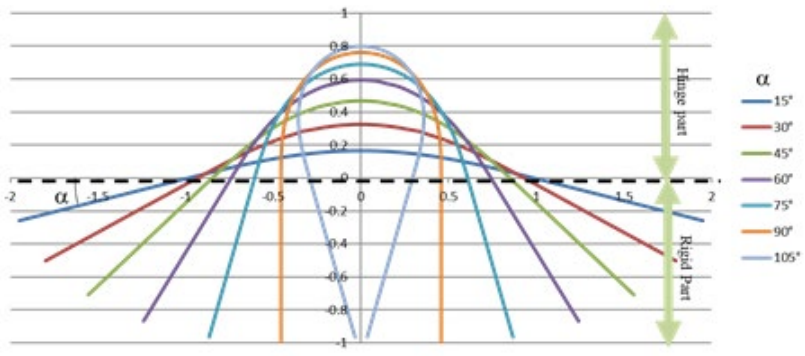


Figure 13. The calculated contour profile of the FRP hinge at bending angle α based on Elastica theory.

5.2. Cutting pattern and module manufacture

The canopy consists of deployable strips and webs. This section describes the cutting pattern and module manufacture.

Because each strip is approximately three meters long and two meters wide, it must be divided into smaller modules considering the cost and easiness in fabrication and transportation. The modules should be less than one meter by three while there should not be more than three cutting modules for easy assembly. Under these requirements, the cutting modules are determined as follows (Figure 14).

The number of the modules is set to three because of the maximum size allowed. A half of each web is integrated to the lower side of each module. The margins for on-site assembly are integrated to the edges of the modules. The webs and margins are integrated to the module via above-mentioned FRP hinges.

The deployable modules have two types of FRP hinges. The ones along the horizontal foldable lines are integrated between panels in each module, and the required fold angle is about 15 degrees. On the other hand, those along the vertical foldable lines are integrated with the assembling margins, which are in turn connected to adjacent margins to complete the linear joint for folding. The required fold angle is about 50 degrees. A higher rotational stiffness is preferred in the horizontal hinge as the hinge more significantly impacts structural stability. Lowering rotational stiffness is preferred in the vertical hinge for deployment. Therefore, the hinge breadth of the horizontal and the vertical flange were set to 4 mm and 8 mm, respectively.

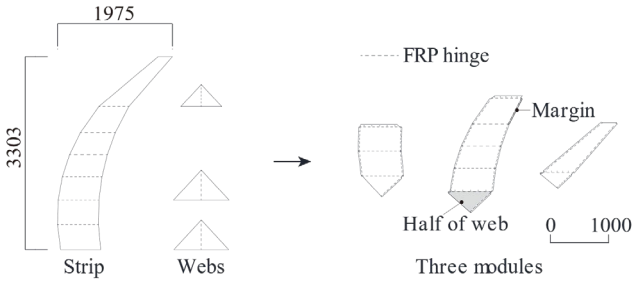


Figure 14. Cutting pattern.

Figure 15 shows the process flow for the prototyping based on the hand-lay-up method. The flange parts with the FRP hinge were separately prepared and finally combined with the main body. For the flange parts CF-epoxy prepregs were stacked on the both sides of a dry glass fabric, which is used as a core, except for the foldable line areas, and then silicon resin (KE-4S-TS, Shin-etsu) was suffused into them, followed by vacuum bagging and curing in an autoclave at 130 ºC under 0.15 MPa. For the main body, each panel was prepared by the lamination of CF prepregs, connected with the finished flange by using bonding film and cured in the same way as described above. The main body and the flange parts were completely consolidated by the curing process.

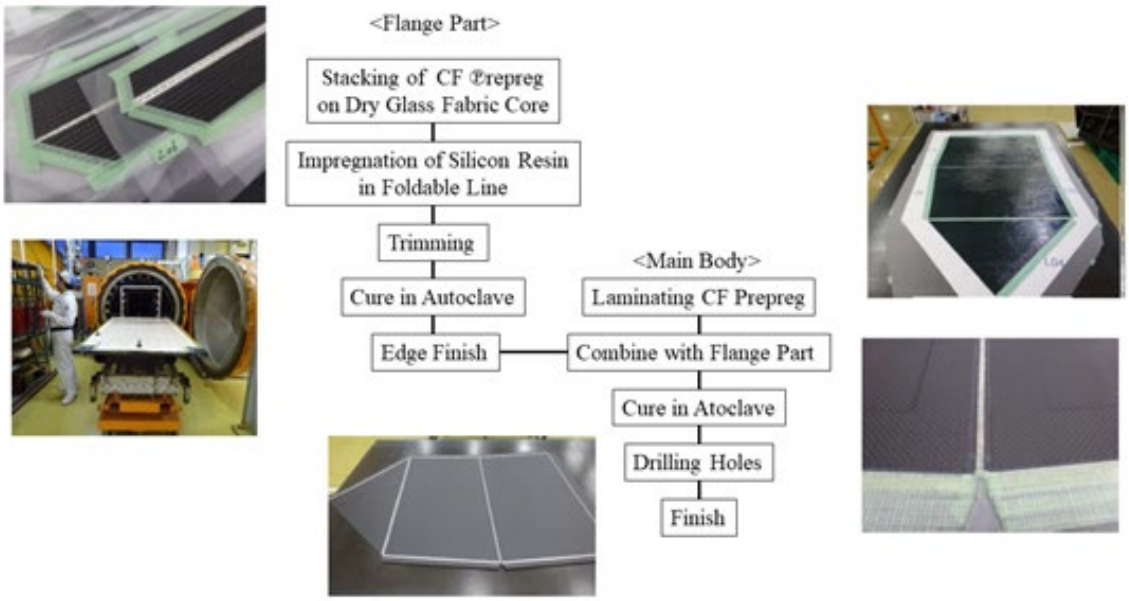


Figure 16. The process flow chart for prototyping the foldable Origami structure.

5.3. Connection detail for on-site Assembly

Watoji joint, a traditional Japanese book binding technique (Figure 16), is applied to the connection between modules. It has several remarkable properties beside the tightness: (1) it is reusable as it does not use bonding material; (2) it can be assembled and disassembled by hand; (3) it is relatively tolerant to manufacturing errors; and, (4) it goes well with origami concept as both were developed for paper art works. The string made of PET is utilized at the connections for its strength and durability.

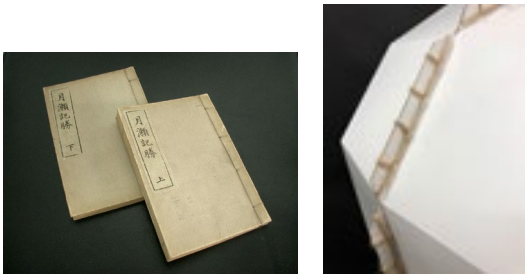


Figure 15. Watoji joint in book binding (left) applied to 1/2 scale model (right)

6. Future Vision

Our fabrication process of composite panels and compliant hinges are based on making hinge parts and assembling them together by manual layout and secondary curing. This process was chosen particularly because of the limitation of available materials and equipment at the time. However, ideally, we can replace this hinge placement process by 2-axis CNC or printing techniques, so we may pattern the creases composed of soft and hard matrix but using a single fiber fabric. We envision that our origami-based approach can lead to developments in automated computational 3D forming based on folding techniques in the future.

Acknowledgements

The authors would like to thank the support from NIKKEN SEKKEI and TEIJIN.

References

[1] Lopez, J. F., and Pellegrino, S., "Folding of Thin-Walled Composite Structures With a Soft Matrix," in *Proceedings of 50th AIAA/ASME/ASCE/AHS/ASC Structures, Structural Dynamics, and Materials Conference*, Palm Springs, CA, 2009.

[2] Todoroki, A., Kumagai, K., and Matsuzaki, R., 2009, "Self-Deployable Space Structure Using Partially Flexible CFRP With SMA Wires," *J. Intell. Mater. Syst. Struct.*, vol. 20, 2009. pp. 1415–1424.

[3] Filipov E. T., Paulino G. H. and Tachi T. "Origami tubes with reconfigurable polygonal cross-sections", *Proc. R. Soc. A,* vol. 472. 2016.

[4] Vierlinger, R.: Octopus. http://www.food4rhino.com/app/octopus/ (2017)

[5] Sadeghipour Roudsari, M., Mackey, C.: Ladybug tools. http://www.ladybug.tools/ (2017)

[6] Karamba3d: https://www.karamba3d.com/

Minimal surface tensegrity networks: The case of an enneper surface pavilion structure

Katherine LIAPI,* Andreana PAPANTONIOU[a]

*,a University of Patras, Greece
Dept. of Architecture, University Campus, Rio, 26500, Greece
kliapi@upatras.gr

Abstract

Minimal surface tensegrity networks constitute a new typology of double layer tensegrity structures that can be formed from the assembly of tensegrity units of square base. Algorithmic processes that permit the exploration of three different types of minimal surfaces, namely of helical, catenoid and enneper, already developed by the authors, were considered for the form exploration of the IASS 2019 tensegrity pavilion structure. A tensegrity enneper network, which is a tensegrity structure the two layers of which are minimal surfaces of enneper geometry, was chosen as the preferred configuration for further exploration. Subsequently a morphological investigation of various configurations of double layer-tensegrity networks of enneper shape was conducted with the utilization of the developed algorithm. The same algorithm is to be used during the construction process to determine all member dimensions and assembly values such as overlapping cable lengths. To facilitate the packaging, transportation and the on-site assembly of the structure, collapsible tensegrity units will be used.

Keywords: tensegrity networks, minimal surfaces, enneper surface, algorithmic design

1. Minimal surface tensegrity structures design: an algorithmic process

Minimal surfaces which are surfaces with zero mean curvature can be also defined as surfaces of the smallest area spanned by a given boundary [1]. .

Minimal surface tensegrity networks constitute a new typology of double layer tensegrity structures that can be formed from the assembly of tensegrity units of square base. The geometric study of minimal surface tensegrity networks has led to a design method that takes into account the constraints determined by the space packing geometry of prismatic tensegrity units. Algorithmic processes that permit the exploration of different types of minimal surfaces have been developed. Specifically three different types of minimal surface tensegrity network, namely of helical, catenoid and enneper geometry, have been studied.

Accordingly three different algorithms have been developed. Each algorithm involves a series of steps which are similar to all three structure types. Therefore, for all surface types, at the first step, by inserting the surface equations and by applying the appropriate transformation equations one of the two layers of the structure is developed. Then a network of points, uniformly distributed on this layer of the structure, is created. Following that, the algorithm creates flat square tiles on this layer, and at the next step, the square tiles are rotated around an axis perpendicular to their plane at their center, until a four square tile pattern, that represents the connection pattern of the bases of four tensegrity units of prismatic form, is constructed on the layer's surface. So, once the first layer of the tensegrity minimal surface is created, the construction of the second layer follows. This time, taking into account that the bases of a tensegrity unit of prismatic form are rotated against each other by a 45 degrees angle, the squares on the second layer are rotated by a 45 degree angle, and scaled until adjacent squares are connected properly. A condition that has to be fulfilled in all three types of minimal surface tensegrity structures is that the

centroids of the squares on the minimal surfaces layers that correspond to the two bases of each tensegrity unit, should fall on a perpendicular axis to both bases.

The developed algorithms can generate tensegrity networks of all three minimal surface types in a graphical environment.

The algorithms for the development of tensegrity surfaces of helicoidal and catenoid shape were developed first. As both the helicoid and the catenoid share the same set of parametric equations which are used for the creation of the first layer of the structure, both types of surfaces can be generated from the same algorithm. In addition the algorithm can generate minimal tensegrity networks the shape of which can be geometrically defined as a transition from helicoid to catenoid (figure 1).



Figure 1: Algorithmically generated minimal surface tensegrity networks: a) Helicoid , b) Transition between helicoid and catenoid

2.1. The case of enneper tensegrity networks

An enneper surface is constructed from the following set of parametric equations.

$$x = u - \frac{1}{3}u^3 + uv^2$$

$$y = -v - u^2v + \frac{1}{3}v^3$$

$$z = u^2 - v^2$$

By following the steps already described in the previous paragraph, these equations have been integrated into an algorithm that can generate various configurations of enneper surface tensegrity networks (figure 2).

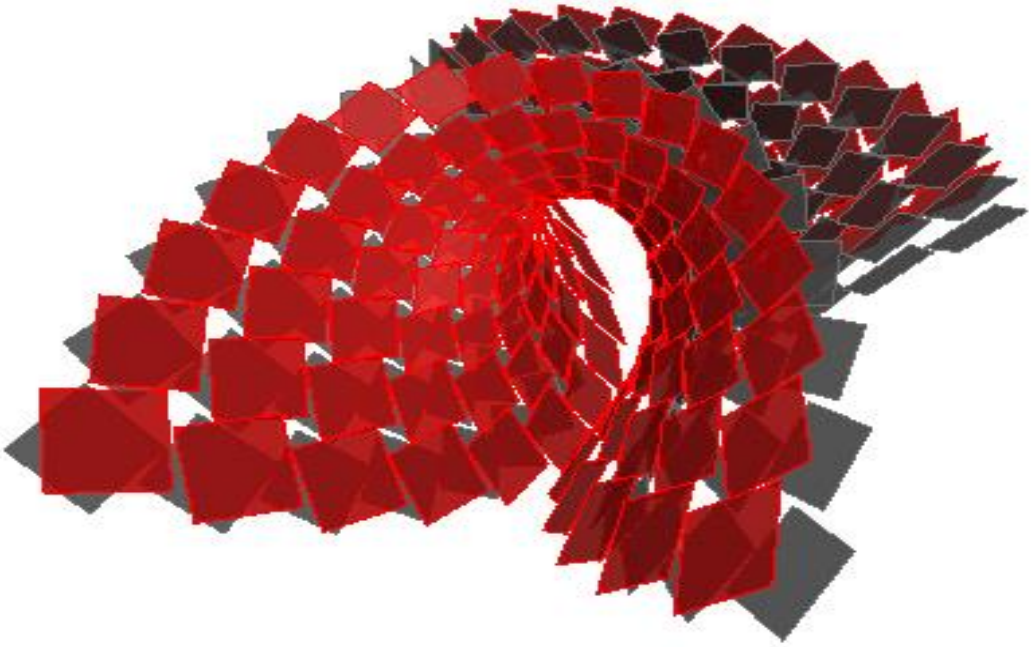


Figure 2: Algorithmically generated minimal surface tensegrity network of enneper geometry.

2. Geometric form studies

The use of the developed algorithms permits the generation in a graphic environment of several digital models of minimal surface tensegrity networks. All three surface geometries were examined during the form exploration of the tensegrity pavilion structure. Finally an enneper geometry has been chosen as the preferred one for further exploration.

Afterwards, with the use of the developed algorithms, a morphological exploration of various configurations of double layer-tensegrity networks of enneper shape has been conducted. The parameters of variation that were considered were: a) a domain value that ranges from 90 to 360 degrees and b) unit size and number on each axis (figure 3). In each instance, once a network was generated, then several digital models that represent only sections of the initial surface were developed on an effort to design a pavilion structure that will also provide a stimulating spatial experience to its guests (figure 4). As structural membranes are also minimal surfaces, several options for membrane surface integration are also explored.

The comparison of the developed digital models of various enneper networks against each other will facilitate the selection process.

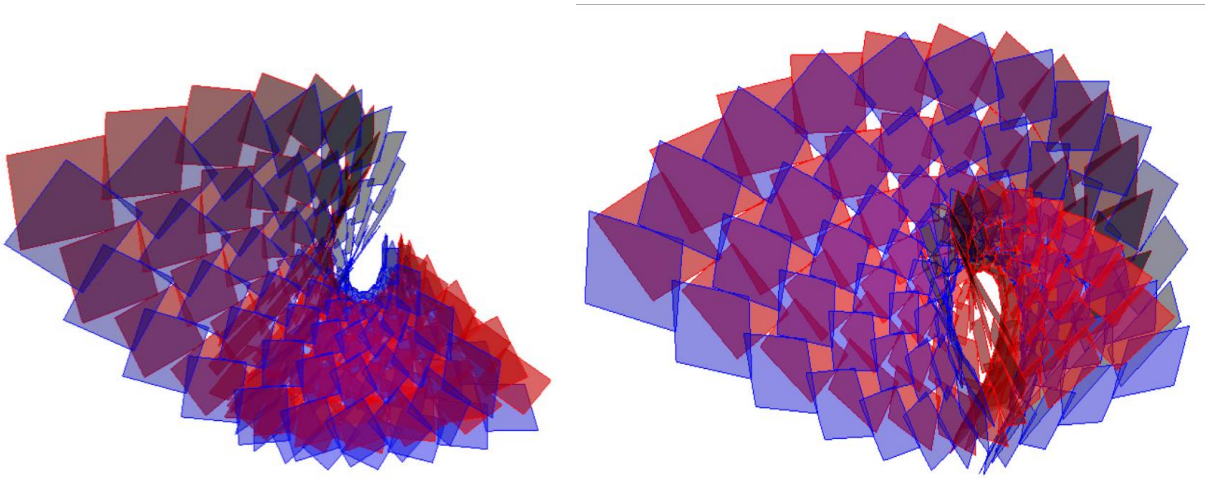


Figure 3: Algorithmically generated minimal surface tensegrity networks of enneper geometry for the same number of units a different domain values

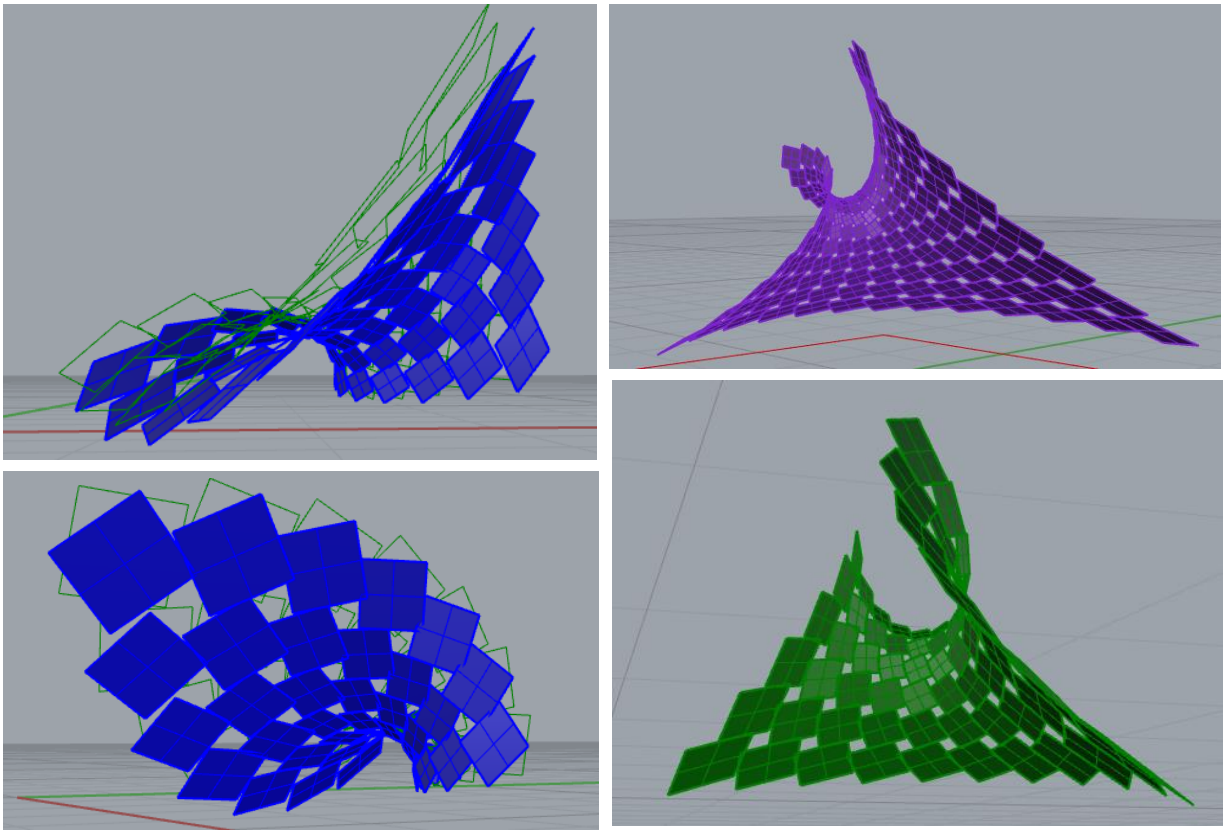


Figure 4: Studies of the proposed enneper surface pavilion's geometric form.

3. Constructability issues

Once the final shape is decided, the developed algorithm will be used to determine the dimensions of all members, the overlapping cable lengths of the adjacent units of the structure, as well as the sizes of the surface elements to be added to the structure after its completion.

To facilitate the transportation and the on site assembly of the structure, a patented method that permits the construction of tensegrity structures from the assembly of collapsible tensegrity units will be used [5]. All units will be pre-assembled and collapsible. A prismatic tensegrity unit is composed of four

rigid members that undertake compression and twelve flexible members, four on each base, and four diagonal ones, that undertake tension. For the deployment the substitution of eight cables, by four continuous ones, where each continuous cable substitutes a diagonal and a base cable, is needed. So, for deploying a unit, a simple mechanism allows the release of the four continuous cables and the unit can collapse in either a vertical or a flat configuration without detaching any cable-ends

Aluminum tubular pipes and wire rope are to be used for the construction of the tensegrity units. Special attention is placed to the design and fabrication of the nodes, as they should allow for unit prestress and, at the same time, facilitate the connection of one unit to another.

.

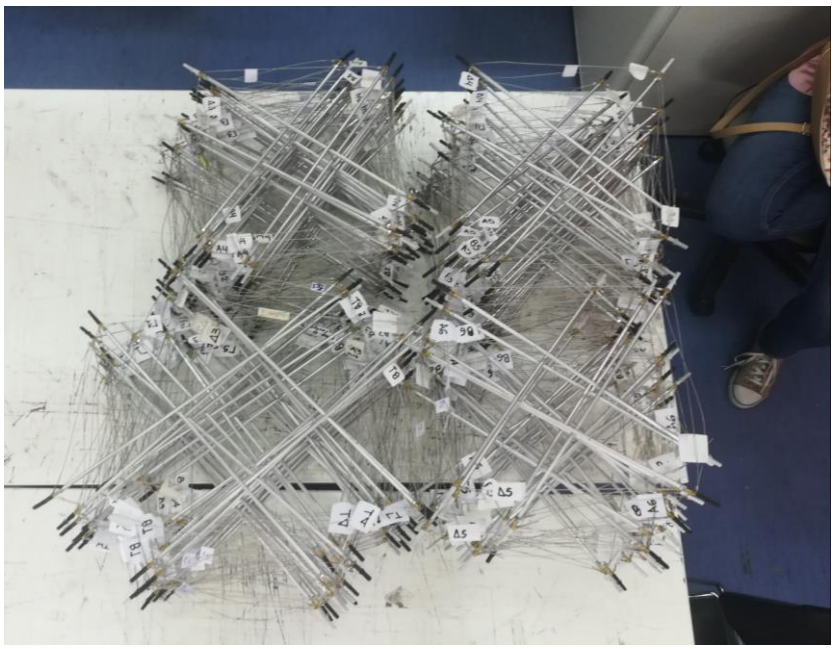


Figure 5: Collapsed tensegrity units in a flat configuration.

Conclusions

The developed algorithms have permitted the experimentation with different morphological variations of all three types of studied minimal surface tensegrity networks. Emphasis was placed on tensegrity structures of enneper surface geometry. The actual construction of the pavilion will prove the validity of the algorithms, while the challenges that will be encountered while constructing the pavilion structure, will be used to improve the algorithms. It is expected that the embedded mathematical processes and technological innovation will be conveyed through the pavilion's form and experience .

References

[1] Velimirović, L.S., Radivojević, Gr., Stanković, M. S., Kostić, Dr., "Minimal Surfaces for architectural constructions", *Facta Universitatis Series: Architecture and Civil Engineering*, Vol. 6, No 1, 2008, pp. 89 – 96.

[2] Liapi K., Papantoniou, A., Nousias, Ch. "Morphological exploration of curved tensegrity networks: towards double-layer minimal surface configurations", in Proceedings of the *IASS Annual Symposium 2017*, *Humburg, Germany, 25-27, 2017,*pp. 254-259.

[3] Liapi, K., 2005 (inventor). "Tensegrity Unit, Structure and Method for Construction", U.S. Patent No 6,901, June 7, 2005.

Proceedings of the IASS Annual Symposium 2019 – Structural Membranes 2019
Form and Force
7 – 10 October 2019, Barcelona, Spain
C. Lázaro, K.-U. Bletzinger, E. Oñate (eds.)

Corn Structure Pavilion

Tonia LUDWIG, Hannah MELZER, Andreas TRUMMER, Christoph HOLZINGER
TU Graz
Technikerstrasse 4/IV
t.ludwig@student.tugraz.at
hannah.melzer@student.tugraz.at

Abstract

In these recent years, helping to preserve the earth has become a present aspect in our society. Since the building industry has a huge impact on the carbon dioxide emission, architects and engineers have begun to research alternative materials for their designs and construction, trying to minimize the consumption of resources and focusing on sustainable products. However, the material palette is still very limited which led to the use of a rather unconventional material, starting a thought-provoking impulse and pushing ourselves to think in different directions. The main structure of the presented design is made of corn starch flips, which are commonly used as packaging material. Providing a design with bio-degradability and light weight material with the effect of self-adhesiveness led to this new material. The flips will be attached to prefabricated components by moisture only. Positive side effects besides the biological aspects, are the transportation and construction. Breaking down the light-weight structure into smaller panels, makes it easy for transportation and setup. The corn starch flips provide the design with an uncomplicated design and construction feature for free form structures. The broad area of applications and the communality of the flips allows easy handling for everyone, from children to professionals.

Keywords: conceptual design, form finding, corn starch flips, preformed, bio-degradability, natural, sustainability, carbon dioxide decreasing

1. Introduction

Being architecture students, we engage with construction in our daily life, on how we build, what we build and with which materials. The materials are becoming more important these days, since the society has reached a point where the resources are slowly lacking. The question of what will happen with the building when it eventually reached the end of its life cycle is given a more and more priority. The designing process actually does go beyond the building phase. Therefore, it is critical for architects to think about the reusability of their designs, since the building industry has an impact of sixty percent on the waste production. [1] The so-called cradle-to-grave design dominates the modern manufacturing. Resources are extracted, shaped into products, sold, and eventually disposed in a "grave" of some kind, usually a landfill or incinerator. [2] The industry needs new products of sustainable goods to renounce of conventional manufactured products. However, not only does the sustainability of the resource has to be a given, but also its entire development, from the raw material through the manufacturing to the outcome.

To think alternatively was the set requirement and to give that thought-provoking impulse a space at the IASS exhibition, literally spoken. Consequently, building a pavilion out of a new-thought material was the first approach for that matter.

Copyright © 2019 by Tonia Ludwig and Hannah Melzer
Published by the International Association for Shell and Spatial Structures (IASS) with permission.

2. Material

Conventional construction materials were made from valuable raw materials that require effort and expense to extract and make a worth of material asset. The cycle of the product means an excess of carbon dioxide.

However, biodegradable materials have a value too. They decompose and return biological nutrients to the soil. Unfortunately, all of these things are heaped in a landfill, where their value is wasted. They are the ultimate products of an industrial system that is designed on a linear, one-way cradle-to-grave model. [2]

The used corn starch flips are a product that is biodegradable to a 100 percent without any limitations, since they are made of corn starch, water and plant-based extracts. [3] In addition, they are an ecologically produced material where the environment stays already preserved during the manufacturing. Furthermore, do the disposing and decomposing have no impact on the environment. Only the amount of carbon dioxide evaporates within the procedure that the product has used up during its growing process before. [4] Hence, the environment will not be affected. The corn starch flips are made of non-genetically modified cultivated plants, in this case economic plants, that grow back every year.

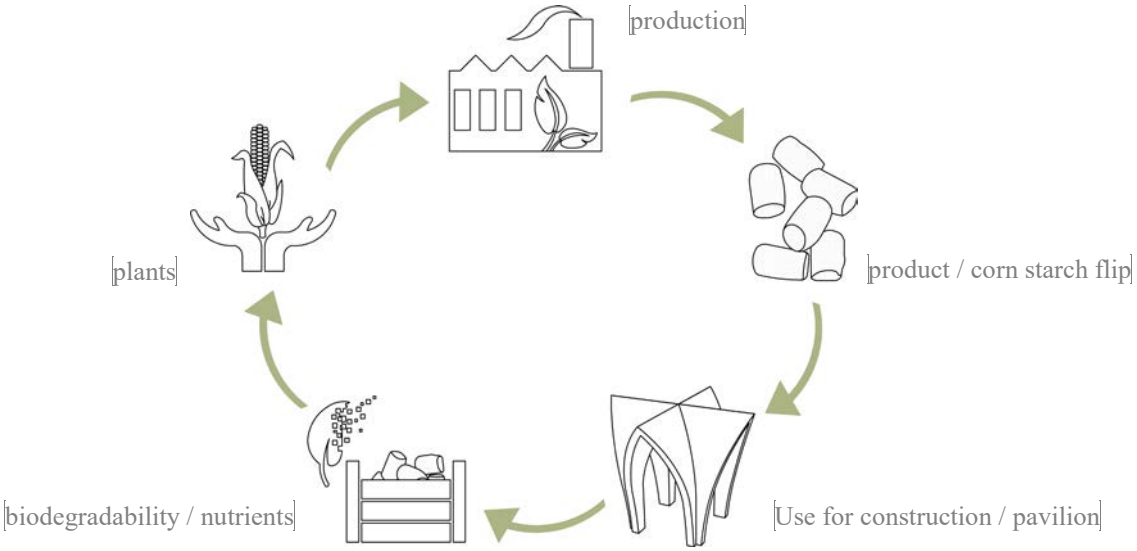


Figure 1: The cycle of biodegradability (cradle-to-cradle) of the corn starch flips

3. Research Methods

The development of constructing with an alternative construction material came with a design competition where the development of a pavilion in a lightweight construction was asked. During the development the concentration laid on the structure and building strategy of the pavilion.

The structure of the pavilion is completely made of corn starch flips, which again reflects the strategy and supports the approach of a low-tech work. Building a pavilion with only one material, without any connecting and bracing elements. During the development different possibilities of connection, as well as the behavior of the corn starch flips were tested. Due to the inexperience with the material its behavior had to be investigated by practical work and eventually reacted to in an architectural aspect. The conclusion that connecting the flips with moisture, as shown in figure 2, would not only be the easiest, but also the most sustainable way.

The construction and design of the pavilion is supposed to exhibit the feasibility of the work with corn starch flips.

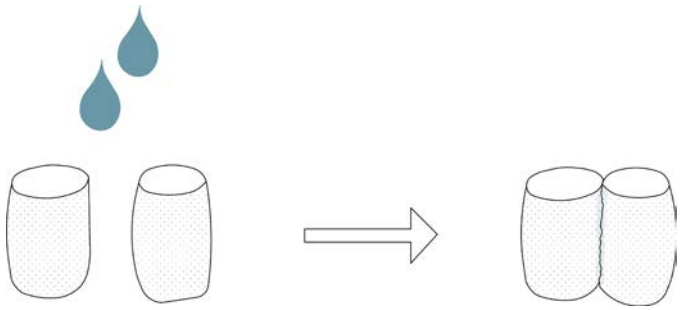


Figure 2: Connection of the material by moisture

4. Results

4.1. Design Process

Dealing with the building material and investigating its behavior build the foundation of the analogue approach to the design process. The pavilion is supposed to accentuate the message of a work with an alternative material which led to choosing a classical design. To underline the thought-provoking impulse, the design of the pavilion is based on a conventional structure that is usually build with reinforced concrete or stone.

The design cites the shape of a lancet arch combined with a ribbed vault. The total height of the pavilion measures 3.75 meters. The architectural challenge of the design however, yields to the wide cantilever of the vaults. The floorplan of the design forms a square. The delicate shaped pillars, that merge into the vaults, are placed in its corner. All four sides of the pavilion are equivalent.

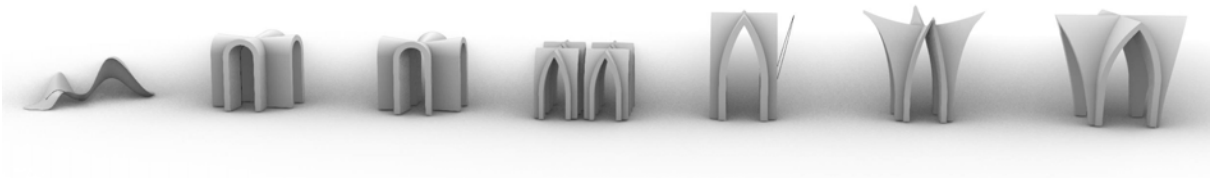


Figure 3: The design evolution / form finding

4.2 Construction

The pavilion is made of 151.200 corn starch flips, that make eight bigger prefabricated components of 18.900 flips. Four pillars that merge into vaults and reach a height of around 3.75m. Each component will be divided into smaller individual panels, as shown in figure 4. The measurements of the individual components are based on the size of transport boxes that were a boundary condition of the competition, with measurements of 1m x 0,6m x 0,75m. The corn starch flips have the form of an irregularly shaped cylinder with a height of 4cm and a diameter of 1cm.

For the fabrication of the components, the flips will be attached to one another by moisture in a laying position and stacked up to a height of 0.75m. Thus, equals an amount of 7 smaller panels that

assemble each component. Each prefabricated element follows that same principle, which yields to 112 panels, that can be assembled to these four components on site. Attaching the corn starch flips in just one layer, the pillars will be executed as hollow sections.

The vaults will be disassembled into smaller triangular shaped panels to achieve the shape of the vault. These triangular shaped panels will be attached to one another in a lying position and will only have the thickness of one layer, that equals about 1cm. In order to accomplish the desired bending, the edges will be beveled and adjusted to each other by slicing them at a certain angle.

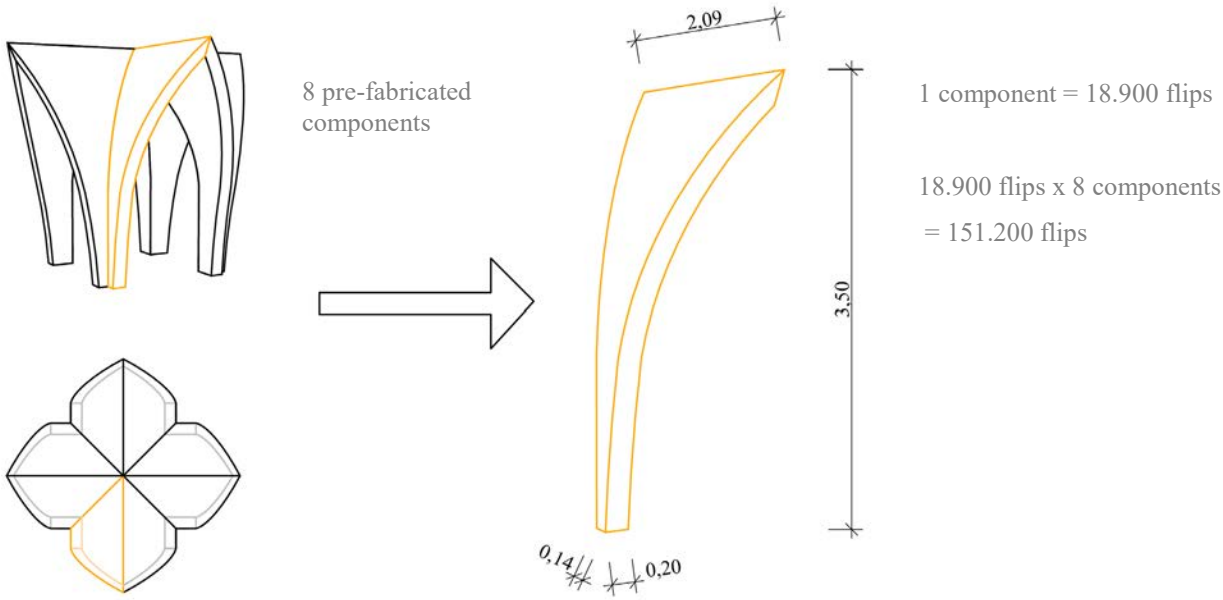


Figure 4: segmentation of the pavilion and quantity of the corn starch flips

The smaller panels will be attached to the bigger components by moisture on site. These components can then easily be attached to each other to form the pavilion.

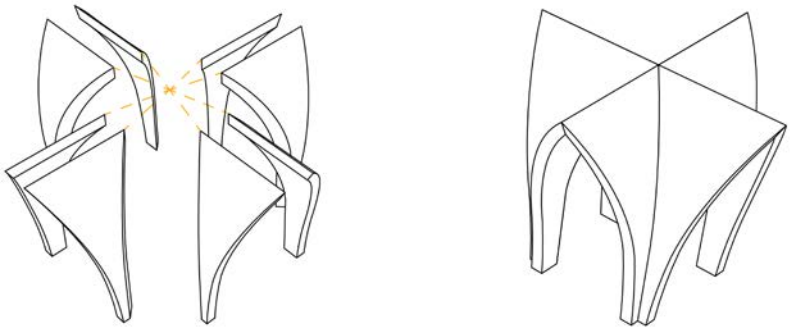


Figure 5: Attaching the components to one pavilion

5. Conclusion

The paper investigated the work with an alternative material in construction and design. The structural design of the pavilion translates the message of a thought-provoking impulse to keep preserving the environment, into an architectural experience by building it with corn starch flips only. The connection of the flips is done by moisture only. No chemicals or mechanical elements are needed. The pavilion exhibits a light-weight structure made of a pure material, that is preassembled in the most possible pure way, to larger segments. Thus, leading to reduced construction time on site.

Acknowledgements

The authors would like to thank Loick Biowertstoffe from Germany and PlayMais Austria for providing us with corn starch flips. The Team of the Institute of Structural Design (TU Graz) for contributing to the project.

References

[1] Adeline Seidel, "Recycling – Architektur/Architektur – Recycling", *in Baunetzwoche #220*, May 5, 2011, pp.

[2] W. McDonough and M. Braungart, *Cradle to Cradle: Remaking the Way We Make Things,* 2002, pp. 27

[3] Loick Biowertstoffe, *Farmfill Premium: Safety Data Sheet*, pp. 1

[4] Loick Biowertstoffe, *Farmfill Premium: Safety Data Sheet*, pp. 2

Proceedings of the IASS Annual Symposium 2019 – Structural Membranes 2019
Form and Force
7 – 10 October 2019, Barcelona, Spain
C. Lázaro, K.-U. Bletzinger, E. Oñate (eds.)

Quipustructure

Manuel ESPINOZA*,André APUMAYTA, Lisseth PACHECO, Karla TORRES, Henry CAEDRO[a]

* Ricardo Palma University. Architecture student
Calle Monte Caoba 182 – Santiago de Surco - Lima
intiespinoza.arq@gmail.com

[a] Escuela Nacional Superior Autónoma de Bellas Artes del Perú. Artist

Abstract

The QUIPUSTRUCTURE Project goal is to create a tensegrity system based on Inca's ancient lightweight construction technology.The use of local materials like bamboo and junco rope combined with the braiding techniques developed by the Incas have demonstrated great structural performance with a low carbon footprint [1]. This ancient technology is being lost, as only two bridges of the Inca´s road system, "Qapac Ñam", remain: Q'eswachaka [2] y Pukayacu [3].The QUIPUSTRUCTURE Project employs these techniques and materials together with tensile fabric and PLA (polylactic acid) joints to achieve a lightweight, modular and sustainable structure for creating shading devices. To test the system, a shading device prototype was fabricated using the "Quipu" mnemotechnical Incas´ artifact as inspiration. This prototype has been developed according to tests and loads analysis to achieve better structural behavior. The use of reed and bamboo on the project generates a low environmental impact and reduces manufacturing and transport costs. On the cultural level, the project gives the ancient Andean communities the opportunity to teach ancestral techniques and constructive philosophy to be used on the fabrication of modular lightweight and deployable structures.

Keywords: Junco, bamboo, lightweight, sustainability, deployable, tensegrity, hybrid, quipu, inkas, tensile fabric, easy assembly, modular, constructive philosophy.

1. Introduction

"Modern engineers can create more sustainable structures if they devote careful attention to nature."

- Brandlin, Daniela & Schexnayder, Cliff.

Quipu, inca artifact with a simple structure but a complex system that has been object of a lot of investigations around the world, was our starting point. Its structure is compose by a backbone called primary cord and Pendant Strings (or secondary cords) attached to the primary one like ribs. In the other hand, quipus are generally composed of cotton or camelid fibers. Our Quipustructure pretends to use this principles in combination with structural knowlegde to create a self-supporting bamboo-junco structure.

In accordance with the current trends in structural design and construction, new materials are investigated for new or equal purposes. Quipustructure explores an hybrid system of bamboo, PLA and vegetal fibers (Junco), selected because of their minimal environmental impact.

Copyright © 2019 by Manuel ESPINOZA, André APUMAYTA, Lisseth PACHECO, Karla TORRES, Henry CAEDRO
Published by the International Association for Shell and Spatial Structures (IASS) with permission.

For the main structure, bamboo was undoubtedly chosen because of its already well-known aesthetic and structural attributes. On the other hand, we needed a strong, good and cheap to produce material like plastic, but the problem was that most plastics are derived from the distillation and polymerization of nonrenewable petroleum reserves. Nevertheless, we had "bioplastics" options, like Polylactic Acid (PLA) derived from renewable resources like corn starch or sugar cane.

For the tensors, vegetal fibers like Junco were thought because its good specific properties. Also, they are lightweigh but at the same time, resistant. In terms of cost, this fibers present lower cost than syntetic ones and we can easily find them on Peru wetlands.

Junco is the less explored material of these three components, a strange fact since in Peru there is a great reference of structures made only of vegetable fibers: Q'eswachaka, the last Inca bridge.

The Q'eswachaka bridge is a suspension bridge over Apurimac River in the southern Andes. It is renewed every year, using traditional Inca techniques and vegetal fibers as raw material that will form the structures, floor, railings, and sides of the bridge. This renovation process, keeps alive the Inca culture and hand-twisted fiber techniques

Despite of the properties mencionated above and the heritage of pre-hispanic techniques, there aren't bigger steps in the structural exploration of this ancient material and that's the importance of this research.

3. From the Vector to the form

"There is no reason why the unknown factors should always be the internal stresses and not, for example, the geometric parameters which define the form itself of the structures, since in this latter case uniformity of stresses and much more complete and efficient use of the material may be obtained.
-Musmeci 1980-

The philosophy of Musmeci follows the representation of the structural behavior with the amount precisely of material. That looked so attractive that we knew from the beginning we'll follow that kind of architecture so we could achieve a form that speaks by itself. The best example is the Muscemi's bridge, a bridge which is supported by a concrete sheet of four contiguous arches fingerlike molded to form made of only one membrane of reinforced concrete (about 30 cm (1 ft) thick). The loads could be read so well, and the design process was no more than a physical of the load direction. Those examples of Architecture in combination with our ideals of the recovery of the ancient techniques. provide us a framework and guidelines we'll pursue in the design process.

The form-finding for the project laid on the Quipu as an extended element that we'll translate into a 3-Dimensional model inscribed inside a virtual space. This virtual space is composed by an octahedron with a triangular grid each side (figure 1). This triangle grid provides an excellent support every structure because the shape cannot be changed when pressure is applied to it. With the virtual space as the framework structure and formal issues could be solve in a manual way. With the concept of the quipu, the interpretation starts with the line vectors of the Quipu transformed into lines that came from a main structure, the arch. As those lines couldn´t stayed in place it was necessary to step up a fabric for tensile purposes. That results into a pre-model reticular structure with some fabric.

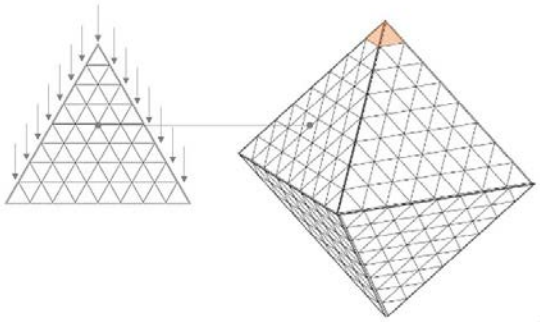


Figure 1:Model of the octahedron Source: Prepared by the authors.

With the initial form it was necessary to explore the geometry, how the structure components works, and how they'll translate into a large scale. Each vector, line and vertex depending of their internal force results in the substitution of a different material or fabrication system. The traction large members translate into a junco rode, it crosses all the structure; the compression members into, Bamboo bars, and the main structure translates into an sectionable Bamboo arch.

4. Building the Structure

The pavilion result was an isostatic structure with a main arch and compress members that came from it, those were tensile by the Junco Rope. It covers an extension of 16 square meters, 4 meters of length each side with just been supported by 2 points each corner. The small-scale prototype results efficiently in order to deliver the best formal choice, but there were limitations in the physical y structural behavior that we need to solve on the larger scale. We start dividing into segments the project, the result: An arch, the compressed members, the Junco and the fabric.

We encourage different challenges in the physical model. For the arch was to make a convince geometry that could resist all the directional loads, so the rise had to be greater and the base bigger than the crown, Then with all the different inside sizes of the ribs it was necessary to make them efficiently in terms of materials, time, production and easy assembly. For that each rib is composed by 4 PLA typical pieces (these are the same for all the ribs) and 3 bars of bamboo. (these vary according to size.). The bamboo compressed members result into a cutting system that could make them packable.

To take the project beyond the preliminary design phase, it was necessary to explore the building manufacturing of the remarkable pieces of the project.

4.1 Materials

One of the main objectives of Quipustructure is that each element of the structure does not compromise the environment regeneration cycle, that's why we use the materials below:

4.1.1. Junco

Schoenoplectus americanus, known as "junco", is a common species on the wetlands from the central coast of Peru. It has an important role in the ecosystem , it is composed by cellulose, hemicellulose, lignin, pectin, waxes, and other components. In structural terms, cellulose and lignin are the main important chemical constituents because the first one provides stability and and fiber strength while

the second one, guarantee rigidity, influence the structure and flexibility of the fibers. In other words, for a better structural behavior, you should look for fibers with a high level of cellulose and low level of lignin

Table1.Chemical proximalofaquatic plant Schoenoplectus americanus (SA) and experimental diets

Composition g/kg	*SA*	*D1 (0% SA)*	*D2 (20% SA)*	*D3 (40% SA)*
Dry matter	98.85	98.85	97.26	97.23
Organic matter	90.2	88.39	87.97	87.66
Asjh	9.8	11.61	12.03	12.34
Ehther extract (EE)	1.83	2.06	2.15	2.19
Crude protein	10.57	13.12	13.96	14.95
Crude fibre	27.04	23.04	22.55	21.7
NFE	50.74	49.56	49.31	48.82
ADF	57.28	54.74	52.47	58.91
ADF	43.77	30.48	31.28	29.74
Cellulose	**27.38**	**21.79**	**21.79**	**21.43**
Hemicellulose	13.51	23.9	21.79	29.17
Lignin	**13.13**	**6.13**	**6.81**	**6.27**
TDN	63.23	62.7	63.07	63.1
Gross energy (GE)	2.8	3.05	3.06	3.07
Digestible energy (DE)	2.24	2.76	2.78	2.78
Metabolixable energy (Me)	1.83	2.26	2.28	2.28

(Puga, 2008). *Feed intake, its utilization and rumen fermentation pattern in sheep fed aquatic plant Schoenoplectus americanus.*

In terms of density, in the field of light structures; it is necessary to look for materials that are not very dense. This characteristic is present in almost all vegetable fibers including Junco due to its porosity. In fact, the density of these fibers is less than fiberglass.

To obtain the fiber it's necessary to do it at any station but summer in Huacho and Chorrillos, local districts of Lima, because the probabilities of pests increases.The process starts in with the extraction of the stem that grows till 2m from the ground, then it goes through a leveling process in which the stems finally have the same size. Finally, those are packed into wads according to the quality and thickness to make them possible to purchase in the market.

The use of junco as its said before is for domestic and handicrafts purpose. So it was necessary to test and analysis the Junco and develop a rode. First, same thickness fibers are selected and are flatten with any cylindrical object bearing down with the weight of the body, then with the flatten fibers it's necessary to spin by hand, the oldest ancient andean method.



Figure 1:Piece of Junco filament bundle. Source: Prepared by the authors.

For the project it was necessary to test the fiber to a tensile test. We prove rodes from 2 to 6 fibers per rode to a tensile stress in order to delivered the best one for our hybrid system. .with the test we choose the 4 and 6 fibers per rode as the best rated to work with the length of the compressed members.

4.1.2. PLA

Polylactic Acid filaments (PLA) is a kind of biodegradable thermoplastic which is used for 3D printing and allows complicated objects elaboration. This material can be processed to be converted in different compounds so it can be used as a substitute of synthetic fibers. Some of the material properties are its resistance to high temperatures (145-160°C), elongation at break (100-160%) and tensile strength (110-145 Mpa.) [4]

For all of this, we choose PLA plastic because we needed a material that can resist tensile strength and elongation at break to sustain the arches of the structure and at the same time, ensure the curvature, avoid the rigid and in the joints of bamboo compress bar members.

4.1.3. Bamboo

The bamboo is a very important plant because of its abundance in the local area, represent low material cost, ease of work as a building material in different structures In general, its use is an environmental advantage because it can replace steel in some cases and concrete for a renewable and sustainable material.The bamboo resistance to compression is relatively high, but it means nothing if we don't specificate the relation between length and diameter of the piece. In the case of shear strength, we have to be careful because it affects directly in the joints. [5]

We use bamboo in parts that works by compressive force, sections of the arch, which were united by the PLA plastic pieces , and finally in the ribs like bars that join the vertex.

Despite its great elastic capacity, it can present certain problems related to durability if certain precautions aren't adopted, some parts of bamboo should be isolated to avoid humidity. Despite of this, the bamboo has been a very important plant for many centuries, not only for the environment, but also for the evolution of construction, as we have just seen.

4.1 Fabrication and Assembly

The vertebra fabrication is similar in every piece and is composed by two typical pieces made by PLA plastic, the central one and other piece that goes in the vertex which join with the ¾" diameter selected bamboo.

The arch is made up by voussoir, which is composed by PLA vertebras and bamboo sections. First of all, the main arch is assembled with a similar system of a stone arch. It starts with the bases to finish in the central voussoir. Every voussoir contains three bamboo arches and four vertebras.

Once the voussoirs are assembled, the points are placed for transport, assembly and sectioned to be join with PLA pieces for the arch system but also can be stretched by the reed rope and the cloth over the structure.

For the placement of the points, it's necessary to create a system that allows to keep the points in place while the reed tensed the system, which was made of 1" diameter bamboo and at each end a PLA piece is added.

The development of the joints between the arch points will be seen in 1:1 scale and must be submitted to error test.

Acknowledgements

We would like to express our very great appreciation to Mr. Sebastian Aste for his selfless and constructive suggestions during the development of this research work. His willingness to give his time so generously has been very much appreciated.

References

[1] P. Magrone, G. Tomasello, S. Adriaenssens, S. Gabriele, Stefano,V. Varano. *Revisiting the form finding techniques of Sergio Musmeci: The bridge over the Basento river: Beyond their Limits.* London Jul,2016

[2] A. Nauta and M. Vergara, *"Simulación de Termofluidos de PLA natural y ABS en el proceso de impresión 3D"*. Ecuador, 2017.

[3] S. Martinez, *"Bambú como material estructural: Generalidades, aplicaciones y modelización a una estructura tipo"*. Valencia, España, 2015.

[4] D. Puga. *Feed intake, its utilization and rumen fermentation pattern in sheep fed aquatic plant Schoenoplectus americanus.* Mexico, Jun 2008.

Proceedings of the IASS Annual Symposium 2019 – Structural Membranes 2019
Form and Force
7 – 10 October 2019, Barcelona, Spain
C. Lázaro, K.-U. Bletzinger, E. Oñate (eds.)

Reviving a Craft through Architecture: Computational Making of a lightweight pavilion based on wire-bending techniques

Vernelle A. A. NOEL *

* Visiting Assistant Professor, Georgia Institute of Technology
245 4th St NW, Atlanta, GA 30332. USA
vernelle@alum.mit.edu

Abstract

This paper presents research on a novel approach to the fabrication of lightweight architectural structures based on a traditional craft of wire-bending specific to Trinidad & Tobago. Wire-bending is a dying craft which was developed in the 1930s in the Trinidad Carnival. In it, wire, fiber glass rods and other linear materials are bent with hand tools to create two-dimensional and three-dimensional structures which are decorated and performed by masqueraders. This research investigates how we might revive this dying craft and explore its possibilities in architecture through computational making. The goal of this paper is to: (1) test a computational description of the craft at the architectural scale; (2) conduct structural tests on materials and connections used in the craft; (3) develop new tectonic descriptions in the craft; and (4) fabricate a lightweight pavilion using these techniques. The paper presents the craft, structural tests and construction of the first pavilion based on it, and concludes with a discussion on the work, and possible next steps.

Keywords: wire-bending, Bailey-Derek Grammar, lightweight structures, craft, fiber glass rods, active bending structures, shape grammars, design computation

1. Introduction

This work situates itself at the intersection of craft, shape grammars, computational making, and active bending structures. Wire-bending is a traditional craft practice from the 1930s in carnival in Trinidad and Tobago. In the practice, static and dynamic linear materials are bent with hand tools to create two-dimensional (2D) and three-dimensional (3D) structures. These structures are then covered, decorated and performed by masqueraders during the carnival (Figure 1). Although the practice is called wire-bending, wire is not the only material used. Other materials used include rattan, fiber glass and PVC rods, just to name a few, with bent wires and adhesive tapes used to make connections (Figure 1).



Figure 1: Photo of a dancing sculpture in the Trinidad Carnival (left), details in the craft of wire-bending (middle and right).

Copyright © 2019 by Vernelle A. A. Noel
Published by the International Association for Shell and Spatial Structures (IASS) with permission.

Shape Grammars are rule-based systems for analyzing, describing, and generating visual or spatial designs (Knight [1]). Developed by Stiny & Gips [2] to generate a series of geometric paintings, shape grammars allow 'recursion and embedding' of shapes for design, with one set of rules having the ability to generate numerous designs belonging to a similar language (Stiny [3]). The system has been used in structural design at the conceptual stage (Mueller and Ochsendorf [4]). Computational Making is a relatively new area of inquiry coming out of shape grammar theory. The field seeks to relate mathematical systems, theories, and technologies in design with situated, embodied acts of making (Knight and Vardouli [5]). This frame is important for craft practices as they are often tied to a social, cultural, and physical environment. The Bailey-Derek Grammar (Noel [6]) is a shape grammar that describes technical knowledge in wire-bending (Figure 2) in the form of rules and steps, and makes that knowledge explicit.

While research into form-finding with fiber-glass rod structures is still in its early stages (Bessai [7]), when it comes to using active linear rods elements to fabricate structures, previous works include bundled fiber-glass rod structures (Bessai [7]); bamboo grid-shells (Krolla [8]); bamboo structures (Nagai [9]); CNC knit and GFRP rod structures (Ahlquist and Lienhard [10]); Ahlquist *et al.* [11]; and form-active hybrid structures (Quinn *et al.* [12]). Additional work exploring computational design, wire-bending, and structures include the creation of digital design and fabrication approaches to wire-bending to increase its accessibility (Noel [13]); and the design and fabrication of a lightweight mobile structure based on digital approaches to the craft (Noel [14]).

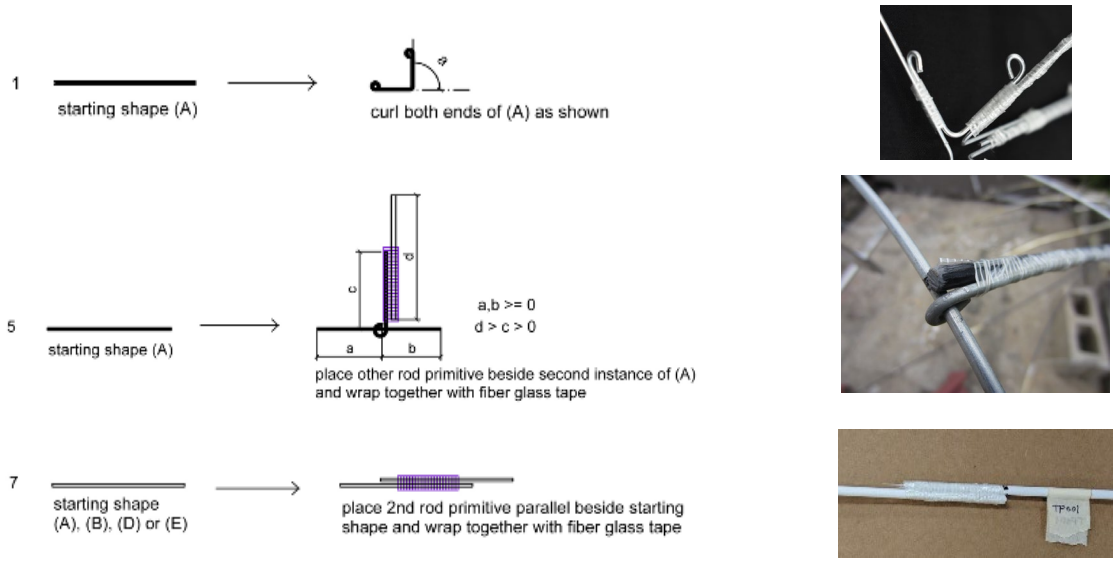


Figure 2: Rules #1, #5, and #7 of the Bailey-Derek Grammar - a computational description of wire-bending with images of corresponding rules on the right.

Unlike the aforementioned studies, this project explores fabrication of a pavilion out of fiber-glass rods built on traditional techniques and tectonics in the craft of wire-bending. The objectives are to: (a) test and apply the computational description of wire-bending (Bailey-Derek Grammar) at the architectural scale; (b) conduct structural tests on materials and connections used in the craft; (c) develop new tectonic descriptions in the craft; and (d) fabricate a lightweight pavilion using these techniques. The design for the pavilion (Figure 3) functions as a diagram with structural requirements becoming clearer as studies, simulations, and tests were conducted.

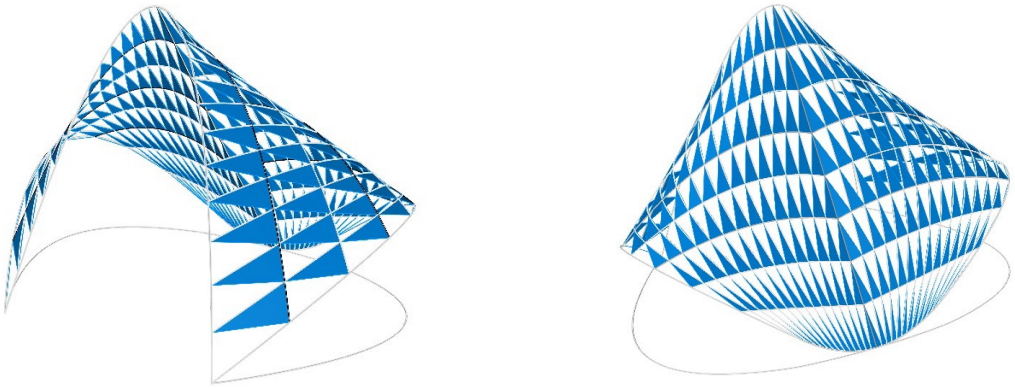


Figure 3: Design of lightweight pavilion. Front perspective (left), and Rear perspective view (right).

The steps taken to explore this craft at the architectural scale include:

1) Conducting structural tests on materials and tectonics in wire-bending;
2) Building a scaled, physical structural model;
3) Building a digital model informed by the physical structural model;
4) Building a physical control model from the new digital model;
5) Building a full-scaled model informed by the control model; and
6) Building the final pavilion informed by the full-scaled model.

2. Wire-Bending

Materials used in wire-bending include wire, fiber glass rods, aluminum rods, plastic rods, rattan, and aluminum flat bars to name a few. The type of material and where it is used in dancing sculptures depends on the structure, weight, the kinetic performance, and movement. The craft is not currently employed in architecture. Based on ethnographic field work, the main means of connecting and securing materials in the craft are through wire-bends and hooks; adhesive tapes; cable ties; and blind rivets (Noel [11]). Adhesive tape is often used in wire-bending because the artifacts in carnival are temporary, de-installed after events, materials are often re-used, and unlike welding adhesive tape allows the movement of connections, and enables quick fixes during fabrication. In this project, we use fiber-glass rods, hollow aluminum rods, and galvanized wire. We also explore three connections from the Bailey-Derek Grammar (Figure 2). Rule #1 shows a wire-bent connector that can be used to connect non-parallel rods together as shown in the photo. Rule #5 shows how a fiber glass rod might be connected to wire in a non-parallel relationship via a short leg of wire looped around the wire on one end with the leg of the wire and the fiber-glass rod wrapped securely with tape. Wire-benders in Trinidad & Tobago call the tight looping of wire around another wire, clinching. Rule #7 shows how fiber-glass, aluminum, or PVC rods are joined when they are parallel to each other.

3. The Project

Objectives

Currently, expert wire-benders – of which there are not many remaining - make design and fabrication decisions based on tacit knowledge developed from their experience and intuitions. A necessary aspect of this project involved testing the performance and limits of different tapes and connections in the craft so that this knowledge became explicit in order to be built upon to extend the craft. We used a Universal Tensile Tester - MTS 55 kip Servohydraulic Load Frame – to examine the tensile strength of Rule #7 using fiber-glass rods and eight different types of tapes. A CNC wire-bender was used to fabricate wire-

bends, reduce the labor-intensive nature of the craft, and achieve consistent bends. In the following sections I describe each step undertaken.

3.1. Structural Tests

Wire-benders currently use masking tape, and fiber glass tape in their work. In this test, I conduct tensile tests on seven different adhesive tapes to gain insight into their limits and employ these results in design and construction. In the experiment, one 3/16" diameter fiber-glass rod was placed beside another with a 2" overlap, then wrapped with tape. Each sample was then tested for tensile strength (Figure 4). Tapes tested (from left to right) include: filament tape; industrial strapping tape; vinyl tape; industrial duct tape; black gaffer's tape; VHB tape; and cloth tape.

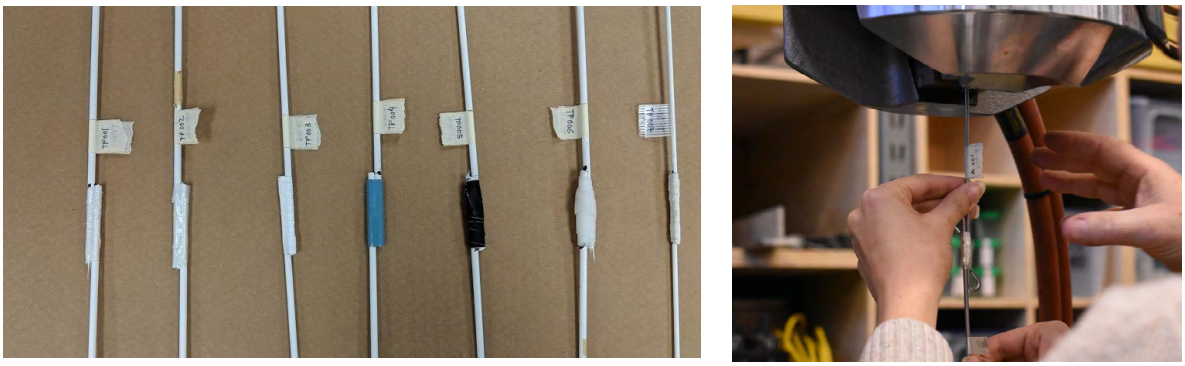


Figure 4: Tapes and rods for tensile tests labelled from TP 001 on the extreme left to TP 007 on the extreme right (left). Insertion of a test specimen in the Universal Tensile Tester (right).

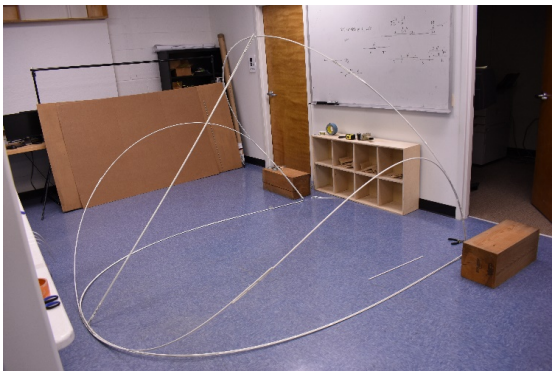
We hypothesized that the top performing tapes would be the VHB tape, industrial strapping tape, duct tape, and vinyl tape, but the results proved otherwise. Results showed that the top three performing adhesive tapes were: (1) Industrial Strapping Tape - 118lbs, 0.21" displacement; (2) Industrial Duct Tape - 118 lbs, 0.55" displacement; and (3) Gaffer's Tape – 100lbs, 0.45" displacement (Table 1) with the VHB tape raking in last place with 20 lbs, 0.90" displacement.

Table 1: Top three performing adhesive tapes for wire-bending rule #7

Rank	Label	Tape Description	Tape Width (in)	Tensile Strength (lb./in.)	Displacement (in.)
1st	TP 002	Industrial Strapping Tape	1/2"	118 (170)	0.21
2nd	TP 004	Industrial Duct Tape	2"	118 (36)	0.55
3rd	TP 005	Black Gaffer's Tape	1"	100 (40)	0.45

3.2. Physical Structural Model

In order to understand the global behavior and performance of the fiber-glass rods for the pavilion, we built a physical model of the main structural members only. This 2/3 scale simulation model (Figure 5a) shed light on the sizes and behaviors of the main structural members, main connections, fabrication, assembly, and erection. Figure 5 shows the main members evaluated in the structural model – the main spine, main curve, front arc, and base arc. A new digital model (Figure 5b) was built based on the final geometry and form of the physical structural model.



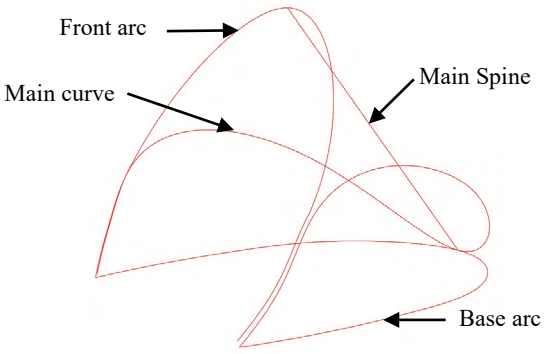
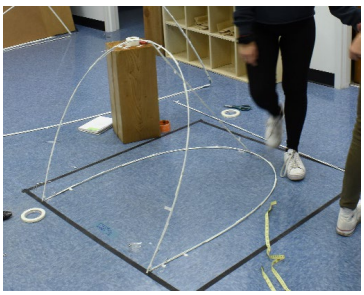
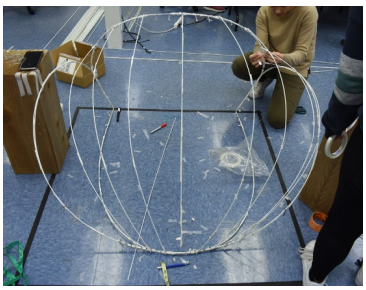


Figure 5: Fig. 5a - Physical structural model (left) at 2/3 scale. Fig. 5b - updated digital model based on behavior of structural model (right).

3.3. Control Model

After redesigning the digital model of the main structure based on the 2/3 scale physical structural model, a 1/3 scale control model of the entire structure was built to give direct feedback on processes, connections, members, logistics, and behavior. The sizes of members in the control model were used to inform construction of the full-scaled model although the scaling of active bending structures depends on the dead load and stability (Lienhard and Knippers [15]; Ahlquist *et al.* [11]). From the control model, failures were documented and strategies were designed and implemented to address them and inform the full-scaled prototype of the pavilion.





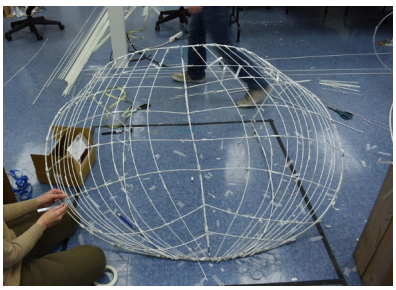


Figure 6: Control Model at 1/3 scale built from updated digital model.

3.4. Full-Scaled Pavilion Model

The final structure for the pavilion was categorized into primary, secondary, and tertiary structures. Materials used included:

(a) Main spine: Bundle of 3No. 1/2" diam. hollow aluminum rods.
(b) Front arc: Bundle of 3No. 3/8" diam. fiber glass rods;
(c) Main curve: Bundle of 3No. 1/4" diam. fiber glass rods;
(d) Base arc: Bundle of 3No. 1/4” and 4 No. 3/16” diam. fiber glass rods;
(e) Secondary members: 2 No. 1/4" diam. fiber glass rods bundled together;
(f) Tertiary members: 1 No. 1/4" diam. fiber glass rod;
(g) Heavy Duty strapping tape;
(h) 1/8” diam. galvanized steel rods;
(i) Overlap length for fiber glass rods: 12”; and
(j) Double-sided neoprene skin.

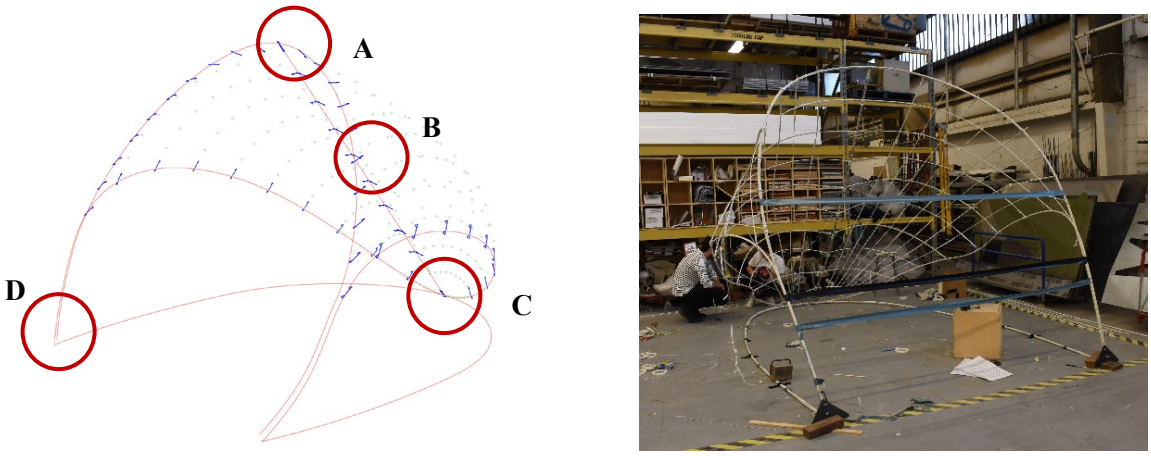


Figure 7: Main areas of focus for tectonics studies (left). Full-scaled erected structure (right)

The main areas of tectonic focus for the pavilion were locations A, B, C, and D (Figure 7). A: where the front arc and the spine meet; B: where the spine, secondary and tertiary rods meet; C: where the base arc and the main curve meet; and D: where the front arc meets the base arc. Due to high stresses in the fiber glass rods, the main curve snapped close to location C during construction. It was repaired by adding a six-foot-long bundle of 3No. 1/4" diam. rods at that location.



Figure 8: Connection details for the pavilion at location A (top left), B (top right), C (bottom left), and D (bottom right).

New tectonics in the craft were developed (Figure 9), with some specific to construction at the architectural scale. Two new features of tectonics in the craft are: (1) parametric connections (Fig. 9a, and 9b); and (2) loops at the ends of wires. The parametric connections permit sliding and may be used to correct errors during fabrication, and/ or encourage interaction with the structure and design in-situ, while making loops at the ends of wires before taping them increases the tensile resistance of

connections. These new connections also take into account bundles comprising more than one rod as currently from ethnographic investigations, only single rods are used (Noel [6]).

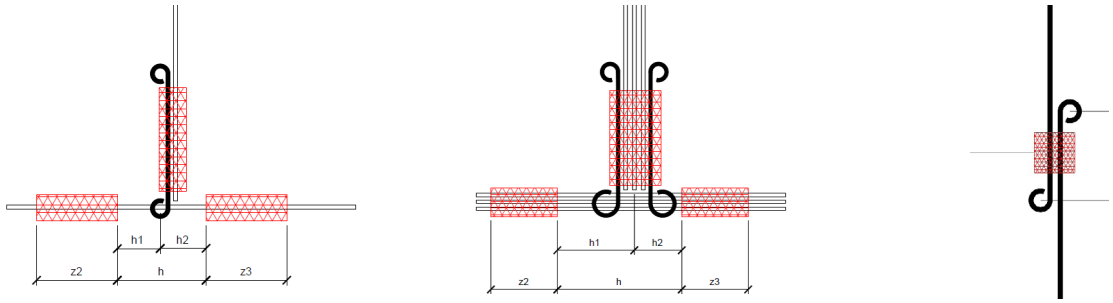


Figure 9: New tectonic connections in wire-bending to aid in application of the craft at the architectural scale. They include parametric connections (Fig. 9a: left and 9b: middle), and the creation of loops at ends of wire (9c).

In this first full-scaled model (Figure 10), we used double-sided neoprene to skin the structure. The fabric was heavy and its dead load had a great effect on the structure which will be revisited in the construction of another full-scaled model.

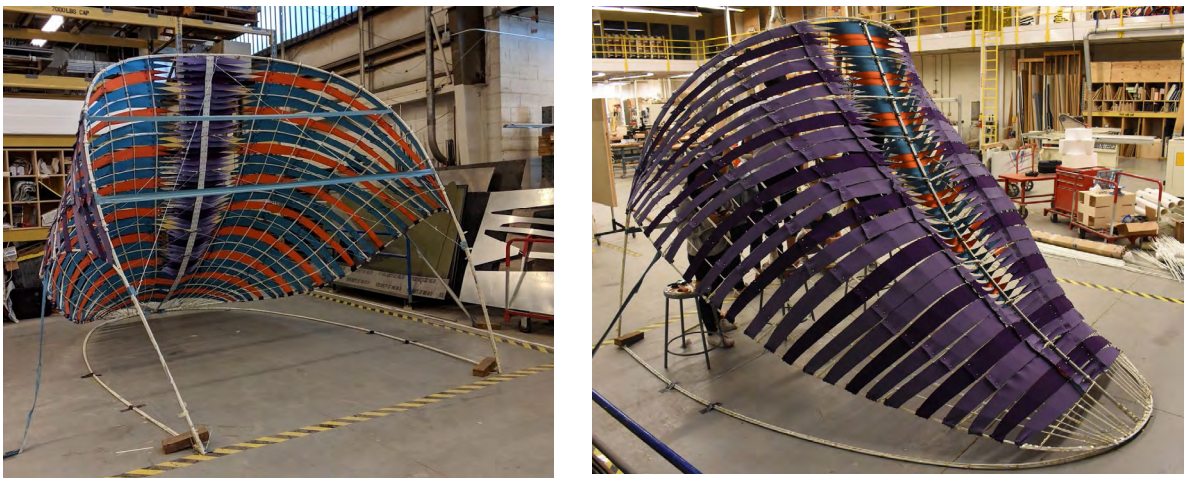


Figure 10: Full-scaled pavilion model. Front view (left) and rear view (right).

4. Conclusion/ Contributions

This research set out to investigate how we might revive the dying craft of wire-bending from Trinidad & Tobago by exploring its possibilities at the architectural scale. This paper outlines the design and construction of a pavilion based on materials and techniques in the traditional craft. We have in this work demonstrated how the computational description of this craft might be used in architecture; how this situated practice with its specific technical knowledge can be transferred to architecture; and explored how this craft might inform active bending structures. We conducted structural tests on materials and connections used in wire-bending to understand the tensile strengths of adhesive tape; connections; and developed new tectonics in wire-bending that include bundles of fiber-glass rods for applications in architecture. By building a series of physical and digital models – each informed by the other, we were able to fabricate a pavilion. Our next step shall include the construction of a full-scaled pavilion that is informed by the behavior of this first full-scaled prototype (Figure 10). Future work will include: (1) investigating greater synthesis between materials, tectonics, behavior, geometry, and form; (2) employing digital simulation tools and Finite-Element-Modeling (FEM) to aid in form-finding; and (3) embedding structural properties and behaviors in the Bailey-Derek Grammar.

Acknowledgements

This work was supported by the Ventulett NEXT Generation Visiting Fellowship from the School of Architecture at the Georgia Institute of Technology. Grateful acknowledgement is given to Niloofar Nikookar, Phuong 'Karen' Tran, Jamieson Pye, Mehmet Bermek, Ashlee Bryant, Shreya Kumar, Shilpa Mehta, Aditi Bharadwaj, Daniel Oddo, Sushmita Tripathi, and Jin Yu for their help in constructing our pavilion in my Spring 2019 Computational Making Course. Special thanks to Pensa Labs for their support.

References

[1] T. Knight, "Applications In Architectural Design, And Education And Practice," Massachusetts Institute of Technology, Report for the NSF/MIT Workshop on Shape Computation, Apr. 1999.
[2] G. Stiny and J. Gips, "Shape Grammars and the Generative Specification of Painting and Sculpture," in *Sciences & Humanities: Models and Applications for the Arts*, Ljubljana, Yugoslavia, 1971.
[3] G. Stiny, *Shape: talking about seeing and doing*. Cambridge, Mass: MIT Press, 2006.
[4] C. Mueller and J. Ochsendorf, "An Integrated Computational Approach for Creative Conceptual Structural Design," p. 6, 2013.
[5] T. Knight and T. Vardouli, "Computational making," *Des. Stud.*, vol. 41, Part A, pp. 1–7, Nov. 2015.
[6] V. A. A. Noel, "The Bailey-Derek Grammar: Recording the Craft of Wire-Bending in the Trinidad Carnival," *Leonardo*, vol. 48, no. 4, pp. 357–365, Jul. 2015.
[7] T. Bessai, "Bending-Active Bundled Structures: Preliminary Research and Taxonomy Towards an Ultra-Light Weight Architecture of Differentiated Components," 2013.
[8] K. Crolla, "Bending Bamboo Rules: Beyond Century-Old Typologies," *J. Archit. Educ.*, vol. 72, no. 1, pp. 135–145, Jan. 2018.
[9] T. Nagai, "Analysis of bamboo truss structure with hand-made rope joint," 26-Sep-2016. [Online]. Available: http://www.ingentaconnect.com/search/article?option1=tka&value1=Analysis+of+bamboo+truss+structure+with+hand.made+rope+joint&pageSize=10&index=1. [Accessed: 04-Sep-2018].
[10] S. Ahlquist and J. Lienhard, "Physical and Numerical Prototyping for Integrated Bending and Form-Active Textile Hybrid Structures," 2013.
[11] S. Ahlquist, J. Lienhard, J. Knippers, and A. Menges, "Exploring material reciprocities for textile-hybrid systems as spatial structures," *Prototyp. Archit. Conf. Pap.*, pp. 187–210, Jan. 2013.
[12] G. Quinn *et al.*, "Calibrated and Interactive Modelling of Form-Active Hybrid Structures," 26-Sep-2016. [Online]. Available: http://www.ingentaconnect.com/content/iass/piass/2016/00002016/00000016/art00005#. [Accessed: 04-Sep-2018].
[13] V. A. A. Noel, "Crafting as Inquiry into Computation - Exploring wire-bending in traditional practice and design education," *Herneoja, Aulikki; Toni Österlund and Piia Markkanen (eds.), Complexity & Simplicity - Proceedings of the 34th eCAADe Conference - Volume 1, University of Oulu, Oulu, Finland, 22-26 August 2016, pp. 311-320*, 2016. [Online]. Available: http://papers.cumincad.org/cgi-bin/works/Show?_id=ecaade2016_075. [Accessed: 12-Aug-2016].
[14] V. A. A. Noel, "From Costuming and Dancing Sculptures to Architecture: The Corporeal and Computational in Design and Fabrication of Lightweight Mobile Structures," in *Future Trajectories of Computation in Design*, Istanbul, Turkey, 2017, pp. 22–41.
[15] J. Lienhard and J. Knippers, "Considerations on the Scaling of Bending-Active Structures," *Int. J. Space Struct.*, vol. 28, pp. 137–148, Dec. 2013.

Proceedings of the IASS Annual Symposium 2019 – Structural Membranes 2019
Form and Force
7 – 10 October 2019, Barcelona, Spain
C. Lázaro, K.-U. Bletzinger, E. Oñate (eds.)

Self-Deploying Tensegrity Structures with Inflatable Struts

Jonathan DESSI-OLIVE [a]*, James CASE [b], Michael KOLINER [a], Vinay TEJA MEDA [b]

[a] Georgia Institute of Technology School of Architecture
245 4th Street NW, Atlanta, GA, USA, 30332
jdo@design.gatech.edu

[b] Uzun + Case, Structural Engineering
1230 Peachtree St NE, Suite 2500, Atlanta, GA, USA, 30309

Abstract

This paper presents research on a hybrid structure system that extends the principles of active-deployed tensegrity structures through a series of prototypes that use inflatable compression struts. These structures combine the advantages of tensegrity and pneumatic structures, resulting in minimum weight with a maximal global volume change. Previous deployable tensegrity structures have been developed that demonstrate self-deploying behavior, but only at small scale. Prototypes that use commonly known three and four-strut geometries were built that use low-pressure inflatable struts, developed to maintain their internal air pressure, resist strut deformation that can occur during deployment, and resist buckling that results from loading the structure. The prototypes presented here precede a large-scale pavilion to be exhibited at the 2019 Form and Force Expo in Barcelona. This paper presents several development prototypes, design and analytical strategies for the inflatable compression struts, load-testing results, as well as drawings of the proposed exhibition structure.

Keywords: tensegrity structures, pneumatic structures, inflatable tensegrity structures, textile composite structures, deployable structures, spatial structures, structural design, structural prototypes.

1. Introduction

Tensegrity structures are considered to be optimal because they maintain their stability with the fewest number of structural members carrying purely axial forces [1]. Since their discovery in the mid-twentieth century, artists, architects and engineers have imagined and proposed several innovative variations and applications for tensegrity structures. This paper presents advancements in a hybridized structure system that extends the principles of active-deployed tensegrity structures through a series of physical prototypes that use pneumatic compression struts. Replacing rigid compression struts with pneumatic members presents an opportunity to maximize the global volume change of the structure before and after it is deployed, while minimizing its overall weight. Though proven to be theoretically possible, no large-scale physical prototypes have yet been developed. *The research presented in this paper is focused on developing assembly strategies for architectural-scale deployable tensegrity structures that use low-pressure air-struts.* Due to the unique combination of two historic structural systems, this paper will first review the origins, historical context, and applications of pneumatic and tensegrity structures in architecture and give an overview of active-deployed tensegrity systems in other fields. Next, theoretical, analytical and design strategies for this hybrid structure system will be described followed by a discussion of a series of physical prototypes, built at increasing scale and technological resolution. Finally, this paper will suggest next steps in the development of a large-scale inflatable tensegrity pavilion structure for the 2019 Form and Force Expo, and speculate on the range of material possibilities and applications such structures may have.

Copyright © 2019 by Jonathan Dessi-Olive, James Case, Michael Koliner, and Vinay Teja Meda
Published by the International Association for Shell and Spatial Structures (IASS) with permission.

2. Background to Pneumatic and Tensegrity Structures

2.1. Pneumatic Structures

Applications of pneumatic (air-supported) structures in engineering and other technical fields far precede their application in architecture. An early example of pneumatic structures being applied to building construction was pioneered by American engineer Wallace Neff, in the early 1940's. The technique, which involved spraying concrete onto rubber balloons as formwork [3], was refined several decades later through systems such as *Domecrete* by Haim Heifetz, and *Binishells* by Dante Bini [4]. In volume one of *Tensile Structures*, Frei Otto [5] included a chapter on that offered an analytical basis for pneumatic structures and helped establish them as a field of building construction. The popularity of pneumatic structures as building technologies culminated with the 1970 Expo in Osaka, Japan, which featured several pneumatic pavilions. Since then, manuals and handbooks on inflatable structures were published [3; 6], including a book of recommendations by the IASS [7]. Inflatable structures are a ubiquitous building technology today, with advances in material, design, and fabrication technologies facilitating their use for many applications in architecture and engineering. Recent innovations such as the 'tensairity' concept [8] use integrated cable-tensioning to give inflatable beam structures increased stiffness, bending, or buckling resistance.

2.2. Tensegrity Structures

The history of tensegrity structures is controversial as several people are credited for their invention; all describing identical structural modules comprising of three compression struts and nine tension cables [2]. The name and concept of tensegrity structures are commonly credited to Buckminster Fuller, whose "tensional integrity" concept dates as far back as the mid 1940's. Kenneth Snelson's 1948 sculpture *X-Column*, is considered to be the first *built* tensegrity structure [2]. Tensegrity structures have scarcely been implemented as superstructures of buildings, due to the difficulty to construct them at large scale. The first building to use a 'true' tensegrity superstructure was built in 2001 for an experimental facility in Chiba, Japan [10]. A current research tread of tensegrity structure research is interested in facilitating their deployment through a range of tactics. One variety uses rigid compression members and external actuating mechanisms [11]. Another variety builds actuating (prestress) capacity into the tension members [12]. A third variety integrate actuation directly into the compression members. Such proposals have been made in aerospace engineering using pneumatic struts, but have only been demonstrated with small scale models [13; 14]. Others have developed analytical and numerical deployment simulation models for inflatable tensegrity structures and proved it was theoretically possible at large scales, but not physically tested or proven [15; 16]. Recently, researchers at Georgia Tech used 3D-printed shape-memory polymers to make self-deploying tensegrity structures at small scale by activating and stiffening strut members through changes in water temperature [17].

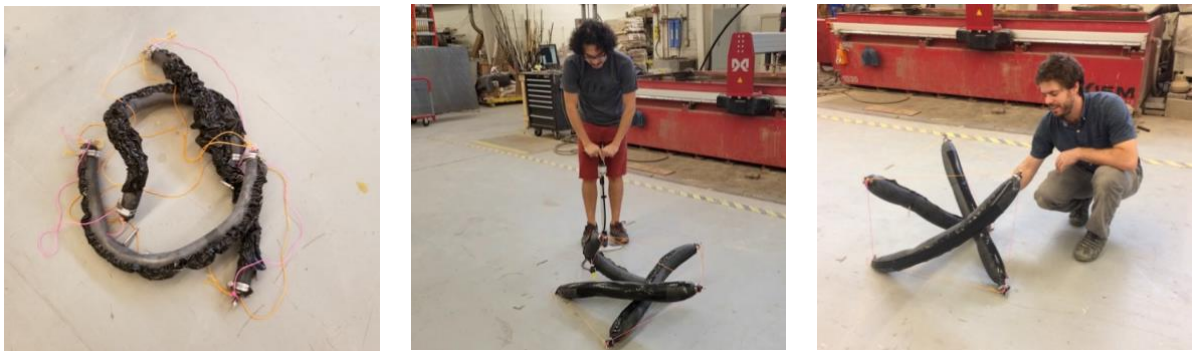


Figure 1: A proof-of-concept prototype of a three-strut deployable inflatable tensegrity structure assembled using rubber bicycle inner-tubes and braided nylon string. [Photos by Jonathan Dessi-Olive and Michael Koliner]



Figure 2: Medium-scale three strut (left) and four strut (right) inflatable tensegrity prototypes using HDPE membranes, PVC pipe caps, and braided steel cable. [Photos by Jonathan Dessi-Olive and Michael Koliner]

3. Overview of Inflatable Tensegrity Structures

This section describes theoretical, analytical and design strategies used to develop an ultralight variety of deployable tensegrity structures that combine the advantages of tensegrity and pneumatic structures. The motivation and methodology of the project is described, as well as the analytical and design challenges posed.

3.1. Motivation and Preliminary Prototypes

Tensegrity structures are known to be one of the most efficient forms of construction, in terms of span-to-weight ratio [1] but are only stable under certain combinations of topology, material stiffness and prestressing. Tensegrity structures that integrate their deploying mechanisms directly into their compression members can achieve a minimum weight structure with significant global volume change. Replacing rigid compression struts traditionally found in tensegrity structures with pneumatic members presents the opportunity to build an even more optimal structure. Using basic geometric and intuitive design guidelines [1; 2], a small proof-of-concept model using was made using bicycle tubes and braided nylon string [Figure 1]. The preliminary prototype validated intuitive concepts, exhibited significant global volume change, and through inflation alone demonstrated self-erection. Following the rubber membrane prototype, two additional prototypes were made with membranes made from several layers of high-density polyethylene (HEPE) tubing and polyvinyl (PVC) plumbing ends, held together with hose clamps [Figure 2]. Somewhat stiffer than rubber, HDPE membranes could handle higher air-pressures and buckled less.

3.2. Design and Analytical Criteria

The preliminary prototype revealed several important considerations that would have to be addressed in seeking to expand on the concept of self-deploying inflatable tensegrity structures. The analytical and design challenges posed by this concept include:

- Achieving a combination of topology and prestress, which result in a stable structure.
- Developing a pneumatic compression strut of minimum weight that has a critical buckling capacity that is larger than the total deployment load of the structure.
- Designing with lightweight materials and components which can be packed into a minimum volume, shipped assembled and inflated on-site as a part of a self-erecting process.

3.2.1. Tensegrity Topology/Design

A basic criterion for this research is achieving stable tensegrity structures through an essential combination of precise topology and sufficient prestress in the compression members. We have chosen to only consider simple and commonly known three and four-strut tensegrity geometries and physically demonstrate the concept of inflatable tensegrity structures at increasing scale and technological resolution. Our focus is on simple geometries of large-scale structures in effort to demonstrate the level of precision that is possible with such a system. Though complex strut configurations would be possible using inflated struts, testing such geometries would likely add unnecessary complications to demonstrating a self-deploying tensegrity structure.

3.2.2. Pneumatic Compression Strut Design

This research addresses the critical issue of how difficult it is to construct tensegrity structures at large-scale through the development of new material schemas for low-pressure compression air struts. These lightweight struts are stiffened with air and must have the capacity to be folded and packed into a much smaller volume when deflated. The struts must as air-tight as possible so the structure can be temporarily freestanding without the need for continuous air feeds. The struts must be sufficiently strong to handle imposed loads – both from prestress and external loads – even at low air pressures. Lastly, shape memory must be accounted for in the material schemas because the struts tend to develop pre-bucking while they are inflated together into their final tensegrity topology.

3.2.3. Materials and Components

Inflatable tensegrity structures have three primary elements: strut membranes, strut end-caps, and tension cables. The strut membranes used in this research have been made of readily available polymeric materials such as HDPE and PVC, which are well suited for applications in inflatable structure. The strut end-caps must be sufficiently rugged to withstand repeated impact from when the structure is deflated, be lightweight and compatible with the membrane material, and include air-couplings and other any other devices to monitor or enhance the performance of the strut. The prototypes presented here all use caps made from PVC pipe ends, steel rod, and brass air-couplings. The tension cables are assumed to carry very low (dependent on the amount of prestress achieved in the compression strut) and made of light gauge steel.

3.3. Structural Analysis

The structural analysis of tensegrity structures is complex because only certain combinations of topology and prestress are feasible – often result in a trial and error analysis. Additionally, tensegrity structures are geometrically non-linear, which necessitates recursive analytical procedures. Finally, the model must incorporate the non-linear properties of the composite air-polymer-steel structure. The four-strut model was derived from a combination of engineering and analogy to known stable four-strut tensegrity topologies [1]. In order to facilitate the design and analysis process, a parametric model was developed using Karamba 3D [18], which allowed for viewing analysis results in real-time as input parameters were modified. Input parameters included topology (number of struts, overall dimensions, angle of rotation, etc.) as well as level of prestress, superimposed loading, and strut/cable properties.

Preliminary analysis was based on incremental loading to capture geometric non-linearity and were reported for two stages results: a prestress stage followed by a superimposed loading stage [Tables 1 and 2]. One advantage to using inflated struts is the magnitude of prestress in each member is correlated to the magnitude of its internal air-pressure. The final configuration from the computational form-finding and analysis tool was validated using SAP [19], which confirmed the strength and stability of the proposed configuration and prestress.

Table 1: Member Forces of four-strut inflatable tensegrity from analysis. [By Vinay Teja Meda and James Case]

	After Applying Initial Prestress (Lbf)	**After Applying Superimposed Loads on the Structure (Lbf)**
Struts	-18.08 (Compression)	-158.16
Top Cables	8.47	74.57
Bottom Cables	5.57	60.38
Ties	13.9	76.16

Table 2: Displacement of an upper compression node. [By Vinay Teja Meda and James Case]

	After Applying Initial Prestress (in)	**After Applying Superimposed Loads on the Structure (in)**
dX	4.42	0.76
dY	-3.00	-0.45
dZ	3.07	0.54

4. Buckling-Resistant Compression Air-Struts

The preliminary prototypes described above [Figures 1 and 2] displayed several strut stability issues. Although inflation pressures were theoretically adequate to maintain structural integrity, premature buckling caused by weak membrane materials was an issue. As the tensegrity prototypes were loaded (both from inflation and from superimposed loads), the inflated struts tended to deform and buckle. In the case of the HDPE membrane, it caused the material to permanently yield into a deformed shape. New material schemas were needed for low-pressure air struts that could better resist buckling – an investigation that is ongoing. Our strategy involves using an integrated steel cable reinforcing system in a manner similar to 'tensairity' [8], which offer increased stiffness to low-pressure pneumatic tubes. Though 'tensairity' has been proven to provide buckling stiffness to inflated members in bending, very little work has been to develop reinforcing strategies for air-struts in compression. Conceptually, the inflatable tube serves to provide prestressing to cables of sufficient strength and stiffness to sustain loads. This is analogous to the effect of tendons in prestressed concrete construction. A computer model of a hybrid strut consisting of a polymer tube reinforced with steel cables was developed.



(a) (b)

Figure 5: Cable-reinforced strut with PVC and nylon composite membrane, and PVC end caps; (a) shown in a four-strut tensegrity configuration with rigid PVC struts; (b) a detail of PVC endcap with integrated brass air intake valve, steel manifold and cables entering nylon sleeve. [Photos by Jonathan Dessi-Olive]

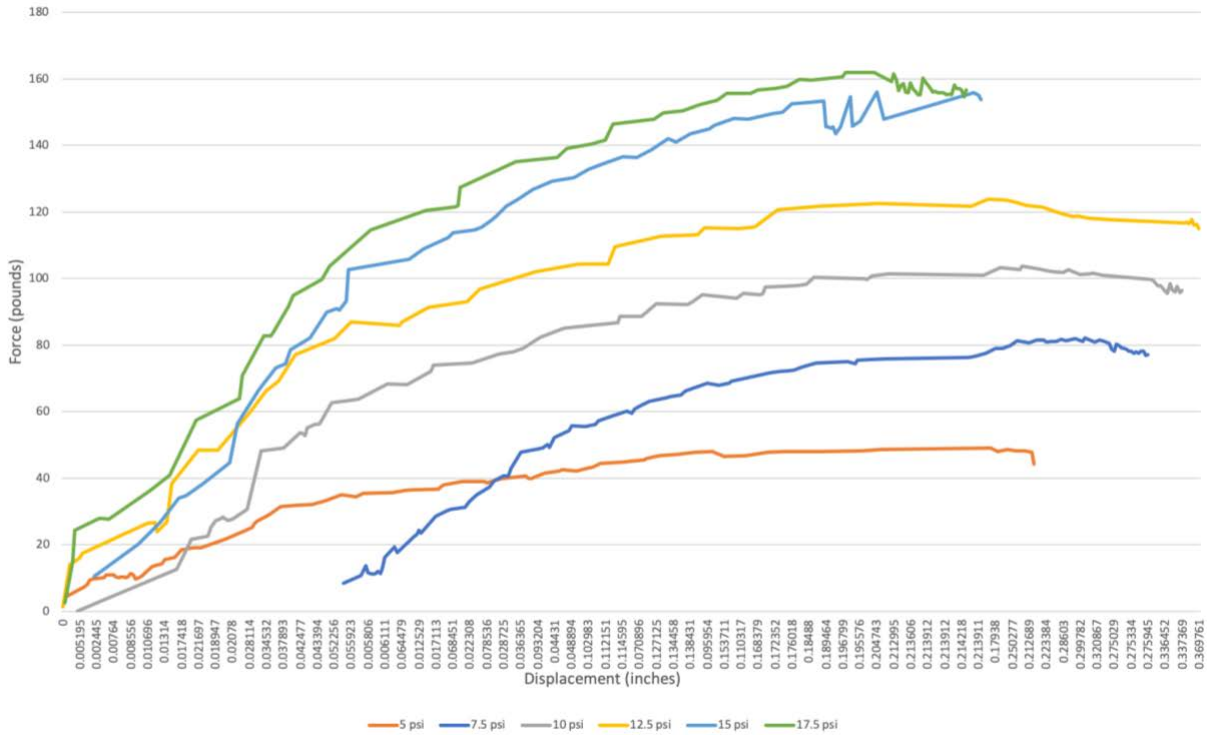


Figure 6: Force displacement graph of the cable-reinforced compression air-strut.

A new strut prototype was built that addressed the issues identified before [Figure 5a] with a membrane schema consisting of an air-tight inner layer of PVC sheeting and two outer layers of woven 'rip-stop' nylon. The PVC sheeting was welded to the PVC cap to make the assembly air-tight, while the nylon layers provided additional stiffness. The PVC caps [Figure 5b] were modified to include a steel manifold that provided points of adjustability for each prestress cable as well as to the overall length of the strut. The prestress cables were strung from the eye-bolts on the manifold into channels sewn into the two-layer nylon sleeve. The cables passed between the two layers of nylon so that would be held in place. An added advantage to this was the ability to precisely 'true' or straighten the compression strut in its fully inflated state. A delicate had to be observed however: while the prestress cables (and the nylon sleeve) have the potential to increase buckling resistance by increasing the stiffness of the strut, one could also imagine causing premature local buckling, or crushing in the membrane, by simply tightening the cables too much. This would be analogous to putting too much post-tensioning in a concrete beam. To confirm our performative assumptions based on computational analysis, the updated compression air-strut was load tested at different air-pressures – graphical results are shown in Figure 6. The tests indicated significant improved performance compared to previous strut designs that used weaker and more flexible membrane materials. The new strut sustained an axial compression force equal to approximately 80% of the axial tension force induced by the air pressure (at all pressure levels except for the minimal 5psf case). The improved performance resulted from increased stiffness provided by the steel prestress cables in combination with the PVC/nylon membrane elements. The non-linear softening at higher loading indicated in the test results is attributed to slipping and imperfect force transfer between the cables and the membrane elements.

5. Self-Deploying Inflatable Tensegrity Prototype

Following the successful tests of the reinforced compression air-strut, four more struts were produced and assembled into a four-strut tensegrity configuration. Thanks to our integrated computational form-finding and structural analysis tools, the geometry of this prototype was far more precise. The struts

were two meters in length, and had less of tendency to buckle due to loading once the structure was fully inflated prestress thanks to the stiffer membrane and reinforcing cables. Most significantly, with sufficient air pressure applied during inflation (enough to overcome gravity and its own weight), the structure has the ability to self-erect without any human intervention. As noted above, there was noticeable slippage between the membrane layers of the struts – a phenomenon that led to the inability to consistently self-inflate the struts into straight configurations when a part of a tensegrity configuration. Based on these observation, the future strut prototypes will use high-performance composite textile membranes and if necessary, have fully bonded cables to ensure consistent geometry and to take advantage of fully composite behavior.

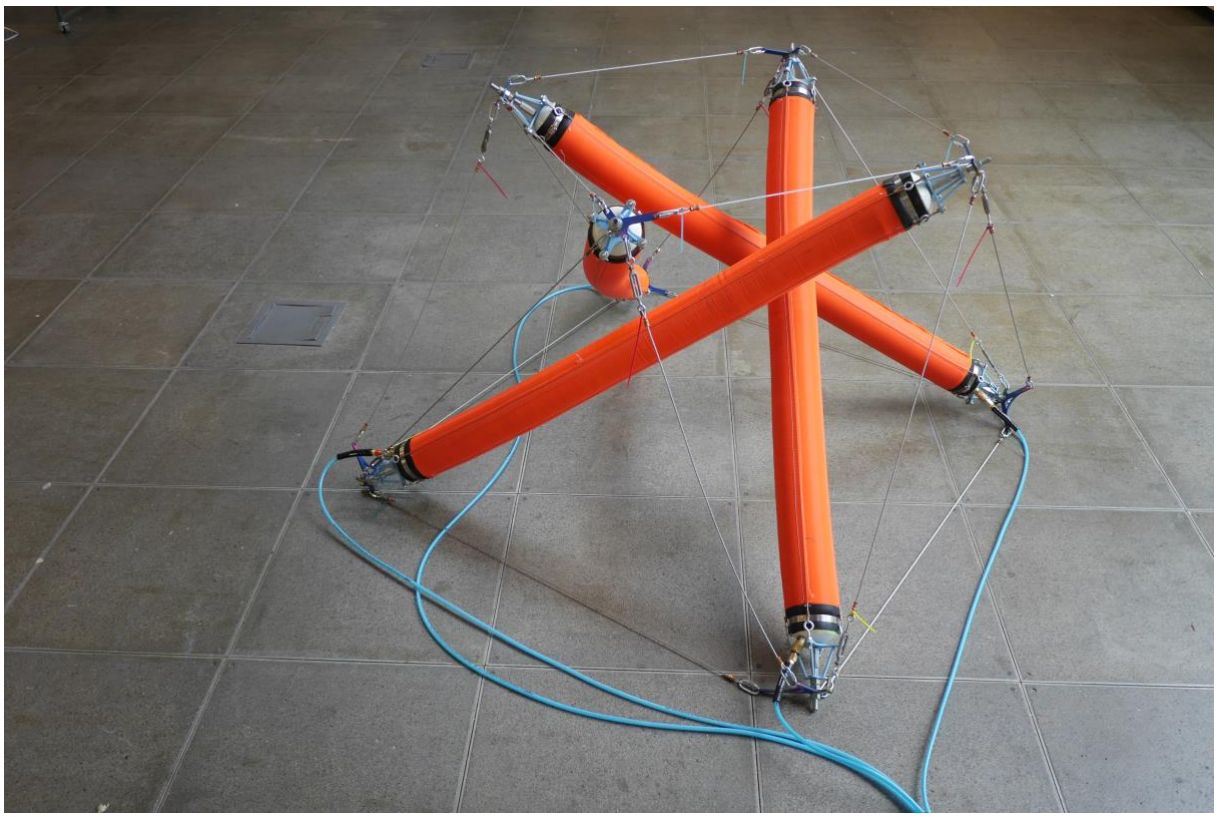


Figure 7: Four-Strut inflatable tensegrity prototype using buckling resistant compression struts.

6. Conclusion / Future Work

The research presented in this paper has focused on developing preliminary construction strategies for architectural-scale deployable tensegrity structures that use low pressure air-struts. Replacing rigid compression struts traditionally found in tensegrity structures pneumatic members presents an opportunity to maximize the global volume change of the structure, and minimize its overall weight. This paper has presented advancements in the field of active-deployed tensegrity structures through a series of physical prototypes that use cable-reinforced pneumatic compression struts. These medium-scale prototypes not only demonstrate that large-scale inflatable are possible, but also will have the ability to self-erect simply by inflating the compression members. The prototypes precede a large-scale structure to be exhibited at the 2019 Form and Force Expo in Barcelona that will demonstrate the concept of self-deploying inflatable tensegrity structures at pavilion scale. With continued develop of buckling resistance and deployment strategies through higher performance textile membranes and more developed reinforcing tactics, there is even greater potential for expanding the material and performative schemata for compression air-struts. This is significant because it suggests potential for this technology to be applied in several contexts and scales. As performative and aesthetic concerns

are address, a wide range of design possibilities and applications arise. At architectural scale, such self-deploying structures could be designed and used for temporary support systems, or work as a part of a larger permanent superstructure. Depending on the application and scale the particular design, anti-buckling strategies, and materials could differ drastically.

Acknowledgements

The authors gratefully acknowledge several of our colleagues at the Georgia Institute of Technology for their valuable advice and support: Glaucio Paulino, Chris Liu, and Russell Gentry. We extend thanks to Michael Gamble, Scott Marble, Zach Brown, and Shrinka Roy. Special thanks to the Georgia Tech School of Architecture, the Georgia Tech School of Civil Engineering, Uzun+Case Engineering and the Ventulett NEXT Generation Fellowship for financial support. Finally, we would like to thank Jake Tompkins in the Georgia Tech Digital Fabrication Lab.

References

[1] H. Furuya, et al. “Concept of Inflatable Tensegrity for Large Space Structures” in Proceedings to the 47th American Institute of Aerospace and Aeronautics Conference, Newport USA, 2006.

[2] Liu, K. Wu, J., Paulino, G.H., and Qi, H.J. “Programmable Deployment of Tensegrity Structures by Stimulus-Responsive Polymers” Scientific Reports. Nature vol. 7:1, 3511, 2017.

[3] Herzog. T. Pneumatic Structures. Oxford University Press, New York, USA, 1976.

[4] Pugnale, A. and Bologna, A. “Dante Bini’s Form-Resistant Shells”. Nexus Network Journal Vol. 19, 2017, 681–699.

[5] Otto, F. Tensile structures. Massachusetts Institute of Technology Press, Cambridge. 1962.

[6] Shapiro, A. et al. The Inflatocookbook, 2nd Printing. Ant Farm. San Francisco, USA. 1973.

[7] Tsuboi, Y. et al. IASS Recommendations for Air-Supported Structures. International Association for Shell and Spatial Structures. Madrid, Spain. 1985.

[8] Tensairity Solutions. <http://www.tensairitysolutions.com/>

[9] Levy, Matthys. “Floating Fabric over Georgia Dome.” Civil Engineering. Vol 61: 11, pg. 34

[10] Kawaguchi, K., & Ohya, S. “Preliminary report of observation of real scale tensegrity skeletons under temperature change.” In Proc. of the IASS, Montpellier, France. 2004.

[11] Veuve, N., Dalil Safaei, S., and Smith, I. “A Deployable tensegrity footbridge that connects at mid-span.” In Proc. of the IASS Symposium, Amsterdam, Netherlands. 2015.

[12] Xu, X., CAI, H., and LUO, Y. “Deployable tensegrity using shape memory alloy springs.” In Proceedings of the IASS Symposium, Tokyo, Japan. 2016.

[13] Murata, S. et al. “Inflatable Tensegrity Module for a Large-Scale Space Structure and its Construction Scenario.” In Proc. to the 56th IAC. Fukuoka, Japan. 2005.

[14] Furuya, H. et al. “Concept of Inflatable Tensegrity for Large Space Structures.” Proc. to 47th AIAA/ASME/ASCE/AHS/ASC. Newport, USA. 2006.

[15] Russell, C. and Tibert, G. “Deployment Simulations of Inflatable Tensegrity Structures.” International Journal of Space Structures, Vol 23, No. 2. 2008. Pg 63-77.

[16] Sinn, T. and Vasile, M. “Deployment simulation of very large inflatable tensegrity reflectors.” In Proc. to 62nd IAC 2011. Cape Town, South Africa. 2011.

[17] Liu, K., Wu, J., Paulino, G.H. and Qi, H.J. “Programmable Deployment of Tensegrity Structures by Stimulus-Responsive Polymers”. Scientific Reports. Vol 7:1, 3511. 2017.

[18] Parametric Eng. Karamba3D. 1.3.1. 2019. Retrieved from <https://www.karamba3d.com>

[19] CSI Software Inc. *SAP2000.* V21. 2019. Retrieved from <https://www.csiamerica.com>

Proceedings of the IASS Annual Symposium 2019 – Structural Membranes 2019
Form and Force
7 – 10 October 2019, Barcelona, Spain
C. Lázaro, K.-U. Bletzinger, E. Oñate (eds.)

The excellence of construction timber details throughout a Tectonic methodology

L. CATALÁ BUSTOS*, P. H. KIRKEGAARD

Department of Engineering, Aarhus University, Denmark
Inge Lehmanns Gade 10, 8000 Aarhus C, Denmark
lcbm92@gmail.com

Abstract

This investigation focuses on enhancing the excellence of the smallest unit of construction: the architectural and structural details, which have the potential to inform the character of the whole, from the first phases of design. This is made by means of a Tectonic methodology, tested through an experimental investigation, where the main material is wood, due to its Tectonic properties. The research carried out to verify the suitability of the proposed methodology consisted of developing a proposal in which both the spatial and structural quality was directly related to the nature of the joints that defined it. Several constructive systems were studied, where the active-bending technique turned out to be the most meaningful. Thus, one of the main objectives with this technique was to traduce material organisation and principles from a scale not very exploited in the construction discipline. The proposal is a wooden pavilion, defined by different curvatures, i.e. an active bending structure, in which the joints play a fundamental role. With this experiment it was demonstrated that the designed joints were the ones that defined both the architectural character and the structural performance of the design. The main benefit of this research is due to the interaction of the technical and artistic aspects during the conceptual design phase, having as a link the constructive details and joints.

Keywords: Tectonics, timber details, design-joint methodology, active-bending structures, experimental investigation, new technology, optimization, integrated early design.

1. Introduction

This article focuses and emphasizes the importance of constructive and architectural details in the early stages of the design process. They are understood as the main elements that develop and manage the structural performance, the architectural appearance, as well as the spatial quality of a design. For this, the research is divided into three fundamental stages:

- Theoretical study of Tectonic philosophy and the role of timber in the art of building.
- Joint methodology proposition
- Experimental investigation to verify the methodology proposed

Thus, under the section The Tectonic paradigm, the Tectonic concept and its repercussion on building design throughout the history is defined. After that, wood is introduced as the material that lead this new paradigm, where thanks to new technologies, processes and advances in material research, its properties and possibilities evolve. This resurgence is stated, by understanding wood, its materiality, and details in a holistic way, to create Tectonic designs, in which the art of building is a poetic combination between construction, structure and architecture.

Hence, this article follows with a proposed methodology, that expects to evaluate the Tectonic quality of a design in which details represent the minimum expression, in order to understand the process as a whole from the conceptual design to manufacturing. It is created based on the following hypothesis:

Copyright © 2019 by L.Catalá Bustos, P.H. Kirkegaard
Published by the International Association for Shell and Spatial Structures (IASS) with permission.

"Through a methodological evaluation of timber joints, the spatial and structural quality of a design may enhance the Tectonics excellence"

Finally, to prove the hypothesis, an experimental investigation is carried out, where both the technical knowledge analysed, as well as the methodology proposed are used to develop a Tectonic design.

2. The Tectonic paradigm

The word *Tectonics* has been studied in architectural theory for quite a few centuries. It derives from the same Greek root that can be found in archi*tect*ure and *tec*hnology, and comes from the Greek word *tekton*, meaning carpenter or builder. Tectonics is a transcendental concept which describes the close relation between material characteristics, structural system and architectural design, as well as the combination of the elements to create the idea of unity. Since the middle of the 19th century, masters as influential as, Gottfried Semper, Karl Bötticher, Eduard Sekler, Marco Frascari or Kenneth Frampton have discussed and investigated the term Tectonics.

Still, this discussion goes ahead one step if more parameters of current importance get into play. Therefore, how this idea of unity evolves and behaves when new technologies or digital tools get into the equation? One of the main obstacles that complicates this informed design is the huge improvements that these progresses brings to the design process. They have allowed the professionalisation and specialisation of multitude jobs and tasks, optimizing, and making them very efficient. However, these processes have been improved independently. Thus, the design process consists of very effective but decontextualized phases, which follow a linear sequence. Consequently, the present challenge, is to use these new technologies to combine the processes mentioned and to reencounter with the Tectonic value. In this way, the conciliation between material properties, structure, form, and design could reach its peak, where Tectonics is again turning into an essential tool.

2.1. Tectonic quality of wood

Thanks to new technologies that allow the designers to explore shapes, structures and forms in a different and novelty way, traditional materials as wood, are being reformulated. This opens a new field of research, in which the classical properties and techniques of wood are adapted and merged with the characteristics that define the current art of building. Wood offers the duality of behaving as a structural material and at the same time being considered as an element that defines spatiality, both external and internally, thus playing a fundamental role in the aesthetic scheme of the work. Hence, wood has demonstrated to have the ability to express the spatiality of a work, while defining the representative and conceptual qualities of the design.

3. Joint methodology at early design stage

3.1. Construction and architectural details

The dictionary definition of detail (*a single piece of information or fact about something*), may be meaningless in architecture, since the scale and features in a project means something different each time. However, an architectural detail is always a connection, which can add value in different ways.

One of the figures that delved deeper into the study of details was Marco Frascari (1945 - 2013), Italian architect and theorist. In his work *The Tell-theTale Detail*, [2] M. Frascari, 1983, defines the details as: "the minimal units of signification in the architectural production of meanings" (p.22). He also defends the ability of details as the elements that enhance invention and innovation through the combination of materials and elements of the building in an aesthetic and functional way. Besides, resuming the concept defined by the school of Beaux Arts, [2] M. Frascari, 1983, takes up this reflection: "The recognition that details themselves can impose order on the whole through their own order" (p. 23).

The objective of this section is to highlight the importance of details, as well as the role they can play in buildings. It is necessary to understand that details not only add value to the structural design, but, depending on the characteristics and conditions, suppose an elementary factor for the definition of concepts such as spatiality, materiality, or acoustics.

Details can define the quality of the architectural design in a building, considering it as a whole. They are also essential elements for the perception of a space, since they can organise in hierarchy different sensations. Rhythmic, tactile, visual, and spatial effects can be coordinated through details. The conception of the architectural space achieved in this way is the result of the associations of visual images of details, with the geometrical proposition embodied in forms, dimensions, and location, developed by touching and walking through buildings.

This brief introduction can be concluded understanding joints as an inspiration, and emphasising that details can solve not only practical functions, but also historical, social and individual meanings. Thanks to detailing, the association between intuitive and rational thinking gives rise to structural poetry as well as to the union of representation and function.

3.2. Timber joint methodology

When proposing a new set of guidelines that may change the conception of the traditional design process, firstly, considering and analysing the establish aspects is essential. Therefore, the perception of details as creators of more complex structures can be understood differently based on how important the connections are. This adaptability goes in favour of the flexibility and creativeness of the design process at the early stages.

It is clear the advantage that the incorporation of the detail and joint design would imply in the conceptual phase of the project, since the structural and architectural value of these elements could be increased in equal parts, while the scope of new materials and its behaviour with traditional and modern techniques would be explored. In this way, the need for a new methodology that is able to inform the designer, about the effects, both structural and architectural, of certain decisions about joints and details, becomes evident. In this case, and as has been analysed so far, the studied material is wood, which requires a new formal language for the new detailing needs, developed by the digital tools.

This methodology aims to establish a series of guidelines for the correct definition of a quality design, based on the complexity and nuances of wood details in the architectural and structural design. In addition, it is important to mention that the intention of this criteria is not to systematise the design process, since it would lose the flexibility and freedom that this phase entails, but to propose certain nuances and parameters to consider for the successful definition of the design, taking advantage of the possibilities that new tools offer.

The proposal is divided into three fundamental phases reflected in figure 1 (left) [1] L. Catalá Bustos, 2018, developed from the most abstract conception of design to the physical design of the proposal. Therefore, it is not only about evaluating the quality of the details in themselves, but also the spatial expressiveness, constructive and structural systems that they produce throughout the process of design.

In this way, the first phase is called *Conception*, in which still very abstract parameters are the most important considerations, where flexibility is the maximum exponent. This first stage is divided into two sub-phases. The first one, focuses on the definition and understanding of the factors that will define the essence of the design, as well as their relationships, to somehow establish certain limitations, as reflected in figure 1 (right) [1] L. Catalá Bustos, 2018. Four fundamental concepts of great importance in the construction sector at present have been established: *costs, sustainability, structural design and architectural expression*. As can be seen throughout the document, the research line of the article focuses on the relationship between structural design and architectural expression, named by the author ‘Tectonics’; so, this link is the one developed.

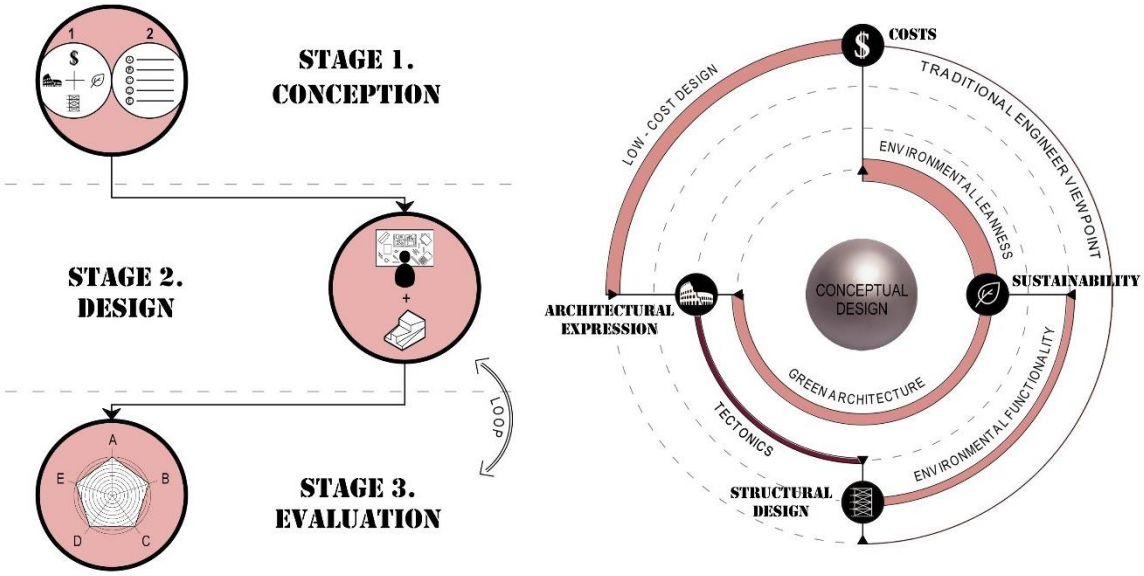


Figure 1: Methodology stages (left). Factors that define the conceptual design (right). [1] L. Catalá Bustos, 2018

Next stage called *Design* lies into the consideration of measurable categories and parameters that characterise the nature of the design and give it a unique identity and quality. Five categories to be considered during the design have been determined. Within them, different singularities and nuances are established, which constitute the main scale of this methodology. These parameters should not be considered at the same time while being designed, but they suppose a guide for the definition of each category, as well as an aid for inspiration while working with conceptual ideas.

Category 1. Matter: *Material combination, materiality, material, material optimization, water, light, colour, texture*.

This category is related to how the matter by itself, as well as in combination with other materials, is able to create textures, to define the space materiality, or to articulate the character of a design in reference to the properties and techniques applied to the material in use. In this way, colour and light play a fundamental role in the essence of a space. Therefore, this category studies the potential of the joint material in relation to the final spatial and structural quality.

Category 2. Principles: *Stress transfer, manufacturing possibilities, connection efficiency, technology used, functionality, accuracy*.

The principle-gesture duality is part of the Tectonics theory, being one of its main relationships. In this case and following the definition that [3] M. F. Hvejsel, 2017 proposes, "[We understand] Principle as describing the structural build-up of the architectural from explaining how it does it" (p. 7). Thus, factors related to the structural and functional design of joints and details, and how they relate to the space they generate are considered.

Category 3. Gesture: *Integration, harmony, symbolism, essence, representation, geographic and cultural context, spatiality, clarity, nuance, structural honesty*.

The 'gesture' is evaluated at the same time as the ‘principle’, both forming an intrinsic relationship in the architectural and structural design. Considering the definition proposed by [3] M. F. Hvejsel, 2017: "[We understand] Gesture as describing the experienced spatial quality of the architectural from explaining what the space does" (p. 7). This category evaluates the importance of details as

representative of the space' essence. Thus, factors such as harmony, symbolism or the cultural context can be the main qualities that a set of details can bring to the proposal.

Category 4. Order: *Rhythm, transition, articulation, main element, symmetry, pause, pattern.*

This is related to the hierarchy that a work can develop based on the details. Thus, depending on the arrangement, form, and relationship of the elements designed, the final result can manage different rhythms that define the space and the user's feeling in one way or another.

Category 5. Translation to the whole: *Simplicity, complexity, scale, form, lightness, heaviness.*

The last category addresses the potential of the detail or element studied when generating the general space and structural system. In this way, the most global conclusions of the previous categories are considered, as well as the inclination towards excellence of the evaluated elements. One of the most important factors within this category is the scale, and how it influences the "buildability" of the designs.

Last phase called *Evaluation*, is developed once a proposal is set. Here, the potential of the categories established in the first stage is evaluated. As can be seen in figure 1 (left) [1] L. Catalá Bustos, 2018, these last two phases are developed iteratively, i.e. a loop between phase 2 and 3 is produced, so that, once the proposed designs have been evaluated, it can be turned back to incorporate the conclusions and improvements obtained because of the evaluation carried out in phase 3.

4. Experimental investigation

Once established the theory that delimit the research, the experimental investigation takes place, where these concepts are applied to a physical design. The main objective is to evaluate, through an experimental investigation, how the joints can increase the quality of the whole design. Therefore, the process aims to integrate an interdisciplinary point of view, in which architecture, structural engineering and timber construction are considered as essential concepts.

4.1. Small-scale experimentation

Throughout this process, physical models on a small scale represent one of the main tools, with which to experiment and understand the most significant nuances of each of the techniques developed. The structural approaches studied are: Active-bending technique and reciprocal frame structures. Different aspects such as buildability, the quality of the joints, the level of practicality, the potential for full-scale development or the difficulty in manufacturing are evaluated throughout this study, to define the most appropriate technique for the next phase of experimentation. To do so, the methodology proposed is used and tested in a small-scale simulation.

Precisely, the duality between the real and exploratory is established as a fundamental premise in the development of the research. The transmission and conditioning of the characteristics studied on a smaller scale into the final models at a real scale, is deeply investigated. This first approach, on a manageable scale, allows the author to capture the subtlest nuances of these systems, while appreciating the importance and quality of details and joints, and how these are developed as the scale increases. These mock-ups show the main advantages and disadvantages of using different techniques, while introducing the challenges that will appear when working with these methods in a larger size.



Figure 2: Small-scale experiments. [1] L. Catalá Bustos, 2018

4.2. Physical model – prototype

The development of the proposal from the conceptual design to construction. was divided into *Design*, *Iteration - optimization*, *production* and *result* stages. The proposed design aims to combine the techniques studied through small-scale models, as well as the Tectonic concepts presented. For this purpose, the methodology proposed has been used to provide the joints and connection elements with the power to define the structural and spatial characteristics of the rest of the work.

Special emphasis will be placed on the development and manufacture of the joining elements, as well as in the production process, which has been treated in two very different ways. Following the slogan '*research by design*', production and construction have been manually developed in the early stages. Once certain assessments and analysis have been achieved, these steps have been industrialised and mechanised thanks to the introduction of more advanced tools and techniques.

The design consists of two main elements: the column module and the roof module. The combination of both generates a basic composite element, capable of creating more complex structures through aggregation or combination actions, as a result of a set of conceptual operations and decisions. In this way, the roof is characterised by being a reciprocal flat structure that is linked to the column, formed by timberfabric modules (concept developed by [4] Y. Weinand, 2017), by active bending.

Since this stage of the research focuses on the evaluation of the proposed methodology, it is used along the design process. In this way, both the methodology and the arrangement, appearance and function of the joints and connections of the design have a fundamental role. Although the elements that constitute the proposal may seem simple, the complexity of the design lies in the connections and details. There are different critical points, which are defined in a way in which, they control the shape, structural performance and spatiality, i.e. if they were different, the result would also change.

4.2.1. Structural performance

The main challenge in this phase of the investigation is to connect both systems or constructive techniques, through connections designed and produced custom-made, in such a way that they are the ones that really define the disposition and characteristics of the design in a Tectonic way. Thus, the connections play a fundamental role in the structural performance of the proposal.

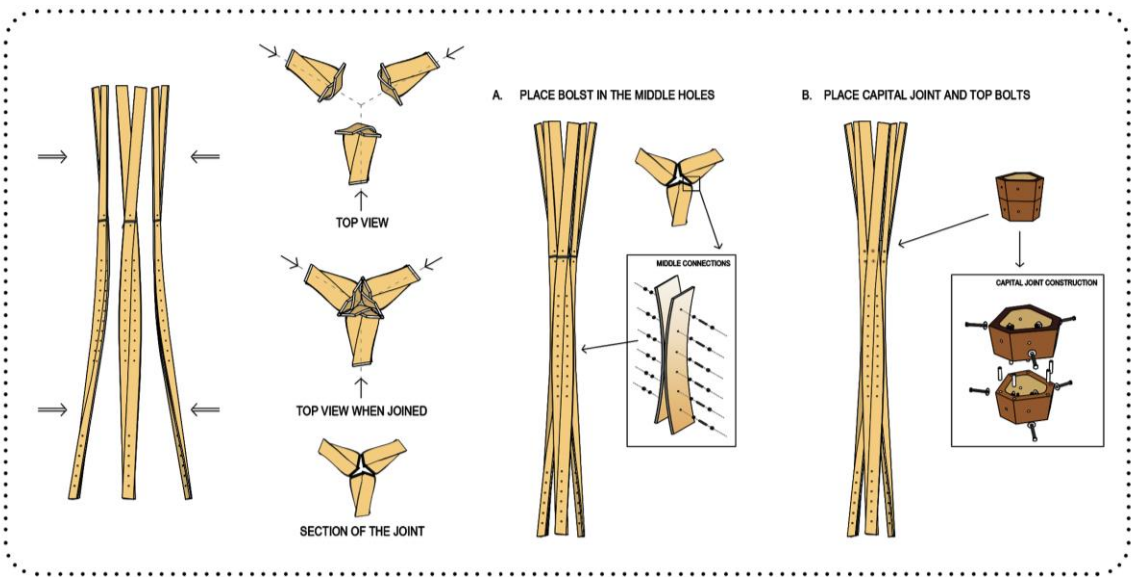


Figure 3: Column production [1] L. Catalá Bustos, 2018

On the other hand, re-dimensioning the connections studied in small-scale experiments, to a prototype on a real scale, is also one of the main challenges. In relation to the active-bending technique, when changing the bending radius and cross-sectional height, residual stresses may change. Therefore, scaling problems will occur due to the change in scale. Thus, considering these changes when building the physical prototype in base on the small-scale experiments experience is fundamental.

In this case, the tests were made experimentally, always considering the strength of the wood used, and the possibilities that the joints offered for the development of the proposal on a real scale. The form-finding method in the studied case was carried out manually, experimenting the stiffness and resistance of the material used.

The connections used at the reciprocal roof, do not force nor deform the module. Therefore, more deformations do not occur because of the join technique. From a structural point of view, each bar behaves as a beam. In this module, each bar bears the supporting force of the one bar resting on it, as well as the dead loads.

On the other hand, reciprocal frames create by themselves a system with convex curvature. This curvature is controlled by the length of the bars, as well as by the distance between the acting and the supporting force. In the studied case, this curvature is forced in order to have a fixed joint in the meeting with the column.

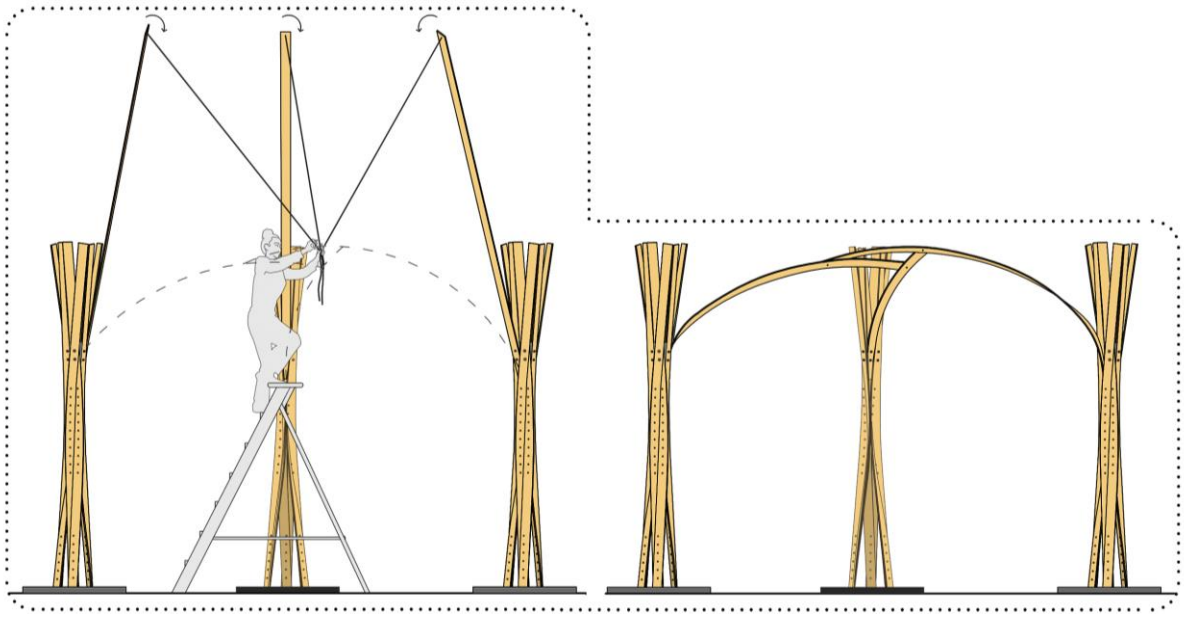


Figure 4: Roof production. [1] L. Catalá Bustos, 2018

5. Conclusion

The process followed both to design and produce the proposal is characterised by having followed the dictates of the Tectonic philosophy. On the other hand, the methodology has been the main design tool, since with this experimental research it was proved its validity.

Finally, highlight that the geometry and structural performance of the proposal is fully defined by the details. In this way, the effectiveness of the methodology has been proven, giving rise to a Tectonic design, where connections establish the unique nature of the proposal. This has been possible, among other things, thanks to the use of digital tools and new technologies, capable of accurately replicating and adjusting the connection elements to fulfil their purpose.

The hypothesis proposed at the beginning of the investigation: *"Through a methodological evaluation of timber joints, the spatial and structural quality of a design may enhance the Tectonics excellence"*, is therefore verified, thanks to the nature of the process and the obtained results. It is worth to mention that a deeper analysis would provide more parameters to improve the research initiated here. In addition of the possible improvements in relation to the design, it should also be noted that the methodology proposed is the first approach made by the authors to the detail-based design. Therefore, by gaining experience and evaluating this procedure again, possible changes and improvements will arise.



Figure 5: Design proposed. [1] L. Catalá Bustos, 2018

Acknowledgements

I would like to express my gratitude to my supervisor Poul Henning Kirkegaard for his priceless advice and encouragement throughout the Master thesis. A special thanks to Povl Filip Sonne-Frederiksen, without whom the thesis that inspires this article, would not have been possible.

References

[1] L. Catalá Bustos, "A Tectonic methodology for timber joints. The excellence of detail in the era of technology throughout an experimental investigation", Master Thesis, Dept. Engineering, Aarhus University, Aarhus, Denmark, 2018.

[2] M. Frascari, "The Tell-the-Tale Detail," *Semiotics 1981*, pp. 325–336, 1983.

[3] M. F. Hvejsel, Gesture and Principle in Urban Tectonics. *Nordic journal of architectural research*, *29*(1), 9-34, 2017.

[4] Y. Weinand, *Advanced timber structures: architectural designs and digital dimensioning*. Basel: Birkhäuser, 2017.

Proceedings of the IASS Annual Symposium 2019 – Structural Membranes 2019
Form and Force
7 – 10 October 2019, Barcelona, Spain
C. Lázaro, K.-U. Bletzinger, E. Oñate (eds.)

Tribute to Kenneth Snelson

Francesca BRUSCIOTTI[a], Ilaria GIANNETTI[a], Andrea MICHELETTI[a]*, Shirley NWOKOYE[a], Diego RUGGERI[b], Giuseppe RUSCICA[c]

[a] Department of Civil and Computer Science Engineering, University of Rome Tor Vergata
Via Politecnico 1, 00133, Rome, Italy
micheletti@ing.uniroma2.it

[b] Lamellazione Srls, Ciampino, RM, Italy

[c] Department of Engineering and Applied Sciences, University of Bergamo, Italy

Abstract

This paper presents the project of a tensegrity pavilion dedicated to the memory of Kenneth Snelson (1927-2016), the American artist who invented tensegrities and popularized them with the sculptures he built worldwide. The shape of the pavilion, based on a combination of X-Modules, is that of a "gate", so that when walking through it, one can observe on the sides and above the transparent "floating-compression" arrangement of struts and cables. The choice of materials employed in the construction – bars in fir-wood for struts and recycled sailing ropes for cables - is also inspired by the Snelson's tensegrity primary plywood "X-Piece", complying with a fabrication and assembly procedure conceived to maximize simplicity and recyclability. The form finding of the pavilion was carried out by energy minimization on a virtual elastic structure, while for the structural design, a linearized static and dynamic analysis was performed considering own weight load and live loads. The geometry developed for the nodal connections between struts and cables has been realized by the Italian company Progetto Legno, according to a customized fabrication process.

Keywords: form finding, tensegrity, x-form.

1. Introduction

We present the project of a tensegrity pavilion for the Form and Force exhibition/competition organized by IASS WG21. The pavilion is dedicated to the memory of Kenneth Snelson (1927-2016), the American artist who invented tensegrities and popularized them with the sculptures he built worldwide [5]. The pavilion's design is based on the sculpture "X-planar Tower" (1962-88), which in turn is derived from Snelson's tensegrity primary plywood "X-Piece" (1948). As Snelson explained in his picture essay, "Tensegrity, Weaving and the Binary World" [1], X-Modules can be combined together in space-filling assemblies which can be extended to any length in all directions. The shape of the presented pavilion, based on a combination of X-modules, is that of a "gate", so that when walking through it, one can observe on the sides and above the transparent "floating compression" arrangement of struts and cables. The choice of materials employed in the construction is also inspired by the X-Piece, complying with a fabrication and assembly procedure conceived to maximize simplicity and recyclability.

Copyright © 2019 by Francesca Brusciotti, Ilaria Giannetti, Andrea Micheletti, Shirley Nwokoye, Diego Ruggeri, Giuseppe Ruscica
Published by the International Association for Shell and Spatial Structures (IASS) with permission.

2. The X-Form

Snelson developed his first sculpure in the autumn of 1948, after attending Buckminster Fuller courses, on structural geometries, at Black Montain College Summer School in North Carolina. As Snelson told, the first “X-Piece” sculpure, was the result of the evolution of a first mobile sculpure concerned with balance of successive modular elements (clay weights) suspended one-to-the-next by means of thread-slings. With the aim to replace the clay weights with additional tension lines to stabilize the modules one to another, he invented "X" kite-like modules, out of plywood. Thus, as Snelson explained “while forfeiting mobility, I managed to gain something even more exotic, solid elements fixed in space, one-to-another, held together only by tension members” [2]. After a further discussion with Fuller in the Black Montain College summer school of 1949, the original X-Piece, kite-like in plywood (Fig. 2), was deveoloped by Snelson in correct tensegrity geometry, replacing playwood struts with metal bars (Fig. 3). In 1959, the original “X-Piece”, together with a series of four “model of tensegrity”, were presented at the MoMA of New York, within the monographic exibithion dedicated to the work of Bukminster Fuller, as a witness of Snelson invention [3]. In 1960, the invention was filed as a patent titled “Continuous tension, discountinuos compression structures” by Snelson (Fig. 2) [4].

The X-Piece turns into a real tensegrity by replacing an “Edge” cable with a strut connected to the structure with four “Sling” cables (Fig. 3). This new structure is stabilized by adding two “Draw” cables. The Draws connects the ends of the new strut to the farthest end of the other two struts, so as to move one strut away from the other, without allowing them to touch each other. The evolution of the X-Piece is the X-form.

What does X-Form consist of? Instead of replacing one Edge cable with a strut, a second X-Module is placed (Fig. 3). This assembly is the first step in a construction process that can be extended indefinitely along the three Cartesian directions.

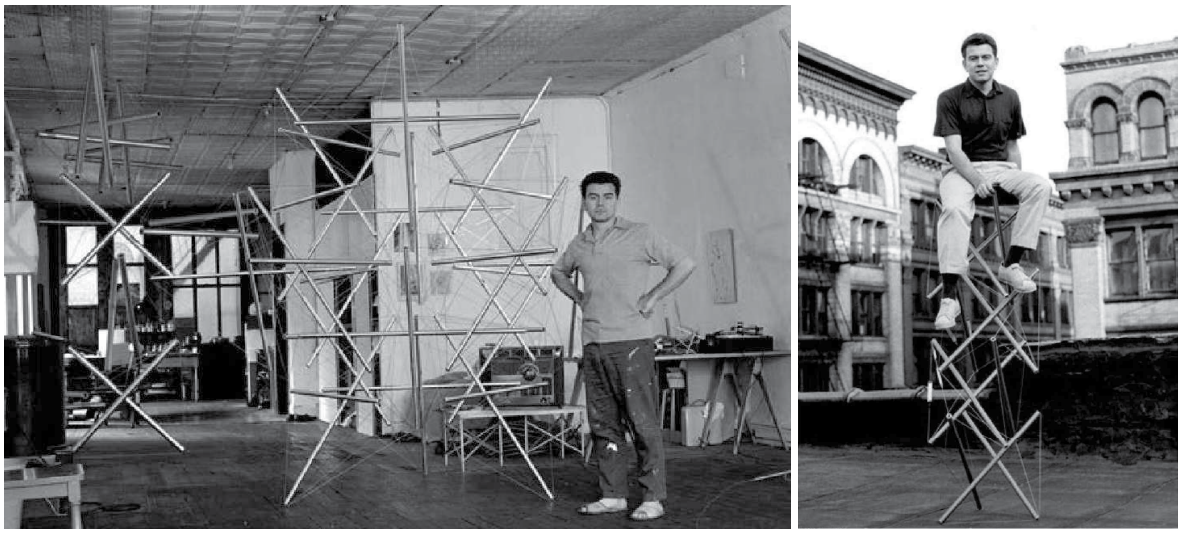


Figure 1: Snelson in his studio in New York in 1960 (left, picture from [5]). Ken On Tower (right, picture from [4])

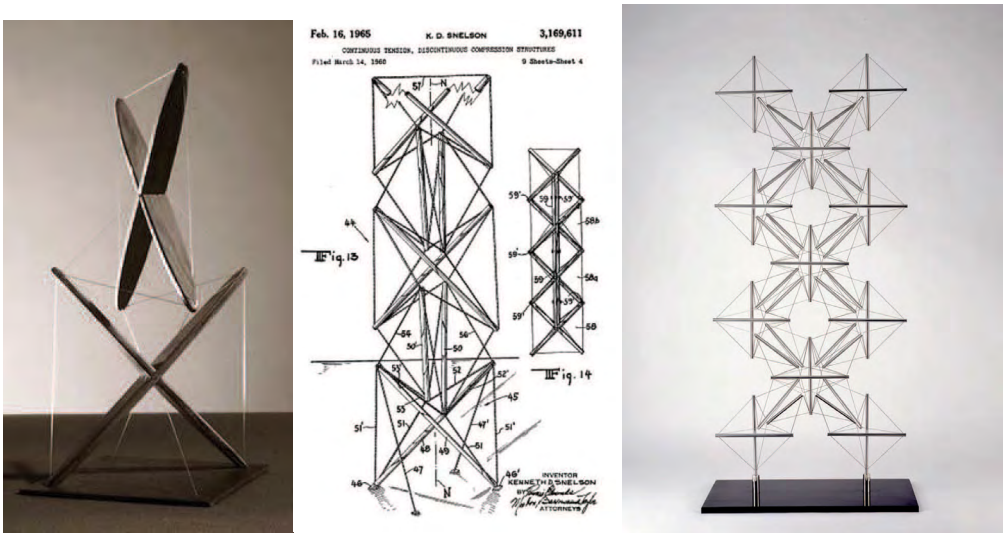


Figure 2: "X-Piece" in plywood, 1948 (left); Snelson Tensegrity patent, 1965 (center); "X-planar Tower" 1962-1988 (right). Pictures from [4].

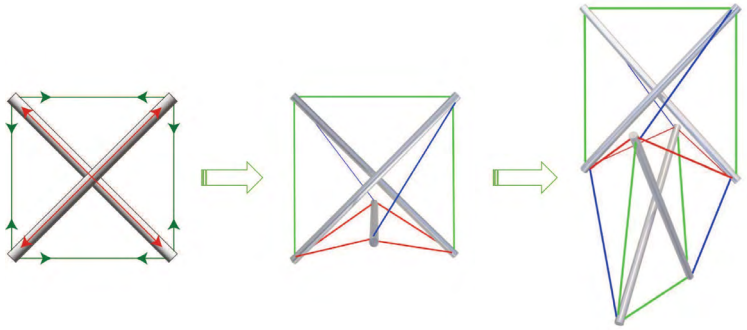


Figure 3: X-Form, assembling modules (pictures rearranged from [1]).

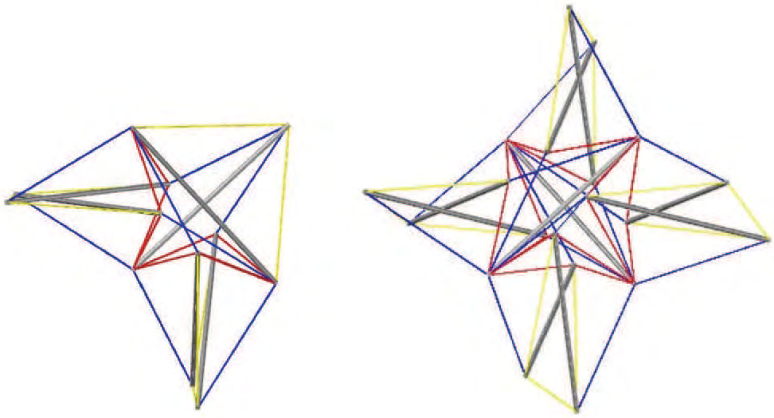


Figure 4: X-Form, angle assembly (left) and star assembly (right).

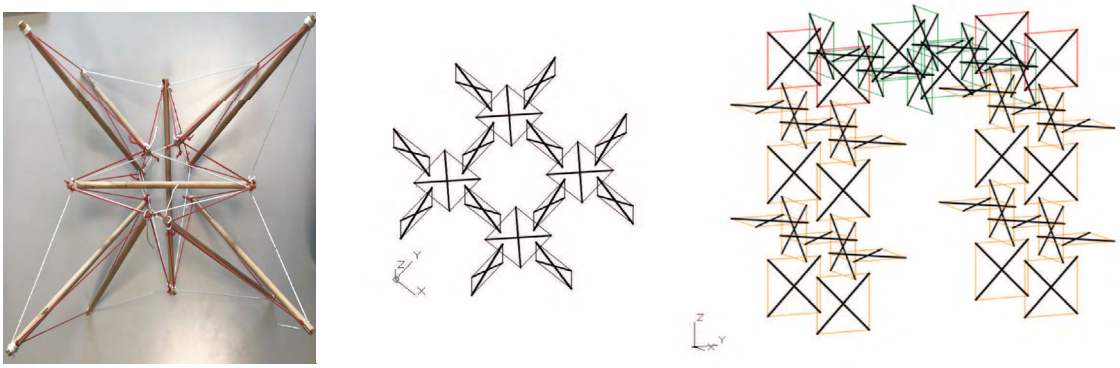


Figure 5: Pavilion geometry: ‘star’ structure (left); ‘plate’ structure (center); angle connection between ‘plates’ (right).

3. Pavillon geometric design

The shape of the pavilion is obtained by laying the X-Form on the top face and the two opposite lateral faces of a cube. The idea is to obtain a “gate”, so that when walking through such structure, one can observe on the sides and above the transparent “floating-compression” [2] arrangement of struts and cables. The way of assembling modules is a critical point in the design process (Fig. 5). A physical model was built on the basis of a “star” of modules, using wooden struts and synthetic cables (Fig. 5, left). Other than experimenting form finding physically, this model provided insight about the problem of determining the level of selfstress that is necessary to apply to cables in order to obtain a uniformly stressed structure.

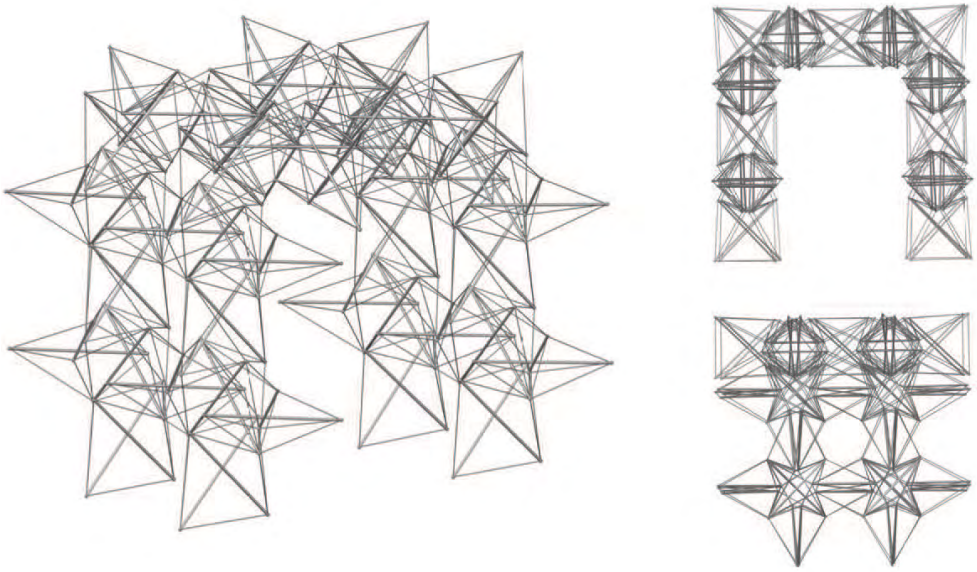


Figure 6: Views of the Pavilion after form finding.

The final solution developed in this study is composed by 88 struts, forming 44 X-Modules, and a multitude of cables. The structure is supported on the ground at four pairs of points, corresponding to the sides of four X-Modules. From these supports, two "walls" consisting of 14 X-Modules each, are erected to connect with the three-dimensional transparent roof, composed by a dense repetition of elements. The walls and the roof are formed by joining stars together. In this way, while on the front the assembly appears with a rectangular feature, on the sides the X-Form appears with its original star-shaped feature, and it looks like it is laying on the ground on single vertices.

4. Realization

The choice of fir-wooden bars for struts is crucial for the realization of the Pavilion. With respect to struts design, the use of wood maximize simplicity and economy in fabrication and assembly procedure. On this purpose, a special node was studied and designed, in order to eliminate additional fitting in the connections between elements. Slits and holes, as shown in Fig. 7, are easily realized at every bar end section to accommodate the ropes. Cross slits allow cables to be positioned and fixed with a simple knot. Holes accommodate the Draw cables, which have the function of tensioning elements for prestressing the structure in a controlled way. Such holes are drilled in an angular fit obtained by flattening the side edges at the end section of the bar (Fig. 7), and the knots are slightly hidden in the flattened area.

Cables are recycled sailing ropes in synthetic fibers. The idea of recycling was the driving concept of the node design, which have been performed in order to optimize the construction process. Indeed, slits and holes allow one to anchor the cables with simple knots and shims - and to adapt to any particular configuration of bars in space, making the structure reusable several times in new forms. On this purpose, the geometry of nodes was studied with the Italian company Progetto Legno, according to a customized fabrication process, thanks to craftsmanship expertise in wooden construction.

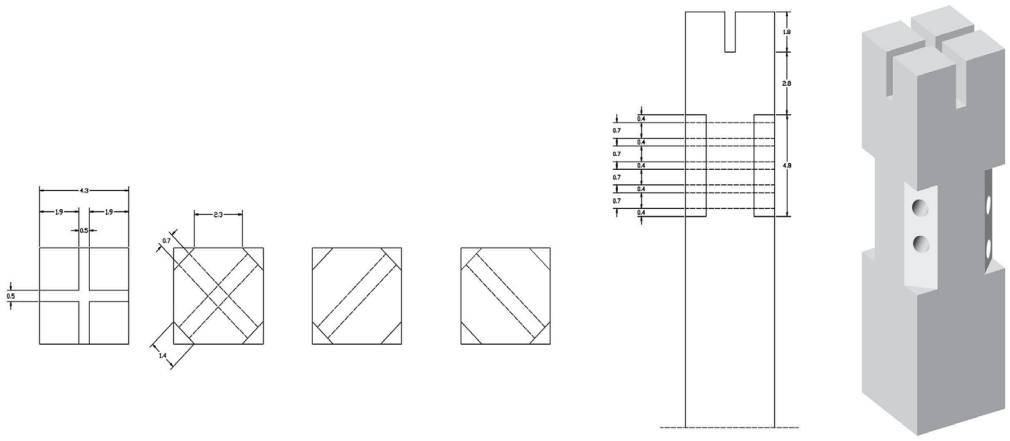


Figure 7: Details of the strut ends.

5. Numerical model: form finding and structural analysis

The design of the pavillion has been perfomed as follows. Once the overall geometry and the X-Form has been decided (structure covering three faces of a cube, relative arrangement of X-Modules), a form-finding procedure has been carried out by minimizing the elastic energy of a virtual structure, with fictitious elastic properties, considering very 'soft' elastic cables. The form-finding allowed us to obtain a pattern of forces in space in stable equilibrium with the desired shape, corresponding to a prestress state in the elements (Fig. 8). Such prestress state is then rescaled to match material properties and loads of the real structure, verifying that maximum allowed stresses are not exceeded (Fig. 9). Finally, fine tuning of geometry and prestress is performed to maximize structural performances. A linearized dynamic analysis is then performed under own weight load to compute natural frequencies and vibration modes (Fig. 10).

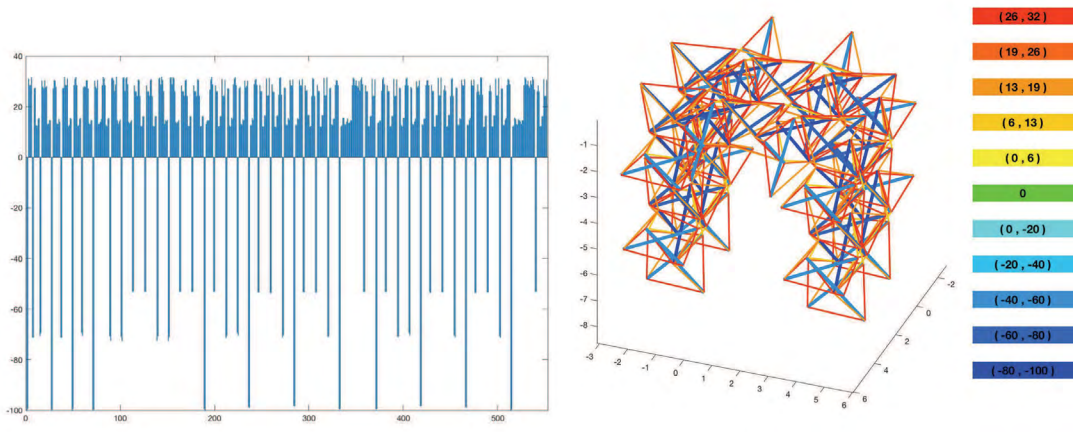


Figure 8: Equilibrium stresses after form finding, bar plot (left) and colormap (right), normalized with respect to a maximum compressive value of -100.

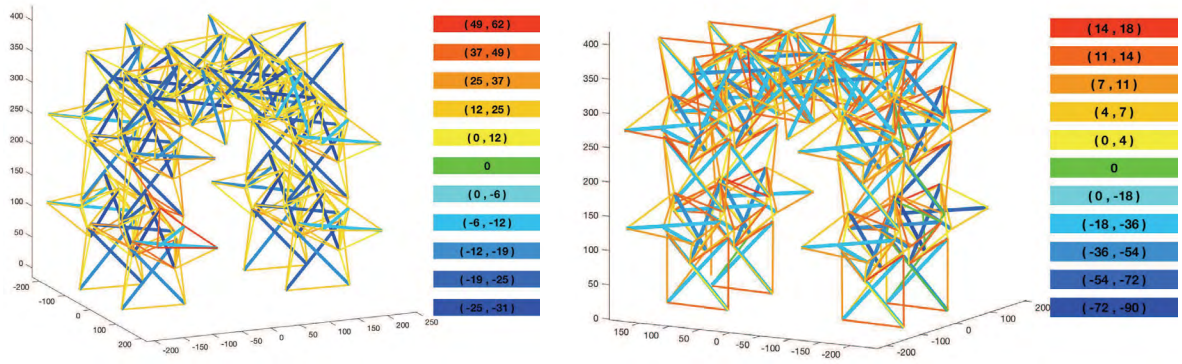


Figure 9: Maximum (left) and minimum (right) stresses, reported as ratio between actual stress and (tensile/compressive) member strength..

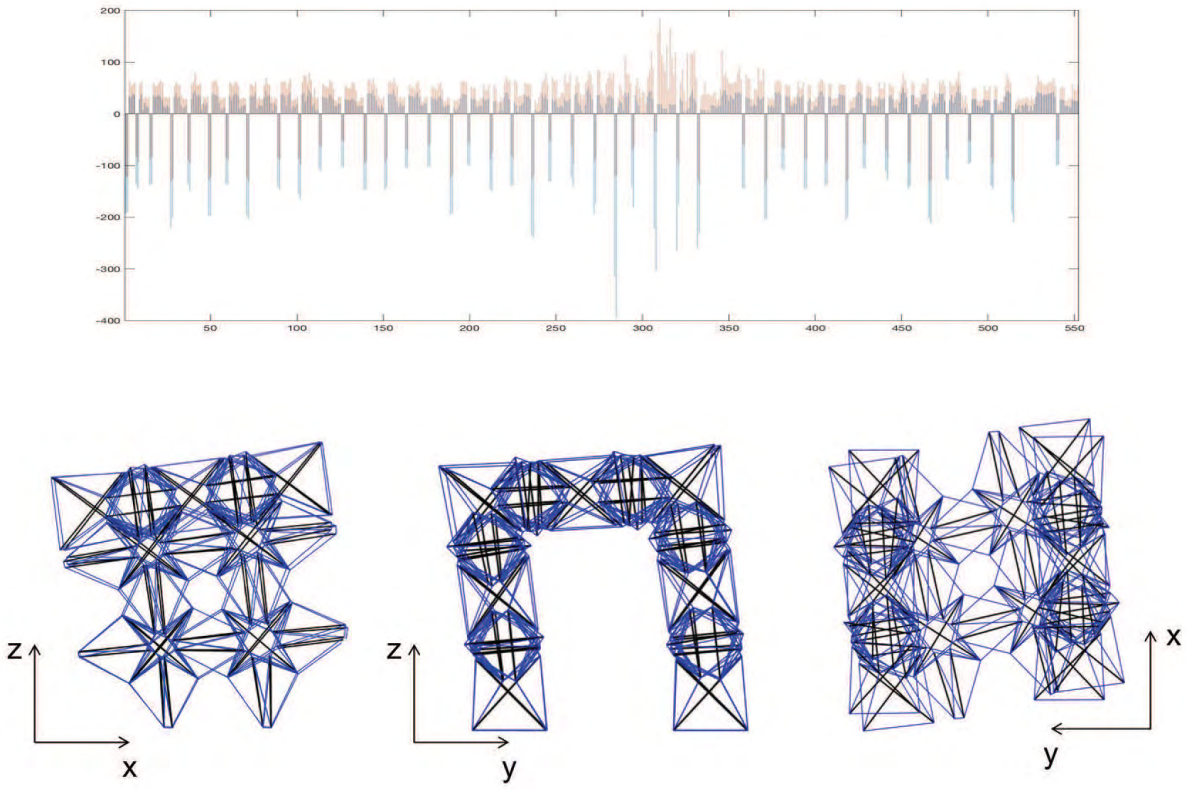


Figure 10: (top) bar plot of the actual member stress in kgf; (bottom, from left to right) deformed shapes in the first, second, and third mode of vibration.

Acknowledgements

We wish to thank professor Stefania Mornati (Department of Engineering and Computer Science – University of Rome Tor Vergata) for putting in contact the academic side and the industry side of this project, within her research interest in wooden contructions. We are grateful to Lorenzo Botti and the company Progetto Legno for providing the wooden struts and performing the machining of the end sections. AM gratefully acknowledges the financial support from the Italian Ministry of Education, University, and Research (MIUR) under the FFABR grant L.232/2016.

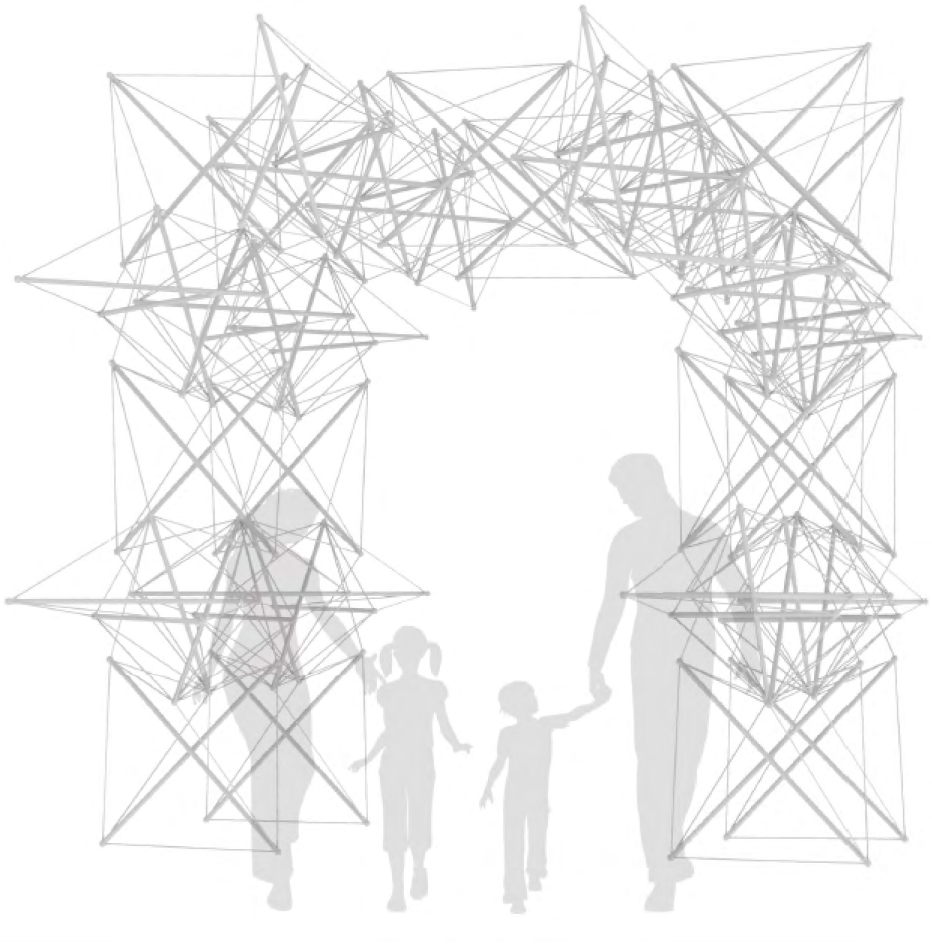


Figure 11: artistic view of the pavilion.

References

[1] K. Snelson, *Tensegrity, Weaving and the Binary World*, 2014, downloaded in 2019 from www.kennethsnelson.net.

[2] R. Motro, *Tensegrity: Structural Systems for the Future*, Kogan Page Science, London, 2003. (Letter from Kenneth Snelson to R. Motro, published in November 1990 in "International Journal of Space Structure").

[3] MoMA Archive, Exhibition 652, Bukminster Fuller, October 23-novembre 22, 1959 Master checklist.

[4] K. Snelson, *The Art of Tensegrity*, International Journal of Space Structures, vol, 27, 2012, pp.71-80

[5] K. Snelson, E. Heartney, *Kenneth Snelson; Art and Ideas*, Kenneth Snelson in association with Marlborough Gallery, New York.

Proceedings of the IASS Annual Symposium 2019 — Structural Membranes 2019
Form and Force
7—10 October 2019, Barcelona, Spain
C. Lázaro, K.-U. Bletzinger, E. Oñate (eds.)

X-Shell Pavilion: A Deployable Elastic Rod Structure

Florin ISVORANU*, Julian PANETTA, Tian CHEN, Etienne BOULEAU[a], Mark PAULY

* LGG-EPFL
Lausanne, Switzerland
florin.isvoranu@epfl.ch

[a] INGENI SA Geneve



Figure 1: The X-Shell pavilion.

Abstract

We present the X-Shell pavilion, a lightweight structure composed of elastic beam elements joined in a special layout that allows easy on-site deployment. The structure's undeployed assembly configuration lies mostly flat and is easy to build, consisting of GFRP rods connected with mechanical fasteners made of aluminum and steel. The structure is deployed simply by either stretching the flat layout or by driving open the angles between rods at the joints. As the structure expands, the constraints imposed by the joints force its beams to bend and the whole structure buckles into its predetermined target shape. Unlike traditional gridshells, our structure does not require boundary supports to maintain its shape. Instead, the structure's shape is directly encoded in the flat layout of its beams, their cross-section geometry, and material properties. The structure can be locked in its deployed configuration just by fixing a few joints. Apart from simplifying deployment, this feature offers several advantages. For instance, it allows the beam ends touching the ground to be mounted on castor wheels without the structure collapsing back into its flat state.

Keywords: Gridshells, deployable structures, physics-based simulation, numerical optimization, computational design.

Copyright © 2019 by Florin ISVORANU, Julian PANETTA, Tian CHEN, Etienne BOULEAU, Mark PAULY
Published by the International Association for Shell and Spatial Structures (IASS) with permission.

1 Introduction

1.1 Concept

X-Shells define a new type of deployable beam structures [2, 1]. They are formed by elastic rods connected in a grid-like network similar to traditional elastic gridshells, but with specific properties that clearly set them apart. The network is assembled in a very compact, usually flat state by connecting beams with rotational hinge joints alternating beams in a scissor type mechanism. The distance between the joints along the beams is non-uniform. As a consequence, the beam network defines an *incompatible* planar linkage mechanism that, when expanded, causes the beams to bend and twist and the entire structure to buckle out of plane towards the desired double-curved target shape.

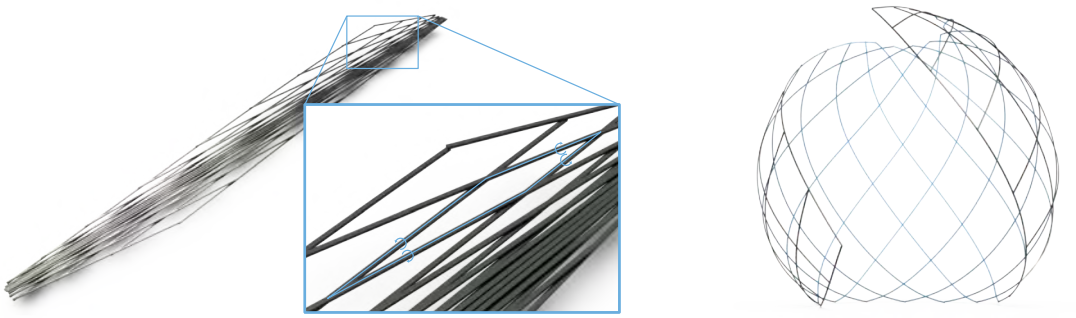


Figure 2: The X-Shell concept: a flat assembly of beams coupled with rotation joints (left, zoomed view) forms an incompatible linkage mechanism that buckles into a programmed 3d shape (right) when deployed by an expansive actuation.

As a new class of gridshell structures, X-Shells do not require any boundary anchors to reach and keep the target shape. Due to the complex interaction between discrete joints and continuously deforming beams, not every X-Shell mechanism is easily deployable or usable architecturally. Exploring the shape space is a challenge requiring specialized simulation and optimization tools.

1.2 Design Tools

We have proposed new computational tools to simulate and optimize X-Shells based on a discrete rod model that allows effective shape exploration [2]. This robust algorithm is complemented with a method for finding sparse actuation layouts in order to efficiently deploy an X-Shell from its compact assembly state to its 3D target state.
The current workflow is limited to forward simulation, although our optimization framework enables the possibility to fit to a reference surface if a good initialization is provided. The design process involves feeding the simulation algorithm with a user generated network of rods, their material properties, and cross-section profile. The tool can then deploy the X-Shell through a range of opening angles with real-time visual feedback. A numerical optimization is applied to optimize the geometry of the deployed and undeployed state. This optimization not only improves the visual quality of the X-Shell, but, more importantly, reduces high local stresses in the structure to ensure easy fabrication and deployment. For details on the algorithms and interfaces used for the design and optimization of the X-Shell pavilion, please refer to [2].

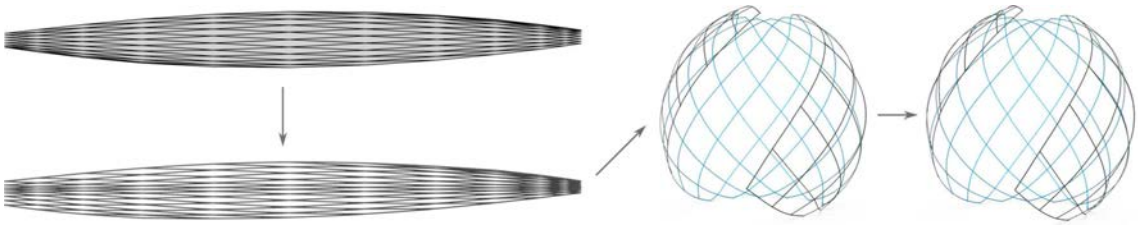


Figure 3: Design pipeline for X-Shells. Our X-Shell simulation framework converts the user-generated rod layout network (upper left) into a coupled assembly of discrete elastic rods and computes its equilibrium in the absence of actuation forces (bottom left). The simulation then drives open the joint angles to obtain the deployed shape (middle), and once the user is happy with the shape, an optimization pass is run to find a nearby X-Shell design with better stress performance (right).

2 Design

2.1 Goals and Constraints

X-Shells are particularly suitable for building temporary lightweight structures. To demonstrate their advantages, we set out to design and build an X-Shell pavilion within a highly constrained design space set out in the Form and Force 2019 pavilion competition: The pavilion bounding box should not exceed 4m × 4m × 4m; it must be self-standing without the need for ground or suspended anchors, but it can be ballasted for stability; it must be transportable, fitting in a maximum of 6 1m × 0.75m × 0.65m cases weighing no more than 32kg; it must be erected/dismantled in one day; and aesthetically, it should reflect the underlying state of the art research and be a pleasant attraction.

2.2 Architectural Typology

The X-Shells design space is quite rich, enabling elegant canopies, intriguing dynamic structures, or biologically inspired shapes. For this particular pavilion project, we are interested in harvesting the purity of their geometric and physical expression, seeking unifying shapes that flow smoothly, integrating wall supports and ceiling into a monocoque structure. Our initial study identified six potential candidates, shown in Figure 4. We settled on the candidate on the lower right as it showcases the free boundaries that distinguish X-shells from conventional elastic gridshells. We also found the design appealing in how it wraps around and embraces its interior during deployment.

3 Construction

X-Shells are easy to build, and from our experiments so far, they are tolerant to construction imprecision. We chose unidirectional GFRP profiles with rectangular 12mm × 8mm cross-sections for the pavilion's beams, based on their properties and availability. The hinge joints employ 3mm diameter 12.9 grade bolts. The connecting sleeves are two-part machined aluminum plates. The bounding box of the deployed X-Shell is 3.2m × 3.2m × 3.6m.

For precise positioning, we laser etched drilling locations and cutting guides directly on the GFRP rods. We then drilled the beams using a bench top drill press aided by a laser cut jig to improve hole alignment (Figure 5) and cut the rods along the etched guides with a band saw.

The X-Shell pavilion is assembled in its flat, low energy state, by pinning corresponding rods until the lattice is complete. While this assembly state has low energy, the energy is not zero: all

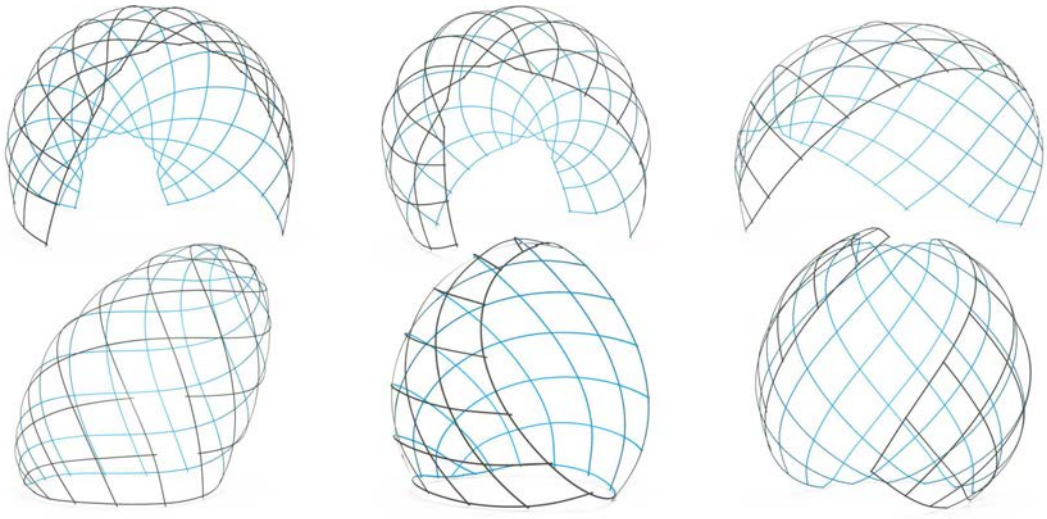


Figure 4: X-Shell pavilion design candidates.



Figure 5: Etching and drilling the GFRP rods.

beams must still incorporate some bending. However, due to the chosen sectional profile of the rods, this compact state remains truly flat. The amount of bending required for the assembly is low enough that it can be manually assembled without power tools, jigs or additional supports. We note that using cross-sections with a higher horizontal aspect ratio could cause the assembly to pop out of plane into a mildly bent shape.

4 Deployment

As an X-Shell mechanism, the pavilion deploys to its designed form from a compact, flat assembly state. Furthermore, to increase transportability, it can be decomposed into shorter, pre-assembled flat sections that join into each other with simple sleeve joints.
Once fully assembled, the pavilion is deployed into the full 3D form by driving open a few of its joint angles, either mechanically or by hand. The X-Shell pavilion can be locked in the deployed state by restricting the lengthening of short quadrangle diagonals using soft stays that clip onto the respective quadrangle joints. Only a few stays suffice to lock the structure open.



Figure 6: Assembly and deployment of the X-Shell pavilion. The aluminum connecting sleeves (upper left) are used to join the separately-assembled scissor linkages of GFRP beams into the full assembly (bottom left, middle). A preliminary manual deployment (right).

5 Performance

We judge the X-Shell pavilion's performance mainly from a structural point of view. Since X-Shells behave as mechanisms, we are interested in analyzing their load behavior and displacements in the deployed state while in the flat (undeployed) and intermediary states we need to assess the internal stresses that could possibly lead to node failure and rod breakage or require excessive deployment forces. Figure 7 plots the pavilion's stress throughout its entire deployment as predicted by our simulation framework. We note that our X-Shell optimization tool is able to substantially reduce the stresses due to beam bending even though the initial design candidate found by forward exploration was already free of any obvious design flaws.

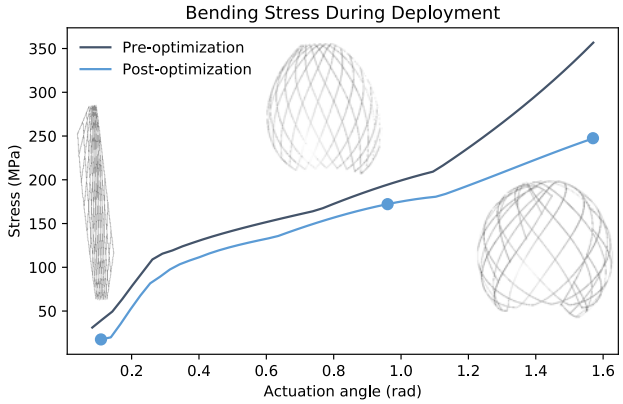


Figure 7: Maximum stresses in the optimized and unoptimized X-shells due to beam bending throughout the deployment process. The inset renderings visualize the deployment stages indicated by the blue disks.

We conducted our analyses using the X-Shell simulation framework [2] to simulate deployment and an Abaqus model for static loading. The current simulation framework and the Abaqus model ignore the drill holes in the rods at the joints. To analyze the structural consequences of the piercings, we separately conducted destructive tests of the rod joints with various piercing sizes and loads; these showed a pin size of 3mm satisfies structural requirements, considering the loads encountered in the X-Shell deployment.

5.1 Experimental Testing

To calibrate our deployment simulations with accurate material parameters and predict the structural integrity of the deployed X-Shell, we conducted four sets of experiments assessing the structural behavior of the GFRP, the sleeve connectors, and the capacity of the joints.

Four point bending along the weak axis of GFRP to derive the Young's modulus. We determined the Young's modulus of the GFRP beams using a four point bending experiment performed on a static load testing machine (Instron 5940 Series Universal Testing Systems) with a load cell capacity of 1kN. A force based loading is imposed at a rate of $1\frac{\text{N}}{\text{s}}$. Rollers are used both at the supports and at the points of load application. The reaction forces and displacements are recorded at 10Hz.

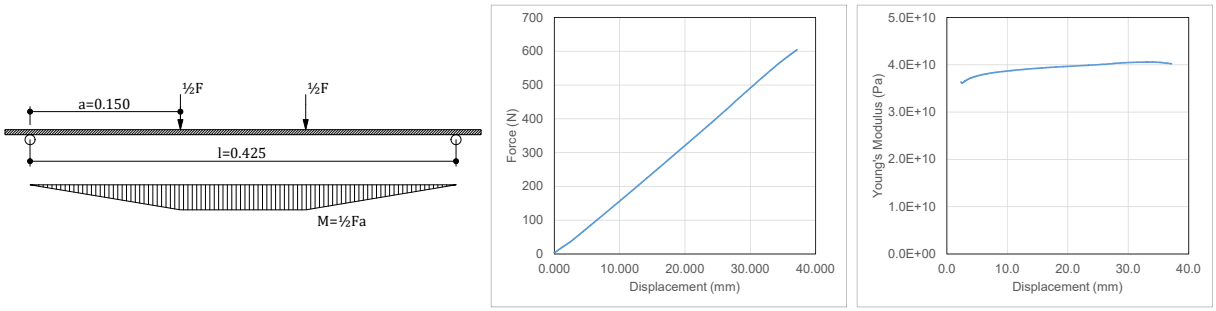


Figure 8: Force/displacement of GFRP under four point bending (left); derived Young's modulus (right).

The resulting force/displacement curve shows a linear relationship for the range of force tested (Figure 8). The analytical solution for the Euler-Bernoulli beam equation under the four-point bending boundary conditions gives us an expression for the displacement at $x = (a = 0.150\text{m})$ under a given force magnitude which can be rearranged to obtain the Young's modulus: $E = \frac{Fa^2}{12dI}(3l - 4a)$, where $l = 0.425\text{m}$, I is the second moment of area, F is the applied force, and d is the downward displacement. Each (F, d) measurement gives us a different estimate of E, as plotted in Figure 8, and we chose $E = 4 \times 10^{10}\text{Pa}$ for use in our simulations.

Four point bending along the weak axis of GFRP with a sleeve connector. We assessed the difference in stress-strain behavior between a simple section and one with a sleeve connector using a second four point bending test. Surprisingly, their bending stiffnesses are virtually indistinguishable (Figure 9), implying that decomposing the X-Shell's beams into segments to satisfy our transportability constraints will not significantly affect the deployed structure's shape or load behavior.

Testing the bolt capacity and delamination. We investigated the potential for local delamination in the direction perpendicular to the fibers. Two beams are connected using a stainless steel M4 bolt with a washer in between. Load up to 550N is applied in compression with no visible failure in either the bolt or the laminates.

Three point bending along the strong axis to obtain material strength. We measured the tensile strength of the GFRP beams by conducting a three point bending experiment

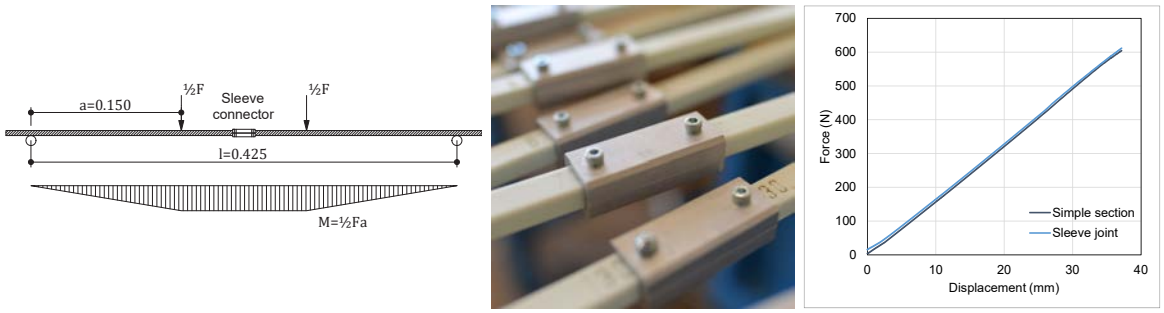


Figure 9: A sleeve connector (left) and the four point bending force displacement plot comparing the bending stiffness of a single GFRP beam to two GFRP beams joined with a sleeve connector (right).

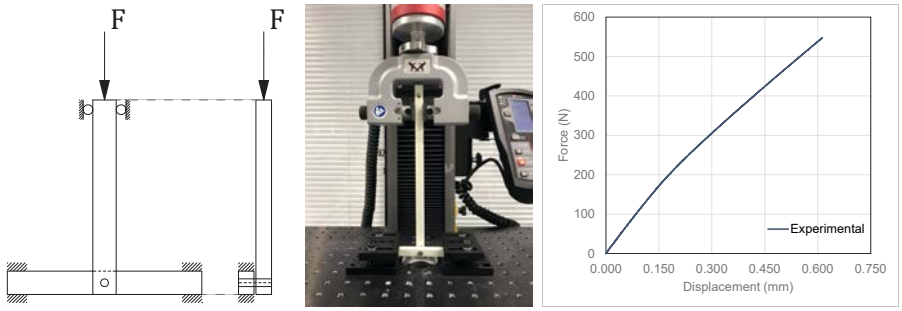


Figure 10: Experimental setup for testing the bolt capacity (left) and results (right).

inducing a large mid span stress at the extremities of the cross section. We used the strong axis to reduce the necessary clearance for deflection. The corresponding analytical solution to the beam equation yields the following expression for the greatest maximum principal stress in the cross-section: $\sigma = \frac{My}{I} = \frac{1}{2}Fl\frac{h}{2}\Big/\frac{bh^3}{12}$.

This linear elasticity-based model agrees with the initial slope of the stress strain curve (Figure 11), but as damage accumulates, the behavior becomes non-linear and the beam fails at approximately 0.014 strain with rupture of fibers on the tension side. The maximum stress reached is conservatively 400MPa. This stress limit is compared with the detailed simulations in the next section to ensure that our design has an adequate safety factor.

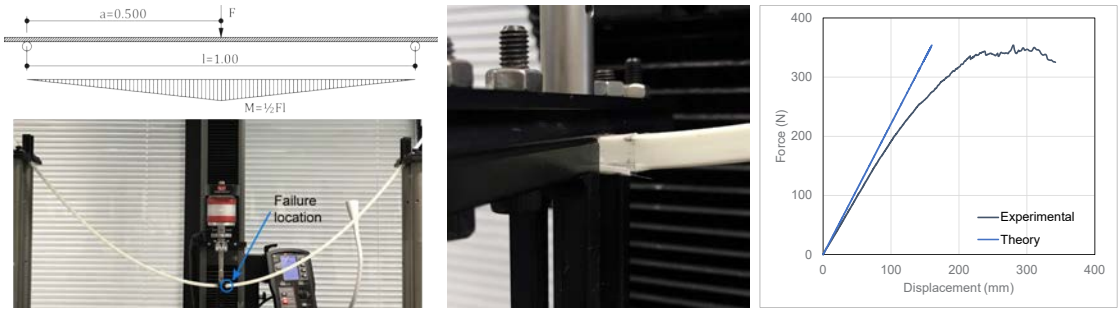


Figure 11: Three point bending experiment inducing failure at mid span (left) with a detailed view (center). The stress strain curve of resulting from the experiment in comparison with theoretical prediction.

6 Detailed Finite Element Simulations

The X-Shells simulation framework [2] does not capture the beam behavior when the cross section has defects such as bolt holes. We perform solid FEA to simulate isolated segments of the deployed structure to demonstrate that the maximum stress remains below the limit in such disturbed regions. As it is unclear where the absolute maximum principal stress will occur within the structure, four different segments are chosen for detailed analysis: the regions of maximum bending stress, twisting stress, joint force, and joint torque (Figure 12).

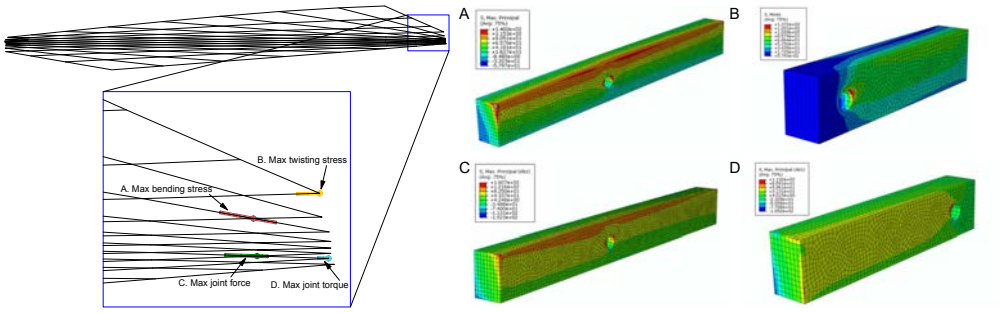


Figure 12: Critical members and their maximum principal stresses computed by Abaqus.

We used Abaqus 14 to simulate the structural behavior using quadratic hexahedral elements. We extracted equivalent forces and torques acting on the segment in question from the X-Shells deployment simulation and applied them to reference points placed at the segment ends and bolt hole centers. These reference points are in turn coupled (in all 6 DOFs) to the faces at the ends of the segment, and to the cylindrical surface made by the bolt hole. To eliminate rigid body motion, one set of forces and torques is replaced by a clamped boundary condition. The cross section is 12mm × 8mm, and the Young's modulus is set at 40 000MPa.
We found stresses concentrate at the rims of the bolt holes and along extreme edges of the cross section. For beam segments on the X-shell boundary, maximum stress occurs only at the bolt holes. We observe an approximate peak stress of 130MPa which offers a safety factor of roughly 3 compared to the experimental capacity of 400MPa.

7 Conclusion

X-Shells are generally easy to build and deploy. Compared to traditional regular elastic gridshells, they have two significant advantages: they do not rely on boundary anchors to develop into the designed shape; and their freedom to eschew boundary constraints enables a much richer design space. These particular advantages make X-Shells highly suitable for mobile and immobile architecture at small and medium scale: pavilions, shelters, concert installations, temporary roof structures, re-configurable domes and canopies.

References

[1] Bouleau, E., Panetta, J., Isvoranu, F., and Pauly, M. X-shell, a new spatial deployable lattice compared to traditional reticulated shells. In *Form and Force 2019: Proceedings of the IASS Annual Symposium 2019* (2019).

[2] Panetta, J., Konaković-Luković, M., Isvoranu, F., Bouleau, E., and Pauly, M. X-shells: A new class of deployable beam structures. *ACM Trans. Graph. 38*, 4 (July 2019).

Proceedings of the IASS Annual Symposium 2019 – Structural Membranes 2019
Form and Force
7 – 10 October 2019, Barcelona, Spain
C. Lázaro, K.-U. Bletzinger, E. Oñate (eds.)

Eco-friendly Mid-rise Apartments Using CLT Panels

Anahita KHODADADI

* Portland State University
Portland, OR
anahitak@umich.edu

Abstract

This paper represents a series of design alternatives for a mid-rise apartment complex, inspired by the configuration of Habitat 67, where the prefabricated modules seem to be stacked chaotically. Unlike Habitat 67, where prefabricated reinforced concrete panels are used for construction, the apartment complex in this project is to be built by structural Cross-Laminated Timber (CLT) panels. In this study, characteristics of Habitat 67 are considered to evaluate the performative characteristics of the generated solutions. The form exploration process in this study is based on a GA+TRIZ hybrid method [1]. First, the design objectives are set, and the Theory of Innovative Problem Solving (TRIZ) is used to define parametric modeling. Then, a genetic algorithm (GA) is employed to generate a wide variety of design solutions. Through the iterative process of form generation, the structural performance, the heating energy demand throughout November to March, the shell cost, the environmental and life cycle impact of the design alternatives are studied. The suitable solutions are explored using Pareto sets and TRIZ matrix of contradictions. Finally, performative characteristics of Habitat 67 are compared with those of the generated solutions, and it is explained how the design objectives and sustainable development of our environment are sought within this project.

Keywords: Form exploration, mid-rise apartment complex, Cross-Laminated Timber (CLT) panels, genetic algorithm, TRIZ, Habitat 67, life-cycle assessment

1. Introduction

In 1967, Moshe Safdie designed Habitat 67 as the Canadian Expo Pavilion. Habitat residential complex gained worldwide admiration as it was an outstanding integration of architecture and structure and could break the traditional form of orthogonal high rises and introduce a new housing topology. Fifty years later, Habitat 67 still seems a spectacular residential project. However, today, the industrialization of building construction is no longer a major concern for architects and engineers. Designers are to find solutions for sustainable development of human-built environment and reduction of building construction impact on global warming, CO2 emission, ozone depletion, and consumption of natural resources. Therefore, if such an innovative project as Habitat 67 were to be built today, the design approach would be different.

Habitat 67 is constructed from 354 identical prefabricated modules stacked in various geometrical configurations to provide 158 apartments (Figure 1). There are 15 models of apartment units that include one to five modules. The units look similar, but the interior space of each house differs from the others. The apartments are soundproofed and heated by a central heating and air-conditioning system. The geometrical and material properties of Habitat 67, along with the cost estimation, are described in Table 1 [2, 3, 4, 5]. The manufacturing site of Habitat 67 was located 300 m away from the site of implementation. The complete modules, whose weight varies between 70 and 90 tons, were hoisted by a giant crane, set up and secured to other units using post-tensioning cables. (Figures 2 and 3) [2].

Copyright © 2019 by Anahita KHODADADI
Published by the International Association for Shell and Spatial Structures (IASS) with permission.



Figure 1: Habitat 67, Montreal, Canada [6]

Table 1: The design properties of Habitat 67

Geometrical properties
354 modules 38×17 ft^2 [7] (12.5×5.7×3.2 m^3 external measurement) Total Height: 36.576 m (120 ft) | 12 stories 15 different modules with an area of 55 m^2 (624 ft^2) Floor plans range from 1 to 4 bedroom apartments and 1 to 3 stories Weight of each module = 70 to 90 tons The area of terraces range from 20-90 m^2 (225 to 1000 ft^2)
Material
Exterior walls of the units: sand-blasted concrete Window frames: brown anodized aluminum
Cost
140,000 CAD per unit Total cost = 140,000 × 158 = 22,120,000 CAD Heating/cooling cost for a one-bedroom apartment of Habitat = 400-600 CAD per month throughout the year [8]. (Heating/cooling cost for a one/two-bedroom apartment in Montreal = 200-300 CAD per month throughout the year)

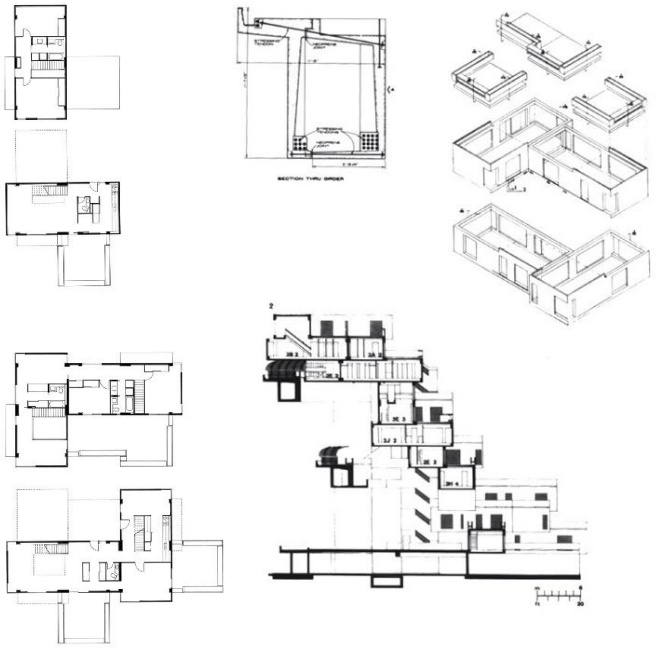


Figure 2: Floor plan of an apartment and constructional details [6]



Figure 3: Prefabrication of the apartment units in the manufacturer's site [9]

2. Configuration processing of the CLT mid-rise residential tower

Habitat 67 includes three clusters of stacked modules. With the same fashion, the residential complex in this project is to be composed of three same clusters of apartment units (Figure 4). In order to reduce the simulation time in this project, only one of the clusters is parametrically modeled and analyzed. Therefore, performative characteristics such as the shell cost, thermal energy demand, weight of structures, and life cycle impact are compared to one-third of the corresponding values in Habitat 67. The configuration of each cluster of apartment units is defined by creating a stack of 12×16×11 (width×length×height) modules whose number of floors is reduced regarding the location of four attractor points on the XY plane (Figure 4). Then, 250 to 500 modules from this basic model are removed randomly to shape the roof gardens and private balconies (a seed value controls the reduction pattern). Each module is 5.8×5.8×3.4 m^3. Then, columns and required structural supports are added to the model where units are not supported by the walls of the lower floors. The geometrical properties of the residential complex are described in Table 2.

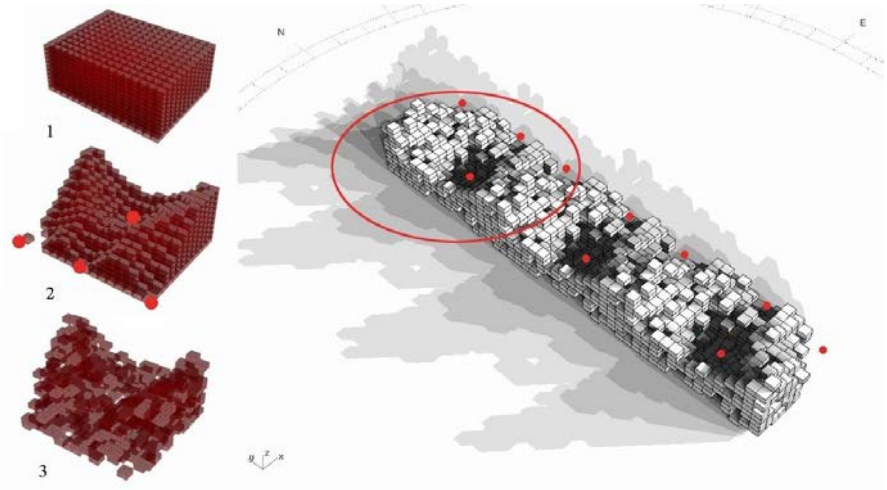


Figure 4: The configuration processing of mid-rise residential complex

Table 2: The geometrical properties of the mid-rise residential complex

Geometrical properties
Habitat module dimension = 12.5×5.7×3.2 = 228 m^3 Habitat maximum height = 36.576 m | 12 stories Assumption: Each residential unit includes two geometrical modules, floor to floor height = 3.4 (11 ft) ⇨ Geometrical dimension of each module = 5.8×5.8 m^2 Height of each apartment module = 3.4×11=37.4 m | 11 stories Area of each apartment module: 5.8×5.8 m^2 (19×19 ft^2) Height of each apartment module: 3.4 m (11 ft) Maximum number of floors: 11

3. Structural and thermal analyses and life cycle impact assessment

The walls, roofs, and floor slabs are all to be made of structural panels. The roofs are expected to be used as roof gardens. Therefore, the appropriate combination of live load and snow load is considered in the structural analysis. Total weight of the structure, its natural frequency, and maximum displacement are obtained through the simulation carried out in Karamba a plugin for Grasshopper [10].

Thermal analysis is carried out for assessment of the Heating Ideal Zone Load for five months, from November 1st to March 31st. In Montreal, heating cost and maintaining the comfortable temperature within these five months are critical while cooling energy demand throughout the year is not important. The thermal analysis is carried out using ArchSIM plugin for Grasshopper [11].

In this design case study, the Life Cycle Assessment (LCA) is carried out to evaluate the magnitude and significance of the potential impacts of the residential building complex on the environment. In this study, the same input data, including the type of occupancy, location, and gross floor area, are truncated

from the model for practical purposes and quick estimation. The Product Declarations of the structural materials, provided by the suppliers, are used to compute the LCA. The LCA assessment in this design project includes global warming potential, acidification potential, ozone depletion potential, total used energy through the life cycle, non-hazardous waste, hazardous waste, and consumptions of freshwater, non-renewable and renewable material.

4. Form exploration of the mid-rise residential complex using the GA+TRIZ method

In this project, the main design objectives are minimizing the environmental impact, reducing the heating energy demand in the cold season, providing a pleasant residential space for the tenants, and maximizing the number of units and total floor area of the apartments. This form exploration method in this study is based on a GA+TRIZ hybrid method [1] (Figure 5).

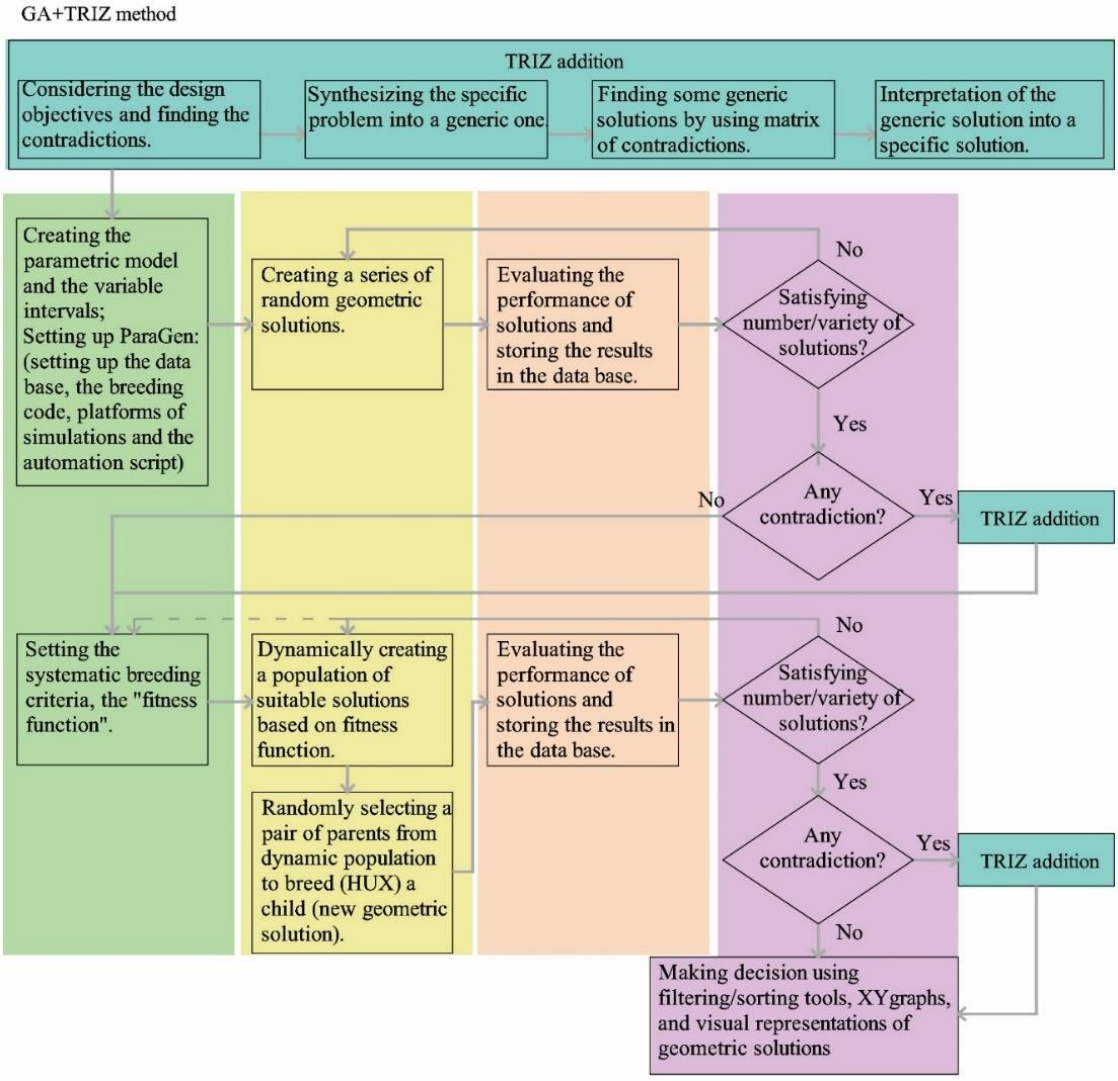


Figure 5: The plan of work in the GA+TRIZ design method [12]

According to the GA+TRIZ method, the design objectives are synthesized into their basic factors and checked for probable conflicts. As a result, the contradiction between the life cycle impact of the building and the amount of structural material or the amount of floor area was revealed. Design alternatives with a greater number of units and amount of total floor area require more consumption of material resources and, as a result, they have greater potential to increase global warming. Referring to the TRIZ inventive principles and the matrix of contradiction [13, 14, 15, 16, 17] made the designer opt for an eco-friendly material such as CLT panels instead of prefabricated reinforced concrete. There are

five reasons for choosing CLT panels as a replacement of prefabricated reinforced concrete in this case study. The first reason is the renewability and low environmental impact of the wood, in particular, its low carbon footprint. Second, CLT panels can be employed in the prefabricated building industry where panels are cut to the required dimensions, engineered and treated to be thermal and fire resistant, and finally erected in-site relatively quickly. Third, the presence of wood can provide the occupants with a pleasant environment and improve the quality of interior space. Fourth, the reason for choosing CLT products and not, for example, light-frame wood construction is to compare two massive constructions that have two different carbon footprints. Fifth, in Canada, in particular in Quebec, forestry is a huge part of the economy, and several companies supply the CLT products for the building industry. Also, the required building codes are provided for architects and engineers to employ CLT products. There are successful examples of CLT residential buildings all over the world, as well as in Canada, that have pushed the boundaries of the CLT industry furthest [18, 19, 20, 21]. Structural specifications of the CLT products used in this design project are provided by Nordic Structures Company [22] in Montreal.

Furthermore, in Habitat 67 prefabricated reinforced concrete panels were used without any thermal insulation. In this project, design analysis suggested thermal insulation of the building for better environmental performance. Moreover, the application of GA+TRIZ form exploration method implies consideration of two separate variables to define the thickness of CLT panels and the thickness of thermal insulation. Taking these actions allow for the resolution of the explained contradiction among the design objectives innovatively.

In the next step of the design procedure, the parametric model of the apartment complex is defined. Then, the database is set, separate models for structural and thermal simulations are created, and the GA-based breeding code is scripted [23, 24]. Details of inputs for structural and thermal analyses are provided in Table 3. The displacement and utilization diagrams of the generated solutions and, the bar charts that show their thermal energy demand from November to the end of March are to be stored in the database.

Table 3: The environmental and structural properties of the mid-rise residential complex

Material and thermal properties
CLT plates density = 500 kg/m^3 ,Conductivity = 0.13 W/mK ,Specific heat 1600 J/kgK Thermal emittance = 0.9 ,Solar absorptance = 0.7 , Visible absorptance = 0.7 Embodied energy =10 MJ/kg , Embodied carbon =0.71 kgCO2/kg
Material cost estimation
CLT structural system cost: Design + material supply +installation = 435-490 CAD/m^2 (40-45 CAD/ft^2) ≈ 450 CAD/m^2 (Exchange rate CAD to USC = 0.75) , Design + material supply +installation = 326 – 367 ≈ 350 USD/m^2
Material and load properties
CLT plates: Spruce-Pine-Fir Density = 400 kg/m^3 (25 lb/ft^3) Thickness = 8-20 cm (3 1/8 – 7 7/8 in) Load case 1 = self-weight + Roof load (promenade roof) of 2.8 kN/m^2 (58.5 psf) [25] Load case 2 = self-weight + residential live load of 1.92 kN/m^2 (40 psf) [25]
Load: 0.01 people/m^2 +11 equipment w/m^2 + 7 lighting w/m^2, 150 lux, continuous dimming, AllOn schedule [26]. Conditioning: heating setpoint: 21C cooling setpoint 26 C Ventilation: Air change per hour = 0.5 ACH Hot water: On | peak flow 0.03 m^3/h/m^2 | 65C supply temperature | All On
Construction
Roof = 95mm CLT + 80mm Rigid foam EPS 035 insulation + 95mm CLT + 20mm Gypsum Fiber Board Partition = 20mm Gypsum Fiber Board + 95mm CLT + 20mm Gypsum Fiber Board Ceiling = 95mm CLT + 30mm Impact sound insulation + 95mm CLT + 20mm Gypsum Fiber Board External floor = 95mm CLT + 80mm Rigid foam EPS 035 insulation + 95mm CLT + 30mm Pine wood Façade = 30mm Pine wood + 80mm rigid foam pur no coating Insulation + 150mm CLT + 20mm Gypsum Fiber Board

According to the described design objectives, a series of design alternatives is generated whose global warming potential is less than 1,000,000 kgCO2eq and ideal total heating energy from November to the

end of March is less than 5000 MJ (Figure 6). Then, the generated solutions are explored to find a series of suitable design alternative whose total floor area is greater than that of the Habitat 67. Figure 7 displays the distribution of solutions regarding their gross floor area and global warming potential. Figure 8 displays the distribution of solutions based on their gross floor area and ideal total heating energy from November to the end of March. In both graphs, solution number 228 has been chosen as a suitable solution. The performative characteristics of solution number 228 are displayed in Table 4.

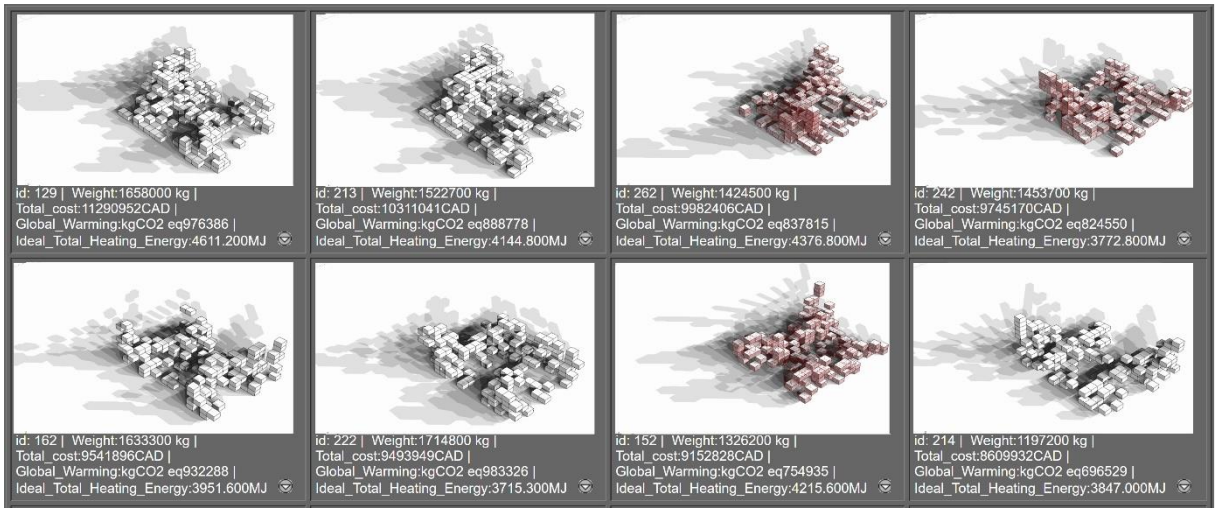


Figure 6: South-East view of the solutions whose global warming potential is less than 1,000,000 kgCO2 eq and ideal total heating energy from November to the end of March is less than 5000 MJ. The solutions are sorted based on their gross floor area in descending order.

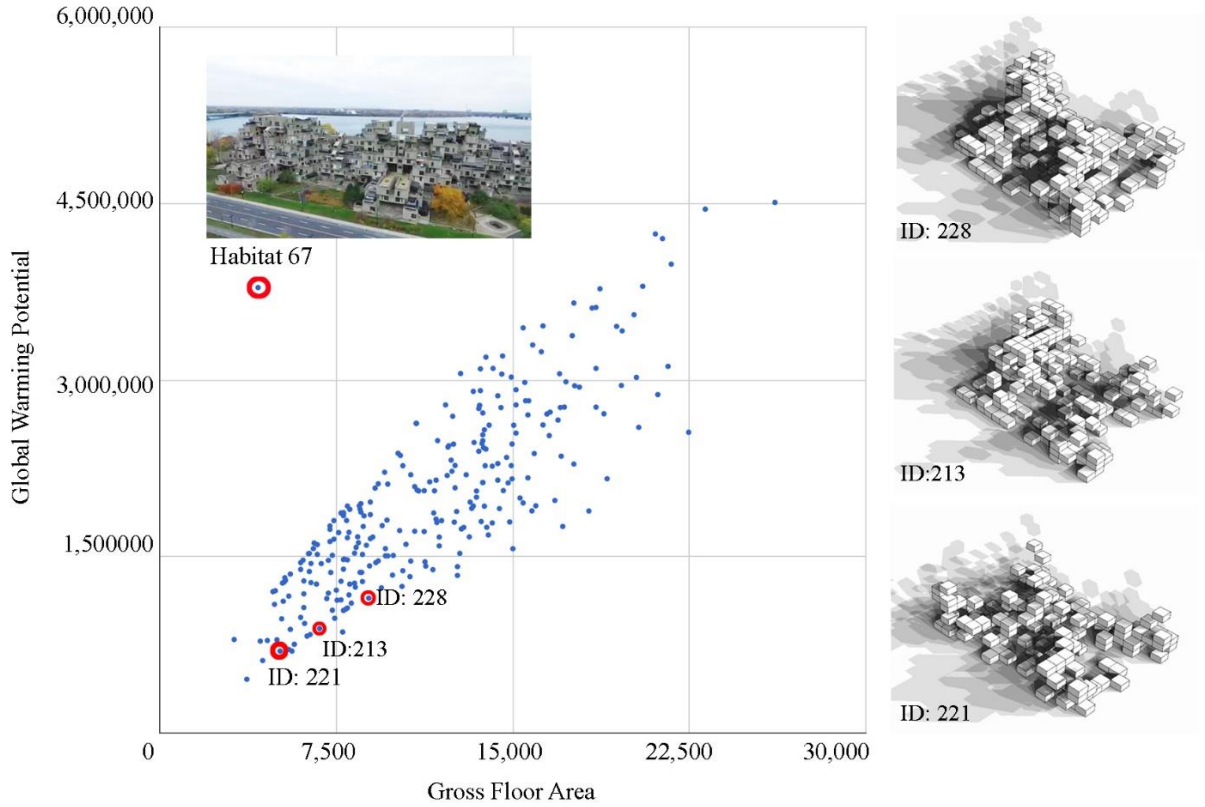


Figure 7: The plot displays the distribution of solutions regarding their gross floor area and global warming potential. Habitat 67 and some of the suitable solutions made of CLT panels are highlighted.

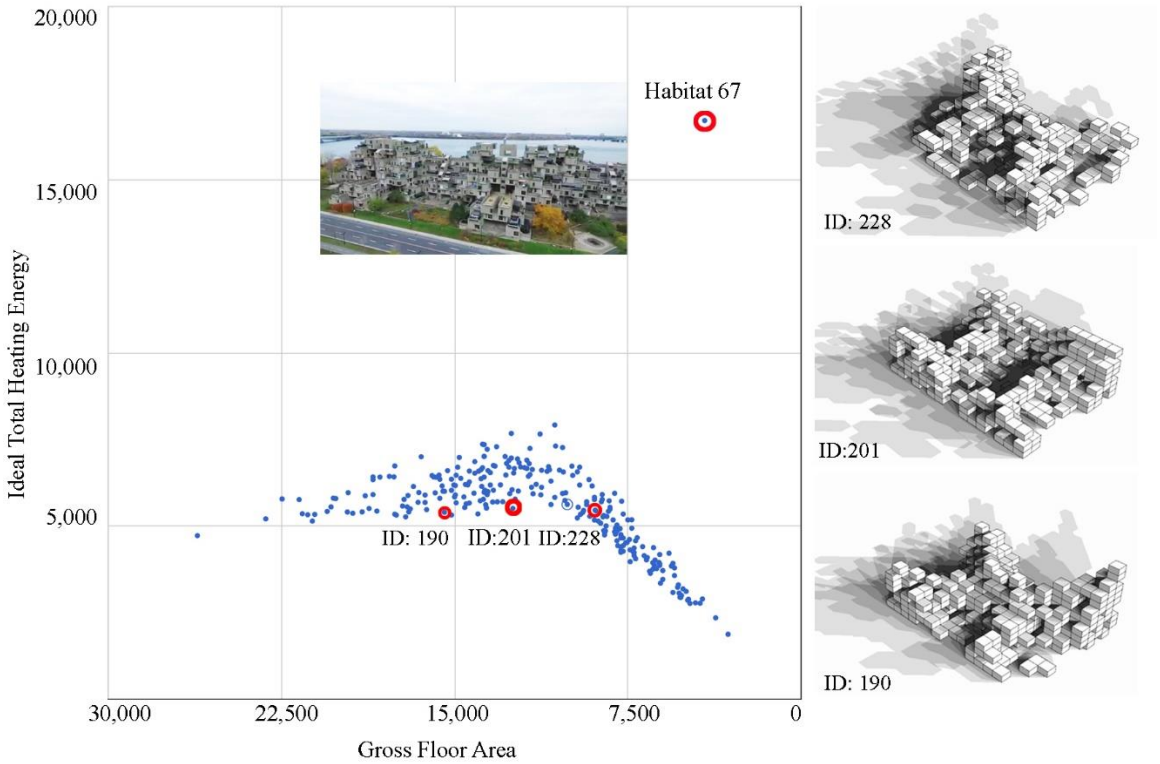


Figure 8: The plot displays the distribution of solutions regarding their gross floor area and ideal total heating energy from November to the end of March. Habitat 67 and some of the suitable solutions made of CLT panels are highlighted.

Table 4: The performative characteristics of solution number 228

Roof_CLT_Thickness	18	CLT_Volume	3866.35	Max_Displacement_Roof	0.516189
Floor_CLT_Thickness	9	Total_cost	13180851.9	Max_Displacement_Floor	0.950771
Wall_CLT_Thickness	9	Facade_Area	15105.52	Natural_Frequency	2.344068
Col_Width	49	Global_Warming	1146864	Mmass_Natural_Frequency	9225.546
Roof_Insulation_Thickness	7	Ozone_Depletion	0.01684	Ideal_Total_Heating_Energy	5437.8
Floor_Insulation_Thickness	6	Acidification	11196.72	Nov_Ideal_Heating_Energy	546.11
Facade_Insulation_Thickness	9	Non_hazardous_Waste	15327745	Dec_Ideal_Heating_Energy	1273.4
G_floor_Area	6627.08	Non_Renewable_Material_Consumption	365445.87	Jan_Ideal_Heating_Energy	1518
Total_Num_Units	264	Renewable_Material_Consumption	3820057.28	Feb_Ideal_Heating_Energy	1263.5
Weight	1913900	FreshWater_Consumption	2446.342	Mar_Ideal_Heating_Energy	836.81

5. Conclusion

It is almost a decade that designers have been more concerned about the sustainable development of human-built environment and reduction of building construction impact on our environment. This paper represents a series of design alternatives for a mid-rise apartment complex, inspired by the configuration of Habitat 67. In contrast to the prefabricated reinforced concrete construction of the Habitat 67, Cross-Laminated Timber (CLT) panels are utilized as the structural components of the residential complex. The application of the GA+TRIZ methodology helped to obtain relatively more suitable solutions by directing the designer to choose better structural material and reduce the life cycle impact and heating energy demand of all generated solutions.

Acknowledgments

My thanks to Professor Peter von Buelow for his support in using ParaGen interface [23] and Hydra Lab at the University of Michigan.

References

[1] A. Khodadadi, "Synergy of a Genetic Algorithm and TRIZ in Conceptual Design," in *International Association of Spatial Structures Annual Symposium (IASS)*, Boston, 2018.

[2] "Étude patrimoniale sur les témoins matériels de l'Expo 67".

[3] *Habitat 67 (Montreal, Canada), Great Spaces, Series 1, Episode 2.* [Film]. Great Spaces TV, 2015.

[4] "Habitat 67 Planning and Architectural Drawings," Canadian Architecture Collection, [Online]. Available: http://cac.mcgill.ca/moshesafdie/habitat/showplans.htm. [Accessed 13 March 2019].

[5] "Homage," Habitat 67, [Online]. Available: http://www.habitat67.com/en/homage/. [Accessed 13 March 2019].

[6] *The Moshe Safdie Archive,* McGill Library.

[7] G. Merin, "AD Classics: Habitat 67 / Safdie Architects," *ArchDaily,* 21 July 2013.

[8] A. Reuben, Director, *Habitat 67: The Transformative Architecture of Montreal.* [Film]. 2018.

[9] J. Kavanagh, Director, *Documentary On Habitat 67 in Montreal.* [Film]. 2012.

[10] "Karamba3D," [Online]. Available: https://www.karamba3d.com/. [Accessed 10 May 2019].

[11] "DIVA," Solemma LLC, [Online]. Available: http://solemma.net. [Accessed May 2018].

[12] A. Khodadadi, "Programmatic Design Methods in Architecture (GA+TRIZ Solution Search Method), Ph.D. thesis," University of Michigan, Ann Arbor, 2019.

[13] V. Souchkov, "Accelaration Innovation with TRIZ," 1997.

[14] W. Eversheim, "TRIZ Methodology," in *Innovation Management for Technical Products: Systematic and Integrated Product Development and Production Planning*, Berlin Heidelberg, Springer Verlag, 2009, pp. 135-153.

[15] M. A. Orloff, Inventive Thinking through TRIZ, A Practical Guide, 2nd ed., Springer, 2006.

[16] G. Altshuller, The Innovation Algorithm: TRIZ, Systematic Innovation and Technical Creativity, Technical Innovation Center, 1999.

[17] G. Altshuller, L. Shulyak and S. Rodman, 40 Principles: TRIZ Keys to Innovation, 2nd ed., Technical Innovation Center, Inc., 2005.

[18] F. Mills, "Top 5: The World's Tallest Timber Buildings," B1M, 4 October 2017. [Online]. Available: https://www.theb1m.com/video/top-5-the-world-s-tallest-timber-buildings. [Accessed 25 March 2019].

[19] T. A. Schuler, "Dalston Works, the Largest CLT Building in the World," *Architect,* 9 October 2018.

[20] "Cecobois Centre d'expertise sur la construction commerciale en bois," [Online]. Available: https://cecobois.com/publications_documents/CECO-11410_Etude_Cas_Origine_paysage_Ang_WEB.pdf. [Accessed 29 March 2019].

[21] "Arbora," Nordic Strcutures, [Online]. Available: https://www.nordic.ca/en/projects/structures/arbora. [Accessed 29 March 2019].

[22] "Nordic X-LAM Cross-Laminated Timber (CLT)," Nordic Structures, 2019. [Online]. Available: https://www.nordic.ca/en/products/nordic-x-lam-cross-laminated-timber-clt. [Accessed 15 March 2019].

[23] P. von Buelow, "ParaGen: Performative Exploration of generative systems," *Journal of the International Association for Shell and Spatial Structures,* vol. 53, no. 4, pp. 271-284, 2012.

[24] A. Khodadadi, "GA-Based Design Exploration of a House: An Interactive Computational Approach," *The International Journal of Design Management and Professional Practice,* vol. 11, no. 3, pp. 13-25, 2017.

[25] SEI/ASCE-7-02 : Minimum Design Loads and Associated Criteria for Buildings and Other Structures, American Society of Civil Engineers, 2013.

[26] "Lighting Levels Guidelines and Definitions," [Online]. Available: http://www.illumenate.com/lightlevels.htm. [Accessed 2 April 2019].

Proceedings of the IASS Annual Symposium 2019 – Structural Membranes 2019
Form and Force
7 – 10 October 2019, Barcelona, Spain
C. Lázaro, K.-U. Bletzinger, E. Oñate (eds.)

Finnish Fins: a novel approach to short-span bridges by the use of stiffening fins

Juan Manuel GARCÍA-GUERRERO *, Gerhard FINK[a], Günther H. FILZ[b]

* Department of Civil Engineering, Universidad Politécnica de Cartagena (UPCT)
Paseo Alfonso XIII 52, 30203, Cartagena, Spain
jm.guerrero@upct.es

[a] Department of Civil Engineering, Aalto University, Finland
[b] Aalto University, ENG | Department of Civil Engineering ° ARTS | Department of Architecture, Finland

Abstract

Using wood as building material has long tradition in many countries, and it is deeply rooted in Finnish culture. The city of Kouvola (Finland) is about to realize a high quality, recreational route for pedestrians and cyclists. In order to improve the functional connections and the recreational activities on the Kymi riverfront approximately a dozen of wooden bridges in a variety of spans in the range of 6 to 10 m, but with the aim to create a "family" of bridges sharing common design aspects. This paper presents an approach for one of the above-mentioned, bridges, where fin-like stiffeners are utilized for stiffening the deck, as form-defining elements for the planar or elastically bent and therefore arched deck, or for other functions destinated to pedestrians as railings, seats, etc. Numerical investigations have been carried out in order to analyze the influence of different parameter on the structural behavior of the bridge, in order to obtain alternatives, different from a classic simple supported deck, that combines aesthetics, sustainability and ease of construction.

Keywords: Timber bridges, conceptual architectural and structural design, bridge engineering, timber shells, bridge aesthetics, parametric design.

1. Introduction

Wood has been used for building since antique in a lot of countries, and specially in Finland, where it is very common in several types of construction. The Finnish tradition of wooden building comprises from the primordial sauna and small houses, to the development of wooden churches and towns, and nowadays to large span structures and multi-story building (see e.g. Norri [1] or Keskisalo [2]). Today the presence of a highly developed Finnish timber industry paired with a strong commitment to sustainability provide the basis for advanced solutions, both structurally and architecturally.

The city of Kouvola is about to realize a recreational route for pedestrians and cyclists. In order to improve the functional connections and the recreational activities on the Kymi riverfront wooden bridges in a variety of spans, most of them in the range of 6 to 10 m are planned to be realized. Even though they will have different structural configurations, they will create a "family" of bridges, sharing common design aspects.

This paper presents a novel approach for one of the above-mentioned, bridges: 6 m span and approximately 1 m in width, where fin-like stiffeners are utilized for three different purposes. Firstly, a set of non-continuous, vertical timber fins is stiffening the deck of a bridge. Secondly, the fins are form-defining elements for the planar or elastically bent and therefore arched deck. Thirdly, the fins will function as railings, seats, etc.

Copyright © 2019 by Juan Manuel GARCÍA-GUERRERO, Gerhard FINK and Günther H. FILZ
Published by the International Association for Shell and Spatial Structures (IASS) with permission.

The general approach and hypothesis are based on the idea that a slender deck of a bridge (or any other structure) can be stiffened by one or more fins. Vice versa, fins can contribute to decrease the thickness and therefore the self-weight of the respective deck. We might think of a traditional wind-surfboard, where a fin can be plugged in. Of course, the fin has no structural meaning in this example but serves as an illustrative and association. In the context of our research, the starting point has been the design for relatively short span bridges made from wood, and mostly thought to be in a natural environment, which might be difficult to access. Therefore, a lightweight, possibly kit-of-parts and environmentally friendly approach askes for this sort of solutions.

From a design and architectural point of view, slender, lightweight solutions are aesthetically and sustainability-wise most interesting. Furthermore, the possibility of dealing with concepts that allow for modular, planar or arched versions, and which are combining structural, spatial and functional requirements seem to offer a huge variety of solutions and combinations. The advantages of such solutions can range from the ease of transport, to the ease of installation, to the flexibility of offered features, to the idea of nearly zero carbon footprint after the life-span of a timber-only structure.

Above-mentioned fins can basically be arranged in all sorts of quantity and pattern, as well as on the top or the bottom side or on both sides of the deck. The number, position and orientation are subject to structural requirements, but also to functional desires. Such functional features can be seating, railing, guiding and information systems and much more. In this sense, reasonable heights for the fins could be in the range of 25 cm for guiding purposes, in the range of 35 to 50 cm for seating and in the range of 100 cm if railing is needed. Therefore, it is easy to understand that the fins´ shape is influenced not only by structural needs, even though these will be the most defining and guiding parameters.

Numerical investigations are carried out in order to analyze the influence of several parameter on the structural behavior of the bridge. Among others (a) the position and orientation of the fins, (b) the overlapping distance between fins, and (c) the geometric characteristics of the fins and the deck have been investigated. Figure 1 illustrates possible realizations of the bridge concept.

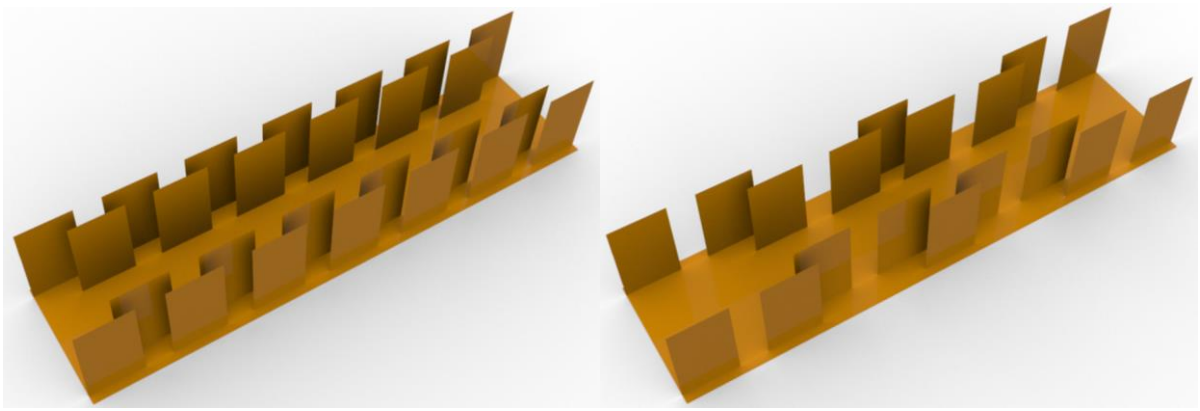


Figure 1: Simple examples of timber bridges stiffened by fins (left, regular pattern, right, irregular pattern).

2. FEM model

The main objective of this study is the investigation of the influence of the position and the geometric characteristics of the fins by using a parametric design approach. For this purpose a simplified numerical model has been selected (see limitations of the FEM).

All bridges presented in this study are composed from a straight deck stiffened by vertical planar fins. The springing points of the deck are pinned, so bridges can be globally considered as simple supported beams. The applied load is limited to pedestrian loads. The bridge is loaded with a vertically, uniformly distributed load of 5 kN/m^2, which corresponds to the pedestrian load model LM-4 defined in EC-1 [3].

In order to investigate and discuss the influence of the dimensions and allocation of fins, reference dimensions have been selected as follows: The span of the bridge L = 6 m, the loaded width of the deck w = 1.5 m, and the thickness of the deck and the fins t = 50 mm. All members are assumed to be Kerto LVL-Q panels, the mechanical properties of the wood are summarized in Table1.

Table 1: Mechanical properties of the reference bridge.

Properties			Unit
Modulus of elasticity Parallel to grain	$E_{0,mean}$	10500	MPa
Modulus of elasticity Perpendicular to grain, edgewise	$E_{90,edge,mean}$	2400	MPa
Modulus of elasticity Perpendicular to grain, flatwise	$E_{90,flat,mean}$	130	MPa
Density	ρ	600	kg/m^3

All the internal forces and deflections shown in this paper have been obtained from FEM models run in SAP2000 (see Computers and Structures, Inc. [4]) The studies carried out are a way to explore the global behavior and some tendencies in the different studies carried out for the paper. As mentioned, the numerical model used here is simplified. The structural analysis of a real bridge design will require a more detailed analysis. The most relevant limitations have been the following:

- The FEM model has been modeled using shell-thin elements, so shear deformation is not considered in the studies. Regarding the mesh size, the maximum size of the finite elements is 0.1 x 0.1 m^2, which is enough to get accurate results considering the size of the bridge.
- The fins and the deck are fully connected, thus, relative movement between fins and deck are not considered. In future studies this connection will be modelized taking into account a possible relative displacement and consequently a reduction of the effectiveness of the fins.
- The transversal deflection is discounted (considering an infinite modulus of elasticity in the transversal direction). Accordingly, only the position of the fins in the main direction of the bridge become relevant. This simplification effects leads to an underestimation of the deck deflection and has to be taken into account for the interpretation of the results of the overlapping length.
- The entire analysis is performed based on the mean properties presented in Table 1, without taking into account modification factors. Thus, the actual deflection will be underestimated.

3. Parameter study

Using the numerical model described in Section 2, a parameter study has been performed. Three different investigations have been carried out so far:

- Fin length
- Fin position
- Number of fins

The investigations are performed for three different fin heights (H_F): H_F = 25 cm (guiding purposes), H_F = 45 cm (seating), and H_F = 100 cm (railing).

The internal forces and deflections are obtained from FEM models run in SAP2000 and postprocessed in Matlab (see The MathWorks Inc. [5]). The geometry for the different studies done in this paper has been modeled and parametrized with Rhinoceros and Grasshopper (see [6]).

The deflection is identified at the middle span (*L/2*) where appear the maximum deflection for a simple supported beam. Stresses have not been considered since they remain low for all the cases considered.

3.1. Fins length

In this case the 6 m span of the reference bridge is stiffened by two fins located at the outmost bridge edges (see Figure 2, left). The parametric study consists on modifying the length of fins (L_F) from 0.1 to 6 m.

The results are illustrated in Figure 2 (right). As expected, the deflection decreases with increasing fin length, and increasing fin height. For short fins $L_F < 3$ m the middle part of the bridge (area with the highest bending stresses) the deck is not strengthen by fins, accordingly, the deflections are significantly larger. If the fin length become larger $L_F > 3$ m they are overlapping in the middle of the bridge and the deflection is decreasing.

As it can be seen in Figure 2 (right), the deflection decreases when the length of the fins increases. It is assumed that for timber bridges, maximum deflection is in a range between $\delta_D = L/200$ and $\delta_D = L/400$ for pedestrian loads (see EC-5 [7]). For easier visibility of the presented outcomes the deflection limit $\delta_D = L/300 = 0.02$ m is illustrated.

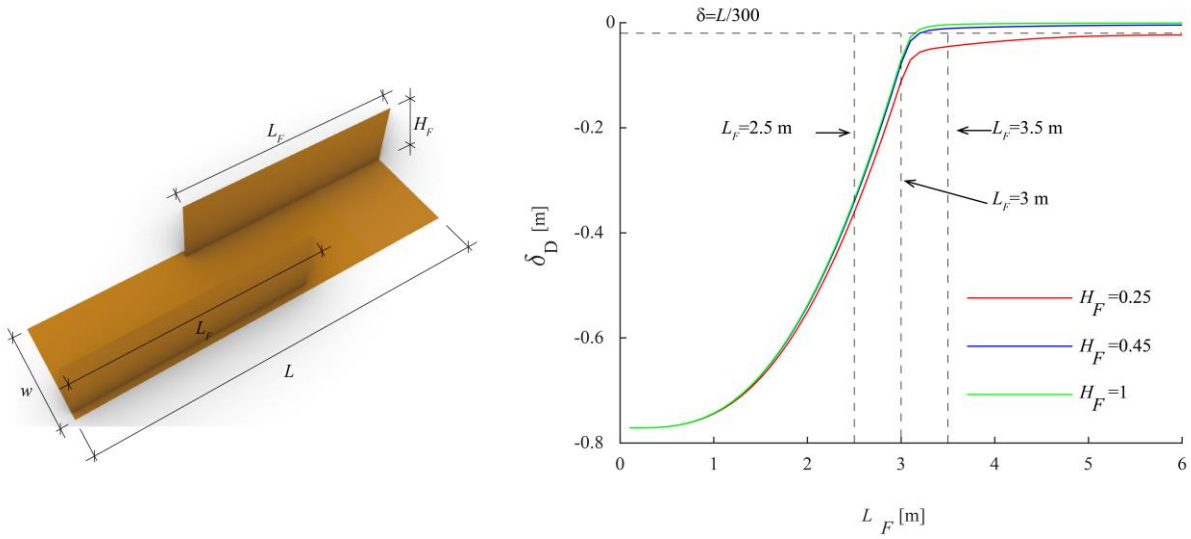


Figure 2: Timber bridge with variable fin length. (left) Schematic illustration, (right) vertical deflection for different fin length and fin heights.

3.2. Fins position

The analysis carried out in this point stiffen the 6 m span of the reference bridge with two fins (one in each edge). The parametric study keep constant the length of the fins and modified only their positions, varying the length of the gap between the fins end and the deck end (L_G). The length of the fins (L_F) is 2.5, 3.0 and 3.5 m, in order to compare with the results of the previous analysis (see Figure 2, right).

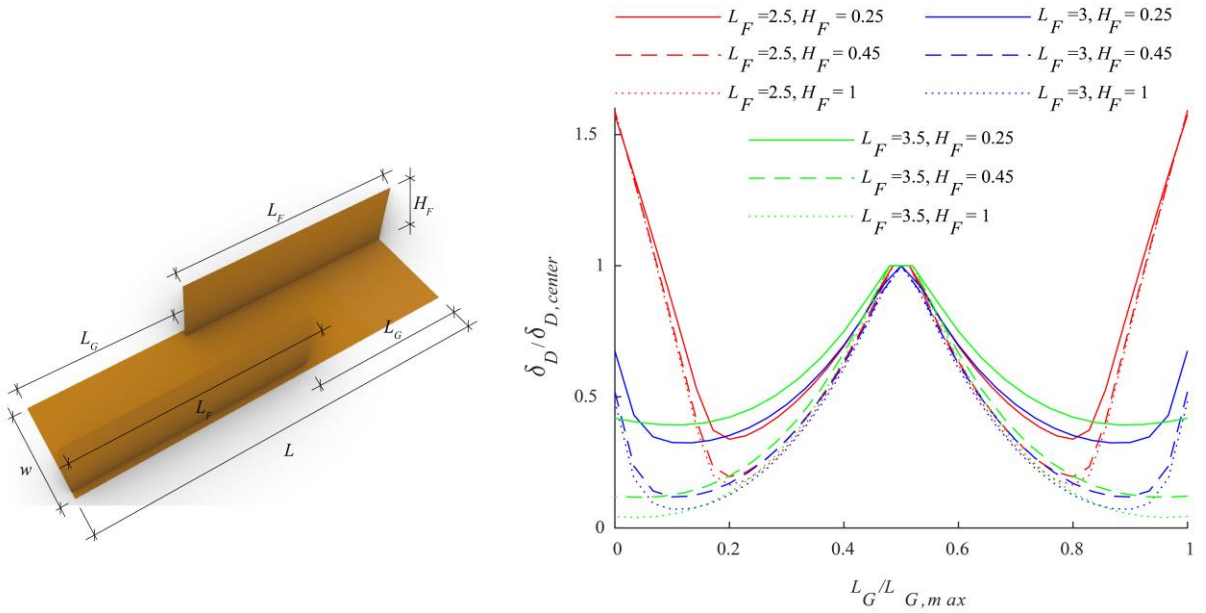


Figure 3: Timber bridge with fins of fixed length and variable position. (left) Schematic illustration, (right) vertical deflection for different length of the gap.

Figure 3 shows the deflection relative to the deflection for centered allocated fins $\delta_{D,center}$ (both fins are located in the center of the deck). The x-axis represents the relative gap L_G to the maximum gap $L_{G,max}$. The maximum gaps are $L_{G,\,2.5} = 3.5$, $L_{G,3.0} = 3.0$ and $L_{G,3.5} = 2.5$ m for the specific fin heights, respectively. As can be seen in Figure 3, maximum deflections occur when the fins are situated at the middle of the bridge or at the ends (for shorter fins). The smallest deflections appear when fins are located in intermediates positions, i.e., between the end of the bridge and the middle span. This position depends on the length of the fins, and only on the height of the fins, if it is large enough compared to the deck thickness. For instance, if $L_F = 2.5$, the minimum deflections occur when the gap is 20% of the maximum gap, for all three fins. Of course, higher fins reduce deflection, but the best position will be always the same for a fixed length of the fins. The graph for relative deflections showed in Figure 3 is symmetric since the fins are displaced to a final state which is similar to the first position they were.

3.3. Variable numbers of fins

This study analyzes the same bridge used in the previous studies, but in this case the number of fins n is variable. In each edge of the bridge there are two lines of fins (external lines an internal lines). The internal lines fill the gaps between the fins situated in the external lines (see Figure 4, left).

The total length of all fins is assumed to be constant (16.8 m), independent from the number of fins n. on. Accordingly, the individual fin length varies from $L_F = 2.8$ m for $n = 6$ (2 fins in each external line) to $L_F = 0.76$ m for $n = 22$ (6 fins in each external line). With an increasing number of fins n the overlapping length between two adjacent fins become smaller.

In Figure 4, absolute deflections δ_D are divided by the minimum deflection $\delta_{D,min}$. The maximum length of overlapping occurs when the number of fins is minimum, i.e., in this study $n = 6$ (2 fins in each external line) whereas the minimum value of overlapping take place for $n = 22$ (6 fins in each external line). As shown in Figure 4, the deflection is higher when the overlapping is lower, i.e., when the number of plates is higher.

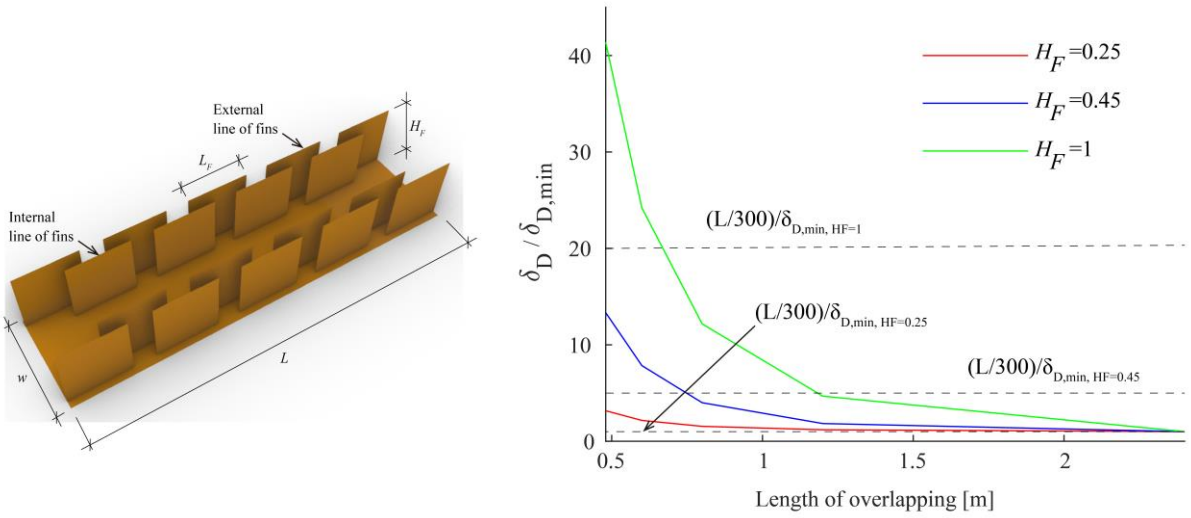


Figure 4: Timber bridge with variable number of fins. (left) Scheme illustration, (right) vertical deflection for different length of overlapping.

4. Conclusion and outlook

This paper presents a novel approach for a short span bridge where fin-like stiffeners are utilized for stiffening the deck, and simultaneously can be used for other purposes such as railings, seats, etc. The idea is driven by the aim of a slender bridge deck, as they are aesthetically and sustainability-wise most interesting.

Numerical investigations are carried out in order to analyze the influence of different parameter on the structural behavior of the bridge. Since the fins should have other than only structural functions the following fin heights were investigated: 25 cm for guiding purposes, 45 cm for seating purposes, and 100 cm for railings. The numerical investigations contain, among others, the position and orientation and geometric characteristics of the fins.

The presented project on the fin-like stiffeners is ongoing and further future studies and improvements are needed, among others:

- The FEM model has to be improved, in particular regarding the limitations described in Section 2.
- The fins orientations different from the longitudinal axis of the bridge (rotated fins) will be investigated in order to analyses the effect on the deflections.
- The application of fins as form-defining elements in order to produce curved shapes, like arched decks.
- Experimental investigations should be carried out in order to validate the numerical investigations.
- Investigation of the long-term behavior of the fin-like stiffeners.

Acknowledgements

The first author wishes to thank the Universidad Politécnica de Cartagena (UPCT, Spain) for the funding provided, through the research project 2007_2420, directed by Dr. Juan José Jorquera-Lucerga. In addition, the first author wishes to thank the Seneca Foundation (Murcia Region, Spain), for the funding

received through a research scholarship (FPI), which allowed for a 4-month research stay at Aalto University, hosted by Dr. Günther H. Filz, Professor of Structures and Architecture.

References

[1] M.-R. Norri, *Timber Construction in Finland*, Museum of Finnish Architecture and Finnish Timber Council, 1996.

[2] M. Keskisalo, "Use of tension rods in wood construction – 14 storeys with laminated veneer lumber as shear walls: Lighthouse Joensuu" in *Internationales Holzbau-Forum IHF 2018*, Garmisch-Partenkirchen, Germany, December 6-7, 2018.

[3] European Committee for Standardization, *Eurocode 1, Actions on structures. Part 2: Traffic loads on bridges*. Brussels, 2003.

[4] Computers and Structures, Inc., *Analysis Reference Manual for SAP2000® v 16*. 2013.

[5] The MathWorks Inc., *Analysis Reference Manual for Matlab R2014*. 2014.

[6] Robert McNeel & Associates, *Rhinoceros 5 for Windows, User's Guide*. 2016.

[7] European Committee for Standardization, *Eurocode 5, Design of timber structures. Part 2: Bridges*. Brussels, 2004.

Proceedings of the IASS Annual Symposium 2019 – Structural Membranes 2019
Form and Force
7 – 10 October 2019, Barcelona, Spain
C. Lázaro, K.-U. Bletzinger, E. Oñate (eds.)

Relationship between bending performance and chip size of strand board made from reed

Takuo NAGAI*

*Lecturer, the University of Shiga Prefecture
2500, Hassakacho, Hikone-city, Shiga, Japan
nagaitakuo@gmail.com / nagai@eurk.jp

Abstract

In this article, we report the development of Reed Strand Board (RSB), which is a strand board made from reed. Recently, reed is little utilized with the decline of reed industries in Japan. The aim of this study is to develop a new effective use of reed. However, the reed in raw state has large variations in strength and dimensions. Therefore it is very difficult to use as a structural material despite having similar tensile strength to wood and bamboo. For the purpose of eliminating the variations of strength and dimensions of the material, a strand board is developed in which reeds are finely cut and chipped and hot pressed with an adhesive. In this paper, we investigate the relationship between the size of reed chip and the bending properties of the board.

Keywords: composite materials, strand board, reed, bending strength, bending modulus

1. Introduction

"Nishi-no-ko Lake" (Western Lake) located in Omihachiman-City, Shiga Prefecture, has the largest area among the endorheic lakes of "Lake Biwa", and has vast reedbeds that are dispersed over the lakefront. In the past, reed has been a valuable resource which supported daily necessities and local industries, marsh-reed screen, reed roofing, etc. However, as such lifestyle and industry has recently declined, the use of reed has greatly diminished. In the case of the Nishi-no-ko Lake, unmanaged reed has grown to the point to whereby the landscape of the lake is significantly impacted, and there are concerns that unattended field expansion could deteriorate and pollute water quality through eutrophication.

A solution of structural applying to this problem can be a sustainable utilization of reed. For this purpose, we have tried to design temporary pavilions [1], [2] using large quantities of reed and held an exhibition to demonstrate construction possibilities as shown in Figure 1.



Figure 1: Reed pavilions [1] (from left to right: Reed Dome 2016, Reed Field 2017, Reed Cocoon 2018)

In these constructions, the reeds were not processed at all and used in raw condition. Although, the reed in raw state has high average tensile strength as shown in the next section, the variation is large.

Copyright © 2019 by Takuo NAGAI
Published by the International Association for Shell and Spatial Structures (IASS) with permission.

Moreover, the dimensions also vary widely among individuals, and it is not easy to use as a structural material in raw state.

For the purpose of eliminating variations in strength and dimensions of reeds, we develop "Reed Strand Board" (RSB) in which reeds are finely cut and chipped and formed together with an adhesive by hot pressing. The mechanical properties, appearance, touch, etc. of the strand board are greatly affected by the manufacturing method. There have been reported some trials. Hermawan *et al.* [3] reported a research to make strand board utilizing construction waste. In recent years, researches to evaluate mechanical properties of Oriented Strand Board (OSB) more accurately (Jin *et al.* [4], Wang *et al.* [5]) are also being conducted.

Since wood waste and scraps can be used as chips for strand boards, it is effective to develop methods for stabilizing strand board performance from the viewpoint of ecology and resource conservation as well. In this paper, with the aim of using reed as a structural material, a basic research on RSB is conducted focusing on the relationship between reed chip size and bending performance.

2. Mechanical properties of reed

In this section, basic characteristics such as dimensions and tensile strength of reed (scientific name: *Phragmites Australis*) are shown. Management of reedbed is generally conducted in a one-year cycle. The reed that grows from spring to autumn is harvested in winter and dried for several months before using later in that year. The reeds used in this research were all harvested one year after germination and stored for about half a year in an indoor warehouse.

Using 217 standing trees of reed, the diameter, thickness, and weight per meter of length were measured by the method shown in Figure 2. In addition, 10 individuals were extracted from each of Sections 1 and 2 within 2 m from the root on the root side, and tensile tests were performed.

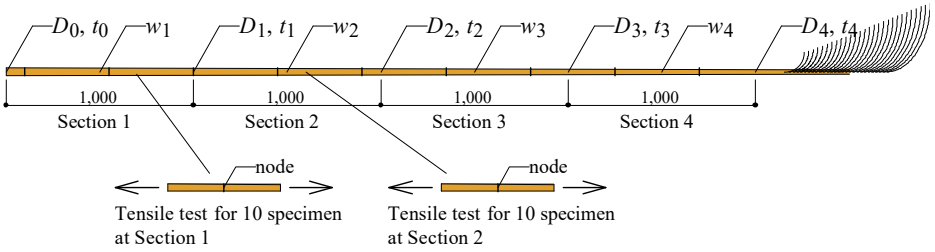


Figure 2: Sampling method of test specimen and measurement items

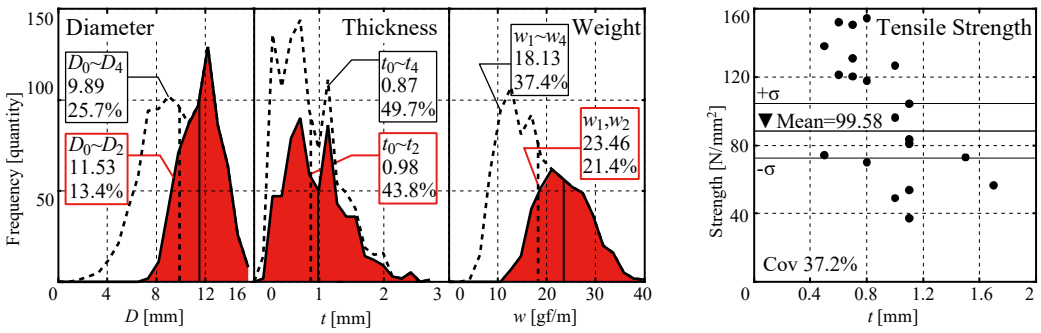


Figure 3: Distribution of measured values (left), scatter plot of tensile strength (right) [2]

The distributions of each value are shown on the left side of Figure 3. The solid line represents the distribution of measured values within 2 m from the root (sections 1 to 2, shaded portions in red), and the dotted line represents the measured values within 4 m from the root (sections 1 to 4). The average (vertical line) and the coefficient of variation (%) are shown in the figure. The diameter and weight

decrease in average value from the root of the reed to the tip, but the stem thickness changes little with the location and the distribution is similar. The average tensile strength shown on the right side of the figure is about 100 N/mm^2, which is equivalent to wood (cedar, cypress) or bamboo generally used in Japan. Tensile failure occurs at the node on the stem. Also, a negative correlation is observed between tensile strength and stem thickness.

3. Manufacturing RSB for test trial

3.1. Manufacturing procedure

The basic preparation procedure of RSB is the same as that of commercially available OSB. Figure 4 shows a procedure of RSB for this test trial. First, the well-naturally-dried reeds are finely crushed using a chipper. Next, the chips are stirred while spraying an adhesive with a spray gun. The adhesive is an aqueous polymer-isocyanate adhesive. This is a kind of thermosetting resin adhesive and is widely used in Japan for the production of laminated wood and CLT. It is certified that the emission of formaldehyde after curing is extremely low, and there is no restriction on the place of use by JIS standard. After thoroughly stirring the reed chips and the adhesive, they are spread in a rectangular mold, and the pressing plates of the hot press are brought into a state of 150 to 200 degrees Celsius, and pressure is applied so as to achieve a target thickness. The RSB in this article is produced with the aim of achieving a specific gravity of about 0.7 after reference to a commercially available OSB. The thickness of the RSB is 10 mm, and the pressure required for that purpose is about 40 to 50 Mpa. The thickness is controlled by a steel plate spacer. The period of pressure application is 6 minutes.



Figure 4: Manufacturing procedure of RSB

Table 1: Parameters of RSB specimen

Name	Target chip Length (mm)	Thickness (mm)	Board size (mm)	Weight (g)	Specific gravity	Adhesive weight ratio (%)
S1	30	10	286 × 289	603.0	0.730	5.571
S2	30	10	275 × 290	556.9	0.698	5.571
S3	30	10	276 × 282	596.6	0.767	5.521
S4	30	10	273 × 282	542.8	0.705	5.521
S5	30	10	279 × 288	646.1	0.804	5.252
S6	30	10	273 × 273	530.4	0.712	5.252
S7	30	10	275 × 285	543.5	0.693	5.169
S8	30	10	275 × 277	542.6	0.712	5.169
L1	70	10	280 × 282	557.9	0.707	5.571
L2	70	10	287 × 287	582.1	0.707	5.571
L3	70	10	265 × 269	526.1	0.738	5.123
L4	70	10	274 × 276	556.4	0.736	5.123
L5	70	10	273 × 273	580.7	0.779	5.368
L6	70	10	278 × 292	590.4	0.727	5.368
L7	70	10	254 × 274	496.7	0.714	5.532
L8	70	10	278 × 278	564.9	0.731	5.532

3.2. Configuration of reed chip in RSB

For each RSB specimen, we investigate the configuration of reed chips. The items are the size (length, width) and angle of reed chips on both surfaces of the board. In the measurement, the average value and the coefficient of variation of each item are calculated over the reed chips randomly extracted from each surface of the specimen. The method of sampling is shown in Figure 5. A grid of 6 squares x 6 squares (one square is 20 mm square) is placed on the center of the board surface, and a reed chip at the center of each square (red dot) is selected. In this way, 36 extracted chips were measured.

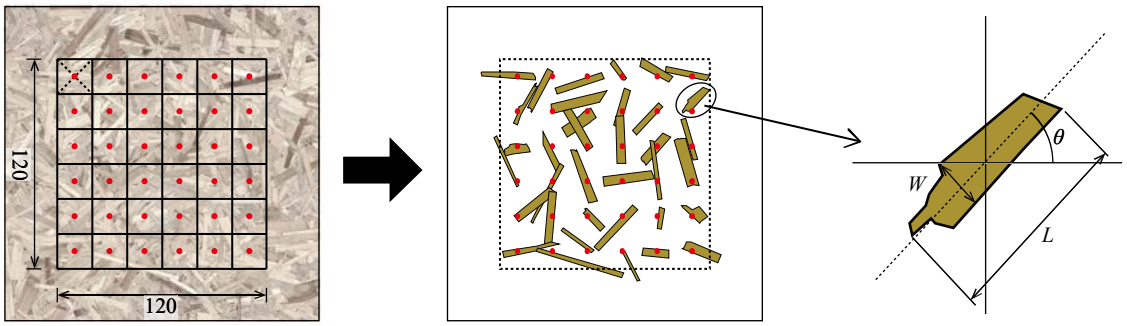


Figure 5: Extraction method of reed chip on board

Table 2 shows the measured values of the chip size and angle of each specimen. The angle was measured in the range of ± 90 degrees, with the span direction of the bending test shown in the next section being zero degree. The mean and variance of the angles are calculated for absolute values. The "Upper surface" and the "Lower surface" of the board are respectively corresponding to each surface at the time of hot pressing.

Table 2: Size and angle of reed chip on board surface (Cov: %)

Name	Upper surface						Lower surface					
	Length (mm)		Width (mm)		Angle (deg.)		Length (mm)		Width (mm)		Angle (deg.)	
	Mean	Cov	Mean	Cov	Mean	Cov	Mean	Cov	Mean	Cov	Mean	Cov
S1	26.8	20.7	4.22	33.5	49.3	55.1	23.6	27.2	4.31	45.7	57.8	39.9
S2	27.5	25.5	5.00	36.8	45.6	53.2	21.4	31.0	3.58	38.6	43.8	57.1
S3	29.6	32.0	5.03	41.5	45.3	55.8	25.4	32.5	3.50	32.6	40.9	58.0
S4	26.2	17.9	4.00	41.7	36.3	64.9	17.1	41.0	3.06	36.9	56.4	35.8
S5	30.1	25.7	4.11	41.3	46.9	49.9	25.3	27.4	4.22	46.4	53.8	43.8
S6	30.1	34.8	4.36	52.7	49.8	42.5	23.1	34.7	4.00	39.1	35.2	61.1
S7	34.0	47.2	4.33	34.8	54.2	49.1	19.6	43.8	4.28	55.5	51.0	51.0
S8	27.0	19.6	4.56	37.1	45.8	51.2	20.7	36.9	3.97	37.3	48.3	52.9
L1	61.5	48.6	5.72	34.6	53.3	42.1	36.1	42.6	4.94	52.4	50.6	43.6
L2	62.5	33.3	5.78	31.9	43.0	57.8	40.0	32.8	4.47	32.3	39.6	63.9
L3	62.9	40.9	5.42	41.4	55.8	40.4	36.0	45.7	3.81	28.9	41.2	68.4
L4	43.2	40.2	4.31	36.2	46.7	53.2	39.5	39.0	4.28	41.1	40.8	56.0
L5	69.1	28.0	4.94	34.7	57.7	35.2	53.1	34.3	5.53	32.6	41.3	64.2
L6	56.4	33.4	5.92	61.4	43.4	53.3	52.3	49.5	5.17	43.9	53.3	44.7
L7	72.2	34.6	5.00	39.4	46.1	53.2	59.2	31.3	5.53	43.4	49.2	39.2
L8	70.1	42.8	5.89	42.7	51.1	49.9	45.5	49.0	4.56	44.6	51.5	48.4

The average chip size on the top surface of "S-series" (S1, S2, …) and "L-series" (L1, L2, …) is sufficiently close to the target value (30, 70 mm) respectively. However, the average chip length is generally smaller on the lower surface than on the upper surface. This is because small pieces are easily accumulated at the bottom when chips are laid in the formwork. The average value of the angles is around 45 degrees for any specimens because the orientation of the chip cannot be controlled in this trial production.

4. Bending test

4.1. Testing method

In order to calculate the bending strength and bending Young's modulus of the RSB specimen, a bending test was conducted by the method shown in Figure 6. The test is a 3-point bending with both ends simple supported, and the span between fulcrums is 210 mm. As described in the previous section, the average chip length is different on the upper and lower surface of the board. Therefore, in order to observe the influence from such condition, the upper surface of each series 1 to 4 is set to loaded surface (the lower surface is in a tensile state), and the lower surface of 5 to 8 is set to loaded surface (the upper surface is in a tensile state).



Figure 6: Bending test condition (left and middle) and failure situation after test of S1 (right)

4.2. Test results and analysis

Figure 7 shows the bending stress-deformation relationship of each test body. The left side of the figure shows the results of "S series", the right shows "L series". The bending stress and deformation are both calculated at the center of the board (loading point).

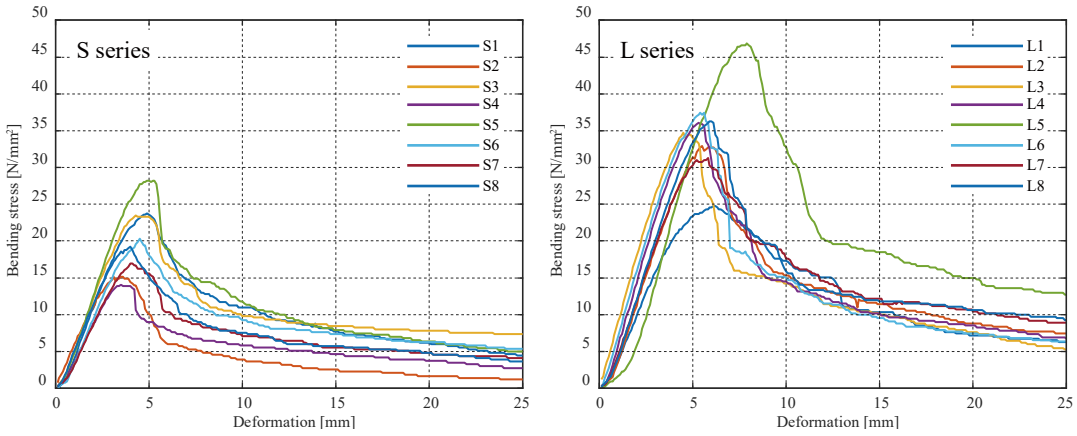


Figure 7: Bending stress-deformation relationship of RSB (left: S series, right: L series)

The main cause of breakage is separation of reed chips on the opposite side of the loading point (center of the span), and almost no tensile breakage of the chip itself occurs. In addition, no particular damage was observed at both end fulcrums. All the specimens show linear behavior up to the maximum load, and the load drops sharply after the maximum load.

Table 3 shows the bending strength and the bending Young's modulus of each specimen. The bending Young's modulus is calculated as secant stiffness connecting a load of 0.4 times the maximum load and the origin. The "L series" is overall superior than the "S series" in both bending strength and bending Young's modulus.

Figure 8 shows the relationship between chip length and bending performance. The bending strength have an evident positive correlation with the chip length. Table 4 shows the correlation coefficients between the chip length on each surface and the bending performance. The values of the bending stress are all 0.7 or more. Therefore, accurate control of the chip length and minimizing the variation is important for stabilizing the bending strength of RSB. However, the bending Young's modulus is not so strongly correlated as the bending strength.

Table 3: Bending strength and bending Young's modulus of RSB

Name	Loaded surface	Bending strength (N/mm^2)	Bending Young's Modulus(N/mm^2)
S1	Upper	23.79	3780.71
S2	Upper	15.12	4233.60
S3	Upper	23.51	4189.21
S4	Upper	14.08	2854.22
S5	Lower	28.23	4485.61
S6	Lower	20.31	3227.28
S7	Lower	16.95	3020.67
S8	Lower	19.24	3901.81
L1	Upper	24.75	3549.51
L2	Upper	32.93	4302.44
L3	Upper	34.71	6583.60
L4	Upper	36.10	5177.06
L5	Lower	46.85	3992.11
L6	Lower	37.39	5942.31
L7	Lower	31.25	4481.99
L8	Lower	36.26	4536.23

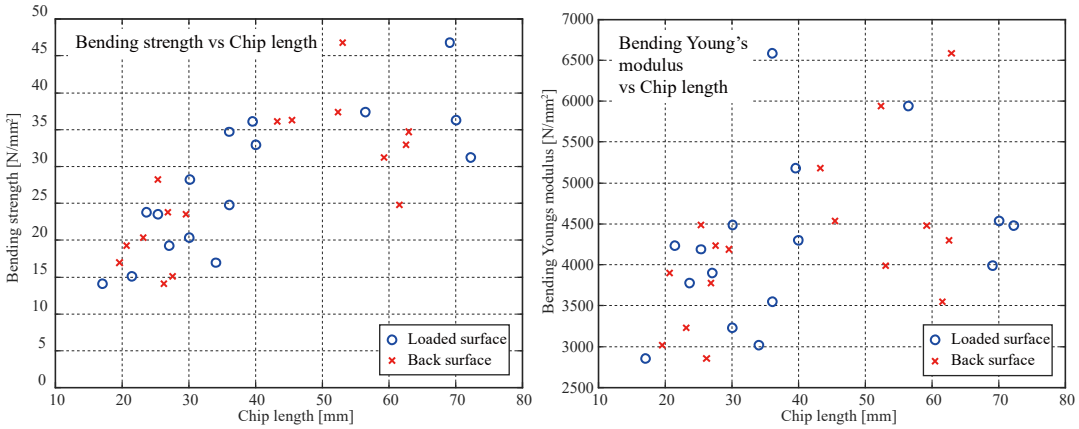


Figure 8: Relationship between bending performance and chip length

Table 4: Correlation coefficient between chip length and bending performance

Surface	Bending strength	Bending Young's modulus
Upper	0.784	0.338
Lower	0.712	0.558

Figure 9 shows the relationship between the bending performance and the angle of the reed chip. In this trial production, the orientation of the chip could not be controlled, so the average angles (absolute values) are concentrated around 45 degrees. In this range, it is difficult to specify the relationship between the chip angle and the bending performance.

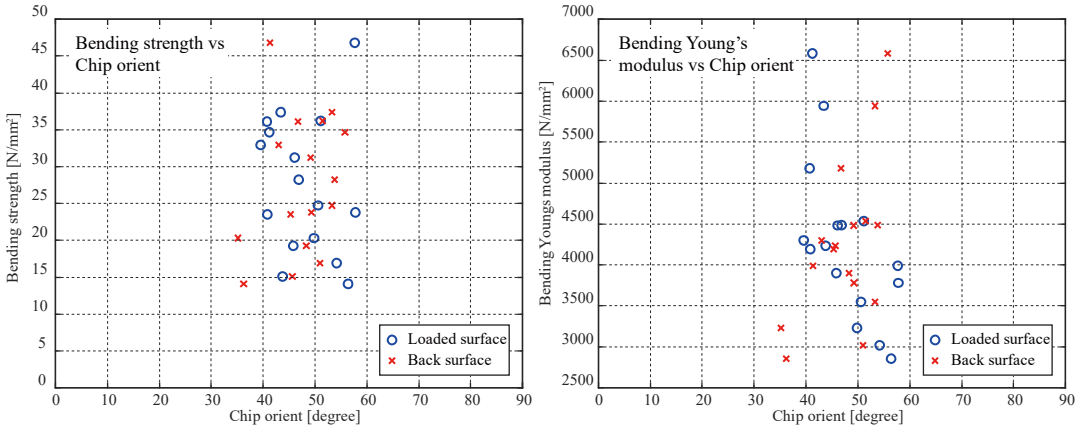


Figure 9: Relationship between bending performance and chip angle

5. Conclusion

In this article, the manufacturing procedure of the strand board using reed and the bending test results were shown. The bending strength of the board have a strong correlation with the chip length, and it was confirmed that a specimen with mean length of 60 mm or more had a sufficient bending strength for structural utilization. Therefore, the development of a method to accurately manage the chip length and minimize the variation is an important challenge to be addressed.

On the other hand, with regard to the bending Young's modulus, the chip length was not so correlated with that. The stiffness might be presumed to have a significant effect on the chip angle. The relation between bending stiffness and chip angle also should be studied in the future.

Acknowledgements

We express great gratitude to Takeyoshi OSADA (CEO, Swood Co., Ltd.) for his technical support and knowledge-giving on strand board, and Akihito MATAURA (Student, The University of Shiga Prefecture) for his many helps in the experimental works. This work is also supported by the Grant-in-Aid for the promotion and enhancement of education and research from The University of Shiga Prefecture (2019).

References

[1] T. Nagai, "Design and construction of temporary pavilion using reed as structural material," in *Recent Innovations in Analysis, Design and Construction of Shell & Spatial Structures: Proceedings of the 12th Asian Pacific Conference on Shell & Spatial Structure (APCS 2018), Penang, Malaysia, October 29-31, 2018,* J. Y. Liew, Mustafasanie M. Y. and K. K. Choong(eds.), 2018. pp. 310-320.

[2] T. Nagai, H. Shirai, T. Matsuoka, "Design and construction of temporary pavilion using reed as structural material," *The AIJ Journal of Technology and Design*, vol. 23, No. 55, pp. 875-880, Oct. 2017. https://doi.org/10.3130/aijt.23.875 (in Japanese)

[3] A. Hermawan, T. Ohuchi, R. Tashima, Y. Murase, "Manufacture of strand board made from construction scrap wood," *Resources, Conservation & Recycling*, vol. 50, Issue 4, pp. 415-426, June 2007. https://doi.org/10.1016/j.resconrec.2006.07.002

[4] B. C. Jin, X. Li, A. Jain, C. González, J. LLorca, S. Nutt, "Optimization of microstructures and mechanical properties of composite oriented strand board from reused prepreg," *Composite Structures*, vol. 174, pp. 389-398, Aug. 2017. https://doi.org/10.1016/j.compstruct.2017.05.002

[5] Zheng. Wang, W. Xie, Y. Lu, H. Li, Zhiheng. Wang, Z. Li, "Dynamic and static testing methods for shear modulus of oriented strand board," *Construction and Building Materials*, vol. 216, pp. 542-551, Aug. 2019. https://doi.org/10.1016/j.conbuildmat.2019.05.004

Proceedings of the IASS Annual Symposium 2019 – Structural Membranes 2019
Form and Force
7 – 10 October 2019, Barcelona, Spain
C. Lázaro, K.-U. Bletzinger, E. Oñate (eds.)

Space truss built with wastes from the sawmill industry

Olivier BAVEREL[a b]* , Tiphaine LE BORGNE[b], Francois ZANINETTI[b], Gerald HIVIN[c],

*olivier.baverel@enpc.fr

a Laboratoire Navier, UMR 8205, Ecole des Ponts, IFSTTAR, CNRS, UPE, Champs-sur-Marne, France
b GSA ENS Architecture de Grenoble, France
c IUT 1 GCCD, Université Grenoble Alpes, France

Abstract

It is well known that wood is difficult to assemble and complex steel system is often used for the joints. The solution proposed in this paper is to limit the use of steel connections by using a specific shape of element to take the shear force, thus linking the top and bottom layers of the space truss that are made of circular logs of small diameter. This proposal is a simpler version of the solution suggested in [5]. The material used for the shear components is waste wood from sawmill when the log is squared, it's mostly composed of bark and sapwood. This part of log is considered as a waste and often used as firewood. This experimentation aims to promote that wood as a structural element in the space truss. The structure was designed by the laboratoire Navier/GSA and ENSAG. It was crafted, erected and tested by the IUT (institute for higher technician). The structure is 6 m by 6 m span and has a height of 0,6 m. The elements that link and brace the top and bottom layer create an hyperboloid that can be simply screwed as the element are tangent to the top circular chord and tangent to the lower circular chord. The structure was tested under symmetrical and asymmetrical loads. The deflections and a detailed observation of the connections during loading was performed using photogrammetry. The behavior of the structure was then compared to the numerical model. Finally, the authors conclude on the economical and environmental aspects of such structures.

Keywords: Architectural geometry, gridshell, hexagonal mesh, free-form surface, rationalization, pavilion

Copyright © 2019 by Olivier BAVEREL, Tiphaine LE BORGNE, François ZANINETTI, Gérald HIVIN
Published by the International Association for Shell and Spatial Structures (IASS) with permission.

1. Introduction

The team of the Navier and GSA lab are working for decades to find structures that reduce the environmental impact of structures [1][2][3][4]. This research propose a new attempt to create structures with a very low environmental impact as it mostly use sawmill industry waste.



Figure 1: view of the structure

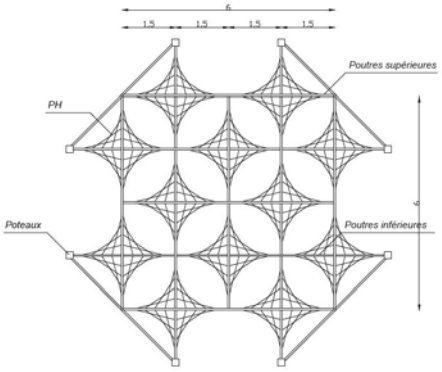


Figure 2 ; Plan view of the configuration

It is well known that wood is difficult to assemble and complex steel system is often used for the joints. The solution proposed in this paper is to limit the use of steel connections by using a specific shape of element to take the shear force, thus linking the top and bottom layers of the space truss that are made of circular logs of small diameter. These logs are usually considered as a waste for the sawmill industry. This proposal is a simpler version of the solution suggested in [5].

The material used for the shear components (in orange on the right of figure 3) is the part of wood which is taken off when the log is squared, it's mostly composed of bark and sapwood. This part of log is considered as a waste and often used as firewood. In our case, it will be cut in two, in order to have two perpendicular sides cut as explained in section 2.

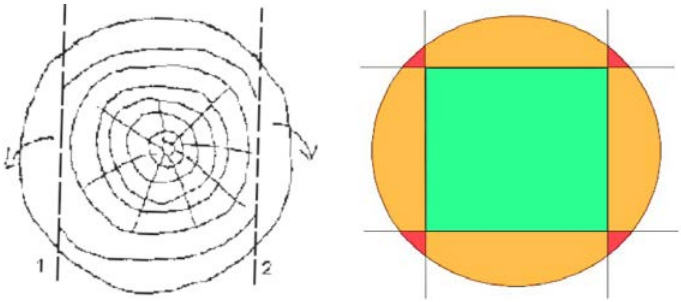


Figure 3: Cutting of the log

Section 2 will explain the different geometrical configurations chosen. It will be based on a hypar to create a space truss. Then the form finding for the connection of the shear element will be detailed, the aim is to link the top and bottom layer. In this section, the morphological potential of these structures will also be discussed. The construction of a prototype is presented in section 3 where the loading test and the comparison with the numerical results are detailed. Finally, the authors conclude on the overall performance of the structure.

2. Formfinding of the structure

The formfinding method shown in this section details how to generate a space truss with the top and bottom layer that could be hypars. The shear elements that link both bottom and top layer will also be hypars and tangent to the logs. An example of such configuration is shown in figure 4.

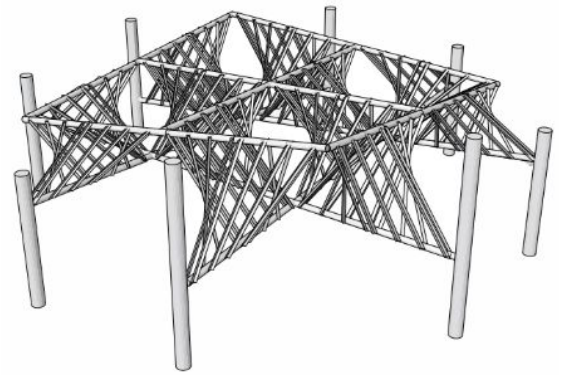


Figure 4 : view of a configuration with top and bottom layer with hypars forms

The raw material used for the hypar is a part of wood mostly composed of bark and sapwood which is not valued. This wood is cut perpendicurlarly to have two flat edges as detailed in the following paragraph.

The first constraint to be taken into account is that beams of the space truss are cylindrical. The wooden element must then be installed tangentially on the beams in order to improve the assembly. They should be cut with a specific angle so that one of the flat sides is tangent to the upper layer while the second side is tangent to the lower layer. If the beams of a layer are connected with a 90 degrees angle, the cut should also be at 90 degrees.

2-1 Modelling methods of a hypar using genetic algorithms

The technique to find the correct position of the shear element that are tangent to the log is to draw circles on the beams of the top and bottom layer. The two circles will be connected by a line (figure 5).

The line must have a right angle with the radius of both circles. This algorithm was implemented and solved with Galapagos. The location of the tangent line to the two circles is found by minimizing the sum of the absolute value of the scalar products between the line and each of the radius to which it is connected. This method is easy to set up and manipulate. However it takes a lot of computing time and gives an approximate position.

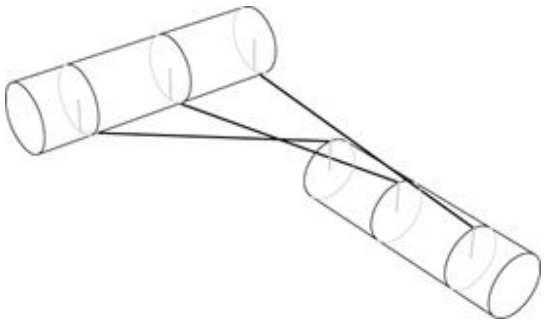


Figure 5: Construction of with the genetic algorithm method

2-2 Modelling methods of a hypar using genetic algorithms

The most accurate method consists in finding the tangent's points positions by a geometric construction. A cylinder of the same diameter (in red in figure 6) as the space truss is drawn passing through the center of the circles at which the hypar must hang. The intersection of this cylinder with the circles makes it possible to draw a line tangent to the two beams at the same time. This method was found by Xavier TELLIER. This is a more accurate but more complex method to implement and requires a large calculation from processor.



Figure 6 Construction of the geometric method

2-3 Morphological potential of the overall structure

The space truss can be transformed in two different ways: by modifying its plane shape or by varying the beams' tilt.

The variation in plane consists of going from an orthogonal grid to a sheared grid (figure 7). However, this variation has the main disadvantage of involving the cutting of the wooden elements at a specific angle for instance in figure 7 the shear element must be cut at an angle of 135 degrees. This would be necessary so that the elements can be tangent to the beams.

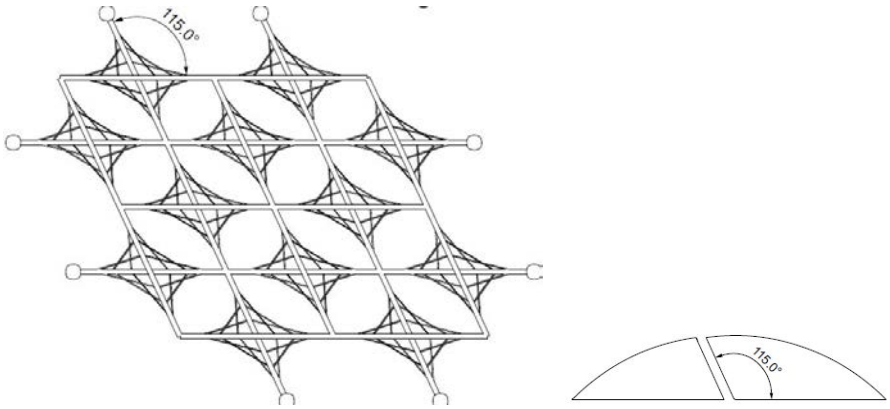


Figure 7: Construction with a shear of the 25 degrees, the shear element should be cut at the same angle

On the other hand, the outcome of plane distortion of the layer has no influence on the cutting of the wooden elements. For this variation, the beams of the two layers are more or less tilted, while keeping the beams completely straight (figure 8) .

The space truss then itself become two hypars linked by hypars. This creates a sense of disorder while maintaining an identical constructive and cutting system for the entire structure. Some prototype were made to prove the accuracy of the algorithm as shown in figure 8.



Figure 8: View of the model with hypar upper and lower layer

3. Prototype :assembling and loading test

3.1 assembling of the prototype

The prototype is 6m by 6m span. First the top layer and lower layer were assembled. The second stage was to create tetrahedra to create and stabilise the space truss as shown in figure 9



Figure 9: First steps of construction

Other diagonals where added, a simple screw was used to connect the diagonal to the top and bottom layers (figure 10).



Figure 10: Different views of the constructed truss

3.2 Loading test

During the loading test some shear elements were added, first the loading was made with one shear element and then 3, 4 and 5. This method allowed the see the improvement of the stiffness of the structure depending on the number of shear component fixed. The loading test was 0,3 KN/m on the bottom layer and 0,35 KN at each node of the bottom layer. The total load was then 75 KN. The structure was loaded with sand bags as shown in figure 11.



Figure 11: Loading of the truss

3.3 Measurement of the deflection

In order to measure the deflection of the structures a photogrammetric technique was used (figure 12). This method is quite simple as it consist of the superposition of the pictures of the structure before and after loading. The measurement of the deflection can then be easily calculated accurately.



Figure 12: technique to measure the deflection

3.4 Comparison with the numerical model

A numerical model was done using Robot structural analysis software. A linear elastic analysis was performed but no eccentricities were taken into account. Figure 13 shows that this eccentricity exist and will give a softer behaviour to the built structure compare to the numerical model. The numerical model assume that the shear element are pinned to the top and bottom layer.

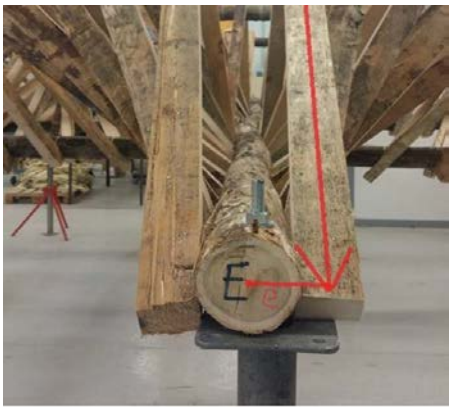


Figure 13: Eccentricities between the log and the shear elements

Number of shear element by hypar	Deflection of the numerical model (mm)	Deflection of the prototype	Weight of the structure (KN)
1	13	22.3	2.27
3	8.5	11.6	2.98

4	7.34	10.2	3.48
5	7.08	8	3.91

Table 1: result from the tests

The result from table 1 show that the numerical model gives as expected lower deflection compare to the real structure. Nevertheless the difference gets lower when the number of shear element increase.

4. Conclusions

The paper presented an original configuration of space truss made out from waste of the sawmill industry. First, different formfinding methods were proposed showing the different possibilities of configuration such as shearing or tilting grid and keeping a simple process to build the configuration. As detailed in the paper the configuration can have top and bottom layer being hypars connected shear elements that are hypars.

A space truss of 6m by 6m span was assembled, tested and compared to an numerical model. The displacements were taken by photogrammetry and the result showed that for hypar made out several shear elements are quite close (around 13%) to the numerical model.

The structure is efficient and cheap to built, the total cost of material was around 12 euros/m2. This is an interesting solution to take the best of the sawmill industry especially when high quality wood is cut such as larch which is also not well suited to be burn in wood stove. The enhance the shear stiffness the hypar could also be continuous like a flat CLT but in this case, it would be 'CLT hypar'.

Acknowledgement

The authors would like to thanks the IUT GCCD of Grenoble Université Alpes, the technicians and the students BASMAISON Alexandre, CATTANEO Léa, LEVET Céline, VERNAY Albin that built and tested the structure.

References

[1] Romain MESNIL, Cyril DOUTHE outhe, Hugo ORTS, Olivier BAVEREL. Isoradial meshes: covering free-form architecture with planar facets *Automation in Construction* November 2017.

[2] Romain MESNIL, Cyril DOUTHE, and Olivier BAVEREL. Fabrication-aware parameterization for the structural optimisation of shell structures. *Engineering Structures*, 2018.

[3] Romain MESNIL, Cyril DOUTHE, Olivier BAVEREL, and Leger Bruno. Morphogenesis of surfaces with planar lines of curvature and application to architectural design. *Automation in Construction*, 2018 .

[4] Romain MESNIL, Cyril DOUTHE, Tristan GOBIN, and Olivier BAVEREL. Form-finding of reciprocal frames with the method of translations. *Automation in Construction*, 2018.

[5] Olivier BAVEREL, Pierre CHALAS, Vincent RICHEFEU, Gerald HIVIN: Proposal for a lowtech wooden space truss, July 2018 Conference: Proceedings of the IASS 2018 *Symposium Creativity in Structural Design*, Boston, Massachusetts, USA.

Proceedings of the IASS Annual Symposium 2019 - Structural Membranes 2019
Form and Force
7-10 October 2019, Barcelona, Spain
C. Lázaro, K.-U. Bletzinger, E. Oñate (eds.)

Sustainable design concepts for short span, timber-only structures

Gerhard FINK[*], **Gengmu RUAN**[a], **Günther H. FILZ**[b]

[*] Department of Civil Engineering, Aalto University, Finland
Rakentajanaukio 4 A, 02150 Espoo, Finland
gerhard.fink@aalto.fi

[a] Department of Civil Engineering, Aalto University, Finland
[b] Aalto University, ENG | Department of Civil Engineering ° ARTS | Department of Architecture, Finland

Abstract

In this study, a novel, low-tech design concept for short span structures is introduced. The structural system is entirely based on wooden products, mainly salvaged material. Individual timber boards with uniform or variable dimensions are connected with hardwood nails to load bearing members. The paper introduces the design concept and explores features and design possibilities ranging from different spans with related thickness of the deck, to integrated seating, signs or railing. The approach is driven by the following three guiding aspects: firstly by the limitation of the possible timber board patterns, which result from the used material; secondly by the assembly process, which aims for the ease of use and its robustness against assembly-errors; thirdly by the arrangement of the nails, which allows for the highest possible grade of flexibility in design and material uses and which respect the aforementioned aspects.

Keywords: Sustainability, timber structure, salvaged material, architecture, low-tech, conceptual design, wood nails, natural trails

1 Introduction

The construction sector is one of the major contributors to environmental burden. In Europe buildings cover about 40% of the total energy consumption and 36% of CO2 emissions [1]. However, the European targets, such as the reduction of the greenhouse gases until 2019 (40% compared to 1990), are ambiguous. This and other targets of the European commission and other institutions indicate the importance of reducing the environmental impacts throughout the entire construction sector. Accordingly, sustainable and more environment-friendly structural concepts and structures are becoming increasingly relevant.
Timber, as a natural grown building material, can play a key role in this process, in particular due to its large potential of reducing CO2 emissions. So far, the full environmental potential of timber has not yet been realised. Currently, the share of re-used and recycled timber is very limited. The same applies for recovery of construction and demolition waste. One example is salvaged timber material from the fabrication process of engineered wood products or from construction processes that is mainly incinerated for energy recovery.

Copyright © 2019 by Gerhard Fink, Gengmu Ruan and Günther H. Filz
Published by the International Association for Shell and Spatial Structures (IASS) with permission.



Figure 1: Salvaged material from a four weeks period from a regional housing company.

In this paper a design concept for short span timber structures using salvaged material connected with wooden fasteners is presented. The most relevant aspects for the design concept are introduced and preliminary results from the experimental investigations are summarized. The paper concludes with an outlook to further investigations and the potential for structures and other applications.

1.1 Salvaged material

Considering the entire construction sector, including strength grading and the fabrication of engineered wood products, a large amount of salvaged timber material can be recognised. Examples for salvaged timber material are:

- Strength grading: Cut-offs or rejection
- Manufacturing process of engineered wood products: Cut-offs
- (Pre-)fabrication process: Cut-offs of timber boards due to e.g. over length
- CNC milling of plate elements: Cut-out of openings (windows, doors, etc)
- Concrete formwork and falsework

The dimensions and quality of the salvaged material varies between the examples above, however, in most cases the material has structural quality. As already mentioned, salvaged wood material is currently mainly incinerated for energy recovery, but the potential is quite large: Figure 1 illustrates the salvaged material of a four week period from a regional housing company. Considering the large timber product industry, e.g. the yearly roundwood consumption of Finnish sawmills is more than 27 million m^3 (2018, [2]), the large environmental potential of using salvaged material become obvious.

2 Application-based design concept

The below presented design concept using salvaged material connected with wooden fasteners might be appropriate for a wide range of applications, but within the framework of this paper the applications are limited to natural trails including short span bridges. Natural trails are widely used in Finland, in particular in wetlands in order to make nature easier and more safely



Figure 2: Example of a natural trail crossing a smaller creek near the Kymi riverfront.

accessible for the society (Figure 2). A large amount of these trails are located in areas with particular attention to the nature, such as natural parks; accordingly, an appropriate place for a timber-only applications. Natural trails are not always, but usually, made from structural timber. The most common approach is to assemble the deck from timber boards that are regularly supported. The distance between the supports (span) depends on the ground (wetland, dryland, river, etc.), the quality of the timber boards used for the deck and the pedestrian traffic. Nevertheless, the span of the deck typically is limited to a range of 1.5 to 4 meters. Even though the span is limited, structural timber is used, that can be also applied to other applications.

As a novel, low-tech design concept for short span structures, our approach is driven by the motivation to create nail-laminated timber decks from salvaged material using wooden nails (Figure 3). In order to achieve this aim the following aspects were considered:
Above-mentioned low-tech design concept is understood as the counterpart to high-tech and refers to an approach, which is developed under the aspects of easy function, easy production, easy service, robustness and easy maintenance (see also Filz [4]).
The proposed concept follows the main principles of nail-laminated timber decks (see e.g. Gutkowski and Williamson [3]). However, the here presented structural system is entirely based on wooden products. From an environmental perspective any use of salvaged material would be beneficial as it would either substitute non-sustainable materials or substitute sustainable materials that can be applied in for other purposes. The used timber is supposed to be salvaged material from regional companies, which guarantees sustainable solutions. So, the wood industry itself serves as a source for the short span load bearing members. Accordingly the available material will come in variable but sufficient quality, and it will vary much in length, and cross-sectional dimension. The variation of the dimensions of timber boards has direct impact on the configuration and resulting patterns of the decks. It is aimed to use the timber boards without further processing, like cutting, milling, or plaining. However, further processing is still possible if needed.
The above-mentioned variety in available material results in irregular patterns. Since the upper deck surface is supposed to be planar (Figure 3), the variation of the board widths can be easily

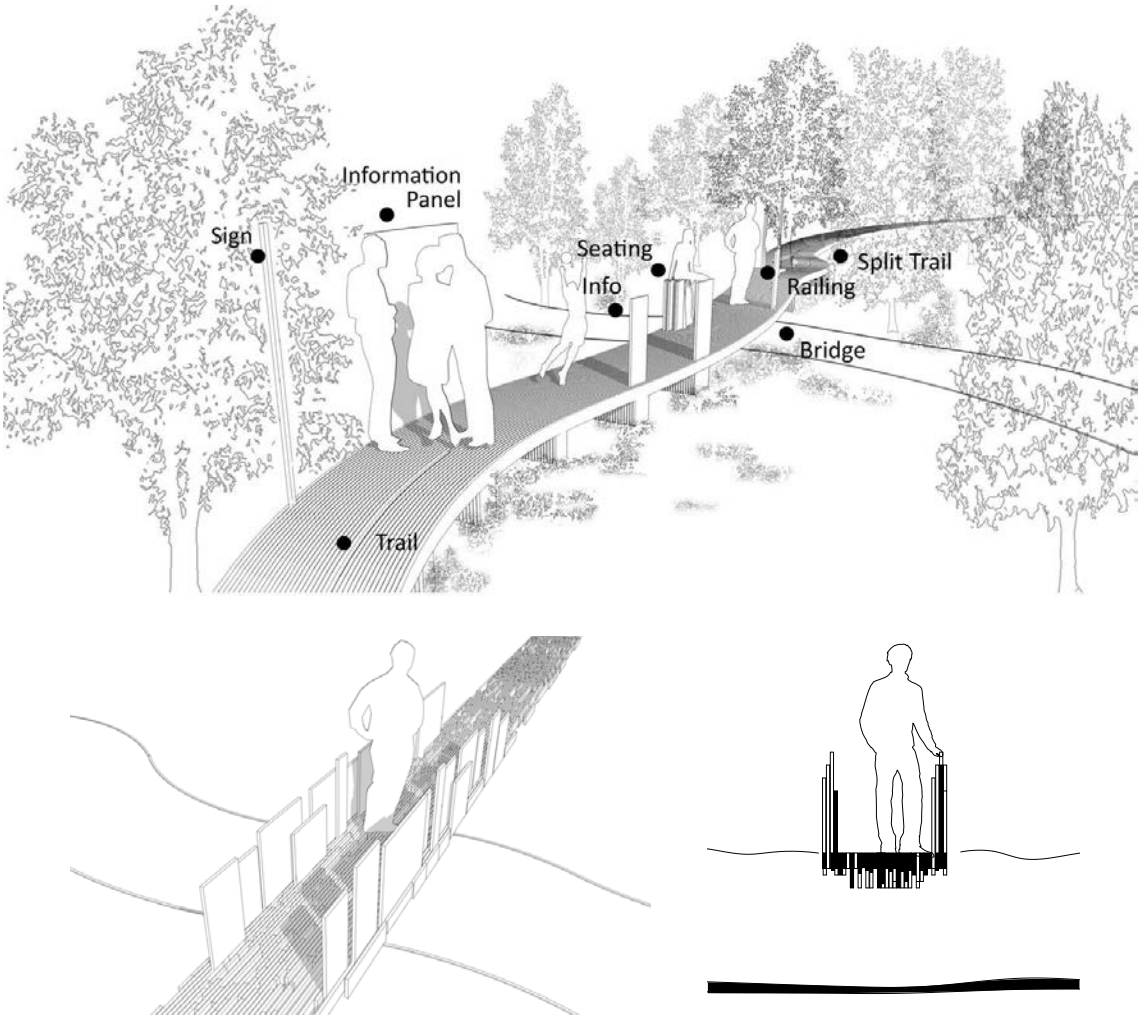


Figure 3: (top) Design concept illustrating a set of possible applications, (bottom, left) railings proposal, (bottom, right) cross-section.

handled by having variable deck thicknesses, and even be advantageously used to increase the cross-sectional height at longer spans. Considering a reduction in self-weight and/or varying board width, the deck-patterns become even more irregular and show a certain percentage of perforation.

One of the novelties of our study, is that the individual timber boards with uniform or variable dimensions are connected with hardwood nails from LignoLoc® to load bearing members. The hardwood nails are fabricated out of compressed beech wood permeated with resin. The resin positively influence the durability and thus allow outdoor applications, however, in the long run, the project is aiming for timber-only structures. The mechanical properties of the wooden nails allows the use of pneumatic nailing devices without pre-drilling. After assembling the wood nails they form a bond with the surrounding timber, it was one of the aims of this project to utilize this effect for the design. Due to the high strength requirement wood nails with a relatively large diameter of 4.7 mm to 5.3 mm are used. The application of nails with large diameter without pre-drilling, result in high splitting forces. Accordingly, particular attention has to be taken on

the minimal board thickness, the distance between the single nails as well as their distance to the edge of the timber board.
The assembly is assumed to happen on site from individual pieces or small prefabricated units. In this regard, the selection of appropriate nail patterns for the connection of boards represents a guiding parameter not only for the stability and the design aspect, but also for the ease of assembly process, and simultaneously for its robustness against assembly-errors. Even though long cut-offs or even full length boards from rejection for example due to warp might be available from sawmills, our approach focused on very short boards with less than one meter length. Depended on the selected nail diameter, the nail patterns are defined by the distance between the single nails as well as their distance to the edge of the timber board. Accordingly, shorter boards are more restrictive for the generation of board patterns and the percentage of perforation.

Referring to above described, systematic analysis and pruning of unwanted design points based on parameters of interest, the design space has been well defined. Its first exploration features design possibilities and functionalities ranging from different spans with related thickness of the deck, to straight and curvilinear path planning in plan and in longitudinal section, to integrated seating, signs or railing, and much more (Figure 3).

3 Experimental investigations

Experimental investigations to realize the connection between adjacent timber boards using hardwood nails have been performed. Due to the variable dimensions of the salvaged material different nail patterns have been investigated. As mentioned above, the project is in conceptual phase and, accordingly, the main purpose for the preliminary experimental investigation is expand the knowledge needed to optimise the design concept and not only to validate the approach. This also explains the limited scope of the experimental work.
Below, a short summary of selected parts from the ongoing, experimental investigations can be found. A comprehensive study based on more intense testing will be presented after finalising the experimental investigations.

3.1 Material and method

The preliminary part of the experimental investigation contains (I) shear tests on single nails and nail groups in order to find suitable nail orientation (Figure 4, left), and (II) bending tests on nails connections to identify appropriate nail pattern (Figure 5).

For the investigation two different types of timber boards been used; the selection has been performed in order to utilize the potential of one regional housing company:
- Cross-sectional dimensions: $w \times t = 123 \times 48$ mm, strength grade: C24
- Cross-sectional dimensions: $w \times t = 100 \times 25$ mm, quality: pl/vl (flat surface/export quality)

Several different board and nail arrangements were investigated. For the specific arrangements, appropriate wooden nails with variable length ($l = 65, 75, 90$ mm) and variable nail diameter ($d = 4.7, 5.3$ mm) have been used.

3.2 Shear tests – Nail orientation

For the shear test three timber boards ($w \times t = 123 \times 48$ mm) are connected with two wooden nails, one nail from each side. In order to utilize the bond of the wooden nails with the surrounding timber, the nails are allocated with variable nail orientation $\alpha = 0, 30, -30°$. The tests

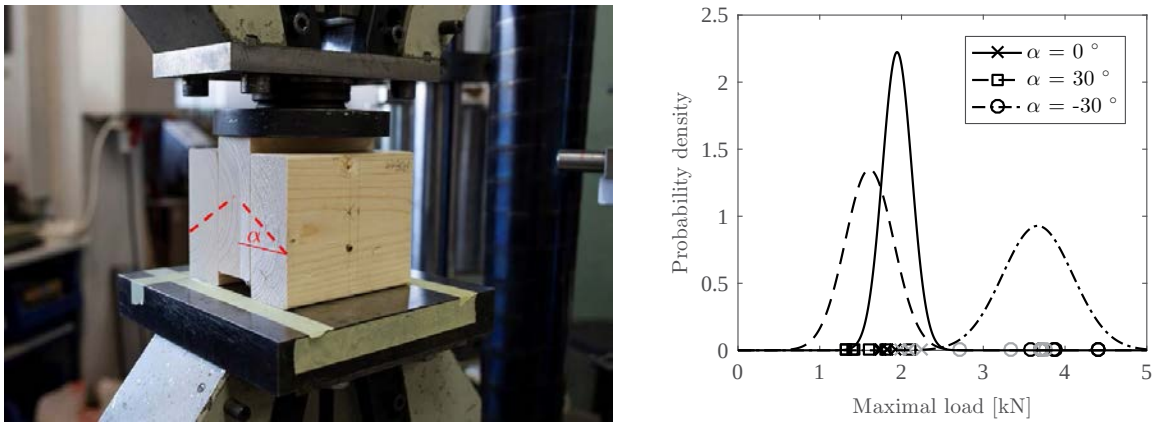


Figure 4: Shear tests: (left) one test sample with $\alpha = 30°$, (right) test results. The black symbols indicate $d = 4.7$ mm and the grey symbols indicate $d = 5.3$ mm

.

were performed with two different nail diameter ($d = 4.7, 5.3$ mm). The results (Figure 4, right) clearly indicate the potential of tensile loaded wood nails ($\alpha = -30°$), whereas the influence of the nail diameter d seems to be small (the black symbols indicate $d = 4.7$ mm and the grey symbols indicate $d = 5.3$ mm). At this point it has to be mentioned that further investigations with larger inclination $\alpha = 45°$ were planned. However, when manufacturing the samples many fabrication errors accrued, mainly due to the smaller edge distance, and accordingly this test series has not been investigated.

3.3 Bending tests – Nail pattern

Bending test have been performed in order to identify appropriate nail pattern. Therefore several different nail pattern were investigated. In Figure 5 two test samples are exemplary illustrated. The left samples shows a connection of three timber boards $t = 25$ mm. The connections contains six nails $l = 75$ mm, $d = 47$ mm (each nail is connected to all three timber boards). The nails are inclined in opposing direction; half of the nails with $\alpha = 30°$ and half of the nails with $\alpha = -30°$.
In the right sample in Figure 5 illustrated a connection of three timber boards $t = 48$ mm. The connections contains two times seven nails $l = 75$ mm, $d = 53$ mm (each nail is connected to two timber boards). The nails are inclined in opposing direction $\alpha = 30°$ and $\alpha = -30°$.
The results from the bending test indicate a large potential for the design approach. However, the tests also indicated some challenges that have to be considered in the design. In particular the splitting force in thin timber boards requires large end distances.

3.4 Further steps

It is planned to fabricate a test bridge as illustrated in Figure 6 and perform bending tests in order to identify the load bearing capacity. Furthermore, the long term behaviour of the nails bridge deck will be planned on a prototype.

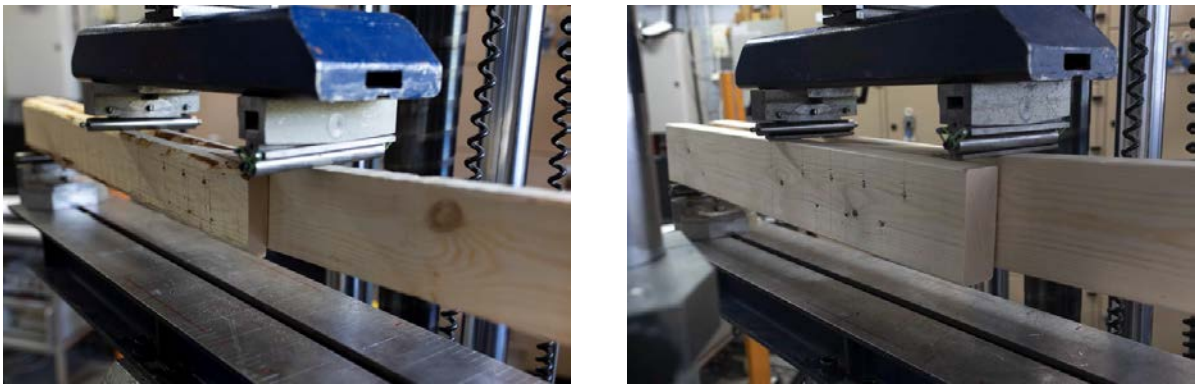


Figure 5: Bending tests: (left) test sample with three $t = 25$ mm timber boards and six inclined nails $\alpha = 30, -30°$; (right) test sample with three $t = 48$ mm timber boards and two times seven inclined nails $\alpha = 30, -30°$.



Figure 6: Bridge deck: (left) possible arrangement of the timber boards to form a the bridge deck; (right) possible application (here the timber boards are not connected with wood nails).

4 Conclusion

In this paper, a novel, low-tech design concept for short span structures is introduced. The approach is driven by the motivation to create nail-laminated timber decks from salvaged material using wooden nails. Salvaged timber material is available in sufficient quality, but variable length, and variable cross-sectional dimension. The variety in available material results in irregular patterns. The upper deck surface is supposed to be planar (Figure 3), the variation of the board widths can be easily handled by having variable deck thicknesses, and even be advantageously used to increase the cross-sectional height at longer spans. Considering a reduction in self-weight and/or varying board width, the deck-patterns become even more irregular and show a certain percentage of perforation.
The approach is driven by three guiding aspects: firstly by the limitation of the possible timber board patterns, which result from the used material; secondly by the assembly process, which aims for the ease of use and its robustness against assembly-errors; thirdly by the arrangement of the nails, which allow for the highest possible grade of flexibility in design and material use and which respect the aforementioned structural and architectural potential in sustainable design approaches and low-tech considerations.

5 Acknowledgements

This research project was supported by Beck Fastener group who provide the wooden nails for this project and the pneumatic nailing device. We thank Kouvola city, Elementit-E Oy and Kouvola innovation Oy for the support in this project.

References

[1] EC European Commission [online]. Accessed 20 May 2019, available at: https://ec.europa.eu/energy/en/topics/energy-efficiency/buildings

[2] Luke, Natural Resources Institute Finland [online]. Accessed 20 May 2019, available at: https://stat.luke.fi/en/uusi-etusivu

[3] R. M. Gutkowski and T. G. Williamson, "Timber Bridge: State-of-the-Art", Journal of Structural Eingineering, vol. 109, issue 9, pp. 2175-2191, 1983.

[4] G. H. Filz, Low-tech or high-tech? "cut.enoid.tower" – Three times two facets of irregularity. In Textile Composites and Inflatable Structures VI – Proceedings of the 6th International Conference on Textile Composites and Inflatable Structures, Structures Membranes, pp. 250-257, 2013.

Proceedings of the IASS Annual Symposium 2019 – Structural Membranes 2019
Form and Force
7 – 10 October 2019, Barcelona, Spain
C. Lázaro, K.-U. Bletzinger, E. Oñate (eds.)

Form-finding and structural modification of a hybrid cable-strut system

Rasoul ASGHARI[a], Karim ABEDI[*], Mohammadreza CHENAGHLOU[b]

[*] Professor of Structural Engineering, Sahand University of Technology, Tabriz-Iran
k_abedi@sut.ac.ir

[a] PH.D candidate of structural Engineering, Sahand University of Technology, Tabriz-Iran

[b] Professor of Structural Engineering, Sahand University of Technology, Tabriz-Iran

Abstract

Cable domes are the most efficient structural application of tensegrities. Stability of these structures is achieved using compression ring in the boundary region of dome, which contradicts the free-standing principle of tensegrity systems. Application of a tensegrity ring, instead of the reinforced concrete or steel truss compression rings, together with a cable dome results in a hybrid cable-strut structure. In the present study, the form-finding of a modified hybrid structure has been presented. In the studied configurations, two different arrangements in tensegrity ring and also two connecting methods between the ring and cable dome were considered. Because of the importance of prestress forces and their distribution in the behavior of cable-strut structures, the proximity of prestress force values between two parts of hybrid structure was chosen as comparison criterion. In order to obtain an efficient combination between two structural parts, form-finding results of the studied hybrid cases were compared with those of the previously proposed hybrid structure. Based on the findings of the present study, it was concluded that the proposed hybrid structure has a very better prestress force distribution and also is much more efficient in comparison with the previous proposed model.

Keywords: Cable dome, tensegrity ring, hybrid structure, form-finding, force density, optimal prestress distribution

1. Introduction

Tensegrities are the structural systems whose main components are cables and struts. Snelson [1] defined tensegrity as a structure with discontinuous compression and continuous tension characteristics. After the 1980s, they were employed as structural systems and cable domes were introduced as one of the most efficient forms of the tensegrity systems. Cable domes contain compression ring in the boundary region which provide the stability of structure. Therefore, presence of the compression ring is in contrast with the self-support characteristic of tensegrity systems. At first, Wang [2] using triangular simplexes and later Yuan *et al.* [3] by modifying triangular simplex introduced tensegrity rings. Application of tensegrity ring instead of the compression ring, results in creating a new hybrid cable-strut system. In cable-strut structures, the geometry must be consistent with a self-stress or prestress mode which obtain from the form-finding process. Previously presented form-finding methods can be categorized in statical and kinematical methods [4]. In statical methods, setting a relationship between the forces of members of a structure with a given topology and its equilibrium configuration and then analyzing this relationship are dominant in form-finding. In this category, the force density method is the most widely used method [5, 6] which will be employed in this study.

Pellegrino and Calladine [7] obtained self-stress modes and mechanisms of tensegrity structures by Gaussian elimination method and Singular value decomposition (SVD) method. Yuan and Dong [8] presented feasible integral prestress mode concept using the inherent geometrical symmetry of cable

Copyright © 2019 by Rasoul ASGHARI, Karim ABEDI, Mohammadreza CHENAGHLOU
Published by the International Association for Shell and Spatial Structures (IASS) with permission.

domes. Yuan *et al.* [9] presented double singular value decomposition method to obtain integral prestress modes of cable domes. Tran *et al.* [10] using the force density method and symmetry characteristics, presented a numerical method to determine the initial prestress of cable dome structures. Koohestani [11] proposed a form-finding method based on genetic algorithm by minimizing eigenvalues of the force density matrix. Shekastehband *et al.* [12] studied self-stress modes of a tensegrity system numerically and experimentally, using linear programming and presented a practical method to apply self-stress modes to these structures. Chen *et al.* [13] investigated optimal prestress design of a Kiewitt dome using quadratic programming algorithm. Lu *et al.* [14] presented geometrical characteristics and form-finding of a semi-regular tensegrity ring and described combination of this ring with a cable dome. However, they investigated only one hybrid structure.

Based on previous studies, in this paper, combination of modular tensegrity ring and Levy-type cable dome has been considered. In order to create the tensegrity ring, two types of arrangement for modules were considered and connecting of the ring and cable dome parts was done in two different ways. Form-finding of the studied structures was carried out using the force density method and linear programming and then feasible prestress modes were found. In the studied structures, if the prestress forces of the ring part and cable dome part are close together, there will be an optimal distribution of forces over the structure. Through comparison the results, the best structural combination was chosen to achieve the most optimal distribution of prestress forces.

2. Configuration of studied hybrid cases

Cable domes have initially been developed in two general forms with radial (Geiger dome) and triangulated patterns (for example Levy dome). The main disadvantage of radial type is its low resistance to the horizontal loads. In order to obtain a more efficient configuration, Rębielak [15] introduced the concept of crystal tension-strut structures by transformation of component parts of the crystal space frame. Two main structural parts of cable domes are central cable-strut system and boundary compression ring. Structural system of the compression ring in the initial cable domes was reinforced concrete or triangular steel–truss (Figure 1). In addition to stated problems above, both of these two compression rings are more rigid in comparison with central cable-strut part of the cable dome structure. If a tensegrity ring is used instead of compression ring, its flexibility in comparison with two previous compression rings, will lead to its better participation in load carrying.



Figure 1: **i)** Levy cable dome; compression ring made of **ii)** reinforced concrete (Geiger dome), **iii)** steel truss (La Plate dome in Argentina (2012)) and **iv)** proposed tensegrity ring by Lu *et al.* [14]

In this study, tensegrity ring and also hybrid model proposed by Lu *et al.* [14] have been named as "Ring **I**" and "reference model" (Figure 1-iv), respectively. In their model, the feasible prestress forces in the ring part of hybrid structure were very larger than those in the cable dome part, which it was the main problem of their model. This leads to an inappropriate force transmission between two structural parts. In this study, the reference model was modified so that another arrangement for the ring and also different connecting method between two structural parts were considered. In order to obtain an efficient hybrid case, the results of proposed model were compared with those of the reference model and also with each other.

2.1 Creating tensegrity ring

Tensegrity ring contains 16 semi-regular modules which obtain form applying a trapezoid transformation on a regular module. Figure 2 shows initial regular module and its transformed shape by a distortion on the lower square (EFGH) so that except nodes B, D, G and H, other nodes are adjusted. Modules of the ring will have θ angle relative to horizontal plane. Nodal coordinates of the new module have been presented in relationships (1) and (2) [14].

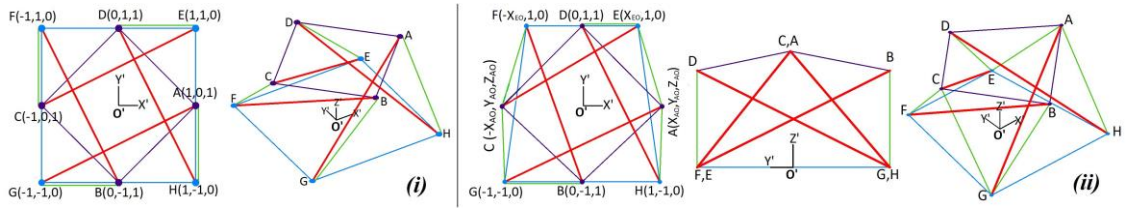


Figure 2: Geometry of the **i)** regular tensegrity module and **ii)** Semi-regular module

$$x_{AO'} = 1 - \tan\frac{\pi}{n}\cos\theta + \tan\frac{\pi}{n}\left(z_{AO'}\sin\theta - y_{AO'}\cos\theta\right)\ ,\ y_{AO'} = -\frac{{x_{EO'}}^2 - 2x_{AO'}x_{EO'} + 2x_{AO'} - 1}{(x_{EO'}+1)^2}\ ,\ z_{AO'} = \frac{2x_{AO'}}{x_{EO'}+1} \tag{1}$$

$$x_{EO'} = 1 - 2\tan\frac{\pi}{n}\cos\theta\ \ ,\ \ \frac{x_{E'}}{x_{EO'}} = \frac{x_{A'}}{x_{AO'}} = \frac{y_{A'}}{y_{AO'}} = \frac{z_{A'}}{z_{AO'}} = R\ \sin\frac{\pi}{n} \tag{2}$$

where, for example, $x_{AO'}$ denotes the x-coordinate of node A, n is the number of modules, R and θ have been shown in Figure 3-ii. Modules are assembled in two ways inside the tensegrity ring. In ring **I** (related to reference model), semi-regular module is replicated uniformly in the circular direction. In ring **II** (proposed here), the module is mirrored with respect to plane $\overline{AEH}$ at its location in the ring and the resulted pair of modules is replicated in the circular direction (Figure 3-i). Based on these relationships, geometry of the resulted tensegrity ring were created in FORMIAN configuration processing software.

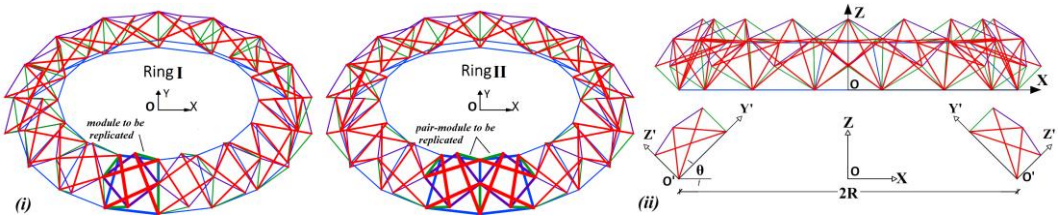


Figure 3: ring I and II in **i)** 3D view and **ii)** side view

2.2 Combination of ring and cable dome

The tensegrity ring and Levy cable dome should be combined in a way that the new hybrid structure has an efficient structural behavior. If the distribution of prestress forces in cable dome part and ring part are close to each other, it will be named as an "*optimal prestress distribution*". In this paper, a Levy-type cable dome (Figure 1-i) is combined with a tensegrity ring. Ridge cables of Levy dome can be connected in two ways to the tensegrity ring; connecting to upper chord nodes of ring (node D in Figure 2) or to lower chord nodes (nodes E, F in Figure 2). These two connecting methods have been named "connecting type **A**" and "connecting type **B**", respectively (Figure 4). Extra cables and struts were used in connecting type A for connecting two parts (dashed lines in Figure 4).

Divisions of tensegrity ring and cable dome in circular direction is equal to 16. Grouping of elements in dome-type cable-strut systems is essential in the form-finding method used here, which is shown in Figure 5 for studied hybrid structures. Based on geometric symmetry, each type of rings is divided into 15 groups. In hybrid structures with connecting type **A** and type **B**, three and two support conditions, were considered, respectively, which one node of each of them have been shown in Figure 5. In all

models, parameters *R, θ,* span length of the cable dome and other dimensions are according to Figure 4. Finally, the studied hybrid structures are given in Table 1.

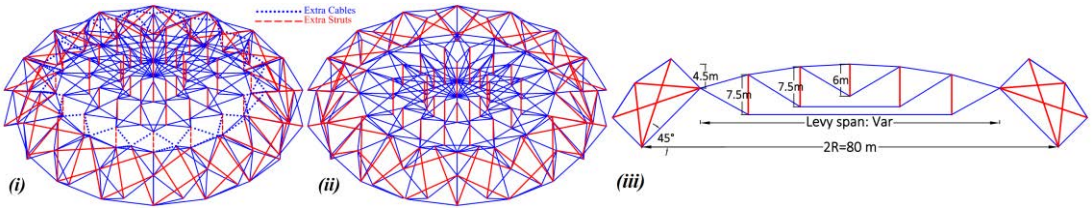


Figure 4: Hybrid structure with **i)** connecting type **A** (related to reference model), **ii)** connecting type **B** (proposed here) and **iii)** dimensions of cable dome part

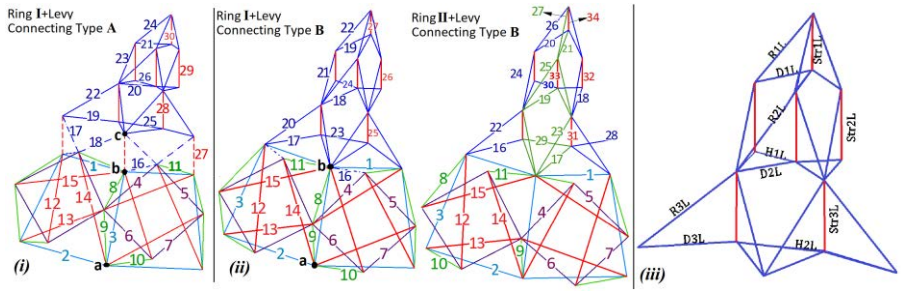


Figure 5: Grouping of elements in **i)** reference model and **ii)** proposed cases; **iii)** labels of groups in cable dome

Table 1: The studied hybrid structures

H.Case 1:	*"Ring **I**+Levy_Connecting Type **A**"*	*H.Case 3:*	*"Ring **II**+Levy_Connecting Type **A**"*
H.Case 2:	*"Ring **I**+Levy_Connecting Type **B**"*	*H.Case 4:*	*"Ring **II**+Levy_Connecting Type **B**"*

3. Form-finding analysis of the studied hybrid structures

A set of suitable and feasible prestress forces should be obtained through form-finding process for each cable-strut structure before any structural behavior analysis. Due to the high application and simplicity of programming, the force density method together with double singular value decomposition technique and linear optimization method were used to determine initial prestress mode.

First step is to obtain equilibrium matrix of structure. For a structure with b elements and n free nodes and n_f fixed nodes, connectivity matrix $\boldsymbol{C}_s$ is partitioned into parts $\left[\boldsymbol{C}_{(b\times n)}, \boldsymbol{C}_{f(b\times n_f)}\right]$ corresponding to free and fixed nodes. In the absence of external loads, the nodal equilibrium equations are as follows:

$$\boldsymbol{E}\,\boldsymbol{d} = \boldsymbol{0} \quad \xrightarrow{\text{in which}} \quad \boldsymbol{E}_{3n\times b} = \begin{pmatrix} \boldsymbol{C}^T diag(\boldsymbol{C}\boldsymbol{x} + \boldsymbol{C}_f\boldsymbol{x}_f) \\ \boldsymbol{C}^T diag(\boldsymbol{C}\boldsymbol{y} + \boldsymbol{C}_f\boldsymbol{y}_f) \\ \boldsymbol{C}^T diag(\boldsymbol{C}\boldsymbol{z} + \boldsymbol{C}_f\boldsymbol{z}_f) \end{pmatrix}, \; \boldsymbol{d} = \{d_1, d_2, \dots, d_b\}^T \;, \; d_i = t_i/l_i \tag{3}$$

in which, $\boldsymbol{E}$ and $\boldsymbol{d}$ are the equilibrium matrix and force densities vector, respectively; $\boldsymbol{x}, \boldsymbol{y}, \boldsymbol{z}$ ($\in \mathbb{R}^n$) and $\boldsymbol{x}_f, \boldsymbol{y}_f, \boldsymbol{z}_f$ ($\in \mathbb{R}^{n_f}$) are the nodal coordinate vectors in free and fixed nodes, respectively and d_i, t_i and l_i are force density, axial force and length of element i, respectively.

3.1 Singular value decomposition (SVD)

Vector of prestress forces must satisfies three basic conditions; Self-equilibrating, Symmetry and Feasibility conditions. For equilibrium matrix $\boldsymbol{E}$ with rank r_E, SVD decomposition is as follows:

$$\boldsymbol{E} = \boldsymbol{U}_{3n\times 3n}\boldsymbol{V}_{3n\times b}\boldsymbol{W}^T_{b\times b} \tag{4}$$

where $\boldsymbol{U}$ and $\boldsymbol{W}$ are orthogonal matrices and matrix $\boldsymbol{V}$ includes singular values of $\boldsymbol{E}$. Matrix $\boldsymbol{W}$ can be partitioned as $[\boldsymbol{W}_{r_E}, \boldsymbol{W}_{b-r_E}]$ in which $\boldsymbol{W}_{b-r_E}$ contains $s = b - r_E$ independent self-stress modes $\mathbf{s}_i$ that satisfy only self-equilibrating condition:

$$\boldsymbol{S}_{b\times s} = \boldsymbol{W}_{b-r_E} = [\boldsymbol{s}_1, \boldsymbol{s}_2, \dots, \boldsymbol{s}_s] \tag{5}$$

3.2 Double singular value decomposition

The integral prestress modes satisfy both self-equilibrating and symmetry conditions. Assuming $\boldsymbol{X}$ as integral prestress mode, it is expressed as a linear combination of the independent self-stress modes as follows [9]:

$$\boldsymbol{X}_{b\times 1} = \boldsymbol{s}_1\alpha_1 + \boldsymbol{s}_2\alpha_2 + \cdots + \boldsymbol{s}_s\alpha_s \tag{6}$$

where α_i values are a set of participation coefficients of independent self-stress modes. It is assumed that the structure contains h groups of members and therefor $\boldsymbol{X}$ can be expressed as:

$$\boldsymbol{X}_{b\times 1} = [x_1\ x_1\ x_1 \dots x_i\ x_i\ x_i \dots x_h\ x_h\ x_h]^{\boldsymbol{T}} = [\boldsymbol{e}_1 \cdots \boldsymbol{e}_i \cdots \boldsymbol{e}_h]_{b\times h}[x_1 \dots x_i \dots x_h]^{\boldsymbol{T}}_{h\times 1} \tag{7}$$

in which, x_i is the prestress of members in ith group. Column vector $\boldsymbol{e}_i$ is related to ith group in which, values in position of this group members are +1 and -1 for cables and struts, respectively and zero for others. Combining equations (6) and (7), results in the following equation:

$$\widehat{\boldsymbol{S}}\,\widehat{\boldsymbol{\alpha}} = \mathbf{0} \xrightarrow{in\ which} \widehat{\boldsymbol{S}}_{b\times(s+h)} = \left[\begin{array}{ccc|ccc} \vdots & \vdots & \vdots & \vdots & \vdots & \vdots \\ \boldsymbol{s}_1 & \cdots & \boldsymbol{s}_s & -\boldsymbol{e}_1 & \cdots & -\boldsymbol{e}_h \\ \vdots & \vdots & \vdots & \vdots & \vdots & \vdots \end{array}\right] \quad , \quad \widehat{\boldsymbol{\alpha}}_{(s+h)\times 1} = \begin{Bmatrix} \boldsymbol{\alpha} \\ \boldsymbol{x} \end{Bmatrix} = [\alpha_1 \cdots \alpha_s |\ x_1 \cdots x_h]^T \tag{8}$$

First application of SVD was on the matrix $\boldsymbol{E}$ to obtain independent self-stress modes. The second decomposition (DSVD) is on the matrix $\widehat{\boldsymbol{S}}$ as below:

$$\widehat{\boldsymbol{S}} = \widehat{\boldsymbol{U}}\widehat{\boldsymbol{V}}\widehat{\boldsymbol{W}}^{\boldsymbol{T}} \tag{9}$$

Assuming the rank of matrix $\widehat{\boldsymbol{S}}$ equal to $\acute{r}$, the number of integral prestress modes is $\acute{s} = (s + h) - \acute{r}$. Vectors between rows $s + 1$ to $s + h$ and columns $\acute{r} + 1$ to $\acute{r} + \acute{s}$ of matrix $\widehat{\boldsymbol{W}}$ are considered as integral prestress modes $\boldsymbol{g}_{\boldsymbol{i}}(\in \mathbb{R}^{h\times 1})$ which each of them contains the prestress of members in h groups. If $\acute{s} = 0$, the geometry of structure must be modified; If $\acute{s} = 1$ and the obtained integral prestress mode satisfies uniaxial behavior condition too, this mode is a feasible mode, otherwise the geometry of structure must be modified; If $\acute{s} > 1$, there are more than one integral prestress mode and in general, none of them satisfy feasibility condition. In this case, a linear combination of integral prestress modes must be used to achieve feasible prestress mode (satisfies all three conditions):

$$\widehat{\boldsymbol{X}} = \boldsymbol{g}_1\beta_1 + \boldsymbol{g}_2\beta_2 + \cdots + \boldsymbol{g}_{s'}\beta_{s'} \tag{10}$$

Finding a set of participation coefficients β_i, so that $\widehat{\boldsymbol{X}}$ satisfies the feasibility conditions, leads to an optimization problem. These conditions are $\sum_{k=1}^{s'} g_i^k\beta_k > 0$ and $\sum_{k=1}^{s'} g_j^k\beta_k < 0$ for cable group i and strut group j, respectively. This optimization problem can be converted to the famous linear programming problem using some modifications [16]: 1) A series of artificial variables ε_i are added to inequalities and minimizing sum of these variables is chosen as the objective function; 2) Inequalities related to cable groups are multiplied in (-1); 3) For convergence improvement, absolute zero on the right hand of inequalities is replaced with the machine zero (*–eps)*. If groups *1* to *c* and *c+1* to *h* are the cable and strut groups, respectively, feasibility conditions will have the form of equations (11). Linear programming problem in MATLAB software is also as equation (12).

$$\sum_{k=1}^{s'} -g_i^k\beta_k + \varepsilon_i \le -eps\ \ i = 1{:}c\ \ \ and\ \ \ \sum_{k=1}^{s'} g_i^k\beta_k + \varepsilon_i \le -eps\ \ , i = c+1{:}h \tag{11}$$

$$min\, \boldsymbol{f}^T\boldsymbol{x}\ \ such\ that\ \{\boldsymbol{A}\boldsymbol{x} \le \boldsymbol{b}\ \ \ (i),\ \ \ \boldsymbol{A}_{eq}\boldsymbol{x} = \boldsymbol{b}_{eq}\ \ \ (ii),\ \ \ \boldsymbol{l}_b \le \boldsymbol{x} \le \boldsymbol{u}_b\ \ \ (iii)\} \tag{12}$$

After forming required matrices of problem (12) and solving it, vector $\boldsymbol{\beta}$, containing the participation coefficients, and then feasible integral prestress mode $\widehat{\boldsymbol{X}}$ are obtained. In order to obtain prestress forces, values of $\widehat{\boldsymbol{X}}$ which are force densities, should be multiplied in the length of members. Assuming vector $\boldsymbol{l}(\in \mathbb{R}^{h\times 1})$ containing length of each group members, prestress forces of groups will be as follows:

$$\boldsymbol{PF}_{feas} = diag(\boldsymbol{l})\hat{\boldsymbol{X}} \tag{13}$$

4. Numerical results

After the configuration processing and grouping of members in FORMIAN software, form-finding process inputs containing the nodal coordinates, connectivity of members and support nodes were obtained. The form-finding of structures was carried out in MATLAB software according to the explained method in the section 3. In the current section, feasible prestress forces for different hybrid structures are presented and compared. The number of groups in both rings **I** and **II** are identical, so in all models, prestress forces vectors were normalized with respect to 13th group which had usually maximum prestress value. Prestress force of this group was set to -1 and the forces of other groups were expressed as a multiple of it. In the following tables, strut groups have been shown with bold letters. Groups related to Levy dome part have been separated by double lines from other groups. Phrases "Bot, Top and inc" are related to bottom layer, top layer and inclined cables of ring part respectively; phrase "str" is related to struts and phrase "ext" means the extra members used to connect two parts of ring and dome. In the groups of dome part, letters "D, R and H" are related to diagonal, ridge and hoop cables, respectively, and letter "L" also implies Levy dome. Numbering of groups are also given in Figure 5.

Table 2 and 3 give feasible prestress forces in the case of ring **I** for two connecting methods between ring and dome that are "*H-Case 1*" (reference model) and "*H-Case 2*" hybrid structures, respectively. These two cases will be compared in order to select one of the connecting methods between two parts so that an optimal distribution of prestress forces in cable dome part is obtained.

Table 2: Feasible prestress forces of "H-Case 1" hybrid structure (reference model)

Groups	Supp(a)	Supp(b)	Supp(c)	Groups	Supp(a)	Supp(b)	Supp(c)	Groups	Supp(a)	Supp(b)	Supp(c)
G1-Bot1	0.0105	0.359	0.098	G11-inc4	0.411	0.194	0.512	G21-D1L	0.003	0.015	0.024
G2-Bot2	0.487	0.974	0.367	**G12-str1**	-0.844	-0.921	-0.752	G22-R3L	0.022	0.125	0.204
G3-Bot3	0.666	0.304	0.741	**G13-str2**	***-1.000***	***-1.000***	***-1.000***	G23-R2L	0.015	0.085	0.139
G4-Top1	0.405	0.523	0.460	**G14-str3**	-0.651	-0.499	-0.830	G24-R1L	0.025	0.144	0.223
G5-Top2	0.458	0.662	0.563	**G15-str4**	-0.781	-0.657	-0.783	G25-H2L	0.047	0.269	0.439
G6-Top3	0.357	0.390	0.318	G16-inc(ext)	0.019	0.011	0.055	G26-H1L	0.017	0.099	0.161
G7-Top4	0.705	0.769	0.629	G17- (ext)	0.056	0.323	0.030	**G27-str(ext)**	-0.027	-0.158	-0.014
G8-inc1	0.434	0.115	0.277	G18- (ext)	0.056	0.323	0.030	**G28-strL3**	-0.010	-0.058	-0.094
G9-inc2	0.340	0.430	0.483	G19-D3L	0.012	0.068	0.111	**G29-strL2**	-0.004	-0.025	-0.041
G10-inc3	0.721	0.786	0.643	G20-D2L	0.004	0.024	0.039	**G30-strL1**	-0.020	-0.117	-0.192

Table 3: Feasible prestress forces of "H-Case 2" hybrid structure

Groups	Supp(a)	Supp(b)	Groups	Supp(a)	Supp(b)	Groups	Supp(a)	Supp(b)
G1-Bot1	0.0111	0.4212	G10-inc3	0.6963	0.6542	G19-D1L	0.0058	0.0261
G2-Bot2	0.2493	0.2867	G11-inc4	0.4622	0.4467	G20-R3L	0.0491	0.2218
G3-Bot3	0.7477	0.7695	**G12-str1**	-0.8154	-0.7661	G21-R2L	0.0335	0.1514
G4-Top1	0.3851	0.3722	**G13-str2**	***-1.0000***	***-1.0000***	G22-R1L	0.0564	0.2552
G5-Top2	0.4389	0.5646	**G14-str3**	-0.7069	-0.8036	G23-H2L	0.1056	0.4775
G6-Top3	0.3452	0.3243	**G15-str4**	-0.7959	-0.6897	G24-H1L	0.0388	0.1754
G7-Top4	0.6812	0.6400	G16-inc(ext)	0.0322	0.1154	**G25-strL3**	-0.0227	-0.1026
G8-inc1	0.4651	0.2745	G17-D3L	0.0268	0.1211	**G26-strL2**	-0.0099	-0.0447
G9-inc2	0.3436	0.4336	G18-D2L	0.0095	0.0431	**G27-strL1**	-0.0460	-0.2082

In the combination of ring **II** and cable dome with connecting type **A**, namely the "*H-Case 3*" hybrid structure, no proper prestress mode was found for any support conditions and it's results is not given here. Prestress forces in similar model with connecting type **B**, namely the "*H-Case 4*" hybrid structure have been given in Table 4. In this case, some groups in dome part are divided into two distinct groups and the number of groups increases. Prestress forces of Levy dome part, given in Table 2 and 3, have been compared in Figure 6-i. Considering the support condition (b), which is common between two structures, as the comparison basis, it can be seen that prestress forces of dome part of hybrid structure for the case of connecting type **B** in comparison with the case of connecting type **A** have been increased approximately to 1.77 times. In structures with support condition (a), this ratio is 2.25 times.

Table 4: Feasible prestress forces of "H-Case 4" hybrid structure

Groups	Supp(a)	Supp(b)	Groups	Supp(a)	Supp(b)	Groups	Supp(a)	Supp(b)
G1-Bot1	0.019	0.445	**G12-str1**	-0.780	-0.780	G23-R3Lb	0.049	0.284
G2-Bot2	0.480	0.272	**G13-str2**	***-1.000***	***-1.000***	G24-R2La	0.027	0.194
G3-Bot3	0.765	0.765	**G14-str3**	-0.776	-0.776	G25-R2Lb	0.044	0.194
G4-Top1	0.452	0.452	**G15-str4**	-0.873	-0.866	G26-R1La	0.042	0.327
G5-Top2	0.452	0.452	G16-D3La	0.031	0.150	G27-R1Lb	0.078	0.327
G6-Top3	0.330	0.330	G17-D3Lb	0.026	0.160	G28-H2La	0.110	0.615
G7-Top4	0.651	0.652	G18-D2La	0.010	0.055	G29-H2Lb	0.113	0.610
G8-inc1	0.904	0.893	G19-D2Lb	0.010	0.055	G30-H1L	0.041	0.225
G9-inc2	0.814	0.813	G20-D1La	0.009	0.033	**G31-strL3**	-0.024	-0.132
G10-inc3	0.666	0.666	G21-D1Lb	0.003	0.033	**G32-strL2a**	-0.010	-0.057
G11-inc4	0.543	0.543	G22-R3La	0.055	0.284	**G33-strL2b**	-0.010	-0.057
						G34-strL1	-0.049	-0.267

Therefore, in the reference model, with modifying only the connecting method between two parts to the proposed connecting type **B**, distribution of prestress forces of hybrid structure becomes more optimal than that of the reference model. Prestress forces of Levy dome part given in Table 2 and 4 have been compared in Figure 6-ii. It shows that changing both the connecting method and also the type of ring in hybrid structure of reference model to the connecting type **B** and ring **II** (both proposed in this study) cause that prestress forces of cable dome part increase averagely 2.26 times. This means that modifying both connecting method and ring type, leads to a very optimal distribution of prestress forces of hybrid structure in comparison with the previous case in which only the connecting method had been changed.

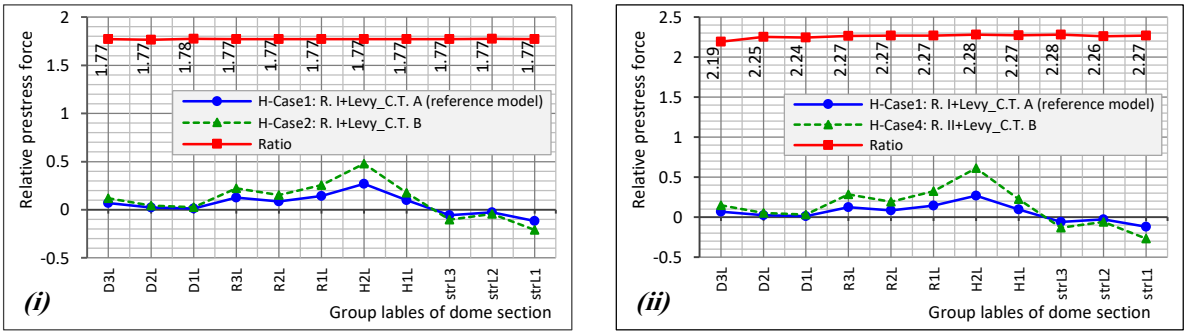


Figure 6: Effect of changing **i)** only the connecting method between two parts and **ii)** both connecting method and ring type in the relative prestress forces of cable dome part of hybrid structure

5. Conclusion

In the present paper, form-finding and modifying of a hybrid cable-strut structure, consisting of a tensegrity ring and a Levy cable dome, have been studied. The reference model and then, new modified hybrid system was described in details. Two types of ring with different arrangement of modules and also two methods for connecting of two parts of hybrid structure were considered. Form-finding of the studied models, were done in MATLAB software and results for all structures were compared with each other. The optimal distribution of prestress forces was defined as a case in which prestress forces of two parts are close together. Prestress forces of dome part for different hybrid structures were compared in order to obtain the best hybrid structure.

Firstly, the difference of results between two connecting methods was investigated. The previously proposed hybrid structure of "*H-Case 1*" was selected as "reference model". It was found that prestress forces in cable dome part of the "*H-Case 2*" hybrid structure with support condition (b) are about 1.77 times of those in reference model. This ratio in the case of support condition (a), is about 2.25 times. Considering two types of tensegrity ring, the results of "H-Case 4" hybrid structure and reference model were compared. It was found that prestress forces of the cable dome part in this hybrid structure are averagely 2.26 times of those in the reference model. Accordingly, changing only the connecting method between two parts of ring and dome or changing simultaneously the connecting method and ring type

to the proposed cases of this study, leads to a more optimal distribution of prestress forces over the hybrid structure. Therefore, the overall results obtained in this study are as follows:

1) To create tensegrity ring, it is recommended that the ring **II** to be used in which the tensegrity modules in circular direction are mirrored with respect to each other;

2) To connect tensegrity ring and cable dome in hybrid structure, connecting type **B** is recommended in which the dome boundary nodes are connected to the inner side of lower chord of the tensegrity ring.

References:

[1] K. Snelson, "Continuous tension, discontinuous compression structures," U.S Patent NO 3169611, 1965.

[2] B.-B. Wang, "Tensegrity structures as' ring beams'," *Bulletin of the International Association for Shell and Spatial Structures*, vol. 37, pp. 31-39, 1996.

[3] X. Yuan, Z. Peng, S. Dong, and B. Zhao, "A New Tensegrity Module "Torus"," *Advances in Structural Engineering*, vol. 11, pp. 243-251, 2008.

[4] A. Tibert and S. Pellegrino, "Review of form-finding methods for tensegrity structures," *International Journal of Space Structures*, vol. 26, pp. 241-255, 2011.

[5] H.-J. Schek, "The force density method for form finding and computation of general networks," *Computer methods in applied mechanics and engineering*, vol. 3, pp. 115-134, 1974.

[6] K. Linkwitz, "Form finding by the "direct approach" and pertinent strategies for the conceptual design of prestressed and hanging structures," *International Journal of Space Structures*, vol. 14, pp. 73-87, 1999.

[7] S. Pellegrino and C. R. Calladine, "Matrix analysis of statically and kinematically indeterminate frameworks," *International Journal of Solids and Structures*, vol. 22, pp. 409-428, 1986.

[8] X. Yuan and S. Dong, "Integral feasible prestress of cable domes," *Computers & structures*, vol. 81, pp. 2111-2119, 2003.

[9] X. Yuan, L. Chen, and S. Dong, "Prestress design of cable domes with new forms," *International Journal of Solids and Structures*, vol. 44, pp. 2773-2782, 2007.

[10] H. C. Tran, H. S. Park, and J. Lee, "A unique feasible mode of prestress design for cable domes," *Finite Elements in Analysis and Design*, vol. 59, pp. 44-54, 2012.

[11] K. Koohestani, "Form-finding of tensegrity structures via genetic algorithm," *International Journal of Solids and Structures*, vol. 49, pp. 739-747, 2012.

[12] B. Shekastehband, K. Abedi, and N. Dianat, "Experimental and numerical study on the self-stress design of tensegrity systems," *Meccanica*, vol. 48, pp. 2367-2389, 2013.

[13] L.-m. Chen, Y.-y. Zhou, and S.-l. Dong, "Overall Self-stress Modes Analysis and Optimal Prestress Design of the Kiewitt Dome," *Journal of the International Association for Shell and Spatial Structures*, vol. 56, pp. 113-123, 2015.

[14] J. Lu, X. Dong, X. Zhao, X. Wu, and G. Shu, "Form-finding analysis for a new type of cable–strut tensile structures generated by semi-regular tensegrity," *Advances in Structural Engineering*, vol. 20, pp. 772-783, 2017.

[15] J. Rębielak, *Shaping of Space Structures: Examples of Applications of Formian in the Design of Tension-strut Systems*: Oficyna Wydawnicza Politechniki Wrocławskiej, 2005.

[16] J. Quirant, N. Kazi-Aoual, and R. Laporte, "Tensegrity systems: the application of linear programmation in search of compatible selfstress states," *Journal of the International Association for Shell and Spatial Structures*, vol. 44, pp. 33-50, 2003.

Proceedings of the IASS Annual Symposium 2019 – Structural Membranes 2019
Form and Force
7 – 10 October 2019, Barcelona, Spain
C. Lázaro, K.-U. Bletzinger, E. Oñate (eds.)

Optimization of initial prestress for cable-strut systems with multiple symmetric self-stress modes

Pei ZHANG*[1, 2]

* [1]College of Civil and Transportation Engineering, Hohai University, Nanjing, 210098, China; [2]State Key Laboratory of Subtropical Building Science, South China University of Technology, Guangzhou 510005, China
1 Xikang Road, Nanjing, Jiangsu
zhangpei250131@163.com

Abstract

This study mainly focuses on initial prestress design of symmetric cable-strut systems with multiple symmetric self-stress modes. A novel optimization model for the determination of combination coefficients of independent symmetric self-stress modes is presented, where the global rigidity of the structure is employed as the objective function. A penalty function is used to consider both hard and soft constraints including stability conditions, unilateral property of members and prestress distribution evenness. Two strategies of the genetic algorithms with and without incorporating isolation niche technique are developed to solve this optimization problem respectively. A typical numerical example is tested to validate the efficiency of the present approaches.

Keywords: Cable-strut system; Initial prestress; Global rigidity; Optimization; Genetic algorithms

1. Introduction

A cable-strut system is a lightweight spatial structure consisting of compression members (called struts) surrounded by a network of tension members (called cables), including tensegrities, cable domes, cable trusses and other prestressed pin-jointed cable-strut assemblies. Since the rigidity of a cable-strut structure is the result of a self-stressed equilibrium between cables and struts, it would not maintain a certain shape until appropriate initial prestress is assigned. Therefore, the determination of initial prestress is one of the key issues for this kind of structures. In most of the existing researches, the shapes and self-stress states of cable-strut structures are to be determined simultaneously in order to discover novel shapes, which are characterized as form-finding [1]. However, in this paper we only focus on seeking reasonable distribution of initial prestress for cable-strut structures with given shapes and specified arrangement of members, which are usually known as force-finding [2].

As a basic work of force-finding, the independent self-stress modes of a pin-jointed cable-strut assembly can be identified through singular value decomposition (SVD) of equilibrium matrix proposed by Pellegrino [3]. Quirant et al. [4] presented the application of linear programmation in search of feasible self-stress modes in modular tensegrity grids without considering the structural stability. Recently, some heuristic algorithms such as the simulated annealing algorithm [2], the ant colony systems algorithm [5], etc. have been adopted for determining the initial prestress with the consideration of feasibility, stability and other specific requirements. However, the inherent symmetric properties of tensegrity structures were not taken into account in aforementioned studies.

Actually, the cable-strut structures usually have symmetric properties. Kangwai and Guest [6] employed group representation theory to block-diagonalise the equilibrium matrix of a symmetric structure. Yuan and Dong [7] presented a practical method based on the group division of members, where all members in each group are assumed to have the same internal force. Nevertheless, the

Copyright © 2019 by Pei Zhang
Published by the International Association for Shell and Spatial Structures (IASS) with permission.

methods mentioned above are only available for the structures with single symmetric self-stress mode, and so far only a few researches [8] have been carried out to investigate the case that multiple symmetric states of self-stress exist.

For structures with multiple symmetric states of self-stress, the prestress distribution is defined as the linear combination of independent symmetric self-stress modes. In this paper, a novel optimization model for the determination of combination coefficients is developed, which selects the global rigidity of the structure as the objective function. A penalty function is used to consider both hard and soft constraints including stability conditions, unilateral property of members and prestress distribution evenness. Two types of the genetic algorithms—simple GA (SGA) and isolated niche GA (INGA)—are employed to search for the optimized prestress mode respectively. Numerical example shows the accuracy and efficacy of the proposed method.

2. General concepts associated with initial prestress

2.1. Self-stress modes

Considering a pin-jointed assembly with b members and n degrees of freedom, the self-equilibrium equations at nodes can be written in the form [3]

$$\mathbf{An} = \mathbf{0} \tag{1}$$

where $\mathbf{A} \in \mathbb{R}^{n\times b}$ is the equilibrium matrix of the structure containing the orientations of members, $\mathbf{n}$ is the vector consists of the tension in each member. Let r denote the rank of $\mathbf{A}$ and s=b-r. By means of the singular value decomposition (SVD) of $\mathbf{A}$, the general self-stress state $\mathbf{n}$ can be expressed as [3]:

$$\mathbf{n} = \mathbf{s}_1\alpha_1 + \mathbf{s}_2\alpha_2 + \cdots + \mathbf{s}_s\alpha_s \tag{2}$$

where the vectors $\mathbf{s}_i \in \mathbf{R}^{\mathrm{b}}$ (i=1, 2, …, s) are independent self-stress modes.

2.2. Symmetric states of self-stress

The prestress distribution, which not only satisfies the nodal equilibrium condition but also conforms to geometrical symmetry, is called symmetric state of self-stress in this study. Considering a cable-strut structure with g groups of members, a symmetric state $\hat{\mathbf{n}}$ has the form as [9]:

$$\hat{\mathbf{n}} = [\bar{\mathbf{e}}_1\ \bar{\mathbf{e}}_2 \ldots \bar{\mathbf{e}}_g]\,\boldsymbol{\beta} \tag{3}$$

where $[\bar{\mathbf{e}}_1\ \bar{\mathbf{e}}_2 \ldots \bar{\mathbf{e}}_{\mathrm{g}}]$ is the member group matrix composed of a set of normlized basis vectors and $\boldsymbol{\beta}=\{\beta_1 \ldots \beta_{\mathrm{i}} \ldots \beta_{\mathrm{g}}\}^{\mathrm{T}}$ consists of the combination coefficients of $\bar{\mathbf{e}}_i$ (i=1, ..., g). Substituting Eq. (3) into Eq. (1) gives

$$\mathbf{A}\,[\bar{\mathbf{e}}_1\ \bar{\mathbf{e}}_2 \ldots \bar{\mathbf{e}}_{\mathrm{g}}]\,\boldsymbol{\beta} = \mathbf{0} \tag{4}$$

Similarly, the solutions of $\boldsymbol{\beta}$ in Eq. (4) lie in the nullspace of $\mathbf{A}[\bar{\mathbf{e}}_1\ \bar{\mathbf{e}}_2 \ldots \bar{\mathbf{e}}_{\mathrm{g}}]$ with a general form as

$$\boldsymbol{\beta} = [\boldsymbol{\beta}_1\ \boldsymbol{\beta}_2 \ldots \boldsymbol{\beta}_h]\,\boldsymbol{\eta} \tag{5}$$

where h represents the dimension of the nullspace of $\mathbf{A}[\bar{\mathbf{e}}_1\ \bar{\mathbf{e}}_2 \ldots \bar{\mathbf{e}}_{\mathrm{g}}]$; $\boldsymbol{\beta}_{\mathrm{i}}$ (i=1, … , h) are a set of orthonormal basis of that subspace, which can also be obtained through singular value decomposition of $\mathbf{A}[\bar{\mathbf{e}}_1\ \bar{\mathbf{e}}_2 \ldots \bar{\mathbf{e}}_{\mathrm{g}}]$; $\boldsymbol{\eta}$ is an arbitrary vector of h real coefficients.

When Substitute Eq. (5) into Eq. (3), the general form of symmetric states of self-stress is given by

$$\hat{\mathbf{n}} = [\hat{\mathbf{s}}_1\ \hat{\mathbf{s}}_2 \ldots \hat{\mathbf{s}}_h]\,\boldsymbol{\eta} \tag{6}$$

where $\hat{\mathbf{s}}_i = [\bar{\mathbf{e}}_1\ \bar{\mathbf{e}}_2 \ldots \bar{\mathbf{e}}_g]\boldsymbol{\beta}_i$ (i=1, 2, …, *h*) are independent symmetric self-stress modes.

2.3. Feasible symmetric states of self-stress

The prestress distribution simultaneously satisfying self-equilibrium equation of nodes, geometrical symmetry of structures and unilateral property of members is called feasible symmetric state of self-stress, and be notated by $\tilde{\mathbf{n}}$. Obviously, $\tilde{\mathbf{n}}$ can be expressed as:

$$\tilde{\mathbf{n}} = [\hat{\mathbf{s}}_1\ \hat{\mathbf{s}}_2 \ldots \hat{\mathbf{s}}_h]\boldsymbol{\eta} = [\bar{\mathbf{e}}_1\ \bar{\mathbf{e}}_2 \ldots \bar{\mathbf{e}}_g][\boldsymbol{\beta}_1\ \boldsymbol{\beta}_2 \ldots \boldsymbol{\beta}_h]\boldsymbol{\eta} \tag{7}$$

However, the real coefficients $\boldsymbol{\eta}$ should make each element of $\boldsymbol{\beta}$ (=$[\boldsymbol{\beta}_1\ \boldsymbol{\beta}_2 \ldots \boldsymbol{\beta}_h]\boldsymbol{\eta}$) be positive:

$$\boldsymbol{\beta} = [\boldsymbol{\beta}_1\ \boldsymbol{\beta}_2 \ldots \boldsymbol{\beta}_h]\boldsymbol{\eta} > \{0\} \tag{8}$$

An automatic linear iteration program for the determination of $\boldsymbol{\eta}$ can be found in Ref. [9].

3. Optimization of initial prestress

Depending on the dimension of the linear space $\mathbf{U}_{\text{iss}}$ spanned by symmetric self-stress modes, there are two cases in general: (1) *h*=1; (2) *h*>1. In former case, we only need to determine the prestress level, which should provide sufficient rigidity for load bearing and prevent cables from slack. This problem can be solved easily by one-dimensional search method such as golden section method [7]. In latter case, the procedure to determine the combination coefficients $\boldsymbol{\eta}$ of $\hat{\mathbf{s}}_i$ in Eq. (6) can be separated into two stages: firstly determine a unit coefficient vector $\boldsymbol{\eta}$ satisfying $\boldsymbol{\eta}^{\mathrm{T}}\boldsymbol{\eta}$=1; then, determine the prestress level that is exactly the same with the situation that *h*=1. In this section, we only focus on the first stage with the following practical considerations.

3.1. Global structural rigidity

Define the global structural rigidity as the capability of the structure to resist the most flexible deformation mode. For a given pin-jointed cable-strut structure, the minimum eigenvalue of tangent stiffness matrix **K**, denoted by $\lambda^{\mathbf{K}}_{\min}$, can evaluate the global structural rigidity since it represents the second-order term of the increment of total potential energy resulting from the most flexible deformation mode $\mathbf{d}_{fle}$ [10]. In order to avoid the confusion of material selection, we consider the situation that the axial stiffness of members is much greater than their current internal forces (this would be typical for cable-strut structures used in civil engineering field and constructed by stiff materials, e.g., steel cables). In this case, the most flexible mode must be an inextensional mechanism with the expression as

$$\mathbf{d}_{fle} = \mathbf{D}_{\text{inm}}\boldsymbol{\gamma} \tag{9}$$

where $\mathbf{D}_{\text{inm}}$ contains all the independent inextensional mechanisms, and $\boldsymbol{\gamma}$ is a unit combination coefficient vector.

Denote the geometric stiffness matrix associated with the unit prestress distribution as $\bar{\mathbf{K}}^{\mathrm{G}}$. The prestress stability is guaranteed if the quadratic form $\bar{\mathbf{Q}}$ of $\bar{\mathbf{K}}^{\mathrm{G}}$. Let $\bar{\mathbf{Q}} = \mathbf{D}^{\mathrm{T}}_{\text{inm}}\bar{\mathbf{K}}^{\mathrm{G}}\mathbf{D}_{\text{inm}}$, and $\mathbf{Q} = \varepsilon\bar{\mathbf{Q}}$ where ε represents the level of the prestress. $\mathbf{d}_{fle}$ can be characterized by the eigenvector of **Q**, associated with the minimum eigenvalue $\lambda^{\mathbf{Q}}_{\min}$. To evaluate the global rigidity, it is more convenient to use $\lambda^{\mathbf{Q}}_{\min}$ instead of $\lambda^{\mathbf{K}}_{\min}$ since the material properties of members do not need to be considered. Noting that $\lambda^{\mathbf{Q}}_{\min} = \varepsilon\lambda^{\bar{\mathbf{Q}}}_{\min}$, we choose the following objective function for the determination of normalized prestress mode as

$$\max \lambda^{\bar{\mathbf{Q}}}_{\min} \tag{10}$$

Eq. (10) imply the condition of $\lambda_{\min}^{\bar{\mathbf{Q}}} > 0$ make the structure to be prestress stable.

3.2. Super stability and the unevenness of the prestress mode

In addition to ensure the prestress stability and maximize the structural rigidity, the following two factors are also taken into account in this section: (1) If $\bar{\mathbf{Q}}$ is positive definite, and $\bar{\mathbf{K}}^{\mathrm{G}}$ is positive semi-definite, the structure is stable irrespective of selection of materials and level of prestress, named super stability [10]. In linear algebra, the positive semi-definiteness of $\bar{\mathbf{K}}^{\mathrm{G}}$ can be identified if the minimum eigenvalue of $\bar{\mathbf{K}}^{\mathrm{G}}$ is non-negative:

$$\lambda_{\min}^{\bar{\mathbf{K}}^{\mathrm{G}}}(\boldsymbol{\eta}) \geq 0 \tag{11}$$

(2) From a designer's point of view, the selected prestress mode should be as even as possible, which may significantly reduce the construction cost [2,5]. Here, the coefficient of variation (CV) is utilized to describe the unevenness of the prestress mode, given by

$$\mathrm{CV} = \frac{\sqrt{\sum_{i=1}^{b}(|n_i| - \bar{n})^2}}{\bar{n}} \tag{12}$$

where $\bar{n} = \sum_{i=1}^{b}|n_i|/b$ is the average of the absolute value of internal forces. Hence the evenness of prestress can be improved by making CV of prestress mode be lower than a user-specified value.

3.3. Definition of the optimization model

Note that the objective function $\lambda_{\min}^{\bar{\mathbf{Q}}}$ is implicitly determined by the variables $\boldsymbol{\eta}$ which should satisfy the unilateral constraint described by Eq. (8) as well as the normalization condition. Thus, the determination of normalized prestress mode of a pin-jointed assembly can be modeled by following constrained optimization problem:

$$\begin{aligned} &\max\ \lambda_{\min}^{\bar{\mathbf{Q}}}(\boldsymbol{\eta}) \\ &s.t.\ \begin{cases} \text{hard} \begin{cases} \text{(i)}\ \boldsymbol{\eta}^{\mathrm{T}}\boldsymbol{\eta} = 1 \\ \text{(ii)}\ [\boldsymbol{\beta}_1\ \boldsymbol{\beta}_2\ \ldots\ \boldsymbol{\beta}_h]\,\boldsymbol{\eta} > \{0\} \end{cases} \\ \text{soft} \begin{cases} \text{(iii)}\ \lambda_{\min}^{\bar{\mathbf{K}}^{\mathrm{G}}}(\boldsymbol{\eta}) \geq 0 \\ \text{(iv)}\ \mathrm{CV}(\boldsymbol{\eta}) < a \end{cases} \end{cases} \end{aligned} \tag{13}$$

3.5. Genetic algorithms

In this paper, the binary-coded genetic algorithms are employed to solve the above optimization problem of prestress mode determination. A brief introduction of the basic genetic operators is presented in this section. Emphasis is placed on the new features of GA used in this paper.

3.5.1. Genetic operators of SGA

Reproduction procedure: an alternative method called Ranking Selection (RS) is employed in this study as reproduction operation. Using RS, the amount of $p_r \times N$ chromosomes that have relatively worse fitness function values are discarded, while $p_r \times N$ chromosomes with better fitness are

reproduced (N denotes the population size and p_r is a user-defined proportional parameter in the interval [0, 1]).

Crossover and mutation procedure: In this procedure, the elite-preservation with an elitist proportion parameter p_e is adopted, i.e. the first $p_e \times N$ individuals from the current population are retained, while the rest $N(1\text{-}p_e)$ individuals are put into the mating pool waiting for the implementation of crossover and mutation. Then, according to the fitness rankings, the $N(1\text{-}p_e)$ chromosomes in the mating pool are divided into $N(1\text{-}p_e)/2$ pairs.

3.5.2. The utilization of INGA

In this study, the genetic algorithm based on isolated niche (abbreviated as INGA) is also presented to find more global optimums simultaneously. Based on the principle of INGA, we design the basic procedure as follows:

```
Generate the initial population randomly with m1×m2 size;
Rearrange all the individuals in decreasing order according to their fitness values;
Assemble m2 niches based on the similarity of the fitness value;
While (the terminate condition is not satisfied)
    For (m niches)
        Each niche evolves independently along the track given in Section 3.5.1;
    End for
    If (the threshold of generation number is achieved)
        Compare the fitness of the best solution in each niche;
        Replace the worst niche with a new one which has the same size;
        Protect the new niche for certain periods;
    End if
End while
```

3.5.3. Constraint handling strategy

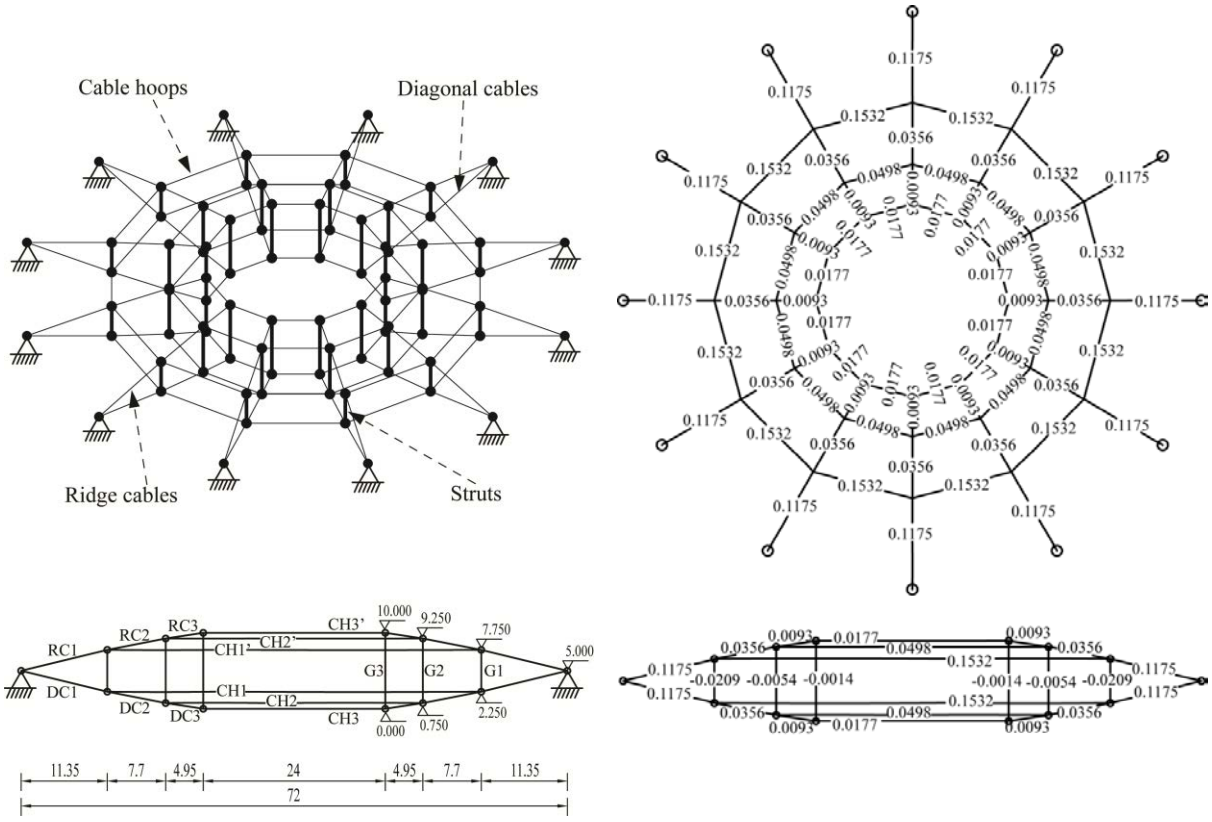
In this paper, the penalty function is used to handle the violations of the inequality constraints, which can be formulated as:

$$f(\boldsymbol{\eta}) = \lambda_{\min}^{\bar{\mathbf{Q}}}(\boldsymbol{\eta}) - \sum_{i=1}^{p}[0,\gamma_i]\cdot\left|\lambda_{\min}^{\bar{\mathbf{Q}}}(\boldsymbol{\eta})\right| \tag{14}$$

In Eq. (14), p denotes the number of inequality constraints (herein p=3); γ_i (i=1, 2, 3) are user-specified penalty parameters corresponding to constraints (ii), (iii) and (iv) in Eq. (13) respectively. The alternative operator "—[]" returns zero as the solution satisfies the ith inequality constraint. Otherwise, it returns γ_i to penalize the infeasible solution. Since the hard constraint (ii) is higher than soft constraints (iii) and (iv) in priority, it should be ensured that $\gamma_1<\gamma_2$ as well as $\gamma_1<\gamma_3$.

4. Illustrative example

Figure 1:(a) shows a spatial cable-truss with an inner hoop, which consists of 84 nodes (72 free nodes, 12 constrained nodes) and 228 members (192 cables, 36 struts). We divide the members into 15 groups notated by RC1, RC2, RC3, DC1, DC2, DC3, CH1, CH1', CH2, CH2', CH3, CH3', G1, G2 and G3 respectively, as indicated in Figure 1:(a). Then, an orthonormal basis of $\mathbf{U}_{iss}$ can be formulated as $[\bar{\mathbf{e}}_1 \ldots \bar{\mathbf{e}}_{15}]\boldsymbol{\beta}_1$, $[\bar{\mathbf{e}}_1 \ldots \bar{\mathbf{e}}_{15}]\boldsymbol{\beta}_2$, $[\bar{\mathbf{e}}_1 \ldots \bar{\mathbf{e}}_{15}]\boldsymbol{\beta}_3$ (see Table 1 for details), where $\boldsymbol{\beta}_1$, $\boldsymbol{\beta}_2$, $\boldsymbol{\beta}_3$ compose of a basis of the nullspace of $\mathbf{A}[\bar{\mathbf{e}}_1 \ldots \bar{\mathbf{e}}_{15}]$. Since none of them satisfy the unilateral requirements of the members, the automatic linear iteration program presented in Ref. [9] is carried out to search for a feasible symmetric state of self-stress, the result of which is shown in Figure 1:(b).



(a) Dimension (m) and member groups (b) A feasible symmetric state of self-stress

Figure 1: A cable truss with an inner hoop

To determine the unit coefficient vector $\boldsymbol{\eta}$ of $\widehat{\mathbf{s}}_i$ (i=1, 2, 3), the optimization model given by Eq. (13) is solved by using SGA and INGA proposed in Section 3.5, respectively. In *Scenario*-1, the main parameters of the SGA are set as follows: the population size is N=12; the mutation probability is P_m=0.05. The penalty factors γ_1, γ_2, γ_3 corresponding to constraints (ii), (iii), (iv) in Eq. (14) are taken as 0.8, 0.3, 0.3 respectively. The threshold of CV in constraint (iv) is empirically set to 0.54. After a series of runs, we get the optimized result as $\boldsymbol{\eta}_1$=[-0.5872 0.6045 -0.5383]^T. The corresponding prestress mode $\mathbf{n}_1$ with an object value equal to $\lambda_{\min}^{\bar{\mathbf{Q}}} = 2.8883\times10^{-3}$ is given in Table 1. Figure 2 shows a typical convergence history in 50 generations. As observed, the best individual has converged to the optimum solution after 36 generations. Then the algorithm no longer generates the offspring superior to the existing one. On the other hand, the CV value of the best individual in each generation does not exceed the pre-specified threshold since the fifth generation.

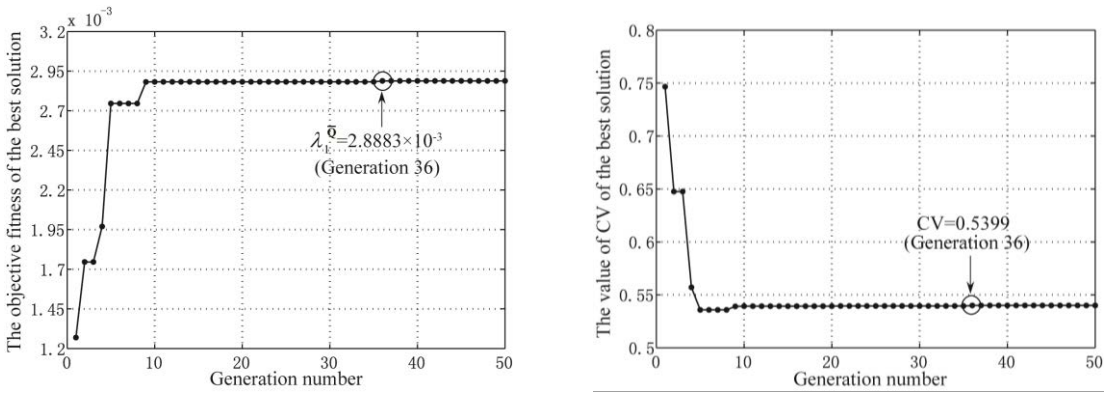
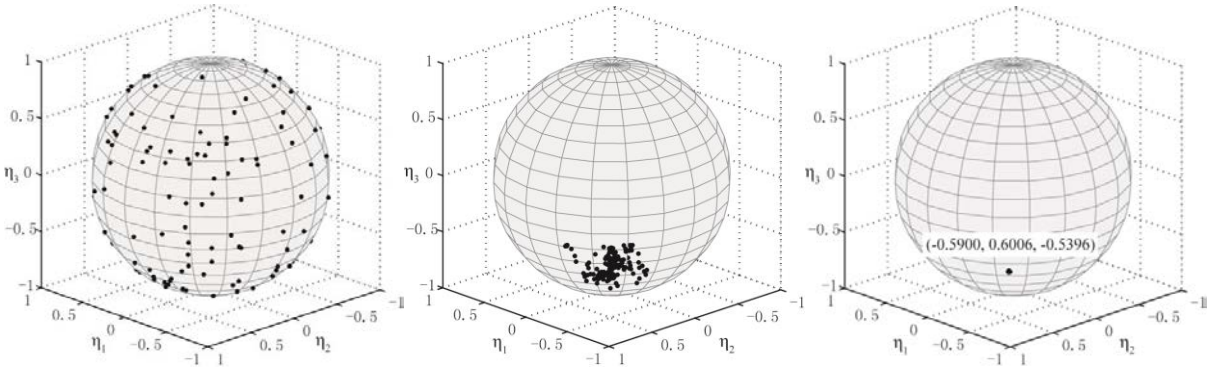


Figure 2: The evolution process of the best objective fitness and the corresponding value of CV in *Scenario*-1

In *Scenario*-2, the INGA presented in section 3.5.2 is employed to solve the same problem. Compared with SGA used in *Scenario*-1, the population size of INGA is raised from 12 to 135 to get a much stronger global searching ability, where the initial population includes 15 niches totally and each niche includes 9 individuals respectively. Noting that the normalized coefficient vector $\boldsymbol{\eta}$ consists of three components denoted as η_i (i=1, 2, 3) in this example, the individuals in the solution space have to locate on a unit sphere, shown in Figure 3. As observed, the initial chromosomes generated randomly are uniformly distributed in the admissible space. Then, after 15 generations, most of the solutions quickly move toward a relatively small area, and after 50 generations all solutions almost converge at a single point which agrees very well with the result obtained in *Scenario*-1.



(a) Initial population (b) Generation 15 (c) Generation 50

Figure 3: Population distribution in the search space at different generations in *Scenario-2*

Table 1 compares the prestress mode shown in Figure 1 (b) with the optimized results obtained in this section. As observed, the minimum eigenvalue of $\overline{\mathbf{Q}}$ associated with $\mathbf{n}_2$ is equal to 1.2346×10^{-3}, while the CV value of $\mathbf{n}_2$ is equal to 0.9945. Obviously, these two parameters, representing the global rigidity of the structure and the unevenness of the prestress distribution respectively, are much more improved for the optimized prestress modes $\mathbf{n}_1$.

Table 1: The comparison of three prestress modes derived from different ways

Member groups	A basis of the symmetric self-stress space $\mathbf{U}_{iss}$			$\mathbf{n}_1$ obtained through optimization method	$\mathbf{n}_2$ obtained through a stochastic way
	$\hat{\mathbf{s}}_1$	$\widehat{\mathbf{s}}_2$	$\hat{\mathbf{s}}_3$		
RC1/ DC1	-0.0420	0.0663	-0.0987	0.1179	0.1175
RC2/ DC2	-0.0536	0.0896	-0.0040	0.0878	0.0356
RC3/ DC3	-0.0842	0.0029	-0.0003	0.0513	0.0093
CH1/ CH1’	0.0227	-0.0453	-0.1778	0.0550	0.1532
CH2/ CH2’	0.0592	0.1644	-0.0070	0.0684	0.0498
CH3/CH3’	-0.1608	0.0055	-0.0005	0.0980	0.0177
G1	-0.0004	0.0015	0.0225	-0.0110	-0.0209
G2	-0.0024	-0.0167	0.0007	-0.0091	-0.0054
G3	0.0126	-0.0004	0	-0.0077	-0.0014
$\boldsymbol{\eta}_1$	-0.6955	0.6468	-0.3129		
$\boldsymbol{\eta}_2$	-0.5872	0.6045	-0.5383		
$\boldsymbol{\eta}_3$	-0.0969	0.2973	-0.9499		

$\bar{\lambda}_1^{Q}$ ($\times 10^{-3}$)	2.8883	1.2346
The value of CV	0.5399	0.9945

5. Conclusion

A systematic procedure is presented for initial prestress design of cable-strut structures with given shapes and specified arrangement of members. For structures with multiple symmetric states of self-stress, an optimization model for the determination of combination coefficients of independent symmetric self-stress modes is developed, which selects the global rigidity of the structure as the objective function. Meanwhile, a penalty function is employed to consider the inequality constraints associated with stability conditions, unilateral property of members and prestress distribution evenness. Two types of the genetic algorithms—simple GA and isolated niche GA—are carried out to solve the proposed optimization problem respectively. Numerical example shows that the results derived from those two scenarios can significantly improve the objective fitness compared with the one gained through the use of an automatic linear iteration program.

Acknowledgements

This work was supported by the Open Project Funded by State Key Lab of Subtropical Building Science, South China University of Technology (No. 2019ZB24), the Fundamental Research Funds for the Central Universities (No. 2018B00914), and the Project Funded by the Priority Academic Program Development of Jiangsu Higher Education Institutions (PAPD).

References

[1] A. G. Tibert, and S. Pellegrino, –Review of form-finding methods for tensegrity structures," *International Journal of Space Structures*, vol 26, pp. 241-255, 2011.

[2] X. Xu and Y. Luo, –Force finding of tensegrity systems using simulated annealing algorithm," *Journal of Structural Engineering*, vol 136, pp. 1027-1031, 2010.

[3] S. Pellegrino, –Structural computations with the singular value decomposition of the equilibrium matrix," *International Journal of Solids and Structures*, vol 30, pp. 3025-3035, 1993.

[4] J. Quirant, –Selfstressed systems comprising elements with unilateral rigidity: Selfstress states, mechanisms and tension setting," *International Journal of Space Structures*, vol 22, pp. 203-214. 2007

[5] Y. Chen, J. Feng and Y. Wu, –Prestress stability of pin-jointed assemblies using ant colony systems," *Mechanics Research Communications*, vol 41, pp. 30-36, 2012.

[6] R. D. Kangwai, S. D. Guest and S. Pellegrino, –Introduction to the analysis of symmetric structures," *Computers and Structures*, vol 71, pp. 671-688, 1999.

[7] X. F. Yuan and S. L. Dong, –Integral feasible prestress of cable domes," *Computers and structures*, vol 81, pp. 2111-2119, 2003.

[8] L. Chen and S. Dong, –Optimal prestress design and construction technique of cable-strut tension structures with multi-overall selfstress modes," *Advances in Structural Engineering*, vol 16, pp. 1633-1644, 2013.

[9] P. Zhang and J. Feng, –Initial prestress design and optimization of tensegrity systems based on symmetry and stiffness," *International Journal of Space Structures*, vol 106, pp. 68-90, 2017.

[10] J. Y. Zhang and M. Ohsaki, –Stability conditions for tensegrity structures," *International Journal of Solids and Structures*, vol 44, pp. 3875-3886, 2007.

Proceedings of the IASS Annual Symposium 2019 – Structural Membranes 2019
Form and Force
7 – 10 October 2019, Barcelona, Spain
C. Lázaro, K.-U. Bletzinger, E. Oñate (eds.)

Optimization of tensegrity lattice with truncated octahedral units

Makoto OHSAKI*[a], Jingyao ZHANG[a], Kosuke KOGISO[a], Julian J. RIMOLI[c]

*[a]Department of Architecture and Architectural Engineering, Kyoto University
Kyoto-Daigaku Katsura, Nishikyo, Kyoto 615-8540, Japan
ohsaki@archi.kyoto-u.ac.jp
[b] School of Aerospace Engineering, Georgia Institute of Technology, Atlanta, GA 30332, USA

Abstract

An optimization method is presented for tensegrity lattices composed of eight truncated octahedral units. The stored strain energy under specified forced vertical displacement is maximized under constraint on the structural material volume. The nonlinear behavior of bars allowing buckling is modeled as a bi-linear elastic material. As a result of optimization, a flexible structure with degrading vertical stiffness is obtained to be applicable to an energy absorption device or a vertical isolation system.

Keywords: tensegrity, optimization, strain energy, truncated octahedral unit

1. Introduction

Tensegrity structures are a class of self-standing pin jointed structures consisting of thin bars (struts) and cables stiffened by applying prestresses to their members [1, 3]. Because the bars are not continuously connected, i.e., they are topologically isolated from each other, these structures are usually too flexible to be used as load-resisting components of structures in mechanical and civil engineering applications. However, by exploiting their flexibility, tensegrity structures can be utilized as devices for reducing impact forces, isolating dynamic forces, and absorbing energy, to name a few applications [5]. Lattice structures consisting of tensegrity units are extensively studied to construct a flexible large-scale structure [7, 8]. Wave-propagation properties are also studied [6, 9].

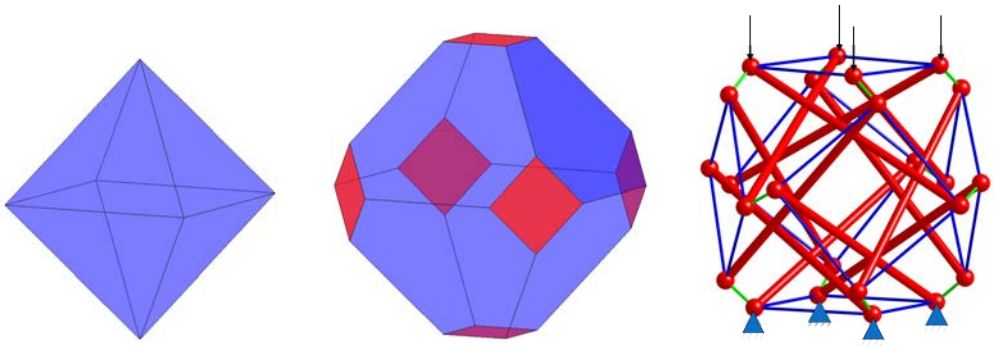
In this study, an optimization method is presented for a recently introduced tensegrity lattice whose unit cell consists of eight truncated octahedral units with threefold symmetry [5]. The objective function to be maximized is the strain energy under specified forced vertical displacement. It is demonstrated in the numerical examples that a stiff structure with degrading tangent stiffness is obtained by maximizing the strain energy. We also show that, for cases where instabilities are present, adding horizontal bars effectively stabilizes the structure.

The remainder of the paper is organized as follow. In Sections 2 and 3 we introduce the basic properties and the configurations of the structure to be studied. In Section 4 we formulate the optimization problem, followed by numerical case studies in Section 5. The conclusions of this work are laid out in section 6.

2. Basic properties of truncated octahedral tensegrity structure

Consider a regular truncated octahedral tensegrity structure as shown in Fig 1(c). The vertices of the octahedron in Fig. 1(a) is removed to generate the truncated octahedron in Fig. 1(b). The members of the tensegrity structure consist of cables and bars, which have tensile and compressive forces, respectively. The cables of the truncated octahedral tensegrity are classified into the edge cables lying on the original edges of the truncated octahedron and the cutting cables lying on its cut edges. The bars are located inside of the truncated octahedron. Hence, a regular truncated octahedral tensegrity structure consists of 24 nodes, 12 bars, 24 cutting cables, and 12 edge cables.

Copyright © 2019 by M. Ohsaki, J. Y. Zhang, K. Kogiso and J. J. Rimoli
Published by the International Association for Shell and Spatial Structures (IASS) with permission.



(a) (b) (c)

Figure 1: Generation of regular truncated octahedral tensegrity structure; (a) regular octahedron, (b) truncated octahedron, (c) truncated octahedral tensegrity.

Due to symmetry of the structure, members in each of three types have the same length, and have the same prestress, and accordingly, have the same force density, which is defined as the axial force divided by the member length. Denote the force densities of the edge cables, cutting cables, and bars as q_{e}, q_{c}, and q_{b}, respectively. Define a and b as

$$a = \frac{q_{\mathrm{e}} + q_{\mathrm{b}}}{2}, \quad b = \frac{q_{\mathrm{e}} - q_{\mathrm{b}}}{2} \tag{1}$$

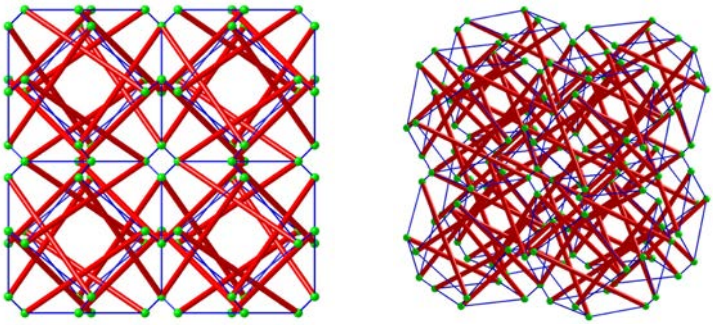
where $b > 0$ is to be satisfied. For the self-equilibrium of a tensegrity structure in 3-dimensional space, its force density matrix necessarily has four zero eigenvalues [1, 3]. From this non-degeneracy condition, we have the force density q_{c} of cutting cables solved as follows [2]:

$$q_{\mathrm{c}} = \frac{b^2 - 5a^2 + \sqrt{a^4 + 14a^2b^2 + b^4}}{4a} \tag{2}$$

for which we need $a > 0$ for proper signs for the force densities as well as *super-stability* of the resulting structure. The scaling parameter β is used to adjust the level of force densities as $\beta\mathbf{q}$. Since the force density matrix is also scaled by β at the same time, the self-equilibrium equations remain to be satisfied by the same configuration.

It is known that a regular truncated octahedral tensegrity has only one mode of prestress and 19 infinitesimal mechanisms. Furthermore, this structure is known to be *super-stable* when $q_{\mathrm{e}} = 1.0$ and $-1 < q_{\mathrm{b}} < 0$, which means that it is always stable irrespective of material properties as well as level of prestress [4], if yielding of cables and buckling of bars are not considered.

Eight units of regular truncated octahedral tensegrity structures are combined to obtain the tensegrity lattice as shown in Fig. 2. The units are combined symmetrically with respect to the horizontal plane and the two vertical planes. The four nodes of each truncating section are connected to those of another unit, where one of the duplicate cables at each connection is removed. Hence, the number of members is 336, and the number of nodes is 96 in this eight-unit tensegrity lattice.



(a) (b)

Figure 2: Undeformed shape of eight-unit tensegrity lattice; (a) plan/elevation, (b) diagonal view.

3. Large-deformation analysis under forced vertical displacement

In this work, a large-deformation analysis and optimization is carried out for the eight-unit tensegrity lattice in Fig. 2. For more details about the generation of this structures and its fundamental mechanical properties we refer the reader to reference [5]. Let l_0 and l denote the length of a member before and after deformation, respectively, under axial force f. We are particularly interested in the deformation regime for which bars undergo buckling. A bilinear elastic model is used for representing buckling behavior of a bar. The relation between compressive axial force $|f|$ and axial contraction $|\Delta l| = |l - l_0|$ of a bar is shown in Fig. 3, where f_b is the Euler buckling load. Stiffness EA of the bar is zero after buckling. When the member is in prebuckling range, its strain energy is calculated from

$$S = \frac{EA}{2l_0}(l - l_0)^2 \tag{3}$$

After buckling, its strain energy is obtained as

$$S = \frac{f_b^2 l_0}{2EA} + f_b \left| l - l_0 - \frac{f_b l_0}{EA} \right| \tag{4}$$

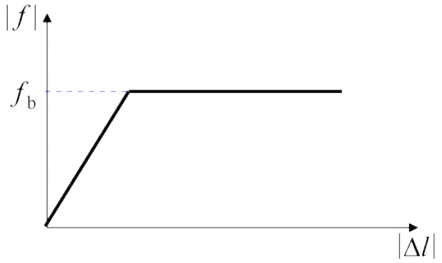


Figure 3: Bilinear elastic buckling model between compressive axial force $|f|$ and contraction $|\Delta l|$ of a bar.

The Euler buckling stress for the bars is computed from the slenderness ratio, and tension in bars is allowed. The yield stress of cables is assumed to be sufficiently large so that cables remain in elastic range, and its strain energy is computed from Eq. (3). Slackening of cable is checked after obtaining the optimal solution. Tangent stiffness matrix is derived as the sum of linear stiffness matrix and geometrical stiffness matrix. Forced displacement is applied incrementally, and unbalanced forces are reduced using Newton iteration at each step.

4. Formulation of optimization problem

Let L_b and L_c denote the total lengths of bars and cables, respectively. The cross-sectional areas of bars and cables are denoted by A_b and A_c, respectively, which are chosen as design variables. Objective function is the strain energy S stored before reaching the specified vertical displacement at the top layer. Here, for simplicity, the strain due to initial prestress is included in evaluation of the total strain energy. The constraints are given as follows so that the total structural volume does not change from the initial volume V_0:

$$A_b L_b + A_c L_c = V_0 \tag{5}$$

Another variable is β denoting the scaling parameter representing level of prestress that is multiplied to forces of all cables and struts at the initial undeformed state. The force density q_b (<0) of bars is considered as a parameter to obtain optimal solutions of various shapes, while the force density of the edge cables is fixed at $q_e = 1.0$. Note again that the shape is determined by the force density only; therefore, the undeformed shape does not change during the optimization process. A small value is assigned for the radius of gyration of the section so that Euler buckling precedes the yielding of a bar.

The optimization problem for finding A_b, A_c, and β for maximizing the total strain energy $S(A_b, A_c, \beta)$ is formulated as

$$\begin{aligned} &\text{Maximize } S^*(A_b, A_c, \beta) \\ &\text{sunject to } A_b L_b + A_c L_c = V_0 \\ &\qquad A_b^L \le A_b \le A_b^U,\ A_c^L \le A_c \le A_c^U \\ &\qquad \beta^L \le \beta \le \beta^U \end{aligned} \tag{6}$$

where the superscripts 'U' and 'L' are the upper and lower bounds of the variables.

5. Numerical examples

We optimized an eight-unit tensegrity lattice as shown in Fig. 2. The members are assumed to be made of steel material with Young's modulus $E = 2.05\times10^5$ N/mm^2. Let the *nominal volume* of the structure denote the volume of the cuboid in which the structure is inscribed. The volume of the surrounding cuboid is $8\times0.004 = 0.032$ m^3; i.e., shape of the structure is scaled to have the nominal volume of 0.032 m^3 for each configuration defined by q_b. Since length of the bar is about 170 mm, the radius of gyration is assumed to be 1.2 mm so that elastic buckling occurs before yielding.

In the bottom plane, the *z*-directional displacement is constrained at all nodes, *x*- and *y*-directional displacements are constrained at a node, and *x*- or *y*-directional displacement is constrained respectively at two of the remaining nodes. This way, rigid-body displacements and rotations are constrained allowing expansion of the bottom square. On the other hand, the 16 nodes in the top layer are enforced to move 80 mm in negative *z*-direction constraining rigid-body displacement and rotation in the similar manner as the bottom plane. The deformation is computed using displacement increment method with 1.0 mm at each step. A small stiffness $EA/100$ is assigned for a bar after buckling to stabilize the process.

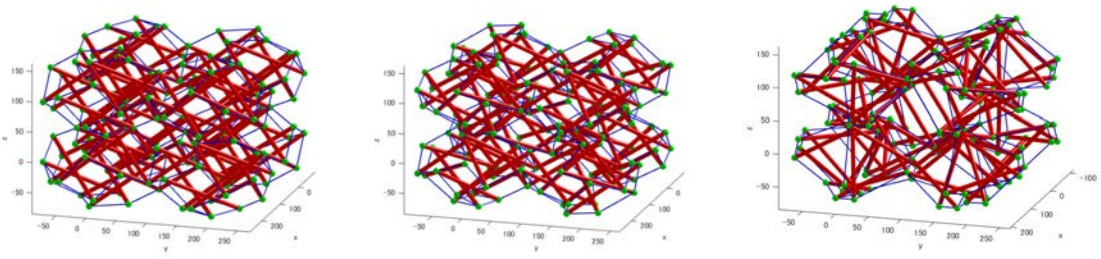
As noted in Sec. 2, each truncated octahedral unit is super-stable when $-1 < q_b < 0$ while q_e is fixed at. Therefore, the parameter q_b is varied as –0.3, –0.4, –0.5, –0.6, and –0.7. The lower and upper bounds for the cross-sectional areas are 0.1 mm^2 and 10.0 mm^2, respectively, for all members including cables and bars. The specified total volume of members is 2.2687×10^3 mm^3. The lower and upper bounds of the stress level β are 0.2 and 20.0, respectively. The optimization problem is solved using sequential

quadratic programming available in the function *fmincon* of the optimization toolbox of MATLAB Ver. 2018.

Table 1: Optimization results.

q_b	A_s (mm^2)	A_c (mm^2)	β	S (Nm)
–0.3	0.9179	0.1000	1.6536	9601
–0.4	0.9806	0.1000	1.7617	10130
–0.5	1.0456	0.1000	1.9449	14185
–0.6	1.1106	0.1000	1.9451	23137
–0.7	1.1742	0.1000	1.8395	37734

Optimal solutions as well as the optimal objective values are listed in Table 1 for various values of q_b. The cable cross-sectional area has its lower-bound value for all cases, and the cross-sectional area of bars and the objective function value increase as q_b is decreased. The stress level β mostly increases as q_b is decreased. The deformed shapes of optimal solutions are shown in Fig. 4. As seen from the figure, the length of strut decreases as q_b is decreased; accordingly, the squares at the truncated vertices become smaller and the initial stiffness increases.



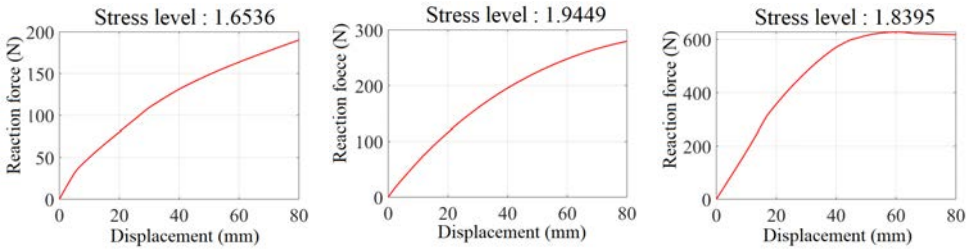
(a) $q_b = -0.3$ (b) $q_b = -0.5$ (c) $q_b = -0.7$

Figure 4: Deformed shape of optimal solutions.

Relation between the vertical downward displacement of top nodes and the sum of vertical reaction forces at all top nodes are plotted in Fig. 5. As seen from the figure, the vertical stiffness decreases as the downward displacement is increased. Furthermore, the maximum reaction force increases as q_b is decreased. The structure has a limit point instability for $q_b = -0.7$; i.e., it has a snap-through behavior if the deformation is controlled by the vertical load instead of the vertical displacement.

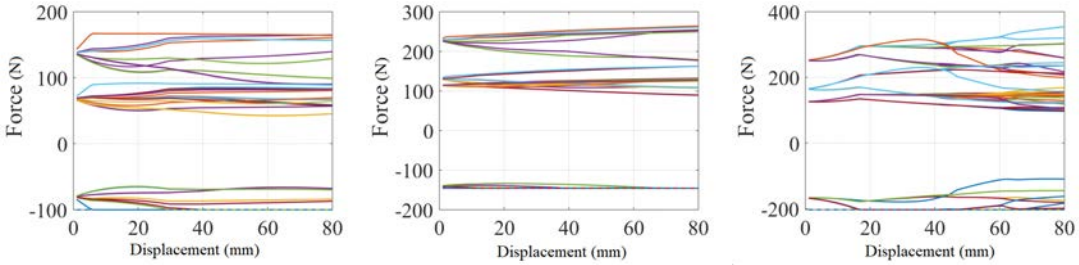
The member forces are plotted with respect to the vertical displacement in Fig. 6. Note that the axial force has positive value in tensile state. Although we do not consider slackening or yielding of cables, the cable forces have non-smooth distributions, which is caused by buckling of bars. It is seen from the results that the number of buckled members increases as vertical displacement is increased.

Although the optimal structures have positive vertical stiffness except for the case of $q_b = -0.7$, horizontal stiffness may be lost when q_b is small due to shear deformation of the upper and lower units. To prevent instability in horizontal direction, additional bars are attached as shown in Fig. 7 in one or two of the top, bottom, and middle layers of the lattice. Optimization is carried out for $q_b = -0.7$ and –0.8, because a smaller value of q_b is effective to have more strain energy.



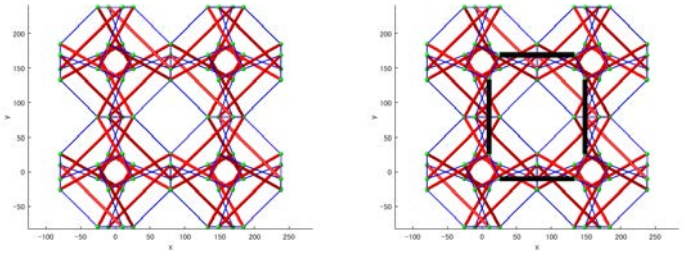
(a) $q_b = -0.3$ (b) $q_b = -0.5$ (c) $q_b = -0.7$

Figure 5: Relation between vertical displacement and reaction force.



(a) $q_b = -0.3$ (b) $q_b = -0.5$ (c) $q_b = -0.7$

Figure 6: Relations between vertical displacement and member forces.



(a) (b)

Figure 7: Additional bars in eight-unit lattice; (a) without bars, (b) with four additional bars.

Table 2: Optimization results of eight-unit lattice with additional four bars in various patterns of layers.

Layers for adding bars	q_b	A_s (mm^2)	A_c (mm^2)	β	S (Nm)
Top	–0.7	1.1294	0.1000	1.8137	38338
	–0.8	1.1825	0.1000	1.8103	38549
Top and middle	–0.7	1.0879	0.1000	1.5261	44891
	–0.8	1.1322	0.1000	1.5060	72591
Top and bottom	–0.7	1.0879	0.1000	1.7596	37265
	–0.8	1.1322	0.1000	1.6076	63305
Top, middle, and bottom	–0.7	1.0493	0.1000	1.3264	62863
Middle	–0.7	1.1294	0.1000	1.8230	38653
	–0.8	1.1825	0.1000	1.6698	66019

Optimization results are listed in Table 2. For example, 'top' means that four bars are added in the top layer. The deformed configuration, force-displacement relation, and load-displacement relation are shown in Fig. 8 for $q_b = -0.7$ with bars in the middle layer.

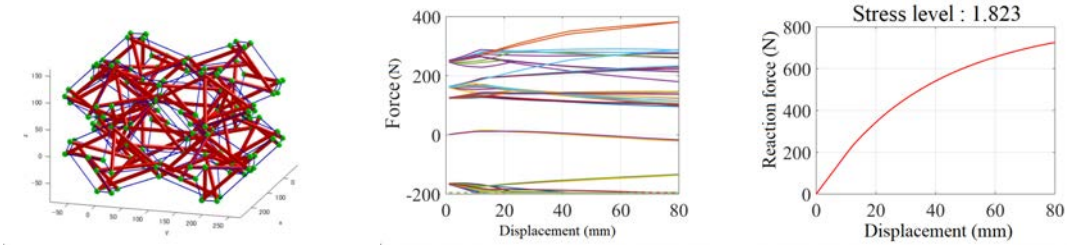
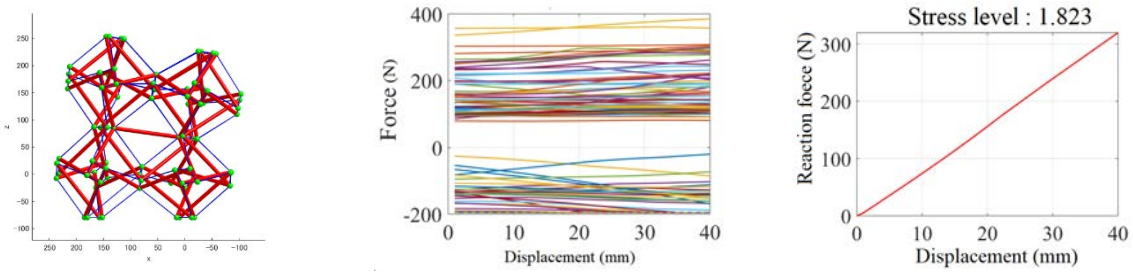


Figure 8: Property under vertical loading of the optimal solution for $q_b = -0.7$ with bars in top and bottom layers; (a) diagonal view of deformed shape, relation between displacement and axial forces, (c) relation between displacement and reaction force..

Shear stiffness in *x*-direction is next investigated after application of vertical displacement of 30 mm. The condition of forced vertical displacement is replaced to application of vertical loads that are equal to the reaction force at the forced displacement of 30 mm.

It was found that the structure is still unstable for the shear deformation, if the support conditions at the bottom layer are not modified. Therefore, all bottom nodes are pin-supported after application of downward displacement of 30 mm. The deformed configuration, histories of member forces, and load-displacement relation are shown in Fig. 8 for $q_b = -0.7$ with bars in the middle layer. The rocking deformation may be suppressed depending on the boundary conditions for practical application as, e.g., base isolation of structures. Suppression of rocking may lead to further stabilization of the structure. It has been confirmed that the vertical load-displacement relation remains almost the same after constraining the nodes in the bottom layer.



(a) (b) (c)

Figure 9: Property under horizontal loading of the optimal solution for $q_b = -0.7$ with bars in top and bottom layers; (a) elevation of deformed shape, relation between displacement and axial forces, (c) relation between displacement and reaction force.

6. Conclusions

An optimization method has been presented for tensegrity lattices composed of eight truncated octahedral units. The stored strain energy under specified forced vertical displacement is maximized under constraints on the structural material volume. It has been shown in the numerical examples that a flexible structure with degrading vertical stiffness is obtained as a result of optimization. Although structures generally retain compression stiffness even after large deformations, in some cases shear stiffness is lost. This issue can be addressed on those optimal solutions by adding four bars in some of the layers of the lattice. In this way, a tensegrity lattice with flexibility in vertical direction and adequate shear stiffness can be obtained to be applicable to an isolation system for vertical motion.

Acknowledgements

This research is partly supported by SPIRITS program of Kyoto University.

References

[1] J. Y. Zhang and M. Ohsaki, Adaptive force density method for form-finding problem of tensegrity structures, Int. J. Solids and Struct., Vol. 43, No. 18-19, pp. 5658--5673, 2006.

[2] J. Y. Zhang, M. Ohsaki and F. Tsuura, Self-equilibrium and stability of regular truncated hexahedral and octahedral tensegrity structures, *Int. J. Solids Struct*., 2019.

[3] J. Y. Zhang and M. Ohsaki, *Tensegrity Structures: Form, Stability, and Symmetry*, Mathematics for Industry 6, Springer, 2015.

[4] J. Y. Zhang and M. Ohsaki, Stability conditions for tensegrity structures, Int. J. Solids and Struct., Vol. 44, No. 11-12, pp. 3875-3886, 2007.

[5] J. J. Rimoli and R. K. Pal, Mechanical response of 3-dimensional tensegrity lattices, *Composites Part B*, Vol. 115, pp. 30–42, 2017.

[6] J. J. Rimoli, A reduced-order model for the dynamic and post-buckling behavior of tensegrity structures, *Mechanics of Materials*, Vol. 116, pp. 146–157, 2018.

[7] L.-Y. Zhang *et al*., Automatically assembled large-scale tensegrities by truncated regular polyhedral and prismatic elementary cells, Composite Structures, Vol. 184, pp. 30-40, 2018.

[8] X.-Q. Feng *et al*., Design methods of rhombic tensegrity structures, Acta Mech. Sin., Vol. 26, pp. 559-565, 2010.

[9] F. Fabbrocino and G. Carpentieri, Three-dimensional modeling of the wave dynamics of tensegrity lattices, Composite Structures, Vol. 173, pp. 9-16, 2017.

Proceedings of the IASS Annual Symposium 2019 – Structural Membranes 2019
Form and Force
7 – 10 October 2019, Barcelona, Spain
C. Lázaro, K.-U. Bletzinger, E. Oñate (eds.)

A geometrical approach to assess levels of structural robustness in statically indeterminate concrete elements

Aurélie DESCHUYTENEER*, Denis ZASTAVNI[a], Jean-François REMACLE[b]

*[a] Structures & Technologies, Faculty of architecture, architectural engineering, urbanism (LOCI), UCLouvain
Place du Levant 1 (L5.05.02), 1348 Louvain-la-Neuve, Belgium
aurelie.deschuyteneer@uclouvain.be
[b] Applied Mechanics and Mathematics (MEMA), Institute of Mechanics, Materials and Civil Engineering (IMMC), UCLouvain

Abstract

Graphic statics represents a powerful tool in the field of structural design, because the reciprocity between form and force diagrams allows constant and simultaneous control of both the geometry and magnitude of internal forces. The 21st century reinterpretation of graphic statics within interactive parametrical software has allowed its extension; in particular, admissible geometrical domains have been developed, which represent the set of permissible positions for the nodes of the force diagram. In the context of robustness assessment, admissible geometrical domains can indicate the range of alternative force distributions that can be activated in the structure in case of an unexpected event (such as loss of structural members, support displacement or increase of applied loads). This paper shows how computerized graphic statics can be employed to indicate the level of robustness of statically indeterminate reinforced concrete structures. The analysis of a simple case study highlights the set of potential force redistributions that can be activated in the structure, as well as their relative efficiency. The influence of the reinforcement layout on the range of possible force redistributions inside concrete is also outlined.

Keywords: structural robustness, structural design, graphic statics, strut-and-tie modelling, reinforced concrete, static indeterminacy, plastic theory.

1. Introduction

Structural robustness can be defined as a structure's aptitude to survive unforeseen or unexpected events, without being damaged to an extent that is disproportionate to the original cause (EN1990 [1]). This property is fundamental in ensuring human safety. Robustness became a compulsory Eurocode requirement after the terrorist attacks of September 11, 2001 (Gulvanessian and Vrouwenvelder [2]).

Many types of robustness assessment approaches are found nowadays in the literature (see Cavaco *et al.* [3] or Sorensen *et al.* [4] for more details). These approaches are all based on a numerical analysis of the structure's capacities for redistribution and resistance, calculated for given failure scenarios and for a design that has been determined beforehand. This leads to two main drawbacks. First, predefining potential failure scenarios does not allow one to cover the total range of events that could happen during the structure's lifetime. Secondly, applying numerical methods to previously designed structures makes these methods difficult to appropriate by project authors. Moreover these methods do not allow interaction with the design in seeking for optimal robustness performance.

To overcome these limitations, the authors of this paper have worked on a complementary approach to structural robustness, based on a geometrical rather than a numerical assessment (Zastavni *et al.* [5]). The approach enlarges the original method of graphic statics, in order to obtain a visual, interactive

Copyright © 2019 by Aurélie DESCHUYTENEER, Denis ZASTAVNI, Jean-François REMACLE
Published by the International Association for Shell and Spatial Structures (IASS) with permission.

and damage independent robustness indicator: the admissible geometrical domain, which shows the set of potential force redistributions inside given structures. Section 2 first reviews graphic statics' main hypotheses. It then details how structural constraints can be added to the original method and, finally, shows how these constraints can be used to build the admissible geometrical domains that indicate the level of robustness. Section 3 illustrates the geometrical robustness analysis of a statically indeterminate reinforced concrete beam.

2. Geometrical robustness assessment

2.1. Graphic statics

Graphic statics was a method established in the 19th and 20th century for structural analysis (Maxwell [6]), further applied to trusses, arches and beams. The principle of graphic statics is to use a common framework to represent both the structure and its internal forces. For continuous structures, these forces are obtained from replacing the structure's principal internal stresses by their resultant normal force, forming what is called a strut-and-tie network (Muttoni *et al.* [7]). The strut-and-tie network gives graphic statics' form diagram *D*, from which the reciprocal force diagram *D** is drawn such as to respect (Zalewski and Allen [8]):

- parallelism: each bar *i* of the form diagram is related to a unique reciprocal bar *i** in the force diagram, such that the difference in angle between them is always zero;
- equilibrium: all the bars that connect in a same node in one of the diagrams have reciprocal bars that form a closed polygon in the other. Inversely, all the bars belonging to a same polygon in one of the diagrams must join in a unique node in the other;
- boundary: all bars and nodes of the strut-and-tie network have to remain entirely inside the defined structural envelope, and constraints and displacements have to be respected at nodes where external or support loads are applied;
- yield: material resistance must not be exceeded in any part of the structure. This consists in verifying that length L_{i*} of each bar *i** of the force diagram conforms to:

$$L_{i*} \leq F_i = \sigma_e A_i \tag{1}$$

where F_i is the maximum axial force in bar *i* supposing that *i* is uniformly and fully stressed, σ_e is the material effective strength supposing a perfect rigid-plastic and thus ductile material behavior (Kostic [9]), and A_i is the areas chosen for the bars of the strut-and-tie network. Yield criterion makes strut-and-tie modeling applicable to any type of structure composed of any kind of material.

2.2. Constraint-based graphic statics

Graphic statics can be coupled to a set of geometrical constraints, which allow the conditional manipulation of the nodes in both reciprocal diagrams (Fivet [10]). These constraints are used to define affine relationships between the diagrams' nodes, such as relative position, proximity or equidistance. For example, considering the structure of Figure 1, the dark grey surface in force diagram *D** gives the set of positions that can be taken by the highlighted red node to ensure that:

- force magnitudes in the strut-and-tie network are below 10kN, defining the circular boundaries of the grey area;
- the strut-and-tie network remains inside the dashed rectangle in Figure 1's form diagram *D*, defining the linear boundaries of the grey area.

If the red node were to be given another position inside *D**'s dark grey area, this would result in drawing an alternative reciprocal strut-and-tie network in form diagram *D* that would still respect the

abovementioned constraints. Hence, *D**'s dark grey area can be seen as a representation of the set of alternative force distributions that can happen in the structure, given some initial design constraints.

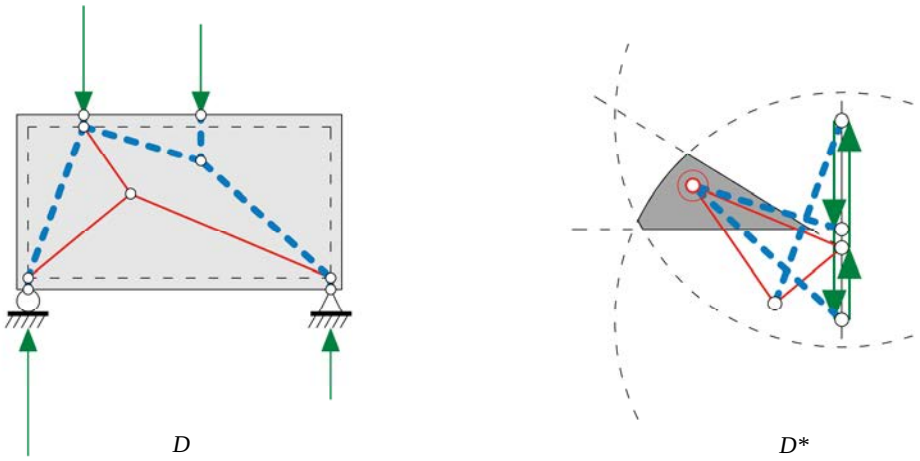


Figure 1: Constraining nodal positions in graphic statics' reciprocal diagrams
(with struts in dashed blue and ties in plain red)

2.3. Admissible geometrical domains

In the context of robustness assessment, the set of possible force distributions inside a structure, given by force diagram's dark grey area, can be used to depict the structure's aptitude to find alternative structural workings in case of hazard. These force distributions are safe solutions to the structural problem: since they verify the conditions mentioned in Section 2.1, they satisfy the Lower Bound Theorem of Plastic Theory (Heyman [11]).

Sets of alternative structural workings will be called admissible geometrical domains. These domains can be used as early indicators of robust design: the larger their area, the more potential force distributions there are and the more robust the structure will be. The geometrical approach to robustness can thus be used by practitioners to gain insight into the redistribution properties of the design they are currently working on. As it is visual and potentially interactive, the method can help comparing design options and help orienting early design. Moreover, admissible geometrical domains are damage independent robustness indicators: thus damage (loss of a structural member, support displacement, increase of applied loads, etc) that could potentially happen during the structure's lifetime does not have to be predicted.

It has been shown in Section 2.2 that alternative force distributions can be reached in a structure by changing nodal positions in the strut-and-tie network, thus changing the network's shape. Another manner of redistributing forces inside a structure is to change nodal connections in the strut-and-tie network, thus changing the network's topology. The combination of both shape and topology problems is known as the layout problem, meaning a change in nodal position and connectivity at the same time (Rothwell [12]). In this case, the structural problem becomes highly complex: as an unbounded number of strut-and-tie networks are solutions, admissible geometrical domains are difficult to obtain. However, in practice, the process of modelling the states of internal forces as strut-and-tie networks can often result in a shape or a topology problem only, depending on the structure to be analyzed. For example, designing unreinforced masonry structures for robustness is reduced to a shape problem, as only funicular paths of internal forces can be activated in the structure (Deschuyteneer *et al.* [13]). It will here be shown how the topology problem can be implemented for the geometrical robustness assessment of reinforced concrete deep structures.

3. Case study example

3.1. Description of the structure

The example developed here consists in a reinforced concrete deep beam, which is 2.1m long, 1.1m high and 20cm thick (Figure 2). It is simply supported, and loaded at the top by a vertical point load Q = 10kN. For the sake of the exercise, steel rebars are placed inside the beam as depicted by the layout of dashed lines $F_{i=0...10}$, the outer ones being placed at 5cm from the edge of the beam.

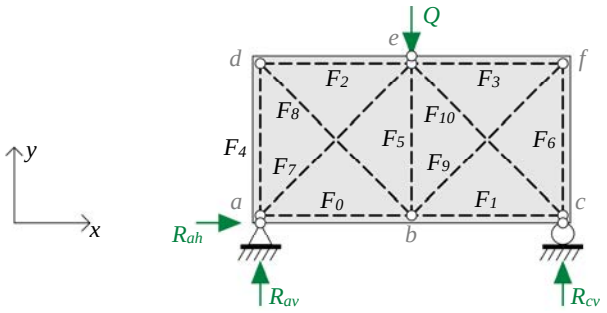


Figure 2: The structure under consideration with its nodal grid and candidate bars

Following the graphic statics approach, internal stresses inside such a continuous structure can be represented by a resultant strut-and-tie network. The set of valid strut-and-tie networks defines the structure's admissible geometrical domain, depicting its level of robustness in terms of force redistributions. In the present case, possible paths for the networks' ties are limited to locations where rebars are present, according to the layout of dashed lines $F_{i=0...10}$. Supposing the same hypothesis for struts, this means that the set of possible strut-and-tie networks can be described by a unique topology, composed of 6 nodes and 11 bars. Assessing the structure's level of robustness thus consists in finding the set of internal force distributions that follow the given topology, and for which material resistance is not exceeded in any bar. To speed up the analysis of the structural problem, a numerical pre-processing will first be applied in order to obtain the limit combinations of internal forces, as these will be the only pertinent ones for obtaining the structure's admissible geometrical domain.

3.2. Structural analysis through equilibrium matrix and Gauss-Jordan elimination

The structure's equilibrium equations are first written in a matrix format such that (A | b) x = 0. This equilibrium matrix possesses 12 lines, one for each node's –x and –y directions. It has 14+1 columns, one per bar F_i, one per reaction force R_i and one for the external load Q = 10kN:

$$\underbrace{\begin{bmatrix}
1 & 0 & 0 & 0 & 0 & 0 & 0 & 0.71 & 0 & 0 & 0 \\
0 & 0 & 0 & 0 & 1 & 0 & 0 & 0.71 & 0 & 0 & 0 \\
-1 & 1 & 0 & 0 & 0 & 0 & 0 & 0 & -0.71 & 0.71 & 0 \\
0 & 0 & 0 & 0 & 0 & 1 & 0 & 0 & 0.71 & 0.71 & 0 \\
0 & -1 & 0 & 0 & 0 & 0 & 0 & 0 & 0 & 0 & -0.71 \\
0 & 0 & 0 & 0 & 0 & 0 & 1 & 0 & 0 & 0 & 0.71 \\
0 & 0 & 1 & 0 & 0 & 0 & 0 & 0 & 0.71 & 0 & 0 \\
0 & 0 & 0 & 0 & -1 & 0 & 0 & 0 & -0.71 & 0 & 0 \\
0 & 0 & -1 & 1 & 0 & 0 & 0 & -0.71 & 0 & 0 & 0.71 \\
0 & 0 & 0 & 0 & 0 & -1 & 0 & -0.71 & 0 & 0 & -0.71 \\
0 & 0 & 0 & -1 & 0 & 0 & 0 & 0 & 0 & -0.71 & 0 \\
0 & 0 & 0 & 0 & 0 & 0 & -1 & 0 & 0 & -0.71 & 0
\end{bmatrix}}_{F_i}
\underbrace{\begin{bmatrix}
1 & 0 & 0 \\
0 & 1 & 0 \\
0 & 0 & 0 \\
0 & 0 & 0 \\
0 & 0 & 0 \\
0 & 0 & 1 \\
0 & 0 & 0 \\
0 & 0 & 0 \\
0 & 0 & 0 \\
0 & 0 & 0 \\
0 & 0 & 0 \\
0 & 0 & 0
\end{bmatrix}}_{R_i}
\underbrace{\begin{bmatrix}
0 \\ 0 \\ 0 \\ 0 \\ 0 \\ 0 \\ 0 \\ 0 \\ 0 \\ -1 \\ 0 \\ 0
\end{bmatrix}}_{Q}
\begin{bmatrix}
F_0 \\ F_1 \\ F_2 \\ F_3 \\ F_4 \\ F_5 \\ F_6 \\ F_7 \\ F_8 \\ F_9 \\ F_{10} \\ R_{ah} \\ R_{av} \\ R_{cv} \\ 10
\end{bmatrix}
= 0 \qquad (2)$$

Matrix (2) is composed of 12 equations (12 lines) and has 14 unknowns (11 F_i's and 3 R_i's). Thus it is *14 – 12 = 2* times indeterminate. To solve the associated system, two indeterminate unknowns can be chosen, let them be F_0 and F_1 (as highlighted in green in both matrices (2) and (3)). This means that all the other internal forces $F_{i=2...10}$ and reaction forces R_i can be expressed as a function of F_0, F_1 and Q only. To obtain the equilibrium equations under this simplified form, a Gauss-Jordan elimination can be performed on matrix (2), for which the two columns corresponding to the indeterminate unknowns have been placed just before the column of the external loads. This gives:

$$\left[\begin{array}{cccccccccccc|cc|c}
1 & 0 & 0 & 0 & 0 & 0 & 0 & 0 & 0 & 0 & 0 & 0 & -1 & 0 & 0.5 \\
0 & 1 & 0 & 0 & 0 & 0 & 0 & 0 & 0 & 0 & 0 & 0 & 0 & -1 & 0.5 \\
0 & 0 & 1 & 0 & 0 & 0 & 0 & 0 & 0 & 0 & 0 & 0 & -1 & 0 & 0.5 \\
0 & 0 & 0 & 1 & 0 & 0 & 0 & 0 & 0 & 0 & 0 & 0 & -1 & -1 & 1 \\
0 & 0 & 0 & 0 & 1 & 0 & 0 & 0 & 0 & 0 & 0 & 0 & 0 & -1 & 0.5 \\
0 & 0 & 0 & 0 & 0 & 1 & 0 & 0 & 0 & 0 & 0 & 0 & 1.41 & 0 & 0 \\
0 & 0 & 0 & 0 & 0 & 0 & 1 & 0 & 0 & 0 & 0 & 0 & 1.41 & 0 & -0.71 \\
0 & 0 & 0 & 0 & 0 & 0 & 0 & 1 & 0 & 0 & 0 & 0 & 0 & 1.41 & -0.71 \\
0 & 0 & 0 & 0 & 0 & 0 & 0 & 0 & 1 & 0 & 0 & 0 & 0 & 1.41 & 0 \\
0 & 0 & 0 & 0 & 0 & 0 & 0 & 0 & 0 & 1 & 0 & 0 & 0 & 0 & 0 \\
0 & 0 & 0 & 0 & 0 & 0 & 0 & 0 & 0 & 0 & 1 & 0 & 0 & 0 & -0.5 \\
0 & 0 & 0 & 0 & 0 & 0 & 0 & 0 & 0 & 0 & 0 & 1 & 0 & 0 & -0.5 \\
\hline
 & & & & & & & & & & & & \mathbf{a} & \mathbf{b} & \mathbf{c}
\end{array}\right]
\left[\begin{array}{c}
F_2 \\ F_3 \\ F_4 \\ F_5 \\ F_6 \\ F_7 \\ F_8 \\ F_9 \\ F_{10} \\ R_{ah} \\ R_{av} \\ R_{cv} \\ F_0 \\ F_1 \\ 10
\end{array}\right]
= 0 \qquad (3)$$

To guarantee admissible sets of internal force distributions inside the topology, material resistance must not be exceeded in any part of the structure. This means that the following inequality has to be verified for each bar F_i of the network:

$$-F_{C,max} \leq F_i \leq F_{T,max} \qquad (4)$$

with $F_{C,max}$ as the maximum axial force in the struts, and $F_{T,max}$ these in the ties. These forces depend on the strength class and on the cover for concrete struts, and on the number and diameter of rebars for steel ties. For C25/30 concrete (f_{cd}^* = 14MPa) and for circular struts the radius of which equals the cover (e=5cm) we find $F_{c,max}$ = 110kN; for 2Ø12 BE500s steel rebars (f_y = 435MPa) we have $F_{T,max}$ = 98.4kN. Based on matrix (3), inequality (4) can be rewritten for bars $F_{i=2...10}$ as:

$$-F_{C,max} \leq F_i = -(aF_0 + bF_1 + cQ) \leq F_{T,max} \qquad (5)$$

with coefficients *a*, *b*, and *c* given in the last three columns of matrix (3). Note that the same reasoning could be applied for constraining reaction forces R_i between specific values. However, for the sake of the present example, these forces will remain unbounded. (4) and (5) thus give 11 pairs of inequalities, which have to be verified by the combinations of internal forces in each strut-and-tie in order to be admissible in terms of internal forces. From a geometrical point of view, these inequalities car be turned into half plane equations in a 2D graph (the dashed lines in Figure 3), with the –x axis standing for the force inside bar F_0 and the –y axis for those in F_1. The light grey surface of Figure 3, formed inside the dashed boundary lines, then depicts the set of valid combinations (F_0, F_1) which are solutions to the structural problem. In particular, the six corner points of this surface are associated with (F_0, F_1) combinations for which the corresponding strut-and-tie network has reached yielding in two bars.

The light grey surface of Figure 3 can further be analyzed, by assessing the efficiency of the strut-and-tie networks associated to each of its valid point coordinates (F_0, F_1). The efficiency is obtained from the formula given by Maxwell in 1890 [14], later reinterpreted by Baker *et al*. [15]:

$$\sum_i L_{t,i}F_{t,i} + \sum_j L_{c,j}F_{c,j} = \sum_i L_{t,i}A_{t,i}\frac{F_{t,i}}{A_{t,i}} + \sum_j L_{c,j}A_{c,j}\frac{F_{c,\mathrm{j}}}{A_{c,j}} = V_t\sigma_{e,t} + V_c\sigma_{e,c} \qquad (6)$$

This means that the sum of the products of each bar length in tension in the form diagram $L_{t,i}$ by its corresponding length (force) in the force diagram $F_{t,i}$, plus the same sum of products for compressive bars (with c indices), is directly proportional to the volume of material V that has to be implemented in the strut-and-tie network to carry the applied load. As in equation (1), $\sigma_{e,t}$ and $\sigma_{e,c}$ values give material effective strength for both steel and concrete; $A_{t,i}$ represents the rebars area and $A_{c,j}$ the maximum circular area that can be given to the concrete struts (which is a function of the cover). Equation (6) then helps ranking the set of possible internal force combinations in the strut-and-tie by order of efficiency: the less volume needed the more efficient the structure is. Efficiency is given by the polygonal curves in Figure 3, with the associated values in [kNm]. Equation (6) also helps assessing that combination ($F_0 = F_1 = 5kN$) gives the most efficient path for internal forces among the set of valid ones: this path is the one associated with a minimum volume of material, thus giving the smallest solution to equation (6).

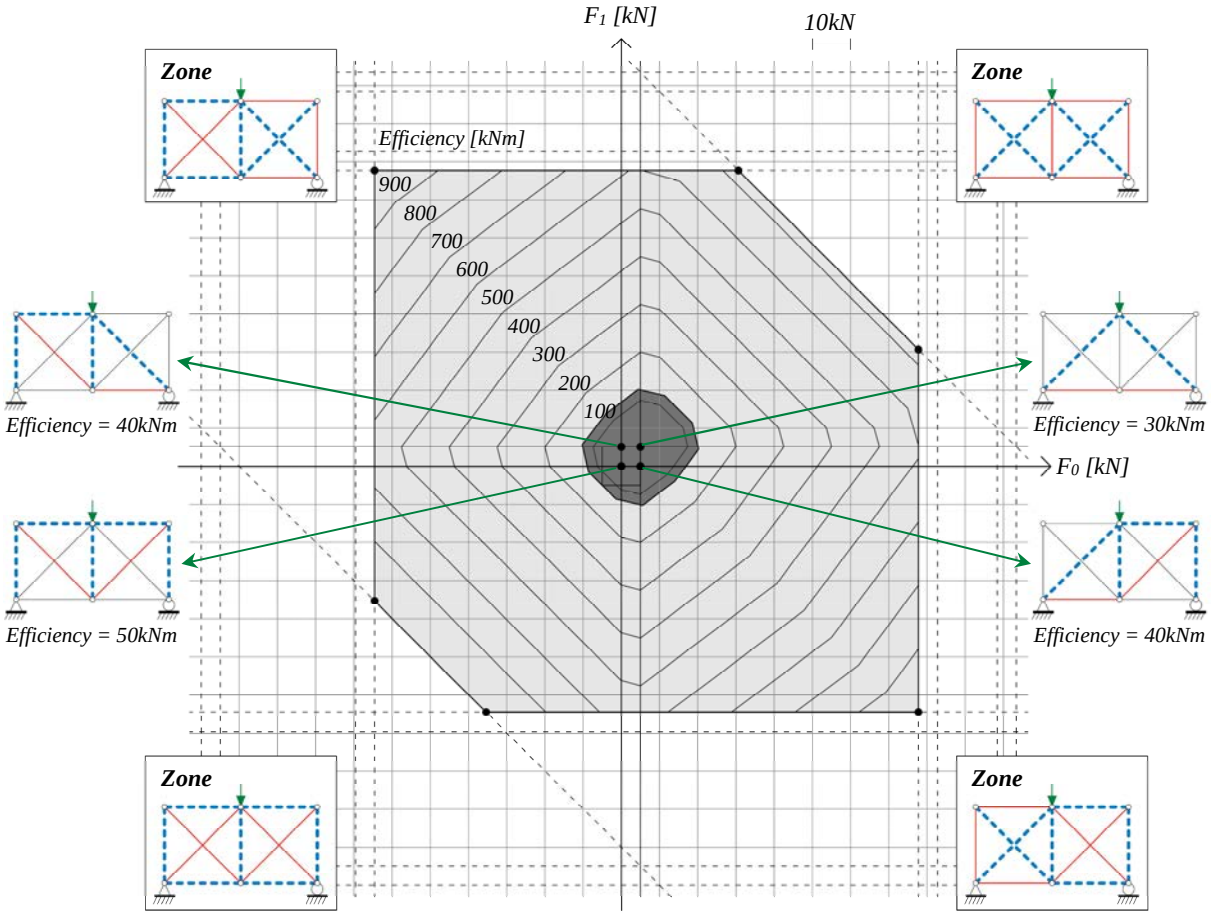


Figure 3: The solution surface associated with the structural problem, representative combinations of internal forces inside the strut-and-tie network topology and related curves of efficiency

The solution surface of Figure 3 can be used to relate the location of rebars in concrete to the level of robustness of the associated structure in terms of force redistributions. Here Figure 3 has been obtained for a structure in which tensile forces can be activated in any bar of the initial strut-and-tie topology (see Figure 2). If the rebar layout was to be limited to bars F_0, F_1, F_8, and F_9 only

(corresponding to a classical rebar layout for this type of structure), the solution space would be limited to the square area comprised between the four central nodes of the solution surface. Hence, this reduced rebar layout would still provide some redistribution properties to the structure, even if at a lower level.

Figure 3 also helps knowing whether a given combination of internal forces is relevant or penalized by the self-stress state. Relevant combinations are defined as the ones at least as efficient as the one for which forces F_0 and F_1 are opposite to those in the most efficient strut-and-tie network. For the present structure, the combination of internal forces leading to maximal efficiency (30kNm) is the one for which $F_0 = F_1 = 5kN$. Thus pertinent combinations of internal forces are the ones at least as efficient as the solution for which $F_0 = F_1 = -5kN$. The associated solution sub-surface is given by the dark grey area in Figure 3.

3.3. Conversion into admissible geometrical domains

To assess geometrically the capacities for force redistributions of the given structure, the 6 corner points of the solution surface of Figure 3 give the 6 possible limit combinations of internal forces (F_0, F_1). These are associated with the 6 strut-and-tie networks that determine the boundaries of the admissible geometrical domain. In this case, the domain is composed of 8 segments – some are partly superimposed –, as depicted in light grey in Figure 4's force diagram *D**. This domains represents the capacity of the given structure to redistribute internal forces. The strut-and-tie network represented in Figure 4's form diagram *D* is associated to the bottom right point of Figure 3's light grey solution surface, reached when F_0 = 7.775kN and F_1 = -6.458kN. This solution yields bar F_7 in compression (in light blue) and bar F_9 in tension (in orange).

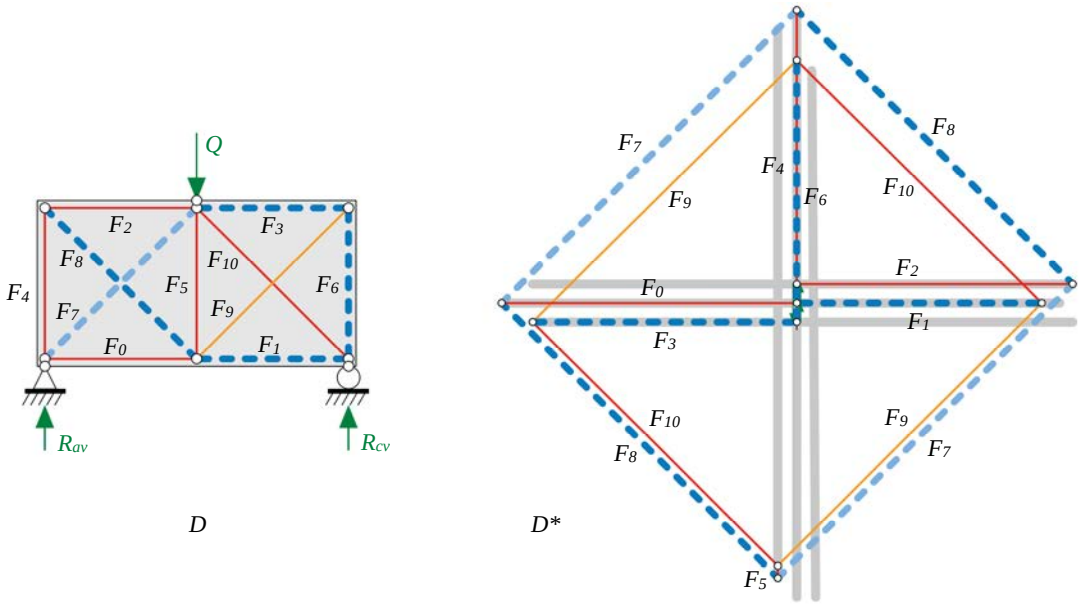


Figure 4: Admissible geometrical domain depicting the structure's level of robustness in terms of force redistributions

4. Conclusion and perspectives

This paper presents a geometrical method that helps characterizing levels of structural robustness. Based on graphic statics and strut-and-tie modeling, the method develops admissible geometrical domains as robustness indicators. Domains depict the range of possible nodal positions inside given structures, indicating their capacity for force redistributions. Hence, comparing domain areas for several rebar configurations helps highlighting the loss or gain in the aptitude to redistribute forces.

As the proposed geometrical method is visual, it can easily be appropriated by project authors at the design stage. When implemented into parametric software (such as Geogebra or Grasshopper under Rhino), the method can further be turned into an interactive tool, showing which design parameters will enhance robustness properties as well as efficiency. In particular, for concrete structures, the method can help choosing a pertinent rebar layout in order to reach required robustness performances.

Even if it helps understanding the basic functioning of the geometrical approach for robustness assessment, the case study presented in this paper remains quite simplistic. In order to be fully useful to study realistic structures, the method is now being extended to:

- larger structures, with more bars;
- structures with several external loads;
- structures with multiple supports and external static indeterminacy;
- structures with holes modeling openings (doors or windows);
- structures for which bars of the initial grid are not limited to orthogonal and 45° angles.

References

[1] EN1990: Eurocode 0 - basis of structural design.

[2] H. Gulvanessian and T. Vrouwenvelder, "Robustness and the Eurocodes", *Structural Engineering International*, vol. 16(2), pp. 167-171, 2006.

[3] E. Cavaco, J. R. Casas and L. Neves, "Quantifying redundancy and robustness of structures" in *IABSE Workshop Helsinki Report 100*, pp. 78-99, 2013.

[4] J.D. Sorensen, E. Rizzuto, H. Narasimhan and M. H. Faber, "Robustness: theoretical framework", *Structural Engineering International*, vol. 22(1), pp. 66-72, 2012.

[5] D. Zastavni, A. Deschuyteneer and C. Fivet, "Admissible geometrical domains and graphic statics to evaluate constitutive elements of structural robustness", *International Journal of Space Structures*, vol. 31(2-4), pp. 165-176, 2016.

[6] J.C. Maxwell, "On reciprocal figures and diagrams of forces", *Philosophical Magazine*, vol. 27(4), pp. 250-261, 1864.

[7] A. Muttoni, J. Schwartz and B. Thürlimann, *Design of concrete structures with stress fields*, Birkhaüser, Basel, Switzerland, 1997.

[8] W. Zalewski and E. Allen, *Shaping structures: Statics*, New York: John Wiley and Sons, 1998.

[9] N. Kostic, *Topologie des champs de contraintes pour le dimensionnement des structures en béton armé*, PhD thesis, Ecole Polytechnique Fédérale de Lausanne, 2009.

[10] C. Fivet, *Constraint-Based Graphic Statics, a geometrical support for computer-aided structural equilibrium design*, PhD thesis, Université catholique de Louvain, 2013.

[11] J. Heyman, *Basic structural theory*, Cambridge: Cambridge University Press, 2008.

[12] A. Rothwell, *Optimization methods in structural design*, Solid Mechanics and its Applications 242, Springer International Publishing, 2017.

[13] A. Deschuyteneer, J.-F. Rondeaux and D. Zastavni, "Structural assessment of masonry arches using admissible geometrical domains", *11th International Conference on Structural analysis of Historical Constructions*, Cusco, Peru, 2018.

[14] J.C. Maxwell, *The scientific papers*, University Press, Cambridge, United Kingdom, 1890.

[15] W.F. Baker, A. Beghini and A. Mazurek, "Applications of structural optimization in architectural design", *Proceedings of the Structures Congress*, Chicago, USA, 2012.

Proceedings of the IASS Annual Symposium 2019 - Structural Membranes 2019
Form and Force
7-10 October 2019, Barcelona, Spain
C. Lázaro, K.-U. Bletzinger, E. Oñate (eds.)

Form-finding method of cable-net structures using Grassmann algebra and mass-points

Maja BANIČEK*, Krešimir FRESL[a], Mario UROŠ[a], Tomica KOSTRIC[b]

*,a Faculty of Civil Engineering, University of Zagreb, Croatia
Kačićeva Street 26, Zagreb, Croatia
mbanicek@grad.hr
b Tenso Ltd, Ante Kovačića 34, Varaždin, Croatia

Abstract

In the paper, an application of Grassmann algebra and weighted points, called mass-points, to the Force Density Method (FDM) for cable-net structures is described. In classical mechanics, point represents location in space, and vector represents a force acting on that point with added mass. In this way, it is possible to study geometry using fundamental principles of mechanics. Procedure for determining the centre of mass-points is closely related to finding the position of a free node of cable-net structure based on FDM. The method presented in this paper is iterative, based on mass-points, where points represent fixed nodes, their masses represent force densities in cables of structure, and centre of the mass-points represents the position of a free node, whose coordinates are unknown. The procedure is presented through an example of a simple cable-net structure consisting of only one free node. Since the form-finding in the form diagram is studied using principles of mechanics, it is possible to construct the reciprocal force polygon using obtained centres of the given mass-points. Applying the method described in this paper, an example of a cable-net structure is shown in the form diagram whereas force polygons are assembled in the force diagram.

Keywords: graphic statics, reciprocal diagrams, form diagram, force diagram, mass-points, Grassmann algebra, Plücker coordinates, form-finding, equilibrium-finding

1 Introduction

Methods of graphic statics are used to evaluate the global equilibrium of structural systems and to determine the flow of internal axial forces in structural elements only by geometric operations. Since the actual trends in architecture give structures with complex and irregular geometry, there is an increasing need for an interactive tool that would enable direct and simultaneous control over the shape of the structure and internal forces caused by external loads, and thus finding an effective geometry of the structure at an early stage of structural design. Graphic statics methods are based on the construction of two reciprocal diagrams: the form diagram which shows the geometry of structure (location of internal nodes and supports, external loads and lengths of structural elements) and the force diagram where polygons of forces, assembled of vectors, represent equilibrium of internal forces in structural elements, forces in supports and external loads.

Copyright © 2019 by Maja Baniček, Krešimir Fresl, Mario Uroš and Tomica Kostric
Published by the International Association for Shell and Spatial Structures (IASS) with permission.

By attaching masses to points, it is possible to study geometry applying basic principles of mechanics (Goldman, [1]). On the other hand, using force densities and an iterative method node by node, the minimal shape of a cable-net structure can be obtained. In every step of the procedure, each free node is considered as an unknown, and its adjacent nodes are considered as supports. The similar procedure, based on an iterative method and force densities, has already been described by Enrique *et al.* [2]. The geometrical procedure of the form-finding, presented in this paper, is performed by adding corresponding masses as the given force densities to the adjacent, fixed nodes and by applying Grassmann algebra of mass-points to find the centre of the given mass-point system. In classical mechanics of particles, finding the centre of given weighted points coincides with the point at which the resultant weight of the given mass-point system acts.

2 Grassmann algebra of mass-points and vectors

2.1 Mass-points

In Grassmann algebra points are expressed as quadruples $P = (m, x, y, z)$, where $m \neq 0$ is a (generalized) mass of the point. Such a point is called the mass-point and we will denote it as a pair (m, mP). Division of the last three coordinates by the first one gives a normalized point $(1, mP/m) = (1, P) = (1, x/m, y/m, z/m)$, and $\mathrm{P} = (x/m, y/m, z/m)$ represents the position of mass-point (m, mP) in Cartesian coordinates. The expression $\mathbf{v} = (0, \vec{v}) = (0, x, y, z)$ represents a point at infinity, where $\vec{v}$ is a vector directed from the origin to the point (m, mP).

2.2 Lines and Forces

A line can be specified as a span of two points, namely by progressive product of two points in the form $l = (\mathbf{l_0}, \bar{\mathbf{l}}) = P_1 \wedge P_2 = (m_1, x_1, y_1, z_1) \wedge (m_2, x_2, y_2, z_2) = (l_{01}, l_{02}, l_{03}, l_{23}, l_{31}, l_{12})$, where $l_{ij} = x_i y_j - x_j y_i$ are homogeneous coordinates of a line, called Plücker line coordinates (Plücker [3], Pottmann and Wallner [4]). For such a line, the distance between two normalized points, that is the length of the line segment, can be determined as: $|l| = \sqrt{l_{01}^2 + l_{02}^2 + l_{03}^2}$.
A force can also be expressed in Plücker line coordinates $F = (\mathbf{f_0}, \bar{\mathbf{f}})$, where the first part represents vector $\mathbf{f_0} = (f_{01}, f_{02}, f_{03})$ of the force F, and the second part represents moment vector $\bar{\mathbf{f}}$ of $\mathbf{f_0}$ about the origin of the coordinate system. Also, the condition $\mathbf{f_0} \cdot \bar{\mathbf{f}} = 0$ must be fulfilled (the same holds for the lines). Force, as in the case of lines, can be expressed as a span of two normalized points $F = P_1 \wedge P_2$. Point P_1 can be regarded as the tail and P_2 as the head of the force F, and the length of the segment is equal to its intensity.

2.3 Operations on mass-points and vectors

Basic geometric operations of Grassmann algebra and their application to graphic statics and static equivalency can be found in Baničeк *et al.* [5]. Here, Grassmann algebra of mass-points and vectors is used to present a graphical method for form-finding of cable-nets applying fundamental principles of mechanics. In this method, mass-points are expressed in Grassmann coordinates of points and vectors as described in sections 2.2 and 2.1.

2.3.1 Point and vector addition

The sum of a given mass-point (m, mP) and a vector $\mathbf{f_0}$, given as a force $F = (\mathbf{f_0}, \bar{\mathbf{f}})$ acting at the point (m, mP), can be expressed as (see Figure 1):

$$(m, mP) + (0, \mathbf{f_0}) = (m, mP + \mathbf{f_0}) = \left(1, \frac{mP + \mathbf{f_0}}{m}\right) = \left(1, P_1 + \frac{\mathbf{f_0}}{m}\right) \tag{1}$$

In mechanical interpretation, the given vector $\mathbf{f_0}$ represents a force $F = (\mathbf{f_0}, \bar{\mathbf{f}})$ acting on the mass m and pulling the point $(1, P)$ to the new position $(1, P+\mathbf{f_0}/m)$. Physically, the expression $\mathbf{f_0}/m$ represents velocity and varies inversely with the mass, while the vector $\mathbf{f_0}$ represents momentum vector (Goldman, [1]).

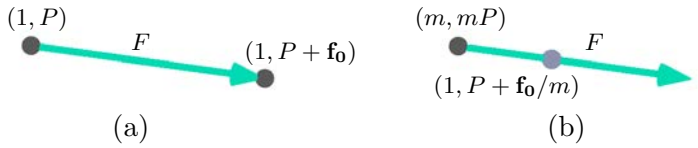


Figure 1: Addition of the mass-point (m, mP) and vector $F = (\mathbf{f_0}, \bar{\mathbf{f}})$, (a) $m = 1$, (b) $m \neq 0, 1$

2.3.2 Centre of mass-point system

According to well-known Archimedes' law of the lever of two mass points (Grassmann [6]), we can find the centre $(m_c, m_c P_c) = (m_1 + m_2, m_1 P_1 + m_2 P_2)$ of two given mass-points as a sum of their coordinates and masses. The mass-centre $(m_c, m_c P_c)$ is also the balancing point of the given mass system, so the sum of moments of the two masses, called mass moments (Browne [7]), about the mass-centre must vanish:

$$m_1 \cdot d_1 - m_2 \cdot d_2 = 0 \tag{2}$$

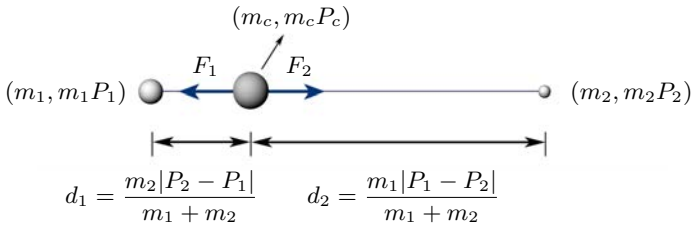


Figure 2: Archimedes' law of the lever

Consider the lever shown in Figure 2 as a cable-net structure consisting of two tensioned cables connected in the node $(m_c, m_c P_c)$. Since forces F_1 and F_2 in the node $(m_c, m_c P_c)$ must be in equilibrium, the condition (2) can be written in the form:

$$F_1 - F_2 = 0 \tag{3}$$

In mechanics of particles, mass-point has inertia. Thus, the effect of a force acting on two points with different masses will be less in the case of the larger mass (larger inertia), and conversely. In other words, translations d_1 and d_2 from the point of the same mass $m_c = m_1 + m_2$ will depend on the force magnitude pulling the mass m_c to the new position (Figure 3a and 3b). Since the two given mass-points uniquely determine the mass-centre, two forces S_1 and S_2 will translate the mass m_c from the point $(1, P_1)$ or $(1, P_2)$ to the point $(1, P_c)$ by the distance d_1 or d_2 accordingly. Therefore, the position of the point $(1, P_c)$ is determined in the form:

$$(1, P_c) = (1, P_1 + d_1) = \left(1, P_1 + \frac{\mathbf{f_{01}} \cdot m_2}{m_1 + m_2}\right),$$

$$(1, P_c) = (1, P_2 + d_2) = \left(1, P_2 + \frac{\mathbf{f_{02}} \cdot m_1}{m_1 + m_2}\right).$$

From equations (1) and (2) it can be seen that the force F_1 in the left cable is equal to $m_1 \cdot d_1$ and the force F_2 in the right cable is equal to $m_2 \cdot d_2$, as shown in the force diagram in Figure 3c. Notice that the expression of the two forces are the same as in the case of force densities with cable force $F = q \cdot l$, where q is force density and l is length of the cable.

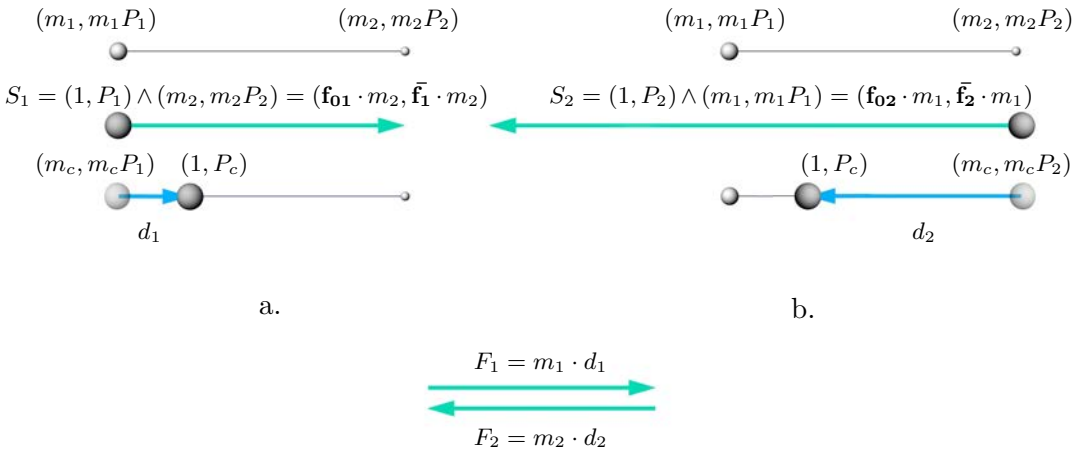


Figure 3: Geometric interpretation of Archimedes' law of the lever

For a mass-point system consisting of an arbitrary number of n mass-points, the mass-centre can be found iteratively, starting with the first two points and by adding in each step of the iteration one of the remaining masses. The equilibrium-finding procedure of the mass-centre, as shown in Figure 3, can be graphically followed in the force diagram. In the next section, we will show the construction of the force diagram for an arbitrary number of mass-points.
The sum of the coordinates of the given mass-points gives us the centre of the mass-points system. To find the position of the centre of the mass-points we can also use the following equation (Möbius [8]):

$$(m_c, m_c\mathbf{P}_c) = \left(\sum_{n=1}^{n} m_i, \sum_{n=1}^{n} m_i\mathbf{P}_i\right) \tag{4}$$

As seen from the expression (4), only operations of addition and multiplication by scalar are used. Therefore, it could be computationally more efficient for preforming of the form-finding because it lets us avoid, or at least postpone, operations of the division until the end of the procedure, thus achieving results with better accuracy.

3 Application of the mass-points algebra to the form-finding

3.1 Equilibrium of a free node and force diagram construction

Using Archimedes' law and the procedure of finding the mass-centre, described in the previous section 2.3.2, it is possible to graphically obtain the equilibrium position of a free node of a cable-net structure by using the iterative method for finding the centre of mass system. The procedure will be applied to the example of a free node in the form diagram, shown in Figure 4a, and will be simultaneously followed by polygons of internal forces in the force diagram.

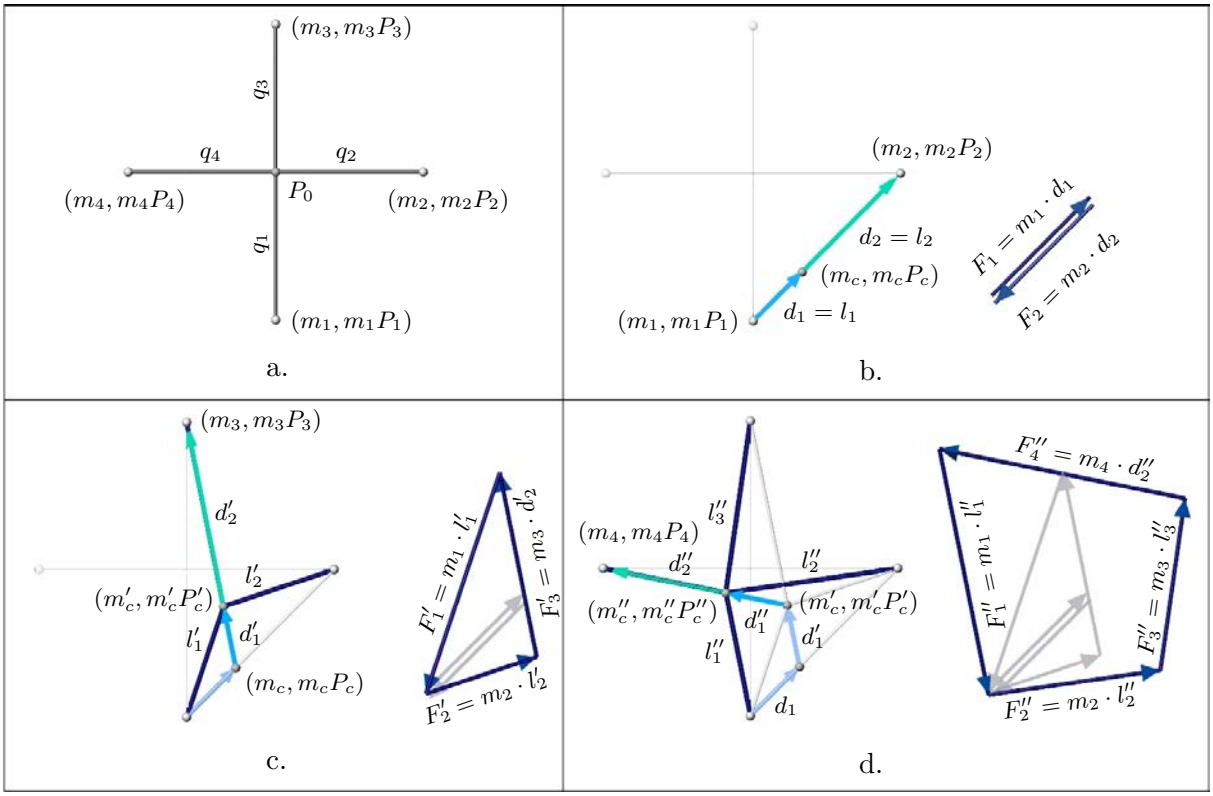


Figure 4: Iterative graphical procedure for form-finding of a free node

Let us consider a single node cable-net system shown in Figure 4. For the free node P_0, connected to fixed points $P_i, i = 1, 2, 3, 4$ with four pre-stressed cables, we can determine its equilibrium position using procedure for finding the mass-centre. Point of the free node is given as a normalized point $P_0 = (1, x_0, y_0, z_0)$ and points of the fixed nodes are given in the normalized form $P_i = (1, x_i, y_i, z_i), i = 1, 2, 3, 4$. The values q_i in Figure 4a present force densities or tension coefficients in corresponding cables.

Before we start the procedure, the given force densities are removed from cables and attached to the corresponding fixed nodes in terms of masses $m_i = q_i$. Therefore, the coordinates of the fixed

nodes becomes Grassmann coordinates of the mass-points $(m_i, m_i P_i) = (m_i, m_i{\cdot}x_i, m_i{\cdot}y_i, m_i{\cdot}z_i)$. Such points form a mass system; thus, the equilibrium-finding for the free node P_0 can be carried out.

First iteration step of the equilibrium-finding is to determine centre of the first two masses $(m_1, m_1 P_1)$ and $(m_2, m_2 P_2)$ (Figure 4b). The system consisting of two mass-points can be regarded as a two-cable structure, and the centre of masses can be obtained as described in section 2.3.2. That is,

$$(1, P_c) = (1, P_1 + d_1) = \left(1, P_1 + \frac{\mathbf{f_{01}} \cdot m_2}{m_1 + m_2}\right)$$

The distances d_1 and d_2 are also the lengths of the two cables. Thus, magnitudes of the forces in the cables are equal and opposite orientated. In order to construct the force diagram, magnitudes of forces F_1 and F_2 can be calculated as products of the corresponding masses and lengths of cables (Figure 4b right).

As mentioned before, for a mass-point system consisting of n arbitrary number of mass-points the mass-centre can be found iteratively, starting with the first two points and by adding in each step of the iteration one of the remaining masses. In the similar way, the equilibrium position of a single node, connected to the fixed nodes with n cables, can be obtained using mass-points. So, the next step is to attach the third mass to existing two-mass system $(m_c, m_c P_c)$. In this way, a new two-mass system $(m'_c, m'_c P'_c)$ (Figure 4c), where the new mass is the sum of the three masses $m'_c = m_1 + m_2 + m_3 = m_c + m_3$, and its location are determined by pulling the mass m'_c of the new system with the force $S_3 = (1, P_c) \wedge (m_3, m_3 P_3) = \mathbf{f_{02}} \cdot m_3$ from the point $(1, P_c)$ for the distance d'_1:

$$(1, P'_c) = (1, P_c + d'_1) = \left(1, P_c + \frac{\mathbf{f_{02}} \cdot m_3}{m_1 + m_2 + m_3}\right) \tag{5}$$

For the example shown in figure 4a, the last iteration step is attaching the fourth mass to the existing two-mass system $(m'_c, m'_c P'_c)$. The new mass-system $(m''_c, m''_c P''_c)$ has the mass $m''_c = m_1 + m_2 + m_3 + m_4 = m'_c + m_4$ and it is translated from the point $(1, P'_c)$ by the force $S_4 = (1, P'_c) \wedge (m_4, m_4 P_4) = \mathbf{f_{03}} \cdot m_4$ to the new position:

$$(1, P''_c) = (1, P'_c + d''_1) = \left(1, P'_c + \frac{\mathbf{f_{03}} \cdot m_4}{m_1 + m_2 + m_3 + m_4}\right) \tag{6}$$

3.2 Application to a cable-net structure

Applying the procedure for a single node, described in section 3.1, finding the shape of the cable-net structure (Figure 5) is carried out by using an iterative method node by node until equilibrium of the given cable net structure is established. For this example, in all cables the force density values are set to 1 except for the boundary cables, where the values are set to 2, and for the inner cable loop, with the force densities set to 3.

To construct the force diagram from the obtained form diagram, we have developed a computer program based on Bow's notation [9] of nodes and forces and the approach by Micheletti [10]. The code of the program is written in GhPython [11] (Python interpreter component and plug-in for Grasshopper [12] and Rhinoceros [13]). After the equilibrium of each node is found, the code calculates forces F_i of each cable by multiplying obtained lengths l_i by their corresponding masses m_i, where $i = 1...n$ number of cables connected at the considered node. To determine the

lengths of the cables, we can apply the expression of line segment as a span of two normalized points, that is: $|l_i| = \sqrt{l_{i01}^2 + l_{i02}^2 + l_{i03}^2}$.

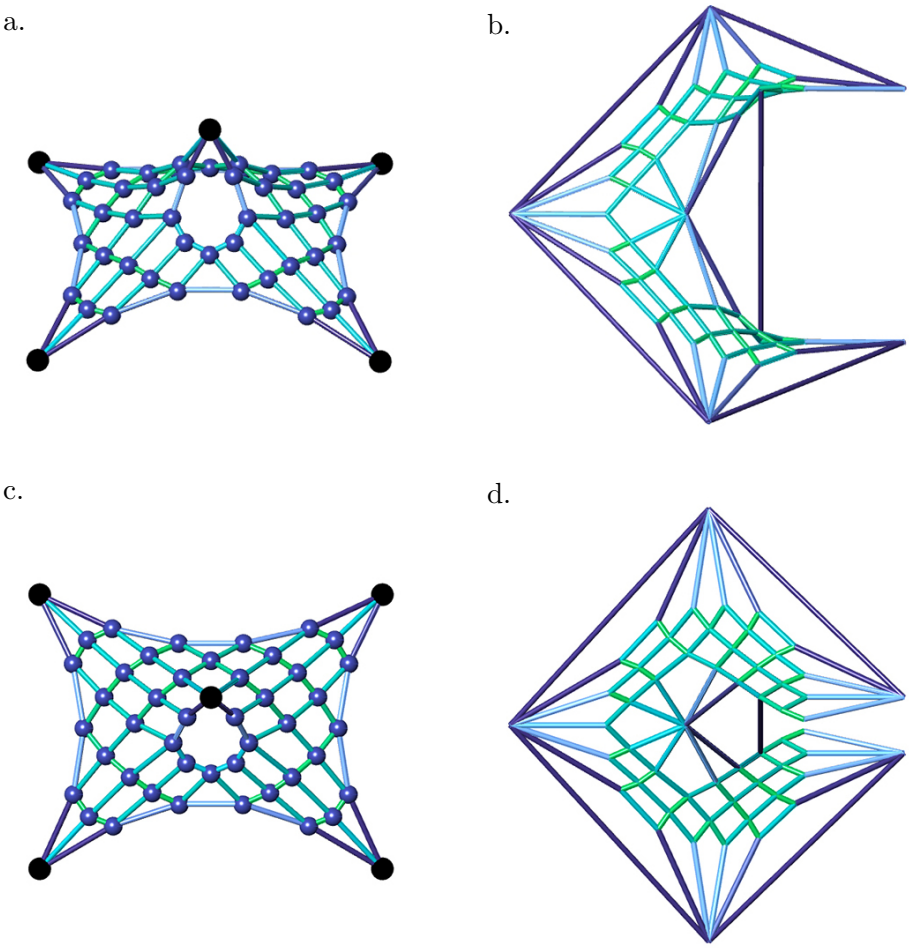


Figure 5: Form-finding of the given cable-net structure using presented graphical iterative method (a. and c. form diagram; b. and d. force diagram; a. and b. 3D view; c. and d. top view)

4 Conclusion and future work

By adding masses to points, it is possible to study geometry by using fundamental mechanical principles. This was applied to a single node problem using described Archimedes' law and thereafter to an example of a cable-net structure using the method node by node. The method presented in the paper allows user to simultaneously explore structural shape in the form diagram and internal forces in the force diagram, and if one applies the tension-compression analogy, the method is convenient for both cable-net and self-supported structures.
The method could also be graphically described with Hooke's law of the spring system, where the position of a free node can be obtained iteratively using the equation $F = k\mathbf{x}$, where F is

the force acting on the spring, $\mathbf{x}$ represents elongation of the spring, and k is a positive constant that characterizes spring stiffness. If one compares Hooke's law and Archimedes' law approach, it is clear that the elongation $\mathbf{x}$ is equal to $d = \mathbf{f_0} / \sum m_i, i = 1, ..., n$, while the spring stiffness k is equal to $m_c = \sum m_i, i = 1, ..., n$.
Similarly, the form-finding of a free node could be described by Newton's second law of motion used in dynamics of particles. When a particle of mass m is acted upon by force F, acceleration of the particle and the force must satisfy the relation $F = m\mathbf{a}$.
Since the graphical method can be described using basic principles of mechanics, they are convenient in engineering education for geometrical study and understanding of iterative methods, evaluation of global equilibrium as well as understanding internal equilibrium of structures.

References

[1] R. Goldman, *Rethinking Quaternions: Theory and Computation*, Morgan and Claypool Publishers, 2010.

[2] L. Enrique, P. Block. and J. Schwartz, "Form-finding method for prestress-dominant surface structures using graphic statics", *Proceedings of the International Association for Shell and Spatial Structures (IASS) Symposium 2015*, August, 2015, Amsterdam, Netherlands.

[3] J. Plücker, "On a new geometry of space", *Philosophical Transactions of the Royal Society of London*, vol. 155, pp. 725-791, 1865.

[4] H. Pottmann, J. Wallner, *Computational Line Geometry*, Springer, Berlin, Heidelberg, 2001.

[5] M. Baniček, K. Fresl and I. Kodrnja, "Some examples of static equivalency in space using descriptive geometry and Grassmann algebra", *Proceedings of the International Association for Shell and Spatial Structures (IASS) Symposium 2018*, July, 2018, MIT, Boston, USA.

[6] H. Grassmann, *A New Branch of Mathematics: The "Ausdehnungslehre" of 1844 and Other Works*, (Transl.: C. L. Kannenberg), Open Court Publishing, 1995.

[7] J. Browne, *Grassmann Algebra Volume 1: Foundations: Exploring extended vector algebra with Mathematica*, Melbourne: Birkhauser, Quantica Publishing, 2012.

[8] A. F. Möbius, *Der barycentrische Calcul*, Verlag von J.A. Barth, Leipzig, 1827.

[9] R. H. Bow, *Economics of construction in relation to framed structures*, London, 1873.

[10] A. Micheletti, "On generalized reciprocal diagrams for self-stressed frameworks", *International Journal of Space Structures*, vol. 23(3), pp. 153-166, 2008.

[11] R.McNeel & Assoc., *GhPython 3D*, http://www.food4rhino.com/app/ghpython, (accessed: 28.5. 2019.)

[12] R.McNeel & Assoc., *Grasshopper 3D*, http://www.grasshopper3D.com, (accessed: 28.5. 2019.)

[13] R.McNeel & Assoc., *Rhinoceros 3D*, http://www.rhino3d.com, (accessed: 28.5. 2019.)

Proceedings of the IASS Annual Symposium 2019 - Structural Membranes 2019
Form and Force
7-10 October 2019, Barcelona, Spain
C. Lázaro, K.-U. Bletzinger, E. Oñate (eds.)

From Polyhedral to Minimal Surface Funicular Spatial Structures

Mostafa AKBARI[*,a], **Masoud AKBARZADEH**[a], **Mohammad BOLHASSANI**[a,b]

[a] Polyhedral Structures Laboratory, School of Design, University of Pennsylvania, Philadelphia, USA
Pennovation Center, 3401 Grays Ferry ave. Philadelphia, PA, 19146
akbariae@upenn.edu

[b] Bernard and Anne Spitzer School of Architecture, The City College of New York
141 Convent Avenue, New York, NY, 10031

Abstract

The structural performance of cellular polyhedral funicular geometries in 3D graphic statics(3DGS) relies heavily on the buckling performance of the system; if the edges of the form diagram are immediately translated to structural members. In addition, the spatial geometry of the nodes makes the fabrication process quite challenging. This paper proposes a novel approach to translate a cellular polyhedral geometry into a polyhedral surface-based structure in 3DGS that is comparable to the widely known minimal surface geometries in the context of structural design, bridging the gap between cellular polyhedral geometry and surface-based structure. Using such minimal surface structures for materialization in place of polyhedral geometry in 3DGS improves the structural performance of the system and facilitates its fabrications process (Figure 1). The proposed approach introduces a new typology of funicular spatial structures consist of a minimal surface for a given boundary condition. Followed by introducing the computational procedure to generate such geometries, the paper concludes by evaluating the mechanical performance of a cellular specimen and a funicular minimal surface structure, based on the same polyhedral geometry with the same volume of construction material (see Figure 1).

Keywords: Funicular spatial structure, 3D Graphic statics, Minimal surface, Shell structure

1 Introduction

1.1 Mininal surface geometries and their structural applications

Minimal surfaces are a subset of anticlastic surfaces which have reliable structural performance due to their specific morphology [17].They are surfaces of minimal area between any given boundary conditions which cover the boundary with the least amount of material, weight and area. In nature, we can find such geometries from an equilibrium of homogeneous tension, for instance in a soap film, which have been an inspiration for designers and engineers to expand the borders of light weight structures [9]. At each point on the minimal surface, if we consider k_1 and k_2, the principle curvatures, the mean curvature would be zero ($H = (k_1 + k_2)/2 = 0$) and the Gaussian curvature would be a negative value ($G = k_1 \times k_2 < 0$). If we consider a minimal surface's discretization as a pin-jointed net, at each interior vertex, two edges are

Copyright ©2019 by [Mostafa AKBARI, Masoud AKBARZADEH, Mohammad BOLHASSANI]
Published by the International Association for Shell and Spatial Structures (IASS) with permission.

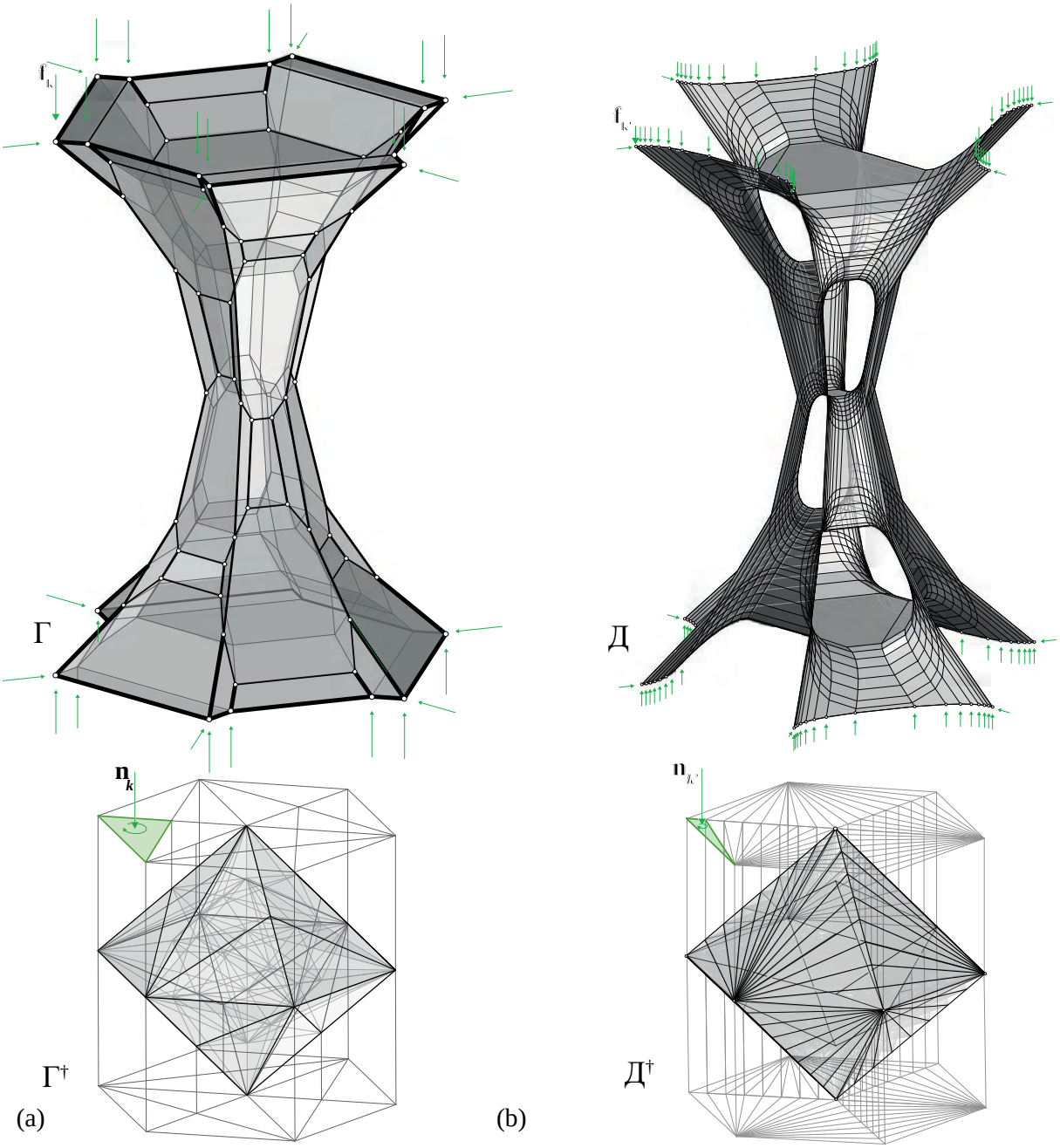


Figure 1: (a) Form and force diagram of a cellular polyhedral specimen in 3DGS; (b) form and force diagram of a translated shellular polyhedral minimal surface.

curved downwards (standing), and other two curved upwards (hanging) to make an anticlastic curvature on the surface (Figure 3a).
In small scales, minimal surface geometries such as Gyroid, Schwarz P, or Schwarz W are used as space-filling, rigid micro-structures to produce light-weight and high-performance materials [11, 17]. These are two-manifold, single-layer, spatial structures which lately have been named 'Shellular' [10].Recent studies show that the high surface-to-volume ratio in shellular geometries

enhances the mechanical performance of the system [10]. Besides, their excelled structural performance are quite useful if used as non-clogging tissue engineering scaffolds or compact light-weight fuel cells with high energy density [10, 20].
Frei Otto was one of the pioneers that utilized mathematical and structural qualities of mininmal surfaces in large scale projects such as German pavilion for expo 1968 and Munich Olympic stadium. Many other architects and engineers also attracted by these surfaces' structural and morphological qualities and used them for the design of light weight structures such as Felix Candela, Sergio Musmeci, and Michael Burt, to name but three [9, 21, 15] (Figure 2).



Figure 2: Minimal surface as large-scale structures; (a) Frei Otto's soap film experiment[22], (b) Los Manantiales restaurant by Felix Candela[13], (c) Bridge over the Basento by Sergio Musmeci[5].

1.1.1 Form finding for minimal surface geometries

The geometry of a minimal surface could not be freely chosen and conceived directly, due to the intrinsic interaction between form and forces, and requires a form-finding technique for design application [19, 12] (Figure 2). This process can be applied both in physical or computational method. Frei Otto as one of the pioneers of physical form finding has worked in multiple techniques such as soap film within a boundary or prestressed hanging fabric or cable nets (Figure 2a). The computational methods can be considered both in geometric stiffness family such as Force Density Method (FDM) or in dynamic equilibrium family such as Dynamic Relaxation (DR) or Particle Spring System(PS) [19]. Although a minimal surface's shape can be achieved by finding the shape of equilibrium for an isotropic prestress field with various tools which commonly are based on a method by Pinkall and Polthier [16, 18], there is no geometric method to construct these surfaces for a given set of boundary conditions.

1.2 Problem statement and objectives

Exploring an unlimited variety of funicular spatial structural typologies is now feasible using 3D (polyhedral) graphic statics [1]. These structural forms have polyhedral configurations including vertices, edges, faces, and cells where the edges of the cells can be materialized as members of a structure with a cross section associated with the magnitude of the force (area of the reciprocal face) in the force diagram. The structural performance of cellular polyhedral structures relies heavily on the buckling performance of the members [8]. Besides, if the loading scenario changes, the mechanical behavior of the system will immediately alter. Moreover, the fabrication process of such system is quite challenging because of their complex spatial configurations. Unlike polyhedral systems, minimal surface structures consist of a continuous surface where the internal forces are distributed on a surface with a consistent mean curvature rather than the cross-section of the members. However, the link between the cellular funicular geometry and spatial minimal surface is left unknown.

In this research, we intend to investigate a creative method to design a compression-only, spatial minimal surface geometry for a given boundary condition using three-dimensional graphic statics (3DGS). Thus, we will; (i) provide a method to generate anticlastic polyhedral geometries using 3DGS ; (ii) describe an approach to generate periodic minimal surface geometries as an aggregation of spatial surfaces; (iii) convert a cellular funicular geometry into spatial minimal surface geometry for a given boundary condition and applied loads and explain the required computational set up for this purpose; and finally (iv) compare the structural performance of the generated cellular and shellular structures for the same boundary conditions under the applied load using the same volume of material.

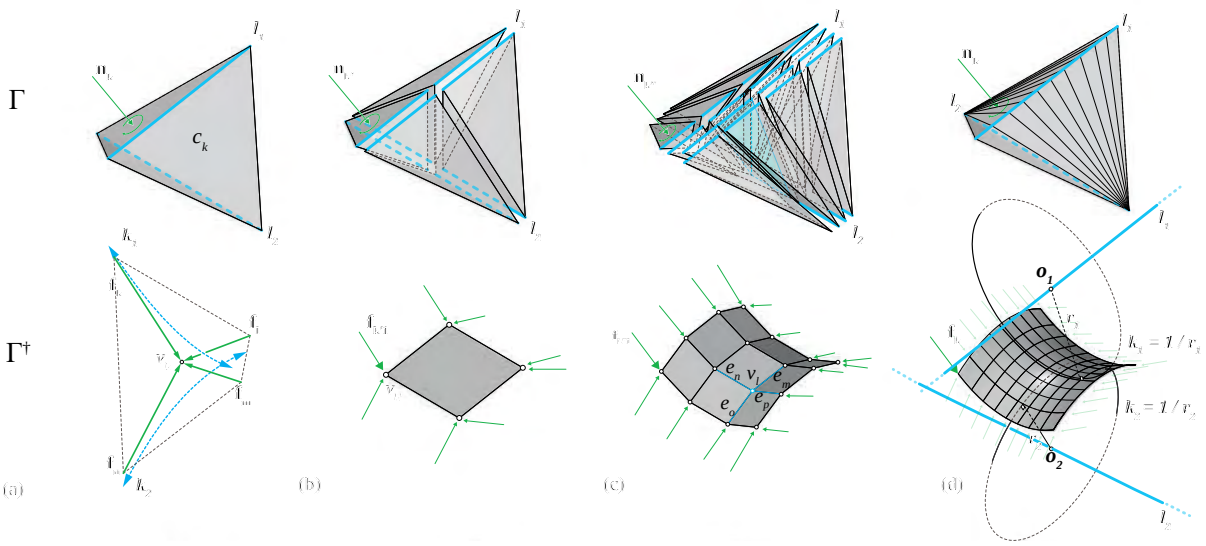


Figure 3: The process of designing an anticlastic surface as a form diagram via subdividing the single polyhedron in the force diagram;(a)single node, (b)4 nodes, (c)16nodes (d)smooth subdivided anticlastic surface with curvatures and axes.

2 Methodology

2.1 Generating anticlastic polyhedral geometry

Subdividing the force diagram as a form finding technique results in a variety of topologically-different structural forms for a given boundary condition and loading scenarios [2, 4]. There are specific types of subdivision rules resulting in a polyhedral surface geometries with synclastic or anticlastic properties. Figure 3 shows a subdivision process that translates a single node in equilibrium into an anticlastic surface. In this process, the two highlighted edges of the global force diagram, l_1 and l_2, are subdivided to construct the surface in each step. Note that in each step of the subdivision, l_1 and l_2 are divided into equal number of segments such that each segment of the former will establish a tetrahedron with its associated segment in the latter (Figure 3b,c). Further subdividing those edges will result in a smoother surface in the form diagram (Figure 3b,c).
However, for this subdivision to work, the force cells should only consist of tetrahedrons. This results in each node, v_l, on the surface to be connected only to four other nodes with two *hanging*

edges, e_n and e_p, and two *standing* edges, e_o and e_m which establishes the negative Gaussian curvature. Moreover, the resulting anticlastic surface of Figure 3 in the form diagram is only subjected to the applied loads from sides with no load applied to the nodes on the surface. As shown in Figure 3c and d, the curvature axis in an anticlastic surface is a subdivision axis in the reciprocal force diagram (l_1 and l_2). More tetrahedron is the direct results of subdivision in the force diagram and subsequently, an smoother anticlastic surface form diagram will be generated as its outcome.

2.1.1 Generating periodic minimal surface geometry using 3DGS

Each minimal surface without self-intersection subdivides R^3 into two segregated regions, each of which is connected and forms a 3D labyrinth [6, 7]. The two labyrinths interpenetrate each other with the surface as their common interface. The geometry of the minimal surface changes when the angle of these labyrinth changes. Figure 4 shows the way two skew labyrinths of l_i and l'_i shape the minimal surface in between (Figure 4a,b) and how their different angles change the geometry of the minimal surface (Figure 4c,d). For instance, according to Figure 4d, axis l_i and l'_i shape surface s_1 in between, while l_i and l'_k shape surface s_2. In fact these two are both part of a bigger surface with same topology but only in different angles.
In 3DGS technique, in a force diagram the angle of subdivisions between the axes can change the geometry of the diagram [3]. According to Figure 4, if we consider l_i and l'_i as minimal surfaces' labyrinths, it can be observed that they play the role of subdivision axes in the force diagram ($e^{\dagger}_k || l_i$ and $e^{\dagger}_{k'} || l'_i$) (Figure 4a,c) and the role of labyrinths in the form diagram (Figure 4b,d) which are the surface's curvature axes as well (Figure 3d). For a specific type of minimal surface, if we identify the topology of the minimal surface by finding its labyrinths, its force diagram can be subdivided based on the labyrinths in order to find the reciprocal funicular geometry in 3DGS.

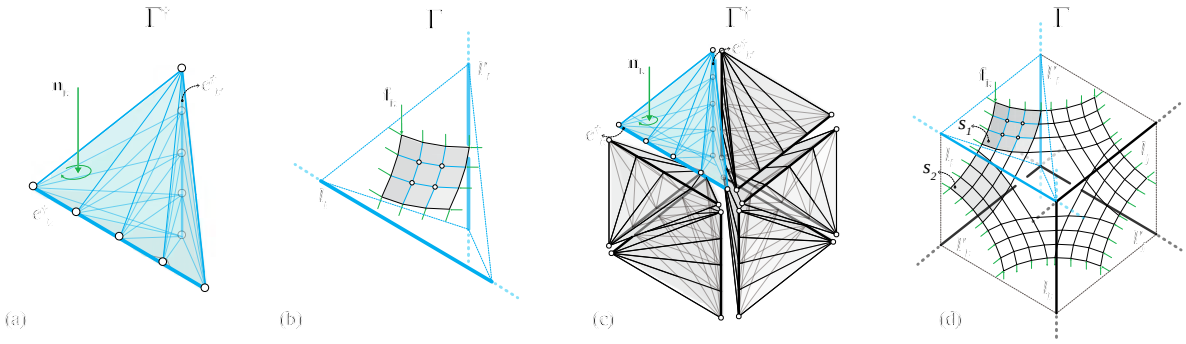


Figure 4: The position of labyrinths in both force and form diagrams of a module of Schwarz P surface, (a) single tetrahedron as force diagram subdivided to 16 tetrahedrons, (b) reciprocal form diagram, (c) Aggregation of the Force diagram, (d) the resulting form diagram of a module of Schwarz P surface.

Similarly, we can explore different aggregations of an anticlastic node to achieve well-known minimal surfaces' typologies based on their labyrinths. We designed three types of continuous porous minimal surface modules, known as Gyroid(G), Schwarz Premitive(P), and Schwarz iWp(W) (Figure 5). For each surface, for a certain boundary condition in the force diagram (the cube), the minimal surface's labyrinths have been located in the global force and each two

skew lines from each groups of labyrinths have been connected together as a tetrahedron (as shown in the Figure 4). Then these tetrahedrons have been subdivided in 3D in order to increase the resolution of the minimal surface's form diagram (Figure 5).

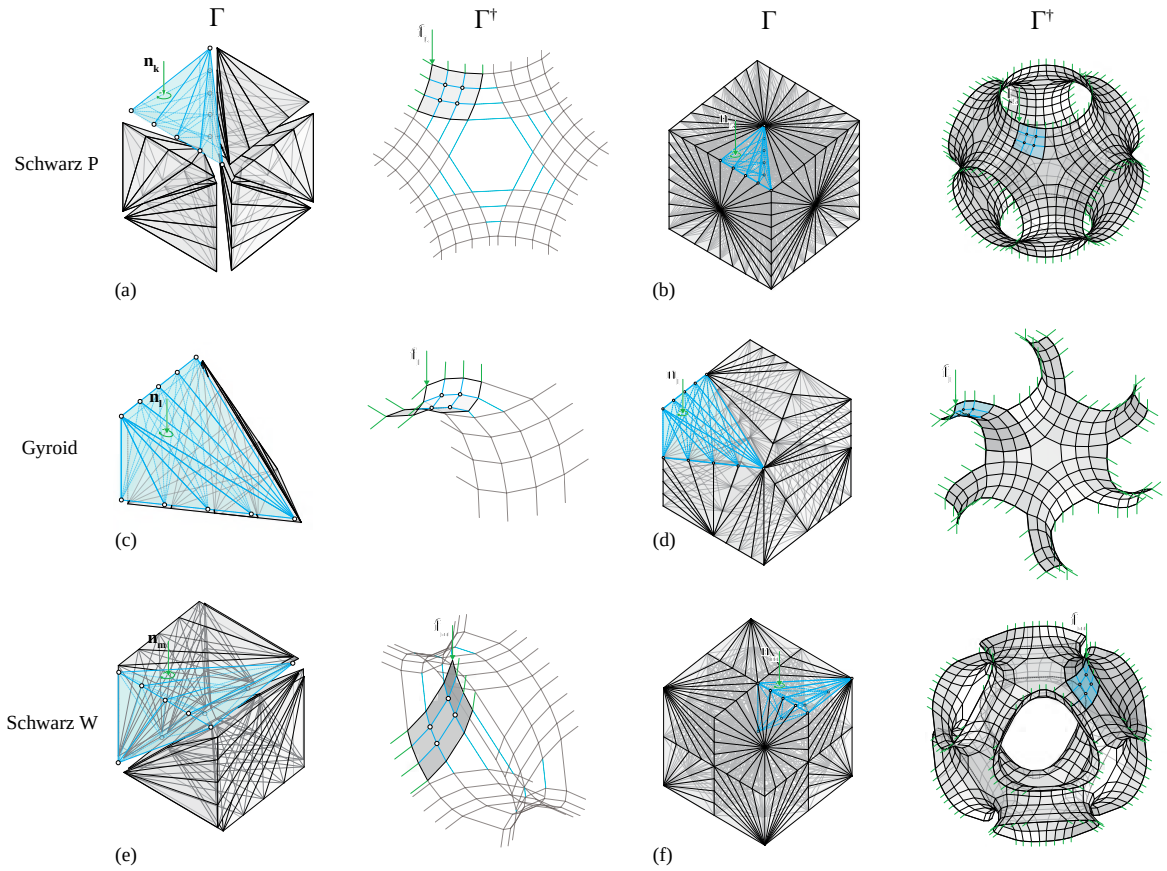


Figure 5: The process of designing three well-known minimal surface modules via 3DGS: (a) force and diagram of a module of Schwarz P surface, (b) force and form diagram of a unit of Schwarz P surface; (c, d) force and form diagrams of Gyroid's surface and its primitive module; (e, f) force and form diagrams of Schwarz W surface and its primitive module.

2.2 Shellular minimal surface for a given boundary condition

The ultimate goal of this research is to translate a funicular, compression-only geometry into a compression-only minimal surface structure called shellular geometry for the same given boundary conditions and applied loads. For a given polyhedral form, we should find the topology of the two labyrinths that translate the polyhedral form into a continuous surface with two-manifold geometry, dividing the space into two separate sub-spaces. In that case, the topology (connectivity) of these sub-spaces/labyrinths can be used to subdivide the force diagram and generate a shellular version of the cellular form for the given boundary conditions.
We can formulate the problem of finding the labyrinths in the form into the following question: how many faces we can remove from the cellular geometry of the form without removing any edge from the system such that, at the end, every edge is connected to two and only two faces?

The following assumption is necessary for the method to work: *each cell within the polyhedral group should have only and only three-valency vertices.*

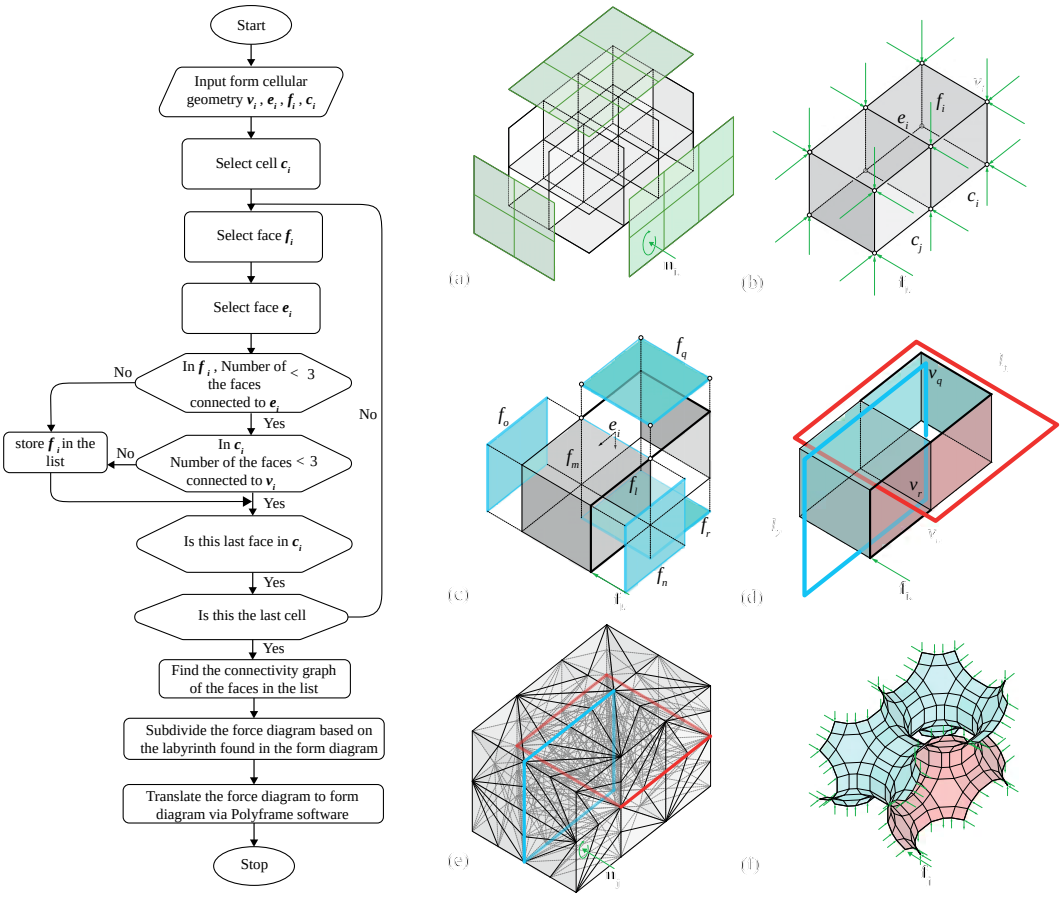


Figure 6: Left; The computational flowchart for translating a cellular spatial structure to funicular minimal surface. Right; (a) cellular geometry's force diagram ,(b) cellular geometry's surface-based form diagram, (c) extracting extra faces to make a 2-manifold geometry ,(d) labyrinths, (e) shellular geometry's force diagram, (f) shellular geometry's form diagram.

2.2.1 Computational setup

We can use a brute-force algorithm to find the topology of the labyrinths in the form diagram as explained in the following steps: to tackle the problem, lets start from a single cell in a form polyhedron found for a given boundary conditions [3, 14]. For the first cell c_i, we visit its faces f_{i-n} and store the vertices v_i and edges e_i and remove faces until each edge, e_i is only connected to two and only two faces in the cell (Figure 6c). In this case, each vertex v_i will only be connected to two faces within a cell. In the next step we move to the adjacent cell c_j, where we already have the shared face from the previous cell. Now, we should start by parsing the edges of the shared face, and for each edge of the face, we remove a face of a cell that will make the vertex-face connectivity more than 2 in a cell, and edge-face connectivity more than 2 in whole geometry. By parsing all the cells and removing all the extra faces we will end up

with a network of faces that divides the space into two sub-spaces. The connectivity of each sub-space will provide the topology of the labyrinth that should be used to subdivide the force polyhedron to get the shellular funicular geometry (Figure 6a–f).

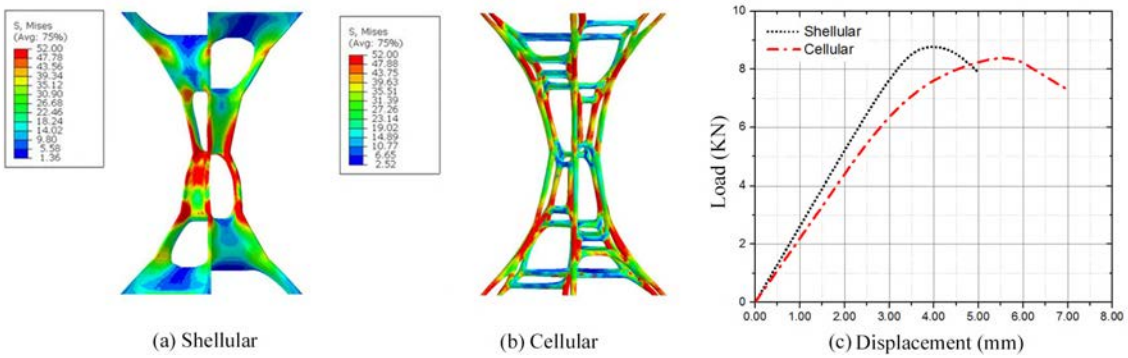


Figure 7: (a) Mises stress contour of shellular specimen , (b) Mises stress contour of cellular specimen, (c)Load-displacement curves of cellular and shellular specimens

2.3 Preliminary numerical study

A numerical structural analysis is performed to study the mechanical behavior of two cellular and funicular minimal surface structures shown in Figure 1 made out of PLA with identical volume. A tetrahedral meshes consist of approximately half a million elements are generated for both specimens using elastic perfectly plastic behavior with similar boundary conditions, loading speed and type of elements. Although a better performance is expected for the shellular specimen, preliminary load-displacement curves showed that the shellular specimen carry slightly more load and less displacement at the final stage compare to the cellular specimen (see Figure 7). This was mainly due to formation of stress concentration at the sharp edges of the shellular specimen. Mises stress patterns are shown in 7, stress concentration can be observed in the shellular specimen at the sharp edges. On the other hand, maximum stress is distributed along the extend length of members in the cellular specimen.

3 Conclusion and future work

This paper discussed a novel technique to bridge the gap between cellular polyhedral and shellular funicular geometry in 3DGS. We showed that it is possible to generate a shellular polyhedral geometry using 3DGS. Also we showed that shellular funicular geometry is a cellular geometry with particular subdivision that decreases the edge lengths and take advantage of a consistent distribution of internal forces in order to make the geometry structurally reliable and to facilitate the process of fabrication.
It is clear that many aspects of the proposed methodology require further explorations to establish a comprehensive theory of minimal surface funicular spatial structure which could be concerned with optimizing shellular structures load capacity via subdivision, mathematical definition of shellular system in 3DGS, and improving the computational algorithm, to name but a few.

References

[1] M. Akbarzadeh. *3D Graphic Statics Using Polyhedral Reciprocal Diagrams*. PhD thesis, ETH Zürich, Zürich, Switzerland, 2016.

[2] M. Akbarzadeh, T. Van Mele, and P. Block. Compression-only form finding through finite subdivision of the external force polygon. In O. J.B. and R. Tarczewski, editors, *Proceedings of the IASS-SLTE Symposium 2014*, Brasilia, Brazil, 2014.

[3] M. Akbarzadeh, T. Van Mele, and P. Block. On the equilibrium of funicular polyhedral frames and convex polyhedral force diagrams. *Computer-Aided Design*, 63:118–128, 2015.

[4] M. Akbarzadeh, T. Van Mele, and P. Block. Spatial compression-only form finding through subdivision of external force polyhedron. In *Proceedings of the International Association for Shell and Spatial Structures (IASS) Symposium*, Amsterdam, August 2015.

[5] F. CANESTRINI. Ponte musmeci, 1975.

[6] W. Fischer and E. Koch. Genera of minimal balance surfaces. *Acta Crystallographica Section A*, 45(10):726–732, 1989.

[7] W. Fischer and E. Koch. Crystallographic aspects of minimal surfaces. *Le Journal de Physique Colloques*, 51(C7):C7–131, 1990.

[8] A. T. Ghomi, M. Bolhassani, Nejur, and M. Akbarzadeh. The effect of subdivision of force diagrams on the local buckling, load-path and material use of founded forms. In *Proceedings of the International Association for Shell and Spatial Structures (IASS) Symposium 2018*, MIT, Boston, USA, July 2018.

[9] L. Glaeser. *The work of Frei Otto*. The Museum of Modern Art, 1972.

[10] S. C. Han, J. M. Choi, G. Liu, and K. Kang. A Microscopic Shell Structure with Schwarzs D-surface. *Scientific Reports*, 7(1):13405, 2017.

[11] S. C. Han, J. W. Lee, and K. Kang. A new type of low density material: Shellular. *Advanced Materials*, 27(37):5506–5511.

[12] W. Lewis. Computational form-finding methods for fabric structures. *Proceedings of The Ice - Engineering and Computational Mechanics*, 161:139–149, 01 2008.

[13] M. Miller. Los manantiales / felix candela, 1910.

[14] A. Nejur and M. Akbarzadeh. Polyframe beta: a geometry-based structural form finding plugin for rhinoceros3d. https://www.food4rhino.com/app/polyframe, 2018.

[15] F. Otto. *Tensile Structure*. The MIT Press, 1952.

[16] U. Pinkall and K. Polthier. Computing discrete minimal surfaces and their conjugates. *Experimental mathematics*, 2(1):15–36, 1993.

[17] Z. Qin, G. S. Jung, M. Jeong Kang, and M. J. Buehler. The mechanics and design of a lightweight three-dimensional graphene assembly. *Science Advances*, 3:e1601536, 01 2017.

[18] E. Schling, D. Hitrec, and R. Barthel. Designing grid structures using asymptotic curve networks. pages 125–140, 09 2017.

[19] D. V. C. W. Sigrid Adriaenssens, Philipe Block. *Shell structures for architecture, form finding and optimization*. Routledge, 2014.

[20] B. Trembacki, E. Duoss, G. Oxberry, M. Stadermann, and J. Murthy. Mesoscale electrochemical performance simulation of 3d interpenetrating lithium-ion battery electrodes. *Journal of The Electrochemical Society*, 166:A923–A934, 01 2019.

[21] L. Velimirovi, G. Radivojevi, M. Stankovi, and D. Kostic. Minimal surfaces for architectural constructions. *Facta Universitatis - series : Architecture and Civil Engineering*, 6, 01 2008.

[22] S. Zexin and H. Mei. Robotic form-finding and construction based on the architectural projection logic. *IOP Conference Series: Materials Science and Engineering*, 216:012058, 06 2017.

Proceedings of the IASS Annual Symposium 2019 – Structural Membranes 2019
Form and Force
7 – 10 October 2019, Barcelona, Spain
C. Lázaro, K.-U. Bletzinger, E. Oñate (eds.)

Geometric approach to form finding of a spoke wheel system: Mathematical explanations

Hiroki TAMAI*

*Nikken Sekkei
Chiyota-ku Tokyo
tamai.hiroki@nikken.jp

Abstract

The author extended the concept of the affine spoke wheel roof system, not by explicitly defining any circles with different radii but rather by implicitly laying out identical isosceles. The extended concept allows a designer to choose a more arbitrary compression ring shape for covering an asymmetry plan shape with a spoke wheel system, as well as to determine the self-equilibrium geometry and prestresses without resorting to sophisticated nonlinear calculations. In fact, any closed convex curve with conditional smoothness can be graphically converted to a self-equilibrium spoke wheel structure. This paper gives more mathematical explanations to the two remarkable properties of the equilibrium geometry of spoke wheel structures that are generated by the extended-affine method. 1) The equilibrium ring geometry that minimizes the sum of the squares of the ring's segment length forms the evolute of other equilibrium rings that minimizes the variance of the segment length, polylines of which connect between different radii. 2) The limit curve of the evolute polyline is a cycloid. The paper also demonstrates the corresponding graphical construction steps of such geometry.

Keywords: form finding of spoke wheel structure, graphic form finding

1. Introduction

The form finding of a spoke wheel roof structure is a highly nonlinear problem as it requires simultaneously determining the geometry of ring and radial cables, flying struts, compression ring as well as ensuring self-stressed equilibrium such that there are only axial forces. While such difficulty lies in the general form of the problem, the affine concept provides a relatively simple approach to determine a circular or oval spoke wheel structure behaving in self-equilibrium. Schlaich Bergermann Partner first applied the concept to a circular roof and later for an oval roof by selecting geometry based on a three-centered arc for the tension and compression rings [1]. However, the application of the concept was limited to a simple and symmetric oval geometry [2].

The author extended the concept of the affine spoke wheel roof system, not by explicitly defining any circles with different radii but rather implicitly by laying out identical isosceles [3[3]. The extended concept allows a designer to choose a more arbitrary plan shape to cover with a spoke wheel system and to determine the self-equilibrium geometry and prestresses without sophisticated nonlinear calculations. In fact, any closed convex curve with conditional smoothness can be graphically converted to a self-equilibrium spoke wheel structure.

The investigation of various equilibrium forms generated by the extended-affine concept showed two relations in the geometry of spoke wheel structures in self-equilibrium states. 1) The ring shapes that approximates different ellipses with the minimum variation of segment lengths can always be generated as the involute of a unique polyline. The evolute polyline was found to be a sector of another equilibrium shape that likewise satisfies the extended-affine concept, as well as minimizing

Copyright © 2019 by Hiroki TAMAI
Published by the International Association for Shell and Spatial Structures (IASS) with permission.

the sum of squared lengths of the ring. 2) A numerical comparison indicated that the evolute polyline approaches to a cycloid when the number of segments increases to infinity [3].

This paper revisits these findings in order to give more mathematical explanations and the corresponding drawing steps. Along with the proof of the geometric link, the paper demonstrates how to draw these equilibrium forms without resorting to the nonlinear programming to find the lengths of ring segments.

2. Definition of terms

This section defines the terms used specifically for this paper with their background, if necessary, so that the mathematical explanations in the following sections should be clear.

Affine method : The word affine is not used with mathematical exactness in this paper. Rather it is used to refer to the method reported by Bergermann [1]. The term was used to describe the non-computational form finding method of spoke wheel systems by setting the equal angles to inner tension and outer compression rings in relation to each radial cable in the form of a circular and a three-centered-arc aka korbborgen. However, since the basic affine concept was developed, in fact, only on concentric arcs, a ring shape needed to be patched by several circles. Therefore, application was limited to circular or elliptic shapes.

Extended affine method, Isosceles method : The author extended the above *affine method* for more general graphical form finding of spoke wheel systems with more arbitrary shapes [3], by freely laying out similar isosceles, or implicitly connecting the isosceles bases to configure inner and outer rings. This method does not have center points of circles, while the above-mentioned *affine method* have one or a few. Therefore, the extended affine method, in theory, can translate any arbitrary closed convex curve into an equilibrium spoke wheel geometry, while the lengths of the radial cables, i.e. roof overhang, are constrained by the curvature. In this method, similar isosceles as many as the axes of roof geometry are laid out adjacent to each other along the legs; the legs define the lines of radial cables, and two closed polylines, the segments of which are set parallel to the bases of the isosceles, define tension and compression rings. Or more directly, the ring polyline can be determined by translating edges of a regular polygon to the points of tangency on the given closed convex curve [3].

A polygon that is generated by the *extended affine method (or isosceles method)* or satisfies the *extended affine rule* is equivalent to a convex polygon whose inner angles are all equal but the side lengths may not be equal. The tension and compression rings are defined one another by translating the sides of the polygon inward for a tension ring or outward for a compression ring by a constant distant. It must be noted that the translation of the sides does not make the two polygon similar to each other; the tension and compression rings cannot be scaled to one another.

Involute polyline, involute polygon : An involute polyline or polygon is defined as a open or closed polygonal line inscribed in the involute curve of a polyline at the points where the rotational radius of the involute changes. The step change of the rotational radius occurs when the center of rotation jumps from a vertex to another on the polyline seen as its evolute.

Evolute polyline, evolute polygon : An evolute polyline appears as a special case of evolute where the centers of the curvature of the involute jumps, corresponding to the step change of the rotational radius. The polyline connecting the discrete locus is referred to as *evolute polyline* or *evolute polygon* if it is closed.

3. Propositions on equilibrium geometry of spoke wheel structure

This section gives two propositions about the geometric links of spoke wheel structures in self-equilibrium states, previously reported by the author [3].

3.1. Proposition 1: On evolute and involute of a spoke wheel ring of in equilibrium

The evolute polyline of a polyline connecting two points with all angles in-between equal and with minimum sum of the squared deviation of the lengths can be obtained by scaling a unique polyline with all angles equal and with minimum sum of the squared length. (Figure 1)

3.2. Proposition 2: On the limit curve of the rings with minimum squared lengths

The limit curve of the evolute polyline in the Proposition 1 is a cycloid; the evolute polyline, which is a quadrant of a polygon with equal major radii and all equal angles, as well as a minimal sum of the squared lengths, approaches to a cycloid when the number of segments increases to infinity. (Figure 2)

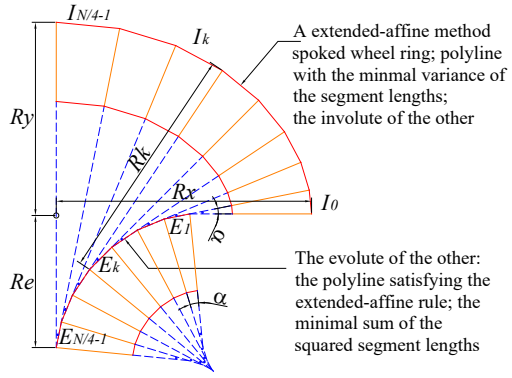


Figure 1: Involute and evolute polylines

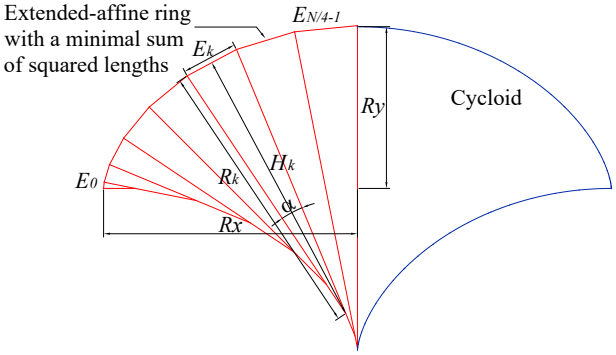


Figure 2: Extended-affine ring and cycloid

4. Mathematical explanation

This section provides mathematical proofs on the above-stated propositions. They are based on the set of equations that are derived from the necessary conditions for the minimums of the associated objective functions in terms of ring segment lengths, i.e. polygon side lengths. In preparation for the proofs, the two minimization problems for the sum of squares and the sum of the squared deviation of the lengths of the ring segments are mathematically stated as below.

Let N be the number of dividing a compression ring, and let the set of segment lengths E_k $(0 \leq k \leq n-1 \leq N-1)$ be a portion of the ring under discussion. Then, the problem to find E_k to minimize the sum of the squared lengths for a polygon or a polyline as a part of it, with all equal inner angles but with different side lengths is stated as follow.

$$\arg\min_{E_k \in \mathbb{R}} \sum_{k=0}^{n-1} {E_k}^2 \tag{1}$$

subject to the constraints

$$\sum_{k=0}^{n-1} E_k \sin(k\alpha + \alpha_0) = D_x, \qquad \sum_{k=0}^{n-1} E_k \cos(k\alpha + \alpha_0) = D_y \tag{2), (3}$$

, where

$$\alpha = \frac{2\pi}{N}. \tag{4}$$

The constraint equations (2) and (3) impose the extended affine rules and the conditions for the polyline to connect the two points with coordinates $(D_x, 0)$ and $(0, D_y)$. Note that specifying the two points will not lose generality of the statement. Here, α_0 depends on how the configuration intersect to the global orthogonal axis. Typically,

$$\alpha_0 = \begin{cases} \dfrac{\alpha}{2}, & \text{if one of the legs of the first isoceles is pararel to the global X axis} \\ 0, & \text{if the base of the first isoceles is perpendicular to the global X axis.} \end{cases} \tag{5}$$

By constructing a Lagrange function using Lagrange multipliers λ_x and λ_y with a factor of -2 on each constraint just for later convenience,

$$\begin{aligned} \mathcal{L}_E(E_k, \lambda_x, \lambda_y) = \sum_{k=0}^{n-1} {E_k}^2 - 2\lambda_x \left(\sum_{k=0}^{n-1} E_k \sin(k\alpha + \alpha_0) - D_x \right) \\ - 2\lambda_y \left(\sum_{k=0}^{n-1} E_k \cos(k\alpha + \alpha_0) - D_y \right) \end{aligned} \tag{6}$$

the problem is rewritten as follows.

$$\underset{E_k,\, \lambda_x,\, \lambda_y \in \mathbb{R}}{\arg\min}\ \mathcal{L}_E(E_k, \lambda_x, \lambda_y) \tag{7}$$

Similarly, the problem to find the set of segment length I_k $(0 \le k \le n-1 \le N-1)$ to minimize the sum of the squared deviation of the segment lengths is stated as follow, where $\bar{I}$ is the average of I_k.

$$\underset{I_k \in \mathbb{R}}{\arg\min} \sum_{k=0}^{n-1} (I_k - \bar{I})^2 . \tag{8}$$

subject to the constraints

$$\sum_{k=0}^{n-1} I_k \sin(k\alpha + \alpha_0) = D_x, \qquad \sum_{k=0}^{n-1} I_k \cos(k\alpha + \alpha_0) = D_y \tag{9), (10}$$

, where $\alpha = \frac{2\pi}{N}$ and α_0 are given as equations (4) and (5) respectively. By applying the Lagrange multiplier method,

$$\begin{aligned} \mathcal{L}_I(I_k, \lambda_x, \lambda_y) = \sum_{k=0}^{n-1} (I_k - \bar{I})^2 - 2\lambda_x \left(\sum_{k=0}^{n-1} I_k \sin(k\alpha + \alpha_0) - D_x \right) \\ - 2\lambda_y \left(\sum_{k=0}^{n-1} I_k \cos(k\alpha + \alpha_0) - D_y \right) \end{aligned} \tag{11}$$

$$\underset{I_k,\, \lambda_x,\, \lambda_y \in \mathbb{R}}{\arg\min}\ \mathcal{L}_I(I_k, \lambda_x, \lambda_y) \tag{12}$$

For calculating a set of E_k or I_k $(k = 0 \sim n)$ for an n-segment polyline to connect the two points with a sectorial angle of $2\pi\frac{n}{N}$, the number of segments n $(\le N)$ can be chosen arbitrarily. For discussing the minimum sums of the squares or the squared deviation of the polygon side lengths, n can be set to $\frac{N}{4}$ or $\frac{N}{2}$ for the sake of clarity because the optimal polygon minimized as such should be symmetric. In such a case, D_x and D_y can be referred to as major and minor radii for $n\alpha = \frac{\pi}{2}$ or diameters $n\alpha = \pi$, depending on which is greater.

4.1. A proof of Proposition 1

Suppose that an involute polyline I_k and an evolute polyline E_k are related via radii of rotation R_k for $k = 0 \sim n-1$ with $n = \frac{N}{4}$. This is expressed as

$$I_k = 2\,R_k \sin\frac{\alpha}{2} \tag{13}$$

$$R_k = \sum_{j=0}^{k} E_j \tag{14}$$

Eq.(13) and Eq.(14), when substituted in the Lagrangean (11), give

$$\begin{aligned}\mathcal{L}_I(R_k,\lambda_x,\lambda_y) = \left(2\sin\frac{\alpha}{2}\right)^2 \sum_{k=0}^{n-1}(R_k-\bar{R}\,)^2 - 2\lambda_x\left(2\sin\frac{\alpha}{2}\sum_{k=0}^{n-1}R_k\sin(k\alpha+\alpha_0)-D_x\right)\\ - 2\lambda_y\left(2\sin\frac{\alpha}{2}\sum_{k=0}^{n-1}R_k\cos(k\alpha+\alpha_0)-D_y\right)\end{aligned} \tag{15}$$

$$\min_{R_k>0,\,\lambda_x,\,\lambda_y} \mathcal{L}_I(R_k,\lambda_x,\lambda_y) \tag{16}$$

When Eq.(13) and Eq.(14) are substituted, the equality constraints Eq.(9) and (10) change the forms as follow.

$$2\sin\frac{\alpha}{2}\sum_{k=0}^{n-1}R_k\sin(k\alpha+\alpha_0)-D_x=0, \qquad 2\sin\frac{\alpha}{2}\sum_{k=0}^{n-1}R_k\cos(k\alpha+\alpha_0)-D_y=0 \tag{17), (18}$$

Given $\alpha_0=\frac{\alpha}{2}$, the form of the LHS of Eq.(17), (18) are changed as follow by applying arithmetic progression formula, analogy to Lagrange's trigonometric identities [4].

$$\begin{aligned}&2\sin\frac{\alpha}{2}\sum_{k=0}^{n-1}\left(\sin(k\alpha+\alpha_0)\sum_{j=0}^{k}E_j\right)-D_x = 2\sin\frac{\alpha}{2}\sum_{j=0}^{n-1}E_j\left(\sum_{k=j}^{n-1}\sin(k\alpha+\alpha_0)\right)-D_x\\ &= 2\sin\frac{\alpha}{2}\sum_{j=0}^{n-1}\left\{E_j\frac{\sin\left(n\frac{\alpha}{2}\right)\sin\left((n-1)\frac{\alpha}{2}+\alpha_0\right)-\sin\left(j\frac{\alpha}{2}\right)\sin\left((j-1)\frac{\alpha}{2}+\alpha_0\right)}{\sin\frac{\alpha}{2}}\right\}-D_x\\ &= \sum_{j=0}^{n-1}E_j\,(-\cos(n\alpha)+\cos(j\alpha))-D_x = \sum_{j=1}^{n-1}E_j\cos(j\alpha)-(D_x-R_0) \quad \because n\alpha=\frac{\pi}{2}, E_0=R_0\end{aligned}$$

$$\text{LHS of Eq. (18)} = 2\sin\frac{\alpha}{2}\sum_{k=0}^{n-1}\left(\cos(k\alpha+\alpha_0)\sum_{j=0}^{k}E_j\right)-D_y = \left(R_{n-1}-D_y\right)-\sum_{j=1}^{n-1}E_j\sin(j\alpha)$$

Thus Eq.(15) can rewritten as below, with $\bar{R}$ denoting the mean of R_k.

$$\begin{aligned}\mathcal{L}_I(R_k,\lambda_x,\lambda_y) = \left(2\sin\frac{\alpha}{2}\right)^2 \sum_{k=0}^{n-1}(R_k-\bar{R}\,)^2 - 2\lambda_x\left(\sum_{j=1}^{n-1}E_j\cos(j\alpha)-(D_x-R_0)\right)\\ - 2\lambda_y\left(\left(R_{n-1}-D_y\right)-\sum_{j=1}^{n-1}E_j\sin(j\alpha)\right)\end{aligned} \tag{19}$$

This imply that the equality constraints can be translated into those of the evolute polyline E_k. Note that at this point, neither (D_x-R_0) nor $\left(R_{n-1}-D_y\right)$ is known. We now calculate the derivatives with respect to I_k to obtain the necessary conditions for minimal of $\mathcal{L}_I(I_k,\lambda_x,\lambda_y)$ as

$$I_k = \lambda_x \sin(k\alpha + \alpha_0) + \lambda_y \cos(k\alpha + \alpha_0) + \bar{I} \quad for\ k = 0 \sim n-1 \tag{20}$$

In addition to Eq. (10), (9). Take the summation of the both sides of Eqs.(20) as follow,

$$\begin{aligned}\sum_{k=0}^{n-1} I_k &= \lambda_x \sum_{k=0}^{n-1} \sin(k\alpha + \alpha_0) + \tilde{\lambda}_y \sum_{k=0}^{n-1} \cos(k\alpha + \alpha_0) + \sum_{k=0}^{n-1} \bar{I} \\ 0 &= \lambda_x \sum_{k=0}^{n-1} \sin(k\alpha + \alpha_0) + \lambda_y \sum_{k=0}^{n-1} \cos(k\alpha + \alpha_0) \quad \because \sum_{k=0}^{n-1} I_k = \sum_{k=0}^{n-1} \bar{I} \\ &= \lambda_x \sin(n\alpha) \sin\left(\frac{(n-1)\alpha}{2} + \alpha_0\right) + \lambda_y \sin(n\alpha) \cos\left(\frac{(n-1)\alpha}{2} + \alpha_0\right) \\ &= \lambda_x \sin\left(\frac{n\alpha}{2}\right) + \lambda_y \cos\left(\frac{n\alpha}{2}\right)\end{aligned}$$

Since we suppose $\sin(n\alpha) \neq 0$ and $\alpha_0 = \frac{\alpha}{2}$, we obtain

$$\lambda_y = -\lambda_x \quad \text{when } \frac{n\alpha}{2} = \frac{\pi}{4}. \tag{21}$$

Consequently, I_k and $\bar{I}$ in Eqs.(20) are replaced with R_k and $\bar{R}$ respectively and rewritten as

$$R_k = \sqrt{2}\,\lambda_x \sin\left(\left(k + \tfrac{1}{2}\right)\alpha - \tfrac{\pi}{4}\right) + \bar{R} \quad \text{for } k = 0 \sim n-1 \tag{22}$$

Notice that in case that $k = 0 \sim \frac{N}{2} - 1$ and $\frac{n\alpha}{2} = \frac{\pi}{4}$, the series of R_k is symmetric about the base line, i.e zero radian. That is, $R_{n-1-k} - \bar{R} = -(R_k - \bar{R})$. Thereofre, when $k = 0$,

$$R_{n-1} + R_0 = 2\bar{R}\,. \tag{23}$$

Plugging in Eqs.(22) and add both sides, Eq.(17) and (18) can be reduced to the relation of D_x, D_y and $\bar{R}$ as follow.

$$\begin{aligned}D_x + D_y &= 2\sin\frac{\alpha}{2} \sum_{k=0}^{n-1} \left(\sqrt{2}\,\lambda_x \sin\left(\frac{2k+1}{2}\alpha - \frac{\pi}{4}\right) + \bar{R}\right) \sqrt{2} \sin\left(\frac{2k+1}{2}\alpha + \frac{\pi}{4}\right) \\ &= 2\sqrt{2}\bar{R} \sin\left(\frac{n\alpha}{2}\right) \sin\left(\frac{n\alpha}{2} + \frac{\pi}{4}\right) \\ &= 2\sqrt{2}\bar{R} \sin\left(\frac{\pi}{4}\right) \sin\left(\frac{\pi}{2}\right) \\ \therefore D_x + D_y &= 2\bar{R}\end{aligned} \tag{24}$$

Equalizing Eqs.(23) and (24) yield

$$D_x - R_0 = R_{n-1} - D_y\,. \tag{25}$$

Now the constraint terms in Eq.(19), replaced with $D_x - R_0 = R_E$ and $R_{n-1} - D_y = R_E$, can be interpreted as those for the evolute polygon subject to the equal major and minor radii R_x and R_y.

$$\begin{aligned}\mathcal{L}_I(R_k, \lambda_x, \lambda_y) = \left(2\sin\frac{\alpha}{2}\right)^2 \sum_{k=0}^{n-1} (R_k - \bar{R}\,)^2 - 2\lambda_x \left(\sum_{j=1}^{n-1} E_j \cos(j\alpha) - R_E\right) \\ - 2\lambda_y \left(R_E - \sum_{j=1}^{n-1} E_j \sin(j\alpha)\right).\end{aligned} \tag{26}$$

Therefore, to prove the proposition, we shall show that Eqs. (22) minimize Eq.(6) (with $D_x = D_y = R_E$) as well.

$$\mathcal{L}_E = \sum_{k=1}^{n-1} {E_k}^2 - 2\lambda_x^E \left(\sum_{j=1}^{n-1} E_j \cos(j\alpha) - R_E \right) - 2\lambda_y^E \left(R_E - \sum_{j=1}^{n-1} E_j \sin(j\alpha) \right) \qquad ((6a)$$

Because Eqs.(2) and , (3) are already satisfied, $\frac{\partial \mathcal{L}_E}{\partial E_k} = 0$ is to be shown.

$$E_k = \lambda_x^E \sin(k\alpha) + \lambda_y^E \cos(k\alpha) \;\; for\; k = 1 \sim n-1 \qquad (27)$$

Plug in Eqs.(27) to Eqs.(2) and , (3) and equalize them to obtain $\lambda_x^E = \lambda_y^E$ as follow.

$$\lambda_x^E \sum_{k=1}^{n-1} \sin(k\alpha)\cos(k\alpha) + \lambda_y^E \sum_{k=1}^{n-1} \cos^2(k\alpha) = \lambda_y^E \sum_{k=1}^{n-1} \sin(k\alpha)\cos(k\alpha) + \lambda_x^E \sum_{k=1}^{n-1} \sin^2(k\alpha)$$

$$\left(\lambda_x^E - \lambda_y^E\right) \sum_{k=1}^{n-1} \sin(k\alpha)(\cos(k\alpha) - \sin(k\alpha)) = 0 \qquad \because \sum_{k=1}^{n-1} \sin^2\left(\frac{\pi}{2} - (k\alpha)\right) = \sum_{k=1}^{n-1} \sin^2(k\alpha)$$

$$\therefore \qquad E_k = \lambda_x^E(\cos(k\alpha) + \sin(k\alpha)) \;\; for\; k = 1 \sim n-1 \qquad (27a)$$

Recall that $E_k = R_k - R_{k-1}$ and plug in Eqs.(22) to express E_k with λ_x that satisfies Eq.(12).

$$E_k = \lambda_x \sqrt{2} \left\{ \sin\left(k\alpha - \frac{\pi}{4} + \frac{\alpha}{2}\right) - \sin\left(k\alpha - \frac{\pi}{4} - \frac{\alpha}{2}\right) \right\} = 2\sin\left(\frac{\alpha}{2}\right) \lambda_x(\cos(k\alpha) + \sin(k\alpha)) \qquad (27b)$$

Compare Eq.(33a) and Eq.(33b) to obtain $\lambda_x^E = 2\sin\left(\frac{\alpha}{2}\right)\lambda_x$. This imply that λ_x and E_k are the minimizer of modified Lagrangean

$$\tilde{\mathcal{L}}_E = \frac{1}{2\sin\left(\frac{\alpha}{2}\right)} \sum_{k=1}^{n-1} {E_k}^2 - 2\lambda_x \left(\sum_{j=1}^{n-1} E_j \cos(j\alpha) - R_E \right) - 2\lambda_y \left(R_E - \sum_{j=1}^{n-1} E_j \sin(j\alpha) \right) \qquad (6b)$$

, which essentially has no effects on the optimizer set of E_k. This concludes the proof.■

For supplemental, Eq.(17), (18), (22) and (24) can be further solved for λ_x, and Eq.(6) in a similar way for λ_x^E independently. They result in

$$\lambda_x = \frac{D_x - D_y}{2\sin\frac{\alpha}{2}\left(n - \frac{1}{\sin\alpha}\right)}, \qquad \lambda_x^E = \frac{2\,R_E}{n - 1 + \cot\alpha}. \qquad (28), (29)$$

These results can also confirm $\lambda_x^E = 2\sin\left(\frac{\alpha}{2}\right)\lambda_x$ when $D_x - R_0 = R_E$ and $R_{n-1} - D_y = R_E$.

4.2. A proof of Proposition 2

Let r and θ denote the radius and the rotation angle of two circles rolling over both sides of the base respectively. Figure 3 illustrates the property that the evolute of a cycloid is exactly the same cycloid it originates from. Also let R and Θ denote the radius and the angle of the rotation of the normal vector at each point of the cycloid generated by the rolling circle. The radius of the rotation of a normal is defined as the distance from a point on the cycloid on the "positive" side of the base to the center of curvature at the point, which is actually the point of tangency on the other cycloid on the "negative" side. The angle of rotation of a normal is

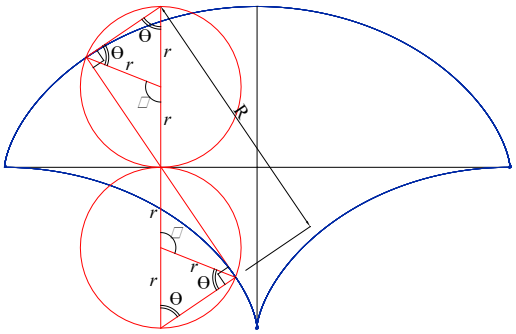


Figure 3: Radius of rotation of a cycloid

defined as the accumulated change of the direction of the normal vectors along a cycloid, measured from the base. Given that *r* is constant, the figure demonstrates that *R* is expressed as a function of θ, and it can be further replaced by Θ (with capital), noticing that $\Theta = \frac{\theta}{2}$, and $R_x = \pi r$. Here, R_x represents the length of the translational move of the rolling circle with the parameter from θ to π.

$$R(\theta) = 4r\cos\left(\frac{\pi-\theta}{2}\right) = 4r\sin\left(\frac{\theta}{2}\right) = 4\frac{R_x}{\pi}\sin(\Theta) = R(\Theta) \tag{30}$$

The necessary conditions for minimum $\mathcal{L}_E(E_k, \lambda_x, \lambda_y)$ that are obtained from the derivatives of $\mathcal{L}_E(E_k, \lambda_x, \lambda_y)$ with respect to $E_k, \lambda_x, \lambda_y \in \mathbb{R}$ are given as

$$E_k = \lambda_x \sin(k\alpha + \alpha_0) + \lambda_y \cos(k\alpha + \alpha_0) \;\; for\; k = 0 \sim n-1 \tag{31}$$

and equations (2) and , (3). Substituting (31) into , (3) yields

$$\lambda_x \sum_{k=0}^{n-1} \sin(k\alpha + \alpha_0)\cos(k\alpha + \alpha_0) + \lambda_y \sum_{k=0}^{n-1} \cos^2(k\alpha + \alpha_0) = D_y \tag{32}$$

Suppose that the polygon is symmetric about both major and minor axes, and let us take the half of the symmetric polygon in the positive Y quadrants, to apply the necessary conditions for the minimal. Then the dividing number *N* shall be even. Let us take $\frac{N}{2}$ for *n*, i.e. $n\alpha = \pi$, and suppose *n* is also even. Correspondingly, D_y should be set equal to zero. While the second summation is non zero, the first summation vanishes as follows.

$$\begin{aligned}(32)\ 1\text{st term} &= \sum_{k=0}^{\frac{n}{2}-1} \left\{\sin(k\alpha + \alpha_0)\cos(k\alpha + \alpha_0) + \sin\left(\frac{2k+n}{2}\alpha + \alpha_0\right)\cos\left(\frac{2k+n}{2}\alpha + \alpha_0\right)\right\} \\ &= \sum_{k=0}^{\frac{n}{2}-1} \{\sin(k\alpha + \alpha_0)\cos(k\alpha + \alpha_0) - \cos(k\alpha + \alpha_0)\sin(k\alpha + \alpha_0)\} = 0\end{aligned}$$

Therefore, $\lambda_y = 0$.

Let R_x be the radius in the direction of the horizontal axis, i.e. $D_x = 2R_x$. When the equation (31) with $\lambda_y = 0$ is substituted, the equation (2) takes the form of

$$\begin{aligned}2R_x = D_x = \lambda_x \sum_{k=0}^{n-1} \sin^2(k\alpha + \alpha_0) &= \lambda_x \sum_{k=0}^{n-1} \frac{1}{2} - \lambda_x \sum_{k=0}^{n-1} \cos(k2\alpha + 2\alpha_0) \\ &= \frac{N\lambda_x}{4} - \lambda_x \frac{\sin(n\alpha)}{\sin(\alpha)}\cos\big((n-1)\alpha + 2\alpha_0\big) \\ &= \frac{N\lambda_x}{4} \; when\; \alpha_0 = \frac{\alpha}{2}, \qquad \text{yielding } \lambda_x = \frac{8R_x}{N}\end{aligned}$$

, and

$$E_k = \frac{8R_x}{N}\sin(k\alpha + \alpha_0) \quad for\; k = 0 \sim n-1. \tag{33}$$

The altitude H_k to the base of each isosceles is expressed with E_k, and substituting Eq.(33) and $\alpha = \frac{\pi}{N}$

$$H_k = \frac{E_k}{2}\frac{1}{\tan\frac{\alpha}{2}} \quad for\; k = 0 \sim n-1 \tag{34}$$

When N goes to infinite,

$$\lim_{N\to\infty} H_k = \lim_{N\to\infty} \frac{4R_x}{\pi}\sin\left(k\frac{2\pi}{N}+\alpha_0\right)\frac{\frac{\pi}{N}}{\tan\frac{\pi}{N}} = \frac{4R_x}{\pi}\sin\left(k\frac{2\pi}{N}+\alpha_0\right) \quad \because \tan\frac{\pi}{N}\to\frac{\pi}{N}$$
$$= 4\frac{R_x}{\pi}\sin 2\pi\frac{(k+\delta)}{N} \quad \text{with } 0\le\delta\le 1, \text{and replacing by } \Theta = 2\pi\frac{(k+\delta)}{N}$$
$$= 4\frac{R_x}{\pi}\sin\Theta \qquad \text{for } 0\le\Theta\le\frac{\pi}{2} \tag{35}$$

Similarly by plugging in the side length of each isosceles

$$R_k = \frac{E_k}{2}\frac{1}{\sin\frac{\alpha}{2}} \quad for\ k = 0\sim n-1 \tag{36}$$

$$\lim_{N\to\infty} R_k = 2\pi\frac{(k+\delta)}{N} = 4\frac{R_x}{\pi}\sin\Theta \qquad \text{for } 0\le\Theta\le\frac{\pi}{2} \tag{37}$$

Recall Eq.(30). Eq.(35) implies that the polyline defined by Eq.(34) circumscribes the cycloid expressed by Eq.(30) when $N\to\infty$, while Eq.(37) implies that the polyline defined by Eq.(34) inscribes the same. This completes the proof. ■

4.3. Graphical construction

Given a number of division *N*, the unique polygon spanning between equal radii, with equal inner angles as well as with the minimal sum of the squared lengths, can be graphically constructed by applying Eq.(27) and scaling it to a prescribed radius R_E. Figure 4 illustrates the steps. For any aspect ratio of major and minor axes, a ring with a minimal variance of segments can be drawn as an involute of the evolute polygon. Depending on what are prescribed, Eq.(28), (29) can be applied.

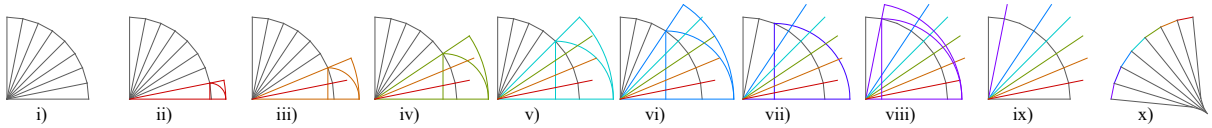


Figure 4: Graphical construction steps for an extended-affine polygon with the minimal sum of squared lengths

4. Concluding remarks

Two propositions on equilibrium forms of spoke wheel rings generated by the extended affine method have been proved. 1) Given a number of vertices, the evolute polygon of a polygon with all equal angles and a minimal variance of side lengths to approximate an elliptic shape is a unique polyline with equal angles with the minimal squared lengths. 2) The evolute polyline approaches to a cycloid when the number of vertices increases to infinite. A few questions remain, including proof for cases where the number of division is not a multiple of 4, i.e. two orthogonal axes of symmetry do not exist, as well as an explanation to the well-known property of cycloid that the involute of a cycloid is the same cycloid. Also, more various application should be demonstrated from practical aspect.

References

[1] R. Bergermann, K. Göppert, "Das Speichenrad – Ein Konstruktionsprinzip für weitgespannte Dachkonstruktionen", *Stahlbau* 69, 2000, Heft 8.

[2] K. Göppert, K. Stockhusen, T. Moschner, "Estadio Jornalista Mario Filho, Rio de Janeiro", *Stahlbau* 83, 2014, Heft 6.

[3] H. Tamai, "On a family of equilibrium geometry of a spoke-wheel structure: Geometric approach to form finding of a spoke wheel system", *Creativity in Structural Design: Proceedings of the IASS Annual Symposium 2018*, Boston, USA, July 16-20, 2018.

[4] Knapp, Michael P. "Sines and Cosines of Angles in Arithmetic Progression"

Proceedings of the IASS Annual Symposium 2019 — Structural Membranes 2019
Form and Force
7—10 October 2019, Barcelona, Spain
C. Lázaro, K.-U. Bletzinger, E. Oñate (eds.)

A new equivalent continuum model for gridshells

Maria Luisa REGALO*, Stefano GABRIELE[a], Ginevra SALERNO[a], Valerio VARANO[a]

* Polytechnic of Bari, Dep. of Civil Engineering and Architecture-Sciences
Via E. Orabona, 4, 70126, Bari, Italy
marialuisa.regalo@poliba.it

[a] Roma Tre University, Archit. Dept., LIMeS-Applied Mathematics and Structural Mechanics Lab.,
Via della Madonna dei Monti, 40, 00184, Rome, Italy

Abstract

In this work, an equivalent continuum of gridshell model is proposed through two different constitutive identification procedures. These are both based on the selection of a Reference Elementary Volume (REV), used to obtain the equivalent elastic constants. The REV is flat in the first procedure, while it is curved in the second one. The two identifications are compared in order to discuss the effect of the surface curvature in the constitutive coupling between the membrane and bending behaviors of the equivalent shell. The numerical validation of the identification procedures is made by means of different examples, comparing the gridshell response and the equivalent shell response in terms of mechanical work.

Keywords: gridshell, discrete homogenization

1 Introduction

A gridshell is a reticulated shell; thus, it has a curved surface like a shell, but its structure is concentrated into pin-jointed truss elements such as a reticulated structure. This kind of structures may be analysed as systems of discrete elements through extensions of the ordinary theories for structural frameworks, or alternatively they may be analysed as continua.
Having an equivalent continuum of a gridshell could be advantageous for better understanding the global mechanical behaviour of the gridshell, in relation to its final shape (that could be obtained by means of a form finding process or defined by an analytical surface). For instance, in the literature the equivalent continuum approach is used to evaluate the global buckling load of the gridshell [1], and the same approach has been used to design the Mannheim Multihalle one [2]. Furthermore, an equivalent continuum model could be used for exploring in a more efficient way a design space of target shapes [3] or, once the shape is fixed, to study the optimal directions of the grid lines with respect to the principal lines of the surface [4].
Several approaches to identify an equivalent continuum of a reticulated shell have been proposed in the literature, as referenced in [5]. Moreover, the approach of the equivalent continuum is largely used also in several application fields, such as periodic brickwork [6] and, recently, in nanostructures [7] [8] [9].
In all of them, the key issue is a proper definition of the equivalent stiffness describing the

Copyright © 2019 by Maria Luisa Regalo, Stefano Gabriele, Ginevra Salerno, Valerio Varano
Published by the International Association for Shell and Spatial Structures (IASS) with permission.

transition from the *fine* model to the *coarse* one, that is, from the gridshell model to the continuous shell. Since the dimensions of the grid's module are relatively small compared to the overall dimensions of the whole structure, the identification procedures reported in [5], neglect the surface curvature. Furthermore the distortion of the pattern is also negleted. Actually, the grid cannot be composed of squares and equilateral triangles on doubly curved surfaces.
The aim of this work is to assess the influence of the surface curvature in the characterization of the equivalent continuum of a gridshell with zero gaussian curvature. Therefore, two different identification procedures (a standard and a novel one) are introduced and compared. A numerical validation of both shows that the novel procedure, which acounts for the shell curvature, is more accurate than the standard one.

2 Fine and coarse models and methodological aspects

Throughout the paper, we consider as fine model a quadrangular mesh of continuous beam elements connected through cylindrical joints, assuming the shape of a barrel vault within 3D space. The grid is triangulated by truss elements to provide in-plane shear stiffness.

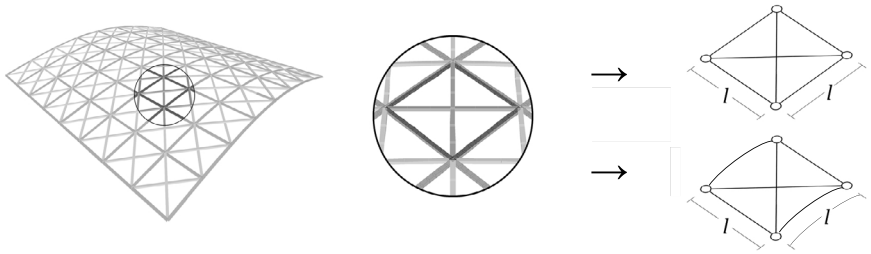


Figure 1: Selected REVs in the fine model

As coarse model we select a Donnell shell, whose equations are given in [10]. For this shell we identify the elastic coefficients for membrane and flexural behaviour, but not the shear ones. The identification process starts from the choice of a Representative Elementary Volume (REV) in the fine model and the selection of a continuous region in the coarse model of the same area as that occupied by REV.
Then, applying monoaxial external forces to the REV, case by case we solve the elastic problem and require work equality of the two models under the same deformation.
For the sake of comparison, in the identification procedure we consider two different REVs, one flat and one curved, shown in Figure 1, of characteristic length l. Both REVs are composed of six elements, four beams and two pin-jointed bars, i.e. the diagonals. The beams are in common to two contiguous modules, and so the beams have been considered with half area of their cross-sections and half inertia moment, for reasons of periodicity.
Finally, in the case of the curved REV we make use of some simple intermediate models, immersed within 2D spaces and derived from the fine model.

2.1 Intermediate models immersed in 2D space

The behaviour of the barrel gridshell may be analysed through simplified models immersed in 2D spaces by imposing homogeneous deformations in the identification procedures. In particular, the behaviour of the curved REV can be analysed by means of the two simple models, shown in Figure 2 and acting in the planes $\mathbf{e_1 e_3}$ and $\mathbf{e_2 e_3}$.

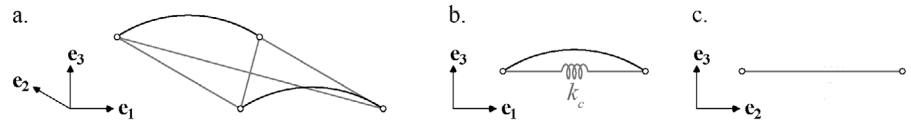


Figure 2: a. Curved REV; b. Equivalent arch-and-spring model; c. Equivalent beam model

The arch-and-spring model, shown in Figure 2.b, is equivalent to the curved REV under axial deformation in direction $\mathbf{e_1}$ and bending deformation around $\mathbf{e_2}$. As a consequence, the arch cross section doubles that of the single arch in the REV, while the stiffness of the spring is equal to the stiffness of the system composed of the two diagonals and the two straight beams under the given axial deformation. So, calling k_{a1} and k_{b1} the axial and bending stiffness of the arch, respectively, and k_c the stiffness of the spring, it holds that:

$$k_{a1} = \frac{EA_b}{l} \qquad k_{b1} = \frac{EJ_b}{l} \qquad k_c = \frac{4\alpha \sin^2(\alpha/2) EA_b A_d}{l\Big(2\alpha^3 A_d + \big(\alpha^2 + 4\sin^2(\alpha/2)\big)^{3/2} A_d\Big)} \tag{1}$$

where E is the elastic modulus of the material; $A_b/2$, $J_b/2$ are the area and the inertia moment of the cross section of the arches and beams, respectively, in the REV; A_d is the cross-section area of the diagonals, l is the common lenght of arches and beams and α is the center angle subtended by the curved REV.
Similarly, the beam in Figure 2.c is made equivalent to the curved REV under axial deformation in direction $\mathbf{e_2}$ and bending deformation around $\mathbf{e_1}$. Thus, the axial and bending stiffnesses of the equivalent beam, named k_{a2} and k_{b2}, are:

$$k_{a2} = EA_b + \frac{2\alpha^5 EA_b A_d J_b}{2c_3\big(3(\alpha - \sin(\alpha)) - c_3\alpha\big) A_b A_d l^2 + 2c_3 c_4 \alpha^2 A_d J_b + c_1 \alpha^2 A_b J_b} \qquad k_{b2} = EJ_b \tag{2}$$

where:

$$c_1 = \big(2 + \alpha^2 - 2\,\cos(\alpha)\big)^{3/2} \qquad c_3 = 1 - \cos(\alpha) \qquad c_4 = \alpha - \sin(\alpha) \tag{3}$$

3 Identification procedures

3.1 Identification of flat REV

The flat standard REV is composed only of straight elements (see Figure 1). By solving the elastic problems depicted in Figures 3.a and 4.a, we find the relations between the external actions, N_1 and M_2, and the relative deformations, which hold:

$$N_1 = \frac{E}{2}\left(A_b + \frac{\sqrt{2}}{2}A_d\right)\epsilon_1 + \frac{\sqrt{2}}{4}EA_d\epsilon_2 \tag{4}$$

$$M_2 = \frac{EJ_b}{2}\chi_2 \tag{5}$$

where ϵ_1, and ϵ_2 are the axial deformations in direction $\mathbf{e_1}$ and in direction $\mathbf{e_2}$, respectively, and χ_2 is the curvature with respect to $\mathbf{e_2}$.
Now, applying the equivalent monoaxial stress states to the continuum region, depicted in Figures 3.b and 4.b, under the assumption that the deformations in the REV and in the continuous

region are the same, the constitutive relation for the coarse model derives:

$$\begin{bmatrix} N_{11} \\ N_{22} \\ M_{11} \\ M_{22} \end{bmatrix} = \begin{bmatrix} \bar{A}_{11} & \bar{A}_{12} & 0 & 0 \\ & \bar{A}_{22} & 0 & 0 \\ & & \bar{B}_{11} & 0 \\ sym & & & \bar{B}_{22} \end{bmatrix} \begin{bmatrix} \epsilon_1 \\ \epsilon_2 \\ \chi_1 \\ \chi_2 \end{bmatrix} \tag{6}$$

with

$$\bar{A}_{11} = \frac{E}{l}\left(A_b + \frac{\sqrt{2}}{2}A_d\right) \qquad \bar{A}_{12} = \frac{\sqrt{2}}{2}\frac{EA_d}{l} \qquad \bar{A}_{22} = \frac{E}{l}\left(A_b + \frac{\sqrt{2}}{2}A_d\right) \tag{7}$$

$$\bar{B}_{11} = \bar{B}_{22} = \frac{EJ_b}{l} \tag{8}$$

Due to the presence of diagonal elements, the constitutive law for the membrane behaviour of the equivalent continuum presents some out-of-diagonal couplings. The coefficients given in Eqs. (7) (8) correspond to those found in [**?**].

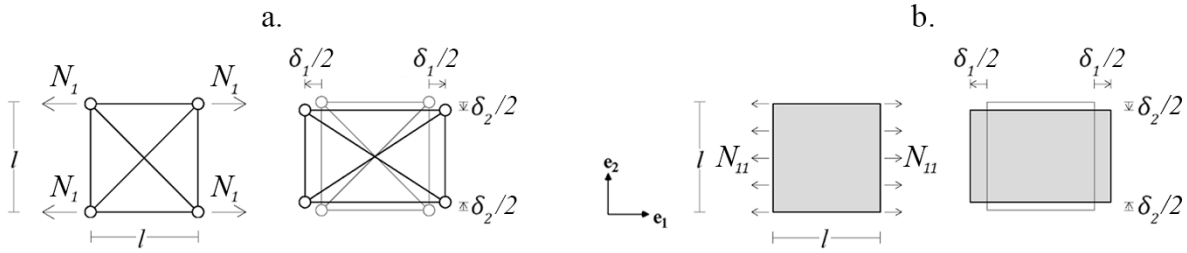


Figure 3: Axial forces and deformations in the fine model (a) and in the coarse model (b)

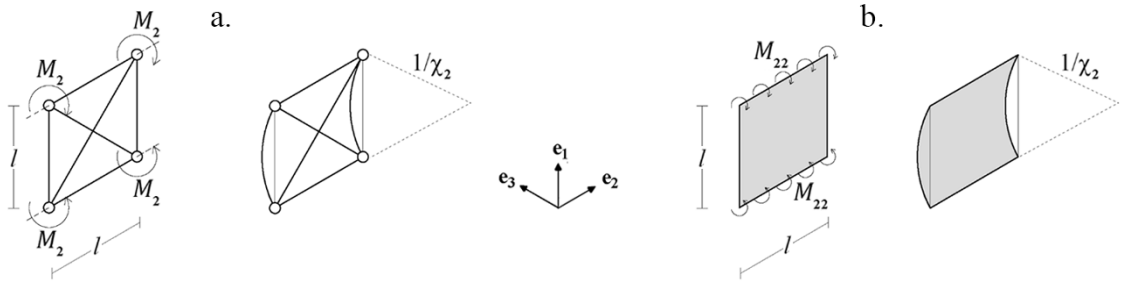


Figure 4: Bending forces and deformations in the fine model (a) and in the coarse model (b)

3.2 Identification of the curved REV

3.2.1 The equivalent arch

In the case of the curved REV, the identification procedure needs an intermediate step, that is the identification of a continuum arch equivalent to a system of arch-and-springs (see Figure 5), defined in section 2.1.
Similarly as before, the identification of the elastic constants of the equivalent arch is addressed by solving the two elastic problems shown in Figure 6, in which the axial and bending behaviour

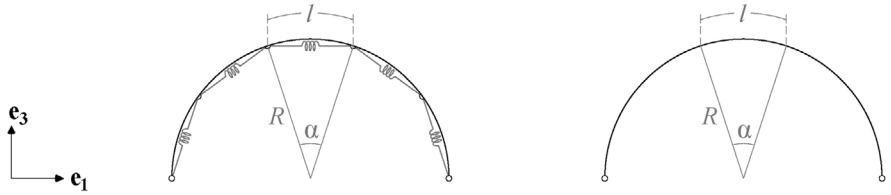


Figure 5: The arch-and-spring REVs and the equivalent arch model

are analysed separately. In principle, this hypothesis could imply some errors in the identification procedure, but our numerical results show that in the considered case these errors are negligible.

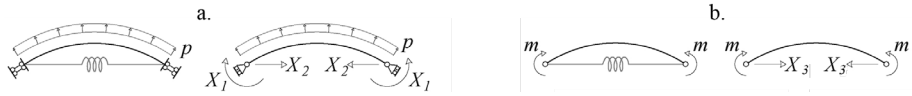


Figure 6: The elastic problems solved for the curved REV

The two elastic problems are solved by the force method. The solution of the axial problem (Figure 6.a) provides the values of the unknowns X_1 and X_2:

$$X_1 = \frac{4c_3(2c_3 - \alpha\sin(\alpha))pA_dJ_bl^2}{2\alpha^3(\alpha^3 + c_3c_4)A_dJ_b + c_1\alpha^3A_bJ_b + 2c_3(c_4\alpha - 4c_3)A_dA_bl^2} \tag{9}$$

$$X_2 = \frac{16\alpha^2\sin^3(\alpha/2)pA_dJ_bl}{2\alpha^3(\alpha^3 + c_3c_4)A_dJ_b + c_1\alpha^3A_bJ_b + 2c_3(c_4\alpha - 4c_3)A_dA_bl^2} \tag{10}$$

and of the average value $\overline{\epsilon}$ of the axial deformation:

$$\overline{\epsilon} = \frac{\alpha^2p(2\alpha^3A_d + c_1A_b)J_bl}{EA_b(c_1\alpha^3A_bJ_b + 2\alpha^3(\alpha^3 + c_3c_4)A_dJ_b + 2c_3(c_4\alpha - 4c_3)A_dA_b)} \tag{11}$$

Then, the axial elastic constant A_1 of the equivalent arch, defined as the ratio between the axial force pR and the average axial deformation $\overline{\epsilon}$, is given by:

$$A_1 = \frac{EA_b\big(2c_3(c_4\alpha - 4c_3)A_dA_bl^2 + 2\alpha^3(\alpha^3 + c_3c_4)A_dJ_b + c_1\alpha^3A_bJ_b\big)}{\alpha^3J_b\big(2\alpha^3A_d + c_1A_b\big)} \tag{12}$$

For the bending problem (Figure 6.b), the force method provides the unknown X_3:

$$X_3 = \frac{4\alpha\sin(\alpha/2)\big(\alpha\sin(\alpha) - 2c_3\big)mA_bA_dl}{\Big((c_3 - 4)c_3\alpha + \sin(\alpha)\big(6c_3 - \alpha\sin(\alpha)\big)\Big)A_bA_dl^2 - 2\alpha^2(\alpha^3 + c_3c_4)A_dJ_b - c_1\alpha^2A_bJ_b} \tag{13}$$

and the mean curvature $\overline{\chi}$:

$$\overline{\chi} = \frac{c_1\alpha^3A_bJ_b + 2\alpha^3(\alpha^3 + c_3c_4)A_dJ_b + 2c_3(c_4\alpha - 4c_3)A_dA_bl^2}{\alpha\Big(c_1\alpha^2A_bJ_b + 2\alpha^2(\alpha^3 + c_3c_4)A_dJ_b + 2c_3\big(3(\alpha - \sin(\alpha)) - c_3\alpha\big)A_dA_bl^2\Big)}\frac{m}{EJ_b} \tag{14}$$

Then, the flexural elastic constant B_1 of the equivalent arch, defined as the ratio between the applied couple m and the mean curvature $\overline{\chi}$, is given by:

$$B_1 = \frac{\alpha\Big(c_1\alpha^2A_bJ_b + 2\big(3(\alpha - \sin(\alpha)) - c_3\alpha\big)c_3A_bA_dl^2 + 2(c_3c_4 + \alpha^3)\alpha^2A_dJ_b\Big)EJ_b}{c_1\alpha^3A_bJ_b + 2(c_4\alpha - 4c_3)c_3A_bA_dl^2 + 2(c_3c_4 + \alpha^3)\alpha^3A_dJ_b} \tag{15}$$

3.2.2 The equivalent shell

The intermediate 1D models of the equivalent arch and beam are the ingredients for the definition of the equivalent shell. While the elastic constants of the equivalent arch, A_1 and B_1, has been found in the previous section, the axial and bending elastic constants of the equivalent beam are clearly $A_2 = k_{a2}$ and $B_2 = k_{b2}$.
For each stress state, we impose the same deformation to the shell model and to the intermediate model, we equate the internal works and thus obtaining the corresponding elastic coefficient of the shell model. For example, under uniform stress along direction $\mathbf{e_1}$, the following equations hold:

$$\begin{cases} N_{11} = A_{11}\epsilon_1 + A_{12}\epsilon_2 \\ 0 = A_{12}\epsilon_1 + A_{22}\epsilon_2 \end{cases} \qquad N_1 = A_1\epsilon_1 \qquad N_1 = N_{11}l \tag{16}$$

from which we derive:

$$\frac{A_1}{l} = \frac{A_{11}A_{22} - A_{12}^2}{A_{22}} \qquad \nu_1 = \frac{A_{12}}{A_{22}} \tag{17}$$

Analogously, we obtain:

$$\frac{A_2}{l} = \frac{A_{11}A_{22} - A_{12}^2}{A_{11}} \qquad \nu_2 = \frac{A_{12}}{A_{11}}. \tag{18}$$

Then, by using Eqs.(17) (18), we derive:

$$A_{11} = \frac{A_1}{l(1-\nu_1\nu_2)} \qquad A_{12} = \frac{\nu_2 A_1}{l(1-\nu_1\nu_2)} \qquad A_{22} = \frac{A_2}{l(1-\nu_1\nu_2)} \tag{19}$$

In similar way, it can be easily obtained that:

$$B_{11} = B_1/l \qquad B_{22} = B_2/l \tag{20}$$

Finally, the elastic coefficients of the equivalent shell are given in terms of the stiffness and geometrical parameters of the fine model:

$$\begin{aligned} A_{11} &= EA_b \frac{c_1 A_b J_b l\alpha^3 + 2\,c_3 A_b A_d l^3(c_4\alpha - 4\,c_3) + 2\,A_d J_b l\alpha^3(c_3 c_4 + \alpha^3)}{c_0 J_b l^2 \alpha^3(c_1 A_b + 2\,A_d\alpha^3)} \\ A_{12} &= -\frac{4\,c_3 E\alpha}{c_0 l(c_1 + 2\,\alpha^3)}\left(A_b + \frac{2\,c_5 A_d\alpha^3}{c_1(1+c_5)}\right) \\ A_{22} &= \frac{E}{c_0 l}\left(A_b + \frac{2\,A_d c_5\alpha^3}{c_1(1+c_5)}\right) \end{aligned} \tag{21}$$

$$\begin{aligned} B_{11} &= \frac{EJ_b}{l}\frac{c_1 A_b J_b + 2\,c_3 A_b A_d l^2\big(\alpha^2\big(2+\cos(\alpha)\big) - 3\,\sin(\alpha)\big) + 2\,A_d J_b\alpha^3(\alpha^3 + c_3 c_4)}{c_1 A_b J_b\alpha^3 + 2\,c_3 A_b A_d l^2(c_4\alpha - 4\,c_3) + 2\,A_d J_b\alpha^3(\alpha^3 + c_3 c_4)} \\ B_{22} &= \frac{EJ_b}{l} \end{aligned} \tag{22}$$

where:

$$\begin{aligned} c_0 &= 1 - \frac{16 c_3 J_b\alpha^5(c_1 A_b + 2\,A_d\alpha^3)(c_1 A_b(1+c5) + 2\,c_5 A_d\alpha^3)}{c_1 A_b(1+c_5)(c_1 + 2\,\alpha^2)^2(c_1 A_b J_b\alpha^3 + 2\,c_3 A_b A_d l^2(c_4\alpha - 4\,c_3) + 2\,A_d J_b\alpha^3(\alpha^3 + c_3 c_4)} \\ c_2 &= 2\,\alpha^3 + c_1 \qquad c_5 = \frac{c_1 A_b J_b\alpha^3}{2\,c_3 A_d\alpha\big(A_b l^2\big(2\,\alpha + \alpha\cos(\alpha) - 3\,\sin(\alpha)\big) + c_4 J_b\alpha^2\big)} \end{aligned} \tag{23}$$

4 Numerical simulations and conclusions

In the previous sections we demonstrated that the constitutive identification of curved gridshells leads to a non trivial solution, for which Eq.6 is represented by two different continua, one found in Section 3.1, the other in Section 3.2, namely continuum A (CA) and continuum B (CB). In order to validate the two identification procedures, we numerically tested and compared the response of the fine model with that of the coarse models.

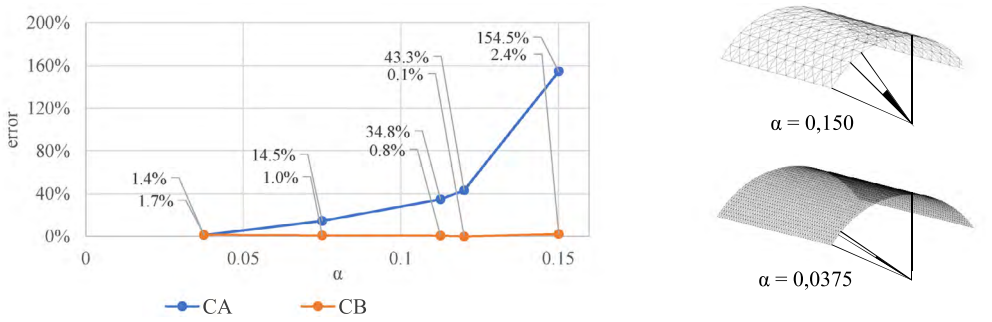
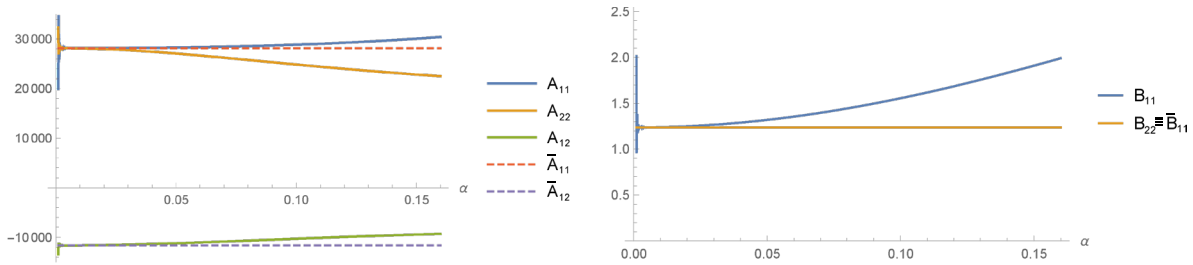


Figure 7: Percent error of CA and CB from the fine model with respect to α

The numerical analyses are carried out with the finite element software SAP2000 [11]. The geometry of the selected gridshell is depicted in Figure 7 and its modeling details can be found in [4]. The model is analysed under uniform vertical load with one longitudinal straigth edge supported by pins and other one by rollers. Then, two equivalent shells are modelled with the same shape and analysed under the same load and boundary conditions.



(a) *Membrane elastic constants* (b) *Flexural elastic constants*

Figure 8: Elastic constants obtained by curved and flat REV for different values of α

SAP2000 allows to define a layered section; therefore, for the CA we define a section composed of two layers, the first one is a membrane with the elastic constants given by (7), and the last one is a plate with the elastic constants given by (8). In the same way, the CB has a layered section, but the elastic constants of the membrane layer are given by (21), while those ones of the bending layer are given by (22).
Figure 7 shows the error (%) in the response of the two equivalent continua with respect to the fine model, this error is evaluated in terms of mechanical work. Five tests are done in which the reference fine model has the same radius and dimensions, but different mesh sizes. As Figure 7 shows, when the mesh size is dense, that is α approaches to zero, the two shells have a similar response and this is also very close to that of the gridshell. Increasing the parameter α, CA is

ever further from the fine model. On the contrary CB is not affected by α. Interestingly, Figure 8 shows that the elastic constants of CB change substantially with α. In conclusion this work proposes a novel approach to take into account the curvature effect in the equivalent continuum modeling of gridshells. The simple numerical example of a barrel gridshell demonstrates how the solutions can widely diverge if starting from a flat REV. This work can form the basis of a methodological approach for equivalent continuum modeling of gridshells with double curvature.

References

[1] S. Malek, T. Wierzbicki and J. Ochsendorf, "Buckling of spherical cap gridshells: A numerical and analytical study revisiting the concept of the equivalent continuum," *Engineering Structures*, vol. 75, pp.288-298, Sep. 2014.

[2] E. Happold and W.I. Liddell, "Timber lattice roof for the Mannheim Bundesgartenshau," *Engineering Structures*, vol. 53(3), pp.99-135, Mar. 1975.

[3] S. Gabriele, V. Varano, G. Tomasello, D. Alfonsi, "R-Funicularity of form found shell structures" in *Engineering Structures*, vol. 157, pp.157-169, Feb. 2018.

[4] M.L. Regalo, G. Salerno and V.Varano, "Numerical assessment of the funicularity of timber grid shells" in *Creativity in Structural Design: Proceedings of the IASS Annual Symposium 2018, Boston, USA, July 16-20, 2018,.*

[5] V.Gioncu, "Buckling of Reticulated Shells: State-of-the-Art," *International Journal of Space Structures*, vol.10(1), pp. 1-46, Mar. 1995.

[6] G. Salerno and G. de Felice, "Continuum modeling of periodic brickwork," *Solids and Structures*, vol.46(5), pp. 1251-1267, Mar. 2009.

[7] A. Genoese, A. Genoese, N.L Rizzi and G. Salerno, "On the derivation of the elastic properties of lattice nanostructures: The case of graphene sheets," *Composites Part B: Engineering*, vol.115, pp. 316-329, Apr. 2017.

[8] A. Genoese, A. Genoese, N.L Rizzi and G. Salerno, "Force constants of BN, SiC, AlN and GaN sheets through discrete homogenization," *Meccanica*, vol.53(3), pp. 593-611, Feb. 2018.

[9] A. Genoese, A. Genoese and G. Salerno, "Elastic constants of achiral single-wall CNTs: Analytical expressions and a focus on size and small scale effects," *Composite Part B: Engineering*, vol.146, pp. 207-226, Aug. 2018.

[10] S.P. Timoshenko and J.M. Gere, *Theory of Elastic Stability*. New York: McGraw-Hill, 1961.

[11] "Structural Software for Analysis and Design SAP2000." [Online]. Available: https://www.csiamerica.com/products/sap2000. [Accessed: 26-Mar-2019].

Proceedings of the IASS Annual Symposium 2019 – Structural Membranes 2019
Form and Force
7 – 10 October 2019, Barcelona, Spain
C. Lázaro, K.-U. Bletzinger, E. Oñate (eds.)

Applications of Timber Gridshells for Humanitarian Assistance and Disaster Relief Efforts

Thomas B. IMHOFF*, Samar R. MALEK

*United States Naval Academy
590 Holloway Road, Annapolis, MD, 21402
tbimhoff@yahoo.com

Abstract

From 1970 to 2000, 68 percent of United States naval operations were categorized as Humanitarian Assistance and Disaster Relief (HA/DR). These relief efforts identified a need for deployable, lightweight structures, capable of sheltering a large area. Large-span shelters are necessary in HA/DR because they provide space for community gathering, emergency services, educational facilities, and worship. Gridshells are a solution to this need because of their portability and efficiency. Formed from flat, linear members bent on-site into a curved surface, gridshells are relatively large structures that can be built without the use of heavy machinery. To broaden the use of gridshells, this paper quantifies the effects of asymmetric loading and bracing on their performance, as both are likely occurrences in HA/DR. The design requirements and constraints for the gridshell were established by fieldwork in Athens, Greece and by international building codes. The structural analysis included a parametric study that assessed the effects of the grid density, bracing patterns, and load cases (gravity, asymmetric, and point loads) on the failure load. These results, along with the design constraints, governed the design of the HA/DR gridshell. The constructability was evaluated with small-scale models and a half-scale prototype. Having verified the structural performance, deployment mechanisms, storage schemes, and joint movements, gridshells were proven to be solutions that meet the distinct needs in HA/DR efforts.

Keywords: gridshells, humanitarian assistance, disaster relief, parametric studies, bracing, asymmetric loads

1. Introduction

Between 1970 and 2000, 68% of United States naval operations involved responding to a humanitarian crisis [1]. Since then, the U.S. and other world navies have continued to respond swiftly to Humanitarian Assistance and Disaster Relief (HA/DR) missions. During a crisis, distressed regions require food, water, temporary shelter, and medical services. Military forces, especially expeditionary naval forces, are designed for quick reaction and have the material resources to provide support during these situations. Among these supplies are the means to build small shelters designed to hold four to eight people. The lack of heavy machinery and infrastructure in relief zones often prevents larger structures from being built, despite the need for large sheltered spaces for community gathering, dining, worship, education, and emergencies. This need is largely overlooked in HA/DR response, but if properly researched, gridshells could offer a solution because of their deployable construction methods, structural performance, and inherent beauty.

2. Problem Statement

Most gridshells are designed to support symmetric distributed loads and are braced with additional material to increase the stiffness of the structure. In order to further advance gridshell technologies and

Copyright © 2019 by Thomas B. Imhoff and Samar R. Malek.
Published by the International Association for Shell and Spatial Structures (IASS) with permission.

adapt them for new applications such as HA/DR, additional research must investigate how these structures perform under non-traditional load cases, as well as the measurable effects of bracing.

A parametric study focused on understanding the factors that affect the structural performance of gridshells was conducted to answer these questions. Additionally, the specific considerations that affect the constructability and design of an HA/DR gridshell were identified and evaluated in order to adapt and broaden their use.

3. Background

Timber gridshells are a subset of shell structures formed by bending an initially flat lattice into a curved surface. The dominant failure mode for gridshells is global shell buckling under a symmetric distributed load [2]. The primary concern with buckling is generally the ability of the shell to support its self-weight, a gravity-based symmetric distributed load [3]. Gridshells rely on their global curvature to support loads. Their catenary shape makes the structures efficient, yet poses a risk because slight deviations can lead to global buckling.

Asymmetric loads are particularly difficult for gridshells to handle because of their tendency to cause global deformation, leading to global buckling failure. Some asymmetric load cases are documented, though these are limited to point loads associated with maintenance personnel climbing a top large shells [4]. In these cases, the loads were not considered the dominant load due to the scale of the shell and therefore were considered negligible.

Bracing a gridshell with diagonal members can improve its strength and stiffness, thereby increasing its load capacity and resistance to buckling. By nature, gridshell lattices lack in-plane shear stiffness [5]. The lack of shear stiffness allows the double curvature of the shell to form properly, yet after construction the shell must be stiffened. Joint tightening is effective for stiffening shells with small deformations, but shells with large deformations require additional members [4, 5]. No previous or ongoing research investigates the amount, frequency, and orientation of additional bracing.

4. Methodology

To achieve the ultimate objective of designing a gridshell for HA/DR, the following actions were taken:

1) Quantified the effects of bracing and asymmetric loads on the structural performance of gridshells through a parametric study.
2) Established constraints for an HA/DR gridshell using fieldwork and international standards.
3) Selected the most feasible design to carry forward based on the parametric study and constraints.
4) Built small-scale models to test the constructability of the proposed design.

4.1 Parametric Study

Rhinoceros, a 3D modelling software, was used with Grasshopper, a graphical algorithm editor, to conduct the parametric study. Karamba is a Finite Element Analysis (FEA) engine for Grasshopper that was used for the structural analysis. The varied parameters were grid density, bracing pattern, and load case (gravity, asymmetric, and point loads). The global buckling factor for each variation was calculated, but factors such as overall mass, member utilization, number of joints, maximum height, and maximum supported load were also recorded.

The global shape of the candidate gridshell was a 15 m clipped square with four corner supports, each with three distinct touchdown points (Figure 1). The gridshell was form-found using *Karamba* where each egress arch was fixed to an entrance height of 2 m. The computational model mimicked the material properties of wood with a modulus of elasticity of 105 MPa and a yield strength of 0.13 MPa. The initial member cross-section was 3 cm by 7 cm. The gridshell was modeled as a continuous lattice

in a single plane, though in reality, single layer gridshells are made up of two layers of stacked beams. A continuous lattice shell and a true single layer shell exhibit the same overall trends and yield results within 15% of one another [6].

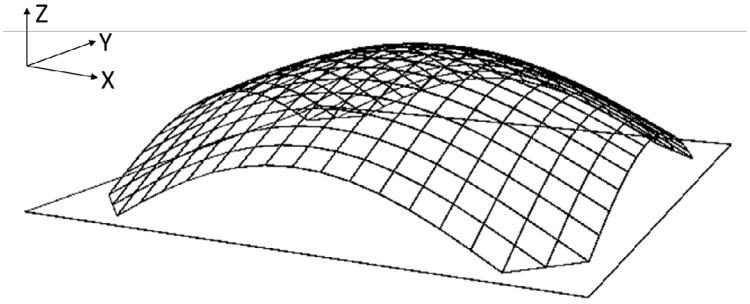


Figure 1: Candidate gridshell used for parametric study

The grid density varied from 8 by 8 to 30 by 30. The bracing schemes were defined as: "half" or "full," depending on whether all or only half of the grids were braced; "continuous" or "discontinuous" depending on if the members braced single or multiple cells (Figure 2).

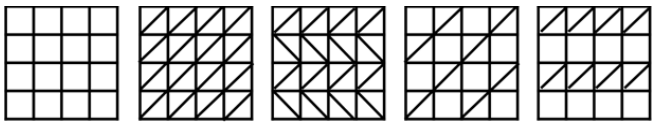


Figure 2: (left to right) – unbraced, full continuous, full discontinuous, half continuous, half discontinuous

Each iteration was subjected to four load cases: a symmetric distributed load, an asymmetric distributed load, a centered point load, and an off-centered point load in a single quadrant of the shell. Table 1 details the range of each parameter. A total of 204 models were evaluated.

Table 1: List of varied parameters and their ranges

Grid Density	Bracing Scheme	Load Case
8, 10, 12, 14, 16, 18, 20, 22, 24, 26, 28, 30	• Unbraced • Half braced, continuous* • Half braced, discontinuous • Full braced, continuous • Full braced, discontinuous	• Symmetric distributed load • Asymmetric distributed load • Centralized point load • Decentralized point load

* select models only

4.2 Design Criteria for HA/DR

The design constraints for HA/DR structures were established by conducting field work in Athens, Greece and using relevant international standards. Refugee populations and non-governmental organizations (NGO) in Athens indicated that community gathering and central spaces were culturally significant. Physical shelter from the elements was important for displaced populations, as was the emotional support provided by a shared community. Gathering spaces that provide for both physical and emotional needs were deemed necessary, yet few structures currently address those needs.

In addition to the situational constraints, the International Building Code, International Fire Code, American Society of Civil Engineers Minimum Design Loads, and the Sphere Handbook (a set of minimum standards for HA/DR response) laid out the engineering requirements for the structure [7, 8, 9, 10]. The standards dictated various classifications and dimensions for the shell and yielded a final design load of: a uniform downward pressure of 287 Pa on the surface, a horizontal wind pressure of 259 Pa on a single side of the shell, and a concentrated point load of 1.33 kN anywhere on the structure. The final structure must withstand this load case in order to be considered a viable solution.

In addition to the standards, the HA/DR gridshell was constrained by the dimensions of intermodal freight containers. The U.S. Navy and many aid organizations use these containers to transport supplies, thus the shell and all of its components must fit easily into the 6.1 m or 12.2 m long variety.

4.3 Constructability Study

To address the constructability of the model, two small-scale models were built prior to the half-scale prototype. The small-scale models did not mimic the *exact* design of the gridshell selected for HA/DR; rather, they were designed to evaluate fabrication methods and building techniques. The small-scale shells were approximately 1:25 scale with respect to the proposed HA/DR gridshell.

The beams for the first model, Model A, were hand cut from 3.175 mm thick high density fiberboard (HDF) into 6.35 mm wide strips. HDF was selected because of its isotropic material properties and relative pliability; however, when subjected to bending stress with such a small cross-section, the material was largely inadequate. The second model, Model B, was constructed using the same global dimensions as the previous shell, but now with 1.524 mm thick acrylic plastic cut into 10 mm strips. Acrylic plastic was an improvement from HDF because it was still isotropic, but stronger and more flexible than HDF. Additionally, Model B was fabricated with a CNC laser cutter to improve the precision of the dimensions.

Improving on Model A and B, a half-scale prototype was built using 9 mm thick, marine grade okoume plywood cut into strips 38.1 mm wide. Okoume is often used to manufacture racing sailboats and was selected because it is both lightweight and flexible. The prototype established realistic manufacturing, transportation, assembly, and forming methods for gridshells designed for HA/DR.

5. Results

5.1 Parametric Study

The results of the parametric study are presented below in terms of the applied load case. Though the grid density ranged from 8 by 8 to 30 by 30, all of the shells with a grid density less than 16 by 16 experienced local member failure in an unbraced condition and therefore were not included. The overall trends are discussed in each load case section, and the design selection is detailed at the conclusion of this section.

5.1.1 Symmetric Distributed Loads

When subjected to a symmetric distributed load, adding a half bracing scheme caused an average increase in maximum supported load by 27% for a 34% increase in weight, regardless of grid density. Adding a full bracing scheme caused an average increase in maximum supported load by 53% for a 66% increase in weight from an unbraced state. Varying grid density did not have a significant impact on the maximum supported load, instead additional bracing accounted for significant jumps. These jumps indicate that when subjected to a symmetric load, full bracing most improves a gridshell's maximum supported load, followed by half bracing, and subsequently an unbraced shell.

5.1.2 Asymmetric Distributed Loads

Applying asymmetric distributed loads to the gridshell presented significant problems. The buckling factor initially decreased as grid density increased, but beyond a grid density of 22 the difference in structural performance was minimal, as each bracing scheme's buckling factor fell within ± 0.11 buckling factors of the group average. The maximum supported load shows that additional bracing improved the load carrying capacity of the shell by an average of 33% and 92%, regardless of grid density, when half and full bracing schemes were added respectively. Much like the behavior of the shell subjected to a symmetric distributed load, bracing greatly improved the buckling load capacity.

5.1.3 Point Loads

With respect to the centered point load, as grid density increased from 16 to 30 and additional bracing was added, the buckling factor increased by an average of 36%. The half bracing scheme showed the highest increase between the initial and final grid density (16 to 30) with 56%. The off-center point load showed that as grid density and bracing increased, both the buckling factor, and maximum supported load by association, increased. On average, the buckling factor of the half braced shell was 6% higher and the buckling factor of the fully braced shell was 57% higher relative to an unbraced shell subjected to either point load.

For the fully braced shell, the type of continuity of the bracing did not have a significant impact on its structural performance. Both full continuous bracing schemes and full discontinuous bracing schemes consistently produced results within 10% of one another. Half continuous bracing was difficult to simulate due to software indexing limitations, thus only select cases at grid densities of 10, 20, and 30 were tested. However, when testing these select cases, half continuous bracing consistently exhibited higher performance, regardless of load case or grid density, compared to half discontinuous bracing. The results of these tests indicated that while the continuity of the bracing did not affect the full bracing schemes significantly, continuous bracing consistently outperformed discontinuous half bracing schemes by an average of 37% across all load cases and grid densities tested.

5.1.4 Design Selection

A pavilion suited to shelter 150 to 200 people, and to be built with heavy machinery, typically weighs between 53.4 and 66.7 kN [11]. In HA/DR, using heavy machinery is not an option and thus decreasing the structure's weight will improve the portability and construction of the shelter. The HA/DR gridshell was designed to weigh 25% of current solutions, approximately 13.3 ± 2.2 kN. This weight range lies between the grid densities of 18 and 22, where the average weight of the half-braced shell and fully braced shell was 11.3 kN and 14 kN respectively. Using this technique, a specific region of the results became the focus of the selection process. Within this region, the results indicated that with respect to symmetric distributed loads, adding additional bracing improved the maximum supported load, while increasing grid density showed little effect. Regarding asymmetric distributed loads, additional bracing again improved both the maximum supported load and the buckling factor. Results indicated that generally speaking, lower grid densities in this region improved structural performance in both measures. The results of the centered and off-center point load indicate that additional bracing improved performance, as did increasing grid density. Given the trends, a region within each grid density subsection was selected as an "ideally suited region" for HA/DR structure. Figure 3 illustrates the selected weight regions and the ideally suited regions in the results.

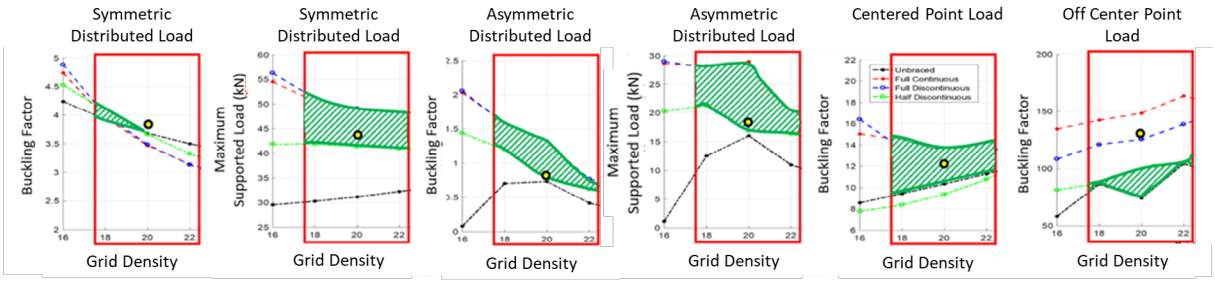


Figure 3: Summary of structural performance for each load case with the optimal performance range highlighted and the 20 by 20, half continuous braced shell indicated

Half continuous bracing was difficult to simulate due to software indexing limitations, thus only select cases at grid densities of 10, 20, and 30 were tested. The results of these tests indicated that while the continuity of the bracing did not affect the full bracing schemes significantly, continuous bracing consistently outperformed discontinuous half bracing schemes. This trend was extrapolated to all grid

densities. Plotted the results of the half continuous bracing scheme at a grid density of 20 revealed that the structure's performance fell within or outperformed the ideally suited region each time. In order to further save weight, and to improve resistance to symmetric and asymmetric distributed loads, the final design for HA/DR was selected as a continuous half braced shell with a grid density of 18.

5.2 Design and Construction of HA/DR Gridshell

5.2.1 Small-Scale Models

The hole measurements for Model A (high density fiberboard) initially failed to consider the sliding of the beams that occurs during assembly and the stress concentrations. Shown in Figure 4, Model B (acrylic plastic) solved the issue of stress concentrations with wider members and stronger material. To alleviate the issue of misaligned holes, the CNC laser cutter cut slots approximately three times the diameter of the original hole. The laser cutter allowed each member to be cut to exact, unique dimensions; however the use of slots showed that the dimensions were similar enough to use a common member size in future iterations. An advantage of gridshell structures is the ease in which they can be constructed, and by creating common member sizes that advantage can become even more pronounced.

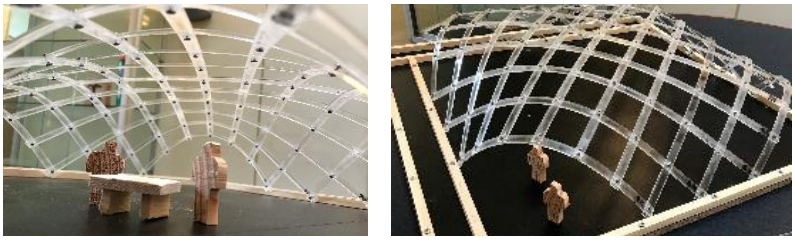


Figure 4: Model B – the acrylic plastic shell from inside and above (figurines scaled to 2 m)

5.2.2 Half-Scale Prototype

Based on the results of the parametric studies, constraints, and small-scale models, a half-scale prototype was built to prove the concept of a mobile, easy to assemble structure for HA/DR. The shell consisted of three standard beams, each made up of 2 to 3 segments. The segments of each beam were interchangeable to ensure that assembling the shell was convenient and could be built with a team of laborers and a few trained individuals. The segment lengths for the prototype were based on the material available, namely 1.22 m by 2.44 m plywood sheets. Four additional beams were required to secure the touchdown points and slotted bracing members were also included.

The prototype's joints were designed with bolts that protruded above the shell to allow additional bracing material to be added with ease. The small-scale models indicated that installing continuous bracing would be easier than discontinuous bracing. Continuous slotted bracing was applied by securing the bracing on one side of the structure using the protruding screws mentioned earlier. The bracing member was bent over the structure, using its own weight to aid in the process, and secured at each new location in a piecewise fashion. Figure 5 details a section cut of the installed bracing.

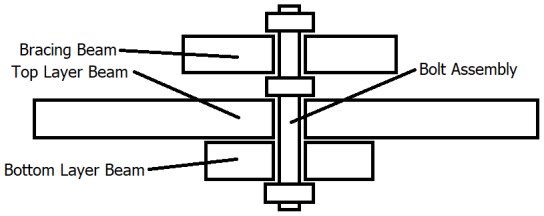


Figure 5: Prototype joint design with upper bolt protrusion to support bracing installation

A computer rendering of the deployment of the shell shows that when subjected to an inverse gravity load, the four egress arches of the shell "pop-up" first, followed by the center of the shell (Figure 6). Larger scale shells can be assembled in this fashion without the use of heavy machinery, if each of the egress arches are initially lifted before pulling and pushing the center upwards.

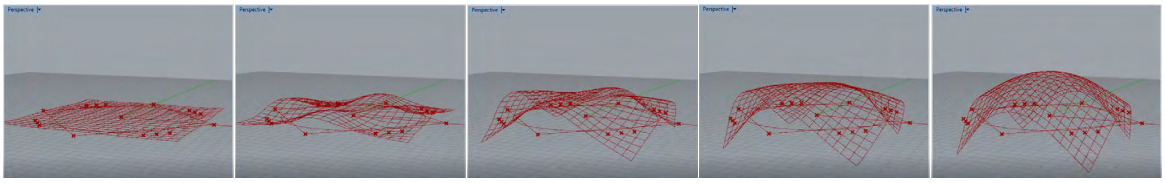


Figure 6: Time lapse of gridshell assembly when subject to an inverse gravity load

The prototype proved successful (Figure 7). The fabrication process was made easier due to the standard member lengths, slot sizes, and hole locations. Assembling the lattice and forming the shell was made possible by using tensioning straps beneath the structure, weights at each support location, and laborers pushing upwards from the center. Compared to previous work, the shell's area coverage relative to the material utilized was much higher [12].

5.2.3 Full-Scale Design

The prototype demonstrated the feasibility and practical application of a gridshell structure in HA/DR. The full-scale shelter would have a 15 m clipped square footprint, a grid density of 18 by 18, a half continuous bracing scheme, a maximum height of 5.3 m and a uniform cross-section of 4 cm by 7 cm. The structural analysis concluded that the full-scale HA/DR gridshell could withstand 352 Pa of downward pressure (22% more than required), 2.2 kPa of horizontal pressure (8.5 times higher than required), and a 21 kN point load (16 times higher than required). Without bracing, the structure would fail. As a result, the final shell will not only withstand the most strenuous load cases presented by HA/DR, but will do so in a mobile and easy to assemble package (Figure 7a).

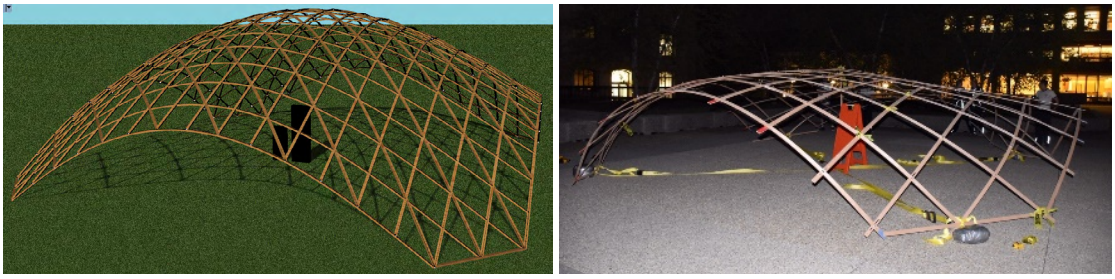


Figure 7: (left to right) – Computer rendering of final proposed HA/DR gridshell, Final half-scale prototype

6. Conclusion

The role of the U.S. Navy and other world navies is vital in HA/DR response. There is a distinct and unfulfilled need for structures capable of sheltering large populations in these types of situations. Traditional building methods are inadequate for this application because of limited infrastructure and a lack of machinery accessible in disaster relief zones. Gridshell structures are capable of spanning large areas using a lattice that can be easily assembled on-site and constructed using only hand tools. When properly braced, gridshell structures are highly effective in carrying load and can withstand the non-ideal loading conditions presented in HA/DR environments. Compared to an unbraced shell, adding bracing to half of the structure increases the buckling load by an average of 27%, 33%, and 6% when subjected to symmetric distributed, asymmetric distributed, and point loads respectively. Subjected to the same three load cases, but with full bracing, the buckling load increases by 53%, 92%, and 57% compared to an unbraced shell. In addition to their structural performance, these shells can be made using standard slotted members that are easily packaged into standard shipping containers when

designed with HA/DR and mobility in mind. Follow on research includes adding a membrane cladding to the shell to shelter inhabitants, investigating the effects of varying bracing member cross section on overall structural performance, and varying the support conditions.

Acknowledgements

The Office of Naval Research and the United States Naval Academy's Trident Scholar Committee were instrumental in providing resources for this project. Professor David Polatty, Director of the Naval War College Civilian-Military Humanitarian Response Program, provided valuable input and expertise as an external collaborator. Mr. Nick Hlavaty and Mr. Dave Majerowicz made the construction of the gridshells possible.

References

[1] W. E. Cobble, H. H. Gaffney, and D. Gorenburg, *For the Record: All U.S. Forces' Responses to Situations, 1970-2000 (with additions covering 2000-2003)*. Alexandria, Virginia: Center for Strategic Studies, 2005.

[2] S. Adriaenssens, L. Ney, E. Bodarwe, and C. Williams, "Dutch Maritime Museum: Form-finding of an irregular faceted skeletal shell- Part a," in *Proceedings of the IASS Annual Symposium 2009, Valencia*, 2009, pp. 1349-1355.

[3] J. Knippers and T. Helbig, "Recent Developments in the Design of Glazed Grid Shells," *International Journal of Space Structures*, vol. 24, no. 2, pp. 111-126, 2009.

[4] E. Happold and W. I. Liddell, "Timber lattice roof for the Mannheim Bundesgartenschau," *The Structural Engineer*, vol. 53, no. 3, pp. 99-135, 1975.

[5] D. Naicu, R. Harris, and C. Williams, "Timber Gridshells: Design methods and their application to a temporary pavilion.," presented at the World Conference on Timber Engineering, Quebec City, 2014.

[6] S. McCormick, C. Besjak, S. Korista, and W. Baker, "Shell of Steel," *Civil Engineering-ASCE* vol. 73, no. 4 pp. 68-73, 2003.

[7] International Code, Council, *International Building Code*, 2018.

[8] International Code Council, *International Fire Code*, 2015.

[9] American Society of Civil Engineers*, Minimum Design Loads for Buildings and Other Structures*, 2002.

[10] Sphere, *Sphere Handbook: Humanitarian Charter and Minimum Standards in Humanitarian Response*, 2018.

[11] "Cedar Pavilion with Aluminum Roof," *http://www.costco.com*, 2019.

[12] M. Vassallo and S. Malek, "Design and Structural Analysis for a Deployable Gridshell Shelter," in the *Interfaces: Architecture. Engineering. Science: Proceedings of the IASS Annual Symposium 2017, Hamburg, Germany, September 25-28, 2017,* A. Bögle and M. Grohmann (eds). pp. 1-8.

Proceedings of the IASS Annual Symposium 2019 – Structural Membranes 2019
Form and Force
7 – 10 October 2019, Barcelona, Spain
C. Lázaro, K.-U. Bletzinger, E. Oñate (eds.)

Fabrication-aware design of architectural envelopes using surfaces with planar curvature lines

Xavier TELLIER* [a b], Cyril DOUTHE[a], Laurent HAUSWIRTH[b], Olivier BAVEREL[a c]

* [a] Laboratoire Navier UMR8205, Ecole des Ponts, IFSTTAR, CNRS
77455 Champs-sur-Marne - MLV Cedex 2 - France
xavier.tellier@enpc.fr

[b] Université Paris-Est, Laboratoire d'Analyse et de Mathématiques Appliquées
[c] GSA / ENS Architecture Grenoble

Abstract

The shape of a complex freeform architectural envelope is usually generated by methods such as NURBS that offer a great design freedom, but that do not take into account fabricability. This often leads to higher than expected building costs. In this article, we present how a forgotten family of surfaces – namely, surfaces with planar curvature lines – can be used for a rationalized design of gridshells. We propose a discrete model of these surfaces, that enjoys properties that simplify the fabrication of all the elements of a gridshell: beams, nodes, and cladding panels. We propose an intuitive generation method, that allows a real-time exploration of the entire family of surfaces with planar curvature lines. Finally, we show how this method can be used to design a great variety of envelope shapes.

Keywords: Conceptual design, architectural geometry, gridshell, fabrication-aware design

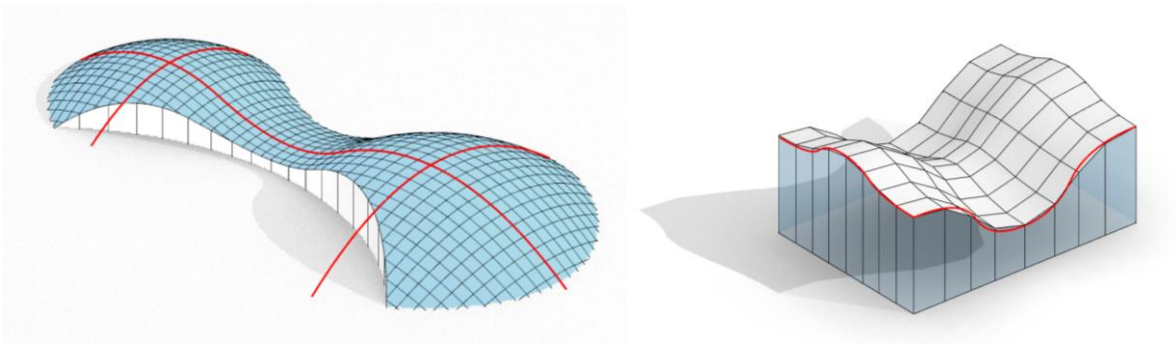


Figure 1: Surfaces with planar curvature lines. Left: The HippoHaus in Berlin [1], revisited as a junction of five patches with planar curvature lines. Right: A building roof, with mesh edges aligned with a façade.

1. Introduction

The fabrication of doubly-curved building envelopes has a been the source of significant engineering challenges in the past few decades. These challenges have led to the emergence of a new field of research, that is often referred to as construction-aware design, fabrication-aware-design, shape rationalization or architectural geometry [2]. For steel-glass envelopes, research has focused on methods to generate quad meshes with properties such as planar faces, torsion-free nodes, and offset, as these yield strong benefits over triangular meshes: lower node complexity [3], better light transmission [4], reduced waste in panel fabrication, and possibility to build multi-layer systems. A special attention was devoted to circular and conical meshes, which combine all these properties together.

Copyright © 2019 by Xavier TELLIER, Cyril DOUTHE, Laurent HAUSWIRTH, Olivier BAVEREL
Published by the International Association for Shell and Spatial Structures (IASS) with permission.

Methods to obtain these properties can be split in two main categories: bottom-up and top-down approaches. In bottom-up methods, the fabrication constraints are taken into account at the time of generation of the shape. The most popular method in this family are scale-trans meshes and rotational meshes [4]. In these methods, subspaces of planar quad meshes can be intuitively explored by controlling two guiding curves. Some more recent research has shown that many other types of surfaces and properties can be attained from this generation method ([5], [6]). [7], [8] and [9], on the other hand, propose optimization algorithms to deform a mesh under geometric constraints. In top-down approaches, also referred to as post-rationalization methods, the shape is first designed without consideration of construction properties. An optimization process is applied afterwards to improve the constructability. Many examples are discussed in [2].

Bottom-up methods are very convenient design tools to explore meshes for a known geometric constraint, but they require a knowledge of the fabrication method at an early stage of the project [10]. On the other hand, top-down methods can be used in a later phase of the project, but there is no guarantee that they will yield a mesh that fulfills all the desired constraints. For example, optimizing a quad mesh to make its face planar and have offsets will tend to align the edges with the principal curvature directions [3]. This process can alter significantly the appearance of the mesh, and might poorly fulfill the desired constraints, especially if the mesh topology is not compatible with the one of the curvature lines. As a rule of thumb, the more constraints are desired, the less likely post-rationalization is going to succeed.

In this paper, we present an overview and results of the work fully detailed in [11]. We investigate the generation of circular quadrangular meshes for which all lines are planar. More precisely, we mean that the edge polylines of any quad strip are planar. We will describe these meshes as having planar curvature lines, even though this term is usually reserved for surfaces. This work is related to the one presented in [12] that looked at circular meshes for which curvature lines are planar in only one direction. The planarity property can be used to simplify beam fabrication and for aesthetic aspect. Given these strong geometric constraints, the generation of these meshes is badly suited for post-rationalization. We therefore introduce a bottom-up method, which uses two guiding curves as an input. Using the fact that circular meshes are discrete equivalents of surfaces parametrized by curvature lines [13], the method is based on the discretization of surfaces with planar curvature lines. The method enables a real-time exploration of the entire design space.

In section 2, we will present our discrete model of surfaces with planar curvature lines and its fabrication properties for gridshells. In section 3, we will describe an effective generation process. Finally, in section 4, we will show this method can be used to design rationalized gridshells.

2. Geometric model and structural applications

2.1. Discrete model

Surfaces with planar curvature lines have been thoroughly studied in the XIXth century by the eminent geometers of the time, such as Monge, Darboux, Adam, and Bonnet. They discovered plenty of fascinating geometrical aspects, such as surprising construction methods, properties of the unit normals, underlying partial differential equations, and transformations into surfaces with spherical curvature lines. The topic went fully explored in the differential geometry point of view, and remained nearly untouched for a century. However, the power of computers and the advances in discrete differential geometry has recently aroused a regain of attention and also shed a new light on classical differential geometry work.

In particular, a natural discrete equivalent of surfaces parametrized by curvature lines turned out to be quadrangular circular meshes [14], which are meshes for which each face is inscribed in a circle. Because of the many interesting applications of circular meshes to architecture (which will be detailed in the next section) we propose a discrete model of surfaces with planar curvature lines by circular

meshes for which each line is planar, as shown in Figure 2. Circular meshes have straight edges, but can be covered with cyclidic nets, which are surfaces with piecewise circular curvature lines: these can be used as a geometric base for grid with circular beams. In [11], we show that a circular mesh with planar lines can be covered with a cyclidic net where the successive arcs of circle of any curvature line are coplanar.

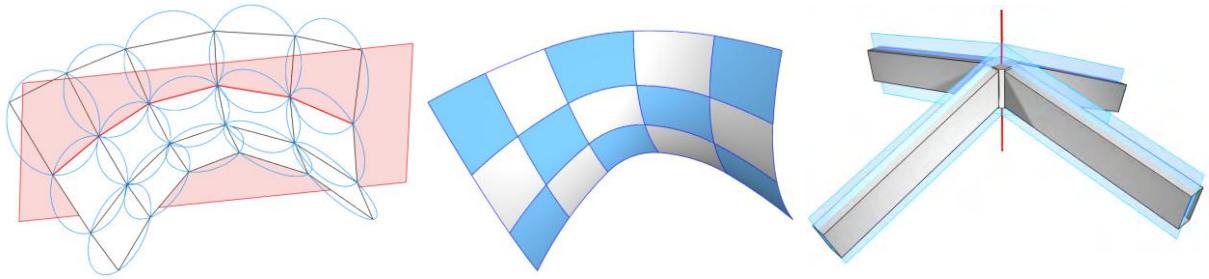


Figure 2: Left: circular mesh with planar curvature lines (straight edges, flat faces). Middle: Cyclidic net (planar piecewise circular edges, curved faces). The corner of each patch coincides with the vertices of the left mesh. Right: A torsion free node. Such node can be built on a circular mesh.

2.2. Fabrication properties

Circular meshes with planar curvature lines offer the following properties, that can simplify significantly the fabrication of a gridshell – most of them being illustrated in Figure 3:

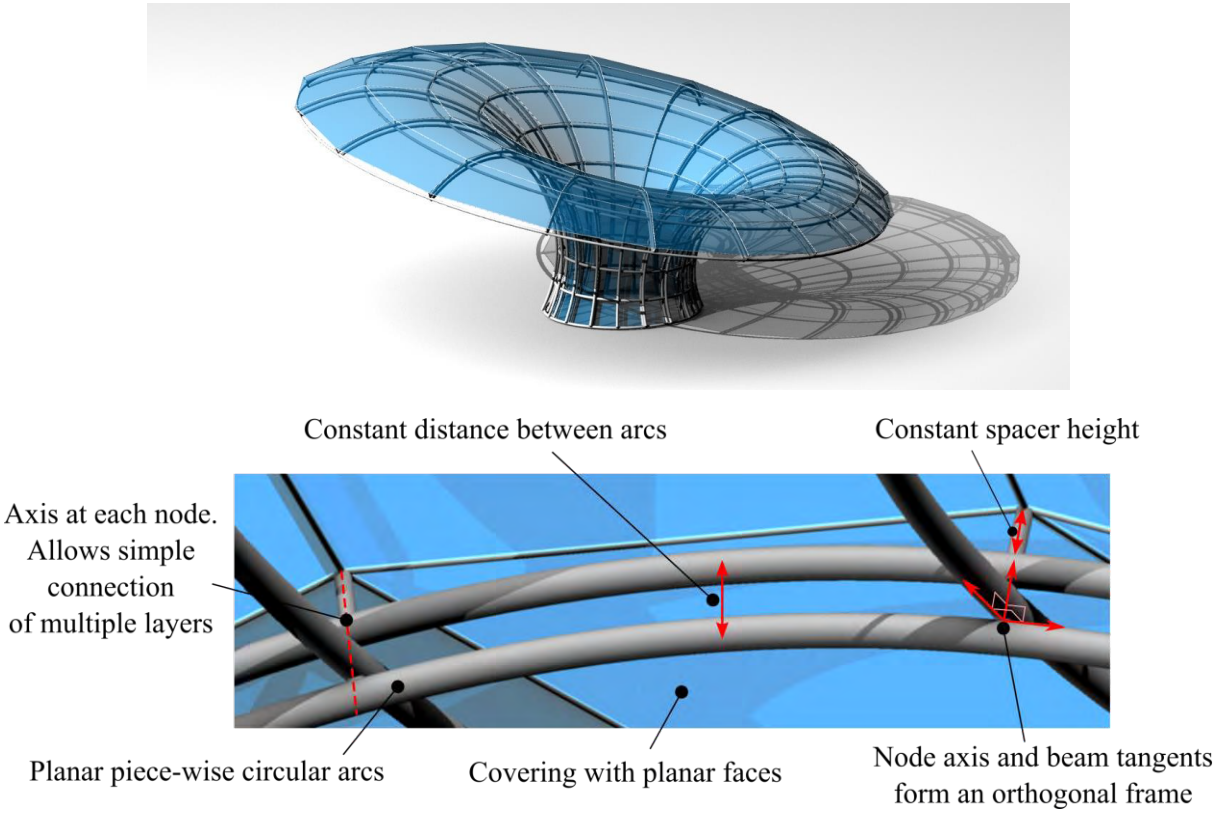


Figure 3: A shading structure demonstrating the fabrication properties

Planar quadrangles: Allows covering by flat sheet material, such as planar glass panels.

Planar beams: Planar beams are usually much easier to fabricate than nonplanar ones. This is particularly true for glulam beams and roller bent steel profiles.

Construction from straight or circular beams: A grid of straight beams can be constructed on the edges of the circular mesh. A grid of piecewise circular beams can also be constructed using cyclidic nets. For example, in the structure shown in Figure 3, the radial beams are planar biarcs, and the horizontal beams are circles.

Torsion free nodes: Each node can be assigned an axis, such that the plane of symmetry of the beam section meet on this axis, as shown in Figure 2 (right). This property simplifies significantly the fabrication of the node, in particular if deep sections are used.

Offsets: Multiple layers can be assembled, such that the distance between layers is constant. For example, in Figure 3, the distance between two radial biarcs is constant. This allows to stack them on both sides of the horizontal circular beams without shims. Furthermore, the spacers between the top beam layer and the glass corners have a constant length, and can thus be standard throughout the whole structure.

Node repetition: At the nodes, beams cross at 90°, and the node axis is orthogonal to the beams. This property, combined with the offset, allows to design a standard node connection for the whole structure.

An example of a structure that uses most of these properties is the Schubert Club Band Shell (US), shown in Figure 4. These properties were obtained by constraining the building shape to a portion of torus, which is a particular surface with planar curvature lines.

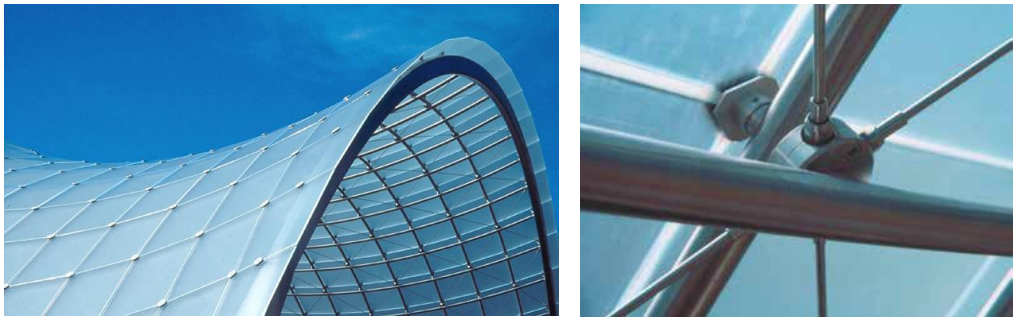


Figure 4: Schubert Marine Club Band Shell. Left: Overview. Right: connection detail (©Brian Gulick) (pictures courtesy of James Carpenter Design Associates)

Another way to use these properties is suggested in Figure 5, where a primal structure is made of trusses with circular members and constant diagonal length. Trusses are assembled via nodes that are all identical. This type of structure would have applications for temporary structures such as concert venues.

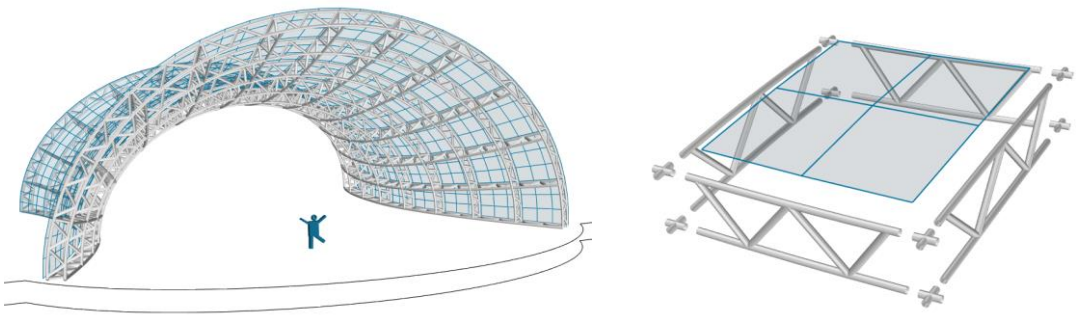


Figure 5: Temporary show venue with a demountable structure. Nodes are standard, truss members are circular, covering can be made with planar faces.

3. Generation method

In order to obtain the geometric properties described in the previous section, we developed a bottom-up generation method. The generation steps are the following, as illustrated in Figure 6. More details and proofs that our construction works are provided in [11].

1/ The designer draws two planar guide curves that intersect at 90°. The respective planes of the guide curves may or may not be orthogonal. Both curves are sampled into points. Then, at the intersection of the two curves, the normal vector to the tangent vectors is calculated. This normal is then propagated along the curves as a rotation-minimizing frame (i.e. a frame that does not undergo any torsion along the curves, also referred to as Bishop frame).

2/ The unit normals of the subdivision points correspond to points on the unit sphere, which lie on two circles.

3/ We build two sets of circles on the unit sphere, such that:

- At each normal point, there is one incident circle from each set;
- Any circle from a set is orthogonal to all the circles of the other sets.

There is actually one degree of freedom to construct these two sets of circles, which corresponds to the different ways a sphere can be mapped by orthogonal circles, as shown in Figure 7. We parametrize this degree of freedom by the angle θ, which locate the position of the "North pole-South pole axis". This choice of parameter highlights the symmetries: for example, $\theta = +180°$ and $\theta = -180°$ correspond to the same case where is axis is at infinity. One trivial case is the mapping by parallels and meridians, which corresponds to $\theta = 0$.

4/ We build a mesh for which vertices are the intersection points of the circles. This mesh is circular [11].

5/ We apply a Combescure transform, computed as in [5], to deform the mesh so that it fits the two guide curves.

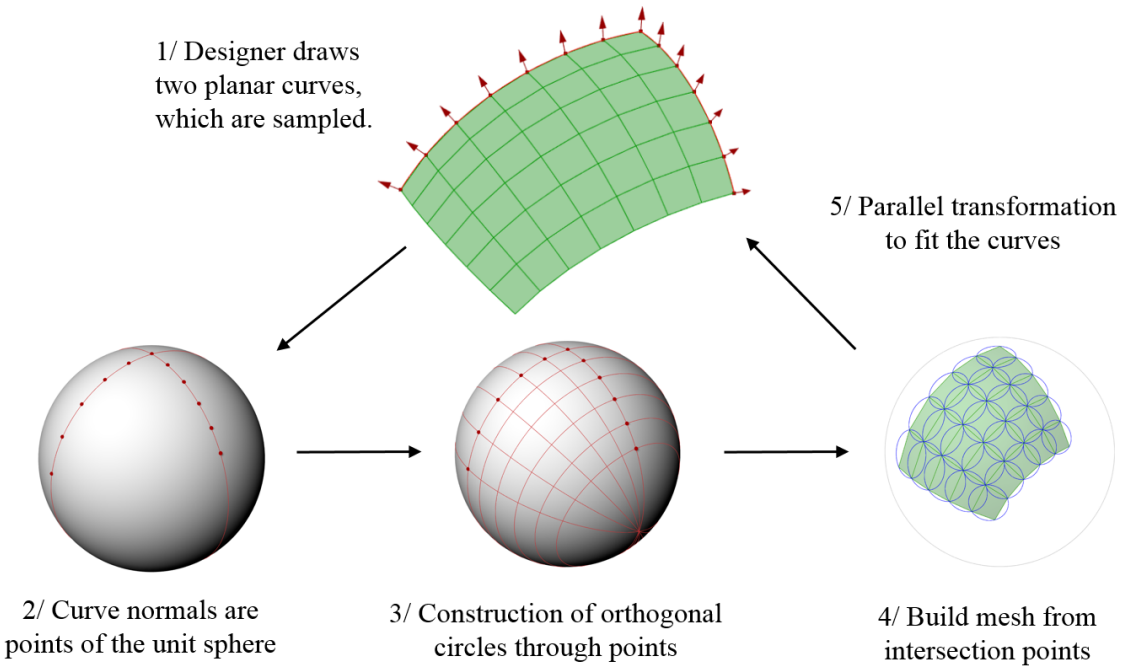


Figure 6: Generation process

The user does not see the spheres and the steps 2 to 4, they just see the mesh appearing on the curve they drew since the process is automatized. The method being simple, it runs very fast. Generation time

is below 75ms for a large 100x100 mesh on a desktop with 3.5GHz processor and 16GB RAM. The user can therefore interact in real time.

One important property is that, if guide curves are arcs of circle, then all the curvature lines are also inscribed in arcs of circles. This property is demonstrated in [11], it allows to generate structures made entirely of circular arcs or biarcs (or n-arcs), such as the structure shown in Figure 3.

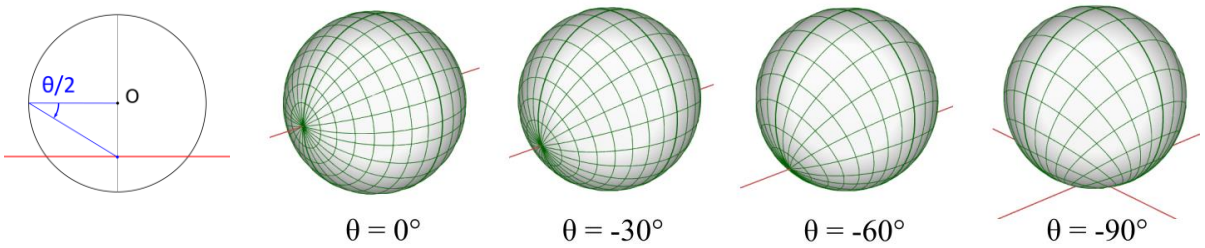


Figure 7: The degree of freedom θ corresponds to the different ways a sphere can be mapped by orthogonal circles

4. Designing with surfaces with planar curvature lines

By controlling the two guide curves and the parameter θ, the entire family of surfaces with planar curvature line can be explored. A rich variety of shapes becomes accessible, as shown in Figures 1, 3, 8 and 9 (guide curves are highlighted in red).

Figure 9 shows circular meshes that can be obtained from two guide curves by varying only the parameter θ. We observe that the cases $\theta = 0$ and $\theta = \pm 180°$ give molding surfaces, a subfamily of Monge surfaces: they are the surfaces generated by the motion of planar curve that slides along another planar curve, with a rotation such that the plane of the sliding curve remains orthogonal to the tangent of the second curve. Our method gives access to surfaces in-between, and surfaces with planar curvature lines can be understood as a generalization of molding surfaces. The planarity of the curves can be visualized in the top and side views.

As detailed in [11], the parameter θ can be adjusted such that the surface edges are contained in a target plane. This allows for example to align the mesh of a roof with the facade, as shown in Figure 1.

In a large envelope, the beams do not need to be planar along the whole length of the building, as multiple beams need to be spliced together anyway. Our method can be used to generate surfaces with piecewise planar curvature lines. This enlarges significantly the design freedom. An example is shown in Figure 8, where two pairs of guide curves are used (one in blue, one in red). The lines circling around the structure belong to four different planes, while the radial beams are planar. For the dome in Figure 1, the longitudinal beams belong to five different planes, while the transverse beams are planar.

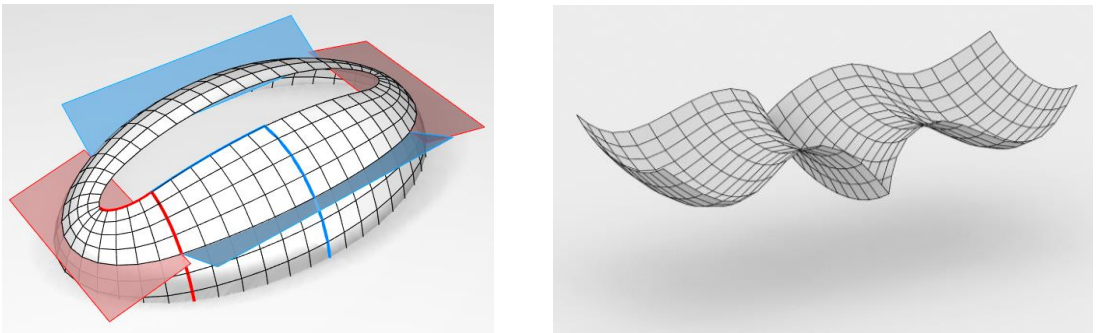


Figure 8: Left: Surface with piecewise planar curvature lines. Right: Surface with a crease.

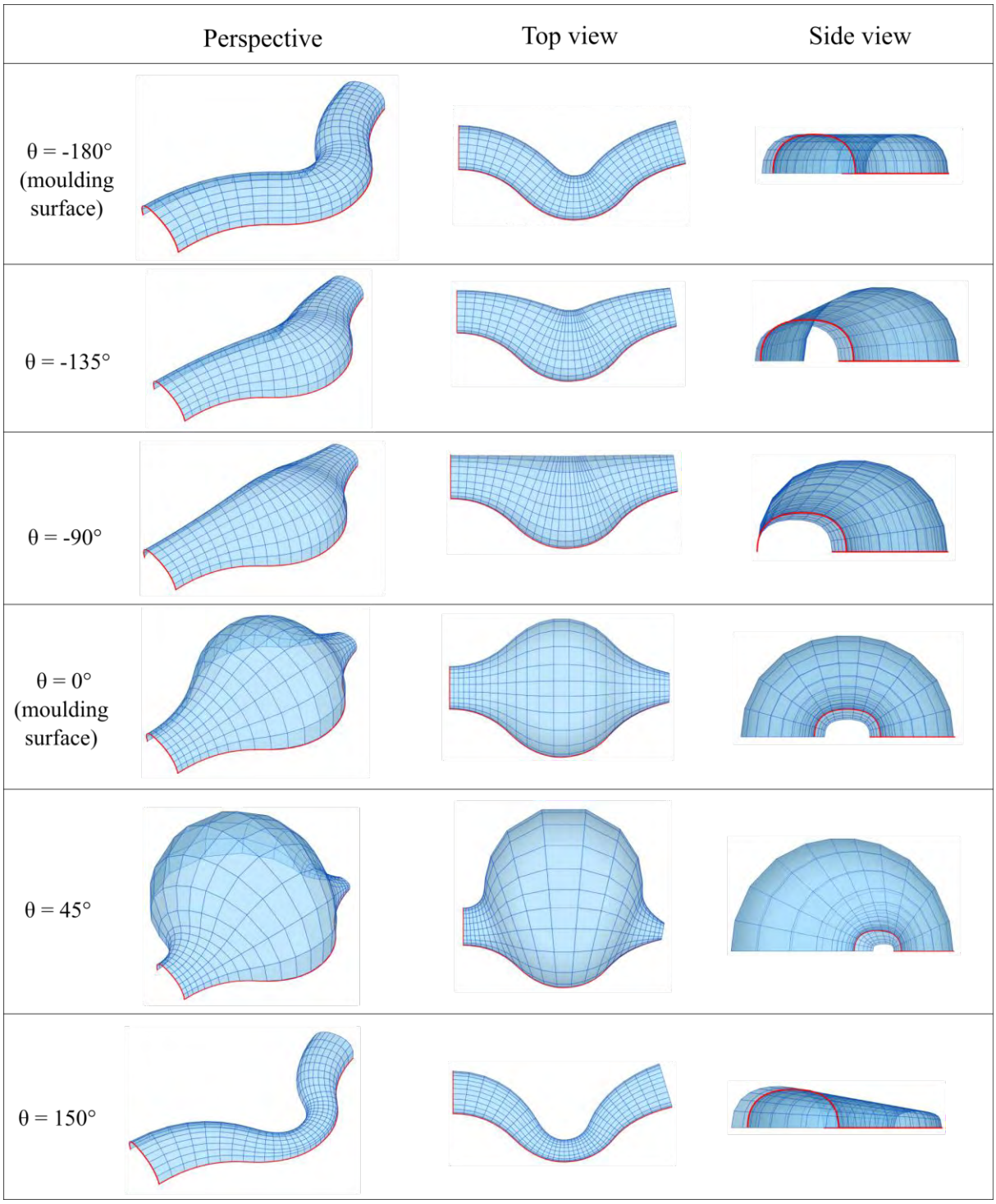


Figure 9: Family of meshes that can be generated from two guide curves with different values of θ

5. Conclusion

Surfaces with planar curvature lines offer a wide panel of forms, and have many properties useful for the fabrication of a double-curvature structure. We proposed a fast generation method that allows a designer to explore intuitively the whole design space. The many properties of these surfaces can be used to expand the shape potential of traditional gridshell fabrication methods, but that can also be used to develop new ways to build complex shapes with relatively simple fabrication means.

Acknowledgements

This work is supported by Labex MMCD (http://mmcd.univ-paris-est.fr/). The authors would like to thank Romain Mesnil for helpful discussions.

References

[1] J. Schlaich and H. Schober, "Glaskuppel für die Flusspferde im Zoo Berlin," *Stahlbau*, vol. 67, pp. 307–312, 1998.
[2] H. Pottmann, "Architectural Geometry and Fabrication-Aware Design," *Nexus Netw. J.*, vol. 15, no. 2, pp. 195–208, 2013.
[3] Y. Liu, H. Pottmann, J. Wallner, Y.-L. Yang, and W. Wang, "Geometric modeling with conical meshes and developable surfaces," *ACM Trans. Graph.*, vol. 25, no. 3, p. 681, 2006.
[4] J. Glymph, D. Shelden, C. Ceccato, J. Mussel, and H. Schober, "A Parametric Strategy for Freeform Glass Structures Using Quadrilateral Planar Facets," *Autom. Constr.*, vol. 13, no. 2, pp. 187–202, 2004.
[5] R. Mesnil, "Structural explorations of fabrication-aware design spaces for non-standard architecture," Université Paris-Est, 2017.
[6] C. Douthe, R. Mesnil, H. Orts, and O. Baverel, "Isoradial meshes : covering elastic gridshells with planar facets," *Autom. Constr.*, vol. 83, pp. 222–236, 2017.
[7] Y.-L. Yang, Y.-J. Yang, H. Pottmann, and N. Mitra, "Shape Space Exploration of Constrained Meshes," *ACM Trans. Graph.*, vol. 30, no. 6, 2011.
[8] C. Jiang, C. Tang, M. Tomicic, J. Wallner, and H. Pottmann, "Interactive Modeling of Architectural Freeform Structures – Combining Geometry with Fabrication and Statics," *Block, P., Wang, W., Knippers, J., Ed. - Adv. Archit. Geom.*, pp. 94–108, 2014.
[9] B. Deng, S. Bouaziz, M. Deuss, A. Kaspar, Y. Schwartzburg, and M. Pauly, "Interactive design exploration for constrained meshes," *CAD Comput. Aided Des.*, vol. 61, pp. 13–23, 2015.
[10] G. Austern, I. G. Capeluto, and Y. J. Grobman, "Rationalization methods in computer aided fabrication: A critical review," *Autom. Constr.*, vol. 90, pp. 281–293, 2018.
[11] X. Tellier, C. Douthe, L. Hauswirth, and O. Baverel, "Surfaces with planar curvature lines: discretization, generation and application to the rationalization of curved architectural envelopes," *Autom. Constr.*, vol. (accepted), 2019.
[12] R. Mesnil, C. Douthe, O. Baverel, and B. Léger, "Morphogenesis of surfaces with planar lines of curvature and application to architectural design," *Autom. Constr.*, vol. 95, pp. 129–141, 2018.
[13] A. I. Bobenko, *Surfaces from Circles*. Series: Oberwolfach Seminars, Vol. 38, 2008.
[14] H. Pottmann and J. Wallner, "The focal geometry of circular and conical meshes," *Adv. Comput. Math.*, no. 29(August), pp. 249–268, 2006.

FORM and FORCE

Proceedings of the IASS Annual Symposium 2019 - Structural Membranes 2019
Form and Force
7-10 October 2019, Barcelona, Spain
C. Lázaro, K.-U. Bletzinger, E. Oñate (eds.)

The design, fabrication and assembly of an asymptotic timber gridshell

Emil ADIELS*, Cecilie BRANDT-OLSEN[a], Johanna ISAKSSON[b], Isak NÄSLUND[b], Karl-Gunnar OLSSON, Emil POULSEN[c], Chris J. K. WILLIAMS

* Department of Architecture and Civil Engineering
Chalmers University of Technology
412 58 Gothenburg, Sweden
emil.adiels@chalmers.se

[a] BIG Engineering
[b] BuroHappold Engineering
[c] CORE Studio Thornton Tomasetti

Abstract

This paper describes and discuss the design, fabrication and assembly of an asymptotic gridshell built of plywood laths. The overall question concerns how geometry, structural action, and efficient production can interplay and inform spatial design. The environment is a two-day workshop where architects, engineers and researchers with specialization in structural and digital design cooperate with undergraduate students in a compulsory parametric design and digital fabrication course. The gridshell shape is based on an Enneper surface of threefold rotational symmetry with a boundary baseplate inscribed within a circle of 4.5 m in radius. Utilizing the concept of asymptotic curves, which are surface curves whose osculating plane coincides with the tangent plane of the surface, the structure was built using planar straight laths of plywood made using manually operated drills and saws.

Keywords: Gridshell, differential geometry, parametric design, active bending, structures , timber, education .

1 Introduction

Throughout the history of construction architects and engineers has sought strategies to reduce the cost of production and use of material without limiting our spatial experience or the performance of the design. Schlaich-Bergerman designed numerous roofs with planar quadrilateral panels[1] while Otto, Happold and Liddell connected continuous timber laths into a flat grid that was formed into the gridshell, like a sieve, creating stiffness in Mannheim Germany[2]. For students aspiring to work in the intersection between architecture and engineering these architects and engineers from the history, with knowledge, skills and attitudes intertwined into a creative working environment, are important role models. The question is how this connection between geometry, space and structure can be best explored and taught to serve as inspiration for deeper studies in the respective fields as well as illustrating how mathematics can support virtual and physical explorations of space and form. We investigated this question by building a

Copyright © 2019 by by Emil ADIELS, Cecilie BRANDT-OLSEN, Johanna ISAKSSON Isak NÄSLUND, Karl-Gunnar OLSSON, Emil POULSEN, Chris J K WILLIAMS
Published by the International Association for Shell and Spatial Structures (IASS) with permission.

gridshell, figure 1, in a three dimensional shape with students from the double degree program in architecture and engineering at Chalmers.



Figure 1: The asymptotic gridshell built during two days in the workshop in December 2018 by the students based on design provided by the workshop leaders, photo: Martin Skarby.

2 Interdisciplinary teaching in an experimental culture

Architecture and Engineering(A&E) is a dual degree program (MArch. and MSc.in Engineering) at Chalmers University of Technology, training students in interdisciplinary design methods combining different areas of knowledge and skills related to both engineering and architecture. The educational program includes mathematics, applied mechanics, building materials, history of architecture, design tools as well as design of architectural projects and experimental workshops integrating mathematics, mechanics and art. These workshops have explored topics such as masonry shells, membranes and weaved structures through both theory and application, figure 2a) - b).

In 2017 the course *Parametric Design - Digital Tools*(3 ECTS) was initiated with the aim to teach bachelor A&E students in basics of parametric design and digital fabrication. In nine days of teaching roughly six days covers parametric design basics, extraction of production data and digital fabrication methods. Examination are through smaller design exercises and projects. The last two and half days consists of a workshop which aim is to summarize the course by building a temporary structure for a indoor exhibition space . In the 2017 workshop a geodesic gridshell was built and is described in Adiels *et al* [3], see 2. The well working format, 4.8 out of 5 in the student evaluation, was kept for the 2018 workshop, but a new geometrical concept that links shape and structure to rational and efficient building process was developed by the group of organizers. This group consists of architects and engineers from both academy and industry with specialism in computational design. As the exhibition would take place in the old testing facility at Chalmers the fabrication could be done on site utilizing the institutions wood-workshop, which facilitates tools and machines for processing wood including a CNC for

plywood boards.



Figure 2: a) Building a of freeform vault on actively bent gridshell the course "Material Laborations" [4] b) Soap films and membranes was invested a workshop in the course "Virtual Tools in a Material Culture" c) and d) shows the geodesic grid-shell built in the workshop 2017 in this course. [3]

3 Asymptotic lines in gridshell design

The geometrical concept for the workshop and the design of the structure to be built has three main requirements: The underlying theory needs to able to be presented in a comprehensible way based on the student's prior knowledge. The design must enable a rational production process linked to the design such that it can built in just two days activating all forty students. It should also be transparently implemented in a parametric environment such that the students can learn and modify it for future projects.

Asymptotic lines are special curves on a surface that has zero normal curvature. Extruding these curves in the normal direction these developable surfaces can be unrolled both straight and planar without distortion. This concept can be utilized in gridshell design to be built with straight planar laths. Asymptotic lines can be found at the top of a torus or physically along the free edges of a prestressed membrane, as in figure 2b. Asymptotic lines are restricted to anticlastic surfaces and surfaces of zero Gaussian curvature. For the former there exist two asymptotic directions in each point while in the latter only one. This is evident looking at *Mohr's circle of curvature*[5], figure 3. Knowing the magnitude and direction of the principal curvatures one can find the asymptotic directions using Mohr's circle or *Euler's theorem*[6], knowing normal curvature to be zero.

$$\kappa_n = k_1 \cos(\phi)^2 + k_2 \sin(\phi)^2 \tag{1}$$

$$\phi \pm \arctan\left(\frac{-k_1}{k_2}\right) \tag{2}$$

The principal directions bisect the angle between the asymptotic directions, but not necessarily the other way around. Only on minimal surfaces the two principal curvatures are equal and opposite, therefore the asymptotic directions are found at a 45° angle to the principal directions.

Inspired by the work of Schling *et. al*[7], a series of scale model prototypes where designed and constructed, all of them following the asymptotic curves. Specifically, three mechanical properties and features were studied: The curvature and bending capacity related to the choice of cross section. The built-in structural mechanism allowing to reshape the structure from a flat shape to a three-dimensional shape. The by active bending built in strain energy creating

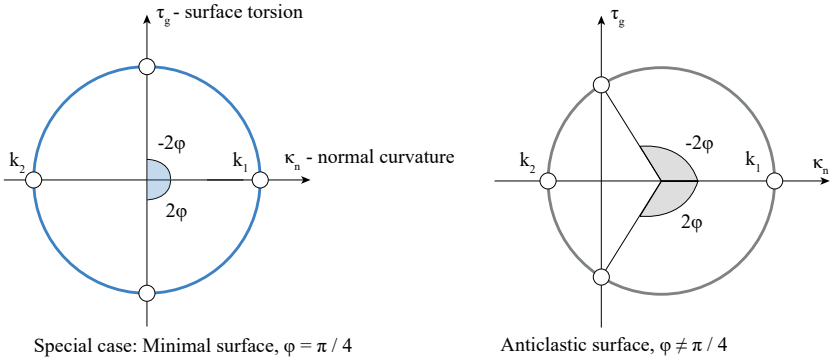


Figure 3: Mohr's cirlce of curvature where the axis represents the normal curvature κ_n and surface torsion τ_g. The blue circle represent a minimal surface where κ_1 and κ_2 are of equal magnitude with opposite sign, therefore the asymptotic directions are given with $\phi = \pi/4$ and form right angles. For the grey case $\phi \neq \pi/4$ and therefore the asymptotic directions are not orthogonal to each other.

a capacity to support the erection of the structure. Figure 4 shows a case where this built in energy where sufficient to reshape the structure without extra supplied external work. Figure 5 and [8] shows the finally chosen case, an Enneper of 3-fold symmetry, where the inner friction requires extra amount of external work to support the erection.



Figure 4: Small physical model of Enneper surface. It was built using planar straight 1mm plywood laths, slotted together. It can be made flat but the inbuilt energy in combination with structure being a mechanism makes it transform into an average shape between the purely geometrical and flat state[9].

4 Prepatory studies

The Enneper surface was chosen due to that it is an anticlastic shape which reminds of shell form which also creates a defined interior space. The openings also create a potential exterior space connected to the structure. The symmetry would also ensure a reduced number of unique elements which speeds up the production process and lessening the probability of errors.
Going further the final dimensions of the grid and the structure would be set to fit the exhibition, creating a space. Also, further analysis of the individual laths and the behaviour during erection and the in-plane. A time-efficient fabrication procedure must also be ensured along with generation of necessary drawings and production data.

The laths were chosen to be 100 mm wide and made from six mm thick birch plywood boards. To create the slots a method was designed using a drill and regular chop saw set to cut. By pre-calibrating the saw this method would not require much prior experience in carpentry. When

evaluating the bending behaviour of these laths it became clear that the slots would attract a lot of stresses causing them break unexpectedly. The limiting curvature was therefore hard to predict and the results varied from decent to bad[10]. Therefore, a test-rig was made where the curvature was plotted, and the laths tested[11]. It was observed that by weakening the lath, i.e. making more cuts, the stress distribution increasing the curvature limit. The test-rig was essential during the design process as well as during the workshop evaluating laths in areas with high curvature.

One of the unknowns was how the structure, being a mechanism with little in-plane stiffness, would perform and behave. The unknowns in the analysis was the quality of the manually made elements and the actual kinematic behaviour in the nodes. The structure was modelled FEM-models were made using different conditions in the nodes as well with and without active bending accounted. The results were compared to the small-scale model to forward with the design. During these exercises, with the presumptions that it would be indoors and temporary, the structure seemed to have enough stiffness in the plane to not cause a collapse, even though it was still believed to be quite flexible. Therefore, no bracing was designed since it would complicate the production

To simulate the erection the small-scale model was compared to a simulation of continuous spline elements using the dynamic relaxation method[12]. At this stage it was interesting to know both the amount of force necessary and the best position to avoid failure or collapse. Since the numerical method was using rods the physical model seemed more accurate and it was easier orchestrate different possible scenarios. The worst case seemed to be when flat since then the laths would have maximum curvature and no twist, meaning the laths will be relieved some of its stresses while being erected.

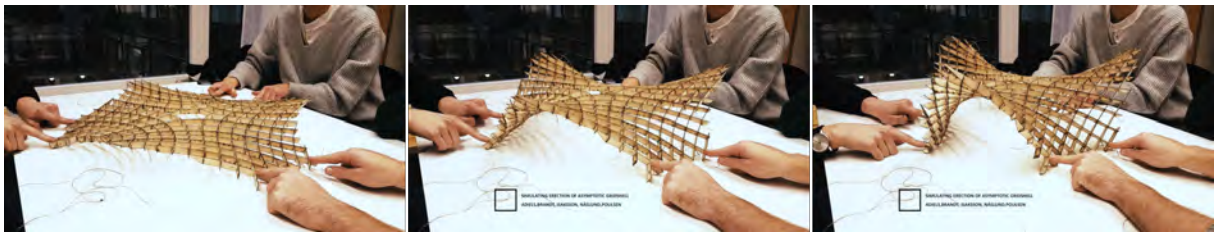


Figure 5: Physical models were made to understand the structural behaviour during erection and trying to understand the best strategy for erecting the structure. [8]

To generate the final geometry of the grid a custom script for constructing asymptotic lines was implemented in the parametric environment using Euler's theorem, equation 1. The grid layout was adjusted using a heuristic approach. This model would be used to construct all the production drawings. The necessary joints were placed in areas with low curvature. Since the geometry would need to be flat initially slots requires to be slightly bigger than in the erected state. By generating a flat configuration of the geometry digitally each slot in the lath could be individually designed based on the nodal angles in the flat state. To avoid to many drills three different slots sizes were chosen. The entire structure was built from nine laths that was repeated six times and were built from thirty elements. In plan the structure took the shape roughly like a six sided polygon with three sides of five meter and three of four meter. The

height in the middle was designed such that one could stand upright in the centre.

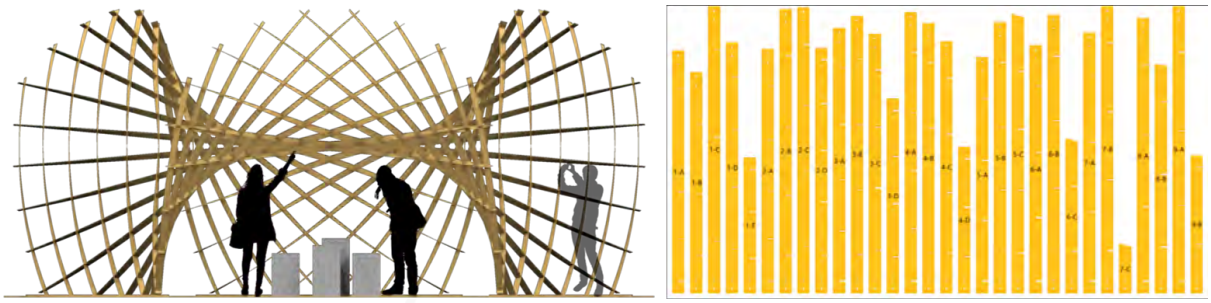


Figure 6: a) The asymptotic gridshell design based on a Enneper surface of 3-fold symmetry. b) The thirty drawings needed to produce all the laths.

5 Workshop

The workshop started with two lectures to prepare the students. The first covering the concept with the underlying theory from differential geometry. In the second lecture the design process was described along with a tutorial through the parametric model[13], which generates the geometry and all production drawings associated. The lectures ended with describing the different workstations for fabricating the laths as well as the base plate to anchor the structure. Each student was then responsible to signing up before the production process would start.



Figure 7: Fabrication of the laths using paper templates a) drilling holes for the slots and the joints. A paper template was printed aid this process b) The slots were finished using a pre-calibrated chop saw, cutting halfway through the width of the lath c) The laths were assembled into full length using two m6 bolts and nuts.

The first day of construction aimed to fabricate all structural elements. The laths were cut up in the correct width in the wood-workshop and transported into exhibition hall for final processing, figure 7a)-c). In the big hall four groups of four people were assigned to process them, each equipped with two drills and a chop sow, which was pre-calibrated for making the slots. Two groups shared a separate chop saw for cutting the lengths. In order to make the process run smoothly paper templates printed out from the parametric model. When all the elements were drilled and cut the rest of the students assembled them into their full length. The base plates were milled using the CNC in the wood-workshop and consisted of two layers of 18 mm birch plywood which were glued together.

The second day started by connecting the baseplates together into a frame and assembling all the laths into a flat grid, see figure 8 and [14]. A computer model visualizing the structure flat was a great during this process. Strings were tied around the nodes to avoid separation during erection. When assembled the flat grid was lifted onto trestles so that it could pushed into along the edges into shape, as in figure 5. The structure was pushed using only manual power to be able to push it slowly and with care, due to the brittle nature of the laths. When pushed into the correct position the laths were fixed in milled cavities in the base plates. Three cables going was connected through a flying steel ring in middle to reduce the displacement in the openings. The workshop ended with a seminar summarizing the workshop and lectures from the invited guests. In the evening structure was used for a book release party with students from the entire Architecture and Engineering program.



Figure 8: a) connecting the laths into a flat grid shown in b). c) - d) the structure was erected by pushing the structure with manual force, photo: Brobäck, Ivarsson & Skarby. [14]

6 Discussion

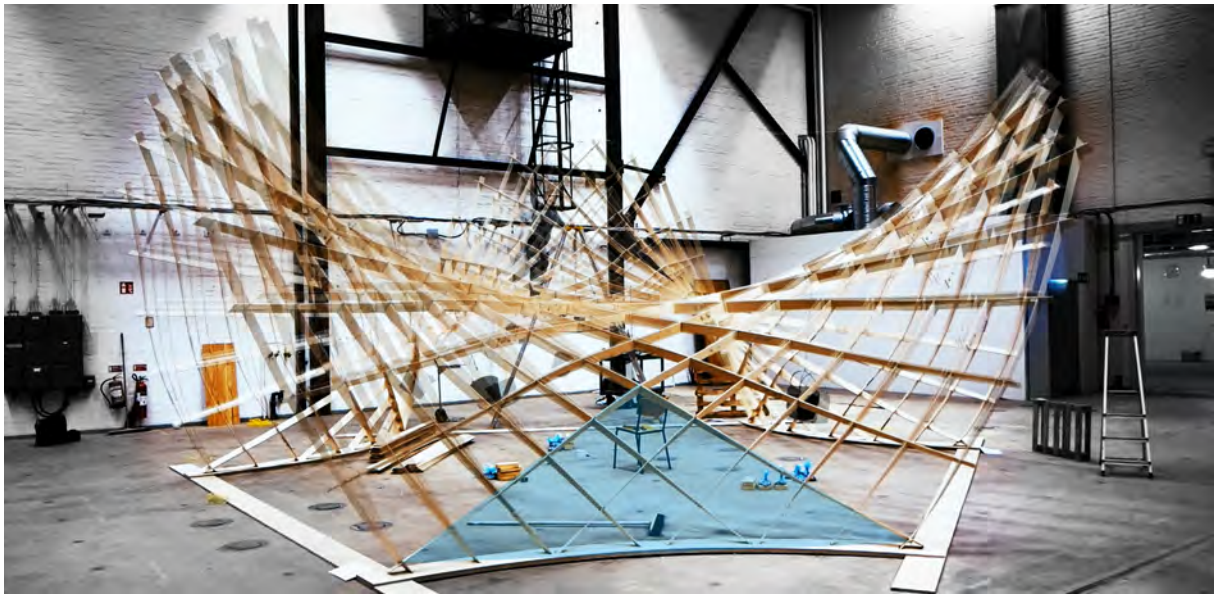


Figure 9: The mechanism in the system was apparent and triggered by motions in the tangent plane. While in motion the rigid parts system could be read, three triangles along the boundaries of the base-plates, coloured blue in this picture. More investigations could be done to find strategies the most optimal places to lock the system using a minimum amount of bracing.

The structure was built on time, it did not collapse and there were no major incidents during the production meaning that the preparations were enough. The reception from the students was overall very positive and one felt they had taken ownership of the structure during these two days. In the course evaluation the course received an average rating of 4.8 out 5 and the workshop was mentioned, both this year and prior year, as a very good segment and exercise.

The built-in mechanism in the structure is necessary for the erection but disadvantageous in its 3-dimensional form. An optional seminar for the students was arranged to discuss how these mechanisms effect the in-plane stiffness and if there are simple strategies increase to lock these mechanisms, without bracing the entire system. The mechanism was evident and could be activated through motions in the tangent plane. While in motion one could read three triangles, coloured blue in figure 9, which was stiff and rigid due the fixed boundary along the baseplates. Adding three cables to the system, going cross each opening from each base plate, the stiffness the tangent plan was noticeably increased. This could be something to investigate further for future workshops in which the structure utilizes a mechanism for the erection.

References

[1] J. Glymph et al. "A parametric strategy for free-form glass structures using quadrilateral planar facets". In: *Automation in Construction* 13.2 (2004), pp. 187–202.

[2] E. Happold and W. I. Liddell. "Timber Lattice Roof for the Mannheim Bundesgartenschau." In: *Structural Engineer* 53.3 (1975), pp. 99–135. ISSN: 14665123.

[3] E. Adiels et al. "Design , fabrication and assembly of a geodesic gridshell in a student workshop". In: *IASS Symposium 2018 "Creativity in Structural Design"*. 2018, pp. 1–8.

[4] E. Adiels. *Workshop exploring crafts and structural behaviour of masonry, Mariestad, 2017 on Vimeo*. 2018. URL: `https://vimeo.com/254638151` (visited on 05/29/2019).

[5] A. W. Nutbourne. "A circle diagram for local differential geometry". In: *The mathematics of surfaces*. Ed. by J. A. Gregory. 1984, pp. 59–71.

[6] D. J. Struik. *Lectures on classical differential geometry*. 2nd. Dover, 1988.

[7] E. Schling et al. "Design and construction of curved support structures with repetitive parameters". In: *Advances in Architectural Geometry*. Ed. by L. Hesselgren et al. Gothenburg: Klein Publishing GmbH (Ltd.), 2018, pp. 140–165.

[8] E. Adiels. *Simulating the erection procedure of the Asymptotic gridshell on Vimeo*. 2019. URL: `https://vimeo.com/312943826` (visited on 05/23/2019).

[9] E. Adiels. *Plywood structure from asymptotic curves of an Enneper surface on Vimeo*. 2019. URL: `https://vimeo.com/311905217` (visited on 05/23/2019).

[10] E. Adiels. *Evaluating the curvature limit of the laths during the design process of the asymptotic gridshell on Vimeo*. 2019. URL: `https://vimeo.com/338520213`.

[11] E. Adiels. *Test rig for evaluating the capacity of the laths of the asymptotic gridshell. on Vimeo*. 2019. URL: `https://vimeo.com/338556892` (visited on 05/29/2019).

[12] S. Adriaenssens et al. "Designed of a strained timber gridshell". In: *Shell Structures for Architecture: Form Finding and Optimization*. Routledge, 2014, pp. 89–102.

[13] E. Adiels et al. *Github repository*. 2019. URL: `https://github.com/archengtech/chalmersworkshop-dec2018` (visited on 05/26/2019).

[14] E. Adiels. *Asymptotic Gridshell - Timelapse on Vimeo*. 2019. URL: `https://vimeo.com/337822771` (visited on 05/29/2019).

Proceedings of the IASS Annual Symposium 2019 – Structural Membranes 2019
Form and Force
7 – 10 October 2019, Barcelona, Spain
C. Lázaro, K.-U. Bletzinger, E. Oñate (eds.)

Research on adobe bricks for sustainable/ traditional building

Călin G.R. MIRCEA*[a], Gabriela A. CĂLĂTAN[b], Andreea-Terezia MIRCEA[a]

*[a] Technical University of Cluj-Napoca, Romania
28, Memorandumului Street, 400114 Cluj-Napoca, Romania
calin.mircea@dst.utcluj.ro

[b] INCD URBAN-INCERC Bucharest, Romania

Abstract

Clay mixtures can be successfully used to build masonry bricks, mortars, plasters and finishes. However, present-day buildings involve severe performance requirements and admissibility criteria, much more easy to accomplish with modern materials. Despite this reality, the most important features of sustainable building can be achieved from natural, traditional materials, derived directly from the environment. Straw, clay or wood are obtained from local, often family-run businesses, supporting the local development and cultural independence of the region. Considering that the production of these materials is environmentally friendly, the transport is done only locally, they demand less embedded energy during the building phase than the conventional ones. After the end of service they do not leave harmful waste, or hard to decompose, because the structure itself is completely biodegradable. In this context, a research was performed to improve the mechanical performance of local adobe bricks and the workability of the fresh mixture, along with the study of a wide span of natural additives. The Paper aims to emphasize the results made in the field of eco-friendly building materials, to analyze the most beneficial mixes, and to highlight significant contributions for revaluation of traditional and local construction materials meant for sustainable building.

Keywords: sustainability, environmentally compatible structures, adobe bricks, mechanical performance, natural materials, green building, traditional building materials,

1. Introduction

Modern buildings involve severe performance requirements and admissibility criteria, easy to be achieved with fashionable materials. However, nowadays some of the key issues of the current global economic and social context with impact on the built environment are: the issue of conservation of natural resources along with the protection of landscape and bionetwork, the economic issue, and the issue of present-day designs trending to use techniques from vernacular architecture.

The most important features of sustainable building can be accomplished from natural and traditional materials, derived directly from the environment. The objective is to build with simple techniques that don't further pollute the environment, consume more fossil fuel, or unnecessarily extract resources. For such buildings, less material and energy is consumed than for conventional ones. Against the background of an increasingly accelerated industrialization, traditional materials, primarily intended for housing, have been poorly promoted on the buildings' market.

Developing new solutions from the historical and traditional experience in order to provide superior performance is currently become a priority in civil engineering research. An ever-increasing turn towards tradition arises from the need of society to have its own identity, to keep in touch with the identity of the nation it originates from, and not to lose the traditions that define it [1]. As already known, clay mixtures can be successfully used to build masonry bricks, mortars, plasters and finishes.

Copyright © 2019 by Călin G.R. MIRCEA, Gabriela A. CĂLĂTAN, Andreea-Terezia MIRCEA
Published by the International Association for Shell and Spatial Structures (IASS) with permission.

These materials have been effectively used for thousands of years, and moreover, nowadays' technology largely eliminates their conventional limitations. Traditional buildings made from these above mentioned materials are price accessible. The work techniques have large impact on local occupation opportunities, generating local jobs and integrating people within their communities.

2. Sustainable building with environmental friendly materials

In sustainable building, the recent trend of green-building construction concept underlines the importance of an environment-friendly management of materials throughout their entire life-cycle, from resource extraction, during the fabrication phase, on-site installation, use, maintenance and post-utilization. In this regard, Life Cycle Assessment (LCA) may be used as a technique for determining the potential environmental aspects associated with products, processes and activities, through production, usage, and disposal, by identifying and quantifying energy and materials used and wastes released to the environment [2], [3], [4].

Some building materials are based on the use of new innovative technologies, others seek to revive verified centuries-old methods. The latter have the advantage that it is easier to anticipate and evaluate their characteristics as well as their in-situ behavior. New technologies require intensive testing, beginning with the concept phase, laboratory tests, in-situ behavioral tests, and what is often the most difficult, to assess their durability. Achieving sustainable building with environmental friendly materials involves the combination of advanced technologies, to attain and operate with low impact on the environment, ensuring the user's safety and comfort for a long time, also to meet aesthetical and functional parameters, and to easily recycle or reintegrate into the natural environment the generated waste from construction and demolition works.

Each geographic area, according to climate, natural resources, spiritual and secular customs, is characterized by the typology of local constructions. Traditional buildings stand for an architectural style based essentially on local needs and materials, reflecting the tradition of the place. Local clay mixtures can be used successfully for masonry, masonry mortars, plaster and ecological finishes, and at the same time they satisfy the performance requirements and admissibility criteria specific to the industrialized materials. Constructions made of unburnt bricks can be found all over the world, mainly in rural areas, both in less developed countries as well as in the economically developed ones [1], [5]. Because of these, many countries have proposed and implemented standards that regulate the earth housing construction. In this aim a research was performed in order to improve the mechanical performance of local adobe bricks and the workability of the fresh mixture. In addition, a wide span of natural additives was studied, resulting in a total of over 50 mixtures, the most beneficial ones being meant for sustainable traditional building.

Adobe bricks type masonry units (Figure 1) represent handmade construction materials, usually obtained by pressing an earth based mixture into an open timber frame or by casting the composition in a metallic mould.



Figure 1: Adobe specimens made from clay mixtures with different proportions of additions [1]

3. Appropriate mixes for adobe bricks

The main raw material needed for manufacture of adobe bricks is clay. Clay is a product of erosion of feldspar and other minerals. The usual term of loam does not represent a standardized composition, but rather it means the clay material extracted from a natural deposit. To determine the suitability of loam for a specific application, it is necessary to know its composition. Depending on the site of extraction location it contains varying amounts of clay, silt, sand, aggregate and water, and results in specific properties. According to their ratio there are defined several types of clay based compositions.

Adobe masonry composition contains different proportions of clay (as main row material, extracted from a natural deposit), sand and various organic matter additive of animal or vegetal provenience. The bricks' material can be dispersed reinforced with animal or vegetal fibers. In conformity with literature [5], [6] an amount of minimum 5% but no more than 50% clay in the loam extracted from the natural deposit is optimal for achieving adobe bricks. The literature refers to this building material [6] as being clean, environmentally friendly, easy obtained with little financial and energy effort, which adapts to users' needs, which helps to regulate indoor air relative humidity, with no toxic emissions, fire resistant, as well as resistant to insects, rodents and mold attack [7], [8], [9], [10]. Some shortcomings about adobe bricks are indicate by the literature, and include the reduced resistance to water, reduced resistance to seismic actions, the necessity of more frequent maintenance and repairs than in case of industrial construction materials, in addition to the effort needed to establish the optimal composition of clay - sand - additions, these varying from one extraction location to another [11], [12], [13], [14], [15].

For achieving the experimental mixes it was used soil extracted from a site in Valea Drăganului, Cluj County, Romania. The granulometric analysis was determined according to prescriptions [16], by sieving method. The granulation characteristics in correlation with data from the literature indicated that this soil is in accordance with the chosen purpose, having a sandy loam-type composition, as indicated in Figure 2. In order to improve the mechanical performances of masonry as well as the workability of the fresh mixture, following additions were studied, both theoretically and experimentally: bone glue, sodium hydroxide (NaOH), salt (NaCl), bran, borsch, milk whey, ash, throughout more than 50 mix recipes.

Previous experimental studies were conducted [17] regarding the effectiveness of natural fiber disperse reinforcement in the adobe bricks. The results indicate an improved mechanical strength and a better thermal conductivity of the clay composite material. The variation of physic-mechanical parameters was influenced by the type of the organic material, hemp fiber or straw, and by the amount of material entered in the mixture. According to this, for the considered clay mixture composition, it was set an optimum addition of hemp fibers, in amount of 9-10% by volume, respectively an optimal straw addition, in amount of 30-40% by volume. All samples achieved the balanced moisture through natural drying and under careful observation, their appearance and the development of cracks being visually tracked.

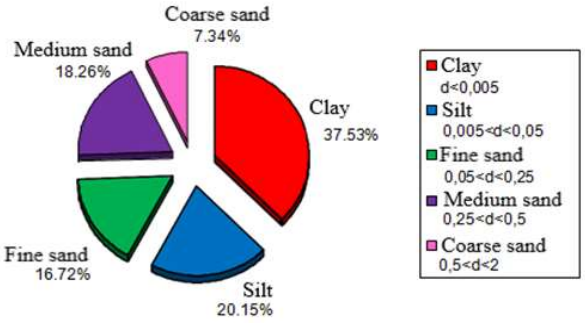


Figure 2: Characteristic texture of the sandy loam-type composition [6]

The thermal conductivity was determined based on the heat transfer property of the samples with a thermofluxmetric method for an average temperature between plates, of 10ºC. The sample, dried in an oven till to a constant mass, was placed in the apparatus for determining the thermal conductivity. The sample thickness was measured automatically by the apparatus. It was recorded the thermal conductivity of the specimen. A comparative representation of the analyzed samples with straw and hemp fiber additions (Figure 3), make them comparable in terms of thermal conductivity, with other building materials, as lightweight aggregates concrete, with perlite concrete or granulite concrete.

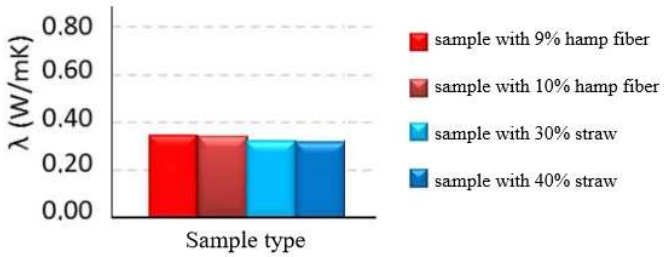


Figure 3: Comparative representation in terms of thermal conductivity [6]

The results obtained from the experimental research are shown in Figure 4, and represent the variation of compressive strength, flexural tensile strength, and thermal conductivity depending on the amount of vegetal fibers included in a clay mixture

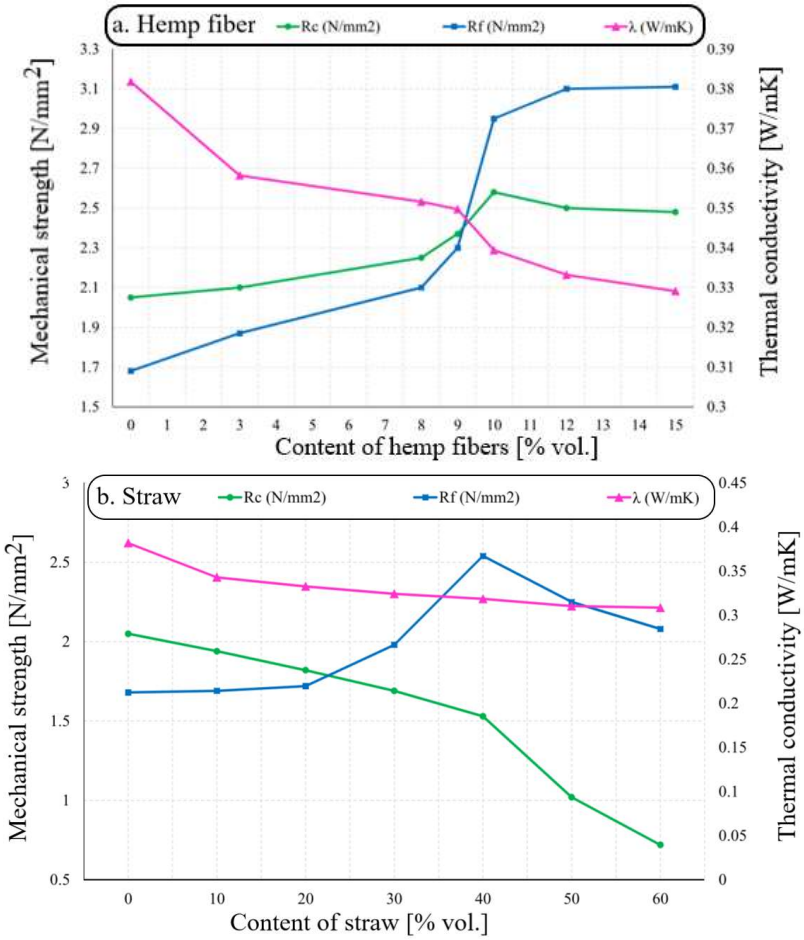


Figure 4: Variation of compressive strength, flexural tensile strength, and thermal conductivity [17]

Experimental results indicate a decreasing trend in workability, axial contraction, crack risk, and thermal conductivity as the amount of vegetal material increases in the mix. The flexural tensile strength, Rf, was determined by applying a concentrated load at half of the distance between the supports, and the compressive strength, Rc, on the two resulted halves of the specimen.

The research emphasizes that the most beneficial additives were the bone glue and sodium hydroxide. The optimal concentration of bone glue is 1.25% to achieve compressive strengths of about 4.1 MPa at 40 days (higher concentrations lead to mold grows). Bone glue was purchased in granular form and dissolved in water. An addition of 2% sodium hydroxide (NaOH as maximum purity substance, routinely used in the laboratory) provides a better workability of the mixture and helps dissolve the bone glue faster. Table 1 summarizes a comparison of the results with similar referred researches.

Table 1: Comparison of adobe bricks performance [1]

Characteristic \ Reference	[5]	[18]	[19]	[20]	***A1**
Axial contraction [%]	15.0	-	17.1	25.0	**6.5**
Compressive strength [N/mm^2]	3.30	2.40	0.32	10.2	**4.10**
Flexural strength	0.63	-	-	-	**1.40**
Density [kg/m^3]	1748	1960	1050	1700	**1900**
Thermal conductivity [WmK]	-	-	0.45	0.59	**0.38**

***A1** – mix with sand 35 % and bone glue 1.25 %, Valea Drăganului /România

4. Recycling of adobe bricks

As a sustainable material adobe bricks are also recyclable. The experimental research provides evidence that the recovered clay material can be used again in new adobe elements without losing their qualities. Recycled clay material was obtained by recovering, crushing and shredding of specimens made from the optimal clay mixture, previously used in other experimental testing which did not required that the surface of the specimens to be treated with impregnating solutions, like linseed oil, beeswax dissolved in oil, beeswax dissolved in siccative oil, paste lime, hydraulic lime or animal fat [21]. After the recovered clay material has been brought to a satisfactory degree of grinding, it was sieved through a sieve with mesh size of 4 mm. This sieve was chosen because the maximum grain size used for the initial mixture (optimum mixture) was 4 mm. Thus it was considered that by sieving the granulometric fractions would not be modified.

The witness specimen was conceived from the established composition, as the optimal one from the experimental research. The mix included sandy loam, sand, bone glue and paste lime, in proportions of 35% sand and 65% binder (composed of 79% sandy loam, 1% bone glue and 2% paste lime). The required water was established as 33% reported to the dry material mass. There were made three sets of witness specimens: optimal mixture, optimal mixture with straw addition and optimal mixture with hemp fiber addition, the proportion of vegetal fibers were determined during previous experimental research [17]. The recycled clay mixture was obtained by soaking in water until the required consistency. It was mixed with water in the same proportions as for the witness specimens. This new mixture had a much better workability than the initial one, achieving as well a better compaction while casting in the mould. Also, after the drying process, through elimination of the interleaved water from the elementary sheets of clay, it produced a better internal link in the material. The specimens tested for mechanical strength were evaluated in following combinations: mixture of recycled clay material without vegetal fibers, mixture of recycled clay material with straw addition and mixture of recycled clay material with hemp fiber addition.

In terms of mechanical strength, the specimens achieved from recycled clay had an increasing of compressive strength in all three analyzed cases, in comparison with their similar witness specimens

(Figure 5). Based on the experimental research results, it can be appreciate that the recovered clay from waste of old adobe bricks type masonry elements can be recycled and used again in order to achieve new elements of the same kind. The physico-mechanical performances of the newly manufactured adobe bricks are not negatively affected by using recycled clay material. Moreover, the composition obtained on the basis of recycled clay allows the disperse reinforcement with vegetal fibers, like straw or hemp fibers.

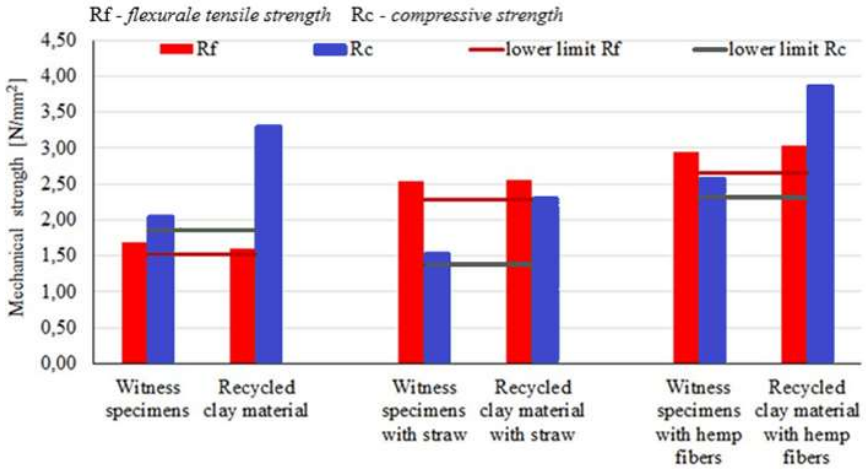


Figure 5: The influence of recycled clay on mechanical strength in different mixtures [6]

5. Conclusions

The current global economic and social context has a high impact on the built environment. Vernacular architecture has been losing ground over the last period of time, as modern methods prevail. The buildings themselves were often beautiful, and many of the old techniques employ natural materials and simple concepts that are energy efficient. Developing new solutions from the historical and traditional experience in order to provide superior performance, to improve technology and to obtain more resistant, comfortable and durable structures is currently become a priority in civil engineering research. The terms related to natural building refers to any sort of construction that is accomplished with the use of natural materials primarily (as opposed to the use of industrial materials), and ways of building that minimize the use of products that require considerable embodied energy for their manufacture or transportation. Building with adobe bricks ensures the responsible use of natural resources in present-day designs combined with traditional construction techniques from vernacular architecture. Due to the possibility of reusing and totally recycling of these materials, it contributes to conservation of natural resources along with the protection of landscape and natural balance, to diminish of pollution, as well as to energy savings, along with the providing of a cleaner and healthier living environment.

References

[1] G.A. Călătan, *Contributions on implementation of local and traditional solutions in sustainable housing*, PhD Thesis, Technical University of Cluj-Napoca, Romania, 2018.

[2] P. Vegh, "Designing Environmentally Compatible Structures", *Proceedings of the 11th International Seminar on Environmentally Compatible Structures and Structural Materials*, IASS WG 18 on ECS, A.T. Mircea (Ed.), pp. 13-22, Cluj-Napoca, Romania, 2014.

[3] A.T. Mircea, "Responsible management of waste - an essential aspect of sustainable construction", *Proceedings of the 11th International Seminar on Environmentally Compatible Structures and Structural Materials*, IASS WG 18 on ECS, A.T. Mircea (Ed.), pp. 89-96, Cluj-Napoca, Romania, 2014.

[4] A.T. Mircea, "Study upon applying Multi-Criteria Analysis to the selection of building materials", *Proceedings of the 28th IBIMA Conference "Vision 2020: Innovation Management, Development Sustainability, and Competitive Economic Growth"*, Seville, Spain, 2016.

[5] G. Minke, *Building with earth. Design and technology of a sustainable architecture*, Birkhäuser, Publishers for Architecture Basel Berlin Boston, 2006.

[6] G. Călătan, A. Hegyi, C. Dico, C. Mircea, "Experimental research on the recyclability of the clay material used in the fabrication of adobe bricks type masonry units", *Procedia Technology 181*, pp. 363 – 369, 2017.

[7] F. Pacheo-Torgal, S. Jalili, "Earth construction: Lesson from the past for future eco-efficient construction", *Construction and Building Materials 29*, pp. 512-519, 2012.

[8] M.R. Parra-Saldivar, W. Betty, "Thermal behaviour of adobe construction", *Building and Environment 41*, pp. 1892-1904, 2006.

[9] J. Revuelta-Acosta, A. Garcia-Diaz, G.M. Soto-Zarazua, E. Rico-Garcia, "Adobe as a sustainable material: A thermal performance", *Journal of Applied Sciences 10 (19)*, pp. 2211-2216, 2010.

[10] Waitakere City Council, *Sustainable home guidelines: Earth building*, Oakland, 2008.

[11] M. Blondet, G.G. Villa, S. Brzev, *Earthqake-resistant construction of adobe buildings: A Tutorial*, EERI/ IAE, World Housing Encyclopedia, Oakland, California, 2011.

[12] A.S. Elnashai, B. Gencturk, O.S. Kwon, Y. Hashash, et al., "The Maule (Chile) Earthquake of February 27, 2010. Consequence assessments and case studies", Urbana (IL), Mid-America Earthquake Center, 2010.

[13] M.L. Germana, "Early modern adobe period in Sicily: Recent finds", *Earthen Architecture: Past, Present and Future*, Mileto, Vegas, Garcia Soriano & Cristini (Eds), Taylor & Francis Group London, pp. 163-168, 2015.

[14] D. Silveira, H. Varum, A. Costa, "Influence of the testing procedures in the mechanical characterization of adobe bricks", *Construction and Building Materials 40*, pp. 719-728, 2013.

[15] D. Silveira, H. Varum, A. Costa, T. Martins, H. Pereira, J. Almeida, "Mechanical properties of adobe bricks in ancient constructions", *Construction and Building Materials 28*, pp. 36-44, 2012.

[16] SR EN ISO 14688:1-2018 Investigaţii şi încercări geotehnice. Identificarea şi clasificarea pământurilor. Partea 1: Identificare şi descriere.

[17] G. Călătan, A. Heghyi, C. Dico, C. Mircea, "Determining the optimum addition of vegetable materials in adobe bricks", *Procedia Technology* 22, pp. 259-265, 2016.

[18] G.T. Ciurileanu (Cioca), I. Bucur Horvath, "The new vernacular based architecture", *JAES, Section Civil Engineering and Installations*, 2011.

[19] P. Lertwattanaruk, J. Choksiriwanna, *The Physical and Thermal Properties of Adobe Brick Containing Bagasse for Earth Construction*, Thammasat University, Pathumthani 12121, Thailand, 2011.

[20] E.A. Okunade, *The effect of wood ash and sawdust admixtures on the engineering properties of a burnt laterite - clay brick*, Department of civil engineering, University of Ado-Ekiti, P.M.B. 5363, Ado-Ekiti, Nigeria, 2013.

]21] G. Călătan, A. Heghyi, C. Dico, C. Mircea, "Surface waterproofing methods of clay bricks used in vernacular constructions", *Proceedings of the 15th International Multidisciplinary Scientific GeoConference and EXPO-SGEM2015*, Albena, Bulgaria, pp. 287-294, 2015.

Proceedings of the IASS Annual Symposium 2019 – Structural Membranes 2019
Form and Force
7 – 10 October 2019, Barcelona, Spain
C. Lázaro, K.-U. Bletzinger, E. Oñate (eds.)

Parametric design and LCA for temporary structures: structural material options and optimization of multiple installation cycles using genetic algorithm

Carlotta MAZZOLA*, Salvatore VISCUSO [a], Carol MONTICELLI [a], Alessandra ZANELLI [a]

* Textile Architecture Network (TAN),
DABC, Politecnico di Milano; via G. Ponzio 31, Milano 20133, Italy,
carlotta.mazzola@polimi.it

[a] Textile Architecture Network (TAN),
DABC, Politecnico di Milano; via G. Ponzio 31, Milano 20133, Italy,

Abstract

In continuity with the growing LCA-integrated design approaches, this paper presents a method for integrating LCA datasets into a parametric model to assess and optimize the environmental impact of a temporary building during the design phase. A temporary structure built with reversible technologies, the TemporActive Pavillion (TA), is used as a case study to present and verify the proposed methodology. In the first analysis, the parametric model is used to estimate the environmental impacts of three alternative building systems during the early design and therefore guiding the designer towards the most eco-aware choice with respect to the project requirements. In the second analysis, genetic optimization solvers are used to define the number of the needed life cycles to minimize the environmental impacts of a temporary structure compared to the single-use scenario.
Results show that the method can support the designer in the early design stage in choosing the most appropriate material and technological option, taking into account also the eco-efficiency requirements. Further developments are needed for making the method less theoretical but usable as a design-supportive tool in the architectural practice.

Keywords: temporary architecture, lightweight structures, environmental impacts, LCA, parametric model, genetic algorithm, optimization, design process

1. Introduction

1.1. LCA-integrated approaches in the design process

The Life Cycle Assessment (LCA) is a widely used methodology for assessing the environmental impacts of a project. Since this is a time-consuming procedure with a high degree of uncertainty (e.g. building components specifications, usage, end-of-life scenarios) that required the expertise of skilled professionals, there is an increasing demand in introducing LCA approaches in the architectural practice. Especially when is used during the project development and not as an ex-post evaluation tool, LCA can support non-expert designers to evaluate the environmental impact of multiple design variables from the early design stage [1] and therefore select the most appropriate design choice in relation to the project requirements.

Recently, LCA tool integrated in 3D CAD software are becoming more and more widespread. BIM-integrated LCA tool such as Impact and Tallys are used in the detailed design phase to evaluate the environmental performance of the project. However, the large amount of information necessary to build the model makes the application of BIM not practicable in the early design stage and more suitable for

Copyright © 2019 by Carlotta Mazzola, Salvatore Viscuso, Carol Monticelli, Alessandra Zanelli
Published by the International Association for Shell and Spatial Structures (IASS) with permission.

large scale projects [1]. With the aim of providing design-integrated approaches to LCA, limited researches on the topic propose the integration of LCA analysis in parametric software to evaluate and optimize the environmental impacts of the building. Heeren *et al.* [2] described a method that uses a parametric model for identifying drivers of both operational and embodied environmental impact of a residential building. In this example, the geometry is integrated as one input parameter and other parameters (i.e. material, design, operation and exogenic building properties) are varied in order to compare the environmental performance of two material variants. The development of design-integrated LCA parametric tools overcomes manual and time-consuming bill of quantities input. The inclusion of LCA datasets in a parametric model from the early design can be a great assistance for the designer because data input such as the geometry or materials definition can be modified and adjusted in later design stages [3]. Where a LCA analysis is to be combined with other analyses such as structural analysis and daylighting parameters, they can be integrated into the parametric model. For instance, Otovic *et al.* [4] combined energy and indoor climate design with LCA into an integrated dynamic model.

The advantages of integrating LCA into a parametric model are multiple:

i) the parametrically-defined inputs of the model (i.e. boundary conditions, building geometry, materials, structural system) can be selected based on the specificity of each project and with the aim of the study;

ii) since in early design there is limited information and all the environmental data are not always available, preliminary assessment can be performed considering generic materials data (even though no producer-specific choices on the materials or precise quantities are known at this stage) and later updated, refined and detailed during the design development in relation to a higher definition of the project (e.g. quantity, materials information, technical choices, etc.);

iii) the resulting environmental performance of different design variants can be easily compared;

iv) the interoperability with other design software (e.g. Rhino Grasshopper, Karamba, EnergyPlus) makes LCA real-time feedback possible during the whole project development and not only as an ex-post evaluation tool.

1.2. Durable temporariness and cycles of use

Lightweight temporary structures are increasingly common within the framework of complex-shaped spatial structures. In terms of design, the lightness means both weight reduction (therefore using lighter, more performative and/or less materials) and limiting the environmental impacts of the project. For this kind of structures, which meet specific project requirements such as the easy transportability and mountability, the environmental impact assessment can represent an important decision supportive criterion for the designer from the conceptual design phase [3]. In the common practice, the multiple cycles of use that a temporary structure can carry out are not considered, although these are primarily reversible and demountable structures. The concept of "durable temporariness" -opposed to the disposable practice- suggests the reuse of temporary architecture and/or its building components after the first use. In this sense, it is particularly relevant to perform a Life Cycle Assessment (LCA) that consider the whole life cycle (therefore considering the multiple service-lives of a structure) from the early stage of design to guide the designer to the most appropriate material and technological choice in relation to the context, the project requirements and its eco-profile [5].

2. Aim of the study

One of the recurrent themes running through the research works of the research group TAN (Textile Architecture Network) at Politecnico di Milano is the consideration of the time variable (therefore structures' life-span and materials durability) as a key decision-making factor during the entire design process of lightweight structures.

The method presented in this paper integrates LCA datasets into a parametric model with the aim of:

i) providing a tool to evaluate the real-time environmental impacts of different material solutions during the early design stage; and

ii) quantifying the scenarios of use cycles needed for the minimization of the environmental impact generated by the pre-use phase (i.e. production of materials and components) of a temporary structure compared with the single-use.

3. Methodology: data selection and algorithm construction

The method presented in this paper incorporates simplified LCA into the design process by integrating LCA datasets in a parametric model to assess and reduce the environmental impact of the project and support the designer from the early design stage. A parametric model developed in Rhinoceros Grasshopper™ [6] with the plugin Tortuga is used to give an overview of the environmental impact of the building. The parametric model is dynamically connected with Ecoinvent database V3 that served as a reference source for obtaining the life cycle inventory data. The environmental data of the materials have been obtained by the LCA tool SimaPro [7] using EPD 2007 calculation method (in accordance with ISO 21930:2017) and added to the customized Excel spreadsheet. Since some detailed information may not be available at the early design stage, the proposed method must be able to give results even if not all the fields are completed. Those missing data can be replaced in the parametric model as the data become available.

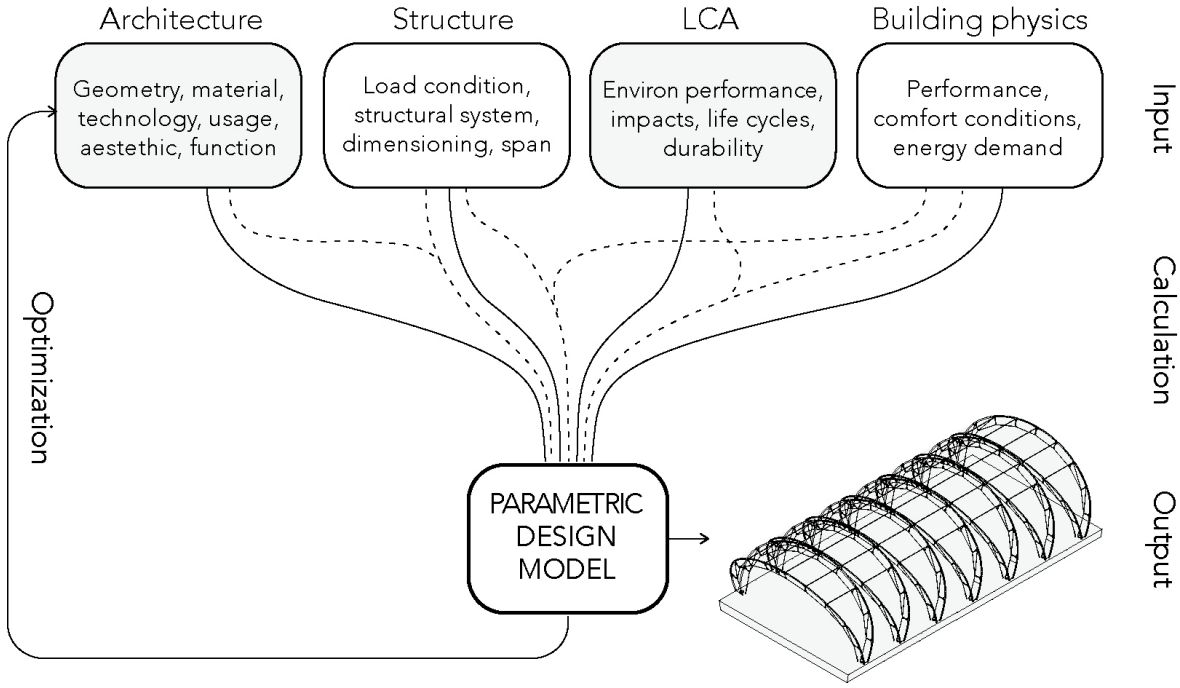


Figure 1: Schematic workflow of a parametric design model embedding different project specifications (e.g. architectural , structural analysis, LCA, building physics aspects) and interfaces (dashed lines) during the design process. The gray boxes are the analysis considered in this paper.

For lightweight temporary and demountable structures, the operational phase of the building during the use (cooling/heating energy consumption, maintenance and substitution) has a much lower contribution than embodied energy demand in the production, construction and end-of-life phase [8]. The environmental impact assessment presented in this paper includes only the pre-use phase; therefore, the operational and end-of-life are neglected.

The presented approach is applied on case study of a temporary structure with reversible technologies, the TemporActive Pavilion (TA) (Figure 1). The temporary pavilion consists of 2.00x7.00 m self-supporting modules, reaching a maximum height of 3.50 m, made of double-wing shape arches that are designed to be structurally efficient and extremely lightweight [9].

In the first analysis, the parametric model is used to estimate the environmental impacts of three alternative building systems. This preliminary assessment is meant to support the designer in the early design for evaluating multiple design alternatives with simplified data input (e.g. geometry, structure, material). In the second analysis, genetic algorithms are used to quantify the number of cycles of use necessary to minimize the environmental impact of a temporary structure.

4. First analysis: LCA of three structural/material options

This work has been carried out during the conceptual design of the TA pavilion to assess, together with other project requirements, the environmental impacts of technical and material solutions. Three options with different materials and the related structural systems are compared to estimate the environmental impacts' level and therefore deepen the advantages and limits of each one. This preliminary eco-efficiency evaluation is later combined with the other design requirements to find the most effective solution. Does the greater sustainability and minimization of the environmental impacts of the project correspond to an optimization of the production processes (reducing the waste materials), of the efficiency of the transportation and storage (in relation to the volume), of the erection phase and maintainability in the operational phase?

During the TA design development, Eco-design strategies developed for membrane architecture [10] were computed as a preliminary assessment of the environmental performance of the materials' choice (i.e. quantities of materials used) in relation with the design ones, before a more specific LCA. Their verification helps to point out the pros and cons of membrane materials and the correct exploitation of their characteristics.

First principle [Perimeter / Area] 47 / 250 = 0,19 (to be verified P / A < = 0,6)

Second principle [Weight Envelope (We) / Weight fixing system (Ws)] 75 / 27 = 2,78 (to be verified We / Ws > 1 towards bigger and bigger values)

Subsequently, LCA had been carried out for three solutions, in which the shape was kept fixed and only the materials and the size of the structural profiles were varied. To perform the first evaluation a simplified linear structural model made of two arches and seven struts was used and three parametrically defined material and structural profile variations were considered:

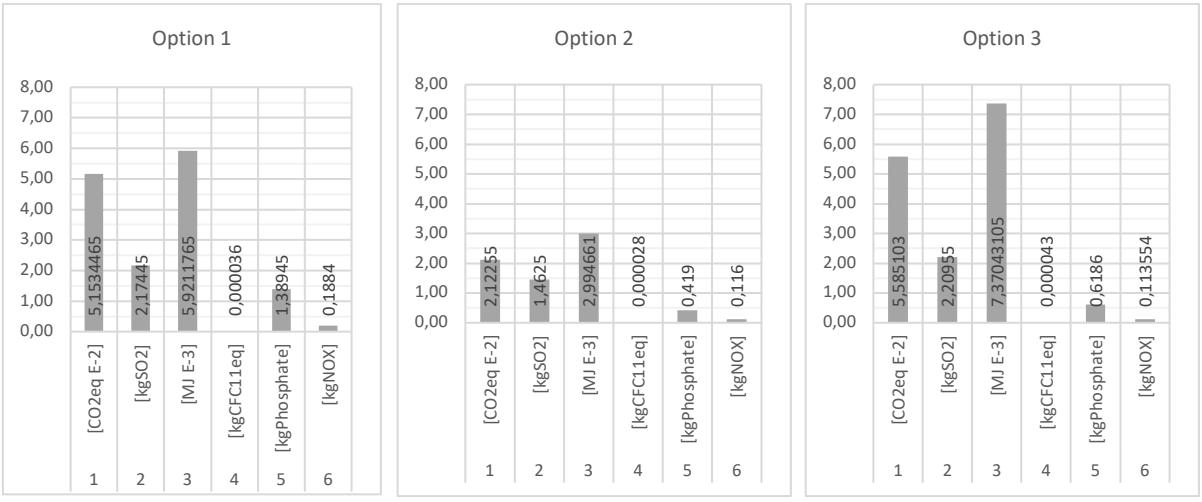
- Option 1. Cross-laminated timber profile 100x150 mm and struts with cross-section 50x80 mm;
- Option 2. Galvanized steel tubes ⌀60 mm, 3 mm thickness and struts ⌀40 mm, 3 mm thickness;
- Option 3. Bending active restrained system: Glass Fiber Reinforced Polymers (GFRP) profile made of triple tubes ⌀26 mm, 3,5 mm thickness combined with stainless steel restraining cables ⌀8 mm; struts: coupled GFRP tubes ⌀26 mm, 3,5 mm thickness.

The geometry, which only consisted of the linear framework of the vertical elevation structural elements, is input using a 3D CAD model. The functional unit considered in the first analysis is one self-supporting module made of two inclined arches and seven struts. The shape, dimension and thickness of the structural profiles are controlled in the parametric design software Grasshopper™. Since this preliminary assessment is meant to be used in an early design stage, all the inaccuracies introduced by this simplified modelling can be neglected.

Through the algorithm built in Grasshopper with Tortuga plugin, the environmental impact assessment of each material per functional unit has been carried out, measured by six LCA indicators typically considered in the Environmental Product Declaration (EPD).

Table 1: Environmental impact of the three material and structural variants assessed with EPD indicators by combining environmental material data obtained from LCA datasets with quantities of the geometric model

Id.	Impact	U.m.	Option 1 Steel | 137 kg	Option 2 CLT | 195 kg	Option 3 GFRP | 73 kg
1	Global Warming Potential	CO2eq	515.34465	212.255	558.5103
2	Acidification	kgSO2	217445	14625	220955
3	Depletion of Non-Ren. Energy	MJ	5921.1765	2994.661	7370.43105
4	Ozone Depletion Potential	kgCFC11eq	0.000036	0.000028	0.000043
5	Eutrophication	kgPO4	138945	0.419	0.6186
6	Formation Tropospheric Ozone	kgNOX	0.1884	0.116	0.113554



Firstly, focusing only on the LCA results, we can confirm that the ultra-lightness of some solutions (i.e. option 3) is not linearly corresponding to eco-efficiency, even when compared to lightweight (i.e. option 1) and more massive/traditional solutions (i.e. option 2). Option 2 is the heaviest solution in terms of weight but with the lower eco-profile. As the table above (Table 1) show, the impact categories with a considerable difference in the results for the three solutions are the Global Warming Potential (GWP) and the Depletion of Non-Renewable Energy (MJ); also the Eutrophication impact during the SST production is higher than the other two options. The cross-laminated timber option, with an advantaged production process due to the natural origin of the material that is ready to be shaped, has a low environmental impact profile.

The environmental performance is one of the criteria that should be combined with the other project requirements to choose the optimum solution. Combining these outputs with the other TA project requirements, the scenario can influence the choice of a different option that the one with the best eco-efficiency performance.

The use of lighter and more efficient structural materials leads to minimizing the building elements and, therefore, to develop high-efficient structures [4]. The structural materials lightness of temporary structures means both transportability of the building components (i.e. lower volume) and easy set-up (i.e. no machinery required for the construction, buildable by non-expert installers). As shown in Figure 2, the Option 3 results the optimal one with respect to the project requirements. Nonetheless, due to the higher eco-profile and to the project pre-requirements of the temporary use (which means easy (dis)assembly), the verification of the materials durability and the reusability of the system becomes one of the most important requirements for temporary structures.

		OPTION 1 Steel	OPTION 2 CLT	OPTION 3 GFRP hybrid
PRODUCTION PROCESS	Environmental impact	● ●	●	● ●
	Production waste	●	● ● ●	●
TRANSPORTATION PHASE	Storage volume	● ●	● ● ●	●
	Weight	● ●	● ● ●	●
INSTALLATION PROCESS	Need for building machinery	● ●	● ● ●	●
	Expertise of the installers	● ●	● ●	●
	Erection time	●	●	●
USE PHASE	Material durability	●	●	●
	Maintenability	●	● ●	●
END OF LIFE SCENARIO	Reciclability	●	● ●	● ● ●

Figure 2: Checklist of the project requirements for the three analysed options

5. Second analysis: Optimization of the environmental impact considering multiple cycles of use of temporary structure

The possibility of reassembling the structure several times during the life span of the building is an aspect that should be considered in the environmental impact assessment of temporary structures, to orient the designer to the most appropriate material and technical solutions. Since the expected lifespan and material durability of temporary structures are often larger than the effective use of the structure, it is essential to consider not only the environmental impacts of the structure single-use in its short service life but of multiple cycles of use in the whole life cycle of the structure. Consequently, the research, following the first static validation, focused on a multi-variable study through the use of a parametric optimization solver. In the second analysis, the ultra-lightweight structure (i.e. option 3) was taken as a reference to assess the number of cycles of use necessary to make it more eco-efficient, exploiting as much as possible the initial higher impacts' eco-profile, instead of producing new structures for future uses, causing additional environmental impact. The second analysis is the answer of the following research question: by setting possible scenarios of minimization of the total environmental impacts for the ultra-lightweight option, how many use cycles can the components undergo, compared to the single use scenario?

The functional unit in this case is enlarged to the whole TA Pavilion, which means seven modules that is seven times the functional unit of the first analysis. The input geometry is derived from a detailed 3D model developed in Rhinoceros, in which the thicknesses of the materials are given parametrically. Through the evolutionary solver Galapagos for Grasshopper, different parametric variables (i.e. geometry, materials, quantities, cycles of use, etc.) can be linked alternatively to a fitness function of the genetic algorithm in order to optimize the remaining variables, the genotypes. In this case, by setting the fitness input in search of the minimum environmental impact obtainable, the algorithm allowed to calculate the minimum number of reuse cycles necessary to reduce the impact of the materials used. The minimization was made component by component and they were later combined considering the cycles of use of the entire structure. The results were compared with the single-use scenario.

The scenarios evaluated in this analysis are: reducing of 20%, 40%, 60%, 80%, 100% the environmental impacts with respect to the impacts related to the single use. The hypothesis of the % reduction scenarios comes as similitude from the latest advises of the European protocol LEED v4 of reducing the impacts compared to a similar existing building. (i.e. 10% reduction of the impacts for the GWP).

Only the pre-use phase was considered in the environmental impact assessment and therefore the operation and end-of-life phase were neglected. The duration of one cycle of use was set six months. The maximum functional life span of the TA Pavilion was set to ten use cycles, therefore five years. The fitness function used in this evolutionary solver process is the following (1):

$$\sigma_{\times} = \sqrt{\frac{\sum_{i=1}^{N}(\times_i - \overline{\times})^2}{N}} \cong 0 \quad \text{(asymptotically equal to 0)} \tag{1}$$

$\sigma_{\times} = Standard\ deviation \quad \times_i = LCA\ result\ per\ each\ impact\ category\ /Num.\ of\ reusing\ cycles\ \overline{\times} = reference\ value\ (-20\%\ of\ Tot\ LCA\ result\ per\ single\ use;\ -40\%; \ldots), N = Impact\ categories\ (population)$

The function measures the amount of variation of genotype values from reference data. Standard deviation obtained from low impact reductions indicates that the data points tend to be close to the reference of the set, while a high standard deviation indicates that the data points are spread out. For instance, to guarantee at least an impact reduction of 60%, the obtained minimum numbers of reusing cycles (depending on the material, from 2 to 7 times) represent the genotypes within the fixed range (1-10 cycles) that produce the value of standard deviation asymptotically closest to 0.

Table 2: Single-use LCA results of the TA, measured component by component and total impact

		Basement		Vertical structure			Envelope	
Impact category	**U.m.**	**GFRP beams**	**OSB Panel**	**GFRP tubes**	**SS cables**	**SS joints**	**PVC Crystal**	**Total** (single use)
Global Warming Potential	CO2eq	5840.275	13.658	3607.223	817.695	1210.690	4623.434	**19720.197**
Acidification	kgSO2	20.713	0.094	12.793	4.569	7.026	13.950	**71.939**
Depletion of Non-Ren. Energy	MJ	81495.99	192.71	5033.688	8275.34	12823.95	**112883.85**	**316343.20**
Ozone Depletion Potential	kgCFC11eq	0.000486	1.7705e-6	**0.0003**	0.000044	0.000064	0.00006	**0.00126**
Eutrophication	kgPO4	5.612	0.027	3.467	1.389	2.167	1.7617	**17.891**
Formation Tropospheric Ozone	kgNOX	0.981	0.0075	0.605	0.283	0.416	**39.810**	**42.708**

Table 3: Reusing cycles per building component and standard deviation from reference values

Building component	**Material**	**Reusing cycles (1 cycle = 6 months; 10 cycles max)**				
		-20% of single use	**-40% of single use**	**-60% of single use**	**-80% of single use**	**-100% of single use**
Basement	GFRP beams	2	4	7	9	10
Floor	OSB Panel	1	2	2	4	10
Arches	GFRP tubes	1	1	4	10	10
Restr. system	Stainless steel cables	2	5	6	10	10
Connectors	Stainless steel profiles	1	2	5	8	10
Envelope	PVC Crystal foil	2	3	3	6	10
	$\sigma_{\times}$	**0.163982**	**1.014501**	**1.63637**	**3.383748**	**12939.73**

The results indicate that the scenario -20% environmental impacts reduction is satisfied by the reuse of two building components (i.e. the GFRP beams and the Stainless Steel Cables) for a second time. When the reduction is -40%, all the components except for the GRFP tubes that have to be reused for more cycles. And the same is for the rest of the reduction scenarios.

This is a theoretical assumption but it gives important indications for the strategies of reuse of components and the optimization of the reuse. The presented parametric model optimized with genetic algorithm solver is aimed to indicate an environmentally compatible strategy also for optimizing the connection systems between the components in the case they have to be reused, while it should be implemented in order to support the designers decisions in the case of the same reuse for the same system or in other systems and for different functions.

Conclusions

The paper presented an improved methodology for the environmental impact assessment of temporary structures, by integrating LCA datasets into a parametric model. At this stage, the approach is in progress. The aim of the research is to proceed with further investigations in order to define a useful tool to support the designer from the early design stage to evaluate eco-efficient design options considering the whole project life cycle. Some meaningful paradigms, that also derived from other investigations, are recurrent in the interpretation of the analysis results: in the Environmental Analysis, the functional context and the specific requirements for each project must be systematized with the LCA assessment results for a better technological choice; if the project has a temporary nature, fundamental is the consideration of predicted life span and the use cycles since the design phase.

The further developments of the research aim to refine the methodology, by considering other variables and integrating them into the parametric design model, and provide a more valuable and user-friendly design-supportive tool addressed to the architects.

References

[1] A. Höllberg, J. Ruth, "LCA in architectural design—a parametric approach.", *The International Journal of Life Cycle Assessment, 21*(7), pp. 943-960, 2016.

[2] N. Heeren, C. L. Mutel, B. Steubing, Y. Ostermeyer, H. Wallbaum, & S. Hellweg, "Environmental Impact of Buildings: What Matters?", *Environmental science & technology*, *49*(16), pp. 9832-9841, 2015.

[3] E. Meex, A. Höllberg, E. Knapen, L. Hildebrand, & G. Verbeeck, "Requirements for applying LCA-based environmental impact assessment tools in the early stages of building design", *Building and Environment*, *133*, pp. 228-236, 2018

[4] A. P. Otovic, L. M. Jensen, K. & Negendahl, "Expansion in number of parameters-simulation of energy and indoor climate in combination with LCA", *2016 ASHRAE Annual Conference*, 2016.

[5] C. Monticelli, A. Zanelli, "Life Cycle Design and efficiency principles for membrane architecture: towards a new set of eco-design strategies", *Procedia Engineering*, *155*, pp. 416-425, 2016.

[6] Grasshopper™, https://www.grasshopper3d.com

[7] Pre Consultant, Sima Pro 8, https://simapro.com/global-partner-network/pre-consultants/

[8] M. Grosso, & F. Thiebat, "Life cycle environmental assessment of temporary building constructions", *Energy Procedia*, *78*, pp. 3180-3185, 2015.

[9] C. Mazzola, B. Stimpfle, A. Zanelli, R. Canobbio, "TemporActive Pavillion: first loop of design and prototyping of an ultra-lightweight temporary architecture, in: *Proceedings of the TensiNet Symposium 2019* "Softening the Habitats", Politecnico di Milano, Milan, Italy, pp. 390-401, 2019 (DOI: 10.30448/ts2019.3245.40)

[10] C. Monticelli, A. Zanelli, "Application and validation of eco-efficiency principles to assess the design of lightweight structures: case studies of ETFE building skins", in: *Proceedings of the IASS Annual Symposium 2017* "Interfaces: architecture. engineering. science", International Association for Shell and Spatial Structures (IASS), 25-28 September, Hamburg, Germany, pp. 1-10. 2017

Proceedings of the IASS Annual Symposium 2019 – Structural Membranes 2019
Form and Force
7 – 10 October 2019, Barcelona, Spain
C. Lázaro, K.-U. Bletzinger, E. Oñate (eds.)

Towards Methodology of Life Cycle Analysis for Structural Reuse

Kateryna KUZMENKO [a,b]*, Cyril DOUTHE [a], Adelaide FERAILLE [a], Olivier BAVEREL [a]

[a,]* Laboratoire Navier, Ecole des Ponts ParisTech, UMR 8205, IFSTTAR, CNRS
6-8 Av. B. Pascal, 77455 MLV Cedex 2
kateryna.kuzmenko@enpc.fr

[b] Kardham C&H Architecture, 10 rue du Débarcadère 75017 Paris

Abstract

This paper presents a case study of a whole life-cycle analysis of shell-nexorade hybrid constructive system. A reuse scenario was established for the end-of-life phase and a method for environmental analysis of reclaimed structures was developed. The results of the construction phase show that the contribution of digital fabrication process in fairly significant to the overall result. The end-of-life study demonstrated that even within the low reclaim rate of elements, the reuse scenario produces less environmental burden than the disposal, however in some figures it can be less performant than the initial structure. The variables are proposed to control the pertinence of reuse solutions.

Keywords: LCA, Reuse, Nexorades, Digital fabrication, Fabrication-aware design, End-of-Life

1. Introduction

The general awareness of the urgency of environmental situation in construction sector fashioned a development of various design strategies for enhancement of building performances. Those optimization and rationalization technics though rarely deal with more than one phase of life-cycle of a system. Thus, most of today's energy regulation policies focus on the operational phase of a building, e.g. heating, cooling, water use etc.[1]. As far as France is concerned, a recent slight progression towards a life cycle performance of those policies, engendered a hot debate on ecological character of different construction materials, with a succeeding popularity of timber high-rise buildings [2].

The ongoing reinvention of lightweight construction systems within the digital design-to-production workflow, mainly occurring in academia [3], [4], keeps demonstrating a significant reduction of materials in construction elements. Finally, the newborn awareness of the severity of the end-of-life phase of building and construction elements (often reduced to disposal), prompted a recourse to the re-use principle in architecture and structural design [5].

The limit of the single-phase approach is therefore perfectly displayed by the classical example of impact transfer in life cycle of a system happened in building industry when the energy efficiency of operational phase was achieved though the exterior insulation of building envelope, creating the circumstances were embodied energy of insulation material is weightier than the savings of operational energy it supposed to bring [6].

A similar phenomenon of impact transfer from one phase of life-cycle to another is presented in the part 4.1 of this paper, within the description of the case study: a timber shell-nexorade hybrid structure. The efficiency of the structure was achieved with the digital design-to-production workflow, and by doing so, the environmental load of robotic construction system turns out to be as significant as the one of the materials.

Copyright © 2019 by K.Kuzmenko, C.Douthe, A.Feraille, O.Baverel
Published by the International Association for Shell and Spatial Structures (IASS) with permission.

In this paper we focus on the end-of-life phase of the construction system mentioned above, within the same problematics of the potential burden-shift when only single life-cycle phase performance is addressed. The reuse potential of the system is investigated within the feasibility study effectuated by the 1st year students of Ecole des Ponts ParisTech. A method for evaluation of the performance of structural reuse solution is proposed.

2. Reuse in Architecture and Structural Design

For the sake of numbers: within the actual growth of population and the tendency for urbanization, the need in terms of new construction for the next 40 years was estimated around 230 billions of square meters [7], when the scarcity of resources tackles already [8] and the productivity in construction sector has barely increased since 90ties [9]. In addition to that, only in 2014 in France construction sector has generated 227,5 tons of waste, 80% of which is inert, i.e. ready for reuse [10].

From historic perspective, the practice of reuse have always existed in construction. In general, before the industrialization the easiest way to get building materials was to deconstruct some buildings from nearby. For example, In XVII century in Rome, Maffeo Barberini used the Colosseum as a quarry for marble and stones for his palaces. He also recycled all the bronzes of the Pantheon into the cannons of Castel Sant'Angelo and the Baldacchino in San Pietro. Unfortunately, his coevals have not shared his sustainable vision, concluding to "*what the barbarians didn't do, Barberini did for them"* [11].

Nowadays, within the rise of awareness of the environmental burden of buildings' demolition, there was a recourse happening to the re-use principle in architecture and structural design. Thus, a few academic works have already been exploring the design challenges related to stock-based structural form-finding [12], [13]. Several design proposals were developed in the field of structural up-cycling [14], with a particular interest to skies [15]. Some of non-structural applications of reuse were attained in full-scale architectural realizations, e.g. Headquarter Council of the EU in Brussels or Circular Pavilion in Paris.

In this paper we stay within theoretical framework of structural reuse, which could be defined as sort-of meta-recycling were the elements are barely transformed after their first use and thus preserve their form and function in the subsequent life-cycles.

The case study proposed to investigate the question is the structure built for the occasion of 20 years of the new site of Ecole des Ponts ParisTech, by the team of Navier Laboratory. Also known as R2 pavilion, the structure demonstrates diverse researches on structural morphology, constructive geometry and robotic fabrication processes conducted in the laboratory for last decades.

3. Description of the Structure

The shell-nexorade hybrid constructive system has been described in details in [16], [17]. A swift recap is however presented below.

3.1. Design

Largely known as reciprocal frames, the structural family was rebranded into Nexorades in late 90ies by Baverel and Nooshin [18]. Constituted of load bearing members supporting each other in a cyclic manner along their sides, this specific arrangement of beams makes them connect by pairs and thus provides a significant simplification of assembly. The structural type of pavilion was baptized as shell-nexorade hybrid, due to the elegant blend of both principles. The membrane behavior was achieved by the introduction of the flat panels, acting like bracing elements and transforming the grid of beams into the discrete shell structure.

The planarity of the bracing quad panels was held within marionette method [19] in order to ensure their fabrication flair as well as to avoid the coupling between bending and axial forces. The initial

surface was meshed with planar quads, then using translation method [20] the T-joints were generated, preserving the planarity of quad panels.

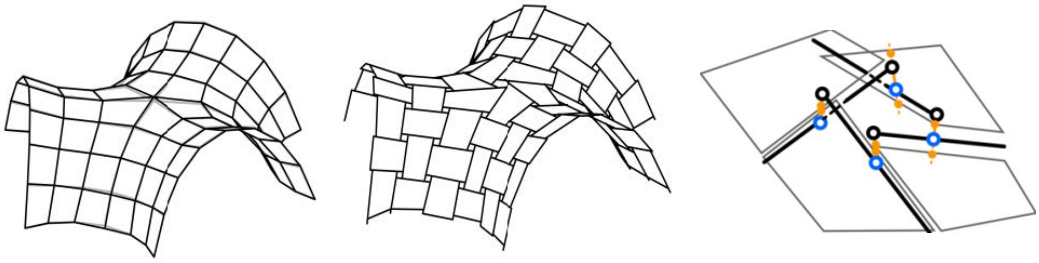


Figure 1. PQ-mesh transformation to reciprocal frame(left); Marionette technic for planarity of quads (right) [17]

3.2. Fabrication

Most of design choices of the project were made within the fabrication-aware strategy [21] , which could be briefly described as the geometry rationalization technic oriented to manufacture constraints. Thus, the final structure is composed of 102 straight glulam beams and 48 flat plywood panels, each of which is non-standard. The totality of formal and manufacturing complexity was centralized into beam's geometry and assured by 6 axes robotic milling. As follows, the panel fabrication was abridged to a mere CNC cut. The layout scheme of the robotic platform of Ecole des Ponts ParisTech is shown in Figure 2.

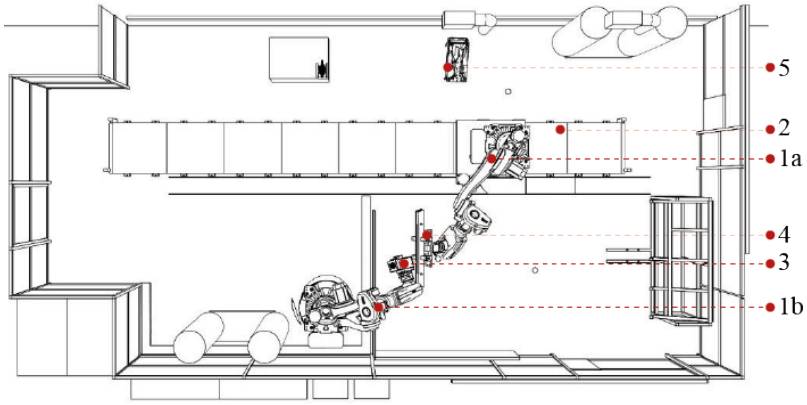


Figure 2. Top view of layout of robotic fabrication platform: 1a) Gripped Robot; 1b) Fixed Robot ; 2) Track ; 3)Milling head ; 4) Pneumatic gripper ; 5) Circular saw [16]

3.3. Assembly

The assembly of the structure represents the most low-tech part of the construction process. It basically demands some drilling skills and some specific crews, may be set against the wood fibers [22]. According to author it can be handled by 2 persons [17], back in time though the human resources needed to figure one were 6 PhD students, 2 Academic Researchers and 1 Professor.

3.4. Reuse Scenario

As it was mentioned before, the feasibility study for reuse was developed with the first-year students of Ecole des Ponts ParisTech. The purpose of the project was to introduce to students the principles of circular economy and its underlying methodological challenges in terms of structural design and life-cycle analysis. It was decided to imagine a structure made of flat or singly-curved nexorade in order to assure its low-tech construction process. The student project is depicted in Figure 3.

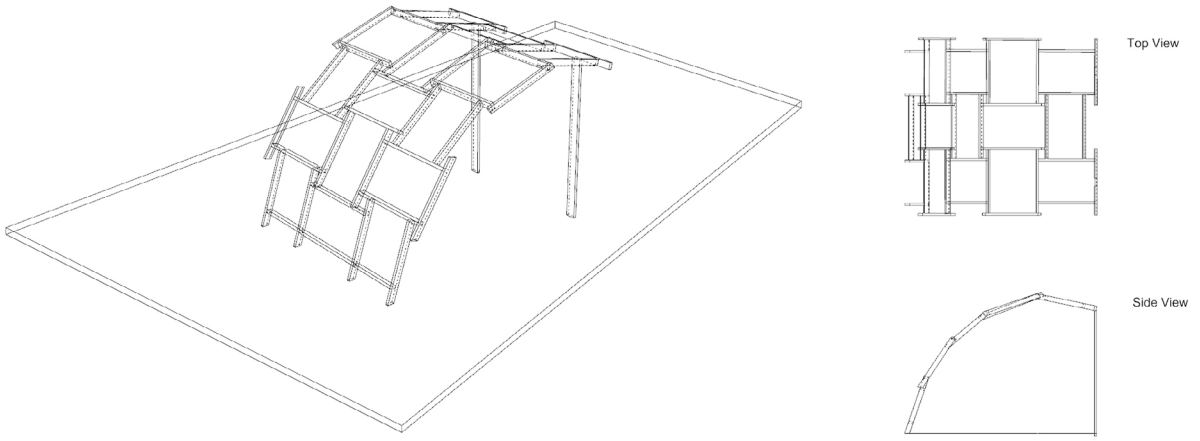


Figure 3. Nexorade made of beams from shell-nexorade hybrid structure

In this paper we skip all structural and geometrical details of the design proposal and focus on the reuse-feasibility part of the study. Therefore, in the first place, the state of elements was investigated on the matter of their reuse capacity. As the pavilion was built in autumn 2017 and was neither protected nor covered, the decay of elements was easily perceptible within the visual examination. Thus, observing a significant degradation of panels (moisture and cracks), it was decided then to only consider beams as the reuse inventory. Again, within the criteria of moisture and cracks presence, the beam's conditions were examined and noted: A for good state, B for intermediate state, C for deplorable state and thus unusable. In general, most of unusable beams were situated on the exterior array of the structure, i.e. the most exposed parts; the cracks are situated on the beam's extremities around the screws. To sum up: 0% of panels' and 40% of beams' total volume are reused.

4. Environmental Assessment of the Structure

The Life Cycle Assessment method was used to evaluate the environmental impact of the system. Framed by International Standards 14040 et 14044 [23], [24] the method consists on tracking all the energy and recourses needed for production, exploitation and end-of life of a system. In building sector, we particularly distinguish the operational impact of the system (heating, cooling, etc.) and the embodied impact (materials and processes deployed during building life-cycle). The present study quantifies the embodied impact.

EcoInvent 3.2 cut-off database was used for the life-cycle model constitution within the OpenLCA software. All the inventory was modeled with its market version, i.e. pass-mark transport, which gives us a universal model of processes independent from geographical location. Recipe midpoint (H) method of impact calculation was chosen, following the ILCD Handbook recommendations [25]. The system boundaries of effectuated study were settled from cradle to grave or A1-D according to norm EN 15804. Yet, the analysis was separated on two parts as it addresses two different problematics. A detailed description of every part is presented below.

4.1. Cradle-to-Gate Analysis

The fundamental problematics of this part dwells into the ongoing development of automation in construction. The virtuosity of the fabrication processes as well as the serial production of bespoke elements enabled by robotics and numerically controlled machine, initially was theorized as the very next industrial revolution that was supposed to supersede the mechanical era of standardization. Lately, a promising improvement achieved in matter of productivity [26], as well as efficiency of construction elements [4], [27], [28], fashioned a general belief into the sustainable potential of digital

technologies in construction sector. This section interrogates this question. Therefore, within the case-study of highly efficient shell-structure designed computationally and fabricated robotically, we evaluate hereby the possible trade-off between efficiency of the structure and environmental load of robotic construction system.

A few academic studies have already explored the topic. Agusti-Huan et al. have effectuated a foremost work in the field, comparing digitally fabricated elements with ones fabricated conventionally [29], [30], concluding that digital fabrication processes do not really count in total results, comparing to the potential in terms of material reduction they bring. The system boundaries of the analysis were cradle-to-gate, without consideration of end of life phase. Also, the construction technology studied was very experimental and hardly represents the future industrial robotic fabrication cells. Krieg et al. have also performed an LCA study of an innovative timber structure [31]. The constructive system was compared with its alternatives, differentiating materials and fabrication technics. The stiffness of the structure was referred as functional unit and only the GWP indicator was considered. The results show that even if the embodied carbon of materials is still more important than the one of robotic construction system, the second does contribute to global result. Not much information on inventory is given, but apparently, only the energy consumption of robot was taken into account. As follows, the significant amount of CO_2 dew to the fabrication phase might be related to the German type of electricity, i.e. coal-fired.

In current case study a specific focus was made on the methodology for taking into account robotic construction system. Therefore, the detailed life cycle model of robotic fabrication system was assembled and a sensitivity study on its outlay to the process of reference was effectuated within two assumptions. The first one reflects an idealistic scenario of the entire production process: one week by machine, which is greatly optimist for the research project but still does consider both the production time and the machines set-up period. The second scenario accounts an actual duration of parametrization, set up and fabrication period at the time: two months for robotic cell and two weeks for CNC cell. Important to note that the energy consumption remains the same in both scenarios.

The real results of the structure's fabrication process are shown by the second scenario but taking into account the industrial immaturity of the robotic construction technic as well as the research character of the project, we rather consider the first scenario as the accurate. Both scenarios are depicted on the Figure 4.

4.2. Reuse Analysis

4.2.1.Methodology

Reuse as well as recycling practice is usually covered by the principle of allocation in LCA discipline. Allocations are generally defined as a partitioning of environmental impact between various co-products of a system. Therefore, as the end-of-life phase typically contains multiple outputs, some of which can be reused, recycled or valorized energetically, the allocations deal with the redistribution of those eventual benefits between different life cycles. Concretely, in the present case-study the methodological challenge is to define if the reused structure inherits the part of environmental burden associated with virgin material production, transportation etc. of initial construction, and in affirmative, does the initial construction gets some environmental credits.

Between today's most used allocation methods we mainly distinguish the cut-off method, the avoided burden approach and the technique of 50/50. In the case of cut-off, the load of the end-of-life phase is directly assigned to the functional unit of the first system, and therefore, the succeeding system of reuse/recycling gets the zero value for material's input. The avoided burden method accounts the elements of reuse entering the system with negative values. Finally, the technic of 50/50 partitions the impact between the cycles.

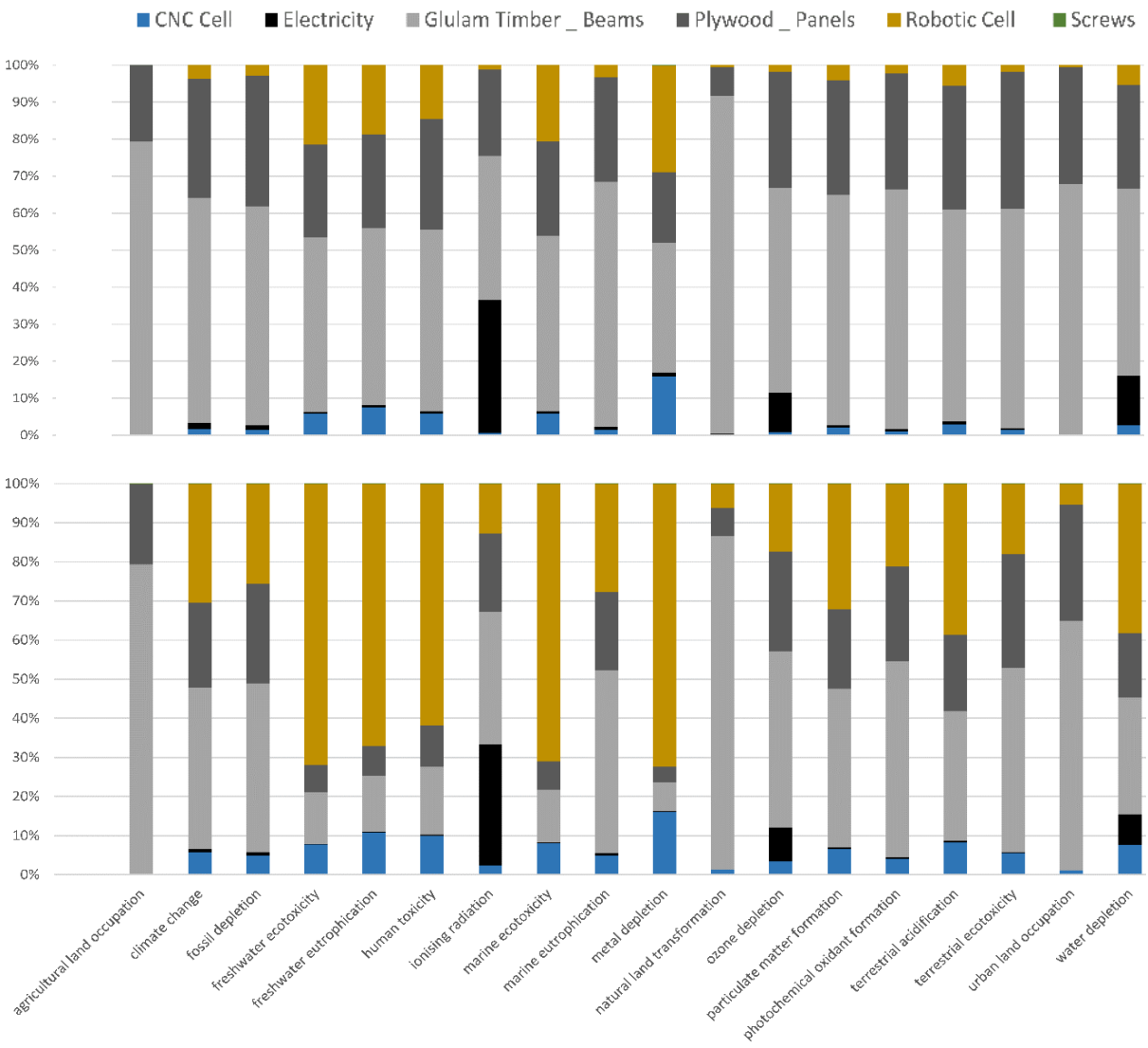


Figure 4. Environmental impact of shell-nexorade hybrid structure: 1st Scenario (above), 2nd Scenario (below)

Obviously, depending on the allocation technic chosen the resulting environmental character of reused content will be significantly different, yet a few studies confirm the thesis [32], [33].

Historically, the negotiation took place within the case of aluminum beverage can [34]. The recycling rate of a can is relatively high, despite a systematic need of primal material re-injection [35]. Still, even considering a substantial requirement in terms of infrastructure and energy for recycling, the main environmental burden comes from primary ingot production and thus renders the first life-cycle of the can significantly loader than others. Therefore, there are two schools of thought on the question of can's life-cycle: either it is "born-live-die-repeat" model composed of separated systems sharing the burden in one of three manners described above, or it is a one large lifespan including multiple recycling loops. The question undoubtedly is deeply ontological and back to the Dark Age would necessitate a Pope's opinion on it.

We propose to articulate the question of system boundaries around the type of actor's involvement: inclusive and exclusive. The exclusive approach represents most of current practices of reuse and recycling. The actor recuperates the materials from previous user and has only a vague information on

their former service. The reuse actor deploys one of previously described allocation schema in adequation to its project.

Inclusive approach consists on expand the boundaries as well as the functionality of the system, integrating the cycles of reuse and recycling. The burden of the system will therefore cumulate itself but so will the years of service and the service itself. The approach takes place in case all the life cycles have been provided by the same group of actors. For example, if one designs a structure with a view it to be easily disassembled for potential reused, we consider that as an expansion of the system boundaries associated to the prolonged life and augmented functionality brought by reusability.

4.2.2. Case study analysis

Within the present study we adopt the inclusive approach, as the both projects were developed by the same actor, i.e. Navier laboratory. The system boundaries include two succeeding lifes of the structure with no end-of-second-life hypothesis. Consequently, the expanded system continues to accumulate the square meters of envelope's surface (S) as well as the impact (I) produced by every use. The time of service (T) equally piles up. The functional unit of the expanded system is defined as one sqm of envelope per year $FU = m^2 * year$, meaning that within the proposed model, the reuse rate of materials is as important as the durability of every solution.

Table 1 resumes the impacts associated to every use-scenario within two indicators: Climate Change and Human Toxicity, where the first one has an inherent decreasing behavior and the second one requires some improvements for the *Reuse* part. Concretely, *1st Use* depicts the cradle-to-gate phase of the system (cf. Part 4.1). *Disposal* describes the end-of-life scenario where all the beams are landfilled, and all the panels are incinerated. *Reuse* scenario is based on the student's project and thus comprises the creation of additional 36 sqm of structural envelope for 2 years of additional exploitation, it also includes the disposal of not reused elements (landfill for beams; incineration for panels). The *Extended Reuse* scenario is a hypothetical increase of the reuse project functionality reached by doubling it service period to 4 years, and expanding its surface of envelope by 30%, i.e. to 47 sqm.

Table 1. Description of every *use* scenario within two indicators

	Total Impact per Use		Functional Unit Progress **m^2 * year**	Impact Progress per Functional Unit	
	Climate Change [kg CO_2 Eq]	**Toxicity Human [kg 1,4-DCB Eq]**		**kg CO_2 Eq / m^2 year**	**kg 1,4-DCB Eq / m^2 year**
1st Use	1001,2	978,3	82 m^2 * 3 years	4,07	3,9
Disposal	1990,9	3242,5	82 m^2 * 3 years	8,09	13,2
Reuse	1994,4	3244,3	118 m^2 * 5 years	3,4	5,5
Reuse _ Extended	1994,4	3244,3	129 m^2 * 7 years	2,2	3,6

Figure 4 depicts the progress of system's performance within all the indicators of Recipe method of calculation. The *1st Use* performance of the system were taken as a basis of the comparison.

Thus, within all the indicators the reclaimed structure produces less burden than the disposal of all the elements. The impact of reuse scenario has a general tendency to decrease comparing to the 1st Use scenario, except for five indicators: Freshwater Ecotoxicity, Freshwater Eutrophication, Human Toxicity, Marine Ecotoxicity and Metal Depletion. As follows, hypothetical extension of project's functionality improves pointedly the environmental performance of the reclaimed structure and, except for the metal depletion indicator, fetches it down to the level of initial structure.

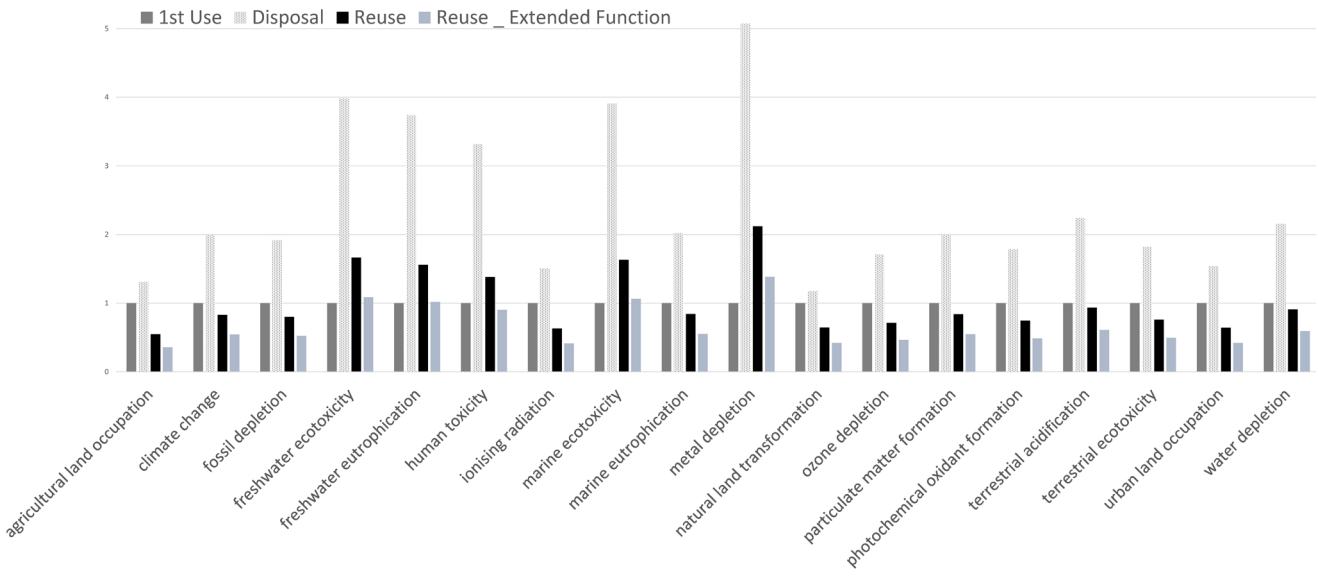


Figure 4. Evolution of system's performance

Results & Discussion

The full life-cycle assessment performed on the shell-nexorade hybrid constructive system has led to two groups of findings. First of all, the results of cradle-to-gate phase have demonstrated an occurring of a significant impact transfer in system's life-cycle caused by the robotic construction technology. The importance of the industrial immaturity parameter of robotic technology was tested within the sensitivity study and demonstrated the promising routes for the improvement of global environmental character of the system. Yet, the current findings show that robot counts as much as materials, which means that in future, the optimization design strategies relying on robotic construction technology for production part should take into account the environmental load of the last.

Secondly, the end-of-life analysis was conducted within the reuse scenario. A methodology was developed for evaluation of environmental performance of reuse solutions when both the initial and the reclaimed structures are designed by the same group of actors. The results of the case-study have shown an equal significance of two parameters: the reuse rate of elements and the durability of every solution. The production means of every solution also count substantially: the studied structure was reclaimed within the low-tech construction process, but still was more impacting that the first one within five indicators. Thus, by having a multi-indicator analysis, the choices of construction technology can vary from one life-cycle to another in order to equilibrate the burden between different indicators.

Conclusion:

The continuing growth of the awareness of environmental urgency in construction sector has led to the emergence of different sustainable design strategies, including the one of reuse. However, those current design practices have tendency to address a unique phase of the life cycle and the present study have demonstrated the limits of that approach. The second part of this study proposes a method for the reuse solution's performance control based on two criteria. The case study confirmed the pertinence of the established model, as in some figures the studied project needed some significant extensions of its functionality in order to assure a decreasing behavior of the system's impact.

The proposed method could also be applied to the emerging practice of design for reuse. A reuse potential of structural system can thus be quantified.

In closing, automation in construction is today's one of the major research topics in building sector. In early 2000, numerical control machines were supposed to shift the industry towards mass-customization, in middle 2010, robotics puts up a front to tackle the environmental problem of the sector. Yet, for multiple reasons of legal and technological inertia, the mass-customization is barely ready to advent, and the environmental impact of automation remains to be studied.

Acknowledgements:

The authors are grateful to the students of Ecole des Ponts ParisTech: Pierre Bessac, Matthieu Glikson, Paule-Claire He-Xie, Mila Rouyer, Adrien Sarrade, whose project provided the feasibility data for the present study. Their interest to the topic and involvement into the project have fairly inspired this research.

Many thanks to Charlotte Roux and Myriam Saadé for their support.

References:

[1] « Les exigences de la réglementation thermique 2012 », *ADEME*. [En ligne]. Disponible sur: https://www.ademe.fr/particuliers-eco-citoyens/habitation/construire/exigences-reglementation-thermique-2012. [Consulté le: 28-févr-2019].

[2] « Construction : les tours en bois font leur promotion », *Les Echos*, 12-sept-2017. [En ligne]. Disponible sur: https://www.lesechos.fr/2017/09/construction-les-tours-en-bois-font-leur-promotion-182002. [Consulté le: 09-juin-2019].

[3] « Block Research Group ». [En ligne]. Disponible sur: http://block.arch.ethz.ch/brg/project. [Consulté le: 18-déc-2018].

[4] « Institute for Computational Design and Construction ». [En ligne]. Disponible sur: https://icd.uni-stuttgart.de/?page_id=17788. [Consulté le: 01-févr-2019].

[5] « Matière grise | Expositions | Pavillon de l'Arsenal ». [En ligne]. Disponible sur: http://www.pavillon-arsenal.com/fr/expositions/9858-matiere-grise.html. [Consulté le: 09-juin-2019].

[6] M. Rivallain, « Étude de l'aide à la décision par optimisation multicritère des programmes de réhabilitation énergétique séquentielle des bâtiments existants », Paris-Est, Paris, France, 2013.

[7] UN Environment and International Energy Agency, « Towards a zero-emission, efficient, and resilient buildings and construction sector. Global Status Report 2017. », Global Status Report, 2017.

[8] World Economic Forum et BCG, « The critical challenge for engineering, construction, and infrastructure companies is to increase productivity. »

[9] McKinsey & Company, « REINVENTING CONSTRUCTION: A ROUTE TO HIGHER PRODUCTIVITY », McKinsey Global Institute, Executive Summary, févr. 2017.

[10] SOeS, MINISTÈRE DE L'ENVIRONNEMENT, DE L'ÉNERGIE ET DE LA MER, « Entreprises du BTP : 227,5 millions de tonnes de déchets en 2014 », p. 4, 2017.

[11] « The Pantheon », *Pantheon Roma*. [En ligne]. Disponible sur: http://www.pantheonroma.com/en/the-pantheon.html. [Consulté le: 09-juin-2019].

[12] J. Brütting, J. Desruelle, G. Senatore, et C. Fivet, « Design of Truss Structures Through Reuse », *Structures*, nov. 2018.

[13] A. Mureşan, J. Brütting, J. Cañada, D. Redaelli, et C. Fivet, « Design Space of Modular Slab Systems with Discrete Stiffness Distribution and Irregular Column Layout », p. 8, 2018.

[14] O. BAVEREL, A. FERAILLE, et M. BROCATO, « Environmentally Compatible Spatial Structures: some Concepts from the Reuse of Manufactured Goods », *Journal of the International Association for Shell and Spatial Structures*, p. 311-320.

[15] S. Colabella, B. D'Amico, E. Hoxha, et C. Fivet, « Structural Design with Reclaimed Materials: an Elastic Gridshell out of Skis », p. 11, 2017.

[16] R. Mesnil, T. Gobin, et O. BAVEREL, « Form Finding and Design of a Timber Shell-Nexorade Hybrid », présenté à Advances in Architectural Geometry, Gothenburg, Sweden, 2018.
[17] C. Douthe *et al.*, « Design and construction of a shell-nexorade hybrid timber structure », présenté à Proceedings of the IASS Annual Symposium 2018, Boston, USA, 2018.
[18] O. BAVEREL, « Nexorades: a family of interwoven space structures », University of Surrey, Surrey, England, 2000.
[19] R. Mesnil, C. Douthe, et O. Baverel, « Marionette Mesh: From Descriptive Geometry to Fabrication-Aware Design », 2016.
[20] R. Mesnil, C. Douthe, O. Baverel, et T. Gobin, « Form finding of nexorades using the translations method », *Automation in Construction*, vol. 95, p. 142-154, nov. 2018.
[21] H. Pottmann, « Freeform architecture and fabrication-aware design », *Computers & Graphics*, vol. 36, nº 5, p. 306, août 2012.
[22] Wurth, « Guide pratique de la visserie ». 2014.
[23] International Organization for Standardization, *ISO 14040 : 2006 « Environmental management -- Life cycle assessment -- Principles and framework »*. .
[24] International Organization for Standardization, *ISO 14044 : 2006 « Environmental management -- Life cycle assessment -- Requirements and guidelines »*. .
[25] European Commission, Joint Research Centre, et Institute for Environment and Sustainability, *International reference life cycle data system (ILCD) handbook general guide for life cycle assessment: provisions and action steps.* Luxembourg: Publications Office, 2011.
[26] C. Gosselin, R. Duballet, Ph. Roux, N. Gaudillière, J. Dirrenberger, et Ph. Morel, « Large-scale 3D printing of ultra-high performance concrete – a new processing route for architects and builders », *Materials & Design*, vol. 100, p. 102-109, juin 2016.
[27] R. Duballet, O. Baverel, et J. Dirrenberger, « Space Truss Masonry Walls With Robotic Mortar Extrusion », *Structures*, nov. 2018.
[28] M. Rippmann, A. Liew, T. Van Mele, et P. Block, « Design, fabrication and testing of discrete 3D sand-printed floor prototypes », *Materials Today Communications*, vol. 15, p. 254-259, juin 2018.
[29] I. Agustí-Juan, F. Müller, N. Hack, T. Wangler, et G. Habert, « Potential benefits of digital fabrication for complex structures: Environmental assessment of a robotically fabricated concrete wall », *Journal of Cleaner Production*, vol. 154, p. 330-340, juin 2017.
[30] I. Agustí-Juan et G. Habert, « Environmental design guidelines for digital fabrication », *Journal of Cleaner Production*, vol. 142, p. 2780-2791, janv. 2017.
[31] O. D. Krieg, S. Bechert, A. Groenewolt, R. Horn, et A. Menges, « AFFORDANCES OF COMPLEXITY: EVALUATION OF A ROBOTIC PRODUCTION PROCESS FOR SEGMENTED TIMBER SHELL STRUCTURES », p. 8.
[32] A. L. Nicholson, E. A. Olivetti, J. R. Gregory, F. R. Field, et R. E. Kirchain, « End-of-life LCA allocation methods: Open loop recycling impacts on robustness of material selection decisions », in *2009 IEEE International Symposium on Sustainable Systems and Technology*, Tempe, AZ, USA, 2009, p. 1-6.
[33] L. Gonda et M. Degrez, « End-of-life Management of Computers in Brussels: Environmental Comparison of Two Treatment Chains », *Procedia CIRP*, vol. 69, p. 968-973, janv. 2018.
[34] P. Americas et B. Street, « Final Report: Can LCA PE Americas », *Final Report*, p. 127.
[35] Rajat Nag, « LIFE CYCLE ASSESSMENT OF ALUMINIUM CAN AND GLASS BOTTLE FOR PACKAGING OF 500 ml BEER », p. 1258817 Bytes, 2016.

FORM and FORCE

Proceedings of the IASS Annual Symposium 2019 - Structural Membranes 2019
Form and Force
7-10 October 2019, Barcelona, Spain
C. Lázaro, K.-U. Bletzinger, E. Oñate (eds.)

A unified approach for shell analysis on explicitly and implicitly defined surfaces

D. Schöllhammer*[a], T.P. Fries[b]

[a,b] Institute of Structural Analysis, Graz University of Technology, Lessingstr. 25/II, 8010 Graz, Austria, www.ifb.tugraz.at

[a] schoellhammer@tugraz.at, [b] fries@tugraz.at

Abstract

The Kirchhoff–Love shell theory and the Reissner–Mindlin shell theory, are reformulated in the frame of the tangential differential calculus (TDC) using a global Cartesian coordinate system. The resulting equations enable shell analyses on explicitly and implicitly defined surfaces, which generalizes the classical shell equations, which strictly rely on parametrizations resulting in curvilinear coordinates on the shell geometry. Hence, the new approach based on the TDC is more general as it also enables shell geometries implied by zero-isosurfaces where no curvilinear coordinates exist. In the case of parametrized surfaces, the numerical results confirm that the approach is equivalent compared to classical theory.

Keywords: Tangential differential calculus; Isogeometric analysis; Manifolds; Kirchhoff–Love shells; Reissner–Mindlin shells

1 Introduction

Shells are thin-walled structures which appear in a wide range of applications due to their high bearing capacity. In the modelling process, the shell is reduced to its middle surface Γ resulting into partial differential equations (PDEs) on surfaces Γ embedded in the physical space $\mathbb{R}^3$.
In the classical shell theory, a local coordinate system with co- and contra-variant base vectors, implied by a parametrization of the middle surface, is introduced, see, e.g., [1], [2]. The use of the curvilinear coordinates makes the approach rather complex and less intuitive. Alternatively, the surface PDEs may also be derived in the global Cartesian coordinates system, where the employed surface operators are defined in the frame of the tangential differential calculus (TDC) [3]. This approach is frequently used for PDEs on manifolds, see, e.g., [4]–[8], however, so far often related to transport and flow problems on manifolds. The major advantages the TDC are: the obtained surface PDEs do not rely on a parametrization, i.e., on curvilinear coordinates and enables a more compact implementation.
Herein, the classical shell models, i.e., Kirchhoff–Love shells and Reissner–Mindlin shells, are derived in the frame of the TDC using the global Cartesian coordinate system. The derivation includes all important mechanical quantities such as normal (membrane) forces, bending moments, transverse shear forces and the equilibrium in strong form. The resulting shell equations are valid no matter whether a parametrisation is available or not.

Copyright © 2019 by D. Schöllhammer
Published by the International Association for Shell and Spatial Structures (IASS) with permission.

For the numerical solution of the obtained shell boundary values problems (BVPs), the presented model equations may be considered in the frame of the Surface FEM, see e.g. [9], as usual. However, in contrast to the classical model equations based on curvilinear coordinates, the proposed equations are also applicable to recent finite element approaches such as CutFEM or TraceFEM, see, e.g., [10], where a parametrization of the middle surface does not exist.
The outline of the paper is as follows: In Section 2, a brief introduction into the TDC is given. In Section 3, the shell models are derived in the frame of the TDC and implementational aspects are considered. In Section 4, numerical results are presented.

2 Preliminaries

Surfaces may be defined explicitly or implicitly. In the first case, the surface is defined through a bijective map $\boldsymbol{x}(\boldsymbol{r}) : \hat{\Omega} \to \Gamma$ from the parameter space $\hat{\Omega}$ to the real domain Γ. The map can be globally defined or may also be an atlas of local, element-wise maps. In the latter case, the surface is implicitly defined following the level-set method. Independently of the surface definition there is a unit normal vector $\boldsymbol{n}_\Gamma$ and at the boundary of the shell $\partial\Gamma$, there is the local triad $(\boldsymbol{t}_{\partial\Gamma}, \boldsymbol{n}_{\partial\Gamma}, \boldsymbol{n}_\Gamma)$ with $\boldsymbol{t}_{\partial\Gamma}$ being the tangent vector pointing in the direction of the boundary and the co-normal vector $\boldsymbol{n}_{\partial\Gamma}$ pointing "outwards" of the domain and being perpendicular to $\boldsymbol{t}_{\partial\Gamma}$ and $\boldsymbol{n}_\Gamma$.
The TDC provides a framework to define surface operators which are valid on explicitly and implicitly defined surfaces. The tangential gradient of a scalar-valued function $u(\boldsymbol{x})$ on the surface Γ is defined as $\nabla_\Gamma u(\boldsymbol{x}) = \mathbf{P}\cdot\nabla\tilde{u}$, where $\mathbf{P} = \mathbb{I} - \mathbf{Q}, \mathbf{Q} = \boldsymbol{n}_\Gamma \otimes \boldsymbol{n}_\Gamma$ are projection operators, $\boldsymbol{n}_\Gamma$ is the unit normal vector and $\tilde{u}$ is an arbitrary, but sufficiently smooth, extension of u in a neighbourhood of Γ. The equivalent expression for parametrized surfaces is $\nabla_\Gamma u(\boldsymbol{x}(\boldsymbol{r})) = \mathbf{J}\cdot(\mathbf{J}^{\mathrm{T}}\cdot\mathbf{J})^{-1}\cdot\nabla_{\boldsymbol{r}} u$, where $\mathbf{J}$ is the Jacobi matrix and $\nabla_{\boldsymbol{r}} u$ is the gradient in the parameter space. For vector-valued functions $\boldsymbol{v}(\boldsymbol{x})$ or second-order derivatives of scalar-valued functions $\boldsymbol{v} = \nabla_\Gamma u(\boldsymbol{x})$, there are two different gradients, i.e, the directional gradient $\nabla_\Gamma^{\mathrm{dir}}\boldsymbol{v}(\boldsymbol{x}) = \nabla\tilde{\boldsymbol{v}}\cdot\mathbf{P}$ and the covariant gradient $\nabla_\Gamma^{\mathrm{cov}}\boldsymbol{v}(\boldsymbol{x}) = \mathbf{P}\cdot\nabla_\Gamma^{\mathrm{dir}}\boldsymbol{v}(\boldsymbol{x})$.
The Weingarten map $\mathbf{H} = \nabla_\Gamma^{\mathrm{dir}}\boldsymbol{n}_\Gamma = \nabla_\Gamma^{\mathrm{cov}}\boldsymbol{n}_\Gamma$ is a symmetric, in-plane tensor, i.e., $\mathbf{H} = \mathbf{P}\cdot\mathbf{H}\cdot\mathbf{P}$ and its two non-zero eigenvalues are the principal curvatures $\kappa_i = -\mathrm{eig}(\mathbf{H})$. For a more detailed introduction to the TDC, we refer to, e.g., [3], [7].

3 The shell equations

In this section, the Kichhoff–Love shell and the Reissner–Mindlin shell are derived in the frame of the TDC using a global Cartesian coordinate system. For the sake of simplicity, we restrict ourselves to infinitesimal deformations and rotations and a linear elastic material governed by Hooke's law with a constant shifter is assumed. With this assumption an analytical pre-integration with respect to the thickness is possible and one may identify stress resultants.
The middle surface Γ of a shell Ω can be implicitly defined with the zero-isosurface of a signed-distance function $\phi_{\mathrm{SDF}}(\boldsymbol{x}) : \mathbb{R}^3 \to \mathbb{R}$. The shell body of thickness t is then defined by

$$\Omega = \left\{\boldsymbol{x} \in \mathbb{R}^3 : |\phi_{\mathrm{SDF}}(\boldsymbol{x})| \leq t/2\right\} \ . \tag{1}$$

Alternatively, if the middle surface is parametrized with a map $\boldsymbol{x}_\Gamma(\boldsymbol{r})$, the domain of the shell is explicitly defined by

$$\Omega = \left\{\boldsymbol{x} \in \mathbb{R}^3 : \boldsymbol{x} = \boldsymbol{x}_\Gamma + \zeta\boldsymbol{n}_\Gamma(\boldsymbol{x}_\Gamma)\right\} \tag{2}$$

where ζ is the coordinate in thickness direction $|\zeta| \leq t/2$.

3.1 Kinematic

In the linear shell theory the cross-section remains straight after the deformation, but not necessarily orthogonal to the middle surface due to transverse shear deformations $\boldsymbol{\gamma}$, see Fig. 1. The displacement $\boldsymbol{u}_\Omega$ of a point $\boldsymbol{P}$ in the shell continuum is determined by the difference between the spatial and reference configuration and can be decomposed into

$$\boldsymbol{u}_\Omega(\boldsymbol{x}_\Gamma, \zeta) = \boldsymbol{u}(\boldsymbol{x}_\Gamma) + \zeta \boldsymbol{w}(\boldsymbol{x}_\Gamma) \tag{3}$$

where $\boldsymbol{u}(\boldsymbol{x}_\Gamma)$ is the displacement of the middle surface and $\boldsymbol{w}(\boldsymbol{x}_\Gamma)$ is the difference vector, modelling the rotation of the shell director, see Fig. 1.

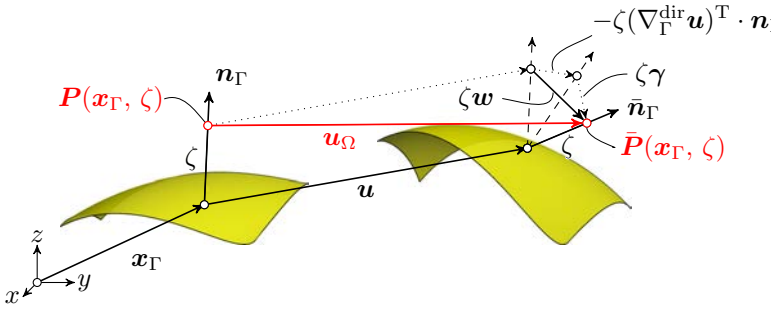


Figure 1: Displacement field $\boldsymbol{u}_\Omega$ of a shell. The yellow surfaces are the undeformed (left) and deformed (right) middle surface Γ. Objects in the spatial configuration are denoted with a bar.

With the assumption that the thickness of the shell does not change after the deformation, the difference vector $\boldsymbol{w}$ is tangential and is defined as in [8]

$$\boldsymbol{w}(\boldsymbol{x}_\Gamma) = -[\nabla_\Gamma^{\mathrm{dir}}\boldsymbol{u}(\boldsymbol{x}_\Gamma)]^{\mathrm{T}} \cdot \boldsymbol{n}_\Gamma(\boldsymbol{x}_\Gamma) + \boldsymbol{\gamma}(\boldsymbol{x}_\Gamma) \ . \tag{4}$$

If transverse shear deformations are taken into account, Eq. 4 represents the Reissner–Mindlin kinematic and the difference vector is denoted as $\boldsymbol{w}_{\mathrm{RM}}$. Due to the transverse shear deformations, the deformation of the middle surface and the rotation of the normal vector are decoupled, which results into two unknown fields, i.e., $\boldsymbol{u}$, $\boldsymbol{w}_{\mathrm{RM}}$.
As well-known for the case of increasingly thin shells, the transverse shear deformations are decreasing and become rather small compared to the first term in Eq. 4. Therefore, the transverse shear deformations can be neglected, resulting into the kinematic of the Kichhoff–Love shell. The difference vector is then only a function of $\boldsymbol{u}$, i.e., $\boldsymbol{w}_{\mathrm{KL}} = -[\nabla_\Gamma^{\mathrm{dir}}\boldsymbol{u}]^{\mathrm{T}} \cdot \boldsymbol{n}_\Gamma$, which results only in one unknown field, i.e., $\boldsymbol{u}$, for the Kirchhoff–Love shell.
For both shell models the linearised strain tensor $\boldsymbol{\varepsilon}_\Gamma$ is defined by the symmetric part of the surface gradient of the displacement field $\boldsymbol{u}_\Omega$, i.e., $\boldsymbol{\varepsilon}_\Gamma(\boldsymbol{x}) = \mathrm{sym}[\nabla_\Gamma^{\mathrm{dir}}\boldsymbol{u}_\Omega(\boldsymbol{x})]$ and is split into an in-plane strain $\boldsymbol{\varepsilon}_\Gamma^{\mathrm{P}}$ and a transverse shear strain $\boldsymbol{\varepsilon}_\Gamma^{\mathrm{S}}$. The in-plane strain is defined by a double projection with $\mathbf{P}$ and is divided into a membrane and bending strain by [7], [8]

$$\boldsymbol{\varepsilon}_\Gamma^{\mathrm{P}} = \mathbf{P} \cdot \boldsymbol{\varepsilon}_\Gamma \cdot \mathbf{P} = \boldsymbol{\varepsilon}_{\Gamma,\mathrm{M}} + \zeta\boldsymbol{\varepsilon}_{\Gamma,\mathrm{B}} \ . \tag{5}$$

The in-plane membrane strain for both shell models becomes

$$\boldsymbol{\varepsilon}_{\Gamma,\mathrm{M}} = \frac{1}{2}\left[\nabla_\Gamma^{\mathrm{cov}}\boldsymbol{u} + (\nabla_\Gamma^{\mathrm{cov}}\boldsymbol{u})^{\mathrm{T}}\right] \ . \tag{6}$$

Inserting the assumptions for both shell models, the bending strains are

$$\boldsymbol{\varepsilon}^{\mathrm{RM}}_{\Gamma,\,\mathrm{B}} = \frac{1}{2}\left[\mathbf{H}\cdot\nabla^{\mathrm{dir}}_{\Gamma}\boldsymbol{u} + (\nabla^{\mathrm{dir}}_{\Gamma}\boldsymbol{u})^{\mathrm{T}}\cdot\mathbf{H} + \nabla^{\mathrm{cov}}_{\Gamma}\boldsymbol{w}_{\mathrm{RM}} + (\nabla^{\mathrm{cov}}_{\Gamma}\boldsymbol{w}_{\mathrm{RM}})^{\mathrm{T}}\right] , \tag{7}$$

$$\boldsymbol{\varepsilon}^{\mathrm{KL}}_{\Gamma,\,\mathrm{B}} = -\left[\boldsymbol{u}^{\mathrm{cov}}_{,ij}\cdot\boldsymbol{n}_{\Gamma}\right] . \tag{8}$$

The transverse shear strains are defined by a projection with $\mathbf{Q}$ as defined in [8]

$$\begin{aligned}\boldsymbol{\varepsilon}^{\mathrm{RM}}_{\Gamma,\,\mathrm{S}}(\boldsymbol{u},\,\boldsymbol{w}) &= \mathbf{Q}\cdot\boldsymbol{\varepsilon}_{\Gamma} + \boldsymbol{\varepsilon}_{\Gamma}\cdot\mathbf{Q} \\ &= \frac{1}{2}\left[\mathbf{Q}\cdot\nabla^{\mathrm{dir}}_{\Gamma}\boldsymbol{u} + (\nabla^{\mathrm{dir}}_{\Gamma}\boldsymbol{u})^{\mathrm{T}}\cdot\mathbf{Q} + \boldsymbol{n}_{\Gamma}\otimes\boldsymbol{w} + \boldsymbol{w}\otimes\boldsymbol{n}_{\Gamma}\right] ,\end{aligned} \tag{9}$$

$$\boldsymbol{\varepsilon}^{\mathrm{KL}}_{\Gamma,\,\mathrm{S}}(\boldsymbol{u},\,\boldsymbol{w}) = \mathbf{0} , \tag{10}$$

where in the case of Kirchhoff-Love shells, the transverse shear strain is zero due to the kinematic assumptions, from above.

3.2 Constitutive equation and stress resultants

The shell is assumed to be linear elastic and, as usual for thin structures, the Lamé constants are chosen such that the stress in normal direction is eliminated, hence, $\boldsymbol{\sigma}_{\Gamma}(\boldsymbol{x}) = 2\mu\boldsymbol{\varepsilon}_{\Gamma}(\boldsymbol{x}) + \lambda\mathrm{tr}[\boldsymbol{\varepsilon}_{\Gamma}(\boldsymbol{x})]\mathbb{I}$, where $\mu = \frac{E}{2(1+\nu)}$ and $\lambda = \frac{E\nu}{1-\nu^2}$. A decomposition in a similar manner as above and an analytical pre-integration with respect to the thickness leads to the stress resultants.
The symmetric, in-plane moment tensor $\mathbf{m}^{\mathrm{i}}_{\Gamma}$ is defined as

$$\mathbf{m}^{\mathrm{i}}_{\Gamma} = \int_{-t/2}^{t/2}\zeta\,\mathbf{P}\cdot\boldsymbol{\sigma}_{\Gamma}\cdot\mathbf{P}\;\mathrm{d}\zeta = \frac{t^3}{12}\boldsymbol{\sigma}_{\Gamma}(\boldsymbol{\varepsilon}^{\mathrm{i}}_{\Gamma,\mathrm{B}}) , \tag{11}$$

where $\mathrm{i} = \{\mathrm{RM}, \mathrm{KL}\}$ indicates the shell model. The moment tensor has two non-zero eigenvalues, which are the principal moments m_1 and m_2. The effective normal force tensor $\tilde{\mathbf{n}}_{\Gamma}$ is equal for both shell models and is

$$\tilde{\mathbf{n}}_{\Gamma} = \int_{-t/2}^{t/2}\mathbf{P}\cdot\boldsymbol{\sigma}_{\Gamma}\cdot\mathbf{P}\;\mathrm{d}\zeta = t\boldsymbol{\sigma}_{\Gamma}(\boldsymbol{\varepsilon}_{\Gamma,\mathrm{M}}) . \tag{12}$$

Similar to the moment tensor, the effective normal force tensor is also a symmetric, in-plane tensor. Note that for curved shells this tensor is *not* the physical normal force tensor, but occurs in the weak form, see Section 3.4. In case of a curved shell, the physical normal force tensor is $\mathbf{n}^{\mathrm{real,\,i}}_{\Gamma} = \tilde{\mathbf{n}}_{\Gamma} + \mathbf{H}\cdot\mathbf{m}^{\mathrm{i}}_{\Gamma}$ and is, in general, not symmetric.
For the Reissner–Mindlin shell, the transverse shear force tensor is determined with

$$\boldsymbol{\Upsilon}^{\mathrm{RM}}_{\Gamma} = \int_{-t/2}^{t/2}\mathbf{Q}\cdot\boldsymbol{\sigma}_{\Gamma} + \boldsymbol{\sigma}_{\Gamma}\cdot\mathbf{Q}\;\mathrm{d}\zeta = t\boldsymbol{\sigma}_{\Gamma}(\boldsymbol{\varepsilon}^{\mathrm{RM}}_{\Gamma,\mathrm{S}}) . \tag{13}$$

The resulting transverse shear force vector is given by $\boldsymbol{q}^{\mathrm{RM}} = \boldsymbol{\Upsilon}^{\mathrm{RM}}_{\Gamma}\cdot\boldsymbol{n}_{\Gamma}$. The transverse shear forces in the Kirchhoff–Love shell model can only be obtained with equilibrium considerations and is given as

$$\boldsymbol{q}^{\mathrm{KL}} = \mathbf{P}\cdot\mathrm{div}_{\Gamma}\mathbf{m}^{\mathrm{KL}}_{\Gamma} . \tag{14}$$

It is noteworthy, that in the case of parametrized surfaces the obtained expressions are equivalent compared to the classical theory, see, e.g., [1], [2], [11]. In the case of flat shells, the kinematic simplifies significantly and one may easily derive the stress resultants of the well-known Reissner–Mindlin plate, Kirchhoff plate and the $2d$ shell.

3.3 Equilibrium in strong form

Based on the stress resultants from above, one obtains the force and moment equilibrium for a curved Reissner-Mindlin shell in terms of the TDC in strong form as

$$\mathrm{div}_\Gamma \mathbf{n}_\Gamma^{\mathrm{real}} + \mathbf{Q} \cdot \mathrm{div}_\Gamma \boldsymbol{\Upsilon}_\Gamma^{\mathrm{RM}} + \mathbf{H} \cdot \boldsymbol{q}^{\mathrm{RM}} = -\boldsymbol{f} \ , \tag{15}$$

$$\mathbf{P} \cdot \mathrm{div}_\Gamma \mathbf{m}_\Gamma^{\mathrm{RM}} - \boldsymbol{q}^{\mathrm{RM}} = -\boldsymbol{c} \ , \tag{16}$$

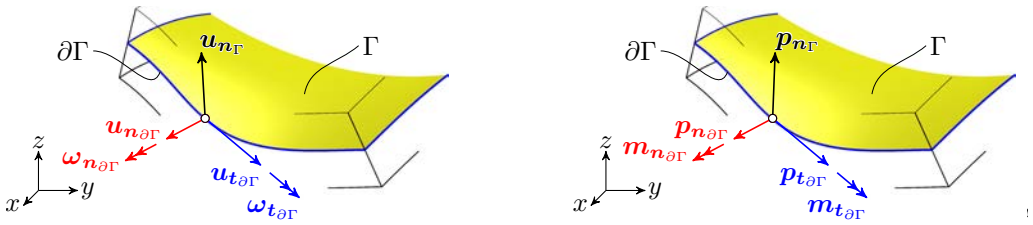
with $\boldsymbol{f}$ being the load vector per area and $\boldsymbol{c}$ being a distributed moment vector on the middle surface Γ. The equilibrium is a system of second-order PDEs for the unknown fields $\boldsymbol{u}$, $\boldsymbol{w}_{\mathrm{RM}}$. The first PDE represents the force equilibrium and the second PDE is the moment equilibrium. The strong form of the equilibrium for the Kirchhoff–Love shell is a fourth-order PDE and represents the force equilibrium

$$\mathrm{div}_\Gamma \mathbf{n}_\Gamma^{\mathrm{real}} + \boldsymbol{n}_\Gamma \mathrm{div}_\Gamma \boldsymbol{q}^{\mathrm{KL}} + \mathbf{H} \cdot \mathrm{div}_\Gamma \mathbf{m}_\Gamma^{\mathrm{KL}} = -\boldsymbol{f} \ , \tag{17}$$

for the unknown field $\boldsymbol{u}$. Note that Eq. 17 can also be obtained with the equilibriums of the Reissner–Mindlin shell, if Eq. 16 is inserted into Eq. 15 with $\boldsymbol{c} = \mathbf{0}$. In order to rewrite the second term in the force equilibrium, the identity $\mathbf{Q} \cdot \mathrm{div}_\Gamma \boldsymbol{\Upsilon}_\Gamma^{\mathrm{RM}} = \boldsymbol{n}_\Gamma \mathrm{div}_\Gamma \boldsymbol{q}^{\mathrm{RM}}$, which holds for symmetric tensors with $\mathrm{tr}(\boldsymbol{\Upsilon}_\Gamma^{\mathrm{RM}} \cdot \mathbf{H}) = 0$, is used. Lastly, the transverse shear force vector $\boldsymbol{q}^{\mathrm{RM}}$ and moment tensor $\mathbf{m}_\Gamma^{\mathrm{RM}}$ are replaced by the quantities of the Kirchhoff-Love shell model and Eq. 17 is determined.
In the case of parametrized surfaces the obtained equations (Eq. 15 - Eq. 17) are equivalent compared to the classical shell theory based on local coordinates, see, e.g., [1]. However, the obtained equilibriums are valid for both *explicitly* and *implicitly* defined surfaces. Therefore, the formulation in the frame of the TDC is a generalization of the classical shell equations.

3.3.1 Boundary conditions

With mechanical meaningful boundary conditions the complete BVPs of the two shell models are defined. The displacements and rotations at the boundary are illustrated in Fig. 2(a) and the conjugated forces and bending moments are shown in Fig. 2(b).



(a) displacements and rotations (b) forces and moments

Figure 2: Decomposition of displacements, rotations, forces and bending moments along the boundary $\partial\Gamma$ in terms of the local triad ($\boldsymbol{t}_{\partial\Gamma}$, $\boldsymbol{n}_{\partial\Gamma}$, $\boldsymbol{n}_\Gamma$).

The difference vector at the boundary is decomposed into the rotations $\boldsymbol{\omega}_{\boldsymbol{t}_{\partial\Gamma}} = (\boldsymbol{w} \cdot \boldsymbol{n}_{\partial\Gamma})\boldsymbol{t}_{\partial\Gamma}$ and $\boldsymbol{\omega}_{\boldsymbol{n}_{\partial\Gamma}} = (\boldsymbol{w} \cdot \boldsymbol{t}_{\partial\Gamma})\boldsymbol{n}_{\partial\Gamma}$ and the corresponding bending moments are given with $\boldsymbol{m}_{\boldsymbol{t}_{\partial\Gamma}} = (\boldsymbol{n}_{\partial\Gamma} \cdot \mathbf{m}_\Gamma \cdot \boldsymbol{n}_{\partial\Gamma})\,\boldsymbol{t}_{\partial\Gamma}$, $\boldsymbol{m}_{\boldsymbol{n}_{\partial\Gamma}} = (\boldsymbol{n}_{\partial\Gamma} \cdot \mathbf{m}_\Gamma \cdot \boldsymbol{t}_{\partial\Gamma})\,\boldsymbol{n}_{\partial\Gamma}$.

In case of the Reissner–Mindlin shell, all of the quantities above can be directly prescribed as Dirichlet boundary conditions, see Fig. 2(a), and Neumann boundary conditions, see Fig. 2(b). A table of common support type is given in [8].
The situation for Kirchhoff–Love shells is more complex due to the absence of transverse shear deformations. In particular, the rotation $\boldsymbol{\omega}_{\boldsymbol{n}_{\partial\Gamma}}$ is a function of $\boldsymbol{u}$ at the boundary. Therefore, $\boldsymbol{\omega}_{\boldsymbol{n}_{\partial\Gamma}}$ can not be chosen independently of $\boldsymbol{u}$. As a result of this, the drill moment $\boldsymbol{m}_{\boldsymbol{n}_{\partial\Gamma}}$ is split into forces and the well-known effective boundary forces and corner forces are introduced

$$\tilde{p}_{\boldsymbol{t}_{\partial\Gamma}} = p_{\boldsymbol{t}_{\partial\Gamma}} + (\mathbf{H}\cdot\boldsymbol{t}_{\partial\Gamma})\cdot\boldsymbol{t}_{\partial\Gamma}\, m_{\boldsymbol{n}_{\partial\Gamma}} \;, \qquad \tilde{p}_{\boldsymbol{n}_{\partial\Gamma}} = p_{\boldsymbol{n}_{\partial\Gamma}} + (\mathbf{H}\cdot\boldsymbol{t}_{\partial\Gamma})\cdot\boldsymbol{n}_{\partial\Gamma}\, m_{\boldsymbol{n}_{\partial\Gamma}} \;,$$
$$\tilde{p}_{\boldsymbol{n}_{\Gamma}} = p_{\boldsymbol{n}_{\Gamma}} + \nabla_{\Gamma} m_{\boldsymbol{n}_{\partial\Gamma}}\cdot\boldsymbol{t}_{\partial\Gamma} \;, \qquad F_C = m_{\boldsymbol{n}_{\partial\Gamma}}\big|_{+C}^{-C} \;,$$

where $+C$ and $-C$ are points close at a corner C. The possible boundary conditions for the Kirchhoff–Love shell are the displacements ($u_{\boldsymbol{t}_{\partial\Gamma}}$, $u_{\boldsymbol{n}_{\partial\Gamma}}$, $u_{\boldsymbol{n}_{\Gamma}}$) and the rotation $\omega_{\boldsymbol{t}_{\partial\Gamma}}$ with the effective conjugates forces ($\tilde{p}_{\boldsymbol{t}_{\partial\Gamma}}$, $\tilde{p}_{\boldsymbol{n}_{\partial\Gamma}}$, $\tilde{p}_{\boldsymbol{n}_{\Gamma}}$) and the bending moment $m_{\boldsymbol{t}_{\partial\Gamma}}$. A detailed derivation of the effective boundary forces and common support types is given in [7].

3.4 Equilibrium in weak form

The equilibriums in strong form are converted to weak forms by multiplying Eq. 15, Eq. 16, Eq. 17 with suitable test functions $\boldsymbol{v}$ and integration over the domain. With the divergence theorem for surface operators [7], the weak form of the equilibriums for the Reissner–Mindlin shell are

$$\begin{aligned}\int_{\Gamma} \nabla_{\Gamma}^{\mathrm{dir}}\boldsymbol{v}_u : \tilde{\mathbf{n}}_{\Gamma} + (\mathbf{H}\cdot\nabla_{\Gamma}^{\mathrm{dir}}\boldsymbol{v}_u) : \mathbf{m}_{\Gamma}^{\mathrm{RM}} + (\mathbf{Q}\cdot\nabla_{\Gamma}^{\mathrm{dir}}\boldsymbol{v}_u) : \boldsymbol{\Upsilon}_{\Gamma}^{\mathrm{RM}}\,\mathrm{d}A &= \int_{\Gamma}\boldsymbol{v}_u\cdot\boldsymbol{f}\,\mathrm{d}A + \int_{\partial\Gamma_{\mathrm{N},\boldsymbol{u}}}\boldsymbol{v}_u\cdot\hat{\boldsymbol{p}}\,\mathrm{d}s \;,\\ \int_{\Gamma} \nabla_{\Gamma}^{\mathrm{dir}}\boldsymbol{v}_w : \mathbf{m}_{\Gamma}^{\mathrm{RM}} + \boldsymbol{v}_w\cdot\boldsymbol{q}^{\mathrm{RM}}\,\mathrm{d}\Gamma &= \int_{\Gamma}\boldsymbol{v}_w\cdot\boldsymbol{c}\,\mathrm{d}\Gamma + \int_{\partial\Gamma_{\mathrm{N},\boldsymbol{w}}}\boldsymbol{v}_w\cdot\hat{\boldsymbol{m}}_{\partial\Gamma}\,\mathrm{d}s \;,\end{aligned} \tag{18}$$

where $(\boldsymbol{v}_u, \boldsymbol{v}_w)$ are the test functions for the displacements and the difference vector. The corresponding function spaces for $(\boldsymbol{v}_u, \boldsymbol{v}_w, \boldsymbol{u}, \boldsymbol{w})$ are subspaces of the $\mathcal{H}^1(\Gamma)^3$ Sobolev space and a standard C^0-continuous discretization is sufficient. Note that $\boldsymbol{v}_w$ and $\boldsymbol{w}$ are *tangential* vectors. The continuous weak form of the equilibrium for a Kirchhoff–Love shell is

$$\int_{\Gamma} \nabla_{\Gamma}^{\mathrm{dir}}\boldsymbol{v}_u : \tilde{\mathbf{n}}_{\Gamma} - \boldsymbol{\varepsilon}_{\Gamma,\mathrm{B}}^{\mathrm{KL}}(\boldsymbol{v}_u) : \mathbf{m}_{\Gamma}^{\mathrm{KL}}\,\mathrm{d}\Gamma = \int_{\Gamma}\boldsymbol{v}_u\cdot\boldsymbol{f}\,\mathrm{d}A + \int_{\partial\Gamma_{\mathrm{N}}}\boldsymbol{v}_u\cdot\tilde{\boldsymbol{p}} + \omega_{\boldsymbol{t}_{\partial\Gamma}}(\boldsymbol{v}_u) m_{\boldsymbol{t}_{\partial\Gamma}}^{\mathrm{KL}}\,\mathrm{d}s \;. \tag{19}$$

Due to the presence of second-order derivatives in the second term, the corresponding function spaces for $(\boldsymbol{v}_u, \boldsymbol{u})$ are subspaces of the $\mathcal{H}^2(\Gamma)^3$ Sobolev space, which requires at least a C^1-continuous discretization. From an implementational point of view, this requirement is the most important difference between the two shell models.

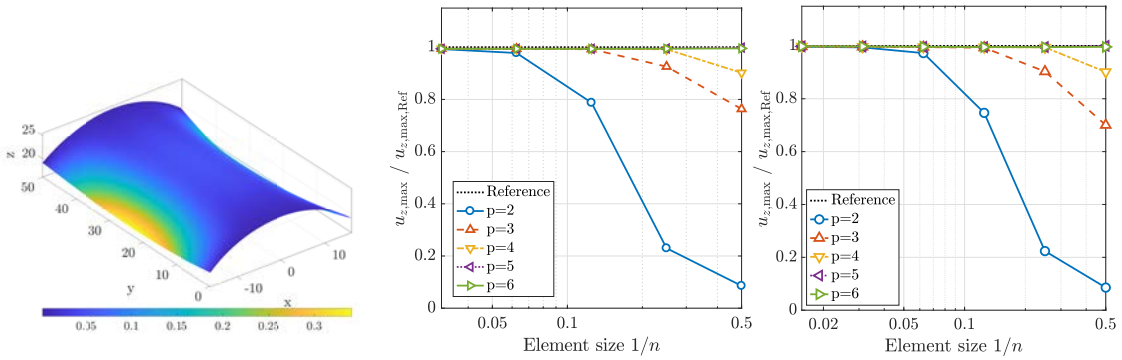
3.5 Implementational aspects

The continuous weak forms in the frame of the TDC allow a discretization with two fundamentally different finite element approaches such as the Surface FEM, see, e.g., [7], [8], or with the TraceFEM, see, e.g., [10]. Herein, a Surface FEM approach based on isogeometric analysis (IGA) proposed by Hughes et al. [12] is used for the discretization of the continuous weak forms of both shell models. An advantage of this method is the high continuity within the patch, which

enables improved convergence properties and smooth forces and moments. In addition, the C^1-continuity requirement of the Kirchhoff–Love shell is easily satisfied. For both shell models, the boundary conditions are enforced weakly with Lagrange multipliers. For the Reissner–Mindlin shell, the constraint on the difference vector is enforced with an additional Lagrange multiplier [8].
The formulation of the PDE with the TDC also leads to a more compact implementation compared to classical theory and a sharper split between application and finite element technology is possible. In particular, the surface operators are applied to shape functions independently of the concrete application, which is an advantage for general purpose FEM implementations. For further information about implementational aspects of using the TDC, we refer to, e.g., [7], [8].

4 Numerical results

As an example, the Scordelis–Lo roof from [13] is taken. Other benchmark examples, e.g., partly clamped hyperbolic paraboloid, clamped flower shaped shell, etc., are considered [7], [8], but omitted herein for the sake of brevity.
The Scordelis–Lo roof is a cylindrical shell with $R = 25, L = 50$ and an subtended angle of 80°. The shell is supported with rigid diaphragms at its ends and is loaded by gravity forces $\boldsymbol{f} = [0, 0, -90]^{\mathrm{T}}$. The material parameters are: Young's moduls $E = 4.32 \times 10^8$ and Poisson's ratio $\nu = 0$. In the convergence analyses, the largest vertical displacement $u_{z,\max}$ is compared with a reference displacement $u_{z,\max,\mathrm{Ref}} = 0.3024$ as given in reference [13]. In Fig. 3(a) the deformed shell is illustrated. The colours on the surface indicate the Euclidean norm of the displacement field $\boldsymbol{u}$.



(a) disaplacements $\boldsymbol{u}$ (b) convergence of the KL shell (c) convergence of the RM shell

Figure 3: Scordelis–Lo roof: (a) displacement field $\boldsymbol{u}$ scaled by one order of magnitude, (b) results of the convergence analyses with the Kirchhoff–Love shell, (c) results of the convergence analyses with the Reissner–Mindlin shell.

The example is computed with both shell models and the results of the convergence analyses are presented in Fig. 3(b) and Fig. 3(c). In particular, the problem is computed with uniform knot spans with $n = [2, 4, 8, 16, 32, 64]$ elements per side and the order is varied up to $p = 6$.
It is clearly seen, that the expected results are achieved, with increasing accuracy for higher orders of the (NURBS) shape functions. Transverse shear locking effects in Fig. 3(c) are not pronounced and a further treatment of locking apart from order elevation is not considered herein and would be beyond the scope of this work.

5 Conclusions and outlook

We have presented a parametrization-free reformulation of the linear shell theory for two important shell models based on the TDC using a global Cartesian coordinate system, which generalizes the classical shell equations. Based on the stress resultants, the equilibrium is given in strong form and the boundary conditions for each model are investigated in detail. In the derivation of the shell models, the differences of the two shell models are analyzed and their consequences on the implementation are emphasized. The results confirm that the proposed approach is equivalent compared to the classical shell theory when a parametrization, hence, local coordinates are available. In our future works, the obtained shell models are discretized on implicitly defined surfaces with the TraceFEM. Furthermore, the presented approach based on the TDC is applied to non-linear problems such as membranes and shells within the finite strain theory.

References

[1] Y. Başar and W.B. Krätzig, *Mechanik der Flächentragwerke*. Braunschweig: Vieweg+Teubner Verlag, 1985.

[2] M. Bischoff, E. Ramm, and J. Irslinger., "Models and Finite Elements for Thin-walled Structures", in *Encyclopedia of Computational Mechanics Second Edition (eds E. Stein, R. Borst and T. J. Hughes)*, 2017.

[3] M.C. Delfour and J.P. Zolésio, *Shapes and Geometries: Metrics, Analysis, Differential Calculus, and Optimization*. Philadelphia: SIAM, 2011.

[4] G. Dziuk, "Finite elements for the Beltrami operator on arbitrary surfaces", in *Partial Differential Equations and Calculus of Variations*. Berlin: Springer, 1988, pp. 142–155.

[5] T.P. Fries, "Higher-order surface FEM for incompressible Navier-stokes flows on manifolds", *Int. J. Numer. Methods Fluids*, vol. 88, pp. 55–78, 2018.

[6] P. Hansbo and M.G. Larson, "Finite element modeling of a linear membrane shell problem using tangential differential calculus", *Comp. Methods Appl. Mech. Engrg.*, vol. 270, pp. 1–14, 2014.

[7] D. Schöllhammer and T.P. Fries, "Kirchhoff-Love shell theory based on tangential differential calculus", *Comput. Mech.*, 2018, https://doi.org/10.1007/s00466-018-1659-5.

[8] D. Schöllhammer and T.P. Fries, "Reissner-Mindlin shell theory based on tangential differential calculus", *Comp. Methods Appl. Mech. Engrg.*, vol. 352, pp. 172–188, 2019.

[9] J. Kiendl, K.-U. Bletzinger, J. Linhard, and R. Wüchner, "Isogeometric shell analysis with Kirchhoff-Love elements", *Comp. Methods Appl. Mech. Engrg.*, vol. 198, pp. 3902–3914, 2009.

[10] M.A. Olshanskii and A. Reusken, "Trace finite element methods for PDEs on surfaces", *Lecture Notes in Computational Science and Engineering*, vol. 121, pp. 211–258, 2017.

[11] R. Echter, B. Oesterle, and M. Bischoff, "A hierarchic family of isogeometric shell finite elements", *Comp. Methods Appl. Mech. Engrg.*, vol. 254, pp. 170–180, 2013.

[12] T.J.R. Hughes, J.A. Cottrell, and Y. Bazilevs, "Isogeometric analysis: CAD, finite elements, NURBS, exact geometry and mesh refinement", *Comp. Methods Appl. Mech. Engrg.*, vol. 194, pp. 4135–4195, 2005.

[13] T. Belytschko, H. Stolarski, W.K. Liu, N. Carpenter, and J.S.J Ong, "Stress projection for membrane and shear locking in shell finite elements", *Comp. Methods Appl. Mech. Engrg.*, vol. 51, pp. 221–258, 1985.

Proceedings of the IASS Annual Symposium 2019 – Structural Membranes 2019
Form and Force
7 – 10 October 2019, Barcelona, Spain
C. Lázaro, K.-U. Bletzinger, E. Oñate (eds.)

Application of a Computer Aided Design Program for Shells with Aluminum Alloy Gusset Joints—Case Study

Shaohan ZONG*, Xiaonong GUO, Shaojun ZHU, Qiang ZENG, Yu CHEN

*Department of Structural Engineering, Tongji University
No.1239 Siping Road, Yangpu District, Shanghai, China
Shzong@tongji.edu.cn

Abstract

The Shanghai Planetarium, due for completion in 2020, will be the world's largest planetarium. An inverted dome with a span of 41.9 m (137.5 ft) is one of the most attractive parts in the building. This dome is a bowl-shaped single-layer latticed shell with aluminum alloy gusset joints, and it satisfies the requirements of both architectural aesthetic and structural rationality. However, the workload will be burdensome if the inverted dome is designed by the traditional design method. This paper introduces an effective method to simplify the process of preparing construction drawings. The 2D shop drawings of joints and members, as well as the 3D model of the shell, can be generated automatically with the program in the ObjectARX-based platform, to assist the manufacture and assembly of the shell. Compared with the conventional method, this newly-developed program can make the design process more automatic and efficient.

Keywords: inverted dome, aluminum alloy single-layer spheritic latticed shell, aluminum alloy gusset joint, auto-drawing program, ObjectARX-based platform

1. Introduction

The Shanghai planetarium is due for completion in 2020 and will be the largest planetarium in the world, with a construction area of approximately 38000 square meters, as shown in Figure 1. It is characterized by its graceful appearance and complex structure form. And the superstructure is composed of three parts: the large cantilevered steel structure, the inverted dome and the spherical cinema. As a representative structure in the planetarium, the inverted dome [1] is a typical aluminum alloy single-layer spherical latticed shell.

Aluminum alloy (AA) spatial structures have been widely applied in the field of building, with some outstanding advantages of attractive appearance, light weight, high corrosion resistance, accurate manufacture and easy assembly [2]~[3]. Nowadays, there have been many aluminum alloy spatial structures built in China, such as Nanjing International Exhibition Center [4], Shanghai International Gymnastic Center [5], and Shanghai Science and Technology Museum [6].

The single-layer latticed shell is one of the most commonly used structure forms in AA spatial structures, and its geometric shape is comprised of triangular meshes generated by dividing a spherical or ellipsoidal surface. Besides, H-shaped AA members and aluminum alloy gusset (AAG) joints are commonly adopted in most single-layer shells. The AAG joint [7]~[9] connects the upper and lower cover plates with the members at the intersection with fasteners. Moreover, the AAG joint is easy to machine and assemble, and can avoid the reduction in the strength of aluminum alloy caused by welding.

Copyright © 2019 by Shaohan ZONG, Xiaonong GUO, Shaojun ZHU, Qiang ZENG, Yu CHEN
Published by the International Association for Shell and Spatial Structures (IASS) with permission.

This paper is mainly divided into the following two parts: the introduction of the AA inverted dome in the Shanghai planetarium, and an ObjectARX-based program used to automatically and quickly draw up construction drawings.



Figure 1: Architectural rendering of the Shanghai Planetarium

2. Structural form

The architectural form of Shanghai Planetarium embodies the orbital motion of celestial bodies. The inverted dome and the spherical astronomical hall symbolize three celestial bodies in a dynamic orbit motion system. As one part of the main structure, the inverted dome serves as a viewing platform and allows people to observe celestial movement indoors or outdoors. The full model, construction site and interior view of the inverted dome are shown in Figure 2~Figure 4.

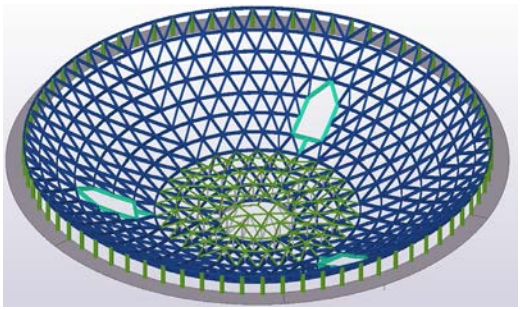


Figure 2: The model of the dome

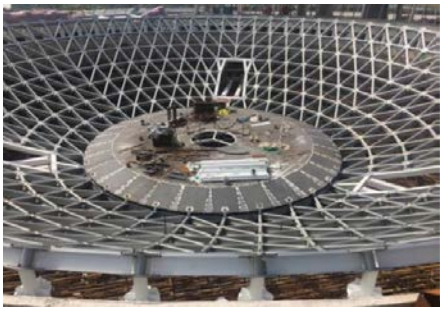


Figure 3: Construction site of the dome



Figure 4: Interior view of the dome

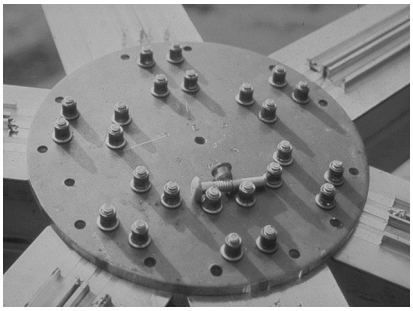


Figure 5: Aluminum alloy gusset joint

2.1. Superstructure

The inverted dome is a bowl-shaped aluminum alloy single layer latticed shell with AAG joints. Its span and height are 42 m and 8.7 m, respectively; and the edge length of triangular meshes is 2 to 3 m. In addition, a steel structure platform is assembled at the bottom of the inverted dome. Tourists can

reach the platform to watch the sky and celestial bodies through three steel doorways. And the frames of these doorways are strengthened by H-shaped steel members.

The section of the aluminum alloy members is H-300×120×8×10 (shown in Figure 6), and the sides of members are sealed with sealing plates for aesthetic and waterproof requirements. Besides, for the convenience of construction and the secure connection between members and sealing plates, the snap-fit connection is introduced, as shown in Figure 7. Furthermore, aluminum alloy latticed shells are commonly used as the roof structure of spatial structures. In order to meet the installation requirement for glass curtain walls, the detail for connecting members and glass curtain walls is put forward.

All the gusset plates are made of aluminum alloy except the gusset plates of rings 1~4 and ring 11. This is because the upper gusset plates of rings 1~4 need welding with the steel tubes of the steel platform, and the lower gusset plates of ring 11 need welding with the steel supports. Therefore, these gusset plates are made of stainless steel to avoid the reduction in the strength of aluminum alloy after welding.

Compared with the conventional single-layer shell, this inverted dome has better stability [6]. The major reason is that the members mainly resisted the tension and bending moment owing to the distinctive inverted morphology. Besides, this inverted dome has enough reserves of strength and stiffness.

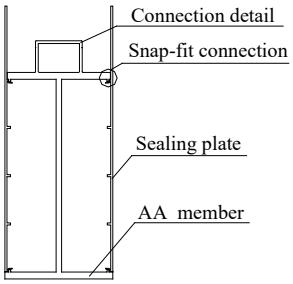


Figure 6: H-shaped AA member

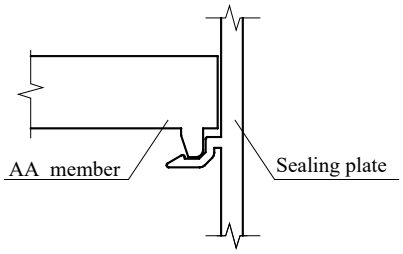


Figure 7: Snap-fit connection

2.2. Steel supports

The inverted dome is supported by short steel column supports, and the supports are fixed in the steel reinforced concrete ring beam by anchor bars. And the anchor bars should be bent and welded on the steel embedded in the ring beam when they touch each other. The connection method between the gusset plate and short steel column is welding. Moreover, arc stiffening plates are set between the gusset plates to improve the bearing capacity of the joint. The connection detail of steel support is shown in Figure 8.

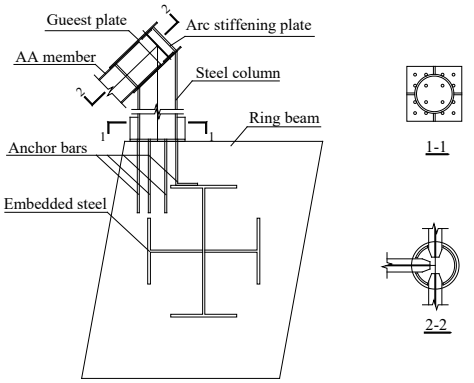


Figure 8: Connection details among the support, shell and ring beam

3. System for preparing construction drawings

For a single-layer latticed shell, the preparation of shop drawings of joints and members is a heavy workload after the structural design and analysis. Thus, it is essential to develop a simple and reliable method to automatically produce structural drawings.

In this project, ObjectARX [10] was introduced to finish the drawing task. ObjectARX is a software package developed by Autodesk Company to redevelop AutoCAD. It is based on C++ and can access AutoCAD graphic database quickly. ObjectARX application is a dynamic link library, which can share the address space of AutoCAD and directly call the functions in AutoCAD. The development environment of this system is Microsoft Visual Studio 2008, ObjectARX 2010 and AutoCAD 2010.

Figure 9 illustrates the execution process of this program, which is divided into three phases: (1) calculating, organizing and inputting the geometric parameters of joints and members; (2) preparing and running the program; (3) outputting and collating the construction drawings.

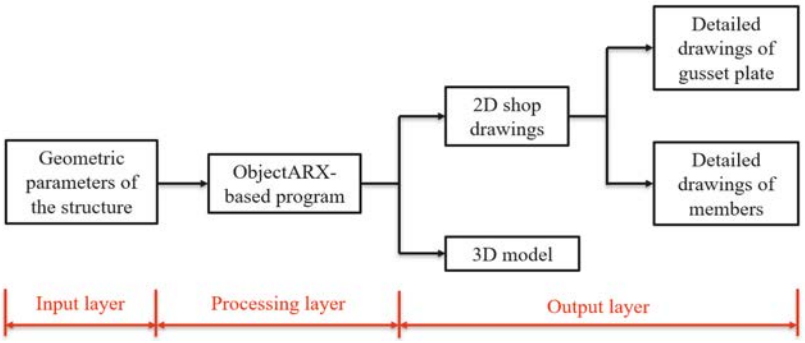


Figure 9: Execution process of the program

3.1. Calculation of geometric parameters

Before running the drawing program, the relevant geometric information of joints and members should be obtained through a sequence of programs. The calculation process is shown in Figure 10. Based on the geometric information of the whole structure, the angle relationships among the gusset plate and its adjacent members are obtained, such as the angle between the axis of a member and the normal vector of a gusset plate at the same joint, and the angle between the projection vectors of two members in the tangent plane of the gusset plate. Then, the detailed parameters of all the members and joints can be calculated. On the whole, the acquisition sequence of geometric information is from the whole shell to the single member or joint.

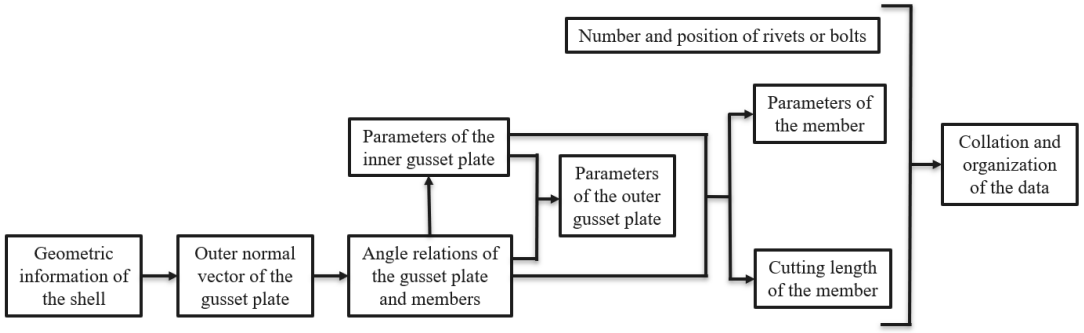
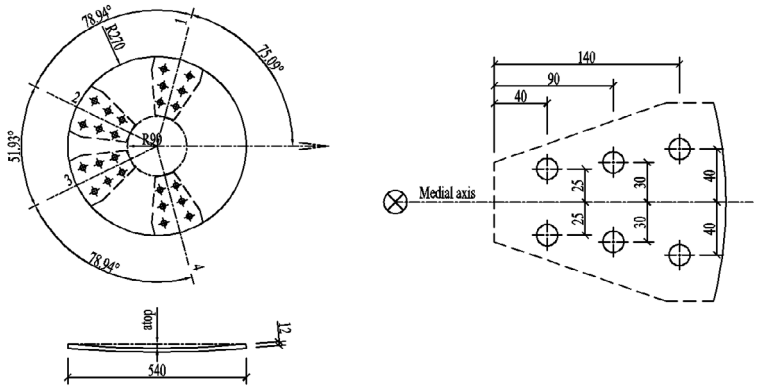


Figure 10: Calculation process of the geometric information of the shell

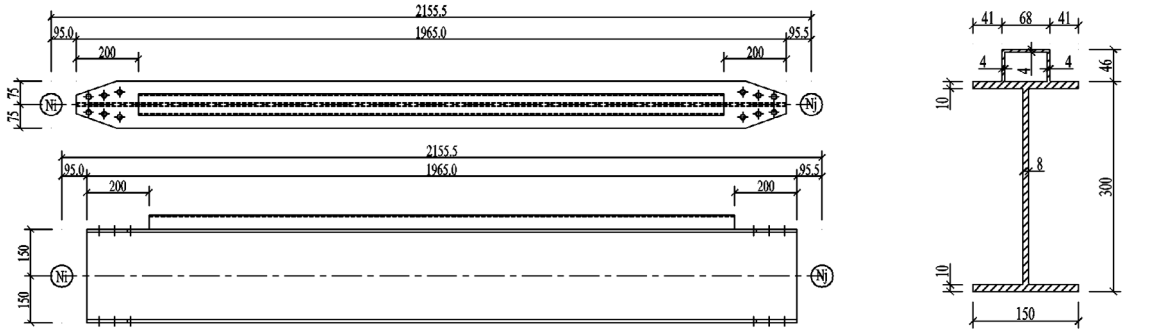
3.2. Two-dimensional shop drawing

This program is able to generate the shop drawings of joints and members automatically and quickly. Figure 11 and Figure 12 exemplify the generated shop drawings, including the top view and front view of the gusset plate and member, and the detail of rivet holes. Moreover, this program can output all the information of joints and members (such as the series number of joints and members, the radius and the sagitta of gusset plates, the angle between adjacent members, the length of members, the number and the radius of rivet holes, etc.) in parameter tables, which can be provided for workers to consult. The spherical structure form determines the adoption of arched gusset plates (shown in the front view of the gusset plate), resulting in an obvious improvement on both the bearing capacity and initial bending stiffness of AA gusset joints compared with plane gusset plates.



(a) Top view and front view (b) Arrangement of rivets

Figure 11: Detailed drawings of the gusset plate



(a) Top view and front view (b) Section of the member

Figure 12: Detailed drawings of the member

3.3. Three-dimensional model

The program can also produce the three-dimensional solid model in AutoCAD. Figure 13 is the 3D model drawing of the aluminum alloy inverted dome, in which the members and gusset joints can be precisely drawn. Designers can collate 2D shop drawings through the 3D model, thus avoiding production losses caused by wrong shop drawings. Figure 14 illustrated the local details of the joint zone. It can be seen that this program cuts the members near the joint zone by Boolean operation, which can more truly represent the morphology of the reticulated shell after completion.

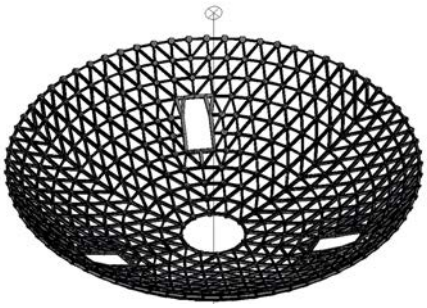


Figure 13: 3D model of the dome

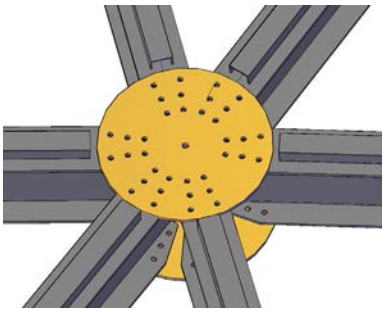


Figure 14: Local details of the joint zone

4. Conclusion

This paper introduces the structural characteristics of the inverted dome in the Shanghai planetarium, and an ObjectARX-based program for automatically and quickly generating 2D shop drawings and a 3D solid model.

The inverted dome has an excellent structural morphology not only with mechanical rationality but also with architectural aesthetics. Besides, owing to the inversion of the shell, its members mainly bear the tension and bending moment, leading to a positive impact on the stability of the dome.

During the design and construction process of spatial structures, it is inevitable to revise or even redraw the construction drawings and shop drawings. ObjectARX based on Visual C++ and AutoCAD provides a good solution for enormous drawing tasks. By using efficient programs, the heavy workload can be handed over to the computer, thus significantly reducing manpower and time costs. The efficiency of this method has been validated in the construction of the inverted dome.

The developed program is currently suitable for regular single-layer reticulated shells. In order to better meet the needs of practical engineering, the further work is to adapt the program to more complicated structural morphology, such as spatial free-form surface, which can dramatically reduce time costs and manpower costs.

References

[1] Y. Li, H. Jia, S. Jia, L. Zhang and J. Gao, "Structural design on inverted dome aluminum alloy latticed shell of Shanghai Planetarium," *Building Struction*, vol. 48, pp. 30-33, Jul. 2018 (in Chinese).

[2] Z. Shen, X. Guo and Y. Li, "State-of arts of research on aluminum alloy structures," *Journal of Building Structures*, vol. 28, pp. 100-109, Dec. 2007 (in Chinese).

[3] L. Yang, S. Wei, Q. Zhang, et al. "Aluminum reticulated spatial structures: state of the art and key issues," *Journal of Building Structures*, vol. 34, pp. 1-19, Feb. 2013 (in Chinese).

[4] C. Hao, J. Qian, T. Song, et al. "Research and application of aluminum alloy grid structure Journal of Building Structures," *Journal of Building Structures*, vol. 24, pp. 70-75, Dec. 2003 (in Chinese).

[5] Q. Ju, and L. Zhu, "An introduction to aluminum alloy dome roof structure of Shanghai International Gymnastic Center," *Journal of Building Structures*, vol. 19, pp. 33-41. Jun. 1998(in Chinese).

[6] X. Zhou, L. Yang, Y. Li, et al., "Structural analysis of the shell of Shanghai Science and Technology Museum," *Building Structures*, vol.33, pp. 55-57, Jan. 2003 (in Chinese).

[7] X. Guo, Z. Xiong, Y. Luo, L. Qiu, and J. Liu, "Experimental investigation on the semi-rigid behaviour of aluminum alloy gusset joints," *Thin-Walled Structures*, vol. 87, pp. 30-40, Feb. 2015.

[8] X. Guo, Z. Xiong, Y. Luo, et al. "Application of the component method to aluminum alloy gusset joints" *Advances1 in Structural Engineering*, vol. 18, pp. 1931-1946, 2015.

[9] Z. Xiong, X. Guo, Y. Luo, and H. Xu, "Numerical analysis of aluminum alloy gusset joints subjected to bending moment and axial force," *Engineering Structures*, vol. 152, pp. 1-13, Dec. 2017.

[10] C. McAuley, *Programming AutoCAD 2000 Using ObejectARX*, Ireland, 2000.

[11] X. Guo, Z. Xiong, Y. Luo, et al. "Experimental study on arch plate of aluminum alloy gusset joint," in *14th National Symposium on Modern Structural Engineering, Tianjin*, *China,* 2014 (In Chinese).

Proceedings of the IASS Annual Symposium 2019 - Structural Membranes 2019
Form and Force
7-10 October 2019, Barcelona, Spain
C. Lázaro, K.-U. Bletzinger, E. Oñate (eds.)

Biaxial tensile analysis in a high tenacity polyester fabric

Carolina Suzin, Marianna Coelho* and Peter Gosling[a]

* Universidade do Estado de Santa Catarina
Rua Paulo Malchitzki, 200, Departamento de Engenharia Civil
coelhomarianna@gmail.com

[a] School of Engineering
Room 2.14, Drummond Building
Newcastle University
Newcastle upon Tyne, NE1 7RU

Abstract

The biaxial test is essential for measuring the mechanical properties of anisotropic composite materials such as structural membranes (yarns and coating), where the material properties are a function of the orthotropic stress state. Those membranes comprise a woven cloth that is then coated, to protect the yarns of the fabric from environmental degradation, and to enable joining. The yarns are made of fibrils, formed into bundles, and then twisted. They are woven to form the base cloth, with the weave pattern and yarn tensions variables within this manufacturing process. The base cloth is coated on both sides. The coating medium permeates the base cloth. Both the coating and yarns have nonlinear characteristics. When the textile is loaded, the coated base cloth changes geometry, adding geometric nonlinearity. There are also fewer than ten biaxial test machines worldwide. The work was carried out with biaxial tensile tests in Brazil in a high tenacity polyester fabric. Deformation was measured with a Digital Image Correlation (DIC) equipment through the registration and image tracking. The test protocol used was based in the European Standard EN17117 [1] and Japanese Protocol [2] adding some load ratios.

Keywords: Textile Membranes. Biaxial Tensile Test. Membrane Structures.

1 Introduction

Membrane structures are composites with yarns disposed of in a plane coated matrix. Yarns are usually made of polyester fibers. Some membranes have superficial coated protection. Membranes are produced in rectangular bands with 30 meters of length and from 3 to 5 meters of width [3].
Membrane wiring is in two main directions: warp and weft, according to Figure 1. In the fabric wiring process, the warp yarns are straight and tightened, and the weft years go over and under the warp yarns. So, in the warp directions, there is a more pronounced ripple. Thus, the mechanical properties for these fabrics will be anisotropic, and the behavior will depend on the

Copyright © 2019 by Carolina Suzin, Marianna Coelho and Peter Gosling
Published by the International Association for Shell and Spatial Structures (IASS) with permission.

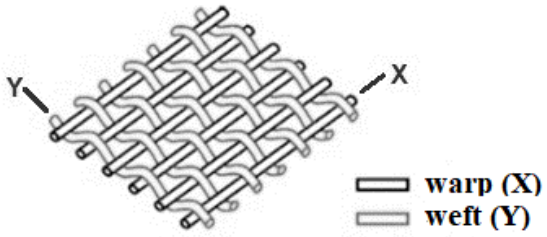


Figure 1: Yarn wiring in a polyester fabric

force orientation relating to the yarn directions. A biaxial tensile test is necessary to predict material behavior [4].
A uniaxial tensile test is usually used for polyester fabric, but this test does not consider the orthotropic or anisotropic material behavior. The method used nowadays is the biaxial tensile test in a plane with cruciform samples, stretching the fabric in both directions. Through monitoring the applied forces and measuring the strains, it is possible to have the stress-strain material relation [4].
According to the standard EN 17177:2018 [3], in a biaxial tensile test, a cruciform sample is loaded biaxially in the fabric plane. The loads are applied cyclically in the warp and weft directions simultaneously. Stress and strain measures are used to analyze the fabric properties.

2 Material and methods

In this work, samples of high tenacity polyester fibers were tested in the biaxial tensile state. According to the producer, the material has the following information: - Fabric name: UNISOL; material yarns: high tenacity polyester; yarn type: 920 Dtex (warp and weft); Tensile strength: warp 115 kgf/5cm and weft 105 kgf/5cm; Additions: anti-UV and antifungal; weldable and sewable; 100% waterproof.
The number of cruciform samples analyzed was seven, oriented in the warp and weft directions. The center of the sample had 150mm x 150mm. The length for each branch was 280mm. To avoid the stress concentration in the sample, the corners were rounded with a radius of 13mm and slits were cut in the four branches with 80mm of length and 15mm of width. For the edging, a length of 200mm was used to fasten the samples in the machine. The geometry used for the samples is shown in Figure 2.
A tensile biaxial machine developed and constructed in the State University of Santa Catarina tested the samples. The machine is shown in Figure 3. The biaxial tensile tests were cyclic with different load ratios. The load ratios are related to the tensile warp direction: weft direction. These load ratios were: 1:pretension, pretension:1, 1:1, 1:2, 2:1, 1:3, 3:1, based on the European Standart EN 17117-1 [1] and the Japanese protocol MSAJ/M-02-1995 [2]. In the present work, for each load ratio, a sample was tested until failure. The pretension was 100N, determined when the sample was taut without wrinklings. The displacement velocity was 10mm/min the temperature during the experiments varied from 25,2^{o}C to 28,1^{o}C.
A Digital Image Correlation (DIC) measured the strains and displacements on the samples. This

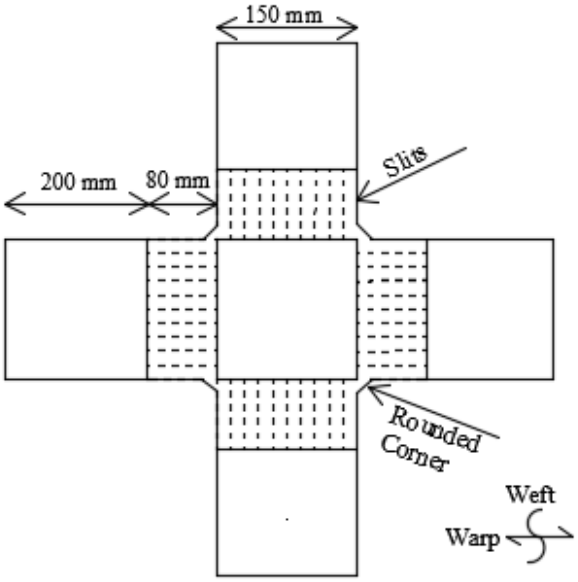


Figure 2: Cruciform samples

DIC equipment is from the Dantec Dynamic company, Q-400 model, and the software is Instra 4D. The material has a solid white color painted with random points using black spray paint for plastic and acrylic.

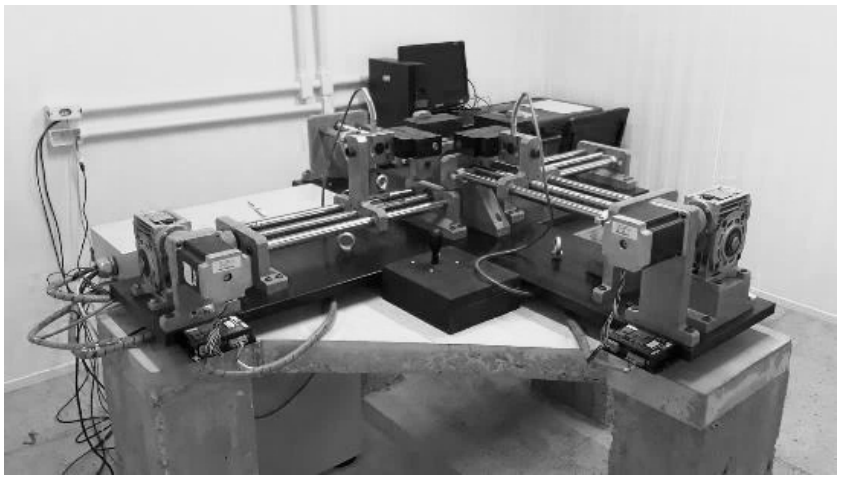


Figure 3: Tensile biaxial machine

3 Results

In the load ratio of 1:1, the material showed in the first load cycles a linear elastic behavior, and in the next cycles, the behavior is elastoplastic. The elastic behavior also increases in nonlinearity. The material presents large strains, around 16%. This material behavior is also observed for the load ratios of 1: pretension, pretension:1, and 1:2.

The load ratio of 2:1, showed in the first cycle that the warp has an elastoplastic behavior with nonlinear behavior increase in the next cycles. On the other hand, the weft showed a linear elastic behavior in the first cycle and nonlinear elastoplastic behavior in the next cycles. In the load ratios of 1:3 and 3:1, the behavior characterization was not possible.
Two photos were selected to visualize the strain field, one from the beginning of the test and the other from the end. The strains are higher in the branches of the samples and lower in the middle, which is the interest area. That was the expected behavior, found for all samples, respecting the Saint-Venant law. Figures 4 and 5 showed the strain field for the load ration of 1:1.

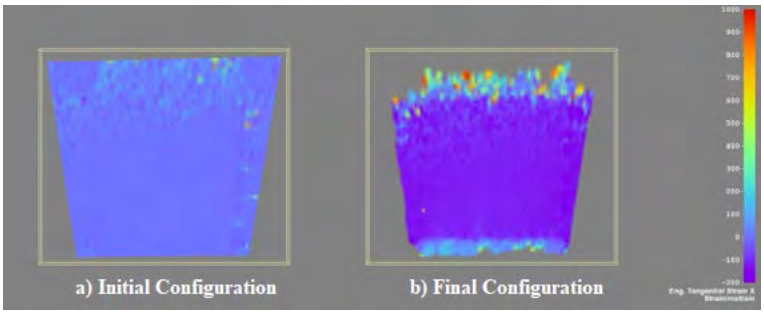


Figure 4: Warp results for the sample with load ratio of 1:1. a) Initial and b) final configuration

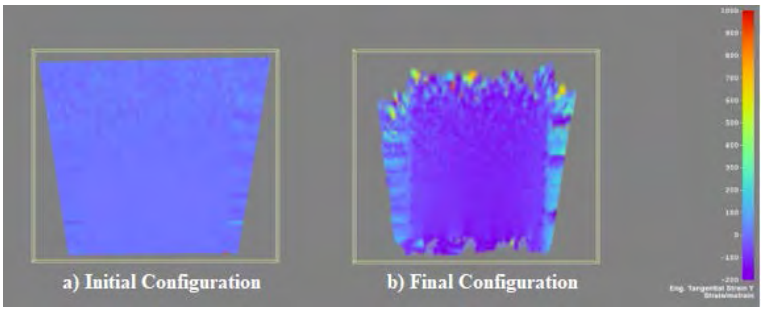


Figure 5: Weft results for the sample with load ratio of 1:1. a) Initial and b) final configuration.

3.1 Shear

Figure 6 presents the stress shear versus strain shear graphic. The values are very low on the test with an increase close to the failure, due to the presence of large strains and yarn distortions. The strain shear values were low compared to the values of strain in x or y-direction. Figure 7 showed with DIC pictures that the strain shear values were closed to zero. This behavior happened for all samples.

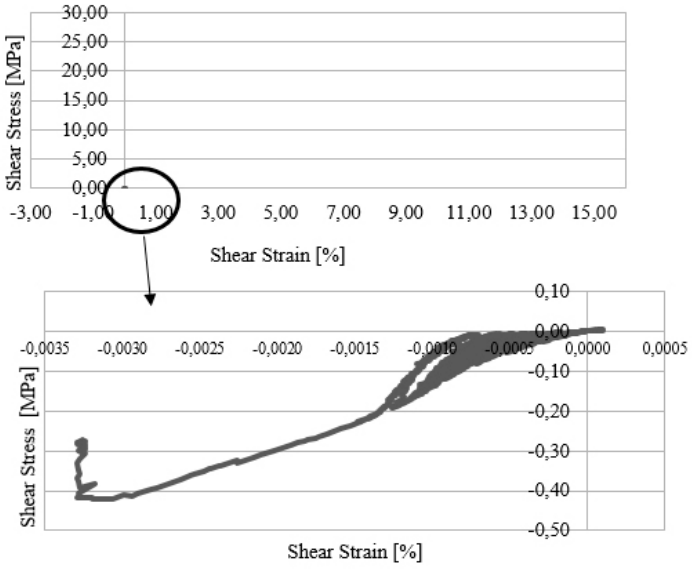


Figure 6: Shear stress versus shear strain for load ratio of 1:1

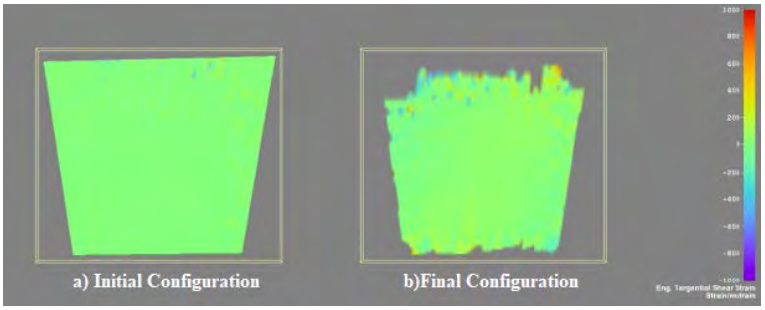


Figure 7: Strain shear for sample with load ratio of 1:1. a) Initial configuration, and b) final configuration

3.2 Warp-weft behavior

A comparison for warp and weft, considering the stress-strain behavior showed the distinct behavior for each yarn direction. The stress-strain graphics were for the same load ratio. The load ratios considered in this analysis was: 1:1 (warp and weft), 2:1 (warp) and 1:2 (weft), and 1: pretension (warp) and pretension:1 (weft). Figures 8 and 9 showed the different behavior for warp and weft, proving that this material does not have an isotropic behavior. On the other hand, Figure 10 showed results more similar for warp and weft. This result was for cases when one of the axes had just a fixed pretension, and the other axis had a load increment. The pretension considered for those tests was 100N. This test is similar to a uniaxial test. This results showed that considering just uniaxial tests for this type of material; it did not provide real material behavior.

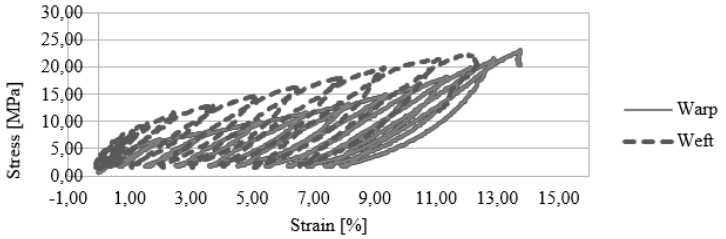


Figure 8: Stress versus strain for 1:1 (warp) and 1:1 (weft)

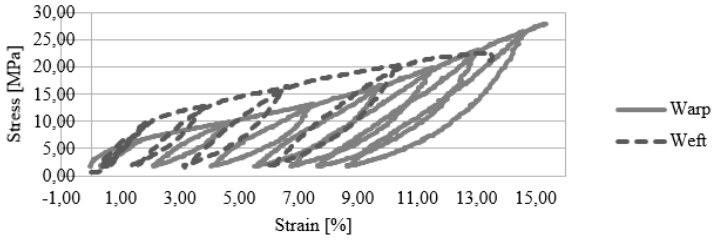


Figure 9: Stress versus strain for 2:1 (warp) and 1:2 (weft)

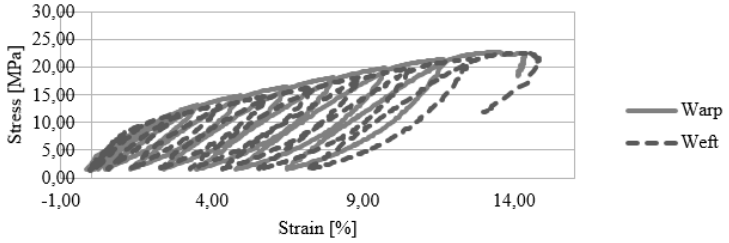


Figure 10: Stress versus strain for 1:pretension (warp) and pretension:1 (weft)

4 Conclusion

The material behavior of membranes subjected to a biaxial tensile test for different load ratios was presented. The results confirmed that for a high tenacity polyester fabric, the behavior is not isotropic and showed the importance to perform biaxial tensile tests. The results from the biaxial test also showed that initially the material behavior is linearly elastic, and with the load increase for each cycle, the behavior is nonlinear elastoplastic. In the tests with a load ratio of 1:3 and 3:1, it was not possible to characterize the mechanical material behavior. Therefore, we recommend to use in further analysis the following load ratios: 1:0,25, 0,25:1, 1:05, 0,5:1, 1:0,75 e 0,75: 1. The test with load ratios of 1: pretension and pretension:1 showed similar results for warp and weft directions and the behavior for other load ratios differs for warp and weft. The samples used in this work did not present shear. Therefore the samples had stress and strain in principal directions, showing a biaxial state.

5 Acknowledgements

This research was supported by FAPESC, (Scientific and Technological Research Support Foundation of Santa Catarina State) - 2015TR482, Newton Fund - EP/N002059/1, and CNPq (National Counsel of Technological and Scientific Development) - 457486/2014-7. We thank our colleagues from the Department of Mechanical Engineering from the State University of Santa Catarina who provided insight and expertise that greatly assisted the research.

References

[1] EN 171171:2018, "Rubber or plastics-coated fabrics - Mechanical test methods under biaxial stress states. Part 1: Tensile stiffness properties", Reino Unido, 2018.

[2] MSAJ/M-02-1995, "Testing Method for Elastic Constants of Membrane Materials". in *Standard of the Membrane Structures Association of Japan*, Tokyo, Japo, 1995.

[3] J. P. Borges Filho. *Projeto de Tensoestruturas em Membrana com Aplicao de Programao No-Linear*, Phd Thesis in Structural Engineering, Universidade de Brasilia, Brasilia, 2006.

[4] M. R. P. Chivante. *Avaliao Experimental das Relaes Tenso-Deformao de um Tecido de Fibra de Vidro Recoberto com PTFE*, Master dissertation in Civil Engineering, Universidade de So Paulo, So Paulo, 2009.

Proceedings of the IASS Annual Symposium 2019 – Structural Membranes 2019
Form and Force
7 – 10 October 2019, Barcelona, Spain
C. Lázaro, K.-U. Bletzinger, E. Oñate (eds.)

Geometric and structural analysis of existing vaults using parametric surfaces

Joram TUTSCH*, Cleo REIHL [a], Rainer BARTHEL [a]

* Chair of Structural Design, Technical University of Munich
Arcisstr. 21, 80333 Munich, Germany
joram.tutsch@tum.de

[a] Chair of Structural Design, Technical University of Munich

Abstract

Besides common geodesic techniques, 3D-laser scanning plays an increasingly important role in surveying existing structures. However, this technique creates an abundance of data, which must subsequently be analyzed, rationalized and transformed into usable geometry. In this paper we present four different methods to approximate point clouds of single or double curved historic vault structures by using parametric NURBS surfaces. The focus lies not only on the representation of the groins and ribs but mainly on the accurate geometric modelling of the webs in between. A verification of the mean distance between the points of the cloud and the generated surfaces shows adequate accuracy for three of the four approaches. In a case study of a pointed vault with lunette caps, the benefit of a continuous surface formulation is illustrated. By analyzing the Gaussian curvature we can identify critical domains of the entire surface. Finally, a structural analysis evaluates the possible impact on the global load-bearing behavior.

Keywords: reverse engineering, historical vaults, point clouds, existing geometry, geometric modelling, investigation, NURBS surface, surface fitting, least square method



Figure 1: Illustration of fitting surface (red) to point cloud (grey) of the case study

Copyright © 2019 by Joram Tutsch, Cleo Reihl and Rainer Barthel
Published by the International Association for Shell and Spatial Structures (IASS) with permission.

1. Introduction

Setting up numerical models of existing structures can be an ambitious challenge for engineers. In the case of historic vaults, accurate geometric information is needed, and more frequently produced by fully automatic terrestrial laser scanners (TLS). If not being transformed to conventional 2D plans, this abundance of three dimensional data is commonly processed to triangulated meshes using different toolkits of CAD-software [1].

New approaches use curves and surfaces, based on Non-Uniform Rational B-Splines (NURBS), to approximate the real geometry [2]. A reduction of numerical costs is expected, as well as an increase of geometrical precision [3]. Therein the focus is on fitting the bounding ribs or groins to the point cloud, which – in a mathematical sense – fully defines the webs in between. Depending on the shape and dimensions of the webs, this semi-parametric process can lead to large deviations between model and reality.

In this paper we present four methods which generate digital models of the webs by using parametric free-form surfaces and full geometric information of the point cloud. Moreover, we illustrate techniques for a geometrical validation, as well as a geometric and a structural analysis.

To demonstrate their practical benefits, these concepts are adapted to different kinds of real vaults: a pointed vault with lunette caps, a groin vault with domed webs and a sail vault.

2. Methods

2.1. Parametric Modelling

When aiming to generate a model that contains as much geometric information out of a 3D point cloud as possible, two options exist. We either can triangulate the data points and obtains a mesh that approximates the point cloud via plane triangles or we can approximate the point cloud to a curved surface, namely a parametric NURBS surface. We have investigated four different approaches using parametric NURBS representation.

2.1.1. Basic Geometry Template (BGT)

A straight-forward method to generate a continuous surface that represents the point cloud is to use a parametric template. This basic form can be adapted to the point cloud by manually adjusting different parameters such as span, height, support angle, etc. (fig. 1). Barthel summarizes several geometric dependencies for all kinds of groin vaults [4]. In doing so, the shape of the webs is determined by the dimensions of groins and free edges.

2.1.2. Lofting

The second approach uses lofted surfaces [5], [6]. A lofted surface is a parametric surface interpolating between consecutively positioned cutting lines. It is produced by the following steps:

- Triangulate the point cloud to a mesh
- Project a regular grid of points vertically onto that mesh (fig. 2a)
- Interpolate all points in line with one cutting line (fig. 2b)
- Loft the cutting lines to a surface (fig. 2c)

The lofting process is done by interpreting the cutting lines $C_k(\xi)$ as ξ-parameter-curves of the parametric NURBS surface $S(\xi, \eta)$. Each curve has a constant η-value and is only dependent on ξ:

$$C_k(\xi) = S(\xi, \eta_k) \tag{1}$$

Only a part of the geometrical information of the point cloud is taken into consideration. Hence, the lofting approach is a local interpolation.

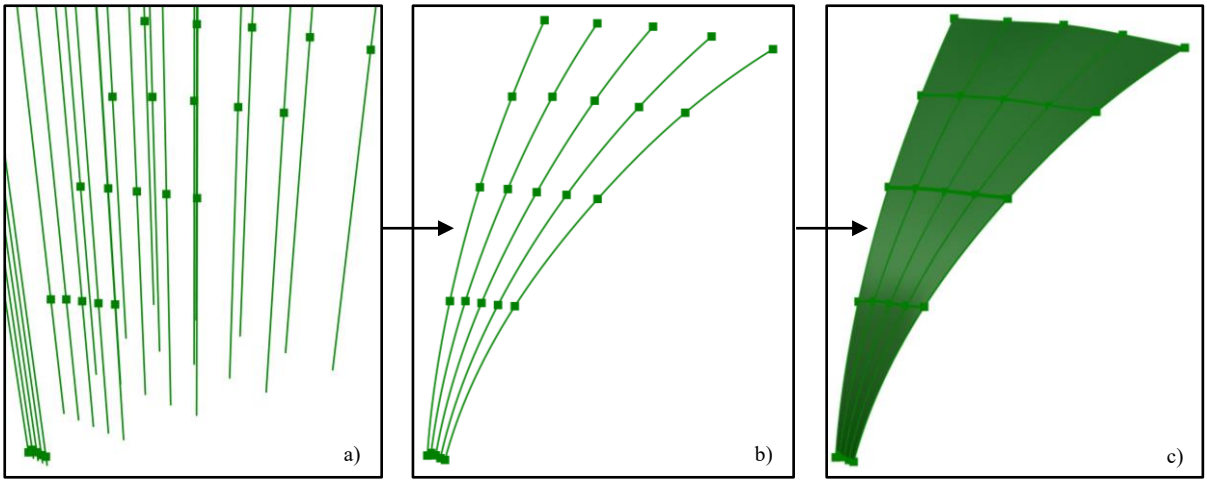


Figure 2: Visualized process of generating a lofted surface out of a point cloud:
a) vertical projection, b) cutting lines and c) final lofting surface

2.1.3. Least Square Method (LSM)

An optimization problem is formulated that minimizes the distance d_k between the point cloud and the parametric surface (e.g. [6], [7], [8]). This is done by minimizing the sum of the squared distances between each point D_k of the point cloud and its related foot point X_k on the surface (fig. 3). Since the shape of the surface is mainly defined by its control points $P_{i,j}$, their initial positions are modified in such a way that the sum of the squared distances is minimized while $d_k = |D_k - X_k|$.

$$min\, f(P_{i,j}) = \sum {d_k}^2 \tag{2}$$

The surface is defined as

$$S(\xi,\eta) = \sum_{i=1}^{n} \sum_{j=1}^{m} R_{i,j}^{p,q}(\xi,\eta) P_{i,j} \tag{3}$$

with $R_{i,j}^{p,q}(\xi,\eta)$ being the basic function of order p and q and $P_{i,j}$ being the control point positions. The variables n and m mark the number of control points in each direction.

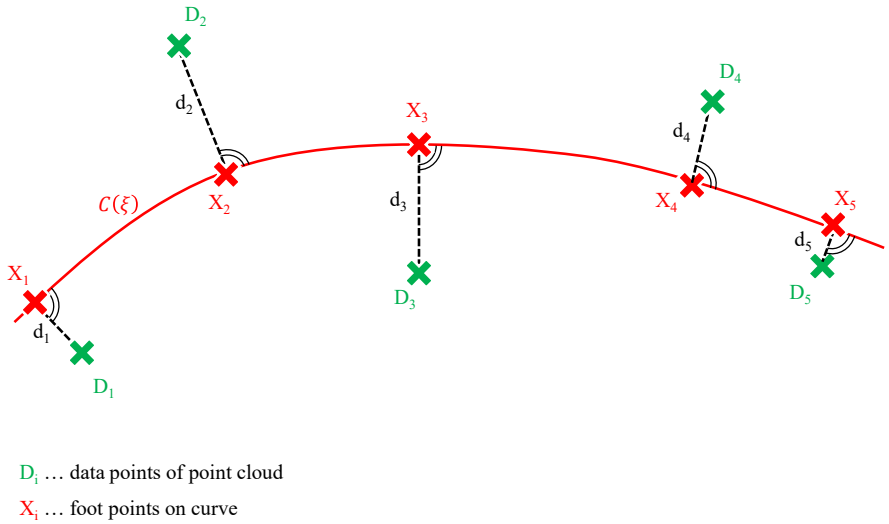


Figure 3: 2D-definition of cloud points, foot points and local distances of cloud points to surface points

A practical approach is formulated to implement the LSM to a CAD environment, here *Rhinoceros* (Robert McNeel & Associates, V.5) was used. The following decisions are made to simplify the method:

- Foot points are found by projecting the data points onto the NURBS surface. For each point of the point cloud the point on the surface is found which is closest to the data point.
- Knot vector and weights for the NURBS surface are either predefined before the optimization or instead of a general NURBS surface, a B-Spline surface is used.
- Number of control points and order of NURBS surface is predefined before the optimization.
- Initial control point positions are predefined before optimization.

2.1.4. Mesh2Surface (M2S)

The three introduced methods can be compared with commercial solutions, e.g. the Plug-in for *Rhinoceros: Mesh2Surface*. This software uses the mesh that is generated by triangulating the point cloud and fits a surface with the mesh

2.2. Geometric Analysis

2.2.1 Quality of surface approximation

To assess the quality of the generated surfaces we introduce two criteria:

- Mean distance d_m between surface and data point
- Distribution of distances

The mean distance gives a good estimation for the accuracy of the surface: a lower value indicates a more precise fitting. A graph of distribution of distances immediately makes the accuracy visible.

2.2.2 Surface curvature

In contrast to meshing, all methods described above produce continuous surfaces. Hence, it is possible to investigate these surfaces by means of geometrical analysis. At each point of the surface the two principal curvatures k_1 and k_2 can be determined [10]. They are perpendicular to each other, representing the highest (k_1) and lowest (k_2) curvature at that point and indicating the two principal curvature directions (fig. 4).

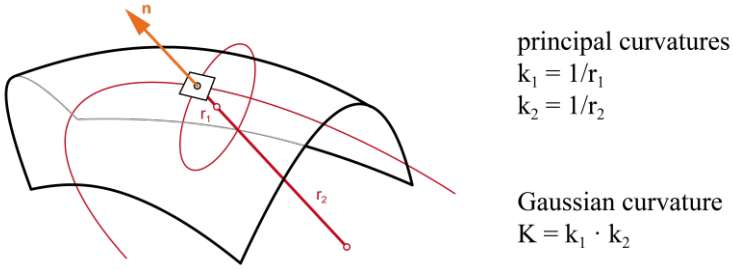


Figure 4: Principal curvatures with corresponding radii and Gaussian curvature at a certain point (by [10])

From these two principal curvatures, the Gaussian curvature ($K = k_1 \cdot k_2$) is calculated and visualized within the digital model. The basic shape of historic vaults is either single curved ($K = 0$, e.g., barrel or pointed vault) or positive synclastic ($K > 0$, e.g., sail vault or dome). The geometry of these constructions is based on circles, ellipses or parabolas and the Gaussian curvature will be constant or change slightly.

In contrast to that basic shape, the real geometry has irregularities. An integral analysis of the Gaussian curvature includes identifying (i) an intense change of K and (ii) anticlastic areas with $K < 0$. Depending on their global position, these domains potentially pose a greater threat of local failure and stress peaks.

3. Results

3.1. Geometrical verification

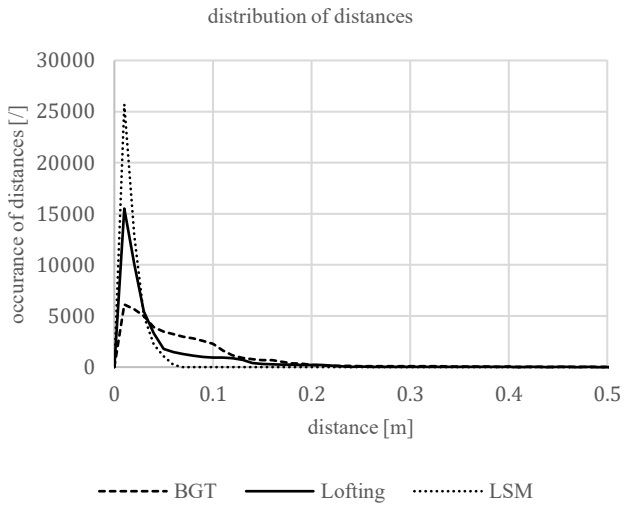
We implemented three geometric modelling approaches – BTG, Lofting and LSM (2.1) – as well as the analysis of accuracy (2.2.1) for three different point clouds of real vaulted structures. The distribution of distances are displayed in table 2.

Table 2: Analysis of distribution of distances for three real structures

a) Groin vault with domed webs



number of data points [/]:
~47 000

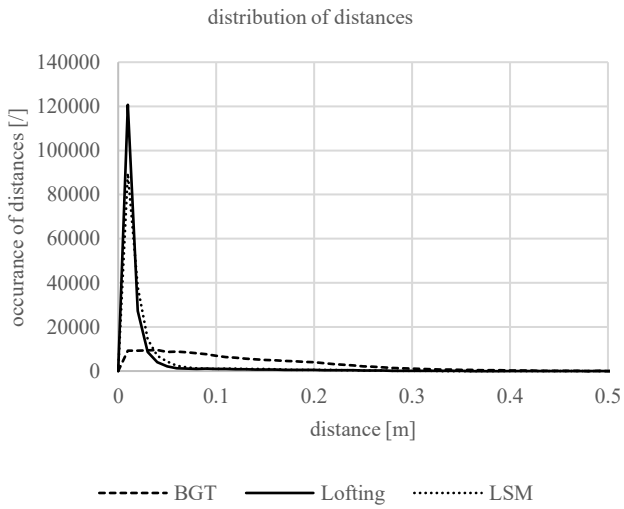


BGT	*Lofting*	*LSM*
max. distance [m]: 1.460 mean distance [m]: 0.067	max. distance [m]: 0.544 mean distance [m]: 0.038	max. distance [m]: 0.064 mean distance [m]: 0.012

b) Pointed vault with lunette caps

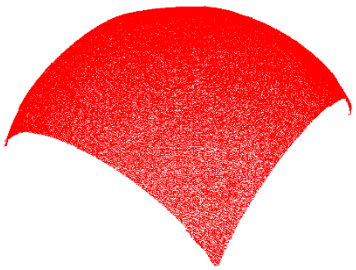


number of data points [/]:
~165 000

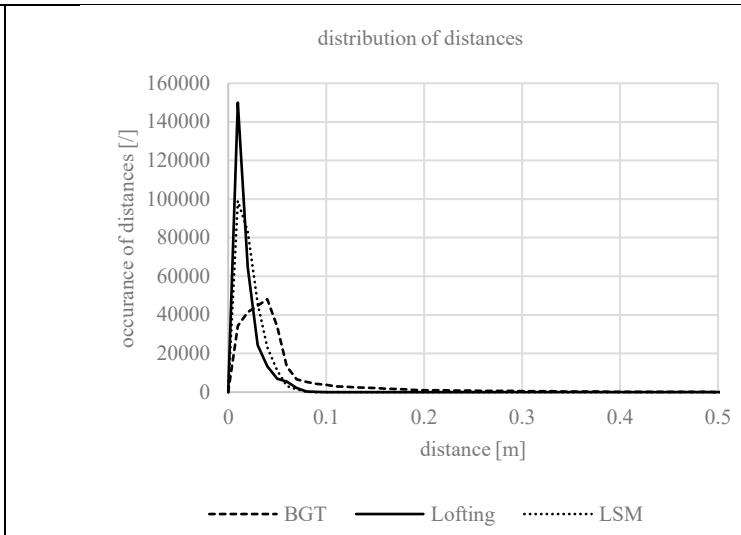


BGT	*Lofting*	*LSM*
max. distance [m]: 0.826 mean distance [m]: 0.116	max. distance [m]: 0.382 mean distance [m]: 0.019	max. distance [m]: 0.375 mean distance [m]: 0.024

c) Sail vault



number of data points [/]:
~267 000



BGT	*Lofting*	*LSM*
max. distance [m]: 0.805 mean distance [m]: 0.051	max. distance [m]: 0.264 mean distance [m]: 0.013	max. distance [m]: 0.092 mean distance [m]: 0.016

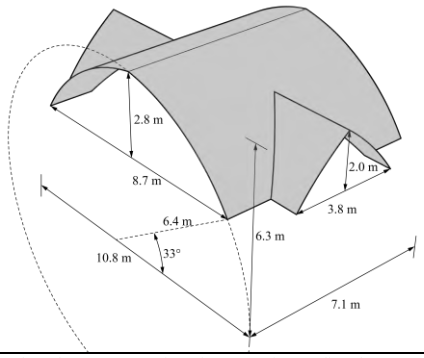
For all three cases, the distribution of distances shows that the BTG is the least accurate method as it results in the largest mean distances. According to that criteria, for vaults b) and c) the lofting method generates the most accurate surface; for vault a) the LSM generates the best fitting surface. This also corresponds to the distribution of the distances. For a small value of the mean distance, the distribution curve shows a small, high peak – most data points lie within a small distance from the surface.

3.2. Case study: pointed vault with lunette caps

3.2.1 Construction and parameters for analysis

We applied the above methods to the real example of a Romanesque church located in southeast Germany (see also: fig. 1). The main aisle has a pointed vault with lunette caps. Table 3 sums up the basic geometry and the chosen parameters for the computation.

Table 3: Parameters for structural analysis

Material and Geometry	Specific weight $\gamma = 20$ kN/m³ Young's modulus $E = 300$ kN/cm² Shear modulus $G = 120$ kN/cm² Poisson's ratio $\nu = 0.25$ Compr. strength $\beta c = -2000$ kN/m² Tens. strength $\beta t = 60$ kN/m² Vault thickness $d = 0.25$m Support height corresponding to opening angle of 57°	
Supports and loads	Non-linear horizontal supports at web edges can only take compression forces; Linear fixed supports at the springing lines; characteristic loads resulting only from dead load	
FEM Computation	"Isotropic degradation" (Dlubal 2012; Shell elements (2D quadrangles or triangles) based on Reissner-Mindlin theory; Theory of 1st order (geometrical linear)	

3.3.1 Gaussian curvature analysis of webs

We applied the above methods to the case study of a Romanesque church.

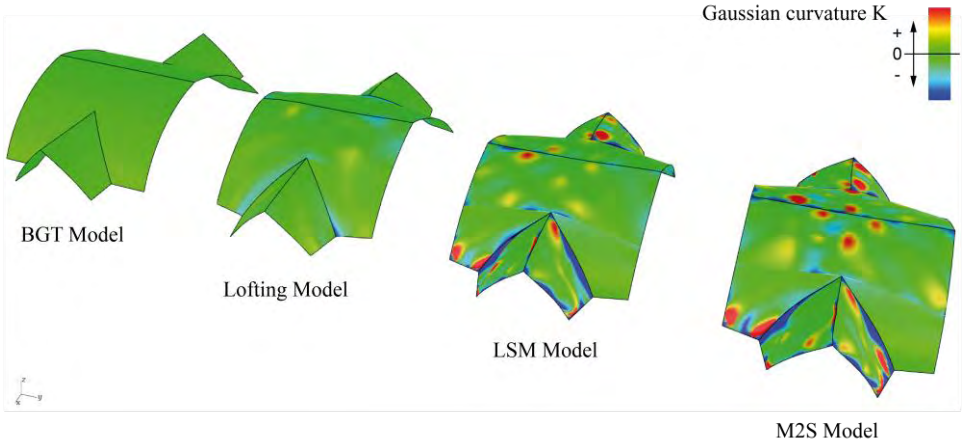
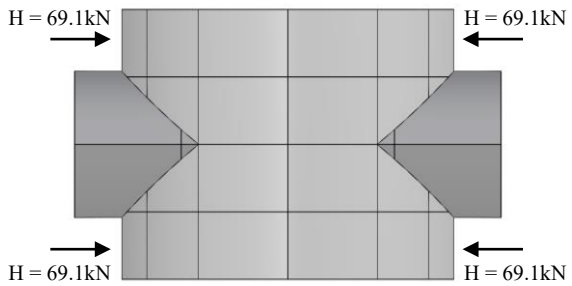
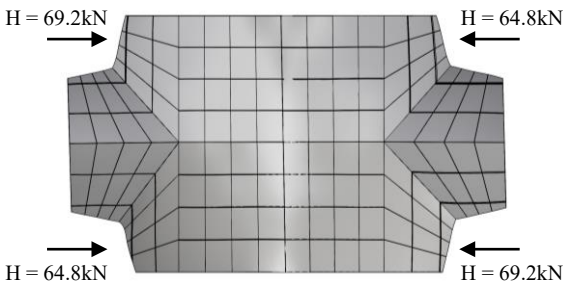
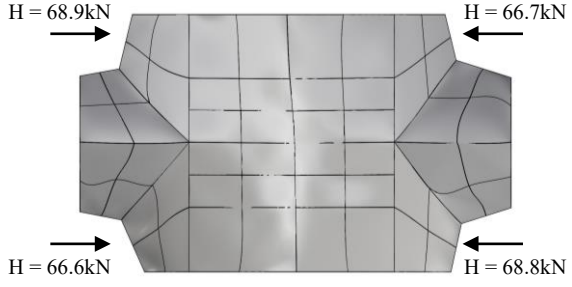
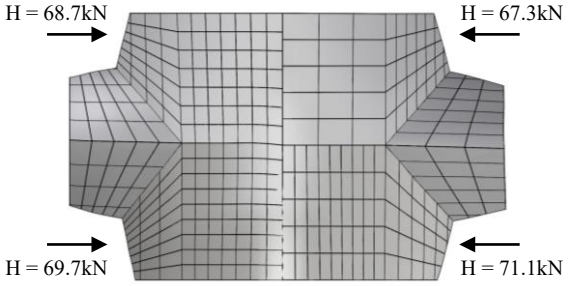


Figure 5: Gaussian curvature analysis of four different geometric approaches

As expected, the BGT approach has no Gaussian curvature (green), since all surfaces have single curvature. Within the other models, we can identify domains with double curvature. Circular-shaped areas (yellow or red) – particularly in the LSM and M2S models – indicate local bulges to the intrados or extrados at many locations in the webs. Elongated bluish areas are anticlastic surface domains and can mainly be identified along the groins of the lunette caps.

3.3.3 Verification of thrust

Table 4: Resulting horizontal thrust for generated models

BGT	Lofting
	
LSM	**M2S**
	

Since the IGA approach is not yet able to analyses masonry structures, we applied a valid FEM-analysis in *RFEM* (Dlubal Software GmbH, V.5) using the boundary conditions and material models mentioned above. Table 4 shows the horizontal component of the integrated lateral support thrusts.

As expected, the BGT model yields symmetric support forces. The three other models show deviations up to ±7%. Yet, the equilibrium of horizontal forces is fulfilled.

4. Discussion

All modelling strategies that consider the discrete shape of the webs lead to reasonable results. The analysis of the mean distance between point cloud and model surfaces identified a significant advantage for the free-form models (lofting, LSM and M2S) over the BTG model. It was expected that a higher accuracy would be obtained than for models that refer only to the groin geometry. Nevertheless, we had to deal with new problems, such as edge fitting, folding or offsetting [10].

In contrast to common meshed FE models, the continuous shape can be investigated by tools for curvature analysis. The integral analysis of the Gaussian curvature seems to be an appropriate tool for detecting local failures in the webs. A possible congruence of principal stresses and principle curvature is much more complicated and not yet being discussed. Furthermore, these kinds of parametric surfaces are particularly suited for analysis using IGA methods [11].

Beside these geometric features, our case study has illustrated another important issue: even the global load-bearing can change to a certain degree – in our case up to ±7 % of the expected thrust. Therefore, the real geometry of the webs can certainly represent a possible cause of damage to historical vaults.

Finally, it should be emphasized that the methods presented require further research and optimization. Nevertheless, our studies have shown that free-form parametric modelling of webs, based on 3D laser scans, has both academic and practical relevance.

References

[1] H. Pottmann, A. Asperl, M. Hofer, A. Kilian, „*Architectural Geometry*," Bentley, 2007.

[2] E. Grillanda, A. Chiozzi, F. Bondi, A. Tralli, F. Manconi, F. Stochino, A. Cazzani, "Numerical insights on the structural assessment of historical masonry stellar vaults: the case of Santa Maria del Monte in Cagliari," *Continuum Mechanics and Thermodynamics*, vol 3/4, 2019.

[3] A. Buchanan, N. Webb, "Creativity in Three Dimensions: An Investigation of the Presbytery Aisles of Wells Cathedral," *British Art Studies*, Issue 6, 2018.

[4] R. Barthel, "*Tragverhalten gemauerter Kreuzgewölbe*," Dissertation, University Karlsruhe, 1991.

[5] H. Park, "An Approximate Lofting Approach for B-Spline Surface Fitting to Functional Surfaces," *International Journal of Advanced Manufacturing Technology*, vol 18 (7), pp. 474–482, 2001.

[6] L. Piegl, W. Tiller, "*The NURBS Book*," (2nd ed.). Berlin, Heidelberg: Springer, 1997.

[7] J. Bureick, H. Neuner, C. Harmening, I. Neumann, "*Curve and Surface Approximation of 3D Point Clouds*," 2016.

[8] S. Flöry, "*Fitting B-Spline Curves to Point Clouds in the Presence of Obstacles*," Diploma thesis, Technical University Vienna, 2005.

[9] E. Schling, "*Repetitive Structures*," Dissertation, Technical University of Munich, 2018, DOI: 10.14459/2018md1449869.

[10] C. Reihl, "*Geometrische Abbildung und Berechnung von Mauerwerksgewölben*," Masterthesis (unpublished), Technical University of Munich, 2019.

[11] M. Breitenberger, A. Apostolatos, B. Philipp, R. Wüchner, K.-U. Bletzinger, "*Analysis in computer aided design: Nonlinear isogeometric B-Rep analysis of shell structures*," Computer Methods in Applied Mechanics and Engineering 284, 2015, 401–457

FORM and FORCE

Proceedings of the IASS Annual Symposium 2019 — Structural Membranes 2019
Form and Force
7—10 October 2019, Barcelona, Spain
C. Lázaro, K.-U. Bletzinger, E. Oñate (eds.)

Isogeometric Analysis in the Design Process of Lightweight Structures

Anna M. BAUER*, Roland WÜCHNER[a], Kai-Uwe BLETZINGER[a]

*,[a] Chair of Structural Analysis, Technical University of Munich
Arcisstr. 21, 80333 München, Germany
am.bauer@tum.de

Abstract

This contribution will give a brief overview of isogeometric analysis (IGA) and its requirements and challenges. The smooth basis functions and the seamless link to CAD provide a lot of possibilities in the design of structures. Especially for lightweight structures, where form and force are highly interacting, this direct link is beneficial. Geometric design and mechanical properties are available in the same environment and can be manipulated simultaneously in order to optimize the shape and stress distribution in the final state of equilibrium. Furthermore, inverse methods can easily be used in order to design the mounted structure. Forward-analysis, such as a simulation of the mounting, has only to be considered in the second step to compute potential normal forces. This can be applied to lightweight structures, e.g. bending-active structures, tensile membranes, prestressed cable nets and combinations of those structures.

Keywords: lightweight structures, CAD-integrated design, isogeometric analysis, active-bending

1 Introduction

The design of lightweight structures is very complex as their shape and load bearing behavior are highly interactive. Usually, apart from some standard cases, it is not possible to just "draw" a structure in equilibrium. Structural feedback is a vital element in the design process. This used to be physical models such as those by Heinz Isler or Frei Otto. Nowadays, these physical models are often replaced by computational models and structures can become more complex and bigger. Furthermore, more effects can be considered. Bending-active structures are a subcategory of lightweight structures. Their design is especially difficult since the assembled structure has to consider the mounting process. This is usually done by laying out flat rods and pulling them with cables and forces into the desired shape. The final form can e.g. be influenced by changing the flat layout. However, getting this initial layout, which results in the closest possible shape to the design idea, can be difficult. It would be beneficial to be able to start the computation with a configuration close to the intended design. Inverse methods are needed in order to retrieve correct stress-strain information from the already deformed state. This is possible with certain assumptions about the initial geometry. The stresses and strains can then be computed based on these assumptions. Similar approaches already exist in literature as e.g. by Bellmann [1] and in other software as e.g. in [2].
In addition to applying this inverse approach in an elegant way as shown later, isogeometric analysis (IGA) gives the possibility of integrating the computational workflow into the design

Copyright © 2019 by Anna M. Bauer, Roland Wüchner and Kai-Uwe Bletzinger
Published by the International Association for Shell and Spatial Structures (IASS) with permission.

environment. Isogeometric analysis, as originally introduced by Hughes *et al.* [3] is a rather new approach within finite element analysis. In contrast to long-established approaches, that require a substitution of the CAD model by a finite element model, IGA skips this step by using the same parametric description also for the analysis. The basis functions are usually Non-Uniform B-Splines (NURBS). Isogeometric B-Rep Analysis (IBRA) as introduced by Breitenberger *et al.* [4] takes this a substantial step further and includes the topology information as well. This implies that one can generate the FE input with the same methods as for the pure shape design. Moreover, the analysis result has the same discretization as the input and can therefore be used in the same manner.
This contribution will briefly show the basics of continuum mechanics with focus on the changes that have to be made in order to be able to start the computation on an already assembled structure. The potential of this inverse computation in the context of isogeometric analysis will be illustrated by several examples. Moreover, the benefits of CAD-integration will be demonstrated with a hybrid structure subjected to several consecutive analysis steps.

2 Isogeometric Analysis

The main difference of isogeometric analysis to a classical FEM approach are the basis functions which are used to describe geometry and deformations. These are usually Non-Uniform Rational B-Splines. NURBS use a parameter space and control points $\mathbf{P}$ in the geometry space to define the geometry (see Fig. 1). The respective basis functions N are defined by a polynomial degree and the knot vector in each dimension of the parameter space.

$$\mathbf{S}(u,v) = \sum_i \sum_j \frac{N_i(u) \cdot N_j(v) \cdot w_{ij}}{\sum_k \sum_l N_k(u) \cdot N_l(v) \cdot w_{kl}} \cdot \mathbf{P}_{ij} \tag{1}$$

where u and v are the parametrical coordinates. Moving a point $\mathbf{X}(u,v)$ along the surface $\mathbf{S}(u,v)$ can easily be achieved by changing the parametrical coordinates.

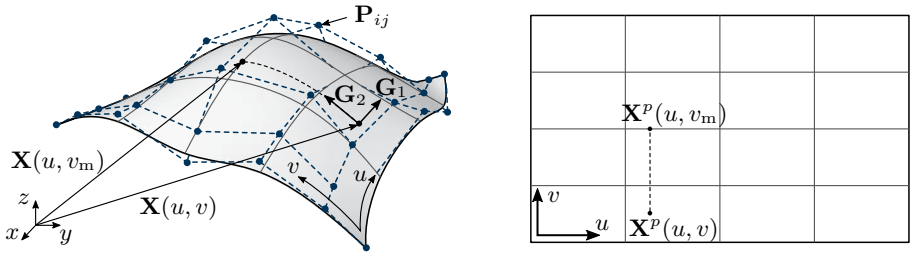


Figure 1: NURBS surface in geometry and parameter space.

3 Inverse Method

The basis of the inverse approach is the *Principle of Virtual Work*.

$$\delta W = -\delta W_\mathrm{int} + \delta W_\mathrm{ext} = -\int_\Omega \mathbf{S} : \delta\mathbf{E}\, dx + \int_\Omega \mathbf{B} : \delta\mathbf{u}\, dx + \int_\Gamma \mathbf{t} : \delta\mathbf{u}\, dx = 0 \tag{2}$$

Green-Lagrange strains $\mathbf{E}$ and energetically conjugated 2nd Piola-Kirchhoff stresses $\mathbf{S}$ can be derived by continuum mechanics. The components of the strain E_{ij} are defined as

$$E_{ij} = \frac{1}{2}\left(\mathbf{g}_i \cdot \mathbf{g}_j - \mathbf{G}_i \cdot \mathbf{G}_j\right) \tag{3}$$

where $\mathbf{G}_i$ and $\mathbf{G}_j$ are the local base vectors of the geometry. They correspond to a local fiber length and can also be used for measuring geometric properties such as curvature. Note that capital letters always refer to the initial configuration and small letters to the actual deformed configuration.
The stresses are referred to the initial unstressed configuration in the standard approach (see Fig. 2(a)). Strains and stresses can be computed for every arbitrary geometry configuration. The isogeometric parameter space allows geometry refining, i.e. adding degrees of freedom, and still being able to get the link between reference and actual configuration. When releasing the geometrical form apart from the intended Dirichlet boundary conditions the system deforms towards its equilibrium state.

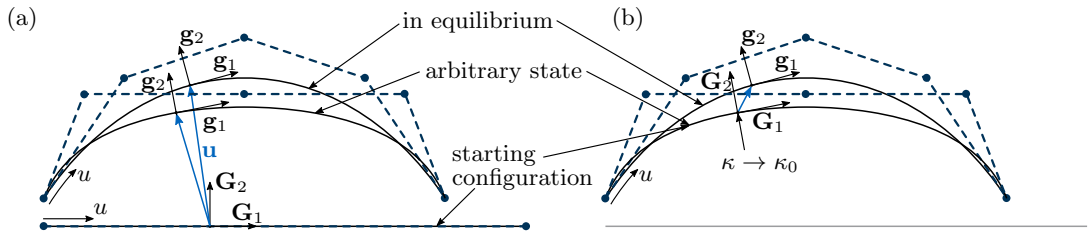


Figure 2: Geometry configuration with base vectors for: (a) standard approach and (b) inverse approach

The here described inverse approach distinguishes itself from the standard procedure by not starting the search for equilibrium in the initially unstressed state but in an arbitrary deformed state (see Fig. 2(b)). The initial configuration is not modeled explicitly but considered by certain assumptions which will be described in the following sections. The integration is then performed in the first deformed configuration. This strategy is appropriate for a certain type of structures. One primary condition is that large in-plane strains are not expected or that the initial integration area can be derived from additional assumptions. A more complex cutting pattern analysis has to be conducted in order to consider such large in-plane strains correctly.

3.1 Inverse bending

The term related to bending in the *Principle of Virtual Work* can be derived by the change in curvature $\boldsymbol{\kappa}$.

$$\delta W_{\text{int}}^{\text{bend}} = \int_{A/L} \mathbf{m} : \delta\boldsymbol{\kappa}\, dx \quad \text{with} \quad \mathbf{m} = I \cdot \mathbf{D} \cdot \boldsymbol{\kappa} \text{ and } \boldsymbol{\kappa} = (\boldsymbol{\kappa}_{\text{act}} - \boldsymbol{\kappa}_{\text{initial}}) \tag{4}$$

The reduced integration domain is defined by A for surface elements and L for curve elements. The respective moment of inertia for each bending axis is denoted as I and is a result of the pre-integration over the cross section. The change of curvature is purely defined by the geometry, hence can be computed by the base vectors.

The curvature of an initially flat structure is zero and can therefore directly be used for computing the actual strains and stresses in a given geometry. One of the most simple and illustrative examples is the elastica. A single beam is bent by bringing its two ends together as shown in Fig. 3.

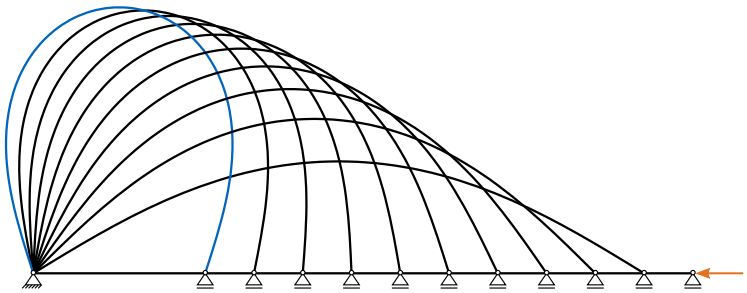


Figure 3: Straight beam bent to elastica shape by bringing its two ends together.

The same result for the two Dirichlet boundary conditions of the beam can be obtained by drawing an arbitrary initial shape with respective length and support positions as shown in Fig. 4. All three initial shapes have the same relaxed state which match the reference solution from bending the initially straight beam in shape and forces. This is independent of the how close the starting and the equilibrated geometry are.

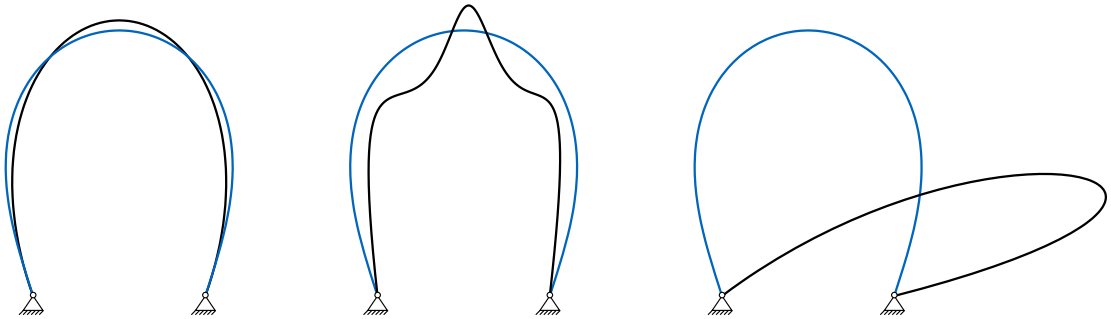


Figure 4: Inverse method for bending applied to three starting shapes (black) with the same boundary conditions as the elastica in Fig. 3 and its equilibrated shape (blue).

3.2 Inverse torsion

The method of the inverse approach can also be used for torsional forces. However, curve and surface elements have to be treated differently. The approach for beam elements is in general the same as for bending. The change of the twist is used for computing the torsional moment. If the reference twist is set to zero, as it is for an initially untwisted rod, one can use the evolving torsional moments to obtain equilibrium. The main task for designers is to define the orientation of the cross section in the actual state.
A simple example, which contains bending and torsion, is a beam with the shape of a quarter circle. The cross section is twisted increasingly around the center line with a final twist of 90°. When releasing this state with the inverse method the beam deforms back into the assumed straight, untwisted state as shown in Fig. 5.

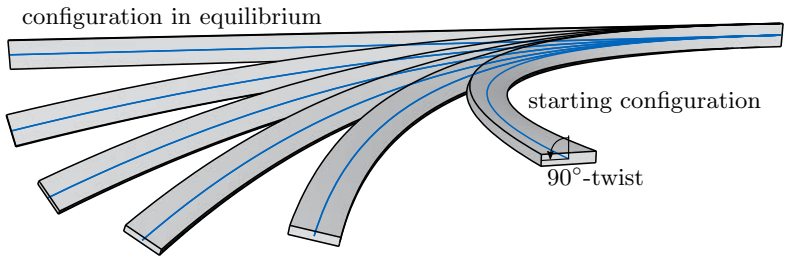


Figure 5: Application of inverse torsion and bending to a twisted and bent beam with all states from starting configuration to relaxed configuration.

In contrast to the beam, there is no specific term related to torsion in the Kirchhoff-Love shell theory as used by Kiendl *et al.* [5]. Fig. 6 shows the same structural problem as Fig. 5 but is modeled by a shell. Fig. 6(a) takes only bending stresses into account. Consequently, a flattening happens. However, the result is not a straight strip but a curved one.

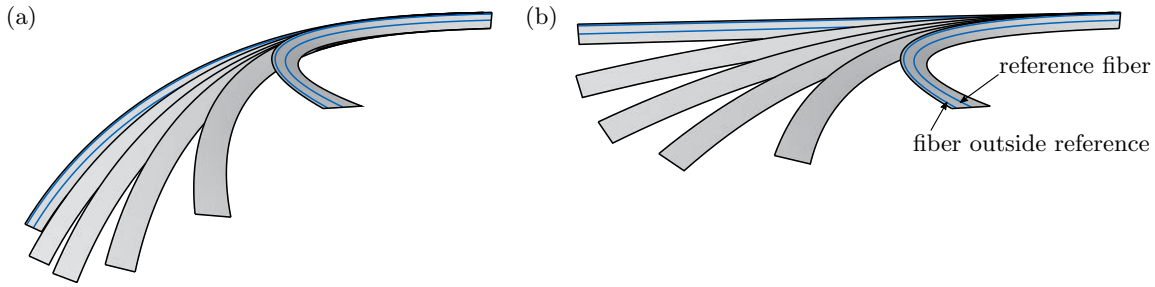


Figure 6: Twisted and bent shell as starting configuration with two respective fibers (blue): (a) Application of inverse bending and (b) application of inverse torsion and bending.

This is due to different lengths of the fibers in the starting configuration as indicated in Fig. 6. If this varying length can be interpreted as result of torsion, one can also pursue a different approach. Twisting results in different elongations and therefore different strains and stresses in the fibers. Fibers close to the center line are less stretched than fibers on the outside if the length of the strip is maintained. This is called helix-torsion and is described in more detail by Lumpe and Gensichen [6]. By defining one initial fiber length, which corresponds to the length of the base vector, for all fibers, as is the case for initially straight shells, one can also consider this twisting effect for shells. Note that the reference length is not necessarily constant along the longer dimension of the shell.
The reference fiber length can easily be defined when using NURBS for the FE model. The whole surface is described by one entity $\mathbf{S}(u, v)$ and is not subdivided into several smaller elements as is usually the case for classical finite elements. The new metric G_{ij} is simply computed by

$$G_{11}(u, v) = \mathbf{G}_1(u, v_{\text{ref}}) \cdot \mathbf{G}_1(u, v_{\text{ref}}) \tag{5}$$

$$G_{22}(u, v) = \mathbf{G}_2(u, v) \cdot \mathbf{G}_2(u, v) \tag{6}$$

$$G_{12}(u, v) = G_{21}(u, v) = G_{12}(u, v) \cdot \frac{\|\mathbf{G}_1(u, v_{\text{ref}})\|}{\|\mathbf{G}_1(u, v)\|} \tag{7}$$

if the fiber length is pointing in $\mathbf{G}_1$-direction. The position of the reference fiber is described by v_{ref} on the surface. If $\mathbf{G}_2$ is the respective fiber direction the indices as well as u and v have to be swapped.
Applying this modification to the bent and twisted quarter circle results in a relaxation as shown in Fig. 6(b). The released strip finds its equilibrium in a flat and straight configuration. A more detailed evaluation and large scale application can be found in Schikore *et al.* [7].

4 Application examples

4.1 Gridshell

A good application example is a bending-active gridshell. The final shape should be close to a part of a sphere. Therefore, a regular grid is projected onto a sphere. The projected curves are then used as starting configuration for the structural analysis. The beams have a circular cross section in order to provide same bending stiffness in every direction. Each end is fixed by a simple support and the beams are coupled with each other by hinges. The inverse method is used to derive the stress-strain state. The final structure in equilibrium varies slightly from the starting assembly as can be seen in Fig. 7. By removing unnecessary supports the gridshell finds a flat equilibrated state which can be used for a simplified initial assembly of the rods on the ground. Note that the flat configuration still has bending moments in the rods as they are curved.

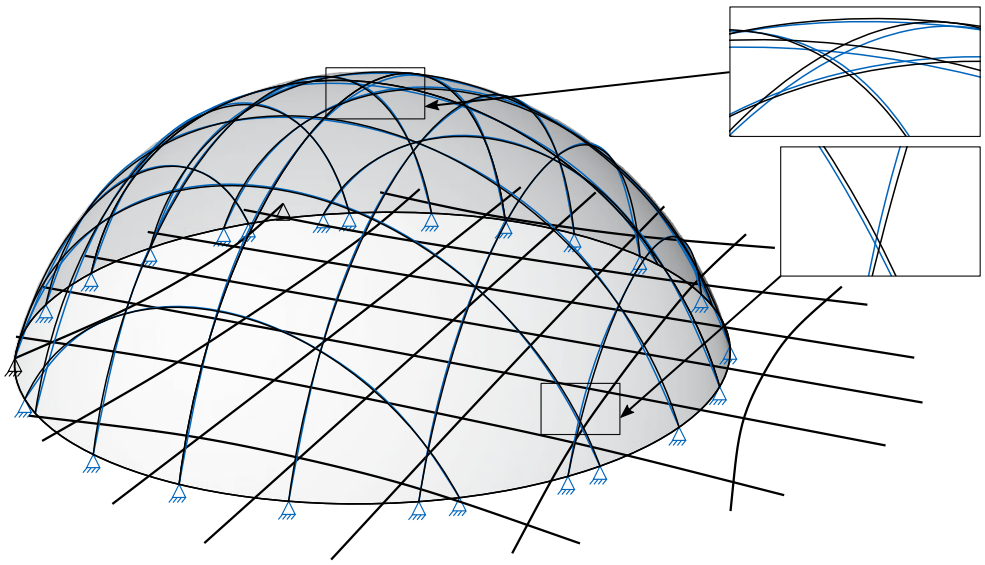


Figure 7: Spherical gridshell with starting assembly (black), relaxed configuration(blue) and flat assembly pattern for the straight rods.

The results of the inverse method are verified by taking the flat assembly with remaining bending moments, remodeling it with a new discretization and pushing it into shape again. The maximum distance between the beams of the forward and backward analysis is 0.6577096mm where the diameter of the gridshell on the ground is 11.31m and the height is 3.95m. The maximum bending moment differs with 0.154%.

4.2 Hybrid structure

The CAD-integration aspect of IGA becomes especially appealing if the analysis result is used in a follow-up analysis since there is no transformation involved. This allows also for a parametric workflow, which is especially beneficial for lightweight structures, where form and forces cannot be treated separately.
The CAD-integrated workflow with several analyses is exemplified by a hybrid structure (see Fig. 8). Two connected and bent beams constitute the initial configuration. Their shape can either be bent in place in a forward analysis or derived with the inverse approach. A membrane roof is added in between. As a membrane's stiffness lies in the combination of curvature and prestress, a form finding analysis has to be conducted to find an equilibrium state. The initial geometry of the membrane component can directly be derived by a loft through the two respective (parametrically defined) subparts of the bent rods. Note that the position of the membrane is independent of the FE-"nodes" of the curve elements within IGA. The beams generate a soft support during the form finding. Their deformation due to the prestressing of the membrane is directly considered. The form finding result can then also be used in a structural analysis for e.g. wind or for a cutting pattern analysis as presented by Goldbach *et al.* [8].

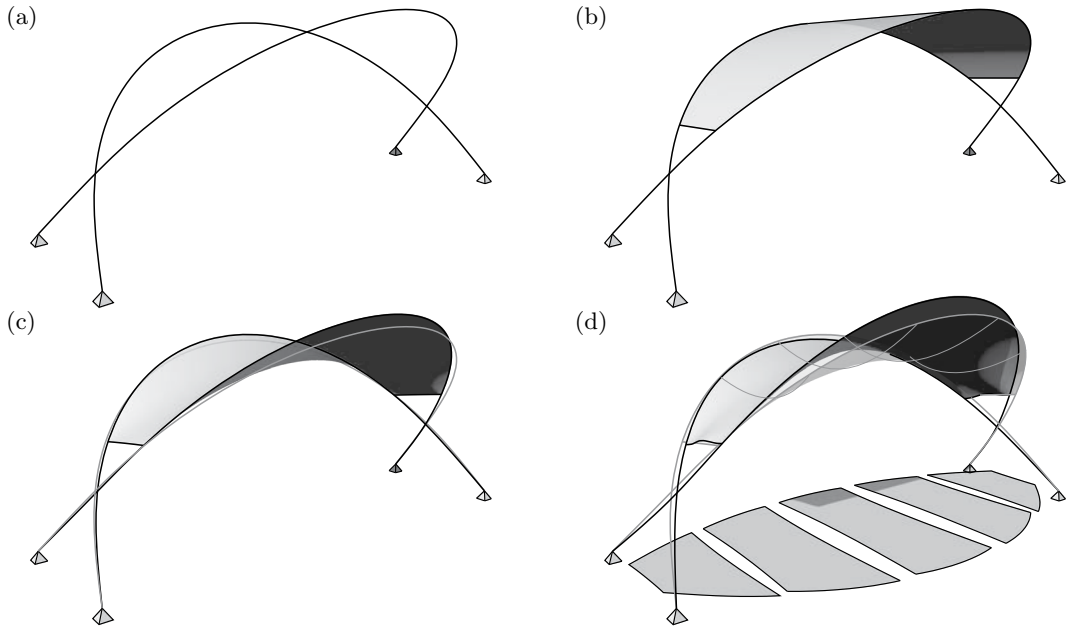


Figure 8: Hybrid structure: (a) bent supporting structure, (b) initial form finding geometry, (c) form finding result and (d) structural analysis for wind and cutting pattern.

5 Conclusion

This contribution gave a brief introduction to isogeometric analysis and possible application scenarios in lightweight design. The focus was set on the design process and how to simplify it by geometrical assumptions. These can be made for certain types of structures in order to compute backwards stresses and strains of already assembled structures. Two special cases of this inverse approach, namely bending and torsion, were elaborated for shells and beams. The

described approach has the advantage that one can skip the modeling of the whole mounting process in the first design phase. The method can be used for finding a state of equilibrium for some chosen boundary conditions or the initial unstressed shape of all members. However, this is restricted to structures which are not subjected to large normal strains.
Two benefits of isogeometric analysis were highlighted by application examples in this contribution. The first showed a potential utilization of the inverse approach for the design of a gridshell. The second example presented the potential of isogeometric analysis in a multi-analysis design process.

References

[1] J. Bellmann, "Active bending starting on curved architectural shape," in *Structural Membranes 2017: Proceedings of the VIII International Conference on Textile Composites and Inflatable, Munich, Germany, October 9-11, 2017* K.-U. Bletzinger, E. Oñate and B. Kröplin Eds., International Center for Numerical Methods in Engineering (CIMNE), 2017. pp. 265-274.

[2] C. Brandt-Olsen, *K2Engineering*, (Software). Available on https://github.com/CecilieBrandt/K2Engineering.

[3] T. Hughes, J. A. Cottrell and Y. Bazilevs, "CAD, finite elements, NURBS, exact geometry and mesh refinement," *Computer Methods in Applied Mechanics and Engineering*, vol. 194(39-41), pp. 4135-4195, Oct. 2005.

[4] M. Breitenberger, A. Apostolatos, B. Philipp, R. Wüchner, and K.-U. Bletzinger, "Analysis in computer aided design: Nonlinear isogeometric B-Rep analysis of shell structures," *Computer Methods in Applied Mechanics and Engineering*, vol. 284, pp. 401-457, Feb. 2015.

[5] J. M. Kiendl, K.-U. Bletzinger, J. Linhard and R. Wüchner, "Isogeometric shell analysis with kirchhoff-love elements," *Computer Methods in Applied Mechanics and Engineering*, vol. 198(49-52), pp. 3902-3914, Nov. 2009.

[6] G. Lumpe and V. Gensichen, *Evaluierung der linearen und nichtlinearen Stabstatik in Theorie und Software: Prüfbeispiele, Fehlerursachen, genaue Theorie*. Berlin: Ernst W. + Sohn Verlag, 2014.

[7] J. Schikore, A. M. Bauer, R. Barthel and K.-U. Bletzinger, "Large torsion on elastic lamella grid structures," in *Form and Force: Proceedings of the IASS Annual Symposium 2019 - Structural Membranes 2019, Barcelona, Spain, October 7-10, 2019* C. Lázaro, K.-U. Bletzinger, and E. Oñate Eds., 2019.

[8] A.-K. Goldbach, and K.-U. Bletzinger, "Cad-integrated parametric design cycle for structural membranes," in *Form and Force: Proceedings of the IASS Annual Symposium 2019 - Structural Membranes 2019, Barcelona, Spain, October 7-10, 2019* C. Lázaro, K.-U. Bletzinger, and E. Oñate Eds., 2019.

Proceedings of the IASS Annual Symposium 2019 – Structural Membranes 2019
Form and Force
7 – 10 October 2019, Barcelona, Spain
C. Lázaro, K.-U. Bletzinger, E. Oñate (eds.)

Large torsion on elastic lamella grid structures

Jonas SCHIKORE*, Anna M. BAUER[a], Rainer BARTHEL, Kai-Uwe BLETZINGER[a]

*Technische Universität München
Department of Architecture, Chair of Structural Design, Arcisstr. 21, 80333 München
Jonas.schikore@tum.de
[a] Department of Civil-, Geo.- and Environmental Engineering, Chair of Structural Analysis

Abstract

Elastically curved grid structures pose great potential to simplify fabrication as the structure may consist of straight elements [1]. However, for assembly, erection and load bearing the structures restraint forces need to be considered. While bending stresses are well explored, nonlinear normal stresses due to torsion (helix-strain) are often neglected. For large twists of lamella profiles in a practical scale, the helix-strain effects need to be considered as they amount significantly to the lamellas torsional stiffness and utilization. For lamella profiles, calculations according to Lumpe and Gensichen [2] can be simplified. The "Inverse"-method allows simulations using the final shape as initial simulation geometry and therefore reduces the complexity of static calculations. This paper presents a method to consider helix-strain effects for the simulation of lamella grids using the IGA "Inverse"-method. This method has been applied to simulate the behavior of a grid structure as central element of a canopy. A simplified simulation offered valuable information about the flat state at assembly and necessary forces to erect the grid structure.

Keywords: elastic gridshell, helix-torsion, Isogeometric Analysis, Formfinding, asymptotic networks, active bending

1. Introduction

Grid structures are suitable for highly efficient lightweight constructions. Creating curved grid geometries however, goes with constructional complex solutions. An elegant approach is to use elastic deformation to create curvature [3]. The *Multihalle* (Mannheim 1972) is an impressive example for this method. Frei Otto managed to create a doubly curved gridshell out of straight timber beams by bending and torsion. Since then this method has fascinated architects and engineers and has been improved and applied on later projects such as the *Wealds Downland Gridshell* or *Saville Gardens*.

The shape of elastically bent structures is subject to minimum strain energy laws and limited by material and profile strain capacities. The local beam stiffness parameters directly specify these restrictions. A prevalent approach is to keep the section stiffness for bending and torsion low to minimize these restrictions.

New designs, such as the research pavilion "InsideOut" (2017), at the TUM (Figure 1) use an asymptotic curve network, where lamella sections are deformation by bending on the weak axis and torsion [4]. A first commercial application of a canopy for a business hotel is currently under construction. The erection process benefits from these restrictions as the grid structure follows a predefined shape turning from flat to spatial without the need for a form giving scaffolding.

Copyright © 2019 by Jonas Schikore, Anna.M. Bauer
Published by the International Association for Shell and Spatial Structures (IASS) with permission.




Figure 1: "Inside/Out" Pavilion, TUM [Foto by Felix Noe] and Hotel Canopy [Rendering by Denis Hitrec]

To control the elastic mechanisms, strain energy states and effects of large deformation need to be carefully considered. Large torsional deformations of sections with large polar moment of inertia go along with normal stresses according to the theory of helix-torsion [2]. Conventional FEM-Beam elements do not consider those effects. For lamella profiles, the use of shell elements seems appropriate.

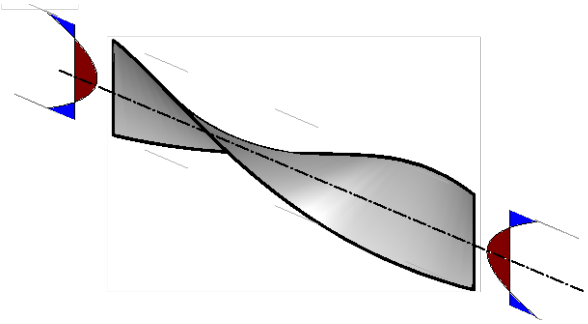


Figure 2: helix-strain due to torsion (red: compression, blue: tension)

Simulating the complete construction process of elastically bent grid structures, starting from straight beam elements is very complex and time intensive. With non-regular grids, the beam elements need to be stepwise connected during simulation. The "Inverse"-Method provides a faster solution.

In chapter 2.1, this paper evaluates the impact of helix-strain in a practical scale. Therefore, calculations quantify resulting stresses, torsional moments and strain energy due to helix-strain of a lamella section. Furthermore, in chapter 2.2, a new approach using IGA is presented to respect the effects of helix-strain using the "Inverse"-Method for simulating elastically bent lamella grid structures. Finally, in chapter 2.3, this method was applied on real scale canopy to predict the structures behavior during erection. The natural shape of the structure was evaluated.

2. Methods

2.1. Calculation of helix strain effects

To evaluate the impact of helix-strain in a practical scale, the torsional effect of a representative lamella element has been investigated.

2.1.1 Calculation set up

The material parameters are set according to steel: $E = 21000$ kN/cm^2 ; $G = 8000$ kN/cm^2

A lamella profile with dimensions of t x h = 2,5 x 100 mm and 1000 mm length was twisted by 90° as shown in Figure 3.

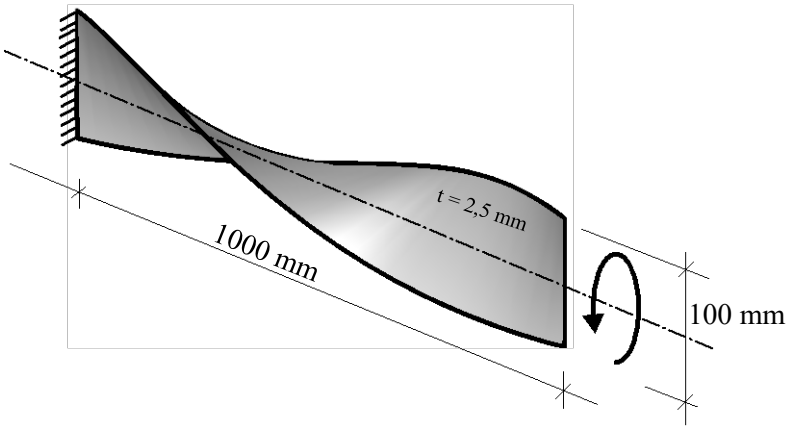


Figure 3: lamella calculation model

2.1.2 Manual Calculation:

For a lamella profile, where $h >> t$, calculations regarding the helix torsion are simplified with the following assumption:

Simplification of moments of inertia:

$$I_r = \int_A r^4 dA \sim t \int_{-h/2}^{h/2} z^4 dz = \frac{th^5}{80} \; ; \; I_p \sim I_y = \frac{th^3}{12} \tag{1}$$

For a lamella profile with $h >> t$, the normal stresses due to helix-strain:

$$\sigma_{x,Helix-strain}(x,z) = \frac{1}{2} E\left(z^2 - i_p^2\right)\vartheta'^2 \tag{2}$$

The torsional moment of a lamella due to helix-strain:

$$M_{t,Helix-strain} = \frac{1}{2} E(I_r - i_p^2 I_p)\vartheta'^3 \tag{3}$$

The strain energy of a lamella due to helix-strain in normal direction:

$$E^F_{t,Helix-strain} = \frac{1}{2} \int_0^L \frac{1}{9} E I_r \vartheta'^4 \tag{4}$$

The strain energy of a lamella due to St.Venant torsional shear:

$$E^F_{t,St.Venant} = \frac{1}{2} \int_0^L G I_t \vartheta'^2 \tag{5}$$

2.1.3 FEM-Calculation

FEM-Calculation (R-FEM5) are performed in Th.III.O. using beam or shell components of element size 1cm. The edges of the lamella, i.e. endsections, are fixed to stay in plane, but overall elongation or shortening is set free.

2.2. Implementation of Helix-strain to the "Inverse"-Method with IGA

The problem while designing structures with rather large torsion in the built state is that the different elongations of the fibers over the cross section can only be considered if one models the full twisting in a classical finite element approach. However, this is rather complicated for a structure consisting of several lamellas. It is beneficial to draw the assembled structure and then compute backwards the stresses and deformations. For the bending stresses this is simply possible by referencing the actual curvature to an initial zero-curvature which results in respective bending moments [5]. This is valid for

initially flat stripes. Applying this method for the stresses related to the helix torsion is not directly possible as the initial local length related to the finite element has to be known a priori. This is not possible for an arbitrary discretization. In the case of initially straight lamellas with constant height, one can assume that the initial local length is constant over the height. However, the fiber is getting longer when measuring the fiber length outside of the centerline in the twisted configuration (see Figure 4). If the computation starts from this geometry, the strain would be referred to a varying fiber length over the cross section which is not in accordance with the assumed initial geometry of the lamella. By choosing one local reference length over the cross section the stresses resulting from of helix torsion can be represented. Note that this reference can vary over the length of the beam if the elements are not equal sized as usually the case in complex models. Furthermore, the reference fiber is not necessarily restricted to the center line.

For a twisted profile, where ends are not fixed in longitudinal direction, helix compression and tension stresses will be in equilibrium. Therefore, the fiber of distance i_p (radius or gyration) to the centerline experiences no strain.

$$\sigma_{x,Helix-strain}(x,z) = 0 = \frac{1}{2}E\left(z^2 - i_p^2\right)\vartheta'^2 \rightarrow z = i_p = \sqrt{\frac{1}{12}}h \rightarrow v_{p,ref} = 0{,}5 + \sqrt{\frac{1}{12}}h \quad (6)$$

The reference fiber may be set to this position accordingly.

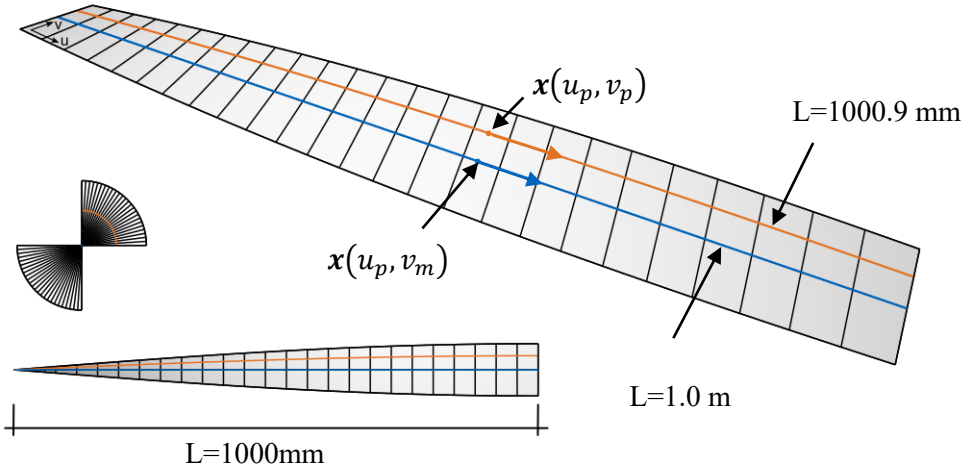


Figure 4: Twisted lamella with different fibers over the height and evaluation point $\boldsymbol{x}(u_p, v_p)$ with related base vector point at the mid $\boldsymbol{x}(u_p, v_m)$.

Isogeometric Analysis applies Non-Uniform Rational B-Splines (NURBS) for the representation of finite elements within the structural analysis. This implies that a lamella can be represented by a surface $\boldsymbol{S}(u,v)$ with one parameter space described by u and v.

$$\boldsymbol{S}(u,v) = \sum_i^n \sum_j^m R_{ij,pq}(u,v) \cdot \boldsymbol{P}_{ij} \text{ with } u \in [u_0, u_1] \; and \; v \in [v_0, v_1] \quad (7)$$

The computation of the reference length for a certain reference fiber can easily be derived from the parameter space as only one coordinate has to be varied. It is independent of the element discretization and storing information about neighbor elements and/or reference elements as needed for classical FEM can be avoided.

However, the following assumptions have to be made. Every lamella is supposed to be straight in the unstressed configuration. The cross section has to be constant and the discretization in cross section direction has to be perpendicular to the center line in order to consider helix-torsional effects.

Furthermore, the center line is restricted to zero curvature around the strong axis of the lamella as it is for asymptotic lines.

2.3. Simulation and erection of a canopy structure

The canopy structure consists of a lamella grid with a stiff steel frame. The grid is designed by finding an asymptotic curve network on an anticlastic design surface. The top part is covered with an arch supported membrane. The lamella grid is shaped by elastic deformation of initially straight lamella strips. Therefore, the grid is assembled flat and pulled into its spatial position. In flat state, lamellas are bent around their weak axis, in spatial state, lamellas are additionally bent and twisted. The lamella section parameters are chosen under the specification to deform mainly elastically. Stainless steel of with $R_{p,0.2}$ = 300 N/mm^2 was used for the lamella profiles.

To control the erection process, it is essential to determine the shape, which the structure is likely to adopt. In this context an analysis of minimum strain energy was executed using the IGA "Inverse"-Method. The design grid was supported statically determined to avoid any restraints. The lamella strips are connected only in translation at the intersecting lines thus a scissor hinge is modeled. In a first step the self-weight was turned off. In a second simulation self-weight was respected and the design grid was supported according to the erection set up. This simulation gave information about the necessary forces to induce the design shape. On site, the necessary force to erect the structure was measured to verify calculations.

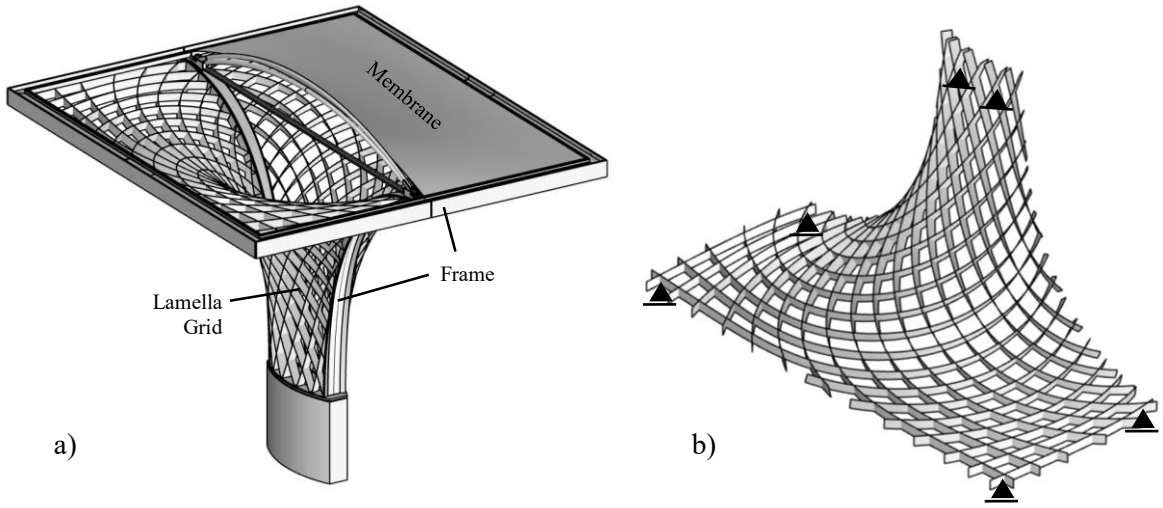


Figure 5: a) construction b) static system of "pulled up" state simulation

The simulation of the erected position may be seen as rough prediction of necessary pull up forces. The nodes of the real structure have slots of 50 mm within the lamellas to create centric nodes. These slots are weakening of the profiles capacities and therefore affect the grids behavior. The simulation model does not include those slots. The lamella thickness, however, has been chosen with the specification, that the slotted sections are capable to perform elastic when applying the necessary curvature to the lamellas. This consideration has been necessary to avoid kinks due to plastification at the nodes.

3. Results

3.1. Evaluation of helix-strain impact

The displayed graphs (Figure 6) show torsional moments and strain energy due to St. Venant shear stresses (bottom portion, grey) and normal helix shear stresses (top portion,blue).

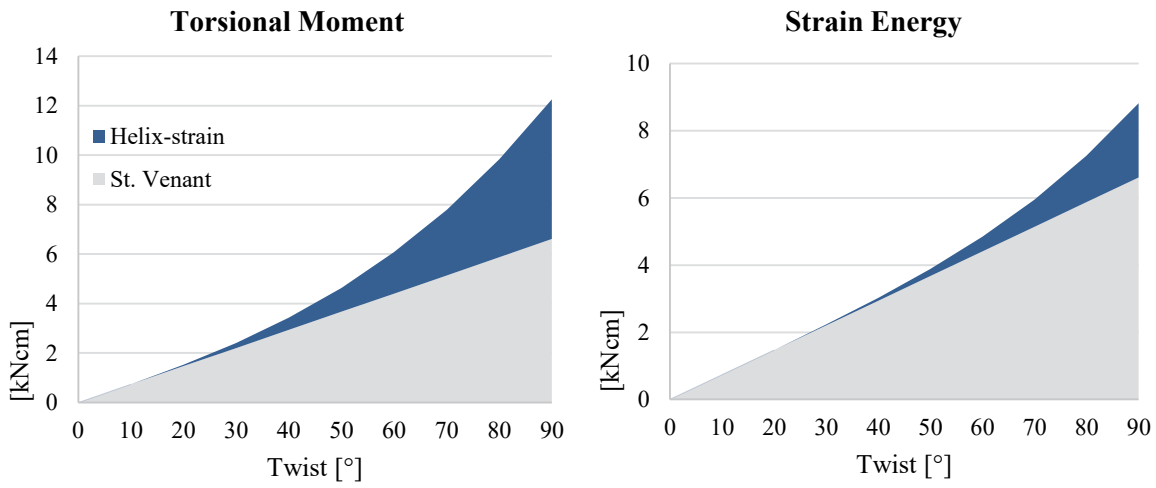


Figure 6: torsional moment and strain energy due to lamella torsion up to 90°

The effects due to helix-strain are nonlinear (Figure 6). A 90° lamella twist results in a torsional moment of 12,25 kNcm with a ratio of 54% due to St. Venant and 46% due to helix-strain. The ratio of induced strain energy due to helix-strain and St. Venant shear is 70% to 30% respectively. Besides the amount of torsion, the lamellas height affects the helix-strain significantly (see eq. 1)

FEM-Calculations verify these effects and show that simplifications lead to negligible differences.

3.2. Evaluation of the "Inverse" Method in IGA

The "Inverse"-method of considering helix torsion results in stresses and Moments (Figure 7).

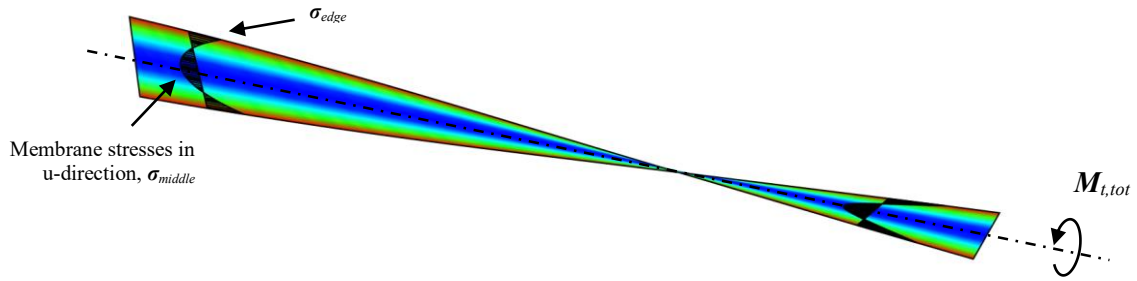


Figure 7: normal stresses of 90° twisted lamella using IGA "Inverse"-Method

The distribution of membrane stresses along the section hight matches the expected quality. The lamella does not significantly deform as expected for a constantly twisted lamella. A comparison with the calculation methods used in chapter 2.1 verifies the "Inverse"-Method as deviations to the other methods results are small.

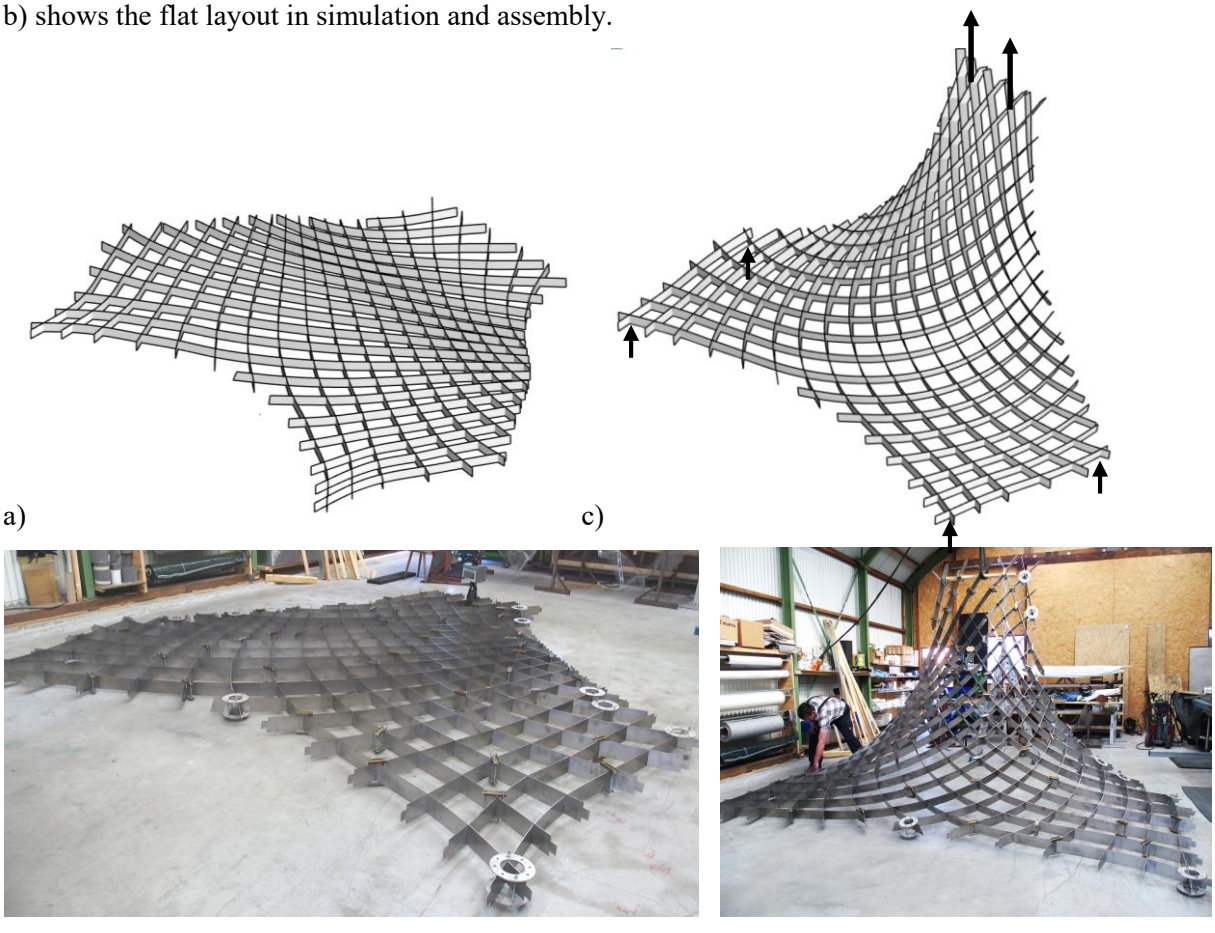
An overwie of the results according to their calculation method is shown in Table 1:

Table 1: Result overview of 90° single lamella twist

	manual calculation	**FEM** beam	**FEM** shell	**IGA** (Inverse)
$M_{t,St.V.}$ *[kNcm]*	6,61	6,44	not measured	not measured
$M_{t,Helix}$ *[kNcm]*	5,64	-	not measured	not measured
$\mathbf{M}_{t,total}$ *[kNcm]*	12,25	6,44	12,92	12,132
σ_{edge} *[kN/cm²]*	43,2	0	44,9	42,2
σ_{middle} *[kN/cm²]*	-21,6	0	-22,8	-21,6

3.3. Evaluation of the canopy simulation and erection

The grid structure found its energy minimum in the flat state. Besides torsion, also bending decreased from erected to flat state. The flat grid layout was used to assemble the grid on the floor. Figure 8 a) and b) shows the flat layout in simulation and assembly.



a) c)

b) d)

Figure 8: a) Simulation of grid structure relaxation, b) Photo: flat lamella grid, c) Pull up simulation, d) Photo: Pull up of structure

The second simulation (Figure 8c) showed, that for a chosen pull-up setting a force of ~1,2 kN is necessary to erect the lamella grid. This result matches about the measured erection force of ~1,3 kN (Figure 8d). The calculation shows, that no fixation in downward direction on the floor is needed to keep the grid partly on the floor as self-weight was sufficient enough.

4. Conclusion

The resistance of a lamella profile to torsion due to helix-strain effects rises to a significant portion for large twists. For conventional torsional deformation, those effects may be small. For large deformations as for elastically bent grid structures the effects may be unneglectable. The impact can be quantified on a reference element or even for a whole design grid by measuring the geometric values of curvature along the profiles. Calculation methods according to Lumpe and Gensichen [2] may be simplified for lamella sections with minor deviation.

Conventional beam elements do not consider helix-strain effects and are therefore questionable if used for the simulation of elastically twisted profiles, or formfinding of elastic grids. The "Inverse"-method has several advantages in the design process as the static simulations can start from the assembled state. The described method allows to consider helix-strain effects for the "Inverse"-method with minor deviation to conventional simulation strategies.

The simulation of a grid structures state of minimum strain energy is useful to characterize the elastic structures behavior during assembly and erection. While for some cases, the flat state is the "natural" state of the grid (as for the canopy), for other grid geometries the structure may tend to adopt to spatial shape.

5. Acknowledgements

We thank Dr. Eike Schling for the architectural design of the canopy structure and collaboration. We also thank Thomas Brandl and his experienced staff for technical assistance and assembly of the canopy.

References

[1] E. Schling, "Repetitive Structures, Design and construction of curved support structures"*, Munich, Germany, 2018*

[2] G. Lumpe, V. Gensichen, "Evaluierung der linearen und nichtlinearen Stabstatik in Theorie und Software" *Bauingenieur Praxis*, Berlin, Aug. 2014.

[3] J. Lienhard, "Bending-Active Structures. Form-finding strategies using elastic deformation in static and kinematic systems and the structureal potentials theriein"*, Stuttgart, Germany, 2014*

[4] E. Schling, M. Kilian, H. Wang, J. Schikore, H. Pottmann, "Design and Construction of Curved Support Structures with Repetitive Parameters", Advances in Architectural Geometry 2018*, Gothenburg, Sweden, September, 2018*

[5] A. M. Bauer, R. Wüchner and K.-U. Bletzinger, `` Isogeometric Analysis in the Design Process of Lightweight Structures," in *Form and Force: Proceedings of the IASS Annual Symposium 2019 - Structural Membranes 2019, Barcelona, Spain, October 7-10, 2019* C. Lázaro, K.-U. Bletzinger, and E. Onate Eds., 2019.

Proceedings of the IASS Annual Symposium 2019 – Structural Membranes 2019
Form and Force
7 – 10 October 2019, Barcelona, Spain
C. Lázaro, K.-U. Bletzinger, E. Oñate (eds.)

Numerically inflating air domes

Jürgen Bellmann*, Andrés von Breymann[a]

* SOFiSTiK
D 85764 Oberschleissheim, Germany
Email juergen.bellmann@sofistik.de

[a] SOFiSTiK, andres.vonbreymann@sofistik.at

Abstract

This document shows how to analyze the inflating process of a cable reinforced air dome. The main intention is not the calculation itself but the advantage of defining a regular cable net in the ground view. With this method the definition of a regular mesh on a double curved surface can be simulated. The first figure shows the regular cable mesh in the ground view before lifting. The following figures show an inflating stage and the final form including the membrane. The advantage of a cable net reinforced membrane is the possibility to achieve a nearly straight roof height in the middle part of the dome.

Keywords: membrane structures, form finding, inflatable domes

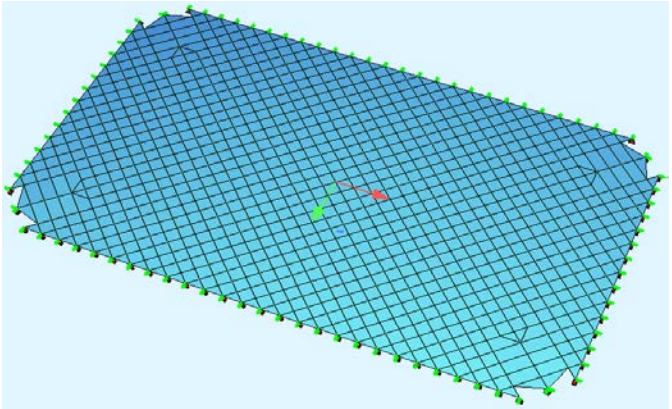


Figure 1: Regular cable net mesh placed on the flat ground

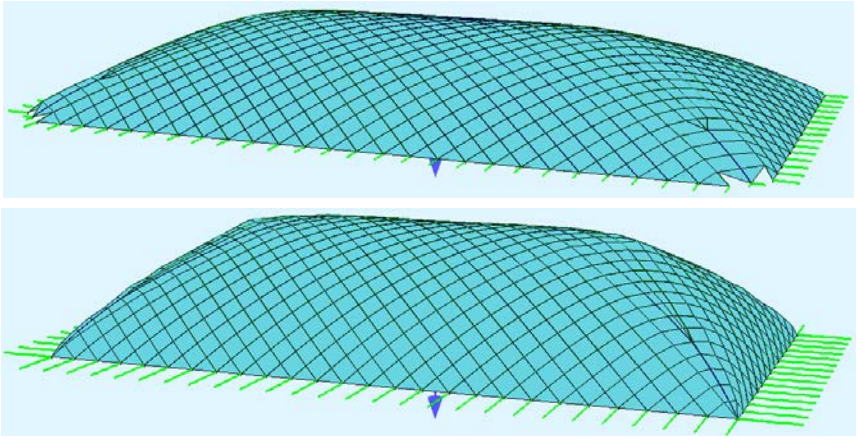


Figure 2: Inflating construction stage and final shape

Copyright © 2019 by Jürgen Bellmann, Andrés von Breymann
Published by the International Association for Shell and Spatial Structures (IASS) with permission.

1. Introduction

To be able to use an inflated dome also in the edges, a soap film prestress is not practicable. In the following figure the height in the corner is not sufficient for a person standing there:

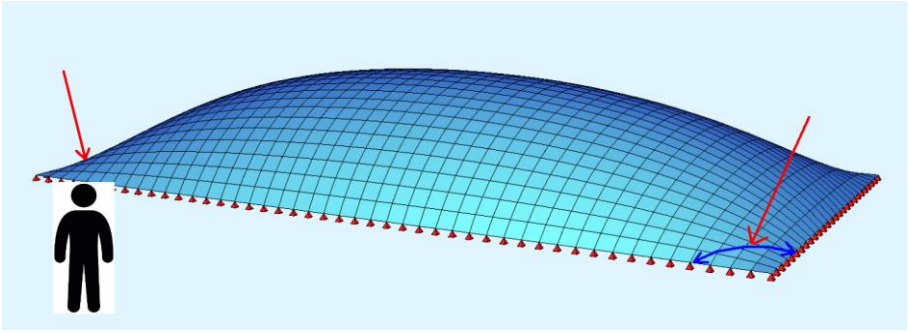


Figure 3: Membrane with inflated soap film on rectangular area -> height problem in the edge

That results in the requirement of using an orthotropic prestress in the membrane, especially the prestress in the diagonals of the corner should be much lower than the prestress in other regions. The following figure shows the cable normal forces of the dome in solution of figure 2:

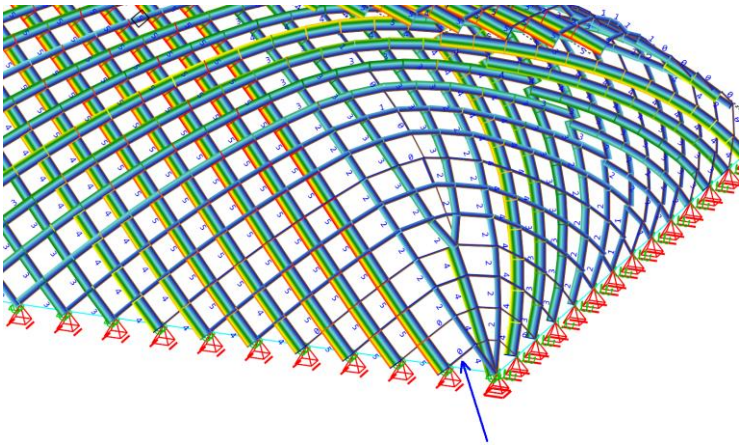


Figure 4: cable normal forces of the dome: diagonal cables in the corner: N=0

This allows the membrane and the cable net to rise quickly in the corner so that a person in the corner has enough headroom.

A second aspect is that the shape of the dome should be flat in the middle part. This can also only be achieved by an orthotropic prestress:

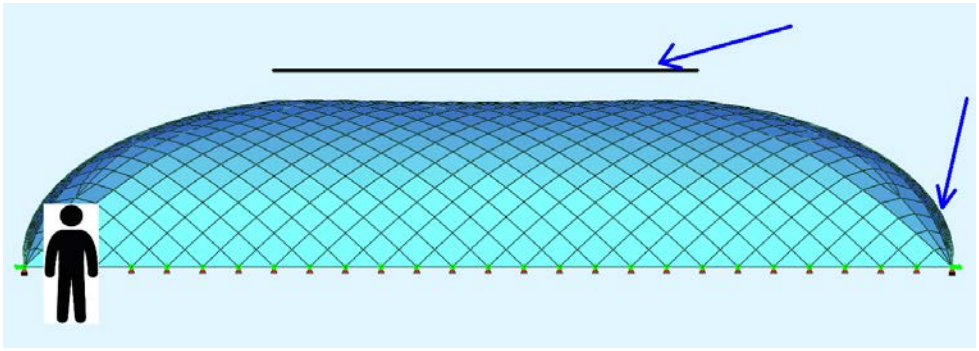


Figure 5: Flat top only possible with an orthotropic prestress, side part nearly vertical

2. Prefabrication of a partial regular cable mesh

To make the fabrication easy and cheaper it is best to prepare a regular mesh of the cables in the ground view. This means that the cable net can first be prepared easily on the flat ground as shown in figure 1. In our example the mesh has a constant distance of 2.121m. That means that 95% of all cable connections can be prepared with a constant cable length of 2.121m. Only some cables must get a shorter initial length. This of course requires a movement of the previous flat prepared mesh on the ground. Figure 6 shows the necessary shortening of 28 cables in a quadrant:

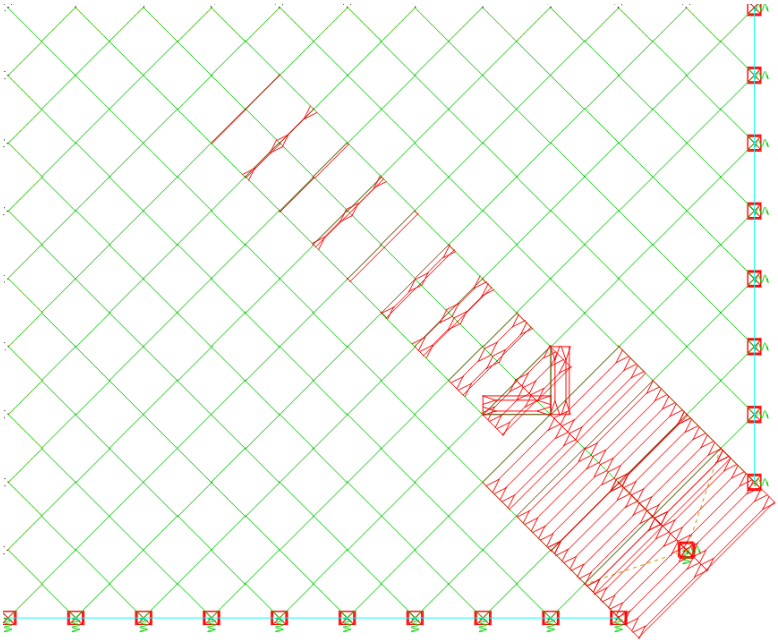


Figure 6: Necessary shortened cables – all other cables have constant length 2.212m

3. Numerically inflating the dome

The trick described in this paper is now to start with an initial flat constant mesh on the ground and shorten some cables during the lifting analysis.

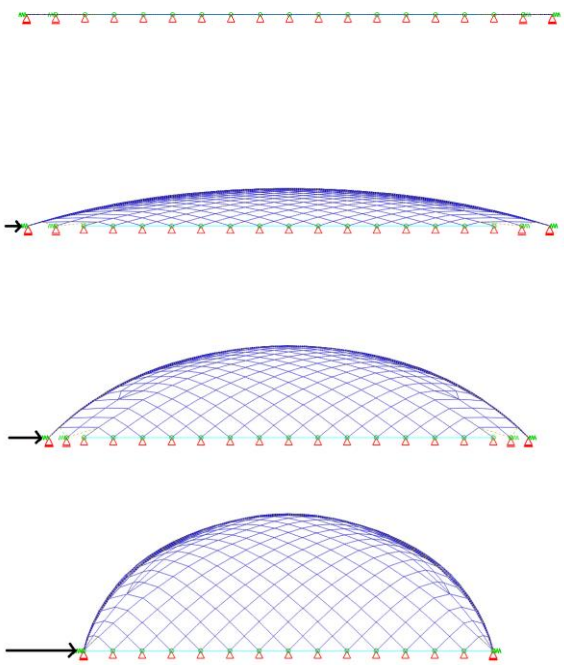


Figure 7: Simultaneous inflating, support movement and cable shortening

Figure 7 shows some construction stages of the numerical analysis where from step to step the boundary supports are moved, some cables are shortened and a slight air pressure is applied to lift the membrane with the cables.

The membrane is introduced as a soap film element. That means that it will not get a stress change due to the deformations during lifting. It is mainly added to apply a constant air pressure vertical to the deformed cable net.

The cables itself are stiff elements. That means that 95% of them keep their initial length (with a slight elongation due to the increasing normal force). Only 5% of the cables change their length during this numerical lifting procedure.

By manual iteration of the shortening of the 5% cables the desired final shape can be optimized.

4. Wind loading

All further real loads as wind now act on this final shape with the real stiffness of all cables and the membrane, if necessary with nonlinear warp and fill characteristic [1].

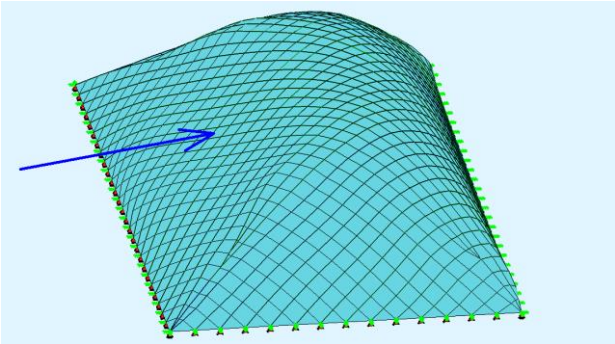


Figure 8: Side wind on the final membrane, deformations multiplied with factor 2

In this analysis the wind loading is assumed to be a short time loading and the volume of the air inside the dome is kept constant. The initial internal air pressure was 0.10 kN/m2, the maximum wind loading on the left 0.40 kN/m2. The wind deforms the membrane towards the inside an increases the inner air pressure from 0.10 to 0.56 N/mm2. This increased inner air pressure now loads the whole membrane from inside. This technique is described in [2], figure 9 shows the principle:

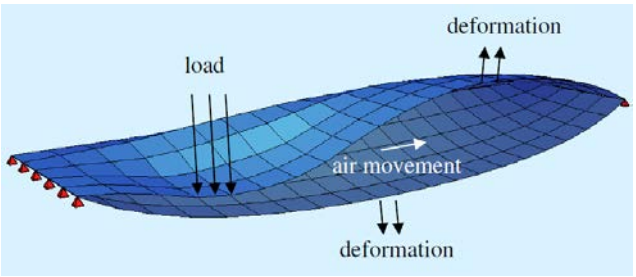


Figure 9: Effect of a constant air volume on a short term loading on an air cushion membrane

References

[1] J. Bellmann, "Experience on the implementation of a nonlinear material model for membrane fabrics," *VI International Conference on Textile Composites and Inflatable Structures*, Structural Membranes 2013.

[2] J. Bellmann, "Air volume elements for distribution of pressure in air cushion membranes," *VI International Conference on Textile Composites and Inflatable Structures, Structures*, Structural Membranes 2011.

Proceedings of the IASS Annual Symposium 2019 – Structural Membranes 2019
Form and Force
7 – 10 October 2019, Barcelona, Spain
C. Lázaro, K.-U. Bletzinger, E. Oñate (eds.)

The new German standard DIN 18204-1: Design of tents and halls with PVC-coated polyester fabrics

Natalie STRANGHÖNER*, Jörg UHLEMANN*

*University of Duisburg-Essen, Institute for Metal and Lightweight Structures, Universitätsstr. 15, 45141 Essen, Germany
natalie.stranghoener@uni-due.de

Abstract

With DIN 18204-1, since 2003 a design and product standard has existed in Germany which has standardized the design of tents and halls made from light PVC-coated polyester fabrics. In 2018, it has been extensively revised, restructured and extended to the standard series DIN 18204 "Components for enclosures made of textile fabrics and plastic films". The title is more general now, aiming to cover also other structures than tents and halls in future like e. g. ETFE-roof structures. However, the published Part 1 of this standard series regulates the design of tents and halls which are made from PVC-coated polyester fabrics classified in three material classes. Besides updates in the normative references, the structure has been fundamentally modified. Material specifications have been purified and adapted to new test standards. Moreover, the design concept has been gently revised. The semiprobabilistic design concept and the rules for connections and edge details now include latest scientific knowledge and provides technical specifications for the fabric materials to be used. The new part 101 regulates the conformity assessment for tents and halls. The present contribution describes the background of DIN 18204-1:2018-11 and -101:2018-11 and shows how the concept and the specifications can be utilized in the current development of the CEN Technical Specification for Membrane Structures.

Keywords: Design standard, product standard, tents, halls, membrane structures, polyester fabrics, materials specification, assessment of conformity

1. Introduction

The special feature of DIN 18204-1:2007-05 [1], published for the first time in 2003 and last time in 2007, was that it represented simultaneously a product and design standard. Basically, it could be applied to many textile components, not only to "simple" halls and tents. In the past, it was occasionally used for the design of small membrane roofs. However, it was mainly used for the design, calculation and manufacturing of tent halls with primary structures, see examples in Figure 1. Corresponding "tent tarpaulin" materials were specified in detail in three different material classes.

DIN 18204-1:2007-05 has now been comprehensively revised and published in two parts as DIN 18204-1:2018-11 "Components for enclosures made of textile fabrics and plastic films – Part 1: Structures and tents" [2] and DIN 18204-101:2018-11 "Components for enclosures made of textile fabrics and plastic films – Part 101: Conformity assessment for tents and halls according to DIN 18204-1" [3]. The revision was necessary because the standard references were no longer up to date. In this context, DIN 18204-1 was directly restructured in such a way that it can be supplemented in future by further parts to be newly developed, e. g. for product specifications for technical membranes of textile architecture, cushion constructions made of PVC-coated polyester fabric and constructions made of plastic films. Furthermore, the design concept was carefully revised, the material specifications purified and adapted to new testing standards.

Copyright © 2019 by Natalie Stranghöner, Jörg Uhlemann
Published by the International Association for Shell and Spatial Structures (IASS) with permission.



Figure 1: Examples of halls and tents conform to DIN 18204-1 (Source and ©: Röder Zelt- und Veranstaltungsservice GmbH)

The present contribution describes the background of DIN 18204-1:2018-11 and -101:2018-11 and shows how the concept and the specifications can be utilized in the current development of the CEN Technical Specification for Membrane Structures, see also [4].

2. Specifications for materials und connections

DIN 18204-1:2018-11 contains specifications for materials and connections. Basically, a distinction is made between three material classes: Z 1, Z 2 and Z 3, see Table 1. The strength requirements have physically not changed compared to the previous standard, but the values for the tear resistance have been adjusted to the new European evaluation procedure stated in [5] in such a way that they reflect the same physical tear strength.

With regard to the keder edges, however, it turned out in the final phase of the revision process that the previous specifications were inadequate. The strengths of the keder edges are only specified as a function of the keder diameter and the test temperature. Herewith they are completely independent of the Z-class of the material. This means that the higher strengths of the upper Z classes cannot be utilised. However, since the keder verification can be decisive for the overall verification in the presence of significant continuous loads (prestress), it becomes obvious that this is a serious shortcoming which can lead to a conservative design. It is strongly recommended to eliminate this – safe sided – inadequacy in a future revision of the standard. For this purpose, extensive series of tests are required which adequately cover all failure modes of keder edges. In the meantime, a simplified verification of the keder edge under strict conditions is proposed as a verification of the weld seam, see detailed explanations in the following section.

Table 1: Specifications for materials and joints according to DIN 18204-1:2018-11

	Row	Parameter		According to	Tarpaulins		
					Class Z 1	Class Z 2	Class Z 3
Coated fabric	1	Fabric		DIN EN ISO 2076	Polyester (PES)		
	2	Coating		-	Soft polyvinylchloride (Soft-PVC)		
	3	Area-related total mass; g/m²		DIN EN ISO 2286-2	≥ 450	≥ 580	≥ 650
	4	Tensile Strength[a] f_u; kN/5 cm; Warp/Fill	at 23°C	DIN EN ISO 1421 V1	2,0 / 1,6	2,5 / 2,5	3,0 / 3,0
	5a	Strain at break in %			≥ 15 / ≥ 15		
	5b	Maximal strain at 10 % of the tensile strength after row 4; Warp/Fill			≤ 2 / ≤ 6		
	6	Tear strength[a]; kN; Warp/Fill		DIN EN ISO 1875-3	0,1 / 0,1	0,13 / 0,13	0,2 / 0,2
	7	Adhesion strength[a]; N/5 cm		DIN EN 15619:2014-07, Annex B	100	100	100
Panel (tarpaulin)	8a	Weld seam strength[a]; 15 mm ≤ b^b < 40 mm; kN/5 cm; Warp/Fill		In the style of DIN EN ISO 1421 V1	at 23 °C: min. 70 % of the tensile strength after row 4 at 70 °C: min. 40 % of the tensile strength after row 4		
	8b	Weld seam strength[a]; b^b ≥ 40 mm; kN/5 cm; Warp/Fill			at 23 °C: min. 80 % of the tensile strength after row 4 at 70 °C: min. 60 % of the tensile strength after row 4		
	9a	Strength[a] $f_{K,u}$ of keder edges; kN/5 cm	⌀ 8 mm	In the style of DIN EN ISO 1421 V1	at 23 °C: 0,8 at 70 °C: 0,30		
	9b		⌀ 10 mm		at 23 °C: 1,0 at 70 °C: 0,60		
	9c		⌀ 12 mm		at 23 °C: 1,2 at 70 °C: 0,80		

[a] Every single value, minimum
[b] Weld seam width *b*

3. Design concept

2.1. General

All references to standards have been updated. Actions must be applied according to the series of DIN EN 1991-1 [6], taking into account the corresponding national annexes DIN EN 1991-1/NA. Load combinations, partial safety factors and combination coefficients have to be applied according to DIN EN 1990 [7]. DIN 18204-1:2007-05 already included a semiprobabilistic safety concept, so that there are no major changes regarding this issue. The partial safety factors were already identical to the current ones according to DIN EN 1990. Only the combination factors for snow at high altitudes and for wind are higher according to DIN EN 1990 than according to the former version of DIN 18204-1. The partial safety factor for prestress has not been modified and is $\gamma_F = 1.35$.

As in principle, the safety level of DIN 18204-1:2007-05 has been approved by the German building authorities and experts in the field of membrane structures. Common sense has easily been achieved to keep this safety level also for the revision of the standard. Therefore, the applied strength reduction factors were adapted to take account of long-term loads, environmental influences and elevated temperature in such a way that the new verifications essentially lead to an identical utilisation of the components. The revision of the design concept was essentially carried out by the Deutsches Institut für Bautechnik (DIBt – German Institute for Building Technology) in close cooperation with the authors.

2.2. Design situations

Instead of three defined "load combinations" in DIN 18204-1:2007-05, four "design situations" are used in DIN 18204-1:2018-11:

- Design situation 1 (winter storm)

G ⊕ P ⊕ W ⊕ S without influence of elevated temperature;

- Design situation 2 (summer thunderstorm)

  G ⊕ P ⊕ W with influence of elevated temperature;

- Design situation 3 (continuous stress)

  G ⊕ P with influence of elevated temperature;

- Exceptional design situation (exceptional snow load)

  G ⊕ P ⊕ W ⊕ S without influence of elevated temperature.

The first three design situations essentially correspond to the previous load combinations. The combination coefficients in design situation 1 are in some cases higher than before, see previous explanations. Design situation 3 "continuous stress" formally corresponds to the previously third load combination "continuous actions". In the previous version, ¼ of the snow load had to be considered in addition to the actual permanent loads. In the revised version, on the other hand, the strength-reducing effect of elevated temperature is taken into account under continuous loading and, at the same time, snow load is consequently not taken into account. The fourth design situation creates a new, exceptional load combination that only applies to increased snow loads in northern Germany to cover snow drifts by wind in that landscape which can yield to rather high snow loads. This additional consideration of a regional peculiarity corresponds to the current rules of the DIBt.

In the various design situations, various strength reduction factors on the resistance side are used to calculate the resistances for the base material, the weld seams and the keder edges. The influence of an elevated temperature is taken into account on the resistance side by strength reduction factors A_{mod} defined as a function of the design situation, see following subsection.

Although a controlled pretensioning is generally not applied in the field of tent halls – with just one exception: pneumatically pretensioned cushions for thermal optimisation, which are not covered by DIN 18204-1 – the design concept anchored in DIN 18204-1 is generally formulated and also takes into account a pretensioning of the textile components. With only minor changes, the design concept can also be used for prestressed components of textile architecture, which has already been used in practice in some cases.

2.3. Resistance of the base material

The load bearing capacity of the base material is given by the tensile strength according to Table 1, divided by the product of the strength reduction factor A_{mod} and the partial safety factor γ_M. Unfortunately, DIN 18204-1:2007-05 provided only values for the product $A_{mod} \cdot \gamma_M$ and did not specify the individual values for the strength reduction factor A_{mod} (or the subfactors for the individual damaging influences) and for the partial safety factor γ_M. Although the different A_{mod} strength reduction factors for the individual damaging influences are not known, the difficulty aroused to define A_{mod} for two design situations: firstly "winter storm" and secondly, the new exceptional design situation.

The strength reduction factors $A_{mod} \geq 1$ are based on the A-factor concept, which is widely used not only in Germany covering various strength-reducing influences. A-factors are frequently used for the strength-reducing influence of "long-term loads" (A_1), environmental conditions (A_2) and elevated temperature (A_3). While the latter is very easy to determine experimentally, values for the first two A-factors are still often taken from Minte's dissertation [8] as no other reliable information are available. Due to this, intensive research in this field is carried out at the Institute for Metal and Lightweight Structures of the University of Duisburg-Essen aiming to achieve correction factors for modern materials, e. g. [9], [10]. The A-factors have been used mostly unchanged since the 1980s, although

there have been many new developments with regard to material formulations and processing techniques, so that it can be assumed that the strength reduction factors have to be adjusted.

2.4. Resistance of weld seams

The basis for the determination of the load bearing capacity of the weld seams are the strengths of the base material specified in Table 1, reduced by multiplication with a reduction factor $\alpha_w \leq 1$ depending on the design situation and the weld seam width and – identical to the base material – divided by the product $A_{mod} \cdot \gamma_M$ depending on the design situation. In addition to a purely editorial revision of the concept, α_w values for the new exceptional design situation were added. Moreover, a design verification format for hemstitch pockets was missing. These are often used in tent hall construction, but load bearing capacities were not defined up to now. For this reason, a new design verification has been added saying that for a spread angle equal or smaller 23°, see Figure 2, the design verification can be carried out as defined for weld seams. The background is that in the case of a spread seam with a large spread angle, the transverse tension on the seam surface is large and thus premature peeling of the weld seam or – in case of a good seam quality – premature peeling of the coating from the fabric becomes the dominant failure mode. On the other hand, below a certain limit angle, it can be expected that the fracture mechanisms dominating flat weld seams will occur in the spread seam, i. e. failure at the seam edge, and thus comparable strengths will be achieved.

To determine the possible limit spread angle φ, tensile tests on welds and hemstitch pockets carried out at 23 °C and 70 °C in recent years were re-evaluated at the Essen Laboratory for Lightweight Structures (ELLF) of the Institute for Metal and Lightweight Structures of the University of Duisburg-Essen covering materials of textile architecture with spread angles up to φ = 14.8°. A detailed description of this re-evaluation and further tests can be found in [4]. In summary, on this basis it can be established – at least for the examined coated polyester fabrics for textile architecture – that up to an angle of 14.8° the peeling of hemstitch pockets does not occur more frequently than with flat seams and that both variants up to this limit spread angle can be sensibly covered by a single provision.

These observations also correspond very well with data from practice [16] and from literature: Seidel [17] reports when limiting the spread angle to a maximum of 15° that in practice, peeling of the weld seam can be avoided.

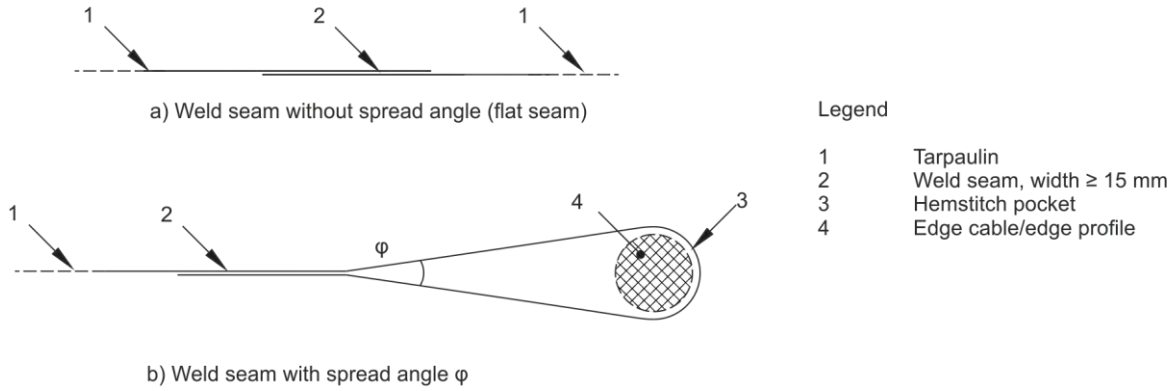


Figure 2: Weld seam without and with spread angle

However, even larger spread angles are used in tent hall constructions. For this reason, especially produced hemstitch pockets were examined in the ELLF to clarify this question. In two test series, hemstitch pocket tensile tests were carried out on two materials made of PES/PVC fabric from different manufacturers at 23 °C and 70 °C. The spread angle of these hemstitch pockets was approximately φ = 23.8°, see Figure 3. Parallel to this, tensile tests were carried out on flat seams. The

parallel tested flat seams met the strength requirements of Table 1. The hemstitch pockets showed good-natured behaviour even at the angle $\varphi = 23.8°$: The strengths were consistently higher than those of the control flat seams. In a test series at 70 °C, always peeling of the hemstitch seams occurred, in one case combined with breakage at the seam edge, but the strength was on average about 35 % higher than the strength of the flat seams and showed a very low scatter. In the other test series, fractures and combing out at the seam edge or even material fractures occurred with correspondingly high strength values, see exemplary Figure 4. Apparently the transverse tension, which equals 10% of the tensile force at $\varphi = 23.8°$, begins to become the dominant force component at this spread angle – at least at high temperatures and for some materials – even if this is not yet reflected in the strengths of the available test results.

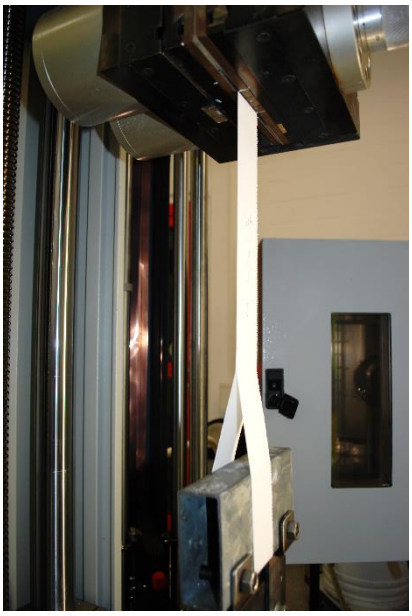


Figure 3: Example of a hemstitch pocket during tensile testing

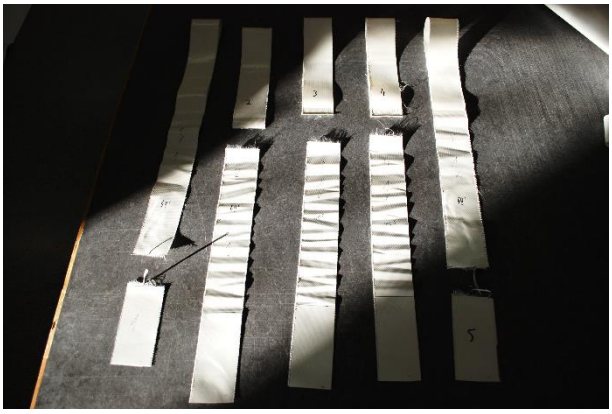


Figure 4: Examples of hemstitch pockets after tensile testing: Fractures at the seam edge or material fracture

Finally, based on the presented results the limit spread angle was rounded to $\varphi = 24°$ and specified in DIN 18204-1:2018-11.

It is proposed to adopt this concept for the Technical Specification for Membrane Structures. Of course, not all numbers can be easily transferred: for instance, the given α_w-values relate to the rather thin tent materials and rather narrow weld seams. However, the method verifying the weld seam of a hemstitch pocket like a flat weld seam up to a limit spread angle is transferable to textile architecture using the experimentally verified limit spread angle of $\varphi = 14.8°$ for materials of textile architecture.

2.5. Resistance of keder edges

The basis for the determination of the load bearing capacity of the keder edges are the strengths for keder edges specified in Table 1, divided by the product $A_{mod} \cdot \gamma_M$ specified for keder edges, depending on the design situation. As stated previously in section 2, an uneconomical shortcoming in already given provisions was detected as the strengths of keder edges are only based on the keder diameter but not on the strength of the tent material, which might lead to a very conservative design, see chapter 2. To solve this issue, further testing is necessary. The results can be implemented in the next revision of DIN 18204-1. In the meantime, a simplified design verification has been implemented which allows to verify the keder edge like a weld seam for the following conditions:

1. a folded keder edge is used, see Figure 5 (i. e. not the usual keder flag in tent construction made of material coated on one side),
2. the size and hardness of the keder rope is selected in such a way that it cannot slip out of the keder profile.

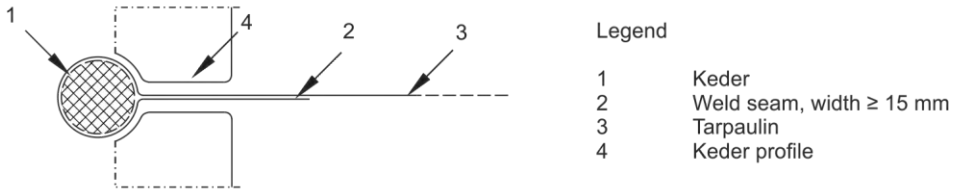


Figure 5: Folded keder edge

3. Proof of conformity

In Germany, the type of proof of conformity required by public law is decisive with regard to the provisions of a technical standard like DIN 18204. The requirements under public law are laid down in the Model Administrative Provisions – Technical Building Rules (MVV TB) [18].

MVV TB defines a certificate of conformity “ÜZ” for "PVC-coated polyester fabrics" by a recognised certification body. In addition to factory production control, this includes regular external monitoring of the material suppliers (coaters). DIN 18204-101:2018-11 specifies the frequency of external monitoring. For most product properties it is fixed to once every five years. Only with regard to the fire behaviour of flame-retardant materials the monitoring frequency is annually.

On the other hand, for the construction product "textile fabrics (tarpaulins) for halls and tents" only a declaration of conformity from the manufacturer (producer of the ready-made tarpaulin) is required after a once-only testing of the construction product by a recognised testing laboratory (confirmation of conformity “ÜHP”). Manufacturers of the tarpaulins must carry out their own factory production control. This consists of inspection of the incoming fabric, marking and regular inspection of the weld seam and keder edge strengths. The strength values required in Table 1 must be verified by an initial test for each weld seam and keder edge type to be used. During fabrication, "weld seams of each welding machine shall be subjected to a test per 1000 operating hours, but at least once every six months, in accordance with DIN EN ISO 1421 for each type of seam used. (...) In addition, a visual inspection of weld specimens shall be performed for each machine, each working day and each time the material is changed. This is done manually by peeling a weld seam sample. The test is passed when the fabric is exposed on one side of the peeled sample."

4. Conclusions

The series of DIN 18204 "Components made of textile fabrics and foils" has been extensively revised in the last two years. The final versions of DIN 18204-1:2018-11 and -101:2018-11 have been presented and discussed covering PVC-coated polyester fabrics and structures made of them. The materials are thinner, lighter and less strong than those used in textile architecture. Nevertheless, the design concept is also applicable to textile architecture in principle. It covers all aspects of permanent buildings and considers prestress. Weld seams with spread angles up to 14.8° in hemstitch pockets could be shown to behave not worse than flat weld seams in PVC-coated polyester fabrics of textile architecture. Larger angles were proven for lighter tent materials but are, however, not used in textile architecture. Folded keder edges like they are common in textile architecture can be verified according to DIN 18204-1:2018-11 as flat weld seams in case they adhere to given strict conditions. These and the presented rules for conformity assessment can be used for orientation in the development of the Technical Specification for Membrane Structures.

References

[1] DIN 18204-1:2007-05, Raumabschließende Bauteile aus textilen Flächengebilden und Folien (Zeltplanen) für Hallen und Zelte – Teil 1: PVC-beschichtetes Polyestergewebe (Components for enclosures made of textile fabrics and plastic films (awnings) for structures and tents – Part 1: PVC coated polyester base fabric).

[2] DIN 18204-1:2018-11, Bauteile aus textilen Flächengebilden und Folien – Teil 1: Hallen und Zelte (Components for enclosures made of textile fabrics and plastic films – Part 1: Structures and tents).

[3] DIN 18204-101:2018-11, Bauteile aus textilen Flächengebilden und Folien – Teil 101: Konformitätsnachweis für Hallen und Zelte nach DIN 18204-1 (Components for enclosures made of textile fabrics and plastic films – Part 101: Conformity assessment for tents and halls according to DIN 18204-1).

[4] J. Uhlemann, N. Stranghöner, „Zelthallen aus PVC-beschichtetem Polyestergewebe nach aktualisierter Normenreihe DIN 18204," *Stahlbau*, vol. 87, pp. 640-648, July 2018.

[5] EN 1875-3:1997-11, Rubber- or plastics-coated fabrics – Determination of tear strength – Part 3: Trapezoidal method.

[6] EN 1991-1, Eurocode 1: Actions on structures, series of standards with their respective current parts.

[7] EN 1990:2002, Eurocode: Basis of structural design.

[8] J. Minte, *Das mechanische Verhalten von Verbindungen beschichteter Chemiefasergewebe*, Dissertation, RWTH Aachen University, Aachen, 1981.

[9] H. Asadi, J. Uhlemann, N. Stranghöner, "Water infiltration impact on tensile strength and breaking strain of architectural fabrics," *Advances in Structural Engineering*, vol. 21, pp. 2605-2616, 2018.

[10] H. Asadi, J. Uhlemann, T. Stegmaier, V. von Arnim, N. Stranghöner, "Investigations into the long-term behaviour of fabrics", *Proceedings of the International Conference on Textile Composites and Inflatable Structures, STRUCTURAL MEMBRANES 2017, Munich, Germany, October 9-11,* K.-U. Bletzinger, E. Oñate and B. Kröplin (Eds.), 2017.

[11] B. Stimpfle, personal communication, January 2018.

[12] M. Seidel, Tensile surface structures. Ernst & Sohn, Berlin, 2009.

[13] MVV TB – Muster-Verwaltungsvorschrift Technische Baubestimmungen (Model Administrative Provisions – Technical Building Rules), August 2017, www.dibt.de.

Proceedings of the IASS Annual Symposium 2019 – Structural Membranes 2019
Form and Force
7 – 10 October 2019, Barcelona, Spain
C. Lázaro, K.-U. Bletzinger, E. Oñate (eds.)

A review on environmental and economic potential of robotic construction in actual scale driven by structural optimization

Odysseas KONTOVOURKIS*, George TRYFONOS, Panagiota KONATZII

*Department of Architecture, University of Cyprus
P.O. Box 20537, 1678 Nicosia, Cyprus
kontovourkis.odysseas@ucy.ac.cy

Abstract

Nowadays, the application of robotic construction techniques in real scale structures is an emerging direction of technological development, which is rapidly growing with various examples coming to the fore. Studies have shown that their implementation in complex design solutions is advantageous as regard their economic aspect in comparison with conventional construction processes mainly due to their ability to minimize material waste and eliminate the use of formworks, in addition to their positive environmental impact when structural optimization, e.g. topology optimization is applied. This paper reviews on relevant works on this research direction with emphasis on robotic construction processes and particularly on 3D Printing (3DP) and Adaptive Casting (AC), together with their influence that can bring to the building industry in terms of their environmental impact and cost, taking into account structural optimization as medium to reduce required materials. Simultaneously, recent developments in this area of research, currently undertaken in our research laboratory are demonstrated. The aim is to discuss and draw conclusions, formulating at the same time a theoretical framework for understanding and applying automation and robotic techniques in the construction industry based on their sustainable potential.

Keywords: Robotic construction, 3D printing, adaptive casting, structural optimization, environmental impact, cost, sustainable potential.

1. Introduction

Recently, an increasing trend on the implementation of robotic construction approaches in construction scale examples is observed, especially for physical production of complex design morphologies due to their advantages and particular their economic feasibility, if this is compared with conventional construction processes, whose cost increases exponentially depending on their design complexity [1; 2]. Apart from this, other advantages include their ability to reduce errors during construction, to minimize material waste and to eliminate the use of formworks, which are evidence of their sustainable potentiality in the construction industry. Also, their environmental impact is considerably reduced when structural optimization, e.g. topology optimization, is applied during the design stage, aiming at material reduction and cost minimization.

Within this framework, a number of topologically optimized designs have been implemented in actual scale, although their construction was achieved by using conventional construction methods [3]. Among others, the project Unikabeton incorporated topology optimization as a method for structural calculation of canopy's structural system, which in turn was manufactured using a formwork produced through CNC milling [4] and the project Shanghai Himalaya utilized discretized result derived from topology optimization for on-site construction based on concrete casting [5]. This direction has been evolved further with the application of robotic construction techniques, e.g. robotic 3D printing or adaptive formwork casting, aiming at the seamless process from design to fabrication. In one category

Copyright © 2019 by Odysseas KONTOVOURKIS, George TRYFONOS, Panagiota KONATZII
Published by the International Association for Shell and Spatial Structures (IASS) with permission.

of examples, emphasis was given on small or medium scales fabrication such as the project by [6] where topology optimization was applied in form-finding stage and then Additive Manufacturing (AM) was implemented for the production of steel nodes in a tensegrity structure and the project by [7] where integration with static analysis and shape optimization as part of brick design and fabrication was conducted. In another category of examples and particularly in the work by [8], form-finding via topology optimization and finite element modeling were introduced and large-scale 3D printing of two pedestrian bridges was conducted. In another project by [9], the investigation integrated design with robotic 3D printing to provide an alternative approach on robotic toolpath planning combined with topologically optimized results.

Furthermore, the relation with sustainable aspects of design, e.g. material reduction, and specifically examples that address the environmental impact and in parallel investigate the cost of design solutions and their correlation with robotic construction techniques, have been investigated in examples like the work by [10], where a custom-made end-effector tool was utilized during production of a conventional wall with minimum thickness, improving at the same time the environmental performance of the structure. With regard to environmental impact and cost analysis of 3D printing case studies, examples like the work by [11] discussed the role of 3D printing methods and particularly the application scale, process cost, construction time and material type and the work by [2] conducted an economic analysis of the manufacturing process in conjunction with environmental analysis of a three-dimensional composite-type concrete printing.

Similarly, in the application of adaptive casting mechanisms in construction industry, connections with sustainable aspects, e.g. material reduction through topology or structural optimization, provide a positive impact on the building industry, especially due to the large cost of formworks in the overall cost of standard construction approaches. Examples like the project TailorCrete by [12] produced a large number of column shapes using a flexible mold. In another work by [13] temporary concrete formworks were produced using hot wax casting and then solidifying in order to reduce waste material and minimize environmental impact. In addition, the introduction of environmental impact analysis in this area of research, for instance through Life Cycle Analysis (LCA), allows the selection of solutions that fulfilled in the best possible way sustainable criteria. Examples like the project Iceformwork by [14] evaluated the environmental impact and energy required during construction and the examples by [15; 16] compared conventional and advanced processes for masonry construction. In addition, assessment on robotic productivity including cost and time using as example the construction of non-conventional masonry was conducted in the example by [17], showing a tendency towards the investigation of automated solutions by taking into account environmental and economic criteria.

Although, works in this research direction have been already conducted, these have not been fully systematized within a general framework. Also, examples have been found fragmented and this imposes the need for further and in depth investigation with regard to their sustainable potential in construction industry. This will allow a more thorough and comprehensive investigation regarding environmental impact and cost, taking into account structural optimization as medium to reduce required materials. The current paper attempts to contribute further in this research direction by demonstrating two case studies, currently undertaken in our research laboratory with emphasis on 3D Printing (3DP) and Adaptive Casting (AC). The aim is to discuss and draw conclusions, formulating at the same time a theoretical framework for understanding and applying automation and robotic techniques in the construction industry based on their sustainable potential.

2. 3D Printing and Adaptive Casting case studies overview

This paper, briefly demonstrates two case studies currently conducted in our research laboratory that focuses on 3DP and AC techniques using structural optimization as medium to assist form-finding. This is done in the early design stage where design decision making is influenced by construction

performance and aims at reducing environmental impact and cost during construction in actual scale [18, 19].

2.1. 3D Printing – Geometric and structural optimization

In this case, the investigation focuses on the integration of Topology Optimization (TO) principles with 3D Printing (3DP) in order to achieve a seamless process from form-finding to robotic construction with the aim to reduce material but also to maximize stiffness of structures. Towards this direction, an approach has been developed for toolpath planning based on infill design and optimization, mainly to solve issues arising due to the irregular morphology of complex structures and particularly the overhang angles, which impose limitations during fabrication stage.

2.1.1. 3DP toolpath generation based on TO principles

Starting from a given solid geometry that represents a building component used in non-conventional brick walls with specific overhang and material volume, the TO plug-in Ameba (a) based on Bio-directional Evolutionary Structural Optimization (BESO) [20] in the parametric design environment of Grasshopper (b) is utilized in order to give a first inside on the TO results regarding loading and mass distribution in the body of structure. Then, an infill pattern in the form of a hexagonal grid is applied, achieving an even distribution of the material and hence a more lightweight structure. The distribution of Von Mises values is used for relative stretching and loosening of infill pattern using Kangaroo physics-based engine (c). Then, material density mapping is conducted based on the TO and deformed infill results by controlling extruder's speed in order to achieve deposition of thicker or thinner material filament on each hexagon's edge. Table 1 shows the initial solid geometry and various infill patterns generated for 3DP.

Table 1: Initial solid geometry and infill patterns with variety in their thickness

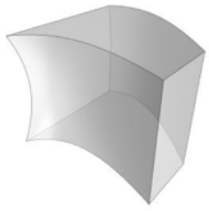
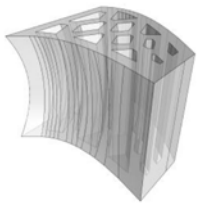
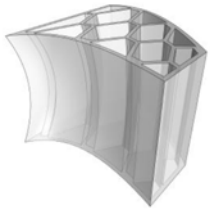
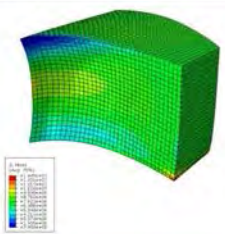
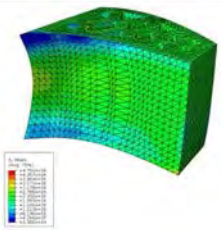
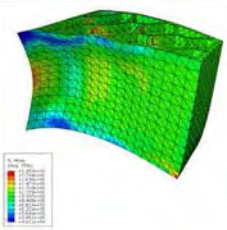
Solid geometry	Infill – thickness 12 mm	Infill - thickness 4 mm
		

Table 2: FEA results for solid geometry, for infill with thickness 12 mm and 4 mm. In each case, maximum compressive strength and total material volume is calculated

Cases	Solid geometry	Infill – thickness 12 mm	Infill – thickness 4 mm
Von Mises			
Compressive strength (MPa)	19.09	2.12	0.99
Volume (cm^3)	1833.1	1600.17	645.6

The results are analyzed using the FEA software ABAQUS CAE (d) in order to evaluate compressive strength with the aim of being within the allowable limits. Material properties used for FEA analysis are based on [21] and are defined for adobe as follows: Mass Density(ρ)= 1400, Poisson ratio=0.3, Young's modulus=300e^6, Yield stress=20 e^6, Inelastic strain=0.0035, Yield stress=2 e^6 and Cracking strain=0.0001. The optimized results are used for toolpath planning based on the parametric-integrated algorithm developed in [22]. Table 2 indicates FEA results for solid geometry, infill with 12 mm thick filament and infill with 4 mm thick filament for 3D printing execution.

2.2. Adaptive casting – Geometric and structural optimization

The second study focuses on a static-performance driven investigation based on a parametric-design and static analysis workflow by integrating a suggested AC mechanism for automated construction in actual scale. The aim is to develop a comprehensive process that include the development of variable designs and in parallel allow evaluation of solutions in accordance with material minimization and static adequacy of non-conventional forms, which face limitations during physical execution based on standard construction approaches [19].

2.1.1. Adaptive Casting driven by parametric design and static analysis

In this case, a variety of brick geometries are parametrically investigated, representing brick typologies used as wall openings for shading-lighting and natural ventilation purposes. The parameters influencing design solutions are associated with the rotation of opening and boundary limitations based on the criteria imposed on the European Eurocode regarding holes/openings of brick elements. The design typologies have dimensions for openings ranged from 20x20mm to 70x70mm, differences in openings thickness from the middle to the edges ranged from 40mm to 80mm and rotation angle ranged from 0^0 to 45^0 degrees (Figure 1). The suggested custom-made AC mechanism enables the production of any given brick typology within the parametric design limits. Briefly, the mechanism, which is supported at the edge of an industrial robot, consists of two parts, the press and pressing containers that are actuated using linear and rotational actuators, enabling reconfiguration of formwork according to the desired shape.

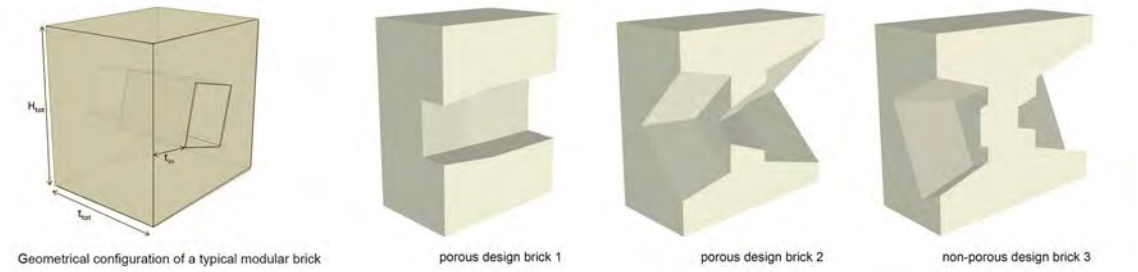
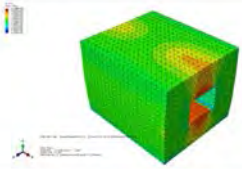
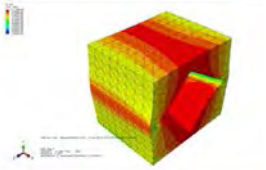


Figure 1: Examples of brick typologies produced by the AC mechanism

The minimum and maximum compressive strength of brick typologies is calculated using the software ABAQUS CAE (d) based on the same adobe material mixture and properties used in 3DP case but also on two other materials, concrete and a hybrid mixture of clay and cement. Results show that concrete brick typologies have larger compressive strength compared to the other two materials. Specifically, the compressive strength in case of concrete material is 10.241 MPa minimum and 34.537 MPa maximum, in case of clay with the addition of cement is 0.15 MPa minimum and 1.30 MPa maximum, while in the case of adobe material the minimum is 0.274 MPa and the maximum is 1.7 MPa. Table 3 shows minimum and maximum compressive strength in case of adobe material with respective brick typologies.

Table 3: FEA results for brick typologies with the minimum and maximum compressive strength in case of adobe material

Minimum compressive strength – Case 3a0		Maximum compressive strength – Case 1d45	
			

3. Environmental impact and economic potential of automated mechanisms

In this section, the suggested 3DP and AC processes are analyzed in terms of their environmental impact and economic potential. Then, the results are compared and discussed.

3.*1. Environmental impact analysis of 3DP and AC processes*

In the context of environmental impact analysis, carbon dioxide emission values are obtained through the OneClick LCA digital platform (e) in case of a building element produced through 3DP (element with infill 12 mm thickness) and in case of a brick module among the 24 brick design typologies produced through AC (element case 2) using the above-mentioned materials. Also, the same material volume (1600 cm^3) in both processes is applied, which allows a comparison of the results, as opposed to the use of different material volumes that might influence proportionally their increase or reduction in relation to carbon dioxide emissions. The LCA analysis takes into account Construction materials (A1-A3), Transportation to site (A4), Construction/installation process (A5) and Deconstruction (C1-C4).

Table 4 shows the results of LCA with the inclusion of energy consumption during Construction/installation process (A5). As it is observed, same values appear in A1-A4 and C1-C4, where higher emission values are recorded in the concrete material and lower values in the adobe material. The same applies for carbon dioxide emission values, where for adobe material the values range from 4.65-4.67 kgCO2, for clay with cement the values range from 4.73-4.98 kgCO2 and for concrete the values range from 5.02-5.26 kgCO2. The comparative analysis of both procedures shows value differentiation at Construction/installation stage. Particularly, the global warming and primary energy values are higher in the 3DP process.

Table 4: Global warming and primary energy consumption results of analysis for the three materials and the two construction processes

LCA - Robotic construction procedures		Global warming (kg CO2e)			Primary energy (MJ)		
		Adobe	Concrete C20/25	Clay	Adobe	Concrete C20/25	Clay
A1-A3	Construction materials	3,78E-3	4,96E-1	1,6E-1	9,24E-2	2,46E0	5,14E-1
A4	Transportation to site	1,78E-2	2,56E-2	2,01E-	2,58E-1	3,77E-1	2,92E-1
A5	Construction/installation process **-Adaptive casting**	4,62E0	4,62E0	4,62E0	7,93E1	7,93E1	7,93E1
A5	Construction/installation process **- 3D printing**	4,76E0	4,76E0	4,76E0	8,15E1	8,15E1	8,15E1
C1-C4	Deconstruction	1,24E-2	3,9E-2	1,67E-	3,7E-1	9,56E-1	4,94E-1

As part of the Construction/installation process (A5), the energy consumption throughout the life cycle of the modular bricks and the energy required by the mechanisms during the robotic construction procedures are also taken into account, both for 3DP and AC based on the following equations:

$EP_{E\text{-}et} = 3D\,printer\,machine$

$$EP_{rp} = E_{-et}\,(linear\,actuator + motor\,stepper) + laptop + robotic\,arm$$

Where $EP_{E\text{-}et}$ and EP_{rp} are energy needed by the end-effector tool and the robotic procedure

Where E-et is the energy for AC mechanism manufacturing

In case of 3DP, the energy consumed during the robotic procedure is calculated as the summation of the energy required by the robotic arm, the laptop and the 3DP mechanism. The total energy value is 2.54kWh. In case of AC, the energy consumed is calculated as the energy needed by the 3DP machine to produce the parts of formwork, the energy needed for the actuators as well as the energy required to produce the brick module. The total energy required for AC tool manufacturing and for brick module production is 2.39 kWh.

3.2. Cost analysis of 3DP and AC mechanisms and processes

In this sub-section the cost for 3DP and AC processes are estimated (Table 5). For each process, the cost is related to the cost of the end-effector tool and the robotic construction process in total and is calculated as follows:

$$C_{E-et} = E_{cost}\,(3d\,printing) + L_{cost} + M_{cost}$$

$$C_{rp} = E_{cost} + CM_{cost} + L_{cost}$$

Where $C_{E\text{-}et}$ and C_{rp} are the cost for end-effector tool manufacturing and the overall robotic construction process respectively.

Where E_{cost} is energy cost, L_{cost} is labor cost, M_{cost} is cost of mechanisms and tools and CM_{cost} is the cost of materials.

Table 5: 3DP and AC cost inputs and overall cost calculation for end-effector mechanisms and for robotic construction process

Cost inputs - 3D Printing						Total cost	
$E_{cost(E\text{-}et)}$	$L_{cost(E\text{-}et)}$	$M_{cost(E\text{-}et)}$	$E_{cost(rp)}$	$CM_{cost(rp)}$	$L_{cost(rp)}$	$C_{E\text{-}et}$	C_{rp}
N/A	N/A	N/A	4,87 cent/kWh	0.225 cent	6.90 €	1197 €	7.98 €
Cost inputs – Adaptive Casting						Total cost	
$E_{cost(E\text{-}et)}$	$L_{cost(E\text{-}et)}$	$M_{cost(E\text{-}et)}$	$E_{cost(rp)}$	$CM_{cost(rp)}$	$L_{cost(rp)}$	$C_{E\text{-}et}$	C_{rp}
2.32 cent/ kWh	211.47€	472.69 €	4.58 cent/kWh	0.225 cent	2.20 €	689.392 €	2.87 €

The cost for the manufacturing of the custom-made AC mechanism is the summation of the cost of materials and mechanical parts, the cost of energy consumed during manufacturing as well as the labor cost. The cost of energy is calculated based on the cost of electricity in Cyprus. Also, in this case, 24 hours of work is required for the manufacturing of the end-effector tool and the labor cost amounts to 211 € approximately. The total cost of AC manufacturing is estimated at 689.39 €. The total cost of 3DP industrial mechanism is 1197 €. The cost for the robotic construction process of one building element is, in case of AC 2.87 € per modular brick every 5 min and in case of 3DP 7.9 € per building element every 47 min.

3. Conclusion

In this paper, the environmental impact and economic potential of automated construction mechanisms is discussed with emphasis on 3DP and AC, as part of the research work currently undertaken in our research laboratory. Results show obvious opportunities and sustainable potentialities for implementing these emerging techniques in the construction industry, mainly due to their flexible use in large variety of design typologies as opposed to conventional approaches where one-off construction solutions are introduced, particularly in complex design cases. The structural optimization plays a decisive role in this process, due to its great impact in early design stage, where decisions on morphologies that minimize material volume and maximize static performance are necessary to be taken into account. An indispensable part in the process of material minimization is the selection of the appropriate material mixtures. The opportunities provided by eco-friendly materials, especially due to their ecological and recyclability properties, in combination with the ability of design, structural optimization and automated fabrication techniques to investigate best performance of design results under investigation, might open opportunities for new sustainable construction approaches to come to the fore.

Acknowledgements

The authors would like to express their thanks to Christos Georgiou for his contribution in the structural optimization of the example presented on 3DP case study.

References

[1] R.A. Buswell, R. Soar, M. Pendlebury, A. Gibb, F. Edum-Fotwe and A. Thorpe, "Investigation of the potential for applying freeform processes to construction", in Proceedings of the 3rd international conference on innovation in architecture, engineering and construction (AEC) 2005, Rotterdam, The Netherlands, 2005. pp. 141–150.

[2] G. De Schutter, K. Lesage, V. Mechtcherine, V. N. Nerella, G. Habert and I. Agusti-Juan, "Vision of 3D printing with concrete — Technical, economic and environmental potentials", *Cement and Concrete Research*, vol. 112, pp. 25-36, 2018.

[3] H. Ohmori, "Computational Morphogenesis: Its Current State and Possibility for the Future", *International Journal of Space Structures*, vol. 25(2), pp. 75-82, 2010.

[4] A. Søndergaard and P. Dombernowsky, "Unikabeton Prototype". In Glynn R. & Sheil B. (Authors), Fabricate 2011: Making Digital Architecture, London: UCL Press, pp. 55-60, 2017.

[5] S. Mostafavi, M. Morales Beltran and N. Biloria, "Performance Driven Design and Design Information Exchange", Stouffs, Rudi and Sariyildiz, Sevil (eds.), Computation and Performance – Proceedings of the 31st eCAADe Conference – Volume 2, Faculty of Architecture, Delft University of Technology, Delft, The Netherlands, 2013, pp. 117-126.

[6] S. Ren and S. Galjaard, S., Topology optimization for steel structural design with additive manufacturing, 2015.

[7] J.J Del Coz Díaz, P.J García Nieto, F.P Álvarez Rabanal, A. Lozano Martínez-Luengas, "Design and shape optimization of a new type of hollow concrete masonry block using the finite element", *Engineering Structures*, vol.33(1), pp. 1-9, 2011.

[8] P. F. Yuan, Z. Chen, and L. Zhang, "Form finding for 3d printed pedestrian bridges", T. Fukuda, W. Huang, P. Janssen, K. Crolla, S. Alhadidi (eds.), Learning, Adapting and Prototyping - Proceedings of the 23rd CAADRIA Conference - Volume 1, Tsinghua University, Beijing, China, 2018. pp. 225-234.

[9] Z. Chen, L. Zhang and P. F. Yuan, "Innovative design approach to optimized performance on large-scale robotic 3d-printed spatial structure", M. Haeusler, M. A. Schnabel, T. Fukuda (eds.),

Intelligent & Informed - Proceedings of the 24th CAADRIA Conference - Volume 2, Victoria University of Wellington, Wellington, New Zealand, 2019. pp. 451-460.

[10] N. Hack, W. Lauer, F. Gramazio, M. Kohler, "Mesh mould: robotically fabricated metal meshes as concrete formwork and reinforcement", 1th international symposium on ferrocement and textile reinforced concrete 3RD ICTRC

[11] P. Wu, J. Wang, X. Wang, "A critical review of the use of 3-D printing in the construction industry", *Automation in construction*, vol.68, pp.21-31, 2016.

[12] F. Gramazio and M. Kohler: 2011, "TailorCrete, 2009-2013". Available from: (accessed 31 March 2019).

[13] S. Oesterle, A. Vansteenkiste and A. Mirjan, "Zero Waste Free-Form Formwork", Proceedings of the Second International Conference on Flexible Formwork, BRE CICM, University of Bath, 2012. pp. 258-267.

[14] V. Sitnikov, 2019, "Ice Formwork for High-Performance Concrete: A Model of Lean Production for Prefabricated Concrete Industry", *Structures*, 18, pp. 109-116, 2019.

[15] I. Agustí-Juan and G. Habert, "Environmental design guidelines for digital fabrication", *Journal of Cleaner Production,* vol.142 (4), pp. 2780-2791, 2017.

[16] F. Gramazio, M. Kohler, S. Langenberg, "Fabricate: Negotiating Design & Making", gta Verlag, Zurich, 2014.

[17] B. G. de Soto, I. Agustí-Juan, J. Hunhevicz, S. Joss, B. T. Adey, "Productivity of digital fabrication in construction: Cost and time analysis of a robotically built Wall", *Automation in Construction,* vol. 92, pp.297-311, 2018.

[18] O. Kontovourkis, G. Tryfonos and C. Georgiou, "Robotic additive manufacturing (RAM) with clay using topology optimization principles for toolpath planning: the example of a building element", *Architectural Science Review*, 2019, DOI: 10.1080/00038628.2019.1620170

[19] O. Kontovourkis, and P. Konatzii, "Design-static analysis and environmental assessment investigation based on a kinetic formwork driven by digital fabrication principles", In O. Kontovourkis ed. Proceedings of the 6th eCAADe Regional International Symposium: Sustainable Computational Workflows. Nicosia: University of Cyprus, pp. 131-140, 2018.

[20] D. Li, W. Liao, N. Dai, G. Dong, Y. Tang, and Y. M. Xie. "Optimal Design and Modeling of Gyroid-Based Functionally Graded Cellular Structures for Additive Manufacturing." *Computer-Aided Design,* vol.104, pp. 87–99, 2018.

[21] R. Illampas, V. G. Loizou, and I. Ioannou, "Effect of straw fiber reinforcement on the mechanical properties of adobe bricks", Sixth Biot Conference on Poromechanics July 9–13, Paris, France, 2017.

[22] O. Kontovourkis, and G. Tryfonos, "Integrating parametric design with robotic additive manufacturing for 3D clay printing: An experimental study". Proceedings of the 35th International Symposium on Automation and Robotics in Construction. Berlin, pp. 909-916, 2018.

(a) Ameba: https://ameba.xieym.com/index_en/.
(b) Grasshopper: https://www.grasshopper3d.com/.
(c) Kangaroo: http://kangaroo3d.com/.
(d) ABAQUS: https://www.3ds.com/products-services/simulia/products/abaqus/
(e) OneClick LCA: https://www.oneclicklca.com/

Proceedings of the IASS Annual Symposium 2019 – Structural Membranes 2019
Form and Force
7 – 10 October 2019, Barcelona, Spain
C. Lázaro, K.-U. Bletzinger, E. Oñate (eds.)

An Automated Reconfiguration Sequence Process of a Bar-Linkage Structure

Maria MATHEOU*, Ibrahim CHAMSEDDINE[a,b], Michael KOKKOLARAS[a], Marios C. PHOCAS

* Department of Architecture, University of Cyprus,
Kallipoleos St. 75, 1678 Nicosia, Cyprus
matheou.maria@ucy.ac.cy

[a] Department of Mechanical Engineering, McGill University,
817 Sherbrooke St. West, Montreal, Quebec H3A 0C3, Canada

[b] Department of Integrated Mathematical Oncology, H. Lee
Moffitt Cancer Center and Research Institute, 12902 USF
Magnolia Drive, Tampa, FL, 33612 USA

Abstract

Rigid bar structures can undergo shape transformations through mechanical actuators at the joints. A reconfiguration approach recently applied by the authors is based on the 'effective 4-bar' concept, using a sequence of one degree-of-freedom motion steps by selectively releasing four joints of the primary members at a time and engaging brakes installed on each individual joint and one geared electrical motor at the base. In following, an automated reconfiguration sequence process is proposed. The initial and target configuration for a planar 9-bar linkage system considered are defined on the basis of a quasi-ellipsoid shape of 5.42 and 4.49 m height respectively and 4.66 m span. The numerical studies have been conducted with the software MATLAB and Simulink for a Model Based-Design. All geometrical, mass and inertia characteristics of the planar 9-bar linkage are exported through the dynamic analysis software program Solidworks Essentials and implemented in the algorithmic model as blocks. A closed feedback loop reads all different motion patterns of the locked and unlocked joint angles for each step, while at the same time the simulation model in Simulink is updated automatically. The obtained results demonstrate that the design of reconfigurable structures can benefit from an automated analysis of possible sequences, from the initial to the target position, further enabling respective optimization tasks in achieving better performance and efficiency.

Keywords: Reconfigurable structures, Motion planning, Reconfiguration sequence, Adaptive direct search algorithm.

1. Introduction

Motion analysis plays a key role for the reconfiguration process involved in transformable structures considering the multi-objectives of performance, efficiency, technical simplicity of the structure and control design. Transformable architectural structures have variable geometrical and mechanical properties in order to adapt in real-time to changing external functional, environmental, or loading conditions. Rigid bar structures can undergo shape transformations through mechanical actuators at the joints. The number of integrated actuators should, however, be limited due to the associated weight increase and design complexity. Along these lines, rigid bar structures may support shape transformations through integration and replacement of primary members and joints with mechanical

Copyright © 2019 by Maria MATHEOU, Ibrahim CHAMSEDDINE, Michael KOKKOLARAS and Marios C. PHOCAS
Published by the International Association for Shell and Spatial Structures (IASS) with permission.

actuators. Kinetic structures of different typologies and mechanisms have been developed in recent years, primarily in terms of deployable structures, in relation to requirements of temporary environments, aerospace and technological progress, Pellegrino [1]. In particular, tensegrity structures, i.e. self-stressed systems composed of tension and compression members, are characterized by their physical properties in providing a holistic and integrated composition of embedded active control. Also, the specific typology comprises autonomous and self-supported systems that are capable of effectively transferring external loading, Gantes [2].

In terms of minimizing energy consumption in deployable tensegrity systems, dynamic models have been presented for solving the kinematics of systems with one, two and three degrees-of-freedom (DOF), with consequent simplification of the systems through replacement of the compression members with pneumatic actuators and the tension members with variable length or spring elements, Hanaor [3]; Tibert [4]; Adam and Smith [5]. In such cases, even if the actuators are locked, the stiffness of the system decreases under external loading, Arsenault and Gosselin [6-9]. In addition, control through pneumatic actuators, does not enable the systems to have adequate stiffness during transformation, nor to undergo large transformations, Bel Hadj, et. al. [10]. Although structures with embedded actuators in place of primary joints or members are usually designed to use a small number of components, in order to achieve a maximum number of shape adjustments, implementation requires designers to deal with an increase of the structure self-weight, depending on the number and characteristics of the actuators used, complex mechanisms and energy-inefficient operation.

From a control perspective, performing structural reconfigurations requires an appropriate feedback control system with actuators, sensors, as well as suitable motion planning and control algorithms, Fox and Kemp [11]. The potential of active control of civil engineering structures was identified and initiated both, theoretical and experimental work in the field, Yang and Soong [12]. Active structural control in tensegrity structures refers to mechanisms that involve shape control using active struts or cables, Korkmaz [13]. Shape-controlled prototype structures realized either for experimental investigations, or specific architectural applications, have been fairly limited and remain mostly at a conceptual research level (e.g. parametric associative digital design and 3D graphical representation techniques). Further insight to related design, modeling, assembly and control aspects can be gained through experimental testing of full- or small-scale reconfigurable structures incorporated with a control system.

The authors have been engaged in the application of the effective 4-bar reconfiguration approach on rigid bar-linkage systems, implementing a direct or cable-driven actuation, Phocas, Christoforou and Matheou [14] and Matheou et al. [15], in simulations and experimentally, Matheou et al. [16]. The current paper refers to a principal planar arch-like frame consisting of a 9-bar linkage. The initial and target configuration for the planar system are defined on the basis of a quasi-ellipsoid shape of 5.42 and 4.49 m height respectively and 4.66 m span. The objective of this study is to investigate different motion patterns of a 9-bar linkage model, from the initial to the target position in an automated reconfiguration process. Among the joints of the 9-bar linkage, the two joints connected to the ground are always unlocked to allow for the motion of the linkage. In the current study, a closed feedback loop provides all different motion patterns of the locked and unlocked joint angles for each step of each possible reconfiguration. The proposed automated analysis of possible sequences, from the initial to the target position, should further enable respective optimization tasks in achieving better performance and efficiency.

2. Reconfiguration Approach and Motion Planning

The reconfiguration approach of the 9-bar linkage presented in Figure 1 is based on the effective 4-bar concept, using a sequence of 1-DOF motion steps by selectively releasing four joints of the primary members as proposed in Christoforou, et al. [17] and Christoforou, et al. [18]. Different intermediate configurations depend on the motion planning, in order to adjust the system joints to the desired values

during the motion steps involved from the initial to the target position. For each intermediate step of the 9-bar linkage only one joint angle is adjusted. Furthermore, in the current study an additional motion planning constraint has been applied. The three joints that remain unlocked after each step will also participate to the next effective 4-bar definition.

For simulation purposes, an initial design of the 9-bar linkage has been applied including all the intermediate steps form the initial to the target position. Hinge-connected beam members with sections of 2x UPN 120/100 mm and 1.75 m length synthesized the 9-bar linkage. Aluminum of 69.6 GPa elastic modulus and 241.3 MPa yield strength is assigned to the beam members. The initial and target configurations of the systems are given by θ_i= [102,168,144,144,144,144,144,168,102]^T and θ_f= [54,144,120,168,144,168,120,144,54]^T degrees of the internal n-bar angles, respectively. The joints of the 9-bar linkages are assumed to be controlled through electromagnetic brakes. Figure 2 shows the scheduling table for a specific control sequence applied to realize the required shape adjustment. The corresponding reconfiguration steps of the systems motion sequence are shown in Figure 3.



Figure 1: The planar 9-bar linkage in its initial and target position.

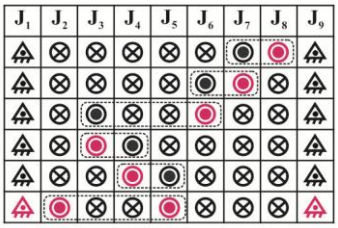


Figure 2: Scheduling table for a control sequence adopted to realize the required shape adjustment (⊗: locked joint, ⊙: unlocked joint, ∆: pivoted–to–the-ground joint, shaded symbols represent the currently adjusted joints).

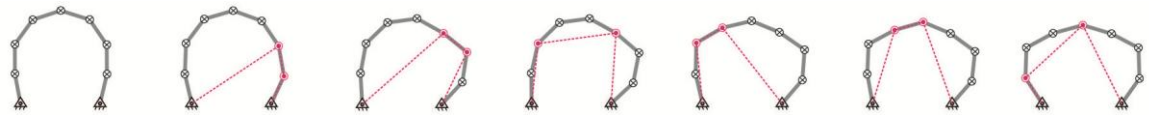


Figure 3: Reconfiguration steps of the 9-bar linkage.

3. Simulation and Analysis Study

The automated reconfiguration sequence process refers to the investigation of the motion patterns of the 9-bar linkage, involving seven different intermediate steps, from an initial to a target configuration. The numerical studies have been conducted with the software MATLAB and Simulink for a Model Based-Design.

All geometrical, mass and inertia characteristics of the planar 9-bar linkage have been exported through the dynamic analysis software program Solidworks Essentials and implemented in the algorithmic model as blocks. Constant gravity has been set to z axis, in parallel to the structural system. As shown in Figure 4, each of the nine joints of the structure in the Simulink Model represents a block of the 'Revolute Joint' connecting all the links through a hinge with one rotational degree of freedom. All the 'Revolute Joint' blocks identify the joint angles set in MATLAB with a 'Signal Builder' block according to time. A 'Simulink-PS Converter' is connected with the 'Revolute Joint' in order to convert the unitless Simulink input signal to a Physical Signal from MATLAB to Simulink. If sensing is activated in the 'Revolute Joint' block, then the selected output could be included in the simulation model through PS-Simulink Converter in the MATLAB base workspace, as shown in Figure 5. A closed continuous feedback loop reads all different motion patterns of the locked and unlocked joint angles for each step, while at the same time the simulation model in Simulink is automatically updated. Different motion patterns of the reconfiguration sequences, defined by respectively different intermediate steps, are automatically implemented in Simulink model giving rise to the user to create a comprehensive overview of the structure's locomotion. For future design purposes an optimization algorithm could be implemented to enable an optimization-driven analysis as shown in Figure 6.

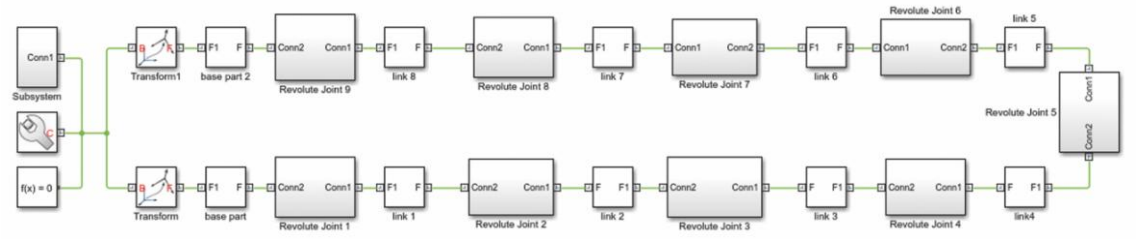


Figure 4: Simulink model with all blocks and subsystems.

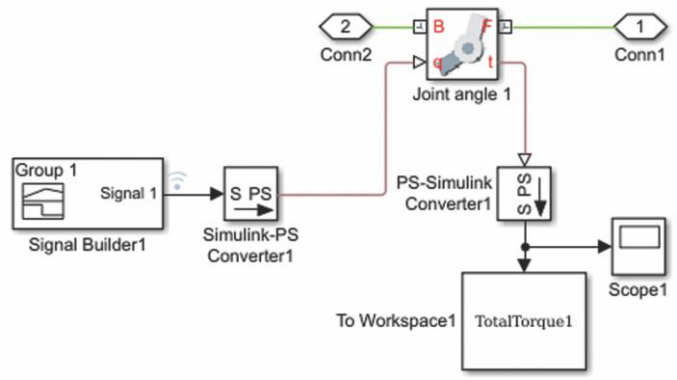


Figure 5: Subsystem of the 'Revolute Joint 1'.

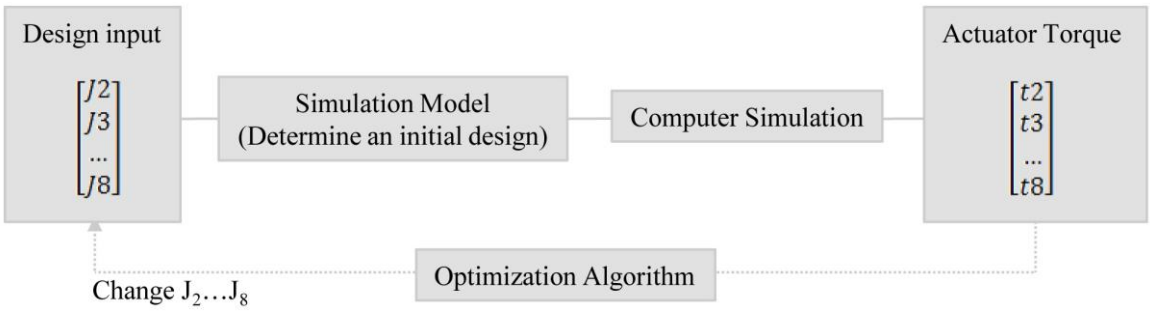


Figure 6: Automated process of the reconfiguration sequence.

4. Conclusions

In the current paper an automated reconfiguration sequence process is proposed for a planar 9-bar linkage structure. The reconfiguration approach is based on the 'effective 4-bar' concept, using a sequence of one degree-of-freedom motion steps by selectively releasing four joints of the primary members at a time. At kinematics level, the motion control approach has been implemented in preserving minimum structure self-weight and energy consumption during reconfigurations, whereas any target configuration of the system is only achieved through the base actuation. Besides the evaluation of the system kinematics, the work carried out reveals the integration potentialities of MATLAB and Simulink giving rise to an automated continuous feedback loop. Future research on the topic includes application of automated optimization processes with regard to the reconfigurations of the structure under uniform distributed vertical and horizontal loading.

Acknowledgements

The research study in the current paper has been conducted in the frame of the Research Funding Program: Marie Sklodowska-Curie Research and Innovation Staff Exchanges (RISE) "OPTARCH – Optimization Driven Architectural Design of Structures", H2020-MSCA-RISE-2015.

References

[1] S. Pellegrino, ed., *Deployable Structures*. International Center for Mechanical Sciences, CISM courses and lectures, 412, 2001.

[2] C.J. Gantes, *Deployable structures: Analysis and Design*. Southampton: WIT Press, 2001.

[3] A. Hanaor, Tensegrity: Theory and application. *Beyond the cube*. J.F. Gabriel Ed., John Wiley & Sons, pp. 385-408, 1997.

[4] G. Tibert, *Deployable tensegrity structures for space applications, PhD Thesis*, Royal Institute of Technology, 2002.

[5] B. Adam and I.F.C. Smith, "Active tensegrity: A control framework for an adaptive civil-engineering structure," *Computers and Structures*, vol. 86, no. 23-24, pp. 2215-2223, 2008.

[6] M. Arsenault and C. Gosselin, "Kinematic, static and dynamic analysis of a planar 1-DOF tensegrity mechanism," *Mechanical Design*, vol. 127, no. 6, pp. 1152-1160, 2005.

[7] M. Arsenault and C. Gosselin, "Kinematic, static and dynamic analysis of a planar 2-DOF tensegrity mechanism," *Mechanism and Machine Theory*, vol. 41, no. 9, pp. 1072-1089, 2006.

[8] M. Arsenault and C. Gosselin, "Kinematic, static and dynamic analysis of a spatial 3-DOF tensegrity mechanism," *Mechanical Design*, vol. 128, no. 5, pp. 1061-1069, 2006.

[9] M. Arsenault and C. Gosselin, "Kinematic and static analysis of a 3-PUPS spatial tensegrity mechanism," *Mechanism and Machine Theory*, vol. 44, no. 1, pp. 162-179, 2009.

[10] A.N. Bel Hadj, L. Rhode-Barbarigos and I.F.C. Smith, "Analysis of clustered tensegrity structures using a modified dynamic relaxation algorithm," *Solids and Structures*, vol. 48, no. 5, pp. 637-647, 2011.

[11] M. Fox and M. Kemp, *Interactive Architecture*. New York: Princeton Architectural Press, 2009.

[12] J.N. Yang and T.T. Soong, "Recent advances in active control of civil engineering structures," *Probabilistic Engineering Mechanics*, vol. 3, no. 4, 179-188, 1998.

[13] Korkmaz, S, "A review of active structural control: Challenges for engineering informatics," *Computers and Structures*, vol. 89, no. 23-24, pp. 2113-2132, 2011.

[14] M.C. Phocas, E.G. Christoforou and M. Matheou, "Design, motion planning and control of a reconfigurable hybrid structure," *Engineering Structures*, vol. 101, no. 10, pp. 376-385, 2015.

[15] M. Matheou, M.C. Phocas, E.G. Christoforou, and A. Müller, "On the kinetics of reconfigurable hybrid structures," *Building Engineering*, vol. 17, pp. 32-42, 2018.

[16] M. Matheou, M.C. Phocas, E.G. Christoforou and A. Müller, "Comparative Analysis on Two Actuation Methods of 9-bar Systems through Kinematics Analysis and Experimental Testing," in *AIMETA 2017, XXII Conference*, The Italian Association of Theoretical and Applied Mechanics, Salerno, Italy, 2017.

[17] E. Christoforou, A. Müller and M.C. Phocas, "Motion planning for shape-controlled adaptable buildings resembling topologically closed-loop robotic systems," in *36th Mechanisms and Robotics Conference (MECH), ASME 2012 International Design Engineering Technical Conferences*, Chicago, 2012.

[18] E.G. Christoforou, A. Müller, M.C. Phocas, M. Matheou and S. Arnos, "Design and control concept for reconfigurable architecture," *Mechanical Design*, vol. 137, pp. 042302-1 – 042302-8, 2015.

Proceedings of the IASS Annual Symposium 2019 – Structural Membranes 2019
Form and Force
7 – 10 October 2019, Barcelona, Spain
C. Lázaro, K.-U. Bletzinger, E. Oñate (eds.)

Structural Optimization of Tubular Steel Wind Turbine Towers with Respect to Buckling

Konstantina G. KOULATSOU*, Kyriakos-Alexandros CHONDROGIANNIS, Charis J. GANTES

*School of Civil Engineering
Institute of Steel Structures
National Technical University of Athens
konkoulatsou@gmail.com

Abstract

As attention on wind energy is progressively increased, wind turbine towers grow in height and the blades become longer in order to better exploit the available wind potential. As a result, actions on the towers are also increased and their safe and cost-effective design is important for the further development of the wind energy sector. A commonly used type of wind turbine tower is the tubular steel tower which offers several structural advantages and has dominated the market over other alternatives, such as truss-type towers. The tubular wind turbine tower is composed of a number of cylindrical and/or conical shells, manufactured in the factory and erected on site by means of bolted ring flange connections. In the present article, the buckling design of an actual 120m tall wind turbine tower is described, aiming towards optimizing the tower with respect to weight, hence also cost, and taking properly into account restrictions pertaining to fabrication, transportation and erection. Among several constraints that the tower design has to satisfy, in the present paper only buckling is addressed, based on Eurocode 3 recommendations for steel shells, as well as on nonlinear finite element analyses, and taking into account realistic action effects in normal and extreme conditions. Namely, initial results obtained by verifications according to EN1993-1-6 are then compared to numerical results from non-linear finite element analysis accounting for geometrical and material nonlinearity and imperfections (GNMNIA). Thus, areas where the tower wall thickness has margins for reduction are identified, so that in future work an optimized tower design can be achieved.

Keywords: wind turbine towers, tubular steel towers, stress design, buckling analysis, non-linear analysis, imperfection analysis

1. Introduction

For the purpose of the present research, an actual wind turbine is used with a tower of approximately 120m height. The wind turbine tower consists of five cylindrical parts and one conical part at the top, which are transported to site and are erected and bolted together on site with preloaded bolts. The lower five parts have a constant outer diameter equal to D_{ext}=4300mm, which is the largest size that can be transported by truck, while their thickness varies along the height of the tower from t=60mm to t=16.5mm from base to top. The upper part of the wind turbine tower has a conical shape, with external diameter varying from D_{ext}=4300mm to D_{ext}=3685mm from bottom to top, while the thickness of the sixth part remains constant and equal to t=15mm.

The material of the tower shell is steel of grade S355 with nominal yield stress equal to f_y=355MPa and f_y=335MPa for tower shell thickness smaller or equal to t=40mm and larger than t=40mm

Copyright © 2019 by Konstantina G. KOULATSOU, Kyriakos-Alexandros CHONDROGIANNIS, Charis J. GANTES
Published by the International Association for Shell and Spatial Structures (IASS) with permission.

respectively. Corresponding nominal values of ultimate stress are f_u=510MPa and f_u=470MPa , while elasticity modulus is equal to E=210GPa.

The design of the wind turbine tower is performed according to EN1993, Part 1-6, "Strength and stability of shell structures", EN1993-1-6:2007 [1]. The fabrication quality class for the wind turbine tower is considered equal to B; however, the effect of fabrication quality class will be also investigated and presented.

2. Verification of the tower according to EN1993-1-6

The verification of the wind turbine tower is performed at characteristic points along its height for the corresponding design forces taking into account realistic action effects in normal and extreme conditions, as obtained by means of aeroelastic simulations, in which the tower has been modeled with beam elements of equivalent cross-sections. Each set of design effects taken into account consists of a maximum design force/moment and its corresponding design forces/moments. Checks according to EN1993-1-6 [1] have been performed by means of analytical calculations and spreadsheets that have been developed for that purpose.

The ultimate limit states to be considered for the design of steel shells are:

- LS1: Plastic failure limit state
- LS2: Cyclic plasticity

  As in our case, cycles of loading and unloading do not produce yielding in tension nor in compression, this limit state is not applicable.
- LS3: Buckling

  Buckling limit state is checked for all actions causing compressive normal and shear stresses on the tower shell. As a result, the tower is checked against meridional (axial) buckling, circumferential (hoop) buckling and shear buckling.
- LS4: Fatigue

  The limit state of fatigue is the condition in which repeated cycles of increasing and decreasing stress lead to the development of a fatigue crack. Fatigue is not considered in the present paper.

2.1. LS1 check – Plastic limit verification

For the verification of this limit state, the design stresses shall satisfy the condition

$$\sigma_{eq,Ed} \leq f_{eq,Rd} \tag{1}$$

where $\sigma_{eq,Ed}$ is the equivalent design stress and $f_{eq,Rd}$ is the von Mises design strength. Analytical description of the plastic limit state can be found in EN1993-1-6 [1].

2.2. LS3 check – Buckling verification

For the verification of this limit state, the design stresses shall satisfy the following conditions,

- for meridional (axial) buckling

$$\sigma_{x,Ed} \leq \sigma_{x,Rd} \tag{2}$$

where $\sigma_{x,Rd}$ is the axial buckling resistance of tower shell

- for hoop (circumferential) buckling

$$\sigma_{\theta,Ed} \leq \sigma_{\theta,Rd} \tag{3}$$

where $\sigma_{\theta,Rd}$ is the circumferential buckling resistance of tower shell

- for shear buckling

$$\tau_{x\theta,Ed} \leq \tau_{x\theta,Rd} \tag{4}$$

where $\tau_{x\theta,Rd}$ is the shear buckling resistance of tower shell

- for the combined buckling check of meridional, hoop and shear buckling

$$\left(\frac{\sigma_{x,Ed}}{\sigma_{x,Rd}}\right)^{k_x} - k_i \cdot \left(\frac{\sigma_{x,Ed}}{\sigma_{x,Rd}}\right) \cdot \left(\frac{\sigma_{\theta,Ed}}{\sigma_{\theta,Rd}}\right) + \left(\frac{\sigma_{\theta,Ed}}{\sigma_{\theta,Rd}}\right)^{k_\theta} + \left(\frac{\tau_{x\theta,Ed}}{\tau_{x\theta,Rd}}\right)^{k_\tau} \leq 1.0 \tag{5}$$

Analytical description of the buckling limit state can be found in EN1993-1-6 [1].

For the buckling verification it is assumed that the critical buckling length corresponding to each tower cross-section is equal to the length of the corresponding part, e.g. it is the length between two ring flanges. Moreover, depending on each part's length, its diameter and its thickness, the part is categorized as long, medium or short cylinder. In our case, all parts are categorized as long cylinders. Finally, it is important to clarify the boundary conditions of each part. EN1993-1-6 [1] distinguishes between three boundary conditions, BC1 (clamped), BC2 (pinned) and BC3 (free). For the base of the tower boundary conditions are assumed to be BC1, while at the ring flanges boundary conditions are assumed to be BC2.

2.3. Verification results of analytical checks

In Figure 1, all exploitation ratios along the height of the tower for all characteristic positions of the tower derived from equations (1) to (5) are illustrated. The horizontal axis of the diagram represents the exploitation ratios while the vertical axis of the diagram represents the height of the tower. Fabrication quality class for the verification of the tower is considered equal to B.

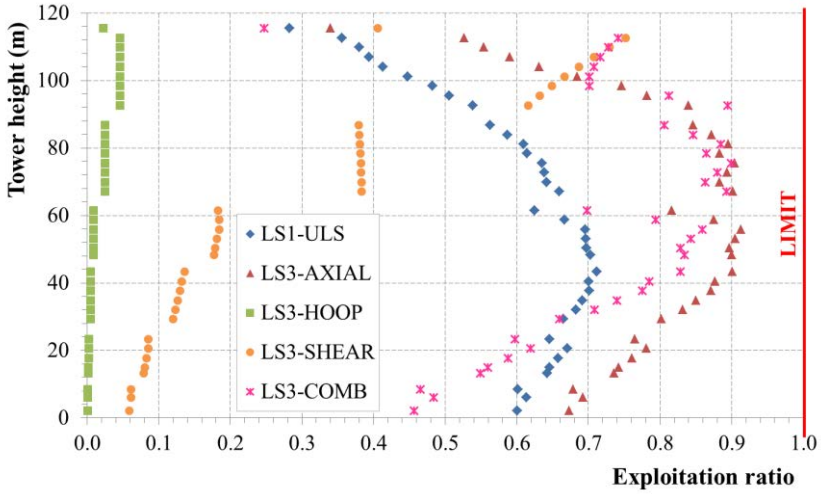


Figure 1: Exploitation ratios along the height of the tower for plastic limit and buckling verifications

In general, buckling is more adverse than plastic limit state, as expected given the height of the tower. The meridional buckling check is dominant over the height of the tower, with the exception of the upper 20m, where torsion-induced shear buckling governs. The maximum exploitation ratio is obtained from the meridional buckling check at a height of approximately 63m and is equal to 0.913 (<1.0).

2.4. Effect of fabrication quality class

EN1993-1-6 [1] distinguishes between three fabrication classes, A (excellent), B (high) and C (normal). For better fabrication class the amplitude of imperfections to be used for buckling checks is smaller. Therefore, the capacity ratios of buckling checks (LS3) depend on fabrication class, while capacity ratios of plastic limit checks (LS1) are independent of fabrication class. In Figure 2, the exploitation ratios illustrated along the height of the tower are derived from meridional buckling state, as it is the most onerous state, and for all fabrication quality classes.

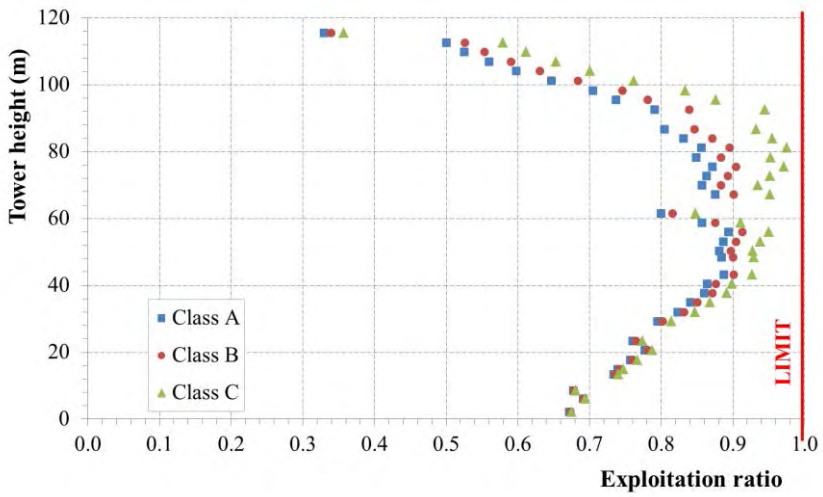


Figure 2: Exploitation ratios along the height of the tower for meridional buckling verification and for all fabrication quality classes

As expected, for better fabrication class, the exploitation ratios are lower. For worse fabrication class, the maximum exploitation ratios occur at higher positions over the tower.

3. Wind turbine tower numerical model

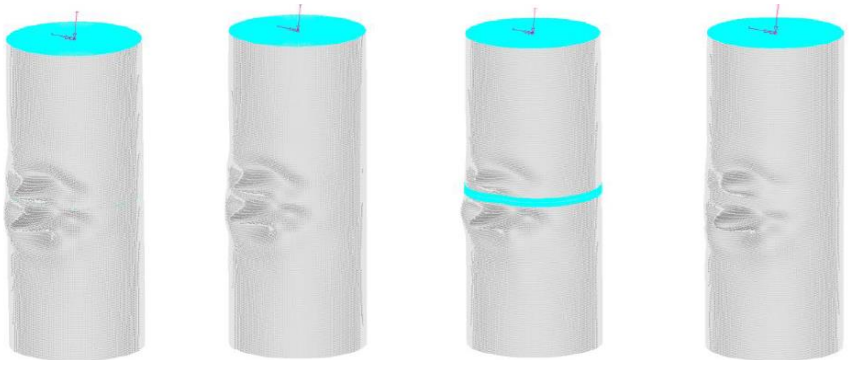
In order to employ a reliable and computationally effective numerical model for the tower analysis, several models with different types and meshing of finite elements were investigated. The ideal numerical model of the tower would be to model all the parts with 3d solid finite elements. However, this would result in a heavy model that would be very difficult to handle. For this purpose, three models were investigated: (a) The pylon shell is modeled with shell elements and the ring flanges with beam elements representing the section of both flanges acting together, taking into account the geometrical eccentricity between flange axis and shell mid-surface by means of rigid elements. (b) Both the pylon shell and the ring flanges are modeled with shell elements with the shell elements representing the section of both flanges acting together, (i) considering that the tower shell extends up to the mid-surface between the two flanges, and (ii) taking into account the tower shell trim due to the flange thickness by means of rigid elements. (c) Both the pylon shell and the ring flanges are modeled with 3d solid elements. For the investigation, linearized buckling analysis is performed.

The different models have been compared for the case of two cylindrical shells of 5m height with external diameter equal to D_{ext}=4300mm and a uniform thickness equal to t=50mm, which are connected together via two ring flanges with width equal to b=270mm and thickness equal to t_f=140mm each. The lower shell is fixed at its base, while the upper shell is free at its top, with a rigid node where loads are applied. The thickness of the shell near the flanges is reduced to t=38mm, in order to direct buckling failure there.

Initially linearized buckling analyses are performed for the different models. In Figure 3 the critical load factors of models (a), (b-i), (b-ii) are compared with the load factor of model (c), and a

satisfactory convergence is observed. In order to extend this conclusion, geometrically and material nonlinear imperfection analyses are also performed for the three simpler models (a), (b-i), (b-ii), using a more accurate geometry, being part of the actual structure, taking now into account the variable thickness of the tower and a larger in height segment in order to intensify the effect of geometric non-linearity. Initially, linearized buckling analysis is performed in order to obtain the first critical buckling modes (Figure 4). The first buckling mode is then used as shape of geometrical imperfection for the nonlinear analysis, while the size of the imperfection is calculated according to EN1993-1-6 [1] for fabrication quality class A.

In Figure 5 the stress distributions obtained from GMNIA at the ultimate point of the analysis are illustrated. Comparing the load factors, a satisfactory convergence is also achieved. As a result derived from both linearized buckling analysis and GMNIA, model (a) with the pylon shell modeled with shell elements and the ring flanges with beam elements taking into account the geometrical eccentricity with rigid elements can be used for the verification of the wind turbine tower.



(a) $\lambda_{cr,a}$=12.75 (b-i) $\lambda_{cr,b\text{-}i}$=12.74 (b-ii) $\lambda_{cr,b\text{-}ii}$=13.37 (c) $\lambda_{cr,c}$=13.04

Figure 3: 1st buckling modes and critical load factors of (a), (b-i), (b-ii), (c) models

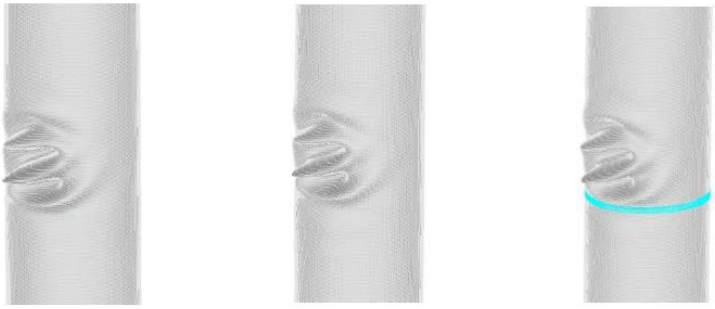
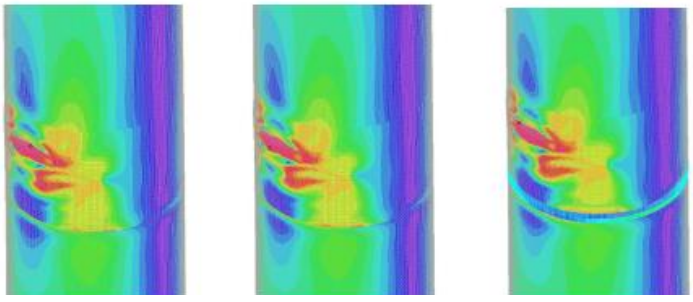


Figure 4: 1st buckling modes and critical load factors of (a), (b-i), (b-ii), (c) models



(a) $\lambda_{u,a}$=1.270 (b-i) $\lambda_{u,b\text{-}i}$=1.268 (b-ii) $\lambda_{u,b\text{-}ii}$=1.277

Figure 5: GMNIA stress distributions at the ultimate point of the analysis of (a), (b-i), (b-ii) models

4. Wind turbine tower verification with finite element analysis

The wind turbine tower verification is now also performed via nonlinear finite analysis with geometrical and material imperfections (GMNIA), employing model (a) of paragraph 3, namely modeling the tower with shell elements and the ring flanges with beam elements. In order to assess the buckling potential at different locations over the tower, successive models of parts of the tower below each flange are analyzed. Each model is loaded with the corresponding design forces/moments at its upper flange. GMNIA is performed taking into account an initial geometrical imperfection with the most unfavorable shape of the five primary buckling modes, determining the size according to EN1993-1-6 [1] and the assumed fabrication quality class. The size of imperfection is calculated for all three fabrication quality classes, A, B and C and the corresponding GMNI analyses are performed.

Due to size restrictions, the results of the GMNIA of only one part of the wind turbine tower are presented. Similar analyses and checks have been performed for all parts. The part of the tower chosen to illustrate the results is the forth from the bottom, approximately between levels +46m and +65m. The cylindrical shell has a uniform external diameter equal to D_{ext}=4300mm, while its thickness varies along its height from t=33mm to t=25mm from base to top. Design forces are imposed on the model at the ring flanges at level +65m. The 1st buckling mode, used as shape of the initial imperfections is illustrated in Figure 6, and their size calculated according to EN1993-1-6 [1] is illustrated in Table 1 for the three different fabrication quality classes.

Table 1: Imperfection size according to fabrication quality class and ultimate load factors

fabrication quality class	**gauge of length l_{gx} (m)**	**thickness t (mm)**	**imperfection size $\Delta_{w,eq}$ (mm)**	**$r_{R,GMNIA}$**
A	0.43	24.5	6.1	1.221
B	0.43	24.5	9.8	1.101
C	0.43	24.5	15.3	1.010



Figure 6: 1st buckling mode of tower part

In Figure 7, the equilibrium paths of the examined tower part are illustrated for the three fabrication quality classes, A, B and C, while the ultimate load factors, from which the exploitation ratios resulted, are also presented in Table 1. The horizontal axis of the equilibrium paths corresponds to the horizontal displacement of the top of the tower part and the vertical axis corresponds to the load

factor. Part of the deformed shape of the tower and the corresponding effective stresses at the ultimate point are illustrated in Figure 8.

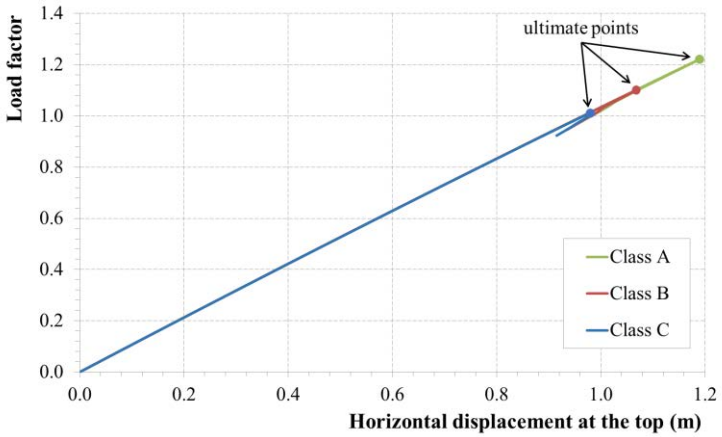


Figure 7: Equilibrium paths of examined tower part for fabrication quality classes A, B and C

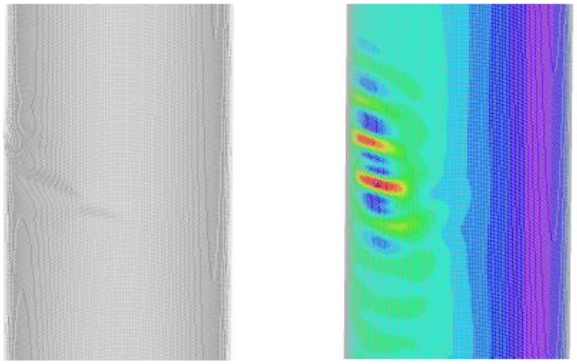


Figure 8: Deformed shape and effective stresses of examined tower part at the ultimate point

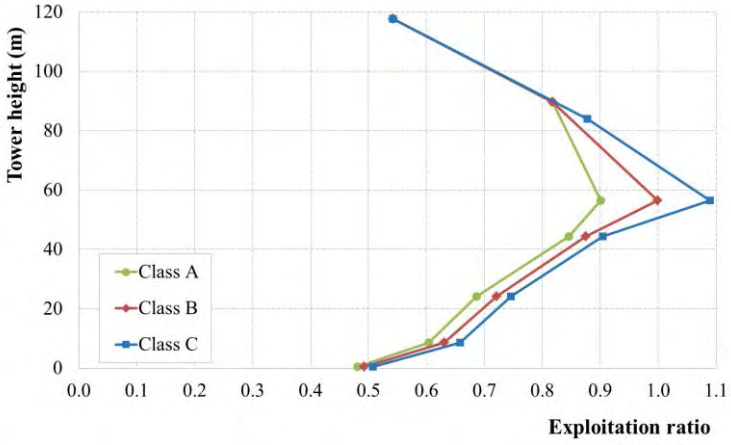


Figure 9: GMNIA exploitation ratios of entire tower for fabrication quality classes A, B and C

The verification procedure described above was applied to all tower parts with their corresponding geometry, design forces and imperfections. The results of this procedure are illustrated in Figure 9 by means of exploitation ratios along the height of the tower. As expected, for worse fabrication quality class, the exploitation ratios are higher and closer to failure. For the wind turbine tower investigated in this project, the most onerous results from the analyses are approximately at 60m height. It should be

noted that in case of fabrication quality class B, the exploitation ratio is 1.0, which means that the tower is marginally safe, while in case of fabrication quality class C, the exploitation ratio is 1.1, indicating buckling failure.

5. Comparison of analytical and numerical results and discussion

The comparison between the analytical and numerical verification of the wind turbine tower is illustrated in Figure 10. For the analytical results, an exploitation ratio envelope is presented encompassing the plastic limit state as well as the buckling state, meridional, hoop, shear buckling and their combination, for fabrication quality class B. The presented numerical results are those derived from the process described in section 4, also for fabrication quality class B.

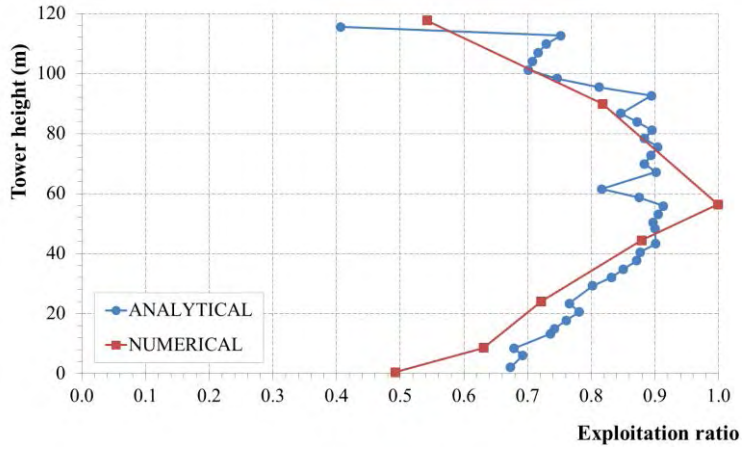


Figure 10: Maximum exploitation ratios of analytical and numerical verifications

In general, analytical and numerical results are in good agreement, apart from the middle of the tower where the numerical exploitation factor is larger than the corresponding analytical exploitation factor.

It is also observed that in lower and upper parts of the tower smaller exploitation ratios are observed, thus identifying the potential of shell thickness reduction and optimization with respect to buckling. This potential will be explored in future work, considering also the effects on fatigue checks and on avoiding tower resonance with the turbine's 1P and 3P rotation frequencies.

Acknowledgements

This research has been supported by the OptArch project: "Optimization Driven Architectural Design of Structures" (No: 689983) belonging to the Marie Skłodowska-Curie Actions (MSCA) Research and Innovation Staff Exchange (RISE) H2020-MSCA-RISE-2015.

References

[1] European Committee for Standardization, *Eurocode 3: Design of Steel Structures – Part 1.6: Strength and Stability of Shell Structures*, 2007.

[2] European Committee for Standardization, *Eurocode 1: Actions on Structures – Part 1.4: General Actions – Wind Actions*, 2010.

[3] International Standard, *IEC 61400-1: Wind Turbines – Part 1: Design Requirements*, 2005.

[4] Det Norske Veritas (DNV), Wind Energy Department, Risø National Laboratory, *Guidelines for Design of Wind Turbines*, 2002.

[5] Germanischer Lloyd, *Guideline for the Certification of Wind Turbines*, 2010.

[6] J.G. Teng and J.M. Rotter, *Buckling of Thin Metal Shells*, Spon Press, 2004.

Proceedings of the IASS Annual Symposium 2019 – Structural Membranes 2019
Form and Force
7 – 10 October 2019, Barcelona, Spain
C. Lázaro, K.-U. Bletzinger, E. Oñate (eds.)

How to gain from loss – Heinz Isler's Haba project and its testing under critical load

Giulia BOLLER*, Matthias BECKH

*ETH Zurich, Institute of Technology in Architecture (ITA), Chair of Structural Design
Stefano-Franscini-Platz 1, 8093 Zurich (CH)
boller@arch.ethz.ch

Abstract

The paper focuses on Isler's building for the Haba Company in Uster (1972), to understand how its monitored destruction led to the improvement of the overall typology. When the structure was torn down in 1980, Isler carried out full-scale tests on the built structure, adapting – even though with different evaluation criteria – the methodology to the experiments he usually conducted on small-scale physical models. Isler constantly not only used models to conduct a variety of tests in the design process, but also measured the built shells to better understand their long-term behavior. Haba gave him the unique possibility to test a built structure under critical load. Out of that, he gained further knowledge about the structural behavior of his shells which most probably influenced his later projects. The study is based on materials of the Isler archive of ETH Zurich. It considers the results of the loading test of the Haba shell, which was jointly conducted by the Swiss Research Institute EMPA and ETH Zurich. The experimental approach throughout the entire lifecycle of the building helped Isler to widen the knowledge on the structural behavior of his shells and thus to improve their design. The monitored destruction of one building thus secured an improvement in the design and performance of the next shells to come, and helped their preservation in good conditions, unlike other projects. The changed perspective allows for more profound insights into Isler's methodology, establishing a permanent dialogue between the designer and his small-scale and full-scale models.

Keywords: concrete shells, pneumatic form, models, full-scale test

1. Introduction

Any collapse, whether accidental or intentional, can help to understand the behavior of specific structures, to inform future projects by learning from the previous errors. It is particularly important for projects realized with a certain level of complexity in geometry, since the design developed through model tests, both physical and digital, has sometimes difficulties in the definition of their appropriate structural behavior. Especially in the past and in the case of shells, innovative concepts had troubles both in design and in construction, since their theoretical understanding and the technology related to them were not as advanced as today.

A famous example of an accidental collapse that contributed to improve the design solution is the first construction's attempt for the Church of Palmira by Félix Candela, built in 1958 in Cuernavaca (Mexico) [1]. The saddle type of hyperbolic paraboloid was chosen as a pure form standing alone on the hill. During the decentering, though, the upper part of the building collapsed because of problems related to

Copyright © 2019 by Giulia BOLLER, Matthias BECKH
Published by the International Association for Shell and Spatial Structures (IASS) with permission.

the construction. As a result, Candela modified its original design, increasing the thickness of the higher edge and reducing its height.

On the other hand, Heinz Isler took advantage from the intentional collapse of the industrial shells for the Haba Company, built in 1972 in Uster (Switzerland), to collect knowledge for his further projects. The monitored destruction with specific load patterns represented a unique opportunity for conducting full-scale tests on one of Isler's most famous industrial shells, almost ten years after the building's completion. Here, the engineer explored the structural behavior of the Haba shells under critical load conditions, until their definitive collapse.

2. Heinz Isler and the use of physical models

Heinz Isler (1926-2009) is considered one of the most prolific shell builders in the world: between 1954 and 2009 he built over one thousand shells and is well-known for his experimental approach to shell design based on the use of physical models. Isler used physical models for a wide range of forms, materials and scales, throughout the entire design process, from the initial concept to the built shell, and beyond. In his work, the model represents a working method, that gave him the possibility to explore design and construction in an iterative way. It becomes a tool both for scientific research and communication [2], representing something already realized, but at the same time exploring a design still to be made.

Heinz Isler not only tested his shells on small-scale physical models, but he also used his buildings as full-scale models. His periodical surveys on the sites to measure the short-term and long-term behavior of his shells is well known [3], defining specific aspects of design, both architectural and structural, that needed to be improved afterwards. He tested the global behavior of the shell in his laboratory on small-scale physical model, through his *Fingerstatik* [4]. On the site of his realized shell, instead, he looked for specific aspects of the structural behavior, such as crack patterns, deformations along the edge beams, shell deformation and resistance under punctual critical load. In this way, the model, both in small-scale and in full-scale, represents the crucial step where it is possible to gain a tactile as well as visual information [5], to better explore different possibilities in design and construction by understanding the structural behavior as well as the architectural space.

3. Haba AG as a full-scale physical model

The pneumatic shells that Heinz Isler developed for the company Haba AG represent one of the crucial steps in his shell explorations, testing on full-scale the design solution with the help of experts from the Swiss Research Institute EMPA and the Swiss Federal Institute of Technology ETH. These shells are part of Heinz Isler's most numerous buildings, spread all over the Swiss industrial landscape and developed through his well-known pneumatic membrane physical model [6]. During the Seventies, the production of Isler's industrial shells decreased in number because of the economic crisis that affected the country. From this perspective, the Haba project, being built in 1972, represents this phenomenon well: it is one of the few projects that was publicly demolished in 1980, in favor of a more functional industrial building.

The project is composed of two pneumatic shells in reinforced concrete, 17 x 17 m and 7 m high, confined by prestressed edge beams and a central polyester skylight of 4.50 m diameter. Without any additional support, a crane is integrated in the edge beam, widening its lower side and adding a small opening in the cross-section. This integral crane beam is similar to the one developed in the project for the Moser company in 1964 in Lyssach [7]. The rectangular form is supported by six columns. The thickness of the shell is 8 cm, which was Isler's standard thickness for pneumatic shells, in order to prevent instability problems, as he had pointed out in 1979 in Stuttgart [8].



Figure 1: The two pneumatic shells of the company Haba AG, Uster, 1980 [gta Archive]

The Haba shells were built in a single construction phase in 1972. Just few years later, in 1979, the client decided to demolish them. For an engineer like Heinz Isler, this occasion was obviously a great opportunity to conduct some demolition tests on full-scale. During his multiple previous experiments, indeed, he had already answered a lot of questions about shell design, but some of them were still with a pure theoretical understanding of the problem [9]. For this reason, Heinz Isler immediately called his client and asked to develop some tests under critical load on the industrial shells. The agreement was reached, with a time window of two weeks between the end of building's use and the final demolition of the structure.

The Swiss Research Institute EMPA, under the supervision of prof. Hans Hugi and prof. Hans Hauri (ETH) together with Heinz Isler, tested the building from 22nd to 30th April 1980. From the academic and research perspective, the exploration on the Isler's pneumatic shells strengthened the knowledge about reinforced concrete shells, a typology that was quite often used in that period, but at the same time helped them to bring together their theoretical background with the practical experience. They wanted to compare these tests with the new outcomes from analytical methods. On the other hand, the engineer Isler wanted to identify potential weak points in the design and construction development of his famous industrial shells, to improve further his design typology, but at the same time to define the possible interventions needed on his existing buildings. At the time of the Haba's tests, indeed, he had already realized more than 450 industrial shells, just in Switzerland. It is not by chance that the company Bösiger AG, his most trusted contractor, was also involved in the exploitation of these tests.

4. Testing under critical load

Due to budget and time restrictions, seven different tests were identified, to be conducted directly on the building site: load test of a short edge beam at the mid-point, load test at the mid-point of a continuous edge beam, shear test of a column, punching test on the shell, load test on the circular upstand at the skylight opening, pulling out of the crane beam suspension, as well as other material tests such as the evaluation of the concrete compressive strength and its module of elasticity. The load was applied with oil-hydraulic cylinders through a system of threaded rods and cross beams put on site. For the measurements, two different methods were applied, based on the needed accuracy: a levelling device and a hose level.

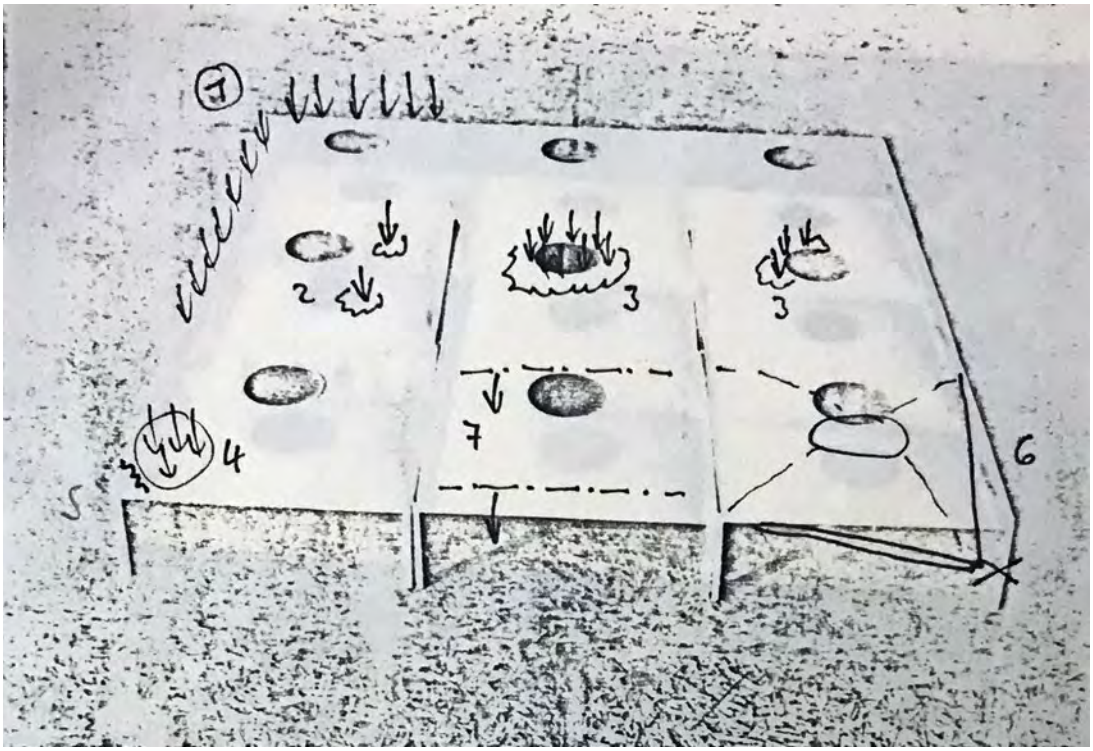


Figure 2: Tests defined for Isler Shells [gta Archive]

First of all, a core drill removed concrete cylinders from the slabs and the beams, with a diameter of 50 mm, to identify the properties of the concrete originally used and to evaluate the needed appropriate tests. The measured E-module was 40'600 - 44'800 N/mm^2 in the slab, whereas 44'400 - 50'300 N/mm^2 in the beam. At the same time, the compressive strength in the slab was about 59 N/mm^2 and in the beam about 71 N/mm^2. In both cases, the values registered were quite high in comparison with the concrete defined in Bösiger's contract prior the construction works, dated October 1970. It was used concrete PC 350 BS (35 N/mm^2 of compressive strength) for the beams, PC 400 BS (40 N/mm^2 of compressive strength) for the columns and PC 350 BS (35 N/mm^2 of compressive strength) for the shells. The much higher results are probably referred to the use of high-quality concrete, with good aggregates, poured and vibrated correctly, thanks to the great experience of the contractor Bösiger, but at the same time the adopted concrete probably strengthened its own properties in the long-term period, since the building was realized eight years before these tests.

The load tests on the edge beams, both the one at the mid-point on the short length and the one on the continuous beam on the long length, highlighted the good properties of the prestressed elements. In both cases, some reference points were defined along the perimeter to measure the deformations. The initial load was set to 10 kN and was increased in steps of 30-50 kN until an applied load of 250 kN was reached. At that point the reinforcement bars started to yield. In the short beam, the breaking load was reached with a load of over 350 kN and a deformation of over 60 mm. The cracks started to become visible, but their dimensions were negligible. In the continuous beam, the maximum deformation was 20 mm, with an applied load of 250 kN. In both cases, the beams were able to respond with an approximately pure elastic behavior to loading conditions much higher than the service loads.



Figure 3: Load test on the edge beam [gta Archive]

The shear test on the column (cross-section 50 x 50 cm) was realized by applying single loads on the edge beams (65 cm high) at either sides of the corner. The deformations were measured in relation to the applied load. Similar to the previous tests, the beam demonstrated an elastic behavior up to the maximum applied load of 1200 kN, when the tests were stopped.

The punching test on the shell was done by applying multiple different loads in a circular arrangement around the skylight, at 2 m distance from the edge beam. Six different punching tests were conducted, with different loading areas. Independently from their position and the local inclination of the shell, the tensile forces were always applied vertically towards the ground. Where the load application area was bigger the breaking load was reached with a load of 240 kN. For small load application areas, instead, the critical load was reached with a load value of 90-100 kN.

The last two tests referred to the specific details of the shell (the circular upstand at the skylight and the crane beam suspension detail) were done in similar ways. Due to the insulation panels, it was not possible to follow the crack development, but it appeared that these elements behaved well from the structural point of view: their resistance was much higher than the one originally expected.

Additionally, two more invasive explorations were carried out, after the official tests by EMPA and right before the destruction of the entire building. Firstly, a corner column was removed to study the shell behavior without one support.

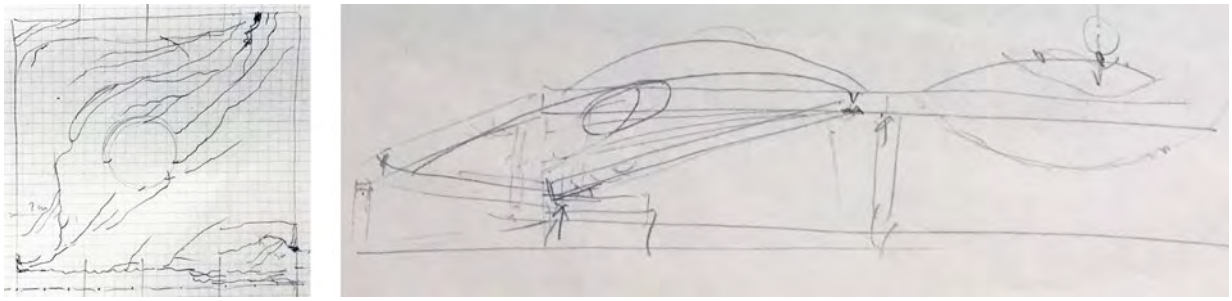


Figure 4: Cracks appeared on the shell roof and collapse mechanism due to column removal [gta Archive]

The second test, instead, was developed simulating the attack of an hypothetical meteorite on the roof, under dynamic applied load.



Figure 5: Demolition of the Haba shells [gta Archive]

5. Conclusion

The outcome of the tests was the publication on the ETH Bulletin [10] and on the journal of the Institute for Structural Engineering at ETH. There was even an internal agreement prior the tests, stating that Heinz Isler should have approved every document before any publication. Especially in this case, he was worried about the unexpected outcomes of the tests as well as the possibility to reveal some secrets of his successful industrial shells. For a precise technical publication of the different tests carried out for

the Haba project, Isler would have waited quite a long time. Interestingly, indeed, a specific publication was released in 1997, almost twenty years after it [11]. Before, he just presented a contribution in a conference organized by Ekkehard Ramm in 1982 [12], in an overview about the stability of thin concrete shells. Here, Isler highlighted the importance of the correct form, the quality of the material and the quality of the construction phases. The tests on the Haba project were thus brought to strengthen the concept, putting the accent on the high quality of his design, proved by the tests under critical load. This was the main aspect that helped Isler to promote further his shell production, becoming one of the most famous shell builders in the world.

The tests on the Haba project confirmed the design and construction quality of his shells. In the EMPA report, although never mentioned in the official publications, there is a short note on concrete quality that could have become potentially critical for Isler's broad shell production. The cracks on the building, indeed, gave the possibility to explore locally the state of the concrete shell. It appeared that in some cases the concrete structure was strongly porous and the steel reinforcement highly corroded. This was due to the characteristics of the 7.5 cm-thick insulation panels, which had two major roles: lost formwork in the construction process and internal finish of the building.



Figure 6: Punching test on the shell, with the insulation panels visible from the shell's inner side [gta Archive]

The insulation panels used in Isler's shells were made of not compact elements. This caused the local problem highlighted: the liquid part of the poured concrete penetrated in the panel's cavities and thus the concrete layer lost the correct balance between aggregates and water, increasing the concrete porosity and decreasing its resistance. At the same time, the corrosion of the reinforcement bars caused internal cracks and reduced the material resistance. The panels, acting as internal finish, were hiding any trace of it. These typology of insulation panels had been used from the very beginning of his career and they had always hided the possibility to inspect the interior side of the concrete layer, causing then a big problem in the prevision of the manifestation of this phenomenon. Even if reported as a short note and never published officially, this detail could have forced Isler to find a suitable solution to the problem, both for preservation of the existence and to improve the quality of his further shells. Although his tests were more in the direction of understanding the structural behavior under critical load, he apparently got some insights in the needed improvement of some crucial construction details, by the confirmation of the good structural behavior of his industrial shells.

[1] M. Garlock, D. Billington, *Félix Candela. Engineer, Builder, Structural Artist*, Princeton: Princeton University Art Museum, 2008, pp. 128-141

[2] S. Chadarevian, N. Hopwood, *Models: the third dimension of science*. Stanford: Stanford University Press, 2004, pp. 1-15

[3] H. Isler, "Generating shell shapes by physical experiments", in *Bulletin of the international association for shell and spatial structures*, Copenhagen, vol. 34, pp. 53-63, Sep. 1993

[4] From a conversation with Hans Glanzmann, Heinz Isler's collaborator in the model workshop, in an interview with Joseph Schwartz, Matthias Beckh, Giulia Boller and Rainer Schützeichel, Zurich, March 28th, 2018

[5] E. S. Ferguson, *Engineering and the Mind's Eye*. Boston: MIT Press, 1993, pp. 102-107

[6] H. Isler, "New Shapes for Shells – Twenty Years After", in *Bulletin of the international association for shell and spatial structures*, Madrid, vol. 71/72, pp. 9-26, 1979

[7] J. Chilton, *Heinz Isler. The Engineer's Contribution to Contemporary Architecture*, London: Thomas Telford Ltd., 2000, pp. 54-55

[8] H. Isler, "Zur Korrelation von Formgebung und Stabilität bei dünnen Schalentragwerken", in *Weitgespannte Flächentragwerke*, Stuttgart, vol. 2, pp. 175-188, 1979

[9] H. Isler, *Schalen Versuche Uster 1980*, unpublished, p. 2

[10] T. Frangi, "Bruchversuche in Betonschalen", in *Bulletin der Eidgenössischen Technischen Hochschule Zürich*, Zurich, vol. 157, pp. 16-17, July 1980

[11] H. Isler, "Monitoring of Built Shell Structures and a Destruction Test of two Fullsize Shellroofs", in *Experimental model research and testing of thin-walled structures*, Prague, pp. 391-396, Sep. 1997

[12] H. Isler, "The Stability of Thin Concrete Shells", in *Buckling of shells,* Berlin, pp. 645-672, 1982

Proceedings of the IASS Annual Symposium 2019 – Structural Membranes 2019
Form and Force
7 – 10 October 2019, Barcelona, Spain
C. Lázaro, K.-U. Bletzinger, E. Oñate (eds.)

Preservation and reuse of reinforced concrete hyperbolic paraboloid shells in the UK

Marisela MENDOZA* and John CHILTON[a]

*MArch Architecture Course Leader
School of Architecture Design and Built Environment, Nottingham Trent University, NG1 4BU, UK.
marisela.mendoza@ntu.ac.uk

[a] The University of Nottingham
Department of Architecture & Built Environment, University Park, Nottingham NG7 2RD, United Kingdom
john.chilton@nottingham.ac.uk

Abstract

During the 1950s concrete shell structures, including hyperbolic paraboloid 'hypar' structures, gained a foothold in Britain's architectural and engineering realm. Amongst the 'hypar' structures built during this period, those designed by Sam Scorer – Lincoln Motor Car Company Showroom, 1958-59, and a petrol station canopy at Markham Moor, 1960-61, as well as the John Lewis Warehouse, Stevenage, by Yorke, Rosenberg and Mardal (YRM), 1963, Queensgate Market Hall, Huddersfield, 1970, by Seymour Harris Architects, and the former Commonwealth Institute, London, by Robert Matthew, Johnson-Marshall and Partners, 1960-62, are some of the most iconic and representative. These structures bear witness to the technological developments in the construction sector as well as the government plans to support the economic growth of Post-War Britain. However, and as is true for most concrete shell structures in the world, these structures have dealt with the challenge of preservation and reuse in different ways, and some of them have been at risk of loss. At present, these structures have been listed Grade II or II* by Historic England, due to their architectural value. This paper gives account of the current use and state of these and other reinforced concrete shell structures in the UK.

Keywords: preservation and reuse, reinforced concrete shells, hypars, Sam Scorer, Hajnal-Kónyi, YRM, Felix Candela.

1. Introduction

Post-War and Post-Austerity planning policies and technological advancements in the construction sector and in particular the fast development and use of reinforced concrete as the 'modern material' brought a new dimension and challenge in the architectural scene in Britain. Amongst some of the most representative structures that portrayed the zeitgeist of this new period were the iconic concrete shells built from the early 1950s to the late 1960s. These structures were iconic not only due to their striking shapes but also for their innovative construction technology as well as for their socio-cultural value. Imported expertise and technology were crucial to the inception and later development of concrete hypars in Britain. In 1959, the American company: O'Neil Ford and Associates were commissioned to erect, in Bedford, the first Texas Instrument Factory outside the US. It is worth to mention that Ford had gained previous experience in the field of inverted concrete hypars to roof industrial buildings through his collaboration with Felix Candela in Texas. Some other early concrete hypars designed and built in Britain were developed by the architect Hugh Segar (Sam) Scorer (1923-2003), with engineer Kálmán Hajnal-Kónyi (1898-1973), including an experimental shell for the Charnos factory in Ilkeston, Derbyshire in 1959 - demolished a couple of years later [1]. However, their most representative hypars include Lincoln Motor Car Company Showroom, 1958-59, and a petrol station canopy at Markham

Copyright © 2019 by Marisela Mendoza and John Chilton
Published by the International Association for Shell and Spatial Structures (IASS) with permission.

Moor, 1960-61. Another early example of early inverted concrete hypars were the shells to roof the Mound Stand of the Gloucestershire County Cricket Club ground at Bristol (1959), which was demolished in 2013. The project was developed by the architect T.H. Burrough and the engineers Derek Bond of Clarke Nicholls & Marcel. Some years later, Clarke Nicholls and Marcell would collaborate with YRM, one of the most representative post-war practices in Britain, and the architect Felix Candela (1910-1997) to design a warehouse for the John Lewis Partnership at Stevenage in 1963 – the building is still in use as a warehouse. Finally, the last inverted concrete hypar shells built in Britain were those to roof the Queensgate Market Hall at Huddersfield in 1969-70. This paper provides an account of the most representative inverted hypar shells built in Britain during the 1950s and late 1960s and which are still in use either retaining its original purpose or being adapted to a serve a different purpose.

2. Hypars designed by Sam Scorer and Kálmán Hajnal-Kónyi

Issues related to the preservation and reuse of hypar shells in the UK are first discussed for three examples designed by Lincoln architect Sam Scorer in collaboration with engineer Kálmán Hajnal-Kónyi. It should be noted that both were present at the first Congress of IASS, in Madrid, in 1959.

2.1. Brayford Pool Restaurants, Lincoln, UK - Former Motor Company Showroom (1958-59)



Figure 1: Linked hypar shells at Brayford Pool, Lincoln, UK: (top) front view showing 'V' shaped columns (bottom) roof showing the continuous rooflights separating the shells on one axis [Photos: John Chilton]

In 1958-59 the architect/engineer team of Scorer and Hajnal-Kónyi designed the largest hyperbolic parabolic roof to be built in the UK at that time, a showroom for the Lincoln Motor Car Company, on a prominent site on Brayford Pool, Lincoln, Fig.1(top). Composed of four hypar surfaces, each 47.5 x 47.5ft (14.7 x 14.7m) and generally less than 2.5" (63mm) thick, the roof is supported on two 'V' shaped columns on one axis, with a continuous edge beam linking the column tops and adjacent shells, and two plain rectangular columns on the other. Slender 6.5" (165mm) diameter steel columns at the external high points control vertical movement due to wind forces. On one axis the shells are separated by a continuous rooflight 10.8ft (3.3m) wide, Fig.1(bottom). Because of site restrictions horizontal thrusts could not be taken by inclined supports so column tops are connected diagonally by prestressed concrete tie beams [2]. Later, the structure was reused as a branch of the Lincolnshire County public library for

a number of years. Described as *"…exceptionally imaginative car showrooms*", the shells were Grade II listed, in 2000 [3]. The shells are currently home to cafés and restaurants.

2.2. Markham Moor filling station, UK (1960-61)

Subsequently, the same partnership designed a simple canopy for Markham Moor petrol filling station, near Retford, Nottinghamshire, in 1960-61. With plan dimensions of 60 x 60ft (18.3 x 18.3m) and rising to 37.4ft (11.4m) at the highest points, it has a distinctive form with elegant curved and tapering edge beams. It stands on four substantial vertical column supports, raising it 5ft (1.5m) above ground level. In the late 1980s, a Little Chef restaurant was constructed under the canopy, Fig 2(a). In 2003 improvements were proposed to an adjacent road junction, which would require its demolition. However, following a national campaign to save the innovative structure, it was saved and in 2012 it was listed Grade II, by English Heritage [1][4]. This gives the structure statutory protection from demolition, extension or alteration without permission from the local planning authority. Sadly, today the shell and restaurant site is abandoned, Fig 2(b).



Figure 1: The Markham Moor hypar canopy, UK, (a) with Little Chef restaurant [Source: https://commons.wikimedia.org/wiki/File:Sam_Scorer,_Little_Chef_-_geograph.org.uk_-_173949.jpg : Richard Croft / *Sam Scorer, Little Chef* / CC BY-SA 2.0] and (b) abandoned state in August 2017. [Photo: John Chilton]

2.3. Church of St John, Lincoln, UK (1962-3)



Figure 3 (a) and (b): Truncated hypar shell Church of St John , Lincoln, UK [Photos: John Chilton]

Scorer and Hajnal-Kónyi's third collaboration was for the Church of St John, Lincoln, UK, Fig.3(a). This is a single hypar surface, in which the high points have been truncated Fig.3(b). It was not initially loved by the public, with reported remarks such as "*…the design of this church will shock most ordinary people. Did the architect have his inspiration on a wet Monday after an acute attack of indigestion?*" Due to its function as a church in a well-populated area of the city it has never been under threat of demolition. In fact, as an important example of ecclesiastical architecture of the 20th century, it too was listed, in 1995, ensuring its preservation for the foreseeable future. In the listing the church is described as a *"…major contribution to church architecture of this period, combining innovative architectural*

thinking with advanced liturgical planning". It is interesting to note that a rather similar truncated hypar shell was built in Rostock, in the former GDR (East Germany), in 1970/71, by architects Gisbert Wolf, Rudolf Lasch and Kurt Tauscher, with engineer Ulrich Müther.

3. Inverted 'umbrella' hypars

3.1. John Lewis Warehouse, Stevenage, UK.

The fast demographic and economic growth in the city of London and the subsequent urban sprawl after the War had an impact on the operational activities of industrial and retail businesses. The well-established John Lewis Partnership (JLP), located in central London, was not an exception. After the War the Partnership was finding an increasing difficulty to maintain its distribution centre in central London, particularly the handling of lorries in and out of London to the various John Lewis stores in the country. Furthermore, the Partnership had two top priorities first, to move into an open plan building to avoid the inconveniences they were experiencing in their multi-storey building in London and second, to find a convenient location that could be relatively near to the headquarters in London and to be effectively connected with the various shops they had around the country [6]. New Towns in Britain, particularly those close to London, offered ample space for the one-storey building the Partnership was looking for and they also provided a relatively close distance from the central store in London. Furthermore, and having its roots in the Garden City movement, New Towns were also attractive as they offered a good quality life for Partnership's employees. In 1959 Felix Candela was invited by the British Council and the Concrete Association to give a series of lectures in the UK. During this visit he met F.R.S. Yorke (1906-1962) – from the prestigious architecture firm YRM (Yorke, Rosenberg and Mardall) - and who a few years later would invite him to collaborate in the design of a new warehouse for the John Lewis Partnership in Stevenage New Town [6]. YRM's architectural proposal for the warehouse was comprised of a rectangular plan, 465 ft. long by 330 ft. to accommodate five bays transversely and fifteen longitudinally Fig.4(a).



Figure 4: (a) John Lewis Warehouse, Stevenage, UK (b) interior view [Source: John Lewis Archives]

The bays were roofed by rectangular inverted hypar shells of 60 ft. (18.2m) long and 31ft. wide tilted to allow in diffuse north light, illustrated in Fig.4(b). Like other warehouses previously built by Candela in Mexico the hypars had a 4 in. diameter rain pipe running down the centre of the columns: 13 ft. high and 2 ft. square section.

Speed in the construction process was paramount and an efficient and systematic construction strategy using only fifteen sets of half-shell formwork as illustrated in Fig.5 to cast all 75 thin-shells made of it a rather unique structure. The innovative and ingenious use of a hinged formwork, unprecedented in Candela's work, both in Mexico and the USA, facilitated a faster transfer of the formwork from shell to shell during the casting process as the hinges would allow the formwork to drop flat and it would only

be necessary to lower it sufficiently to detach it from the concrete before transferring it to cast the next shell. This lowering operation was carried out by just two men and it had a significant impact on the rapid construction process at a rate of three shells per week [7]. Conversely to the inverted hypar shells that Candela built in collaboration with O'Neil Ford in the USA, those of the John Lewis Warehouse followed more closely the careful selection of fine formwork planks thus providing a richer material expressivity to the texture of the exposed concrete of the shells' soffit.



Figure 5: Sets of half-shell formwork, John Lewis Warehouse, Stevenage, UK. [Source: John Lewis Archives]

The architectural uniqueness of the John Lewis Warehouse was recognised by English Heritage – renamed Historic England since 2015 - and was awarded grade II listed status in 1988 praising how the original method of roofing had turned a warehouse into architectural poetry [8]. In 2018 the Warehouse was sold to the American Multinational Wholesale Corporation, Costco. In July 2018 the Comet newsletter announced: 'Under the Costco plans the building will retain its Grade II-listed idiosyncratic reinforced concrete roof, designed by the noted architect Felix Candela'[9].

3.2. Queensgate Market Hall, Huddersfield, UK.

Following the comprehensive plans for re-building Britain after the War, officially published in 1947 in the Town and Country Planning act, Huddersfield's borough architect worked on a challenging development plan to regenerate the town centre. At the beginning of the 1950s the footprint of a ring road and areas for compulsory purchase had been identified. In 1963 the Council put forward a public consultation and exhibition of the regeneration plan which identified two key areas. One of these two areas, the Murrayfield scheme, included the demolition of the existing neo-gothic Market Hall (1878-80) which was rather contentious as the community was very appreciative of it and it also was a building of architectural value [10].

The Murrayfield Real Estate Company appointed the Seymour Harris Partnership architects to developed phase II and Kenneth Wood was appointed as the project's architect. The architect Gwynfor Edwards Roberts, member of Kenneth's team, was assigned to study the most economically efficient proposal for an enclosed market. Roberts was by then well acquainted with reinforced concrete shells and he was positive of the potential they had in covering the proposed market. Roberts worked on a series of iterations, from one-single inverted hypar (85 x 38m) to a twenty-one free-standing asymmetric inverted hypars (17m x 9.5m) to cover an area of 54,850 sq. ft [11]. Roberts iterations and final design were highly influenced and informed by the markets that Felix Candela had previously built in Mexico and most importantly by a visit that Roberts made to study the inverted hypars of the John Lewis Warehouse. Roberts' design was not only responsive to the functional programme but it also carefully considered natural light and ventilation by alternating and increasing the columns' height gradually from North to South thus creating openings for fresh air ventilation and natural light as illustrated in figure Fig.6(a).



Figure 6: (a) Interior and (b) south façade Queensgate Market Hall, Huddersfield, UK. [M. Mendoza 2017]

The iconic character of the market was not only framed by the striking shape of the inverted hypar shells but also by the art work developed by the artist Fritz Steller which includes the steel figures on the interior east wall of the market and the ten ceramic panels on the south elevation of the market. These ceramic panels, the largest of their kind in Britain, provided a rich character to the south façade following the rhythm of the exposed inverted hypars as illustrated in Fig.6(b).

Queensgate Market Hall officially opened on the 6th of April 1970 bringing the communities excitement and interest of the press, the editor of the Huddersfield Day Examiner wrote: 'Architecturally, the new Market Hall is one of the most interesting buildings to have been erected in Huddersfield for many years'[12]. However, and despite five decades of successful operation, the Queensgate Market Hall has been at risk of partial and total demolition. In 2003 Kirklees Metropolitan Council announced the 'Queensgate Revival' redevelopment plan for Huddersfield centre town in which the demolition of the market was proposed. After this announcement two significant events took place to support and secure the preservation of the market. The first of these two events were the application from the Twentieth Century Society to list the Huddersfield Library and the Queensgate Market Hall (February 2004); the second was the establishment of the Huddersfield Gem group in 2004 to promote the Market Hall through social and cultural events [13]. Despite being awarded grade II listing by English Heritage, in August 2005, Kirklees Council announced, in October 2006, a regeneration plan which included the demolition of eight of the twenty-one inverted umbrellas of the Market Hall. Conversely to the lack of appreciation from Kirklees Council, the Concrete Society's Certificate of Excellence was awarded to the Queensgate Market Hall in November 2007. Following the community consultation [14] and appeal from English Heritage the 'Queensgate Revival' redevelopment plan did not proceed, and the market continued in operation to celebrate its 40th anniversary in 2010. Keeping the building in use, and fit to its original purpose, has been instrumental to safeguard the future and integrity of the structure which will be 50 years old in 2020.

4. The Design Museum (former Commonwealth Institute), London

The most recent hypar shell preservation project in the UK is the refurbishment of the former Commonwealth Institute to create a new home for London's Design Museum. Under construction from 1960 and opened by the Queen in 1962, the former Commonwealth Institute, in London's Holland Park, was Grade II* listed on 12th October 1988 [15]. Designed by the architects Robert Matthew, Johnson-Marshall and Partners, with structural engineers A. J. and J. D. Harris of Harris and Sutherland. The Government-funded project was subject to financial restraints and was supported by donations 'in-kind' of materials from Commonwealth countries. It has been reported [16] to have been described as '*…possibly the most outstanding example of architects and engineers in post-war Britain constructing something for (almost) nothing*'. The original brief is said to have been for a 'tent in the park' but this is disputed by Brawne [17]. Drawn up between 1958 and 1960, the brief was influenced by recent reinforced concrete shells constructed in Mexico by Félix Candela and the symbolism of enclosing all nations of the British empire under one large roof. The result was the first hyperbolic paraboloid concrete shell roof to be constructed in London [17] and one of the most prominent built in the UK. The central

55 x 55 m shell [17] is enclosed by 4 separate warped surfaces [15]. The latter are not shells and are composed of inclined prestressed concrete ribs supporting a deck of wood wool slabs.



Figure 7: The Design Museum (former Commonwealth Institute), London [Source: https://commons.wikimedia.org/wiki/File:Commonwealth_Institute,_Kensington,_London_10.jpg, Edwardx [CC BY-SA 4.0 (https://creativecommons.org/licenses/by-sa/4.0)]]

The building became disused in 2005 [18]. In 2007, a search began to find a new function and five architectural practices were invited to make proposals for alternative uses for "reinjecting life into the modernist monument" [19]. Subsequently, architects Office for Metropolitan Architecture (OMA) in collaboration with Allies and Morrison, with Arup as structural engineers, were engaged to design what has become the new home for London's Design Museum, Fig.7. A key part of the brief was the retention of its distinctive copper-clad hyperbolic parabolic roof. To enable the insertion of additional accommodation for the new use, the whole existing roof, amounting to about 2000 tonnes, had to be temporarily supported, with a limitation of only ± 5mm differential settlement between supports [20]. The project is an exemplar of investment in the preservation of historic hypar structures in the UK.

5. Conclusions

Most hypar shells were originally designed to cover open long-span spaces with quite specific functions. When these functions are no longer appropriate the shells often find themselves to be under threat of demolition, as it is difficult to find a suitable alternative use. The majority of the hypar shells described here have been preserved principally because they have been listed, due to their perceived architectural merit. Although most are still in use, the function has changed for some and this has assisted in their preservation. In the case of the Markham Moor filling station canopy, the reuse that resulted in it being the roof of an architecturally inferior restaurant has detracted from its appreciation as an elegant structural form. On the other hand the multi-million pound refurbishment of the Commonwealth Institute, to create London's Design Museum, has shown that if an appropriate alternative function can be found, sympathetic remodelling can preserve and enhance the historic hypar architecture. Furthermore, the excellent condition of the inverted 'hypars' of the John Lewis Warehouse and the Queensgate Market Hall can be attributed to the fact that they have maintained their original purpose, as a warehouse and a market, respectively, and to the architectural and historic value that the owners and communities have recognized in them.

References

[1] K. Szynalska, *Sam Scorer A lesser known architect of the twentieth century*, Masters thesis, University College London, September 2010, available at, http://eprints.lincoln.ac.uk/6004/1/sam_scorer_karolina_szynalska.pdf (Accessed 29th May 2019)

[2] Anon, "A concrete hyperbolic roof over a Lincoln garage", in *Concrete Quarterly*, Number 44, pp. 11-12, January-March 1960.

[3] Historic England, "Lincolnshire Motor Company Showrooms", 2000, available at https://historicengland.org.uk/listing/the-list/list-entry/1392689 (Accessed 13th June 2019)

[4] Historic England, "Canopy to former petrol station", Markham Moor, 2012, available at https://historicengland.org.uk/listing/the-list/list-entry/1402678 (Accessed 13th June 2019)

[5] Historic England, "Church of St. John", 1995, available at https://historicengland.org.uk/listing/the-list/list-entry/1388800 (Accessed 13th June 2019)

[6] M. Mendoza, "Felix Candela's First European Project: The John Lewis Warehouse, Stevenage, New Town," *Architectural Research Quarterly*, 19-2 (2015), pp. 149-169.

[7] Anon., "New Warehouse at Stevenage", in *The Builder*, 206 (28 February 1964), pp. 459-60.

[8] Anon., "Stevenage Partners: 300+ years of service", *in Distribution Chronicle Stevenage* (22 January 2010), p. 14-15.

[9] Asher J.P., "Work starts on Stevenage Costco ahead of planned July 2019 opening", in *The Comet*, 11 July 2018.

[10] M. Mendoza, "Construction of the 21 inverted hyperbolic paraboloid concrete shells to roof the Queensgate Market Hall, Huddersfield", *in Building Histories: The Proceedings of the Fourth Annual Construction History Society Conference, Cambridge, 7-9 April, 2017,* Campbell J.W.P., Baker N., Driver M., Heaton M., Pan T., Tutton M., and Yeomans D., Eds, CHS Cambridge 2017.

[11] C. R. Marsden, "*An Exploration of the Development of Huddersfield's 1970 Market Hall: Architectural Decoration with Cheap Greens; An Architect's Dream?"*, MRes thesis, 2012, available at http://eprints.hud.ac.uk/id/eprint/18045/1/cmarsdenfinalthesis.pdf (Accessed 29th May 2019)

[12] Anon., "Queensgate market still popular: Controversial gem celebrates 40 years", Huddersfield Daily Examiner, 2 April 2010.

[13] Huddersfield gem: http://www.monoculartimes.co.uk/huddersfieldgem/ Last visited 12 June 2019.

[14] Anon., "Model view of the town centre", *Huddersfield Examiner*, 26 June 2003.

[15] Anon, "The Commonwealth Institute – a concrete 'tent' in Holland Park", in *Concrete Quarterly*, Number 56, pp. 2-5, January-March 1963.

[16] J. Merrick, "Building study: the new Design Museum by John Pawson, OMA, and Allies and Morrison", in *Architects' Journal*, 18 November, 2016, available at https://www.architectsjournal.co.uk/buildings/the-design-museum-by-john-pawson-oma-and-allies-and-morrison/10014902.article?blocktitle=big-picture-story&contentid=13625 (Accessed 10th June 2019)

[17] M. Brawne, "Commonwealth Institute, South Kensington", in *The Architectural Review*, Vol. 133, April 1963, 260-266

[18] Historic England, Commonwealth Institute, Grade II* listing, 2019, available at https://historicengland.org.uk/listing/the-list/list-entry/1227441 (Accessed 10th June 2019)

[19] Office for Metropolitan Architecture, "Design Museum, London", available at https://oma.eu/projects/design-museum, (Accessed 10th June 2019)

[20] Oasys, "Design Museum London", 2019, available at https://www.oasys-software.com/case-studies/design-museum-london/, (Accessed 10th June 2019)

Proceedings of the IASS Annual Symposium 2019 – Structural Membranes 2019
Form and Force
7 – 10 October 2019, Barcelona, Spain
C. Lázaro, K.-U. Bletzinger, E. Oñate (eds.)

Preservation and reuse of reinforced concrete shells in Guatemala

Victor Daniel POZUELOS POLANCO*, Mauricio René SOSA, Sandra CASTILLO GALLUSSER, Germán Antonio MELÉNDEZ FUENTES

*Colectivo Cubiertas Ala de Guatemala,
3a. Avenida 12-76 Zona 14, Guatemala City
arq.pozuelos@gmail.com

Abstract

Reinforced concrete shells were first introduced in Guatemala during the 1950s by Guatemalan engineer Mauricio Castillo Contoux who, with his brother Pierre, signed a technical consultancy alliance agreement with the Mexican firm Cubiertas Ala led by Spanish architect Félix Candela. Cubiertas Ala de Guatemala designed, planned and built over forty shell structure projects in Guatemala and other Central American countries including temples, an auditorium, banks, factories, residential houses, an acoustic shell and gas stations, some of which have become reference points in Guatemala's modern architecture. Our commitment, as a research team, over the past 5 years, has been to identify, document and promote the preservation of each of these constructions. Our findings show that, fifty years later, most of the structures are in good condition and used as originally planned for. Additionally, we have been able to present the results of our studies at different universities in Guatemala and abroad. This document records the most important and best preserved structures in Guatemala and our experience in the documentation process, which we believe will help create and promote awareness regarding the cultural heritage of reinforced concrete shells in our region.

Keywords: Shell structure, Guatemala, heritage, Castillo Contoux, awareness

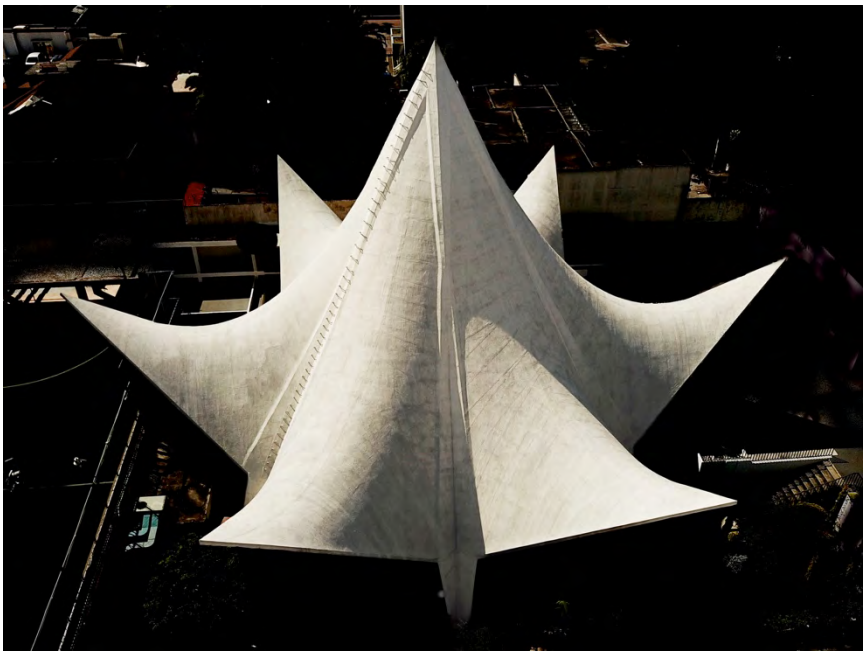


Figure 1. Photo of the exterior of the Shaarei Binyamin Jewish Synagogue, built in 1959. (Photo: John Turton, 2017)

Copyright © 2019 by Victor Daniel POZUELOS POLANCO, Mauricio René SOSA, Sandra CASTILLO GALLUSSER, Germán Antonio MELÉNDEZ FUENTES
Published by the International Association for Shell and Spatial Structures (IASS)with permission.

1. Introduction

The 1950s was a decade of great importance for the history of Guatemalan architecture in which projects marking the emergence of Modernism in the country were built. Given the absence of a School of Architecture in Guatemala[1], many young aspiring architects emigrated to Mexico, the US and Europe[2] to study architecture. Upon their return, the teachings of renowned experts at the time led to the implementation of the International style that had been quite successful in other countries.

Guatemala was undergoing a strong modernization process that required significant changes to the city's image and the few existing architects were flooded with commissions demanding quick, affordable and aesthetic solutions. This reality led to the development of proposals for concrete shell structures in Guatemala that would part with the country's traditional and conservative architectural style and place concrete shell structures in the limelight. The popularity and success of these structures yielded buildings that are now architectural icons and which shapes evidence the country's important construction progress during that period.[3]

It has now been over sixty years since Cubiertas Ala de Guatemala, S.A. built the country's first concrete shell structure: that of the Francisco Vela Auditorium for the Faculty of Engineering, in 1957, giving way to a period of great importance in terms of construction that includes over forty projects in which a variety of hyperbolic paraboloids were used.

The work performed by Cubiertas Ala de Guatemala has been researched and documented by both Guatemalan professionals and Mexican scholars and has enabled the dissemination of its significant architectural contribution in written communication and international conferences. «BAM»

2. Concrete Shells in Guatemala

Guatemalan Civil Engineer Mauricio Castillo Contoux[4] travelled to France in 1954 to specialize in prestressed concrete structures at the prestigious École Nationale des Ponts et Chaussées, where his curiosity regarding new challenges led him to study the work of Spanish Engineer Eduardo Torroja and French Engineer Eugène Freyssinet, introducing him to concrete shell structures. Later on, his interest in these structures led him to contact Spanish Architect Félix Candela, who was living in exile in Mexico. In Guatemala, Modernism was taking its first steps under the guidance of leading young architects filled with innovative ideas.

At the same time, their passion for and the challenge of building new shapes leads Engineers Mauricio and Pierre Castillo Contoux, jointly with Architect Félix Candela, to establish the company Cubiertas Ala de Guatemala, with Engineer Mauricio Castillo acting as its representative for Central America. The company would be in charge of providing new and ambitious projects with technology and fascinating hyperbolic paraboloid shapes to attend to the entire Central American market.

The professional relationship and friendship between Candela and Mauricio Castillo is one of the ingredients that quickly lead to the commercial success of Cubiertas Ala de Guatemala. Castillo relied on the direct expert advice of Candela, whose reputation was worldly renowned in 1957, and who shared his experience with Mauricio through regular correspondence in which he provided recommendations on construction, structural calculations and design. Thus, from the start, the Guatemalan company was able to ensure work of the highest quality.

Cubiertas Ala de Guatemala's first commission was to design and build the auditorium of the Faculty of Engineering of Universidad de San Carlos de Guatemala. Given that the university was in the process of building the university complex known as Ciudad Universitaria[5], the new home for the Faculty of Engineering required new technological construction system solutions that would serve as symbols of their progress and turn its buildings into true icons of an era filled with magnificent architectural expression.





Figure 2. Photo of the exterior of the Francisco Vela auditorium, during construction in 1957 at the Universidad de San Carlos de Guatemala. (Photo: Copy from the photographic archive of the Castillo family)

Figure 3. Photo of the interior of the Francisco Vela auditorium, built in 1957 at the Universidad de San Carlos de Guatemala. The building is currently in optimum conditions. (Photo: John Turton, 2015)

The construction of the auditorium gained immediate notoriety. Castillo's design included details, provided by Candela, on construction and techniques to build the formwork and perform the concrete casting work. The exchange of letters was fruitful. In one letter, Candela states: *«The world's interest in this type of construction has evidently awakened and many are interested in venturing into this field, though it is also true that there is great amount of confusion regarding the design of these structures, which is a major obstacle for those starting out without the correct advice and experience. The road to clarify the arising inquiries is long and difficult. Therefore, I believe that we will always be favored by our years of experience and the projects we have built».*[6]

This is how Cubiertas Ala de Guatemala introduced concrete shells and became the first country in all of Central America to experiment with reinforced concrete hyperbolic paraboloid shapes. Its success was immediate since many projects required affordable as well as aesthetic solutions. The impact made by the university's auditorium caught the attention and awakened the interest of many architects who had graduated in different parts of the world. And so, since 1957 and throughout the 1960s, Cubiertas Ala de Guatemala designed, calculated and built over forty concrete shell structures with different architects in Guatemala and Central America.





Figure 4. Photo of the Acoustic Shell, designed by Candela and Castillo, built in 1960. Located at Parque de la Industria is currently in optimum conditions. (Photo: José Mata 2017)

Figure 5. Photo of shell structures built in series for market places in 1960. The system was also used for factories. (Photo: Copy from the Castillo family photographic archive).

3. Preservation

Properties built with concrete shells and that are part of the catalogue of historical buildings declared as the Nation's Historical and Cultural Heritage Sites, include the Penthouse of the Instituto Guatemalteco de Seguridad Social (Guatemalan Social Security Institute), located in Guatemala City's Civic Center[7] and the Francisco Vela Auditorium, in Ciudad Universitaria[8], both in the Guatemalan capital. Studies and proposals are currently being carried out for other shell structure projects that are located in the jurisdiction of the city's historical center to be included among Guatemala's structures of historic and cultural significance given that they contain elements of a unique architectural trend and constitute a structural element that is no longer built.

The concrete shell structures are an innovative construction element that while making use of the force transfers also provides an important aesthetic solution. Religious temples are included among the best preserved structures. Cubiertas Ala de Guatemala built and designed five hyperbolic paraboloid projects in Guatemala, each with formal features that distinguish them from others given that the task team in charge of each project aimed to design a structure offering different sensations in each temple, through their shape and space.

The Shaarei Binyamin Jewish Temple and Cristo Rey Lutheran Church, are among the most prominent temples, both containing solutions corresponding to their function and which interior space offers a unique spatial experience using their overall size to create a monumental work of architecture. In the words of Castillo: *«They have mainly been used on projects which interior and exterior aspect seeks to identify a given function or a clearly defined architectural and plastic expression, as in the case of the religious temples».*[9]

The first temple, the Champagnac Church, was built in 1958; the last, the Church of San Ignacio de Loyola, in 1967. All of these temples were built over sixty years ago and, despite the huge impact of the earthquake that shook Guatemala in 1976 and the effects of time, are in perfect condition.



Figure 6. Photo of the interior of the Cristo Rey Lutheran Church, built in 1963. It is currently in optimum conditions. (Photo: José Mata, 2017)



Figure 7. Photo of the exterior of the Shaarei Binyamin Jewish Synagogue, built in 1959. It is currently in optimum condition. (Photo: José Mata 2017)

4. Reuse

As previously stated, the majority of buildings are still used for the purposes they were originally built for and, therefore, are preserved in good condition. Those which surroundings have been altered are those intended for market places, which due to the urban sprawl of the cities are exposed to different phenomena such as the saturation of their interior spaces, very humid areas and environmental pollution, among others. All of this leads to the emergence of different building material pathologies that in the long run, due to the inadequate maintenance performed by their owners or administrators,

have a negative effect on the structures. Buildings used for industrial and commercial purposes, like the market places, are vulnerable in many aspects due to the space usage dynamics they experience throughout the course of time. In the case of the first two, these have preserved the original concept for which they were built. We can, for example, mention the Ducal and Nestlé factories which interior and exterior structural shell system and finishes remain in optimum condition.





Figure 8. Photo of the market in Chiquimula during construction in 1961. (Photo: Copy from the Castillo family photographic archive)

Figure 9. Photo of the current state of the market in Chiquimula. (Photo: Victor Daniel Pozuelos 2017).

Another example is that of the Klee commercial premises housing a Banco Agromercantil «BAM» banking agency and the GENTRAC machinery agency, both built in the 1960s. Though modifications to these buildings do not allow the shell surface elements to be appreciated from the outside, their interior, free of false ceilings, exhibits such elements and has enabled the appropriate conservation of the facilities.

The shell structures recovered through architectural interventions yielded fortunate results since the architects in charge of each project were aware of the importance of the structure and proposed designs in which the concrete shell recovers its prominence. Thus, the shell structure again produces its unique spatial perception and sculptural characteristic.





Figure 10. Photo of the interior of the BAM bank agency, built in 1964. It is currently in optimum condition. (Photo: John Turton 2015)

Figure 11. Photo of the interior of the GENTRAC machinery agency, built in 1964. It is currently in optimum condition (Photo: Victor Daniel Pozuelos 2018).

5. Research and Dissemination

Our task team has documented approximately 70% of the 46 structures that we know were built by Cubiertas Ala de Guatemala. It is interesting to point out that of those structures that have been documented, 90% have not changed the use for which they were built and only 4 were demolished. Of these, one gas station was demolished to "standardize gas stations and convenience stores" and one restaurant, located in Parque de la Industria, was demolished to build a parking lot. All the documented projects are located in Guatemala, but we know of the existence of one temple in El Salvador and two factories in Honduras.

DESCRIPTION	YEAR	No.	DOCUMENTED
RELIGIOUS TEMPLES	1958-1966	6	5
BUILDINGS FOR VARIOUS USES	1957-1968	7	6
FACTORIES	1960-1969	5	4
COMMERCIAL PREMISES	1963-1966	6	4
RESIDENCES AND OFFICES	1958-1965	8	6
MARKET PLACES AND BUS STATIONS	1961-1966	8	4
GAS STATIONS AND OTHERS	1958-1968	6	3
TOTAL		46	32

Table 1: Summary of concrete shell structures built by Cubiertas Ala de Guatemala in Central America

To date, the majority of concrete shells are still standing. There is no record of any structural failure in or damage to such caused by the constant quakes that have historically impacted the country.[10]

The documentation and dissemination of the projects executed by Cubiertas Ala de Guatemala began when Félix Candela commissioned Mauricio Castillo to write about Latin America for the «Coloquio Internacional sobre Progreso de las Estructuras Lainares en los últimos diez años y su desarrollo futuro», held in Madrid in 1969 and published by the International Association for Shell and Spatial Structures (IASS). Nonetheless, it was not until 2010, the year of Candela's centennial, that Dr. and Architect Juan Ignacio del Cueto, head researcher at UNAM, Mexico, presented an exhibit at the Mexican Embassy in Guatemala, where Castillo Contoux's work is included. This event awakens the interest in researching concrete shell-built structures, and marks the formation of the task team that has since then documented and identified these projects. Dissemination has been key in this process, as well as participating in the following national and international conferences: Conmemoración 50 años del Templo Cristo Rey (Guatemala 2016), 6th Structural Engineers World congress (México 2017), Seminario Moderno de la Arquitectura Nacional (Guatemala 2017), La estela de Félix Candela a 20 años de su muerte (México 2017), Encuentro Nacional de estudiantes investigadores (Guatemala 2018), III Congreso Internacional Hispano-americano de Historia de la Construcción (México 2019).





Figure 12. Photo of the restaurant at Parque de la Industria, built in 1960, demolished to build a parking lot. (Photo: Copy from the Castillo family photographic archive)

Figure 13. Photo of the Shell gas station on Avenida de las Américas, built in 1962, demolished to build another gas station. (Photo: Sandra Castillo, 2005)

6. Conclusions

Constructions performed by Cubiertas Ala de Guatemala constitute a major contribution to Guatemalan architecture for they preserve the legacy of Felix Candela and Mauricio Castillo Contoux in their buildings. Almost all these constructions are standing, in optimum preservation condition and hold the original spaces for which they were designed.

In addition to studying and documenting these structures, national and international exhibits and conferences regarding such have awoken the interest of architecture and construction professionals and students, and have even served to motivate the preservation of these structures among their owners.

Acknowledgements

We wish to express our gratitude to John Turton, José Mata, Roberto Antonio Prado, Roberto Castañeda, Mábil Hernández, Juan Ignacio del Cueto, Docomomo capítulo Guatemala, for their invaluable collaboration.

References

[1] The first Faculty of Architecture in Guatemala was established on September 5, 1958; Roberto Aycinena Echeverría, graduated from UNAM, Mexico, served as the faculty's first dean.

[2] The most prominent architects were: Pelayo Llerena Murúa, who graduated from the University of Illinois, USA. Jorge Montes Córdova, who graduated from the Alabama Polytechnic Institute, USA. Carlos Haeussler Uribio, who graduated from the Universidad Nacional Autónoma, Mexico. Raúl Minondo Herrera, who graduated from the Harvard University, USA. Max Holzheu, who graduated from Eidgeno Essische Technische Hochschule, ETH, in Zürich, Switzerland.

[3] Monterroso, Raúl. 2008. *Moderna: guía de arquitectura moderna de la Ciudad de Guatemala* / texts by Raúl Monterroso, Gemma Gil; photos by Andrés Asturias. Guatemala: el Librovisor, Ediciones Alternativas el Centro Cultural de España/Guatemala.

[4] Mauricio Castillo Contoux obtained his degree as a Civil Engineer from the Universidad de San Carlos de Guatemala in 1953. In 1962, he studies structures at Oklahoma State University, National Science Foundation.

[5] Cazali Ávila, Augusto. 2001. 50 años de Autonomía Universitaria. In *Historia de la Universidad de San Carlos de Guatemala época republicana: (1821-1994).* Editorial Universitaria Colección Monografías, 305. USAC. Guatemala.

[6] Letter written by Félix Candela to Mauricio Castillo Contoux, Mexico City, dated September 8, 1957. The letter belongs to the Castillo family correspondence archive.

[7] The Civic Center of Guatemala City was declared as the Nation's Historical and Cultural Heritage Site through Ministerial Resolution number 189-2014 dated March 5, 2014

[8] Central Campus of Universidad de San Carlos de Guatemala, declared as the Nation's Historical and Cultural Heritage Site through Ministerial Resolution number 1199-2011 dated December 19, 2011.

[9] Castillo Contoux Mauricio, 1969 "General Report. Session V. Central and South America, Mexico." *Coloquio internacional sobre Progreso de las Estructuras Laminares en los últimos diez años y su desarrollo futuro*. *Bulletin of the International Association for Shell and Spatial Structures*, No. 48, pp. 43-49, Madrid, Spain.

[10] Sixteen earthquakes have been recorded throughout the Republic of Guatemala from 1957 to 2017. INSIVUMEH (s.f.). «Principales eventos sísmicos del siglo XX en Guatemala».

Proceedings of the IASS Annual Symposium 2019 – Structural Membranes 2019
Form and Force
7 – 10 October 2019, Barcelona, Spain
C. Lázaro, K.-U. Bletzinger, E. Oñate (eds.)

Strengthening of the Hypar Shell in Magdeburg with Carbon Reinforced Concrete – Design and Calculations

Alexander SCHUMANN*, Manuel HENTSCHEL[a], Robert ZOBEL[b], Manfred CURBACH*

*Technische Universität Dresden
Institute of Concrete Structures, 01062 Dresden, Germany
Alexander.schumann1@tu-dresden.de

[a] CarboCon GmbH, Ammonstraße 72, 01067 Dresden, Germany
[b] IBB Ingenieurbüro Baustatik Bautechnik, Altcoschütz 17, 01189 Dresden; Germany

Abstract

Carbon reinforced concrete is a high potential possibility for the strengthening of existing buildings. When utilizing this innovative material, the load-capacity can be increased impressively, by thin strengthening layers of only 10–15 mm. Therefore, carbon reinforced concrete is a perfect fit for the restauration or strengthening of existing steel reinforced concrete structures, which cannot carry any more loads resulting from the self-weight of an additional component. In this paper the current status of the hypar shell in Magdeburg (Germany) with relating problems and damages as well as the planned strengthening of the hypar shell with carbon reinforced concrete will be described. In detail the concept of the design and the calculation for the strengthening layers will be introduced. More over some important facts of the design and the recalculation of the CRC strengthening will be shown, e.g. taking into account the interaction of bending moment and normal forces or the consideration of the pre-deformation of the hypar shell. At the end, an outlook of the future work for the project will be given.

Keywords: shell structure, concrete shell, hypar shell, damages, restauration, retrofitting, strengthening, carbon reinforced concrete, CRC, textile reinforced concrete, TRC, design, strengthening concept.

1. Introduction

Due to various reasons, nowadays a great number of structural elements have to be strengthened or restored. One possible method for the strengthening of steel reinforced concrete (RC) structures is the use of carbon reinforced concrete (CRC). The huge advantages of the composite material CRC compared to conventional strengthening methods, e.g. shotcrete, are well-known (e.g. high strengths of the carbon grids and high resistance against corrosion) and already proved in academic researches [1]-[5] as well as by practical projects [6], [7]. Although, much research with CRC has already been finished, many aspects still need to be further investigated or discussed. For example, there are already many experimental investigations, calculation methods and design recommendations for enhancing the flexural strength of RC elements with CRC, see [8], but no practical project has yet been carried out without further additional investigations. Therefore, in this paper the calculations and the design model of a strengthening measure will be described by means of a hypar shell in Magdeburg, which is to be strengthened with a 10 mm thin CRC layer at the top and the bottom of the RC shell structure.

2. The hypar shell in Magdeburg

The hypar shell in Magdeburg, Germany, was built in 1967 by Ulrich Müther [10], see fig. 1. The shell structure is one of Magdeburg's attractions because of its beautiful thin structure. The roof was made of reinforced concrete with a planned thickness of 70 mm (in real the thickness of the shell was only 50

Copyright © 2019 by Alexander SCHUMANN, Manuel HENTSCHEL, Robert ZOBEL, Manfred CURBACH
Published by the International Association for Shell and Spatial Structures (IASS) with permission.

mm) by a span of 48 m × 48 m. The building had to be closed in 1997 due to enormous damages over time caused by deficiencies in the construction, which now became visible. Figure 1, for example, shows some damages from 2017. The first defects occurred shortly after completion in 1967. A continuous progression of the damage of the whole structure made it necessary to close the building.



Figure 1: Condition of Magdeburg's hypar shell in 2017; view and examples of current damages of the shell structure (photos: S. Wilhelm)

In order to protect this landmark of the city of Magdeburg from demolition, however, the city of Magdeburg has been searching for a suitable redevelopment concept for many years. Initially, the focus was on conventional refurbishment concepts, e.g. through strengthening with shotcrete [11]. However, these and other variants did not prove to be effective in terms of the special character of the load-bearing structure and its authentic preservation. The progress made in the development of the innovative carbon reinforced concrete technology enabled a breakthrough in finding a solution [12].

3. Strengthening of the hypar shell with CRC

In the course of an intensive feasibility study, it was proven that it is possible to strengthen the shell structure with CRC [12]. Based on this, a corresponding design planning for reinforcement with carbon concrete was carried out.

Two preferred variants for the strengthening of the shell with CRC were found. For both variants, the ready-mixed fine grained concrete Pagel TF10 [13], which was specially developed for the strengthening of RC structures with textile and carbon reinforced concrete, respectively, was to be used. The difference lies in the type of carbon grids. Variant 1 dealt with a carbon grid according to the first general building approval for strengthening with TRC in Germany [14], [15]. In variant 2, a biaxial carbon grid based on [14], but modified to improve the mechanical characteristics was considered. Therefore, two different strengthening concepts were developed. Variant 1 could be carried out analogously to [14] without additional investigations. Two layers of carbon grid would be required as the carbon grid was developed for static strengthening in one main load-bearing direction. On the other hand, there is variant 2, which is not regulated—that means, an approval in individual cases (ZiE) is required—, but which requires only one layer by using a biaxial grid with a higher tensile strength and better bond behavior. For a detailed description of the variant discussion with different carbon grids, please refer to [12]. After comparing the two concepts, it was decided to use the modified biaxial grid for the strengthening of the Müther's shell in Magdeburg.

Finally, the hypar shell in Magdeburg will be strengthened with a 10 mm thin CRC layer on the top and on the bottom of the shell structure. So, the desired goal of restoring the durability and serviceability of the shell structure can be achieved. Furthermore, the CRC layers will increase the load-bearing capacity

by 50% compared to the actual state. The construction work on site of the concrete shell is planned for the end of 2019.

4. Design of the carbon reinforced concrete strengthening

For the strengthening of existent RC structures, design models und calculation methods are already available, e.g. [8]. But for the design and calculation of the CRC layers for this project the already known design models could not be used efficiently because of the interaction between the bending moments and the normal forces. Due to this fact it was not a priori obvious, at which point of the whole shell structure the critical areas are. So the static proof of the hypar shell had to be verified with a simplified bending moment-normal forces (m-n) interactive diagram. This diagram was created based on the determined material resistances of the strengthened cross section, taking into account the uniaxial tensile force $n_{t,Rd}$, the uniaxial compressive force $n_{c,Rd}$ and the pure bending moments m_{Rd} using linear interpolation between the values of the material resistances (fig. 2). Thereby, a rather conservative assumption was made by linearize the course of the m-n interactive diagram in comparison to the more lifelike nonlinear course based on the interaction between normal forces and bending moments.

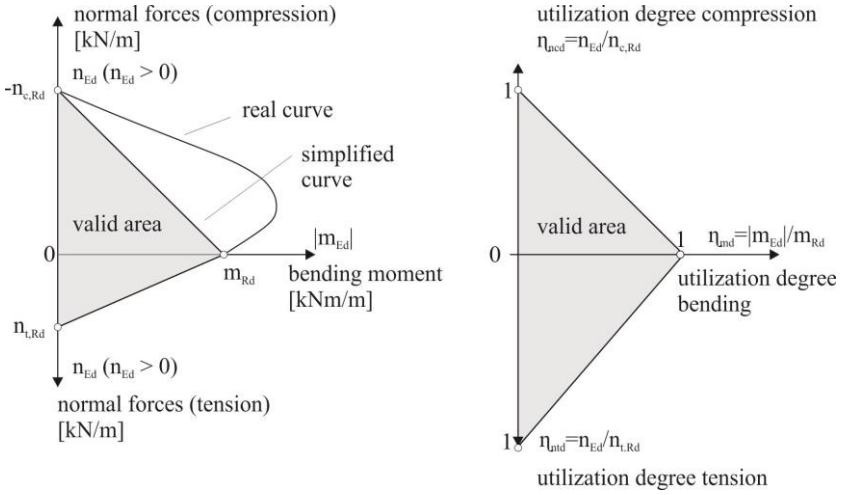


Figure 2: Principle of the m-n interaction diagram (graphic: Alexander Schumann)

To determine the design internal forces of the hypar shell, a finite element model was created from the project partner Prof. Rühle, Jentzsch & Partner. In addition to the permanent loads (e.g. dead load of the load bearing structure itself, additional death loads, skylights etc.) and the variable loads (e.g. caused by wind and snow) the different states of construction of the CRC strengthening were also considered closely.

For the calculation of the CRC-layers following assumptions were made (referring to Figure 3 and Figure 4):

- The Hypothesis of Bernoulli (plain sections remain plain) is valid.
- The cracked cross-section areas, the concrete tensile strength is neglected.
- There is rigid bond between reinforcement (carbon and steel9 and concrete.
- The strain distribution is linear across the height of the cross section.
- Idealized stress-strain curves are used for all materials, compare [16], [8].
- The tensile force distribution between the reinforcing steel and the carbon grid is neither depending on the different strain stiffnesses of the materials nor on the bond characteristics of both materials.

With those assumptions the maximal bending capacity $\mathbf{m_{Rd}}$ of a with CRC strengthened cross-section was calculated according to Figure 3 and Figure 4. In those figures the external forces and the internal

forces as a result of the strain state of a strengthened RC cross section with CRC is shown. With this iterative process the bending moment capacity can be calculated, which is already described detailly in the literature [8], [17]. More over in Figure 4 the consideration of the pre-deformation is illustrated.

The capacity of the normal forces of the strengthened slab in compression ($\mathbf{n_{t,Rd}}$) and tension ($\mathbf{n_{c,Rd}}$) was calculated according to the cross-sections and the ultimate strengths of the various materials. For the determination of the compression strength of the strengthened cross-section the carbon grid was not considered. As a assumption, the strength of the fine-grained concrete was defined analogous to the existent concrete strength. This assumption was made on the safe side of the design of the concrete shell.

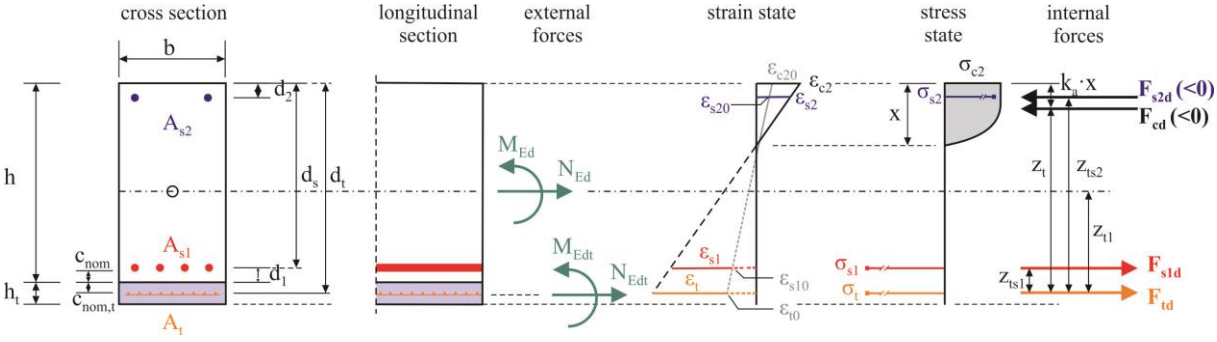


Figure 3: Strains, stresses, internal and external forces shown on a strengthened cross section, tensile forces at the bottom surface of the shell (graphic: Robert Zobel)

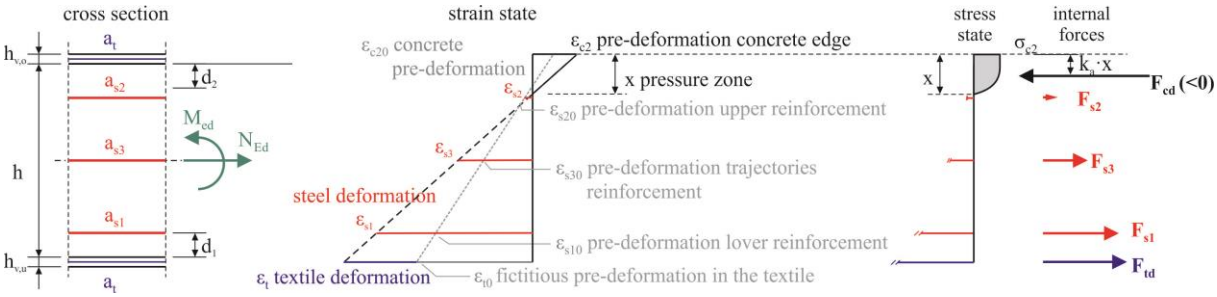


Figure 4: Strains, stresses, internal and external forces shown on a strengthened cross section, tensile forces at the top surface of the shell (graphic: Robert Zobel)

Generally, the RC shell is characterized by an upper and a lower bending reinforcement as well as a trajectories reinforcement (reinforcement layer at the shell's mid-surface, see figure 3). Due to the variations in the reinforcement distribution of the origin RC shell as well as the varying current conditions of the reinforcement, the shell was divided into eight areas with different reinforcement cross sections. Considering the pre-strain state of the shell, the material resistances $n_{t,Rd}$, $n_{c,Rd}$ and m_{Rd} of the strengthened hypar shell were determined for every different reinforcement cross section.

Besides the bending and the carbon reinforcement also the trajectories reinforcement was taken into account for the determination of m_{Rd}. If existing, the bending reinforcement (made of steel) located in the compression zone was considered as compressive reinforcement to calculate the material resistance $n_{t,Rd}$. At the same time, the textile carbon grid does not function as a compression reinforcement. Only the thin layers of additional concrete are factored for the determination of $n_{c,Rd}$.

Using the determined material resistances, m-n interaction diagrams for each of the different reinforcement cross sections can be generated. With the prove that the design values of the design internal forces n_{Ed} [kN/m] and m_{Ed} [kN/m] for all load combination, are within the permissible range of the m-n interaction diagram, the design of the ultimate limit state (ULS) of the

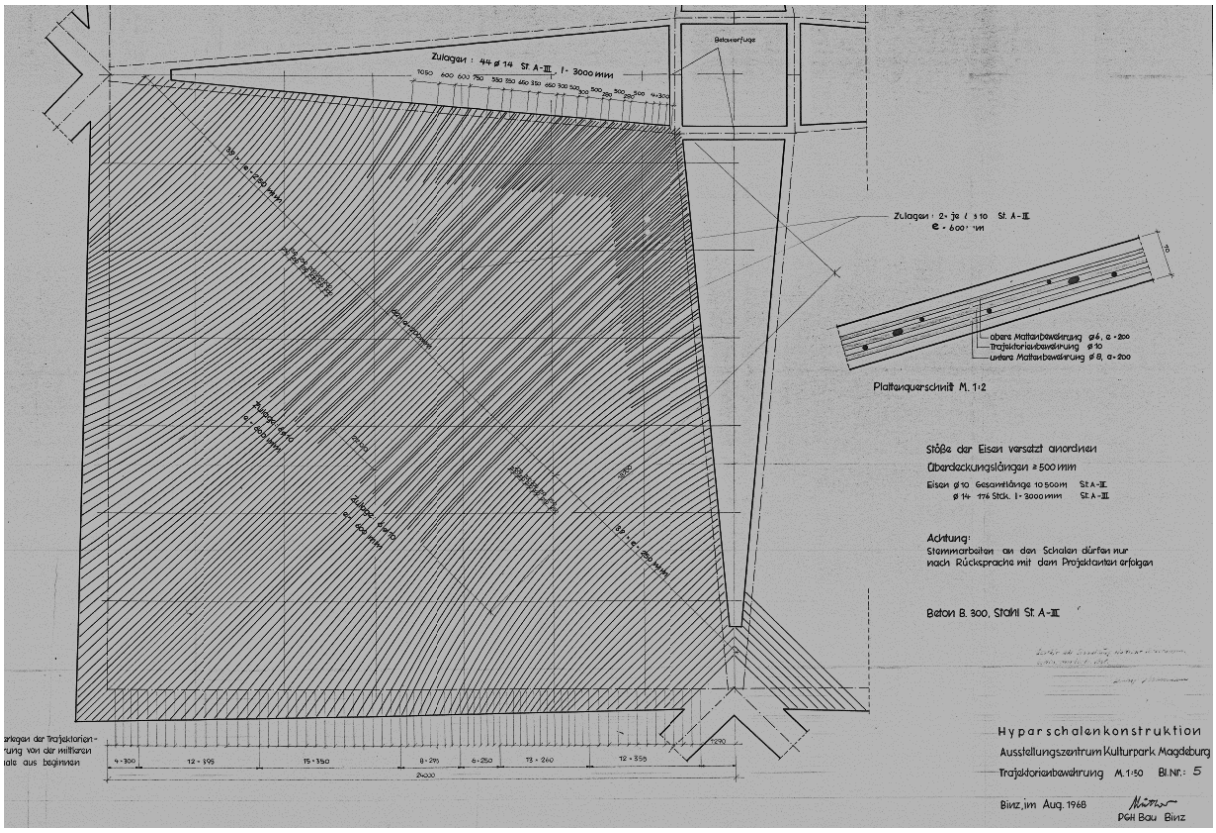


Figure 5: Historical reinforcement drawing of the hypar shell in Magdeburg [18]

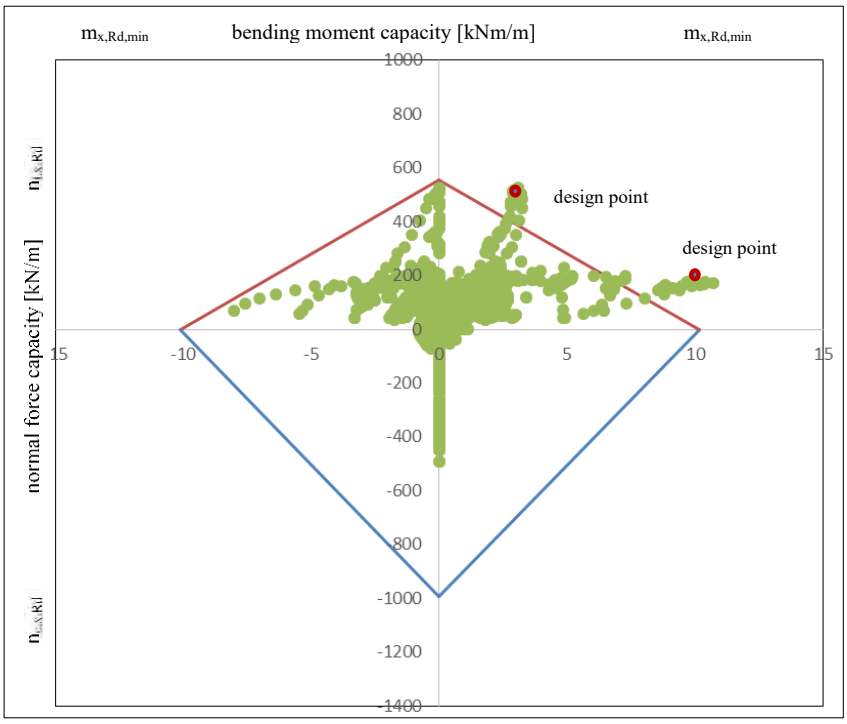


Figure 6: Cross section 1, m-n interactive diagram, essential values are highlighted in red (graphic: Robert Zobel)

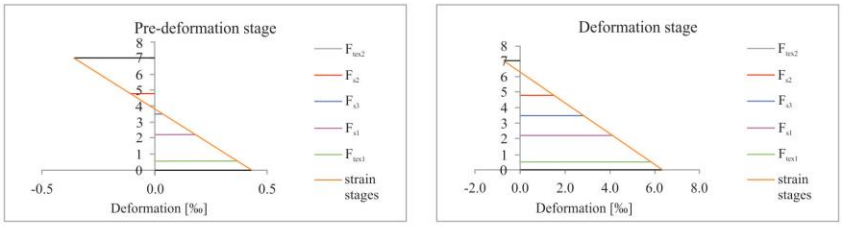
Step 1: External forces

External Moment M_{Ed} = 2.8 kNm

External Force N_{Ed} = 420.0 kN (tension)

Step 2: Pre-deformation stage

strain stages	strain stages	maximum values
ε_{cv} = 0.75 [‰]	$\varepsilon_{cv,fk,0}$ = -0.36 [‰]	ε_{c2u} = -3.86 [‰]
ε_{c} = 0.27 [‰]	$\varepsilon_{c,0}$ = -0.25 [‰]	ε_{c2u} = -3.50 [‰]
ε_{s2} = 1.49 [‰]	$\varepsilon_{s2,0}$ = -0,11 [‰]	
ε_{s3} = 2.81 [‰]	$\varepsilon_{s3,0}$ = -0.03 [‰]	
ε_{s1} = 4.14 [‰]	$\varepsilon_{s1,0}$ = 0.18 [‰]	
ε_{t} = 5.87 [‰]	$\varepsilon_{t,fk,0}$ = 0.37 [‰]	ε_{tud} = 6.25 [‰]
$\varepsilon_{t,new}$ = 5.87 [‰]		
ε_{bottom} =6.38 [‰]	$\varepsilon_{bottom,fk}$ = 0.43 [‰]	



Step 3: Ultimate limit stage

d_{tex} = 5.50 [cm]
d_{s1} = 4.80 [cm]
$z_{t,1}$ = 3.00 [cm]
z_{ts1} = 1.70 [cm]
z_{ts3} = 3.00 [cm]
z_{ts2} = 4.3 [cm]

concrete compression force
x = 0.74 [cm]
α_R = 0.18
k_a = 0.34
z = 6.25 [cm]
F_c = -18.82 [kN]

steel force
σ_{s2} = 21.17 [kN/cm²]
F_{s2} = 29.85 [kN]
σ_{s3} = 37.09 [kN/cm²]
F_{s3} = 304.85 [kN]
σ_{s1} = 22.95 [kN/cm²]
F_{s1} = 32.36 [kN]

textile force (tension)
σ_t = 109.94 [kN/cm²]
F_t = 71.76 [kN]

$\sum H = 0$
$M_{Ed,t}$ = -9.80 [kNm]
$M_{Rd,t}$ = -9.80 [kNm]
$M_{Ed,t} / M_{Rd,T} = 1$
$A_{tex,req}$ = 0.65 [cm²]
$A_{tex,\ exist}$ = 0.71 [cm²]
$A_{tex,req} < A_{tex,\ exist}$

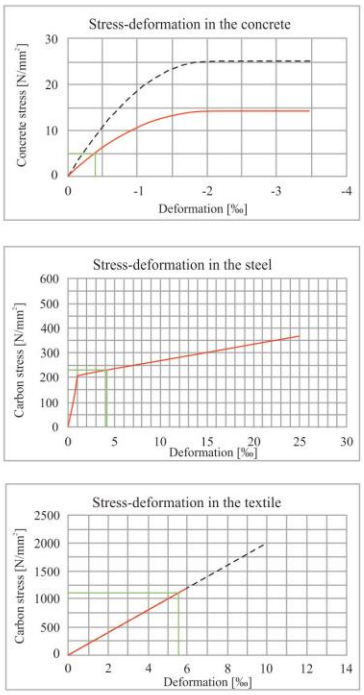


Figure 7: example for the iterative calculation (graphic: Alexander Schumann)

strengthened hypar shell can be performed (see Figure 6). Ensuring to be on the safe side, always the maximum design internal forces were combined with one another. A separation of the internal forces by groups of load combinations does not occur.

Additionally, some of the calculated values were outside of the permitted area in the m-n interactive diagrams of the different cross sections. The majority of these calculated values can be traced back to singularities, but unfortunately, not all of them (see Figure 6, red highlights). Finally, based on an interactive design method, a separate proof of these points were made (see Figure 7). This was possible because the course of the function of the m-n interactive diagram is rather a conservative estimate of the actual nonlinear interaction between normal force and bending moment.

In fig. 7, the exemplary process for the calculation of one data point which was not proved by the simplified m-n interactive diagram is shown. At first, for the given load stages the pre-deformation state of the hypar shell was determined. Based on this, the bending moment capacity of the cross-section considering the normal force and the different reinforcements was defined. Therefore, the already known iterative calculation method for RC structures strengthened with TRC or CRC was used, e.g. [8].

With the previously described method the strengthening layers for the concrete shell was calculated and designed for the whole structure. More over with this simplified method an easy and efficient design of the strengthened shell with one CRC layer on the top and the bottom of the existent concrete shell was possible. But, for the final design of the strengthening layers more aspects and proofs had to be considered which were not described in this paper. Exemplary the aspects of the end anchorage of the carbon grids can be mentioned. For the end anchorage of the carbon grids for this shaped concrete shell different solutions had to be developed. All aspects of the planning of the strengthening of the Hyparshell in Magdeburg with CRC had to be checked and proved by an approval for this special application.

5. Conclusion and Outlook

The strengthening of the hypar shell in Magdeburg in Germany is currently one of the biggest projects for the strengthening with carbon reinforced concrete in Germany nowadays. All advantages of CRC for strengthening of RC structures can be shown impressively within this project. The whole building envelope can be saved of demolition with only 10 mm thin layers of CRC on the top and the bottom of the shell structure.

In this paper, the current condition of the concrete shell was described. The design and the calculation procedure for the strengthening with CRC was shown. In detail, the calculation of the flexural strengthening in consideration of the interaction between normal forces and bending moments was described by the use of a simplified bending moment – normal forces interactive diagram. With this method, an effective calculation of the strengthening layer with CRC could be provided.

Acknowledgements

We thank the city of Magdeburg, especially the ‘Eigenbetrieb Kommunales Gebäudemanagement (KGm)’ for giving the opportunity to strengthen the hypar shell in Magdeburg with carbon reinforced concrete. Moreover we would like thank our partners at Prof. Rühle, Jentzsch & Partner, who were responsible for the calculations and proves of the existing concrete shell.

References

[1] L. N. Koutas, Z. Tetta, D. A. Bournas, T. C. Triantafillou, “Strengthening of Concrete Structures with Textile Reinforced Mortars: State-of-the-Art Review”. *J. Compos. Constr.*, vol. 23, pp. 1-20, 2019.

[2] A. Peled, A. Bentur, B. Mobasher, *Textile Reinforced Concrete*. Series: Modern Concrete Technology No 19, CRC Press: Boca Raton, FL, USA, 2017.

[3] T.C. Triantafillou (Ed.), "Textile Fibre Composites in Civil Engineering", Woodhead Publ./Elsevier, 2016.

[4] D. Bournas, "Strengthening of existing structures: Selected case studies", In Textile Fibre Composites in Civil Engineering; Triantafillou, T.C., Ed., Woodhead Publ./Elsevier, 2016, 2016, Chapter 17, pp. 389–411.

[5] S. May, A. Schumann, S. Bergmann, M. Curbach, J. Hegger, "Shear Strengthening of Reinforced Concrete Structures with Carbon Reinforced Concrete," in *Concrete – Innovations in Materials, Design and Structures: Proceedings of the fib Symposium, Krakow, Poland, May 27-29, 2019*.

[6] F. Schladitz, M. Tietze, M. Lieboldt, A. Schumann, M. P. Garibaldi, M. Curbach, "Carbon reinforced concrete in construction practice," in Engineering the Delevoping World, Kuala Lumpur, Malaysia, April 25-27, 2018.

[7] A. Al-Jamous, "Instandsetzung der historischen Betonbrücke in Naila". Beton- und Stahlbetonbau 112, 9, pp. 623-628, 2017.

[8] S. Scheerer, R. Zobel, E. Müller, T. Senckpiel-Peters, A. Schmidt, M. Curbach, "Flexural Strengthening of RC Structures with TRC – Experimental Observations, Design Approach and Application" Applied Sciences 9, 1322, pp. 1-18, 2019.

[9] A. Schumann, S. May, M. Curbach, "Experimental Study on Flexural Strengthening of Reinforced Concrete Structures with Carbon Reinforced Concrete", in *Concrete – Innovations in Materials, Design and Structures: Proceedings of the fib Symposium, Krakow, Poland, May 27-29, 2019*.

[10] M. Ludwig, "Formwork Virtuoso" Ulrich Müther (1934 – 2007), Exploring the Müther-Archive", in *Interfaces: architecture.engineering.science – Proc. of the IASS Annual Symp. 2017*, Bögle, A.; Grohmann, M. (Eds.), Hamburg: HCU & IASS, 2017, book of abstracts: p. 196, full paper published digitally: paper no. 9998, 10 pages.

[11] R. Jähnel, G. König, G. Schenck, N. V. Tue, "Hyparschale Magdeburg" Bautechnik 79, 8, pp. 516-522, 2002.

[12] M. Hentschel, A. Schumann, H. Ulrich, S. Jentzsch, "Sanierung der Hyparschale Magdeburg", Bautechnik 96, 1, pp. 25-30, 2019.

[13] Homepage Pagel Feinbeton TF10,"https://www.pagel.com/de/produkte/betoninstandsetzung/tf10-tudalit-freinbeton/, Dresden, June 2019.

[14] Deutsches Institut für Bautechnik (DIBt), "Verfahren zur Verstärkung von Stahlbeton mit TUDALIT (Textilbewehrter Beton), 1st ed.; Approval no. Z-31.10-182; DIBt", Berlin, Germany, 2014, update 2016."

[15] S. Scheerer, E. Schütze, M. Curbach, "Strengthening and Repair with Carbon Concrete Composites – the First General Building Approval in Germany", in: Mechtcherine, V.; Slowik, V.; Kabele, P. (Hrsg.): *Proc. of SHCC4 – Int. Conf. on Strain-Hardening Cement-Based Composites, 18.-20.9.2017 in Dresden (Germany)*. Dordrecht: Springer, 2018, pp. 743-751.

[16] DIN EN 1992-1-1:2011-01, "Eurocode 2: Design of concrete structures – Part 1-1: General rules and rules for buildings; German version EN 1992-1-1:2004 + AC:2010" Jan. 2011.

[17] M. Curbach, F. Schladitz, R. Zobel and J. Weselek, "Eine Vision wird Realität: Der Betonbau der Zukunft ist nachhaltig, leicht, flexible und formbar – dank Carbon" Prüfingenieur, pp. 20-35, 2017.

[18] U. Müther, "Original plan of Ulrich Müther of the hypar shell in Magdeburg from 1968".

Proceedings of the IASS Annual Symposium 2019 – Structural Membranes 2019
Form and Force
7 – 10 October 2019, Barcelona, Spain
C. Lázaro, K.-U. Bletzinger, E. Oñate (eds.)

A parametrized design space for pneumatic flood barriers

Alexander NIEWIAROWSKI*, Sigrid ADRIAENSSENS, Ruy Marcelo PAULETTI [a]

* Department of Civil & Environmental Engineering, Princeton University
59 Olden Street, Princeton, NJ 08544, USA
aan2@princeton.edu

[a] Polytechnic School at the University of São Paulo

Abstract

Inflatable flood and storm-surge barriers based on existing pneumatic dam technology promise several economic and environmental advantages over traditional structures such as sea walls. The numerical modeling of such structures must consider the complex hydrodynamic loads, the flexibility of the structure, and the ensuing fluid-structure interaction. With regards to form, to date, studies in the literature have only considered simple semi-cylindrical geometries. This work is motivated by the hypothesis that the barrier's resistance to fluid loads can be optimized by improving upon this typical design, for example, by introducing double curvature (corrugations). To this end, this paper reviews a suitable finite element model and then presents a parametrization of the design space for this type of pneumatic structure, based on the analytical solution of the volume maximization problem for cylindrical pneumatic membranes. The qualitative behavior of some of these geometries under a hydrostatic load is assessed numerically.

Keywords: pneumatics, membranes, shape parametrization, inflatable dam, hydrostatic loading, finite element modeling

1. Introduction

Pneumatic membrane structures have found numerous architectural and structural engineering applications. Inflatable flood and storm-surge barriers based on existing pneumatic dam technology promise several economic and environmental advantages over traditional structures such as sea walls. The numerical modeling of such structures, which is the subject of past [1] and ongoing work, must consider the complex hydrodynamic loads, the flexibility of the structure, and the ensuing fluid-structure interaction. The pneumatic membrane barrier itself is analyzed using a total Lagrangian formulation based on an isoparametric reference configuration, similar to [2]. The fluid flow is modeled via the two-phase incompressible Navier-Stokes equations using an arbitrary Lagrangian-Eulerian (ALE) formulation. The numerical method of choice is the finite element method.

Once a system can be modeled, it can be optimized; while the internal pressure is perhaps the most important design variable, it is hypothesized that the barrier's resistance to hydrodynamic loads can be optimized by improving upon the typical cylindrical design of inflatable dams, for example, by introducing double curvature (corrugations). To this end, this paper explores a parametrization of the design space for this type of pneumatic structure, based on the analytical solution of the volume maximization problem for cylindrical pneumatic membranes [3]. The design space becomes a set of admissible mappings from the isoparametric domain to the initial configuration. A parametric study or shape optimization problem can be then posed as an optimization of the coefficients of these mappings, with state variables in the governing PDEs. To demonstrate the parametrization approach, the effects of design parameters (such as transverse support width, cross-sectional length, the frequency and amplitude of crown and base corrugations in the longitudinal direction) are assessed qualitatively in terms of the deflection resulting from a hydrostatic load. This paper is a necessary stepping stone to more rigorous

Copyright © 2019 by Alexander Niewiarowski, Sigrid Adriaenssens, Ruy Marcelo Pauletti
Published by the International Association for Shell and Spatial Structures (IASS) with permission.

shape optimization studies of pneumatic barriers subjected to hydrodynamic loads and is of relevance to the practitioner and researcher interested in the design of non-traditional pneumatic structures.

2. Pneumatic membrane finite element model

2.1 Background

The numerical modeling of pneumatic membrane structures, though a mature area of research, continues to warrant attention. Interest in pneumatic dams in particular first became evident in the 1980s and 1990s, with several studies on equilibrium [4] and dynamics [5]. More recently, Streeter et al applied dynamic relaxation to the problem of pneumatic storm surge barriers in particular [6]. Although the current work is motivated more by design than analysis, it builds on previously presented numerical models [1]. The finite element model used in the present work mostly follows Bonet et al. [2] and Schweizerhoff [7]. It is implemented using the open-source FEM library FEniCS [8]. The key ideas are summarized in this section.

2.2 Mathematical model and solution

Similar to [1], [2], the pneumatic barrier (Figure 1) is analyzed with a total Lagrangian formulation based on an isoparametric reference configuration where the only unknown is the displacement field with respect to an arbitrary initial configuration $\boldsymbol{\phi_X}$ (Figure 2). The barrier is assumed to be a rubber membrane structure with negligible bending stiffness and is supported by a fixed mass of air. Instead of explicitly modeling the internal air, adiabatic Boyle's law is used to establish an inverse pressure-pressure relationship.

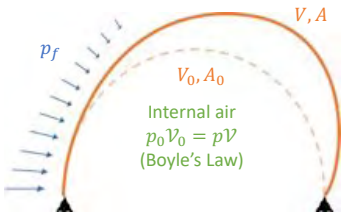


Figure 1: The pneumatic membrane problem

As shown in [7], the internal air pressure p in the current configuration can be expressed in terms of the displacements $\boldsymbol{u}$. The equilibrium position of the membrane is found by minimizing the total potential energy of the coupled system, $\Pi(\phi)$, which is the summation of membrane strain energy, external loads, and internal gas pressure:

$$\Pi(\phi) = \Pi_{int}(\phi) - \Pi_{ext}(\phi) - U_{air}(\mathcal{V}) \tag{1}$$

Here the total internal energy, $\Pi_{int}(\phi)$, of the rubber membrane can be described as the integral over the membrane volume of the hyper-elastic incompressible neo-Hookean strain energy function,

$$\Pi_{int}(\phi) = \int_{V_0} \psi(\boldsymbol{C})\, V_0 = \frac{\mu}{2}\int_{V_0} (tr(\boldsymbol{C}) + \det(\boldsymbol{C})^{-1} - 3)\, V_0 \tag{2}$$

where ϕ is the mapping from the initial to the current configuration, $\boldsymbol{C} = \boldsymbol{F}^T\boldsymbol{F}$ is the right Cauchy-Green strain tensor, $\boldsymbol{F}$ is the deformation gradient defined using the (generally not orthonormal) convected tangent basis vectors, and μ is the shear modulus. Interested readers are referred to the study by Bonet et. al. for details on the kinematic formulations [2].

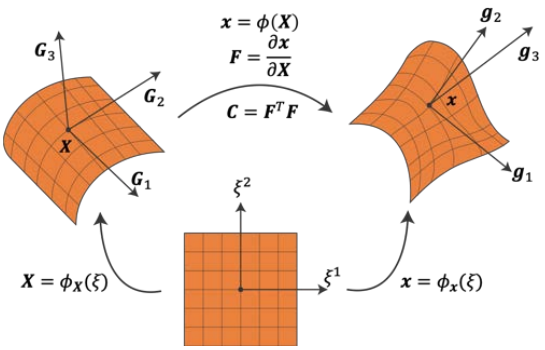


Figure 2: Membrane kinematics showing the parametric, initial, and current configuration, and relevant quantities

The potential energy of the external fluid pressure is given by:

$$\Pi_{ext}(\phi) = \int_{A_0} p_f \boldsymbol{g_3} \cdot \phi dA_0 \tag{3}$$

In this study, only hydrostatic loads are considered. Finally, the potential energy of the enclosed air is simply the integral of the internal pressure over the enclosed volume $\mathcal{V}$:

$$U_{air}(\mathcal{V}) = \int p(\mathcal{V}) d\mathcal{V}\,, \qquad \mathcal{V} = \frac{1}{3}\int_{A_\xi} \boldsymbol{x} \cdot \boldsymbol{g}_3 dA_\xi \tag{4}$$

The equilibrium configuration is found by minimizing the total potential energy using a standard Newton-Raphson scheme. The details of this procedure are omitted from this paper, but can be found in [2], [7]. However, it is worth mentioning that the resulting linear system for the incremental displacement $\mathbf{\Delta u}$ takes on the form:

$$\left(\mathbf{K}_T - k_g \boldsymbol{a} \otimes \mathbf{a}\right)\Delta\mathbf{u} = -\mathbf{F} \tag{5}$$

The term $k_g \boldsymbol{a} \otimes \boldsymbol{a}$ arises from the finite element discretization of the term relating the internal air pressure p to the volume $\mathcal{V}$ and constitutes a rank-one update to the tangent stiffness matrix $\mathbf{K}_T$, where k_g is a constant and $\mathbf{a}$ is the assembled normal vector. Even though this term gives rise to a full matrix, the computations can be performed relatively cheaply using the Sherman-Morrison formula:

$$\Delta\mathbf{u} = -\mathbf{K^{-1}F} + \frac{k\mathbf{K^{-1}aF}}{1 + k\mathbf{aK^{-1}a}}\mathbf{K^{-1}a} \tag{6}$$

3. Shape parametrization

Parametric design studies can provide designers with insights on structural behavior and lead to more efficient designs. With advances in computational techniques such as automated symbolic adjoint derivation [9], such studies can be automated with the use of shape and topology optimization algorithms. In both the manual and automated approaches, a representation or parametrization of the geometry is needed. In the broad field of shape optimization, many geometry parametrization methods are available. The use of NURBS is a relatively new area of interest [10], especially in the context of isogeometric analysis. However, unlike three-dimensional solid structures, pneumatic membranes are inherently two-dimensional in nature. This suggests that any parametrization should be in terms of curvilinear, rather than cartesian coordinates. Furthermore, there exists the notion of "viable" pneumatic geometries, meaning that only a subset of all possible geometries will be structurally useful after inflation.

As discussed in the previous section, the solution to the membrane equilibrium problem requires the mapping $\boldsymbol{\phi_X}$ from the parametric to the initial configuration: $\boldsymbol{X} = \boldsymbol{\phi_X}(\boldsymbol{\xi})$. With these observations, the approach presented in this paper involves placing some restrictions on the function $\boldsymbol{\phi_X}$ and then making the coefficients of this function available as the design parameters.

3.1 Basis for the parametrization approach

Considering, momentarily, a pneumatic barrier with a constant cross section, the geometry can be characterized by the length L of its cross section and the distance between the supports $W := cL$, for some $c \leq L$. Perhaps the simplest case of this type of structure is that of a semi-cylindrical barrier with fixed radius R, whose initial configuration can be described by the mapping:

$$\boldsymbol{X} = \boldsymbol{\phi_X}(\boldsymbol{\xi}) = \begin{matrix} Rcos(\xi^1) \\ T\xi^2 \\ Rsin(\xi^1) \end{matrix} \tag{7}$$

for $\boldsymbol{\xi} \in [0, \pi] \times [0, T]$. In this particular case, $L = \pi R, W = 2R, c = \frac{2}{\pi}$, and T is the longitudinal length. In what follows, this type of mapping will be generalized to yield more diverse geometry.

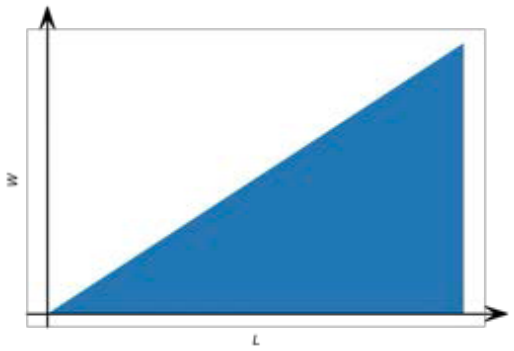


Figure 3: In 2D, the design space Ω_D is completely characterized by L and W. This design space can be visualized in the first quadrant considering the inequality $W \leq L$ (support width cannot exceed the cross-sectional length).

3.2 Parametrization by inflated shape

It is important to remark that for any pneumatic membrane structure analyzed in the manner of this paper, the initial configuration itself is arbitrary; the final equilibrium solution (of the inflated and externally loaded membrane) is not dependent on the initial configuration. In other words, for a given structure, there exist infinitely many possible initial configurations to choose from (as it is possible to draw infinitely many curves of length L between two points separated by distance W).

To define a unique initial cross section, a family of curves parametrized by L and W is needed. An ideal parametrization would yield an initial configuration that is close to the inflated configuration without external loading. Such a parametrization would conceivably accelerate convergence of the solution, and if used in a fluid-interaction study, would also minimize fluid mesh distortions if arbitrary Lagrangian-Eulerian (ALE) methods were employed to ensure compatibility between the fluid and structure [1].

Under a small strain assumption, it is possible to develop such a parametrization. Considering (1), if the strains are small, and no external loads are present, then the total potential energy of the system $\Pi(\phi)$ approximately reduces to that of the internal pressure. By treating the membrane as a two-state material (inextensible under tension, slack under compression), the equilibrium can be found by maximizing the difference between the initial and final volumes:

$$\min \Pi(\phi) = \max\left(p_0 \int_{A_0} \frac{1}{3}(\boldsymbol{x} \cdot \boldsymbol{g_3} \det(\boldsymbol{F}) - \boldsymbol{X} \cdot \boldsymbol{G_3} \det(\boldsymbol{F}_0)) d\xi^1 d\xi^2\right) \tag{8}$$

As shown by Ligarò and Barsotti [3], the following analytical solution is available for the special case of cylindrical and axisymmetric membranes:

$$\begin{aligned} \boldsymbol{X}^1(\xi) &= A\cos\left(\xi^1 \frac{L}{R}\right) + B\sin\left(\xi^1 \frac{L}{R}\right) + C \\ \boldsymbol{X}^3(\xi) &= \sin\left(\xi^1 \frac{L}{R}\right) - B\cos\left(\xi^1 \frac{L}{R}\right) + B \end{aligned} \tag{9}$$

$$A = -\frac{W}{2}, \qquad B = -\frac{W}{2}\frac{\sin(\eta)}{(1-\cos(\eta))}, \qquad C = \frac{W}{2} \tag{10}$$

The above equations constitute a 2D parametrization of a family of circles (in the *x*-*z* plane) with radius $R = \frac{L}{\eta}$ and center at $\boldsymbol{C} = (-C, -B)$. The geometrical ratio $\eta = \frac{L}{R}$ is obtained from the implicit equation:

$$(\xi^1 \eta)^2 - 2(1 - \cos(\eta)) = 0 \tag{11}$$

Note that Ligarò and Barsotti [3] consider the 1D parametric space $\xi \in [0, L]$, whereas this work considers the parametric unit square, $\boldsymbol{\xi} \in [0,1] \times [0,1]$.

$$\phi_{\boldsymbol{X}} \coloneqq \boldsymbol{\xi} \to \boldsymbol{X}(\boldsymbol{\xi}, L, W) \;\; \forall\, L, W \in \Omega_D \tag{12}$$

3.3 Extension to 3D

To make progress, the second parametric coordinate ξ^2 is now introduced to describe the longitudinal direction. For example, the simple semi-cylinder from (7) can be rewritten as:

$$\begin{aligned} \boldsymbol{X}^1(\boldsymbol{\xi}) &= \cos\left(\xi^1 \frac{L}{R}\right) + B\sin\left(\xi^1 \frac{L}{R}\right) + C \\ \boldsymbol{X}^2(\boldsymbol{\xi}) &= T\xi^2 \\ \boldsymbol{X}^3(\boldsymbol{\xi}) &= A\sin\left(\xi^1 \frac{L}{R}\right) - B\cos\left(\xi^1 \frac{L}{R}\right) + B \end{aligned} \tag{13}$$

With the above expressions for the radius and center, the cross section can now be varied in the longitudinal direction by introducing an amplitude parameter a, frequency parameter ω, and the longitudinal length T:

$$\begin{aligned} \boldsymbol{X}^1(\boldsymbol{\xi}) &= (aR\sin(\omega\pi\xi^2) - R)\cos(\pi - \xi^1\pi) - C_x \\ \boldsymbol{X}^2(\boldsymbol{\xi}) &= T\xi^2 \\ \boldsymbol{X}^3(\boldsymbol{\xi}) &= (aR\sin(\omega\pi\xi^2) - R)\sin(\pi - \xi^1\pi) - C_y \end{aligned} \tag{14}$$

For example, varying ω with $c = 2/\pi, L = 0.25\pi,\ T = 2,$ and $a = 0.15$ results in the family of geometries seen in Figure 4. Further control of the geometry can be achieved by supplying expressions for $L, R, or\ \eta$.

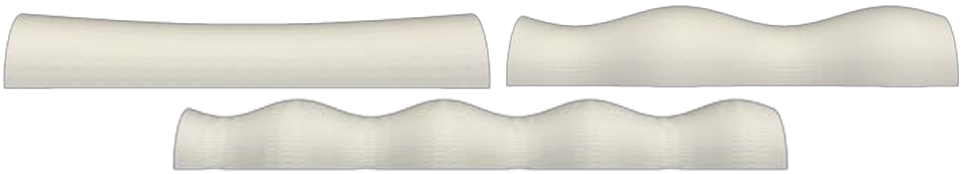


Figure 4: Example geometries with varying $\omega, \omega \in \{1,4,8\}$, $c = 2/\pi$, $L = R\pi$, $T = 2$, and $a = 0.15$

4. Parametric study

To demonstrate the geometry parametrization introduced in the previous section, this paper presents a parametric study of a pneumatic dam under hydrostatic conditions (Figure 5). In this study, a pneumatic barrier is loaded by a hydrostatic pressure distribution on one side (Figure 5). This pressure field is calculated analytically based on the depth, where the depth is equal to the maximum retention capacity of the barrier (the supremum of cross-sectional z coordinates). The current membrane position vector $\boldsymbol{x}$ is used to calculate the z coordinates upon which the hydrostatic pressure depends.

$$z = \boldsymbol{x} \cdot \hat{\boldsymbol{k}}$$

$$p = \rho g\left(z_{sup} - z\right) \; if \; z \leq z_{sup} \; else \; 0$$

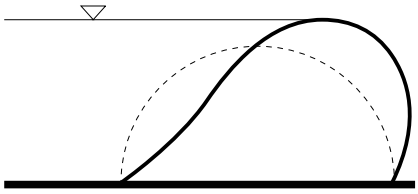


Figure 5: Typical pneumatic dam under hydrostatic conditions

For this study, the following non-dimensional quantities and values are introduced. Radius to thickness ratio, $R/H = 25$, the shear modulus to internal pressure ratio $\mu/p_0 = 40$, and the hydrostatic contribution $R\rho g/\mu = 0.144$. The barrier is pinned along its length, while the end edges are restrained in the ξ^2 direction only. The geometry is initialized with fixed radius $R = 0.25$. The results (pressure and radial stretch) for the case of the semi-cylinder (13) are shown in Figure 6.

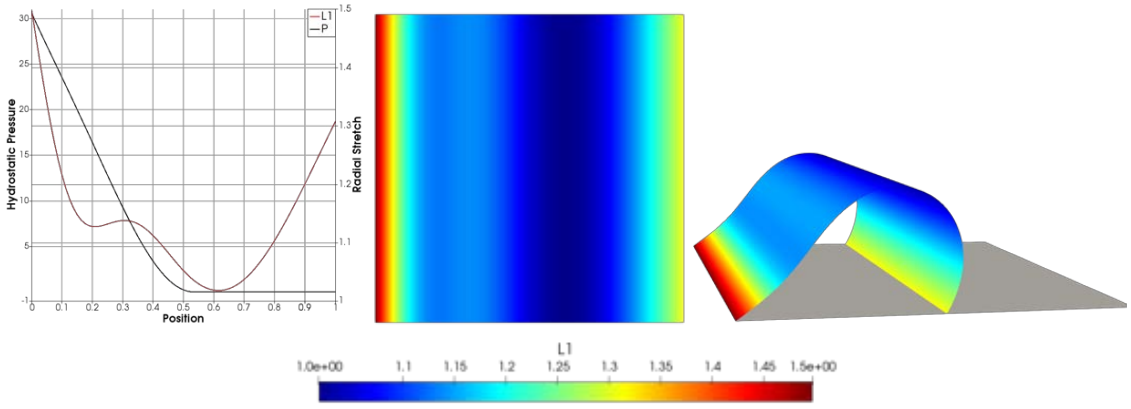


Figure 6: Hydrostatic loading of semi-cylindrical barrier

Next, the effect of the corrugations (Figure 4) is examined. It is apparent that increasing the number of corrugations over a fixed length significantly changes the strain pattern in both inflated, and loaded

conditions (Figure 7). More corrugations locally increase the radial stretches, while also resulting in longitudinal stretches smaller than 1. This type of strain pattern is an indicator of wrinkling in membranes structures. Further studies will need to investigate how wrinkled barriers handle hydrodynamic loads (i.e. stress concentrations) and if need be, how to eliminate wrinkled states from the design space.

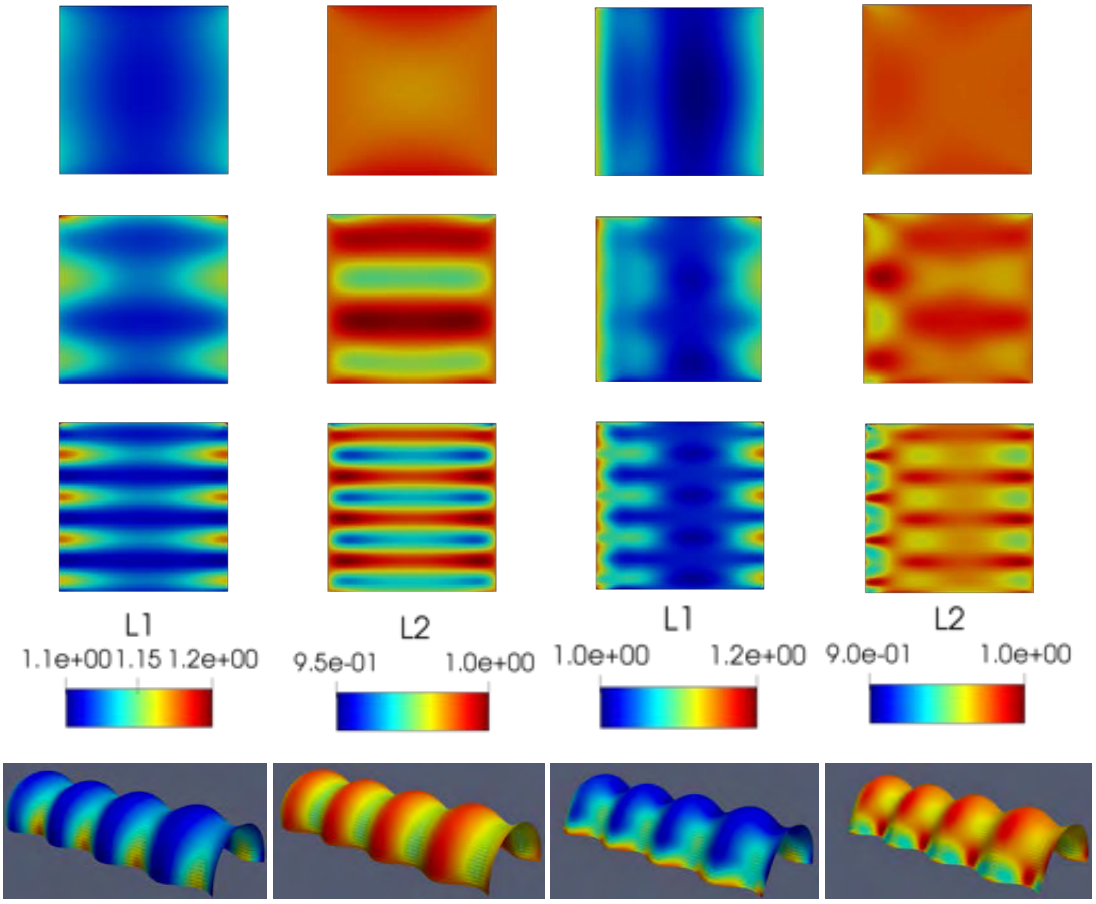


Figure 7: Radial (L1) and longitudinal (L2) stretches for the inflated (left) and hydrostatically loaded (right) barriers with omega 1,4,8.

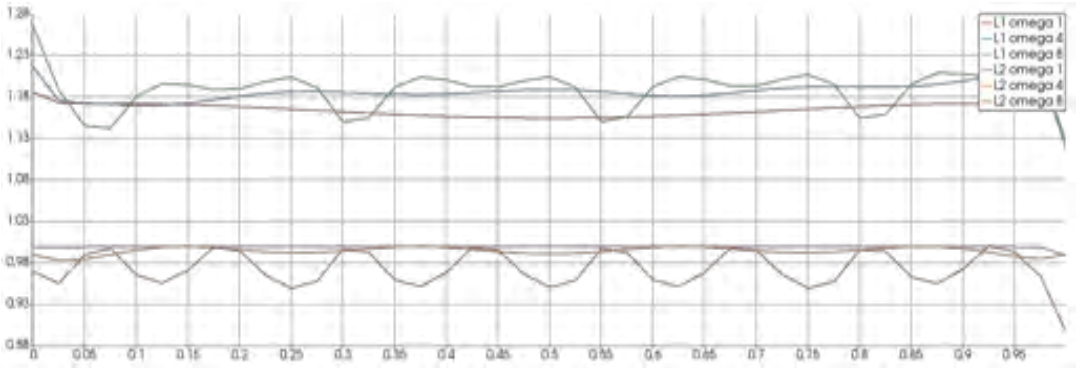


Figure 8: Variation in radial (L1) and longitudinal (L2) stretch along the wet pinned support for different values of omega

4. Conclusions and future work

This study presented a possible shape parametrization approach for pneumatic dams. After a review of appropriate numerical modeling techniques, it was shown that the initial shape can be uniquely described by a chosen cross sectional length and support width with the use of an analytical solution to the inflation of an inextensible membrane. A few samples from the resulting design space were modeled under a hydrostatic load to show the viability of the approach.

The presented parametrization approach enables multiple future research directions. First, the complexity of the parametric equations can be increased, for example, by setting L as a function of the longitudinal coordinate. to include asymmetric corrugations, although it is expected that the inflation of such geometries may result in slack states. More generally, other analytical equilibrium formulas, namely, equilibrium shapes under hydrostatic loading as presented by should be investigated in a similar approach. The use of these parameterizations in a shape optimization study is also a compelling research topic.

Acknowledgements

This material is based upon work supported by the Princeton Environmental Institute at Princeton University, as well as the Princeton University-University of Sao Paulo Collaborative Partnership.

References

[1] A. Niewiarowski, A. Rock, S. Adriaenssens, and M. Chiaramonte, "Pneumatic storm surge barriers subject to hydrodynamic loading," in *Creativity in Structural Design: Proceedings of the IASS Annual Symposium 2018*, 2018.

[2] J. Bonet, R. D. Wood, J. Mahaney, and P. Heywood, "Finite element analysis of air supported membrane structures," *Comput. Methods Appl. Mech. Eng.*, vol. 190, no. 5–7, pp. 579–595, Nov. 2000.

[3] S. S. Ligarò and R. Barsotti, "Equilibrium shapes of inflated inextensible membranes," *Int. J. Solids Struct.*, vol. 45, no. 21, pp. 5584–5598, Oct. 2008.

[4] R. Watson, "A note on the shapes of flexible dams," *J. Hydraul. Res.*, vol. 23, no. 2, pp. 179–194, 1985.

[5] J.-C. Hsieh and R. H. Plaut, "Free vibrations of inflatable dams," *Acta Mech.*, vol. 85, no. 3–4, pp. 207–220, Sep. 1990.

[6] M. Streeter, L. Rhode-Barbarigos, and S. Adriaenssens, "Form finding and analysis of inflatable dams using dynamic relaxation," *Appl. Math. Comput.*, vol. 267, pp. 742–749, Sep. 2015.

[7] T. Rumpel and K. Schweizerhof, "Volume-dependent pressure loading and its influence on the stability of structures," *Int. J. Numer. Methods Eng.*, vol. 56, no. 2, pp. 211–238, 2003.

[8] A. Logg, K. A. Mardal, and G. N. Wells, "Automated solution of differential equations by the finite element method," *Lect. Notes Comput. Sci. Eng.*, 2012.

[9] P. E. Farrell, D. A. Ham, S. W. Funke, and M. E. Rognes, "Automated Derivation of the Adjoint of High-Level Transient Finite Element Programs," *SIAM J. Sci. Comput.*, vol. 35, no. 4, pp. C369–C393, Jan. 2013.

[10] W. A. Wall, M. A. Frenzel, and C. Cyron, "Isogeometric structural shape optimization," *Comput. Methods Appl. Mech. Eng.*, vol. 197, no. 33–40, pp. 2976–2988, 2008.

Proceedings of the IASS Annual Symposium 2019 – Structural Membranes 2019
Form and Force
7 – 10 October 2019, Barcelona, Spain
C. Lázaro, K.-U. Bletzinger, E. Oñate (eds.)

Inflated cushions under uniformly distributed loading

Slade GELLIN*, Romuald TARCZEWSKI[a]

*Buffalo State College
Buffalo NY USA
gellins@buffalostate.edu, sgellin@birdair.com

[a] Wroclaw University of Technology, Wroclaw Poland

Abstract

The study of inflated cushion structures under active bending is continued with application of a uniformly distributed load. The methodology of previous studies is employed to produce numerical results. These results are compared and contrasted to those obtained for inflated cushion structures under a central point force.

Keywords: inflatable cushions, active bending, *elastica*, central difference method

1. Introduction

A series of papers (Gellin and Tarczewski [1-3]) published in IASS symposium proceedings presented theoretical studies to describe the behavior of inflated cushion structures deployed into arched shapes under active bending to span a particular distance. In [1], it was demonstrated that this behavior was equivalent to the classical *elastica* problem of Love [4]. In [2], the authors extended the methodology of [1] to include the behavior of these structures under a mid-span point load. It was noted in that paper that the methodology was limited to deriving shapes that did not include inflection points, and that a modification of the methodology would be required to derive shapes for forces of greater magnitude which would potentially include them. Such a modification was successfully made in [3], in which the authors noted that the methodology used would have greater potential for future studies.

In this paper, the authors successfully use the methodology of [3] to derive shapes and load data for inflated cushion structures under a uniformly distributed load, such as weight and, to a lesser extent, snow loads. Results indicate that these structures exhibit much stiffer behavior than when under the same total load as an equivalent mid-span point force.

2. Description of the physical system and assumptions

The physical system is that studied by Tarczewski *et al* [5 - 7]. The physical structure consists of the three groups of elements: modular inflated cushions, tension cables and cross-braces, as shown in Figure 1, left. The latter are optional and are used to increase the structural height. This can also be done by increasing the thickness of the cushions, in the whole structure or part thereof (variable rigidity of the structure). The structure may be shaped as an arc or a single or double curved shell.

The flat structure is assembled at ground level as a near mechanism. It is stabilized and finally shaped in the self-erection process. The essence of the process is the introduction into the structure forces that cause its large deformation (uplift) and give the rigidity. The forces are introduced by pulling the bottom tension cable, thus reducing the distance between the supports. The system becomes bending-active. Figure 1, right, shows a general idea of this process.

Copyright © 2019 by Slade Gellin and Romuald Tarczewski.
Published by the International Association for Shell and Spatial Structures (IASS) with permission.

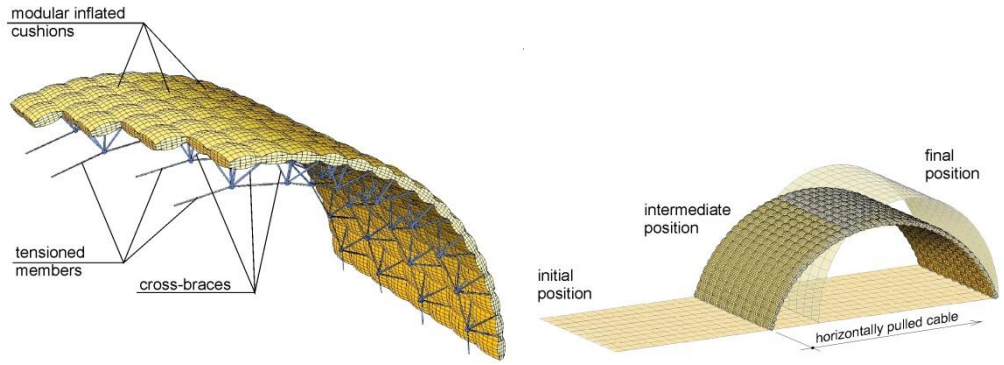


Figure 1: Typical configuration of modular inflated shell (left); process of self-erection (right)

The structure is assumed to behave elastically, in that a bending stiffness *EI* is assumed constant. The authors realize that this is probably not the case; however, the purpose of the theoretical studies is to understand the non-linear behavior due to the bending-thrust interaction without further complication due to non-linear bending stiffness.

3. Derivation of the equations

Figure 2 is a free body diagram of the general case to be studied. It also indicates the key geometric and mechanical parameters.

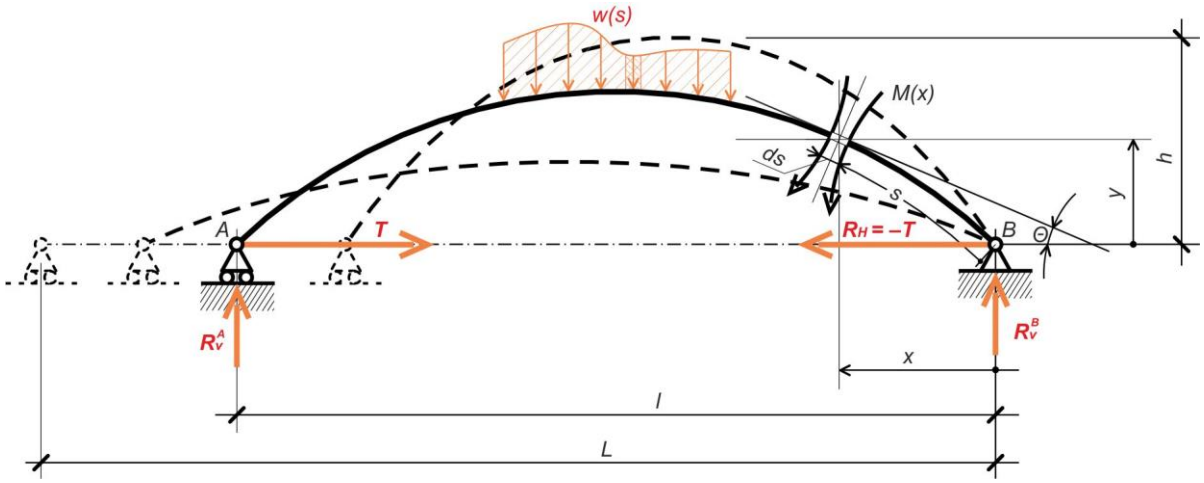


Figure 2: Free body diagram for an inflated cushion structure in active bending under a vertical distributed load

The equilibrium equations for this structure were derived in [2]; specifically:

$$EI\left(\frac{d^2\theta}{ds^2}\right)+T\sin\theta+V\cos\theta=0$$
$$\frac{dV}{ds}=w \tag{1}$$

For the case studied in this paper, $w(s) = w_0$, a constant. The second equilibrium equation can be solved to yield:

$$V = -\frac{w_0 L}{2}\left(1 - 2\frac{s}{L}\right) \tag{2}$$

This can be directly substituted in the first equation to yield a single, non-linear differential equation for $\theta(s)$. This equation is solved by the methodology introduced in [3]. Essentially, it is a central difference shooting method. The domain of the solution is one half of the structure due to the symmetry of the loading. This symmetry demands that $\theta = 0$ at mid-span. Furthermore, since the bending moment is zero at the supports, the first derivative of θ is zero there as well. Since the central difference method is primarily used for initial value problems, a guess for θ_0, the value of the rotation at the supports, must be made. Another condition that needs to be satisfied is that the x coordinate at mid-span must equal half the chosen value of ℓ. The second parameter that must be guessed is the tension in the rope, T. The two parameters are varied by trial and error until the two mid-span conditions are satisfied.

The shapes are determined by the two first order equations:

$$\begin{aligned} \frac{dx}{ds} &= \cos\theta \\ \frac{dy}{ds} &= \sin\theta \end{aligned} \tag{3}$$

The bending moment distribution is determined by recognizing that Equation (1) is a first order equation for the bending moment. These equations are solved by central difference method as well with zero initial condition. It can be shown as a check on the computations that the moment at mid-span can be calculated as:

$$M_c = Ty_c - \frac{w_0 L}{2}\bar{x} \tag{4}$$

Here, y_c is the deflection at mid-span and $\bar{x}$ is the average x coordinate of the shape. In all cases, the difference between the two procedures was less than 0.1%.

A series of cases were examined for ascending values of w_0L/P_E, where P_E is the Euler buckling load of the inflated cushion structure before erection. As in [3], convergence becomes more difficult above certain values of this load parameter. The results below offer a clue as to the cause of this effect.

4. Results

As in [3], two main cases are considered, $\ell / L = 0.50$ and $\ell / L = 0.75$. The derived shapes are displayed in Figure 3, below. For the first case, inflection points in the half-shape are clearly visible for the larger values of w_0L / P_E. For the second case, the half-shape displays an inflection point only for the largest value of w_0L / P_E indicated.

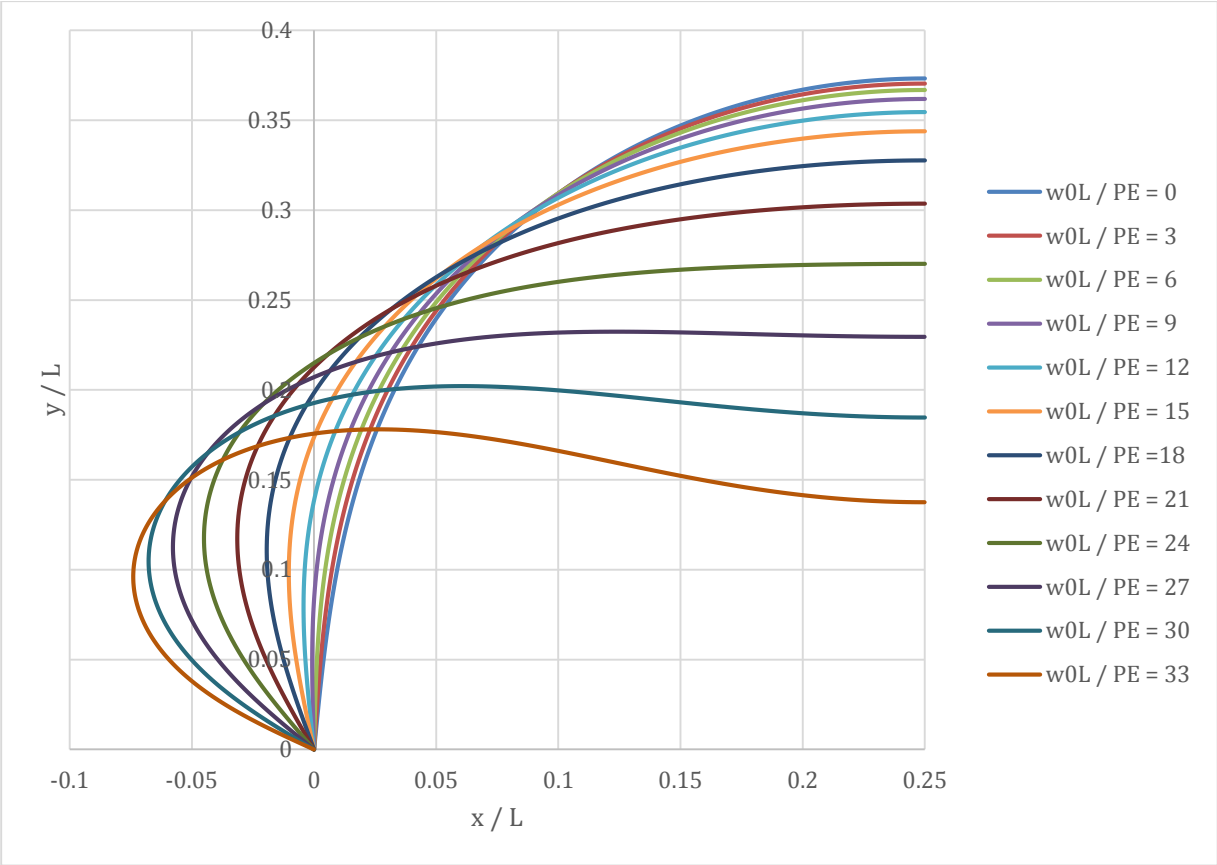


Figure 3(a): Half shape for $\ell / L = 0.50$

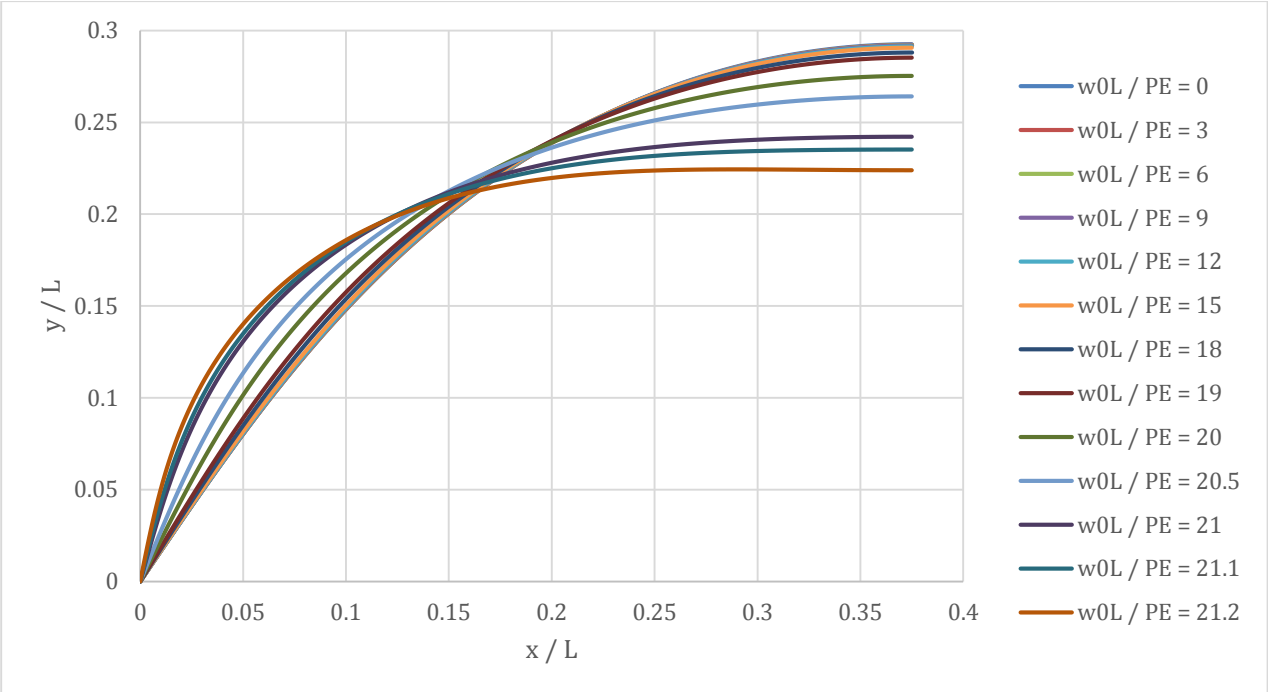


Figure 3(b): Half-shape for $\ell / L = 0.75$

Figure 4 displays the tension in the draw rope. For the first case, a surprising decrease in the tension is displayed for values of w_0L / P_E just below the onset of inflection points. The second case exhibits virtually linear increase in rope tension with applied load, until inflection points appear, where the tension begins increasing more rapidly.

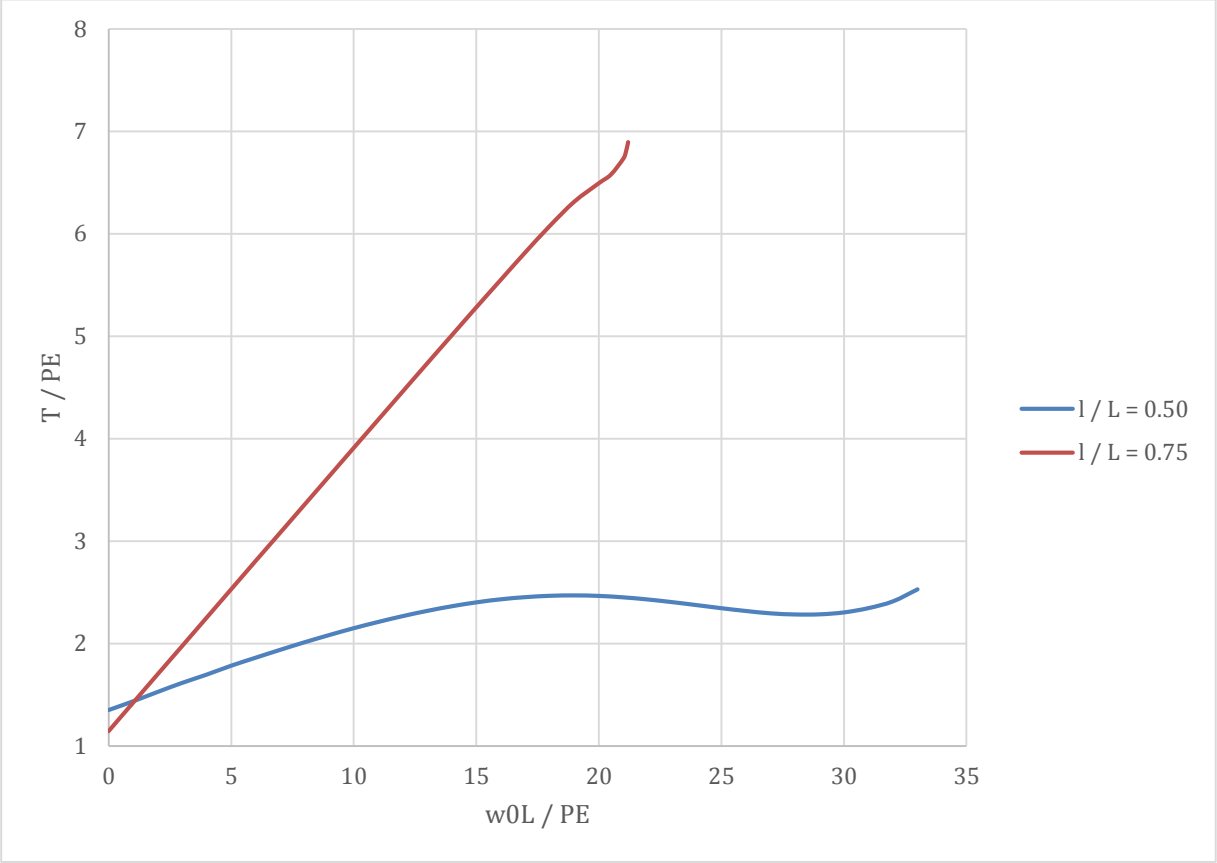


Figure 4: Tension in the draw rope

Figure 5 displays bending moment data for the two cases. For both cases, the maximum bending moment occurs at mid-span before moving closer to the supports. For the first case, the transition begins relatively smoothly with increasing load. When the mid-span moment, M_c, becomes negative then the presence of an inflection point is indicated. This occurs when w_0L / P_E exceeds about 25. For the second case, the moment at mid-span and the maximum moment, M_{max}, remain almost constant; then there is a relatively sudden and sharp departure from this value occurring above w_0L / P_E = 20. It is also seen that if the shape does not change significantly and a linear relation between the tension in the rope and the applied load exists, that the bending moment distribution could remain virtually constant. Equation (4) analytically explains this assertion.

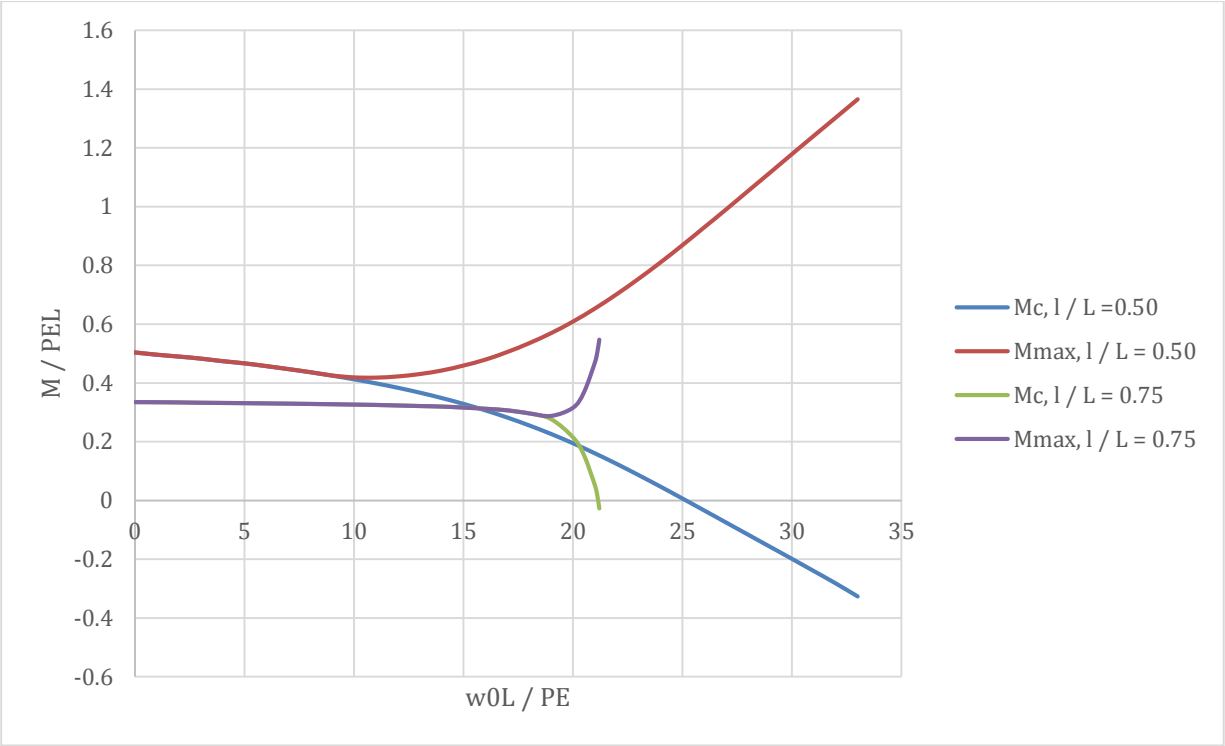


Figure 5: Bending moments

Figure 6 displays the secant stiffness of the structure normalized by the classical bending stiffness:

$$k_0 = \frac{5}{384}\frac{w_0 L^4}{EI} \tag{5}$$

In the first case, the stiffness decreases smoothly; in the second case, the stiffness seems to vary wildly for smaller load values. This could be due to precision issues on the mid-span deflection which is varying very slowly for the smaller load values. The decrease for larger load values is fairly smooth, but much more dramatic than for the first case.

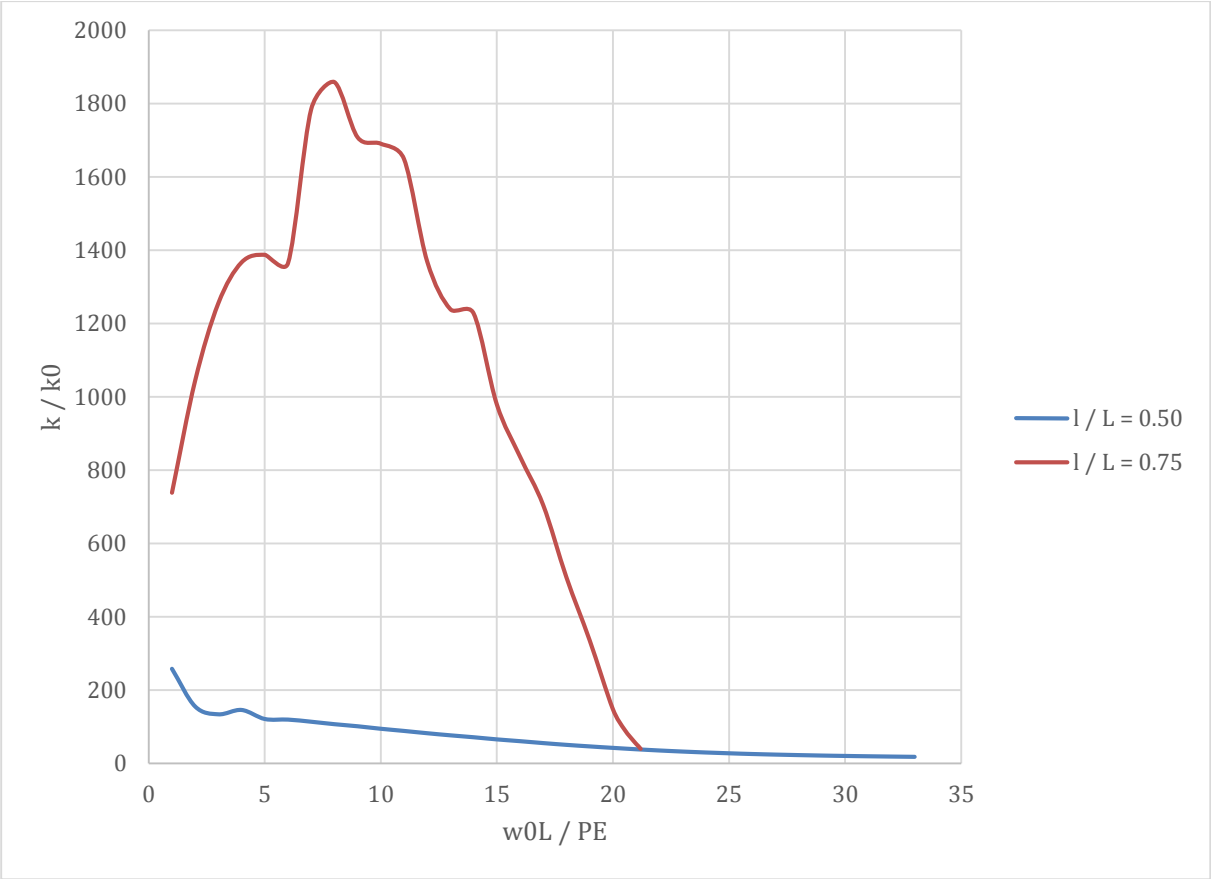


Figure 6: Mid-span stiffness

It is important to note the similarities and differences with the results of [3]. In both cases, the structures generally display decreasing stiffness with increasing load. For $\ell / L = 0.50$, the central moment steadily decreases while the maximum moment decreases, then increases, for both sets of results. For $\ell / L = 0.75$, however, these moments remain almost constant, until there is a relatively extreme decrease in central moment with an equally extreme increase in maximum moment. Somewhat related to this phenomenon is a nearly linearly increasing rope tension with applied load and virtually no change in shape. These phenomena are qualitatively different from the corresponding results of [3]. For both span values, the total applied load that can be supported is approximately 3 times that of the corresponding point load.

5. Conclusion and future work

A methodology developed for analyzing *elastica* structures, such as the inflated cushions described herein, has been successfully applied for the case of a uniformly distributed load. Results are similar to those found for these structures under a central point force with some interesting differences when the deflected span is 0.75 of the structure length. Future work may include analyzing these structures under non-symmetric loads.

Acknowledgements

The first author would like to thank Birdair, Inc. and its parent company Taiyo-Kogyo Corporation for support of this work.

References

[1] S. Gellin and R. Tarczewski, "Inflatable cushions, active bending and the *elastica*," in *IASS 2016, Spatial Structures in the 21st Century, Tokyo, September 26 – 30, 2016,* K. Kawaguchi, M.Ohsaki and T. Takeuchi Eds., 2016

[2] S. Gellin and R. Tarczewski, "Extension of *elastica* methodology to inflated cushions under applied transverse loading," in *IASS 2017, Interfaces: architecture, engineering, science, Hamburg, September 25 – 28, 2017,* A. Bogle and M. Grohmann Eds., 2017

[3] S. Gellin and R. Tarczewski, "Point force on inflated cushions with inflection points," in *IASS 2018, Creativity in Structural Design, Boston, July 16-20, 2018,* C. Mueller and S. Adriaenssens Eds., 2018

[4] A.E.H. Love, *A Treatise on the Mathematical Theory of Elasticity (4th ed).* Dover, 1944

[5] R. Tarczewski, "Post-tensioned modular inflated structures," *Computational Methods in Applied Sciences,* vol.3, pp. 221-239, 2005.

[6] R. Tarczewski, "Physical modeling of modular inflated shells – an initial research," in *Lightweight Structures in Civil Engineering,* pp. 40-44, 2005.

[7] R. Tarczewski *et al*., "Improvement of the system of modular inflated shells by means of physical modeling," in *Structural Membranes,* pp. 1-8, 2011.

Proceedings of the IASS Annual Symposium 2019 – Structural Membranes 2019
Form and Force
7 – 10 October 2019, Barcelona, Spain
C. Lázaro, K.-U. Bletzinger, E. Oñate (eds.)

Some improvements on the static analysis a large pneumatic envelope

Ruy M.O. PAULETTI*, Karina B. ROCHA, Paula M. BOLELLI

* Polytechnic School, University of São Paulo, São Paulo, Brazil
P.O. Box 61548, 05424-970, São Paulo, Brazil
pauletti@usp.br

Abstract

This paper presents some results on a current investigation on the influence of internal volume variation on the structural response of the large, cable-reinforced pneumatic envelope. The system has been previously studied with respect to membrane wrinkling and adherent or sliding conditions between cables and membrane. It was shown that these factors are significant to the determination of the system's deformation and overall stress and load distributions. However, due to restrictions of the SATS analysis code, the study so far considered constant internal pressure and a rough estimative of wind loads, according to static wind pressure coefficients adapted from the literature. The program is currently being improved to allow updating of the internal pressure and the system stiffness according to the deformation of the membrane envelope. The paper assesses the response of the pneumatic envelope to wind pressure loads determined from more exacting CFD analysis, comparing the results with previous analyses, where the wind pressures were defined according to practice standards and some educated guessing.

Keywords: membrane structures, pneumatic structures, nonlinear analysis, wind loads, pneumatic stiffness.

1. Introduction

We considered the static response of the cable-reinforced, pneumatic membrane envelope shown in Figure 1(a). It has been installed to cover the site of a new nuclear power plant during the process of ground preparation remaining on site for only 6 months. The structure had a roughly rectangular plant, 110m x 86m, 30 meters high, and was anchored to a perimeter concrete wall. One of the smaller sides displays a semi-circular inclusion, which breaks the symmetry of the system. The membrane material was a PVC-coated, polyester fabric, and the envelope was reinforced by seven cables laid over the membrane, aligned with the longest direction and transversally constrained by fabric straps, but otherwise capable of sliding. A relatively small internal pressure $p_0 = 100 N/m^2$ was specified for the design of the structure, and, due to its short lifetime, a reduced basic wind pressure $q = 245 N/m^2$ was estimated. However, wind tunnel tests were deemed too costly, for such a temporary structure, and the response of the structure for wind loads was studied considering two limit conditions, given by the cylindrical and spherical domes, for which pressure coefficients are known.

In previous papers ([1–4]) we discussed the influence of cable sliding and membrane wrinkling to the response of the same structure. Our previous analyses suggested that for winds acting in directions parallel to the cables, much larger displacements are observed when cable sliding is considered, whilst maximum stress values are reduced, when compared to the full-adherence condition. Besides, even though the average normal load on a cable, under the hypothesis of full adherence, is roughly equal to the uniform normal load acting on the same cable, under frictionless sliding conditions, large variations of the normal load can be observed in the case of full adherence. We also concluded that

Copyright © 2019 by Ruy M.O. Pauletti, Karina B. Rocha, Paula M. Bolelli
Published by the International Association for Shell and Spatial Structures (IASS) with permission.

due to the small internal design pressure, large portions of the membrane envelope would become wrinkled and prone to flutter, when the membrane was subjected to design loads. The contractor for the pneumatic delivery maintenance argued that full redundancy of real pressurizing system was available, so the internal pressure could be actively controlled, by activating the extra air pumps. That was indeed required during the system operation. Wrinkled conditions are nevertheless interesting, from an academic point of view, so we continued the study of the membrane considering the original, low initial internal pressure.

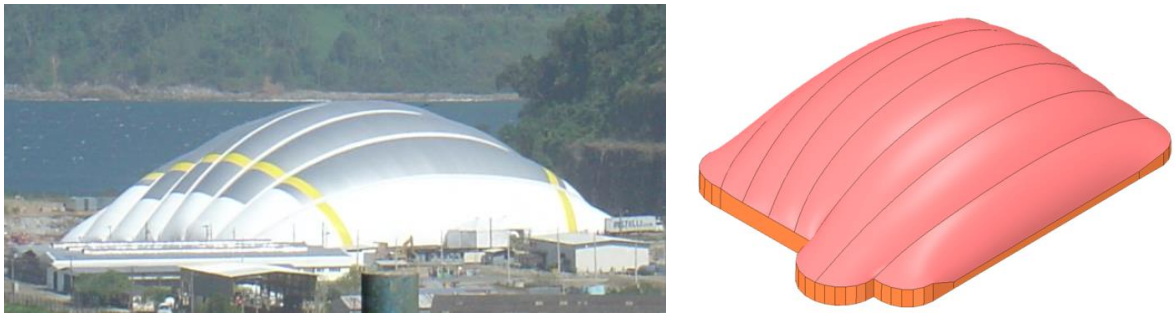


Figure 1: (a) A large pneumatic dome reinforced by sliding cables; (b) geometry of the pneumatic envelope, under internal pressure, as determined by SATS and transferred to Ansys/Fluent for CFD analysis

2. Wind pressure coefficients determined by Ansys/Fluent

In this paper, we check our original educated guesses about the wind pressures around the pneumatic envelope by performing CFD analyses, using Ansys/Fluent CFD analysis code. The geometry of the envelope, as originally determined by SATS, was imported to Ansys, and recreated as a solid object, obtained by extrusion of the membrane surface (Figure 1(b)). This solid was then subtracted from a rectangular box, with dimensions 400m x 600m x 150m, thus defining the control volumes for the CFD analyses shown in Figure 2. We considered two wind cases: longitudinal and transversal winds, for a velocity of 20 m/s, perpendicular to the inlet face. At the outlet facet, the pressure is zero. For all the other faces, slip boundary conditions were assumed.

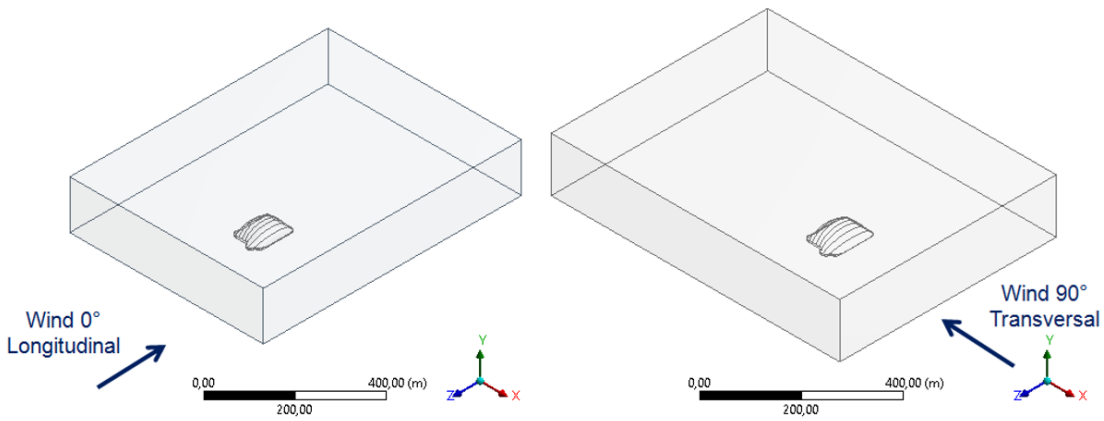


Figure2: Control volumes for CFD analyses, for longitudinal and transversal wind actions

The air was considered as an incompressible fluid with a density $1.23kg \cdot m^{-3}$ and a viscosity $1.795kg \cdot m^{-1} \cdot s^{-1}$. We assumed turbulent steady flow conditions, and the standard *k*-ε turbulence model was adopted, with default parameters. This are typical hypotheses for models at the scale of membrane structures, with satisfactory results for most turbulent flows. We used an ANSYS academic license and the size of our models should be rather modest. That leaded us to reduce the density of the membrane discretization as shown in Figure 3, which compares the original mesh used in SATS with the discretization of the envelope surface considered in Fluent.

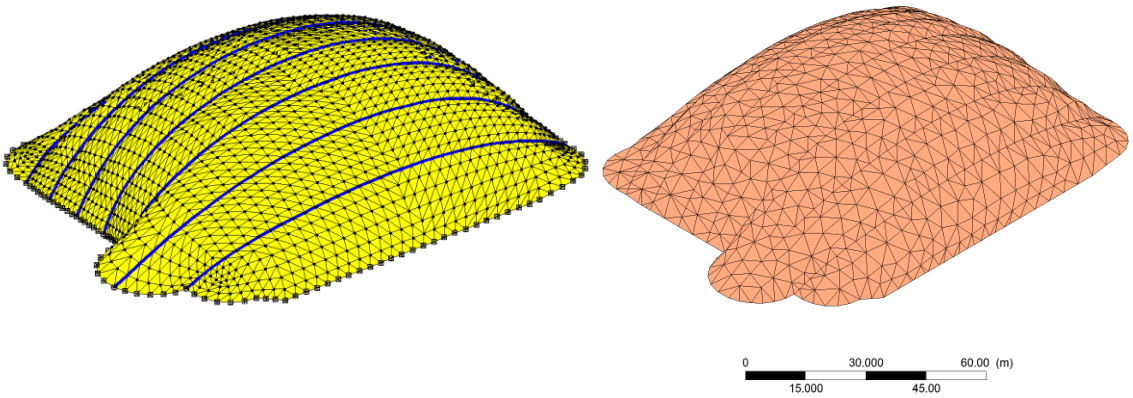


Figure3: Original SATS mesh and Ansys/Fluent mesh, to reduce the cost of the CFD problem

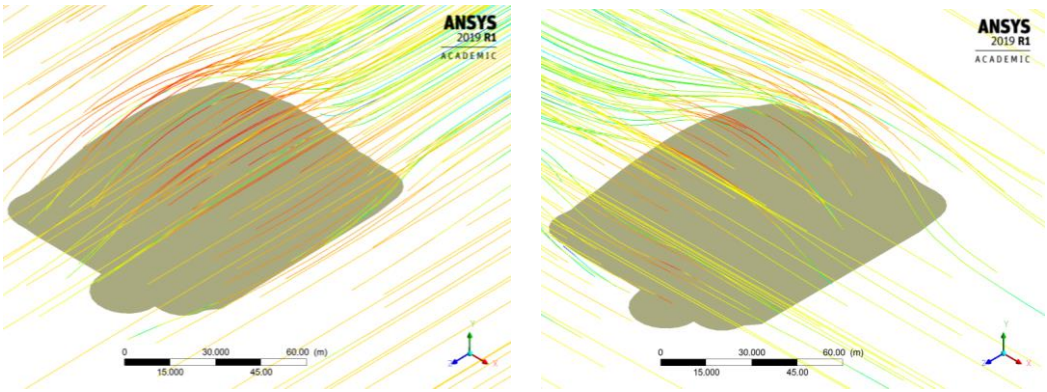


Figure 4: Streamlines for the longitudinal and transversal wind conditions

Figure 4 depicts the streamlines around the pneumatic envelope, for the two wind conditions we considered. Figure 5(a) shows the total pressure coefficients of the wind acting on the pressure envelope surface, in the case of longitudinal wind. Figure 5(b) shows the same coefficients for the case of transversal wind. It is seen that the lobes of the envelope surface, which exist due to the action of the reinforcing cables, provoke minor perturbations on the field of pressure coefficients, as compared to a smooth surface. Overall, the pressure coefficients determined by CFD analyses agree with the '*educated guessing'* assumed during our previous analyses. In fact, we have previously studied a set of plausible pressure distributions, considering as limit conditions the cases of the cylindrical and spherical domes, for which pressure coefficients are well established. Although our current CFD models indicate some zones of high compression (i.e., pressures acting inward the volume) close to the envelope rim, at windward side, values averaged over larger regions are in good

agreement with our previous estimates. The main difference is the occurrence of some compression at the leeward side of the envelope, close to its rim, for the case of longitudinal wind.

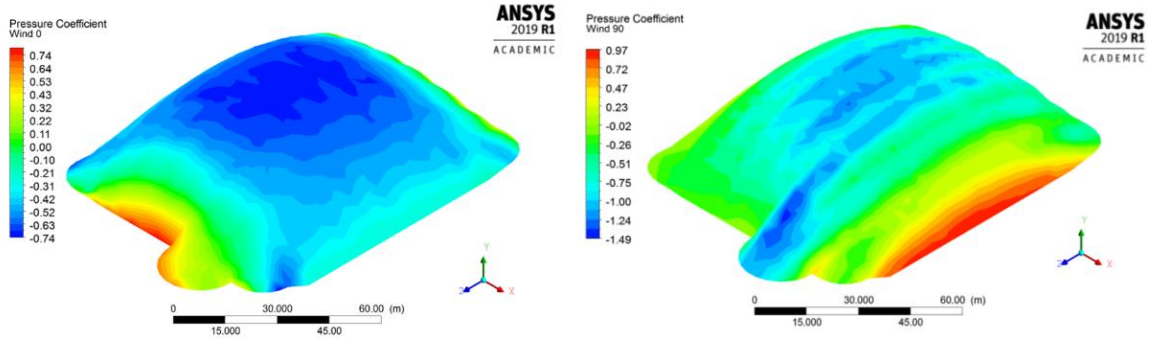


Figure 5: Wind pressure coefficients, for (a) longitudinal and (b) transversal wind conditions.

3. Structural response of the pressure envelope under wind loads

Structural analyses were performed with the aid of our in-house SATS finite element code. For easy transfer of wind loads, we kept the same mesh as used in Fluent. Displacements at the borders were restrained, and the membrane was initially subjected to internal pressure load only. An initial superficial stress $S_0 = 1,0 kN/m$ was adopted, i.e., an initial membrane stress $\sigma_0 = 1,0 MPa$, for a nominal thickness $t=1mm$. An elastic modulus $E = 1.0 GPa$ was adopted for the membrane. All the analyses were performed using full Newton Method, with the tangent stiffness calculated either analytically or by a finite-differences procedure. A relative error $\left(\|\mathbf{g}\| / \|\mathbf{g}_0\|\right) \leq 10^{-3}$ was adopted, which was shown to be enough to preserve quality of results. Results were further confirmed using a DRM procedure.

3.1. Response of the pneumatic envelope to internal pressure

Figure 6 shows the displacement norms and the 1st and 2nd principal stress fields (σ_1 and σ_2 fields) for the case of internal pressure loading, considering frictionless sliding conditions for the cables and allowing for membrane wrinkling. The maximum displacement reached 0.13m, on the top of the dome. The initial geometry was determined in previous analysis, considering adherent cables, but due to the small displacements, we opted for not updating the initial mesh. Except from some stress concentrations at the corners and the semi-circular inclusion (maximum σ_1 about 3.5MPa), the principal stress fields are smooth, with a maximum σ_1 stress about 2.5MPa at the top of the dome. Incipient wrinkling is observed at the regions of geometric discontinuity. Results were similar to those obtained in our previous papers, which were produced with more refined meshes.

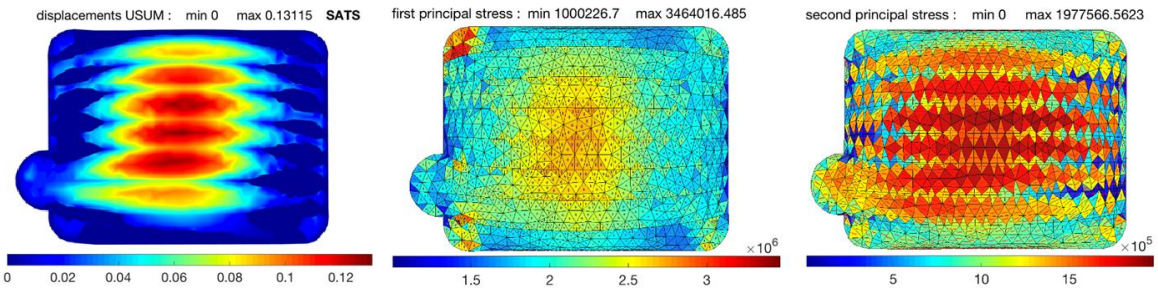


Figure 6: internal pressure loads; (a) displacement norms; (b) σ_1 on elements; (c) σ_2 on elements.

3.2. Response of the pneumatic envelope to internal pressure + longitudinal wind

Figure 7 shows results for the case of internal pressure superposed with longitudinal wind pressures. Results were obtained both with NRM and DRM with good agreement between both methods. The maximum membrane displacement reached 1.65m, inward the envelop, both at the windward and the leeward regions. The maximum σ_1 stress reached about 8.2MPa on the top of the dome. Also, the σ_2 stresses are maximum at this region, reaching about 6.4MPa. The stress results compare well with our previous models. Inspection of the principal stress fields and principal stress directions shown in Figures 7(b/c) allows to understand the basic clasp mechanisms by which the membrane responds to the wind action and provides the analysis with a better understanding of the behavior of the structure. The reader of the digital version of this paper is invited to zoom in these figures to identify the principle stress directions, plotted at the centroid of each element.

Some difference was observed between the displacement fields, since in our previous analyses the membrane moved inward only at the windward region. This difference is due to the occurrence of some inward wind pressures at the leeward side, as determined by our CFD model, and is also reflected on the wrinkling regions. Our current model presents wrinkling at both windward and leeward regions, whilst little wrinkling was observed on the leeward side of the envelope, during our previous studies. This difference alleviates the anchor loads on the rim of the structure at the leeward side, but does not alter the design load envelope, since it encompasses winds along other directions. Overall, the agreement of the current and previous results is a good indication of the effectiveness of our previous guesses for design purposes.

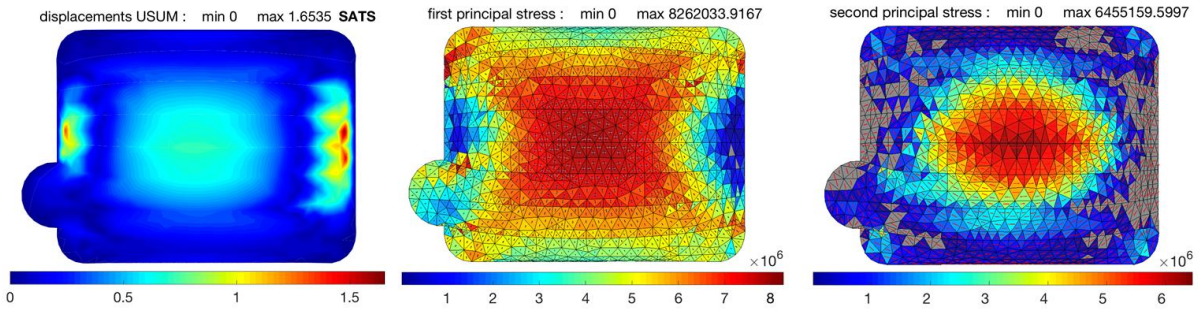


Figure 7: internal pressure + longitudinal wind loads; (a) displacement norms; (b) σ_1 on elements; (c) σ_2 on elements.

3.3. Response of the pneumatic envelope to internal pressure + transversal wind

Figure 8 shows results for the case of internal pressure superimposed with transversal wind pressures. Maximum displacements were about 2.67m at the windward side of the envelope. A maximum σ_1 stress about 11.5MPa is observed at the border corners, at windward side, where a large portion of the membrane is on a wrinkled state. Outside the corner regions, maximum σ_1 stress reaches about 8.0MPa, at the top of the dome. Once again, these results compare well with previous analyses, where wind loads were estimated on educated guessing. However, in our previous analyses, the maximum displacement reached only 0.8m due to smaller pressure intensities estimated for this region.

Widespread wrinkling is observed at both windward and leeward regions. The top of the dome remains in taut conditions, with σ_2 stresses about 5MPa. In our previous models, wrinkling was concentrated at the windward region, but the top of the model presented roughly the same stress level as does the current model. That reflects the differences on the wind pressure fields, determined suing Ansys/Fluent, if compared to our previous estimates. inspection of the principal stress fields and

principal stress directions shown in figure 8(b/c) allows to understand the basic clasp mechanisms by which the membrane responds to the wind action.

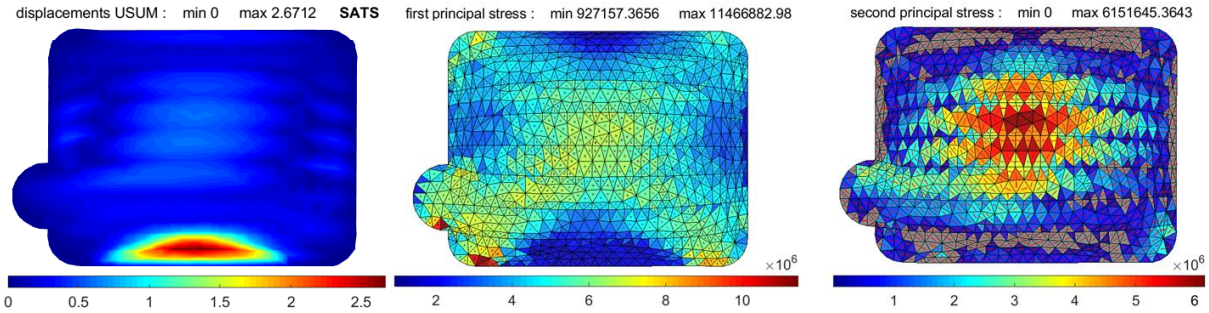


Figure 8: internal pressure + transversal wind loads; (a) displacement norms; (b) σ_1 on elements; (c) σ_2 on elements.

4. Pneumatic loads and stiffness

We are currently implementing variable pneumatic loads and stiffness on our in-house SATS finite element program. A report of our preliminary results will be provided during IASS 2019 conference and forthcoming papers. In the sequel, we provide a brief summary of our approach.

Upon discretization, the problem of *equilibrium of a membrane structure* can be expressed as *finding a displacement vector* $\mathbf{u}^*$ such that $\mathbf{g}(\mathbf{u}^*) = \mathbf{p}(\mathbf{u}^*) - \mathbf{f}(\mathbf{u}^*) = \mathbf{0}$, where $\mathbf{g}(\mathbf{u})$ is *a residual force vector*, $\mathbf{p}(\mathbf{u})$ is the internal load vector and $\mathbf{f}(\mathbf{u})$ is the external load vector. This problem can be solved –within a vicinity of a solution $\mathbf{u}^*$ – iterating Newton's recurrence formula,

$$\mathbf{u}_{k+1} = \mathbf{u}_k - \left(\left. \frac{\partial \mathbf{g}}{\partial \mathbf{u}} \right|_{\mathbf{u}_k} \right)^{-1} \mathbf{g}(\mathbf{u}_k) = \mathbf{u}_k - (\mathbf{K}_k)^{-1} \mathbf{g}(\mathbf{u}_k),$$

where we define the *tangent stiffness matrix*

$$\mathbf{K} = \frac{\partial \mathbf{g}}{\partial \mathbf{u}} = \frac{\partial \mathbf{p}}{\partial \mathbf{u}} - \frac{\partial \mathbf{f}}{\partial \mathbf{u}} = \mathbf{K}_{\text{int}} + \mathbf{K}_{ext} \ ,$$

and where $\mathbf{K}_{\text{int}}$ is the internal stiffness matrix, comprising geometrical and constitutive effects, and $\mathbf{K}_{ext}$ is the external stiffness matrix.

4.1. External nodal loads and stiffness for constant net transversal pressure

We consider that each membrane element under a uniform net transversal pressure $\Delta p = p_1 - p_2$, where p_1 and p_2 are the absolute pressures acting on both sides of the element. For open systems, $p_1 = p_{atm} + \Delta p_1$ and $p_2 = p_{atm} + \Delta p_2$, thus the relative pressure values Δp_1 and Δp_2 can also be considered, since the base atmospheric pressure p_{atm} cancels out. We assume constant values for these terms, and that the element unit vector is oriented outward the element side 1, thus, a positive net pressure $\Delta p > 0$ acts opposite to the element orientation. With the above definitions, the external load vector of a triangular membrane element can be expressed as

$$\mathbf{f} = \mathbf{f}_g + \mathbf{f}_p = \frac{V_0^e \rho_0}{3}\begin{bmatrix}\mathbf{g}\\ \mathbf{g}\\ \mathbf{g}\end{bmatrix} - \frac{\Delta p A^e}{3}\begin{bmatrix}\mathbf{n}\\ \mathbf{n}\\ \mathbf{n}\end{bmatrix}$$

where $\mathbf{f}_g$ are forces due to self-weight, $\mathbf{f}_p$ are forces due to the net transversal pressures, V_0^e and ρ_0, are respectively the volume of the element and the density of the material at the reference configuration, $\mathbf{g}$ is the gravity acceleration, $A^e = A^e\left(\mathbf{u}^e\right)$ is the element area and $\mathbf{n} = \mathbf{n}^e\left(\mathbf{u}^e\right)$ its unit normal vector. From the above expression, a consistent *external stiffness matrix* can be straightforwardly obtained, as shown in [5]. The result is recast below:

$$\mathbf{K}_{ext} = -\frac{\partial \mathbf{f}}{\partial \mathbf{u}} = \ldots = \frac{\Delta p}{6}\begin{bmatrix}\mathbf{\Lambda}_1 & \mathbf{\Lambda}_2 & \mathbf{\Lambda}_3\\ \mathbf{\Lambda}_1 & \mathbf{\Lambda}_2 & \mathbf{\Lambda}_3\\ \mathbf{\Lambda}_1 & \mathbf{\Lambda}_2 & \mathbf{\Lambda}_3\end{bmatrix}$$

where $\mathbf{\Lambda}_i = \text{skew}(\mathbf{l}_i), i = 1,2,3$, are skew-symmetric matrices, whose axial vectors are given by $\mathbf{l}_i = \mathbf{x}_k - \mathbf{x}_j$, with indices $i, j, k = 1,2,3$ in cyclic permutation. We remark that although $\mathbf{k}_{\text{ext}}$ is an asymmetric matrix at the element level, all the non-symmetric stiffness terms corresponding to the internal nodes of any patch of triangular elements cancel out, thus if boundary nodes are constrained, there is no degree of freedom associated to them, therefore the global $\mathbf{K}_{\text{ext}}$ is symmetric, and the system is indeed conservative [6]. If, however, pressure varies along the surface in a generic way, there is no guaranty on the symmetry of $\mathbf{K}_{\text{ext}}$, even thou the boundary is fully restrained.

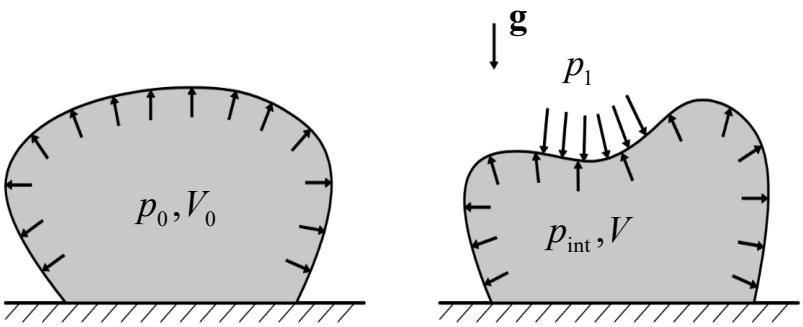


Figure 9: Initial and current configuration of a pneumatic envelope. Adapted from Bonet *et al*. [7].

4.2. External nodal loads and stiffness for pneumatic envelopes

In the case of the pneumatic system depicted in Figure 9, the internal pressure also provides a 'volumetric stiffness', a component of the external stiffness which corresponds to a reluctance of the pressure envelope to alter its volume. The higher the internal pressure, the more relevant this term can be. Bonet *et al.* [7] and Rumple, Schweizerhof and Hassler [8,9] present some alternative approaches to cope with volume variations.

We assume Boyle's law for adiabatic conditions, such that the pneumatic internal pressure is given by

$$p_{\text{int}}(\mathbf{u}) = \frac{p_0 V_{tot}^0}{V(\mathbf{u})}$$

where p_0 and p_{int} are the absolute values of the internal pressure acting on the internal side of the pneumatic envelope ('side 2'), at the initial and current states, respectively. In Figure 10 we plot the variation of the absolute value of internal pressure for a pneumatic envelope with initial internal pressure $p_0 = 1\,atm$ and unit initial volume $V_0 = 1\,m^3$, for positive and negative volume variations ΔV . When volume is reduced to $V_0 / 2$ (i.e. $\Delta V = -0.5\,m^3$, $\Delta V = +1.0\,m^3$) the internal pressure is doubled. When the volume is doubled (i.e. $\Delta V = +1.0\,m^3$), the internal pressure reduces to $p_0 / 4$.

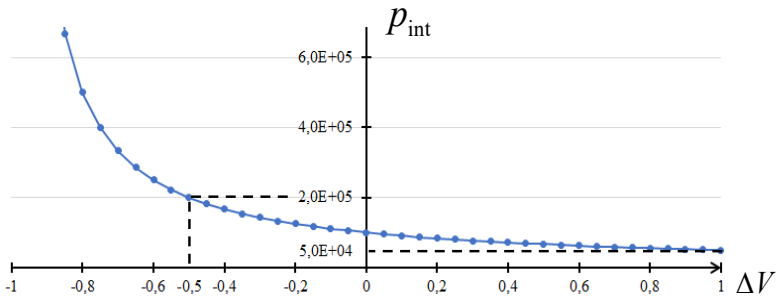


Figure 10: Absolute values of the internal pressure, as a function of the variation of the envelope volume

The total volume of the pneumatic envelope is calculated as

$$V_{tot} = \int_V dV = \frac{1}{3}\int_\Omega \mathbf{x}\cdot\mathbf{n}\, dA \simeq \frac{1}{3}\sum_{e=1}^{n_e} \mathbf{x}_c \cdot A^e \mathbf{n} \ .$$

The external side of the pneumatic envelope experiences a transversal pressure given by $p_1 = p_{atm} + \Delta p_w$, where Δp_w is a fluctuation of the pressure around the base atmospheric pressure, usually produced by wind actions (thus the subscript w). Therefore, the net transversal pressure experienced by the membrane element is

$$\Delta p = p_{atm} + \Delta p_w - \frac{p_0 V_{tot}^0}{V(\mathbf{u})},$$

which is positive if acting inwards the pneumatic envelope.

The external load vector acting on the element is thus

$$\mathbf{f} = \mathbf{f}_g + \mathbf{f}_p = \frac{V_0^e \rho_0}{3}\begin{bmatrix}\mathbf{g}\\ \mathbf{g}\\ \mathbf{g}\end{bmatrix} - \left(p_{atm} + \Delta p_w - \frac{p_0 V_{tot}^0}{V(\mathbf{u})}\right)\frac{A^e}{3}\begin{bmatrix}\mathbf{n}\\ \mathbf{n}\\ \mathbf{n}\end{bmatrix}.$$

After a somewhat lengthy derivation, to be presented in forthcoming papers, we arrive at the external stiffness of a triangular element under wind and pneumatic loads:

$$\mathbf{k}_{ext} = \frac{p_{atm} + \Delta p_w - p_{\text{int}}}{6} \begin{bmatrix} \boldsymbol{\Lambda}_1 & \boldsymbol{\Lambda}_2 & \boldsymbol{\Lambda}_3 \\ \boldsymbol{\Lambda}_1 & \boldsymbol{\Lambda}_2 & \boldsymbol{\Lambda}_3 \\ \boldsymbol{\Lambda}_1 & \boldsymbol{\Lambda}_2 & \boldsymbol{\Lambda}_3 \end{bmatrix} + \frac{p_{\text{int}} A}{18 V_{tot}} \begin{bmatrix} \boldsymbol{\Phi}_1 & \boldsymbol{\Phi}_2 & \boldsymbol{\Phi}_3 \\ \boldsymbol{\Phi}_1 & \boldsymbol{\Phi}_2 & \boldsymbol{\Phi}_3 \\ \boldsymbol{\Phi}_1 & \boldsymbol{\Phi}_2 & \boldsymbol{\Phi}_3 \end{bmatrix},$$

where $\boldsymbol{\Phi}_i = -\mathbf{n}\left(\mathbf{x}_j \times \mathbf{x}_k\right)^T$, with indices $i, j, k = 1, 2, 3$ in cyclic permutation.

The above formulation is being implemented on SATS and preliminary results will be reported during IASS 2019 Symposium, as well as on forthcoming papers.

Acknowledgements

The first author of this paper acknowledges the steady support of FAPESP – São Paulo Research Foundation to his researches on cable and membrane structures.

References

[1] R.M.O. Pauletti (2010), "Some issues on the design and analysis of pneumatic structures", Int. J. Structural Engineering, 1 (3/4), pp. 217-240.

[2] RM.O. Pauletti and E.S. Almeida Neto (2011), 'A finite-difference approximation to Newton´s Method Jacobian Matrices' IABSE-IASS Symposium. London, 2011.

[3] RM.O. Pauletti, D.M. Guirardi (2013), 'Implementation of a simple wrinkling model into Argyris' membrane finite element', VI International Conference on Textile Composites and Inflatable Structures, Munich, 2013.

[4] R.M.O. Pauletti and S. Gellin, "The influence of cable sliding on the structural response of a large pneumatic envelope". Proceedings of the International Association for Shell and Spatial Structures (IASS) Symposium 2015 - Future Visions. 17 - 20 August 2015, Amsterdam.

[5] R.M.O. Pauletti, Static Analysis of Taut Structures. In Textile Composites and Inflatable Structures II. Dorderecht: Springer-Verlag, 2008, 117-139.

[6] M.J. Sewell, On configuration dependent loading. Arch. Rat. Mech. Anal. 23, pp. 327-351, 1967.

[7] J. Bonet, R.D. Wood, J. Mahaney, P. Heywood, Finite element analysis of air supported membrane structures, Comp. Methods Appl. Mech. Eng., vol. 190, no. 5–7, pp. 579–595, 2000.

[8] T. Rumpel, K. Schweizerhof, Volume-dependent pressure loading and its influence on the stability of structures. Int. J. Numer. Meth. Engnr. 56, n. 2, pp. 211-238, 2003.

[9] T. Rumpel, K. Schweizerhof, M. Hassler, Efficient Finite Element Modelling and Simulation of Gas and Fluid Supported Membrane and Shell Structures. Computational Methods in Applied Sciences, pp.153-172, 2005.

Proceedings of the IASS Annual Symposium 2019 – Structural Membranes 2019
Form and Force
7 – 10 October 2019, Barcelona, Spain
C. Lázaro, K.-U. Bletzinger, E. Oñate (eds.)

Do we need technical specifications for membrane structures?

Bernd STIMPFLE*

* formTL ingenieure für tragwerk und leichtbau gmbh
güttinger straße 37, 78315 radolfzell
bernd.stimpfle@form-TLde

Abstract

The development of a common European code for membrane structures is in progress. Does this process improve the quality of our structures? Are there benefits for all of us? This paper presents the progress of the Eurocode for membrane structures, and shows with examples the importance to include the membrane structures from the beginning in the design process.

Keywords: standardization, membrane structures, integrated design

Introduction

Few national design codes for membrane structures are available today. They cover specific types, such as air halls, temporary structures or mechanically tensioned structures with specific constraints. Since long time discussions are going on, how to create a commonly agreed design code. It should provide the common practice on verification, design approach and quality standards.

Starting with the European project TensiNet a first step has been done into that direction. In 2008 the TensiNet organisation, the follow-up network that has been established after the European project, implemented a working group Specifications and Eurocode. This resulted in the standardisation committee CEN/TC 250 WG5, formed in 2010 with the target to elaborate an Eurocode on membrane structures.



Figure 1: Tensinet Design Guide, Tensinet Master Document, SaP report [TensiNet and CEN TC250WG5]

Copyright © 2019 by Bernd Stimpfle
Published by the International Association for Shell and Spatial Structures (IASS) with permission.

This working group has meanwhile prepared a SaP report, which is a background document of the actual state of the art in different countries, and is giving also an outlook on a future Eurocode. Now the next step towards this Eurocode for membrane structures, the preparation of a technical specification TS, is in progress.

Reasons for a common standard

The experts in the field are capable to develop membrane projects without an Eurocode. So why should they work on the new standard, and at the same time help their competitors?

There are many different reasons and opinions. Probably as many as we have participants in that field.

- All agree on the fact that this helps to increase the market.
- We all want to have our technology seen as an established building technology and not only a niche market with high risk.
- With harmonised safety levels, and commonly agreed quality standards, we improve the quality of our industry and we avoid doubts of our clients.
- Once all players respect the same high quality standards this will result in a fair competition.
- By being involved in this standardisation process, one can influence the result and later be satisfied with the final result.

Understanding membrane structures

Membranes are often seen as cladding, treated as add-ons applied to the building or the structure. But this is neglecting at the same time beneficial and unfavourable impacts, as shown with the folowing examples:

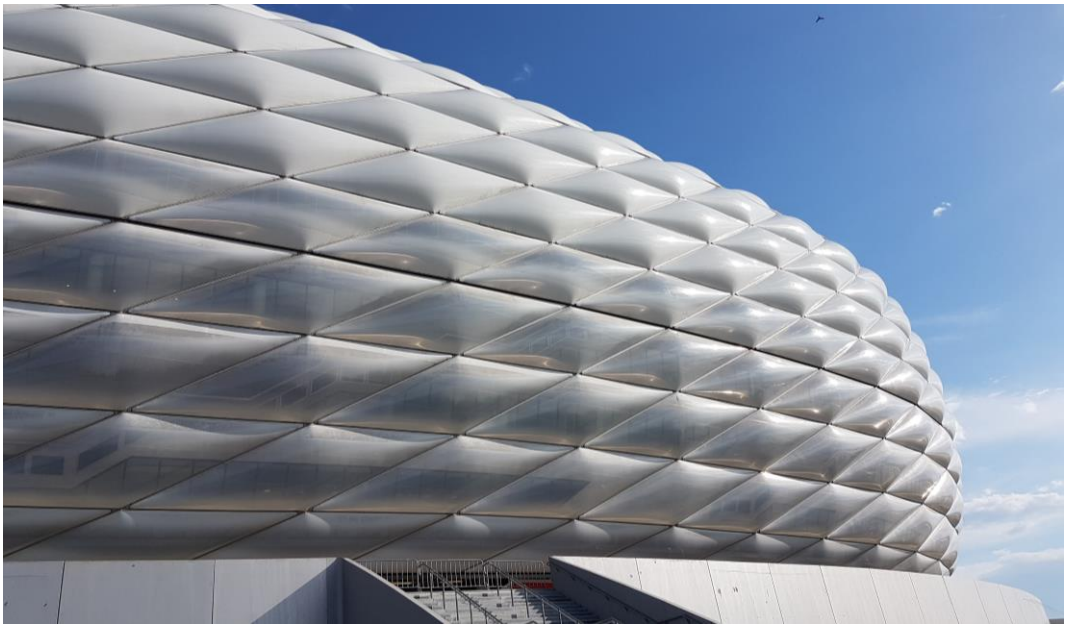


Figure 2: Allianz Arena [formTL]

The roof structure of the Allianz Arena for example has been designed without taking into account the ETFE façade. Just the self-weight has been taken into account. This resulted in another 50 % of steel weight that was required to realize the secondary structure. With an integrated design we suppose that only a small amount of additional steel would have been needed to apply the cushions on the structure.

Furthermore the primary structure of seating bowl and roof has been subdivided with expansion joints in order to minimize constraints due to thermal expansion. Due to the long cantilevers of the roof, one

can easily immagine the large deformation in these joints. The ETFE envelope had to be realised as a continuous surface. Therefore in the roof area the secondary structure is sitting on rather long pin jointed struts, compensating the differential movement of the primary structures underneath. Large spring elements brace the ETFE grid, and keep the constraints acceptable low. In the façade each rhombic cushion has flexible corners and compensating the deformation of the bowl redistributed over the full length of the façade. Knowing this from the beginning, it would have been an easy task to provide a continuous primary structure, and reduce the cost of the façade.

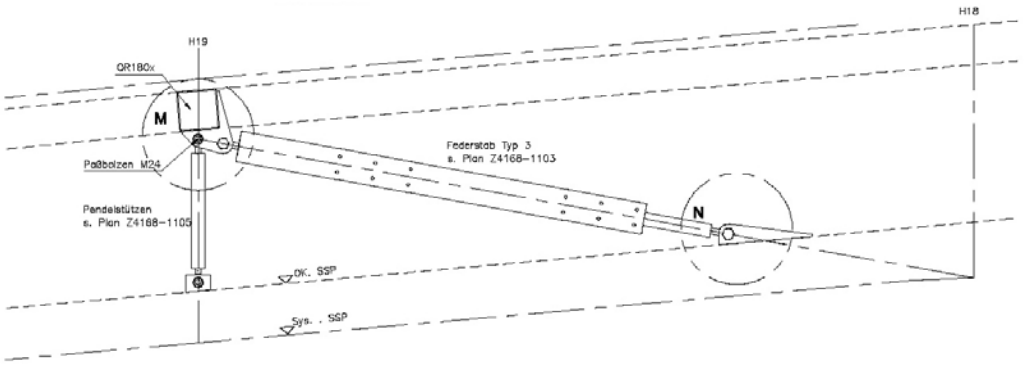


Figure 3: upstand with spring packet [formTL]

The same happened to the Unilever façade, which has been treated as a simple façade too, which was supposed to transmit just the external forces due to wind to each slab, and the self weight of the façade in one slab. Due to the diagonal orientation of the façade the self weight creates a bending moment, which leads to much higher vertical reactions loads.



Figure 4: Unilever Hamburg, ETFE foil façade [formTL]



Figure 5: steel frames and connection to the building [formTL]

Therefore it was necessary to build stiff and heavy steel frames to couple the high tensile forces resulting from the single layer ETFE façade. Difficult built-in parts, instead of the initally foreseen resin anchors, were needed to fix the façade in the prestressed concrete slabs.

The proof engineer of the Dresden Castle ETFE roof answered to the engineers when they sent the analysis of the cushions: “I do not check the roof tiles either”



Figure 6: Dresden Castle, canopy of the small courtyard [Jürgen Lösel]



Figure 7: steel grid with cushion cladding [formTL]

Integrated design must be the future

Integrated design is elementary in our business. Neglecting this will never end in excellent and economic structures.

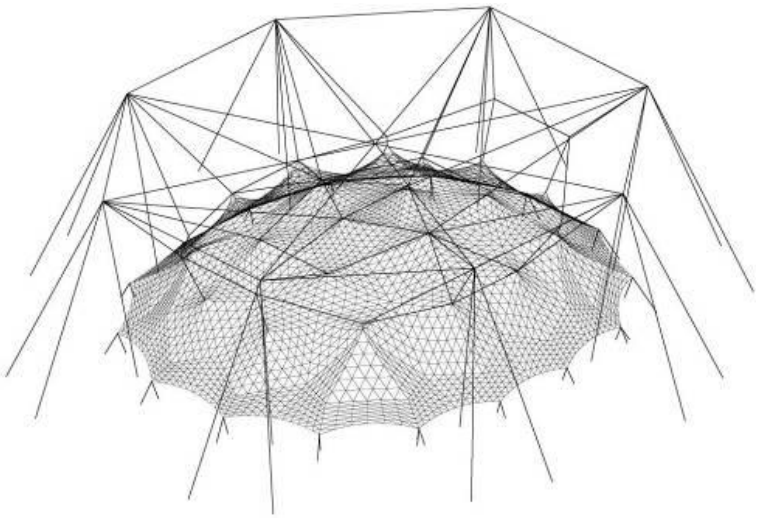


Figure 8: combined analysis model of the Velodrome in Abuja [formTL]

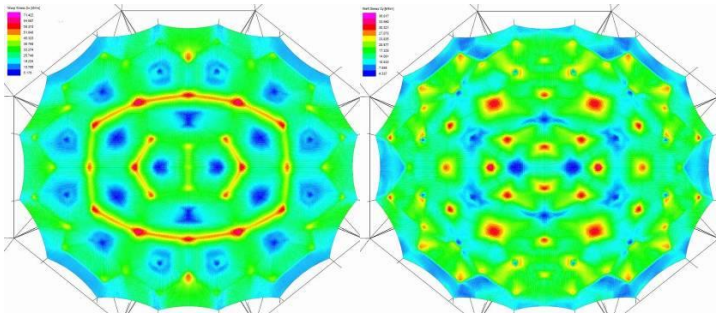


Figure 9: stress results example [formTL]

Large deformation of membrane structures helps to redistribute the loads within the structure, and reduce local stress peaks. The steel and cable can be used much more efficently, and the stress results show up much more homogeneous and realistic.

Conclusion

As mentioned here, there are different opinions for an Eurocode, so are for example some interested in an increased market, and wouldn‘t care about safety levels, and others are mainly interested to minimise the administration process for approval.

The ongoing standardisation process is needed to keep and to improve the quality of our structures. It helps that others treat our business with the required seriousness to the benefit of all.

If we contribute to an Eurocode for structural membranes, we take part in the decision process, and will get finally a document that fits with our needs.

References

[1] Prospect for European Guidance for the Structural Design of Tensile Membrane Structures, Support to the implementation, harmonization and further development of the Eurocodes, JRC Science and Policy Report, European Commission, Joint Research Centre, Editors: M. Mollaert, S. Dimova, A. Pinto, St. Denton, EUR 25400 EN, European Union, 2016

[2] Design Recommendations for ETFE Foil Structures, TensiNet, 2013

[3] Analysis and design of membrane structures: Results of a round robin exercise, Engineering Structures, Volume 48, March 2013, Pages 313-328

Proceedings of the IASS Annual Symposium 2019 – Structural Membranes 2019
Form and Force
7 – 10 October 2019, Barcelona, Spain
C. Lázaro, K.-U. Bletzinger, E. Oñate (eds.)

Strength values of ETFE-foils correlated to limited residual strains

Natalie STRANGHÖNER*, Felix SURHOLT*, Jörg UHLEMANN*

*University of Duisburg-Essen, Institute for Metal and Lightweight Structures, Universitätsstr. 15, 45141 Essen, Germany
natalie.stranghoener@uni-due.de

Abstract

In uniaxial tensile tests, ETFE-foils exhibit two inflexion points where the stiffness changes. They are correlated to different residual strains after unloading. As unloading is usually not carried out in uniaxial tensile tests, the residual strain after unloading is usually unknown. But: to enable the design engineer to assess at which stress level noticeable plastification starts, this knowledge is crucial. Nowadays, the various existing design concepts used in practice are based on different definitions of these inflexion points, commonly called yield points. Hereby, the residual strain after unloading is not considered at all. However, taking into account that ETFE foil structures usually exhibit biaxial stress states, the design is highly recommended to be based on biaxial mechanical behaviour of the material instead of uniaxial strength values. For this reason, uni- and biaxial tensile tests at load ratios of 1:1 and 2:1 have been performed in order to define strength values corresponding to 0.2% residual strain. Herein, the foils have been stressed to a predefined load level which yield to 0.2% residual strain directly after unloading before reverse creep occurs. The objective was to determine load levels and thus strength and stiffness values which correlate to a limited spontaneous residual strain. The achieved knowledge will strengthen the fundament for defining an appropriate design concept for ETFE-foil structures as an objective of the current development of the Technical Specification for Membrane Structures.

Keywords: ETFE-foil, stress-strain behaviour, residual strain, ETFE design concept, uniaxial, biaxial.

1. Introduction

ETFE-foils for membrane structures are convincing due to their light weight, translucency and persistence. The first use of ETFE took place in the eighties of the last century with the construction of the mangrove hall at Burgers' Zoo in Arnhem, Netherlands, see Figure 1. In the beginning, only synclastic, pneumatically pre-stressed cushion constructions were built using ETFE-foils. However, the trend is towards less curved or towards flat constructions and thus constructions with less geometric rigidity. Due to the decrease in geometric stiffness, a suitable method for determining the material properties, strength and stiffness values – modulus of elasticity, Poisson's ratio, yield strength or proof stress at defined strain, creep and relaxation behaviour – is becoming increasingly important. In Germany, foil structures in the building industry always need single case approvals by the German building authorities, so that for each project the characteristic values describing the mechanical behaviour of the used materials are determined individually. For this, in general, uniaxial tensile tests are performed to determine the mechanical characteristics as the – so called – yield strength, elongation at break, 10%-strain stress and elastic constants using stress-strain diagrams. However, ETFE-foils show a different mechanical behaviour in uni- and biaxial tensile tests. For this reason, the authors of this contribution claim that mechanical properties of ETFE-foils used in biaxial tensioned structures should

Copyright © 2019 by Univ.-Prof. Dr.-Ing. habil. N. Stranghöner, Dr.-Ing. J. Uhlemann, F. Surholt, M.Sc.
Published by the International Association for Shell and Spatial Structures (IASS) with permission.



Figure 1: ETFE cladding of the mangrove hall at Burgers‘ Zoo in Arnhem, Netherlands
(Source and ©: Vector Foiltec GmbH, Andreas Braun, Hammeln)

be consequently determined in tensile tests under biaxial loading as long as a correlation between uni- and biaxial material behaviour has not been derived.

Furthermore, no official design guide for ETFE-foils is currently available. Different suggestions exist to calculate ETFE-structures, see e. g. [1], [2], which base on different approaches, e. g. the two descriptive inflexion points, commonly called yield points, which are visible in uniaxial stress-strain curves, or the stress at 10% strain.

The aim of the present contribution is to experimentally determine stress values of ETFE by uniaxial tensile tests and biaxial tensile tests at load ratios of 1:1 and 2.1 which result in approximately 0.2 % residual strain after unloading in order to evaluate the stress level at which noticeable plastification starts. This stress level might be called 0.2 % proof stress. With the limitation of the working stress referring to 0.2 % residual strain directly after unloading before reverse creep occurs, in the following called instantaneous 0.2 % residual strain, it shall be ensured that the material behaves approximately linear-elastic. In addition, due to the viscoelastic material behaviour of ETFE, the instantaneous residual strain of 0.2 % will decrease with stressless time passing. Considering that ETFE structures are usually subjected to biaxial stresses, biaxial resistance values have been derived and are recommended for design purposes. Biaxial strength values have been determined which refer to 0.2 % residual strain. The uni- and biaxial strength values may deviate from each other due to their different material behaviour in uni- and biaxial tensile tests.

The achieved knowledge will strengthen the fundament for defining an appropriate design concept for ETFE-foil structures as an objective of the current development of the Technical Specification for Membrane Structures.

2. Material behaviour

ETFE (ethylene tetrafluoroethylene) belongs to the group of organic-synthetic materials and thus to thermosoftening plastics. It is assumed that ETFE is a homogeneous material with isotropic characteristics so that the material behaviour can be described by one modulus of elasticity and one Poisson’s ratio up to the point when viscoelastic or viscoplastic material behaviour starts.

To determine ETFE’s stress-strain behaviour – characteristic material values and stiffness parameters – uni- and biaxial tensile tests have been performed in the frame of the presented investigations. For uniaxial tensile tests, strip specimens have been used according to EN ISO 527-3 [3] and for biaxial tensile tests, cruciform specimens, see Figure 2.

The tensile behaviour of ETFE changes under uni- and biaxial loading. Figure 3 illustrates the tensile performance of ETFE in an uniaxial tensile test executed at $T = 23°C$ with a load rate of $v_T = 100$ mm/min. It becomes apparent that ETFE exhibits two inflexion points where the stiffness visually changes.

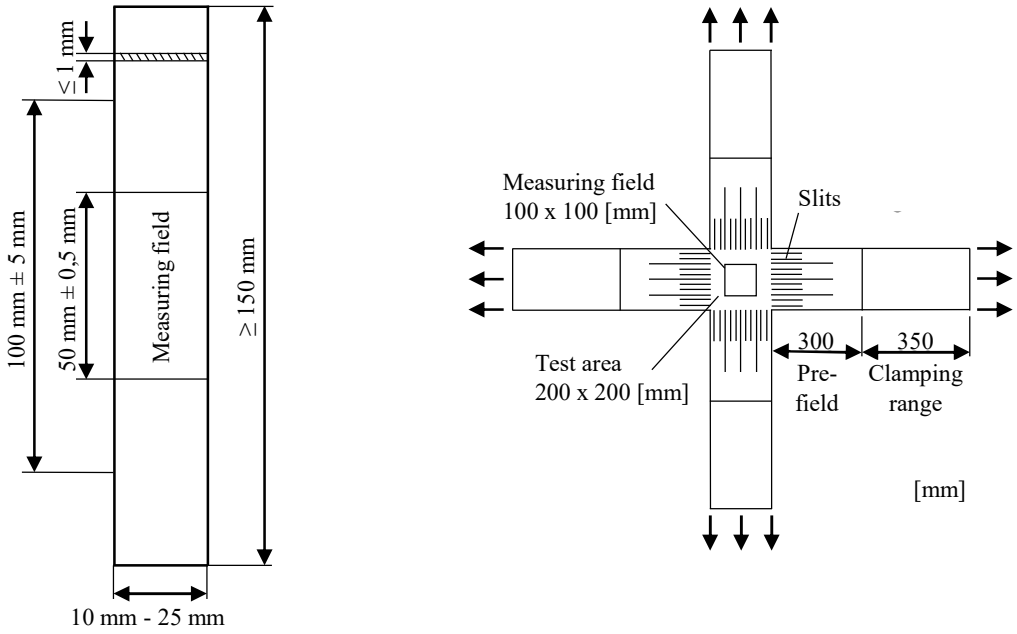


Figure 2: Specimens for uni- (left, [3]) and biaxial (right) tensile tests

The first inflexion point occurs at ~16 MPa. Here, the material properties change from predominant linear-elastic to predominant viscoelastic and the material becomes softer. At the second inflexion point at about 22 MPa, the predominant material behaviour changes from viscoelastic to viscoplastic. Here, ETFE starts to yield. For this reasons, the second inflexion point might be called yield point from the author's point of view. To call the first inflexion point yield point as well – as commonly done in practice – seems not be appropriate as yielding cannot be observed. At the second inflexion point, a disproportionate increase in elongation is observed without an increase in stress up to the point when hardening occurs. Finally, the foil breaks at its ultimate tensile strength.

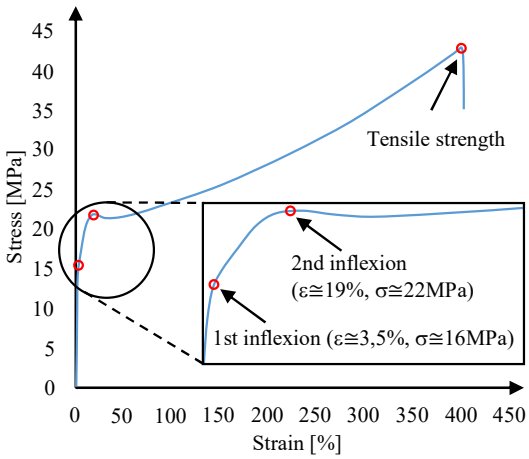


Figure 3: Typical uniaxial material behaviour of ETFE (1:0, T = 23°C, v_T = 100 mm/min)

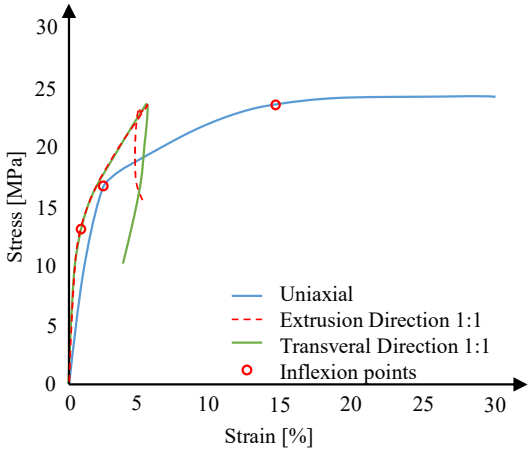


Figure 4: Comparison between uni- (1:0) and biaxial (1:1) material behaviour of ETFE (T = 23°C, v_T = 100 mm/min)

Figure 4 shows a comparison of the uni- and biaxial tensile performance under comparable testing conditions. It becomes obvious that ETFE shows a stiffer material behaviour in biaxial tensile tests. Due to the fact that in practice ETFE structures are predominant biaxially tensioned, the biaxial material behaviour is pivotal.

In typical biaxial tensile tests with cruciform test specimens, only the first inflexion point becomes visible. This is due to the geometry of the cruciform specimens. In a biaxial tensile test with a cruciform test specimen as shown in Figure 2 (right), the arms start to yield before the measuring field in the centre of the test specimen is stressed up to the second inflexion point and yielding can start, so that no further stress increase can occur in the measuring field. Therefore, no second inflexion point can be observed in biaxial tensile tests with cruciform specimens. Nevertheless, to determine stress levels resulting in 0.2 % residual strain immediately after unloading, cruciform specimens are used due to the advantage of knowing the governing stress and strain in the measuring field.

3. Current design recommendations for ETFE structures

Currently, ETFE structures – at least in Germany – are always designed with single case approvals by the regional building authority where different approaches are applied in the design process depending on the design engineer involved. At present, on European level, a Technical Specification (TS) for Membrane Structures [4] is under development mirrored by the relevant national standardization committees. This TS aims to specify the design of tensile membrane structures. A first draft is set up and will be further developed in the coming two years. Relying on the general Eurocode philosophy, the guideline distinguishes between Ultimate Limit State (ULS) and Serviceability Limit State (SLS). In ULS, partial safety factors are applied to the actions/action effects on the one side and resistances on the other side covering the load bearing capacity of the considered member/detail and the material strength by various characteristic values with $\gamma_{M0} = 1.1$ for general member behaviour and $\gamma_{M1} = 1.5$ for joints at the current stage. Hereby, the design resistance value f_{Rd} is determined as the minimum of f_{1Rd} and f_{2Rd} as follows:

$$f_{Rd} = \min \begin{pmatrix} f_{1Rd} = f_{y23} / \gamma_{M0} \\ f_{2Rd} = f_{uw\,23} / \gamma_{M1} \end{pmatrix} \tag{1}$$

where f_{y23} refers to the 5 %-fractile of the strength value corresponding to second inflexion point of at least five uniaxial tensile tests at T = 23°C and f_{uw23} reflecting the 5 %-fractile of the strength value corresponding to the short term tensile strength of at least five seam tests at T = 23°C. In the current draft of the TS, the recommended value for the second inflexion point is given to $f_{y23} = 21$ MPa which results to $f_{1Rd} = 19$ MPa. Up to now, the seam strength is defined to $f_{uw23} = 30$ MPa which leads to $f_{2Rd} = 20$ MPa. It has to be mentioned that the value for the seam strength is still under discussion as higher values are achievable in practice. Depending on the fabrication quality achieved by different manufacturers, this value can be enhanced to $f_{uw23} = 33$ MPa. But to do so, it has to be ensured, that this enhanced strength can be achieved by most of the manufacturers. As it can be easily imagined, this topic is still under discussion. The authors like to propose to define high quality requirements for welding in a separate execution part of the TS to ensure a high quality of the weld seams and to enable higher strength values for the weld seams which are decisive for design.

To consider environmental effects, load duration and temperatures, several modification factors k_{age}, k_{long}, k_{perm}, k_{temp*} are introduced which reduce the design resistance f_{Rd} for different load conditions. These modification factors k can be experimentally determined or taken from the TS as follows:

- $k_{age} = 1.05$ environmental effects,
- $k_{long} = 1.2$ long term effects,
- $k_{perm} = 1.8$ permanent long term effects,
- $k_{perm} = 3.5$ single layer foils; permanent long term effects e. g. prestress,
- $k_{temp0} = 0.7$ temperature effects; 0°C and
- $k_{temp50} = 1.2$ temperature effects; 50°C.

ETFE-foils might plastify. Of course, this might be allowable depending on the project (e. g. for cushion structures), but the design engineer should have control of the stress leading to plastification.

Other design concepts, e. g. developed by Moritz [5], refer to the stress values of the second inflexion point under different environmental conditions, e. g. low and high test temperatures or load speeds. In the approach of Saxe [6], stress values for different temperatures were experimentally determined:

- $R_{k(0°C)}$ = 15 MPa
- $R_{k(23°C)}$ = 12 MPa
- $R_{k(35°C)}$ = 10 MPa

These fixed strength values refer to an approximately linear-elastic material behaviour modified by the modification factor k_{mod} which considers the load rate resulting in e. g. k_{mod} = 0.5 for snow loads and k_{mod} = 1.8 for wind loads. Furthermore, the latter approach by Saxe refers to cyclic determined stress levels resulting in 0.25 % residual strain under high load rates with 10 sec. per load cycle depending on the test temperature. Figure 5 illustrates the determined strength levels depending on the test temperature.

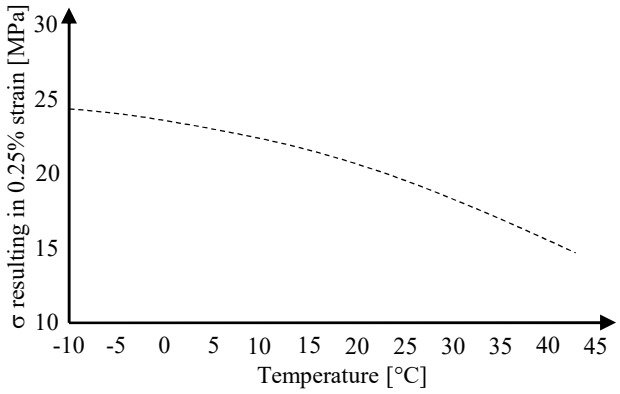


Figure 5: Stress levels determined under "high" load rates resulting in 0.25 % residual strain [6]

With the definition of a working stress corresponding to 0.2 % instantaneous residual strain after unloading, the foil's plastification is known. Further permanent residual strain can be excluded. In addition, the 0.2 % instantaneous residual strain decreases over stressless time passing. Furthermore, Maywald and Mißfeld [7] claim that ETFE exhibits hardening characteristics under cyclic loading, so that even higher stresses could be allowed after cyclic loading than correlated to the 0.2 % strain-stress after one single loading. Based on the approach of Saxe, stress levels for uni- and biaxial tension states with load ratios 1:1 and 2:1 have been experimentally determined to ensure 0.2 % or less instantaneous residual strain directly after unloading. These results are presented in the following.

4. Experimental investigation into the stress level resulting in 0.2 % instantaneous residual strain

4.1. General

In order to determine the desired stress values, uni- and biaxial tensile tests have been carried out. Uniaxial tensile tests have been performed using strip specimens according to EN ISO 527-3, see Figure 2 whereby both foil directions, extrusion (ED) and transversal direction (TD), have been investigated. Former research showed that both foil directions can be treated as isotropic, e. g. [6], [8]. Furthermore, biaxial tensile tests have been performed under stress ratios 1:1 and 2:1 (ED:TD) reflecting the most common stress ratios in ETFE cushion type structures: 1:1 covers quadratic or circular cushions, 2:1 covers rectangular cushions. Finally, statistical evaluations of the strain values per stress level have been carried out.

4.2. Uniaxial tensile tests

The 0.2 % instantaneous residual strain has been determined on virgin ETFE foils with a thickness of 200 µm. To examine the stress level which yields to the 0.2 % instantaneous residual strain, several ETFE specimens have been stressed to varying predetermined stress levels σ_{max} under a constant load rate of 0.25 kN/m/s ≙ 1.25 MPa/s. After reaching the predetermined stress level, the foils have been unloaded with the same load rate, see Figure 5, and the instantaneous residual strain was measured.

Repeating this procedure with different stress levels, the desired stress level correlated to a 0.2 % instantaneous residual strain has been determined iteratively.

According to the hint in [6] that a working stress level of 12 MPa at room temperature, T = 23°C, results in 0.25 % residual strain, firstly σ_{max} = 11 MPa has been investigated. Despite the $\Delta\sigma_{max}$ = 1 MPa lower stress, these tests resulted in an average 0.25 % instantaneous residual strain after unloading. The deviations from the results given in [6] might be caused in the deviating load rates, since the load rate has an influence on ETFE's material behaviour. With an increase of the load rate, ETFE becomes stiffer.

A further decrease of σ_{max} to a stress level of 10.8 MPa resulted in an average 0.23 % residual strain with a coefficient of variation of 19.9 % in ED. The residual strain of the tests in TD average at 0.29 % residual strain with a coefficient of variation of 24.5 %. If, however, the standard deviation is considered, it can be seen that the strains at maximum stress and the residual strains are comparable in their magnitude: 0.06 % strain and 0.05 % strain in ED and 0.12 % strain and 0.11 % strain in TD, respectively. Table 1 shows the results of the uniaxial tensile tests. The same magnitude of standard deviation leads for the much smaller residual strains to much higher coefficients of variation. Due to the small values, the explanatory power of the coefficient of variation becomes less meaningful. The low deviation of strain at max stress in both foil directions confirms the high degree of homogeneity. With an average of 0.23 % residual strain in ED, 10.8 MPa leads to an insignificant deviation from the nominal limit of 0.2%, so that 10.8 MPa can be assumed as the stress limit. Figure 7 illustrates the measured hysteresis of the uniaxial tensile tests in ED and TD.

Table 1: Results of uniaxial tensile tests with nominal stress 10.8 MPa

Foil direction	Test number	Max Stress [MPa]	Strain at max stress [%]	Residual strain [%]
ED	1	10.76	1.52	0.22
	2	10.76	1.59	0.28
	3	10.77	1.46	0.17
	4	10.77	1.39	0.12
	5	10.75	1.56	0.25
	6	10.76	1.52	0.24
	7	10.76	1.50	0.24
	8	10.76	1.50	0.24
	9	10.76	1.54	0.25
	10	10.76	1.54	0.25
Average	-	10.76	1.51	0.23
Standard deviation	-	0.01	0.06	0.05
Coefficient of Variation [%]	-	0.05	3.69	19.87
TD	1	10.75	1.65	0.30
	2	10.75	1.58	0.27
	3	10.75	1.64	0.29
	4	10.75	1.73	0.37
	5	10.75	1.50	0.21
	6	10.75	1.60	0.29
	7	10.75	1.68	0.37
	8	10.77	1.34	0.15
	9	10.75	1.71	0.38
	10	10.75	1.65	0.31
Average	-	10.75	1.61	0.29
Standard deviation	-	0.01	0.12	0.07
Coefficient of Variation [%]	-	0.06	7.20	24.50

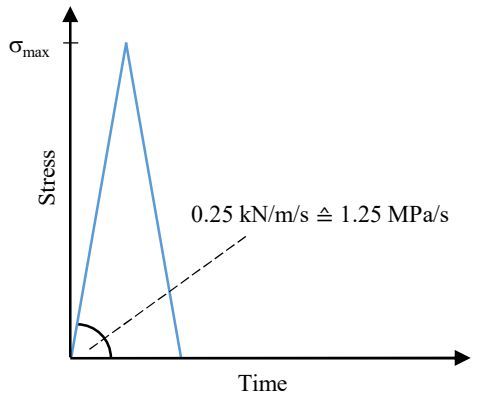


Figure 6: Load protocol for the uniaxial tests

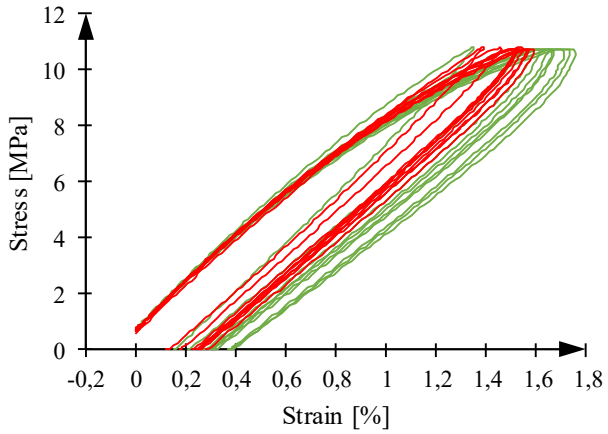


Figure 7: Results of the uniaxial tensile tests in ED (red) and TD (green), ten tests each; σ_{max} = 10.76 MPa, 200 µm

4.2. Biaxial tensile tests

Comparable to the uniaxial tests, in the biaxial tensile tests, the stress values have been determined in such a way that they result in a 0.2 % instantaneous residual strain for the load ratios 1:1 and 2:1 for a 250 µm thick ETFE-foil. In order to determine the desired stress level iteratively, the same procedure has been used as applied in the uniaxial tests.

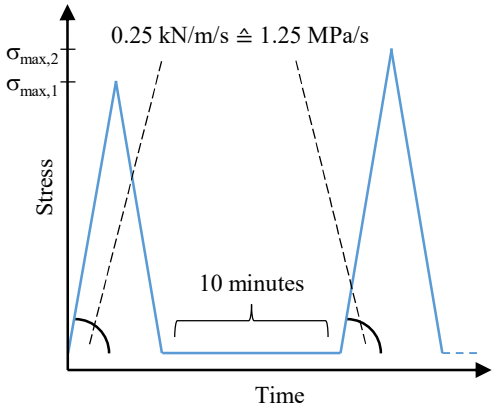


Figure 8: Biaxial test protocol for determining the stress level resulting in 0.2 % residual strain

To minimize the required material, preliminary tests for different maximum load levels have been carried out with one test specimen. For this reason, 10 minutes hold time at the minimal stress has been set between the different stress levels, see Figure 8. The hold time ensured that the ETFE foil could recover from the previous load. With the assumption of ETFE being stiffer under biaxial loading, the first investigated stress level has been set to σ_{max} = 13 MPa for both load ratios 1:1 and 2:1 wherein 13 MPa represents the major stress in load ratio 2:1 in practice. With each step, the stress levels increased by $\Delta\sigma_{max}$ = 0.5 MPa. With this procedure, the stress level yielding to 0.2 % instantaneous residual strain has been determined. Finally, the achieved stress level has been validated by testing virgin material.

With the help of the described procedure, stress levels between 19 MPa and 19.25 MPa for a load ratio of 1:1 and between 20 MPa and 20.75 MPa for a load ratio of 2:1 have been determined. The subsequent biaxial validation tests on virgin material for 1:1 with a stress level of 19 MPa resulted in an average 0.12 % residual strain with a coefficient of variation of 16.7 % in ED and an average 0.15 % residual strain with a coefficient of variation of 7.9 % in TD. Again, due to the low standard deviation of 0.02 % strain and 0.01 % strain in ED and TD, respectively, the coefficients of variation are misleading. For a load ratio of 2:1 loaded to 20 MPa, the standard deviation became 0.03 % strain at an average residual strain of 0.10 % with a coefficient of variation of 33.3 % in ED. In TD the average residual strain was -0.02 % with a standard deviation of 0.01 % strain. Figure 9 and Figure 10 show the experimentally determined stress-strain paths of the biaxial tensile tests for the load ratios 1:1 and 2:1. Furthermore,

comparative biaxial tests for the first load ratio have been carried out and loaded up to a maximum stress of 20 MPa. While for the load ratio 2:1 the average residual strain was 0.10 % in major direction, the average residual strain for the same stress level yield to 0.41 % for ED and 0.45 % for TD with coefficients of variation of 7.0 % and 5.9 %, respectively, see Figure 9. Herewith, it can be concluded that an increase of $\Delta\sigma_{max}$ = 1 MPa results in an average increase of 0.3 % residual strain and 0.4 % strain at maximum stress.

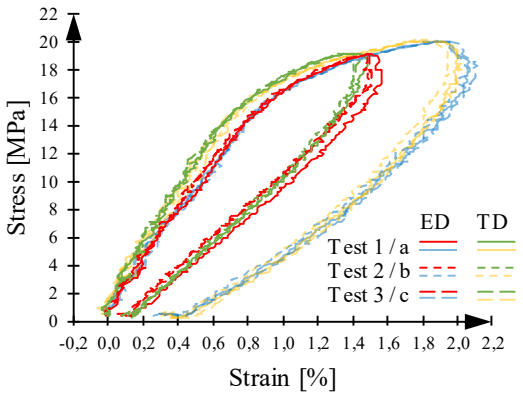


Figure 9: Results of the biaxial tensile test, three tests each (1:1, σ_{max} = 19 MPa / 20 MPa, 250 µm)

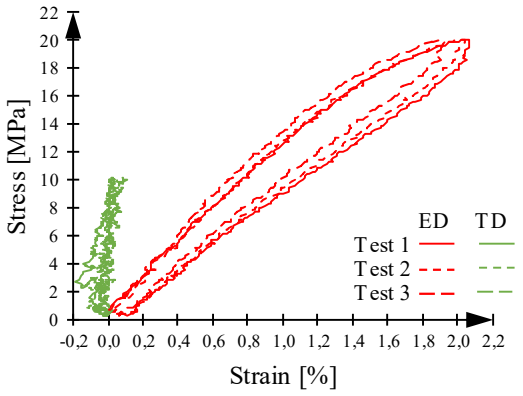


Figure 10: Results of the biaxial tensile test, three tests each (2:1, σ_{max} = 20 MPa, 250 µm)

6. Conclusion

In this contribution, investigations into the determination of a stress value are presented which results in an instantaneous 0.2 % residual strain after unloading. This stress might be called 0.2 % proof stress. Due to the viscoelastic material behaviour of ETFE, the residual strain decreases further when time elapses after unloading. Uni- and biaxial tensile tests at load ratios of 1:1 and 2:1 clearly show that ETFE-foils behave considerably stiffer under biaxial tension. Under uniaxial loading, the investigated ETFE-foils can be stressed up to 10.8 MPa resulting in approximately 0.2 % instantaneous residual strain after unloading. In comparison to the uniaxial material behaviour, ETFE can be stressed in biaxial tests up to 19 MPa under a load ratio of 1:1 and up to 20 MPa under a load ratio of 2:1 yielding to residual strains less than 0.2 %. Furthermore, the biaxial tests have shown that under a load ratio of 2:1, the inflexion point at which the stiffness visually changes is not strongly formed. Furthermore, it could be shown, that ETFE behaves less stiff under a load ratio of 2:1 than under 1:1. Nevertheless, simultaneously, the viscoelasticity is less distinct. Overall, for the load ration of 2:1, slightly higher stresses are allowable resulting in 0.2 % instantaneous residual strain.

In the current draft of the Technical Specification for Membrane Structures, the design resistance f_{Rd}, which has to be modified by k-factors, is determined by applying stress values achieved by uniaxial tensile testing referring to the second inflexion point, commonly called yield point in literature. However, the second inflexion point occurs at high strain values with unknown plastic residual strain. In contrast, in this contribution stress values have been determined resulting in 0.2 % residual strain which might be called 0.2 % proof stress. Herewith the strength value belongs to a specified plastic strain and herewith the magnitude of plastification is known. Based on the presented study, the design resistance f_{Rd} and the biaxially determined 0.2% proof stress for load ratio 1:1 can be defined to 19 MPa in both cases although originating from different approaches. Nevertheless, the experiments show that a biaxial stress of 19 MPa results in less than 0.2 % residual strain, so that the uniaxially determined 19 MPa might be used for design purposes. It is obvious, that ETFE-foils exhibit different material behaviour under uni- and biaxial loading. For this reason, it is highly recommended to base the future design concept on the biaxial material behaviour of ETFE foils.

References

[1] R. Houtman (Ed.), *TensiNet European Design Guide for Tensile Surface Structures Appendix A5: Design recommendations for ETFE foil structures*, TensiNet, Brussels, 2013.

[2] N. Stranghöner, J. Uhlemann et al., *Prospect for European Guidance for the Structural Design of Tensile Membrane Structures, Support to the implementation, harmonization and further development of the Eurocodes*, JRC Science and Policy Report, European Commission, Joint Research Centre, Editors: M. Mollaert, S. Dimova, A. Pinto, St. Denton, EUR 25400 EN, European Union, 2016.

[3] EN ISO 527-3:2018, *Plastics – Determination of tensile properties – Part 3: Test conditions for films and sheets (ISO 527-3:2018)*.

[4] CEN Technical Specification "Membrane Structures", internal draft, CEN/TC 250 WG 5, April 2019 (unpublished).

[5] K. Moritz, *ETFE-Folie als Tragelement*, PhD Thesis, Technische Universität München, Munich, Germany, 2007.

[6] K. Saxe, *Zur Berechnung und Bemessung von ETFE-Folientragwerken*, in: N. Stranghöner, K. Saxe (Eds.), Essener Membranbau Symposium 2012, Shaker Verlag, Aachen, Germany, 2012.

[7] C. Maywald, M. Mißfeld, *Zum Alterungsverhalten von ETFE-Konstruktionen in der Architektur*, Stahlbau 87 (2018), No. 7, pp. 663-672.

[8] L. Schiemann, *Tragverhalten von ETFE-Folien unter biaxialer Beanspruchung*, PhD Thesis, Technische Universität München, Munich, Germany, 2009.

Proceedings of the IASS Annual Symposium 2019 – Structural Membranes 2019
Form and Force
7 – 10 October 2019, Barcelona, Spain
C. Lázaro, K.-U. Bletzinger, E. Oñate (eds.)

The calibration of the partial factors for the design of a typical hypar membrane structure

Elien DE SMEDT*, Marijke MOLLAERT[a], Robby CASPEELE[b], Lincy PYL[a]

*Vrije Universiteit Brussel
Pleinlaan 2, 1040 Etterbeek
Elien.De.Smedt@vub.be

[a] Vrije Universiteit Brussel
[b] Universiteit Gent

Abstract

Membrane structures are widely used for various functions, although there does not exist a unified design approach as there exists for conventional buildings (partial factor framework, Eurocode). Specific for most membrane structures is that they have doubly curved shapes, they are pre-tensioned and exhibit a non-linear structural behaviour. The current article investigates an existing calibration method to obtain the partial factors to be used for the design of a typical hypar membrane structure. The reliability analysis is performed using a First Order Second Moment method in combination with Latin Hypercube Sampling. The study is performed for the load cases snow load and wind uplift load.

Keywords: hypar membrane structure, reliability index, optimization function, Latin Hypercube Sampling.

1. Introduction

Membrane structures exist in various forms and scales for temporary and permanent use. Over the years, the design of membrane structures is greatly improved and is currently well established. Several countries have their own design guidelines [1]. However, a uniform design approach, such as the Eurocodes [2], does not exist. Within CEN TC 250, Working Group 5 is currently working on a standardised design approach for membrane structures [3]. In order to propose for membrane structures a partial factor framework as described in the Eurocode, specific research combining structural design and reliability analysis is needed. Methods to perform the reliability analysis of membrane structures are proposed by Gosling et al. [4] and De Smedt et al. [5]. Gosling et al. determined the most influential parameters of the considered membrane structure by means of a sensitivity analysis. Afterwards, the reliability index is found using First Order Reliability Analysis. De Smedt et al. discussed a preliminary reliability analysis on a hyperbolic paraboloid (hypar) cable-net structure, which structural behaviour is similar to the behaviour of a hypar membrane structure. The reliability analysis was performed using a First Order Second Moment (FOSM) method in combination with Latin Hypercube Sampling (LHS).

This article proposes a method to perform the reliability analysis and to calibrate the partial factors to be used in the design of a specific hypar membrane structure. The partial factor for prestress, snow load and wind uplift load are evaluated. The proposed calibration method is based on the method described in De Smedt et al. [5]

Copyright © 2019 by Elien De Smedt, Marijke Mollaert, Robby Caspeele and Lincy Pyl.
Published by the International Association for Shell and Spatial Structures (IASS) with permission.

2. Description of the hypar membrane structure

The studied membrane structure is a hyperbolic paraboloid (hypar) with two high and two low points (Figure 1). The considered material is a Type I PVC-coated polyester membrane. The in-plane distance from low point (LP) to high point (HP) is 6 m. The height of the high point is 2 m. The membrane is tensioned between four points by means of a turnbuckle in each corner point. The turnbuckles have a length of 0.5 m.

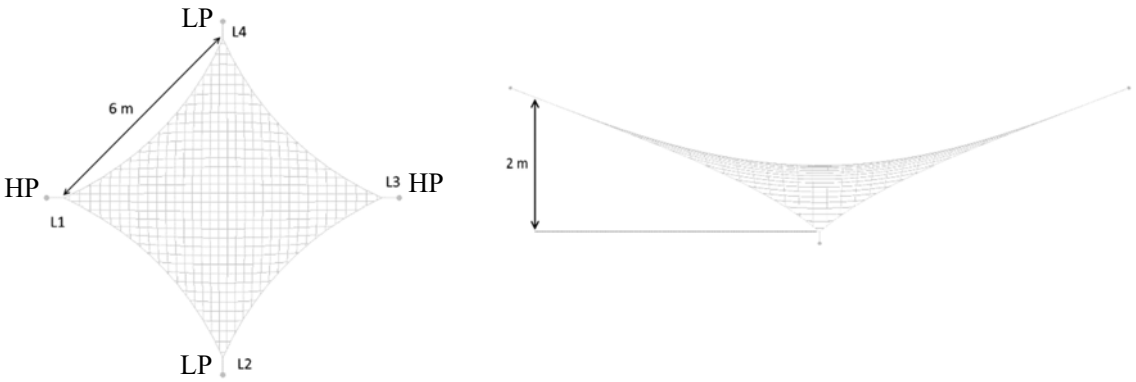


Figure 1: Top view (left) and side view (right) of the hypar membrane structure.

The prestress for hanging and arching direction is set at 4.0 kN/m. For the dimensioning, the membrane is submitted to two load cases: a snow load of 0.5 kN/m² and a wind uplift load of 1.0 kN/m². Usually, the hanging direction of the membrane is dimensioned under snow load (reduced stress in the arching direction) and the arching direction under wind uplift load (reduced stress in the hanging direction). The membrane is designed following the method described in the Prospect for European Guidance for the Structural Design of Tensile Membrane Structures (SaP report) [3]. The condition in equation (1) has to be met:

$$\sigma_{memb} \leq \frac{f_u}{\gamma_m . k} \tag{1}$$

where σ_{memb} is the membrane stress, f_u is the ultimate tensile strength, γ_m is the material safety factor (= 1.4, according to the German Standard [6], [7]), k is the strength reduction factor (= 3.6, SaP-report [3]). Note that $\frac{f_u}{k}$ is called the reduced strength f_{red}. Normally, an existing membrane is selected with a specific thickness, stiffness and strength for hanging and arching direction. In this study, to calibrate the investigated partial factors accurately, the membrane must be optimally dimensioned. So, for each design (each considered set of partial factors) the membrane properties are different and do not correspond to an existing material type.

3. Structural reliability analysis: the calibration method

The proposed calibration method is a minimization process as described by Madsen et al. [8] and Sorensen et al. [9]. The hypar membrane structure is designed according to a range of partial factors for prestress γ_p (1, 1.2, 1.35), snow load γ_s (0.5, 1.0:0.1:2.0, 2.5) and wind uplift load γ_w (0.5, 1.0:0.1:2.0, 2.5). The reliability index is calculated for each design and compared to the target reliability index. The partial factors used in the design for which the difference between the reliability index and the target reliability index is the smallest are retained. The used target reliability index is set according to the Eurocode for a reliability class two and a 50 years reference period (3.8, see Table 1) [2]. For the reliability analysis a First Order Second Moment Method is used in combination with Latin Hypercube Sampling (LHS).

Table 1: Target reliability indexes according to Eurocode, for a 50 years reference period [2].

Reliability class	Minimum values for β
	50 years reference period
RC3	4.3
RC2	3.8
RC1	3.3

First, the important parameters in the structural analysis of membrane structures are selected. The stochastic models of the parameters are determined based on literature or expert advice.

3.1. Parameters and stochastic models

For the reliability analysis, the considered parameters are the elastic stiffness in hanging direction $E_{warp}t$ and in arching direction $E_{fill}t$, the reduced strength in hanging direction $f_{red,warp}t$ and in arching direction $f_{red,warp}t$, the length of the turnbuckles $L_{tb,1-4}$, and the load cases Q_{snow}, Q_{wind}. In Table 2, an overview is given of the parameters and their stochastic model.

Table 2: Stochastic models of the parameters used in the reliability analysis.

Parameter	Distribution	Mean value	COV	Unit
$\boldsymbol{E_{warp}t}$	Normal	$E_{warp}t^*$	0.07	kN/m
$\boldsymbol{E_{fill}t}$	Normal	$E_{fill}t^*$	0.07	kN/m
$\boldsymbol{f_{red,warp}t}$	Normal	$f_{red,warp}t^*$	0.10	kN/m
$\boldsymbol{f_{red,fill}t}$	Normal	$f_{red,fill}t^*$	0.10	kN/m
$\boldsymbol{L_{tb,1-4}}$	Normal	0.50	0.005	m
$\boldsymbol{Q_{snow}}$	Gumbel	0.55	0.30	kN/m²
$\boldsymbol{Q_{wind}}$	Gumbel	0.70	0.35	kN/m²

The variation of length of the turnbuckles is considered as an installation uncertainty which leads to an indirect uncertainty on the geometry of the membrane and the prestress in the membrane.

The stochastic models for the snow load and the wind uplift load are derived from Holicky et al. [10]. Stochastic models of the elastic stiffness of hanging and arching direction, the reduced strength of hanging and arching direction, and the length of the turnbuckles are based on expert advice.

For each design, sets of the considered parameters are generated. Each set contains different values for the same parameter based on the corresponding stochastic model (type of distribution, mean value, coefficient of variation, etc.). For the generation of the sets LHS is used.

3.2. Optimization function

The following optimization function $W(\gamma)$ [11] is used to calibrate the partial factors:

$$W(\gamma) = \sum_{j=1}^{L} w_j(\beta_j(\gamma) - \beta_t)^2 \quad (2)$$

where w_j is the importance of each reference case j, $\beta_j(\gamma)$ is the calculated reliability index for the considered design and β_t is the target reliability index (= 3.8). In this study only one reference case is analysed and formula (1) can be rewritten as followed:

$$W(\gamma) = (\beta_j(\gamma) - \beta_t)^2 \quad (3)$$

The limit state function considered in this study to obtain the reliability index is an Ultimate Limit State function. The function includes the resistance R of the membrane and the effect E, being the stress in the membrane, $z = R - E$ [2]. The resistance and the effect are normally distributed, and the reliability index is calculated as followed:

$$\beta = \frac{\mu_z}{\sigma_z} \quad (4)$$

where μ_z is the mean value of z and σ_z is the standard deviation.

4. Results

The hypar membrane structure is designed according to combinations of the partial factor for prestress, snow load, and wind uplift load. The combinations are made for three different partial factors for prestress (1, 1.2 and 1.35), and thirteen partial factors for snow load and wind uplift load (0.5, 1.0:0.1:2.0, 2.5). The designs are evaluated under normal use. This means that the reliability analysis is done without a partial factor for the prestress and the loads.

For each design the reliability index is calculated considering the hanging and the arching direction separately. Afterwards, the optimization function *W* (equation (3)) is used to find the most suitable combination of partial factors for this hypar membrane structure. In Figure 2, the optimization function for the reliability analysis under snow load is visualised and in Figure 3, the reliability analysis under wind uplift load is visualised. The coloured curves correspond to the *W* values obtained for the structural dominant direction (increase of tension), i.e. regarding the hanging direction under snow load or the arching direction under wind uplift load. The results corresponding to the structural non-dominant direction, i.e. regarding the arching direction under snow load and the hanging direction wind uplift load, are displayed in grey. For the optimization function under snow load and wind uplift load the minimum value *W* of the hanging and the arching direction is retained.

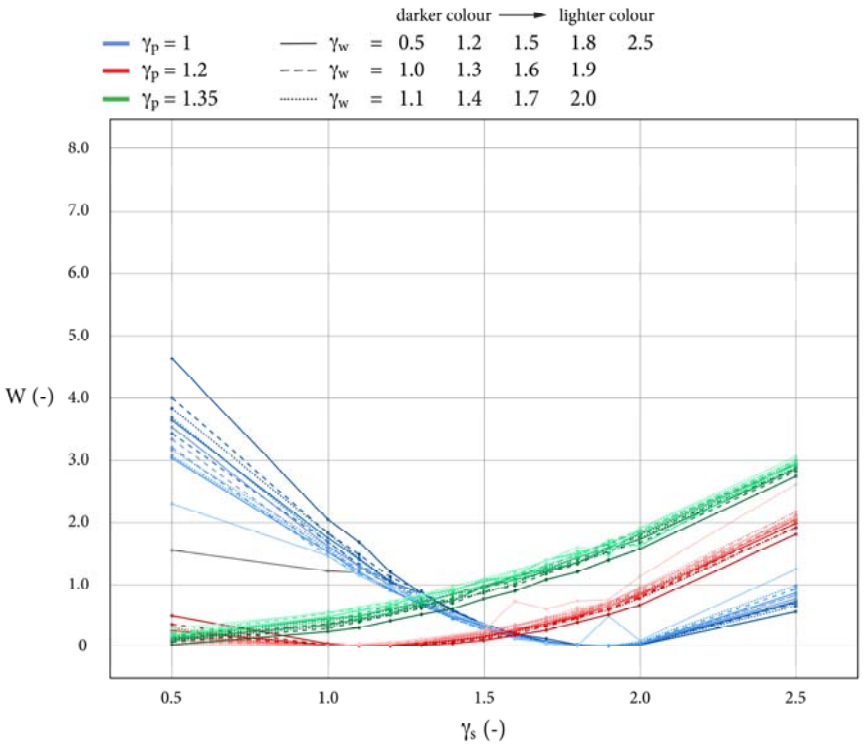


Figure 2: Optimization function under snow load.

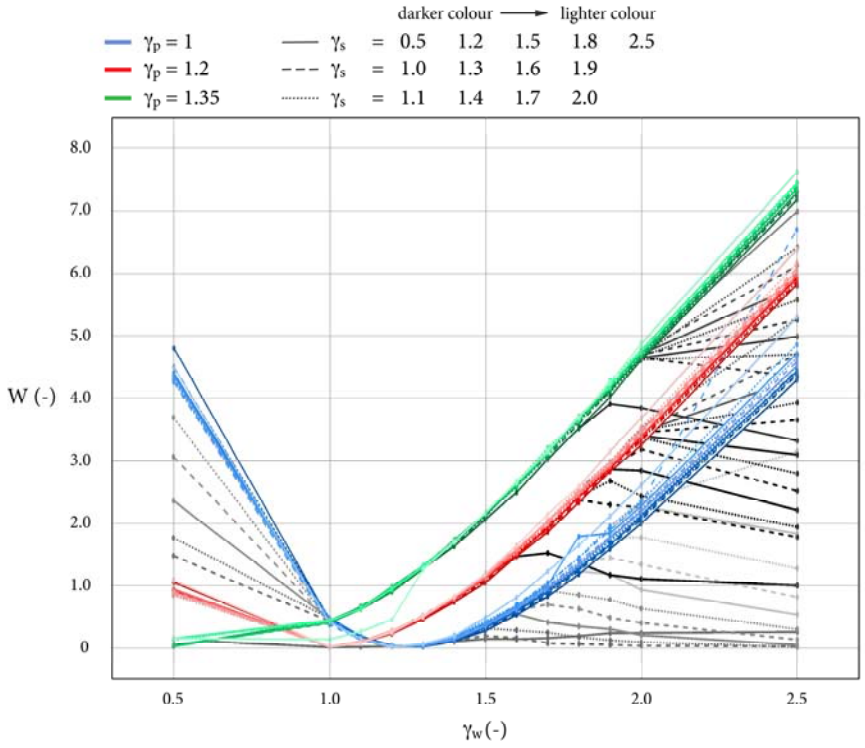


Figure 3: Optimization function under wind uplift load.

The optimization function W(γ) under snow load

Figure 2 contains three distinct groups of curves, blue, red and green curves. Each group represents a different partial factor for prestress for the dimensioning, γ_p = 1, 1.2 and 1.35, respectively. For an increase of γ_s for the dimensioning, the curves γ_p = 1 and 1.2 start high, reach a minimum and increase again. The designs left from the minima fail while the designs right from the minima are over-dimensioned according to the set target reliability index of 3.8. It is noted that the values on the x-axis for γ_s and the names of the curves (curves γ_w) relate to the factor for which the hypar membrane structure is designed. For curves γ_p = 1.35 the minimum would be reached for γ_s < 0.5. For higher values of γ_p the minimum is reached for smaller values of γ_s. The obtained partial factors for the reliability analysis under snow load are given in Table 3. The smallest *W* value (= 0) is obtained for two sets of partial factors: γ_p = 1.0, γ_s = 1.9 and γ_w = 1.1 and γ_p = 1.2, γ_s = 1 and γ_w = 1.7. The structural dominant direction (the hanging direction) is determinant for the smallest *W* value.

The optimization function W(γ) under wind uplift load

On Figure 3, the minimum (*W* = 0.0004) is obtained for γ_p = 1.2, γ_s = 1.0 and γ_w = 1.0. The smallest *W* values for reliability analysis under wind uplift load are given in Table 4. The structural dominant direction (the arching direction) is determinant for the smallest *W* value. For the reliability analysis under wind uplift load, for γ_p = 1, 1.2 and 1.35, a large spread is noticed between the grey curves for higher values of γ_w (γ_p = 1 for γ_w = 1.4 – 2.5, γ_p = 1.2 for γ_w = 1.6 – 2.5, γ_p = 1.35 for γ_w = 1.8 – 2.5). This means that in the structural non-dominant direction (the hanging direction) high stresses can occur under wind uplift load. Also, for the curves γ_p = 1 with γ_w < 1, it is possible that in the hanging direction high stresses exist under wind uplift load.

Table 3: Obtained partial factors with corresponding *W* and *β* values for the reliability analysis under snow load.

Reliability analysis under snow load				
γ_p	γ_s	γ_w	*W* (-)	*β* (-)
1	1.9	1.1	0	3.8
1.2	1.0	1.7	0	3.8
1.35	Minimum not reached			

Table 4: Obtained partial factors with corresponding *W* and *β* values for the reliability analysis under wind uplift load.

Reliability analysis under wind uplift load				
γ_p	γ_s	γ_w	*W* (-)	*β* (-)
1	1.9	1.2	0.0043	3.87
1.2	1.0	1.0	0.0004	3.82
1.35	Minimum not reached			

From the graphs in Figure 3 it is noticed that the partial factor for prestress has pronounced influence on the calibration of the partial factors (blue, red and green curves). Note that the difference between the obtained reliability indices for the different sets of partial factors, shown inTable 3 and Table 4, is small (3.80 until 3.87).

Eventually, both load cases are considered in the optimization function to obtain the set of partial factors for the studied hypar membrane structure.

The optimization function W(γ) considering both load cases

In Figure 4, the results of the optimization function combining both load cases are visualised. This means that the minimum *W* values are retained from both load cases (snow load and wind uplift load) and both directions (hanging direction and arching direction). Like in the reliability analysis under snow load and wind uplift load, the curves γ_p = 1.35 do not reach a minimum in the considered range of partial factors. The minimum *W* values (= 0) correspond to the minimum value obtained for the optimization function under snow load (Table 3) for two sets of partial factors, namely γ_p = 1.0, γ_s = 1.9 and γ_w = 1.1 and

γ_p = 1.2, γ_s = 1 and γ_w = 1.7. The structural dominant direction under snow load (the hanging direction) is determining the smallest *W* value.

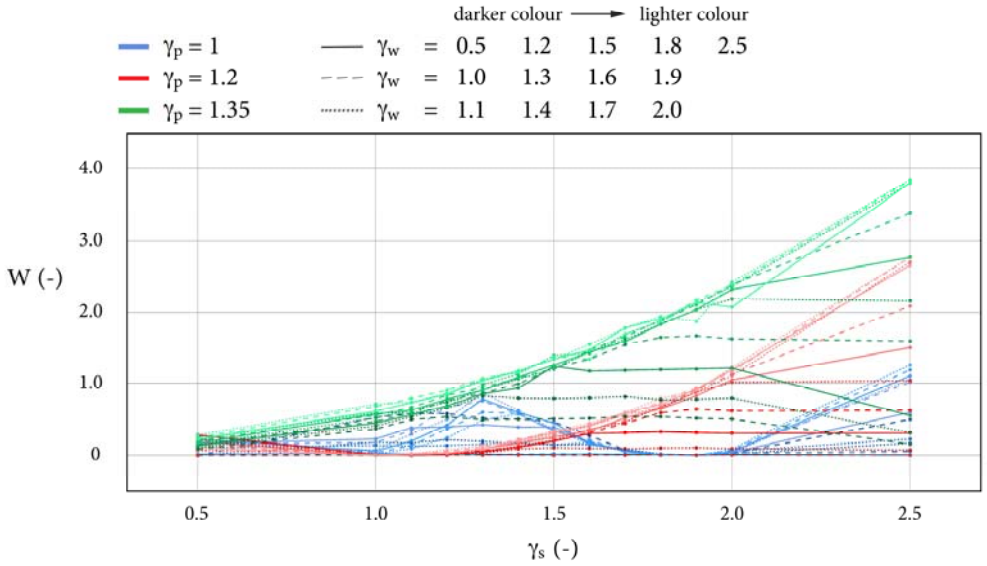


Figure 4: The optimization function considering the minimum *W* value.

Notice that the curves γ_p = 1 (blue curves) do not have one distinct minimum. For γ_s = 0.5 – 1.3, the curves γ_w ascend. The *W* values in this range correspond to the hanging direction under wind uplift load. In the range γ_s = 1.3 – 2.5, the curves γ_w reach a minimum. The *W* values in this range correspond to the hanging direction under snow load.

The obtained partial factor sets, γ_p = 1.0, γ_s = 1.9 and γ_w = 1.1 and γ_p = 1.2, γ_s = 1 and γ_w = 1.7, are specific for the investigated hypar membrane structure. For the calibration of the partial factors for prestress, snow load and wind uplift, more references cases (different rise-to-span ratio, small, medium and large-scale structures, different topologies, …) should be investigated. The results, based on a higher variety of structural shapes, would be more pronounced.

6. Conclusion

In this article a calibration method for the partial factors for prestress, snow load and wind uplift load is proposed and evaluated for a specific hypar membrane structure.

Considering the reliability analysis under snow load, the hanging direction is conclusive for the calibration of the partial factors. For the reliability analysis under wind uplift load, the arching direction is conclusive.

With the reliability analysis under wind uplift load it is found that the hanging direction (the structural non-dominant direction) appears in the graphs representing the optimization function. This means that the membrane stress in the arching direction under snow load and the hanging direction under wind uplift load can be important for the reliability analysis and should be included in the calibration process.

For the calibration of the partial factors for the considered hypar membrane structure, the hanging direction and arching direction of both load cases are taken into account, which results in two partial factor sets: γ_p = 1.0, γ_s = 1.9 and γ_w = 1.1 and γ_p = 1.2, γ_s = 1 and γ_w = 1.7. Note that this is the outcome

for one hypar membrane structure. In order to propose partial factors for the prestress, snow load and wind uplift load, more reference cases should be investigated.

The proposed method to perform the reliability analysis is applicable to other membrane shapes besides the studied hypar membrane structure.

Further research is needed to find partial factors that can be used for a wider scope of membrane structures. More reference cases should be investigated.

References

[1] M. Mollaert and B. Foster, *European Design Guide for Tensile Surface Structures*. TensiNet, 2004.
[2] CEN, 'EN 1990: Eurocode 0: Basis of Structural Design'. European Committee for Standardization, 2001.
[3] N. Stranghöner *et al.*, 'Prospect for European Guidance for the Structural Design of Tensile Membrane Structures', European Commission. Joint Research Centre., JRC Science and Policy Report.
[4] P. D. Gosling, B. N. Bridgens, and L. Zhang, 'Adoption of a reliability approach for membrane structure analysis', *Structural Safety*, vol. 40, pp. 39–50, Jan. 2013.
[5] E. De Smedt, M. Mollaert, L. Pyl, and R. Caspeele, 'Reliability-based analysis of tensile surface structures designed using partial factors', in *Life-Cycle Analysis and Assessment in Civil Engineering: Towards an Integrated Vision*, Ghent, 2019, p. 468.
[6] J. Minte, 'Das mechanische Verhalten von Verbindungen beschichteter Chemiefasergewebe', Thesis, RWTH Aachen, 1981.
[7] DIN, 'Tragluftbauten - DIN 4134'. 1983.
[8] H. O. Madsen, S. Krenk, and N. C. Lind, *Methods of Structural Safety*. Mineola, NY: Dover Publications, 2006.
[9] J. D. Sørensen, I. B. Kroon, and M. H. Faber, 'Optimal reliability-based code calibration', *Structural Safety*, vol. 15, no. 3, pp. 197–208, Sep. 1994.
[10] M. Holicky and M. Sykora, 'Stochastic Models in Analysis of Structural Reliability.', presented at the The International Symposium on Stochastic Models in Reliability Engineering , Life Sciences and Operations Management, Beer Sheva, Israel, 2010.
[11] J. Ching and K.-K. Phoon, 'A quantile-based approach for calibrating reliability-based partial factors', *Structural Safety*, vol. 33, no. 4, pp. 275–285, Jul. 2011.

Proceedings of the IASS Annual Symposium 2019 – Structural Membranes 2019
Form and Force
7 – 10 October 2019, Barcelona, Spain
C. Lázaro, K.-U. Bletzinger, E. Oñate (eds.)

A Showroom with a Mesh Structure in Roppongi, Tokyo: Design and Construction

Yuma SAITO*, Ryo WATADA[a], Takashi OSHIMA*, Takuya KINOSHITA[a], Ikuya HANAOKA*

* Design Department, Tokyo Main Office, Takenaka Corporation
1-1-1, Shinsuna, Koto-ku, Tokyo, Japan.
Email saitou.yuuma@takenaka.co.jp

[a] Research&Development Institute, Takenaka Corporation

Abstract

The Roppongi 7-Chome Project is a small-scale showroom building in Roppongi, Tokyo. The design concept is based on an image of future life and involves a building composed of translucent walls and roofs. With this concept in mind, we designed a space using a structural system called a *mesh structure*. The mesh structure is composed of panels fabricated from steel flat bars, and it forms a lattice shape. The panels are braced to ensure planar rigidity and for reinforcement against buckling. We performed topology optimization for the brace layout considering fabrication constraints, and we ensured that the brace layout within the mesh structure can be automated while reflecting the designer's plans. As a result, the design concept was successfully realized in a short time.

Keywords: Mesh structure, Topology design of bracing, Translucent wall-like panels

1. Introduction

The Roppongi 7-chome Project is a small-scale showroom building that was planned in Roppongi, Tokyo (Figures 1 and 2); this building is being used to promote electric cars. Our design concept, which is based on an image of future life, is a building that is composed of translucent walls and roofs. We have specifically sought to create a new spatial effect using wall panels of translucent aluminum filled with fine holes that produce a gradated pattern by gradually changing the hole layout. The building comprises a tubular volume penetrating a house-shaped volume (Figures 3 and 4). The exterior and interior surfaces of both the house-shaped and the tubular volumes are covered with aluminum. The indoor space is restricted to the interior of the tubular volume; the interior of the house-shaped volume is a semi-outdoor space.

This service period of the building is about two years, and a short execution period of 13 months (from design to the completion of construction) was required.

Copyright © 2019 by Yuma SAITO, Ryo WATADA, Takashi OSHIMA, Takuya KINOSHITA, Ikuya HANAOKA
Published by the International Association for Shell and Spatial Structures (IASS) with permission.



Figure 1: External appearance (Photo: Inoue Noboru)

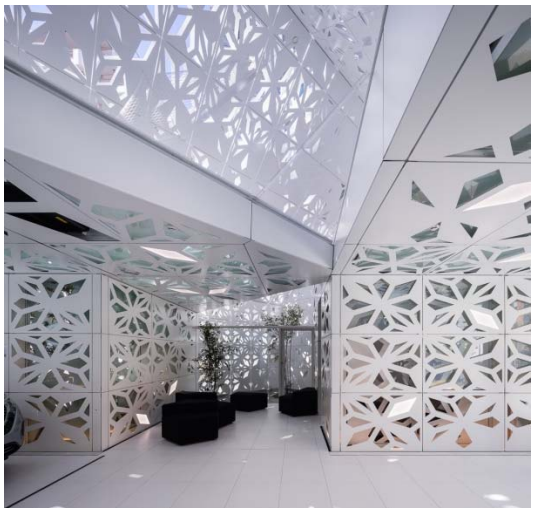


Figure 2: Internal appearance (Photo: Inoue Noboru)

Table 1: Architectural overview

Building site	Roppongi, Tokyo
Design and construction	Takenaka Corporation
Total floor area	88.1m^2
Height	8.3m
Structure type	Steel construction
Completion date	28 February 2019

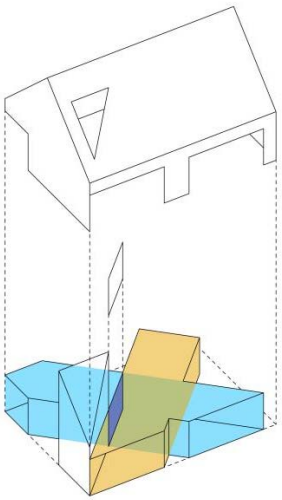


Figure 3: Building configuration

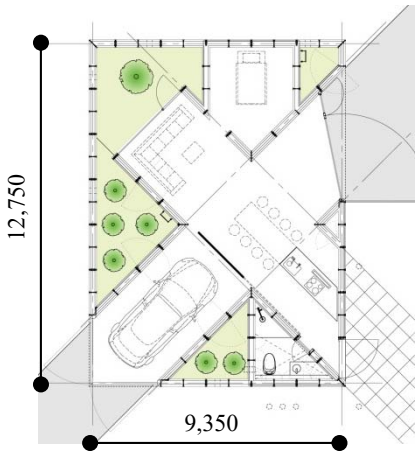


Figure 4: Floor plan of first floor

2. Structural concept

As per the design concept, we considered creating a structure comprising translucent wall-like structural elements; although reinforced concrete box-shaped wall structures and cross laminated timber (CLT) panel constructions are examples of structures fabricated with wall-like elements, fabricating translucent walls in these structures is difficult. Therefore, we considered designing a structure with translucent wall-like panels using steel frames.

As shown in Figures 5 and 6, we fabricated a panel by assembling steel flat bars (structural member) in a lattice shape based on the pattern of the aluminum panel (non-structural member) to form a *mesh structure*, which would constitute the entire building. The flat bars are disposed along the strong axis in the out-of-plane direction of the panel. As the projected area of the mesh structure was very small, it would function as a translucent wall and thus the design concept would be realized.

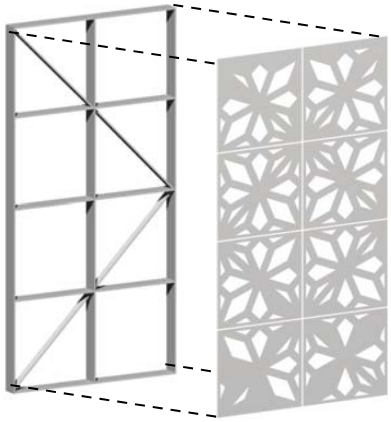


Figure 5: Conceptual diagram



Figure 6: Mesh structure panel after fabrication

3. Characteristics of the mesh structure

Steel flat bars are not generally used as compressed members because they tend to buckle in the out-of-plane direction. However, in the proposed mesh structure, the steel flat bars are arranged in the form of a lattice with a fine pitch, and braces are placed appropriately to stiffen the bars in the direction of the weak axis; this enables increasing the allowable compressive stress (Figure 7). Therefore, these flat bars arranged in the form of a lattice can be used as compressed members, which makes it possible to build the entire structure using only flat bars. Further, because flat bars are arranged in a fine pitch in the mesh structure, they can also be used as a finishing base; therefore, an additional secondary steel frame member—to be used as the finishing base—is not required.

The present construction has a basic lattice of 850 mm × 850 mm, and the sizes of the flat bars are mainly 16 mm × 150 mm and 19 mm × 150 mm.

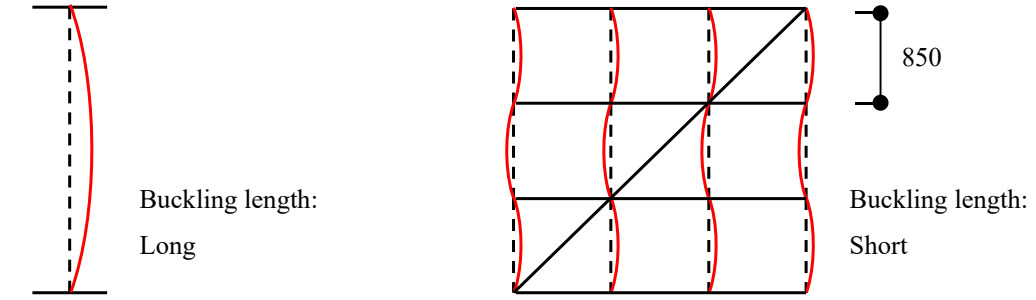


Figure 7: Buckling length of mesh structure

4. Jointing system of mesh structure

The mesh structure panels are manufactured by factory welding the flat bars. As shown in Figure 8, notches are cut at intersections in the flat bar, and the flat bars are inserted into each other and joined using the *cross notch joint* weld.

Panel-to-panel jointing is performed using high strength bolts at the site. Since the panels may contain manufacturing defects like size deviations because of problems such as welding distortion, we designed a *gap joint system* that can absorb such defects by providing a clearance of 10 mm between panels and bolting them with a filler plate in between, as shown in Figure 9.

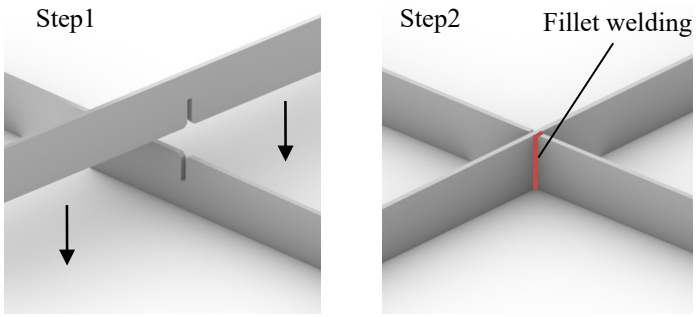


Figure 8: Cross notch joint

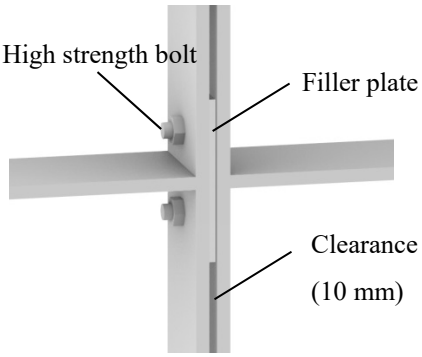


Figure 9: Gap joint system

5. Structural planning using mesh structure

As noted previously, the building structure comprises a tubular volumes penetrating through a house-shaped volume (Figure 10); the vertical force of the roof generates a thrust on the top of the walls, widening the roof because it is house shaped. In the mesh structure, a pin joint is placed between the panels, and hence, the roof is easily opened by thrust. However, in our proposed structure, the tube-like volume (inner tube) counters the force of the thrust and prevents the roof from opening, which stabilizes the building frame. Braces are placed at both the outer frame and the inner tube to bear the seismic force.

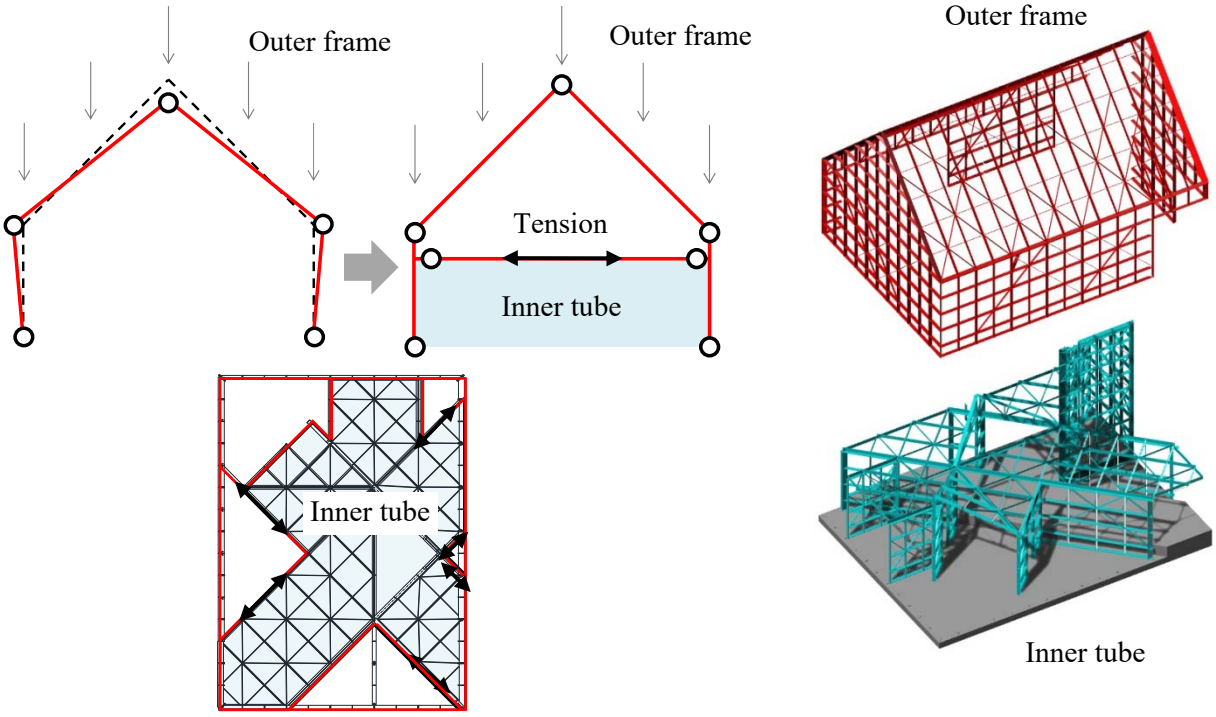


Figure 10: Structure of the frame

6. Panel division

The mesh structure is constructed by first assembling the panels of the wall and then those of the roof. Panel division considerably affects the workability of panel erection; it also affects the structural analysis because the bolt joints between the panels are pin joints. Therefore, panel division was decided by coordinating with the constructor at the design stage (Figure 11). Owing to construction

requirements, the panels were divided to improve transportation efficiency; further, to ensure that the panels are as self-supporting as possible during erection, corner panels were fabricated as L-shaped panels.

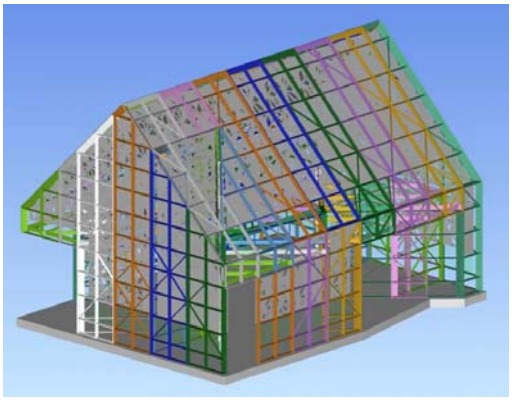
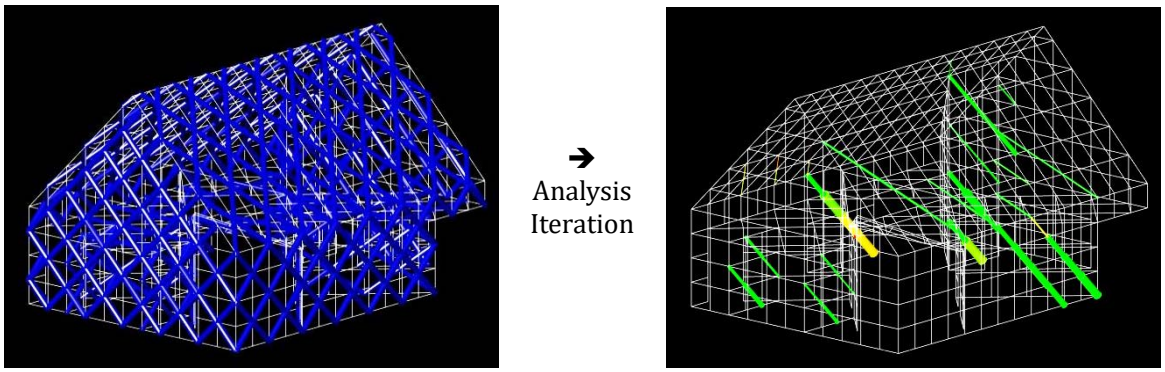


Figure 11: Panel division

7. Automation by computational design

Topology optimization was utilized for designing the layout of the braces of the building. As shown in Figure 12, a brace layout was generated through iterative calculations using a model wherein braces were placed at all possible locations (Figure 12(a)); penalties were gradually assigned to small-stress braces, which were then deleted (Figure 12(b)).



(a) (b)

Figure 12: Automation of brace layout

While automating the brace layout, the structural designer's idea is reflected by setting a rule that considers the manufacturability of the steel frame. Vertical members at the corners of the building are inclined at an angle of 45° to the axis of the member; therefore, fitting the braces in these parts is difficult, as can be seen from Figure 13. Thus, the designer suggested avoiding placing braces at the corners of the building, and accordingly, we set a rule that assigns a large penalty during topology optimization and tends to avoid braces in the corners of the building (Figure 14).

Thus, we devised a structure wherein although the placement of braces in the corners of the building was basically avoided, braces were still placed at corners where they were indispensable from a mechanics point of view. Topology optimization was performed by creating a program using Grasshopper (For details regarding the optimization method, refer to the continuing paper subtitled “Topology design of bracing”).

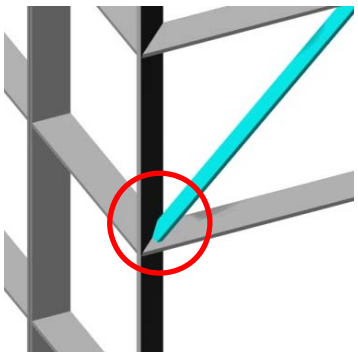


Figure 13: Fitting diagram of a brace at a corner

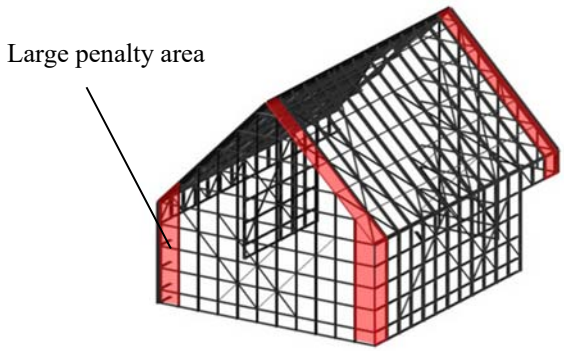


Figure 14: Large penalty area

Once the brace layout was decided, the thickness of the flat bars constituting the panel was determined by cross-section optimization using Grasshopper and Karamba. The optimized cross section was directly converted into a BIM model using Grasshopper Tekla Live Link and delivered to the constructor. Using this design flow, we could complete the frame plan and cross section design in a very short time after deciding the basic architectural plan and we could communicate the design contents to the constructor (Figure 15).

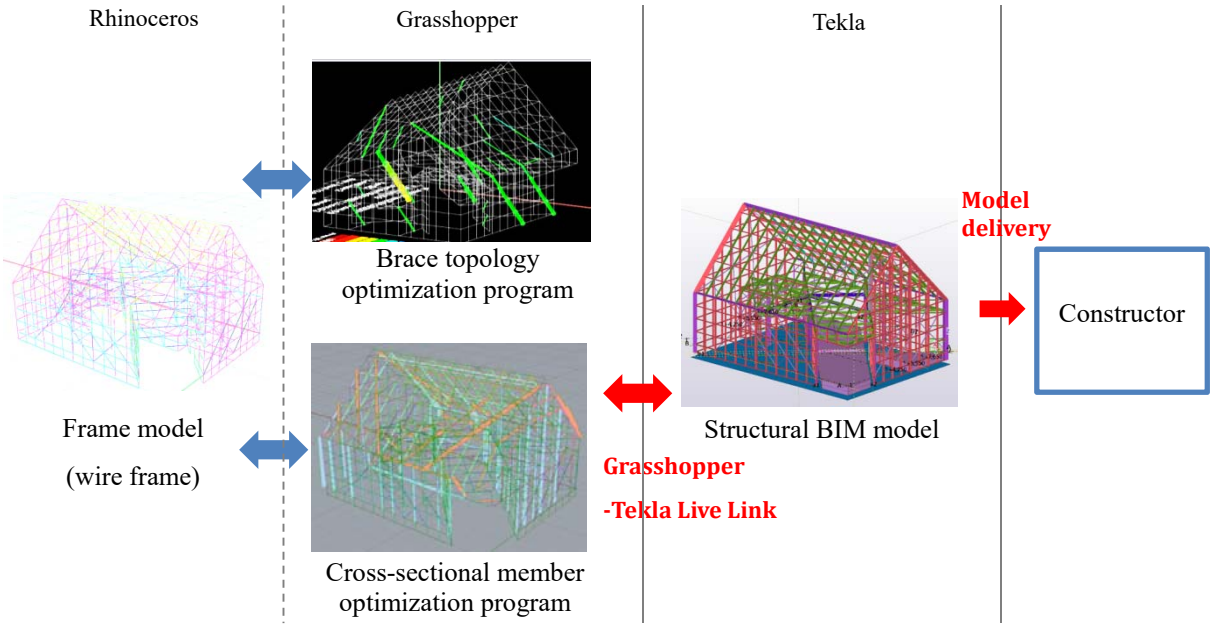


Figure 15: Flow of design automation flow

8. Review using VR

The design content was reviewed using virtual-reality (VR) devices. The details were verified by walking around in the structural model wearing VR goggles (Figure 16). Problems regarding the details of parts with intricately connected panels could be identified and solved at the design stage.

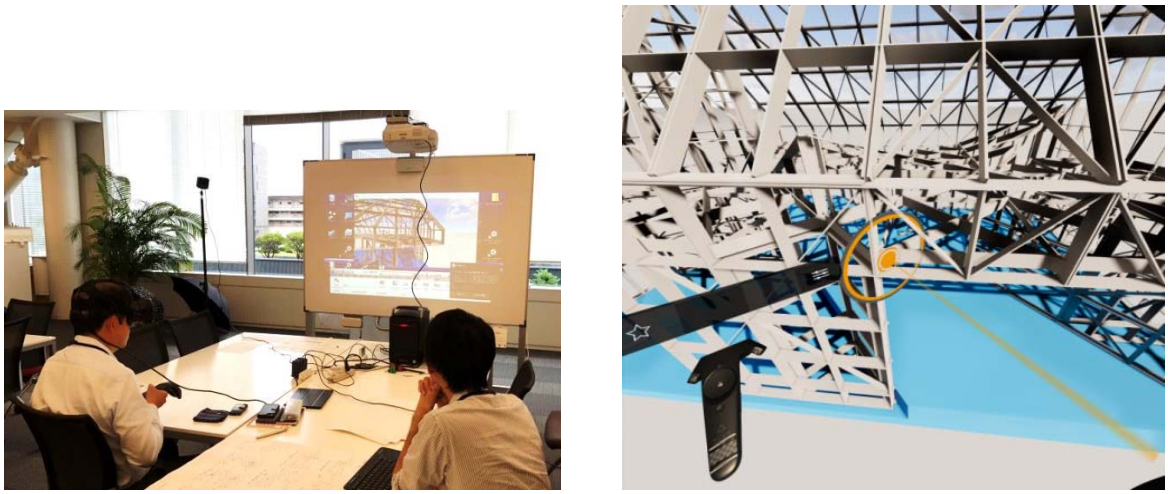


Figure 16: Review using VR

9. Construction

Since the steel frame could be constructed on site using only bolt connections, the construction was efficiently completed in a short period of time (Figure 17). After construction, the mixed-reality (MR) device HoloLens (Figure 18) was used for inspecting the structure. The frame design model was displayed on the HoloLens and was superimposed on the actual frame, thus verifying that the parts had been installed as per the design. In addition, a model with color codes for the thickness and material of each member was prepared and used to confirm that the thickness and material were in accordance with the design (Figure 19).



Figure 17: Construction process



Figure 18: HoloLens on construction site

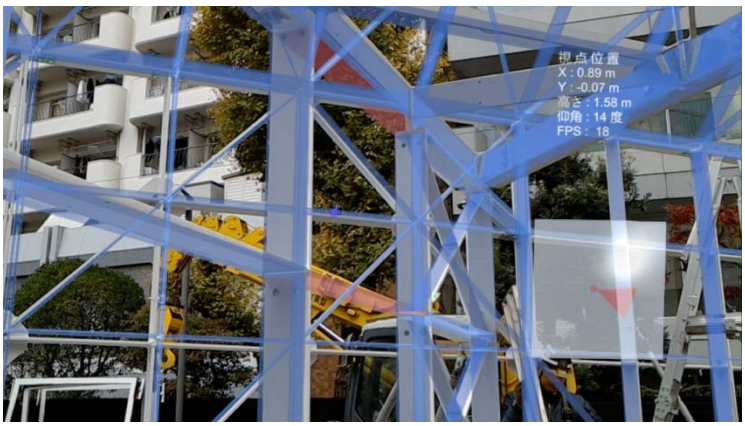


Figure 19: Superimposed view through the HoloLens

10. Conclusion

We devised a structural design using a mesh structure and successfully realized an architectural concept for constructing an entire building with translucent elements (Figure 20). In addition, automated optimization and design and construction using VR and MR technology enabled us to complete the design and construction in a short time.



Figure 20: Internal appearance (Photo: Inoue Noboru)

Proceedings of the IASS Annual Symposium 2019 – Structural Membranes 2019
Form and Force
7 – 10 October 2019, Barcelona, Spain
C. Lázaro, K.-U. Bletzinger, E. Oñate (eds.)

A Showroom with a Mesh Structure in Roppongi, Tokyo: Topology Design of Bracing

Ryo WATADA*, Yuma SAITO [a], Takuya KINOSHITA*, Takashi OSHIMA [a]

*Research & Development Institute, Takenaka Corporation
5-1, 1-chome, Otsuka, Inzai-shi, Chiba, Japan.
Email watada.ryou@takenaka.co.jp

[a] Design Department, Tokyo Main Office, Takenaka Corporation

Abstract

In this paper, we propose a method to determine the layout of diagonal braces in a lattice-type grid composed of vertical and horizontal materials. To determine the placement of bracing, we used the fully stressed design method considering the thickness of the braces, which are proportional to the areas of them, as a variable, the value of which keeps getting updated until the tensile stress generated in all the braces reaches the specified target tensile stress. To obtain a clear and realistic placement, upper and lower limits were placed on the thickness applying power-law penalization. The differences in the difficulties in the placement of bracing for manufacturability reasons are also considered by changing the rate of increase of the penalties mentioned above. This method was applied to the Roppongi 7-Chome Project, a small-scale showroom in Roppongi, Tokyo.

Keywords: Mesh structure, Topology design of bracing, Fully stressed design, conceptual design

1. Introduction

Many methods have been proposed for applying optimizing structural design. Examples include a method based on mathematical programming such as the Solid Isotropic Material with Penalization (SIMP) method [1] and the homogenization method [2], and evolutionary methods such as the Evolutionary Structural Optimization (ESO) method [3]. Although a fully stressed design is an algorithm that pioneered the study of these structure optimizations and is distinguished from optimization methods used for minimizing strain energy under constrained capacity conditions, it is a method that offers designers many suggestions from an easily understandable process. In particular, the nature of the fully stressed design's simple and easily understandable process is highly advantageous for practical building designs, where a structural design that is easily understandable for designers and third parties is necessary while reflecting the unique constraints of each project with limited designing time.

In this study, we developed a method based on a fully stressed design that uses brace plate thickness as a variable for the topology design of bracing members in current construction projects. Here, a penalty parameter [4] was introduced to the fully stressed design to establish placement priority owing to reasons such as setting the upper and lower limit values of the brace plate's thickness and workability, which are constraints in practical design. Through the method proposed herein, the need for a bracing configuration that satisfies the abovementioned constraints are shown in a numerical example.

The method proposed herein was applied in the Roppongi 7-Chome Project (opened in March 12, 2019). For details of the project, please refer to the continuing paper subtitled "Design and Construction". It is noteworthy that although this development was intended to be applied to the same project, it can also be applied to any general project.

Copyright © 2019 by Ryo WATADA, Yuma SAITO, Takuya KINOSHITA and Takashi OSHIMA
Published by the International Association for Shell and Spatial Structures (IASS) with permission.

2. Formularization

2.1. Topology design of bracing

Consider the grid-type frame in the XY-plane shown in Fig. 1. In the frame shown in Fig. 1, point A is a pin support, points B, C, and D are roller supports that restrict movement in the Y-direction, and load P is applied to point C in the X-direction as an external force. Let us consider a section within the frame panel as shown in Fig. 1(b), and the issue of placing braces for both end pin joints that are effective only for the tensile axial force. The number of diagonals of all panels on which braces can be placed is denoted by m, and the number of each diagonal position is denoted by i $(i = 1, \dots, m)$. The width and thickness of the braces placed on each position i are b_i and t_i, respectively. However, diagonal lines with no placed braces may appear. In these cases, $t_i = 0$. Hence, an arbitrary bracing configuration (topology design) can be expressed with t_i.

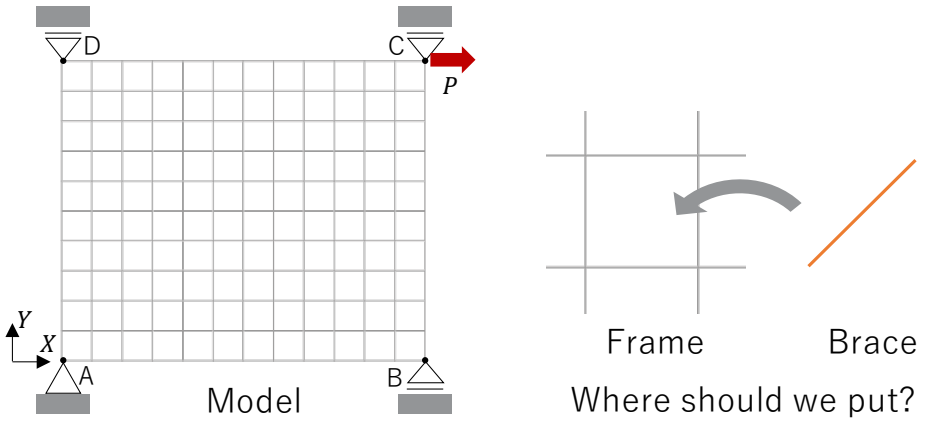


Figure 1: Topology design of bracing for flat grid-type frames

2.2. Formularization using fully stressed design method

The fully stressed design method is a classical method to determine the bracing configuration mentioned in the previous section. The fully stressed design method is an algorithm that finds the arrangement of members that produce a uniform stress in all members through iterative calculations. The condition in which all members exhibit uniform stress can be regarded as an ideal state with no wasted members. The method repeatedly updates the thickness of the plate such that the degrees of stress for all members converge to the predetermined target stress degree σ_T. Here, $\sigma_T(>0)$ is the target value of the axial stress in the tensile direction that occurs in each brace, and the thickness of each brace plate t_i is updated and converged repeatedly such that the axial stress level generated in all positions of the brace σ_i $(i = 1, \dots, m)$ conform with σ_T. Here, the variable $k = 0,1,2, \dots$ that expresses the number of repeated steps is introduced, and the plate thickness and axial stress of member i in step k are $t_i^{[k]}$ and $\sigma_i^{[k]}$, respectively. The updated step of the plate thickness in each position i is expressed in the following equation.

$$t_i^{[k+1]} = \begin{cases} t_i^{[k]} \left(\dfrac{\sigma_i^{[k]}}{\sigma_T} \right)^{\alpha} & \left(\sigma_i^{[k]} > 0 \right) \\ 0 & \left(\sigma_i^{[k]} \leq 0 \right) \end{cases} \quad (k = 0,1,2, \dots) \tag{1}$$

Here, α is called the mitigation coefficient and it is set to satisfy $0 < \alpha \leq 1$.

2.3. Introduction of penalty parameter for fully stressed design method

In the bracing design that is ultimately determined by the fully stressed design, although all braces bear the same degree of tensile stress, the plate thicknesses vary in size. These include those that are either excessively thick or thin to be manufactured realistically. Therefore, in this study, when braces are placed at a certain position ($t_i > 0$), a constraint is considered in which the plate thickness is a value between a predetermined upper limit t_i^U and a lower limit t_i^L. That is, the brace plate thickness t_i in all candidate positions $i(i = 1, \ldots, m)$ shall satisfy either of the following two equations.

$$t_i = 0 \tag{2a}$$

$$t_i^L \le t_i \le t_i^U \tag{2b}$$

To determine the bracing configuration in which the plate thickness (obtained at the end) satisfies either equation (2a) or (2b) in the fully stressed design, an effective plate thickness $t_{i,\mathrm{eff}}^{[k]}$ is introduced in the stress analysis using the following example for each bracing plate thickness herein $t_i^{[k]}$.

$$t_{i,\mathrm{eff}}^{[k]} = \begin{cases} \left(\dfrac{t_i^{[k]}}{t_i^L}\right)^{p-1} t_i^{[k]} & \left(0 < t_i^{[k]} < t_i^L\right) \\ t_i^{(k)} & \left(t_i^L \le t_i^{[k]} < t_i^U\right) \\ t_i^U & \left(t_i^U \le t_i^{[k]}\right) \end{cases} \tag{3}$$

Here, $p(\ge 1.0)$ represents the penalty parameter [4]. The relationship between the fixed plate thickness $t_i^{[k]}$ and effective plate thickness $t_{i,\mathrm{eff}}^{[k]}$ in equation (3) is shown in Fig. 2. As shown in Fig. 2, when $p = 1.0$, the relationship between $t_i^{[k]}$ and $t_{i,\mathrm{eff}}^{[k]}$ is a straight line throughout the entire range in $0 < t_i^{[k]} < t_i^{\mathrm{U}}$, and both values are consistent. However, when p becomes larger, $t_{i,\mathrm{eff}}^{[k]}$ becomes smaller than $t_i^{[k]}$ in the $0 < t_i^{[k]} < t_i^L$ range.

In the fully stressed design method, as large fluctuations in stress and plate thickness appear in each position during the initial step, adding a penalty from the initial step using the first equation in equation (3) may result in unstable calculations that will not converge to a rational solution. Therefore, in this study, the value of penalty parameter p was set to increase gradually from 1.0 as the fully stressed design step k increases. The penalty in step k is denoted as $p^{[k]}$, and is increased gradually at every Δp according to $p^{[k+1]} = p^{[k]} + \Delta p$ from $p^{[0]} = 1.0$ at the start of the iterative calculation. Based on the above, the algorithm of the revised fully stressed design method is shown in Fig. 3. Here, the contents added herein from the original fully stressed design method are shown in red.

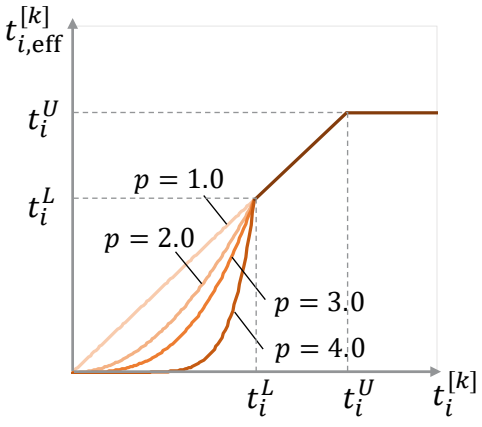


Figure 2: Upper and lower limit values of plate thickness considered with penalty parameter

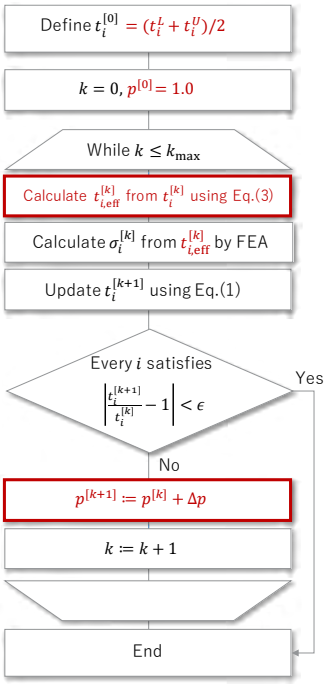


Figure 3: Revised fully stressed design method

2.4. Setting placement priority

In the structure design, it is necessary to arrange the members while considering the ease of construction other than mechanical properties. For example, it is desirable to avoid the easy placement of members in positions that would complicate construction as shown in Fig. . Similarly, the places that we wish to avoid configuring as much as possible in comparison to a normal part are herein defined as a "deprioritized part". The difference in priority for the member placement of a normal part and a deprioritized part can be expressed by changing the penalty step width Δp of both members. In this case, step width Δp_i that corresponds to the deprioritized member i should be made relatively larger in contrast to a normal part. Hence, a deprioritized part exhibits a sharper penalty increase compared with that of a normal part, resulting in the members being eliminated first (Fig. 4). However, even at a deprioritized position, some of the members will not be eliminated regardless of the Δp_i value if a large plate thickness exceeding t_i^L is required from the first iteration.

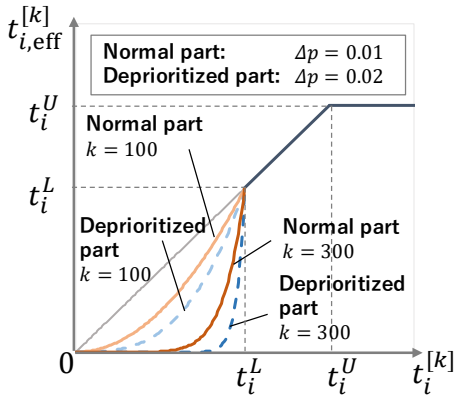


Figure 4: Placement priority is considered by setting multiple penalty-parameter increment sizes

3. Example analysis

3.1. Numerical example 1

As a numerical example, the method is applied to the model in Fig. 1. The units used hereinafter are N, mm, or a combination thereof, and their expressions are omitted in the text and figures. The load is set to $P = 200 \times 10^3$. Additionally, a downward-sloping bracing configuration with an applied compressive force when a load is applied is removed in advance for simplicity. Therefore, the number of braces m is the same as the number of panels, 120. The width of the bracing b_i is 75 for all braces. The upper and lower values of the plate thicknesses are $t_i^L = 6.0, t_i^U = 16.0$ $(i = 1, \ldots, m)$, respectively, and are established with the initial step plate thickness $t_i^{[0]} = (t_i^L + t_i^U)/2 = 11.0$. The target value of the axial stress that the brace bears is $\sigma_T = 50$ in all braces. The grid member is a flat bar with dimensions 150×19.0 and is placed such that the cross section of the weak axis is orthogonal to the plane surface. The end of the flat bar is a pin joint. The mitigation coefficient α is 0.6, and the penalty parameter increment Δp is 0.01. Rhinoceros and its plugin grasshopper [5] are used in the coding, and Karamba 3D Ver. 1.3.1 (grasshopper's plugin) [6] is used in the structure analysis. It is noteworthy that to maintain numerical stability during structure analysis, the microscopic plate thickness $t_{i,\mathrm{eff}}^{[k]} = 0.1$ is considered as a dummy member even at the position of the eliminated brace.

The results of the analysis are shown in Fig. 5. Here, Figs. 5(a), (b), and (c) show the bracing configuration and the axial stress load for each brace at steps $k = 0$, $k = 10$, and $k = 200$. It is noteworthy that the bracing configuration is cylindrical with a radius proportional to the plate thickness of each brace, the plate thickness of each arranged brace is labeled in its brace position, the

axial stress load for each arranged brace is expressed in a color contour, and only braces that satisfy $t_i^{[k]} \geq 0.2$ are shown in each graph in Fig. 5. Additionally, Figs. 6 (a), (b), and (c) show the distribution diagrams at $k = 0$, $k = 10$, and $k = 200$, with the horizontal axis representing the brace plate thickness satisfying $t_i^{[k]} \geq 0.2$, and the vertical axis representing the axial stress, and shall be called $t - \sigma$ maps. The red line in the same graph connects two points together, i.e., (t_i^L, σ_T) and (t_i^U, σ_T). The objective of the method proposed herein is to determine the bracing configuration such that the distribution of the plate thicknesses and tensile stress loads for all braces are positioned above this line.

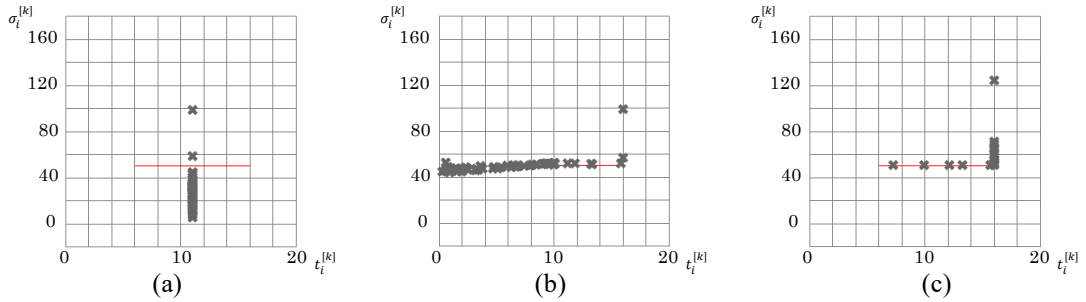
According to Fig. 5(a), in the initial step $k = 0$, $t_i^{[0]} = 11.0$ for all positions, the axial stresses are large in the areas surrounding the diagonal line and become smaller as the distance from the line increases, thus rendering the distribution less uniform. This can be confirmed in Fig. 6, where the plotted points are aligned vertically. In Figs. 5(b) and 6(b) where iterative calculations were performed 10 times, although the axial stress is approximately 50, which is similar to σ_T, it primarily includes those that are less than $t_i^L = 6.0$ in the plate thickness distribution. Contrastingly, in Fig. 5(c) where the max k value is $k = 200$, braces with plate thicknesses less than t_i^L are eliminated owing to the effects of the penalty parameter, thus leaving behind only braces surrounding the diagonal line. These plate thicknesses are contained between the predetermined upper and lower limit values $t_i^L = 6.0$ and $t_i^U = 16.0$.

Additionally, it can be confirmed that the stress is maintained at a value close to the target $\sigma_T = 50$ (except for one portion). This can be confirmed in Fig. 6(c), where each of the points is generally contained in the range of the target red line. Although it can be confirmed from Fig. 5 that a large axial stress is generated locally in the vicinity of points A and C, it is owing to the upper limit value t_i^U set to the plate thickness. In the actual design, it is desirable to establish separate design considerations for members with these locally generated large axial stresses.



(a) (b) (c)

Figure 5: Numerical example 1: Distribution of brace plate thickness and axial stress in each step; (a)$k = 0$, (b) $k = 10$, (c) $k = 200$



(a) (b) (c)

Figure 6: Numerical example 1: Distribution of brace plate thickness $t_i^{[k]}$ and axial stress $\sigma_i^{[k]}$ in each step ($t - \sigma$ map); (a)$k = 0$, (b) $k = 10$, (c) $k = 200$

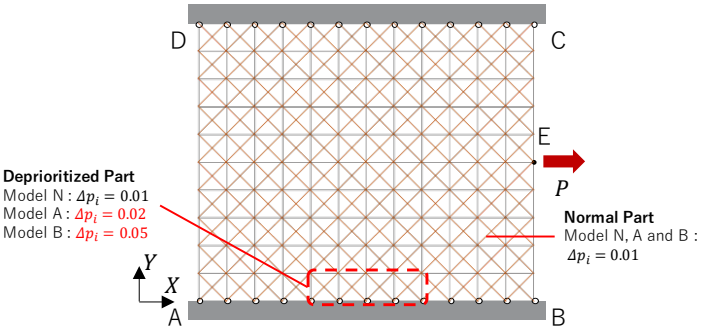
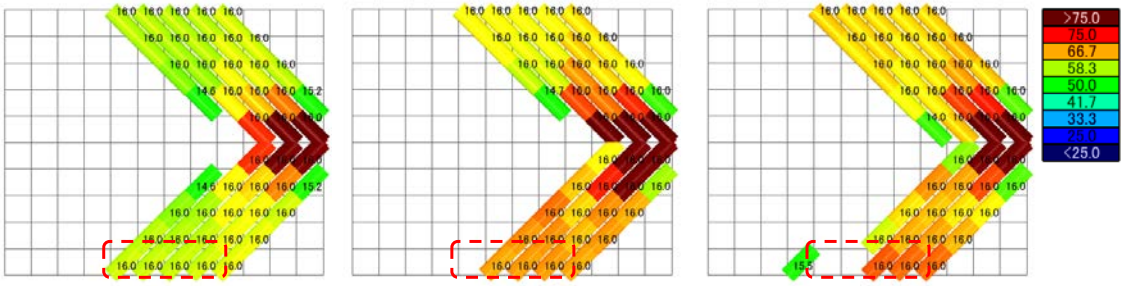


Figure 7: Two-fixed-sides model. Here, the position of the reduced placement priority is shown with a dotted red line.

Table 1: Table of other data

Number of braces	m	240
Brace width	b_i	75
Upper brace plate thickness limit	t_i^U	16
Lower brace plate thickness limit	t_i^L	12
Load	P	500×10^3
Target axial stress value	σ_T	50
Cross section of grid member		FB-150×19
Mitigation coefficient	α	0.6



(a) (b) (c)

Figure 8: Difference in results owing to consideration of placement priority; (a) Model N, (b) Model A, (c) Model B.

3.2. Numerical example 2

Next, we consider a model with two pin-supported vertical sides, as shown in Fig. 7. Here, we considered reducing the brace placement priority to be lower than the normal part at the positions within the dotted red frame in Fig. 7, and examined three cases (Models A, B, and N) against $\Delta p_i = 0.01$ for the normal part. The penalty parameters at the positions within the dotted red frame are 0.02 for Model A, 0.05 for Model B, and 0.01 (undetermined placement priority) for Model N. Other data are shown in Table 1.

The results of the bracing configuration for Models N, A, and B when $k = 200$ are shown in Fig. 8. In Model N where the placement priority is undetermined according to Fig. 8(a), a shape is obtained in which the top and bottom are symmetrical. Contrastingly, in Model A of Fig. 8(b), the brace with deprioritized parts contains one less than that of the same position in the upper region. In Model C of Fig. 8(c), the priority is even lower, resulting in even fewer braces within the dotted red frame.

4. Application in Roppongi Project

The method was applied in the Roppongi 7-Chome Project. The building according to Fig. 9 is a three-dimensional structure in which the surfaces of the outer walls, roof, inner walls, and floor are formed with grid panels using flat bars. The method was applied to determine the bracing configuration required to resist horizontal forces during an earthquake.

A horizontal seismic force is set in four directions (±X and ±Y directions) as an external force where seismic coefficient is 0.3. The determined bracing configuration is superimposed using the method for each direction, and the final bracing configuration is determined. Additionally, because braces in the corner positions shown in Fig. 10 are difficult to construct, as shown in Fig. 11, the placement priority is lowered and the penalty parameter increment for these positions are set to twice that of a normal part. Other data are shown in Table 2.

Figs. 12 (a)–(d) show the results of the brace configuration and $\sigma - t$ map at steps $k = 1$ and $k = 200$ for each loading direction. As shown in Fig. 12, a clear bracing configuration is obtained in each direction. The bracing that extend from the wall surfaces to the roof surfaces were obtained by analyzing the entire structure as one body. Fig. 13 shows the results of the superimposed bracing configuration obtained in each direction. Based on these results, the configuration used in the actual design was decided, as shown in Fig. 14.

5. Conclusion

The primary conclusions of this study are as follows:

1. The bracing configuration design method was proposed in a grid-type frame that used a fully stressed design. In this method, the bracing plate thickness obtained in the end can be maintained within specified upper and lower limit values by introducing penalty parameters in the fully stressed design.

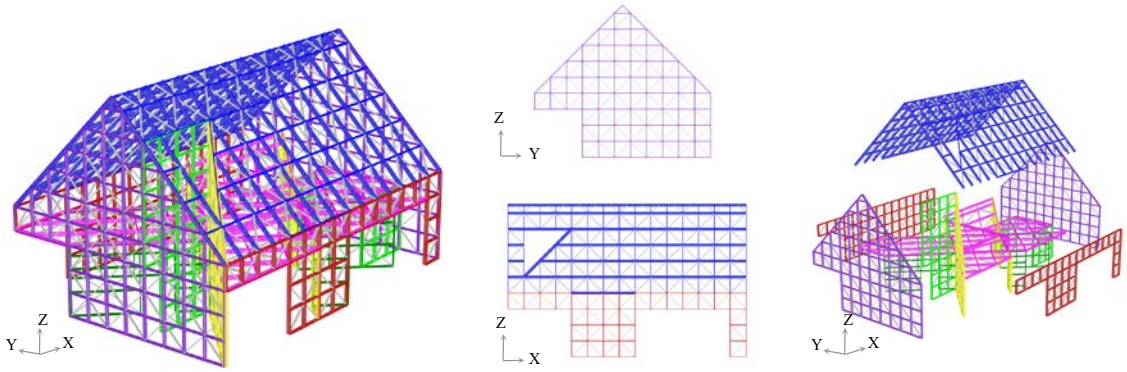


Figure 9: Application in Roppongi Project; (a) Model image (b) Elevation view (c) Grid walls, roof and floor

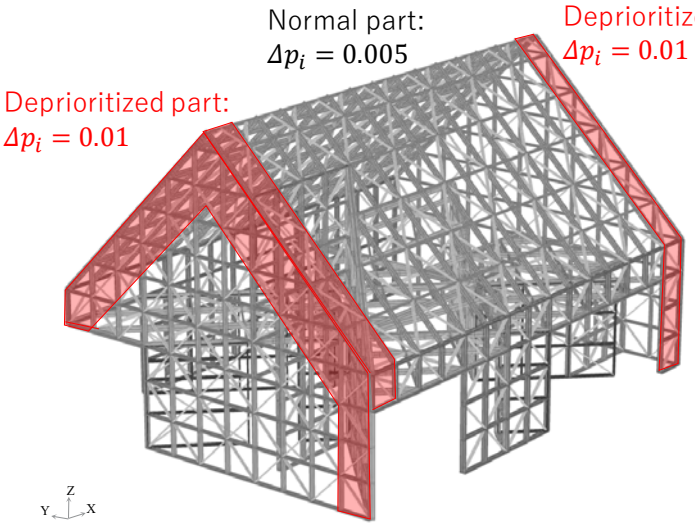


Figure 10: Setting placement priority

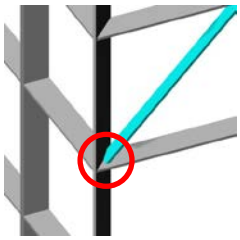


Figure 11: Position where construction is difficult

Table 2: Table of other data

Number of braces	m	549
Brace width	b_i	75
Upper brace plate thickness limit	t_i^U	16
Lower brace plate thickness limit	t_i^L	6, 8 (outer walls) 2 (roof, inner walls) 1 (floor)
Target axial stress value	σ_T	50
Cross section of grid member		FB-150×19
Mitigation coefficient	α	0.6

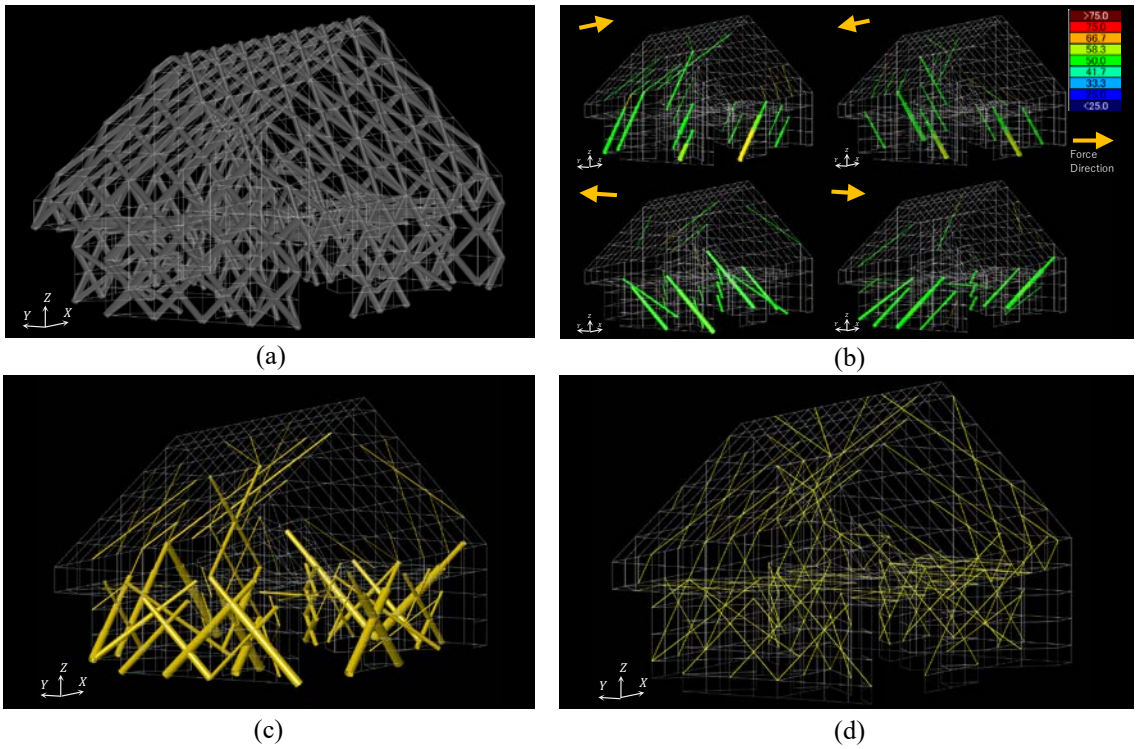


Figure 12: Topology design of bracing; (a) Initial state of the analysis, (b) Aanalyzed results of configuration, (c) Obtained bracing, (d) Configuration used in actual design

2. By changing the increased speed of the penalty parameters in each member position, the member configuration priority could be set.

3. This method was applied in the Roppongi 7-Chome Project. By utilizing this method, we could obtain the possible manufacturing range of the plate thickness while considering construction difficulty, and efficiently determine an effective bracing configuration against external forces.

References

[1] M. P. Bendsøe and O. Sigmund, *Topology optimization : theory, methods and applications,* Springer, 2003.

[2] M. P. Bendsøe and N. Kikuchi, "Generating Optimal Topologies in Structural Design Using a Homogenization Method", *Computer Methods in Applied Mechanics and Engineering*, Vol. 71, pp. 197-224, 1988.

[3] Y. M. Xie and G. P. Steven, "A simple evolutionary procedure for structural optimization", *Computers and Structures*, Vol. 49, pp. 885-886, 1993.

[4] M. P. Bendsøe, "Optimal shape design as a material distribution problem.", *Structural and Multidisciplinary Optimization*, Vol. 1, No. 4, pp. 193-202, 1989.

[5] Robert McNeel & Associates, *RHINO USER GUIDE,* Jul. 2015.

[6] C. Preisinger, *Karamba User Manual*, Oct. 2016.

Proceedings of the IASS Annual Symposium 2019 – Structural Membranes 2019
Form and Force
7 – 10 October 2019, Barcelona, Spain
C. Lázaro, K.-U. Bletzinger, E. Oñate (eds.)

Ariake Arena - Seismically-isolated Large-Space Roof Structure -

Yuki HAMADA*, Masahiro HOSHINO*,Masanori SAKATA*,Sou YONEDA*,Masaki TABEI*,
Hiroshi ITO[a], Masari KAWAI[a]

* Takenaka Corporation
1-1,1-chome, Shinsuna, Koto-ku, Tokyo, Japan
hamada.yuuki@takenaka.co.jp

[a] KUME SEKKEI Co.,Ltd.

Abstract

The Ariake Arena will be used as one of the venues for the Tokyo 2020 Olympics and Paralympics. The main structural element of the stand structure section was made a reinforced concrete structure with high rigidity. A steel structure was adopted for the core framing structure at the four corners that bears the horizontal force of the roof section in the event of an earthquake. This structural plan provides sufficient value in terms of both rigidity and bearing strength. For the roof structure, a steel plane truss was adopted based on erection of the large space roof using the traveling construction method. To mitigate the danger of the ceiling and suspended equipment falling during a major earthquake, a seismically isolated roof structure in which the seismic isolation devices are placed directly beneath the roof was adopted.

Keywords: steel spatial structures, seismically-isolation.

1. Introduction

Ariake Arena is scheduled to be used as the venue for volleyball and wheelchair basketball in the 2020 Tokyo Olympics and Paralympics, respectively. Following these competitions, the venue will be used for sporting events as well as concerts and the like. The main characteristics of the design and construction for this project were ① the exterior of the arena, which is characterized by an elevation shape that opens upward and outward and a roof shape that is convex in the downward direction; ② the large span roof structure that is seismically isolated; and ③ the use of the traveling method to construct the roof. These features were indispensable measures needed to achieve the architectural given conditions for the building, which were "minimization of the air volume inside the main arena while still ensuring the spectator capacity, based on the restricted site conditions" "reducing the response acceleration spectrum of the roof section, from the standpoint of ensuring the safety of the ceiling and suspended equipment" and "construction of the building in a short period of time."

2. Overview of building plan

Location:	1-19 Ariake, Koto Ward, Tokyo
Total floor area:	Approximately 47,000 m^2
No. of floors:	5 aboveground stories
Height:	36.7 m
Structural form:	Roof seismically isolated structure
Type of structure:	Steel, reinforced concrete, steel-reinforced concrete
Skeleton form:	(2F - 5F) Rigid frame structure with braces,
	(1F) Rigid frame structure with earthquake-resisting walls



Figure 1: Overview of building plan & exterior perspective view (As of October 2015, Tokyo)

Copyright © 2019 by Yuki Hamada Takenaka Corporation
Published by the International Association for Shell and Spatial Structures (IASS) with permission.

Fig. 1 shows an exterior perspective view of the plan.The complex consists of a Main Arena placed on the north side and a Sub-Arena placed on the south side of the site. The roof of the main arena is a large span roof measuring approximately 120m x 130m. The spectator seating can accommodate 15,000 spectators, a necessary condition for holding volleyball matches in international sports competitions. The floor configuration places the parking area, machine room and athlete locker rooms on the 1st floor, the concourse and spectator seating on floors 2 through 4, and the video adjustment room, electrical room, etc. on the 5th floor. Fig. 2 shows the 2F framing plan and framing elevation.

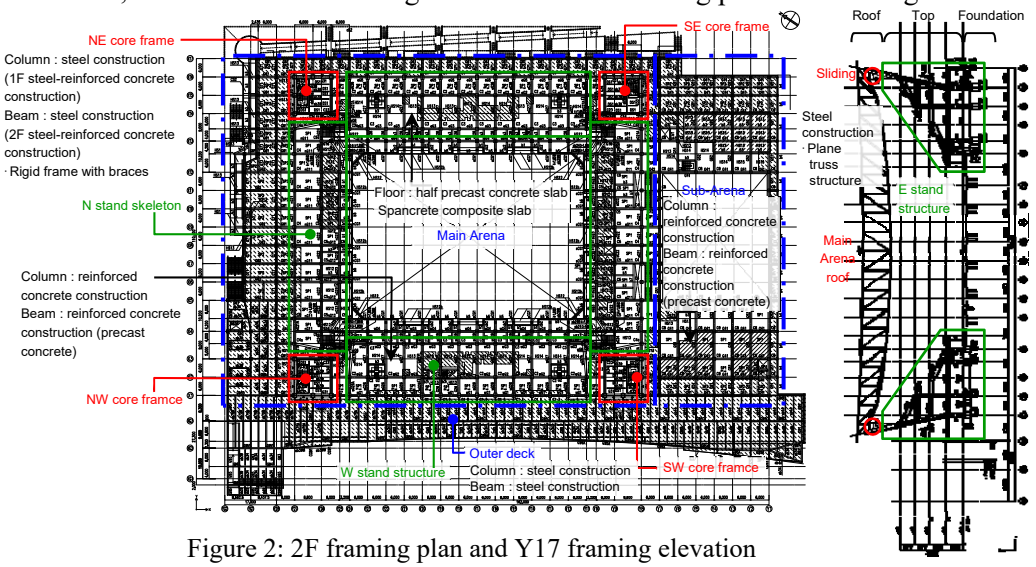


Figure 2: 2F framing plan and Y17 framing elevation

3. Overview of structural plan

3.1. Configuration of individual structures

The structural configuration of the arena comprises the following: [the roof structure,] constructed with a plane truss structure that achieves a large span; [the seismic isolation layer with seismic isolators,] located directly beneath the roof truss; and [the upper structure] that supports the roof truss.

The upper structure can be divided into two sections: the stand structure, which is the main area in which spectators are present, and the core framing structure at the four corners where the stairs and elevators are placed. Both of these sections are structurally integrated. The structural configuration also includes the foundation structure, which is made up of the existing concrete piles that support the building from the bearing stratum (located up to approximately 60m beneath the surface of the ground) and the mat-slab and footing beams.

Fig. 3 shows the structural diagram. Table 1 shows the materials used in the construction.

Table 1: Materials used

Location	Floor	Type of structure	Concrete strength	Main members			
			Skeleton	Columns (truss strut members / diagonal members)		Girders (truss upper and lower chord members)	
				Steel frame	Reinforcements	Steel frame	Reinforcements
Roof structure	Roof	S	SN490B STKN490B BCP325			SN490B	
Upper structure	1-5	S RC SRC	Fc30 Fc36 Fc48 Fc60	HBL385B STKN490B BCP325B SN490B	SD590 (*1) SD490 (*1) σy785 (*2) SD295A (*2)	HBL385B SN490B	SD490 (*1) SD390 (*1) σy785 (*2) SD295A (*2)
Foundation structure	Foundation	RC	Fc36				SD490 (*1) SD295A (*2)

*1: Main reinforcement
*2: Stirrup

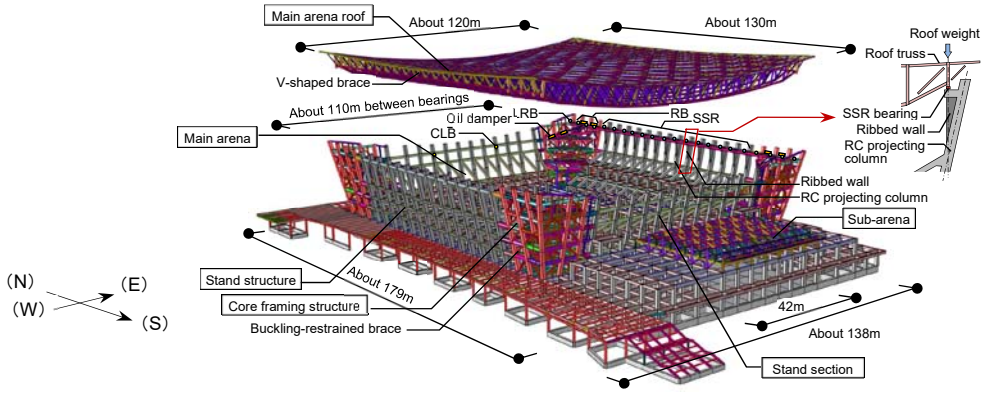


Figure 3: Structural diagram

3.2. Roof structure

A plane truss of steel construction was adopted for the roof structure, based on the use of the traveling method for the construction. In order to mitigate the danger of the ceiling and suspended equipment falling during a major earthquake, a seismically isolated roof structure in which the isolation devices were placed directly beneath the roof was adopted. The roof truss comprises 22 main trusses and 7 connecting trusses arranged orthogonally to the main trusses. The main trusses were placed at intervals of 6m, with a truss depth of approximately 6.4m to 9.0m and a roof span of approximately 120m. To construct the roof structure, the traveling method was used in which each of the trusses was assembled separately on top of a gantry erected on top of the Sub-Arena and then sent out in the direction perpendicular to the truss. To ensure the self-supporting performance of the roof during the construction, the trusses were designed as unidirectional trusses with respect to long-term load and bidirectional trusses with respect to short-term load such as wind and seismic load. Horizontal braces were provided on the upper chord surface of the roof to ensure in-plane rigidity. Fig. 4 shows a structural diagram of the roof structure and the seismic isolation layer.

3.3. Seismic isolation layer

Because the roof supporting section of the stand structure has cantilever columns with comparatively low rigidity placed perpendicular to the exterior wall, 28 low-friction sliding supports with rubber pads (SSR) are provided so the horizontal force produced in the roof section is not transmitted to the stand structure during an earthquake. In the core framing structure that can secure high rigidity in every direction, 4 lead rubber bearings (LRB), 12 rubber bearings (RB) and 8 oil dampers (OD) in each direction (for a total of 16) are provided so the horizontal force produced in the roof section during an earthquake is intensively transmitted to the core framing structure. On the top of the north and south exterior walls, 2 cross linear bearings (CLB) are provided on each surface (for a total of 4) to control vertical deformation during wind and seismic loading.

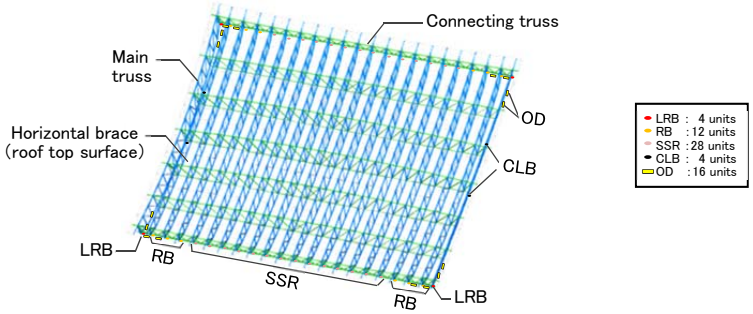


Figure 4: Structural diagram of roof structure and seismic isolation layer

3.4. Upper structure

The architectural plan for the 1st floor called for many walls to be placed, and the stand structure was made a rigid frame structure with earthquake-resisting walls of reinforced concrete. Reinforced concrete rigid frame structures were used for the 2nd floor and above where lines of movement via the concourse and so on needed to be secured. The cantilever column sections that support the roof truss were provided with a ribbed wall to ensure rigidity, and the positions of the roof support points were adjusted so bending moment would not be produced at the base of the columns during long-term loading. The core framing structures at the four corners that are subjected to horizontal force from the Main Arena roof in the event of an earthquake were made rigid frame structures with steel-reinforced concrete earthquake-resisting walls on the 1st floor and rigid frame structures with steel braces on the 2nd floor and above. Steel buckling-restrained braces (earthquake-resistant braces) were provided to ensure high rigidity and bearing strength.

Most of the columns and girders in the stand structure were of precast concrete construction to shorten the construction time. In addition, the members placed in the boundary between the core framing structure and the stand structure were reinforced to integrate the two structures.

3.5. Foundation structure

The foundation for the building was made a pile foundation constructed using the existing concrete piles that offer high supporting capacity and have an axial diameter of 400Ø - 1,200Ø. The ends of the piles were set in firm ground at a depth of N value 60 or greater. The bearing stratum is inclined (GL- approximately 30m to approximately 60m) that becomes gradually lower from the northwest section to the southeast section of the site, so a ground survey was conducted at a total of 38 locations to appropriately determine the pile end depth. A footing beam structure was used in locations where equipment pits were needed, and a mat-slab was provided in sections where pits were not needed.

3.6. Earthquake-resistant design

3.6.1. Earthquake-resistant design policy

- In order to confirm earthquake-resistant safety, the behavior of the building during a ground motion of the presumed level was evaluated, and it was confirmed that the earthquake-resistant performance targets were met.
- The evaluation of building behavior was conducted by means of a static elastoplasticity analysis (using the load incremental method) and a multi mass system multiple bar graph model.
- The direction of input for the ground motion was in two directions (X, Y) perpendicular to the plane.
- Member settings were conducted using the allowable stress level design method, using the static horizontal load during an earthquake and stationary vertical load designed based on the results of the preliminary response analysis.

3.6.2. Earthquake-resistant safety targets

Table 2 shows the targets for the earthquake-resistant safety of the roof structure and upper structure.

Table 2: Earthquake-resistance targets and design conditions for roof structure and upper structure

Loading case	Description of load		Roof structure	Upper structure	Roof structure	Upper structure
			Acceleration	Story drift Story plasticity	Member design	Member design
L1 (Level 1)	Earthquake that occurs rarely	Considered dynamically	Horizontal 200gal or less	1/200 or less 1.0 or less	No greater than short-term allowable stress	No greater than short-term allowable stress
L2 (Level 2)	Earthquake that occurs very rarely	Considered dynamically	Horizontal 300gal or less	1/100 or less 2.0 or less	No greater than short-term allowable stress	Maximum plasticity $\mu \leq 4.0$, no greater than ultimate strength

3.6.3. Design conditions for seismic isolation members

The shear force and deformation applied to the seismic isolation level in the event of an earthquake were evaluated using the maximum stress values in the seismic response analysis. In the seismic response analysis, variations in the seismic isolation materials were taken into consideration. Table 3 shows the design conditions for the seismic isolation members. The criterion for bearing pressure on the tension side was -1.0 N/mm^2.

Table 3: Design conditions for seismic isolation materials

Ground motion	Item		Design conditions
Ground motion that occurs rarely	Bearing pressure of laminated rubber － shear strain	σ_{01}-γ_1	No greater than stable deformation *1
	Clearance of moving parts	δmax（mm）	250mm (γ: 125%) or less
Ground motion that occurs very rarely	Bearing pressure of laminated rubber － shear strain	σ_{02}-γ_2	No greater than performance assurance deformation *1
	Clearance of moving parts	δmax（mm）	450mm (γ: 225%) or less

*1 Defined based on the relationship between bearing pressure and shear strain that is determined for each apparatus diameter.

4. Overview of structural design

4.1. Design of roof structure

The design of the roof structure was conducted using a fully three-dimensional model of the roof structure section including the seismic isolation devices. A static analysis was conducted using the horizontal seismic coefficient of 0.3G and vertical seismic coefficient of 0.4G, set based on the results of the Level 2 seismic response analysis conducted with a multi mass system multiple bar graph model. Subsequently, the section design was conducted so the members would be within the short-term allowable stress level even when long-term load + horizontal and vertical seismic load were considered simultaneously. Moreover, in order to consider the effect of dynamic behavior, a dynamic analysis was conducted with the response acceleration directly beneath the seismic isolation layer, obtained from the Level 2 response analysis for the entire building, considered as input acceleration applied to the roof model. The analysis confirmed that there were no problems with structural safety in the section that had been established. Fig. 5 shows the results of the analysis of the roof structure.

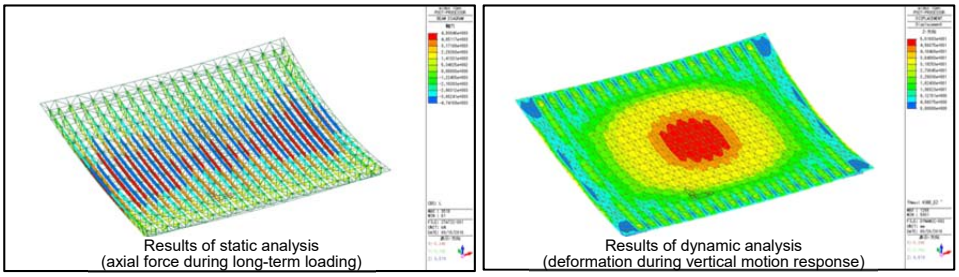


Figure 5: Results of roof structure analysis

4.2. Design of upper structure

A tentative response analysis was conducted using a multi mass system multiple bar graph model, and design story shear force values encompassing the values for maximum story shear force during a Level 1 earthquake that were obtained from this analysis were finalized. A static elastoplasticity analysis was conducted for the design story shear force, and the analysis confirmed that the stress produced in each member together with the force produced over the long term would be within the target values with respect to a Level 1 earthquake.

The study of the upper structure with respect to a Level 2 earthquake was done by first setting values for story shear force and external force distribution profile that encompass the values for maximum story shear force during a Level 2 earthquake that were obtained from the Level 2 seismic response

analysis. A static elastoplasticity load incremental analysis was conducted using this distribution profile and, using the step at which the set design story shear force during a Level 2 earthquake was exceeded on all levels, it was confirmed that the stress at that step was within the target value with respect to a Level 2 earthquake.

5. Overview of seismic response analysis

5.1. Static elastoplasticity analysis

Table 4 shows the size of the shear force coefficient at each of the loading levels on the 1F and seismic isolation layer in the static elastoplasticity load incremental analysis. The maximum plasticity rate of members was 1.0 or less for all members in the roof structure and, in the upper structure, was 2.76 for columns and 3.54 for large beams, confirming that the established criteria had been met.

Table 4: Story shear force coefficients at each loading level

Floor	Loading level	X direction	Y direction
Seismic isolation layer	Response equivalent to earthquake that occurs only very rarely	0.300	0.300
1F	For first-order design	0.261	0.278
	Response equivalent to earthquake that occurs only very rarely	0.575	0.564

5.2. Overview of response analysis in the event of an earthquake

The time history response analysis model for horizontal ground motions is modeled with the 1F column base position as fixed and each of the core framing structures in the four corners and the stand structures on the four sides as one equivalent shear multiple mass point system model, with the roof structure above the seismic isolation layer as one mass point. Attenuation was set for each element, as h = 2% for steel and h = 3% for steel-reinforced concrete with respect to the first-order characteristic frequency. The value was set to h = 0% for the seismic isolation layer.

5.3. Eigenvalue analysis

Table 5 shows the natural periods derived from the eigenvalue analysis. The eigenvalue analysis was conducted by extracting the roof structure and upper structure with the seismic isolation members as the boundary and conducting the analysis for the roof structure and upper structure with the lowest section fixed. The overall system was shown for the case in which the rigidity of the seismic isolation layer was the equivalent rigidity (in the event of a Level 2 ground motion) for the shear strain (when γ = 200%) caused by an earthquake that occurs only very rarely.

Table 5: Natural period

Rigidity of seismic isolation members	Order	Overall		Roof structure	Upper structure	
		X direction	Y direction	3-dimensional model	X direction	Y direction
		Natural period (sec)		Natural period (sec)	Natural period (sec)	
In the event of a Level 2 earthquake (γ: 200%)	1st-order	3.65	3.65	0.77	0.43	0.48
	2nd-order	0.43	0.48	0.60	0.40	0.47
	3rd-order	0.41	0.47	0.57	0.34	0.41

5.4. Ground motions for analysis

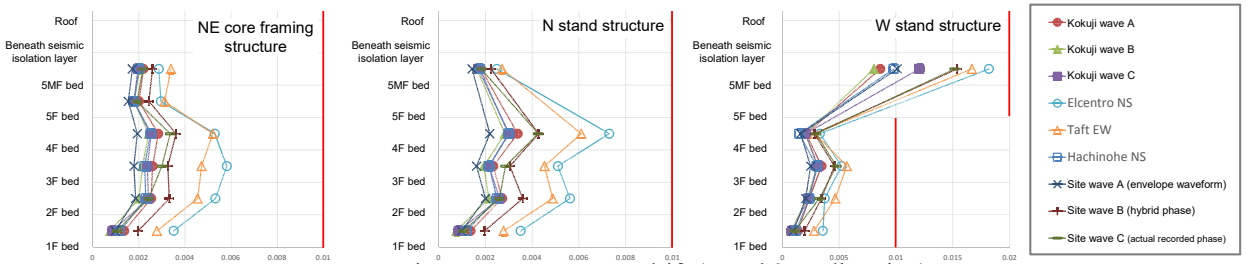
A preliminary response analysis was conducted using all ground motions determined from the results of PS logging at three different locations in the support layer, and the seismic wave that produced the maximum story drift response in the Main Arena roof for each wave was selected and used for the seismic response analysis. Table 6 shows the ground motions used for the seismic response analysis that was conducted for this building.

Table 6: Maximum velocity and acceleration of design horizontal ground motion

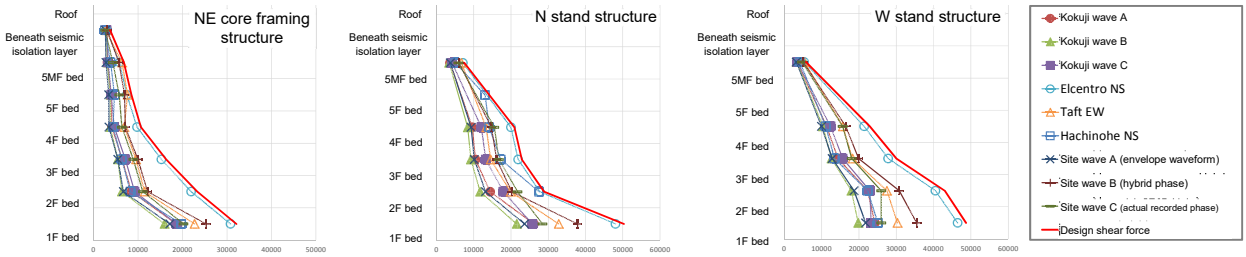
Type	Name of seismic wave used	Level 1 ground motion		Level 2 ground motion	
		Velocity (cm/s)	Acceleration (cm/s^2)	Velocity (cm/s)	Acceleration (cm/s^2)
Seismic waves conforming to Kokuji spectrum	Kokuji wave phase (Kobe)	14.4	75.8	71.2	276.6
	Kokuji wave phase (Kushiro)	13.0	65.6	64.5	236.8
	Kokuji wave phase (random)	11.4	68.5	55.1	237.6
Fault earthquake simulated seismic waves	Site wave (envelope waveform)	-	-	61.5	251.1
Long period seismic waves	AIJ long period ground motion (hybrid phase)	-	-	42.6	481.2
	AIJ long period ground motion (actually recorded phase)	-	-	43.8	326.4
Observed seismic waves	EL CENTRO 1940NS	25.0	255.5	50.0	511.0
	TAFT 1952EW	25.0	248.5	50.0	497.0
	HACHINOHE 1968NS	25.0	174.5	50.0	349.0

5.5. Results of seismic response analysis

A response analysis for a Level 1 and Level 2 ground motion was conducted, and in each case the results confirmed that the target performance had been satisfied. Fig. 6 shows the story shear force coefficient and story drift in the X direction for the NE core framing structure, N stand structure and W stand structure.



Maximum response story drift (Level 2, X direction)



Maximum response shear force (Level 2, X direction)

Figure 6: Maximum response story drift and maximum response shear force (Level 2, X direction)

Fig. 7 shows the energy absorption ratio for the seismic isolation members (Kokuji Kobe L2). Roughly 65% of the seismic input energy was absorbed by the seismic isolation members (LRB, RB, oil dampers), roughly 25% was absorbed by internal viscosity attenuation, and roughly 10% was absorbed by strain energy. This confirmed that the roof section acted effectively to absorb the energy applied to the building as a whole.

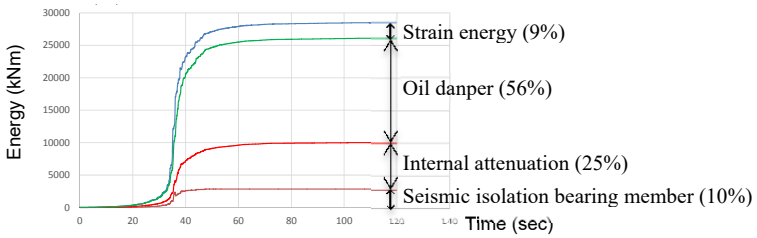


Figure 7: Seismic energy absorption ratio

6. Overview of wind resistance design

6.1. Study policy

The design wind load was established with the velocity pressure set in accordance with Notification No. 1454 of the Building Standards Law, and with the reoccurrence period corrected to 500 years. The wind force coefficient was set as follows based on the results of wind tunnel tests.

6.2. Establishment of wind force coefficient

Wind tunnel experiments were conducted in order to set the wind load that would act on the planned building. The average wind force coefficient for the roof as a whole was a negative value in all of the wind directions in the experiments, and the minimum value was -0.56 for a wind direction of 260°. The average wind force coefficient for the seismic isolation bearing section was a negative value in almost all of the wind directions in the experiments, and the minimum value was -2.12 for a wind direction of 140° at location b8 (the wind direction at which this location would be upwind). The fluctuating wind force coefficient for the roof as a whole was great for the wind direction blowing directly on the outer wall surface, and the maximum value was 0.23 for a wind direction of 270°. The fluctuating wind force coefficient for the seismic isolation bearing section was great when the location in question was upwind, and the maximum value was 0.66 for a wind direction of 210° at location b7. Fig. 8 shows the minimum value for the structural framework wind force coefficient for the wind acting on seismic isolation bearing sections b1 - b8, as well as the wind direction for that wind.

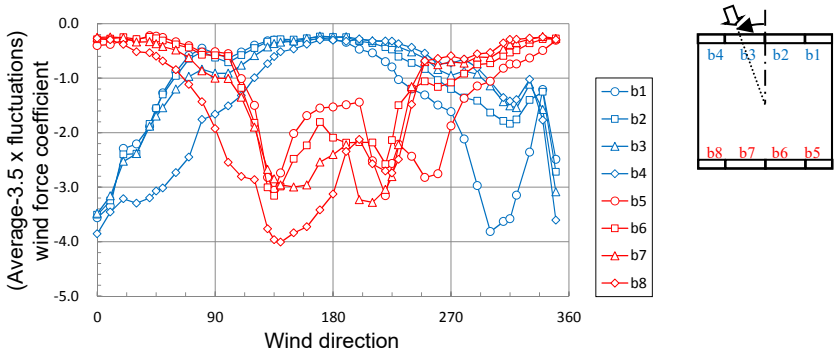


Figure 8: Relationship between structural framework minimum wind force coefficient and wind direction angle for seismic isolation bearing sections b1 - b8

6.3. Study of soundness of overall building and seismic isolation devices

The velocity pressure that corresponds to a wind load with a reoccurrence period of 500 years was 1170 N/m^2, and the design wind load for the roof surface determined by multiplying this value by the wind force coefficient was -1568 - 433 N/m^2. Accordingly, the effect of the wind load on the roof as a whole was extremely small in comparison to the weight of the roof itself, confirming that the wind load for a wind with a reoccurrence period of 500 years would not be a dominant factor for the design, in that lifting and the like caused by the upward wind load would not be produced. Similarly, the wind load acting on each of the seismic isolation bearing sections was confirmed to not pose problems for structural safety, in that tensile stress would not be produced in the seismic isolation devices.

7. Conclusion

This paper has discussed the structural design of the Ariake Arena. The authors would like to express their appreciation to Professor Masao Saito, the Tokyo Metropolitan Government Finance Bureau, and Kume Sekkei Co., Ltd. for their substantial assistance regarding the design of this structure.

Proceedings of the IASS Annual Symposium 2019 – Structural Membranes 2019
Form and Force
7 – 10 October 2019, Barcelona, Spain
C. Lázaro, K.-U. Bletzinger, E. Oñate (eds.)

Buckling strength of timber grid shell roof with steel connections considering rotational stiffness

Shun NAKAJIMA[a], Yuki TERAZAWA , Toru TAKEUCHI*
Toshiyuki OGAWA , Yoshihiro YAMAZAKI , Hiroyasu SAKATA

*Tokyo Institute of Technology
O-okayama 2-12-1-M1-29, Meguro-ku, Tokyo 152-8550, Japan
Takeuchi.t.ab@m.titech.ac.jp

[a] Former Graduate student, Tokyo Institute of Technology (NIHON SEKKEI. INC.)

Abstract

In this paper, the authors propose effective steel connections to achieve high bending stiffness and strength for timber grid-shell structures and confirm their performance through real size mock-up tests. In light of the test results, the buckling strengths of 24 m-span timber grid-shell roof structures with and without diagonal bracing roofs are discussed. The theoretical buckling strength including the rotational stiffness at connections is derived using a continuum shell analogy and compared with the results of discrete FEM analyses. Reduction factor equations of buckling strength as a function of in-plane/out-of-plane bending stiffness ratio and rotational stiffness are proposed, and their validity is confirmed.

Keywords: Grid shell, Timber-steel composite, Connection, Buckling, Continuum shell analogy

1. Introduction

In recent years, lattice shell roofs have become popular on timber structures to create a long span space that is both lightweight and aesthetically pleasing. This research proposes several types of steel connections for timber lattice shells that will improve structural performance and architectural appearance. The out-of-plane flexural strength and rotational stiffness of the proposed connections are examined by performing full-scale experiments. Based on the test results, the elastic buckling strength of 24 m-span timber grid shells with and without diagonal bracing roofs are discussed. Their theoretical buckling strength including the rotational stiffness at connections are derived using a continuum shell analogy and compared with the results of discrete FEM analyses. Finally, the reduction factor equations of buckling strength as a function of in-plane/out-of-plane bending stiffness ratio of the timber member and two directional rotational stiffness at the connection are proposed, and the validity of the equations is confirmed.

2. Mock-up test of timber-steel connections

The dimensions of the mock-up single-layer timber lattice shell are assumed to be 24 m × 24 m × 3.2 m, as shown in Figure 1. In this type of single-layered grid shell, the rotational stiffness at connections significantly affects their buckling strength. To achieve reliable connections with high bending stiffness and strength, three types of hybrid connections using steel elements are proposed, as shown in Figure 2. In Figure 2(a), rectangular laminated timber members are fixed to a tee flange section with lag screws. The tee length is set to be 1.5 times the height of the timber member (300 mm) and is referred to as TB300. TB440 has the same configuration but uses a tee length of 2.0 times the height of the timber member (Figure 2(b)). A connection using an H-

Copyright © 2019 by S.Nakajima, Y.Terazawa, T.Takeuchi, T.Ogawa, Y.Yamazaki, H.Sakata
Published by the International Association for Shell and Spatial Structures (IASS) with permission.

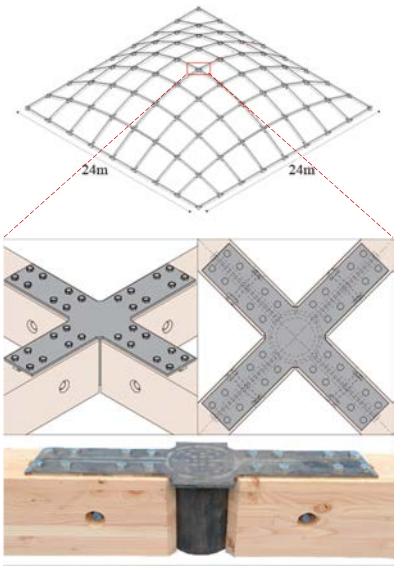


Figure 1: Latticed shell roof with timber-steel hybrid connections

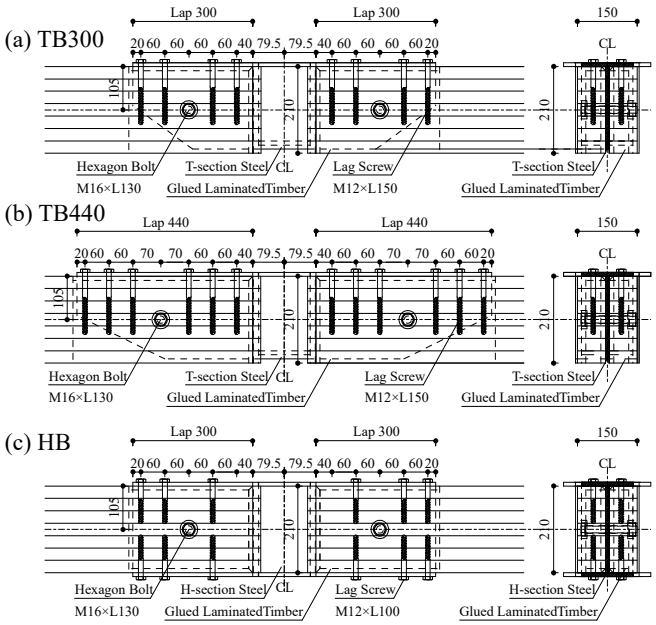


Figure 2: Hybrid connection types

bracket grasping timber member between two flanges with lag screws is referred to as HB (Figure 2(c)). These connections have resistance to out-of-plane bending moments owing to the pull-out force of the lag screws and bearing force between the timber members and the steel flanges. Tests on three specimens for each type of connection are conducted to confirm the rotational stiffness, flexural strength, and fracture mode with respect to out-of-plane and in-plane bending.

Monotonic bending tests for each connection type are conducted to confirm their bending stiffness and strength. The test setup is shown in Figure 3. The size of the timber members and connections are designed assuming the 24 m grid shell shown in Figure 1, and the material used for the specimens are shown in Table 1(a) and (b). Laminated timber members are composed of Canadian pine lamina of grade E105-F300 (E=10.5 GPa, F=30 MPa). Three specimens are tested in each connection along the out-of-plane (strong) axis in the positive and negative directions [1] and in the in-plane (weak) axis [2]. The test results are summarized in Table 2. In general the stiffness is higher in TB440, and the strength is higher in HB. The normalized rotational spring at connection $\kappa = K_\theta l/EI$ ranges between 10 and 20, and the bending strength against the timber member M_{max}/M_b is between 0.37 and 0.87, which is much higher than in conventional timber connections.

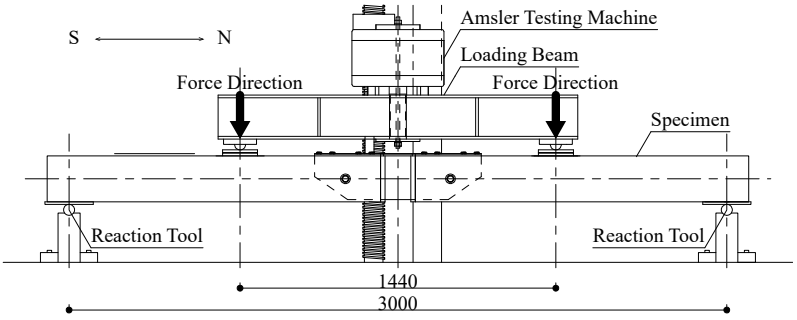


Figure 3: Setup of bending test for connections

3. Elastic buckling analyses of grid shell including connection stiffness

Using the test results, the buckling strength of a 24 m × 24 m-span grid shell roof as shown in Figure 4 is investigated as a function of the sectional stiffness ratio I_z/I_y and the connection

Table 1 Characteristic value of constituent material

(a) Glued laminated timber

Tree species	Composition	Strength grade	Direction	Bending Young's modulus (kN/mm^2)	Bending strength (N/mm^2)	Moisture content (%)	Specific gravity (-)
Douglas fir	Specific symmetric	E105-F300	Out-of-plane	16.9	64.2	9.9	0.55
			In-plane	15.2	48.9		

(b) Steel connection

Part	Steel grade	Young's modulus (kN/mm^2)	Yield strength (N/mm^2)	Tensile strength (N/mm^2)
Web	SM490A	2.09×10^2	346	511
Flange				

Table 2 Rotational stiffness and bending strength obtained by the experiment

	Out-of-plane (positive)			Out-of-plane (negative)			In-plane (negative)		
connection type	TB300	TB440	HB	TB300	TB440	HB	TB300	TB440	HB
Average of rotational stiffness K_θ(kNm/rad)	5870	11012	5377	7311	7369	5377	697	1295	1438
Coefficient of variation of 3 samples CV	0.25	0.30	0.27	0.34	0.44	0.27	0.33	0.11	0.18
Normarized rotational stiffness κ	11.6	21.8	10.7	14.4	14.6	10.7	-	-	-
Average of maximum bending strength M_{max} (kNm)	13.0	20.7	30.2	28.88	26.19	30.2	13.0	15.6	15.8
Coefficient of variation of 3 samples CV	0.04	0.12	0.04	0.06	0.10	0.04	0.12	0.03	0.06
M_{max}/M_b	0.37	0.59	0.87	0.55	0.59	0.87	0.20	0.24	0.25

stiffness ratio $K_{\theta z}/K_{\theta y}$. The following parameters are used: 1) The roof is set as either a "Grid model" without diagonals or a "Braced model" with steel rod diagonals. The load is assumed to be evenly distributed; 2) The half subtended angle φ uses values of 20º, 30º, 40º, 50º; 3) Connections are modeled as either detailed model (D) or simple model (S); 4) The cross-sectional shape is either square (S193, I_z/I_y=1.0) or rectangular (R240, I_z/I_y =0.18) with the same I_y; 5) The out-of-plane rotational stiffness of the connection is varied between rigid (R), TB300(T3), TB440

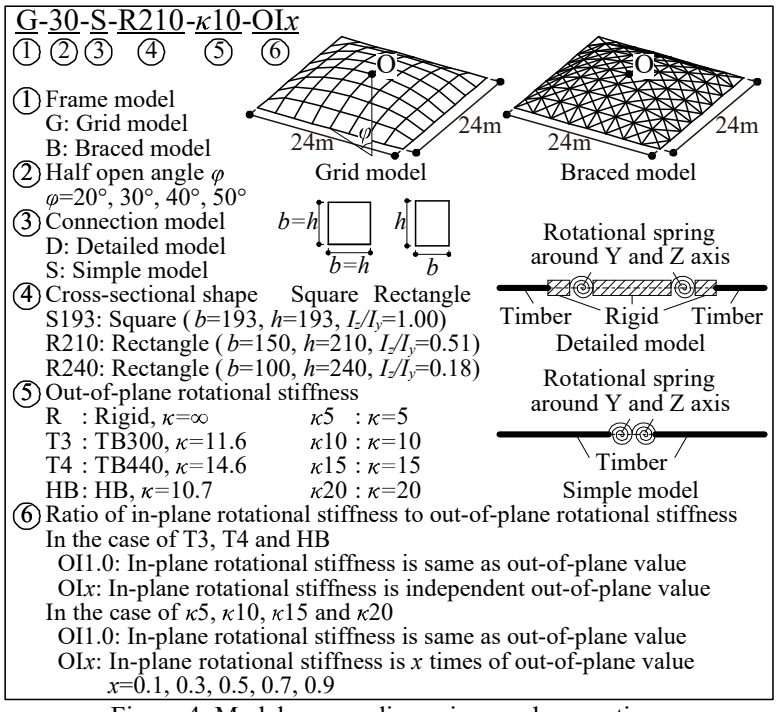


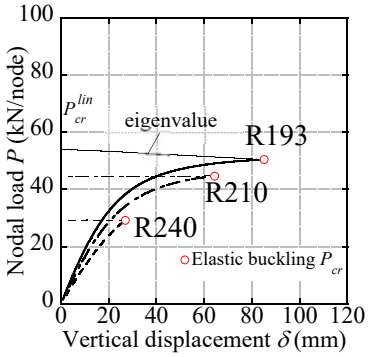
Figure 4: Model names, dimensions and properties

(T4), HB (HB), with κ=5 (κ 5), κ=10 (κ 10), κ=15 (κ 15), κ=20 (κ20); 6) Ratio of the in-plane rotational stiffness of the connection to out-of-plane rotational stiffness is varied between $K_{\theta z}/K_{\theta y}$ =1.0 (OI1.0) and $K_{\theta z}/K_{\theta y}$=0.1, 0.3, 0.5, 0.7, 0.9 (OIx, x=0.1, 0.3, 0.5, 0.7, 0.9). For T3, T4 and HB, the connection stiffness values shaded in Table 2 are used. The half subtended angle φ is defined at the ridge of the roof. No initial imperfection is assumed. The properties used for the tested connections are shaded in Table 3.

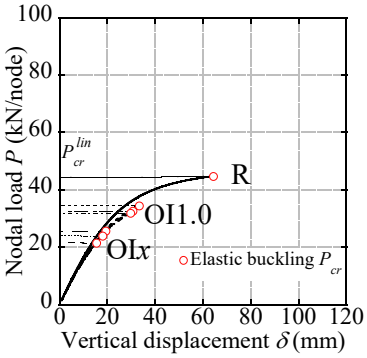
A push-over analysis including geometric nonlinearity under incremental arc-length method control is carried out, together with buckling eigenvalue analyses. Results with the simple model (S) give more conservative values than the detailed model (D). Parts of the obtained results are shown in Figure 5. When I_z/I_y is reduced (Figure 5(a)) and $K_{\theta z}/K_{\theta y}$ is reduced (Figure 5(b)), the elastic buckling strength P_{cr} is reduced. From Figure 5(b), the buckling strength of tested connections (OIx) is estimated to be reduced to approximately half of those with a rigid connection (R). Examples of the buckling modes at the point of elastic buckling are shown in Figure 6.

Table 3 Member properties of studied lattice shell

Parts	Material	Cross-sectional shape	Moment of inertia for Y axis I_y (mm^4)	Moment of inertia for Z axis I_z (mm^4)	Ratio of moment of inertia I_z/I_y (-)	Young's modulus E (kN/mm^2)	Shear modulus G (kN/mm^2)
Lattice member	Specific symmetrical composition glulam E105-F300	Square (S193) 193.1×193.1	1.16×10^8	1.16×10^8	1.00	13.1	0.87
		Rectangle (R210) 150.0×210.0		5.91×10^7	0.51		
		Rectangle (R240) 100.5×240.0		2.03×10^7	0.18		
Brace	SS400	Rod φ9	322	322	1.00	2.05×10^2	78.8

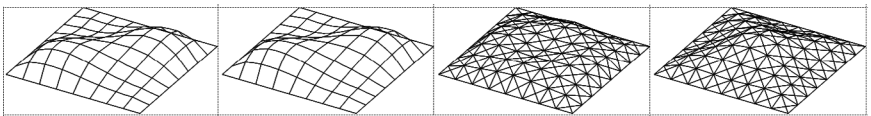


(a) Effect of sectional proportion I_x/I_z (R)



(b) Effect of spring ratio $K_{\theta x}/K_{\theta z}$ (R, T3, T4, HB)

Figure 5: Elastic buckling strength with different out-of-plane/in-plane stiffness (G-30-S)



(a-3) G-30-S-S193-κ20-OI0.1 | (b-3) G-30-S-R210-κ20-OI0.1 | (c-3) B-30-S-S193-κ20-OI0.1 | (d-3) B-30-S-R210-κ20-OI0.1

Figure 6: Elastic buckling modes (G,B-30-S-S193,R210-κ20-OI0.1)

4. Buckling strength evaluation using continuum shell analogy

Buckling strength evaluation formulae are derived using a continuum shell analogy. The stiffness of

the continuous shell plate can be expressed as follows.

In-plane: $\begin{Bmatrix} n_x \\ n_y \\ n_{xy} \end{Bmatrix} = \begin{bmatrix} K_{1111} & K_{1122} & 0 \\ K_{1122} & K_{2222} & 0 \\ 0 & 0 & K_{12} \end{bmatrix} \begin{Bmatrix} \varepsilon_x \\ \varepsilon_y \\ \gamma_{xy} \end{Bmatrix}$ (1a) Out-of-plane $\begin{Bmatrix} m_x \\ m_y \\ m_{xy} \end{Bmatrix} = \begin{bmatrix} D_{1111} & D_{1122} & 0 \\ D_{1122} & D_{2222} & 0 \\ 0 & 0 & D_{12} \end{bmatrix} \begin{Bmatrix} \kappa_x \\ \kappa_y \\ \kappa_{xy} \end{Bmatrix}$ (1b)

From the balance of complementary strain energy, each component can be expressed using the equations in Table 4. For $K_{1111}=K_{2222}(=K)$ and $D_{1111}=D_{2222}(=D)$, elastic buckling strength P_{cr}^{lin} of the Grid model and the Braced model can be expressed by Eq. (2) ([3], [4]).

$$P_{cr}^{lin} = \frac{4l^2}{R^2}\sqrt{\frac{2\left(D+D_{1122}+D_{12}\right)}{2/\left(K+K_{1122}\right)+1/K_{12}}} \tag{2}$$

In the Grid model, $K_{1122}= D_{1122}=0$ and K_{12}/K is negligible, Eq.(2) can be reduced to Eq.(3).

$$P_{cr}^{lin} = \frac{4l^2}{R^2}\sqrt{2\left(D+D_{12}\right)K_{12}} \tag{3}$$

For G and torsional effects, D_{12}/D is negligible in timber, so Eq.(3) can be further reduced to Eq. (4).

$$P_{cr}^{lin} = \frac{4l^2}{R^2}\sqrt{2DK_{12}} \tag{4}$$

In recommendations from the AIJ [4], the following buckling strength reduction factors due to the connection stiffness are introduced. However, the effects of I_z/I_y and $K_{\theta z}/K_{\theta y}$ are not included.

$$P_{cr(\kappa)}^{ela} = \alpha_0 \times \beta(\kappa) \times P_{cr(\infty)}^{lin} \tag{5}$$

Average: $\beta(\kappa) = \begin{cases} 0.47\log_{10}(\kappa)+0.34 & (1 \le \kappa \le 10 \quad : \text{Low stiffness}) \\ 0.19\log_{10}(\kappa)+0.62 & (10 \le \kappa \le 100 \ : \text{Moderate stiffness}) \\ 1.0 & (100 \le \kappa \quad : \text{High stiffnes}) \end{cases}$ (6)

Minimum: $\beta(\kappa) = \begin{cases} 0.365\log_{10}(\kappa)+0.28 & (1 \le \kappa \le 100 : \text{Low and moderate stiffness}) \\ 1.0 & (100 \le \kappa \quad : \text{High stiffness}) \end{cases}$ (7)

where, α_0 is a knock-down factor due to imperfection and geometric nonlinearity ($\cong$ 0.5). From Eq. (2), the following reduction factor equations considering the effects of sectional proportion I_z/I_y are proposed, where, $I_z/I_y=m$, and $K_{\theta z}/K_{\theta y}=n$.

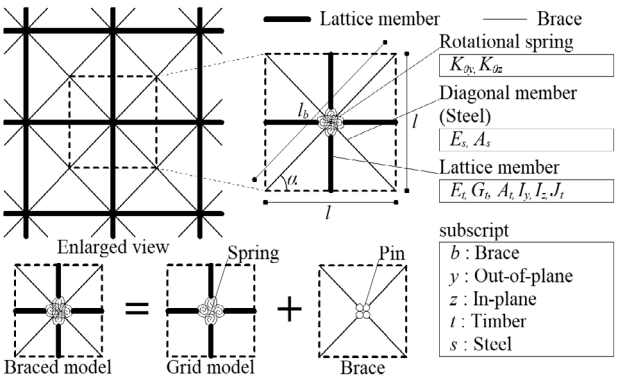


Fig. 7 Enlarged view of Braced model

Table 4 Rotational stiffness of each connections

Effective stiffness	Grid model	Braced model
$K_{1111}(=K)$	$\frac{E_t A_t}{l}$	$\frac{E_t A_t}{l}+\frac{E_s A_s}{\sqrt{2}l}$
K_{1122}	0	$\frac{E_s A_s}{\sqrt{2}l}$
$K_{2222}(=K)$	$\frac{E_t A_t}{l}$	$\frac{E_t A_t}{l}+\frac{E_s A_s}{\sqrt{2}l}$
K_{12}	$\frac{1}{l^3/(6E_t I_z)+l^2/K_{\theta z}}$	$\frac{1}{l^3/(6E_t I_z)+l^2/K_{\theta z}}+\frac{E_s A_s}{\sqrt{2}l}$
$D_{1111}(=D)$	$\frac{1}{l/E_t I_y+2/K_{\theta y}}$	$\frac{1}{l/E_t I_y+2/K_{\theta y}}$
D_{1122}	0	0
$D_{2222}(=D)$	$\frac{1}{l/E_t I_y+2/K_{\theta y}}$	$\frac{1}{l/E_t I_y+2/K_{\theta y}}$
D_{12}	$\frac{G_t J_t}{l}$	$\frac{G_t J_t}{l}$

$$\gamma_i = P_{cr(\kappa)}^{lin} \Big/ \left(P_{cr(\kappa)}^{lin} \big|_{m=1} \right) \tag{8}$$

Grid model: $$\gamma_{i.g}^{con}(\kappa) = \sqrt{\frac{1/(1+2/\kappa)+a_m}{1/(1+2/\kappa)+a_1} \cdot \frac{2/\lambda_1^{\,2}+1/6+(1/n)(1/\kappa)}{2/\lambda_m^{\,2}+1/(6m)+(1/n)(1/\kappa)}} \tag{9}$$

Braced model: $$\gamma_{i.b}^{con}(\kappa) = \sqrt{\frac{\dfrac{1}{1+2/\kappa}+a_m}{\dfrac{1}{1+2/\kappa}+a_1} \cdot \frac{\dfrac{2}{1+2s_1}\dfrac{1}{\lambda_1^{\,2}}+1\Big/\left\{1\Big/\left(\dfrac{1}{6}+\dfrac{1}{n}\dfrac{1}{\kappa}\right)+s_1\lambda_1^{\,2}\right\}}{\dfrac{2}{1+2s_m}\dfrac{1}{\lambda_m^{\,2}}+1\Big/\left\{1\Big/\left(\dfrac{1}{6m}+\dfrac{1}{n}\dfrac{1}{\kappa}\right)+s_m\lambda_m^{\,2}\right\}}} \tag{10}$$

When the connection is rigid, $\kappa = \infty$ and $1/\kappa = 0$. Eq. (10) describes the Grid model and Eq. (11) the Braced model:

$$\gamma_{i.g}^{con}(\infty) = \sqrt{\frac{1+a_m}{1+a_1} \cdot \frac{2/\lambda_1^{\,2}+1/6}{2/\lambda_m^{\,2}+1/(6m)}} \tag{11}$$

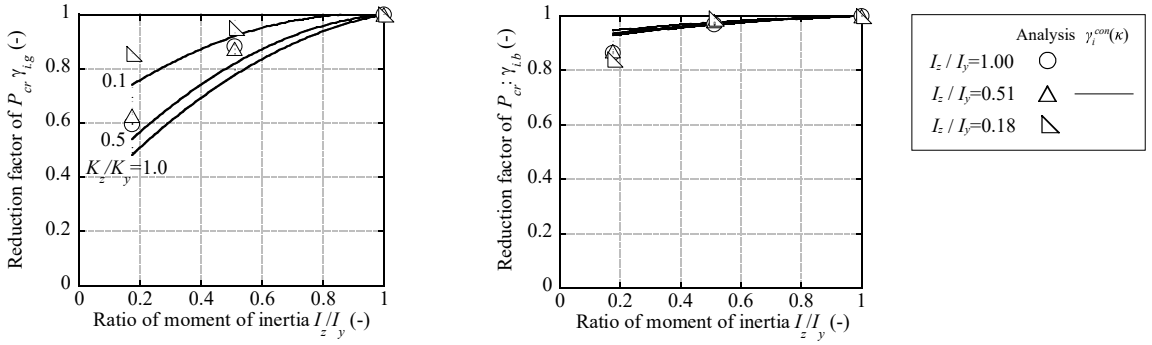
$$\gamma_{i.b}^{con}(\infty) = \sqrt{\frac{1+a_m}{1+a_1} \cdot \frac{\{1/(1+2s_1)\}\left(2/\lambda_1^{\,2}\right)+1/\left(6+s_1\lambda_1^{\,2}\right)}{\{1/(1+2s_m)\}\left(2/\lambda_m^{\,2}\right)+1/\left(6m+s_m\lambda_m^{\,2}\right)}} \tag{12}$$

$$a_m = G_t J_t \Big/ \left(E_t I_{ty}\right) = (4/5)\, jm \tag{13}$$

$$\lambda_m^{\,2} = A_t l^2 \big/ I_y = 12 l^2 m / b^2 \tag{14}$$

$$s_m = E_s A_s \Big/ \left(\sqrt{2} E_t A_t\right) = E_s A_s \Big/ \left(\sqrt{2} E_t h^2 m^{1/2}\right) \tag{15}$$

The values obtained from Eq. (9), (10) are compared with FEM analyses in Figure 8. In the grid model, Eq. (9) results in more conservative values than the numerical results. In the braced model, Eq. (10) overestimates for a lower I_z/I_y, but generally matches the numerical analyses results. This error is caused because the shear stiffness K_{12} of the roof panels in the Braced model is underestimated when neglecting axial deformations of the timber chords.



(a) Grid model (κ=10) (b) Braced model (κ=10)

Figure 8: Reduction factor of buckling load (φ=30º)

From Eq. (2), the reduction factors including the effects of $K_{\theta z}/K_{\theta y}$ can be expressed as follows.

Grid model: $$\beta_{ik.g}^{con}(\kappa) = \sqrt{\frac{1/(1+2/\kappa)+a_m}{1+a_m} \cdot \frac{2/\lambda_m^{\,2}+1/(6m)}{2/\lambda_m^{\,2}+1/(6m)+(1/n)(1/\kappa)}} \tag{16}$$

Braced model: $$\beta_{ik.b}^{con}(\kappa) = \sqrt{\frac{\dfrac{1}{1+2/\kappa}+a_m}{1+a_m} \cdot \frac{\dfrac{2}{1+2s_m}\dfrac{1}{\lambda_m^{\,2}}+\dfrac{1}{6m+s_m\lambda_m^{\,2}}}{\dfrac{2}{1+2s_m}\dfrac{1}{\lambda_m^{\,2}}+1\Big/\left\{1\Big/\left(\dfrac{1}{6m}+\dfrac{1}{n}\dfrac{1}{\kappa}\right)+s_m\lambda_m^{\,2}\right\}}} \tag{17}$$

Eq. (16) can be also expressed as Eq. (18).

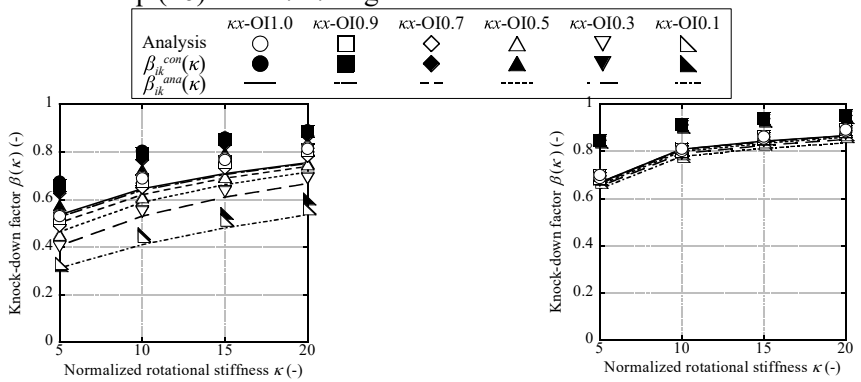
$$\beta_{ik.g}^{con}(\kappa) = \kappa\sqrt{\frac{1}{(\kappa+2)(\kappa+6\,m/n)}} \times k_g \times d_g \tag{18}$$

$$k_g = \sqrt{1+\frac{\left(2/\lambda_m{}^2\right)(6m/n)(1/\kappa)}{\left(2/\lambda_m{}^2\right)+1/(6m)+(1/n)(1/\kappa)}} \quad (19), \qquad d_g = \sqrt{1+\frac{2a_m}{1+a_m}\frac{1}{\kappa}} \tag{20}$$

In the Grid model, K_{12}/K is negligible and $1/\lambda_m{}^2 = 0$, $k_g = 1$. Because D_{12}/D is negligible and $a_m = 0$ and $d_g = 1$ in timber, then Eq.(18) becomes;

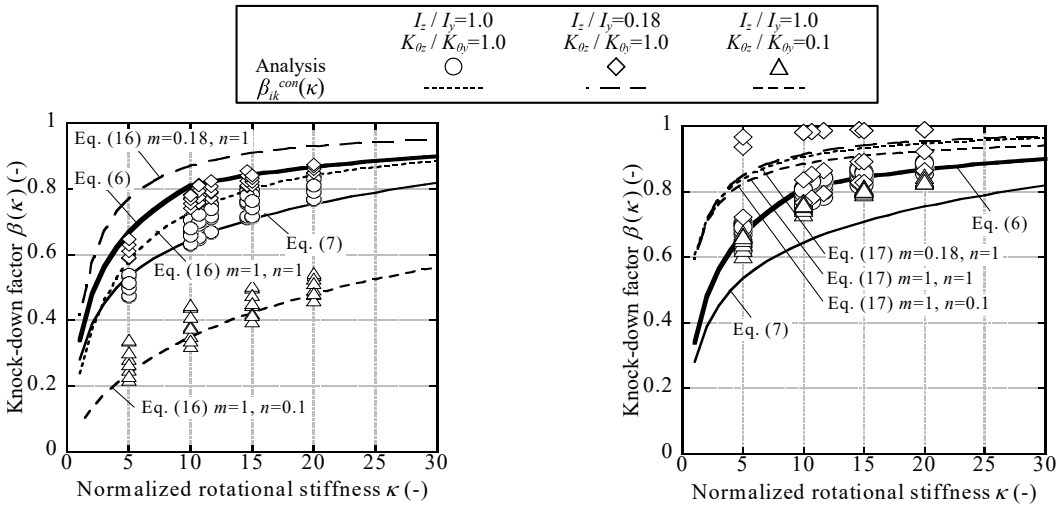
$$\beta_{ik.g}^{con}(\kappa) = \kappa\sqrt{\frac{1}{(\kappa+2)(\kappa+6\,m/n)}} \tag{19}$$

The values obtained from Eq. (16), (17) are compared with FEM analyses in Figure 9. The proposed equations generally give more conservative results for the numerical analyses. Eq. (16), (17) are also compared with Eq. (6), (7) in Figure 10. In the Grid model (Figure 10 (a)), the proposed Eq. (16) gives values between those of Eq. (6) and (7) when m=n=1, and also provides the appropriate reduction values due to $K_{\theta z}/K_{\theta y}$. In the Braced model (Figure 10 (b)), the proposed Eq. (17) gives higher estimated values than the analyses, which is caused by overestimating K_{12} and neglecting axial deformation of the timber chord. In general, the reduction due to $K_{\theta z}/K_{\theta y}$ is not significant in the braced model, and with Eq. (16) with m=n=1 gives conservative values for all the cases.



(a) Grid model (κ=10) (b) Braced model (κ=10)

Figure 9: Knock-down factor (φ=30º)



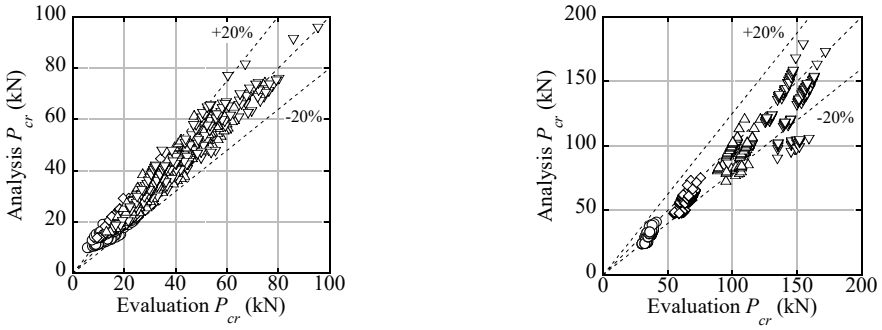
(a) Grid model (b) Braced model

Figure 10: Knock-down factor compared with AIJ recommendations

Finally, the elastic buckling strength can be expressed as Eq. (33):

$$P_{cr.ik(\kappa)}^{ela} = \alpha_0 \times \beta_{ik}^{con}(\kappa) \times \gamma_i^{con}(\infty) \times \left\{ P_{cr(\infty)}^{lin} \middle|_{m=1} \right\} \tag{33}$$

The validity of the proposed method is shown in Figure 11, compared with numerical analyses. Generally the proposed equations give consistent values with errors of approximately ±20%. For the proposed connections (κ=10–15, I_z/I_y=0.51 and $K_{\theta z}/K_{\theta y}$=0.1–0.3), β_{ik}^{con} is evaluated at approximately 0.4–0.5 for the Grid model and 0.7–0.8 for the Braced model in the case of a 24 m-span shell roof with φ=30º.



(a) Grid model (κ=10) (b) Braced model (κ=10)

Figure 11: Validity of proposed method against numerical analyses

5. Conclusions

The obtained conclusions are summarized as follows.

(1) The proposed three steel connections for timber members gives an adequate stiffness with κ=10–20 and M_{max}/M=0.37–0.87.
(2) The elastic buckling strength is reduced, especially in the Grid model, owing to the in-plane member stiffness ratio I_z/I_y and the in-plane connection stiffness ratio $K_{\theta z}/K_{\theta y}$.
(3) The buckling strength derived from the continuum shell analogy, including the effects of I_z/I_y, and $K_{\theta z}/K_{\theta y}$, gives values generally agreeing well with FEM analyses in grid-shell roofs.

Acknowledgements

The authors would like to express sincere thanks to Mr. Hiroaki Harada of NIKKEN SEKKEI Ltd., and Kenichi Hayashi of Nippon Steel Engineering Co. Ltd.

References

[1] Harada, H., Nakajima, S., Yamazaki, Y., Matsui R., Hayashi, K., Sakata, H. and Takeuchi, T.: Rotational Stiffness and Bending Strength of Steel Connections in Timber Lattice Shell, *Journal of Structural and Construction Engineering (Transactions of AIJ)*, Vol. 83, No. 746, pp. 577-587, 2018. 4 (in Japanese)

[2] Nakajima, S., Yamazaki, Y., Sakata, H., Takeuchi, T., Harada, H., and Hayashi, K.: Rotational Stiffness along Negative Out-of-plane and In-plane Directions for Steel Connections in Timber Grid-Shell Roof, *Journal of Structural and Construction Engineering (Transactions of AIJ)*, Vol. 84, No. 760, pp. 831-841, 2019. 6 (in Japanese)

[3] Kato, S., Yamashita, T.: Evaluation of elasto-plastic buckling strength of two-way grid shells using continuum analogy, *J. Space Structures*, Vol. 17, No. 4, pp. 249-261, 2002

[4] Architectural Institute of Japan: AIJ Recommendation for Design of Latticed Shell Roof Structures, 2016. 11 (in Japanese)

Proceedings of the IASS Annual Symposium 2019 – Structural Membranes 2019
Form and Force
7 – 10 October 2019, Barcelona, Spain
C. Lázaro, K.-U. Bletzinger, E. Oñate (eds.)

Calculation and classification method of member importance of spatial latticed structure in service

Yunsong LI*, Yongfeng LUO[a], Qi NIE[b]

*Department of Structural Engineering, Tongji University
1239, Siping Road, Shanghai, China
yunsongli@tongji.edu.cn

Abstract

The current member importance calculation methods are majorly based on linear elasticity assumption and Alternative Path Method (APM), lacking the consideration of spatial latticed structure's nonlinearity characteristics and actual possibility of a member being completely destroyed. In this paper, a calculation and classification method of member importance was proposed based on strain energy. Firstly, the concept of total strain energy of spatial latticed structure in critical state of overall stability was introduced, and the total strain energy was calculated based on load-displacement relationship. Next, the member importance factor (IMF) was defined by the reduction rate of total strain energy caused by member damage. Then, the effect of different minor damage cases acting on the member was studied. Finally, the classification method was proposed based on safety assessment criterion and IMF of members, and structural members was divided into important members, general members and unimportant members. For numerical simulation, member importance coefficients of single-layer spherical latticed shells under uniform load with different span length were studied. The numerical results show that the quantity and position of important members that should be determined by actual condition, and the distribution of important members wouldn't be influenced by span length.

Keywords: spatial latticed structure in service, member importance factor, strain energy, classification method

1. Introduction

The detection and identification of steel structures in service is almost on member level, and the safety of the whole structure is based on the safety of the members. The quantity of actual structural members is often greatly, and the cost of detecting all members is high. Thus, the Chinese detection code [1] suggests to use sampling method in detection and identification. The sampling detection method usually divides the members into important members and general members, and different detection and identification solutions will be used for the two kinds of members respectively. However, the current testing and identification codes [1-2] do not give a suggestion about the quantitative classification method of members. Meanwhile, compared with frame structure, the research on the IMF of spatial latticed structure is relatively few.

The importance evaluation of structural members is not only related to the mechanical properties of the structural system, but also depends on the load conditon, as in LP. Ye *et al* [3]. The energy-based methods determine the IMF by the change of structural strain energy based on APM, as in Ye *et al* [3], or LM. Zhang and XL. Liu [4]. And the stiffness-based methods determine IMF by the change of the overall stiffness of the structure, as in CM. Liu and XL Liu [5], or LS. Luo and YF. Luo [6]. The stress ratio-based method determines IMF by the change of the average stress ratio, as in XB. Hu and JR. Qian [7]. However, ZX. Zhao [8] pointed out that all the above methods are based on linear elasticity assumption and could not apply to reticulated shell structures who have strong nonlinearity. At the

Copyright © 2019 by Yunsong LI, Yongfeng LUO, Qi NIE
Published by the International Association for Shell and Spatial Structures (IASS) with permission.

same time, in the practical structures, the possibility of complete failure of the existing structural members is very low, and the APM is not suitable for the detection and identification of the structures in service.

At present, there is also no accurate method or theory that could be used for member classification in application. And DJ. Wang [9] suggested to classify members according to their role in structural function and failure result, X. Liu [10] suggested to classify members based on cumulative frequency and the quantitative member classification method which assumed that the members with cumulative frequency of IMF greater than 80% were important members.

In order to solve the problem of the calculation and classification of member importance of spatial reticulated structure in service, and considering the actual damage cases of its members, this paper proposed a calculation and classification method of member importance based on strain energy and K-medoids algorithm.

2. Calculation method of total strain energy

2.1. Calculation of Structural strain energy

Strain energy is the energy stored by the structure undergoing deformation with external forces. For the conservative structure system, the external work should be fully stored in the structure, transformed into the strain energy of the structure, and its total strain energy U should be equal to the sum of the strain energy of all the member and nodes. If the initial state strain energy before the structure is loaded is zero, then the total strain energy after the structure is loaded is equal to the work done by the external load, which can be expressed as:

$$U = \sum_{\mathrm{e}} U^{\mathrm{e}} = W_{\mathrm{ext}} \tag{1}$$

$$W_{\mathrm{ext}} = W_{\mathrm{ext}}^{\mathrm{Node}} + \sum_{\mathrm{e}} W_{\mathrm{ext}}^{\mathrm{e}} \tag{2}$$

where U^{e} is the strain energy of elements, W_{ext} is the work done by external load, e is every element, $W_{\mathrm{ext}}^{\mathrm{Node}}$ is the work done by node load, $W_{\mathrm{ext}}^{\mathrm{e}}$ is the work done by non-node load.

For spatial latticed shells, node load work can be computed as

$$W_{\mathrm{ext}}^{\mathrm{Node}} = \sum_{i} W_{\mathrm{ext}}^{i} = \sum_{i} \int_{\mathrm{L}} f_{\mathrm{N}}(i)\, du(i) \tag{3}$$

where i is node number, W_{ext}^{i} is the work done by node node on node i, L is the deformation path, f_{N} is the load vector on node i, $du(i)$ is the displacement differential of node i.

2.2. Strain energy at limit state

Overall instability is one of the main failure forms of spatial reticulated structures, as mentioned in YF. LUO *et al* [11]. When the load reaches the extreme point, the tangent stiffness matrix of the structure is singular, and the structure reaches the limit state of the overall instability. Considering that the total strain energy of the structure can reflect the load and stiffness performance of the structure, this paper takes the total structural strain energy of the structure when the structure reaches the limit state of the overall instability as the parameter to reflect the structural property.

Due to the limitation of mechanical theory, numerical calculation method is mainly used in the calculation of total strain energy of structure. ZC. Zhu *et al* [12] suggested that in the nonlinear incremental calculation of the structure, for a generic iteration step i, the incremental equilibrium equation can be written as

$$K_{\mathrm{T}i}\Delta U_i = \Delta P_i \tag{4}$$

where $K_{\mathrm{T}i}$ is tangent stiffness matrix, ΔU_i is incremental displacement vector, ΔP_i is incremental load vector.

Multiply each side of Eq. (4) by the transpose of ΔU_i, the equation is obtained as follows:

$$\Delta U_i^{\mathrm{T}} K_{\mathrm{T}i}\Delta U_i = \Delta U_i^{\mathrm{T}}\Delta P_i \tag{5}$$

Then, the work done by incremental load vector in step i can be expressed as

$$\Delta w_i = \Delta U_i^{\mathrm{T}}\Delta P_i \tag{6}$$

When $\Delta w_i = 0$, the energy in the structural system reaches the standing value state, and the structure is in the overall stable critical condition. Thus, $\Delta w_i = 0$ can help to judge whether structure is in the limit state.

Assume that the structure reaches the critical state of overall instability after n steps. The total work can be expressed as the sum of the work in every load step:

$$U = W_{\mathrm{ext}} = \sum_{i=1}^{n} \Delta U_i^{\mathrm{T}} P_i \tag{7}$$

According to Eq. (7), the total work U at the limit state is associated with load pattern and structural stiffness matrix, which means U is a physical quantity that can reflect the ultimate bearing capacity and overall deformation ability of the whole structure.

3. Calculation and Classification Method

3.1. Importance factor

During the service time of structure, due to various adverse factors, such as the environment, cracks, corrosion, deformation and other damages may happen in the structure. Then the structure's bearing capacity will be reduced by these damages. It is generally believed that the damage of the structure is the loss of the local stiffness. In the existing member importance calculation methods, the influence of a member on the whole structure system is mostly calculated based on APM. E. Zio [12] stated that APM amplify the risk of the member and is an extreme method which should be used carefully. In actual condition, the member generally would not be completely destroyed. Therefore, APM should not be used when calculating the IMF of the members. Thus, this paper defines the loss of local stiffness of the structure as the reduction of the cross-sectional area of a single member.

Under ultimate load, the contribution of a member to the total strain energy of the structure directly reflects the role of a member in the structural system. Therefore, the importance of member is measured by the change of the total strain energy of the structure with the cross-sectional area reduction of the member, and total strain energy reduction coefficient is used as the member importance factor which can be written as

$$I_k = \frac{U_0 - U_k}{U_0} = 1 - \frac{U_k}{U_0} \tag{8}$$

where I_k is the k^{th} member's importance factor, U_0 is the total strain energy of the initial structure, U_{k} is the total strain energy of structure with cross-sectional area reduction in the k^{th} member.

3.2. Classification of members

In this paper, it is found that the IMF is more likely a discrete variable, and its cumulative frequency curve is a segmented discontinuous curve. So, the existing classification method of members based on continuous cumulative frequency curve is not suitable for single-layer spatial reticulated structure.

The number of members in a single-layer reticulated shell structure is often limited, and IMF of the members is also discrete, which means K-medoids algorithm could be used for the classification of such data, as in H.S. Park [14]. The algorithm clusters a subset of objects with adjacent distances, and finally gets compact and independent clustering results, as shown in Fig. 1. The K-medoids algorithm calls the actual center point (or the most central point) of each cluster as the central point of the cluster, and the rest of the object are called non-central points.

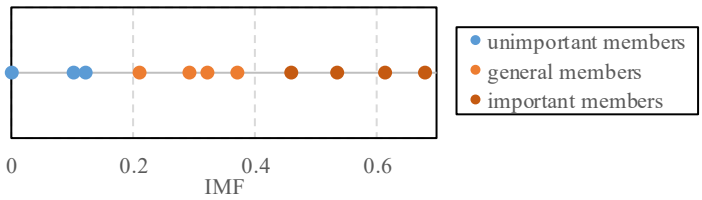


Figure 1: Importance factors clustering results

When classifying data, all data is given in a dataset X which should only contain description properties, without category properties. And the number q of clustering subsets should be given in advance. The goal of the K-medoids algorithm is to minimize its cost function, which is represented by the square sum of the distance of all data to its nearest center point

$$\min \quad E = \sum_{i=1}^{q} \sum_{p \in X_i} \left\| p - m_i \right\|^2 \tag{9}$$

where X_1、X_2、⋯、X_q are clustering subsets, m_1、m_2、⋯、m_q are cetral points, and p is non-central point.

Based on the K-medoids algorithm, this paper proposes the specific classification process of member importance, which is shown as follows:

Step 1. The member importance factors of all members are calculated and recorded as dataset X;

Step 2. Randomly select q importance factors as the center points, and assume that each center point represents an initial clustering subset. Then, other non-central points in dataset X are assigned to a cluster with the minimum distance to a center point At the same time, calculate the cost of this classification according to the Eq. (9), and record the cost as E_1;

Step 3. Randomly select a center point O_i from the current q center points and select a non-center point O_h. Replace the O_i with O_h to generate a new set of center points. Recluster non-central points in dataset X and calculate the cost of this classification according to Eq. (9), and record the cost as E_2;

Step 4. If the E_2 is smaller than E_1, the center point O_i should be replaced with the non-center point O_h; Conversely, O_i should not be replaced with O_h.

Step 5. Repeat steps (3) and steps (4) until all central points and all non-central points have been selected. The classification result at this time is the optimal classification result of member importance.

3.3. Calculation and Classification Method

In order to solve the problem of calculation and classification of member importance of spatial reticulated structures in service, this paper proposes a method based on total strain energy U and K-medoids algorithm. In this paper, the member importance factor I_k is defined by the reduction

coefficient of the total strain energy U of the structure with the cross-sectional area reduction, and after the importance factors of all members is obtained, the classification is carried out according to the K-medoids algorithm. This paper suggests to divide the members into 3 categories: important members, general members and unimportant members, which also means clustering subsets number q=3.

The concrete steps of the calculation and classification method of member importance can be given as follows:

Step 1. The ultimate bearing capacity analysis of the perfect structure model is carried out, and the total structural strain energy U_0 of the perfect model is calculated according to the Eq. (7).

Step 2. According to the actual situation, reduce the cross-sectional area of the k^{th} member by a certain proportion in the numerical model. Then, the ultimate bearing capacity analysis of the structural model with member damage should be carried out, and the total structural strain energy U_k is calculated according to Eq. (7).

Step 3. Repeat Step 2. until all the members are analyzed.

Step 4. Calculate importance factors of all the members according to Eq. (8).

Step 5. Classify all the members, and determine the quantity and the distribution position of important members, general members and unimportant members.

4. Numerical example

4.1. K6 shell model

The K6 shell model is shown in Fig.2, whose span is 40m and height is 10m. The structural members are steel pipes. And the section size of the rib rod and the ring rod are 133×4.0, the section size of inclined rod are 114×3.0. The constitutive model of the structural members are assumed to be ideal elastic-plastic model with yield strength f_y=235MPa, Young's modulus E=2.06×10^{11}Pa, and Poisson's ratio v=0.3. The dead load of the structural members are equal to 0.3kN/m^2, the live load is assumed to be a uniform load equal to 0.5kN/m^2. The joints between structural members are assumed to be rigid and the supports in the circumference of the shell are considered as fixed-hinge support.

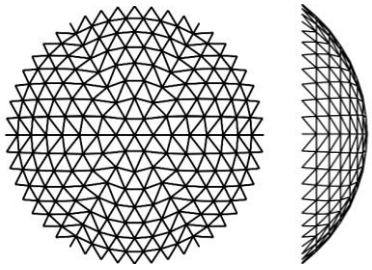


Figure 2: FE model of K6 shell

4.2. Cumulative frequency of IMF

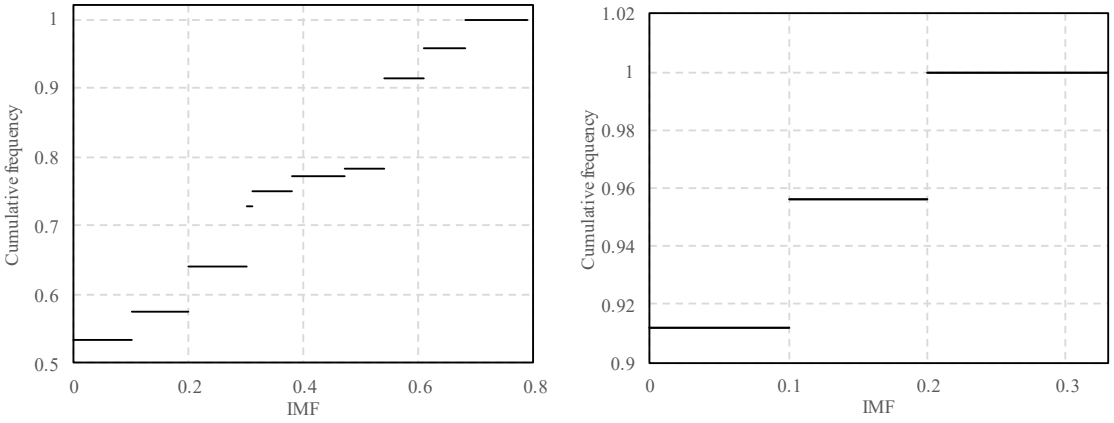
In order to illustrate the distribution characteristics of the IMFs of single-layer spatial reticulated structure, this subsection analyzes two cases of member with cross-section area reduction of 50% and 10%. The IMFs and its frequency and cumulative frequency are shown in Table 1, Table 2 and Fig.3.

Table 1: Frequency number of IM with a 50% cross-sectional area reduction

IM	0	0.1	0.2	0.3	0.31	0.38	0.47	0.54	0.61	0.68
Frequency	294	24	36	48	12	12	6	72	24	24
Cumulative frequency	0.533	0.576	0.641	0.728	0.750	0.772	0.783	0.913	0.957	1.000

Table 2: Frequency number of IM with a 10% cross-sectional area reduction

IM	0	0.1	0.2
Frequency	504	24	24
Cumulative frequency	0.912	0.956	1.000



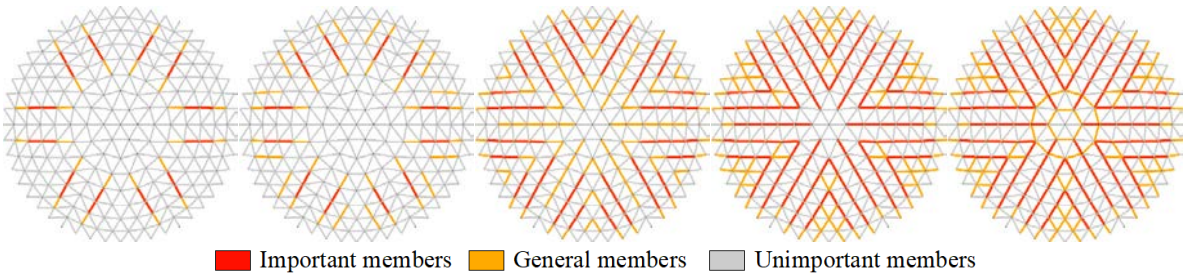
(a) 50% (b) 10%

Figure 3: Cumulative frequecny curve with cross-sectional area reduction

Table 1, Table 2 and Fig.3 show that the IMFs of K6 shell is discrete variable, but not continuous variable, and its cumulative frequency curve should not be approximated by continuous function. Meanwhile, under different area reduction degree, the IMFs may vary greatly. For example, there are only 3 cases of member importance factors with the cross-sectional area reduction of 10%, while there are 10 cases with the cross-sectional area reduction of 50%.

4.3. Damage degree

In order to study the influence of area reduction degree on member importance classification, 5 kinds of member reduction degrees are selected for analysis, which are 10% to 50% and the interval is 10%. The member importance classification results under different reduction degrees are shown in Fig.4.



(a) 10% (b) 20% (c) 30% (d) 40% (e) 50%

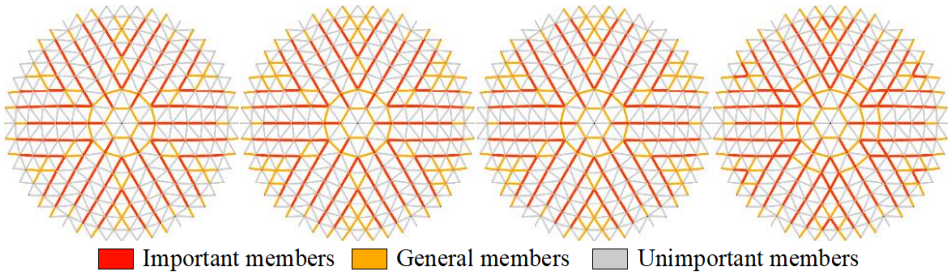
Figure 4: Importance clustering results with different cross-sectional area reduction

Fig.4 shows that under different reduction degrees, the number of important members is quite different. With the increase of the reduction degree of the cross-sectional area, the number of important members increases gradually, which also means the number of members that have a greater impact on the ultimate bearing capacity of the whole structure increases gradually. And at the same time, the number of general member increases, and the number of unimportant member decreases gradually.

Fig.4 also shows in different area reduction degree, the quantity and distribution position of important members are quite different. Therefore, in engineering application, the quantity and distribution position of important members should be determined according to the actual condition of all the members.

4.4. Span

In order to study the influence of span on the importance classification of members, 4 kinds of span length are selected, which are 30m, 40m, 50m and 60m. The rise-span ratio of all shells is 1/4, the member reduction degree is 50%, rod section size is described in section 4.1. The member importance classification results under different structural spans are shown in Fig.5.



(a) 30m (b) 40m (c) 50m (d) 60m

Figure 5: Importance clustering results in different span length

Fig.5 shows that with other conditions unchanged, the classification result of member importance is basically unchanged in different span length, which also means that the span length has no effect on member importance classification.

5. Conclusion

In this paper, a rational calculation and classification method of member importance for spatial reticulated structure in service has been proposed. Some conclusions can be given as follows:

(1) The cumulative frequency curve of member importance factor in K6 spatial reticulated shell structure is segmented discontinues.

(2) The quantity and distribution position of important members are not same in different damage degree. In practical engineering application, the quantity and distribution location of important members should be determined according to actual condition of members.

(3) When other conditions remain the same, the span length has no effect on the member importance classification results.

Acknowledgements

This work was supported by National Natural Science Foundation of China (No. 51678431). And the following colleagues helped in carrying out the analysis: Dr. Jun Liu, Dr. Xu Yang and Dr. Yujian Zhang; their contributions are sincerely acknowledged. In addition, Yunsong Li would like to thank Prof. Hongsheng Wang for his guidance in phenomenology.

References

[1] Ministry of Housing and Urban-Rural Development of the People's Republic of China, *Standard for appraisal of reliability of civil buildings: GB 50292-2015.* Beijing: China Architecture Industry Press, 2015. (In Chinese)

[2] Ministry of Housing and Urban-Rural Development of the People's Republic of China, *Standard for inspection and appraisal of high-rise and complicated steel structures: GB 51008-2016.* Beijing: China Planning Press, 2016. (In Chinese)

[3] LP. Ye, XC. Lin, Z. Qu, XZ. Lu, P. Pan, "Evaluating method of element importance of structural system based on generalized structural stiffness," *Journal of Architecture and Civil Engineering*, vol. 27, no. 1, pp. 1-6, Mar. 2010. (In Chinese)

[4] LM. Zhang, XL. Liu, "Network of energy transfer in frame structures and its preliminary application," *China Civil Engineering Journal*, vol. 40, no. 3, pp. 45-49, Mar. 2007. (In Chinese)

[5] CM. Liu, XL. Liu, "Stiffness-based evaluation of component importance and its relationship with redundancy," *Journal of Shanghai Jiaotong University*, vol. 39, no. 5, pp. 746-750, May 2005. (In Chinese)

[6] LS. Luo, YF. Luo, "A practical method for evaluation of members importances of existing spatial structures," *Structural Engineers*, vol. 33, no. 2, pp. 109-114, Feb. 2017. (In Chinese)

[7] XB. Hu, JR. Qian, "Study on alternate path method of structural progressive collapse analysis," *Sichuan Building Science*, vol. 33, no. 4, pp. 8-13, Apr. 2008. (In Chinese)

[8] XZ. Zhao, S. Yan, YY. Chen, "A review on progressive collapse study for large-span space structures," *Journal of Building Structures*, vol. 34, no. 4, pp. 1-14, Jan. 2013. (In Chinese)

[9] DJ. Wang, "Methods of existing structural system in safety comprehensive assessment," M.S. thesis, Dept. Str. Eng., Xi'an University of Architecture and Technology, Xi'an, China, 2011. (In Chinese)

[10] X. Liu, "Safety assessment method of existing large span steel structures," Ph.D. dissertation, Dept. Str. Eng., Tongji Univ., Shanghai, China, 2008. (In Chinese)

[11] YF. L, H.Q. H, H.W. L, *Stability of steel structures - The theory and implement*. Beijing: China communication press, 2010. (In Chinese)

[12] ZC. Zhu, Y. Xiang, YF. Luo, "Characteristic stiffness method for static stability analysis and assessment of spatial structure," *Journal of Zhejiang University (Engineering Science)*, vol. 51, no. 11, pp. 2112-2120, Nov. 2017. (In Chinese)

[13] E. Zio, *Computational methods for reliability and risk analysis*. Beijing: National defense industry press, 2014. (In Chinese)

[14] H.S. Park, C.H. Jun, "A simple and fast algorithm for K-medoids clustering," *Expert System with Application*, vol. 36, no. 2, no. 3336-3341, Feb. 2009.

Proceedings of the IASS Annual Symposium 2019 – Structural Membranes 2019
Form and Force
7 – 10 October 2019, Barcelona, Spain
C. Lázaro, K.-U. Bletzinger, E. Oñate (eds.)

Configurations based on crystallographic parameters and system stability of reticulated domes

K. RANJITH [a]*, S. Arul JAYACHANDRAN [a]

[a] Department of Civil Engineering,
Indian Institute of Technology Madras
Chennai, 600036, India
* Email: ranjithkolakatil@gmail.com

Abstract

Single layer domes are part of many long-span structural systems. Low dead load makes it more economical without compromising on the stiffness. Most of the standard dome configurations use triangulation as the primary unit. Geodesic dome, diamatic dome, and Schwedler's dome have triangulated geometries, and this has been studied by many authors. Based on topological studies, different polygonal shapes such as kite geometry can be utilized as the primary unit for dome configuration, and they are architecturally pleasing. In this paper, crystallographic nomenclature is introduced in the development of parameterized skeleton dome configurations using kite geometry. A reticulated structural shape is a combination of elements like vertices, edges, faces, and cells. They are expressed with the help of three parameters – dimensionality, valency, and extent. In the structural design of such domes, the member design follows codes of practice. However, the global behavior is the key to a stable dome design, for which there is no guidance in codes of practice. The global stability of one of the new dome configurations is studied with geometrically and materially nonlinear analysis (GMNA). From the study, a framework for global stability limit states and the type of analysis are proposed for reticulated metal domes.

Keywords: Dome configuration, Crystallography, Lattice structure, System stability, Global limit states

1. Introduction

Space structures are common around the world as they provide large span roofs without any intermediate supports. The roofs of indoor sports stadiums, community halls, and swimming pools are constructed with different spatial structures. Domes are one of the spatial structures where double curvature plays a crucial role in load carrying capacity [1]. Arch is structurally efficient in load carrying as the system subjected to mainly axial force, and the member utilized to its maximum capacity during axial forces. In three-dimensional space, similar behavior can be observed in domes as the double curvature helps in effective load transfer and makes sure that the structure is lightweight. Domes can cover large volume with least surface area. It is highly energy efficient and has a more significant role to play in the present era and the one that to come. Greenhouses built by geodesic domes are examples of energy efficient structures. Most of the domes are spherical, and their basic units are triangles. Geodesic domes, Schwedler's domes, and diamatic domes are created with triangulation as the basic unit [2]. Different dome configurations are possible by taking inspiration from nature and crystallography. Nature is a great teacher, and the structures available in nature are in the most stable forms. Buckminster Fuller got the inspiration for the creation of geodesic domes from Icosahedron, one of the platonic polyhedra available. Similar way, creation of different dome configurations by applying different concepts related to crystallography is possible. The parameters of structures like dimensionality and valency [3] help in parameterizing the configuration and creating a

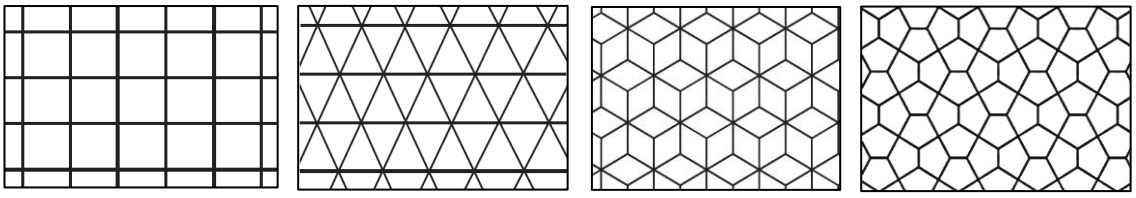
Copyright © 2019 by Ranjith K and Arul Jayachandran S.
Published by the International Association for Shell and Spatial Structures (IASS) with permission.

nomenclature of the domes. In this way, the creation of the dome configuration becomes simple when information related to parameters of structures are available to the user.

In this paper, a dome configuration with the help of crystallographic parameters is explained in the first part. Crystallographic parameterization is utilized for the nomenclature of the different type of reticulated dome configurations. Global stability analysis is conducted for one of the dome configurations created, and the effect of shallowness is studied. From the studies, different global limit states are proposed, which encompasses various global buckling modes of single layer reticulated domes. First time in literature, a prescriptive guideline is evolved, which can specify the type of analysis required depending on the geometrical parameters of domes.

2. Parameterized dome configuration

Most of the conventional domes are made with triangulation as the basic unit. Triangulated structures provide the most stable structural forms in reticulated single layer profiles. But, when clients and architects are demanding innovative and aesthetically pleasing structures, one has to go for different kinds of configuration other than the standard patterns. Here comes the importance of crystallography in dome configurations. Various crystal lattices can be studied to find the best patterns that can be utilized in the dome configurations. The repetitive pattern in crystals can be represented by points which are separated by different distances in different directions. This collection of points is known as lattices [4]. Various lattice structures are available starting from simple forms like square lattices and triangular lattices to more complex lattices like pentagonal lattices (Figure 1). Different two-dimensional lattices based on topological studies created and the same lattices are utilized for different dome configurations. Defining the parameters of structures have great significance in the creation of different lattices. These parameters help to establish different relations between elements of structures, which will be valuable in the configuration of the domes. Any structure is defined as the interrelations between different elements. Vertices, edges, faces, and cells are known as the elements of the structures, and the combination of these elements form the structure.



(a) Square lattice (b) Triangular lattice (c) Dice pattern lattice (d) Pentagonal lattice

Figure 1: Different two-dimensional lattice structures

2.1. Parameters of structure

As per Arthur L Loeb, there are three parameters for structures - dimensionality, valency, and extent [3]. Dimensionality is related to the degree of freedom. The vertex is having dimensionality 0 as it is fixed to a location in a structure. Similar way, the dimensionality of edge, face, and cell is 1, 2, and 3, respectively. Structures can be redefined as the systems of interconnected elements having different dimensionalities. Valency was used initially in Chemistry to define the combining power of an element. Here, Valency of an element of particular dimensionality defined as the number of elements of different dimensionality that meets this given element. To understand the valency, consider the tetrahedron (Figure 2). Here the edge valency of the vertex is three as the vertex connected to three edges. Similar way, the face valency of the vertex is three, and the cell valency of the vertex is two. Valency defined for other dimensionalities like edges, faces, and cells in a manner as mentioned above. There are 12 types of valences in a three-dimensional structure. Extent is the third parameter which defines the measurable quantities like length, area, and volume for dimensionality 1, 2, and 3 respectively. Above mentioned three parameters will guide to define a structure, and the same can be

extended to the configuration of reticulated structures like domes. Different mathematical relations derived for dome configurations are described in the next section.

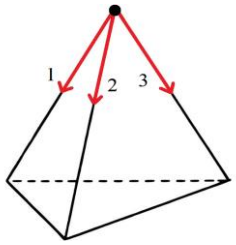


Figure 2: Edge valency of a vertex explained in a Tetrahedron

2.2. Mathematical relations between parameters of structures

Many mathematical relations are obtained with different parameters of structures. One of the important relationship existing is the Euler-Schaefli equation, which connects the elements of different dimensionality (Equation 1). Here 'j' is the total number of dimensions used in the system, and 'N_i' represents the number of elements of dimensionality 'i'. For example, 'N_0' represents the number of vertices, and 'N_1' represents the number of edges and so on. This equation used for creating lattices or patterns in the two-dimensional and three-dimensional state. Simplified version for two-dimensional (Equation 2) and three-dimensional (Equation 3) states are described below.

$$\sum_{i=0}^{j}(-1)^i N_i = 1 + (-1)^i \tag{1}$$

$$N_0 - N_1 + N_2 = 2 \tag{2}$$

$$N_0 - N_1 + N_2 - N_3 = 0 \tag{3}$$

This equation makes sure that the configuration formed is in the closed form state, and it restricts the number of valences based on the equation derived (Equation 4) from the Euler - Schlaefli relation. Here subscript represents the dimensionality of valency. For example, 'V_1' represents edge valency of a vertex and 'V_2' represents face valency of a vertex. Similar restrictions can be obtained for different elements. Hence the unknown elements of different dimensionalities can be found out from the known elements from the Euler- Schlaefli equation. This relation is used for systems having any number of dimensions.

$$V_1 - V_2 + V_3 = 2 \tag{4}$$

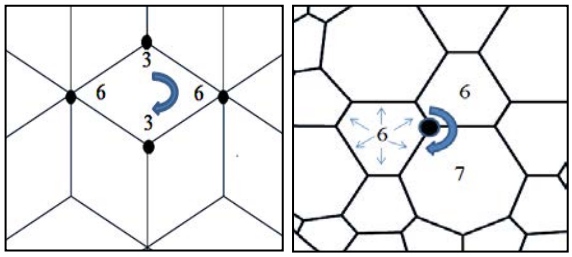
The equations mentioned above make sure the configuration of different types of domes by varying the parameters like valency and extent.

2.3. Nomenclature of domes

The existing dome configurations have names based on the inventor or the geometric pattern. The geodesic dome is obtained from the geodesic sphere, and the ribbed dome have main structural components as ribs. Hence, we have a limited number of domes based on their names. In a particular dome itself, we can have varieties of dome configurations by modifying the parameters of structure. To the author's knowledge, there is no unique nomenclature of domes available, and one has to go through the complete details to know the geometry of the dome. A nomenclature method is followed here for domes based on the crystallographic parameters. The nomenclature is based on two approaches used in plane tessellations - vertex configuration and face configuration [5]. Elements of different dimensionalities are incorporated in the nomenclature so that the configuration can be identified from the nomenclature itself.

To understand the nomenclature, one has to study the topology of different types of dome configurations. A configuration can be of faces having same edge valency or vertices having same

edge valency. There can also be complex patterns where the combination of the above two patterns coexists. Nomenclature of the first two kinds of patterns explained here. For configurations having edge valency of all the faces equal, the edge valency of vertices used in the nomenclature (Figure 3a). Here "V" indicates that the edge valency of vertices is not unique in the configuration. The number of digits represents the vertex valency of the face. Each digit represents the edge valency of each vertex in the face, and it is arranged in the clockwise direction. For configurations having the same edge valency for all the vertex, a slightly different approach is followed for nomenclature (Figure 3b). This approach is identical to the Schlaefli symbol that defines tessellations and regular polytopes [5]. No letter prefixed here as the vertex has same edge valency throughout the configuration. Here the number of digits represent the face valency of a vertex. Each number represents the edge valency of each face adjacent to the vertex in the clockwise direction. The third type of configuration where the faces and vertices are not unique, a combination of the above two nomenclature methods to be followed.



(a) (b)

Figure 3: Explanation for the nomenclature: (a) V.3.6.3.6: Configuration of faces having the same edge valency (b) 6.7.6: Configuration of vertices having the same edge valency

New dome configurations can be created by studying the topology of different lattices and different parameters of structures (Figure 4). Various relations that interconnect different elements make sure that the dome is geometrically stable. The same nomenclature explained earlier followed for these domes. As the basic unit or mesh is not triangulated, pin-jointed connections are not adequate for the domes. Rigid joints make sure that the dome is structurally stable. As the present industry provides efficient rigid connectors, the member connections will not affect the structural stability. These derived configurations are aesthetically more pleasing, and architects will find it more interesting. These geometries are restricted to single layer domes in the present study.

3. Stability investigations on new dome configuration

The dome configurations based on lattices and crystallographic parameters subjected to geometrical and material nonlinear analysis (GMNA) to understand the behavior in different load conditions. One model of 10 m span named dice kite tiling dome (Figure 5) used in this study. The members are designed considering member buckling as per IS 800-2007 [6]: the Indian Standard code of practice for general construction in steel, which is very similar to Eurocode-3: code of practice for structural steel design in the Europe [7]. Hollow circular tube of outer diameter 60 mm and thickness 3 mm chosen as the member cross section and slenderness ratio of members kept in between 100 to 120. Material behavior is adopted as Elasto-Plastic. Finite element analysis software ABAQUS [8] used for the study. Two kinds of load distribution used to study the behavior of dome configuration. One is by applying a concentrated load on the apex, and the other one is by applying concentrated forces on all the nodes. The behavior studied by varying the rise to span ratio from 1:10 to 1:4 for the chosen model. Wind load effect also observed by selecting different nodes in the dome geometry.

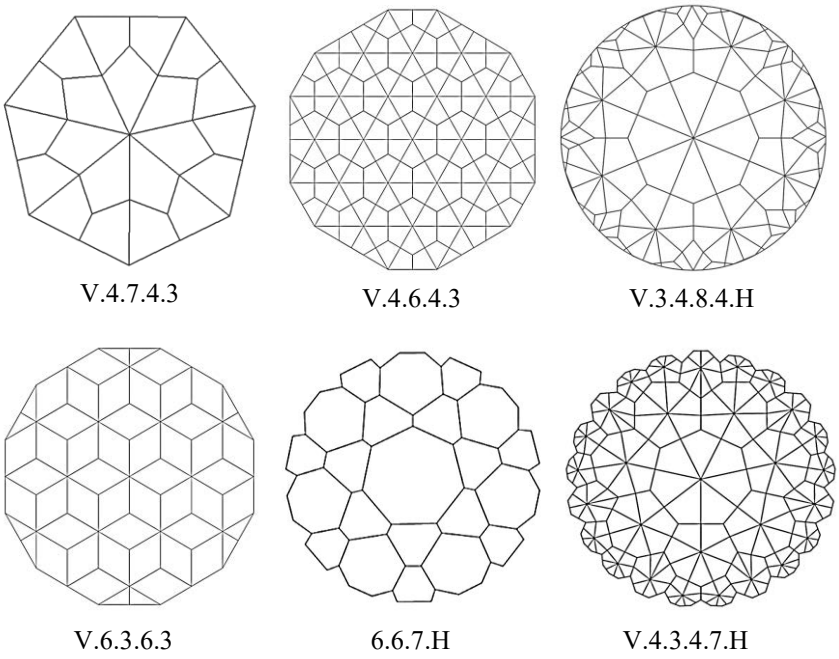


Figure 4: Different dome configurations created using crystallographic parameters

The behavior of the dome under concentrated load at the apex is studied, and results are plotted (Figure 6). The dome is undergoing snap-through buckling, and the load capacity is 70 kN. Deflected shapes at various stages included in the same figure by marking at different stages in the load-deflection curve. Point loads applied on all the nodes as collateral loads and behavior under different load ratios studied (Figure 7). The ratio of apex load to the ring load is varied and plotted in the same graph. Load at the crown node is defined as the apex load and the point loads applied at other nodes defined as ring loads for simplicity. Hence, '1:1' denotes that the loads having the same magnitude in both apex and ring nodes and '1:2' denotes that the magnitude of ring node loads is twice the magnitude of apex load. The same behavior studied by varying the rise to span ratio of the dome. The ring load stabilizes the dome geometry, and the probability of snap-through buckling reduced. Load ratio 1:1 does not cause snap-through buckling for any of the cases where the rise to span ratio varied from 1:8 to 1:4. Deflected shape of the dome during failure presented for the rise to span ratio 1:10 (Figure 8a) and 1:4 (Figure 8b) for the load ratio of 1:1. For load ratio 1:2, the ring nodes undergo snap-through buckling. The chance of snap-through buckling increases when the rise reduces in this dome configuration. The effect of wind load also studied for the same dome as per the IS 875 (Part 3) - 2015 [9], Code of practice for design wind loads for buildings and structures in India. The variation of external pressure distribution around a spherical surface shown in Figure 9. The projected area of the dome is used to calculate the pressure on the surface. Three different nodes are chosen on the dome surface to study the behavior of the dome configuration under wind load (Figure 10), and load-deflection curves obtained from the nonlinear analysis (Figure 11). A large part of the dome surface is subjected to the uplifting force, and there is literally no chance of snap-through buckling. The dome fails by yielding of its members. The nodes which lie in the plane perpendicular to the wind direction moves up, and the nodes near to the windward side (Node 2 in this case) moves down.

Similar studies can be conducted for other configurations, and efficient domes can be identified. Geometrical parameters like rise to span ratio and load ratio can be identified based on the performance. In the present case, the load ratio of 1:1 and the rise to span ratio in the range 1:6 to 1:8 has been demonstrated to be optimum.

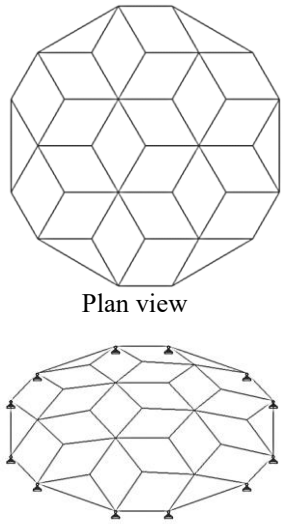


Fig 5: Dice kite tiling dome

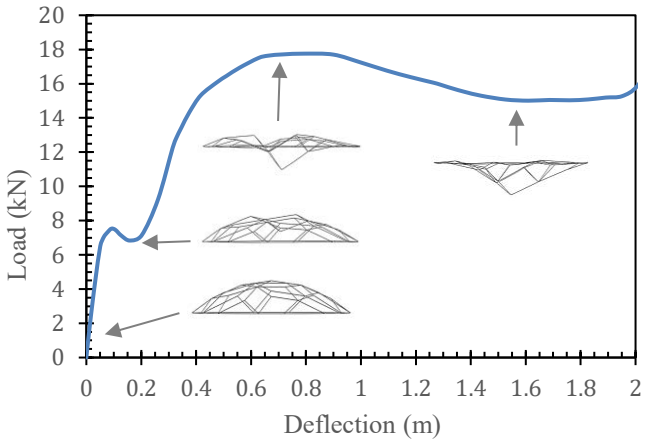
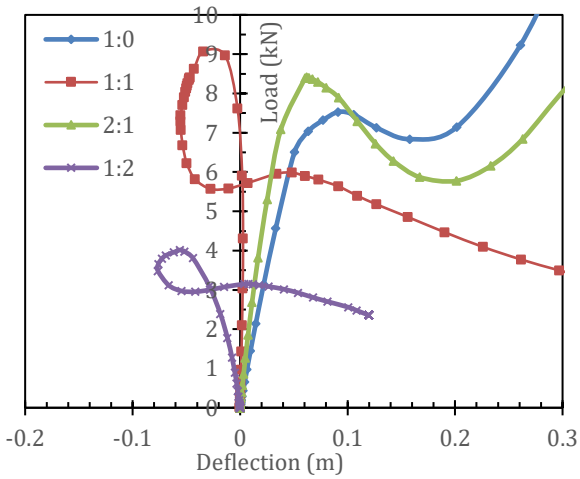
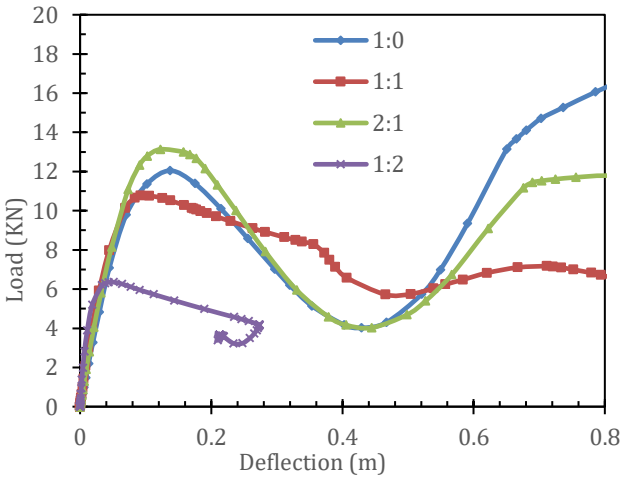


Fig 6: Load deflection curve for apex load (R:S = 1:10)



(a) R:S = 1:10

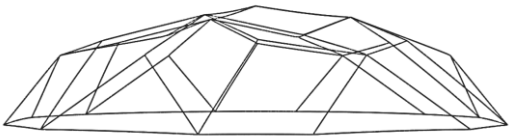


(b) R:S = 1:4

Figure 7: Load deflection curve for different apex to ring load ratio



(a) R:S = 1:10



(b) R:S = 1:4

Figure 8: Deflected shape of the dome during failure for load ratio 1:1

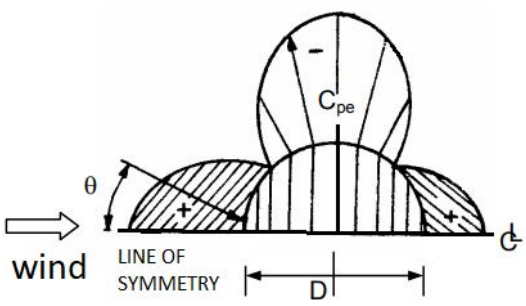


Figure 9: Distribution of external pressure around the spherical surface (IS 875 Part 3: 2015)

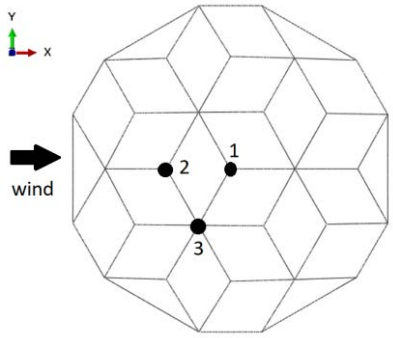


Figure 10: Nodes chosen for studying the behavior of the dome under wind action

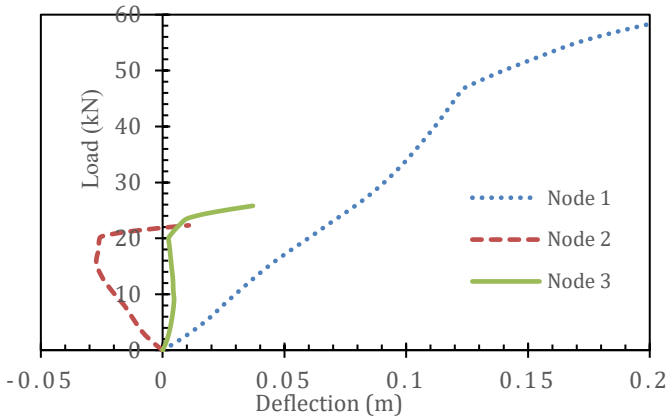


Figure 11: Load deflection curve for different nodes on the dome surface under wind action

4. Limit state of buckling for domes

In various design codes available all over the world, guidelines are given for the design of individual members. Design of tension member, compression member, and members under the combined action of bending and axial forces are provided in separate chapters in IS 800-2007 and Eurocode 3: Part 1-1. There have been no guidelines for system stability or overall structural stability effects in structures like reticulated metal domes. As geometry plays a vital role in structures like reticulated metal domes, separate guidelines for the overall design is required. As per the studies on the new dome configurations, global limit states for reticulated domes proposed here. Although one example is presented in this paper, extensive studies are carried out in [10]. A prescriptive method is given for the type of analysis required for a dome based on the global limit state under which the dome will fall. Three global limit states proposed for the reticulated domes. They are the plastic limit state (LS1), buckling limit state (LS2) and snap through buckling limit state (LS3).

4.1. Plastic limit state (LS1)

The ultimate limit state where the reticulated structure develops the zone of yielding in patterns such that its ability to resist increased load is deemed to be exhausted. It is closely related to the small deflection theory, plastic limit load, or plastic collapse mechanism. Here the linear analysis is sufficient as the deflections are small.

4.2. Buckling limit state (LS2)

The ultimate limit state where the reticulated structure suddenly loses its stability under member compression. It either leads to the large displacement or collapse as the structure is unable to carry the load. This limit state is the most critical one as the member buckling happens suddenly, and it causes catastrophic failure. Here members and connections are appropriately designed to avoid the failure. Members can fail by net section rupture in case of bolted connection or gross section yielding in tension. Ball joints can fail by fracture of the node or pull out of the members from the nodes. Members can also fail by buckling perpendicular to the dome plane or along the dome plane. Here geometrically and materially nonlinear analysis (GMNA) is compulsory.

4.3. Snap through buckling limit state (LS3)

The ultimate limit state where the shell structure suddenly loses its stability under membrane compression and snap into a shape where structure carries the load by membrane action. The entire structure or part of the structure toggle down, and individual members are not undergoing any buckling. The shallowness of the dome increases the chance of this type of failure. As the rise to span

ratio decreases, the chances of snap-through buckling increases. Here geometrical and material nonlinear analysis (GMNA) or at least geometrical nonlinear analysis (GNA) is required.

Based on the geometrical parameters of the dome, including the rise to span ratio, the decision can be made on which type of global limit state dominates for the given structure. Once the type of global limit state is known, the designer can choose the appropriate analysis for the structure from a pre-qualified list of "type of analysis". This method will simplify the choice of appropriate analysis and design procedure with respect to the overall design of the domes.

5. Conclusions

Crystallographic nomenclature is implemented into the development of parameterized dome configurations. Parameters of structures and topological study of lattices are used to create new dome configurations. Face and vertex configurations are applied in the nomenclature of reticulated domes. This nomenclature helps to distinguish between different types of dome configuration topologies. One dome configuration is selected from the new configurations developed, and geometrical and material nonlinear analysis (GMNA) is performed. The behavior of the dome under apex load, gravity load, and wind load is studied. The following observations are summarized: Apex load alone can cause snap-through buckling of the structure. Ring loads have a stabilizing effect when the apex load to ring load ratio is 1:1. The behavior of the dome studied by changing the rise to span ratio of the dome. As the rise to span ratio decreases, the chances of snap-through buckling increases. In the wind load analysis, the snap-through effect is not observed as the wind uplift is significant on most portion of the dome surface. The structure fails by yielding of the members during wind load dominance. Even though guidelines are available for member design in different design codes of practice, there is no design guideline which considers the system stability of reticulated metal domes. From the study of global stability, three kinds of global limit states proposed, and the required type of analysis for each limit states are recommended. Buckling limit state (LS2) is the critical limit state as it can cause catastrophic failure, and sufficient care should be given to avoid such failure.

References

[1] Z.S. Makowski, *Braced domes, their history, modern trends, and recent developments*, Architectural Science Review, Volume 5, no. 2, pp. 62-79, 1962.

[2] Z.S. Makowski, *The analysis, design, and construction of braced domes*, Granada Publishing, London, 1984.

[3] Arthur Loeb, *Space Structures: Their Harmony and Counterpoint*, Springer Science + Business Media, LLC, United States, 1991.

[4] C. Giacovazzo, H.L. Monaco, D. Viterbo, F. Scordari, G. Gilli, G. Zanotti, and M. Catti, *Fundamentals of Crystallography*, Oxford University Press, New York, 1992.

[5] Walter Steurer and Sofia Deloudi, *Crystallography of Quasicrystals - Concepts, methods, and structures*, Springer Series in Materials Science, 2009.

[6] IS 800-2007, *Indian Standard code of practice for general construction in Steel*, Bureau of Indian Standards, 2007.

[7] EN 1993-1-1, *Eurocode 3: Design of Steel Structures, Part 1-1: General rules and rules for buildings*, European committee for standardization, 2005.

[8] Abaqus CAE *Standard User's Manual*, Version 6.9, Simulia, 2009.

[9] IS: 875 (Part 3), *Code of Practice for Design Loads (Other than Earthquake) for Buildings and Structures – Part 3: Wind Loads,* Bureau of Indian Standards, 2015.

[10] Ranjith K., "*System instability investigation on single layer reticulated metal domes",* Master of Science-thesis, Indian Institute of Technology Madras, Chennai, India, 2019.

Proceedings of the IASS Annual Symposium 2019 – Structural Membranes 2019
Form and Force
7 – 10 October 2019, Barcelona, Spain
C. Lázaro, K.-U. Bletzinger, E. Oñate (eds.)

Damage evaluation index of long-span spatial grid structure

Xiaohui ZHANG*, Jianguo CAI[a], Jian FENG[a]

* School of Civil Engineering, Southeast University
Sipailou 2#, Nanjing 210096, China
383129416@qq.com
[a] School of Civil Engineering, Southeast University

Abstract

Based on the double indexes of energy and displacement, this paper evaluates the damage of the structure, and puts forward a new dynamic damage index D value, which can classify the damage degree of the structure into four grades: basical intact, slight damage, medium damage, serious damage and collapse. In the form of structure, the long-span prestressed double-layer composite torsional reticulated shell is taken as the research object, and the two joints, three joints, four joints and six joints of the structure are respectively removed, including a total of six models. The equivalent load unloading method considering the initial conditions is used to analyze the collapse failure of the structure after removing the joints. The damage degree of the structure can be quantified by using the dynamic damage index D value of the structure, which is more conducive to the damage study of the long-span spatial structure.

Keywords: long-span spatial structure, dynamic damage index, sensitivity analysis, classification of damage grade.

1. Introduction

At present, when studying the damage index of long-span spatial structures, single index is considered more[1-3], but it can not accurately evaluate the damage of structures. In view of this situation, this paper proposes a double index considering energy and displacement to evaluate the damage of the structure, which can evaluate the damage of the structure more accurately and quantify the damage of the structure well. In this paper, the long-span prestressed double-layer composite torsional reticulated shells are studied. In this paper, the long-span prestressed double-layer composite torsional reticulated shell is studied, and the damage is quantified by using the new index.

2. Project summary

In this paper, the Qingyuan Gymnasium in Guangdong Province, China, is taken as an analysis object. The structural system is a long-span prestressed double-layer composite torsional reticulated shell, which consists of three-way cross truss. As shown in Fig. 1 and Fig. 2, the upper part of the gymnasium is composed of six torsional reticulated shells. The center of the torsional reticulated shell is connected with the hexagonal three-way flat grid, and the adjacent torsional reticulated shells are connected with each other through daylighting belts. The lower part is composed of six reinforced concrete columns. The building area of the structure is 5450 m^2, the diagonal span of the structure is 68.418 m, the cantilever is 12.615 m, and the height of the structure is 2.8 m.

Copyright © 2019 by Xiaohui Zhang
Published by the International Association for Shell and Spatial Structures (IASS) with permission.

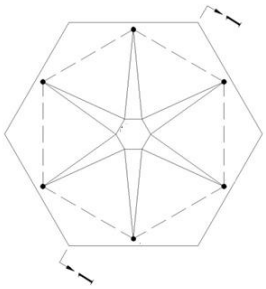


Figure 1: Layout of the structure

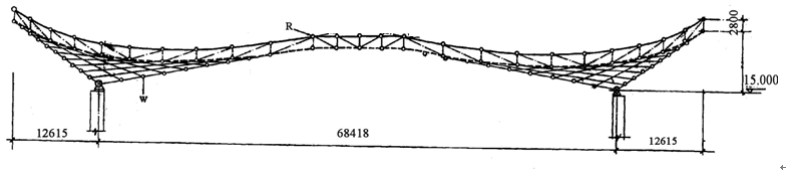


Figure 2: 1-1 sectional drawing of the structure

The structural member is selected from the following cross section: a solid round steel bar with a prestressed cable equivalent size of 80, and a standard tensile strength of 1870 MPa; The dimensions of roof members are as follows: ϕ60×3.5、ϕ68×3.5、ϕ76×3.5、ϕ83×3.5、ϕ89×3.5、ϕ95×3.5、ϕ102×3.5、ϕ114×4、ϕ121×4、ϕ133×4、ϕ140×4.5、ϕ152×4.5、ϕ168×4.5、ϕ180×5、ϕ194×5、ϕ203×6、ϕ219×6、ϕ219×8、ϕ245×6.5、ϕ273×6.5、ϕ299×7.5、ϕ351×8.0，The steel used for round steel pipe is Q345; Concrete column section size is 1200 mm × 1200 mm. SAP2000 was used to establish the model, and all the connections between the steel members of the model are hinged. The joints between the upper roof and the lower pillars adopt rubber bearings. The plane size of the rubber bearings is 500 mm × 750 mm, and the total thickness is 67 mm. The rubber bearings are treated equivalently. The horizontal direction is constrained by spring, the effective stiffness of spring is 7780 kN/m, and the vertical stiffness is infinite. The built finite element model is shown in Fig. 3.

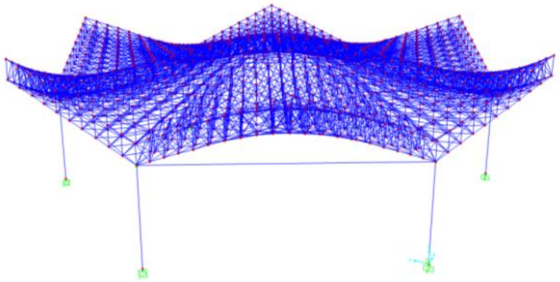


Figure 3: Finite element model

3. Analysis of structural damage

3.1. Dynamic damage index *D* of structure

At present, there is little research on the evaluation index of the damage of long-span spatial grid structures under unexpected loads. This paper evaluates the damage of structures based on the double index of energy and displacement. Energy reflects the overall failure of the structure, but can not give the specific form of structural failure; Deformation is another important indicator of the degree of structural failure, it reflects the maximum displacement response of the structure, but it can not reflect the plastic cumulative energy dissipation of the structure. Therefore, the dynamic damage index *D* is put forward by combining the energy and displacement, which can more accurately reflect the degree of structural damage. The calculation of the dynamic damage index *D* is as shown in the formula (1).

$$D = \frac{\delta_m}{\delta_u} + \frac{\beta}{E_u}\int dE \tag{1}$$

Where δ_m is the maximum displacement response of the structure under unexpected loads; δ_u is the ultimate displacement of the structure under static load; β is the coefficient of the structural system,

usually taken as 1.0; $\int dE$ is the plastic cumulative energy dissipation of the structure under unexpected loads. E_u is the ultimate energy dissipation. The first term on the right side of equation (1) is the ratio of the maximum displacement response of the structure to the ultimate displacement of the structure under static load, reflecting the development of the ductile displacement of the structure. The second term on the right side of equation (1) reflects the ratio of plastic cumulative energy dissipation to ultimate energy dissipation, reflecting the development of structural plastic cumulative energy dissipation.

3.2. Classification of dynamic damage of structures

Table 1: Classification of dynamic damage

Damage grade	Basic intact	Slight damage	Medium damage	Serious damage and collapse
Phenomenon description	There are almost no members whose stress ratio exceeds the limit, and there are no damages. Structural displacement is not large, it will not cause damage to water, electricity, instruments and other equipment. It does not need to be repaired after the disaster.	A small number of components in the structure enter into plasticity, resulting in minimal damage. The displacement of the structure is not large, and it will not cause damage to water, electricity, instruments and other equipment. The cost of repairing the structure after the disaster is not high.	A certain number of members in the structure enter into plasticity, and the structure produces certain damage. Structural displacement is large, causing certain damage to water, electricity,instruments and other equipment. After the disaster, the cost of repair is higher.	There are many plastic members in the structure, and the damage is very serious. Structural displacement is very large, causing damage to water, electricity, instruments and other equipment. After the disaster, the cost of repair is very high. The structure has lost its bearing capacity and collapsed.
Dynamic damage index D	$0 \le D < 0.3$	$0.3 \le D < 0.4$	$0.4 \le D < 2.0$	$2.0 \le D$

Table 1 divides the dynamic damage of the structure into four grades: basical intact, slight damage, medium damage, serious damage and collapse. These four grades correspond to the dynamic damage index D. When calculating the dynamic damage index of the structure, the damage situation of the structure can be judged. The damage degree of the structure can be quantified, which is more conducive to the damage study of long-span spatial structures.

3.3. Structural Sensitivity Location

According to document [4], the area where the sensitive member is located is shown in Fig. 4(according to the symmetry of the structure, take the 1/4 structure), which is located in the support area, the daylighting zone zone, the space truss zone and the side truss. Because the sensitive area is the weak part of the structure, in order to fully grasp the failure mechanism of the structure, the joints dismantled in this paper are located in these areas.

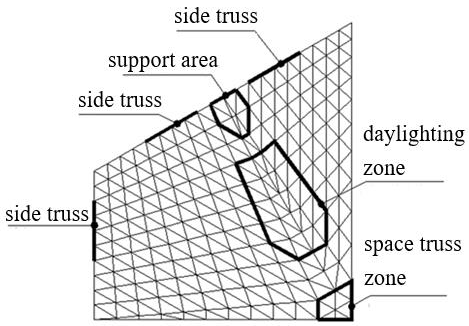
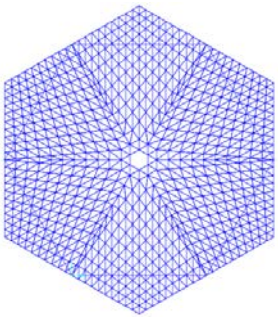
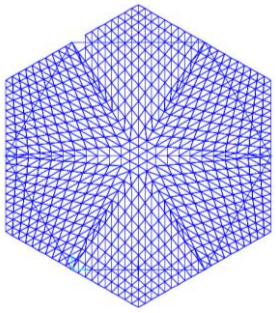


Figure 4: Sensitive areas(1/4 structure)

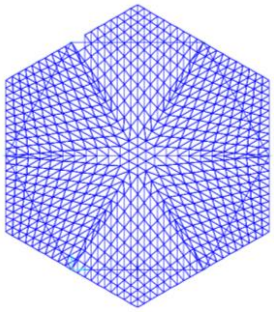
3.4. Structural sensitivity location



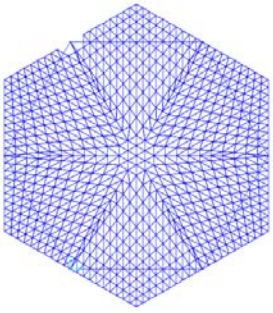
(a) Removing the space truss center 2 joints



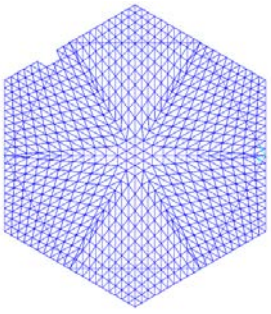
(b) Removing 2 joints near the support



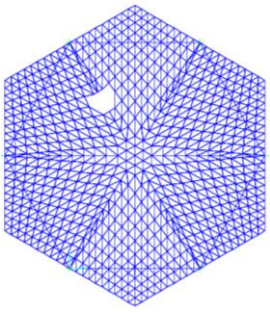
(c) Removing the 3 joints near the support



(d) Removing 4 joints near the support



(e) Removing the side truss 4 joints



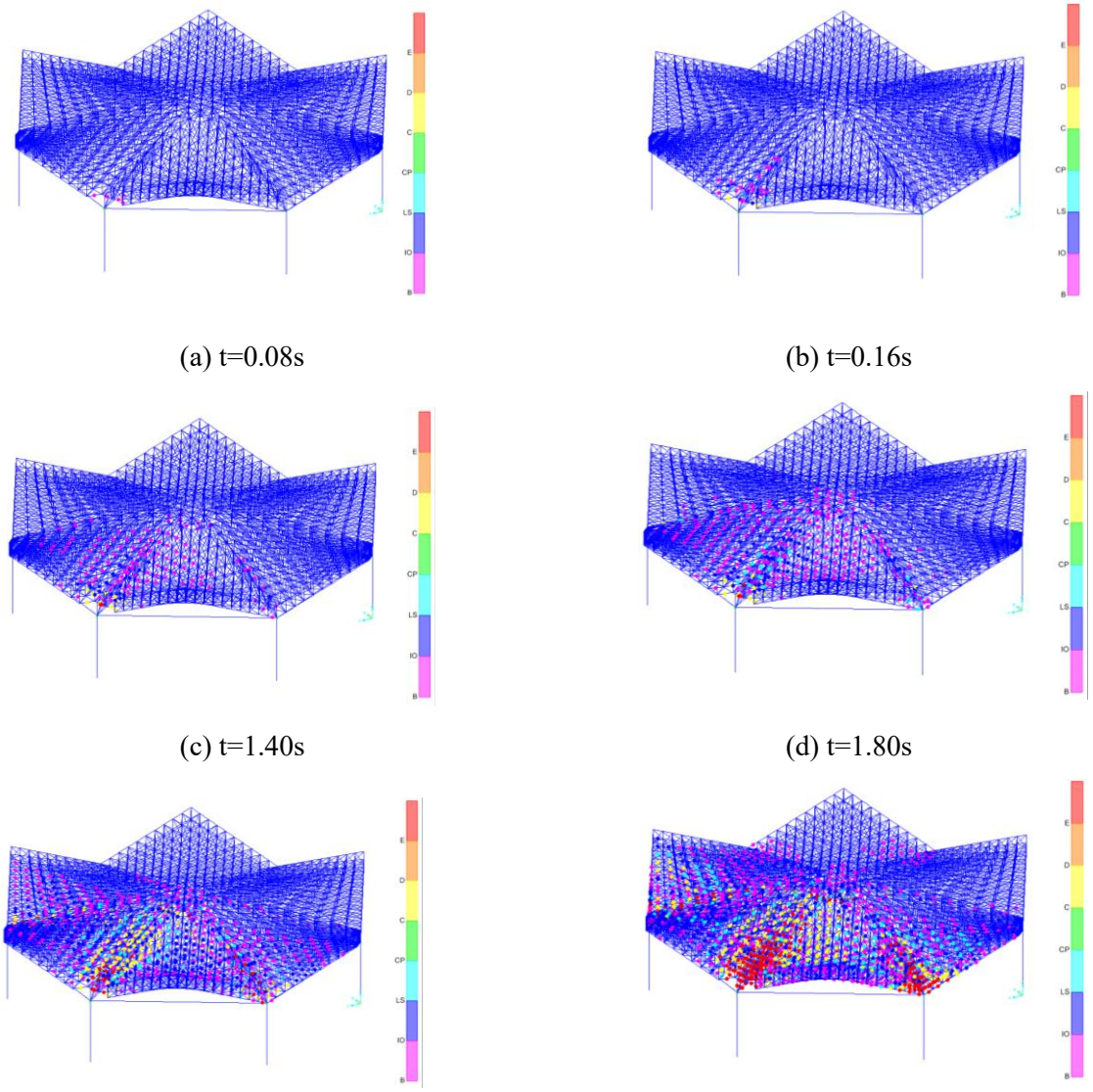
(f)Removing the daylighting band 4 joints

Figure 5: Location diagram of the removed joints

According to the literature [4], the destruction of the structure by removing the members is very small. This paper studies the destruction of the structure after removing the joints. Similar to the method of dismantling the member, dismantling the joint means dismantling the joint and the member connected with it. In order to comprehensively analyze the effect of joint failure on the overall structure, several joints in the sensitive region of Fig. 4 are removed. Firstly, the joint with higher force is removed, and then the joint adjacent to it is removed. The model determined by trial calculation includes two, three, four and six joints. The location of the dismantled joints is shown in Figure 5, where (a) is the removal of two joints in the center of the space truss, and (b), (c), (d) are the two, three, and four joints removed near the support, (e) is the four joints removed by the side truss, and (f) is the six joints removed by the daylighting belt.

3.5. Dynamic damage index D of structures with different joints removed

The ultimate displacement δ_u of long-span prestressed double-layer composite torsional reticulated shells under static load is -698 mm, and the ultimate plastic energy dissipation E_u is 1.95e^7 kN mm. In this section, the model of dismantling four joints is taken as an example for specific description. The specific removal position is shown in Figure 5(d).



(a) t=0.08s (b) t=0.16s

(c) t=1.40s (d) t=1.80s

(e) t=4.60s (f) t=5.28s

Figure 6: Development process of plastic hinge

Figure 6 shows the development process of the plastic hinge after removing the four joints near the support. In the process of dynamic time history analysis, when t=0.08s, the plastic hinges first appear near the dismantled four nodes. When t=0.16s, the number of plastic hinges begins to increase near the supports. When t=1.40s, the plastic hinges begin to develop toward the twisted reticulated shells on both sides. When t=1.80s, the development of plastic hinges on twisted latticed shells on both sides is more sufficient. As time goes on, when t=4.60s, it can be seen from figure (e) that nearly half of the structural areas begin to appear plastic hinges. From the development of plastic hinges, the development of plastic hinges near the dismantled joints and the adjacent two supports is more stringent. After that, the plastic

hinges continued to develop. When t = 5.28s, as shown in figure (f), the plastic hinges developed sufficiently in six torsional reticulated shells, and the structure had lost its bearing capacity.

According to formula (1), the *D* value of the four joints near the support is calculated. The maximum displacement δ_u is -10482mm, the plastic cumulative energy dissipation of the structure $\int dE$ is 9.81e^7 kN mm. Substituting these values into the formula (1):

$$D = \frac{\delta_m}{\delta_u} + \frac{\beta}{E_u}\int dE = \frac{-10482}{-698} + \frac{9.81e^7}{1.95e^7} = 20.0480$$

The damage grade of the structure can be seen directly from the *D* value. The structure has serious damage and collapse. The calculations of the other five models are shown in Table 2.

Table 2: Classification of dynamic damage

Model	Maximum nodal displacement(mm)	Plastic cumulative energy dissipation(kN mm)	*D*	Damage grade
Model 5(a)	203	2.55 e^4	0.2921	Basic intact
Model 5(f)	203	6.08e^4	0.2939	
Model 5(e)	213	1.16e^5	0.3111	Slight damage
Model 5(b)	214	1.44e^5	0.3140	
Model 5(c)	407	4.12e^6	0.7943	Medium damage
Model 5(d)	10482	9.81e^7	20.0480	Serious damage and collapse

It is easy to see from Table 2 that after calculating the dynamic damage index D, the damage grade can be quickly judged and the structural damage can be quantified.

4. Conclusion

In this paper, based on the double indexes of energy and displacement, a new dynamic damage index D is proposed, which is more accurate in evaluating the damage of long-span spatial structures. At the same time, the damage degree of the structure is classified into four grades: basic intact, slight damage, medium damage, serious damage and collapse, which can quantify the damage of the structure, and is more conducive to the damage study of long-span spatial structures.

References

[1] Shiata A,Sezoen MA.The substitute structure method for seismic design in reinforced concrete[J].Journal of the Structural Division,ASCE,1976,102(1):1-18.

[2] Krawinkler H,Zourei M.Cumulative damage in steel structures subjected to earthquake ground motions[J].Computers&Structures,1983,16:1-4.

[3] Banon H ,lrvlne HM.Seismic damage of reinforced concrete frame[J].Journal of the Structural Division ,ASCE,1981,107(9):1713-1729.

[4] ZHANG Xiao-hui, LONG Hai-fang, SHEN Bo, et al. Progress collapse analysis of long-span prestressed steel reticulated shell structure [J]. Journal of Guizhou University (Natural Sciences), 2016, 33(4): 112-117.

Proceedings of the IASS Annual Symposium 2019 – Structural Membranes 2019
Form and Force
7 – 10 October 2019, Barcelona, Spain
C. Lázaro, K.-U. Bletzinger, E. Oñate (eds.)

Influence of length tolerances in space frames' resistance

Gabriel RUIZ [a], Mikel MONASTERIO* [b], Sergio GONZÁLEZ [b], Josu GOÑI [b], Rebeca ROSENKRANZ [b], Guillermo BLANCO [b], José Miguel RICO [a]

[a] Professor, School of Architecture
University of the Basque Country (UPV/EHU)
Plaza Oñati 2, 20018, San Sebastián, Spain

* [b] LANIK I, S.A.
Mundaiz 8, 20012, San Sebastián, Spain
mmonasterio@lanik.com

Abstract

Space frames have been used in construction for years. Different systems have been developed and thousands of structures have been built. Their design and calculation is simple for a structural engineer, thanks to the matrix of stiffness method. Their main challenges lay on their geometry, optimization and manufacturing. One of their strength is that they are highly hyper-static structures. If one element fails, efforts are redistributed so that the structure will not collapse. However, the hyper-staticity may also become a problem if the bars are not manufactured with accurate tolerances. Despite the common use of space frames, no deep researches have been made on this field. Therefore, there are no unified criteria for them and it relies on the accuracy of each manufacturer. The study was based in the ORTZ system, which has been used in space frames by Lanik since 1978, and was divided into two parts. First of all, the manufacturing tolerances of the system were checked, measuring 1288 bars of variable dimensions and obtaining the length-distribution errors of a built system. Later, in order to study the effect of tolerances, 14 projects were analysed. In each of them, the length variation of the bars has been applied as a load case. The differences in length follow a normal distribution, with a zero-mean (no error) and 10 different standard deviations, equivalent to manufacturing tolerances. The research shows that standard deviations of 0.8 mm lead almost to double the utilization factor of at least one of the bars, considering section resistance and buckling. In conclusion, although these small tolerances of tenths of millimetres are not usual in steel structures, they become necessary in spaces frames. Designers and manufacturers should take this into account in order to avoid problems. However, this study has been done using linear calculations and only shows the effect on the worst bar; therefore, a deeper study shall be done, studying non-linear effects and push-over analyses.

Keywords: space frame, manufacturing, tolerances, ortz, statistic, distribution, hyperstatic, sofistik, buckling

1. Introduction

Since the development of the ORTZ system in the 70's, Lanik started building space frames. Lanik has always been concerned about tolerances, which led to the requirement of reaching a total tolerance of 0.4 mm. However, with the expansion of the use of this kind of structures, these sharp tolerances may have not been taken into account. Hence, the dissertation of Gabriel Ruiz [1] explored this field, showing the influence of length tolerances in the maximum utilization factor of the bars in a space frame.

Copyright © 2019 by Gabriel Ruiz, Mikel Monasterio, Sergio González, Josu Goñi
Published by the International Association for Shell and Spatial Structures (IASS) with permission.

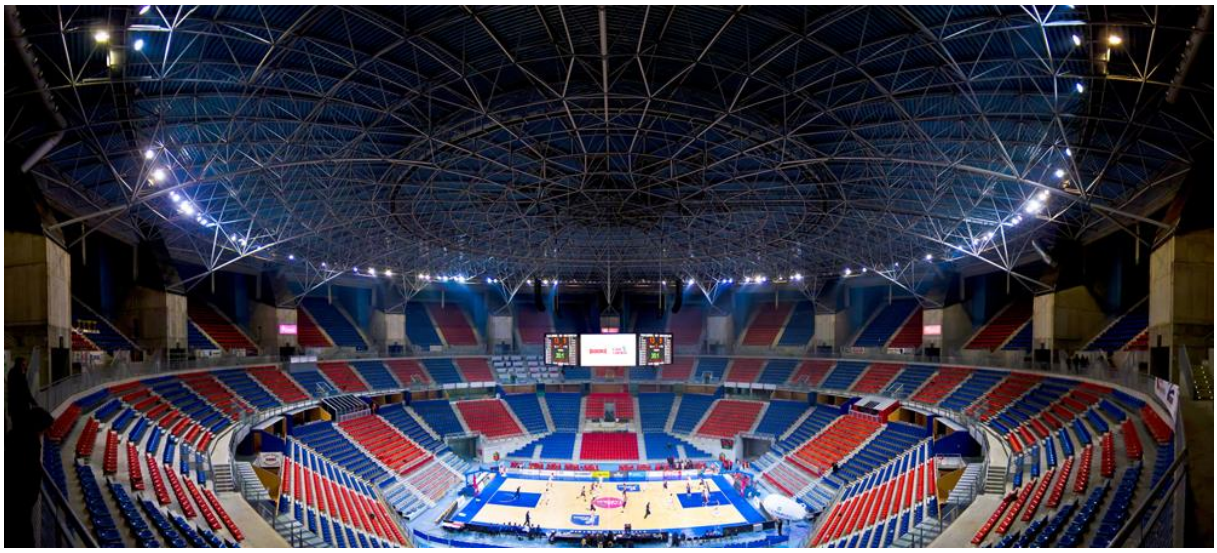


Figure 1: Space frame of Fernando Buesa Arena in Vitoria-Gasteiz (Spain) [Lanik]

1. A first approach: an easy calculation of a single bar

In order to understand the significance of the aforesaid influence, an easy example could be made. A common bar of a space frame is 3 m length, it is a CHS tube with a 88.9 mm diameter and a 3 mm width and S275 steel. It can bear up to a maximum design compression force of N_{Ed} = 100 kN. As it is common in space frames, it shall be considered with a pinned connection in both nodes. According to Eurocode EN 1993-1-1, its resistance to tension forces is $N_{t,Rd}$ = 222.64 kN and its buckling resistance $N_{b,Rd}$ = 103.50 kN. Therefore, its utilisation factor is 0.966, which means it is working at a 96.6% of its resistance. This is quite normal in a space frame, where all the elements are very optimised.



Figure 2. Bar buckling in compression test [Lanik]

If the bar were manufactured with standard tolerances for steel construction, it could be made with an extra length of, for example, 1 mm. Then, it would have to be accommodated in its place, between the other bars of the structure. Space frames are very hyper-static structures, with no internal grades of freedom, so other bars would force the analysed bar into its theoretical position and dimension: the aforementioned 3 m length. This would cause an extra compression effort in the bar, which can be

easily calculated: 1 mm in 3000 mm is a 0.033% strain, taking E = 210000 MPa and A = 809.59 mm^2, it gives an extra compression of 56.67 kN. With this extra effort, the bar could buckle.

2. Effect on big structures

The previous calculation cannot be extrapolated directly to a complete structure, but it gives a glance of its effect. In a space frame, if a beam is manufactured 1 mm longer than its theoretical length, it will introduce a geometrical variation that will affect its working ratio, since the rest of the structure will try to force it to its original length (of course, this will not be fully achieved). Depending on the stiffness and real dimensions of the surrounding bars, it will adopt a final length. What's more, the length error on the bars will not be constant; there will be shorter and longer bars; they will follow a statistical distribution.

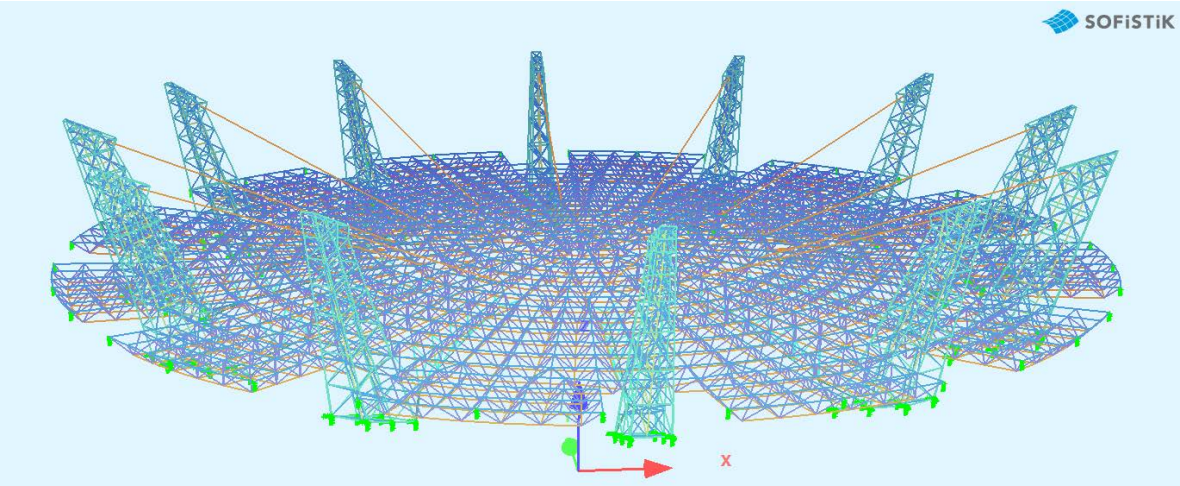


Figure 3: Space frame of Fernando Buesa Arena in Sofistik [Lanik]

3. Calculation method

In order to analyse the influence of manufacturing lengths, 14 structures were selected. These projects are shown in Table 1, and, as it can be seen, there are different geometries and sizes. Their space frames were recalculated adding a calculation hypothesis with a length error in each bar.

Table 1: Selected projects

Project ID	Nodes	Bars	Project ID	Nodes	Bars
1	389	1455	**8**	247	897
2	796	2978	**9**	250	903
3	917	3491	**10**	902	3521
4	83	256	**11**	1001	4071
5	492	1506	**12**	659	1955
6	1449	5565	**13**	81	293
7	246	892	**14**	284	1041

As explained before, fabrication errors cause a lengthening or shortening of bars. This deviation affects all the bars in the structure, so the imperfection was introduced randomly in all of them. A standard distribution was used for the error, with a mean of zero (no error) and different standard deviations, from 0.1 mm to 8 mm, as shown in Table 2. An error in millimetres was assigned to each bar, following the distribution.

Although the explained procedure seems to be correct, the application of the standard distribution on all the bars of the structure may come up with different results, depending on which bars received the largest errors. This is caused because the distribution on the bars has infinite possibilities. Therefore,

the distribution of errors should have been applied several times and then, the average of the results should be taken. However, the calculation time would have grown exponentially. In order to reach a reasonable compromise, 5 calculations were done. The distribution was applied 5 times for each deviation and each project. Then, the results were averaged.

Table 2: Applied distributions

Mean	Std. deviation	No. of calculations
0	0.1	5
0	0.2	5
0	0.4	5
0	0.6	5
0	0.8	5
0	1	5
0	2	5
0	4	5
0	6	5
0	8	5

Calculations were done in the Sofistik software, using linear analysis and linear materials. The aforementioned errors were transformed to strains, in order to introduce them in local X directions, as it is shown in Figure 4.

```
LC NO  15  TITL  'H15-Imperfecciones'
beam from       10001    type ex pa      0.105535852
beam from       10002    type ex pa      -0.085508914
beam from       10003    type ex pa      -0.069306764
beam from       10004    type ex pa      -0.059440259
beam from       10005    type ex pa      -0.111728367
beam from       10006    type ex pa      0.033488739
beam from       10007    type ex pa      -0.083263314
beam from       10008    type ex pa      0.195726882
beam from       10009    type ex pa      0.252036017
beam from       10010    type ex pa      0.376455683
beam from       10011    type ex pa      -0.319718034
beam from       10012    type ex pa      0.422412073
beam from       10013    type ex pa      -0.518951985
beam from       10014    type ex pa      -0.209019638
beam from       10015    type ex pa      -0.098628993
```

Figure 4: Length errors applied in Sofistik as a loadcase

In order to simplify the calculations and to focus on the effect of the length imperfections, only two hypotheses have been done. First of all, only permanent loads are taken into account. After that, both permanent loads and imperfections are introduced. For each hypothesis, the maximum utilisation factor of the structure is obtained. Finally, the difference between the factor with and without imperfection is the utilisation factor increase that is used as a result.

4. Results

14 projects, 10 standard deviations and 5 distributions for each one, led to a total of 700 calculations in the research. Table 3 shows all the complete results for one of the analysed projects. The utilisation factor is increased almost linearly when the standard deviation of imperfections increases. In this case, the standard deviation of 1 mm amplifies the utilisation factor on a 100% of utilisation.

Table 3. Complete results for project 1

Project	St.dev.	Calcul.no.	U.F. Only Perm	U.F. Perm+Imperf	Difference (Utilisation factor increase)	Utilisation factor increase (mean)
1	0.1	1	0.385	0.423	0.038	0.050
		2	0.385	0.427	0.042	
		3	0.385	0.460	0.075	
		4	0.385	0.459	0.074	
		5	0.385	0.407	0.022	
1	0.2	1	0.385	0.445	0.060	0.085
		2	0.385	0.440	0.055	
		3	0.385	0.522	0.137	
		4	0.385	0.440	0.055	
		5	0.385	0.504	0.119	
1	0.4	1	0.385	0.776	0.391	0.284
		2	0.385	0.672	0.287	
		3	0.385	0.621	0.236	
		4	0.385	0.602	0.217	
		5	0.385	0.675	0.290	
1	0.6	1	0.385	0.949	0.564	0.510
		2	0.385	0.887	0.502	
		3	0.385	0.935	0.550	
		4	0.385	0.754	0.369	
		5	0.385	0.952	0.567	
1	0.8	1	0.385	1.242	0.857	0.933
		2	0.385	1.340	0.955	
		3	0.385	1.220	0.835	
		4	0.385	1.350	0.965	
		5	0.385	1.440	1.055	
1	1	1	0.385	1.680	1.295	1.153
		2	0.385	1.330	0.945	
		3	0.385	1.660	1.275	
		4	0.385	1.390	1.005	
		5	0.385	1.630	1.245	
1	2	1	0.385	2.240	1.855	2.315
		2	0.385	2.520	2.135	
		3	0.385	2.810	2.425	
		4	0.385	2.520	2.135	
		5	0.385	3.410	3.025	
1	4	1	0.385	5.410	5.025	4.591
		2	0.385	4.970	4.585	
		3	0.385	4.960	4.575	
		4	0.385	4.280	3.895	
		5	0.385	5.260	4.875	
1	6	1	0.385	7.270	6.885	6.905
		2	0.385	7.270	6.885	
		3	0.385	7.140	6.755	
		4	0.385	5.830	5.445	
		5	0.385	8.940	8.555	
1	8	1	0.385	11.300	10.915	11.575
		2	0.385	11.700	11.315	
		3	0.385	13.700	13.315	
		4	0.385	10.500	10.115	
		5	0.385	12.600	12.215	

Table 3 also shows that the distribution of errors influences the results, as explained before. For example, with a standard deviation of 0.6, the maximum utilization factor is 0.949 and the minimum 0.754. However, the 5 calculations that were done minimize this effect and only their average is used for comparisons.

After the analysis of all the projects, Table 4 has been done. In spite of some exceptions, the influence of length tolerances is similar in the analyzed structures. Figure 5 and Figure 6 show the same information in a chart.

Table 4. Results for all the projects

Std. Dev. Projects	0.1	0.2	0.4	0.6	0.8	1	2	4	6	8
1	0.050	0.085	0.284	0.510	0.933	1.153	2.315	4.591	6.905	11.575
2	0.048	0.081	0.345	0.514	0.635	0.987	2.187	5.633	7.679	9.663
3	0.061	0.162	0.555	0.685	1.049	1.565	3.869	9.679	10.273	13.521
4	0.013	0.109	0.413	0.604	0.875	0.809	3.552	6.768	9.022	11.540
5	0.050	0.155	0.464	0.666	0.767	1.662	2.837	5.884	8.163	9.178
6	0.113	0.278	0.520	1.032	1.289	1.789	4.264	7.963	13.141	16.454
7	0.008	0.086	0.254	0.529	0.851	1.018	2.154	5.031	7.142	11.475
8	0.006	0.014	0.159	0.311	0.528	0.772	1.860	3.398	5.846	9.138
9	0.025	0.098	0.375	0.616	0.949	1.343	2.391	5.202	8.066	10.652
10	0.000	0.078	0.250	0.592	0.899	0.975	2.537	5.104	9.637	13.051
11	0.012	0.073	0.253	0.434	0.854	1.081	2.540	6.380	9.894	13.683
12	0.007	0.056	0.189	0.438	0.567	0.843	2.154	4.345	7.460	8.943
13	0.074	0.169	0.391	0.598	0.960	1.124	2.150	4.297	7.018	10.450
14	0.050	0.180	0.390	0.723	0.972	1.547	2.979	6.700	9.702	14.796
Mean	**0.037**	**0.116**	**0.346**	**0.589**	**0.866**	**1.191**	**2.699**	**5.784**	**8.568**	**11.723**

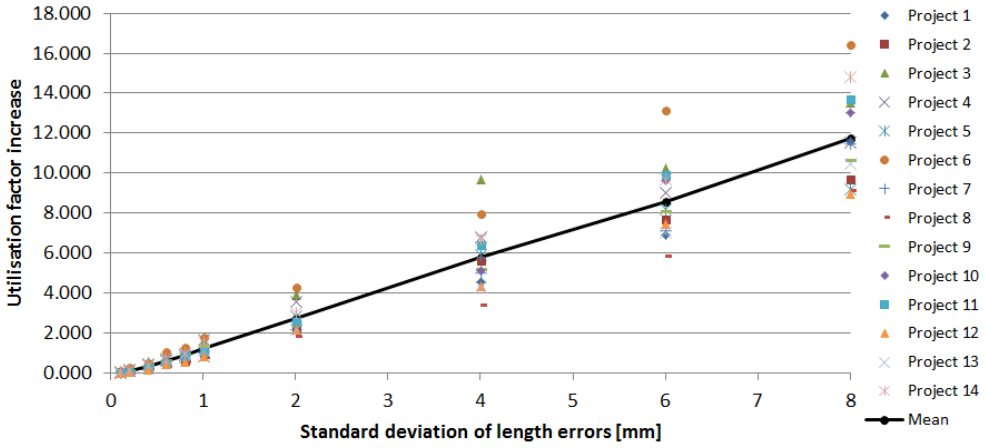


Figure 5. Results of all the projects

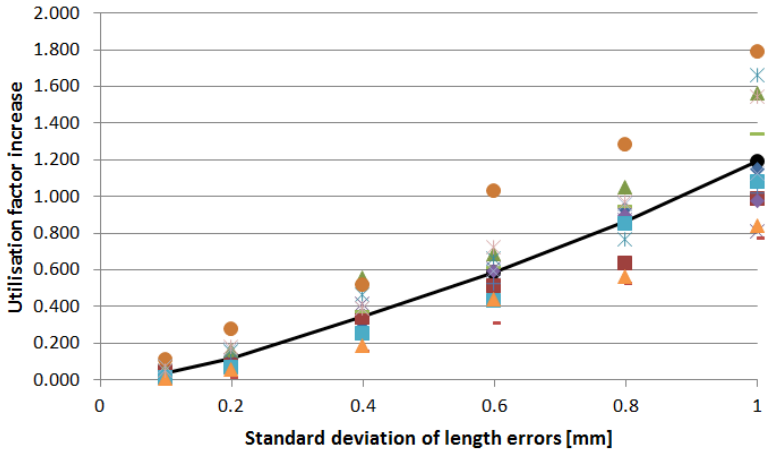


Figure 6. Results of all the projects (Detail: standard deviation between 0.1 and 1)

A regression analysis can be done with the results of the different projects. As shown in Figure 5, the relation between length errors and utilisation factor is quite linear. The mean could be approximated using one of the following equations:

Linear: $$y = 1.4872 \cdot x - 0.2437 \quad (1)$$

Polynomial: $$y = 0.0054 \cdot x^2 + 1.4462 \cdot x - 0.2153 \quad (2)$$

5. Conclusion and further analysis

This study concludes that length errors have an influence in the spaces frames' resistance. Therefore, manufacturing processes have to be designed and oriented to ensure sharp tolerances that are compatible with a space frame.

What's more, if the manufacturing tolerance is known, the increase of utilisation factor could be easily obtained following the equations (1) or (2). Calculations were done without taking into account any own parameter of Lanik's ORTZ system. Therefore, the results of the dissertation [1] and this paper do not apply only for ORTZ system but also for all the space frames systems in the market.

Furthermore, the study has opened new paths of investigation. On the one hand, the calculations have only been done using linear analysis. On the other hand, the results take into account the maximum utilisation factor of the structure, which is related to only one bar. Even if the worst bar were over its limit, the remaining ones may not be affected by the phenomenon. A deeper research may be advisable and could analyse non-linear effects and push-over.

Finally, the dissertation only analyses the calculation results in different and complete structures. Physical tests may be interesting. For example, small structures or octahedrons could be manufactured with precise tolerance values and their actual efforts checked, using dynamometers or strain-meters.

References

[1] G. Ruiz, "Incidencia de las tolerancias de fabricación en la seguridad de las estructuras spaciales" (Incidence of manufacturing tolerances in the safety of space structures), Ph.D. dissertation, Spain: School of Architecture, University of the Basque Country (UPV/EHU), 2015.

[2] L. Irisarri, J. Martinez and J. Goñi, "Past, present and future of the space frame Market: LANIK experience," in *IASS Symposium*, Valencia, Spain, 2009.

[3] J. Chilton, Space Grid Structures, Architectural Press, 1999.

Proceedings of the IASS Annual Symposium 2019 – Structural Membranes 2019
Form and Force
7 – 10 October 2019, Barcelona, Spain
C. Lázaro, K.-U. Bletzinger, E. Oñate (eds.)

Load factor to be applied to buckling design of cylindrical lattice shells under asymmetric snow loads

Yutaka NIHO*, Shiro KATO[a], Shoji NAKAZAWA[a]

*National Institute of Technology, Kure College, Department of Architecture and Structural Engineering
ZIP code 737-8506, 2-2-11, Aga-Minami, Kure city, Hiroshima prefecture, JAPAN
niho@kure-nct.ac.jp

[a] Toyohashi University of Technology, Department of Architecture and Civil Engineering

Abstract

This paper investigates the relationship between reliability index and snow load factor for buckling design for a simply supported cylindrical latticed shell roof under simultaneous action of both dead load and asymmetric snow load. The snow distribution as a main target is assumed in a way that the snow depth on the half of the arch direction is half of the amount the other half arch. The snow fall depth is here assumed 50 cm evaluated as 100-year return period, and probability is assumed as Gumbel probability with 100-year reference period. The probability distribution of ultimate strength including geometrical and material nonlinearities is approximately evaluated based on a first-order perturbation. The reliability is calculated in terms of a relationship of γ_s-to-β for design use.

Keywords: Cylindrical lattice shells, Load factor, Reliability index, Buckling Design, asymmetric snow loads

1. Introduction

Cylindrical lattice shells are light-weight roof structures on account of super high strength. The structures are well suited to roofs of sport halls, gymnasia, hangers and other large span buildings. On the other hand, excessive reduction of structural members may induce a risk of buckling leading to collapse. Therefore, any cylindrical latticed shell has to be designed with the objectives to prevent the buckling. With the above mentioned background, many researchers have studied buckling behavior and buckling strength of cylindrical latticed shells for many years. With recent researches, IASS working group No.8 has compiled invaluable results [1] in 2014 with respect to buckling of reticulated shells.

Since load factors for design is one of the keys in design, several papers for load factors and reliability for single layer latticed shells have been recently published [2, 3, 4]. The papers have focused especially relationships between reliability index β and snow load factor γ_s or global load factor γ_n applied to design for single layer latticed domes mainly under uniformly distributed snow load [2, 3]. On the other hand, less papers have been found for reliability design on single layer cylindrical latticed shells under non-uniform snow load [3, 4] in authors' knowledge. Based on the present discussion, this paper presents a study to formulate for calculating failure probability for a simply supported cylindrical latticed shell subject to non-uniform snow load. Based on a reliability analysis, the paper clearly represents a numerical scheme and several results of the relationship between reliability index β and snow load factor γ_s to be applied in member proportioning.

2. Cylindrical Lattice Shell for Analysis

2.1. Configuration of lattice shell

Figure 1 shows a study target of a cylindrical latticed shell with an equilateral triangle grid pattern. Each

Copyright © 2019 by Yukata Niho, Shiro Kato, Shoji Nakazawa
Published by the International Association for Shell and Spatial Structures (IASS) with permission.

grid is composed of a longitudinal member which is horizontal to the *X*-axis and two diagonal members crossing at α=60 degrees to the *X*-axis. Each member is connected rigidly to nodes.

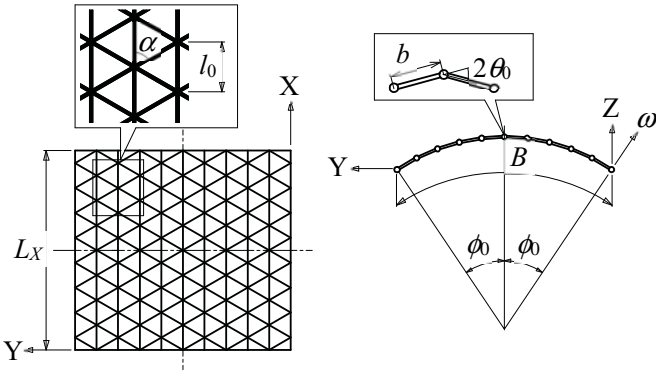


Figure 1: Geometry of the analytical model [5]

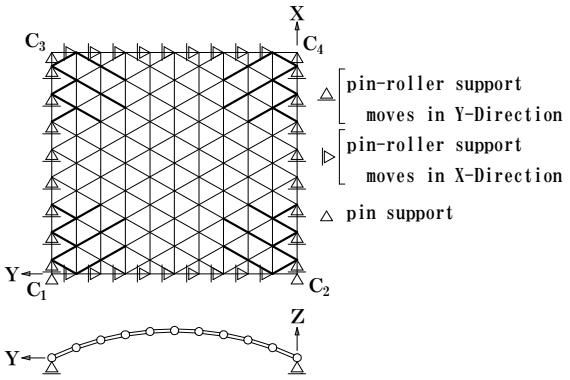


Figure 2: Boundary condition for analysis [5]

The repetition number in the *X*-axis, n_X, is 8 and that of in the arch direction, n_B, is 10. The member length for each member l_0 is 4m. A characteristic parameter θ_0, that is called a subtended half angle of members on the gabled sides, is applied (Figure 1). The value θ_0 is restricted to 4 degrees in this paper. The parameter θ_0 is defined using a half open angle ϕ_0 of the arch as follows.

$$\phi_0 = n_B \cdot \theta_0 \tag{1}$$

2.2. Boundary condition

The lattice shell is supported by pins and rollers with no displacements in *Z*-direction as shown in Figure 2. Nodes on the gabled arches of C_1-to-C_2 and C_3-to-C_4 can move in parallel with the *X*-direction, while nodes on the two straight edges of C_1-to-C_3 and C_2-to-C_4 can move in parallel with the *Y*-direction. On the other hand, the four corners of C_1, C_2, C_3 and C_4 are supported by pins with no displacements in the three directions. Three rotations in the *X*-, *Y*- and *Z*-direction are not restrained at any node.

2.3. Assumption of reference shell; diameter and thickness of members

With respect to diameter and thickness of members, a typical model is first set up as a reference shell in advance of investigation of failure reliability. The geometry and boundary condition are described in the above sections. For the reference shell, members are classified into two groups; members for an inner area and members along boundaries. Considering a tendency of single layer cylindrical lattice

shells applied so far, member slenderness ratio λ_0 of the inner members is selected as 40 for brevity. The value λ_0 is defined with respect to 4.0 m as the member length l_0. With respect to thickness distribution of tubular sections of inner members, based on a preliminary analysis of axial force distributions under uniform loading, the distribution is assumed as shown in Figure 2, where the thickness of members marked with thin lines is assumed 5 mm, while the thickness of members shown in bold lines is assumed 8 mm around and near from edges. Here the thickness of the reference shells is denoted by $t_{0(n)}$, and $t_{0(n)}$ corresponds to 5mm for the members with marks of thin lines, and 8 mm for the bold lines. For definition of the representative thickness of the reference thickness, 5 mm is denoted by $t_{0(r)}$ and often referred in later explanations.

One of the reasons to adopt a little larger thickness of 8mm for members around the corners is to keep a situation that, the members around supports C_1, C_2, C_3 and C_4, being subject to large stresses, remain stable not to buckle until the lattice shell reaches its ultimate strength. On the other hand, the member slenderness ratio of members on the four boundaries is assumed half times the value λ_0 of inner members, and their thickness for the reference shell is assumed 10 mm to keep the members remain elastic until ultimate strength of shells.

Since this paper investigates failure probability of the cylindrical lattice shells of which member sections are proportioned for a factored design load of dead load and snow load, the thickness of members, being different from those of the reference shell, is first proportioned to adapt to the factored load. The load combination and the thickness distribution of members are later explained in this section for reliability analysis.

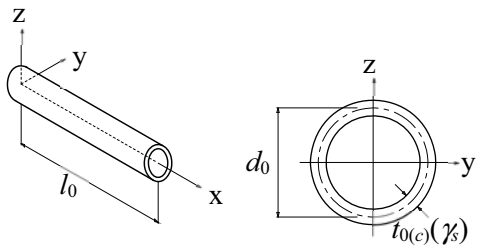


Figure 3: Steel tubular section [5]

2.3.1. Diameter of inner members

The diameter of each of inner members, d_0, is assumed based on member slenderness ratio λ_0 by the following equation.

$$d_0 = 2 \cdot \sqrt{2} \cdot \frac{l_0}{\lambda_0} \tag{2}$$

where l_0 is 4 m for the member length except for members on the four boundaries. Here member slenderness λ_0 is assumed 40, and the value d_0 of all members are same as 282.3 mm except for edge members. For the edge members on the four boundaries, λ_0 is assumed half of those for the inner members. Therefore in the case of λ_0=40, the diameters for members are either 282.3 mm or 565.7 mm.

2.3.2. Thickness of members of lattice shell to be studied for reliability

Thickness of each of inner members for reliability analysis described later is calculated in proportion to a uniform factored design load $P_{v(n)}(\gamma_s)$ per one node for dead load and uniform snow load.

$$P_{v(n)}(\gamma_s) = A_{node} \cdot (\gamma_d \cdot p_{d(n)} + \gamma_s \cdot p_{s(n)}) \tag{3}$$

where $p_{d(n)}$ and $p_{s(n)}$ are nominal design loads per unit surface, A_{node} is defined as the influence loading area of one node, γ_d is a load factor for $p_{d(n)}$ and γ_s is also a snow load factor to be applied in LRFD

design, and A_{node} is defined as follows using the member length l_0.

$$A_{node} = \frac{\sqrt{3}}{2} \cdot l_0^2 \tag{4}$$

In this study, γ_d is assumed 1.1 referring to AIJ LRFD recommendations, and γ_s is varied as 1.0, 1.25. 1.5, 2.0, 2.5. 3.0, and 3.5 for assuming the thickness of the lattice shells to be studied for reliability. Based on an experience so far, the dead load $p_{d(n)}$ is assumed 0.8 kN/m^2, and $p_{s(n)}$ is calculated as the product of design snow depth $h_{s(n)}$ for 100-year return period and nominal snow density $\rho_{s(n)}$. The depth $h_{s(n)}$ and the density $\rho_{s(n)}$ are assumed here to be 0.5 m for 100-year return period and 2.83 kN/m^3 [5], respectively. Consequently, $p_{s(n)}$ is 1.415 kN/m^2, and A_{node} is 13.86 m^2 per one node using 4.0 m for l_0.

We focus the nominal buckling strength of the reference shell mentioned previously. The member arrangement and other geometries including the diameter and thickness distribution of tubular sections are those just mentioned above for the reference shell. The nominal buckling strength is denoted by $P_{cr(n,0.2)}$ in this paper. However, the applied load as nominal is assumed as a uniform load proportional to dead load. It is assumed to be the same nominal strength which is evaluated as the ultimate load per one node based on elastic-plastic buckling analysis considering a geometric imperfection with 0.2 times the equivalent shell thickness t_{eq}. The value t_{eq} is defined by the following equation.

$$t_{eq} = 2 \cdot \sqrt{3} \cdot \frac{l_0}{\lambda_0} \tag{5}$$

Reflecting the geometry of the reference shell with λ_0=40 and l_0=4,000 mm, the amplitude of the imperfection w_{i0}=69.2 mm as $0.2t_{eq}$, where the equivalent shell thickness is 346 mm. A notice should be marked for the imperfection mode, and the adopted mode is the one which leads the lowest elastic plastic buckling load among first three buckling modes, being abbreviated here for brevity. As for $P_{cr(n,0.2)}$ as a nominal value, the yield stress is assumed $\sigma_{y(n)}$=235N/mm^2 for the strength class of 400 kN steel, and the nominal value $P_{cr(n,0.2)}$ is evaluated as 86.88 kN per one node with 13.86 m^2 for A_{node}.

Returning to the shell to be studied for reliability, the load is the factored design load $P_{v(n)}(\gamma_s)$ defined by Eq.(3), and the uniform load distribution over the surface is similar to dead load. Then, the thickness of each member $t_{0(c)}(\gamma_s)$ of the shell under $P_{v(n)}(\gamma_s)$ can be assumed by Eq.(6) using the thickness $t_{0(n)}$ and buckling strength $P_{cr(n,0.2)}$ of the reference shell.

$$t_{0(c)}(\gamma_s) = \frac{P_{v(n)}(\gamma_s)}{P_{cr(n,0.2)}} \cdot t_{0(n)} \tag{6}$$

The thickness $t_{0(n)}$ is 5 mm or 8 mm for inner members depending on members marked with thin lines or bold lines in Figure 2, and those of the edge members are 10 mm. Table 1 is a list of lattice shells designed for the factored loads $P_{v(n)}(\gamma_s)$, and for example they are denoted by S2.50 for γ_s=2.50. And the member thickness $t_{0(c)}(\gamma_s)$ is calculated by Eq. (6), corresponding to the inner members with $t_{0(r)}$=5 mm as their representative thickness of the reference shell. They are marked with thin lines in Figure 2. For "bold" members (see Figure 2), $t_{0(c)}(\gamma_s)$ is 1.6 times the value shown in Table 1.

Table 1: Thickness of members depending on snow load factor γ_s; the members correspond to those of the reference shell with thickness $t_{0(r)}$=5 mm, which are marked by thin solid lines in Figure 2.

γ_s for uniform snow load	1.00	1.25	1.50	2.00	2.50	3.00	3.50	3.86
Name of shell	S1.00	S1.25	S1.50	S2.00	S2.50	S3.00	S3.50	reference
$P_{v(n)}(\gamma_s)$ [kN]	31.80	36.70	41.60	51.41	61.21	71.01	80.82	86.88
$P_{cr(n,\,0.2)}$ [kN]	86.88							86.88
$t_{0(c)}(\gamma_s)$ for members [mm]	1.83	2.11	2.39	2.96	3.52	4.09	4.65	$t_{0(r)}$=5.00

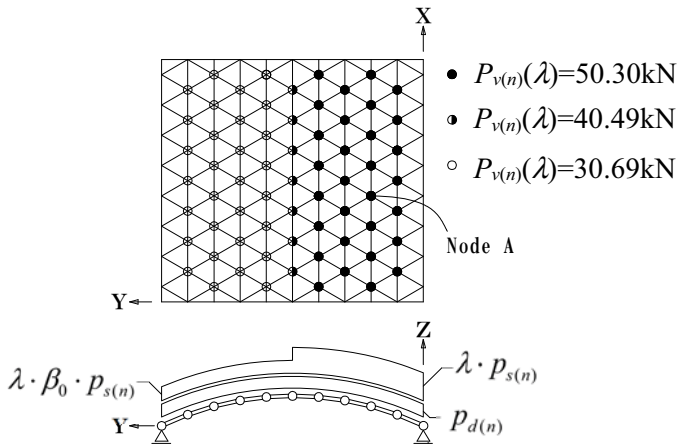


Figure 4: loading conditions for obtaining the buckling strength (β_0=0.5, λ=2.0 in Eq.(7))

3. Reliability Analysis

3.1. Loading conditions for obtaining the buckling strength

The model to be analyzed for reliability, such as S2.50 for example as introduced in previous section, is subjected simultaneously to both uniform dead load and asymmetric snow load, as shown in Figure 4.

The load per one node $P_{v(n)}(\lambda)$ is calculated as follows using a generalized load incremental factor λ for snow load given by Eq.(7). This equation is applied to approximately find the buckling strength of the shells in Table 1.

$$P_{v(n)}(\lambda) = \begin{cases} \left(p_{d(n)} + \lambda \cdot p_{s(n)}\right) \cdot A_{node} & \text{(for right part of arch)} \\ \left(p_{d(n)} + \lambda \cdot \dfrac{1+\beta_0}{2} \cdot p_{s(n)}\right) \cdot A_{node} & \text{(for central part)} \\ \left(p_{d(n)} + \lambda \cdot \beta_0 \cdot p_{s(n)}\right) \cdot A_{node} & \text{(for left part)} \end{cases} \tag{7}$$

where only snow load is incremented, β_0 expresses the degree of non-uniformness in load, and 0.5 is assumed for β in this study.

3.2. Average and coefficients of variation of buckling strength of analyzed shell

For reliability analysis of buckling, the probability of buckling load considering elastic plastic properties are required. In this study, the probability distribution of buckling strength under asymmetric loading is assumed as log-normal with average strength $\mu(P_{cr})$ and coefficient of variation $v(P_{cr})$. Despite of snow load distributions and other related parameters, the average strength $\mu(P_{cr})$ is assumed to be obtained as an elastic plastic buckling load just based on the average values of related probability parameters, while the present study adopts E, t, σ_y and λ_0 for probability variables. The parameters denote Young's modulus, thickness of tubular sections, yield stress and member slenderness ratio, respectively in this order. Accordingly, the average strength $\mu(P_{cr})$ is replaced by $P_{cr(c)}$, which is evaluated by using the average values $E_{(c)}$, $t_{(c)}$, $\sigma_{y(c)}$ and $\lambda_{0(c)}$ of their variables respectively. On the other hand, the coefficient of variation is assumed approximately based on a first order perturbation expressed as follows.

$$v(P_{cr}) = \sqrt{(a_1 \cdot v_1)^2 + (a_2 \cdot v_2)^2 + (a_3 \cdot v_3)^2 + (a_4 \cdot v_4)^2} \tag{8}$$

where the coefficients a_1, a_2, a_3 and a_4 are those obtained as the sensitivity coefficients for perturbation [3], and v_1, v_2, v_3 and v_4 are the coefficient of variations of E, t, σ_y and λ_0. The details of Eq.(8) are

abbreviated here for brevity.

Cylindrical lattice shells are sensitive to geometric imperfections, and accordingly the value $P_{cr(c)}$ is evaluated considering initial imperfection. The adopted imperfection distributions are the first three lowest linear buckling modes, and the maximum amplitude w_{i0} is assumed by Eq.(9) using a parameter δ_i based on the equivalent shell thickness t_{eq} of Eq.(5).

$$w_{i0} = \delta_i \cdot t_{eq} \tag{9}$$

Accordingly, six types of initial imperfection are adopted depending on positive and negative values for δ_i. Then six values of the buckling strength are obtained for the same amplitude of imperfection w_{i0}. And, the minimum of them is selected and obtained as its buckling strength $P_{cr(c)}$. The ratio δ_i shown in this equation is assumed as 0.1, 0.2, 0.3, 0.4 or 0.5 abbreviating the sign.

The average of buckling strength $P_{cr(c)}$ thus obtained using load distribution of Eq.(7) is shown in Table 3 depending for the shells of S1.00 to S3.50. Here $P_{cr(c)}$ denotes the strength at node A of Figure 4 on the right half of the shell. We need a notice that the average of the buckling strength is the one for the shell with the thickness $t_{0(c)}(\gamma_s)$ of tubular sections given in Table 1.

Based on Eq.(8), the coefficients of variations are also evaluated by assuming the coefficients of variation of E_s, t, σ_y and λ_0.The coefficient of variations are assumed as shown in Table 4 together with the sensitivity coefficients a_i (see ref. [3]).

Table 2: Assumptions for stochastic variables [5]

stochastic variables	Average	Coefficient of variation	Probability distribution
Young's modulus E	205kN/mm^2	0.087	log-normal
member thickness t	$t_{0(c)}(\gamma_s)$(see table 1)	0.03	log-normal
yield strength σ_y	310N/mm^2	0.081	log-normal
member slenderness λ_0	40	0.084	log-normal

Table 3: Average of buckling strength on the model $P_{cr(c)}$(Node A:See Figure 4)(Unit:kN)

Shell Name	Ratio of amplitude of imperfection δ_i					
	0.0	0.1	0.2	0.3	0.4	0.5
S1.00	40.08	36.70	33.68	30.79	28.31	26.25
S1.25	46.03	42.15	38.66	35.33	32.47	30.08
S1.50	52.01	47.67	43.70	39.95	36.69	33.97
S2.00	63.88	58.60	53.70	49.09	45.06	41.69
S2.50	75.72	69.52	63.67	58.23	53.41	49.40
S3.00	87.47	80.37	73.61	67.34	61.76	57.10
S3.50	99.33	91.32	83.65	76.55	70.19	64.89

Table 4: Sensitivity coefficients a_i and coefficient of variation for buckling strength, $v(P_{cr})$

Sensitivity coefficient		variation	Ratio of amplitude of imperfection δ_i					
	Stochastic variables		0.0	0.1	0.2	0.3	0.4	0.5
a_1	Young's modulus	0.05	0.520	0.495	0.462	0.436	0.401	0.401
a_2	Member thickness	0.02	0.964	0.978	0.982	0.987	0.983	0.982
a_3	Yield strength	0.05	0.520	0.506	0.518	0.498	0.491	0.466
a_4	Member slenderness	0.084	-1.355	-1.474	-1.535	-1.638	-1.696	-1.764
Coefficient of variation for buckling strength of the analytical model $v(P_{cr})$			0.133	0.140	0.144	0.151	0.155	0.160

Table 5: Failure probability [5]

Reliability index β	1.5	2.0	2.5	3.0	3.5	4.0
Failure probability p_f	0.067	0.023	0.0062	0.0014	0.00023	0.000032

3.4. Reliability function

Reliability function Z is assumed by Eq.(10) for the loading condition shown in Figure 5.

$$Z = P_{cr} - (p_d + h_s \cdot \rho_{s(n)}) \cdot A_{node} \tag{10}$$

where the snow load on the left half surface slips down reducing to $\beta_0 \cdot h_s \cdot \rho_{s(n)}$, and the snow load on the other right half remains as same as the uniform snow load.

Failure probability p_f is defined as follow.

$$p_f = Prob(Z \le 0) \;\; ; \quad p_f = 1 - \Phi(\beta) \; ; \beta = \frac{\mu_z}{\sigma_z} \tag{11}$$

where the coefficient of variation for dead load is 0.1 while the average being same as its nominal value, and μ_z and σ_z are average and standard deviation for the reliability function Z. Reliability index β is calculated here based on AFOSM. Relationship between failure probability and reliability index is shown in Table 5 [5].

4. Results and Conclusions

Figure 6 is a relationship of p_f-to-γ_s in the case of loading condition of Figure 5 and Eq.(7). Six lines respectively correspond to the imperfection amplitude ratio δ_i. The result in Figure 6 is interpreted in terms of β-to-γ_s relationship, showing the load factor γ_s required to satisfy the reliability index β. The case, for example, picked up for β=3.0 and δ_i=0.2 in Table 6 means that the load factor γ_s=2.59 is required in the case of loading condition of Eq.(7).

This paper presents a scheme to evaluate the reliability index considering the non-uniform snow distribution and proves that the scheme works well to obtain the numerical results as β-to-γ_s relationship.

Acknowledgements

Authors would like to express their appreciation to Nohmura Foundation for Membrane Structure's Technology for the financial partial support.

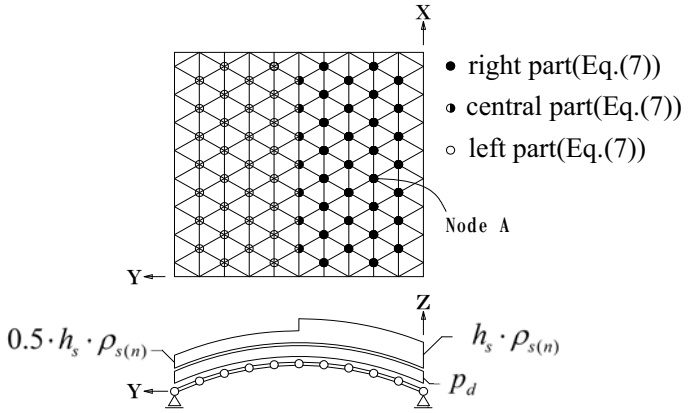


Figure 5: Non-uniform load (β_0=0.5, Eq.(10))

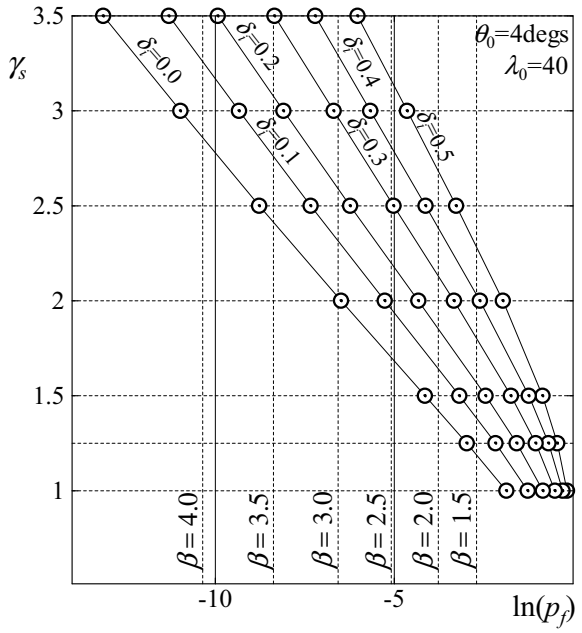


Figure 6: Scatter diagram for failure probability and snow load factor

Table 6: Minimum required value for snow load factor γ_s read from Figure 6

β	Ratio of amplitude of imperfection δ_i					
	0	0.1	0.2	0.3	0.4	0.5
1.5	1.19	1.38	1.57	1.80	2.03	2.28
2.0	1.42	1.64	1.85	2.13	2.38	2.68
2.5	1.70	1.96	2.20	2.52	2.81	3.16
3.0	2.02	2.32	**2.59**	2.96	3.29	3.70
3.5	2.41	2.76	3.08	3.51	3.88	4.35
4.0	2.86	3.26	3.61	4.10	4.52	5.06

References

[1] IASS WG8, "(DRAFT) Guide to buckling load evaluation of metal reticulated roof structures," October, 2014

[2] S. Kato and T. Yanagisawa, "Reliability analysis of buckling of reticulated single layer roofs of general form under vertical loads," *Journal of IASS, Vol. 57, No.3,* September 2016, pp.227-244

[3] S. Kato, T. Yoshino Y. Niho and S. Nakazawa, "Discussions on loads factor for reticulated shells under snow load," *Proceedings of the IASS Annual Symposium 2018, MIT, Boston, USA, July 16-20, 2018,* July 2018

[4] S. Kato, Y. Niho, T. Yanagisawa and S. Nakazawa, "Buckling and reliability of cylindrical lattice shell under snow load," *Proceedings of the IASS Annual Symposium 2017, Hamburg, Germany, September 25-28, 2017,* September 2017

[5] S. Kato and Y. Niho, "Evaluation of relationship between global load factor and reliability index for buckling of cylindrical latticed shells under snow load —the case of uniform load and simple support boundary —", *Steel Construction Engineering, Vol.102*, *Japanese Society of Steel Construction,* June 2019 (in Japanese; to be published)

Proceedings of the IASS Annual Symposium 2019 – Structural Membranes 2019
Form and Force
7 – 10 October 2019, Barcelona, Spain
C. Lázaro, K.-U. Bletzinger, E. Oñate (eds.)

Proposal of new roof support considering seismic performance

Yoichi MUKAIYAMA *, Shiro KATO [a], Shoji NAKAZAWA [a]

* TOMOE Corporation
16-13, Tsukishima 4-chome, Chuo-ku, Tokyo, 104-0052, Japan
mukaiyama@tomoe-corporation.co.jp

[a] Toyohashi University of Technology

Abstract

The steel roofs of gymnasiums or factories are generally supported by reinforced concrete structure. In this type of structures, pin supports or roller supports are installed at the base of steel roofs and atop of reinforced concrete structure. In 2011 Tohoku earthquake and in 2016 Kumamoto earthquake, the damages around the supports were reported. Therefore, the present paper proposes a new support to refrain from the damage due to strong earthquake. Seismic performance in the span direction is discussed in the present paper by elasto-plastic dynamic response analysis. Through the results obtained ductility factor of the energy absorbing members, amount of horizontal displacement between column and support, the stress of the steel members of roof are investigated and proved the applicability of this supports.

Keywords: Steel roofs on RC-frame, Energy absorbing member, Ductility factor, Dynamic response analysis

1. Introduction

As damage to spatial frame structures in the Great East Japan Earthquake of 2011 and Kumamoto earthquake of 2016, many damages on the support of the steel roofs have been reported. As observed in the damage cases, most of these damages are caused by out-of-plane deformation of the RC substructure. In the case of pin support, it is considered that these damages are caused by the fact that the shear force input from the substructure is not properly evaluated in the design. On the other hand, in the case of looseness support, it is expected that the looseness assumed in the design was not appropriate.

It is considered that the above-mentioned damage is rather small because the recent support of the roof is designed in consideration of 1/100 or 1/200 out-of-plane deformation of the substructure. However, if a severe earthquake is assumed, the gymnasium will be used as a shelter, so it is an important task to secure additional security for the support. Therefore, the present paper proposes a new support to suppress the force input to the roof structure and anchor bolt of the support by introducing a mechanism to absorb energy in the support. Based on elasto-plastic response analysis, the effectiveness of the proposed method is discussed.

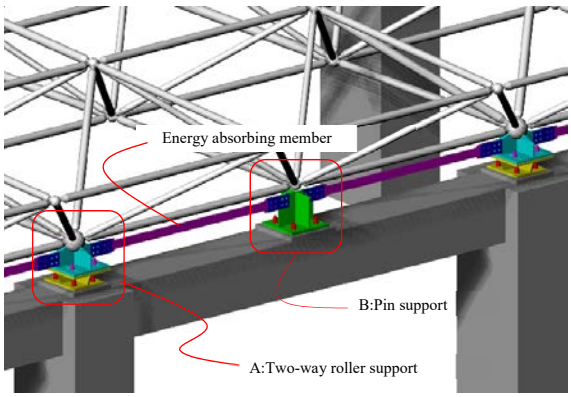
2. Configuration and design method of the proposed support system

The configuration of the proposed support system is illustrated in Figure 1. Support A is a 2-way directional roller support that transmits the vertical load from the roof structure. Support B is a pin support and is not connected to the truss members of the roof structure. The movable part of Support A and Support B are connected by a plate, and this member is an energy absorbing member.

Copyright © 2019 by Yoichi MUKAIYAMA, Shiro KATO, Shoji NAKAZAWA
Published by the International Association for Shell and Spatial Structures (IASS) with permission.

The out-of-plane horizontal force of RC substructure is not input to the roof structure by the roller mechanism of Support A. On the other hand, the tangential horizontal force is transmitted to Support B via the plate. Accordingly, the horizontal seismic force input to the roof structure is transmitted by Support B parallel to the RC substructure. By yielding the plate subjected to strong earthquake, the shear force generated in the anchor bolt is suppressed, and a tension braced framework is constructed between the RC substructure and the truss roof.

As a concept of the seismic design of the proposed support system, the roof truss is designed to be elastic against the seismic force corresponding to the required horizontal load capacity of the substructure. The plate, which is an energy absorbing member, is designed to be elastic against the seismic force. Also, the plate is designed to yield before the anchor bolt reaches its ultimate strength. As a result, it is considered possible to design the plate to yield against unexpected seismic force and to suppress damage around the truss and anchor bolt. If a strong earthquake occurs, it is possible to easily restore the roof's performance by replacing the yielding plates.



"Pin support" is not connected with the steel members of roof.

Figure 1: Configuration of the proposed support system

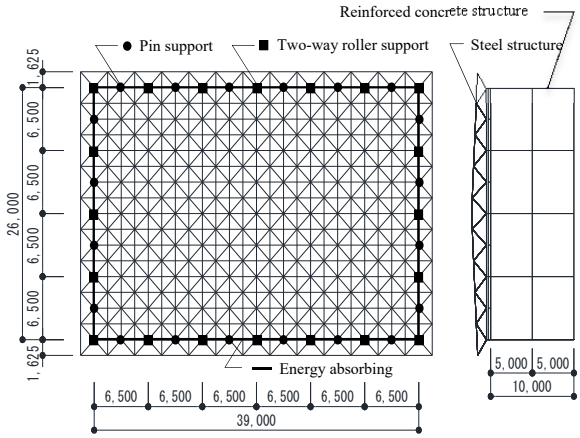


Figure 2: Analysis model

3. Analysis model

3.1. Shape of analytical model and modeling of bearing

Figure 2 shows the analytical model, and Figure 3 illustrates the modeling of the support system. As shown in Figure 2, the analysis model is a space structure of the roof type consisting of the system truss of the upper steel frame and the RC substructure. The span is 26 m, the length in the longitudinal direction is 39 m, and the length of the column grid is 6.5 m in both the span direction and the longitudinal direction. As illustrated in Figure 3, the plastic area of the energy absorbing member is 4 m in total, 2 m on each side of the beam, and plasticization in the analysis is assumed to occur in this part. Furthermore, since the energy absorbing member uses a plate, no compressive force acts on the member.

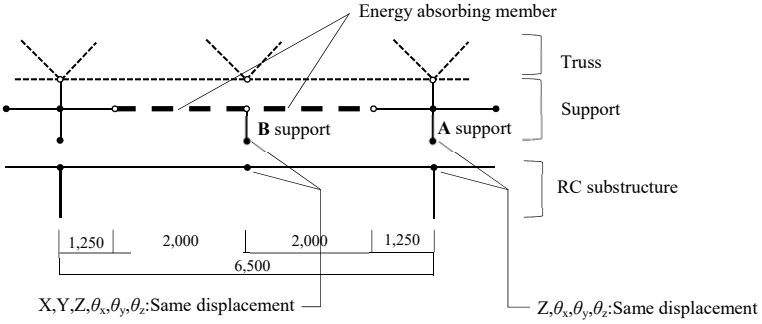


Figure 3: Modeling of the support system

3.2. Design of RC substructure

Two types of analytical models, frame model and shear wall model, are considered as RC substructure. In the frame model, the beam is designed as a special moment frame. The shear wall model is a model in which a seismic shear wall is added to a column and beam designed as a special moment frame. Weight is the same for both models. The cross sectional dimension of the column is 1000 × 800, and the cross sectional dimension of the beam is 600 × 650, 500 × 800, 500 × 1300 from the top.

Table 1 lists the seismic load of the roof structure obtained from the required horizontal strength of RC substructure. Based on the safe side approximation of the seismic shear coefficient C_i of RC substructure, the value of C_i of the roof structure is set to 0.5 in the frame model and 0.6 in the shear wall model.

Table 1: Seismic load

		Frame Model	Shear Wall Model
Importance factor	I	1.250	1.250
Structural characteristic factror	Ds	0.300	0.350
Shape factor	Fes	1.000	1.000
Regional coefficient	Z	1.000	1.000
Vibration characteristic factor	Rt	1.000	1.000
Layer shear force distribution coefficient	Ai	1.317	1.317
Standard shear coefficient	Co	1.000	1.000
Seismic force coefficient	Ci	0.494	0.576
Seismic force coefficient for design	Ci	0.500	0.600

3.3. Design of the roof truss

The design loads (DL: 1000 N/m^2, SL: 690 N / m^2, WL: 1200 N/m^2, EQ: C_i = 0.6) of the roof truss are set, and the designed sizes of upper and lower chord members in the truss roof are *P*-101.6×3.2 to *P*-165.2×4.5, and the sizes of lattice members are *P*-60.5×2.3 to *P*-114.3×3.5.

3.4. Analysis model and energy absorbing member cross section

Table 2 lists the numerical parameters of analytical models. A cross-sectional area of the energy absorbing member of each analytical model is also listed in Table 2. The weight of the roof is set to 1000 N/m^2, and the cross section of the member is determined based on the yield stress 23.5 kN/cm^2 of the energy absorbing member. Since the structure is due to seismic input in the span direction in the response analysis, the seismic load of the roof is transmitted to the RC substructure with eight energy absorbing members on both end faces. Necessary cross-sectional areas are calculated for the frame model and the shear wall model, and a model in which the cross-sectional area is about 1.0 times and about 1.5 times, respectively, is set.

Table 2: Numerical parameter of analytical models

	RC substructure	Ci	Area of energy absorbing member
MODEL-1	Frame model	0.5	3.52x1.0→4.0cm^2
MODEL-2	Frame model	0.5	3.52x1.5→6.0cm^2
MODEL-3	Shear wall model	0.6	4.26x1.0→4.5cm^2
MODEL-4	Shear wall model	0.6	4.26x1.5→6.5cm^2

3.5. Input ground acceleration

The input direction of earthquake motion is span direction. The simulated earthquake motions are that adapt to the design acceleration spectrum (5% damping factor, Soil type 2) of damage limit level in seismic design code in Japan. Using the phase characteristics of recorded ground motion waves, six simulated earthquake motions are generated. The magnitude of earthquake motion is represented by the seismic intensity λ_E. Elastic-plastic seismic response analysis is performed while increasing λ_E from 1.0 to 5.0 in increments of 1.0. Note that λ_E = 1.0 is corresponding to the earthquake motion at

the damage limit level, and λ_E = 5.0 is the earthquake motion at the safety limit level. Table 3 lists the phase characteristics of the recorded ground motion, and Figure 4 illustrates the acceleration response spectrum of the six simulated ground motion.

Table 3: Phase characteristics of the recorded ground motion

No.	Phase characteristics
1	El Centro (1940) NS
2	Taft (1952) EW
3	Miyagi (1978) NS
4	Kobe(1996) NS
5	Hachinohe (1968) NS
6	Sendai501 (1962) NS

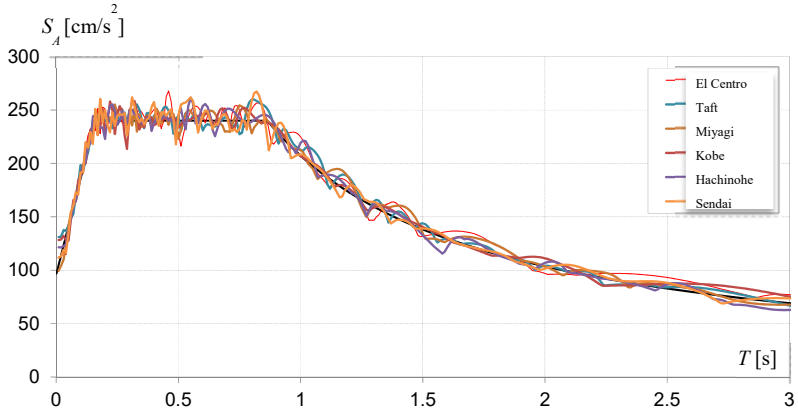


Figure 4: Acceleration response spectrum (h=5%, λ_E = 1.0, damage limit level)

4. Analysis results

4. 1. Natural frequency and natural vibration mode

Table 4 illustrates the natural period and effective mass ratio of the mode excited in the span direction (Y direction) for MODEL-1 and MODEL-3. The corresponding mode shapes are illustrated in Figure 5 and Figure 6, respectively. There are three dominant modes (1) out-of-plane vibration mode of substructure longitudinal surface, (2) Y direction vibration mode of the roof, and (3) Y direction (tangential direction) vibration mode of the end surface.

Since the stiffness and weight of the columns of the frame model and the shear wall model are the same, the natural periods of the modes vibrating in the out-of-plane direction of those longitudinal surfaces are equal. On the other hand, the natural period of the modes vibrating in the tangential direction of the end surfaces differs greatly depending on the presence or absence of the seismic resistance wall. Thus, it is expected that the out-of-plane response of the longitudinal surface will not change much depending on the presence or absence of a seismic wall.

Focusing on the effective mass ratio, the sum of the effective mass ratio of the dominant three modes of the frame model is 83%, while that of the shear wall model is 49%. It is expected that the shear wall model has a large effect of other modes.

Table 4: Natural period and effective mass ratio

	No.	Natural period T(sec)	Effective mass ratio(%)
MODEL-1	3	0.364	30.6
	8	0.279	33.4
	18	0.153	19.0
MODEL-3	3	0.364	29.1
	10	0.240	12.1
	28	0.084	8.1

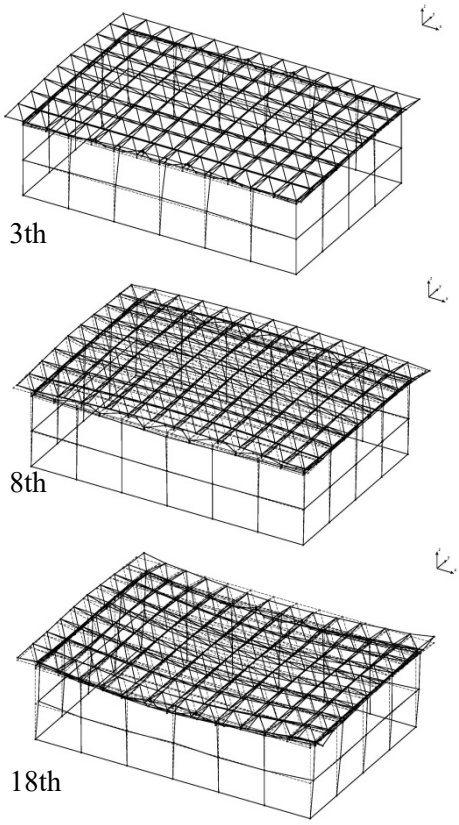


Figure 5: Mode shape (Model-1)

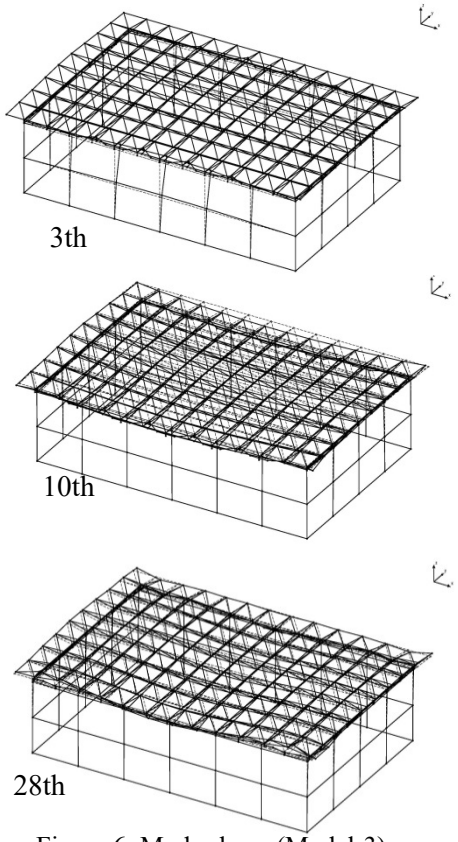


Figure 6: Mode shape (Model-3)

4. 2. Time History Response Analysis

The roof truss member is assumed to be elastic in performing time history response analysis. The hysteresis characteristic of the energy absorbing member is assumed to be a slip model. The RC substructure takes material nonlinearity into consideration, and its hysteresis characteristic is degrading trilinear model. The damping matrix is assumed to be a Rayleigh damping matrix with damping ratio 2% for two dominate natural period of 0.36 seconds and 0.15 seconds. For time history response analysis, SNAP, which is nonlinear analysis software for an arbitrary-shaped three-dimensional frame, is used.

4.2.1. Response Displacement of Top of RC Substructure

The response displacements of the top of RC substructure of MODEL-1 and MODEL-3 are illustrated in Figure 7 and Figure 8, respectively. These responses are the displacements in the excitation direction (Y direction) with respect to the center of the longitudinal surface and end surface due to severe earthquake motion (λ_E = 5) with El Centro phase. The response of the end surface is due to the response of the frame at end surface, and the response at the center of the longitudinal surface is related to the response of the independent column.

The response displacement of the top at the end surface is greatly affected by the presence or absence of the seismic resistance wall. The response displacement with the seismic wall is less than 1/10 of the response without the seismic wall. On the other hand, the response displacement of the independent column shows the same response regardless of the presence or absence of the seismic wall. Therefore, in both models, the response of the frame at the end surface and the response of the independent column are independent of each other, and the influence of the response between the two is small. In addition, residual deformation due to plasticization is observed in the independent column.

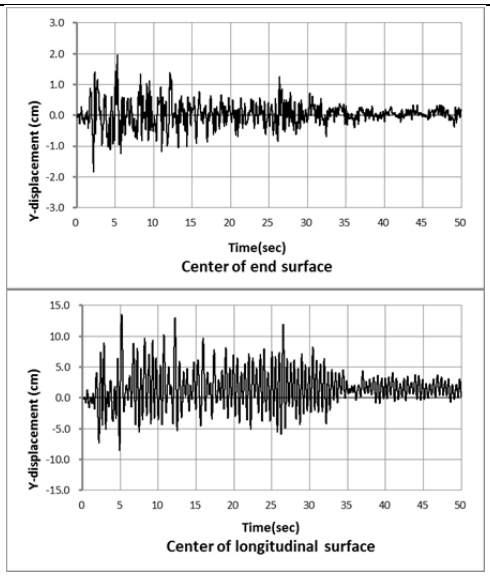


Figure 7: Displacements of the top of RC (Model-1)

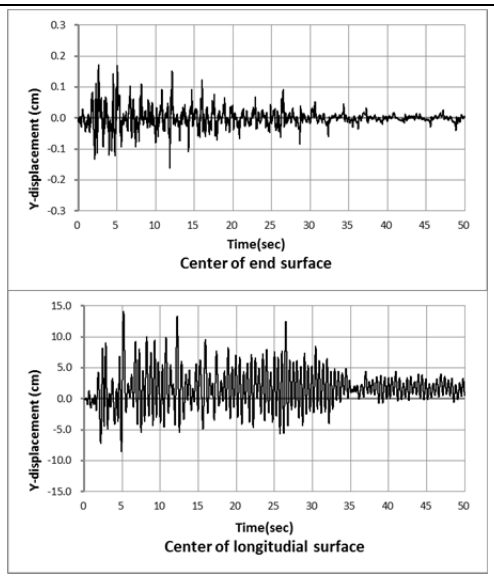


Figure 8: Displacements of the top of RC (Model-3)

4.2.2. Effects of energy absorbing members

In this section, a comparison between the conventional one-way support system and the proposed support system is discussed. A conventional one-way support is modeled by a model that assumes linear elasticity by increasing the cross section of the energy absorbing member. Here, the objected structure for analysis is MODEL-3 with a shear wall.

Figure 9 illustrates the response shear force at Support B bearing the horizontal force at the center of the end surface subjected to severe earthquake motion $\lambda_E = 5$ with phase No. 1 (ElCentro). As shown in Figure 9, the conventional support responds mainly with the roof's vibration period, but the response of the proposed support has nonlinearity due to the plasticization of the energy absorbing member. The maximum response shear force of the proposed support is reduced by about 100 kN compared to the conventional support, and the effect of the proposed bearing can be confirmed. Figure 10 shows the response axial force of the lattice member near the support. The response axial force also responds in the same cycle as the support shear force. In the proposed bearing, the maximum axial force of the lattice member is smaller than the short-term allowable strength, which confirms the effectiveness of the proposed support system.

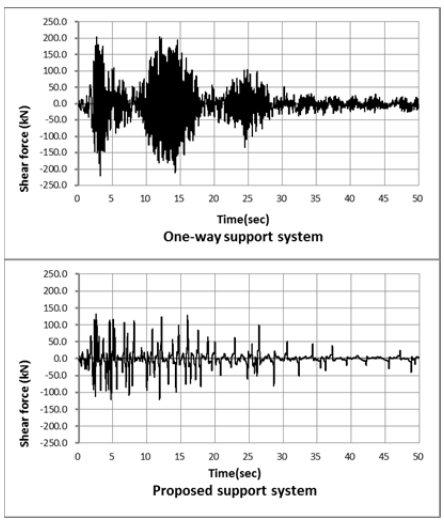


Figure 9: Shear force at Support

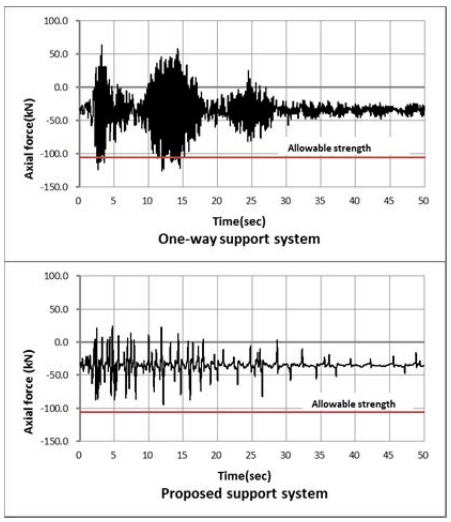


Figure 10: Axial force of the lattice member

4.2.3. Displacement difference of the support

Figure 11 to Figure 14 show the maximum value of the difference in displacement between the roof structure and the RC substructure. This displacement difference is the amount of looseness required for the support. The vertical axis of the graph is the acceleration magnification λ_E, and the horizontal axis is the displacement difference.

The displacement difference at the end face corresponds to the deformation of the energy absorbing member. In consideration of the ductility factor of the energy absorbing member, the critical input ground motion level are λ_E = 3 for MODEL-1 and λ_E = 4 for MODEL-2 and 3, respectively. The displacement difference of the model with the shear wall is smaller than that of the model without the shear wall. The reason for this is considered to be that the cross-sectional area of the energy absorbing member is large, and in the model with the seismic wall, the response of the frame at the end surface is suppressed small. In the frame model, it is necessary to allow some allowance in the cross section of the energy absorbing member.

The displacement difference on the longitudinal surface is mainly caused by the displacement of the independent column, and is affected by the deformation of the frame at the end surface and the energy absorbing member. Although not described in detail, the maximum deformation of the independent column alone is small in model variability, and the maximum deformation corresponding to the input ground motion level of λ_E = 5 is about 12.7 cm on average. The maximum deformation corresponds to a value slightly exceeding the story drift angle 1/100. Therefore, it is considered appropriate that the necessary amount of looseness in the out-of-plane direction of the support portion is 1/100 or more of the story deformation angle of the RC substructure. In MODEL-1 in which the cross-sectional area of the energy absorbing member is small, the displacement difference is also large because the deformation of the energy absorbing member is large.

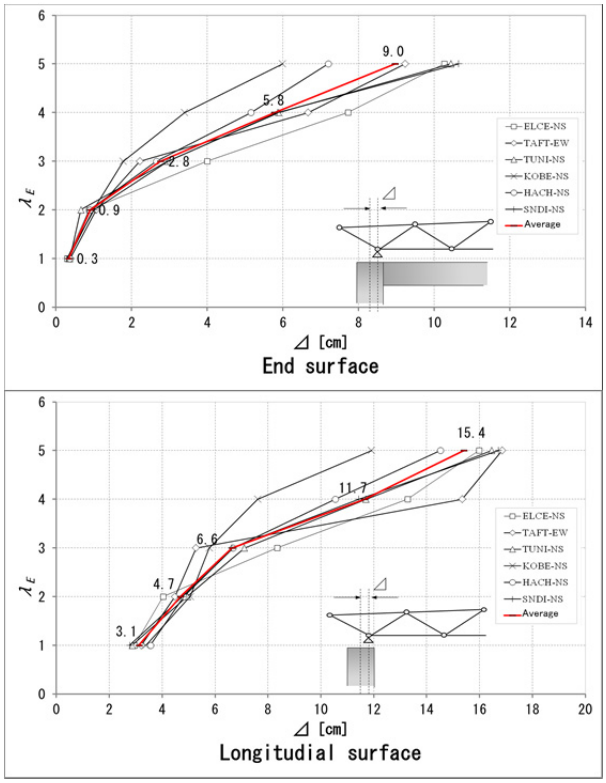


Figure 11: Displacement difference (Model-1)

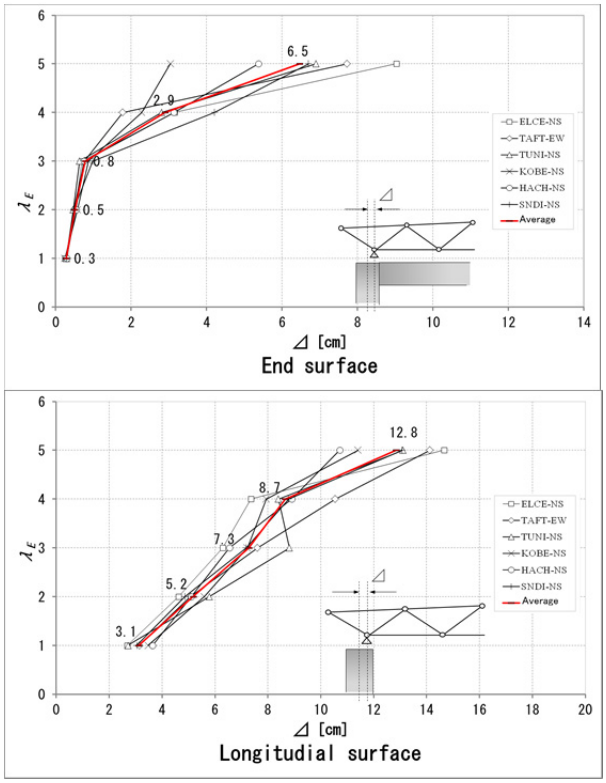


Figure 12: Displacement difference (Model-2)

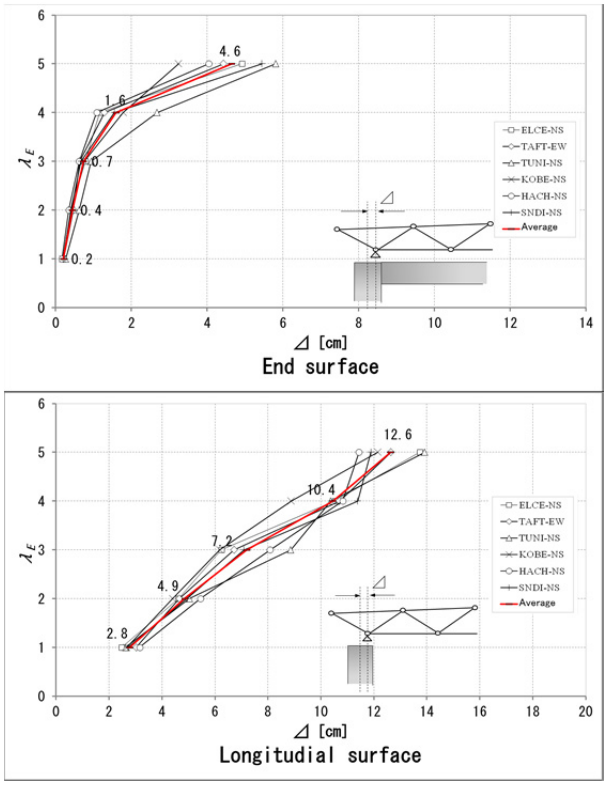


Figure 13: Displacement difference (Model-3)

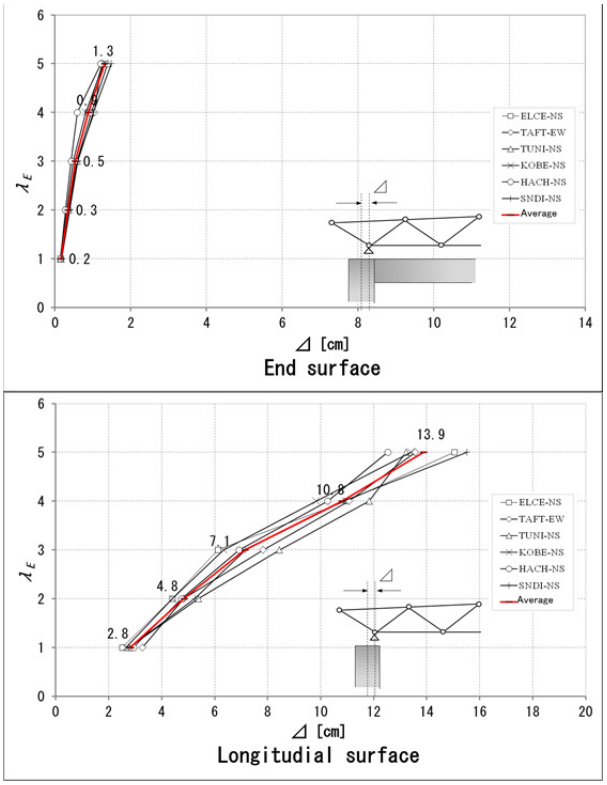


Figure 14: Displacement difference (Model-4)

5. Conclusion

In this research, a support system for suppressing damage to the roof truss and anchor bolt at the time of earthquake was proposed for the installation roof, and its behavior was analyzed. The conclusions obtained are shown below.

1) In the response of RC substructure, the out-of-plane vibration of the girder column and the vibration of the end frame are independent, and the degree of both effects is small.

2) Compared with the conventional support system, the proposed support system which introduced the energy absorbing member can suppress the reaction force of the support and the axial force of the truss member, and its effectiveness can be confirmed.

3) As to the presence or absence of shear walls, the model with shear walls has a small response of the end face frame and can reduce the looseness of the support.

References

[1] JAPAN ASSOCIATION FOR BUILDING RESEARCH PROMOTION (JABRP) : *Report on Damage of Steel Roofs on RC-frame in the Great Tohoku Earthquake*, 2012 (in Japanese)

[2] The joint editorial committee for the report on the Great East Japan Earthquake Disaster : *Report on the Great East Japan Earthquake Disaster, Building Series Vol.3, Structural Damage to Steel Building, Structural Damage to Shell and Spatial Structures*, 2014.9 (in Japanese)

Proceedings of the IASS Annual Symposium 2019 – Structural Membranes 2019
Form and Force
7 – 10 October 2019, Barcelona, Spain
C. Lázaro, K.-U. Bletzinger, E. Oñate (eds.)

Seismic Response Evaluation of Long-span Domes Supported by Multi-storey Substructures Incorporating Spine Frames

Deepshikha NAIR*[a], Yuki TERAZAWA[a], Ben SITLER[a], and Toru TAKEUCHI[a]

[a]Takeuchi Laboratory
Department of Architecture and Building Engineering
Tokyo Institute of Technology
M1. 4F-406 2-12-1 Ookayama Meguro-ku Tokyo, Japan
nair.d.aa@m.titech.ac.jp

Abstract

This study aims to investigate the seismic response characteristics of domes of span 150m. It is found that in comparison with the medium-span domes (span∼60m), the periods of these long-span domes are longer resulting in a greater contribution from the higher modes to the response. The acceleration distributions, especially the vertical accelerations in the roof are also sensitive to the dominant mode shapes of these higher modes. In addition, the response is influenced by the substructure characteristics, which is investigated by incorporating multiple damped spine frames in a multi-storey substructure. A simple design procedure incorporating the effects of higher modes based on response spectrum analysis and equivalent linearisation procedure is proposed to evaluate the equivalent static loads of the roof using amplification factors. The accuracy of the proposed method is validated using nonlinear response history analysis.

Keywords: long-span domes, earthquake design, equivalent static loads, higher mode effects, spine frames, metal spatial structures

1. Introduction

In the past decade, there has been a rise in the number of long-span steel spatial structures incorporating response control strategies, which has further propelled the need to investigate and present simple design methods for practising engineers. This paper studies the response characteristics of double layered long-span domes. By using response spectrum analysis (RSA) and equivalent linearisation techniques, the maximum acceleration distributions in the horizontal and vertical directions are expressed using amplification factors by taking the effects of higher modes into account. These distributions are then used to obtain the equivalent static loads for design.

2. Analysis models

Takeuchi et al. [1] have studied medium-span domes in the past and have concluded that when the depth to span ratio of the dome is sufficiently large, the response characteristics become simpler. The response can be explained using just the 4 dominant modes which are named as O1, O2, O2.5 and I (Figure 1). The dome is a double-layered dome with a depth-to-span ratio (d/L) of about 1/50 and a half subtended angle (θ) of 30° (Figure 2). The span is 150 m. The domes are modelled as single-layered domes and the

Copyright © 2019 by Deepshikha Nair & Toru Takeuchi
Published by the International Association for Shell and Spatial Structures (IASS) with permission.

out-of-plane stiffness of the roof members are multiplied by factor of about 60 to represent an equivalent double layered dome [1]. The dome consists of rigidly jointed circular hollow sections and was designed for a uniform 3 kPa dead load which includes an allowance for acoustic panels.

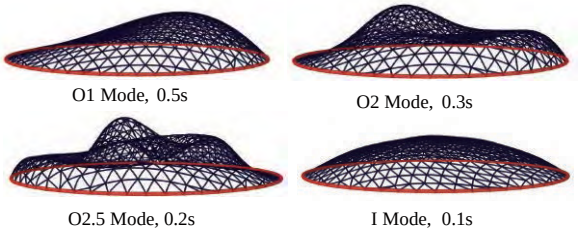


Figure 1: Four principal modes: Periods and mode shapes of the dome

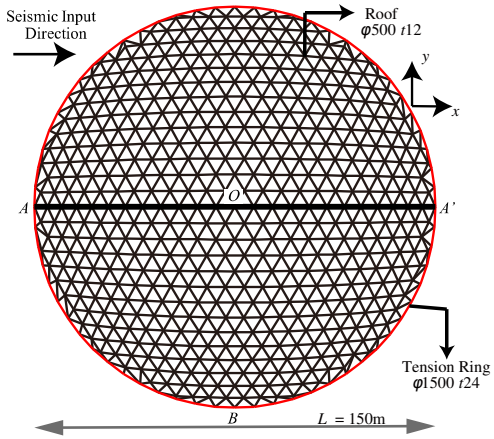


Figure 2: Ridge line shown in the plan view

The effects of a multi-storey substructure on the roof response are analysed by adding the dome roof model to a multi-storey substructure. 3-D analysis models were constructed in ETABS [2] and SN490 steel was adopted for all frame and roof members. The choice of the models is inspired from the recent trend of large scale realised indoor stadiums or sports arenas with seating capacities of around 20,000 people. The frame sections and mass distribution are summarized in Table 1.

Table 1: Model Information

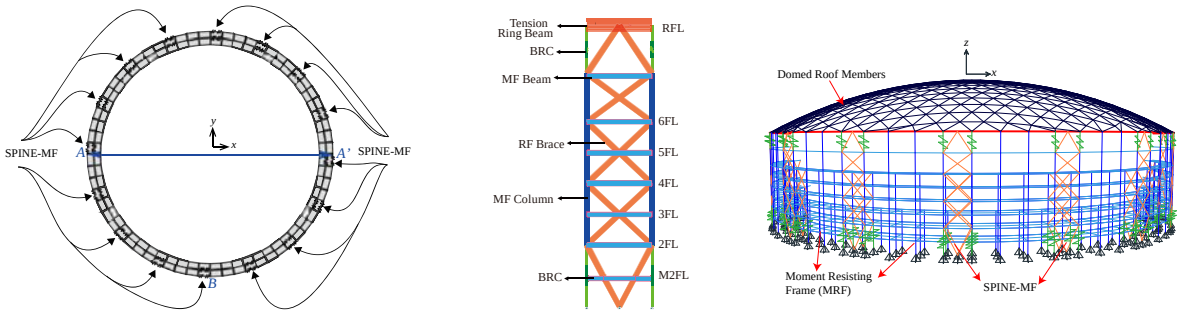
(a) Frame Sections Data

Member	Section Shape	Section Size (mm)
Roof Member	CHS	ϕ500 t12
Tension Ring	CHS	ϕ1500 t24
MF Column	SHS	600×600×25
MF Beam	I/Wide Flange	588×300×12×20
RF Brace	I/Wide Flange	600×600×19×19

(b) Model Mass Data

Storey	Height (m)	Weight (kN)
RFL	32	54018
6FL	21	18304
5FL	17.5	28507
4FL	14	28507
3FL	10.5	41121
2FL	7	41121
M2FL	3.5	41121

The substructure consists of a moment resisting frame (MRF) enveloping 16 pairs of spine frames [3] spaced equidistant around the perimeter (Figure 3) and was designed using seismic design shear forces and *Ai* distribution defined in the Japanese code [4]. The spine frame utilises a stiff elastic braced steel frame with replaceable energy-dissipating members (buckling restrained braces or BRBs) inserted vertically (here, the BRBs are referred to as buckling restrained columns (BRC)). The main parameters used to design the axial force-displacement of BRBs were determined assuming a post yield stiffness ratio of 2% following the design guidelines given in [5]. The Spine-MF model employs MRF with rigidly jointed beam-column connections. An additional model with pinned beam-column connections was also included (Spine-P) to investigate the effects of low post-yield stiffness of the substructure. The contribution of the MRF towards the lateral stiffness is negligible in the Spine-P model.



(a) Plan view: location of Spine frames

(a) Section view: Spine frame

(c) 3-D view of the combined model

Figure 3: Different views of the analysis models

2.1. Effects of substructure stiffness

The dynamic characteristics of the dome is investigated using a simple supporting substructure consisting of one storey of columns which are pin supported at the base (Table 1a). The connections between the tension ring and both substructure and roof are assumed to be pin connected. The models are named as D30-α where α is the substructure stiffness amplification factor. The major vibration modes of the roof mainly consist of the three principal mode shapes, O1, O2, and I (Figure 4). It can be seen that the first mode is not necessarily dominant. Moreover, the number of modes required to obtain a combined mass participation of 90% is larger than conventional multi-storey structures. As the substructure stiffness increases, the mode with the highest participation factor gradually shifts from O1 to O2. When compared with the prominent vibration modes of a medium-span dome [1], the periods of these modes are longer, as seen by mapping these modes on the target design spectrum (BRI-L2) (Figure 5). The spectrum corresponds to a Level-2 earthquake as per the Japanese Building code [4]. Equation 1 defines the design acceleration (S_a(cm/s^2)). In the case of domes with stiff substructure, all the prominent modes lie on the constant acceleration (maximum acceleration) region. In comparison, all but the O1 mode lie on the region with lower acceleration in the medium-span case (Figure 5). This implies that the magnitude of roof excitation of long-span roofs may be up to two times greater than the medium-span case, with greater contribution from the higher modes.

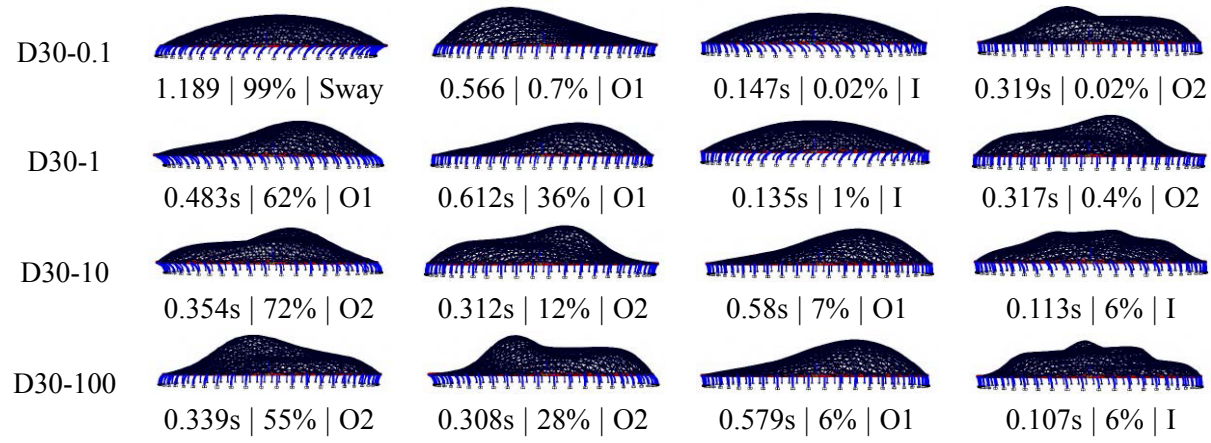


Figure 4: Major vibration modes: Periods & mass participation factors along the *x*-direction

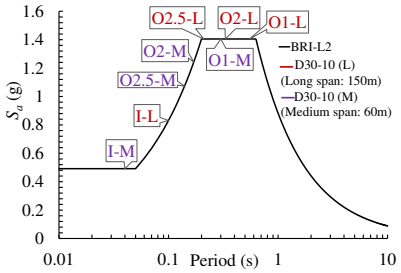
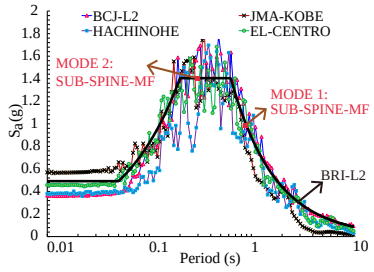


Figure 5: Prominent modes mapped on the spectrum

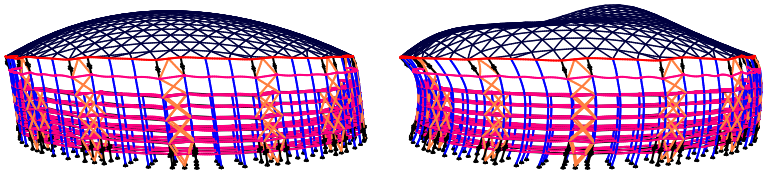
$$S_a(T) = \left\{ \begin{array}{cc} 350D_h & (T \leq 0.05) \\ 350D_h(T/0.05)^{(1+log(5/7)log4)} & (0.05 < T \leq 0.2) \\ 1000D_h & (0.2 < T < \pi/5) \\ 1000D_h/(T/2\pi) & (\pi/5 \leq T) \end{array} \right\} \quad (1)$$

$$D_h = \sqrt{(1+75h_b)/(1+75h_o)} \quad (2)$$

The mode shapes of the first two modes of the combined model Spine-MF are shown in Figure 6. The periods were found to be very close to the corresponding periods of their substructure models (Figure 6a). The first mode is essentially a combination of the translational sway mode of the substructure and the roof's O1 mode. In the second mode, the O2 roof mode (higher mode) is excited as the period 0.34s coincides with the roof's O2 mode (Figure 1).



(a) Substructure modes on the design spectrum



(b) Mode:1 0.94s, 63% (c) Mode:2 0.34s, 25%
Mode shape, Period and Mass Participation

Figure 6: (a) Design acceleration spectrum and (b-c) Two dominant modes of Spine-MF

3. Roof response using amplification factors

Takeuchi et al. [1] demonstrated that the seismic roof response of a medium-span dome can be evaluated in a simple manner using amplification factors derived from the response characteristics of a simple lumped mass arch model. The same fundamental concepts were applied to long-span domes in this study. The procedure to obtain the horizontal and vertical amplification factors F_{Hi} and F_{Vi} are briefly described below where θ is the half subtended angle, $R_T = T_{eq}/T_R$ is the ratio of equivalent period of the SDOF (single degree of freedom model) to that of the roof O1 mode, $R_M = M_{EQ}/M_R$ is the ratio of SDOF model to roof mass and the calibration factor C_V is taken as 1.88 as proposed by Takeuchi et al. [1]. To account for harmonic resonance (when $R_M > 2$ and $R_T \sim 1$) the modified amplification factors $F_H^{'}$ and $F_V^{'}$ for the equivalent period (T_{eqi}) are calculated using Equations 3 and 4.

$$F_{Hi} = \left\{ \begin{array}{cc} 3 & (0 < R_{Ti} \leq 5/16) \\ \sqrt{5/4R_{Ti}} & (5/16 < R_{Ti} \leq 5/4) \\ 1 & (5/4 < R_{Ti}) \end{array} \right\}, {F_{Hi}}' = \sqrt{{F_{Hi}}^2 + \frac{1}{\left(1-{R_{Ti}}^2\right)^2 + \left(1/R_M\right)^\theta}} \quad (3)$$

$$F_{Vi} = \left\{ \begin{array}{cc} 3C_V\theta & (0 < R_{Ti} \leq 5/16) \\ (\sqrt{5/R_{Ti}} - 1)C_V\theta & (5/16 < R_{Ti} \leq 5) \\ 0 & (5 < R_{Ti}) \end{array} \right\}, {F_{Vi}}' = \sqrt{{F_{Vi}}^2 + \frac{1}{\left(1-{R_{Ti}}^2\right)^2 + \left(1/R_M\right)}} \quad (4)$$

3.1. Proposed acceleration distribution incorporating higher modes

A modified acceleration distribution is proposed to include contributions from higher modes of the roof. Amplification factors for the ith mode are denoted as F_{Hi} and F_{Vi} ; where x and y are the coordinates of roof nodes with $\{x,y\}$ = {0,0} as the centre and L is the span of the dome (Equations 5-7).

1. Horizontal acceleration distribution: Since the horizontal acceleration is not particularly sensitive to the dominant mode shapes, Equation 5 [1] is sufficient to capture the response in the horizontal direction.

$$A_{Hi}(x,y) = A_{Heqi}\{1 + (F_{Hi} - 1)\cos\frac{\pi\sqrt{x^2+y^2}}{L}\} \tag{5}$$

2. Vertical acceleration distribution: Previously, the equation for vertical acceleration distribution was formulated exclusively based on the O1 mode (Takeuchi et al. [1]). Here, it is proposed to adopt a weighted acceleration distribution that includes contributions from the O2 and O2.5 mode shapes, as required (Figure 1). The distribution of the vertical acceleration should be selected according to the excited roof mode. For example, if a certain mode of the structure exhibits the roof in O1 mode, then the vertical acceleration contribution for that mode should be determined from Equation 6. Similarly, if the mode consists solely of the translational sway of the substructure, A_{Vi} may be taken as zero.

- O1 mode:

$$A_{Vi}(x,y) = A_{Veqi}F_{Vi}\frac{x}{\sqrt{x^2+y^2}}\sin\frac{2\pi\sqrt{x^2+y^2}}{L} \tag{6}$$

- O2 mode:

$$A_{Vi}(x,y) = \begin{Bmatrix} A_{Veqi}F_{Vi}\frac{x}{\sqrt{x^2+y^2}}\sin\frac{2\pi\sqrt{(2x)^2+(2y)^2}}{L} & (|x| \le L/4) \\ A_{Veqi}F_{Vi}\frac{0.5x}{\sqrt{x^2+y^2}}\sin\frac{2\pi\sqrt{(2x)^2+(2y)^2}}{L} & (|x| > L/4) \end{Bmatrix} \tag{7}$$

4. Equivalent static loads

The steps of revised design procedure (Figure 7) to estimate the equivalent static loads of long-span domes considering the plasticity of substructure and incorporating the higher mode effects are described in this section.

Step 1 Obtain the substructure periods (T_i) corresponding to n dominant modes with a combined participation factor of at least 90% ($\Sigma\beta_i$>90).

Step 2 Allowing the moment frame beams and BRBs to yield, perform nonlinear pushover analysis on the substructure models using the force distributions as per the first mode. Calculate the ratio of the post-yield stiffness to the elastic stiffness K_2/K_1 from the bi-linearized curves (Figure 8).

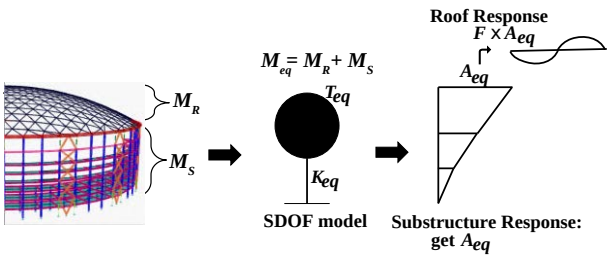


Figure 7: Simplified illustration of design procedure

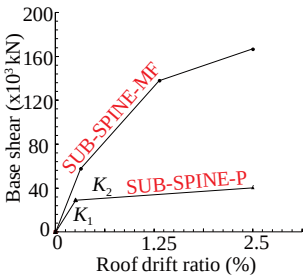


Figure 8: Pushover curves of the substructures

Step 3 Use the *Ai* distribution (as per the Japanese code or any other suitable seismic design shear force distribution) and the design acceleration spectrum to obtain the maximum elastic acceleration distribution of the substructure. The acceleration at the top storey is adopted as the peak elastic acceleration A_i (where i is the mode number). This approach is considered to be consistent with the contemporary multi-storey design concepts [6].

Step 4 The equivalent stiffness (K_{eqi}) and equivalent damping ratio (h_{eqi}) are obtained using the equivalent linearisation procedure proposed by Kasai et al. [7], which estimates the peak response of elasto-plastic systems. For each of the modes, assume a starting value of ductility ratio μ_i and iterate h_{eqi} and K_{eqi}/K_1 using Equations 8-11 until μ_i converges, where the subscript (j) is the jth step of the iteration. Next, for each of the modes, calculate the equivalent (secant) period T_{eqi} and the peak inelastic accelerations A_{Heqi} and A_{Veqi} of the SDOF model using Equations 12-14.

$$K_{eqi}/K_1 = 1/\mu_i + (1 - 1/\mu_i)K_2/K_1 \tag{8}$$

$$h_{eqi} = h_{oi} + \frac{2(K_1/K_2)}{\pi\mu_i} \ln \frac{K_1/K_2 + \mu_i - 1}{(K_1/K_2){\mu_i}^{K_2/K_1}} \tag{9}$$

$$D_{hi} = \sqrt{(1 + 25h_{oi})/(1 + 25h_{eqi})} \tag{10}$$

$$\mu_{i(j)} = \mu_{i(1)} D_{hi(j-1)} / \sqrt{K_{eqi(j-1)}/K_1} \tag{11}$$

$$T_{eqi} = T_i \sqrt{K_1/K_{eqi}} \tag{12}$$

$$A_{Heqi} = A_i D_{hi} \sqrt{K_{eqi}/K_1} \tag{13}$$

$$A_{Veqi} = A_i \sqrt{K_{eqi}/K_1} \tag{14}$$

Step 5 After obtaining the peak response of the substructure, use Equations 3-7 to calculate the roof amplification factors and obtain the peak roof acceleration distribution for each mode.

Step 6 Combine the modal accelerations at each node using Equations 15 to obtain the envelope of peak roof accelerations. This study uses the absolute summation rule. Similarly, the peak displacements can also be obtained. Finally, evaluate the equivalent static seismic forces for design for each node from the nodal mass m_k and acceleration $A_H(x, y)$ or $A_V(x, y)$ at position (x,y). Apply the forces to perform a static analysis to obtain the response.

$$A_H(x, y) = \sum_{i=1}^{n} |\beta_i A_{Hi}(x, y)| \text{ and } A_V(x, y) = \sum_{i=1}^{n} |\beta_i A_{Vi}(x, y)| \tag{15}$$

5. Accuracy of the proposed method

NLRHA was performed on the combined models (Spine-MF and Spine-P) to validate the proposed design procedure permitting the beams in MRF and BRCs to yield. The proposed design procedure was applied using the first two dominant modes. Four input ground motions (El-Centro, Hachinohe, BCJ-L2 and JMA-Kobe) were used, each are spectrally matched to the BRI-L2 design spectrum (Figure 6a). 2% Rayleigh damping was applied to the first two dominant modes.

The acceleration distributions along the ridge line A-O-A' is shown in Figure 9 and the main parameters of the inelastic response are summarised in Table 2. The combined response obtained using the proposed method (Section 5) was labelled as 'PROPOSED' while the modal contributions ($|\beta_i A_{Hi}(x, y)|$ or $|\beta_i A_{Vi}(x, y)|$) of the first and second modes are labelled as 'MODE-1' and 'MODE-2'. The response calculated as per Takeuchi et al. [8], which only considers the first mode of the substructure (with β_1 equal to 100%), are labelled as 'PREVIOUS'. The results are in good agreement with the results obtained from NLRHA. The excitation of the O2 mode (higher roof mode) is evident from the dual peaks

appearing in the distribution of vertical acceleration. The results for Spine-P confirm that only considering first mode for response underestimates the peak accelerations. Including the predominant higher modes significantly improves the accuracy of response estimation.

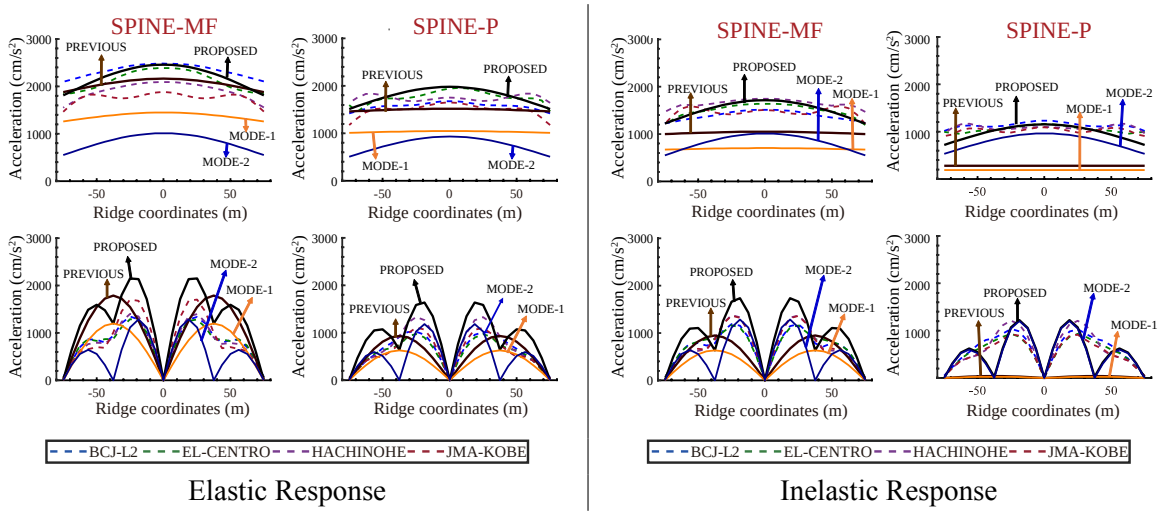


Figure 9: Horizontal acceleration (top) and Vertical acceleration (bottom)

Table 2: Main Parameters: Proposed method

Mode	β_i (%)	T (s)	D_h	K_{eq}/K_1	μ	T_{eq} (s)	A_{Heq} (cm/s^2)	A_{Veq} (cm/s^2)
(i) Spine-MF								
1	67	0.91	0.69	0.65	3.27	1.13	1000	1500
2	25	0.31	1.00	1.00	1.00	0.31	2200	2200
(ii) Spine-P								
1	68	1.18	0.42	0.21	5.80	2.58	300	700
2	23	0.32	1.00	1.00	1.00	0.32	2300	2300

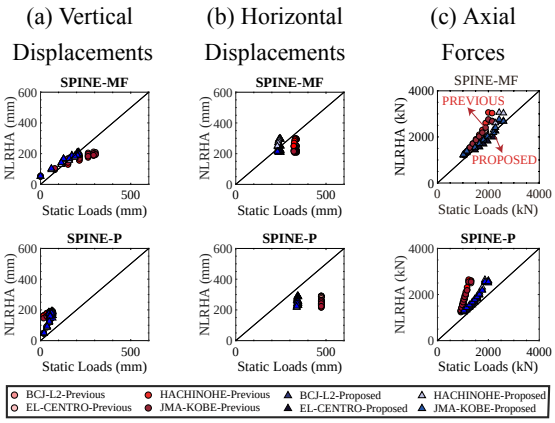


Figure 10: Accuracy of the proposed method

The substructure yields for all the models in the first mode, significantly reducing the first mode contribution to the overall response, evident from the reduced A_{Heq1} and A_{Veq1} values. In the case of Spine-P, the contribution of the first mode to the overall response was negligible compared to the second mode (Figure 9(b)). This is due to the negligible post-yield stiffness of the substructure evident from the near elastic-perfectly-plastic pushover curve (Figure 8). This results in a longer equivalent period (T_{eq1}) and larger response reduction ($D_h \sim 0.4$) explaining the low values of peak accelerations A_{Heq1} and A_{Veq1}. However, the substructure is still elastic in the second mode, resulting in T_{eq2} lying in the maximum acceleration region of the response spectrum causing high A_{Heq2} and A_{Veq2} values. This also suggests that there is a need to introduce response control strategies that can effectively reduce the response not only of the first mode but also of the significant higher modes.

The axial forces along the ridge line obtained using the proposed accelerations (Section 4) as equivalent

static load coefficients and the calculated displacements of the models are compared with the corresponding maximum results obtained from NLRHA as shown in Figure 10. The response values were found to be generally consistent with the NLRHA results despite the proposed accelerations being slightly conservative. The results from the 'PREVIOUS' method underestimate the actual response values. The proposed method gives a better correlation of the response values as can be seen from the plots.

6. Conclusions

From this investigation, the following conclusions are drawn:

1. The contribution of higher modes lying on the constant acceleration region of the design spectrum with significant values of participation factor must be included when estimating the peak design accelerations of long-span domes despite the elongated natural periods of the combined structures.
2. For substructures lacking the stiff moment frames, due to the near elastic-perfectly-plastic behaviour of substructure, significant reduction in accelerations is expected when judged from the first modal response. However, the higher modes of the substructure remain elastic resulting in the large combined accelerations.
3. Yielding of a multi-storey substructure was incorporated using equivalent linearisation technique in the proposed design procedure. Adding damped spine frames proved to be effective in reducing the roof response. The response estimated by this method are in good agreement with those obtained from NLRHA and this method is considered suitable for the preliminary design stage of such large-scale structures.

References

[1] T. Takeuchi, T. Ogawa, and T. Kumagai, "Seismic response evaluation of lattice shell roofs using amplification factors," *Journal of the IASS*, vol. 48, pp. 197–210, 2007.

[2] E. L. Wilson, *CSI Analysis Reference Manual For SAP 2000, ETABS, SAFE and CSI Bridge*. Berkeley: Computer & Structures Inc, 2015.

[3] X. Chen, T. Takeuchi, and R. Matsui, "Simplified design procedure for controlled spine frames with energy-dissipating members," *Journal of Constructional Steel Research*, vol. 135, pp. 242–252, 2017.

[4] *The Building Standard Law of Japan on CD-ROM*. The Building Center of Japan, 2016.

[5] T. Takeuchi and A. Wada, *Buckling-Restrained Braces and Applications*. JSSI, 2017.

[6] T. Takeuchi, T. Kumagai, H. Shirabe, and T. Ogawa, "Seismic response evaluation of lattice roofs supported by multistory substructures," in *Shell and Spatial Structures: Structural Architecture - Towards the future looking to the past. IASS Symposium*, (Venice, Italy), p. 362, December 3-6 2007.

[7] K. Kasai, H. Ito, and A. Watanabe, "Peak response prediction rule for a SDOF elasto-plastic system based on equivalent linearization technique," *Journal of Structural and Construction Engineering (Transactions of AIJ)*, vol. 68, no. 571, pp. 53–62, 2003.

[8] T. Takeuchi, T. Ogawa, and T. Kumagai, "State-of-arts views on response control technologies on metal space structures," in *Proceedings of IASS 2009*, no. 6506, (Valencia, Spain), September 28-October 2 2009.

Proceedings of the IASS Annual Symposium 2019 – Structural Membranes 2019
Form and Force
7 – 10 October 2019, Barcelona, Spain
C. Lázaro, K.-U. Bletzinger, E. Oñate (eds.)

Shell-like and member buckling of latticed shells made of H-shaped steel

Tetsuo YAMASHITA*, Kai KAGEYAMA[a]

*Prof., School of architecture, Kogakuin University
A2514, 1-24-2, Nishi-Shinjuku, Shinjuku-ku, Tokyo, Japan
tetsuo_y@cc.kogakuin.ac.jp

[a] Kanebako Structural Engineers, Completed master's program in Kogakuin University

Abstract

This paper is about elastic buckling of latticed shells made of H-shaped steel. We have to consider not only shell-like buckling but also in-plane member buckling around the weak axis of H-shaped section. However, even when member buckling appears as the 1st mode in an eigenvalue analysis, sometimes out-of-plane shell-like buckling actually occurs due to geometric nonlinear effect. This study specifies the watershed condition between member and shell-like buckling and presents an index to estimate buckling type and the knockdown factor. Effective length for in-plane member buckling is also derived.

Keywords: latticed shells, H-shaped steel, effective length, member buckling, shell-like buckling, knockdown factor, geometric nonlinearity

1. Introduction

Many beautiful steel latticed shell roofs have been constructed all over the world. Some latticed shells are made of H-shaped steel [1] (Figure 1). Advantages of the use of H-shaped section are, 1) easy and economical fabrication of full-rigid connection, 2) sufficient out-of-plane bending stiffness to prevent shell-like buckling (Figure 2a), etc. However, the second moment of inertia around the weak axis is so poor that shells are prone to in-plane member buckling (Figure 2b), which is more frequent than pipe-made shells.

To estimate buckling load and type, linear buckling eigenvalue analysis is commonly used. However, due to geometric nonlinearity, overall shell-like buckling can occur prior to member buckling, even when member buckling appears in the 1st eigenmode. Therefore, tracing the nonlinear equilibrium path is requested in the design recommendations [2,3] when member buckling appears in the lowest eigenmode. Moreover, Chan proposed the direct method which uses elastic nonlinear (second order) analysis in design [4]. But elastic nonlinear analysis requires a certain level of skill and assumption of appropriate imperfection. But there have been few available studies on how to determine the worst imperfection.

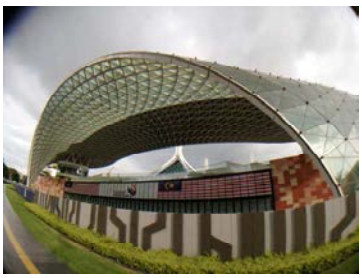


Figure 1 Latticed shell made of H-shaped steel[1]

The present study investigates the watershed condition between in-plane member and out-of-plane shell-like buckling under geometric nonlinearity. Spherical latticed shells made of H-shaped steel are supposed for study, where member buckling appears in the 1st eigenmode. An index to estimate buckling type and elastic nonlinear buckling load is proposed. Effective length in member buckling also has been specified according to the boundary condition.

Copyright © 2019 by Tetsuo Yamashita and Kai Kageyama
Published by the International Association for Shell and Spatial Structures (IASS) with permission.

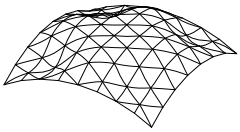


Figure 2a Out-of-plane shell-like buckling

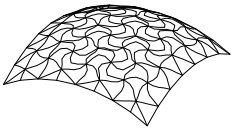
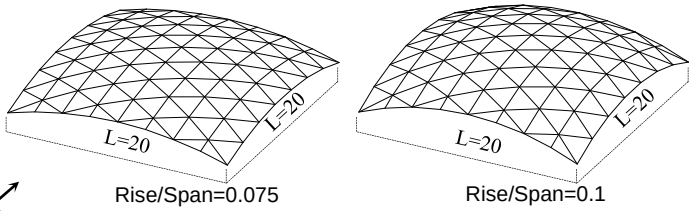


Figure 2b In-plane member buckling



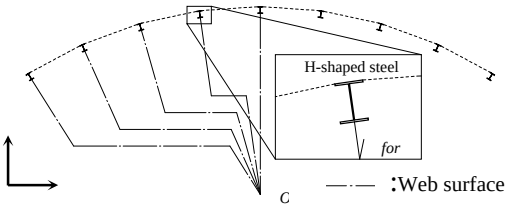
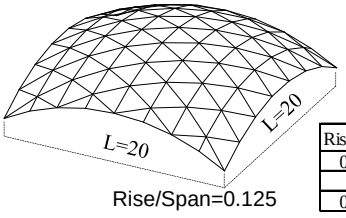
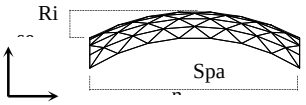


Figure 5 Orientation of H-shaped section





Rise/Span	L [mm]	l_0 [mm]	R [mm]	θ_0 [rad]
0.075	2000	2825.0	34083	0.041
0.1		2860.7	26000	0.055
0.125		2910.6	21250	0.068

Figure 3 Latticed shells for study

2. Elastic Latticed shells for study

2.1. Geometry

Spherical latticed shells on square plan are supposed for the present study (Figure 3). The X and Y spans are 20m x 20m. The radius of curvature (denoted by R) was determined so that the rise-span ratios at the center arcs were 0.075, 0.1 and 0.125. The lattice configuration is nearly equilateral triangle and the average member length (denoted by l_o) is approximately 2.9m. l_o, θ_o and R relate as expressed in Eq.(1).

$$\theta_0 = \frac{l_0}{2R} \tag{1}$$

The definition of θ_o is given in Figure 4.



Figure 4 θ_0

2.2. Load and boundary condition

In the FE analysis, static gravity load was equally given on all the nodes. The load per one node was calculated by multiplying the roof area per one node $\left(=\sqrt{3}l_0^{\,2}/2\right)$ by the distributed roof load.

Two boundary conditions were assumed. The nodal displacement on the boundary was constrained but the rotation was free in the "pin-supported" shells. In the "roller-supported" shells, only Z (vertical) displacement was constrained. Actually many latticed shell roofs are supported on high steel columns, which cannot resist the horizontal thrust, thus the roller-support is more realistic.

2.3. Determination of weak-axis rigidity considering eigenmode

The web plates of H-shaped sections were installed within the surface defined by the member axis and the center of spherical shell (Figure 5). The second moment of inertia about the strong axis (denoted by I_x) and the section area (denoted by A) of the H-shaped sextion were commonly assumed 2000cm^4 and 25cm^2, respectively. The lowest member buckling load (denoted by q_{cr-m}^{lin}) primarily depends on the weak-axis second moment of inertia (denoted by I_y). I_y was parametrically determined using FE eigenvalue analysis so that the lowest shell-like buckling load q_{cr-all}^{lin} found in a higher eigenmode was approximately 1.5, 2.0 or 2.5 times of q_{cr-m}^{lin}. Table 1 indicates the section properies, where H,B,t_w and t_f are the section height, flange width, web and flange thickness,respectively. Some of the B/t ratios are unrealistically large since local buckling is neglected in this study. Hereafter, a latticed shell is represented by a sign as 'Rise/span ratio_Boundary condition_$q_{cr\text{-}all}^{lin}/q_{cr\text{-}m}^{lin}$', such as 0.1_Pin_2.5.

Table 1 Cross section properties of H-shaped members

Model							Linear Buckling Analysis				
Rise/Span	Boundary	$q_{cr-all}^{lin}/q_{cr-m}^{lin}$	H x B x t_w x t_f	A [cm^2]	I_x [cm^4]	I_y [cm^4]	$q_{cr-m}^{lin}[kN/m^2]$	mode	$q_{cr-all}^{lin}[kN/m^2]$	mode	$q_{cr-all}^{lin}/q_{cr-m}^{lin}$
0.075	Pin	1.1	200 x 167.3 x 2.93 x 5.82	25	2000	455	70.6	1	77.1	7	1.09
		1.25	200 x 154.7 x 2.85 x 6.36	25	2000	392	61.2	1	76.9	15	1.26
		1.5	200 x 138.9 x 2.72 x 7.18	25	2000	321	50.4	1	76.7	27	1.52
		2.0	200 x 118.9 x 2.50 x 8.60	25	2000	241	38.1	1	76.4	37	2.01
		2.5	200 x 105.1 x 2.28 x 9.94	25	2000	193	30.6	1	76.1	45	2.49
0.1		1.1	200 x 191.7 x 3.05 x 5.01	25	2000	588	116.1	1	126.8	7	1.09
		1.25	200 x 178.4 x 2.99 x 5.42	25	2000	513	101.9	1	126.5	17	1.24
		1.5	200 x 160.0 x 2.89 x 6.12	25	2000	418	83.7	1	125.9	28	1.50
		2.0	200 x 137.2 x 2.71 x 7.28	25	2000	313	63.4	1	125.2	37	1.97
		2.5	200 x 121.5 x 2.53 x 8.38	25	2000	251	51.0	1	124.6	48	2.44
0.125		1.1	200 x 216.4 x 3.14 x 4.39	25	2000	741	170.7	1	187.7	7	1.10
		1.25	200 x 201.3 x 3.09 x 4.75	25	2000	645	149.8	1	187	18	1.25
		1.5	200 x 181.0 x 3.00 x 5.33	25	2000	527	123.8	1	186.1	28	1.50
		2.0	200 x 155.4 x 2.85 x 6.32	25	2000	396	93.9	1	184.7	37	1.97
		2.5	200 x 137.9 x 2.71 x 7.24	25	2000	317	75.6	1	183.6	49	2.43
0.075	Roller	1.5	200 x 146.5 x 2.79 x 6.76	25	2000	354	42.7	1	64.0	29	1.50
		2.0	200 x 125.4 x 2.58 x 8.07	25	2000	266	32.4	1	63.7	43	1.97
		2.5	200 x 111.0 x 2.38 x 9.32	25	2000	212	26.1	1	63.4	61	2.43
0.1		1.5	200 x 168.3 x 2.94 x 5.78	25	2000	459	67.2	1	102.3	30	1.52
		2.0	200 x 144.4 x 2.77 x 6.87	25	2000	345	51.3	1	101.5	45	1.98
		2.5	200 x 128.0 x 2.61 x 7.89	25	2000	276	41.5	1	100.9	55	2.43
0.125		1.5	200 x 190.4 x 3.05 x 5.05	25	2000	580	92.2	1	140.5	29	1.52
		2.0	200 x 163.5 x 2.91 x 5.97	25	2000	435	70.8	1	138.8	44	1.96
		2.5	200 x 145.2 x 2.78 x 6.83	25	2000	348	57.4	1	137.5	53	2.40

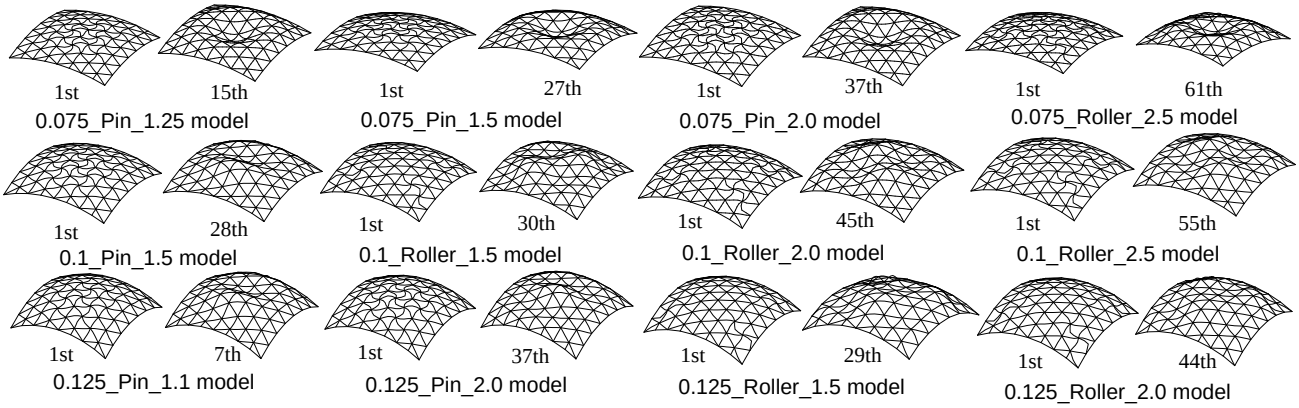


Figure 6 Eigenmodes in linear buckling

3. Linear buckling analysis

3.1. Buckling mode

The used FE code was MSC-MARC2017[5]. Figure 6 illustrates the eigenmodes. Shell-like buckling was found in the high-order modes. For example, the lowest shell-like buckling mode is the 27th eigenmode on the 0.075_Pin_1.5 shell. In general, the member buckling in the pin-supported shells was observed in the central area while in the peripheral in the roller-supported shells.

3.2. Shell-like buckling load

Eq.(2) has been proposed to calculate linear buckling load on spherical latticed shells based on the classical shell theory [2,3]. The continuum analogy is also introduced.

$$q_{cl-all}^{lin} = \frac{4}{R^2}\sqrt{DK\left(1+\nu_B+\frac{D_{xy}}{D}\right)\frac{1}{\frac{K}{2K_{xy}}+\frac{1}{1+\nu}}} \qquad \left(K=\frac{3\sqrt{3}}{4}\frac{EA}{l_0}, K_{xy}=\frac{EA\sqrt{3}}{4l_0}, D=\frac{3\sqrt{3}}{4}\frac{EI_x}{l_0}, D_{xy}=\frac{EI_x\sqrt{3}}{2l_0}\right) \quad (2)$$

where K, K_{xy}, D and D_{xy} are the effective stiffness of latticed surface (in-plane axial, stiffness, out-of-plane bending and twisting, respectively). ν and ν_B are the effective Poisson's ratio regarding the in-plane axial and out-of-plane bending strain. 1/3 can be taken for both on the equilateral triangular

lattice. *E* and *G* are the Young's and shear modulus of the material. *A* and I_x are the area and second moment inertia about the strong axis of the member section.

Figure 7 shows the ratios of the FE to the classical buckling load ($\gamma_{all} = q^{lin}_{cr-all} / q^{lin}_{cl-all}$) in correlation to $q^{lin}_{cr-all} / q^{lin}_{cr-m}$. The values of γ_{all} are about 1.1 on the pin-supported shells and 0.9 on the roller-supported shells. Both show a good agreement between the two calculations.

3.3. Effective length for member buckling

Several members simultaneously bend in in-plane member buckling. Taking the full-length as the effective length [2] might lead an excessive underestimation. For a membrane state where a lattice unit is subjected to the two orthogonal membrane forces equally (Figure 8), the effective length can be theoretically determined using Timoshenko's energy method [6].

The equivalent nodal forces to the membrane force are illustrated in Figure 8. Equilibrium leads an expression on the same axial compression in the three members (denoted by *N*).

$$N = \frac{P}{\sqrt{3}} \tag{3}$$

Buckling deformation for the diagonal and horizontal members is assumed to sine functions as illustrated. Equating the change in the total potential energy to zero, the buckling nodal force P^t_{cr-m} is obtained as Eq.(4).

$$P^t_{cr-m} = \frac{2\sqrt{3}\pi^2 EI}{l^2} \tag{4}$$

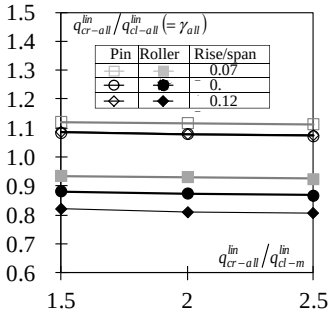


Figure 7 Ratio of FE to classical buckling load

Then the effective length is found to be 0.7 in the expression of the buckling member force $N_{cr\text{-}m}{}^t$

$$N^t_{cr-m} = \frac{\pi^2 EI}{\left(l/\sqrt{2}\right)^2} \cong \frac{\pi^2 EI}{(0.7l)^2} \tag{5}$$

The effective length also can be obtained using linear FE analysis. The member most prone to buckle in a latticed shell is found using Eq.(6) [2].

$$\lambda_{(i)} = \frac{\pi^2 EI_y / l_{(i)}{}^2}{N_{0(i)}} \qquad i = 1, 2, \cdots, m_c \tag{6}$$

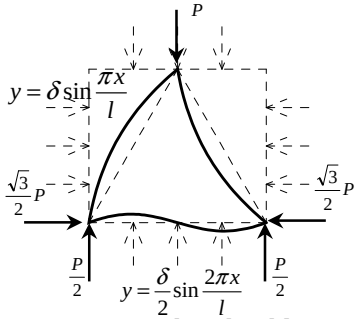


Figure 8 Member buckling in two-way membrane forces

where $N_{0(i)}$ is the axial compression of the i-th member for the unit load. m_c is the number of the compressed member. To find the member most prone to buckle, the full-member length is temporarily taken for $l_{(i)}$ and iteration to find the minimum $\lambda_{(i)}$ (denoted by $\lambda_{(E)}{}^{lin}$) is needed. The member with $\lambda_{(E)}{}^{lin}$ is chosen as the member most prone to buckle. The effective length is obtained by Eq.(7).

$$\lambda^{lin}_{cr-m} = \frac{\pi^2 EI_y}{\left(kl_{(E)}\right)^2 N_{0(E)}} \qquad \therefore kl_{(E)} = \sqrt{\frac{\pi^2 EI_y}{\lambda^{lin}_{cr-m} N_{0(E)}}} \tag{7}$$

where $_{(E)}$ represents that the value is of the member most prone to buckle. $\lambda_{cr\text{-}m}{}^{lin}$ is the load factor corresponding to $q_{cr\text{-}m}{}^{lin}$. The effective length factor *k* is calculated as indicated in Table.2. The value of *k* is about 0.7 for the pin-supported shells and 0.5 for the roller-supported shells.

As illustrated in Figure 9, the axial compression distributes quite uniformly in the pin-supported shells. It is similar to the assumed membrane state in the theoretical derivation of Eq.(5). On the other hand, tensioned members are connected to the buckled member in the roller-supported shells. The tensioned members obstruct the buckling of the connected compressed member so that the effective length factor becomes smaller than that in the pin-supported shells.

Table 2 Effective buckling length

			λ_E^{lin}	λ_{cr-m}^{lin}	$\lambda_E^{lin}/\lambda_{cr-m}^{lin}$	$l_{b(E)}$	k
0.075	1.1	Pin	237.1	487.7	0.49	2084.9	0.70
	1.25		204.5	423.2	0.48	2078.6	0.70
	1.5		167.3	348.5	0.48	2071.7	0.69
	2		125.5	263.3	0.48	2063.9	0.69
	2.5		100.4	211.5	0.47	2059.7	0.69
0.1	1.1		378.9	822.6	0.46	2093.4	0.68
	1.25		330.3	722.0	0.46	2086.2	0.68
	1.5		269.0	593.2	0.45	2077.0	0.67
	2		201.7	449.1	0.45	2067.2	0.67
	2.5		161.4	361.3	0.45	2061.4	0.67
0.125	1.1		546.1	1252.0	0.44	2126.6	0.66
	1.25		475.5	1099.0	0.43	2118.1	0.66
	1.5		388.7	908.0	0.43	2106.9	0.65
	2		291.5	688.9	0.42	2094.6	0.65
	2.5		233.2	555.0	0.42	2087.4	0.65
0.075	1.5	Roller	78.5	295.4	0.27	1541.7	0.52
	2		58.8	224.1	0.26	1531.7	0.51
	2.5		47.0	180.4	0.26	1526.3	0.51
0.1	1.5		115.7	476.3	0.24	1520.0	0.49
	2		86.6	363.5	0.24	1505.3	0.49
	2.5		69.2	293.9	0.24	1496.6	0.49
0.125	1.5		157.1	676.2	0.23	1552.1	0.48
	2		117.5	519.1	0.23	1531.9	0.48
	2.5		93.8	421.3	0.22	1519.7	0.47

4. Geometric nonlinear buckling behavior

4.1. Initial imperfection

Two types of imperfection, member-buckling imperfection being proportional to the 1st eigenmode and shell-like-buckling imperfection proportional to the higher shell-like buckling mode, were given to all the FE models. The amplitude was 1/1000 of l_o in the member-buckling imperfection [7] and 1/1000 of the larger span in the shell-like buckling imperfection [2,3]. Hereafter, a model name with the member buckling imperfection is specified by "_m" and by "_all" with the shell-like buckling imperfection.

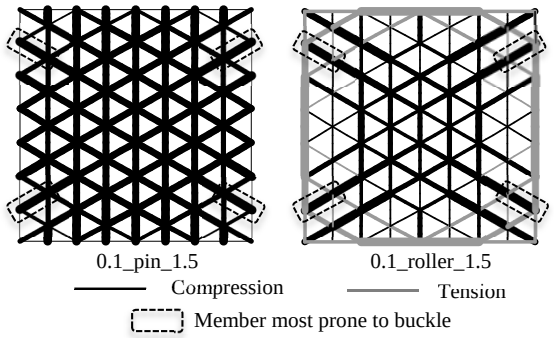


Figure 9 Axial force distribution

4.2. Nonlinear behavior

Two kinds of knockdown factor in elastic nonlinear buckling are defined by Eq.(8).

$$\alpha_{0-m} = \frac{q_{cr}^e}{q_{cr-m}^{lin}}, \qquad \alpha_{0-all} = \frac{q_{cr}^e}{q_{cr-all}^{lin}} \tag{8}$$

where $q_{cr}{}^e$ is the elastic buckling load which was specified as the load at the bifurcation or at the limit point. The Riks-Ramm arc-length analysis was employed. Figure 10 summarizes typical examples of the nonlinear load-displacement paths with the corresponding buckling mode. The buckling mode specified as the incremental vector at the buckling point did not necessarily agree with the 1st eigenmode illustrated in Figure 6.

Shell-like buckling occurred where $q_{cr-all}^{lin}/q_{cr-m}^{lin} \leqq 1.5$ in spite of the 1st eigenmode as for the pin-supported shells. The values of $\alpha_{o\text{-}m}$ distribute 0.88～1.08 while $\alpha_{o\text{-}all}$ distribute 0.46～0.72 (contained in Table 3). It is noteworthy that the buckling type of the 0.075-Pin shells was affected by the given imperfection type. Regarding the roller-supported shells, shell-like buckling occurs where $q_{cr-all}^{lin}/q_{cr-m}^{lin} \leqq 2.0$. The values of $\alpha_{o\text{-}m}$ distribute 0.85～0.99 while $\alpha_{o\text{-}all}$ distribute around 0.4. As for the shallow roller-supported shells, member buckling is also observed in the shell-like buckling but these cases are classified into the shell-buckling.

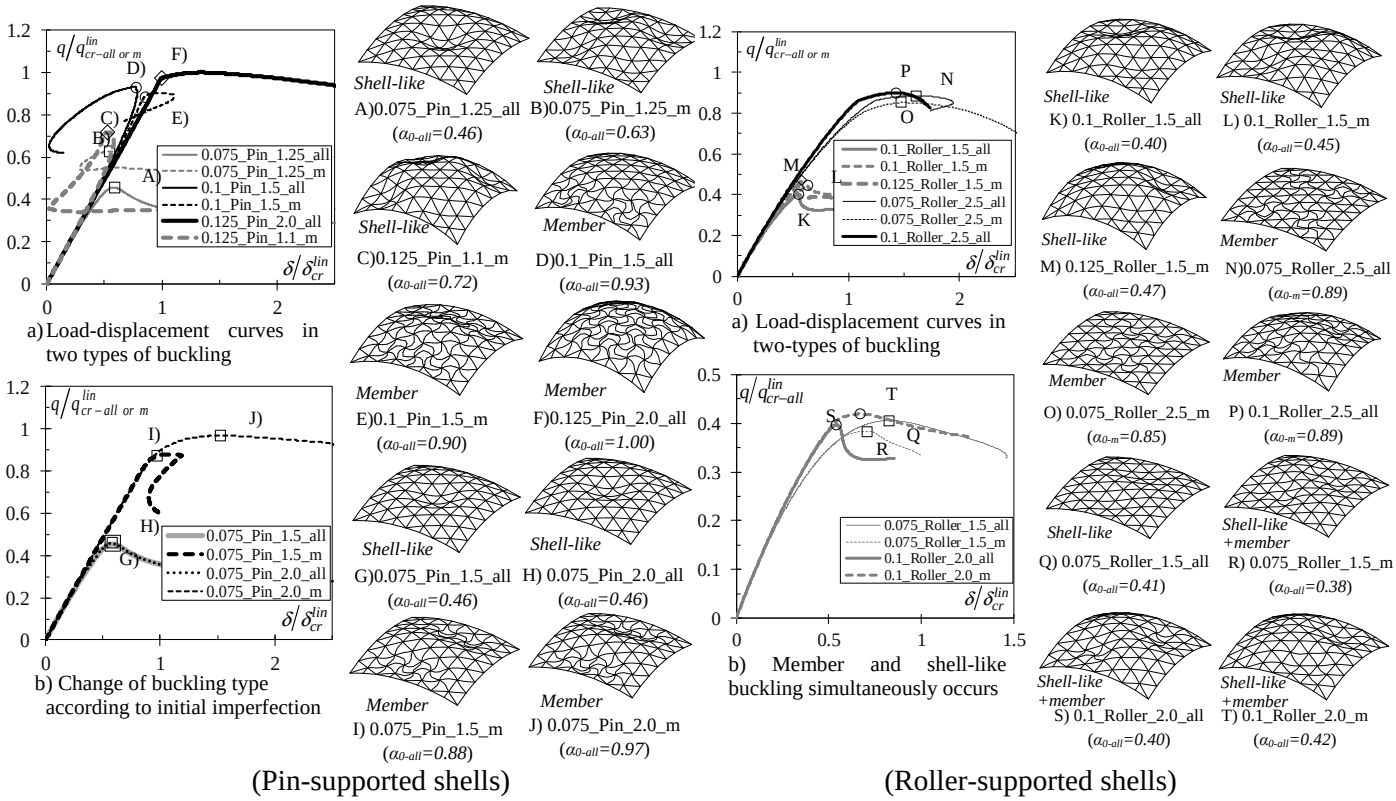


Figure 10 Elastic geometric nonlinear behavior

5. Buckling type

5.1. Condition of shell-like buckling

The condition when shell-like buckling occurs prior to member buckling is expressed by Eq.(9).

$$\alpha_{0-all} \cdot q_{cr-all}^{lin} \le \alpha_{0-m} \cdot q_{cr-m}^{lin} \tag{9}$$

This is transformed to Eq.(10).

$$\frac{q_{cr-all}^{lin}}{q_{cr-m}^{lin}} \le \frac{\alpha_{0-m}}{\alpha_{0-all}} \left(= \alpha_H\right) \tag{10}$$

α_H mainly depends on the boundary condition and the geometry as indicated in Figure 12 The avarage is 1.58 on the pin-supported shells and 2.18 on the roller-supported shells.

Table 3 Knockdown factor in elastic buckling analysis

Rise/Span	Boundary	$\frac{q_{cr-all}^{lin}}{q_{cr-m}^{lin}}$	Initial imperfection type			
			Member buckling mode proprtional		Overall buckling mode proprtional	
			member $\alpha_{0\text{-}m}$	overall $\alpha_{0\text{-}all}$	member $\alpha_{0\text{-}m}$	overall $\alpha_{0\text{-}all}$
0.075	Pin	1.1		0.63		0.46
		1.25		0.63		0.46
		1.5	0.88			0.46
		2.0	0.97			0.46
		2.5	1.04		1.01	
0.1		1.1		0.66		0.64
		1.25		0.65		0.64
		1.5	0.90		0.93	
		2.0	0.98		0.99	
		2.5	1.03		1.08	
0.125		1.1		0.72		0.71
		1.25		0.71		0.70
		1.5	0.94		0.96	
		2.0	0.99		1.00	
		2.5	1.04		1.01	
0.075	Roller	1.5		0.38		0.41
		2.0		0.42		0.40
		2.5	0.85		0.89	
0.1		1.5		0.45		0.40
		2.0		0.42		0.40
		2.5	0.93		0.89	
0.125		1.5		0.47		0.43
		2.0		0.44		0.42
		2.5	0.99		0.95	

5.2. Index to estimate buckling type and knockdown factor

An index called as the shell-likeness factor, has been proposed for pipe-made latticed shells to estimate the buckling type [2,3]. The index and the condition of shell-like buckling is expressed by Eq.(11).

$$\xi_0 = \frac{12\sqrt{2}}{\lambda_0 \theta_0} \geq 4 \qquad (11)$$

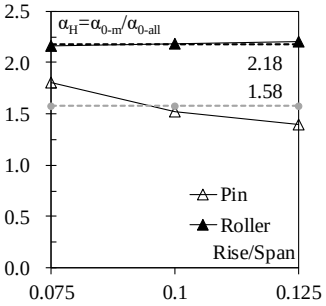


Figure 12 Knockdown factor ratio

where λ_o is the member slenderness calculated using l_o. But another index is required for H-shaped-steel-made shells. Under geometric nonlinearity, the condition of shell-like bucking is expressed by Eq.(10), where the two linear buckling loads q_{cr-m}^{lin} and q_{cr-all}^{lin} can be expressed applying the classical shell theory.

$$q_{cr-m}^{lin} = \frac{\pi^2 EI_y}{\left(kl_{(E)}\right)^2} \cdot \frac{2\sqrt{3}}{\gamma_N R l_o} \qquad \left(\gamma_N = \frac{N_{0(E)}}{N_{0g}}\right), \qquad q_{cr-all}^{lin} = \gamma_{all} \cdot q_{cl-all}^{lin} \qquad (12)$$

Where $N_{0g}\left(=q_0 R l_o / 2\sqrt{3}\right)$ is the member axial force under two equal and orthogonal membrane forces. $N_{0(E)}$ can be determined by linear FE analysis using Eq.(6). The value of γ_N distributes about 1.0 on the pin-supported shells but 2.5～3.0 on the roller-supported shells. By unifying Eqs.(2)(10)(11)and (12), another index ξ_H to estimate the buckling type is derived. The expression of ξ_H and the conditon of shell-like buckling is given as follows:

$$\xi_H = \xi_0 \frac{\alpha_H I_y l_0^{\,2}}{\gamma_N \gamma_{all} I_x \left(kl_{(E)}\right)^2} \geq \frac{48}{\pi^2} = 4.86 \qquad (13)$$

Some coefficients (α_H, k and γ_{all}) have to be empirically determined as indicated in Table 4.

From the distribution of knockdown factors illustrated in Figure 13, two regression functions of ξ_H are obtained for the two boundary condiitions.

$$\alpha_0 = \frac{0.53}{1+14.1\times\exp\left\{6.92\times\left(\xi_H - 5.31\right)\right\}} + 0.46 \qquad \left(\text{pin-supported}\right)$$
$$\alpha_0 = \frac{0.55}{1+14.5\times\exp\left\{10.3\times\left(\xi_H - 4.96\right)\right\}} + 0.39 \qquad \left(\text{roller-supported}\right) \qquad (14)$$

Elastic nonlinear buckling load can be estimated by multiplying the approximated knockdown factor to the linear buckling load.

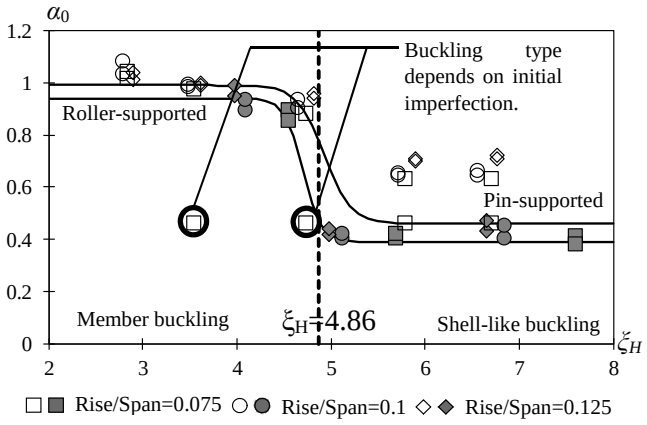


Figure 13 Estimation of knockdown factor by ξ_H

Table 4 Coefficients empirically determined

		Pin	Roller
Knockdown factor ratio	α_H	1.56	2.18
Buckling length coefficient	k	0.7	0.5
Buckling load analysis coefficient	γ_{all}	1.10	0.87

6. Conclusions

In-plane member buckling is likely to occur in the elastic buckling of latticed shells made of H-shaped steel. However, even when in-plane member buckling appears in the 1st eigenmode, shell-like buckling can firstly occur due to geometric nonlinearity. This study has specified the watershed condition for each buckling type in geometric nonlinear behavior. Shell-like buckling occurs when the ratio $q_{cr-all}^{lin} / q_{cr-m}^{lin}$ is less than or equal to 1.5 as for the pin-supported shells, and 2.5 as for the roller-supported shells. Moreover a new index ξ_H to estimate buckling type has been derived as expressed in Eq.(13). Shell-like buckling occurs where $\xi_H \geqq 4.86$. A regression function of ξ_H also has been proposed to estimate the knockdown factor. However, ξ_H contains some constants empirically determind thus it is available within a certain limit.

Acknowledgements

Funding by Grant-in-Aid for Scientific Research (C) from the Japan Society for the Promotion of Science is gratefully acknowledged.

References

[1] H. C. Saw, K. K. Choong, V.W. Tong, S. K. Wong, K. S. Chew, S.T. Tang, Iconic Roof of Setia SPICE Convention Centre Penang Malaysia – Architectural and Engineering Aspect of Organic Form Single Layer Latticed Grids Steel Shell Roof, *Proceedings of the 12th Asian Pacific Conference on Shell & Spatial Structures, APCS2018*, pp.14-24, 2018.10

[2] AIJ, *Recommendation for Design of Latticed Shell Roof Structures (in Japanese)*, AIJ, 2016.11

[3] IASS WG8, *(Draft) Guide to Buckling Load Evaluation of Metal Reticulated Roof structures*, IASS,2014

[4] S. L. Chan, Y. P. Liu, S. W. Liu, A New Codified Design Theory of Second-order Direct Analysis for Steel and Composite Structures – From Research to Practice, *Structures Volume 9*, pp.105-111, 2017.2

[5] MSC Software, Marc® 2017, *Volume A: Theory and User Information, Volume B: Element library*, 2017

[6] S. P. Timoshenko, J. M. Gere, *Theory of elastic stability second edition*, McGraw-Hill Book Company, Inc., 1961.

[7] AIJ, *Japanese Architectural Standard Specification JASS6 Steel Work*, AIJ, 2015.3(in Japanese)

Proceedings of the IASS Annual Symposium 2019 – Structural Membranes 2019
Form and Force
7 – 10 October 2019, Barcelona, Spain
C. Lázaro, K.-U. Bletzinger, E. Oñate (eds.)

Structural design of "Steel Pavilion"

Motoki UCHIYAMA*, Hirokazu NOZAWA, Masahito OHNO, Takumi KOBAYASHI

*Takenaka Corporation, Design Department
4-1-13 Hommachi, Chuo-ku, Osaka, Japan
uchiyama.motoki@takenaka.co.jp

Abstract

This paper introduces a construction project of an office building of a steel fabricator, adjacent to its own plant. We have provided the areas in the building with three-dimensional and multi-faceted connections by using the geometry of the Voronoi division for the spatial structure, which has led to a space configuration that will activate communication between the employees working in different departments in the office. We have also realized the "Steel Pavilion" which demonstrates the advanced steel fabrication technology that the steel fabricator has, by employing three structural features: (1) "Steel plate shear wall", (2) "Sandwich steel plate slab" and (3) "Cross-hatch braces". For structural analysis of such a special structure, we used the data generated by a computational design tool. The authors devised the methods to efficiently convert the complex Voronoi shape data between the analysis tools and validate the structural performances.

Keywords: Voronoi division, computational design, BIM, buckling analysis.

1. Introduction (project overview)

This project is construction of an office building of a steel fabricator Sanei Kensetsu, adjacent to its own plant. Since the client Sanei Kensetsu produced the steel structure of its own new building, we were requested to create what we call "Steel Pavilion" that represents an advanced steel fabrication technology. Furthermore, the client is actively working on Building Information Modelling ("BIM") as a steel fabricator. Therefore we faced the unusual conditions under which the project's requirements were to utilize BIM and make efforts to achieve a complex-shaped steel structure. The building dimensions are 21 meters by 92.4 meters and approximately 13 meters in height. All the footing beam are made of steel, like the superstructure, in order to achieve the labour saving and construction period reduction during the foundation work. (Figure 2)



Figure 1: 3D rendering of the building

Copyright © 2019 by Motoki Uchiyama, Hirokazu Nozawa, Masahito Ohno and Takumi Kobayashi
Published by the International Association for Shell and Spatial Structures (IASS) with permission.



Figure 2: Footing beam structure

2. Main frame structures

2.1. Spatial structure by Voronoi division

Encouragement of communication between the employees working in this office and between the departments, as well as development of the steel processing techniques into architectural representations, was assigned as a challenge in this project. As a means of resolving this issue, it was decided to use the geometry of the Voronoi division for the spatial structure and provide the areas in the building with three-dimensional and multi-faceted connections (Figure 3 (left)). The structure was designed so that the steel framework become the architectural representation by using the boundaries between the Voronoi divisions for the main steel frames made of pipes with a diameter of 318.5 mm (Figure 3 (right)).

In order to meet the client's requests for the connections and sizes of the required rooms with complicated shapes using the Voronoi division, we performed a parametric study through programming using Rhinoceros and its plugin Grasshopper, optimized the result by modeFRONTIER and determined the shape (Figure 4).

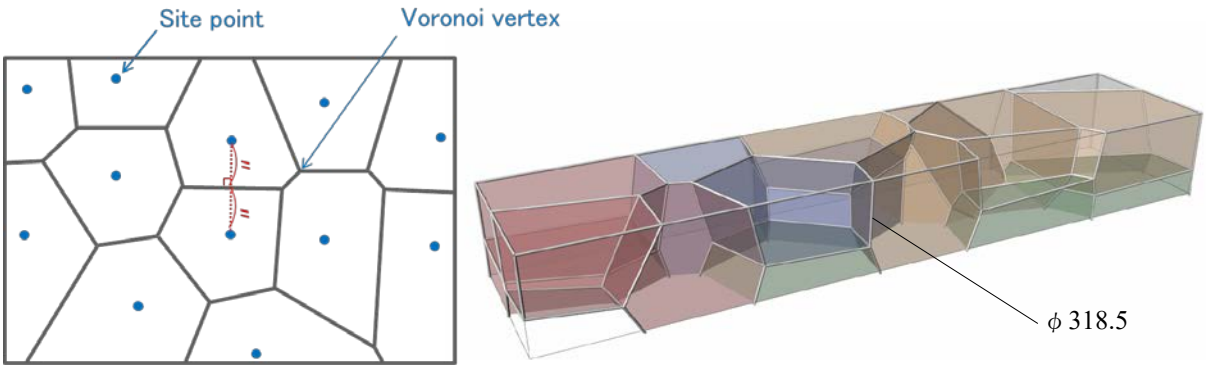


Figure 3: Voronoi division (left) and main frames by Voronoi division of space (right)



Figure 4: Study by programming; Rhinoceros and Grasshopper (left) and modeFRONTIER (right)

2.2. Joints of main frames

The main frames arranged along the boundaries between the Voronoi divisions are made of round pipes, 318.5 mm in diameter by 12.7 mm. Since three or four round pipes are jointed at the Voronoi points that correspond to the nodes between main frames, we aimed to simplify the joints by pin-jointing of most of the beam members to the columns (Figure 5).

At the seven points which are hard to make pin joints due to architectural or structural reasons, the complicated shapes of the rigidly joined nodes were achieved by using the cast steel as shown in Figure 6.

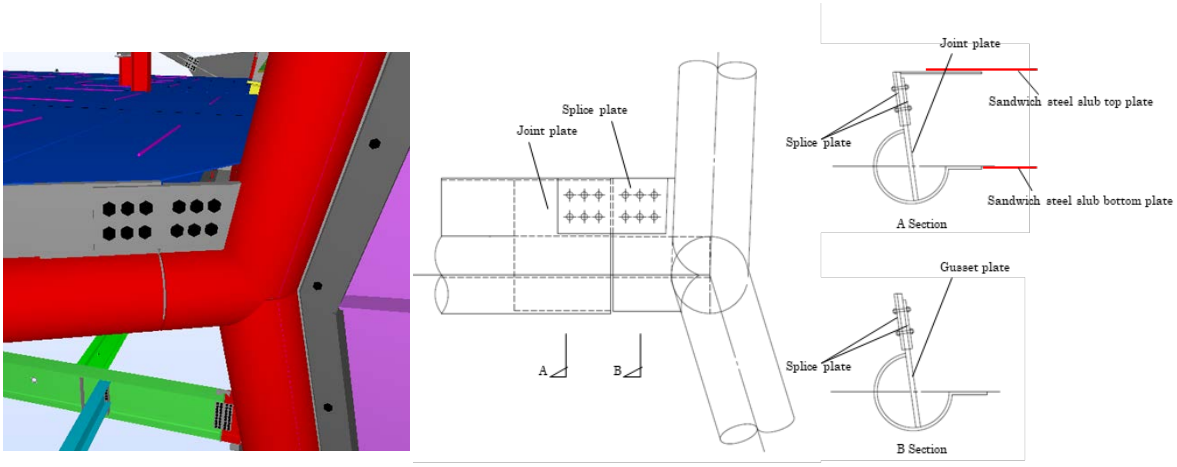


Figure 5: Illustration of model (left) and sectional view (right)

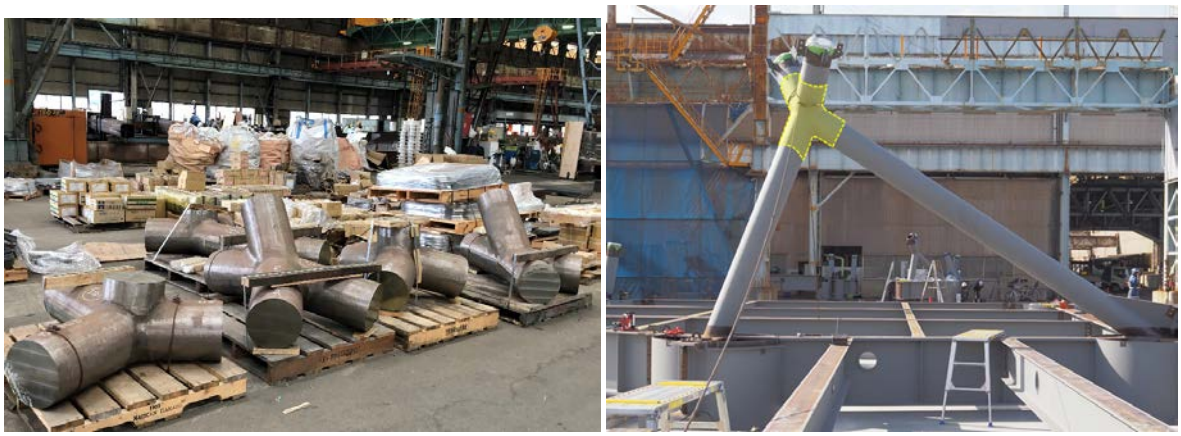


Figure 6: Elements of Cast steel (left) and Shape of node made of cast steel (right)

3. Structural planning

There are three structural features:

1. "Steel plate shear wall" with buckling stiffening ribs of 2D Voronoi shape.

2. "Sandwich steel plate slab" which is a structural floor composed of steel plates.

3. "Cross-hatch braces" which are made to be seismic elements by crossing multiple narrow steel pipes.

By using these special structural elements, we have realized the "Steel Pavilion" which expresses the fabricator's advanced steel manufacturing technology.

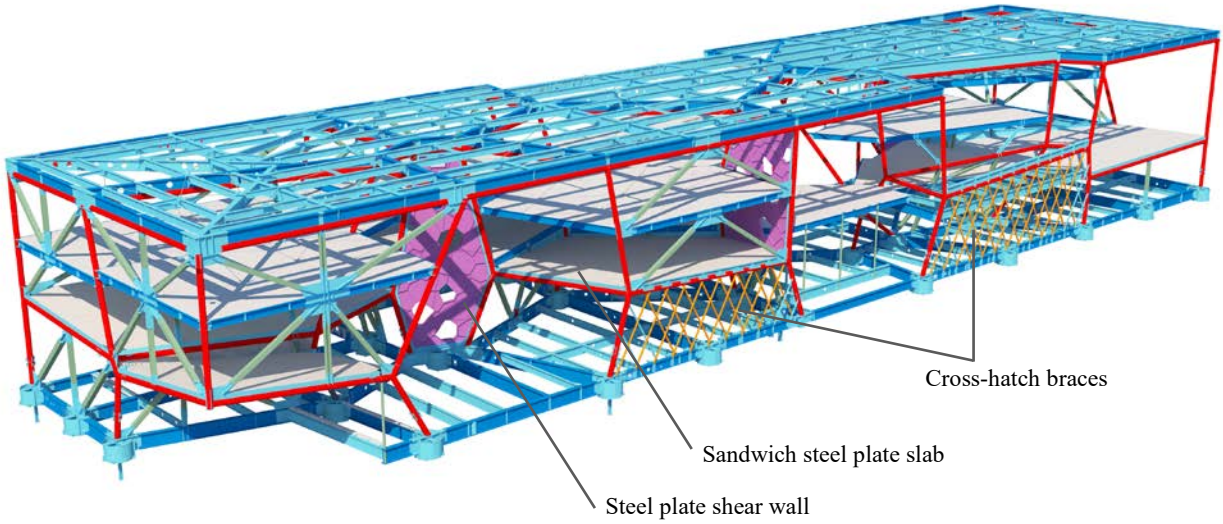


Figure 7: Overall view of steel structure

3.1. Steel plate shear wall

When a shear wall is used as a seismic element in a general building, the wall is often made of reinforced concrete. In this building, however, steel plate shear walls are used to represent the concept of "Steel Pavilion" more strongly. Furthermore, the validity as an architectural representation was also enhanced by using the Voronoi division, which was employed as a three-dimensional spatial structure, for the shape of buckling stiffening ribs (Figure 8).

In the structural analysis of a steel plate shear wall, it is especially important to perform a detailed study of the buckling stiffening ribs arranged in the 2D Voronoi shape. Specifically, it was verified that when the horizontal force for design was caused to work, the buckling load factor exceeded one (1), and consequently no buckling occurred.

The smaller the buckling stiffening ribs' grid, the larger the buckling load factor, which results in enhancement of the safety against buckling. On the other hand, the dimensions of the ribs' grid should be optimal for architectural representation. In order to perform both architectural and structural studies more efficiently, we built a system using Rhinoceros and Kramba, a component of Grasshopper, and performed a parametric study (Figure 9). Once the shape was determined, we performed a more detailed validation by using Midas iGen and confirmed structural safety (Figure 10).



Figure 8: 3D rendering of steel plate shear wall

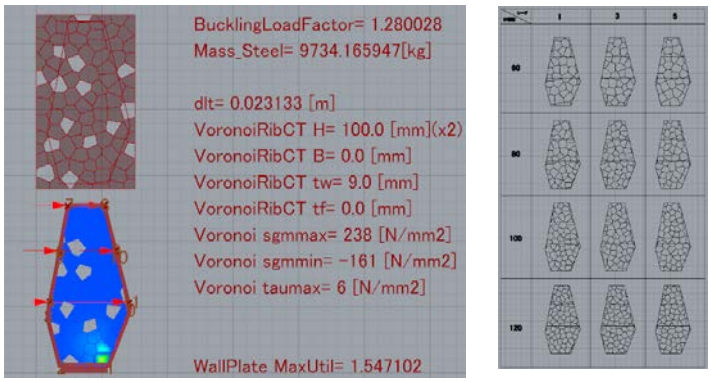


Figure 9: Analysis on buckling (left) and parametric study (right)

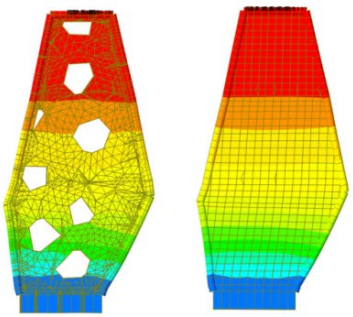


Figure 10: Analysis using Midas iGen

3.2. Sandwich steel plate slab

A sandwich steel plate slab was applied to this building, which led to a reduction of the total thickness of the floor from that in case of the RC slab applied to a normal building and thus realized the representation of a floor which is light in weight so as not to interfere with the representation of the Voronoi boundaries by the main frame. Moreover, use of only steel for structural members including the slab has enabled us to achieve a purer representation of the "Steel Pavilion" concept (Figure 11).

The beams that form the outer circumstances of a sandwich steel plate slab have two patterns: The steel pipe frames along the Voronoi boundaries (Figure 12 (left)) are used for one of them, and the beams are made of 400 mm high H-shaped steels (Figure 12 (right)) in the other case. The 2.4 meter grid in the slab is composed of H-shaped steels or 6 mm thick ribbed plates. A sandwich steel plate slab consists of 6 mm thick steel plates welded to the top and bottom of the outer beams and 2.4 meter grid.

Figure 13 (left) shows the stress diagram of a typical slab. For the stresses, it was confirmed that the

maximum principal stress of the steel materials was not more than the allowable stress. It was also verified that the responses as a result of the floor vibration analysis were under V-70, the allowable value for offices or equivalent, specified by the AIJ (Architectural Institute of Japan) [1], which tells that the building has adequate habitability [1]. (Figure 13 (right))

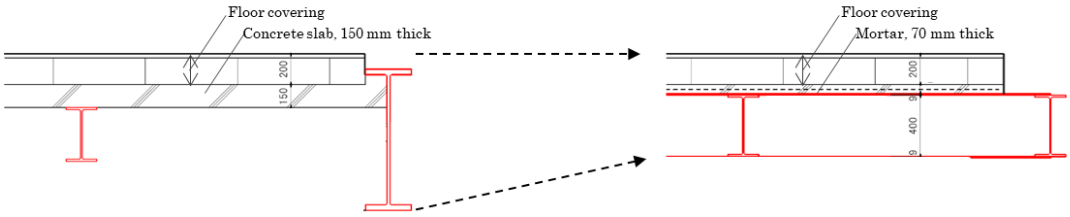


Figure 11: Comparison of sectional views between general method (left) and steel plate slab (right)

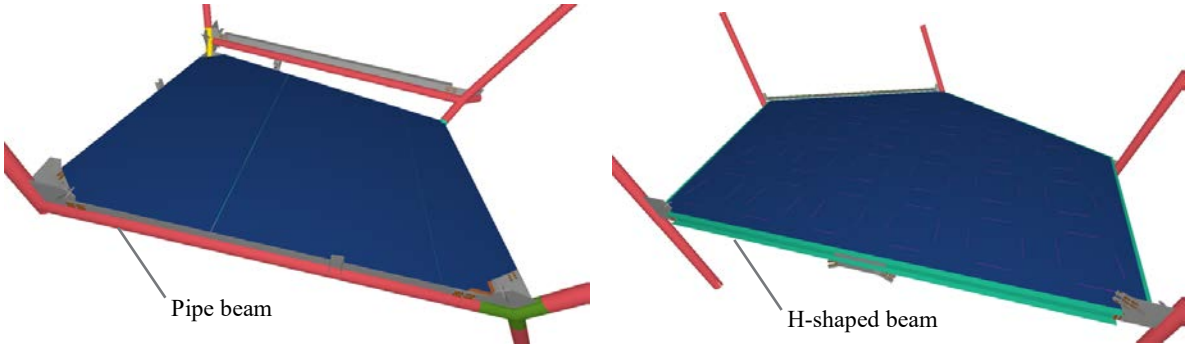


Figure 12: Configuration of steel plate slab; round pipes (left) and H-shaped steels (right) in outer beam

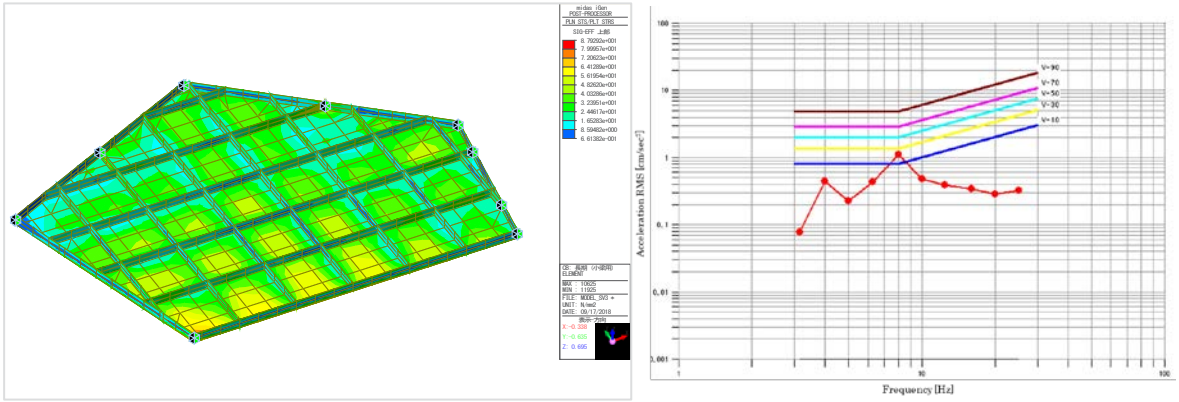


Figure 13: Stress diagram (left) and Habitability Evaluation (right)

3.3. Cross-hatch braces

Most of seismic braces in this building are installed where they are concealed by aluminium panels or louvers so as not to stand out for architectural aesthetics. However, we were requested to represent the seismic braces as architectural design at two points on the ground floor on the east side, which is the main facade of the building. Hence, consistency with the architectural design was aimed at by arranging small-diameter steel pipes in a cross-hatch pattern, at the same positions as the support members for cladding. Additionally, the cross braces were arranged so that their two-dimensional positions might be shifted from each other by directions to avoid interference between braces and ensure workability (Figure 14 (left)).

Like a steel plate shear wall, it is critical to ensure safety of cross-hatch braces against buckling. The buckling lengths of the braces were reduced by providing ties at the intersections of the two-dimensional shifted braces as shown in Figure 14 (right), the result of which has indicated that the buckling load factor meets the requirement of one (1) or more, proving that the safety against buckling is ensured.

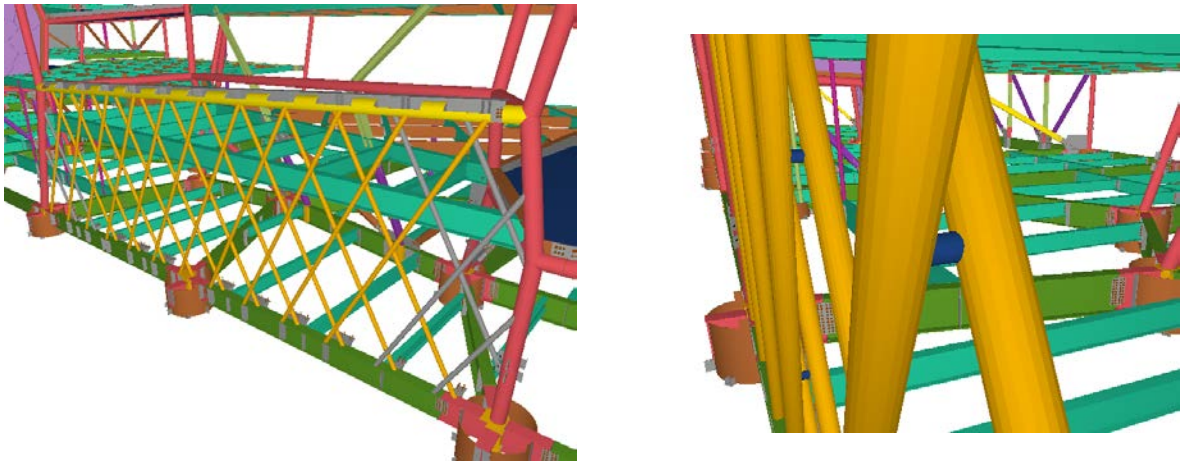


Figure 14: Cross-hatch braces (left) and ties at their intersections (right)

4. Use of computational design and BIM tools

For this project, in the initial stage we carefully planned a data linkage system both for the computational design tool in the design stage and for the BIM tool in the construction stage, which kept the consistency of a complicated shape from the basic design stage through the construction stage and minimized reworking caused by inconsistency between the data, consequently realizing a more efficient seamless flow (Figure 15).

Using the Voronoi shape determined by study in the initial stage, we proceeded with the basic design by inputting the 3D data including the architectural details and structural members on the Rhinoceros software. Thus we intend to share the images by making use of the VR and a 3D printer.

In the detailed design stage, the coordinates of the Voronoi division were output on the basis of the above data, and then ArchiCAD was used for the architectural modelling, Midas for the structural analysis modelling, Tekla for the steel structure modelling, and Rebro for the MEP modelling. The data was developed as stated above and created to completion. We proceeded with the detailed design while using the Solibri software to check that the models produced by different professions were consistent with each other by overlapping them.

Since complicated details which could not be represented in two-dimensional drawings were generated in various places, a regular meeting for confirming the steel structure model was held weekly, where the related people shared the TEKLA model and determined the details in various places. A new production management system using BIM is built, such as approval of member ordering by confirming the TEKLA model and CAM utilization for steel frame processing. Besides, we are taking up a new, leading-edge challenge, such as a trial of an inspection method by overlapping a BIM model with actual steel products, using the MR (Mixed Reality) technology (Figure 16).

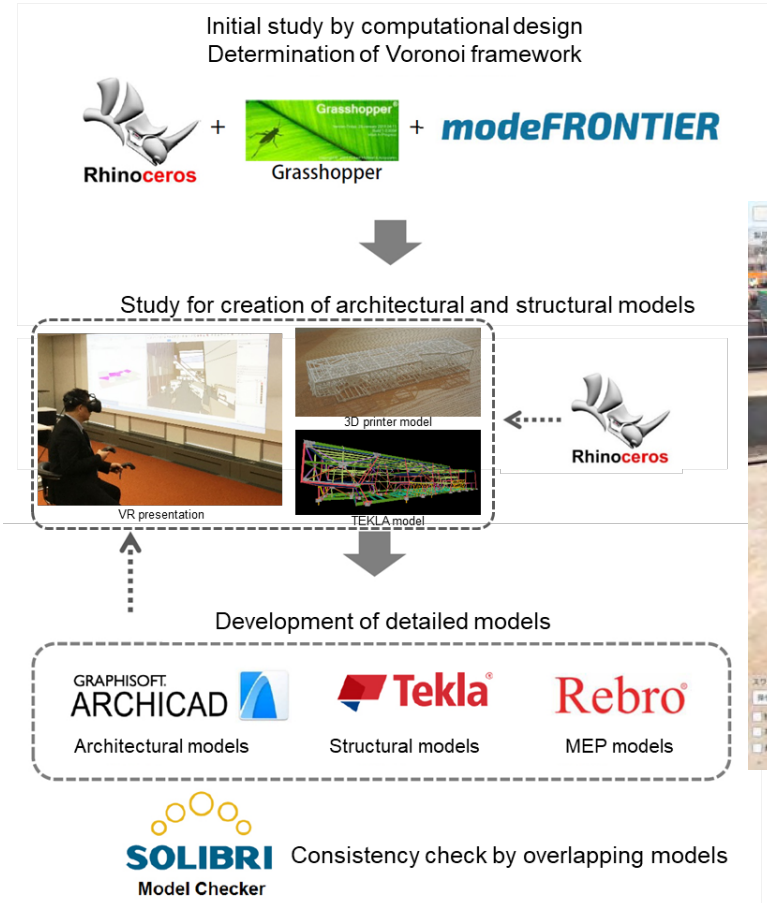


Figure 15: Flow chart of data delivery



Figure 16: Use of MR

5. Conclusion

In this project, we were able to create a complicated and attractive architectural spaces by the Voronoi divisions, employing the design method that uses a computational tool. We also invented various special structural systems using steel, which enabled us to realize the concept of "Steel Pavilion" to make an appeal about the steel fabricator's advanced technology. In addition, an efficient seamless flow with minimized reworking was built from the design stage modelling through the BIM in the construction stage.

In the future, we would like to further develop the design method using a computational tool and the seamless data flow throughout the whole project, and make efforts to create more innovative architectural spaces.

References

[1] AIJ (Architectural Institute of Japan), *Guidelines for the evaluation of habitability to building vibration*, (2nd ed.). AIJ, 2004.

Proceedings of the IASS Annual Symposium 2019 – Structural Membranes 2019
Form and Force
7 – 10 October 2019, Barcelona, Spain
C. Lázaro, K.-U. Bletzinger, E. Oñate (eds.)

Study on Equivalent Static Seismic Force of Free-Form Reticulated Shell Roofs Supported by Substructures

Shoji NAKAZAWA*, Takumi IWATA[a], Yuji TAKIUCHI[b], Shiro KATO[a]

* Toyohashi University of Technology, Department of Architecture and Civil Engineering
1-1, Tempaku-cho, Toyohashi, Aichi, 441-8580, Japan
nakazawa@ace.tut.ac.jp

[a] Toyohashi University of Technology, Department of Architecture and Civil Engineering

[b] aT ROBOTICS Inc.

Abstract

The present paper discusses about equivalent static seismic force distributions of free-form reticulated shells with edge beams supported by substructures, and proposes a scheme to the seismic force. First, in order to analyze the response characteristics of the shell roof structure, dynamic eigenvalue analysis is performed. Based on the analysis of effective mass ratio and maximum strain energy corresponding to each mode, the response of the shell roof structure is revealed to be mainly due to the response of the first mode. Therefore, an equivalent two degree of freedom model for simulating the vibration of the shell roof structure and the substructure is established, and the equivalent static load of the roof structure taking the response characteristics of the substructure into consideration is evaluated. Several numerical parameters, such as yield shear coefficients and initial shear stiffness, are set to investigate the influence on seismic force. Finally, comparisons between the maximum responses obtained from the time history response analysis and the maximum responses obtained from the proposed equivalent seismic load are illustrated, and the validity of the equivalent seismic force of the free-form reticulated shells is examined.

Keywords: Equivalent static seismic load, Free-form reticulated shell, Substructure, Two degree of freedom model

1. Introduction

Recently, with the development of BIM and 3D CAM system, design examples of free-form reticulated shells tend to increase. Since the mechanical properties of the free-form reticulated shell largely depend on its shape, many investigations on optimal design have been performed [1, 2].

In addition, analysis of the buckling characteristics of the free-form surface lattice shell generated by the optimal design method and research on ultimate strength have also been studied. On the other hand, there are few types of research on analysis of response characteristics of free-form reticulated shells, evaluation of equivalent static seismic force and proposal of seismic performance evaluation method. In previous research [3], for the free-form reticulated shell supported by the substructure, the estimation method of the maximum response and equivalent static seismic load by modal analysis based on the response spectrum considering two dominant modes wew proposed. However, the response amplification characteristics of the shell roof structure by the substructure have not been sufficiently discussed.

Copyright © 2019 by Shoji NAKAZAWA, Takumi IWATA, Yuji TAKIUCHI, Shiro KATO
Published by the International Association for Shell and Spatial Structures (IASS) with permission.

Therefore, in this research, the free-form reticulated shell determined by the strain energy minimization method is targeted. First, the influence of the dynamic characteristics of the substructure on the response amplification of the shell roof structure is analyzed. Focusing on the fact that the dominant mode of the shell roof structure is one, and an equivalent two degree of freedom model is established. Furthermore, the estimation of maximum responses of the roof structure considering the dynamic characteristics of the substructure, and the calculation method of equivalent static seismic load are proposed. Moreover, the validity of the proposed method is examined based on the comparison with the results of time history response analysis.

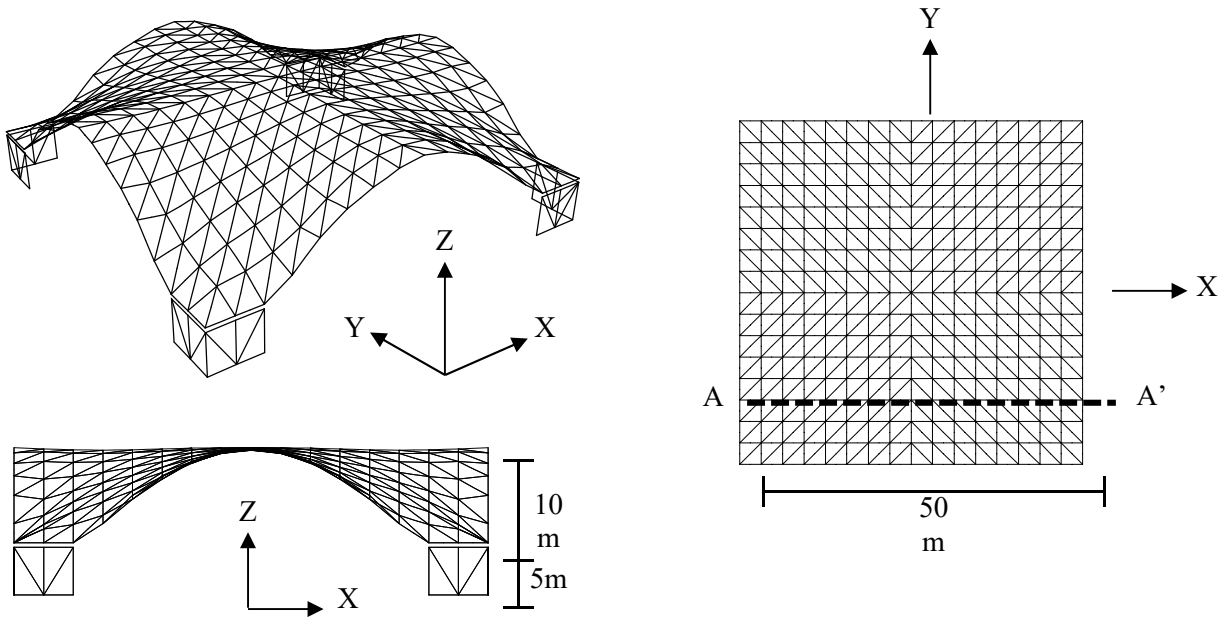


Figure 1 Numerical model

2. Numerical model

The analytical model illustrated in Fig.1 consists of a shell roof structure and a substructure. The length of one side of the analytical model is 50 m. The rise of the shell roof structure is 10 m and the height of the substructure is 5 m.

2.1 Shell roof structure

The shell roof structure investigated in this paper are shallow steel single layer reticulated shells consisting of rigidly jointed tubular members, and the shapes are generated by a shape optimization considering minimization of strain energy due to dead load [2,3]. The members of the shell roof structure are assumed to be steel pipes. The slenderness ratio of the ridge members is assumed to be 30, and the slenderness ratio of parallel and diagonal members is assumed to be 60.

The dead load P_0 is assumed to be 0.8 kN/m^2. The design load P_d considering both dead load and snow load which is assumed to be 2.75 kN/m^2. The member thicknesses of the roof structure are determined in such a way so that the ultimate strength P_{cr} of the shell roof structure exceeds P_d. Table 1 lists cross-sectional properties of the members. The weight $M_R g$ of the roof structure is equal to 1927.7 kN.

The value of P_{cr}/P_d. of the designed shell roof is 1.25. It is confirmed that the ultimate strength of the designed shell roof structure is greater than the design load. Also, the safety factor P_{cr}/P_0 of the structure with respect to the dead load P_0 corresponds to 4.41.

As a result of dynamic eigenvalue analysis of the shell roof structure without substructure, the natural period ${}_1T_R$ of the first mode is 0.736 sec, and the effective mass ratio ${}_1\rho_R$ is 29.4%. Since the maximum strain energy of the first mode is 98% of the sum of the maximum strain energy of the first to 200th modes, it is expected that the first mode is the dominant mode of the shell roof structure.

Table 1 Cross-sectional properties of the members

	Ridge member	Pararell member	Diagonal member
Dinomiter D [mm]	304.6	153.3	216.3
Thikness t [mm]	10.0	6.5	8.0
Area A [cm^2]	92.6	30.0	52.4
Moment of inartia I [cm^4]	20100	1618	5688

2.2 Substructure

The substructure is composed of buckling restrained braces with bi-linear hysteresis characteristics, and it consists of eight braces in one direction. The weight $M_S\,g$ of the substructure is equal to 120.3 kN. The total weight $M_T g$ (= $M_R\,g + M_S\,g$) of the objective structure is 2050 kN. Thus, the ratio R_M of the total weight $M_T g$ to the weight of the structure is 1.06. In this study, the cross section A_{BR} of the brace is determined for the four design yield layer shear coefficients, C_{yd} (= 0.2, 0.3, 0.4, and 0.5). The values of R_T corresponding to C_{yd} = 0.2, 0.3, 0.4, and 0.5 are 0.69, 0.56, 0.49, and 0.44, respectively. Moreover, A_{BR} is set for five natural period ratios R_T (= 0.1, 0.5, 1.0, 2.0, and 5.0). Here, R_T is the natural period ratio of the shell roof structure and substructures. Table 2 lists the values of R_M, T_0, R_T and A_{BR} of each analysis model. T_0 is an elastic natural period of the substructure when the shell roof structure is assumed to be a rigid body.

Table 2 Numerical parameters

	R_T					C_{yd}			
	0.1	0.5	1.0	2.0	5.0	0.2	0.3	0.4	0.5
R_M	1.06								
${}_1T_R$ [sec]	0.736								
T_0 [sec]	0.074	0.368	0.736	1.472	3.680	0.507	0.414	0.358	0.321
A_{BR}[cm^2]	195.12	7.81	1.95	0.49	0.08	4.12	6.17	8.23	10.29

3. Input ground motion

The earthquake motions are input in X-direction. The input earthquake motions are artificial earthquake motions simulated on the design acceleration response spectrum specified by Notification No.1457 of Japan Building Code [3], corresponding to the soil layer for the medium soil Type II. To prepare the twelve artificial ground motions the phases of recorded earthquake accelerations such as El-Centro NS and Taft EW, which are often utilized for seismic design in Japan are used in this study, λ_E represents a seismic intensity, and λ_E =1.0 corresponds to the serviceability limit level. The acceleration response spectra of twelve artificial ground motions are illustrated in Figure 2.

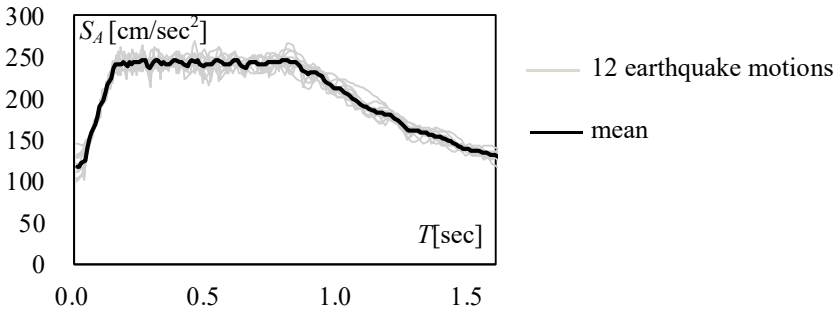


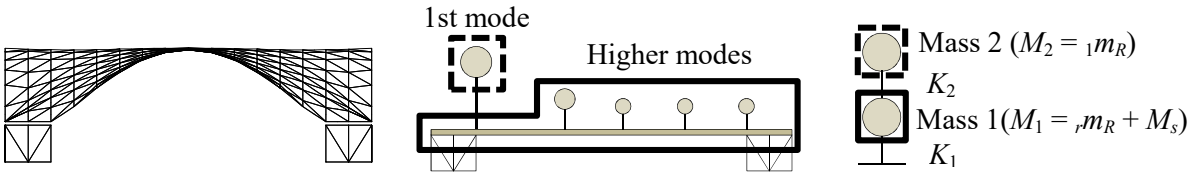
Figure 2 Acceleration response sepctram of twelve artificial ground motions (λ_E =1.0, h=5%)

4. Static Seismic Load of Free-Form Surface Lattice Shell Supported by Substructure

4.1 Replacement of the equivalent two degree of freedom model

In this study, in order to consider the response amplification of the shell roof structure caused by the substructure, an equivalent two degree of freedom model based on a parallel multi degree of freedom model is adopted. It is known that the space structure supported by the substructure can be replaced by the model as shown in Fig.3(b) using the vibration mode of the shell roof structure [4, 5].

The shell roof structure targeted in this study mainly has two types of vibration modes. The former is a first mode that greatly affects the vertical displacement, axial force, and bending moment although the natural period is relatively long and the effective mass ratio is not very large. The latter are higher order modes that have short natural periods and affect horizontal displacement and layer shear force. The natural periods of the high-order modes are sufficiently short compared to the natural period of the first mode, and assuming these modes as rigid-body modes, it can be replaced by the equivalent two degree of freedom model as illustrated in Fig.3(c). This methodology has already been applied to single layer cylindrical lattice shell roofs [6].



(a) Full model

(b) Parallel multi degree of freedom model

(c) Two degree of freedom model

Figure 3 Replacement of the equivalent two degree of freedom model

As shown in Fig.3(c), M_1, M_2, K_1, and K_2 represent mass and stiffness of each point. In this study, ρ_m and γ are numerical parameters defind as

$$\rho_m = \frac{M_1}{M_2}, \quad \gamma = \frac{\omega_1}{\omega_2}, \quad \omega_1 = \frac{K_1}{M_1}, \quad \omega_2 = \frac{K_2}{M_2} \tag{1}$$

4.2 Equivalent static seismic load of shell roof structure

The horizontal and vertical equivalent static seismic loads ${P_{EH}}^i$ and ${P_{EV}}^i$ of the shell roof structure in consideration of the substructure are given as

$${P_{EH}}^i = {}_1{P_{EH}}^i + {}_r{P_{EH}}^i, \quad {P_{EV}}^i = {}_1{P_{EV}}^i \tag{2}$$

where ${}_1P_{EH}{}^i$ and ${}_1P_{EV}{}^i$ are equivalent static seismic loads in the horizontal and vertical directions corresponding to the first mode, respectively. ${}_rP_{EH}{}^i$ is a static seismic load in the horizontal directions due to the higher-order mode. ${}_1P_{EH}{}^i$, ${}_1P_{EV}{}^i$, and ${}_rP_{EH}{}^i$ are given as

$$\begin{cases} {}_1P_{EH}{}^i = m_i \cdot {}_1\beta_X \cdot {}_1\phi_x{}^i \cdot \alpha_2 \cdot A_{\max} \\ {}_1P_{EV}{}^i = m_i \cdot {}_1\beta_X \cdot {}_1\phi_z{}^i \cdot \alpha_2 \cdot A_{\max} \end{cases} \tag{3}$$

$${}_rP_{EH}{}^i = (1 - {}_1\rho_R) \cdot m_i \cdot \alpha_1 \cdot A_{\max} \tag{4}$$

in which ${}_1\beta_X$ is a participation factor in the X direction of the 1st mode of the roof structure, and ${}_1\phi_X{}^i$, ${}_1\phi_Z{}^i$, are X and Z direction components of the 1st mode vector of the roof structure. $A_{\max}$ (= 96 cm/sec^2) is the maximum ground acceleration.

The values of $\alpha_1 A_{\max}$ and $\alpha_2 A_{\max}$ correspond to the maximum response accelerations ($a_{1\max}$ and $a_{2\max}$) of Mass 1 and Mass 2 of the equivalent two degree of freedom model, respectively. The values of α_1 and α_2 are the amplification factors with respect to $A_{\max}$. α_1 and α_2 are evaluated based on the equivalent two degree of freedom model.

$$\alpha_1 = \frac{a_{1\max}}{A_{\max}}, \quad \alpha_2 = \frac{a_{2\max}}{A_{\max}}, \quad S_{p0} = \frac{S_A({}_1T_R, {}_1h_R)}{A_{\max}} \tag{5}$$

On the other hand, the seismic load of the shell roof without the substructure is given assuming that α_1 = 1.0 and α_2 $A_{\max}$ = $S_A({}_1T_R,{}_1h_R)$. Here, $S_A({}_1T_R,{}_1h_R)$ is the value of absolute acceleration response spectrum corresponding to first mode of the shell roof structure, and is denoted as S_{p0} $A_{\max}$. The amplification factor α_H of the horizontal shear force of the roof structure supported by the substructure against the horizontal shear force of the roof structure without the substructure, and the amplification factor α_V for the seismic load in the vertical direction are given as

$$\alpha_H = \frac{{}_1\rho_R \cdot \alpha_2 + (1 - {}_1\rho_R) \cdot \alpha_1}{{}_1\rho_R \cdot S_{p0} + (1 - {}_1\rho_R)}, \quad \alpha_V = \frac{\alpha_2}{S_{p0}} \tag{6}$$

4.3 Calculation of response amplification factor

By solving the vibration equation of the equivalent two degree of freedom model shown in Section 4.1, it is possible to obtain the response amplification factors of the shell roof structure in consideration of the substructure. The maximum response value of each mass can be evaluated based on ABS method (absolute value sum), SRSS method (square-sum-square), and AVE method (average of ABS and RSS). For example, the ABS evaluation of maximum absolute accelerations of Mass 1 and Mass 2 is given as

$$\begin{aligned} a_{1(ABS)} &= \left|{}_1\beta \cdot S_A({}_1T, {}_1h)\right| + \left|{}_2\beta \cdot S_A({}_2T, {}_2h)\right| \\ a_{2(ABS)} &= \left|{}_1\beta \cdot {}_1\Phi \cdot S_A({}_1T, {}_1h)\right| + \left|{}_2\beta \cdot {}_2\Phi \cdot S_A({}_2T, {}_2h)\right| \end{aligned} \tag{7}$$

in which ${}_sT$, ${}_s\beta$, and ${}_s\Phi$ are s-th natural period, participation factor and the value of mode vector, respectively. These values can be easily calculated from the equivalent two degree of freedom model.

$${}_sT = \frac{2\pi}{{}_s\omega} = \frac{2\pi}{\omega_2 \cdot {}_s\Omega_1}, \quad {}_s\beta = \frac{\rho_m + {}_s\Phi}{\rho_m + {}_s\Phi^2}, \quad {}_s\Phi = \frac{1}{1 - {}_s\Omega^2}$$

$${}_1\Omega^2, {}_2\Omega^2 = \frac{(1+\gamma^2)\rho_m + 1}{2\rho_m} \mp \sqrt{\left(\frac{(1+\gamma^2)\rho_m + 1}{2\rho_m}\right)^2 - \gamma^2} \tag{8}$$

Fig.4 illustrates the amplification factors α_H and α_V. In the region where R_T is around 1.0, the values of α_H and α_V become large, and the response amplification of the roof structure appears notably. In the region where R_T is close to 0.0, which corresponds to the roof structure supported by high rigidity substructure or without the substructure, the values of α_H and α_V are close to 1.0. In the region where R_T is large, the values of α_H and α_V tend to be small.

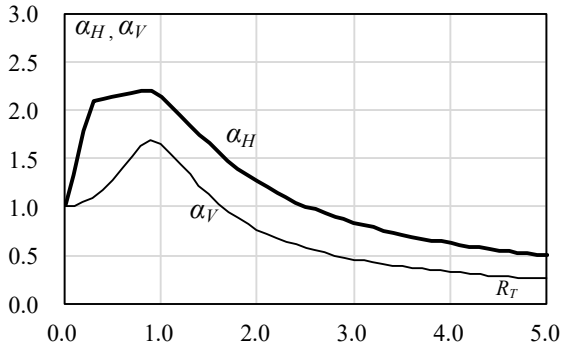


Figure 4 amplification factors α_H and α_V.

5. Evaluation of maximum responses by using proposed static seismic load

5.1 Distribution of maximum responses along A-A' line (R_T = 1.0)

In order to examine the validity of the proposed equivalent static seismic load, we compare the maximum response values calculated by using the proposed seismic load with the maximum response value of linear response analysis. Fig.5 illustrates a comparison of the distribution of horizontal displacement, vertical displacement and axial force along A-A' line at R_T = 1.0. The nodal point on line A-A' includes a point where response displacement and member axial force are quite large. The marks □, ◇ indicate the maximum responses due to the equivalent static seismic loads caused by the first mode and the higher modes, respectively. As the maximum responses calculated by the time history response analysis, the mean value (μ) and the mean value + standard deviation ($\mu + \sigma$) of the maximum responses due to twelve simulated earthquake motions are also shown in Fig.5. As observed in Fig.5, it is confirmed that the maximum response value is roughly evaluated to the safe side by the proposed equivalent static seismic load.

5.2 Maximum axial force of shell roof structure

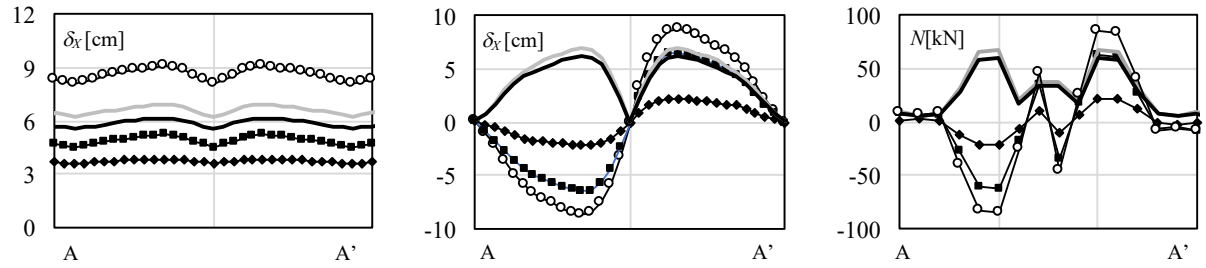
Fig.6 shows a comparison of the maximum axial forces of the shell roof structures excluding R_T = 1.0. sN is a maximum axial force evaluated by the proposed equivalent static seismic load, and ${}_dN$ is a maximum axial force calculated by time history response analysis. As shown in Fig.6, in all models, the values of sN are evaluated larger than the values of ${}_dN$. Therefore, it is confirmed that the maximum response can be evaluated on the safe side by using the equivalent static seismic load.

Although only the result of maximum axial force is shown here, it is confirmed that the maximum vertical displacement and bending moment can be evaluated on the safe side by using the equivalent static seismic load.

5.3 Shear force coefficient of shell roof structure

The shear coefficient can be estimated in the process of calculating the response amplification factor. Fig.7 illustrates a comparison of the shear force coefficient of shell roof structure. The dashed black and gray lines indicate the maximum shear coefficient due to the equivalent static seismic loads caused by the first mode and the higher modes, respectively. The solid line is the evaluated maximum

shear coefficient. As the maximum responses calculated by the time history response analysis, the mean value (μ) and the mean value + standard deviation ($\mu + \sigma$) of the maximum responses due to twelve simulated earthquake motions are also shown in Fig.7. As observed in Fig.7, it is confirmed that the maximum shear coefficient is roughly evaluated to the safe side by the proposed equivalent static seismic load. However, in the models with R_T = 2.0 and 5.0, it is confirmed that the horizontal displacement and layer shear coefficient evaluated on the slightly dangerous side by using the equivalent static seismic load.



(a) Horizontal displacement (b) vertical displacement (c) axial force

■ : 1st mode [Eq.(3)] ◆: Higher mode [Eq.(4)] ○: 1st mode + higher mode [Eq.(2)]

—— : time history response analysis (μ) ——: time history response analysis ($\mu + \sigma$)

Figure 5 Distribution of horizontal displacement, vertical displacement and axial force (R_T = 1.0)

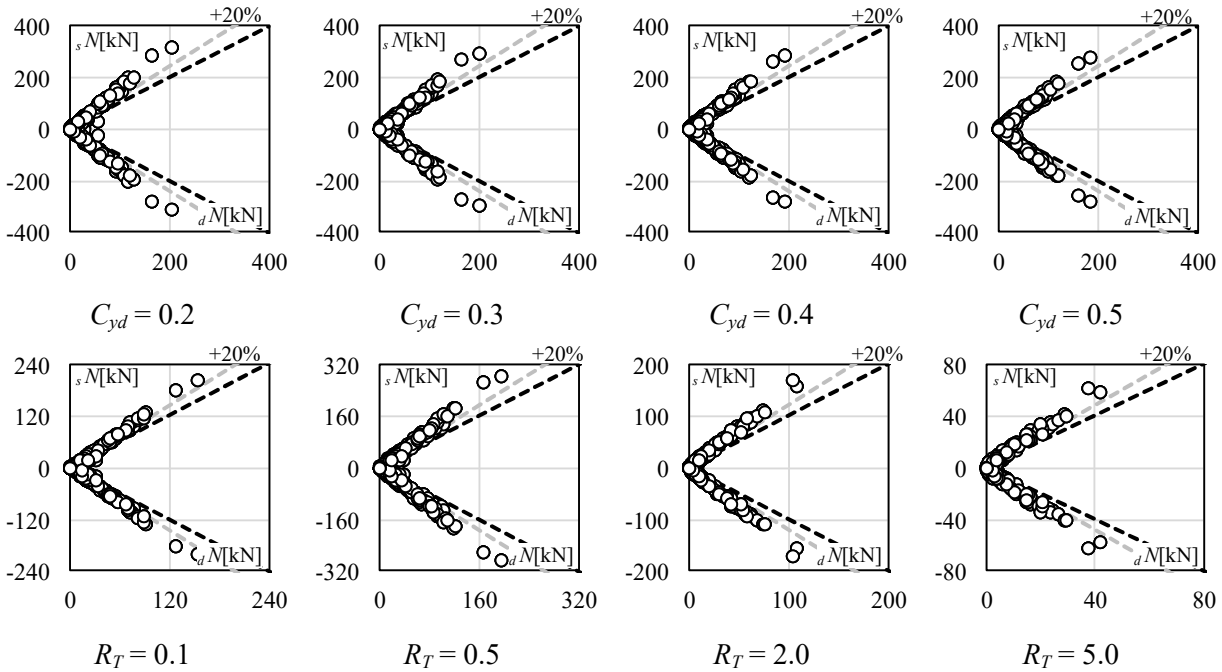


Figure 6 Maximum axial forces of the shell roof structures

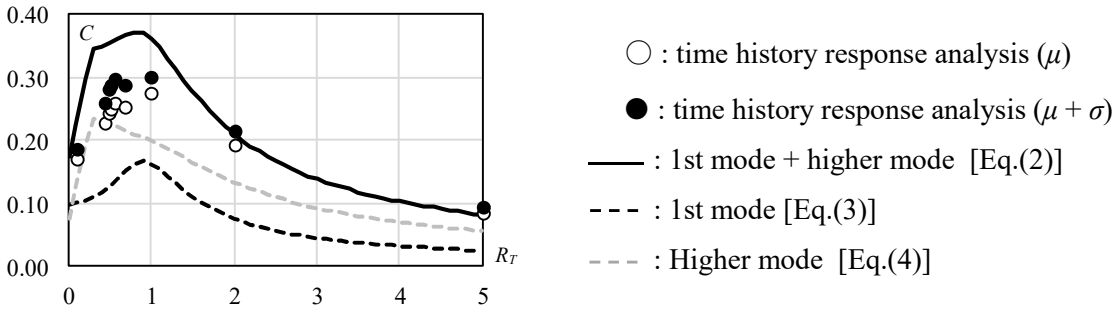


Figure 7 Shear force coefficient of shell roof structure

6. Conclusion

The present paper discusses about equivalent static seismic force distributions of free-form reticulated shells with edge beams supported by substructures, and proposes a scheme to determine the equivalent seismic load. An equivalent two degree of freedom model is established by using the dominant mode of roof structure. The equivalent static seismic load considering the substructure is formulated based on modal analysis, the response amplification factors α_H and α_V are evaluated without timehistory response analysis.

In order to examine the validity of the proposed equivalent static seismic load, maximum responses calculated by the proposed seismic load are compared with the maximum responses calculated by linear time history response analysis. It is confirmed that the maximum responses roughly evaluated to the safe side by using the equivalent static seismic load.

In addition, even if the substructure is plasticized, it seems that this method can be applied by using the equivalent linearization method. A detailed examination will be a future investigation.

References

[1] E. Ramm, "Shape Finding of Concrete Shell Roofs'', *Journal of IASS*, 2004;45; 29-39

[2] Y.Takiuchi, S.Kato, S.Nakazawa, "Buckling strength maximization approach for free-form of single layer reticulated shells'', *Proceedings of the IASS Symposium 2016*, Tokyo, Japan, 2016.

[3] S.Kato, Y.Takiuchi, S.Nakazawa, "Two modes evaluation of seismic loads for free-form single layer reticulated shell structures supported by substructures'', *Proceedings of the IASS Symposium 2017*, Hamburg, Germany, 2017.

[4] S. Nakazawa, S. Kato T.Takeuchi, S. D. Xue, C. Lazaro, "State-of-the-art of Seismic Response Evaluation Methods for Metal Roof Spatial Structures'', *Journal of the Int. Assoc. for Shell and Spatial Structures*, Vol.53, No.2, June n.172, pp.117-130, 2012.

[5] S.Kato, Y.Konishi, S.nakazawa, "Push-Over analysis and static estimation of seismic responses of large steel space structures'', *Proceedings of the IASS Symposium 2003*, Taipei, 2003.

[6] Shoji NAKAZAWA, Haruki MAEDA, Shiro Kato, "Study on Equivalent Static Seismic Force of Single Layer Cylindrical Latticed Shells Roofs'', *Proceedings of the IASS Symposium 2018*, July 16-20, 2018, MIT, Boston, USA, 2018

Proceedings of the IASS Annual Symposium 2019 – Structural Membranes 2019
Form and Force
7 – 10 October 2019, Barcelona, Spain
C. Lázaro, K.-U. Bletzinger, E. Oñate (eds.)

Roof structural design for Fukui Prefectural Gymnasium located in heavy snowfall region

Shinsuke YAMAZAKI*, Chikamasa OKUNO[a], Hiroki YODA[a]

*KUME SEKKEI Co., Ltd Structural Engineer Division
2-1-22 Shiomi, Koto-KU, Tokyo 135-8567, Japan
Shinsuke.Yamazaki@kumesekkei.co.jp

[a] KUME SEKKEI Co.,Ltd Structural Engineer Division

Abstract

This paper describes the structural design of the Fukui Prefectural Gymnasium, which spans a length of 53 m. Fukui City is located in one of the heaviest snowfall regions of Japan. The falling snow depth and design load for this region should be 2.0 m and 6,000 N/m^2, respectively, according to the Japanese Building Standards Act and the regulation of Fukui Prefecture. The roof structure is a steel parallel arch truss beam with sufficient rigidity. In addition, the Steel Reinforced Concrete (SRC) columns on the ground floor are placed diagonally so that a large thrust force does not occur on the second floor of the truss leg, and the axial force is transmitted smoothly to the foundation. Pre-stressing is introduced on site to the foundation beam to reduce the thrust force. The whole structure, from the roof of the steel frame to the foundation beam, has stable equilibrium. Moreover, the roof frame is a light frame and is able to create an open space by reducing the depth of the center to 400 mm.

Keywords: snowfall region, arch truss, steel, thrust force, pre-stressed foundation beam.

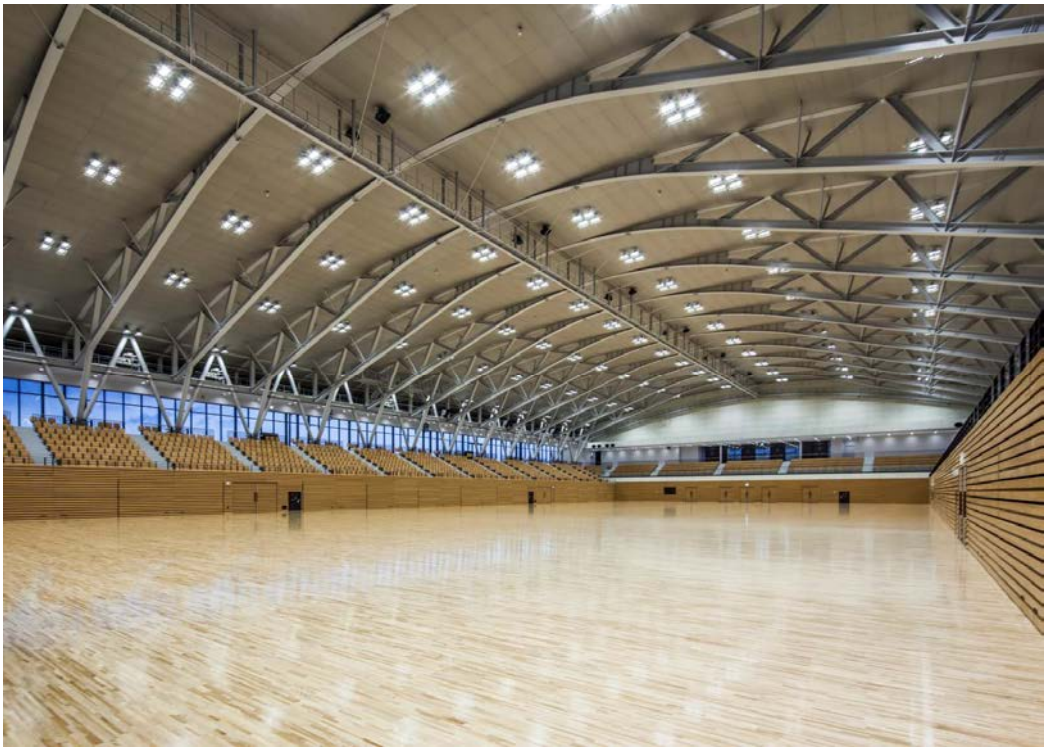


Figure: Parallel arch truss beams of the main arena

Copyright © 2019 by Shinsuke YAMAZAKI, Chikamasa OKUNO, Hiroki YODA
Published by the International Association for Shell and Spatial Structures (IASS) with permission.

1. Introduction

The new Fukui Prefectural Gymnasium is one of the facilities in the overall maintenance plan of the athletic park in Fukui City (Figure 1). The main entrance of this gymnasium is near "Peaceful Place", which is the center of the athletic park. We expected the athletics stadium and the baseball stadium around the place to be united. The main entrance has a large blowout space named "Sports Mall", which has a wide glass screen. We intended to revitalize the park by making people playing in the gymnasium visible from the outside (Figure 2). The shape of the arena behind the sports mall is designed to follow the contours of the Fukui mountain range.

The gymnasium is arranged so that the main arena and sub arena are parallel to the sports mall, which will be the main movement line because the main arena will be used for competitions and events and the sub arena will be used by people on a daily basis. It has a simple layout plan to make it easy for people to use.

2. Architectural scheme

General information about the building

Name of building: Fukui Prefectural Gymnasium Location: Fukumachi, Fukui City, Fukui Prefecture

Building area: 13,914.66 m^2 Total floor area: 11,090.96 m^2

Maximum height: 17.66 m Number of stories: 2 stories above ground

Audience seats: main arena = 3,960 seats, sub arena = 200 seats



Figure 1: Bird's-eye view of the athletic park



Figure 2: The glass screen exterior of the sports mall

3. Structural scheme

General information about the structure planning

Structure of second floor: Steel frame construction

Structure of ground floor: Reinforced concrete (RC) and steel reinforced concrete (SRC) construction

Foundation type: Pile foundation (precast concrete Pile)

Structure type: Rigid frame with earthquake resisting wall (ground floor), rigid frame with brace (second floor)

Construction period: April 2015 to March 2017 (24 months)

3.1. Total plan

The ground floor has partially RC and SRC construction and the second floor has a steel frame construction. The gymnasium consists of three parts—the main arena, sub arena, and sports mall (Figure 3, 4). The sports mall, with a width of approximately 130 m, connects the main arena to the sub arena. These 3 parts have no expansion joints and are a single structure. By not using expansion joints, it is possible to give the glass screen of the sports mall a continual design, an important consideration for preventing water leakage due to snowdrift.

The structure type of the ground floor is rigid frame with earthquake resisting wall, and second floor is rigid frame with brace. The steel frame of second floor is covered on the rigid RC platform of ground floor.

Furthermore, the regulation of Fukui Prefecture prescribes the addition of the snow load. According to the building standard law in Japan, the long-term snow load is reduced to 70%, but in the regulation of Fukui, the long-term snow load must be 100%. Because the snow depth is 2 m, and the unit weight is 30 N/cm/m^2, as defined by the law, the long-term snow load for design should be 6,000 N/m^2.

Because there are many detached houses around the park, a low and gentle arch shape with a reduced roof height was required.

From the above conditions, the roof structure of the main arena and the sub arena was parallel arch truss beams with high stiffness.

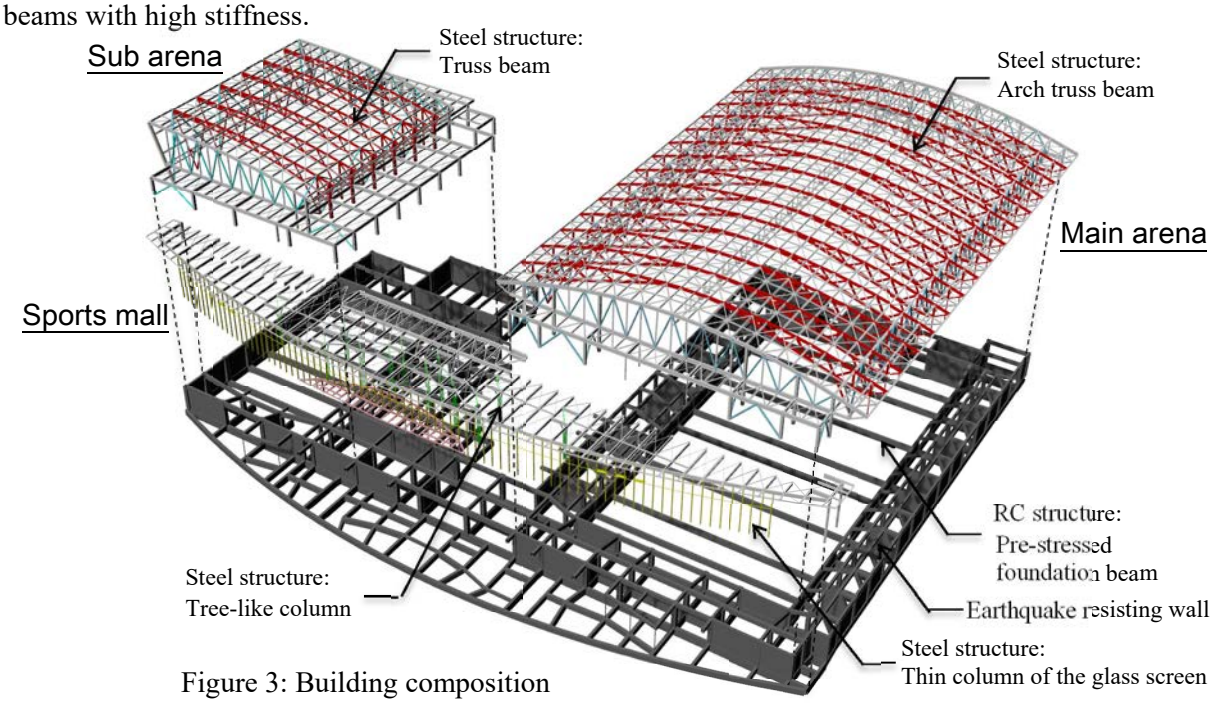


Figure 3: Building composition

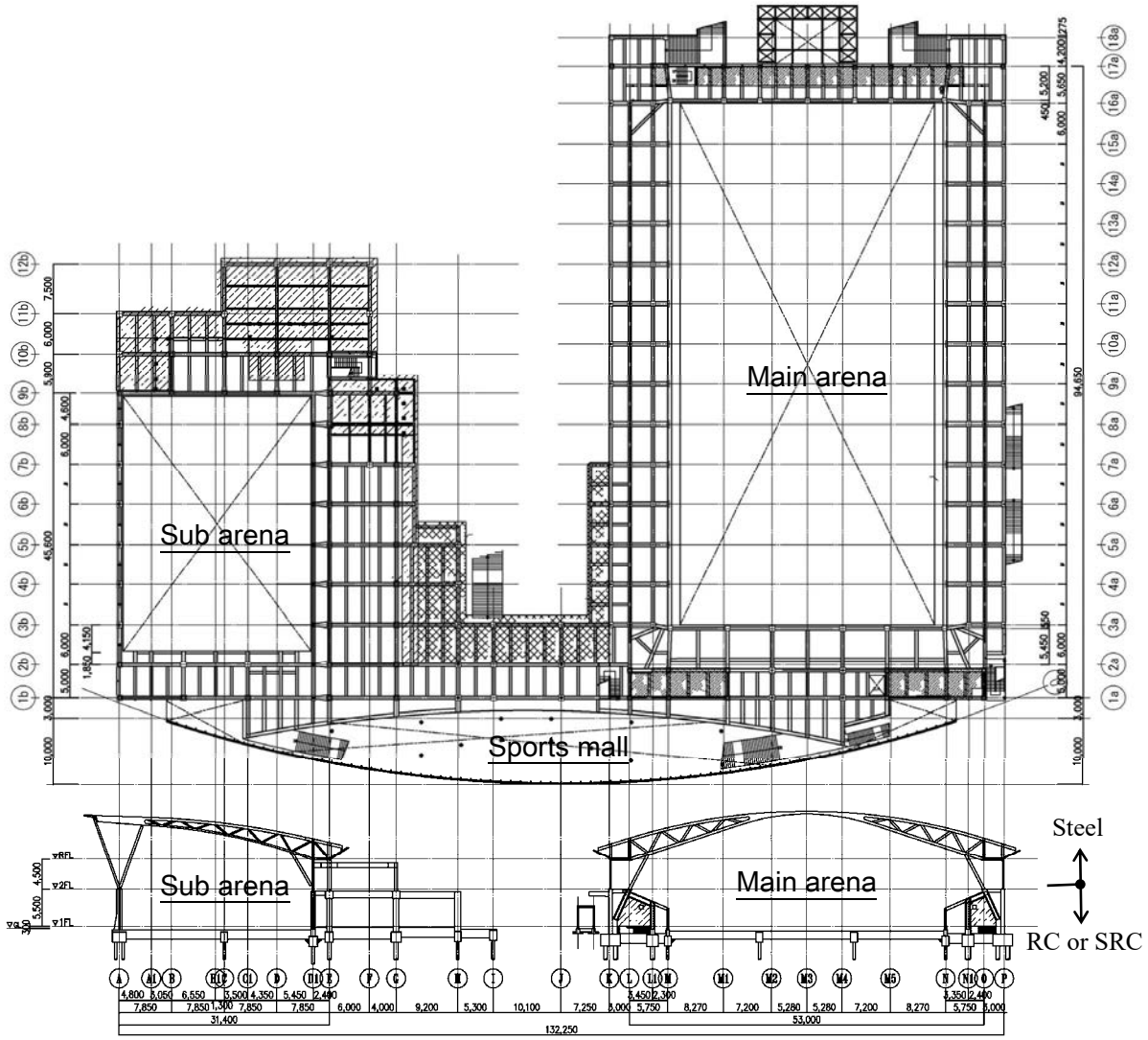


Figure 4: Framing plan on second floor, and framing elevation on Line 4a(4b).

3.2. Foundation structure

The foundation type is pile foundation supported by a 30 m deep sandy gravel layer, and the pile type is precast concrete pile. The pile length is 29 m, and the pile diameters are from 400 mm to 700 mm.

3.3. Main arena structure

The roof of the main arena has a parallel arch truss beam with a 53 m span. The arch truss beam consists of parts of H-shaped steel. The upper chord members are H-390×300, the lower chord members are H-400×350, and the diagonal members are H-300×300 or H-250×250. The truss beam depth of the center is 400 mm, and the depth of the end is 3,000 mm (Figure 5). The long-term load is transmitted as an axial force by the arch effect. The leg parts of the truss beam are ϕ 355.6 mm steel pipes (Figure 6, 7), because these members also need to support bending moment in case of earthquake, in addition to long-term axial force. An image of the flow of force under long-term loading is shown in Figure 8, and the stress analysis result is shown in Figure 9. The maximum deformation of the center of the truss beam is 87.1 mm (deflection angle to span is 1/608) at the long-term load considering the snow load of 2 m in depth. Because the truss legs are attached diagonally to the second floor, the ground floor columns that support the truss legs are placed diagonally to transmit axial force to the foundation.

To smoothly transmit the thrust force in the diagonal column, six RC wall units are arranged on the ground floor on one side to give enough rigidity. In order to reduce the thrust force generated in the piles, the foundation beams connecting both sides across the arena are pre-stressed on site to support the thrust force.

Although it is legally necessary to consider the snow load as a long-term load, in reality it is a variable load since most of the year there is no snow. If the pre-stressing force introduced to the foundation beam is excessive, a stress will be generated in the pile due to axial contraction of the foundation beam. Therefore, when the snow load is 100% (=6,000 N/m^2), the design target for the foundation beam allows the tensile stress to be generated in the concrete and is set within the tensile strength of the concrete. The snow load level, the thrust force generated on the foundation beam, and the pre-stressing force introduced are shown in Table 1. The thrust force of 17,800 kN at a snow load of 100% is reduced to 2,784 kN (= 17,800 kN – 15,016 kN) by the pre-stressing force. At a snow load of 70%, the thrust force is reduced by the pre-stressing force, and no tensile force occurs.

Thus, the whole structure, from the roof of steel frame to the foundation beam, has stable equilibrium.

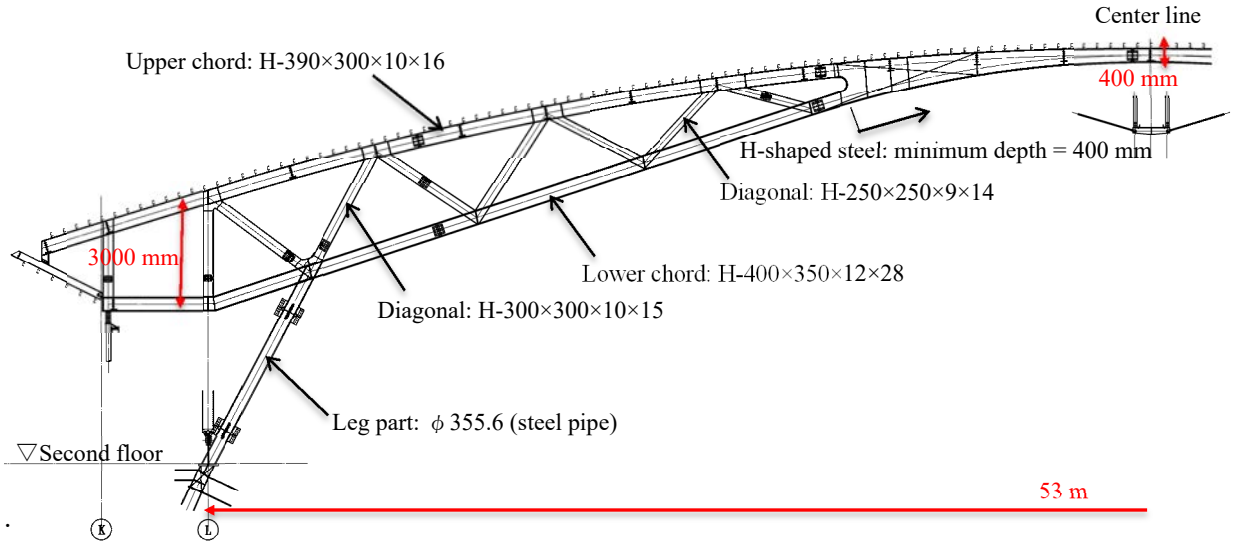


Figure 5: Steel detail of the arch truss beam of the main arena



Figure 6: The interior of the main arena

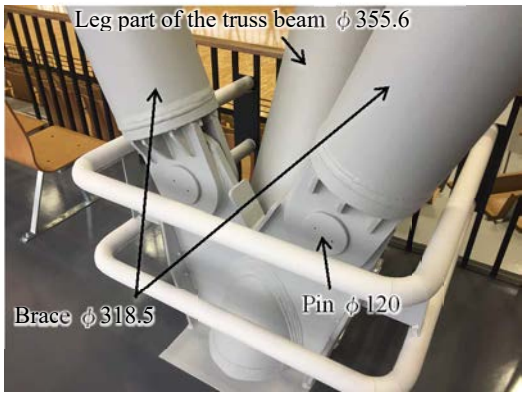


Figure 7: The leg part of the truss of the main arena

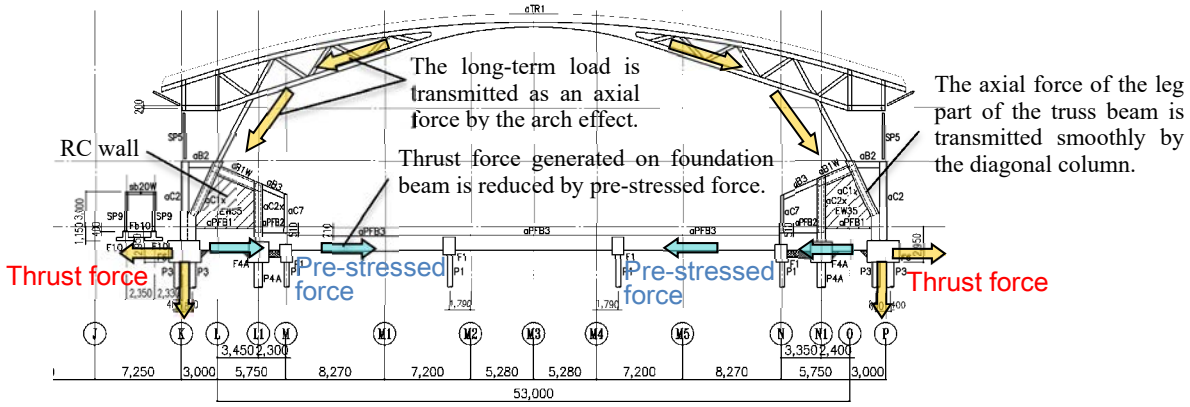


Figure 8: Flow of force at the arch truss beam of the main arena.

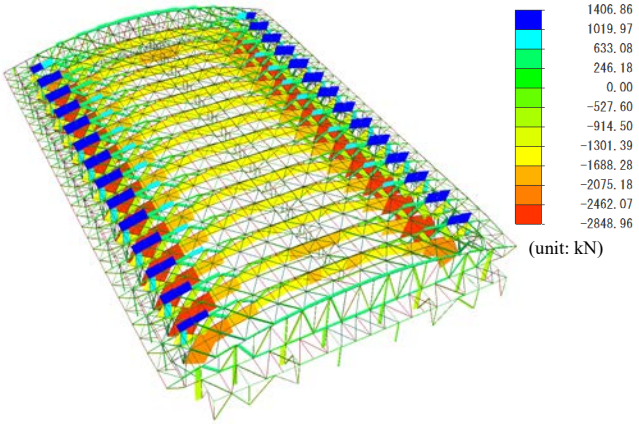


Figure 9: Stress analysis results of the main arena (Axial force diagram of long-term load).

Table 1: Thrust force and pre-stressed force of the foundation beam

Snow load		Thrust force (total value)	Pre-stressed force (total value)
(%)	(N/m^2)	(kN)	(kN)
100	6000	17800	15016
70	4200	13900	
35	2100	9300	
0	0	4750	

3.4. Sub arena structure

The roof of the sub arena has a parallel truss beam with a 29 m span. The truss beam is hung on diagonal columns placed on both sides. The truss beam also consists of parts of H-shaped steel. The upper chord members are H-400×200, the lower chord members are H-250×250, and the diagonal members are H-200×200 (Figure 10). The diagonal column is ϕ 318.5 mm steel pipe (Figure 11). Unlike the main arena's arch effect, the truss beam in the sub arena mainly experiences bending stress. Therefore, a large thrust force is not generated. The stress analysis result is shown in Figure 12. The maximum deformation of the truss beam is 45 mm (deflection angle to span is 1/644) at the long-term load considering the snow load of 2 m in depth.

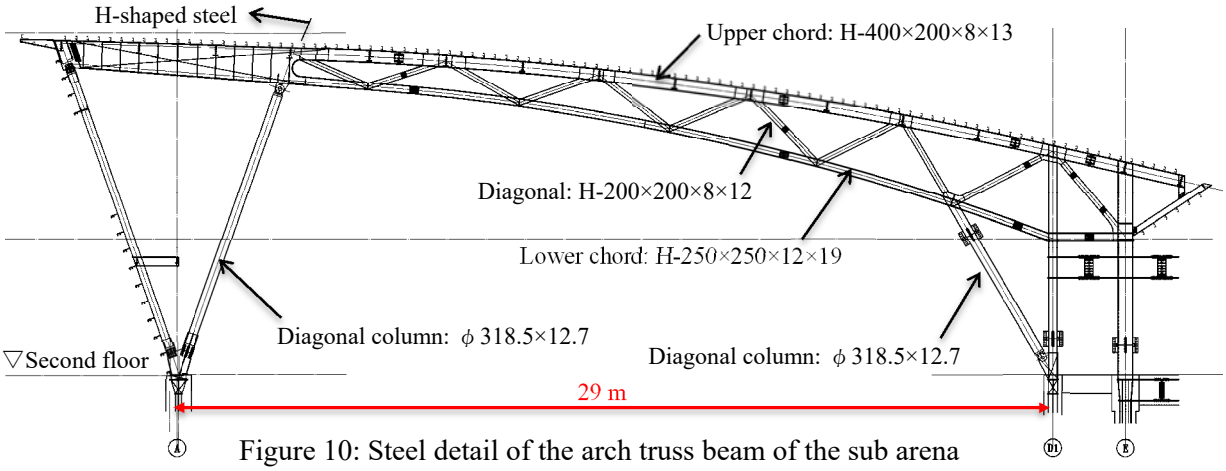


Figure 10: Steel detail of the arch truss beam of the sub arena



Figure 11: Interior of the sub arena

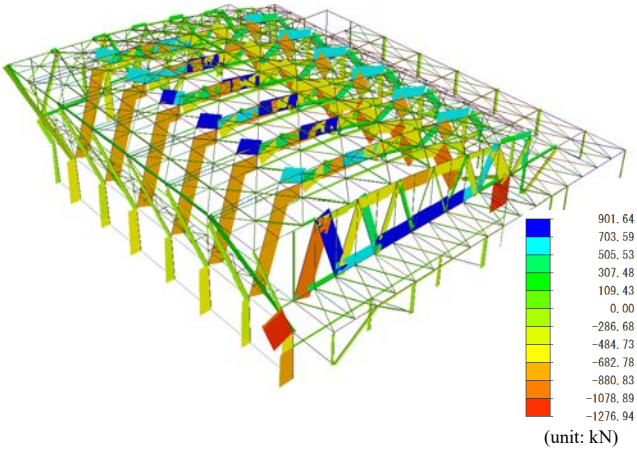


Figure 12: Stress analysis results of the sub arena

3.5. Sports mall structure

The sports mall entrance is approximately 130 m in length with thin steel columns placed at 1500 mm intervals on the glass screen side and tree-like steel columns support the roof of the mall (Figure 13).

The section of the thin steel column is a 200mm×100mm rectangular steel pipe. In order to stiffen the weak axis direction of these columns, 32mm×100mm steel flat bars are arranged at the center of the column. These flat bars get sufficient rigidity through jointing with stairs on both sides of the mall (Figure 14). The tree-like steel column is a combination of four bent steel columns (Figure 15).

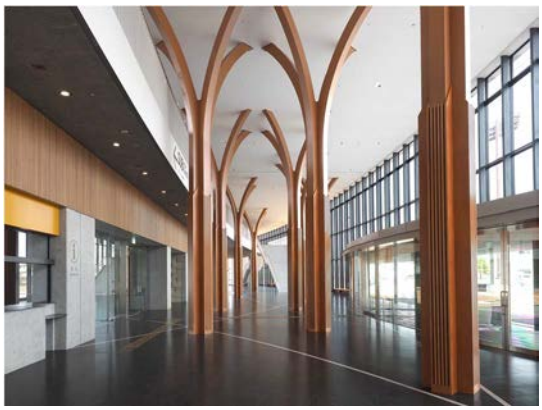


Figure 13: Interior of the sports mall



Figure 14: Junction of the thin column and stair

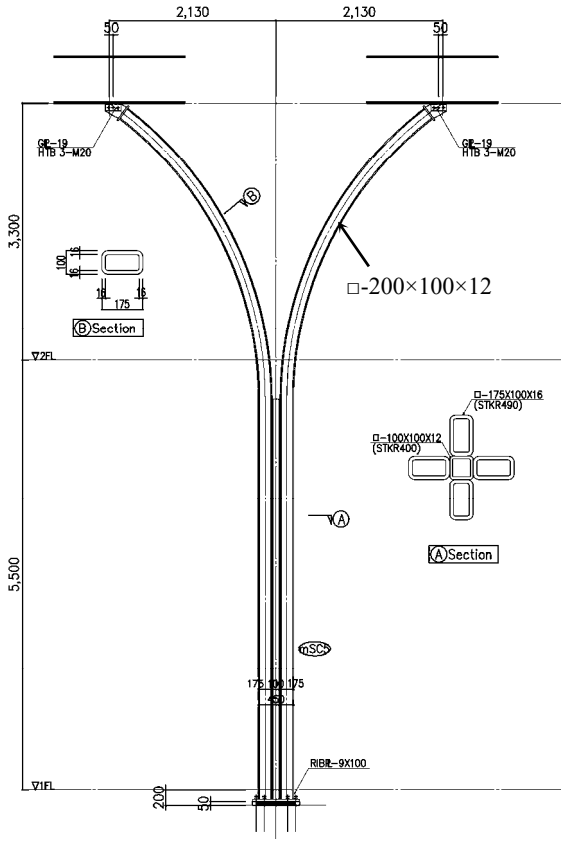


Figure 15: Steel detail of the tree-like column

4. Construction plan of the main arena

One truss beam was divided into 8 pieces ranging from 9.5 m to 11.3 m in length and manufactured at the factory. It was constructed while being supported by five temporary supports (Figure 16). An analysis simulating the state of each construction stage was performed, and a control value for deformation during construction was set. As determined by analysis after removing the support, the maximum deformation was 11.2 mm (Figure 17).

Based on this result, a 12 mm camber was provided at the center of the truss beam. In addition, the allowable value of deformation when removing the supports was set to 12 mm, and the limit value was set to 21 mm. The measured values of deformation at the time of removing supports are shown in Figure 18. The deformation tended to be large between line 9 and line 11, but the 12 mm camber had been almost cancelled, and all were within the allowable value.

5. Conclusion

The construction site is one of the heaviest snowfall areas in Japan; it is a severe condition for the gymnasium with a large space roof in a region where a large snow load of 6,000 N/m^2 must be supported as a long-term load. Under these conditions, the truss beams are reduced to 400 mm in the center by having a balanced shape throughout the whole structure using truss beam arch effects, ground floor diagonal columns, and pre-stressed foundation beams. In addition, the roof frame became a light frame, and was able to create an open space.

Acknowledgements

The authors wish to express their gratitude to the owner and those involved at the designing team for their cooperation at each design stage.

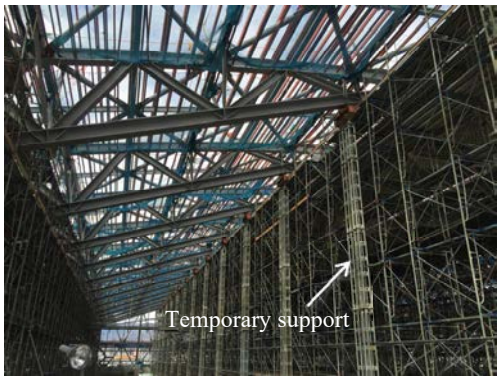


Figure 16: Condition of the support

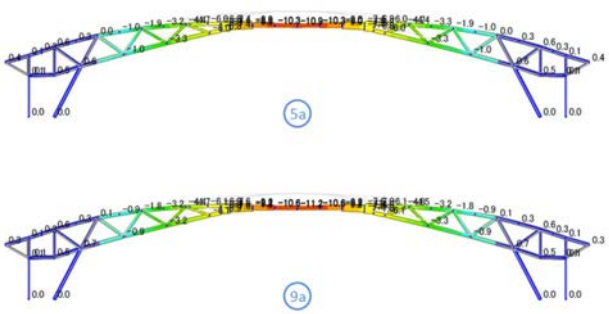
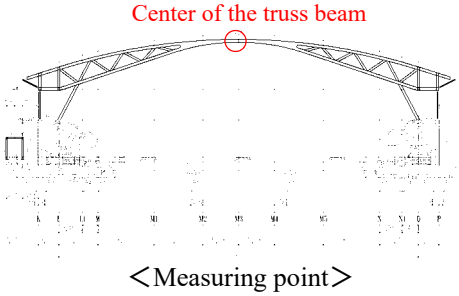


Figure 17: Result of analysis when removing the support



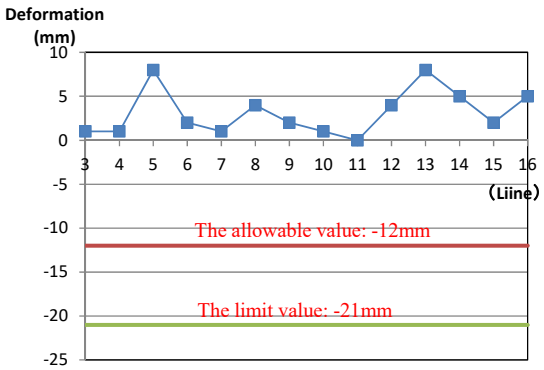


Figure 18: Measured deformation value against designed value of the center of the truss beam

Proceedings of the IASS Annual Symposium 2019 – Structural Membranes 2019
Form and Force
7 – 10 October 2019, Barcelona, Spain
C. Lázaro, K.-U. Bletzinger, E. Oñate (eds.)

Curved-crease Paperfolding Shell

Duks Koschitz

Pratt Institute
Brooklyn NY 11238, USA
duks@pratt.edu

Abstract

Given the geometric constraint of curved-crease paperfolding which type of shell can be designed and fabricated that uses a single surface folded along curves with compliant hinges? This research project with undergraduate architecture students resulted in building a free standing shell that withstands most forces within the surface. The specific geometry is based on mirror reflections of a general cylinder. The structure was realized with vulcanized paper, a recyclable material that is malleable while moist and becomes stiff again after it dried. This enables a building process in two phases: The first phase consists of making a flat assembly. The second phase is comprised of lifting the assembly with pulleys, folding it into its final configuration and setting it into a base rail.

Keywords: Curved-crease paperfolding, Compliant hinge, Single-surface shell

1. Introduction

1.1. Context

The requirements that created the context for this project are based on a grant by the IDC foundation that afforded us to construct this project during a studio course in the undergraduate school of architecture at Pratt Institute (students: Sharon Broyn, Xuechen Chen, Chafiq Ennaoui, David Huh, Bharati Kodnani, Yen Chi Lee, Shaun Mehta, Jonathan Ovshayev, Massi Sur-ratt, Yuheng Wu, Runyu Zheng). The pedagogical ambitions frame the project in the sense that participating students are supposed to learn problem solving by realizing a small structure at full scale. Regarding the material choice and technique of construction we defined the following requirements. The material should be readily available, low-cost, non-toxic during fabrication and fully recyclable. The ambition is to find a material that is not typically used in construction as to insure innovative solutions during the detailing phase of the project.

1.2. Selecting constraints

In order to create a rigorous case study we impose the constraint that the structure has to be made by folding the entire shell from a single flat surface assembly. We used a simple array of strings and pulleys to lift the surface, wet it and fold it.

The United Nations predict that the existing footprint of all cities globally will have to double by 2050 [1] and we are interested in finding novel ways of building that are light and fast. The manufacturing of a flat (2D) building assembly that can be formed into its final configuration on site has many benefits. We can eliminate form-work or scaffolding and avoid the use of complex 3D manufactured parts, which saves energy and is efficient in terms of material use. Our main architectural reference is Frei Otto's Multihalle in Main [2], it was erected with scaffolding towers inside the shell, while the wooden grid was tightened. We aspire to find a single-surface solution with similar characteristics (see Fig.1).

Copyright © 2019 by Duks Koschitz
Published by the International Association for Shell and Spatial Structures (IASS)with permission.



Figure 1: Side view of final project

2. Geometry and Design

2.1. The geometry of Curved Creases

Curved creases have been explored by artists, designers and geometers since the 16th century when table decorations consisted of elaborate arrangements made of cloth napkins [3]. Josef Alber's students used curved creases in his 'Vorkurs' at the Bauhaus and since the 1960's [4]. We should also consider the work of David Huffman [5] Ron Resch [6], Poul Christiansen [7], Hiroshi Ogawa [8] and Kurt Londenberg [9], all conceived in the 1970's. In more recent years origami artists and compu-tational folding experts have further explored curved creases [10] and Haresh Lalvani has produced large column covers and architectural components [11]. However there exist very few examples at the scale of a pavilion that architects can learn from [12].

Modeling curved creases in 3D software is difficult as we still don't know a general mathematical description of the behavior of a curved crease. A survey of available computational approaches to model curved creases shows that deriving design me-thods is not trivial [13], [14], [15].

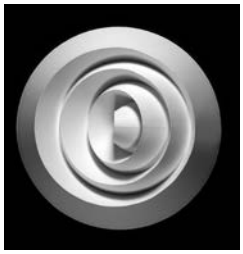


Figure 2: Design by David Huffman with reflected cones (photo by Tony Grant).

2.1. The selected Design Approach

The selected design approach for this project is based on manipulating developable surfaces that are extruded and quasi 'folded' with mirror operations. The four types of developable surfaces are a plane, a general cylinder, a general cone and a tangent surface. They can be thought of as input surfaces,

which are subjected to mirror re-flected. This means that the user is working with the final curved surfaces in 3D rather than editing a crease pattern in 2D. In order to devise a step-by-step method we used ORI-REF by Jun Mitani for initial studies [16]. The software allows a user to manipulate a relative coordinate system to locate mirror reflections. As the software is only meant for experimentation we subsequently used Rhino3d as production tool for accuracy (see Fig. 3). The design process was based on iterating through many versions and making paper models at every stage.

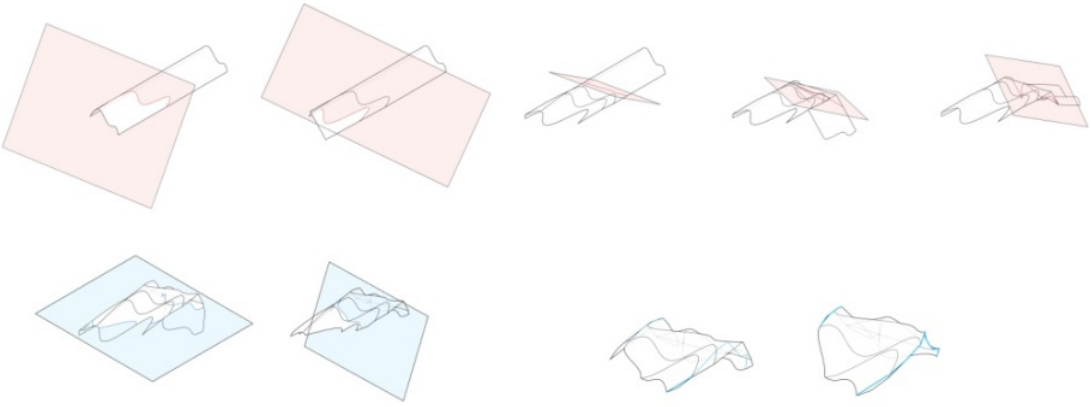


Figure 3: above: Mirror reflections. below: Clipping planes for boundary (fig. by Xuechen Chen).

Physical models made of paper served several purposes such as receiving feedback on surface deformations under stress by pushing down on the model with one's finger. They also proved practical to test rib systems (see Fig. 4). Decisions related to the final design were agreed upon as a team via two one-week long competitions. One mail goal consisted of finding two appropriate base curves that would serve as guide rails on the ground (see Fig.5).



Figure 4: Sketch models with proposals for seam locations and ribs.

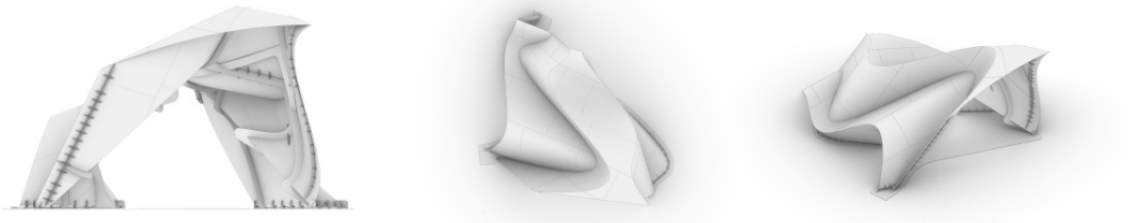


Figure 5: Renderings of final design (fig. by Xuechen Chen).

2.3. Preliminary Analysis

A preliminary finite element analysis showed that substantial forces occur along the creases. Both compression and tension forces concentrate in some areas along the bottom of the structure, which

ultimately resulted in a tear in the final prototype. The forces in the areas further away from the creases appear reasonable given the properties of vulcanized paper, but the moment forces in the compliant hinges clearly required stiffening of the folding angles.

3. Making a Prototype

3.1. Material and Assembly

Vulcanized paper was invented as one of the first plastics. The paper pulp is treated with acid such that the bonding properties between molecules change. The result is a paper-like product that is stronger. The paper is malleable while wet and can dry in a deformed state. We exploit this property to fold the creases along perforations while the material is soft and then wait for the creases to harden.

Compliant hinges have several advantages related to fabrication and structural performance. They provide folding accuracy and material continuity that is beneficial in terms of force transfer within the surface. The constraint of creating the entire 2D assembly first meant that the creases needed to be folded while the material was malleable and weak. This in turn necessitated a pulley system supported by tripod cranes (see Fig.6) to support the assembly during construction. Once the surface was in the correct position and dry and we could install the ribs and folding guides.

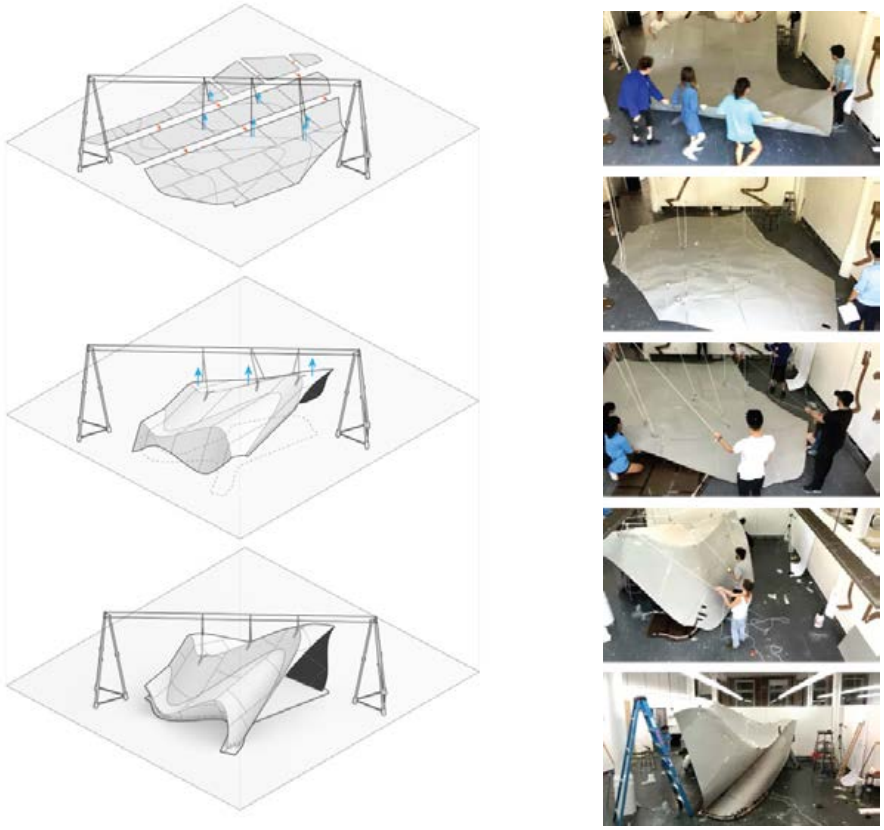


Figure 6 : Assembly sequence from flat to fully folded (fig. by Xuechen Chen).

3.2. Digital Coordination of 2D Fabrication

The flat assembly required careful coordination as sub-assemblies needed to be CNC-cut and connected using specific sequences. The parametric model was set up such that panel to panel seams would get adjusted when seams crossed creases. Sub-assembly to sub-assembly connections were reinforced by laminating patches of vulcanized paper on specific areas. The digital file also took bolt alignments and holes for rib connection into consideration (see Fig.7).

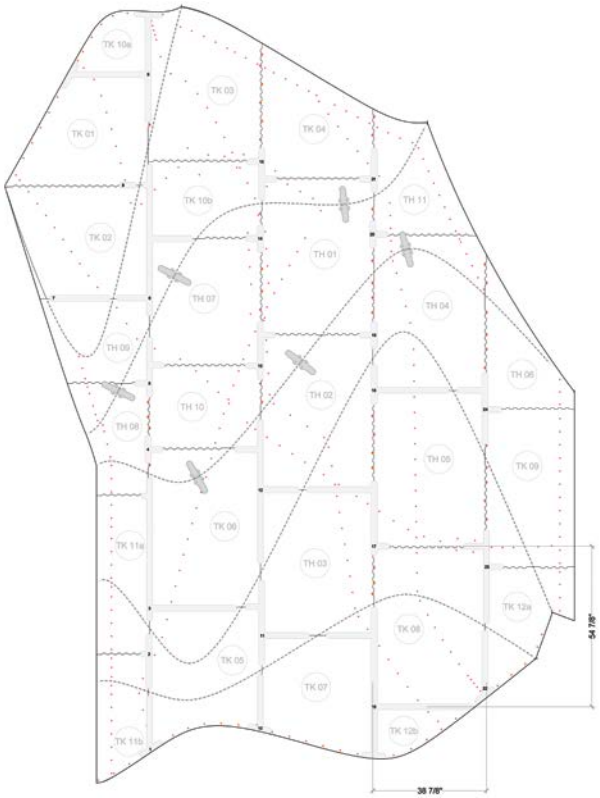


Figure 7 : Layout of sub-assemblies with creases, seams, patches, guide holes and lifting anchors.

3.3. Details for the flat Assembly

As the material is not a conventional building material we had to develop the tectonics of the flat assembly. This required full-scale prototyping of the following conditions: **perforations for compliant hinge, panel-to-panel seam, sub-assembly to sub-assembly seam, lifting tabs.**

After much iteration of perforation patterns for the creases, we decided to use material continuity that has a 4 : 1 ratio of length to surface thickness. This ratio resulted in very few failures during the folding process (see Fig. 8 and 9). The panel to panel seams were designed with a saw tooth pattern that worked well for positioning, but did not perform well in tension. Laminated patches turned out to be surprisingly difficult to attach in the field. The lifting tabs performed well and did not deform the sheet in any way, but more lifting locations would provide more accurate support while the assembly is not attached to the base rail (see Fig. 9).

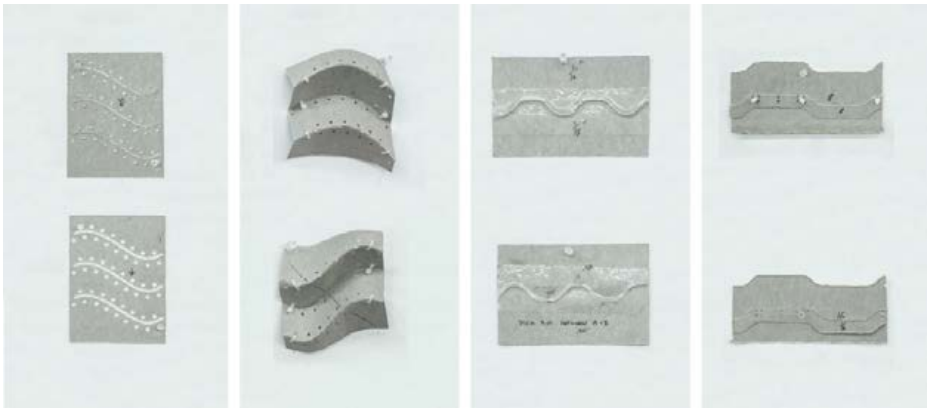


Figure 8 : Prototyping: CNC cutting, Folding, Panel-to-panel seam, Laminated patch.



Figure 9 : Curved crease with rib fasteners, Lifting tab.

3.4. Locating Ribs and Stiffeners As the material

The constructed solution relies on four main ribs and two series of linear stiffeners, which we call fish bones. The ribs and stiffeners are located in six planes and their location is optimized such that they cross through as may creases as possible while remaining close to surface normals (see Fig.10). The rational is based on ease of assembly and maximal stiffening of crease angles. The fish bones are mostly located along a ruling, which means they are straight and easy to install. In some cases we used perpendicular fins to ensure a correct alignment along the surface normal.

We want to point out that the main forces are being taken on by the sheet itself and that the ribs do not engage the ground in several locations. We did not succeed in creating a true monocoque structure, but can report that the ribs made of Masonite did not take on the role of a primary structural system. The configuration of the ribs allowed us to stiffen the folding angle in relevant areas.

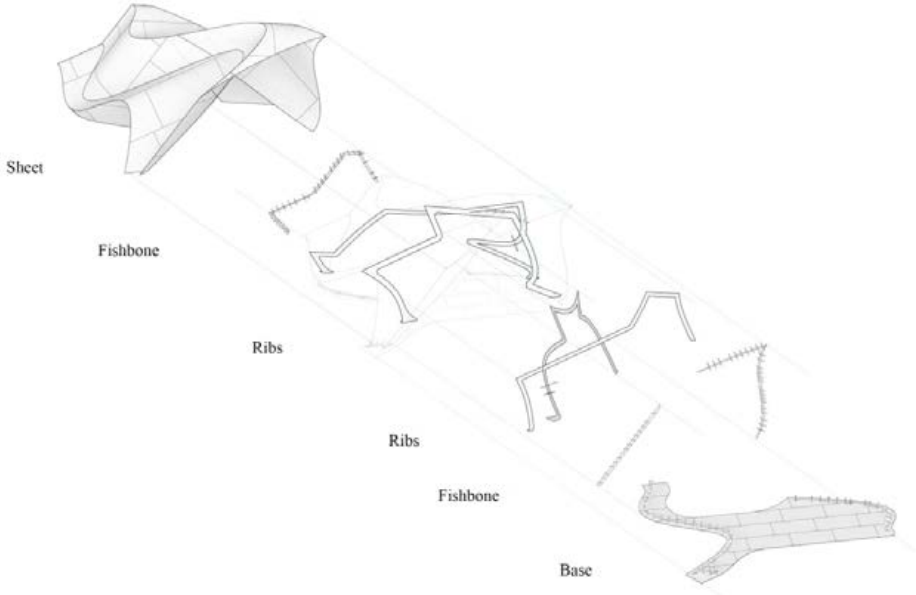


Figure 10 : Diagram with folded sheet, fish bones, main ribs and base rail. (fig. by Xuechen Chen).

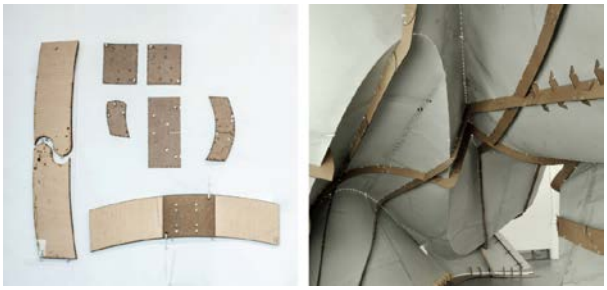


Figure 11 : Prototyping ribs and connections, Installed ribs and stiffeners.

3.5. The Base Rail

The base proved to be an essential device to ensuring the correct position of the folded surface. Guides and upright tabs made in plywood were used to clamp the sheet to the base rail (see Fig.12). The base rail is attached to a ground surface that provides accurate location details for guide shoes that hold the rail.



Figure 12 : Base rail details and assembled base rail.

3.6. The Curved-crease Paperfolding Shell

The final structure was installed over a period of three days and was exhibited for two weeks (see Fig.13). After ten days a panel to panel seam stared to show signs of fatigue, which resulted in a tear after two more days.



Figure 13 : Front view of structure. Back view of structure.

4. Findings and Discussion

4.1. Structural Failure and Assembly Issues

We identified several issues and areas for improvement. The structure showed damage due to tensile forces in certain areas. The patches tended to delaminate in the high-stress areas identified by the FE analysis. The panel to panel connections should have been designed with tension forces in mind. One such seam ripped over the course of two days (see Fig.14).

Creating compliant hinges that can bend during the building process, but subsequently take on moment forces once folded, is a difficult issue to resolve. Lamination of larger areas and small stiffening elements may perform better than the ribs we used. The floor rail proved very useful during the building process, but should be designed to be able to take on tensile forces.



Figure 14 : A tear at a panel to panel connection widened between day 7 and 9 of the exhibition.

4.2. Future work

Dovetail Connections In order to provide support in tension at the panel to panel seams dovetail configurations should be used. The issue of surface continuity can be addressed by using wider patches and better hardware.

Elimination of Ribs and better Angle Stiffeners Future work should investigate stiffening of folding angles without continuous ribs. Prefolded patches that are laminated into the crease may provide a solution here.

Pulley Simulation In order to better predict how the surface folds, more accurate folding simulation will be necessary. The dynamic pulley system we used is the right conceptual approach, but it needs to be simulated to better plan the process.

References

[1] UnitedNations Homepage, http://www.un.org/development/desa/en/news/population/2018-world-urbanization-prospects.html.
[2] Otto, F., Mutschler, C.: Multihalle. Spector Books (2018)
[3] Sallas, J.: Gefaltete Schönheit. Frieburg im Breigau und Wein (2010)
[4] Adler, E.: A New Unity! The Art and Pedagogy of Josef Albers. Univ. of Maryland (2004)
[5] Wertheim, M.: Cones, Curves, Shells, Towers: He Made Paper Jump to Life. New York Times. http://www.theiff.org/press/NYThuffman.html. (2004)
[6] Resch, R. The Topological Design of Sculptural and Architectural Systems. In: Proceedings of AFIPS Conference, 42:643–50. (1973)
[7] Klint P.V.J.: Le Klint Lighting. www.ylighting.com/search/ field_brand/brand-23242.
[8] Ogawa, H.: Forms of Paper. Van Nostrand Reinhold (1972)
[9] Londenberg, K.: Papier Und Form, Design in Der Papierverarbeitung. Krefeld (1972)
[10] Demaine, E., Demaine, M., Koschitz, D., Tachi, T.: Curved Crease Folding: A Review on Art, Design and Mathematics. In: Taller, Longer, Lighter - Meeting Growing Demand with Limited Resources. London, England (2011)
[11] Lalvani,H.: Bend the Rules of Structure. Metropolis Magazine. http://www. metropolis-mag.com/html/content_0603/mgo/ (2003)
[12] Wilcox, G., Yates, H.: Patent Application. Foldable Shelter Structure with Zig-Zag Roof Profile (1968)
[13] Kilian, M., Flöry, S., Chen, Z., Mitra, N., Sheffer, A., Pottmann, H.: Curved Folding." In ACM SIGGRAPH 2008 Papers, 75:1–75:9. SIGGRAPH '08. New York, NY, USA: ACM. doi:10.1145/1399504.1360674 (2008)
[14] Geretschlaeger, R.: Folding Curves. In: Origami 4, 151–64. A K Peters. 151-164 (2009)
[15] Kergosien, Y., Hironoba, G., Tosiyasu L. K.: 1994. Bending and Creasing Virtual Paper. IEEE Computer Graphics and Applications 14 (1): 40–48. (1994)
[16] Mitani, J.: ORI-REF: A Design Tool for Curved Origami Based on Reflection (2011)

FORM and FORCE

Proceedings of the IASS Annual Symposium 2019 – Structural Membranes 2019
Form and Force
7–10 October 2019, Barcelona, Spain
C. Lázaro, K.-U. Bletzinger, E. Oñate (eds.)

Design of Novel Origami Shell Structures

Zeyuan He*, Simon D. Guest

* Department of Engineering, University of Cambridge
Trumpington Street, Cambridge CB2 1PZ, UK
zh299@cam.ac.uk

Abstract

A developable quadrilateral creased paper is the union of a planar region (the paper) and a quadrilateral mesh embedded on this paper. In this article we will present some design methods for constructing a shell structure based on three different types of rigid-foldable and developable quadrilateral creased papers. Each type mentioned in this article can approximate different types of surfaces. The first two types of quadrilateral creased papers also have the "self-locking" property – the rigid folding motion halts at the final rigidly folded states due to clashing of panels, and the final rigidly folded state forms the approximation. Each of the examples has a one degree of freedom unique rigid folding motion.

Keywords: rigid origami, rigid-foldability, approximation

1 Introduction

This paper will present some design methods for constructing a shell structure, which are based on different types of rigid-foldable and developable quadrilateral creased papers. A developable quadrilateral creased paper is the union of a planar region (the paper) and a quadrilateral mesh embedded on this paper.

Deployable shell structures are often considered for temporary shelters [1]. For such applications the shell structure needs to have the following properties: (1) enough structural strength and low self-weight (preferably portable by one person); (2) small packaged volume; (3) easily deployable (without the use of heavy lifting devices). It has been shown that origami has great potential for designing structures with those properties [1, 2], since (1) the rigid folded plates of these structures provide enhanced structural performance in the deployed form; (2) origami folds permit easy packaging in a small volume. Considering the design of an origami-inspired shelter, [3, 4] provide multi-objective shape optimization methodologies which balance the priorities of structural performance and energy efficiency, including dimension control and material selection. Some other shape design methods and shelter examples can be seen in [5, 6]. Based on the shape provided by origami design, it will then be possible for soft wall (canvas) and rigid wall solutions to be packaged, assembled, deployed and fixed to become a practical shelter.

In this paper we will enlarge the range of possible design of such shell structures by applying the techniques developed in [7] and considering new types of rigid-foldable quadrilateral creased paper. Here three design examples for a shell structure, each based on one of these types, will

Copyright © 2019 by Zeyuan He, Simon D. Guest
Published by the International Association for Shell and Spatial Structures (IASS) with permission.

be discussed in detail. The first example is the developable case of the "parallel repeating" type, which is generated with rows of parallel inner creases; the second one is the developable case of the "orthodiagonal" type, which is generated with several parallel straight line segments; and the third one is the developable case of the "longitudinal linear repeating" type, which is newly discovered [8] and has less regular rigid folding motion than the other two types.

2 Design Method with the Parallel Repeating Type

In this section we will present the design method for the parallel repeating type of rigid-foldable quadrilateral creased paper. This method can generate an approximation to a surface where a planar target curve f is scanned along a planar datum curve g. The angle between the plane containing f and the tangent vector of g, can be adjusted. With given f and g, an example of the parallel repeating type is shown in Figure 1(a). Here all the rows of inner creases are parallel, and all the columns are straight lines. If the number of inner vertices in the longitudinal and transverse directions are m (m is odd) and n, there are $m+2$ parallel rows and $n+2$ straight line columns in the crease pattern. In Figure 1(b), the second left column (colored green) approximates f at the final rigidly folded state, and the middle row (colored red) approximates g at the final rigidly folded state. Note that the first and last column of panels are designed to halt the rigid folding motion by clashing of panels. Then the geometric parameters of the crease pattern are the sector angles on the middle row, and the length of all the inner creases colored red and green.

The algorithm to determine the above geometric parameters are listed below.

(1) From the creased paper we choose, the target curve $f : I \ni t \to (x(t), y(t)) \in \mathbb{R}^2$ is approximated by a polyline, and the angle ξ between adjacent line segments is constant (Figure 1(c)). In order to be approximated, f should satisfy the following condition: there exists a rotation $\theta \in [0, 2\pi)$ and a shear transformation of magnitude $\pi/2 - \xi$, $\xi \in [0, \pi]$, s.t. after the affine transformation $f \to \overline{f}$ described below, $\overline{f}$ is monotone decreasing.

$$\begin{bmatrix} \overline{x}(t) \\ \overline{y}(t) \end{bmatrix} = \begin{bmatrix} 1 & -1/\tan\xi \\ 0 & 1/\sin\xi \end{bmatrix} \begin{bmatrix} \cos\theta & \sin\theta \\ -\sin\theta & \cos\theta \end{bmatrix} \begin{bmatrix} x(t) \\ y(t) \end{bmatrix} \tag{1}$$

The proof of this condition and the approximation of f based on the above shear transformation are provided in Proposition 2 of [7]. With ξ chosen, the length of inner creases colored green d_i ($1 \le i \le m+1$) can be obtained.

(2) Approximate g by a polyline (Figure 1(d)), then the lengths of inner creases colored red l_i ($1 \le i \le n-1$) can be obtained. Consider the projection of the plane containing each column of inner creases, the angles between these projections and each line segment of the polyline (measured from the same side) are named δ_i ($1 \le i \le 2n-2$), which can be calculated directly. In Figure 1(d) all the projections are perpendicular to the tangent vector of g, but other choices are also possible.

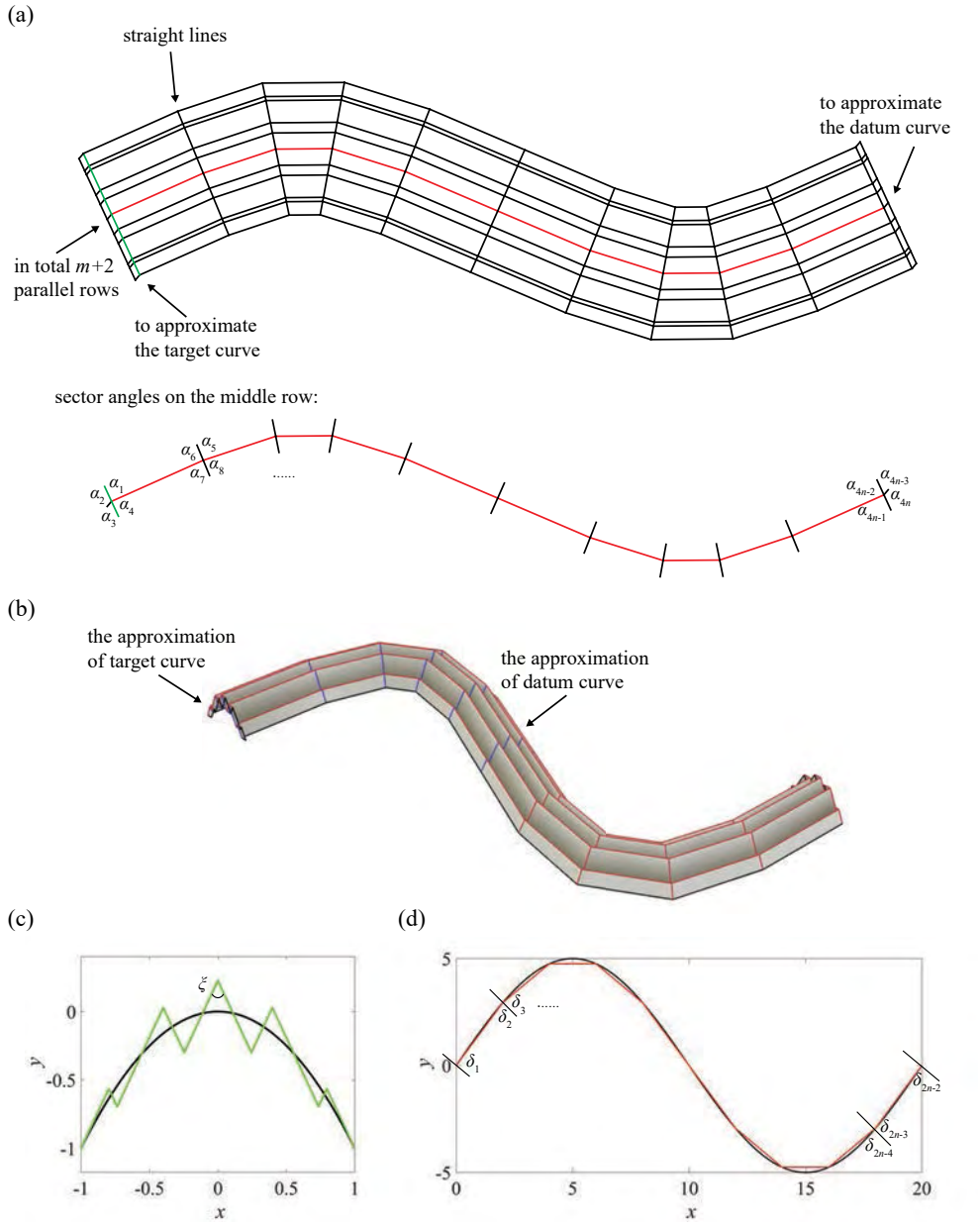


Figure 1: The approximation of the parallel repeating type. (a) shows the crease pattern. Here all the rows of inner creases are parallel, and all the columns are straight lines. There are $m = 9$ rows and $n = 11$ columns of inner vertices. The second left column (colored green) approximates the target curve $f = -x^2$ $(-1 \le x \le 1)$ at the final rigidly folded state, and the middle row (colored red) approximates the datum curve $g = 5\sin(\pi x/10)$ $(0 \le x \le 20)$ at the final rigidly folded state. (b) shows the approximation, where the first and last column of panels are designed to halt the rigid folding motion by clashing of panels. This figure is plotted by Freeform Origami [2], where the mountain and valley creases are colored red and blue. (c) is the approximation of the target curve (colored green). Here the angle ξ between adjacent line segments is constant. (d) is the approximation of the datum curve (colored red). Consider the projection of the plane containing each column of inner creases, the angles between these projections and each line segment of the polyline (measured from the same side) are named δ_i $(1 \le i \le 2n-2)$.

(3) Calculate all the sector angles on the middle row α_i $(1 \leq i \leq 4n)$:

$$\begin{aligned}
\alpha_3 &= \frac{\pi - \xi}{2} \\
|\cos\alpha_4| &= \cos\delta_1 \cos\alpha_3 \\
\frac{\tan\alpha_{4i+3}}{\tan\delta_{2i}} &= \frac{\tan\alpha_{4i}}{\tan\delta_{2i-1}} \ (1 \leq i \leq n-1) \\
\frac{\cos\alpha_{4i+4}}{\cos\delta_{2i+1}} &= \frac{\cos\alpha_{4i+3}}{\cos\delta_{2i}} \ (1 \leq i \leq n-2) \\
|\cos\alpha_{4n}| &= \frac{\cos\alpha_{4n-1}}{\cos\delta_{2n-2}} \\
\alpha_{4i-3} &= \pi - \alpha_{4i} \ (1 \leq i \leq n) \\
\alpha_{4i-2} &= \pi - \alpha_{4i-1} \ (1 \leq i \leq n)
\end{aligned} \tag{2}$$

(4) With α_i $(1 \leq i \leq 4n)$, d_i $(1 \leq i \leq m+1)$ and l_i $(1 \leq i \leq n-1)$, draw the creased paper.

From direct geometric analysis, at the jth $(2 \leq j \leq n)$ column of inner creases, the angle between adjacent inner creases is not ξ. However, we can still write the curve approximated by the nth column as an affine transformation of f, which is given in [7]. If $m, n \to \infty$, the approximation from each column will become f, hence this type can approximate a surface where a planar target curve f is scanned along a planar datum curve g.

3 Design Method with the Orthodiagonal Type

In this section we will present the design method for the orthodiagonal type. This method can approximate a cylindrical developable surface where a planar target curve f is scanned along a planar datum curve g. Here each column or row of inner creases are co-planar, and each plane containing a column of inner creases is orthogonal to each plane containing a row of inner creases. With given f and g, an example of the orthodiagonal type is shown in Figure 2(a). All the columns are straight lines and parallel to each other, and the sector angles in different rows satisfy certain equations. If the number of inner vertices in the longitudinal and transverse directions are m (m is odd) and n, there are $m+2$ rows and $n+2$ straight line columns in the crease pattern. In Figure 2(b), the second left column (colored green) approximates f at the final rigidly folded state, and the middle row (colored red) approximates g at the final rigidly folded state. Note that the first and last column of panels are designed to halt the rigid folding motion by clashing of panels. Then the geometric parameters of the crease pattern are all of the sector angles, and the length of all the inner creases colored red and green.

The algorithm to determine the above geometric parameters is listed below.

(1) Approximate f by a polyline (Figure 1(c)) which turns left and right alternately. Thus the lengths of inner creases colored green d_i $(1 \leq i \leq m+1)$ can be obtained. Then calculate the angle between adjacent line segments β_i (measured from the alternating sides, $1 \leq i \leq m$).

(2) Approximate g by a polyline, and find the lengths of inner creases colored red l_i $(1 \leq i \leq n-1)$. Calculate the angle between adjacent line segments γ_i (measured from the same side, $1 \leq i \leq n-2$).

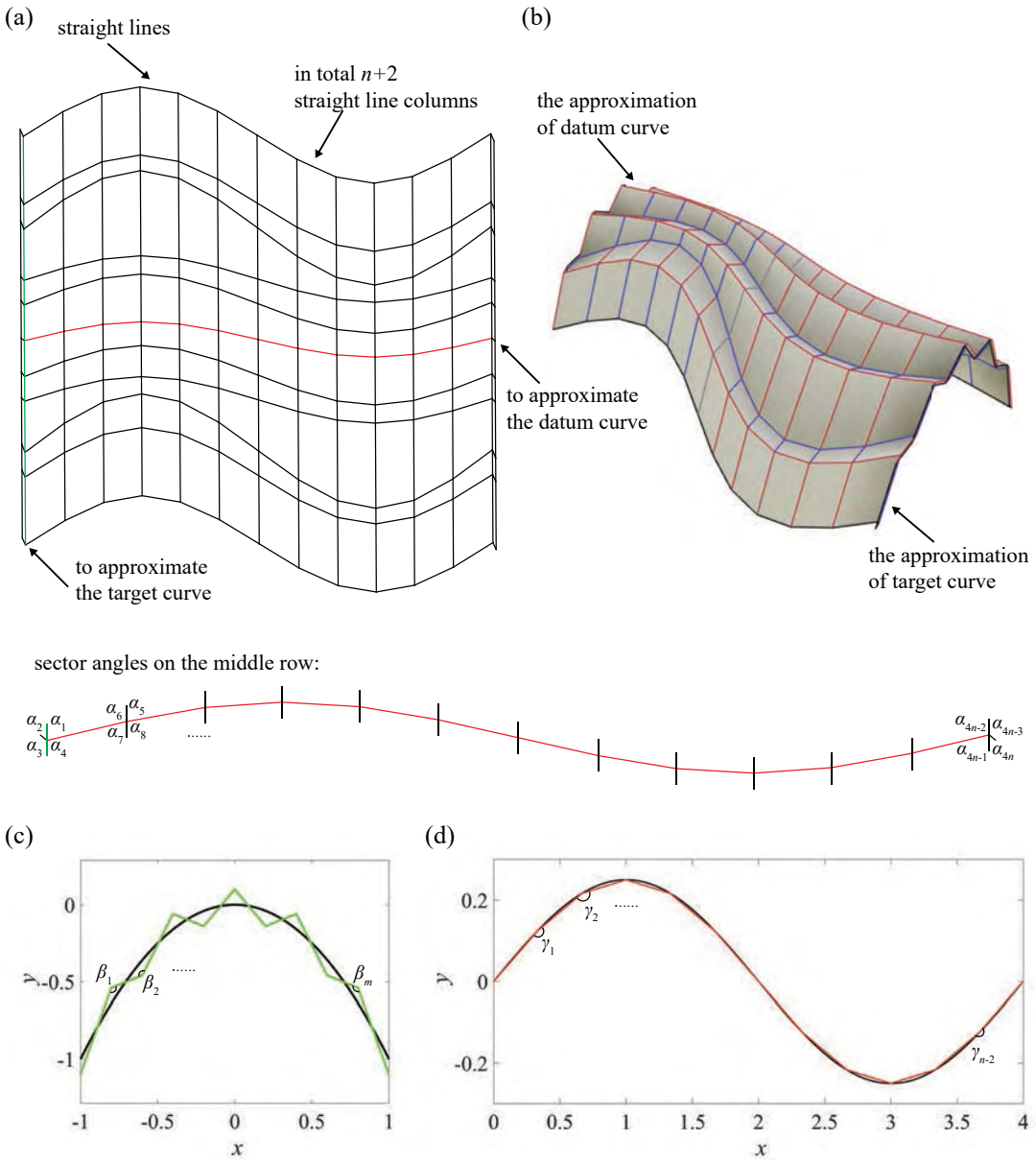


Figure 2: The approximation of the orthodiagonal type. (a) shows the crease pattern. Here each column or row of inner creases are co-planar, and each plane containing a column of inner creases is orthogonal to each plane containing a row of inner creases. There are $m = 9$ rows and $n = 13$ columns of inner vertices. The second left column (colored green) approximates the target curve $f = -x^2$ $(-1 \leq x \leq 1)$ at the final rigidly folded state, and the middle row (colored red) approximates the datum curve $g = 0.25\sin(\pi x/2)$ $(0 \leq x \leq 4)$ at the final rigidly folded state. (b) shows the approximation, where the first and last column of panels are designed to halt the rigid folding motion by clashing of panels. This figure is plotted by Freeform Origami [2], where the mountain and valley creases are colored red and blue. (c) is the approximation of the target curve (colored green). The angles between adjacent line segments are β_i $(1 \leq i \leq m)$, which are measured from the alternating sides. (d) is the approximation of the datum curve (colored red). The angles between adjacent line segments are γ_i $(1 \leq i \leq n-2)$, which are measured from the same side.

(3) Choose α_0 s.t. $\pi/2 < \alpha_0 < (\pi + \beta_{(m+1)/2})/2$, then calculate all the sector angles α_{ij} $(1 \le i \le m, 1 \le j \le 4n)$, α_0 controls the angle between the tangent vector of g and the plane containing f:

$$\begin{gathered}
\alpha_{i,3} = \alpha_{i,4n} = \frac{\pi + \beta_i}{2} \ (1 \le i \le m) \\
\alpha_{(m+1)/2,4} = \alpha_0 \\
\alpha_{(m+1)/2,4j-1} = \pi - \alpha_{(m+1)/2,4j-4} \ (2 \le j \le n) \\
\frac{\cos\alpha_{(m+1)/2,4j}}{|\cos\alpha_{(m+1)/2,3}|} = \cos(\gamma_{j-1} - \arccos\frac{\cos\alpha_{(m+1)/2,4j-1}}{|\cos\alpha_{(m+1)/2,3}|}) \ (2 \le j \le n-1) \\
\frac{\tan\alpha_{i,4j}}{\tan\alpha_{i+1,4j}} = \frac{\tan\alpha_{i,4j-1}}{\tan\alpha_{i+1,4j-1}} \ (\frac{m-1}{2} \ge i \ge 1, 1 \le j \le n-1) \\
\alpha_{i,4j+3} = \pi - \alpha_{i,4j} \ (\frac{m-1}{2} \ge i \ge 1, 1 \le j \le n-1) \\
\frac{\tan\alpha_{i,4j}}{\tan\alpha_{i-1,4j}} = \frac{\tan\alpha_{i,4j-1}}{\tan\alpha_{i-1,4j-1}} \ (\frac{m+3}{2} \le i \le m, 1 \le j \le n-1) \\
\alpha_{i,4j+3} = \pi - \alpha_{i,4j} \ (\frac{m+3}{2} \le i \le m, 1 \le j \le n-1) \\
\alpha_{i,4j-3} = \pi - \alpha_{i,4j} \ (1 \le i \le m, 1 \le j \le n) \\
\alpha_{i,4j-2} = \pi - \alpha_{i,4j-1} \ (1 \le i \le m, 1 \le j \le n)
\end{gathered} \tag{3}$$

(4) With α_i $(1 \le i \le 4n)$, d_i $(1 \le i \le m+1)$ and l_i $(1 \le i \le n-1)$, draw the creased paper.

From direct geometric analysis, at the jth $(2 \le j \le n)$ column of inner creases, the angle between adjacent inner creases is still β. We can also write the curve approximated by the nth column as an affine transformation of f, which is given in [7]. If $m, n \to \infty$, the approximation from each column will become f, and since the planes containing each column are parallel, this type can approximate a cylindrical developable surface that a planar target curve f is scanned along a planar datum curve g.

4 Design Method with the Longitudinal Linear Repeating Type

In this section we will introduce the design example for the new type of rigid-foldable quadrilateral creased paper, as shown in Figure 3(a). Here the input sector angles are $\alpha_1, \beta_1, \gamma_1, \delta_1 \in (0, \pi)$ (colored red). We can solve $\alpha_2, \beta_2, \gamma_2, \delta_2$ numerically from the four equations in (4), and hence all the sector angles in Figure 3(a) are known. These equations are derived in [9].

The next step is to tessellate the sector angles in Figure 3(a) to generate a infinitely extendable rigid-foldable quadrilateral creased paper. It is possible to adjust the length of a row (colored red) and a column (colored green) of inner creases. These lengths are required to fully determine the creased paper once the input sector angles are given. In each row, the sector angles repeat every four columns of inner vertices; in each column, the sector angles repeat every two rows of inner vertices. Note that each row of inner creases are co-planar thoughout the folding, while each column of inner creases are not co-planar. For this new type of crease pattern, it is unclear how we can describe the surface that can be approximated. One possibility is to approximate a target curve f scanning along a line g, where the curvature of f will increase or decrease monotonously. We provide an example in Figure 3(b), where f is approximately an arc.

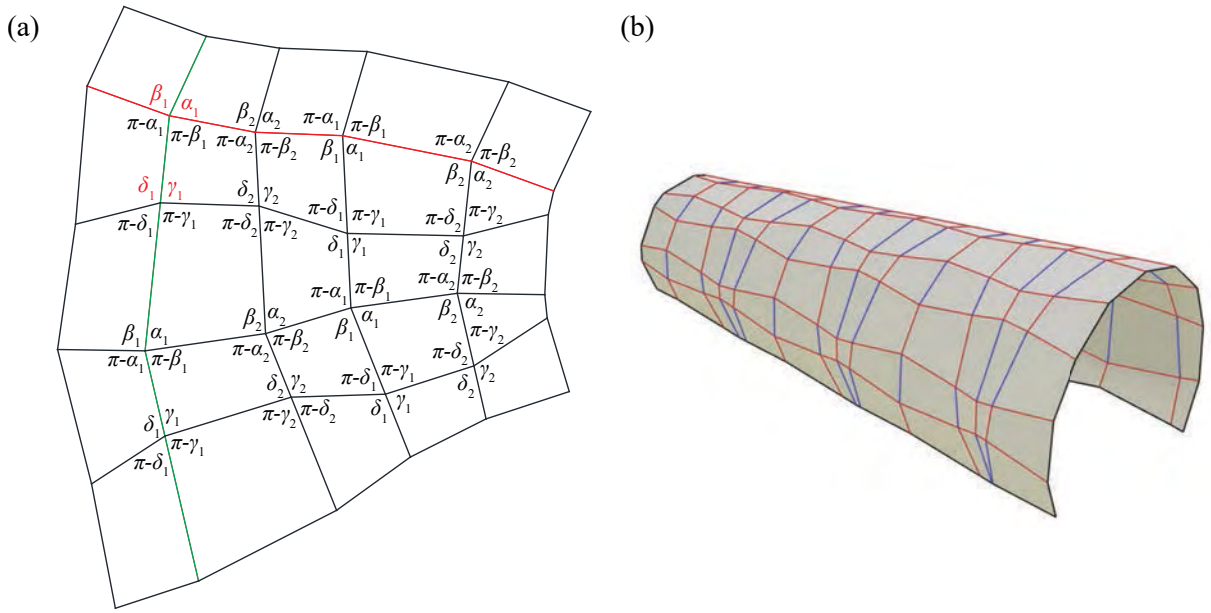


Figure 3: The longitudinal linear repeating type. (a) illustrates the relation among the sector angles, where the input sector angles $\alpha_1, \beta_1, \gamma_1, \delta_1$ are colored red, and $\alpha_2, \beta_2, \gamma_2, \delta_2$ are solved numerically. All the sector angles and the length of a row (colored red) and a column (colored green) of inner creases determine the entire creased paper. In each row, the sector angles repeat every four columns of inner vertices; in each column, the sector angles repeat every two rows of inner vertices. (b) is an approximation of a circular shell, where the radius of the cross section r mototonously increases to $1.67r$. Here the sector angles are $\alpha_1 = 85°, \beta_1 = 80°, \gamma_1 = 95°, \delta_1 = 100°$; $\alpha_2 = 91.23°, \beta_2 = 86.23°, \gamma_2 = 106.23°, \delta_2 = 76.23°$. The length of inner creases on the second left column are set to be equal. The length of inner creases on the middle row is randomly chosen. (b) is plotted by Freeform Origami [2], where the mountain and valley creases are colored red and blue.

$$\begin{aligned}
\beta_1 + \alpha_2 - \gamma_1 - \delta_2 &= 0 \\
\alpha_1 + \beta_2 - \gamma_1 - \delta_2 &= 0 \\
\sin\gamma_1 \sin\gamma_2 - \sin\delta_1 \sin\delta_2 &= 0
\end{aligned}$$

The last equation can be chosen from

$$c = \frac{\sin\dfrac{\alpha_1 - \beta_1}{2}\sin\dfrac{\beta_2 + \alpha_2}{2}}{\sin\dfrac{\alpha_1 + \beta_1}{2}\sin\dfrac{\beta_2 - \alpha_2}{2}} = k\sqrt{\frac{\sin(\delta_2 + \gamma_2)\sin(\gamma_1 - \delta_1)}{\sin(\delta_2 - \gamma_2)\sin(\gamma_1 + \delta_1)}}$$

or

$$\begin{aligned}
c = \frac{\cos\dfrac{\alpha_1 - \beta_1}{2}\cos\dfrac{\beta_2 + \alpha_2}{2}}{\cos\dfrac{\alpha_1 + \beta_1}{2}\cos\dfrac{\beta_2 - \alpha_2}{2}} &= k\sqrt{\frac{\sin(\delta_2 + \gamma_2)\sin(\gamma_1 - \delta_1)}{\sin(\delta_2 - \gamma_2)\sin(\gamma_1 + \delta_1)}} \\
k = 1 \quad \text{if} \quad (\gamma_1 + \delta_1 - \pi)(\gamma_2 + \delta_2 - \pi) &> 0 \\
k = -1 \quad \text{if} \quad (\gamma_1 + \delta_1 - \pi)(\gamma_2 + \delta_2 - \pi) &< 0
\end{aligned} \tag{4}$$

Remark 1. The design example shown in Figure 3(a) is a periodical solution of the longitudinal linear repeating type in [8], but is not the only case. It is possible to get some non-perodical solutions numerically, and the rigidly folded states can reach some other shapes. Since equation (4) is highly non-linear, there might be no solution or only degenerated solutions for a given set of input sector angles.

5 Conclusion

This paper demonstrates three methods to approximate different types of surfaces based on the developable case of three types of rigid-foldable quadrilateral creased papers. For the first two types, the first and last column of panels are designed to halt the rigid folding motion by clashing of panels. All the quadrilateral creased papers used in this paper have a unique one degree of freedom rigid folding motion.

References

[1] A. P. Thrall and C. P. Quaglia, "Accordion shelters: A historical review of origami-like deployable shelters developed by the US military," *Engineering structures*, 59:686–692, 2014.

[2] Tomohiro Tachi, "Freeform rigid-foldable structure using bidirectionally flat-foldable planar quadrilateral mesh," *Advances in architectural geometry*, pages 87–102, 2010.

[3] F. J. Martínez-Martín and A. P. Thrall, "Honeycomb core sandwich panels for origami-inspired deployable shelters: Multi-objective optimization for minimum weight and maximum energy efficiency," *Engineering Structures*, 69:158–167, 2014.

[4] C. P. Quaglia, N. Yu, A. P. Thrall, and S. Paolucci, "Balancing energy efficiency and structural performance through multi-objective shape optimization: Case study of a rapidly deployable origami-inspired shelter," *Energy and Buildings*, 82:733–745, October 2014.

[5] Ting-Uei Lee and Joseph M. Gattas, "Geometric design and construction of structurally stabilized accordion shelters," *Journal of Mechanisms and Robotics*, 8(3):031009, 2016.

[6] Niels De Temmerman, Marijke Mollaert, Tom Van Mele, and Lars De Laet, "Design and analysis of a foldable mobile shelter system," *International Journal of Space Structures*, 22(3):161–168, 2007.

[7] Zeyuan He and Simon D. Guest, "Approximating a Target Surface with 1-DOF Rigid Origami," *in Origami 7: The proceedings from the seventh meeting of Origami, Science, Mathematics and Education*, volume 2, pages 505–520. Tarquin, 2018.

[8] Zeyuan He and Simon D. Guest, "On Rigid Origami II: Quadrilateral Creased Papers," *arXiv preprint arXiv:1804.06483*, 2018.

[9] Ivan Izmestiev, "Classification of flexible Kokotsakis polyhedra with quadrangular base," *International Mathematics Research Notices*, 2017(3):715–808, 2017.

Proceedings of the IASS Annual Symposium 2019 – Structural Membranes 2019
Form and Force
7 – 10 October 2019, Barcelona, Spain
C. Lázaro, K.-U. Bletzinger, E. Oñate (eds.)

Exploration of Compliant Hinges in Origami-based Structures

Yves KLETT*, Peter MIDDENDORF, Fabian MUHS, Stefanie WEIDNER[a], Werner SOBEK[a], Walter HAASE[a]

*Institute of Aircraft Design, University of Stuttgart, Pfaffenwaldring 31, 70569 Stuttgart, Germany
klett@ifb.uni-stuttgart.de

[a]Institute of Lightweight Structures and Conceptual Design, University of Stuttgart
Pfaffenwaldring 7+14 70569 Stuttgart, Germany

Abstract

The term "origami" is usually associated with the outcome of a given folding process rather than the process itself. Once we focus on the folding, every piece of origami becomes a (more or less intricate) mechanism and can provide a wealth of inspiration to efficiently design kinematic structures from flat sheets. A critical point for origami-based structures made for real-world applications that need to be produced from thicker materials is the availability of practical hinge concepts that need to meet several requirements, including ease and economy of manufacture, robustness, and longevity. Compliant hinges show promise with regard to these requirements. Recently introduced plastically annealed lamina emergent origami (PALEO) combines this concept with non-trivial programmable states to which a given structures will return elastically without any additional actuators or external stimuli. This paper explores the potential of PALEO structures intended for use as facade elements, which are one focus of the Collaborative Research Centre 1244 "Adaptive Skins and Structures for the Built Environment of Tomorrow" at Stuttgart University. Issues of design, manufacturing, scalability, longevity and feasibility of origami-inspired structures in an architectural context will be addressed and augmented by data gathered from finite element analysis and real-world mechanical testing of selected structures.

Keywords: origami, compliant mechanism, facade, adaptivity, skins, civil engineering, functional integration

1. Introduction

A facade is the interface of a building between its interior and exterior. It can either establish a direct connection to the surrounding environment or insulate the inside from the outside. Facades also significantly influence the visitor's first impression of the building. This makes them to one of the most important architectural elements of a building. Yet, facades need to be more than just the appealing outer layer, like a skin they both need to shelter the inhabitant, but also interact with the environment and provide a comfortable working and living space in general.

Meeting these requirements is a challenging task, especially in changing environments. Adaptive facades that can change their appearance and functionality (e.g. influencing building physical characteristics) have become a relevant research topics. Some preliminary stages of adaptation are already present in architecture, mostly as kinematic shading systems. An extension of existing concepts is of great interest to provide new opportunities to design adaptive building skins that can change their physical properties and their appearance. Relevant building-physical properties include amongst others thermal and acoustical aspects, but also ventilation, optical properties and energy-saving.

Copyright © 2019 by Yves Klett et al.
Published by the International Association for Shell and Spatial Structures (IASS) with permission.

Since external or internal parameters can change instantly, hourly, daily or seasonally, the timeframe of a possible adaptation can vary between short-term, mid-term and long-term. Considering the broad spectrum of all of these aspects can result in micro-, meso-, or macro-sized adaptive solutions.

2. State of the art in adaptive facades

The current state of art for adaptive kinematic facades mainly happens on a macro-scale. A good overview is presented by e.g. [1]. Two prominent examples include the facade of SDU Kolding Campus in Denmark and the Al-Bahar Tower facade in Abu Dhabi. These two solutions provide very appealing versions of shading systems that can adjust the solar input to the glazing.



Figure 1: SDU Kolding Campus (source: https://www.sdu.dk/en/om_sdu/byerne/kolding)

In these examples, linear actuators open and close the shading devices once a day according to a preset program, which prevents direct solar radiation. Implemented sensors can recognize a change in weather condition, e.g. overcast sky, increase in wind-speed and cause the actuators to react correspondingly.

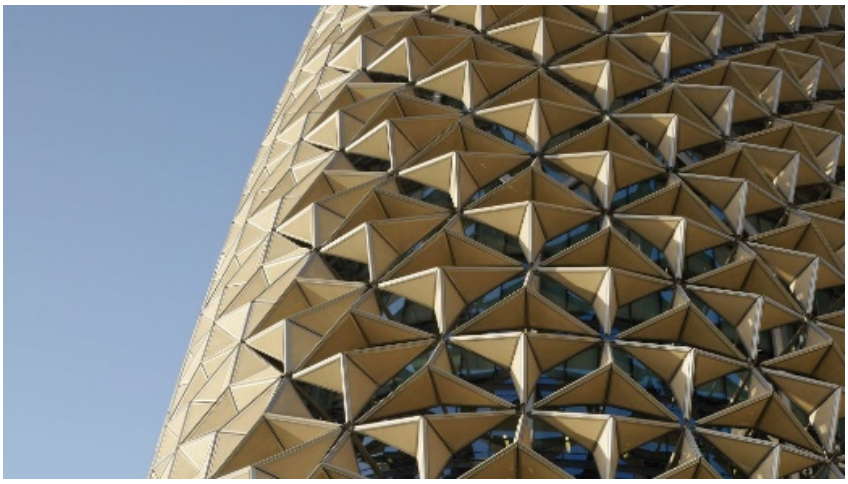


Figure 2: Al Bahr tower shading (source: https://www.ahr.co.uk/Al-Bahr-Towers)

On the one hand, there are many benefits of such a system. The cooling energy can be reduced, whilst still allowing floor to ceiling glazing even in a desert and enabling a visual reference to the outside. On the other hand, it requires a fully functioning facade as an inner layer and the size of the shading devices necessitates a solid substructure, as well as powerful actuators to activate the elements. This leads to an

additional resource consumption and thereby an increase in embodied energy. Moreover, the functionality of those large-scale shading systems is limited in windy conditions.

Of course, the design and actuation methods vary greatly, generating multiple different solutions which can also influence ventilation or include photovoltaic panels, but most current kinetic facade systems follow a similar principle and are applied as adaptive shading elements. A nice overview over adaptive facade systems is provided by [2].

Most existing solutions experiment with the concept of adapting a facade to provide changing shading or insulation but use conventional mechanical means to realize macroscopic changes in appearance and functionality (Figure 3). They quite often do not provide superior performance when compared to conventional solutions like standard blinds but derive attractivity by providing mostly optically new ways to change the look of a building.

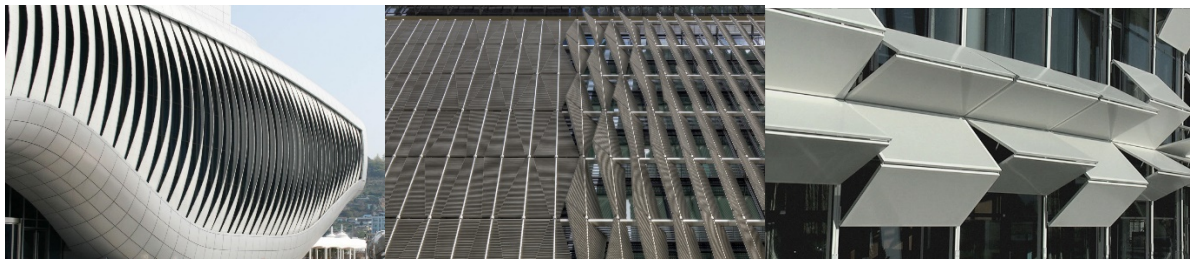


Figure 3: Macroscopic kinematic facade examples (left to right: One Ocean Pavillon Yeosu https://www.knippershelbig.com/en/one-ocean-pavillon-yeosu , Q1 ThyssenKrupp Quarter Essen: https://www.archdaily.com/326747/q1-thyssenkrupp-quarter-essen-jswd-architekten-chaix-morel-et-associes/510bd274b3fc4b21ce00008f-q1-thyssenkrupp-quarter-essen-jswd-architekten-chaix-morel-et-associes-photo, Kiefer Technic Showroom https://www.archdaily.com/89270/kiefer-technic-showroom-ernst-giselbrecht-partner/kiefertechnic_10).

3. Origami as inspiration for facade constructions

Current origami research provides a lot of inspiration to efficiently generate mechanisms that are based on flat base materials, with a great potential for the change of shape and texture of surfaces by a minimal number of necessary actuators. Origami tessellations with one degree of kinematic freedom (so-called rigid origami) can be used as a template for kinematic surfaces that change their texture on a mesoscopic level with very limited actuation, but a huge variety of appearance. There is an infinite number of tessellations that by their very nature form intricate mechanisms, giving designers and engineers a large choice to design visually appealing and functionally relevant solution (see Figure 3).

Moreover, the comparatively fine-grained texturing of origami-inspired surfaces does increase the specific bending stiffness of resulting panels. Just like more standard corrugations, the crease lines in the surface add stiffness to a structure. The static properties of tessellations in light-weight construction as sandwich cores have been the focus of recent research [3].

Translating origami into the building skin or facade context raises several challenges. While the mechanism inherent in any (rigidly foldable) origami structure immediately provides a way to model kinematic variability, the actual realization of larger moving structures that need to withstand taxing environmental and mechanical loads is not trivial.

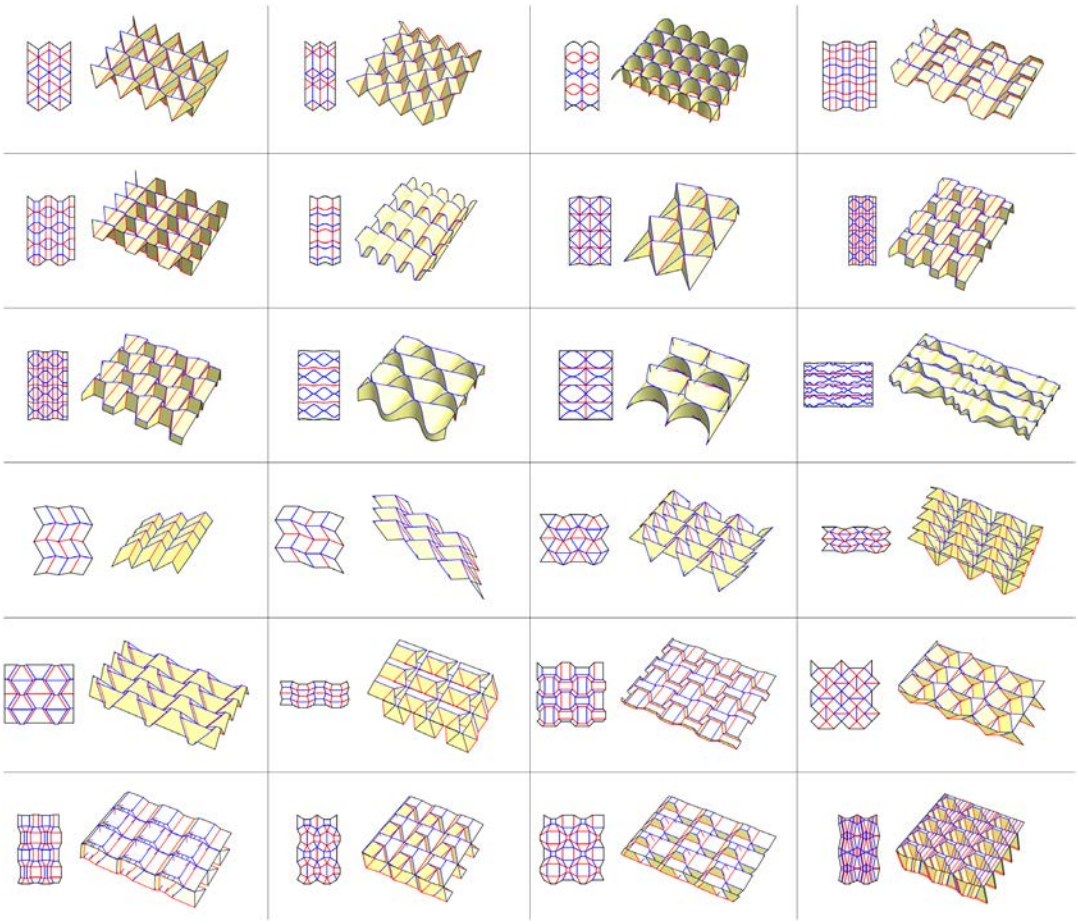


Figure 4: A small selection of rigid foldable tessellations [3].

The design of efficient hinges that enable movement is a critical aspect for origami-based structures and a key point here. Generally, origami creases are used as hinges for thin, paper-like materials. With increasing material thickness, this does not work anymore, and alternatives to enable movement must be provided. The quite recently developed field of thick origami deals with some of these issues [4,5]. Straightforward hinge concepts include piano-type and membrane hinges, each with their own strengths and weaknesses, but even here the placement and realization of hinges is not necessarily a simple affair.

4. Compliant hinges as enabler for origami-based surfaces

Compliant mechanisms constitute a very interesting field of mechanical engineering. The general principle is to use the elasticity of any given material to transfer forces and displacements between points, without the need for classical additional components like bearings and connectors.

Some advantages of compliant mechanisms include simplicity and ease of manufacturing, reliability, cost of production, and the principle is used extensively in different application areas, from microelectromechanical systems (MEMS) to rocket engine positioning [6].

The presented solution for generating compliant hinge sections in origami-based structures has been introduced in the past [5], and has been gradually extended to origami [7,8]. Compliant hinge areas are manufactured by removing material from a sheet, reducing the local stiffness in these areas and providing an arbitrarily large range for elastic deformation. The result is an elastic mechanism that

retains to a large degree the kinematic behavior of the underlying origami tessellation, and works without any additional components.

A more recent addition to the lamina emergent origami is the introduction of a annealing process, which resets the stresses in a given structure at a given, non-flat target state [9]. This results in a threedimensional lamina emergent mechanism that has the tendency to return to the target state without any additional external actuation or stimulus. This behavior removes a number of problems compared to position-indifferent hinge systems like piano or membrane hinges, which can get caught up in singular geometric configurations, and need additional safeguards to avoid undesirable lockups or geometric bifurcations.

An example is shown in Figure 5, with a plastically annealed lamina emergent mechanism (PALEO) transforming quickly from a compact packed state into a threedimensional target state.

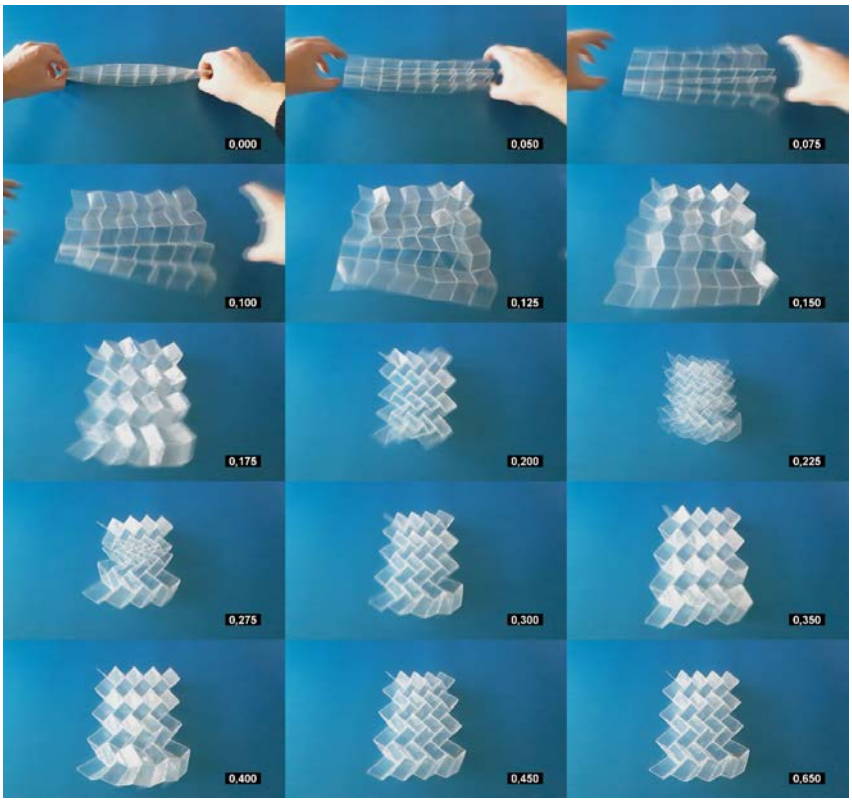


Figure 5: Automatic depoloyment of a PALEO made from 0.2mm thick PET. The structure deploys very dynamically without additional external stimulus or actuation. The text denotes the time elapsed in seconds after release [7].

Potential benefits of the application of compliant hinges in new facade systems may include:

- the possibility to generate meso-scaled texture changes in large surfaces with a minimum number of actuators
- large design freedom to design the adaptive surface according to functional and aesthetic considerations
- generation of lightweight facade structures by using meso-scale patterned surfaces

- simple integration of various, kinematics-related functionalities into the facade, including ventilation, shading, acoustic and thermal insulation
- ease of manufacturing and economic manufacture, by machining readily available flat base material
- high redundancy by the provision of multiple alternative load paths in the compliant hinge area
- suitability for thermoplastics, metals and composite material in many varieties
- high reliability of the hinge function and robustness against environmental impacts (icing, corrsion, ageing)
- virtually noiseless function
- low maintenance

Challenges posed by moving to compliant hinge concepts:

- choice of the most beneficial tessellation design with regard to functionality
- proper design of elastic and fatigue behavior
- potentially non-linear and multi-dimensional changes of surface forms compared to linear, one-dimensional solutions like blinds, necessitating new design paradigms
- design of efficient mechanical building-facade interfaces to
- product design to meet certification standards, e.g. with regard to fire resistance

5. Proof of concept

To show the applicability for materials and material thicknesses relevant for civil engineering and architectural use, a larger element was manufactured from 2mm strong polycarbonate. The polycarbonate provides a transparent material with excellent elastic and fatigue properties, and can be machined and annealed with standard means.

The torsion bar pattern for the Miura-ori type unit cell was designed by refining an initial guess and by confirming the results by finite element analysis (Figure 6) [10]. Using a combination of Rhino3D and Mathematica scripts, a machining program for a standard 3-axis milling machine was generated and single cells and a larger 4x3 cell grid was manufactured (Figure 7).

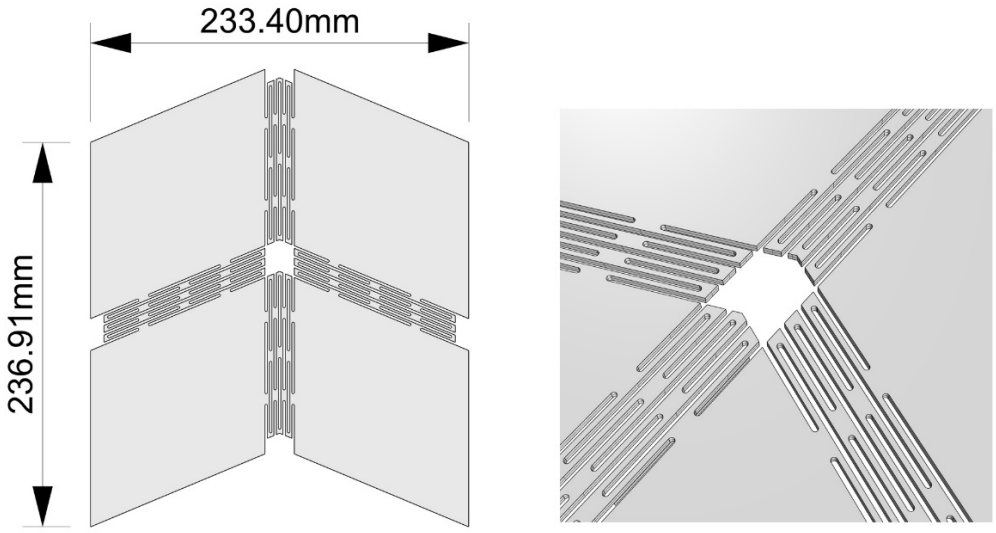


Figure 6: PALEO unit cell for 2mm polycarbonate sheet material.

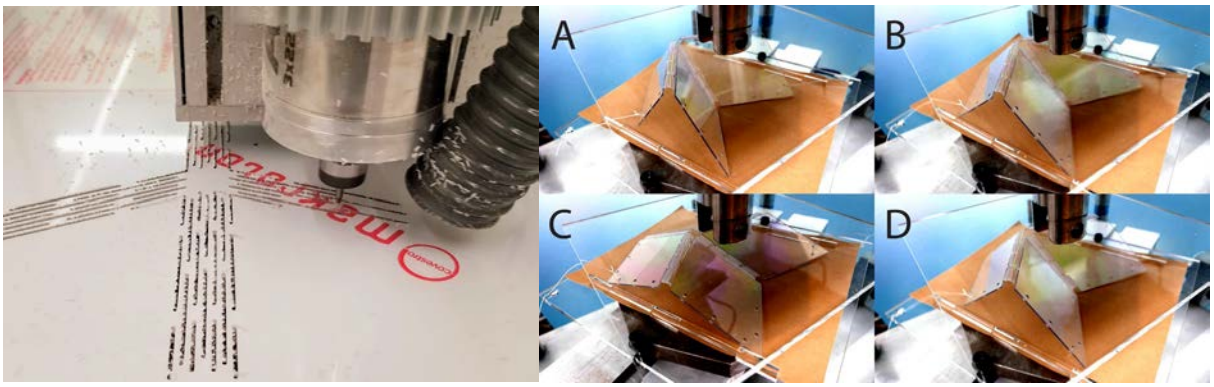


Figure 7: Left: Milling of the PALEO grid from 2mm polycarbonate. Right: Cyclic testing of a unit cell module.

A cyclic test of the single cells was conducted, where the unit cell was subjected to a compressive force. The cells performed reliably in this test, and reached a lifetime between 200.000-800.00 cycles before a fault could be detected. These first results are encouraging for the application in real-world scenarios, where a large number of actuations can cumulate over decades of the facade element lifetime.

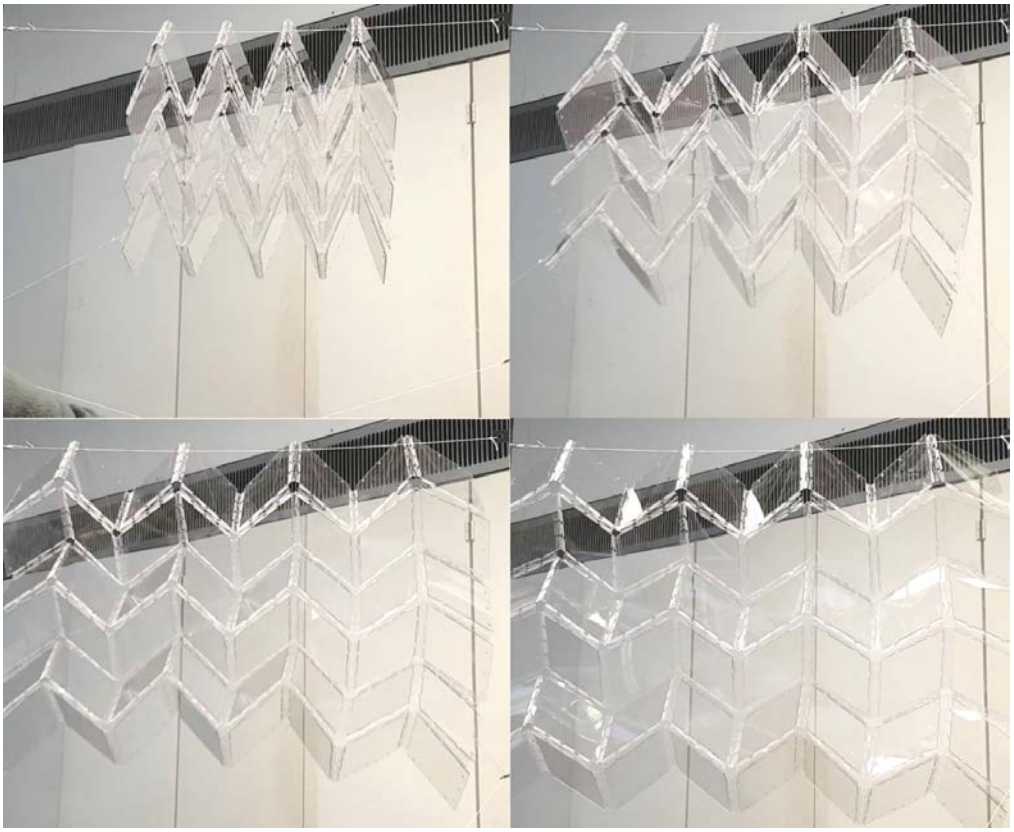


Figure 8: 4x3 PALEO matrix, manufactured from one sheet of polycarbonate. Actuation is carried out by a simple pulley arrangement, with just one actuation vector.

A 4x3 cell grid was also manufactured from a sheet of about 1000x800mm² polycarbonate and installed in a simple frame to demonstrate the shape change caused by a simple pulley arrangement that pulls on

the two lower edges of the structure. The mechanism works reliably, and does need only small forces for successful actuation (Figure 8).

For an application in architecture, many challenges need to be addressed, including installation, kinematic compatibility, actuation and material choice. The general concept however provides potential for the design and economic manufacture of lightweight, kinematic elements for adaptive building skins.

Conclusion

Compliant hinges and PALEO elements for the application in adaptive facades can be used to design origami-based elements that may be applied for future buildings. They can provide a simple way to generate meso-scale texture changes in facades with a small number of actuators. The mesoscopic patterning can provide benefits in terms of lightweight performance and manufacturing cost, and physically and design-wise open up new ways to generate structures with adaptive characteristics.

Acknowledgements

The work described in this paper was conducted in the framework of the Collaborative Research Centre 1244 "Adaptive Skins and Structures for the Built Environment of Tomorrow" funded by the German Research Foundation (DFG - Deutsche Forschungsgemeinschaft). The authors gratefully acknowledge the support.

References

[1] K. Zvironaite, A. Knol, und S. Kneepens, *A playful way through the world of moving facades*, available online: https://repository.tudelft.nl/islandora/object/uuid:cabfd871-7ea9-465a-9f78-2a24fdcb9430?collection=research

[2] K. Herter, *Adaptive Gebäudehüllen - Kategorisierung nach Funktionalität sowie die quantitative Analyse und Bewertung von Energie- und Materialeinsparungen*, master thesis, Universität Stuttgart, ILEK, 2018

[3] Y. Klett, *Auslegung multifunktionaler isometrischer Faltstrukturen für den technischen Einsatz* ISBN 978-3-8439- 1025-5, Dissertation Universität Stuttgart, 2013.

[4] T. Tachi, 2011. *Rigid-foldable thick origami*. *Origami*, *5*, pp.253-264.

[5] J. Ku, E. Demaine, *Folding Flat Crease Patterns with Thick Materials*. ASME. *J. Mechanisms Robotics.* 2016;8(3):031003-031003-6. doi:10.1115/1.4031954

[6] L. Howell, *Compliant Mechanisms*. No. ISBN 9780471384786. Wiley, 2001

[7] Ohshima, Tachi, Tanaka, and Yamaguchi. *Analysis and design of elastic materials formed using 2D repetitive slit pattern*. In Proceedings of the International Association for Shell and Spatial Structures (IASS), 2015

[8] Nelson, Lang, Pehrson, Magleby and Howell, *Facilitating deployable mechanisms and structures via developable lamina emergent arrays.* Journal of Mechanisms and Robotics, (3), Mar., pp. 031006–031006–10, 2016

[9] Y. Klett, *PALEO: Plastically Annealed Lamina Emergent Origami* in IDETCIE 2018, Québec, Canada, http://dx.doi.org/10.1115/DETC2018-85983, 2018

[10] Y. Klett, P. Middendorf, F. Muhs, *Analysis of Static and Dynamic Behavior of Thick-Walled PALEO elements*, IDETCIE 2019, Anaheim, USA.

[11] Y. Klett. *Folding perspectives: Joys and uses of 3D anamorphic origami*. In P. Wang-Iverson, R. J. Lang, and T. Tachi, editors, Origami 6. ISBN: 978-1-4704-1874-8, 2016

Proceedings of the IASS Annual Symposium 2019 – Structural Membranes 2019
Form and Force
7 – 10 October 2019, Barcelona, Spain
C. Lázaro, K.-U. Bletzinger, E. Oñate (eds.)

Folding a dome

Florian TUCZEK

Freier Architekt
Annenstr. 7, 04315 Leipzig, Germany
ft@dome-scape.com

Abstract

When a dome has to be built of many components, it should be preassembled as a whole to be folded for transport. Because a dome surface is not developable without cutting many gaps, the surface of built foldable sheet domes shows a fold relief, mostly an origami diamond pattern, counteracting a dome's good small surface-area-to-volume ratio, compared to a cubic building. However, a nearly smooth surface of quad facets offers a folding solution, based on symmetry and modularity.

Keywords: modular origami, kirigami, deployable structure, quad faceted surface, intentional buckling, snap through, semi-rigid material

1. Introduction

In a model scale, substantially double-curved, faceted surfaces can be folded of one single blank without cutting gaps, if the superfluous areas, instead of being cut off, are folded into 180° folds either standing inside as seams perpendicularly to the reference surface [1] or lying tangentially to the outer surface increasing the surface area like cooling ribs [2]. In a built scale, there would be too much superfluous material counteracting again the relatively good A/V ratio of a hemisphere. Besides, large blanks are not available on market; they could be produced only on site.

The proposed plane quad mesh surface subdivision [3] equals topologically that one of Catmull and Clark [4]. In addition, it shows symmetric, straight running, tapered columns of plane quads in an array of isosceles trapezoidal facets defined by two sets of planar polygonal curves enabling folding.

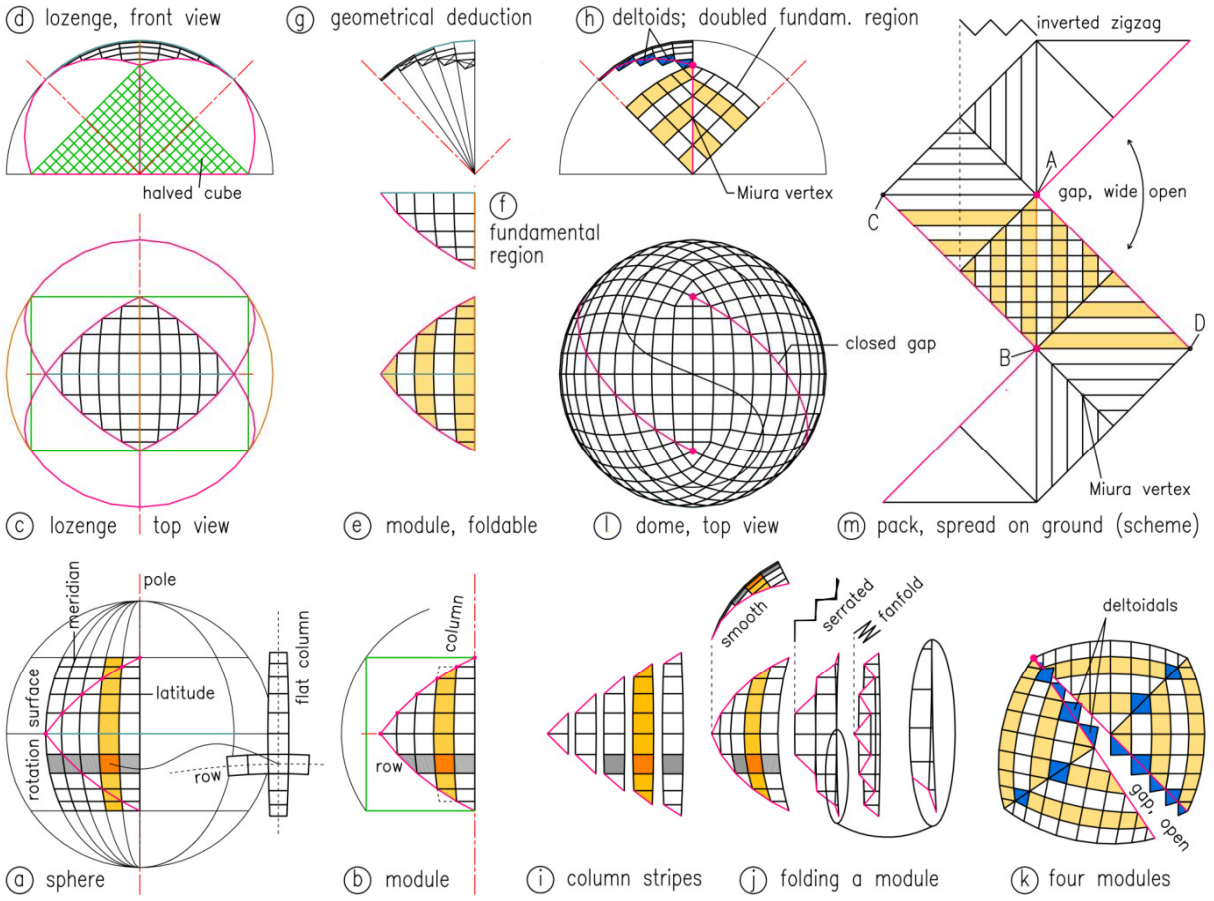
Triangulated thin shells of sheet material could be folded similarly along geodesic curves made as polygonal creases, but they are unstable without folded ribs acting as struts on the edges. Thin shells of pentagons or hexagons are stable, but not foldable because they lack planar continuous curves for folding. This applies equally to other quad-faceted shell surfaces than the proposed one.

2. Geometric preconditions for folding

Imagine a spherical surface that is subdivided by parallels of latitude and meridians (Figure 1a). Their intersections define isosceles trapezoidal facets, hereinafter simply called trapezoids. The facets form an array of rows between great circle arcs and of columns between small circle arcs. The straight lines that define later only slight creases within each column of the unfolded shell surface are parallel. The trapezoids of a row are conjoined at their equal non-parallel lines defining later acute folds. Each row runs slightly curved on the surface. Its facets are equal (see Fig. 1a on the right).

Trapezoids had been occurred already in scale-trans surfaces. [5]. These surfaces need not be rotational, but in order to avoid several oblong, small, or acute facets, scale-trans shells are restricted to be shallow. According to [3], portions of rotation surfaces can be combined to form a higher shell shape (Figs. 1c, 1d). Like the subdivision of a conventional geodesic dome, the presented meta-geodesic one is based on an imagined polyhedron, here a diagonally halved cube (Fig. 1d, green) instead of a half icosahedron.

Copyright © 2019 by Florian TUCZEK
Published by the International Association for Shell and Spatial Structures (IASS) with permission.



Figures 1a to 1m: The design of the dome – geometric base – folding options

Two triangular modules can be combined to form a lozenge-shaped shell-portion, hereinafter simply called lozenge, by conjoining them at their common base side (orange). A lozenge has a homogeneous scale-trans surface. A module (Fig. 1e) can also be halved along its symmetry line (teal) to result in two fundamental regions. A fundamental region (Fig. 1f) is the geometric surface unit. It can be mirrored virtually in the planes of its three plane border curves (purple, teal, orange) to result in a spherical shell.

The vertex points (purple) of small triangles at the equal sides of each module coincide with the vertex points of cut off trapezoids Figs. 1a, 1b). The goal of the novel geometry had been to have only quad facets. So, the precondition was to make two adjoining mirror-symmetrical small triangles of adjoining modules coplanar in order to fuse them into a deltoidal quad (Fig. 1h, blue). The deltoidal shapes were geometrically constructed depending on the regularly subdivided equator line (Fig. 1g, teal). That is why the parallel lines between the trapezoids of a column are not equidistant. So, the surface is geometrically exactly deduced. It could be automatically generated via software.

2.1. Combining equal shell portions as built modules

Because the trapezoids of two curved columns - adjoining each at one of its equal, oblique sides being parts of a planar polygonal curve in the shell surface - are equally inclined to the plane of this curve as a shallow mountain fold, they can be folded close to each other to be parts of two flattened columns (Figs. 1i, 1j). So, several columns of thin material can be stacked compactly face to face when they are folded up and down alternatingly. After this, the polygonal curves being then two symmetric sides of the resulted flat pack are less curved than before.

Folding doesn't work without warping each originally and finally flat facet temporarily. Energy is needed to overcome resistance in the state of warping. The longer the column is, or the higher the rise of the column's border curve is, the higher is this resistance. Finally, the folds could buckle unwantedly and the facets could crumple. By combining rotation surfaces, too oblong columns are avoided.

2.2 Folding more than an isolated shell portions

The initial assumption was that each lozenge has to be a separate pack to be deployed and assembled as one of several lozenges on site. Before building a small dome (Fig. 1l), one single large-scale lozenge (Figs. 1c, 1d) of it was made and folded. It seemed to be foldable only if its border is free, that is, if it is neither adjoined to another lozenge along said hypotenuses nor fixed on a rigid plane. The border is strongly deformable indeed and gives the opportunity to begin a wanted valley fold from there. The border of the unfolded lozenge sagged completely to the flat ground to end its movability. The facets were warped hereby, but the substantially synclastic curvature of the lozenge was maintained. When turned upside down however, a lozenge can be rolled together in both directions of the array of facets. This deformability can be limited by adjoining lozenges breaking the parallelism of the fold lines. However, trying to interconnect two such unfolded lozenges without formwork was already arduous.

A one-piece solution to erect the dome was found by recalling two facts: 1. As intended, each deltoid consists of two small triangles. 2. As tested long before, two fundamental regions (Fig. 1h) can be coupled along their longest side (purple) by folding deltoids alternatingly into sloping ridges or sloping valleys in a Miura-like manner. Because of these facts, modules can be conjoined at their longest side to fold them interdependently.

A shell of cohering modules can't be folded if not at least one gap remains to be closed between two of them. Each gap must be bridged by adding deltoidal facet parts, hereinafter called deltoidals, exceeding the module's border at one side of the gap inside or outside in order to overlap each a small triangle at the other side of the gap, in a connection being as reversible as the folding process itself (Fig. 1k).

3. Snap effect – controlled buckling from a shallow mountain to a deep valley

Each facet of a lozenge is warped in a zigzag-folded state (Fig. 1j) while its four edge lines remain straight. The fact that each long fold is a polygonal curve instead of being one straight line causes resistance against accomplishing the deployment: Across the middle of the fold there is compression, across its ends there is tension. The resulting tendency of a serrated lozenge to fold back has to be redressed. Energy is needed to transform deep valley folds durably into shallow mountain folds.

Complete changes of lozenges away from the serrated relief state (Fig. 1j), or towards it, are possible only by switching subsequently each vertex pyramid into an opposite position: An unfolding pack can be deployed finally by intentionally snapping up, vertex by vertex along each valley fold line, a concave vertex pyramid into a shallow convex one. As well, a deployed, substantially curved surface can change into a folding pack only after intentionally making it buckle, e. g. by making it snap trough locally, vertex by vertex, to change a convex vertex pyramid into a concave one along each second polygonised fold curve of the shell surface.

The parallel creases between facets within each column are important to form vertex points in order to control folding and unfolding. Omitting them by changing the polygonal curves into smooth curves for curved folding would cause danger by randomly and rapidly extending valleys, unhindered by vertices.

To avoid unintended buckling, the sheet material should be resistant to in-plane shear forces, not too compressible elastically, that is, be unable hereby to evade sideways by unwanted buckling. Moreover, the dihedral angles between completely deployed facets must not be too close to 180°, the surface creases must not be too flat. So, the maximal frequency is 6. The frequency number means the number of facets at each of a module's three sides. If it is lower than 4, snapping trough is possible only by crumpling. If it exceeds 6, snapping is too easy.

Regarding only one single shallow vertex pyramid, snapping is enabled by slight elastic compression near its apex: in the sheet material in the four facet areas as well as across the creases acting as living hinges. Correspondingly, it is enabled by elastic tensional stretching afar from the apex, that is, near the next vertices. Because anticlastic faceted surfaces don't have vertex pyramids, there is no opportunity for snapping. This insight was the reason to discard finally shells that include anticlastic regions.

4. Scale models and small domes

A first scale model of fairly thick material indicated already that fan folding a shell works geometrically as assumed although the folded pack was still thick (Figs. 2, 3, 4). Such a shell with rather stiff edges is clearly stable by folded slab action. Then, a small dome shell was built of thin material, with hinged folds, to show whether it is also stable despite a truss is missing. Because of the quad shape of its facets, the dome is assumed to act as a hybrid of a plate shell and a truss shell where facets act as plates and crease zones act as bars [6].

The first solution to conjoin the column stripes was to add standing abutting gluing tabs still causing dead load; the doubled fold tabs are bulky in the folded and unfolded pack. They hinder a fold from changing flexibly at a moving vertex from valley to ridge. So they were cut away from blanks of a small 3.05m-done still under construction. The second solution was to add gluing tabs lying flat at the reference surface. But they imply an eccentricity out of the reference surface.to be mastered geometrically by a layer change from stripe to stipe and from module to module. This eccentricity restricted it to a small model scale – also for exploring anticlastic curvature. In a larger scale, a simple butt joint within one layer is easier to build and sufficient against mainly membrane forces.

While the joint design depends on scale, the basic design concept of all examples was the same: By having pivoted the virtual basic cube 45° in a horizontal axis, all 12 modules could be arranged in the pack along one single folding path having an S-shape (Fig. 1l). So, the deployed dome has only two gaps to be closed. (Fig. 2, purple).

4.1. A carton model of a 4 frequency dome

To explore the folding behaviour, a smaller frequency seemed to be sufficient. The model was made of photo carton, admittedly somewhat too thick and rigid, 260g/m², but apt to test if the folding mechanism works principally. The stripes were glued together by flat tabs according to the afore described second solution. So, differing from Fig. 1k, the connecting deltoids are an integral part each of the stripes lying alternatingly in the inside layer along one side of the gap, and in the outside layer along the other side. According to Figure 1k, deltoids were provided not only there. But each second one was still arranged wrongly here, So, deltoids were forcibly folded (Fig. 3) and bulky in the pack.

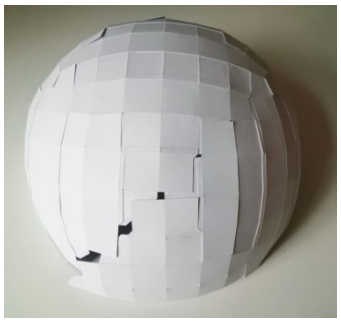


Fig. 2: An opening gap.



Fig. 3: Four modules, still curved.



Fig. 4: The nearly folded pack.

4.2. A 5 frequency 3.05 m dome made of milk carton

To master the scale effect, its material had to be tougher than normal cardboard, still flexible, and rigid against unintended creasing within a facet. So, milk carton, PP-coated paperboard, 390 g/m², was

chosen. The radius-to-thickness ratio is 1.523 m / 0.6 mm = 2538. Even if a static height of 5 mm is conceded because of the shallow mountain folds between facets, the ratio is still 305.

All edges of each column stripe blank were wrapped with adhesive tape to prevent deterioration by both: splicing of the paperboard core by compression, and delamination of the PP-skins from the paperboard by shear force. Then, the blanks were conjoined by adhesive PP packing tape, 4 cm inside and outside. Initially there was no formwork to position abutting blank edges exactly to each other. But the first module – built by conjoining arduously line segment by line segment – could serve as formwork.

A deltoidal facet part was added to one triangular facet at the end of each stripe of the one single layer of milk carton alternatingly inside and outside at one of both sides of an open gap according to Fig. 1k. To fix the reversible interlocking linkage formed by the deltoids, hook and loop tape sections, 2 cm x 7 cm were stuck on all overlapping facets. Further deltoids along irreversible joints between modules added at first were removed later because they are not necessary to reach and maintain the final surface. Feared sagging valley folds between coplanar small triangles of adjoining modules didn't occur.



Fig. 5: Unfolding on the ground according to Fig. 1m



Fig. 6: Further snaps, impossible on ground.



Fig. 7: Asymmetric configuration



Fig. 8: The rising dome before closing the second gap.

At the first erection without experience in this scale, not a single seam was broken even when a wind gust grabbed a still exposed, movable larger region of the deployed shell. But along 1,5 cm, the corners of six unfolding cohering modules at a gap end were drawn 1 cm apart despite of a reinforcement by additional tape. One seam of this pack item was broken this time, but only this time.

Figures 1 to 4 show the second one of four erections of the dome. At first, the pack was extended on the ground as wide as possible without snapping - according to Fig. 1m. The four middle modules were easily snapped out by lifting them together. The result was a ship shape still visible in Figure 7. But snapping out further valley folds became difficult, as can be seen there in the front. Larger regions had to be lifted to continue unfolding. This was the reason to turn the shell inside out for the next time.

During the third erection, all 12 modules were unfolded and snapped out on ground in six pairs having each a curved surface. So, it was possible to lift them by moving them more independently from each other, that is, without constraints, before removing the valleys between them. However, it got clear that the span of the spread arms of one person was too short to hold both gap ends at the upper lozenges. So, at least one side could sag down again before having reached the final position. It was wrong to compensate this more than before by lifting one sagged side too high: In a hanging state, the modules can be easily snapped out indeed. But the outer modules came to close to the centre and had to be pushed outwards. Before closing the gaps, the weakened regions around at least one of both gap ends sagged down again, as shown already in Fig. 8, to get again an arbitrary crumpled shape leaving wrinkles in facets or creases. But the PP-skins remained intact. The stability of the final dome was not affected. The deployed dome was able to withstand vertical loads, but it should be fixed all around because the wind bent the loose base inwards at the lee side of the moving dome because the plane ground was not smooth.

Like in the precedent carton model, one single intentional snap-trough in the deployed surface didn't move recognisably the surrounding eight vertices. But pushing strongly a hand on the outer surface affects several vertices. The dome looked like a dented ping pong ball. However, this didn't affect the stability of the shell as a whole - in contrast to more than one bar at a node of a truss shell - because it is a "hybrid" shell between plate action and truss action, according to [6]. Admittedly, a vertex where three or four modules abut can sag down unintentionally because it was made not precisely enough.

Snapping out a fold within a module begins at a free border of the module and passes then a Miura vertex being too difficult to unfold at first. It is not a problem to make snap out more than one vertex in same time by one push. Folding needs more care than unfolding - especially a less compressible sheet material in this scale: Beginning folding at one open end of a fold at a module's border is easy. In its middle, snapping through simply a vertex point as already described is still easy – by pressing the vertex point to the inside. But at the end of the fold, the ridge has to be changed fluently point by point into a valley. This fluent change from ridge to valley should not exceed the end of one fold-line segment between two facets before pressing somewhat down both ridge line segments running nearly parallel to that line segment. Ignoring this leads to crumpled facets. Differing from unfolding, folding a long valley of a module has to begin at the Miura vertex, which is more difficult to be folded later.

4.3. A 5 frequency 2.54 m dome made of milk carton

The length of the base side (Figs. 1e, 1l, orange) of a module between both gap ends was reduced to a human scale – by reducing the new dome's diameter. Only this was the reason for the reduction. The initially flat facets are again slightly concave on the outside. This might be caused by thermally induced plastic expansion of the inner facet area and by compression at the surrounding folds acting as bars.

The first erection was: trying to unfold and snap out in same time asymmetrically the pack from its one end of to the other. This trial to save site ground area was a regress. So, the dome was folded together again according to that one after the 3.05m-dome's second erection. The second 2.54m-dome's erection was: forming three ship shapes of 4 modules each, lifting the middle one and removing the two folds between them. The third and fourth erections were conceptless. Near each of both upper gap ends, a fold end between two longest column strips was ripped apart. Nevertheless, folding together began in a well-considered manner by snapping in at first only the longest folds, which form the edges of a ridge roof.

So, for the fifth erection, the systematic change of configurations was clear: Recalling this dome's polyhedral base: a cube, by approximating a diagonally halved cube (Fig. 1d) whose both ridge roof sides are quadrats composed each of 2 x 2 modules and, whose both gables comprise 2 modules each. The valleys on the halved cube's edges were snapped out between six already curved surfaces: the horizontal top ridge at first, the four verges starting from the bottom and ending on the top. Two bottom ends of these verges buckled because they have to support also the two upper four modules (between points A, B, C, D in Fig. 1m) that temporarily spanned like a bridge. Reinforcing them later didn't help.

As in intermezzo, the fourth erection of the old, somewhat larger dome having the same fold design when turned inside out showed that it is not stiff enough for this temporary cubic arrangement.

During the sixth erection of the 2.54 m dome, only a few modules were spread on the ground. Besides, they remained this time in their zigzag relief even when they were lifted in the middle to form the ridge roof shape. But before, there were still asymmetric configurations (Fig. 9) because both hands would be needed again already to support the unfolding object temporarily.



Fig. 9: Only one gable stands



Fig. 10: The ridge roof configuration



Fig. 11: First module snapped out



Fig. 12: All sides snapped out, edges still recessing

A second 2.54 m dome was built to have an unwrinkled surface. For more elegance, the seam tape width was reduced outside to 2,5 cm and compensatively increased inside to 5cm. Differing from Fig. 1k, each (blue) deltoid, provided now only along one side of the gap, received a diagonal crease in order to facilitate the insertion of the upper gap side between the protruding deltoids. Paired Neodym magnet discs instead of hook and loop fasteners were too weak.

The author lifted the valley fold between points A and B (in Fig. 1m) and kept it in shape with both hands (Fig. 13) until the lifted unfolding object stood partly on the ground. Then, two times, one hand was free to turn four outer modules around the middle to close a gap. A better procedure will be: By lifting the spread pack as before, by inversely pivoting the four middle modules around the central axis, the author's twisted spine, and by letting both outer regions of four modules unmoved on the ground, the gap borders could be moved towards each other twice in same time to form the ridge roof without trouble or, help from outside. This will need a V profiled yoke supporting also points C, D.

This time, the gaps were closed and locked (Fig. 14) before smoothening the surface by snapping out the folds. Unexpectedly, this was possible without crumpling – in contrast to snapping in vice versa: Beginning at the Miura vertex points led to valley creases with a blocking mountain peak in their middle.



Fig. 13: Pack, lifted to pivot 4 middle modules



Fig. 14: Snapping out the closed zigzag relief



Fig. 15: Closed zigzag relief configuration



Fig. 16: The final 2.54 m dome

5. Conclusions and future work

The presented dome was proven to be foldable principally into a fanfold pack. It is generally stable and efficient without any substructure if the borders are fixed on the flat ground. So, such a shell can undoubtedly be realised in a larger scale. This individual, novel approach still focusses on qualities going to be quantifiable by measurements and calculations. Unfolding and folding are not equal because the unfolded state is the less constrained one, originating from building unfolded modules.

Simply a double part leg sling hanging on a crane will serve as hoisting device. The upper part of the sling will be twisted before lifting the spread pack at the ends of the middle fold via a cross beam preventing this fold from snapping out too early or from buckling. Two additional cables will lift said points C and D. So, the four middle modules can be pivoted as a whole around the central axis. Besides, a portable snap tool may be useful. It will reach three parallel fold line segments. Two arms with suction tamps will move along each of them and extend, or contract, perpendicularly each to the shell surface. So, arbitrary movements and unpredictable temporary forces will be avoided.

The large-scale semi-rigid material could be a squeezable hollow-core sheet of plastic being reinforced by carbon fibre. Its thickness is principally limited by the geometric imperfection of a folded Miura vertex. The deployed thin shell could act as one single cohering middle layer interconnecting thick rigid sandwich panels added at its both sides. This structure could be strengthened by applying prestress: tension to the foldable middle layer and compression to the added panels, by either pressing wedge-profiled bars into the joints between them or, by oversizing each panel slightly and mitring its edges.

References

[1] T. Tachi, "Freeform origami tessellations by generalizing Resch's patterns," in P*roceedings of the ASME 2013 International Design Engineering Technical Conferences and Computers and Information in Engineering Conference IDETC/CIE 2013, Portland, Oregon, USA, August 4-7, 2013,* ASME, 2013.

[2] R. Lang, http://langorigami.com/artwork/otomipot16/ .

[3] F. Tuczek, *Double Curved Shell*, US Patent 7,591,108 B2, Sep. 22, 2009, Figs. 34–39, 42.

[4] E. Catmull and J. Clark, "Recursively generated B-spline surfaces on arbitrary topological meshes," *Computer-Aided Design*, vol. 10, No. 6, pp. 350., Nov. 1978.

[5] A. Bögle, P. Cachola Schmal and I. Flagge, eds.. *leicht weit - Light Structures - Jörg Schlaich Rudolf Bergermann,* Munic; Prestel, 2003. pp. 113-129.

[6] H. Almegaard, A. Bagger, J. Gravesen, B. Jüttler and Z. Sír, "Surfaces with Piecewise Linear Support Functions over Spherical Triangulations," in *Proceedings of the 12th IMA international conference on mathematics of surfaces 2007, Sheffield, UK, September 04-06,* Springer, 2007, pp. 42–63, Fig. 1.

Proceedings of the IASS Annual Symposium 2019 – Structural Membranes 2019
Form and Force
7 – 10 October 2019, Barcelona, Spain
C. Lázaro, K.-U. Bletzinger, E. Oñate (eds.)

Frame model for analysis and form generation of rigid origami for deployable roof structure

Kentaro HAYAKAWA*, Makoto OHSAKI

*Department of Architecture and Architectural Engineering, Kyoto University
Kyoto-Daigaku Katsura, Nishikyo, Kyoto 615-8540, Japan
se.hayakawa@archi.kyoto-u.ac.jp

Abstract

Various models and methods have been developed for design and analysis of rigid origami. Rigid origami is a transformable polyhedron which consists of rigid flat panels connected by rotational hinges. However, very few methods have been proposed for form generation of rigid origami with a simple but not regular crease pattern. It is essential to obtain a simple crease pattern in terms of constructability when we apply rigid origami to deployable structures in architecture. In addition, it is important to develop a new model that can be used consistently throughout the process of form generation and analysis of the kinematics of rigid origami. In this paper, we present the authors' recent studies and their extensions about form generation of a developable and rigid-foldable polyhedron that approximates a curved surface with a simple crease pattern using a frame model which is simple but enables us to use the same variables in form generation, evaluation of kinematic indeterminacy and large-deformation analysis using a general finite element analysis software.

Keywords: rigid origami, deployable structure, frame model, form generation, finite mechanism

1. Introduction

Rigid-foldable origami, or rigid origami, is a kind of polyhedral origami whose facets do not deform either in-plane or out-of-plane directions throughout the folding process. Its facets and crease lines can be substituted with rigid panels and hinges, respectively. This feature is well suited to engineering application especially for architectural deployable structures, because mechanism of rigid origami does not rely on the property of its material, i.e., it is scalable and applicable to large scale structures. Although there are some applications of the concept of origami [1] in the architectural scale, there are only few examples because of the difficulty in designing rigid-foldable mechanism.

There are some typical rigid-foldable crease patterns such as Miura-ori [2], Resch's pattern [3] and waterbomb tessellations. However, we often cannot just apply them to architectural purposes because of the various demands of the shape of the building reflecting its floor plan and its exterior design. Therefore, it is important to develop a method for form generation of a general-shaped rigid origami, or the general polyhedron which satisfies the conditions for rigid-foldability and developability or flat-foldability. Tachi [4,5] formulated the geometric constraint of general quadrilateral mesh origami and presented the method for form finding of rigid-foldable quad mesh origami. Although his method is available for arbitral quad mesh origami, a known crease pattern such as Miura-ori, discrete Voss surface [6] or the hybrid surface of them is used as the initial configuration for form finding because it must satisfy the geometric condition for rigid-foldability. A typical crease pattern is also used to approximate a target surface by rigid origami; e.g., Dudte *et al*. [7] used generalized Miura-ori, and Zhao *et al*. [8] used generalized waterbomb tessellations. However, the generated crease lines tend to be the repetition of the similar pattern. It is difficult to obtain the polyhedra which have various degrees of freedom (DOFs) using a typical crease pattern.

Copyright © 2019 by Kentaro Hayakawa, Makoto Ohsaki
Published by the International Association for Shell and Spatial Structures (IASS) with permission.

In our resent paper [9], we proposed a method for approximating a curved surface with a rigid-foldable polyhedral origami which does not rely on a typical crease pattern. Only the developability and rigid-foldability of polyhedron are considered and the condition for flat-foldability is not incorporated. When a polyhedron is developable to a plane, the sum of angles between adjacent crease lines around each interior vertex needs to be equal to 2π. Although this necessary condition seems to be simple, it is not easy to directly obtain a shape of polyhedron satisfying this condition if a typical crease pattern is not used. Thus, we formulated an optimization problem to minimize the sum of errors of angles at the all interior vertices so that the generated polyhedron satisfies the condition for developability. Optimization starts from a triangulated curved surface to be approximated. If there isn't any unfolded or flat-folded crease line, the number of DOF of triangular mesh origami with E_{out} edges on the boundary is equal to $E_{out} - 3$ [5]. It is sometimes too large for the deployable structure in architecture. Therefore, to reduce the DOF, constraints are sequentially assigned so that the normal vectors of specified adjacent triangular facets are parallel. By removing (fixing) the crease lines between them, we can obtain a polyhedron that has both triangular and polygonal flat facets. Existence of infinitesimal mechanism is confirmed by singular value decomposition (SVD) of the linear compatibility matrix, and existence of finite mechanism is investigated by large-deformation analysis, because the generated polyhedron may not have a finite folding mechanism, i.e., cannot be continuously developed to a plane.

A frame model has been developed in Ref. [9] to carry out the procedure of form generation and evaluation of the mechanism of the polyhedron using the same model. The frame model enables us to use the same variables in each process, evaluate the kinematic indeterminacy by SVD in the same manner as the frame model of linkage mechanism [10], and carry out large-deformation analysis using general finite element analysis software. However, in Ref. [9], the type of surface is limited to a rectangular grid, and some optimization results are presented in Ref. [11]. In this study, we extend the results in Ref. [9] and derive the compatibility conditions of the coordinates of nodes of frame model for an arbitrarily triangulated surface. The compatibility conditions in the general form can be used for designing any specific type of polyhedron. In addition, the number of independent variables can be reduced using the compatibility conditions.

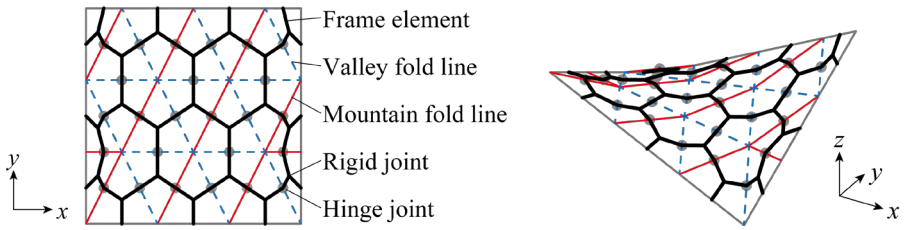


Figure 1: Frame model

2. Frame model

2.1. Models for analysis of rigid origami

Unstable truss model [12] and rotational hinge model [13] are generally used to analyze the kinematics of rigid origami. The former consists of rigid bars pin-jointed at each vertex. The positions of vertices are used as variables. It is convenient to directly use the positions of vertices of polyhedron; however, complicated configuration is often needed to restrain the deformation in out-of-plane direction if one or more polygonal facets such as quadrilateral, pentagon or hexagon are included in the model. The latter consists of rigid panels connected by hinges. The rotational angles of hinges on edges are used as variables. The angles are constrained so that a closed loop around each interior vertex cannot separate. Although folding state is easily demonstrated using the rotational hinge model, conversion of variables

is necessary for dealing with the shape of polyhedron. In addition, it is difficult to construct a finite element model for large-deformation analysis using general finite element analysis software.

In this paper, frame model [9] as shown in Fig. 1 is used for design and analysis of rigid origami. In Fig. 1, black bold lines, red solid lines and blue dotted lines represent frame element of frame model, mountain fold crease lines and valley fold crease lines, respectively. Frame elements are connected by hinges at the nodes on crease lines and rigidly connected at the nodes on facets. In case of a triangle mesh polyhedron, a node on an edge is located at its center point and a node on a facet can be arbitrarily defined, e.g., the centroid of each triangle facet in Fig. 1. If there is any polygonal flat facet, it is assumed as the combination of triangular facets and nodes are also located at the center points of the edges of these triangles. Variables for form generation and analysis of the mechanism are the coordinates of the nodes on edges of triangular facets. They satisfy the compatibility condition such that the end points of the edge shared by adjacent triangular facets meet at the same point.

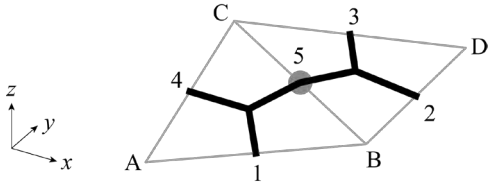


Figure 2: Adjacent triangular facets

2.2. Compatibility conditions of frame model

In this section, we formulate the compatibility conditions of the coordinates of the nodes on edges of frame model when the polyhedron is homeomorphic to a disk. As shown in Fig. 2, let 1-5 denote the indices of the nodes and A-D denote the indices of the vertices on adjacent triangular facets. Since the node on the edge is located at its center point, the position vector $\mathbf{q}_{\mathrm{B}}$ of vertex B is written as

$$\mathbf{q}_{\mathrm{B}} = \mathbf{r}_5 + \mathbf{r}_1 - \mathbf{r}_4 = \mathbf{r}_5 + \mathbf{r}_2 - \mathbf{r}_3 \tag{1}$$

where $\mathbf{r}_i \ (i = 1,2,\ldots,5)$ represents the position vector of node *i*. The position vector of vertex C is also represented by the position vectors of nodes in the same manner. Thus, the relation among the position vectors of nodes is obtained as

$$\mathbf{r}_1 - \mathbf{r}_4 = \mathbf{r}_2 - \mathbf{r}_3 \ \Leftrightarrow \ \mathbf{r}_1 - \mathbf{r}_2 + \mathbf{r}_3 - \mathbf{r}_4 = \mathbf{0}\,. \tag{2}$$

Let x_i^e, y_i^e and z_i^e denote *x*-, *y*- and *z*-coordinates of the node *i* on edge. Eq. (2) can be rewritten in the matrix form as follows:

$$\begin{bmatrix} 1 & -1 & 1 & -1 \end{bmatrix} \begin{pmatrix} x_1^e \\ x_2^e \\ x_3^e \\ x_4^e \end{pmatrix} = 0\,, \ \begin{bmatrix} 1 & -1 & 1 & -1 \end{bmatrix} \begin{pmatrix} y_1^e \\ y_2^e \\ y_3^e \\ y_4^e \end{pmatrix} = 0\,, \ \begin{bmatrix} 1 & -1 & 1 & -1 \end{bmatrix} \begin{pmatrix} z_1^e \\ z_2^e \\ z_3^e \\ z_4^e \end{pmatrix} = 0\,. \tag{3}$$

When the number of interior edges and all edges of the polyhedron are E_{in} and E, respectively, E_{in} equations similar to Eq. (3) can be obtained for all interior edges, and the compatibility conditions of the coordinates of the nodes on edges are written as

$$\mathbf{C}_0\mathbf{x}^e = \mathbf{0}\,, \ \mathbf{C}_0\mathbf{y}^e = \mathbf{0}\,, \ \mathbf{C}_0\mathbf{z}^e = \mathbf{0} \tag{4}$$

where $\mathbf{x}^e$, $\mathbf{y}^e$ and $\mathbf{z}^e$ are the vectors consisting of x_i^e, y_i^e and z_i^e $(i = 1,2,\ldots,E)$, respectively, and $\mathbf{C}_0$ is the $E_{in} \times E$ matrix whose elements are −1, 0 or 1. When the rank of $\mathbf{C}_0$ is *R*, Eq. (4) can be rewritten using the full rank $R \times E$ matrix $\mathbf{C}$ as

$$\mathbf{C}\mathbf{x}^e = \mathbf{0},\ \mathbf{C}\mathbf{y}^e = \mathbf{0},\ \mathbf{C}\mathbf{z}^e = \mathbf{0}. \tag{5}$$

In fact, R is equal to $E-V$, and considering Euler's polyhedron theorem, $E-V=F-1$ is satisfied where V and F represent the number of vertices and facets of the polyhedron. The equation $R=F-1$ is inductively proved when we suppose that a triangular facet is sequentially added to the polyhedron. Therefore, the coordinates of $E-V$ nodes on edges are obtained from those of V independent nodes. In addition, since the coordinates of the nodes on facets can be arbitrarily assigned, they can be represented by the linear combinations of the coordinates of the nodes on edges as

$$\mathbf{x}^f = \mathbf{D}_f\mathbf{x}^e,\ \ \mathbf{y}^f = \mathbf{D}_f\mathbf{y}^e,\ \ \mathbf{z}^f = \mathbf{D}_f\mathbf{z}^e \tag{6}$$

where $\mathbf{x}^f$, $\mathbf{y}^f$ and $\mathbf{z}^f$ are the vectors consisting of x-, y- and z-coordinates of the nodes on facets, and $\mathbf{D}_f$ is the $F\times E$ matrix. On the other hand, the coordinates of the vertices of polyhedron can also be represented by the linear combinations of the coordinates of the nodes on edges in the same way as Eq. (6). Let $\mathbf{p}^x$, $\mathbf{p}^y$ and $\mathbf{p}^z$ denote the vectors of x-, y- and z-coordinates of vertices, which are written as

$$\mathbf{p}^x = \mathbf{D}_p\mathbf{x}^e,\ \ \mathbf{p}^y = \mathbf{D}_p\mathbf{y}^e,\ \ \mathbf{p}^z = \mathbf{D}_p\mathbf{z}^e. \tag{7}$$

Therefore, we can define the polyhedron and its frame model using the coordinates of the V independent nodes on edges.

2.3. Reduction of variables

Let $\bar{\mathbf{x}}^e$ denotes the vector consisting of x-coordinates of the V independent nodes on edges and $\hat{\mathbf{x}}^e$ denotes the vector of x-coordinates of the remaining $E-V$ nodes on edges. According to the first equation in Eq. (5), $\hat{\mathbf{x}}^e$ is written as

$$\begin{bmatrix}\hat{\mathbf{C}} & \bar{\mathbf{C}}\end{bmatrix}\begin{pmatrix}\hat{\mathbf{x}}^e\\ \bar{\mathbf{x}}^e\end{pmatrix} = \hat{\mathbf{C}}\hat{\mathbf{x}}^e + \bar{\mathbf{C}}\bar{\mathbf{x}}^e = \mathbf{0} \Leftrightarrow \hat{\mathbf{x}}^e = -\hat{\mathbf{C}}^{-1}\bar{\mathbf{C}}\bar{\mathbf{x}}^e \tag{8}$$

where $\bar{\mathbf{C}}$ and $\hat{\mathbf{C}}$ are the matrices whose columns are the columns of $\mathbf{C}$ corresponding to $\bar{\mathbf{x}}^e$ and $\hat{\mathbf{x}}^e$, respectively, and $\hat{\mathbf{C}}$ is a $(E-V)\times(E-V)$ regular matrix. Similar equation as Eq. (8) can be formulated for y- and z-coordinates of the nodes on edges. From Eqs. (6), (7) and (8), the coordinates of all the nodes of frame model and the vertices of polyhedron can be obtained from the coordinates of independent nodes on edges as follows:

$$\mathbf{x} = \begin{pmatrix}\bar{\mathbf{x}}^e\\ \hat{\mathbf{x}}^e\\ \mathbf{x}^f\end{pmatrix} = \begin{bmatrix}\mathbf{I}_V\\ -\hat{\mathbf{C}}^{-1}\bar{\mathbf{C}}\\ \mathbf{D}_f\begin{bmatrix}\mathbf{I}_V\\ -\hat{\mathbf{C}}^{-1}\bar{\mathbf{C}}\end{bmatrix}\end{bmatrix}\bar{\mathbf{x}}^e = \mathbf{G}\bar{\mathbf{x}}^e,\ \ \mathbf{y} = \begin{pmatrix}\bar{\mathbf{y}}^e\\ \hat{\mathbf{y}}^e\\ \mathbf{y}^f\end{pmatrix} = \mathbf{G}\bar{\mathbf{y}}^e,\ \ \mathbf{z} = \begin{pmatrix}\bar{\mathbf{z}}^e\\ \hat{\mathbf{z}}^e\\ \mathbf{z}^f\end{pmatrix} = \mathbf{G}\bar{\mathbf{z}}^e \tag{9}$$

$$\mathbf{p}^x = \bar{\mathbf{D}}_p\bar{\mathbf{x}}^e,\ \ \mathbf{p}^y = \bar{\mathbf{D}}_p\bar{\mathbf{y}}^e,\ \ \mathbf{p}^z = \bar{\mathbf{D}}_p\bar{\mathbf{z}}^e \tag{10}$$

where $\bar{\mathbf{D}}_p$ is the matrix whose columns are the columns of $\mathbf{D}_p$ corresponding to the independent components of the coordinates. Therefore, we can reduce the number of variables using Eqs. (9) and (10).

$\bar{\mathbf{C}}$ and $\hat{\mathbf{C}}$ can be obtained from $\mathbf{C}_0$ by using the algorithm presented by Zhang *et al.* [14]. The reduced row-echelon form (RREF) [15] is used to effectively specify the independent set of nodes. The RREF of any finite matrix can be defined by the sequence of elementary row operations, and it has the following properties:

(a) The first nonzero element in any nonzero row is 1.

(b) In any column which contains the leading 1 of each nonzero row, 1 appears only once and all the other elements are 0.

(c) Because of (a) and (b), the columns which contains such leading 1 are independent of each other.

(d) The RREF saves the rank of any matrix. It is equal to the number of columns which contains such leading 1.

Thus, the RREF of $\mathbf{C}_0$ contains $E-V$ independent columns which has the leading 1 of the nonzero rows. These columns correspond to $\widehat{\mathbf{C}}$ and the remaining columns correspond to $\overline{\mathbf{C}}$.

3. Form generation

The procedure of form generation of a developable and rigid-foldable polyhedron is shown in Fig. 3. The target surface is defined using a Bézier surface. Some polyhedra which have different DOFs can be generated by optimization, and we choose the best solution considering the result of the analysis of the finite mechanism. If there is no suitable solution, a different pattern of triangulation is tried [9].

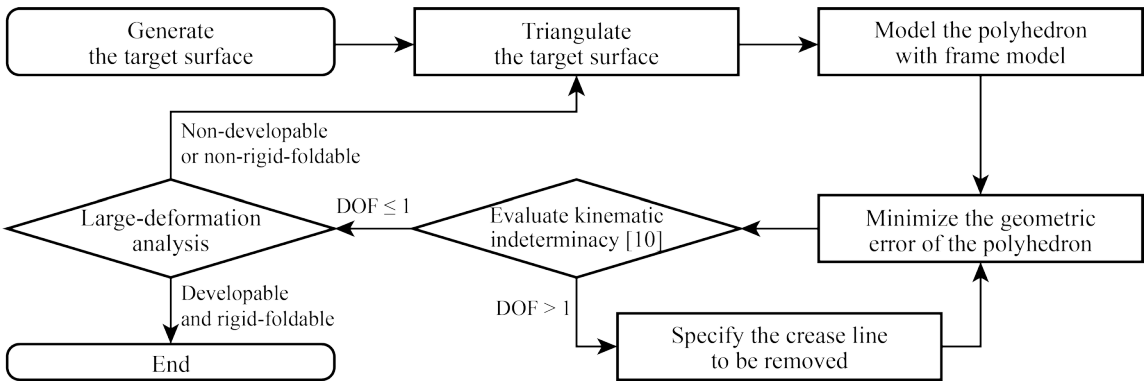


Figure 3: Flowchart for generating a rigid-foldable polyhedron [9]

Let $\mathbf{X}=\left(\overline{\mathbf{x}}^{e\mathsf{T}},\overline{\mathbf{y}}^{e\mathsf{T}},\overline{\mathbf{z}}^{e\mathsf{T}}\right)^{\mathsf{T}}$ denote the vector of the coordinates of independent nodes on edges, which are the design variables of the optimization problem. The condition for developability of the polyhedron with set of interior vertices V_{in} is written as

$$F_1(\mathbf{X})=\sum_{v\in V_{in}}\left(\sum_{k=1}^{f_v}\theta_{v,k}(\mathbf{X})-2\pi\right)^2=0 \tag{11}$$

where $\theta_{v,k}(\mathbf{X})$ is the kth angle between crease lines around the vth interior vertex and f_v is the number of crease lines connected to the vth interior vertex. To reduce the DOF, a polyhedron with polygonal flat facets is generated by assigning a condition to make specified pairs of normal vectors of adjacent triangle facets to be parallel, and by removing the crease lines between them. Let E_D represent a set of crease lines to be removed. The condition for removing crease lines is written as

$$F_2(\mathbf{X})=\sum_{e\in E_D}\left\|\mathbf{n}_{e,1}(\mathbf{X})\times\mathbf{n}_{e,2}(\mathbf{X})\right\|^2=0 \tag{12}$$

where $\mathbf{n}_{e,k}$ $(k=1,2)$ are unit normal vectors of facets connected to the eth crease line. Since $F_1\geq 0$ and $F_2\geq 0$ are satisfied for any $\mathbf{X}$, we minimize the sum of them; $F(\mathbf{X})=F_1(\mathbf{X})+F_2(\mathbf{X})$ and when it converges to approximately zero, optimization is regarded as successful.

The difference between $z_i^e(\mathbf{X})$ and the z-coordinate of the projected point of node i onto the target surface along with z-axis is denoted by $\Delta z_i^e(\mathbf{X})$. The upper bound of the absolute value of $\Delta z_i^e(\mathbf{X})$ is represented by $\Delta \bar{z}_i^e$. Throughout the process of optimization, the outline of the polyhedron projected to xy-plane is constrained not to deform and the vertices at the corners of the polyhedron are constrained not to move. Therefore, the x-coordinates $p_v^x(\mathbf{X})$ of vertices v $(v \in V_y)$ on the y-directional boundary of the polyhedron, the y-coordinates $p_v^y(\mathbf{X})$ of vertices v $(v \in V_x)$ on the x-directional boundary of the polyhedron and the z-coordinates $p_v^z(\mathbf{X})$ $(v \in V_c)$ of the vertices at the corners of the polyhedron are constrained to the specified values $\bar{p}^x$, $\bar{p}^y$ and $\bar{p}^z$ respectively, where V_y, V_x and V_c are the sets of vertices on the y-directional boundaries, the x-directional boundaries and at the corners of the polyhedron, respectively. The upper bounds and lower bounds of $\theta_{v,k}(\mathbf{X})$ are denoted by $\theta_{\max}$ and $\theta_{\min}$. The optimization problem is written as a nonlinear programming (NLP) problem as follows:

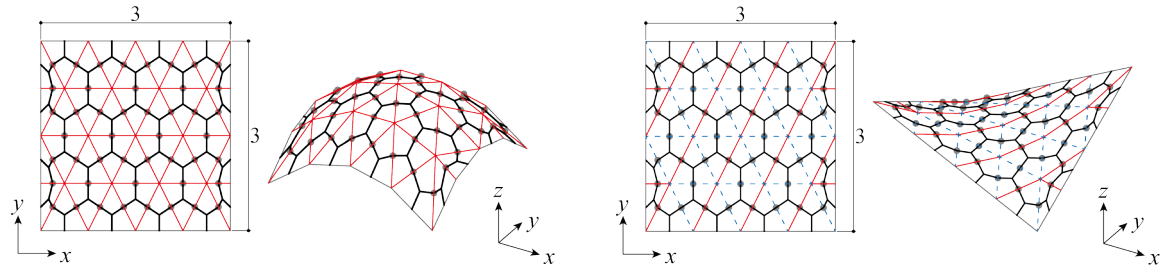
$$
\begin{aligned}
\text{Minimize:} \quad & F(\mathbf{X}) = F_1(\mathbf{X}) + F_2(\mathbf{X}) \\
\text{subject to:} \quad & \theta_{\min} \le \theta_{v,k}(\mathbf{X}) \le \theta_{\max} && (v \in V_{in};\ k = 1,2,\ldots f_v) \\
& -\Delta \bar{z}_i^e \le z_i^e(\mathbf{X}) \le \Delta \bar{z}_i^e && (i = 1,2,\ldots,E) \\
& p_v^x(\mathbf{X}) = \bar{p}_v^x && (v \in V_y) \\
& p_v^y(\mathbf{X}) = \bar{p}_v^y && (v \in V_x) \\
& p_v^z(\mathbf{X}) = \bar{p}_v^z && (v \in V_c)
\end{aligned}
\tag{13}
$$

In the same manner as in Ref. [9], the crease lines to be removed are sequentially chosen. First, the optimization problem is solved with E_D empty. Let γ_e denote the dihedral angle between the adjacent facets sharing eth edge representing the crease line. The edge corresponding to the smallest difference of γ_e to π is added to E_D. Then, we solve the optimization problem (13) again.

4. Examples

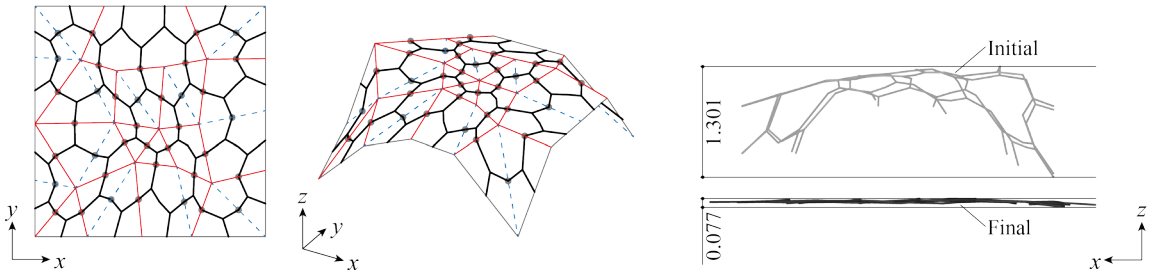
Optimization problem (13) is solved using SLSQP (Sequential Least SQuares Programming) for NLP available in the Python library SciPy. Kinematic indeterminacy is calculated using SVD in NumPy of a Python program, and large-deformation analysis is carried out using Abaqus 2016.

Two examples are shown in Fig. 5 (Model 1) and Fig. 6 (Model 2). The initial shapes of them are shown in Fig. 4. The parameters for optimization are set as $\theta_{\max} = 2\pi/3$, $\theta_{\min} = \pi/6$ and $\Delta \bar{z}_i^e = 0.25$. The number of independent nodes of frame model is 27, which is equal to the number of vertices of the polyhedron. The results of optimization as well as the kinematic indeterminacy (DOF) and the error in large-deformation analysis are summarized in Table 1. The generated polyhedra can be regarded to satisfy the conditions of developability and existence of polygonal facets with good accuracy. It has been confirmed by the large-deformation analysis that both examples can be continuously developed to a plane without deformation of their facets, i.e. they are rigid-foldable.



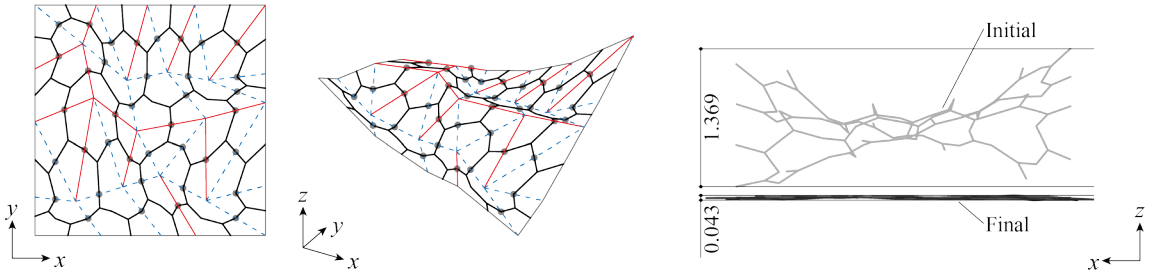
(a) Model 1 (b) Model 2

Figure 4: Initial shapes



(a) Optimal shape (b) Large-deformation analysis

Figure 5: Model 1



(a) Optimal shape (b) Large-deformation analysis

Figure 6: Model 2

Table 1: Result of optimization, evaluation of DOF and large-deformation analysis

	Model 1	Model 2
$F(\mathbf{X})$	1.918×10^{-11}	1.858×10^{-11}
Max. error of $\sum\theta_{v,k}$ from 360 (deg.)	1.319×10^{-4}	1.307×10^{-4}
Max. error of γ_e $(e\in E_D)$ from 180 (deg.)	1.251×10^{-4}	9.573×10^{-5}
Max. $\lvert\bar{z}_i^e\rvert$	0.250	0.250
DOF	5	5
Max. absolute value of strain throughout the large-deformation analysis	1.875×10^{-5}	3.509×10^{-5}

5. Conclusion

The conclusion of this paper is summarized as follows:

a) The compatibility condition of the coordinates of the nodes of frame model has been formulated so that the end points of the polyhedron's edge shared by adjacent triangular facets meet at the same point. The formulation is independent of the type and method of triangulation, and can be systematically incorporated as the constraints of optimization problem for form generation of rigid-foldable origami surface.

b) The number of variables can be reduced using the compatibility condition of frame model. The independent set of nodes is effectively specified using RREF of the compatibility matrix. It has been shown that the number of independent nodes is equal to the number of vertices of the polyhedron.

c) It has been confirmed by the numerical examples that the matrix $\overline{\mathbf{C}}$ and $\hat{\mathbf{C}}$ can be obtained effectively using the method proposed by Zhang *et al.* [14] and the number of independent nodes of frame model is as same as the polyhedron's vertices. We carried out optimization successively to reduce the DOF of the mechanism, generated a polyhedral surface with a heptagonal facet.

References

[1] P. M. Reis, F. L. Jimenez and J. Marthelot, "Transforming architectures inspired by origami," *Proceedings of the National Academy of Sciences of the United States of America*, vol. 112 (40), pp. 12234-12235, Oct. 2015.

[2] K. Miura, "Method of packaging and deployment of large membranes in space," *The Institute of Space and Astronautical Science report*, Report No. 618, pp. 1-9, Dec. 1985.

[3] R. D. Resch, "Self-supporting structural unit having a series of repetitious geometrical modules," United States Patent No. 3,407,558, 1968.

[4] T. Tachi, "Generalization of rigid foldable quadrilateral mesh origami," *Journal of the International Association for Shell and Spatial Structures*, vol. 50, pp. 173-179, Dec. 2009.

[5] T. Tachi, "Geometric considerations for the design of rigid origami structures," in *Spatial Structures-Permanent and Temporary: Proceedings of the IASS Annual Symposium 2010, Shanghai, China, November 8-12, 2010*, 2010. pp. 458-460.

[6] W. K. Schief, A. I. Bobenko and T. Hoffmann, "On the integrability of infinitesimal and finite deformations of polyhedral surfaces," in *Discrete Differential Geometry (Oberwolfach Proceedings)*, 2007, pp. 67-93.

[7] L. Dudte, E. Vouga, T. Tachi and L. Mahadevan, "Programming curvature using origami tessellations," *Nature Materials*, vol. 15 pp. 583-588, Jan. 2016.

[8] Y. Zhao, Y. Endo, Y. Kanamori and J. Mitani, "Approximating 3D surfaces using generalized waterbomb tessellations," *Journal of Computational Design and Engineering*, vol. 5, pp. 442-448, Oct. 2018.

[9] K. Hayakawa and M. Ohsaki, "Form Generation of rigid-foldable origami structure using frame model," *Journal of Environmental Engineering (Transactions of AIJ)*, vol. 84 (760) pp. 597-605, Jun. 2019. (in press)

[10] M. Ohsaki, S. Tsuda and Y. Miyazu, "Design of linkage mechanisms of partially rigid frames using limit analysis with quadratic yield functions," *International Journal of Solids and Structures*, vol. 88-89, pp. 68-78, Jun. 2016.

[11] K. Hayakawa and M. Ohsaki, "Optimization approach to form generation of rigid-foldable origami for deployable roof structure", Proc. in *Proceedings of The World Congress of Structural and Multidisciplinary Optimization* (*WCSMO 13)*, *Beijing*, *China*, *May 20-24, 2019,* 2019, Paper No. A050457.

[12] M. Shenk and S. D. Guest, "Origami folding: A structural engineering approach," in *Proceedings of Fifth International Meeting of Origami Science, Mathematics and Education (Origami5)*, P. Wang-Iverson, R. Lang and M. Yim Ed., CRC Press, 2011, pp. 291-303.

[13] T. Tachi, "Simulation of rigid origami." in *Proceedings of Forth International Meeting of Origami Science, Mathematics and Education (Origami4)*, R. Lang Ed., AK Peters, 2009, pp. 175-187.

[14] J. Y. Zhang, M. Ohsaki and Y. Kanno, "A direct approach to design of geometry and forces of tensegrity systems," *International Journal of Solids and Structures*, vol. 43, pp. 2260-2278, Apr. 2006.

[15] G. J. Borse, *Numerical Methods with MATLAB: A Resource for Scientists and Engineers*. International Thomson Publishing Inc., 1997.

Proceedings of the IASS Annual Symposium 2019 – Structural Membranes 2019
Form and Force
7 – 10 October 2019, Barcelona, Spain
C. Lázaro, K.-U. Bletzinger, E. Oñate (eds.)

Fabrication of three-dimensional curved surface using ETFE film by stretching drape strips considering friction contact conditions

Quang Hieu BUI*, Masaya KAWABATA[a]

*Doctoral Student, Graduate School of Urban Innovation, Yokohama National University, Japan
Yokohama National University, N5-3 Building of Architecture, Room 603, Yokohama 240-8501, Japan
quanghieu022000@gmail.com

[a] Associate Professor, Graduate School of Urban Innovation, Yokohama National University, Japan
kawabata-masaya-gx@ynu.jp

Abstract

In the manufacture field of plastics, high strengthening by drawing of films is general. It is easy to draw uniaxial direction, however, there have been few cases that performed biaxial elongation, especially in three-dimensional (3D) shape. This paper presents the experiments of fabrication of 3D curved surface of ETFE tensile membrane structures by drawing the drape strips considering the friction contact conditions. In addition, the analytical method which can solve the geometrical nonlinearity, the material nonlinearity and the nonlinearity of friction contact conditions is proposed too. The results of the experiments showed that the 3D smooth curved surfaces could be established with the sufficiency of prestress of around the first yield point of ETFE film. The observed slides between ETFE and supporting galvanized steel arches and the measured prestress during the experiments confirmed the validity of the proposed analytical method for the 0.3 of static friction coefficient between ETFE film and galvanized steel arches. Moreover, the reduction of rigidity of the structures was seen at the pressure of around 1.3kPa in the pressurization tests.

Keywords: ETFE film, friction contact, tensile membrane structures, three-dimensional smooth curved surfaces, fabrication technique.

1. Introduction

In the manufacture field of plastics, high strengthening by drawing of films is general. It is easy to draw uniaxial direction, however, there have been few cases that performed biaxial elongation, especially in three-dimensional (3D) shape [1]. This paper presents the experiments of fabrication 3D curved surface of ETFE tensile membrane structures by drawing the drape strips considering the friction contact conditions.

The saddle type of tensile membrane structure is investigated in this paper. This structure comprises the rectangular outside frame, two supporting galvanized steel arches and ETFE film. The part of the film between two arches is called by the middle part, while the parts between arches and outside frame are called by the corner parts. The dimension of this structure is two by four meters. The *15%* of rise ratio, which is the ratio between the height of arch and the short span of structure, is investigated in this paper. The long direction indicates the machine direction of the film (*MD* direction), while the short direction shows the transverse direction (*TD* direction).

First, the form finding analysis is carried out with several prescribed prestress ratios between *MD* and *TD* directions for both middle and corner parts. Second, the cutting pattern analysis based on the mathematical approach [2] produces the drape strips which correspond to the shapes obtained from the form finding. Third, these drape strips are connected by heat seal lines into the specimens, and the

Copyright © 2019 by Quang Hieu BUI, Masaya KAWABATA
Published by the International Association for Shell and Spatial Structures (IASS) with permission.

boundary of these specimens is drawn to introduce the prestress of tension. The values of drawing boundary are determined to guarantee the sufficiency of prestress and the absence of wrinkling. Finally, the pressurization test is carried out to confirm the strength of the structure after above construction stage.

In addition, the analytical method which can solve the geometrical nonlinearity, the material nonlinearity and the nonlinearity of friction contact conditions is proposed in this paper. In the proposed analytical method, the total Lagrangian formulations are established for both the triangular membrane element and the node-to-node contact element, and the analytical procedure is also suggested.

The results of the experiments showed that the 3D smooth curved surfaces could be established with the enough prestress of around the first yield point of ETFE film. The observed slides between the ETFE and supporting arches and the measured prestress during the experiments confirmed the validity of the proposed analytical method for the *0.3* of static friction coefficient between ETFE film and galvanized steel arches. In addition, the reduction of rigidity of the structures was seen at the pressure of around *1.3kPa* in the pressurization tests.

2. Experiments

2.1. Process of experiments

The experiments were carried out in three phases as shown in Figure 1.

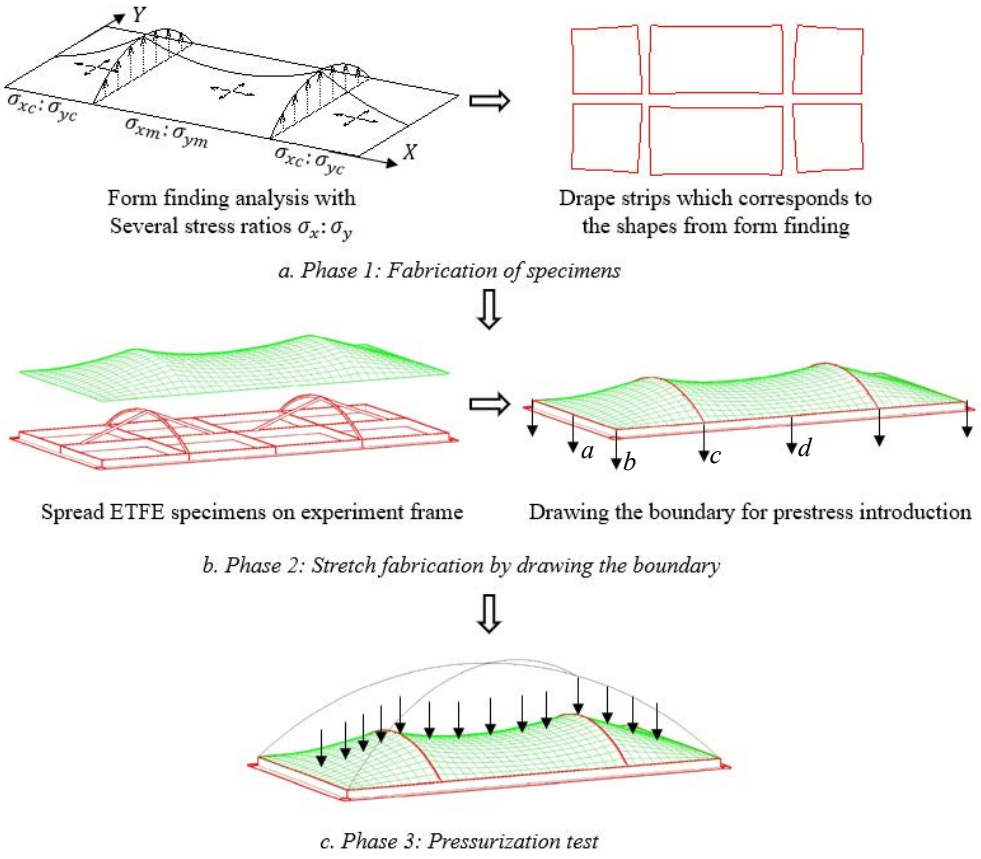


Figure 1: The process of experiments

The dimensions of the frame of experiments are shown in Figure 2. It should be noted that all dimensions are in millimeter unit.

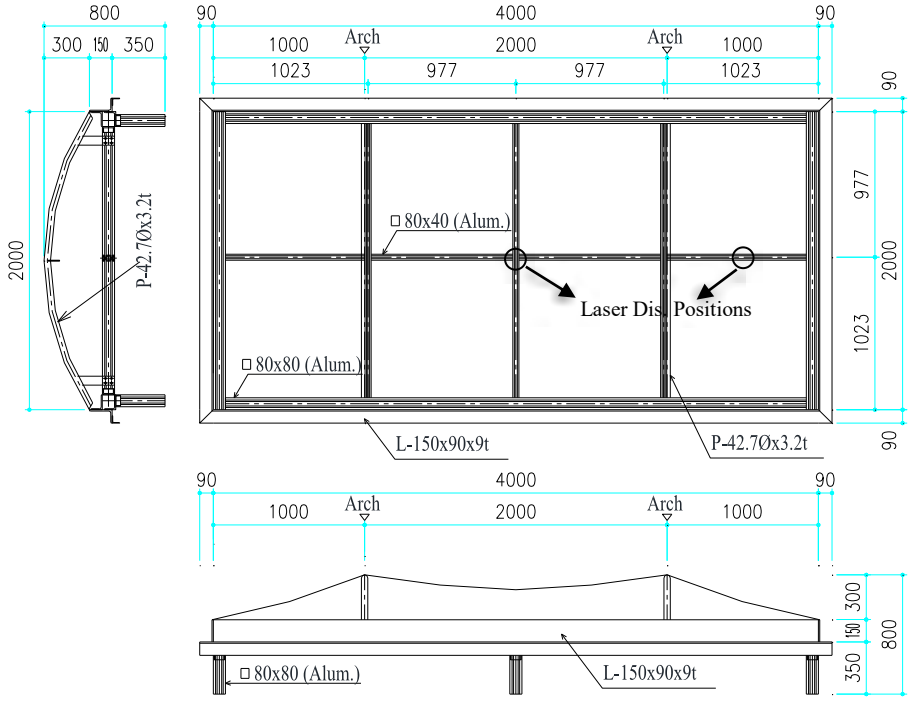


Figure 2: The process of experiments

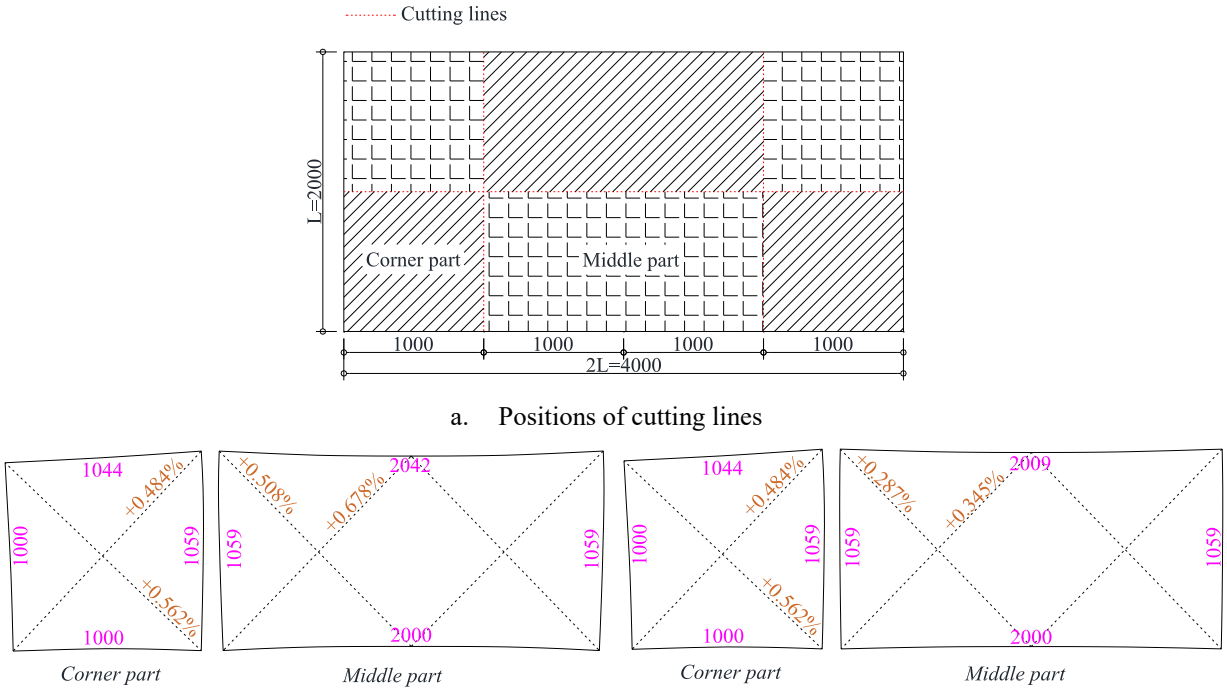
2.2. Specimens

The MD direction is named by *X* direction and the TD direction is named by *Y* direction in this paper. The isotropic stress surface method [3] was used for form finding. It is assumed that the membrane has a very small Young's modulus and the initial stress ratios between MD and TD directions (σ_x: σ_y) are shown in Table 1. It should be noted that (σ_{xc}: σ_{yc}) and (σ_{xm}: σ_{ym}) are prescribed stress ratios for the corner part and the middle part, respectively.

Table 1: Prescribed stress ratios between MD and TD directions in form finding analysis

Specimens	Stress ratio	
	σ_{xc}: σ_{yc}	σ_{xm}: σ_{ym}
DD1511	3:1	1:1
DD1531	3:1	3:1

The least-squares minimizations flattening approach [2] was used in this paper for cutting pattern analysis. The cutting lines and the results of drape strips for specimens DD1511 and DD1531 are shown in Figure 3. The numbers show the lengths of cutting lines, while the percentages indicate the expansions of the lengths of drape strips and the corresponding lengths of the form finding shapes in Figure 3b and Figure 3c. In this experiment, each type of cutting pattern shapes had two specimens named as DD1511*a/b* and DD1531*a/b* in the following parts. It should be noted that the thickness of ETFE film was 250μm, and the dot printed type of this film was used.



a. Positions of cutting lines

b. DD1511

c. DD1531

Figure 3: The position of cutting lines and shapes of drape strip

2.3. Values of boundary drawing

The values of drawing at four special boundary positions are shown in Figure 1b, while those values at other positions are interpolated linearly. The values of *a*, *b*, *c* and *d* are input step by step to introduce the prestress on the film during the experiments. The target prestress is around the first yield point of ETFE film, so the values of *a*, *b*, *c* and *d* are determined to guarantee the sufficiency of prestress. In addition, the limited values of *a*, *b*, *c* and *d* are 80*mm* due to the setup of experiments, and the relations between *a*, *b*, *c* and *d* are controlled by the absence of wrinkling. The experiments were carried out in five steps as shown in Table 2.

Table 2: Values of boundary drawing

	a (mm)	b (mm)	c (mm)	d (mm)
Step 1	0	0	0	0
Step 2	10	10	10	10
Step 3	20	15	20	20/25*
Step 4	30	20	30	30/40*
Step 5	40	30	40	40/50*

* The first value was used for DD1511*a/b*, while the second value was used for DD1531*a/b*

2.4. Pressurization tests

The pressurization tests were carried out after around ten hours of stretch fabrication phase. The internal pressure was input by the compressor. The process of pressure is described as follow: *0kPa* → *0.5kPa* → *0kPa* → *1kPa* → *0kPa* → *1.5kPa* → *0kPa* → *2kPa* → *0kPa.*

3. Analytical method

In the static analysis of geometrical nonlinearity of tensile membrane structures, it is preferable to use a dense mesh of primitive elements rather than a coarse mesh made up higher order elements [3]. Therefore, the work in this paper focuses on triangular membrane elements with three nodes and nine degrees of freedom per element. In addition, the dimensions of supporting frames are usually much smaller than that of membrane. As a result, the node-to-node contact elements are used to model the contact between the membrane and supporting galvanized arches approximately. The total Lagrangian formulations for both triangular membrane and node-to-node contact elements could be referred in the works of the authors of this paper [4]. The analytical procedure is suggested in this study.

3.1. Suggested analytical procedure

The stick-slip phenomenon could be occurred frequently within the assumptions of this study. When the slide condition is adapted, the slide direction is updated by the friction contact forces of node-to-node element in previous stick condition. On the other words, the stiffness and slide direction of node-to-node contact element were independent with the incremental nodal displacements from the discrete time t to the discrete time $t + \Delta t$. This work improved the convergence criteria during the static loading process.

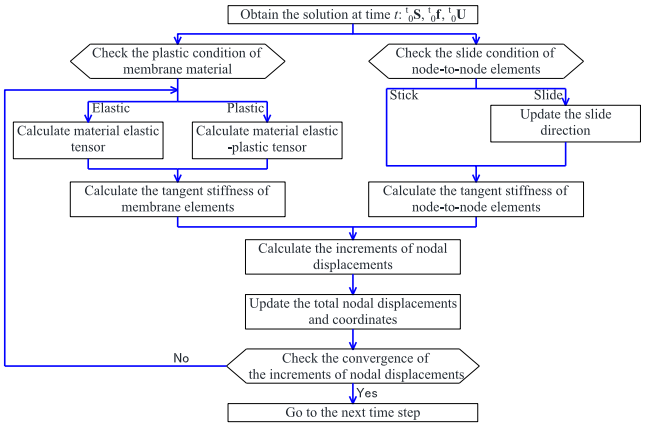
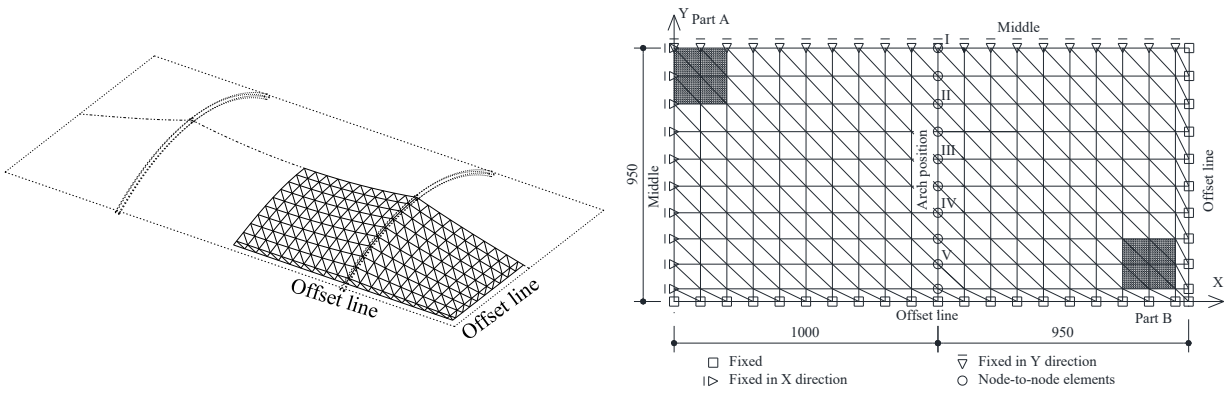


Figure 4: The suggested analytical procedure



a. Model of a quarter of specimens b. Boundary conditions

Figure 5: Analytical model of stretch fabrication phase

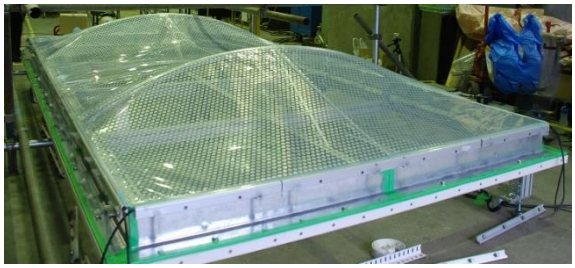
3.2. Analytical modeling of stretch fabrication phase

Figure 5 shows the assumptions for analytical models of stretch fabrication tests. The models of a quarter of specimens, which have 400 triangle membrane elements and 10 node-to-node contact elements, are used to predict the behavior of ETFE film and friction contact between the film and supporting galvanized steel arches. The initial shapes of those models are adapted from the results of form finding analysis. The offset points are assumed in fixed conditions, and the motions of these points, which were observed in the experiments, are used as the input forced displacements conditions. The material properties for ETFE film are determined based on the uniaxial tension test [4], [5]. The static friction coefficient between ETFE film and galvanized steel arch can be utilized by 0.3 [6].

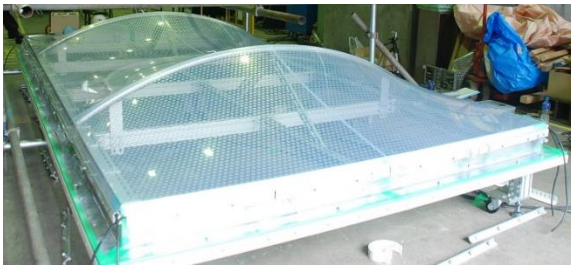
4. Results of experiments and analyses

4.1. Three-dimensional smooth curved surfaces

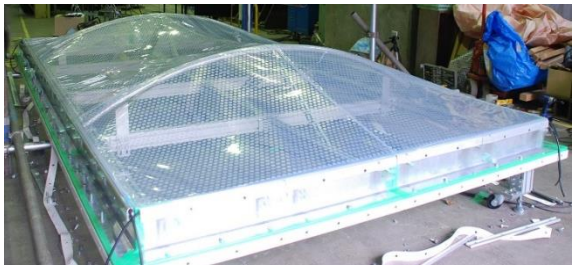
The 3D curved surfaces without wrinkling could be established by the suggested boundary drawing values as shown in Table 2. Figure 6 represents the initial and final shapes of specimens DD1511*a* and DD1531*a*.



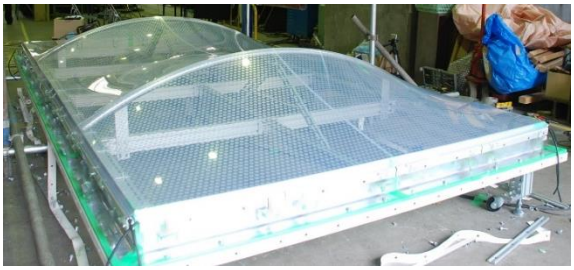
a1. DD1511*a*, Initial shape



a2. DD1511*a*, Final shape (step 5)



c1. DD1531*a*, Initial shape



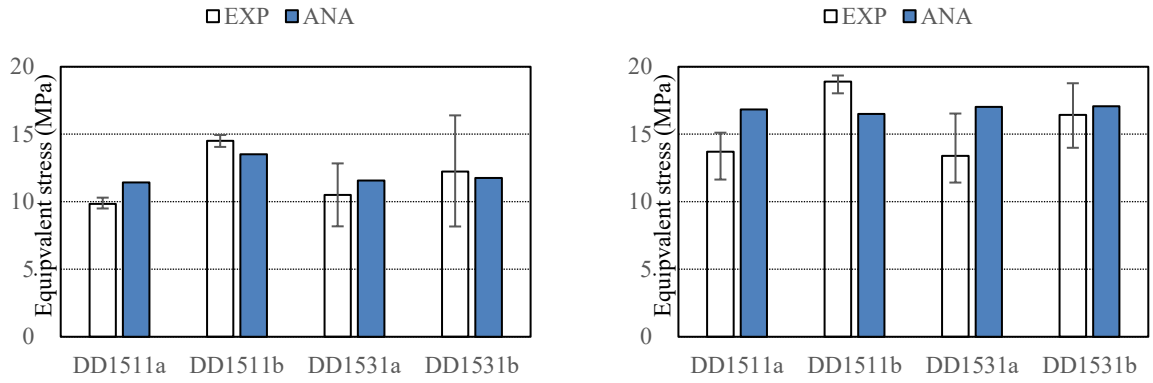
c2. DD1531*a*, Final shape (step 5)

Figure 6: Three-dimensional smooth curved surface

4.2. Equivalent stress

The lengths of four edges and two diagonals of part A and part B, which were shown in Figure 5b, were measured by the paper tapes and caliper during the experiments. These measured values are used to calculate the pre-tensile strains on ETFE film, and the equivalent stress can be obtained by these strains.

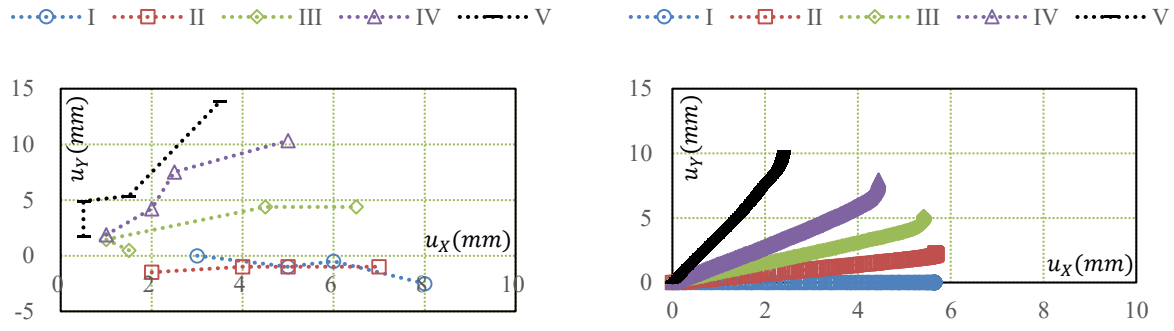
Figure 7 represents the equivalent stress of part A and part B in both experiments and analyses. The experiment results are shown in bar and error bar type, while the results of analyses are presented by solid bar. The high agreement between the two results are seen.



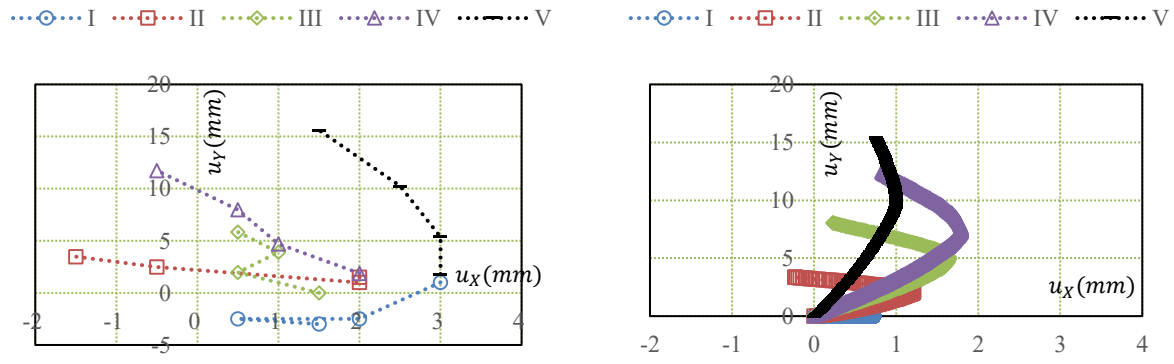
a. Part A b. Part B

Figure 7: Equivalent stress of part A and part B

4.3. Observed sliding values



a1. DD1511*a*, Experiment a2. DD1511*a*, Analysis



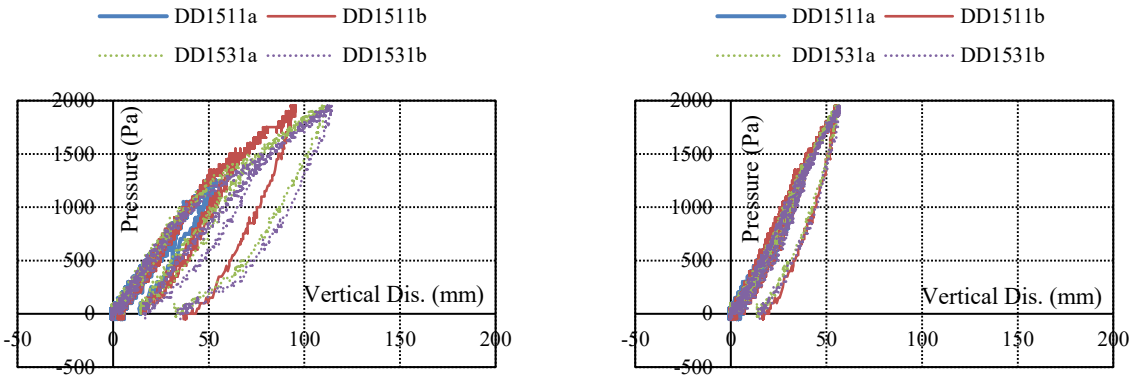
b1. DD1531*a*, Experiment b2. DD1531*a*, Analysis

Figure 8: Observed slides in both experiments and analyses

Figure 8 represents the observed slides between ETFE film and galvanized steel arch at five points (Figure 5b) in both experiments and analyses. The good agreement was seen, and the validity of analytical procedure was confirmed. It should be noted that 200 equal load steps were used in the analyses.

4.4. Results of pressurization tests

The vertical displacements of ETFE film were measured by the laser displacement meters during the pressurization test. The positions of laser displacement meters are shown in Figure 2. Figure 9 shows the results of pressurization tests. The reduction of rigidity of the structures was seen at the pressure of around 1.3kPa in these tests.



a. Middle part b. Corner part

Figure 9: Results of pressurization tests

5. Conclusion

This paper showed the experiments on the fabrication of ETFE tensile membrane structures considering friction contact conditions. The possibility of fabrication of the high-rise smooth curved surface by stretching drape strips of several prescribed stress ratios was confirmed. In addition, the results of suggested analytical method are in high agreement with the results of experiments for the 0.3 of static friction coefficient between ETFE film and galvanized steel arch.

Acknowledgements

The support for experiments from Taiyo Kogyo Cooperation and all members of Space Structure Laboratory of Yokohama National University is gratefully acknowledged.

References

[1] M. Kawabata, E. Jeong, and K. Nishikawa, *Curved surface fabrication and strengthening of film structures by stretching plane film*, Proceeding of IASS 2008 Symposium, Acapulco Mexico, 2008.

[2] B. Tabarrok, Z. Qin, *Form finding and cutting pattern generation for fabric tension structures,* Microcomputers in Civil Engineering, Vol.8, pp. 337-384, 1993.

[3] B. Tabarrok, Z. Qin, *Nonlinear analysis of tension structures*, Computers & Structures Vol. 45, No. 5/6, pp. 973-984, 1992

[4] Q. H. Bui, M. Kawabata, *Total Lagrangian formulation for ETFE membrane structure considering friction contact*, Journal of Structural Engineering, Architecture Institute of Japan, Vol. 65B, pp. 465-475, 2019

[5] T. Yoshino, S. Segawa, K. Oda, *Material characteristics of ETFE film under the bi-axial tension and stress-displacement analysis considering the elasto-plastic characteristics*, Research Report on Membrane Structure, The Membrane Structures Association of Japan, 2004

[6] Technical report, The Chemours Company, 2017

Proceedings of the IASS Annual Symposium 2019 – Structural Membranes 2019
Form and Force
7 – 10 October 2019, Barcelona, Spain
C. Lázaro, K.-U. Bletzinger, E. Oñate (eds.)

Application of parametric design tools for the roof of the C³ technology demonstration house – CUBE

Iurii VAKALIUK*, Michael FRENZEL, Manfred CURBACH

* TU Dresden, Institute of Concrete Structures
01062 Dresden, Germany
iurii.vakaliuk@tu-dresden.de

Abstract

The C³ project (Carbon Concrete Composite) is currently one of the largest research projects in the German construction industry. A significant number of results of this project are brought together in the C³ technology demonstration house "CUBE" which is assumed to be constructed of steel and both glass and carbon reinforced concrete members. This paper introduces the design and development of the house's roof shell. For that, the software solutions Rhinoceros 3D + Grasshopper 3D were used as the main algorithmic environment. Methods and specially developed tools that were used to model and compare multiple structural solutions of the load-bearing shell as the main part of the roof are presented. The paper additionally describes an overview of the important aspects that are of particular interest within the CUBE project which are part of the key works, such as the design workflows and manufacturing strategies of the appropriate shape of the formwork, as well as of the insulation and biaxially oriented carbon reinforcing grids.

Keywords: carbon reinforced concrete (CRC), textile reinforced concrete (TRC), shell, Rhinoceros, Grasshopper, parametric design, building, 3D model

1. Introduction

In 2012, the German Federal Ministry of Education and Research (BMBF) announced the funding program "Twenty20 – Partnership for Innovation" (German: Zwanzig20 – Partnerschaft für Innovation) [1] with about 500 million euros at its disposal which were to be invested into solutions for economic and socially important challenges. Ten projects were funded – one of them is the project "Carbon Concrete Composite – C³" (in short: C³ project) [2]. Currently, it is one of the largest research projects in the German construction industry, and it is funded from 2014 until 2021. More than 160 partners are involved in the development of the building material carbon reinforced concrete (CRC) from design to calculation to construction within more than 50 subprojects [3], [4], [5]. The common goal is to bring CRC onto the German market by 2025 with a reliable value-added chain. The BMBF and the involved companies have been funding the C³ project with 45 and 20 million euros respectively.

One of the C³ subprojects is the project C3-V3.1 "C³ technology demonstration house – CUBE" [6] which started in 2017 and will run until 2021. With a total budget of about 5 million euros, it is a significant project. The main goal of the project and of the erection of a demonstration house is to show that the C³ construction method has progressed so far that the building's entire process chain can be completed, including a sophisticated architecture, design, planning, structural calculation, approval and tendering procedures, precast and in-situ construction and operation. Additionally, the aim is to demonstrate that non-metallic reinforcement, in the broadest sense - and carbon reinforcement in particular - in combination with concrete results in a high-performance composite material that is very durable, very resistant to compression and tension and allows aesthetically demanding and diverse constructions. The visualisation of the front view of the CUBE building is shown in Figure 1.

Copyright © 2019 by Iurii Vakaliuk, Michael Frenzel and Manfred Curbach
Published by the International Association for Shell and Spatial Structures (IASS) with permission.



Figure 1: Front view of the CUBE building, visualisation: Iurii Vakaliuk

2. The C³ technology demonstration house – CUBE

In autumn of 2017, students of civil engineering and architecture from the HTWK Leipzig, FH Aachen, (both in Germany) and the Università di Camerino in Ascoli (Italy) developed and manufactured different basic concepts for the C³ tech demo house [7] in the frame of a workshop. The elaborated concepts served as inspiration for the architects of the office HENN, Berlin, which was contracted to prepare the preliminary design. In February 2018 out of four design concepts, the "TWIST" concept (Figures 1 and 2) was chosen because it fulfilled best the defined requirements of an aesthetically demanding architecture with landmark effect which can be realised with carbon reinforced concrete considering the local urban planning situation and environment of the TU Dresden campus where the house will be erected.

The building consists of two identically twisted roof shells, a two-storey unit ("Box"), two wings and a steel-glass façade. While the Box is to be made of prefabricated carbon reinforced concrete members (beams, walls, columns and slabs), the roof shells and the continuing wings are to be manufactured with carbon reinforced shotcrete. The twisted roof shells are supported linearly by steel beams and steel columns. Both shells are connected in the ridge area either directly or via a roof light stripe/top window band which allows the light to enter into the building. The building has a length of about 24.1 m without and 40 m with the wings and a width of 7.2 m. Thus, the house has a ground and gross floor area of approximately 24.1 m × 7.2 m (174 m²) and of 220 m², respectively. It accommodates a presentation room (97 m²), a domestic technology room (38 m²), three laboratory/measuring rooms (33 m²) and restrooms.

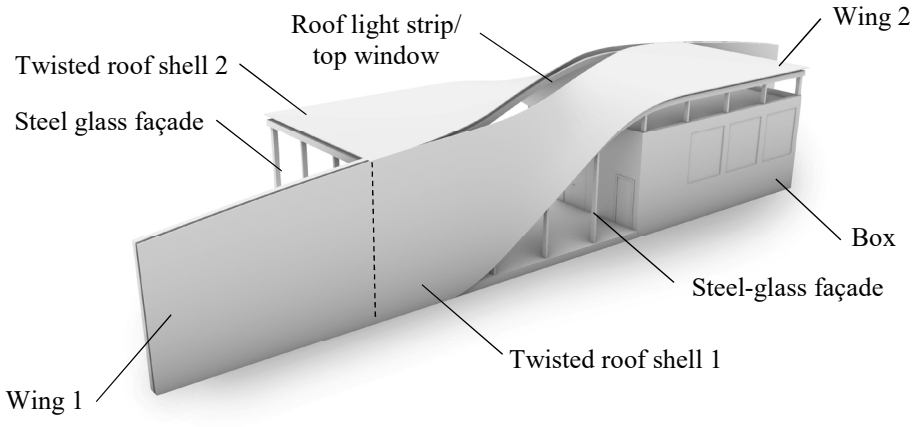


Figure 2: Components of the C³ tech demo house CUBE

In order to develop the shape of the twisted roof shells and have full possible flexibility in the parametrical adjustment of the shell geometry, it was decided to model the shell by developing appropriate algorithms within the Rhinoceros 3D + Grasshopper 3D software environment [8], [9]. For the structural analysis, the Dlubal RFEM software tool [10] was used. One of the most important challenges of the project was to establish a reliable and efficient workflow between multiple software packages as well as between partners of the project in fields of architectural planning, structural design and construction.

3. Structural analysis

After the first stage of the preliminary design, the next step was the implementation of a whole set of design procedures. Such procedures form an iterative process of the structural component's optimisation and update. As a result, a set of possible solutions was developed. Figure 3 shows the most different structural solutions that were discussed during the design and structural analysis in a particular stage of the project development. Figure 3 (a) shows the very first discussed solution with a smooth surface of the twisted roof shell, but it is partially improved with ribs in both directions to reduce deflections in the horizontal area. Next, Figure 3 (b) represents an approach in which the whole shell is solved completely as a "waved" structure. The waves, in turn, are oriented transversally, along with the generators presented in chapter 4, to form beams similar to those shown in the previous solution. The solution represented in Figure 3 (c) can be considered as an extension of the very first solution. Thus, the beams come from one side to the opposite side of the twisted roof shell. As it is known from structural theory, a ribbed solution helps to reduce the self-weight, but it keeps the bending stiffness at the appropriate level.

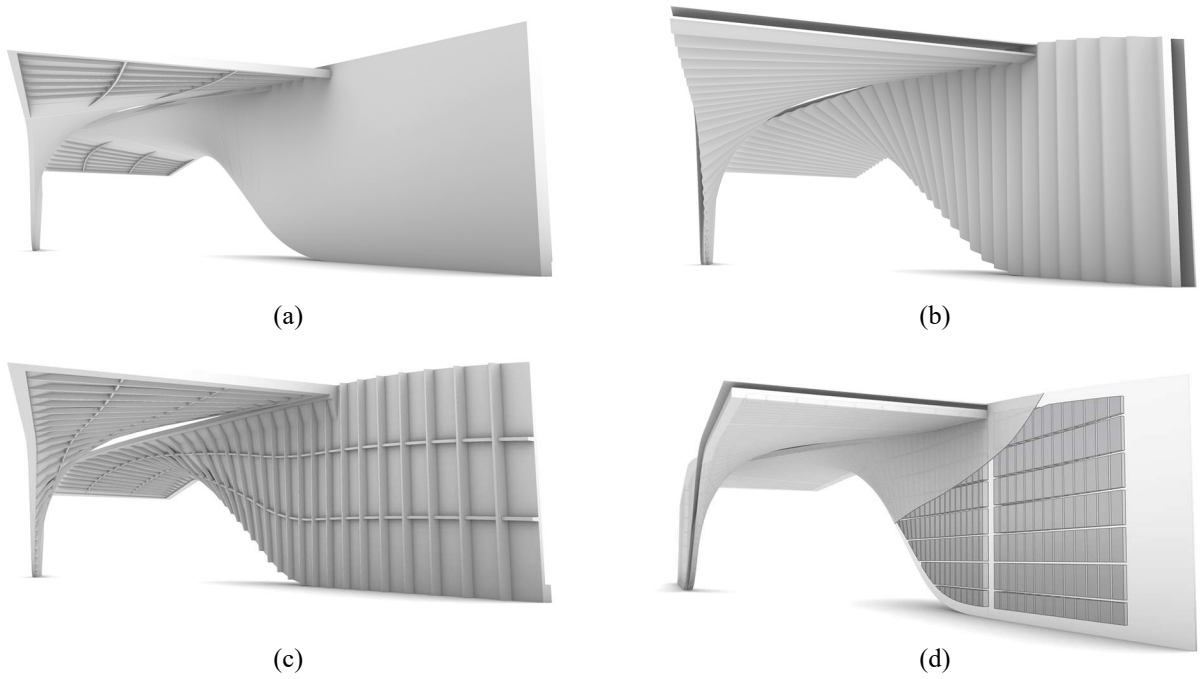


Figure 3: Various structural solutions of the twisted roof shell; (a) – solid cross-section with partially placed ribs in the zone with largest deflections, (b) – "waved" solution, (c) – solid cross-section with longitudinal and transversal ribs (T-cross-section), (d) – a final hollow-core solution with internal voids

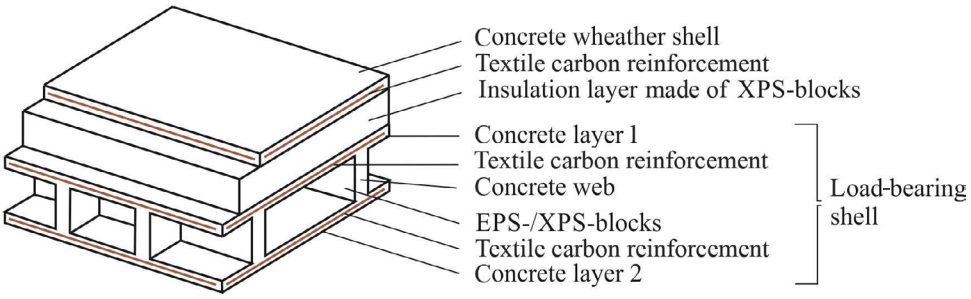


Figure 4: Principal structure of the twisted roof shell

To further improve the structural performance of the load-bearing shell, it was decided to create a hollow-core structure (see Figure 4). The voids inside the load-bearing shell are assumed to be prepared using either expanded or extruded polystyrene (EPS, XPS) specially cut blocks. The general view of the last solution is provided in Figure 3 (d). As these materials are included in the proof of thermal insulation, a relatively thin roof structure can be realised overall.

The 3D model of the CUBE's twisted roof shell was developed with the help of Rhino 3D and Grasshopper 3D software package [8], [9]. But in order to perform a reliable and comprehensive structural verification, a special model was prepared to be imported into an external calculation software solution. To do so, Dlubal RFEM calculation software package [10] was selected. The RFEM model is represented in Figure 5. It can be seen that the model comprises a sequence of lines that represent the shape of the shell and form the shell objects with required properties for the structural calculation. The development of the RFEM model together with the main 3D model made it possible to have parametrical freedom for the structural calculations or in other words have an instant update, in case of some changes, of the key model properties such as total dimension, roof inclination, distribution of structural elements, etc. In addition, it enabled the development of a range of 3D models and other related data to cover different aspects of the twisted roof shell. For instance, there was a model that represented just the load-bearing part of the shell (from Figure 4), and another model that comprised data to calculate the behaviour of the connection between the load-bearing shell and the weather shell.

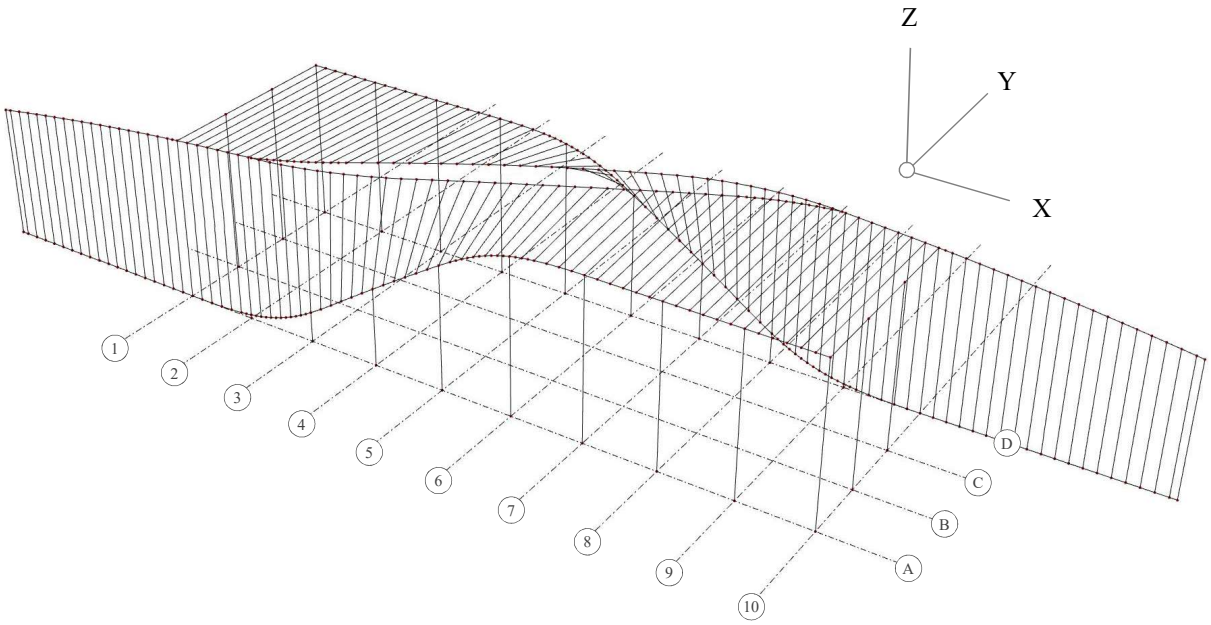


Figure 5: Structural model in Dlubal RFEM [10]

4. Textile carbon reinforcement

After the CUBE roof geometry preparation was completed, according to the range of architectural constraints and the structural analyses, the next step was the development of appropriate data for all steps of the manufacturing process. One of those steps is the preparation of the textile carbon reinforcement fragments to be integrated into the concrete of the twisted roof shell. As can be seen, from Figure 3, and especially in Figure 5, the CUBE geometry has been developed as a conoidal ruled surface. Therefore the main focus within the project was on the behaviour of ruled surfaces $S \subset \mathbb{R}^3$ in general, which are defined in mathematical form [11] by equation (1)

$$\boldsymbol{x}(s,t) = \boldsymbol{b}(s) + t\,\boldsymbol{\delta}(s), \quad t \in \mathbb{R} \tag{1}$$

where $\boldsymbol{b}(s)$ and $\boldsymbol{\delta}(s)$ represent a *directrix* and a *generator* of a ruled surface respectively. For the purpose of the CUBE project, a direction of the generator vectors for all ruled surfaces are accepted to be parallel to the global plane *YZ*, according to the coordinate system provided in Figure 6 (b). Thus, the generator vectors can be expressed as $\boldsymbol{\delta_i} = [0 \quad y_i \quad z_i]^T$. Such selection of the generators is governed by the necessity to have straight beams reinforced with rigid rebars and located transversely to the longitudinal direction of the CUBE building. Also, such beam orientation helps to transfer loads appropriately between both twisted roof shells of the CUBE building.

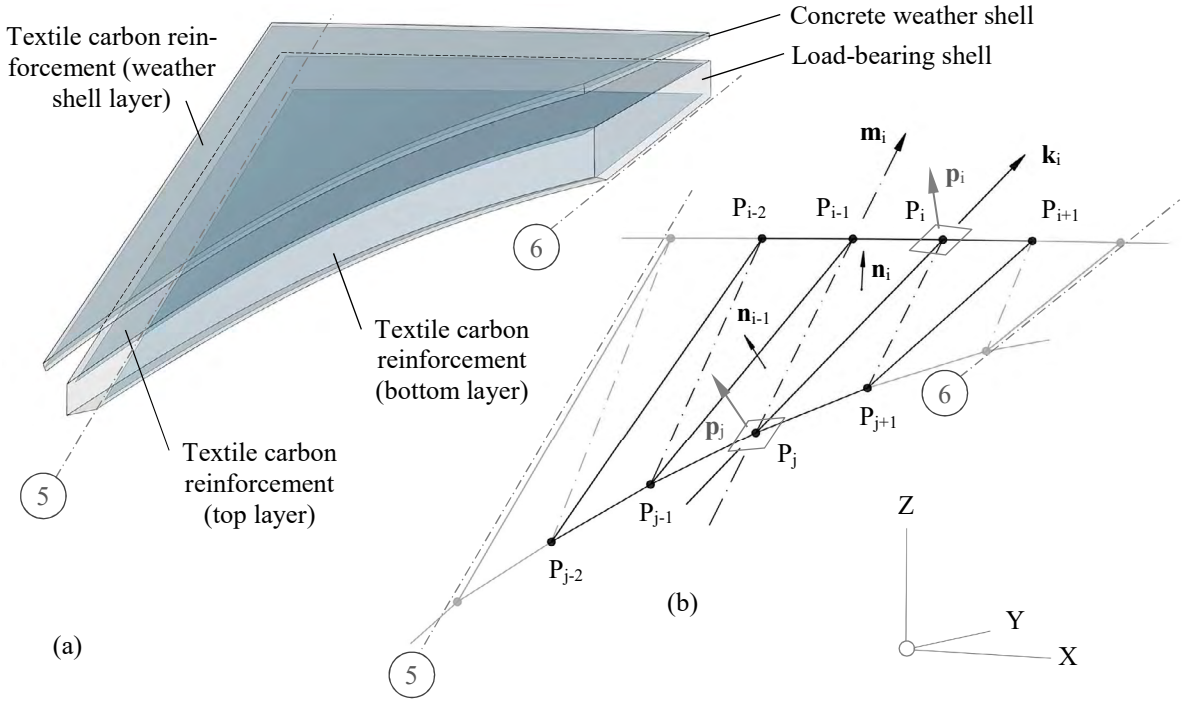
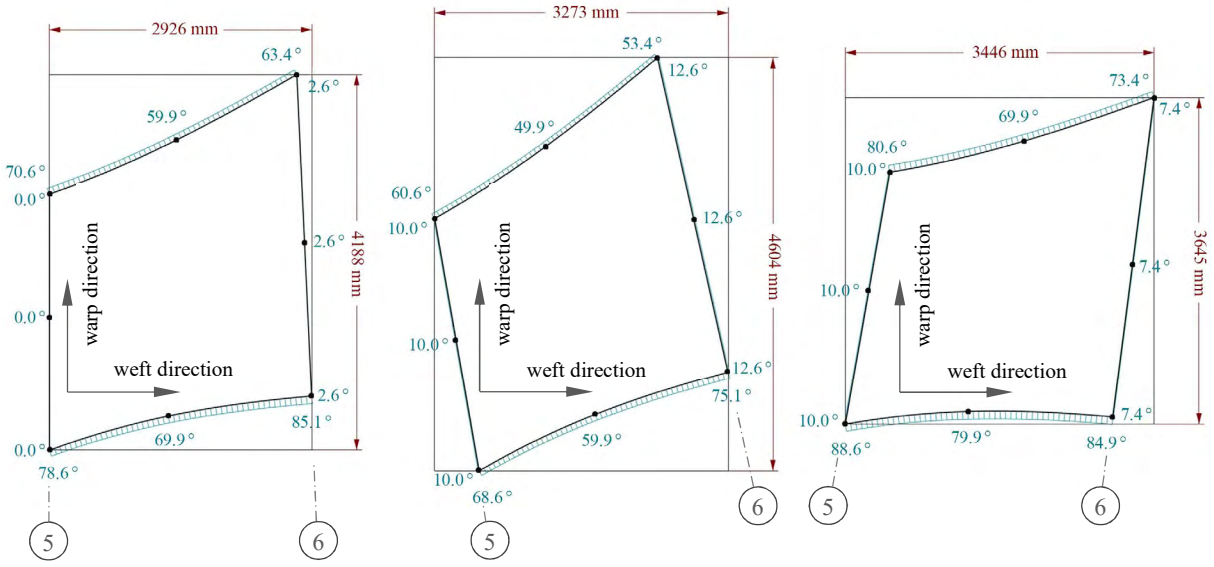


Figure 6: Key components of the textile reinforcement flattening procedure; (a) – textile carbon reinforcement layers within the load-bearing shell; (b) – geometry approximation via triangulation

Figure 6 (a) shows the position of the top and bottom textile carbon reinforcement layers within the load-bearing shell. In order to flatten the selected textile fragments, a special design textile preparation tool was developed. The tool is based on the approximation by triangulation of the original geometry, provided in Figure 6 (b). It can be seen from the figure that the textile fragment is subdivided into a sequence of triangles, where generators of the ruled surface are used as edges of the triangles. The flattening procedure itself is driven by a simple sequence of linear transformations. Where a set of normal vectors $\boldsymbol{n_i}$, rotational axes $\boldsymbol{m_i}$, $\boldsymbol{k_i}$ and boundary points P_i, P_j are required as input data to launch the transformation procedure. The selected way of creation of the ruled surface brings some drawbacks as well. Thus, for instance, the curvature analysis throughout the whole shell shows that Gauss-curvature

is equal or less than zero value ($K \leq 0$) in general for the twisted roof shell. Deviations from zero value have a higher magnitude in the middle of the CUBE's shell and vanish approaching to both ends of the building. Consequently, it can be stated that according to the ruled surface properties [12], the geometry of the textile reinforcement fragments is not developable. To manage such a problem, further optimisation of the textile fragment positions was required to find the most appropriate dimensions and configuration of the cut-offs. A feasible way is the approximation of the most critical undevelopable regions with stripes. Such an approach helps to minimize the relative rotation of the tangent planes at the end points P_i, P_j and by this, it make the selected textile fragment close to the developability condition $\boldsymbol{p}_i \times \boldsymbol{p}_j = 0$ [13].

The textile preparation tool, mentioned above, was developed in such a way to provide the possibility to adjust the position of the final textile cut-out with the purpose of optimising the direction of the textile yarns at the edges of the reinforcement fragments. Thus, Figure 7 (a) represents the original position of the reinforcement fragment from Figure 6 (a) after the flattening procedure. As a result of the flattening procedure, all data that is required for production is generated as shown in Figure 7 (a), such as the net area of the fragment, the total area of the textile mat and boundary dimensions of the textile mat. Figure 7 (b) and Figure 7 (c) show the possible rotation of the textile fragment by 10 degrees counterclockwise and clockwise respectively with the aim to find the most appropriate orientation of the textile yarns. The orientation itself is one of the critical parameters that effect reinforcement behaviour due to the orthotropic nature of the textile reinforced concrete. Therefore, the provided figures contain diagrams, at the edges of cut-offs, that show the magnitude of the angle between the edge point and the warp direction. By this, the deviations of the yarn resulting direction from the required "ideal" direction can be detected.



(a) Mat area: 15.0 m^2
Net area: 8.9 m^2

(b) Mat area: 12.3 m^2
Net area: 8.9 m^2

(c) Mat area: 12.6 m^2
Net area: 8.9 m^2

Figure 7: Textile reinforcement fragment positioning; (a) – initial position with no rotation, (b) – counterclockwise rotation by 10 degrees, (c) – clockwise rotation by 10 degrees

5. Production method

Within the CUBE project, one of the most important questions is how to cast the load-bearing shell. In order to construct the structural solution for the twisted roof shell, the mentioned voids are assumed to be generated by placing either EPS- or XPS-blocks. Figure 8 shows all the blocks that need to be produced and the corresponding subdivision into groups according to their functionality. There are two

groups within the twisted roof shell: group 1 with internal structural blocks and group 2 with blocks for thermal insulation. Also, there is group 3 with the blocks required to construct the hollow-core structure of the wings.

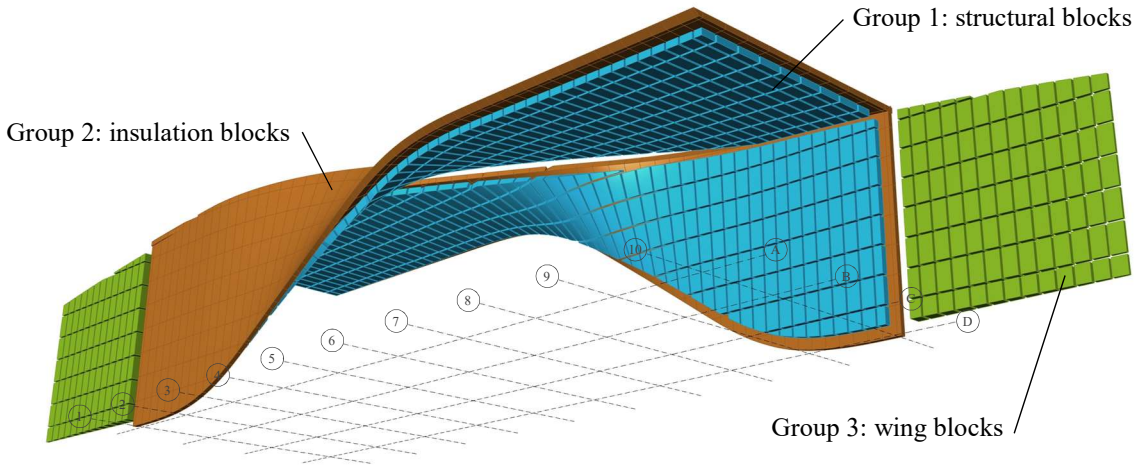


Figure 8: Groups of EPS-/XPS-blocks

From the figure and from the introductory chapters, it can be seen that the whole CUBE twisted roof shell is subdivided into two equivalent parts with an equal number of blocks. Thus, it may be stated that each part comprises approximately 900 blocks. Some of them are nearly equal, some of them are significantly different. With a purpose to reduce expenses, within the scope of the project, different optimisation approaches were considered. For instance, certain blocks can be replaced with an equivalent rectangular block in order to save time and expenses during the precision cutting phase. Alternatively, it is possible to find blocks with nearly similar dimensions, within an acceptable margin of error. This approach simplifies the production by reducing the time for the development of unique blocks.

According to the description provided before in the paper, the load-bearing shell was developed as a ruled surface. The same approach was applied to all surfaces including EPS-/XPS-blocks. Thus, all the formwork and thermal insulation blocks can be manufactured via hot wire cutting. Figure 9, shows some of the blocks with the related boundary boxes required for the development of the correct cutting routine.

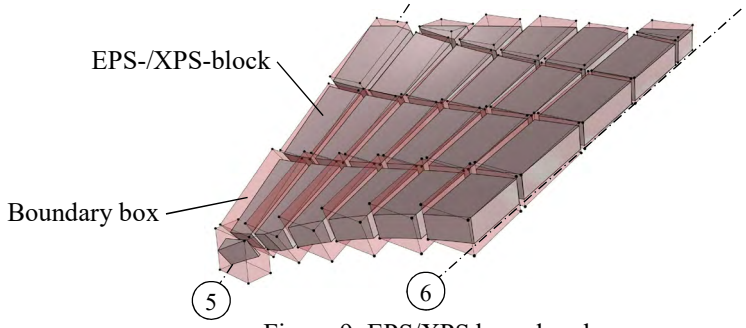


Figure 9: EPS/XPS boundary boxes

It may be seen from the figure that in general, the predominant number of blocks may be manufactured by cutting four sides with the hot wire and keeping two other sides completely flat. Of course, there are also blocks that have a different number of cutting surfaces. Additionally, it should be mentioned that the whole generating procedure of 3D geometry of EPS-/XPS-blocks with related boundary boxes was programmed within the Rhinoceros 3D + Grasshopper 3D software environment [8], [9]. The data were developed in such a way that can be exported and recognized easily by the project contractors that are responsible for the production.

6. Summary

To conclude, it may be stated the paper includes only a basic, introductory description of the CUBE project and its design stages in particular. By this, it follows that the project itself is a huge database of important structural solutions, software developments, design achievements and consequently a good source of experience for all project participants to be used in future projects. Finally, the knowledge obtained is important for further introduction into the construction industry of the non-metallic reinforcement solutions along with high-performance concrete.

Acknowledgements

The authors thank the Federal Ministry of Education and Research (BMBF) for funding the project and the involved project partners Institut für Betonbau, HTWK Leipzig; AIB GmbH, Bautzen; ASSMANN Beraten + Planen AG, Dresden; and HENN GmbH, Berlin for the design and engineering support. The authors are particularly grateful to the members of the Institute of Geometry of the TU Dresden who support the project by giving mathematical background and multiple workshops like "Line Geometry for Lightweight Structures (in short: LGLS)" summer school for the development of ruled surface design and preparation of various manufacturing procedures.

References

[1] "German Federal Ministry of education and research (BMBF)," 31-May-2019. [Online]. Available: https://www.unternehmen-region.de/de/zwanzig20---das-programm-1780.html.

[2] "Carbon Concrete Composite," 31-May-2019. [Online]. Available: https://www.bauen-neu-denken.de/en/.

[3] F. Schladitz, M. Tietze, M. Lieboldt, and M. Curbach, "Carbon and concrete - the future of construction?," *Bridges and Structures Sustainability - Seeking Intelligent Solutions. IABSE Conference Report, Guangzhou, China*, vol. 106, pp. 240-241 (abstract, full paper published digitally, 11 p.), May 2016.

[4] M. Tietze, A. Kahnt, F. Schladitz, S. Scheerer, and M. Curbach, "C^3 − Carbon reinforced concrete – construction of the future," *Concrete - Innovation and Design: Proceedings of 13th fib Symposium 2015, Copenhagen, Denmark*, p. 479 (abstract, full paper on 9 p.), May 2015.

[5] M. Curbach, F. Schladitz, and G. Müller, "Carbon concrete - from research to real life (Carbonbeton - von der Forschung zur Praxis)," *BWI - BetonWerk International*, vol. 1, pp. 36–41, 2017.

[6] "TU Dresden, Institute of Concrete Structures, C3-V3.1: C^3 technology demonstration house – CUBE," 31-May-2019. [Online]. Available: https://tu-dresden.de/bu/bauingenieurwesen/imb/forschung/Forschungsfelder/TRC-C3/C3-vorhaben/C3-V3.1?set_language=en.

[7] M. Rossi and S. Kirmse, *C^3 Vision. Ideas, projects and models for the first building in Carbon Concrete Composite.* M. Curbach, U. Häußler-Combe U. Eds, addprint AG, 2018.

[8] "McNeel Europe SL, Rhinoceros 3D, Version 6.0," 31-May-2019. [Online]. Available: https://www.rhino3d.com/.

[9] "Robert McNeel & Associates, Grasshopper 3D, Version 6.0," 31-May-2019. [Online]. Available: https://www.grasshopper3d.com/.

[10] "Dlubal Software GmbH, RFEM, Version 5.19," 31-May-2019. [Online]. Available: www.dlubal.com.

[11] K. L. P. Rose, "Modeling Developable Surfaces from Arbitrary Boundary Curves," Master Thesis, The University Of British Columbia, 2007.

[12] E. Hartmann, "Geometry and Algorithms for Computer Aided Design," Department of Mathematics Darmstadt University of Technology, 2003.

[13] S. Kolmanic and N. Guid, "The Flattening of Arbitrary Surfaces by Approximation with Developable Stripes," University of Maribor, Slovenia, 2002.

Proceedings of the IASS Annual Symposium 2019 – Structural Membranes 2019
Form and Force
7 – 10 October 2019, Barcelona, Spain
C. Lázaro, K.-U. Bletzinger, E. Oñate (eds.)

Design space exploration for high-performance greenhouse design

Demi FANG*, Alpha ARSANO, Nathan BROWN, Christoph REINHART, Caitlin MUELLER

*Massachusetts Institute of Technology (MIT)
Cambridge, MA, USA
dfang@mit.edu

Abstract

This paper presents a case study in utilizing design space exploration techniques for the design of a greenhouse that extends the growing season for vegetables in Portola Valley, California. The work synthesizes disparate fields of research: greenhouse design and performance-driven early-stage design. The design problem involves variables relating to geometry and glazing ratio, which are adjusted to meet objectives based on lighting, thermal, and structural performance. Design space explorations are conducted to test greenhouse design rules of thumb, such as the importance of south-facing surfaces and the tradeoff between lighting and thermal performance that dictates glazing ratios. The results demonstrate how design space exploration techniques can validate and potentially augment these rules of thumb in greenhouse design, demonstrating a workflow for exploring and selecting design options that extend the growing season of select crops.

Keywords: conceptual design, design space exploration, optimization, multi-objective optimization

1. Introduction

The design of high-performance buildings has its roots in principles and rules of thumb but has recently been augmented by simulations in structural, lighting, and thermal performance. By integrating simulation programs with parametric frameworks, designers gain additional insight into complex design problems. Sampling and multi-objective optimization (MOO) techniques have demonstrably offered ways to systematically and widely explore complex design spaces for high-performance buildings [1]–[4]. Because of its inherent design complexity, particularly in tradeoffs between thermal and lighting performance, the greenhouse constitutes one such high-performance building that could benefit from the application of these techniques that permeate the design of other high-performance structures. The use of light and energy simulations for evaluating the performance of agricultural spaces, such as [5], are not uncommon; however, few to no existing work describe how sampling or optimization techniques participate in the greenhouse design process by enabling an exploration of the complex design space.

1.1 Design approach for evaluating greenhouse performance

State-of-the-art tools for greenhouse design primarily target the maximization of crop output for commercial purposes [6]. Conversely, the primary design objective of the greenhouse presented in this paper is to extend the growing season for a miscellaneous variety of vegetables. This overarching objective is not only more appropriate for hobby growing purposes, which was the client's stated degree of interest, but also demonstrates a workflow for designing for year-round greenery, which has been shown to have improve human health in urban areas [7].

Copyright © 2019 by FANG, ARSANO, REINHART, MUELLER.
Published by the International Association for Shell and Spatial Structures (IASS) with permission.

1.2 Principles of the design space

The design space represents the domain of possible designs given the constraints and variables of a given design problem. Linking each design to objectives, or performance scores, can enable designers to systematically understand the design problem at hand and make more informed design decisions.

The term "design space exploration" refers to the process of understanding how different design decisions affect the design objectives. Several options exist for systematically and automatically exploring the design space: 1) *sampling* gives an unbiased overview of the design space, while 2) *multi-objective optimization (MOO)* can be particularly useful in evaluating a set of best solutions (called the Pareto front) considering tradeoffs among different objectives, in other words biasing the exploration of the design space towards better-performing designs. As will be demonstrated through this applied design study, both techniques can be valuable for the designer: the unbiased sample of the design space can allow the designer to verify the scope of constraints and expected results, while MOO can enable a more efficient and directed search for better-performing designs.

1.3 Data visualization

As the number of variables and/or objectives in a given design problem increases, it becomes more complex to convey the results of evaluating the design space. In this paper, new data visualization techniques for conveying the particular design space at hand are proposed.

2. Methodology

The design problem was formulated in the Grasshopper plug-in for Rhinoceros 6.

2.1 Design constraints and variables

The greenhouse design was constrained by some context-specific requirements: the square footage was limited to 11.15 m^2 and the maximum height to 2.44 m (Figure 1, left). Within those design constraints, a base typology was developed with geometric design variables along with window-to-wall ratios (WWR) for design freedom (Figure 1, right). Because the site slopes downwards towards the southwest, the structure is built into the slope to utilize thermal mass of the upslope earth on the north face of the structure, a side which does not receive much sun.

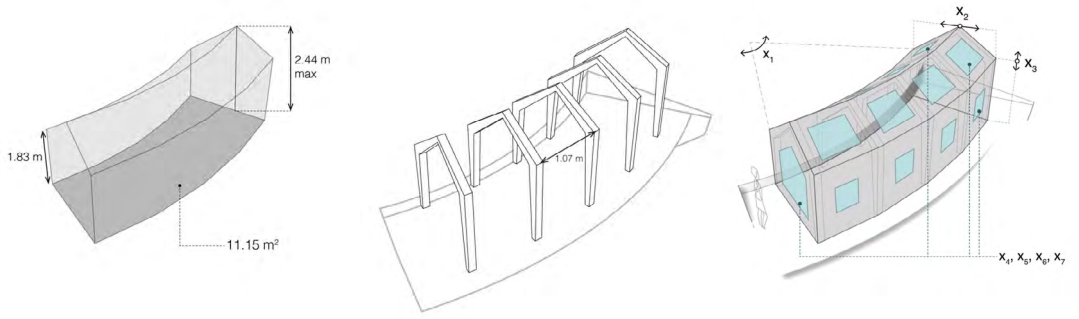


Figure 1. Design constraints (left, middle) and variables (right).

Of the 7 variables selected to formulate the design space, 3 are geometric and 4 are glazing-related. The bounds on the variables were design decisions based on the context of the design problem. The variables are summarized in Table 1.

A few geometric constraints in the parametric model were implicitly captured by variable bounds; for example, a footprint area of 11.15 m^2 (maximum under design constraints) is maintained, meaning the north-south width of the greenhouse varied with the angle of embrace x_1. Furthermore, a target spacing

of 1.07 m was maintained between structural frames, meaning the number of structural frames also varies with the angle of embrace x_1. The north wall height was also maintained at 1.83 m, and the peak frame height at 2.44 m.

Table 1. Details of variables making up the design space.

Variable	Type	Description	Bounds
x_1	Geometric	Angle of embrace of global geometry	0.15π to 0.35π rad
x_2	Geometric	Normalized location of peak of frame, where higher values corresponds with more northern positions	0.05 to 0.95
x_3	Geometric	Height of south-facing wall	1.52 to 2.13 m
x_4	Glazing	Window-wall ratio of north-facing roof	0.20 to 0.80
x_5	Glazing	Window-wall ratio of south-facing roof	0.20 to 0.80
x_6	Glazing	Window-wall ratio of east- and west-facing walls	0.20 to 0.80
x_7	Glazing	Window-wall ratio of south-facing wall	0.20 to 0.80

2.2 Design objectives

The lighting and thermal objectives for the design problem were constructed such that the favorable performance corresponded to extension of the growing season. The structural performance objective favors efficient use of materials.

2.2.1 Lighting performance

The DIVA plug-in was used for lighting and thermal performance simulations [8]. Typical Meteorological Year (TMY) data for the site was interpolated based on neighboring regions and verified against real-time collected data from an on-site weather station.

A common metric for understanding the amount of light received by plants is Daily Light Integral (DLI), which is a daily average value measuring the amount of light received in the photosynthetically active radiation (PAR) spectrum, the spectrum of interest for plants. DLI (units of moles per m^2 per day) can be converted directly from illuminance (units of lux, or lumens per m^2), an instantaneous measure of light from the visible spectrum and a common output from state-of-the-art daylighting simulations. The key intermediate conversion factor is photosynthetic photon flux density (PPFD) (units of micromoles per m^2 per second), or the number of photons that are received by a surface at each second. The photosynthetic photon flux (PPF) of sunlight is equivalent to 54 lux.

To begin the conversion, it must first be determined how illuminance data is output from the simulation program, since illuminance is an instantaneous measurement. The Grasshopper DIVA component outputs illuminance as an hourly average. Because DLI is a daily average value, every 24 values must be averaged together to get a daily average illuminance ($\text{Illuminance}_{\text{daily}}$).

$$\text{Illuminance}_{\text{daily}}[\text{lux}] \times \left[\frac{1\ \text{PPF sunlight}}{54\ \text{lux}}\right] = \text{PPFD}\ \left[\frac{\mu\text{mol}}{\text{m}^2 \times \text{s}}\right] \times \left[\frac{1\ \text{mol}}{10^6\ \mu\text{mol}}\right] \times \left[\frac{86400\ \text{s}}{1\ \text{day}}\right]$$
$$= \text{DLI}\ \left[\frac{\text{mol}}{\text{m}^2 \times \text{day}}\right]$$

The client's stated interest for greenhouse function was for extending the growing season for various vegetables. Different types of vegetables require different levels of light [9], [10]. To simplify these

requirements into a manageable number of metrics for the scope of this early-stage design study, two thresholds were developed. The first threshold required minimum DLI of 10 mol m^2/day, representing light requirements for vegetables such as lettuce and cucumbers; while a second threshold with DLI of above 20 mol m^2/day represented light requirements for vegetables such as tomatoes.

The conversion of illuminance data to DLI results in 365 DLI values – one for each day of the year – for each of *n* discretized grid spaces in the footprint of the greenhouse. In order to collapse 365*n* values into a single performance value, for any given greenhouse design, the proportion of floor area receiving an average DLI across a season under each threshold was constructed as a light performance objective. By subdividing lighting performance into seasons, it was possible to gain additional insight into light performance for different parts of the year so that seasonal recommendations could be made. The decision to quantify those average DLIs under a given threshold was made to ensure that a lower score corresponded with a better lighting performance.

For this study it was assumed that a plant could be placed in the entire floor area of the greenhouse. A future step in the design study could examine the spatial distribution of lighting performance in a given design in order to make spatial design recommendations, such as utilizing poorer-performing grid spaces as circulation paths for specific designs or highest-performing grid spaces as placement of higher-threshold vegetables.

2.2.2 Thermal analysis

As with lighting performance, the thermal requirements for different types of vegetables varies [11]. Hardy vegetables like lettuce thrive in temperatures ranging from 16 to 18°C, while warm-season crops such as cucumbers and tomatoes require temperatures ranging from 18 to 30°C. For the scope of this design study, the latter range of temperatures was assumed as a requirement for better thermal performance. This assumption is a simplification but can undergo further refinement in future stages of the design study in order to be inclusive of other types of vegetables.

For any given greenhouse design, temperature for each of 8760 hours in a year was available for the whole space. Unlike lighting performance, this data has no spatial dimension, so the objective scores are quantified as the proportion of the year for which the temperature exceeds the desired range and the proportion of the year in which the temperature undershot the desired range.

Assuming high insulation of the greenhouse floor and thermal separation where the greenhouse touches the earth, the north wall and the ground surface are set to be adiabatic surfaces. Natural ventilation is turned on with a setpoint of 18°C and a range of outdoor temperatures 18-35°C for open windows. An air exchange rate of 0.35 is set for infiltration.

For simplicity, humidity is not modeled in this study. While plants have humidity requirements, usually the evapotranspiration of plants in greenhouses guarantees sufficient humidity; oftentimes moisture needs to be extracted from the air to prevent excess humidity. Evapotranspiration does play a role in the cooling of plants and the authors acknowledge that the simplification of omitting this model may affect the accuracy of thermal performance.

2.2.3 Structural performance

The structural system selected was an arced series of timber portal frames with rectangular cross-sections. Structural performance was analyzed using the Karamba plug-in [12], applying load combinations on primary members only per ASCE 7-10. The auto-selection of section sizes was applied for the structural members. The mass of the resulting system was recorded to represent the embodied energy or structural efficiency of the structural system of any given greenhouse design. Unlike the other objectives, this objective score was not normalized from 0 to 1 but instead given in units of kg.

A summary of the design objectives is provided in Table 2.

Table 2. Details of objectives in the design space.

Objective	Type	Description	Bounds
1	Lighting	Proportion of floor area receiving average DLI < 10 [mol m^2/day] in the spring	0 to 1
2	Lighting	Proportion of floor area receiving average DLI < 10 [mol m^2/day] in the summer	0 to 1
3	Lighting	Proportion of floor area receiving average DLI < 10 [mol m^2/day] in the fall	0 to 1
4	Lighting	Proportion of floor area receiving average DLI < 10 [mol m^2/day] in the winter	0 to 1
5	Lighting	Proportion of floor area receiving average DLI < 20 [mol m^2/day] in the spring	0 to 1
6	Lighting	Proportion of floor area receiving average DLI < 20 [mol m^2/day] in the summer	0 to 1
7	Lighting	Proportion of floor area receiving average DLI < 20 [mol m^2/day] in the fall	0 to 1
8	Lighting	Proportion of floor area receiving average DLI < 20 [mol m^2/day] in the winter	0 to 1
9	Thermal	Proportion of the year too hot (above 30 C)	0 to 1
10	Thermal	Proportion of the year too cold (below 18 C)	0 to 1
11	Structural	Mass of optimized members	Non-negative

2.3 Design space exploration

The design space exploration done in this work is implemented with the Design Space Exploration plug-in [13]. Because the optimization component in this package works to minimize objectives, all of the objectives in Table 2 were constructed such that a lower score corresponded with better performance.

Because of the two "classes" of variables in the design problem and the heightened complexity of understanding a design space with many variables and objectives, a hierarchy in the design process was established (Figure 2).

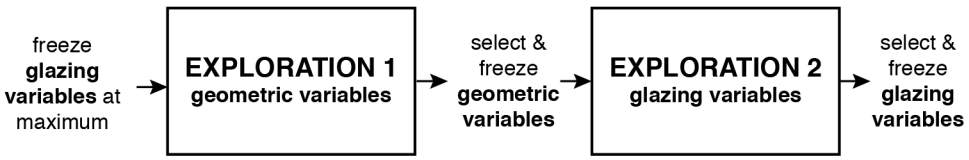


Figure 2. Sequence of design space explorations within overall proposed design process.

3. Results

3.1 Insights from design space sampling

Design space sampling represents an unbiased insight into the design problem. The purpose of sampling is not necessarily to select a design but to benchmark assumptions and to understand the extents of the design space with the given variables and constraints.

800 designs were generated using Latin hypercube sampling, first of different combinations of geometric variables with WWR variables (Figure 3). Each row of the figure represents the same data but color-coded to each of the 3 geometric variables, while each column of the figure corresponds to a different performance area. Lighting and thermal performance have multiple objectives and are displayed as separate parallel coordinate charts (columns 1-3 in Figure 3). Because structural performance only has one objective, the x-axis of its plot (column 4 in Figure 3) maps to the geometric variable in question.

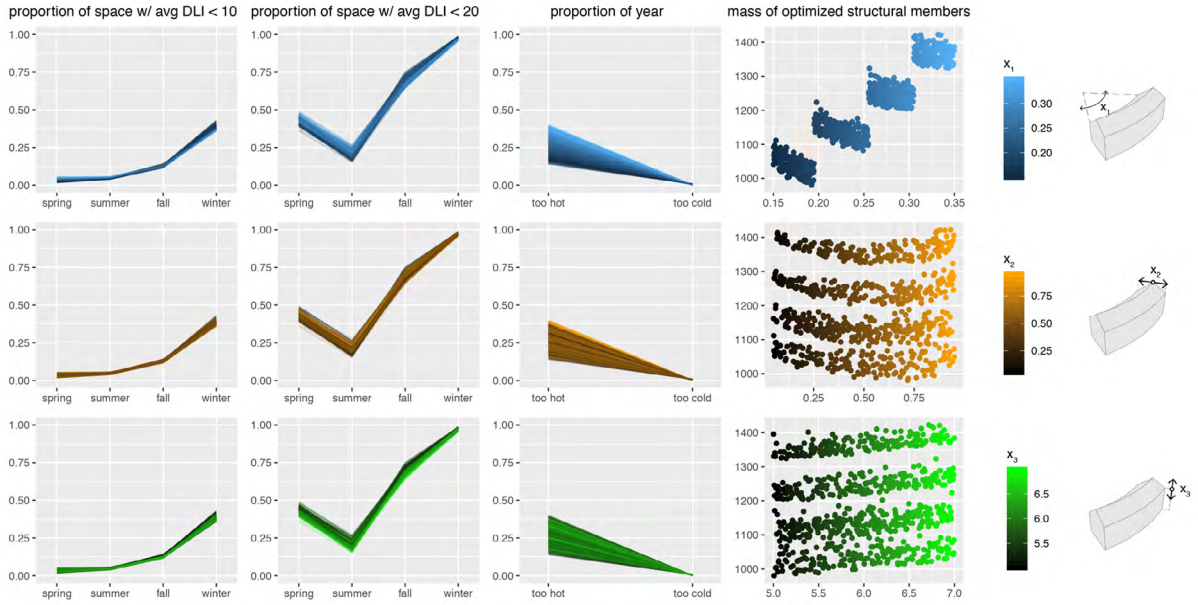


Figure 3. Sample of 800 designs from varying geometric variables by Latin hypercube method. Objectives are charted on the y-axis of each plot, with lower numerical score corresponding with better performance. Columns 1 and 2 represent lighting performance, column 3 represents thermal performance, and column 4 represents structural performance.

In the second step of design space exploration, one of the geometric variable combinations was selected and 800 designs were generated using Latin hypercube sampling of different combinations of WWR (Figure 4). The figure reads similarly to Figure 3 but without the structural objective because WWR variables have no effect on structural performance.

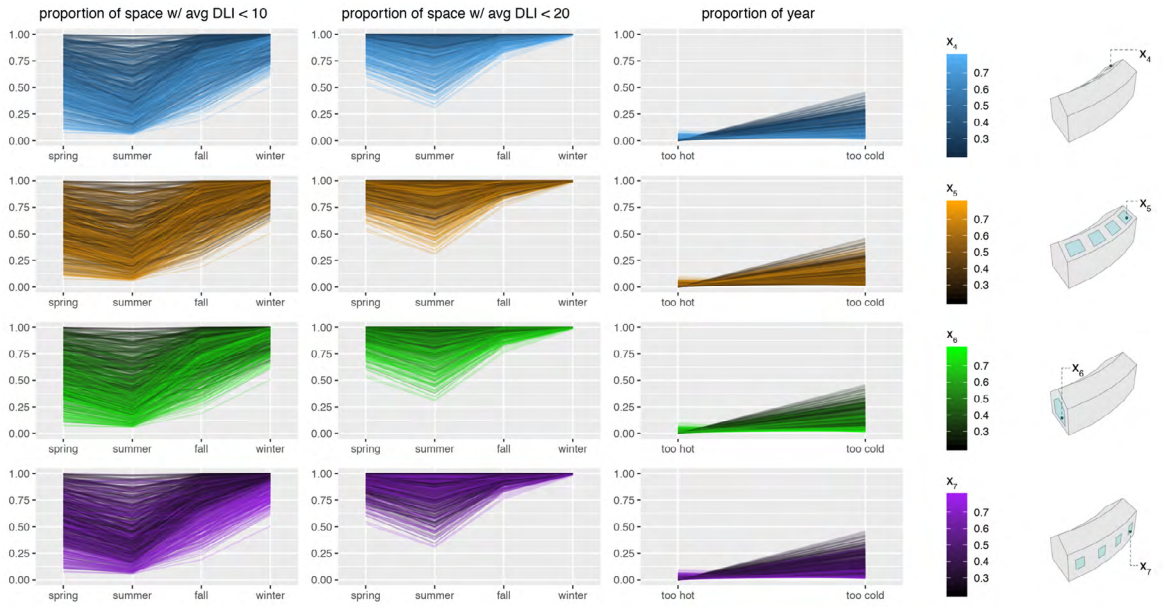


Figure 4. Sample of 800 designs from varying WWR variables by Latin hypercube method. Objectives are charted on the y-axis of each plot, with lower numerical score corresponding with better performance. Columns 1 and 2 represent lighting performance, and column 3 represents thermal performance.

Both sampling exercises and their data visualizations, through the spread of the lines in the parallel coordinate plots and trends in color mappings, give insight into how evaluating design space verifies and augments greenhouse design rules of thumb. These insights are summarized in Table 3.

Table 3. Insights from design space sampling.

	Design space of geometric variables (x_1, x_2, x_3)	Design space of glazing ratios (x_4, x_5, x_6, x_7)
Rules of thumb confirmed	Geometry plays little role in thermal and lighting performance. Symmetry in structural frames is favorable for efficiency.	Glazing ratios on south-facing surfaces are key for light availability. A tradeoff exists between lighting and thermal performance in determining glazing ratio.
Additional insight (specific to the design context) gained	Number of frames governs structural efficiency There is a slight tradeoff between lighting and structural performance in determining the south wall height, involving the extremes of about 12% less space with sufficient lighting vs. about 7% increase in mass.	The tradeoff between lighting and thermal performance involves the extremes of getting insufficient light 100% of the year vs. getting too hot 25% of the year.

3.2 Insights from multi-objective optimization

Multi-objective optimization is a more directed search through the design space for designs with better performance evaluations. The two design space explorations were repeated but with multi-objective optimization in 10 generations of population 100. The final generation of 100 designs represent the

Pareto front of the design space. For each design space exploration, only the Pareto front is considered in the following results.

The Pareto front from varying geometric variables at maximum WWR is represented in Figure 5. Because only the 100 designs on the Pareto front are represented, a "catalog"-type visualization is used with bar overlays representing collapsed objective scores for each design. This visualization enables designers to simultaneously assess the look of the greenhouse and its relative performance with other best-performing designs.

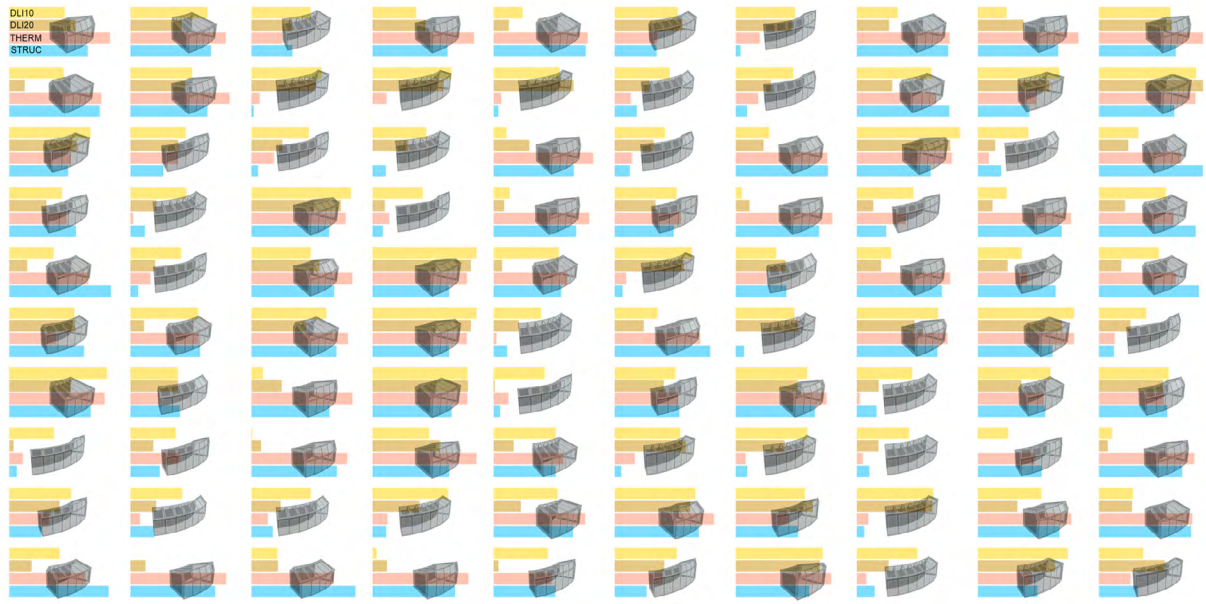


Figure 5. Resulting designs from the Pareto front of designs on geometric variables, with performance scores overlaid on top. The bars are mapped to the minimum and maximum scores of all 100 designs, with longer bars representing better performance.

The catalog visualization can give us a snapshot of the best designs from the study. For example, in Figure 5, a few "typologies" of geometries can be picked out – a long and skinny footprint, or a footprint with a stockier aspect ratio. Through the catalog, the designer can see the range of performance possibilities for each typology and make informed decisions based on these discrepancies. For an even improved experience of selecting from the catalog, the catalog could be interactively sorted by geometry or by specific performance values.

One of these geometric designs is selected for the next step of MOO. The geometric variables from design 93 (Figure 5 bottom row, third from left) are selected. The Pareto front from varying WWR variables of this selected geometric design is represented in Figure 6. This overlay of WWR variables and performance gives designers a snapshot of how different WWR combinations for the same geometric design can offer different ranges within the best-performing set of designs.



Figure 6. Resulting designs from the Pareto front of designs on WWR variables. The WWR combination for each design is represented by the vertical bars (legend in top right), with performance scores overlaid on top. The bars are mapped to the minimum and maximum scores of all 100 designs, with longer bars representing better performance.

4. Conclusions

In this paper, the applicability of different design space exploration techniques was demonstrated on the design of a greenhouse. A hierarchical and sequential separation of variables for a two-step procedure was useful in eliminating excess complexity in understanding the design problem. Sampling proved to be an effective first tool at understanding and verifying the extents of the design space. The insights gleaned from sampling were especially useful in both verifying the original hypotheses of the design problem, demonstrating how computational tools can expand the designer's knowledge of the design problem. Multi-objective optimization was useful in making relative comparisons among the better-performing designs.

4.1 Limitations and further work

While focus was placed on the methods of navigating the design space, simplifications and assumptions were made in various aspects of the simulations, particularly in energy simulations. The refinement of evapotranspiration modeling, ground thermal mass, and other thermal modeling details could further improve the evaluation of the design space. Furthermore, the interconnection of thermal and lighting objectives for a successful growing season was not yet implemented in the construction of objective values. Implementing this consideration would improve the relational insights given from thermal and lighting performance and potentially augment the verified rules of thumb.

The data generated for the content of this paper was used to train and test surrogate models for each simulation. These surrogate models demonstrated accuracy within 8% and show the potential for these data sets to alleviate computationally intensive simulations, the often-cited barrier of exploring the design space. Combined with aforementioned improvements to the performance evaluation framework, this process could become a compelling example of how conventional design processes can be augmented by strategic explorations of the design space.

Acknowledgements

Khadija Benis provided references early on in the research process for plant growth requirements.

References

[1] N. C. Brown and C. T. Mueller, "Design for structural and energy performance of long span buildings using geometric multi-objective optimization," *Energy Build.*, vol. 127, pp. 748–761, Sep. 2016.
[2] R. Evins, "A review of computational optimisation methods applied to sustainable building design," *Renew. Sustain. Energy Rev.*, vol. 22, pp. 230–245, Jun. 2013.
[3] C. Waibel, "Simulation-based optimization of buildings and multi-energy systems," Dr. Sc. Thesis, ETH Zurich, Zurich, Switzerland, 2018.
[4] J. Haymaker *et al.*, "Design space construction: a framework to support collaborative, parametric decision making," *J. Inf. Technol. Constr. ITcon*, vol. 23, no. 8, pp. 157–178, Jun. 2018.
[5] K. Benis, C. Reinhart, and P. Ferrão, "Development of a simulation-based decision support workflow for the implementation of Building-Integrated Agriculture (BIA) in urban contexts," *J. Clean. Prod.*, vol. 147, pp. 589–602, Mar. 2017.
[6] *Virtual Grower 3*. United States Department of Agriculture, 2017.
[7] B. Matthias, A. Egorov, P. Mudu, T. Wolf, C. W. Thompson, and M. Martuzzi, "Effects of urban green space on environmental health, equity and resilience," in *Nature-Based Solutions to Climate Change Adaptation in Urban Areas*, Cham: Springer, 2017, pp. 187–205.
[8] *DIVA*. Solemma LLC, 2016.
[9] M. Dorais, "The use of supplemental lighting for vegetable crop production: light intensity, crop response, nutrition, crop management, cultural practices," presented at the Canadian Greenhouse Conference, 2003.
[10] L. Schiller and M. Plinke, *The Year-Round Solar Greenhouse*. Gabriola Island, BC, Canada: New Society Publishers, 2016.
[11] G. E. Welbaum, "Vegetable History, Nomenclature, and Classification," in *Vegetable Production and Practices*, UK: CABI, 2015, p. 486.
[12] C. Presinger and Bollinger+Grohmann, *Karamba*. 2018.
[13] N. Brown, J. Felipe, R. Danhaive, V. Jusiega, A. Nimrick, and C. Mueller, *Design Space Exploration*. Digital Structures, 2019.

Proceedings of the IASS Annual Symposium 2019 — Structural Membranes 2019
Form and Force
7—10 October 2019, Barcelona, Spain
C. Lázaro, K.-U. Bletzinger, E. Oñate (eds.)

DigitalTWIN improving future gridshell installations

Fabian C. SCHMID*, Philipp KOPRIWA*, Martien TEICH*

* seele
Gutenbergstraße 19, 86368 Gersthofen, Germany
Email: fabian.schmid@seele.com, Web page: http://www.seele.com

Abstract

Ensuring an optimized design and installation of gridshell structures, optimization of geometry, tools and workflows are set up mostly parametrically. Such projects and constructions are still realized without a continuous data exchange and automated use of parameters and constraints at the manifolded interfaces. This makes a flexible implementation of digital tools, a fast and easy data aquisition for integrated analysis difficult and elaborately nowadays [1]. The authors provide a summary on gridshell projects, to identify relevant challenges within the necessary workflows[2]. Results of a current research project are highlighted afterwards. Renowned partners representing industry and research are developing digital tools and tech-nologies to enable the integration and automation of services, processes and workflows along the building life cycle. Based on the early results, the consortium developed three use cases that address relevant issues and the interfaces between planning, manufacturing, installation and building operation. Especially the assembly support with augmented reality technology is highlighted in the paper. First demos were realized to evaluate the user interface for the workers and to specify the necessary computer infrastructure on site. The authors will highlight positive and negative experiences gained with the first demos and make suggestions to enable an easy integration of digital tools in a projects workflow and to ensure an intuitive, safe and secure data and knowledge exchange for the future.

Keywords: digital tools, installation, construction site, project management, design processes

1 Design Processes for Gridshell Structures

Gridshell design is typically driven by either geometric parameters or structural constraints and principles nowadays. Parametrically defined principles enable an interconnected processing of the component's geometries. Studying options with differently weighted optimization parameters takes place in multiple iterations. The iterative design process and visual reviews are necessary to ensure a smooth and steady flow of the meshes as well as balanced proportions of the components within the design stages. [2, 3]
Principal geometry and design intent are provided by the design team to enable the analysis, checks and categorizations in order to offer alternatives, share experiences and ideas by specialist subcontractors during tender phase. In addition, local constraints for an efficient fabrication and installation come into the discourse.

Copyright © 2019 by F. Schmid, P. Kopriwa, M. Teich
Published by the International Association for Shell and Spatial Structures (IASS) with permission.



(a) Welded steel construction (b) Tolerance checks (c) Surface finish

Figure 1: Steel work supply chain - part 1 [Image: © seele]

The optimization of a structure focuses typically on material, geometry or topology. The relevance of several optimization objectives depends on the design intend. Typical topics, which are outlined by subcontractors more deeply are the glass panels' inclination, their planarity, member lengths and node angles, the principal detailing for the nodes and the edge beam. From the beginning, parametric programming is crucial from the outset for all stakeholders to enable a rapid survey of possible alternatives parallel to the several design and optimization phases. [1]
The models are generated with different intentions in mind. A subcontractors model has integrated more details for fabrication, logistics and processing topics. An additional benefit of retracing and understanding different perspectives and resulting parameters, dependencies and influences is an acceleration of the design approach to determine process and design options faster and more purposeful. [1]
A significant complexity is the available construction period combined with increasingly differentiated assemblies. The summarized experience of three projects reflects challenges and optimization goals of gridshell projects within the last decades.
The gridshell structure for the Westfield shopping mall in London/UK (2008) was dominated by the seamless integration of the CNC-controlled milling of the nodes straight out of the 3D model. The challenge for the shopping mall Chadstone in Melbourne/Australia (2017) was logistics and installation to ensure on-schedule execution within a tight schedule. The design had to take into account weather conditions, local work requirements, and a joint manufacturing and preassembly in Europe and Australia. Figure 1 shows a welded steel structure and the processing within steelwork manufacturing before shipping. Figure 2 shows the quality assurance in the warehouse, the transport to the construction site and a continuous installation process.
The roof for the Moynihan Train Hall in New York/USA (2018) took an extended approach. The multiple requirements of the design intent, thermal and solar requirements, site conditions and the prefabrication of unitized panels and their installation technology were considered and implemented accordingly.
The advancements of gridshell design and optimization of gridshells are possible through a continuous development of Computer-Aided Design (CAD) software and hardware technology, the automated control of production machines using CNC (Computer Numerical Controlled), CAM (Computer-aided manufacturing) technology, and digital data processing in logistics that enables tracking and tracing through every stage. [1] Limitations associated to fabrication, precision, individuality of components and the organization of the assembly process were enhanced and design options seems to expand faster than before. The disadvantage is that project's processes are still characterized by numerous manual adjustments, transfers and interface conflicts. A con-



(a) Checks at the warehouse (b) Logistics to the site (c) Assembly and installation

Figure 2: Steel work supply chain - part 2 [Image: © seele]

tinuous and coordinated dataflow between the involved parties is challenging due to numerous developments regarding methods, tools and technologies connected with the buzzword "Building Information Modelling". Some good approaches fail because of the business model used and the market specific lack of trust. The stakeholders involved make insufficient use of predefined project coordination tools, as no transparency is provided on data sovereignty, data protection and further effects. [1]

Focusing on the projects goals, simplification of data interconnection and administrative effort is required to enable the team to succeed successfully and fast. The preparation of alternatives and the decision making process needs to be supported by interconnected data covering all involved parties. Beside those topics, which are relevant in general for construction projects, gridshells are suitable to test and transfer a highly automated and holistic design approach. It interconnects manufacturing processes on the specialist subcontractor's side. Today those tools are used for different purposes in the architects office, engineering offices, in preparation for the fabrication or for logistics. A combination and coordination of these functions, would likely lead to a higher level of consistency. It is necessary to exchange and edit the data using standardized interfaces as known in automation engineering with a semantic content to enable a faster and wider research in early project stages with more potential alternatives due to automatically accessible data from involved partners.

The use and testing of new technologies and numerous IT solutions for the building sector shows an additional experience. Integration and data exchange between software solutions is an issue for programming and updating sequences (especially for specifically programmed tools). The greatest challenges currently seems to be in the integration of varying IT systems, ensuring plausible and secure data transfer and satisfying usability. True collaboration not hindered or slowed by administrative restraints still seems a vision of the future. [1]

The multi-facetted topics and the constantly changing and complex mixture of interests and roles characterize construction projects and justify the differences to product offers in other industries. In particular, the lack of equal parts, technological innovations and project-specific new combinations of processes are added to the challenging market situation. In order to maintain this special characteristics of building projects and a high-quality building culture, it is important to quickly adapt and further develop the experience of other leading industries. In other industries, the product responsibility of a manufacturer typically leads to a better combination of such information and the networking of different data sources. This market organization structure enables automation technology or the automotive industry to create, process and administer comprehensive and largely consistent digital product models with integrated,

automated and standardized processes. In this context, the term Digital Twin is used to express that there is a - more or less - complete, digital and functional description of a component or product.
'Digital Twins' also exist in construction industry and the building sector. However, often only with individual partners for their respective field of activity and in distributed IT systems. Simple access to information at a later date or from other project partners is not possible without manual effort. The interpretation, which information drives a Digital Twin is very different. The use of 3D component data is sometimes referred to as a Digital Twin or Building Information Modeling.
Nevertheless, geometry and object-specific metadata - such as material, production batch or installation location - are not sufficient to gain a comprehensible, retrospective understanding of the numerous project decisions for the projects resulting from individual preparatory work and discourse. Instead, the planned variants, the defined solution and the actual processes as well as the resources used for it, should be documented continuously. Most of this information already exists today, but little attention is paid to it. It is either destroyed or it is not available for a networked data exchange.
In other leading industries, comprehensive networking of data sources and the coupling of simulation models, for example, are essential. Such industries can provide important orientation for the construction industry when dealing with digital planning or management. In the application of some tools, methods or approaches, however, the different nature of the market structure in the construction sector also becomes obvious. The research project DigitalTWIN, in which seele and Werner Sobek, among others, are involved, aims to accelerate this critical transfer of solutions and implement it safely and easily in the work processes between project partners and along the entire value chain. Figure 3 shows the emerging challenge of integrating diverse digital tools through a coordination of processes and tools characteristics in order to open up new technologies like smart data analysis, data and knowledge management, as well as networked communication.

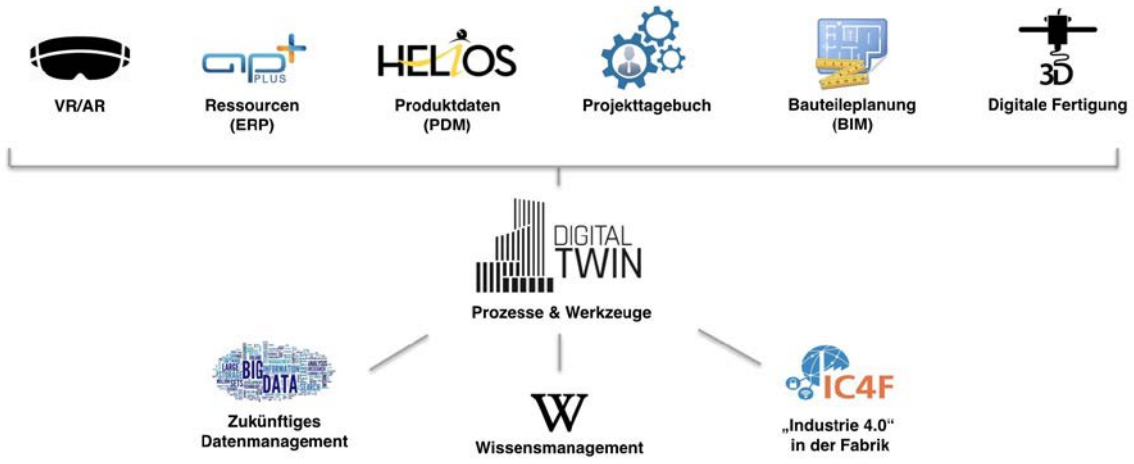


Figure 3: System integration as a major challenge [Image: © se commerce]

2 Research Objectives

In a project to be completed by 2021, renowned project partners representing industry and research develop digital tools and technologies to enable the integration and automation of services, processes and workflows along the value creation chain in the construction industry. DigitalTWIN — Digital Tools and Workflow Integration for Building Lifecycles – focuses on a better understanding of systemic dependencies and interactions. The challenges of the construction sector are constantly changing responsibilities over the whole building lifecycle, different international standards and regulations as well as constantly changing partners in design, fabrication and operation. The project's aim is that an open platform architecture, more advanced broadband communication systems and computer vision technologies should simplify planning, production and coordination with the building site. The solutions shall provide a reliable, flexible and upgradable communication and management infrastructure.
Based on market and technological analysis, the consortium developed three illustrative Use Cases that address relevant issues and the interfaces between planning, production and building operation. The use cases refer to different stages of a building lifecycle, take into account a diverse number of stakeholders and the successively increasing linking of object information, processes, tools and people.

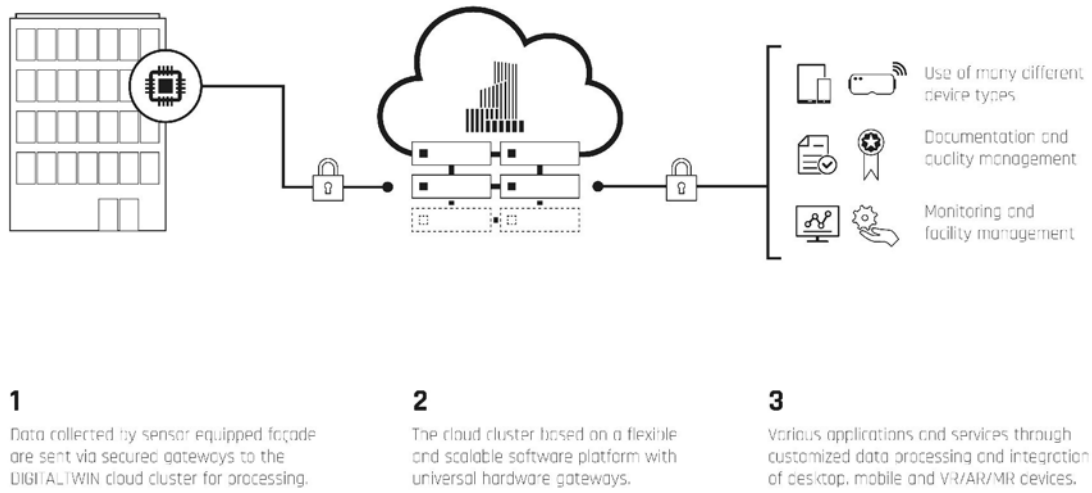


Figure 4: Use Case 1: Facility management and maintenance support [Image: © se commerce]

Use Case 1 addresses the easy availability and visualization of live measured data at the building through the Digital Twin using edge cloud and cluster computing technologies. A multi-layered façade system ensures long-term and low-maintenance use. To offer the customer a maintenance service that is optimized and target-oriented, the conditions of the glass elements are continuously monitored. The acquisition of temperature, humidity and air pressure values also enables weather data to be recorded in detail for facility management. The shared use of measurement data by users, operators, product manufacturers and consultants is a typical use case for the development and management of a collaborative Digital Twin. This use case allows the devel-

opment of fundamental platform features, the integration of specific algorithmic analysis and the implementation of AR technologies. Figure 4 shows a schematic view of the relevant topics.

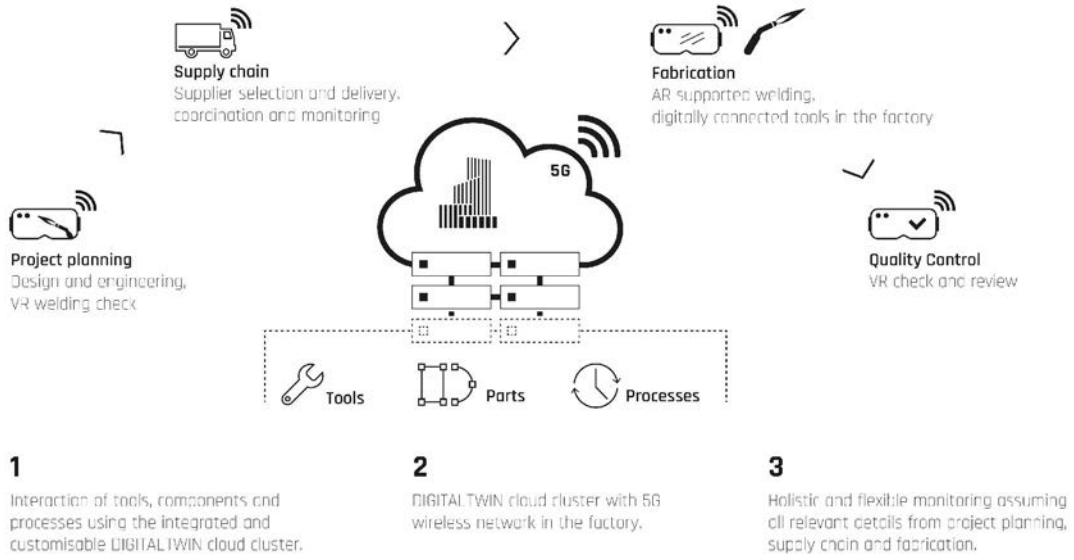


Figure 5: Use Case 2: Digital quality assurance for welding works [Image: © se commerce]

Use Case 2 addresses a virtual welding documentation and inspection on the shop floor. Interconnecting all data within the planning, supply chain management and fabrication processes is a key to enable a remote inspection of welding seams using a precise Digital Twin. All information relating to planned and actual geometry, base material, tools and machines used, settings as well as measurement and scan data are provided accordingly for inspection and documentation. The capabilities of new computer vision technologies for applications under difficult operating conditions is also investigated. Figure 5 shows a schematic view of the relevant topics.
Use Case 3 addresses the issue of more effective and efficient installation using digital tools and task-related interconnected information. The use of mixed reality technology in safety glasses will provide users relevant information, which is currently documented and communicated on drawings. A gridshell construction will be used to demonstrate the complete process chain from parametrical design, assembly planning and logistics to assembly support on site. Installers will be able to see installation sequences and identify and localize correct parts and tools. Furthermore, they can document various work steps, such as verifying the correct component position or correct tightening torques of bolts. Figure 6 shows a schematic view of the relevant topics.

3 Digital Tools on Site, necessary pre-processes and data dependencies

For the last use case, mixed reality technology with video glasses has been identified as an important, forward-looking technology. The use on the construction site makes sense, as integration into safety glasses will be possible in the future and safe operation is possible without the need to carry devices and tools. In addition, the new technology makes it possible to develop a flexible and simple hardware integration in future IT environments.

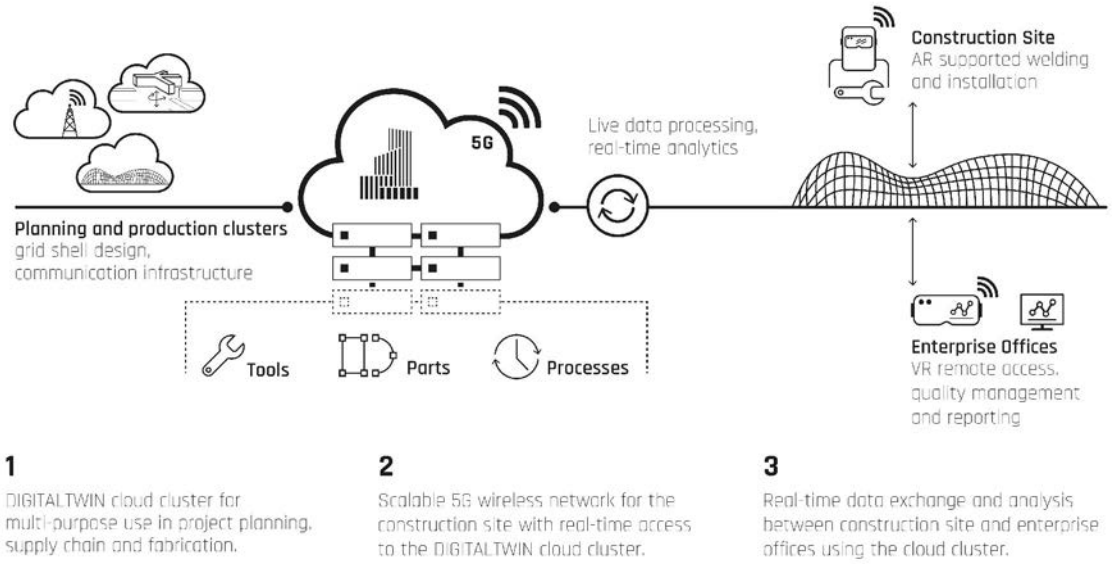


Figure 6: Use Case 3: Assembly support with MR/AR-technology [Image: © se commerce]

A first demo was realized, which addresses the problem of intuitive positioning and the verification of installation within tolerances. A steel node, which is typically used for large gridshell constructions can be moved, rotated and tilt. The Hololense supports finding the right position within installation on site and checking tolerances on the fly. The computer vision technology gives these additional information and indicates, where to move the object and when you reach the right position.

Installers commissioned with the assembly of components must first familiarize themselves with complex processes. Usecase 3 deals with the simplification of assembly processes, supported by digital tools, such as augmented reality glasses, in which the real environment is connected with virtual 3D objects in real time. And for this use case a first demo was realized, which addresses the problem of intuitive positioning and the verification of installation within tolerances. A steel node, which is typically used for large grid constructions can be moved, rotated and tilted by the user for demonstration purposes.

These movements along the x-, y- and z-axis are reproduced by a camera mounted statically in the room. First, the registration of the node takes place at a defined starting position, which is calibrated by using markers. After that an arbitrary target position is defined in the system at which the node is finally to be mounted by the user in the simulated construction site environment. For the tracking of movements, the camera creates an edge detection by means of grayscale adjustment and thus continuously locates the position of the node. In order to support the user with Microsoft HoloLens AR glasses, the created data on the target position as well as the tracked live position are technologically transmitted to the data glasses at runtime by so-called web sockets.

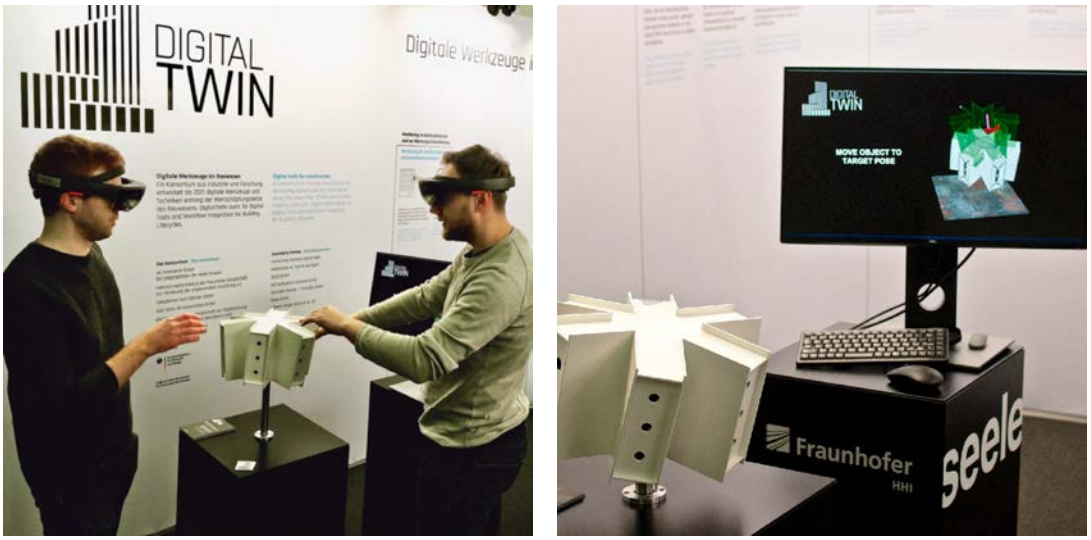
In the mixed-reality world of HoloLens, the user is assisted by colored arrows that indicate the direction in which the node should be guided to the target position. By rotating and tilting the steel node into the right direction, the corresponding direction arrow is increasingly minimized. If the user succeeds in completely minimizing all direction arrows, the object has arrived at

the target position where the node is to be mounted later, e. g. by screwing it together. In addition to arrows, so-called gizmos for distance checks in the corresponding tolerance ranges and a visual checklist are displayed, which indicates the correct alignment along the axes by means of percentage values for the accuracy of the assembly and finally by confirmation hooks. Once the node has been mounted in the correct location, the system also transmits a visually projected 3D reference node overlaid on the real node in green. The UI and the operator guidance in the HoloLens have already been brought into the second version for the demonstrator by user feedback. The next aim is to use the HoloLens camera to perform the registration of the object that is currently being performed by the auxiliary camera. In the future, the components to be assembled on a construction site will be recognized directly with the data goggles and assigned to the corresponding assembly position.
Figure 7 shows a construction site of a gridshell project using scaffolds, manual and digital measuring devices in combination to adjust parts of the steel structure and the resolving assembled structure. Figure 8 shows the connected IT technology and a steel node as an example to demonstrate an intuitive and integrated installation process and tolerance check.



Figure 7: example for an installation on site [Image: © seele]

An important lesson learned from testing assembly support with mixed reality is that the solution is seen as a good substitute for a large number of individual working steps needed today. Gestures can be trained to operate the system, even if it is necessary to gain additional knowledge regarding a clear and reliable control system for the construction site. It is obvious that today's software solutions do not yet allow an automated scene configuration and thus a context-related data rendering. The necessary networked data is simply unavailable and the software solutions have not yet been developed integrating fully data exchange with special software and workflows of the building context. It is also foreseeable that the necessary data needs a solution for broadband communication for many different participants on site. This makes it obvious that a successful use of digital tools in routine operation on the construction site is dependent by many different aspects. In particular the interface technology for data exchange, the communication technology for the construction site and the system integration based on a simple, flexible platform ecosystem are relevant topics.



(a) MR/AR support positioning a steel node (b) Accompanying visualization of the results

Figure 8: Demo: Positioning and the verification of tolerances [Image: © se commerce]

4 Interoperability and system integration using scaleable and flexible ICT

A networked Digital Twin with mapping of object, process and tool data should be this simple collection point of a wide variety of information. It can reduce the loss of information at critical interfaces and in the course of construction projects. The consistency of data formats and model contents is relevant for planning. For use on the construction site, the integration of tools, ease of use and situational use are added. Due to the heterogeneity and lack of standardization, the data format and structure have to be adjusted, developed and tested each time. Until reliable standards are implemented, the only way to work effectively on a project is to coordinate processes, data exchange and data management openly and at an early stage with partners. [4] Furthermore, it is noticeable that digital tools occasionally encourage the consideration of secondary issues. Irrelevant adjustments to the accuracy of a model despite much greater tolerances in execution mean that some designs lack a working tolerance concept at the design stage. At the same time, experience in steel and aluminium construction with CNC machines shows that the preparation effort for digitally conceived design approaches is lower than for shaped, modeled designs. Digital tools do not automatically guarantee a correct design or a design description adapted to the manufacturing process - but they can be an important aid. For this, a closer exchange between partners as well as the early consideration of manufacturing processes and procedures is important. Planning, production and operation must be thought and managed more closely together. For flexible, trustworthy partner networks, the corresponding infrastructures are not yet in place that enable transparent project structuring and organization as well as simple and quick operability.

Since many different partners are involved along the planning and the building life cycle, reliable use of data formats and interface definitions across software generations and ecosystems is important - a requirement which, however, receives too little attention due to the current hype surrounding BIM and the existing market conditions of software solutions for planners, manufacturers and operators. Manufacturers outbid each other with additional features and functions,

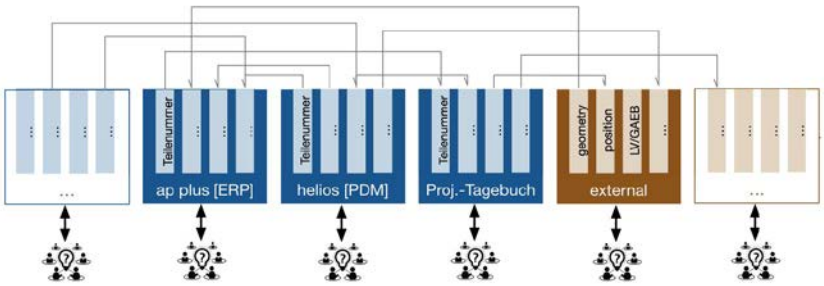


Figure 9: Typical direct linking of software solutions [Image: © se commerce]

without producing any notable advances in compatibility or taking the market's requirements for data sovereignty and data security seriously.
In other industries there is a better combination of such information and data sources - not least due to the product responsibility typically clearly assignable to a manufacturer. This enables industries such as automotive and aircraft construction to create, process and administer comprehensive and largely consistent digital images of their products using integrated and standardized processes. In this context, the term Digital Twin is used. This refers to a more or less complete and functional description of a component or product in digital form.
Digital Twins already exist in the construction industry - but so far only in individual companies and only for individual tasks. The understanding of what information forms a Digital Twin also varies greatly. For example, the use of 3D construction part data is sometimes referred to as a Digital Twin or Building Information Modeling. In other industries, the process goes much further; there, comprehensive networking of data sources and coupling of simulation models are already common (suggests industry wide use: somewhat weaken: in use). The solutions developed here can provide the construction industry with important clues for the future use of digital planning tools. The DigitalTWIN research project aims to accelerate this critical transfer of solutions and make it safe and easy to apply along the entire value chain.
Figure 9 shows a schematic example for interconnected software solutions in a grown ecosystem. On the other hand, web technologies and digital web-based platforms guide to simple to use, multi-functional environments for example in business to consumer services. Interestingly, the use of such solutions for project management tools leads to mistrust and concerns between project partners. Research projects such as scaleIT or DigitalTWIN address these concerns, with the aim of developing a trustworthy networkable cloud cluster infrastructure that enables data sovereignty and data protection in the construction project as well as with regard to the software providers.
Figure 10 shows a schematic new way to interconnect software solutions within an enterprise using web-based and open source technologies. The platform is also useable in a cluster network to enable the collaboration of different departments, different project groups or companies. An

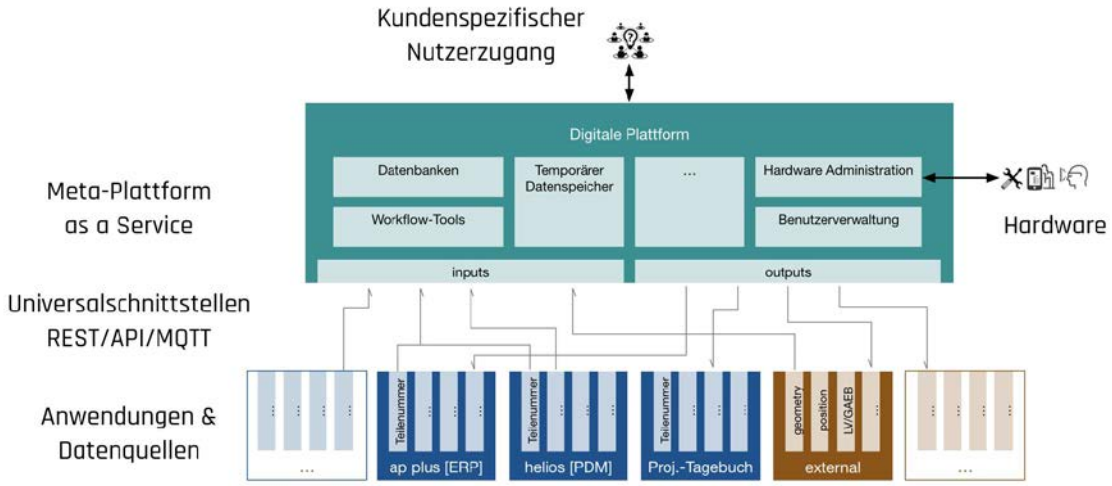


Figure 10: Integrating software, hardware and processing tools [Image: © se commerce]

additional important characteristic is a user-specific access to all connected software solutions and data storages without the need to learn individual expert user interfaces.

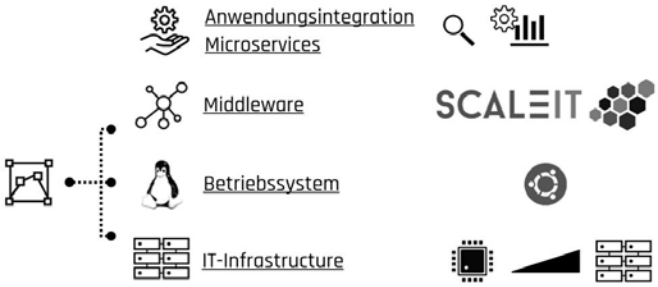


Figure 11: Technology stack of an open source, flexible and scaleable platform [Image: © seele]

For planners as well as for manufacturing companies, the change that digitalization brings, can only be positively shaped if an open discourse between stakeholders, employees and software developers is established. With many digital tools, usability and administration are so complex that a lot of time has to be spent on preparing and merging the data or programming interfaces. A further problem is the difficult operability of many software solutions - complex training courses with little lasting learning success are the result. This leads to a lack of interest and the continued use of a limited set of functions. In design offices, it can also be observed that, despite increasing digitalization, the number of hand-drawn sketches is increasing - employees have to visualize the geometry in order to understand certain dependencies. This is characteristic of the entire planning process. Planning processes will therefore long be an interplay of analog and digital steps. Accordingly, the digital tools must enable the exchange of information in a consistent and simple manner.

Such trustworthy, open and secure basic infrastructures are important for the long-term operation of buildings in addition to the manufacturing industry. To be able to provide IT infrastructure not only after completion, but also during the construction phase and with the possibility to let different partners and trades participate, is a basic prerequisite for an improvement of the processes during the construction phase, a faster commissioning and system integration for the building operation and a flexible exchangeability and further use of technology during maintenance and other services for users and operators.
The results of the first demos and the technical investigation on the use cases in the research project show that developments regarding IT infrastructure for manufacturing purposes of small and medium-sized enterprises can be transferred and extended to the market situation of the construction industry and the construction site. The open, flexible and adaptable technology stack from scaleIT was identified as an important component. It makes big data, web-based, open source technologies flexibly usable with regard to the hardware selection (microcontroler to service cloud), offline or online architecture as well as the administration of networked data of various formats and sources. Figure 11 shows the principal layers of the technology stack. Software development and user specific programming can be handled on the top layer by the use of microservices, which are developed agile and lean using e.g. docker software-containers. the stack is designed to be used even in complex cluster configurations, which will also enable and simplify digital cooperation between different stakeholders in the long term. The development of a trustworthy and easy-to-use IT infrastructure like scaleIT, which meets the European requirements for data protection, privacy, copyright, quality and the needs of small and medium sized enterprises is an important prerequisite for the successful long-term digitalization of the construction industry.

5 Conclusion

Digital Twins, Industry 4.0 and BIM: All three terms have one essential thing in common: they are keywords that aim to point out the relevance of digitalization for society and the economy and the need for action. Their broad interpretation makes sense because they affect almost all market participants and ensure that the topic is relevant. For planners and manufacturing companies alike, the changes that digitalization can only be positively shaped if an open discourse is established in order to jointly find industry-specific answers to concerns and opportunities.
Project experience shows that today the use of valuable resources for administrative work that is unavailable for the primary tasks associated with the project and the core challenges continues to grow. Interfaces to planners, subcontractors or general contractors, for example, must be redefined, tested and adhered to from project to project. With many digital tools, usability and administration are so complex that a lot of time has to be spent on preparing and merging the data or preparing the programming of user interfaces. Also obvious is the often not self-explanatory operability of software solutions: complex training courses with little learning success are the result. This also leads to a lack of interest in dealing with new digital tools and a limited, familiar function set is used for many different tasks: "We know, but we do it manually with Excel lists". This response from critical users should not be underestimated, as lists, documents, hand-drawn sketches or whiteboard sketches are also relatively simple and convey the feeling of autonomy and controllability.
Even an own small database applications can only be set up by experienced users or experts from project experience. Furthermore, despite the numerous digital tools on offer, many employees keep their personal notebooks. This is where important information is noted during meetings,

although the diversity of this information is kept out of further processing. Protection of privacy, data and copyright are reasons for this. However, these analogous work steps are also important arguments for finding solutions. In the design office it can be observed that despite increasing 3D design, the number of hand sketches in front of the screens is increasing. This is due to the need for employees to visualize the geometry in order to understand certain dependencies.
This is characteristic of the entire planning process. Today, there are many design and development steps that serve the development of solutions and are characterized by analog working methods. The conversion into descriptive models or data as well as their further development is implemented more efficiently with digital tools. Planning processes will thus long be an interplay of analog and digital steps. Accordingly, the tools must enable the exchange of information in a consistent and simple manner.
A holistic system understanding and the development of an open platform architecture, more advanced broadband communication systems and computer vision technologies influence the guiding principals and the research work. The approach uses web and big data technologies for a new information technology backend. The frontend shall provides a reliable, flexible and upgradable communication and management infrastructure in an easy to use way connecting planning, production and building site for advanced projects. [3]

6 Acknowledgements

The research project DigitalTWIN is supported by the Federal Ministry for Economic Affairs and Energy (BMWi) and it is part of the Smart Service World II funding program.

References

[1] F. Schmid, S. Marinitsch, M. Teich and C. Timm, "Metal and Glass gridshell Design: Flexible Integration of Digital Design and Fabrication Tools", *Proceedings of IASS Annual Symposia: IASS 2018 Boston Symposium*, Boston, USA, July 16-20, 2018, IASS 2018.

[2] T. Spitzer, H. Eder, C. Bauchinger, I. Volkhausen, S. Peters, S. Engelsmann, C. Dengler, and C. Fischer, "Freeform gridshell for Chadstone Shopping Centre, Melbourne", *Proceedings of IASS Annual Symposia, IASS 2017 Hamburg Symposium*, Hamburg, Germany, September 25-28, 2017, IASS 2017.

[3] "Digital tools for the building sector". `https://d-twin.eu/en/` [Online; accessed 23-Jan-2019].

[4] "Scaleable ICT for Increasing Productivity in Mechatronics Manufactureing". `https://scale-it.org/en/the-project.html/` [Online; accessed 14-Jun-2019].

Proceedings of the IASS Annual Symposium 2019 – Structural Membranes 2019
Form and Force
7 – 10 October 2019, Barcelona, Spain
C. Lázaro, K.-U. Bletzinger, E. Oñate (eds.)

Novel Parametric Knowledge Modelling approach applied to Viaducts

Maria GKIOKA[*], Jeroen COENDERS[a], Rob NIJSSE[b], Sander van NEDERVEEN[c], Sander PASTERKAMP[d], Arend RUTGERS[e]

*White Lioness technologies
Van Diemenstraat 118, Amsterdam, Netherlands
mariagkioka@white-lioness.com
[a] White Lioness technologies
[b,c,d] Delft University of Technology
[e] A&E Architecten

Abstract

This paper presents a novel approach to modelling and documenting design knowledge: to use parametric technology to explicitly store knowledge which exists in a group of people (such as a company), so that it can be reused over many projects and grow over time when more projects are designed. This approach has been applied and tested on a test case of common concrete viaducts. The outcome constitutes the first iteration of the development of a parametric viaduct design platform, aimed for architects and structural engineers. The motivation was to counter the fragmentation of the Architecture, Engineering & Construction (AEC) industry, where each discipline encapsulates different knowledge areas, which results in miscommunication and the loss of valuable information and time. The suggested methodology aims at combining the BIM principles [1] with the concepts of parametric and associative design, as well as visual programming [2] to develop a common design platform for the architect and the structural engineer. Such a platform ensures that both disciplines are working on the same design and merges their different knowledge areas into one model. The knowledge model evolves from a top-down UML diagram into a user-friendly, parametric platform for viaduct design implemented in Dynamo [3].

Keywords: concrete viaducts, conceptual design, parametric design, associative design, knowledge model, BIM

1. Introduction

This research project investigates the development of a knowledge-based, parametric platform and the extent to which the knowledge around an infrastructure project can be integrated and stored on such a platform. While Building Information Modelling (BIM) aims at resolving the miscommunication within the project design team, BIM technologies are often characterised by a limited design flexibility, which discourages the practitioners from adopting an integrated design approach from the early design stages. To tackle this, the knowledge model of this research project is based on BIM principles, considering associative modelling with local and global design parameters, in an attempt to identify patterns, create links and produce an efficient, computational design approach and a final 3D visualisation of the viaduct.

This research project focuses on defining the recurrent steps of the design and tracking the implicit information, which is usually hidden behind the project's requirements and the designer's intuition [4].

Copyright © *2019 by Maria GKIOKA, Jeroen COENDERS, Rob NIJSSE, Sander van NEDERVEEN, Sander PASTERKAMP, Arend RUTGERS*
Published by the International Association for Shell and Spatial Structures (IASS) with permission.

The resulting platform enables the engineer/architect to access, interpret and act on the available information. The infrastructure project under investigation is a common concrete road viaduct over traffic. This project type is chosen for its repetitive design process, which restrains the architectural freedom and the available functional choices.

2. Methodology

The methodology for this research project is based on an ontology, composed of various systems and subsystems (components) which have their own requirements and goals in a local level, but are also connected to each other, so as to meet global requirements. As an ontology, the viaduct includes a set of concepts, entities, properties and functions, as well as relationships and semantics [5]. The output of this approach is a generic viaduct design template which can serve as a starting point for similar projects. In the aforementioned template, the abstract needs and requirements of a project can be converted into functional and technical input, processed on the platform and the final output can be visualised.

The first step of the research project is to define how the viaduct components are related and the requirements which steer the design. As a second step the translation of the aforementioned knowledge into an associative, parametric model is attempted. The structural analysis of the bridge is also integrated into the platform, so that the communication between the architect and the structural engineer can be facilitated. An outline of the process can be seen in Figure 1.

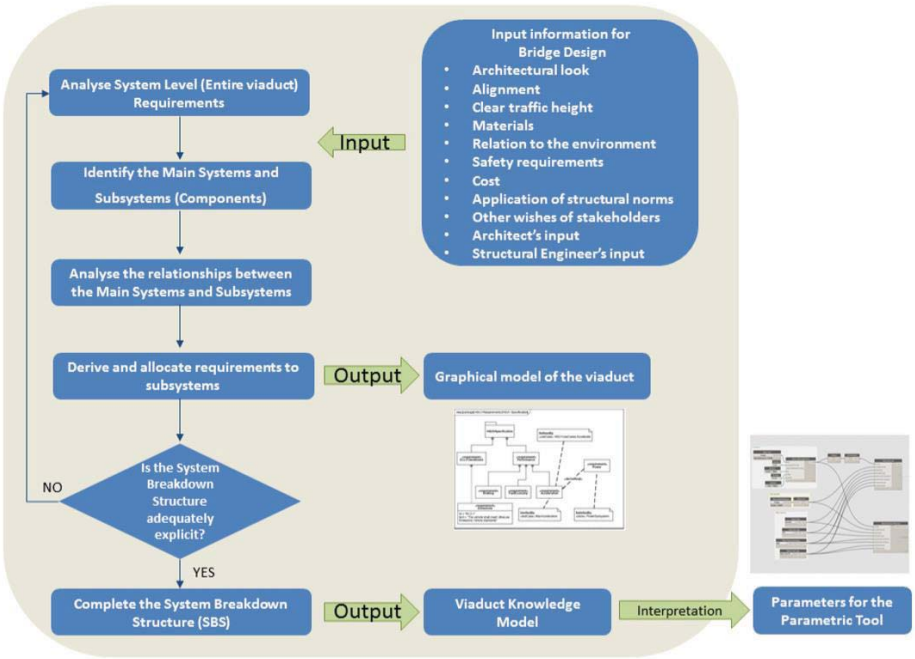


Figure 1: Development of the knowledge model and its relation to the Parametric Model

2.1. Development of the Knowledge Model

The aim of a knowledge model is to capture, formalise and implement the knowledge of the AEC practitioners into a digital design tool, incorporating automated, as well as semi-automated tasks [6]. One of the most important, yet elusive elements, associated with a knowledge model is the experience of the design team. In order to capture the latter, the parameters defined in the model are specified after discussion with practitioners at BAM A&E, the architectural and engineering department of a major Dutch contractor.

One of the objectives of the knowledge model is to define which information is relevant during each design phase and therefore request the right level of input from the designer. For instance, in preliminary design the choice of the deck prefab beams type is not required, since it can be decided at a later stage.

The knowledge model of this research project focuses on three main components: the deck, the abutments and the pier. Those components function as a system, since the design needs of one influence the design needs of the others. The knowledge model documents the interaction between those components by introducing a generic viaduct design, which includes all possible designs within the set design space.

2.2. UML diagram

Initially, the viaduct is seen as a system with a top-down structure and a UML [7] model is developed to outline the relationships between the components on a higher level. The UML model contains the main components of the viaduct, as well as their main design parameters. Through this model the propagation of the design changes and the influence of each design choice on the rest of the model can be monitored. An important step in establishing a connection between the UML model and the parametric/associative model is to clarify the semantics of the relationship between them.

2.3. Parametric Model

The strict top down structure of the UML model facilitates the definition of the system components and the interaction among them. The findings of this step, along with a further investigation of the topological interdependencies of the components, are used to develop a parametric model, based on a bottom up approach. Parametric design is by essence non-destructive, meaning that one model contains all the previously explored solutions, as well as the ones yet to evaluate [8], which can highly benefit the design process, by enabling an interactive feedback loop. This parametric model is developed in Dynamo [9].

The development process requires a constant re-evaluation of the defined parameters, namely specifying the shape and qualities of each component, so as to address the design needs of the viaduct. The Dynamo model constitutes a fully parametric design algorithm, where the user is able to create numerous designs, within an expandable design space. The whole viaduct model is built around two alignments, the 3D alignment of the viaduct and the 2D alignment of the road underneath, which are part of the initial input. A user interface is added to the model in order to guide the user through the parameters that need to be defined. The visualisation of the final design can be seen in Figure 2.

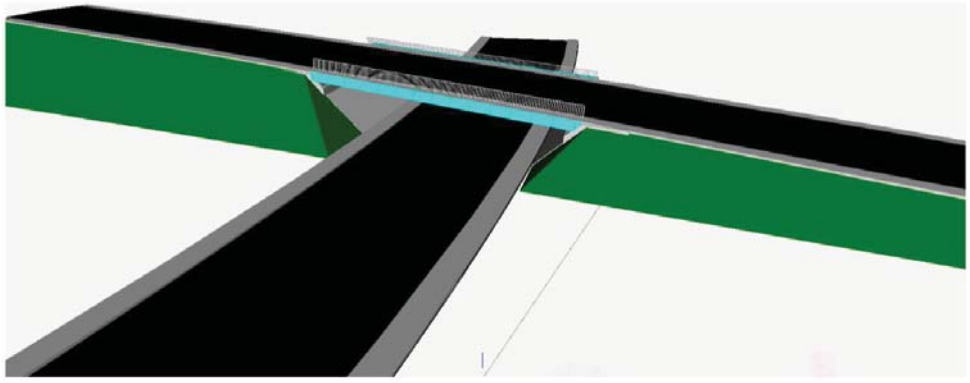


Figure 2: Visualisation of viaduct in Dynamo

The development of the script is incremental, in order to ensure that the complexity is gradually introduced to the model and ensure the credibility of the final parametric model. Two main tools are employed: Visual Programming (Dynamo) and Python. The connection between the applications is illustrated in Figure 3.

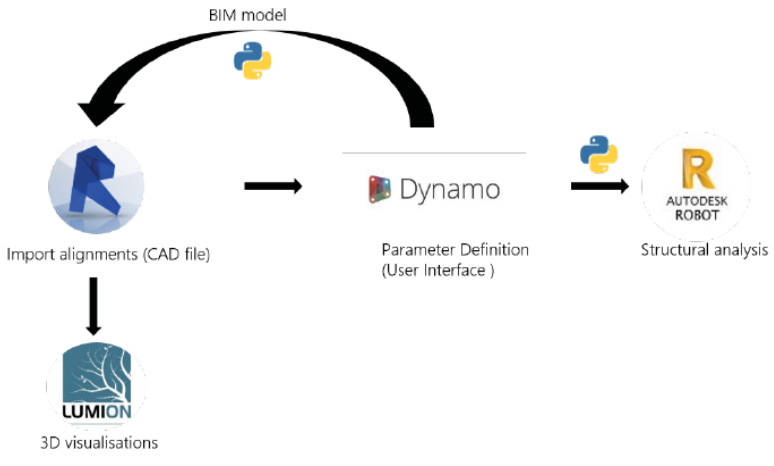


Figure 3: Overview of linked applications

2.4. Design Parameters

The design parameters of this research project have been derived from the study of the requirements and the input of the AEC practitioners. The total number of parameters is 82 and a list of them is presented in Table 1.These parameters are divided in three categories, according to the level to which the designer can influence them. Those categories are the following:

User-Defined parameters: User-defined parameters reflect the level of design freedom in the model. This parameter type can be seen in Table 1 (no colour). A number of user-defined parameters can be symmetrical, which means that the same design choice can be applied for both (or more) instances of one object, which reduces the overall design complexity. E.g the cornices on both sides of a viaduct are usually the same, so the designer needs to define the object only once.

Default parameters: The default parameters do not have an impact on the design. The values of those parameters can be predefined, as they refer to standardised components or standardised dimensions of components. This parameter type is denoted with light grey in Table 1.

Immutable parameters: This category is closely related to the scope limitations of the platform. The user cannot influence these parameters, as they define the scope of the research. For instance, the abutments of the viaduct can only be of type bankseat, therefore the abutment type is an immutable parameter. This parameter type is denoted with dark grey in Table 1.

Table 1: Parameter list

Element Name	Number of Instances	Parameters
Viaduct	1	Alignment
		Slope (side 1)
		Slope (side 2)
		Road width underneath the viaduct
		Pier
Deck	1	Width
		Slab Thickness
		Crossfall
		Tolerances
		Asphalt Layer
		Clearance Height
		Curved/Straight Edges
Railings	2	Position on Curb
		Inclination
		Shape of Vertical and Horizontal Bars
		Distance between Vertical Bars
		Number of Horizontal Bars
Edge Elements	2	Shape
		Size
		Length of each element
		Tolerance
		Position
		Cutting at Wing Walls
Abutments	2	Type
		Shape (6 parameters)
		Vertical Translation
		Location
		Angle of Skewness
		Cut for Approach Slabs
Bearings	n	Dimensions (3 parameters)
		Position
		Number
Approach Slabs	2 arrays	Dimensions (3 parameters)
		Position
Wing Wall	4	Shape
		Dimensions (3 parameters)
		Position
Pier	0 or 1	Position
		Number of Columns
		Diameter of Columns
		Dimensions of Pier Beam (2 parameters)
		Pier Beam Cut to Skewed Angle
Surroundings	-	Embankment angle

The percentage of each parameter type in relation to the whole parameter set can be seen in Table 2.

Table 2: Design parameters

Parameter Category	Number	Percentage of Total Parameters
User-Defined (non-symmetrical)	42	51.2%
User-Defined (symmetrical)	30	36.6%
Default	30	36.6%
Immutable	10	12.2%

3. Structural Analysis

The structural analysis of the viaduct is also considered at a conceptual level, by linking the parametric model directly to the structural analysis application. This eliminates the need for each practitioner to develop individual models on multiple applications. To achieve this, Robot [10] is linked to the

Dynamo model via Python. All structural analysis parameters, the generation of the FE model and the linear analysis execution are defined and controlled in Dynamo and the structural engineer uses the Robot environment simply to assess the analysis results.

The scope of the structural analysis is limited to the deck of the viaduct, considering prefabricated beams. The output of the structural analysis provides an overview of the resulting forces and the behaviour of the slab. The Robot model can be seen in Figure 4.

From this model the following can be derived:

1. Effect of prestressing on the slab.
2. Behaviour of the viaduct under the applied loads
3. Reactions at the supports and shear reinforcement in the beams.

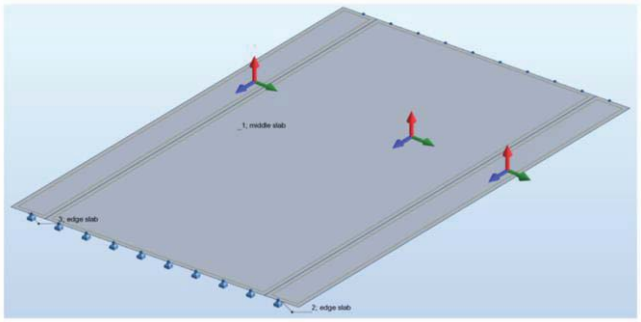


Figure 4: FE deck model in Robot

3.1 Structural analysis assumptions

The following assumptions have been made for the structural analysis.

3.1.1. General assumptions

The structural analysis is conducted at the full service stage of the viaduct ($t = \infty$). The prefab beams and the in situ concrete layer are assumed to work together as one composite section. The deck of the bridge is modelled as orthotropic plate elements.

3.1.2 Supports

Point supports which restrict the vertical movement are employed, in order to simulate the effect of the bearings. The location of the supports is defined automatically in Dynamo, based on the dimensions of the abutments.

3.1.2. Loads and load combinations

The loads are automatically placed on the deck, according to its geometry and distribution of notional lanes. The following loadcases are considered:

Dead Load: The dead load is considered for the whole model.

Asphalt Load: The asphalt load is applied on the carriageway as a uniformly distributed load.

Edge Load: A line load is applied at the edges of the viaduct to include the loads of the curb, the edge elements, the parapet and the railings.

Traffic Loads: Uniformly distributed loads and a tandem system are considered according to EC2 [11]. The location and magnitude of the loads are automatically generated in Dynamo.

3.2. Structural result validation

The result validation of this conceptual study by the researcher is limited to the following three verification methods, since the goal of the research project is to conduct a first iteration towards the development of a knowledge model for parametric viaduct design. Those methods are:

1. Visual Verification: Check whether the viaduct has the expected behaviour under the applied loads.

2. Sum of reactions: Check whether the sum of the reactions equals the sum of the applied loads.

3. Comparison with analytical solutions: The Guyon-Massonnet method [12] was employed to define the load distribution on the beams and verify the results of the structural analysis in Robot.

4. Test Case

The platform is tested on an actual project to assess its efficacy and the value it can bring to its execution. The Hoevelaken project (designed by BAM A&E) includes the construction of new common concrete viaducts in the area of Hoevelaken (the Netherlands), as well as the expansion of existing ones. The outcome of this research has been assessed, using the Hoevelaken Quality Team requirements for the new viaducts, which provide guidelines about the conceptual design. These guidelines focus on the function of the viaducts, the visual impact of the design, the relation to the surroundings and the user experience, as well as ensure that the design is cohesive.

The total number of requirements in this category is 56, of which 24 could be met by the platform. This proves that the platform can be an important asset during the design phase, since the interpretation of the requirements by the designers can be visualised easily, discussed and agreed upon. In Table 3, a list of the met requirements is given, along with their subdivisions.

Table 3: Requirements met by the platform

Category	Number of Requirements
Cohesive Design	3
Span and Clearance Height	2
Deck Curvature	2
Viaduct - Environment relation and Abutment Type	2
Detailings of Edges	7
Pier Location and Design	4
Slopes	4
Total	**24**

5. Conclusion

This research project investigates a novel approach to viaduct design, in an attempt to facilitate the communication among the team members and develop a parametric design platform which encapsulates their accumulative knowledge.

The results of this conceptual study indicate that the designers can highly benefit from such an approach. Indeed in the case of a symmetrical viaduct design the number of user-defined parameters are 30 out of 82 (36.5%). This means that the design time can be drastically reduced, since 63.5% of the design issues considered in this study are automatically addressed by the platform. Testing the platform using actual design requirements, further underlines the benefits of this approach, since 24 out of 56 (42.8%) requirements could be addressed using the platform.

A more automated design process, supported by parametric design, allows the designer to focus on the creative and challenging parts of the design process and drastically reduce the amount of time needed for the mundane parts of it. Moreover, through visual programming, the parametric model's logic is transparent and available to the designer, rather than hidden in a "black box".

An important constraint are the tools that were used in this research project, since the increased complexity of the model and the dense relationships between the components reduce the computational speed. This could be resolved by changing the tools that were employed in this research project and moving the knowledge model to the cloud, in order to fully benefit from the suggested approach.

Acknowledgements

The authors would like to acknowledge Delft University of Technology, BAM A&E and White Lioness technologies for their guidance and involvement in this research project.

References

[1] C. Eastman, P. M. Teicholz, R. Sacks and K. Liston, BIM Handbook: a Guide to Building Information Modeling for Owners, Managers, Designers, Engineers and Contractors. Hoboken, NJ, Wiley, 2011.

[2] J. Coenders, "NetworkedDesign: Next generation infrastructure for computational design", Ph.D. dissertation, Dept. Civil Eng., TU Delft, Delft, Netherlands, 2011.

[3] R. Aish and E. Mendoza, "DesignScript: a Domain Specific Language for Architectural Computing", in Proceedings of the International Workshop on Domain-Specific Modeling 2016, Amsterdam, the Netherlands, October 30 – November 4, 2016, pp.15-21.

[4] M. Bernal, J. R. Haymaker, and C. Eastman, "On the role of computational support for designers in action". *Design Studies 41*, 2015, pp.163–182.

[5] M. P. Nepal, S. Staub-French, R. Pottinger, and A. Webster, "Querying a building information model for construction-specific spatial information", *Advanced Engineering Informatics 26,* no.4, 2012, pp.904–923.

[6] M. Sandberg, P. Jensen, and I. Ramic, "Knowledge-based bridge design", *19th IABSE Congress, Strockholm,* 21-23 September 2016, pp. 328–336.

[7] J. Rumbaugh, I. Jacobson, and G. Booch, "Unified Modeling Language Reference Manual", Pearson Higher Education, 2004

[8] R. A. Danhaive, and C. T. Mueller, "Combining parametric modeling and interactive optimization for high performance and creative structural design", *in Proceedings of IASS Annual Symposia, Amsterdam Symposium: Future Visions – Computational Design*, August 2015, pp. 1-11,

[9] DynamoBIM, DynamoBIM, 2017 [online], Retrieved September 10, 2017, from http://www.dynamobim.org/

[10] Autodesk, Robot, 2017, [online] Retrieved October 25, 2017, from http://www.autodesk.com/products/ robot-structural-analysis/overview

[11] Eurocode 1: Actions on structures—part 2: Traffic loads on bridges (EN No. 30). British Standards Institution, 2003

[12] P. P. Xanthakos, "Theory and design of bridges", John Wiley & Sons, 1994

Proceedings of the IASS Annual Symposium 2019 – Structural Membranes 2019
Form and Force
7 – 10 October 2019, Barcelona, Spain
C. Lázaro, K.-U. Bletzinger, E. Oñate (eds.)

Review of parametric strategies for design optimization of built structures

Sanjay SOMANATH [*], Vanessa REED [b], Robert CARPENTER [b], Sarah DAVIDSON [a], Jack WU [a], Paolo BECCARELLI [a],

*Department of Architecture and Built Environment - University of Nottingham
University of Nottingham, University Park, Nottingham NG7 2RD
sanjay.somanath@nottingham.ac.uk

[a] University of Nottingham
[b] I2O Ltd.

Abstract

A survey of several workflows for the optimization of various objectives involved in the design of buildings using parametric design tools are presented. A greater emphasis is placed on workflows targeted towards the structural optimization of the building. A general design optimization workflow is identified, and a new consolidated workflow is presented. Further, an overview of the tools and methods implemented in each of the steps is presented in order to encourage more designers to explore the utility of combining opensource tools in their parametric design workflow. It is also found that no singular tool, method or approach is objectively superior. Rather, the selections of these tools, methods and approaches must take into consideration the specific needs of the problem, feasibility of acquiring the tool, the capabilities of the tools and user preferences, extent of collaboration as well as the required level of accuracy the project requires.

Keywords: Parametric design, BIM, IFC, Structural Analysis, Optimization.

Abbreviations

AEC – Architecture Engineering and Construction
BIM – Building Information Modelling
BPA – Building Performance Analysis
CAD – Computer Aided Design
CAE – Computer Aided Engineering
FEM – Finite Element Method
FEA – Finite Element Analysis
IFC – Industry Foundation Classes
IGA – Isogeometric Analysis
MOO – Multi-Objective Optimization
MOP – Multi-Objective Optimization Problems
NURBS – Non-uniform rational basis spline
PDE – Partial differential equation
RSM – Response Surface Methodology
SDK – Software Development Kit
SFMT – Simultaneous Failure Mode Theory

1. Introduction

Traditionally the AEC industry is extremely slow to change, mostly due to technology being the driver of the change rather than an enabler of change driven by the user/designer [1]. However, given enough time, stability and reliability of new technology and most importantly the increase in business drivers to force the use of this technology such as – increasing multidisciplinary collaboration, need for sustainable design and construction, demand better data management for various end of construction stages the

Copyright © 2019 by Sanjay SOMANATH, Vanessa REED, Robert CARPENTER, Sarah DAVIDSON, Jack WU, Paolo BECCARELLI
Published by the International Association for Shell and Spatial Structures (IASS) with permission.

adoption of new technologies supporting geometrical modelling such as BIM, in the AEC industry is very promising [2].

1.1. Traditional design Processes

In the traditional design process the stages of development are typically linear[3]. Initial stages primarily focus of form development and functional aspects of the design and gradually move towards detailed design stage where other performance factors can be analysed and improved [4], [5]. The initial form development stage focuses on the aesthetics and generally are driven by the project architect and further delivered to a structural engineer to develop the design further with a suitable structural system. However, this process is done towards the end of the design stage[6] when majority of the design would have been decided on resulting in a lot of constraints for further steps on the design stage. This linear approach generally results in limited communication and mutual understanding between architects and structural engineers [7]. The introduction of complex CAD tools has now allowed designers to perform conceptual structural, occupant comfort and sustainability [8], [9] analysis at the early design stages [7].

1.2. Parametric design and neutral file formats for data exchange

Further to the introduction of early stage design tools, the increased accessibility of parametric design tools has made the initial design process more fluid and iterable. Current industry practices still haven't completely bought in to the parametric design process entirely and still use multiple models independently resulting in a large amount of duplication, simplification, translation, abortive and redundant design efforts [10] [4].
Integrating all the stages in the design process using a parallel design workflow that exchanges information through a neutral file format can result in numerous benefits reducing the amount of duplication and expediting the design process as well as improving collaboration between different disciplines [11].
Neutral file formats such as IFC have the ability to contain customizable attributes as the information is required to be exchanged. Designers can use this information for interoperability between software and tools as well as filter out the data at different levels of detail for various types of analysis as well as the use of multi-objective solvers capable of heuristic problem solving [10].

1.3. Optimization of objectives in the AEC design process

Some of the earliest optimization in the form development stages have been demonstrated through the works of Antoni Gaudi [12] and Frei Otto[13] with their use of inverted catenary chains and soap-film models to represent behaviors of shapes on larger scales. With the advent of new computation tools and methodologies the complex field of optimization is becoming more and more accessible to architects and engineers alike.

In the field of AEC, there are several highly specialized and technical disciplines [14] that require to inform each other and work together to resolve a problem at different stages of the project, right from the design to construction and operation.[15] In most of the cases engineering problems need to be optimized by taking two or more opposing criteria such as minimizing weight and minimizing the stiffness of a structural member [8], [15] or to maximize daylight factor while reducing thermal heat gain into the envelope of a building and controlling the cost of the solutions [8], [9]. Such optimization problems are called Multi-Objective Optimization Problems (MOP) in literature [5], [15], [16]. One important distinction indicated by Nguyen, Reiter and Rigo [17, p.] on the topic of optimization in the context of building performance simulations is that the objective of the above mentioned optimization is not always to find a singular solution that maximizes or minimizes the objective function but can also be used to determine multiple sub-optimal solutions that can be further developed by the designer/engineer or even to study the problem using a sensitivity analysis [17], [18] or approximation methods like RSM [18]. The importance of structure and energy[19] as early design objectives has already been covered in literature [16].

2. Overview of analysis tools and methodologies

Structural Analysis – It is the process of utilizing the set of mechanical theories that obey the physical laws required to predict the behavior of a structure in order to determine the deformations, internal forces and stresses. Several methodologies have been implemented in literature to perform structural analysis on buildings that rely on either analytical formulations or numerical approaches such as FEM. [20]

This survey presents structural analysis methodologies that have been implemented with the larger overview of parametric and multidisciplinary capabilities that can be optimized using one of several optimization methods.

2.1. Basic Concepts and Definitions

FEA – FEA can be achieved using numerical approaches called FEM. Traditional FEM is solved using various genres of PDE and the suitability of these equations are decided by the structural engineer based on the type of problems and the boundary conditions. With the introduction of computational solvers and software with user friendly GUI, the selection of tools to solve the problems are significantly simplified. One approach to introducing parametric capabilities to FEM is using open-source FEM solvers such as OOFEM [21] to communicate with structural pre-processors like MIDAS [22] through interoperability tools like DONKEY [23] using a neutral file format in Grasshopper [7], [24]. A similar workflow is used in [4], [16] where the solver, preprocessor, interoperability tool, interoperability format and post processors are used to achieve the same final goal using Karamba [25], Grasshopper, Geometry Gym [26], Rosetta [27], and Autodesk Robot Structural Analysis.

Isogeometric Analysis – Traditional FEA solvers require a labor-intensive process called polygonal meshing [28], where the 3D bounding element representing the geometry of the object to be analyzed is divided into discreet polygons in order to perform FEM on complex geometry. IGA can bypass this step by taking advantage of the NURBS geometry representation method used in popular commercial 3D modelling programs such as Rhino [29]. The NURBS geometry can be created in Grasshopper and then can be converted in the T-Spline geometry using the Autodesk T-Spline plugin for Rhino in order to be analyzed by an analysis solver called the IGA Shell Solver [28] KIWI!3D [3] is another plugin for Grasshopper capable of performing IGA .

RSM – The response surface modelling of design constraints can be done by taking a multivariate polynomial model representation of a problem and solving them through a sample size to record the "experimental" solutions of the problem. Once the RSM is used to construct performance functions, the problem can then be further optimized using various algorithms and approaches [18].

A common pattern seen in the workflows surveyed above is that there needs to be a process to parametrically model and control the design problem and then maintain the parametric information and control while the model is structurally analyzed, in addition to this the results from the analysis must be identifiable with the configuration of the parametric model. In all surveyed examples, these tasks are performed by disjointed and usually opensource add-ons to popular parametric-visual programming tools such as Grasshopper. However, there do exist more robust workflows that utilize integrated commercial tools that provide parametric modelling and analysis capabilities within the same package. Examples of such tools are Bentley's Generative Components (GC) [30] and COMSOL Multiphysics. The structural model can be modelled within GC or COMSOL Multiphysics while being assigned to parametric control variables and the variables can further be packaged to define a new variable that controls the overall form of the geometry reducing the number of decision variables for further post processing of analysis data [31] either within an existing optimization package or an external optimization package through a live link [30].

Simultaneous Failure Mode Theory (SFMT) – One of the earliest methods used to determine the optimal structural conditions that result in the minimization of the strength to weight ratio is the SFMT. The basic concept being that the requirement for optimum structural configuration of members is a

combination that results in all the failure modes occurring simultaneously for the possible design variables [32]. This theory can be used to setup the graphical model of the global structural system within a 3D modelling tool capable of parametric control as well as seamless and lossless bi-directional communication with an analysis platform.

Several traditional structural design tools such as Bentley's STAAD Pro can also be used for a parametric generative design process by defining loading trees created through a pre-processor interface to create a .std input file according to user defined values [33], either directly or through the OpenSTAAD library. However, to achieve comparable levels of automation and convenience to other workflows surveyed in this paper, it would require high levels of programming capabilities and further expertise in order to implement an automated optimization algorithm to the design process.

Similar workflows have been explored within a more robust BIM environment using tools such as Autodesk Revit , Ansys and custom plugins developed through the Revit API [34] and even including a point cloud based approach to capture as built site data - SolidWorks ScanTo3D to reconstruct structures that have already been built but don't have reliable construction data [34]. Standalone opensource tools such as Ebes [35] have been used to frame the numerical model and can be further integrated with a compatible optimization package called JMetal [35] to close the feedback loop required for Multi Objective Optimization [15].

With regards to overall parametric control the two software packages that stand out due to their industry wide use and robust support structure are Bentley's Generative Components and McNeel's Rhino + Grasshopper package with its extended plugin family. Generative components in combination with Bentley MX for parametric control and Bentley Triforma for modelling documentation and Rhino-Grasshopper in combination with Infograph [36], Oasys GSA for structural analysis, Salamander [37] and StructuralComponents to communicate with the finite element solvers [38].

3. Overview of tools for Neutral File Format Conversion

3.1. Background to Neutral File Formats

For several years there have been efforts to create a neutral file format for data exchange within the AEC industry but now with the added incentivisation of greater levels of sustainability of data handling in the industry, this goal is now achievable through BIM [2] and more specifically due to the efforts of the International Alliance for Interoperability (IAI) [11].

3.2. Improvements and add-ons to IFC

By no means is IFC a complete solution[11], [39] for collation and exchange of data between AEC disciplines [11] but given the recent international adoption of the schema as a CAD-CAD vehicle [40] IFC is the most mature of the neutral file formats having already been tested for its compatibility with structural analysis through structural analysis tools [39], [41]. There is also development of other infrastructure for technology transfer through the integration of STEP, CIMSteel and IFC that is used as an extension to the existing IFC schema though a model called sCAsD [14]. The sCAsD infrastructure is capable of incorporating four model schemata, namely the dynamic analysis schema, FEM schema, structural analysis results schema, and the relationships schema [14]. One approach proposed to overcome the constant need to reproduce the IFC file to provide the downstream disciplines with the most up to date file is to integrate the parametric modelling and analysis tools, either directly or through plugins [4], [42] or through a BIM based approach [42], [43] like Geometry Gym, a plugin that allows communication to other software through IFC or proprietary software SDK's, Chameleon [44] a Grasshopper plugin that allows the exchange of data through the gbXML file format [42], GRevit [45] a Grasshopper plugin that supports multiple software interaction through a network communication protocol, VisualARQ [46] a BIM extension to Rhino that allows users to call existing BIM libraries in VisualARQ and use BIM features in the Rhino environment through IFC, BIMScript by BIMObject is

a tool that allows for BIM content creation as well as a free scripting language that allows users to author BIM object attributes, JumpingFrog|Robot [47], a plugin that allows not only for exchange of data between Autodesk Robot Structural analysis and Grasshopper but also to import results and perform smart post-processing of the information etc.
Grasshopper in particular has a healthy ecosystem of dedicated users and developers that keep the list of interoperable software that Grasshopper can communicate with steadily increasing. IFC based systems being only one of the ways this is possible. Grasshopper through Geometry Gym can communicate to a number of industry standard analysis software such as Ansys, Robot, Tekla, SAP2000, Oasys GS and many more using a combination of text-based file formats and API interaction [10]. Other third-party releases of GeometryGym are also capable of exchanging information for steel detailing through the Steel Detailing Neutral Format (SDNF).
Commercial architectural and BIM software are now beginning to integrate the neutral file format and parametric tool integration into their software packages, one example of a significant move in this direction is by ArchiCAD by Graphisoft that has an ArchiCAD-Grasshopper link feature that allows simultaneous modelling and editing of parametric 3D geometry with BIM properties in on ArchiCAD through Grasshopper.

4. Overview of Optimization methods reviewed

As mentioned above in 1.3, in most engineering problems the functions that need to be optimized are usually made up of a combination of two or more opposing objectives. The process of systematically optimizing a collection of objective functions is known as multi objective optimization (MOO) [48].

Performing a sensitivity analysis once the parametric model and analysis models have been set up in order to make decisions on the objective functions and decision variables can be extremely beneficial and time saving for the designer and the wider project team. When multiple criteria contribute towards the objective function it is generally advisable to gauge the significance of each criteria by conducting a sensitivity analysis on the criteria and mapping the value of the function while keeping all the other criteria constant [18]. For example, a sensitivity analysis is conducted on ANSYS through APDL (the native ANSYS programming language) or using other tools to implement the Morris Method of Sensitivity Analysis [30].

4.1. Basic Concepts and Definitions

A key term to be defined in the subject of MOO is a Pareto Optimal condition. A Pareto Optimal condition can be defined as a condition where it is impossible to improve one aspect of the condition without drastically making the other aspects worse. There are other terms such as compromise solutions and ideal points that refer to a situation where a true Pareto Optimal solution is not feasible.

When a multi-objective optimization problem is posed, it usually requires maximizing or minimizing of a set of objective functions. The reader is referred to [48] for a comprehensive survey of multi-objective optimization methods for engineering. Even though there are several methods to attain the Pareto Optimal Point of a problem [48], from an engineering and design point of view this may not always be desirable. What is more useful to Architects and Building engineers is to be presented with Multi-modal [31] compromise solutions, regardless of the availability of a Pareto optimal point and then use their professional judgement and understanding of the subject and other collaborative subjects to decide.

Due to this collaborative nature of AEC, with many specialized subjects being involved in the design process, setting up a MOO problem may be too computationally expensive or may result in no optimal solutions. This is where heuristic solutions may be more suitable for the problem. Due to the requirement of a global, discreet and multi-objective method, evolutionary multicriteria optimization methods are suitable for these types of problems [5], [15], [49] These include NSGA-II [15], [49], SPEA2 [15], [49], (c)MOEA/D[15], Close Harmony Improvisation [31], Simulated annealing [50] etc.

There are several software packages that incorporate metaheuristic optimization methods such as NSGA-II, MOEA/D that contain inter-application communication capabilities such as Simulated Annealing and Evolutionary solvers provided within Galapagos [51], a built-in solver within Grasshopper, jMetal to optimize objective functions set up in Ebes [15], Genetic Algorithm solvers provided in the MATLAB optimization Toolbox™ [18], ModeFRONTIER [52] is a comprehensive multidisciplinary optimization platform with inter-software capabilities and has been used in optimization of large sports building envelops [53]

Problems with high levels of unpredictability may be better evaluated using stochastic, non-parametric methods such as historical simulation and Monte-Carlo simulations [49]

Shape and size optimization problems in structural design have been solved in the past using similar methodologies as the methods mentioned above but these methods present with several limitation such as inability to converge even to local minima [8]. One solution that overcomes these limitations is Topology Optimization , the guiding principle in the use of topology optimization for structural optimization is that form-follows-force and material is only used based on the loads and the boundary conditions [8]. Topology optimization follows the same technique as FEM, where an element is broken down to several smaller fragments allowing for discrete analysis of each fragment. Among the various numerical methods for topology optimization, Evolutionary Structural Optimization (ESO) and Bidirectional Evolutionary Structural Optimization (BESO) by Mike Xie and Grant Steven have been studied thoroughly in literature [54].

TopOpt [55] is a topology optimization package for Rhino3D and Grasshopper developed by the Århus Architect School, Technion and DTU, capable of performing Topology optimization for various applications such as acoustic modelling, energy harvesting, fluid dynamic simulations etc. [56]. Octopus [57] is another multi-objective optimization toolkit employing evolutionary algorithms that has been used for shape optimization of building envelopes [58] amongst other BPA optimizations [19], [59]. Ameba [60] and TopoStruct [61] + Millipede [62][63] are plugins for Grasshopper that bring BESO topology optimization capabilities within a parametric environment.

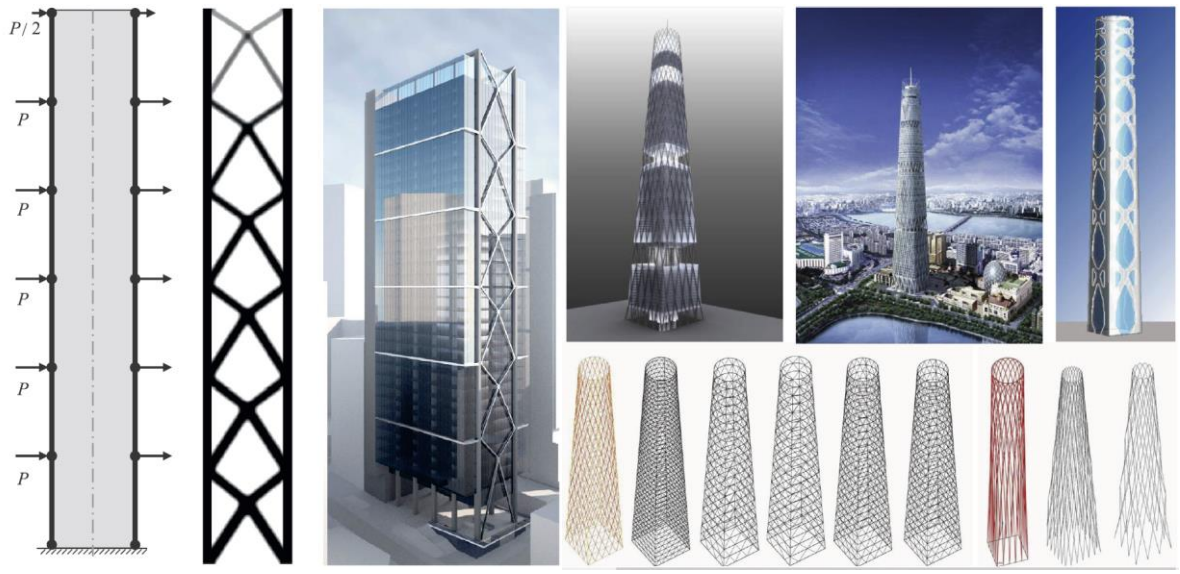


Figure 1 Topology Optimization and Parametric Setup of Highrise buildings [8]

Table 1 Analyzed workflow of Case Studies

Case Studies	**Reference**	**Architectural Form Finding**	**Modelling of the Architectural/Structural System**	**Numerical Modelling/Cost Function**	**Interoperable File conversion**	**Structural Analysis**	**FEM Analysis**	**Other Analysis**	**Optimization Methods**
Kurilla's Annelida bridge	[7]		✓	✓		✓			
Self-supporting Leonardo's bridge	[7]		✓	✓		✓			
Geometric Death Frequency-141	[7]		✓	✓		✓			✓
126 bar spatial truss structure	[64]					✓			✓
A 36-story frame structure	[64]					✓			✓
Origami-inspired deployable shelter	[64]		✓		✓	✓			
Modular façade design for an office building	[4]		✓	✓				✓	✓
Pavilion truss	[4]		✓	✓	✓	✓			✓
Thin Concrete Shell	[12]	✓	✓	✓	✓	✓			✓
NREL Phase VI wind turbine blade	[28]		✓			✓	✓		
NREL 5 MW wind turbine blade	[28]		✓			✓	✓		
HUT-600 project	[11]		✓		✓			✓	
Structural Optimization problem	[49]			✓		✓	✓	✓	✓
Design of a cable-stayed bridge	[15]		✓	✓		✓			✓
Design of a lightweight composite triangular truss	[18]		✓	✓				✓	✓
Bridge supported by two parabolic arches (Basket Handle arch bridge)	[31]		✓	✓		✓	✓		✓
Transmission Tower	[33]		✓	✓		✓			✓
Stadium Roof	[40]	✓	✓		✓	✓		✓	
Castle of Haut-Koenigsbourg	[34]		✓	✓	✓	✓	✓		✓
Competition entry for the Austrian Pavilion of the EXPO2010	[38]		✓	✓		✓			
Scheme Design for Coastal Canopies	[38]	✓	✓	✓		✓			
NSP Arnhem transfer hall	[38]	✓	✓	✓		✓			
Kurilpa tensegrity bridge	[38]		✓	✓	✓	✓			✓
Cable stay bridge option study	[38]		✓	✓		✓			✓
Window Frame Analysis	[30]		✓	✓				✓	✓
World Trade Centre Tower One spire	[8]	✓	✓	✓		✓			✓
Multitower Bridge-Zendai Competition	[8]	✓	✓	✓		✓			✓
Structure Similar to Exchange House - London	[65]	✓	✓	✓		✓	✓		✓

5. Integrated AEC design approach

Comparing existing case studies that have incorporated various methodologies we can observe a generic workflow in *Table 1* for the design process that enables the designers to further optimize the design parameters using computational methods [16], [42]. One key element that is not automated is the initial form finding process since it requires cognitive evaluation of the risks, opportunities and constraints of a design project. However, once the initial form-finding has been developed, preliminary refinement to the design can be achieved by developing a parametric computational model capable of bidirectional communication of design and analysis data [66]. Establishing bidirectional communication capabilities in the parametric model is key to enable parallel development of the design stage and improve multidisciplinary collaboration throughout the design process.

Combining all the key stages of design development observed in the case study projects a parametric workflow can be generalized as follows –

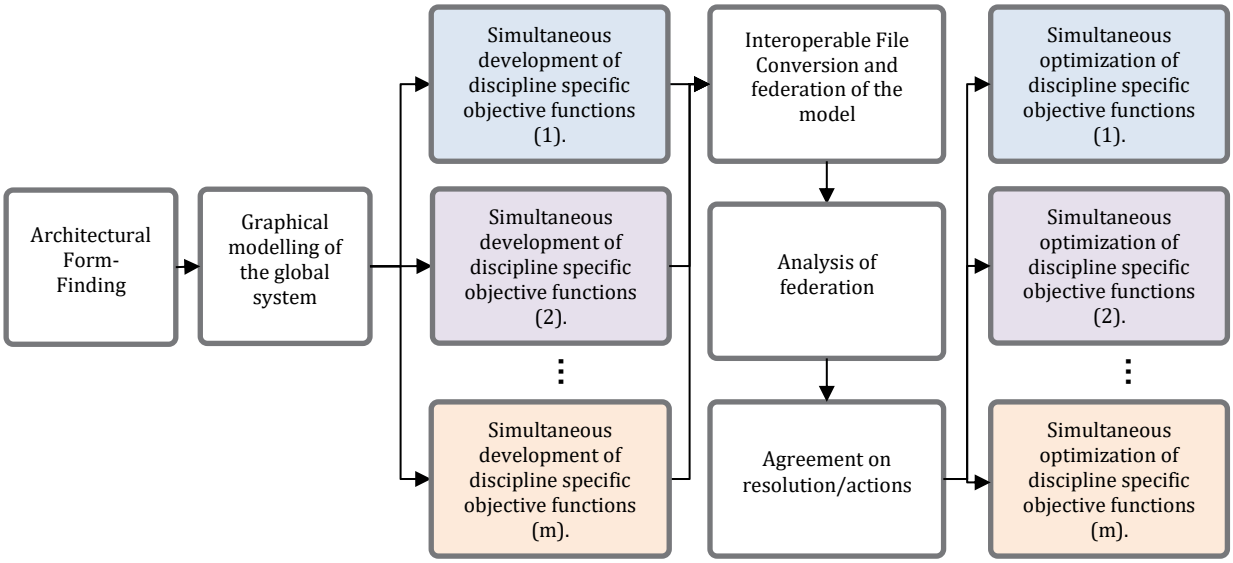


Figure 2 Generalized parametric workflow for interdisciplinary collaboration

The general set of vectors representing the multi-objective optimization problem can be posed as follows

$$Min\, f(x_m) = (f_1^m(x_m),\ f_2^m(x_m),\ \dots,\ f_{nm}^m(x_m)) \quad (1)$$

$$\textbf{s.t}\ x_m \in \mathbf{X}$$

Where m is the number of multi-objective objective optimization vectors with independent variables x_m.

The feasible design space X where feasibility implies that none of the constraints of the problems are violated.

The function $f(x_i)$ could be described as a function to minimize heat gain in the structure and $f(x_j)$ could be described as a function to minimize weight of the structural system, where $f(x_i)\ and\ f(x_j)$ have no interdependent variables.

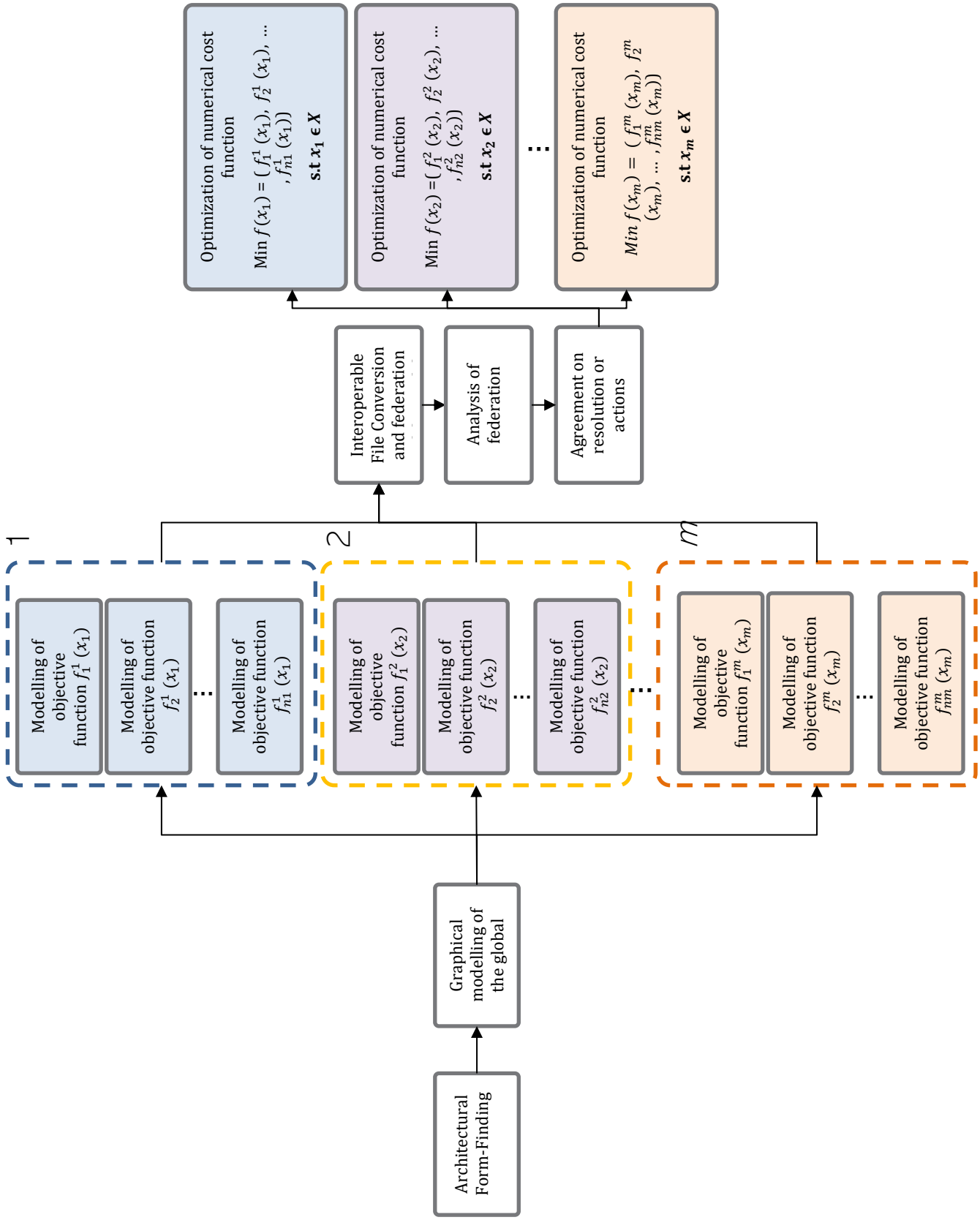


Figure 3 Proposed workflow for an integrated optimization approach for AEC design

6. Conclusion and further work

Design and analysis are at the core of the AEC industry and several workflows have been proposed over the years to incorporate efficient arrangements of these processes. However, over the recent years with the increase in computational accessibility to architects and engineers through parametric design and analysis tools like Grasshopper, dynamo, Tekla etc. these workflows need to be re-assessed and updated to be able to exploit the capabilities provided by these tools. Multi-Objective Optimization too is no longer purely in the domain of statistics, data analysis and computer science. Rather, the spread of the opensource computation community is increasing the accessibility of high-quality optimization algorithms and toolkits for a generic designer or engineer to exploit. The frameworks that are proposed to integrate these interdisciplinary exercises must be validated and re-adapted to create an increasingly robust. No single tool or software can be considered a generic solution to all the various design problems faced by engineers and architects but a single robust framework that integrates the tools together is of great value to provide direction to those involved in the development of the tools. Change in the AEC industry must be initiated through a ground up approach rather than simply be software generated. Further trial and research are required on the comparative application of the tools and strategies mentioned in this review on real-world case studies to identify the benefits and disadvantages of various tools depending on the design problem.

References

[1] K. A. Davis and A. D. Songer, "Technological change in the AEC industry: a social architecture factor model of individuals' resistance," in *IEEE International Engineering Management Conference*, Cambridge, UK, 2002, vol. 1, pp. 286–291.

[2] N. Gu and K. London, "Understanding and facilitating BIM adoption in the AEC industry," *Automation in Construction*, vol. 19, no. 8, pp. 988–999, Dec. 2010.

[3] P. Längst, A. M. Bauer, A. Michalski, and J. Lienhard, "The Potentials of Isogeometric Analysis Methods in Integrated Design Processes," p. 11, 2017.

[4] R. Aguiar, C. Cardoso, and A. Leitão, "Algorithmic Design and Analysis Fusing Disciplines," p. 10, 2017.

[5] L. Grunske, "Identifying 'good' architectural design alternatives with multi-objective optimization strategies," in *Proceeding of the 28th international conference on Software engineering - ICSE '06*, Shanghai, China, 2006, p. 849.

[6] RIBA, *Plan of Work for Design Team Operation, Reprinted from RIBA Handbook, 1973 Edition*. RIBA, 1973.

[7] L. Svoboda, J. Novák, L. Kurilla, and J. Zeman, "A framework for integrated design of algorithmic architectural forms," *Advances in Engineering Software*, vol. 72, pp. 109–118, Jun. 2014.

[8] L. L. Beghini, A. Beghini, N. Katz, W. F. Baker, and G. H. Paulino, "Connecting architecture and engineering through structural topology optimization," *Engineering Structures*, vol. 59, pp. 716–726, Feb. 2014.

[9] E. Touloupaki and T. Theodosiou, "Optimization of Building form to Minimize Energy Consumption through Parametric Modelling," *Procedia Environmental Sciences*, vol. 38, pp. 509–514, 2017.

[10] J. Mirtschin, "Engaging Generative BIM Workflows," p. 8.

[11] J. Plume and J. Mitchell, "Collaborative design using a shared IFC building model—Learning from experience," *Automation in Construction*, vol. 16, no. 1, pp. 28–36, Jan. 2007.

[12] C. Gomes, M. Parente, M. Azenha, and J. C. Lino, "An integrated framework for multi-criteria optimization of thin concrete shells at early design stages," *Advanced Engineering Informatics*, vol. 38, pp. 330–342, Oct. 2018.

[13] R. Muslimin, "Parametric, grammatical, and perceptual iterations on structural design synthesis," *AIEDAM*, vol. 32, no. 3, pp. 269–281, Aug. 2018.

[14] M. Hassanien Serror, J. Inoue, Y. Adachi, and Y. Fujino, "Shared computer-aided structural design model for construction industry (infrastructure)," *Computer-Aided Design*, vol. 40, no. 7, pp. 778–788, Jul. 2008.
[15] G. R. Zavala, A. J. Nebro, J. J. Durillo, and F. Luna, "Integrating a multi-objective optimization framework into a structural design software," *Advances in Engineering Software*, vol. 76, pp. 161–170, Oct. 2014.
[16] N. Brown, S. Tseranidis, and C. Mueller, "Multi-objective optimization for diversity and performance in conceptual structural design," p. 12, 2015.
[17] A.-T. Nguyen, S. Reiter, and P. Rigo, "A review on simulation-based optimization methods applied to building performance analysis," *Applied Energy*, vol. 113, pp. 1043–1058, Jan. 2014.
[18] S. Ju, R. A. Shenoi, D. Jiang, and A. J. Sobey, "Multi-parameter optimization of lightweight composite triangular truss structure based on response surface methodology," *Composite Structures*, vol. 97, pp. 107–116, Mar. 2013.
[19] M. R. Asl, M. Bergin, A. Menter, and W. Yan, "BIM-based Parametric Building Energy Performance Multi- Objective Optimization," p. 10.
[20] K.-H. Chang, *Product Performance Evaluation using CAD/CAE: The Computer Aided Engineering Design Series*. Academic press, 2013.
[21] B. Patzák, "OOFEM — an Object-oriented Simulation Tool for Advanced Modeling of Materials and Structures," *Acta Polytechnica*, vol. 52, no. 6, p. 8, 2012.
[22] L. Svoboda, *MIDAS - Multifunctional Interface between Design And mechanical response Solver*. 2014.
[23] L. Kurilla, *DONKEY: Structural Evaluation Assistant*. 2016.
[24] D. Rutten, *Grasshopper*. Robert McNeel & Associates, 2007.
[25] C. Preisinger, "Linking Structure and Parametric Geometry," *Archit Design*, vol. 83, no. 2, pp. 110–113, Mar. 2013.
[26] J. Mirtschin, "Generative Models Utilized for Superior Design Development," *Proceedings of IASS 2011*, 2011.
[27] J. Lopes, "Portable Generative Design for CAD Applications," p. 8, 2011.
[28] M.-C. Hsu, C. Wang, A. J. Herrema, D. Schillinger, A. Ghoshal, and Y. Bazilevs, "An interactive geometry modeling and parametric design platform for isogeometric analysis," *Computers & Mathematics with Applications*, vol. 70, no. 7, pp. 1481–1500, Oct. 2015.
[29] *Rhinoceros*. Robert McNeel & Associates, 2018.
[30] J. Zajas and P. Heiselberg, "Parametric study and multi objective optimization of window frame geometry," *Build. Simul.*, vol. 7, no. 6, pp. 579–593, Dec. 2014.
[31] K. Martini, "Optimization and Parametric Modelling to Support Conceptual Structural Design," *International Journal of Architectural Computing*, vol. 9, no. 2, pp. 151–166, Jun. 2011.
[32] N. G. R. Iyengar, "Optimization in Structural design," p. 8.
[33] Z. C. Muda, K. N. Mustapha, R. C. Omar, F. Usman, M. A. Alam, and S. Thiruchelvam, "Optimization of Structural Design for Sustainable Construction of Transmission Tower Based on Topographical Algorithm," *IOP Conf. Ser.: Earth Environ. Sci.*, vol. 16, p. 012023, Jun. 2013.
[34] X. Yang, M. Koehl, and P. Grussenmeyer, "Parametric Modelling of As-Built Beam Framed Structure in BIM Environment," *Int. Arch. Photogramm. Remote Sens. Spatial Inf. Sci.*, vol. XLII-2/W3, pp. 651–657, Feb. 2017.
[35] F. Luna, G. R. Zavala, A. J. Nebro, J. J. Durillo, and C. A. C. Coello, "Solving a Real-World Structural Optimization Problem with a Distributed SMS-EMOA Algorithm," in *2013 Eighth International Conference on P2P, Parallel, Grid, Cloud and Internet Computing*, 2013, pp. 600–605.
[36] *InfoGraph*. Aachen, Germany: InfoGraph Gmbh.
[37] P. Jeffries, *Salamander 3*. Denmark: Ramboll Group A/S, 2017.
[38] A. Rolvink, R. van de Straat, and J. Coenders, "Parametric Structural Design and beyond," *International Journal of Architectural Computing*, vol. 8, no. 3, pp. 319–336, Sep. 2010.

[39] C. Wan, P.-H. Chen, and R. L. K. Tiong, "Assessment of IFC's for Structural Analaysis Domain," p. 21.
[40] D. Holzer, R. Hough, and M. Burry, "Parametric Design and Structural Optimisation for Early Design Exploration," *International Journal of Architectural Computing*, vol. 5, no. 4, pp. 625–643, Dec. 2007.
[41] M. Weise, P. Katranuschkov, T. Liebich, T. L. Consulting, and R. J. Scherer, "Structural Analysis Extension of the IFC Modelling Framework," p. 20.
[42] P. Janssen, "Parametric BIM Workflows," p. 10.
[43] G. Gudnason and R. Scherer, *eWork and eBusiness in Architecture, Engineering and Construction: ECPPM 2012*. Taylor & Francis, 2012.
[44] H. Jacobs, *Chameleon*. 2017.
[45] M. Thumfart, *Grevit*. .
[46] *VisualARQ*. Barcelona, Spain: Asuni, 2019.
[47] *JumpingFrog|Robot*. weArk.
[48] R. T. Marler and J. S. Arora, "Survey of multi-objective optimization methods for engineering," *Structural and Multidisciplinary Optimization*, vol. 26, no. 6, pp. 369–395, Apr. 2004.
[49] C. A. Coello, A. Hernández Aguirre, and E. Zitzler, Eds., *Evolutionary multi-criterion optimization: third international conference, EMO 2005, Guanajuanto, Mexico, March 9-11, 2005: proceedings*. Berlin ; New York: Springer, 2005.
[50] C. Tort, S. Şahin, and O. Hasançebi, "Optimum design of steel lattice transmission line towers using simulated annealing and PLS-TOWER," *Computers & Structures*, vol. 179, pp. 75–94, Jan. 2017.
[51] D. Rutten, "Galapagos: On the Logic and Limitations of Generic Solvers," *Architectural Design*, vol. 83, no. 2, pp. 132–135, Mar. 2013.
[52] *modeFRONTIER*. eSTECO.
[53] D. Yang, Y. Sun, and M. Turrin, "Multi-objective and multidisciplinary design optimization of large sports building envelopes: a case study.," p. 15, 2015.
[54] X. Huang and M. Xie, *Evolutionary Topology Optimization of Continuum Structures: Methods and Applications*. Wiley, 2010.
[55] D. Maier, *TOPOPT*. Technical University of Denmark, Israel Institute of Technology and Aarhus School of Architecture.
[56] M. Sasaki and O. Sigmund, "Discrete topopt formulation," *Mechanical Engineering*, p. 16.
[57] R. Vierlinger and K. Bollinger, "Accomodating Change in Parametric Design," 2014.
[58] L. Zhang, L. Zhang, and Y. Wang, "Shape optimization of free-form buildings based on solar radiation gain and space efficiency using a multi-objective genetic algorithm in the severe cold zones of China," *Solar Energy*, vol. 132, pp. 38–50, Jul. 2016.
[59] Y. Ashour and B. Kolarevic, "Optimizing Creatively in Multi-Objective Optimization," p. 8.
[60] *Ameba*. XIE Technologies.
[61] K. Sawako and M. Panagiotis, *TopoStruct*. .
[62] K. Sawako and M. Panagiotis, *Millipede*. .
[63] P. Michalatos and A. O. Payne, "Working with Multi-Scale Material Distributions," p. 8, 2013.
[64] M. Kim, "A Study on Efficient Approaches for Grasshopper Programming in Architectural Design Process," *Korean Journal of Computational Design and Engineering*, vol. 21, no. 4, pp. 453–461, Dec. 2016.
[65] W. F. Baker, A. Beghini, and A. Mazurek, "Applications of Structural Optimization in Architectural Design," in *20th Analysis and Computation Specialty Conference*, Chicago, Illinois, United States, 2012, pp. 257–266.
[66] L. Qin, X. Deng, and X. Liu, "Industry foundation classes based integration of architectural design and structural analysis," *J. Shanghai Jiaotong Univ. (Sci.)*, vol. 16, no. 1, pp. 83–90, Feb. 2011.

Proceedings of the IASS Annual Symposium 2019 – Structural Membranes 2019
Form and Force
7 – 10 October 2019, Barcelona, Spain
C. Lázaro, K.-U. Bletzinger, E. Oñate (eds.)

Proposal of design method of natural and rational tree-structure based on computational hanging upside-down simulation

Chisato EGUCHI, Noritoshi SUGIURA, Hiroyuki TAGAWA*

*Mukogawa Women's University
1-13 Tozaki-cho, Nishinomiya, Hyogo, 663-8121, JAPAN
tagawa@mukogawa-u.ac.jp

Abstract

In our previous study, a physical hanging upside-down model was created to obtain structurally rational configuration of a tree-structure supporting a free-surface shell roof, which was still close to the designer's image. Then, simulation of computational hanging upside-down model of unstable truss structure was conducted to correct nodal coordinates slightly so that the equilibrium holds at each joint due to axial member forces only. However, trunks and branches obtained were all straight lines, similar to most existing tree-structures, which gave artificial rather than natural impression. In this study, a design method to obtain "natural" and "rational" tree-structure based on hanging upside-down simulation is proposed. First, a shape of a tree-structure is obtained using physical model similar to actual trees. The 3D geometric data is computed through photogrammetric processing and the finite element model is created. Computational simulation of the hanging upside-down model is conducted applying the dynamic relaxation. Bending stress values before and after the hanging upside-down simulation is evaluated. Finally, architectural design of a natural and rational tree-structure, which has slightly curved trunks and branches but still has bending stress within admissible level, is proposed.

Keywords: tree-structure, morphology, upside-down model, dynamic relaxation, physical model, computational model

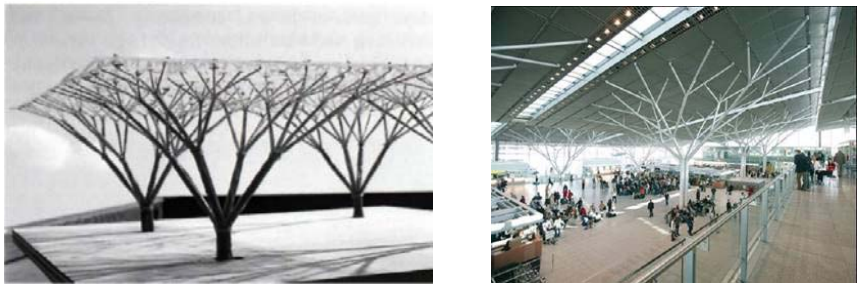
1. Introduction

The tree structure, the use of which was first proposed by Frei Otto in 1960 and implemented at Stuttgart airport as shown in Figure 1, is a fascinating structural form that can be used to create a large space owing to its organic design. In a tree structure, from the perspective of structural rationality, it is desirable that the loads are transmitted with axial forces only. In order to find an axial-force-resistant form of a tree structure, various methods [1]-[6] have been proposed. However, it is difficult to satisfy both a free form envisioned by a designer and the structural rationality simultaneously.

In our past study [7],[8], a "classical" experimental approach comprising a physical hanging upside-down model as shown in Figure 2 was used to obtain an axial-force-resistant form of a tree structure subjected to gravity loading. Further, structural analyses were conducted using the finite element model based on the 3D configuration data obtained through photogrammetric processing in order to evaluate how axial-force-resistant the scaled model and the full-scale structure are.

In this research, a method to correct the 3D configuration model such that it becomes more axial-force-resistant by conducting "computational" hanging upside-down simulation applying dynamic relaxation to the computational hanging upside-down model of the unstable truss structure is proposed. Further, to be more generalized, it is examined whether more "natural" configuration of the tree-structure with curved trunks and branches, which possesses structural rationality simultaneously, can be obtained by the "physical" and "computational" hanging upside-down models.

Copyright © 2019 by Chisato EGUCHI, Noritoshi SUGIURA, Hiroyuki TAGAWA
Published by the International Association for Shell and Spatial Structures (IASS) with permission.



(a) Model for tree-structure (b) Stuttgart airport

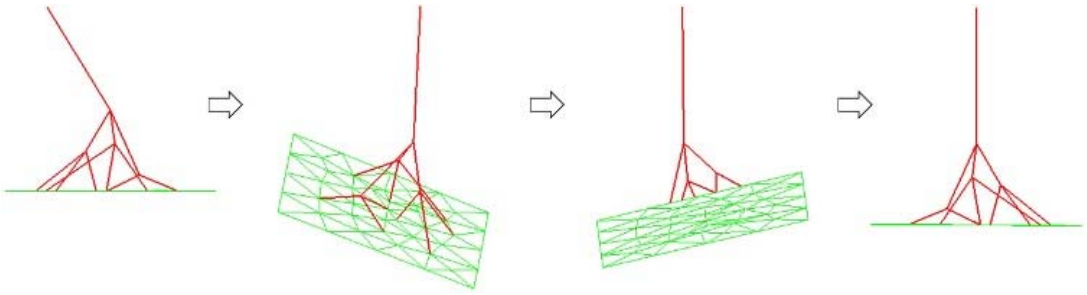
Figure 1: Tree-structure proposed by Frei Otto



Figure 2: Physical hanging upside-down model

2. Small adjustment by simulation of computational hanging upside-down model

The configuration of tree-structure obtained by the "physical upside-down model" is not completely axial-force-resistant and somewhat small bending moment is activated even under gravity loading. Therefore, if the hanging upside-down model is modeled by truss element, it becomes unstable structure and the static analysis is difficult to be carried out when the hanging upside-down simulation is conducted. Therefore, the dynamic relaxation method is used for the simulation of the hanging upside-down model and dynamic analysis is carried out assuming the mass and fictitious damping. It is believed that the state where the structure does not oscillate and is at almost rest is in the self-equilibrium condition. An example of the dynamic relaxation is shown in Figure 2. The inclined trunk becomes upright at rest after the oscillation.



(a) Initial state (b) at 10^{th} step (c) at 100^{th} step (d) at 1000^{th} step

Figure 2: Simulation using dynamic relaxation for hanging upside-down model

The computational hanging upside-down model corresponding to the physical model shown in Figure 2, in which all trunks and branches are straight, is created as shown in Figure 3. All elements are modeled by truss element. This truss structure is unstable in nature. The hanging upside-down simulation is conducted using the dynamic relaxation for gravity loading. Then, the coordinates of the

nodes of the deformed shape at rest, which is nearly in self-equilibrium for gravity loading, is obtained. The models created before and after the adjustment by the hanging upside-down simulation are analyzed for the gravity loading. The contour plots of the maximum and minimum combined stress are shown in Figure 4 for the model before the adjustment and Figure 5 for the model after the adjustment. As shown in these figures, the maximum and minimum stress values are reduced from 173.7 N/mm^2 and -221.0 N/mm^2 to 96.6 N/mm^2 and -140.0 N/mm^2, respectively, after the adjustment by the hanging upside-down simulation [8].

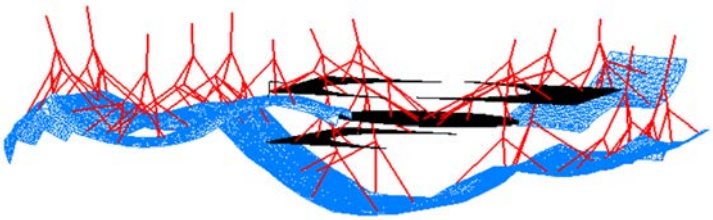
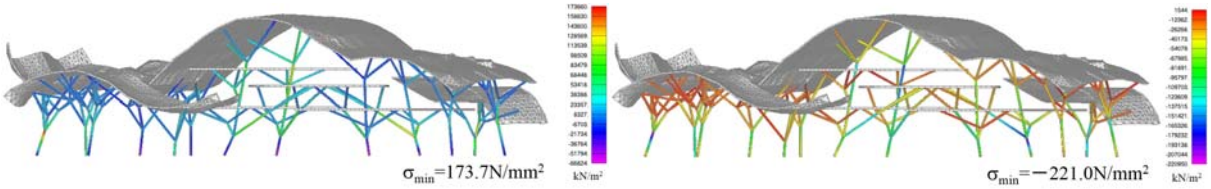
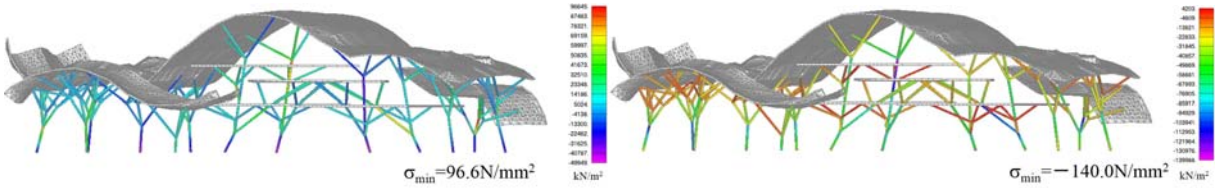


Figure 3: Computational hanging upside-down model



(a) Maximum combined stress (b) Minimum combined stress

Figure 4: Gravity analysis results for the model before adjustment by hanging upside-down simulation



(a) Maximum combined stress (b) Minimum combined stress

Figure 5: Gravity analysis results for the model after adjustment by hanging upside-down simulation

3. Design procedure to create more “natural” and “rational” tree-structure

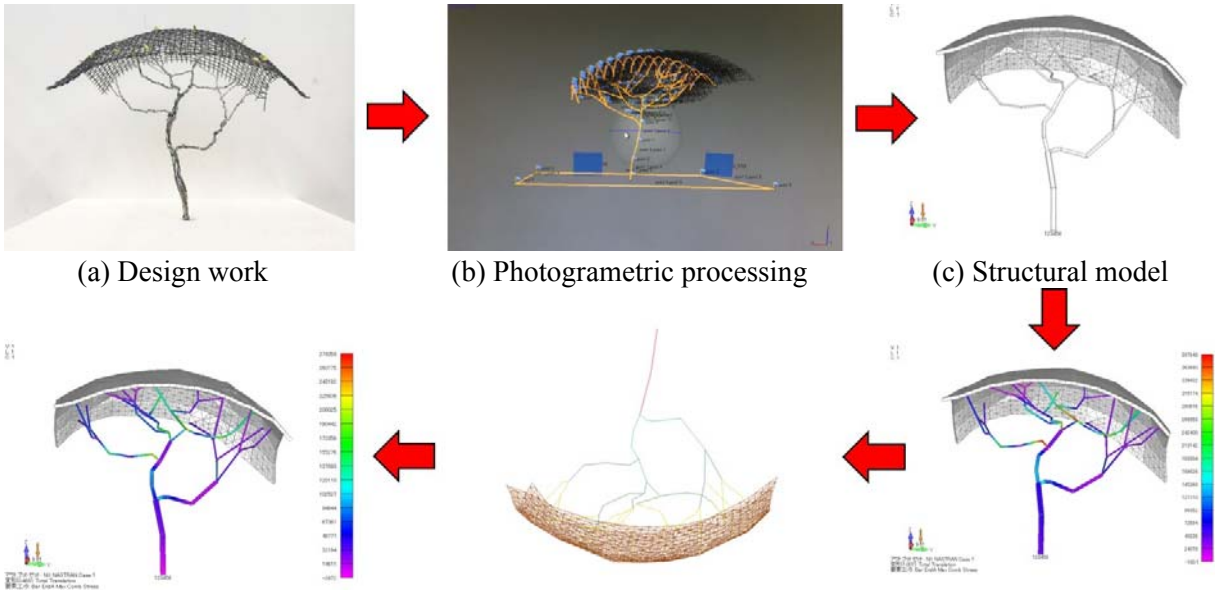
All trucks and branches are straight in a tree-structure obtained from the physical hanging upside-down model due to the gravity loading as shown in Figure 1. The possibility of more “natural” tree-structure, which consists of “curved” trunks and branches and possesses still structural rationality, is explored in this study. The design procedure to create the “natural” and “rational” tree-structure is summarized in Figure 6 using a tree-structure model with one trunk as an example.

1. A work of tree-structure with curved trunks and branches is created as shown in Figure 6(a).
2. The photogrammetric processing is conducted for this work to produce an original configuration model as shown in Figure 6(b).
3. The finite element model corresponding to the configuration model is created as shown in Figures 6(c).
4. Structural analysis is conducted for the finite element model as shown in Figure 6(d).
5. The hanging upside-down simulation for the model with truss element or beam element with very small flexural rigidity is conducted using the dynamic relaxation to find the self-equilibrium state

as shown in Figure 6(e).

6. The 3D configuration is modified according to the deformed shape at rest in the hanging upside-down simulation and structural analysis is conducted as shown in Figure 6(f).

Both results for the models before and after the adjustment by the computational hanging upside-down simulation such as Figures 6(d) and 6(f) are compared to evaluate whether the hanging upside-down simulation using the dynamic relaxation is effective or not to reduce the stress due to bending.



(a) Design work (b) Photogrametric processing (c) Structural model

(f) Structural analysis (e) Hanging upside-down simulation (d) Structural analysis

Figure 6: Design procedure for more "natural" and "rational" tree-structure

4. Application to architectural design of tree-structure with four trunks

A physical model of a tree-structure with four trunks are applied to the architectural design. A span of the trunks is 10 m and a circle with 4 m diameter is removed from the roof at the center providing a well-hole. The material of the tree and the roof is steel pipe and the roof is made by space frame. The diameters of the trunks and branches are 200 mm, 150 mm and 100 mm and the thickness is 30 mm, 20 mm and 8mm. The steel material is assumed to be elastic with an elastic modulus of 205 kN/mm^2 and the density of 7.85 ton/m^3.

The analysis results for the model before the adjustment by the hanging upside-down simulation are shown in Figure 7. The maximum and minimum stress of the trunks and branches in the tree-structure is 40.2 N/mm^2 and −43.8 N/mm^2, respectively.

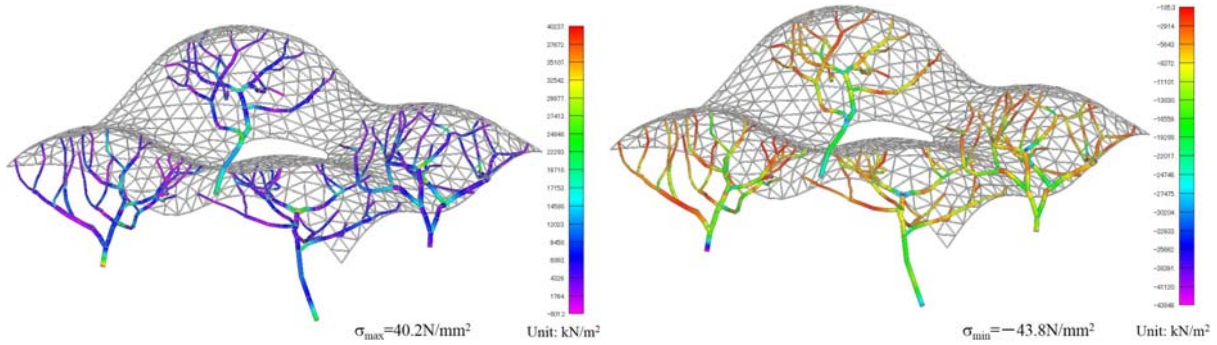


Figure 7: Analysis results for the model before adjustment by hanging upside-down simulation

(1) Modification by hanging upside-down model with truss elements

The computational handing upside-down simulation is conducted to adjust the shape to be more axial-force-resistant. If the model is completely changed to a truss structure, all curved trucks and branches are straightened due to tensional forces resulting from gravity loading and if and some trunks and branches are so long that the compatibility condition is not satisfied, these are slacked in compression as shown in Figure 8. Some of these elements are outside of the space frame roof.

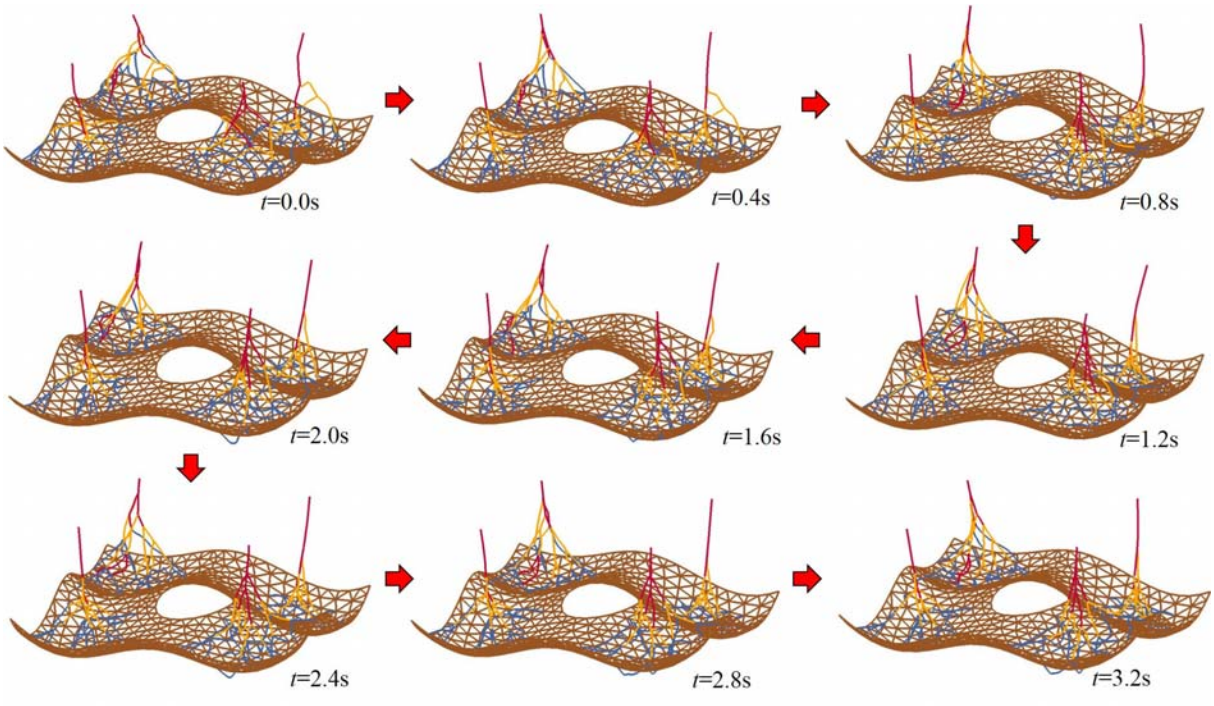


Figure 8: Deformed shape for the model with truss elements after hanging upside-down simulation

(2) Modification by hanging upside-down model comprising of beam elements with 0.0005*EI*

Therefore, the hanging upside-down simulation is conducted with the model using beam elements with small moment of inertia of the sections. The analysis results for the model obtained by the hanging upside-down simulation with the model with 0.0005 times moment of inertia (*EI*). The result for the hanging upside-down simulation is shown in Figure 9. The analysis results for the model obtained by the hanging upside-down simulation with the model with 0.0005*EI* are shown in Figure 10. The maximum and minimum stress of the tree-structure is 29.1 N/mm^2 and −31.9 N/mm^2, respectively, which are almost half of the result shown in Figure 7.

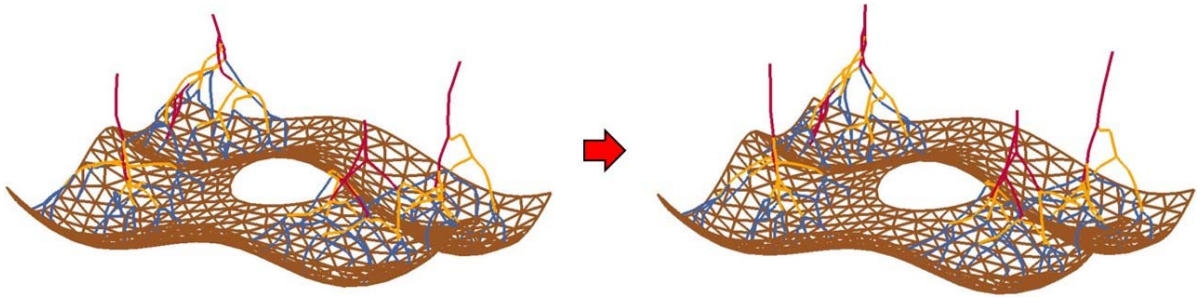
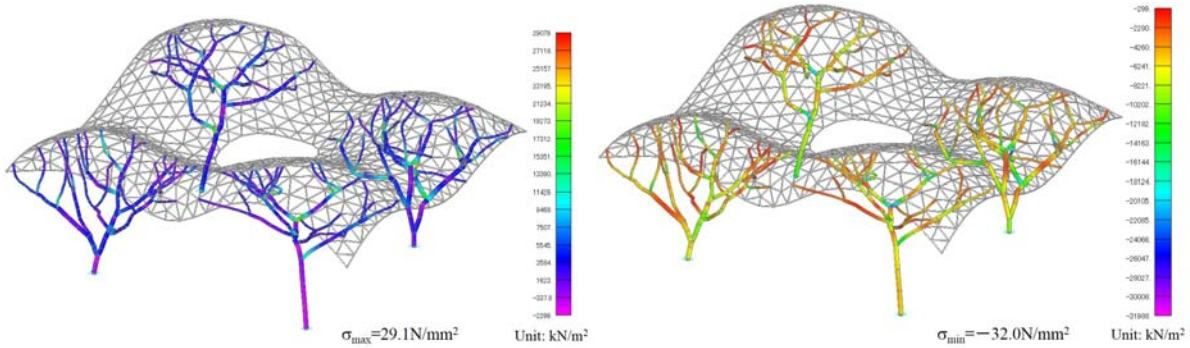


Figure 9: Deformed shape of model with 0.0005*EI* before and after hanging upside-down simulation



(a) Maximum combined stress (b) Minimum combined stress

Figure 10: Analysis results for model after adjustment by hanging upside-down simulation

(3) Modification by hanging upside-down model comprising of beam elements with 0.0001*EI*

If the model with 0.0001*EI* is used for the hanging upside-down simulation, a part of the branches are outside of the roof as shown in Figure 11. As a result, the maximum and minimum stress of the tree-structure is 35.3 N/mm^2 and −38.6 N/mm^2, respectively, which are larger than the values in Figure 12.

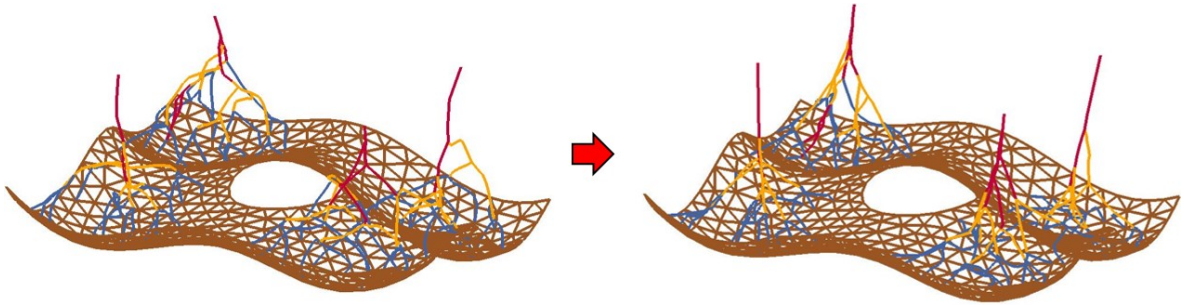


Figure 11: Deformed shape of model with 0.0001*EI* before and after hanging upside-down simulation

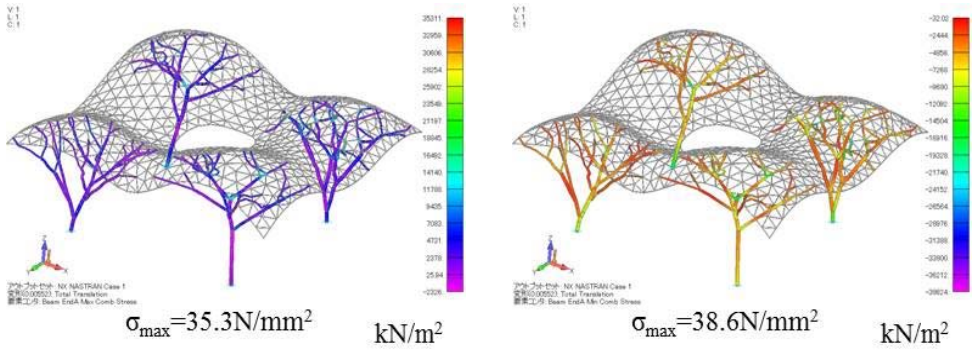


Figure 12: Analysis results for the model after adjustment by hanging upside-down simulation

(4) Transition of strain energy after modification

The rate of decrease in strain energy for the models corrected with the flexural stiffness ratio is shown in Figure 13. It is found that as the flexural stiffness ratio decreases, the strain energy decreases. When the 0.0005*EI* is used for the correction, the strain energy becomes 0.48 times that of unmodified model.

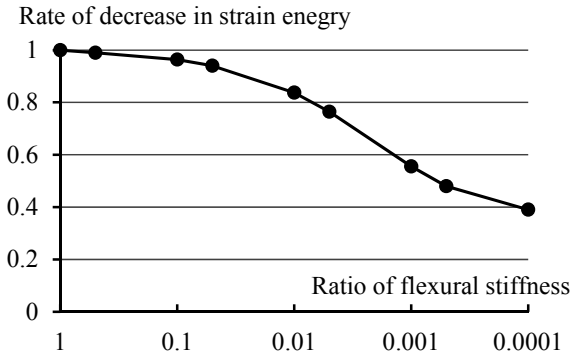


Figure 13: Rate of decrease in strain energy corresponding to the ratio of flexural stiffness used for adjustment by hanging upside-down simulation

An example of the application to the architectural design is illustrated in Figure 14.



Figure 14: Architectural design

5. Conclusion:

In this study, the design process of more natural and rational tree-structure using the physical and computational hanging upside-down models is investigated.

References

[1] Hajime Sakai, Masao Saitoh, Akira Okada, Naoya Miyasato, Nobuyuki Morinaga, "Basic study on structural morphogenesis of tree-shaped structure", Summaries of technical papers of annual meeting, AIJ, 2006.9 (in Japanese)

[2] Peter von Buelow, "Following a thread: a tree column for a tree house", Proceedings of IASS symposium, Beijing, 2006

[3] Peter von Buelow, "A geometric comparison of branching structures in tension and compression versus minimal paths", Proceedings of IASS symposium, Venice, 2007

[4] Jeffrey Hunt, Walter Haase, Werner Sobek, "A design tool for spatial tree structures", Journal of the International Association for Shell and Spatial Structures, Vol. 50(1), pp.3-10, 2009

[5] Kazuki Imazawa, Mutsuro Sasaki, "Representation of shape using Lindenmayer system—computational morphogenesis of tree rahmen", Summaries of technical papers of annual meeting, AIJ, 2013.8 (in Japanese)

[6] Jinglan Cui, Guangchun Zhou, Makoto Ohsaki, "Design of tree-type support structure of free-form shell generated using fractal geometry", Proceedings of IASS symposium, Tokyo, 2016

[7] Chisato Eguchi, Noritoshi Sugiura, Hiroyuki Tagawa, "Form-finding of tree-structure supporting free-surface shell utilizing hanging upside-down model", Summaries of technical papers of annual meeting, AIJ, 2017.9 (in Japanese)

[8] Chisato Eguchi, Noritoshi Sugiura, Hiroyuki Tagawa, "Architectural and Structural Design of Tree-structure supporting Free-surface Shell Roof using Hanging Upside-down Model", Proceedings of the IASS Symposium 2018, Creativity in Structural Design, July 16-20, 2018, MIT, Boton, USA

Proceedings of the IASS Annual Symposium 2019 – Structural Membranes 2019
Form and Force
7 – 10 October 2019, Barcelona, Spain
C. Lázaro, K.-U. Bletzinger, E. Oñate (eds.)

Seeing Numbers: Considering the Effect of Presentation of Engineering Data in Design

Sam C. JOYCE*, Grace GUO, Bianchi DY, Nazim IBRAHIM, Ate POORTHUIS

* Meta Design Lab,
Singapore University of Technology and Design
8 Somapah Rd, Singapore, 487372
sam_joyce@sutd.edu.sg

Abstract

Computing has made detailed design analysis across all engineering domains types easier to produce, this has as a result generated significantly more design data than before. Similarly, tools like parametric modelling, and BIM have also allowed for differentiated design options to be generated faster and at lower human effort than previous design methods. This is leading to what the authors call "big- design-data"; large amounts of data which rather than being passively collected, have been generated during design and analysis of options. This data suffers from the same issues of data volumes and complex relationships (albeit not as large as classical big-data) and so in need of visualisation and interpretation to allow for meaningful insight which in turn can result in effective decisions. This paper explores the details of the issues and considerations of visualising data for designers and engineers specifically in relation to design decision making; identifying relevant research that supports how one may approach sense making in this big-design-data context.

Keywords: Data visualisation, Design Decision Making, Engineering Analysis, Design Exploration, Optioneering

1. Introduction

Engineering is a classically data-rich environment; with modern analysis providing us with increasingly more comprehensive engineering data. When matched with parametric design it is possible and increasingly common to swiftly generate large ranges of design variations with integrated analysis workflows; thus, data volumes are multiplied vastly [1]. This has allowed engineers to explore the solution space thoroughly by considering many design options and possibilities [2] [3]. However, this has been at the price of imposing more intellectual load on designers, specifically in decision making which requires understanding of complex relationships between design variables and performance outcomes.

Methods such as optimisation have since given way to "optioneering" and "optimisation based exploration" [4][5], whereas optimisation was supposed to provide a 'singe shot' solution, in fact it showed that most design problems do not have one dominant solution but are complex problems, with no definitive solution or stopping rule as we have independent performance variables which trade off each other and the priorities between them are still being defined and change and where satisficing is often required [6]. And whilst optimisation is very useful it often represents the start and understanding of a design process and evaluation rather than the initially claimed "solution" [7].

Copyright © 2019 by Sam C. JOYCE, Grace GUO, Bianchi DY, Nazim IBRAHIM, Ate POORTHUIS
Published by the International Association for Shell and Spatial Structures (IASS) with permission.

In this context although the content of any engineering analysis is of the most importance, the visual presentation of information can be shown to have a significant impact on the accuracy of understanding and insight by the consumer of this data [8]. Whilst the accuracy of engineering data itself can be rigorously verified, by contrast our perception of information when shown in tables, summarized, or as a visualisation has been shown to be highly subjective and open to influence from cognitive biases [9][10]. Unfortunately, this is the critical point that the data is consumed for decision making, thus it is important for engineers to understand the impact that presentation of complex data.

This paper seeks to highlight important visualization issues related to engineering design. Seeking to present empirically proven cognitive visual biases that should be avoided and how to make the clearest and best use of data for accurate, well informed and impartial decisions by engineers, but also clients, and other team members.
The work considers these issues:

1. User fidelity of understanding of data is significantly affected by types of data and the method used to display it; recommending the best and worst combinations.
2. The amount of design data, the number of options, and how they are compared will significantly affect human intuitive comparisons away from rational selective decisions. Looking to limits of understanding large data sets and how to control this complexity.
3. Widely used existing engineering analysis tools often generate data that is hard to visually digest, specifically in the context of decision making. Recommending how this can be reduced by simple but carful changes to those data visualizations.

To validate these insights and recommendations, this research makes use of existing work in visualization-based fields. And shows new empirical research from the authors.

2. Visual Fidelity – Understanding the data

A vital but often underappreciated mechanic of data visualisation is that the consumer of the chart is interpreting an abstract spatial graphic into a comparative understanding of the represented data. The principal benefit being that they allow for faster consumption of large amounts of data, however an inherent issue is that users are not directly being shown values, unlike a table for example, thus, they are open to misinterpretation and visual biases; thus the visualisation designer cannot be sure of the accuracy of user interpretation. We may call this ‘visual fidelity’ relating to the accuracy (bias) of the user’s impression of the data as compared to the actual underlying data.

One of the earliest known cases in the application of data visualisation is also an example of the benefits but also issues: In 1858 nursing manger Florence Nightingale wanted to bring focus on the significantly larger number of deaths due to preventable or controllable diseases (epidemic, endemic, and contagious) in the Crimean War as compared to combatant death. To do this she developed a presentation using an early use of a rose plot to effectively show the impact of illness and compelled the army to make the decision to support her medical efforts saving many lives. It must be noted however that this visualisation is biased in how it presented information. As Tufte [11] points out users are inclined to compare the area of the bar rather than the length, so due to the radial placing of the bars it adds visually even more weight to those on the outside of the bar; in this case conveniently (for Florence Nightingale) visually exaggerating the deaths due to preventable illnesses. Thus, in just this example we see both the benefits for insight and decision making, but also opportunity for accidental or intentional misrepresentation of the actual data.

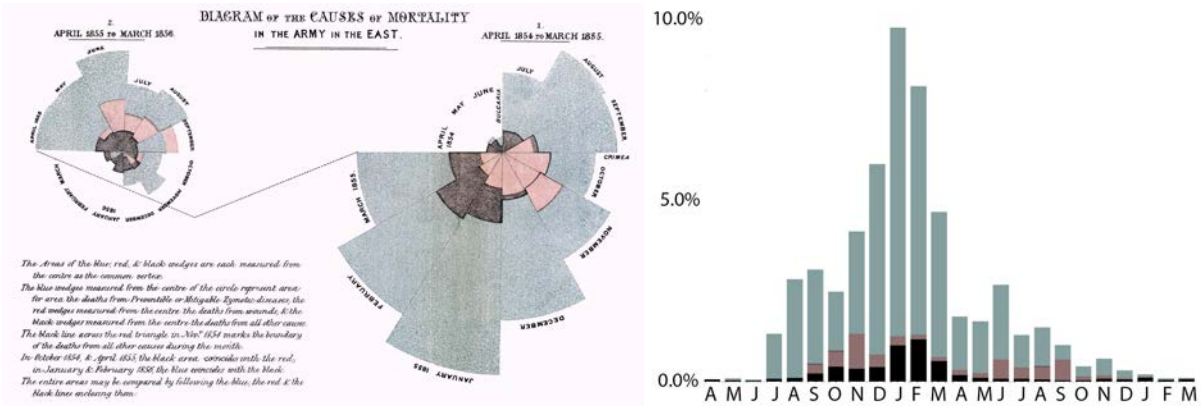


Figure 1: Left except from Florence Nightingale's presentation of soldier deaths due to preventable diseases (blue), wounds (red), and other causes (black). The deaths are measured by length from the centre, however due to the angular change notice the representative area is larger and more exaggerated. This can be compared to the same data shown as a length and area proportionate bar chart on the right.

2.1 The possibilities in the visualization of data

Before discussing issues of accuracy when interpreting data visualisations, it is worth considering what the capabilities and degrees of freedom available in simply making visualisations. Much of the theory is covered in Jacques Bertin's 1967 work *Semiology of Graphics* [12], where the basic visual marks that human vision can appreciate as data where laid out. In this he identified seven main visual properties (shown in figure 2), 4 are location based: position, size, orientation and shape (of a point/icon etc.), and 3 others which are colour or pattern based: colour, value (darkness), texture/hatching. This work was focused towards cartography so these are demonstrated to be unique when applied to points, lines, and areas (effectively 0D, 1D and 2D, representations). Each of these methods can be used to encode data. These properties are compositable; meaning that they can be combined and still retain the sperate data elements, effectively meaning that on one piece of paper a single point can encode up to 8 pieces of information as it can be placed in 2D and then leverage the other 6 methods.

At the same time, it is worth noting that data can also have different types. In data visualisation typically they are categorised into 3 types:

1. Scalar (a continuous or discrete number, which can be normalised or not)
2. Ordinal (the relative order of a set, without any magnitude, 1st, 2nd 3rd etc.)
3. Categorical (the grouping of things into similar categories)

Whilst most data in engineering is scaler being number based, we also see use of categorical to relate to selection of options (steel section type, bracing types, number of significant dynamic modes etc.) and we may also rank options in terms of preference or similar, thus creating ordinal data. We should also consider more broadly that scalar data comes in many forms such as discrete numbers such as integers, but also the distribution

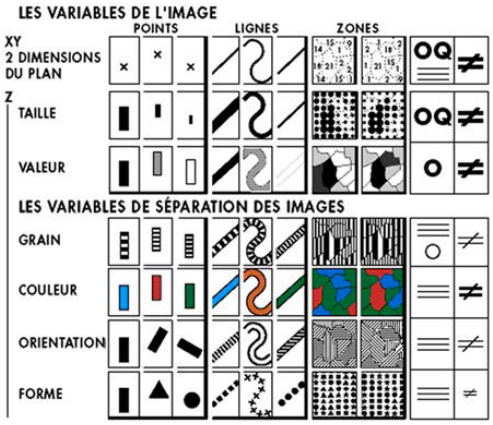


Figure 2: Reproduction of Bertin's representation [12] of different ways for displaying visual differences (vertical) and what a range geometric elements point, line, area (horizontal).

2.2 Visual chart type choice – what charts are better?

Understanding that different visualisations have varying levels of accuracy raises the question: which charts are better to use for engineering data? In this aspect some reach has already been undertaken; most notably by Cleveland & McGill [8], in this work they developed an approach to measure how accurately users were able to identify the underlying data relationships. In these cases they identified that when developing basic visualisations such as bar charts, pie charts, etc. have better performance in relation to accuracy and speed of interpretation.

The authors have recently undertaken similar work with designers and design students [13], in this case using a questionnaire testing 7 different chart types (shown in figure 3) was conducted and the relative sizes as a percentage asked to 123 participants resulting in 4602 questions answered. The findings reinforced Cleveland showing that spatial designers act in a similar way as others, and are as susceptible to visual biases including those relating to area length. The results enforced that bar charts result in greater accuracy and speed of data interpretation as compared to other methods, the results of which can be found in figure 4.

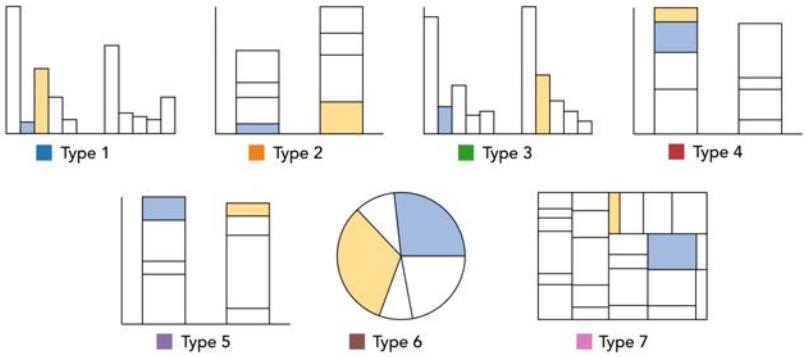


Figure 3: Except from authors experiment showing the 7 chart types used. In all of these cases users were asked to find the relative sizes between the yellow and blue sections and measured on their speed and accuracy.

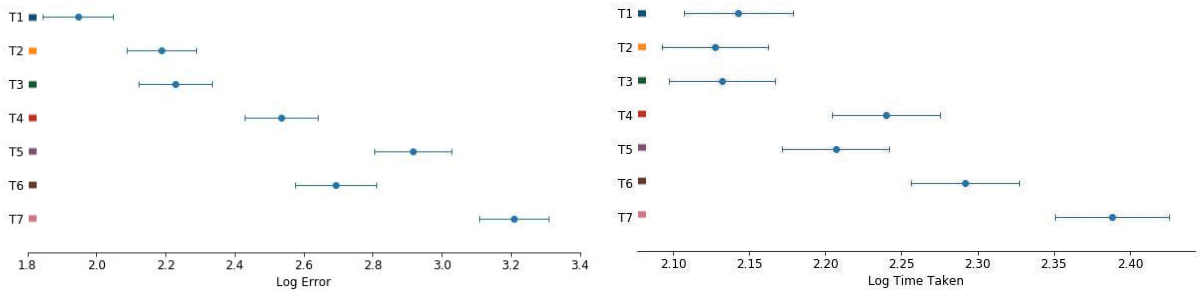


Figure 4: Accuracy (bias) and time taken for an experiment undertaken with a population of 123 architects, engineers, and students of both topics. Showing the accuracy on the left and speed on the right (lower is better in both cases) for each chart type.

This work has been extended by Talbot et al. [10] who explore the effectiveness of various visual properties on the accuracy of data understanding but with respect to the three data types (scalar, ordinal, categorical). The properties where categorised into these visually different aspects: Position, Hue, Texture, Connection, Containment, Density, Saturation, Shape, Length, Angle, Slope, Area and Volume(3D), this is from the user viewpoint as seen, hence the differences as compared with Bertin's which is from the view point as drawn. In these cases they were able to identify for each type which was better, this is shown as an order in figure 5. Using this we may consider engineering data and see that spatial changes rather than colour or hatching are better to use for scalar data.

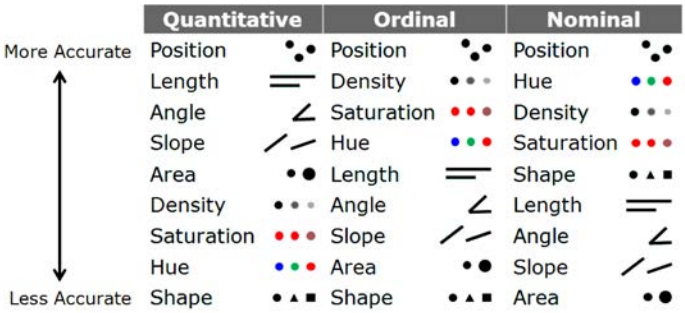


Figure 5: The relative accuracy of different visualisation properties as seen in relation to the data type, reproduced from Mackinlay 1986 [14]

2.3 Colour scales

As shown in [14] colour and figure 5, the visual accuracy of colour has a wide range of effectiveness which is highly influenced by the data shown with it. This is of critical importance to engineers as the uses of colour is very good for categorical and ordinal data low in accuracy for scalar data types. This points to a major failing in the presentation methods of FEM analysis, which use the HSV or "rainbow" type colour schemes used to show stresses and similar data mapped onto the 3D model in almost all commercial software. Interestingly it shows that using traditional bending moment diagrams which rely on spatial information (essentially a continuous line chart, mapped on to the structural element) are actually very effective. However, these suffer from being confusing when used in 3D. Thus, colour is a flawed but perhaps necessary method to show quantitate data, but we must be aware of its limitations.

Research which has looked more thoroughly at the correct and effective use of colour is by Cynthia Brewer for initial application in choropleth maps for showing magnitudes of cartographic areas [15].

This work looked carefully at the use of colour scales and the ideal colour differences required for accurate identification for two types: categorical/qualitative differences and scalar/quantitative differences. Whilst categorical requires pallets of discrete colours that are different and identifiable between one another. Ordinal requires a logical series of colours that can be identifiable along a scale. Brewer identified that for numbers the range of the numbers effects what is the most easily interpretable to use. For numbers that are along a continuous range colour scales with a background colour and one dominant colour that gets darker are better. This is effective in part because it uses saturation as well a colour to differentiate the values which is more accurate according to Macinlay. Furthermore, diverging number scales which is of special interest to engineers as many values range from zero with both +ve and -ve sign, such as stresses require a neutral background colour a zero moving to a single colour at maximum and another at minim. In both cases it is worth noting that red green comparisons should be avoided as for colour blind users the difference between these (if at the same saturation or value) is imperceptible.

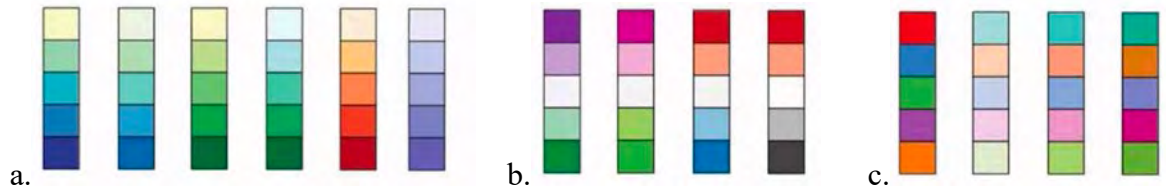


Figure 6: Specific colour ranges designed to be most effective for given data types: (a) for continuous ranges, (b) for continuous but diverging numbers, and (c) for categorical values, designed for colour bind users, reproduced from Harrower and Brewer 2003 [15]

3. Scale of data understanding and human limitations

What has been shown above are issues and findings pertaining to single charts and the display of generic information, but there are more questions that arise when considering the context of decision making. There is still much work that is required in this field that needs to be done to explore how one considers comparing design options in ways that improve accuracy and removes bias. One issue is the level of 'band-width' that humans are able to retain in short time memory relatively few individual elements, a diagram compresses this into an easier image to remember mentally capturing general relationships better than individual numbers.

The role of seeing relationships reduces cognitive load. However, there is little research which actually looks at this and none found to explore this in a design decision making context. Of interest is how many values and how many options could be considered in any one chart, and like Cleveland which visual methods are better. It can be shown in charts (for example figure 7) that there is a limit to how much data can be included before it is illegible, but this has not been tested yet and this this is fertile ground for research.

5. Conclusions

The modern situation of generation of powerful computer driven methods to generate and analyse designs, presents a new frontier of "Big Design Data" but at the same time a challenge in the development of computer augmented design. It requires careful thought and consideration to ensure that this data is truly leveraged, by interpretation and insight. In some way our current situation as a community may represent something of a state of 'technical-debt' or even 'visual-debt', whereby we as designers have got to a stage where we are not able to adequality make use of all the data as a result of our relative lack of development in AEC industry to improve how we see the data. and do research to actually verify it helps.

However arguably building designers are well equipped to improve this situation, they understand the complex spatial organisation and relationships, and how to make clarity of this. Thus it is an open challenge to consider not just *what* the data is but *how* it will be shown and *what* it will be used for. Taking the display of data as a design challenge in-an-of itself that the community needs to own and address.

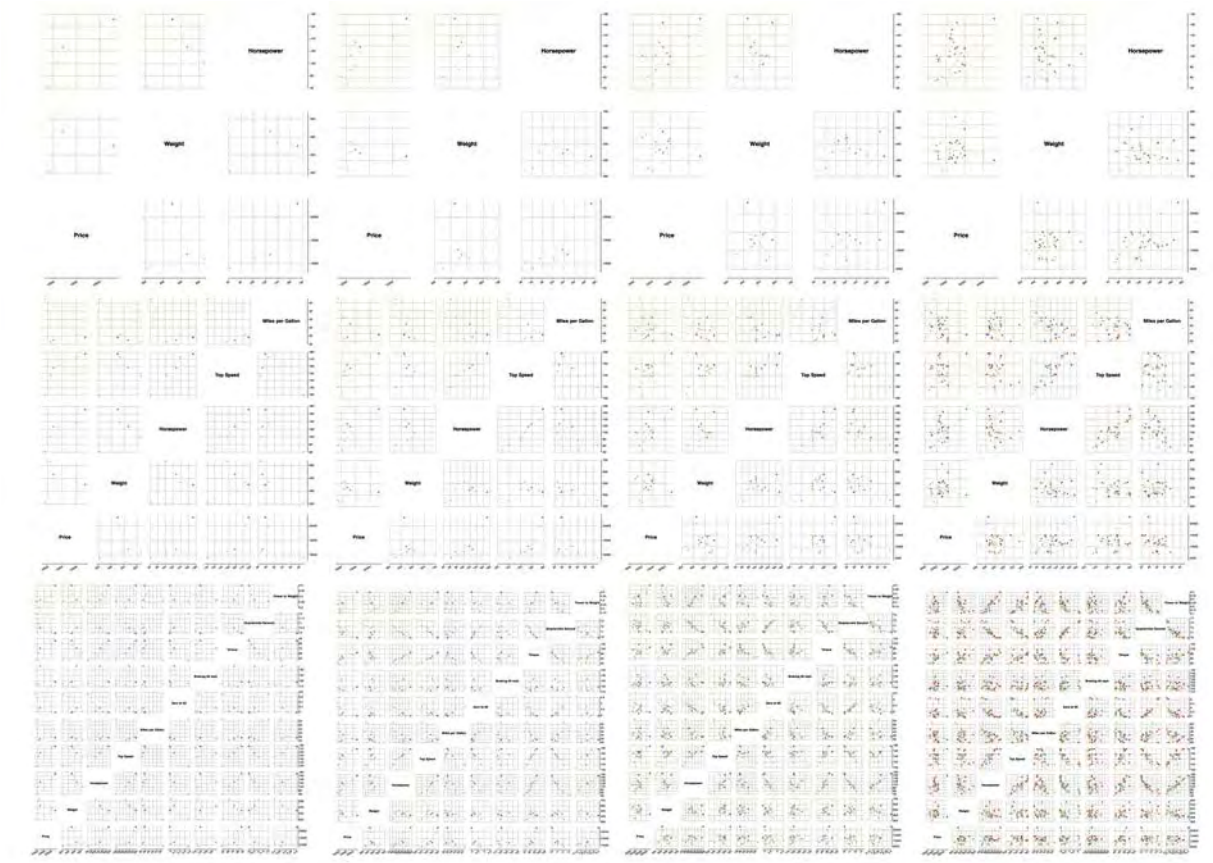


Figure 7: Example multi-valued data visualisations, shown as an array of matrix scatter using the same data but ranging from 3 to 5 to 10 metrics (top to bottom) and 5, 10, 20 and 40 options (left to right). The more data shown the more complex visualisations become with issues of readability.

Acknowledgements

The material reported in this document is supported by the SUTD-MIT International Design Centre (IDC). Any findings, conclusions, recommendations, or opinions expressed in this document are those of the author(s) and do not necessary reflect the views of the IDC.

References

[1] Aish, R., Fisher, A., Joyce, S. and Marsh, A., 2012, October. Progress towards multi-criteria design optimisation using DesignScript with SMART form, robot structural analysis and Ecotect building performance analysis. In Association for Computer-Aided Design in Architecture (pp. 47-56). ACADIA.

[2] Evins, R., Joyce, S.C., Pointer, P., Sharma, S., Vaidyanathan, R. and Williams, C., 2012, May. Multi-objective design optimisation: Getting more for less. In Proceedings of the Institution of Civil Engineers-Civil Engineering (Vol. 165, No. 5, pp. 5-10). Thomas Telford (ICE Publishing).

[3] Tsigkari, M., Chronis, A., Joyce, S.C., Davis, A., Feng, S. and Aish, F., 2013, April. Integrated design in the simulation process. In Proceedings of the Symposium on Simulation for Architecture & Urban Design. Society for Computer Simulation International.

[4] Mueller, C.T., 2014. Computational exploration of the structural design space (Doctoral dissertation, Massachusetts Institute of Technology).

[5] Brown, N., Tseranidis, S. and Mueller, C., 2015, August. Multi-objective optimization for diversity and performance in conceptual structural design. In Proceedings of IASS Annual Symposia (Vol. 2015, No. 20, pp. 1-12). International Association for Shell and Spatial Structures (IASS).

[6] Rittel, H.W. and Webber, M.M., 1973. Dilemmas in a general theory of planning. Policy sciences, 4(2), pp.155-169.

[7] Bradner, E., Iorio, F. and Davis, M., 2014, Parameters tell the design story: ideation and abstraction in design optimization. In Proceedings of the symposium on simulation for architecture & urban design (p. 26). Society for Computer Simulation International.

[8] Cleveland, W.S. and McGill, R., 1985. Graphical perception and graphical methods for analyzing scientific data. Science, 229(4716), pp.828-833.

[9] Heer, J. and Bostock, M., 2010, April. Crowdsourcing graphical perception: using mechanical turk to assess visualization design. In *Proceedings of the SIGCHI conference on human factors in computing systems* (pp. 203-212). ACM.

[10] Talbot, J., Setlur, V. and Anand, A., 2014. Four experiments on the perception of bar charts. *IEEE transactions on visualization and computer graphics*, *20*(12), pp.2152-2160.

[11] Tufte, E.R., 2001. The visual display of quantitative information (Vol. 2). Cheshire, CT: Graphics press.

[12] Bertin, J., Berg, W.J. and Wainer, H., 1983. Semiology of graphics: diagrams, networks, maps (Vol. 1, No. 0). Madison: University of Wisconsin press.

[13] Grace, G., Dy, B., Ibrahim, N., Poorthuis, A., Joyce, S. C., 2019, Re-examining the use of `convenient' test participants in graphical perception experiments, In processdings of IEEE VIS 2019 Confrecne, Vancouver (in process)

[14] Mackinlay, J.,1986, Automating the design of graphical presentations of relational information. ACM Transactions on Graphics, 5(2):110-141

[15] Mark Harrower & Cynthia A. Brewer (2003) ColorBrewer.org: An Online Tool for Selecting Colour Schemes for Maps, The Cartographic Journal, 40:1, 27-37

Proceedings of the IASS Annual Symposium 2019 – Structural Membranes 2019
Form and Force
7 – 10 October 2019, Barcelona, Spain
C. Lázaro, K.-U. Bletzinger, E. Oñate (eds.)

The combination of SQL database queries and stochastic search methods used to explore generative design solutions

Peter VON BUELOW*

*University of Michigan
Ann Arbor, Michigan, USA
pvbuelow@umich.edu

Abstract

ParaGen is a method that has been developed over the past several years at the University of Michigan's Taubman College. ParaGen combines both a GA and a SQL database for solution exploration and performance optimization. Multi-performance optimization has been successfully demonstrated on numerous problems using stochastic algorithms like GAs. But for many problems which include visual aspects of form, like architectural design, quantitative performance values alone are not the only criteria needed to search for a good design. In architecture as in other design fields with a visual component, aesthetics, human comfort and other qualitative aspects need to be considered. By allowing designers to make visual comparisons of solution forms that have been found through performance driven search, ParaGen is able to respond to both quantitative and qualitative aspects of design. In this paper an example is given where a combination of quantitative performance criteria along with qualitative criteria based on the designer's visual selection are used to search for better performing structural forms.

Keywords: performance optimization, generative design, parametric, data-driven optimization, genetic algorithms

1. Introduction

The exploration of a range of possible solutions as a means of searching for new solutions has long been seen as a valuable tool in the design process. Numerous studies in the latter half of the 20th century attempt to describe or even formularize this process. Some form of exploration is generally common to these methods. Osborn describes "ideation, piling up alternatives by way of ideas"[1]. Koberg and Bagnall describe ideation as a way to "generate options" and "search out all possible ways of realizing the major goals."[2] Most stochastic optimization techniques, such as genetic algorithms (GAs), include a search operator which essentially explores the solution space in search of good solutions. Unfortunately most GAs do not maintain a history of the search progress and only have a 'memory' of the current generation. So although these techniques do "generate options" the do not really "pile up alternatives" since they lack any recorded memory of the search. Of course one solution is to simply store the solutions as they are generated, but a more useful approach is to actually incorporate a database with a structured query language (SQL) into the search process so that solutions are not only saved, but more importantly can later be explored interactively. This is much closer to Osborn's concept of ideation.

Copyright © 2019 by Dr.-Ing. Peter von Buelow.
Published by the International Association for Shell and Spatial Structures (IASS) with permission.

The ParaGen method links both a SQL database and a GA to form a tool which can both search using performance criteria and explore the broader scope of possible solutions [3]. It is intended for use in the early stages of design development when form exploration is desired. But at the same time ParaGen is able to bring a higher level of performance information into consideration which allows for more effective form exploration at the early stages of design development.

2. The ParaGen method

ParaGen is a method rather than a specific piece of software. It combines four basic components:

1. A genetic algorithm to search for new solutions
2. A parametric form generator to realize the solutions
3. Analysis software to find performance characteristics
4. A SQL database to store solution characteristics and performance data

In addition, descriptive images are saved and linked to the data. This enables the solutions to be searched using both quantitative performance values and qualitative images. It is also possible to guide the GA using either a fitness function based on SQL queries of the performance values or by using breeding populations selected based on user (visual) preference. The procedure is repeated in cycles until good solutions are found. Figure 1 shows the procedure.

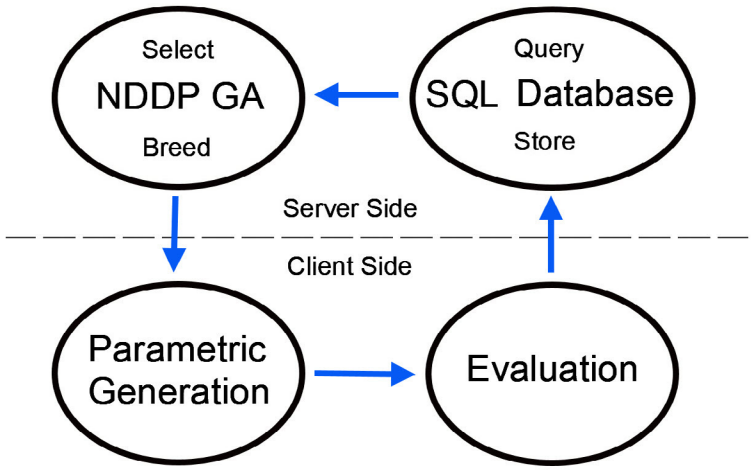


Figure 1: An outline of the ParaGen method

The ParaGen method is conceived to run in a parallel processing environment using a single web server and some number of clients in parallel. In this way longer evaluations such as daylighting analysis or complex wind analysis can run in parallel for greater efficiency. ParaGen is based on a Non-Destructive Dynamic Population GA (NDDP GA) [4]. Rather than traditional generational structures which eliminate less fit solutions from the breeding population, ParaGen stores all solutions in a database and dynamically creates a breeding population based on a SQL query at the moment of breeding. Parents from this population are then bred using half-uniform crossover (HUX) [5]. In the first step, the NDDP GA produces a new solution either by selection and breeding or by selection and mutation or by random generation (usually to start the process). This new 'child' is then downloaded in the form of a CSV file to a client machine where in step 2 it is read into some parametric software which produces the geometry based on the values supplied by the CSV file. In the third step, this geometry is analyzed for whatever performance characteristics are relevant. This is often possible within the parametric software using

plugins, or it may require the geometry to be passed (usually in DXF format) to some specialized software. In either case the resulting performance values along with descriptive images are uploaded in the fourth step to the SQL database on the server. The GA then accesses the database in selecting parents to breed the next child and the cycle continues [6].

Initially, the GA code generates some number of random solutions to populate the database. Once the data and images for solutions are stored in the database, designers can browse through them using the web interface and SQL queries. Both the performance data and the images are then linked, enabling both quantitate and qualitative information to be viewed together. In an NDDP GA the breeding population is

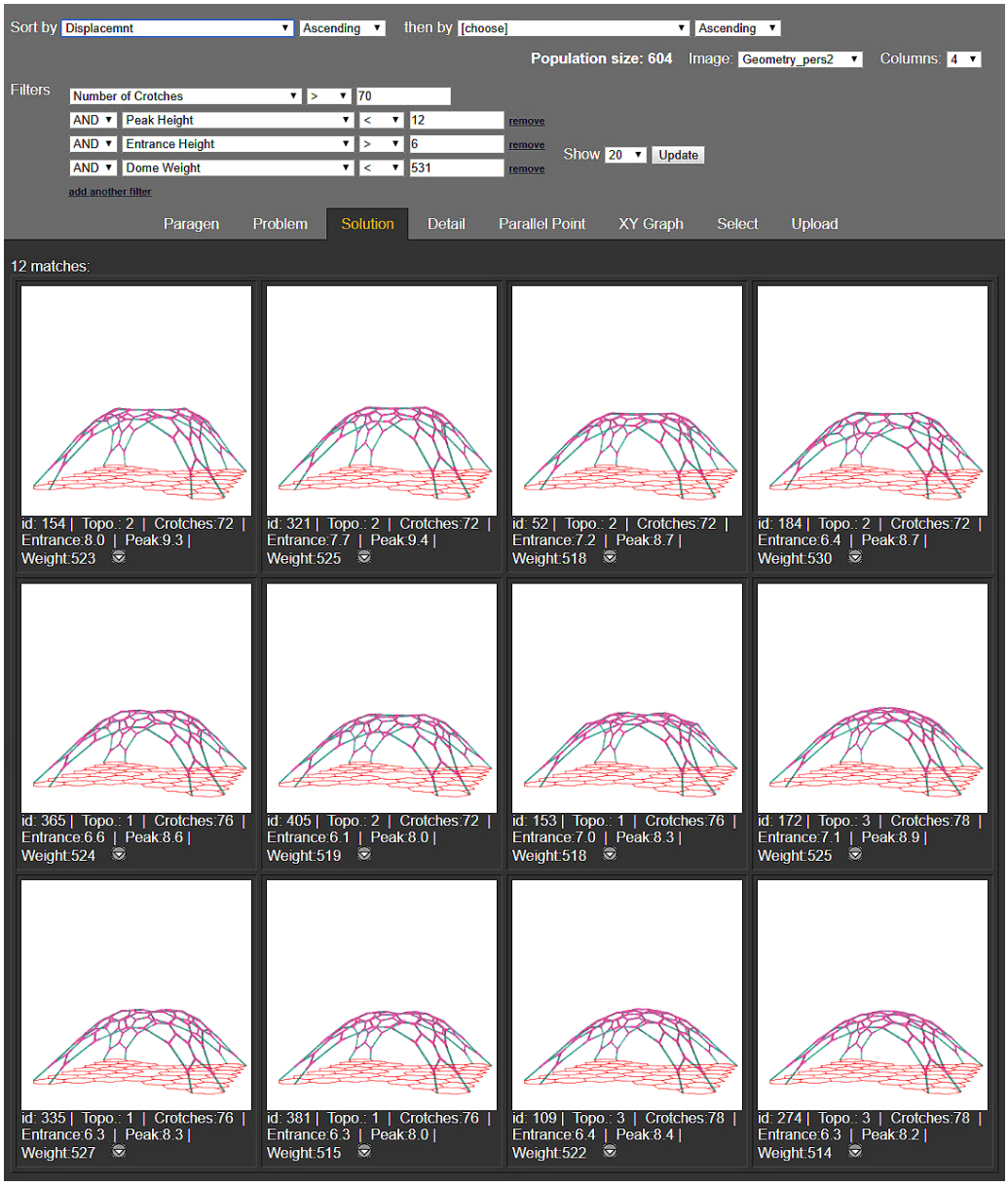


Figure 2: A SQL query defined in the ParaGen interface with the resulting set of solutions

selected from the database using a SQL query each time a new child is bred. The query contains both soft (flexible) design constraints as well as optimization fitness criteria. In the ParaGen method, constraints can be seen as having two forms – hard and soft. The hard constraints are coded into the definition of the parametric model and cannot be changed without altering that base model definition. The soft constraints, on the other hand, are used to focus or limit the scope of the design space being searched. In other words the full design space is defined by the parametric model, but the search space used for breeding is restricted to a part of the full design space limited by the SQL query. The intent of limiting the breeding population is to focus on a particular (optimal) area of the design space. Initially, by using either randomly generated solutions or by systematically scanning the design space, the search space equals the full design space. But the goal is to search that space for the "better" solutions as defined by the SQL query. This search is made flexible in order to follow the exploratory nature of early design by altering the SQL query. In this way the designer can steer the search procedure to explore different areas of the design space. SQL queries are designed to be efficient in searching a database for certain desired items based on multiple attributes. Figure 2 shows an example of a SQL query given through the ParaGen website and the resulting set of solutions.

3. Selection using SQL

ParaGen is able to make use of SQL queries in different ways is searching the design space. Three ways which are illustrated below are:

1. Quantitative values for geometry and performance
2. Conflicting performance values using Pareto sets
3. Qualitative considerations combined with other values

3.1. Selection based on quantitative values

In the example shown in Figure 2, designs for an irregular wooden reticulated dome are searched based on five criteria or constraints:

1. the number of joints is greater than 70
2. the peak center height is less than 3.7 m. (12 ft.)
3. the entrance (arch) height is greater than 1.8 m. (6 ft.)
4. the material weight is less than 240 kg. (530 lbs.)
5. the deflection is minimized

The first four constraints can be seen listed under "Filters" and the last criterion which minimizes displacement is show at the top as "Sort by…Ascending". The total selection is then limited in number (in this case 12). This in effect produces a breeding population from which a pair of parents are randomly chosen and bred in the GA. In this way the SQL query becomes the fitness function for the GA. The size of the breeding population is controlled by the query limit parameter, set in this example to 12. So after meeting the first four constraints, the 12 with the least deflection (sort by displacement ascending) become the breeding population. As new solutions are found that meet the first four constraints and have less deflection, they enter into the breeding population. It would also be possible not to set the population limit criterion (12 in this case) or perhaps replace it with a set constraint like the other four – for example require deflection less than some certain amount. In such a case the breeding population would gradually increase but could be restricted (re-focused) periodically by adjusting any of the five constraints or add additional constraints. Unlike generational GAs that build a breeding population through successive generations, the fitness function for the NDDP GA can be changed at any time without restarting the

whole process. Because all solutions are maintained in the SQL database, changing the GA fitness function merely shifts the focus of search in the database.

3.2. Selection based on Pareto sets

Architectural design problems often contain conflicting parameters. For example one might want to increase span to give more column-free open space, but at the same time reduce structural weight in order to reduce cost. These would be conflicting parameters. A common solution is to seek some trade-off solution whereby the two (or could be more) parameters are adjusted to give a balanced performance. GAs have for some time used Pareto sets as the breeding populations to search for the best (non-dominated) trade-off solutions [7]. ParaGen also uses Pareto sets to explore conflicting multi-objective goals [6]. Figure 3 shows a graph of a set of solutions from the wood dome example. The Pareto frontier (level 1) is highlighted with the red dots. By clicking on the dots, images of the solutions are shown. This can quickly show the relationship between the form and the graphed quantities and allow the designer to choose among the options based on visual qualities.

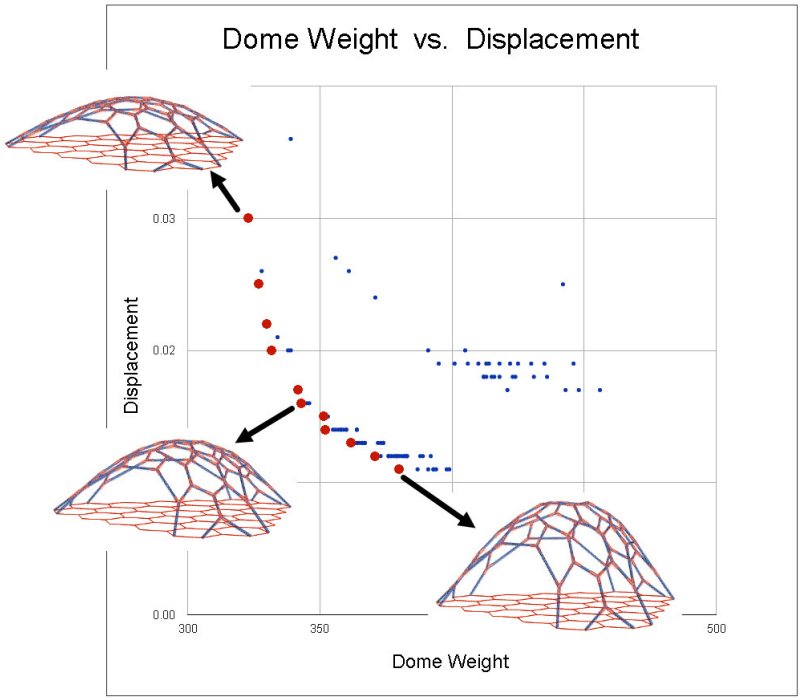


Figure 3: A graph showing the first level Pareto set. Selected images show the range of form.

The database can also store the Pareto level number for each solution. From any pair of conflicting parameters the Pareto frontier as shown in Figure 3 can be calculated and stored. The frontier as shown is considered level 1. The next level behind this (one level less optimal) is level 2. Behind level 2 is level 3 and so on. Having more than one level adds depth to the set being considered either for breeding or simply viewing more options. Any number of sets of parameters can be chosen for Pareto calculations. Each Pareto set is listed in the database as a column (or field) which holds the Pareto level number for each solution. Pareto sets can also be based on more than two parameters although beyond three is hard to visualize or graph. Again, by using the SQL filters on the solution array page, the different visual images

of the Pareto solutions can be scrolled through. Figure 4 shows the full set of images from the Pareto level 1 set shown in Figure 3.

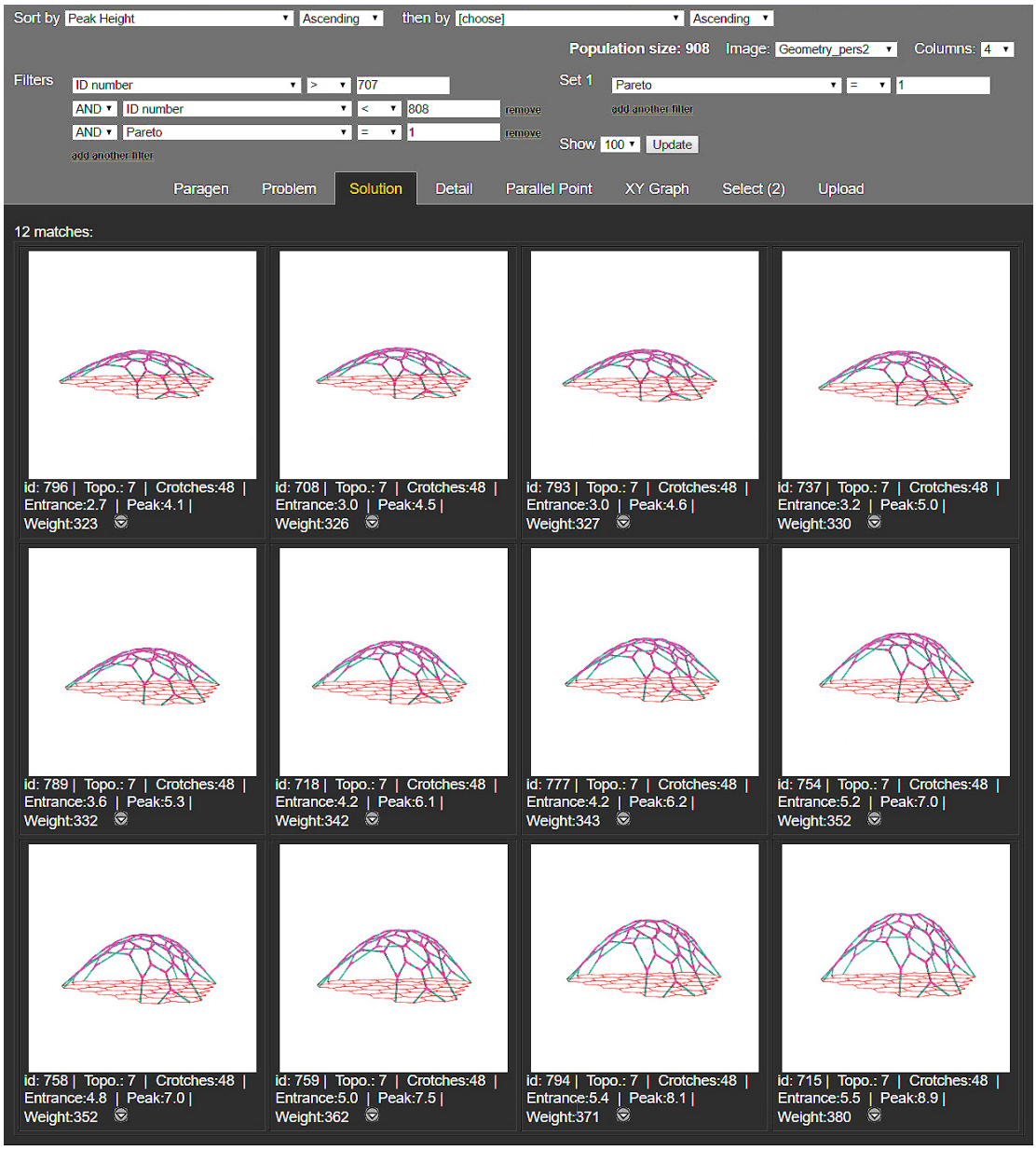


Figure 4: Solutions from the Pareto frontier shown in Figure 3.

3.3. Selection based on user selection

The breeding population may also be selected from the database based on qualitative visual criteria of the designer. Any desired combination of filters and sorts can be chosen to allow the designer to visually explore the solutions in the database. Each solution has a unique identifying number and by specifying a list of these solution numbers chosen by the designer, the GA can use this list as the breeding population.

As an example, using a full set of Pareto level 1 solutions from the wood dome problem (a total of 68 solutions), 20 solutions were selected by the designer based on visual criteria of aesthetics and usability. These 20 solutions were then taken as a breeding set to produce 100 further solutions. From these new solutions the dome shown in Figure 5 was chosen as meeting the aesthetic interest of the designer as well as having fairly good performance.

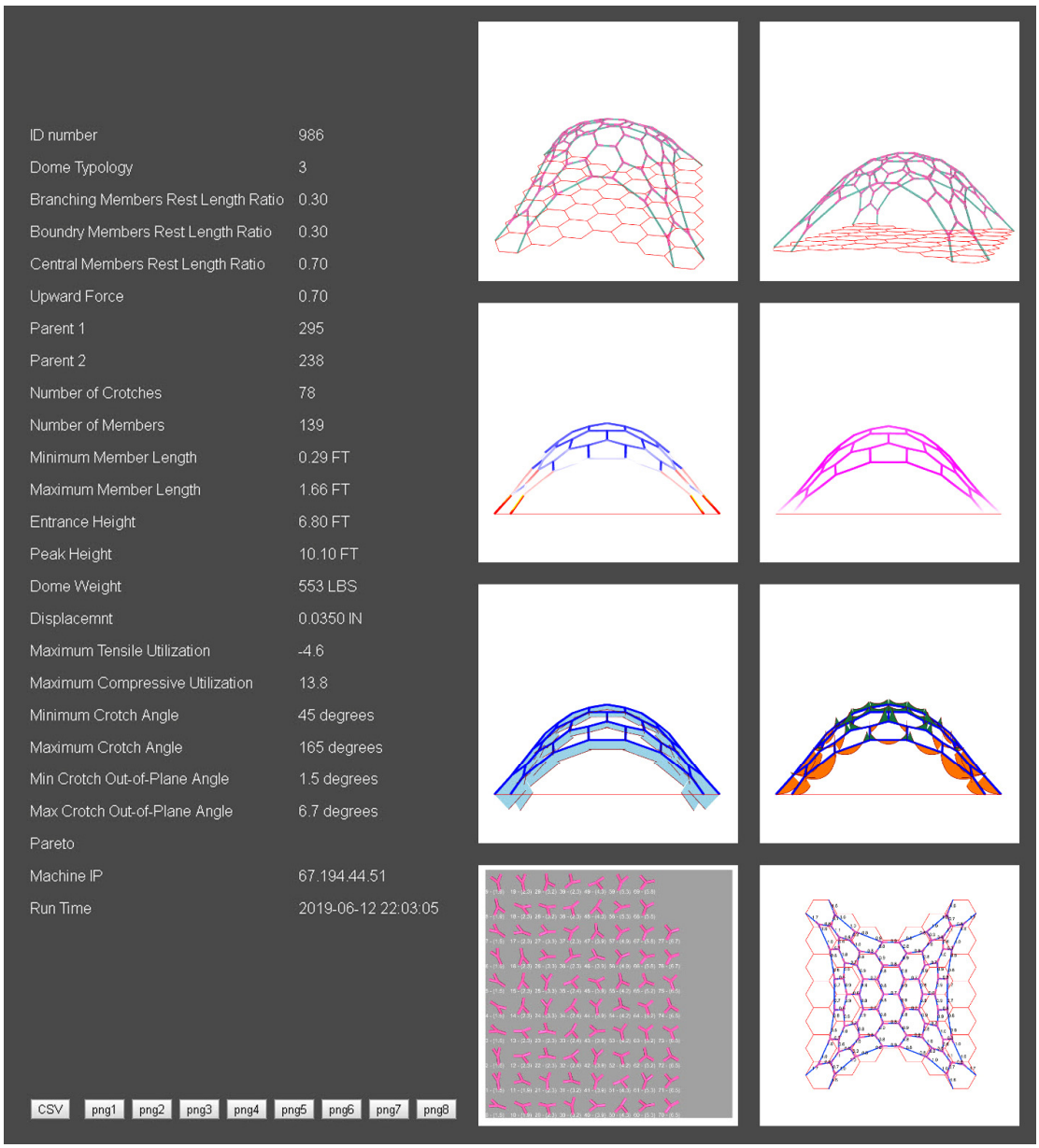


Figure 5: A chosen design generated from the designer selected population. ParaGen can show an overview page of any selected solution which includes all images along with all generating and performance data.

4. Conclusion

Through a simple design example of a reticulated wood dome, some advantages were demonstrated in the use of a SQL database together with a genetic algorithm to search for good solutions. ParaGen, developed at the University of Michigan, combines both an optimizing GA and a SQL database for solution exploration in the early phases of design. ParaGen uses SQL queries to both focus the GA search direction and to provide the designer with post processing, interactive search of the generated solutions. Because a variety of images can also be linked to the stored data, visual and qualitative aspects of the design can be considered in the evaluation process. Using selections made from these visual images, it is also possible to further direct the search for new solutions. In this way ParaGen is able to include both quantitative and qualitative aspects of a design in the exploration process. The result is a more complete consideration of the problem and ultimately a better solution.

Acknowledgements

The author wishes to thank the University of Michigan Taubman College for support over the years of the ParaGen project and the Hydra Lab for parallel computing.

References

[1] A. Osborn, *Applied Imagination – Principles and Procedures of Creative Writing*, Scribner's, Oxford, England, 1953.

[2] D. Koberg and J. Bagnall, *The Universal Traveler,* William Kaufmann, Inc., Los Altos, USA, 1972.

[3] P. von Buelow, "ParaGen: Performative Exploration of Generative Systems" in *Journal of the International Association for Shell and Spatial Structures*. Vol. 53 (2012) No. 4, pp. 271-284.

[4] P. von Buelow, . "Techniques for More Productive Genetic Design: Exploration with GAs using Non-Destructive Dynamic Populations" in *Adaptive Architecture* eds. P. Beesley, O. Khan and M. Stacey. Proceedings of the Association for Computer-Aided Design in Architecture 2013 International Conference. October 24-26, 2013. Cambridge, Ontario, Canada.

[5] L. Eshelman, "The CHC Adaptive Search Algorithm: How to Have Safe Search When Engaging in Nontraditional Genetic Recombination", in: *Foundations of Genetic Algorithms*. Morgan Kaufmann Publ., San Mateo, California. 1991. pp. 265-283

[6] P. von Buelow, "Choosing parents to produce better preforming children: a comparison of selection methods used for evolutionary search". in *Interfaces: architecture . engineering . science*, (IASS 2017). Sept. 25-28, 2017. Hamburg, Germany.

[7] K. Deb, *Multiobjective Optimization using Evolutionary Algorithms*. Wiley, 2001.

Proceedings of the IASS Annual Symposium 2019 – Structural Membranes 2019
Form and Force
7 – 10 October 2019, Barcelona, Spain
C. Lázaro, K.-U. Bletzinger, E. Oñate (eds.)

Multi-objective optimization of reciprocal timber layouts from reclaimed stock elements

Dario PARIGI, Lars DAMKILDE

Aalborg University, Department of Civil Engineering
Thomas Mann vej 23, 9220 Aalborg, Denmark
dp@civil.aau.dk

Abstract

The constructive dimension of structures becomes more important today as the question of sustainability encompasses a broader scope in regards to material use. The inclusion of construction constraints within the digital design process enable novel design approaches, such as design and construction based on reuse of reclaimed material. Reciprocal structures were used in the past for different purposes, but in this context, it is worth noting their use for solving the practical issue of spanning distances especiallly in slabs when the available elements were shorter than the span. The use of reciprocally connected elements allows defining a set of variables that allows adapting to design constraints and goals related to structure and construction. Computational strategies are investigated to generate layouts that are able to span planar configurations with non-standard reclaimed elements. This work presents an optimization study for the design of standardized structural layouts for floors and/or walls, using the SPEA-II Multi Objective method. A set of geometrical and material parameters are defined for modelling the panel architecture, while competing objective functions are defined related primarily to aspects such as structural lightness and efficiency in construction. The results are presented in the form of Pareto optimal sets, from which conclusions can be drawn for the design of cost effective panels from reclaimed elements.

Keywords: reuse, upcycling, reciprocal structures, sustainability, tectonics, construction, optimization, timber structures, sustainability.

1. Introduction

In the past two decades, timber construction has gained revival due to its environmental value and particularly due to the reductions in the building's embodied energy [1]. However the rise in demand of construction timber poses challenges in the long-term adequacy of world timber supply.

Construction based on reuse avoids sourcing new material, reduces superfluous waste, and requires little energy. However, designing a structure from a stock of reclaimed elements entails a change of paradigm. (Bruttning et al. [2]). Consideration of material and construction constraints can lead and strengthen designers´ attention to material and resource use from the early design stages, and enable new paradigms in design. This work presents an optimization study for the design of standardized structural layouts for floors and/or walls using the constructional logic of reciprocal structures. Using the SPEA-II Multi Objective method, set of geometrical and material parameters are defined, while competing objective functions are defined related primarily to aspects such as structural lightness and efficiency in construction.

Copyright © 2019 by Dario PARIGI, Lars DAMKILDE
Published by the International Association for Shell and Spatial Structures (IASS) with permission.

2. Opportunities by using the principle of structural reciprocity

The principle of reciprocity is based on the use of load-bearing elements which, supporting one another along their spans and never at the ends, compose a spatial configuration with no clear structural hierarchy (Pugnale and Sassone [4]). Reciprocal structures were used in the past for different purposes, but in this context, it is worth noting their use for the practical purpose of spanning longer distances when using short elements, connected with aligned axis (figure 1).

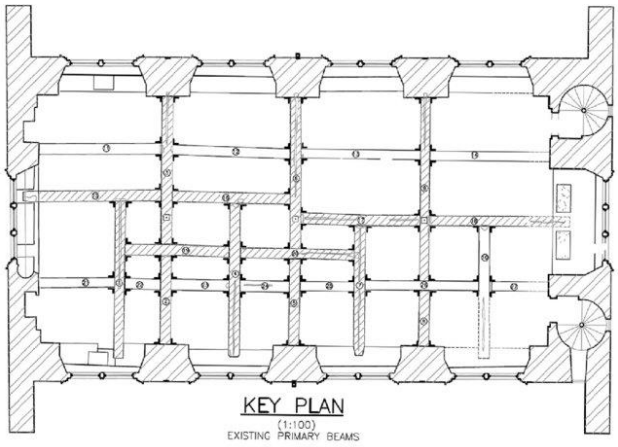


Figure 1: Wollaton Hall, sub-floor structure survey. This layout shows an irregular pattern of timber shortbeams which was clearly conceived not to be seen. Image: Ed Morton, The Morton Partnership LTD, London, UK (sourced from Pugnale and Sassone[3],)

The possibility to span long distances with short elements constitute an opportunity with respect to the reuse of a set of non-regular, reclaimed elements. In particular, this opportunity is formulated on the basis of an intrinsic feature of reciprocal configurations, the fact that elements are supported along their span rather than at their ends: this characteristic allows a higher degree of freedom while arranging the bars in a configuration. The position in which an element meet the supporting element is called engagement length and affects the length of the elements themselves. The possibility to vary this postion in turn means that the length of the elements can be adjusted. Thus this variable can be used to fit a set of non-regular elements to a structural layout.

Utilizing this logic, the following work will investigate whether a set of reclaimed elements, of varying and non-regular length, could be fitted, minimizing cut-offs and material waste, for the purpose of creating a structural grid.

3. Embedded tectonics

The premises of this work are rooted in a research field that extend the notion of pre-rationalization in architecture as the process of modelling and embedding in the geometrical model the tectonic of construction. This notion is referred as “embedded tectonics” (Parigi & Damkilde [4])

Pre-rationalization can be defined as a process in which logically applied constraints pre-determine the architectural geometry, limiting the design to a family of geometries, which are known to be buildable Attar et al. [5]. On the other hand, pre-rationalization can be understood as the process that, by incorporating the logic of construction in a computational environment, allows conceiving geometries bottom up, from a set of physical constraints related to the assembly logic and assembly parts, fostering design search and exploration.

Through early incorporation of material and construction constraints, the designer finds itself with more opportunities for experimentation: the construction logic become a part of the design, and determine original design choices that doesn´t necessarily lead to a family of well-known geometries. On the contrary, with the possibility of inclusion of specific material and construction constraints, it opens the door to complex, structurally optimal yet construction-aware geometries.

Within this notion, novel approaches to structural optimization, that encompass material use and the reuse of material, construction methods and structural performance are posible. In this paper, this notion wiill be embraced through the case study of fitting a set of stock elements to a given plan layout. Rather than the creation of non-standard geoemtries, this work has the goal of the generation of standard

geometries through non-standard components. The complexity of the goemetry is found at a local level, in the complex interaction between elements size and disposition, rather than at a global level.

4. Geometry of reciprocal structures

Even simple reciprocal configurations could be challenging to model due to their recursive nature. Elements are typically organized in "supernodes", around which bars are arranged in a recursive manner as "fans". In a fan, each bar is at the same time supporting and supported by the connecting elements. The fans can have a clockwise (CW) or counter-clockwise (CCW) direction, that affects the elements connectivity.

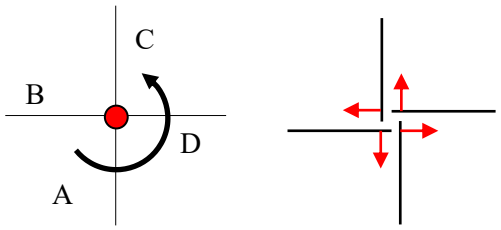


Figure 2a: a supernode where bars are arranged in a CCW fan

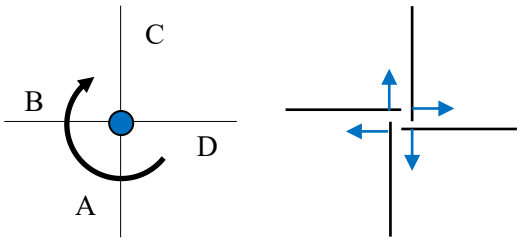


Figure 2b: a supernode where bars are arranged in a CW fan

In a clockwise direction, in a fan with bars A, B, C, D, the bars are arranged with the following connection rule, following the scheme b_i-b_j, where bi is the supported bar and bj is the supporting bar : A-B, B-C, C-D, D-A (figure 2a). In an anti-clockwise direction, in a fan with bars A, B, C, D, the bars are arranged with the following connection rule: A-D, D-C, C-B, B-A (figure 2b).

The recursive nature of the geometry of fans manifests itself when physical constraints are set for the meeting of the bars. The geometry could then be understood as a characteristic that emerges from the parameters set at the joints (how and where bars should meet) and from the bars connectivity and length. In previous research, the author D. Parigi focused on the solution of the geometry of large configurations based on the constraint of the parameter of the joints. The outcome of such research was the development of the Reciprocalizer a module for Grasshopper (Parigi and Kirkegaard [6]). In the Reciprocalizer the only free parameter, among the ones listed before as the fundamental parameters for the geometry of reciprocal structures, was the bars length. The bars length was a parameter that was left free, while the bars connectivity and the physical constraints at the joints could be set as goal. Letting free the bars length allowed to achieve a geometric solution with almost any configuration set up at the joint: a geometrically compatible solution was always achieved.

Conversely, in this work the focus has shifted from the parameters at the joint to the bars length. The typical behaviour related to the non-hierarchical nature of reciprocal structures is retained, i.e. the modification of one bar´s length will affect the whole configuration, rather than just the immediately adjacent bars. The geometric problem is in this study further refined to encompass a specific subset of planar reciprocal configurations where the joint is defined as such:

i. joint axis: the elements are meeting along the axis, i.e. the eccentricity is 0, and the elements meet at 90 degrees (and consequently, the elements can only translate on the adjacent elements but not rotate with respect to the original position);
ii. elements connectivity: fans must be arranged to always alternate clockwise and counter-clockwise direction.

The constraints above have the objective to focus on the primary objective of investigating the use of optimization algorithm in the combinatorial problem of maximization of the use of existing stock element in the spanning of regular span.

5. Geometric constraints

5.1 The joint axis

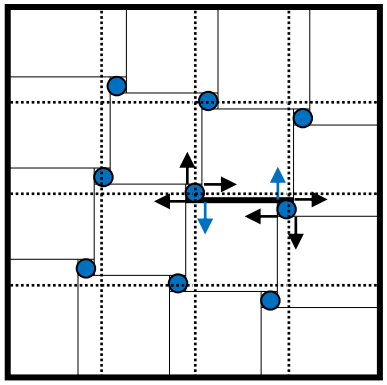


Figure 3a: arrangement of supernodes with CW configurations and the initial bars position (dotted lines)

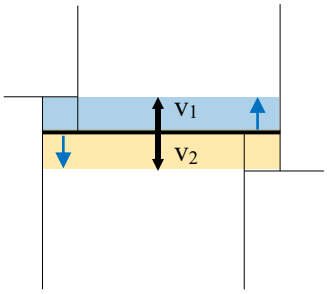


Figure 3b Mobility of a bar in CW configuration

The elements axis are meeting along the axis, i.e. the eccentricity is 0, and the elements are meeting at 90 degrees. The joint is imagined as a simple doweled connection.. As typical for reciprocal structures, always a maximum of two elements meet at every joint, maintaining the connection simple and attainable with standardized components.

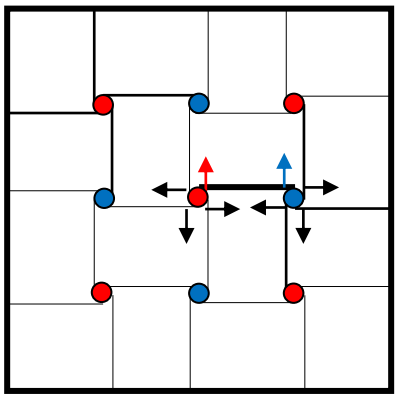


Figure 4a: arrangement of supernodes with alternating CW and CCW fans (initial bars position is omitted for similarity to Figure 5a)

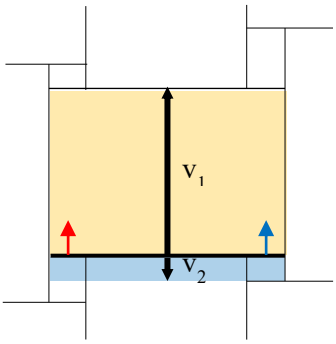


Figure 4b: Mobility of a bar in CW-CCW configuration.

5.2 Elements connectivity

This work will focus on configurations that have fans that alternate clockwise and counter-clockwise direction. For each bars the mobility, i.e the range in which the bars is allowed to reposition along the supporting bars, mantaning the bars connectivity unaltered, is evaluated. It is favourable to maximize the mobility of the bars since it is the main parameter on the basis of which the bars can be rearranged to fit the stock elements size. In a configuration where all fans are CW (or CCW), (figure 3a), the bars mobility is limited since the nodes of the bars must move in opposite direction. Since the parallelism must be maintained, a certain degree of mobility, defined with the length of v1 and v2 (figure 3b) is only achieved when bars have sufficiently moved away from the starting position. Conversely, in a configuration where CW fans and CCW are alternated (figure 4a), each node of a bars will move towards the same direction in order to create in each end respectively a CW and a CCW fan. The mobility, similarly defined with the length of v1 and v2 (figure 4b) spans the whole length of the supporting bars. The configuration of figure 4a is used as the primary configuration in this work for benchmarking the combinatorial algorithm, and it is based on a quadrangular grid of elements.

6. Stock optimization algorithm

The stock optimization algorithm is set up from two basic set of data: the stock set of bars, the connectivity of the bars configuration, and the panel dimension to cover. The algorithm can be described

with the following parts: initialization, the problem variables and the fitness function, the optimization and assignment engine.

6.1 Initialization: virtual ballroom algorithm

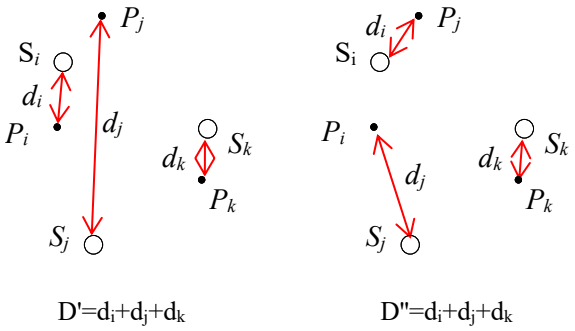


Figure 5. D'>D"

In the initialization step the bars are assigned to a corresponding bar in the stock set . The corresponding bar is assigned in order to minimize the length difference between the bars of the two sets, therefore minimizing the starting value of material waste.

The assignment of the bars is performed with a global evaluation of the material waste. Consequently, not necessarily bars with a small difference in length will be assigned one to another, since a different coupling of elements could produce a better overall waste.

If we visualize the length difference as a physical distance between points, we can create two set of points P and S, representing respectively the set of bars and the stock elements, and propose the problem of coupling the points from the two sets to minimize the overall distance between the couples. While it may seem intuitive to associate S_i with P_i, and S_k with P_k, physically close, and consequently S_j with P_j, the overall distance would not be minimized, as shown in figure 5. Which assignment should we choose between al the possible combinations? It is possible to detect the coupling that produce the minimum distance with a brute force algorithm, that calculates all the possible combinations between the points of the two sets. However the number of possible combinations increases exponentially with the number of elements in the two sets. In order to efficiently perform this assignment, a *virtual ballroom algorithm* is employed. The algorithm enable to minimize globally the distance between two sets with the use of a Genetic Algorithm and a fitness function described as the total distance between the coupled elements.

At the end of this initiali stage, to each bar of the configuration a stock bar is assigned. Note that if the initial configuration all the bars have the same length, the goal bars are assigned taking the closest matching bars in the stock set randomly, since there is no hierarchy between the bars. However, in general cases, a first optimization is the result of this initialization phase.

6.2 Fitness function and variables

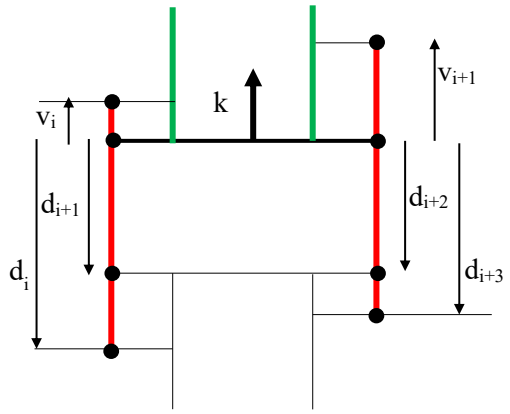


Figure 6: Evaluation of upper and lower bounds

At this stage, for each bar an objective length is assigned by the virtual ballroom algorithm among the stock elements. A penalty factor is added when the bars exceed the stock length of the bars to minimize assigning the bars to shorter stock elements: in this case, the stock element cannot be used.

The variables of the problem is a matrix that contains the of translation vectors for each bar. The translation vectors in turn determines the position of each bar along the supporting bars span, and consequently the value of engagement length, a characteristic value at each bar end node. Every bar can translate in the 2d plane, along the supporting bars, without rotations, along two opposite directions *d* or *v* with respect to a characteristic

direction vector *k* defined for each bar. The bounds of the direction vectors d and v are chosen as the smaller length respectively between the vectors v_i; v_{i+1}, .., v_n and the vectors d_i; d_{i+1}, .., d_n (figure 6).

6.3 Engagement length optimization

A gradient based algorithm minimizes the distance to the goal length of the bar assigned in the initialization of the algorithm. At this stage, one solution to the problem is allowed, determined by the initial bars assignment. Depending on the availability of initial stock elements size, a solution is found.

6.3.1 Benchmark

A benchmark test is set up for testing the optimal assignment of bars in a 24 bars square configuration following the connectivity of figure 6a. A set of random length stock element is created with length in a range from 1,5 to 3,5 meters. Since the starting mesh of elements is regular, the initial assignment engine will assign the stock elements to the configuration elements randomly since there is no parameter to rank the elements with. The initial material waste is 16 meters. The engagement length optimization reduced the waste to 4 meters. The results are consistent from one run to the other, and the runtime is approximately 30 seconds with a processor Intel(c) i7-6500 CPU @2.50 GHz Dual core.

6.3 Assignment engine

Due to the interdependency of bars position, and the orthogonality rule, and the typology, the adjustment of one bar affect the length of two supported bar simultaneously. In the case of a configuration based on alternating CW CCW fans in a quadrangular grid, as a consequence of the connectivity each bar has at its side a twin bar with identical length. If the initial assignment the two "twin" bars were assigned two different length, the difference in length would be wasted. The consequence is that the initial assignment of bars could also be optimized. An additional algorithm is therefore used for the assignment of bars. The input is a vector for the assignment of bars to the stock elements. The engagement length algorithm will optimize the placement of the bars to fit best the stock bars. The assignment engine uses a Genetic Algorithm to find the best combination between the configuration bars and the stock bars.

6.3.1 Assignment engine benchmark

A benchmark test is set up for testing the optimal assignment of bars in a 24 bars configuration. First a goal configuration is set up (figure 7a), the length of the bars measured, and sorted into a stock elements set (figure 7b). The benchmark tests whether the stock bars are assigned to the original position of the goal configuration, to warrant zero waste. The assignment engine provided the expected results, with a run time of approximately 10 minutes with a processor Intel(c) i7-6500 CPU @2.50 GHz Dual core. It is posible to note how, despite the right assignemnt of bars in order to obtain zero waste material, the configuration is not completely overlappping the goal configuration; this can be explained by the fact that some group of bars could be shifted and moved rigidly without affecting the bars lenght (figure 7c)

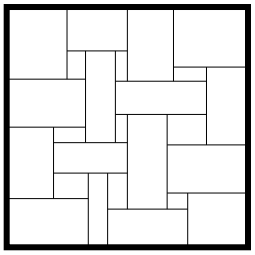


Figure 7a : goal configuration

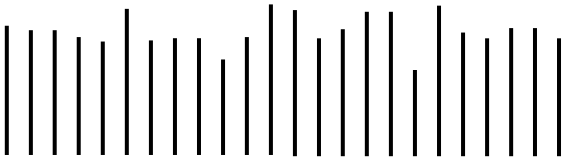


Figure 7b: stock elements size obtined from goal configuration

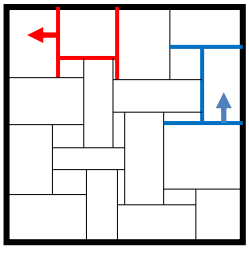


Figure 7c: optimized configuration

6.4 Multi-objective optimization

Multiple solutions to the combinatorial problem exists: while there could be one absolute best solution based on the amount of waste material, a larger set of solutions can also be found with higher material waste, with higher waste material with comparable waste material. A further evaluation allows to add another layer of information to the solution space. Since the variation of the engagement length and the associated elements length affects the structural performance of a structural reciprocal arrangement, a multi-objective optimization using the SPEA-II method, based on the simultaneous evaluation of the waste material and the structural efficiency of the configuration is performed. The organization of the solutions in a Pareto front detects the optimal trade-offs between waste material and structural efficiency. The input to the optimization is a vector for the assignment of bars to the stock element.

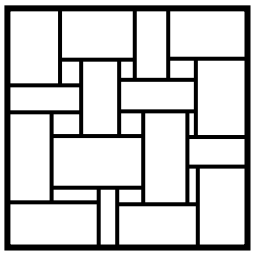


Figure 8a: Sol A

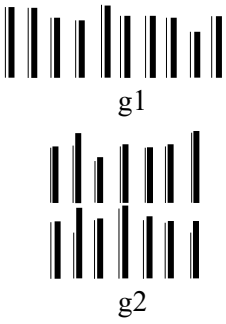


Figure 8b: assignment (thick lines from stock)

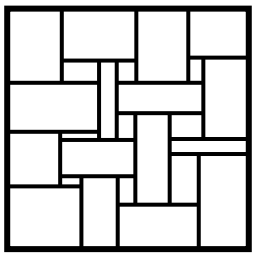


Figure 9a: Sol F

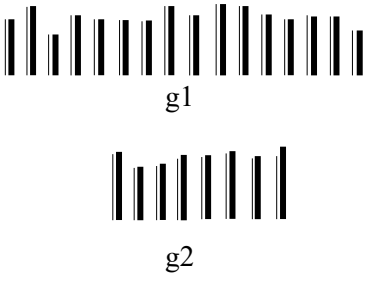
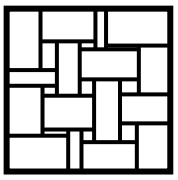
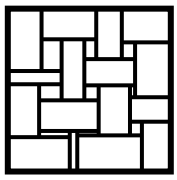


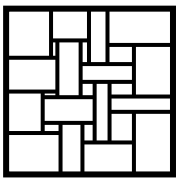
Figure 9b: assignment (thick lines from stock)



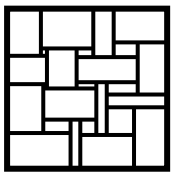
Sol B



Sol C



Sol D



Sol E

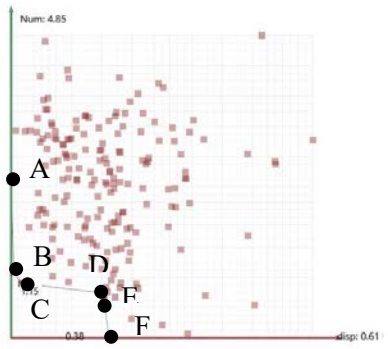


Figure 10: Pareto front

	Displ [cm]	Waste [m]
Sol A	3,7	3.07
Sol B	3,77	1,96
Sol C	3,8	1,81
Sol D	4,4	1,7
Sol E	4,45	1,64
Sol F	4,5	1,15

Figure 10: Pareto front solutions objective values

6.4.1 Benchmark

A benchmark configuration with 24 elements is defined to cover a square surface of 8x8 meters. A stock of 24 elements is defined with random length from 1 to 4 meters. The multi-objective algorithm detects

6 solutions (sol. A B C D E F) on the Pareto front that constitute the optimal trade-offs between optimal stock waste and structural stiffness. The solutions at the extreme of the Pareto front are visualized together with the corresponding stock use (Figure 8a and 9a). For each solution bars assignement are grouped in group *g1*, where bars are utilized to the exact stock length, and in group *g2*, where the stock bars must be adjusted to fit the compatibility of the solution (Figure 8b and 9b).

7. Conclusions

This work presented an optimization study for the design of standardized structural layouts for floors and/or walls using the constructional logic of reciprocal structures. Using the SPEA-II Multi Objective method it is possible to evaluate a set of solutions that minimize material waste while providing different degrees of structural stiffness. Further studies will investigate the application to three dimensional structures and different reciprocal patterns.

References

[1] Fang D., Mueller C., Joinery connections in timber frames: analytical and experimental explorations of structural behavior, *Proceedings of the IASS Symposium 2018 Creativity in Structural* Design July 16-20, 2018, MIT, Boston, USA

[2] J. Brütting, J. Desruelle, G. Senatore, C. Fivet, "Optimum Truss Design With Reused Stock Elements" *, Proceedings of the IASS Symposium 2018 Creativity in Structural* Design July 16-20, 2018, MIT, Boston, USA

[3] Pugnale A., Sassone M., Structural Reciprocity: Critical Overview and Promising Research/Design Issues, Nexus Network Journal 2014; 16

[4] D. Parigi, L. Damkilde, D "Multi-dimensional form finding: structure, construction and sustainability" *, Proceedings of the 4th International Conference on Structure and Archtiecture,* July 24-26, 2019, Lisbon, Portugal

[5] Attar R., Aish R., Stam J., Brinsmead D., Tessier A., Glueck M., Khan A., Embedded rationality: a unified simulation framework for interactive form finding, Int. J.Archit. Comput. 8 (2010) 399–418

[6] Parigi D., Kirkegaard P.H., The Reciprocalizer: an agile design tool for reciprocal structures, Nexus Network Journal, Vol.16, no.1, 2014.

FORM and FORCE

Proceedings of the IASS Annual Symposium 2019 — Structural Membranes 2019
Form and Force
7—10 October 2019, Barcelona, Spain
C. Lázaro, K.-U. Bletzinger, E. Oñate (eds.)

Buckling behavior of open-top, stocky flat bottom tanks subject to wind load

Andreas JÄGER-CAÑÁS*, Peter KNÖDEL[a]

* EHS beratende Ingenieure für Bauwesen GmbH
Am Alten Rathaus 5, 34253 Lohfelden, Germany
a.jaeger_ehs@t-online.de

[a] Karlsruhe Institute of Technology, Steel & Lightweight Structures

Abstract

Flat bottom tanks are widely employed to store liquids, such as water, sludge and oil. In many cases, no roof is necessary to cover the tank or a floating roof is built. When these structures are exposed to wind a complex bearing behavior develops since the load pattern is nonlinearly distributed around the circumference. In recent years standard relevant research was mostly conducted on slender structures, such as chimneys and silos, which lead to first design recommendations. However, for stocky flat bottom tanks, no design procedures are yet proposed. This paper aims at taking a closer look on flat bottom tanks subject to wind load. Decisive parameters such as the radius-to-thickness ratio r/t, stiffness of the wind girder I, length-to-radius ratio l/r and the role of the imperfection amplitude are studied with a parametric finite element analysis. It is shown that the complex behavior imposes a challenge to prepare a design recommendation valid for a broad range of geometries, which allows economical results.

Keywords: Steel structure, buckling, cylindrical shell, flat bottom tank, wind load

1 Introduction

Flat bottom tanks are used to store liquids such as oil, sludge and water. In many cases floating roofs are used to cover the tank or it is left open. Depending on its purpose, bins may become quite thin-walled. Biogas digesters may reach a radius-to-thickness ratio (r/t) of up to 10000 while oil storage tanks are usually not thinner than $r/t \approx 3000$.
While very thin walls allow quite economical structures, local and global buckling due to wind becomes a critical issue in the design process of flat bottom tanks. Depending on toxicity of the stored medium, local buckling between two ring stiffeners may not be permitted. In this case, rather thick shells are required because local and global buckling are tackled with the same design check. In the other cases, when local buckling may be neglected, the failure of the wind girder becomes the decisive critierion.
The wind load results in a compressive force in the girder as well as in bending due to the ovalization of the tank. The stiffness of the eaves ring hence is crucial for the overall stability of the flat bottom tank with larger diameters and higher tanks requiring stronger wind girders.

Copyright © 2019 by Andreas Jäger-Cañás and Peter Knödel
Published by the International Association for Shell and Spatial Structures (IASS) with permission.

For this paper, a parametric study was prepared, which dealt with most influencing aspects. The r/t ratio was varied between 500 and 5000 at a fixed thickness of $t = 10\,\text{mm}$ to represent a large range of practical geometries. The height-to-length ratio l/r was chosen either to 0.5 or 1. Rather weak up to quite strong wind girders were studied using local and global imperfection patterns with several amplitudes.
The parametric study revealed the complexity of the subject. Besides the studied parameters does the boundary have an impact on the resistance as it impedes ovalization at the tank foot and allows the shell to carry the wind load via membrane forces. An attempt to propose a design procedure requires much more research as the evaluation of the finite element calculations showed.

2 Research on cylindrical shells subject to wind loads

Ansourian [1] prepared a remarkable contribution to the field of wind induced buckling of tanks and silos when he proposed a minimum stiffness for the eaves ring (eq. 1, *WG* for wind girder).

$$I_{\text{WG}} = 0.048 t^3 l \tag{1}$$

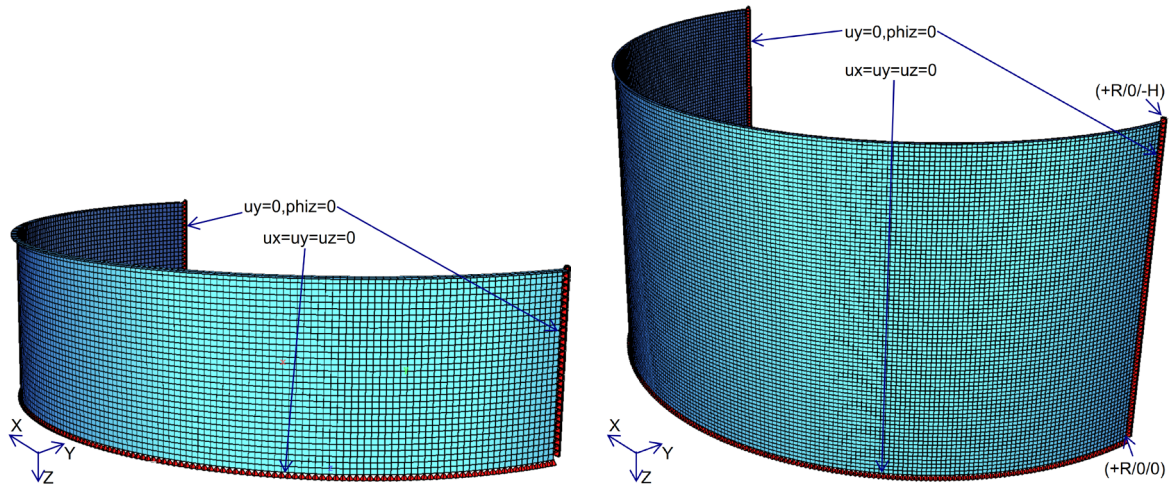
Peter Knödel [9] studied the impact of wind on the design of very thin-walled tanks with a $r/t \geq 5000$. He proposed to calculate the size of the wind girder using eq. 2.

$$W_{\text{WG}} = 7 \cdot 10^{-8} \, (2r)^2 \, l \; q_{\text{p}} / \left(3 \; \left[\text{kN/m}^2\right]\right) \tag{2}$$

with: q_{p} as the design wind load at the stagnation meridian in kN/m^2
Gettel [7] intensively studied the role of the imperfection on the buckling behavior of slender, chimney like shells. He proposed the use of a natural longitudinal imperfection as an easy to generate and mechanically compatible shape deviation, valid even for deep amplitudes. Chen [3] studied slender shells with $3 \leq l/r \leq 15$ subject to wind load. He determined the consequence of the imperfection shape derived from a linear buckling analysis (LBA) and a geometrically nonlinear analysis (GNA) in this length range. Chen concluded that for less slender clyinders, the eigenform shape deviation is the prefarable choice. A finite element study [8] focussed on the influence of the flexibility of discrete anchors on the buckling resistance. It was shown that a flexible lower boundary may crucially reduce the strength of the shell since it favors ovalization. The author team of Qing Shuai [2] analyzed typical cylindrical shells with stocky to very slender aspect ratios. They applied the codified (EN 1993-1-6 [5] and EN 1993-4-1 [6]) numerical procedures on the cylinders using a weld depression depresssion according to Rotter [10]. Qing Shuai *et al.* determined the imperfect shape using LBA. The numerical calculations, a materially and geometrically analysis of the imperfect structure (GMNIA) yielded almost the same resistance as if determined by a materially and geometrically analysis (GMNA).

3 Model, parameters and procedure of the numerical study

The tank shell was modeled using four-node shell elements with linear deformation interpolation. In the circumferential direction the mesh size was chosen according to eq. 4 with the factor $k_{\text{imp}} = 0.05$ and an element height to length ratio of roughly one. The wind girder has been attached as an eccentric beam with a rectangular shape and a width of four times the thickness. Its dimensions were determined following the provisions of EN 14015 [4] (eq. 3). Only half of the shell has been modeled due to load and geometrical symmetry. At the ground the cylinder is fixed rigidly but free to rotate. The basic analysis system is depicted in fig. 1.



(a) $r/t = 500$, $l/r = 0.5$, $k_{\mathrm{WG}} = 2$ (b) $r/t = 5000$, $l/r = 1.0$, $k_{\mathrm{WG}} = 0.1$

Figure 1: Model – overview of mesh and boundary conditions

Table 1: Parameters of the study

r/t	l/r	k_{WG}	k_{imp}	imperfection shape
500	0.5	0.1	0.005	1st buckling eigenform local (BuE1)
1000	1.0	0.5	0.010	2nd buckling eigenform local (BuE2)
1500		1.0	0.016	buckling eigenform global (BuEG)
2500		2.0	0.025	natural frequency eigenform (NEF)
5000			0.050	natural longitudinal imperfection (NL)

The imperfection depth is determined following EN 1993-1-6 [5], which relates the equivalent imperfection amplitude to measurements according to eq. 4. The factors k_{imp} for the codified fabrication tolerance quality classes (FQC) are indicated in tab. 1 together with the parameters used for the geometries analyzed.

$$Z = 0.058\,(2r)^2\,l\frac{V_{\mathrm{w}}^2}{45^2}\cdot k_{\mathrm{WG}} \tag{3}$$

with: V_{w} as 3 second wind gust velocity in m/s and k_{WG} according to tab. 1

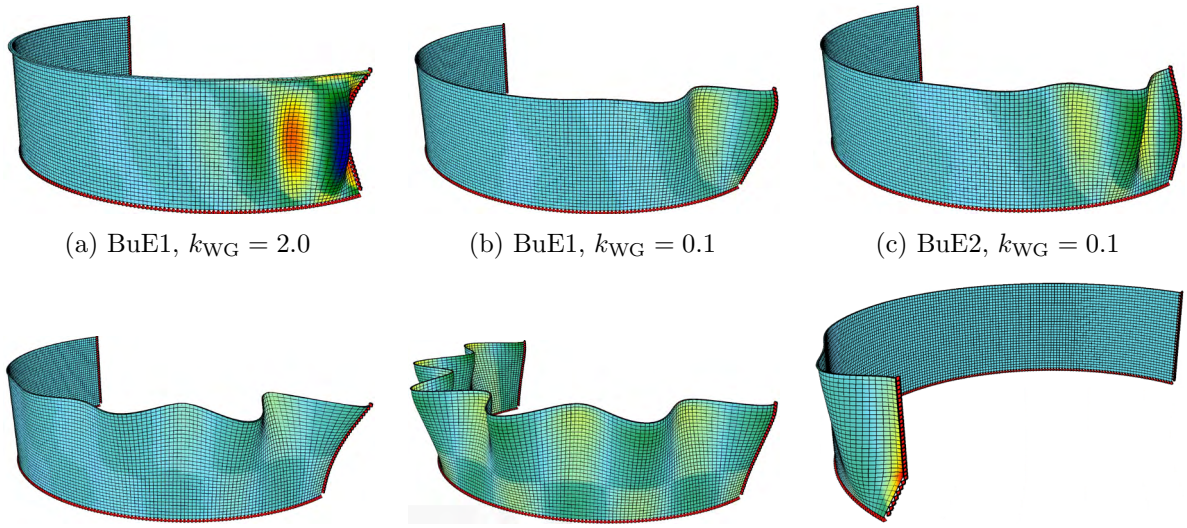
$$\Delta w_{\Theta,\mathrm{eq}} = 2.3\left(l^2 rt\right)^{0.25} k_{\mathrm{imp}} \tag{4}$$

The load pattern is described via the wind pressure factor C_{p}, for which the (corrected) equation (eq. 5) has been adopted from EN 1993-4-1, annex C [6] for a single tank.

$$\begin{aligned} C_{\mathrm{p}} = {} & -0.54 + 0.16\,(l/d) + [0.28 + 0.04\,(l/d)]\cos\theta + [1.04 - 0.20\,(l/d)]\cos 2\theta \\ & + [0.36 - 0.05\,(l/d)]\cos 3\theta - [0.14 - 0.05\,(l/d)]\cos 4\theta \end{aligned} \tag{5}$$

with: θ as the angle of rotation around the circumference $\leq 180°$ and $l/d = l/(2r) \geq 0.5$

A simplified elastic-ideal plastic material law is employed with a modulus of elasticity E equal to $210\,000\,\mathrm{N/mm^2}$, yield strength f_{y} of $235\,\mathrm{N/mm^2}$ and a tensile strength f_{u} of $236\,\mathrm{N/mm^2}$.



(a) BuE1, $k_{\mathrm{WG}} = 2.0$ (b) BuE1, $k_{\mathrm{WG}} = 0.1$ (c) BuE2, $k_{\mathrm{WG}} = 0.1$

(d) BuEG, $k_{\mathrm{WG}} = 0.1$ (e) BuEF, $k_{\mathrm{WG}} = 0.1$ (f) NL, $k_{\mathrm{WG}} = 0.1$

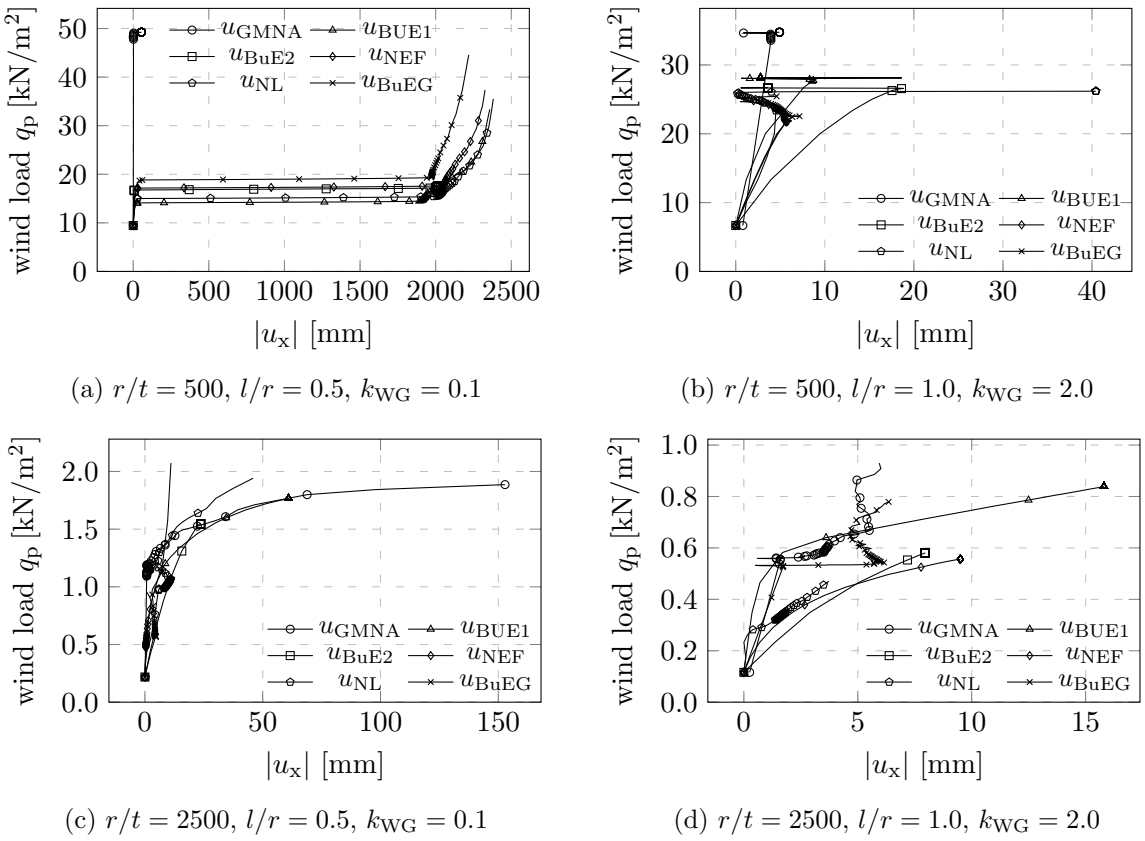
Figure 2: Imperfection shapes, $r/t = 500$, $l/r = 0.5$

The impact on the resistance of several imperfection shapes according to tab. 1 was studied (fig. 2). For the global buckling shape an artifical load (linearly decreasing around half of circumference from maximum value at windward meridian to zero) was imposed on the wind girder and a LBA was performed to derive global buckling shapes. The natural longitudinal imperfection was determined following the proposal of Gettel [7]. Each shape deviation was studied with its positive and negative amplitude using the Newton-Raphson scheme (limit load F_{NR}) employing a GMNIA. Only if the imperfection reduced the strength compared to a GMNA, a subsequent quasi-static analysis was performed starting with small increments of $F_{\mathrm{NR}}/1000$, which were increased as soon as a sudden rapid increase of the total deflection was detected.

4 Results of the numerical study

4.1 Typical load-deflection curves

The stocky tank with a r/t-ratio of 500 and a very weak wind girder (fig. 3a) has a global first buckling eigenform (fig. 2 b). Despite the GMNA all further analysis show a huge gain in resistance with few deformation. At the bifurcation point, which is equal to a change of the load bearing behavior, the stiffness of the shell is lost so that huge deflection occurs that may reach more than two meters in the simulation because the wind girder provides a weak flexural support even in the buckled configuration so that numerically a convergence still is achieved. At about two meter deformation a further increase of the capacity is possible. However, in practice, the deformation is inacceptably big so that the buckling capacity should be deemed as reached at the biforcuatioon point.
With $l/r = 1$ and a strong wind girder as shown in fig. 3b, a higher resistance is achieved and the deformation of the wind girder is crucially reduced. The maximum bearable wind load is about half of what the more stocky version of this geometry parameters would allow. A stronger eaves ring allows higher knockdown factors (relation of resistances $\alpha = r_{\mathrm{GMNIA}}/r_{\mathrm{LBA}}$). When a very weak stiffener as shown in fig. 3a is used, α reaches not more than about 0.30, while for



(a) $r/t = 500$, $l/r = 0.5$, $k_{WG} = 0.1$

(b) $r/t = 500$, $l/r = 1.0$, $k_{WG} = 2.0$

(c) $r/t = 2500$, $l/r = 0.5$, $k_{WG} = 0.1$

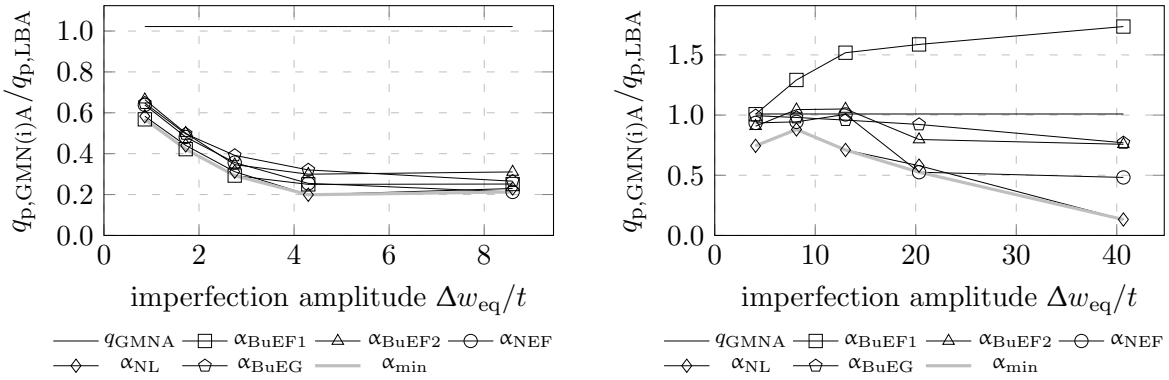
(d) $r/t = 2500$, $l/r = 1.0$, $k_{WG} = 2.0$

Figure 3: Load-deflection curve of node in mid height for $k_{imp} = 0.016$

the heavy ring in fig. 3b a α value of about 0.67 is determined. Sudden changes of direction of the load-deflection curves in fig. 3b show that the interaction of local and global buckling is numerically more unstable than global buckling alone (fig. 3a).
If all parameters are kept and only the r/t ratio is changed to 2500, the outcome of the simulation is basically the same as for $r/t = 500$. As can be seen in figs. 3c and 3d, weak stiffeners allow large deflections before a failure is achieved while stronger stiffeners cause buckling at much smaller deformation. The achievable wind load is less for higher tanks, even if the wind girder is very strong. This is due to the loss of stiffening by the lower boundary and the higher bending moments in the shell. Sudden changes of the direction of the deformation are a hint for multiple bifurcations and hence changes of load bearing mechanisms.
Determining the buckling resistance from the load-deflection curves is quite challenging, especially when an economical yet not unsafe estimate shall be accomplished. Some curves show a continuos shape, hence may undergo snap-through buckling while others indicate multiple bifurcation points. However the latter may indicate higher load bearing capacity than the continuous curves.

4.2 Imperfection sensitivity

Cylindrical shells are known to be imperfection sensitive, especially against uniform loads such as axial compression. However, tanks and silos are less sensitive against circumferential compression and shear. In the case of wind, the load pattern is nonlinearly distributed around



(a) $r/t = 500$, $l/r = 0.5$, $k_{WG} = 0.1$ (b) $r/t = 2500$, $l/r = 1.0$, $k_{WG} = 2.0$

Figure 4: Imperfection sensitivity of two parameter combinations for $k_{imp} = 0.016$

the circumference and combines hoop compression at the stagnation meridian with shear at the flanks. Especially for the thin-walled tanks, the axial compression approximately ninety degrees around the circumference away from the stagnation zone may cause buckling before the loss of stability due to wind is reached.

In the figs. 4a and 4b typical sensitivity curves are plotted. In the case of $r/t = 500$ a steady decrease independently of the imperfection shape is observed as the amplitude gets deeper. A lower limit is reached at the level of FQC C (second symbol from the right).

Thinner shells show a different behavior. In case of $r/t = 2500$ some imperfections may even increase the capacity instead of decreasing it. The strength is almost linearly reduced as the the amplitude increases.

Neglecting the result of the first buckling eigenform of $r/t = 2500$ yields a scatter of capacities around fifty percent in both presented cases. It is obvious that multiple imperfections have to be studied before a clear judgement of a cylindrical shells subject to wind load is possible.

To provide an overview of all parameter combinations, the minimum values of the knockdown factor of each parameter combination is depicted. It can be observed that more stocky tanks usually reach higher capacity. This is mostly due to the influence of the boundary on the ovalization. Eaves rings of longer shells are less stabilized so that ovalization has a larger impact on the stability.

Up to the imperfection amplitude necessary for FQC C, normally the resistance steadily decreases. However, when deeper imperfections are used, higher resistances are calculated. However, since the standard EN 1993-1-6 [5] demands an additional check with a decreased imperfection amplitude, this behavior is not crucial for design purposes.

Most likely, the increasing resistance with increasing amplitude, which is observed for $r/t = 5000$ is due to numerical difficulties. For such thin shells the meridional compression force, which is induced by the imperfection may trigger axial buckling. Especially at small imperfection amplitudes, no significant bending moments develop so that the membrane stress state can cause axial buckling because there is no restraint by bending half-waves or close stiffeners.

No clear function may be deduced from the numerical calculations for all the parameters under condideration. Hence, much more work is required to fully understand and capture all the features of the buckling behavior of thin-walled shell subject to a wind load.

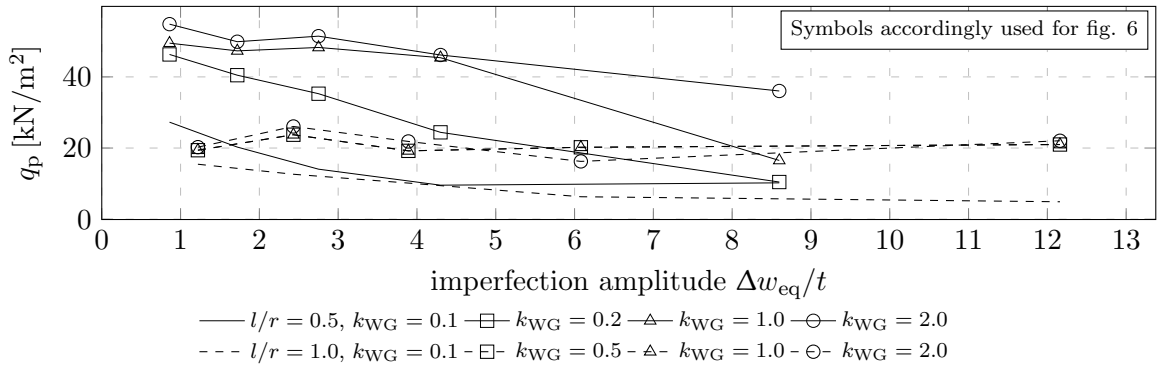
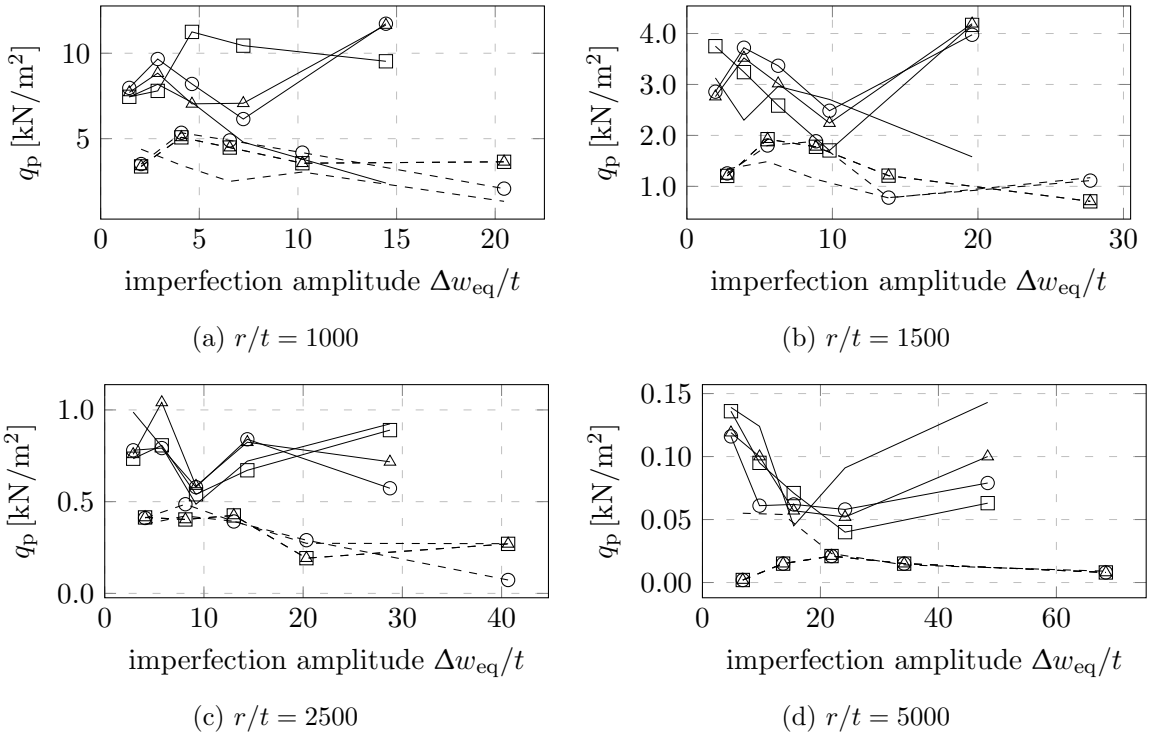


Figure 5: Imperfection sensitivity of parameter combinations for $r/t = 500$



(a) $r/t = 1000$

(b) $r/t = 1500$

(c) $r/t = 2500$

(d) $r/t = 5000$

Figure 6: Imperfection sensitivity of parameter combinations for $1000 \leq r/t \leq 5000$

5 Conclusion

A parameteric study on open top, flat bottom tanks with r/t-ratios between 500 and 5000 and a l/r ratio of 0.5 and 1.0 subject to a wind load was presented. Several influences on the buckling behavior and capacity were studied, such as the stiffness of the wind girder as well as the imperfection shape and its amplitude.

When weak stiffeners are built, huge deformations may occur before a global failure is detected, which makes it difficult to determine a realistic resistance. Strong stiffeners allow for higher capacity at smaller deformation. It was observed that normally more stocky tanks bear higher wind loads compared to higher cylinders.

Different imperfection shapes may yield fewest capacity at a given imperfection depth so that it is not possible to determine *the* worst imperfection and, in any case, multiple shape deviations should be checked in the design process.
To deduce formulae suitable for a design format much more research is required. More studies that systematically focus on decisive parameters would be very helpful to give practitioners a tool, which they could efficiently use for their daily work.
The final outcome of this study is that in most cases tanks and silos of the considered aspect ratios with $r/tr \leq 1500$ can be built in whole Europe and in many places European wide stocky cylindrical shells with $r/t = 2500$ can be constructed with confidence.

References

[1] P. Ansourian. On the buckling analysis and design of silos and tanks. *Journal of Constructional Steel Research*, 23:273–284, 1992.

[2] Q. S. Cao, Y. Zhao, and R. Zhang. Wind induced buckling of large circular steel silos with various slenderness. *Thin-Walled Structures*, 130, 2018.

[3] L. Chen. *Buckling of circular steel cylindrical shells under different loading conditions*. PhD thesis, The University of Edinburgh, Edingburgh, 2011.

[4] EN 14015: Specification for the design and manufacture of site built, vertical, cylindrical, flat-bottomed, above ground, welded, steel tanks for the storage of liquids at ambient temperature and above. Standard, CEN, Brussels, 2005.

[5] EN 1993-1-6: Eurocode 3 - Design of steel structures - Part 1-6: Strength and stability of shell structures. Standard, CEN, Brussels, 2007.

[6] EN 1993-4-1: Eurocode 3 - Design of steel structures - Part 4-1: Silos. Standard, CEN, Brussels, 2007.

[7] M. Gettel. *Ersatzimperfektionen für den numerischen Beulsicherheitsnachweis stählerner Kreiszylinderschalen*. PhD thesis, Institute of statics and dynamics of structures, University of Leipzig, Leipzig, 2008.

[8] A. Jäger-Cañás, B. Justus, and K. Thiele. Buckling of thin-walled steel shells with closely spaced, discrete and flexible anchors under wind load. In *Shell Structures: Theory and Applications: Proceedings of the 11th International Conference 'Shell Structures: Theory and Applications, (SSTA 2017)'*, volume 4, Dansk, 2017. CRC Press.

[9] P. Knödel and T. Ummenhofer. Design of squat steel tanks with r/t > 5000. In *IASS Symposium 2004 Montpellier*, Montpellier, 2004.

[10] J. Rotter and J.-G. Teng. Elastic stability of cylindrical shells with weld depressions. *Journal of Structural Engineering*, 115(5):1244–1263, 1989.

Proceedings of the IASS Annual Symposium 2019 — Structural Membranes 2019
Form and Force
7—10 October 2019, Barcelona, Spain
C. Lázaro, K.-U. Bletzinger, E. Oñate (eds.)

Calculation of static deformation of membrane structures under the load of ponding water

Navaneeth K. Narayanan[*,b], **Roland Wüchner**[b] **and Joris Degroote**[a,c]

[*] Department of Flow, Heat and Combustion Mechanics, Ghent University
Sint-Pietersnieuwstraat 41, 9000 Ghent, Belgium
navaneeth.kodunthirappullynarayanan@ugent.be

[a] Department of Flow, Heat and Combustion Mechanics, Ghent University
[b] Chair of Structural Analysis, Technical University of Munich
[c]Flanders Make, Belgium

Abstract

Ponding refers to a phenomenon of accumulation of water on top of a structure. Even though most light weight membrane structures are designed to prevent its occurrence, it can be initiated in some cases during rainfall by an event such as drifted snow settling on the surface of the structure causing a local depression of the membrane structure. The present work proposes a method to calculate the static deformation of a membrane structure due to a given volume of ponding water. The method involves coupling of a structural solver for the membrane and a volume conserving solver representing the static behavior of an incompressible fluid. The coupling is performed in a partitioned manner with the linearized behavior of the incompressible fluid incorporated in the structural equations to accelerate the coupling iterations. Using this method, the final deformation of the structure due to ponding is calculated by applying loads due to a fixed volume of water.

Keywords: ponding, partitioned coupling, volume conserving solver, hydrostatic load

1 Introduction

Membrane structures are very efficient in carrying loads compared to the materials usage, but these structures undergo significant surface movement when loaded, making them vulnerable to the formation of a water pond. Rainfall along with an event such as snow settling or some dead loads on the structure can trigger accumulation of water in local depression. If the structure is not stiff enough this can cause more deflection leading to more ponding and so on. This cycle of increasing deformation and water accumulation may increase the load indefinitely resulting in structural collapse or failure. For the cases where the structure is much stiffer with good draining characteristics, the excess water will drain, resulting in a stable pond. However, even in this case if the rain is accompanied by strong winds, the wind flow around the structure may induce large oscillations. In 2011, during the Pukkelpop festival held in Kiewit (Belgium), a strong wind interacting with ponding water led to huge swaying of tents eventually resulting in the collapse of the structure. Studying such cases will involve fluid structure interaction (FSI) simulation between the membrane structure, the ponding water and the wind flow.

Copyright © 2019 by Navaneeth K. Narayanan, Roland Wüchner and Joris Degroote
Published by the International Association for Shell and Spatial Structures (IASS) with permission.

In order to simulate such systems it is necessary to find the static deformation of the membrane structure under the load of the ponding water. This will be the pre-processing step for the FSI simulation. The other applications of this analysis include floating caps of oil storage tanks [9], and optical reflector forming using ponding loads [7]. Some of the older works on studying the ponding on membranes include the work of Szyszkowski and Glockner [8] who studied ponding stability and deformation on spherical inflatables, where they solved axi-symmetric membrane equations with the hydrostatic loads. Tuan [7] focused on large deformations and strains of initially flat, simply supported circular membranes under gradually accumulated fluid pressure. He used fourth-order Runge-Kutta numerical integration with an iterative finite element analysis using shell elements to calculate the deformation due to the ponding. However, these studies only involved axi-symmetric geometries. One example of a general approach is presented in the work of Bown *et al.* [3], where an in-house structural code inTENS is coupled with a shallow water solver in a partitioned method to analyse ponding on tensioned membrane structures.
The idea presented in the current work is similar to Bown *et al.*, except here a volume conserving solver is used instead of a transient shallow water solver. The volume conserving solver conserves the given volume of incompressible fluid with a constraint that the top surface is normal to gravity, thus representing the free surface of the fluid in static condition. The coupling iterations are accelerated by adding the linearized static behaviour of the fluid under gravity in the structural solver. In terms of implementation this will translate into adding the load stiffness matrices to the tangent stiffness matrix of the membrane elements and a linear update of the top surface in the non-linear iterations of the structural solver. The required load stiffness matrices are mentioned shortly in the later sections but this has been extensively discussed in [1, 2], where the authors derive all the tangent stiffness matrices from the principle of virtual work. In each coupling iteration, hydrostatic load is applied on the structure based on the plane's height and the volume-conserving solver updates the plane's height depending on the deformation of the structure in order to conserve a given volume of water. When the convergence is achieved in the partitioned iterations, the deformed shape of the structure is determined. The following sections discuss the proposed volume-conserving solver and how it is coupled to a structural solver in KRATOS [4], an open-source finite element framework. At the end, an example is presented where the static deformation of the membrane structures is calculated due to the accumulation of an incompressible fluid.

2 Mathematical models

2.1 Hydrostatic load

Consider a membrane surface denoted by $\partial\Omega_s$ containing a certain volume of incompressible fluid. The free surface of the fluid, denoted by $\partial\Omega_f$ is perpendicular to gravity. The wetted region of the membrane, $\partial\Omega_{fs}$ experiences hydrostatic pressure proportional to the height of the free surface from the fluid above. If the gravity is along the z-direction then mathematically, the traction at a point P with z-coordinate, z on the structure can be stated as:

$$\begin{aligned} \mathbf{t} &= -\gamma_f(z - z_f)\mathbf{n} && \partial\Omega_{fs} \\ \mathbf{t} &= \mathbf{0} && \partial\Omega_s \setminus \Omega_{fs} \end{aligned} \tag{1}$$

where, z_f is the z-coordinate of the free surface, γ_f is the specific weight of the fluid, $\mathbf{n}$ is the outward unit normal vector at the point P. Figure 1 clearly indicates the symbols and terminologies used.

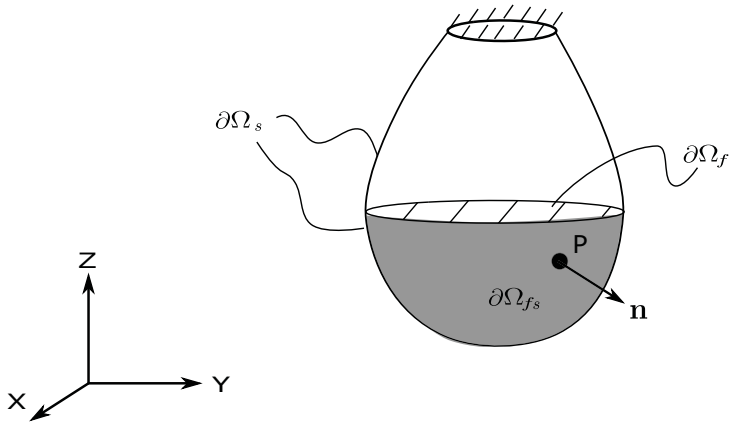


Figure 1: Hydrostatic loading by a fluid on a membrane.

2.2 Structural equations

the variational formulation of the static non-linear membrane in its reference configuration can be written as

$$-\int_{\partial\Omega_s^0} h\ \mathbb{S} : \delta\mathbb{E}\ dS + \int_{\partial\Omega_s^0} \mathbf{t}_0 \cdot \delta\mathbf{u}\ dS = 0, \tag{2}$$

where $\mathbb{S}$ and $\mathbb{E}$ are the second Piola-Kirchhoff stress tensor and the Green-Lagrange strain tensor, respectively. The first term in the equation 2 is the virtual internal work (δW_{int}) and the second term is the external virtual work (δW_{ext}), corresponding to the virtual displacement $\delta\mathbf{u}$. With the assumptions of large displacement and small strains, we only consider the Saint-Venant Kirchhoff material law, equation 3, in the numerical example presented in this paper.

$$\mathbb{S} = 2\mu\mathbb{E} + \lambda\mathbb{E} : \mathbb{I} \tag{3}$$

The tangent stiffness matrix of the membrane elements ($\mathbb{K}_{mem}$) can be obtained by discretising equation 2 and deriving δW_{int} by the nodal displacement vector $\hat{\mathbf{u}}$. For more details on the derivation of membrane elements, please refer to [10]. For the case of hydrostatic loading, δW_{ext} can be written in the current configuration by using equation 1 giving

$$\begin{aligned}\delta W_{ext} &= \int_{\partial\Omega_{fs}} \delta\mathbf{u} \cdot p\mathbf{n} ds \\ &= -\int_{\partial\Omega_{fs}} \delta\mathbf{u} \cdot \gamma_f(z - z_f)\mathbf{n} ds.\end{aligned} \tag{4}$$

In the equation 4, the external work term is calculated based on z_f determined by the volume conserving solver. By linearizing the discretized form of equation 4 and subtracting it from the membrane tangent stiffness matrix the convergence speed of the coupling iterations between the structural and the volume conserving solver can be improved. Even though, the free surface is moved by the volume conserving solver in every coupling iteration to conserve a given volume of water, the water level should also change during the non-linear iterations of the structural

solver. This is not directly performed by the volume conserving solver as it was found to be unstable in some numerical experiments. Actually, if the volume conserving solver was used in structural iterations, the external coupling iterations is not required and the convergence will be much faster. But for the algorithm to be more robust, it was decided to perform the coupling external to the structural solver with the linear update of the free surface inside the non-linear iterations of the structure, given by

$$Dz_f[\mathbf{u}] = \Delta z_f = \frac{-\int_{\Omega_{fs}} \Delta\mathbf{u}\cdot\mathbf{n}\ ds}{A_f}. \tag{5}$$

The linearization of the external work term from the hydrostatic pressure in the equation 4 is given by

$$\begin{aligned} D\delta W_{ext}[\mathbf{u}] = &-\gamma_f \int_{\partial\Omega_{fs}} \delta\mathbf{u}\cdot Dz[\mathbf{u}]\ \mathbf{n}\ ds + \gamma_f \int_{\partial\Omega_{fs}} \delta\mathbf{u}\cdot Dz_f[\mathbf{u}]\ \mathbf{n}\ ds \\ &-\gamma_f \int_{\partial\Omega_{fs}} \delta\mathbf{u}\cdot(z-z_f)\ D\mathbf{n}[\mathbf{u}]\ ds. \end{aligned} \tag{6}$$

Substituting $Dz[\mathbf{u}]$ from equation 5 we get

$$\begin{aligned} D\delta W_{ext}[\mathbf{u}] = &-\gamma_f \int_{\partial\Omega_{fs}} \delta\mathbf{u}\cdot Dz[\mathbf{u}]\ \mathbf{n}\ ds - \frac{\gamma_f}{A_f}\left(\int_{\partial\Omega_{fs}} \delta\mathbf{u}\cdot\mathbf{n}\ ds\right)\left(\int_{\partial\Omega_{fs}} \Delta\mathbf{u}\cdot\mathbf{n}\ ds\right) \\ &-\gamma_f \int_{\partial\Omega_{fs}} \delta\mathbf{u}\cdot(z-z_f)\ D\mathbf{n}[\mathbf{u}]\ ds. \end{aligned} \tag{7}$$

Discretizing equation 7 using the shape functions matrix $\mathbb{N}$ and the nodal displacement vector $\hat{\mathbf{u}}$, we can write the equation 7 in terms of the load stiffness matrix $\mathbb{K}_p$, the incremental nodal displacement vector $\Delta\hat{\mathbf{u}}$ and the virtual displacement $\delta\hat{\mathbf{u}}$. The discretized equation for each membrane element inside the wetted region Ω_{fs} is given in equation 8, which is assembled in a global matrix to give $\mathbb{K}_p$.

$$\begin{aligned} D\delta W^e_{ext}[\mathbf{u}] =&\delta\hat{\mathbf{u}}^{eT}\left\{-\gamma_f \int_\xi\int_\eta \mathbb{N}^T\tilde{\mathbf{n}}\mathbf{e}_z^T\mathbb{N}\ d\xi d\eta - \frac{\gamma_f}{A_f}\left(\int_\xi\int_\eta \mathbb{N}^T\tilde{\mathbf{n}}\ d\xi d\eta\right)\left(\int_\xi\int_\eta \tilde{\mathbf{n}}^T\mathbb{N}\ d\xi d\eta\right)\right. \\ &\left.-\gamma_f \int_\xi\int_\eta (z-z_f)\left(\mathbf{g}_\xi\times\frac{\partial\mathbb{N}}{\partial\eta} - \mathbf{g}_\eta\times\frac{\partial\mathbb{N}}{\partial\xi}\right)\ d\xi d\eta\right\}\Delta\hat{\mathbf{u}}^e \\ =&\delta\tilde{\mathbf{u}}^T\mathbb{K}^e_p\Delta\tilde{\mathbf{u}}^e \end{aligned} \tag{8}$$

with the corresponding virtual external work for each element,

$$\begin{aligned} \delta W^e_{ext} &= -\delta\hat{\mathbf{u}}^{eT}\gamma_f \int_\xi\int_\eta \mathbb{N}^T(z-z_f)\tilde{\mathbf{n}}\ d\xi d\eta \\ &= \delta\hat{\mathbf{u}}^{eT}\mathbf{F}^e_p \end{aligned} \tag{9}$$

In equation 8 and 9, the integration is performed in the parametric domain, where the unit normal vector $\mathbf{n}$ is replaced by the normal vector $\tilde{\mathbf{n}}$ using the relation, $\mathbf{n}\ ds = \tilde{\mathbf{n}}\ d\xi d\eta$. In equation 8, $\mathbf{g}_\xi$ and $\mathbf{g}_\eta$ are the basis vectors at any point in the element. In the current work, only constant strain triangle (CST) elements are considered with the numerical integration based on Gauss quadrature. For the elements that are cut by the free surface the integration is performed by dividing the cut triangles and performing Gauss integration on the triangles that are below the free surface, as shown in the figure 2. The final equation after the assembly for arbitrary $\delta\tilde{\mathbf{u}}$ is solved in every non-linear iteration of the structure, until convergence, giving

$$\begin{aligned} &\delta\tilde{\mathbf{u}}^T \left(\mathbb{K}_{mem} - \mathbb{K}_p\right) \Delta\tilde{\mathbf{u}} = \delta\tilde{\mathbf{u}}^T \left(\mathbf{F}_p - \mathbf{F}_{mem}\right) \\ \implies &\left(\mathbb{K}_{mem} - \mathbb{K}_p\right) \Delta\tilde{\mathbf{u}} = \mathbf{F}_p - \mathbf{F}_{mem} \end{aligned} \tag{10}$$

where $\mathbf{F}_{mem}$ is the global internal force vector of the membrane. In each non-linear structural iteration the global hydrostatic force vector $\mathbf{F}_p$ is calculated based on the position of the free surface which is updated according to equation 5.

3 Volume conserving solver

The volume conserving solver consists of two components: a volume calculation algorithm and a iterative algorithm to conserve a given volume. The volume of $\partial\Omega_{fs}$ in figure 1 can be calculated using the relation,

$$V_f = \int_{\partial\Omega_s} (z - z_f)\mathbf{e}_z \cdot \mathbf{n} ds \tag{11}$$

and its derivative with respect to z_f,

$$\frac{\partial V_f}{\partial z_f} = \int_{\partial\Omega_s} -\mathbf{e}_z \cdot \mathbf{n} ds = A_f \tag{12}$$

where A_f is the area of the free surface. The integration in equation 11 and 12 is performed numerically using Gauss quadrature, in the same way as explained in the previous section. In the current work, leap-frogging Newton's method is used for conserving a given volume. This method is discussed in detail in [6]. It consists of a Newton step followed by a pseudo secant step. The main advantage of this method is that it only involves one derivative evaluation, like Newton's method and yet it can attain cubic convergence. The Newton method and leap-frogging method were tested for volume conservation with a complicated geometry and it was found that the leap-frogging Newton was much more robust and had faster convergence rate than Newton's method. Hence, it was chosen over the other. The equation used for iteration to conserve the volume is given in equation 13, with the function f and x_n being the difference between the current volume and the target volume $(V_f^n - V_t)$, and the z-coordinate of the free surface at the n^{th} iteration, respectively. The derivative of function, f' is given by equation 12, which is the area of the free surface at the n^{th} iteration.

$$\begin{aligned} \tilde{x}_n &= x_n - \frac{f(x_n)}{f'(x_n)} \\ x_{n+1} &= x_n - \frac{f(x_n)^2}{f'(x_n)\left(f(x_n) - f(\tilde{x}_n)\right)} \end{aligned} \tag{13}$$

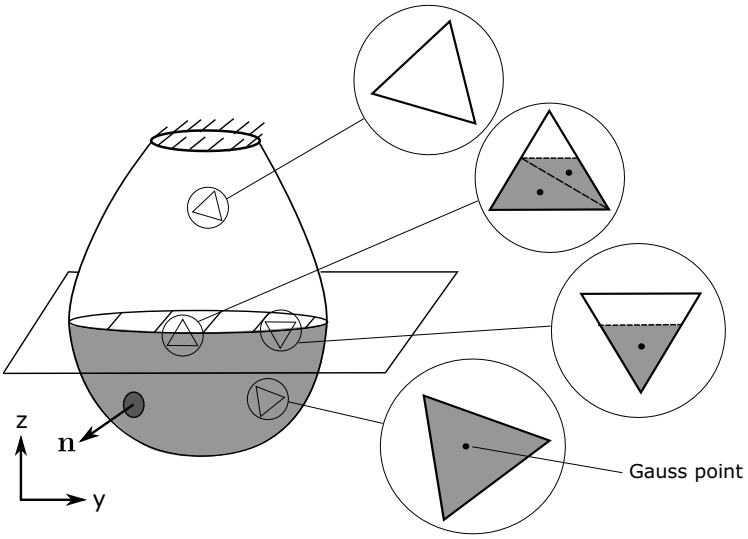


Figure 2: Gauss integration in the wetted region.

4 Partitioned coupling

The static structural deformation under the load of a given volume of fluid, V_t is obtained when the variational equation of the structure, equation 2, and boundary conditions given in equation 1 are satisfied with fluid volume $V = V_t$. The solution of the problem is obtained by iterating between structural solver and volume-conserving solver until the norm of the displacement change between the iterations is under a certain tolerance. Because the linearized part of the fluid is added in the structural system, there was no need to use any convergence accelerators like Aitken or IQNLS [5]. This claim is also supported by the numerical experiments that were carried out. For example, in the numerical example presented in the paper, for most of the fluid volume the number of coupling iterations was around 3 or 4.

5 Numerical example: Ponding on a pnuematic membrane structure

Before performing the simulation of this case, the volume conserving solver was validated with a known case where the enclosed volume was already known. The partitioned coupling between the solvers was also validated with the numerical results presented in table 2 of [7]. Here, the maximum vertical displacements corresponding to four different fluid volumes were compared and were found to be in very close agreement. In the numerical example presented in this paper, we consider an inflated thin-walled membrane hemisphere with Young's modulus $E = 7 \times 10^6\ N/m^2$, Poisson ratio $\nu = 0.45$ and thickness $t = 0.002\ m$. A difference in pressure of $p = 0.5\ kPa$ compared to the atmospheric pressure is applied at the internal surface. To get the perfect hemisphere of diameter $D = 10\ m$ after the application of pressure, an isotropic normal pre-stress calculated from the formula $\sigma_{mem} = pD/4t = 1.2MPa$ is applied on the membrane with zero shear stress. The hemisphere is clamped at the bottom boundary and for reducing the computational time only a quarter section of the hemisphere is simulated considering the symmetry of the problem. To start the ponding process, we first apply a dead load of $w = 1\ kPa$ on the top surface of the membrane enclosed by a circle of radius $R_{dead} = 1.736\ m$ as a seed event. Due to the dead load, there will be a local depression in the hemisphere. In

the created depression, a hydrostatic load due to different volumes of water was applied. The results are obtained by running the partition coupling iterations with various target volumes as input in the volume conserving solver. In all the simulations considered in the example, the volume conserving solver is initialized from the topmost point of the undeformed hemisphere. The vertical displacements of top most point of the hemisphere corresponding to the different fluid volumes are given in table 1. Figure 3 shows the deformed shape of a cut section of the hemisphere for $V_t = 1.6\ m^3$. The distance from the free surface is scaled to positive and negative values very close to zero to show the wetted surface of the hemisphere.

Table 1: Vertical displacement of the top most point of the hemisphere (u_z) and vertical position of the free surface (z_f) for different volume of water (V_t).

$V_t\ [m^3]$	0.0	0.8	1.6	2.4	3.2	4.0
$u_z\ (m)$	-0.972	-2.442	-3.709	-4.950	-6.214	-7.531
$z_f\ (m)$	N.A.	7.986	6.950	5.887	4.774	3.590



(a) Distance from the free surface.

(b) Deformed geometry with mesh.

Figure 3: Deformed geometry of inflated the hemispherical membrane due to the ponding of water with $V_t = 1.6\ m^3$.

6 Conclusion and Outlook

An algorithm for calculating the static deformation of a structure due to ponding load from a fixed volume of fluid was developed. The algorithm involved partitioned coupling of a structural solver and a volume conserving algorithm, responsible for maintaining a constant volume of fluid on the structure. The linearized contribution of the fluid behavior was added in the structural iterations to accelerate the coupling. The obtained deformation will be used as the initial condition for the FSI simulation of the membrane structure, ponding water and wind flow.

7 Acknowledgements

The authors gratefully acknowledge the funding of the Research Foundation – Flanders (FWO) for this work (project number G086517N).

References

[1] T. Rumpel and K. Schweizerhof, "Hydrostatic fluid loading in non-linear finite element analysis," *International Journal for Numerical Methods in Engineering*, vol. 59(6), pp. 849-870, 2004.

[2] C. Hoareau and J.-F Deü. "Non-linear finite element analysis of an elastic structure loaded by hydrostatic follower forces," *Procedia Engineering, Elsevier*, vol. 199, pp. 1302-1307, 2017.

[3] A. Bown, T. Makin and D. Wakefield, "Beyond Static Analysis: Investigation of Membrane Structure Performance Using Time Stepping, Transient and Progressive Analyses," *Procedia Engineering*, vol. 155, pp. 1877-7058, 2016.

[4] P. Dadvand, R. Rossi and E. Oñate, "An object-oriented environment for developing finite element codes for multi-disciplinary applications, "Archives of computational methods in engineering," vol. 17(3), pp. 253–297, 2010.

[5] J. Degroote, "Partitioned Simulation of Fluid-Structure Interaction." *Archives of Computational Methods in Engineering*, vol. 20(3), pp. 185-238, 2013.

[6] J.B. Kasturiarachi, "Leap-frogging Newton's method," *International Journal of Mathematical Education in Science and Technology*, vol. 33(4), pp. 521-527, 2002.

[7] C. Y. Tuan, "Ponding on circular membranes" *International journal of solids and structures*, vol. 35, pp. 269-283, 1998.

[8] W. Szyszkowski and P. Glockner "Finite deformation and stability behaviour of spherical inflatables subjected to axi-symmetric hydrostatic loading" *International journal of solids and structures*, vol. 20, pp. 1021-1036, 1984.

[9] H. I. Epstein and T. J. Strnad, "Liquid-filled, liquid-supported, circular structural membranes," *Computers & structures*, vol. 21, pp. 443-451, 1985.

[10] R. L. Taylor, E. Onate, P. -A. Ubach, "Finite element analysis of membrane structures" *Textile composites and inflatable structures*, pp. 47-68, 2005.

Proceedings of the IASS Annual Symposium 2019 – Structural Membranes 2019
Form and Force
7 – 10 October 2019, Barcelona, Spain
C. Lázaro, K.-U. Bletzinger, E. Oñate (eds.)

Efficient aeroelastic analysis of wind loads on inflatable hangars

Roberto FLORES*, Enrique ORTEGA[a]

* International Center for Numerical Methods in Engineering (CIMNE)
C. Gran Capitán s/n, 08034 Barcelona, Spain
rflores@cimne.upc.edu
[a] Serra Hunter professor at Escola Superior d'Enginyeries Industrial, Aeroespacial y Audiovisual de Terrassa (ESEIAAT), Universitat Politècnica de Catalunya, Spain

Abstract

Wind loads play a crucial role in inflatable structures. Unfortunately, design loads from safety regulations grossly overestimate the real aerodynamic forces. Thus, a more accurate estimation of wind loads is desirable. Conventional CFD approaches (e.g. LES) struggle with the complexities of the flow field (intricate geometry and massive flow separation) and require a very high computational effort. We present a cost-efficient tool for the aeroelastic analysis of inflatable hangars. It uses a staggered solution scheme with an explicit finite-element structural solver and potential flow aerodynamics. To account for large areas of separated flow typical of blunt shapes, a semi-empirical correction is applied to the inviscid solution. The streamlines of the potential solution are computed and, for each one, the separation point is predicted with Stratford's criterion. Finally, an empirical correction is applied to the inviscid pressure field. We present validation benchmarks as well as a real life application example. Over the majority of the flow field, the pressure field agrees well with high-fidelity computations, yielding similar global loads for structural sizing. This is achieved with a small fraction of the computational effort required by conventional CFD approaches

Keywords: inflatable structures, aeroelasticity, wind loads, low-fidelity methods

1. Introduction

From the point of view of analysis and design, inflatables pose special challenges, such as material characterization and structural response (both highly nonlinear), airtightness and shape stability. A typical case is the study of wind loading. The combination of low stiffness and reduced inertial mass increases the importance of the coupling between the structural and aerodynamic fields.

The first numerical tools for fluid-structure interaction (FSI) analysis of inflatables appeared in the early 90s. Air was modeled using panel methods with finite element (FE) techniques used for the structure. This methodology has proven very effective for streamlined shapes where the flow is mostly attached. Higher-fidelity FSI methods with full volume discretization incur in much higher computational cost.

In a production environment, time and computer resources are limited. Hence, methods yielding acceptable accuracy with minimal cost are necessary. Furthermore, potential users of the analysis tools have limited training in continuum mechanics and numerical analysis. To address these constraints, CIMNE & ESEIAAT co-developed a simplified simulation code, initially intended for ram-air parachutes (see https://www.cimne.com/parachutes). The solution is based on potential flow aerodynamics, explicit FE structural dynamics and staggered FSI coupling; see [1,2]. Here, we extend this methodology to simulate wind effects on inflatable structures, correcting for the special features of the flow around blunt bodies. The procedure is outlined in sections 2 and 3, and a real-life example is

Copyright © 2019 by Roberto Flores & Enrique Ortega
Published by the International Association for Shell and Spatial Structures (IASS) with permission.

presented in section 4 to illustrate the performance achieved. The most relevant conclusions are drawn in Section 5.

2. Overview of the simulation approach

We outline briefly the main characteristics of the numerical model. For further details the reader is referred to [1].

2.1. Structural modeling

The structural solver is based on a large-displacement dynamic FE formulation. A wrinkling model is used to account for the lack of compression stiffness in cables and membranes. When computing stresses, small tensile strains are assumed, but arbitrarily large compressive strains are allowed to account for wrinkling. The equations are advanced in time with an explicit second-order scheme. A numerical dissipation model with Rayleigh damping and bulk viscosity is used to control local high-frequency modes that are not well resolved by the staggered coupling adopted. This approach is simple and inexpensive, but care must be taken to avoid contamination of the solution with spurious viscous forces. Guidelines for tuning the damping parameters are given in [1,3].

The solver models cables, membranes and 3D solids using 2-node linear, 3-node triangular and 4-node tetrahedral elements, respectively. Line elements are used for simulating the anchoring and stabilization cables, fabric seams and reinforcement tapes. The solid tetrahedral elements model ballasts and any other suitable components. If the deformations of the parts discretized with volume elements are negligible compared with the rest of the structure, groups of solid elements can be lumped into rigid bodies to reduce the model complexity.

Different types of kinematic constraints and analytical contact with pre-defined surfaces are available to accommodate the different support conditions found in real life. In addition, it is possible to prescribe time-varying tube pressurization (for inflation and deflation analyses) and several types of distributed loads (e.g. fixed-direction and follower) to simulate wind and snow actions.

2.2. Aerodynamic modeling

The flow is solved with a low-order unsteady panel method using doublets and sources. Constant strength panels lower complexity and computational cost. Also, the discretization is simplified because exact matching between panels is not required. Wake rollup is included via time-steeping technique. Unsteady added mass effects are also simulated, and drag forces on cables and simple bodies are accounted for by means of empirical coefficients. For this work, the unsteady capabilities of the solver have not been used, only steady-state results are presented.

The atmospheric boundary layer is model with an exponential wind profile according to the Eurocode 1 standards (EN 1991-1-4: wind actions, see [4]). In the context of potential flow, boundary layers can be approximated as a uniform far-field inflow velocity plus a local velocity correction at the surface of the structure that depends on the distance to the ground. Hence, the irrotationality of the velocity field is preserved.

Although simple and effective, the inviscid solution approach is only suitable for solving attached flows. The next section describes the strategy to include the effect of separation.

3. Flow detachment correction

In flows with extensive and well-defined areas of detached flow, experiments show that the pressure field over the areas where the boundary layer remains attached does not differ much from an inviscid solution. The main differences appear in the separated area because the pressure recovery downstream of the separation point stops and the time-average pressure in the near-wake becomes almost constant. Since in blunt body problems pressure is the main contribution to the aerodynamic forces, these

observations suggests a simple correction of the inviscid solution. At the beginning of each time step the inviscid solution is used to predict the separation points. Next, the pressure downstream of the detachment area is corrected by keeping the value constant. Finally, the corrected pressure field is transferred to the FE solver to calculate the structural response.

There are numerous methods in the literature that combine approximate boundary layer solutions and empirical data to estimate the point of separation [5,6]. In this work, Stratford's method [7] is used due to its efficiency and acceptable accuracy. As the criterion was developed for 2D and axisymmetric problems [8], it is applied along the flow streamlines. The method can be applied to fully turbulent and laminar-turbulent flows. It yields an averaged (quasi-steady) pressure field accounting for separation. The main implementation details of the procedure are described next.

3.1. Streamline calculation

The first step for the correction of the inviscid solution is to recover the flow streamlines. To this end, the inviscid solver computes the velocity and pressure at the center of each panel in the solid surface. The velocity field is normalized and a linked-list is constructed to identify, for each surface panel *i*, its corresponding downstream panel *i+1*. The search is performed over the nearest panels, skipping those already tagged. Panels where flow reversal takes place are also marked at this stage.

Using the linked-list, the streamlines are constructed starting from the forward stagnation areas until there are no remaining downstream panels or flow reversal occurs (which indicates the rear stagnation area has been reached).

3.2. Prediction of separation points

Stratford's model predicts the detachment of incompressible high-Reynolds flows using a two-layer approach. Closer to the surface, in the inner part of the boundary layer, the pressure forces are balanced by the gradient of the viscous stresses. In the outer layer the flow is assumed nearly inviscid, and the pressure forces are balanced by inertial forces through variation of dynamic pressure. The model formulation and validation examples can be found in [7]. In the present work, the guidelines given in [5, 9] are followed with the objective to emphasize the implementation aspects.

It is assumed that the points $\boldsymbol{x}_i$ along each streamline can be connected by straight lines, so the distance between them is approximately the Euclidean distance between the centers of the panels. In streamline coordinates the first point (stagnation point) is located at the origin $x_0=0$ and the position of the downstream points $i=1,2,\ldots n$ is calculated as $x_i = x_{i-1} + \left\| \mathbf{x}_i - \mathbf{x}_{i-1} \right\|$. For each streamline the position of the point of maximum velocity x_m is determined. When applicable, the transition location $x_t < x_m$ at which the flow switches to fully turbulent is also stored. This can be prescribed (user-input) or calculated with a suitable transition criterion. The downstream position of the separation point x_s is the solution sought.

The characteristic points are shown in figure 1, where the position is plotted against $\left(1-\overline{C}_p\right)$. The parameter $\overline{C}_p$ is the pressure coefficient at a point referred to the conditions at the point of maximum velocity x_m

$$\overline{C}_p = \frac{p-p_m}{q_m} = 1 - \frac{q}{q_m} \tag{1}$$

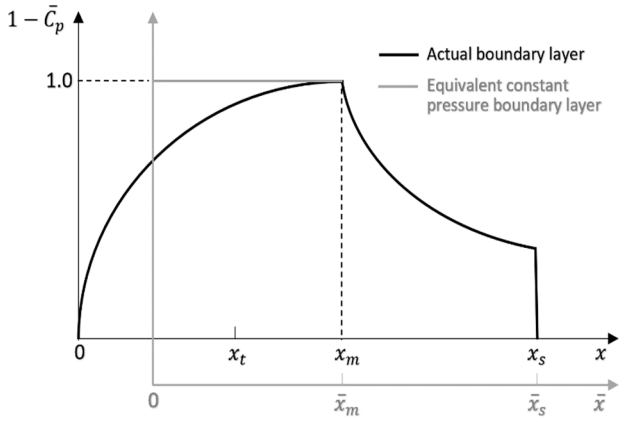


Figure 1: Actual and equivalent pressure distributions along a streamline and characteristics points [9]

An additional coordinate system $\bar{x}$ is depicted in figure 1, intended for general cases including boundary layer transition and favorable pressure gradients (the original criterion only applies to fully turbulent boundary layers with adverse pressure gradients). To treat these cases, Stratford made the assumption that at $x=x_m$ the actual velocity profile can be assimilated to that of a flat-plate turbulent boundary layer whose leading edge is located at $\bar{x}_0 = x_m - \bar{x}_m$. Hence, $\bar{x}_m$ is the length of an equivalent constant pressure region over which a turbulent boundary layer would develop the same momentum thickness θ as the actual laminar-turbulent boundary layer over the distance x_m. The velocity profile at this point is approximated by a power-law $u/U_m = (y/\delta)^{1/n}$. With these considerations, Stratford's criterion for the location of the separation point can be expressed as [9]

$$\left(2\bar{C}_p\right)_s^{(n-2)/4}\left(\bar{x}\frac{d\bar{C}_p}{dx}\right)_s^{1/2} = N\beta\left(10^{-6}\overline{\mathrm{Re}}\right)^{1/10} \tag{2}$$

where subscript *s* indicates values measured at the separation point, $\overline{\mathrm{Re}} = U_m\bar{x}_m/\nu$ and

$$N = 11.36\frac{(n-2)^{(n-2)/4}}{(n+1)^{(n+1)/4}(n+2)^{1/2}} \tag{3}$$

In equation (1) the empirical parameter β depends on the shape of the boundary layer near separation. Values of β=0.66 and 0.73 are suggested in [39] depending on the sign of $d^2\bar{C}_p/dx^2$. Following [9] we adopted a value n=6 for the boundary layer shape parameter. Using these values, the separation criterion becomes

$$\frac{\left(2\bar{C}_p\right)_s\left(\bar{x}\frac{d\bar{C}_p}{dx}\right)_s^{1/2}}{\left(10^{-6}\overline{\mathrm{Re}}\right)^{1/10}} = S(x) = \begin{cases} 0.35 & \text{for} \quad d^2\bar{C}_p/dx^2 < 0 \\ 0.39 & \text{for} \quad d^2\bar{C}_p/dx^2 \geq 0 \end{cases} \tag{4}$$

Eq. (3) is evaluated at each point x_i along the streamline starting from the x_0 and separation is predicted where S(x) reaches the indicated values.

The length of the equivalent boundary layer $\bar{x}_m$ needed to compute $\overline{\mathrm{Re}}$ in Eq. (3) is obtained from [9]

$$\bar{x}_m = 38.2\left(\frac{\upsilon}{U_t x_t}\right)^{3/8}\left[\int_0^{x_t}\left(\frac{U}{U_t}\right)^5 dx\right]^{5/8} + \int_{x_t}^{x_m}\left(\frac{U}{U_m}\right)^3 dx \tag{5}$$

where the transition location x_t can estimated with Michel's method [10]. It is based on a correlation for the local momentum thickness given by

$$\mathrm{Re}_{\theta,t} = \frac{U(x)\theta(x)}{\upsilon} \approx 2.9\,\mathrm{Re}_{x,t}^{0.4} \tag{6}$$

where the subscript t denotes values measured at the transition point. We compute the momentum thickness $\theta(x)$ using Thwaite's method [9]

$$\theta(x) = \frac{0.45\upsilon}{U_m^6}\int_0^x U^5(x)dx \tag{7}$$

Note that the separation distance $\bar{x}_s$ predicted by Eq. (4) must be corrected to take into account the actual boundary layer length. Thus, the real separation point is $x_s = x_m + (\bar{x}_s - \bar{x}_m)$.

4. Application example: two-way coupled solution of an inflatable hangar with wind loads

We study a Buildair's H20 inflatable hangar [11] subject to lateral wind (β=90º. The hangar's internal width and height are 20.5 m and 10.25 m, respectively. It is built using 11 tubes (3.5 m in diameter each) that make up a total length of 31.2 m. The discrete model (figure 2) uses 21374 quadrilaterals elements for the fabric (split internally into triangles by the structural solver) and 8014 line elements for the anchoring cables, seams and reinforcements. A symmetry plane is included to model the ground surface. For the aerodynamic simulation, an atmospheric wind profile with basic velocity 90 km/h is prescribed according to the EN 1991-1-4 standards. The Reynolds number based on the outer hangar's diameter is about $47 \cdot 10^6$, high enough that fully turbulent flow can be assumed. An inflation pressure of 3000 Pa is applied to the tubes. The fabric is a pvc-coated polyester with Young's modulus of 0.38 GPa, 0.5 mm thickness and surface density of 590 g/m^2. The reinforcements have a Young's modulus of 2.5 GPa, 2 mm thickness, 50 mm width and linear density 85 g/m.

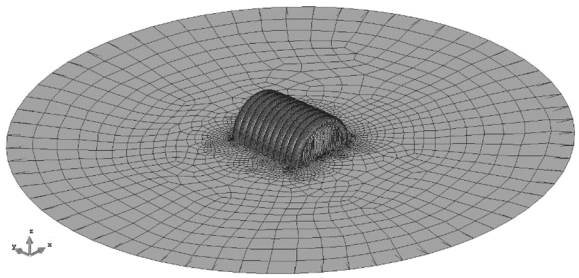


Figure 2: Buildair H20 hangar discrete model and symmetry plane

The objective of the analysis is to determine the steady-state deformations and stresses caused by the wind loads. The steady two-way coupled solution requires 26 s of physical simulation time. This takes about 1 hour CPU-time running in a desktop computer with an Intel Core2 Quad Processor Q9550 @ 2.83 GHz (using 4 cores). The predicted flow separation area and the corrected pressure field are shown in figure 3. The solution captures the main features of the flow around the hangar satisfactorily, although small higher-pressure areas appear at the rear of the hangar. These are not completely eliminated the detachment correction, probably due to a stagnant flow that disrupts the streamlines

over this area. However, since only a small surface is affected, the impact on the overall loads is negligible.

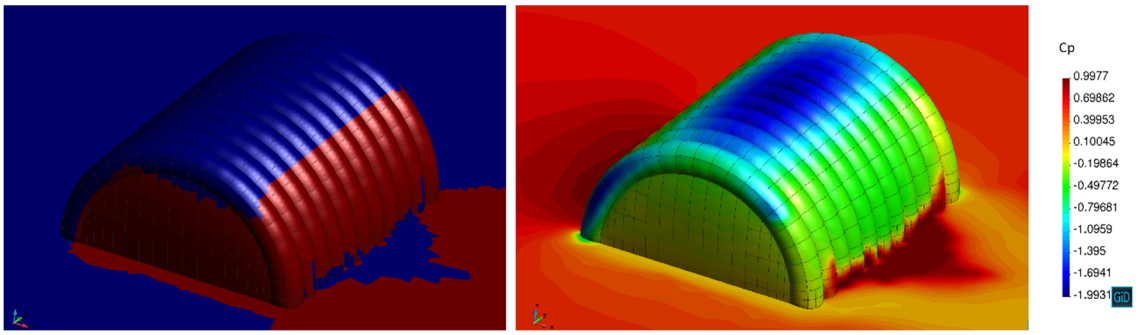


Figure 3: H20 under lateral wind. Views of the detached flow area (left, colored in red) and the corrected Cp field (right) obtained for the steady-state problem solution

The steady pressure distribution calculated along the central tube (#6) is compared in Figure 4 with higher-fidelity CFD results and standard design loads from EN 1991-1-4. The CFD results have been computed with the incompressible Navier-Stokes solver Tdyn [12], using the Spalart-Allmaras turbulence model and law-of-the-wall boundary conditions. Although building regulations consider neither the exact shape of the hangar nor the aeroelastic redistribution of loads, these estimations are often used in preliminary design when specific results are not available. Hence, it is useful to have a measure of the differences expected in such cases. There is a good agreement between our coupled solution and the CFD calculation for the windward side, although the suction peak obtained is higher (about 20%) and somewhat displace3d downstream with respect to the high-fidelity result. The detached flow area is well captured by our solution and the overall comparison is satisfactory. Regarding the loads computed from the EN 1991-1-4 standard, these underestimate the maximum and minimum pressures compared to our results and the CFD solution.

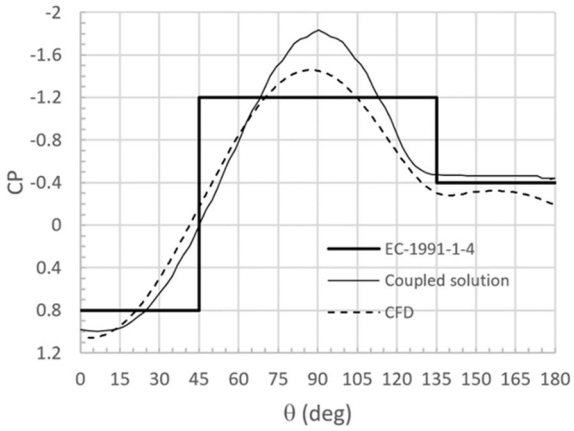


Figure 4: Cp distributions calculated along the central tube of the hangar H20 for a lateral wind condition. Comparison of coupled solution with CFD and standard design loads

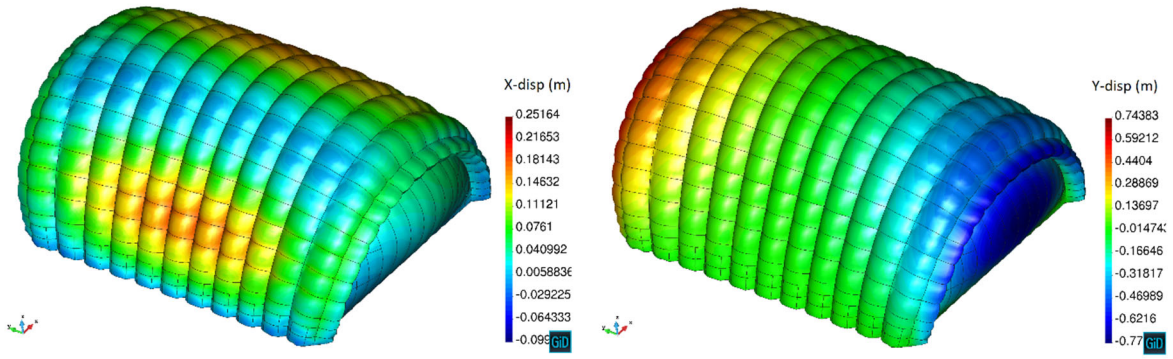


Figure 5: H20 transverse (left) and longitudinal (right) displacements (displacement magnification x5)

Figure 5 shows the computed horizontal displacements. The maximum lateral and longitudinal displacements are 0.25 and 0.75 meters, respectively. As shown in figure 6 (left) the maximum vertical displacement of the roof is 0.55 m. The figure also displays the reaction forces at the anchor points (right). Finally, the fabric principal stresses are plotted in Figure 7.

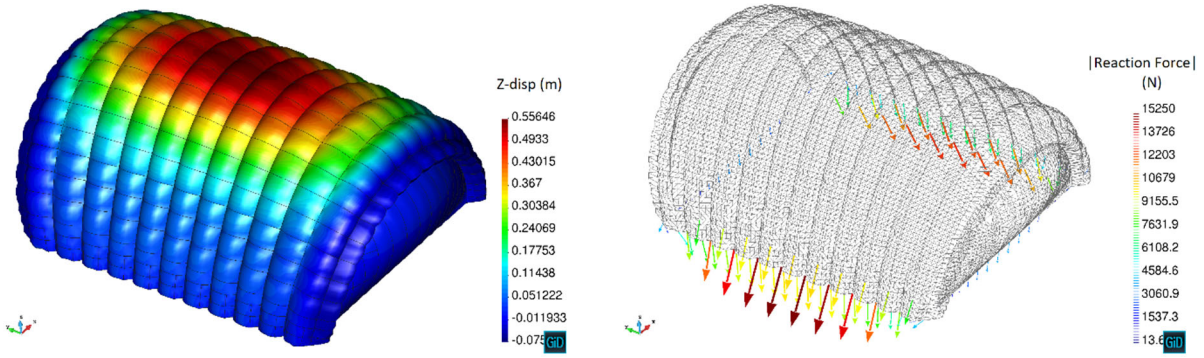


Figure 6: H20 vertical displacements and anchoring reaction forces (displacement magnification x5)

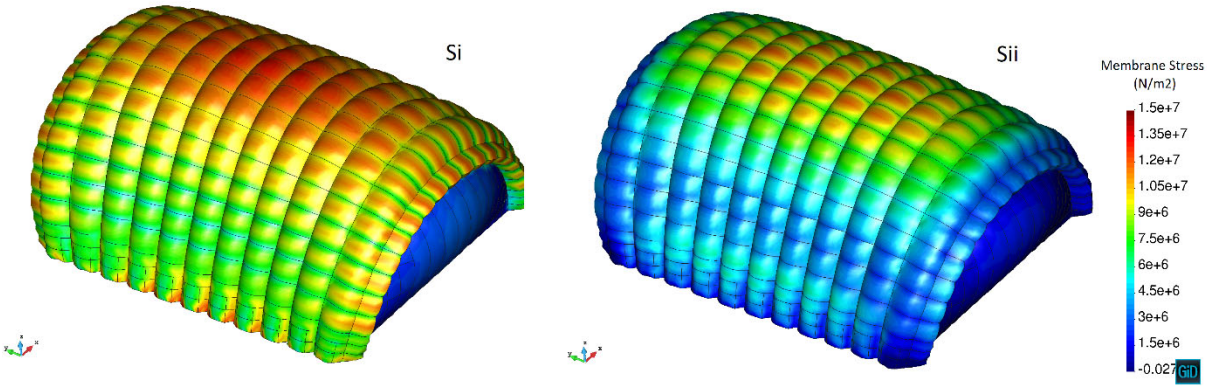


Figure 7: H20 fabric principal stresses S1 and S2 (displacement magnification x5).

4. Conclusions

We presented a cost-effective approach to aeroelastic analysis of inflatable structures under wind loading. It combines explicit finite-element structural dynamics and enhanced potential flow aerodynamics. The inviscid flow field is modified to take into account the massive flow separation

typical of bluff shapes. The potential solution is used to predict the detached flow areas (using Stratford's method) and the pressure field is corrected accordingly.

Overall, the results obtained indicate that the enhanced aerodynamic model can estimate wind loads on inflatable bluff structures with reasonable accuracy, at a small fraction of cost of high-fidelity CFD approaches. It can prove especially useful in the design of structures with unconventional characteristics, where standard design practices become unreliable.

Acknowledgements

The authors wish to thank BuildAir Inflatable Structures Solutions S. A. (www.buildair.com) for providing analysis models, test data and many other useful inputs during the development of this work.

References

[1] R. Flores, E. Ortega and E. Oñate, "Simple and efficient numerical tools for the analysis of parachutes," *Engineering Computations*, vol. 31, issue 5, pp. 957-985, 2014.

[2] E. Ortega, R. Flores and J. Pons-Prats, "Ram-Air Parachute Simulation with Panel Methods and Staggered Coupling," *Journal of Aircraft*, vol. 54, issue 2, pp. 807-814, 2017.

[3] D. de la Torre, E. Ortega and R. Flores, *PARACHUTES. A computer program for calculating ram-air parachutes. User's manual*. CIMNE publications, 2015.

[4] N. Cook, *Designers' Guide to EN 1991-1-4 Eurocode 1: Actions on structures, general actions part 1-4. Wind actions*. Thomas Telford Publishing, 2007.

[5] T. Cebeci, G.J. Mosinskis and A.M.O. Smith, *Calculation of Viscous Drag and Turbulent Boundary-Layer Separation on Two-Dimensional and Axisymetric Bodies in Incompressible Flows*. Report MDC-J0973-01, Douglas Aircraft Co, 1970.

[6] P.M. Gerhart and L.J. Bober, *Comparison of several methods for predicting separation in a compressible turbulent boundary layer*. NASA TM X-3102, 1974.

[7] B.S. Stratford, "The prediction of separation of the turbulent boundary layer," *Journal of Fluid Mechanics*, vol. 5, issue 1, pp. 1-16, 1959.

[8] A.M.O. Smith, "Stratford's turbulent separation criterion for axially-symmetric flows," *Journal of Applied Mathematics and Physics (ZAMP)*, vol. 28, issue 5, pp. 929-939, 1977.

[9] A.M. Kuethe, A.M. and C.Y. Chow, *Foundations of Aerodynamics. Bases of Aerodynamics Design*. John Wiley & Sons, 1997.

[10] R. Michel, *Etude de la Transition sur les Profiles d'Aile; Etablissement d'un Critére de Determination de Point de Transition et Calcul de la Trainee de Profile Incompressible*. ONERA Report, 1951.

[11] Buidair's outstanding projects - Hangars - H20 Poland. Available online, last checked May 2019. http://www.buildair.com/projects-delivered/hangers-h20-poland/

[12] E. Oñate, F. Flores and J. Marcipar, "Membrane Structures Formed by Low Pressure Inflatable Tubes. New Analysis Methods and Recent Constructions." in *Textile Composites and Inflatable Structures II, Stuttgart, Germany, October 2-4, 2005*, Springer, 2008, pp. 163-196.

Proceedings of the IASS Annual Symposium 2019 – Structural Membranes 2019
Form and Force
7 – 10 October 2019, Barcelona, Spain
C. Lázaro, K.-U. Bletzinger, E. Oñate (eds.)

Experiment Study on Wind Resistant Performance of Standing Seam Roof System with Anti-wind Clip

Tao WU*, Ying SUN[a], Wei LIU[b], Zhenggang CAO[c],

* Key Lab of Structures Dynamic Behavior and Control of China Ministry of Education, Harbin institute of Technology, Harbin, 150090, China
202 Haihe Rd., Nangang District, Harbin 150090, China
Email: Wutao21y@163.com

[a] sunnyhit@sina.com
[b] Changchun Vanke Co., Ltd.
[c] caohit@hit.edu.cn

Abstract

Wind uplift failure occurred repeatedly in the standing seam roof system. On the one hand, there is a big difference between the modeling of the standing seam roof system in foreign countries and that in China, so the research results cannot be directly used. On the other hand, most domestic researches focus on the static performance of roof systems without anti-wind clip. The static experiment and dynamic loading experiment of the standing seam roof system were carried out, and the response change, ultimate bearing capacity and failure mode of the roof system under load were obtained. The research shows that the standing seam roof system has two main failure modes: occlusion failure and tearing failure, and the use of anti-wind clip and loading method will change the failure mode of the roof system. At the same time, dynamic loading, increasing the plate width and the spacing between the anti-wind clips, and not using the anti-wind clips will all reduce the ultimate bearing capacity of the roof system.

Keywords: Standing seam roof system, Anti-wind clip, Ultimate bearing capacity, Static experiment, Dynamic loading experiment

1. Introduction

Because of its excellent waterproof performance and changeable shape, the standing seam roof system is favored by the designers. However, due to the weak connection between the support and roof plates, the wind uplift failure of the standing seam roof system occurred many times under strong winds, as shown in Figure 1, and brought great economic losses and adverse social impacts.

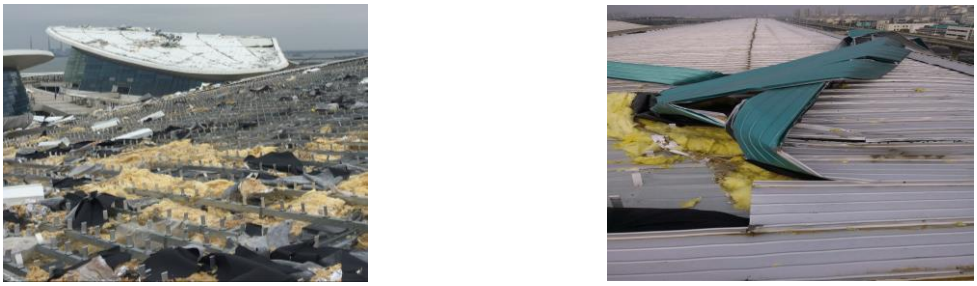
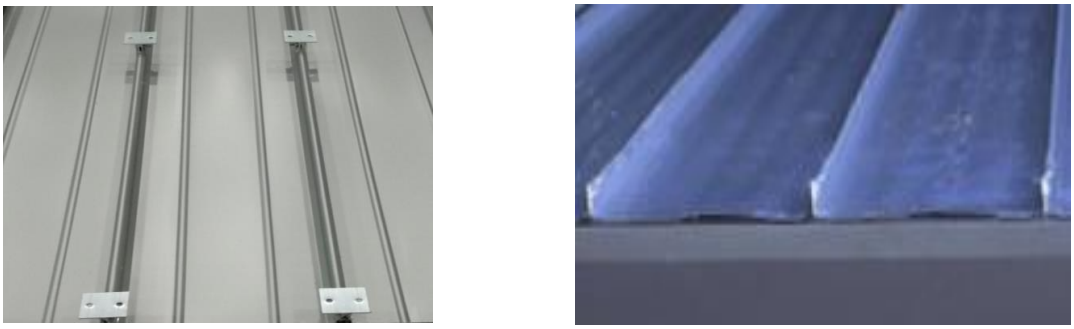


Figure 1: Wind uplift accident of standing seam roof system

Copyright © 2019 by Tao WU, Ying SUN, Wei LIU, Zhenggang CAO
Published by the International Association for Shell and Spatial Structures (IASS) with permission.

Standing seam roof system is not a new type of roof system, and its application is not overnight. In foreign countries, the standing seam roof system is widely used in slope roof with a slope of more than 3 degrees. Therefore, foreign scholars also conducted a lot of experimental and numerical studies on its wind resistance performance[1-4], and formed a standard wind resistance test method for roof system[5-6]. However, there is a big difference in the shape between domestic and foreign standing seam roof systems, as shown in Figure 2. Relevant research results cannot be directly adopted, so it is necessary to carry out independent research. Qin, Yu et al.[7-8] carried out experimental research and analyzed the changes of mid-span displacement and stress of roof system under load. Chen et al.[9] studied the influence of plate width, plate thickness and other parameters on the key response and ultimate bearing capacity of the roof system by means of simulation, and proposed a formula for fitting the ultimate bearing capacity of the roof system. Luo, Shi et al.[10-11] studied the simplified numerical model of standing seam roof system, and respectively proposed the use of spring element and two-step analysis method to simulate the restraint effect of support on roof plate.



a) Roof system in China b) Roof system in abroad

Figure 2: The comparison of standing seam roof system in China and abroad

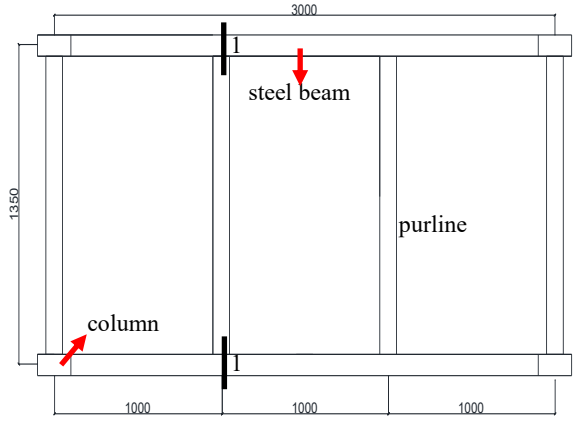
However, it is noted that most of the above experiments and numerical studies did not consider the influence of anti-wind clip on the wind resistance performance of the standing seam roof system, and the studies were all aimed at the static performance of the roof system.For this reason, static experiment and dynamic loading experiment were carried out. First, the influence of model parameters on the ultimate bearing capacity of roof system was studied. Second, the difference between dynamic load and static load is studied.

2. Static experiment and dynamic loading experiment

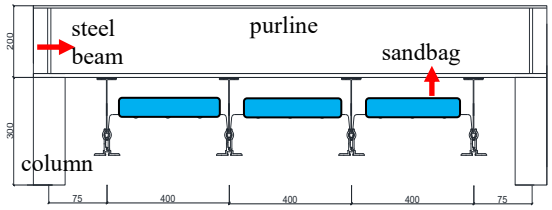
Four static experiments and two dynamic loading experiments were carried out. The loading device, measuring device and model parameter information of each working condition were introduced in this section.

2.1. Static experiment

According to the results of the literature[7-11], the ultimate bearing capacity of each experiment condition was estimated, and the static loading device was designed accordingly, as shown in Figure 3. During the experiment, the sandbag was used for reverse loading until the component was destroyed. Strain gauge and laser displacement meter are used to collect the strain and seam displacement of the roof plate. The roof system parameters under the four experiment conditions are shown in Table 1.



a) Top view of loading device



b) 1-1 cross-section of loading device

Figure 3: Loading device

Table 1: Parameter information of static experiment condition

Condition	Plate width/mm	Spacing of anti-wind clip/mm	Anti-wind clip
1	300	1000	×
2	300	1000	√
3	400	1000	√
4	400	500	√

2.2. Dynamic loading experiment

The dynamic loading experiment of roof system was carried out according to domestic and foreign codes[6,12]. The loading device and measuring device are shown in Figure 4. The results of previous numerical simulation show that the gravity direction of roof system has little effect on its wind resistance performance. In the experiment, gradient cyclic load is applied to the roof system through the pressure valve until the component is destroyed. The roof plate strain and seam displacement were also collected, and the failure process of the roof system was recorded with a camera. The roof system parameters under the two experiment conditions are shown in Table 2.

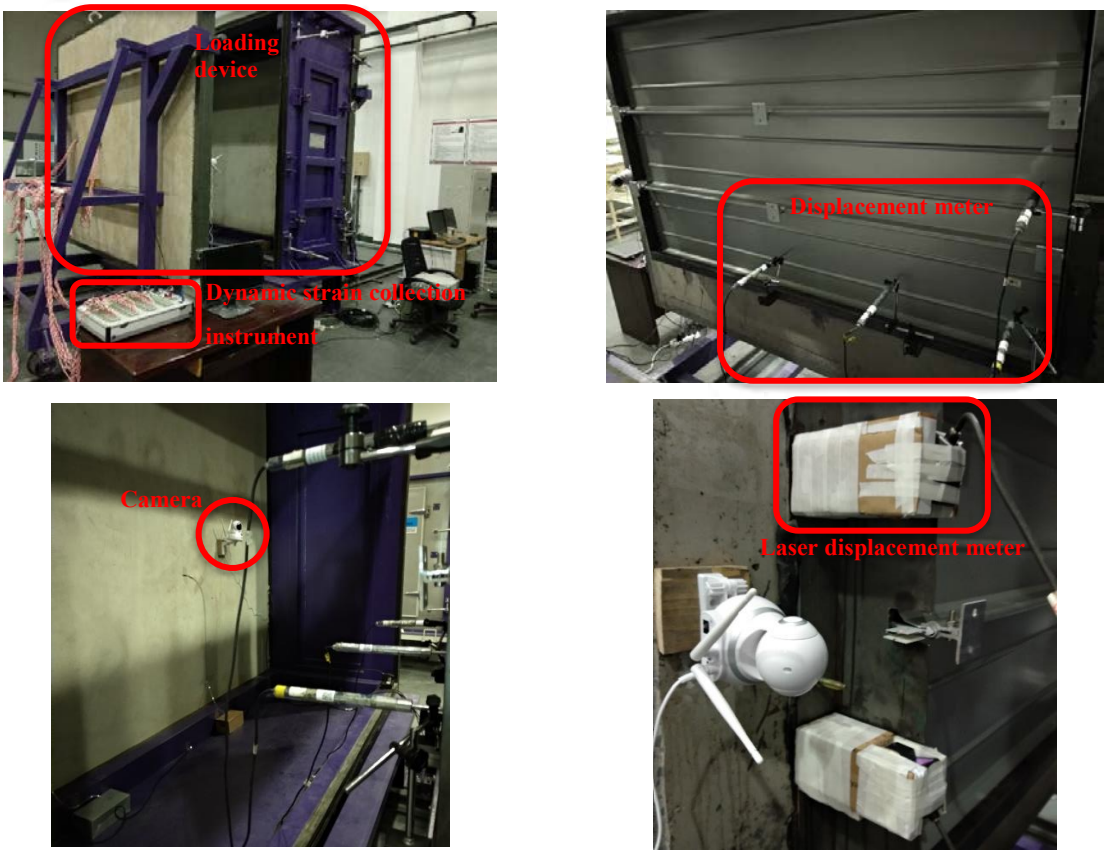


Figure 4: Loading device and measuring device

Table 2: Parameter information of dynamic loading experiment condition

Condition	Plate width/mm	Spacing of anti-wind clip/mm	Anti-wind clip
5	300	1000	√
6	400	1000	√

3. Experiment results

Through the above static experiment and dynamic loading experiment, the failure modes, ultimate bearing capacity, and the corresponding seam displacement and maximum roof stress at the failure time of the standing seam roof system are obtained, as shown in Table 3. In general, the main failure modes of the standing seam roof system are occlusion failure and tearing failure. Occlusion failure occurs when the seam displacement exceeds 1.8mm, and tearing failure occurs when the maximum roof stress exceeds the ultimate strength 280MPa. In case 3, compared with case 1, the ultimate bearing capacity of the roof system was more than doubled by using the anti-wind clip. Similarly, in working conditions 2, 3 and 4, it can be found that increasing the plate width and the spacing between anti-wind clips will reduce the bearing capacity. In addition, compared with conditions 2 and 3, it can be found that dynamic loading reduces the bearing capacity of the roof system and may change the failure mode of the roof system in working conditions 5 and 6.

Table 3: Summary of experiment results

Condition	Seam displacement /mm	Maximum roof stress /MPa	Ultimate bearing capacity /kPa	Failure mode
1	1.81	225	3.4	Occlusion failure
2	1.17	282	7.6	Tearing failure
3	1.85	264	6.0	Occlusion failure
4	1.21	298	12.0	Tearing failure
5	1.35	291	6.0	Tearing failure
6	1.46	287	3.5	Tearing failure

4. Conclusion

The results show that (i) with anti-wind clip can obviously improve the bearing capacity of roof system more than double. When there is no anti-wind clip, roof plate separation occurs at the joints of the roof plates, resulting in the occlusion failure. but the stress of the roof plate is lower than the yield strength. For the roof system with anti-wind clip, the anti-wind clip improves the occlusal strength of the joints, and makes the stress of the roof plate near the anti-wind clip increase rapidly to the ultimate strength, and then causes tearing failure. (ii) The capacity of the roof system is increased by the installation of anti-wind clips, the reduction of plate width and the spacing between the clips. (iii) The failure mode of roof system mainly depends on the maximum stress of roof plate and the lateral displacement of joints. When the maximum stress of the roof exceeds the ultimate strength first, the tearing failure occurs. When the lateral displacement of the roof plate at the joints reaches 2mm first, the occlusion failure occurs.(iv) Dynamic loading will reduce the bearing capacity of roof system and change the failure mode.

References

[1] F. Habte, M. A. Mooneghi, A. G. Chowdhury, et al, "Full-scale testing to evaluate the performance of standing seam metal roofs under simulated wind loading," *Engineering Structures*, vol. 105, pp.231-248, Dec. 2015.

[2] S. Farquhar, G. A. Kopp, D. Surry, "Wind Tunnel and Uniform Pressure Tests of a Standing Seam Metal Roof Model," *Journal of Structural Engineering*, vol. 131, pp. 650-659, Apr. 2005.

[3] A.A.EI Damatty, M. Rahman, O. Ragheb, "Component testing and finite element modeling of standing seam roofs," *Thin-Walled Structures*, vol. 41, pp. 1053-1072, Nov. 2003.

[4] M.Ali Hosam, E.Senseny Paul, "Models for standing seam roofs," *Journal of Wind Engineering & Industrial Aerodynamics*, vol. 91, pp. 1689-1702, Dec. 2003.

[5] ANSI/FM 4474-2004, *Test Standard for Evaluating the Simulated Wind Uplift Resistance of Roof Assemblies Using Static Positive and Negative Differential Pressures*. USA: 2004.

[6] European Organization for Technical Approvals (EOTA). *Guideline for European technical approval of systems of mechanically fastened flexible roof waterproofing membranes, ETAG 006.* Brussels: EOTA, 2000.

[7] G. P. Qin, X. X. Zhang, C. Sun, "Experimental research and numerical analysis of an aluminum-alloy roof system under wind uplift load," *Industrial Construction*, vol. 46, pp. 169-173,. 2016.(in Chinese)

[8] J. H. Yu, L. C. Li, L. Gai, Y. B. Xu, and X. Y. Yan, "Node test study on wind resistance bearing capacity of the standing seam metal roof system," *Building Structure*, vol. 45, pp. 83-86, Sep. 2015. (in Chinese)

[9] Y. Chen, *Loading bearing capacity of the standing seam roof system under the wind load.* Beijing: Beijing Jiaotong University, 2015. (in Chinese)

[10] Y. F. Luo, X. J. Zheng, X. N. Guo, D. Z. Li, and Z. Hu, "Loading behavior analysis of an aluminum alloy roof structure system under wind loads," *Journal of Chongqing University*, vol. 36, pp. 94-100. Oct. 2013. (in Chinese)

[11] J. Shi, Q. L. Zhang, Z. Dong, "Numerical simulation and experimental analysis on aluminium alloy roof panel," *Building Structure*, vol. 36, pp. 98-100. Jun. 2006. (in Chinese)

[12] *Test methods for wind uplift resistance of single-ply roof assemblies: GB/T 31543—2015*. Beijing: Standards Press of China, 2015

Proceedings of the IASS Annual Symposium 2019 – Structural Membranes 2019
Form and Force
7 – 10 October 2019, Barcelona, Spain
C. Lázaro, K.-U. Bletzinger, E. Oñate (eds.)

First Code of Practice for Rubber Gates in Germany

Ralf GURT*, Martin DEUTSCHER[a]

*,[a]Bundesanstalt für Wasserbau (BAW, Federal Waterways Engineering and Research Institute)
Kußmaulstraße 17, 76187 Karlsruhe (Germany)
ralf.gurt@baw.de

Abstract

In a designing phase of a construction, a tool for the calculation of internal forces and a design approach are needed. For rubber gate membranes the latter is not normative available. A complete calculation of the internal forces of a rubber gate membrane in all areas was not possible in the past. In the middle-section, the membrane forces can already be determined since the 60s of the last century, however this approach is not applicable to the discontinuous areas around the sidewalls and the clamping lines. Over the next few years, the Federal Waterway and Shipping Administration of Germany intends to increasingly use the technology of rubber gates on the federal waterways. Since no European standards are available, the Federal Waterways Engineering and Research Institute (Bundesanstalt für Wasserbau - BAW) was commissioned to develop a design concept for rubber gates. For this purpose, complex numerical simulations are used to determine the stress at key points in the rubber membrane. A normalization and tabulation of the relevant internal forces allows a proof in the ultimate limit state without complex numerical calculations. Recently, our design approach has been published as a BAW Code of Practice.

Keywords: numerical simulations, rubber gates, stress concentrations ultimate limit state

1. Introduction

The Federal Waterways and Shipping Administration (WSV) operates over 300 weirs, half of which are more than 60 years old. Consequently, there will be a high demand for reconstruction over the next several years. Although steel hydraulic engineering closures have a long service life of up to 70 years, on average they have to be comprehensively maintained every 15 to 20 years. The WSV decided to use a lesser known technology at some weirs and to use rubber gates as weir shutters. The WSV would also like to define the rubber gates as a new standard for federal waterways.

Rubber gates are elastic weir shutters in which a rubber membrane is attached to the solid weir structure in such a way that a dam body with a tight interior is created. The rubber membrane generally consists of an elastomer with several polyester or polyamide fabric layers that serve as reinforcing elements. Rubber gates are controlled simply by the introduction and discharge of air or water into the membrane. Water filled rubber gates are better suited for regulating the upstream water level and controlling the discharge [1]. Therefore, water filled rubber gates are preferred for the federal waterways. An example of this construction type has been realized in Marklendorf at the River Aller 2006, see Figure 1. Characteristic for rubber gates is the load transfer via the membrane and the clamping construction into the solid weir body. This allows large weir field widths (Figure 2) and a simple design of the solid weir body.

Copyright © 2019 by Ralf Gurt, Martin Deutscher (Federal Waterways Engineering and Research Institute)
Published by the International Association for Shell and Spatial Structures (IASS) with permission.



Figure 1: Downstream side of the rubber gate Marklendorf at the River Aller with a gate height of 2.35 m



Figure 2: Rubber Gate Au near Kempten in Allgäu with a span width of 62.4 m

Rubber gates are constructions that must be proven like other weir shutter systems. There is no normalized design approach for the rubber membrane with the exception of Japanese design standard, which has been used to implemented the largest amount of installations worldwide. The BAW Code of Practice “Schlauchwehre – Teil B: Nachweis der Tragfähigkeit von Membranen wassergefüllter Schlauchwehre im Binnenbereich“ [2] [Inflatable gates – Part B: Verification of the load-bearing capacity of membranes of water-filled inflatable gates on inland waterways] is intended to close the gap and describe a Eurocode-conforming design approach in accordance with DIN EN 1990 [3] for the WSV. Additional parts of the Code of Practice are in preparation: "Hydraulics of rubber gates" (Part A) and "Material testing of rubber membranes" (Part C).

2. Calculation of membrane forces and design approach

2.1 Previous approaches

A standardized design of the rubber membrane requires a standardized calculation of the relevant internal forces. The complex geometry of a tubular membrane in the raised state with folds and multidimensional curvatures cannot yet be calculated analytically. Anwar [4] published approaches to analytical calculation for the rubber membrane forces in the undisturbed middle section as early as 1967. Differential equations based on pressure differences and the geometry of the rubber gate have been solved [4]and thus membrane forces in the rubber membrane in flow direction are determined. In 1985 Watson [5] expanded and improved the approaches of Anwar. Both approaches are based on the membrane theory and the negligence of the dead weight. As described in [1, 6] a width-related, characteristic membrane force T_k with

$$T_{\mathrm{k}} = \frac{1}{4}\,(2\,\alpha - 1) \cdot \rho \cdot g \cdot h_{\mathrm{s}}^2 \tag{1}$$

is calculated for water-filled weirs with full backwater. Here α is an internal pressure coefficient, which in case of water filling represents the proportion of the inside water pressure head h_{i} and the upstream water level h_{OW}. Further, ρ is the density of water, g the gravitational constant and h_{s} the dam height.

In Japan, a technical standard for rubber gates was developed by the former "Japan River Association" in 1987. In the 2000 issue of the guideline, the analytical membrane force is also determined according to equation (1) [7]. A general "safety factor", which is better called an overall factor, of 8.0 was introduced for the consideration of further influences from the edges and the degradation of the membrane [7]. The current revision from 2015 by the "Ministry of Land, Infrastructure and Transport, River Bureau" of Japan was translated into English by PIANC WG 166 [8].

Research in the BAW pointed out that a more detailed modelling of the composite material is necessary for a qualitative evaluation of the structural stability of rubber membranes. Since 2014, extensive and essential investigations for the structural design of rubber gate membranes have been carried out [9].

2.2 Numerical simulations

The numerical calculations are executed with the LS-DYNA software. The large deformations that a rubber membrane runs through during the simulation can be reproduced with this software. The hydrostatic internal and external pressures from water load can be replaced by energetically equivalent load vectors. Hence, there is no need to model the water itself. The first numerical models used simple, homogeneous and isotropic material laws. The largest part of the cross-section consists of an elastomer, see Figure 3. Compared to the eccentrically inserted fabric layers, elastomers have higher compression stiffness and much lower tension stiffness. Therefore, a homogenized material cross-section is not sufficiently accurate, as already shown in [6].

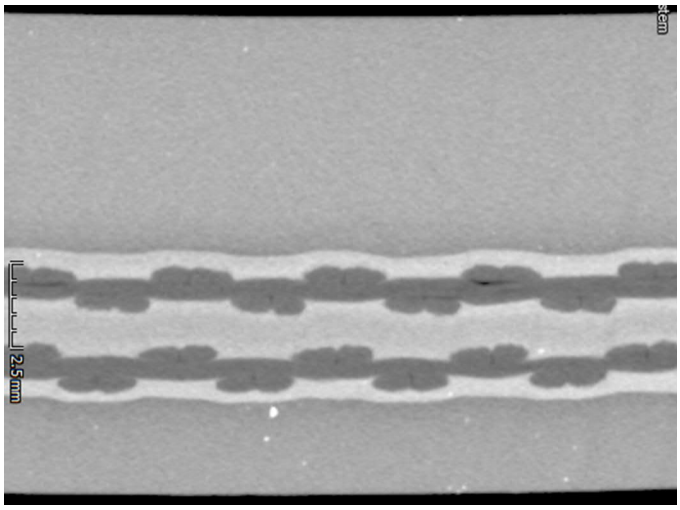


Figure 3: Cross-section of a typical rubber membrane

The experience made in the field of laminated safety glass can be used to model the composite material of rubber membranes. The modelling of the composite behaviour of a flexible foil between two float glass plates is described in [10]. Transferred to the modelling of a rubber membrane, this means a separation of the material into individual elements. In this way, the elastomer and the fabric can be represented by their respective properties each in an own element. The fabric layers responsible for load transfer are combined in a single element layer in the geometric centre of gravity of the fabric layers. The materials are coupled via the element nodes. The effects of a more accurate modelling can be seen in the bending properties and the stresses resulting from bending. The stresses in the areas of bearing and folds are significantly lower, which is consistent with the practical experience on existing installations and the design rules from Japan. A purely optical comparison between the different approaches to material modelling and reality can be seen in Figure 4. This shows a much more precise mapping of the folds.



Figure 4: Optical comparison of the numerical modelling approaches with a real rubber gate in the fold area - left: Modelling with homogenised cross-section; centre: real weir; right: modelling with fabric reinforcement according to membrane theory with the new composite modelling method

The modelling of the composite material in this way offers the additional advantage that the results of the simulation can be displayed directly by selecting the fabric elements. Figure 5 shows that higher tensile stresses occur in the area of folds (A), at the clamping line (B) and in the transition between weir bottom and sidewall (C).

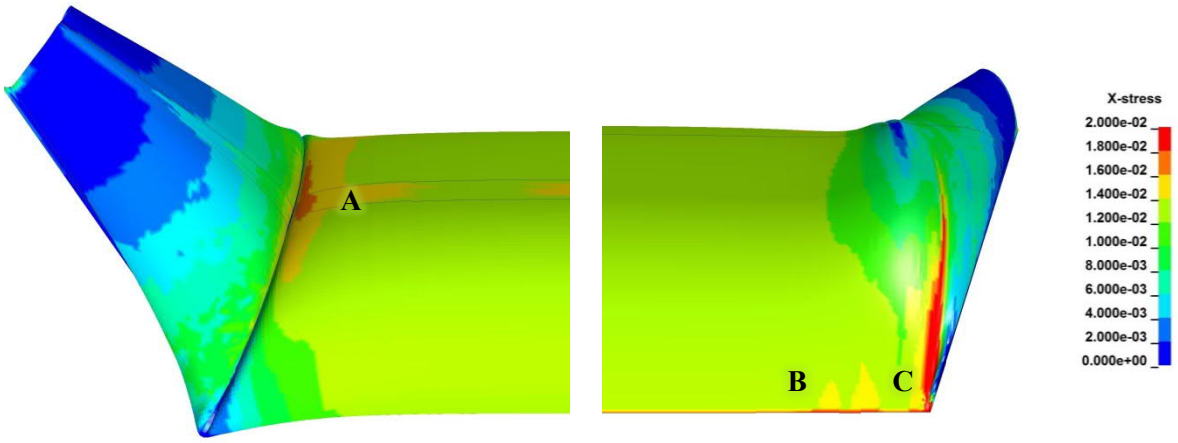


Figure 5: 3D view of a numerical rubber gate model with stresses in circumferential direction (warp) in kN/mm² - left: View from the downstream side; right: View from the upstream side

With the help of routines written specially with Matlab, the calculation results from LS-DYNA can be rewritten to a 2D view. For this purpose, the membrane geometries or meshes (3D) of the calculation must first be converted to a flat form in order to determine the 2D coordinates of the element nodes. For this the input geometry is unfolded with Matlab. This results in a 2D-layout with normalised values. The stress values from LS-DYNA are normalized with the analytical, width-related membrane force according to equation (1). This results in unitless stress concentration factors (SCF_i) with

$$SCF_i = \frac{\sigma_{\mathrm{Ek},i} \cdot d_\mathrm{f}}{T_\mathrm{k}} . \tag{2}$$

Here $\sigma_{\mathrm{Ek},i}$ is the characteristic stress in an area i of the rubber membrane, d_f the thickness of the fabric element in the numerical simulation and T_k the characteristic width-related membrane force according to equation (1).

An exemplary representation can be seen in Figure 6. In the middle-section the SCF in warp direction is 1, as the value from the analytics agrees with the numeric simulations.

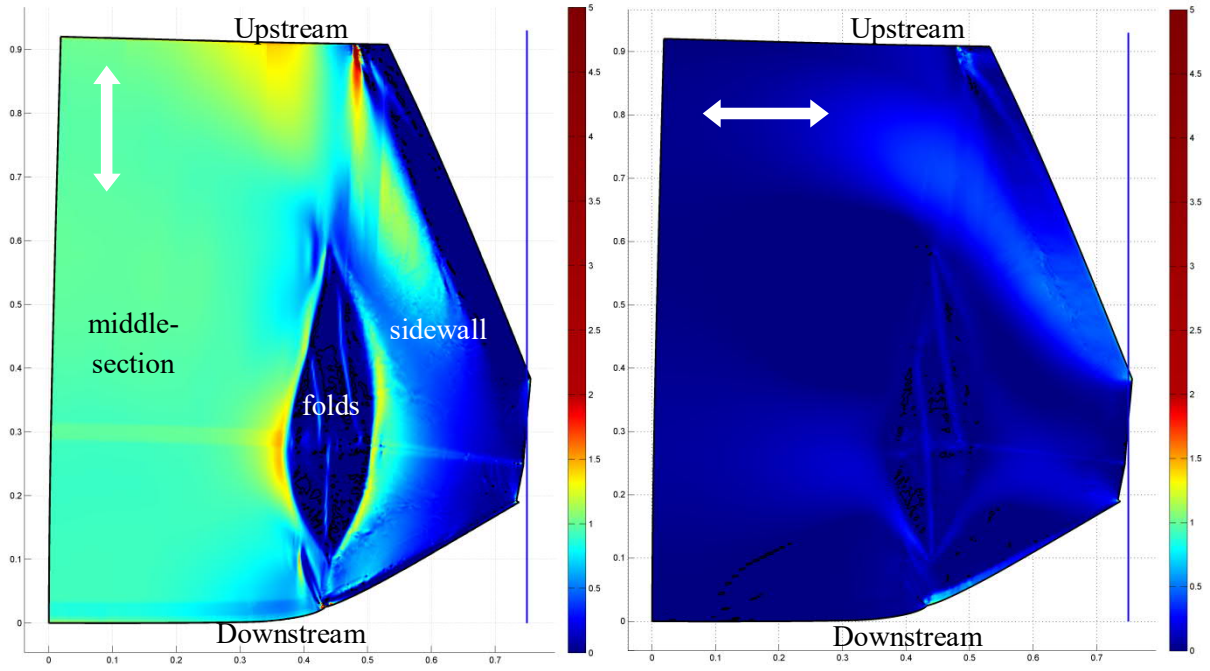


Figure 6: Illustration of stress concentration factors in a 2D view - left: SCF in warp direction; right: SCF in weft direction

There are no analytical possibilities to determine a reference value in the transverse direction, corresponding to the weft direction, therefore these membrane forces are also normalized with T_{k}.

3. Dimensioning of a rubber gate membrane according to BAW Code of Practice

BAW Codes of Practice are introduced by the Federal Ministry of Transport and Digital Infrastructure (BMVI) as a set of rules for the federal waterways. The design approach for rubber gate membranes is based on DIN EN 1990 [3]. Thus, the design parameters for the design at the limit state must be compared with the load carrying capacity

$$E_{\mathrm{d}} \leq R_{\mathrm{d}} \,. \tag{3}$$

On the side of action, the design values of the effects of the actions $E_{\mathrm{d},i}$ are determined with

$$E_{\mathrm{d},i} = \gamma_F \cdot \sigma_{\mathrm{Ek},i} \cdot d_{\mathrm{f}} = \gamma_{\mathrm{F}} \cdot SCF_i \cdot T_{\mathrm{k}} \qquad \text{in N/mm.} \tag{4}$$

According to DIN EN 1990 [3] it is possible to apply the partial safety factor γ_{F} for membrane structures to the effects instead of to the actions. Values for SCF_i are given in BAW Code [2]. Then, using the height of the gate to be designed and the selected internal pressure, the relevant parameters on the side of actions can be determined without highly complex numerical procedures, if the boundary conditions for the stress concentration factors are taken into account.

The design value of the material resistance $R_{\mathrm{d},j}$ is determined with

$$R_{\mathrm{d},j} = \xi \frac{R_{\mathrm{k},j}}{\gamma_{\mathrm{M},j}} \quad \text{in N/mm.} \tag{5}$$

Here ξ is an overall reduction factor to consider ageing and creep resistance, $R_{\mathrm{k},j}$ is the characteristic, width-related material resistance with j for warp and weft direction, as well as the joints. The partial safety factors $\gamma_{\mathrm{M},j}$ are to be derived statistically from material investigations. A total reduction factor of $\xi = 0.33$ for a service life of 30 years is derived from Japanese [7] and BAW studies. The value of the total reduction factor can be used for the design and has to be validated with the material to be installed. The ageing is investigated parallel to the usage on ageing samples. An adjustment of the service life is possible when the results of the ageing tests show less aging than estimated in the design phase. If ageing is worse than expected, the membrane must be replaced at the recalculated time.

4 Summary and Outlook

The investigations at the BAW have succeeded in quantifying the relevant design parameters and converting them into a manageable stress concentration factor concept for the proof at the ultimate limit state.

The Code of Practice will be introduced by the Federal Ministry of Transport and Digital Infrastructure for the area of federal waterways in the course of 2019 and is then available at baw.de.

In future, the boundary conditions for the stress concentration factors, such as type of clamp construction and material combinations, are to be extended.

References

[1] M. Gebhardt, “Hydraulische und statische Bemessung von Schlauchwehren,” Dissertation, Institut für Wasser und Gewässerentwicklung - Bereich Wasserwirtschaft und Kulturtechnik, Universität Karlsruhe (TH), Karlsruhe, 2006.

[2] R. Gurt, “BAWMerkblatt: Schlauchwehre - Teil B: Nachweis der Tragfähigkeit von Membranen wassergefüllter Schlauchwehre an Binnenwasserstraßen,” Entwurf, Karlsruhe, Aug. 2018. Accessed on: Apr. 08 2019.

[3] *Eurocode: Grundlagen der Tragwerksplanung*, 1990, 2010.

[4] H. O. Anwar, “Inflatable Dams,” *Journal of the Hydraulics Devision, ASCE*, vol. 93, no. Paper 5239, pp. 99–119, May. 1967.

[5] R. Watson, “A note on the shapes of flexible dams,” *Journal of Hydraulic Research*, vol. 23, no. 2, pp. 179–194, 1985.

[6] R. Gurt, M. Deutscher, and M. Gebhardt, “Design and Analysis of Reinforced Rubber Membranes for Inflatable Dams,” in *Structural Membranes 2015: VII International Conference on Textile Composites and Inflatable Structures*, E. Oñate, K.-U. Bletzinger, and B. Kröplin, Eds., Barcelona, 2015, pp. 306–317.

[7] Ministry of Land, Infrastructure and Transport, River Bureau, “Technologische Standards für Schlauchwehre (unveröffentlichte Übersetzung aus dem Japanischen im Auftrag der BAW),” 2000.

[8] M. Gebhardt *et al., Inflatable Structures in Hydraulic Engeneering: PIANC Report N° 166*. Bruxelles, 2018.

[9] R. Gurt, “Entwicklung eines Bemessungskonzeptes für den Nachweis der Tragfähigkeit von Schlauchwehrmembranen,” in *BAWForschungskompendium, Forschungskompendium Verkehrswasserbau 2017*, Bundesanstalt für Wasserbau, Ed., Karlsruhe: Bundesanstalt für Wasserbau, 2018, pp. 45–46.

Proceedings of the IASS Annual Symposium 2019 – Structural Membranes 2019
Form and Force
7 – 10 October 2019, Barcelona, Spain
C. Lázaro, K.-U. Bletzinger, E. Oñate (eds.)

High performance computing of wind-induced pressures on various domes under real conditions

Tetsuro TAMURA*, Yong CAO, Yuki NAGAO, Hidenori KAWAI, Koji NISHIGUCHI[a], Makoto TSUBOKURA[a]

*Department of Architecture and Building Engineering, Tokyo Institute of Technology
Nagatsuta, Yokohama, 226-8502, Japan,
tamura.t.ab@m.titech.ac.jp

[a] Riken Center for Computational Science, RIKEN

Abstract

In this study, high performance computing (HPC) was performed for estimation of wind-induced pressures on various kinds of dome using the K computer (Japanese supercomputer). Focusing on the super critical Reynolds number (Re) and complexity of a long span roof of actual open stadium, real conditions are set up for discussing aerodynamic characteristics of a dome. Using the LES model for strong wind, this study numerically elucidates wind flow patterns and unsteady pressures around a dome with various shapes and provides the information of wind load acting on a dome under the real conditions for a wind resistant design.

Keywords: wind engineering, high-performance computing

1. Introduction

In this study, in order to accurately estimate pressures acting on the roof of various domes for wind resistant design, high performance computing (HPC) was performed using the K computer (Japanese supercomputer). Design wind loading on a dome should be obtained under real conditions such that the Reynolds number (Re) is in the supercritical regime from the fluid mechanical sense and the long span roof of actual open stadium is complexly attacked by the strong wind. Thus far the wind tunnel experiment has been performed using the roughened model instead of real roof surface for assuming to realize the supercritical regime. However this kind of imitation causes the different wind loading, because basic supercritical condition shows more drastic change of wind pressures on a curved roof. Recent advancement of HPC has made it possible to compute the supercritical flow around a bluff shaped object [1]. Also, by the sophisticated numerical technique based on the Cartesian coordinate system [2] for the actual space structure, very complicated flows interacting with long span roof can be solved. The objective of this study is to numerically clarify wind flows and pressures around various domes and discuss adequacy for the estimation of wind load under the real conditions.

2. Aerodynamics of a hemispherical dome at subcritical and supercritical Reynolds numbers

2.1. Numerical methods

Two numerical methods are used to predict the wind-induced pressures on a dome. One is the finite-volume method traditionally based on body-fitted unstructured grid. The code is FrontFlow/red (FFR) which has been intensively optimized for high-performance computing and was applied high-Re flows around a sphere, golf ball and vehicles (Tsubokura et al. [3]; Muto et al. [4]). The other method is

Copyright © 2019 by Tetsuro TAMURA, Yong CAO, Yuki NAGAO, Hidenori KAWAI, Koji NISHIGUCHI, Makoto TSUBOKURA
Published by the International Association for Shell and Spatial Structures (IASS) with permission.

under the framework of the building cube method (Nakahashi [5]), but the structure-fluid boundary is treated by the topology independent immersed-boundary approach (Onishi et al. [6]). This method is well-suited for massive computation with high parallel efficiency, and is called CUBE.

2.2. CUBE and FFR for predicting wind-induced pressure and flow field in the subcritical Re regime

The numerical accuracy of CUBE in the prediction of wind-induced pressures on a hemispherical dome is first examined by comparing to the widely-validated FFR. At the inlet of two solvers, the same dataset is input, i.e., the turbulent boundary layer with a thickness of 20.1D (D is the diameter of the dome). The Reynolds number is $Re_H = U_H D/\nu = 2 \times 10^4$, where U_H is the wind velocity at the height of the dome. The Cartesian grid system in the symmetry plane of the dome that is used for CUBE code is shown in Figure 1, where the minimum cell size adjacent to the dome is $\Delta \approx 0.002$. The total cell size is 140.1 million for CUBE code. For the CUBE solver, the convective and diffusion terms are spatially discretized using the second-order central-difference scheme, while 5% of the first-order upwind scheme is blended to estimate the convective flux on the cell face. The fractional-step method is used for time marching. The semi-implicit Crank-Nicolson method is used to treat the convective and diffusion terms. The semi-implicit velocity equation and Poisson equation are solved using the red/black successive over-relaxation (SOR) method. The time step is set as 5×10^{-4} such that the maximum Courant number is around 0.3.

The unstructured grid system used for the FFR solver is similar to Figure 3. For comparison, the similar numerical schemes as the CUBE solver are used as much as possible. No turbulence model is adopted. The second-order central-difference scheme that is blended with 5% upwind scheme is used for spatially discretizing the convective and diffusion terms in the region around the dome. The SMAC method is used for time marching and the Euler implicit scheme is used for all terms. The time step is chosen to ensure the maximum Courant number less than 1.0.

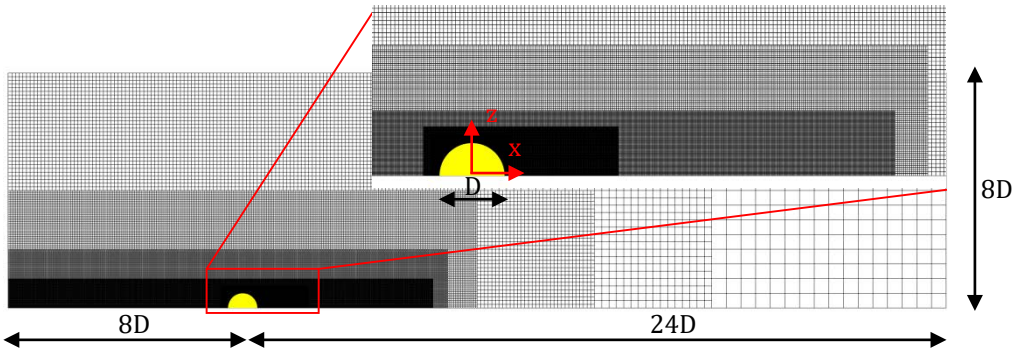


Figure 1: Grid system in the symmetry plane of the dome used for CUBE code.

Figure 2(a) shows the mean pressure distributions on the longitudinal center-line of a hemisphere, and Figure 2(b) shows the mean flow topologies obtained by FFR and CUBE. Good agreement of pressures can be recognized among the numerical results and the experimental data. Furthermore, the flow topology is consistent between two solvers. The critical points, like the frontal stagnation point, the separation point, the focus and the saddle point in the wake, agree well with each other between two solvers. Moreover, the unsteady flow characteristics are captured by both solvers: horseshoe vortex system, shear layer instability and large-scale wake oscillation. The instantaneous separation points occur at the crest of the dome for both solvers, which is typical for the subcritical-Re flows.

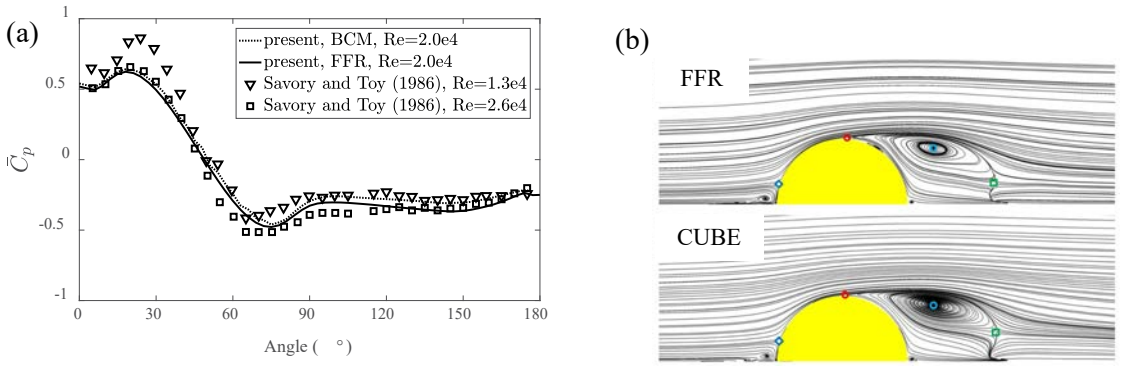


Figure 2: (a) Mean pressure distributions on longitudinal center-line. (b) Mean flow field in the symmetry plane.

2.3. Aerodynamics of a dome in the supercritical Re regime

The Reynolds number effects are investigated by using the high-resolution unstructured grids, with a focus on the supercritical-Re status. The Reynolds numbers contain Re=7×10^4, 1.4×10^5, 3×10^5, 5×10^5, 7×10^5. The grid system is shown in Figure 3. The mesh resolution is expected to be fine enough to predict supercritical-Re flows, according to the experiences in sphere, circular and rounded-corner square cylinder (Muto et al.[4]; Cao and Tamura [1][7]). In this study, the height of the first-layer mesh nearest the dome is 0.0002D, and the lateral resolution is 0.003D. The steady power-law inflow profile (with the power index 1/6) is set at inlet. The thickness of boundary layer is comparable to the height of the dome. A small rectangular barrier is placed downstream the inlet in order to generate the turbulence intensity. The dynamic Smagorinsky model is used. The 2~3% upwind scheme is blended into the second-order central-difference scheme in discretizing the convective term. The other numerical schemes are kept the same as the previous section.

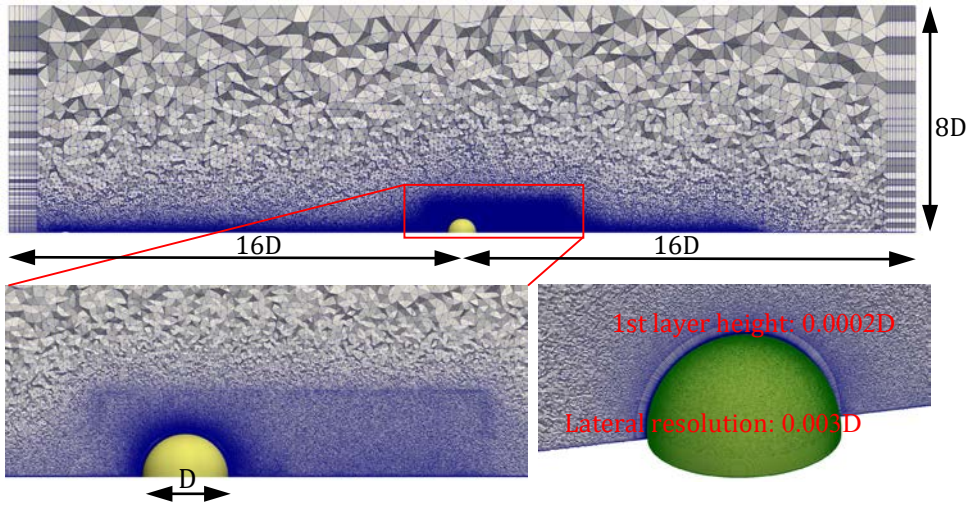


Figure 3: Unstructured grid system used for FFR code.

Figure 4 shows the mean drag and lift coefficients and the mean pressure distribution, which are varied with Reynolds numbers. Strong Re effects are observed. The critical Re is $Re_{cr}\simeq2\times10^5$. Beyond Re_{cr}, the drag decreases and the lift increases significantly. The pressure distributions at the supercritical Re are similar to the counterparts of a sphere or a circular cylinder. Much lower negative pressures act on the crest of the hemisphere and a greater pressure recovery is observed in the downstream part of the body, in comparison with that at the subcritical Re. Figure 5 shows the instantaneous flow fields at the subcritical and supercritical Re. The recirculation zone behind the hemisphere is shrunk greatly at the

supercritical Re, which is induced by the delay of the separation point. As a result, the wake is much thinner.

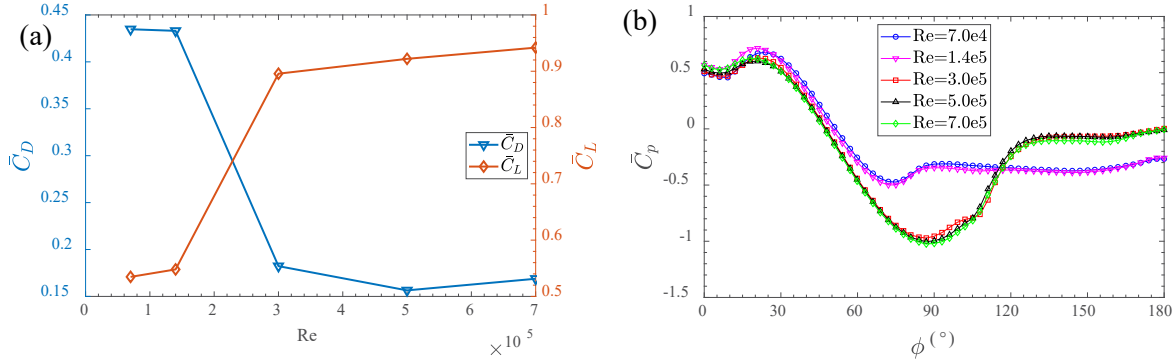


Figure 4: (a) Mean drag and lift coefficients against Re; (b) mean pressure distributions against Re.

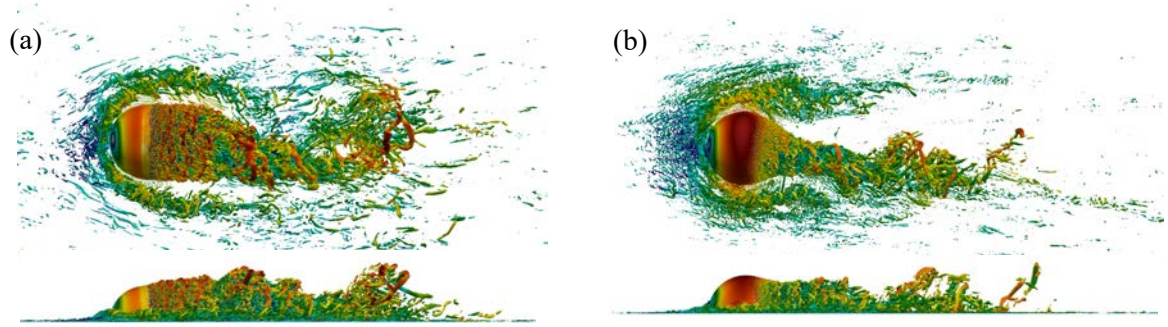


Figure 5: Flow structures at the subcritical (a) and supercritical (b) Re.

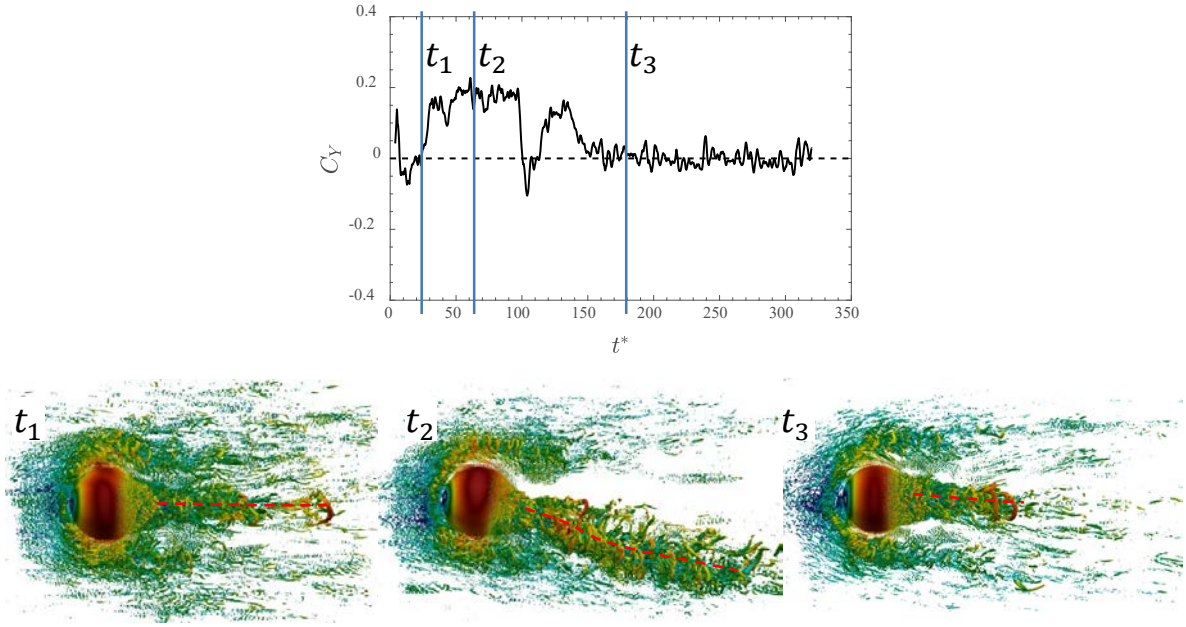


Figure 6: Wake patterns at different instants in the supercritical Re regime.

In addition, an interesting phenomenon of the wake shedding is observed, as shown in Figure 6. Three instants are chosen, i.e., t_1, t_2 and t_3. The orientation of the shedding appears to be locked

around a certain azimuthal direction at t_2, at least for long intervals of time. The inclined shedding pattern leads to much lower negative pressure on one side of the hemisphere than the other. It is reflected in the positive lateral force C_Y with a large magnitude. However, the nearly symmetric shedding at t_1 and t_3 has very small C_Y magnitude. This phenomenon was also observed in the supercritical-Re regime behind a sphere (Taneda[8]; Constantinescu and Squires[9]).

3. Aerodynamics of a dome with open type long span roof (3 pages by Nishiguchi and Nagao)

3.1. Problem formulation

In order to accurately predict the wind flow around the dome model, we introduce LES based on BCM (Building Cube Method) which is formulated on the very fine Cartesian mesh system (Onishi et al., 2013). Recent high-performance computing (HPC) technique has developed distinctly, so high-resolution computation becomes able to be applied to flows around a complicated configuration such as actual dome structure. Very fine mesh system by BCM can solve this problem, supported by the external forcing technique at the boundary named IBM (Immersed Boundary Method). Also, BCM uses the mesh system consisting of cubes and cells in the Cartesian grid. Each cube has 16 by 16 by 16 cells, and then the algorithm of computation is quite simple. As a result, the efficient solver on high performance computing is realized for parallel algorithm where the load balance is appropriately obtained at each core.

The turbulent field around dome is resolved in a high resolution for the complicated shape of buildings using LES-based Building Cube Method (BCM-LES) by Jansson[2]. The boundary condition in BCM-LES is imposed using volume constraint IBM developed by Patankar et al[10]. It shows the advantage in modelling the no-slip boundary condition for complex geometry with highly physical approach. .

3.2. Numerical conditions and models

Firstly, this study reproduce the configuration of a typical dome with open type long span roof. Then, the BCM grid is generated as shown in figure 7. The minimum grid size is 0.78m and the number of grid is approximately 85 million. For the inflow condition, the inflow turbulence generated is imposed to inlet surface assuming AIJ category III. The inflow turbulence is generated in the driver region using the semiperiodic boundary condition by Nozawa and Tamura[11]. The other calculation conditions are shown in Table 1

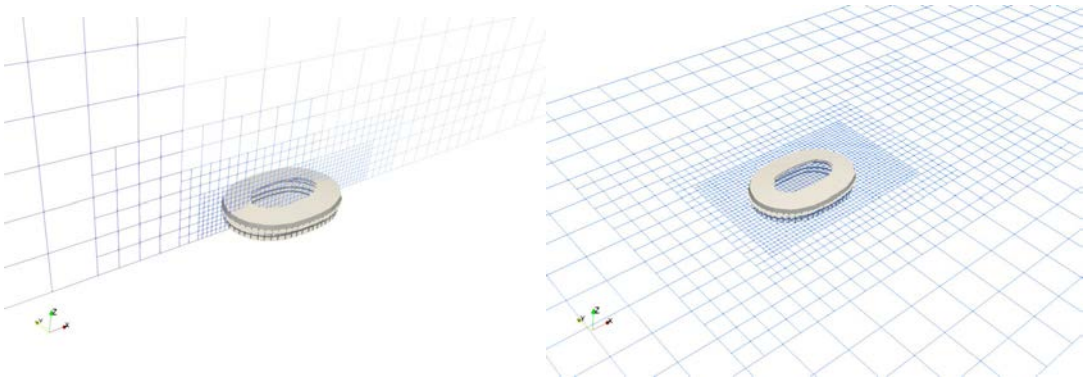


Figure 7: Side and top view of the computational grid for the simulation of rigid open type dome (336・228・52.4m) at the center of the longitudinal (left) and horizontal (right) axis

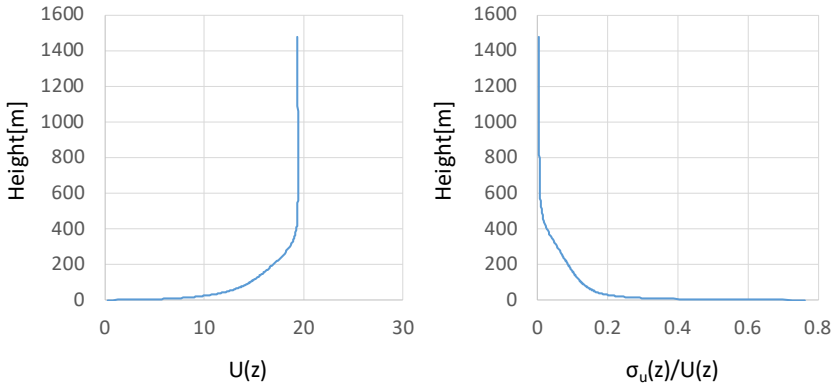


Figure 8: Inflow turbulence profile of dome model

Table 1: Calculate condition of dome model

Re	30000
Resolution	dt=0.005, 0.78m (Minimum)
Time integration	2nd order Crank-Nicolson
Spatial discretization	Convective term: 2nd order Central+5% Upwind, Diffusion term：2nd order Central
Boundary condition	Wall：Volume constraint IBM, Side,Top：Slip Inlet：inflow turbulence Outflow：convective
Pressure solver	Solver: Multigrid Poisson Solver Iteration number: 30 Pressure convergence:1d-5

3.3. Inside and outside flows and pressures in the rigid open type dome

Firstly, the distribution of velocity and pressure on xy plane is shown in Figure 9. In the target building, the side wall is opened in the upper part of audience seats and the wind comes into the inside area of target building through the opened parts in the wind ward side of target building. Also, the the flow separates from the side of target buiding and the shear layer appears. Focusing on the pressure distribution, the separation bubble with low-pressure strucuture occurs from the separation area (area A shown in figure 9).

Figure 10 shows the the distribution of velocity and pressure on xz planes and figure 11 shows the stream line in the outside and inside of target building. In figure 11, the flow comes to inside of the building from the opened area of windward side (area B in figure 10) and the circulation flow appears below the large roof.

On the other hand, above the roof, the flow sepatates from the edge of roof in windward. In the pressure distribution of figure 10, the structure with low pressure appears near the windward edge of large roof. Then, focuing on the area around leeward roof (around area C in figure 10), the flow separates upward and downward. The separated flow downward causes the circulation flow in the inside area of target building as shown in figure 11.

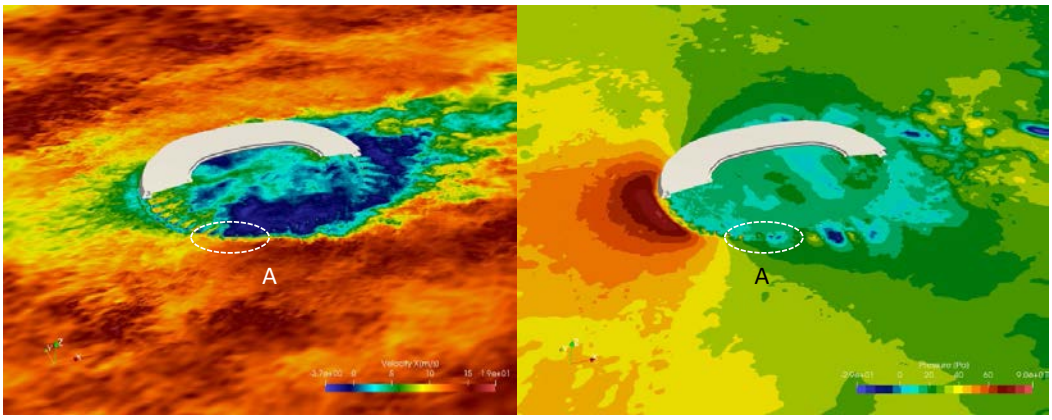


Figure 9: Wind velocity (left) and wind pressure (right) acting on inside and outside of rigid open type dome at the dome opening height (Z=31m) of the horizontal axis

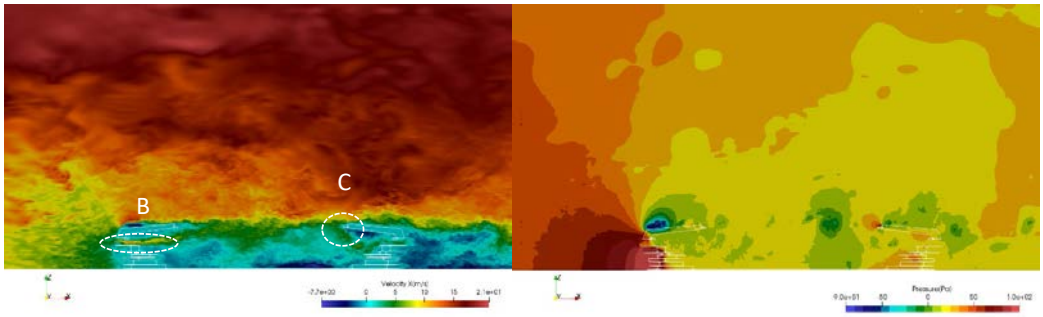


Figure 10: Wind velocity (left) and wind pressure (right) acting on inside and outside of rigid open type dome at the center of the longitudinal axis

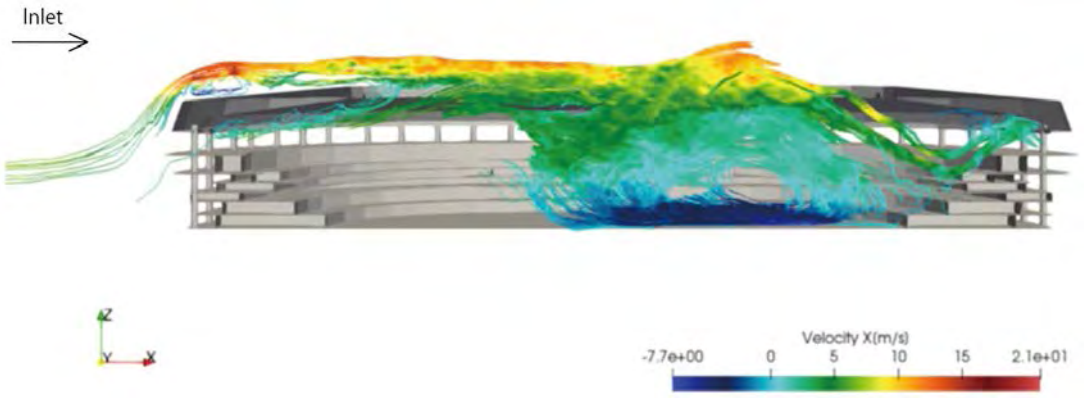


Figure 11: Side view of the streamlines of wind velocity at the center of the longitudinal axis

4. Conclusions

This study performed high performance computing for estimation of wind-induced pressures on various domes based on the LES technique. For numerical scheme and discritization, unstructured grid system and Cartesian coordinate grid system were installed. Physical mechanism of wake vortex structures was discussed analyzing the unsteady velocity fields behind a hemispherical dome in the subcritical and supercritical Re regime. Very special phenomena such as an inclined vortex shedding pattern can be observed in some time of a supercritical case. Also a very complicated dome was dealt with in order

to clarify the interaction of the unsteady flows between the inside and outside of an open dome. Wind pressures acting on various dooms were provided for the wind resistant design of a long span roof.

References

[1] Cao, Y., Tamura, T. (2017). Supercritical flows past a square cylinder with rounded corners. *Physics of Fluids*, *29*(8), 085110.

[2] Jansson, N., Bale, R., Onishi, K., & Tsubokura, M. CUBE, A scalable framework for large-scale industrial simulations. The International Journal of High Performance Computing Applications, 1094342018816377., 2018

[3] Tsubokura, M., Kobayashi, T., Nakashima, T., Nouzawa, T., Nakamura, T., Zhang, H., ... Oshima, N. (2009). Computational visualization of unsteady flow around vehicles using high performance computing. *Computers & Fluids*, *38*(5), 981-990.

[4] Muto, M., Tsubokura, M., Oshima, N. (2012). Negative Magnus lift on a rotating sphere at around the critical Reynolds number. *Physics of Fluids*, *24*(1), 014102.

[5] Nakahashi, K. (2003). Building-cube method for flow problems with broadband characteristic length. In *Computational fluid dynamics 2002* (pp. 77-81). Springer, Berlin, Heidelberg.

[6] Onishi, K., Obayashi, S., Nakahashi, K., Tsubokura, M. (2013). Use of the immersed boundary method within the building cube method and its application to real vehicle cad data. In *21st AIAA Computational Fluid Dynamics Conference*(p. 2713).

[7] Cao, Y., Tamura, T. (2018). Aerodynamic characteristics of a rounded-corner square cylinder in shear flow at subcritical and supercritical Reynolds numbers. *Journal of Fluids and Structures*, *82*, 473-491.

[8] Taneda, S. (1978). Visual observations of the flow past a sphere at Reynolds numbers between 10 4 and 10 6. *Journal of Fluid Mechanics*, *85*(1), 187-192.

[9] Constantinescu, G., Squires, K. (2004). Numerical investigations of flow over a sphere in the subcritical and supercritical regimes. *Physics of fluids*, *16*(5), 1449-1466.

[10] N. A. Patankar, P. Singh, D. D. Joseph, R. Glowinski, T. W. Pan, A new formulation of the distributed Lagrange multiplier/fictitious domain method for particulate flows, *Int J. of Multiphase Flows*, 26, pp.1509-1524, 2000,

[11] Nozawa, K. and T. Tamura, Large eddy simulation of the flow around a low-rise building immersed in a rough-wall turbulent boundary layer, Journal of Wind Engineering and Industrial Aerodynamics, 90, No. 10, 1151-1162, 2002

Proceedings of the IASS Annual Symposium 2019 – Structural Membranes 2019
Form and Force
7 – 10 October 2019, Barcelona, Spain
C. Lázaro, K.-U. Bletzinger, E. Oñate (eds.)

Numerical simulation of an inflated structure for an aircraft hangar

Jose Manuel GONZALEZ*, Javier MARCIPAR[a], Carles ESTRUCH[a],
Eric CUARTERO[a], Eugenio OÑATE[b]

*Technical University of Catalonia (UPC)
Campus Nord – Building C1 C/ Jordi Girona 1-3 08034 Barcelona
josem.gonzalez@cimne.upc.edu

[a] BuildAir – Ingeniería y Arquitectura
[b]International Center for Numerical Methods in Engineering (CIMNE)

Abstract

BuildAir S.A. has projected and built the H75 hangar in Jeddah (Saudi Arabia) for aircraft storage and maintenance tasks. The hangar is mainly conceived as a set of inflatable tubes where the stiffness is provided by the internal pressure and the stability of the structure is assured by a textile straps network. The structural analysis and design of this structure involves complex structural concepts due to the specificity of the structural elements employed which makes the problem highly non-linear. In this paper, the numerical simulation of the hangar and its structural units is presented as well as some structural and numerical conclusions and/or recommendations coming out from the work developed in the H75 structural analysis. The lack of standards for wind loads over this type of structures lead to oversized pressure distribution over the hangar. To improve the knowledge about the wind loads a coupled fluid-structure interaction is being developed a Panel Method approach for the fluid. Preliminary and promising results for an inflatable hangar are also presented.

Keywords: inflated structures, structural conception, internal pressure, equivalent static pressure, membrane elements, structural design, stabilization, fluid-structure interaction, potential flow.

1. Introduction

The H75 inflatable hangar is the largest inflatable structure ever conceived, designed and built in the world and the major engineering challenge in the history of Buildair [1], a company specialized in the design, manufacturing and construction of inflatable structures for a range of applications in engineering and architecture (www.buildair.com).

The main function of the inflatable hangars built by Buildair is to serve as shelter for aircrafts storage, construction and maintenance tasks. The H75-SAEI hangar will be set-up in Jeddah Airport Base (Kingdom of Saudi Arabia) and has been designed to host an Airbus 300 or a Boeing 777-200ER, during an expected lifetime of 7 years. The erection of the H75 hangar in the Jeddah airport took place on the last week of July 2019.

2. Project requirements

The design procedure of the H75 hangar must hold the Saudi Building Code SBC 301 "*Loads and forces requirements*", following local regulations and customer's demands.

Copyright © 2019 by J.M. Gonzalez, J. Marcipar, C. Estruch, E. Cuartero, E. Oñate
Published by the International Association for Shell and Spatial Structures (IASS) with permission.

The structure must be stable under its own weight, the internal pressure in the tubes and the pressure produced by a wind speed over the structure in every direction, according to the norm.

The Saudi Build Code establishes that the basic wind speed corresponds to a 3-second gust speed at 10 m above ground in exposure category C for the city of Jeddah, where the hangar is set-up. Accordingly, the basic wind speed is 152 Km/h. This basic speed obtained from the KSA norm is equivalent in terms of pressure to 83 Km/h of mean wind speed assuming the European norms.

The deformation of the structure is limited by functional and safety requirements, and so a minimum distance from the structure to the plane must be preserved for the projected actions.

3. Structural conception

The H75 inflatable hangar has been conceived as a membrane-strap-anchorage system to ensure the stability and functionality requirements in front of the external and internal actions projected.

The inflatable tubes are the main structural item of the hangar. They are PVC membrane made and filled with air by means of a blowing engines system. The (low) internal pressure inside the tubes (usually around 20 mbar) provides the required stiffness for the structure with a very low weight [2].

The stability of the tubes is ensured by an ***innovative straps network*** conceived as a cage surrounding the inflated membranes with two main objectives: limit the deformation of the tubes and transmit the internal forces to the anchoring points.

The different types of straps around the tubes present a very well defined role into the system: straps following the tube axis direction (*spines*, *ribs*) of the tube bear the bending forces reducing the deformation in this direction. Straps placed around the tubes (*braces*) keep their cohesion and bear the circumferential component of the stress and deformations in the membrane mainly produced by the internal pressure. Straps placed in the interphase between tubes (*radials*, *crosses*) enlarge the stiffness in this plane, very relevant for transversal loads like lateral wind.

Straps are connected to each other to configure a network in such a way that forces over the membranes are transmitted through the straps to the anchorage points in the form of axial forces.

This basic structural conception of the hangar as a novel ***membrane-strap-anchorage system*** is shown in Figure 1.

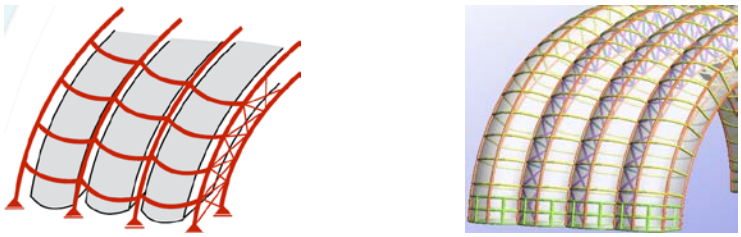


Figure 1. Inflated tube – straps network system – anchorage to the ground

4. Structural analysis of the main body

4.1 Geometrical definition

The main body of the H-75 hangar is defined by thirteen inflated tubes with an elliptic shape where free horizontal width is 75 m and free vertical height is 25.5 m, while the same outer lengths are 90 m and 33 m. These dimensions are projected to lodge an aircraft from fleet A330 and fleet B777-200 ER whose largest length measured at the wings is 59 m.

In the longitudinal direction of the hangar, the tubes are defined from tube number one as the front side to tube number 13 as the back side. A 2.3 m gap is left between tubes 7 and 8 due to safety requirements.

The total longitudinal size of the hangar is 95.8. Figure 2 shows the geometrical definition of the structure compared to aircrafts dimensions.

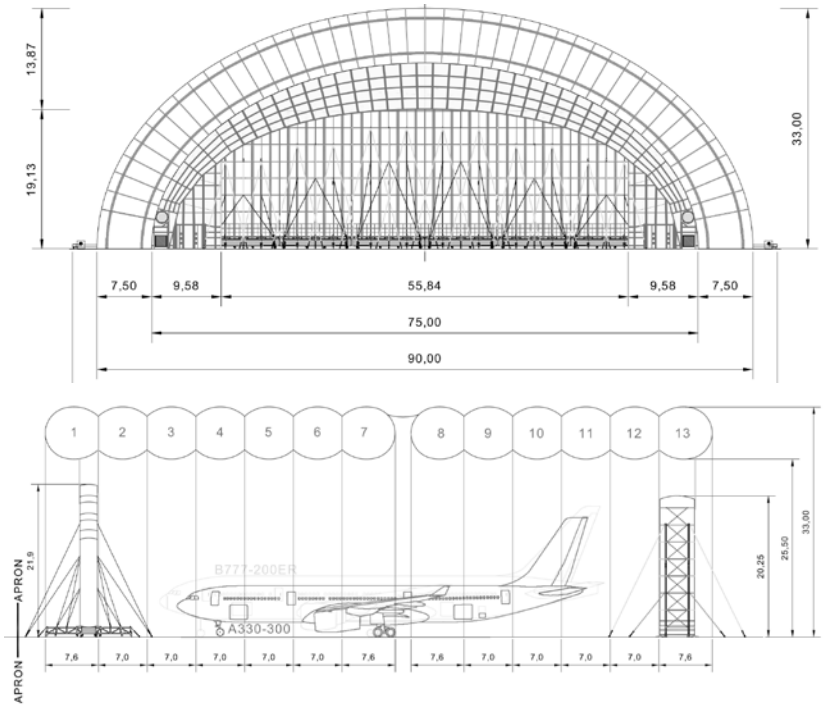


Figure 2. Geometrical definition of the main body. (a) Front view (b) Lateral view

4.2 Structural units

The main body is conceived as a cluster of structural units according to their role in the structural behavior in front of the loads. The main structural units are:

1. The inflated tubes and the joints involved (welded and sought)
2. The straps network including the sewing joints and shackles involved.
3. Anchorage devices for all the structural units.

The **inflated tubes** bear the internal pressure that produced the shear and bending rigidity to hold the loads acting over the structure and minimize deformations of the hangar. They are limited by the resistance of the membrane and the constructive joints.

The inflated tubes are bounded by a **net of straps** to assure its stability and to keep the structure inside the limits of admissible deformations, transmitting the internal forces to the ground. Different types of straps have been projected depending of the structural behavior and internal forces expected, as depicted in Figure 3.

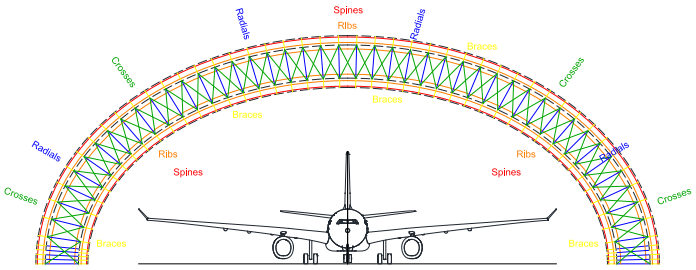


Figure 3. Straps network. Typologies and location

Membranes and straps network presented above transmit the internal forces produced in the structure to the ground by means of **anchorage devices**, mainly anchorage plates and eyebolts. These become another structural unit of the hangar which reclaims a structural analysis in two aspects: the resistance of the anchorage device and the resistance of the anchorage to the ground.

4.3 Numerical model

4.3.1 Structural elements

The geometry of the hangar has been modeled using different types of finite elements according to every particular structural behavior.

Inflated tubes are closed membranes, but also the waterproof layer, the curtains at the enclosures and the emergency exit layer. Membranes have been modeled using *linear membrane triangles* [3].

The straps network has been modeled by means of *linear unidimensional elements* that assume tension axial forces only as depicted in the Figure 4. They are modeled embedded in the membranes assuming they transmit a part of the axial load through the anchor points or by friction.

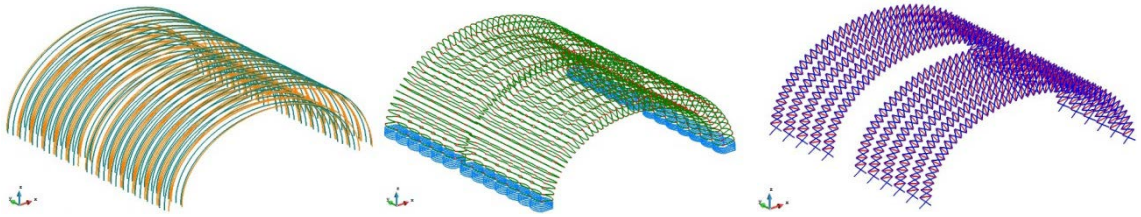


Figure 4. Numerical model of the straps network (a) spines and ribs (b) braces (c) radials and crosses

The whole numerical model is conformed by 77073 *linear membrane triangles* for the membranes, and 37613 *linear unidimensional elements* for the straps, which means the model is built with 114686 finite elements, defined by 41934 nodes with 3 degrees of freedom per node.

Figure 5 shows a general view of the numerical model built for the numerical simulation.

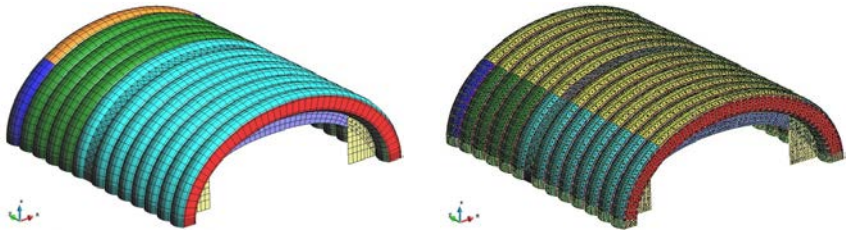


Figure 5. Numerical model of the main body. (a) geometry (b) mesh

4.3.2 Loads over the main body

The loads over the structure considered in the numerical simulation are the self-weight of the structural components, the internal pressure inside the tubes and wind loads.

The **self-weight** of the main body concerns to the structural elements involved: the membranes for the tubes, for the front and back curtains and the waterproof sheet, and the straps network.

The working **internal pressure** in the tubes of the main body is prescribed to 1500 Pa (15 mbar) during its lifetime. For safety reasons, the structure is projected and designed for an internal pressure of 2500 Pa (25 mbar) for peak wind loads scenario.

The determination of the **pressure distribution due to wind** has been performed in accordance to the Saudi Arabian standard SBC 301, which defines a design value for the wind speed.

As mentioned, the Saudi Build Code establishes a basic wind speed (V) corresponding to a 3-second gust speed at 10 m above ground in exposure category C for the city of Jeddah, where the hangar is going to be built. Accordingly, the basic wind speed is 152 Km/h.

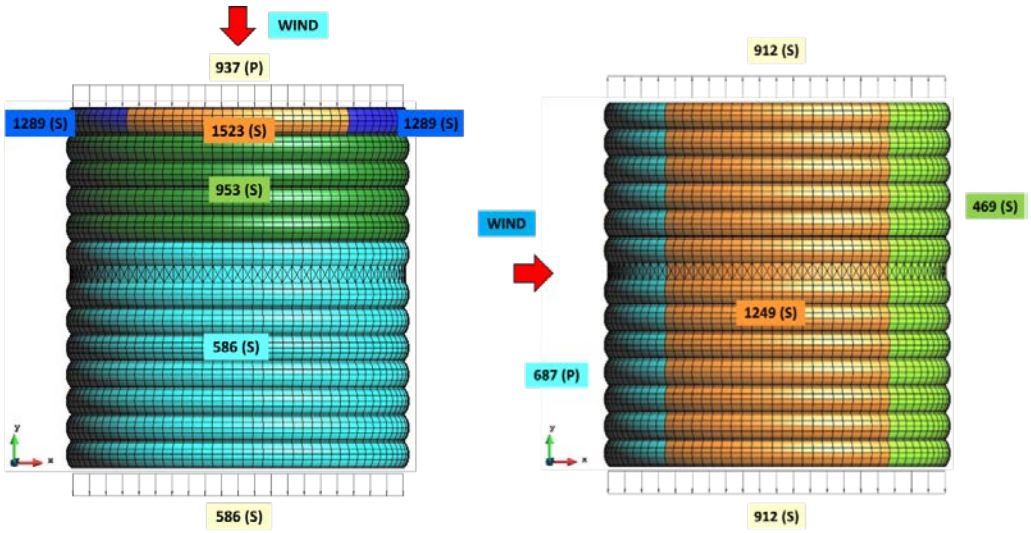


Figure 6. Pressure distribution due to (a) Frontal wind (b) Lateral wind

The design pressure is q_z=1171,8 Pa to fulfill the Saudi standards. However, European standards have been accepted as reference to define the wind loads over the structure. The pressure loads due to wind obtained from European norm EN 13782 for an equivalent pressure are represented in Figure 6 for both load cases – frontal and lateral wind – showing the different exposed zones, and the values applied for pressure (P) or suction (S).

4.3.3 Boundary conditions

The stability of the main body of the hangar is performed by means of anchorage plates and eyebolts. The boundary conditions are modeled by set of nodes where the displacements are prescribed to zero and the rotations are free, corresponding to the anchoring points of the tubes, the straps and curtains.

4.3.4 Mechanical problem features

The numerical simulation has been performed assuming elastic behavior of the whole structure.

The numerical simulation of the main body of the hangar implies a mechanical geometrically non-linear problem because of the large displacements potentially observed in the deformation, especially in the membranes. This problem is solved using an iterative procedure based on the prediction-correction, load control and stabilization algorithms.

The numerical simulation has been performed using the calculation code RAMSeries from *Compass Ingeniería y Sistemas* [4] and the pre-post processor Gid developed by the *International center for Numerical Methods in Engineering (CIMNE)* [5].

4.4 Structural analysis and design of the membranes

One of the main requirements of the hangar is the safety of the aircraft. Figure 7 shows the transversal displacement (wind direction) due to lateral wind which is the critical case for deformation. The maximum transversal displacement is 3.66 m located in the central part of the hangar. The closest point

of the membranes to the wing of the hangar is 4.82m far. The displacement of this point reduces this distance to 1.73m in the worst wind scenario.

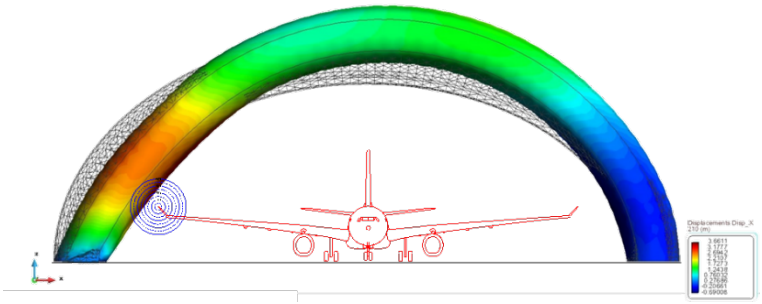


Figure 7. Transversal displacement of the main body over undeformed hangar

The membrane used for the inflated tubes of the main body of the hangar is *SIOEN TT0117E*. The characteristic strength of the membrane is f_{tk} = 270 daN/5m. The safety factor is γ_M = 2,5 which leads to a design strength (f_d) of 108 daN/5cm.

Tubes are reinforced in the extremes by means of the so called *thimble*, built with a second membrane wrapping the extreme of the tube. The strength of these zone is considered the addition of both strengths leading to a design strength of 216 daN/5cm.

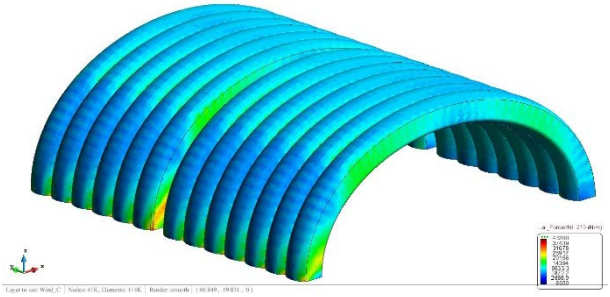


Figure 8. Maximum main axial forces over the membrane of the inflated tubes

The maximum axial force observed is 213 daN/5cm which holds the resistance criteria. Figure 8 shows the representation of the maximum main axial force over the membranes. As observed, the whole membranes are under this strength limit.

4.5 Structural analysis and design of the straps

The design of the straps network involves a characteristic strength (f_k) provided by the manufacturer which leads to a design strength (f_d) considering a safety factor γ_M which depends on the equivalent diameter.

The maximum axial forces over the *spines* or *ribs* are 140,1 kN from the frontal wind case. For a design strength f_d = 167 kN the design axial force in the *spines* hold the resistance criteria with SF = 3.2.

The maximum axial forces over the *braces* are 28.4 kN from the lateral wind case. For a design strength f_d = 34 kN the design axial force in the *braces* hold the resistance criteria with a safety factor SF = 4.8.

The maximum axial forces over the *radials* are 10.4 kN from the lateral wind. For a design strength f_d = 12.5 kN the design axial force in the *radials* hold the resistance criteria with a safety factor SF =5.0.

The maximum axial forces over the *crosses* are 40.6 kN from the lateral wind case, out of the numerical concentrations observed due to boundary conditions. These straps do not hold the resistance criteria. An

additional 50 mm wide strap reinforcement is added to this set to increase the design strength up to 41 kN. The joint of 75 and 50 mm wide straps now holds the resistance criteria with a safety factor SF =5.0.

4.6 Structural analysis and design of the anchorages

The anchorage system of the main body of the hangar is mainly made up steel plates. The continuum body verification is performed by means of numerical simulation using the finite element method.

The maximum vertical and horizontal reactions are 245.8 kN and 95.1 kN respectively.

The numerical simulation of critical plate is presented in Figure 9, in terms of displacements (modulus in mm) and distribution of Von Mises stresses.

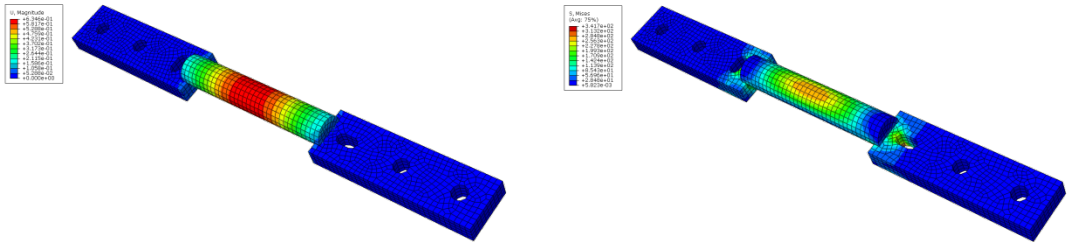


Figure 9. Numerical simulation of anchoring plates. (a) displacements (b) Von Mises stresses

High stress level in terms of Von Mises stress is found in the cylinder-plate joint and edges of the holes to fix anchors. The latter do not represent a problem, since they are caused by a singularity of the numerical model. This stress concentration is due to the edge conditions set in the numerical analysis and would not cause any problems in the real component. Maximum displacements are predicted to be 0.63 mm in the central section of the cylinder which is acceptable.

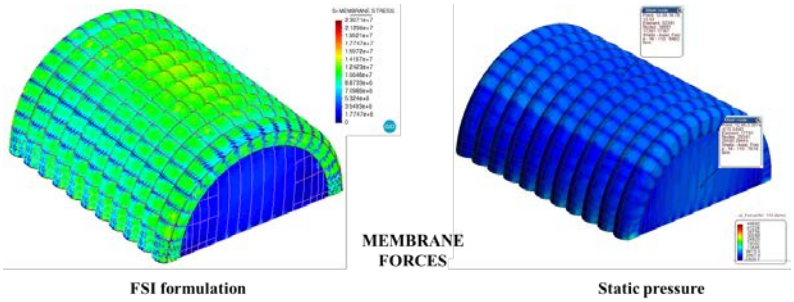
5. Next steps in numerical simulation of inflatable hangars

The main load over the inflatable hangar is the wind load defined using the norms for temporal structures and building dimensions because of the lack of standards. The approximation of these loads usually means an oversized pressure distribution over the hangar.

More realistic pressures over the membranes can be obtained using well-known CFD numerical methods. However, this numerical simulation usually reclaims a great amount of computing power and time which makes this option difficult to implement in the design procedure of a hangar.

At this point, a new coupled fluid-structure formulation it's being considered based in a potential flow using a Panel Method approach for the fluid, to improve the knowledge about the real wind loads. An FSI calculation code is being developed specifically for inflatable hangars [6].

Some preliminary results have been obtained for lateral wind over a small hangar built by BuildAir (H20) and shown in Figure 10 comparing the results of both numerical approximations: static pressure and fluid-structure interaction



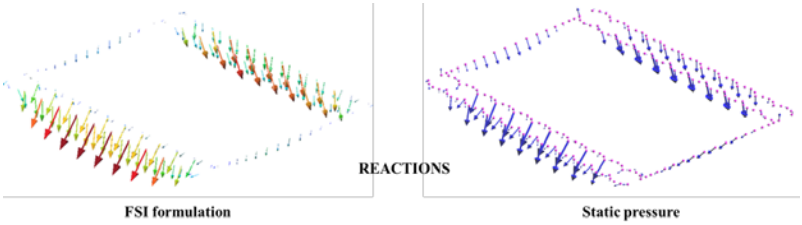


Figure 10. Static pressure vs FSI method. (a) stresses over membranes (c) reactions

Table 1 compares results from both methods. A reduction in forces can be appreciated in most cases, especially in the membranes and the anchorages which could reduce the amount of material employed.

Table 1. Numerical results comparison: static pressure vs FSI method

Magnitude	FSI method	Static pressure
Displacements	0.24 m	0.65
Membrane tubes	7.5 kN/m	6.5 kN/m
Membrane curtains	1.7 kN/m	7.6 kN/m
Straps forces	18.6 kN	32.5 kN
Reactions	15.6 kN	37.1 kN

6. Conclusions

This paper describes the structural analysis and design procedure of H75 inflatable hangar, conceived, designed and built by BuildAir. H75 is a singular structure due to its structural conception where the rigidity is provided by air pressure, its size, being the world largest inflatable hangar ever built, its shape or the lack of standards to define the procedure.

In this innovative context, numerical simulation is crucial to approach the structural response of the hangar. Structural and numerical assumptions have been made related to geometry, loads and bounds into a highly non-linear problem. Numerical simulation has led to a solution holding the structural requirements and resistance criteria with the safety factors required for every structural component.

7. References

[1] J. Marcipar, E. Oñate and J.M. Canet "Experiences in design analysis and construction of lowpressure inflatable structures", *Textile composites and inflatable structures*. pp. 241-257, (2005), Springer.

[2] E. Oñate E, F. G. Flores F.G and J. Marcipar (2008) "Membrane Structures Formed by Low Pressure Inflatable Tubes. New Analysis Methods and Recent Constructions". In: Oñate E., Kröplin B. (eds) *Textile Composites and Inflatable Structures II. Computational Methods in Applied Sciences, vol 8.* Springer, Dordrecht

[3] R. L. Taylor, E. Oñate and P. A. Ubach, "Finite element analysis of membrane structures", *Textile composites and inflatable structures*. pp. 47-68, (2005), Springer.

[4] "RAMSeries Reference manual", "RAMSeries Theory manual" Compass Ingeniería y Sistemas (www.compassis.com)

[5] GiD. "The personal pre and postprocessor" version 14.0 (2018) International Center for Numerical Methods in Engineering (CIMNE) (www.gidhome.com)

[6] E. Ortega, R. Flores and J. Pons-Prats, "Ram-Air Parachute Simulation with Panel Methods and Staggered Coupling", *Journal of Aircraft, vol. 31*, pp. 807-814, 2017.

Proceedings of the IASS Annual Symposium 2019 – Structural Membranes 2019
Form and Force
7 – 10 October 2019, Barcelona, Spain
C. Lázaro, K.-U. Bletzinger, E. Oñate (eds.)

Wind analysis of an air-inflated membrane structure

Krisztián HINCZ*, Sherly Joanna POOL BLANCO[a], Mauricio GAMBOA-MARRUFO[b]

* Department of Structural Mechanics, Faculty of Civil Engineering,
Budapest University of Technology and Economics
Műegyetem rkp. 3., Kmf. 63., Budapest, Hungary
hincz.krisztian@epito.bme.hu

[a,b] Structural Engineering Group, Engineering Faculty,
Autonomous University of Yucatan

Abstract

Air-inflated structures are portable, very light structures with small folded/uninflated volume and with extremely short set-up and dismantling time. Air-inflated structures were built with larger and larger spans in the previous years. Since the building codes do not provide the pressure coefficients of membrane structures, normally they are determined by the help of wind tunnel tests or CFD (Computational Fluid Dynamics) calculations. In the course of the current research the pressure coefficients of a structure composed of six air-inflated arches were determined through wind tunnel tests. The main steps of the research were: a) The determination of the pressure coefficients of the structure by means of wind tunnel tests. The pressure coefficients were determined for different wind directions in the cases of a closed and an open set-up (structures with and without end walls). b) The nonlinear static analysis of the structure based on the determined pressure coefficients. c) Wind tunnel tests of the model of a deformed shape of the structure (the deformed shape was determined numerically using the pressure coefficients of the inflated structure). d) Comparison of the pressure coefficients of the inflated structure (without external loads) and the pressure coefficients of the deformed shape. The aim of the last step of the research was to analyze the efficiency of the wind tunnel tests of a rigid model in the case of a structure with large deformations.

Keywords: air-inflated membrane structures, wind load, wind tunnel test, dynamic relaxation method.

1. Introduction

Tensile membrane structures supported by masts (Figure 1) and arches (Figure 2) provide environmentally friendly solutions for covering large areas with exciting, aesthetic surfaces. One of the most difficult tasks during the design and analysis of membrane structures is the determination of the wind load on the doubly curved surface of the structure. On the one hand, the site wind speed and dynamic pressure are given by the different design codes (for example [1] or [2]). On the other hand, the pressure coefficients (c_p) for different doubly curved surfaces are not provided by the design codes, they can be determined by expensive and time consuming wind tunnel tests or CFD calculations. In the case of structures with smaller span (and smaller budget for the analysis), the pressure coefficients are often approximated on the basis of previous tests on similar surfaces. For example the pressure coefficients determined by wind tunnel tests for different tensile membrane structures are presented in [3], [4] and [5]. The models for the wind tunnel tests of different tensile structures can be seen in Figure 3. The European Standard [6] gives general pressure coefficients for hyperbolic surfaces for two different load cases. Load case 1 means suction

Copyright © 2019 by K. Hincz, S. J. Pool Blanco, M. Gamboa Marrufo
Published by the International Association for Shell and Spatial Structures (IASS) with permission.

on the whole surface with a constant c_p value of -0.7, load case 2 means positive pressure on the whole roof with a constant c_p value of +0.3. Although this is a quite rough approximation, this is often used during the design of small tensile structures.



Figure 1: Mast supported tensile membrane structures in Hungary



Figure 2: Arch supported tensile membrane structures in Hungary, (Photos: D. Hegyi and Gy. Galaskó)

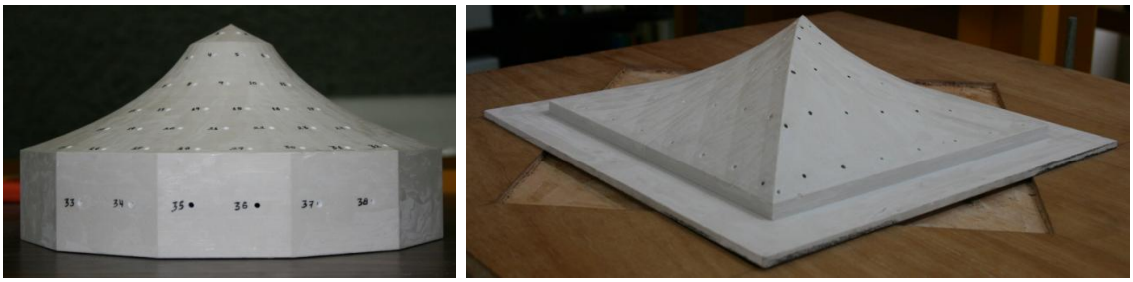


Figure 3: Models for previous wind tunnel tests

Besides the membrane structures tensioned by mast, arches and cables, the pneumatic structures are, nowadays, also more and more popular. The two main groups of pneumatic structures are air supported structures and air inflated structures. In the case of air supported structures the whole covered space is closed and there is overpressure in the building, hence such structures have special entrances (Figure 4). On the other hand, air-inflated structures are composed of closed inflated walls, tubes and cushions, but the covered space can be open (Figure 5).



Figure 4: Entrance of an air-supported membrane structure in Cambridge, USA



Figure 5: Air-inflated hangar of Lufthansa Technik Budapest, (Photos: Budapest Airport)

The current research deals with the wind analysis of a structure composed of six air-inflated arches. The 3 main steps of the research were: a) The determination of the pressure coefficients on the external and internal surfaces of the inflated structure by wind tunnel tests. The pressure coefficients were determined for 3 different wind directions. b) The nonlinear static analysis of the structure on the basis of orthotropic membrane material, given internal pressure and the experimentally determined pressure coefficients. c) Wind tunnel tests of the model of a deformed shape of the structure (the deformed shape is determined numerically using the pressure coefficients of the inflated structure). Comparison of the pressure coefficient field of the inflated structure (without external loads) and the pressure coefficient field of the deformed shape (for one chosen wind direction). Similar analysis was completed previously for a conical tensile membrane structure [4].

2. The analysed structure

2.1. Geometry of the analysed structure

The analysed structure is composed of six air-inflated, circular arches. The size of the covered rectangular area is 13 m x 26 m, the height of the structure is 13 m. The inner radius of the inflated arches is 10 m, the outer radius is 13 m. The top view and the front view of the structure can be seen in Figure 6. The cross section of the structure with the relevant sizes can be seen in Figure 7.

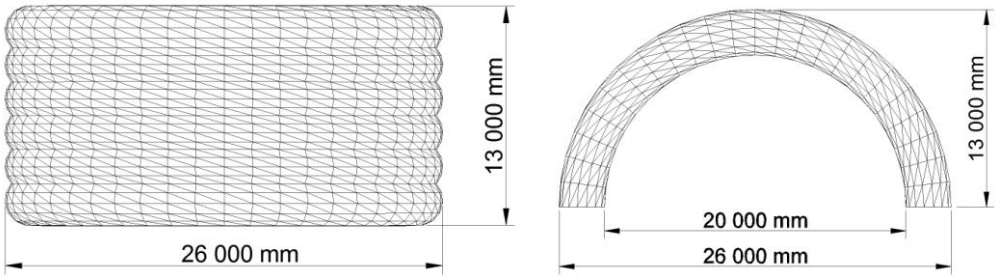


Figure 6: The top view and the front view of the analysed structure

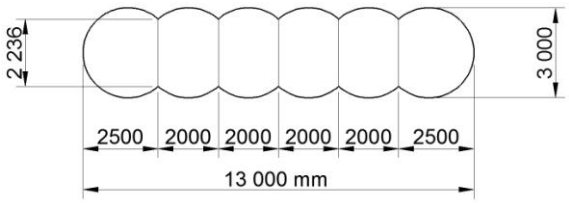


Figure 7: Cross section of the structure

2.2. Mechanical model

The doubly curved, synclastic surface of the structure was approximated with a network of thin, planar triangular elements. The membrane forces and the deformed shape of the inflated and loaded structure were determined by the Dynamic Relaxation Method (DRM). DRM is a step-by-step, numerical method which is especially suitable for the analyses of tensile structures (Day [7], Barnes [8]). The material of the membrane was supposed to be linear elastic and orthotropic with the same modulus of elasticity in warp and fill directions (E_w=E_f=400 kN/m, G=10 kN/m, ν_{wf}=ν_{fw}=0.3). Warp direction was supposed to be "parallel" with the centerline of the inflated arches. (Fill direction is perpendicular to warp direction.) The internal pressure in the inflated arches was p=25 mbar. The joints at the ground were fixed before inflating the structure and they were supposed to be fixed during the static analysis also. The membrane forces in warp and fill directions in the inflated structure can be seen in Figures 8 and 9. The 3-3 numbers beside the colour scales are the minimum, average and maximum values of the membrane forces. The membrane forces in warp direction are larger at the outer side than at the inner side of the arches. The distribution of the membrane forces in fill direction is even with the exception of the regions close to the supported joints. The average value of the membrane forces is approximately two times larger in fill direction than in warp direction.

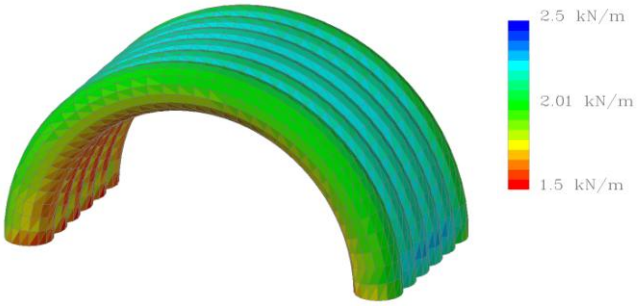


Figure 8: Membrane forces in warp direction in the inflated structure

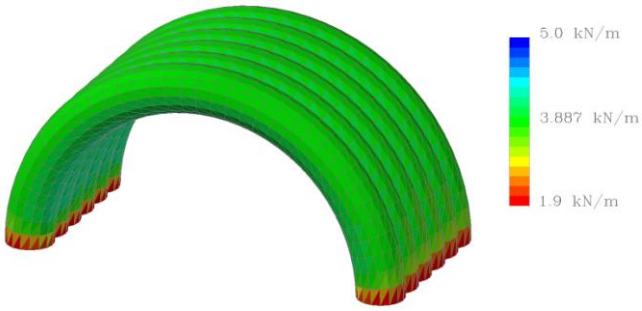


Figure 9: Membrane forces in fill direction in the inflated structure

3. Pressure coefficients of the original, inflated shape

The model of the original, inflated shape for the wind tunnel tests can be seen in Figure 10. The model was analysed with and without end walls. The pressure coefficients of the closed and the open model were determined for 3 different wind directions. Figure 11 presents the pressure coefficient of the open model in the case of wind load parallel with the (theoretical) planes of the centrelines of the arches. The pressure coefficient distribution of the closed structure in the case of the same wind direction can be seen in Figure 12. (The pressure coefficient fields for other two wind directions will be presented at the Symposium.)



Figure 10: The model of the open structure for the wind tunnel tests

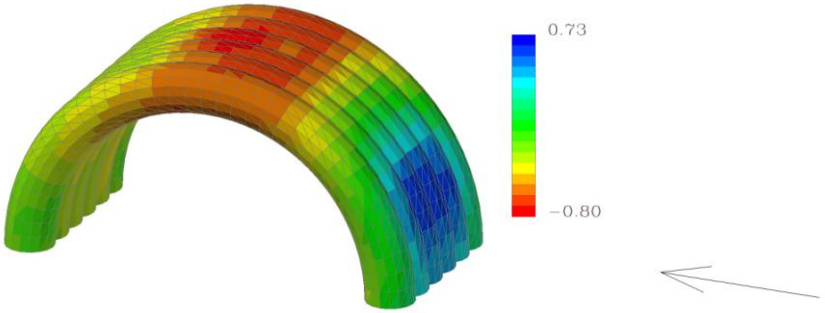


Figure 11: The pressure coefficient field of the open structure (the arrow shows the wind direction)

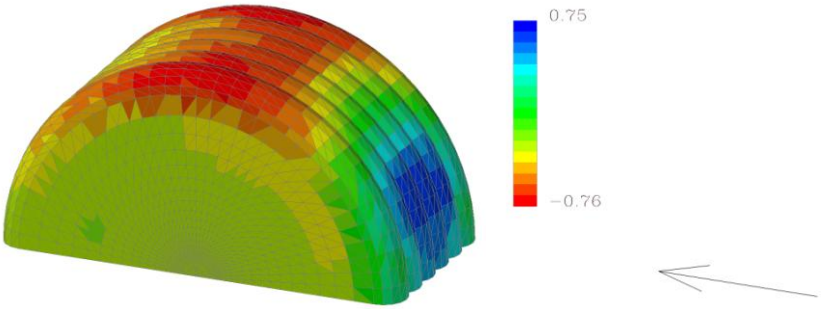


Figure 12: The pressure coefficient field of the closed structure

4. Static analysis of the structure under wind load

The membrane forces and the displacements were calculated for different wind directions and different dynamic pressure values using the pressure coefficients determined by wind tunnel tests. The results for the open model in the case of wind direction parallel with the theoretical planes of the centrelines of the arches can be seen in Figures 13-15. The dynamic pressure was selected to q=1.52 kN/m (recommended by the Mexican Standard [2]).

Figure 13 presents the membrane forces in warp direction. The minimum value can be detected at the outer side of the inflated arches at the windward side of the structure. The black elements in the figure show that there is a relatively small slack area, where the tension in warp direction equals to zero. The maximum values in warp direction can be detected at the inner side of the inflated arches at the windward side of the structure. It can be seen in Figure 14 that the distribution of the membrane forces in fill direction is even with the exception of the regions close to the supported joints. The maximum of the displacements is approximately 2.7 m and it can be detected at the slack area at the windward side of the structure (Figure 15).

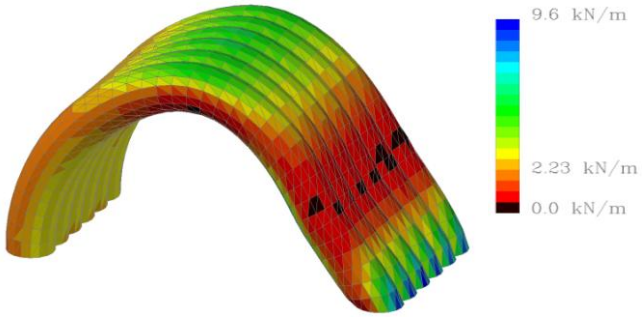


Figure 13: Membrane forces in warp direction under wind load

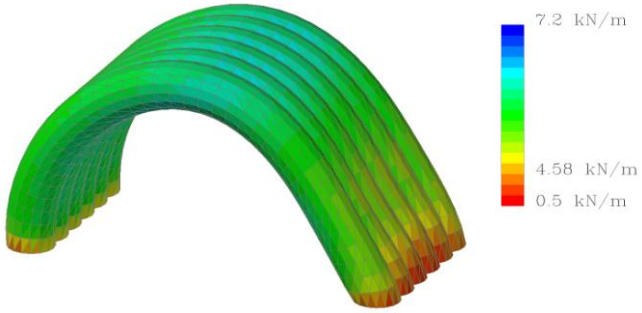


Figure 14: Membrane forces in fill direction under wind load

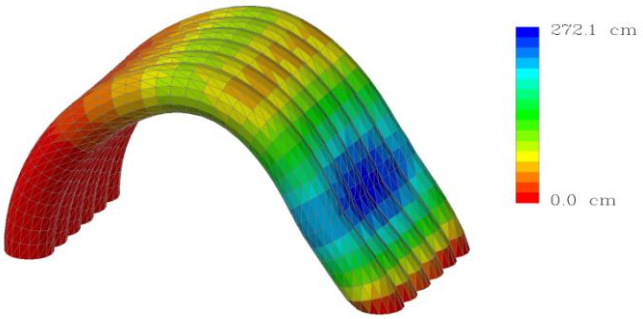


Figure 15: Displacements of the structure under wind load

5. Model of the deformed shape

The next step of the research was the determination of the pressure coefficients of the deformed shape of the structure. The model of the deformed shape for the wind tunnel tests can be seen in Figure 16. The wind tunnel tests were completed, the evaluation of the results and the determination of the pressure coefficient distribution is still in progress. They will be presented at the Symposium.



Figure 16: Model of the deformed shape for the wind tunnel tests

6. Conclusion

The paper presents the first steps of the deformed shape wind analysis of an inflated structure. The pressure coefficients of the surface of the membrane were determined by wind tunnel tests. The membrane forces and the deformed shapes of the structure were calculated using the Dynamic Relaxation Method. In the next step of the research the rigid model of one chosen deformed shape was subjected to wind tunnel tests and results are ready to be analysed. The pressure coefficients of the inflated shape (without external load) and the pressure coefficients of the deformed shape will be compared to analyse the efficiency of the wind tunnel tests of rigid models in the case of the design and analysis of inflated structures.

Acknowledgements

This work was supported by NKFI under Grant K119440.

References

[1] European Standard EN 1991

[2] Mexican Standard, Manual de diseno de obras civiles, Diseno por viento, Mexico, 2008

[3] K. Hincz and M. Gamboa-Marrufo, "Wind analysis of an arch supported tensile roof" in *Spatial Structures - Permanent and Temporary: Proceedings of the IASS Annual Symposium 2010, Shanghai, China,* 13 p., 2010.

[4] K. Hincz and M. Gamboa-Marrufo, "Deformed shape wind analysis of tensile membrane structures", *Journal of Structural Engineering (ASCE)*, vol. 142(3), Paper: 04015153, 5 p., 2016.

[5] B. Foster, M. Mollaert, European Design Guide for Tensile Surface Structures, TensiNet 2004.

[6] European Standard EN 13782:2005

[7] A. S. Day, "An introduction to dynamic relaxation", *The Engineer,* pp. 218-221, 1965.

[8] M. R. Barnes, "Form-finding and analysis of prestressed nets and membranes", *Computers and Structures,* vol. 30, pp. 685-695, 1988.

Proceedings of the IASS Annual Symposium 2019 – Structural Membranes 2019
Form and Force
7 – 10 October 2019, Barcelona, Spain
C. Lázaro, K.-U. Bletzinger, E. Oñate (eds.)

3D-Printed Formwork for Integrated Funicular Concrete Slabs

Andrei JIPA[*], Cristián CALVO BARENTIN[b], Gearóid LYDON[c], Matthias RIPPMANN[b], Georgia CHOUSOU[a], Matteo LOMAGLIO[a], Arno SCHLÜTER[c], Philippe BLOCK[b], Benjamin DILLENBURGER[a]

[*, a] Digital Building Technologies, ETH Zürich
Stefano-Franscini-Platz 1, HIB E23, 8093, Zürich, Switzerland
jipa@arch.ethz.ch

[b] Block Research Group, ETH Zürich
[c] Architecture and Building Systems, ETH Zürich

Abstract

This paper describes how 3D-printed formwork can be used to facilitate the integration of functional features in structurally optimised concrete slabs. The weight of concrete slabs represents the largest portion of the weight of a concrete framed, multi-storey building. Despite this significant share, slabs are usually designed as monolithic, oversized boxes due to various construction constraints. Optimised design alternatives, featuring funicular shapes, differentiated ribs, profiled soffits and hollow sections use significantly less material and can moreover integrate building services within the thickness of the slab, such as heating, cooling and ventilation. Nevertheless, both the optimised external geometry and the internal network of functional voids present very complex fabrication challenges for concrete. This is because standard commercial formwork systems are not suitable for bespoke designs. To address this limitation, this research demonstrates how fused-deposition 3D printing can be used for the fabrication of custom formwork for a functionally integrated concrete slab. The resulting prototype efficiently uses material and integrates provisions for an active beam ventilation system within the standard structural depth of the slab (Fig. 1). All these intricate geometric features are achieved with an ultra-lightweight 3D-printed formwork, which weighs less than 15 kg for the 660 kg concrete slab.

Keywords: concrete, funicular structures, functional integration, formwork, 3D printing, digital fabrication, concrete slab, active beam, embodied energy, sustainability



Figure 1: Integrated Funicular Concrete Slab prototype, built using 3D-printed formworks [A. Jipa]

Copyright © 2019 by Andrei Jipa, Cristián Calvo Barentin, Gearóid Lydon, Matthias Rippmann, Georgia Chousou, Matteo Lomaglio, Arno Schlüter, Philippe Block, Benjamin Dillenburger
Published by the International Association for Shell and Spatial Structures (IASS) with permission.

1. Context

Buildings are responsible for around 48% of the global energy consumption through their construction, operation and deconstruction [1]. Recent innovations have helped reduce operational energy significantly, while recent studies have shown the imperative importance of addressing the embodied energy as well [2]. This research acknowledges the benefits of a holistic approach, where the biggest impact can be achieved by addressing the operational and embodied energy of a building in parallel.

The biggest impact on embodied energy in buildings comes from concrete, which is the most used material globally [3], and as regards concrete buildings, slabs are the biggest material consumers [4]. Currently, the vast majority of slabs are built in reinforced concrete due to their simple construction and due to the advantages this material has for providing thermal mass, fire insulation and soundproofing. But conventional slabs cast with flat shuttering panels result in oversized, monolithic concrete boxes with big embodied energy values.

Designing more material-efficient slabs can indirectly lead to further material savings in the vertical structure and foundations of a building and therefore it can have an important benefit in reducing the embodied energy of a building. This research investigates a sustainable fabrication method based on fused deposition modelling (FDM) for formwork, suitable for lightweight, functionally integrated, bespoke funicular concrete slabs which address all stages of the life-cycle energy.

2. State of the Art

Through structural optimisation, the volume of material needed to carry loads in a slab can be significantly reduced [5, 6]. An inevitable aspect of the resulting geometries is that their complexity poses fabrication challenges. Aside from enabling material efficiency through optimised topologies, complex geometries can significantly extend the spectrum of solutions to common architectural design problems with new aesthetics. Structurally, complex designs can be solutions to reducing stress and increasing stiffness, while functionally, complexity can ensure precise enclosure for bespoke building services and smart assembly details and interfaces.

2.1. Standardised Slabs

Reusable flat-panel formwork systems are efficient and cost-effectiveness, but not suitable for non-standard geometries. For non-flat slabs, mass-produced formwork systems exist as well. Voided Biaxial Slabs, create large voids inside ribbed or waffle concrete slabs with plastic containers, Perforated Waffle Slabs allow for the integration of services and Filigree Wide Slabs combine prefabrication with in-situ concrete casting. However, these formwork solutions are very restrictive and not feasible for the fabrication of bespoke slab designs.

2.2. Non-standard Slabs

Direct digital fabrication through concrete-extrusion 3D printing could bypass the need for complex formworks altogether. However, several fabrication challenges regarding the integration of reinforcement and cold joints between layers have limited the application of this technology in load-bearing slabs, which need to resist considerable bending stresses. Another type of direct digital fabrication, through binder-jet additive manufacturing, has been proposed for the fabrication of compression-only slabs [5]. However, this process produces a sandstone composite with an organic binder, which, unlike cement, cannot be used directly in buildings yet, due to fire protection, user health and safety regulations.

Several strategies for non-standard, digitally fabricated formworks have been developed as well, subtractive CNC processes being the most applicable. The Unikabeton slab prototype was fabricated using CNC milling, based on a topology optimised design featuring a ribbed soffit [7]. CNC milling in

this case has a relatively big geometric freedom, but it is a time-consuming process generating large amounts of waste, with geometric limitations dictated by tool-head accessibility.

Additive manufacturing has also been used for concrete slab formworks [8]. The Smart Slab uses mainly binder-jet 3D printing to create the formwork for the soffit of an 80-m^2 structurally efficient slab that integrates functionality in an inhabited building. However, binder-jetted formworks can weigh more than half the mass of the concrete slab itself and are difficult to recycle.

2.3. Submillimetre 3D-Printed Formworks

Additive manufacturing has the largest geometric freedom when compared to other digital fabrication techniques. Manufacturing disposable formworks for one-of-a-kind parts in heavy binder-jetting is a very fast, but wasteful process, as illustrated by the Smart Slab. To avoid this issue, this research investigates FDM, an alternative additive manufacturing technology, to produce very thin shells that can act as formwork. This has been previously investigated for the fabrication of spatial elements and columns, but so far not for slabs [9].

3. FDM 3D-Printed Formwork

The aim of this research is to investigate FDM as a sustainable fabrication method suitable for efficient, bespoke funicular concrete slabs. FDM is a widely available 3D-printing technology in which molten material is extruded and hardens immediately after deposition. The deposition happens in consecutive horizontal layers, which are generated by slicing a digital model. FDM has access to a wide variety of plastics (biodegradable, water-soluble, fibre-reinforced, flexible, conductive, low-shrinkage, bioplastics etc). Furthermore, despite some fabrication limitations such as the inability to produce unsupported cantilevers, FDM is unique among the different 3D printing technologies for its capability of producing in large scale freestanding parts with very thin geometric features, such as walls as thin as 0.4 mm.

Unlike the previous approaches, FDM is also suitable for producing complex internal void geometries. For example, such internal structures can precisely define ducts for heating, ventilation and air conditioning (HVAC) and other building services. However, once the concrete hardens, the internal formwork becomes inaccessible and it is no longer possible to mechanically remove it. Thus, due to its ability to produce very thin submillimetre shells, FDM is perfectly suited for stay-in-place formwork having a negligible environmental impact and contribution to the overall weight of the slab.



Figure 2: The resulting section shows the thin concrete shells, the upstand ribs, the stay-in-place EPS formwork, acting as insulation, as well as the hydronic coil and the pipework necessary for the active beam. [A. Jipa]

4. Integrated Funicular Concrete Slabs

The proposed method was tested for the fabrication of a one-to-one, integrated funicular concrete slab (IFCS) prototype. The prototype represents one half of a conceptual slab measuring 2.6 m × 2.6 m ×

0.25 m. As a tool for communicating the advantages of the IFCS systems, the prototype is built as a sectional model (Fig. 2), with the cut line going through the middle of the slab, thus revealing the complexity of the internal structure, as well as the integrated building services. The prototype was exhibited in the ETH Pavilion at the World Economic Forum (WEF) in Davos in January 2019. The prototype was developed to test the construction of a slab based on 3D-printed formwork which enables material reduction and smart functional integration.

4.1. Reducing embodied energy

Recent research has demonstrated that the use of funicular floors composed of curved shells and stiffening ribs (Fig. 3) has the potential to reduce material (up to 70%) and implicitly embodied energy [5, 10, 11].

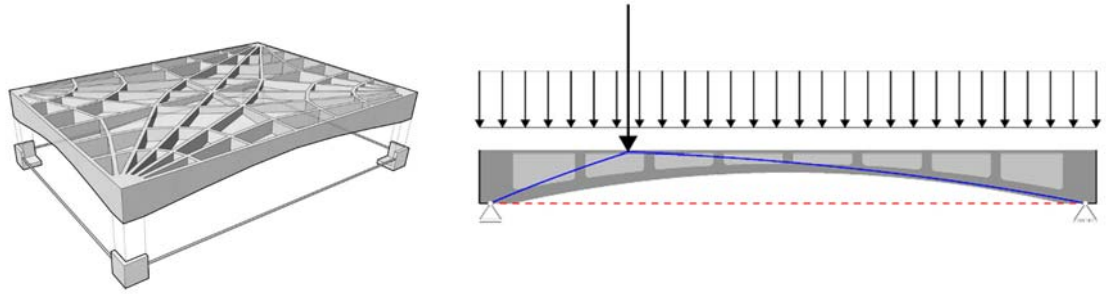


Figure 3: A rib-stiffened floor and its section showing the internal thrust lines (solid) terminating at supports and generating horizontal forces, which can be taken either by ties (dashed) or horizontal restraints. [M. Rippmann]

The structural principle of such vaulted rib-stiffened slab systems is based on shallow arching action to initiate compressive stresses rather than exclusively on flexural normal stresses, leading to lightweight and stiff structures. Resulting horizontal thrusts can be taken either by ties or horizontal restraints at the supports. The ribs allow a floor plate to be supported on the topside by transmitting the loads to the vault, as well as stiffening the structure, the latter being important for resisting asymmetric loading. The structural geometry of such funicular floors results in very low stresses allowing for the use of alternative materials with almost no tensile capacity but with low embodied carbon. The 3.4 m^2 IFCS prototype required 275 L of concrete, which represents only 32.5% of the volume of its bounding box.

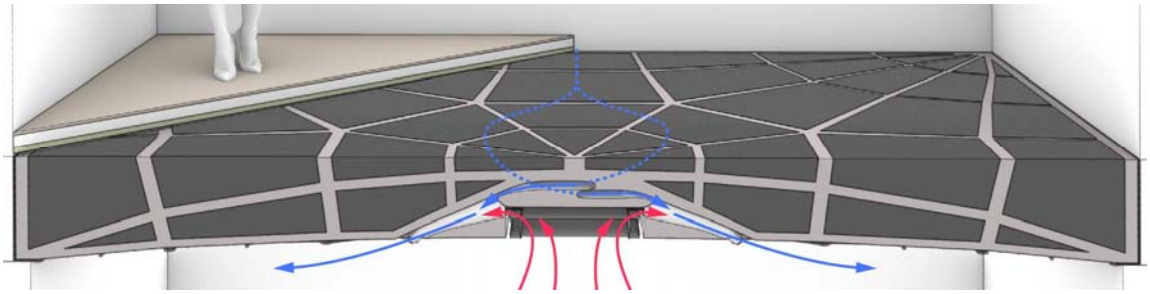


Figure 4: The active beam model uses the primary supply air (dotted blue lines) to induce room air (red lines) onto the hydronic coil and deliver heating or cooling (blue lines) to the associated zone. [M. Rippmann]

4.2. Reducing operational energy

Compliance with climate change mitigation scenarios will require the adoption of decarbonised energy technologies on a large scale [12]. This adjustment will involve improvements to embodied energy for the construction phase and operational energy used to run buildings. Oversizing of HVAC systems is a

well-documented problem for the construction industry [13]. Applying an integrated approach to building design has been identified as a method to reduce equipment oversizing.

The building systems for the funicular floor are focused on the design of a custom ventilation ducting system and the housing of an active beam (Fig. 4). The active beam consists of a hydronic coil (heat exchanger) that is connected to a two-pipe water distribution system. Heating or cooling can be supplied to the conditioned room via a changeover valve. This performance is achieved by mixing the primary supply air and the induced air from the room within the active beam. Computational fluid dynamics modelling was used to evaluate the ventilation performance (Fig. 5).

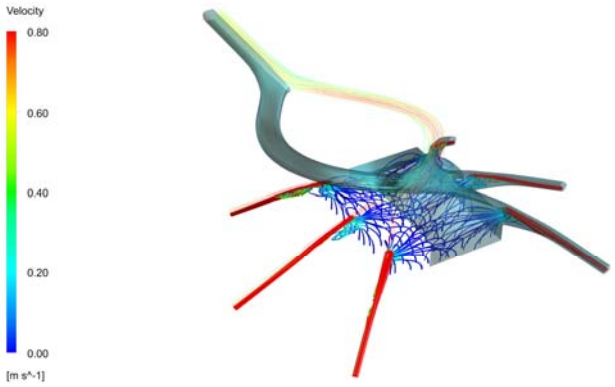


Figure 5: CFD analysis of the concept for the 3D-printed ventilation duct. This model provides an estimate of the induction ratio of the zone airflow. [G. Lydon]

A significant benefit of the highly integrated fabrication approach is a reduction of the building space that is typically required for HVAC equipment. For commercial buildings in densely populated cities, previous research has shown that this space saving can increase the usable floor area of the building [14]. In addition, the thermal storage properties of the exposed concrete volume can be utilised to regulate the internal environment passively [15]. This effect is termed thermal mass, and it is achieved in combination with buoyancy-driven natural ventilation when there is a temperature difference between the internal air and the concrete mass. The resulting time lag in internal air temperature can reduce the usage of operational energy at peak times. As the external 20-30 mm layer of concrete volume is the crucial one, the thinness of the structure should not greatly influence the passive performance [16].

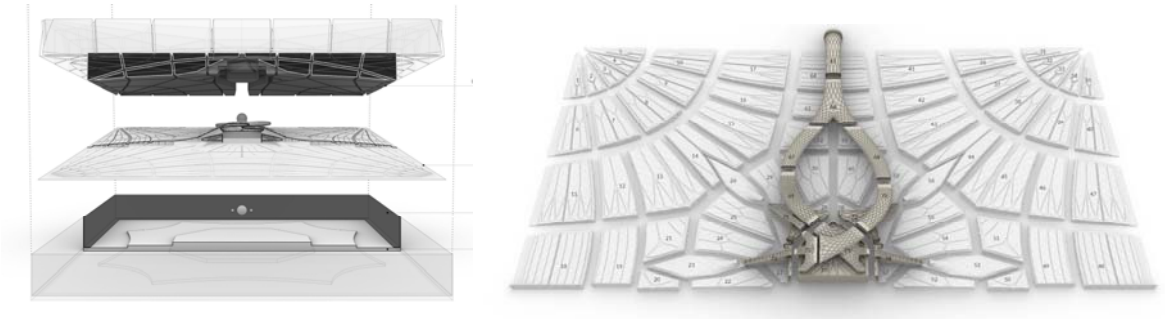


Figure 6, left: The formwork system for the IFCS, including the flat panel side supports, the FDM formwork and the hot-wire cut EPS blocks. Right: the FDM formwork discretised in 76 unique parts. [G. Chousou]

5. Fabrication

The total surface area of the articulated IFCS soffit and inner structures is 21.03 m^2, two and a half times larger than the surface of a conventional solid slab. This increase in surface area and the complex geometric features resulting from the structural and functional optimization processes, significantly

increase the challenge to create the necessary formwork. To define the precise spatial distribution of the concrete, three different fabrication systems were used for the manufacturing of the formwork. Standard panels were used to define the flat sides of the prototype, while digital fabrication was employed for the more intricate geometries: FDM for the soffit and internal ducts, and CNC hot-wire cutting for the geometry of the upstand ribs. Each method was used taking into account its particular advantages and geometric limitations (Fig. 6).

5.1. CNC Hot Wire Cutting

CNC hot-wire cutting of expanded polystyrene (EPS) foam blocks was used for defining the upstand ribs and the internal surfaces of the concrete shells. This technology was used for its efficiency, as it is suitable for relatively simple prismatic objects, with few faces and with no closed cavities and undercuts. Only ruled surfaces are possible, therefore some of the double-curvature surfaces, such as the shells, had to be approximated, but deviations were minimal. The 84 individual voids were fabricated using 485 dm^3 of EPS, weighing around 10 Kg on a custom four-axis turntable CNC wire cutter. Occupying 65% of the volume of the slab, the EPS blocks are a stay-in-place formwork which takes the role of thermal insulation.

5.2. 3D-Printed Disposable Formwork

The doubly-curved soffit of the slab, featuring ornamental ribs reflecting the funicular rib pattern, was based on a disposable FDM formwork system (Fig. 7). The challenge identified in the literature regarding FDM formwork is the hydrostatic pressure exerted by concrete during casting, which can damage the fragile plastic formwork. A linear function of the height of the cast, the hydrostatic pressure is small for slabs, compared to walls and columns. Previously, solutions to use counter-pressure materials and use accelerated concrete mixes have been proposed, however these methods increase significantly the complexity of the fabrication process [17].

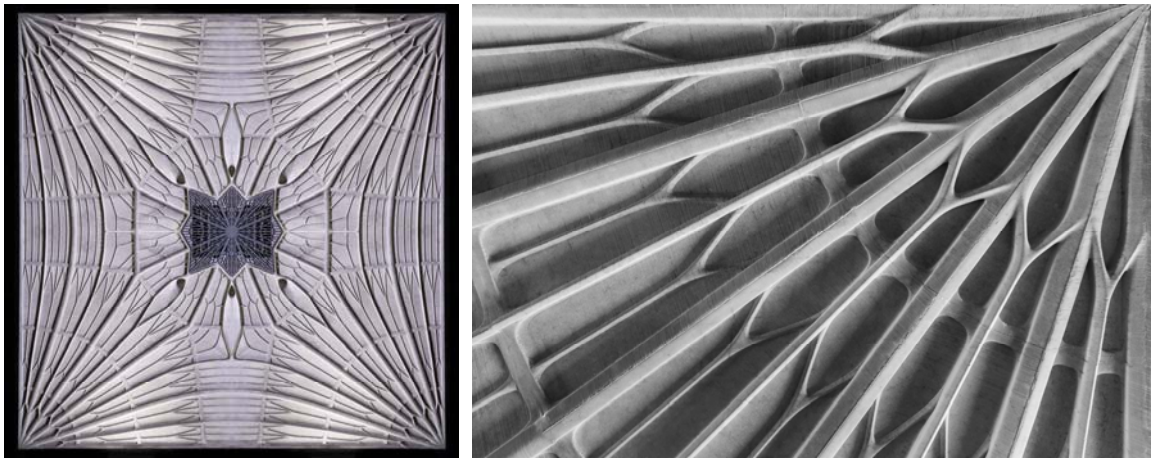


Figure 7, left: Overall view of the soffit of the IFCS. Right: detail of the expressive, articulated soffit. [A. Jipa]

In order to address the challenge of the hydrostatic pressure, the formwork for the IFCS prototype was produced by locally reinforcing the thin shell formwork with a grid of 3D-printed ribs, evenly spaced at 20 mm from each other. This sparse grid of ribs is significantly faster to print than a thick solid shell, and provides the necessary stiffness to the FDM formwork during casting.

5.3. 3D Printed stay-in place Formwork

The ducts for the active beam system, as well as the housing for the hydronic coil were fabricated using 3D-printed stay-in-place formwork. The complex network of ducts is designed to cross the upstand

concrete ribs in strategic locations and distribute the single air inlet through six smaller outlets into the internal space. The resulting geometry has ducts with non-circular sections varying between 10 and 80 mm, smoothly tapered according to the CFD simulation.

The ducting system also features a grid of stiffening ribs on its external surface which is in contact with the concrete. On the one hand, this grid stiffens the pipes to withstand the hydrostatic pressure, and on the other hand it increases the bonding area with the concrete, preventing delamination due to concrete shrinkage. Thus, after casting, the stay-in-place formwork provides an airtight shell, with no need for an additional duct.

All the 3D-printed formwork parts were produced based on commercial 3D printers with a build volume of 30 × 30 × 60 cm, using a bio-based polymer, polylactic acid (PLA), which is compostable and recyclable. The layer height used was 0.2 mm, with a 0.4 mm nozzle diameter and 0.4 mm shell thickness. Given the limited size of the printers, the formwork was discretized into 76 parts, 63 for the soffit and 13 for the ducts, which were assembled prior to casting through a chemical welding process.

6. Discussion and Outlook

IFCS are complex design solutions which require high levels of interdisciplinary cooperation and a significant investment during the design phase [18]. Digital fabrication tools naturally extend computational design processes and make integrated design-to-production pipelines possible. A software tool can seamlessly integrate structural optimization and building services specification, CFD and static analysis, and finally produce all the necessary digital fabrication data. Therefore, digital fabrication can deliver the necessary flexibility to provide multifunctional products to the built environment. Specifically for the IFCS, the design of the 3D-printed formwork system involved the discretization of the formwork, the generation of the auxiliary stiffening ribs, the integration of alignment features, referencing grooves and automatic labelling. Subsequently, each individual part was spatially oriented in order to minimize the amount of auxiliary support structures needed to optimise FDM fabrication times.

Fabrication times are the main drawback of FDM in comparison to other 3D printing technologies, and in particular binder jetting which has been used previously for producing formwork. However, while binder-jet 3D-printed formwork can weigh more than 100 Kg/m^2 of slab [8], FDM only needs a 0.8 mm thick shell and weighs only 3.72 Kg/m^2 of slab. Thus, only 14.6 Kg of plastic were used for the formwork for the entire IFCS prototype. This is a good solution for bespoke, single-use disposable formwork systems, because waste material is reduced to a minimum. The PLA used for the IFCS is also recyclable, and therefore it could be a suitable replacement for the less sustainable EPS foam blocks used as formwork for the upstand ribs. The drawback of this extreme material reduction is the fragile nature of the resulting formwork panels, which are well-suited for prefabrication in a controlled environment, but would need to be stiffened further in order to avoid risks related to on-site fabrication.

7. Conclusion

This research showed how a holistic approach to energy efficiency, addressing all phases of the life-cycle of a building can have significant synergies and a bigger impact than an uncoordinated approach. Smart HVAC systems, integrated in material-efficient structural slabs present multi-disciplinary design challenges and result in complex, difficult to fabricate shapes. While slow, the geometric freedom of 3D printing can overcome this challenge and if used efficiently as a formwork system, it is a sustainable fabrication approach which generates minimal amounts of waste.

Acknowledgements

The authors would like to thank the industry partner of the project, BASF Schweiz AG for supporting the concrete development and casting process, Holcim (Schweiz) AG for providing materials, Francesco Ranaudo, the ETH Foundation and the NCCR Digital Fabrication.

References

[1] M. K. Dixit, "Life cycle embodied energy analysis of residential buildings", *Renewable and Sustainable Energy Reviews*, vol 79, pp. 390–413, 2017.

[2] C. De Wolf, M. Ramage, and J. Ochsendorf, "Low Carbon Vaulted Masonry Structure", *Journal of the International Association for Shell and Spatial Structures,* vol 57 (4), pp. 275, 2016.

[3] Concrerte most used material

[4] C. Georgopoulos, A. Minson. "Sustainable concrete solutions", John Wiley & Sons, 2014.

[5] M. Rippmann, A. Liew, T. Van Mele and P. Block, "Design, fabrication and testing of discrete 3D sand-printed floor prototypes", *Material Today Communications*, vol. 15, pp. 254-259, 2018.

[6] A. Jipa, M. Bernhard, M. Meibodi and B. Dillenburger, "3D-Printed Stay-in-Place Formwork for Topologically Optimized Concrete Slabs.", *TxA Emerging Design + Technology*, pp. 96–107, San Antonio, Texas, 2016.

[7] A. Søndergaard and P. Dombernowsky, "Unikabeton prototype", *Fabricate: Making Digital Architecture*, pp. 56–61, 2011.

[8] A. Jipa, M. Meibodi, R. Giesecke, D. Shammas, M. Leschok, M. Bernhard and B. Dillenburger, "3D-Printed Formwork for Prefabricated Concrete Slabs", *3D Construction Printing*, Melbourne, Australia, 2018.

[9] A. Jipa, M. Bernhard, B. Dillenburger, "Submillimeter Formwork", *Emerging Design + Technology,* pp. 9, 2017.

[10] A. Liew, L. Gardner, and P. Block, "Moment-curvature-thrust relationships for beam-columns.", *Structures*, vol. 11, pp. 146-154, Elsevier, 2017.

[11] D. L. López, D. Veenendaal, M. Akbarzadeh and P. Block, "Prototype of an ultra-thin, concrete vaulted floor system.", *Journal of the International Association for Shell and Spatial Structures*, vol. 15, pp. 1-8, 2014.

[12] B. V. Mathiesen, H. Lund, K. Karlsson, "100% Renewable energy systems, climate mitigation and economic growth", *Applied Energy*, vol. 88 [2], pp.488-501, 2011

[13] S. Sorrell, "Making the link", *Energy Policy*, vol. 31 [9], pp. 865-878, 2003.

[14] A. Schlueter, A. Rysanek and F. Meggers. "3for2: Realizing Spatial, Material, and Energy Savings through Integrated Design." *CTBUH Journal*, vol. 2, pp.40-45, 2016.

[15] D. Yang, Y. Guo, "Fluctuation of natural ventilation induced by nonlinear coupling between buoyancy and thermal mass", *International Journal of Heat and Mass Transfer*, vol. 96, pp. 218-230, 2016.

[16] G. P. Lydon, J. Hofer, Z. Nagy and A. Schlueter, "Thermal analysis of a multifunctional floor element", *Proceedings of the Third IBSPA Building Simulation and Optimisation Conference*, Newcastle, England, 2016

[17] F. Gramazio, M. Kohler, R. J. Flatt, M. Hutter, E. Lloret, T. Wangler, L. Reiter, M. Wermelinger, T. Ulrich, F. Scotto, "Method of vertical forming of a concrete wall structure and apparatus therefor.", *EP17209534.1*, 2018.

[18] G.P. Lydon, J. Hofer, B. Svetozarevic, Z. Nagy, A. Schlueter, "Coupling energy systems with lightweight structures for a net plus energy building", *Applied Energy*, vol. 189, pp. 310-326, 2017.

Proceedings of the IASS Annual Symposium 2019 - Structural Membranes 2019
Form and Force
7-10 October 2019, Barcelona, Spain
C. Lázaro, K.-U. Bletzinger, E. Oñate (eds.)

An exploration of 3d printing design space inspired by masonry

Paul CARNEAU[a], Romain MESNIL[b], Nicolas ROUSSEL[a], Olivier BAVEREL[a,c,d]

[a] Navier, UMR 8205, École des Ponts, IFSTTAR, CNRS, UPE, Champs-sur-Marne, France
paul.carneau@enpc.fr

[b] École des Ponts ParisTech, Champs-sur-Marne, France
[c] ENSA Paris-Malaquais, Laboratoire Gometrie Structure Architecture, France
[d] ENSA Grenoble, France

Abstract

This paper describes an approach of a process-aware exploration of the design space of building components constructed by extrusion of cementitious material (or concrete 3d printing). In an attempt to broaden the geometries that are being printed today, and to build cantilevers, vaults and domes without using temporary support, we look back at construction techniques used in masonry structures, and analyse the stability of the fabrication process at the scale of the brick, the layer and the final structure. Those strategies are applied to 3d printing with regards to the material properties and the technological aspects of the process. Three examples are actually printed to validate the approach, namely a Nubian vault, a dome and an arch, all without temporary support. Finally a framework for generation of printable geometries and corresponding toolpaths is proposed.

Keywords: 3d printing, cementitious material, funicular shell, masonry, digital fabrication, robotics, form finding

1 Introduction

1.1 Context

Additive fabrication of cementitious material - or mortar 3d printing - has known a rapid expansion in the last decade which has led to multiple innovations in term of material rheology, printing technology (robotics and extrusion head) and their applications. Research has focused on finding the best mortar for printing, on the formation of "cold joints" at the interface between layers or on the potential reinforcement of the printed structures. A field that is yet to explore is the design space of printable geometries.
3d printed geometries are limited by the resistance of the fresh material and the printing process. Non standard geometries have been achieved by use of external supports [5]. However, it is not satisfying as a sustainable solution due to costs and environmental impact of such temporary structures. The challenge is hence to solve the problem of printing free of temporary support and yet without loosing architectural freedom or structural efficiency.
This paper proposes a geometry exploration of printable structure that does not require external support. In a first part we look at 3d printing processes that have been developed so far based

Copyright © 2019 by P.Carneau, R. Mesnil, N. Roussel and O. Baverel
Published by the International Association for Shell and Spatial Structures (IASS) with permission.

on two asymptotic strategies in terms of material and technology. Then in a second part, we present three examples of ancient masonry brickworks and their implementation using 3d printing process. Finally we propose a framework for generation of geometries and corresponding toolpaths.

1.2 Previous works

Based on what has been done so far by the different actors in the field of 3d printing - academics or industrials actors - the strategies in place can be bounded by two asymptotic strategies in terms of material properties described by Roussel in [7], robotic complexity and control of the process.

- a **pure extrusion process** which is the most common strategy in use up to this day. It consists in printing with a 3-axis robot (namely a printing head mounted on a gantry bridge) moving in Cartesian coordinates, extruding a material that does not go through a phase change and which has an initial yield stress relatively high (500 Pa to 1kPa). The shape of the layer is given entirely by the shape of the nozzle. The extrusion occurs in successive horizontal planes (some talks of 2.5D printing) and the only way for this technology to create global cantilever is by creating corbels with the layers (local cantilevers).

- a **sheared material deposition** is the opposite strategy using a 6-axis robot to print layers that are not inevitably horizontal. This strategy is introduced in [4]. The mortar used goes through a phase change in the extrusion head by addition of additives giving to the material a low initial yield stress (100 Pa) but a high structuration rate. The layer is shaped by squeezing it between the nozzle and the previous layer. Different layer's heights can be obtained just by changing the printing parameters.

As Pegna mentioned in [6], 3d printing can be seen as a new approach to masonry. 3d printing and masonry are additive manufacturing processes sharing the disadvantage of using a material with a poor tensile strength. Historically, masonry builders have developed strategies to overcome this issue and build cantilevered structures without the use of temporary supports. From these strategies, many of which are detailed in [2] by Auguste Choisy, we can cite the creation of corbels, the inclination of layers of a dome, the construction of barrel vault by successive inclined arches or the development of squinches by the Persians.

1.3 Method statement

Due to the poor mechanical properties of the fresh mortar, 3d printing main difficulty lies in the stability of the structure during the fabrication. By analogy to masonry, this issue can be tackled at different scales. The scale of the section when the material is extruded, the scale of the layer and the scale of the overall structure in its final configuration. In this paper, we explore similarities between masonry and 3d printing through three examples. Each representing a topology and a construction strategy developed by masonry builders. We analyse the printing parameters at play for the realisation of such structures, in terms of material properties and fabrication technology. The aim is to push the boundaries of the design space of printable geometries and propose a framework for the design of such structures and the generation of corresponding toolpaths.

2 Masonry and 3d printing

2.1 Planar cantilever

2.1.1 The geometry

The first example is an opening in a wall, so a cantilever in two dimensions. The crossing takes the shape of a pointed arch. The wall is made of a double layer for two purposes. First, this is a way to have a closed toolpath and avoid having to stop and start the printing set up. Secondly, it allows for the overall thickness of the wall to evolve with the height. It is wider at the base than at the top, providing more stability to the wall. Fig.1 illustrates the geometry of this two dimensional crossing.

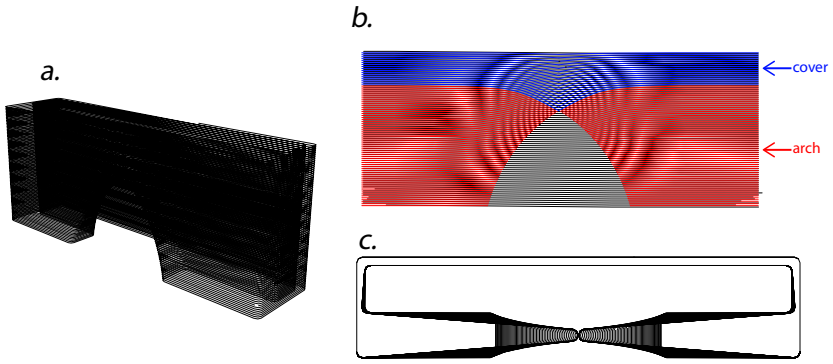


Figure 1: Toolpath of the 2D crossing. a.*3D view*, b. *front view* with distinction between upper and lower parts, c. *top view*

The main difficulty in this example is to ensure the local stability of a layer around the opening, by avoiding the material to flow after the extrusion. The strategy chosen to tackle this problem is to incline the layers in order to avoid any local cantilever in the layer which would create bending.
By doing so, the contact surface is maximised between two consecutive layers, and the material only sees pure shear stress.
This is achieved by slicing the geometry not horizontally as it is usually the case, but by offsetting the layers on the object surface with a constant distance, until the two half-arches connect. This can be done using Adiels *et al.* slicing algorithm described in [1] and initially intended for masonry structures. The result is a set of layers that bend downwards near the opening (see Fig.1.b). In the upper part (the *cover*), the distance between layers increases locally to compensate gradually for the non-planarity of the layers until reaching a horizontal level.

2.1.2 The printing process

In practice, the printing head connected to the robot rotates so that the extrusion nozzle remains tangent to the surface of the object at all times. This makes full use of the 6-axis robot and its capacity to reach any target in space with different orientations. The strategy described above ensure the stability of the material locally, just after the extrusion.
The overall structural system of each half of the wall that ensure global stability until the arch is complete, is inspired by a construction technique used to build Gothic vault without formwork (see Fig.2.*left*). The cantilever structure itself remains in compression thanks to the

stone-weighted rope device, working in tension. In our case, the tensile stresses are located in the walls. For such a structure, reinforced concrete could help achieve much higher cantilevers.

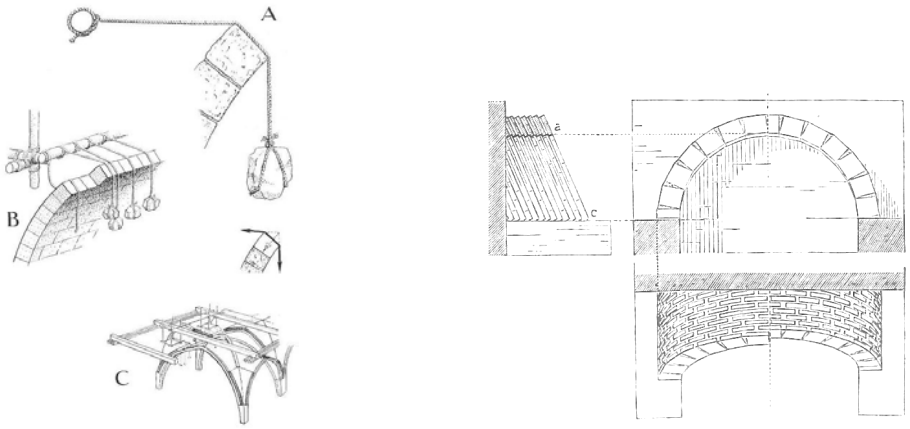


Figure 2: *left:* The stone-weighted rope device for erecting Gothic vaults (John Fitchen, *The Construction of Gothic Cathedrals, 1961, fig. 69, p.182*), *right:* Nubian vault construction by Auguste Choisy from "L'Art de btir chez les Byzantins"

In practice the printing process can be divided in two part, one for the bottom and another for the upper part of the object.

- in the lower part, all parameters - printing speed and extrusion flow rate - are kept constant.
- in the upper part, the flow rate q_c is kept constant. In order to compensate for the thickness increase in the layer and keep the same width d, the speed c_r is decreased locally with respect to mass conservation relation 1.

$$Q_c = c_r \cdot h \cdot d \tag{1}$$

with Q_c the flow of concrete, c_r the speed of the robot, h and d the height and width of the layer.



Figure 3: Wall opening

2.1.3 Observations and limitations

In this example, we managed to print a two dimensional arch (see Fig.3) with a global inclination of 37° and a maximum local inclination up to 60° in the upper part of the arch. This demonstrates the local stability of a layer even with high inclination can be achieved given that the material's initial yield stress is sufficient. Consequently, a global cantilever can be obtained by 3d printed.

2.2 Translated vault

The second example is a barrel vault, built with a technique developed by the Nubians in Egypt, examples of which are still standing after over 3300 years. This technique allows to built barrel vault without any temporary support. The construction can then be assimilated to a horizontal extrusion of an inclined arch, where each layer is supported by the previous ones (see Fig.2.*right*).

2.2.1 Construction sequence

Throughout construction of a Nubian vault, each layer experiences three phases in terms of stresses. By considering one layer in particular, the three phases are as follows:

- The first phase corresponds to the extrusion of the material. At this stage, it has to withstand its own self-weight to avoid local collapse of the layer. Since the layer is inclined, the stress in the material is higher than when extruded horizontally. The material's initial yield stress must be adapted to the layer inclination angle θ.
- once the layer is fully in place, it starts behaving as an arch in compression. In the same time, it has to withstand the loads brought by successive new layers. In 3d printing, that means, the structuration rate of the material A_{thix} has to be sufficient so that the stress accumulated by the addition of layers stays below the yield stress τ_c at all times. The higher the angle with the vertical θ is, the higher is the influence of the new layers.
- the third phase appear when the addition of new layers has no influence anymore on the stress state of our considered layer. Since the structure evolves horizontally, the layers are not continuously loaded as in vertical extrusion. This characteristic of Nubian vault fabrication make them not limited in length.

To summarise, if $\theta = 0$ (layers are vertical), the initial stress in the material is maximum but the layer reaches its final state quickly. With a high inclination angle θ, the initial stress is lower but the permanent regime is reached later.

2.2.2 Toolpath generation

The geometry of the vault is generated using form-finding method leading to a funicular shape under self-weight. The vault once finished, is fully in compression. This is permitted by the absolute precision of a robot in space. Indeed, for a masonry vault built manually, the shape has to be approximated by arcs of circle, so that a mason can follow the geometry using simple tools (wire, level, etc.). This shows that architectural freedom brought by digital fabrication can support a design process where shape follows forces.

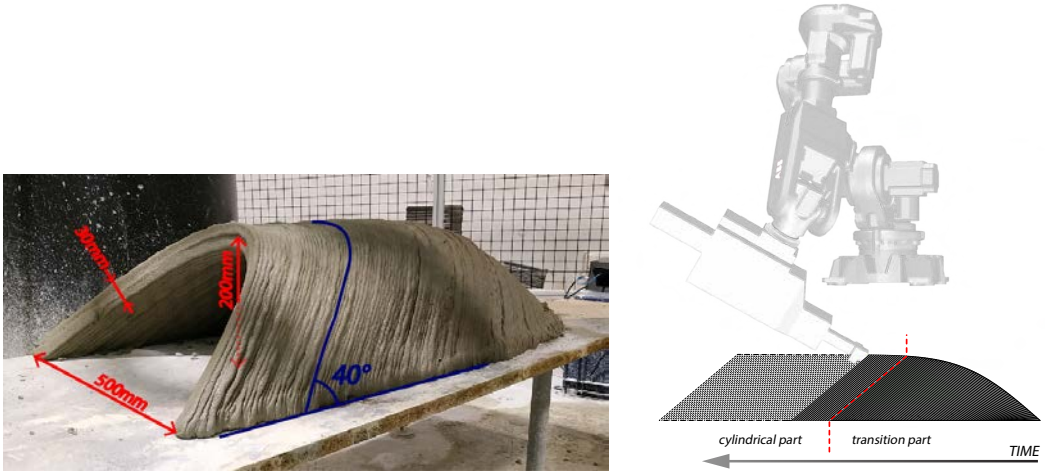


Figure 4: *left:* 3d printed Nubian vault and its dimensions - *height*, *width*, and *thickness*, *right:* slicing of the vault

In masonry, the Nubian vault usually takes support on a vertical gable wall (see Fig.2.*right*). This lead to discontinuous first layers and it has to be avoided for 3d printing process due technical difficulty to stop and restart the set-up. The 3d printing vault then has to start from a fully horizontal layer before shifting to inclined arches. Fig.4 shows the dimensions of the printed vault.
In this example, the layers are all planar. They come from the intersection of the vault surface with a set of planes. In the transition part, the planes inclination gradually increase from horizontal to 40°. This inclination is then kept constant all the way through the cylindrical part (see Fig.4.*right*).
The frames describing the orientation of the robot are generated from those layer curves. For each point on the curve, we define the vector tangent to the curve and the vector normal to the vault surface. The extrusion nozzle orientation is given by the cross product of those two vectors (illustrated in Fig.5). This way, the contact surface between two layers is maximised and always the same. In practice, by adding the robot accessibility constraints, the maximum inclination of the frame with the horizontal is set to 60° (this angle is reached at the apex of the vault).
As a result, the path of the robot is planar, but its orientation gives torsion to the layers. The final step in the generation of the toolpath is the setting of the printing parameters. For this vault, the speed of the robot in the cylindrical part is set at 200mm/s, keeping a constant inter-layer time of 10s.

2.2.3 Results

This example validate the possibility to 3d print barrel vaults without temporary support in a similar way it is done in masonry. It shows that the material can be printed with an inclination up to 60° without collapsing, pointing out in the same time the pertinence of a 6-axis robot to broaden the range of printable geometries.

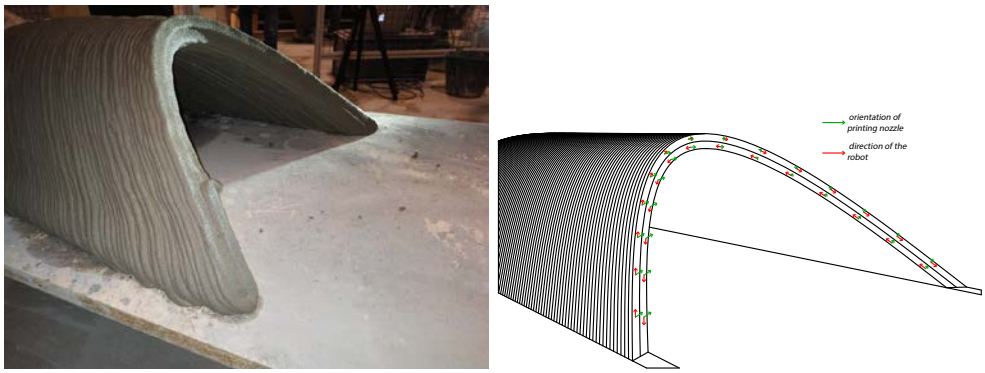


Figure 5: Printing path and local orientation of the extrusion nozzle

2.3 Dome

The last example is a dome with a square base. Circular squinches are generating at each corner and spandrels link them together to reach a horizontal circular perimeter (see Fig.6). From there up, the geometry consists in a simple hemispherical dome, described by Cowan as a *true dome* in [3]. The slope of the squinches in the corners have an inclination of 45°.

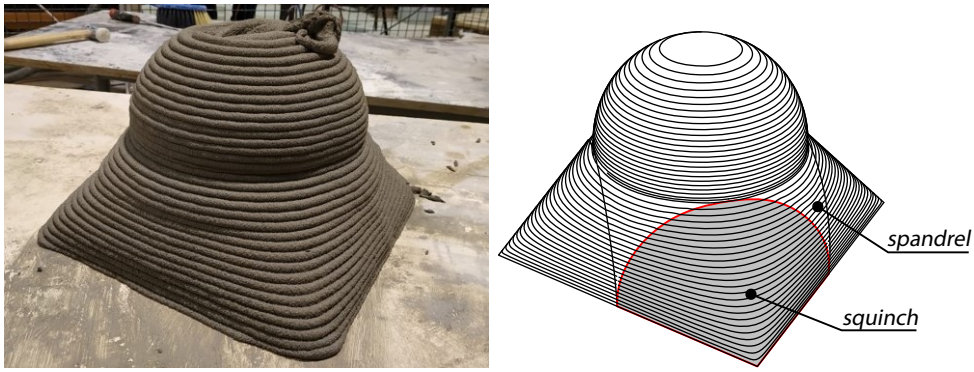


Figure 6: Dome on squinches

The goal of this example is to show the potential and imitations of printing with a 3-axis robot, moving in Cartesian coordinates and hence unable to modify the orientation of the nozzle. The layers are all horizontal, and the height between them is constant.
In addition to that, all the parameters remain unchanged during the printing. Consequently, the cantilever is made by corbelling layers on top of each other and creating local cantilevers. In this configuration, the material requires a high enough initial yield stress. Once a layer is complete, the stability is ensured structurally by the apparition of compressive rings.
The slicing strategy used for the generation of the geometry and the toolpath is simple and fast compare to the ones described in previous parts. However, it comes with limitations:

- the local cantilevers of the layers induce bending in the material. Since this cantilever increases with the inclination of the surface of the dome (see Fig.7.*left*), the stress in the material gets higher as the print goes. This leads to a local collapse of the layers closed to the top of the dome.

- in addition to the increasing stress in the material, the geometry of the structure makes the layer's length decreases the more it goes up (Fig.7.*right*). Since the robot speed is constant, the inter-layer time decreases proportionnally to the length. Thus the last layers have less time to build thixotropy and increase their yield stress accentuating the risk of failure.

To summarise, this strategy advantages lay in the simplicity to generate the toolpath for the robot and the easy movement of the robot reducing the risks of clashes and simplifying the calibration process. On the other hand, the slicing eventually leads to an increase of the stresses in the material, accentuated by an increase of the loading rate.

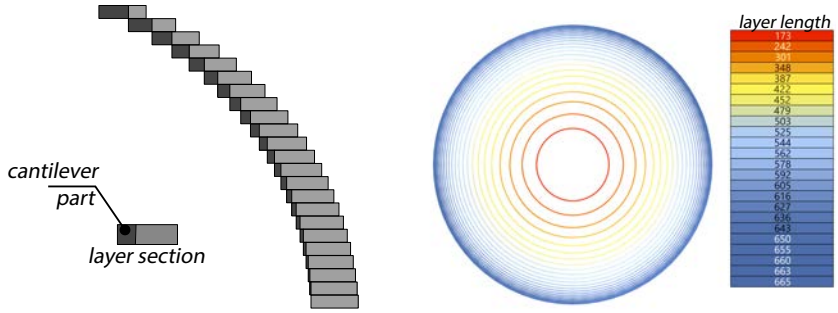


Figure 7: *left:* effect of corbelling on a spherical dome with gradual increase of the cantilever, *right:* decrease of the layer's length (in mm)

3 Results

The examples presented in this paper help to show the similarities between masonry construction techniques and mortar 3d printing process. Using different structural typologies, namely a two dimensional opening, a barrel vault and a dome, we can draw general conclusions in regards to printable geometries and toolpath generation. The challenges being to ensure stability of the printed object during fabrication and mechanical efficiency of the final structure accounting for the material used.
Those examples show that 3d printing process faces challenges of stability at different scale. The local scale of the component, where the material must withstand its on weight as soon as it is extruded. The strategy chosen to perform the global cantilever, is translated at the layer's scale to either a local cantilever inducing bending moment in the material, or an inclined layer, where contact is maximised between layers and the stress is mainly shear. At the scale of the layer, a structural subsystem is set in place - arches for the barrel vault, or compression rings for the dome - that ensure its stability by making the material work mainly in compression. Finally, both for masonry and 3d printing, the targeted final geometry must be as closed as possible to the funicular of the structure under its own weight. The structure is then fully in compression, and the lack of reinforcement can be justified.
The aim of the authors is to generalised this process to free-formed shapes in order to extend furthermore the design space of printable geometries.

4 Conclusion

This paper presents an exploration of printable geometries, aiming at building structures without the use of temporary supports. It shows the possibility to print cantilever structures even with a material with poor tensile strength and in this way, validates the approach of finding inspiration in masonry techniques. The problem of stability of the structure is tackled by dividing it in different scales, the scale of the material just after the extrusion, the scale of the layer and the scale of the final structure.
Eventually, expending the boundaries of printable geometries can address the need for architectural freedom while providing answers to environmental issues such as wastes generated by complex temporary structures and a solution to reduce fabrication costs and delays.

References

[1] E. Adiels, M. Ander and C. Williams, "Brick patterns on shells using geodesic coordinates" in *Interfaces: architecture.engineering.science: Proceedings of the IASS Annual Symposium 2017.* Hamburg, Germany, September 25-28, 2017.

[2] A. Choisy, "L'art de batir chez les Byzantins", 1883.

[3] H. J. Cowan, "A history of masonry and concrete domes in building construction" in *Building and Environment.* Volume 12, January 1977. pp. 1-24.

[4] C. Gosselin, R. Duballet, Ph. Roux, N. Gaudilliere, J. Dirrenberger, and Ph. Morel, "Large-scale 3d printing of ultra-high performance concrete a new processing route for architects and builders" in *Materials & Design.* Volume 100, June 2016, pp 102-109.

[5] S. Lim, R. Buswell, P. Valentine, D. Piker, S. Austin, and X. De Kestelier, "Modelling curved-layered printing paths for fabricating large-scale construction components" in *Additive Manufacturing.* Volume 12, Part B, October 2016, pp 216-230.

[6] J. Pegna, "Exploratory investigation of solid freeform construction" in *Automation in Construction.* Volume 5, 1997, pp 427-437.

[7] N. Roussel, "Rheological requirements for printable concretes" in *Cement and Concrete Research.* May 2018.

Proceedings of the IASS Annual Symposium 2019 – Structural Membranes 2019
Form and Force
7 – 10 October 2019, Barcelona, Spain
C. Lázaro, K.-U. Bletzinger, E. Oñate (eds.)

Design and Manufacturing of The First Freeform 3D-Printed House

Platt BOYD*, David GOODLOE, Melody REES, Bruce HILBERT

*Branch Technology, Inc.
1530 Riverside Drive, Suite B; Chattanooga, TN 37406
david.goodloe@branch.technology

Abstract

Branch Technology has developed a novel additive manufacturing process for construction applications called Cellular Fabrication (C-FAB™). This technology enables a "freeform" extrusion process wherein material solidifies in open space to create a lattice structure at large scale and geometric complexity. To date, Branch Technology has completed several lattice shell structures using C-FAB™ that are the largest Freeform 3D printed structures in the world. This paper documents the next generation research and development to unite the novel technology with existing construction methods, ultimately creating a high-performance composite building enclosure system. C-FAB™ construction holds the potential to transform the nature of grid-shell and spatial structure solutions currently available in the AEC industry. This paper presents findings on a case study structure enclosing more than 280m². Named *Curve Appeal*, the structure represents a potential future of construction, combining additive manufacturing, industrial robotics, conventional building materials, and prefabricated modular construction methodologies. Organized in 3 sections, this paper will begin with an overview of the composite product for the construction industry. Because composites are inherently complex and include many variables, it is key to quantify structural boundary conditions, load cases and long-term assumptions. Finally, this paper will discuss a new digital discretization process for complex geometries. With the convergence of material science, prefabrication, AM, and direct digital fabrication, full composite structural shell assemblies can be created and tailored to any design, geometric, or engineering parameters.

Keywords: additive manufacturing, 3D-printing, shell structures, optimization, advanced manufacturing, robotics, autonomy, composites, structured-grid generation, C-FAB™

1. Introduction

Branch Technology is an architectural fabricator specializing in a new method of large-scale 3D-Printing called Cellular Fabrication (C-FAB™). To date, Branch has completed the world's largest 3D-printed structures with this capability, including a permanent 14-meter by 7-meter tall bandshell pavilion in Nashville, TN that debuted at the Annual IASS Symposium in Boston in 2018. This 3D-printed matrix product exists primarily to introduce Branch Technology's patented technology. The long-term goal for the technology, however, is to use C-FAB™ in combination with conventional construction materials to create custom prefabricated composite panels. Benefits of this system include cost-effective geometric design freedom as well as labor efficiencies, resource stewardship, high performance enclosure systems, and ease of construction. The composite assembly allows architects and builders to achieve high-performance enclosure systems with highly complex shapes. *Curve Appeal* as a project is used to accelerate, develop and scale the prefabricated composite panels into a market-ready product for commercial sales. Many compelling solutions came out of this process that are also extremely relevant to the future of shell structure construction.

Copyright © 2019 by Branch Technology; Platt Boyd, David Goodloe, Melody Rees, Bruce Hilbert
Published by the International Association for Shell and Spatial Structures (IASS) with permission.

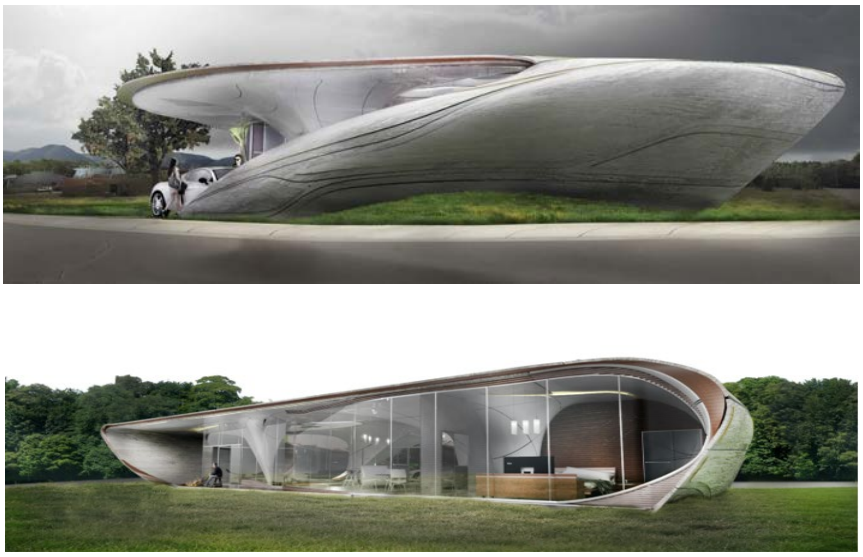


Figure 1 - Curve Appeal

2.0. Product – Composite Overview

The first challenge of the project was to define and develop the basic composite— the prefabricated wall assembly for commercial use. Materials include the 3D printed matrix and foam insulation while processes include large-scale 3D printing, large-format foam filling and containment, material formulation, and 7-axis robotic milling. Lean manufacturing principles were implemented through rigorous operating procedures to manufacture and maneuver parts within a shop environment.

2.1. Product – Materials Used

Branch Technology has the ability to 3D-print with a number of high-strength thermoplastic polymers that are robust, rigid, weathering-resistant, and recyclable. *Curve Appeal* is printed with carbon-fiber reinforced ABS. A small 1kg test block of this material the size of a CMU block can support over 13,350 N of compressive force. Itself a composite fiber-reinforced polymer, this ABS formulation is so structurally robust that it was the only material used in Branch's permanent bandshell pavilion in Nashville - a structure that is engineered to code standards and can support 30cm of snow accumulation, 7cm of ice buildup, a 145 km/h wind-load, and a 3X safety factor. *Curve Appeal*'s matrix structure, while strong on its own, gains a significant structural integrity when the composite panels are finished with insulating spray foam, glass-fiber reinforced concrete (GFRC),

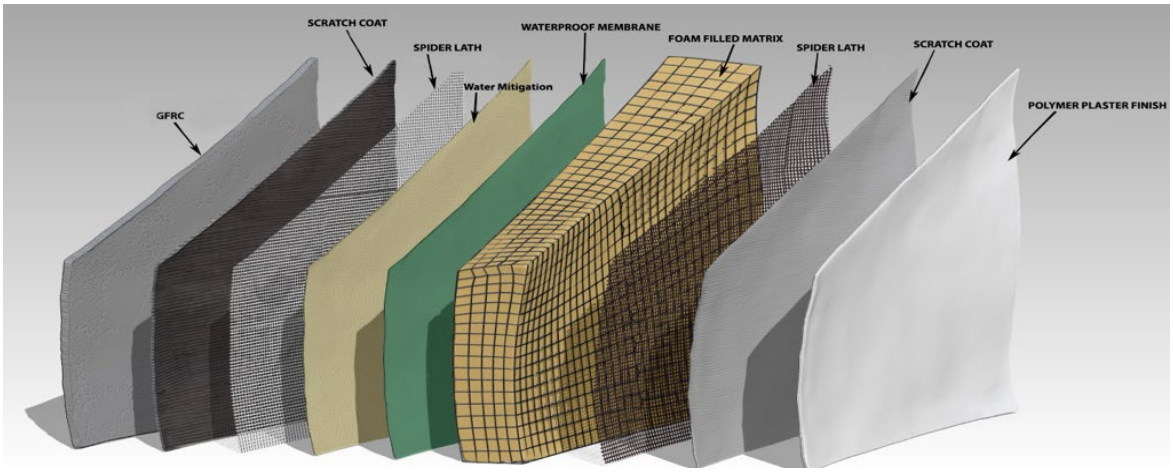


Figure 2 - A typical exploded section of the composite with field applied architectural finishes.

and other incremental layers. With these added materials, the same lightweight block that supported over 13,350 N can now support over 44,000 N.

All processes were developed first at a small scale and with the help of industry experts. Foaming material science and application methods were tested in laboratories where mixture ratios could be adjusted in real-time. In addition, multiple methods of application were investigated, including spraying, pouring and filling, to balance chemical reactions of the material and scalability of the process. Variables including flow rate, expansion, containment, speed, and temperature were taken into consideration for planning control processes and eventual commercial application. Because Branch embraces the responsibility of creating a clean and safe work-cell environment with state-of-the-art mechanical systems and modified industry standard equipment, the team selected a 0.91kg low-VOC pourable foam for process implementation. It should be noted that this product may be the first in the industry to utilize expandable foam in such a custom, monolithic format. Predecessors include SIP panels who use this material very effectively and in a large format, but at a fraction of the overall size and with minimal geometric complexity.

A milling process was also developed to control the product's final finish. All surfaces need to be smooth and regular. The outer surfaces must accept the architectural finishes and the connecting edges must submit to standardized tolerances, structural bonding and, most critically, thermal and water mitigation for environmental control. The largest printed part was 7m x 1.4m x 2m and contained both overcutting and undercutting. Shell construction is often an additive process -making 3D printing a suitable technology for such construction. The milling process is an additional process employing high levels of accuracy and repeatability to achieve a desirable surface finish.

2.2. Product – Composite Connectivity



Figure 3 - The multi-modal 3D printing process and

The issue of panel-to-panel connections was the next mystery to solve. How do colossal building components come together in the field in a way that is simple and fast? To resolve this issue, Branch reevaluated printing capabilities. While C-FAB^{TM} freeform printing was known and developed, Branch had never incorporated FDM (fused deposition modeling) into its printing process alongside Freeform elements. FDM was trialed on various parts and was discovered to have desirable strength-to-weight properties. The team tested the integration of both printing methods wherein FDM plates were used as reinforcing edges and C-FAB^{TM} as volume-filling structural elements. Flat reinforced edges could be connected to one another with construction fasteners such as decking screws. The tensile pull-out strength of these fasteners when tested to failure was excellent – many times the strength of wood-embedded fasteners. The development of these FDM plates yielded a highly controllable, multi-modal 3D-printing process entirely executed from one program and one machine system. The result was a novel and industrialized process for creating robust field connections using 3D-printing.

This connection typology allowed parts to be indexed for placement in the field while also acting as permanent connection means. However, after further structural analysis was conducted, additional connection typologies were required to resolve issues such as uplift and some tensile or compression

forces— especially at cantilevering roof joints, columns and structural girder parts. The team developed a series of four connection types of standard structural details and utilized hardware such as that produced by the manufacturer, Simpson Strong Tie. Other connection details included the use of off-the-shelf, bolted structural steel angles to attach printed parts to the concrete slab.

3.0. Material Characterization of the Composite

In addition to characterizing the composite product through its constituent materials, it was equally important to characterize it by quantifying structural boundary conditions and long-term performance assumptions based on existing material data. The following analysis includes descriptions of the components and some of the performance variables that were utilized in the engineering process.

3.1 Additional Performance Criteria

In addition to structural capacity, Branch has determined several other performance criteria where the composite product must perform well in order for it to serve as a high-performance building enclosure. These performance criteria include:

- Fire propagation
- Water mitigation
- Air infiltration
- Thermal breaks
- Thermal insulation value
- Water vapor resistance
- Weather and aging

Branch has begun working with a specialty facade consultant to engineer the product for code compliance in each of these critical performance areas. Product design is being supported by a United States National Science Foundation (NSF) Small Business Innovation Research (SBIR) Grant dedicated to engineering the composite product for code compliance. *Curve Appeal* will be the first demonstration of the composite product serving more than a structural role and will become a market-ready product.

3.2 Structural Engineering - Boundary Conditions

The process of structurally engineering *Curve Appeal* as a whole was dependent on a great collaboration between Branch Technology and structural engineering firm Skidmore, Owens, and Merrill (SOM). Branch Technology conducted small and large-scale sample testing of composite beams and panels that provided the appropriate boundary conditions for SOM's finite-element analysis (to be discussed below) and complete structural engineering.

One of the most valuable tests was ASTM C78 four-point bending (flexural) tests that measured load vs. deflection, shown below.



Figure 4 - ASTM C-78 test before and after beam failure.

Comparison testing was conducted to quantify the load-capacity difference in flexion between the bare matrix (truss) beam and a composite beam. Like it's enhanced compression load capacity, the composite beam's flexural load capacity also improved 2-3X compared to the bare matrix.

Once a greater understanding of the composite structure's behavior under sudden loading was understood, Branch also had to come to greater understanding of the composite structure's long-term behavior under sustained loading - a property known as creep. Creep testing involved the test set-up shown below, where a long spanning beam was supported on CMU blocks with a slow-action load (here, gravity) applied on the middle of the top face. The creep testing took place over the course of 9 months and, as is evidenced by the plots below, shows clear material stabilization over time, similar to concrete.



Figure 5 - Two composite specimen being tested for long-term creep effects.



Figure 6 - Graphical results of two composite specimen being tested for long-term creep effects.

Armed with enhanced knowledge of these boundary conditions, structural engineering was completed to account for any design vulnerabilities. With 3D-printing and direct digital fabrication, small tweaks to geometry are not hard to incorporate between design and fabrication. This benefit of direct digital manufacturing allowed for a much shorter production timeline because:

1. There was no need for iterations of shop drawings. Changes could be made directly in the 3D-model.
2. Sections of the structure that had previously been finalized could be released for printing even while finalization of more complex parts continued

Once parts were finalized, they proceeded into Branch Technology's proprietary digital production software stack that creates the internal geometry to drive the robot through its path for printing the panelized sections.

4.0. Digital Production

To date, there are limited ways to construct shell structures. Often the structure is broken down into small elements like brick, rebar or timber members which are tortured into shape on-site. The process is extremely labor and time intensive— also there is a disconnect in the translation from drawing to built form.

A critical part of the project was to create an improved direct digital fabrication software process. How can architectural design models be translated into machine path plans capable of manufacturing highly accurate building components? The answer was to develop algorithms that could subdivide continuous geometric space into discrete topological elements that could then be processed with a software package capable of outputting robotic motion control programing. The collective programming would thus enable Branch's 3D printers to create C-FAB™ elements in the built world.

4.1 Digital Production: Panelization

The project demanded a new method for initial processing of the architectural model into parts, termed panelization. Similar to an egg slicer, the volume is sliced vertically and horizontally. The architectural model is then output into 136 colossal sized parts, dimensionally complex in form and each unique. The process begins with a 3D model of a building created as a singular closed NURBS or mesh volume. Based on structural forces and robotic build envelope, a 3-dimensional grid is developed with which the continuous geometry can be spliced. Manufacturing tolerances print orientations and reinforcing edges were processed using Rhino/Grasshopper scripts. Each panelized part is then processed to generate the C-FAB™ matrix grid and robotic path plans.

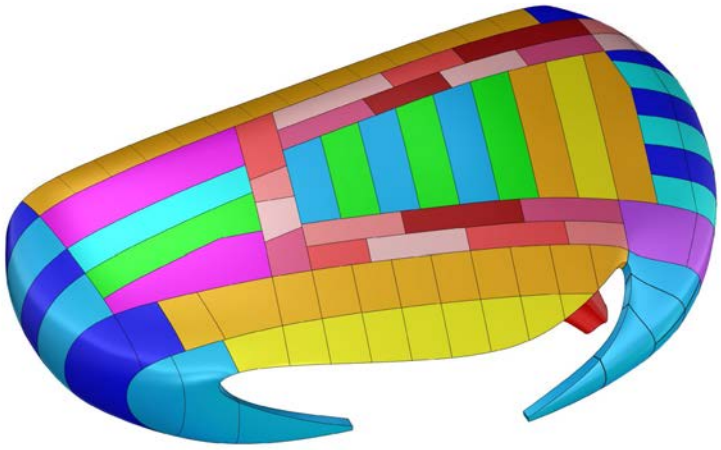


Figure 7 - This image displays the 3 dimensional panelization utilizing a 1.25m grid.

4.2 Digital Production: Gridding and Path Planning Algorithms

The structures generated by Branch Technology are created through the utilization of structured grids originally developed for aerospace and other engineering applications. These grids conform to the surfaces and fill the volumes of the designed structures. The structured grids are then used to create the extrusion sequence and resulting robotic code through a process known internally as path planning. Virtually all of the software used to grid and path plan the parts for Curve Appeal has been created by Branch Technology, and interact w/graphical interfaces through Rhino/Grasshopper.

The process of creating a structured grid is usually labor intensive. As such, Branch developed a set of interfaces to Rhino, including a primary gridding tool, to expedite the process. First, a gridding plan is generated for each of the parts. This blocking plan is essentially a set of under-dimensioned but geometry conforming structured grids. Once these grids are in place, they are re-dimensioned in order to appropriately size the segment lengths for our printing process. To ensure the quality of lengths and angles, the nodes of the grid are smoothed utilizing a point-centered, gradient-based methodology similar to the one described by Karman and Hilbert for use in unstructured grids [2, 3, 4]. The particular implementation utilizes a two-point step method originally developed by Barzilai and Borwein [1]. The custom gridding tool has a number of tools that allow for the creation of quality structured grids such as the ability to add "slices" at points wherever the user deems necessary and the addition of FDM plates onto parts. In addition, the software has the ability to create singular disconnections between structured

blocks, called transitions, that allow the grid spacing to be controlled in areas where such control would be difficult in a simply-connected structured grid.

Once the grid is complete, it is processed through a Grasshopper script whose end result is the robotic code that prescribes the extrusion path. This process is the aforementioned path planning and involves decisions about print order as well as part placement to accommodate robotic reach. Also generated during this phase are a number of ancillary files such as a complete wireframe and pictures for production reference.

5.0 Brief Conclusion

Through robotic additive manufacturing, prefabrication, and direct digital fabrication capabilities, this revolutionary method of construction stands to enhance construction productivity, resource use, and design freedom - transforming the nature of grid-shell and spatial structure solutions available today.

References

[1] Jonathan Barzilai and Jonathan M. Borwein. Two-point step size gradient methods. IMA Journal of Numerical Analysis, 8(1):141–148, jan 1988.

[2] Christopher B Hilbert. Tetrahedral mesh optimization and generation via topological transformations and gradient based node perturbation. Ph.d. dissertation, University of Tennessee at Chattanooga, 2015.

[3] Steve L. Karman. Adaptive Optimization-Based Smoothing for Tetrahedral Meshes. In 53rd AIAA Aerospace Science Meeting, Kissimmee, Florida,2015.

[4] Steve L. Karman and Nicholas J. Wyman. Automatic Unstructured Mesh Generation with Geometry Attribution. In AIAA Scitech 2019 Forum. American Institute of Aeronautics and Astronautics (AIAA), Jan 2019.

Proceedings of the IASS Annual Symposium 2019 – Structural Membranes 2019
Form and Force
7 – 10 October 2019, Barcelona, Spain
C. Lázaro, K.-U. Bletzinger, E. Oñate (eds.)

Fabrication of Topology Optimized Concrete Components Utilizing 3D Printed Clay Mould

Sihan WANG*, Kunsheng HUANG[a], Zixun HUANG [a], Michele SODANO*, Weishun XU [a], Felix RASPALL*

*Architectural and Sustainable Design
Singapore University of Technology and Design,
8 Somapah Road, Singapore
sihan_wang@mymail.sutd.edu.sg

[a] College of Civil Engineering and Architecture, Zhejiang University

Abstract

This paper presents the result on the development of an additive manufacturing approach to fabricate topology optimized concrete components, discuss the challenges associated with the clay mould printing process and its assembly. Our intention is to improve the fabrication process that increases efficiency without losing accuracy. We introduce a prototype of a concrete shelf to access the ability of such process in fabricating large-scale artifacts. We believe steps towards advancing the fabrication process of clay mould will accelerate its application in concrete manufacture.

Keywords: Clay Mould, Robotic Fabrication, Additive Manufacture, Topology Optimization, Concrete.

1. Introduction

In the past two decades, the principles of Additive Manufacturing (AM) with cementitious material have been substantially developed to manufacture freeform concrete components. These AM techniques, for example, Contour Crafting - concrete extrusion AM [1] and D-shape project - concrete binder jetting AM [2] present advanced options to concrete construction leading to high production rate, more geometry freedom and cost reduction [3].

One of these techniques introduces a robotic technology to fabricate clay moulds via AM extrusion, for the casting of freeform concrete components using Self Consolidating Concrete (SCC) [4]. Its manufactural process is similar to other mould production which involves fabrication of mould segments, assembly, casting, demoulding and post processes. Once the concrete cures, the clay is demoulded and can be recycled for subsequent prints. Thus, this method takes advantage of AM to enable the production of freeform geometries and the recyclability of clay to overcome the wastage of extensive one-off formworks.

In this paper, we apply the AM clay technique to fabricate freeform topology optimized concrete components. Our main research objective is to develop a fabrication process which is suitable for designated geometry that improves the fabrication efficiency without losing the accuracy. We firstly introduce the design and fabrication of a concrete shelf as a prototype. In addition to the overall fabrication procedures, we present the fabrication of hollows with various cross-section topologies. This

Copyright © 2019 by Sihan WANG, Kunsheng HUANG, Zixun HUANG, Michele SODANO, Weishun XU, Felix RASPALL
Published by the International Association for Shell and Spatial Structures (IASS) with permission.

further contributes to the expansion of achievable geometry range which offers the flexibilities in terms of AM clay with more geometrical varieties. At last, we discuss the result and our future development.

2. Topology optimization

Topology optimization is no longer a novelty in architecture and civil engineering since the first discussion by Bendsøe & Kikuchi [5]. It can be used in structural design to reduce the material consumption of elements, allocating matter only to the areas where it is required. The resulting parts are highly material-efficient, but their geometry is usually highly complex. Therefore, the feasibility of such efficient structures is limited by the manufacturing process, which enhances our intention to overcome the challenges in the fabrication of such customized components with complex geometries.

In this paper, we utilized topology optimization as a form-finding strategy to design a shelf for the exhibition of 3D printed ceramic artifacts. The optimization was executed in Millipede [6], a plugin for Grasshopper. We designed a boundary region for 2D optimization with a dimension of 2368mm (L) X 576mm (H) to fit in the exhibition space. Subsequently, according to the result of principal stress lines (white color in Figure 1a), we drew the boundary of the front view to form the geometry and gave it a shelf depth of 200mm. Consequently, the design of shelf represented a multi-hole geometry based on 2D topology optimization as shown in Figure 1b.

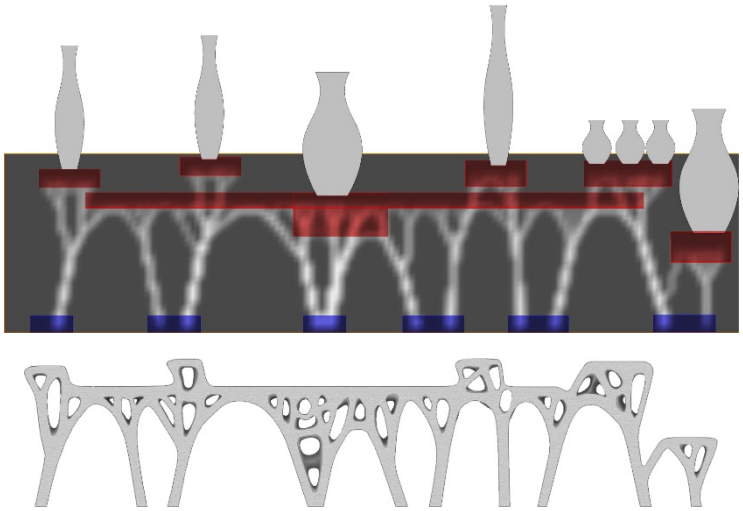


Figure 1. Topology Optimization of the shelf. Top: Dark grey is the optimization boundary, Blocks in red represent the load and ones in blue are the support. Bottom: Finalized geometry based on the principal stress lines with a dimension of 2213mm (L) X 474mm (H) X 200mm (D) and a volume of 64.80 liters.

3. Fabrication

In this section, we will introduce the fabrication of the prototype. It is initiated with a brief introduction of the experiment setup. This is followed by the fabrication procedures: 1. Fabrication of clay mould segments; 2. Assembly and reinforcing clay moulds; 3. Concrete casting.

3.1. Experiment setup

We utilized a KUKA KR 90 R3100 robot arm to control the motion of material deposition (Figure 2, left), with a bespoke end effector. Regarding the extruded clay which represents the outline of the wall and the geometries of cavities for plants to grow must have sufficient stiffness to maintain the shape when sustaining concrete casting, we considered two main factors of the clay extrusion mechanism: the necessary torque to extrude rather viscous material and the precise material deposition rate. In this scenario, we opted the ram pump mechanism to execute a constant clay extrusion (Figure 2, right). This extrusion system consisted of a NEMA 34 stepper motor, a 1: 40-reduction gearbox with cylinder, piston with frames.

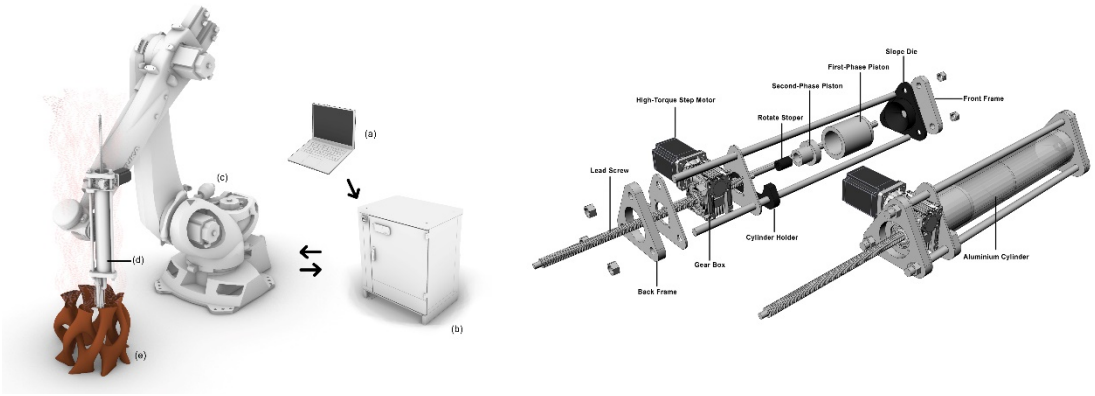


Figure 2. Workcell Setup. Left: Diagram of Setup, (a) Personal computer, (b) Robotic arm controller, (c) Robotic arm as positioning apparatus, (d) Extrusion system and end effector, (e) Printed clay mould. Right: Assembly of clay pump.

The printing material remained the same from the authors' previously research: terracotta clay with 35-40% water ratio through extrusion. We first calibrated the clay AM system to match the extrusion velocity with the nozzle movement speed that facilitated a constant filament deposition. In the case of our pump, each round per minute (rpm) of the motor rotation could extrude 1/90 ml of clay. In this case, to match up a 100 mm/s nozzle movement speed, we set the rpm as 72 for 8 mm nozzle diameter with the printing layer height of 1mm.

3.2. Clay AM extrusion

Considering the overall size and weight of the shelf prototype, we decided to split the fabrication into 4 segments as demonstrated in Figure 3, due to limited manpower. Although this was contradictory to the result of structural optimization, it remained the strategy to investigate our main objective, to improve the fabrication process in terms of the efficiency.

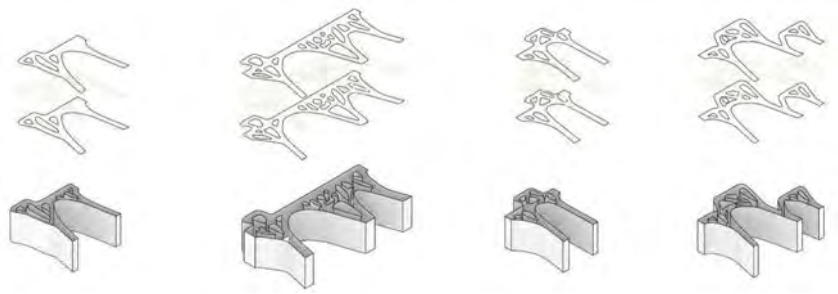


Figure 3. Segmentations of the topology optimized shelf.

Once these geometric models were generated, we subsequently converted them to mesh triangulations for mainly interoperability and precomputation of discretization. The machine paths for our printing setup were produced by contouring the geometry. Our approach here was to translate the machine paths for direct drive of the robotic system. Additional work is required for one to one mapping between the digital and physical artifact within tolerance. Such processes involving computation were executed in the visual programming environment of Rhinoceros / Grasshopper which produces geometric representations of machine paths and converted to robot code using Taco software add-on.

When it came to physical printing, we considered three deficiencies when printing each segment within one process: 1. To fabricate such topological complex objective, the nozzle had to travel inefficiently between prints as red lines in Figure 4, 2. The start and end of each extrusion could cause deformation on the deposited artifact, especially those holes with small cross-section areas, and 3. To switch the extrusion motor on / off caused a postponement for acceleration. In this scenario, we decided to print the interior holes and the boundary envelop of each segment respectively other than print them together as a whole. In addition, for each printing, we transferred the original contoured printing path which was a series of closed curves into one spiral curve to implement a smooth nozzle movement.

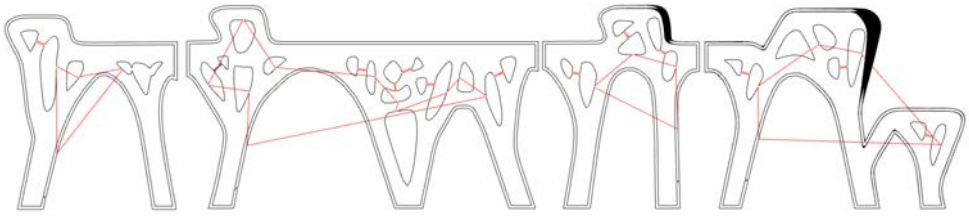


Figure 4. The top view of the printing path for each segment. The black represents the paths where it distributes clay and the red is the nozzle movement without extrusion. In this print job, the wasted nozzle moving distance might increase 15.6% of printing time (5984.6m of extrusion length and 935.1m of free nozzle traveling) exclude the time wastage on motor acceleration.

Besides the concept of printing mould components separately, we also practiced the topological variation in height of each hole as rendered in Figure 5, left. The total printing time to produce every mould components was 16 hours and 38 minutes. This excluded the reprinting of 3 failures out of 33 components representing the interior topological holes.

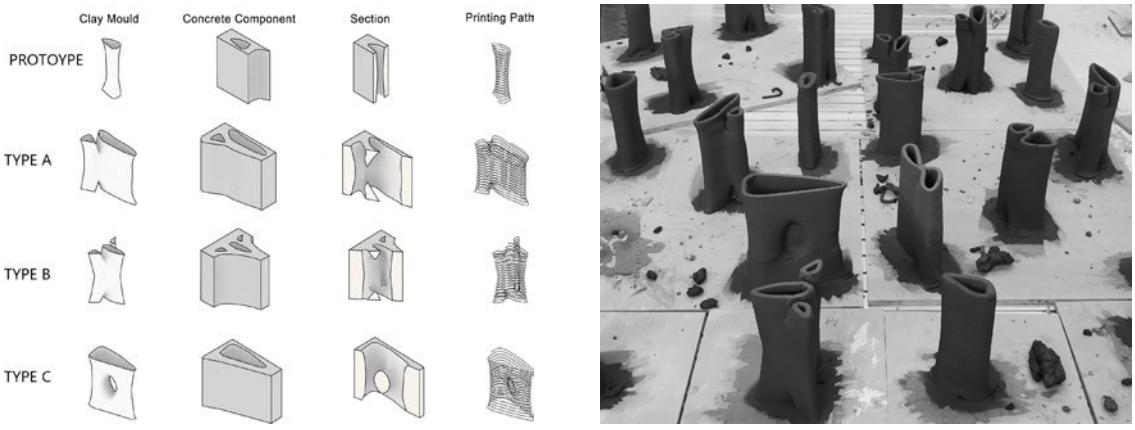


Figure 5. Variations in the topologies of holes. On the left, we present four types of topologies with the geometries of the moulds, concrete components after casting with sections and the printing paths. On the right is a portion of printed works.

3.3. Concrete casting

After the printing of mould components and their post processes, we proceeded to the concrete casting. Our intention was to maintain the humidity of clay mould till concrete casting to avoid the potential surface crack due to dried clay mould absorbing water from concrete, according to Wang et al. [7]. However, the humid clay mould brought another challenge that the deformation of mould would occur during casting due to the pressure exerted by concrete. In this circumstance, the printing of clay mould had to reach a sufficient thickness to sustain the concrete pressure. Nevertheless, it came along with the trade-off between less deformation, a thicker mould as more material to be distributed in a longer time, and shorter printing time.

To response, we proposed the sandbox support as a reinforcement for the clay moulds in Figure 6. Firstly, we placed each piece of interior mould that represented a topological hole into the envelop mould. Subsequently, we surrounded the clay mould with a box made of middle-density fiberboards (MDF) and filled the gap in between with sand. Finally, we cast in concrete with a with the paste of fine aggregates, cement, water and plasticizer (3:2:1:0.005), waited for 24 hours for the concrete curing and demoulded.

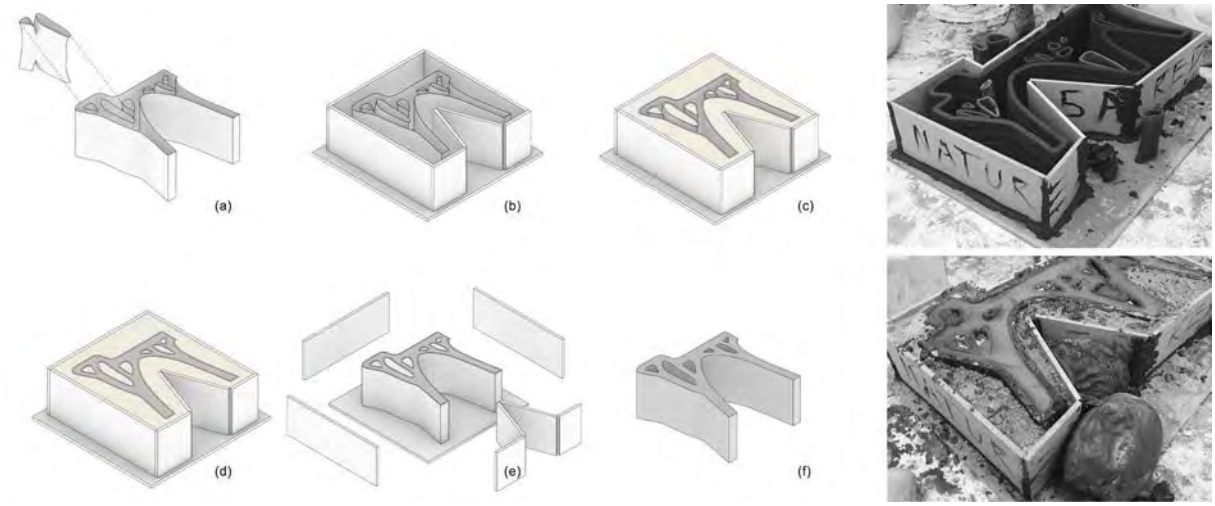


Figure 6. Mould assembly and concrete casting. Left: (a) Assembling 3D printed clay components into the mould for monolithic casting, (b) Surrounding the mould with MDF, (c) Filling the gap between clay and MDF with sand, (d) Casting concrete, (e) Removing sandbox support, (f) Demoulding clay. Photos on the right are fabrication in progress.

4. Result and discussion

We put the fabricated shelf components side by side as presented in Figure 7. There were 64.80 liters of the concrete cast and 47.88 liters of clay distributed as mould that more than 95% was recycled.



Figure 7. Completed shelf.

Through the fabrication process, we detected three flaws as demonstrated in Figure 8: 1. The minimum width of the branch was set as 12mm which resulted in a crack after casting, 2. The sand as support was not condensed that caused the deformation on the longest side of the shelf, and 3. When printing with a sinuous path in a small area, the redundancy of material distribution might cause a displacement.



Figure 8. Flaws in fabrication. From the left: cracks, deformation of concrete casting and displacement in printing.

In response to these, we propose investigating the concrete paste to satisfy the demand for the casting of ultra-thin components. The infilling process of sandbox support has to be secured that the sand is dense and the boundary box is stiff. As for the displacement in printing, we hypothesize that by reducing the extrusion velocity while maintaining the nozzle movement speed, less material will be distributed that retards the redundancy. These hypotheses may be verified in our further research.

5. Conclusions and further development

We presented part of the development for a digital fabrication technology aiming to achieve the topological complexities of concrete artifacts. We highlighted our approach to shorten the total fabrication time which mainly takes place in the additive manufacturing process by mould segmentation and building sandbox support. However, such an approach comes along with trade-offs. Firstly, the mould segmentation is limited by geometry, which means it can not be applied as a general solution to all cases. Although sandbox support seeks a balance between machine fabrication and manpower regarding efficiency, it violates the concept of automation in digital fabrication. Lastly, sand as support ruins the elegance of 3D printed clay mould that it causes trouble in clay recycling since they mix together.

In architecture, the development of software for Computer Aided Design keeps pushing the boundary of design aesthetics and structural efficiency. The demand for materializing these design work has become an ultimate objective that involves researches on novel material and fabrication techniques. We research on concrete since it is one of the most used materials in construction representing workability and durability. When utilizing AM clay mould, we further overcome the difficulties in shaping concrete and the wastage of customized mould. In this scenario, our research will retain the testing of clay extrusion under various printing configurations which aims to understand the behaviors of clay printing in terms of shaping and mechanical performance. Besides, concrete casting will be practiced based on the result of clay AM to determine the successful casting strategies according to deflection and surface finish.

To conclude, we demonstrated positive steps towards fabricating large-scale concrete artifact via additive manufacturing clay mould. There remains a lot more to be investigated to access a better understanding of the material behavior, thus, leading to the control of the fabrication process. We believe such researches will implement the manufacture of concrete components with intricate geometries towards lower costs and potentially higher efficiency.

Acknowledgments

This project was executed in the robotics lab of Zhe Jiang University as a result of a collaborative course with SUTD. We would like to thank the rest of the group members who helped the fabrication process, Li Zaixi, Ding Yufeng, Zhang Xizhi, and Liu Housen.

References

[1] Khoshnevis, B. (2004). Automated construction by contour crafting - Related robotics and information technologies. Automation in Construction, 13(1), 5–19. https://doi.org/10.1016/j.autcon.2003.08.012

[2] Cesaretti, G., Dini, E., De Kestelier, X., Colla, V., & Pambaguian, L. (2014). Building components for an outpost on the Lunar soil by means of a novel 3D printing technology. Acta Astronautica, 93, 430–450. https://doi.org/10.1016/j.actaastro.2013.07.034

[3] Perrot, A., Rangeard, D., & Pierre, A. (2016). Structural built-up of cement-based materials used for 3D-printing extrusion techniques. Materials and Structures/Materiaux et Constructions, 49(4), 1213–1220. https://doi.org/10.1617/s11527-015-0571-0

[4] Wang, S., Philippe, M., Ho, K. and Stylianos, D.: 2016, Clay robotics: A hybrid 3D printing casting process, Proceedings of the International Conference on Sustainable Smart Manufacturing (S2M), Lisbon, 83-88.

[5] Bendsøe, M. P., & Kikuchi, N. (1988). Generating optimal topologies in structural design using a homogenization method. Computer methods in applied mechanics and engineering, 71(2), 197-224.

[6] Michalatos, P., & Kajima, S. (2014). Millipede. Grasshopper Plug-in.

[7] Wang, S., Conti, Z.X., and Felix, R. (2019). Optimization of Clay Mould for Concrete Casting Using Design of Experiments. In Intelligent & Informed - Proceedings of the 24th CAADRIA Conference (pp. 283-292).

Proceedings of the IASS Annual Symposium 2019 – Structural Membranes 2019
Form and Force
7 – 10 October 2019, Barcelona, Spain
C. Lázaro, K.-U. Bletzinger, E. Oñate (eds.)

High-Performance Corrugated Concrete Shell Construction on Bending-actuated Robotically 3D-printed Formworks

Xiang WANG*[c], Kam-Ming Mark TAM*[b], Dalma FÖLDESI[a], Hyerin LEE[a], Jung In SEO[a], Anna VASILEIOU[a], Youyuan LUO[c], Chun Pong SO[c], Xiao ZHANG[c], Zain KARSAN[a], Gene Ting-Chun KAO[b], Liming ZHANG[c], Hua CHAI[c], Philip F. YUAN[c], Philippe BLOCK[b]

*Tongji University & Swiss Federal Institute of Technology in Zurich
Shanghai, People's Republic of China & Zurich, Switzerland
18310021@tongji.edu.cn & tam@arch.ethz.ch

[a] Department of Architecture, School of Architecture and Planning, Massachusetts Institute of Technology
[b] College of Architecture and Urban Planning, Tongji University
[c] Block Research Group, Institute of Technology in Architecture, Swiss Federal Institute of Technology in Zurich

Abstract

Additive manufacturing (AM) has expanded possibilities for materialising structures that achieve strength through intelligent, but complex geometries. However, conventional AM techniques, such as thermoplastic fused deposition modelling (FDM), also rely on material with low strength and stiffness, which limit their full-scale building construction applications. This paper articulates one of several design-fabrication strategies jointly developed by MIT, ETHZ and Tongji researchers in a workshop to respond to this challenge: FDM is optimised for producing self-supporting scaffold that can be printed flat and bent in-place on site—scaffolds whose strength are built gradually via additional structural material application. Inspired by principles of shallow arching action and structural corrugation, this paper—part 2 in the series—develops an AM-enabled multi-phased construction method for creating a walkable full-span structure capable of accommodating live structural loads. The feasibility of the novel assembly process is demonstrated with the construction of a bridge measuring approximately 5-metre in span. The produced prototype illustrates one alternative design-fabrication strategy leveraging force-explicit equilibrium design methods to synthesise the advantages of vernacular and digital manufacturing techniques—resulting in new possibilities for the materialisation geometrically complex, live-load-bearing and moderate-span concrete structures with minimal form-work.

Keywords: additive manufacturing, formwork, surface corrugation, bending active, concrete, shallow vault

1 Introduction

To engineers interested in structural performance, robotics-enabled additive manufacturing (AM) is a research area eliciting strong interests due to its potential to realise structures achieving strength through intelligent, but complex geometries, which are difficult to realise under traditional construction methods. But while AM—complemented by advances in digital computation and industrial robotics—have been transformed into reliable and rapid methods for producing end-use parts ranging from human to modest architectural scales, the application of the technology has rarely extended beyond architectural structures with limited design requirements, such as sculptures or pavilions. Applications are especially limiting for AM techniques with fabrication efficiency appropriate for mass production, such as thermoplastic-based Fused Deposition Modelling (FDM), which relies on material with low strength and stiffness, and idiosyncratic processes introducing imperfection and weakness to the artefacts [1]. Consequently, the application of AM has remained limited in practical building constructions.

Copyright © 2019 by Xiang WANG, Kam-Ming Mark TAM
Published by the International Association for Shell and Spatial Structures (IASS) with permission.

2 Literature Review

Acknowledging the limitations in state-of-the-art robotics-enabled AM, researchers have pursued alternative applications for AM in construction, and developed methods for generating designs informed by their process constraints. One alternative AM application is to use the technique to develop self-supporting scaffold for complex structurally informed geometries—a scaffold upon which the final structural material, such as concrete or bricks, can be incrementally applied to build up the required structural strength. The approach therefore synthesises the advantages of traditional and digital fabrication methods to respectively achieve structural strength and stiffness, and geometrical customisability and complexity—in the process creating novel resource-efficient methods for producing concrete formwork at reduced material and labour intensity. Prominent research in this area include the use of AM-produced lattices [2] and digitally knitted textiles membranes [3] as respectively containers and surfaces for later concrete infill and casting.

Given the paramount role of geometry in determining structural performances, researchers applying AM to architecture have also developed methods for optimising the structural geometry and internal material distribution of AM-produced parts[4]. Transferable lessons may also be learnt in design-build research based on material with unconventionally low structural strength and stiffness, such as recycled or organic material [5]—projects wherein the strength achievable in the weak material is maximised by synthesising tried-and-true principles on structural efficiency, such as the preferencing of funicular, compression-based and doubly-curved forms, and the employment of geometrical-based and force-explicit methods of design exploration, like Graphic Statics, that offer designers good capabilities for controlling and accommodating structural forces and material constraints respectively.

3 Context and Design Concept Formulation

3.1 Workshop Introduction

Evident in the research reviewed above is the importance of structural geometry in activating the limited strength and stiffness of weak materials—enabling formworks based on the weak materials to sustain the stresses and strains imposed on them by the incremental application of the final structural material. The final built-up structure in turn benefits from the heightened strength and stiffness realised through the formwork's structural geometry—designed and optimised with smart computational methods, and produced using AM technologies that support customisability and complexity.

The synergistic opportunities presented by the combination of concepts discussed above provided the motivation for the diverse collection of students and researchers from Massachusetts Institute of Technology (MIT), Swiss Federal Institute of Technology (ETHZ), and Tongji University (TJU) that convened in the design-build workshop hosted by TJU's Professor Philip Yuan during January 2019. Spanning over an 18-day period, this workshop commenced with 3 days of instructions on foundational computational structural design topic. This was followed by a 3-day ideation period wherein students worked in pairs to propose a human-scale structure to be constructed via incremental application of a structural material on FDM-produced scaffolds. These generated ideas were then synthesised into 2 consolidated designs that were developed, prototyped, fabricated and assembled over the remaining 12 days. Presented in the remainder of this paper is the development of one of the two concepts pursued.

3.2 Material Design Concept: Corrugated Shallow Vault

One compelling design trajectory emerged from the ideation exercise was the investigation of funicular structures embodying principles of shallow vaulting action, which were ambitiously programmed as ramps or bridges (Figure 1-1)—in other words, floor-like spanning systems accommodating live loads at magnitudes conducive to basic building occupancy.

The concept of developing expressively sculpted shallow vaults as viable floor system alternatives to conventional slabs captivated the organisers of the workshop—it is also substantiated with structural logic and precedents. With proper restraints, shallow vaults (Figure 1-2), which are activated via axial compressive stresses, are structurally more efficient than flexural, or bending-dominated slabs [6].

However, the structural feasibility of shallow vaults as robust floor systems is contingent upon the adequate provision of structural stiffeners, such as a network of ribs, for resisting asymmetric live loads [6][7]. In the context of this exercise, the stiffening option most sufficiently developed was the strategy of corrugating a funicular surface geometry into a series of ridges or folds (Figure 1-2b).

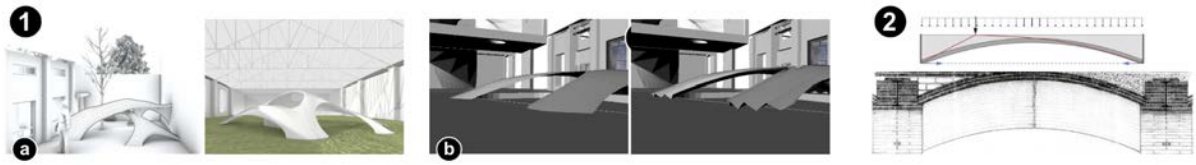


Figure 1: (1-a) Ideated design concepts, with (1-b) some materialisation by corrugation; (2) Ribbed shallow vault floor.

Surface corrugation is one of three standard shell stiffening methods, which also include the thickening of shell thickness, and the introduction of stiffening ribs as discussed previously [8]. There was significant compatibility of the strategy to the workshop's goal of developing AM-produced thermoplastics-based formwork with minimal support requirements—as revealed in the authors' own numerical analyses showing that materialisation of the shallow geometry without corrugation by thermoplastic-based AM would result in formworks experiencing problematically high creep deformation under initial concrete application. In contrast, the increased structural depth achieved through surface corrugation would substantially reduce creep deformation to levels that could be feasibly managed. Other advantages of surface corrugation included relative fabrication and assembly ease with respect to the facilities available in the workshop, and expressive aesthetical quality. In view of the reasons discussed here, the proposal to develop a live-load-bearing spanning structures converged towards a corrugated shallow vault system.

4 Design Methodology

4.1 Overall Workflow

The process to develop and materialise the corrugated bridge design consisted of the two primary stages of **(I)** Design development [**§6**]; and **(II)** Fabrication and assembly [**§7]**. In anticipation of uncertainties in the novel and complex design and fabrication strategy, **(0)** Comprehensive prototyping was introduced in parallel at the beginning to quickly articulate and implement the design in full [**§5]**, in order to identify issues requiring further resolution in the sub-steps of I and II.

The structure of the paper's remaining sections mirrors the aforementioned. Specifically, the implementation began with **(I-1A)** Global geometry and pattern refinement, which incorporated **(I-1B)** equilibrium form-finding [6.1], and concluded with the output of a 2.5-D quad-mesh of the form-found geometry (Figure 2-1,2). Next, the **(I-2)** intrinsic striping of the shallow vault was computed to obtain the corrugation layout. Using the quad-mesh as the centre-surface, and parameters characterising the design's structural depth, the corrugation geometry was generated (Figure 2-3), and **(I-3)** Planarised to ensure that the corrugation strips or folds would be developable, so that they could be additive manufactured flat. Finally, the planarised quad-mesh of the corrugated surface in 3-D space was further **(I-4)** Discretised into a dense infill pattern corresponding to the layout of filament to be extruded via AM [§6.2] To improve the strength achievable in the AM-produced formwork, all parameters identified in the process above, which include the local variations in the formwork's structural depth and infill pattern density, were optimised in a procedure developed in §6.2. Next, edges from the optimised infill pattern were then **(II-1)** assigned respectively to their corresponding panel groups by location [**§6.3**], where they were **(II-2)** sequenced together into robotic print trajectories, post-processed and **(II-2)** converted into instructions for the industrial robot arms, which **(II-3)** extruded the parts. Finally, the flat printed panels were **(II-4)** Transported to site, **(II-5)** Assembled into components [**§7]**, and **(II-6)** Combined together into their final location on site [**§7]**.

All fabrication described in this paper—encompassing both prototyping and final production—were conducted in the shared robotic production facilities of Archi-Union and Fab-Union. The setup utilised

two KR 120 R1800 nano industrial robot arms, which were mounted with a custom extrusion module with a nozzle diameter of 8 mm that were developed by researchers at FabUnion. Polylactic acid (PLA) was used as the final printing material.



Figure 2: Results of various implementation workflow's substages: (1-5) I-1A, I-1B, I-2, I-3, I-4

4.2 Boundary Conditions and Structural Analysis

As Figure 3 shows, the corrugated bridge featuring multiple curved spans, which create two primary walkways connected at their midspans, was designed over a concrete fish pond situated within the private courtyard of Archi-Union in the Yangpu District of Shanghai, China. The geometric profile of the pond—wedge-shaped—dictated the variable lengths of the bridge's two primary walkways (at 4.5m and 5.5m). Additional constraints were also imposed on the bridge's support conditions: the owner has requested that the bridge's connections to the site made easily dismantlable.



Figure 3: Final design on site: (Left) Plan view; (Right) Elevation view

A safety reduction factor of 2.0 applied to the strength property of all materials included in various structural analytical models developed throughout the course of this project. The material strength of the plastic filament, which was needed to predict the behaviour of the formwork under initial concrete application, was set according to tensile tests conducted on structural joints AM-produced under a fabrication setup identical to the one used by this workshop. Requirements on concrete thickness, which directly imposes stresses on the formwork, and steel reinforcement were determined based on the objective to support a uniformly distributed live load of 1 kN / m^2—approximately equivalent to supporting at least one person per square metre.

5 Initial Design Resolution and Prototyping

5.1 Structural System Detailing

The design of the final assembly system sought to balance several competing structural and fabrication objectives, which included maximising structural strength, and minimising both total concrete weight, and construction complexity. To this end, a staged assembly process was conceived (Figure 4-1) whereby the assembled thermoplastic planar strips acted as a formwork for a coating of glass-fibre reinforced concrete (GFRC) approximately 2 cm in thickness—incrementally applied over a steel wire mesh covering the entire folded plastic formwork. Once the initial concrete sufficiently cured, the internal space enclosed by the corrugation was applied with a second layer of concrete, which (i) included steel reinforcement to provide the bridge's bending capacity for resisting live loads, was made into a hollow cross section by the deployment of AM-produced triangular-shaped voids, and (iii) embedded a steel wire mesh in its surface slab to provide the capacity for compressive and tension forces to be transferred in the directions traverse to the alignments of the corrugation. Finally, metal studs were applied along the creases of the bridge's top fold to fasten the two concrete layers. Four welded and stiffened steel boxes (Figure 4-2a)—one for each of the bridge's four access points—were

provided the vaulted bridge's anchoring. These boxes were in turn welded onto L-shaped steel parts hung from the pond's ledge—resulting in friction-fitted supports that are detachable.

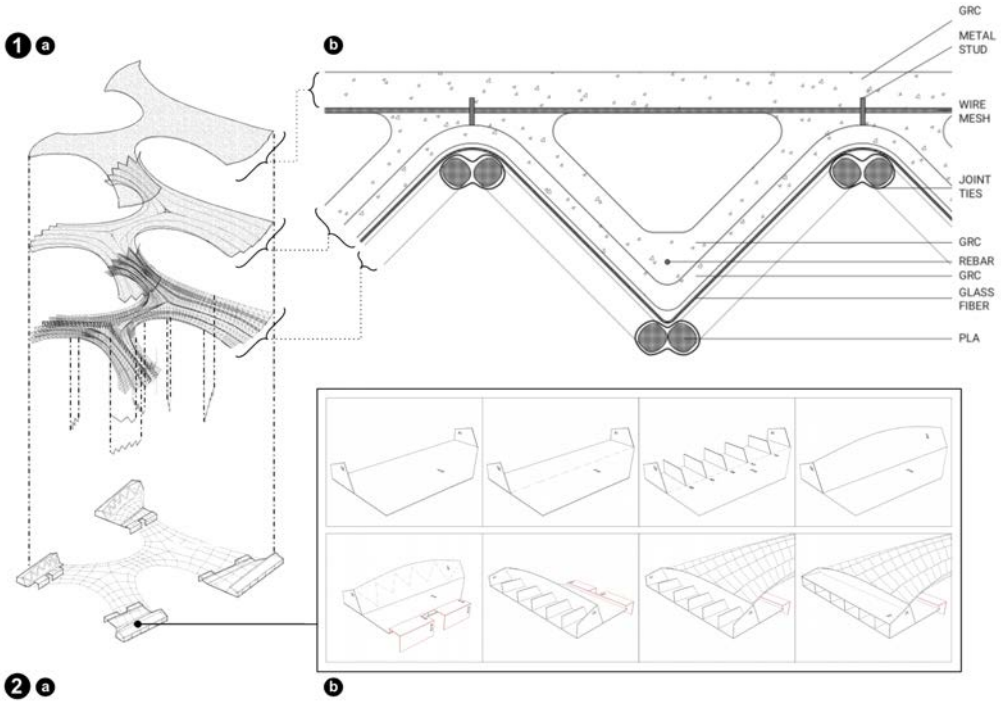


Figure 4: Finalised structural assembly detailing: (1) Main shallow vaulted bridge; and (2) Steel connections.

5.2 Prototyping and Testing

The initial structural assembly design described in the preceding section were implemented in a series of simplified prototypes at 1:2 scale. While these studies generally demonstrated the proposal's feasibility, a number of problems were also observed. Table 1 documents a selection of these challenges and failures, and the strategies the team elaborated in later sections to address them.

Description	**Proposed Resolution**
P-1.) Extensive vertical creep deformation in the plastic formwork as concrete was applied **P-2.)** The formwork splayed in the direction traverse to the corrugation during concrete application **P-3.)** Substantial propagation of structural failures in the area around the bridge's main singularities, which are situated approximately at the two main walkways' mid-spans—failures that affected predominately members traverse to the corrugation direction. **P-4.)** Bending actuation of the panels was difficult; there was a clear trade-off between achieving the required strength to prevent failure, and maintaining sufficient flexibility to allow bending.	**R-1.**) The bridge's geometry would be cambered so that the formwork would deform to the correct funicular geometry with concrete application. Also, temporary poles would be added to prop the formwork. **R-2.)** Printed 'combs' with significantly greater relative strength and stiffness were introduced—fitted to the underside of the formwork at strategically points to help maintain its shape, and to provide its capacity to transfer forces laterally prior to concrete completion [**§7**] **R-3.)** The final bidirectional form and force explorations would focus on reducing the forces in the direction traverse to corrugation [**§6.1**] **R-4.)** Both the infill pattern density and the structural depth of the formwork would be locally optimised to reduce filament forces [**§6.2**]

Table 1: Description of issues observed during prototyping, and their corresponding proposed resolutions

6 Design Development

6.1 Geometry and Topology Development

Since the topology used for form-finding effectively prescribes the bounds of the design space of achievable equilibrium geometries, both topology and geometry were investigated in parallel in the form-finding process. This began with the consolidation and adaptation of the initial design concepts

formulated in **§1** for the final site condition—resulting in a closed planar surface defined by a sequence of curvatures modelled in Rhinoceros 5.0 that outlined the planimetric footprint of the shallow vault bridge. The surface boundary served as inputs in Grasshopper 3-D components implementing *compas_pattern*, which is a library of topology exploration algorithms that enabled user-defined singularities to be integrated in quad-mesh generation [9]. In quad-meshes, singularities refer to vertices with a valency other than 4, or 3 in the case of boundary vertices. Singularities are important because they carry significant structural, fabrication, and aesthetic implications [10], as demonstrated in Figure 5-L, whereby the placement of singularities could result in mesh discretisation creating unusable, or irrational corrugation pattern.

As is the case in the exploration of topology, the form-finding development—implemented using both RhinoVault and compas_tna within respectively Rhinoceros 5.0 and Grasshopper 3-D—was guided by fabrication and structural considerations. Specifically, efforts were made to reduce the forces in the direction traverse to the corrugation orientation Figure 5-R—a direction in the formwork with compromised force flow prior to concrete completion owing to the geometric perturbation introduced by corrugation. Formal constraints were also embedded to improve the manufacturability of form-found results, such as by setting lower bound limits on the length of segments, which reduced the occurrences of tightly folded strips that would render concrete application infeasible.



Figure 5: Key concepts in geometry and topology exploration: (Left) Singularity and strip collection for corrugation; (Right) Forces oriented traverse to alignment of corrugation.

6.2 Corrugation, Planarisation & Infill Pattern Generation

With the conclusion of the geometry and topology exploration, the mesh geometry representing the form-found bridge's centre-surface was determined, and subsequently folded into its corrugated form. The process first subdivides each quad-face in the smooth form-found surface geometry in halves. Next, mesh vertices in the subdivided (pre-folded) mesh were translated either above or below the mesh surface according to their local vertex normals and locally assigned structural depth—resulting in a V-shaped corrugation cross section module per each original quad-face. Finally, the folded quad-mesh geometry was planarised to ensure the developability of printed strips. and subdivided along the corrugation direction according to local density parameters—creating the final dense tessellated infill pattern embedding all edges to be additive manufactured.

In view of the failures observed in (**§5.2-P.4**), the local structural depths and infill pattern densities of the formwork were optimised in an integrated optimisation procedure that sought to minimise the number of tessellation edge members with utilisation approaching failure—according to results computed in a Finite Element (FE) model constructed using Karamba 3-D, which is a plug-in for Grasshopper 3-D. To avoid premature local optimisation, the optimisation was staged—beginning with an evolutionary algorithm varying both depth and density (Figure 6-2A), and followed by a gradient-based optimisation targeting structural depth (Figure 6-2B), and subsequently density (Figure 6-2C).

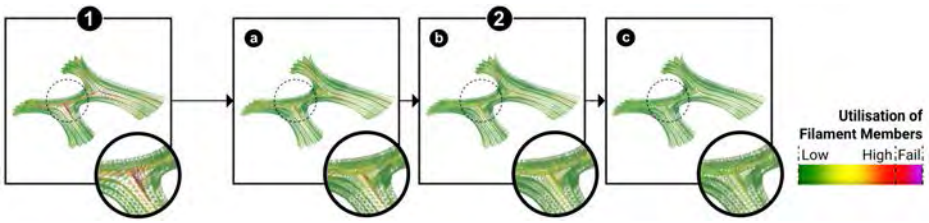


Figure 6Figure 5: Results from staged optimisation of infill pattern to reduce utilisation and failure of filament members

6.3 Panelisation

Following optimisation, the edges embedded in the dense tessellated mesh strips were grouped according to their assigned panels by their locations. The panelisation scheme that best balanced the goals to reduce the number of discrete parts, and to maintain sufficient flexibility for assembly ease, was determined via prototyping. Figure 8-2B presents this layout, wherein the vault was partitioned into 5 primary components each composed of 4-5 corrugation channels (8, or 10 strip panels)—4 components for the 4 halves together composing the 2 walkways, and 1 component for the connection bridge between the 2 walkways at their midspan.

7 Implementation III: Fabrication & Assembly

To create the print instructions for the robotic arms, the edges assigned per panel were extracted, parsed and post-processed using a custom software developed by the authors called FURobot, which sequenced edge segments within the mesh according to their location, type (e.g.: along, or normal to corrugation direction), and structural importance, which may demand uninterrupted material continuity (e.g. boundary outline of panels). On the whole, the 50 print programmes corresponding to each strip-panel were printed over a period of 4 days—totalling more than 1,200 m of filament length.



Figure 7-B describes the overall assembly and erection procedure—beginning with the assembly of the corrugated strips onsite into the 5 pre-defined bridge components. The process involved the fitting of the panels onto the printed comb, which acted as both stiffeners and guides, and the use of zip-ties and bolts for the fastening of panels (Figure 7-A). Components forming the two primary walkways or spans of the bridges are then joined, and successively relocated to their installation location where they were fastened to the steel plate anchors using zip (Figure 7-B3). With the plastic formwork fully assembled, installed on site and fastened (Figure 7-B4), a fine steel mesh with a 6 mm density was then applied onto the plastic formwork—followed by the incremental application of the first layer of concrete according to the description outlined in §5.1 (Figure 7-B5). Allowing the initial layer of concrete to cure for one week, the final layers of concrete, which included the surface slab, were applied (Figure 7-B6)—resulting in the completed shallow vaulted bridge as Figure 8 shows. In total, approximately 3,500 to 4,000 kg of concrete was poured.



Figure 7 Images showing fabrication and assembly execution

8 Conclusion

This paper documents a multi-phased design-fabrication strategy jointly developed by researchers from MIT, ETHZ and TJU in a workshop to create a walkable full-span funicular shallow vault capable of accommodating live structural loads. Specifically, the novel technique approximates a complex shallow compression-only form in a series of folded AM-produced scaffold panels to create a corrugated profile

with increased structural depth, which augments the shell's structural stiffness to support an initial layer of incrementally applied concrete. The corrugated concrete in turn supports a final layer of concrete filling the interior spaces enclosed by the corrugation to create a robust continuous system of structural stiffeners and diaphragm. An integrated form-finding method was devised to simultaneously optimise the vault's locally varying structural depths, and infill pattern densities—while incorporating fabrication and assembly considerations, and the properties of the printing material. The proposed framework—demonstrated through a completed prototype—highlights the potential for the synthesis of digital and traditional fabrication techniques through smart structural computation to open new possibilities for materialising geometrically complex, live-load-bearing and moderate-span concrete structures with limited formwork requirements.



Figure 8 Images of completed bridge

References

[1] K-M. M. Tam, J. R. Coleman, N. Fine., and C. T. Mueller. "Stress line additive manufacturing (SLAM) for 2.5-d shells," *Journal of the International Association for Shell and Spatial Structures*, vol. 57, no. 4, pp. 249-259, Dec 1.

[2] N. Hack, W.V. Laurer, F. Grammazio, M. Kohler, and W. Brameshuber. "Mesh Mould: Robotically Fabricated Metal Meshes as Concrete Formwork and Reinforcement," in *FERRO-11: Proceedings of the 11th International Symposium on Ferrocement and 3rd ICTRC International Conference on Textile Reinforced Concrete, Aachen, Germany, June 07-10, 2015,* RILEM Publications SARL, 2015. pp. 347-359.

[3] M. Popescu, M. Rippmann, A. Liew, "Concrete shell built using a cable-net and knitted formwork," *DETAIL structure*, vol. 1, pp. 10-11, 2019.

[4] K. M. M. Tam, D. J. Marshall, M. Gu, J. Kim, Y. Huang, J. Lavallee, and C.T. Mueller, "Fabrication-aware structural optimisation of lattice additive-manufactured with robot-arm," *International Journal of Rapid Manufacturing*, vol. 7, no.2/3, pp.120 - 168, 2018.

[5] Block Research Group. ETH Zurich Pavilion, New York City, USA, 2015 http://www.block.arch.ethz.ch/brg/project/eth-ideas-city-pavilion-new-york-ny-usa. Accessed: May 31, 2019.

[6] A. Liew, D. López López, T. Van Mele, and P. Block, "Design, fabrication and testing of a prototype, thin-vaulted, unreinforced concrete floor," in *Engineering Structures*, vol. 137, 2017, pp. 323-335.

[7] *Guastavino/Collins Collection*. Drawings and archives. Avery Library, Columbia University.

[8] S. Malek, and C. Williams, "The Equilibrium of Corrugated Plates and Shells," *Nexus Network Journal*, vol 19., 2017. pp 619-627.

[9] R. Oval, M. Rippmann, R. Mesnil, T. Van Mele, O. Baverel, P. Block, "Feature-based Topology Finding of Patterns for Shell Structures," *Automation in Construction*, vol. 103, pp. 185-201, Feb. 2019.

[10] A. Schiftner, J. Balzer, "Statics-sensitive layout of planar quadrilateral meshes," in *Advances in Architectural Geometry*, 2010, C. Ceccato, P. Hesselgren, M. Pauly, H. Pottmann, and J. Wallner Eds., Springer, 2010. pp. 221–236.

Proceedings of the IASS Annual Symposium 2019 – Structural Membranes 2019
Form and Force
7 – 10 October 2019, Barcelona, Spain
C. Lázaro, K.-U. Bletzinger, E. Oñate (eds.)

Optimized Internal Structures for 3D-Printed Sandwich Elements

Hyunchul KWON*, Benjamin DILLENBURGER

*Chair of Digital Building Technologies, ETH Zurich
Stefano-Franscini-Platz 1, HIB E 23, 8093 Zürich, Switzerland
kwon@arch.ethz.ch

Abstract

The paper describes how internal structures for Fused Deposition Modeling (FDM) 3D Printing (3DP) can optimize the structural capacity of large-scale freeform sandwich elements for architecture. FDM enables the mold-less fabrication of plastics, allowing cost-effective production of geometrically complex artifacts. FDM can be used for the fabrication of large-scale freeform sandwich panels. To 3DP large elements, often a wide extrusion diameter is chosen. This leads to higher strength of parts and the reduction of fabrication-time, but also to heavier components. Thus, achieving structural integrity while maintaining lightness remains the challenge. Instead of increasing the material thickness, the research focuses on the 3DP of infill to reinforce the overall structure efficiently. While conventional infill strategies are limited to vertical extrusions, a more performative inner structure – namely 3D lattices oriented in multiple directions – can be adopted allowing the realization of functionally-graded, structurally-optimized sandwich structures. The research investigates a strategy of utilizing the 3D lattice infill structures for large-scale applications in order to optimize the weight-to-strength ratio of freeform FDM 3D-printed double-shell structures. The paper describes the investigation of the parametric design of infill structures, the fabrication strategy, the structural evaluation, and the full-scale 3DP demonstration of a chaise lounge as a sandwich, double-shell structure (Fig. 1).



Figure 1: Cross section image of full-scale 3D-printed chaise lounge showing structurally-optimized internal structure [Developed with Moon Young Jeong and Frank Cheng-Huang Lin, photographed by Jetana Ruangjun]

Keywords: freeform sandwich element, 3D lattice internal structure, structural optimization, functional gradient, 3D printing, fused deposition modeling, lightweight building component.

1. Introduction

In architecture, using lightweight building components has significant benefits: efficient transport to construction sites, easy assembly, and reduction of embodied energy in buildings. Lighter building elements can have a positive impact on the overall structure of buildings and can allow long structural spans and cantilevering structures with minimal material.

Copyright © 2019 by Hyunchul Kwon, Benjamin Dillenburger
Published by the International Association for Shell and Spatial Structures (IASS) with permission.

One construction principle for lightweight structures is sandwich panels. Sandwich panels consist of a lightweight core layer sandwiched between two surface layers. One can distinguish between different sandwich panels as either composites, which use different materials for the core and the shells, or monolithic sandwich constructions, where the core and shell are fabricated from the same material. Adhesive and/or cohesive layers can provide a mechanical connection between the shells and the core. Enclosing thick, lightweight architected material cores such as foam or honeycomb-structures between two thin and stiff layers of sheet material improves the mechanical properties of the material significantly. "Architected" in this context refers to a particular spatial configuration of material which gives it different properties compared to its monolithic state. Sandwich structures typically obtain efficient bending strength, as the thickness of the core enables a high area moment of inertia by separating the stiff sheet layers with a thick core. The sheets work in in-plane compression and tension, while the core works in shear and transverse compression.

Sandwich structures are widely used whenever reducing weight is a key design goal, such as in the aerospace industry, but also increasingly in sporting and automotive applications such as for helmets and surf-boards. In architecture, they are used mainly for their excellent weight-to-strength-ratio, vibration absorption and for their thermal and acoustic insulation properties for facade panels.

2. Fabrication of sandwich panels: state-of-the-art

Due to the increasing demand for freeform geometries in contemporary architecture, there is a need for bespoke sandwich panels. However, the applications of sandwich structures as 3D shells are limited by the high costs of tooling and molding required for conventional forming operations.

The direct fabrication methods for sandwich panels limit them to flat 2D shapes, and usually rectangular boundaries. Typically, cores of sandwich panels are made from polymer or metallic foams. Other materials, such as Nomex (aramid fiber reinforced paper) and aluminum honeycombs are also used. The cores are mechanically bonded with adhesives or roll-bonded at high temperatures on both sides to light, stiff sheet materials. The flat panels can be subsequently 3-dimensionally formed through specialized tooling, such as pressing or deep drawing but the cost of these processes are very high while geometric freedom is still limited [1]. There is, therefore, a commercial motivation for exploring new fabrication methods for freeform sandwich panels with reduced tooling costs.

3DP has enabled the mold-less fabrication of plastics, allowing the cost-effective production of geometrically complex artifacts. Among the different 3DP technologies, FDM is the most widespread technology due to its simple hardware setup, accessibility and wide range of available materials, in which molten material is extruded and hardens instantly after deposition. FDM can produce large-scale elements with reasonable speed (20–100 L/h) and various resolutions in the range of 0.1 mm to 9 mm layer-height.

In architecture, FDM has already been investigated for the prefabrication of sandwich-structured building elements. Relevant precedents investigated geometric complexity and physical performance criteria such as thermal insulation, ventilation, shading [2, 3], and structural reinforcement through Carbon Fibre-reinforced Plastic (CFRP) add-on 3DP [4]. To fabricate large FDM 3D-printed elements, a wide extrusion diameter is often chosen (up to 9 mm) [5]. This leads to higher strength of parts and the reduction of fabrication-time, but also to heavier components. Thus, achieving structural integrity while maintaining lightness remains one of the biggest challenges of FDM 3DP.

3. 3DP structurally-optimized sandwich panels

Instead of increasing the material thickness, this research investigates how one can reinforce freeform FDM 3D-printed sandwich structures effectively by integrating 3D infill core structures, in order to optimize the weight-to-strength ratio. These infill structures can be 3D-printed without support structures, hence minimizing the fabrication-time.

The strategy aims to fabricate the external face shells of the panel along with a minimal 3D lattice internal structure for stiffness in a single process. Through this process, geometric freedom is inherited from the 3DP process of the outer shell, while the anisotropic stiffness of the core is achieved through a structurally-oriented 3D core, maintaining the lightness of the structure.

Moreover, due to the nature of the monolithic materiality and singular fabrication process of FDM 3DP, adhesion failure between face shells and core can also be avoided, addressing one of the largest mechanical challenges in conventional manufacturing, e.g. for foam cored metal/plastic sandwich structures.

Furthermore, 3D core structures are not limited to uniform shapes but can also be adapted to complex freeform geometries. These 3D core scan be functionally-graded and optimized for specific loads and in response to specific failure modes in order to address performance-limiting mechanisms. Due to local adaptability to specific load cases, 3D-printed cores can structurally be more efficient than random cellular structures. Performance benefits and reduced weight can be achieved by using 3D-printed complex-shaped sandwich panels with functionally-graded cores [6].

The presented approach consists of the investigation of the geometric system of the core structures and the development of the related fabrication strategy.

3.1. Geometric system

Until recently, conventional infill strategies for FDM have been limited to vertically-extruded geometries, regardless of their shapes [7]. Lately more performative inner structures have been investigated through the design and fabrication of custom cores with optimized lattice geometries which work in uniaxial tension [8, 9]. However, FDM 3DP of 3-dimensionally optimized inner structures require 3D-printed additive support, [10] especially for geometrically complex elements [11], which slows down the fabrication process. In large-scale fabrication, this critically increases the manufacturing-time.

Building components require strength in various directions. Thus, the main structural principle of the core pattern aims to achieve orthotropic structural behavior. In order to obtain this, the investigated 3D core is constituted of multi-directional lattice units which are 3-dimensionally anisotropic showing uniform stiffness [8, 9]. With a specific geometric arrangement, avoiding any large overhangs, the 3D lattice core can be completely free of the requirement of temporary support structures, enabling each lattice to become the support for another (Fig. 2).

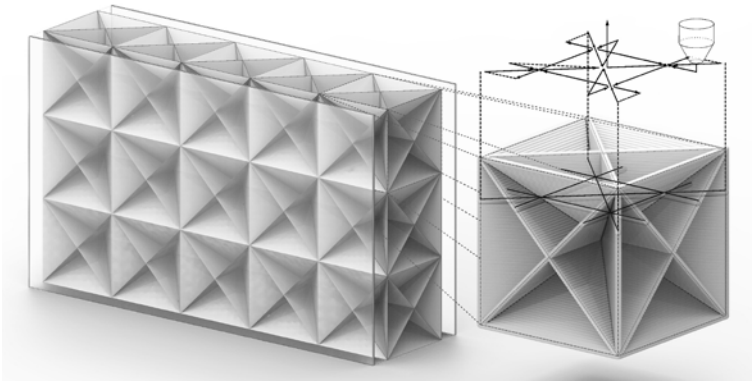
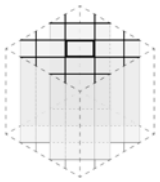
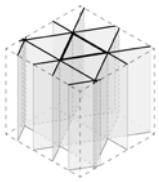
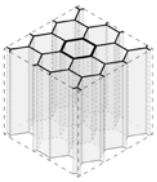
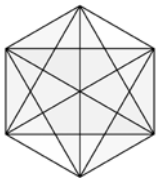


Figure 2: (left) Investigated 3D lattice system structure for sandwich panels; (right) A unit of the 3D lattice core allowing non-supportive FDM 3DP with efficient 3DP-path

In comparison with conventional vertically-extruded structures, Table 1 shows the investigated 3D lattice core.

Table 1: Geometric features of investigated different core compositions in units

Conventional 3DP patterns of vertical infill cores [7]			3D lattice core [8, 9]
Rectangular	Triangular	Hexagonal	
			

3.2. Fabrication setup

To materialize the investigated strategy of creating a sandwich panel and its core design in large-scale, a six-axis industrial robot arm (ABB IRB 1600 8 kg payload 1.45 m reach) is used, with the integration of a custom tool-head extruding Polylactic acid (PLA) thermoplastic material. The tool is designed to extrude a 2.5 mm diameter of PLA, which is significantly smaller than other large-scale FDM extrusions (up to 9 mm) [5], in order to be able to 3D print lighter structures with a higher resolution.

4. Structural tests

4.1. Design of experiments

The research assesses the mechanical properties of the investigated 3D lattice cores by comparing a set of 3D-printed sandwich beams consisting of vertically-extruded infill structures. Three common patterns of conventional 3DP infill structures – triangular, rectangular and hexagonal – are included, consisting of typical source shapes (Fig. 3).

The sandwich beams are designed to have overall dimensions of 160 mm x 40 mm x 40 mm for the uniaxial three-point bending test and 40 mm x 40 mm x 40 mm for the uniaxial compression test. Considering the anisotropic nature of 3DP technology due to the deposition process, the layer orientation is assumed to influence the structural performance of the material. Therefore, all the specimens are 3D-printed along the same orientation. For the compression test, two different orientations are tested with 1) the load and 3DP build-up directions in parallel, and 2) the load and 3DP build-up directions in orthogonal (Fig. 3 right), to compare the orthotropic structural behavior.

Each specimen is designed to have the same amount of material – 212 g for the bending test and 53 g for compression (density of 829 kg/m³ with a relative average deviation of 1.4%) in order to compare under the same weight-to-strength ratio condition. Consequently, the fabrication required roughly the same amount of time for each specimen: ≈80 minutes for bending test samples (256 mm³) and ≈20 minutes for compression test samples (64 mm³).

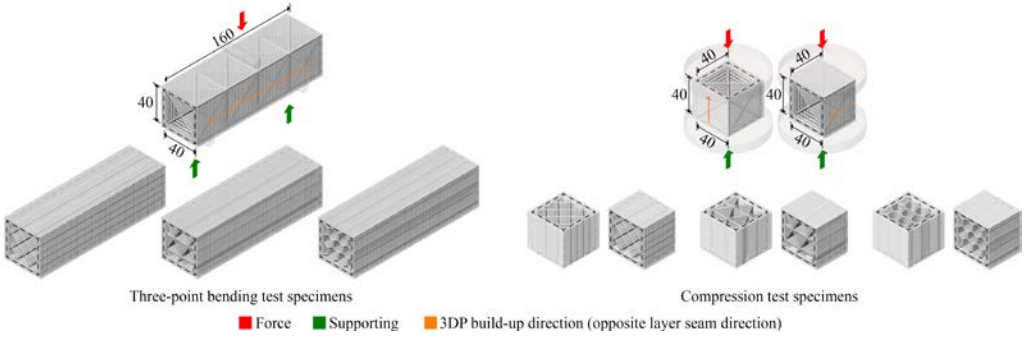


Figure 3: Sandwich-structured beams for structural tests; Four core units are embedded into the outer shell

4.2. Mechanical testing

The bending test and compression test were performed using a mechanical tester (ZWICK Universal testing machine Type 1484) with a 200 kN load cell at a loading rate of 1 mm/min. The bending test was carried out with a span length of 120 mm. All the bending test samples failed in shear with fracture. Compressive strength of each specimen was measured until the value decreased to 80% from the maximum measured. No fracture was observed (Fig. 4).



Figure 4: (left three) Shear failure of test piece of 3-point during bending test; (right two) Shortened test pieces of two different orientations of compression test

The mechanical properties of the sandwich-structured beams are presented in Figure 5. On the one hand, as expected, the result of the bending test shows the investigated 3D lattice cored sandwich structure attaining the highest strength among others (1.11 to 1.53 times stronger on average).

On the other hand, in the compression test for the specimens in which the 3DP build-up direction is oriented in the parallel direction of the load, the conventional triangularly infilled specimens obtain the highest strength (avg. 45 MPa) while the 3D lattice cored specimen has the second highest (avg. 36 MPa). It can be inferred that because the nature of uniaxial compression is carried in one direction, the conventional vertically-extruded patterns can be structurally more advantageous especially when the same amount of material is used. Moreover, the triangle is, in this case, the strongest geometry that can be found. Thus, among the conventional 3DP core patterns, the triangular infill shows the highest structural efficiency in all the compressive and bending strength tests, while the hexagonal core has the lowest.

While comparing the absolute strength values between both sets (different orientations) from the compression tests, it is found that only the 3D lattice structure shows the relative orthotropic behavior for both orientations of the specimens, while vertical 3D-printed structures have very low compressive strength in opposite directions of the 3DP build-up. Overall, the 3D lattice cored sample shows the highest compressive strength (avg. 24 MPa), presenting the largest differences in ratio from being 1.3 to 2.03 times stronger than others.

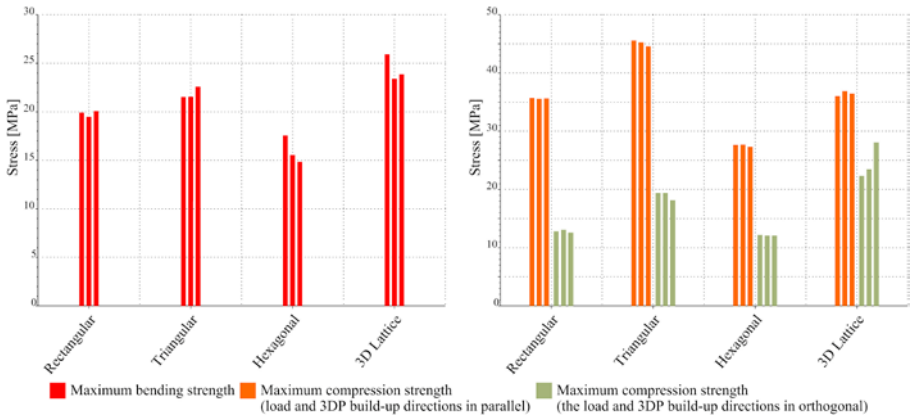


Figure 5: Strength characteristics of tested sandwich-structured specimens; Each peak indicates the maximum strength the specimens bore; (left) Flexural strength; (right) Compressive strength

5. Large-scale demonstration: 3DP of LevisErgon chaise lounge

To demonstrate the ability to scale up the proposed fabrication approach and to investigate the adaptability of the geometric system to various complex geometries, a shape of the Surf Lounger chaise longue created by the industrial designer Karim Rashid [12] is selected and reinterpreted for the proposed 3DP fabrication process. As a sandwich, double-shell structure, it contains an optimized, 3D-printed core. Here, the investigated 3D lattice core units are functionally-graded and adapted for specific loads by placing and orienting the lattice structure along the flow of forces [13].

The design of the LevisErgon chaise lounge is optimized to the load case of a sitting person (up to 120 kg). By adapting a computationally-generated structural-flow (compressive and tensional stress vector fields), the design system allows the core structure to follow the force fields creating an optimal 3D wave infill structure, the efficient continuous-path generation and the support-free 3DP (Fig. 6, Fig. 7 left).

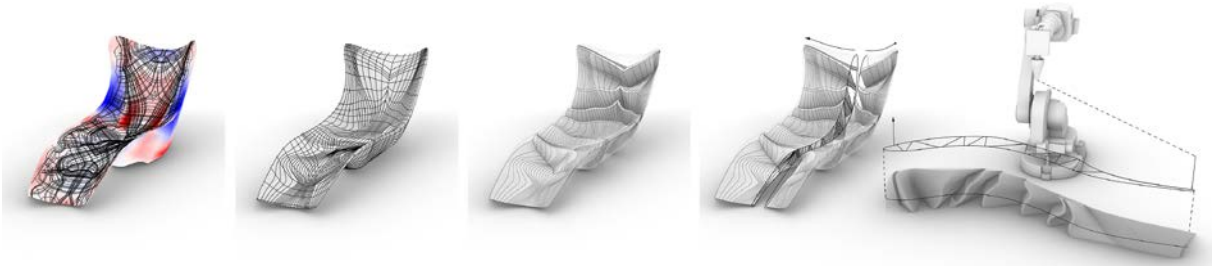


Figure 6: Design and fabrication of LevisErgon [Created by Moon Young Jeong and Frank Cheng-Huang Lin]

Consequently, the structurally-optimized 3D core structure enables the weight of the chaise lounge to surmount to less than 15 kg. Along with the core structure, the computationally generated geometry shows the implementation of design features with structural roles (Fig. 7 right): the individual plastic layers are 3D-printed with variable layer-height following the force fields; the honeycomb-shaped holes further reduce material.



Figure 7: (left) View of structural-flow oriented 3D lattice core; (right) Structurally-oriented 3DP layers and weight reduction enabled by strategic perforation [Developed with Moon Young Jeong and Frank Cheng-Huang Lin, photographed by Jetana Ruangjun]

Consequently, the chaise lounge, with dimensions of 1.7m x 0.7m x 0.7m, could be 3D-printed with a thickness of just 3mm, reducing the weight (Fig. 8 left). The chair has been in use at multiple exhibitions such as the Olma Fair 2018 in St. Gallen and the Implenia BIM Community Days 2018 in Winterthur (both indoor and outdoor) and has so far not shown any cracks or other failures (Fig. 8 right).

With its ergonomic design, intricate details and its optimized geometry, the robotically 3D-printed LevisErgon chair showcases the potential of a strong interplay between digital fabrication and computational design.



Figure 8: (left) The lightweight 3D-printed demonstrator can be easily lifted [Model: Frank Cheng-Huang Lin]; (right) Actual use of the chair at ETH Zurich [Model: Maria Margherita Innocenti] [Developed with Moon Young Jeong and Frank Cheng-Huang Lin, photographed by Jetana Ruangjun]

6. Discussion and outlook

Only the FDM 3D-printed 3D lattice core structures achieved a comparable compressive strength in opposite directions of the 3DP build-up. However, the observed strength is still substantially lower (32% of strength loss) compared to the strength of the sample in which the load and 3DP build-up directions are oriented in parallel. This is mainly because of the orthotropic nature of FDM 3DP resulting in weak inter-layer bonding [14].

As a possible solution to overcome the low-bonding strength, previous research has investigated how multi-directional add-on 3DP of continuous CFRP enables efficient, opposite structural reinforcement with minimum material use [4]. In combination with this additional reinforcement method, the strength of the 3D lattice cored sandwich element is expected to increase radically, preventing shear fracture from bending test.

The tested specimen presented in this paper consists of shells closed on four sides with various inner structures. Additional tests will be conducted with larger sandwich panels without side-walls. Furthermore, larger scale experiments integrating CFRP add-on 3DP on 1:1 facade-elements will be investigated to test the proposed construction system for architectural applications. The identified outlook for large-scale fabrication consist of the following:

- 3DP of plastic sandwich units that can easily be assembled for a building-scale structure.
- Investigation of an integrated joint strategy to connect the units.

While the material used in the experiments, PLA, has some shortcomings regarding its usage in architectural applications (i.e. fire resistance), the presented findings could also be relevant for other FDM 3DP systems.

7. Conclusion

The paper describes a method of fabricating sandwich elements consisting of structurally-optimized 3D infill structures for architectural use. The presented experiments have shown substantial structural improvement of bending strength and similar compressive strength in multiple orthogonal directions. The 3D-printed chaise longue demonstrates the architectural applicability of functionally-graded core structures to freeform sandwich structures at large-scale. The proposed strategy could be used for the prefabrication of building components such as double-shell structures (internal-walls, partition-walls, and facade-panels), promising a more efficient construction process through achieving lightness, with no waste material, and greater design freedom.

Acknowledgements

The LevisErgon was developed for a thesis of the 2017/18 MAS ETH DFAB [13] and the exhibition of ETH Zurich at the Olma Fair 2018. The MAS ETH DFAB is a one-year full-time educational program jointly organized by Digital Building Technologies (DBT) and Gramazio Kohler Research, and of the

NCCR Digital Fabrication. The authors would like to thank a number of partners whose dedication helped fulfill the research described in this paper: Moon Young Jeong, Frank Cheng-Huang Lin (2017/18 MAS ETH DFAB), Dr. Juanita Schläpfer-Miller, Annina Ziltener (Zurich-Basel Plant Science Center), Daniela Villiger (Compresso), Michael Lyrenmann, Philippe Fleischmann (NCCR Digital Fabrication), Andrei Jipa, Angela Yoo (DBT), Rafael Pastrana, Jetana Ruangjun (2017/18 MAS ETH DFAB), Maria Margherita Innocenti, Jun Su, Ying-Shiuan Chen, Wei You (models) and HAL Robotics (software support).

References

[1] K. P. Jackson, J. M. Allwood, and M. Landert, "Incremental forming of sandwich panels," *Journal of Materials Processing Technology*, vol. 204(1-3), pp. 290-303, Aug. 2008.

[2] M. Mungenast, "Fluid Morphology – 3D-printed functional integrated building envelope," in *Conference Proceedings of the 12th Conference of Advanced Building Skins, Bern; Switzerland, October 2-3, 2017,* Advanced Building Skins GmbH, 2017, pp. 109-124.

[3] M. Tenpierik, M. Turrin, Y. Wattez, T. Cosmatu, and S. Tsafou, "Double Face 2.0: A lightweight translucent adaptable Trombe wall." *SPOOL*, vol. 5(2-), Apr. 2018.

[4] H. Kwon, M. Eichenhofer, T. Kyttas and B. Dillenburger, "Digital Composites: Robotic 3D Printing of Continuous Carbon Fiber-Reinforced Plastics for Functionally-Graded Building Components," in *Robotic Fabrication in Architecture, Art and Design 2018, Zurich; Switzerland, September 12-14, 2018,* J. Willmann, P. Block, M. Hutter, K. Byrne and T. Schork Ed., Springer, 2018, pp. 363-376.

[5] C. E. Duty, V. Kunc, B. Compton, B. Post, D. Erdman, R. Smith, R. Lind, P. Lloyd and L. Love, "Structure and mechanical behavior of Big Area Additive Manufacturing (BAAM) materials," *Rapid Prototyping Journal*, vol. 23(1), pp. 181-189, Jan. 2017.

[6] J. Parthasarathy, B. Starly and S. Raman, "A design for the additive manufacture of functionally graded porous structures with tailored mechanical properties for biomedical applications," *Journal of Manufacturing Processes*, vol. 13(2), pp. 160-170, Aug. 2011.

[7] M. Fernandez-Vicente, W. Calle, S. Ferrandiz and A. Conejero, "Effect of infill parameters on tensile mechanical behavior in desktop 3D printing," *3D printing and additive manufacturing*, vol. 3(3), pp. 183-192, Sep. 2016.

[8] IceSL, "Cubic, tetrahedral and hierarchical infills," in *online Icesl.loria.fr, available at: https://icesl.loria.fr/pages/features/tetrahedral-infills/,* accessed Jun. 15 2019, 2015.

[9] H. Y. Sarvestani, A. H. Akbarzadeh, A. Mirbolghasemi and K. Hermenean, "3D printed meta-sandwich structures: Failure mechanism, energy absorption and multi-hit capability," *Materials & Design*, vol. 160, pp. 179-193, Dec. 2018.

[10] J. Vanek, J. A. G. Galicia and B. Benes, "Clever support: Efficient support structure generation for digital fabrication," *Computer graphics forum*, vol. 33(5), pp. 117-125, Aug. 2014.

[11] D. A. Ramirez, L. E. Murr, S. J. Li, Y. X. Tian, E. Martinez, J. L. Martinez, ... and R. B. Wicker, "Open-cellular copper structures fabricated by additive manufacturing using electron beam melting," *Materials Science and Engineering: A*, vol. 528(16-17), pp. 5379-5386, Jun. 2011.

[12] K. Rashid, "Furniture Project Surf Lounger," in *online Karimrashid.com, available at: http://www.karimrashid.com/projects/#category_1/project_204,* accessed Jun. 15 2019, 2010.

[13] M. Y. Jeong and F. C. H. Lin, "Lightweight Complexity," in *thesis of 2017/18 Master of Advanced Studies ETH in Architecture and Digital Fabrication, September, 2018, Zurich; Switzerland,* H. Kwon Supervisor.

[14] B. Peters, "Solar bytes pavilion," In *Robotic Fabrication in Architecture, Art and Design 2016, Sydney; Australia, March 18-19, 2016,* D. Reinhardt, R. Saunders and J. Burry Ed., Springer, 2016, pp. 326-337.

FORM and FORCE

Proceedings of the IASS Annual Symposium 2019 - Structural Membranes 2019
Form and Force
7-10 October 2019, Barcelona, Spain
C. Lázaro, K.-U. Bletzinger, E. Oñate (eds.)

Potentials of 3D Printing Technique in Optimum Design of Reinforced-Concrete Elements

A. Baghdadi*, C.Müller, H. Kloft

* TU Braunschweig Inst. für Tragwerksentwurf
Pockelsstrasse 38106 Braunschweig. Email:a.baghdadi@tu-braunschweig.de

Abstract

This paper discusses some potentials of the steel printing-technique, in reinforcing the concrete elements. This study enjoys robotic manufacturing and structural science toward a new construction approach. Wire and Arc Additive Manufacturing (WAAM) enables the designer to Print Free-Form-Bar (PFB) in place as reinforcement and/or anchor inside of the concrete in optimum shapes. The optimum shapes of PFB can improve the stress-distribution in the concrete and force-transmission in the steel. This technique can be used to form the embedded PFB in the concrete, e.g shear-connectors. The targets of utilizing printing-technique are increasing the stiffness of the whole element and having a more uniform stress distribution in both materials. In this study, the variables include shapes, locations and dimensions of the embedded PFB. The study develops some components of optimal printable patterns by means of Finite Element(FE) simulations and experimental tests. The geometries and printing component are described and the accuracy of the analysis are proved by experimental tests. The results revealed that specimens enjoying printing-potentials can have more optimum structural performance.

Keywords: Printing Technique, Free Form Bar, Stress Distribution, FE-Analysis, Concrete Elements

1 Introduction

The digitalization of planning and production in the last years is developed to accelerate the logical manufacturing process toward the next generation of construction industry [1]. Concrete and steel printing techniques have a remarkable impact on the construction digitalization process, in which the application procedures, conveying and compacting are performed simultaneously [2], while additional frame-work is not utilized [3].
Concrete can be printed by spraying concrete founded in 1919 [4] and in order to reinforce the printed concrete, some methods are proposed. One of the methods places the horizontal re-bars during the printing process, between the concrete layers. In the other method a robot produces and locates complex free-form meshes or re-bars by technique as cutting and welding, as successfully employed in the production of a complex structural wall [5]. Another straightforward approach benefits form fibre-reinforced in the concrete [6], which especially in the field of high-performance composites material has a wide range of advantages. Nonetheless, by this additive-material, concrete production becomes complex, while this material regarding the structural necessities cannot be selected instead of continuous re-bar [7]. In addition to the concrete printing technique and mentioned reinforcing methods, wire and arc additive manufacturing (WAAM) enables the producer to Print Free-Form-Bar (PFB). The studies confirmed

Copyright © 2019 by A. Baghdadi, C.Müller, H. Kloft
Published by the International Association for Shell and Spatial Structures (IASS) with permission.

the satisfying performance of this technique, which can be more developed by investigating the ribs(profile) over the bar, increasing the steel printing speed and properties of the material [1]. Employing robotic additive manufacturing in printing steel and concrete, prepares new digitalized production approach for creating sophisticated free-form geometries [8].
To enjoy the additive manufacturing technique, as a challenging opportunity, advanced shape optimization tools found their way into the structural industry. One of the most effective optimization methods is topology optimization [9], which instead of size and shape optimization may lead to an entirely new geometry [10]. The optimum geometrical design of PFB in the concrete can also be categorized as topology optimization. The PFB should be formed respecting the usages of the embedded section, to resist against different types of loads and fulfil different structural requirments, in uniuqe forms. For instance, PFB can be designed as shear connectors in composite construction for resistance against the pullout forces by incresing the tangential and frictional resistance [11]. Studies proved that changing routine structural details may considerably improve the performance of the elements. For instance, dipping the elements in the concrete instead of using extra steel plates can develope the performance of the elements(e.g. steel columns) [12], under cyclic shear and bending forces [13]. This performance is dependent on the embedding depth, innovative geometry and detailing of the embedded steel. These details can improve, rotational stiffness [14], investing more energy and enjoying the sustain performance by large inelastic deformations [15]. The elements can also, be designed regarding the school of Shape-following-force [1], and the necessary details can be freely manufactured by the digitalized techniques.
Up to know, different studies for developing the digital manufacturing of unlimited PFB geometries are addressed. The present paper, numerically and experimentally, studies the behaviour of a few embedded PFB in un-reinforced concrete under pull-out tests, to discuss the potentials of 3D printing technique.

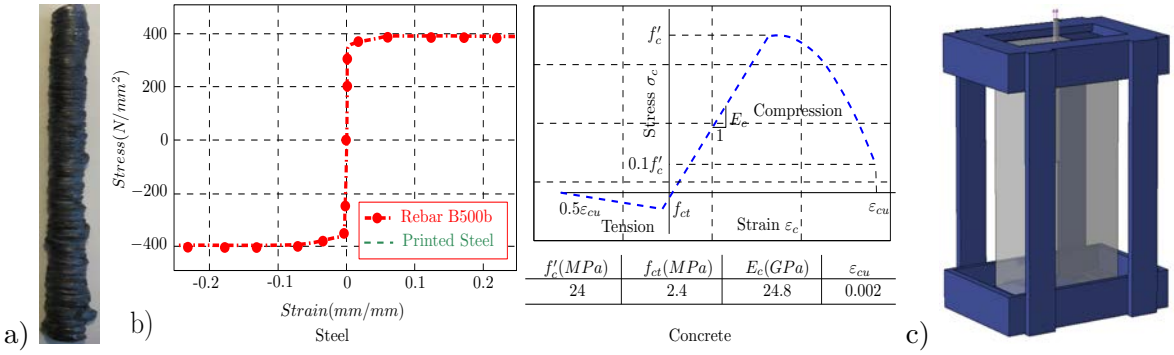


Figure 1: a) Printed steel, b) Steel and concrete properties, c) Testing setup

2 Methodology:

Manufacturing Producer: Two approaches are particularly interesting for the production of building elements by additive welding. 1- Layer-wise driving of webs, e.g. for the production of complex hollow profiles or free-form metal sheets and 2- Spot welding process, that is initiated at one point only for a short interval of less than one second, when the robot is not in motion. By means of the Spot welding technique, the complex geometry of the re-bars can be produced precisely according to the designed 3D models, as selected in this study. The PFB are printed

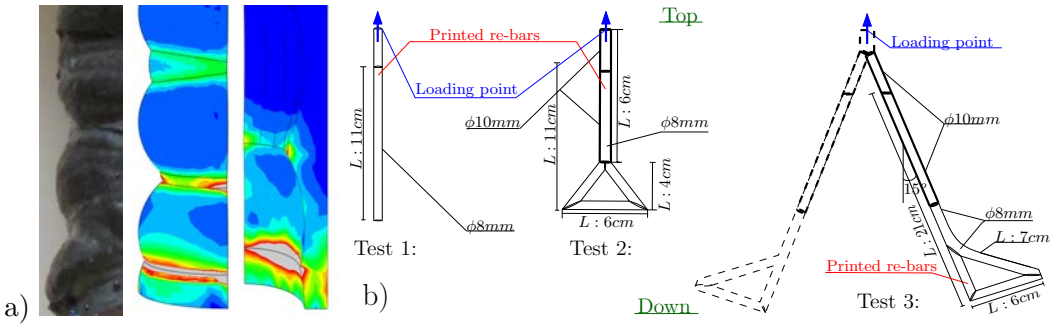


Figure 2: a) Micro photo and schematic stress in a printed ribs, b) Geometires of the disscussed moleds

at the Digital Building Fabrication Laboratory (DBFL), owning a CNC-controlled 5-axis portal milling machine, a 6-axis heavy-duty robot and a WF 60i ROBACTA DRIVE welding robot for Cold Metal Transfer (CMT) arc welding [16] process. With the special feature, the pulsation and a high-frequency back and forth movement of the welding wire are controlled by means of a processing unit. As a result, welding material drops better and are detached from the wire. Additionally, the temperature is reduced to prevent unwanted deformation. The path-plannings of the robot are modeled in Grasshopper(Rhinoceros 3D), and fed with information such as the switching and pausing the welding-robot frequency to avoid overheating.

Analytical Modeling: In the numerical simulation the testing setup and properties are generated in Abaqus 6.14-2, regarding its ability in modeling behaviour of both steel and concrete materials along with different tangential properties, Fig(1). Regarding the nonlinear behaviour of the material, the complexity of geometrical surfaces and the defined interaction Dynamic-Explicit as the producer is selected. In order to define the steel the bi-linear model and for the definition of concrete, the Concrete-Damage-Plasticity as the most realistic and precise behaviour is selected. This property definition can simulate the crush and cracking procedure in the concrete, in which strain-stress properties should be defined for tension and compression along with damage parameters. In order to have a relevant simulation of the contact between steel and concrete, cohesive contact is selected. In the interaction module Adhesion, Detachment, Slip and Friction are simulated. In addition, the Hard-Contact is defined in Abaqus for the friction-less interference between steel and concrete surface.

Experimental Modeling: In addition to initial tests and correspond to the numerical simulation, physical Free-Form-Bars are printed and embedded in concrete. Universal testing machine (IAM 50KN) is used for pulling the re-bar out of the concrete boxes to assess the stiffness and performance of the models. Due to using the material testing machine a specific consideration for preventing the movement of concrete-cube is essential, hence a robust steel-cage is prepared. The steel-cage is connected strongly to the machine to fix the concrete while acting as supports only on the top side of the concrete-cube. The cage simultaneously prepares enough space in the top-side to let the re-bar be pulled out by the testing machine, as similarly simulated in Abaqus, Fig(1,c).

3 Discussion:

WAAM can be utilized to form PFB paralleled to principle stress, as stirrups-bar against shear and/or as embedded cages to ensure the bars remain firmly anchored in a field with continued properties, etc. Hence, three geometries step-wise are discussed to structurally address the

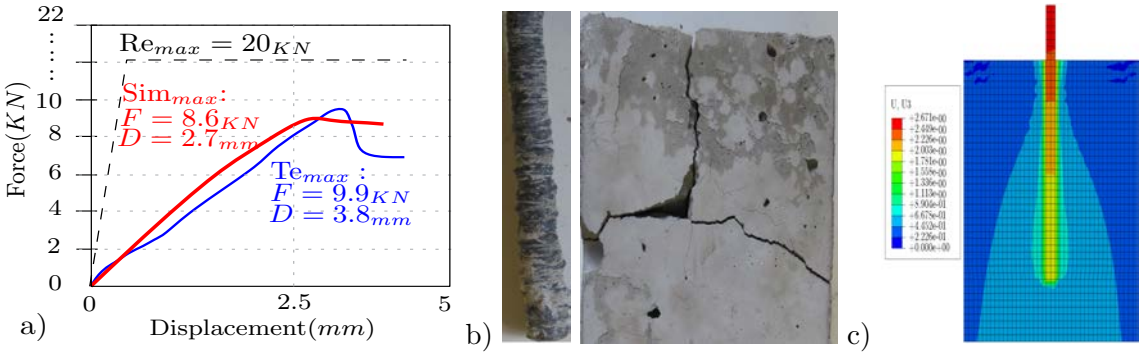


Figure 3: Test1: a) Force(F)-Displacment(D) diagram by FE simulation(Sim)) and experimental tests(Te) along with Re-bar tension capacity(Re_{max}), b) Printed re-bar and concrete after the tests, c) Simulated deformation contour(mm).

impression of using the potentials of printers in the manufacturing of unique complex geometry. In the first geometry, the performance of the printed steel is similar to the normal straight re-bars, in which the adhesion in the surfaces between the concrete and PFB is the most effective component. Then, curvature and branches are regarded in two other models steel loops.

3.1 Straight Elements:

By the cohesive behaviour should be no slippage between the concrete and the steel, in which the adhesion resists against the shear-stress. In conventional reinforces 25-30% of resistance happens due to concrete-steel adhesion and 70-75% due to the roughness of the ribs over the re-bars. However, commonly the ribs(profiles) are bigger on the surfaces of the printed re-bars in compare to the conventional re-bars. From the other side, the modulus of elasticity and tensile strength, in the printed steel is 20% less than normal steel [17]. As a result of the more adhesiveness and less strength, the essential bond length(development length) of the printed re-bar can be shorter. Hence, generally in calculations and in comparison with the conventional design, the resistance of the ribs is more critical. In addition to steel and bonding-surface, the third component which resists against the transformed load is the concrete. Improving the quality of the concrete and strength, in addition to distributing the load in the further distance, increases the adhesiveness between PFB and the concrete. Nonetheless, the focus of this study is on the potential of PFB to distribute the stress wider and deeper in concrete. Hence the PFB is designed, in a way to avoid any failures in steel.
Figure(2a) displays an image of ribs form printed steel and the simulated schematic stress. The simulation displays locally similar deformation in the two material and suitable cohesion, in initial steps of the loading process. However, the stress concentration and asymmetry in the printed steel in detail is considerably more than conventional re-bars and can lead to non-predicted damage and yield in the elements. The concentration of stress is more in the troughs on the surface of the steel, which is actually the area where the re-bar has the smallest cross-section and should be selected as the calculative dimensions. This issue can lead to a micro-scale smash in the bonding surface, which eases the slip of re-bar. However, this stress concentration is not limited to printed re-bar, but the PFB is more sensitive. Additionally, reducing the surface-roughness by minimizing the dimensions of the ribs in the entrance part of the PFB (similar to wooden-screws) comforts deeper force transition. Another point in the PFB geometries is the formation of sharp-angle points, that causes a high concentration of stress in the steel

and concrete. This issue becomes more important by the use of branches and loops in these geometries. In conventional reinforcement, this issue is elaborated by using curved and flat elements. This point should be considered in designing of printed geometries.
Figure(3), displays the performance of the pulled out straight printed steel. The force-displacement diagrams based on the average amount of the tests and the simulation results are plotted. Additionally, photos of the cracked concrete and printed steel after the tests along with the deformation of full geometry are addressed, which is calculated by Abaqus. In this geometry, the re-bars emerge from concrete without any rupture in the steel and due to an entire crush in the concrete, under $9.9KN$ axial-force. In case of having less surface-roughness (smaller ribs) over the printed steel, the emerge could be accrued by a slight slip and local damage around the steel.
An efficient difference between conventional re-bars and PFB is the capability of the printers in manufacturing the re-bars with non-prismatic cross-sections. These non-prismatic sections, with the different area to perimeter ratios, enables the designer to control the amount of transmitted load through bonding-surface in compare with the load which remains in re-bar for deeper concrete. For instance, printers can convert the circular-cross-section to an ellipsoidal-cross-section, aiming optimum area to perimeter ratios. Differently, based on some simulations, changing the axis-angle of the straight re-bars, under the same direction of forces, brings more compressive force(stress) between re-bar and concrete. Increasing the rotational angle from vertical to horizontal, leads to bending moment and more stress, especially in the primary parts of the re-bar(top side) and transfers more force via bonding surface in this area, in a horizontal direction. In other words, this deviation reduces the depth of vertical stress propagation. Accordingly, this deviation is more profitable in dipper parts, otherwise can have destructive effects.

3.2 Looped Elements:

In addition to rotating the re-bar, non-prismatic cross-sectional and optimizing the adhesiveness of the printed elements, manufacturing completely closed steel-loops by 3D printers is possible. Which is not readily available on routine reinforcements for each element in a unique shape. By the loops, the aims are bringing more stability against the slip of the re-bar, semi-confinement of the concrete and trying to transfer the force to a greater level of the concrete. Which in case of preventing the rupture in the PFB increases the strength of the full element.

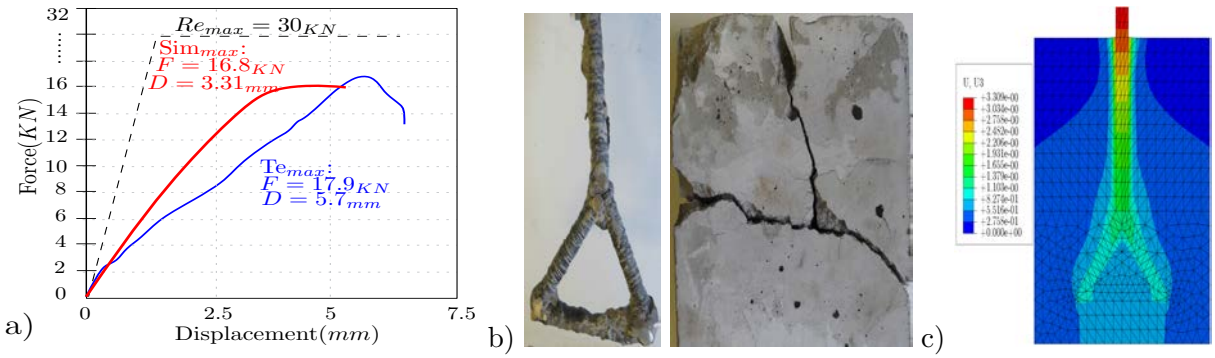


Figure 4: Test2: a) Force(F)-Displacment(D) diagram by FE simulation(Sim)) and experimental tests(Te) along with Re-bar tension capacity(Re_{max}), b) Printed re-bar and concrete after the tests, c) Simulated deformation contour(mm).

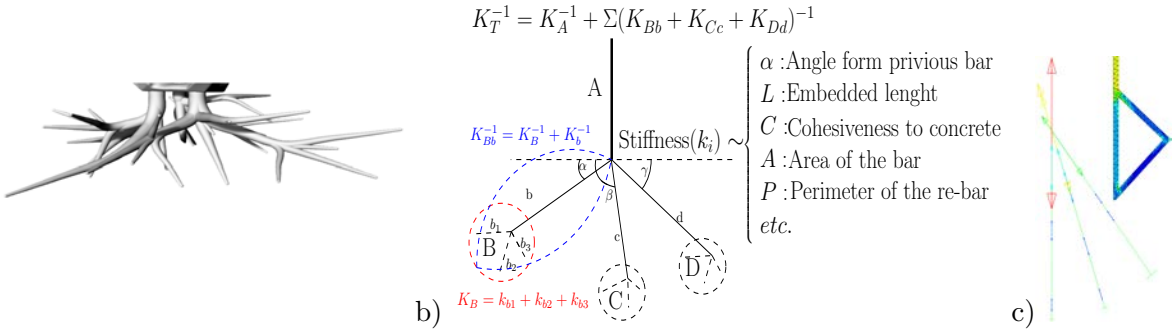


Figure 5: a) Symbol of PFB roots b) Seris of Stiffness(force divition) in re-bar banches c) Shematic effect of deviation and branches under

Figure(4), displays the performance of the printed steel with a loop at the end. The force-displacement diagrams as an important criterion from the average amount of the tests along with the simulation results are plotted. In comparison to the previous geometry it can be concluded that adding a ring in the printing process, can improve the stiffness by around 40%. In preparation for these tests, it is found that some failures in the PFB happen in places with a sudden change in the dimension of the cross-section, which may match with the place of the formation of the ring and changes in stiffness. This issue is faced as a gradual change in the dimensions of cross-sections during the printing process.

3.3 Branched Elements (Test(3)):

Additionally, closed printed rings will inevitably be in branched in some parts. In manufacturing the branches, which is not possible by ordinary reinforcement, the proper angle and the change in the dimensions of the branched re-bars are the discussion point. Creating branches makes it also possible to distribute the force in an optimal form to have wider concrete under stress. The amount of the transmitted force by each branch is depended on the stiffness(K) of that branch in compare with the summation of all other stiffness(ΣK_i). The re-bars perform series or parallel with each other, which makes it possible to be calculated as springs, Fig(5). The amount(percentage) of gathered force(by each branch) is related to several component, e.g. Angle(α), Perimeter(P), Area(A) Cohesiveness(C) in bonding-surface and Length(L) of each individual branch. Also, in an efficient design, this force division depends on the probable branches and circles at the end of each branch, subsequently. An Efficient design should properly transmit the force from the highest part of the PFB to the lowest level of that gradually and symmetrically in a wide area of concrete. In the configuration of branches, such as trees, deeper roots have smaller dimensions that ease the touch with more soil(here concrete). Optimum design is not an easy task due to involving noticed influential parameters. In many cases, for example, due to the large angle in a branch or the early transfer of force to concrete, it simply causes areas with high stress in both concrete and steel, in addition to stress-free areas in lower regions. This fact indicates the importance of using optimization algorithms appropriately along with additive manufacturing toward optimum designs, which should be discussed in future studies.

By considering the mentioned points and potentials of WAAM, a plethora of geometries can be optimally calculated and designed. As a simple and basic example, a geometry with a ring and a non-prismatic section is designed (Fig(2)). However, due to limitations in the testing-machine

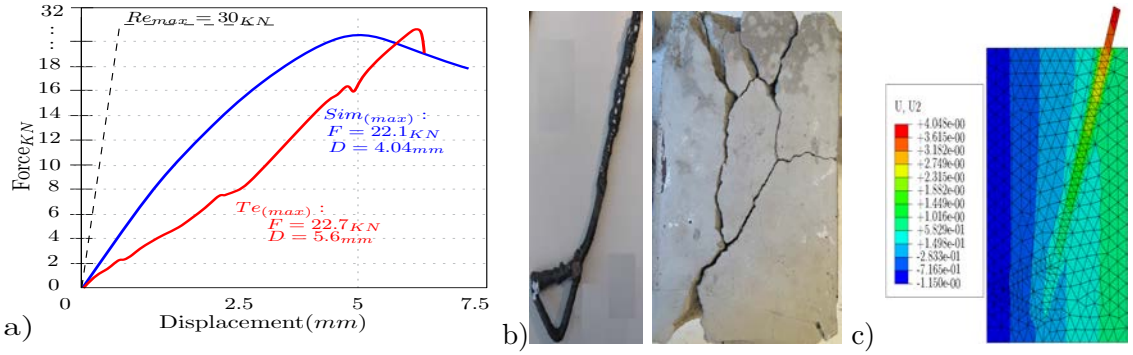


Figure 6: Test3: a) Force(F)-Displacment(D) diagram by FE simulation(Sim)) and experimental tests(Te) along with Re-bar tension capacity(Re_{max}), b) Printed re-bar and concrete after the tests, c) Simulated deformation contour(mm).

and to reduce the costs of analysis, half of the symmetric geometry is tested and simulated. The geometry of PFB due to its depth needs to resist against higher force to cause a complete disruption in concrete, while as mentioned, the optimization targets are preventing internal rupture and slip of the steel. In this model, with gradual changes in the dimension of the cross-section, increasing depth and adding curvature, it is attempted to transfer the force to a greater depth of concrete, which leads to over 30% more stiffness than the previous models, Fig(6). In fact, this geometry enjoys a wide area of concrete, which increases the overall capacity of the element by aids of additive manufacturing, without any yield in steel as an optimum design.

4 Conclusion and Outlook:

Additive manufacturing and digital construction have become recently the subject of rapidly growing activities. Since utilizing the reinforced concrete is essential in a wide range of structures and regarding the ability of the steel printers, it is obligatory to discuss and develop the potentials of this technique and the differences of this usage, to bring the technology of steel printers forward. This present at hand briefly describes the potential of 3D steel printers in developing the geometries which can be printed and used to resist against pulling-out similar to a shear-connector. The selected tools for production and evaluations are 3D arc welding robotic printers, numerical FE simulation software(Abaqus) and universal testing machine to pull the printed re-bars out of concrete. It can be concluded that: 1- The creation of curvature and loop, as the potentials of additive manufacturing and robotic printers, can lead to an optimal distribution of stress in concrete. 2- Establishing branches in PFB, similar to the root of trees, for greater penetration, increases the stability of re-bar in the concrete and the adhesiveness between PFB and concrete. 3- Re-bars should be designed and printed with an optimal non-prismatic section to transfer forces in greater depth and wider distribution. 4- Reducing the surface-roughness at the beginning of the PFB (here top side) optimizes the absorbed forces via the bonding-surface through the length of PFB.

References

[1] Viktor, et al. 3D-printed steel reinforcement for digital concrete construction Manufacture, mechanical properties and bond behaviour. Construction and Building Materials 179 (2018): 125-137.

[2] Ott J., Neudecker S., Petri J., Kloft H., Generative concrete spraying of a free-form chair a case study IASS, 2015.

[3] Muether U., Spritzbeton-Kuppel des Planetariums Wolfsburg, Beton-Stahlbetonbau, 1985.

[4] Neudecker St., et al. A new robotic spray technology for generative manufacturing of complex concrete structures without formwork. Procedia CIRP 43 (2016): 333-338.

[5] N. Hack, et al., Mesh Mould: An onsite, robotically fabricated, functional formwork, in: 11th High Perform. Concr. Concr. Innov. Conf., Troms, Norway, 2017.

[6] V. Mechtcherine, V.N. Nerella, Incorporating reinforcement in 3D-printing with concrete, Beton- und Stahlbeton 113 (2018), https://doi.org/10.1002/ best.201800003. first publ. online: 27.4.2018.

[7] V. Mechtcherine, Novel cement-based composites for the strengthening and repair of concrete structures, Constr. Build. Mater. 41 (2013) 365373.

[8] C. Gosselin, et al., Large-scale 3D printing of ultra-high performance concretea new processing route for architects and builders, Materials & Design, vol. 100, pp. 102-109, 2016.

[9] P. Christensen and A. Klarbring, An introduction to structural optimization. [Dordrecht]: Springer, 2009.

[10] E. Holmberg, Topology optimization considering stress, fatigue and load uncertainties, Ph.D, Linkping University, 2018.

[11] Heristchian, M., P. Pourakbar. Tensile behaviour of tapered embedded column bases. (2014): 485-499.

[12] Grauvilardell JE, et al. Synthesis of design, testing and analysis research on steel column base plate connections in high-seismic zones, Structural Engineering Report No ST-04-02, Department of Civil Engineering, University of Minnesota, October 1, 2005.

[13] Nakashima S. Response of Steel Column Bases Embedded Shallowly into Foundation Beams, Proceedings of the Eleventh World Conference on Earthquake Engineering, Acapulco, Mexico, 1996.

[14] Hitaka T, et al. CFT Column Base Design and Practice in Japan, Proceedings of the International Workshop on Steel and Concrete Composite Construction (IWSCCC-2003), Report No. NCREE-03-026, National Centre for Research in Earthquake Engineering, Taipei, Taiwan, October 8-9, 2003, pp. 35-45.

[15] Morino S, et al. Strength and stiffness of CFT semiembedded type column base, Proceedings of the International Conference on Advances in Structure, Sydney, Australia, 2003, pp. 3-14.

[16] Contreras, Rafael Felix ,Estudio De La Soldabilidad Entre Materiales DisÍMiles A6061-T6/Acero Dp900 Galvanizado, Unidos Por El Proceso Cmt,2018.

[17] Mechtcherine, Viktor, et al. "3D-printed steel reinforcement for digital concrete constructionManufacture, mechanical properties and bond behaviour." Construction and Building Materials 179 (2018): 125-137.

Proceedings of the IASS Annual Symposium 2019 – Structural Membranes 2019
Form and Force
7 – 10 October 2019, Barcelona, Spain
C. Lázaro, K.-U. Bletzinger, E. Oñate (eds.)

Study on Static and Dynamic Behavior of Roof Structures Consisting of Radially Arranged Cables under Strong Winds

Akira OSHIUMI*, Akira OKADA[a], Naoya MIYASATO[a],
Shuzo HIROISHI[b], Takuto YAGASAKI[c]

* NIKKEN SEKKEI, Ltd., Tokyo, Japan
2-18-3, Iidabashi, Chiyoda-ku, Tokyo, 102-8117, Japan
akira.oshiumi@gmail.com

[a] Professor Nihon University, Tokyo, Japan
[b] Associate Professor Nihon University, Tokyo, Japan
[c] Graduate Student, Nihon University, Tokyo, Japan

Abstract

In Japan, it is assumed that there will be many new constructions of stadiums with roofs and expansions and renovations of stadium roofs in the future. In this paper, the authors focused on a roof structure consisting of radially arranged cables in which cables are radially arranged between the inner tension ring and the outer compression ring. This structure has been adopted extensively both for new and renovated roofs on the stadiums outside of Japan, but there are no cases adopted in Japan. One of the factors is wind load. Since this structure is a lightweight structure, the wind load is generally dominant. In the case of Japan, wind load is larger than in many places in the world due to the influence of typhoons. Deformation and stress are also considered to be larger than in many places in the world. Various studies on this structure have been conducted in the past, but detailed studies on structural behavior during strong winds have not yet been published. In this paper, with a view to adopt this structure in Japan, the authors consider the structural characteristics under wind load. The authors conducted wind tunnel tests using scale models, conducted static and dynamic studies by numerical analysis, and documented detailed structural behavior under strong wind loads.

Keywords: lightweight structure, stadium, tension structure, cable, wind tunnel test, time history response analysis

1. Introduction

In recent years, regulations have been set in detail for stadiums in Japan. For example, it is recommended that the roofs of the stadiums cover all of the audience seats. However, many existing stadiums do not have roofs that cover all the audience seats. Therefore, it is assumed that there will be many new constructions of stadiums with roofs and expansions and renovations of stadium roofs in the future. In this paper, the authors focused on a roof structure consisting of radially arranged cables, which has been used in many new constructions and renovations in recent years at stadiums outside of Japan. This structure is a lightweight structure in which cables are radially arranged between the inner tension ring and the outer compression ring. However, there are no cases adopted in Japan. In this paper, with a view to adopt this structure in Japan, the authors consider the structural characteristics and accumulate basic knowledge for structural planning.

Copyright © 2019 by Akira OSHIUMI, Akira OKADA, Naoya MIYASATO, Shuzo HIROISHI, Takuto YAGASAKI
Published by the International Association for Shell and Spatial Structures (IASS) with permission.



Mercedes-Benz Arena (Germany)

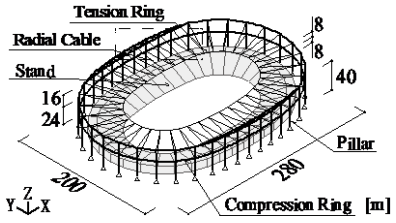


Stadium Maracana (Brazil)

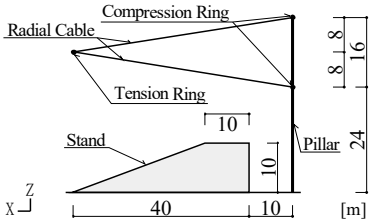
Figure 1: Examples of the structure

2. Consideration and examination model

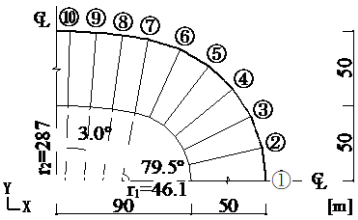
Since this structure is a lightweight structure, wind load is generally dominant, and wind resistant design is the most important design issue. Although previous research about this structure has reported on the basic properties and behavior against seismic load, detailed examination on the structural behavior under strong winds has not been discussed on. Therefore, the authors conducted a study based on wind tunnel tests using a scale model and numerical analysis. In this paper, an examination model was constructed referring to existing repair cases outside of Japan. The planar shape of the examination model is an elliptical shape, and the stand and the roof are structurally separated. The roof was composed of one tension ring and two compression rings, and the tension ring was located at the center of the two compression rings height. In addition, with reference to the previous report [1], the upper part of the compression ring has double compression rings arranged on the long side to add branch pipes and diagonal members in order to improve the out-of-plane rigidity.



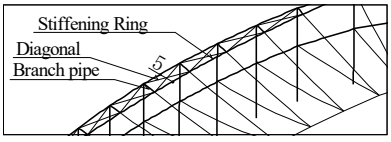
a) Experiment Model



b) XZ section



c) XY plane



d) Stiffening ring detail

Figure 2: Outline of model

Table 1: Structural specifications

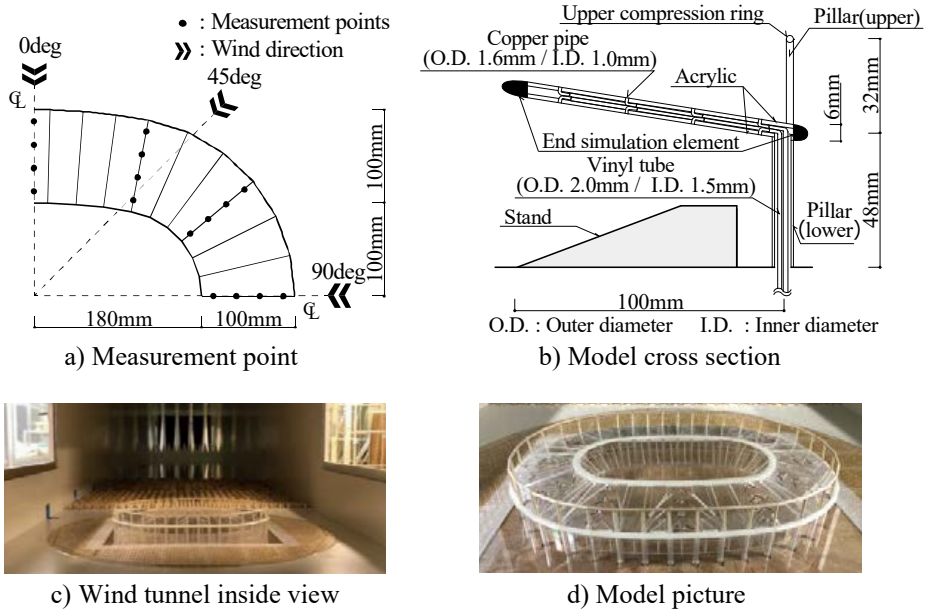
■Structural specifications of the frame		
(Pillar)	STK400	φ1320.8×36
(Compression Ring)	STK400	φ1270×36
(Stiffening Ring)	STK400	φ1016×28
(Branch Pipe)	STK400	φ762×22
(Diagonal)	Tie Rod	φ90

■Structural specifications of the cable (Locked coil rope & Non-pressure bearing)						
Tension Ring	10-φ100					
Radial Cable	(Lower)			(Upper)		
	short side	(①～⑥)	2-φ72	short side	(①～⑥)	2-φ86
	corner	(⑦)	φ82	corner	(⑦)	φ90
	long side	(⑧～⑩)	φ68	long side	(⑧～⑩)	φ56

3. Wind Tunnel Test

3.1. Outline of Wind Tunnel Test

For the purpose of grasping the wind pressure characteristics of the examination model, a wind tunnel test with a rigid model was carried out. The outline of the wind tunnel test is shown Figure 3, and test conditions are shown Table 1. The wind tunnel model was an acrylic rigid model with a scale of 1/500 that was composed of columns, compression rings, stands, and membrane attached at the position of the lower radial cable. In addition, a total of 96 measurement holes were provided at the upper and lower surfaces of the roof at 48 points each. The wind direction was set to 0 degrees in the long side direction and 90 degrees in the short side direction, and a total of three cases were targeted at a 45-degree pitch from 0 degrees to 90 degrees. The test air flow used the boundary layer turbulence equivalent to category Ⅲ of surface roughness in Recommendations for Loads on Buildings in Japan. The wind speed and turbulence intensity at the model eaves height of this test is 6m/s and about 0.2. The measurement was performed simultaneously at all measurement points for about 10 minutes (about 13 minutes at full scale) with a sampling frequency of 800 Hz. The evaluation time was in total 10 minutes, from 1.7 minutes in to about 13 minutes of full scale conversion. The influence of the pressure-introducing tube was corrected from the pressure transfer characteristic of the pressure measuring device.



a) Measurement point b) Model cross section

c) Wind tunnel inside view d) Model picture

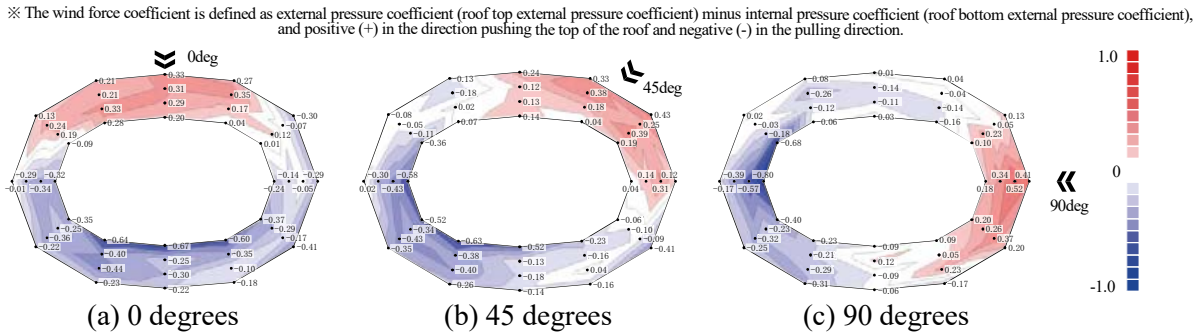
Figure 3: Outline of wind tunnel test

Table 2: Experimental conditions

Wind tunnel device	Eiffel type wind tunnel device (1.2m×0.9m)
Air flow (assumed air flow)	Boundary layer turbulence (category of surface roughness III)
Reference wind velocity (eaves height)	6m/s
Sampling frequency ,time	800Hz, about 10sec
Model, Air flow, Time scale	1/500, 4/27, 27/2000
Wind direction	0, 45, 90deg

3.2. Wind tunnel test results and considerations

The measurement was performed ten times at each wind direction, and ensemble averaging was performed. A mean air pressure coefficient at the wind directions of 0 degrees, 45 degrees, and 90 degrees is shown in Figure 4. Against the wind direction, positive pressure was shown near the eaves of the upwind roof, negative pressure was shown at the tip of the downwind roof, and negative pressure was shown at the tip of the downwind roof. In addition, it was found that no large air pressure coefficient occurred in the roof surface in the direction perpendicular to the wind. In addition, it was confirmed that the downwind side roof has a larger absolute value of the air pressure coefficient than the upwind side roof. It is thought that the wind flowing into the stadium pushed up the lower surface of the downwind side roof.



(a) 0 degrees (b) 45 degrees (c) 90 degrees

Figure 4: Mean air pressure coefficient

4. Numerical analysis

4.1. Numerical analysis overview

Static analysis and time history response analysis were performed on the model using the results obtained from the wind tunnel test. The numerical analysis overview is shown in Figure 5. The radial cable was modeled with eight elements joined by pins to grasp the dynamic behavior at the time of tension loss. The joint of the pillar base and the joint between the upper compression ring and pillar head was a pin that could be rotated only in the direction of the radial cable attached to each pillar. Also, in the joint between the lower compression ring and the pillar, a virtual material was provided on the pillar, and the virtual material and the compression ring were pin-joined. This is because the torsional moment generated in the compression ring is not transmitted to the pillar. The long-term load was set to 20N/㎡ assuming the weight of the roof membrane material and self-weight. The wind load was loaded as a concentrated load at the 4 nodes of the lower radial cable, using the reference velocity pressure calculated from the reference wind velocity 41 m/s at the roof eaves height, the wind force coefficient obtained in the wind tunnel test, and the load area. The wind force coefficient was used for the average wind force coefficient for static analysis, and the time history data of the wind force coefficient was used for time history response analysis. In addition, static analysis was performed in advance, and the initial tension force not causing tension loss was calculated under the wind load of all wind directions in which the wind tunnel test was performed. As a result, the amount of initial tension force introduced to the tension ring at the time of long-term load became 25,000kN. About 160kN was the tension force generated by the long-term load. The damping ratio was 1% for first order and second order in Rayleigh damping, seeing the reference [2].

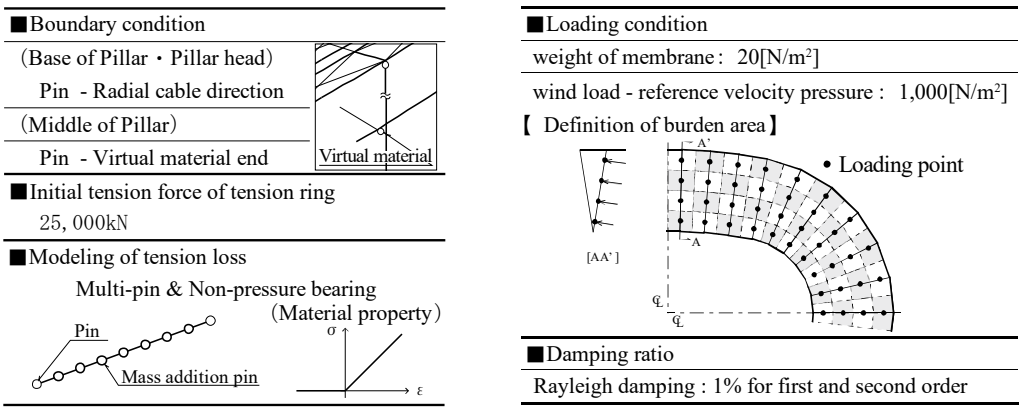
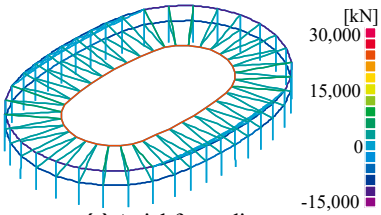


Figure 5: Numerical analysis overview

4.2. Static analysis result and Consideration

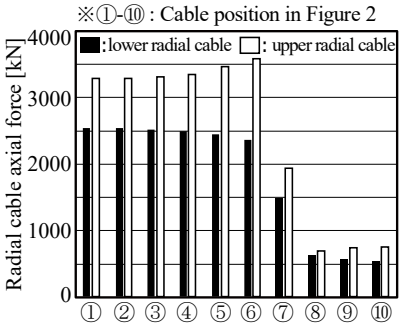
The axial force distribution under long-term loading at the initial tension force of 25,000kN is shown in Figure 6. It was confirmed that the axial force was distributed almost equally between the tension ring and the upper and lower compression rings, and that the absolute value of the axial force of the tension ring and the sum of the axial force of the upper and lower compression rings showed almost the same value. Moreover, the axial force of the radial cable increased in the order of the long side, the corner, and the short side.



(a) Axial force diagram

(b) Axial force distribution

Tension ring	25,050[kN]
Upper compression rings	-14,590[kN]
Lower compression rings	-10,640[kN]



(c) Axial force distribution of the radial cable

Figure 6: Axial force distribution under long-term loading

The relationship between the load at the time of wind load of 0-degree and 90-degree wind direction, the lower radial cable center vertical displacement, and the upper stage compression ring horizontal displacement is shown in Figure 7. Focusing on the vertical displacement in the wind direction, it was confirmed that the lower radial cable was deformed significantly vertically downward on the upwind side and vertically upward on the downwind side. In addition, the vertical displacement of the long side at a 0-degree wind direction is larger than that at the short side at a 90-degree wind direction. It is considered that the initial tension force of the long side radial cable is small and the geometric rigidity is small. On the other hand, it was confirmed that the horizontal displacement was such that the upwind side was deformed inward and the downwind side was deformed outward both at a 0-degree and a 90-degree wind direction.

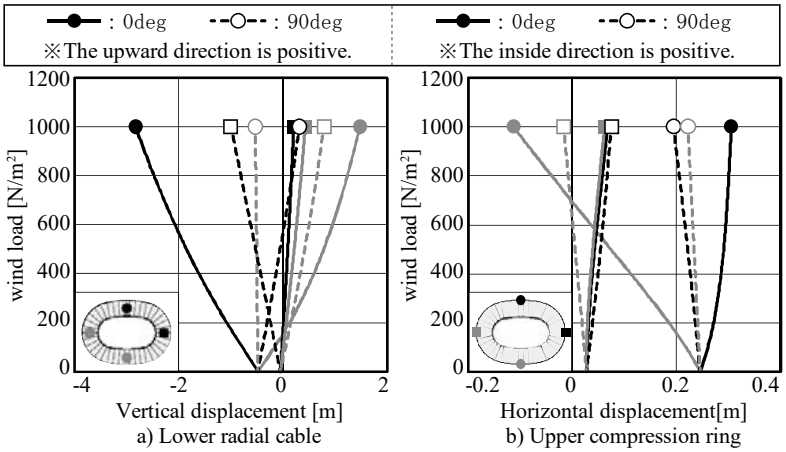


Figure 7: Static analysis result (PS 25,000kN)

4.3. Dynamic analysis result and Consideration

4.3.1. Eigenvalue analysis

Prior to time-history response analysis, an eigenvalue analysis was carried out for the purpose of grasping the basic vibration characteristics of the model. In the eigenvalue analysis, geometric rigidity accompanying the axial force generated in the tension ring and the radiation cable by the initial tension force and long-term load was considered. The eigenvalue analysis result is shown in Figure 8. In the figure, the first and second natural periods and eigenmodes in the X, Y and Z directions are shown.

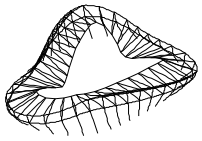
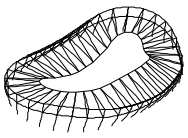
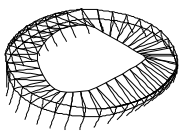
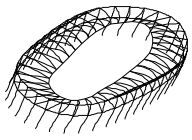
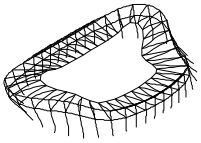
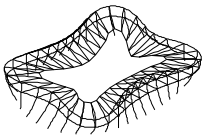
X Direction	Y Direction	Z Direction
1st Order Mode	1st Order Mode	1st Order Mode
T=1.94sec	T=2.34sec	T=2.47sec
		
2nd Order Mode	2nd Order Mode	2nd Order Mode
T=1.37sec	T=1.53sec	T=1.44sec
		

Figure 8: Eigenvalue analysis result (PS 25,000kN)

4.3.2. Time history response analysis results and Consideration

The time history response analysis results of the lower radial cable central vertical displacement, the upper compression ring horizontal displacement, the tension ring axial force, and the radial cable axial force at wind directions of 0 degrees and 90 degrees are shown in Figure 9. A time history waveform lasting 30 seconds from 200 to 230 seconds of the total evaluation time of 600 seconds is shown, and the average value shown in the figure is an average of the total length of 600 seconds. When the average value of the time history response analysis was compared with the result of static analysis, it showed almost the same value.

(i) Focusing on the vertical displacement, in the case of a wind direction of 0 degrees, only the long side is largely deformed in the vertical direction. On the other hand, in the case of the wind direction of 90 degrees, it was understood that both the short side and the long side were significantly deformed in the vertical direction. This is considered to be due to the low geometric rigidity of the long side, and it was understood that the long side produces large vibrations even when low wind load is applied.

(ii) It was confirmed that the horizontal displacement of the long side and the short side of the wind direction at 0 degrees and 90 degrees shows the behavior with almost the same periodicity. Moreover, it was confirmed that the phase of the period of the horizontal displacement of a long side part and a short side part is shifted half cycle. This is considered to be due to the influence of the eigenmode.

From the above, it was understood that the value of the static analysis result and the average value of the time history response analysis showed almost the same value. However, these results suggest that it is necessary to grasp the vertical vibration characteristics and the influence of the eigenmode on horizontal displacement of the long side by time history response analysis.

(iii) The axial force fluctuation of the tension ring showed almost the same value regardless of each time. Therefore, it was suggested that no axial force difference occurs in the ring, and the design sliding force of the joint becomes relatively small.

(iv) The axial force fluctuation of the upper and lower of the radial cable showed a nearly line-symmetrical waveform at each part. From this, it was understood that the upper and lower radial cable were resisting together. In addition, although the loss of tension of the upper radial cable at the long side was confirmed at the wind direction of 0 degrees, the impact tension fluctuation of the upper and lower radial cable accompanying the loss of tension was not confirmed.

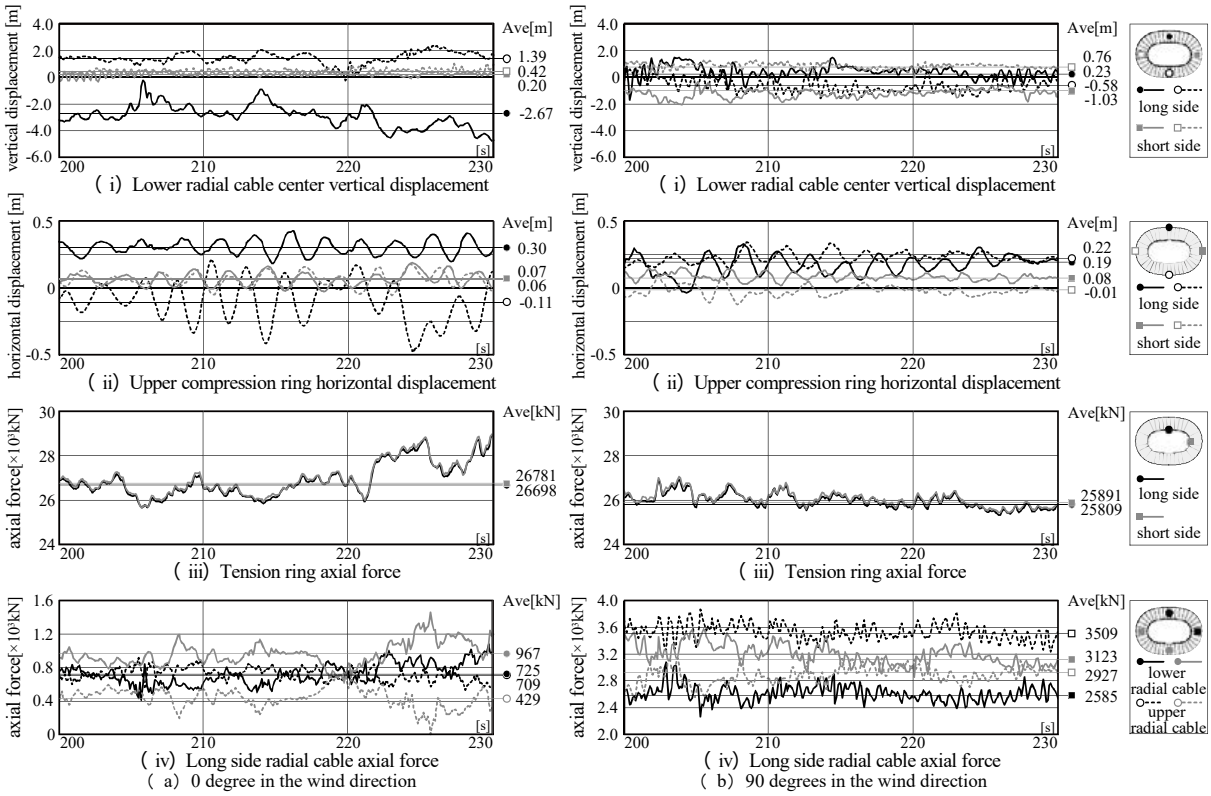


Figure 8: Time history response analysis result (PS 25,000kN)

5. Conclusion

In this paper, wind tunnel experiments and numerical analysis were conducted to understand the structural behavior of the structure and to accumulate data for structural planning under strong wind. These examinations suggested the necessity of evaluation by time history response analysis as well as static analysis for this structure. In the future, the authors plan to conduct experimental studies using a small-scale model and to study detailed equivalent static wind loads.

Acknowledgements

The authors would also like to express their gratitude to Jonathan Harrison for assistance in the editing of this paper.

References

[1] Koike, T., Okada, A., Miyasato, N., "Basic Study on the Mechanical Behavior of Roof Structures Consisting of Inner Tension Ring and Radially Arranged Cables," Abstracts of Annual Meetings of the Architectural Institute of Japan, Structure I, pp. 1065-1070, 2018.

[2] Aizawa, J., Saito, M., "Experimental Study on Basic Dynamic Behavior of Shizuoka Stadium," Abstracts of Annual Meetings of Architectural Institute of Japan, Structure I, pp. 899-900, 2002.

[3] Japanese Architectural Institute, "Recommendations for Design of Cable Structures," Japanese Architectural Institute, 1994.

[4] A. Okuma, et. al., "Wind Tunnel Experiment Guidebook for Practitioners," The Building Center of Japan, 2008.

[5] J. Schlaich and R. Bergermann, "Light Structures," Prestel Publishing, 2004.

Proceedings of the IASS Annual Symposium 2019 – Structural Membranes 2019
Form and Force
7 – 10 October 2019, Barcelona, Spain
C. Lázaro, K.-U. Bletzinger, E. Oñate (eds.)

Tile Vault Construction on Bending-actuated Robotically 3D-printed Formworks

Xiang WANG*[c], Kam-Ming Mark TAM*[b], Alexandre BEAUDOUIN-MACKAY[a], Benjamin HOYLE[a], Molly MASON[a], Zhe GUO[b], Weizhe GAO[b], Ce LI[b], Weiran ZHU[b], Zain KARSAN[a], Gene Ting-Chun KAO[c], Liming ZHANG[c], Hua CHAI[c], Philip F. YUAN[c], Philippe BLOCK[b]

*Tongji University & Swiss Federal Institute of Technology in Zurich
Shanghai, People's Republic of China & Zurich, Switzerland
18310021@tongji.edu.cn & tam@arch.ethz.ch

[a] Department of Architecture, School of Architecture and Planning, Massachusetts Institute of Technology
[b] College of Architecture and Urban Planning, Tongji University
[c] Block Research Group, Institute of Technology in Architecture, Swiss Federal Institute of Technology in Zurich

Abstract

Additive manufacturing (AM) has expanded possibilities for materialising structures that achieve strength through intelligent, but complex geometries. However, conventional AM techniques, such as thermoplastic fused deposition modelling (FDM), also rely on material with low strength and stiffness, which limit their full-scale building construction applications. This paper articulates one of several design-fabrication strategies jointly developed by MIT, ETHZ and Tongji researchers in a workshop to respond to this challenge: FDM is optimised for producing self-supporting scaffold that can be printed flat and bent in-place on site—scaffolds whose strength are built gradually via additional structural material application. This paper—part 1 in the series—uses FDM to produce bendable panels that can form highly curved scaffolds for thin-tile vaulting. The feasibility of the novel assembly process is demonstrated with the construction of a large-scale pavilion measuring seven metre in diameter, where seven overlapping flexible panels robotically 3D printed with eight layers of PLA material create a load-bearing scaffold for thin-tile applications. The produced prototype illustrates one alternative design-fabrication strategy leveraging force-explicit equilibrium design methods to synthesise the advantages of vernacular and digital manufacturing techniques—resulting in new possibilities for the materialisation of complexly curved thin-tile vault construction without intensive labour and formwork requirements.

Keywords: additive manufacturing, formwork, tile vaulting, thin-tile, bending active, geometry processing

1 Introduction

To engineers interested in structural performance, robotics-enabled additive manufacturing (AM) is a research area eliciting strong interests due to its potential to realise structures achieving strength through intelligent, but complex geometries, which are difficult to realise under traditional construction methods. But while AM—complemented by advances in digital computation and industrial robotics—have been transformed into reliable and rapid methods for producing end-use parts ranging from human to modest architectural scales, the application of the technology has rarely extended beyond architectural structures with limited design requirements, such as sculptures or pavilions. Applications are especially limiting for AM techniques with fabrication efficiency appropriate for mass production, such as thermoplastic-based Fused Deposition Modelling (FDM), which relies on material with low strength and stiffness, and idiosyncratic processes introducing imperfection and weakness to the artefacts [1]. Consequently, the application of AM has remained limited in practical building constructions.

Copyright © 2019 by Xiang WANG, Kam-Ming Mark TAM
Published by the International Association for Shell and Spatial Structures (IASS) with permission.

2 Literature Review

Acknowledging the limitations in state-of-the-art robotics-enabled AM, researchers have pursued alternative applications for AM in construction, and developed methods for generating designs informed by their process constraints. One alternative AM application is to use the technique to develop self-supporting scaffold for complex structurally informed geometries—a scaffold upon which the final structural material, such as concrete or bricks, can be incrementally applied to build up the required structural strength. The approach therefore synthesises the advantages of traditional and digital fabrication methods to respectively achieve structural strength and stiffness, and geometrical customisability and complexity—in the process creating novel resource-efficient methods for producing concrete formwork at reduced material and labour intensity. Prominent research in this area include the use of AM-produced lattices [2] and digitally knitted textiles membranes [3] as respectively containers and surfaces for later concrete infill and casting.

Given the paramount role of geometry in determining structural performances, researchers applying AM to architecture have also developed methods for optimising the structural geometry and internal material distribution of AM-produced parts[4]. Transferable lessons may also be learnt in design-build research based on material with unconventionally low structural strength and stiffness, such as recycled or organic material [5]—projects wherein the strength achievable in the weak material is maximised by synthesising tried-and-true principles on structural efficiency, such as the preferencing of funicular, compression-based and doubly-curved forms, and the employment of geometrical-based and force-explicit methods of design exploration, like Graphic Statics, that offer designers good capabilities for controlling and accommodating structural forces and material constraints respectively.

3 Context and Design Concept Formulation

3.1 Workshop Introduction

Evident in the research reviewed above is the importance of structural geometry in activating the limited strength and stiffness of weak materials—enabling formworks based on the weak materials to sustain the stresses and strains imposed on them by the incremental application of the final structural material. The final built-up structure in turn benefits from the heightened strength and stiffness realised through the formwork's structural geometry—designed and optimised with smart computational methods, and produced using AM technologies that support customisability and complexity.

The synergistic opportunities presented by the combination of concepts discussed above provided the motivation for the diverse collection of students and researchers from Massachusetts Institute of Technology (MIT), Swiss Federal Institute of Technology (ETHZ), and Tongji University (TJU) that convened in the design-build workshop hosted by TJU's Professor Philip Yuan during January 2019. Spanning over an 18-day period, this workshop commenced with 3 days of instructions on foundational computational structural design topic. This was followed by a 3-day ideation period wherein students worked in pairs to propose a human-scale structure to be constructed via incremental application of a structural material on FDM-produced scaffolds. These generated ideas were then synthesised into 2 consolidated designs that were developed, prototyped, fabricated and assembled over the remaining 12 days. Presented in the remainder of this paper is the development of one of the two concepts pursued.

3.2 Material System Design Concept: Tile Vault

As Figure 1-A shows, one prominent design trajectory emerged from the 3-day ideation exercises was the exploration of complexly curved funicular geometries featuring intertwining arching spans, which amorphously transitioned between various architectural elements, such as supports, roof, ramps, and seating at various scales and heights, and meandered expressively to create various spiralling or circular global geometry motifs. Of interest were designs investigating materialisation strategies motivated by AM manufacturability considerations (Figure 1-B), such as the reconstruction of doubly curved vaulted surfaces as singly curved surfaces that were folded to create stiffened V-shaped-like cross sections. Moreover, these panels were connected and arranged in such a way that bending was induced in their

assembly. Consequently, the elastic behaviour of these formworks was activated—transforming them into stabilising bending active systems with improved rigidity and arching and shell properties in their final deformed states.

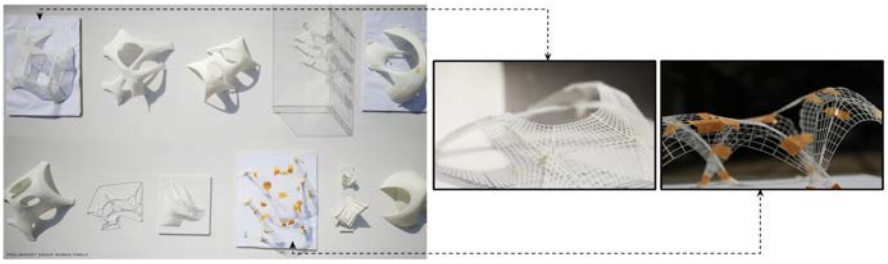


Figure 1: (Left) Complexly curved and intertwining funicular geometries; (Right) Materialisation as bending actuated folds

The proposal to develop AM as a technique for producing stable and rigid formworks with minimal support requirements to enable complex funicular geometries to be built—by the bending actuation of folded surfaces that could be printed flat—appealed the workshop organisers. There is a potential for the technique to address challenges limiting the construction of complexly curved funicular surfaces under traditional tile vaulting methods.

Also referred to as 'thin-tile', or 'Catalan' vaulting (Figure 2-1), thin vaulting is a 600-year old construction technique for constructing compressive spanning structures that has been applied in regions around the Mediterranean. Typically employing a lightweight sandwich of thin structural tiles in conjunction with rapid setting gypsum mortar, the technique provides enables tiling in temporarily unsupported space, which reduces formwork requirement [6]. While adequate for basic geometries, the application of traditional tile vaulting techniques has proved more challenging for the diverse range of complexly curve funicular geometries that could be generated in an era of rapidly advancing computational form-finding tools. A commonly cited open problem is the need for strategies to better guide and support respectively the accurate and stable construction of the complex funicular geometries. Researchers have developed efficient computational strategies to simplify and automate the production of falsework systems [7] (Figure 2-2), and to optimise the tiling assembly sequence to minimise formwork requirement. However, such strategies remain infant in their developments, and are beset by a number of limitations: for instance, elaborate formworks and complex assembly may still be needed. Furthermore, the construction of formworks—even when simplified—could still create obstacles in the site of assembly that frustrates inspection and quality control [7].



Figure 2: Design projects embodying thin tile vaulting: (1) New York City's City Hall station by Rafael Guastavino; (2) Computationally enabled vaulting with innovative and automated formwork production

4 Methodology

4.1 Overall Workflow

Motivated to contribute to the modernisation of tile vaulting constructions through AM, the aforementioned pairwise teams then consolidated into a single group to begin conceiving, developing, and implementing a design-fabrication workflow for developing AM-produced formwork for tile vaulting, as explained in Figure 3, which began with **(0)** consolidating the architectural concepts explored and specifying them on site. **(I)** Next, the converged topology and geometry design was

iteratively developed in parallel—informed initially by the anticipated formwork panelisation layout [**§5.2**]. Completing form-finding, **(II-1)** the obtained funicular geometry was then partitioned into discrete parts, and **(II-2)** simplified and reconstructed as developable singly curved surfaces for AM manufacturability [**§5.3**]. In parallel, **(III)** extensive prototyping was conducted to calibrate the formwork pattern, material thickness, and the panelisation to achieve a balance in the material strength and flexibility of the printed panels to ease their bending actuation during assembly [§6.1]. Informed by the prototyping investigations, **(IV-1)** the surface parts were then discretised or tessellated into dense meshes representing the filament layout to be printed via AM. Next, (**IV-2)** the mesh edges of adjacent panels were then extracted and grouped in a strategic way to create an overlapping panelisation scheme [**§6.2**]. Finally, **(V)** a custom programmed robotic path planner parsed the regrouped panel edges—sequencing and post-processing the edges as needed to create the series of print programmes for the industrial robot arm to execute.

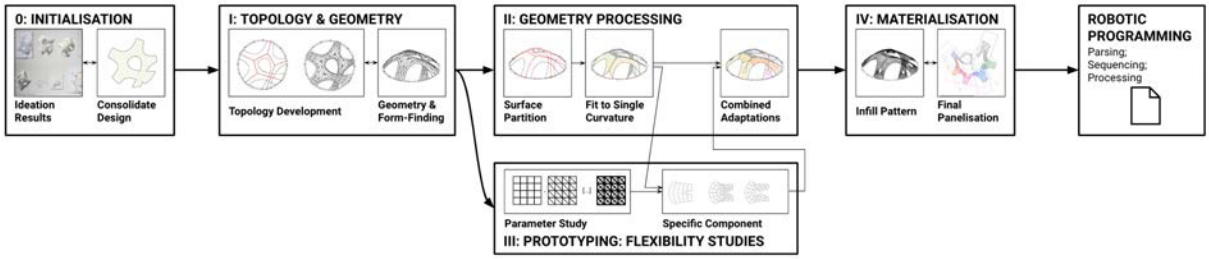


Figure 3: Design workflow implemented to develop AM-produced bending actuated thin tile formwork

All fabrication described in this paper—encompassing both prototyping and final production—were conducted in the shared robotic production facilities of Archi-Union and Fab-Union. The setup utilised two KR 120 R1800 nano industrial robot arms, which were mounted with a custom extrusion module with a nozzle diameter of 8 mm that were developed by researchers at FabUnion. Polylactic acid (PLA) was used as the final printing material. The robotics-enabled additive manufactured plastic panels were relocated to site, where they were erected, and assembled together before tile application.

4.2 Site and Boundary Conditions

Figure 4-L shows the space allocated for constructing the final thin-tiled pavilion—situated within the public courtyard of Archi-Union office's main public entrance, which can accommodate an architectural intervention with a maximum bounding volume dimension of 7m × 7m × 2m once setbacks from the windows and the existing roof structure were considered.

5 Implementation 1: Conceptualisation, Design Development and Rationalisation

5.1 Idea Consolidation and Site Specification

Upon further development on the initial design ideas, the proposal converged to a concept that embodied both the meandering and circumscribing global geometry motifs. The refined tile-vault boundary features 5 inward-leaning arches that are supported and enclosed by a circular perimeter boundary ring at their bases, and connected as a continuous spiral at their top—a spiral with one end crossing over its other end, as Figure 4-C shows. To simplify fabrication and assembly, this boundary ring was designed as a series of modular individual steel curve segments with interlocking joints—allowing a strong and rigid connection to form between the segments, as Figure 4-R shows. These ring segments were placed on custom footings to accept the tile-vault's thrust.



Figure 4: (*Left*) Site plan; (*Centre*) Consolidated global geometry concept; (*Right*) Boundary ring

5.2 Geometry and Topology

The process to finalise the funicular geometry began with discretisation of the converged design boundary (Figure 4-C) into a fine mesh that could be used as the basis form diagram required for form-finding. Within the context of this design proposal, since the meandering sequence of arches would be split into halves to be folded and bent, the discretisation of the boundary surface incorporated as its edge features a series of curves approximating the surface's midlines, as Figure 5-1B shows. Both quad- and triangular-based meshing methods from *compas* and *compas_pattern*[8] were explored as tools for further refinement by discretisation (Figure 5-1C). For crucial components where careful control of material behaviour is required, custom algorithms were developed within Grasshopper 3-D to create the discretisation layout from a network of algorithmically generated NURBs curves.

Obtaining a fine mesh, the form-finding procedure was then initiated. The key challenge to form-finding for this design—given the clear geometrical prescription and crossing over of spans—was the maintaining of geometry control to ensure that the form-found surfaces would not only satisfy the defined constraints, but would also result in a smooth usable geometry without self-intersections, and not substantially different in plan from the initial basis diagrams. To that end, the Graphic-Statics-based tool RhinoVault was used for the control it offered in setting geometric targets—both in height and plan—during the form-finding process. Through successive iterations, the final form-found geometry, as Figure 5-2A. shows, was obtained.

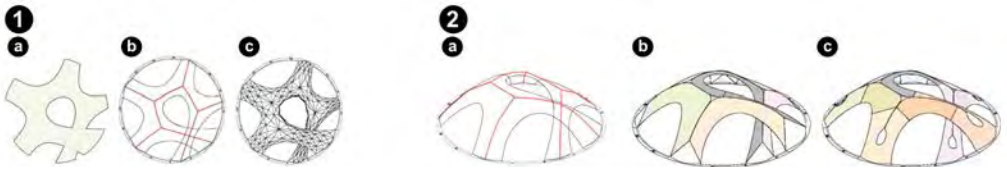


Figure 5: Geometry development concepts: (1) Mesh discretisation for form-finding; (2) Single curvature fitting

5.3 Geometry Rationalisation

Next, the spiralling form-found surface was split into discrete strips according to their midlines and the preliminary layout (Figure 5-2A). To ensure the strips' developability, so they could be additive manufactured on a flat printing platform, the strip geometries were simplified and reconstructed as singly curved strips in an optimisation procedure that sought to minimise the geometric deviation between the original form-found geometry and the simplified, refitted surface (Figure 5-2B). Further reducing panelisation complexity, and to provide structural and material continuity at key junctions of the vault's load paths, the half-strips that composed each of the vault's bases were consolidated into a single continuous panel per base (Figure 5-2C).

6 Implementation 2: Materialisation Design

6.1 Calibration: Strength & Flexibility

Motivated to improve the capacity of the printed panels both to assume the desired geometry when assembled and actuated, and to withstand the stresses induced by bending actuation and tiling application, extensive prototyping was conducted to optimise the materialisation process. This task encompassed the optimisation of robotic fabrication parameters and infill pattern generation, which refers to the tessellation of the fine mesh discretisation used for form-finding (Figure 5-1C). into the filament layout to be extruded via AM. In the context of this workshop, the problem of materialisation was challenging because the fabrication parameters available for adjustment affecting either strength or stiffness, such as the material thickness, generally set the two properties in competition. Consequently, the calibration of material strength and flexibility relied predominately on the design variation within the panels' infill pattern, such as by topology modification or density redistribution.

A two-phase investigation to calibrate infill pattern generation was pursued. Firstly, the implications of infill patterning variation to material flexibility was investigated generically at 1:1 scale. As Figure 6-

1 shows, these investigations adjusted both the subdivision magnitude, and the design of the internal topology within the quadrilateral faces composing the infill patterns. The initial tests also investigated various print material, material thickness, and path sequencing parameters. Next, the generic studies were transferred to the design of prototypes for critical components of the vault, such as panels corresponding to its various base footings. While the studies demonstrated that double curvature could not be induced stably within flat printed panels, the investigations to introduce single curvature did achieve some success. Specifically, the feasibility of inducing the base footings into bulged cone-shaped surfaces (Figure 6-2a)—primarily singly curved, but also with regionalised double curvature—were developed by modifying the panels' boundaries, and by adopting radial-like tessellation approximately aligned to the cones' curvature (Figure 6-2b,3c). The resulting prototype exhibited improved stiffness and rigidity (Figure 6-2d). In summary, the finalised infill pattern featured edge lengths ranging from 5 to 15 cm—with 2-edge diagonalisation of the quadrilateral faces, as Figure 7-3 shows.

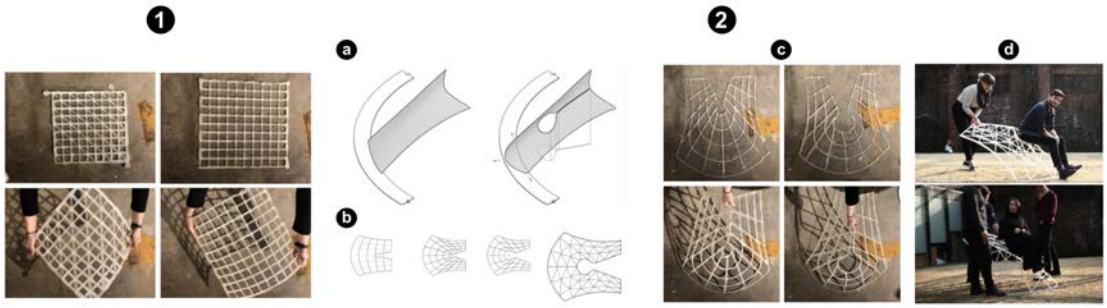


Figure 6: Investigations on material strength and flexibility, with studies on (1) General patterning; and prototyping on the (2) Base support components.

6.2 Panelisation Strategy

Applying additional simplifications, the panelisation layout was simplified to a scheme requiring only 7 panels—6 strips centred on the 6 bases that are connected to 1 centrally spiralling strip. The infill pattern edges were then assigned by their location to the 7 panels—with the edges organised into 2 primary filament layers based on their orientations (one layer containing the grid edges, and a second layer containing the grids' diagonalization, as Figure 7-2). To improve the distribution of both stress and strains introduced by the bending actuation, the panels were modified to include regions of overlaps (Figure 7-1)—regions where a pair of adjacent panels would each contribute one of the two primary constituent layers needed to complete the layering (Figure 7-2). Finally, these regrouped infill pattern edges were unrolled along with their assigned singly curved surfaces into a planarised state (Figure 7-4), where they were then parsed, sequenced, processed and converted into programmed robotic paths.

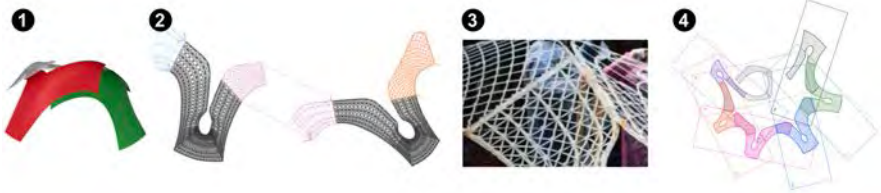


Figure 7: (1) Overlapping panelisation concepts; and their implications to (2) infill patterning; (3) materialisation; (4) global layout

7 Implementation 3: Final Production

7.1 Fabrication and Assembly

In total, the several panels encompassed a total print length of 2,200 m and required approximately 750 hours to print. The printed parts were relocated to site, and assembled piecemeal one base support at a time. Temporary bracing for the strip-panels were provided through a series of triangular trusses fitted

underneath the shell formwork, and by the deployment of support poles inserted below the shell structure at an average density of 4 poles / m^2—poles that also doubled as a height adjustment and validation mechanism to ensure the geometric fidelity of the as-built formwork.

In anticipation of difficulties and uncertainties in the fabrication and bending actuation process, efforts were made to model the structural behaviour of the panels during assembly—realised in 2 independent studies examining 2 types of structural actions at 2 different scales. Using Abacus, the first set of analyses applied non-linear Finite Element Analysis (FEA) to simulate the bending actuation of individual footing panels, in order to identify regions with elevated bending-induced structural stresses and strains (Figure 8-3-Top) where heat gun application during assembly, which improves local malleability of the material, could be especially beneficial in reducing the likelihood of crack formations (Figure 8-2-Top). The second set of structural analyses modelled the as-built assembly in its entirety (Figure 8-3-Bottom)—including the location of fasteners and temporary supports—using FEA with linear elastic assumption, in order to identify areas with high creep or stress requiring further bracing.

7.2 Tiling

Reflecting the workshop's motivation to hybridise traditional and digital fabrication method, the tile selected for application on the assembled geometry is a type of clay brick commonly found in vernacular constructions in the Yangtze River delta region of China enveloping the site. Binding of the tiles, which measured approximately 200 mm × 100mm × 20 mm, relied on a custom prepared fast-setting cement mortar incorporating an additive called 801 adhesive. As with traditional tile vaulting methods, a total of three layers were applied. Structural stability considerations informed the tiling layout: Figure 9-R shows the close alignment of the tiling orientation at the top and bottom layers to the vault's force paths and principal curvatures, which are approximately equivalent in this design. For the intermediate layer, tiles were applied at a 45 degrees rotation to provide sufficient overlaps with the two sandwiching layers. Approximately 4'500 tiles were applied on the vault, which measures approximately 30 m^2 in area—completed over a period of 4 days. Figure 9 documents the completed pavilion.

8 Conclusion

This paper documented a multi-phased design-fabrication strategy jointly developed by MIT, ETHZ and TJU researchers in a workshop for developing bendable panels that can form highly curved scaffolds for tile vaulting. Specifically, the design-fabrication implementation articulated in this paper began with iterative topology and geometry exploration informed by panelisation considerations using compas_pattern and RhinoVault. To generate the panels' fabrication geometries, an optimisation procedure then fitted the complex doubly-curved funicular geometry into a series of singly curved surface folds corresponding to panelisation. The panels were then discretised into a printable infill pattern informed by extensive materialisation studies investigating the trade-off between the material strength and flexibility of the panels. The integrated procedure resulted in formworks that could be two-dimensionally printed, and bent in-place and assembled on site. In doing so, the project highlights the potential in synthesising digital and traditional fabrication techniques through smart structural computation to open new possibilities for the materialisation of geometrically complex thin tile vaults at reduced fabrication complexity.



Figure 8: Erection and assembly documentation and strategy: (1) General steps; (2) Connection details and formwork bracing; (3) FEA studies enabling localised fabrication support



Figure 9: Finished tiled vault

References

[1] K-M. M. Tam, J. R. Coleman, N. Fine., and C. T. Mueller. "Stress line additive manufacturing (SLAM) for 2.5-d shells," *Journal of the International Association for Shell and Spatial Structures*, vol. 57, no. 4, pp. 249-259, Dec 1.

[2] N. Hack, W.V. Laurer, F. Grammazio, M. Kohler, and W. Brameshuber. "Mesh Mould: Robotically Fabricated Metal Meshes as Concrete Formwork and Reinforcement," in *FERRO-11: Proceedings of the 11th International Symposium on Ferrocement and 3rd ICTRC International Conference on Textile Reinforced Concrete, Aachen, Germany, June 07-10, 2015,* RILEM Publications SARL, 2015. pp. 347-359.

[3] M. Popescu, M. Rippmann, A. Liew, "Concrete shell built using a cable-net and knitted formwork," *DETAIL structure*, vol. 1, pp. 10-11, 2019.

[4] K. M. M. Tam, D. J. Marshall, M. Gu, J. Kim, Y. Huang, J. Lavallee, and C.T. Mueller, "Fabrication-aware structural optimisation of lattice additive-manufactured with robot-arm," *International Journal of Rapid Manufacturing*, vol. 7, no.2/3, pp.120 - 168, 2018.

[5] Block Research Group. ETH Zurich Pavilion, New York City, USA, 2015 http://www.block.arch.ethz.ch/brg/project/eth-ideas-city-pavilion-new-york-ny-usa. Accessed: May 31, 2019.

[6] J. Ochsendorf, *Guastavino vaulting*, the art of structural tile. New York: Princeton Architectural Press, 2010.

[7] L. Davis, M. Rippmann, T. Pawlofsky, P. Block, "Innovative funicular tile vault: A prototype vault in Switzerland," *The Structural Engineer*, pp. 46-56, Nov. 2012.

[8] M. Rippmann, L. Lachauer, and P. Block, "Interactive Vault Design", *International Journal of Space Structures*, vol. 27. no. 4, pp. 219-230, Dec. 2012.

Proceedings of the IASS Annual Symposium 2019 – Structural Membranes 2019
Form and Force
7 – 10 October 2019, Barcelona, Spain
C. Lázaro, K.-U. Bletzinger, E. Oñate (eds.)

Digital Fabrication of a Timber Bridge

Laetitia KONING*, Stijn JOOSTEN[a]

*ARUP Amsterdam
Naritaweg 118, Amsterdam, the Netherlands
Laetitia.Koning@arup.com

Abstract

Research on digitally fabricated timber structures has focused on design for an architectural rather than a load-bearing purpose. To fulfil a load-bearing and civil engineering purpose, the design needs to address outdoor conditions, a large number of load cases, strict safety requirements, and a strong focus on connection design with sufficient strength and stiffness. This is examined through a case study: the design of a timber frame bridge with interlocking joints that is fabricated using CNC-milling techniques. A strong focus is put on the design, structural calculation, optimization, detailing and testing of the connections and their integration in the global design.

Keywords: Digital fabrication, reciprocal grid structure, timber, Japanese connections, interlocking joints, optimization, CNC-milling

1. Introduction

Rapid developments of both new (digital) fabrication techniques and innovative software facilitate the possibility to design, check and construct objects with great complexity and uniqueness without a large price tag. In the building sector, architectural research institutes take the lead in the application of these new techniques by showcasing digitally fabricated art installations and architectural structures.[1] The next step will be to enter the world of civil engineer by designing and building structures with a load-bearing purpose.

To realize this, the design needs to address outdoor conditions, a large number of load cases, strict safety requirements, and a strong focus on connection design with sufficient strength and stiffness. This is examined as part of the Master's Thesis *Digital Fabrication of a Timber Bridge* [2] through a case study: the design of a timber frame bridge fabricated using CNC-milling. A strong focus is placed on the design, structural calculation, optimization and detailing of the connections and their integration in the global design.

2. Description case study

First, the case study was defined to address the gaps in the knowledge about digital fabrication mentioned above.

It has been decided to design a bridge to study a civil engineering application, dealing with many load combinations and a structural function.

A reciprocal grid is applied with integrated connections to obtain a single material structure, which limits the production process to one robot or machine and speeds up and simplifies the assembly process. Lap joints, known from ancient Japanese woodworking, had lost their popularity due the high labour intensity and great skills needed for the fabrication process. However, new fabrication techniques like

Copyright © 2019 by Laetitia Koning and Stijn Joosten
Published by the International Association for Shell and Spatial Structures (IASS) with permission.

CNC-milling enable the revival of this kind of joints. They allow for the connection of beams with different sizes, approaching from different angles and can accommodate the eccentricity required to create a double curved free-form surface with straight beams. Furthermore, interlocking joints have a higher strength and stiffness than the currently applied nailed and glued connections in digitally fabricated timber projects. [3][4] Finally, they fit into a complete digital fabrication and assembly process, in contrast to welded or 3D-printed steel connections.

A timber structure is applied, because it is easily modified and thus suitable for digital fabrication. In specific, it is chosen to Azobé to address outdoor cases.

A double-curved surface was chosen as the starting point for the shape of the bridge, to show the possibility to fabricate structures with freedom of shape when applying digital fabrication. Figure 1 gives an impression of the design of the bridge.

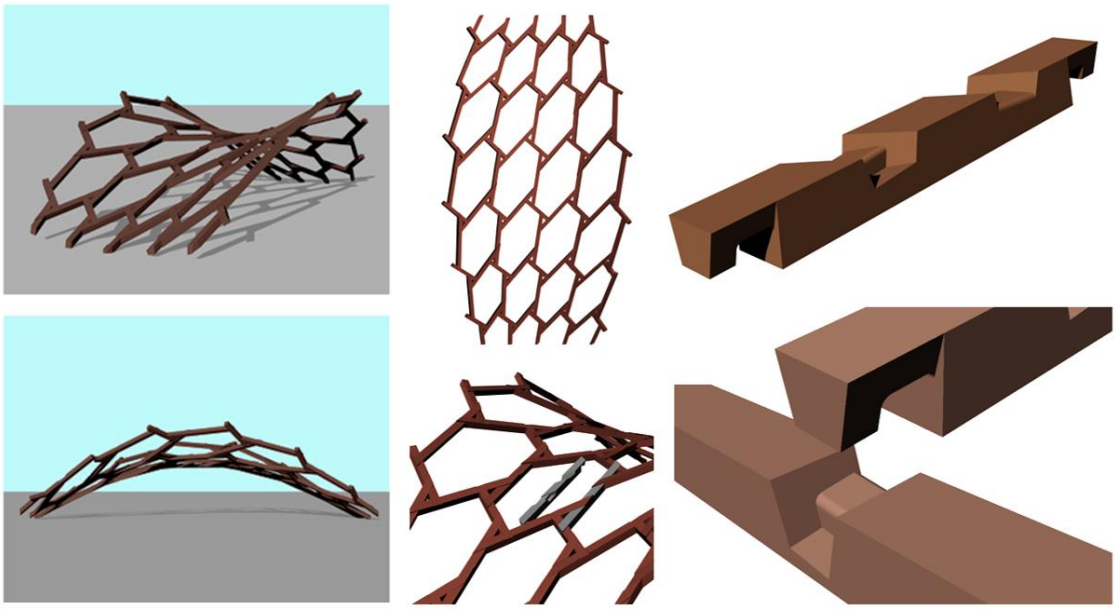


Figure 1 Impressions of the design of the case study bridge

3. Design process

The great design freedom which is obtained when applying digital fabrication also comes with a price: a large complexity of design. The ability to individually optimize all members in a structure and design structures with freedom of shape results in a large uniqueness off all elements. Furthermore, the statical indeterminacy of gridshell structures results in a large interdependence of the separate parts. Additionally, the embedment of the connections in the beam results in a relation between the dimensions of the beams and the connections. This altogether results in a large number of design parameters and a strong relation between them, which makes it hard to decouple design steps. However, designing all parts simultaneously results in a lack of starting points. Therefore, an iterative design process is applied in which first the global design is addressed, secondly the connection design and finally the integration of both.

3.1 Global design

The global design of the bridge is created parametrically using the Grasshopper plugin for Rhino. The geometric model is converted into a structural model using the Finite Element (FE) plugin for Grasshopper called Karamba. The advantage of this workflow is that changes can be easily made and

that instant feedback on the structural behavior of the design is given. To retain a fast feedback loop, traffic load optimization is not carried out per element. Instead, several chessboard load patterns are predefined, covering the most governing traffic load cases. A set of twelve important load combinations combining dead-, wind and crowd load is applied according to NEN-EN 1990 and NEN-EN 1991.[5][6]

Next, a cross section and shape optimization are implemented, aiming to minimize the material usage. Because built-in cross-section optimization algorithms only existed for concrete and steel sections, a custom python script was written to iteratively find the minimum cross section of each timber beam according to the eurocode. All beams are checked in accordance with NEN-EN 1995-1, considering all 12 load cases.[7] A reduced cross-sectional area is used for the checks to account for the decreased cross section size at the location of the connection.

Due to the complex relation between the shape of the bridge and the mass of the structure, an evolutionary solver is used to find the optimal shape. For each design alternative, a shortened version of the aforementioned cross section optimization is applied to effectively estimate the mass.

3.2 Connection design

Here, the focus is shifted from the global design to the connection design of the lap joints. As a result of the freeform shape of the bridge, each connection in the structure is unique. To avoid having to design each connection individually, the connection is described in a parametric way. Each connection is defined by four parameters associated to the global design and seven parameters related to the size and shape of the connection, see Figure 2.

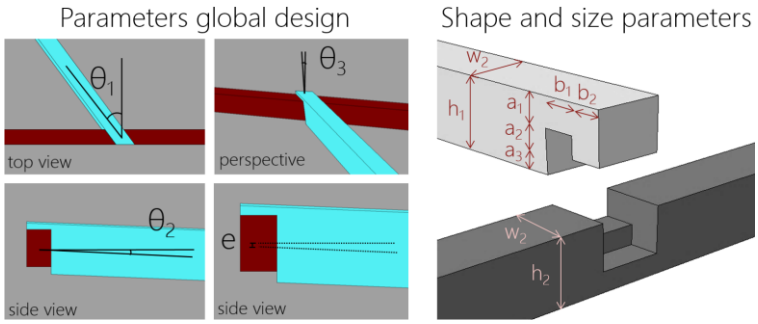


Figure 2 Parameters defining the connection design

A few adjustments have been made to the design, benefiting the structural behavior and the assembly process, see Figure 3.

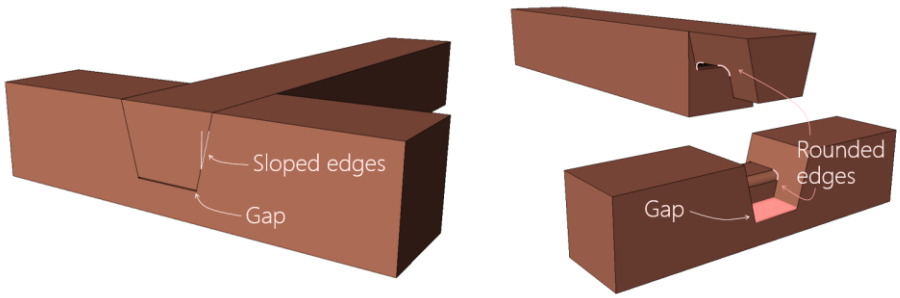


Figure 3 Detailing connection

The next step is the structural verification of the connections. Although lap joints have been applied since thousands of years, only limited information is available about the structural calculation of the connection since the design process was mainly based on trial and error. Current research on the

structural behavior of interlocking joints is mainly focused on numerical modelling of specific types of connections resulting in computationally intensive models with only limited applicability in design. [8] Engineering firms that apply CNC-milling techniques commonly apply codes and guidelines that are only applicable to standard designs. Both methods are therefore not suitable for a parametric workflow. A parametric workflow requires a quick calculation method which is suitable for a wide range of design alternatives.

Therefore, as part of this study, a calculation method is developed in which the stresses and capacities for all critical planes are calculated, see Figure 4. Each plane is verified for axial and shear strength, considering the aforementioned twelve load cases and the orientation of each plane with respect to the grain direction.

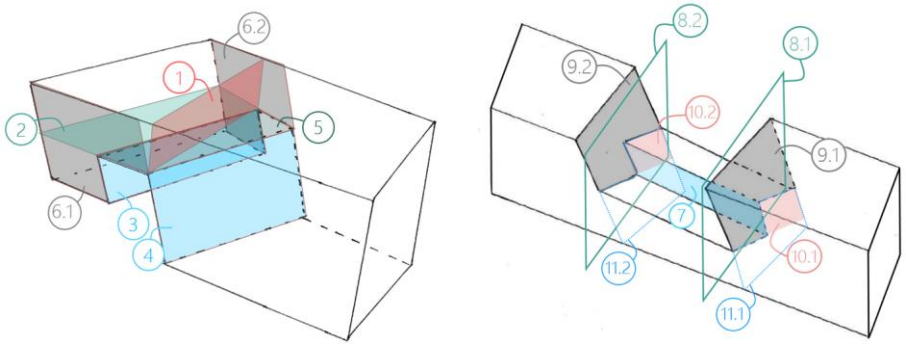


Figure 4 Critical planes

3.3 Integration

After running through a first design iteration at global and connection level, both must be integrated. The seven beam forces and four shape parameters following from the global design have to be linked to the seven parameters defining the connections, see Figure 5.

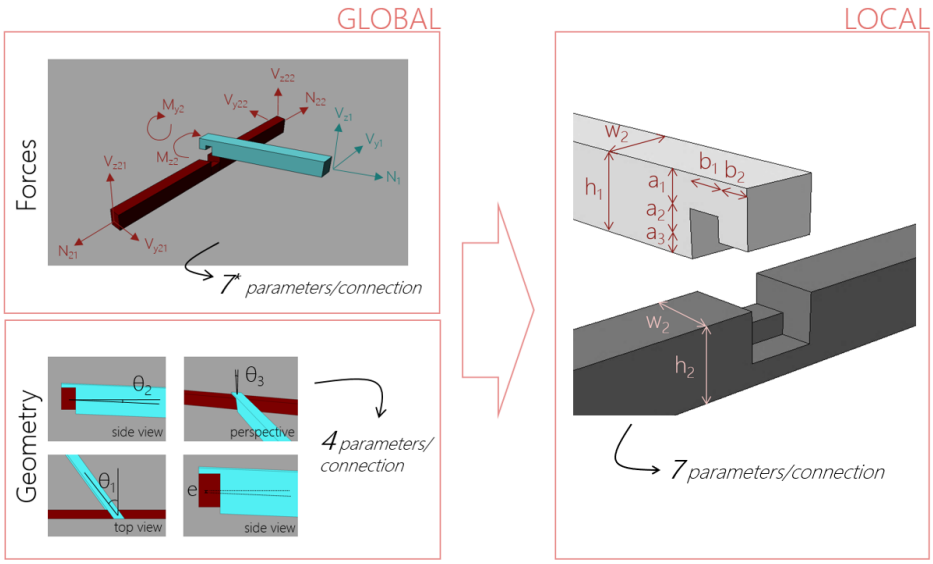


Figure 5 Design challenge: linking parameters on global and local level

The large amount of unique connections, the large number of parameters and the complex relation between them makes it difficult to directly link the parameters of the global design to suitable connection dimensions. Using machine learning to predict suitable dimensions is proven to speed up the connection

design process in the first design phase, in which still a lot of changes to the design are made. When the design is adjusted, the algorithm can instantaneously predict the dimensions of the altered connections based on the new force distribution. Nevertheless, this method requires the input of a database with a large amount of designs with their performance, which is time-consuming to construct. Therefore, an alternative method is to apply the same dimensions to all connections and spend more time on adjusting the design of the ones that don't fulfill the requirements.

4. Testing

The application of new fabrication techniques is often associated with a lack of knowledge on the structural behavior of the new material or type of design. In this case, the largest source of uncertainty is related to the shear capacity of the notched connection. The Eurocode prescribes a calculation method based on the fracture energy of softwoods (NEN-EN 1995-1-1, section 6.5.2).[7] Previous research has indicated that this method is not suitable when hardwood is applied. [9]

Additionally, it is common to apply screws just after the notch in order to prevent the member to crack along the grain. In that case, the shear capacity of the member is governed by the withdrawal capacity of the screw instead of the shear of the timber. Several guidelines and handbooks (e.g. EC5, DIN 1052:2008 and APA) give approaches to calculate the withdrawal capacity of screws. However, capacity calculated by different approaches are very varied, see Figure 6. For this reasons tests have been performed at Delft University of Technology, both on the capacity unreinforced and reinforced notched members.

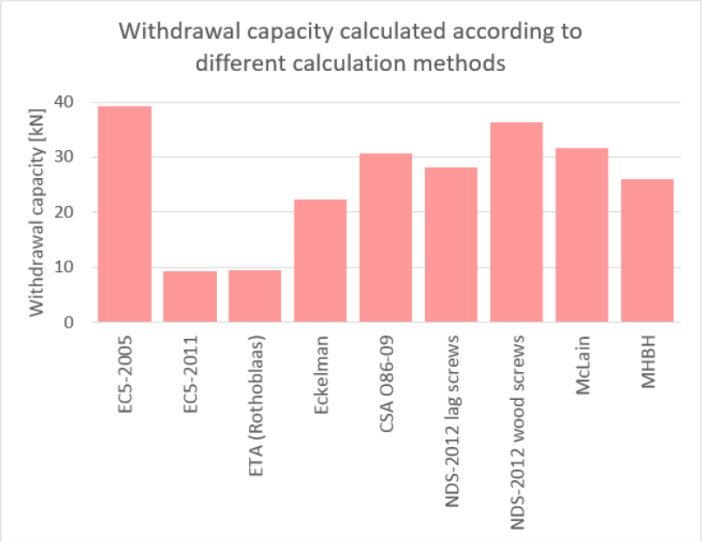


Figure 6 Withdrawal capacity according to different calculation methods

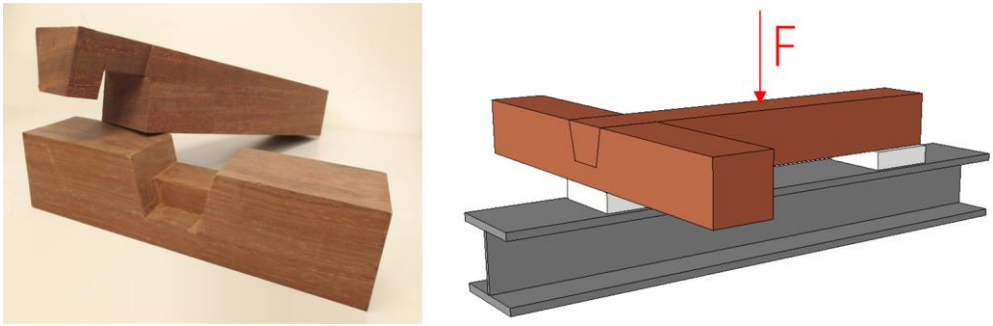


Figure 7 Test specimen (left) and model of the test setup (right)

Four types of specimens were tested: specimens with sharp edges and specimens with rounded edges, both unreinforced and reinforced with screws, see Figure 8

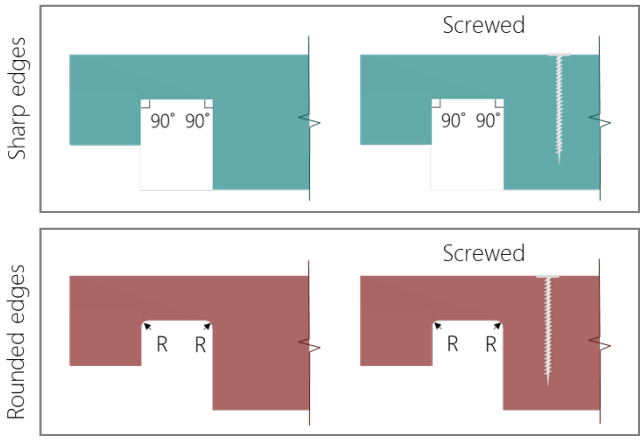


Figure 8 Types of test specimens

The tests show that the calculation method from the Eurocode does not adequately predict the shear strength of notched members made in Azobé and therefore additional research on the fracture energy of hardwoods is required to develop a more accurate prediction method.

Rounded edges and screws were expected to increase the shear capacity of the notched beam. This was confirmed by lab tests. The tests showed an increase in capacity with a factor 1.6 when rounded edges are applied instead of sharp edges. Applying rounded edges in combination with screws resulted in an increase with a factor 3.0. Additionally both adjustments increased the ductility of the connection. Therefore, it is recommended to always apply rounded edges since an increase in capacity is obtained without increasing the amount of material, the weight and fabrication time. Screws preform even better, but the increase in capacity should we weighted against the increase of fabrication costs and time. This applies to all types of structures with notched members, including for example lock gates or timber roof structures.

5. Recommendations and conclusions

Major benefits of the application of digital fabrication techniques are the ability to design structures with a great freedom of shape and uniqueness of structural parts. This allows for the structural optimisation at both global (shape and member) level and connection level. However, this large design freedom results in a huge amount of design parameters, complicating the design process. The complexity is dealt with through the application of a completely parametric iterative workflow in combination with digital design tools like evolutionary solvers and machine learning algorithms.

In order to enable the assessment of large number of design alternatives, design strategies are developed to speed up and optimise the design process. One of the strategies is confining the problem by for example reducing the amount of load cases, limiting the amount of design parameters, simplifying the design, decoupling design steps. Furthermore, a simplified calculation method is developed in order to get quick feedback for each design alternative. Another applied strategy is to determine the effectiveness of design iterations and defining an acceptable error.

Another complication that is associated with digital fabrication is the lack of knowledge regarding unusual shapes and materials. Codes and handbooks are aimed at standard sections and applications and therefore often not applicable. For this reason experiments should be carried out in order to define the structural behaviour.

Altogether, this research has demonstrated that it is possible to use Azobé to fabricate connections with the required freedom of shape and as confirmed by lab tests, structural function. This together paves the way to apply digital fabrication of timber structures in civil engineering.

References

[1] Gramazio Kohler Research, ETH Zürich, *Additive Robotic Fabrication of Complex Timber Structures,* 2012-2017, URL: http://gramazio-kohler.arch.ethz.ch/web/forschung/e/0/0/0/184.html

[2] Koning, L.F.M. (2018) *Digital Fabrication of a Timber Bridge* (Master's Thesis), Retrieved from http://resolver.tudelft.nl/uuid:0298448c-5bad-4760-9382-06d58ed07edc

[3] Philipp Eversmann, Fabio Gramazio, and Matthias Kohler. *Robotic prefabrication of timber structures towards automated large-scale spatial assembly.* Construction Robotics, Aug 2017. ISSN 2509-8780

[4] Søndergaard, A., *Topology Optimization of Spatial Timber Structures,* 2015, URL: http://gramazio-kohler.arch.ethz.ch/web/e/forschung/300.html

[5] Eurocode 0: Basis of strcutal design, nen-en1990+a1+a1=c2=2011-nl

[6] Eurocode 1: Actions on structures

[7] Eurocode 5: Design of timber structures, nen-en1995-1-1+c1+a1=2011-nl

[8] C. Chen, H. Qui, and L. Yong. *Flexural behaviour of timber dovetail mortise and tenon joints*. Elsevier - Construction and Building Materials, pages 366 – 377, 2016. doi: https://doi.org/10.1016/j.conbuildmat.2016.02.074.

[9] van Otterloo, J.R. (2013) *Force distribution and connection strength in timber lock gates* (Master's thesis) Retrieved from http://resolver.tudelft.nl/uuid:57cc1e2a-ed31-44b8-a32a-d52aba5d720f

Proceedings of the IASS Annual Symposium 2019 – Structural Membranes 2019
Form and Force
7 – 10 October 2019, Barcelona, Spain
C. Lázaro, K.-U. Bletzinger, E. Oñate (eds.)

Into lightness: Furniture as Proxies for radical experimental Structural Design using Advanced Manufacturing

Carlos BANON*, Felix RASPALL*, Hui Ping TOH*

* Singapore University of Technology and Design
8 Somapah Road. 487372 Singapore
carlos_banon@sutd.edu.sg

Abstract

Following the tradition of architects Charles and Ray Eames, Frank Gehry, Jean Prouvé and Greg Lynn, the paper presents research pertaining to application of structural design using furniture as proxy to understand and empirically test experimental structural hypothesis. Five state-of-the-art designs by the authors explore the opportunities and challenges in the area of structural performance, material selection and transition, mechanical properties, manufacturing process and assembly procedure. All projects investigate the load distribution through lean structure members, the proportion of supporting points on the ground with respect to material mass, the slenderness ratio of the structural member and the overall span and applied force capacity in functional load cases. This process demonstrates the effectiveness of experimental furniture design to bridge the gap between intuitive structural knowledge and digital simulations, and to provide hint on the implication of structural strategies in the field of architectural design and to solve complex challenges at the level of conceptualization, development of components and assembly workflow.

Keywords: Additive Manufacturing, Structural Design, 3D Printing, Geometry, Form Finding, Spatial Structures, Generative Design, Furniture, Proxies.

1. Introduction

The use of digital manufacturing has opened opportunities for innovation in structural design. The high cost of architecture scale makes experimentation unfeasible. Furniture design opens opportunities for exploration, experimentation and prototyping. New fabrication process like Additive Manufacturing (AM), Computer Numerical Control (CNC) and Thermo-Forming, in combination with parametric digital design tools, can be applied using furniture as test-case that provide substantial resolution for structural design consideration, before upscaling it to building or structural designs.

The increasing interest of AM in the construction industry still conflicts with limitations in build volume of printed components, and high cost of production for higher strength capacity materials. Parametric digital models in combination with FEM analysis help elude the fabrication of physical prototypes, reducing the cost during the design development. However, they are unable to provide crucial empyrical data solely obtained when operating with actual and functional components. Working with tables as the chosen furniture type, makes it necessarily to think about structural challenges that entail horizontal surfaces and linear elements that transfer its load, enabling the proxies to be scalable to a slab-beam-column system [1]. The investigation is founded on three full-scale completely functional designs which explore fundamental structural strategies and geometric transition and connections through dissimilar materials to pursue lightness in architectural design. The paper discusses our methodology, results and conclusions.

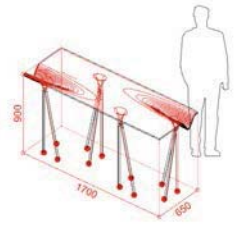
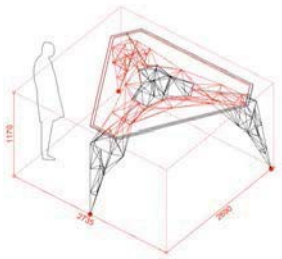
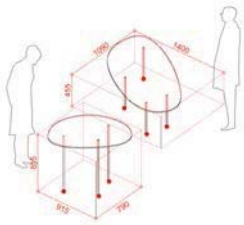
Copyright © 2019 by Carlos BANON, Felix RASPALL, Hui Ping TOH
Published by the International Association for Shell and Spatial Structures (IASS) with permission.

2. Methods

The proposed methodology demonstrates the efficacy of experimental and furniture design as fully functional proxies to mediate between intuitive structural principles and digital simulations, constituting an effective process to solve complex challenges at the level of conceptualization, optimization of components and assembly workflow [2].

A compehensive process from design to ultimate manufacturing and assembly using digital fabrication, is covered by the research, including the following stages: (1) Parametric model and structural optimization using bespoke algorithms, (2) Structural performance and optimization, (3) Survey, selection and implementation of advance manufacturing techniques, (4) Detailing, fabrication and assembly workflow. The research is based on three build 1:1 proof-of-concept designs, following the four steps of the abovementioned toolchain.

Table 1: Digital fabrication processes and geometric properties of the selected three build test-cases.

	1. OH Platform	***2. AIR Table***	***3. Bamboo Gradshow***
Surface	Thermo-Formed	6-Axis CNC	3-Axis CNC
Nodes	Resin Casting on SLS with PA Nylon	Binderjetting Steel with Bronze	Entry level FDM with PLA
Contact Points	12	3	3 - 4
Bounding Box	X 1.70 , Y 0.65 , Z 0.90 m	X 2.73 , Y 2.69 , Z 1.17 m	XY (0.90-1.40) , Z (0.40-0.75)
			

2.1. Custom parametric models using bespoke algorithms.

The three test-cases described in this paper are part of an ongoing research initiated in 2016 on 3D Printed Architecture (Raspall and Bañón, 2016), using bespoke 3D Printed components as functional parts of actual built designs [3]. Taking advantage of 3D printing and CNC technologies, out investigation targets free form and non-standardized components as a way to mediate between complex geometries and efficiently respond to the many singularities where standard components become a limitation.

Parametric Modelling allows to work at the level of the overall design simultaneously with the scale of the smaller components. By doing that in an early stage, structural efficiency, costing, aesthetics, geometric continuity and resolution are iteratively addressed by a combination of bespoke algorithms using Grasshopper for Rhinoceros as common platform.

2.2. Structural Performance and Optimization

Once the design is conceptualised, a deeper optimization of the structure is performed. As part of our custom workflow, we explored Ansys Workbench and Karamba to assess results to better understand the structural behaviour. In all the designs, a generative optimization using Galapagos for single goals, and Opossum for multiple design targets, was performed to determine the angle, length and position of the supports respect to the table top. In all the cases, the thickness of the members was not considered a

variable in order to centre the research into a broader geometric optimization rather than a local study of each member.

2.3. Survey, selection and implementation of advance manufacturing techniques

Our research investigates the feasibility of AM to produce functional components in architectural design, with the main objective of designing and fabricating complex parts capable to extend geometric continuity through dissimilar materials, and to achieve a high degree of intricacy at the connection level. In this research we explored three different manufacturing techniques:

2.3.1. Resin Casting on SLS with PA Nylon.
Taking full advantage of the high resolution that this fabrication method confers, we explored epoxy resin casting on thin 1mm shell to strengthen its mechanical properties to meet the structural requirements while reducing printing costs. This method was used in the OH Platform.

2.3.2. Binder jetting Steel with Bronze
Despite the high cost of production, mechanical properties make this 3D printing process very suitable for high-performance structural design with an ultimate strength of 496 MPa. Using binder jetting techonology, the resulting composite is 60% steel and 40% bronze, with a resolution good enough to print intricated connection details. This process was used in the AIR Table.

2.3.3. FDM with plant-based polymer PLA
In order to meet tigh budget constraints, entry level printers such as Ultimaker and Sindoh were also explored to fabricate functional components. It is a very suitable technology when budget is very tight, but impacts the thickness and dimension of the design as mechanical properties are relatively low. This process was used in the Bamboo Gradshow.

2.4. Detailing, fabrication and assembly workflow

The research challenged a full Design to Fabrication process with no drawings produced at any stage of the detailing workflow. Only digital STL files were generated to fabricate each of the bespoke 3D Printed components, and Excel sheets with lenghts for the standard bars.

The iteration between digital models and physical objects was drastically accelerated with the use of 3D printing, as physical prototypes were made overnight and tested the following day. Quick adjustments regarding the interfacing of structural elements, assemblability, manufacturability and aesthetic effects were possible, accelerating the design and production of the designed objects.

3. Results

Three parallel projects were developed from September 2017 until October 2018 as part of this research, all of them structured to enable the development of the aforementioned four steps in real life cases. Presented in chronological order, each one of the project focuses on different aspects.

3.1. OH Platform

The OH table was designed as an experimental display platform for the Venice Biennale of Architecture and Urbanism, and SUTD's Open House in 2018. The structural premise was to hover a very thin 12mm surface, pleated on two corners to increase its rigidity over a forest of very slender columns. A total of sixty 1700mm x 650mm units were produced, allowing different combinations into linear or two-dimensional arrays, where the surface's pleats align and helps provide a sense of continuity to the extended surface.

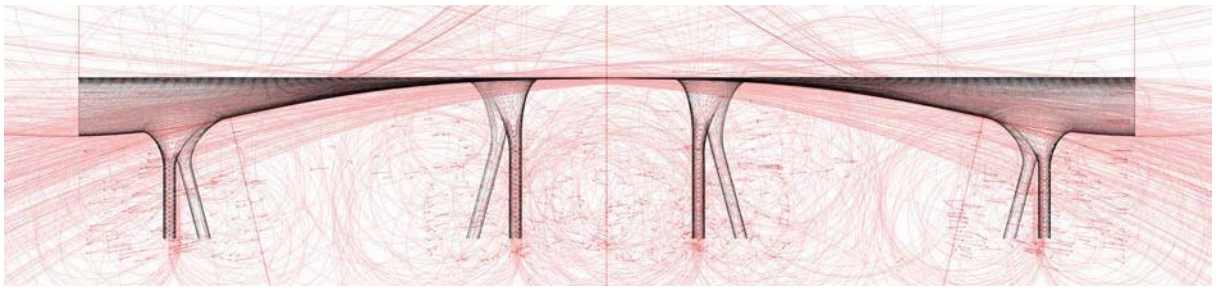


Figure 2: analysis of geometric continuity between table surface, nodes and supports.

The table's top is a thermo-formed acrylic solid surface sheet that describes a smooth yet tight curvature. This geometric move adds inertia to the table allowing it to be stiff without a substructure and adds appeal to the design. The surface is supported by 12 thin aluminium legs, clustered in four tripods, to reduce the leg's visual presence. The positioning of the tripods was defined through a careful structural analysis using FEM to reduce the deflections and increase the stiffness. The connection of legs to the surface was resolved with a complex geometry part that interpolates the geometries and creates an effect of seamless continuity between all elements. The connecting pieces were 3D printed in high performance nylon and fitted with a threaded connector that allows the legs to be dismounted for storage and transportation. The tables gently rest on twelve rounded 3D-printed supports adjustable in height that confer great stability to the system while conferring an aesthetic of visual lightness.



Figure 2: Left, axonometric drawing of all components; center, 3D Printed node with threaded connectors embedded; right, 3D Printed adjustable leg tips.

Several challenges were present at the initial stages of the design. First, the intention of bending a solid surface using a Gauss curve in tight radius of 20mm which was beyond the recommendations of manufacturers. Several prototypes were conducted to demonstrate the bending possibilities of the material with no visible cracks. Second, the use of polymer 3D printing for structural components was an uncertain approach. Through prototyping, the right geometry, process and machine setting was established (see Figure 2). The final design includes threaded inserts that allow the legs to be disassembled and add strength to the part. Third, 3D printed was required because the complexity of geometry and the relatively small production volume of 60 tables. However, the short production schedule required development of 3-dimensional packing strategy to maximise the number of parts

produced in a single printing session. As a result, more than 240 nodes and 2,000 leg tips were produced over the course of a week. This strategy can be used for future projects and helps in the viability of 3D printing for mass production.

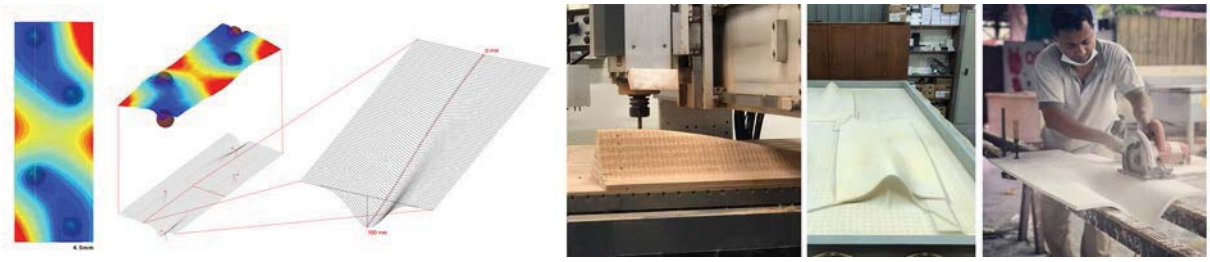


Figure 3: This is a typical figure/photo/table caption [with credits and/or references as appropriate]

The design combines and improves in novel ways existing design and manufacturing methods. It demonstrates a more daring curvature for solid surface materials beyond what has been tested before. It showcases the possibilities of 3D printing for production purposes and implements new algorithms that optimize the production time. For the first time, three different material technologies, solid surface, 3d printed connectors and aluminium legs were aesthetically and functionally merged into a single product. The use of structural analysis tools, in combination with physical prototypes, enabled the use of a single solid surface sheet as a table material without substructure (see Figure 3)



Figure 4: Left: 3D printed nodes; center: epoxy resin casting with threaded steel rods; right: detachable tripod.

The project had strict budget and schedule constraints, which determined much of the execution decisions. 60 tables needed to be designed for less than US$400 each, over the lapse of three months. Two successful thermoforming prototypes with manufacturers allowed the commencement of production of the table tops. Independently, the design of the connector and legs was conducted in house. Over 10 prototypes were used to refine and validated the aesthetic and functional performance of connectors, which need to structurally attach to the table tops and detachable legs. For the production of the connectors, a custom nesting algorithm was produced to improve the printer's proprietary software and accelerate the production schedule. Once the nodes were printed, the threaded connectors were installed and secured with epoxy resin (see Figure 4). The final element was the adjustable leg tip, which was also design and printed in house.

Geometrically, the design seeks for continuity and slenderness, hiding the dissimilar materials and fabrication processes win a singular, minimalistic table. When tables are combined, the two ripples align and give the surface a sense of continuity (see Figure 5) while creating a mesh of very slender fibrous-looking supports underneath.



Figure 5: Left, aggregation of two tables; middle: front view; right: pleated surface and 3D printed connector.

3.2. AIR Table

The second project presented in this paper takes full advantage of advanced metal printing technology in a furniture system that can be customized for multiple applications. In addition, the project demonstrates a design philosophy that engages with material economy through design, using stainless-steel tubes 6mm in diameter and a table top made of white Corian which was chamfered, and the bottom hollowed out using a 6-axis CNC Router. AIR Table's apparent structural prowess pushes the limit of materials and therefore aims to inspire the curiosity and audacity to its users by transferring the heavy load of the table top to only three contact points. [4]

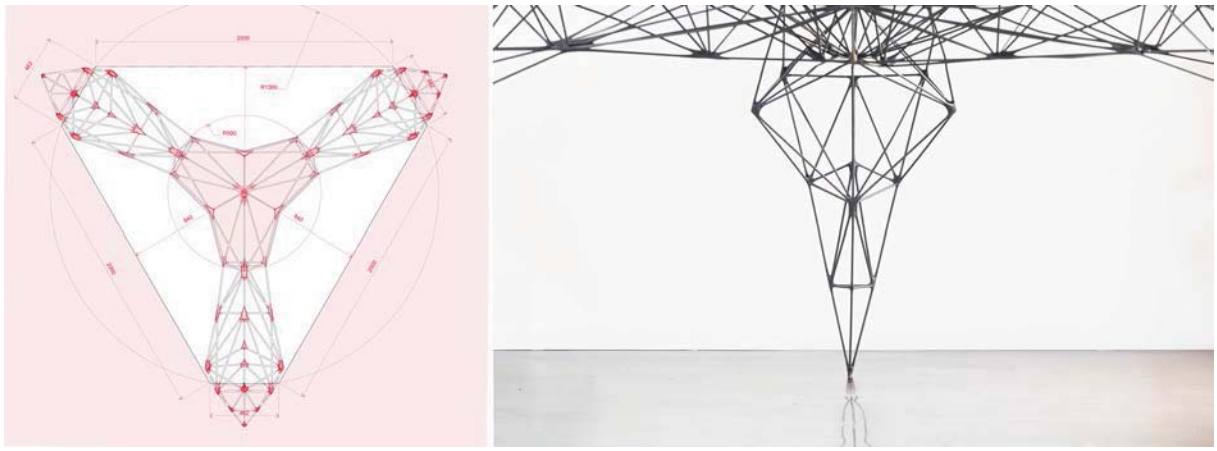


Figure 6: Left, floor plan of the AIR Table; Right, front view of one of the supports,

Through a generative wireframe model, the structural nodes placement was done according to structural performance and optimization considerations using Karamba, avoiding self-intersections in the generation of the intricated tetrahedral network (Figure 6). A total of 84 nodes were generated with a bespoke script refined using T-Splines, and 3D-printed with 420 Stainless Steel using binder jetting technology. The end of each bar and the corresponding tip of each node was threaded for connecting purposes. The connection detail was a difficult technical challenge because of the small section of the bars (6mm), which was resolved through substantial prototyping, trial and error and refinement.

The assembly strategy began from the centre of the table and radiated outwards, one bar at a time, towards each leg of the table. The whole process took approximately 30 days to complete by one full-time researcher. The inherent stiffness of the growing connected geometries made it easier to propagate the connections in a single direction than to join two completed parts of the system together. To attain the perfect fit that the whole system was designed for, each bar had to be calibrated carefully

as they needed to rotate into two nodes simultaneously. At the level of details, the design intends for an almost invisible connection that makes the node and bar seamless (Figure 7).

The table, which spans a total 3m, is 108kg heavy and is able to withstand a uniform load of 2kN with an average deflection of 6.4mm with no visible signs of buckling.

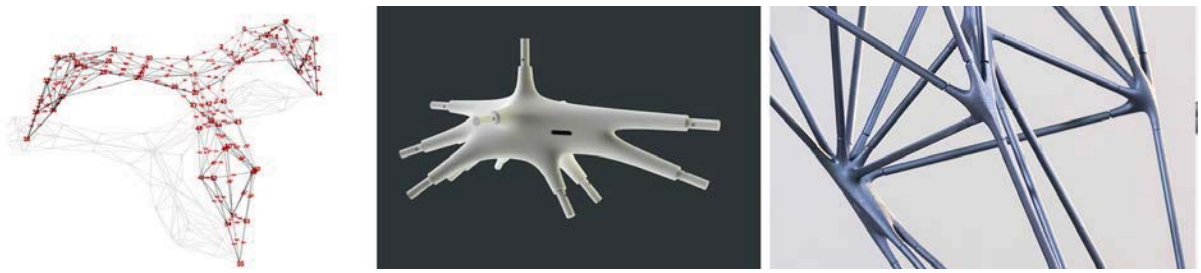


Figure 7: Left, generative structural model; center: digital model of a node; right: nodes and bar connected.

3.3. Bamboo Gradshow

The third project described in this paper was developed for the SUTD Grad Show in 2018. It consisted on a series of 31 customised curve-profile tables supported on vertical bamboo poles. Although the structural principle is relatively straightforward slab-column problem, the seamless connection between dissimilar materials within a reduced budget framework was the real challenge.

The design of each of the table tops was digitally generated using an algorithm that creates a 2D convex hull polygon derived from the objects to be displayed and generates a smooth curve around it. Each of the boards were CNC-ed in 18mm birch plywood and 12mm Corian acrylic board (Figure 8).

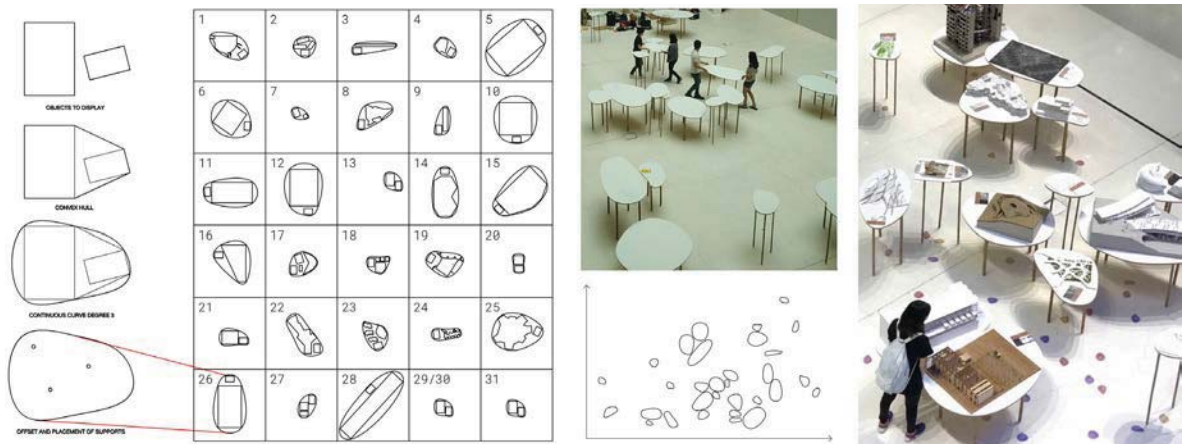


Figure 8: Left, tale top generation; center, layout of the exhibition using scatter a plot graph; right: exhibition at the National Design Centre in Singapore, 2018.

Bamboo was chosen as the material for the vertical supports, in order to explore the work with material imprecisions. The project builds on previous research done by the authors in 3D Printed Frames, using computation to analyse the irregularities in each bamboo pole and process the data to optimize the structural design to create connectors that perfectly fit each bamboo profile (Figure 9). In accordance, 3D printing enables the fabrication of bespoke connectors required at no additional effort. In this way, the unpredictability is used as a design gain in a very precise and controlled manner, combining cutting-edge process with vernacular materials like bamboo to augment its potential.

A total of 112 bamboo poles were cut to length, and its end sections digitized using a 2D scanner. This information was transferred to a script that analyse the structural capacity of each pole, assign it to the

optimal position in the tables and create the precise geometry of the connector, which were parametrically designed and printed in inexpensive PLA biopolymer. The bottom side of the joints and the leg caps are also designed to fit every unique piece of bamboo.

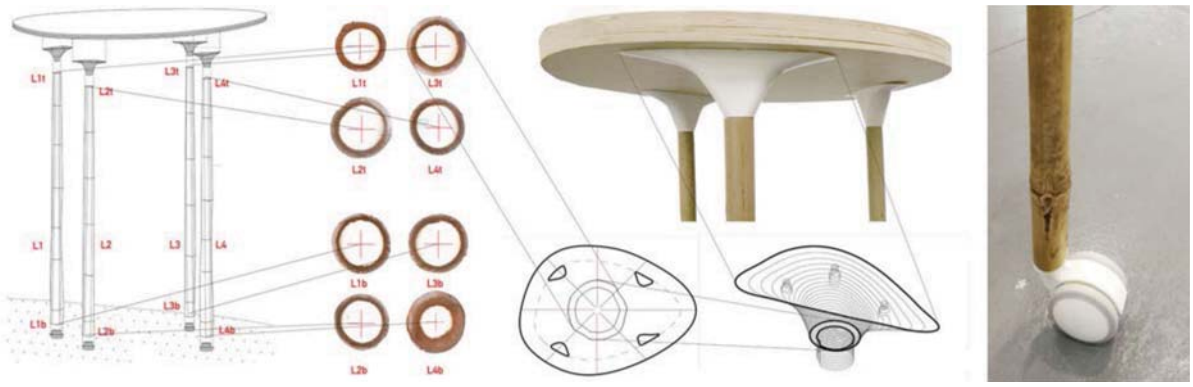


Figure 9: Left, axonometric drawing of all components; middle: scanned sections of the bamboo poles; bottom-right: 3D model of the connection node; top-right: built prototype.

The script generates the space for the steel screws which mechanically connect the nodes with the table tops, making the assembly process a very unchallenging and extremely efficient. Some problems were encountered with the larger connecting pieces that were printed with low-density infill material. Those were reprinted with a higher density setting in order to withstand bigger horizontal shear forces.

4. Conclusion: submission of contributions

The three table projects demonstrate the effectiveness of using furniture projects as a model for developing experimental structural principles and novel construction technologies. The three structural principles, modeling methods and fabrication processes were tested from concept to final materialization in functional 1:1 scale. This furniture scale design and fabrication exercise provides evidence of the modeling processes, structural hipothesis and assembly detailing. Through this, the scalability to architectural scale is accelerated, reducing the uncertainties in the initial experimental hypothesis.

By working at the scale of furniture using AM, complex structural challenges are tackled both digitally and empyrically in an increased speed. This allows for large amount of data collection from direct experience which will inform the digital models to be better simulate actual conditions, and to explore innovative structural strategies subject to be taken to a larger scale.

Acknowledgements

We would like to thank all sponsors and researchers for their support; OH Platform: F. Amtsberg, Yuxin, J. Chong, L. Hongzhe, Y. Goh; AIR Table: J. Chong, A. Toh, Zabir, Nurin and Nazri; Bamboo Gradshow: Caroline, T. Yu Jie, J.W. Chen, Roxanne, S. Narendran, Xin Ling and G. Chek.

References

[1] J. E. Gordon, Structures: Or Why Things Don't Fall Down, London: The Folio Society, 2003.

[2] F. Otto and J. M. Songel, Conversation with Frei Otto, New York: Princeton Press, 2010.

[3] F. Raspall, and C. Banon: 2016, "vMESH: How to print Architecture?", *Proceedings of SIGRADI 2016, 394-398.*

[4] F. Raspall, C. Banon, and J. C. Tay, "AirTable: Stainless steel printing for functional space frames", in Intelligent & Informed. Proceedings of the 24th International Conference of the Association for Computer-Aided Architectural Design Research in Asia (CAADRIA) 2019, Paper 632 (Preprint), Hong Kong, 2019.

Proceedings of the IASS Annual Symposium 2019 – Structural Membranes 2019
Form and Force
7 – 10 October 2019, Barcelona, Spain
C. Lázaro, K.-U. Bletzinger, E. Oñate (eds.)

Metal-reinforced Membranes - Electroplating high-strain membranes into metal shells

Federico FORESTIERO*, Bruno KNYCHALLA[a]

*FAUST FabricationArchitectureStructure
Elektrastrasse 15, 81925, Munich, Germany
info@faust.co

Abstract

The research presented focuses on the development and evaluation of a novel manufacturing strategy for reinforcing high-strain membranes into rigid metal shells. The mean of reinforcement is electroplating, a process that uses electric current for applying thin metal coatings on conductive formworks. In the proposed manufacturing strategy, high-strain membranes serve as stay-in-place formwork for the electrodeposition of metal. The goal is to define the parameters of the fabrication strategy and to evaluate its potentials and limits. Through a series of physical tests, the steps of electroplating membranes are investigated. The metal-reinforced membrane, after electroplating, maintains its geometry, showcasing its shift from a tensile to a shell structure. In fact, the structural typology transforms from form-active to surface-active. The proposed manufacturing strategy, increasing weather durability and stiffness of high-strain membranes, could be a new solution for fabricating free-form facade panels without the necessity of custom formwork.

Keywords: high-strain membrane, metal shell, electroplating, electroforming, metal reinforced membrane, fabric formwork

1. Introduction

In contemporary architecture simple metallic skins are used as a non-structural cladding system for their superior metallurgical properties [1]. As architectural form develops to structurally optimized or free form shapes e.g. in lightweight construction, the need to generate metallic skins of higher geometric freedom arises. The fabrication of complex metallic elements often requires a multiplicity of operations such as pressing, drilling, machining, deburring and welding during manufacturing, that might not be compliant to the cost and energy sensitive field of architecture. The ability to cost-effectively manufacture complex metallic parts to close tolerances has brought the process of electroplating to application in traditional manufacturing fields such as the automotive industry. Although it is not a universally applicable process, electroplating has proven to produce/reproduce shapes to close dimensional tolerances with net-shape surface quality and superior metallurgical properties [2]. These qualities have long found their way into architectural application. Already in 1854 the gold domes of the Church of the Redeemer in Moscow, then largest Orthodox church in the world, were plated through this electrochemical process. In Cooperation with Moritz Hermann von Jacobi, a German architect and one of the inventors of electro metallic plating, Duke Maximilian von Leuchtenberg established a plant in St. Petersburg, where the gold plating of the copper dome plates was carried out in three wooden tanks that each held over 5000 liters of cyanide solution[3].

Copyright © 2019 by Federico Forestiero and Bruno Knychalla
Published by the International Association for Shell and Spatial Structures (IASS) with permission.



Figure 1: The Church of the Redeemer in Moscow before demolition, between 1854 and 1931 [3].

Even though nowadays electroplating, or electroforming, is used to make near net-shape metal parts for small series production similar to injection molding, it was originally developed as a metal coating method and always needs a substrate or mandrel where metal ions can attach to during the metallic growth [2]. If the goal is to produce various different doubly curved geometry at least minimal formwork is necessary, ideally one that's easily malleable.

High-strain membranes, for example, have been used as a means for a material- and energy efficient fabrication of complex doubly curved geometry due to their ability of being shaped into anticlastic tension-active structures by applying forces in defined areas or points [4]. Furthermore it has been

proven that they can be used as a minimal formwork for conventional fabrication methods [5] when freeform geometry is sought after. However the need for a frame to hold the membrane in place and shape together with its low durability properties make stretchable membranes not applicable for most architectural projects, even though a high degree of freedom in form could be achieved.

By using the time, material and energy efficient strategy of generating doubly curved geometry with elastically deformable membranes and locking them into shape through electroplating, this research aims to create rigid energy and cost effective elements of complex shape with superior metallurgical properties. The scope of this research is to develop a manufacturing strategy for reinforcing high-strain membranes into metal shells.

2. Methods

2.1. Electroplating

The naming of the method ranges between electroplating and -forming, where the first aims to coat a part with a metallic layer and the latter to coat a mandrel that is then removed so that the deposed material becomes a new self-contained element [2]. Electroplating is a process by which metal is deposited upon the surface of a conductive substrate, if non-conductive, the substrate is coated with an electrical conductive paint [6]. The process begins with the suspension of a substrate into a solution of metallic salts (called "electroplating bath") together with solid pieces of the to be deposited metal. Then a current is passed through the solution between the substrate (called "cathode") and the metal (called "anode"). The parameters to influence the plating thickness and quality are: cathode design, anode position in the bath, electrical contact points position and voltage [7]. To avoid uneven metal thickness the substrate is in constant motion during the electroplating process and it is manually rearranged within the bath approximately every 5 hours. Here, copper and nickel are the chosen metals for plating within two different electroplating bath of 1500 x 500 x 500 mm. The tested paintings for the textile are silver, copper and graphene. The fabric used is lycra , a high-strain textile that is continuously woven and elastotulle, woven with an hexagonal pattern and 2 mm holes.

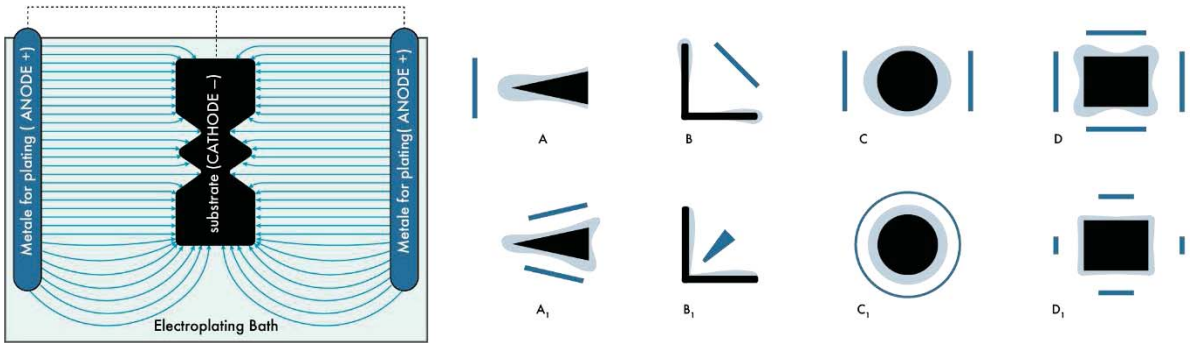


Figure 2: Different electroplated results based on the anode position and shape within the bath [7].

2.2. Elastically deformable structures

Elastically deformable is a structure, when it undergoes large deformations but finds equilibrium shapes through interactions between form, material and forces. Elastically deformed high-strain membranes fall into this category. Shape drivers in this case are tension, anchor points or areas, and relative material properties that can be manipulated to discover a wide range of doubly curved tension equilibrium forms [8].

3. Developments

The manufacturing strategy is developed through a series of physical experiments. The proposed strategy starts from an existing computational design approach [8] and continues to use the digitally produced data for the development of a fabrication strategy (figure 3).

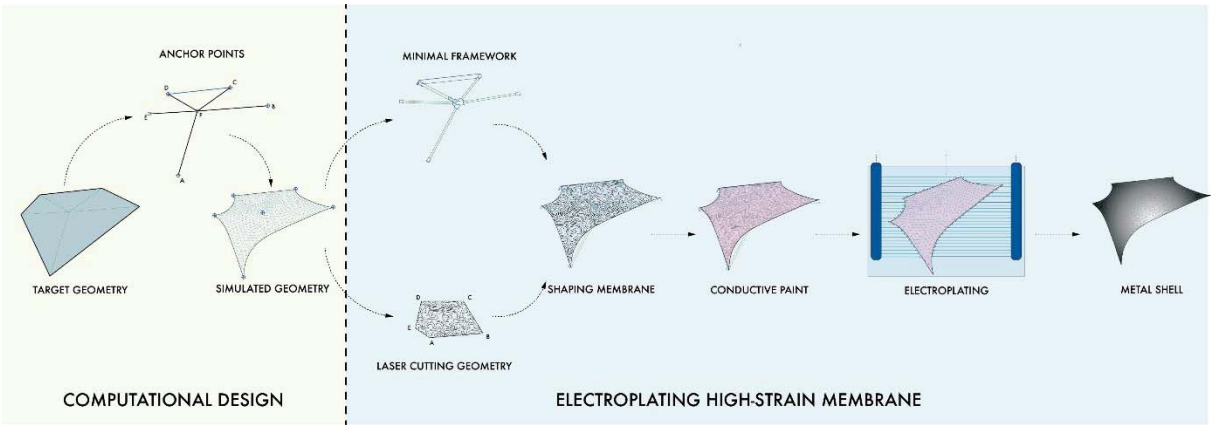


Figure 3: Phase for electroplating a high-strain membrane into a target metal shell.

From a target geometry the anchor points and edge condition are extracted and the deformation of the high-strain membrane upon a minimal framework is digitally simulated using a particle spring based system. With the simulated geometry a minimal framework is fabricated following three strategies: a bounding box with metal wires, a laser cut plastic framework or a simple truss with a single 3D printed node. In preparation for laser cutting the digitally deformed membrane is brought into a flat state by an approximative unrolling algorithm. Once cut the high-strain membrane is easily connected to the framework through thin metal wires and is tensioned to achieve the target geometry. To convert the membrane into a conductive surface, two different types of painting are tested: copper and graphene spray paint. The membrane is left to dry for 30 minutes and afterwards immersed into the electroplating bath. During this process the membrane or substrate works as a cathode receiving metals from either a nickel or a copper anode. To ensure reliable electrical connectivity anode and cathode are connected through multiple copper wires in the vertex of the membrane. These electrical connection points are empirically derived based on geometry, voltage and desired plating thickness. The substrate is left in the bath until its desired plating thickness is achieved. After the electrochemical process is finished the substrate, now a metal shell, is taken out of the electrolyte, washed in a cleaning bath for removing any residual and then finished through a sandblasting process.

To evaluate each phase of this novel manufacturing strategy a series of empirical tests is executed. Multiple variables are changed and their effects investigated in these experiments to define a formula that can lead to the establishment of a standardized process such as. Parameters that where changed are plating material, voltage, thickness/time ratio, framework dimensions and conductive paint.

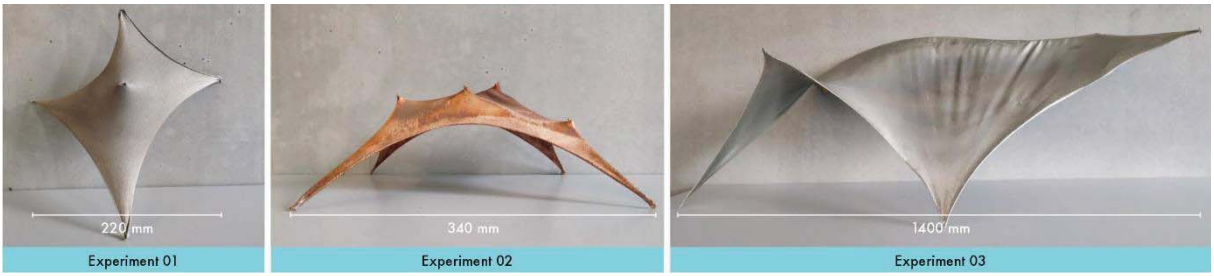


Figure 4: Experiments: 01) nickel plated elastotulle - 02) copper plated elastane - 03) nickel plated elastane.

3.1. Experiment 01

In the first experiment, a single "spike" geometry with five tension points and a bounding box of 250 x 250 x 120 mm produced from elastotulle is tested. The goal is to plate a thin nickel coating maintaining the transparency of the substrate material while increasing its stiffness to achieve a self-supporting metal shell. The substrate is tensioned with metal wires within an aluminum frame to achieve its target shape and successively sprayed with conductive graphene paint. Each vertex of the membrane is connected to the electrical current to insure an even electrical field on the membranes surface. The prepared substrate is immersed in the galvanic bath for 2 hours at constant 2.0 volt.

The reinforced membrane maintains its geometry and its transparency and it becomes a metal shell with a thickness that varies from 0.3 to 0.5 mm (figure 4). During the electroplating process the aluminum frame attracts a high amount of nickel, reducing the speed of the electroplating for the membrane.

3.2. Experiment 02

Here a "multi-spike" geometry with eleven tension points and a bounding box of 400 x 300 x 170 mm, produced from a white elastane is to be manufactured. As a waterproof copper shell in a more durable complex shape is strived for, a layer of more than 1.0 mm thickness should be electroplated. The substrate is tensioned, within a plastic non-conductive frame to reduce its interference on the electroplating process of the substrate. Similarly to the previous experiment the electrical connection points are on the membranes vertexes. The membrane is painted with copper paint to increase the speed of the plating process. The substrate is immersed in the galvanic bath for 35 hours at 1.0 volt.

The plated object has a thickness that varies from 0.6 mm to 1.5 mm with darker areas in the center without plating (figure 4). Especially edge conditions show thickness increases, while plating dramatically decreases towards the center of the surface reaching almost zero. The problem is due to the electric field on the object combined with the applied high voltage. Here especially the anticlastic geometry with multiple spikes creates a series of electrical "valleys" where the bowl effect reduces the electrical field to zero. Exactly in these defined valleys, plating thickness reached its low point.

3.3. Experiment 03

For the third experiment, a double curved surface with four tension points and a fix edge with a bounding box of 1400 x 450 x 500 mm, should be produced from a white elastane. The goal of this test was to produce a watertight object that fills most of our fabrication set-up. Here a new framework, laser cut from metal, was used, rigid enough to take on the tension forces of the larger membrane. The substrate is tensioned within the framework, that was previously coated with non-conductive polyurethane and successively sprayed with graphene. A series of thin wires are connected to the membrane as electrical connection points. Placed within 100 to 150 mm distance, these points should ensure even plating for the larger membrane. The substrate is immersed in the galvanic bath for a total of 30 hours divided in: 10 hours at 2.0 volts, 10 hours at 3.0 volts and 10 hours 3.5 volts.

The plated object has a varying thickness from 0.4 mm to 1.5 mm (figure 4). Furthermore, the final metal shell shows multiple non uniform areas, due to low and uneven tension in the membrane. Additionally during the fabrication process the electrical connection points had to be moved multiple times as vastly heterogenous plating occurred. At this scale the fabrication strategies becomes more complex as additional steps had to be executed half way through the plating process, counteracting the uneven plating.

4. Results

These experiments were the basis for defining an optimized fabrication strategy taking in account all fabrication parameters. Both elastane and elastotulle were successfully plated and the resulting shells can be used for different architectural application for their metallurgical properties. The importance of reducing the complexity and dimension of the frame to avoid any shielding effects became clear. In

conclusion a precise system of 3D printed nodes and metal bars was introduced. By minimizing the dimensions of the framework, a dramatic decrease in shielding effect during the electroplating process was noticed. The copper-based conductive painting used has the highest conductivity properties from the ones that were tested and therefore lead to more equal plating. From the available plating material nickel performed more effectively, as it deposed almost twice as fast as copper on self-similar geometry. During the process of plating, voltage in the electroplating bath should to be low at the beginning and slowly increased to negate burning effects.

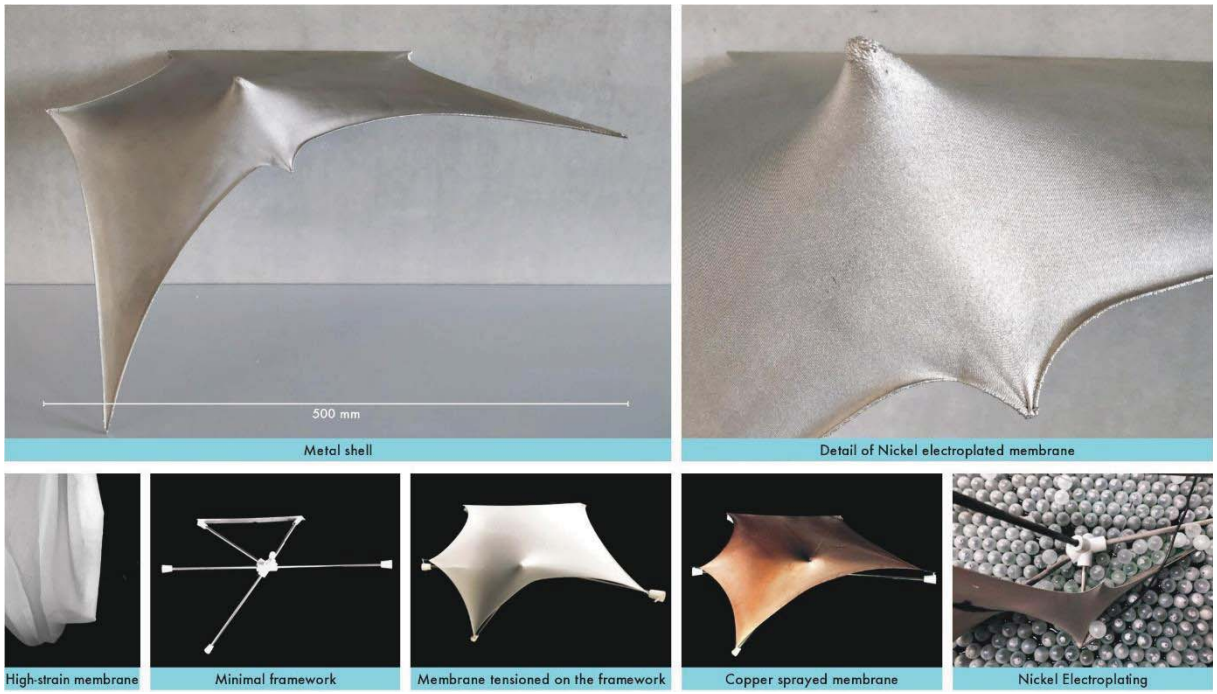


Figure 5: Fabrication process from high-strain membranes to metal shells.

A final watertight facade panel showcase is fabricated to test the efficiency of the fabrication strategy (figure 5). The elastane substrate is tensioned, within a plastic non-conductive frame, and successively sprayed with copper paint. The substrate is then immersed in the galvanic bath for a total of 19 hours divided in: 6 hours at 3.0 volt, 5 hours at 3.5 volts, 2 hours at 4.0 volts and 6 hours at 4.5 volts.

The plated object has a thickness that varies from 1.0 to 1.4 mm. Minimum thickness occurred near the edge of the surface.

5. Conclusions

In this paper, the authors presented an innovative strategy for the fabrication of complex doubly curved metal shells for the building industry. Two fabrication strategies; the shaping of high-strain membranes into anticlastic geometry and electroplating/-reinforcing, where chosen and combined to complement each other. Electroplating has shown its potential as a material-effective and precise way to manufacture highly doubly curved elements with metallurgical properties, while the structural typology transforms from form-active to surface-active as the elastic membrane is permanently locked into shape. Furthermore have these membranes proven their potential as a very suitable substrate layer for the electroplating process, by offering material efficiency, shape flexibility and ease of fabrication. After a series of experiments the fabrication strategy was validated by laboratory scale demonstrators in multiple materials.

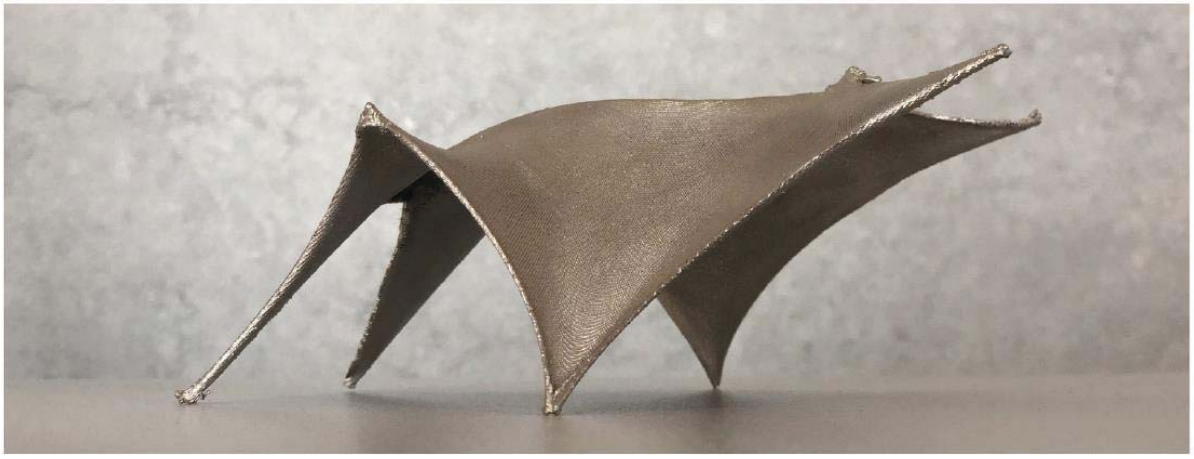


Figure 6: 1.0 mm nickel metal shell manufactured from two elastane substrates individually electroplated.

The developed process is limited by the size of the electrolyte bath and by the capacity of plating equipment. Although there seems to be no direct relationship between electroplating time and part volume or area [2] we found it difficult to produce parts that fill the available bath size. This limitation should be further investigated.

Typical metals that are electroformed successfully are iron, silver, gold, copper or nickel, while the experiments here only included the latter two. This restriction might indicate that the raw outcome of this process finds usage in façade panels or other non-load-bearing application, but can and should be used as part of a more integrative materialization process.

Shape-flexibility and a high amount of control on material disposition combined with a minimal waste and energy approach can make metal reinforced membranes an economical and performative solution for complex metallic skins, bringing the usage of elastically deformable structures to broader architectural application.

6. Outlook

The presented research focuses heavily on the fabrication side of a design to fabrication workflow that should be enhanced by simulation. Further research should be conducted on the design and simulation processes, before and during fabrication.

Form finding simulation methods of high strain membranes are vastly investigated [4] and can and should be implemented into the presented fabrication strategy. From a structural point of view, the typological transformation from form-active to surface-active and its implications on metal shell design could introduce a novel design space for metallic structures that needs to be explored.

Electrochemical simulation methods on the other hand are not yet easy to bring into an architectural design-to-fabrication workflow, as necessary digital interfaces require a multidisciplinary approach to be developed [2]. These simulation models might open up great possibilities for metal-reinforced membranes, like locally manipulatable shell thicknesses with high precision tolerances that are known from industrialized electroplating processes. As size was limited by the available electroplating equipment presented in this paper, further research should focus on scale effects and their impact on the application of this research.

Lastly the process of electrochemically reinforcing membranes should be applied to not only anticlastic but also synclastic substrate to further expand the field of geometric and structural possibilities for this material system.

7. Acknowledgment

This research is supported by the FIT Additive Manufacturing Group, a leading company in Additive Manufacturing and innovative technologies. Especially, the authors would like to thank Leo Schledowitz, for his help during the electroplating and fabrication process.

8. References

1. P. Nicholas, M. Zwierzycki, E. C. Nørgaard, D. Stasiuk, M. Thomsen, C. Hutchinson, *Adaptive Robotic Fabrication for Conditions of Material Inconsistency*, 2017

2. A. McGeough, M.C. Leu , K.P. Rajurka, A.K.M. De Silva, Q. Liu, *Electroforming Process and Application to Micro/Macro Manufacturing*, 2001.

3. L. B. Hunt, *The Early History of Gold Plating*, 1973

4. S. Alquist, A. Menges, *Frameworks for Computational Design of Textile Micro-Architectures and Material Behavior in Forming Complex Force-Active Structures*, 2013

5. D. Veenendaal, M. West and P. Block, "History and overview of fabric formwork: using fabric for concrete casting" *Structural Concrete*, vol. 12 no. 3, pp. 164-177, Aug. 2011.

6. J. Edwards, "Electroplating, A guide for designer and engineers", Committee for Promotion of Electroplating, K&N Press, 1983.

7. D. N. Layton, *Design for Electroplating.* London: The International Nickel Company 1961.

8. S. Suzuki, J. Knippers, *Topology-Driven Form-Finding*, 2017

9. R. Parkinson, "Electroforming: a unique metal fabrication process." *AIFM Galvano Tecnica e Nuove Finiture(Italy)* vol. 9.3 pp 140-142, 1999.

10. L. Ghang and K. Seonwoo, "Case Study of Mass Customisation of Double-Curved Metal Facade Panels Using a New Hybrid Sheet Metal Processing Technique" *Journal of Construction Engineering and Management,* vol. 138, Issude 11, Nov. 2012.

11. J. Knippers, J. Cremers, M. Gabler and J. Lienhard, *Construction Manual for Polymers + Membranes*, Birkhäuser, 2011.

Proceedings of the IASS Annual Symposium 2019 – Structural Membranes 2019
Form and Force
7 – 10 October 2019, Barcelona, Spain
C. Lázaro, K.-U. Bletzinger, E. Oñate (eds.)

Selective Cement Activation (SCA) – new possibilities for additive manufacturing in construction

Daniel TALKE*, Klaudius HENKE[a], Daniel WEGER[b]

*Chair of Timber Structures and Building Construction, Technical University of Munich
Arcisstr. 21, 80333 Munich, Germany
talke@tum.de

[a] Chair of Timber Structures and Building Construction, Technical University of Munich
[b] Centre for Building Materials, Technical University of Munich

Abstract

This article presents research on the additive manufacturing of concrete elements using selective binding of cement. In the process referred to as selective cement activation, fine layers of a dry cement-sand mixture are solidified locally by applying water. This way, layer by layer, complex 3D objects can be created with a high degree of geometric freedom. Initial tests with a prototype 3D printer have demonstrated the potential of the manufacturing method for applications in construction. An updated prototype printer is presented which enables further exploration of the process and its future applications.

Keywords: selective binding, 3D printing, additive manufacturing, free form construction, concrete

1. Introduction

Recent developments in additive manufacturing methods for the construction industry have opened up new possibilities for the design and production of building elements. Various additive manufacturing methods have been developed to create concrete structural components which can be optimized regarding load bearing capability or building physics while at the same time reducing the amount of waste produced.

2. Additive manufacturing in construction

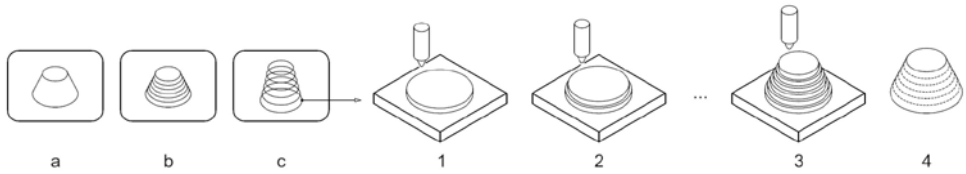


Figure 1: Extrusion process: digital pre-process (a -c) and physical manufacturing (1 -4) [1]

The majority of the research worldwide focus on variations of extrusion-based 3D printing. In general, these methods use pre-mixed concrete which is deposited onto a build platform according to a processed digital 3D model of the desired element. By adding subsequent layers, the complete object can be manufactured without the use of formwork (see figure 1). However, these manufacturing methods are limited in regard to their geometric freedom.

Well known examples for this manufacturing method can be seen in [2] and [3].

Copyright © 2019 by Daniel Talke, Klaudius Henke, Daniel Weger
Published by the International Association for Shell and Spatial Structures (IASS) with permission.

Alternatively, in the process known as selective binding thin layers of particles can be selectively solidified to create a 3D concrete object. Figure 2 shows the general process. As before, a 3D model is processed and translated into machine instructions (figure 2, a-c). However, instead of mixing the material and depositing it, an entire layer of bulk material is spread out onto a build platform and then selectively solidified by applying a fluid component. Layer by layer a 3D object is thus created, entirely encased in surrounding bulk material, which acts as support (figure 2, 1-3). In a final step, the unbound material is removed and could be reused for following prints. Using this method objects with a high degree of geometric freedom can be created.

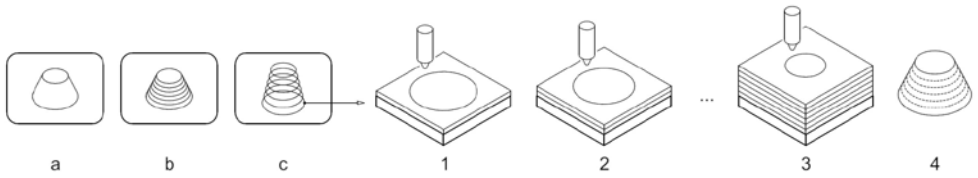


Figure 2: Selective binding process: digital pre-process (a -c) and physical manufacturing (1 -4) [1]

Two main variants of this method are currently being researched at the Technical University of Munich. In the first, referred to as selective paste intrusion, layers of coarse sand (grain size < 3 mm, layer height 3 mm) are selectively bound by depositing a fluid cement paste which infiltrates the voids between the particles. Experiments using this method have proven successful with achieved compressive strengths above 70 MPa after 7 days and good durability against freeze-thaw and carbonation attacks. [4] [5]

The second variant of the selective binding method, and the focus of this article, is the so-called Selective Cement Activation (SCA). Here, the bulk material consists of a dry cement and sand mixture. The hydration process of the cement is then activated by applying water to the layer. Since this method only uses water as an activator the print head can be outfitted with much finer nozzles which allows for a high print resolution. In addition, by using very fine quartz sand (d_{max} = 0.5 mm) as an aggregate, the layer height can be significantly reduced. Put together, the selective cement activation method enables the manufacture of objects with a high resolution in all 3 dimensions. First experiments conducted using a prototype 3D printer achieved material strengths above 16 MPa after 7 days [6]. However, form fidelity and layer cohesion still proved to be problematic. Furthermore, the prototype printer proved difficult to work with, as its print head, build chamber dimensions and particle dispenser volume were insufficient for extensive testing. In order to continue the research on selective cement activation, it was necessary to develop an improved 3D printer.

3. Prototype SCA printer and process description

3.1. Overview of the prototype printer

The first prototype printer for selective cement activation was developed in a recent research project within the DFG (German Research Foundation) priority program 1542 'Light Construction with Concrete'. Aim of the project, in part, was to explore the possibilities of selective cement activation for the use in construction and to determine suitable process parameters and materials. For this, a first prototype printer was developed which allowed the manufacture of specimens for material and contour precision testing. [7]

Due to the promising results of the previous research an improved version of the prototype printer was developed as part of an ongoing DFG transfer project. With its larger build chamber and increased print speed and reliability, the new machine enables the next steps to be taken in material development and research into real-world applications.

The prototype printer (seen in figure 3) is made up of multiple distinct components. Most noticeable is the outer frame with its linear bearing units (a) which are used to raise a three axis CNC portal (b). The build chamber (c) consists of a stationary base platform with movable bounding walls which are connected to the CNC portal and are raised incrementally with each layer. The print head (d) as well as the bulk material dispenser (e) and the compaction roller (f) are also mounted on the CNC portal which ensures that their distance from the bulk material remains constant for each layer. Fluid is supplied by a pressurized water tank (g) and fed through a series of filters before reaching the print head.

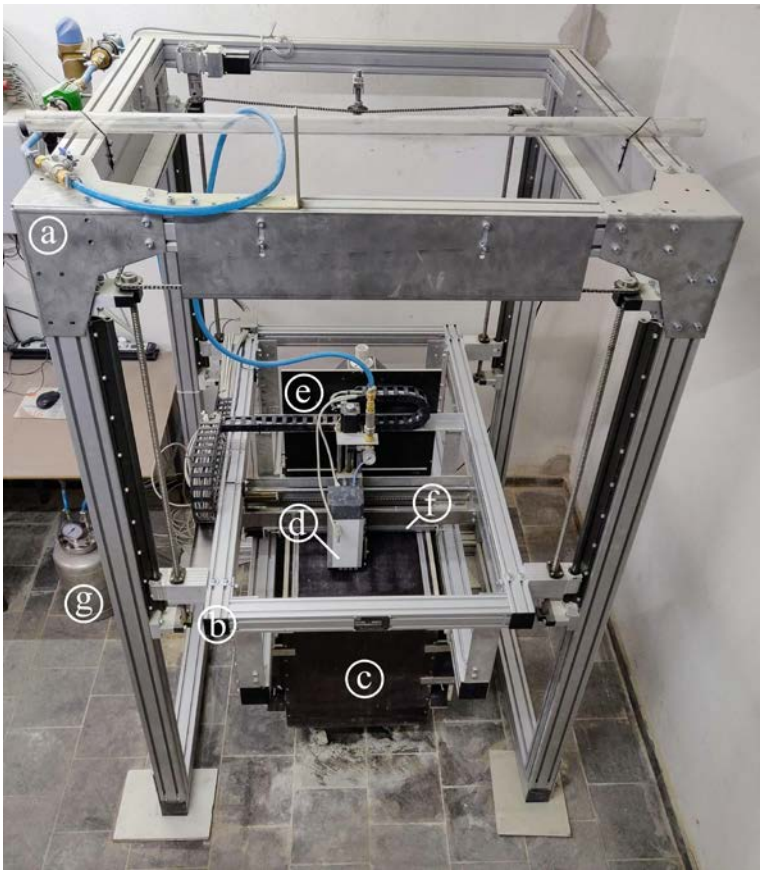


Figure 3: Prototype printer for selective cement activation (a: printer frame, b: CNC portal, c: build chamber, d: print head, e: bulk material dispenser, f: compaction roller, g: pressurized fluid supply)

3.2. Creating the bulk material layer

Before printing, a layer of bulk material must be laid down. For this, the walls of the build chamber with an internal area of 450 mm x 600 mm are raised slightly above the level of the desired layer height. The dispenser, which consists of a hopper with a motorized roller with flexible ridges at its bottom, is filled with the sand-cement mixture. While moving across the build chamber the roller inside the dispenser rotates and forces the bulk material through a sieve. This ensures that agglomerates are broken up and a loose powder layer with a thickness slightly above that of the desired layer height is dispensed onto the build platform (see figure 4).



Figure 4: Freshly dispensed bulk material onto a previous layer. Top left: bulk dispenser unit, right: bulk overflow container.

Since the cement-sand mixture cannot be mixed with water in a conventional way to form concrete, the final strength properties depend heavily on the density of the particles and thus on the packing density of the dry bulk material. In order to create a homogenous layer with a high packing density, the dispenser unit has a compaction roller attached to it. While the dispenser moves across the build chamber, in a first step, the freshly dispensed powder is smoothed by the counter rotating roller and excess material is pushed into an overflow container for reuse. Then, the walls of the build chamber, together with the compaction roller are moved back down again to obtain the desired layer height. Finally, the compaction roller is moved back across the bulk layer with a forward rotation corresponding to its linear velocity, thus compacting the bulk material.

Typically, the machine is set to create layers with a thickness of 1 mm by compacting 1.5 mm of loosely smoothed bulk material. Depending on the cement/sand ratio this results in a packing density between 1.3 and 1.7 g/cm³.

3.3. Printing

Once the layer of cement and sand is laid down and compacted, water is locally applied by the print head to those areas of the layer that are to be solidified. The previous version of the printer was outfitted with a single flat fan nozzle. Apart from limiting the possible geometry of printed objects, the fine water mist which was sprayed onto the surface could not fully penetrate the particle layer, resulting in less cohesion between layers and lower material strength. [6]

In contrast to the previous printhead, the new version consists of 32 individual nozzles. Each nozzle creates a fine water jet which penetrates the layer surface, enabling a better hydration of the particle layer. The deionized water is provided by a pressurized tank and fed through multiple filters before entering the print head. The water pressure is regulated depending on the desired water/cement ratio and penetration depth.

Printing takes place in a two pass system by moving the print head across the build chamber, shifting it by 1 mm and moving it back to its original position, thereby covering 64 mm of the build chamber width. In order to print the entirety of the build chamber this must be repeated for a total of seven times. This is also one of the main factors in determining the print speed of the system, the other being the chosen federate of the CNC portal in accordance with the water pressure to set a specific water/cement ratio. The current setup allows for a print speed of up to 40 layers per hour.

The resolution of the printer is one pixel per one millimeter or 25.4 dpi both in x and y direction. A close up of the resulting print can be seen in figure 5.



Figure 5: Close up of a printed layer with visible individual printed lines.
Printed image dimensions: 68 mm x 35 mm

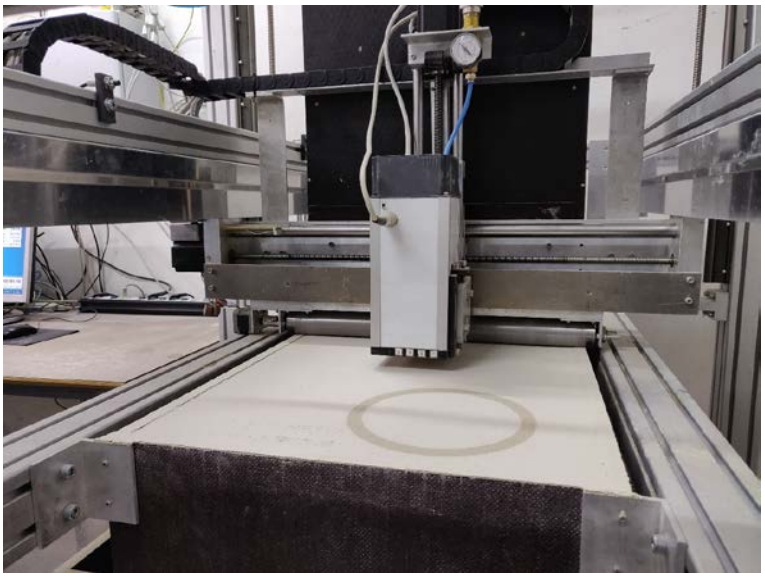


Figure 6: Print head and compacted cement-sand layer during print of a tubular test geometry

3.4. Excavation

Once the last layer is completed (see figure 6), the print is left to rest until the cement has developed enough initial strength for excavation. Depending on the type of cement/sand ratio used, this period can last from a few minutes to multiple hours. Due to the shape of the fine aggregate and cement, as well as the high packing density, the printed objects cannot simply be taken out of the surrounding dry material without risking damage to the objects. Therefore, in a first step, large portions of dry material must be removed with the use of shovels, spatulas and brushes. This material can be reused for subsequent prints. Figure 7 shows the build chamber and printed objects with most of the bulk material removed.

At this point, the printed objects still have an outer coating of cement and sand about 3 mm thick which must be discarded, as it may be contaminated by moisture from the print. This material can be removed by either scraping and brushing the parts clean, where possible, or by spraying the parts with water, thereby washing away the excess material. This latter approach may also function as a form of post-treatment of the parts the effect of which must still be examined.



Figure 7: Printed parts during excavation

A 3D-printed object fabricated by this method can be seen in figure 8. The pipe segment with a length and diameter of 200 mm is an example of an object that is nearly impossible to manufacture using typical concrete formwork.



Figure 8: 3D-printed pipe segment with internal trusses

4. Further research and conclusion

The new prototype printer enables the production of concrete objects with a high level of geometric freedom and detail. In addition to test specimens for material testing, e.g. test prisms for 3 point bending tests, current research is focusing on the possible geometric freedom and shape accuracy that can be achieved using different material and manufacturing combinations. Test objects as seen in figure 9 (left) are used to gauge limits in geometric elements such as minimum shaft and hole diameter or tongue and groove thickness that can be manufactured. The printed specimens are also analyzed using a 3D scanner and evaluation software to determine their deviation from the original cad model (see figure 9, right).

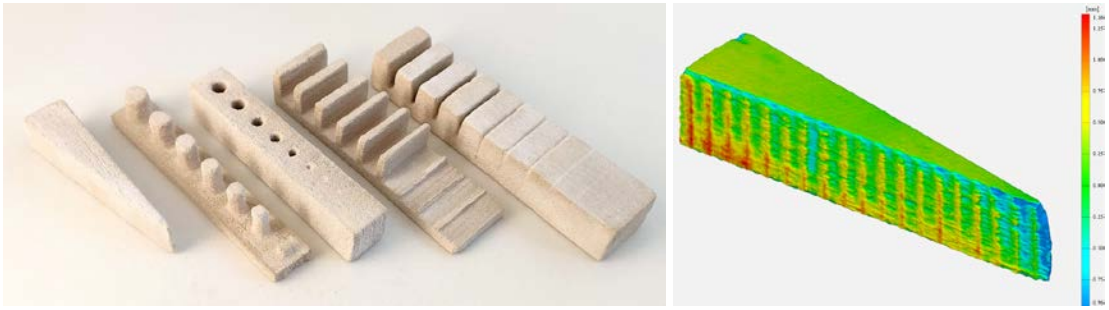


Figure 9: Printed geometric test specimens (left) and comparison of geometric fidelity via 3D scan and evaluation software (right)

First results of examined test specimens show deviations within a range of ± 3 mm of the original cad model. Also, a noticeable increase in deviation is noticeable towards the bottom of the test specimens. This is likely the result of a combination of water dissipating into the surrounding material and further compression of the layers caused by the additional weight.

However, the resulting geometric fidelity and minimal geometric elements are not only limited by the material and print process parameters, but also largely depend on the ability to remove the excess material after printing. For example, even though holes with a diameter as little as 8 mm can be printed, excavating them proves to be difficult after a certain depth. In order to develop design rules for applications in construction, further research and standardized excavation methods are required.

In conclusion, the new prototype printer for selective cement activation provides new possibilities for the manufacturing of concrete elements with a high degree of geometric freedom with material strengths suitable for applications in construction. Further research, especially in regard to material composition, packing density, excavation methods, post-treatment and concepts for upscaling of the process are needed in order to transfer this technology from prototype to real-world applications.

5. Acknowledgements

The research presented here is a collaboration between the Chair of Timber Structures and Building Construction and the Centre for Building Materials, both Technical University of Munich, and the Institute of Building Materials, Concrete Construction and Fire Safety at the Technische Universität Braunschweig.

The research is funded by the DFG (German Research Foundation) in a transfer project ‘Industrial 3D Concrete Printing by Selective Cement Activation - Process, Material, Applications' (project number: 389705984).

6. References

[1] K. Henke, Additive Baufertigung durch Extrusion von Holzleichtbeton. Dissertation. Technical University of Munich, 2016

[2] B. Khoshnevis, Contour Crafting - State of Development. Proceedings of the 10th Solid Freeform Fabrication (SFF) Symposium, Austin, Texas, 1999

[3] N. Cheniuntai, Apis Cor. [Online] Available: https://www.apis-cor.com/. Accessed on: May 27 2019

[4] D. Weger, D. Lowke, C. Gehlen, D. Talke, and K. Henke, “Additive manufacturing of concrete elements using selective cement paste intrusion - effect of layer orientation on strength and

durability," in First RILEM International Conference on Concrete and Digital Fabrication - Digital Concrete 2018, 2019

[5] D. Weger, C. Gehlen, and D. Lowke, "Additive Fertigung von Betonbauteilen durch selektive Zementleim-Intrusion," in Tagungsbericht / Ibausil, 20. Internationale Baustofftagung, Weimar, 2018

[6] D. Lowke et al., "Particle-bed 3D printing in concrete construction – Possibilities and challenges," Cement and Concrete Research, vol. 112, 2018

[7] D. Lowke et al., "3D-Drucken von Betonbauteilen durch selektives Binden mit calciumsilikatbasierten Zementen – Erste Ergebnisse zu betontechnologischen und verfahrenstechnischen Einflüssen," in Tagungsbericht / Ibausil, 19. Internationale Baustofftagung, 2015.

Proceedings of the IASS Annual Symposium 2019 – Structural Membranes 2019
Form and Force
7 – 10 October 2019, Barcelona, Spain
C. Lázaro, K.-U. Bletzinger, E. Oñate (eds.)

3D printed grid shell in ice composite

Arno PRONK*, Irma BOUW, Tessa EZENDAM, Naomi v HIERDEN, Joris VLEESHOUWERS, Dominique vd WEIJDEN

*Eindhoven University of Technology
Vertigo 9.35 PO Box 513
5600 MB Eindhoven
the Netherlands
a.d.c.pronk@tue.nl

Abstract

This paper presents the design of a grid shell that is made of fibre reinforced ice and constructed by combining additive manufacturing with an inflatable mould. While previous fibre reinforced ice structures were constructed by spraying, additive manufacturing with ice has not yet been tested before. Additive manufacturing is a stepwise production technique where material is being added layer by layer, resulting in a high degree of formability. Combining this printing technique with sustainable materials such as ice makes it possible to develop more sustainable structures and building applications in cold environments such as Mars or the poles. To test this application, a grid shell of fibre reinforced ice was designed and eventually constructed. The grid shell was designed by considering the design constraints of the inflatable mould that needed to support the wet ice layers during construction. The structural capacity of the grid shell was enhanced by performing an optimization procedure on the gridlines. In the end, a theoretical failure load calculation shows that the middle part of the structure could carry more than 6000 kg of additional load. To test this finding, the constructed grid shell was loaded on site with approximately 3000 kg, without showing any signs of failure. By designing and testing this innovative object, this project illustrates that additive manufacturing can successfully be applied for other structural applications such as sculptures, moulding and Mars missions.

Keywords: fibre reinforced ice, additive manufacturing, grid shell, optimization, inflatable formwork.

1. Introduction

The current research into using ice and ice composites for construction is part of a larger movement to investigate new sustainable building materials. Ice and water are widely available, cheap, fully circular without producing waste, and they produce little to no CO2 emissions during processing.

In the past centuries, architects and engineers have explored many possibilities to apply ice for building structures. The first well-known examples of ice-based structural objects are igloos. More impressive structures constructed of ice blocks have been around since 1739, when the first ice palace was built in Sint-Petersburg [1]. In 1942, Geoffrey Pyke started to use an ice composite that existed of water mixed with wood fibres [2]. This mixture formed a strong solid mass, much stronger than pure ice. Inspired by the report of Pyke, Max Perutz investigated the properties of ice composites from sawdust and ice and tested, amongst others, the resistance of pykrete against shock loading and creep mechanisms in ice [3]. Later, during the 1980s and 1990s, Tsutomu Kokawa successfully developed a method to spray “snice”, a special wet and easily processable snow, on moulds to construct igloos with a large span [2].

Copyright © 2019 by Arno PRONK, Irma BOUW, Tessa EZENDAM, Naomi v HIERDEN, Joris VLEESHOUWERS, Dominique vd WEIJDEN
Published by the International Association for Shell and Spatial Structures (IASS) with permission.

More recently, an ice research group at Eindhoven University of Technology (TU/e), guided by Arno Pronk, combined ice composites with the spraying method developed by Kokawa [4]. Pronk showed that spraying ice composites increases the composites' strength and resistance to impact and shock-loading. This research showed that a relatively small amount of fibres was required to significantly improve the mechanical properties of ice. In a further research stadium, Pronk replaced the wood fibres in the mixture by cellulose fibres, which have the same impact on the properties of ice [1].

To test his findings, Pronk guided TU/e students in cooperation with other groups to build a number of structures. In 2014, by using these mixtures, the largest igloo dome structure with a span of 30m was realized [4]. In 2016, an attempt was made to construct an ice bridge with a free span of 35 meters [5]. In 2018, the Flamenco tower claimed the position as largest ice tower ever built with a height of 30.5 m [6]. All three structures used an inflatable mould as formwork. The aforementioned achievements show that engineers and design teams are able to successfully realize ice-based (shell) structures with different mixtures and different shapes. Following the success of these building projects, Pronk wanted to further investigate how the processes of 3D printing of ice on an inflatable mould could also be applied in structural applications.

The focus of this paper shifts away from spraying ice composites towards investigating possibilities of 3D printing of ice composites. The reason for this is that 3D printing is a building method that can be used to sustainably print a mould, 3D habitat, sculpture or temporary foundation of ice in cold environments, such as Mars or the poles. To specifically test 3D printing of ice for this project, a grid shell in ice was designed by using an inflatable formwork as supporting structure. Consequently, this project included optimization of the morphology of the grid and the construction and testing of the grid shell structure in Harbin (China).

2. Cellulose reinforced ice

The design group applied a manual extrusion technique, similar to 3D printing, to create a grid shell structure in ice. In order to increase the extrudability, 1.5 grams of Guar Gum and 1.5 grams of Xanthan Gum per litre of water were added to a mixture of water with 8% cellulose fibres. Relevant mechanical data for this composite were derived from experiments by another group of students from the TU/e. Their results are presented in a separate paper [7], but their main outcomes are summarized in Table 1. The cellulose-reinforced ice composite shows plastic behaviour in compression and brittle behaviour in tension, due to which the safety factor for tension was taken somewhat higher compared to the safety factor for compression.

Table 1: Mechanical properties of the used composite

Property	Characteristic value [N/mm^2]	Design value [N/mm^2]
Compressive strength	4.6	1.0
Bending (tensile) strength	3.0	0.3
Modulus of elasticity	550	550

3. Behaviour of shell structures

To analyse the relation between the shape and the mechanical behaviour of a shell, the 'Rain flow analysis' was considered [8]. In this analysis, the behaviour of forces in a shell is compared to the behaviour of water particles that flow along the surface of the shell. From the analysis, it can be stated that the distribution of forces in shells is poor when the applied loading is perpendicular to the surface, and that forces should preferably be guided towards the supports without abrupt changes. Namely,

abrupt changes in force direction will obtain bending moments in the edges of the shell. Furthermore, this analysis in combination with theories from other literature resulted in three additional conclusions on the behaviour of shell structures. Firstly, it can be concluded that a double curved shell has a more equal force distribution compared to a single curved shell [9]. Secondly, the combination of upward and inward curvature increases the strength and stiffness of the shell [10]. Finally, inward curvature of the supports increases the buckling load of the shell structure [10].

4. Parametric design and optimization

In order to create a 3D shape by means of additive manufacturing, a supporting structure is needed to prevent the unfinished grid shell structure from collapsing. An inflatable formwork for temporary support of the grid shell is considered to be effective, reusable, and easy to install and dismantle. Due to the internal pressure, inflatables have a circular shape in at least one cross sectional direction. Therefore, the shape of the inflatable differs from the structurally most favourable shape of a grid shell. A comparison was made between the shape of an inflatable and the shape of a structurally optimized grid-shell. This comparison led to the design of a mould with a double curved surface with three openings and inward curved supports. Subsequently, four different grid patterns were designed on this mould with Rhinoceros and Grasshopper, as shown in Figure 1. The principles behind these grids are summarized in Table 2.

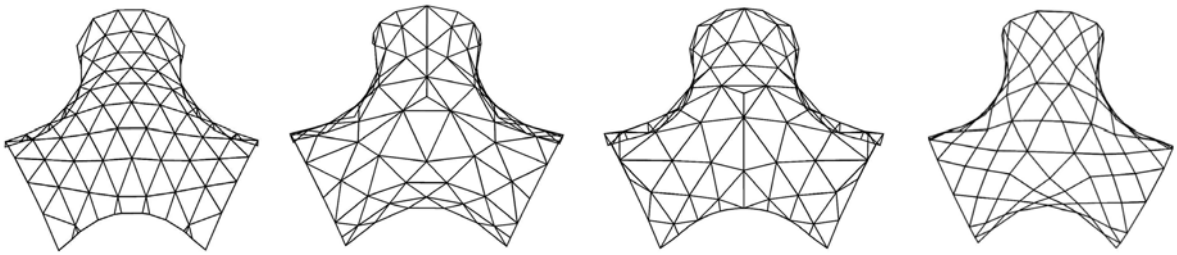


Figure 1: The different grid options that were analysed (from left to right: grid option 1, 2, 3, & 4)

Table 2: Overview of the design principles of the different grid options

Grid option 1: Projection of a triangular mesh on the shell shape	
Advantages: The grid consists of straight, continuous lines on the shell shape.	Disadvantages: The density of the grid at the bottom of the shell shape is lower compared the top, which does not correspond to the expected stress distribution in which higher stresses are expected at the bottom of the shell shape. Furthermore, the grid lines are irregular at the bottom due to the projected grid lines being cut off at ground level.
Grid option 2: Morphology based on strictly horizontal lines and triangles in-between	
Advantages: The grid is denser near the bottom and less dense near the top of the shell, as expected from the stress distribution.	Disadvantages: Direct force transfer to the foundation is prevented due to the presence of kinks in the lines that run from the top of the shell towards the bottom.
Grid option 3: Morphology based on direct force transfer from the top of the shell to the foundation by means of vertically oriented grid lines and triangles in-between	
Advantages:	Disadvantages:

The vertical grid lines allow for direct force transfer from the top to the bottom.	There is some discontinuity of the grid pattern near the openings of the grid shell. In addition, the limited variation in grid density does not correspond with the real stress distribution of the shell.
Grid option 4: Morphology based on continuous lines that are drawn over the solid shell-shape to create a pattern of mainly rhombuses and some triangles	
Advantages: The grid lines are continuous and smooth and they follow the shape of the shell. In addition, the grid density is representing the expected magnitude of stresses, since a denser grid occurs at the bottom compared to the top of the grid shell.	Disadvantages: Rhombic shapes are not stable by themselves, unless the members have a rigid connection in the nodes. As a result, applying rhombic shapes is expected to cause forces, other than compression forces, such as bending moments and shear forces.

The four grid options were analysed by means of FEM analyses and the results were compared. Grid option 3 showed the best results from a structural point of view, since this grid resulted in the least axial stresses under self-weight loading and an equal stress distribution throughout the structure. However, besides a poor architectural appearance, the construction of this grid was expected to be difficult due to the discontinuities that are present near the edges. As a result, the choice was made to optimize a more fragile and open grid (option 4), rather than choosing the structurally best performing grid (option 3). Grid option 4 was subjected to optimization steps that ensured stresses to remain within the limits. This optimization process existed of the subsequent addition of members, while the effect of these additions was monitored. The members that were added in the different steps of the grid optimization process are shown in Figure 2. The outcomes of the optimization analysis showed that the members added in analyses 2 and 3 were the most influential in reducing the deformations and internal stresses in the grid shell. Overall, the optimization of the grid shell resulted in a reduction in deformations of 52%, a reduction in tensile stresses of 56% and a reduction in compressive stresses of 33%. The final design consisted of a grid shell with a pattern that combines quadrilaterals and triangles.

5. Numerical calculations

5.1. Self-weight calculation

After the structure was optimized in shape, size and morphology, a self-weight calculation was performed to verify whether the structure was able to resist its own weight. A density of 980 kg/m3 was used to calculate an ice mixture that consists of 8% cellulose, 0.15% Guar Gum and 0.15% Xanthan Gum. The cross-sectional diameters of the members were 120 mm for the bottom part, 90 mm for the middle part, and 60 mm for the top part. A representation of the structure with the different cross-sections is visualized in Figure 3 with white, green and red struts, respectively.

A self-weight calculation without external loads was assumed to be a sufficiently accurate structural verification due to the openness and small size of the structure (4.0 x 4.0 x 1.8 meter). For the material properties of the ice mixture, a Poisson ratio of 0.15 and a Young's modulus of 550 MPa were used. The internal nodes were modelled as rigid connections, while the nodes at the bottom were hinged connected to the subsurface. The outcome of this self-weight analysis showed that the maximum compression stress was 0.103 MPa and maximum tensile stress was 0.085 MPa, which are both less than the design limits of 1.0 and 0.3 MPa respectively.

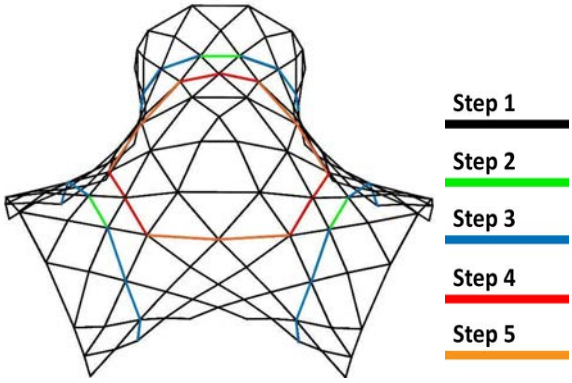


Figure 2: Overview of the members that were being added in the optimization process

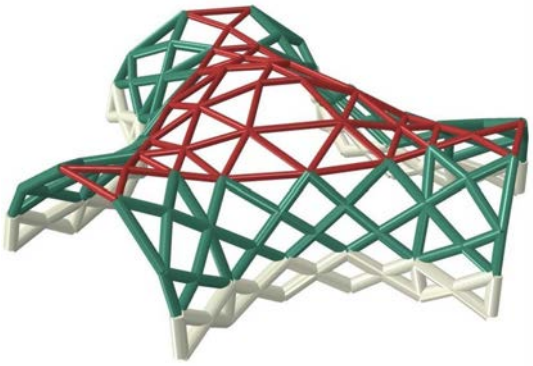


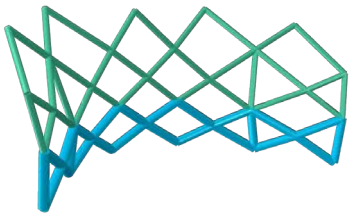
Figure 3: Final grid shell showing the division of the different cross-sections used for the analysis

5.2. Grid shell under construction

During the construction of the grid shell, an inflatable formwork covered by a rope net was used to support the unfrozen ice layers. A numerical study was conducted to investigate the structural behaviour of the grid shell under construction in three steps.

First, the pressure of the inflatable (200 Pa) was modelled as a series of point loads acting perpendicular to the surfaces of the inflatable, which were represented by the grid of the rope net. Assuming an effective width of 100 mm of inflatable pushing against the ropes resulted in a line load of 20 N/m for the ropes. Because large deformations of the rope net were expected, a nonlinear calculation was performed to obtain reliable output. In the second step, the average deformations of the rope net (0.1067 m) and the applied pressure (2 N per node) were used to calculate a fictitious spring stiffness representing the supporting inflatable. This spring stiffness turned out to have a value of 18.75 N/m. In the last step, part of the grid shell under construction was modelled, with the spring supports at the ends and at mid-span of each strut. The struts do not have their final thickness during the construction stage, thus their sections are reduced to 60 mm for the bottom elements and 30 mm for the middle part of the structure. Table 3 shows that the spring supports, representing the inflatable, have a small effect on the stresses and deformations in the grid shell under construction. The stresses seem to decrease slightly as a result of the springs being present. Although both maximum compression and tensile stress are not exceeded for the calculation without springs, the inflatable will still be required as a formwork to support the wet ice mixture during the printing process.

Table 3: Results from the structural analysis for a part of the structure with and without spring supports

Mechanical scheme (cross-sections)		With springs	Without springs	Design value
	Max. tensile stress [MPa]	0.275	0.284	0.300
	Max. compressive stress [MPa]	-0.277	-0.285	-1.000
	Deformation [mm]	5.15	5.40	n/a

5.3. Failure analysis

Lastly, a failure analysis was performed to find the theoretical failure load of the grid shell structure. In

this analysis, 21 point loads were added at the top part of the structure. The loads were only applied on the nodes to prevent a situation in which premature (bending) failure of the bars was governing. All point loads were gradually increased in magnitude until the stress exceeded the characteristic compression (-4.6 MPa) or tensile stress (3.0 MPa) for cellulose-reinforced ice. Figure 4 shows that the structure failed in compression when applying point loads with a value of 2900 N per node, which corresponds with a total mass of approximately 6000 kg on the grid shell structure. A possible reason for failure of the reinforced ice structure in compression rather than in tension is that a shell structure is by nature a compression-based structure, due to its curved shape. Consequently, the magnitude of the compression forces in the grid shell is higher than the magnitudes of the tensile forces. Furthermore, an accumulation of compression in the critical nodes where failure occurs can probably be explained by the connection between elements with different cross-sectional diameters. The bars at the bottom part of the structure have a larger diameter and can therefore provide more stiffness compared to the upper part. This discontinuity seems to lead to an increased stress in the less stiff part, which might be the reason for failure.

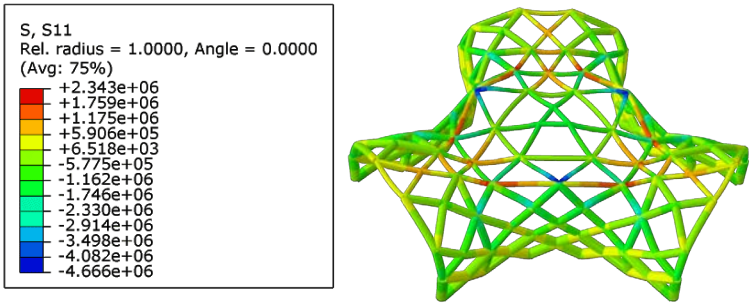


Figure 4: Axial stress distribution [Pa] in the grid shell in the deformed state when a load of 2900 N/node is applied

6. Construction of the grid shell

Several printing methods were tested to find the best printing technique. The tested methods include manual extrusion with piping bags, extrusion with a barrel with overpressure and extrusion with a worm pump. On the short term, the first method appeared to be the most simple and reliable. However, future projects should target the automatization and improvement of the printing process.

To ensure the suitability of the printing process, a test was performed in a cooling cell in Venlo (the Netherlands). From the experiences in this cooling cell, it was concluded that the rope net that held the inflatable mould in place was also a crucial element to allow printing the ice mixture on nearly vertical surfaces. Furthermore, the printing process seemed to be more efficient when the water-cellulose mixture was close to its freezing point at the moment of extrusion, because then the printed material would cure sooner. This way, the curing of the ice composite takes about one hour. The rope net was used as guideline for the printing process as well as for fastening and shaping the inflatable formwork. The net was knotted according to the grid geometry, as exerted from the digital model. The inflatable formwork was 10% oversized and constructed from flat cutting patterns that were welded together. The patterns were made from a PVC coated membrane with polyester fibres.

The final grid shell was built in Harbin (China). To speed up the overall building time, the construction of the grid shell was done in a 24/7 continuous process, starting from the foundation going upwards to the top. By the time that all gridlines had the required structural thickness, LED-lights were attached to the structure, and the supporting inflatable and the scaffolding were removed. Afterwards, the

appearance of both the grid lines and the foundation plate were improved by applying the printing techniques at specific locations that needed smoothening. The final result of the construction process is shown in Figure 5. On January 6th, the structure was tested with a load of approximately 2500-3000 kg. Because the load was lower than the theoretical failure load of 6000 kg, the structure did not fail, as predicted.

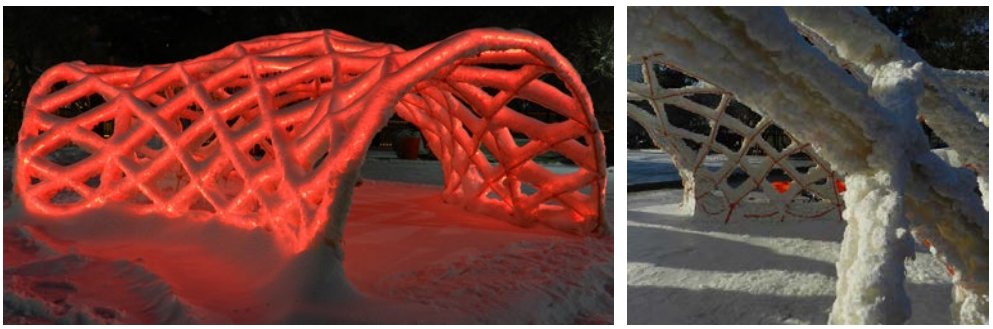


Figure 5: The final result of the constructed grid shell in ice in Harbin, China, and a close-up image of the printed cross-section of a grid member.

7. Discussion

This paper presents research regarding the design and execution of a grid shell structure in reinforced ice constructed by means of a 3D printing process. The main issues related to this topic included the research into the material properties of reinforced ice, the form-finding process of the grid shell design, the research into the formwork that was used during the execution of the grid shell and the investigation of 3D printing techniques to extrude layers of ice. The combination of all the different studies presented in this paper resulted in the development and the construction of a final grid shell design.

This grid shell in ice was successfully designed as can be seen in Figure 5. The gridshell had inward curved supports that seem to contribute to the high stiffness of the structure. It should be noted that the assumed positive influence of inward curvature of the supports was based on literature [10], and it was only checked with a basic calculation in ABAQUS. Further research is necessary to verify this initial calculation. After the final shape of the grid shell was determined, the grid was optimized to enhance the force distribution in the structure. The results of a FEM analysis showed that the final grid shell had sufficient capacity to withstand a substantial additional loading of approximately 6000 kg, next to self-weight. The high stiffness of the structure could possibly be attributed to the variety in grid density applied in accordance with the expected stress distribution. Although the final models for the self-weight calculation with and without additional loading implied simplifications regarding the structural configuration, the results were assumed to be reliable. Further research should target more accurate calculations to predict the structural behaviour of a grid shell subjected to asymmetric loading and a grid shell during construction. If in future projects the size of the grid shell is increased, a grid shell with a triangular mesh will likely be more feasible. In addition, if the manual printing process becomes labour-intensive for large-scale projects, an automated printing process is then probably more desirable.

8. Conclusion

The results presented in this paper indicate that an ice composite grid shell structure can be designed and verified with the help of computer software such as Rhinoceros, Grasshopper and ABAQUS. By combining these software tools, engineers can perform an iterative design process in which a suitable overall shape and grid morphology can be modelled and analysed. The shape of the inflatable mould designed by the TU/e team guided the form finding phase of the grid shell. The structural analyses in

ABAQUS helped to determine the optimal shape and grid morphology by minimizing the overall deformations and the peak stresses in the structure. If engineers in future projects construct their digitally designed and verified structure on an inflatable mould by means of a manual 3D-printing process, it will probably result in a successful end-product that is sufficiently strong to carry both its own self-weight as well as a substantial additional load.

Acknowledgements

The TU/e design team wants to thank the following for their contribution to this project: the 'Harbin Institute of Technology' (HIT) in China for organizing a competition for structural ice, and for arranging a building site for the construction of the grid shell; Elke Mergny for her guidance and advice on modelling in ABAQUS and her extensive reviews on our numerical results; and the employees of the structures laboratory and ice researchers of the TU/e for their help and support.

References

[1] A. D. C. Pronk, N. K. Vasiliev, and J. L. I. F. Belis "Historical development of structural ice," in *Structures and Architecture: beyond their limits: Proceedings of the 3rd International Conference on Structures and Architecture, ICSA 2016, Guimarães, Portugal, July 27-29, 2016,* P. J. S. Cruz Ed. London: CRC Press Taylor & Francis Group, 2016. pp. 339-347.

[2] J. M. Hijl and R. M. F. Pluijmen, "Pykrete dome project," M.S. thesis, Dept. Structural Design, Eindhoven University of Technology, Eindhoven, The Netherlands, 2014.

[3] M. F. Perutz, "A description of the iceberg aircraft carrier and the bearing of the mechanical properties of frozen wood pulp upon some problems of glacier flow," *Journal of Glaciology*, vol. 1, no. 3, pp. 95-104, 1948.

[4] A. D. C. Pronk, A. Bogart, J. M. Hijl and R. M. F. Pluijmen, "The calculation and construction of a 30 meter span ice dome" in *Shells, Membranes and Spatial Structures: Footprints: Proceedings of the IASS-SLTE 2014 Symposium, Brasilia, Brazil, September 15-19, 2014,* R. M. L. R. F. Basil, R. M. O. Pauletti, Eds., 2014

[5] A. D. C. Pronk, R. Blok, M. C. A. J. van Brunschot, A. J. van Lier, F. F. H. van de Mortel, K. K. Williams, T. A. H. van de Nieuwenhof, "Design of Da Vinci's bridge in ice," in *Structures and Architecture: beyond their limits: Proceedings of the 3rd International Conference on Structures and Architecture, ICSA 2016, Guimarães, Portugal, July 27-29, 2016,* P. J. S. Cruz Ed. London: CRC Press Taylor & Francis Group, 2016. pp. 363-375.

[6] J. L. Konings, "Ijsproject in Harbin geslaagd," *Cursor: cursor.tue.nl*, January 13, 2017. [Accessed March 11, 2019].

[7] A. D. C. Pronk, D. Janssen, K. Kara, J. van Laar and H. Willems, "Structural Behavior of Ice Composite for 3D Printing," Dept. Structural Design, Eindhoven University of Technology, Eindhoven, The Netherlands, 2019.

[8] A. Borghart, "Non-Linear Grid Optimization and Rain Analysis on Free Formed Glass Roof," Delft University of Technology, Delft, The Netherlands, 2018.

[9] K. Bletzinger and E. Ramm, "Form finding of shells by structural optimization" *Engineers with Computers*, vol. 9, Issue 1, 1993.

[10] Q. Li, "Form Follows Force: A theoretical framework for Structural Morphology and Form-Finding research on shell structures," Ph.D. dissertation, Dept. Architectural Engineering and Technology, Delft University of Technology, Delft, The Netherlands, 2018.

FORM and FORCE

Proceedings of the IASS Annual Symposium 2019 — Structural Membranes 2019
Form and Force
7—10 October 2019, Barcelona, Spain
C. Lázaro, K.-U. Bletzinger, E. Oñate (eds.)

The world's first sprayed net hyperboloid ice structure

Cameron MILLAR*, John ORR, Qingpeng LI[a], Alfred YEUNG, Arthur CHAN, Matthew SHEASBY, Mar GIMÉNEZ FERNÁNDEZ, Mercedes BAXTER CHINERY, Minghang QU, Stephanie WAI

* Department of Engineering, University of Cambridge
Cambridge, CB2 1PZ, UK
cgm37@cam.ac.uk

[a] School of Architecture and Urban Planning, Nanjing University

Abstract

In the winter of 2018, a team of architects and engineers from the University of Cambridge built the world's first hyperboloid-net ice structure in Harbin, China. A prestressed hemp rope net was sprayed with a cellulose water mix to form a structural sculpture which won the International Ice and Snow Construction Competition to which it was entered. Ice structures have traditionally been constructed from blocks of ice, whereas this project used a variation of Pykrete sprayed onto a flexible formwork. This paper explores areas of ice construction that have been little researched; the spraying of rope nets, difficulties in the construction of ice nodes, and the buckling of struts during construction are discussed. The project proved the viability of sprayed net ice structures and successfully used rope formwork to pretension the ice columns in a design that was both efficient and novel.

Keywords: Hyperboloid, Reinforced Ice, Sprayed net, Structural modelling, Structural analysis

1 Introduction

In October 2018, a team of student engineers and architects from the University of Cambridge designed a structural sculpture using reinforced ice as the main construction material. This was their first experience of construction in ice. The 5m tall hyperboloid lattice had inclined columns of approximately linearly varying diameter from 150mm at the base to 75mm at the top, and is shown in Figure 1. Two timber hexagons made up the top (5m diameter) and bottom (2.5m diameter) planes. This paper discusses a number of topics related to this project: the architectural concept, ice as a construction material, the structural modelling and analysis (including the construction sequence), and some future prospects are given.

Since 1985, Harbin, a city in North East China, has hosted the Ice and Snow Festival [1]. It is the largest ice and snow sculpture festival in the world covering $600,000m^2$ [2]. The tallest sculptures are now $46m$ high, requiring 10,000 workers [2], $110,000m^3$ of ice and $120,000m^3$ of snow [1].

Initially, the festival participants were Chinese, but in the last decade it has become an international festival and competition, encouraging larger and more decorative sculptures, such as

Copyright © 2019 by Cameron MILLAR, John ORR, Qingpeng LIa, Alfred YEUNG, Arthur CHAN, Matthew SHEASBY, Mar GIMÉNEZ FERNÁNDEZ, Mercedes BAXTER CHINERY, Minghang QU, Stephanie WAI
Published by the International Association for Shell and Spatial Structures (IASS) with permission.



Figure 1: The team with the finished structure

the palace in Figure 2. The festival is held from the end of December through to February, and attracts 10 - 15 million visitors [2].
In 2017, Harbin Institute of Technology launched the HIT Ice and Snow Festival, and it soon became a hit on local social media. In the winter of 2018-2019, they hosted the International University Ice Sculpture Competition and the International Ice and Snow Innovation Construction Competition. The University of Cambridge were invited to participate in the Innovation Construction Competition. The brief for the competition was to produce a structural sculpture in ice within a 5x5m square with a maximum height of 5m. The authors investigated a series of designs before constructing a hyperboloid ice lattice.



Figure 2: An Ice Palace at the Harbin International Ice and Snow Sculpture Festival 2019

2 History of Ice

Ice has been used in construction for thousands of years. Ice can only be used in environments with sub-zero temperatures and is only temporary. Early Inuits travelled across what is now Alaska, Canada and Greenland, building ice and snow houses for shelter. The igloos were built of

blocks of snow or ice in a circular form and were good at retaining heat and protecting occupants against wind in harsh conditions.
The first ice palace is said to have been constructed in 1740 in Russia, with huge blocks of ice frozen together with water [3]. During the second half of the 19th century ice palaces were used as centrepieces for popular Scandinavian and North American winter festivals. More recently, the ice hotel industry has developed, with countries such as Canada, Norway and Finland offering rooms sculpted from snow and ice.

2.1 The Invention and Development of Pykrete

During World War II, Geoffrey Pyke developed Pykrete as an alternative to ice, which was up to three times as strong, as well as more durable, flexible, and slower to melt. Pykrete is a frozen composite material, consisting of ice and a form of wood pulp, such as sawdust or paper. The original composition was 14% sawdust by weight [4]. Pykrete was introduced in 1943 as an alternative for ice in the construction of an aircraft carrier (Project Habakkuk) [4]. Whilst scale models were built, the project was never put into action due to the models experiencing buckling and warping.
Subsequent research has been undertaken into Pykrete composition, its uses and potential benefits over ice. Nixon and Smith (1987) researched the fracture toughness of ice composites containing various proportions of newspaper, wood pulp, sawdust or blotting paper [5]. The values of K_{IC} obtained ranged from 5 to 20 times the values obtained for freshwater ice [5]. Houben and Janssen (2013) researched fibre reinforced ice structure, testing the compressive strength of cylinders and beams with varying concentrations of wood pulp [6]. The material properties given in this thesis were used in the analysis of the hyperboloid lattice constructed. One issue still to be solved is the creep experienced during the lifetime of a Pykrete or ice structure. However, as ice structures are temporary, creep can sometimes be neglected.

2.2 Ice as a Structural Material

Ice is often used in construction in the form of blocks due to its high compressive strength and limited tensile strength. Ice can be used as a substitute for unreinforced concrete, or masonry blocks. Igloos and the first ice palaces were built using blocks of ice, usually harvested from local rivers or lakes. The Harbin International Ice and Snow Festival usually uses ice blocks to create its attractions, as seen in Figure 2.
Ice hotel constructors spray special 'wet snow' onto steel moulds, allowing the snow to freeze before removing the moulds. These structures experience an increase in strength as the snow melts and refreezes over time (on a day/night cycle) [7]. Pykrete was sprayed in 2015 by the students of Eindhoven University of Technology over an inflatable to form a thin walled dome [7]. Both forms of construction rely purely on the compressive strength of ice.

2.3 Ice for Spraying

The composition of the ice composite used to construct the net hyperboloid structure was initially chosen to be 2% cellulose paper by weight. If the mixture is too watery, it is not viscous enough to stay on the structure until it freezes. However, the cellulose composition was reduced to 0.6% due to clogging of the nozzles during spraying. When the authors changed the proportion of cellulose paper to 0.3%, the mix became too watery and the structural layers did not build up as quickly.

The mixture was sprayed as fine mist which built up the layers of ice. Direct spraying caused the water mixture to run down the structure, causing ice to build up predominantly towards the base of the structure, and an increase in the size of the icicles. A large volume of waste water was sprayed on the ground and over the ice blocks.

3 Design

A sprayed net design was quickly decided upon due to its aesthetics and because few structures of this type have ever been constructed, giving scope for research and development. The main desire was to have a purely tensile structure during construction which transformed into a purely compressive structure upon release. The authors studied examples of how this could be achieved such as tree structures with top tension rings. This idea developed to become a hyperboloid lattice with tension rings at the top and bottom. The hyperboloid is an inherently stable shape due to the double curvature and has been used widely by engineers including Antoni Gaudi and Félix Candela [8]. The most well known hyperboloid structures are cooling towers [9].
A compression-only structure was desirable due to the limited tensile capacity of ice (over 3 times stronger in compression). This is why many progressive ice structures are shell structures [10]. However, these require inflatable moulds onto which water is sprayed, or tensioned fabric formwork. Both of these are expensive to produce as they must be made uniquely for each structure. In comparison, the rope net is easy to produce in a few hours from materials commonly found in any hardware store.
The beauty of this design was how the formwork became part of the final structure. Ice construction is usually difficult because the formwork required is large and technically challenging as it must hold the water while it freezes (and expands). Through the use of a net, the formwork was easy to design, cheap to produce, and very sustainable. The formwork helped prestress the ice, increasing the overall stability of the structure.
Very few forms allow a tension-only lattice to form a compression-only structure upon release of the loading mechanism. The hyperboloid lattice did this well. At the same time, the structural form was elegant and efficient; as a compression only structure, it had a short load path so transferred the loads applied to it efficiently to the ice foundations.
The authors have seen very few sprayed net ice structures and no papers on this topic. The success of this project demonstrates that this method of construction is feasible for future projects. 3D printing techniques such as that performed by Pronk [11] are becoming more popular due to the ability to build ice structures without the need for complicated and expensive formwork. However, this requires a printer which has a large upfront cost associated with it. In contrast, the sprayed net technique forms similar structures at a lower cost. One downside of the sprayed net technique, compared to the 3D printing, is that a lot of the sprayed cellulose water mix misses the lattice net and is wasted.

4 Architecture

Situated in front of the university main building, the project aimed to inspire curiosity whilst not competing with the grand architectural backdrop, as shown in Figure 3. Taking the form and meaning of a tree, the self-supporting ice structure stood slightly higher than the surrounding tree-line. At 5m tall and 5m wide at the top, it tapered toward the base (2.5m wide), providing a sense of space with a minimal foot-print; serving as a node for congregation, a place to meet others, for members of the university and public alike. The project balanced its potential

imposingness through use of a hyperboloid net structure, in reference to the Shukhov Tower [8]; it minimizes its surface area while maximizing the number of sightlines running through, rendering it more relatable to the human-scale and more reverent to the surroundings. Visitors could also observe icicles on the structure, as seen in Figure 3; an architectural detail that reveals its unique spray-construction process which simulates nature.



Figure 3: The surrounding architecture and icicles

5 Structural Analysis

Finite Element Analysis (FEA) was performed with a range of ice diameters which varied linearly from the base to the top. This was most useful when onsite as it allowed the authors to focus spraying either the top or bottom section of the structure so as to make the sculpture as structurally sound as possible. The buckling modes of Shukhov towers and hyperbolic lattices are well understood and this aided the authors in calculating the buckling loads [8]. Due to the surprisingly warm weather during construction, the desired ice thickness was not achieved. However, the authors still produced a stable structure.

The original design employed a diamond lattice but the structure built included horizontal hoops between nodes. Small scale models of the diamond lattice structure were made from cardboard and wet string, loaded with weights, and then placed in liquid nitrogen. These experiments were successful and showed that even thin-columned hyperboloid lattices could support a large enough load before failure. The model demonstrated the overall stability of the design and allowed for rapid analysis of a range of different geometries. As the weather during construction was warmer than expected, the ice did not grow as quickly as desired. Therefore, horizontal hoops were added to increase the buckling load. The addition of hoops was a major alteration to the design form, considering the aim of using a slender form was to challenge the perception of ice being "chunky".

The FEA clearly showed that the deflection of the structure decreased with the addition of the horizontal hoops. The factor of safety against the buckling of the structure was of the order of 5.0 without the hoops and 6.5 with the hoops. The slanting struts of the upper part of the structure were the weakest part, regardless of the addition of the hoops, as they have the longest

length and smallest cross-section. Therefore, the addition of the hoops only increased the overall stability of the structure slightly. The buckling of the structure dominated the design as the compressive strength of ice is of the order of $3N/mm^2$ and the stress in the ice was of the order of $0.13N/mm^2$.

6 Construction

Two timber hexagons were fabricated for the top and bottom sections and the corners strengthened using plywood. The hemp rope formwork was then constructed by tying figure of eight knots through holes drilled in the plywood. A grid of timber members was fabricated to rest atop the bottom hexagonal frame near the nodes. Three blocks of ice cut from the river, each with a mass of roughly 600 kg, were then placed atop this grid using a forklift to form the ballast. A chainsaw was used to shape the ice blocks to avoid interaction with the ropes.

The top hexagonal frame was lifted using a mobile crane. Crane ropes were attached to each corner of the hexagon before being lifted. Special care was taken to ensure each rope had a similar tension. This was done by pushing the ropes and feeling how taught they were. A total of 1 tonne of load was applied by the crane. When the crane hook was lowered after spraying, this load became a prestress in the ice columns on the order of $0.14N/mm^2$. This prevented the ice from cracking and allowed the column to utilize more of its compressive strength. The prestress also reduced the amount of sag caused by the weight of the rope and water during the spraying process. Therefore, the column would be straighter and deform less under loading.

The ropes were wetted with water using a garden spray bottle. The ropes were then wrapped in toilet roll before spraying commenced. Initial water absorption, allowing the formation of the infant strut, was aided by the wetted toilet paper and the use of hemp ropes, whose natural fibres made them ideal for this purpose. The natural fibres in hemp also allowed a strong bond between the ice and rope to form, preventing pull-out and maintaining the compressive prestress applied.

Where the ropes crossed, they were tied together using cable ties to increase the strength of the node. If the ropes did not touch, the lines of action would be further apart and could cause strength problems at the nodes.

The structure was sprayed continuously over a period of three days, as seen in Figure 4. Each spray lasted ninety seconds and occurred every ten minutes. This was to allow the water to freeze between spray cycles. The water was sprayed using fireman's equipment with an adjustable nozzle at approximately 0.2 l/s. The nozzle required regular cleaning to avoid the build up of cellulose. The structure was sprayed from different angles to avoid build up of ice on only one side of the rope.

A mixture with a much larger cellulose content was used to reinforce the nodes of the structure, which were not achieving sufficient thickness through spraying alone. The horizontal hoops restricted water flow to the bottom of the nodes, hence they were much thinner than desired. The thicker mixture had paste-like qualities and could be easily placed by hand onto areas which needed to be thicker. A cherry picker was used to access parts of the structure which could not be reached from the ground.

To release the structure, the crane hook was lowered by 50mm to remove the load from the crane straps. The straps had frozen so two workers used the cherry picker to remove the ice from them before disconnecting the structure from the crane. The cherry picker was also used to remove any icicles which were considered too large and were causing safety concerns.



Figure 4: Spraying of the structure throughout the night

7 Future Developments

One technical constraint with the construction approach taken was the uneven distribution of strut thicknesses. It was difficult to achieve uniform thickness whilst spraying without a substantial increase in economic costs, for example, spraying at heights using a cherry picker. Furthermore, it was estimated that as much as 90% of spray mix ended up missing the structure, contributing to a higher material cost. A possible improved construction method to address both issues could be adopting a two-stage approach. For example, using moulding or compaction to achieve an acceptable thickness before proceeding to spraying.

A major limitation encountered in performing safety checks was the inaccuracy in the modelling assumptions. During construction, it was observed that the spray does not adhere to the joints as well as they adhere to the struts. Thus, it was inaccurate to model the structure as a uniformly brittle material as the joints would not have acquired sufficient strength. The structure's behaviour when the ice thickness was insufficient to provide a brittle property was not modelled. Should an ice net structure be constructed in the future, the observations from this project concluded that a better model taking care of the varying behaviour of the nodes and struts should be developed. For example, the structure should be checked in 3 separate stages, namely plain ropes, intermediate and fully coated, where its behaviours could drastically differ. The optimal water-to-cellulose ratio was determined on site via trial and error, which resulted in some delay in the spraying process. Using the observations from this project, the authors agreed that the spray mix formula should be decided in the design stage should another similar project commence in the future. Not only would this save construction time, it would also facilitate better modelling of the structural behaviour if the exact composition of the ice is known. The possibility of using enhancing additives, for example, thickening agents like guar gum and xanthan gum, should also be explored in future projects. It was important to find a fluid of the correct viscosity; too viscous and it would clog the nozzle and too watery and the mixture would run off the surface before freezing. Furthermore, creep is a major consideration in ice structural design. No creep analysis was performed throughout the design process due to time limitations. However, it is important that this is researched further. The creep behaviour of the ice should be tested in a laboratory, including the effects of the unusual construction technique.

8 Conclusion

The authors of this paper successfully designed and constructed the world's first hyperboloid lattice ice structure in Harbin, China, using an innovative sprayed net technique. The properties of ice encouraged the use of a form that produced a purely tensile structure during construction and transformed into a purely compressive structure upon release. By prestressing the net, the imperfections associated with the ice struts were reduced and a prestress was applied to the ice struts. Hemp rope was used throughout to improve the bonding with the ice. A water and cellulose mixture was used to spray the structure as it was both stronger and less viscous than conventional ice. Most ice structures require large, complex formwork whereas this construction technique was cheap, sustainable and fast.

References

[1] Edition.cnn.com *'World's largest ice and snow festival kicks off in China'*. [Online]. Available: https://edition.cnn.com/travel/article/harbin-ice-and-snow-festival-2019-china/index. [Accessed 22-May-2019]

[2] Chinahighlights.com *'Harbin International Ice and Snow Festival 2019'*. [Online]. Available: https://www.chinahighlights.com/festivals/harbin-ice-and-snow-festival. [Accessed 22-May-2019]

[3] Arch.mcgill.ca, *'The History of Ice Construction'*. [Online]. Available: http://www.arch.mcgill.ca/prof/sijpkes/ice/History%20-%20Ice. [Accessed 10-May-2019]

[4] Warhistoryonline.com, *'Making An Aircraft Carrier Out of Ice and Sawdust In World War Two'*. [Online]. Available: https://www.warhistoryonline.com/world-war-i/erwin-rommel-earned-germanys-highest-honor-mere-lieutenant-m. [Accessed 10-May-2019]

[5] W. A. Nixon, R. A. Smith. 'The Fracture Toughness of Some Wood-Ice Composites', *Cold Regions Science and Technology*,Volume 14 Issue 2, Pages 139-145, August 1987

[6] F. H. M. E. Janssen, R. W. G. Houben, 'Reinforced Ice Strcutures: Research on the building method for the application of ice composites', Master's Thesis, Department of the Built Environment, Eindhoven University of Technology, Eindhoven, Netherlands, 2013

[7] A. Pronk, N. Vasiliev, J. Belis. 'Historical development of structural ice', in *ICSA*, Guimarães, Portugal, 2016, Pages 339-347

[8] Matthias Beckh, Hyperbolic Strcutures: Shukhov's lattice towers: forerunners of modern lightweight construction, John Wiley & Sons Ltd, 2015

[9] E. Asadzadeh, M. Alam. 'A Survey on Hyperbolic Cooling Towers', *International Journal of Civil and Environmental Engineering*, Volume 8, Number 10, Pages 1079-1091, 2014

[10] A. Pronk, 'The calculation and construction of the highest ice dome: the Sagrada Familia in Ice', in *ISOFF*, Amsterdam, Netherlands, 2015, Pages 1-13

[11] Cursor.tue.nl, *'Gridshell made of ice intended to impress the Chinese'*. [Online]. Available: https://www.cursor.tue.nl/en/news/2018/december/week-2/gridshell-made-of-ice-intended-to-impress-the-chinese. [Accessed 11-May-2019]

Proceedings of IASS Annual Symposium 2019 – Structural Membranes 2019
Form and Force
7 – 10 October 2019, Barcelona, Spain
C. Lázaro, K.-U. Bletzinger, E. Oñate (eds.)

TW-ICE: A Freestanding Ice Shell Pavilion

Rui LIU*, Mark MISTUR

*Kent State University
132 S. Lincoln St. Kent, OH 44242
rliu5@kent.edu

Abstract

TW-ICE, a 10-meter tall freestanding ice shell pavilion formed by two intersecting asymmetrical cones with a scalloped surface, was successfully constructed in January 2019, Harbin, China using removable tension-based soft formwork including ropes and fabric. Its success was based on the knowledge gained from its sister pavilion THRICE built in December 2017. The paper reviews the major structural-formal challenges identified from the construction of THRICE including: excessive sag on the side of the structure with shallowest slope, excessive deformation caused by high elasticity and creep of polypropylene ropes used for its formwork, and out of plane arches at openings to the exterior. By investigating the challenges associated with developing a geometry best suited to the reversal of forces from tension (formwork) to compression (the resultant ice shell pavilion), this paper discusses the design and construction modifications including: (1) increased cone slopes achieved by reducing the diameters of base circles; (2) the use of polyester ropes with higher modulus of elasticity and lower creep compared to polypropylene ropes; (3) pretensioned perimeter ropes along their parabolic paths of the openings to reduce the out of plan segmentation caused by scalloping and (4) improved design of the oculi formed by projecting circles on the tops of the two intersected asymmetrical cones. This research expands on Heinz Isler's investigations into frozen draping fabric forms. Unlike Isler's forms, in addition to removing the temporary column supports, the debonding between the muslin fabric and the frozen water/cellulose mixture allowed the removal of the fabric and interior rope formwork from the interior of TW-ICE – resulting in a freestanding, fabric-free ice shell structure. The study further confirms the soft tension-based formwork using ropes and fabric is feasible for the form-finding and construction of ice shell structures.

Keywords: ice shell, soft tension-based formwork, water cellulose mixture

1. Introduction

Elegant curves can be derived from draping flexible fabric as a structural membrane. Soft, tension-based formwork has been used for concrete casting with the advantages of producing architectural and aesthetic expressions [1-2]. It also has been explored as an architectural form-finding technique for ice shells that celebrate the austere beauty of winter [3-4]. Inspired by Heinz Isler's draped frozen fabric (Figure 1), "THRICE" (Figure 2), a 10-meter-tall ice pavilion consisting of three intersecting asymmetrical cones, was designed and built by a team from Kent State University (U.S.) in December, 2017 at the Harbin International Snow and Ice Construction Festival co-organized by Harbin Institute of Technology (HIT) and the IASS Working Group 21. Flamenco Ice Tower, designed by Pronk et al, the world's largest thin shell ice structures, was also built employing pneumatic construction technique during that same event [5].

THRICE was built by tying three wooden columns to the ground with prestressed, radially arrayed ropes. These ropes were tied to an oculus forming loop attached to the top of each column. The oculi allowed daylight to penetrate deep into the space and were also designed for easy removal of the columns. A fine water cellulose mixture was sprayed to a sewn-to-fit, hydrophilic, orthogonally biased fabric that was draped onto the tension-based formwork. It was expected the resultant ice shell could convert the intersecting cones into a freestanding form acting in compression. However, the construction team was

Copyright © 2019 by Rui Liu and Mark Mistur
Published by the International Association for Shell and Spatial Structures (IASS) with permission.

not able to remove the columns in 2017 due to excessive deflections of the tension structure and insufficient thickness of the ice layer gained during the one-week construction period with an abnormal high temperature (-5 ℃) in December in the City of Harbin.



Figure 1 Draped Frozen Fabric [3]



Figure 2 THRICE [4]

Because of its elegant form and unique form-finding / construction technique adopted by THRICE, Kent State University was invited by HIT again to participate in the 2018-2019 HIT International Ice and Snow Construction Festival. They were joined by five other teams from Eindhoven Institute of Technology led by Arno Pronk, the University of Cambridge led by John Orr, the Tsinghua University led by Weixin Huang, and the HIT led by Peng Luo [6].

Using a similar construction technique to THRICE, and based on lessons learned in 2017, TW-ICE, a 10-meter tall freestanding ice-shell pavilion formed by two intersecting asymmetrical cones with a scalloped surface, was successfully completed in January 2019, (Figure 3a) using removable tension-based soft forms including ropes and fabric as formwork (Figure 3b). This paper reviews the major structural-formal challenges identified from the construction of THRICE and discusses design and construction modifications to develop a form best suited to the reversal of forces from tension (formwork) to compression (the resultant ice pavilion).



(a) Completed Exterior view



(b) Soft tension-based formwork mock-up

Figure 3 TW-ICE

2. From THRICE to TW-ICE

2.1 Lessons learned from THRICE

THRICE, resulted from geometrically complex intersection of three asymmetrical cones, was challenging to be constructed within one-week construction period with unexpected weather conditions. Although local contractors helped continue spraying the water cellulose mixture on the fabric after the construction team returned to U.S., the columns were not able to be removed to prove the feasibility of soft tension-based formwork for thin ice-shell construction due to the distresses identified in the later stage of exhibition.

As discussed in "THRICE – An Ice Pavilion: Reversing Forces from Construction to Completion" [4], greater than expected sag, particularly on the side of the pavilion with shallowest slope. This was the result of inadequate 9.5 mm polypropylene ropes with a relatively small stiffness in the axial direction of the rope (Figure 4a). The sag was exacerbated by the asymmetric melting (temperature and solar generated), creep of the ropes and ice, as well as spraying not supervised by the construction team, which resulted in redistribution of the ice shell weight causing bending of the unremoved columns. Vertical and inclined cracks identified in the late stage of the exhibition were caused by excessive sag exacerbated by movement of the columns (Figure 4b).



(a) Excessive sag on the side with shallowest slope



(b) Cracks identified in the later stage

Figure 4 Issues Identified from THRICE [4]

Important lessons learned from the design and construction of THRICE included:

(1) The complexity of the form should be controlled considering the construction period and experience of the construction team.
(2) The aspect ratio, defined as the ratio between the height and least width of the pavilion, should be increased to help control the excessive sag due to the asymmetric form of the pavilion.
(3) The openings or entrances into THRICE were too large, resulting in segmented hanging ice panels, which affected the overall structural integrity of the pavilion.
(4) Design of oculi should be improved considering the geometry and ease of column removals.
(5) Ropes should be carefully selected to avoid the deflection, creep and resulting sag, which is the most critical to the success of the project.
(6) Due to the unique form and construction technique, the spraying of water cellulose mixture should be completed or supervised by the design team.

These lessons have been implemented into the design, material selection, and construction of TW-ICE.

2.2 Design of TW-ICE

Instead of three intersected conical forms, TW-ICE employed two with base diameters of 5m and 6.5m respectively. The complexity of the form was reduced, but the goal of the project was clear to the design team composed of two faculty advisors and eight students, none of whom were from the previous year's team. It was to demonstrate the feasibility of soft tension-based formwork for thin shell construction using temporary columns, ropes and fabric as the basis for achieving an elegant, expressive, and freestanding ice pavilion. The three conical forms of THRICE were designed to fit within the 10m

cubical side site restrictions with an aspect ratio of 1.02. The overall height of TW-ICE was 10 meters, the same as THRICE, but the aspect ratio increased to 1.54. By increasing the aspect ratio, the slope of the cone was increased with less ice weight applied in the direction perpendicular to the cone to avoid the excessive sag. Two temporary columns, with a height of 8.5 m and 10m respectively, were each offset from their centers a fifth distance of their base radius – also less than THRICE.

Two oculi were formed by projecting two circles with a diameter of 0.9 m and 1.2 m respectively on the tops of the two intersected asymmetrical cones. They were created using rope loops connected to the top of the columns at one point to accommodate 18 and 20 prestressed ropes radially arrayed from each oculus to ground anchors (Figure 5). The issue of out of plane arches at openings to the exterior was addressed by designing smaller opening spanning only two panels with a width of 1.98m at the bottom and a height of 1.8m. They were derived using virtual cylinders to boolean the two cones shown in Figure 5.

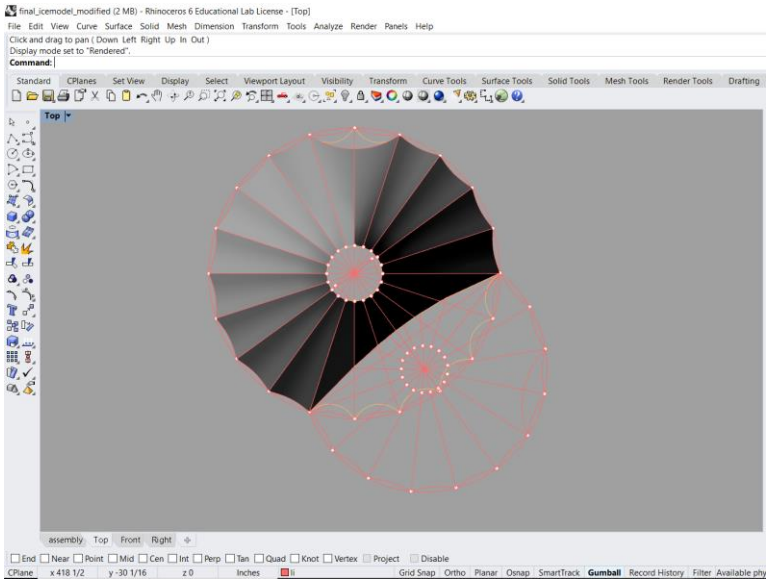


Figure 5 Top view of TW-ICE

2.3 Materials and Fabrication

Like THRICE, the intersecting form of TW-ICE was generated by tying two temporary wooden columns, each with a cross section of 15cm × 15cm, to the ground with prestressed radially arrayed ropes connected to a rope loop attached to the top of each column (Figure 3b). Pretied fixed bowline knots were used to connect the radially arrayed ropes to the two rope loops, and these radial ropes were subsequently anchored to the ground loops by means of adjustable knots. Orthogonally biased, bleached muslin fabric was precut and sewn to form the water/ice substrate. The cutting pattern was created in the Rhino 6.0 by unrolling the surface of intersected cones with maximum width of the fabric panels at the bottom less than 1m to stay within the supplied fabric panel width. The seams of the fabric panels coincide with the ropes. The two fabric cones were attached to each other by means of pre-sewn Velcro seams at the intersection shown in Figure 5.

Polypropylene ropes with a diameter of 9.5mm were used to fabricate the tension-based formwork of THRICE. However, excessive sag was caused by the stretch and creep of the polypropylene ropes. For TW-ICE, the mechanical performance of three types of rope fibers were compared (Table 1). Tenacity is defined as resistance of fiber to breaking (grams/denier), stretch measures the elongation of fiber at break, the coefficient of friction evaluates resistance of fibers to slipping, and creep is one of the mechanisms causing permanent elongations caused by load over a long time period.

As shown in Table 1, nylon fiber stretches the most, polypropylene stretches significantly, and polyester stretches the least making it a better choice to address the sagging issue. Comparing to polypropylene, both nylon and polyester fibers have negligible creep. To control the axial deformation or stretch occurring in the ropes, polyester ropes with a diameter of 15mm were selected to build the soft tension-

based formwork (Figure 6). The estimated stretch in the selected polyester rope is only 30% of that occurring in the polypropylene rope under the same axial tension.

Table 1 Comparison of Rope Fiber Characteristics

Fiber Type	Nylon	Polypropylene	Polyester
Tenacity	7.5-10.5	6.5	7.0-10.0
Stretch	15-28%	18-22%	12-18%
Coefficient of Friction	0.12-0.15	0.15-0.22	0.12-0.15
Specific Gravity	1.14	0.91	1.38
Creep	Negligible	Application Dependent	Negligible



Figure 6 Polyester rope

2.4 Structural Consideration for TW-ICE

A mixture of water and cellulose was sprayed to the fabric draped onto the soft tension-based formwork to form an ice shell at a temperature below -10°C, which converted the intersecting cones into a form acting in compression.

The form of two intersected cones is stable in geometry. The scalloped surface resulted from the weight of water cellulose mixture increased the stiffness of the cross section and helped resist buckling caused by the compression. The load of the ice shell was distributed along the parabolic paths (approximate) of the conical intersection as well as at the two openings formed by boo leaning the cones with a virtual cylinder. The stiffness of the intersecting parabolic arch, as well as the opening arches was increased by a rope stitched into the fabric. The structural integrity of THRICE was also compromised by its two large exterior openings. The heavy segmentation and greater than anticipated scalloping took the resultant arches out of plan. A much smaller design dimension was adopted for TW-ICE. In addition, the perimeter ropes along the openings was pretensioned and anchored to the ground to reduce the out of plan segmentation caused by scalloping.

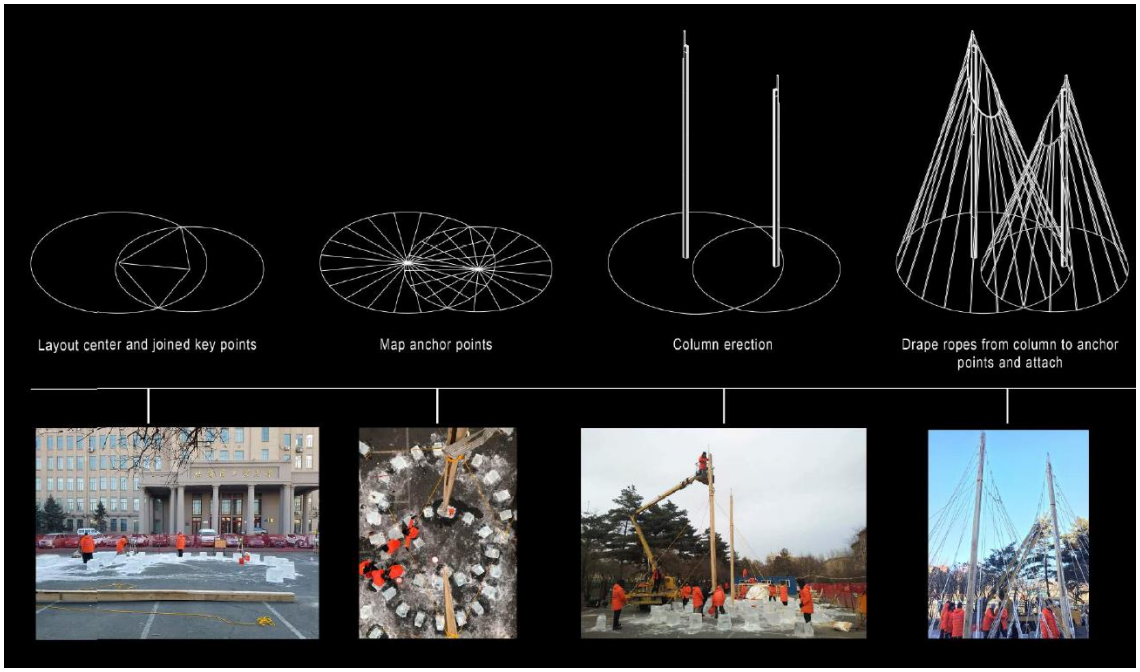
3. Full-scale Structure

3.1 Assembly Procedure

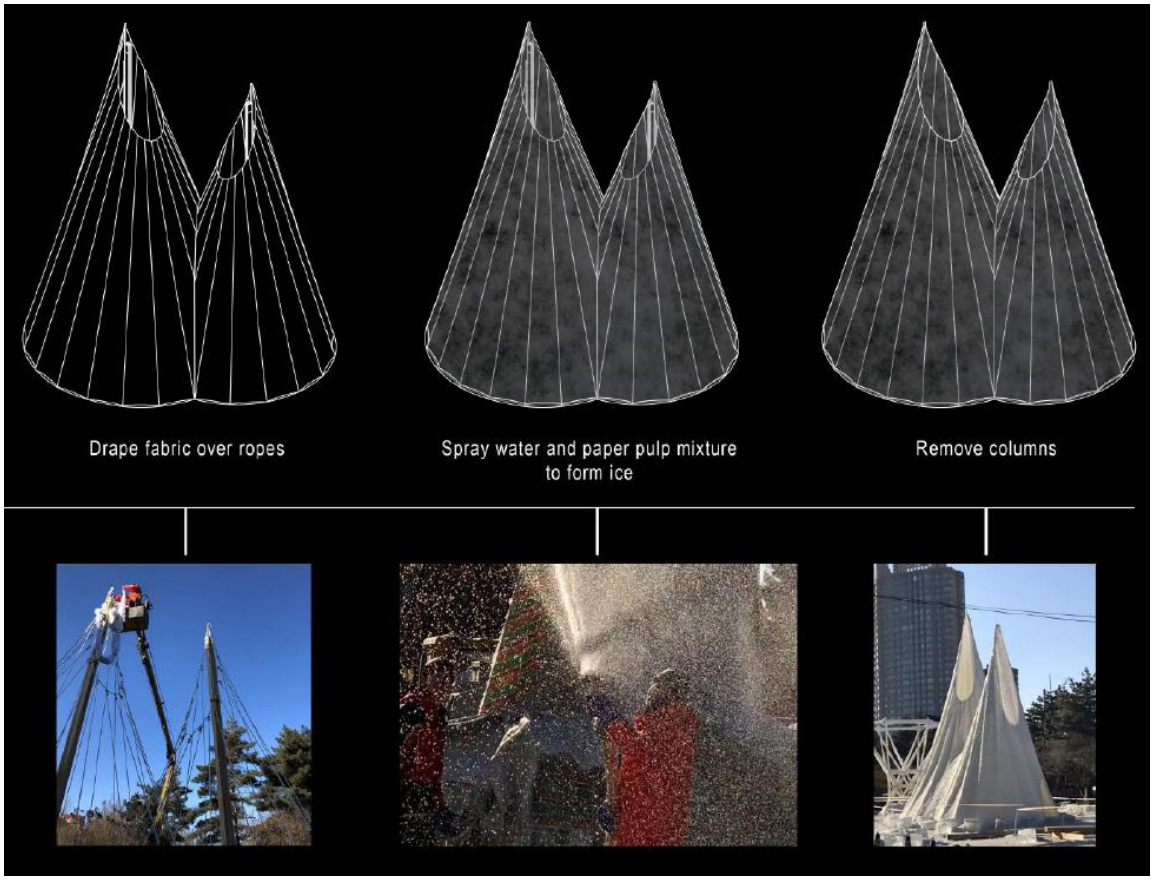
The full-scale construction was completed from December 17 to December 22, 2018 on the main campus of HIT, in Harbin. The construction sequence is documented in Figure 7.

The construction team composed of eight students and two faculty advisors first laid out key nodes on two intersected circles indicating the locations of columns and rope anchors. Half-hitch knots, made from 15 mm polyester ropes, were frozen to the ground, but stayed outside of the ice block anchors to afford adjustable connections to the radially arrayed ropes. Two temporary wood columns were anchored by radial ropes tied to rope loops (oculi) connected to the top of each of the columns. The end of each radially arrayed rope was connected to the knots frozen to the ground. Tensions in these ropes were adjusted to find the final shape of the formwork. After draping the pre-cut, pre-sewn fabric to the

form, a mixture of water of cellulose (approximately 2% cellulose by weight) was sprayed to the fabric, resulting in the predicted scalloped surface between ropes, and a slight curve along the rope due to the weight of the ice shell.



(a) Construction of the soft tension-based formwork



(b) Fabric draping and mixture spraying

Figure 7 Construction of TW-ICE

3.2 Column and Fabric Removal

The spraying was completed on December 21, 2018 to reach a thickness of 8 cm at the bottom of the ice shell. No measurement was made for the thickness of the ice shell on the top, but it was estimated to be 2 cm. However, due to a warm temperature (0 °C during the day) and a snow event, the columns were not removed until January 5, 2019. Removal of columns and fabric are documented in Figure 8 and 9.

The top rope loop was supported by a "Y" shaped steel bar inserted in a steel pipe. The steel pipe was strapped to the top of wood column. The single point connection facilitated the easy separation between the column and ice shell. The higher column was removed first then the shorter column.

An experienced contractor first tied a hanging rope from a crane to the top of column, keeping it from losing its balance to hit the thin ice shell. The ice shell and column were separated by cutting the rope loop at the single support point. Then the column was taken out from the ice shell through the oculus on the top as indicated in Figure 8.

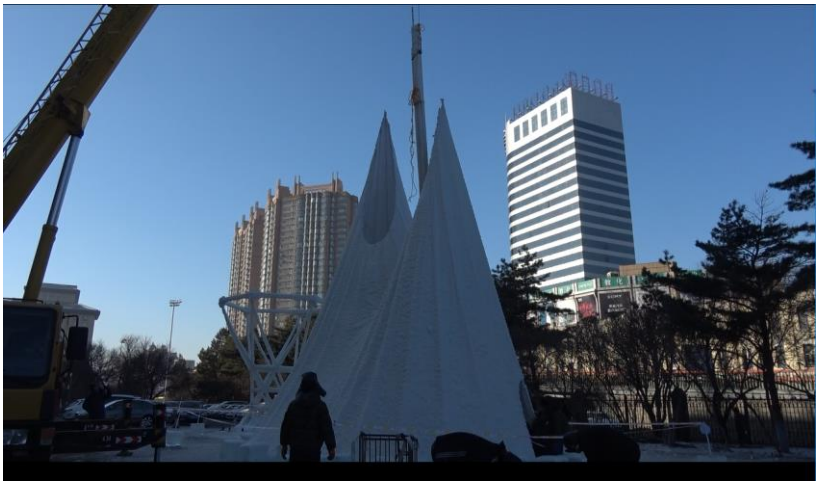


Figure 8 Column removal

The same contractor in a steel basket was lowered down into the ice pavilion through the oculus to cut all the radially arrayed ropes connected to the top rope loop. The rope loops were frozen into the ice shell and they were not able to be removed. But they functioned as the stiffener to increase the stiffness of the ice oculi.

Debonding between the fabric and the ice-shell caused by the sublimation of ice on the interface between the fabric and ice shell was identified in THRICE. The cellulose at the interface between the fabric and ice caused debonding and made it possible to easily remove the fabric from the ice shell. Figure 9 shows the thin fabric being removed top down from the interior of the pavilion.



Figure 9 Fabric removal

The interior and exterior of the completed ice pavilion are shown in Figure 10. The freestanding ice pavilion demonstrated the that design and construction improvements based on the lessons learned from THRICE were successful. Excessive rope sag and out of plane segmentation were controlled. As shown in Figure 10b, ropes at the oculi and along the intersecting arch of the two cones were integrated into the ice shell helping increase the structure's stiffness. The "arch" effect at the intersection play an important role to distribute the load to both side of the pavilion while enabling a large and tall interior space. The oculi designed allowed the daylight to penetrate the pavilion (as well as for the easy removal of the columns), were complemented by the translucent thin ice shell. The tension in the radial ropes were well controlled as indicated in Figure 10c. The teardrop, saddle-shaped occuli, a result of the forces applied to them, were nevertheless a circle seen perpendicular to the ground plane as the intended design shown in Figure 5.



(a) TW-ICE (exterior view) (b) TW-ICE (interior view) (c) Interior with temporary form work

Figure 10 Exterior and interior views of TW-ICE

4. Conclusion

The paper reviews the major structural-formal challenges identified from the construction of THRICE, proposed and implemented design modifications for TW-ICE. Properly selected ropes were the key to the success of TW-ICE, a project that extends Heiz Isler's investigations into frozen draping fabric forms. The soft tension-based formwork was successfully removed from TW-ICE resulting in a freestanding, fabric-free ice shell structure, confirming that soft tension-based formwork using ropes and fabric is feasible for the form-finding and construction of ice-shell structures.

Acknowledgements

The authors would like to acknowledge Harbin Institute of Technology, China and IASS Working Group 21, the organizers of the 2018-2019 HIT International Ice and Snow Construction Festive. Our special thanks are given to Mr. Kun Lv and his employee for his coordination and technical support during the full-scale construction in Harbin.

Our thanks are also given to JoAnn fabrics for providing the fabric material. We also acknowledge Professor Vincent Quevedo from School of Fashion at the Kent State University for assisting the team in fabrication the fabric formwork, Professor Anthony Mirando from Construction Management Program at the Kent State University for helping the team in the mock-up construction, and the following students from the College of Architecture and Environmental Design, Kent State University, who participated in the design and construction of TW-ICE: Benjamin Barry; Yu-Ting Chang; Aidan Crossey; Amanda Harrer; Timothy Jockers; Kentrell Lodge; Fredrick Wolfe; Badr Zabarah.

References

[1] D. Veenendaal, M. West, and P. Block, "History and Overview of Fabric Formwork: Using Fabrics for Concrete Casting," *Structural Concrete*, vol. 12, no. 3, pp. 164-177, 2011.

[2] J. J. Orr, A. P. Derby, T.J. Ibell, M.C. Evernden, and M. Otlet, "Concrete Structures using Fabric Formwork," Structures, vol. 112, pp. 97-105, 2011.

[3] J. Chilton, "Form-finding and Fabric Forming in the Work of Heinz Isler," *Proceedins of 2nd International Conference on Flexible Formwork*, pp. 84-91., 2012.

[4] R. Liu, and M. Mistur, "THRICE – An Ice Pavilion: Reversing Forces from Construction to Completion," in Creativity in Structural Design: Proccedings of the IASS Annual Symposium 2018, MIT, Boston, USA, July 16-20, 2018, C. Mueller and S. Adriaenssens (eds.). (Invited to contribute to Reference [5]).

[5] A. Pronk, M. Mistur, Q. Li, X. Liu, R. Blok, R. Liu, Y. Wu, P. Luo, and Y. Dong. (2019). The 2017-2018 Design and Construction of Ice Composite Structures in Harbin. *Structures*. 18, 117-127.

[6] D. Huylebrouck (2019). Cold and Austere Beaty in Harbin, China. *The Mathematical Intelligencer*. 20-26. https://doi.org/10.1007/s00283-019-09876-w.

Proceedings of the IASS Annual Symposium 2019 – Structural Membranes 2019
Form and Force
7 – 10 October 2019, Barcelona, Spain
C. Lázaro, K.-U. Bletzinger, E. Oñate (eds.)

Adaptable Meshes: A Dynamic Approach to the Construction of Membranes

João COSTA[1,2], Felix KRAEMER[1,3], Christoph BADER[1,4], Jean DISSET and Neri OXMAN*

*Corresponding Author. Massachusetts Institute of Technology, Department of Architecture and Urban Planning, Media Lab
75 Amherst St. E14-433c, 02142 Cambridge MA, USA
neri@mit.edu

[1] First Co-Authors: [2] jpcosta@mit.edu, [3] fkraemer@mit.edu, [4] bader_ch@mit.edu

Abstract

The fabrication of thread-based membranes and panels is typically constrained by the limitations of the underlying scaffold in which it is constructed. In this paper we present an alternative method of developing fiber-based meshes that are the result of ongoing research with the *Bombyx mori* silkworm done by the group and explored previously [1][2]. It consists of a system that uses a heat bonding thread comprised of a polyester core coated in PLA that is deposited by a custom end effector responsible for laying the thread and creating anchor points by heating up and fusing the threads together. This research shows how we can reduce the complexity of the scaffold while increasing the ability to create anchor points within the mesh itself, allowing for a more intricate and adaptable behavior of the system. In this paper we present (1) the mechanism and development of the end effector; (2) the approach for toolpath pre-planning; (3) future steps for the inclusion of a feedback loop capable of interfacing with living organisms.

Keywords: membrane design, thread-based fabrication, biological design, computational design, fabrication system, tool design.

1. Introduction

Within the last five years, the construction of robotically spun meshes has been actively explored as means of controlling fiber distribution on membrane structures, allowing for structural optimization and aesthetic control and curation. Although recent examples [2][3] have successfully demonstrated that the process yields promising results in both structural and architectural realms, designers and engineers still have to conform to the boundaries of fairly limited fabrication mechanisms.

The constraints imposed by (a) the end effector chosen to spin the fiber and (b) the support (i.e. frame) in which the spinning process will occur have a major influence on the possibilities for the development of the toolpath. That is because the current approaches have relied on the spinning process to be done around pre-defined anchor points at the edges of the supporting frame without the possibility of having intermediate anchors within the boundaries of the support which, in its turn, becomes more complex.

Here the authors present a novel approach to the development of membranes which introduces intermediate connections along the surface of the membrane. The process is made possible by the development of a custom end-effector responsible for creating such connections and depositing the yarn that forms the mesh, coupled with a toolpath generation method that allows for the simulation of what the membrane will look like. Furthermore, we propose future steps that aim to implement a feedback

Copyright © 2019 by João COSTA, Felix KRAEMER, Christoph BADER, Jean DISSET and Neri OXMAN
Published by the International Association for Shell and Spatial Structures (IASS) with permission.

loop in which the system will be able to (a) accommodate for any changes resulting from the spinning process and (b) adapt to the addition of living organisms for a combined mesh.

2. End-Effector

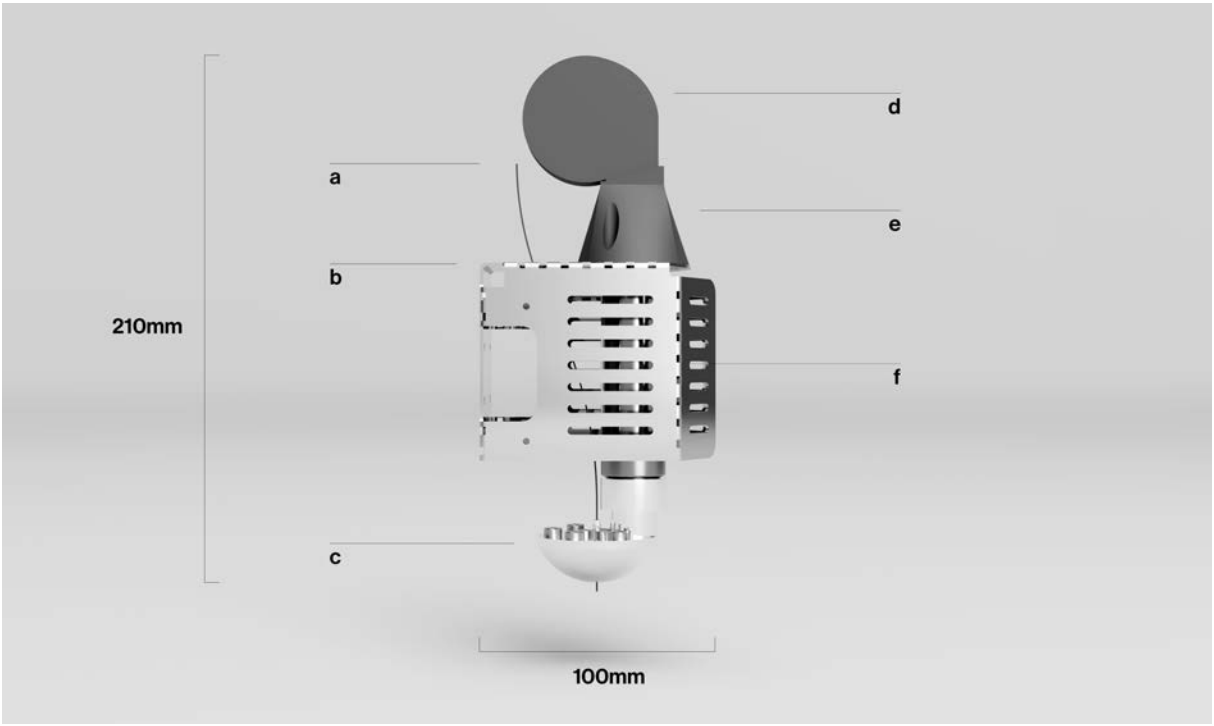


Figure 1: Render of the end-effector and its components. (a) Heat-bonding thread; (b) Stainless steel guard; (c) Aluminum nozzle; (d) Fan; (e) Fan Adapter; (f) Heater.

The custom end-effector can be attached to fabrication systems such as CNC machines or robotic arms. It is responsible for heating up the PLA coating of the thread and fusing it to previously laid out thread, therefore creating connection points. The tool is designed to be in a constant "on" state–meaning it is always heating up the thread–allowing for connections to be made at any stage of the fabrication and releasing the necessity of having to track where existing threads are in order to fuse them together.

2.1. Mechanism

The end-effector works by creating an air flow that starts at the top of the tool, with a 12V fan (**Figure 1(d)**) that goes into the heater (**Figure 1 (f)**) and finally exits through the nozzle (**Figure 1(c)**) where it meets the heat-bonding thread.

The heater consists of spooled nichrome wire that spirals around a ceramic core and is covered by a steel shell. This allows for the cold air flow to pass through and carry the heat over to the nozzle. The ceramic core also houses a thermocouple probe that allows for a feedback control of the temperature. The heating element and thermocouple are controlled by a microcontroller that gives the user access to the temperature control.

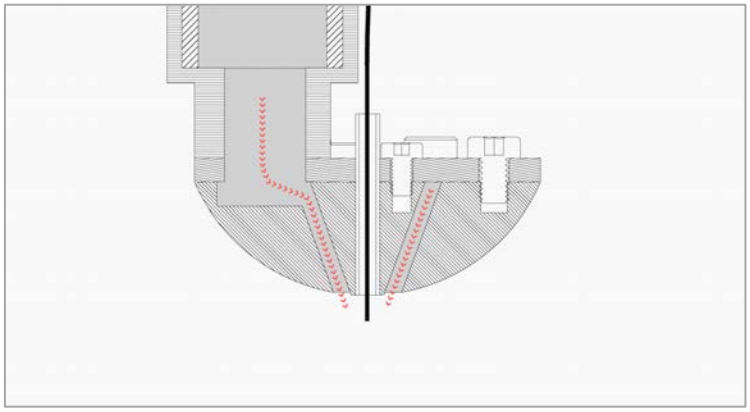


Figure 2: Section view of the nozzle. The red arrows indicate the air flow within the nozzle.

A dome-shaped nozzle is used, allowing the tool to smoothly go over existing threads on the mesh, in any direction these may come from. Since the nozzle is made out of aluminum, its body also gets warm with a thermal focal point where the air exits the nozzle and meets the thread (**Figure 2**).

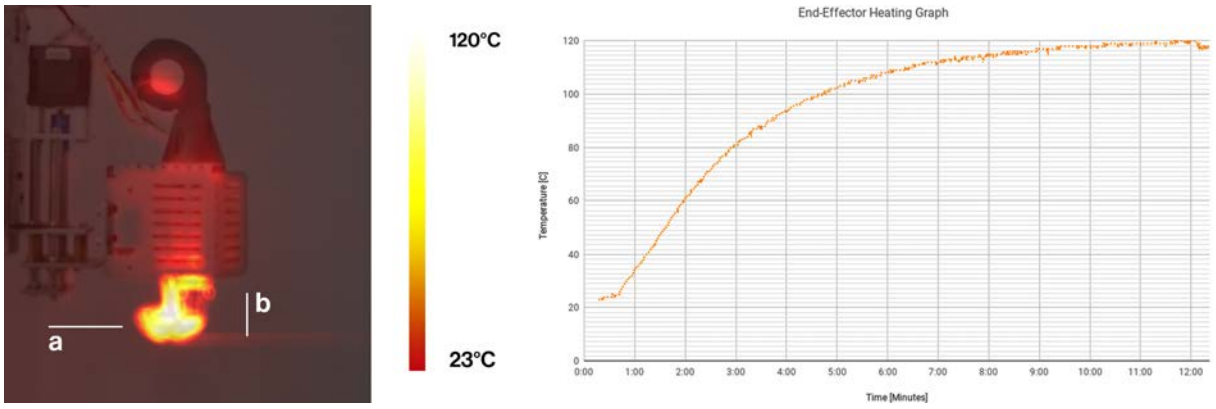


Figure 3: IR heatmap showing heat distribution on nozzle (a) and thread (b). Graph (right) shows heating curve of End-Effector at room temperature.

Due to the thermal inertia of nozzle body, the full target temperature of the nozzle is reached after approximately 11 minutes (**Figure 3**), using 188.6 Watts at a room temperature (22-23°C). However, the heating element and fan already produce a stream of approximately 80°C after 15-20 seconds and the application temperature of the PLA coating (minimum of 120°C) is reached at approx. 4-5 minutes, allowing for displacement of the end-effector and operation of the robotic environment it is mounted in.

PLA coated thread is deposited at a temperature of 120°C (**Figure 3(a)**). The thermal inertia and radiation of the metal nozzle body result in a pre-heating of already deposited thread around the focal point in which new thread is placed.

2.2. Setup and Operation

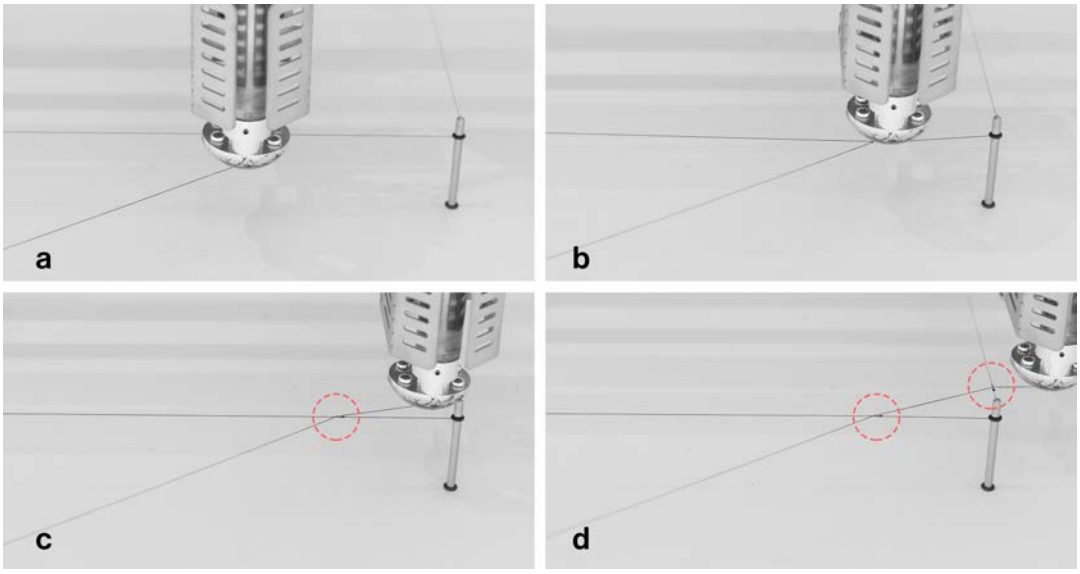


Figure 4: Image sequence showing the creation of two anchor points on a thread frame.

The setup necessary for the system to work is minimal: an outline of the desired membranes created with the heat-bonding thread. The initial shape of the membrane will define the boundaries of the workspace and, within these limits, the anchor points can be created. When compared to previous approaches for fiber-based membranes [2][3] the frames are considerably simplified since the anchor points do not need to be defined beforehand. In the event of a construction of multiple panels with different meshes but same outline this would prove to be an advantage in the fabrication of the modules.

In order to simplify and exhibit the basic behavior of the system, we have used a 300mm x 300mm outline. The sides of the square (made out of heat-bonding thread) were attached to short steel poles that secured the initial setup.

An example of anchor point creation can be seen on **Figure 4**. With the tool starting outside the boundaries of the membrane (**Figure 4(a)**) it crosses one of the sides (**Figure 4(b)**) and fuses the existing thread to the *operation thread* (the thread being fed through the end-effector), creating a first anchor point (**Figure 4(c)**). From that point onwards, every time the operation thread goes over an existing thread it will create a new anchor point (**Figure 4(d)**). With time, the greater the number of existing threads and anchors, the greater is the possibility of creating new connection points.

3. Toolpath Planning and Simulation

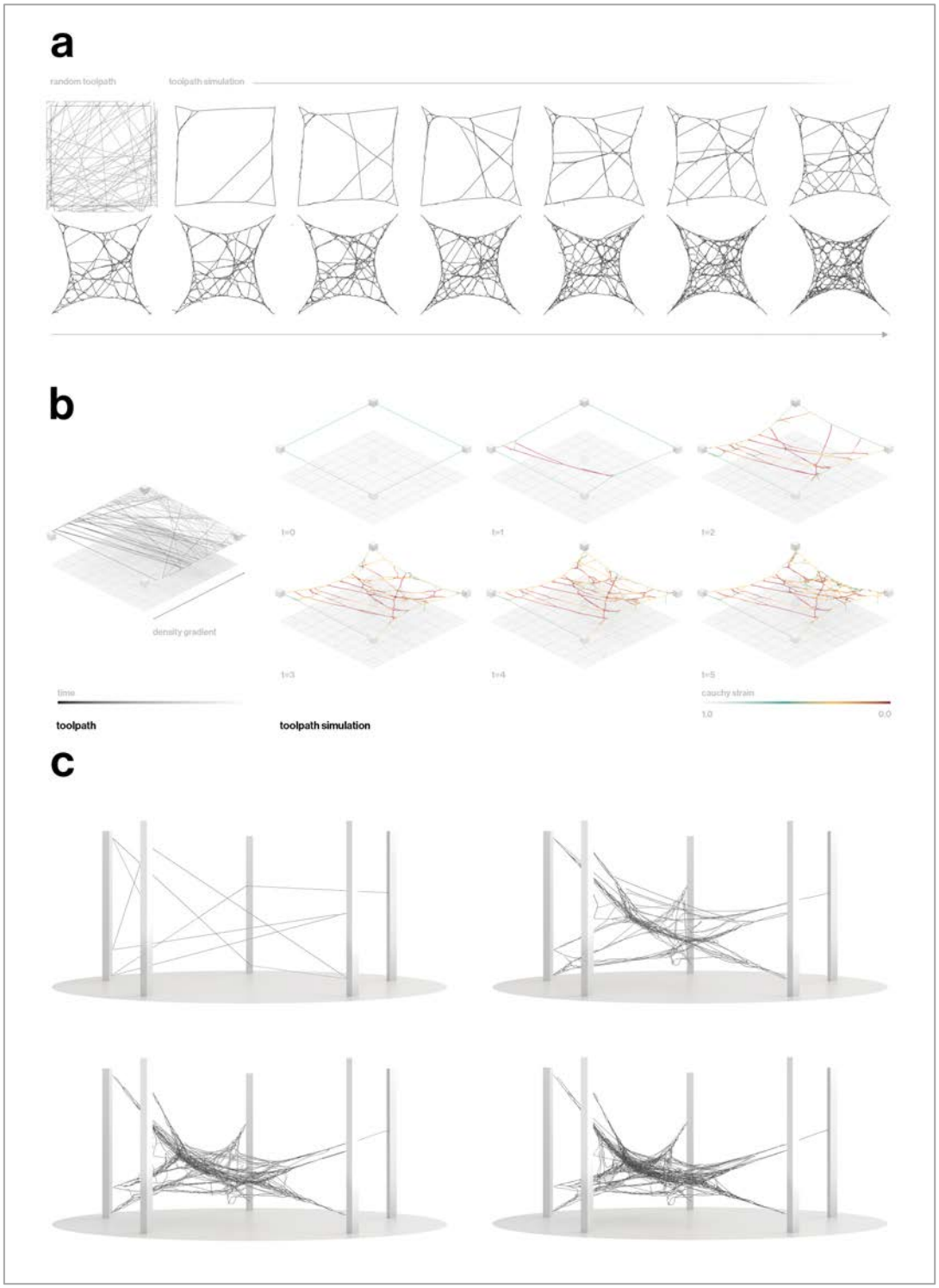


Figure 5: (a) Top view of random toolpath and simulation of intermediate anchor points along time. (b) Deformation and stress variation on the mesh over time. (c) Example of three dimensional membrane application.

Path planning and simulation must work in parallel when utilizing the tool presented here. Similar to CAM software, the visualization of the path itself does not reflect the outcome of the process and therefore a simulation tool was developed.

A basic random toolpath (**Figure 5(a)**) consists of straight lines and does not display the changes the mesh will suffer over time. Factors such as the number of times it goes over the threads, angle of incidence, proximity of anchor points and stress on the anchor points will affect the rate of creating successful connections. Thus the simulation tool, at this stage, is not a perfect prediction of the outcome but works as a guiding tool for displaying an overall density distribution.

It is also important to observe that missing connections and overstress of anchor points (**Figure 5(b)**) are the main cause for loose threads and can be avoided by having (1) constant thread management in order to prevent it from creating slack and (2) increasing the chances of creating connections by moving the end-effector perpendicular to existing threads. Stress reduction can also be achieved by increasing the number of anchor points that will distribute the force within the mesh.

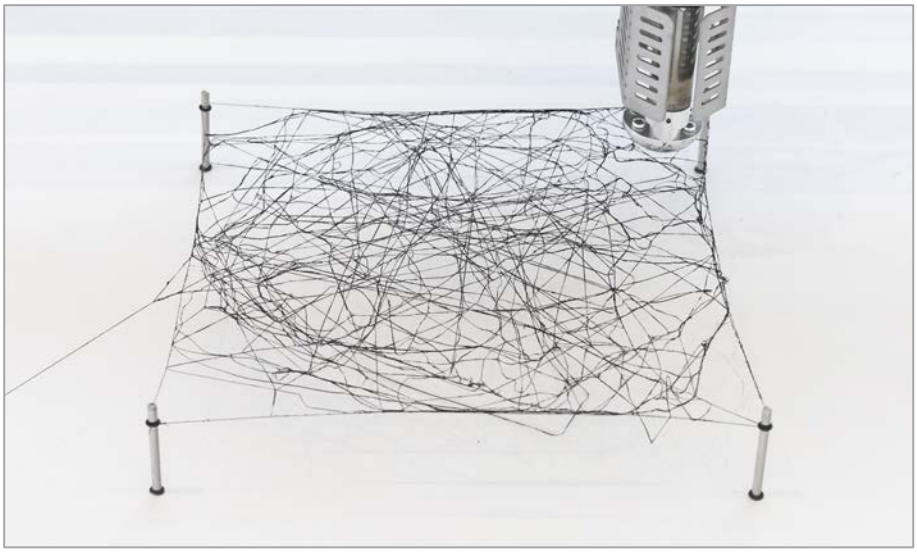


Figure 6: Example of 300mm x 300mm flat mesh.

4. Feedback Loop and Future Steps

Although at the present state the system works mostly as a pre-planned fabrication approach, it offers multiple research directions that can further explore its inherent qualities. The group has been looking into establishing a feedback look with cameras and IR sensors that will enhance the flexibility provided by the tool and path planning.

For instance, one could use this setup not as a means of executing a predefined plan but rather as an on-the-fly-mechanism that is able to "see" what is being created and act based on it. At a first glance, this could be seen as a loss of control on the design of the membrane but, on the other hand, may yield interesting results if guided by a set of rules that allows for the appearance of an emergent behavior and autonomy of the system [4].

Furthermore, we can think of adding new agents to the system that will enhance the autonomy of the system and its flexible character. For instance, the addition of silkworms to the system would provide an interesting factor of unpredictability, "forcing" the machine to adapt the path in order to accommodate and allow for silk deposition which would, in its turn, reinforce the membrane in specific places. Because the system does not have to rely on specific anchor points, it is able to adjust to the

organisms' behavior and create, for example, a path for it to walk on making it as dense or sparse as needed, based on the number of connections it makes.

4. Conclusion

The system and tool presented in this paper can be seen as a step towards an ideal adaptable approach for fabrication of meshes. It suggests that, in order for that to be truly attained, compromises need to be made in the amount of control designers have over the outcome of the process–it does require tools that support this kind of design process but also calls for a change in the way we perceive our interference in the process itself.

That said, it offers a novel form of fabricating membranes in a dynamic manner, one that can adapt to different stimuli from the environment or other additional agents. It is still being explored in a larger scale but has yielded promising results so far which leads us to believe that it can soon be applied in the construction of a larger pavilion-scale structure.

Acknowledgements

The authors would like to acknowledge the support provided by fellow lab mates, in particular Sunanda Sharma and Susan Williams for their contribution to the project.

References

[1] J. Costa, C. Bader, S. Sharma, J. Xu, and N. Oxman. "Spinning Smooth and Striated: Integrated Design and Digital Fabrication of Bio-Homeomorphic Structures across Scales", Creativity in Structural Design *Proceedings of the IASS Annual Symposium 2018,* Boston, USA, July 16-20, 2018

[2] N. Oxman, J. Laucks, M. Kayser, J. Duro-Royo, C. Gonzales-Uribe. "Silk Pavilion: A Case Study in Fiber-based Digital Fabrication," FABRICATE Conference Proceedings, pp. 248-255.

[3] S. Reichert, T. Schwinn, R. La Magna, F. Waimer, J. Knippers, A. Menges. "Fibrous Structures: An integrative approach to design computation, simulation and fabrication for Lightweight, Glass and Carbon Fibre Composite Structures in Architecture based on Biomimetic Design Principles", CAD Journal, Elsevier, Volume 52, July 2014, pp. 27–39

[4] M. A. Bedau, "Weak Emergence", *Noûs*, vol. 31, no. s11, pp. 375–399, 1997.

Proceedings of the IASS Annual Symposium 2019 – Structural Membranes 2019
Form and Force
7 – 10 October 2019, Barcelona, Spain
C. Lázaro, K.-U. Bletzinger, E. Oñate (eds.)

Graded textile shaping: Manufacture of curved cladding panels using multi-material knitted preforms

Ying Yi TAN[1], Yu Han, QUEK[1]

[1]Singapore University of Technology and Design
8 Somapah Road, Singapore 487372
Yingyi_tan@mymail.sutd.edu.sg

Abstract

This paper documents the design and fabrication of a multi-material knitted textile preform to be shaped and laminated into GFRP architectural cladding panels of non-developable and non-orthogonal geometries. The textile design involves incorporating polyurethane (PU) yarns at designated areas alongside a base of glass fibre yarns to compose this preform. This provides localised regions of increased axial stretch which seeks to accommodate to intended geometries and maintain a tensioned surface for direct lamination.

Keywords: CNC-Knitting, Material Design, Textile Hybrid System, GFRP Composite

1. Introduction

Architectural cladding panels of non-developable and non-orthogonal geometries present a challenge to fabricate. One way to manufacture panels of such geometries would to create them out of Glass Fibre Reinforced Polymer (GFRP) composites with current methods in industry adopting mould-making and wet lay-up processes [1]. However, these techniques require extensive amounts of material and manpower respectively: Mould-making methods consume large blocks of expendable material that undergo subtractive manufacturing processes to create the desired geometry; the subsequent Wet lay-up involves multiple people to simultaneously and progressively laminate multiple layers of glass fibre sheets upon the mould surface to attain an intended depth.

Our research presents an alternative method to manufacture curved GFRP laminate panels of such non-standardised geometries. First, we use a customised textile, machine-knitted out of glass fibre yarns, to serve as a flexible stay-in-place formwork and internal composite preform. Next, we insert carbon fibre strips into continuous channels integrated along the textile's boundary edges. We then mount the planar textile upon an adjustable shaping mechanism and flex the bendable strips which creates the desired geometry. Once shaped, we laminate the curved surface with polyester resin to solidify the textile into a curved composite panel. Finally, we can de-mould the panel and reuse the carbon fibre strips for subsequent shaping instances.

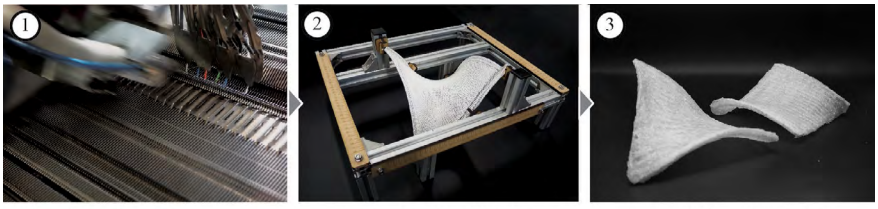


Figure 1: Graded textile shaping fabrication workflow

Copyright © 2019 by Ying Yi TAN, Yu Han QUEK
Published by the International Association for Shell and Spatial Structures (IASS) with permission.

From this, our method capitalises on a modified textile hybrid system with knitted membranes to shape and laminate the textile preform in a material-efficient manner. We tap upon the principles of textile hybrid systems – reciprocal structural configurations consisting of slender bending-active elements with high flexural stiffness which interact with tension-active membranes to maintain the structural stability of the entire assembly [2]. In our case, inherently elastic knitted membranes undergo shaping along their edges using several bending-active elements to produce doubly curved minimal surfaces [3]. In turn, the bending-active elements keep the textile in tension which provides a surface to be directly laminated upon without the need for a hard mould backing.

In this paper, we expand upon our ongoing research [4] by introducing a multi-material textile that has been designed to facilitate geometric shaping. This textile incorporates polyurethane (PU) yarn knitted alongside the base material of glass fibre (GF) yarns at designated regions. Such aims to serve two purposes:

- To broaden the geometric range of our shaping method to non-orthogonal forms (i.e. edges of geometries not bound by a cuboidal box)
- To maintain a tensioned textile surface for direct resin lamination

Akin to functionally graded materials [5], the textile becomes 'graded' in terms of its material composition and microstructure. Sequential stacking of different yarn materials in a specific manner generates zones with higher axial stretch capacity within the same piece of textile to conform to boundary conditions of intended geometries. From this, our paper seeks to achieve the following:

- Exploration and characterisation of GF-PU textiles with different stitch patterns;
- Proposing a computational approach to assign different regions of GF-PU and GF patterns based on input surface geometries;
- Implementing this approach on three non-orthogonal doubly curved geometries

2. Bespoke Knitted Textiles

A review of recent literature shows that bespoke knitted textiles have been designed using methods that fall under one of the three categories: (a) shaping; (b) altering the stitch pattern; (c) integrating a different yarn material.

The first category is typically performed for textile composite preforms, where the membrane's boundaries are widened or narrowed to adhere to an input 3D geometry. This involves merging or splitting of loops to modify the overall shape of the knitted textile. Popescu's and Liu's research both investigate this with the creation of shaped knitted preforms for concrete casting and composite lamination respectively. Installations of Popescu's KnitCandela [6] and KnitCrete bridge [7] and Liu's composite chair [8] all demonstrate implementations of this method.

In the second group, altering stitch patterns essentially modifies the textile's microstructure by varying the way the yarn forms loops in the creation of a piece of textile. Different combinations of needle actions, such as knits, tucks and misses, generate a variety of stitch patterns that exhibit different extents of stretch. This enables the textile to accommodate to either boundary conditions or internal areas within the membrane to facilitate assembly with other external elements. The textile hybrid installations of Hybrid Tower [9] and Isoropia [10], designed and assembled by the Centre for Information Technology and Architecture (CITA), feature this technique: - An elastic *Piquet Lacoste* pattern enables the textile to stretch and interface with tension cables that hold the membrane in place; this contrasts with the less elastic *Interlock* pattern which reinforces the edges of the membrane and tubular pockets that interface with bending-active rods.

The third group employs subsidiary yarn(s) spun from a material that exhibits different mechanical properties from the main yarn. These yarns can be knitted together either as distinct separate zones or as overlapped areas to create localised variations of elasticity/stiffness within the textile. Sharmin &

Ahlquist's work on textile-reinforced composites investigated this technique by integrating yarn materials of increased stiffness (eg. nylon, carbon fibre tow etc.) as a peripheral zone around a central area of elastic "nylastic" yarn [11]. They pre-tensioned the textile and applied resin onto the peripheral zone. This induced a build-up of internal forces within the elastic central area and caused the textile composite to flex into a curved geometry when released from its constraints. In their experiments, they demonstrated how the stiffness of the peripheral zone influenced the eventual deformed geometry.

2.1 Opted Strategy

Although the first category has been commonly adopted for textile composite preforms, machine-knitting shaped glass fibre textiles proves to be a challenge. Shaping involves multiple instances of transferring of the loops across needle beds and this action imposes a strain on yarns. Such strain makes the glass fibre yarns susceptible to tearing as they have lower breaking extensions (4.8%) compared to other yarn materials typically used in fashion industry (e.g. Polyester: 12-15%; Nylon: 15-28%) [12].

Thus, to maintain a textile preform knitted primarily from glass fibre yarns while improving the membrane's extent of stretch, we have opted for a strategy which involves a combination of the latter two categories. This not only incorporates a more elastic yarn into the textile preform, but also customises the way it is being knitted. From this, we explore the design of a multi-material knitted textile featuring a subsidiary polyurethane (PU) yarn knitted alongside the primary glass fibre (GF) yarn at user-defined areas. Such aims to facilitate shaping of the textile membrane by accommodating to curved edge boundaries.

3. CNC Knitting and Multi-Material Textile Design

We select weft-knitted fabrics as our main textile structure due to their higher inherent elasticity compared to the other woven or braided variants that are commonly used as composite preforms. The characteristic intermeshed loops of weft-knitted textiles, created from a single strand or multiple strands of yarns, allows the textile to stretch and form doubly curved surfaces as a single continuous membrane element. Thus, this reduces the need for sewing or stitching in the production of complex curved geometries. Weft-knitting also enables the integration of additional features, such as continuous channels, for the inclusion of the bending-active shaping elements [7].

Our work employs CNC-knitting technology which enables a stitch-by-stitch level of customisation to design and fabricate this multi-material textile preform. We create our textile via a proprietary design software which converts our input into machine instructions. The knitting machine reads these instructions to actuate the needles, yarn carriers and carriage to build row-upon-row of loops from input yarn(s) and this iterative process physically composes the textile. For our case, we see this to be akin to designing for multi-material additive manufacturing, where different yarn materials can be juxtaposed with one another in a desired layout to create a multi-material textile from a single 'print' job.

We explored the combinations of GF (E-glass, 224 tex) and PU yarns (450D Spandex, 100D Polyester) using the Shima Seiki MACH2®XS 15-gauge WHOLEGARMENT weft-knitting machine [13] and knitting at half-gauge. Our stitch patterns referenced the *Milano Interlock* pattern – a *Double Jersey* pattern with *Tubular Jersey* pattern inserted in between every alternate row [4]. Glass fibre yarns form the *Double Jersey* rows, while PU yarns make up the *Tubular Jersey* rows.

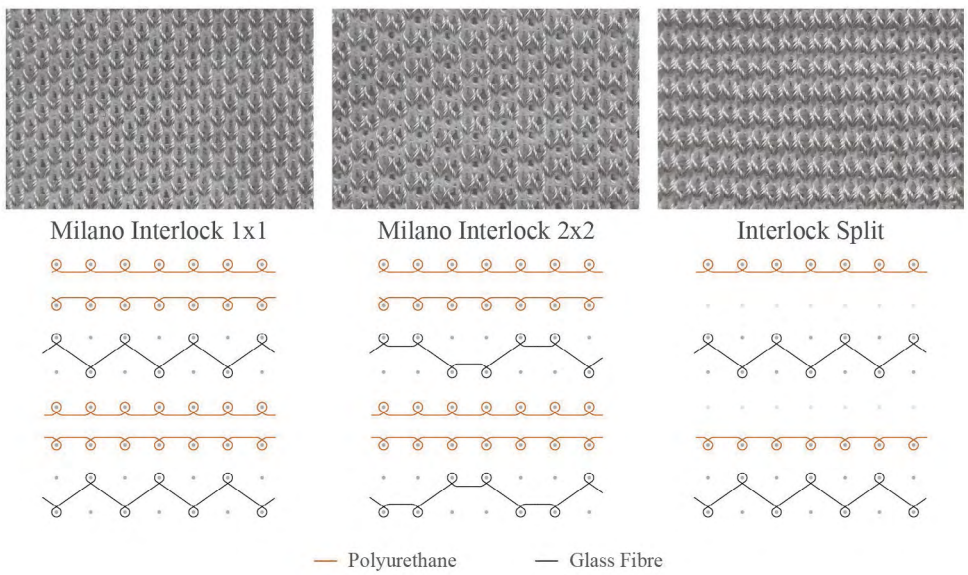


Figure 2: Multi-material *Milano Interlock* Variations and knit notations

Additionally, we characterised each of the patterns by measuring their stitch density (loops/cm) in both the wale-wise (longitudinal) and course-wise (transverse) axes. We also performed uniaxial tensile tests of each of these patterns using the Strip method, ISO-13934-1 standard using the Instron-5943 machine, in the wale-wise (WW) and course-wise (CW) directions. This included specimens made from the GF *Double Jersey* pattern as a form of comparison.

Stitch Pattern	Stitch Density (loops/cm)	
	Wale	Course
Double Jersey *(GF)* [DJ]	8.9	4.0
Milano Interlock 1x1 *(GF-PU)* [M1]	16.7	4.0
Milano Interlock 2x2 *(GF-PU)* [M2]	11.7	4.0
Interlock Split *(GF-PU)* [Split]	9.0	4.0

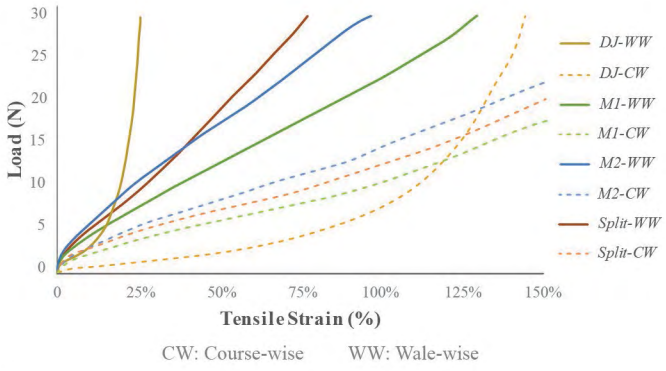


Figure 3: Characterisation and Load-Strain graph of GF & GF-PU patterns

The results from the tensile tests reveal that the GF *Double Jersey* pattern (DJ) has a low initial stiffness but has a steep incline when extended beyond 20% strain in the wale-wise direction and 100% strain in the course-wise direction. In contrast, the GF-PU specimens have a higher initial stiffness but gradually become more linear in their elasticity after being stretched past ~3% strain. This means that these GF-PU patterns can elongate to greater distances without reaching their peak stiffness compared to the GF-only pattern.

4. Designing Multi-Material Textiles

Next, we develop a computational approach to assign PU yarn into designated regions of the primary GF yarn based on input doubly curved geometries. This mapping utilises the GF-PU (*Milano Interlock 1x1*) pattern's greater capacity to stretch than their pure GF (*Double Jersey*) counterpart. The design-to-fabrication process of this multi-material textile is as follows:

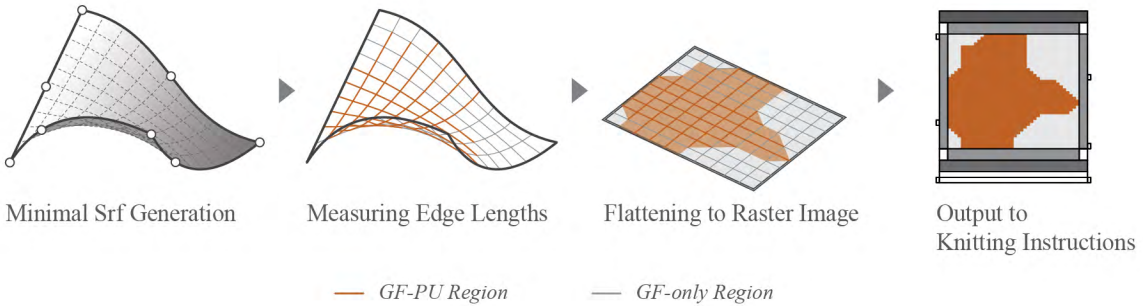


Figure 4: Computational approach to design Multi-Material textiles

1. **Minimal Surface Generation** – Using an input of four boundary curves, a minimal surface is generated by implementing the dynamic relaxation algorithm on a quad-mesh using the Kangaroo plug-in [14].
2. **Measuring Edge Lengths** – The clothed mesh edges are sorted to both course and wale axes and their linear lengths are measured. An initial pretension factor is set, and the mesh is dispatched into regions of GF-only and GF-PU patterns depending on the amount of axial stretch required in each mesh edge.
3. **Flattening to Raster Image** – The mesh is flattened and exported to a 2D raster image, retaining information of the regions of GF-only and GF-PU patterns.
4. **Output to Knitting Instructions** – The raster image is translated into the proprietary software (KnitPaint) using a Python script. It is then developed into machine instructions for the manufacture of the graded knit preform.

4.1 Geometry Input and Fabrication Parameters

We implemented this approach on three non-orthogonal geometries, which we termed as (1) 'Fan', (2) 'Saucer', (3) 'Quarter-Horn'.

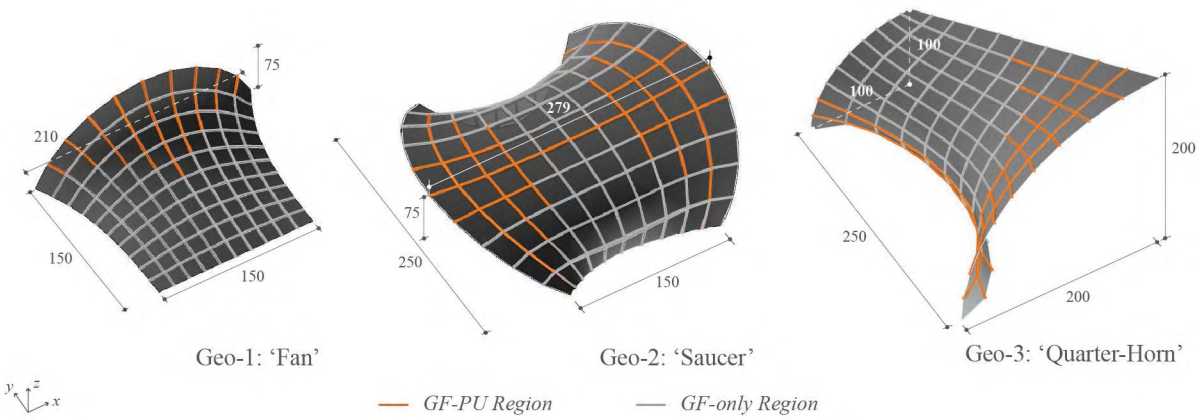


Figure 5: Non-Orthogonal Geometries with assigned material regions

In this study, we scaled down the measured wale-wise axial lengths to 95% and course-wise axial lengths to 80% of their original dimensions to ensure that the textile preform remains in tension after being shaped based on prior resin lamination trials. Subsequently, we referenced the strain percentages from Section 3 and dispatched the clothed mesh edges into different regions. GF-PU *Milano Interlock* pattern consisted of mesh edges that exceeded 120% of the shortest mesh edge in the wale axis, and 200% of the shortest mesh edge in the course axis. The remaining areas adopted the GF *Double Jersey* pattern.

A key consideration when fabricating these multi-material textiles is the change in their physical dimensions resulting from the inclusion of PU yarn in between rows of GF yarn. This change is primarily an increase in the wale-wise direction with a ratio of 3:2, where 3 'stacks' of the GF *Double Jersey* pattern corresponds to the same wale height of 2 'stacks' of the GF-PU *Milano Interlock* pattern. Thus, courses within the textile that have both GF-PU and GF-only patterns would need to be modified to prevent excess of material in the GF-PU pattern region, which might lead to un-tensioned areas after the shaping process.

We implement this through the inclusion of short rows in courses that encounter both GF-PU *Milano Interlock* and GF *Double Jersey* patterns. This entails a separate 'stack' of *Double Jersey* pattern to be knitted in the GF-only areas to even out the difference in wale height for both segments.

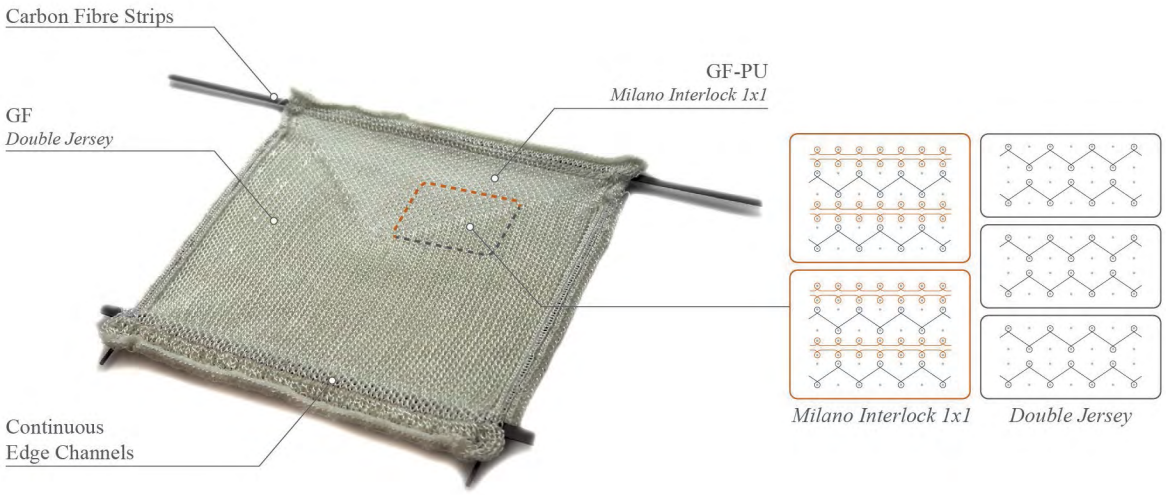


Figure 6: Knitting short rows to equalise the wale heights

Additionally, the use of PU yarns proves to be beneficial when creating the continuous edge channels intended for insertion of the bending-active shaping elements. A *Tubular Jersey* pattern forms these channels with GF yarn knitted on the front needle bed and PU yarn knitted on the back bed. PU yarn improves the grip on the carbon fibre strips to prevent accidental slippage of these members during the shaping process. By using an existing yarn material, this further saves on the number of yarn carriers needed for the manufacture of this multi-material textile preform.

4.2 Textile Shaping and Discussion

The shaping step involves inserting carbon fibre strips along the edge channels along the textile preforms and mounting this assembly upon a custom-made adjustable shaping jig. This jig consists of a network of extruded aluminum rail profiles with MDF laser-cut and 3D printed fixtures. The bending-active carbon fibre strips function as physical manifestations of 'splines' and these can be manipulated by the fixtures which serve as 'control points' positioned along the aluminum rails. As such, these fixtures directly flex the strips and control their curvature in physical space.

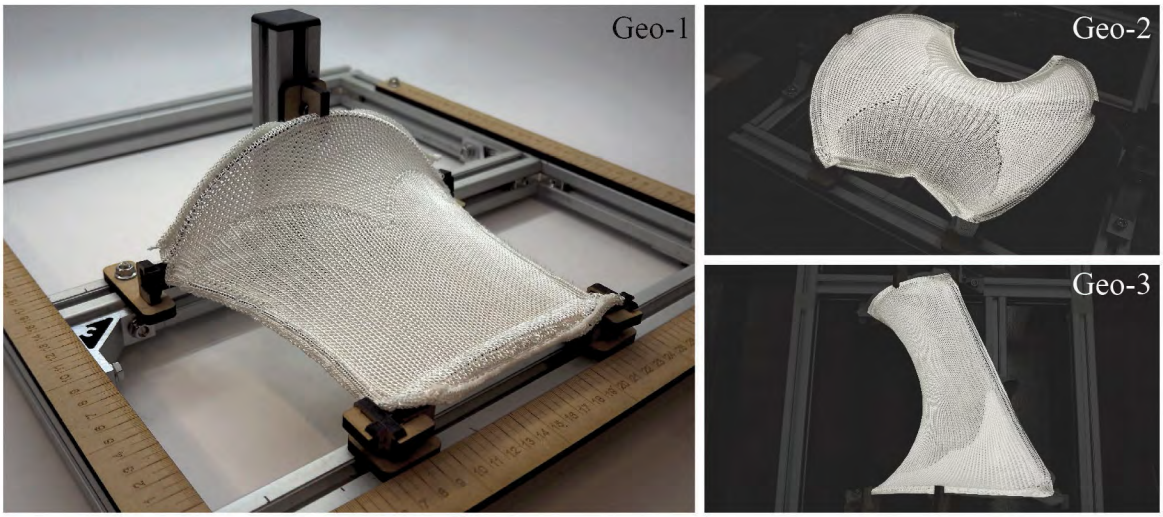


Figure 7: Shaped Graded Textiles

While the symmetrical geometries of 'Fan' and 'Saucer' faced no problems during shaping, the asymmetrical 'Quarter-Horn' geometry was over-tensioned in the course axis and this made it difficult to stretch the geometry to fit the edge strips. The issue could be attributed to referencing the shortest mesh length for the initial dimension when determining the assignment of *Milano Interlock* pattern. The asymmetrical geometry featured a large variation of mesh lengths and our mapping approach resulted in a smaller preform with segments that stretched up to 2.9 times. This led to a proportionate increase of stiffness in the GF-PU pattern, making it a challenge to elongate to fit the boundary conditions. To resolve this, we adjusted the scaling factor course axis from 80% to 90% to ease the shaping process. Thus, it is imperative to limit the maximum amount of stretch experienced by the *Milano Interlock* pattern to prevent too much elongation of the physical textile.

After making the above adjustments, the graded multi-material textiles generally conform well to their respective boundary conditions. The allocation of different yarn materials and stitch patterns further creates a well-tensioned surface to be laminated upon.

5. Conclusion and Future Work

In summary, this paper demonstrates the following:

- Design of multi-material textiles composed from Glass Fibre and Polyurethane yarns to create *Milano Interlock* patterns which feature a higher stretch capacity in both wale-wise and course-wise directions, as compared to the Glass Fibre *Double Jersey* pattern;
- Development and implementation of a computational approach to assign different regions of GF-PU *Milano Interlock* and GF *Double Jersey* patterns based on axial stretch within several non-orthogonal doubly curved geometries.

Future work includes broadening the geometric vocabulary of the shaped textiles to include more complex curved edge conditions, as well as geometries with under-cuts to be done at larger scales. Additionally, there are plans to design for connectivity between each composite panel. This could tap upon the textile-to-textile joining methods to assemble the panels and form a larger continuous surface geometry.

Acknowledgements

This research is supported by the Computational Framework for Functional Textiles project funded by SUTD Digital Manufacturing and Design (DManD) Centre, supported by the Singapore National Research Foundation. The main author would like to extend my gratitude to his advisors, Prof. Sawako Kaijima and Dr. Erwin Viray, for their guidance and mentorship in this thesis. Special thanks to Dr. Oliver Weeger and Prof. Kenneth Tracy for their advice in this segment of the research.

References

[1] Stage One Limited, "Case Study: Chanel – Exhibition Pavilion", 2009.

[2] S. Ahlquist, J. Lienhard, J. Knippers and A. Menges. "Exploring Material Recirpocities for Textile-Hybrid Systems as Spatial Structures," in *Prototyping architecture: The Conference Paper*, pp. 187-210.

[3] J. Lienhard, J. Knippers and A. Menges. "Extending the functional and formal vocabulary of tensile membrane structures through the interaction with bending-active elements vocabulary of tensile membrane structures elements," in *[RE]THINKING Lightweight Structures, Proceedings of Tensinet Symposium, 2013*, pp. 109-118.

[4] Y.Y. Tan and T. L. Lee. "Knit Preform Shaping: Design of Textile Preform and Edge-shaping mechanism for curved composite panel formation," in *Proceedings of the 24th International Conference of the Association for Computer-Aided Architectural Design Research in Asia (CAADRIA) 2019, Wellington: New Zealand, 15-18 April 2019*, vol. 1, pp. 43-52.

[5] Y. Miyamoto, W.A. Kaysser, B.H. Rabin, A. Kawasaki and R.G. Ford. *Functionally Graded Materials: Design, Processing and Applications.* US: Springer Science+Business Media, 1999.

[6] M. Popescu, M. Rippmann, A. Liew, T. Van Mele and P. Block. "Concrete shell built using a cable-net and knitted formwork," in *DETAIL structure*, vol. 1, pp 10-11, 2019.

[7] M. Popescu, L. Reiter, A. Liew, T. Van Mele, R. J. Flatt and P. Block. "Building in concrete with an ultra-lightweight knitted stay-in-place formwork: Prototype of a concrete shell bridge," in *Structures*, vol. 14, pp 322 – 332, June 2018.

[8] Y. Liu, L. Li, P. F. Yuan. "A Computational Approach for Knitting 3D Composites Preforms," in *Proceedings of the 2019 DigitalFUTURES. CDRF 2019.* pp 232 – 246, 2019.

[9] M. Tamke, A. Deleuran, C. Gengnagel, M. Schmeck, R. Cavalho, R. Fangueiro, F. Monteiro, N. Stranghoner, J. Uhlemann, T. H. Homm and M. Ramsgaard Thomsen, "Designing CNC Knit for Hybrid Membrane and Bending Active Structures," in *Structural Membranes 2015, Barcelona, Spain.*

[10] R. La Magna, V. Fragkia, P. Langst, J. Lienhard, R. Noel, Y. Sinke Baranovskaya, M. Tamke and M. Ramsgaard Thomsen, "Isoropia: an Encompassing Approach for the Design, Analysis and Form-Finding of Bending-Active Textile Hybrids," in *Creativity in Structural Design: Proceedings of the IASS Annual Symposium 2018*, Boston, USA, July 16-20, 2018.

[11] S. Sharmin and S. Ahlquist. "Knit Architecture: Exploration of Hybrid Textile Composites Through the Activation of Integrated Material Behaviour," in *Proceedings of ACADIA 2016: Posthuman Frontiers, Michigan, USA,* pp. 254-259.

[12] R. Chattopadhya. "Introduction: Types of Technical Yarns", in *Technical Textile Yarns.* UK: Woodhead Publish Limited, 2010.

[13] Shima Seiki, *Shima Seiki CNC Knitting*, 2019.

[14] D. Piker, Kanagaroo 2.0, 2015.

Proceedings of the IASS Annual Symposium 2019 – Structural Membranes 2019
Form and Force
7 – 10 October 2019, Barcelona, Spain
C. Lázaro, K.-U. Bletzinger, E. Oñate (eds.)

Structural optimization of coreless filament wound components connection system through orientation of anchor points in the winding frames

Marta GIL PÉREZ[a], Niccolò DAMBROSIO*, Bas RONGEN[a], Achim MENGES, Jan KNIPPERS[a]

* Institute for Computational Design and Construction (ICD)
Keplerstrasse 11, University of Stuttgart
niccolo.dambrosio@icd.uni-stuttgart.de

[a] Institute of Building Structures and Structural Design (ITKE), University of Stuttgart

Abstract

Coreless filament winding is a technique where glass and carbon fibre filaments impregnated with epoxy resin are wound freely between two rotating winding scaffolds by a robotic arm. The load induction in the connections of coreless filament FRP components is one of the major challenges when designing with this novel structural system. An efficient fibre layup requires the fibre bundles to be aligned in the direction of the load, taking full advantage of the anisotropic characteristics of the material. In previous research pavilions developed at the University of Stuttgart, the direction of the fibres in proximity of the anchor points was mainly dictated by fabrication constraints (geometry of winding frame). The purpose of this research is to structurally improve the capacity of the connection system in fibrous building components. Load induction in several test specimens, representing different angles of incidence between fibres and winding frames, was investigated under tension and compression forces. Consequently, a computational tool was developed to generate winding frame geometries and optimal orientations of the winding pins (which allow fibres to lay in the direction of the load), and utilised to inform the fabrication setup for the prototyping and production of the components of the Bundesgartenschau 2019 Fibre Pavilion.

Keywords: optimization, frp structures, connection, anisotropic material, test design, computational design.

1. Introduction



Figure 1: BUGA fibre pavilion (left) and one of its components' robotic fabrication setup (right)

This research had the aim to improve the connection design of the BUGA fibre pavilion (Figure 1 left). The pavilion's main load bearing structure, with an ETFE membrane façade on top, is composed of 60 different glass and carbon fibre components wound robotically between frames as shown in the

Copyright © 2019 by Marta GIL PÉREZ, Niccolò DAMBROSIO, Bas RONGEN, Achim MENGES, Jan KNIPPERS
Published by the International Association for Shell and Spatial Structures (IASS) with permission.

fabrication setup of Figure 1 (right). The coreless filament winding technique employs the use of winding frames equipped with winding pins (anchor points) for the fabrication of FRP building elements. The shape of the component gradually emerges from the interaction of the freely spanning fibres as they are progressively hooked around the winding pins by a robotic arm. The winding pins are built in the frame with aluminium sleeves, which remain embedded in the structure after removing the scaffolds, providing a space for bolted connections between components (Figure 2 left). In previously realized coreless filament wound structures [1] [2] the direction of the winding pins on the frame was never considered as a parameter that could be varied in order to improve the overall structural performance of the FRP building element. Depending on the orientation of the winding pin and on the geometry of the winding frame, collisions between the fibres and the edges of the winding frame during the fabrication process generated uncontrolled thinning of the fibre bundles' sections and abrupt deviations of the fibres from the desired direction, creating major structural weaknesses in the finished element. This paper illustrates the design and development of a simplified specimen test that demonstrates how the connections structural capacity of the FRP components can be improved by changing the orientation of the winding pins.

1.1. Overview of previous coreless wound FRP structures connections

In previous FRP structures designed by ICD and ITKE the winding pins and aluminium sleeves were mounted on a frame to keep their directions almost exclusively parallel to each other. Once the cured element was demoulded the embedded sleeves left by the winding pins could be used to join the fibre elements together by means of mechanical fasteners (bolt-nut system) (Figure 2 left and centre). If on the one hand this strategy allowed for an easy bolted connection, on the other hand it created critically weak areas in the component as the fibres had to wrap around the frame during the winding process, drastically reducing their section and deviating from the direction of the load. The first iteration made during the prototyping phase of the BUGA fibre pavilion followed the previous research pavilions' approach by situating the winding anchors in the back of the winding frame as shown in Figure 2 (right), resulting in an extreme kink between the fibres and the pin connection.

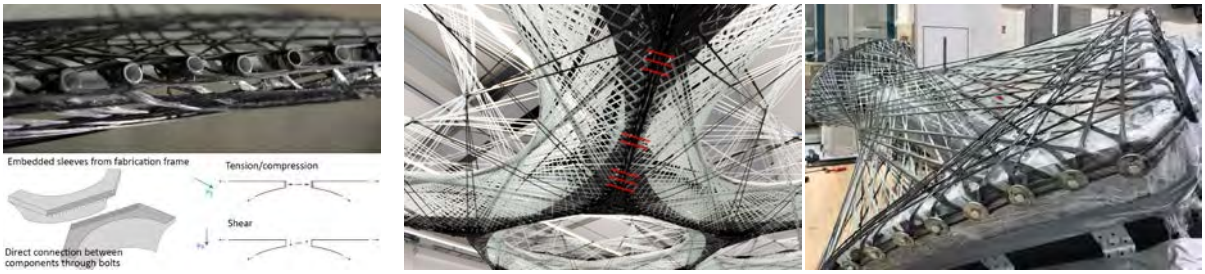


Figure 2: Embedded sleeves from fabrication frame (left) and connection between components (center) at the Elytra Filament Pavilion (Victoria and Albert Museum, London, 2006), and first iteration of the BUGA Pavilion winding frame (right)

1.2. Investigation of the different angles in the BUGA pavilion components

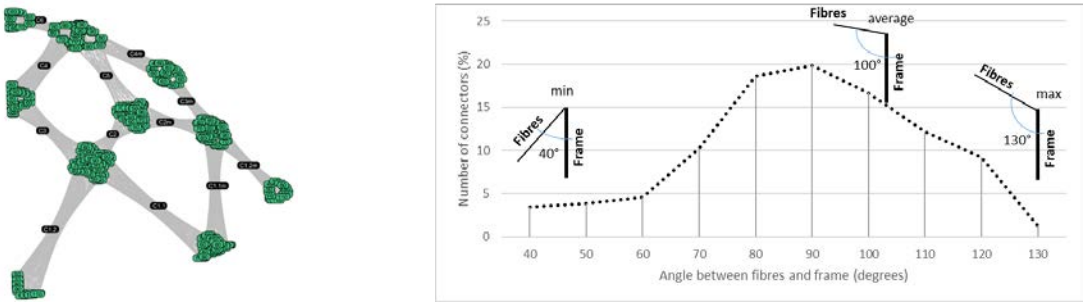


Figure 3: Angle investigation of the components of the BUGA pavilion (left) and percentage of angles (in degrees) between fibres and frame (right)

An initial investigation was made to determine the different fibre incidence angles in the BUGA pavilion components. This survey showed that on average, the fibres approach the winding frame with 100°, with extreme angle cases of 40° as a minimum and 130° as a maximum as shown in Figure 3. These values served as an initial assumption for the connection capacity investigation described in this paper.

2. Connection specimen test set up design

The objective of the test is to investigate the load induction into fibre bundles through steel connectors for coreless winding fibre structures when the angles between fibres and fabrication frame are at a minimum or maximum.

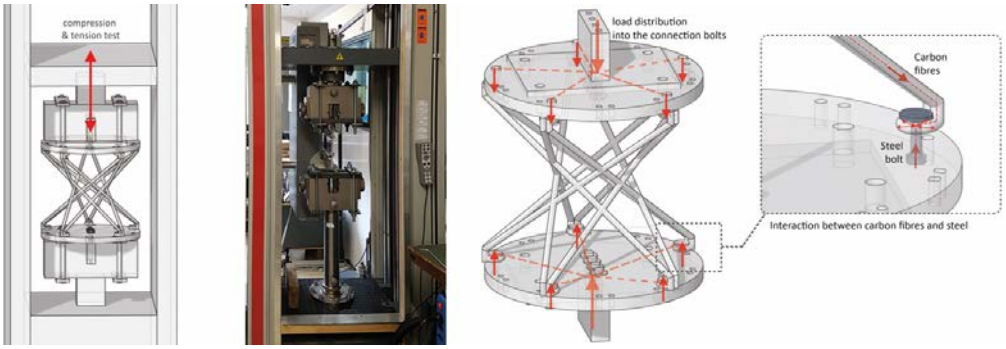


Figure 4: Test concept and setup representation for the 40° angle specimen

2.1. Test setup description

The test setup uses a Zwick Roel – Z100 machine capable of inducing a maximum of 100kN in both tension and compression. The specimen and the setup, represented in Figure 4, are designed to fit into the machine brackets through a steel plate that distributes the loads into a set of connectors attached to the carbon fibre sample structures. Two different specimens are investigated, representing the extreme angles between frame and fibres (40° and 130° as described in the previous section) to determine the load induction and interaction at the connection.

2.2. Specimen design and load assumptions

In order to design the specimen and to study the capacity of the connection, the fibre syntax of the specimen was designed to withstand in buckling more than the possible applied force. With this aim, two FEM models without imperfections were analysed to obtain the first eigenvalue-buckling load given the geometry and assumptions described in Figure 5. The specimen with the 40° fibre arrangement had a buckling failure load of 188kN, while the specimen with 130° angles could withstand 192kN in buckling. Assuming an even distribution of forces and a capacity of about 15kN in each of the M8 bolts in the connections, the target load of the test would be 75kN. This is less than half of the buckling failure load in both cases.

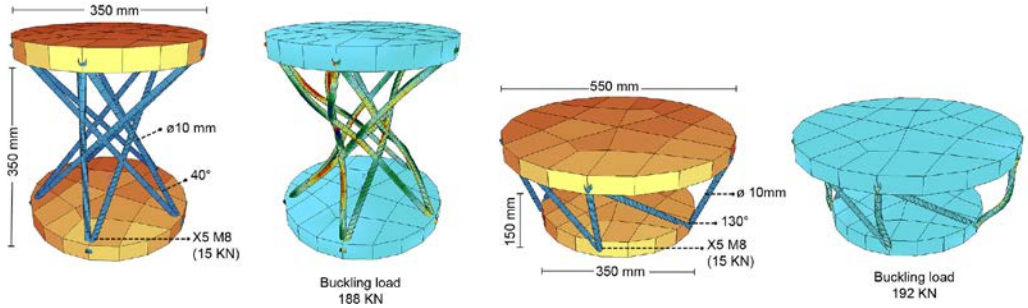


Figure 5: FEM models of the specimens and its first eigenvalue calculated buckling load representing the minimum (left) and maximum (right) angles between fibres and frame

2.3. Specimen robotic fabrication

To keep the quality of the specimen constant, an automated fabrication setup was implemented. The specimens were fabricated in a seven-axes robotic setup consisting of a standard industrial six-axes robotic arm and an external one-axis positioner where the winding frame was fixed. The fibres were impregnated with resin during the winding process by pulling them through a resin bath. A custom made nozzle, mounted on the robot flange as end-effector, was used to place the fibres on the winding frame.

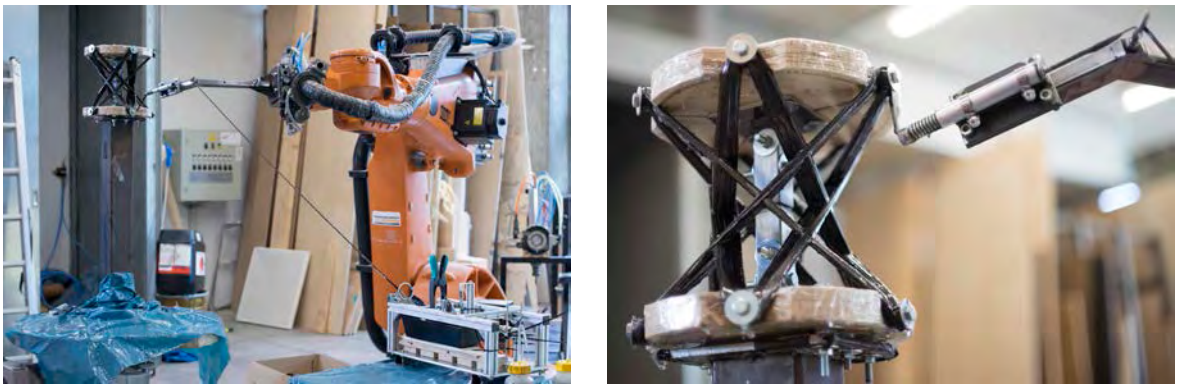


Figure 6: Specimen robotic fabrication

3. Test iterations and results

To simplify the comparison of the results, only the design iterations of the 40° angle test specimen is explained through section 3.1 to 3.3 under the most relevant loading condition, compression. In section 3.4, the results of the 130° specimen are also compared for its final iteration.

3.1. First iteration

For the first iteration, the most unfavourable situation is represented, following the application of the winding frame pin direction of previous projects into the current component frame as explained in section 1.1 and Figure 2 (right). Thus, the pins are situated at the back of the frame and during fabrication the fibres lay at the edge of the frame to hook around the winding anchor. Although this allows a direct connection utilizing a single bolt in the location where the winding pin was, it also creates a double kink caused by the shape of the frame after it is removed (Figure 7).

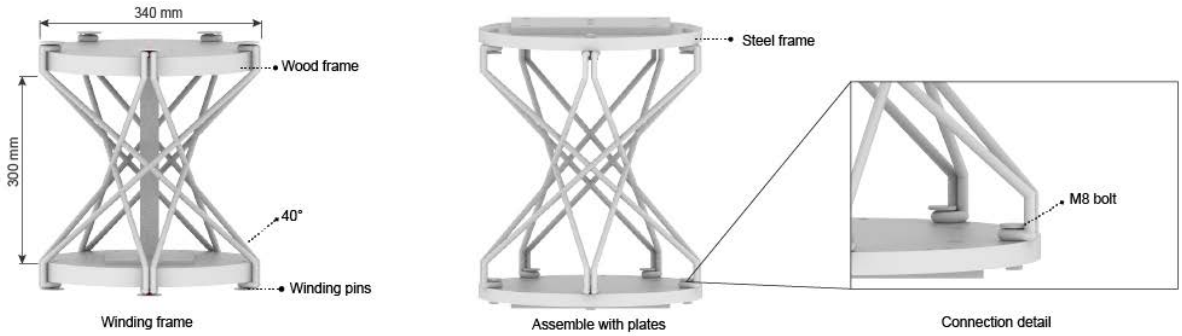


Figure 7: First iteration specimen design

3.1.1. Results and findings

Figure 8 shows the setup and the results of the compression test. The graph on the right side of the figure represents the failure of the specimen with a maximum load of 9.8kN for a deformation of 14.1mm. It can be seen how most of the deformation occurs around the upper kinks of the fibres, since the geometry at this point is not strong enough to transfer the forces and the fibres break under bending at the upper part of the frame.



Figure 8 First iteration results

3.2. Second iteration

To avoid the behaviour which occurred in the first iteration, the winding pins are located this time in the side of the frame as a simple adjustment (Figure 9). The geometric proportions of the specimen are adjusted to keep the same angle of 40° between fibres and frame, and an additional standard L-shape steel piece is introduced for the connection to transfer the loads from the newly designed winding pin, perpendicular to the side of the frame, to the test connection point at the steel frame.

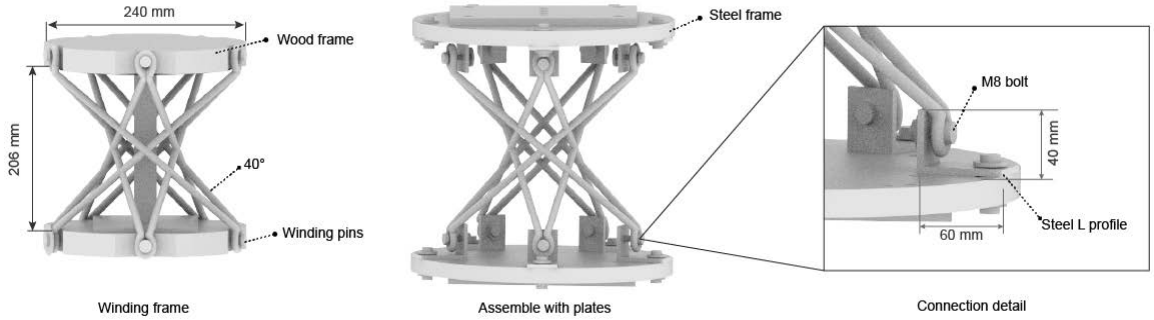


Figure 9: Second iteration specimen design



Figure 10: Second iteration results

3.2.1. Results and findings

The results of the second iteration under compression loads are represented in Figure 10. Here it can be seen how the capacity of the connection is greatly improved by achieving a failure force of 37.6kN for a deformation of 20.5mm. During the test the whole geometry was activated, and the deformation was appreciated evenly distributed along the specimen height. The failure was produced at the bottom of the

specimen where the fibres were touching the steel L profile edge due to friction and bending at this point.

3.3. Third iteration

The two previous iterations showed that the geometry around the winding points is crucial and have a great influence in the transfer of the loads. For that reason, the third iteration is a much more customized design where the winding frame is fabricated following the inclination angle of the fibres allowing the winding pin to be installed perpendicular to the direction of the fibres. In the same way, the steel connector is designed to fit the same geometry as shown in Figure 11.

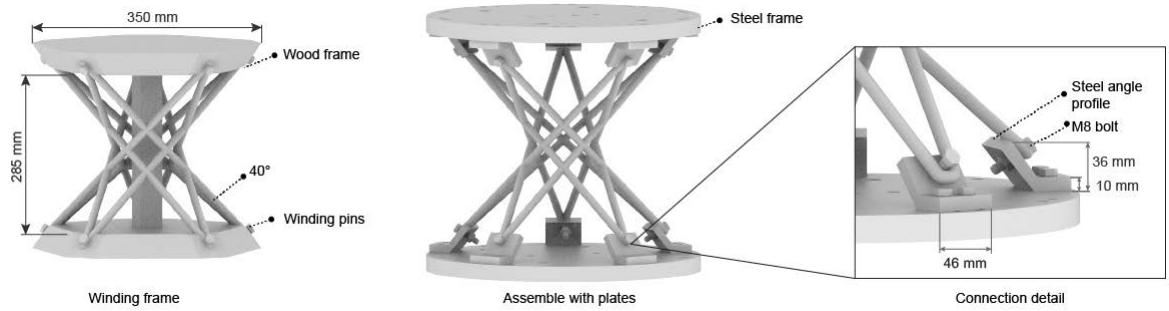


Figure 11: Third iteration specimen design

3.3.1. Results and findings

The results shown in Figure 12 represent the failure of the specimen at 80.6kN with a deformation of 18.8mm. In this iteration, the behaviour of the specimen is similar to the previous one, with an evenly distributed deformation, and the maximum load is achieved at a similar displacement (with just a deviation of 1.7mm). In this case, however, the failure is not produced with the interaction of the steel in bending but at the location where the fibres reach the winding pin in shear, as shown in the middle image of Figure 12.

.



Figure 12: Third iteration results

3.4. Result comparison

Figure 13 represents the result comparison for the three iterations of the 40° specimen. The results show a great improvement in the capacity of the specimen. By achieving a load of 80.6kN at the last iteration, the equivalent capacity of one of the connections is about 20kN, which is higher than the design resistance of the M8 bolt in shear. Therefore, this relationship between the amount of material and bolt size could be used for future connection designs when the angle between fibres and winding frame is eliminated.

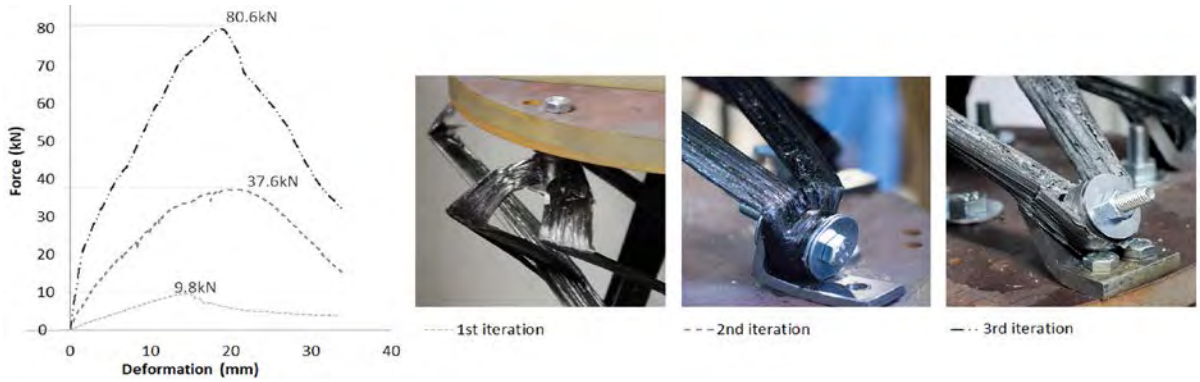


Figure 13: Results comparison for all the iterations of the 40° specimen

In addition, in Figure 14 it can be seen how the maximum load induced for the third iteration of the specimen with 130° is very similar of the ones for the 40° specimen (with just a deviation of 2.4kN which can be originated due to fabrication reasons). These results demonstrate that independently of the geometry and the behaviour of the specimen, the structural capacity is equivalent when using this connection approach where fibres are orientated in the direction of the load.



Figure 14: Results comparison for the third iteration of 40° specimen and 130° specimen

4. Implementation of the design in the BUGA fibre pavilion

This section explains the application of the test findings into the design of the BUGA fibre pavilion.

4.1. Computational tool development



Figure 15: Pin orientation implementation in coreless filament winding frame of the BUGA fibre pavilion

A computational design tool was developed with the purpose of calculating the incidence angle of the fibres with the winding frame and define the optimal orientation of the winding pin. The dihedral angle between the plane containing the component profile curve and the best fitting plane containing all the

digitally simulated fibres converging in one winding pin was calculated for each anchor point. In a second step, for fabrication reasons, the best fitting planes' inclinations were then adjusted to the next value multiple of ten (e.g. 21° becoming 30°). The normal of the adjusted best fitting plane was then used to define the direction of the winding pin. As a result, all the winding pins were mostly normal (with a deviation of max 9°) to the simulated surface of the building element (Figure 15).

4.2. Connection detail of the BUGA components

As a side effect, the holes left in the components once demoulded never have parallel axes. Therefore, an innovative component-component connection system which mediated between two non-parallel edges needed to be developed (Figure 16). To create a planar interface that would allow one component to connect to its neighbours, custom-made steel L-connectors were introduced. The steel L-connectors are characterized by the angle between their two faces: it varies from 40° to 90° in incremental steps of 10°, depending on their location along the edge of the element. Once mounted on the edge of the building component, the vertical faces of the L-connectors formed the required planar interface, and will point outwards allowing for an easy bolted connection to the neighbouring elements.

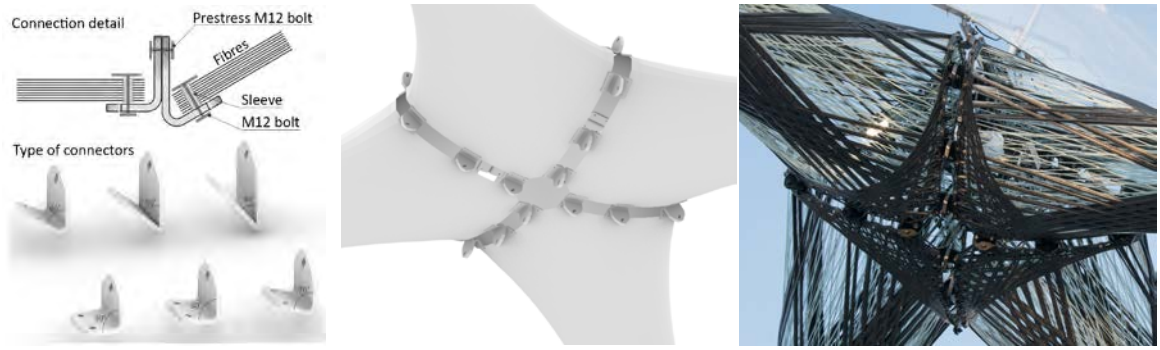


Figure 16: Connection detail and steel L-connectors types (left), 3D of the location of the connections in one node (centre) and constructed components node (right) of the BUGA fibre pavilion

5. Conclusion

This research showed the importance of the connection design for coreless winding FRP structures. As a conclusion from the test iterations, the reduction or elimination of the angle between fibres and winding frame needs to be pursued. For the design of large components and complex geometries this approach will result in a customized design that will require the implementation of computational tools as in the case of the BUGA fibre pavilion. With the help of these tools it was demonstrated that the connection can be optimized both in terms of fabrication and structurally, increasing the performance of the FRP components.

Acknowledgements

The authors would like to express their gratitude to the entire scientific development and robotic fabrication team, including students and support staff, who helped to complete this project. The research has been partially supported by the Deutsche Forschungsgemeinschaft (DFG, German Research Foundation) under Germany´s Excellence Strategy – EXC 2120/1 – 390831618.

References

[1] S. Parascho, J. Knippers, M. Dörstelmann, M. Prado, and A. Menges, "Modular Fibrous Morphologies: Computational Design, Simulation and Fabrication of Differentiated Fibre Composite Building Components", Advances in Architectural Geometry 2014, pp. 29–45, 2014.

[2] M. Prado, M. Dörstelmann, A. Menges, J. Solly, and J. Knippers, "Elytra Filament Pavilion: Robotic Filament Winding for Structural Composite Building Systems", Fabricate 2017, pp. 224–231, 2017.

Proceedings of the IASS Annual Symposium 2019 – Structural Membranes 2019
Form and Force
7 – 10 October 2019, Barcelona, Spain
C. Lázaro, K.-U. Bletzinger, E. Oñate (eds.)

A vaulted multi-storey concrete floor system without external ties, a structural analysis

Frank OMLOO

Catena Beton BV
aan de Fremme 62B, 6269BE Margraten, NL
frank.omloo@catenabeton.nl

Abstract

Vaulted structures are characterised by their high structural efficiency. On the downside, however, they produce a horizontal thrust, which either calls for tension ties or otherwise calls for buttresses. For a basement construction this doesn't pose much of a problem, but for a multi-storey building either solution could be undesirable. This paper examines if there is a third solution to the horizontal thrust problem and apply it to a multi-storey office building. The design is composed of bending stiff columns in combination with a thin concrete slab on top of the vault, which functions as a passable office floor and also contains the tie rods which support the columns. Tension ties underneath the vault can be avoided that way, which is more aesthetic and practical. We will investigate this conceptual design through the elaboration of a square groin vault with a ground plan of 7m. Of special interest is the junction of column, vault and concrete slab, which sits on top of the vault. A preliminary calculation of this design shows that a vault, supported on four bending stiff columns, is a stable and a safe structural building assembly.

Keywords: vault, office building, multi-storey, concrete shell, cross vault.

1. Introduction

A load-bearing vaulted floor or roof construction develops a thrust vector that, either must be absorbed by buttresses, or by tie rods. Buttresses are laborious constructions, using lot's of ground space and requiring a bulk of material. Tie rods underneath a vault are more efficient but architecturally not always desirable [1], [2].



Figure 1: Design of a vaulted floor system without ties underneath the vault.

In this article we will examine whether there may be a third way for stabilising the thrust loads. We will use the columns to transfer the thrust load to the level of the "keystone" of the vault before tying

Copyright © 2019 by Frank Omloo
Published by the International Association for Shell and Spatial Structures (IASS) with permission.

these loads with rods. Therefor the columns need to be bending stiff and capable of transferring shear forces along their longitudinal axis. Figure 2 shows the simple mechanical principle that we are exploring.

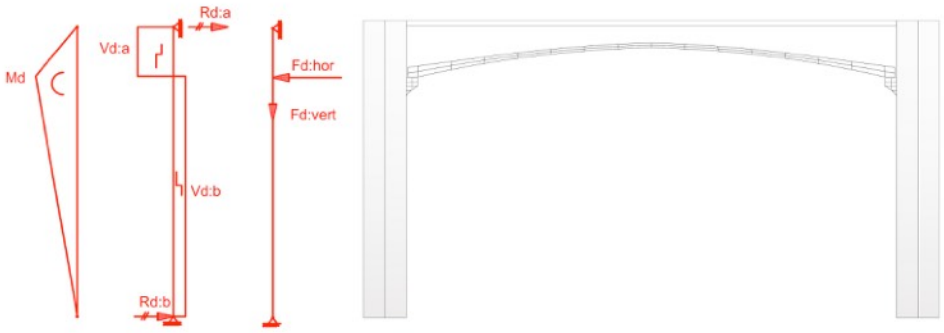


Figure 2: Mechanical principle of floor system, supports are provided by tie rods.

Because a vault is not accessible, we will have to lay a level floor on top of it. The tie rods, which function as the supports for the columns, can therefore be incorporated into this floor without little practical implications. The void between vault and floor will be filled with a light weight material which will uniformly transfer the dead and live loads to the vault.

2. Design

We will examine a square groin vault with a span of 7m. The rise of the vault is 0.65m. See also figures 3 and 4.

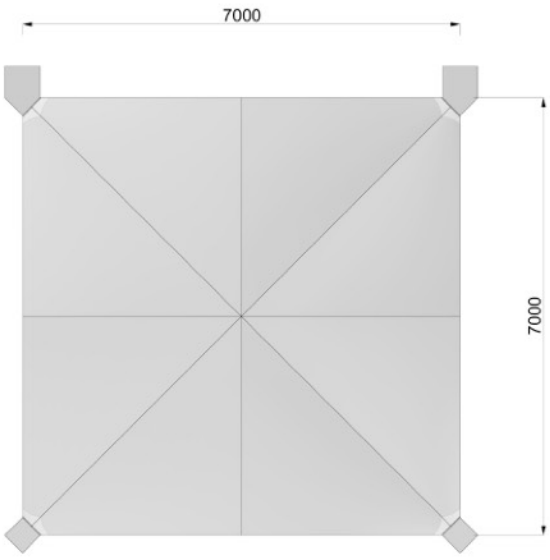


Figure 3: Main dimensions and groins of vault

The catenary of the thrust vector is calculated using graphical statics and is thus determinative for the envelope of the shell [3]. The safety of the structure is defined by the margin of the catenary of the thrust vector with respect to the lower and upper envelope of the shell [4]. Thus, the shell needs a certain thickness to provide for enough safety margin for other load cases, which differ from the initial assumed uniform distributed load.

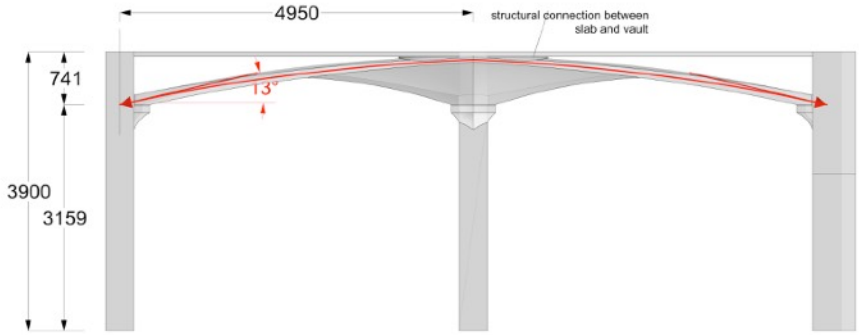


Figure 4: Cross-section along the diagonal groin, showing also the catenary curve

2.1. Non-uniform loads

The Achilles heel of a vault is its sensitivity to a configuration of a loads, other than the initial design configuration, in our case, a uniform distributed load. A dead load is not expected to change, but a live load may vary in time and may not always be present or uniformly distributed on the vault (figure 5). The changing catenaries should all be well within the envelope of the shell.

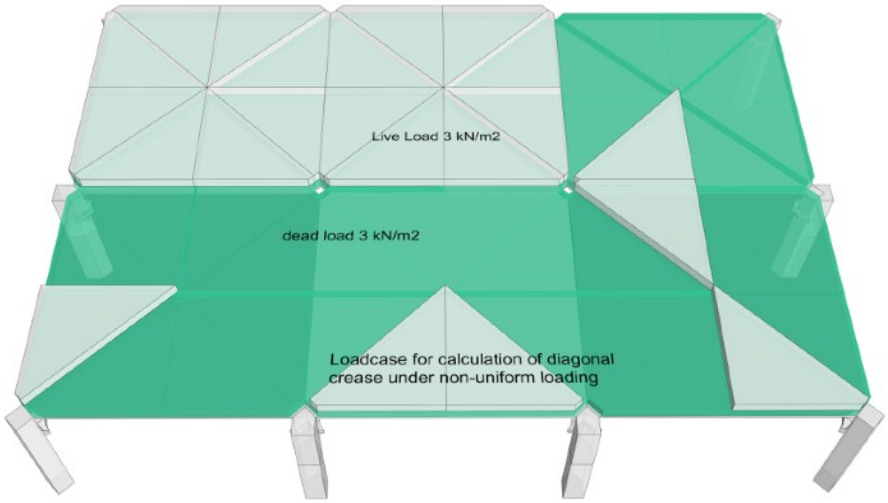


Figure 5: Loading of floor and some possible distributions for the live load

2.2. Imbalance of horizontal thrust loads on the diagonal groin

Figure 9 shows the components of the thrust vectors from the adjacent field segments upon the main diagonal groin. The horizontal component of this vector, the one which is perpendicular to the groin,

leaves no resultant load on the groin, because it is contra-balanced by a component from the opposite field with the same size. However, if on one side of the groin these loads are absent, this equilibrium falls apart. The groin will be pushed aside. The diagonals are initially not equipped for this sidewise loading.
That's why we have opted for a relatively flat design for the vault. This creates a straight beam within the thickness of the shell's envelope (figure 6). The incorporated beam is supported at its both ends. The lower support is established by the column and the second support is established by the level floor at around the "keystone" of the vault. As a result we will have to establish a structural connection between vault and floor (see also figure 6). The floor will be loaded in its plane, something this floor is particularly well equipped for.

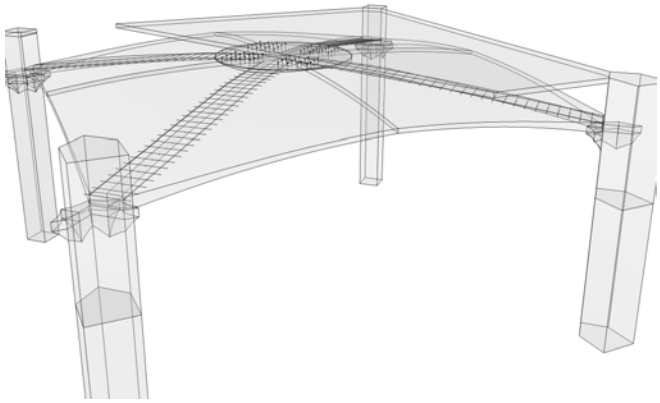


Figure 6: Incorporated beam with reinforcement at the groin and the connection to the slab with dowels.

3. Dimensions

We will check the structural feasibility of a few crucial components in the system. We will not explicitly show the calculation of the vault's envelope. We did check it through the method of graphic statics by William Wolfe [3] and adapted the envelope according a variety of load cases according figure 5. In all cases, the thrust vector is within the envelope of the shell. In the following paragraphs we will calculate the cross-sectional forces of the edge columns and the incorporated beam of the groin.

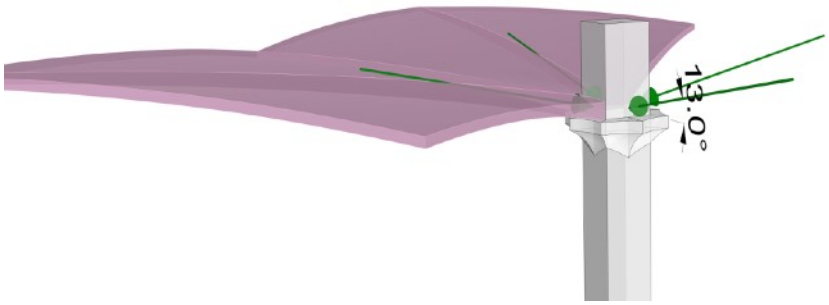


Figure 7: Angle of inclination of the main diagonal groins at their supporting point on the column.

3.1. Edge Columns

In contrast to the centre columns, the edge columns are constantly subjected to thrust loads, just like the buttresses of a classical vault. We must therefore calculate these columns with partial safety factors in place. The ultimate load case for the edge column is a fully loaded vault. We opt for partial factors of 1.2 for the dead loads and 1.5 for the live loads. The vertical load on the edge column from one diagonal groin equals:

$$F_{d:\,vert} = 3.5m \times 3.5m \times (3.0\ kN/m^2 \times \cos 45^\circ\ 1.2 + 3.0\ kN/m^2 \times 1.5) = 99\ kN$$

The angle at which the thrust lines arrive is 13º relative to a horizontal plane (see figure 7). So the horizontal component is:

$$F_{d:thrust} = 99\ kN / \sin 13^\circ = 440\ kN$$

The resulting horizontal load out of two groins is:

$$F_{d:\,hor} = 2 \times 440\ kN \times \cos 45^\circ = 622\ kN$$

The total height of the columns is 3.9m, the moment of bending is thus:

$$M_d = 622\ kN \times 3.16m \times 0.74m / 3.9m = 372\ kNm \text{ (see figure 2)}$$

The resulting tensile force in the tie rods is:

$$R_{d:\,tie:a} = 622\ kN \times 3.16\ m / 3.9\ m = 504\ kN \text{ (see figure 2)}$$
$$R_{d:\,tie:b} = 622\ kN - 504\ kN = 118\ kN \text{ (see figure 2)}$$

The tensile force for each set of ties under an angle of 45º is:

$$F_{d:\,tie} = 622\ kN / \cos 45^\circ / 2 = 439\ kN$$

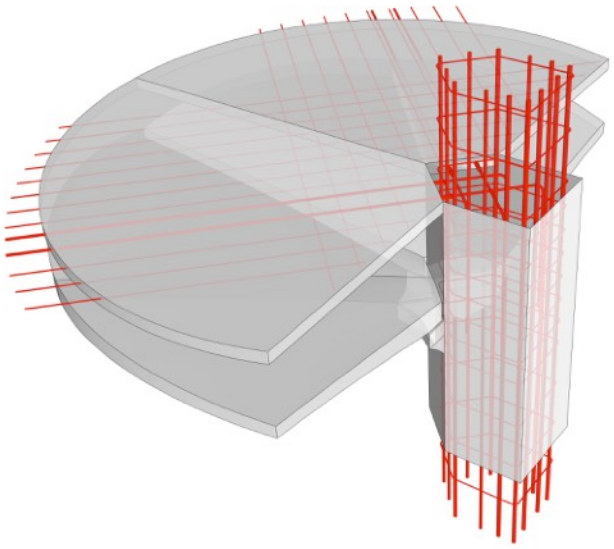


Figure 8: Tie rods, bending force and shear force reinforcement at the junction of vault, column and slab.

3.2. Middle Columns

If one or more vaults are failing due to a catastrophic overloading, the remaining floors and columns should maintain their structural integrity. So the middle columns should resist the thrust loads of the remaining vaults. Because this is a special case of loading, the partial factors may be set to 1.

3.3. Checkerboard

The live loads are not always present or they might not uniformly (see also paragraph 2.1), which will leads to a non-symmetrical loading of the diagonal groins of the vault. Figure 9 gives a decomposition of these thrust vectors. These vectors differ along the diagonal groin according the varying angle of inclination of the segments. These vectors can be decomposed into three components, namely, a vertical component, a horizontal component, parallel to the groin, and a horizontal component perpendicular to the groin. Normally, if the entire vault is subject to an equally large uniform load, the latter doesn't result in a load on the groin because components out of the opposite fields cancel each other out. However, if the opposite fields remain unloaded, this is not the case.
The curvature of the vault is relatively flat. As a result, a beam element has been created within the envelope of the shell, which coincides with the diagonal groin (see also figure 6). We will use this element for its bending capacity and for transferring these horizontal loads to the column and to the top floor.

A uniform load applied to one-fourth of the vault section will maximise the unfavourable effect on the diagonal groin. With a live load of 3 kN/m² and partial safety of 1.5, the total vertical load for each diagonal groin is:

$$F_{d:\,vert} = 7m \times 7m / 4 / 2 \times 3kN/m^2 \times 1.5 = 27\ kN$$

This load is triangularly distributed over the main diagonal groin from bottom to top.

$$Q_{d:\,vert:\,a} = 27\ kN \times 2 / 4.95m = 11\ kN/m$$
$$Q_{d:\,vert:\,b} = 0\ kN$$

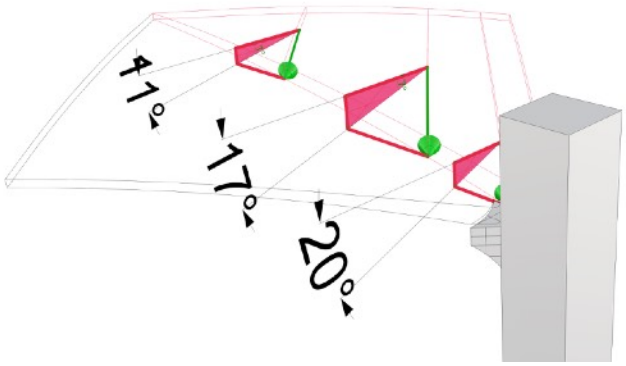


Figure 9: the angle of inclination of the catenaries from the adjacent fields.

The size of the horizontal component perpendicular to the plane of the diagonal can be calculated as a fraction of the vertical component (see figure 9). We take an angle of 20.4° as representative of the value of $Q_{d:\,vert:\,a}$ (near the column) and we will assume that the intermediate values can be linearly interpolated.

$Q_{d:\,horz:\,a}$ = 11 kN/m / tan 20.4º = 30 kN/m
$Q_{d:\,horz:\,b}$ = 0 kN/m / tan 11º = 0 kN/m

With a triangular load from 30kN/m down to 0 kN/m the cross-sectional forces are:

$M_{d:\,c}$ = 30 kN / m × 4.94^2 m / 15.6 = 46.9 kNm
$V_{d:\,a}$ = 30 kN / m × 4.94 m / 3 = 49.4 kN
$V_{d:\,b}$ = 30 kN / m × 4.94 m / 6 = 24.7 kN

The dimensions of the incorporated beam are 400 mm × 75 mm . The required reinforcement for the bending reinforcement is then:

$A_{s:\,bend}$ = 46.9 kNm × 10^6 / 400 / 435 = 269 mm^2
$A_{s:\,shear}$ = 49.4 kN × 10^3 / 435 / 400 = 0.28 mm^2 / mm

4. Conclusion

The proposed construction is feasible. It might be interesting to investigate more and different floor plans for this type of structure, for example a polygonal floor plan. This would introduce more groins per vault which would reduce the magnitude of the thrust vector and opens the way to larger floor spans.
The incorporated beam, which coincides with the groins, seems a practical component for balancing for non-uniform sidewise loading of the groins. Its width and thickness can be easily adapted to different load cases and to different envelopes with respect to different catenaries.

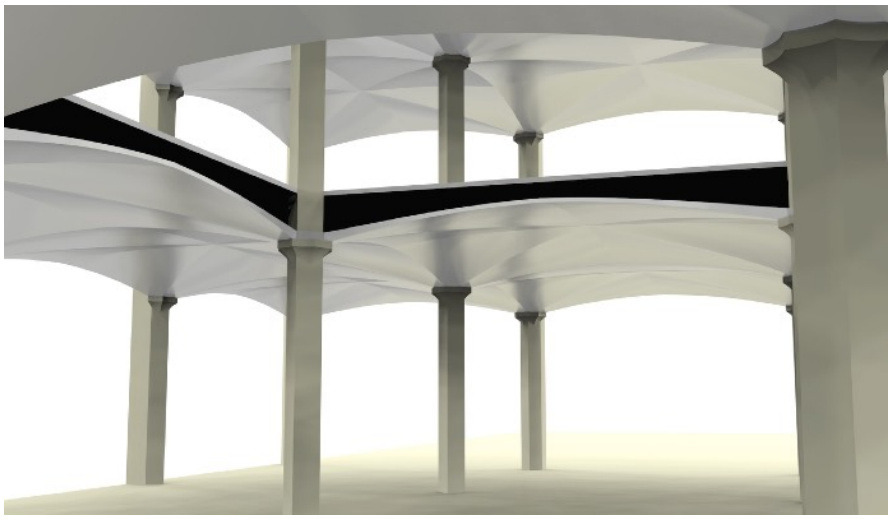


Figure 10: Multi-storey office building with groin vaults

References

1 W. Hawkins, J. Orr, T. Ibell, P. Shepherd and I. Benford, "Prototyping and load testing of thin-shell concrete floors", *Proceedings of the IASS Symposium 2018,* Boston, USA, July 16-20, C. Mueller, S. Adriaenssens (eds.)

2 D. López López, D. Veenendaal, M. Akbarzadeh and P. Block, "Prototype of an ultra-thin, concrete vaulted floor system", *Proceedings of the IASS-SLTE 2014,* Brasillia, Brazil, September 15-19, R. Brasil, R. Pauletti (eds.)

3. William S. Wolfe, "Graphical Analysis" *McGraw-Hill Book Company Inc*., New York, 1921

4. Philippe Block, M. DeJong, J. Ochsendorf, "As hangs the flexible line: equilibrium of masonary arches", *Nexus Network Journal - Vol.8, No.2*, 13-24, 2006

Proceedings of the IASS Annual Symposium 2019 – Structural Membranes 2019
Form and Force
7 – 10 October 2019, Barcelona, Spain
C. Lázaro, K.-U. Bletzinger, E. Oñate (eds.)

Dynamic experiment of integrated ceiling system used in large span office buildings

Shoki ISHIGURO[1*], Tetsuo YAMASHITA[a]

[1*]Graduate Student, Kogakuin University
Tokyo, Japan
dm18003@ns.kogakuin.ac.jp

[a] Professor, School of Architecture, Kogakuin University

Abstract

In 2011, the Pacific coast of Tohoku earthquake caused severe ceiling collapse. The line type integrated ceiling system is widely used in large span office buildings. However, there has been few studies on earthquake response or collapse prevention of a line type integrated ceiling system. We carried out a full scale shaking table experiment of a line type integrated ceiling system. In this study, the effects of the number of clips and the rigidity of the lighting boxes on the ceiling collapse were studied. Vibration of sine wave of constant and linearly increasing amplitude was given to the test body. It was found that the increase of clips reduced in-plane deformation of the ceiling and prevented the collapse triggered by the drop off of the ceiling boards. This explains that the increase of strength and stiffness of the clips could be effective to prevent the collapse of ceiling. The reinforcement of the lighting boxes effectively increased the in-plane rigidity of the ceiling. It contributes to reduce the in-plane deformations of the ceiling and to prevent the collapse as well.

Keywords: Line Type Integrated Ceiling System, Full Scale Shaking Table, Lighting Box, Brace, clip, In-plane Deformations

1. Introduction

During the 2011 off the Pacific coast of Tohoku Earthquake, many buildings suffered ceiling collapse (Photo 1) [1]. A seismic design method for conventional ceilings has been shown in the Ministry of Land, Infrastructure, Transport and Tourism notification [2]. On the grid type integrated ceiling system, several studies on fall and collapse have been conducted [3]. However, there has been few studies on line type integrated ceiling system which has been widely used in large span office buildings. Fig. 1 illustrates the line type integrated ceiling system components. The ceiling boards are connected each other with the H-bars on the T-bar flange. Therefore, the ceiling does not have in-plane bending or shear rigidity. Moreover, the T-bars and H-bars are jointed by vulnerable clips.



Photo 1: Drop of ceiling board in the 2011 quake

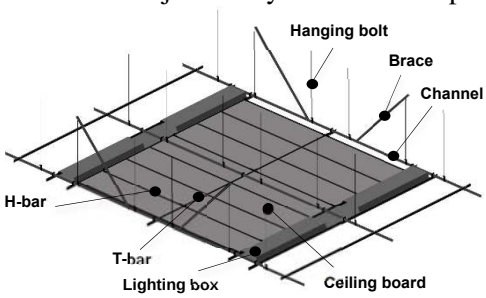
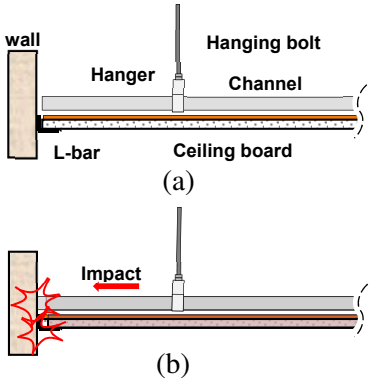


Figure 1: Overview of line type integrated ceiling system

Copyright © 2019 by Shoki Ishiguro and Tetsuo Yamashita.
Published by the International Association for Shell and Spatial Structures (IASS) with permission.

Typically the line type integrated ceiling transfers the inertial force generated by the earthquake to the structure through the non-structural walls around the ceiling (Figs.2). However, it is highly possible that the walls do not have sufficient rigidity and strength for the impact due to the collision of the ceiling boards. Therefore, braces are often installed to transfer the inertial force in Japan. However, the ceiling deformed into arch-like-shape between the braces (Fig.3). Moreover, T-bars are prone to rotate by the collision of the ceiling boards and it easily drop the ceiling boards (Figs.4).



Figures 2: Collision of ceiling boards to wall

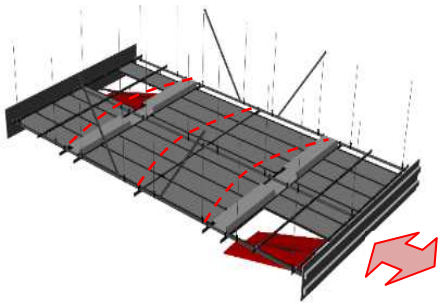
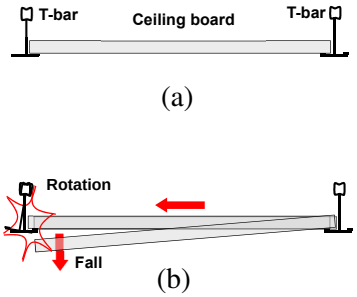


Figure 3: In-plane deformations of ceiling.



Figures 4: Fall of ceiling board due to rotation of T-bar

In this study, dynamic experiments were carried out using the test ceiling where braces and lighting boxes at the both ends of the ceiling were installed to study the effects of the rotation of T-bars and the in-plane deformation on ceiling collapse. The number of clip connecting T-bar and H-bar was changed to study the effect on the rotation of the T-bar (Fig.5). Moreover, the lighting boxes were reinforced to prevent the in-plane deformations of the ceiling (Figs.6).

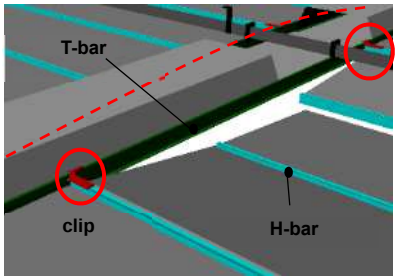
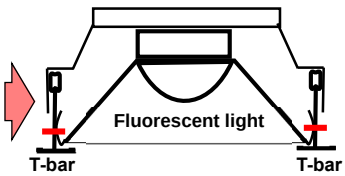
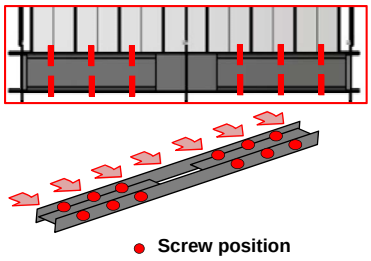


Figure 5: Drop off of H-bar



(a) A cross-section view



(b) Plan view

Figures 6: Reinforced lighting box

2. Experimental overview

2.1. Setup

Fig.7 shows the setup of experiment. We used the full scale shaking table. The test ceiling was suspended from the shaking table. At the both side of the ceilings, a set of strong steel braces was installed to resist inertia force. The vibration was given directly by the horizontal oil jack. The limits of the load, stroke and velocity were 100kN, ±50cm and 100 kine. Figs.8 and table 1 shows the detail of test ceiling. There were five test ceiling. In test ceiling 1-1, about 1/3 of the H-bars were joined to the T-bars by the T-H clips. In test ceiling 1-2, about 2/3 of the H-bars were joined. In test ceiling 1-3, all the H-bars were joined. In test ceiling 2-1, about 1/3 of the H-bars were joined by clip. Moreover, the lighting boxes were reinforced to increase the in-plane bending rigidity. In test ceiling 2-2, the number of the all H-bar were joined and the lighting boxes were reinforced.

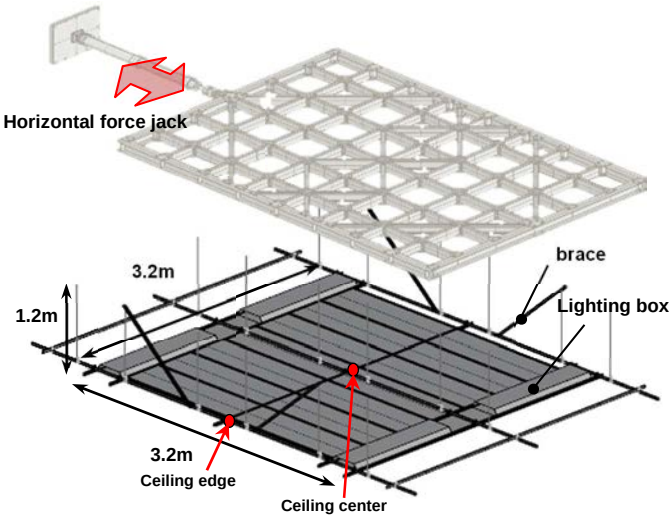
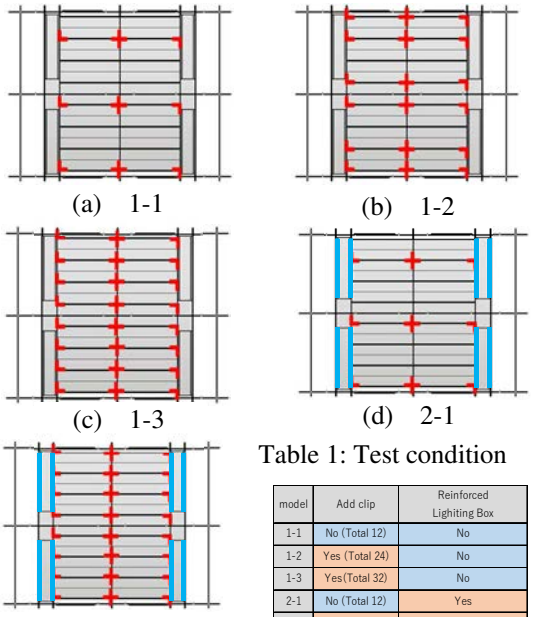


Figure 7: Overview of test ceiling

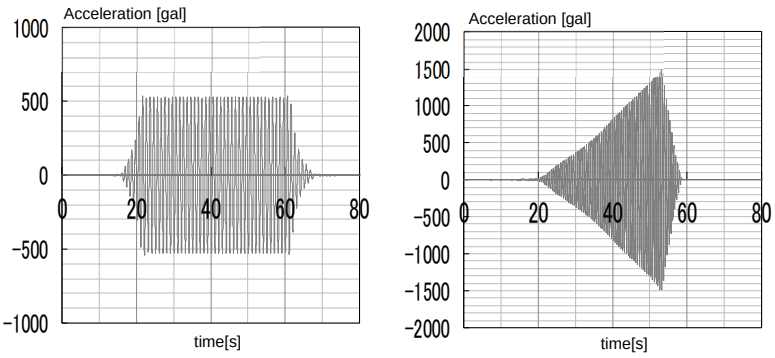


Figures 8: Five test ceilings

Table 1: Test condition

model	Add clip	Reinforced Lighiting Box
1-1	No (Total 12)	No
1-2	Yes (Total 24)	No
1-3	Yes(Total 32)	No
2-1	No (Total 12)	Yes
2-2	Yes(Total 32)	Yes

Figs.9 shows the acceleration given to the test ceiling. The input to the shaking table was called “the input acceleraction data”, the actual acceleration due to the vibration of the shaking table was called “the actual input” and the response of the test ceiling was called “the response”. There were two input acceleraction data. One was the sine wave of constant amplitude with 1 second period. Another was the linearly amplified wave with 0.5 second period. However, the amplitude of the actual input was about 1.4 times at maximum of the input acceleraction data as shown in fig.10.



(a) Sine wave (b) Linearly amplified wave

Figures 9: Input acceleraction data

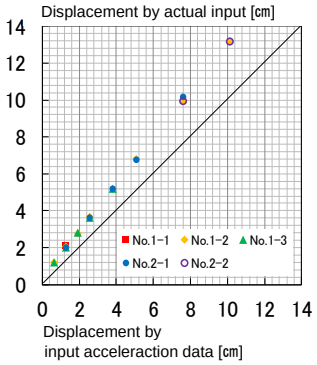


Figure 10: Magnification of input

2.2. Monitoring

We monitored the acceleractions at the shaking table and the ceiling center, the strain of the braces and the in-plane deformation of the ceiling (Fig.11,12). The sampling frequency of the accelerometer and strain gauges is 1000 Hz, the sampling frequency of the displacement gauges is 100 Hz. The noise in the monitored data was removed by the band pass filter.

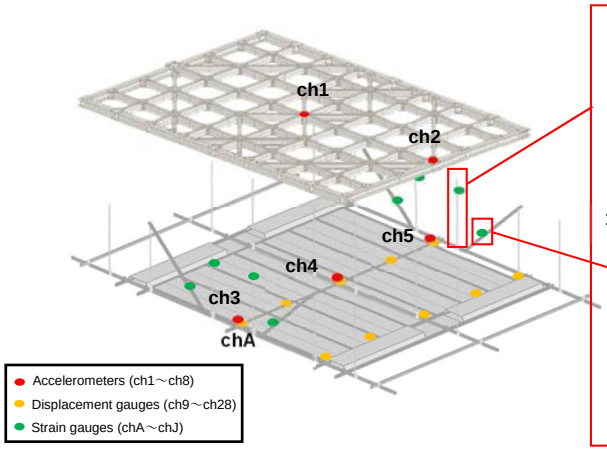


Figure 11: Monotoring location

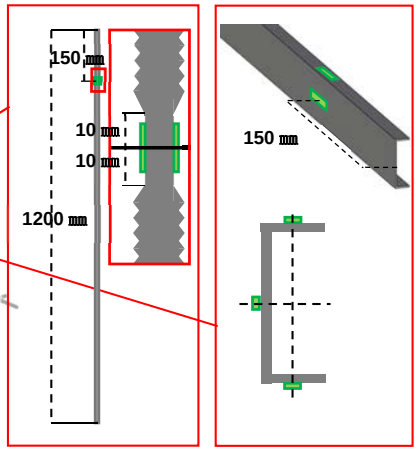


Figure 12: Detail of strain monitoring

Table 2 shows the actual input. First, the sine wave of 1Hz was given to the test ceiling. The amplitude of the sine wave increaseed step by step. We observed the damage in each stage and determined the accleration amplitude given in the next stage according to the degree of damage. If the ceiling did not fall until the 400 gal at the level of input data, the amplitude-increasing wave of 2 Hz was given to the test ceiling. Then we specified the acceleration when the ceiling boards begin to fall.

Table 2: Overview of actual input

Actual Input	Maximum Acceleration[gal]	Maximum Speed[kine]	Maximum displacement[cm]	model				
				1-1	1-2	1-3	2-1	2-2
Sin Wave(1 period)	40	6.4	1.0	▨			▨	▨
Sin Wave(1 period)	80	12.7	2.0					▨
Sin Wave(1 period)	105	16.7	2.7	▨			▨	▨
Sin Wave(1 period)	130	20.7	3.3	▨				▨
Sin Wave(1 period)	200	31.8	5.1	▨		▨		▨
Sin Wave(1 period)	260	41.4	6.6	▨				▨
Sin Wave(1 period)	400	63.7	10.1	▨	▨			
Sin Wave(1 period)	520	82.8	13.2	▨	▨		▨	
Amplitude-Increasing Wave(0.5 period)	Object 1500	Object 120	Object 9.5	▨	▨		▨	

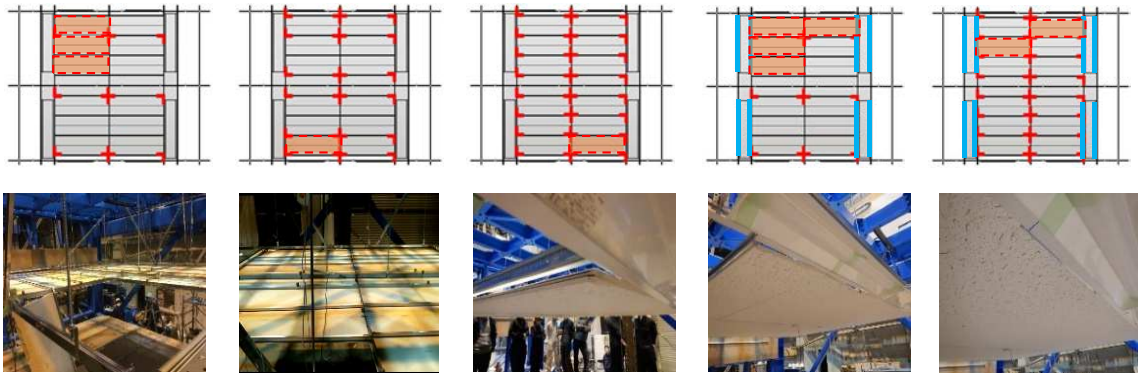
3.Dynamic response and collapse of ceiling

3.1. Damage on ceiling by simple harmonic excitation

Table 3 and Figs.13 show the observed damage to the sine wave. In the test ceiling 1-1, the ceiling boards and the H-bar fell together from the T-bars at about only 80 gal of the actual input.In this test, the ceiling boards fell successively since drop out of the H-bars without the clip triggered the fall-down of the whole ceiling. In the test ceiling 1-2, the ceiling boards fell down by the lateral move of the H-bar at about 200 gal actual input. In the test ceiling 1-3, the ceiling boards dropped out from both the H-bars and T-bars at about 520 gal actual input. In the test ceiling 2-2, there was no noticeable damage even at about 520 gal of the actual input. These results show that the increased clips and the reinforced lighting boxes were effective to prevent the ceiling collapse.

Table 3: Overview of damage to sine wave

Model / Acceleration (gal)	1-1			1-2			1-3			2-1			2-2		
	Gap	Damage	Fall	Gap	Damage	Fall	Gap	Damage	Fall	Gap	Damage	Fall	Gap	Damage	Fall
25															
50			○								○				
75															
100											○				
150						○				○	○				
200										○	○				
300							○				○		○		
400							○	○					○		
Object 800									○						○

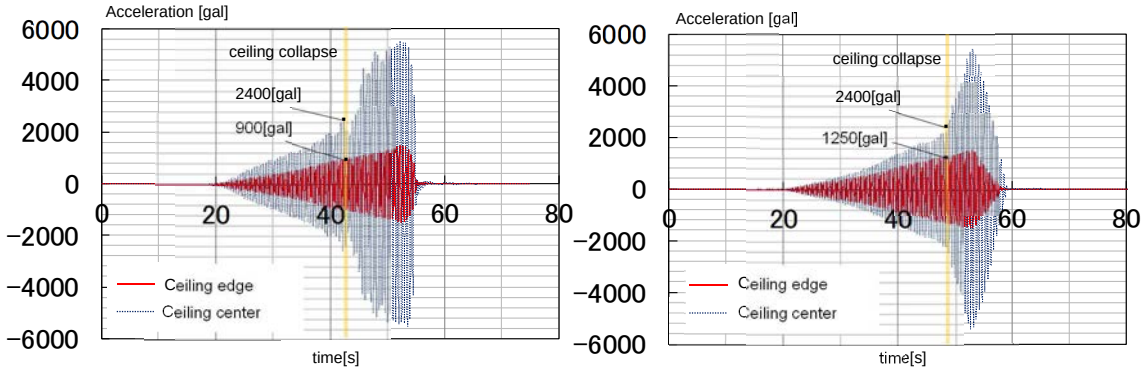


(a) 1-1 (b) 1-2 (c) 1-3 (d) 2-1 (e) 2-2

Figures 13: Damage to sine wave

3.2. Acceleration response to ceiling collapse

Fig.14 shows the observed damage to the linearly amplified wave. In the test ceiling 1-3, the whole ceiling collapsed at about 900 gal of the actual input. The response accerelation of the ceiling was about 900 gal at the both sides while at about 2400 gal at the center at that time. In the test ceiling 2-2, the ceiling collapsed at about 1250 gal of the actual input. The response accerelation was about 1300 gal at both sides while 2400 gal at the center. The response acceleraction at the center was about 2.7 times of the actual input on average in the test ceiling 1-3 while it was about 1.9 times on average in the test ceiling 2-2. This explains that the in-plane rigidity of the ceiling was effectively increased by the reinforcement of the lighting boxes.



(a) 1-3 (b) 2-2

Figures 14: Response and actual input on the linearly amplified wave

The effective acceleration of the ceiling is defined by Equation (1) and specified by the axial force of the braces.

$$A_{ce} = \frac{4 \times N_{br} \times \cos\alpha}{M_{ce}} \qquad (1)$$

where A_{ce} is the effective acceleration of test ceiling. N_{br} is the axial force of the braces calculated by the monitored axial strain. M_{ce} is the mass of test ceiling. α is the brace mounting angle (Fig.15). When the whole ceiling collapsed in the test ceiling 1-3 and test ceiling 2-2, the axial force was about 3.1 kN, the effective acceleration was about 2300 gal in the both tests. It is thought that the effective acceleration almost equal to the monitored acceleration at the center and the whole ceiling collapsed is caused at about 1.9 kN and 2300 gal.

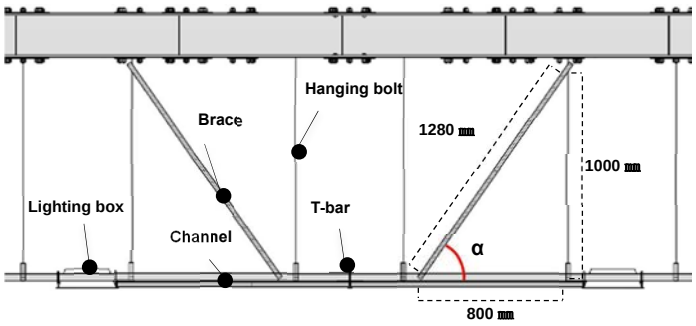
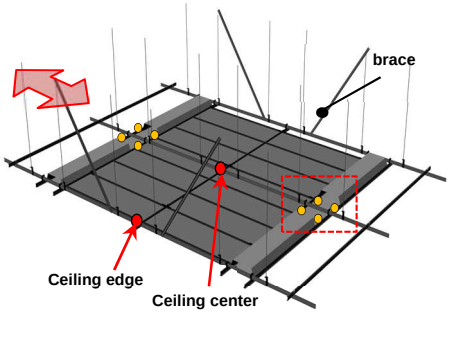


Figure 15: Brace and mounting angle

The falling acceleration of the actual input increased from about 900 gal in the test ceiling 1-3 to about 1250 gal in the test ceiling 2-2, by the reinforced the lighting boxes. However, the T-bar that was the frame material of the lighting boxes was locally buckled by bending stress as illustrated in Fig.16. The stress of the T-bar concentrated at the buckled points where the inner plates to install fluorescent lights made gaps between them (Photo 2). Therefore, it is thought that the bending strength of the lighting boxes can be further increased by the improvement of the reinforcing method.



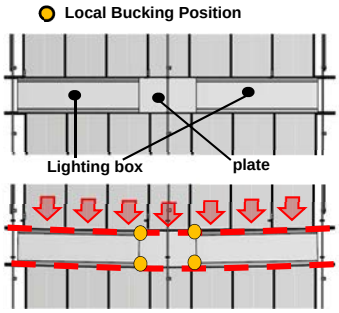


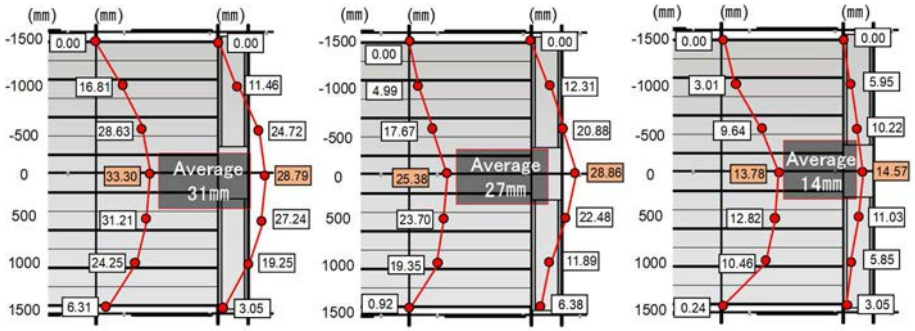
Figure 16: Local buckling by bending stress



Photo 2: Local bucking of T-bar

3.3. In-plane deformation of ceiling

Figs.17 shows the deformations of the T-bar monitored in the test ceiling 1-3, 2-1, 2-2 at about 400 gal of the actual input. The displacement was extremely small at the both sides of ceiling since the braces were installed. However, the displacement was larger at the ceiling center. Therefore, the T-bar and the ceiling deformed into arch-like-shape.



(a) 1-3 (b) 2-1 (c) 2-2

Figures 17: Deformation of T-bar

The in-plane rigidity of the ceiling is defined by Equation (2) and specified by the inertial force of the ceiling and the T-bar deformation at the ceiling center.

$$K_{ce} = \frac{P_{ce}}{\delta_t} \qquad (2)$$

where K_{ce} is the in-plane rigidity of the ceiling. P_{ce} is the inertial force on the ceiling calculated from the effective acceleration and the mass of the ceiling (84.6 kg). δ_t is the lateral deformation at the center of the T-bar. In the test ceiling 1-3, 2-1 and 2-2, the in-plane rigidity of the ceiling were 10.9 N/mm, 12.5 N/mm and 24.2 N/mm.

Comparing the rigidity of the test ceiling 1-3 with the test ceiling 2-2, the in-plane rigidity of the ceiling was about 2.2 times. This indicates that the T-bar deformation is prevented by the reinforced the lighting boxes. The test ceiling 2-1 and the test ceiling 2-2, the in-plane rigidity of the ceiling was about 1.9 times. This indicates that the T-bar deformation is prevented by the increased clips. This result shows that the clip not only prevent the H-bar damage, but also help prevent the T-bar deformation by the H-bar. However, the clip is vulnerable. Therefore, it was found that the T-bar deformation is further prevented by the T-bar and H-bar are rigidly joined by the steel connector that is stronger than current clip.

4. Summary

In this study, full-scale tests of the integrated ceiling system were carried out. In the tests, we focused on the effects of the clips and the lighting boxes to prevent the ceiling collapse due to the in-plane deformations of the ceiling. The findings are summarized as follows:

1) The increased clips not only prevent the ceiling collapse triggered by the drop off of the H-bar, but also reduce the in-plane deformations of the ceiling. But the current clips are very weak and deformable. Therefore, increase of strength and stiffness of the clips could be effective to prevent the collapse of ceiling.

2) The reinforcement of the lighting boxes reduces the in-plane deformations of the ceiling and was effective to prevent the collapse. However, the T-bars which were the frame material of the lighting boxes locally buckled by bending stress. A development of reinforcement method to improve bending strength of the lighting boxes is required.

Acknowledgements

The authors express their gratitude for funding by the Urban Disaster Mitigation Center in Kogakuin University.

References

[1] Ken'ichi KAWAGUCHI, Yasushi OBA, Yosuke NAKASO. FAILURE OF CEILINGS AND ESTIMATION OF ITS IMPACT OCCURRED IN AN AIRPORT BUILDING DURING THE 2011 OFF THE PACIFIC COAST OF TOHOKU EARTHQUAKE. AIJ J. Technol. Des. Vol. 18, No.39, pp.789-793, June., 2012 (in Japanese)

[2] National Institute for Land and Infrastructure Management Ministry of Land, Infrastructure, Transport and Tourism, Japan, Practical Guide on the Technical Standards concerning Measures to Prevent the Fall of Ceilings in Buildings,2013.9 (in Japanese)

[3] Shojiro MOTOYUI, Kaede KAMIJO, Kimcheng TEA, Fumihiko SAKURABA. Study on Structural Characteristics of US-Style Suspended Ceilings subjected to Dynamic Load –Par1,2. AIJ, 2018, pp.989-992 (in Japanese)

Proceedings of the IASS Annual Symposium 2019 – Structural Membranes 2019
Form and Force
7 – 10 October 2019, Barcelona, Spain
C. Lázaro, K.-U. Bletzinger, E. Oñate (eds.)

Experimental Research on the Reinforcement of Cylindrical Concrete Shell with Opening

Naoki GOROUMARU*, Takashi HARA[a]

*,[a] National Institute of Technology, Tokuyama College
Gakuendai Shunan 745-8585 Japan
C13goroumaru@tokuyama.ac.jp

a National Institute of Technology, Tokuyama College. Gakuendai Shunan 745-8585 Japan
t-hara@tokuyama.ac.jp

Abstract

In this paper, the reinforcing method of reinforced concrete cylindrical shell with opening was investigated experimentally. The dimensions of the specimen were 900 mm in the meridian direction, 960 mm in the hoop direction on the horizontal projection plane, and the shell thickness was 20 mm. In experiments, a reinforcing ratio of 0.26% was used. In order to compare the reinforcement effect of the shell with openings, the methods of reinforcement are shown below. All specimens are reinforced around the opening in both hoop and meridional directions instead of the lost reinforcements at the opening (A, B, C). Also, in Pattern B, the conventional diagonal reinforcing bars were arranged. In Pattern C, additional hoop and meridional reinforcing bars were arranged instead of diagonal reinforcing bars to prevent the shearing failure around the opening. Using these models, the reinforcement effect for the shell at the opening portion was experimented concerning the deformation and the load bearing capacity under axial compressive load. Regarding the load carrying capacity evaluation, the compressive failure of the loading point occurred earlier than the failure at the vicinity of the opening and the reinforcing bar buckled. About the stiffening effect due to reinforcing bars, (a) The conventional reinforcement method has sufficient reinforcement effect. (b) The simple reinforcement method proposed in this study had a reinforcement effect, but the amount of rebar was insufficient.

Keywords: shell, compression, experiments, strength, opening, reinforcement

1. Introduction

The reinforced concrete (RC) cylindrical shell structure has the advantages of thin member thickness, light weight, and excellent load resistance. For this reason, the RC cylindrical shell structure is widely used mainly for relatively tall and large cylinder such as water storage tanks, large chimneys, and cooling towers. The reinforcement of the opening is the same as that of the flat plate [1], but in the case of the flat plate, the tilt-up by factory manufacture is predominate and there is little difficulty in construction. In the case of a shell, there are many on-site constructions, and it is often difficult to arrange curved bars at the construction site, and improvements of reinforcement are required [2]. Since cylindrical shell structure is expected to reduce the resources, costs, disaster prevention and disaster reduction, its application to many buildings is expected other than chimneys. In order to enable the safety and easy design and construction of cylindrical shell structures, it is necessary to improve curved diagonal bars in in situ construction. In this research, in order to compensate the reduced strength and improve the workability, a simple reinforcement method was considered, and cylindrical shell concretes with three patterns of reinforcement methods was manufactured and an experimental verification on the

Copyright © 2019 by Naoki GOROUMARU, Takashi HARA
Published by the International Association for Shell and Spatial Structures (IASS) with permission.

reinforcement effect of the opening was examining by obtaining the deformation capacity and the load carrying capacity under the axial compressive load.

2. Experimental analysis

2.1. Specimens

The dimensions of the specimen were 900 mm in the meridian direction, 960 mm in the hoop direction (arc length 1050 mm) on the horizontal projection plane, and the shell thickness was 20 mm. Radius of curvature is 668.7 mm, full opening angle is 88 ° (Figure 1 and Table 1). According to ACI 307[3], that the amount of rebar is 0.2% or more of the concrete cross-sectional area and 2 layers are required. In experiment, φ 3.2 mm and a spacing of 30 mm wire mesh were used (Table 2). In this experiment, considering the reinforcement method of the opening, in order to investigate the reinforcement effect, cylindrical shells with three patterns of reinforcement method are manufactured and the ultimate strength was measured (see section 2.2). The dimensions of the opening are 240 mm in the meridian direction and 260 mm in the circumferential direction. The opening is placed at the center of the specimen. The weight ratio of micro concrete used was water: cement: sand = 1: 2: 4. In order to prevent the adhesion of concrete on the inside the formwork, a specimen was coated with a release agent, a water-reducing agent was added, and the mortar was poured by self-filling. The material properties of the specimen are shown in (Table 3).

Table 1: Specimen size

Symbol	Test body
B(mm)	960
H(mm)	900
T(mm)	20
R(mm)	688.7
θ(°)	88

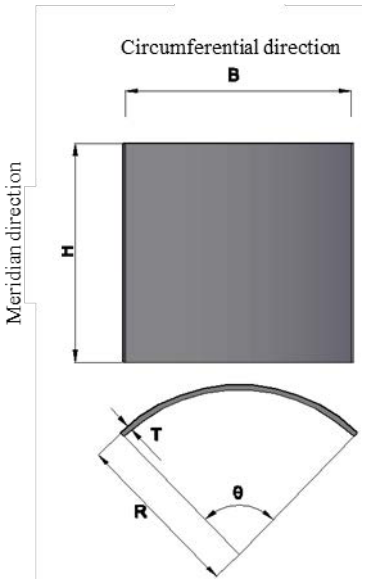


Figure 1: Test specimen (shell) plan view

Table 2: Rebar amount

Rebar	Rebar (Vertical)	Rebar (side)
φ3.2mm	0.25%	0.26%

Table 3: Material property

Concrete	Compressive strength	Modulus of elasticity
	36MPa	33GPa
Rebar	tensile strength	Modulus of elasticity
	235MPa	200GPa

2.2. Reinforcement method

To compare the reinforcing effect of the opening three pattern of reinforcement methods are adopted and manufactured method are shown below (Figure. 3 to Figure. 5). Inserting the reinforcement bars is inserted around the openings of all patterns (A, B, C). In addition, pattern B adds reinforcement bars diagonally at the corner of the openings, and pattern C adds reinforcement bars around the opening in the meridional and circumferential directions. The reinforcement length is L1 from the corner of the opening (Figure 2). Since L1 is the reinforcing bar diameter * 40. It is 3.2 * 40 = 128 mm when φ 3.2 mm of the reinforcing bar are this time, therefore, L1 is 130 mm in this experiment. In the case of diagonal bars, it is 2 * L1, so a 260 mm rebar is arranged at an angle of 45 °. As for the number of reinforcement bars, the number of rebar lost when forming the opening is arranged in the meridian direction and circumferential direction. In this case, five reinforcing bars were arranged. Similarly, 5 diagonal bars are also arranged (Photo 1). As a simple improvement plan for the oblique part of the opening, we have manufactured one in which the sheared diagonal rebar is arranged in the meridian and circumferential direction (Photo 2). In this case as well, 5 bars of reinforcement were arranged. The experiment was carried out with the specimen subjected to the above three patterns of reinforcement.

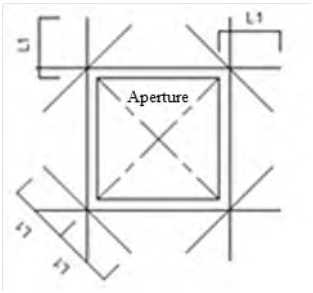


Figure 2: Test specimen (shell) plan view

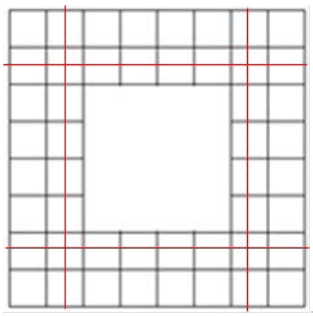


Figure 3: Pattern A

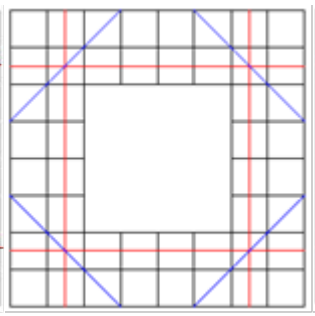


Figure 4: Pattern B

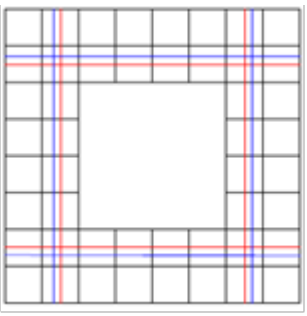


Figure 5: Pattern C



Photo 1: Pattern B



Photo 2: Pattern C

2.3. Experimental method

2.3.1. Loading method

An axial compressive force was applied to the specimen, the maximum axial compressive load of the shell was determined, and the strains were measured up to failure. Five hydraulic jacks were used to apply axial compression. The equipment apparatus used for the test is shown in (Figure. 6).

2.3.2. Supporting method

For the supporting condition of the specimen, five channel steel of 300 mm * 90 mm were installed on both sides of the specimen, and these channels were fixed by the 100 mm *150mm channel. The specimen was housed inside. The steel plate was installed between loading head and specimen and the loading head of the hydraulic jack was divided into five steel plate placed an equidistance on the lower side, and the steel plate was also installed between the steel plate and a specimen and the experiment was conducted under distributed load (Figure. 8).





Figure 6: Experimental device

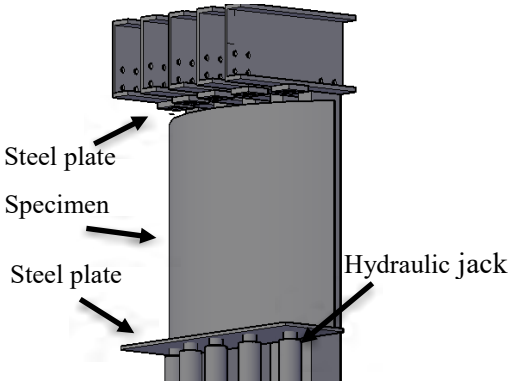


Figure 8: Support condition

2.3.3. Strain measuring method

The strain was measured by a strain gauge installed at 50 mm from the edges of the opening. In addition, the number of gauges was two in meridional direction and is two were in the hoop direction and in addition four closing gauges were installed, and in measuring strains totally, 12 gauges are placed on each surface (Figure. 7). From each point, the axial and flexural strains are evaluated.

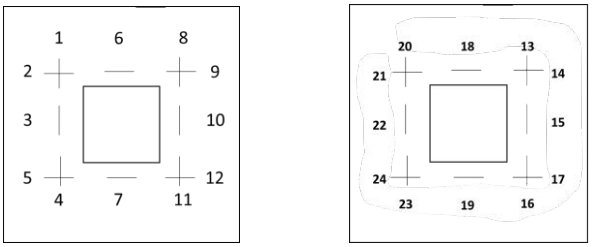


Figure 7: Strain gauge attachment position (left: convex, right: concave)

3. Experimental results

The load-strain diagrams obtained by the experiment are presented. The numbers in the load-strain diagram are indicated correspond to those in Figure 7 where the strain gauges are attached.

3.1. Failure load and failure status

All the test specimen reinforced by of the three patterns A, B, and C were crushed at the portion in contact with the support surface before the vicinity of the opening was crushed. The compressive failure of concrete induces the buckling of the reinforcing bar.

3.1.1. pattern A

The centered portion of the lower hoop edge, where is in the middle of loading jacks was crushed and the rebar buckled (ultimate load is 450kN) (Photo 3).

3.1.2. pattern B

In pattern B was crushed at the top and bottom in the circumferential center. The reason for the decrease in ultimate strength in spite of the placement of the addition diagonal reinforcement is due to the uneven thickness of the specimen. (ultimate load is 400kN) (Photo 4).

3.1.3. pattern C

In pattern C were also was induces by a central compressive failure as like as pattern A. However, the crushed load is close to that of pattern A, and is higher than that of pattern B. But it is difficult to evaluate whether reinforcement effect was effective or not because the thickness of specimen was not uniform. (ultimate load is 450kN) (Photo 5).

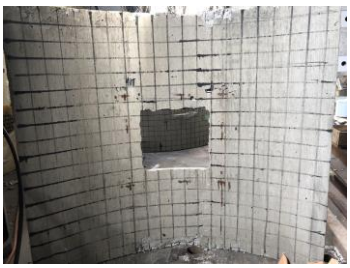


Photo 3: pattern A



Photo 4: pattern B



Photo 5: pattern C

3.2. Load-strain relationship

Figures 9 to 10 shows the relationship between strain and load of the test specimen during loading test. In this figures, the strain in the meridional direction (1-13, 3-15, 4-16, 8-20, 10-22, 11-23) and the strains in the circumferential direction (2-14, 5-17, 6- 18, 7-9, 9-21, 22-24) were determined, and the strains of the specimen due to loading was determined. It is considered that bending deformation occurred in the place where the strains in the meridional direction was not compressed and the strains in the circumferential direction was not tensile. The cause is the initial imperfection of the specimen and experimental apparatus that the loading devices were placed at the loading point so as to overlap with the axis of the specimen, but due to the difference between expensive and the setting position at the assembly stage, or the initial geometrids imperfection of the specimen, the deformation caused by the load applied. In this research, since the specimen was cast with a wooden form, the form expanded and did not have a uniform thickness, so it was not possible to measure the detailed and sufficient strength to be compared in the loading experiment.

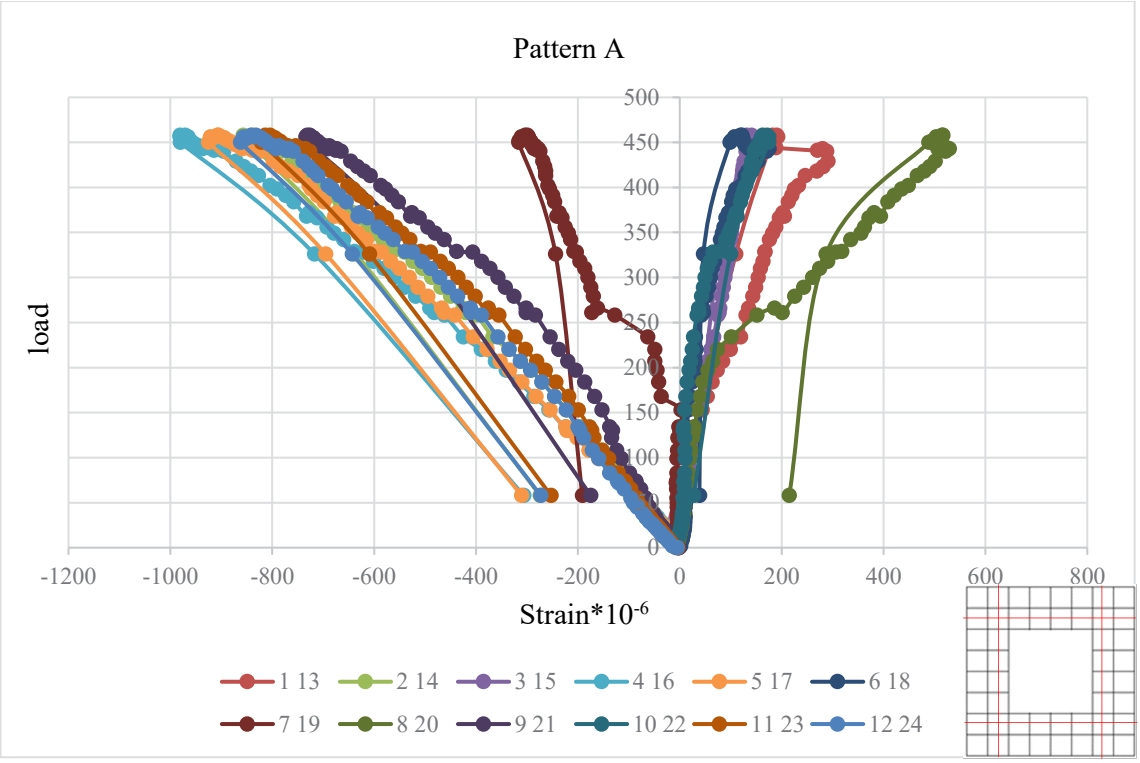


Figure 9: Load-strain graph (pattern A)

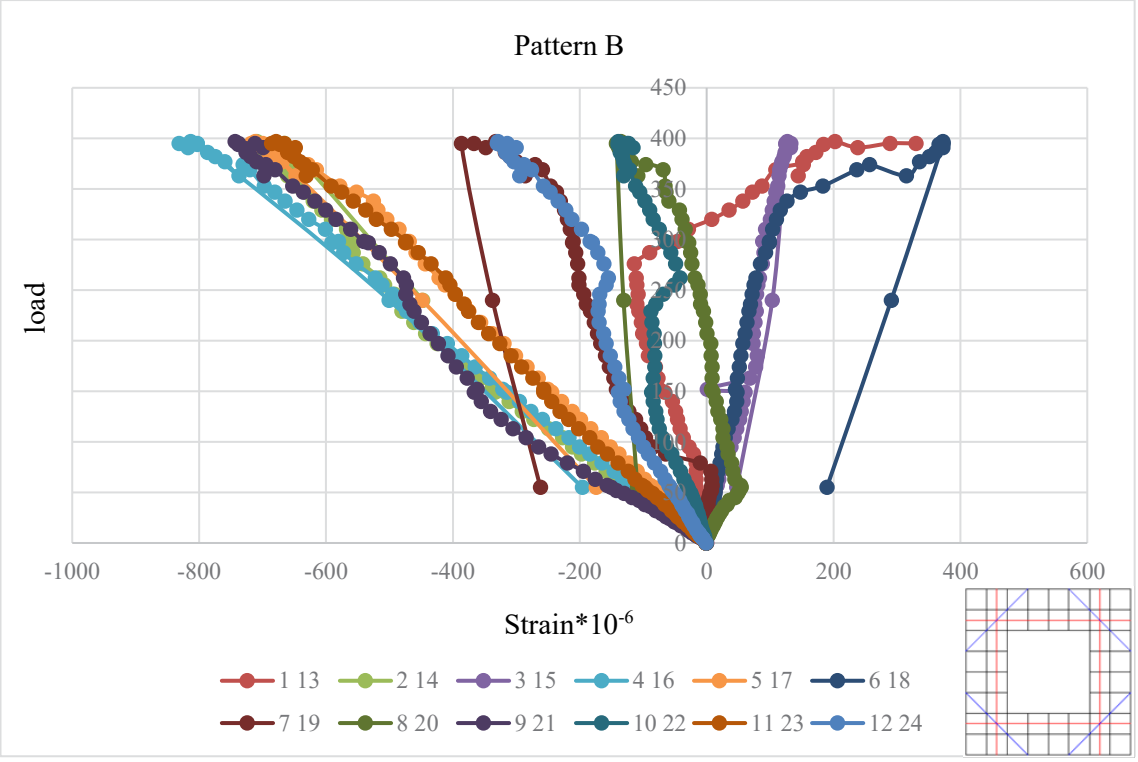


Figure 10: Load-strain graph (pattern B)

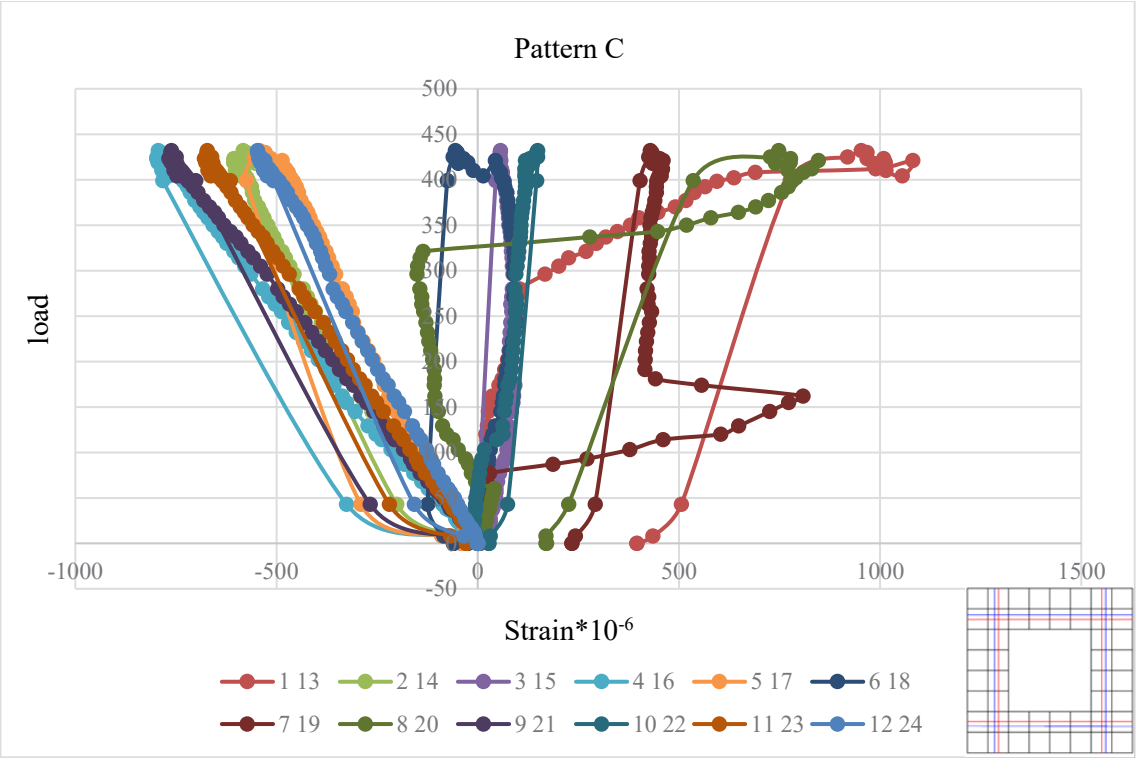


Figure 11: Load-strain graph (pattern C)

3.2.1. pattern A

Shows the load-strain relation in Figure 9. In pattern A, 1-13, 3-15, 6-18, 8-20, and 10-22 are all compressive strain, and others are tensile strain. 1-13, 3-15, 6-18, 7-19 and 8-20 have relatively high rigidity. Others were similar tendencies, among which 4-16 and 5-17 have low rigidity. It can be seen that the overall stiffness is lower than pattern B and pattern C, and reinforcement of the opening is necessary.

3.2.2. pattern B

Shows the load-strain relation in Figure 10. In pattern B, 1-13, 3-15, and 6-18 were compressive strain, and others were tensile strain. R/C shell shows high rigidity in most places. Above all, 1-13, 3-15, 6-18, 7-19 8-20 10-22 and 12-24 have high rigidity. The current reinforcement method is effective because pattern B is generally stiffer than pattern A.

3.2.3. pattern C

Shows the load-strain relation in Figure 11. In pattern C, 1-13, 13-15, 6-18, 7-19, 8-20 and 10-22 were compressive strain, and others were tensile strain. Overall rigidity is high and there are few places with low rigidity. Reinforcement was effective because the overall rigidity is higher than pattern A. The reinforcement method of pattern C is effective because pattern C is more rigid than pattern B depending on the location, and the overall rigidity is also equivalent.

4. Conclusions

In this paper, in order to compensate for the reduced strength due to hole of the shell surface, a simple reinforcement method is considered, and cylindrical shell concrete with three patterns of reinforcement method is manufactured. In addition, we measured deformation capacity and load capacity under axial

compressive load. And the experimental verification about reinforcement effect of opening were conducted. In the experiment, the load-bearing capacity and the strain test of the test specimen due to the load were measured. With regard to load carrying capacity following conclusions are obtained, (a) compression failure both at loading and supporting edges precedes failure before failure near the opening, and the rebar buckles. (b) The specimen did not have a uniform thickness. It is difficult to handle as load capacity evaluation because spacimen is not the same thickness. Therefore, it is necessary to change the form of the specimen from wood to steel and to reinforce the reinforcement along the hoop edges or to increase the thickness of the concrete. Regarding the rigidity effect by reinforcement (c) The existing reinforcement method has achieved sufficient reinforcement effect. (d) The simple reinforcement proposed in this study shows the reinforcement effect, but the same effect as the current reinforcement method is not obtained because of the lack of reinforcement.

References

[1] Architectural Institute of Japan "*Chimney structural design guidelines Structural Design Recommendation for Chimneys*", Tokyo Japan 2007

[2] Sami A. D.A, and Selcuk A "An Investigation of Opening Reinforcement Configurations for Reinforced Concrete Chimneys" *ICCT 2016 INTERNATIONAL CONFERENCE ON INDUSTRIAL CHIMNEYS & COOLING TOWERS 2016*

[3] ACI Committee307 ACI307-08 "*Code Requirement for Reinforced Concrete Chimneys and Commentary American Concrete Institute*", 2008 30p

Proceedings of the IASS Annual Symposium 2019 – Structural Membranes 2019
Form and Force
7 – 10 October 2019, Barcelona, Spain
C. Lázaro, K.-U. Bletzinger, E. Oñate (eds.)

Field Test for a Prefabricated External Prestressed Concrete Wind Turbine Tower

Yuqi CAO *, Renle MA *, Huiqun LIU[a], Feng LIANG[a]

*College of Civil Engineering, Tongji University
Shanghai, 200092, China
09caoyuqi@tongji.edu.cn

[a] Tongji Architectural Design (Group) Co., Ltd

Abstract

The prefabricated external prestressed concrete wind turbine tower is a competitive solution to large-scale turbine for its high stiffness and reasonable cost; as such, a 120-meter-high test tower supporting a 3 MW turbine was built in Eastern China. A series of field test work was done to ensure its reliability. Vibrating-wire strain sensors were adopted for monitoring the strain of key positions during the stressing process and operation period. Pressure sensors were used to monitor the force of prestressed steel strands. Finally, accelerometers were installed to collect the vibration at the top of the tower. The results matched with a previously done shell element model. The vibrating-wire strain sensors results and the measured strand forces proved the feasibility of the structure solution. The natural frequency and damping ratio extracted from the acceleration data could provide reference for sequent modal estimate and seismic design.

Keywords: wind turbine tower, prestressed concrete, field test.

1. Introduction

World's fossil reserves, which have been powering the modern civilization and its industries for the past decades, are now considered as one of the predominant environmental contaminator and greenhouse gas emitters. Consequently, the alternative energy platform with clean and green features becomes more desirable to alleviate these environmental problems. The wind power, which is ubiquitous and sustainable, plays a consequential role in this course. Generally, securing the electricity at higher efficiency and lowering the costs are the key features of the wind energy development. Nowadays, the capacity of a single turbine rises up to megawatts and the supporting tower become higher and slenderer. In this case, the conventional tubular tower scheme may not be the optimal choice. The concrete tower draws more attention for its high stiffness and reasonable cost. The prefabricated external prestressed concrete wind turbine tower is an application of concrete tower and external prestressing. It contains a lower prestressed concrete tube and an upper steel tubular adapter which is connected to the nacelle by the top flange. The concrete tube is segmented along the vertical direction. Except that the base is cast in place, all the segments are prefabricated in factory and then transported to the construction site. The steel strands on the inner side are prestressed to the degree that the segments are tied together under extreme loadings. The diagram is as Fig.1(a) shows.

A model tower was completed in Jiangsu Province, China in 2018. The tower is 120 m high, supporting a 3 MW turbine. The concrete tube is 104 m high, with three major sections: Φ4 500×400, Φ6 600×350 and Φ8 000×350 (in mm) from top to bottom. Sixteen steel strands were prestressed to 3 200 kN to insure the segments are tied together under extreme loadings.

Copyright © 2019 by Yuqi Cao, Renle Ma, Huiqun Liu, Feng Liang
Published by the International Association for Shell and Spatial Structures (IASS) with permission.

Researchers have adopted various sensors to monitor the wind turbine towers. Rolfes *et al.* [1] combined accelerometers and strain gages to detect damage. Hartmann *et al.* [2] built a system consisting of accelerometers, inductive displacement transducers, temperature sensors and an anemometer and developed probabilistic lifetime estimation framework. Botz *et al.* [3] presented monitoring of concrete-steel hybrid tower with accelerometer and strain gauges.

No research has been done on the strain state of this kind of tower in the construction phase and operation phase. The long-term performance of the steel strand is to be investigated. Thus a structural health monitoring system was necessary. Additionally, an acceleration field test needed to be done to obtain the modal property of this innovative structure form. A series of field test have been conducted. This paper shows the outline of the applied methods and gives the major results and further discussions.

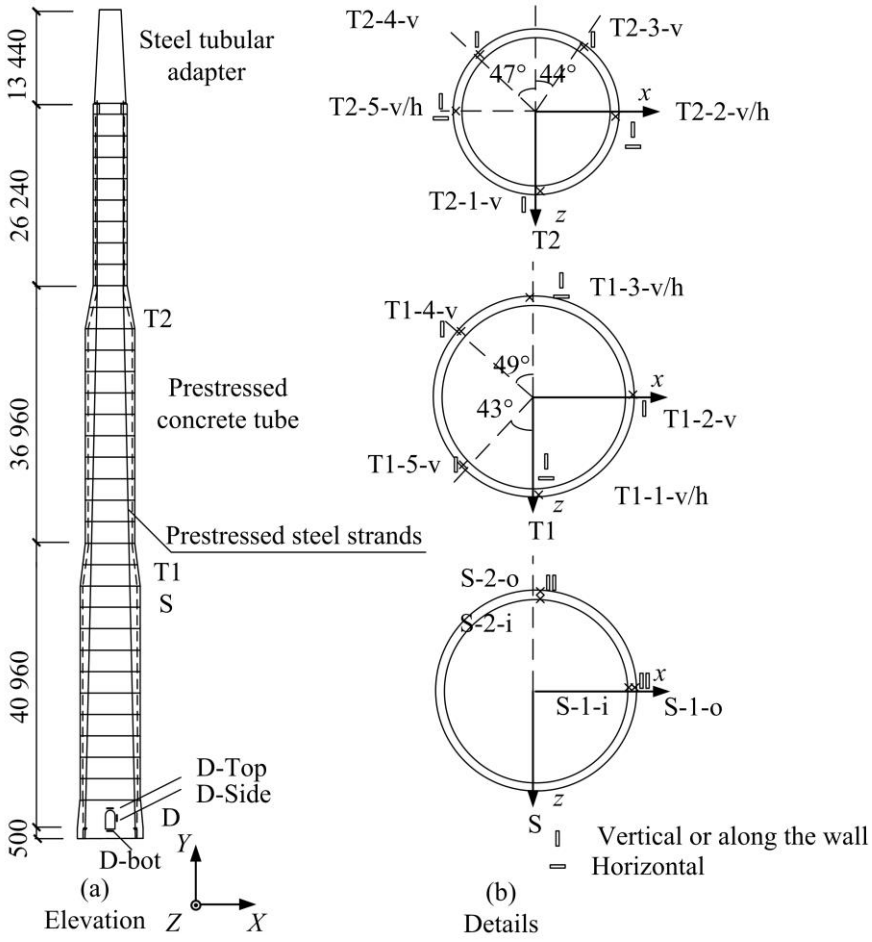


Figure 1: Distribution of the sensors

2. Strain of key positions

The strains of key positions are monitored by the vibrating-wire strain sensors for their excellent anti-jamming capacity and longtime stability. Bai *et al.* [4] used the vibrating-wire strain sensors to capture the occurrence of cracks in wind turbine concrete foundations. The strain is calculated according to eq.(1)

$$\varepsilon=\left(f^2-f_0^2\right)\times k+\left(\alpha_1-\alpha_2\right)\times\left(t-t_0\right) \tag{1}$$

where f is the current frequency, f_0 is the initial frequency, k is the instrument coefficient, α_1 is the thermal expansion coefficient of the vibrational chord, α_2 is the thermal expansion coefficient of the tested material, t is the current temperature and t_0 is the initial temperature.

The sensors were installed in the bottom of two transition segments and around the door in the base. The details and numbering are shown in Fig.1. Four sensors, organized into Group S, were placed vertically in the top of segments of the section Φ8 000×350. Seven sensors, organized into Group T1, were placed in the bottom of the lower transition segment, five along the wall and two horizontally. Seven sensors, organized into Group T2, were placed in the bottom of the upper transition segment, five along the wall and two horizontally. Three sensors, organized into Group D, were placed around the door.

The sensors were installed in the prefabricated segments before cast. Because assembly steel formworks were used, the signal lines were hidden in steel tubes and taken out after form removal. Then f_0 and t_0 were recorded. The signal lines were lengthened and fixed at embedded parts inside the wall. They were released to the ground after transportation and hoisting, before the steel strands were prestressed. The signal lines were connected to the data collecting box. Thus a strain monitoring system was built. Both the stressing process and the operation stage could be monitored.

The system is illustrated by the case of the stressing process. It helped engineers grasp the development of the prestress in the concrete tube. The sixteen steel strands were stressed only once in the following order: ⑩②⑥⑭/⑪③⑮⑦/④⑫⑯⑧/①⑨⑬⑤, if they were numbered from ① to ⑯ counting from the door clockwise as Fig.2 shows.

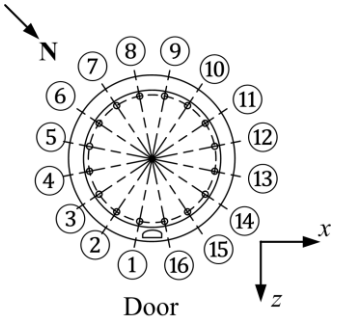


Figure 2: Numbering of the steel strands

A shell element model was built in ABAQUS to analyze the stressing process. The elastic modulus of concrete and rebar were taken as 35.5 GPa and 200 GPa. Linear elasticity was adopted approximately for the concrete stress was no more than 70% of the compressive strength.

The strain of S-2 is shown in Fig.3(a). The development of the prestress was not so idealized before uniform compression formed in the whole section.

The strain development was similar in transition segment T1 and T2. The measured results and simulated results of T2 are shown in Fig.3(b)(c). They varied in synchronization, especially the results of T2-1-v.

The results of D-top, D-side and D-bot are shown in Fig.3(d). Cracks might happen at the top of the door. The crack had a width of about 0.03 mm on account of the gauge length; as such it would not do any harm to the structure safety.

The signal of the sensors stayed stable and the measured strain changed steadily. The safety of the construction process has been proved. The difference between the measured results and the simulation could be explained by the discreteness of the concrete. The results also indicate that the shell element model is precise enough to reflect the general performance of the structure.

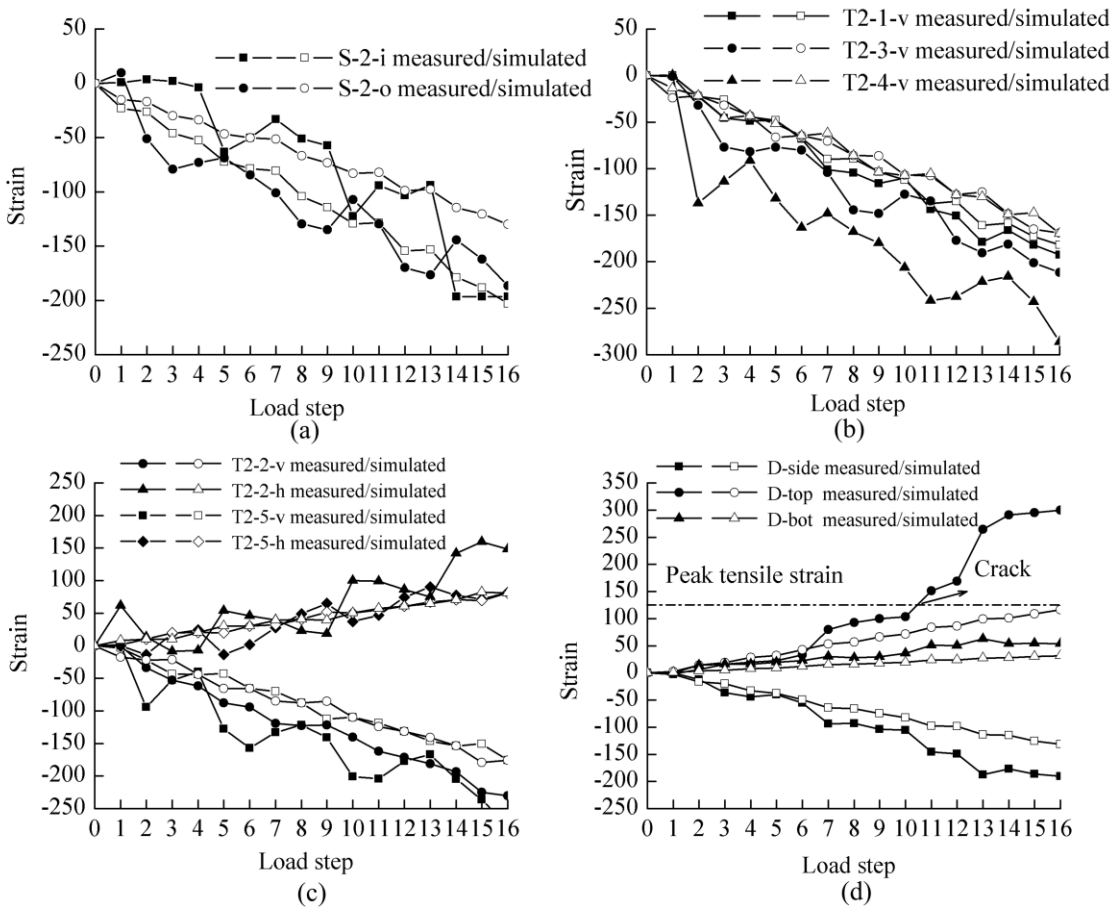


Figure 3: Strain development in the groups of S T2 and D

3. Force of prestressed steel strands

Strands of ①⑤⑬ were picked from the sixteen steel strands. They were the strand near the door, on the windward side and on the lee side in turn. It was difficult to monitor the tension force directly for the pretension force was 3 200 kN and the diameter was 150 mm, protective layer counting in. Pressure sensors were installed under the nuts of the bolts connected to the strands by deviators as Fig.4 shows. Tension force of a strand could be monitored by monitoring the pressure of the four pressure sensors.

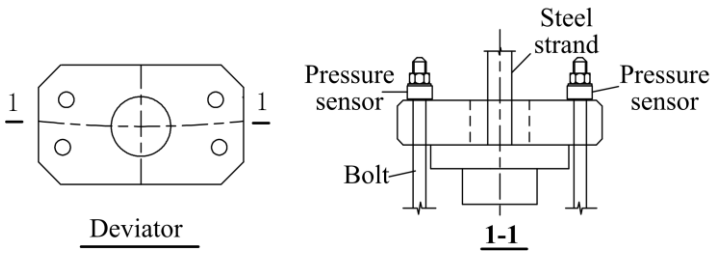


Figure 4: The installation of the pressure sensors

One-week monitoring results are plotted in Fig.5. It can be seen that the force stay stable around 3 200 kN. A step in tension force occurred when the turbine came into operation from the parked state. The

force kept increasing as the power rose. A maximum growth of 4% can be observed compared to the parked state.

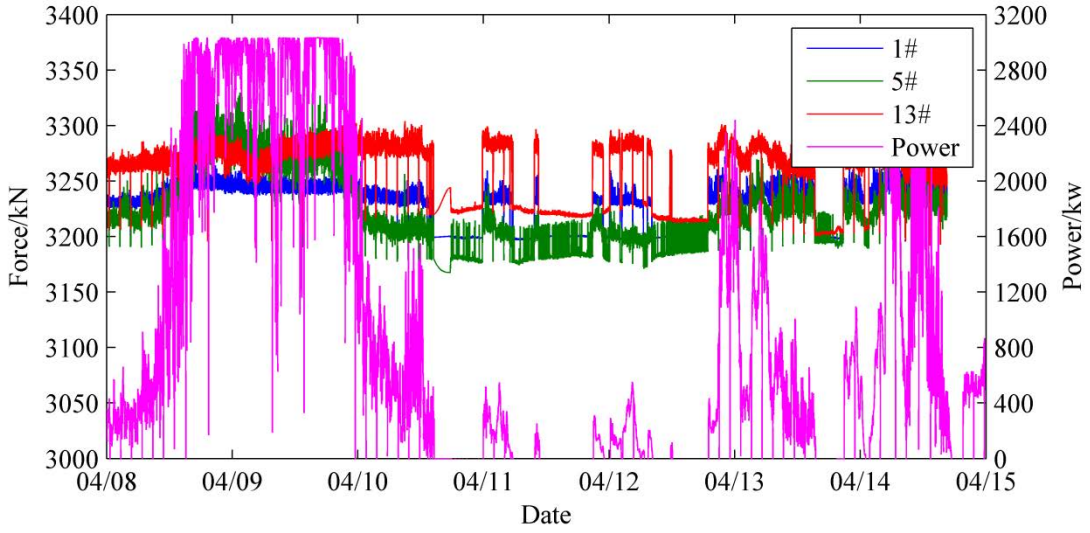


Figure 5: One-week forces monitoring results

4. Acceleration at the top

The tower is a combination of concrete tube and steel tube, thus the damping ratio should lie in between 0.01 and 0.05. Acceleration field test needed to be done to investigate the dynamic characteristics including the basic frequency and the damping ratio. Ma *et al*. [5] and Dai *et al.* [6] provided good examples of acceleration field test. The test was done soon after the turbine was connected into the power system.

As can be seen in fig.6, four accelerometers were installed at the top of the tower, two at the top of the concrete tube and two at the top of steel tube. The accelerometers were attracted to the wall horizontally, pointing to the center of the circular platform. The accelerometers at the same height were perpendicular, one pointing towards the downwind end of the nacelle (1x/2x), and the other to the left when looking toward the downwind end of the nacelle (1z/2z). The sampling frequency was set to be 100 Hz.

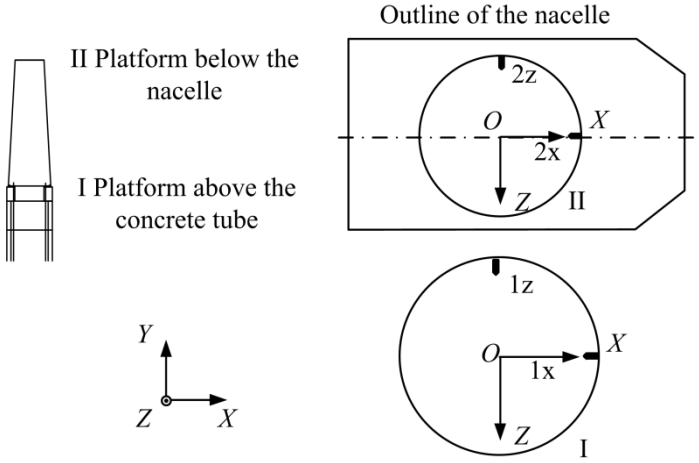


Figure 6: Distribution of the accelerometers

Before the field test, a shell element finite element model similar to model in Chapter 2 was built. Analysis results show that the first two natural frequencies are 0.43Hz and 1.66Hz.

3.1. Parked condition

When the turbine is parked, it is excited by natural excitation which is usually assumed to be uncorrelated Gaussian white noise. Random decrement technique (RDT) was used to identity the modal parameters. The attenuated responses of measuring points are shown in Fig.7. It can be concluded that the damping ratio of the structure is about 4%.

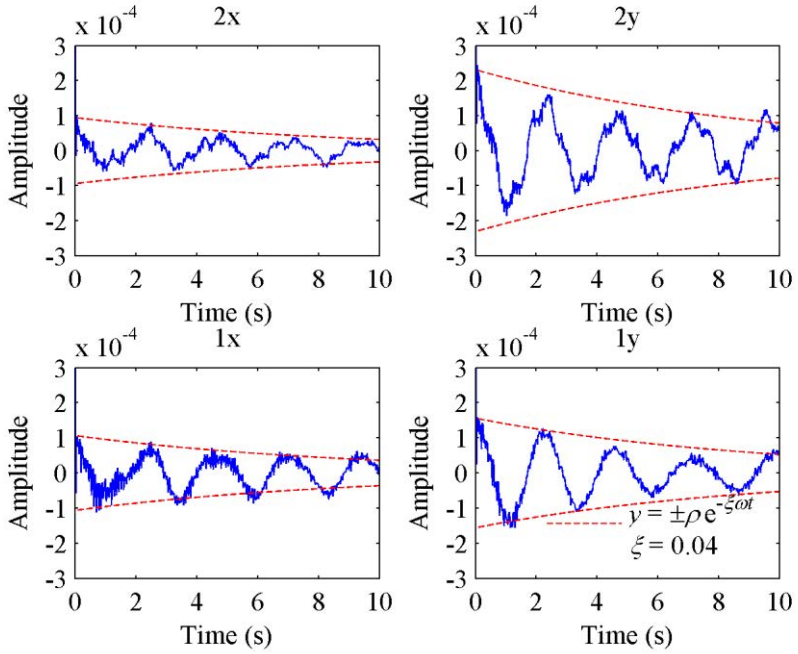


Figure 7: RDT results and damping ratio estimate

3.2 Operation condition

When the turbine is operating, it is also excited by the periodical force derived from the blades. When the wind speed at the hub height is under the rated wind speed, the rotor speed fluctuates with the wind speed, resulting in an unsteady excitation. When the wind speed is over the rated wind speed, the rotor speed stay stable and the pitch angle is adjusted to keep rated output power, resulting in a periodic excitation.

Welch method was applied to estimate the power spectrum of the acceleration data. In Fig.8, *nP* stands for *n* times of the frequency corresponding to the rated rotor speed. The rated speed is 13.75 rpm. P = 13.75/60 = 0.229 Hz. $3P$ = 0.688Hz. It can be seen from the power spectrum of parked condition that the first natural frequency is 0.43 Hz and the second natural frequency is 1.68 Hz. The components of $1P$ and $3P$ are clear in the power spectrum of operation condition besides the first two natural frequencies. It is worth noticing that the amplitude is not draw in log scale. The background components are relatively obvious if compared to other research results. It might be the intrinsic property of this kind of structure whose integrity relies on the prestress of steel strands other than continuous longitude reinforcing rebar.

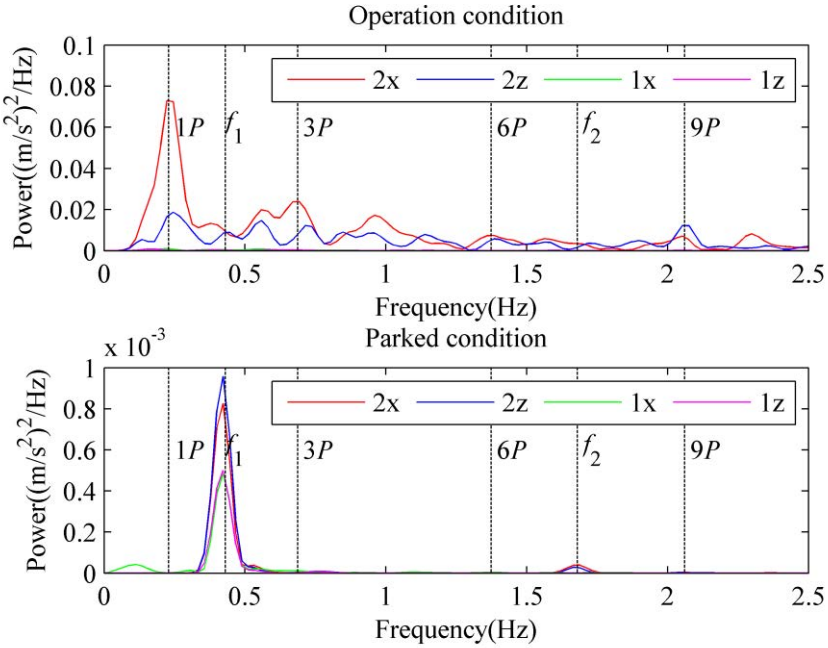


Figure 8: Power spectrum of the acceleration at measuring points

5. Conclusion

The strain monitoring system and the prestressed steel strands force monitoring system have been proved effective. They will serve to monitor the health state of the concrete tube and the prestressed steel strands. The acceleration field test result indicated the first natural frequency of 0.43 Hz and the damping ratio of 4%, providing reference for sequent modal estimate and seismic design.

Acknowledgements

References

[1] R. Rolfes, S. Zerbst and G Haake, "Integral SHM-system for offshore wind turbines using smart wireless sensors," in *Proceedings of the 6th international workshop on structural health monitoring, Stanford, CA, USA, September 11-13, 2007*.

[2] D. Hartmann, K. Smarsly and K.H. Law, "Coupling sensor-based structural health monitoring with finite element model updating for probabilistic lifetime estimation of wind energy converter structures," in *Proceedings of the 8th international workshop on structural health monitoring, Stanford, CA, USA, September 1, 2011*.

[3] M. Botz, S. Oberlaender and M. Raith, "Monitoring of wind turbine structures with concrete-steel hybrid-tower design," in *8th European workshop on structural health monitoring (EWSHM 2016), Bilbao, Spain, July 5-8, 2016*.

[4] X. Bai, M. He and R. Ma, "Structural condition monitoring of wind turbine foundations," *Proceedings of the Institution of Civil Engineers-Energy*, vol. 170, pp. 116-134, Aug. 2017.

[5] R. Ma, Y. Ma and H. Liu, "Ambient vibration test and numerical simulation for modes of wind turbine towers," *Journal of Vibration and Shock*, vol. 30, pp. 152-155, Mar. 2011. (In Chinese)

[6] K. Dai Y. Wang and Y. Huang, "Field testing of an in-service wind turbine tower using a laser based remote sensing method," *Chinese Journal of Engineering*, vol. 38, pp. 1475-1481, Oct. 2016 (In Chinese)

Proceedings of the IASS Annual Symposium 2019 – Structural Membranes 2019
Form and Force
7 – 10 October 2019, Barcelona, Spain
C. Lázaro, K.-U. Bletzinger, E. Oñate (eds.)

Model Fidelity between Automated Simplified Model and Full FEA Model as Compared in SAP2000

Alloy Hudson KEMP

Thornton Tomasetti, Inc.
707 Wilshire, #4450, Los Angeles, CA 90017
akemp@thorntontomasetti.com

Abstract

This report outlines and discusses the methods of analysis performed by TT for the verification of the cold formed steel truss design strategy. The study compares the partial models to a more inclusive FEM model of the same structure to establish the level of fidelity between the results of the two models.The analysis of the combined full model validates the results of the simple model and confirms the simple model is acceptable for use on this project.

Keywords: Cold formed steel, structural model, SAP2000

1. Introduction

For a confidential project in the US [permission to name project or show photos will be sought prior to presentation], Thornton Tomasetti (TT) was retained as the Engineer of Record (EOR) for the façade system. The façade design is an undulating, curved form made from bespoke molded Fiber Reinforced Plastic (FRP) and supported off the main structure by cold-formed steel trusses. The trusses are largely straight members, and the curvature in the FRP panels is accommodated by a curved cold-formed element in the front of the truss and bespoke connections between that respond to the curvature of the panel.

The project schedule was compressed, and the engineering team was challenged to create an analysis process that would be both efficient and sufficiently accurate for our responsibility as Engineer of Record.

2. Purpose of the Study

This report outlines and discusses the methods of analysis performed by TT for the verification of the cold formed steel truss design strategy. The structural calculations of the cold formed steel members is split up in several “partial models” and analyzed with a Finite Element Method (FEM) model. Dividing up any structure into partial models by its nature raises the question regarding the fidelity of the idealization of the structure. The study compares the partial models to a more inclusive FEM model of the same structure to establish the level of fidelity between the results of the two models.

This study will inform if there is sufficient fidelity of the analysis results between a Finite Element Method (FEM) model of the complete model and separate FEM models to justify the use of partial FEM models for the different scope parts of the façade backup structure.

3. Model Setup and Analysis

3.1. Software

Copyright © 2019 by the author.
Published by the International Association for Shell and Spatial Structures (IASS) with permission.

SAP2000 version 20 is the primary structural analysis software used for analyzing the structure and loads. CFS is used to calculate member capacities for axial, shear and bending for cold formed steel and provides results that can be summarized in the form of demand to capacity ratios (DCR's). Excel provides a means of evaluating data from SAP, such as member length and forces, to CFS calculations for design checks, using an automation module.

3.2. Setup

TT uses linear elastic analysis for all FEM models. There is a limited amount of redistribution of stresses allowed by code, accounting for any stress concentrations around fasteners. The geometry of the support structure is stable enough to keep the geometric second order effects of the overall model well under the allowable limit of 10%. This means there is no need to analyze non-linear plastic material or non-linear geometric behavior for the overall FEM model. Local effects are verified in the member checks and detail calculations where applicable.

TT assumes that all truss connections are true pins as applicable, simplifying the effective length factor to 1.0 for all members. This assumption allows the use of the Effective Length Method used for traditional buckling analysis by assuming there are no partial fixities in the trusses.

All truss members are made of cold formed steel, which is available in two grades: 33ksi and 50ksi. All members with a gage thickness of 54mil or heavier shall be 50ksi cold formed steel while all other sections with a lighter gage thickness shall be 33ksi. All of the members used in the models use the 50ksi grade.

The FRP panels have the following key properties: elastic modulus of 1,000ksi, flexural strength of 16ksi and compressive strength of 18ksi.

Both the combined simple model and the combined full model include the secondary steel truss. The secondary steel truss consists of truss chords, web members, compression struts, braces, and straps.

The following sections are typical in both models:

- (2) 800S250-68 – Truss Chords
- (2) 362S200-54 – Truss Webs
- (2) 600S200-68 – Compression Struts
- 5.00x97 – Straps
- (2) 250S162-54 – Braces

3.3. Loads and Load Combinations

3.3.1. Dead and Superimposed Dead Loads

In the analyses performed by TT, dead load is considered to be the self-weight of members. Dead load and superimposed dead load always act in the direction of gravity. In the simplified model, superimposed dead load includes the FRP and Tertiary trusses (bowtrusses) and MEP. These values are as follows:

- FRP = 6psf
- Bowtruss = 3psf
- MEP = 2psf

In the full model, SDL includes MEP only, as the rest of the elements are explicitly modeled.

3.3.2. Live Loads

Live loads apply to any surface of the facade where the angle between the panel and horizontal plane is less than 30 degrees and has open space above it, similar to a sloped roof conditions. The live load applied is 20psf and acts in the direction of gravity.

3.3.3. Wind Loads

Wind loads act normal to surfaces formed by the facade. Positive wind pressure is taken as +20psf and negative wind suction is taken as -25psf.

3.3.4. Seismic Loads

Seismic loads are applied in 3 axes based on the direction of seismic movement being observed.

Two seismic forces of equal magnitude apply to each node of the truss and act in the global x- and y-axes. An envelope case encompasses 8 directions of the seismic force (+ or -; x or y; and in the percentages 100% or 30%). The magnitude of the seismic force applied at the nodes depends on the tributary area of the nodes and the weight, both self and superimposed, of that area and its included elements.

The seismic force in the global z-axis is applied in the gravity direction.

3.3.5. *Loads Due to Seismic Displacement of the Building*

Based on the structural general notes, an interstory drift of H/250 is applied to the model to force seismic displacement of the truss. The displacement applies in the same 8 directions used by the applied component seismic forces and has its own load case.

3.3.6. Combinations

Wind loads act normal to surfaces formed by the facade. Positive wind pressure is taken as +20psf and negative wind suction is taken as -25psf.

The analyses performed by TT conform to the following load combinations.

Table 1 - LRFD load combinations from ASCE 7-10.

Equation #	Load Combination
2.3.2-1	1.4D
2.3.2-2	1.2D + 1.6L + 0.5(L_r or S or R)
2.3.2-3	1.2D + 1.6(L_r or S or R) + (L or 0.5W)
2.3.2-4	1.2D + 1.0W + L + 0.5(L_r or S or R)
2.3.2-5	1.2D + 1.0E + L + 0.2S
2.3.2-6	0.9D + 1.0W
2.3.2-7	0.9D + 1.0E

3.4. Assemblies and Components

3.4.1. Secondary Trusses

The secondary trusses are three dimensional space trusses constructed from cold formed steel sections and gusset plate connections at each node of the truss. All truss members are released for major and minor bending at both ends and released for torsion at one end where applicable while maintaining model stability.

3.4.2. Connections to Primary Structure and Supports

The primary structure supports each truss section at four points. The top two points are restrained vertically while the bottom two are released. The right side truss supports are released laterally while the left side are restrained.

The goal is to release the system as much as possible to prevent the locking in of forces due to temperature changes or forced displacements. Due to the geometry of the façade support structure it is not possible to completely release all the supports. For a complete release, all four supports need to be in a single plane. Since this is not usually the case for this project, some member forces do exist due to "locking in" or "over-constraining" of the FEM model. The connections to the primary structure are purposely angled to minimize this effect.

In other words, the connections to the primary structure, as modelled as supports in the FEM models, are detailed to approach a statically determined system as closely as possible.

3.4.3. Connections between Secondary and Tertiary Systems

The connections transfer the gravity and lateral loads while allowing for building tolerances and construction sequencing. They allow a 17-degree rotation, 1inch (25mm) adjustability in each direction, and for the entire tertiary system to be hung without access from the interior. In both the simplified and full models, this connection element is modeled as an extremely stiff member.

3.4.4. FRP Connection to Tertiary System

The tertiary system supports the FRP panels via stainless steel T-pins. These T-pins are fixed to the tertiary members and fixed to the FRP panels.

T-Pin member release was studied in three models: fixed at both ends (baseline), pinned at FRP and fixed at tertiary (A), fixed at FRP and pinned at tertiary (B).

After analyzing, there was no discernible difference to the forces and moment in the secondary truss members.

The only noticeable difference seen was axial force in the bowtruss chords under thermal loads. The baseline option incurred 1.4kips of force, while connections option A and B developed 0.75kip and 0.69kip, respectively. This is due to the difference in thermal expansion properties between steel and FRP, and the FRP effectively locking in the steel from expanding.

Thus fixed-fixed (baseline) T-pin connection option which was shown to be conservative, and was used in the Full model described in this report.

4. Combined Simple Model

The combined simple model, as the name implies, reduces the number of elements analyzed by excluding the FRP panels, bow trusses, and their connecting elements.

For the simplified model, point loads are calculated in Grasshopper from 3D modeled FRP panel surfaces. These point loads apply to the ends of the "CONN_stiff" elements, which represent the offset of the ball joint connection. The magnitude of these point loads depend on tributary areas from the FRP panels and bow trusses. See Table 2 for a list of loads applied to the simplified model and their corresponding figures for illustrations of the load applications.

Table 0 - Order of Loads Shown for Simplified Model.

Load Case	Load	Applied To
DL	Superimposed Dead Load (FRP Panels and Bowtrusses)	Tertiary Connector

	Superimposed Dead Load (MEP)	Truss Nodes
LL	Live Load	Select Tertiary Connectors
W	Positive (+)	Tertiary Connector
	Negative (-)	Tertiary Connector
E	E-X, E-Y, E-Z due to components and cladding	Tertiary Connector
	E-X_SW, E-Y_SW, E-Z_SW due to self-weight	Truss Nodes
	E-X_BLDG, E-Y_BLDG, E-Z_BLDG Displacement	Support Nodes

5. Combined Full Model

The combined full model is identical to the combined simple model with regard to geometry and load path up to the ball joint element. From the ball joint element, the combined full model includes the king hats, tertiary systems, T-pin elements, and FRP panels.

For the combined full model, area loads such as Wind and Live apply directly to the FRP panels and the forces distribute through the structure. Due to the completeness of the model, it does not require the application of superimposed dead loads due to components and cladding. Application of the superimposed dead load due to MEP is still required. See Table for a list of loads applied to the full model and their corresponding figures for illustrations of the load applications.

Table 3 - Order of Loads Shown for Full Model.

Load Case	Load	Applied To
DL	Superimposed Dead Load (FRP Panels and Bowtrusses)	Not explicitly defined
	Superimposed Dead Load (MEP)	Truss Nodes
LL	Live Load	Select FRP Panels
W	Positive (+)	FRP Panels
	Negative (-)	FRP Panels
E	E-X, E-Y, E-Z due to components and cladding	Tertiary Connector
	E-X_SW, E-Y_SW, E-Z_SW due to self-weight	Truss Nodes
	E-X_BLDG, E-Y_BLDG, E-Z_BLDG Displacement	Support Nodes

6. Results Comparison

6.1. Support Reactions

	Simple Model				**Full Model**				**Compare**
	Global FX (kip)	**Global FY (kip)**	**Global FZ (kip)**	**Resultant (kip)**	**Global FX (kip)**	**Global FY (kip)**	**Global FZ (kip)**	**Resultant (kip)**	**Resultant % of Simple**
DEAD	-	-	5.925	5.925	-	-	5.924	5.924 [1]	100.0%
DL+SDL	-	-	30.063	30.063	-	-	24.523	24.523	***81.6%***
SDL	-	-	20.126	20.126	-	-	14.463	14.463 [2]	***71.86%***
SDL_FRP	-	-	-	-	-	-	9.743	9.743	-
SDL_MEP	-	-	4.136	4.136	-	-	4.136	4.136	100.0%
LIVE	-	-	3.201	3.201	-	-	3.123	3.123	97.6%
WIND(+)	-17.214	26.533	-11.198	33.552	-13.851	22.339	-9.227	27.857	***83.0%***
WIND(-)	21.520	-33.162	14.002	41.939	17.313	-27.924	11.533	34.821	***83.0%***
E-X	-7.223	-	-	7.223	-7.224	-	-	7.224	100.0%

E-Y	-	-7.223	-	7.223	-	-7.224	-	7.224	100.0%
E-Z	-	-	3.780	3.780	-	-	3.780	3.780	100.0%
E-X_SW	-2.913	-	-	2.913	-2.913	-	-	2.913	100.0%
E-Y_SW	-	-2.913	-	2.913	-	-2.913	-	2.913	100.0%
E-Z_SW	-	-	0.687	0.687	-	-	0.687	0.687	100.0%

1. Dead load is of secondary truss elements only and equal between both models.

2. SDL of the FRP and Tertiary trusses (Bowtrusses) are applied in the same case in the Simple model, as "SDL". The SDL from MEP loads is explicitly applied to truss nodes in both models. From the material properties of the Full model, the modeled FRP load is 9.743 kip. Thus the SDL load is derived from subtraction.

The SDL load applied in the Simple model is more conservative than the actual modeled elements.

The Live load applied in the Simple model is also more conservative. This can be attributed to the Grasshopper script which takes the entire area of the FRP, not just the projected area.

The Wind loads applied in the Simple model are consistently 17% conservative. This can be attributed to the Full model – with the mesh modeled explicitly – being more efficient with distributing tributary area to the nodes. The Grasshopper script is more simplistic and may overcount some area. However, this is more conservative and thus it is acceptable.

Overall, the models' resultant reactions are aligned such that the simplified model can be used in lieu of the full model for each bay.

6.2. Member Force Distribution

There is a high degree of fidelity between the simplified model and the full model. In the load cases where the loads are applied to the ends of the ball joint members in the simple model, there can be additional moment on those truss chords. This is due to the ball joint member being fixed to the truss chords in the simple model while being pinned in the full model.

As shown in the images, where the max force in the full model exceeds that of the simplified model, the difference is small enough (less than 2 kip) that it can be ignored. Therefore the simplified model is acceptable for use in design of the trusses.

6.3. Demand to Capacity Ratios (DCR)

The names of each secondary truss members are the same in both the simple and full models, allowing direct comparison of the DCR check. This check is performed with a macro in Excel, which uses strength values computed by CFS through an automation module. Please refer to Appendix 3 for the complete table of DCR results.

Below is a plot of every member's maximum DCR (ultimately what would be used for design).

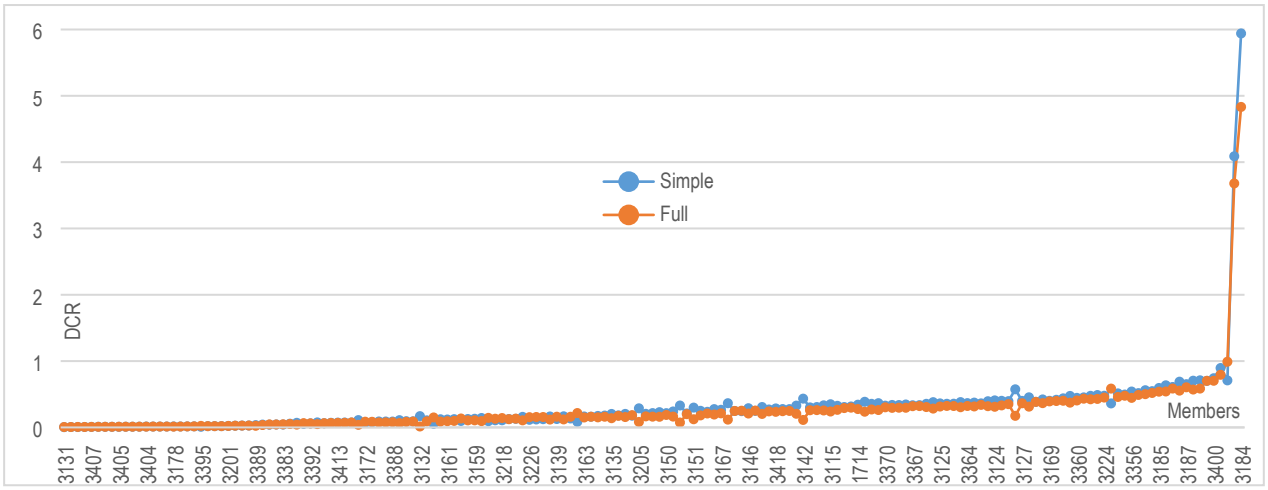


Figure 1 – Plot of maximum DCR per member, for both Simple and Full models. DCR Axis set from 0 to 6.

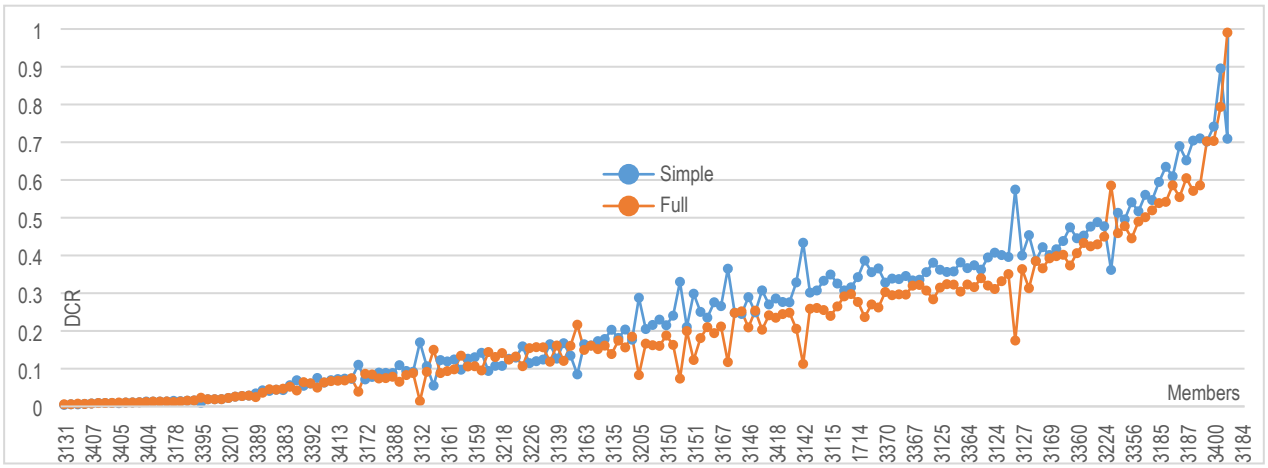


Figure 2 – Plot of maximum DCR per member, for both Simple and Full models. DCR Axis scaled from 0 to 1.

The DCR numbers for each member are very close in magnitude. Generally the simple model members have higher DCRs. The two members that fail the DCR check are the same in both models, with similar magnitudes.

Both models' DCR check show the same two members failing in the same load cases. The simple model's DCR results are slightly conservative here compared to the realistic full model. This is likely due to the larger forces from SDL and Wind as previously discussed.

Name	Section	Length	LoadCase	DCR
3184	(2) 800S200-68	176.414	5_1.2D+1.0L+1.0Eh+1.0Ev	5.940
3184	(2) 800S200-68	176.414	6.1_0.9D+1.0Eh-1.0Ev	4.982
3184	(2) 800S200-68	176.414	7.1_0.9D+1.0Eh+1.0Ev	4.982
3184	(2) 800S200-68	176.414	5_1.2D+1.0L+1.0Eh+1.0Ev	4.120
3189	(2) 800S200-68	193.232	5_1.2D+1.0L+1.0Eh+1.0Ev	4.088
3189	(2) 800S200-68	193.232	5_1.2D+1.0L+1.0Eh+1.0Ev	4.012
3184	(2) 800S200-68	176.414	5_1.2D+1.0L+1.0Eh+1.0Ev	3.639
3189	(2) 800S200-68	193.232	4.1_1.2D+1.0W(+)	3.525
3189	(2) 800S200-68	193.232	4.1_1.2D+1.0W(+)	3.513

Figure 3 - Excerpt of DCR check for simplified model.

Name	Section	Length	LoadCase	DCR
3184	(2) 800S200-68	176.414	5_1.2D+1.0L+1.0Eh+1.0Ev	4.833
3184	(2) 800S200-68	176.414	6.1_0.9D+1.0Eh-1.0Ev	4.107
3184	(2) 800S200-68	176.414	7.1_0.9D+1.0Eh+1.0Ev	4.107
3189	(2) 800S200-68	193.232	5_1.2D+1.0L+1.0Eh+1.0Ev	3.679
3189	(2) 800S200-68	193.232	5_1.2D+1.0L+1.0Eh+1.0Ev	3.534
3184	(2) 800S200-68	176.414	5_1.2D+1.0L+1.0Eh+1.0Ev	3.350
3189	(2) 800S200-68	193.232	4.1_1.2D+1.0W(+)	3.019
3189	(2) 800S200-68	193.232	4.1_1.2D+1.0W(+)	3.016

Figure 4 - Excerpt of DCR check for full model.

7. Conclusions

The analysis of the combined full model validates the results of the simple model and confirms the simple model is acceptable for use on this project.

The base reactions between the two models are nearly identical. The force distribution and magnitude among members is similar in most cases, and understood when not. The deflections (and therefore, stiffness matrix) are also aligned.

The DCR check shows alignment between the models as well. As this is the key calculation in design of the secondary members, it shows that the DCR check of a simplified model can be used in further design of the secondary trusses.

Modeling of tertiary system and the connections between, FRP and connections between is not necessary to achieve a result that is reliably accurate to design the secondary truss members.

Proceedings of the IASS Annual Symposium 2019 – Structural Membranes 2019
Form and Force
7 – 10 October 2019, Barcelona, Spain
C. Lázaro, K.-U. Bletzinger, E. Oñate (eds.)

Reinforcements of the Cylindrical Panel with Opening

Takashi HARA*

* National Institute of Technology, Tokuyama College
Gakuendai, Shunan 745-8585, Japan
t-hara@tokuyama.ac.jp

Abstract

Reinforced concrete (R/C) shell with an opening reinforced by the improved reinforcing method was examined numerically and was compared with that reinforced by the conventional diagonal reinforcements. In this method, only the hoop and the meridional reinforcement was arranged equivalent to the diagonal reinforcements around the corners of an opening. FEM analyses were done to evaluate the efficiencies of the improved reinforcing method comparing with the conventional reinforcing method. From the numerical analyses, the model with improved reinforcing method, that is the replacement of the diagonal reinforcement to the equivalent meridional and hoop reinforcements at corners, shows the slightly smaller initial stiffness and the same load carrying capacity comparing with the model using the conventional reinforcement method under compressive or tensile loads. Both models shows the same crack propagation. From the numerical results under uniformly distributed lateral load, the stiffness and the ultimate load of the improved model show almost the same as those of the conventional model. Although the experimental results to confirm the validities of the improved reinforcement method are required, it will be the useful method to reduce the placement work of diagonal reinforcements at the shell opening.

Keywords: R/C shell, opening, stiffening, numerical analysis, nonlinear

1. Introduction

Reinforced concrete (R/C) cylindrical chimney has a large opening at the lower portion to take in a flue-gas. R/C cylindrical roof has also infrequently openings to take in the sunlight. The region around the hole is prone to decrease the strength and the stress concentration is arisen at the corners. It was reported that R/C chimney with wide opening destroyed due to the earthquake [1].



Figure 1: Collapse of Tupras Chimney[1]

Copyright © 2019 by Takashi HARA
Published by the International Association for Shell and Spatial Structures (IASS) with permission.

Figure 1. shows the stack collapsed under the earthquake Kocaeli in 1999. The stack had large rectangular hole at the lower portion of it. In Figure 1, the dotted line shows the outline of the stack before collapse. The reports concluded that the collapse of the stack caused due to the wide opening and a lack of reinforcement around the rectangular hole.

To prevent the collapse of the structure due to such discontinuity of the structure, many researches have been studied the reinforcement method around the hole. Doh et al. studied the reinforcing method of the flat wall experimentally [2]. In the same manner, the design code of the chimney with hole was recommended by ACI [3]. The thickness of the concrete around the hole is increased and the meridional and hoop reinforcements were placed equivalent to the loss amount of reinforcements at the hole. In addition, the diagonal reinforcements were placed to prevent the corner failures as well. However, in case of placing the diagonal reinforcements in the shell, reinforcing bars have curved shape (Figure 2). In case of placing the diagonal reinforcements in the shell, the placing works are laborious because reinforcing bars have curved shape and diagonal.Sami stated the difficulties to place them and the requirement of improving these works [4].

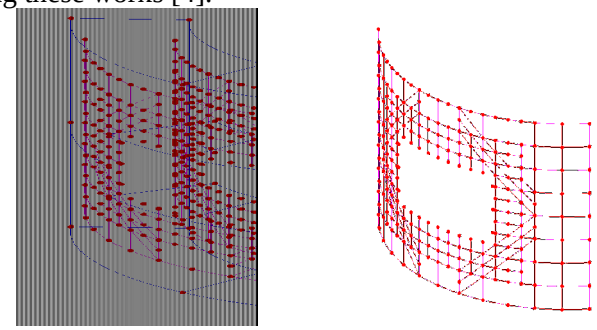


Figure 2: Current reinforcement around the Hole

This paper applied the improved reinforcement method instead of placing the conventional diagonal reinforcements. The improved reinforcement method arranged only the hoop and the meridional reinforcement equivalent to the diagonal reinforcements around the corners. FEM analyses evaluated the efficiencies of the improved reinforcing method comparing with the conventional reinforcing method.

The numerical analyses examined four types of model. One model was R/C panel without hole and three models were R/C panels with hole. These three models contain the model with the conventional reinforcement, the model only with hoop and meridional reinforcements and the model with improved reinforcements. Numerical models were cylindrical panel supported on hoop edges and free along the meridional edges when R/C panel was subjected to the axial compression or the axial tension. In case of the lateral loading, R/C panel was supported on both meridional edges.

The stiffness, the ultimate strength and the crack propagations were compared among these models.

2. Numerical analysis

2.1. Numerical model

Figure 3 shows the configuration of the numerical model. The model is R/C cylindrical panel. Intending to compare the experimental analyses, the model is small. The radius and the opening angle are 693.75mm and 83.08degrees, respectively. The height and the thickness are 900mm and 40mm, respectively. The shell has the rectangular (264mm x 240mm) opening in the middle of the shell panel. The reinforcements are placed in both hoop and meridional directions. The reinforcement ratio is 0.35% in each inner and outer surface [5]. The concrete cover is 5mm. The reinforcing methods adopted in this paper are shown in Figure 4. Figure 4(a) shows the panel without hole. Figure 4(b) shows the panel

with hole and the reinforcements are removed at the hole and no additional reinforcements are placed around the hole edges. In Figure 4(c), the panel with hole has conventional reinforcements [3]. The hoop and meridional reinforcements removed by the hole are placed around the hole, respectively. In addition, the diagonal reinforcements are placed to prevent the local failure. Finally, in Figure 4(d), the hoop and the meridional reinforcements are placed in the same mannor of Figure 4(c) and the diagonal reinforcements are replaced to meridional and hoop reinforcements with the same diagonal reinforcement ratio as shown in Figure 4(c). The material properties adopted in this analyses are shown in Table 1.

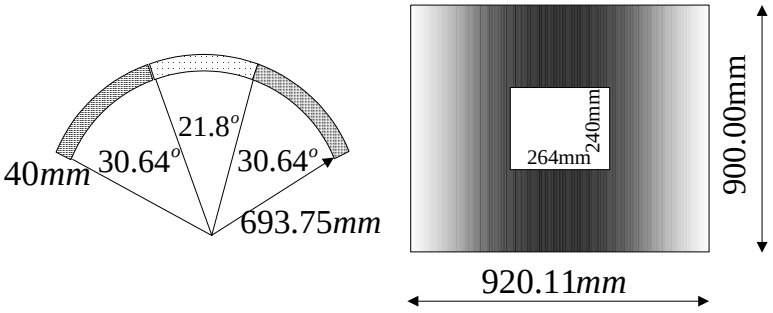
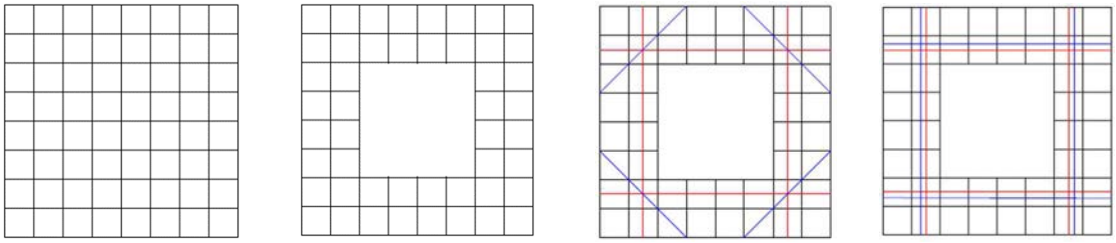


Figure 3: Configuration of R/C panel



(a)Without hole (b)With hole (c) With hole+m+h+d (d)With hole+2m+2h

Figure 4: Reinforcing patterns

Table 1. Material properties

CONCRETE		STEEL	
Elastic Modulus E_c	22.3*GPa*	Elastic Modulus E_s	208*GPa*
Poisson's ratio V	0.20	Hardening Parameter H'	0.01
Compressive Strength f_c'	34.4*MPa*	Yield Strength f_y	235*MPa*
Tensile strength f_t	3.44*MPa*	Tensile Strength f_b	402*MPa*

Figure 5 shows the chimney with hole at lower portion of the shell. In case of the hole is leeward, the compressive load is applied to the shell around the hole when the shell is subjected to the wind load. On the other hand, the tensile force is applied when the hole is windward. In addition, if the shell thickness is small comparing with the shell diameter, the out of plane bending is quite important. Therefore, in this paper, the compressive and the tensile forces as well as the lateral load are applied as the external loads. R/C panels are supported on hoop edges and are free on meridional edges in case of compressive or tensile load. Supporting points are equally placed five portions on the hoop edges. The compressive and the tensile loads are applied to the opposite hoop edge of supporting edge in the meridional direction (see Figure 6). In case of chimney subjected to wind load, the lateral load is applied to R/C panel with hole. R/C panel is supported along the meridional edges (see Figure 7). Figure 7(a) and 7(b) shows the pin-pin support and the pin roller support, respectively.

Each model is divided into 32 elements in hoop direction and 28 elements in meridional direction, respectively. Also, R/C panel is divided into four element through the thickness. Therefore, the shell had at least seven integration points through the thickness.

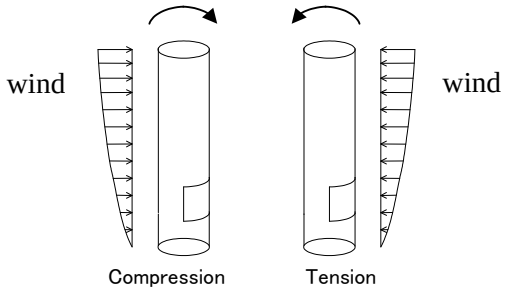
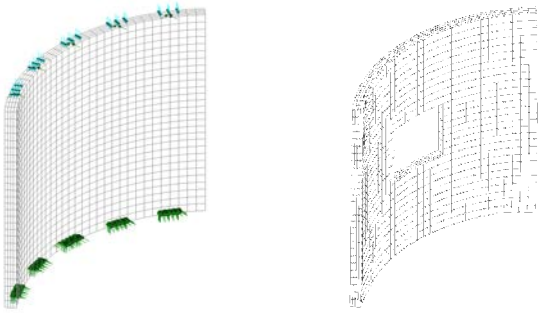
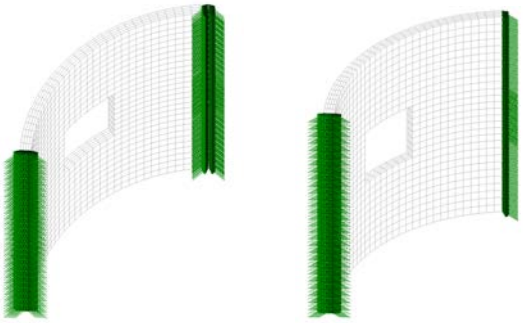


Figure 5: R/C chimney with the hole under wind load



(a) R/C panel without hole (b)R/C panel with hole

Figure 6: Numerical model of R/C panel under compression or tension



(a) R/C panel with pin-pin support (b) R/C panel with pin-roller support

Figure 7: Numerical model of R/C panel under lateral load

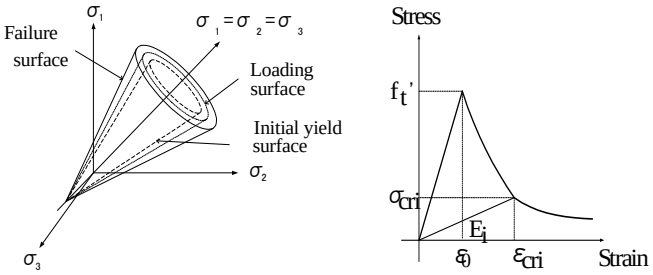
2.2. Numerical procedure

The inelastic behavior of concrete possesses the recoverable strain components and irrecoverable strain components. Under tri-axial stress state, the yield function depends not only on the mean normal stress I_1 but also on the second deviatoric stress invariant J_2 [6]. The yield condition of tri-axial compressive concrete is expressed by Drucker Prager criterion (see Figure 8(a)) [6-7].

$$f(I_1, J_2) = \sqrt{\beta(3J_2) + \alpha I_1} = \sigma_0 \tag{2}$$

where α and β are the constants. Also σ_0 is the equivalent stress.

Parameters adopted in the criterion are defined by the Kupfer's experiment [8]. It is assumed that the initial yield begins when the equivalent stress exceeds $0.3f_c$ (f_c: compressive strength of concrete). Also, the crushing condition of concrete is described as a strain control phenomenon and the crushing condition is defined as like as the yield function [6-7].



(a)Yield surface (b) Stress strain in tension

Figure 8: Stress status

The response of concrete in tension is modeled as a linear-elastic brittle material and maximum tensile stress criteria are employed. After cracking, to evaluate the stiffening of reinforced concrete, the stress reduction of the concrete normal to the cracked plane is assumed as an exponential degradation curve (see Figure 8(b)).

$$\sigma = f_t' \exp\left(-\frac{\varepsilon - \varepsilon_t'}{\gamma}\right), \quad \gamma = \frac{G_f - 0.5 f_t' \varepsilon_{cr} \ell_c}{f_t \ell_c} \tag{2}$$

where f_t' is maximum tensile strength of concrete, γ is the tension stiffing parameter, ε_t' is crack strain, G_f is the fracture energy of concrete, ℓ_c is the cubic root of volume in Gaussian point and ε_{cr} is the strain in crack. γ =0.1 is adopted in this paper due to the characteristics of normal concrete.

The reinforcing bars are considered as steel sheet. The bilinear idealization is adopted in order to model the elasto-plastic stress strain relationship and both the tensile and the compressive states are governed by the same relationship. The reinforcements modele as steel sheets had the same node as the concrete element nodes and were placed at the reinforcing position with the excentricity equivalent to the concrete cover.

3. Numerical results

Applying the numerical procedure mentioned avobe, the stiffness, the ultimate strength and the crack propagations were evaluated under the conditions presented in the previous chapter and the numerical resuilts are compared smomg these models.

3.1. R/C panel under axial compression

Figure 9 shows the load deflection relations of R/C panel under an axial compression. The displacement referenced point is is the top center of the hole. The positive displacement is upward (see Figure 6). The legends are the reinforcing method shown in Figure 4.

The stiffness of R/C panel with hole is smaller than that of R/C panel without hole due to the loss of the shell body. Also, from Figure 9, the ultimate strength of R/C panel with hole stiffened by the conventional method (long dash) is smaller than that R/C panel without hole.

Figure 10 shows the crush and the crack status of R/C panel with hole. R/C panel stiffened by the hoop,

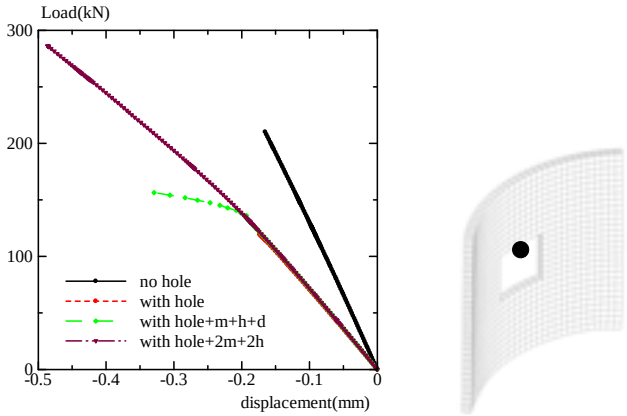
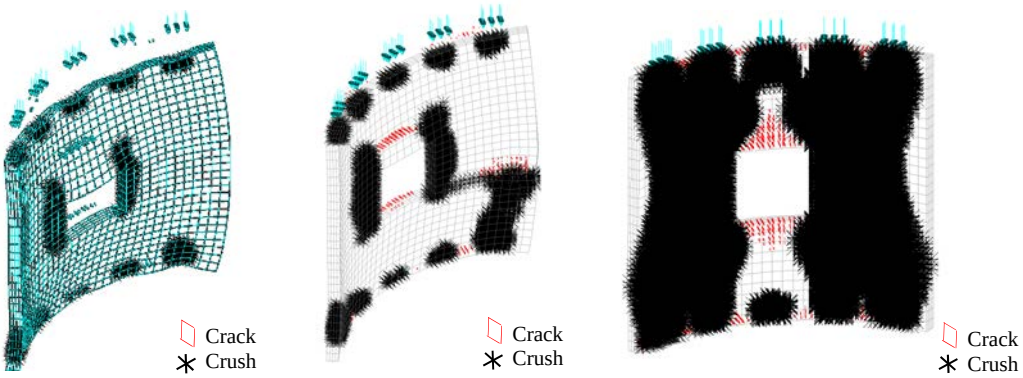


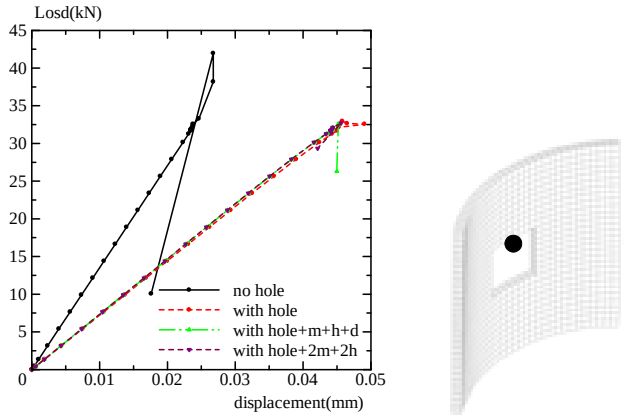
Figure 9: Load deflection relation of R/C panel under compression



(a)with hole (b) with hole +m+h+d (c)with hole with 2m+2h

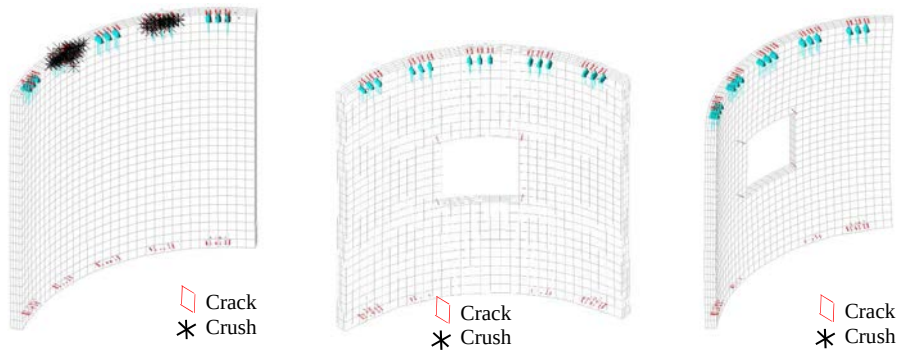
Figure 10: Final failure and cracks under an axial compression

the meridional and the diagonal reinforcements (conventional reinforcement) deforms at right lower portion and fails. However, R/C panel with the hoop, the meridional and both hoop and meridional reinforcement (proposed reinforcement) shows the large crack area. The ultimate strength stiffened ny propoed method is larger than that stiffened by conventional method.



3.2. R/C panel under axial tension

Figure 11 shows the load deflection relation of R/C panel under axial tension



(a)with hole (b)with hole+m+h+d (c)with hole+2m+2h

Figure 12: Final failure and cracks under an axial tension

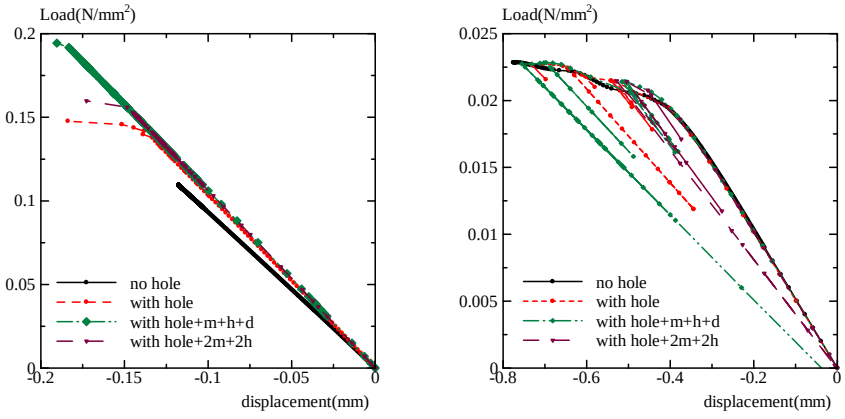
The displacement referenced point is also the top center of the hole. The positive displacement is upward (see Figure 6). The legends are the reinforcement method shown in Figure 4. The stiffness of R/C panel with hole is smaller than that of R/C panel without hole in the same manner. Also, from Figure 11, the ultimate strength and the stiffness of R/C panel with the hole show the same tendencies.

Figure 12 shows the crack and crush pattern at the failure of R/C panel. In case of the unstiffened R/C panel shows the crushing of the loading edge. Ho\wever, R/C panel with hole shows the same status as that stiffened by the conventional and the proposed reinforcements.

3.2. R/C panel under lateral load

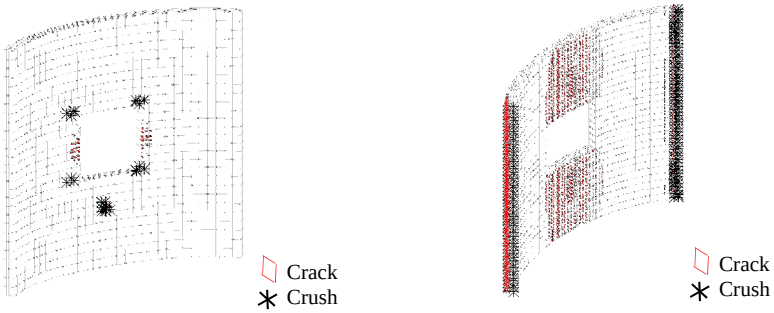
Figure 13 shows the load deflection behavior of R/C panel with hole. R/C panel is subjected to uniformly lateral load. Supporting condition is (a) pin-pin support and (b) pin-roller support (see Figure 7).

In case of R/C panel with pin-pin support, the stiffness of R/C panel with hole is larger than that without hole because the lateral load is reduced by the hole. The ultimate strength of R/C panel stiffened by the conventional reinforcement shows the largest. R/C panel with proposed reinforcement shows also the improvement of the weakness of R/C panel with hole. The stiffness R/C panel with hole shows the same results. In case of R/C panel with pin-roller support, the ultimate strength with all the reinforcement methods does not shows the particular differences. The conventional reinforcing method conrtibute the large ductility of R/C panel with hole. Figure 14 shows the cracking and crashing status.



(a)pin-pin support (b)pin-roller support

Figure 13: load deflection relation of R/C panel under lateral load



(a) pin-pin support (b)pin-roller support

(b) Figure 14: Final failure and cracks of R/C panel under lateral load

4. Conckusions

The deformation and the strength of R/C panel with hole was investigated under the axial load and the lateral load. The conventional reinforcing method was modified to replace the diagonal reinforcement to additional meridional and hoop reinforcements. From the numerical analyses, folowing conclusions are obtained.

(1) R/C cylindrical panel with hole degrade the stiffness under compressive load

(2) R/C panel with hole stiffened by the modified reinforcement shows the same or the larger ultimate strength than that stiffened by the conventional reinforcing method.

(3) The craks of R/C panel at the corners of the hole frequently occure under an axial compressive load. Also, the cracks occur under lateral load when the meridional edges are the pin-pin supported.

The proposed reinforcement method was nuerically effective under the loading und supporting conditions shown in this analysis. It is required to investigate the behabior of R/C panel experimentally and from the comparison of both results, the appropriate design systems will be derived.

References

[1] Huang W., Gould P.L., “Martinez R. and Johnson G., Non-linear analysis of a Collapsed Reinforced Concrete Chimney”, *Earthquake Engineering and Structural Dynamics*, vol.33, pp485-498, 2004

[2] Doh J. H., Fragomeni S., “ Ultimate load formula for reinforced concrete wall panels with openings, *Advances in Structural Engineering”,* vol.9, pp103-115 2006

[3] ACI Committee 307, “*Code Requirements for Reinforced Concrete Chimneys and Commentary*”, ACI, 2008.

[4] Sami A. K., Dovlet A and Selcuk A., “An investigation of Opening Reinforcement Configurations for Reinforced Concrete Chimneys”, *ICCT 2016 International Conference on Industrial Chimneys & Cooling Towers Rotterdam*, pp.213-218, 2016

[5] ACI-ASCE Committee 334, “*Concrete Shell Structures Practice and Commentary, 334.2*”, ACI, 2017

[6] Hinton E., “*Numerical methods and software for dynamic analysis of plates and shells*”, Pineridge press Swansea U.K, 1988

[7] Hara T., “Behavior of Reinforced Concrete Cooling Tower Shell under Lateral Load on Nonuniform Foundation”, *Heat Transfer Engineering*, Vol.38, pp.1127-1134, 2017.

[8] Kupfer H., Hilsdorf K.H., “Behavior of concrete under biaxial stress”, *ACI Journal*, vol.66, pp.656-666 1969.

Proceedings of the IASS Annual Symposium 2019 – Structural Membranes 2019
Form and Force
7 – 10 October 2019, Barcelona, Spain
C. Lázaro, K.-U. Bletzinger, E. Oñate (eds.)

Structural Analysis and Design of a Sectored Cylindrical Vertical Tank

Carlos M. FERRER*, José J. FERRÁN, Miguel REDÓN, Juan B. TORREGROSA, Francisco J. SÁNCHEZ

*U.Construction-DIRA; Universitat Politècnica de València

Camino de Vera s/n; Valencia 46022 (Spain)
Email caferrer@agf.upv.es

Abstract

This paper describes the conceptual design and the structural analysis of a vertical cylindrical partitioned tank for an international chemical Company. Vertical cylindrical tanks are commonly used in the chemical industry around the world as vessels to contain liquids. Most of these plants, because of the size of its plan view, have reduced area for the installation of the container tanks. Many of them have the need to renew their manufacturing process according to the new technologies and requirements. Also, in some cases, the preparation of mixtures is devoted to small areas. The stated conditions led to the idea of designing a partitioned vertical tank. In this case, for the sectored tank, alternative hydrostatic pressure cases may lead to eccentrically loads on above the surfaces. Therefore, bending stresses will occur, together with compression and tension stresses as per its specific tank deformation. Thus, partitioned tanks are classified as Class 3 according to EN 1993-4.2. Taking into account all the above-mentioned, a Finite Element Method calculation should be performed in order to determine the wall thickness fulfilling the structural requirements. This paper describes the particular models designed and the detailed FEM calculation carried out to determine the wall thickness of partitioned tanks, being obtained particular conclusions.

Keywords: Conceptual design, sectored tanks, vertical cylindrical tanks, f.e.m., stainless steel.

1. Introduction

Vertical cylindrical tanks are commonly used in the chemical industry around the world as vessels to contain liquids. Most of these plants, because of the size of its plan view, have reduced area for the installation of the container tanks. Many of them have the need to renew their manufacturing process according to the new technologies and requirements. Also, in some cases, the preparation of mixtures is devoted to small areas. The stated conditions led to the idea of designing a partitioned vertical tank for PPG Ibérica, located at Quart de Poblet, Valencia (Spain) (Figure 1). This chemical industry manufactures coating products for automobiles, trucks and vans factories, construction materials and canned drinks i.e. The coating sector moves many billions of Euros in the market around the world.

After several previous work meetings with the owners, consultants and possible contractors, it was decided to design a vertical stainless-steel tank with four independent sectors that was entrusted to the authors. Because of aesthetic questions, the tank might be cylindrical. The first contractor's projects were based on API 650 standard [1], and they thought that the tank behaves like a membrane in tension. Since the wall thicknesses were very small, we advertise about future problems because the asymmetrically structural behaviour regarding hydrostatic pressures alternation and distribution.

Copyright © 2019 by C. M. Ferrer, J. J. Ferránn , M. Redón, J.B. Torregrosa, F.J. Sánchez
Published by the International Association for Shell and Spatial Structures (IASS) with permission.



Figure 1: Aerial plant view

Taking also account that the liquid contained is hazardous (resins), with a specific weight of 1100 kg/m^3, and following EN 1993-4.2.[2], which clasifies the situation and tank type as Class 3, a finite element method should be used for the design, analysis and calculations, which is the objective of this paper.

2. Vertical sectored cylindrical tank description

The general geometry of the designed vessel is a cylindrical tank with a self-supported conical roof and a stiffened also conical bottom, inside divided in four symmetric vertical compartments throughout four walls in a cross shape intersected at the middle axle of the tank. The cylinder height is 18 m and the diameter 4,6 m which supposes an H/D ratio of 3,913 that means a slender tank. The external cylinder, whose thickness will be object of study and analysis, is projected by curved smooth welded courses, 2 m height and 7,128 m length each. The inner walls, after a particular analysis and conversations with possible contractors, are of plane corrugated 10 mm thick sheets with a constant repetition of 0,674 m in height per each. These are continuously welded at the inner extremes to a central vertical column composed by a square hollow section 250 x 250 x 12 mm, externally reinforced with four channel sections profiles 250 x 60 x 12 mm, which all together form a cross section. These channels section provide more rigidity to the set, and facilitates the assembly and welding of the corrugated shells to the central column. This is also welded to the bottom base until the intersection to the conical covering. At the opposite extreme, intersection with the cylinder, another four channels are disposed, as transition element. The idea is that the inner walls with the channels at the extremes, previously welded, should be welded afterwards to the rest of the tank facilitating the assembly and the welding disposition.

The bottom of the base presents a conical surface with 0,115 m height at the centre and an outside slope of 5%, made of smooth welded shells. To lay the conus to the horizontal base of the concrete foundation, 24 radial vertical stiffeners plates, 15º separated, are disposed varying their height according to the shape of the conus, and annular vertical reinforcement plates, ones disposed to diminishing the free shell of the conus piece, and other, as a vertical small pipe diameter 500mm, at the central area acting as support of the central column. At the opposite side, at the intersection with the curved courses, there is a ring annular plate, externally reinforced with an angular profile.

The tank is top closed with a self-supported conical covering with a central height of 0,492 m, a slope of 21%, and welded to the cylinder, disposing an external reinforcement ring too with 'L' cross section.

Furthermore, the whole of the tank is supported, anchored to the foundation throughout anchor bolt chairs. According to the former calculations 12 chairs are needed, located symmetrically around the perimeter. They are composed of a top plate and 2 gusset plates, and an anchor bolts of 30mm diameter each one.

For the final design, two alternatives were considered as regards to the external cylinder thickness, at the end, the model with an inner reinforcement bracing system was chosen. Geometrically, there are 13 rows of four frames which horizontally constitute one bracing system. Each row is spaced 1,011m in the tank height vertically, inscribed each one inside the circumference of the cylinder transverse section. They are projected with circular hollow sections, 125 mm diameter and 5 mm thickness.

In Figure 2 some views and details of the geometry are depicted for more clarity.

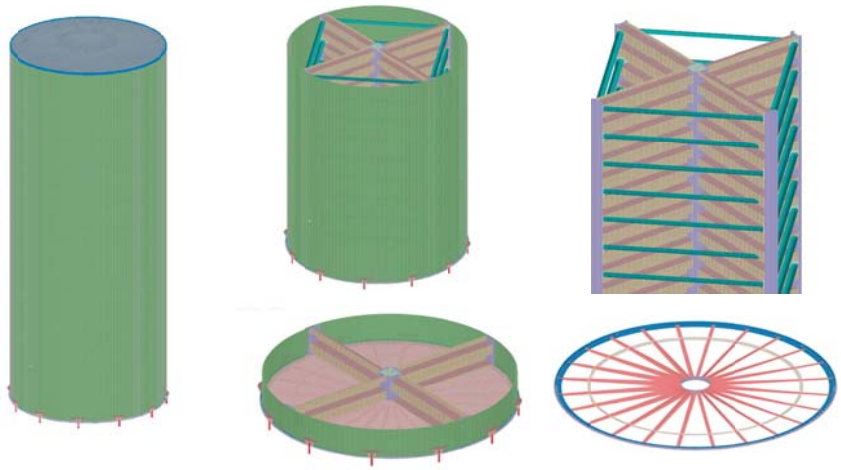


Figure 2: Geometry views: Left, general view; Top, partial section; Right, inner partitions and bracing system; Bottom, bottom tank section and stiffeners at the bottom.

3. Material properties

The whole tank is designed and will be constructed with stainless steel, with the exception of the anchor bolts that will be structural carbon steel. Every part or element steel made should comply the specifications of Eurocode 3 and EN 10088. More concretely the whole stainless steel components should verify EN 1993-1-4 [3] *General rules for stainless steel*. The stainless steel chosen is the austenitic one, grade 1.4306 (equivalent to American AISI 304, and AISI 304 L). According to table 2.1 of the mentioned Eurocode its main mechanical characteristics are:

- Yield stress: f_y = 200 N/mm^2 (Nominal stress corresponding to a 0,2% remainder deformation).
- Ultimate stress: f_u = 520 N/mm^2

Moreover, according to 2.1.3 point, and its comments, is possible to be adopted:

- Elastic modulus: E = 200000 N/mm^2
- Poisson coefficient in elastic behaviour: υ = 0,3
- Transverse shear modulus: $G=E/(2(1+v))$
- Taken account that for frames, cables and bars (affects to angular sections):Yield stress f_y = 180 N/mm^2 and Ultimate stress f_u = 460 N/mm^2
- Anchor bolts, structural steel, 6.8 class, with a Yield stress f_y = 480 N/mm^2 and Ultimate stress f_{ub} = 600 N/mm^2.

4. Actions and loading combinations

The following actions on the model, taken from Eurocodes, have been considered. The particular nomenclature used also appears. The self-weight, G, is taken from the specific weight of stainless

steel: 7900 kg/m^3. Implemented in the software, and according to the geometry, it is self-calculated and considered. For the hydrostatic pressure distribution, *W*, the specific weight of the fluid (mainly resins, taken their greater value) is 1100 kg/m^3 and asking the manufacturer. The maintenance weight on the cover, *S*, taken from Eurocode 1 EN 1991-4 [4] ,of 1 kN/m^2, has been considered. For the snow, *N*, a medium value of 1 kN/m^2, integrating many locations, has been chosen, Eurocode 1, EN 1991-1-3 [5]. For the wind, *V*, to include wide spectra of the Southern Europe, at the coast, beside Mediterranean Sea, and taking account the location of the plant at the East of Spain, Eurocode 1 submits to national specifications. According to this, a value of basic pressure of 0,42 kN/m^2, which corresponds to 26 m/s, has been taken [6].

For the calculation and analysis only the worst combinations have been considered.

Load combination coefficients for Ultimate Limit State (U.L.S.), following, National (Spanish) Specification [7] are:

- Filled tank + gravity loads: (1,35 G + 1,20 W)
- Filled tank + gravity loads: (1,35 G + 1,20 W) + S 1,5 + 0,75 N
- Filled tank + gravity loads + wind: (1,35 G + 1,20 W) + S 1,5 + 0,75 N + 0,9 V
- Empty tank + wind: (0,8 G)+ 1,5 V

Load combination coefficients for deformations analysis Serviceability Limit State (S.L.S.) are:

- Filled tank + gravity loads: (G + W)
- Filled tank + gravity loads: (G + W) + S + 0.5 N
- Filled tank + gravity loads + wind: (G + W) + S + 0,5 N + 0,6 V
- Empty tank + wind (0,8 G) + V

From the whole of the actions, the separately effect of hydrostatic pressures are the worst. As it is known, they grew proportionally with depth. Furthermore, as there are four compartments in the tank, for each combination, an alternation of loading study has been considered, following the sequence indicated in Figure 3.

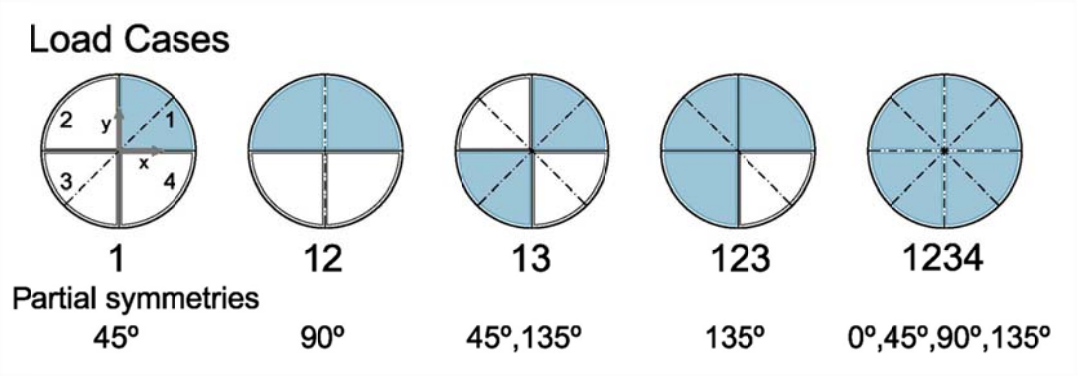


Figure 3: Load cases sequence for hydrostatic pressures loading

5. Thickness determination. Alternatives

Many previous calculations and analysis, study of preliminary designs, work meetings and discussions have been carried out to set the thicknesses for the different elements of the tank.

Since in a conventional tank the cylinder and their courses are the main elements and the most important, a deeper analysis of the thickness of the vessel has been done, and then explained in this article, but already setting as valid the thicknesses of the rest of the compartmented tank.

A deep analysis was carried out, but its extension is out of this paper. Two main alternatives have been considered: the first without any restriction or inner stiffeners, and the second with a stiffener bracing

system formed by CHS stainless steel frames disposed through the tank bottom until 13 m height approximately.

Both alternatives are technically viable. The optimum shell courses uniform thickness for the first alternative is 18 mm. For the second, included the bracing system, is 12 mm. From a structural point of view, the second alternative presents a better behaviour. Only has the inconvenience that its manufacture may be more difficult, but not enough for a specialized contractor. Furthermore, to manage with an 18 mm thickness sheets may be more complex and difficult to find. In need of a definitive economical budget, the second alternative with the bracing system present most of the advantages, and was consensually the model finally adopted.

6. Second alternative results

In this section, the main results for the definitive model: 12mm thickness and with bracing system as exposed in the before point, are offered.

The main results comprised the maximum absolute translations (X,Y,Z) in mm (SLS) and the maximum Von Mises stresses, in N/mm^2 (ULS), for each load combination. The maximum Von Mises stresses, after a rigorous analysis, are provided for different parts of the shell model: at the cylinder 'tummy bellies' (T.B.), at the 'welding seams' between the cylinder courses and the inner walls (W.S.), near or at the base (N.B.) for the bottom courses, at interior partitions(I.P.) (in the inner walls) (Figure 4). As the worst effect in the result (maxima values) is due to aximmetrically hydrostatic pressure loading, these are first offered in the next Table 1 and Figures (5, 6, 7). Subsequently effects, taking account wind loads, result negligible. A selection of them, are presented in the mentioned Figures. As a commentary, only non-linear calculations results are provided.

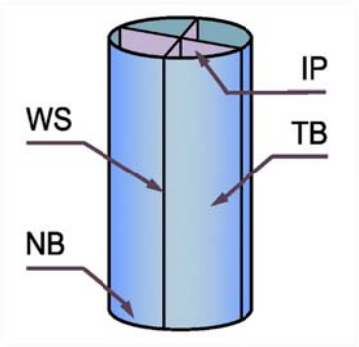


Figure 4: Maximum stresses location scheme

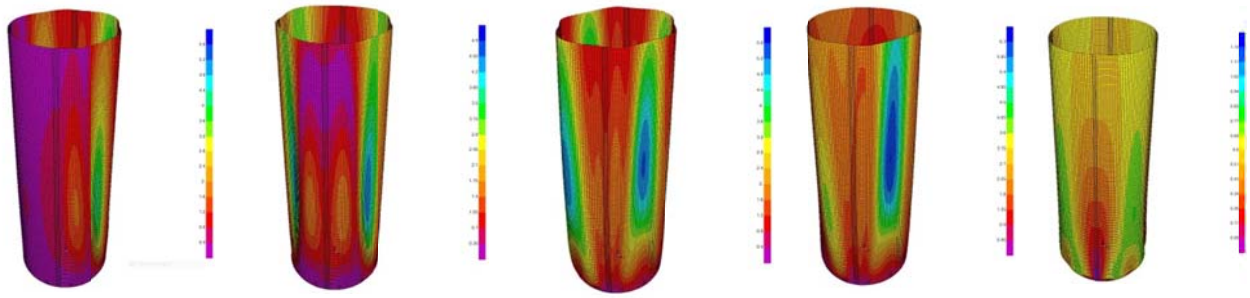


Figure 5: Absolute resultant translations. Left to right: G+1, G+1+2; G+1+3, G+1+2+3, G+1+2+3+4 (in mm)

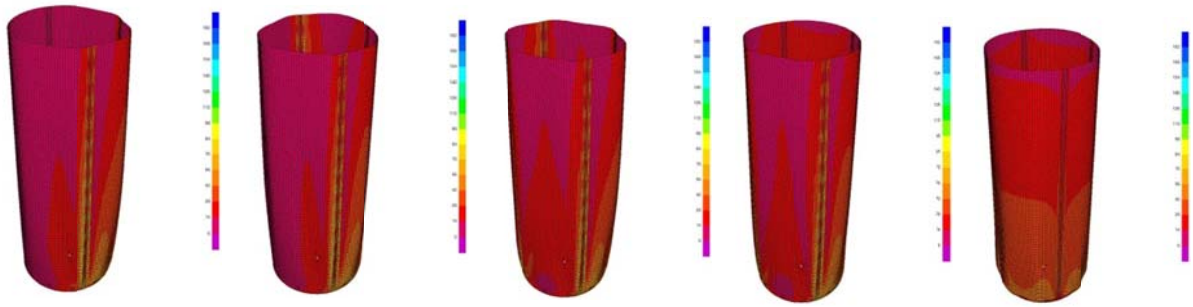


Figure 6: Von Mises stresses for the cylinder. From left to right: idem. Scale from 0 up to 182 N/mm^2

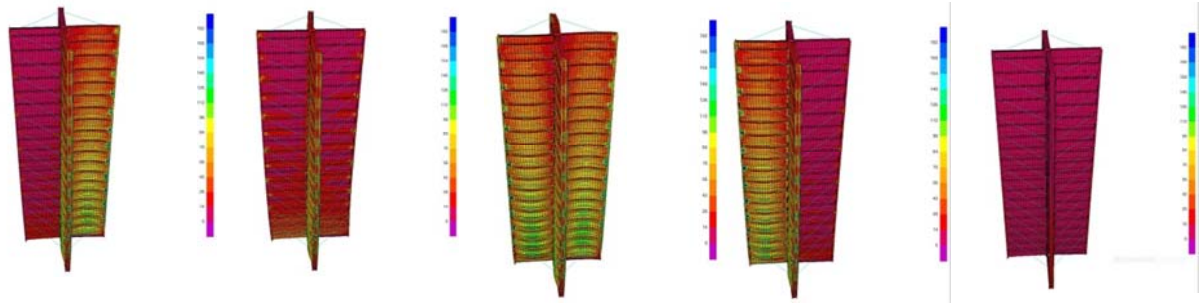


Figure 7: Von Mises stresses for the inside partitions. From left to right: idem. Scale from 0 up to 182 N/mm^2

Table 1: Main results for hydrostatic pressure combinations (self-weight G is included)

Load Combination	Absolute Translation (mm)	Maximum Von Mises Stresses (N/mm^2)			
		T.B.	W.S.	N.B.	I.P.
"1"	4,579	40,32	136,00	55,90	142,40
"1+2"	3,967	41,39	133,56	62,63	139,44
"1+3"	4,465	33,39	132,20	63,43	160,38
"1+2+3"	5,435	41,08	134,30	69,57	137,56
"1+2+3+4"	1,029	36,00	54,15	45,09	16,12

7. Conclusions

Compartmented tanks could be very useful in chemical industries, especially when there is a lack of space for their location or when mixtures are needed in the process.

Because of the aximmetrical loads affecting each compartment, they structurally don't behave as a single tank. In these last, deformations affect mainly to the circumferentially perimeter of the cylinder, usually in tension. In compartmented vertically tanks, the asymmetric structural behaviour affects to the cylinder shape, losing their original form (Figure 8). Furthermore than tension stresses, stresses due to bending moment appear, and the rest of the circumferential perimeter sections have to adapt to these deformations, as their length have to be maintained, forming inward and outward creases.

Because of that, regular or ordinary Specifications and Rules for tanks do not apply at all, being necessary to make a specific model for finite element analysis, which has more complexity of elements and loadings.

A study of the minimal thickness for the cylinder courses that verifies calculation tests (translations, stresses) has been carried out, providing two possible alternatives: one with 18 mm uniform thick; other with 12 mm and with the addition of an inner particular bracing system.

Finally, this last was the chosen solution for a more rigorous analysis.

In this solution, regarding non-linear calculation results for hydrostatic pressures loading combinations for the cases with aximmetrically loading, the worst results on deformations and stresses are obtained. These results are quite similar, affecting especially to the bottom first courses where stresses concentration are greater because of the degree of rigidity and fixing against the free deformation. For 1+2+3 combination the absolute resultant translation is the highest with main deformations in three of the sectors, and one which remains practically unstrained. For the 1+2+3+4 case there is a pressure compensation acting as an entire complete tank, with symmetrically distribution of deformations and stresses, having lower values, and only at the first course together the base because of the restrain to the cylinder deformation which provides the inner walls. In this case, stresses in the inside partitions are very low.

Adding other variable gravitational loads (S and N), generally the results are similar, especially for translations. The magnitude of these loads against the effect of hydrostatic pressures is small. Regarding the stresses, there is a small increase in the creases, especially when the gravitational loads trend to increase them, but against in some areas, i.e. inside partitions, there is a kind of loading compensation which makes them more non-deformable, at avoids the wall extremes free deformation. Stresses increases are very slight.

Conclusions for wind loads analysis, the first one, considering the tank empty, in the two considered directions, and combined with the tank self-weight, throw as results that the effect of wind is scarce compared with hydrostatic pressures load cases (each with their partial safety coefficients), so it can be previously concluded that their combination with other loads, sometimes will very few increase or decrease them according with wind direction and sector loading, but minimally, less than 2%. Thus, wind pressures effect is minimal versus hydrostatic pressure values. By the other hand, the tank remains stable without anchoring for wind loading, although it is interesting to provide them because of other loads (seismic i.e.) or other engineering questions (erection i.e.).

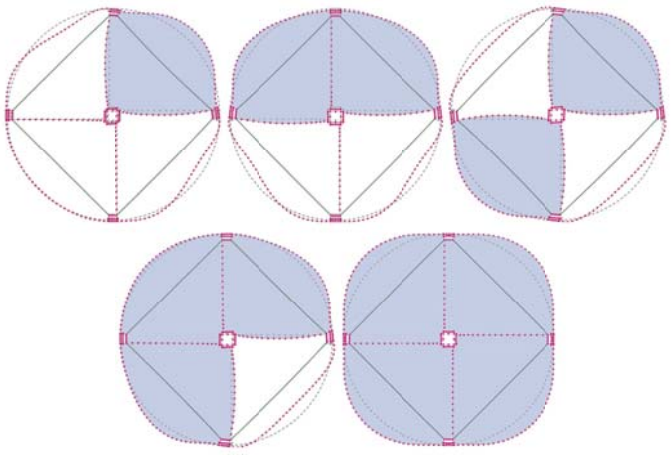


Figure 8: Sectional Deformations (5,8 m Height) for the Alternative 2 (Bracing). Up: 1, 1+2, 1+3. Down: 1+2+3, 1+2+3+4

Acknowledgements

The authors want to acknowledge the support of PPG Ibérica and Folch Ingenieros Consultants S.L. to develop the design and analysis collected in this paper.

References

[1] API-650, Welded Steel Tanks for Oil Storage, American Petroleum Institute (2012)

[2] EN 1993-4.2, Eurocode 3: Design of steel structures – Part 4.2: Tanks (2007)

[3] EN 1993-1-4 Eurocode 3: Design of steel structures. Part 1-4: General rules. Supplementary rules for stainless steel (2006).

[4] EN 1991-4, Eurocode 1: Actions on structures. Part 4: Silos and tanks (2006)

[5] EN 1991-1-3, Eurocode 1: Actions on structures. Part 1-3: General actions. Snow loads (2003)

[6] CTE-DB-SE-AE, Documento básico, seguridad estructural, acciones en la edificación, Ministerio de Fomento (España) (2009)

[7] CTE-DB-SE, Documento básico, seguridad estructural, Ministerio de Fomento (España) (2009)

Proceedings of the IASS Annual Symposium 2019 – Structural Membranes 2019
Form and Force
7 – 10 October 2019, Barcelona, Spain
C. Lázaro, K.-U. Bletzinger, E. Oñate (eds.)

Structural stability analysis of stadium roof

Antonio ČREŠNAR*, Mario UROŠ[a], Petra GIDAK[a]

*IVICOM Consulting LTD, D. Tomljanovića Gavrana 11, 10 020 Zagreb, Croatia
cresnar.antonio@gmail.com

[a] Faculty of Civil Engineering, University of Zagreb, Zagreb, Croatia

Abstract

In this paper the stability of single layered reticulated shell stadium roof is analysed. Preliminary structure geometry is obtained by process of structural optimization according to the tension-compression analogy, which is originally developed for the form finding problems of tensile structures [1]. Final coordinates of nodes are defined by solving nonlinear system of equations in the procedure of form finding of tensile structures. System of equations are solved using force density method for gravity loads. The procedure is applied iteratively until equilibrium [2]. With this procedure more optimal distribution of axial forces is obtained while influence of bending moment for vertical load is reduced to minimum [3]. Stability analysis is carried out and postbucklingbehaviour of the shell is observed [4]. Equilibrium paths are obtained by the finite element method considering geometrical and material nonlinearity to determine load capacity of the structure. The bifurcation points are detected and postbuckling equilibrium paths were developed for various imperfections which are assumed in the form of buckling modes and its linear combination. Several values of extreme amplitudes are considered for each imperfection. Finally, the sensitivity diagrams are constructed. The shape of the structure is the result of optimization process and the buckling modes are close to each other. Consequently, postbuckling branches sharply decrease resulting with extreme imperfection sensitivity.

Keywords:reticulated shell, shape optimisation, stability analysis, postbuckling behaviour, extreme imperfection sensibility.

1. Introduction

Sensitivity to imperfection of members with large slenderness can significantly reduce load bearing capacity of single layered reticulated shell. Closely spaced buckling modes can additionally reduce bearing capacity and sensitivity to imperfection. In this paper the stability with accent to the sensitivity of single layered shell stadium roof is analysed. Bearing capacity depends on amplitude and shape of imperfection. To determine the influence of amplitude and shape of imperfections on stability, analysis will be carried out on the undeformed shape and for two different imperfection shapes with various amplitudes. The obtained results will be a good insight of sensitivity to imperfection of single layered reticulated shells.

2. Geometry and load cases

The shape of the structure is obtained by the process of structural optimization according to the tension-compression analogy (or hanging cloth analogy), which is originally developed for the form finding problems of tension structures. Geometry is a key parameter in the process of structural optimization. The shape of grid pattern must satisfy structural, functional and aesthetic requirements. Span of the initial grid pattern in form finding is 35 m in the minor direction with 5 cables and 55 m in

Copyright © 2019 by Antonio Črešnar, Mario Uroš, Petra Gidak
Published by the International Association for Shell and Spatial Structures (IASS) with permission.

major direction with 12 cables. The span between cables is 5 m. Thus, the grid has a total of 96 nodes, of which 36 are edge nodes with fixed coordinates, and other 60 nodes are free. Coordinates of free nodes are unknowns and are obtained by solving the system of equilibrium equations. Thus, the final shape of grid is found. In the form finding process value of wanted forces in elements was not defined, but for physical possible solution the force must be tensile [2]. The obtained grid is mirrored and based on the tension-compression analogy the shape shown in Figure 1. is obtained. With this procedure more optimum distribution of axial forces is obtained while bending moments for vertical load are reduced to minimum as is shown in Figure 2. [3].

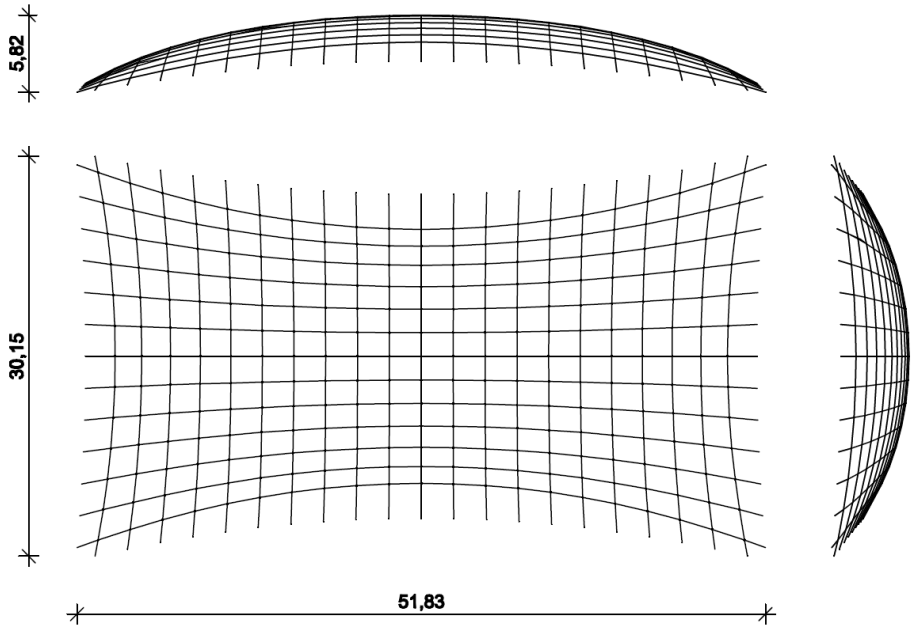


Figure 1: Final shape of the structure [1]

Edge bars are shortened for constructive reasons. The area covered by the shell is irregular. Span of the shell is 30,15 m in the minor, and 51,83 m in the major direction while the height of the shell is 5,82 m. All elements of the shell are steel tube profiles of circular cross section with the diameter of 159 mm and thickness of 6,3 mm. with welded joints while the support nodes are considered as hinges. The total weight of the structure is 293,47 kN.

For the purpose of structural analysis five load cases are taken in consideration: self-weight of the structure, additional permanent load, two cases of snow load and wind load. Additional permanent load is uniformly distributed area load with the value of 0,50 kN/m^2 (cover weight) across the roof. Two cases of snow load are symmetric snow load and asymmetric snow load. Symmetric snow load is uniformly distributed area load with the value of 0,88 kN/m^2 across the roof. Asymmetric snow load is uniformly distributed area load with the value of 1,46 kN/m^2 on one half of the roof and 0,73 kN/m^2 on the other half of the roof. Wind load is nonuniform distributed area load for which values are obtained using interactive curves.

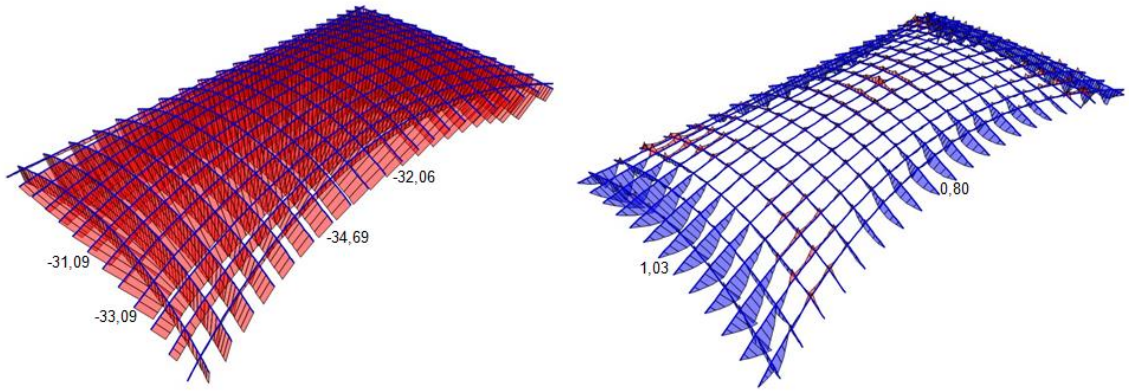


Figure 2: Diagrams of axial forces and bending moments for uniform distributed vertical load [1]

3. Structural stability analysis

Single layered reticulated shell is a complex static system that has no theoretical solution, prescribed procedure or recommendation for load bearing capacity estimation. The shell is characterized by linear fundamental equilibrium path so we can apply eigenvalue problem solution. According to this, eigenvalue and corresponding eigenvector can be calculated. Unfortunately, the obtained value of the critical load is regularly higher than the real value because of imperfection sensitivity. The reason for sensitivity is existence of a cubic member in the expression for energy that causes decrease of the postbuckling branch and occurrence of multiple or close eigenvalues which sometimes makes this decrease very sharp. Plastic yielding also contributes to the decrease of the critical load but is often of secondary importance because the large slenderness of the shell and the small amount of prescribed imperfections often delay plastic yielding at postbuckling branch, after loss of stability [4].

It is not easy to determine the coefficient of critical load reduction factor caused by these effects. We can find that the solution lies in many various collapse experiments, such as those carried out on bars which are the basis of most regulations. Unfortunately, final objects are usually unified, so such experiments are not carried out, except sometimes on scaled models and a small number of samples.

In the case of high values of critical load (10 and more times than predicted) the structure is considered as safe and further stability analysis is not required. Such a high level of safety does not mean that the structure is able to carry ten-time higher load, but that, except for unreliability of the load and the material, the influence of the imperfection significantly decreases its load bearing capacity.

Single layered reticulated shells have small slenderness, so such high level of safety is often overstated. However, lower factor of safety does not guarantee a stable structure, and more strict analysis are needed.

In the lack of the experiment, it is still possible to numerically estimate the single layered shell load bearing capacity based on the function of the equilibrium determined by the application of the geometric and material nonlinear calculation. At this point, it is not difficult to set the maximum imperfection that should be respected during construction but reference shape with minimal bearing capacity remains unknown.

Furthermore, in the case of exceptional nonlinearity, the solution is not unique (there are more possibilities), so iterative procedures in which both geometric and material convergence criteria must be satisfied can lead to the wrong solution.

Load increase in the area of multiple or close eigenvalues must be sufficiently small, and indicators that confirm the overrun of these values are not very reliable because the algorithm could “skip” some eigenvalues and continue uncontrolled by the labile branch. This phenomenon is particularly

dangerous in complete symmetry.

As part of the stability analysis of the considered structure, Euler's critical force was calculated, and nonlinear static and dynamic analysis were performed. Special attention is given to the influence of geometric imperfections and plastic yielding on the load bearing capacity of single layered reticulated shell.

4. Numerical model

The numerical analysis of the stability is performed by the software package SAP2000, v18.0.1. The numerical model consists of bar and surface finite elements. Shell elements are modelled with bar elements. All bar elements are divided into four finite elements. Surface elements are modelled as triangular surface elements without geometric properties just to bear the load on the bar elements without affecting the load bearing system.

5. Linear buckling analysis

Using buckling analysis, it is possible to solve eigenvalue problem. It does not take into consideration geometry changing of the structure and axial force changing in bar elements. In the initial geometry, the value of axial forces of elements are determined which directly, with the length of element, represents its geometric stiffness.

In the buckling analysis, buckling factor (BF) is determined representing factor for multiplication of the initial load so that the structure can lose its stability, i.e. the buckling factor is the ratio between the critical and applied load. For most cases, a product of the buckling factor and the applied load gives a satisfactory value of the critical force.

In the buckling analysis, buckling factors were determined for each loading combination. Only positive values of the buckling factor are taken into consideration because for a negative values buckling is not expected or buckling occurs for reverse directions of the applied load. For practical application the most significant is the first buckling mode because the probability that the structure will be buckled in this way is highest.

Table 1: Buckling factors for load combinations [1]

Load Combination	**Buckling factor *BF***
COMB1 (wind load dominant)	35,828
COMB2 (symmetric snow load dominant)	2,246
COMB3 (asymmetric snow load dominant)	1,845
COMB4 (permanent load)	6,942

Table 1. shows that the loading combination COMB3 including asymmetric snow load has the lowest value of the buckling factor, which means that it gives the lowest value of the critical load. Therefore, this loading combination is relevant for the stability analysis.

6. Nonlinear dynamic analysis

In dynamic analysis, the effect of inertial forces after reaching the critical point "pushes" numerical model in a physically correct direction, usually with no convergence problems. In software package SAP2000 a nonlinear direct integration process of the motion equation was performed.

Geometric nonlinearity with large displacements and moderately large rotation angle is used. This means that a system of equilibrium equations is solved on a deformed configuration during the analysis by taking the necessary data from the previous step in each next iteration step with resetting equilibrium equations until the end of the analysis. A 5 % damping rate is defined which stabilizes the system during nonlinear analysis and reduces inertia effects [5].

During the dynamic analysis execution, a stable time discretization method was used, more precisely the Hilber – Hughes – Taylor method (HHT – α method). This method is suitable for research of stability problem and is recommend for analysis. The method uses only one parameter α with a range of -1/3 to 0. During analysis the value 0 is taken for parameter α [5].

Because time dependent analysis is concerned, it is necessary to define the load time function (the ramp). The ramp is defined as a linear function with initial value of 0 and after 100 seconds the value is 1, i.e. it takes 100 seconds until load reach full value. For dynamic analysis 10000 steps have been taken, which means that one step takes 0,01 second. The smaller the step, the curve will be more precise and smoother, but calculation time will be extended. It is therefore necessary to achieve the appropriate balance between satisfactory precision and cost effectiveness of the procedure. Because of the complex static system, it is desirable to have higher precision of the process.

For the observation of the geometric imperfections influence, the first buckling mode for the relevant load combination COMB3 is selected, as this is the most probable deformed shape of the structure or the direction of the lowest stiffness. The selected buckling mode is asymmetric.

Due to close values of buckling factors and for more complete calculation in the nonlinear dynamic analysis, load combination COMB2 is also taken into consideration. For this combination the second buckling mode is selected which is symmetric.

7. Influence of geometric imperfections

For both observed buckling modes, five models were made in which the value of initial geometric imperfection was varied. The values of the geometric imperfections are 1, 2, 5, 10 and 20 cm. The displacements of the selected buckling shape are scaled so that the principal displacement takes the assigned imperfection value. The resulting shape is a new initial shape of the structure for which a nonlinear dynamic analysis was performed.

The central point of a single layer reticulated shell is imposed as a logical solution of reference point whose displacements will be observed in order to obtain the equilibrium curve. However, in the first selected shape, displacement of the shell's central point is relatively small compared to displacements of other points, while in other selected shapes, the central point of the shell is the inflection point of the buckled shape and therefore is not the best choice for observation.

Nodes at the axis of symmetry are selected as reference points. These nodes have significant value of vertical displacement in observed buckling shape. For the first buckling mode, node 1601 was selected, while for the other buckling mode the node 1137 was selected, as indicated in the Figure 3.

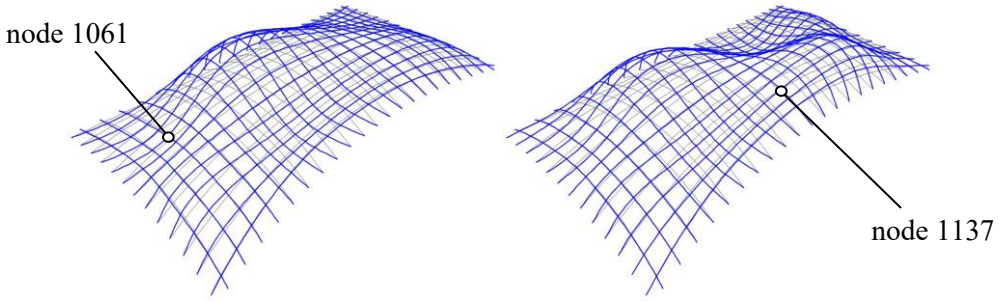


Figure 3: Selected buckling modes and selected nodes [1]

The obtained equilibrium curves calculated by nonlinear dynamic analysis for different values of geometric imperfections for the first buckling mode and load combination COMB3 are shown in Figure 4. It is visible that the system's bearing capacity decreases as geometric imperfections increases. The decrease of bearing capacity is systematically shown in Table 2. The model with the highest geometric imperfection of 1 cm shows the bearing capacity decrease of 5,88 % and the model with the highest geometrical imperfection of 20 cm shows the bearing capacity decrease of 40,75 % compared to the ideal structure.

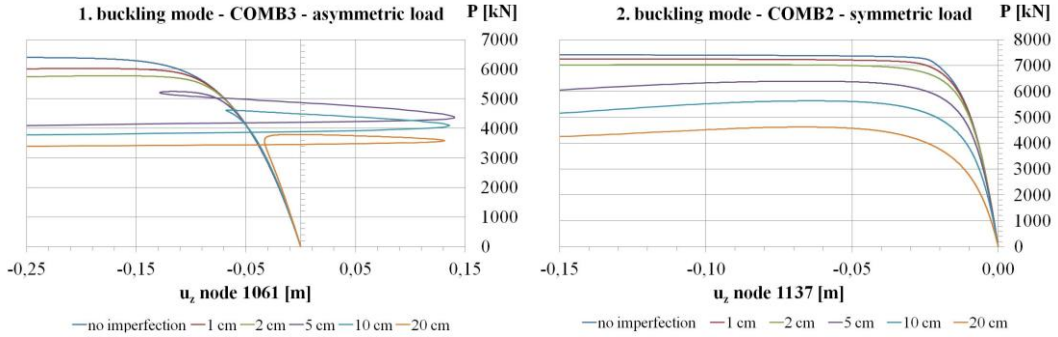


Figure 4: Equilibrium curves for different geometric imperfections for selected load combinations [1]

The obtained equilibrium curves calculated by nonlinear dynamic analysis for different values of geometric imperfection for the second buckling mode and load combination COMB2 are shown also in Figure 4. The reduction of system's bearing capacity as geometric imperfections increases is noticeable, but somewhat lower than for the load combination COMB3. The decrease of bearing capacity is systematically shown in Table 3.

Table 2: Decrease of bearing capacity for selected load combination COMB3 [1]

Largest geometric imperfection [cm]	**Bearing capacity [kN]**	**Decrease of bearing capacity**	
		[kN]	**[%]**
1	6021,63	375,94	5,88
2	5775,51	622,06	9,72
5	5245,79	1151,79	18,00
10	4620,15	1777,42	27,78
20	3790,27	2607,30	40,75

Table 3: Decrease of bearing capacity for selected load combination COMB2 [1]

Largest geometric imperfection [cm]	**Bearing capacity [kN]**	**Decrease of bearing capacity**	
		[kN]	**[%]**
1	7251,94	160,17	2,16
2	7029,97	382,14	5,16
5	6391,80	102031	13,77
10	5631,18	1780,92	24,03
20	4619,66	2792,45	37,67

By drawing the approximation curve through the points representing the critical loads for the corresponding imperfections, the sensitivity curve depending on the imperfection is defined. The sensitivity curves for selected load combinations COMB3 and COMB2 are shown in Figure 5.

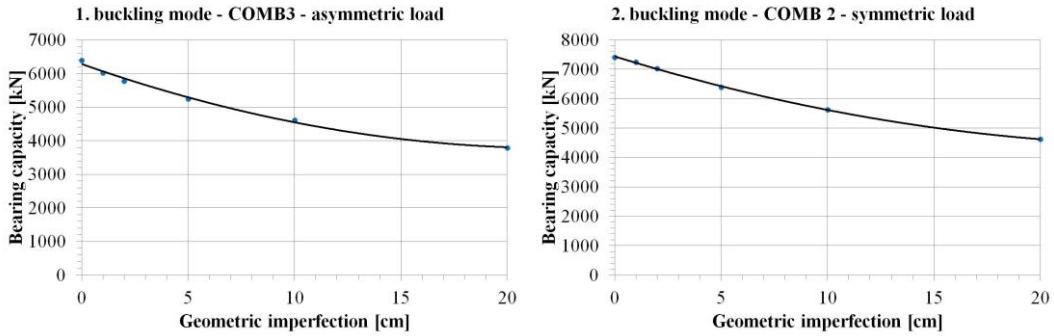


Figure 5: Sensitivity curves for imperfections for selected load combinations [1]

8. Conclusion

From this paper, it is evident that the impact of geometric imperfections on bearing capacity is significant. Single layered reticulated shell obtained by the process of structural optimization has larger bearing capacity than the ordinary shell. Postbuckling branches sharply decrease because buckling modes are close to each other. The result is extreme imperfection sensitivity which is known as compound buckling.

References

[1] A. Črešnar, *Conceptual design of the soccer field roof*, Zagreb, Croatia, 2016.

[2] K. Fresl, P. Gidak and R. Vranić, *Generalized minimal nets in form finding of prestressed cable nets*, Građevinar 65, pp. 13-16, 2013.

[3] M. Uroš, P. Gidak and D. Lazarević, "*Optimization of stadium roof structure using force density method," in 3rd International Conference on Structures and Arhitecture - ICSA* 2016., Guimaraes, Portugal, July 27-29, 2016. Paulo J.S. Cruz Ed, Taylor and Francis Group, 2016. pp. 193-194.

[4] D. Lazarević, M. Uroš and P. Gidak, "*Postbuckling Behavior of Shallow Lattice Dome," in Shell and Spatial Structures – Temporary and Permanent:Proceedingsof the IASS Annual Symposium 2010,* Shangai, China, 2010., November 8-12, 2010., Q. Zhang, L. Yang, Y. Hu Editors, China Architecture & Building Press, 2010. pp. 282-283.

[5] D. Lazarević, M. Anđelić and M. Uroš, *Shaping and analysis of dome structure for the Krešimir Ćosić Hall in Zadar*, Građevinar, 62, pp. 875-886. 2010.

Proceedings of the IASS Annual Symposium 2019 – Structural Membranes 2019
Form and Force
7 – 10 October 2019, Barcelona, Spain
C. Lázaro, K.-U. Bletzinger, E. Oñate (eds.)

Studying the shape of a helical ramp

Marina RYNKOVSKAYA*

* Department of Civil Engineering, Peoples Friendship University of Russia (RUDN University)
6 Miklukho-Maklaya St, Moscow, 117198, Russian Federation
rynkovskaya_mi@pfur.ru

Abstract

The main purpose of this paper is to clarify the classification of helicoids and to introduce several types of helicoids to engineers in terms of geometry, stress-strain behavior and exploitation parameters for the practical tasks. Mathematically helical ramps are usually designed in the shape of a right helicoid which is well-known among civil engineers and designers, while mechanical engineers also know evolvent and convolute helicoids and use them for screws. The paper mostly focuses on the civil engineering and architectural helical structures such as ramps. It is shown that designers generally do not pay proper attention to the way the surface for a ramp can be formed from mathematical point. However, different types of helicoids (and ramps as final structures) show different stress-strain and buckling behavior. The review of existing classifications, methods of calculation and differences in geometry of all five types of ruled helicoids are presented. The clear classification which can be used by both mathematicians and engineers is shown, along with the most appropriate methods for calculation. The geometry and stress-strain behavior comparison of several types of helicoids is done in order to find forms which are the most rational for application to ramps and screw elements of buildings.

Keywords: helical structures, ramps, helicoids, design, form finding.

1. Introduction

Large-capacity parking structures, serving airports, stadiums, entertainment parks, etc., often use flat parking levels with spiral helix ramps for circulation [1]. Sometimes the whole ramp structure can be designed as a big helical structure with parking on slope parts of the ramp, as it was done in Marina-City apartments in Chicago (USA). However the example of the most popular type of the open helical ramps for parking zones is shown in Fig. 1.



Figure 1: Helical ramp for the parking zone (Moscow, Russian Federation) and its model in Maple17.

According to the recommendations for the codes “Parking Structures” [2] “the ramp is the inclined structure designed to move cars between levels in multi-storey car parks; the ramp may be open, i.e. uncovered and fully or partially wall fencing, as well as closed - with walls (fully or partially) and coating protecting it from precipitation”.

Copyright © 2019 by Marina RYNKOVSKAYA
Published by the International Association for Shell and Spatial Structures (IASS) with permission.

The helical ramps are usually designed in the shape of a right helicoid which is well-known among civil engineers and designers, while mechanical engineers also know evolvent and convolute helicoids and use them for screws [3]. From mathematical point of view helicoids according to their geometry may be separated into five types: right closed; oblique closed; right open; oblique open; developable [4]. Some researchers with engineering background show other classifications [3], [5], [6] which in some cases are more reasonable for practice and express the engineering logic. In this paper there is an attempt to unite and structure all the knowledge about the ruled helicoids to show their differences and similarities in order to clarify which type is rational to be used for the particular engineering tasks. The paper mostly focuses on the civil engineering and architectural helical structures such as ramps and helical parts of buildings.

2. Geometry investigation for a helical ramp.

The most generalized ruled helical surfaces can be obtained by the following parametric equations [3], [5]

$$\begin{aligned} x &= x(t,v) = a\cos v - t\sin\gamma\sin v \\ y &= y(t,v) = a\sin v + t\sin\gamma\cos v \\ z &= z(t,v) = pv + t\cos\gamma \end{aligned} \tag{1}$$

a is a radius of the inner boundary cylinder; t is the coordinate of the point on the ruled generatrix, v is a curvilinear coordinate line; p is the pitch of the surface; γ is the inclination angle between the axis of the surface and its ruled generatrix. One of the particular cases of the surface obtained by Eq. (1) is shown in Fig. 2. The differences between some types of helicoids according to mathematical classification is shown in Fig. 3, *a-d*.

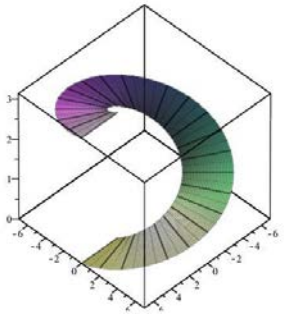


Figure 2: Ruled helical surface mostly used for ramps (model created in Maple17).

Since there is no unite classification for different types of ruled helicoids in engineering practice, most engineers generally call any helical surface “a helicoid” or sometimes “Diny’s helicoid” [7]. However different types of helicoids can be combined in one type only according to mathematical point of view, while from engineering point these surfaces have different properties and consequently can be recommended for different types of structures due to the engineering application. There are two main classifications which can be found in international sources: mathematical and engineering.

The first one is clear from mathematical point of view and consists of two big types (or five particular types): closed helicoids (right and oblique) and open helicoids (right, oblique and developable). In closed helicoids the linear generator intersects the axis of the surface, while in open helicoids the linear generator is tangent to the inner cylinder (Fig. 3, *d*). The difference between right and oblique helicoids is determined by the inclination angle of a linear generator (Fig. 3, *a*): if the generator is a horizontal line (the inclination angle is zero from horizontal plane or $\pi/2$ from the axis), in any other cases (any other inclination angle). The only exception is made for a particular inclination angle for open helicoids: if the inclination angle is equal to a particular (the only one value) the helicoid can be unfold or developed on the plane and in this particular case the surface is called a developable

helicoid. From these five types of ruled helical surfaces the one is the most general – open oblique helicoids because any other four types can be called as particular cases of this surface.

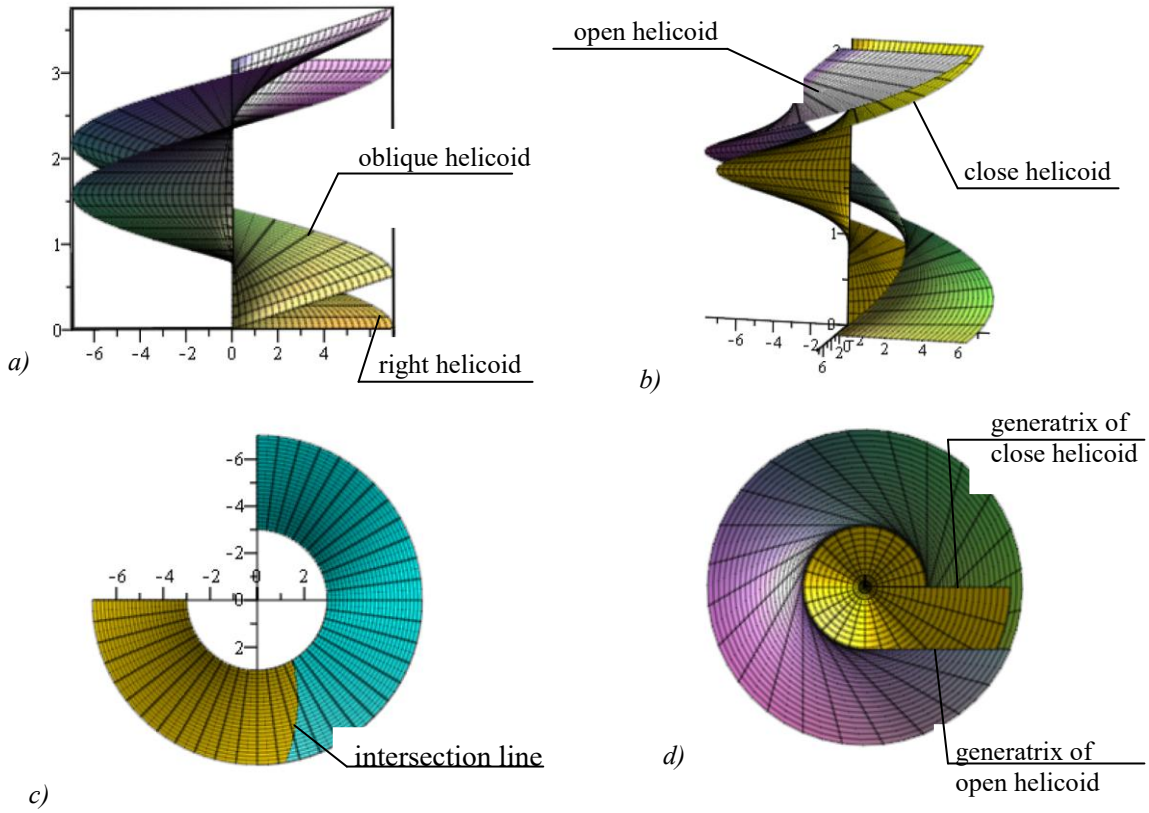


Figure 3: Ruled helical surfaces: *a)* right and oblique close helicoids; *b)* the intersection between right and oblique close helicoids; *c)* right close and right open helicoids; *d)* right close and right open helicoids in projection.

The second classification is more useful from engineering point of view because it expresses the possibility of practical application and consists of five types: right, oblique, developable, pseudo-developable and convolute helicoids. All these five types have the same differences in geometry and properties as the types from mathematical classification, but they have been discovered one-by-one by engineers (separately from mathematicians) and classification has been created in the order of their investigation. In the right helicoid the linear generator intersects the axis of the surface and inclination angle is equal to zero from horizontal plane or $\pi/2$ from the axis. In the oblique helicoid the linear generator intersects the axis of the surface and the angle between the generator and horizontal plane can get any value. Developable helicoid has the linear generator which is tangent not only to the projection of the inner cylinder but also to the curvilinear edge of the helicoids that lays on the inner cylinder (that explains the reason for this surface to be developable). Pseudo-developable helicoid has been investigated after developable helicoid as a case when the inclination angle of the linear generator is equal to zero from horizontal plane (or $\pi/2$ from the axis). And the convolute helicoid has been independently investigated theoretically by geometers and with experiments by mechanical engineers and has the linear generator that is tangent to the inner cylinder and can take any inclination angle to the horizontal line (or the axis).

The material used for these five types of shells will be different, because the surface areas for the five types of helicoids are different, and can be calculated analytically by the following formula

$$S = \int_{u1}^{u2}\int_{v1}^{v2} \sqrt{EG - F^2}\, du dv \tag{2}$$

where *E, F, G* are the coefficients of the first quadratic form of the surface; *u* and *v* are the linear and curvilinear coordinate lines on the surface; u_1 , v_1 , u_2 , v_2 are the coordinates of the beginning and the end of the calculated part of the surface.

The surface areas calculated by this formula for ruled helicoids with fixed geometrical parameters (inner and outer radii) are shown in Table 1.

	Type of helicoid				
	Right	Oblique	Pseudo-developable	Developable	Convolute
Surface area ratio (to the minimal surface))	1	1.13	1.14	1.158	1.158

According to the comparison of the surface areas, the right helicoid has the minimum surface area that is confirmed by its geometrical properties (by the way, the right helicoid is the only one ruled minimal surface known by now [8]).

3. Stress-strain behavior of different types of a helical ramp.

First works on strength analysis of right helicoids are considered to be written by Taylor [9] and Panov [10], where the helical shells were applied to mechanical engineering. In civil engineering, a right helicoid is mainly used and its stress-strain analysis was carried out by Solomon [11], Reissner [12], A. W. Leissa, Hirashima and Iura [13] and many others. Analytical calculation of oblique helicoids can be found in [14]. Developable helicoids are known and used mainly in mechanical engineering [15] and industrial design [16], and their analytical calculation can be found in the works of Krivoshapko [17]. However, all tasks were limited to long helicoids, when the problem from two-dimensional was transferred to one-dimensional. Pseudo-developable helicoid was investigated only by Halabi [18], and the fifth ruled helical surface – a convolute helicoid – was studied only by geometers [19].

There has not been found any works on the comparative analysis of different types of helicoids depending on their stress-strain behavior, geometrical and exploitation parameters, except [20], where two ramps in the shape of oblique and convolute helicoids are calculated. The results show that the ramp in the shape of convolute helicoid shows better stability behavior than the structure in the shape of oblique helicoid, while stresses and strains distributions showed rather inconsistent results, which requires to deeper investigate the stress-strain behavior of these two shells by other analytical approaches.

An attempt to choose the most efficient type of helicoid for solving the problem of pulling the yarn in a spinning machine was undertaken by Nikiforova [21], where the conceptual analysis of a generalized model of a fixed torsion body of a spinning machine in the form of a helical surface is investigated as well as the influence of the helicoid shape on the thread, including the torques arising in the thread. However, the results obtained in [21] are narrowly focused for solving a specific task, and the calculation of the screw element itself was not considered in that work. A new interest in the calculation of helicoidal shells was manifested in [22] and [23], however, it does not mention the division into types of helicoids, as well as in [24], which reviewed various types of helicoids and first indicated inconsistencies of classifications

and terms in various sources of literature and the need to develop a unified classification and approaches to the calculation of helicoids.

4. Practical parameters for future form finding

According to the civil engineering codes [1], [2] for parking, while designing the helical automobile ramp several points should be taken into account:

- transverse slope;
- the height of the storey (hitch height or longitudinal slope for the surface);
- open space along the inner curve line (inner hole or inner cylinder for the surface).

All mentioned above parameters influence the choice for the type of ruled helicoid to be used during the preliminary design. However some other parameters are to be taken into account (which does not exist now in the engineering codes for parking structures) such as:

- which type of the ramp is better for the car that moves along the helical ramp;

- in which form (type of a ruled helical surface) the ramp should be designed.

According to [1]: "a parking ramp slope of 5% or less is preferred, although parking ramp slopes up to 7% are tolerated by the public in very dense urban areas", according to [the International Building Code (IBC)] parking ramp slopes should not exceed a 6.67% slope. The slope can be arranged by the bearing structure shape or by the floor layers. The most effective form (type of the ruled helical surface) can be found in order to organize the most effective car movement.

Due to the information above, the type of a surface for the ramp should be chosen taking into account at least four points:

1) exploitation geometrical parameters (in most cases the ramp is designed with the inner hole; inclination slope will be obtained by the bearing structure or by the layered floor structure);
2) stress-strain and stability behavior (for the particular physical and geometrical characteristics);
3) the minimal weight or consumption of material (the minimal surface area required);
4) manufacturing process (will it be precast or built on the site; in which way the casting will be arranged – obtained from the flat sheet, manufactured step-by-step by means of ruled planks or even fabricated by additive technologies according to the designed model).

5. Conclusion

Since the main purpose of this work is to introduce to the engineers and designers five types of ruled helicoids which can be used for parking helical ramps, the introduction into geometrical, strength and exploitation parameters are presented. The comparison is made by geometrical and stress-strain parameters. According to geometrical investigation the surface area vary from one type to other, which determines different material consumption for the structure. According to the stress-strain analysis the maximum and minimum values of stresses and strains also vary, because of different stresses and strains distribution along the surfaces. Most of the results shown require further investigations in order to find the particular explanation for all differences in stress-strain behavior, as well as deeper geometrical analysis to predict which type of the ruled helicoid will be more effective for automobile ramp. More results will be given during the presentation at the conference.

References

[1] Parking Structures: Recommended practice for design and construction (Manual), The Precast/Prestressed Concrete Institute, USA, 2015.

[2] Recomendations for the codes "SP 113.13330.2016. Parking structures", Moscow, 2016.

[3] S.N. Krivoshapko and M. Rynkovskaya, "Five types of ruled helical surfaces for helical conveyers, support anchors and screws", *MATEC Web Conference*, 95 (2017) 06002, 2017.

[4] https://en.wikipedia.org/wiki/Generalized_helicoid (This page was last edited on 18 April 2018, information from 19.11.2018), 2018.

[5] S.N. Krivoshapko and V.N. Ivanov, "Encyclopedia of analytical surfaces". Switzerland: Springer, 2015.

[6] V. Jean Paul, "On the investigations of ruled helical shells in 2000-2017", *Structural Mechanics of Engineering Constructions and Buildings*, 3, pp. 9-11, 2017.

[7] E. Abbena, S. Salamon and A. Gray, "Modern differential geometry of curves and surfaces with Mathematica". CRC Press, 2017.

[8] M. Rynkovskaya, V.N. Ivanov, "Analytical method to analyze right helicoid stress-strain", Engineering Design Applications, pp. 157-171, 2019.

[9] D.W. Taylor, "The Speed and Power of Ships". Washington: Ransdell Incorporated, 1933.

[10] D.U. Panov, " Calculation of propeller strength". TSAGI proceedings, 288, 1937.

[11] L.I. Solomon, "To the calculation of helicoidal shells". PhD Thesis, Moscow, 1953.

[12] E. Reissner, "Small rotationally symmetric deformations of shallow helicoidal shells". *Journal of Applied Mechanics,* 22-1, pp. 31-34, 1955.

[13] M. Hirashima and M. Iura, "A geometrically nonlinear theory of right helicoidal shells", *Theoretical and Applied Mechanics*, 27, pp. 155-167, 1979.

[14] E.M. Tupikova, "Investigation of V.G. Rekatch's method of stress – strain analysis of the shell of long shallow oblique helicoid form", *Structural Mechanics and Analysis of Constructions*, 1, pp. 14-19, 2016.

[15] R. Anisimov and A. Tarapanov, "Design of the tool for periodic not evolvent profiles", *MATEC Web of Conferences*, 129 01039, 2017.

[16] Y. J. Liua, K. Tangb, W. Y. Gongc and T. R. Wuc, "Industrial design using interpolatory discrete developable surfaces", *Computer-Aided Design*, 43-9, pp. 1089–1098, 2011.

[17] S. N. Krivoshapko, "Geometry and strength of general helicoidal shells", *Applied Mechanics Review*, 52-5, pp. 161-175, 2009.

[18] S.M. Halabi, "Moment theory of thin helicoidal pseudo-developable shells", *Structural Mechanics of Engineering Constructions and Buildings*, 10, pp. 61-67, 2001.

[19] S.F. Pylypaka, "Control of bending of ruled surfaces on an example of a screw conoid", Applied geometry and engineering graphics, 70, pp. 180-186, 2002.

[20] M. Rynkovskaya, A. S. Markovich, M. Gil-Oulbe, S.V. Strashnov, "Numerical experiments on helicoids stress-strain state" (to be published).

[21] E.N. Nikiforova, "Development of mechanics of long fibrous materials for the creation of advanced technologies and equipment in the spinning industry", PhD thesis, Ivanovo, 2004.

[22] N. Edelen, "A conservation approach to helicoidal surfaces of constant mean curvature in R3, S3 and H3", arXiv:1110.1068 [math.DG], 2011.

[23] M. Xia, Q. Yan, D. Zuo and J. Xie, "An investigation on multistage bending of blank sheet into cylindrical tube by experiment and numerical simulation", International Journal of Advanced Manufacturing Technologies, 53, pp. 145-155, 2011.

[24] V. Jean Paul, "A review of geometry investigations of helicoids", *IOP Conference Series: Material Science Engineering,* 371 012029, pp. 1-8, 2018.

Proceedings of the IASS Annual Symposium 2019 – Structural Membranes 2019
Form and Force
7 – 10 October 2019, Barcelona, Spain
C. Lázaro, K.-U. Bletzinger, E. Oñate (eds.)

The Finite Element Analysis of Welding Effect on Wall Joints of Shenzhen Ping An Financial Center Curtain

Lei GU*[a], Xingcun LU[b], Jie CHEN[a], Fang WU[c]

* [a] China Construction Steel Structure Corp. Ltd
No. 3331, Central Road, Nanshan District, Shenzhen 518000, China
gulei_sz@sina.com

[b] Shenzhen Graduate School, Harbin Institute of Technology, Shenzhen 518055, China
[c] Shenzhen Eastern Development (Group) Co., Ltd., Shenzhen 518034, China

Abstract

Welding residual stress has an important influence on the performance of welded components, which is directly related to the quality of the project and the safety of the structure. For loaded structures, it is generally necessary to avoid re-welding. Otherwise, the changes of the temperature and stress fields during the welding need to be investigated so as to ensure the performance of the structure. In Shenzhen Ping An Financial Center, the connectors attached to the columns and beams need to be welded to the loaded main structures, since the glass curtain wall cannot be installed during the construction of the main structure. In the welding process, the balance of the welding residual stress is affected by the different members around the joint. In this paper, three types of three-dimensional finite element models of curtain wall joints are developed by MSC.MARC. Based on the thermoplastic theory, the temperature and the stress fields of the curtain wall joints during the welding process are numerically analyzed. The distribution and the value of the welding residual stress and the area affected by this stress are achieved. These provide references for considering the influence of wielding residual stress on the loaded structures in similar cases.

Keywords: welding residual stress, temperature and stress fields, welding process, finite element analysis, curtain wall joints, distribution.

1. Introduction

During the welding process, the material undergoes complex physical and chemical interactions under the heating effect, leading to the changes of the stress and deformation in the structure. For some simple welded structures, empirical equations or analytical methods can be used to calculate the residual stresses and deformation. However, these methods cannot be applied for the complex structures. The measurement of the residual stress is a complicated process and the corresponding explanations that have been provided are also very limited. Using the non-destructive technique, only the stress state on the surface of the structure can be achieved [1]. Moreover, even using the damage measurement method, the complete three-dimensional stress states inside the component also cannot be obtained [2]. Therefore, extensive studies on the numerical simulation of the welding process have been carried out from the 1960s over the world, since the advantages of finite element analysis are obvious. For example, through finite element analysis, it can simulate the structure with arbitrary complex geometry, and it is easy to realize the analysis of temperature and stress fields. In addition,

Copyright © 2019 by Lei GU, Xingcun LU, Jie Chen, WU Fang
Published by the International Association for Shell and Spatial Structures (IASS) with permission.

the heat transfer problem on the complicated boundary conditions including the contact can also be analyzed by the numerical simulation. The finite element analyisis on the simple welded joints has also been realized in the 1990s [3].

In the research of welding temperature field, the Soviet scientist Rykain simplified the heat source model, and did not consider the influence of temperature on the physical properties of the material [4]. He conducted in-depth research on the heat transfer problems during the welding process, laying a theoretical foundation for the study of welding heat transfer problems. Compared to the simulation of the temperature filed, the simulation of the residual stress filed is more complicated. Moreover, the research of the residual stress is based on the elastoplastic theory, and the start of the research in this area is therefore relative late. In the 1970s, Japanese scholar Ueda Ueda proposed a theory of thermal elastoplastic analysis of welds [5]. This study considered the mechanical properties of materials and temperature, and implemented the analysis on the complex dynamic processes of the stress and strain. Hibbitt and Marcal conducted finite element analysis on the residual stress of welding, and paid more attentions on the prediction of stress and strain fields during the welding. During the last few decades, the numerical simulation of the welding process has been continuously improved, since more and more the factors related to the welding have been considered in the studies and the results of these simulation are constantly close to the real situation [6-7].

MSC.MARC is an internationally advanced nonlinear finite element analysis software with general-purpose. It has linear and nonlinear structural analysis capabilities and can effectively solve the nonlinear heat transfer problem with complex boundary conditions, such as the convection, radiation, and latent heat of phase change during the welding, meeting the analytical requirements for the multiple coupled fields [8]. The calculation of the welding temperature field in the software is equivalent to solve the transient heat conduction equation. The solution of the transient thermal differential equation can be transformed into a variational problem for solving the functional extremum. Then the finite element method is used to discretize the time domain and the spatial domain of the model, and the variational problem is therefore approximately converted into the solution of the linear equations.

In Shenzhen Ping An Financial Center (Figure 1), the connectors attached to the columns and beams attached to V-shaped box column, H-shaped steel column and floor H-shaped steel side beam need to be welded to the loaded main structures, since the glass curtain wall cannot be installed during the construction of the main structure. The distribution of the residual stress around the joint is complicated, and the balance of the residual stress is not realized by the tensile and compressive stress of the same member itself, but is balanced by the different members around the joint. In this paper, three types of finite element models of curtain wall joints are developed by MSC.MARC. Based on the thermoplastic theory, this research pays attention on the numerical analysis on the temperature and the stress fields of the curtain wall joints during the welding process. The distribution and the value of the welding residual stress and the area affected by this stress are achieved. These provide references for considering the influence of wielding residual stress on the loaded structures in similar cases.

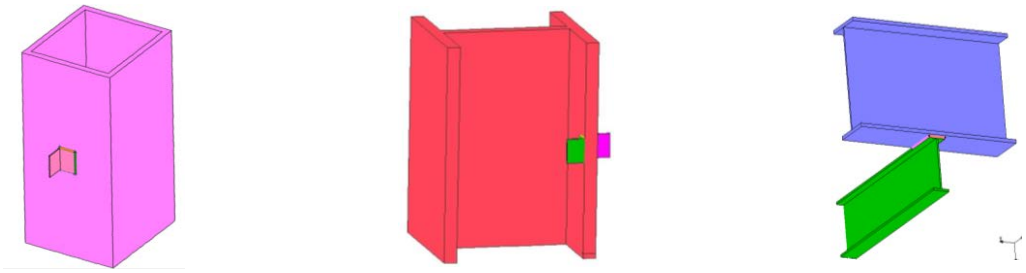


Figure 1: Ping An Financial Center

2. Finite element models of curtain wall joints and main structure

2.1 Geometric size of models

The members with smaller section and thinner plate, which affected more from welding, are selected to develop finite element models for analysis. The specific section size of the models are listed as follows: box column with section of 400 mm×400 mm×25mm, and the corresponding angle steel connector with section of L70mm×70mm×5mm and length of 100mm; H-shaped steel column with section of 600 mm×600 mm×50mm, and the corresponding angle steel connector with section of L70mm×70mm× 5mm and length of 100mm; and H-shaped steel floor beam with section of H500mm×200mm×10mm ×16mm, and the corresponding H-beam connector with section of H250mm×100mm×10 mm×10mm. The developed modes are shown in Figure 2. Fillet welds are employed in the welding. The strength grades of the steel for both the box column and the H-shaped steel floor beam are Q345, and those for the H-shaped steel column and the connectors material are Q390 and Q235, respectively.



a) box-shaped steel column b) H-shaped steel column c) H-shaped steel floor beam

Figure 2: Geometric size of models

2.2 Physical parameters of models

During the welding process, the concentrated input of the welding heat source results in an extremely uneven distribution of the temperature field. The physical properties of the weldment material, such as elastic modulus, thermal conductivity, specific heat capacity, thermal expansion coefficient, etc., increase and vary constantly with increased temperature. In this paper, the physical properties of steel with strength grades of Q235, Q345, and Q390 at specific temperatures are achieved by reference [9], and other values are obtained by interpolation and extrapolation. The initial ambient temperature is taken as 25°C. Table 1 lists the representative material property of Q235 steel.

Table 1: Material properties of steel with strength grade of Q235

Temperature (℃)	Elastic modulus (MPa)	Linear expansion coefficient	Yield strength (MPa)	Thermal conductivity	Density (kg/m^3)	Possion's ratio	Specific heat capacity
25	2.09	12.3	235	33.6	7850	0.29	561
100	2.01	13.7	220	32.8	7850	0.29	561
500	1.72	14.6	160	31.2	7850	0.29	561
1000	0.05	15.8	12	27.6	7850	0.29	561
1500	0.01	15.8	1	27.6	7850	0.29	561
1800	0.01	15.8	1	27.6	7850	0.29	561

2.3 Finite element model

During the welding process, the changes of the temperature and the stress are severe in the welds and the surrounding areas where the welding heat source is concentrated. Thus, a smaller grid is required

for division in the welds and its surrounding areas. For the other areas away from the weld position, the variations of the temperature and the stress is relatively smaller. Moreover, some details of the model can be neglected, and the mesh size can therefore be increased to improve the efficiency of the calculation when its accuracy can be ensured. Since the requirement of the quality of the mesh is high in the analysis of the stress field, and in order to facilitate the application of the load and the convergence of the control, the mapped mesh is used to divide the geometry.

The mesh of the model with solid elements is depicted as Figure 3. The gradient of the temperature near the welds is gradually increased, and the mesh of the weld zone is divided with smaller size of 2 mm×2 mm. The grid uses an 8-node hexahedral full-integration isoparametric element with an element number of 7. Element 7 can be used for both stress analysis and thermal coupling analysis. To avoid the volume locking induced by the incompressibility of the full integration element, the constant dilatation parameter is used to improve the integration method.



a) box-shaped steel column b) H-shaped steel column c) H-shaped steel floor beam

Figure 3: Mesh of models

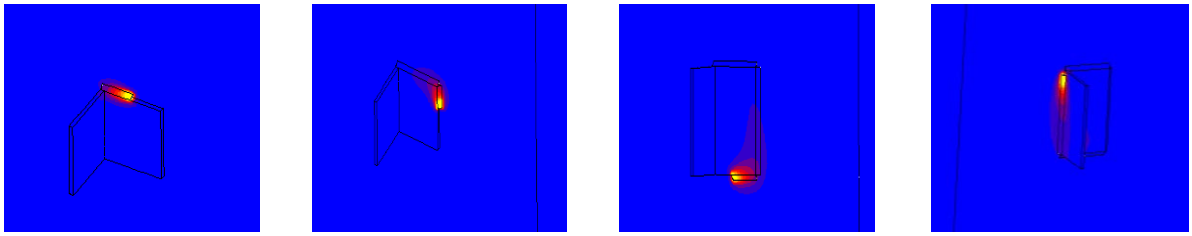
2.4 Thermal coupling analysis method

The coupled field analysis can consider the interaction of two or more physical fields. The coupling analysis of temperature field and stress field is divided into direct method and indirect method. The direct method is to use a coupling element with displacement and temperature degrees of freedom, and performs thermal analysis and structural stress analysis simultaneously. The indirect method is to first perform thermal analysis on the structure and then apply the obtained node temperature as a load in the structural stress analysis. This paper uses the direct coupling method in MSC.MARC for analysis.

3. Analysis of results of welding temperature field and stress field

3.1 Results of welding temperature filed

The temperature field analysis in this paper uses the heat source loading method based on birth-death element. Figure 4 shows the temperature simulation of welding the angle steel to the box column. This method can effectively simulate the dynamic movement of the heat source and the progressive filling of the solder [10]. The welding heat source has a maximum temperature of 1500°C and can reflect the distribution of energy in the direction of penetration.

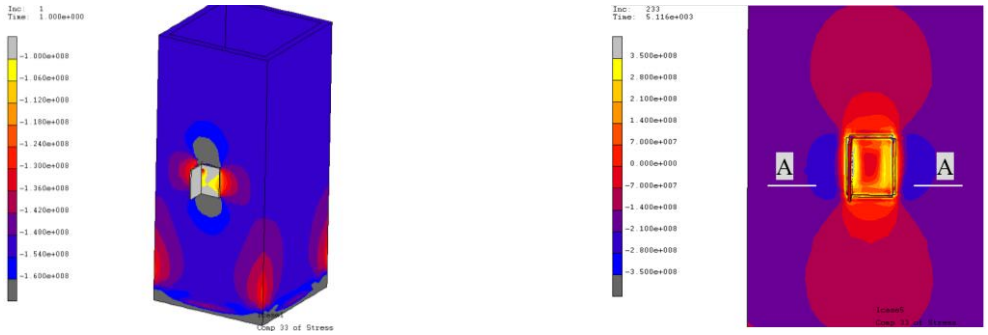


a) *t*=12s, Weld 1 b) *t*=35s, Weld 2 c) *t*=71s, Weld 3 d) *t*=113s, Weld 4

Figure 4: Welding temperature distribution of heat source in connectors at different times

3.2 Results of welding stress field of box column

Since the box column is under load before welding, a vertical compressive stress of 150 MPa perpendicular to its cross section is applied to the box column before the welding simulation. Considering that the box column mainly bears the vertical load, the following analysis is performed on the vertical (Z-axis) stresses on the structure. Under the state of loading, the distribution of the stresses along the Z-direction of the box column immediately after the start of welding at *t*=1s and at the time of the cooling completed to room temperature are shown in Figures 5a and 5b, respectively. It can be seen from Figure 5 that the stress distribution of the structure ranges from -350 MPa to 350 MPa, but only a few regions are in high stress states, and most of the structural stresses are between -210 MPa and -170 MPa. The stresses in the area close to the upper and lower welds vary from -140 MPa to -70 MPa, and those in the area near the left and right welds are between -210 MPa to -170 MPa.



a) at *t*=1s after the start of welding (Pa) b) at *t*=5116s that cooling completed to room temperature (Pa)

Figure 5: Distribution of stress in vertical direction of the box column

Figure 6 shows the distribution of high stress in compression in the thickness direction of the plate, which is only about 4 mm deep. The stress distribution curve along the A-A section in Figure 5 of the box-shaped column in Z-direction is extracted as shown in Figure 7. It can be seen from the curve of Figure 6 that the compressive stress increases continuously and reaches a maximum value along the path of the left and right sides toward the welds 2 and 4, and then the compressive stress changes rapidly to a higher tensile stress at the weld position. Then, between 2 and 4 welds, there is a transition from tensile stress to compressive stress. The peak values of tensile and compressive stresses both reach or approach the yield strength of the steel, but the range and depth of their influences are small. Thus, the welding area is recommended as shown in Figure 8.

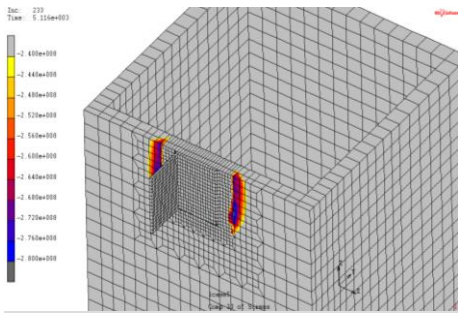


Figure 6: Sectional view of high compressive stress (-280 MPa~-240 MPa) zone (Pa)

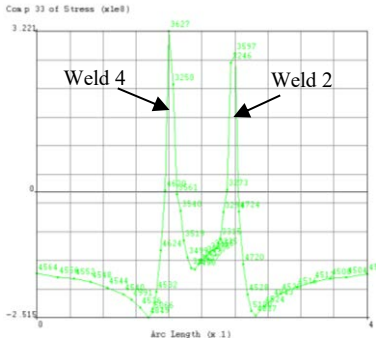


Figure 7: Stress distribution curve of the box-shaped column in Z-direction

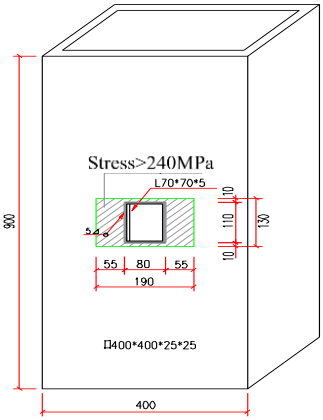


Figure 8: Welding influence range of connectors in the box-shaped column

3.3 Results of welding stress field of H-shaped column

There is an angle steel connector welded to the inner and outer surfaces of one flange of the H-shaped steel column, respectively. The welding process requires that the back angle steel should be welded only after the front angle steel is sufficiently cooled to the room temperature. A vertical compressive stress of -150 MPa is also applied before the welding simulation. Figure 9 shows the stress distribution in Z-direction observed at multiple angles after welding. Figure 10 depicts the main distribution range of the stress, in which the gray part represents the area affected by the welding significantly. It can be seen from Figures 9 and 10 that the compressive stress range of -200 MPa to -120 MPa occupies most areas of the structure, and a dramatic change from high compressive stress to high tensile stress can be observed near the vertical weld seam.

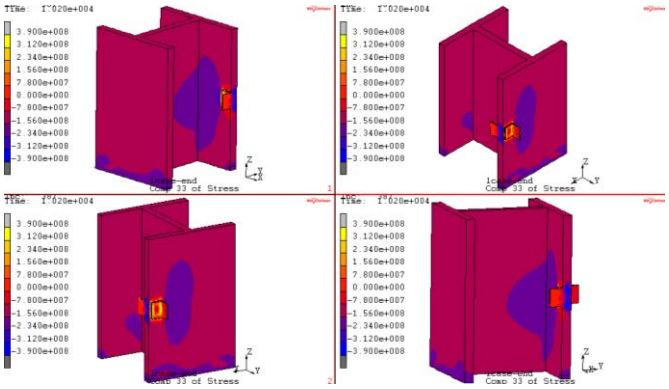


Figure 9: Stress distribution in Z-direction after welding of H-shaped column (Pa)

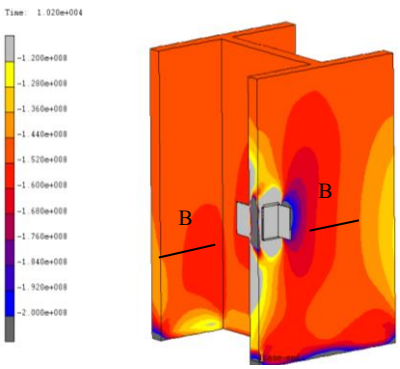


Figure 10: Stress distribution between -200MPa and -120MPa in Z-direction (Pa)

The stress distribution curve of the B-B section of the H-shaped steel column is extracted as shown in Figure 11. It can be seen that the tensile stress is generated at the vertical weld, but the value of tensile stress is small. Specifically, the maximum tensile stress on the cross section is only 30.8 MPa. The maximum compressive stress generated near the vertical weld reaches 280 MPa. It is recommended that the influence range of welding of the H-shaped steel column is shown in Figure 12.

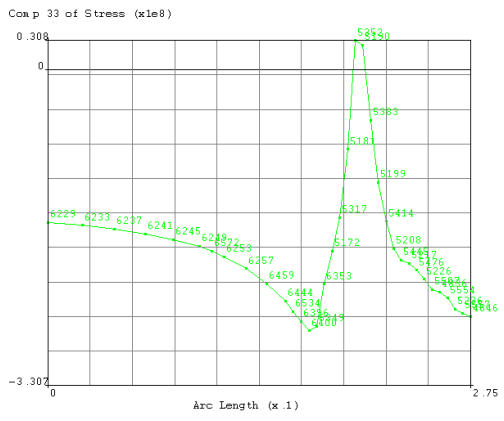


Figure 11: Stress distribution curve of the B-B section of H-shaped column

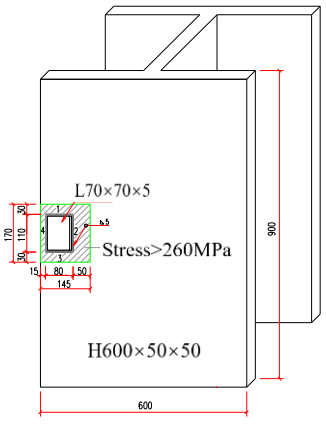


Figure 12: Welding influence range of connectors in the H-shaped column

3.4 Results of welding stress field of H-shaped steel floor beam

Different from the above columns, the curtain wall connector is made of I-beam, and the three sides are welded to the lower flange of the H-shaped steel floor beam of the main structure. The three welds listed as 1, 2 and 3, respectively, as shown in Figure 13. An axial tensile stress of 200 MPa is applied to the floor beam before the tensile welding of the H-beam floor beam. Figure 14 shows the axial welding stress distribution of the floor beam from multiple angles. Figure 15 depicts the cross-sectional stress diagram of the weld 1, in which the high stress is only about 4 mm deep. Figure 16 shows the stress variation curve of the C-C section. It can be observed that most of the main structure is in the tension state, and the tensile stress region of 140 MPa to 280 MPa accounts for most of the main structure. Only a small portion of the areas close to the welds are in the high stress range of 280 MPa to 350 MPa. It is recommended that the area affected by the welding of the floor beam as shown in Figure 17.

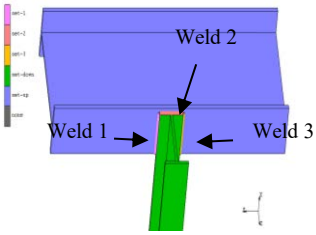


Figure 13: Welds of connectors to the H-shaped steel floor beam

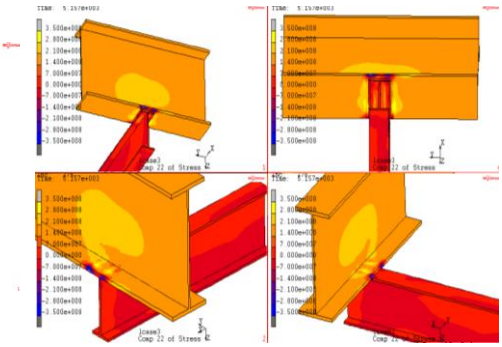


Figure 14: Axial welding stress distribution of the floor beam

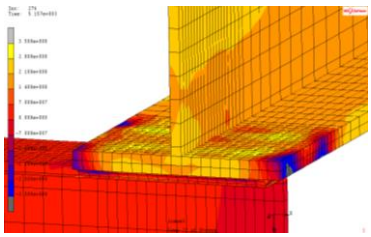


Figure 15: cross-sectional stress diagram of the weld 1

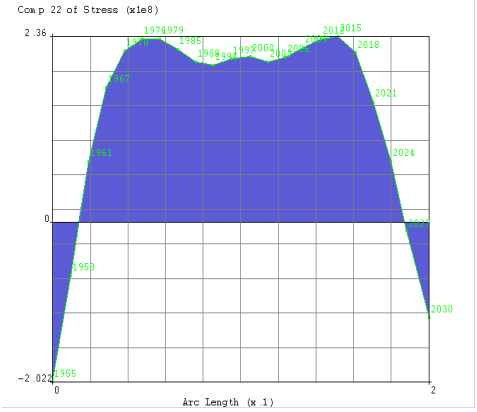


Figure 16: stress variation curve of the C-C section

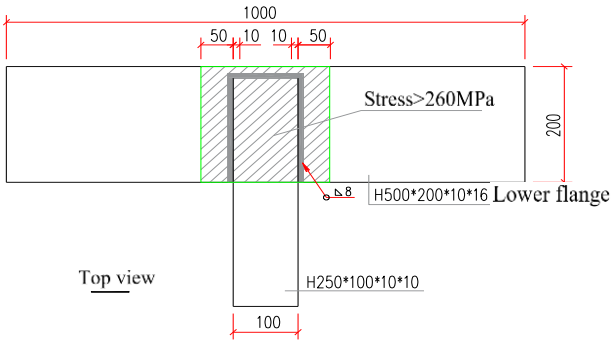


Figure 17: Welding influence range of steel floor beam

4. Conclusions

In this paper, the direct coupling method combined with the birth-death element in MSC.MARC software is used to calculate the dynamic process of temperature field and stress field in the welding construction of the curtain wall joints. According to the finite element analysis, the following conclusions are achieved as following:

(1) The area affected by the welding residual stress of the curtain wall joints is limited, which is mainly around the welds within 60 mm. It is worth noting that the maximum value of the local residual stress is close to the yield stress of the steel.

(2) The depth affected by the fillet weld to the steel plate is about 4mm. Since both the thicknesses of the steel plate and the weld are 5mm, and the local section is therefore strengthened. The welding residual stress does not influence the stress distribution, the stiffness and the bearing capacity of the overall structure.

(3) The research results of this paper provide significant references for determining the curtain wall joints welding effect in the project of Ping An Financial Center.

References

[1] K. H. Luo, "Non-destructive evaluation of residual stress," *Mechanics and Practice*, vol. 25, pp. 7-10, Aug. 2003. (in Chinese)

[2] Q. Q. Liu, Z. S. Liu, S. Song and L. L. Xie, "Research status of measurement for residual stress," *Machine Tool & Hydraulics*, vol. 39, pp. 124, 135-138, Jun. 2011. (in Chinese)

[3] L. J. Lu, S. W. Bai and H. S. Ding, "The research development of finite element simulation in welding joint," *Metal World*, vol. 2 pp. 35-38, 54, 1 Feb. 2008. (in Chinese)

[4] K. L. Lei, B. Y. Xu and H. Zhuang, *The Calculation of Welding Thermal Process*. Beijing: Mechanical Industry Press, 1958. (in Chinese)

[5] D. M, Gong and Y. Lei, "Application analysis of numerical simulation in welding," *Electric Welding Machine*, vol. 42, pp. 58-62, 104, Jun. 2012. (in Chinese)

[6] H D. Hibbitt and P V. Marcal, "A numerical thermo-mechanical model for the welding and subsequent loading of a fabricated structure," *Computers and Structures*, vol. 3, pp. 1145-1174, May. 1973.

[7] H D. Hibbitt, P V. Marcal, and J. R. Rice, "A finite element formulation for problems of large strain and large displacement," *International Journal of Solids and Structures*, vol. 6, pp. 1069-1086, Aug. 1970.

[8] L. Xu, A, Luo and R. J. Yan, "Numerical simulation of multipass welding based on MSC.Marc," *Modern Manufacturing Technology and Equipment*, vol. 2, pp. 42-45, Feb. 2007. (in Chinese)

[9] Y. Z. Jia, Z. H. Ruan and C. W. Zhang, "Numerical analysis on residual stress in direct welded K-joint of steel tubular members," *Transactions of The China Welding Institution*, vol. 32, pp. 97-101, Sep. 2011. (in Chinese)

[10] J. Sun, X. Liu, Y. Tong and D. Deng, "A comparative study on welding temperature fields, residual stress distributions and deformations induced by laser beam welding and CO2 gas arc welding," *Materials & Design*, vol. 63, pp. 519-530, Nov. 2014.

Proceedings of the IASS Annual Symposium 2019 - Structural Membranes 2019
Form and Force
7-10 October 2019, Barcelona, Spain
C. Lázaro, K.-U. Bletzinger, E. Oñate (eds.)

A building of unlimited height

Mats ANDER[a], Jens OLSSON[a], Paul SHEPHERD[b], Robert STUART-SMITH[c,d], Christopher WILLIAMS[a,b*]

[a] Chalmers University of Technology, Gothenburg, Sweden.*
christopher.williams@chalmers.se
[b] University of Bath, UK. [c] University of Pennsylvania, USA. [d]University College London, UK.

Abstract

We consider the overall buckling under own weight of a thin-walled column of circular cross-section and a radius that is a hyperbolic sine function of distance from the top of the column. The maximum stress is limited to a given value, but there is no limit to the height of the column. The wall thickness is determined by consideration of local buckling. It can be made to represent a building by adjusting the own weight of the column to include the weight of the floors, finishes, cladding and imposed load.

Keywords: Tallest building, buckling under own weight, optimization.

1 Introduction

Greenhill [1] was the first to obtain formulae for the buckling due to self-weight of columns of varying vertical profiles, including prisms and cones. But it was not untill 1966 that Keller & Niordson [2] found the optimum profile for a column. Both these papers assumed a material of unlimited strength and Naicu and Williams [3] extended the method to include non-linear elasticity.

In this paper we again combine the effect of buckling with the fact that the vertical stress has to be limited, but take a simpler approach by specifying the column profile, rather than using optimization. We shall assume that the material is linear elastic, but that the stress is limited to a given value.

If the cross-sectional dimensions of a column increase exponentially as one progresses downwards from the top, then the compressive stress due to self-weight can be made to approach a constant value. The same applies to the compressive stress in the columns and walls of a building, where one has to include the weight of floors, finishes and cladding, and imposed loads. Thus, there is no limit to the height of a building based upon stress, if one is prepared to sufficiently increase the footprint of the structure.

If the cross-sectional dimensions of a column (or the vertical structure of a building) increase exponentially downwards, then they must decrease exponentially upwards, which clearly cannot be possible because the structure will become too slender and buckle. Thus in this paper we consider the buckling of a column or building whose profile is described by the hyperbolic sine (sinh) function whose value starts at zero and then approaches the exponential. We will consider a column or idealized building which consists of a thin-walled circular tube whose radius is given by the sinh function and whose wall thickness is controlled by stress and local buckling of the wall.

Copyright © 2019 by Ander, Olsson, Shepherd, Stuart-Smith and Williams
Published by the International Association for Shell and Spatial Structures (IASS) with permission.

2 Buckling of a column under own weight

Let us imagine a column made of a material of constant density ρ, whose cross-sectional area $A(x)$ varies with the distance x below the top of the column. In the case of a building we would need to adjust ρ artificially to include the weight of floors, finishes and so on. The volume of material above a cross-section at x is

$$V = \int_{u=0}^{x} A(u)\,du \tag{1}$$

and the axial stress in the column is

$$\sigma = \frac{\rho g V}{A} \tag{2}$$

where g is the acceleration due to gravity.
Now let us imagine that the column buckles and $y(x)$ is the sideways displacement of the column at x. Then the moment at x due to the weight of the column above is

$$M = \int_{u=0}^{x} (y(u) - y(x))\,\rho g A(u)\,du = \int_{u=0}^{x} y(u)\,\rho g A(u)\,du - y(x)\int_{u=0}^{x} \rho g A(u)\,du. \tag{3}$$

In this equation $\rho g A(u)\,du$ is the weight of an element of height du and $(y(u) - y(x))$ is the lever arm of that weight about the section at x. If we differentiate (3) with respect to x,

$$\frac{dM}{dx} = y(x)\,\rho g A(x) - \frac{dy}{dx}\int_{u=0}^{x} \rho g A(u)\,du - y(x)\,\rho g A(x) = -\frac{dy}{dx}\rho g V \tag{4}$$

in which $\frac{dy}{dx}$ is negative so that $\frac{dM}{dx}$ is positive. If we make the usual assumption in the linear theory of buckling of columns that $\frac{dy}{dx}$ is small, then the curvature is equal to $\frac{d^2y}{dx^2}$ and, for a linear elastic material, $M = EI\frac{d^2y}{dx^2}$ in which E is the Young's modulus of the material, which is assumed to be constant, and I is the second moment of area of the cross-section. Thus from (4),

$$\frac{d}{dx}\left(EI\frac{d^2y}{dx^2}\right) + \rho g V\frac{dy}{dx} = 0 \tag{5}$$

which is equivalent to equation IV(1) of Greenhill [1] and can be solved for y if we know the value of the constants E, ρ and g as well as V and I as functions of x and the boundary conditions.

3 Non-dimensional parameters

We will find it convenient to introduce the non-dimensional parameter,

$$\theta = \frac{x}{h} \tag{6}$$

in which

$$h = \frac{\sigma_{\max}}{\rho g} \tag{7}$$

and σ_{max} is the maximum stress that the material can carry. The maximum value of θ for a prismatic column is 1.0 since the stress at the base will then be σ_{max}. However in our case we shall see that θ can be increased without limit.
We shall use Greek letters to denote non-dimensional quantities, with the exception of σ which is conventionally used for stress.
If the material is assumed to be linear elastic up to σ_{max} we can write the yield strain,

$$\varepsilon_{max} = \frac{\sigma_{max}}{E}. \tag{8}$$

so that

$$\frac{E}{\rho g} = \frac{h}{\varepsilon_{max}}. \tag{9}$$

The rotation of the column due to buckling is

$$\phi = -\frac{dy}{dx} = -\frac{1}{h}\frac{dy}{d\theta} \tag{10}$$

in which the minus sign is there because y decreases as θ increases, so that (4) can now be written

$$\frac{1}{\varepsilon_{max} h}\frac{d}{d\theta}\left(I\frac{d\phi}{d\theta}\right) + V\phi = 0. \tag{11}$$

We now introduce another non-dimensional quantity,

$$\lambda = -\frac{\left(\frac{d\phi}{d\theta}\right)}{\phi} = -\frac{d}{d\theta}(\log\phi) \tag{12}$$

in which the minus sign is there because ϕ decreases as θ increases.
Then $\frac{1}{\varepsilon_{max} h}\frac{d}{d\theta}\left(I\frac{d\phi}{d\theta}\right) = -\frac{1}{\varepsilon_{max} h}\frac{d}{d\theta}(I\lambda\phi) = -\frac{1}{\varepsilon_{max} h}\left(\frac{d}{d\theta}(I\lambda) - I\lambda^2\right)\phi$ so that

$$I\frac{d\lambda}{d\theta} + \lambda\frac{dI}{d\theta} - I\lambda^2 - h\varepsilon_{max} V = 0. \tag{13}$$

In this equation only λ is unknown and we can integrate starting at the top of the column where $\theta = 0$, provided that we know the starting value of λ.
Note that this technique can be used for all column buckling problems to replace a second order differential equation with a first order, but usually there is little point in so doing because the second order equation is linear whereas the first order is not. However in our case they are both non-linear.

4 Local buckling of the column wall

If $R(x)$ and $T(x)$ are the radius and wall thickness of a thin walled circular tube, the cross-sectional area and second moment of area are

$$A = 2\pi RT \quad \text{and} \quad I = \pi R^3 T. \tag{14}$$

In article 11.6 of *Theory of Elastic Stability* Timoshenko and Gere [4] show that the stress necessary to cause local buckling of the wall of a circular tube is equal to

$$\sigma = \alpha E\frac{T}{R} \tag{15}$$

in which the constant $\alpha = \dfrac{\mu}{\sqrt{3(1-\nu^2)}}$ and E is again Young's modulus, ν is Poisson's ratio and $\mu \approx 0.2$ is a factor to take into account approximations in the theory and inaccuracies of manufacture. We shall treat α as known and hence we can calculate T if we know R and E and make the assumption that T is a small as possible consistent with avoiding local buckling of the wall. When the stress is equal to σ_{max}, $\dfrac{T}{R} = \dfrac{\varepsilon_{max}}{\alpha}$, so that if we take $\alpha \approx 0.1$ and $\varepsilon_{max} \approx \dfrac{1}{1000}$ then $\dfrac{T}{R} \approx \dfrac{1}{100}$.
From (2) and (15) we have $V = \dfrac{2\pi\alpha h}{\varepsilon_{max}} T^2$ and therefore $2\pi RT = A = \dfrac{dV}{dx} = \dfrac{4\pi\alpha}{\varepsilon_{max}} T \dfrac{dT}{d\theta}$ so that

$$\frac{dT}{d\theta} = \frac{\varepsilon_{max}}{2\alpha} R. \tag{16}$$

Now let us stipulate that the column radius is given by the hyperbolic sine function as stated in section1,

$$R = \beta h \sinh(\chi\theta) \tag{17}$$

where χ and β are non-dimensional constants that are to be determined. Then $\dfrac{dT}{d\theta} = \dfrac{\varepsilon_{max}\beta h}{2\alpha} \sinh(\chi\theta)$ which has the solution

$$T = \frac{\varepsilon_{max}\beta h}{2\alpha\chi} (\cosh(\chi\theta) - 1) \tag{18}$$

to give $T = 0$ when $R = 0$. Thus

$$\sigma = \frac{E\varepsilon_{max}(\cosh(\chi\theta) - 1)}{2\chi \sinh(\chi\theta)} = \frac{\sigma_{max}}{2\chi} \tanh\left(\frac{\chi\theta}{2}\right). \tag{19}$$

But we also have to ensure that σ is less than or equal to σ_{max} and therefore $\chi = \dfrac{1}{2}$ so that finally, writing

$$\xi = \frac{\theta}{2} \tag{20}$$

we have

$$R = \beta h \sinh\xi \tag{21}$$

$$T = \frac{\varepsilon_{max}\beta h}{\alpha} (\cosh\xi - 1) \tag{22}$$

$$\sigma = \sigma_{max} \tanh\left(\frac{\xi}{2}\right) \tag{23}$$

$$A = \frac{2\pi\varepsilon_{max}\beta^2 h^2}{\alpha} \sinh\xi (\cosh\xi - 1) \tag{24}$$

$$V = \frac{2\pi\varepsilon_{max}\beta^2 h^3}{\alpha} (\cosh\xi - 1)^2 \tag{25}$$

$$I = \frac{\pi\varepsilon_{max}\beta^4 h^4}{\alpha} \sinh^3\xi (\cosh\xi - 1) = \frac{\pi\varepsilon_{max}\beta^4 h^4}{\alpha} \sinh\xi (\cosh\xi + 1)(\cosh\xi - 1)^2. \tag{26}$$

We shall also need

$$\frac{dI}{d\theta} = \frac{\pi\varepsilon_{max}\beta^4 h^4}{2\alpha} \sinh^2\xi \left(3\cosh^2\xi + \sinh^2\xi - 3\cosh\xi\right) = \frac{\pi\varepsilon_{max}\beta^4 h^4}{2\alpha} (4\cosh\xi + 1)(\cosh\xi + 1)(\cosh\xi - 1)^2.$$

5 Integration of the differential equation

We can now substitute the results obtained at the end of section 4 into (13), which produces

$$(\cosh\xi+1)\left(\sinh\xi\left(\frac{d\lambda}{d\theta}-\lambda^2\right)+\frac{1}{2}(4\cosh\xi+1)\lambda\right)-\frac{2\varepsilon_{max}}{\beta^2}=0. \tag{27}$$

If we assume λ and $\frac{d\lambda}{d\theta}$ are both finite as $\theta\to 0$ then the value of λ at $\theta=0$ is $\lambda_0=\frac{2\varepsilon_{max}}{5\beta^2}$ so that

$$\beta=\sqrt{\frac{2\varepsilon_{max}}{5\lambda_0}}. \tag{28}$$

Thus

$$\frac{d\lambda}{d\theta}=\frac{1}{2\sinh\xi}\left(\frac{10\lambda_0}{\cosh\xi+1}-(4\cosh\xi+1)\lambda\right)+\lambda^2 \tag{29}$$

which almost certainly has to be integrated numerically. We cannot use (29) to calculate $\frac{d\lambda}{d\theta}$ at very small values of θ. Instead we have $\frac{d\lambda}{d\theta}=-5\frac{d\lambda}{d\theta}+\lambda_0^2$ so that $\frac{d\lambda}{d\theta}=\frac{\lambda_0^2}{6}$.

```
lambda[0] = 1.401381149d;
for (int i = 1; i <= n; i ++){
  double thetaMidPoint = ((double) i - 0.5d) * delta_theta;
  lambda[i] = lambda[i - 1];
  for (int run = 0; run <= 10; run ++){
    double lambdaMidPoint = (lambda[i - 1] + lambda[i]) / 2.0d;
    double hypcos = Math.cosh(thetaMidPoint / 2.0d);
    double hypsin = Math.sinh(thetaMidPoint / 2.0d);
    double lambdaDash;
    if (run == 0 && i == 1)lambdaDash = lambda[0] * lambda[0] / 6.0d;
    else lambdaDash = (10.0d * lambda[0] / (hypcos + 1.0d)
      - (4.0d * hypcos + 1.0d) * lambdaMidPoint) / (2.0d * hypsin)
      + lambdaMidPoint * lambdaMidPoint;
    lambda[i] = lambda[i - 1] + lambdaDash * delta_theta;}}
gamma[0] = 0.0;gamma[1] = gamma[0] - arbitraryValue * delta_theta;
for (int i = 1; i <= n - 1; i ++){
  double temporary = lambda[i] * delta_u / 2.0d;
  gamma[i + 1] = (2.0d * gamma[i] - gamma[i - 1] * (1.0d - temporary))
  / (1.0d + temporary);}
for (int i = 0; i <= n; i ++)gamma[i] = (gamma[n] - gamma[i]) / gamma[n];
```

Listing 1: Numerical Integration

5.1 Boundary condition at the bottom of the column

If we assume that the bottom of a column of finite height is fully encastré so that the rotation, $\phi=0$, then $\lambda\to\infty$ in (12). Therefore let us introduce $\psi=\frac{1}{\lambda}$ so that

$$\frac{d\psi}{d\theta}=-\frac{1}{2\sinh\xi}\left(\frac{4\varepsilon_{max}}{\beta^2}\frac{\cosh\xi}{\cosh\xi+1}\psi^2-(4\cosh\xi+1)\psi\right)-1 \tag{30}$$

and $\psi\to 0$ at the bottom. However we want to imagine that a given column is actually only part of a larger column which *could* be infinitely tall. If θ is large in (30), $\frac{d\psi}{d\theta}=2\psi-1$ which has the solution

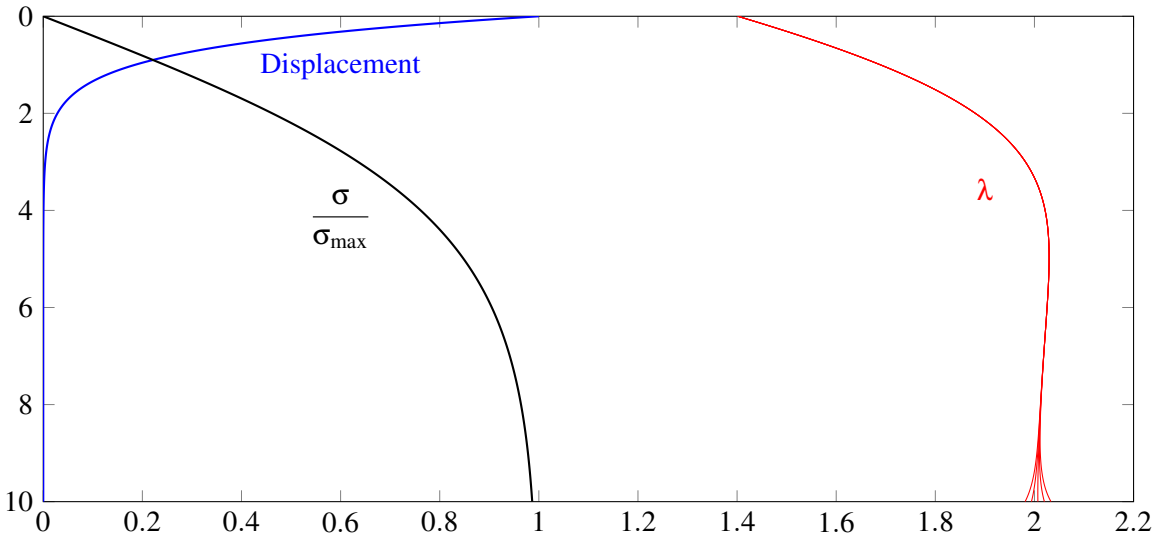


Figure 1: Lateral displacement in blue, $\frac{\sigma}{\sigma_{max}}$ in black and λ in red for different values of λ_0 plotted against non-dimensional distance from top of column $= \theta$ on the vertical axis.

Material	ρ kg/m^3	E GPa	σ_{max} MPa	$\varepsilon_{max} = \frac{\sigma_{max}}{E}$	$h = \frac{\sigma_{max}}{\rho g}$km	$\beta = \sqrt{\frac{2\varepsilon_{max}}{5\lambda_0}}$
Mild steel	7850	200	400	2×10^{-3}	5.0	0.0239
Concrete	2400	20	40	2×10^{-3}	1.7	0.0239
Timber	400	8	30	3.75×10^{-3}	7.6	0.033

Table 1: Approximate Material Properties, $g = 9.81$m/s^2 and the timber is Sitka spruce [5]

$\psi = \frac{1+\eta e^{2\theta}}{2}$ where η is a constant. From this we have to conclude that $\eta = 0$ and so $\psi \to \frac{1}{2}$ and $\lambda \to 2$ as $\theta \to \infty$.

5.2 Numerical integration

We have to integrate (29) numerically starting from λ_0. We can do this repeatedly adjusting the value of λ_0 to satisfy $\lambda \to 2$ for large θ. The core of the code is given in listing1 and the reason for the loop containing the counter 'run' is because we need the value of λ midway between λ_{i-1} and λ_i. y is found by solving the differential equation $\frac{d^2y}{d\theta^2} = -\lambda\frac{dy}{d\theta}$ using $y_{i+1} = \frac{2y_i - y_{i-1}\left(1 - \lambda_i\frac{\delta\theta}{2}\right)}{1 + \lambda_i\frac{\delta\theta}{2}}$. The code automatically sets the maximum displacement to an arbitrary value of 1.0.
The results of the numerical integration are given in figure 1. The values of λ_0 are in the range 1.401381147 to 1.401381151 and the column was split into 25000 segments. There was no change to the results if there were 10 times fewer or 10 times more segments. Thus we can take $\lambda_0 = 1.40$ with sufficient accuracy for practical purposes.

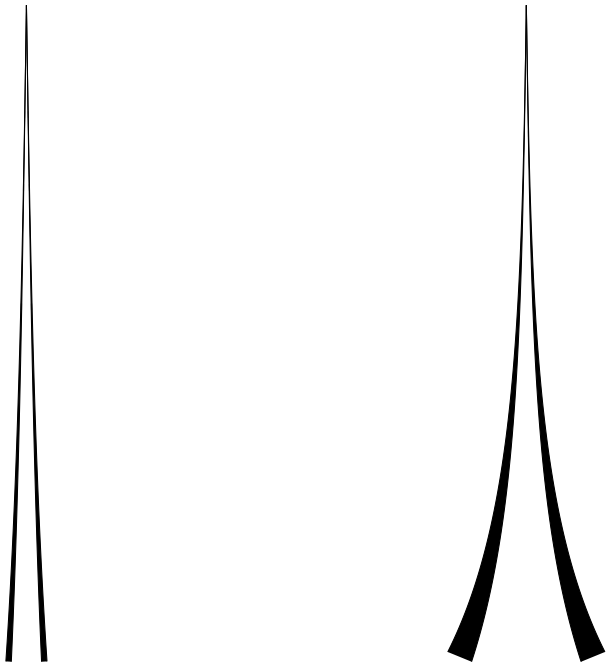


Figure 2: Column profiles with $\theta_{base} = 4$ on the left and $\theta_{base} = 8$ on the right. $\beta = 0.03$ for both.

6 Physical examples, wind and conclusions

Table 1 shows some typical material properties and figure 2 shows plots of columns with different values of the value of θ at the base. The wall thicknesses are exaggerated so that they can be seen. Both columns could be extended infinitely downwards and the column on the left is the top half of the column on the right drawn to a different scale. The value θ at the base has to be multiplied by the value of h in table 1 to give the height of the column. Thus the height of the column on the right in figure 2 is 60km tall.
Clearly this figure is at variance with what one might expect, since the maximum height of existing buildings is of the order of 1km. But we have to include safety factors and also all the weight of floors, finishes, cladding and imposed load which will effectively multiply ρ by some factor, hence reducing h.
We have not considered wind load. If we imagine a column with a conical profile and constant ratio of wall thickness to radius, then the section modulus at any section is proportional to the distance from the top cubed. If we assume that the wind load per unit area is constant, the moment due to wind is also proportional to the distance from the top cubed. Thus the bending stress is the same at all heights. This in turn means that for a column with a hyperbolic sine profile, the wind stresses are greatest at the top. However we have assumed that the ratio of wall thickness to radius tends to zero at the top, although it tends to a constant lower down. Therefore modification of the wall thickness will be required near the top.
Thus we can see that there is no limit to the height of a building, although the amount of material required grows exponentially with height. However tall a building we build, somebody else can come along and build a taller one.

References

[1] Alfred George Greenhill, Determination of the greatest height consistent with stability that a vertical pole or mast can be made, and of the greatest height to which a tree of given proportions can grow, *Proceedings of the Cambridge Philosophical Society, Mathematical and Physical Sciences*, vol. IV, Number II, pp. 65-73, 1881.

[2] Joseph B. Keller and Frithiof I. Niordson, The Tallest Column, *Journal of Mathematics and Mechanics*, vol. 16, pp. 433-446, 1966.

[3] Dragos Naicu and Christopher Williams, The use of dynamic relaxation to solve the differential equation describing the shape of the tallest possible building, *VII International Conference on Textile Composites and Inflatable Structures*, E. Oñate and K.-U. Bletzinger and B. Kröplin editors, 2015

[4] S. P. Timoshenko, J. L. Gere, *Theory of Elastic Stability*, 2nd Edition, McGraw-Hill, 1961.

[5] J. Moore, *Wood properties and uses of Sitka spruce in Britain*, Forestry Commission, UK, 2011.

Proceedings of the IASS Annual Symposium 2019 – Structural Membranes 2019
Form and Force
7 – 10 October 2019, Barcelona, Spain
C. Lázaro, K.-U. Bletzinger, E. Oñate (eds.)

Determination of Mixing Principles of Precast Reinforced Concrete Structures with Hybrid Connections Based on Elastic Displacement Control of Small Earthquake

Ge LI[a], Bin DU[a], Zheng HE*, Guohui HUANG[b], Feng PAN[c]

*State Key Laboratory of Coastal and Offshore Engineering, Dalian University of Technology, Dalian, China
Email:hezheng@dlut.edu.cn

a Dalian University of Technology Dalian, China
b China Machinery International Engineering Design & Research Institute Co., Ltd
c Shanghai Construction No.5 (Group) Co., Ltd, Shanghai, China

Abstract

Precast connections and cast-in-place connections are used to mix and cross reasonably in the height and plane of structure to form a new type of high-rise precast reinforced concrete frame structure with hybrid connections. The expression of the limit value R_0 of the stiffness coefficient of the semi-rigid connections of the single-story structure is derived when it reaches the elastic max story drift limit. Meanwhile, the expression of the limit value of the semi-rigid connection stiffness coefficient is obtained through numerical regression by MATLAB programming. The ETABS is used to model space frame structures, and the elastic response of different arrangements and stiffness values of semi-rigid connections is compared to obtain the preliminary mixing principles of precast concrete structures with hybrid connections. The results show that the elastic response of structures with the semi-rigid connections is better when the semi-rigid connections are arranged evenly along with the height. The influence of the arrangement of the semi-rigid connections in the plane on the elastic responses of the structure has a large relationship with the number of semi-rigid connections but has little relationship with the arrangement position of the semi-rigid connections.

Keywords: precast concrete structure, semi-rigid connections, mixing principles, max story drift, small earthquake.

1. Introduction

Precast concrete (PC) structure has the advantages of easy control of component quality, high construction efficiency, environmental impact and economy in manpower, etc. However, the key to the large-scale application of PC structures lies in whether the precast connection is the weak link of the structure and whether the connection area has strong seismic performance[1]. The flexural strength and rotational stiffness of beam-column connections determine the overall performance of the precast structure and also affects its application in high-rise buildings. Precast connections and cast-in-place connections are used to mix and cross reasonably in the height and plane of structure to form a new type of high-rise PC structure with hybrid connections. This kind of structure can not only rely on the advantages of cast-in-place concrete in stiffness and damping but also make full use of the outstanding designability of precast connections.

At present, most of the research on PC structures focuses on the method of connection [2][3][4], while the research on the overall performance of hybrid connected structures is conducted through the layout and stiffness of precast connections. The key to this structure lies in the layout and stiffness of precast connections. Generally, we treat connections as rigid connections or pin connections and consider that

Copyright © 2019 by Ge Li, Bin Du, Zheng He, Guohui Huang, Feng Pan
Published by the International Association for Shell and Spatial Structures (IASS) with permission.

connections do not transfer bending moments or transfer all bending moments. However, in fact, these connections generally transfer part of bending moments as semi-rigid connections [5][6]. Bljuger [7] first introduced the concept of semi-rigid connection in the PC structure. Sucuoglu [8] used a rotational spring with the stiffness of k to simulate the semi-rigid connection of PC structures and studied the impact of the stiffness of connections on PC structures by deriving the stiffness matrix of beam elements with rotational springs at both ends. Elliott K Set al. [5][6] studied the semi-rigid behavior of PC structure through experiment and numerical simulation, and put forward the theoretical equation to predict the value of resistance moment and rotational stiffness S, thus obtaining the M-θ_r curve. El-sheikh et al. [9] proposed two macro unit models, namely the fiber model and spring model.

For the precast connections of high-rise PC structures with hybrid connections, the elastic story displ. occupies a large proportion of the total displ due to the insufficient connection stiffness. Therefore, based on the elastic displ. requirements of small earthquakes, this paper obtains the mixing principles of PC structure with hybrid connections and the stiffness range of the semi-rigid connections.

2. Analysis of stiffness parameters of semi-rigid connections in single-story structures

Du [10] simplified precast connections to rotational springs as shown in figure 1, through the connection position parameter α (the ratio of connection position to beam length) and the connection stiffness parameter R, which can consider connection position and stiffness changes, based on shear-bending story model. The stiffness matrix of the ith story is derived, as shown in Eq. (17) in [10].

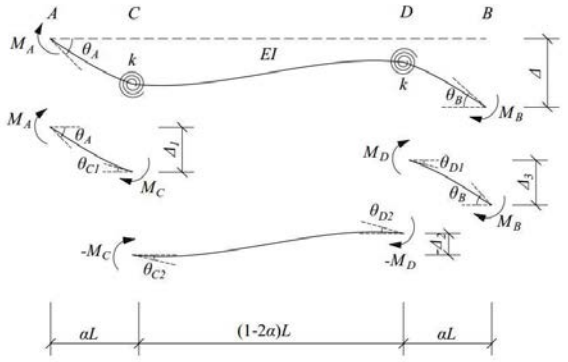


Figure 1: Beam Element with semi-rigid connections

2.1. Derivation of the stiffness parameter formula of the single-story structure

For single-story structure, take i=1, N=*0* and substitute Eq. (17) in [10] into Eq. (19) in [10] to get Eq. (1). From Eq. (2) of the story drift, we can get Eq. (3). The range of values of R and α can be solved by Eq.(3) and Eq.(18) in [10]. Where L_{ci} and L_{bi} respectively represent the length of column and beam, i_{ci} and i_{bi} respectively represent the linear flexural stiffness of column and beam, and m represents the span number of frame, F_1 represents the lateral force in the first story, the stiffness k of the rotational spring represents the stiffness of the connection, denoted by $R=kL_{bi}/(EI_{bi})$. k_{bi} =$12\sum\lambda i_b$ is related to parameters α and R, reflecting the influence of connection location and stiffness, where λ is Eq.(18) in [10]. The values of R and α are discussed below: (1) If α = 0: when $k_{b1}=12mRi_b/(R+6)\geq A$, we can get Eq. (4), where the expression of A is shown in Eq. (6). (2) If R is a fixed value: when $k_{b1}=12mRi_b/(R+24\alpha^2-24\alpha+6)\geq A$ and $1-12mi_b/A\leq 0$, we can get Eq.(5); when $1-12mi_b/A>0$, then $\{\alpha:0\leq\alpha\leq 0.5\}$.

$$x_1 = \frac{F_1\left[4(m+1)i_c + k_{b1}\right]L_{c1}^2}{12(m+1)i_c\left[(m+1)i_c + k_{b1}\right]} \tag{1}$$

$$\theta_1^{'}=\frac{x_1}{H_1}\le[\theta] \tag{2}$$

$$k_{b1}\ge\frac{4(m+1)i_c\left\{-3(m+1)i_c[\theta]+F_1L_{c1}\right\}}{12(m+1)i_c[\theta]\text{-}F_1L_{c1}} \tag{3}$$

$$\left\{R:R\ge\frac{6}{\frac{12mi_b}{A}-1},R\ge0\right\} \tag{4}$$

$$\left\{\alpha:\frac{1-\sqrt{1-(6+R-\frac{12mi_b}{A})/6}}{2}\le\alpha\le\frac{1+\sqrt{1-(6+R-\frac{12mi_b}{A})/6}}{2},0\le\alpha\le0.5\right\} \tag{5}$$

$$A=\frac{4(m+1)i_c\left\{-3(m+1)i_c[\theta]+F_1L_{c1}\right\}}{12(m+1)i_c[\theta]\text{-}F_1L_{c1}} \tag{6}$$

2.2. Case analysis

The calculation model is shown in Figure 2. The section of the column is *500mm×500mm*, the section of the beam is *300mm×600mm*, the beam-column elastic modulus is $E_b=E_c=30000N/mm^2$, the concrete strength is C30, and the concrete strength grade is $f_{cu}=14.5N/mm^2$. When the position parameter α takes different values, the change of the story drift with the stiffness coefficient R is shown in Figure 3. Generally, the story drift decreases with the increase of the connection stiffness parameter R. When R is less than 1, the story drift decreases faster. When R is greater than 5, the story drift decreases slowly and tends to the value of $\alpha=0.5$, that is, the structure tends to be rigid. Taking the limit of story drift $[\theta]=1/550$ based on the Chinese code, and let $F=249.76kN$, {R: R≥0.425} is obtained by Eq.(4). Modeling in ETABS and taking $R=0.425$ as the connection stiffness coefficient, the finite element analysis shows that the story drift is $\theta_1^{'}=1/544$, which basically coincides with $[\theta]=1/550$ to verify the correctness of the deduced formula.

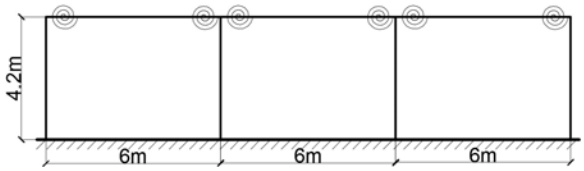


Figure 2: Single-story structure model

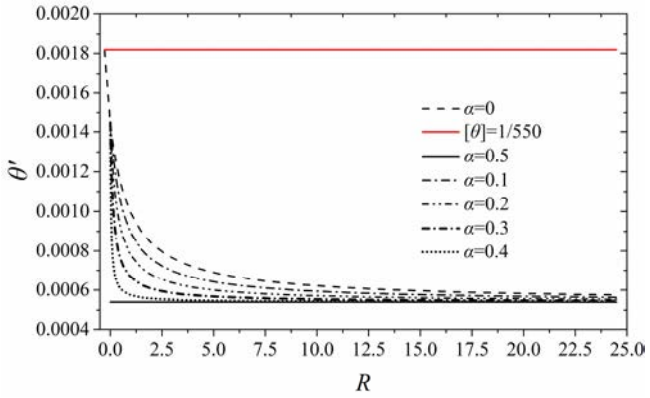


Figure 3: Story drift of single-story semi-rigid structure

3. Analysis of stiffness parameters of semi-rigid connections in multi-story structures

3.1. Programming analysis of multi-story frame structures

For multi-story structures, the total stiffness matrix [*K*] of structures can be obtained from Eq.(17) in [10] and (19) in [10] and is written as $\{F\}=[K]\cdot\{\delta\}$, where [*K*] is shown in Eq. (7) and $k_{i\ (2,3)}$ is the stiffness matrix of the *i*th story and (2,3) is the corner mark of the stiffness matrix of the *i*th story, representing the second row, the third column of the stiffness matrix of the *i*th story, and k_i is the matrix of Eq. (17) in [10], when $N=0$.

$$[K]=\begin{bmatrix}
[k_{1(3,3)}+k_{2(1,1)}] & [k_{1(3,4)}+k_{2(1,2)}] & k_{2(1,3)} & k_{2(1,4)} & & & & & & & & & \\
[k_{1(4,3)}+k_{2(2,1)}] & [k_{1(4,4)}+k_{2(2,2)}] & k_{2(2,3)} & k_{2(2,4)} & & & & & & & & & \\
k_{2(3,1)} & k_{2(3,2)} & [k_{2(3,3)}+k_{3(1,1)}] & [k_{2(3,4)}+k_{3(1,2)}] & k_{3(1,3)} & k_{3(1,4)} & & & & & & & \\
k_{2(4,1)} & k_{2(4,2)} & [k_{2(4,3)}+k_{3(2,1)}] & [k_{2(4,4)}+k_{3(4,2)}] & k_{3(2,3)} & k_{3(2,4)} & & & & & & & \\
 & & k_{3(3,1)} & k_{3(3,2)} & [k_{3(3,3)}+k_{4(1,1)}] & [k_{3(3,4)}+k_{4(1,2)}] & k_{4(1,3)} & k_{4(1,4)} & & & & & \\
 & & k_{3(4,1)} & k_{3(4,2)} & [k_{3(3,3)}+k_{4(1,1)}] & [k_{3(4,4)}+k_{4(2,2)}] & k_{4(2,3)} & k_{4(2,4)} & & & & & \\
 & & & & \vdots & \vdots & \vdots & \vdots & & & & & \\
 & & & & k_{i(3,1)} & k_{i(3,2)} & [k_{i(3,3)}+k_{i+1(1,1)}] & [k_{i(3,4)}+k_{i+1(1,2)}] & k_{i(1,3)} & k_{i(1,4)} & & & \\
 & & & & k_{i(4,1)} & k_{i(4,2)} & [k_{i(3,3)}+k_{i+1(1,1)}] & [k_{i(4,4)}+k_{i+1(2,2)}] & k_{i(2,3)} & k_{i(2,4)} & & & \\
 & & & & & & & & \vdots & \vdots & & & \\
 & & & & & & & & k_{n-1(3,1)} & k_{n-1(3,2)} & k_{n(3,1)} & k_{n(3,4)} & \\
 & & & & & & & & k_{n-1(4,1)} & k_{n-1(4,2)} & k_{n(4,1)} & k_{n(4,4)} &
\end{bmatrix} \quad (7)$$

The equations mentioned above are programmed in MATLAB [11] to obtain the total stiffness matrix of the structure. The seismic action is obtained by the mode decomposition response spectrum method, and then the displ. is obtained to get the max story drift of the structure. Taking twelve-story three-span plane frame as an example, according to the GB50011-2010 [12] and JGJ3-2010 [13], the first story is 4.2m, the other stories are 3.3m; the three-span is 6m, the section of columns in 1-4 stories is *700mm×700mm*, the section of columns in 5-8 stories is *600mm×600mm*, the section of columns in 9-12 stories is *500mm×500mm*, the section size of beam is *300mm×600mm*, the elastic modulus of beam and column is $E_b=E_c=30000N/mm^2$, and the strength of concrete is *C30*. It is the first seismic group, the intensity level of 8, the second site classification. The design basic acceleration is 0.2g. The period and story drift calculated by the program and commercial software such as ETABS and PKPM is compared, where the error of the max story drift is 4.9%. The results show that the results obtained by the program are basically reliable. The variation of the max story drift and T_1 with position parameter α and stiffness parameter *R* is shown in figure 4 and figure 5. The max story drift decreases with the increase of *R*, especially when $0\leq R\leq 10$, the max story drift decreases significantly. Under the same *R*, the max story drift decreases significantly. The max story drift decreases with the position of semi-rigid connections moving inward. It is noteworthy that when the semi-rigid connections are located in the middle of the span, the max story drift does not change with the change of *R*. The main reason is that the mid-span is the position of the reverse bending point, and the rotational stiffness here has no effect on the lateral stiffness of the structure, which is equivalent to rigid connections.

3.2. Regression analysis of multi-story planar frame structures

From 3.1, the critical value of the semi-rigid connection can be determined by numerical regression [14] through MATLAB programming. To simplify the regression analysis, it is assumed that:(1) The change of R_0 (the critical value of stiffness coefficient of semi-rigid connections) is only caused by the change of its own structural factors. Site factors, seismic grade, and other external forces do not lead to the change of R_0. (2) The connections of the structure are located at the beam-column joints, and *R* remains unchanged in a structure. (3) The span of the structure is the same, and the section of the beam remains unchanged. According to 6.3.1 in JGJ3-2010 [15], the section height of the beam in the frame structure

can be determined according to 1/10−1/18 of the calculated span. The section height of the beam should not be less than 1/4 of the section height, nor less than 200 mm. For simplification, the section height of the beam should be 1/12 of the span. The section width of the beam should be 1/2 of the section height of the beam. Considering the different cross-sections of columns in different stories, the cross-sections of columns in every four stories are the same. The regression analysis of 1000 samples shows that the dependent variable R_0 is related to the independent variable m, n, H_b and L_c, and the regression mathematical model is $R_0=a_5 \cdot m^{a1} \cdot \beta^{a2} \cdot n^{a3}+a_4$ (n≥4), where $\beta=H_b/L_c$. The results show that the column width Hc has a no significant effect on the dependent variables, so $H_{c1}=0.5m$, $H_{c2}=0.6m$, $H_{c3}=0.7m$ are kept unchanged. The results of regression analysis are shown in Table 1, where $F \geq F_{\alpha=0.05}=2.09$ and model information of the planar structures is shown in figure 6 (b), (c), (d).

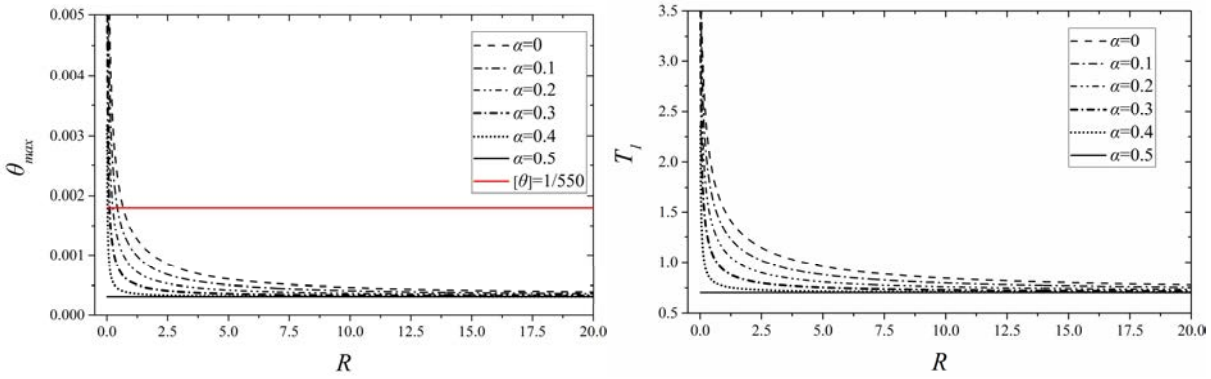


Figure 4: Max story drift of 12-story frame structures; Figure 5: T1 of 12-story frame structures

Table 1: The results of the regression analysis

Model	the results of regression analysis	the judgment coefficient (R^2)	the multiple correlation coefficient (R)	F value
M 2	$R_0=1.85\times10^{-6} \cdot m^{-0.28} \cdot \beta^{-2.96} \cdot n^{3.30}+0.12$	0.9110	0.9545	3.10×10^3
M 4	$R_0=1.06\times10^{-10} \cdot m^{-0.47} \cdot \beta^{-5.53} \cdot n^{4.65}-1.81$	0.7134	0.8446	61.39
M 3	$R_0=6.60\times10^{-12} \cdot m^{-0.66} \cdot \beta^{-6.06} \cdot n^{4.93}+0.18$	0.9023	0.9499	1.23×10^3

4. Analysis of space frame structure

4.1. Model information

In ETABS 2016[15], a twelve-story, seven-piece and three-span frame structures with the same structural information as in 3.1 is established. The release of bending moment at the end of the beam is used to reflect the difference in the stiffness of semi-rigid connections. The structures are modeled by using different R and different positions of semi-rigid connections. The location information of semi-rigid connections of the models is shown in figure 6. Figure 6 (a)-(f) shows the layout of a single piece of the frame with semi-rigid connections. Figure 6 (h)-(k) is the layout of the frame with semi-rigid connections. Only the stiffness and position of semi-rigid connections in these models are different from other information except that the models with -# is four spans.

4.2. Analysis

Table 2 shows the elastic responses of PC structures with different rotational stiffness of connections. The relationship between the elastic responses and the stiffness of the connections is reflected in the M

2 series. With the increase of *R* of the connections, T1, the max story drift and the max top displ. gradually decrease and finally tend to the rigid connection, while the min stiffness-gravity ratio and the min sheer-gravity ratio gradually increase and finally tend to the rigid connection.

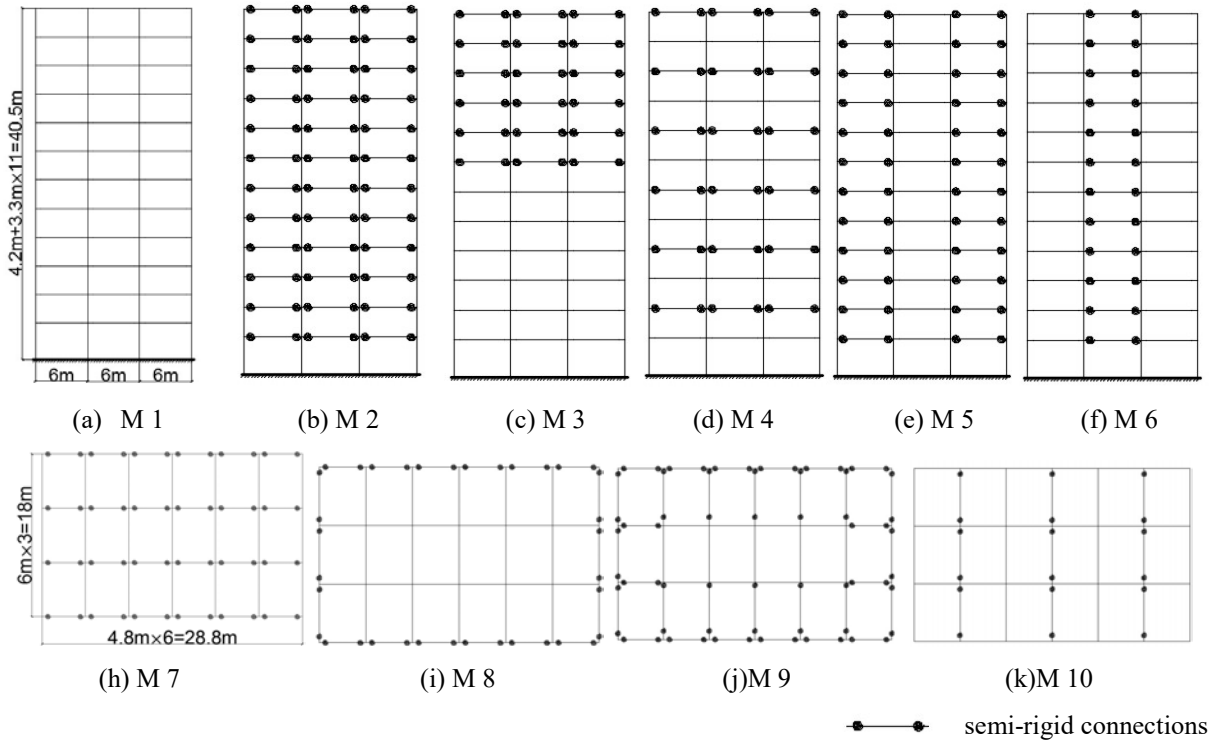


Figure 6. Model information

Table 3 is the elastic response when semi-rigid connections are in different positions. Comparing M 3 with M 4, half of the stories with the semi-rigid connections are used. The max story drift, the max top displ. of Y-direction, the min stiffness-gravity ratio and min shear-gravity ratio of M 4 is smaller than these of M 3. The T1 is bigger than that of M 3. This is due to that the rigid connections are at the bottom of M 3 and the stiffness mainly concentrates at the bottom, while the stiffness distribution of M 4 is uniform along with the height. The stiffness distribution of M 4 is not much different from that of M 5, but the semi-rigid connections are used for the side span of M 5, and the semi-rigid connections are used for the connections equivalent to 2/3 of the three-span structure. In order not to be affected by the number of semi-rigid connections, the models of the four-span structure are established, namely, M 3-#, M 4-#, M 5-#, M 6-#. The other parameters are the same as those of three-span models. Compared with M 4-#, M 5-#, M 6-#, the difference of T1, max story drift, min stiffness-gravity ratio, and min shear-gravity ratio is very small. M 7 reflects the influence of the semi-rigid structure on the overall elastic responses of the frame structure. It can be seen that the longitudinal hinge (M 7-1) has no effect on the lateral story drift of Y-direction, but has a great influence on the longitudinal story drift and the overall stiffness of the structure. The M7-2 meets the requirement of the code after the connections adopt appropriate stiffness. When the appropriate stiffness of connection is adopted (e.g. M 8 and M 9), the response of M 8 and M 9 meets the code limit values. M 10 adopts semi-rigid connections for spans, which shows that reasonable mixing can make the elastic response of the structure meet the requirements of the code. In summary, it can be concluded that (1) when the semi-rigid connections are evenly distributed along the height of the structure (e.g. M4), the elastic response of the semi-rigid connections meets the requirements of the elastic limit of the code and has a certain degree of affluence; (2) when the semi-rigid connections are evenly distributed along the height of the structure, the elastic responses of the structure have a great relationship with the number of semi-rigid connections in the plane, but not with the position of semi-rigid connections in the plane; (3) for the stiffness of longitudinal connections, a

smaller semi-rigid coefficient can be used, which can meet the requirements of the code and meet the characteristics of PC structures, thus having certain economic effects.

Table 2: Elastic response of frame structures with different rotational stiffness of connections.

Model	R	T1(sec)	Min stiffness-gravity ratios	Min Sheer-gravity ratios	Y-direction	
					Max story drift	Max top displ. (mm)
M 1		1.5	27.72	0.043	1/785	37.51
M 2-1	0.5	3.01	7.18	0.028	1/235	124.33
M 2-2	3	2.04	15.04	0.032	1/545	52.48
M 2-3	3.5	1.96	16.25	0.033	1/571	50.27
M 2-4	3.68	1.94	16.69	0.034	1/579	49.68
M 2-5	3.875	1.91	17.07	0.034	1/589	48.88
M 2-6	4.25	1.87	17.83	0.035	1/605	47.67
M 2-7	5.5	1.77	19.99	0.037	1/646	44.92
M2-8	8	1.65	23.09	0.039	1/705	41.56
M2-9	10.5	1.58	25.21	0.041	1/739	39.87
M2-10	17.85	1.49	28.81	0.043	1/797	37.61

Table 3: Elastic response of semi-rigid frame structures with semi-rigid connections at different locations

Model	T1(sec)	Min stiffness-gravity ratios	Min Sheer-gravity ratios	Y-direction		X-direction	
				Max story drift	Max top displ.(mm)	Max story drift	Max top displ.(mm)
M3	1.634	27.73	0.039	1/587	43.62	1/913	32.62
M3-#	1.605	27.92	0.039	1/622	42.49	1/913	33
M4	1.7	21.73	0.038	1/672	43.03	1/913	32.62
M4-#	1.679	21.88	0.038	1/672	42.29	1/913	32.62
M5	1.762	20.06	0.037	1/648	44.7	1/913	32.62
M5-#	1.675	22.08	0.038	1/689	42.1	1/913	32.62
M6	1.617	23.94	0.04	1/722	40.82	1/913	32.62
M6-#	1.678	22.14	0.038	1/691	42.38	1/913	32.62
M7-1	10.021	0.87	0.02	1/786	37.51	1/27.	919.54
M7-2	1.658	23.53	0.039	1/785	37.51	1/698	41.74
M8	2.211	19.55	0.036	1/657	44.48	1/637	46.26
M9	2.165	15.76	0.033	1/673	51.03	1/560	52.37
M10	1.652	22.8	0.032	1/701	41.55	1/913	32.62

5. Conclusion

Some observations and conclusions can be reached at the following:

(1) The range formula of the stiffness coefficient of semi-rigid connections and the elastic response of the structure when the stiffness of the connections change are obtained when the single-story structure and multi-story planar frame structure reach the maximum story drift limit specified by the elastic limit state of small earthquakes. These provide an initial estimate of the stiffness of the connections of PC structures with hybrid connections.

(2) The preliminary mixing principles of the hybrid connections of PC structures are obtained. The results show that the elastic response of the structure is better when the semi-rigid connections are evenly

arranged along with the height; the effect of semi-rigid connections layout on the elastic response of the structure in the plane is related to the number of semi-rigid connections, but not to the location of semi-rigid connections in the plane.; the elastic response of the whole structure can be improved obviously by choosing a reasonable position and stiffness parameters of connections.

Acknowledgments

This research is financially supported by the Natural Science Foundation of China (Grant No. 51878123) and the Fundamental Research Funds for the Central Universities (Grant No. DUT19G208).

References

[1] R. Park, "The fib state-of-the-art report on the seismic design of precast concrete building structures," in *2003 Pacific Conference on Earthquake Engineering, Paper*, 2003, no. 011.

[2] M. J. N. Priestley, "Overview of PRESSS research program," *PCI J.*, vol. 36, no. 4, pp. 50–57, 1991.

[3] S. Pampanin, D. Marriott, and A. Palermo, *PRESSS design handbook*. New Zealand Concrete Society, 2010.

[4] H. Parastesh, I. Hajirasouliha, and R. Ramezani, "A new ductile moment-resisting connection for precast concrete frames in seismic regions: an experimental investigation," *Eng. Struct.*, vol. 70, pp. 144–157, 2014.

[5] K. S. Elliott, G. Davies, M. Ferreira, H. Gorgun, and A. A. Mahdi, "Can precast concrete structures be designed as semi-rigid frames? Pt. 1: the experimental evidence.," *Struct. Eng.*, vol. 81, no. 16, pp. 14–27, 2003.

[6] K. S. Elliott, G. Davies, M. Ferriera, H. Gorgun, and A. A. Mahdi, "Can precast concrete structures be designed as semi-rigid frames? Part 2: Analytical equations & column effective length factors," *Struct. Eng.*, vol. 81, no. 16, pp. 28–37, 2003.

[7] F. E. Bljuger, *Design of precast concrete structures*. Ellis Horwood, 1988.

[8] H. Sucuoglu, "Effect of connection rigidity on seismic response of precast concrete frames," *PCI J.*, vol. 40, no. 1, pp. 94–103, 1995.

[9] M. T. El-Sheikh, R. Sause, S. Pessiki, and L.-W. Lu, "Seismic behavior and design of unbonded post-tensioned precast concrete frames," *PCI J.*, vol. 44, no. 3, pp. 54–71, 1999.

[10] B. Du, Z. He, and G. Huang, "An Estimate on Distribution of Hysteretic Energy Demand in Seismic Precast Concrete Frame Structures," *J. Earthq. Eng.*, pp. 1–27, 2019.

[11] Kwon and YoungW, *The finite element method using MATLAB*. 2000.

[12] Ministry of Housing and Urban-Rural Development of People's Republic of China. *Code for seismic design of buildings (GB50011-2010).* China Architecture & Building Press : Beijing; 2010. (in Chinese).

[13] Ministry of Housing and Urban-Rural Development of People's Republic of China. *Technical specification for concrete structures of tall building (JGJ3-2010).* China Architecture & Building Press Beijing; 2011. (in Chinese)

[14] Kwon and YoungW, *The finite element method using MATLAB*. 2000.

[15] R. R. Hussain, M. Wasim, and S. Hasan, *Introduction to ETABSETABS*. 2016.

Proceedings of the IASS Annual Symposium 2019 – Structural Membranes 2019
Form and Force
7 – 10 October 2019, Barcelona, Spain
C. Lázaro, K.-U. Bletzinger, E. Oñate (eds.)

Elastic buckling behavior of anisotropic latticed shells

Takahiro MATSUDA*,Tetsuo YAMASHITA[a]

* Graduate Student, Kogakuin University,
Tokyo, Japan,
dm18048@ns.kogakuin.ac.jp

[a] Professor, Kogakuin University

Abstract

Today, we can design latticed shells according to guidelines[1,2]. However, in most of these studies, isotropic latticed shells of equilateral triangle grid has been dealt with. There are few studies on buckling behavior of anisotropic latticed shells. In this study, we assumed three types of grids composing latticed shells and parametrically changed the degree of anisotropy. Firstly, we conducted the linear buckling and the geometric nonlinear analysis on the anisotropic latticed shells without imperfection and investigated the knockdown factor. The knockdown factor of the anisotropic latticed shells is higher than that of the isotropic latticed shells. Secondary, we conducted the geometric nonlinear analysis on the anisotropic latticed shells where imperfection was proportional to the buckling mode. The imperfection proportional to the 1st buckling mode minimizes the knockdown factor in almost cases, while some exception on isotropic shells was found.

Keywords: Anisotropic latticed shells, geometric nonlinear analysis, imperfection, knockdown factor

1. Introduction

In design of single layer latticed shells, it is critical to consider buckling. Many studies on buckling of single layer latticed shells have been done, so we can design latticed shells according to guidelines[1,2]. However, in most of these studies, isotropic latticed shells of equilateral triangle grid has been dealt with. There are few studies on buckling behavior of anisotropic latticed shells.

In this study, we conducted the linear FE buckling analysis and the geometric nonlinear analysis on shells composed of triangular, rhomboid and hexagonal lattices(fig.1), where the degree of anisotropy was parametrically changed, and investigated the effect of anisotropy and imperfection on the knockdown factor defined as the ratio of the elastic buckling load p_{cr}^{el} to the linear buckling load p_{cr}^{lin}.

The effective rigidities of lattice surface to express the anisotropy is introduced in this study. [1~5] In order to derive the effective rigidities, the complementary strain energy of a lattice unit (fig.1 solid line) is equaled to that of the corresponding anisotropic continuum plate. (fig.1 dashed line)The in-plane effective rigidities are defined by Eq. (1).

$$\begin{Bmatrix} n_x \\ n_y \\ n_{xy} \end{Bmatrix} = \begin{bmatrix} K_{1111} & K_{1122} & 0 \\ K_{2211} & K_{2222} & 0 \\ 0 & 0 & K_{12} \end{bmatrix} \begin{Bmatrix} \varepsilon_x \\ \varepsilon_y \\ \gamma_{xy} \end{Bmatrix} \tag{1}$$

$$\varepsilon_x = \frac{\partial u}{\partial x} \qquad \varepsilon_y = \frac{\partial v}{\partial y} \qquad \gamma_{xy} = \frac{\partial v}{\partial x} + \frac{\partial u}{\partial y}$$

Copyright © 2019 by Takahiro Matsuda and Tetsuo Yamashita
Published by the International Association for Shell and Spatial Structures (IASS) with permission.

where u and v are the displacement in x and y directions. K_{1111},K_{1122},K_{2211},K_{2222} and K_{12} are the effective in-plane rigidities and $K_{1122}=K_{2211}$, $K_{1122}=\nu_{xy}K_{1111}$, $K_{2211}=\nu_{yx}K_{2222}$($\nu_{xy}$ and ν_{yx} are in-plane poisson's ratio.).

In this study, triangular, rhombus and haxagonal lattices are dealt with. Table1 shows the in-plane effective rigiditeis of the latticed surface where E and A are the Young's modulus and the section area of member. I is the in-plane second moment of inertia. Hereafter, the subscripts $_h$ and $_g$ with the signs are given for the horizontal and diagonal materials, respectively. λ_g is the slenderness ratio of members. Ratio of length, the section area and the in-plane second moment between horizontal material and diagonal material are $h=l_h/l_g$, $a_h=A_h/A_g$ and $i_h=I_h/I_g$, respectively.

The degree of anisotropy is expressed by ξ defined by Eq.(2). The lattice of which ξ is not equal to 1 have orthogonal anisotropy.

$$\xi = \frac{K_{1111}}{K_{2222}} \tag{2}$$

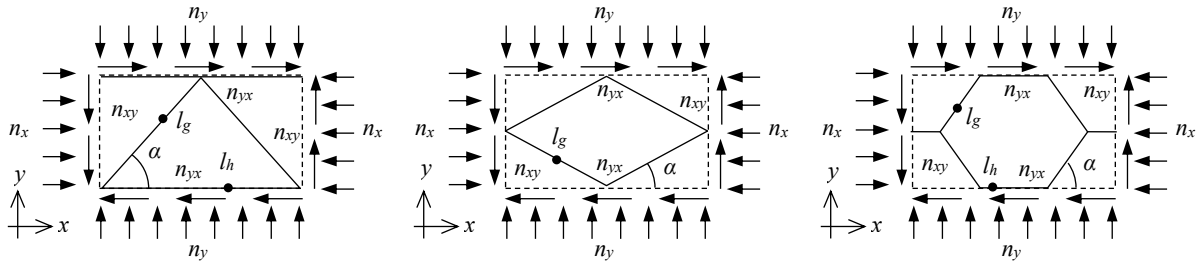


Fig.1 Latticed surface

Table 1 Effective rigidities

	K_{1111}	$K_{1122}=K_{2211}$	K_{2222}	K_{12}
Triangle[1]	$\psi_1\left(\cot^2\alpha+\frac{a_h}{\sin^2\alpha\cos\alpha}\right)$	ψ_1	$\psi_1\tan^2\alpha$	ψ_1
Rhombus[4]	$\psi_1\left(\cot^2\alpha+\frac{12}{\lambda_g^2}\right)$	$\psi_1\left(1-\frac{12}{\lambda_g^2}\right)$	$\psi_1\left(\tan^2\alpha+\frac{12}{\lambda_g^2}\right)$	ψ_1
Hexagon[5]	$\psi_2(\cos\alpha+h)\left(1+\frac{\lambda_g^2}{12}\cot^2\alpha\right)$	$\psi_2\cos\alpha\left(\frac{\lambda_g^2}{12}-1\right)$	$\psi_2\frac{1}{\cos\alpha+h}\left(\frac{2h}{a_h}+\cos^2\alpha+\frac{\lambda_g^2}{12}\sin^2\alpha\right)$	$\frac{2EA_g(\cos\alpha+h)\sin\alpha}{l_g\left\{2(1+h\cos\alpha)^2+\left(\frac{h}{3i_h}+\frac{1}{6}\right)h^2\lambda_g^2\sin^2\alpha\right\}}$
$\psi_1=\frac{EA_g}{l_g}\sin\alpha\cos\alpha,\quad \psi_2=\frac{EA_g}{l_g\sin\alpha\left\{\frac{2h}{a_h}\left(1+\frac{\lambda_g^2}{12}\cot^2\alpha\right)+\frac{\lambda_g^2}{12\sin^2\alpha}\right\}}$				

2. The analysis models

Fig. 2 shows the values of the effective Poisson's ratio for in-plane strain and ξ. The value of ξ equals to 1 when the diagonal angle α(Fig.1) is 60 degrees on triangle and hexagonal grids and 45 degrees on rhombus grid, 45, 60 and 75 degrees were assumed for the triangle and hexagonal grid, and 30, 45 and 60 degrees for the rhombus grid.

The shells for study were a portion of torus surface in which the central section was an arc of the span of approximately 30m.(fig.3) The rise span ratio of the central arc was 0.1 or 0.2. In the triangular grid shells, the center grid was an isosceles triangle with the diagonal members of 3000mm and the diagonal angle α. In the rhomboid and hexagonal grid shells, the center grid of shells had the diagonal members of 3000mm and the diagonal angle α. The member cross section was commonly assumed to be a steel pipe (φ 216.4 × 4.5). The Young's modulus E=2.05×10^5 N/mm^2 and the elastic shear modulus

G=7.94×10^5 N/mm^2. Fig. 4 shows the model name notation, and Table2 shows the numbers of grids in the x and y directions of each model. The shells are pin-supported on the boundary, and subjected to vertical nodal load to all the nodes excluding the outer peripheral nodes. We used the finite element analysis program Marc mentat 2017 [6].

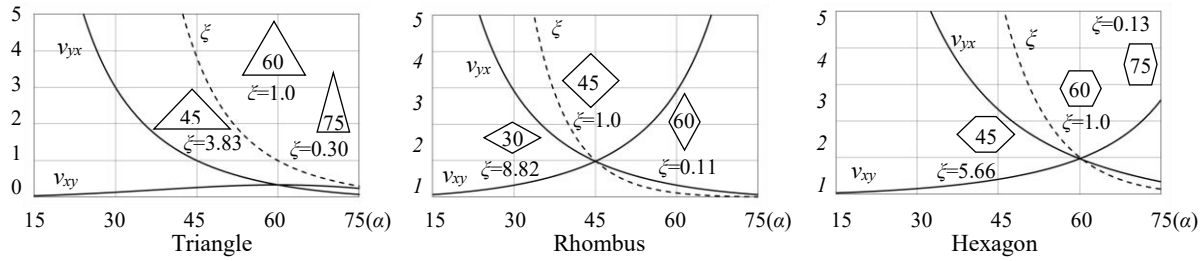


Fig.2 Anisotropy of lattice

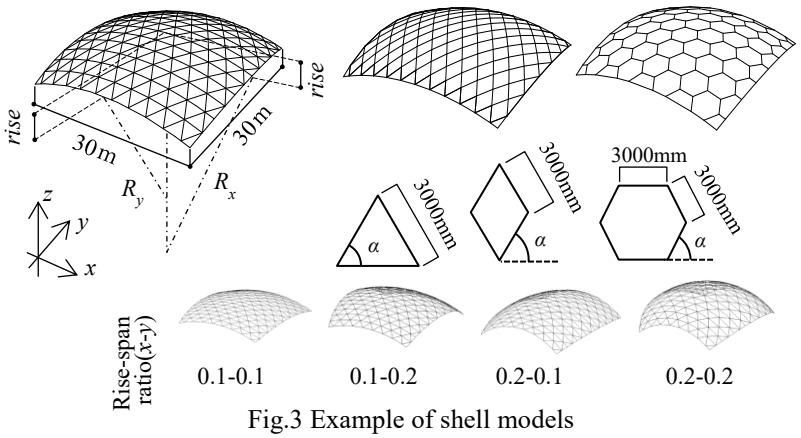


Fig.3 Example of shell models

Table 2 the number of grids

α (deg)	Triangle		Rhombus		Hexagon	
	x	y	x	y	x	y
30			6	11		
45	8	16	8	8	3	7
60	10	12	11	3	4	7
75	22	12			5	6

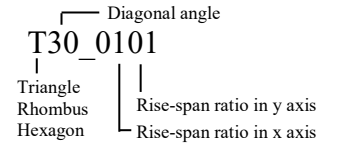


Fig.4 Model name notation

3. Linear buckling analysis

Fig.5 shows the ratios of the i-th linear buckling load $q_{cr}^{lin_i}$ to the 1st linear buckling load $q_{cr}^{lin_1st}$. In triangularly latticed shells, the linear buckling loads of higher order are close to $q_{cr}^{lin_1st}$. In rhomboidally latticed shells where the diagonal angle is not 45°, higher linear buckling loads are far beyond $q_{cr}^{lin_1st}$. In hexagonal latticed shells, higher linear buckling loads are also beyond $q_{cr}^{lin_1st}$ but not as much as the case of the rhomboidally latticed shells. In case of the shells of which ξ *is* equal to 1, the higher linear buckling loads are closed to $q_{cr}^{lin_1st}$ without correlation to the grid configuration.

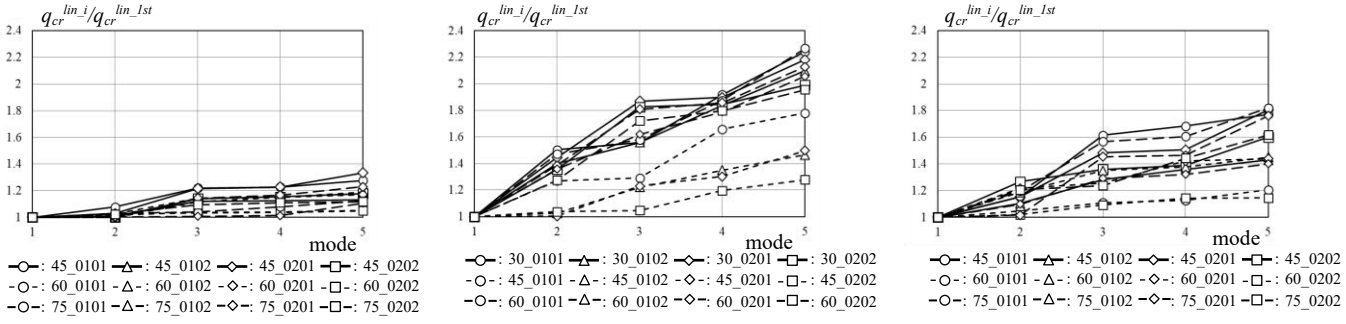


Fig.5 Ratio of higher linear buckling load to 1st linear buckling load

4. Elastic buckling analysis

We performed geometric nonlinear analysis by arc length method (hereinafter elastic buckling analysis). Forty-nine imperfection modes were assumed, which were proportional to the linear buckling mode of the 1st to 49th in the vertical direction with the amplitude δ of 1/500, 1/1000, 1/3000 of the span. The maximum load in the load-displacement curve was regarded as the elastic buckling load q_{cr}^{el}. The knockdown factor α_0 is defined by Eq. (3).

$$\alpha_0 = \frac{q_{cr}^{el}}{q_{cr}^{lin_1st}} \tag{3}$$

4.1. The knockdown factor of shell without imperfection

Fig. 6 shows the knockdown factor of the shells without imperfection (denoted by $\alpha_0^{el_0}$).

1) Triangularly latticed shells

The values of $\alpha_0^{el_0}$ of the triangular latticed shells having anisotropy are approximately 0.8 or more, while the $\alpha_0^{el_0}$ of T60_0101 having isotropy is 0.67. The $\alpha_0^{el_0}$ of the isotropic shells increases as the rise span ratio increased. However, The $\alpha_0^{el_0}$ of the anisotropic shells does not change so much with the rise span ratio.

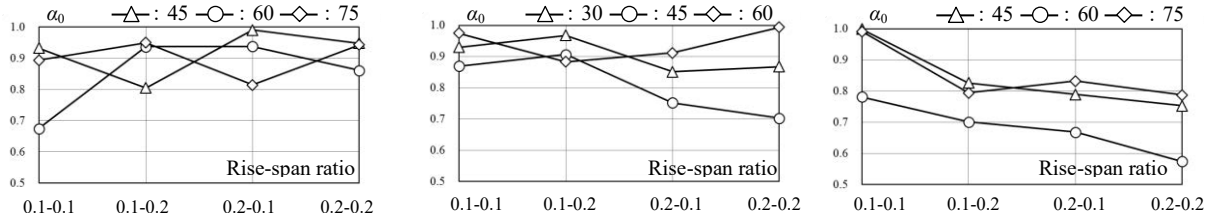
2) Rhomboidally latticed shells

The values of $\alpha_0^{el_0}$ of the shells of which α=30 and 60 degrees with anisotropy are approximately 0.9, and the difference between the linear and the elastic buckling load is small. However, the $\alpha_0^{el_0}$ of R45_0101 and R45_0202 having $\xi = 1.0$ and $R_x \fallingdotseq R_y$ are 0.87 and 0.70, respectively, far below the linear buckling loads. These values are lower than the knockdown factor of the anisotropic shells having anisotropy. Furthermore, the values of $\alpha_0^{el_0}$ of shells of which α=45 degrees decrease as the rise span ratio increase.

3) Hexagonally latticed shells

The $\alpha_0^{el_0}$ of the anisotropic shells are higher than the values of the shells of which $\xi = 1$. The $\alpha_0^{el_0}$ of H45_0101 and H75_0101 are nearly equal 1. In general, the values of $\alpha_0^{el_0}$ of hexagonally latticed shells decrease as the rise span ratio increase.

Summarizing these facts, the values of $\alpha_0^{el_0}$ of the anisotropic shells are higher than the values of ~~a~~ the shells of which $\xi = 1.0$ and $R_x \fallingdotseq R_y$. In addition, the $\alpha_0^{el_0}$ of the shells of which $\xi = 1.0$ is more likely to be affected by the rise span ratio than the anisotropic shells .



Triangle Rhombus Hexagon

Fig.6 Knockdown factor of shells without imperfection

4.2. RS buckling mode

The RS buckling mode, to estimate the lowest limit of elastic nonlinear buckling load, is introduced to find an effective imperfection other than the 1st mode. The energy quotient β_i for the i-th buckling mode calculated by Eq. (4) is called the RS value [7].

$$\beta_i = \frac{U_0}{U} = \frac{\frac{1}{2}\{\phi_i\}^T[K_0]\{\phi_i\}}{\frac{1}{2}\{\phi_i\}^T[K]\{\phi_i\}} \tag{4}$$

where U is the strain energy generated by the i-th buckling mode vector $\{\phi_i\}$, [K] is the linear stiffness matrix, [K_0] is the linear stiffness matrix where the in-plane rigidities are assumed zero.

The minimum value of $\beta_i q_{cr_i}^{lin}$ is called as the RS buckling load (denoted by q_{cr}^{rs}) and the corresponding buckling mode is the RS buckling mode. β_o is defined as the ratio of q_{cr}^{rs} to $q_{cr}^{lin_1st}$.

Table3 shows the 1st and the RS buckling loads and β_o. Fig.7 shows some examples of the RS buckling mode. Yamada [7] demonstrated that the RS method can be used in finding the worst imperfection for latticed domes.

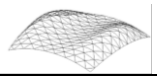
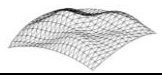
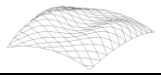
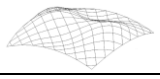
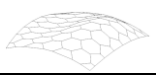
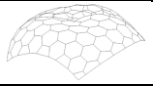
T45_0101	T75_0101	R30_0101	R45_0101	H45_0101	H60_0202
					
symmetric	asymmetric	symmetric	symmetric	asymmetric	symmetric

Fig.7 Examples of RS buckling mode

Table3 RS buckling load

Triangle							Rhombus							Hexagon					
α	Rise-Span ratio	1st mode	RS mode				α	Rise-Span ratio	1st mode	RS mode				α	Rise-Span ratio	1st mode	RS mode			
		$q_{cr}^{lin_1st}$	mode	$q_{cr}^{lin_RS}$	q_{cr}^{rs}	$q_{cr}^{rs}/q_{cr}^{lin_1st}$			$q_{cr}^{lin_1st}$	mode	$q_{cr}^{lin_RS}$	q_{cr}^{rs}	$q_{cr}^{rs}/q_{cr}^{lin_1st}$			$q_{cr}^{lin_1st}$	mode	$q_{cr}^{lin_RS}$	q_{cr}^{rs}	$q_{cr}^{rs}/q_{cr}^{lin_1st}$
45	0101	23.2	5	29.6	7.7	0.33	30	0101	6.3	1	6.3	5.6	0.90	45	0101	3.2	1	3.2	1.7	0.52
	0102	54.9	8	64.5	18.2	0.33		0102	9.0	1	9.0	7.0	0.78		0102	6.2	2	6.8	2.5	0.40
	0201	47.0	7	66.8	19.5	0.42		0201	11.6	1	11.6	9.6	0.83		0201	6.6	2	7.6	2.8	0.43
	0202	89.4	6	109.4	30.7	0.34		0202	15.2	1	15.2	10.9	0.72		0202	10.0	3	13.6	4.9	0.49
60	0101	48.1	9	52.7	20.7	0.43	45	0101	5.6	1	5.6	3.8	0.68	60	0101	2.9	4	3.3	1.7	0.57
	0102	70.0	36	142.9	18.6	0.27		0102	11.3	1	11.3	6.1	0.54		0102	4.7	4	6.5	2.6	0.55
	0201	74.1	5	86.8	26.7	0.36		0201	11.2	1	11.2	6.0	0.53		0201	4.8	5	6.8	2.0	0.43
	0202	160	5	168.4	83.0	0.52		0202	18.7	1	18.7	8.4	0.45		0202	9.4	2	9.6	4.1	0.44
75	0101	37.7	8	46.8	17.3	0.46	60	0101	6.5	1	6.5	5.8	0.90	75	0101	1.9	1	1.9	1.0	0.52
	0102	65.7	10	96.6	16.7	0.25		0102	12.3	1	12.3	10.1	0.82		0102	4.7	4	6.5	2.6	0.55
	0201	79.7	40	127	41.4	0.52		0201	9.3	1	9.3	7.4	0.80		0201	3.7	2	4.0	1.5	0.40
	0202	125	46	247	60.3	0.48		0202	16.6	1	16.6	12.2	0.73		0202	6.1	2	7.4	2.1	0.35

4.3. Imperfection sensitivity

Table4 shows the knockdown factors of the shells without imperfection ($\alpha_0^{el_0}$), the knockdown factors of the shells where the imperfection was assumed proportional to the 1st buckling mode (α_0^{1st}) and the RS buckling mode (α_0^{RS}). The minimum knockdown factor found among the 49 buckling-mode proportional imperfections is also indicated by the sign $\alpha_0^{el_1000}$. In all the cases in Table4, the imperfection amplitude was 1/1000 of the span. The knockdown factors of many shells are minimum when the imperfection proportional to the 1st buckling mode is given. However, the knockdown factors of the T60_0101, T60_0202 and H60_0202 of which ξ =1.0 and $R_x \fallingdotseq R_y$ are minimum when the shells are distorted by the imperfection proportional to the RS buckling mode.

Table4 Elastic buckling load

Triangle							Rhombus							Hexagon						
α	Rise-Span ratio	$\alpha_0^{el_0}$	$\min_\alpha_0^{el_1000}$		α_0^{1st}	α_0^{RS}	α	Rise-Span ratio	$\alpha_0^{el_0}$	$\min_\alpha_0^{el_1000}$		α_0^{1st}	α_0^{RS}	α	Rise-Span ratio	$\alpha_0^{el_0}$	$\min_\alpha_0^{el_1000}$		α_0^{1st}	α_0^{RS}
			mode	$\alpha_0^{el_1000}$						mode	$\alpha_0^{el_1000}$						mode	$\alpha_0^{el_1000}$		
45	0101	0.93	1	0.75	0.75	0.96	30	0101	0.93	1	0.87	0.87	0.87	45	0101	1.00	1	0.86	0.86	0.86
	0102	0.80	2	0.68	0.70	0.69		0102	0.97	1	0.92	0.92	0.92		0102	0.83	1	0.78	0.78	0.82
	0201	0.99	1	0.82	0.82	0.91		0201	0.85	1	0.83	0.83	0.83		0201	0.79	1	0.77	0.77	0.79
	0202	0.95	2	0.81	0.82	0.90		0202	0.87	1	0.85	0.85	0.85		0202	0.75	1	0.73	0.73	0.75
60	0101	0.67	11	0.58	0.67	0.58	45	0101	0.87	1	0.81	0.81	0.81	60	0101	0.78	1	0.71	0.71	0.76
	0102	0.94	1	0.78	0.78	0.90		0102	0.91	5	0.88	0.96	0.96		0102	0.70	1	0.67	0.67	0.70
	0201	0.94	3	0.76	0.78	0.83		0201	0.75	1	0.73	0.73	0.73		0201	0.67	1	0.64	0.64	0.67
	0202	0.86	5	0.62	0.65	0.62		0202	0.70	1	0.67	0.67	0.67		0202	0.57	2	0.55	0.57	0.55
75	0101	0.89	1	0.67	0.67	0.74	60	0101	0.97	1	0.90	0.90	0.90	75	0101	0.99	1	0.85	0.85	0.85
	0102	0.95	4	0.82	0.82	0.98		0102	0.88	1	0.85	0.85	0.85		0102	0.79	1	0.77	0.77	0.79
	0201	0.81	1	0.64	0.64	0.72		0201	0.91	47	0.90	0.94	0.94		0201	0.83	1	0.78	0.78	0.82
	0202	0.94	1	0.76	0.76	0.91		0202	0.99	1	0.94	0.94	0.94		0202	0.79	1	0.76	0.76	0.79

1) Triangularly latticed shells

The α_0 of the triangularly latticed shells decreased with increasing amplitude of imperfection. The rate of reduction depend on the linear buckling mode to be assumed as imperfection. The imperfection minimizing the knockdown factor of the triangularly latticed shells was asymmetric buckling-mode-proportional. Fig.8 compares the values of α_0 where the imperfection was proportional to the 1st and the RS buckling mode.

The knockdown factors are mostly lower when the shells are distorted by the imperfection proportional to the 1st buckling mode than by the RS buckling mode. However, the knockdown factors of T60_0101 and T60_0202 of which ξ =1.0 and $R_x \fallingdotseq R_y$ are minimum when the imperfection is proportional to RS buckling mode. In the case of T60_0101, the knockdown factor when the imperfection is proportional to the RS buckling mode decreases to 0.86 times of the case where the imperfection is proportional to the 1st mode. The knockdown factor of the shells of which ξ =1.0 and $R_x \fallingdotseq R_y$ is lower than that of the anisotropic shells.

Fig.9 shows the ratio of the knockdown factor when the imperfection is proportional the 1st buckling mode to that without imperfection $\alpha_0/\alpha_0^{el_0}$. The values of $\alpha_0/\alpha_0^{el_0}$ are approximately 0.8 when the amplitude of imperfection is 1/1000 of the span. The rate of decrease of $\alpha_0/\alpha_0^{el_0}$ with increasing amplitude of imperfection is hardly affected by the degree of anisotropy.

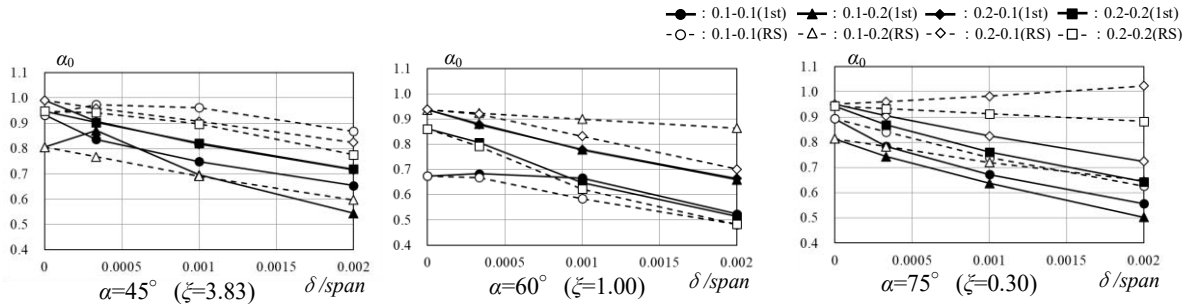


Fig.8 α_0 of triangularly latticed shells with imperfection proportional to 1st and RS buckling mode

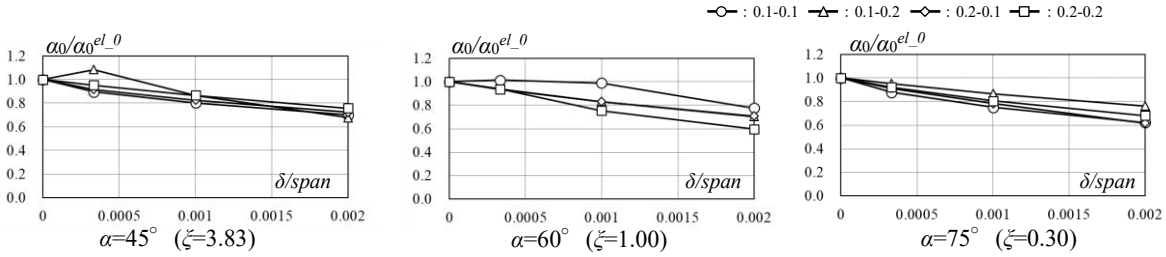


Fig.9 $\alpha_0/\alpha_0^{el_0}$ of triangularly latticed shells

2) Rhomboidally latticed shells

The imperfection minimizing α_0 of rhomboidly latticed shells were proportional to1st buckling mode in all the models. Fig.10 shows the influence of the amplitude on α_0. The knockdown factor of shells of which ξ =1.0 and $R_x \fallingdotseq R_y$ is lower and more strongly affected by the rise span ratio-than the anisotropic shells. Fig.11 shows that the values of $\alpha_0/\alpha_0^{el_0}$ are close to 1 thus the amplitude of the imperfection has little effect on the knockdown factor of the rhomboidly latticed shells.

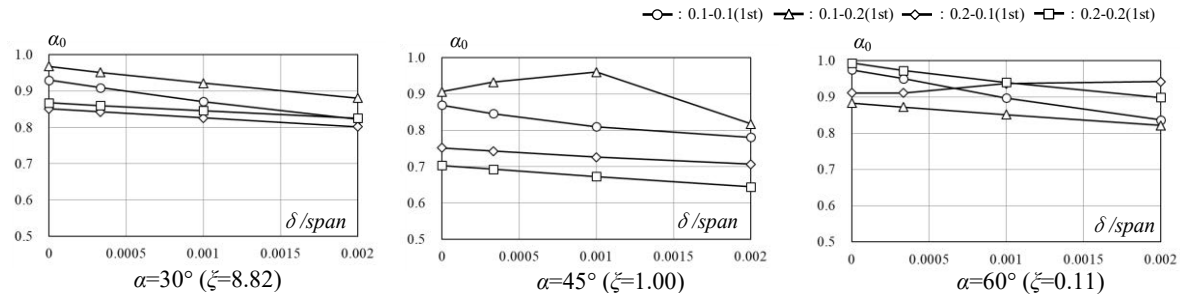


Fig.10 α_0 of triangularly latticed shells with imperfection proportional to 1st buckling mode

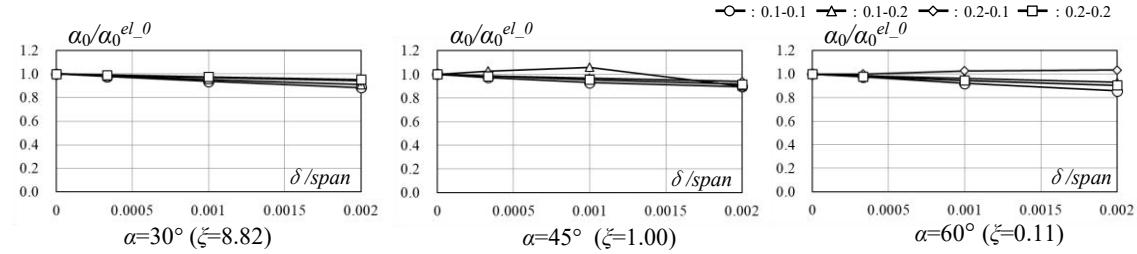


Fig.11 $\alpha_0/\alpha_0^{el_0}$ of rhomboidally latticed shells

3) Hexagonally latticed shells

As shown in Fig.12, The imperfections minimizing the value of α_0 of hexagonally latticed shells are proportional to the 1st buckling mode except for H60_0202. In the case of H60_0202, the knockdown factor is minimum when the imperfection is proportional to the RS buckling mode. Similarly to the triangularly and rhomboidly latticed shells, the knockdown factor of hexagonally latticed shells of which ξ =1.0 and $R_x \fallingdotseq R_y$ is lower than that of the anisotropic shells. Different from other hexagonally latticed shells, the knockdown factor of the H45_0101 and H75_0101 shells decreased significantly with increasing amplitude of imperfection. Fig.13 shows that the values of $\alpha_0/\alpha_0^{el_0}$ are close to 1 thus the amplitude of the imperfection has little effect on the knockdown factor of the rhomboidly latticed shells.

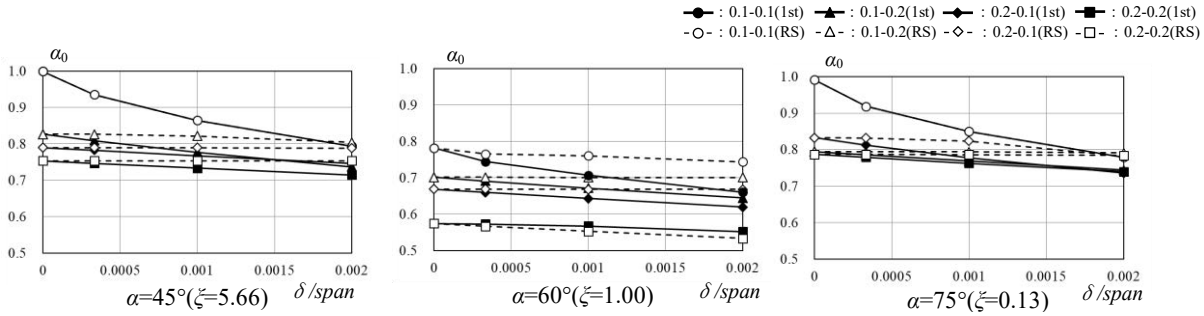


Fig.12 α_0 of Hexagonally latticed shells with imperfection proportional to 1st buckling mode

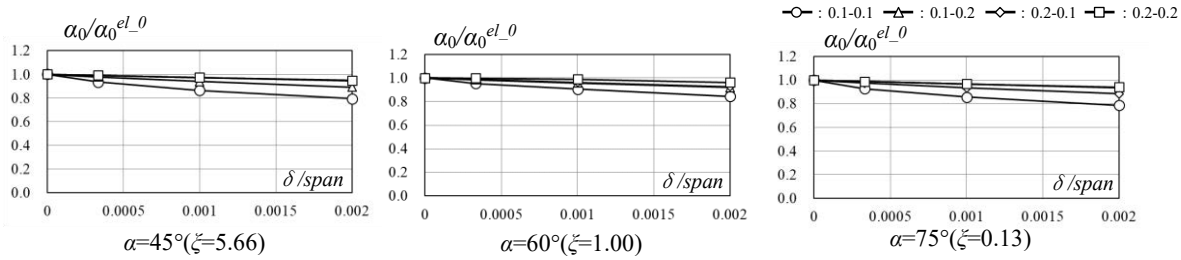


Fig.13 $\alpha_0/\alpha_0^{el_0}$ of hexagonally latticed shells

Summarizing the above observations, the imperfection proportional to the 1st buckling mode minimizes the knockdown factor in almost cases. However, the knockdown factor of shells of which ξ=1.0 and $R_x \fallingdotseq R_y$, is often minimum when the imperfection is proportional to the RS buckling mode. The knockdown factor of a shells composed of lattices with ξ=1.0 is greatly affected by the rise span ratio compared to anisotropy shells.

5. conclusion

We conducted geometric nonlinear analysis on latticed shells composed of triangular, rhomboid and hexagonal lattices varying the degree of anisotropy. The findings of this study are summarized as follows;

1) The knockdown factor of anisotropic shells is relatively high compared with the shells of which ξ = 1.0 and $R_x \fallingdotseq R_y$

2) The knockdown factor of shells of which ξ=1.0 is greatly affected by the rise span ratio compared with the anisotropic shells.

3) The imperfection proportional to the 1st buckling mode is most effective to drop down the knockdown factor in almost cases except the shells of which ξ=1.0 and $R_x \fallingdotseq R_y$, where the imperfection proportional to the RS buckling mode affects most.

4) The rate of decrease of $\alpha_0/\alpha_0^{el_0}$ with respect to the amplitude of imperfection does not depend on the degree of isotropy.

5) In the case of rhomboidly and hexagonally latticed shells,the amplitude of the imperfection has little effect on the knockdown factors.

References

[1] Architectural Institute of Japan (AIJ): Recommendation for Design of Latticed Shell Roof Structures, 2016.11

[2] IASS WG8:(Draft) Guide to Buckling Load Evaluation of Metal Reticulated Roof Structures, 2014.10

[3] Heki K., Saka T.:Analysis of space truss plates –Part 1 Effective rigidity of plates and equation-Transactions of the Architectural Institute of Japan, No. 157, pp. 33-39, 1969.3 (in Japanese)

[4] M.Ohsaki, T.Takeuchi, T.yamashita: Basic theory and design of shell and spatial structure, 2019,2

[5] Jianliang Zhu, Tetsuo Yamashita: Effective rigidity and liner buckling load of hexagonal latticed flat plates subjected to in-plane shear force, Proc. of 11th APCS, 2015

[6] MSC Software: MARC2017,VolA,Theory and User Information

[7] S. Yamada, A. Takeuchi, Y. Tada, K. Tsutsumi,"Reduced Stiffness Analysis using a Commercially Available Code and its Application to Latticed Dome Buckling Problem" Journal of Struct. Construct. Eng., no. 526, pp. 85-92, 1999. (in Japanese)

Proceedings of the IASS Annual Symposium 2019 – Structural Membranes 2019
Form and Force
7 – 10 October 2019, Barcelona, Spain
C. Lázaro, K.-U. Bletzinger, E. Oñate (eds.)

Geometry of the crack-free spherical masonry dome

István SAJTOS*, Orsolya GÁSPÁR, András Á. SIPOS

*Budapest University of Technology and Economics, Department of Mechanics, Materials and Structures
H-1111 Budapest, Műegyetem rkp. 3., Hungary
sajtos@szt.bme.hu

Abstract

Spherical masonry domes are attractive elements of architectural heritage. The often recognizable development of cracks in the meridional direction challenged master builders and later architects and engineers to understand the structural behavior of domes. Membrane theory of shells suggests, that due to the low tensile capacity of masonry, cracks at the lower portion of a hemispherical dome, with constant thickness subjected to its self-weight, are inevitable, as the hoop stresses change sign (from compression to tension). Disregarding the limited tensile capacity of masonry, based on a no-tension material model, the extensive literature of the topic offers various theoretical solutions to this problem. These can be classified in the following way: *a)* the geometry of the middle surface can be altered (resulting non-spherical dome), *b)* a thrust surface, different from the mid-surface, can be obtained still within the dome section, *c)* retaining the spherical middle surface as membrane surface, varying thickness functions can be defined, resulting crack-free domes. Present paper offers an extension to the last approach. A thickness function is defined, which guarantees compression everywhere or at least zero hoop stresses from top to bottom.

Keywords: spherical masonry dome, membrane theory, crack-free dome, variable thickness dome

1. Introduction

Spherical masonry domes are attractive elements of architectural heritage. The spherical form is advantageous in terms of construction and is considered to deliver a spatial message of completeness, eternal power. The often recognizable development of cracks in the meridional direction challenged master builders and later architects and engineers to understand the structural behavior of domes. Membrane theory of shells suggests, that due to the low tensile capacity of masonry, cracks at the lower portion of a hemispherical dome, with constant thickness subjected to its self-weight, are inevitable, as the hoop stresses change sign (from compression to tension). Disregarding the limited tensile capacity of masonry, based on a no-tension material model, the extensive literature of the topic offers various theoretical solutions to this problem. These can be classified the following way:

a) the geometry of the middle surface can be altered (e.g. catenary dome of St. Paul's Cathedral, London, or elliptical paraboloid shape dome),

b) a thrust surface, different from the mid-surface, can be obtained still within the dome section [1],

c) an optimal shape of spherical domes can be found, which retains the spherical middle surface as membrane surface but allows the thickness of the dome to vary [2], [3].

Present paper offers an extension to the last approach.

Copyright © 2019 by István Sajtos, Orsolya Gáspár, András Á. Sipos
Published by the International Association for Shell and Spatial Structures (IASS) with permission.

It is assumed, that the membrane theory is applicable, i.e. the structure is characterized by the middle surface, which is treated as membrane or in other words *thrust surface*. The membrane shell model of the dome is analogous to the catenary shape masonry arch [4]. The middle surface is kept hemispherical and it is loaded by the self-weight of the dome. A suitable thickness function is searched, which results in a crack-free dome. Such a thickness function guarantees compression everywhere or at least zero hoop stresses from top to bottom.

In [2], [3] and [5] such a thickness variation was looked for which results uniform strength i.e. uniform stress either in the meridional or in the circumferential direction. The calculation was based on the membrane shell model. A special case was examined in [2] where the lower part of a uniform meridional stress dome, where tensile hoop stress is developed, was substituted by such a spherical part which has zero stress in circumferential direction. The later problem is generalized and examined in this paper.

2. Membrane shell model of the dome

The membrane theory of shells is assumed to be applicable for a masonry dome. The membrane shell is a special dome where the thrust surface coincides with the middle surface of the shell.

2.1. Assumptions

The middle surface of the dome is a sphere with radius R, but the t thickness of the dome is not fixed a-priori. The thickness is assumed to vary with respect to the meridional angle φ and the function, $t_{(\varphi)}$, is at least continuous and once differentiable. The dome is loaded by its self-weight, g, which is defined by the product of the specific weight, ρ of the masonry material and the thickness t.

The masonry is assumed to be no tension material, having only resistance against compression. The dome cracks for tensile force, but remains crack-free if only compressive membrane forces are developed or one of the membrane forces is not needed to provide equilibrium i.e. that membrane force is zero.

2.2. Equilibrium equations

The masonry dome and its load are rotationally symmetric and so only meridional and hoop membrane forces are developed. The equilibrium equations are written in a polar-coordinate system, Fig. 1a.

From the vertical equilibrium equation of the top spherical cap of the dome the meridional membrane force is, [5], Fig. 1c):

$$N_{\varphi} = -\frac{G_{(\varphi)}}{2R\pi \sin^2 \varphi}, \tag{1}$$

where $G_{(\varphi)}$ is the self-weight of the upper part of the dome above the level where the meridional force is determined.

The hoop force may be determined from the radial force equilibrium equation [6], [7], Fig. 1b.

$$\frac{N_{\varphi}}{R} + \frac{N_{\vartheta}}{R} = -p_r = -\rho t_{(\varphi)} \cos \varphi \tag{2}$$

Calculating the change of the self-weight while φ angle is increased by $\mathrm{d}\varphi$ (see Fig.1a) provides a relation between the derivative of the weight function and the thickness of the dome:

$$\frac{\mathrm{d}G}{\mathrm{d}\varphi} = G'_{(\varphi)} = \rho t_{(\varphi)} 2R^2 \pi \sin \varphi \tag{3}$$

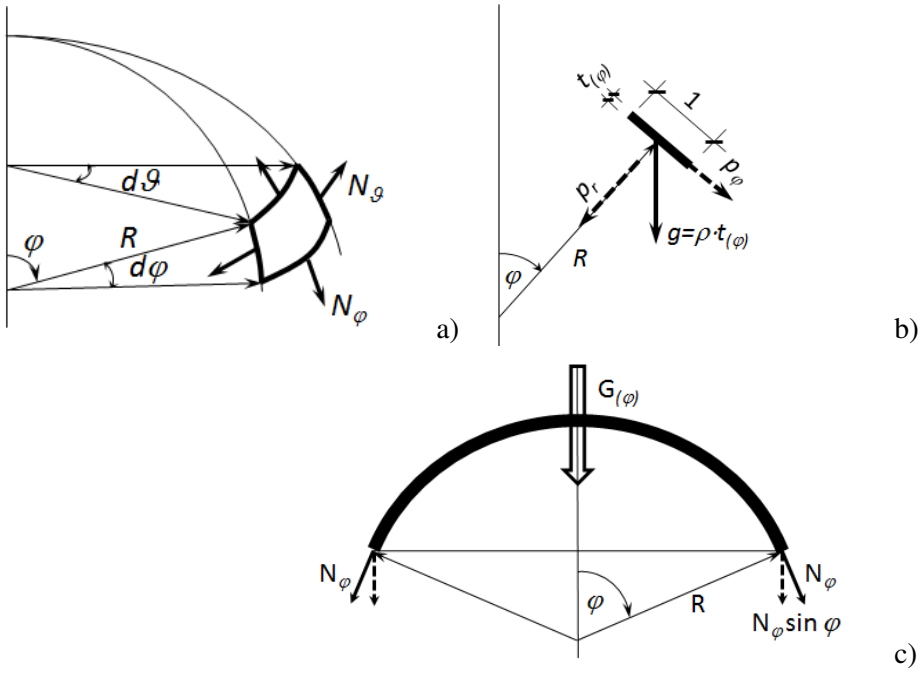


Figure 1: a) The polar coordinate system and membrane forces, b) the self-weight and its resolution, c) vertical equilibrium of the upper spherical cap part

Considering the weight function, *G,* as unknown and combining equations (1)-(3) the hoop force is found to follow.

$$N_\vartheta = \frac{G_{(\varphi)}}{2R\pi \sin^2 \varphi} - \frac{G'_{(\varphi)} \cos \varphi}{2R\pi \sin \varphi} \tag{4}$$

If the weight function is known as a function of the thickness of the dome the membrane forces can be calculated from equations (1) and (4). In case of a dome with constant thickness *G* and *G'* read:

$$G_{(\varphi)} = \rho t_0 2\pi R^2 (1 - \cos \varphi) \text{ and } G'_{(\varphi)} = \rho t_0 2\pi R^2 \sin \varphi \,, \tag{5}$$

where t_0 is the constant thickness itself. Substituting (5) in (1) and (4) the well-known results for the uniform thickness, shelf-weight loaded spherical shell can be determined [6], [7].

3. Crack-free masonry dome

A crack-free state is a natural requirement in case of a masonry dome. Since the meridional membrane force is a compressive force for self-weight, cracks may be caused only by the tensile hoop force.

3.1. Thickness variation of the crack-free masonry dome

If the hoop force is negative or at least zero, $N_\vartheta \leq 0$, then the masonry dome for self-weight is not cracked. Using equation (4) a first order, ordinary differential equation can be obtained. Solution of this differential equation provides such a weight function and so thickness function by the help of equation (3), which result zero or compressive hoop force i.e. the dome is not going to be cracked.

The solution of the $N_\vartheta = 0$ differential equation and the corresponding thickness function are:

$$G_{(\varphi)} = C_1 \tan \varphi \text{ and } t_{(\varphi)} = \frac{C_1}{2R^2 \pi \sin \varphi \cos^2 \varphi} \,, \tag{6}$$

where C_1 is an integration constant, which should be determined from a boundary condition.

The thickness function has a minimum value at $\varphi_0 = 35{,}26°$ independently from the radius of the sphere. If $t_{(\varphi_0)} = t_0$ then C_1 can be determined. Now the thickness function and the weight function read:

$$t_{(\varphi)} = t_0 \frac{2}{3\sqrt{3}} \frac{1}{\sin\varphi \cos^2\varphi}, \tag{7}$$

$$G_{(\varphi)} = \rho t_0 2R^2\pi \frac{2}{3\sqrt{3}} \tan\varphi\ . \tag{8}$$

The thickness function (7) results in a zero hoop force, $N_\vartheta = 0$. If the thickness, and so the weight is decreased not proportionally to the determined thickness variation then the hoop force will be compressive. Otherwise if the weight of the dome is decreased than the dome is compressed circumferentially, too. It means that a crack-free opened masonry dome may be constructed using thickness function (7).

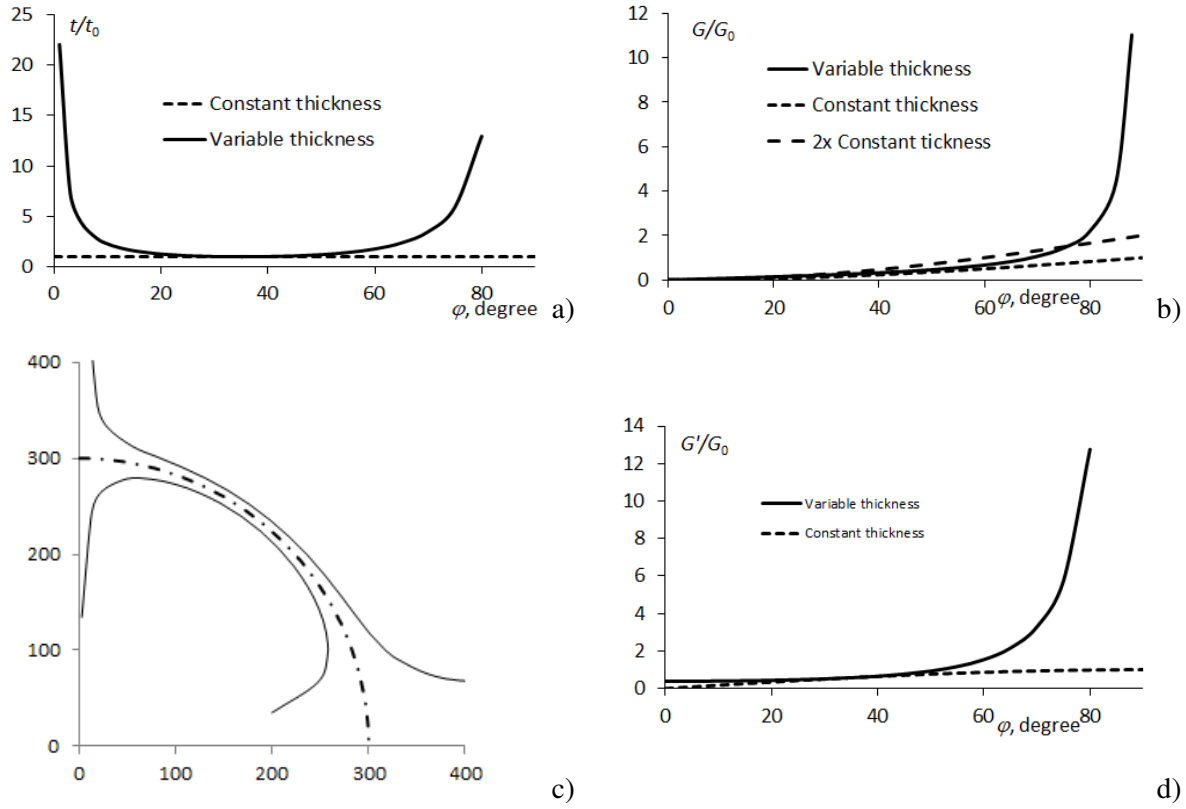


Figure 2: a) the thickness function, b) the weight function, d) thickness variation along the spherical dome mid surface *R*=300 cm, e) derivative of the weight function with respect to the meridional angle

The thickness function is singular at the top, $\varphi = 0$, and at springing, $\varphi = 90°$, Fig. 2a), Fig. 2c). This suggests that the result has limited practical application. But as it is said above, changing the thickness at the top to a finite value results in a compressive hoop stress all over the spherical dome, thus the dome remains crack-free. The infinite thickness required at the bottom can also be disregarded, considering a spherical dome with an opening angle slightly lower than 90°.

Note that if the thickness of a dome with constant thickness is increased, e.g. doubled, the total weight of the dome becomes larger than in the variable thickness case for a large interval of angle of embrace, see Fig. 2b).

3.2. Membrane forces of the crack-free masonry dome

Knowing the weight function $G_{(\varphi)}$ and using equations (1) and (4) the membrane forces can be determined for variable thickness case via

$$N_\varphi = -\rho t_0 \frac{2}{3\sqrt{3}} R \frac{\tan\varphi}{\sin^2\varphi}\,, \tag{9}$$

$$N_\vartheta = 0\,. \tag{10}$$

The membrane forces scaled by the $\rho t_0 R$ product can be seen on Fig. 3. Like the thickness function the meridional membrane force is also singular at the top and at the springing. However the stress is finite for the whole dome and its variation is defined by a cosine function. Note that the meridional force for the variable thickness is nearly identical to the uniform thickness dome, except in the vicinity of the top and springing, Fig. 3a).

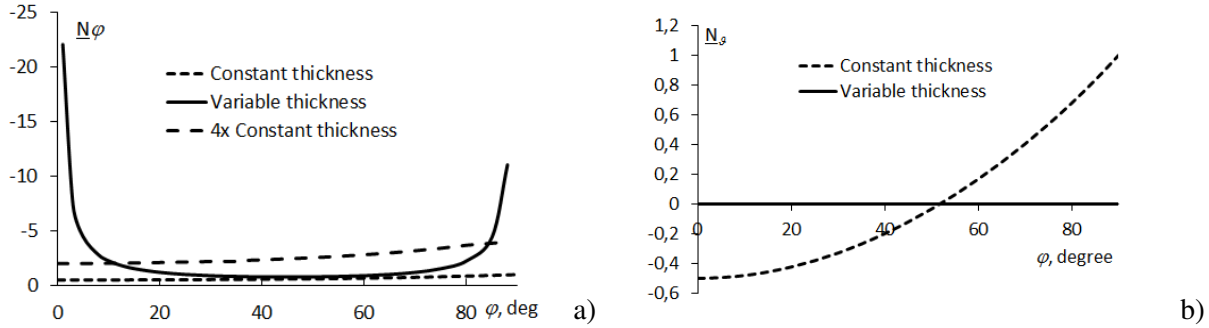


Figure 3: Closed crack-free masonry dome: a) meridional force N_φ, b) hoop force N_ϑ scaled by the $\rho t_0 R$ product

The main difference between constant and variable thickness dome arises in the hoop force. It seems that removing the extra material at the top and springing (see Fig. 2a)) results in a hoop force which is even tension i.e. crack cannot be avoided, Fig. 3b). But as it was mentioned earlier, limited reduction of thickness and mass causes compression in the circumferential direction. This is for example the case of a masonry dome opened at the top.

3.3. Opened crack-free masonry dome

It is suggested to reduce the thickness in the vicinity of the top to make the determined thickness variation more feasible. In the most extreme case an opening is cut at the top of the dome. However the thickness variation (7) is not changed on the remaining part of the dome. The position of the opening level is given by the embrace angle $\varphi_1 > 0$. The new weight function is $G_{(\varphi)} - G_{(\varphi_1)}$ and the corresponding membrane forces from (1) and (4) are:

$$N_\varphi = -\rho t_0 \frac{2}{3\sqrt{3}} R \left[\frac{\tan\varphi}{\sin^2\varphi} - \frac{\tan\varphi_1}{\sin^2\varphi_1}\right], \tag{11}$$

$$N_\vartheta = -\rho t_0 \frac{2}{3\sqrt{3}} R \frac{\tan\varphi_1}{\sin^2\varphi_1}\,. \tag{12}$$

From equation (12) it may be concluded that the hoop membrane force is always compression, so the opened masonry dome is also crack-free with the derived thickness function (7). The membrane force variation is depicted in Fig. 4 and Fig. 5 for $\varphi_1 = 5°$ and $\varphi_1 = 25°$, respectively.

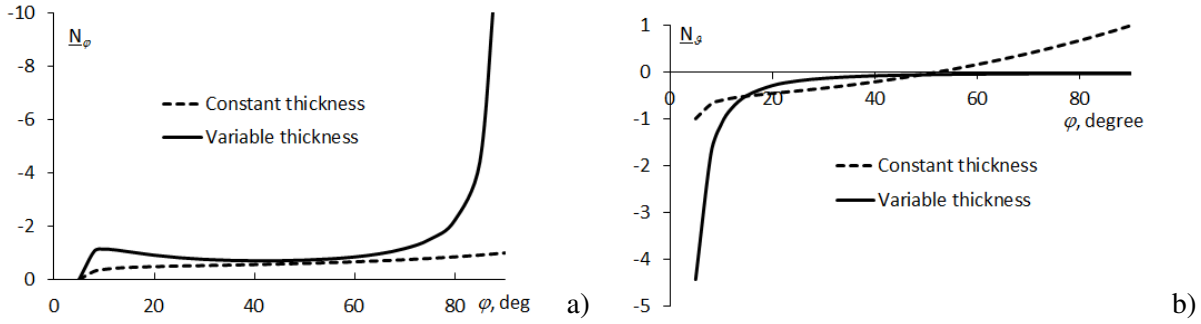


Figure 4: Opened crack-free masonry dome, $\varphi_1 = 5°$: a) meridional force N_φ, b) hoop force N_ϑ scaled by the $\rho t_0 R$ product

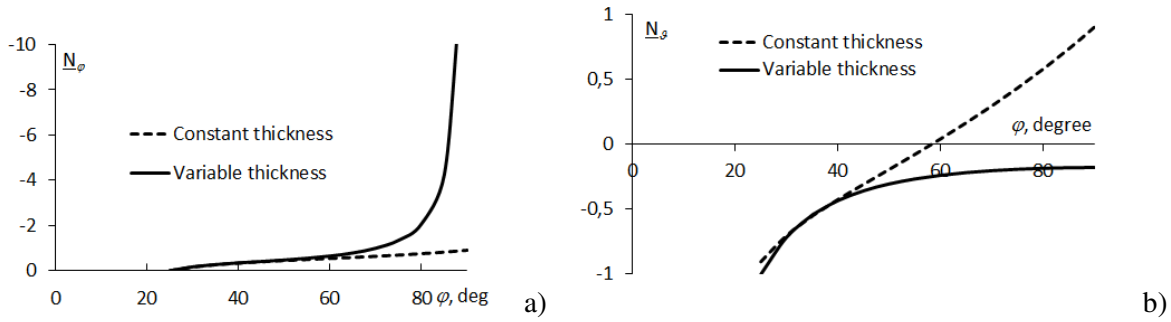


Figure 5: Opened crack-free masonry dome, $\varphi_1 = 25°$: a) meridional force N_φ, b) hoop force N_ϑ scaled by the $\rho t_0 R$ product

It can be seen on Fig. 4 and Fig. 5 that both the meridional and the circumferential membrane forces are compressive forces for the variable thickness case. While in the case of constant thickness case, tension in the hoop direction cannot be avoided although the zero stress hoop force level is lowered for larger opening.

A lantern may be built over the opening if its weight is less than $G_{(\varphi_1)}$ i.e. the membrane forces under opening level are not altered by the weight distribution above the opening level. That is why the top part of the variable thickness masonry dome may be changed for everywhere compressed spherical cap as it was suggested in [2].

Based on Fig. 4 and Fig. 5 it may also be concluded that reducing the thickness around the springing results tension in the hoop direction but the zero hoop force level moving up or down depending on the actual thickness variation.

4. Historical relevance of the findings

Traditional practice and engineering intuition suggest that spherical masonry dome must have larger thickness at springing. There are many historical masonry domes where this kind of thickness variation can be found. But it seems that change in the thickness cannot be arbitrary.

For example, the Pantheon has an opening and increased thickness toward springing. The angle of embrace is less than 90°. But it is known that there are cracks in the lower part of the dome due to tension in the hoop direction [8]. It seems that the proportion of the thickness changing was not

enough to result compressive hoop stress at the bottom of the dome, otherwise the density of the dome is not uniform so (7) cannot be used directly for comparison.

However, it may be claimed that the thickness variation as an effective structural design tool was used in the past. There are many historical buildings were those principles was used to build the dome which were concluded based on thickness function (7). Some may be mentioned among others e.g. church Santa Costanza, Rome; Duomo Vecchio, Brescia; church San Lorenzo, Mantova.

5. Conclusions

Based on the membrane theory of the shells a thickness variation was determined that results in a zero hoop force i.e. even the no tension material masonry dome remains crack-free.

It seems that the determined thickness variation has limited practical application because the thickness is infinite at the top and the springing. But changing the thickness at the top to a finite value results compressive hoop stress all over the spherical dome, thus the dome remains crack free. The infinite thickness required at the bottom can also be disregarded, considering a spherical dome with an opening angle slightly lower than 90°.

The masonry dome opened at the top is such a case that the hoop membrane force is always compression, so the opened masonry dome is also crack-free with the derived thickness function (7).

A lantern may be built over the opening if its weight is less than $G_{(\varphi_1)}$ i.e. the membrane forces under opening level are not altered by the weight distribution above the opening level. That is why the top part of the variable thickness masonry dome may be changed for everywhere compressed spherical cap as it was suggested in [1].

Based on Fig. 4 and Fig. 5 it may also be concluded that reducing the thickness around the springing results tension in the hoop direction but the zero hoop force level moves up or down depending on the actual thickness variation.

Similarly to the thickness function the meridional membrane force is also singular at the top and at the springing. However the stress is finite for the whole dome.

It may be concluded that the determined thickness function for a spherical mid surface enables one to design a rational crack-free masonry dome. The thickness on the top part may be changed nearly freely. While at the springing the determined thickness variation must be kept as it was determined by (7).

Traditional practice and engineering intuition suggest that a spherical masonry dome must have larger thickness at springing. But it seems that change in the thickness cannot be arbitrary. Equation (7) defines that thickness function which may result in crack-free, spherical masonry dome as long as the self-wright of the dome is considered.

Acknowledgements

The support of grants NKFIH 124859 and BME FIKP-VÍZ by EMMI are highly acknowledged.

References

[1] B. Cipriani and W.W. Lau, "Construction Techniques in Medieval Cairo: the Domes of Mamluk Mausolea (1250 AD–1517 AD)": *Proceedings of the Second International Congress on Construction History, Queen's College, Cambridge University March 29-April 2, 2006,* M. Dunkeld Ed., Construction History Society, 2006. Vol. 1, pp. 695-716.

[2] C. Pesciullesi and M. Rapallini and A. Tralli and A. Chianchi, "Optimal spherical masonry domes of uniform strength", *Journal of Structural Engineering*, vol. 123, pp. 203-209, 1997.

[3] H. Nakamura, M. Dow, and G. I. N. Rozvany. "Optimal spherical cupola of uniform strenght: allowance for selfweigth", *Ingenieur-Archiv,* 51: (3-4), pp. 159-181, 1981.

[4] S. Adriaenssens, P. Block, D. Veenendaal and C. Williams (eds.), *Shell Structures for Architecture: Form Finding and Optimization*, Routledge, 2014.

[5] W. Prager, G. N. I. Rozvany, "Optimal spherical cupola of uniform strength", *Ingenieur-Archiv,* vol. 49, pp. 287-293, 1980.

[6] P. Csonka, *Theory and practice of membrane shells*, Akadémiai Kiadó, Budapest, 1987.

[7] W. Flügge, *Stresses in Shells*, Springer Verlag, 1960.

[8] R. Mark and P. Hucthinson, "On the structure of the roman Pantheon", *The Art Bulletin*, vol. 68, No.1., pp. 24-34, 1986.

Proceedings of the IASS Annual Symposium 2019 – Structural Membranes 2019
Form and Force
7 – 10 October 2019, Barcelona, Spain
C. Lázaro, K.-U. Bletzinger, E. Oñate (eds.)

Ordinary analysis of concrete porticoes: a modification of Cholesky's method for graphically solving their equation systems

Agustin.G. LACORT

Higher Technical School of Architecture, University of the Basque Country
Plaza de Oñati, 2, 20018, Donostia-San Sebastián (SPAIN)
agustingregorio.lacort@ehu.eus

Abstract

The present study suggests an accurate, graphic procedure for solving equation systems derived from conventional equilibrium analyses of linear building structures. The procedure comes from a change in method [1] when concrete porticoes are analysed. It is based on the establishment of a link between the operations that factorise the stiffness matrix and the mechanical behaviour of the portico. This link was detected on observing that Cholesky's operations explain the process of equilibrium when the portico cracks progressively. If these cracks are not taken into account, factorisation becomes simpler and coincides with Crout's method. It is suggested that the operations be carried out graphically using the simple mnemonic rules that make up the new procedure. The results are accurate enough when the sketches are drawn freehand in all cases, which facilitates the use of the procedure in the early stages of design. In the course of the exposition the method is justified qualitatively by using Cross's philosophy, the mnemonics are set out and the deflection of a model is obtained graphically. Based on this work, possible lines of research are pointed to for developing further graphic methods that can be used to analyse other types of structure accurately.

Keywords: Spatial porticoes, graphic methods, Cholesky´s method, freehand analysis, Crout´s method

1. Introduction

This study seeks to set out a manual method that can be used to supplement [1,2] for solving equilibrium equation systems for porticoed structures under nodal actions. The procedure suggested is graphic, and reproduces the operations of Crout's method, based on a modification of the Cholesky's by associating it with the mechanical behaviour of the model. The basic algebraic operations are carried out by transforming segments that represent numbers on squares measuring one unit per side (Fig.1) using techniques from the past discussed in recent literature [3]. As in [1,2] it is suggested that they be drawn freehand to save time and maintain the precision of the results, because the perimeters of the squares prevent any major errors from being committed. It is also observed that the size of the squares has no great influence on the result. The study sets out the mechanical interpretation, then describes the modification and finally gives an example.

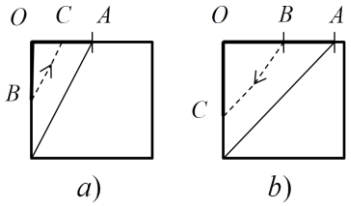


Figure 1. Basic graphic operations: a) OC = OB*OA, b) OC = OB/OA

Copyright © 2019 by <substitute here the name(s) of the author(s) or individual(s) claiming copyright>
Published by the International Association for Shell and Spatial Structures (IASS) with permission.

2. Interpretation

It was observed that the operations in Cholesky's method could be justified from a physical perspective by relating them to the behaviour of the model during the equilibrium process, assuming that it is a concrete structure that cracks progressively. The link was obtained by modifying the mechanical interpretation of the Gauss method suggested in [4] based on Cross's philosophy.

From this perspective the operations in Cholesky's method could be said to derive from a hidden procedure that interprets deflection as a sum of partial deflections (Figs.2b,c,d), each of which is caused by a partial load state, which cracks the model without changing the stresses. That load state has an "active" action (in a continuous line) which produces nodal movements, plus one or more "restrictive" actions (in a discontinuous line) which prevent some nodes from moving. Each deflection has a different number of unknowns, which depend on movement α_i of node i, where the active action operates.

The hidden procedure determines the deflection in two phases and the matrices [B] & [B^t], derived from factorising the stiffness matrix [A], are involved in them. In Phase 1 the partial deflections are obtained with (1), and in Phase 2 the deflection is obtained with (2). These phases are described below in regard to the triangular frame in Fig.2a, whose [A] is (3). This explanation is valid when the exterior momentums are oriented as shown in Fig.1a.

$$[B]\{\alpha\} = \{M\} \tag{1}$$

$$[B^t]\{\theta\} = \{\alpha\} \tag{2}$$

$$\begin{pmatrix} A & B & C \\ B & D & E \\ C & E & F \end{pmatrix} = \begin{pmatrix} \frac{1}{\theta'_A} & r_{AB} & r_{AC} \\ r_{AB} & \frac{1}{\theta'_B} & r_{BC} \\ r_{AC} & r_{BC} & \frac{1}{\theta'_C} \end{pmatrix} \tag{3}$$

2.1. Phase 1: obtaining of the partial deflections

The partial deflections (Figs.2b,c,d) are obtained as a function of so-called "primary" deflections (Figs.2e,k,q), whose load states (referred to as $\underline{A}$, $\underline{B}$ & $\underline{C}$ respectively), crack the model as per Figs.2f,g,h. A description follows of how these primary deflections are obtained by combining load states known as "initial" (Figs.2e,i,l), as per Cross's philosophy, applied to the uncracked model, and each of which is determined by one row in (3).

2.1.1. Primary deflection by state $\underline{A}$ (Fig.2e)

The state in Fig.2e is applied to the model. When equilibrium is reached, the primary deflection is obtained by assuming that the framework cracks as bars AB and AC lose stiffness with no variation in their stresses. This occurs because the inertias I_{AB} and I_{AC} turn into $I_{AB}\sqrt{\theta'_A}$ and $I_{AC}\sqrt{\theta'_A}$ respectively. Thus, θ'_A becomes $\sqrt{\theta'_A}$, the stiffnesses of bars AB and AC vary depending on the direction of rotation of their ends, and the model in Fig.2a becomes the one in Fig.2f.

2.1.2. Primary deflection by state $\underline{B}$ (Fig.2k)

Start by loading the state in Fig.2i on the structure in Fig.2f. Bar AB deflects without the cracking effect due to the direction of rotation of B. Add another state (Fig.2j) similar to that of $\underline{A}$ to allow A to rotate freely. Bars AB and BC are cracked and produce other restrictive momentums in B and C. Then eliminate the restrictive momentum in B by adding another state such as that in Fig.2i whose active

momentum is $\theta'_B\theta_A r^2_{AB}$. If this process is repeated indefinitely the restrictive momentums in *A* and *B* are gradually eliminated, making the nodes rotate freely. When they disappear (Fig.2k) state *B* is obtained. The active momentum of *B* is (4) and makes this node rotate to the extent of (5).

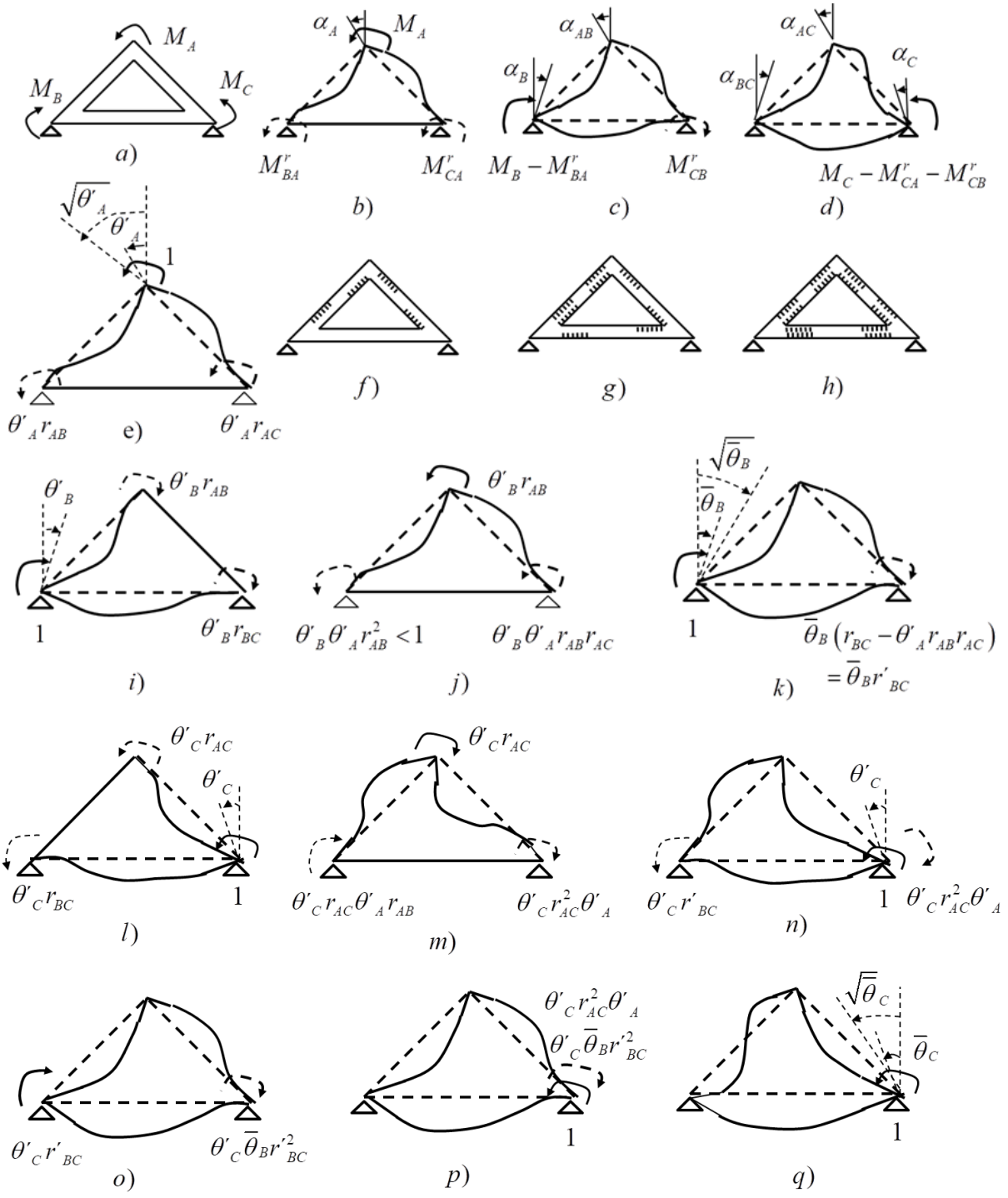


Figure 2. Cholesky's method: mechanical interpretation: a) model; b),c),d) partial deflections; e) "primary" deflection; f),g),h) cracked model; i),j) load states that produce the primary deflection in k); l),m),n),o),p) load states that produce the primary deflection in q)

The primary deflection is obtained by assuming that in this situation bars *AB* and *BC* crack without changing the restrictive momentum in *C* by transforming inertias I_{BA} and I_{BC} into $I_{BA}\sqrt{\bar{\theta}_B}$ $I_{BC}\sqrt{\bar{\theta}_B}$ respectively. Thus, the model in Fig.2f becomes the one in Fig.2g.

$$1+\theta'_B\theta'_A r_{AB}^2+\left(\theta'_B\theta'_A r_{AB}^2\right)^2+.....=\frac{1}{1-\theta'_A\theta'_B r_{AB}^2} \tag{4}$$

$$\frac{1}{1-\theta'_A\theta'_B r_{AB}^2}\theta'_B=\bar{\theta}_B \tag{5}$$

2.1.3. Primary deflection by state C (Fig.2q)

Start by loading the initial state in Fig.2l on the model in Fig.2g. The stiffness of the deflected bars is the initial stiffness due to the direction of rotation in *C*. Allow node *A* to rotate freely by applying another state (Fig.2m) which is added to the previous one to obtain the state in Fig.2n. By adding the state in Fig.2o, which is similar to the one in Fig.2k, to let *B* rotate freely, the deflection in Fig.2p is obtained. The restrictive momentum in *C* is eliminated by applying another load state similar to the one in Fig.2p, and another, smaller restrictive momentum in *C* appears. If this process is repeated indefinitely state C and a rotation in *C* of (6) are obtained. The primary deflection (Fig.2q) is obtained by assuming that the model (Fig.2g) at equilibrium becomes the one in Fig.2h as bars *AC* and *BC* crack as above, so that (6) becomes $\sqrt{\bar{\theta}_C}$.

$$\frac{1}{1-\left(\theta'_C\bar{\theta}_B r'^2_{BC}+\theta'_C r_{AC}^2\theta'_C\right)}\theta'_C=\bar{\theta}_C \tag{6}$$

Finally, the rotations α_i that determine the partial deflections are obtained by applying the load states in Figs.2b.c.d to the structures in Figs.2f,g,h. This is equivalent to solving equation system (1), which is (7).

$$\begin{pmatrix} \frac{1}{\sqrt{\theta'_A}} & 0 & 0 \\ r_{AB}\sqrt{\theta'_A} & \frac{1}{\sqrt{\bar{\theta}_B}} & 0 \\ r_{AC}\sqrt{\theta'_A} & r'_{BC}\sqrt{\bar{\theta}_B} & \frac{1}{\sqrt{\bar{\theta}_C}} \end{pmatrix}.\begin{pmatrix}\alpha_A\\ \alpha_B\\ \alpha_B\end{pmatrix}=\begin{pmatrix} \frac{1}{\sqrt{\theta'_A}} & 0 & 0 \\ \frac{M^r_{BA}}{\alpha_A} & \frac{1}{\sqrt{\bar{\theta}_B}} & 0 \\ \frac{M^r_{CA}}{\alpha_A} & \frac{M^r_{CB}}{\alpha_B} & \frac{1}{\sqrt{\bar{\theta}_C}} \end{pmatrix}.\begin{pmatrix}\alpha_A\\ \alpha_B\\ \alpha_C\end{pmatrix}=\begin{pmatrix}M_A\\ M_B\\ M_C\end{pmatrix} \tag{7}$$

2.1. Phase 2: obtaining of the deflection

The nodal movements are obtained by adding up the nodal rotations of the partial deflections, corrected first to eliminate the influence of the cracks. Each partial deflection is corrected by multiplying each α_i by $\sqrt{\bar{\theta}_i}$ which is equivalent to solving (8).

$$\begin{pmatrix} \frac{1}{\sqrt{\theta'_A}} & r_{AB}\sqrt{\theta'_A} & r_{AC}\sqrt{\theta'_A} \\ 0 & \frac{1}{\sqrt{\bar{\theta}_B}} & r'_{BC}\sqrt{\bar{\theta}_B} \\ 0 & 0 & \frac{1}{\sqrt{\bar{\theta}_C}} \end{pmatrix}.\begin{pmatrix}\theta_A\\ \theta_B\\ \theta_C\end{pmatrix}=\begin{pmatrix} \frac{1}{\sqrt{\theta'_A}} & \frac{\alpha_{AB}}{\theta_B} & \frac{\alpha_{AC}}{\theta_C} \\ 0 & \frac{1}{\sqrt{\bar{\theta}_B}} & \frac{\alpha_{BC}}{\theta_C} \\ 0 & 0 & \frac{1}{\sqrt{\bar{\theta}_C}} \end{pmatrix}.\begin{pmatrix}\theta_A\\ \theta_B\\ \theta_C\end{pmatrix}=\begin{pmatrix}\alpha_A\\ \alpha_B\\ \alpha_C\end{pmatrix} \tag{8}$$

3. Modification

If the transformed inertias of bars *ij* due to cracks are expressed as $I_{ij}.K_i$, with K_i being a figure of less than one, then [*A*] factorised is (9).

$$[B_1][B_2]=\begin{pmatrix} \frac{K_A}{\theta'_A} & 0 & 0 \\ r_{AB}K_A & \frac{K_B}{\overline{\theta}_B} & 0 \\ r_{AC}K_A & r'_{BC}K_B & \frac{K_C}{\overline{\theta}_C} \end{pmatrix}.\begin{pmatrix} \frac{1}{K_A} & r_{AB}\frac{\theta'_A}{K_A} & r_{AC}\frac{\theta'_A}{K_A} \\ 0 & \frac{1}{K_B} & r'_{BC}\frac{\overline{\theta}_B}{K_B} \\ 0 & 0 & \frac{1}{K_C} \end{pmatrix} \tag{9}$$

When $K_i = 1$ the partial deflections are real because the model does not crack, and (9) becomes (10). When $K_i = \overline{\theta}_i$ a similar result is obtained. Both these factorisations match those in Crout's method and the first is suggested here to solve the system graphically. The operations are described below using a method similar to those suggested in [1,2] but with simpler mnemonic rules.

$$[B_1][B_2]=\begin{pmatrix} \frac{1}{\theta'_A} & 0 & 0 \\ r_{AB} & \frac{1}{\overline{\theta}_B} & 0 \\ r_{AC} & r'_{BC} & \frac{1}{\overline{\theta}_C} \end{pmatrix}.\begin{pmatrix} 1 & r_{AB}\theta'_A & r_{AC}\theta'_A \\ 0 & 1 & r'_{BC}\overline{\theta}_B \\ 0 & 0 & 1 \end{pmatrix}=\begin{pmatrix} A & 0 & 0 \\ B & x_1 & 0 \\ C & x_2 & x_3 \end{pmatrix}.\begin{pmatrix} 1 & \frac{B}{A} & \frac{C}{A} \\ 0 & 1 & \frac{x_2}{x_1} \\ 0 & 0 & 1 \end{pmatrix} \tag{10}$$

3.1. Graphic version

The matrix (3) is represented by a stepped area *S* formed by squares measuring one unit per side (Fig.3a). On the left side of the squares are segments referred to as "initial segments", which have the value of the coefficients of (3) located on and below the main diagonal. If the initial segment of a square protrudes from its cell, the sketch can be controlled by reducing all the segments of *S* to a size smaller than one; the deflection is thus obtained by reducing the nodal movements derived from the calculation by the same proportion. The size of the initial segment and that of its square can also be divided by a number *n* before they are drawn, as in Fig.3d. *S* determines the segments of the areas S_1 (Fig.1b) and S_2 (Fig.1c), which represent $[B_1]$ and $[B_2]$ in (10) respectively. These areas and the deflection are obtained graphically by making the following sketches:

3.1.1. Sketch 1

Sketch 1 reproduces the factorising operations, modifying the initial segments of *S*. It uses "Type 1" and "Type 2" auxiliary lines associated with each column in *S*, such as the discontinuous lines in Figs.3f,g,h associated with column 1. For each column in *S* the following are obtained: i) the segments that define a column in S_1. The signs of the segments from the squares below the top squares are changed to leave the unknowns clear (e.g. those of column 1 in Fig.3a are those of column 1 in Fig.3b); ii) the segments in a column of S_2. These are horizontal and are defined by Type 2 lines based on the initial segments, and their signs are changed as in (i) (e.g. *B*/*A* and *C*/*A* in Fig.3c are obtained with *B* and *C* in Fig.3d); iii) modifications of the initial segments in the remaining columns of *S*. These are vertical segments which are obtained by cutting Type 1 auxiliary lines with Type 2 lines. Thus *a* and *b* are determined with the lines in Figs.3f,g and segment *c* with those in Figs.3f,h (Fig.3d). The sign in each case is indicated in square *s,* where the modification is obtained. The signs (*) and (**) result from multiplying the initial segment of square *s* by segments *B* and *C* respectively, changing signs. *a* and *b* (Fig.3d) transform the initial segments of column 2 and *c* transforms that of column 3. If *S* had more rows, the auxiliary lines would determine more modifications, which would influence

other rows in columns 2 and 3 (Figs.3g,h). Then i), ii) and iii) are repeated for column 2 (Fig.3e) using x_1, x_2 and

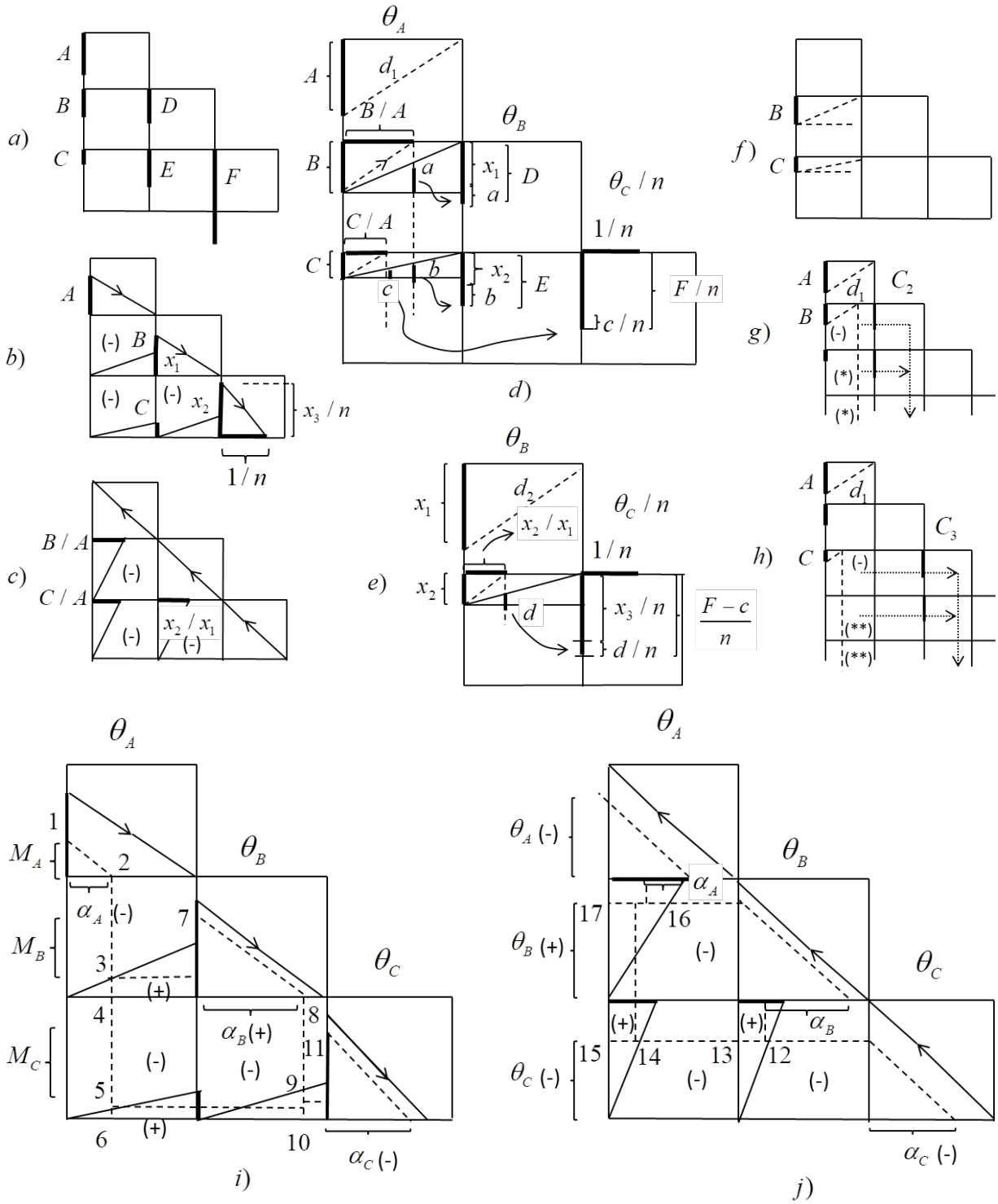


Figure 3. Model in Fig.2a: graphic solving of an equation system: a) area S with initial segments; b) area S_1, c) area S_2; d),e) preparation of Sketch 1; column 1: f) Type 1 lines; Type 2 lines with influence on column 2 (g) and 3 (h); preparation of Sketch 2 (i) and Sketch 3 (j)

(F-c)/n as the initial segments. Finally, in the third column only x_3/n is obtained, since there are no auxiliary lines.

3.1.2. Sketch 2

Sketch 2 (Fig.3i) reproduces on Fig.3b the operations that solve (1) to obtain the α_i in the form of segments, as a function of 1/EI, using the criterion for signs in Fig.4a. This is done as in [1,2], as follows: i) draw line 1-2 considering M_A (negative) to determine α_A; ii) draw line 2-6 to obtain 3-4 and 5-6. Their signs are obtained by multiplying the sign of M_A by that of the square where 3-4 or 5-6 is located; iii) project 3-4 and 5-6 horizontally to column 2; iv) add M_B to 3-4 (positive) and draw line 7-8 to obtain α_B; v) draw line 8-10 to obtain 9-10; vi) add up segments 5-6, 9-10 and M_C (negative) and project the result to obtain α_C.

3.1.3. Sketch 3

Sketch 3 reproduces on S_2 (Fig.3j) the operations that solve (2) to obtain the nodal movements as segments as a function of 1/EI. The procedure is similar to that in Sketch 2: start from α_C to obtain segments θ_C, 12-13 and 14-15. 12-13 and α_B are then used to obtain segment θ_B, and the final rotation is determined by proceeding in the same way.

4. Example

The model considered is that of Fig.4a, made up of equal porticoes joined transversally by articulated bars. The equations are grouped into independent systems expressed as a function of the inertia I in OZ of the columns. There is one system per portico, with the stiffness matrix defined with the flat graph in Fig.4c, and another system whose matrix is determined by the spatial graph in Fig.4d. This can be represented by the subgraph in Fig.4e if the influence of the unknowns eliminated is considered.

It is proposed to factorise the above matrices and obtain the deflection of portico $ABCD$, drawing freehand in both cases on areas S determined by the above graphs and made up of squares measuring 3 cm per side. An exact numerical calculation of the deflection is also made as per [4] with Figs.4c,e. Figs. 4b,f show Sketches 1. In the first case the modification of the segments in columns δ^z takes into account the influence of the four porticoes. Figs. 4g,h show Sketches 2 and 3, and Table 1 compares the results with the numerical values, which took longer to work out. The errors can be considered as acceptable in the knowledge that draughting materials are not used and that the exact value of θ^z_A is small. Repeating the sketches using squares measuring 2 cm and 1 cm per side gives similar results.

Table 1. Deflection of the portico: comparison of results

	Por método gráfico	Por método numérico	Error (%)
δ^x_A	100/EI	112,9/EI	13
θ^z_B	37,5/EI	33,04EI	13
θ^z_A	18,7/EI	14/EI	33

5. Conclusions

Based on this research, the possibility emerges of calculating certain hyperstatic structures commonly found in building graphically and almost exactly by freehand.

Possible lines of research are also pointed to in the developing of further graphic methods that can analyze other types of structure directly and accurately

Acknowledgements

We would like to thank my friend José Múgica, Manager of Tradutecnia, and Chris Pellow for the help that they have provided in translating this manuscript into English.

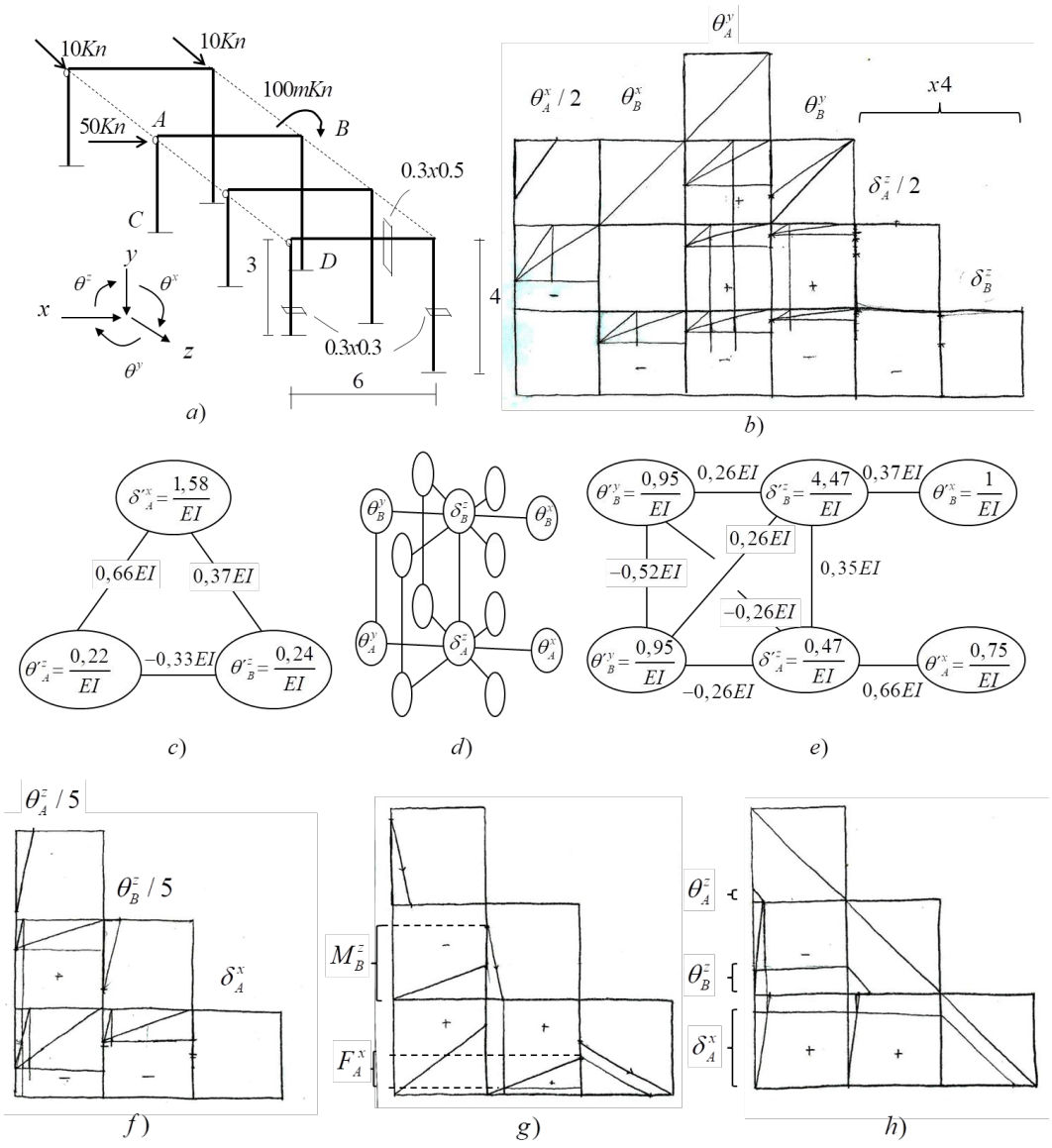


Figure 4. Graphic analysis of a spatial portico: a) model & criterion for signs for nodal movements & actions; b) Sketch 1 in system 2; c) graph 1, graph 2: d) sketch & e) detail; sketches of the portico *ABCD*: f) Sketch 1, g) Sketch 2 & h) Sketch 3 with the resulting deflection

References

[1] A. Lacort, "A Graphic version of Cholesky's method for improving the manual analysis of spatial porticoes", *Proc. Eng.,* Vol. 121, pp. 1007-1012, 2016

[2] A. Lacort, "A freehand method for analyzing certain spatial porticoes almost accurately" *Proceedings of the 3th ICSA*, Guimaraes, Portugal, July 27-29, 2016, CRC Press, pp. 964-971

[3] A. Holme., "Geometry, our cultural Heritage", Springer, 2010

[4] A. Lacort, "Control semigráfico de análisis exacto para ciertas estructuras de edificación" *Inf. Tecnol.*, vol. 3, pp 145-156, 2015

Proceedings of the IASS Annual Symposium 2019 – Structural Membranes 2019
Form and Force
7 – 10 October 2019, Barcelona, Spain
C. Lázaro, K.-U. Bletzinger, E. Oñate (eds.)

Semi Analytical Solution for Material and Geometrically and Material Nonlinear 2d Truss

P. CUNHA*, R. DURAND[a], R. DURAND[b], T. OLIVEIRA[b]

*University of Brazilia
Prédio SG–12, 1º andar, Campus Darcy Ribeiro, Universidade de Brasília, CEP 70910-900, Brasília - DF, Brasil
pedro_flc@hotmail.com

[a] University of Pernambuco, R Acadêmico Hélio Ramos, Cidade Universitária CEP 50740-530 - Recife – PE

Abstract

The analytical and semi-analytical results are important tools for approximate solutions' validation, however, for non-linear analyzes, these results are not calculated trivially. In turn, these results are not found in detail in the literature. Therefore, the main objective of this paper is presenting a semi-analytical solution for Von Mises-type plane trusses, showing the nodal behavior along the equilibrium, for both elastic and non-linear linear materials. Comparisons are presented for the consideration of geometric non-linearity and geometric and material non-linearity. The obtained results were compared with routines implemented via MATLAB, adopting the Co-rotational approach for finite elements and using the displacement method for the nonlinear system's solution. Finally, we show the displacement paths of the monitored node in relation to the abscissa and coordinates axis, in addition, the variation of the resulting force applied in relation to the displacements in the main directions is plotted.

Keywords: Nonlinear geometric analysis. Nonlinear physical analysis. Semi analytical solution.

1. Introduction

Linear analysis is still widely used in the academic environment to determine the displacements, rotations and loads in a structure, because it is more practical and easier to implement. The main difference between the linear analysis and the geometric nonlinearity (GNL) is that, in this second, the equilibrium conditions are conditioned to the current configuration of the structure, after being submitted to a portion of the load.

The material nonlinearity (MNL) is the result of the constitutive relations of the material, **because** from a certain level of loading, the material does not behave linearly (Hooke's Law). According to Lacerda (2014), several materials have a non-linear behavior (NL), such as: nonlinear elasticity, plasticity, viscoelasticity and creep.

Junior (2012) mentions that nonlinear analysis of a structure or the determination of its equilibrium curve can be performed by analytical solutions, incremental, iterative or incremental-iterative procedures. Therefore, it is observed that NL analysis is a tool that needs to be explored in order to obtain results for structural analysis in a way that is closer to reality.

According to Greco (2009) because of its simplicity, the truss is an ideal structure for the study of NL behavior. The purpose of this paper is to present a semi analytical solution for nonlinear geometric and physical analysis of a flat lattice structure, since the exact solution serves as a tool for validation of numerical solutions.

Copyright © 2019 by P. CUNHA, R. DURAND, R. DURAND, T. OLIVEIRA
Published by the International Association for Shell and Spatial Structures (IASS) with permission.

2. Methodology

The truss consists of two bars shown in Figure 1:

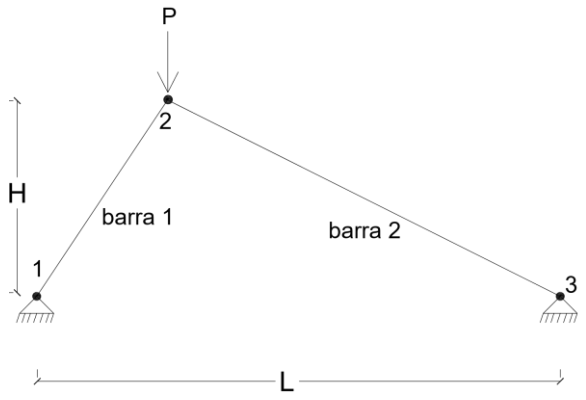


Figure 1: Von Mises type truss undeformed.

The methodology described below was based on Greco (2009). Initially, before the application of the load P, the truss presents an undeformed structure with angles α_0 and β_0. After application of the load, the bars deform as shown in Figure 2.

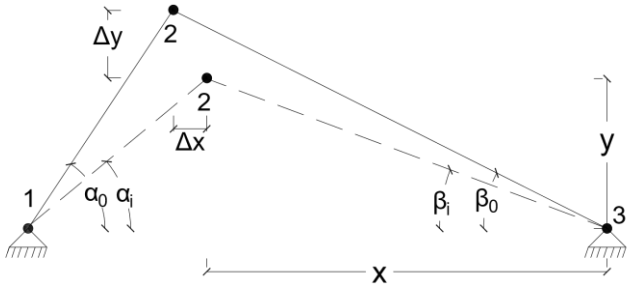


Figure 2: Von Mises type truss deformed.

Applying the method of the nodes to the central node, through the sum of x-direction loads equal to zero:

$$F_1 = \frac{cos\beta_i}{cos\alpha_i} F_2 \tag{1}$$

For the equilibrium of y-direction loads, results in (2) and find a corresponding equation for axial force in bar 2 (F_2).

$$F_1 sen\alpha_i + F_2 sen\beta_i = P \tag{2}$$

Substituting equation (1) into (2):

$$F_2 = \frac{P}{cos\beta_i tan\alpha_i + sen\beta_i} \tag{3}$$

Combining the kinematics of the problem, it is possible to determine two equations that relate the displacements of bars 1 and 2, respectively.

$$\delta_1 = \frac{(L-x)}{cos\alpha_i} - \frac{a}{cos\alpha_0} \tag{4}$$

$$\delta_2 = \frac{x}{cos\beta_i} - \frac{b}{cos\beta_0} \tag{5}$$

2.1 Semi Analytical Solution Considering Geometric Nonlinearity and a Linear Elastic Material

In a first moment, the material will be of the linear elastic type. Applying Hooke's law to bar 1, in the deformed structure:

$$\delta_1 = \frac{F_1 L_1}{E_1 A_1} \tag{6}$$

$$F_1 = \delta_1 E_1 A_1 \frac{cos\alpha_0}{a} \tag{7}$$

Substituting equations (3) into (1):

$$F_1 = \frac{cos\beta_i}{cos\alpha_i}\left(\frac{P}{cos\beta_i tan\alpha_i + sen\beta_i}\right) \tag{8}$$

Now (4) and (8) into (7):

$$\frac{cos\beta_i}{cos\alpha_i}\left(\frac{P}{cos\beta_i tan\alpha_i + sen\beta_i}\right) = E_1 A_1 \left[\frac{cos\alpha_0 (L-x)}{a(cos\alpha_i)} - 1\right] \tag{9}$$

Again, by Hooke's law, for bar 2:

$$\delta_2 = \frac{F_2 L_2}{E_2 A_2} \tag{10}$$

$$F_2 = \delta_2 E_2 A_2 \frac{cos\beta_0}{b} \tag{11}$$

Substituting equations (3) and (5) into (11):

$$\frac{P}{cos\beta_i tan\alpha_i + sen\beta_i} = E_2 A_2 \left(\frac{x(\,cos\beta_0)}{b(cos\beta_i)} - 1\right) \tag{12}$$

It is observed that the left-hand part of the equation (12) is inserted in equation (9), it is possible to determine an expression that does not depend on external loading, as (13):

$$\frac{cos\beta_i}{cos\alpha_i}\left[\left(\frac{x(\,cos\beta_0)}{b(cos\beta_i)} - 1\right)\right] = \frac{E_1 A_1}{E_2 A_2}\left[\frac{cos\alpha_0 (L-x)}{a(cos\alpha_i)} - 1\right] \tag{13}$$

Inserting (5) in (11):

$$F_2 = \left[\frac{x(cos\beta_0)}{b(cos\beta_i)} - 1\right] E_2 A_2 \tag{14}$$

Through equations (15) and (16), obtained by trigonometric relations in Figure 2, it is possible to calculate the values for x and y.

$$x = \frac{L \tan\alpha_i}{\tan\beta_i + \tan\alpha_i} \tag{15}$$

$$y = \frac{L \tan\alpha_i \tan\beta_i}{\tan\beta_i + \tan\alpha_i} \tag{16}$$

Substituting (15) in (13):

$$\left[\frac{cos\beta_i}{cos\alpha_i}\left(\frac{L\tan\alpha_i}{\tan\beta_i+\tan\alpha_i}\frac{cos\beta_0}{b(cos\beta_i)}-1\right)\right]=\frac{E_1A_1}{E_2A_2}\left[\frac{cos\alpha_0\left(L-\frac{L\tan\alpha_i}{\tan\beta_i+\tan\alpha_i}\right)}{a(cos\alpha_i)}-1\right] \quad (17)$$

The input parameters for analytical solution are: $L, a, b, E_1, E_2, A_1, A_2$ and α_i. These will be replaced in (17) and thus the value of β_i is determined.

2.2 Semi Analytical Solution Considering Geometric and Material Nonlinearity

For this study, bar 1 is composed of a non-linear material and bar 2 is linear elastic. The constitutive law of the material is represented by the following hypothetical equation:

$$\sigma_1 = E_1\left(\varepsilon_1 - 3{\varepsilon_1}^2\right) \quad (18)$$

Figure 3 shows the stress x strain curve for equation (18):

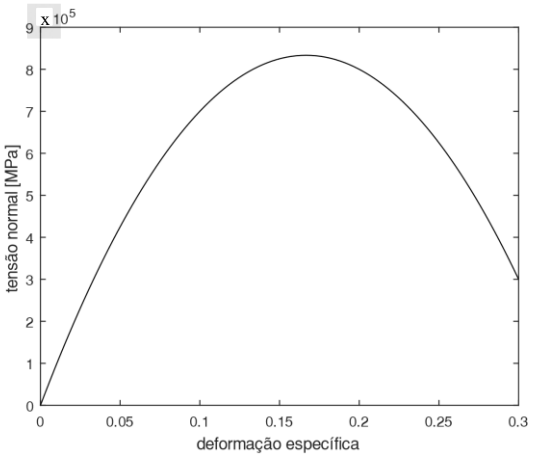


Figure 3: Stress x strain curve for nonlinear material.

Applying (18) to bar 1:

$$F_1 = A_1E_1\left(\varepsilon_1 - 3{\varepsilon_1}^2\right) \quad (19)$$

With:

$$\varepsilon_1 = \frac{L\sin\beta_i cos\alpha_0}{a[sin(\alpha_i+\beta_i)]} - 1 \quad (20)$$

Substituting equations (14) and (19) into (1):

$$A_1E_1\left(\varepsilon_1 - 3{\varepsilon_1}^2\right) = \frac{cos\beta_i}{cos\alpha_i}A_2E_2\left[\frac{x(cos\beta_0)}{b(cos\beta_i)} - 1\right] \quad (21)$$

And finally, by introducing (15) and (20) into (21):

$$\left[\left(\frac{L\sin\beta_i cos\alpha_0}{a[sin(\alpha_i+\beta_i)]}-1\right)-3\left(\frac{L\sin\beta_i cos\alpha_0}{a[sin(\alpha_i+\beta_i)]}-1\right)^2\right]=\frac{cos\beta_i}{cos\alpha_i}\frac{A_2E_2}{A_1E_1}\left[\frac{L\tan\alpha_i}{\tan\beta_i+\tan\alpha_i}\frac{cos\beta_0}{b(cos\beta_i)}-1\right] \quad (22)$$

The input parameters for the calculation of the β_i angle is the same as those used in the analysis for the linear elastic material.

3. Results

The geometric information and materials for the truss presented are shown in Table 1:

Table 1: Material and geometric properties of the material.

A_1 (m²)	A_2 (m²)	E_1 (GPa)	E_2 (GPa)
1,00E-03	1,00E-03	10,00	10,00

Through (17) it is possible to determine values for β_i, then by equations (15) and (16) determine the values of x and y, and subtracting from length L and the height H, respectively, results in Δx and Δy. In (11) the force is calculated on bar 2. Then the stress on bar 1 and the applied force P are determined using equations (1) and (2). Figure 4 presents the results obtained for the horizontal displacement of node 2, which were compared with the software Amaru, developed in finite elements method, and based on the high-performance programming Julia language.

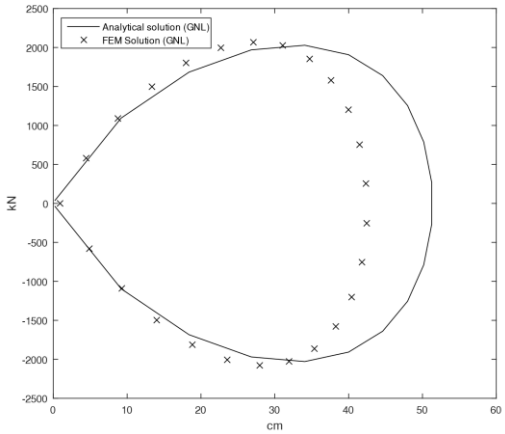


Figure 4: Validation of the results obtained for the horizontal displacement of node 2 to GNL.

The same program was used to validate the y-direction displacement of node 2, according to Figure 5:

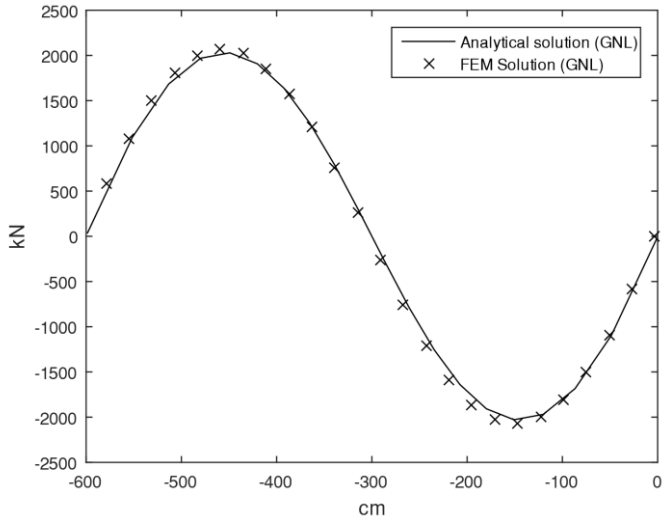


Figure 5: Validation of the results obtained for the vertical displacement of node 2 to GNL.

For equation (22) that includes geometric and material nonlinear analysis, the procedure is similar to that described for (17) and the validated results are shown in Figures 6 and 7:

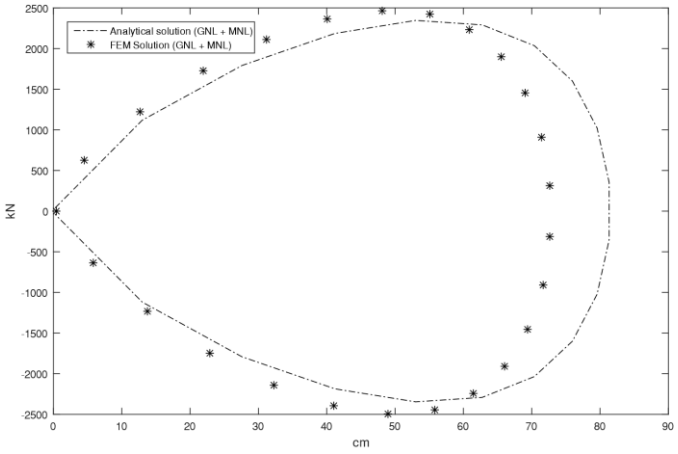


Figure 6: Validation of the results obtained for the x-direction displacement of node 2 for GNL and MNL.

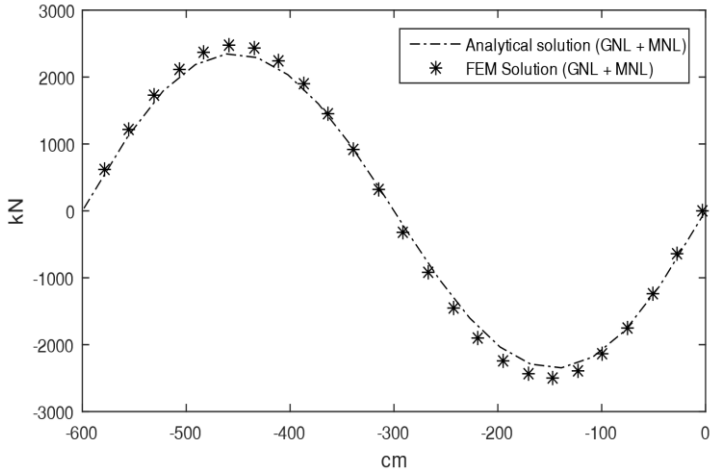
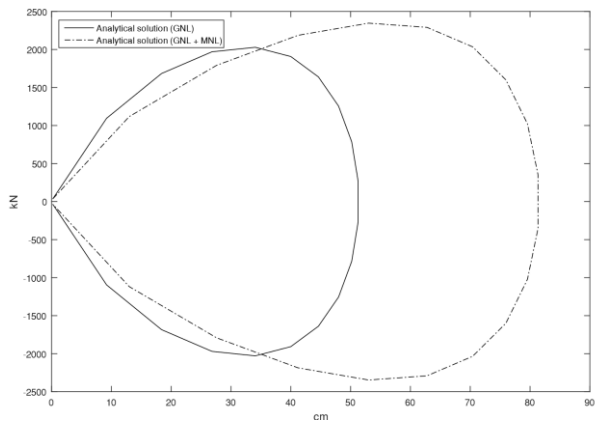


Figure 7: Validation of the results obtained for the vertical displacement of node 2 for GNL and MNL.

On Figures 8 and 9 are compared the results obtained for the analysis considering only the geometric non-linearity and both (GNL and MNL):



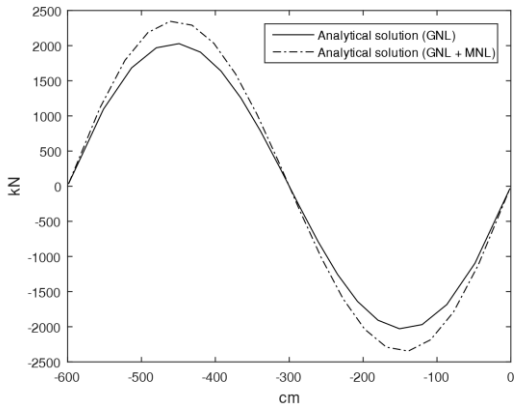


Figure 8: a) Comparison between GNL solution and GNL + MNL for the x-direction displacement node 2. b) Comparison between GNL and GNL + MNL solution for y-direction displacement node 2.

Figure 10 shows the equilibrium path for node 2 in the two cases:

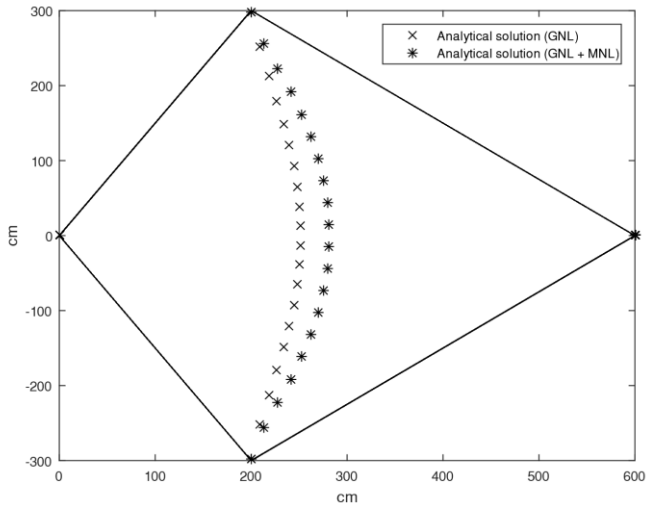


Figure 10: Comparison between GNLG and GNLG + MNL analysis.

Figures 11 and 12 compare the intensities of the axial forces along the x and y-direction displacement of the node, respectively:

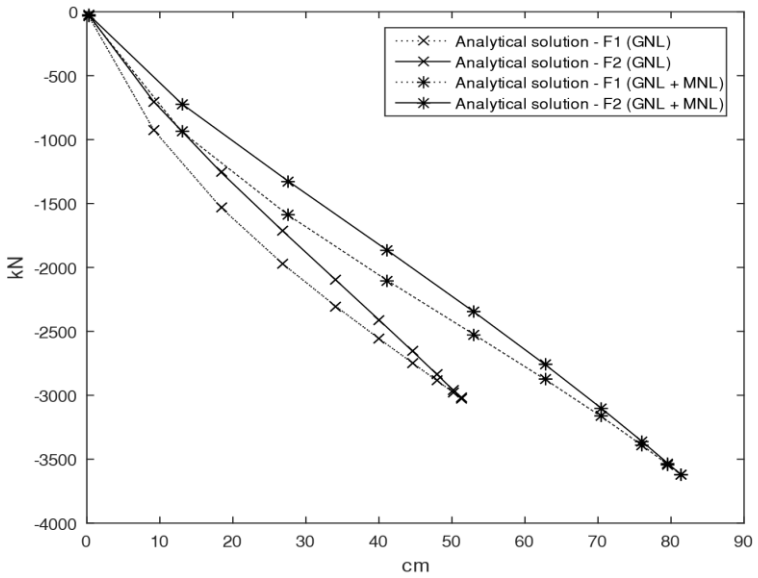


Figure 11: Comparison between GNL and GNL + MNL solution for the x-direction displacement of node 2 and the forces in the bars.

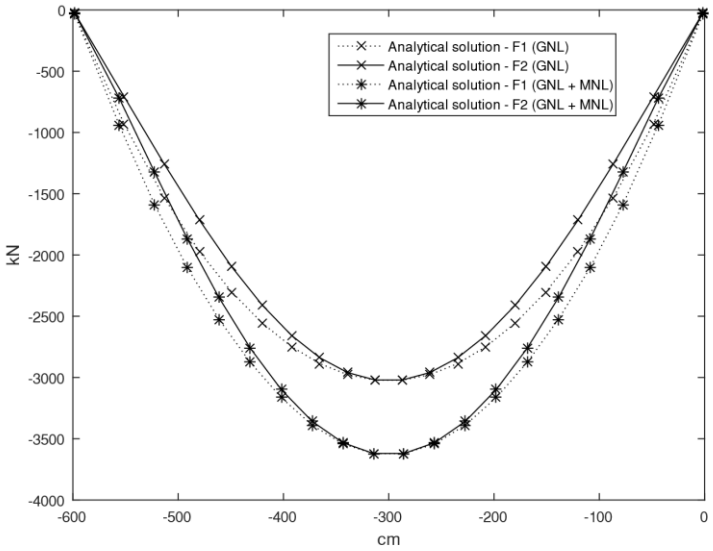


Figure 12: Comparison between GNL and GNL + MNL solution for the vertical displacement of node 2 and the forces in the bars.

4. Conclusion

Although this simple example, it can be seen that the inclusion of geometric and geometric and material non-linearity considerably modifies the values for nodal displacement and forces in the bars. This paper presents analytical solutions for inclusion of nonlinear analysis, it can be used as a tool for validation of numerical models that study NL problems.

References

[1] GRECO, M.; VICENTE, C. E. R. Analytical solutions for geometrically nonlinear trusses. Revista Escola de Minas, págs. 205-214, 62ª edição, 2009.

[2] JÚNIOR, J. C. A. Dimensionamento de pórticos planos baseado em confiabilidade considerando não linearidade geométrica. Universidade Federal de Pernambuco. Dissertação de Mestrado. Recife, 2012.

[3] LACERDA, E. G. M. Análise não linear de treliças pelo método dos elementos finitos posicional. UFRN – Universidade Federal do Rio Grande do Norte. Dissertação de Mestrado. Natal, 2014.

[4] WOOD, R. D.; ZIENKIEWICZ, O. C. Geometrically Nonlinear Finite Element Analysis of Beams, Frames, Arches and Axisymmetric Shells. Computers & Structures, vol. 7, págs. 725-735. 1977.

[5] YANG, Y. B.; LEU, L. J. Constitutive laws and force recovery procedures in nonlinear analysis of trusses. Computer Methods in Applied Mechanics and Engineering, v. 92, p. 121–131, 1991.

Proceedings of the IASS Annual Symposium 2019 – Structural Membranes 2019
Form and Force
7 – 10 October 2019, Barcelona, Spain
C. Lázaro, K.-U. Bletzinger, E. Oñate (eds.)

Before, at the height, after the Tsunami and now of Ogatsu Inkstone Museum: a case on the seashore of Ishinomaki City

Kuniaki ITO*, Junichiro MATSUMOTO[a], Nobuyoshi KOWATARI[b] , Masahiro ONUMA[c]

*Arch. & Prof. Emeritus of TOHOKU Univ.
1-1-7, Kurosuna, Inage-ward, Chiba city 263-0042 Japan
kuniaki1114ito@gmail.com
[a] Director of Junichiro MATSUMOTO Arch. & associates
[b] Director of Architectural Institute of MAIS
[c] Prof. of Tohoku Institute of Technology

Abstract

In 2001, Ogatsu Inkstone Museum was built by the design of Arch. Kuniaki ITO and Arch. Junichiro Matsumoto in the center of Ogatsu Town close to Ogatsu Bay in Miyagi Prefecture. When the big Tsunami attacked the town on March 11th, 2011, this building withstood against its strong wáter pressure and secured goods in the tresury which was located 7 meters above sea level. As the lobby space of the ground level had been surrounded by large glass panes, this building could slide by the enormous torrents allowing the panes to be broken and the sea wáter to rush through the first floor. Furthere more, the building style with conically sharpened figure was effective to mitigate the wáter pressure of the drawing wave of Tsunami. .In spite of the surviving without any structurally serious damage, this museum was demolished by the reason of making the sea walls of the height 9.7m.

Keywords: Tsunami, conically sharpened figure, pilotis, emergency generator, treasury, sea Wall



Fig.1 Withstanding drawing back waves coutesy: Hisao SUGIYAMA

Copyright © 2019 by Kuniaki ITO, Junichiro MATSUMOTO, Nobuyoshi KOWATARI and Masahiro ONUMA
Published by the International Association for Shell and Spatial Structures (IASS) with permission.

1. Introduction

In 1999, Newly planned Ogatsu Inkstone Museum was selected as the working plan for exhibition and storage of precious Inkstones, China Ink Stick, Calligraphy and Writing Brush. The leader of this competition committee was Prof. Saburo Yamashita at that time. The most important Design concepts were it could become the symbol of this harbor town and could survive big Tsunamis almost every fifty years had attacked to this area.

Ogatsu has been known as the place of producing slate stone which is used mainly for roof tiles and Inkstones for calligraphy. This Ogatsu stone had been important industry to sustain people's lives together with fishery in Ogatsu Bay where a lot of nursing rafts were for farming oysters or scallops. But the wharf for ships sank about 1m by the earthquake and Tsunami since before.

The roof facing the mountains was covered by Ogatsu slate-stone as the symbol of the Ogatsu products and in constrast to it, the opposite side of roof facing the bay was covered by Titanium as the easily recognised landmark like a light house. Even after more than ten years since its completion, Ogatsu Inkstone Museum had been looked as clean and beautiful as it was opened until 8 years ago. In 2011, March 11, the great Tsunami attacked Ogatsu town and this building.

2. Design of Ogatsu Inkstone Museum and the Tsunami

The site of this building close to the sea was prepared putting 5m high sea wall from sea level between the site and the sea. This height had been decided by the experience of Chile Earthquake Tsunami 1960. But the great Tsunami exceeded easily this wall to the height of 15.3 m from the ground level which was reclaimed 3m from sea level. Then the height of Tsunami at this place was 18.3m above sea level. The highest point of Tsunami running up to the mountain was almost 42m above sea level.



Fig.2 North elevation



Fig.3 A former Ogatsu Town 2001



Fig.4 Map 2001



Fig.5 At the height of Tsunami 2011



Fig.6 After the Tsunami 2013

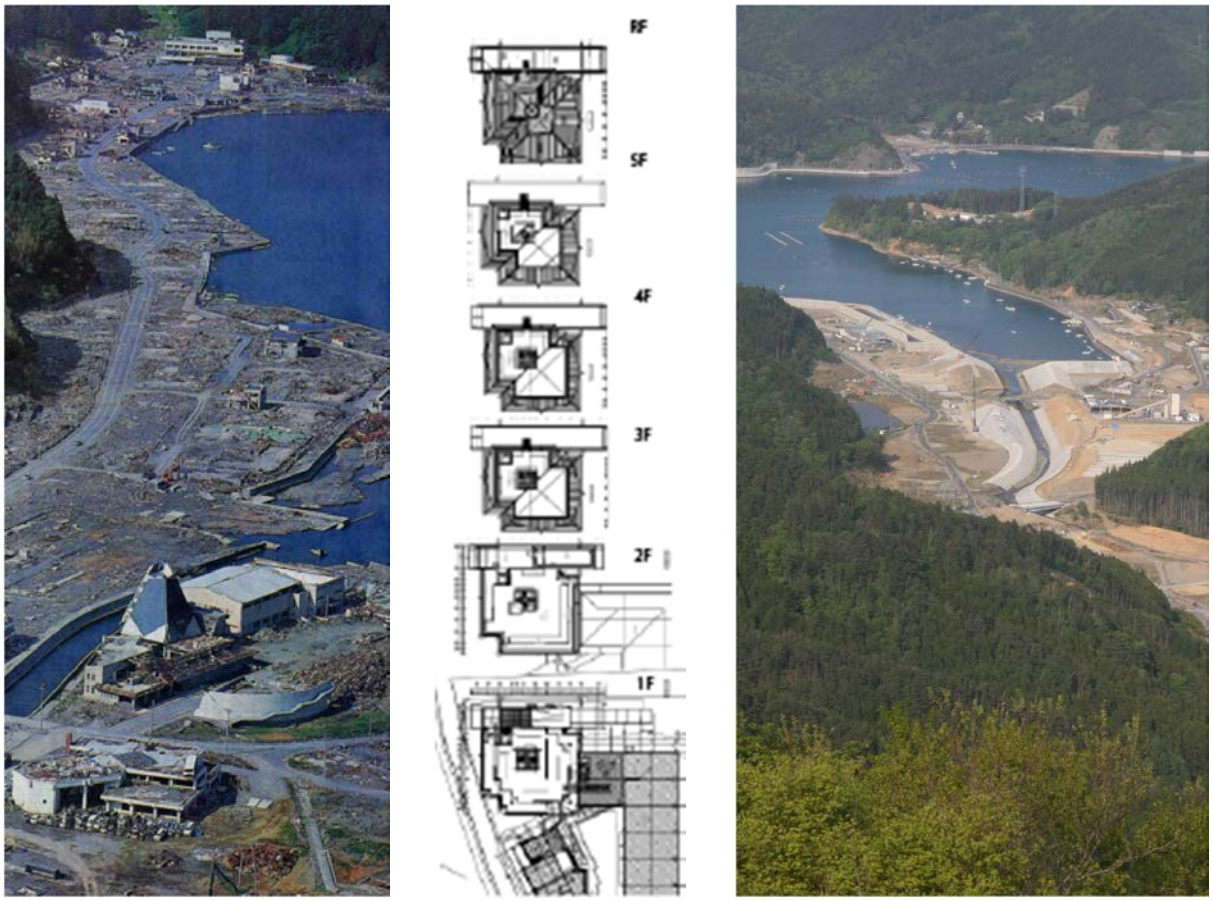


Fig.7 left-Just after the Tsunami (courtesy:Kyodo Press) and right-the old site in May 11, 2019

The author confirmed sharpened pyramid type polyhedra were effective to keep their figures by structural check done after permission to enter. As being shown in Fig.1, Emergency generator Space had been planed on the fifth floor. From this space, people who want to escape to the top could climb up there using ladder for help of helicopter. Opening of sky light was designed like petals open.

Now that this museum was demolished, enormous sea walls began to appear on the seashore area surrounded by mountains . In spite of nothing apparent rule to discuss with dwellers, the sea walls more than 300km length are scheduled to make in several years at the north east of Japan.

Now the site has been surrounded by the bank of more than about 6 meters height from the ground level and the old surfice of the earth could be only found at the corner towards the mountain side.



Fig.8 North side of Ogatsu Bay surrounded by Sea Walls in May 11, 2019 viewed from the south

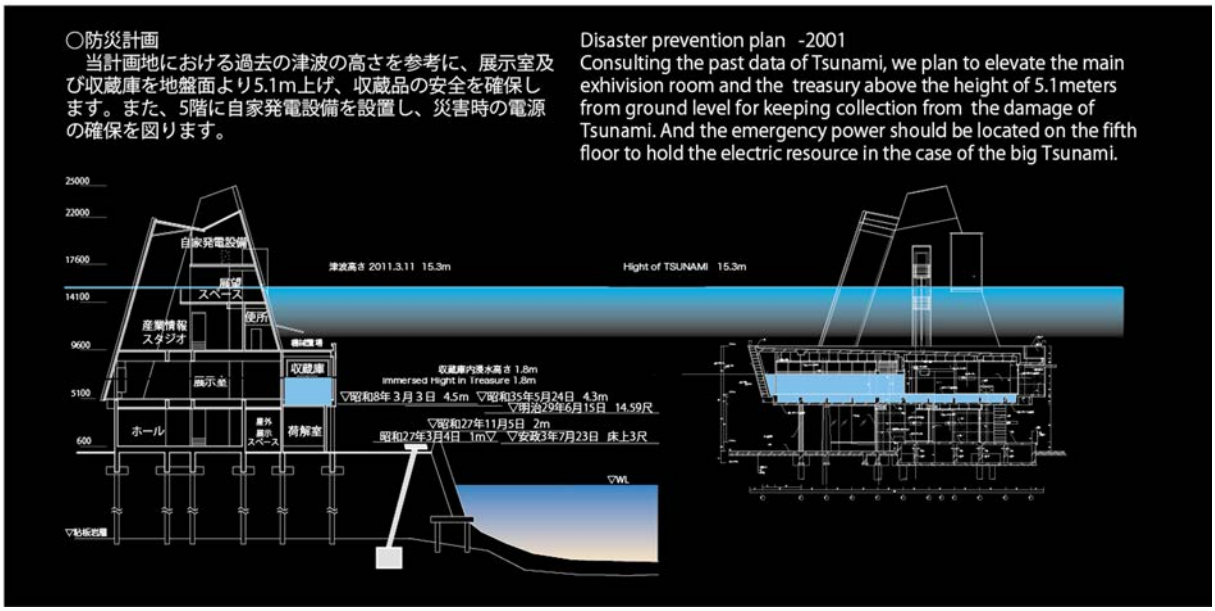


Fig. 9 Original drawing overlaid the Tsunami height and the treasury submergence condition

3. Referencing literature

[1] Yoshinori YOKOYAMA, “Approach leading to the fabricational thinking of social system design”, University of Tokyo Press 2019, P-88,ISBN 978-4-13-043042-5

[2] “Building town-development resistible to disasters-Miyagi Model-”, Miyagi Prefecture, 2017

[3] “Guide Line of Breakwater for Anti Tsunami Design”, Ministry of Land, Infrastructure and transport, 2013

4. Conclusion

This buiding shows how imporatant to consider the fundamental facts over regulated architectural laws to save the total architectural value against the enormous natural power. For that, especially It needs to involve persons who know well about a spirit of the ground, in other words, genius loci.

Acknowledgements

First of all, I must thank the land of Shichigahama (Seven Beaches) Town and people which made my nature for leaving this impressive result about Ogatsu Inkstone Museum. And Museum’s Director, Mr. Takashi Chiba and the director of Inkstone Manufacturers’ Cooperative,Mr. Fumio Sawamura at that time, they were devoted themselves in the despairate conditions for treating a lot of problems incidental to the disaster. Mr. Hisao Sugiyama, who took a series of miracle photos of the museum fleeimg from the Tsunami, gave them to the author and I thank Mr. Kenichi Yamashita, who acted as a go-between for us. Finally I express my deep gratitude to Mr.Kenichi Onuma who incidentally stayed at Ogatsu Ink Stone Museum at the same time the big earthquake happened. Because his incredible story of escaping from Ogatsu impressesd the author the importance of keeping normal mind.

References

[1] K. ITO, “Ogatsu Inkstone Museum and its Titanium Roof”, Japan Titanium Association, No.60(3), pp. 194-196, 2012

[2] M. ONUMA, K. ITO, “The Worth of Maturity in Living Properties”, ICOMOS ISC Theory & Philosophy “The Image of Heritage:Changing Perception, Permanent Responsibilites”, Florence, 2009

Proceedings of the IASS Annual Symposium 2019 – Structural Membranes 2019
Form and Force
7 – 10 October 2019, Barcelona, Spain
C. Lázaro, K.-U. Bletzinger, E. Oñate (eds.)

Constructing form versus constructing architecture - A comparison of two modular buildings using irregular prefabricated panels

Yukun ZHAI, Jingxiang ZHU, Rico S. DIEDERING, Hing Ching LAU

The Chinese University of Hong Kong
506, AIT Building, The Chinese University of Hong Kong, Shatin, NT, Hong Kong
zhai-yukun@link.cuhk.edu.hk

Abstract

Two centuries, two countries, two architects, two buildings and two approaches on modularization. Whereas the former was driven by spatial composition, the other was driven by an act of construction. This paper is a retrospective comparison between the Finnish Pavilion at the 1958 World Expo in Brussels and the New Lawuga School, in Qinghai Province, China, 2015. Although built with different functions in mind, both projects share a formal similarity in the application of the module. Furthermore, both architects put a special formed z-shaped wall and roof panel in the center of their design. But, a closer look reveals the differences in their modularity. The construction driven approach for the New Lawuga School by UNITINNO, found answers to various problems for high altitude building projects. When facing serious climatic conditions in far remote mountain villages like Yushu, the modularization of the Z-shaped panel was presented as an ease of construction. Being not only a solution for transportation and material supply, the modular z-panel formed the structure, the envelope as well as the space. In other words, form follows construction. On the contrary, the Finnish Pavilion by well-known Finnish architect Reima Pietilä designed for the World Expo in Brussels was conceived as the morphological answer to modern modularization. In doing so, construction was reduced to the mere implementation of a modular envelope. Varying in size and proportion, the z-panel became an outer skin only. The module left space and structure unanswered. The in-deep presentation of the two cases serves as an example to question the role of construction in modern architecture.

Keywords: Lawuga School, UNITINNO, Finnish Pavilion at Brussels, Reima Pietilä, Construction-driven, Morphology-driven

1. Introduction

Finnish pavilion at the Brussels World's Fair of 1958 (Fig. 1) was designed by a well-known architect, Reima Pietilä (1923-1993), who is a second generation modernist of Finland after Alvar Aalto (1898-1976). This pavilion is the first project that Pietilä won in an architectural competition after graduating from Helsinki University of Technology in 1953. Expo 58 was the first major World's Fair after World War II marked by many fantastic architectures including the Atomium, a giant model representing atoms, and the Philips Pavilion designed by the office of Le Corbusier. It showed an eagerness to get ride off the dogma of modernism and a prosperity of the post-war life. Next to Norwegian Pavilion, Finish Pavilion showed its own culture by a rhythmical combination of modular wooden panels. A stepped shape volume supported by wooden truss formed the main exhibition hall, and linked by a low cubic volume with big glass windows.

Copyright © 2019 by Yukun ZHAI, Jingxiang ZHU, Rico S. DIEDERING, Hing Ching LAU
Published by the International Association for Shell and Spatial Structures (IASS) with permission.

New Lawuga School at Qinghai Yushu plateau (Fig. 2) was designed by UNITINNO, a team led by Professor Zhu Jingxiang of the Chinese University of Hong Kong. It has a similar form with Finish Pavilion, a stepped type shape composed by Z-shaped panels. But the site condition of New Lawuga School is much different, which is located at an altitude of 3900 meters a.s.l. where has a typical plateau climate with prolonged freezing winter and rapid temperature changes in summer. So the building uses several special techniques to prevent undesirable environment, including a thick insulation layer, metallic claddings, double-glazed windows, Trombe Walls, etc. This two-floor building servers for the children from the local minority nomadic families after the 7.1 Ms earthquake in 2010 and gives a good study environment to the local children.



Figure 1: Finnish Pavilion in Brussels, Reima Pietilä [1]



Figure 2: New Lawuga School in Yushu, UNITINNO

Two buildings built in two countries and two centuries have similar form. Whether they have same nature? Whether the late project made any progress? If the answers are yes, how to describe the fundamental difference of the two?

2. Form generation

2.1 Morphology study of Finish Pavilion

During the designing of Finish Pavilion, Pietilä was researching on architectural morphology which was about the generation of forms, a fundamental principle of architecture. Actually, this research was started by Aulis Blomstedt (1906-1979), a professor of Helsinki University of Technology, for getting a new architectural theory to get rid of "Aalto Style" in Finland. "Blomstedt's theoretical ambition to grasp back to the roots of modern architecture pitted him against Aalto, dividing Finnish architecture into two opposing schools for a long time: one of an Aalto-Romantic and one of a Blomstedt-Harmonic tendency."[1] Pietilä followed the theory of Blomstedt and participated in a summer course at Imatra which was organized by PTAH (Progrès Téchnique Architecture Helsinki) led by Blomstedt. Later, Pietilä developed the research to his stick studies (Fig. 3), which was about form compositions of growing blocks around a single stick. It was also about the mathematic, algebraic and geometric, study of architectural form.

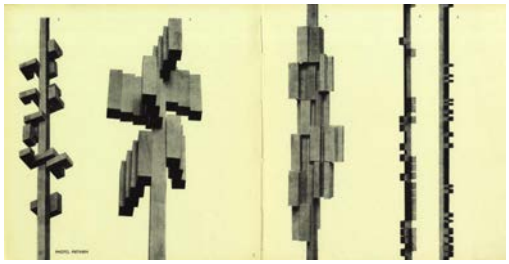


Figure 3: Stick studies by Reima Pietilä [3]

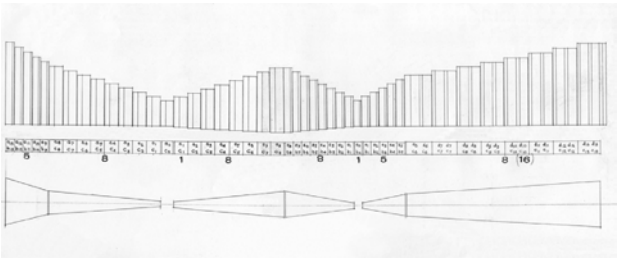


Figure 4: Elevation expand diagram, Finish Pavilion [1]

In the designing of Finish Pavilion, Pietilä combined his morphology study and the modular concept, which he experimented in the university, to generate a rhythmic form of the pavilion. Pietilä said "my Brussels idea had to do with spatial modulation. It came, of course, from Blomstedt. It was an idea for making Finish architecture natural and intellectual at the same time". [2] The main parts of pavilion consisted of 22 parallel parallelepipeds following the basic modules, 0.9m, 1.8m and 2.7m, which are widths of exterior wood panels. The height of these panels increased from 6.1m to 11.7m in the front and 15.2m at the back, with a 0.7m difference between two adjacent modules. From the elevation expand diagram by Pietilä (Fig. 3), we can see the rhythm of the form which followed the number of modules.

2.2 Z-shaped panel system of New Lawuga School

Before designing of New Lawuga School, UNITINNO has finished many lightweight buildings with different systems serving for remote rural areas or natural reserve. In this school project, a large effort was given to find a system that can easily transport, rapidly assemble and get a high quality in an extreme environment. After carrying corresponding researches and studies, the Z-shaped panel was found for effective responding to all-around consideration. Z-shaped panels as main components of wall, roof and floor generated a coherent form of the building (Fig. 5).

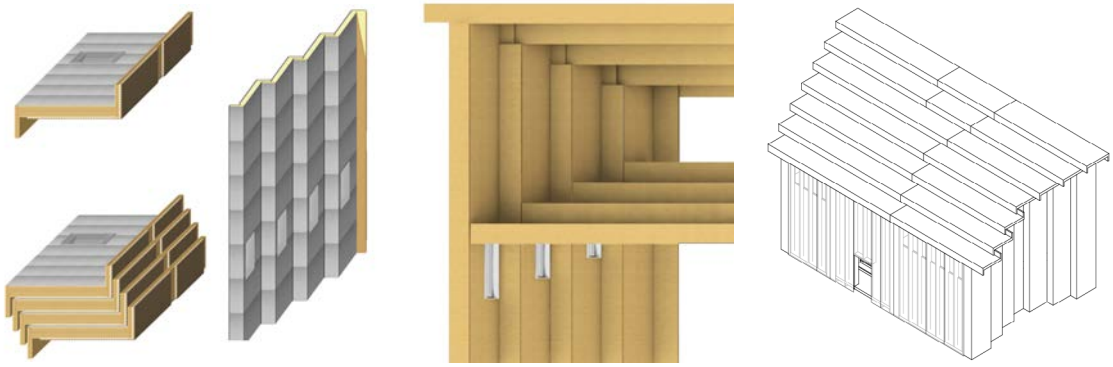


Figure 5: Transportation and assembly of Z-shaped panel, New Lawuga School

The two "wings" of Z-shaped panel at the long edges entrust the spatial defining panels with the structural possibilities. The wings can help prevent the flat panel in the either transportation or construction process. When the Z-shaped panel was placed horizontally as floor or ceiling slabs, the wings became beams overcoming the span; and when it was placed vertically as a wall panel, the wings would help to resist the lateral forces. And when two Z-shaped panels were connected, overlapping "wings" is an easy connection which gives strong structural performance, and provides excellent air-tightness. So just combining Z-shaped panels together we can easily get a high-quality building with a delicate form. It is not a special aesthetic pursuit out of construction.

The size of modular panels is an integrated result responding to multiple requirements of manufacturing, transportation, construction, structural requirement, thermal performance, and the spatial requirement. For example, the peripheral walls panels (150mm thickness) is thicker than the suspended floor panel (90mm thickness); the width of the panels is defined by the raw plywood panel width (1220mm); the length of all panels are limited by 9m for lorry transportation, etc. As a result, the form of building influenced by the material supply and construction requirement to a certain extent.

3. Construction of form

Comparing the generation of the architectural form of two buildings, we can find that one came from the study of morphology theory, another was from the research on construction system. Although the shape of two buildings was looked similar because of the modular concept, the design logics are totally different. For example, the mathematic system, one pursues a harmonic division of numbers and another depend on the size of raw materials. These different have a strong influence on the realization process of two buildings.

In New Lawuga School, the Z-shaped panels are the main structure elements, either erected as walls or placed as the roof (Fig. 6). There are totally 80 nos. of panels, and the installation process of the main building structure took only 8 days by using a crane. The construction of the building started from the erection of the central core (Fig. 7), so that a stable structure could be erected independently. The tolerance due to the construction was shifted to the exterior sides. Following was the installation of the suspended floor panels. After finishing the construction of Z-shaped panels, the architecture is formed without any component from other structure system. The Z-shaped panels are not only the structure components, but also the envelope for protection, the stepped floor for classrooms and the formal generator. The construction of form process is also the construction of structure, enclosures, functions and spaces. One type of component can realize many aspects of the building.

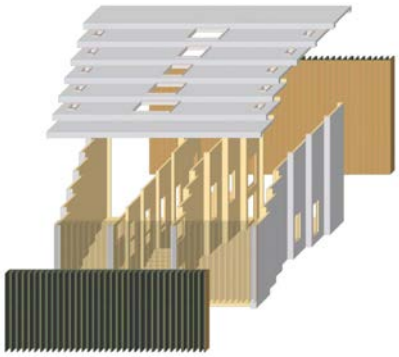


Figure 6: Form and Structure

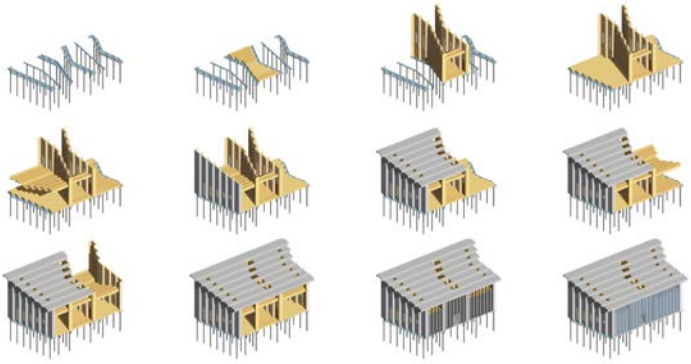


Figure 7: Construction Process, New Lawuga School

In contrast, the form of Finish Pavilion needs to be supported by a structure system composed by new elements. The span of Finish Pavilion along the direction of roof panels could get 38m long, and the roof elements were not in a plane (Fig. 8), so it was a challenge to design a structure that could well fit the stepped shape. From the architect's point of view, it was better to keep the architectural form pure and consistent when looking from outside. The structure should be concealed inside to avoid hurting the completeness of architectural form. Pietilä conceived "its exterior sculpturalism is logically geometric, its structural system is a compromise" [2].

The compromise of the structural solution led that the form of pavilion and the structure were separated to two systems. A stepped sculpture was supported by wooden trusses (Fig. 9). In the end, "the construction was built up on site out of isolated panels attached to columns in contrast to the original

intention of prefabricating the parallelepipeds out of slats and self-supporting H.B.-frames" [1]. The modular form didn't speed up the construction process, but make it more complex and difficult to get a solution of structure. To realize the pure out form, the other types of elements must be introduced as a structure. The modular form only used as an envelope.

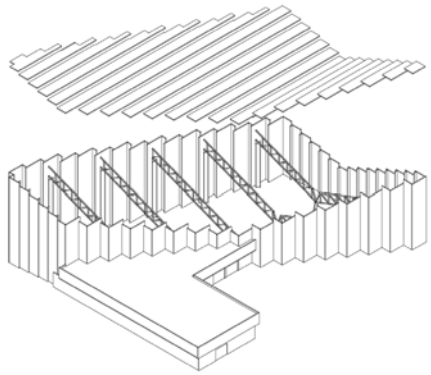


Figure 8: Form and Structure, Finish Pavilion

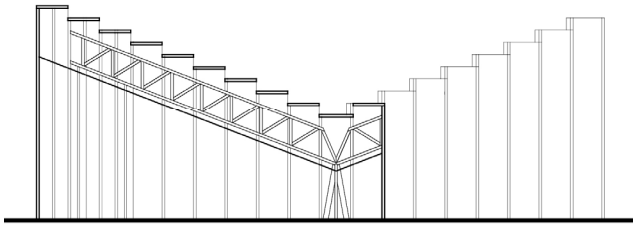


Figure 9: Section, Finish Pavilion

4. Space experience

Looking into the interior of Finish Pavilion, the roof structure and stepped roof were concealed by the yellow-red pine ceiling. What we could see inside was a sloped ceiling consisted by thin wooden grilles (Fig. 10). Sunlight going through louvers was filtered by the grille lighting up the exhibition hall. This reminds us the soft sunshine of Nordic countries which gave a feeling of the Finish culture. But staying in this pale space with Finnish perfume, we could not see the form of the building because of the concealed by the ceiling. For an exhibition building, it should avoid sunlight go into the exhibition hall directly for protection the artworks, but sunlight can easily go through the louver of the stepped roof of Finish Pavilion due to long glass window cast. To filter the strong sunlight, as well as hide the wooden truss, a ceiling was added. It made the interior looked like a simple volume with diffused soft light. But it also interrupted the consistent of architectural form when looking from inside and outside. The modular roof "lost" inside.



Figure 10: Exhibition hall, Finish Pavilion [1]



Figure 11: Classroom, New Lawuga School

In New Lawuga School, the Z-panel system produces a complex spatial geometry characterized with the warm wooden color (Fig. 11). The building consists of a central double height stairway connecting to 4 classrooms. Due to Z-panel system, the two lower level classrooms have a stepped ceiling getting higher at east, while the upper floor rooms are stepped classrooms, with a dramatic ceiling height at the

west. Since the walls are not parallel to each other and opening density Varys too, each classroom acquired an identical spatial ambience.

5. Conclusion: constructing form or constructing architecture

In Finish Pavilion, folding components covering wall and roof shape the volume and outline the space, while the wooden trusses serve as load-bearing structure. Unfortunately, the simplicity of overall volume was messed by entry annex of a very different form. An inclined false ceiling covering the roof faked the expression and revealed the splits between the look and the essence.

In New Lawuga School, those Z-shaped panels generate the building and space, and offer both functions of structure and envelope. The component design leads to radical benefits for the construction of a permanent school on high plateau area.

Both buildings started with folding panels, the shape of which brought structural stiffness and tactile expression. But the interest on the first one rested on the form or expression, while the second one has examined its comprehensive potential to the task.

We may name the two realization approach as morphology-driven or construction-driven: the first one successfully realized an attractive form responding to the surroundings, but not yet extended the attention to every aspects of architecture. The second one selected the component shape for an ease of construction, from making, stacking, transportation to assembly, ended at an architecture of unity, after absorbing each requirement into the initial idea.

Acknowledgements

All of figures about New Lawuga School are from UNITINNO. Figure 1, 4 and 10 are from reference [1]. Figure 3 is from reference [3].

References

[1] Devos, Rika, and Mil De Kooning. "The Merging of Proportion Theory, Morphology and 'National' Imagery in Fifties Modern Architecture: The Pietilä Pavilion at Expo 58". *91st ACSA INTERNATIONAL CONFERENCE.* HELSINKI: July 2013. 15-22.

[2] Quantrill, Malcolm. *Reima Pietilä: Architecture, Context and Modernism.* Helsinki: Otava Pub., 1990, 28-30.

[3] Pelkonen, Eeva-Liisa. "Architectural Morphologies, Ca. 1960." *Getty Research Journal* 9.1 (2017): 161-79.

[4] Pietilä, Reima, Suomen Rakennustaiteen Museo, Alvar Aalto-museo, and Arkkitehtuurimuseo. *Pietilä: Modernin Arkkitehtuurin Välimaastoissa = Intermediate Zones in Modern Architecture.* 2. Painos ed. Helsinki: Jyväskylä: Suomen Rakennustaiteen Museo; Alvar Aalto Museo, 1985,34-41.

Proceedings of the IASS Annual Symposium 2019 – Structural Membranes 2019
Form and Force
7 – 10 October 2019, Barcelona, Spain
C. Lázaro, K.-U. Bletzinger, E. Oñate (eds.)

Exploring Folded Plate Design in Realized Works of Varied Scale and Materials

Ahmet TOPBAS*, Ahmet DEMIR, Burhan KAPLAN, Kimiya JOZAGHI

*ATTEC
Muhurdar Karakolu Sok. 28/2 Moda Istanbul Turkey
topbas@ateknik.design

Abstract

Folded plate behavior can be used very efficiently in structural design with various materials and scales of structures. In this paper, our recent explorative case studies in creative and innovative folded plate design and constructions will be presented in timber, concrete and steel folded plate structures. The examples are for school building roofs, an archeological protection roof, floor systems in ecological architecture, and floors in a residential building. The projects vary in size from couple of hundred square meters to thousands, in coverage area. 5 projects in total will be presented. A timber-and-steel composite roof covered an ancient city ruins where archeological park protection required column-free, asymmetric, and flexible design for a roof. Solid Timber was used in two of the innovative folded plate architectural covers. Traditional steel-brick vaulted floors were replaced with concrete vaults in a similar concept for a residential multi-story building. And lastly a timber frame roof which resembles a classic gabled roof from exterior, was made into an effective beam-purlin folded structure with vertical attic posts removed to create a spacious teachers' room for the art studies building.

Keywords: Folded-plate, timber vault, efficiency of folded structures, steel folded, concrete vault, structural design innovation

1. Introduction

Folded plate construction has been used for structural efficiency in many areas of design in various scales in modern history. From smaller components such as trapezoidal metal deck and cladding under mostly bending forces, to large and ondulating brick walls of the Iglesia de Estacion Atlantida by Eladio Dieste [1] which is under compression and bending can all take advantage of this method. Both elegance and sustainability can be achieved by folded plates. The sustainability mentioned here is certainly the efficient use of materials through structural efficiency.

When we fold a thin plate and use a higher section depth in an alternating manner, we increase the inertia and the critical buckling factor. As we increase the end support constraints against torsion, and perpendicular thrusts occuring between the arch supports of the folds at the supports, we further increase the capacity of the folded plates. In this article we will share our explorations into the method. Some of our built structures and some structures in the design phase with various sizes and material types will be shared.

2. Saint Euphemia Archeological Frescos Protection Canopy

In Sultanahmet-Hagia Sophia, historic peninsula region of Istanbul, there was a discovery of ruins of an ancient church and its frescoed walls in good condition from around 500AD. The Church of St. Euphemia was dedicated to the saint protector of Kadikoy (ancient Khalkedon), and the chapel was a byzantine orthodox pilgrimage site from as early as 1000 years ago. The frescos needed to be protected from weather with a roof while the site was being organized to be an archelogical park.

Copyright © 2019 by Ahmet TOPBAS, Ahmet DEMIR, Burhan KAPLAN, Kimiya JOZAGHI Published by the International Association for Shell and Spatial Structures (IASS) with permission.

The main challenge was to span the canopy covering 250 m^2 without any intermediary columns or supports and with only a 1.75m total structural depth. The canopy shall "fly over" the ruined church wall with wall paintings with only point supports or columns around the perimeter. The ruins on the ground on the center were also of archeological value and the roof construction shall be built with the idea that at some point in the future, the roof could be removed without any harm to the ruins. There were varied proposals by previous engineering teams. One was with intermediary posts sitting on ground platforms, which were precast slabs, but this was too risky for the ruins on the ground. Another proposal was a hanging scheme, but this was against the maximum structural depth requirements that came from the Heritage Committee. Figure 1 shows one of the earlier proposals by other teams compared to our schematic design.



Figure 1: Top: Earlier proposal with supports landing on archeological park. Middle: Our schematic for folded & kinked canopy. Bottom: The way it was built with architectural modifications

We were inspired by moving sculptures and a subsequent roof design of a vineyard building by Santiago Calatrava [3] and proposed ondulating roof schemes: one sinusoidal, and one triangular or kinked as in Figure 1. These designs were finally adapted and somewhat revised to fit an earlier architectural plan approved by the Committee. Figure 2 shows the comparison of the earlier proposal with the finally built scheme. With the help of folding kinks we were able to fit into the depth requirments from the top of columns to the tip of the canopy cantilevers.



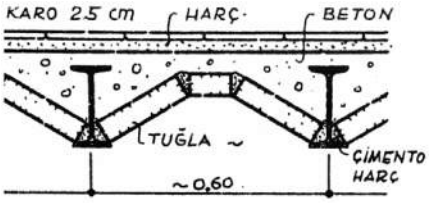


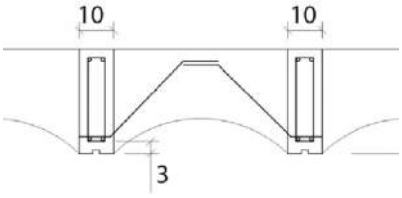
Figures 2a and 2b: Left: Trial assembly in the shop and Right: Kinked canopy in place

The main girder was spanning 22m with only 800mm structural depth to carry the entire canopy mid tributary area and cantilevers. Fabrication and construction of the steel main structure was done carefully with trial assembly in the shop for right fit of various kink angles. Figure 2 includes snapshots from the shop trial assembly and the canopy assembled on site.

3. ParkKare Zonaro Apartments

We designed a floor slab system in an innovative fashion for this apartment building, across from the famed Galata Tower in Istanbul. This was a reconstruction of the original 10 story building which had been made with masonry load bearing walls and terracotta-steel beam vaulted flooring. Following the historic geometry we reconstructed the vaulted flooring with architecturally exposed structural concrete. The concrete vaults are exposed as ceiling decoration as well as their structural purpose. The niches between the arches will be used for the embedded ceiling lighting as well. Before deciding on the form material, we exercised between steel and fiber formwork and went with the fiber option for the vaulted ceilings.This was an efficient, strong, and an easily dismantable form system, as well as helping the asthetics and reference to the historic character. Figure 3 shows the comparison of geometry between the traditional vaulted slabs of Beyoglu region of Istanbul, and the finished vaulted ceilings after the forms were removed.





Figures 3a and 3b: Traditional vault and the concrete exposed vaults we created

The overall thickness required by the Turkish concrete code for the slab was 30cm, for the beams were 30cm thick minimum, and either same shall be used, or deeper beams would have to be used per the code. Therefore, the vaulted concrete slabs descreased the concrete amount used, while providing elegance, but more importantly the reinforcement requirements were decreased as well. Traditionally, one would reinforce such a slab with two way top and bottom reinforcement for gravity, seismic and temperature/shrinkage. A One-way concrete joist system with aereated concrete or other insulating block components in the form between the joists would be a traditional choice too. But these wouldn't have been nearly as elegant and architecturally useful. Figure 4 shows the arched fiber form strips that were placed on top of the flat plywood forms to create the arched vault voids.



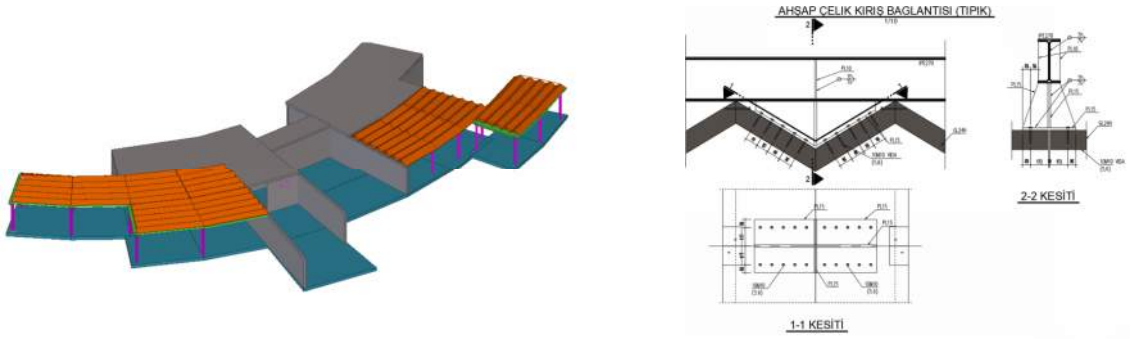


Figures 4a and 4b: Fibre forms, reinforcement on forms, and the view after the forms are removed

4. Hukoy, the Ecological Resting and Education Center, Restaurant Structure

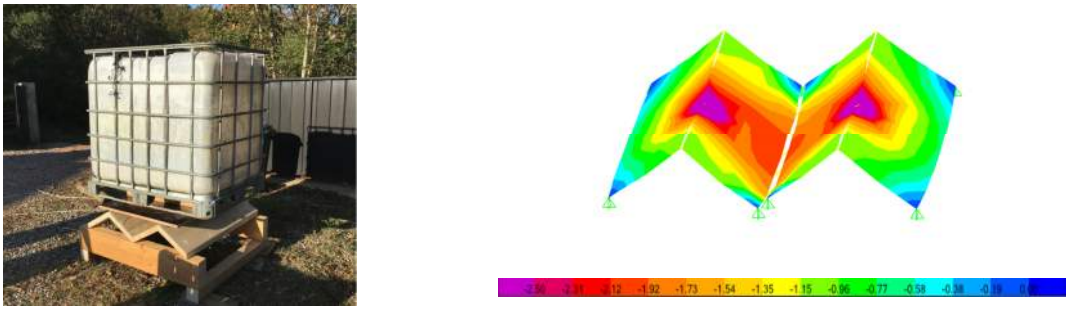
This construction is the load bearing structure for the green roof of a single story restaurant in an ecological resting and education village. A private school is constructing this center with social areas and accomodation units for gatherings of families of students, academia, and other interested guests. Nested in the Taurus Mountains of Mediterranean coast of Anatolia, hiking, resting, and nature observing areas, organic vegetable and fruit growing, agricultural training will be the activities in the complex. We were inspired to further our experiences and by the efficiency and elegance by similar works [2]

We designed the restaurant and the social center for the complex to be built with steel moment frames carrying folded Glulam plates. The GL plates, or sideways-turned beams, positioned at 30 degrees to each other will be filleted and screwed together with lag screws to create a continuous floor plate. On a 6m axis at every steel beam perpendicular to the floor plate, the folded plates will be lag screwed to hanging connectors that are welded to the steel beams. Figure 5 shows the general layout and the detail of the plates which will be hung from the steel frames. The steel beams are set above to hang the plates for simplicity of construction of green roof, but mostly for allowing a plenum for mechanical, piping and electrical services above the vaults. We spanned 6.5m with 10cm thickness with our vaults.



Figures 5a and 5b: The restaurant structure general view and the folded timber roof vault detail

To make sure that the folded plate screwed connection will really behave as calculated, we conducted 1:5 scale test to see the sag under incremental load. The screw connection rigidities obtained from the manufacturer were checked by this test, since it was essential for plates to work together and transfer the combined shear and tension forces without excessive stresses in the wood fiber. This would have caused undesired deflections first, before the strength issues. Figure 6 shows our testing of the sample in the field and our deflected vaults modeled in the FEM software which used spring rigidities for modeling connection screws.



Figures 6a and 6b: Fibre forms, reinforcement on forms, and the view after the forms are removed

5. Roof of the Izmir American College Arts Building, Bristol Hall.

We designed a folded plate scheme for the timber roof with a spin to clear the most area teachers' room and art supply storage. This historic building which is one of the oldest buildings of the century-old school was built in 1927 as an innovative concrete-masonry composite structure of the time. It is the most loved by the alumni and most-relaxing, since it was the music and the arts building of the campus. The existing timber trusses, though, were not as innovative for their timed. The old trusses with multiple posts and no diagonals that teachers could actually work within the story-deep truss, attic space, the veritcal elements were creating much clutter and narrowing the work space for the teachers. Let alone both gravity and seismic load carrying capacity and its connections to the masonry loadbearing perimeter walls were beyond strengthening and repair. A new roof within the old building line would also give opportunities for better air conditioning and access.

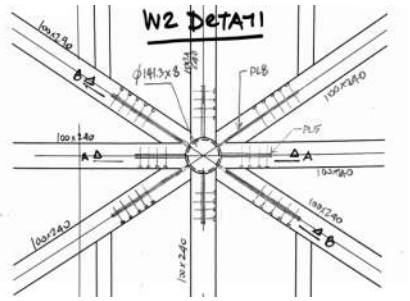


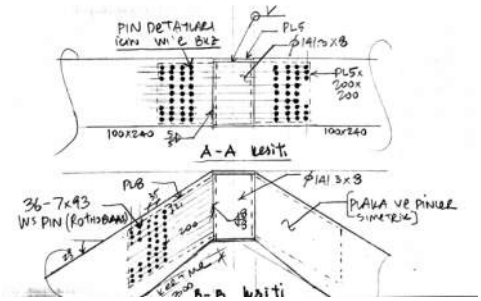




Figure 7a, 7b, 7c: The completed roof looks like an ordinary gabled roof from the outside, but inside a free area is created by the folding of the planes of the beams and the purlins.

The replacement timber gabled roof we designed followed the historic outer lines of the roof, but virtually no vertical elements exists in our design, until a ceiling tapers down to a height less than 1m towards the edges of the roof. We used the eave lines of the historic gable lines to place the major load bearing girders. The purlins, then, were connected to these eave girders creating triangular planes of about max 3m span on the height of a triangle. When we connected all the girders and purlins, a 10m by 23m column-free space was created. Figure 7 shows the completed roof, Figure 8 shows the initial sketches of the joints, where Figure 9 is the node connection in progress for one of the main girder node connections with 8 elements connecting to a single node at different angles.





Figures 8a and 8b: The 8 member connection timber node

The connections created by a cylindrical or a tubular steel shape in their center with connector plates welded on various angles of the girders are key to the system. The angles of the plates welded to the center piece vary in 3 spatial dimensions, and holes were made on them for timber dowels to be inserted in the field. The tight-fit timber dowels were used to take the shear and the moment loads occuring for obtaining fixity, earthquake diaphragm forces, and the eccentricity from the plate lengths. Figure 9a shows the plates in that connection. The efficient system enabled us a column free area with only 24cm of structural depth at the main girders in addition to the warmth and elegance provided by its cover.





Figures 9a and 9b: A special node where 8 girders are rigidly connected around a cylinder

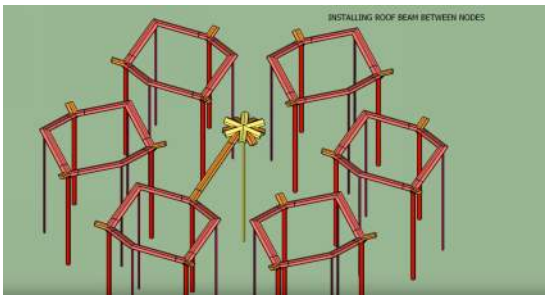
6. Community Center and KinderGarten Roofs of Madac, AlMadinah Academy

The structure I will mention here is a part of a major k12 school development in the city of Madinah in the Kingdom of Saudi Arabia. The community center (CC) including the kindergarten (KG) is one of the 3 building clusters in the school campus and is around 15,000m^2 in architecturally usable space. The folded timber roof will cover the entire space. CC building is a 70cm thick semi-subterranean, elevated concourse slab, circular in plan with a 125m diameter on a 12m grid column line, with two stories of varied buildings carried by it. The concourse is a ceiling for the parking and the drop off areas of school as well as a foundation for the buildings on top of it. The upper story structure is steel with two stories topped off by the timber folded plate roof. Design for the folded plate timber roof was done with CLT triangularly-cut panels supported on V-shaped beams, on circular steel columns. Where the V shaped beams join, a solid block-glued GL node (Rosette) is designed to receive all 12 beams on one node. Typical hexagonal construction module is shown in Figure 10. The system consists of valleys and ridges made up of triangular plates which are linearly connected along edges one-another with screws through V or inverted V beams. This multi-dimensional fold system creates a considerable economy in spanning the roof, that savings from a more traditional gabled girder-purlin system was around 30% in timber cubic meters. The final thickness of the slabs was 120mm and the V beams were 140mm deep only.




Figure 10a and 10b: General architectural rendering and digitally printed model of the folded roof

Where the design required column-free areas for long spans such as the mosque and the exhibition areas, we designed prestressed tie rods and used arching actions between the longer-span columns. The ties are going to be connected and tensioned from short stub columns sticking down from a valley point. This way spans as long as 24m in both directions were crossed with only 120mm thick slabs. The erection sequencing was carefully planned by the team, to make sure that the system was stable during construction, and tolerances can be handled by the method. Snapshots from a method model video study is on Figure 11. This method statement video helped us study the constructability issues.



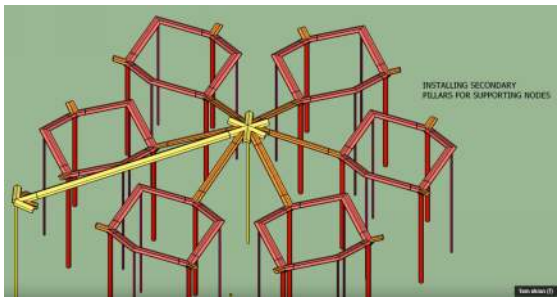


Figure 11a and 11b: Support conditons and loadings of timber node

Rosettes have critical role in folded plate design and they should transfer the all internal forces. As it is known that timber behaves different according to grain and glue is the important factor for this type of block glulem nodes. To consider this critical conditions and see whole behavior of timber node, it is analysed by using solid FEM. Orthotropic material model is used for timber material and glue lines between nodes are modeled with CZM modelling.

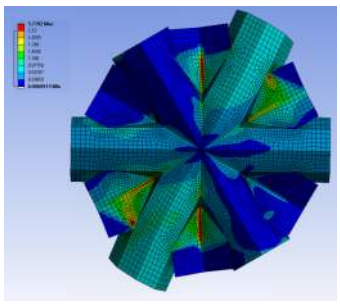
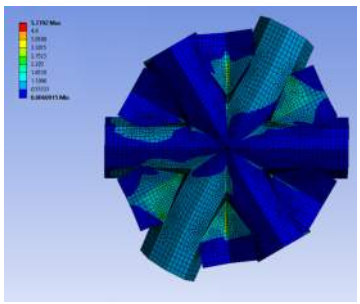
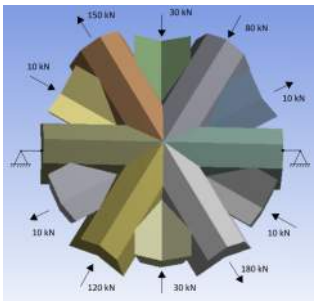




Figure 12a, b, c: Solid analyis stresses and model support conditons and loadings of timber node

Rosettes are loaded according to worse combination and two faces are used for support conditions which are restrained only displacements (Figure 12). They are checked in elastic range according to Eurocode 5. They were analized either as block glulam (Figure 12a) with glue assigned between the faces as CZM model or single solid piece (Figure 12b) which was carved with CNC and modeled without glue.

According to results of analysis, tension stresses perpendicular to grain and shear stresses are both critical condition on some areas and the material working both direction according to grain is needed like CLT or LVL. The next step will be taken with the predictions provided by FEM analysis.At this point physical 1/5 scaled samples will be made and loading tests will be performed to measure critical stresses. Both CLT ve glulam sample will be studied. Sample study for the option considering from the glulam elements. Figure 13 shows the mockup for testing for the first type of node design.



Figure 13: Block-glued mockup

7. The Next Steps

Over the last 5 years, we have been working on different scales and materials with the same idea in mind: the efficiency and elegance of folding in structures. It is the authors' pursuit that innovative approaches creating efficiencies and elegance simultaneously are the most intellectual and satisfying ways of engineering. Folded plates and similarly alternating or reciprocal surface or linear elements have even more and perhaps industrial production qualities in the structural scale. Therefore, the authors will continue to produce, and push the boundaries of this type of construction, improving upon the already-made explorations and combining their aspirations with inspiring international examples.

Acknowledgements

We would like to thank our strategic partners SanalArc, Ahmet Demirel Timber Products, Fibrobeton as well as our client Vehbi Koc Foundation, (VKV) for the chance to develop our ideas and their support for innovation-oriented design.

References

[1] S. Anderson, *Eladio Dieste, Innovation in Structural Art*, New York: Princeton Architectural Press, 2004

[2] C. Werner, M. Robbeler, *Integral Mechanical Attachment for Timber Folded Plate Structures, EPFL Thesis No 6564, 2015*

[3] A. E Yildiz, *Mobile Structures of Santiago Calatrava: Other Ways of Producing Architecture*, METU, Thesis for the Degree of Master of Architecture, 2007

FORM and FORCE

Proceedings of the IASS Annual Symposium 2019 – Structural Membranes 2019
Form and Force
7 – 10 October 2019, Barcelona, Spain
C. Lázaro, K.-U. Bletzinger, E. Oñate (eds.)

Structural Design for a Wide Span Roof Structure made from small to medium cross-section structural wood components

Noriaki YAMADA *

* Yamada Noriaki Structural Design Office Co., Ltd
1-5-63 Kamiosaki Shinagaw-ku 141-0021 Japan
yamada.noriaki@yamadakozo.jp

Abstract

The most abundant, locally available wood in Japan come from standing Sugi Trees in Japanese forest that measure in average 300 to 350mm in diameter which produces solid timbers that measure 120mm thick x 180 to 240mm wide. The Oita Prefecture Martial Arts Sports Center (Showa Denko Martial Arts Sports Center, designed by: Ishimoto Architectural Office; Completed in 2019) is an example of effective and viable use of locally available Solid Sugi Sawn Lumber in its structure. The roof frame structure was designed using 120x240mm in cross section locally available Sugi lumber in 2 to 4 meter lengths. In order to realize an open span roof structure to cover the open field of the main stadium measuring 70m x 100m, a special Arched Truss design that insured structural viability and at the same time ease of construction using the locally available Sugi Lumber was developed. By relying on the Stress (load) Transfer mechanism through the lumber pieces end planes, the shape of the Arch was determined while at the same time the ease of fabrication was insured. Potential gaps at surface to surface joints in the materials as well as shrinkage of the materials were investigated in detail to avoid excessive load concentration points and risk of deformation.

Keywords: Timber frame structure, Large space structure

1. Context of the Structural Design Plans

Regularly available structural lumber sizes in Japan measure 105 or 120mm in thickness with widths starting at 105mm and up at 30mm increments at 2 to 4 meters in length with a maximum of 6 meters. Designing process, costing system and building regulations for the most common Japanese Post & Beam houses are based on standardized structural lumber sizes. Sufficient Structural Performance can be assured for standard residential structures using the standard lumber sizes but for designing the larger and more complex commercial and public structures, larger cross section lumber become necessary in order to satisfy the increased loads and unsupported spans. Due to the difficulty in properly and effectively drying large cross section timbers (high degree of drying expertise, long lead time, fall down risks etc.), Glue-Laminated products, LVL and other engineered structural products are widely used for the design and construction of large wood frame structures. But at the same time, due to the demand and existing lumber processing industry base that produces lumber for finishing application as well as structural lumber based primarily on small to medium size materials, strongly supported and backed by not only the lumber processing industry but also by the regional government entities to maximize use of the product, a special project was launched to design and construct large open span structures using strictly locally produced small to medium size standard structural solid lumber.

2. Overview of the Oita Prefecture Martial Arts Sports Center Complex

The Oita Prefecture Martial Arts Sports Center is a leading example of an innovative use of small to

Copyright © 2019 by Noriaki Yamada
Published by the International Association for Shell and Spatial Structures (IASS) with permission.

medium size standard lumber products produced locally. This structure is an indoor sports complex constructed within the large Oita Sports Park, measuring approximately 16,126m2 in total floor space spread through 3 levels above ground and 1 level underground. It features an open, unsupported span measuring 70m x 100m in the main stadium and a 30m x 100m open, unsupported span in the martial arts center. [Figure 1 and 2] The "Showa Denko Dome Oita" stadium where the 2019 Rugby World Cup Championship is scheduled to be held is located in the same Sports Park and will be linked with the new Sports Center Complex. Plans to utilize the newly completed Sports Center Complex for this upcoming major event is presently underway. The roof structure is Wood Frame utilizing strictly locally produced small to medium size Oita Sugi lumber. The volume used for the roof structure in the main stadium and the martial arts building is 985m3. The following comments are namely of the roof structure in the main stadium.

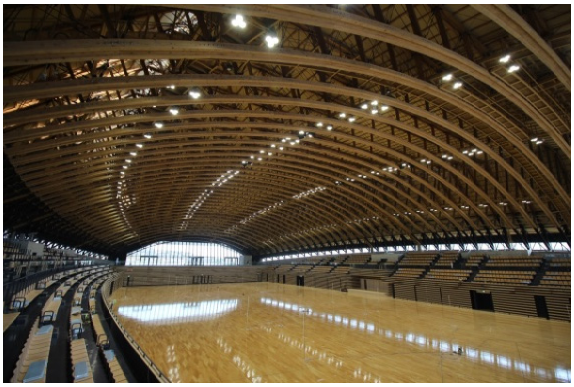




Figure 1: Exterior view after completion, Figure 2: Interior of the Main Stadium

In the Main Stadium, the viewers' stands extend East to West while the North and South faces are Glazed Walls. The Roof Structure is designed from 3 in-plane arched surface section of cylinders shapes on 3 separate vertical load axis and as such the shape or contour of the joint cut surfaces (of the pieces) of all structural wood beams are trapezoidal in shape. The overall shape or contour of the interior space is defined by the 3 arched curves, each floor's horizontal plane and the vertical planes on the North and South sides. Therefor the East and West sides of the structure is oval shaped while the North and South sides are parallel vertical planes. [Figure 3 to 6]



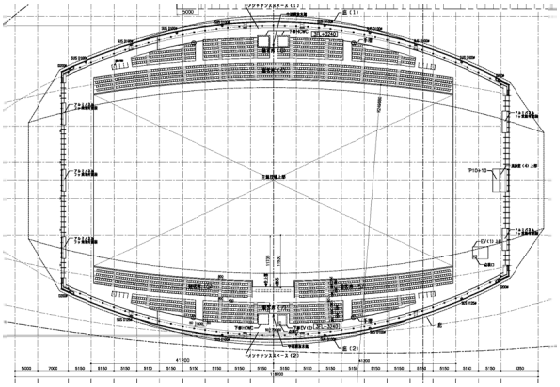


Figure 3: Overall Plan View of Complex, Figure 4: 2F Plan view of Main Stadium

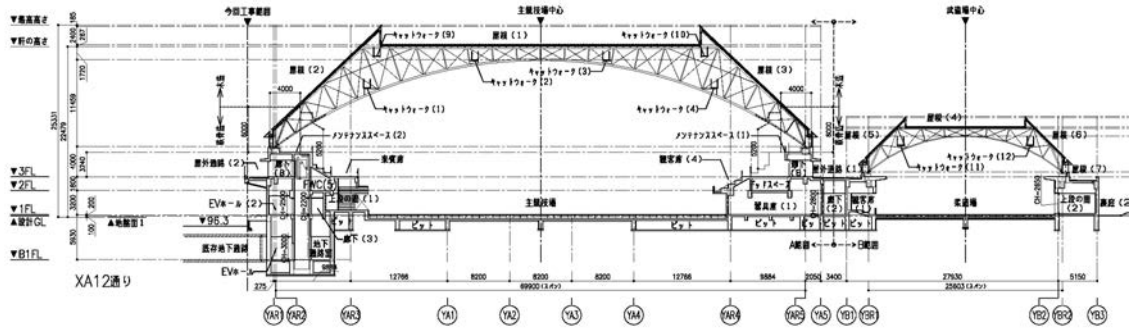


Figure 5: Cross Section details of East-West orientation

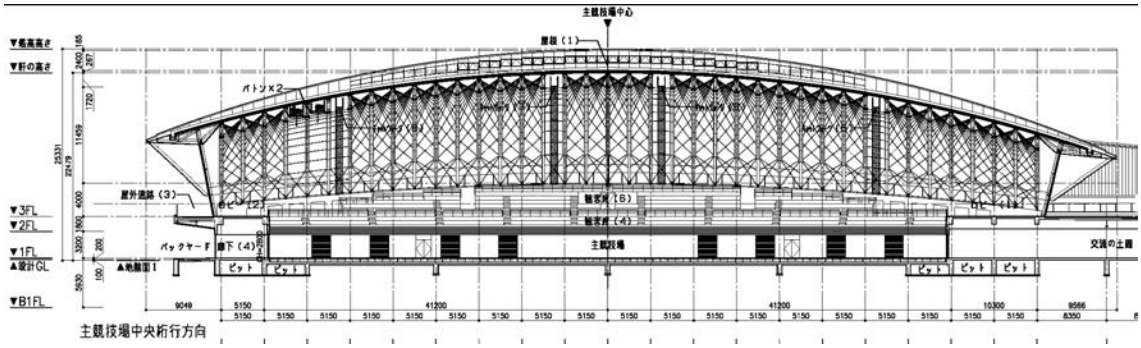


Figure 6: Cross Section of Main Stadium – North-South orientation

In keeping with the project owner's (Prefecture of Oita) wishes and request to utilize as much Sugi lumber produced in Oita as possible and the fact that there are no Glue-Lam manufacturers in the Prefecture and its vicinity, the decision to design and construct the structure strictly with locally available structural Sugi lumber products was made. Detailed discussions were held with the Oita Prefecture's Wood Products Cooperative (Association) in order to determine the type and sizes of structural lumber to be utilized for the project. 120mm thick x 240mm wide x 4,000mm long Solid Structural Sugi Lumber was determined to be the most desirable and most readily available lumber for the project. Larger lumber sizes were found to be difficult, requiring longer lead times, higher costs due to limitations of the diameter of standing trees in the forests, extraction from the forest and materials recovery rates at local sawmills. Although the widely accepted design value (MOE) for Japanese Sugi is E-70, for commercial purposes, it was desirable to keep the application of E-70 rated Sugi to less than 1/3 of the total needed volume for similar cross section sized lumber. Additionally, as the final application of the local Sugi was for constructing large span structural assemblies, it was critical to stabilize the materials dimensionally through proper drying process. At the same time, drying Sugi is difficult and risk effecting "case hardening" or "inner checking" in the product if dried excessively or at a high drying rate. In order to minimize these undesirable results (which are difficult to detect visually) it was decided that Sugi Lumber with 15% M.C. would be used for the bottom chords members (of the truss assembly) which is critical in terms of deformation and Sugi Lumber with M.C. over 20% would be used for other components. After considering the local structural materials production make up and volumes, it was decided that the design and construction of the arched roof truss assemblies would be based on two solid structural lumber cross sections sizes: 120mm thick x 240mm wide and 105mm x 105mm squares.

Due to the overall size of the structure, it must meet the Fireproof Structures guidelines. In order to expose the wood frame of the roof structure for design and eye appeal purposes, the components and roof structure was evaluated under the Fireproof Performance Evaluation Process (Route-C) and

secured a Ministerial Approval/Certification. As fire started on the East-West oriented viewers seating area floor level would raise the temperature high enough to ignite the Wooden Arched Truss structure, the seating area structure was designed and constructed in steel.

3. The Fabrication of the large open space structure with small to medium size lumber

In order to design an unsupported open space structure measuring 70m x 100m with 120mm thick x 240mm wide x 4,000mm long lumber rated at MOE M-50, special design with an eye towards effective and commercially viable fabrication process and format and points of joints have to be considered in earnest. To start with, considerations were given to where and how best to transfer the vertical loads to the lower level of the structure. The North and South ends of the structure incorporated a Glazed Curtain Wall which precluded the placement of heavy and voluminous sub-structures. As the overall unsupported span of the roof on the North-South orientation measured 100m, it was decided to anchor the span behind the viewers seating area in an East-West direction making the overall maximum span a more manageable 70m. Next, as we were restricted to use only relatively short and standard sawn lumber sizes to construct the large span, the basic design chosen was a Planar Arched Truss structure. The main reason behind choosing the Planar Truss Design as opposed to a Three Dimensional Truss Design is the fact that as the configurations of the components at each Joint would become excessively complex and voluminous as the span length changes from truss position to truss position. The design and construction process of the Arched Trusses were as follows.

1) Apply the components that carry the vertical loads on an Arched Form.

2) When horizontal loads are applied to the components of the arched structure, inverse moments are distributed along the center axis of the span; arched components become the bottom chord and the trusses are spaced according to the degree (size) of the bearing moment. [Figure 7 and 8]

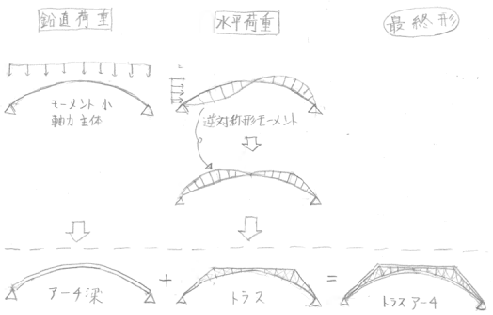
3) At each Truss position, Sawn Sugi Lumber components are jointed lengthwise to create an Arch. It is more efficient to make the Arch form in a quadratic curve but by doing so, the angles of each joint varies throughout the curve making the fabrication process excessively difficult and cumbersome. A circular curvilinear line was chosen as the base line for the Arch. By fixing the rise to span ratio at 1:6 the central angle of the circular arch are the same for all components.

4) In order to make all the cut angles for all the joints of the different spans per grid line the same, the fracture line of the circular geometric shape of the bottom chord was chosen as the central angle in a radial direction for each diffraction point. [Figure 9] Additionally, the angle and position of the bundled (BUB) components were also made the same and as such the basic framework evolved.

5) As the diagonal bracings required in each of the trapezoidal cells in the fundamental frame needed to be longer than 4 m, Tensile Stresses Steel Rods were employed on an cross bracing pattern instead of Lumber and relied strictly on Tension loading to stabilize the assembly.

6) The Arched Trusses were spaced at 2,575mm on center and in order to prevent sideways buckling of the Upper Chord and to insure sufficient horizontal plane strength (diaphragm) of the entire roof structure, strapping was secured perpendicular to the direction of the trusses at 910mm on center spacing and covered with a layer of structural plywood.

7) In order to support 9m outward cantilevered portion of the roof over a large Glazed Curtain Wall at each of the structure, Cantilevered Steel Trusses anchored by Steel Marion Columns were chosen.



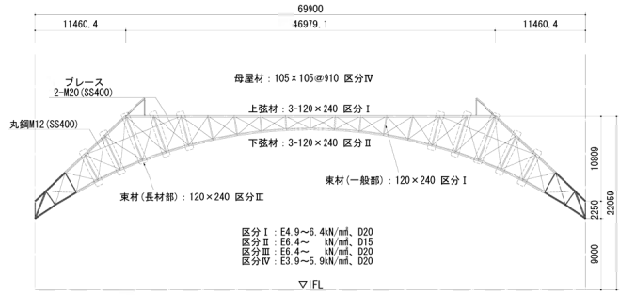


Figure 7: Process of developing the basic Arched Truss Design, Figure 8: Structural Frame Drawings of the Arched Truss

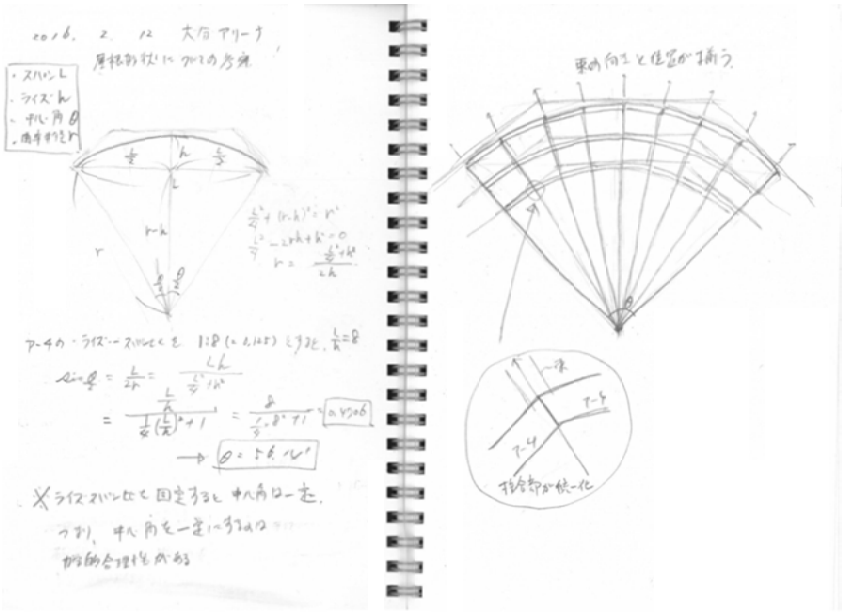


Figure 9: Sorting process for streamlining the mechanical aspects of the joints for the Arched form

4. Planning the ordonnance of the materials

As described in (2), the basic plan for the design of the Arched Truss was completed but we next had to plan the most effective way to utilize the relatively short standard sawn lumber to fabricate the parts and assemble the trusses. We needed to come up with a plan to simplify the joint details vis-à-vis the composition of the materials. We narrowed the lumber cross sectional sizes of the lumber to be utilized to only two sizes (120mm thick x 240mm wide and 105mm x 105mm squares) in an effort to minimize loss and ease of production.

Along with the streamlining of the fabrication process, two challenges were identified. The first issue was how to solve the buckling restrain generated from the relatively high compression loads placed on the Bottom Chords of the Arched Trusses. The lumber pieces selected were 120 thick by 240mm wide Sugi pieces. Each by themselves were not capable to withstand the compression forces that would bear on them so 3 pieces were bundled together but if all 3 pieces were oriented the same way, there was risk for it to buckle along its weakest direction. The second issue that we needed to address was the stress problems at the joints between the bundled bottom chord components and the stainless steel rods. Although we solved the issue of cut angles and partitioning of materials by making all cut angles the same, the angles of the stainless steel rods remained all different. In order to at least ease or

facilitate the fabrication and assembly process the following efforts were implemented. [Figure 10 and 11]

1) In order to minimize the difference in performance in the strong and weak axis of the vertical chord components, 3 pieces of 120mm thick by 240mm wide Sugi pieces were bundled in an "H" pattern and used as the basic shape for all the vertical chord pieces. Single pieces at 120mm thick by 240mm wide were employed in radial direction to tie the top and bottom hanging pieces. With this bundled components, the buckling at the diffraction junctures of the bottom chord were secured. In order to satisfy the horizontal buckling effects of the vertical chord pieces, the abutting bundled components were cross-braced with metal rods.

2) An excessive number of bolts would have been required if we employed bolts and steel place connector systems to direct the compression loads from the top and bottom chord pieces, we relied on the bearing capacity of the wooden components where they joined surface to surface to reduce the number of bolts to a more manageable number.

3) In a similar manner, in order to deal effectively with the differing angles of the steel rod bracing pieces, Flat (steel) Bars welded at the end of the Steel Rods were used enabling the connection of each steel rod with a single high tension stressed bolt. From this single high tension stresses bolt, load forces were distributed through the Flat Steel Bars installed in the Chords to the bundled components and the distributed onto the Chords themselves through the bolts holding the connection in place.

4) Metal Pins and Metal Bolts are the most common components used for joining lumber components but in order to prioritize the surface to surface pressure effect, metal bolts were chosen for connecting the joints.

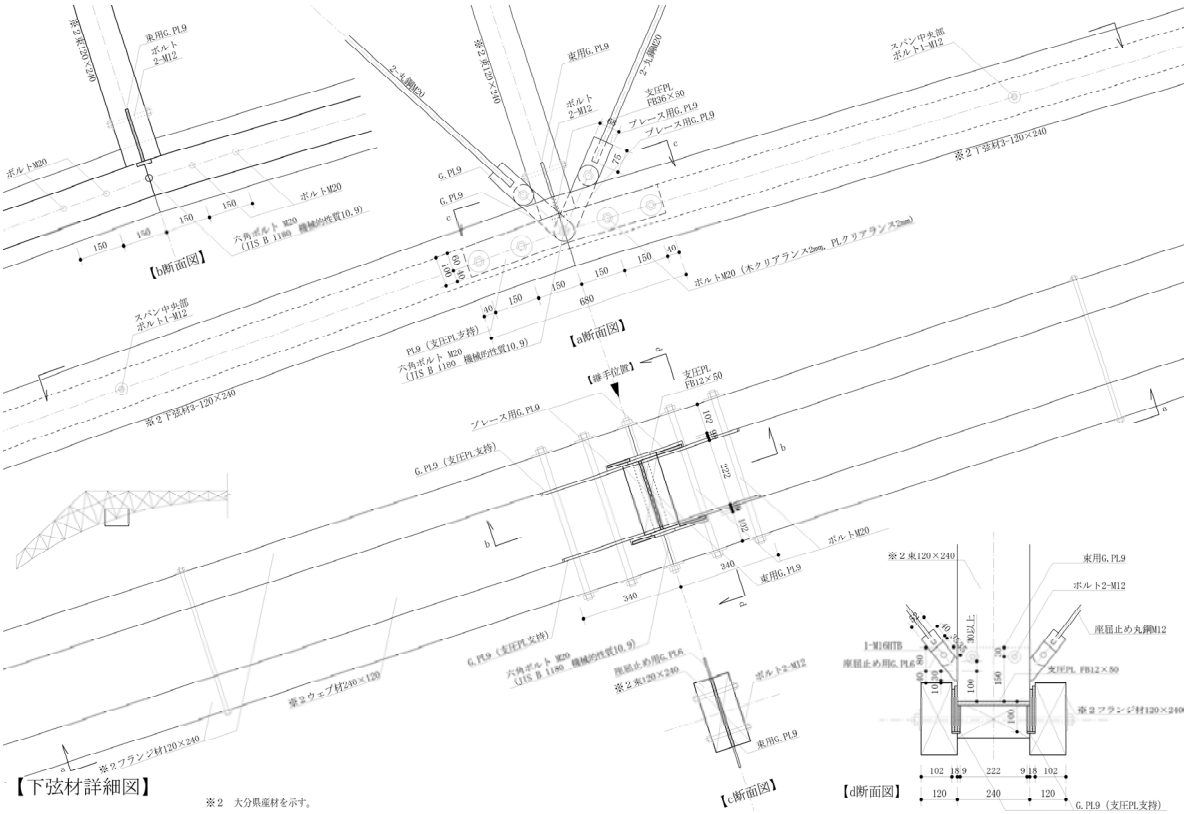


Figure 10: Details of the Bundled Bracing with Steel Plates and Rods



Figure 11: Close-up details of the Joints used for the Trusses in the Main Stadium

5. Construction

In an effort to maximize and improve the communication and sharing of critical information between the Owner, Contractor and the Designer, project status review meetings were held once every 2 weeks after the start of construction on site. Meetings related to the connection joints were held in separate meetings where aspects of ease of assembly and speed, accuracy and quality of the wood surface to surface connection cuts and bolt-hole clearance sizes were minutely discussed and investigated in order to find the best solutions. [Figure 12] Additionally, we tested the effect of the wood drying (Shrinkage) on the metal connector plates and used these results to fabricate two full size mock-ups and used them for evaluating the assembly and installation issues. [Figure 13] We relied on the BIM Software Tekla Structures to produce the working drawings for pre-cutting the wood components and the steel plates.

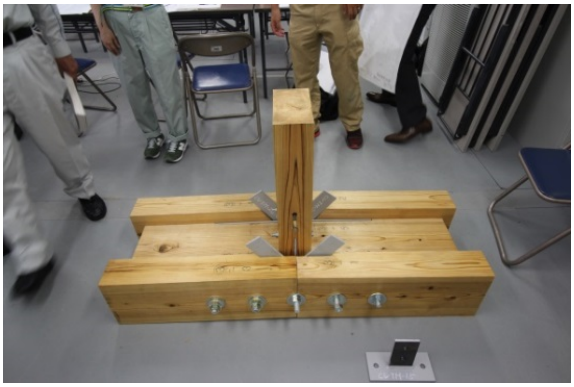


Figure 12: Cut Sample model of the Joint Assembly,



Figure 13: Full size Mock Up (of the Truss Assembly)

In order to insure the transfer of lateral seismic loads from the roof directly to the anchor points behind the viewer seating area, two layers of 24mm thick structural plywood panels were used to insure sufficient horizontal plane stiffness (Diaphragm Stiffness) We relied on the Rhinoceros 3D Modeling Software to produce digital mock ups of the plywood panels that have to be applied to the oval shaped frame structure. The digital information from the mock-up were fed to an automatic panel cutter to pre-cut the plywood panels. As there were concerns regarding the installation of 24mm thick structural plywood panels to an oval shaped frame, tests were conducted to assess the issues and difficulties around shaping the thick plywood panels to a curved frame. [Figure 14 and 15]



Figure 14: Testing the installation of plywood panels,



Figure 15: Installation of structural plywood panels on the roof surface

We employed a 7 stage Jack-Down process at 6mm per stage to lower the Arched Truss Assemblies in place with the final settling flex or deflection measured at roughly 1 to 5 cm. [Figure 16 and 17] In order to estimate the settling and maximum deformation after installation, we created an analytical model taking into consideration the degree of elastic deformation, gaps in the surface to surface joints and degree of shrinkage due to drying of the wood. The analytical model shows that a maximum of 12cm would occur in time and as such degree of deflection on the structure is monitored on continuous basis.



Figure 16: Installation,

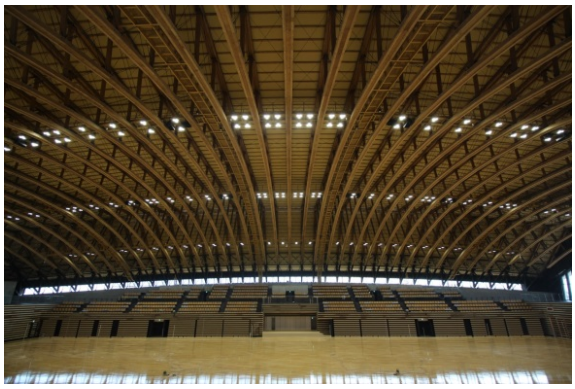


Figure 17: Interior of the Main Stadium

Acknowledgements

The authors acknowledge the valuable contribution from all the people who has involved in this project and of course to my family.

References

[1] N. Yamada, "Structural Design Plans for the Roof Structure over the Oita Prefecture's Multipurpose Martial Arts Sports Centre.es," *Journal of Timber Engineering*, vol. 32 No.2.

Proceedings of the IASS Annual Symposium 2019 – Structural Membranes 2019
Form and Force
7 – 10 October 2019, Barcelona, Spain
C. Lázaro, K.-U. Bletzinger, E. Oñate (eds.)

Structural Design of Gridshells aiming at Lightweight Design and Rapid Assembly

Philip F. YUAN*, Jinxi JIN[a], Li HAN[b], Hua CHAI[c]

**Tongji University
No. 1239 Siping Rd, Tongji University, Yangpu District, Shanghai, China
philipyuan007@tongji.edu.cn

[a] jinjess@tongji.edu.cn
[b] 1810137@tongji.edu.cn
[c] chaihua@tongji.edu.cn

Abstract

Taking Venue B for 2018 World AI Conference as an example, this paper introduces structural design of gridshells aiming at lightweight design and rapid assembly. Steel-timber composite gridshell covers courtyard space in the project. Based on the feedback information of digital visual model, structural design is carried out under interaction between architect and structural engineer to meet the need of lightweight design and rapid assembly. Finally, the span of main gridshell reaches 40 meters, which realizes lightweight and transparent space. The 2000 m^2 double-curved roof was prefabricated and assembled within 2 months. The paper introduces innovative structural design of gridshells and provide a useful reference for large-span steel-wood structures.

Keywords: gridshells, lightweight design, rapid assembly, digital design, steel-wood composite design.

1. Introduction

Located in West Bund in Shanghai, Venue B for 2018 World AI Conference is built to meet the need of meeting space for 2018 World AI Conference. The design and construction should be realized in 100 days, so the whole building is realized by lightweight prefabrication system and rapid on-site construction. The rectangular conference halls are three modular light aluminum bent structure, which enclose two countyards. The courtyards are covered by lightweight steel-timber composite gridshell.

This paper introduces structural design of gridshells in Venue B, which aims at lightweight design and rapid assembly. Lightweight means a light weight structure that achieves high efficiency with less material and efficient structural system. Meanwhile, it also refers to lightweight space quality and atmosphere, which shows free and open attitude the building took towards the riverside environment and the urban public (figure 1). The structural design also aims at rapid assembly, which reflects the comprehensive cognition of construction problems, the accurate grasp of problems and the realization of specific strategies.

Copyright © 2019 by Philip F. YUAN, Jinxi JIN, Li HAN, Hua CHAI
Published by the International Association for Shell and Spatial Structures (IASS) with permission.



Figure1: Steel-timber gridshell of Vunue B for 2018 World AI Conference, Shanghai

2. Structural Design

2.1. Relationship between roof system and supporting system

The courtyards are spatially limited to the triangular space defined by three rectangular meeting spaces. The gridshells need to be coordinated with the the meeting area and riverside environment in terms of form and space, also be adapt to the column system of bent structure on both sides. Using plug-in kangaroo, gridshells can achieve structurally optimized surface under different boundary conditions. Consider the relationship with the surroundings, roof system and supporting system are separated to realize form-finding, which result in a harmonious roof (figure 2). However, the contradiction between form and structure is reflected in the following aspects. Firstly, supporting system cannot balance the horizontal thrust of roof system. Secondly, the height of gridshell is small, which is conducive to the realization of the overall lightweight form, but not conducive to the three-dimensional structure effect.

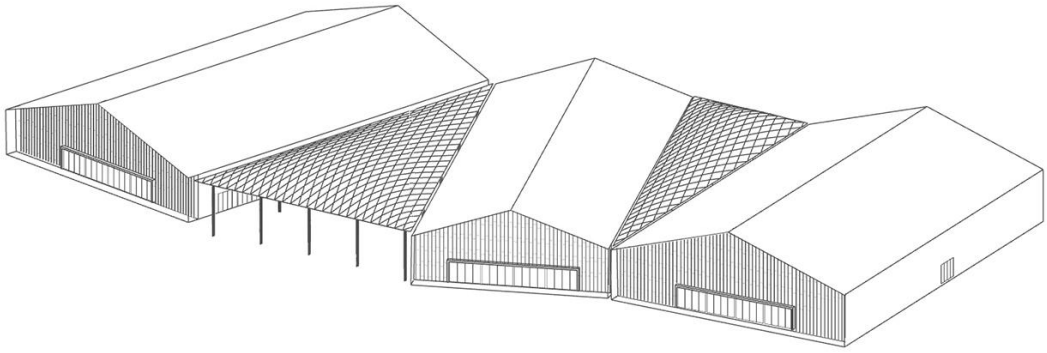


Figure2: The relationship between retangular bent structure and triangle gridshell

Steel-wood composite design is a common design strategy to improve the performance of wood structures. Composite material can resolve the contradiction between structure and form, and the contradiction between roof system and support system. Beam string structure is an ideal solution to improve structural performance of gridshells. It can not only balance the horizontal thrust of the gridshell, but also reduce the cross-section of components and improve stiffness and stability. The shortcoming of the beam string structure is that it sacrifices the net height of space. After the comparison of different beam string structure, the steel strings are finally arranged at three corners. The steel truss in the outer ring and steel string at three corners are used as structural constraints to achieve balance of horizontal thrust. The wood beams corresponding to steel strings are replaced by steel beams.

2.2. Componenent design

The triangular mesh and diamond mesh are common to fit the surface.The triangular mesh has good overall structural performance. But the rigidity and construction of joints are difficult to realize. Also space permeability is bad. The structure efficiency of diamond mesh is lower with longer force transmission route, but the space under diamond mesh is transparent, the joint is simpler and material saving is realized. Considering the requirements of lightweight design and rapid assembly, diamond mesh is used to achieve the gridshell.

The gridshell can be fitted with different components. Full length glulam curved beams can achieve higher joint stiffness, but its processing and construction is complex and time-consuming. Decomposing the gridshell into small components at the joint avoids the problem of time-consuming processing, but the stiffness of joint is weakened, types of components and joints are increased. By contrast, the staggered beams can realize semi-rigid joint connection, optimize the number of components and reduce construction difficulty.

In order to further improve the overall performance of gridshells, steel beams are used near the steel trusses in the outer ring and steel string at three corners. At the same time, short wood beams are added in the middle of the gridshell to enhance the structural integrity, further emphasize the center space. The structural model can be established after component design (figure 3).

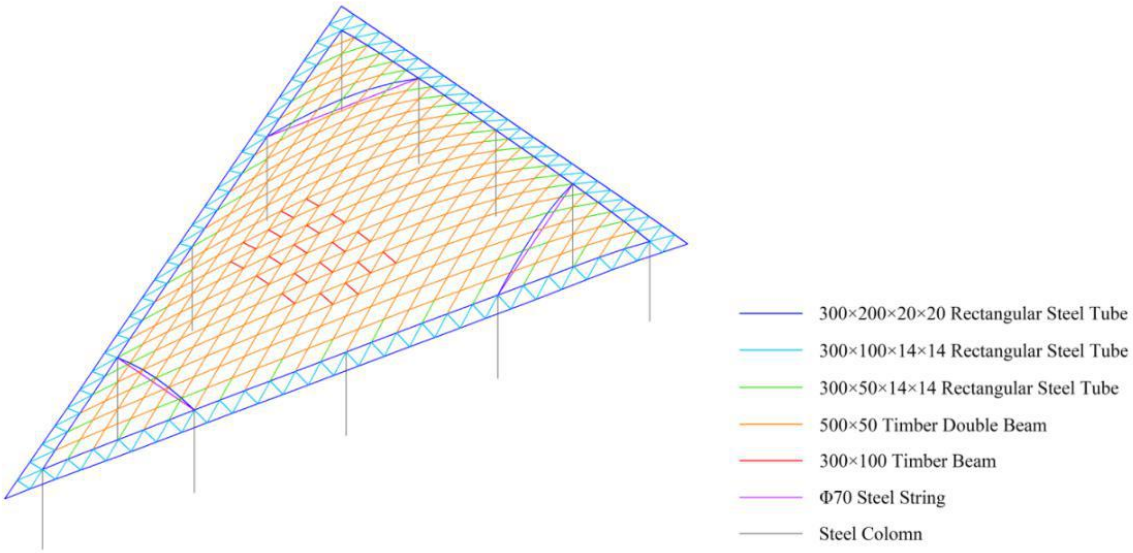


Figure3: Structural Model

The structural analysis is carried out at two levels. The initial structural analysis is carried out in Millipede in Rhino platform. In the process of optimizing the materials and distribution of components, the structural performance of gridshells are improved in different degrees in Millipede. It is an intuitive and synchronous analysis platform, which can effectively connect geometric parameters and structural parameters. What's more, expert analysis was conducted in SAP2000, a general finite element software. The data in SAP 2000 is used to determine the ultimate structural reliability. Consider the staggered beam, the joints are rigidly connected on one side and hinged on the other side. The structural analysis of the steel-wood gridshell was analyzed detailedly (figure 4).

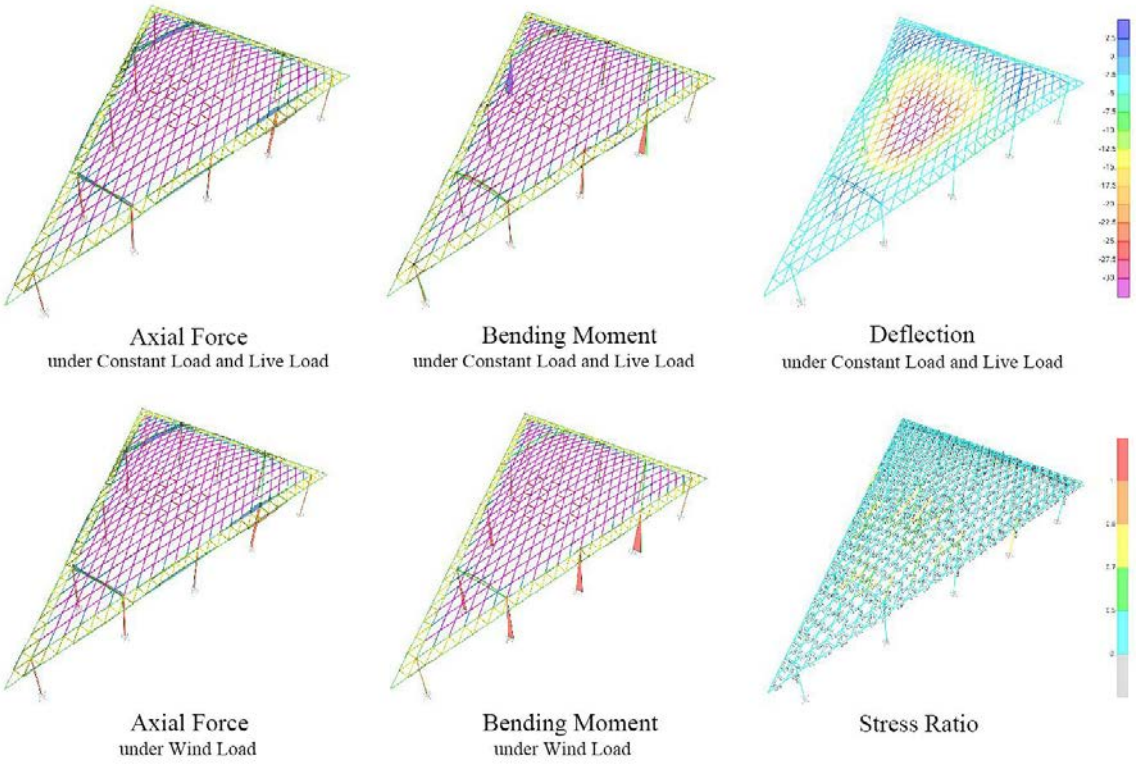


Figure4: Structural Analysis in SAP2000

2.3. Detailed design

Considering reducing the material, improving joint stiffness and eliminating assembly error, the gridshell is further optimized. Use straight beam to fit surface and optimize the single beam into vertical hollow double beam with a thickness of 50mm (figure 5). The straight beam enhances the staggered rhythm of the gridshell. At the same time, the joints are concealed well. Hollow double beams greatly reduce the weight of the roof and strengthen the light floating sensation of the roof. Timber beams are connected by bolt and self-tapping screw. The joint takes into account structural and construction factors, such as installation speed, construction accuracy and good structural rigidity.

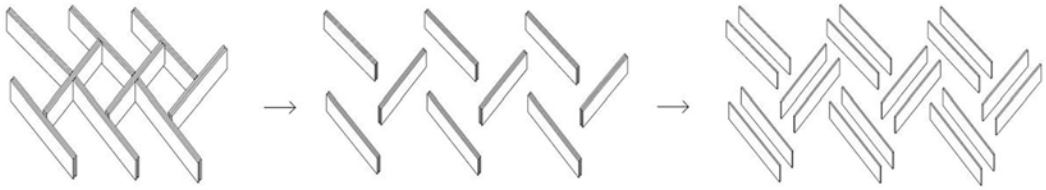


Figure5: Use the straight beam and vertical hollow double beam to fit gridshell surface

3. Prefabricated Construction

3.1 Factory processing

One problem caused by free-form gridshell is that the components are not standardized, the geometric information of 562 wood beams is inconsistent. The design data and construction data are efficiently connected through digital model. Construction-oriented optimization is considered in the design process, such as fitting curved surface with linear component, using bolt and self-tapping screw as

connection. The geometry of wood beam is relatively simple, which can be rapidly processed (figure 6).



Figure6: After construction-oriented optimization, the geometry of wood beam is relatively simple

3.2 On-site Assembly

On-site assembly was based on the 3D model information. Firstly steel columns, steel trusses and steel beams are installed. Then the assembly of wood beam is carried out. Considering the difficulty of assembling staggered wood beams, full scaffold is set up for installation as the operating platform and positioning reference grid. The total station instrument is used for measure and adjustment of construction errors (figure 7).

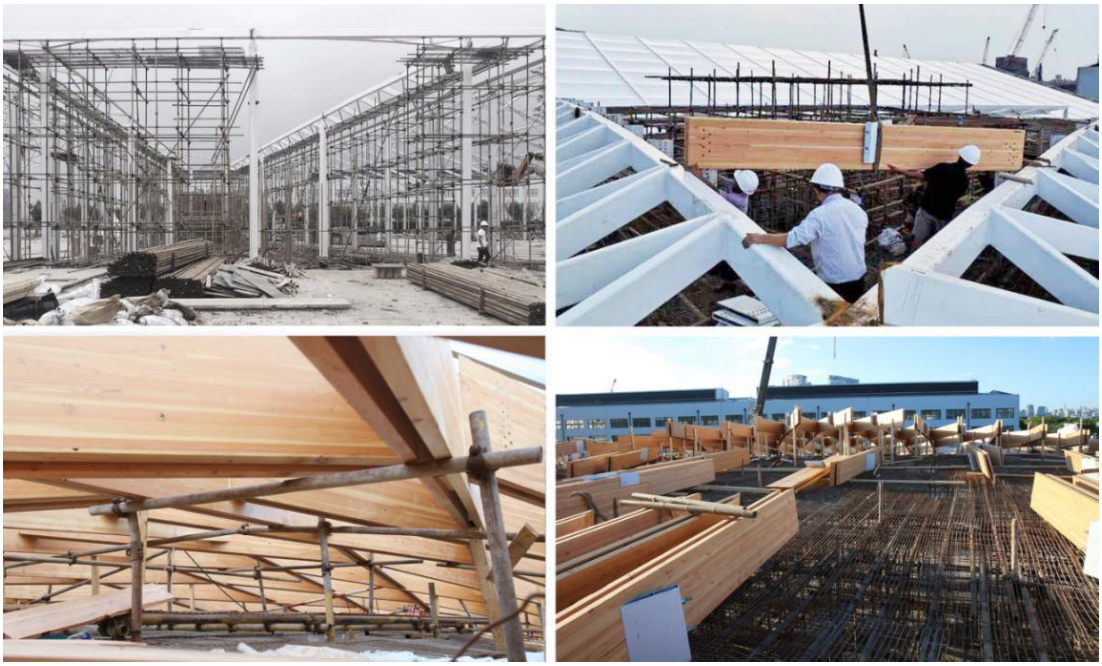


Figure7: On-site assembly

Reasonable design greatly improves the assembly speed and precision of gridshells. Lightweight single wood beam can be carried by 3-4 workers. The components reach a higher degree of installation before lifting and overall combination, which speeds up the installation process. The self-tapping screws perforate wood beam after overall positioning, which realizes rapidly assembly and error adjust (figure 8). The steel strings are tensioned after the installation of the whole structure. Then unloaded the whole structure to realize the final shape.

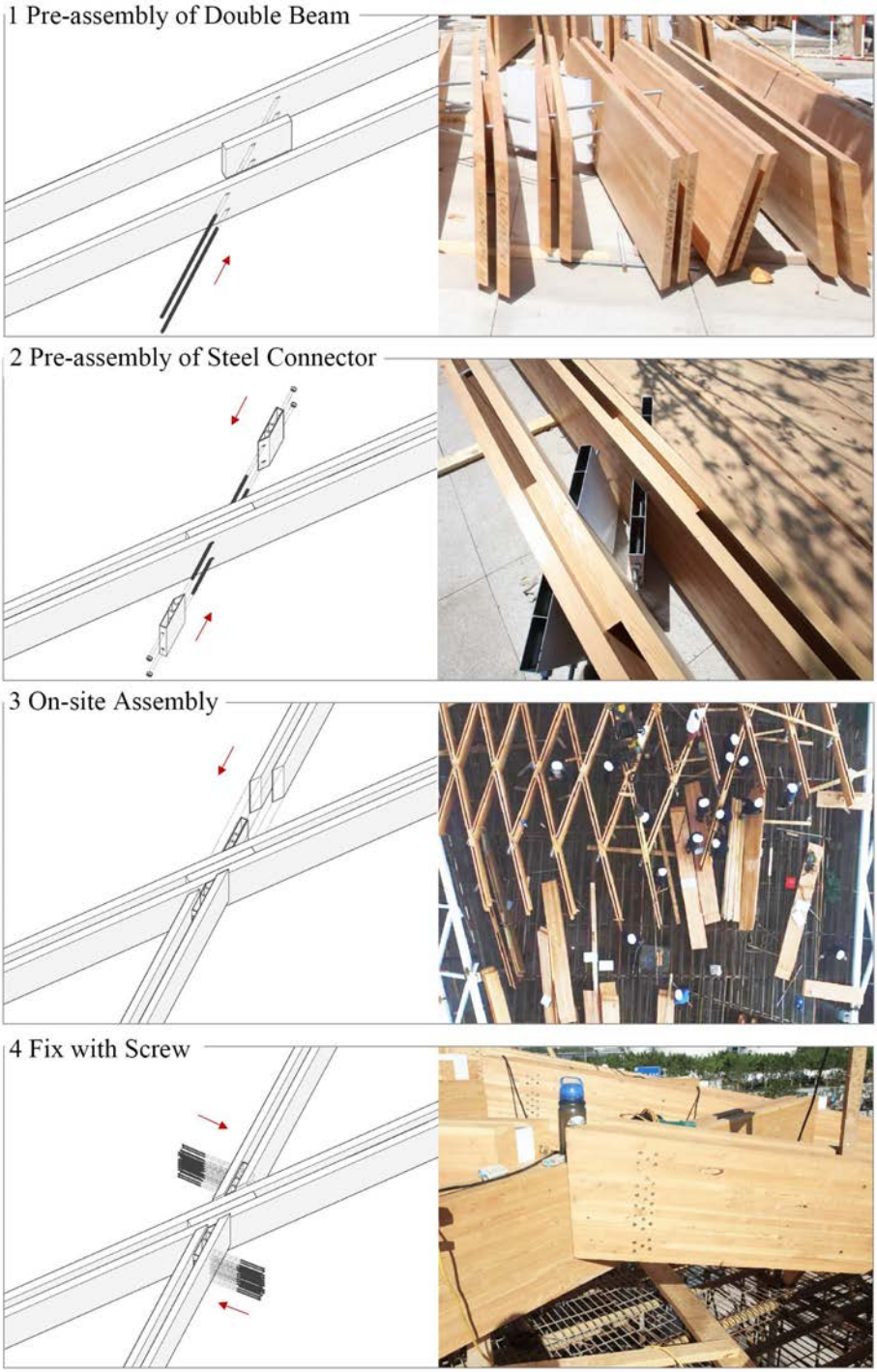
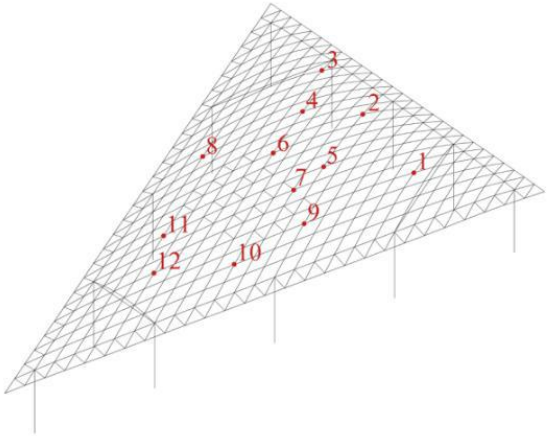


Figure8: the Assemble Process of Gridshell

3.2 Reflection

In the assembly process of wood gridshell, different points in the structure were selected to monitoring the deformation of structural. Height before unloading, height after unloading was monitored and recorded. In the unloading process , the maximum variation of the height difference reached 125mm in the selected point positions, which is much higher than the calculated value. It can be seen that the installation height of the structure did not reach the design height, and the maximum difference in the

selected point positions was about 200mm (figure 9). The main reason is that the joint opening of the timber beam is too large. There's still a large gap between wood beam and bolt after the bolt was inserts into the joint. The component be compressed and force be exerted after structural deformation. That is the mainly reason why the structural height is lower than the design height, which needs to be improved in the future.



Point	Design Height/mm	Height before Unloading/mm	Height after Unloading/mm	Height Difference/mm
1	1867	1830	1820	10
2	2224	2195	2171	24
3	1523	1500	1478	22
4	2676	2570	2490	80
5	2852	2805	2680	125
6	2885	2780	2680	100
7	2710	2650	2540	110
8	2073	1980	1975	5
9	2014	2014	1980	34
10	1467	1415	1390	25
11	1663	1663	1630	33
12	1497	1475	1420	55

Figure9: Deformation Monitor of Gridshell

4. Conclusion

Finally, the construction of 2000m^2 hyperboloid gridshell roof was completed within two months, including one month for prefabrication and one month for on-site assembly. Coherent form and rich space of a gridshell are achieved in a balance of complex forces. The overall form present a complete atmosphere and unique simplicity. As a structural design aiming at lightweight design and rapidly assembly, it provides a beneficial reference for the innovative practice of lightweight steel-wood composite structure and plays a leading role in promoting ecological timber structure in large-span architecture (figure 9).

The practice makes us further thinking the changes digital tools have brought to the workflow of structural design and architectural design. Based on the feedback information of digital visual model, structural design is carried out under interaction between architect and structural engineer. Innovative structural design is completed in this process, which is based on material, mechanics and construction and unifies form and structure. The innovation edge of the construction practice is pushed to a broader field under new tools, and the traditional binary logic of design and construction will be rewritten.

Acknowledgements

This research is funded by the National Natural Science Foundation of China (Grant No.51578378), the Special Funds for State Key R&D Program during the 13th Five-year Plan Period of China (Grant No.2016YFC0702104), the Sino-German Center Research Program (Grant No.GZ1162), and Science and Technology Commission of Shanghai Municipality (Grant No.16dz1206502, GrantNo.16dz2250500,GrantNo.17dz1203405,GrantNo.18dz1205604).

References

[1] J. HOU. "Research on Modern Steel-wood Composite Structure Design," Nanjing: Southeast University, 2006.

[2] K. LIU. "The Tectonic Research on Modern Large-span Wood Structure Achitecture." Nanjing: Southwest Jiaotong University, 2012.

[3] L. MA. "Research on Construction Process of Contemporary Architecture Based on Cocurrent Engineering." Tianjin: Tianjin University, 2016.

[4] A. PICON. "Architecture and the Virtual: Towards a New Materiality." Praxis, 2011(6), pp. 101-111.

[5] F. QIAN, Z. YU, and S.TANG. "Practing the Design of Natatoriums with Timber-Steel Tensile Shell Structure - A Case Study of Natatorium of Chongming." Architectural Journal ,2017(11). pp 48-51.

[6] Y. ZHANG. "Architectural design under the guidance of intelligent construction", in Learning, Prototyping and Adapting: Proceedings of CAADDRIA 2018, Beijing, China, May 16-19, 2018, China Architecture & Building Press, 2018. pp. 418-422.

[7] A. Sigrid, B. Philippe, V. Diederik, et al. "Shell structures for archi- tecture: form finding and optimization." Routledge, London and New York.2014.

[8] F.YUAN. "Research on Digital Structural Performance Morphologies." Journal of Human Settlement in West China, 2014, pp 6-12.

[9] Y. ZHANG. 2018, "Architectural design under the guidance of intelligent construction." proceedings of CAADRIA 2018, pp 418-422.

Proceedings of the IASS Annual Symposium 2019 – Structural Membranes 2019
Form and Force
7 – 10 October 2019, Barcelona, Spain
C. Lázaro, K.-U. Bletzinger, E. Oñate (eds.)

Application of continuous column concept to morphogenesis of super-high-rise building and large spatial stadium

Hiroyuki TAGAWA, Misaki OKADA*, Seika FUJIWARA, Noritoshi SUGIURA

*Mukogawa Women's University
1-13 Tozaki-cho, Nishinomiya, Hyogo, 663-8121, JAPAN
tagawa@mukogawa-u.ac.jp

Abstract

Application of the continuous column concept to morphogenesis of super-high-rise building and large spatial structure is investigated in this study. The continuous column effect is defined as the phenomenon in which, as the flexural stiffness of continuous columns or walls in multistory building increases, drift distribution over structural height becomes more uniform when subjected to earthquake ground motions. In the past research, in order to evaluate the continuous column effects in various framing types quantitatively, inelastic dynamic time-history analyses were carried out for the coupled shear-flexural-beam model, in which lumped mass and spring model is connected to continuous column. Recently, this continuous column concept is applied to the design proposal of a super-high-rise building. Here, many partially-continuous columns are installed to provide the structural continuity, flexibility of floor planning and asymmetric overall configuration. Also, the continuous column concept is applied to the design proposal of large spatial structure. This stadium consists of continuous columns, wooden moment-resisting frames, and membrane roof. In ordinal times, continuous columns support membrane roof. At earthquakes, continuous columns are expected to exert continuous column effects to mitigate the drift concentration in the wooden moment-resisting frames.

Keywords: conceptual design, morphogenesis, continuous column concept, castle tower, five-story pagoda, super-high-rise building, large spatial stadium, seismic response

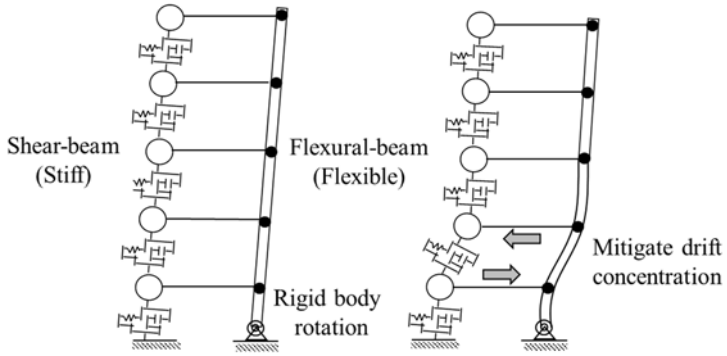
1. Introduction

Elastic columns and walls that are continuous over structural height are likely to mitigate the drift concentration in particular stories, prevent a weak-story collapse mechanism, and thus increase the stability of an entire structure when a multi-story building structure is subjected to earthquake ground motion. This is well known as the continuous column (C.C.) concept [e.g. 1] or the C.C. effects [e.g. 2]. Many modern and traditional architecture have the C.C. For example, wooden five-story pagodas in Japan have "shinhashira", which is located at the center and continuous over the height. It is well known that none of five-story pagodas have never been collapsed even though suffered many large earthquakes. One of many hypotheses is that the "shinhashira" functions as "kannuki", bolt or spring-back in English, and prevents a weak-story collapse mechanism, which is similar to the C.C. effects. Also, the "shinhashira", which is suspended, is believed to play a role of a pendulum, which provides positive restoring force. In this paper, the C.C. concept is briefly explained and the formulation of the coupled shear-flexural-beam models are described. Various ways of the C.C. observed in Japanese traditional architecture such as wooden five-story pagodas and castle towers are described. Seismic control effects of these C.C., which is either fixed or pin-supported at the base or suspended from the top, are investigated through nonlinear dynamic analysis. Finally, examples of application of the C.C. concept to the morphogenesis of a super-high-rise building and a large space stadium are introduced.

Copyright © 2019 by Hiroyuki TAGAWA, Misaki OKADA, Seika FUJIWARA, Noritoshi SUGIURA
Published by the International Association for Shell and Spatial Structures (IASS) with permission.

2. Continuous column effect

The continuous column concept is explained using the coupled shear-flexural-beam model as shown in Figure 1. It is assumed that the stiffness of the shear-beam is assigned so that drift distribution is uniform for design level of external forces and the flexural-beam is supported with pin connection to the ground. When the shear-beam is elastic, it deforms with almost linear distribution over structural height as illustrated in Figure 1(a). In this case, the flexural-beam, which follows to deformation of the shear-beam, rotates as a rigid body around the pin connection and the resistance of the flexural-beam is minimal. However, as the horizontal external forces increase and a particular story in the shear-beam starts to yield and deforms in an inelastic manner, the flexural-beam provides the shear-beam with the resistance to push buck such inelastic deformation occurred in a particular story as illustrated in Figure 1(b). In this mechanism, the flexural-beam mitigates drift concentration occurred in a particular story and prevent a weak-story collapse mechanism.

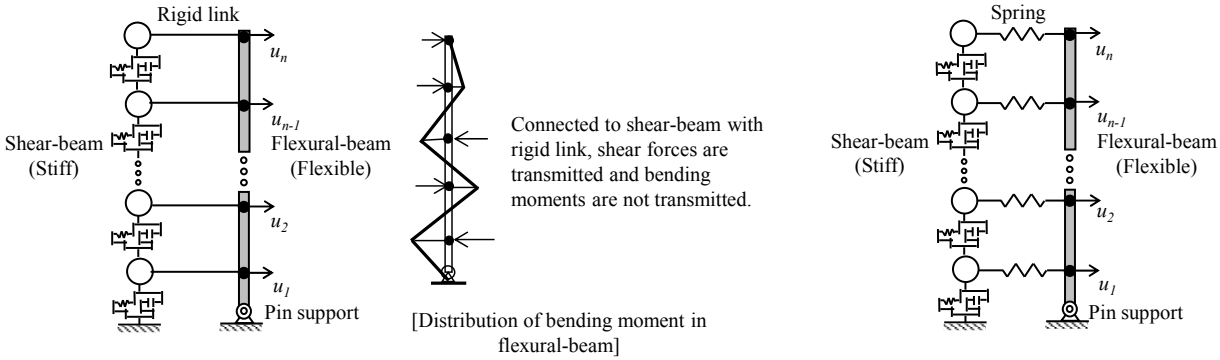


(a) Elastic behavior (b) Inelastic behavior

Figure 1: Continuous column effects in coupled shear-flexural-beam model

3. Mathematical formulation of coupled shear-flexural-beam models

The coupled shear-flexural-beam model and coupled shear-flexural-beam model with spring element as illustrated in Figure 2 are used to evaluate the C.C. effects quantitatively. In the coupled shear-flexural-beam model, shear-beam and flexural-beam are connected with perfectly-rigid link as show in Figure 2(a) and the displacements of the shear-beam and flexural-beam (continuous column) are identical. In contrast, in the coupled shear-flexural-beam model with spring element, the shear-beam and flexural-beam are connected with spring element as shown in Figure 2(b), which gives different displacements of the shear-beam and flexural-beam.



(a) Coupled shear-flexural-beam model (b) Copuled shear-flexural-beam model with spring element

Figure 2: Coupled shear-flexural-beam models

3.1 Coupled shear-flexural-beam model

The kinematic equation of motion for the coupled shear-flexural-beam model shown in Figure 2(a) is expressed in Equation (1). Here, **M** is a mass matrix, **C** is a Rayleigh damping matrix, and $\mathbf{K_s}$ and $\mathbf{K_f}$ are stiffness matrixes of the shear-beam and flexural-beam, respectively, and **u** is a relative horizontal displacements of the structure and u_g is a horizontal displacement of the ground.

$$\mathbf{M}\{d\ddot{\mathbf{u}}\} + \mathbf{C}\{d\dot{\mathbf{u}}\} + (\mathbf{K_s} + \mathbf{K_f})\{d\mathbf{u}\} = -\mathbf{M}\mathbf{l}d\ddot{u}_g \tag{1}$$

The stiffness matrix of the shear-beam, $\mathbf{K_s}$, is expressed in Equation (2). Here, k_i is tangent stiffness of a horizontal spring in the i^{th}-story of the shear-beam.

$$\mathbf{K_s} = \begin{bmatrix} k_1+k_2 & -k_2 & 0 & \cdots & 0 \\ -k_2 & k_2+k_3 & \ddots & \ddots & \vdots \\ 0 & \ddots & \ddots & \ddots & 0 \\ \vdots & \ddots & \ddots & k_{n-1}+k_n & -k_n \\ 0 & \cdots & 0 & -k_n & k_n \end{bmatrix} \tag{2}$$

The stiffness matrix of the flexural-beam, $\mathbf{K_f}$, needs to be expressed in terms of the displacement degrees-of-freedom (DOF). Stiffness matrix of the Bernoulli-Euler beam element $\mathbf{k_{BE}}$ is given by Equation (4). EI_f is flexural stiffness and ℓ is an element length equal to the i^{th}-story height, H_i. The global stiffness matrix is obtained by assembling $\mathbf{k_{BE}}$ as in Equation (5) with the finite element assembly operator **A** and rearranged as in Equation (6). Using boundary condition that the moment input at each node is zero, **M**=**O**, and static condensation, $\mathbf{K_f}$ is obtained as in Equation (9). The flexural stiffness ratio of the flexural-beam, α_{cc}, is define as Equation (10). Here, K_i is the initial stiffness of the i^{th}-story spring.

$$\{F_i^a, M_i^a, F_i^b, M_i^b\}^T = \mathbf{k_{BE}}\{u_i^a, \theta_i^a, u_i^b, \theta_i^b\}^T \tag{3}$$

$$\mathbf{k_{BE}} = \frac{EI_f}{\ell^3}\begin{bmatrix} 12 & 6\ell & -12 & 6\ell \\ 6\ell & 4\ell^2 & -6\ell & 2\ell^2 \\ -12 & -6\ell & 12 & -6\ell \\ 6\ell & 2\ell^2 & -6\ell & 4\ell^2 \end{bmatrix} \tag{4}$$

$$\mathbf{K} = \mathop{\mathbf{A}}_{e=1}^{N_{el}}\left[\mathbf{k}_{\mathbf{BE}}^{e}\right] \tag{5}$$

$$\begin{Bmatrix} \mathbf{F} \\ \mathbf{M} \end{Bmatrix} = \begin{bmatrix} \mathbf{K_{uu}} & \mathbf{K_{u\theta}} \\ \mathbf{K_{\theta u}} & \mathbf{K_{\theta\theta}} \end{bmatrix}\begin{Bmatrix} \mathbf{u} \\ \boldsymbol{\theta} \end{Bmatrix} \tag{6}$$

$$\mathbf{M} = \mathbf{O} \;\; \therefore \mathbf{K_{\theta u}}\boldsymbol{\Delta} + \mathbf{K_{\theta\theta}}\boldsymbol{\theta} = \mathbf{O} \;\; \therefore \boldsymbol{\theta} = -\mathbf{K_{\theta\theta}}^{-1}\mathbf{K_{\theta u}}\mathbf{u} \tag{7}$$

$$\mathbf{F} = \mathbf{K_{uu}}\mathbf{u} + \mathbf{K_{u\theta}}\boldsymbol{\theta} = \mathbf{K_{uu}}\mathbf{u} - \mathbf{K_{u\theta}}\mathbf{K_{\theta\theta}}^{-1}\mathbf{K_{\theta u}}\mathbf{u} = \mathbf{K_f}\mathbf{u} \tag{8}$$

$$\mathbf{K_f} = \mathbf{K_{uu}} - \mathbf{K_{u\theta}}\mathbf{K_{\theta\theta}}^{-1}\mathbf{K_{\theta u}} \tag{9}$$

$$\alpha_{cc} = \frac{EI_f / H_i^3}{K_i} \tag{10}$$

3.2 Coupled shear-flexural-beam model with spring element

The kinematic equation of motion for the coupled shear-flexural-beam model with spring element as shown in Figure 2(b) is given by Equation (11). The relative displacements of the shear-beam and flexural-beam are different, which are denoted as $\mathbf{u_s}$ and $\mathbf{u_f}$, respectively. $\mathbf{M_s}$ and $\mathbf{M_f}$ are mass matrices of the shear-beam and flexural-beam, respectively, and $\mathbf{K_s}$, $\mathbf{K_f}$ are stiffness matrices of the shear-beam and flexural-beam, respectively, and $\mathbf{K_l}$ is the stiffness matrix of the spring element, which is given by Equation (12). Here, $k\ell_i$ is the tangent stiffness of the i^{th}-story spring element. When the shear-beam and flexural-beam are separate, $k\ell_i$ is set to zero. In the contact problem, when the shear-beam and flexural-beam become on contact, $k\ell_i$ is set to very large value.

$$\begin{bmatrix} \mathbf{M_s} & \mathbf{O} \\ \mathbf{O} & \mathbf{M_f} \end{bmatrix} \begin{Bmatrix} d\ddot{\mathbf{u}}_\mathbf{s} \\ d\ddot{\mathbf{u}}_\mathbf{f} \end{Bmatrix} + \mathbf{C} \begin{Bmatrix} d\dot{\mathbf{u}}_\mathbf{s} \\ d\dot{\mathbf{u}}_\mathbf{f} \end{Bmatrix} + \begin{bmatrix} \mathbf{K_s} + \mathbf{K_l} & -\mathbf{K_l} \\ -\mathbf{K_l} & \mathbf{K_f} + \mathbf{K_l} \end{bmatrix} \begin{Bmatrix} d\mathbf{u}_\mathbf{s} \\ d\mathbf{u}_\mathbf{f} \end{Bmatrix} = -\mathbf{M}\mathbf{l}d\ddot{u}_g \tag{11}$$

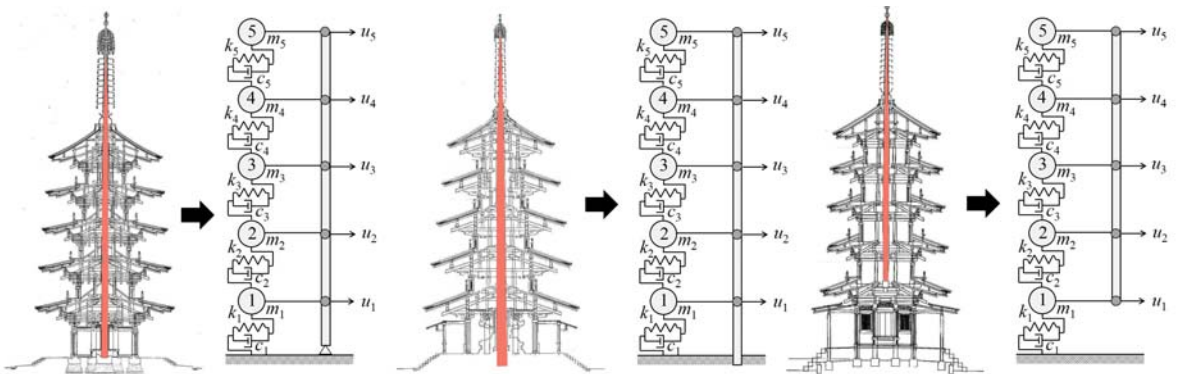
$$\mathbf{K_l} = \begin{bmatrix} kl_1 & 0 & \cdots & \cdots & 0 \\ 0 & kl_2 & \ddots & \ddots & \vdots \\ \vdots & \ddots & \ddots & \ddots & \vdots \\ \vdots & \ddots & \ddots & kl_{n-1} & 0 \\ 0 & \cdots & 0 & 0 & kl_n \end{bmatrix} \tag{12}$$

4. Research on various types of continuous columns

Various types of the arrangement of the C.C. obtained by referring to Japanese traditional architecture such as wooden five-story pagodas and castle towers are investigated through numerical analyses to evaluate these C.C. effects.

4.1 Analysis on continuous column effects inspired by wooden five-story pagodas [3],[4]

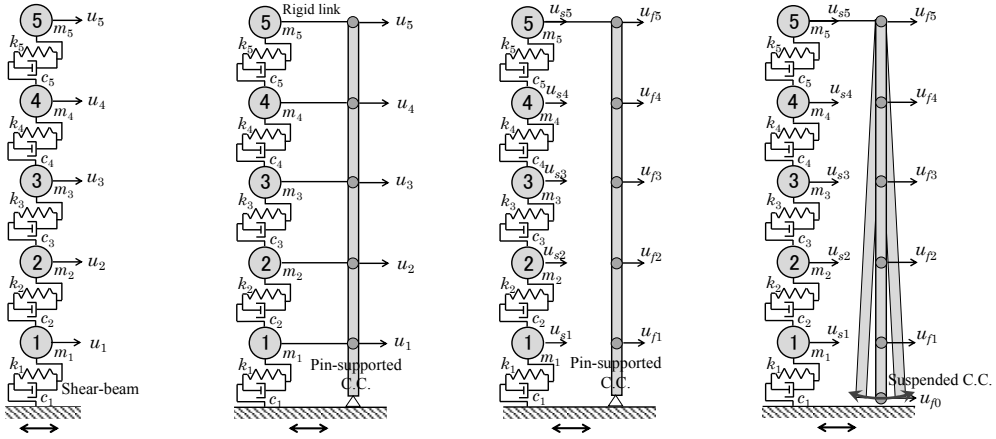
Wooden five-story pagodas in Japan have various types of "shinhashira (central column)", which is similar to the C.C., as shown in Figures 3. At the five-story pagoda in the Daigoji temple, the central column is supported on a foundation stone, similar to "pin-supported", as shown in Figure 3(a). At the Horyuji pagoda, the central column is dug into the ground, similar to "fixed at the base", as shown in Figure 3(b). At the Kaijuusenji pagoda, the central column is supported at the 2nd-story floor level as shown in Figure 3(c). The "shinhashira" is not structural element and is not allowed to be touched by any other component of the pagoda due to the very divine nature of the central column [5]. There is a space between the center column and the tower body, "toshin", and the center column is almost suspended from the top of the tower.



(a) Daigoji pagoda (874-) (b) Horyuji pagoda (607-) (c) Kaijuusenji pagoda (735-)

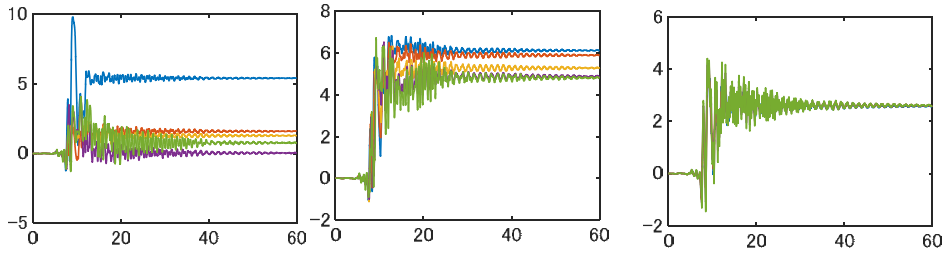
Figure 3: Continuous columns in wooden five-story pagodas

Various types of models as shown in Figure 4 are analyzed with the NF17 record (1995 Kobe earthquake). Shear-beam model only is shown in Figure 4(a), the model with pin-supported C.C. connected to the shear-beam at all stories is shown in Figure 4(b), the model with pin-supported C.C. connected at the top is shown in Figure 4(c) and the model with suspended C.C. is shown in Figure 4(d). The results of the time-history of the story drift angle (SDA) are shown in Figure 5. When there is no C.C., the SDA become very large as shown in Figure 5(a). If the C.C. is present, the SDA decreases as shown in Figure 5(b). If the diameter of the C.C. becomes twice, all SDAs are almost identical due to the C.C. effects as shown in Figure 5(c). If the C.C. is connected to the shear-beam only at the top, the C.C. does not have effects as shown in Figure 5(d). If there is no contact between the C.C. and the shear-beam, suspended C.C. does not have effects as shown in Figure 5(e). If the contact is considered, the C.C. functions as "kannuki", and the SDA decrease as shown in Figure 5(f).

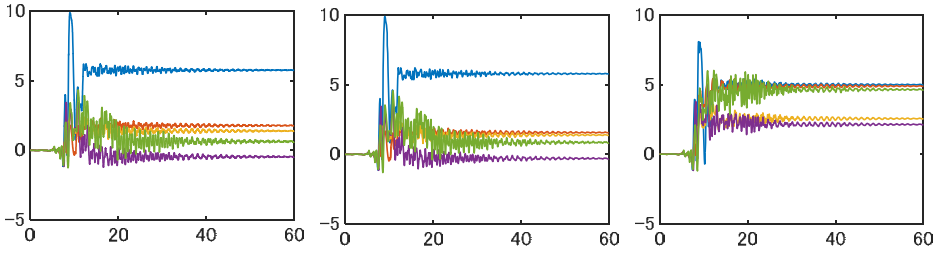


(a) Shear-beam only (b) Pin-supported C.C. (c) Only top connected (d) Suspended C.C.

Figure 4: Analysis models



(a) Shear-beam only (b) Pin-supported, all connected (c) Diameter two times

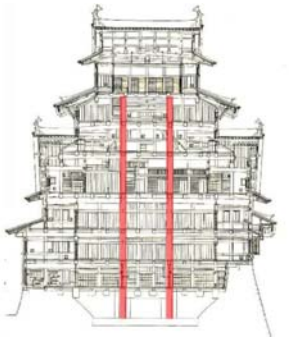


(d) Only top connected (e) Suspended C.C. w/o contact (f) Suspended C.C. w/ contact

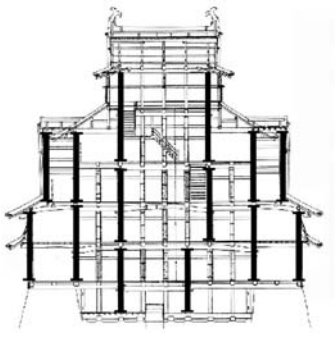
Figure 5: Time-history of story drift angle in five-story pagodas (X-axis: time [s], Y-axis: SDA [%])

4.2 Analysis on continuous column effects referring to castle towers [6]

Castle towers in Japan have the C.C. as shown in Figures 6. In the Himeji castle, the C.C. penetrate overall castle tower as shown in Figure 6(a). In contrast, in the Matsue castle, many partially C.C. are overlapped and as a whole penetrate the castle tower as shown in Figure 6(b). This was due to the lack of long timber enough to penetrate castle tower. Both castles are national treasures.

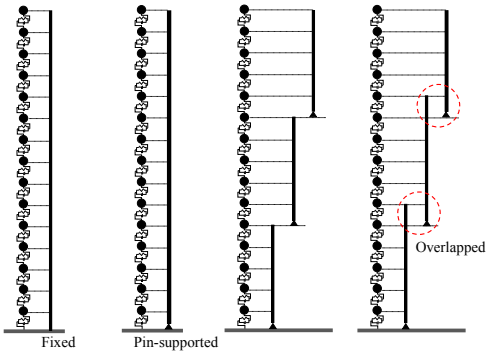


(a) Himeji castle (1346-)



(b) Matsue castle (1611-)

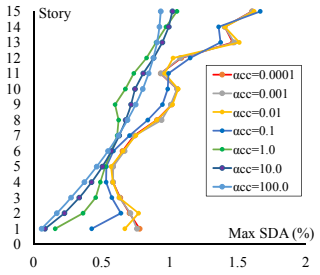
Figure 6 C.C. in Japanese castle towers



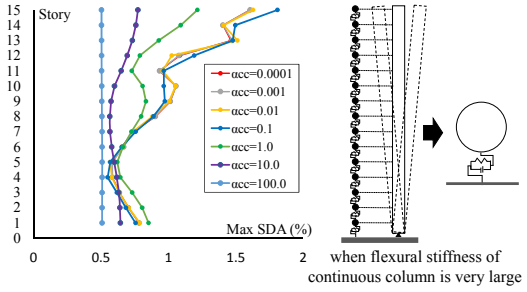
(a) (b) (c) (d)

Figure 7 Models for analysis

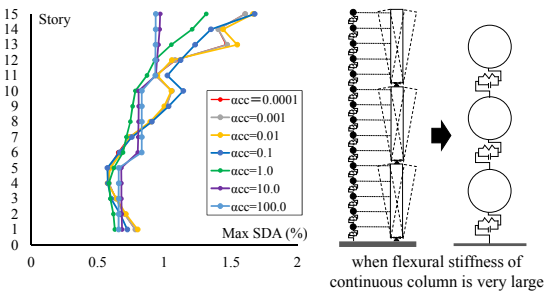
The coupled shear-flexural-beam models as shown in Figure 7 are analyzed. The model in Figure 7(d) has overlapped partially C.C., similar to the Matsue castle. The maximum SDA distributions for various α_{cc} are shown in Figure 8. As shown in Figure 8(c), the model with non-overlapped partially C.C. has similar response to the 3-DOF model as α_{cc} increases. In contrast, as shown in Figure 8(d), the model with overlapped partially C.C. has similar response to the 1-DOF model as α_{cc} increases.



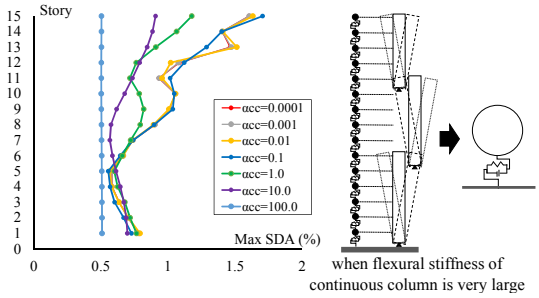
(a) Fixed C.C.



(b) Pin-supported C.C.



(c) Non-overlapped partially C.C.



(d) Overlapped partially C.C.

Figure 8 Distribution of maximum SDA

5. Application of continuous column concept to conceptual design

5.1 Application to super-high-rise building [7]

Recently, this C.C. concept is applied to the conceptual design proposal of a super-high-rise building. Here, many overlapped partially C.C., the idea of which is from the Matsue castle, are installed to provide the structural continuity, flexibility of floor planning and asymmetric overall configuration as shown in Figure 9. The inelastic dynamic analyses were conducted to evaluate the C.C. effects of overlapped partially C.C. This design work won the award of excellence in the 2017 Architectural Institute of Japan (AIJ) annual meeting.

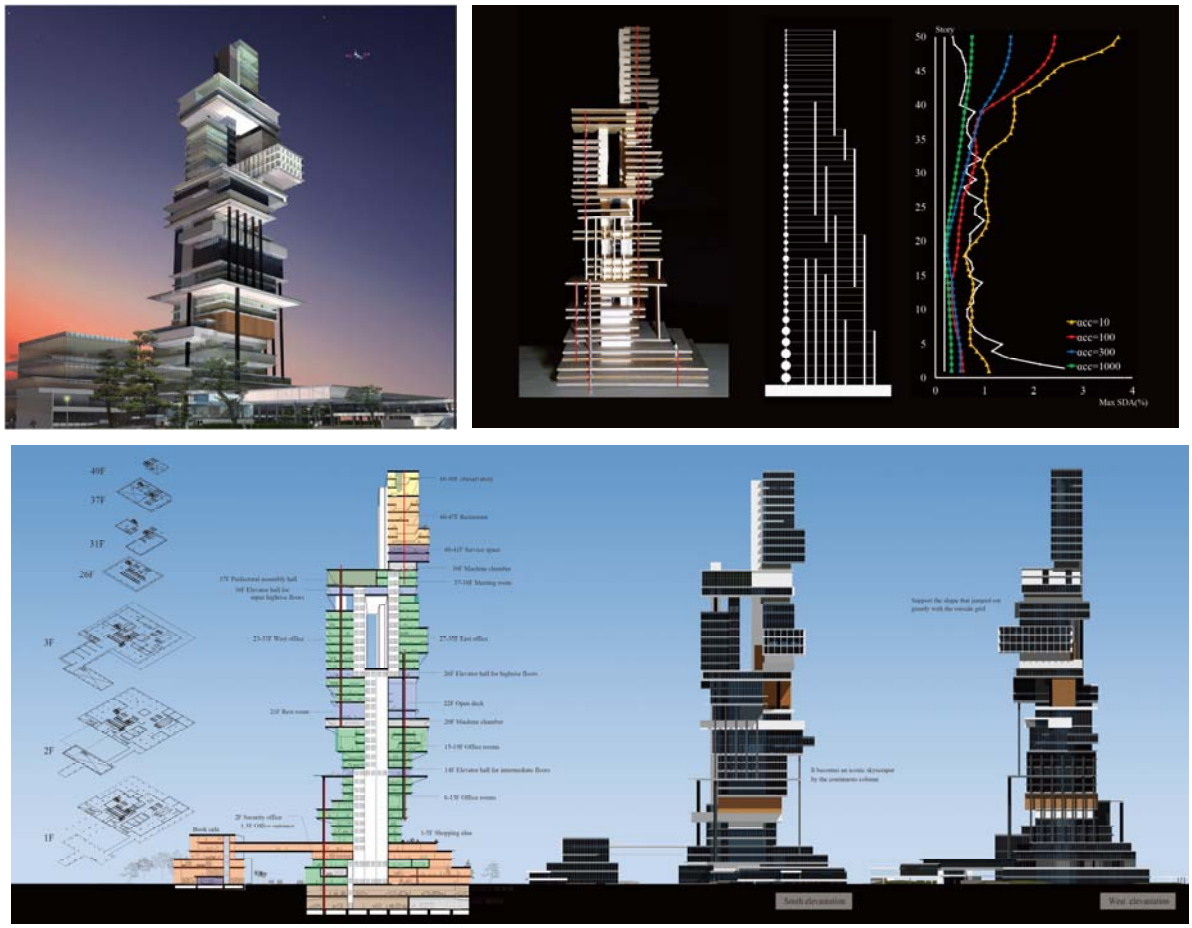


Figure 9: Conceptual design of super-high-rise building

5.2 Application to large spatial stadium [8]

The C.C. concept is applied to the conceptual design proposal of large spatial stadium as shown in Figure 10. It has seldom that the C.C. concept is applied to the design of the large spatial structure such as stadium. This stadium consists of continuous columns, wooden moment-resisting frames, and membrane roof. In ordinal times, many C.C. support membrane roof. At earthquakes, many C.C. are expected to exert the C.C. effects to mitigate the drift concentration in the flexible wooden moment-resisting frames.

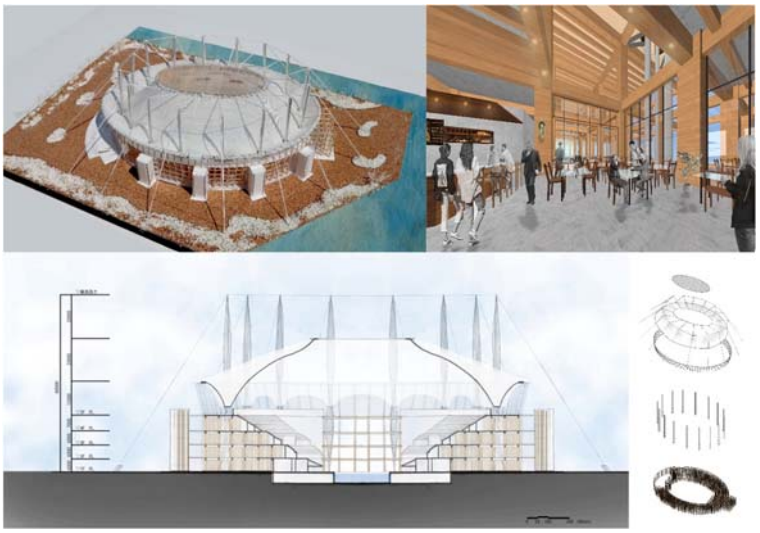


Figure 10: Conceptual design of large spatial stadium

6. Conclusion:

The C.C. effects are evaluated for various types of the C.C. referring to traditional Japanese architecture such as wooden five-story pagodas and castle towers. The application of the C.C. concept to conceptual design of super-high-rise building and large spatial stadium is introduced.

References

[1] MacRae, G.A. The Development of the Continuous Column Concept. *7th International Conference on Urban Earthquake Engineering & 5th International Conference on Earthquake Engineering Joint Conference,* Tokyo, Japan, 2010.3

[2] Tagawa, H., Gregory, M. and Lowes, L. Continuous column effects on gravity columns in U.S. steel moment-resisting frame structures, *Journal of Structural and Construction Engineering.* Architectural Institute of Japan, No. 650, pp.761-770, 2010.4.

[3] Matsumoto, Y., Tagawa, H., Sugiura, N., "Seismic Control Effects of Continuous Column going through Multi-story Structure, Part 2: Continuous Column Effects in Wooden Five-story Pagoda", *Summaries of Technical Papers of Annual Meeting*, AIJ, September, 2017

[4] Fujiwara, S., Tagawa, H., Sugiura S., "Continuous Column Effects of Shinhashira going through Toshin in Wooden Five-story Pagoda, Part 2: Investigation of Shinhashira-kannuki and Shinhashira-furiko Hypotheses", *Summaries of Technical Papers of Annual Meeting*, AIJ, September, 2019

[5] Kawaguchi, M., "On Sophistication of Structural Expression in Japanese Architecture", IASBE Conference NARA 2015, Elegance in Structures, Nara, Japan, 2015

[6] Okada, M., Tagawa, H., Sugiura, N., "Seismic Control Effects of Overlapped Partially Continous Columns referring to Japanese Traditional Architecture, *Summaries of Technical Papers of Annual Meeting*, AIJ, September, 2018

[7] Okada, M., Matsushita, S., Tagawa, S., Sugiura, N., "Consistensy: Skyscraper composed of Spreading Continous Columns, *Summaries of Technical Papers of Annual Meeting*, AIJ, September, 2018

[8] Fujiwara, S., Sugiura, N., Tagawa, H., "Mori of Flying – Swimming Stadium with Continuous Columns –", *Summaries of Technical Papers of Annual Meeting*, AIJ, September, 2019

Proceedings of the IASS Annual Symposium 2019 – Structural Membranes 2019
Form and Force
7 – 10 October 2019, Barcelona, Spain
C. Lázaro, K.-U. Bletzinger, E. Oñate (eds.)

DEM modelling of masonry vaults: influence of brick pattern and infill on stability during supports displacements

Claudio BONI*, Daniele FERRETTI[a], Erica LENTICCHIA[b], Alessandro TASORA[a]

* Student of Civil Engineering at University of Parma
via D. Fenulli, 85 - Reggio Emilia - 42123 - Italy
claudio.boni.94@gmail.com

[a] Department of Engineering and Architecture, University of Parma, Italy
[b] Department of Structural, Geotechnical and Building Engineering, Politecnico di Torino, Italy

Abstract

The paper proposes a discrete element method to study both the effects of brick pattern and infill on the stability of masonry vaults subjected to settlements of the supports. The open-source multi-physics simulation engine ProjectChrono - ChronoEngine, which is an open source C++ library based on a regularized non-smooth contact dynamics approach, was used to model the vaults. In particular, the voussoirs of the vault were modelled with rigid blocks reproducing the brick pattern, whereas the infill was modelled by means of thousands of rigid spheres. Initially, the parameters of the model were calibrated by means of experimental results on three types of vaults (barrel, cross, pavilion) with different brick patterns. Then, a barrel vault was investigated considering six brick patterns, suggested in ancient treatises, and the presence of the infill. Results show that the brick pattern, thanks to interlocking and friction between blocks, provides an equivalent tensile strength of masonry, which affects the behavior of the vault in terms of failure mode and failure load/settlement. Furthermore, the infill causes additional compression, which affects the thrust net configuration and, consequently, the stability of the vault.

Keywords: DEM modelling, masonry vaults, brick pattern, infill, supports displacements.

1. Introduction

Starting from Ancient Roman architecture, masonry vaults have been built for centuries around the world, with different forms and construction techniques. Although in the past masonry vaults were designed and built without structural calculations, ancient builders developed practical rules, mainly based on geometry, for the static equilibrium of these curved structural elements. Only after the 17th century, the stability of vaults begun to be studied mathematically, and builders begun to abandon the everlasting rule of proportions [1]. Although the behavior and structural response of masonry vaults had been analyzed with increasingly refined methods, however, it has always been known that brick pattern influences the structural performance of masonry: an herringbone pattern is always preferred than one composed with vertical stacked bricks. Moreover, the optimal design of brick and stone masonry vaults have frequently been one of the main topic in most historical treaties, in which also the optimal blocks orientation was one of the most investigated issues (e.g. Figure 1). Also the infill of vaults and domes had been a constant issue questioned during centuries, starting from Alberti and Palladio [2] [3]. Today the stability of masonry vaults is studied by means of computational methods, such as finite and discrete element methods, both from a static and dynamic point of view. However, the influence of the brick pattern and the influence of the infill, and how they could affect the stability of the vault, have only scarcely been investigated [4].

Copyright © 2019 by Claudio Boni, Daniele Ferretti, Erica Lenticchia, Alessandro Tasora
Published by the International Association for Shell and Spatial Structures (IASS) with permission.

After the identification of the more common brick patterns, employed in different vaults configurations, the paper illustrates the modelling of a barrel vault chosen as paradigmatic example. The static of six different masonry patterns is analyzed by using the discrete element library ProjectChrono - ChronoEngine [5], developed at the University of Parma. The influence of brick pattern on the stability of masonry vaults subjected to settlements of the supports is studied and discussed. The aim is to evaluate and assess if, considering the same shape, the static behavior changes with the variation of the pattern of the bricks and the presence of the infill.

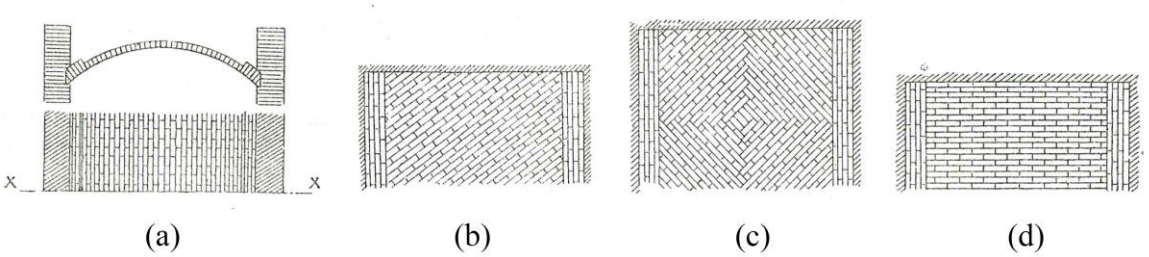


Figure 1: Different brick patterns of a barrel vault in an Italian treatise [6].

2. DEM model

Discrete Element analyses of the vaults were performed using the software ChronoEngine [5], which is an open source C++ library developed for mechanical engineering but also successfully used to study masonry structures in civil engineering [7] [8] [9] [10].

The bricks were modelled with rigid convex blocks ("convex hull") while rigid spheres were used for the infill. In ChronoEngine, contact forces and motion laws for each block are determined considering Newton's Second Law (in the gravity field), Coulomb's Friction Law, and springs/dashpots reactions [7] [8]. It is worth noting that contacts, modelled with springs and dashpots, if properly calibrated (by means of the parameters "Compliance" and "Damping"), can reproduce mortar deformability and the consequent overall deformation of the vault.

The main equation of this DEM approach can be written as:

$$M \cdot \frac{dv}{dt} = f - f_c \tag{1}$$

where M is the mass matrix, containing mass properties of all the discrete elements, v is the velocity vector, t is the time, f is the generalized forces vector (function of time, position and velocity) and f_c is the contact forces vector. Equation (1) is numerically integrated in time and the solution is found through force impulses. The main novelty of this approach consists of a particular stabilizing term that affects the solution and also limits dilatation effect, so that the frictional model remain essentially a non-associative one [7] [8]. This is particularly useful to solve the friction cone complementary problem with low computational burden and to bypass numerical integration inaccuracy. The solution is based on a regularized non-smooth contact dynamics approach [7] [8] that reduces the computational time with respect to other DEM methods permitting to analyze 3D problems with a huge number of bodies.

Another peculiarity of the model is the contact detecting algorithm, which is based on Gilbert-Johnson-Keerthi approach [11]. This method operates on convex surfaces and, in order to solve the problem of degenerate cases, i.e. coplanar faces with infinite contact points, the algorithm is run several times at each time-step with small rotational perturbations on blocks, so as to obtain a finite number of possible contact points [7] [8]. For this reason, number and position of contact points may vary between identical blocks. Moreover, a fictitious offset is generated inwards (parameter "Margin") and outwards (parameter "Envelope") each discrete element to deal with compenetrations and to detect collisions in advance, wiping out initial small geometrical errors [5] [7] [8].

3. Model calibration

The parameters of the model have been calibrated by studying well-known experimental campaigns, including the tests by:

- Hudson and Theodossopoulos [12] on a wooden scale model of gothic barrel vault;
- Vermeltfoort [13] on two full-scale masonry barrel vaults (rectangular and skew);
- Foti et al. [14] on a scale model of a 3D printed cross vault;
- Rossi et al. [15] on a scale model of a 3D printed pavilion vault.

Figure 2 shows the tests modelled by means of ChronoEngine, before and after collapse while experimental and model results are compared in Table 1 in terms of load or displacement at collapse. Considering the inevitable uncertainties, the results are very good. The corresponding values of the main parameters adopted in ChronoEngine after calibration are shown in Table 2.

Table 1: Comparison between experimental and DEM model results in terms of collapse load/displacement.

Test	Experimental	Model	Error
Hudson and Theodossopuolos [12]	132 mm	137 mm	+3.8%
Vermeltfoort [13] (rectangular)	40.7 kN	42.0 kN	+3.2%
Vermeltfoort [13] (skew)[1]	26.0 kN	28.0 kN	+7.7%
Foti et al. [14] (horizontal)[2]	21 mm	22.1 mm	-5.2%
Rossi et al. [15]	9.51 mm	10.5 mm	+10.5%
[1] Mortar joints parallel to the supports; [2] Mean value of three experimental tests.			

Table 2: Values of model parameters after calibration.

Solver	Barzilai-Borwein
Compliance	$1 \cdot 10^{-10}$ m/N
Damping	0.2 kg/s
Envelope	0.002 m
Margin	0.001 m

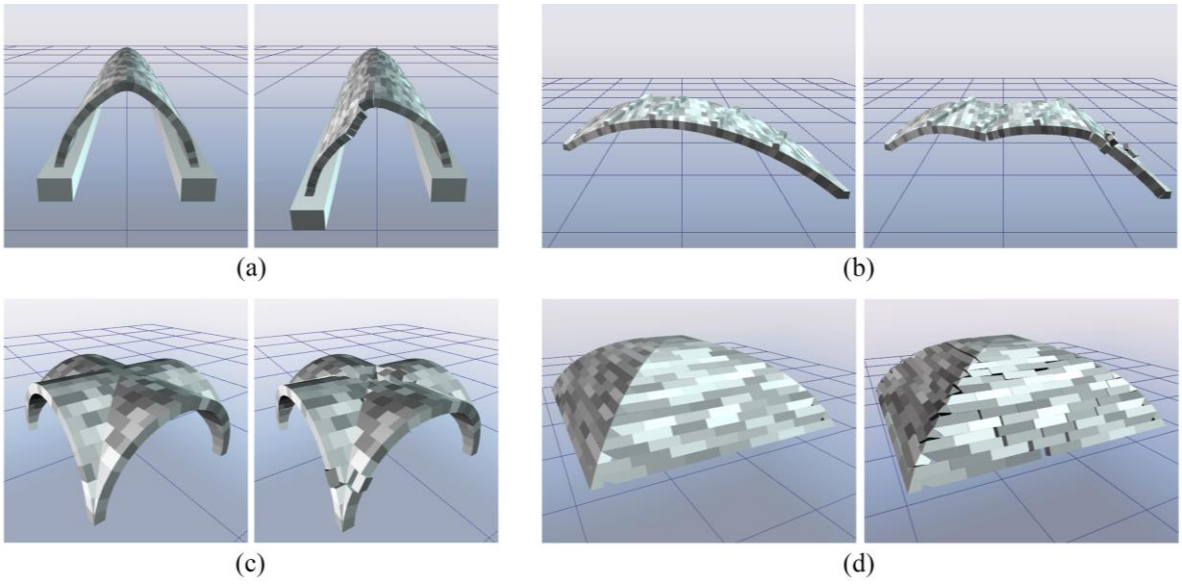


Figure 2: Validation of the DEM model. Pictures show the vault before (left) and after collapse (right): (a) Barrel vault tested by Hudson and Theodossopoulos [12] ; (b) Skew vault tested by Vermeltfoort [13]; (c) Groin vault tested by Foti et al. [14] ; (d) Pavilion vault tested by Rossi et al. [15]

4. Analysis of barrel vaults

The study started from the thesis by Boni [16], which included three types of vaults (barrel, cross, pavilion) with different brick patterns and subjected to displacements (settlements) of the supports up to failure. In the present work, only the paradigmatic behavior of barrel vaults is analyzed.

The effect of both brick pattern and infill on support settlement at failure was investigated on the exemplary vault shown in Figure 3, where the geometric dimensions are also reported. The longitudinal length of the vault was about 5.25 m. Density and friction coefficient were set to 1800 kg/m^3 and 0.5 respectively. Based on the indication guidelines of ancient treatises, six brick patterns were investigated (Figure 4).

The vault was modelled with a number of blocks ("convex hull" type) varying from 314 to 373, depending on the brick pattern. The infill, if present, was made of 1750 spheres, whose density was set equal to 2700 kg/m^3 to take into account the presence of vacuum spaces among spheres in respect of a real loose material. Three types of support displacements were investigated: horizontal on a support, horizontal on two supports, and vertical (Figure 3). All support displacements were applied in a quasi-static mode.

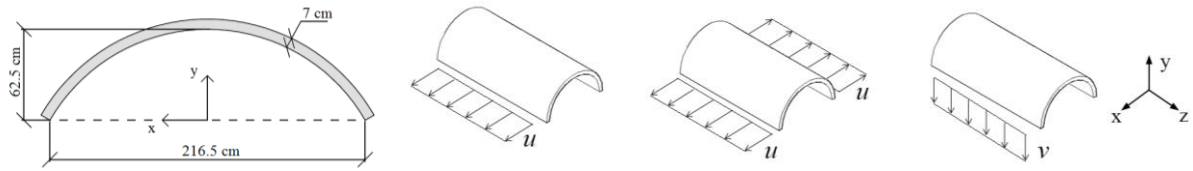


Figure 3: Barrel vault: geometry of the cross section and support settlements analyzed.

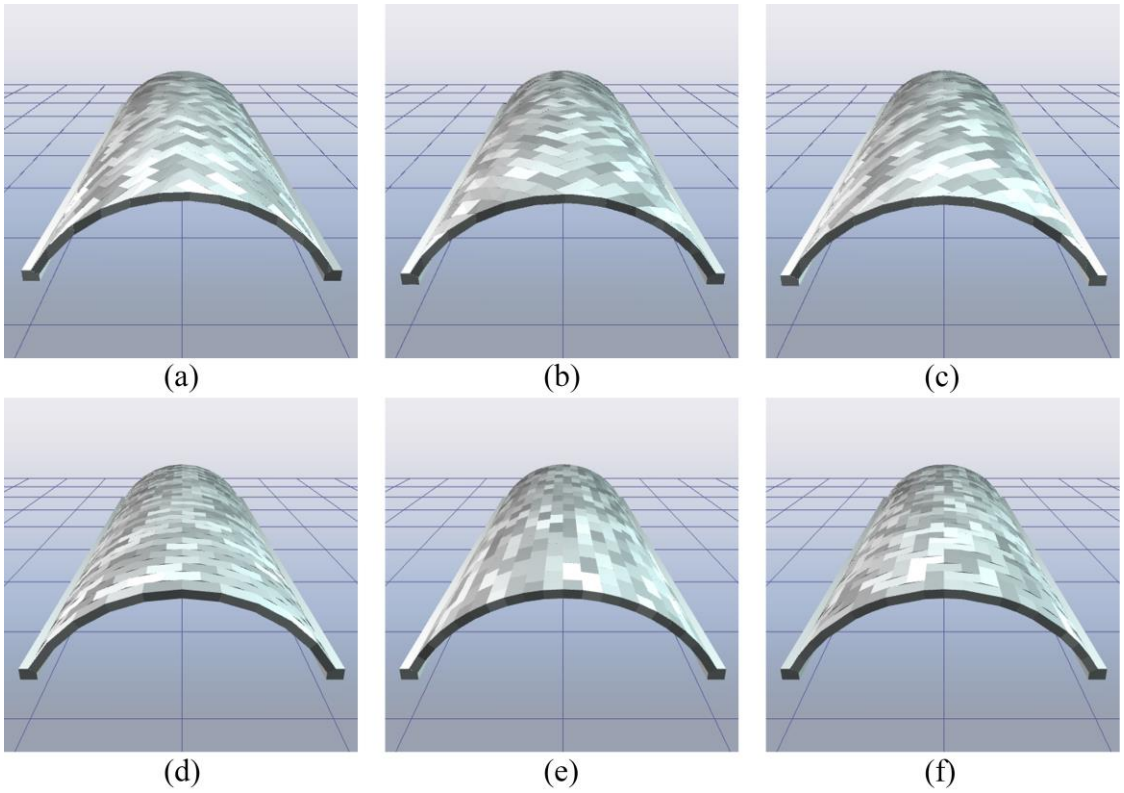


Figure 4: Brick patterns of the analyzed vaults: (a) Herringbone brick rows to center; (b) Herringbone brick rows to edges; (c) Diagonal brick rows; (d) Brick rows perpendicular to supports; (e) Brick rows parallel to supports; (f) Bricks in herringbone configuration.

The aforesaid six different vaults with no infill and different brick patterns were subjected to horizontal displacement of supports. The failure mechanism of the vaults is generally the classical one, evolving from the three-hinge configuration, as shown in Figure 5. Results confirm that the brick pattern influences the settlement at collapse. This is evidenced in Figure 6a, where u is the displacement of the support, and y and y_0 are the actual and the initial positions of a reference point (in a block where the hinge forms), measured in the reference system shown in Figure 3. Initially the curves are subhorizontal and then they display a knee followed by a steep variation, corresponding to collapse. It is possible to notice that the knee point of the curves depends on the brick layout, i.e. with some brick layouts the collapse is deferred.

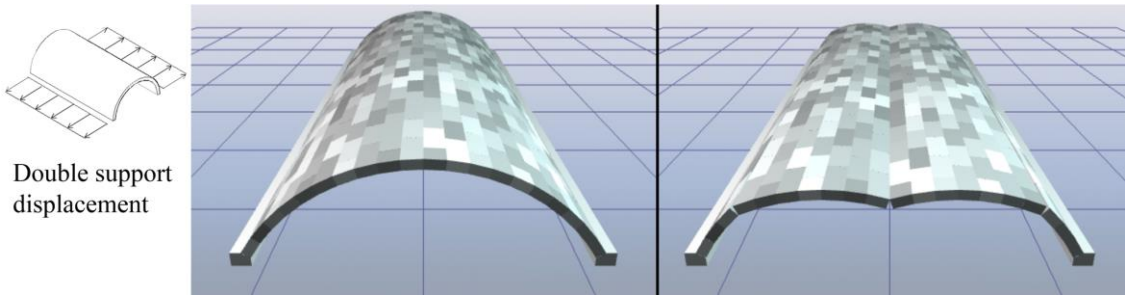


Figure 5: Collapse mechanism for barrel vault with brick rows parallel to supports without infill.

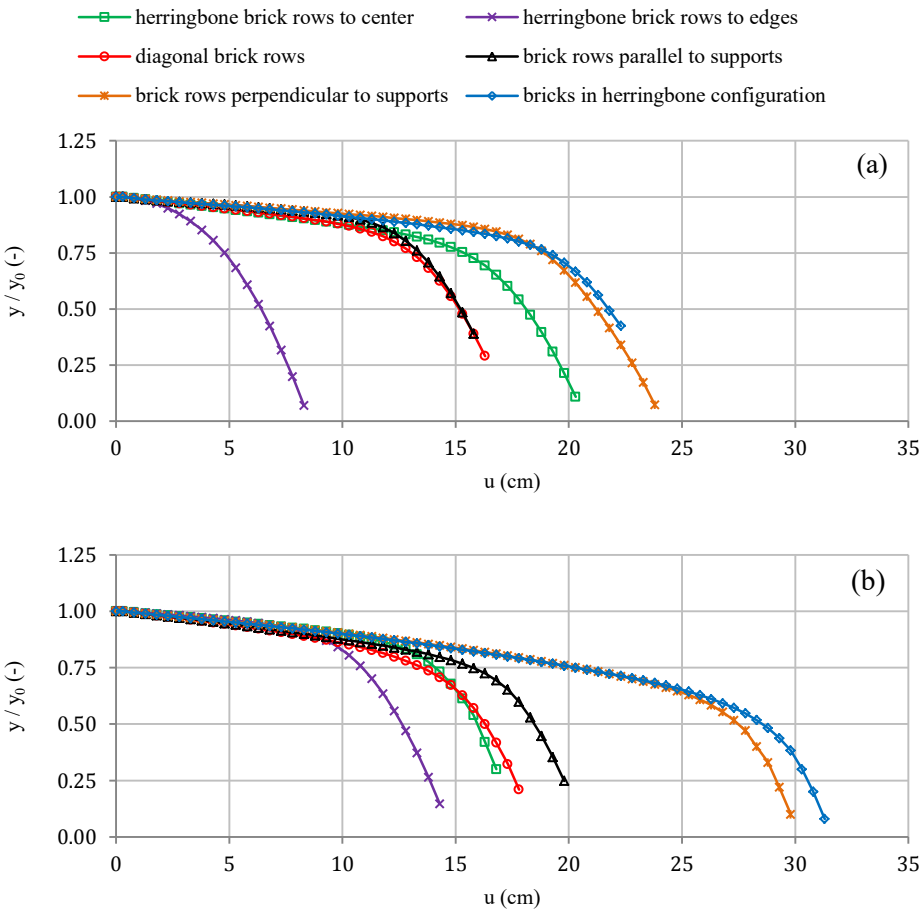


Figure 6: Comparison of the behavior of vaults with different brick patterns. Dimensionless vertical position y/y_0 of a reference point as a function of the horizontal settlement u of one support: (a) no infill; (b) with infill.

Figure 6a shows that the brick layout with herringbone rows to edges is the most sensitive to support displacements (failure occurs for values about 2 cm), while the brick layout with rows perpendicular to supports and the herringbone layout of single bricks are the most performant (failure occurs for displacements of more than 15 cm).

It is worth noting that the brick pattern not only influences the failure displacement, but may also affect the failure mode as can be seen, for example, in Figure 7.

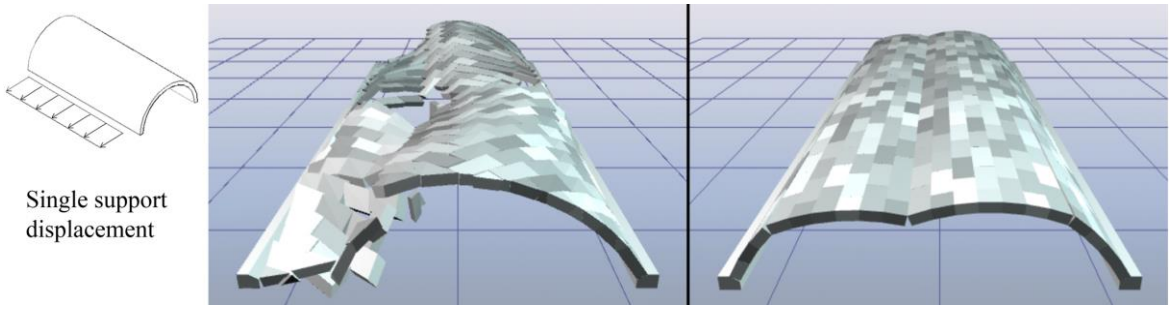


Figure 7: Comparison between two different brick patterns (single support displacement).

The analyses have been repeated considering the infill, which was modelled with spheres. Defining the position of the spheres in a vault of generic shape is a cumbersome process. In the present work, firstly, the voussoirs and the lateral walls are tied together, and the spheres are introduced as free bodies following a defined geometrical scheme (Figure 8a). While spheres are falling, the vault globally shakes in order to tamp the infill (Figure 8b). Secondly, an additional block is used as a bulldozer in order to level the upper surface of the infill (Figure 8c). Then, the final position of the spheres is saved and is used for the subsequent analyses (Figure 9).

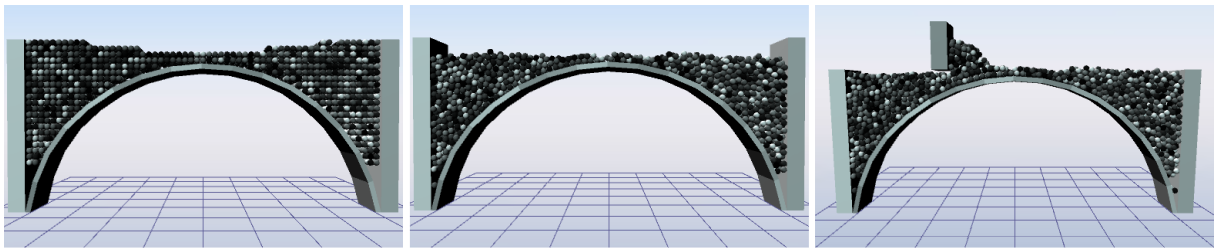


Figure 8: Introduction of the infill: (a) initial position of spheres; (b) position of spheres after shaking; (c) levelling of the infill using an additional block.

Results confirm that the infill generally improves the stability of the vault, i.e. its presence increases the collapse displacement as can be seen in Figure 6b. With the infill, the failure displacement of the vault with herringbone rows to edges goes approximately from 2 cm to 8 cm. In the case of single bricks in herringbone configuration, the displacement goes approximately from 15 cm to more than 20 cm. Moreover, the presence of the infill influences also the failure mechanism, as can be observed comparing Figure 5 and Figure 9.

The previous analyses focused on horizontal settlements because generally the vault is less sensitive to vertical ones. For instance, Figure 10 shows that, in the case of a vault with brick rows parallel to supports, the horizontal failure displacement increases about 30 % with the infill, but is three times in the case of vertical displacements.

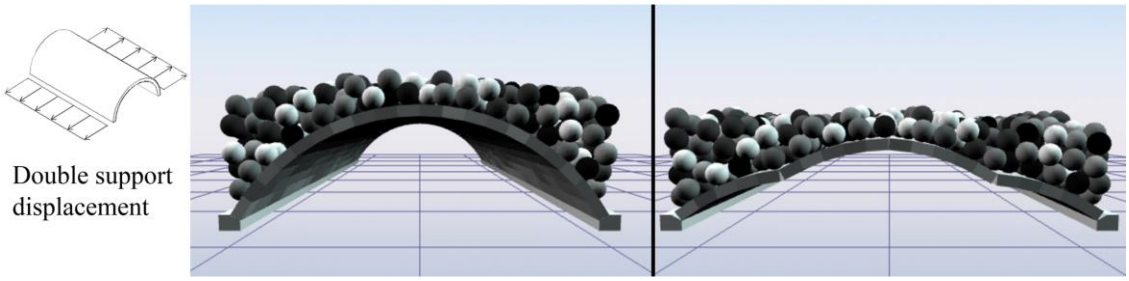


Figure 9: Collapse mechanism for barrel vault with brick rows parallel to supports and infill.

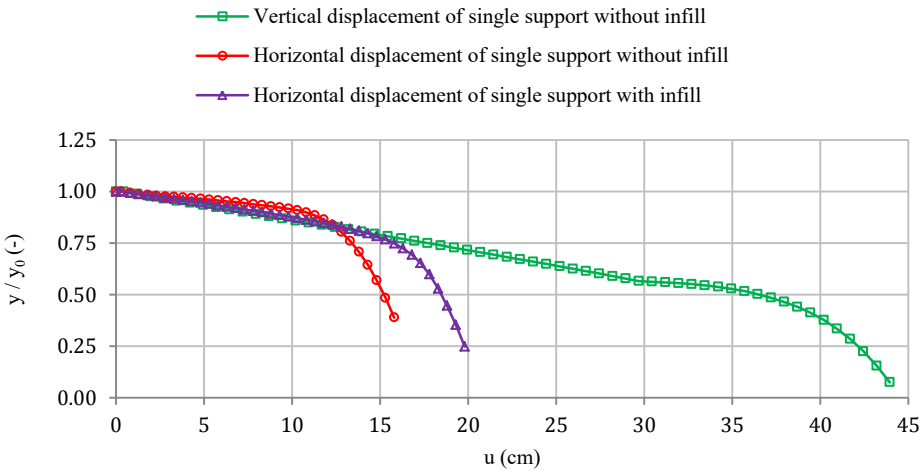


Figure 10: Effects of vertical and horizontal support displacement in comparison for the brick pattern with rows parallel to supports.

5. Conclusions

In the present work, the open-source multi-physics simulation engine ChronoEngine was used for discrete element analyses of vaults. In particular, a barrel vault was analyzed with six different brick patterns suggested in ancient treatises. The voussoirs were modeled with rigid bricks. Thanks to the algorithms of ChronoEngine, it was possible to model the infill by means of thousands of spheres. The vault was subjected to horizontal settlement of the supports, which is one of the main causes of its collapse.

Results show that brick pattern influences the displacement at failure. In particular, the layout of blocks with rows perpendicular to supports displays unexpected strength, while the layout with herringbone rows to edges, which is quite common and well seen by practical rules in handbooks, exhibits the worst performance.

The infill generally increases the failure displacement: this can be explained by the additional dead load, which plays a centering action on the thrust net configuration; on the other hand, the infill, if made of loose material, introduces a lateral pressure that may change the failure mode and may affect the vault stability.

A natural progression of this work is to analyze barrel, cross and pavilion vaults of different geometries, in order to generalize the results. Furthermore, it would be interesting to perform the same analyses on more complex geometrical configurations, such as hemispherical domes on pendentives.

References

[1] J. Heyman, "The stone skeleton," *International Journal of solids and structures*, vol. 2, pp. 249-279, 1966.

[2] L. B. Alberti, *De re aedificatoria*, Firenze, 1450.

[3] A. Palladio, *I quattro libri di architettura*, Venezia, 1570.

[4] A. Tralli, C. Alessandri and G. Milani, "Computational methods for masonry vaults: a review of recent results," *The Open Civil Engineering Journal*, vol. 8, 2014.

[5] "Project Chrono," [Online]. Available: *https://projectchrono.org*. [Accessed 30 Sept 2018].

[6] C. Gelati, *Nozioni pratiche ed artistiche di architettura*, 2nd ed., Torino: Carlo Pasta, 1907.

[7] V. Beatini, G. Royer-Carfagni and A. Tasora, "A regularized non-smooth contact dynamics approach for architectural masonry structures," *Computers & Structures*, vol. 187, pp. 88-100, 2017.

[8] V. Beatini, G. Royer-Carfagni and A. Tasora, "The role of frictional contact of constituent blocks on the stability of masonry domes," *Proceedings of the Royal Society A: Mathematical, Physical and Engineering Science*, vol. 474.2209, 20170740, 2018.

[9] E. Coïsson, L. Ferrari, D. Ferretti and M. Rozzi, "Non-smooth dynamic analysis of local seismic damage mechanisms of the san felice fortress in Northern Italy," *Procedia Engineering*, vol. 161, pp. 451-457, 2016.

[10] D. Ferretti, E. Coisson and M. Rozzi, "A new numerical approach to the structural analysis of masonry vaults," *Key Engineering Materials*, vol. 747, pp. 52-59, 2017.

[11] E. G. Gilbert, D. W. Johnson and S. S. Keerthi, "A fast procedure for computing the distance between complex objects in three-dimensional space," *IEEE Journal on Robotics and Automation*, vol. 4, pp. 193-203, 1988.

[12] J. Hudson and D. Theodossopoulos, "Gothic barrel vaults under differential settlement: the effects of boundary conditions and FRP on structural behaviour," *Key Engineering Materials*, vol. 747, pp. 496-503, 2017.

[13] A. T. Vermeltfoort, "Analysis and experiments of masonry arches," in *Historical Constructions*, Guimarães, Lisbon, 2001.

[14] D. Foti, V. Vacca and I. Facchini, "DEM modeling and experimental analysis of the static behavior of a dry-joints masonry cross vaults," *Construction and Building Materials*, vol. 170, pp. 111-120, 2018.

[15] M. Rossi, C. C. Barentin, T. V. Mele and P. Block, "Experimental study on the behaviour of masonry pavilion vaults on spreading supports," *Structures*, vol. 11, pp. 110-120, 2017.

[16] C. Boni, "Analysis of masonry vaults with discrete element method: brick pattern effect," University of Parma, Italy. Tutors: Ferretti, Lenticchia, Tasora, 2018.

Proceedings of the IASS Annual Symposium 2019 – Structural Membranes 2019
Form and Force
7 – 10 October 2019, Barcelona, Spain
C. Lázaro, K.-U. Bletzinger, E. Oñate (eds.)

Dry self-balanced vaulting technology

V. PARIS*, A. PIZZIGONI[a], G. RUSCICA[a], M. ETEME MINKADA[a], G. MARCHETTI[a], M. PANZERI[a], A. LOCATELLI[a], M. PIEVANI[a], J. GHERARDI[a], M. CASERI[a], F. LOMBARDONI[a],

*University of Bergamo
5, Via Marconi, Dalmine (Bg), Italy
vittorio.paris@unibg.it

Abstract

Starting from the existing historical examples, considering structural and stability principles, the research has been developed within the context of form-finding. To find practical and sustainable solutions that could be relevant to build masonry shells the research has focused on the study of self-balancing dry technology. To pursue this, the form-find has not been applied on the whole shape but just to the masonry blocks geometry. Historical self-balanced building technologies, above all the cross-herringbone method, constitute precious references to begin the search of a self-balanced constructive method. This document provides some indications on how it is possible defining a constructive self-balancing method and, even though the research is still being held, here it is reported the results achieved, the method and principles assumed. In the case study assumed, it has been evaluated a hemispherical dome thus the form-finding process it has been applied to define masonry pattern Structural and geometrical properties are the features which have led to search the masonry pattern. Surely, nowadays technologies as laser cutting or 3D printing allow building easier a wide variety of form-found shape, but these technologies even allow to increase productivity during the stage of prototyping.

Keywords: masonry, dome, self-balancing, additive manufacturing.

1. Introduction

The study here presented is focussed on the issue of self-balancing dry constructions. Several self-balanced technologies are already known [1] [2], more of these were used by the ancient master builders. They have built arches, vaults and domes using masonry for centuries and only based on geometrical concepts, realizing models or prototypes. These ancient forms create impressive architectural spaces that certainly surpass the longevity of contemporary structures. Inspired by the Italian dome of Santa Maria dei Cieli of Montedoro [3] built with cross herringbone technology, this study has the purpose to obtain more practical and sustainable design adapting this historical knowledge to the modern constructions.

There are many reasons for keep using masonry compared to other materials nowadays. The primary advantage is its low environmental impact being minimally processed and low in embodied energy [4]. Another benefit is the thermal mass that can reduce the energy required to heat and cool buildings and the important environmental advantages compared to the material it most often replaces: concrete, which contributes roughly 50% to the 140 million metric tons of construction waste stream generated annually in the United States [5]. Even if recently, it has been paid new attention to masonry structures

Copyright © 2019 by the authors.
Published by the International Association for Shell and Spatial Structures (IASS) with permission.

[6], the methods used to design structurally efficient geometries for arches, domes and vaults are largely unknown in the contemporary structural engineering community.

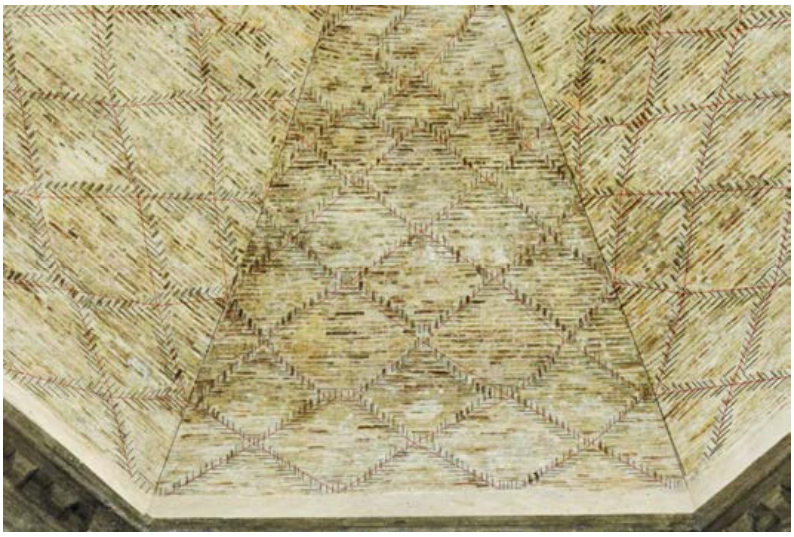


Figure 1: Santa Maria dei Cieli of Montedoro. Cross-herringbone pattern.

In fact, as commonly known, structural engineering practice has generally focused on three main structural criteria: strength, stiffness and stability building. Although these criteria also apply to masonry structures, the third criterion, stability, plays a central role in the design of masonry structures [7]. If the proportions of an arch, vault or dome are correct, the internal compressive forces will be maintained within the masonry, with relatively low compression tensions and consequently, the structures will not have stability problems. This consideration is the result of the analysis of real structures and therefore of loads that can be maintained in real cases. Stiffness is rarely an issue in masonry structures because of the low stresses account for very small displacements due to elastic deformation of the material. Stress plays an important role only when the entire load is focused at a specific point at collapse.
This research focuses on the possibility of building without any false or form-work the hemispherical masonry dome. Moreover, the physical prototypes have been made without mortar: the joints, between the blocks founded, are dry.

2. Some notes on the history of self-balanced masonry structures

Building a self-balanced dome requires peculiar technologies, several self-balanced methods have been developed throughout history. As introduced in section 1.0, the goal of this document is not providing a resume of all those methods, nevertheless, here it has been reported some technologies adopted during history.
The most known technology called "Catalan" or "thin" vaulting was been developed and applied in the Mediterranean area, especially in Spain [7]. Between 1800 century and the beginning of the 1900 century “Catalan” method was systematically applied by Guastavino's family, which exported it to America. The "Catalan" vaults are characterized by their dimension: they are really thin and capable to have a greater span, but certainly, the most relevant feature is their capacity to find the self-balance even under construction, as shown in figure 2.1. This important property can be ascribed to their shapes and even by precautions observed during building phases: the bricks laying with gypsum mortar, and to built by closed courses.

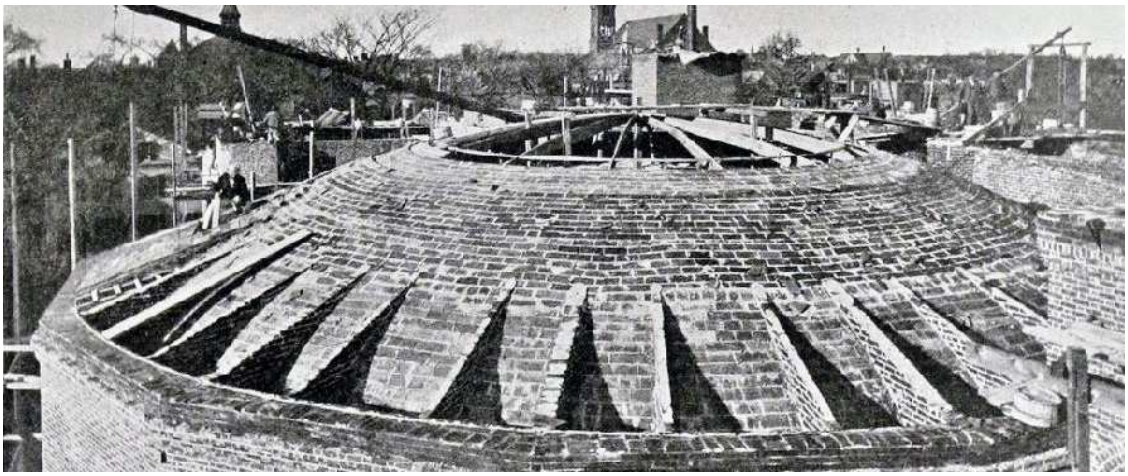


Figure 2.1: Dome of East Boston High School, Diameter 21.34 m, by R. Guastavino Company

Another self-balanced technology is the "Nubian" vaulting [1] figure 2.2. The "Nubian" vaults is an extruded arch similar to the barrel vaults but unlike those, it does not require support during the construction phase. The shape of vaults is parabolic and the bricks courses are laid as shown in figure 2.2. In particular, the arrangement of bricks courses are inclined about 20° respect the vertical and posed in a way to allow to support the next brick and then the next course. Through the "Nubian" technology can be built barrel vaults and cross vaults without using any support. But this technology requires some lateral supports as the wall shown in figure 2.2, as well the process of laying assumes extremely important, especially in the cross vaults.

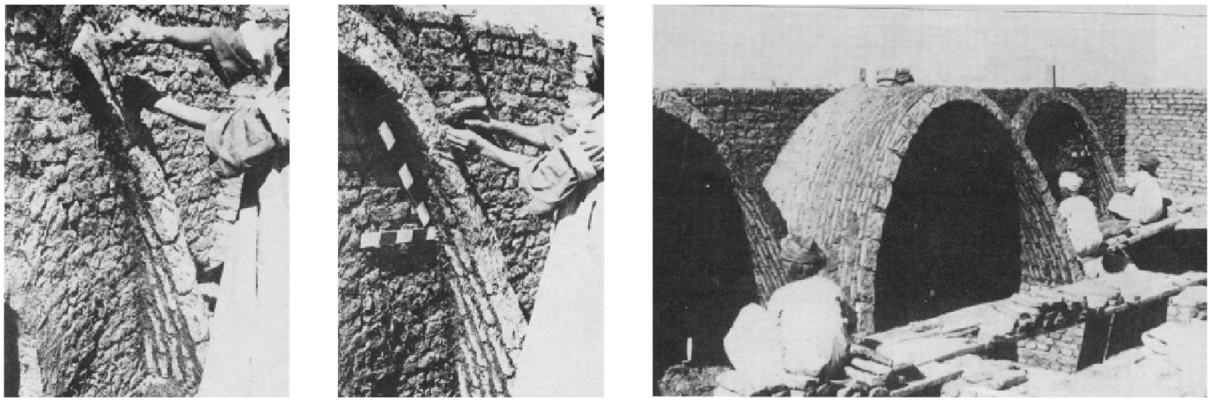


Figure 2.2: "Nubian" vaulting. Several building phases

Certainly, during history, other technologies have been developed [1] as the herringbone technology [3] which was based on a precise manner to arrange the bricks.
From the study of historical self-balanced methods, it is possible to affirm that the self-balanced methods have in common some features: some technologies require the use of a particular kind of mortar, others to adopt precisely masonry pattern, but for all technologies, the process assumes a key role.

3. In search of the equilibrium

Unlike conventional linear elastic methods, the limit state analysis permits to predict the behaviour and the failures of masonry structures. Instead of attempting to calculate the stresses in an overly idealized elastic structure, the safe theorem of plastic design dictates that if one equilibrium state could be found for a structure given under a set of loads, the structure is safe. The static graphics methods permit to visualize the compressive forces paths through the thrust line, a theoretical line that represents one of the possible paths of the compressive forces through the structure. According to the safe theorem of

plasticity [8], the study of the thrust line geometry respect to the geometry of structure analyzed allows affirming if the structure is balanced. Being the instability the most restricted criterion, the geometry of structure assumes a key role in order to determine the equilibrium. The Heyman approach is based on three hypotheses: the absence of tensile strength, infinite compression resistance and no sliding [8]. It can certainly be applied to the complete structures, but under construction, the friction may not be enough to prevent the sliding. Actually, during the building stages, the blocks of masonry structures such as domes, vault or arches not supported by any falsework or formwork exhibit failures to overturning and slipping. The reason is due to the low tensile strength of mortar joints and to the role assumed of the friction. Therefore from Heyman hypothesis, it must be removed: there is no sliding, and then considering a finite value of friction. Under these assumptions, as describe A. Casapulla the unicity of solution is not lost [9].
Considering the example proposed by A. Giuffre [10] and referring to figure 3.1, when the brick is loaded with a parallel force to the surface of the laying plane, when at the brick is applied a parallel force of the laying plane, two collapse mechanisms can occur, depending by its geometry: it can slide away onto the plane or overturning without slipping. The evaluation of safety against overturning can be measured by the η ratio between the M_S stabilizing moment and the M_R overturning moment (1). The overturning moment is given by F_R the external force, while the stabilizing moment is produced by W its weight.

$$\eta = M_S / M_R = (\gamma \cdot b^2) / (2 \cdot F_R) \tag{1}$$

As well the slipping occurs when the magnitude of F_S the applied force is larger than F the friction force (2).

$$F_S \geq F \tag{2}$$

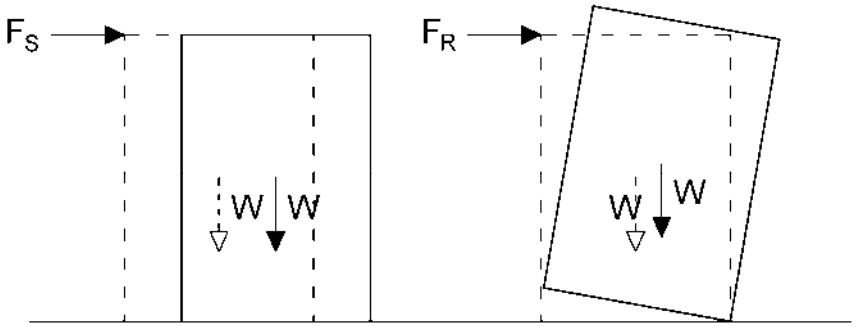


Figure 3.1: collapse mechanisms due to slipping and overturning

To build a double curvature masonry structure without any false or formwork, an equilibrated solution must be found to avoid slippage or overturning. Considering only the interaction between two blocks it is reasonable to affirm that between blocks contact surfaces an F frictional force acts onto contact plane. According to the Coulomb's Equation (2) F is related to μ the friction coefficient and $F_\perp$ the normal force to contact the plane.

$$F = \mu \cdot F_\perp \tag{3}$$

Referring to figure 3.2, an inclined plane of an α angle and assuming that there are no external forces acting, the M_R overturning moment is given by $F_{//}$ the weight component parallel to the laying plane, while the M_S moment stabilizing by $F_\perp$ its perpendicular component (4).

$$\begin{gathered} F_\perp = W \cdot cos(\alpha) \\ F_{//} = W \cdot sen(\alpha) \\ \eta = M_S / M_R = B / H \cdot \cot(\alpha) \end{gathered} \tag{4}$$

The stabilizing moment increases as the base increases, while it decreases as the inclination increases. Instead, the overturning moment grows with increasing height and inclination.
While slipping occurs when $F_{//}$ the component of the weight force parallel to the plane of contact reaches F the friction force. This latest force decreases as the inclination increases, as it depends on the orthogonal component to the weight force laying plane (5) figure 3.2.

$$F_{//} \geq F = \mu \cdot (\gamma \cdot B \cdot H) \cdot cos(\alpha) \tag{5}$$

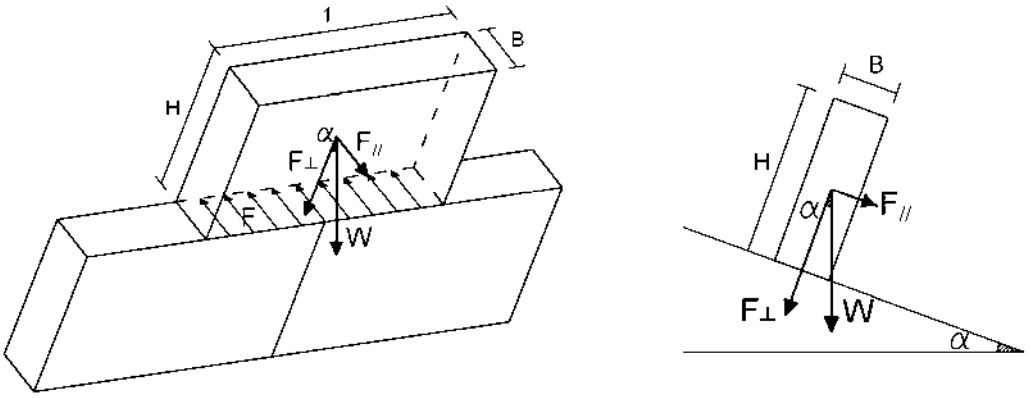


Figure 3.2: collapse mechanisms due to slipping and overturning for tilted brick

Both relations are not satisfied for any α angle thus the (4) (5) proof which the bricks fall. The meaning appears clear considering a hemispherical dome. Near the crown, the bricks collapse, the courses cannot be laid without any support. The resources required to build a dome without any formwork must be found through other resistance mechanisms. Where the mechanism could be found are unknown, it depends on the technology has been adopted.

4. Stereotomy of the blocks

Being the aim to define a dry self-balanced method to build domes using the least number of different modules, it has been chosen to approximate the hemisphere through geodesic polyhedron. Starting from Magnus Wenninger's Spherical models [11], polyhedra are given a particular geodesic notation based on the polygon forming the faces of polyhedra and the number of subdivisions. In particular, it has been chosen the polyhedra identified as {3,5}5.0, figure 4.1D, which represents an icosahedron with faces divided into 25 smaller equal triangles and projecting vertices to the sphere.
Dividing the polyhedron faces in smaller modules, and projecting them onto a hemispherical surface it is possible to obtain a periodic spherical triangular pattern composed by 1500 faces, divided into only fifteen different modules. The pattern of these modules has been adopted to defined the blocks. The pattern shown in figure 4.1A is obtained assembling the modules into hexagonal blocks, the idea which led this composition is to build a dome defining substructure during the construction.
The design of 4.1 B instead has been constituted through the union of two blocks. This subdivision realizes a link between the various levels. Finally, it has been opted to increase the number of bricks by dividing and combining the module, figure 4.1 C.

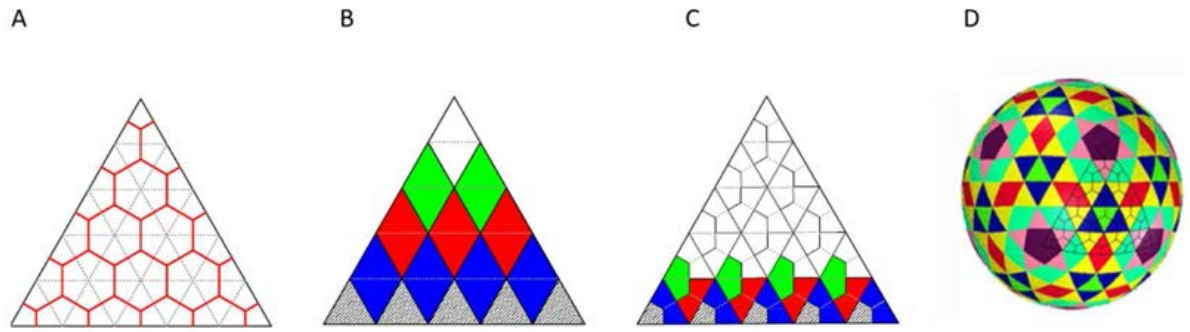


Figure 4.1: A) Polyhedron {3,5}5.0 with hexagonal blocks B) Second blocks composition C) Final blocks composition D) Projected polyhedron on the sphere.

In all three cases, the modules have led the composing of the block- pattern, but the composition was guided from different principles:
- building substructures thus temporary resistance mechanisms, whose role is to provide the self-support of the blocks during building stages (C, A cases);
- create a link between two courses in order to fix the blocks which belong to the upper course at those of the level previously (B case).

5. Tests and construction process

For any different blocks pattern, a building method was tested. To perform the tests, it has been assumed that the joints are dry joint, no mortar was used. As well it has been adopted a strict constructive process: any course can be laid only when the previous course is completed. With this manner the complete block levels already laid can offer support to the next courses.

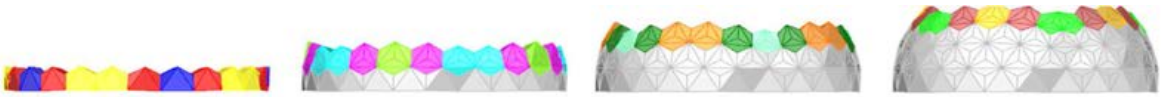


Figure 5.1: Assembly phases from level 1 to 4 corresponding to hexagonal composition of figure 4.1 A).

The first configuration analyzed shown in figure 5.1 is obtained from A) case described in section 4. With these method the blocks are huge, to build a dome of 4 meters radius the dimensions of the block are about 0.7 meters height, and 0.5 meters large. The first 4 levels are composed of 25 hexagonal blocks which then are reduced until of 5 blocks for the next layers. The dome is completed through one hexagonal keystone.
A 3D printed model was made to perform stability tests, which have shown that the inclined contact surfaces couldn't offer enough resources to avoid the sliding. The blocks must be laid in pairs, furthermore, the hexagonal blocks of the uppers levels rotate because they are not enough bounded with the courses before

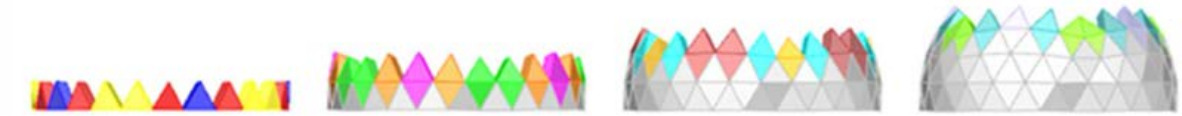


Figure 5.2: Assembly phases from level 1 to 4 corresponding to rhomboidal composition of figure 4.1 B).

The second configuration reported in figure 5.2 and obtained from B) case of section 4., is composed of 150 blocks: 25 triangular geometry at the first level and 125 rhomboidal ones for the rest. Differently, from the A) composition it closed with 5 rhomboids blocks. The geometry assumed permits to bound the blocks between two consequently levels.
The tests highlighted that until near the crown, even the sliding is avoided due to the laying plane, but then both collapse mechanisms manifest.



Figure 5.3: Assembly phases from level 1 to 4 corresponding to the composition of figure 4.1.C

Referring in figure 5.3, C) case of section 4., the last solution consists of an ulterior subdivision of the bricks, this leads to an increase of the difficulty of building, but even the capacity to prevent overturning grows. The blocks have variable size, generally similar to the common bricks, but the shapes are different. Each shape is studied to a specific role, the smaller blocks allow to link two levels and the bigger ones complete the substructures required to find the balance state. The method requires a 425 different blocks shape and unfortunately, during the tests even this solution exhibits failures.
Despite the arrangements, depending on the slope of the contact surfaces, from a level forward the sliding manifests. Thus, under construction, to increase the stability an eccentric load is applied which once the ring is closed can be removed and repeat the procedure for the following rings, figure 5.4.



Figure 5.4: Test configuration of 4.1.C).

6. Conclusion

As proved by the historical technologies developed in different cultures, the desire to find self-balancing technologies is certainly not recent. Today, the new attention about masonry structures due to sustainability drives the rediscovery of many of these lost technologies. From the study of the historical method and the characteristics that guarantee the construction of self-balancing structures can be summarized in two distinct fields:
- the materials, especially of the mortar joints;
- the geometry of the blocks and the whole structures.

The study of historical construction methods combined with the use of contemporary technologies could lead to the definition of economically and energetically sustainable methods. In the ambitious vision to define a dry self-balanced method, the geometry and the stereotomy of the blocks assume extreme importance.
This is also evidenced by the equations (4) (5) in which it is evident that the self-weight system cannot guarantee to avoid sliding or overturning regardless of inclination. For these reasons, it is necessary to identify temporary resistant mechanisms that permit to reach a equilibrate state, even during construction.
The physical tests, although limited, have highlighted the difficulty of building temporary resistance mechanisms. However, the precautions adopted, figure 5.4, allowed the construction of a self-balanced dry model, providing the bases to develop this research.

References

[1] D. Wendland, "Traditional vault construction without formwork: Masonry pattern and vault shape in the historical technical literature and in experimental studies," *International Journal of Architectural Heritage*, 1.4, pp. 311-365, 2007.

[2] M. H. Ramage, J. A. Ochsendorf and P. Rich, "Sustainable Shells: New African vaults built with soil-cement tiles," *Journal of the International Association for Shell and Spatial Structures*, 51.4, pp. 255-261, 2010.

[3] A. Pizzigoni, V. Paris, M. Pasta, M. Morandi and A. Parsani, "Herringbone naked structure," in *Proceedings of IASS Annual Symposia* 2018, International Association for Shell and Spatial Structures (IASS), July 2018, pp. 1-6.

[4] De Wolf, Catherine, M. Ramage and J. Ochsendorf, "Low carbon vaulted masonry structures," *Journal of the International Association for Shell and Spatial Structures*, 57.4 pp. 275-284, 2016.

[5] J. Dahmen and J. F. Muñoz, "Earth masonry unit: Sustainable CMU alternative," *International Journal of GEOMATE,* vol.6, pp. 903-903, Nov. 2013.

[6] A. Heath, M. Lawrence, P. Walker and C. Fourie, C 2009, "The compressive strength of modern earth masonry," in: *11th international conference on non-conventional materials and technologies, Nocmat,* 2009. pp. 6-9.

[7] L. Davis, M. Rippmann, T. Pawlofsky and P. Block, *Innovative funicular tile vaulting: A prototype vault in Switzerland. Structural Engineer, 90.11, pp. 46-55, 2012.*

[8] J. Heyman, *The Stone Skeleton: Structural Engineering of Masonry Architecture*, Cambridge University Press, 1997.

[9] D. D'Ayala and C. Casapulla, *"Limit state analysis of hemispherical domes with finite friction. Historical constructions, possibilities of numerical and experimental techniques"*, 2001, pp. 617-626.

[10] A. Giuffrè, *Letture sulla meccanica delle murature storiche*, 1991.

[11] J. Magnus and Wenninger, *Spherical Models*, Cambridge, 1979.

Proceedings of the IASS Annual Symposium 2019 – Structural Membranes 2019
Form and Force
7 – 10 October 2019, Barcelona, Spain
C. Lázaro, K.-U. Bletzinger, E. Oñate (eds.)

Dual Boundary Element Method applied in aircraft fuselage fatigue analysis

Thiago Arnaud Abreu de OLIVEIRA

*University of Brasília
Asa Norte, SQN 406, Bloco K, Ap. 208, Brasília, Brazil
eng.thiagoarnaud@gmail.com

Abstract

The continuum mechanics deals with the interaction between two bodies in order to analyze the stresses in the domain due to the contact load. In this way, to compute the stresses, it is considered each body as a semi-infinite in extent and having a plane surface. The Boundary Element Method (BEM) appears as a numerical technique for evaluating this type of problem. Using this technique, the boundary is discretized and the stresses are computed in the body domain. This paper consists of the multiscale analysis via Dual Boundary Element Method (DBEM) of fatigue life of aircraft fuselage plate. The macro analysis is evaluated through the stress field in the plate due to continuum mechanics. With this stress field, a micro element, composed by different distribution of cracks, is subjected to fatigue and analyzed by Dual Boundary Element Method (DBEM). This is accomplished using the software BemCracker2D obtaining fatigue life data in each crack increment. For this, advanced computational techniques were developed to evaluate the fracture mechanics behavior with the purpose of ensuring the integrity and the good functioning of the fuselage during its design lifespan.

Keywords: Dual Boundary Element Method, Multiscale Analysis, Fatigue, Aircraft Fuselage

1. Introduction and Theory

From the technical point of view, it is sought to develop structures that are subject to combinations of external loads in a way that works in the usual situation and does not reach the respective Ultimate and Service Limit States [1]. For this, the knowledge of the stress field is a necessary condition to predict the behavior of these elements to avoid combinations that provoke a Limit State.

This paper analyzes the growth of aircraft fuselage subjected to external loads evaluated from the continuum mechanics [2]. In this way, a macro analysis of stresses in a fuselage plate is realized from the theory of the continuum, and after it is analyzed the behavior of the advance of the crack in this plate to evaluate fatigue, residual strength, Stress Intensity Factors, crack path and the deformations at every crack increase. The main objective is to evaluate from the continuum mechanics, cracked fuselage plates when subjected to continuum stresses. And, as specific objectives define crack propagation to obtain fracture mechanics parameters at each increment, such as: Stress Intensity Factors, number of loading cycles (fatigue), deformations and residual strength [3-12].

Fatigue is characterized by a cyclic loading process that causes progressive internal cumulative structural damage. After a certain number of cycles, the cracks can reach critical lengths that can make the structure unstable and, in some cases, lead to collapse. Admitting an elastic half-space body shown in Figure 1. External loads p(x) and q(x) act on the surface over the region from x = -a to x = b while the remainder of the body is free from loads. The stress components σ_x, σ_y, τ_{xy} at all points through the solid are computed according to [13, 14] shown in Equations 1, 2 and 3.

Copyright © 2019 by Thiago Arnaud Abreu de OLIVEIRA
Published by the International Association for Shell and Spatial Structures (IASS) with permission.

$$\sigma_x = -\frac{2y}{\pi}\int_{-a}^{b}\frac{p(s)(x-s)^2}{((x-s)^2+y^2)^2}ds - \frac{2}{\pi}\int_{-a}^{b}\frac{q(s)(x-s)^3}{((x-s)^2+y)^2}ds \quad (1)$$

$$\sigma_y = -\frac{2y^3}{\pi}\int_{-a}^{b}\frac{p(s)}{((x-s)^2+y^2)^2}ds - \frac{2y^2}{\pi}\int_{-a}^{b}\frac{q(s)(x-s)}{((x-s)^2+y^2)^2}ds \quad (2)$$

$$\tau_{xy} = -\frac{2y^2}{\pi}\int_{-a}^{b}\frac{p(s)(x-s)}{((x-s)^2+y^2)^2}ds - \frac{2y}{\pi}\int_{-a}^{b}\frac{q(s)(x-s)^2}{((x-s)^2+y^2)^2}ds \quad (3)$$

2. Methodology

To achieve the objectives a routine was developed in Matlab to automate the stress field derived from continuum mechanics based on [13, 14] and showed in Eqs. 1, 2 and 3. From the stress field, it is analyzed the crack propagation in an infinitesimal element through Dual Boundary Element Method (DBEM) using BemCracker2D [15, 16] to obtain the required parameters. The DBEM has several advantages over other methods, mainly due to the simplified modelling of the cracked area, direct SIF calculation, reduced run times and accurate crack growth simulation [17-19].

2.1. Macro element analysis

Figure 2 shows the model of the continuum problem to be analyzed. *P* and *Q* are normal and shear loads (MPa), respectively, and they can be non-uniform with lengths *a* and *b* (cm). With automation, loads *P*, *Q* (MPa) and *a, b* (cm) will assume the values in Table 1.

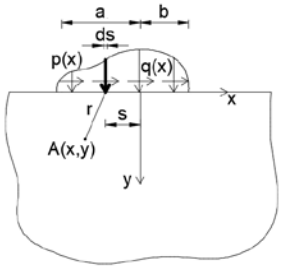


Figure 1: Model of the continuum mechanics

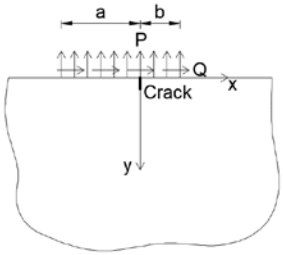


Figure 2: Macro element analysis

Table 1: Loading Series

	P	Q	a	b
Loading Series 1	1000	0	-10	10
Loading Series 2	1000	0	-10	0
Loading Series 3	1000	1000	-10	10
Loading Series 4	1000	1000	-10	0
Loading Series 5	0	1000	-10	10
Loading Series 6	0	1000	-10	0

2.2. Micro element analysis

From the applied external load, the micro element is subject to stress in the directions x (σ_x), y (σ_y), and shear (τ), according to Figure 3. The value is obtained directly from the stress field of Eqs. 1, 2 and 3 considering a square of 1 cm of side located in the origin of the axis (x, y) of Figure 2. The pre-established crack has initial size of 0.1 cm.

3. Results

For the 1 x 1 cm micro element located at the axis origin shown in Figure 2 with a preexisting crack of 0.1 cm size subjected to the loading series 1, 2 and 3 presents the following stress fields indicated in Table 2. Applying these stress fields, the crack growth path and deformation results are shown in Figures 4, 5, 6, 7 and 8 for each loading series, respectively. The objective results of this work are shown in Tables 3, 4, 5, 6, 7 and 8 for each increment of crack of size 0.05 cm.

Table 2: Stress field in the micro element (MPa)

Loads (MPa)	σ_x	σ_y	τ
Loading Series 1	999.87	1000.00	0.00
Loading Series 2	499.94	500.00	318.31
Loading Series 3	999.87	1000.00	999.87
Loading Series 4	0.00	818.31	818.25
Loading Series 5	0.00	0.00	999.87
Loading Series 6	0.00	318.31	499.94

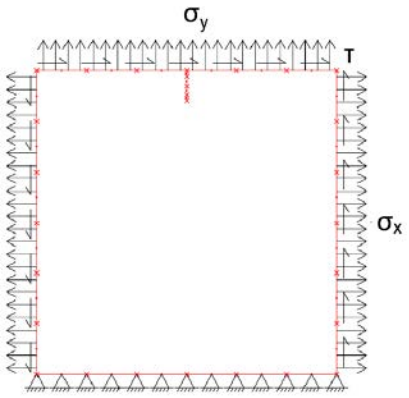
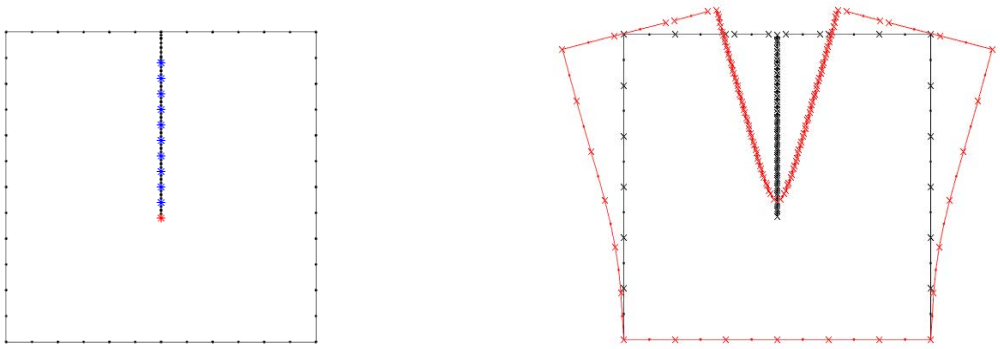
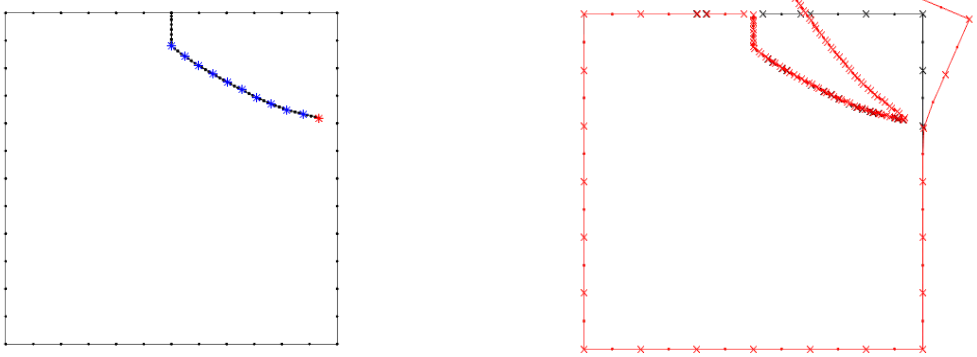


Figure 3: Micro element stress field



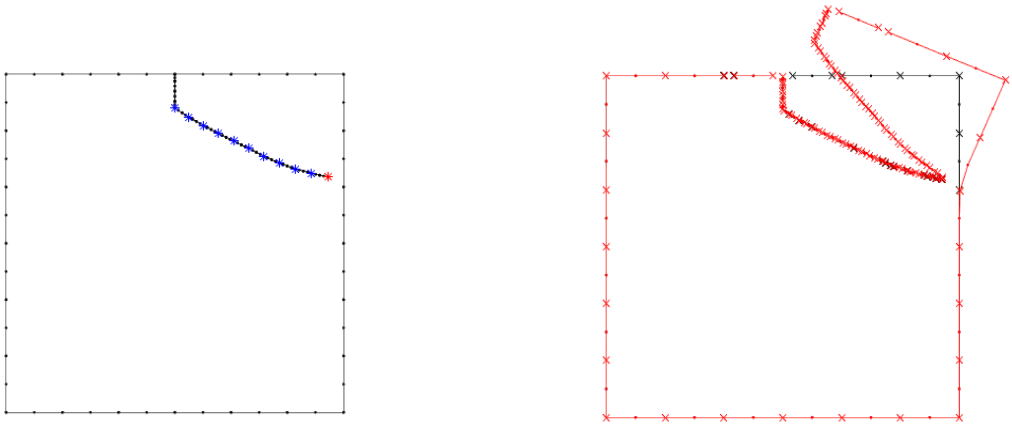
(a) Crack growth (b) Deformed mesh

Figure 4: Fuselage behaviour Loading Series 1



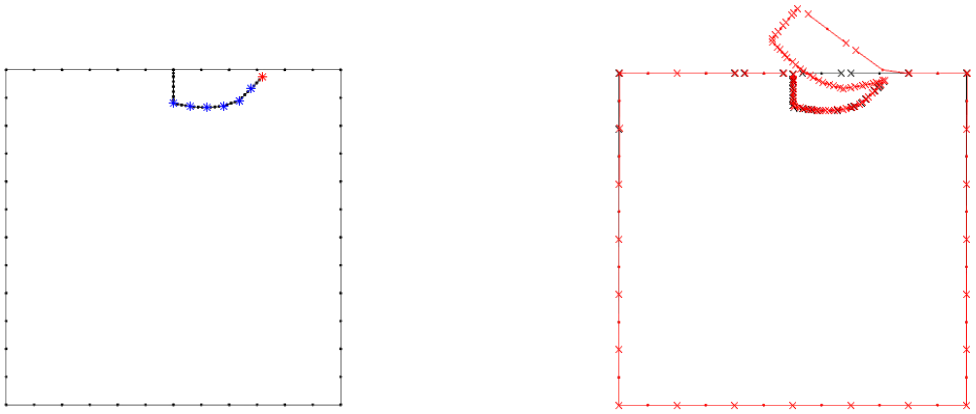
(a) Crack growth (b) Deformed mesh

Figure 5: Fuselage behaviour Loading Series 2



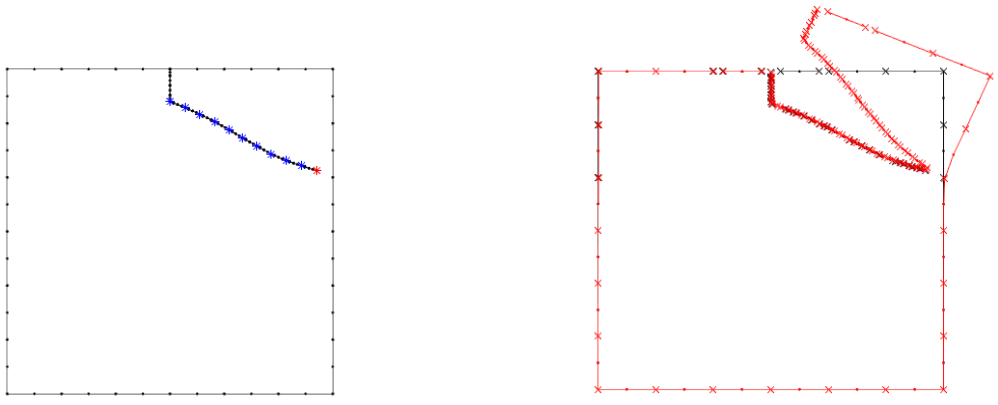
(a) Crack growth (b) Deformed mesh

Figure 6: Fuselage behaviour Loading Series 3



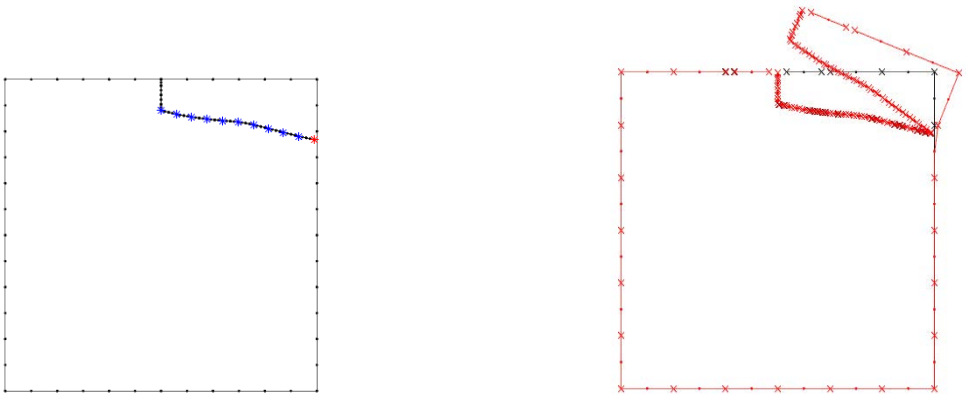
(a) Crack growth (b) Deformed mesh

Figure 7: Fuselage behaviour Loading Series 4



(a) Crack growth (b) Deformed mesh

Figure 8: Fuselage behaviour Loading Series 5



(a) Crack growth (b) Deformed mesh

Figure 9: Fuselage behaviour Loading Series 6

Table 3: Results for Loading Series 1

Crack increment	Residual Strength	Load Cycles	SIF I (MPa√m)	SIF II (MPa√m)	SIF-EQ (MPa√m)
0	0	0	72.0622	-1.99E-12	1
1	0.755681	52.49072	95.3607	3.87E-12	1.32331
2	0.599116	74.93781	120.281	5.71E-12	1.66913
3	0.488826	85.94768	147.419	3.49E-12	2.04572
4	0.407959	91.83705	176.641	5.77E-12	2.45122
5	0.347234	95.2159	207.532	9.02E-12	2.8799
6	0.300915	97.27797	239.477	1.13E-11	3.3232
7	0.265304	98.61077	271.621	1.43E-11	3.76926
8	0.237991	99.52177	302.793	1.37E-11	4.20183
9	0.217433	100.1813	331.422	1.50E-11	4.59911
10	0.202717	100.6895	355.482	1.77E-11	0

Table 4: Results for Loading Series 2

Crack increment	Residual Strength	Load cycles	SIF I (MPa√m)	SIF II (MPa√m)	SIF-EQ (MPa√m)
0	0	0	36.0315	-18.1037	1
1	0.632296	213.5569	73.2124	-0.84049	1.58154
2	0.462899	262.0393	99.9985	-1.30234	2.1603
3	0.352915	280.5802	131.166	-1.60581	2.83354
4	0.269149	288.3648	171.998	-1.84885	3.71541
5	0.200498	291.5654	230.901	-2.1395	4.98759
6	0.143529	292.7709	322.502	-4.36119	6.96725
7	0.097036	293.167	477.023	-6.43715	10.3055
8	0.060193	293.2741	769.099	-7.71436	16.6134
9	0.032617	293.2959	1419.23	-16.9419	30.6589
10	0.015239	293.2988	3037.89	-30.1767	0

Table 5: Results for Loading Series 3

Crack increment	Residual Strength	Load cycles	SIF I (MPa√m)	SIF II (MPa√m)	SIF-EQ (MPa√m)
0	0	0	72.0622	-56.8669	1
1	0.625724	12.19713	180.323	-2.97177	1.59815

2	0.457403	14.90175	246.723	-3.10891	2.18626
3	0.349803	15.9353	322.623	-3.83444	2.85875
4	0.267462	16.37333	421.986	-3.77599	3.73886
5	0.199112	16.55436	566.807	6.25634	5.02231
6	0.14179	16.62216	795.865	-11.0773	7.05268
7	0.094871	16.644	1189.55	-14.2971	10.5406
8	0.057789	16.6497	1953	-19.7375	17.3044
9	0.030269	16.65079	3728.16	-50.1163	33.037
10	0.014518	16.65092	7772.58	-112.564	0

Table 6: Results for Loading Series 4

Crack increment	Residual Strength	Load cycles	SIF I (MPa√m)	SIF II (MPa√m)	SIF-EQ (MPa√m)
0	0	0	-1.03274	-46.5369	1
1	0.462376	58.17771	114.887	-3.02649	2.16274
2	0.295878	68.5422	179.651	-2.94942	3.37977
3	0.204239	71.15631	260.284	-3.69231	4.89622
4	0.13787	71.94176	385.551	-6.18795	7.25323
5	0.067592	72.13344	786.415	-12.7495	14.7947
6	0.023467	72.15182	2241.98	-190.739	0

Table 7: Results for Loading Series 5

Crack increment	Residual Strength	Load cycles	SIF I (MPa√m)	SIF II (MPa√m)	SIF-EQ (MPa√m)
0	0	0	5.26E-12	-56.8669	1
1	0.70775	42.85735	92.7189	-1.92455	1.41293
2	0.533504	66.2019	123.024	-2.15511	1.8744
3	0.41769	76.00086	157.148	-2.50916	2.39412
4	0.323276	80.4276	203.06	2.88698	3.09333
5	0.241713	82.31484	271.616	-2.89937	4.13714
6	0.172536	83.03004	380.51	4.25847	5.79588
7	0.116098	83.26259	565.396	-8.58928	8.61339
8	0.071527	83.32451	917.885	-9.54093	13.9807
9	0.038275	83.33682	1715.07	-24.0966	26.1266
10	0.018188	83.33842	3609.64	-40.1977	0

Table 8: Results for Loading Series 6

Crack increment	Residual Strength	Load cycles	SIF I (MPa√m)	SIF II (MPa√m)	SIF-EQ (MPa√m)
0	0	0.00E+00	-0.40058	-28.4337	1
1	0.535001	304.8075	60.9072	-1.49791	1.86915
2	0.364999	387.2771	89.3236	-1.39278	2.73973
3	0.271768	413.3057	119.968	-1.84095	3.67961
4	0.20842	423.7156	156.436	-2.29929	4.79799
5	0.158883	428.1429	205.199	3.25889	6.29394
6	0.115122	429.9184	283.155	-5.37929	8.68646
7	0.074583	430.5016	437.111	-7.33041	13.4078
8	0.040978	430.6351	795.669	11.3547	24.4033
9	0.018362	430.6535	1775.73	-25.0611	54.4615
10	0.011113	430.6551	2045.23	-1348.8	0

4. Conclusion

The crack paths follow the stress field presented in Table 2. Loading Series 1 result in a linear crack path due to the symmetrical stress field without shear stress. The crack growth in Loading Series 2 is similar to Loading Series 3 since the stress field is almost half of each other. Loading Series 4 and 6 represent a mixture of high and low magnitude of y-normal and shear stress, respectively. In the first case (LS4) the crack is deflected up. In Loading Series 5 there is the crack growth for pure shear stress.

Now, analyzing the numerical results of residual strength and load cycles in Tables 3 to 8 varying the size of application (LS1, LS3 and LS5 a=b=10 cm ; to LS2, LS4 and LS6 a=0 cm and b=10 cm), comparing the Loading Series 1 and 2 (Tables 3 and 4, respectively) with pure external normal stress (P=1000 MPa), neglecting the external shear load. The residual strength reduces and the number of load cycles increases since the micro stress field reduces. For Loading Series 3 and 4 there is a mixture of normal and shear loads (P=1000 MPa and Q=1000 MPa), in these case the residual strength reduces and the number of load cycles increases, again, since the micro stress field reduces. For Loading Series 5 and 6 with pure external shear load (Q=1000 MPa) residual strength reduces and the number of load cycles increases, again, since the micro stress field reduces.

Analyzing the results of Stress Intensity Factors (SIF), there is a mixed mode fracture and higher values of σ_x, σ_y and τ increases SIF I and SIF II depending on the crack direction. For Loading Series 1, SIF I increases and SIF II is zero for each crack propagation. In all other Loading Series both SIF I and SIF II increase for each crack increment.

Acknowledgements

The authors are grateful to the Brazilian National Research Council (CNPq), to the Brazilian Coordination for the Improvement of Higher Education (CAPES) and to Federal District Research Support Foundation (FAP-DF) for the supporting funds for this research.

References

[1] Melchers, R. E. Structural Reliability Analysis and Prediction. 2. ed. Chichester, United Kingdom: Wiley. 456 p, 1999.
[2] T. Oliveira, G. Gomes, F. Evangelista Jr. Multiscale aircraft fuselage fatigue analysis by the dual boundary element method. Multiscale aircraft fuselage fatigue analysis by the dual boundary element method. Engineering Analysis with Boundary Elements 104, 2019.
[3] T. L. Anderson, Fracture mechanics: Fundamentals ans Applications, Boca, Ed., CRC Press, 2005.
[4] D. Broek, The practical use of fracture mechanics, 1 ed., Netherlands: Kluwer Academic Publishers, 1988.
[5] Z. P. Bazant and J. Planas, "Fracture and size effect in concrete and other quasibrittle materials," CRC Press, 1998.
[6] P. C. Paris and F. Erdogan, "A critical analysis of crack propagation laws," Journal of basic engineering, nº 85, pp. 528-534, 1960.
[7] A. A. Griffith, "The phenomena of rupture and flow in solids," Philosophical Transactions of the Royal Society of London, vol. 221, pp. 163-198, 1921.
[8] A. A. Griffith, "The theory of rupture," First International Congress of Applied Mechanics, nº In C. B. Biezeno and J. M. Burgers, pp. 55-63, 1924.
[9] G. R. Irwin, "Analysis of stress and strain near the end of a crack traversing a plate," Journal of Applied Mechanics, vol. 24, pp. 361-364, 1957.
[10] G. R. Irwin, "Onset of Fast Crack Propagation in High Strength Steel and Aluminium Alloys," Sagamore Research Conferece Proceedings, vol. 2, pp. 289-305, 1956.
[11] J. R. Rice, "A path independent integral and the approximate analysis of strain concentration by notches and cracks," Journal of applied mechanics, vol. 35, pp. 379-386, 1968.

[12] J. R. Rice, "The mechanics of crack tip deformation and extension by fatigue," Syrup. on fatigue crack growth, nº ASTM-STP-415, 1967.
[13] Johnson K. L. *Continuum mechanic,* Cambridge University Press, 1985.
[14] Sackfield A., Hills D. A., Nowell D. *Mechanics of elastic continuums*, Butterworth-Heinemann, ISBN**:** 9781483291949, 45-48, 1993.
[15] G. Gomes and M.A.M. Noronha, A B-Rep data structure and object GUI programming to implement 2D boundary elements. International Journal of Applied Mathematics and Computation. 4 (2012) 369-381.
[16] G. Gomes, A. M. Delgado Neto and L. C. Wrobel, Modeling and view of 2D cracks using Dual Boundary Integral Equation (in Portuguese), Brasília/DF, Brazil, DF: Proceedings of the XXXVII Iberian Latin-American Congress on Computational Methods in Engineering, ABMEC/RIPE, 2(6), pp. 120-133, 2016, p. 113.
[17] A. Portela, M. H. Aliabadi and D. P. Rooke, "The Dual Boundary Element Method: Efective implementation for crack problems," International Journal for Numerical Methods in Engineering, vol. 33, pp. 1269-1287, 1992.
[18] A. Portela, M. H. Aliabadi and D. P. Rooke, "Dual boundary element analysis of cracked plates: singularity subtraction technique," International Journal of Fracture, vol. 55, pp. 17-28, 1993.
[19] G. E. Blandford, A. R. Ingraffea and J. A. Liggett, "Two-Dimensional Stress Intensity Factor Computations Using the Boundary Element Method," International Journal Numerical Methods in Engineering, nº 17, pp. 387-404, 1981.

Proceedings of the IASS Annual Symposium 2019 – Structural Membranes 2019
Form and Force
7 – 10 October 2019, Barcelona, Spain
C. Lázaro, K.-U. Bletzinger, E. Oñate (eds.)

Element Force Equation Using Multiple Non-stressed Length for Tensegrity Form-finding

Cho Kyi SOE*, Hiroyuki OBIYA[a], Katsushi IJIMA[a], Muhammad N.b. ZAKARIA[b]

*Graduate School of Science and Engineering, Saga University
1 Honjo Saga, 840-8502, Japan
chokyisoe@gmail.com

[a] Department of Civil Engineering and Architecture, Saga University, Japan
[b] Structures and Material Engineering Department, University of Tun Hussenin Onn Malaysia, Malaysia

Abstract

Tensegrity is an outstanding morphological structure that can be stabilized by its self-equilibrium state under no external force. The equilibrium shape of a self-stressed tensegrity is not identical to the shape of an original geometry, and hence, form-finding is required to investigate the equilibrium configurations even for the simple tensegrity structure. Taking the advantage of tangent stiffness method, we proposed the measure potential of elements and introduced the element force equation using multiple non-stressed length in order to find out a wide variety of equilibrium solutions for the proposed tensegrity even under the same condition of connectivity. In this study, a double-layered pentagonal tensegrity structure is examined and the numerical results show that the diversity of various configurations can be expected by controlling the non-stressed length with multiple setting. Moreover, the potential energy is evaluated to cooperate in categorizing the outcoming solutions systematically. Therefore, this analysis gives higher possibility to obtain the different equilibrium solutions for the form-finding analysis of tensegrity structure.

Keywords: Tensegrity structure, form-finding, multiple non-stressed length, tangent stiffness method

1. Introduction

Tensegrity is a unique morphology which is composed of discontinuous compression members with a continuous network of tension members. Pure tensegrities assume pin-jointed structures where the self-weight of composed elements are neglected and the joints are considered to be frictionless. They can maintain their stability by the pre-stressed tensile members and are in self-equilibrium under no external loading [1]. These structures are especially lightweight, aesthetic, flexible, foldable and deployable which have been taking the interest of many researchers over the last few decades. Due to their superior characteristic properties, various aspects of analyses are found to be conducted in order to meet the required purposes for the investigation of tensegrity structures [2] [3].

Finding its equilibrium shape has become one of the key points for designing tensegrity structures, which is known as form-finding analysis [1]. Most of the existing literatures are conducted on the basis of force density method (FDM) which uses the ratio between the internal force and its corresponding member length [4]. Although it is seemed to be a linear equation, in fact, the application of FDM to self-equilibrium tensegrities without self-weight and external forces requires the determination of the feasible sets of force density by non-linear analysis before solving the linear stiffness equation. FDM cannot make a control over the geometrical properties of a structure such as member length in a direct and exact way [5] [6].

Copyright © 2019 by Cho Kyi SOE, Hiroyuki OBIYA, Katsushi IJIMA, Muhammad N.b. ZAKARIA
Published by the International Association for Shell and Spatial Structures (IASS) with permission.

In this study, the form-finding process is approached by the tangent stiffness method (TSM) with the consideration of geometrical non-linear analysis. Obiya [7] studied and proved the accuracy and versatility of tangent stiffness method and the utilization of TSM can also be made in the equilibrium analysis of plane frame structures [8]. Furthermore, TSM can be used in solving the form-finding problems of tensegrity structures. Obiya *et al*. [9] proposed the virtual stiffness for the equilibrium shape analysis of tensegrity and they evaluated the equilibrium solutions by searching the equilibrium path. Soe *et al*. [10] introduced the virtual potential functions having parameters of element measurement and its differential functions as the element force equations prescribing the element behavior. In FDM, it is only possible to use the element force that is proportional to its length in the linear relation. However, TSM can solve the nonlinear problems that allows us to define any type of element force function. Therefore, we examine the element force equation whose potential function has multiple stoppage points in this paper. It is expected to investigate a wide variety of equilibrium solutions by the application of element force equation with multiple non-stressed length for tensegrity form-finding analysis.

2. Form-finding process by tangent stiffness method

The tangent stiffness method evaluates the geometrical nonlinearity caused by elements' rigid body displacement strictly, because of the tangent geometrical stiffness derived by the differential calculus calculation of balanced equation between the element edge force vector and the nodal force vector. Thus we can make rules about the element behavior inside of the element local coordinate no concern with the tangent geometrical stiffness, and the obtained equilibrium solutions adjust to defined element behavior. In other words, the tangent stiffness gives the usefulness that the element behavior can be defined freely.

2.1. General formulation of TSM

Let the vector of the element edge forces independent of each other be indicated by S, and the matrix of equilibrium which relates S to the general coordinate system by J. Then the nodal forces U expressed in the general coordinate follow the equation.

$$U = JS \tag{1}$$

The tangent stiffness equation is expressed as the differential calculus of equation (1).

$$\delta U = J\delta S + \delta J S = (K_0 + K_G)\delta u \tag{2}$$

in which K_0 is the element stiffness which provide the element behavior in element (local) coordinate, and K_G is the tangent geometrical stiffness, δu is nodal displacement vector in general coordinate.

The main feature of tangent stiffness method is its two stiffness matrix forms in which the behavior of material and geometrical orientation can be emphasized separately. In other words, the pure structural properties can be effectively and strictly controlled without concerning the material properties of the structure.

2.2. Element force equation for setting multiple non-stressed length

In the form-finding process by the tangent stiffness method, we can set the element behavior by defining the measure potentials. Therefore, many types of the element can be used according to the purpose of the analyses. Therefore, we designated the stiffer element as a truss element and for the softer element, the axial force line elements can be defined as the element force equations by differential calculus of the measure potentials of P as in equation (3).

$$N = \frac{dP}{dl} \tag{3}$$

in which N is axial force and l is the length of elements. Actually, we can freely define any of the measure potential or the element force equation (4) for the softer element, whose potential has multiple stoppage points, is examined in order to lead the diversity of solutions. Moreover, equation (5) is the differential of equation (4) to compose the tangent stiffness.

$$N = C(l - l_{01})(l - l_{02}) \dots \dots (l - l_{0n}) \tag{4}$$

$$\delta N = \left(\sum_{i=1}^{n} \frac{1}{l - l_{0i}} \right) N.\delta l \tag{5}$$

in which l_{0n} is the non-stressed length of elements conducting the stoppage points of the potential.

2.3. Tangent stiffness equation for each element

Let α be the components of cosine vector of an axial force line element, which connects node 1 and node 2 of an element, and we can rewrite the equation (1) as:

$$\begin{bmatrix} U_1 \\ U_2 \end{bmatrix} = \begin{bmatrix} -\alpha \\ \alpha \end{bmatrix} N \tag{6}$$

Substituting the equation (6) to the above equation (2), and make it matrix form.

$$\delta \begin{bmatrix} U_1 \\ U_2 \end{bmatrix} = (K_G + K_0)\, \delta \begin{bmatrix} u_1 \\ u_2 \end{bmatrix} \tag{7}$$

Here, we have to notice that the tangent geometrical stiffness K_G can be used for any type of elements regardless of the definition of the element potential. Thus the form of K_G is always as following.

$$K_G = \frac{N}{l} \begin{bmatrix} e - \alpha\alpha^T & -e + \alpha\alpha^T \\ -e + \alpha\alpha^T & e - \alpha\alpha^T \end{bmatrix} \tag{8}$$

On the other hand, K_0 should be prepared according to the element force equations. In case of equation (5).

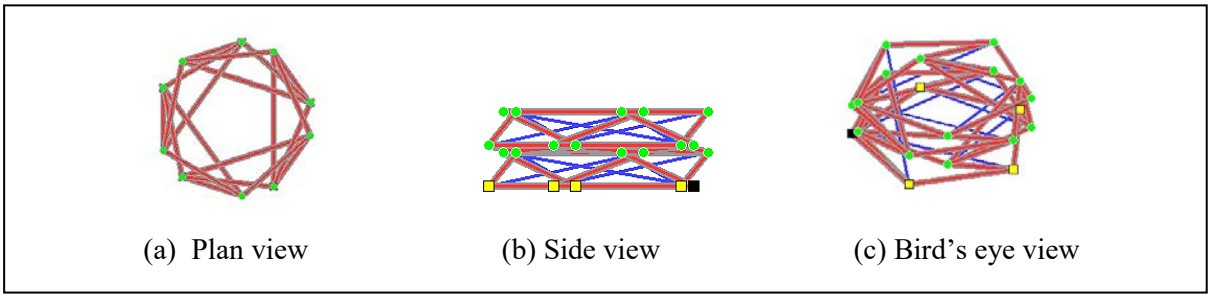
$$K_0 = \left(\sum_{i=1}^{n} \frac{N}{l - l_{0i}} \right) \begin{bmatrix} \alpha\alpha^T & -\alpha\alpha^T \\ -\alpha\alpha^T & \alpha\alpha^T \end{bmatrix} \tag{9}$$

2.4. Total potential energy of each equilibrium solution

Let E be the strain energy for the stiffer element (strut), V is the axial line potential for the softer element (cable) and W is the loss potential of the external force. Then the total potential energy Π can be defined as below.

$$\Pi = E + V - W \tag{10}$$

3. Numerical example



(a) Plan view (b) Side view (c) Bird's eye view

Figure 1: Connectivity and support condition of primary unbalanced configuration

The form-finding analysis is done with a double-layered pentagonal tensegrity structure composed of ten stiffer elements (struts) and twenty softer elements (cables) as shown in figure 1. The application of the measure potential and the virtual stiffness allows us to set a free choice of each coefficient. For this numerical example, we apply the coefficients for stiffer elements in equation (4) as $C=2.0E10^{11}$ and $n=1$ and the non-stressed length is fixed as 7.0 m. Therefore, the stiffer elements behave as the boundary condition for the element distance. On the other hand, the coefficients of softer elements are adopted as $C=1000$ and $n=3$, and the equilibrium shapes are examined with the change of the non-stressed length.

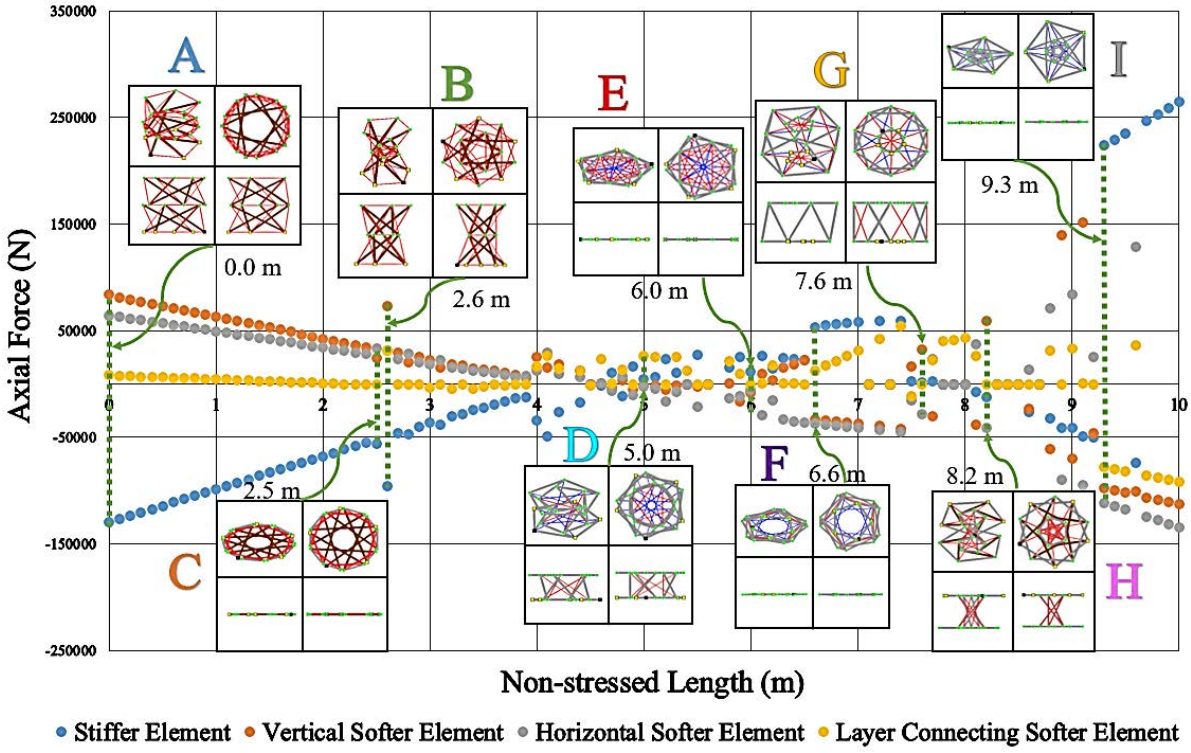


Figure 2: Result of one time analysis of a two-layered pentagonal tensegrity

Figure 2 shows the relation between the non-stressed length and the axial force of the equilibrium solutions resulted from one time analysis from the origin of the primary unbalanced configuration. The shape of each solution is resembled by a set of each dot in four color series of axial force. Axial force of the stiffer element is represented by blue color whereas orange and grey color indicate ones of the vertical and horizontal softer elements and yellow color for one of the connections between layers. The graph in figure 2 shows the discrete solutions obtained by the one time analysis when l_{03} in equation (4) is let to move between the range of 0-10 m with 0.1 m of interval while l_{01} and l_{02} are fixed at 0.1 m and 0.3 m respectively. The total 90 of converged equilibrium solutions are achieved out of 100 trials with the wide diversity of shape formation.

Meanwhile, total potential energy of discrete solutions of one time analysis is checked in figure 3 in order to categorize their similarity. Total 9 series can be expected and each series is denoted by a distinct color and represented by example solutions (A~I). By following the similarity of each color series, it can be organized into total 6 groups in which some color series are found to be related and corresponding to each other. The thick line at 7 m indicates the non-stressed length of softer element become equal to that of the stiffer element. Each solution in each group is picked up and reset as the primary form to conduct the incremental analysis where the non-stressed length of softer element is continuously increased or decreased in order to follow the path of each discrete solution.

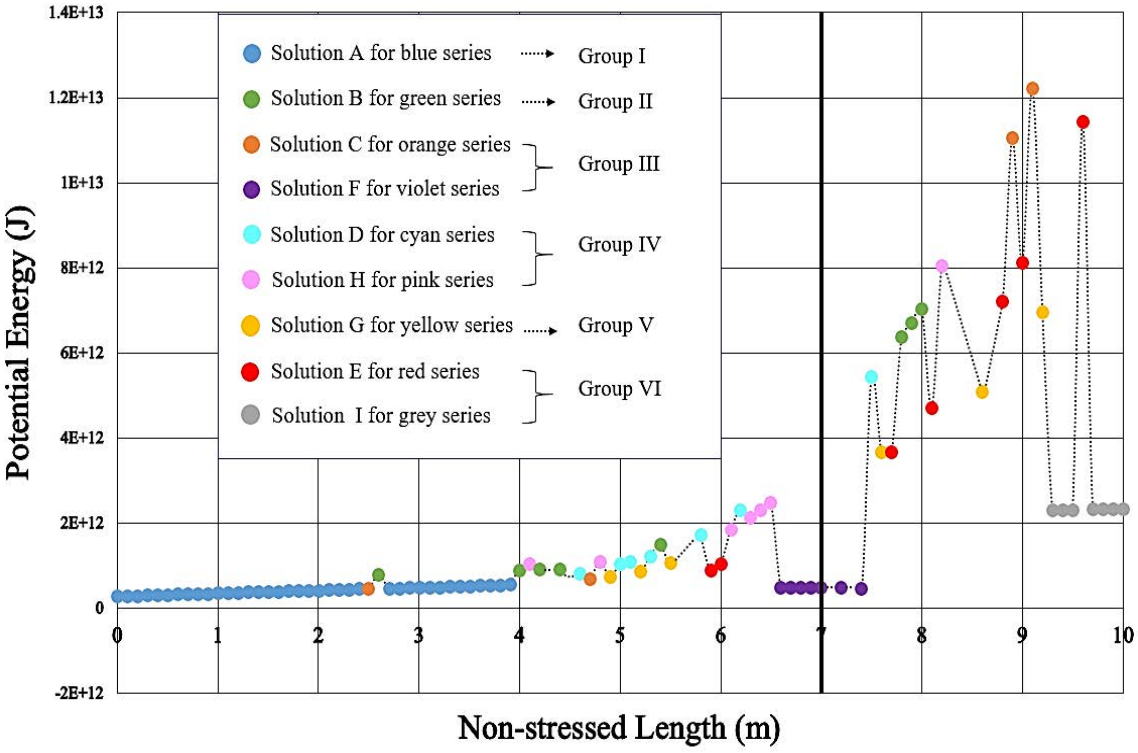


Figure 3: Potential energy for one time analysis

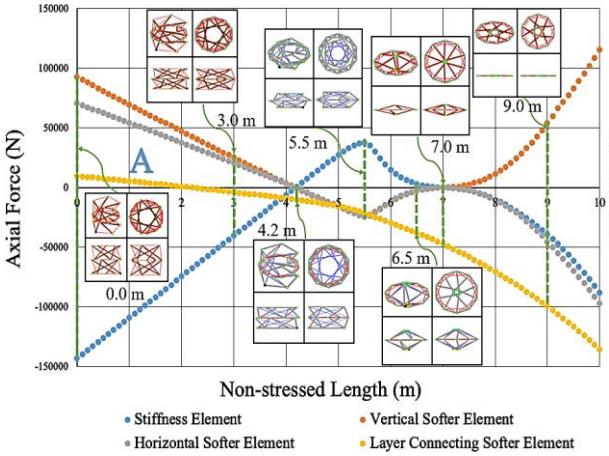


Figure 4: Incremental analysis for Group I

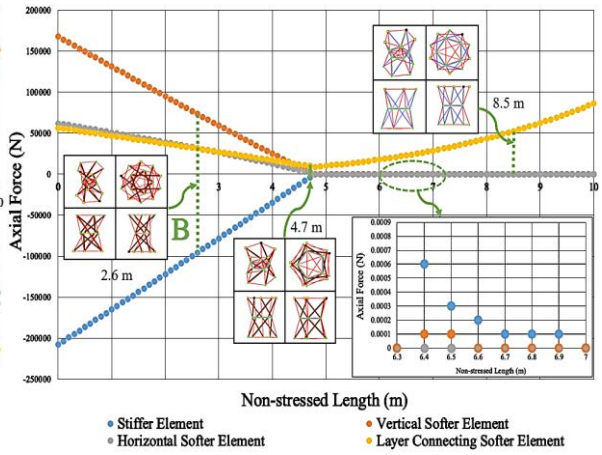


Figure 5: Incremental analysis for Group II

Figure 4 shows the pattern for Group I in which solution A gives the continuous path of equilibrium solutions where the proposed tensegrity structure is smoothly and perfectly folded along with the gradual increment of softer non-stressed length. It can be seen that most of the discrete solutions of blue series from figure 3 fall into this pattern, forming the strongest path. Figure 5 is for the solution B of Group II in which the three dimensional solution suffers a large amount of difference in axial force after the critical point of 4.7 m where the axial force of layer connecting softer element is much larger compared to that of vertical and horizontal softer elements. These small amount of axial forces are zoomed-in and attached in the figure 5.

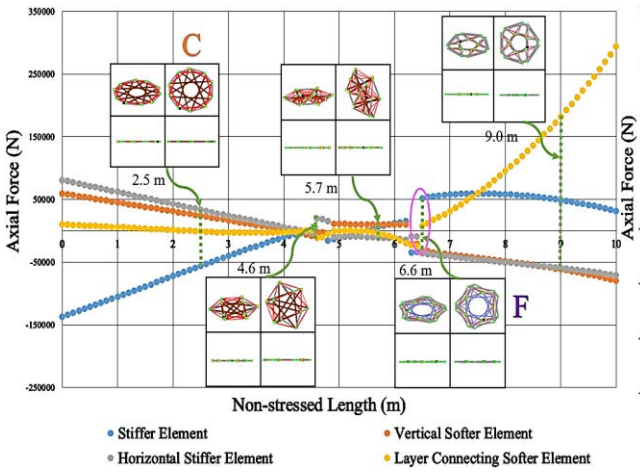


Figure 6: Incremental analysis for Group III

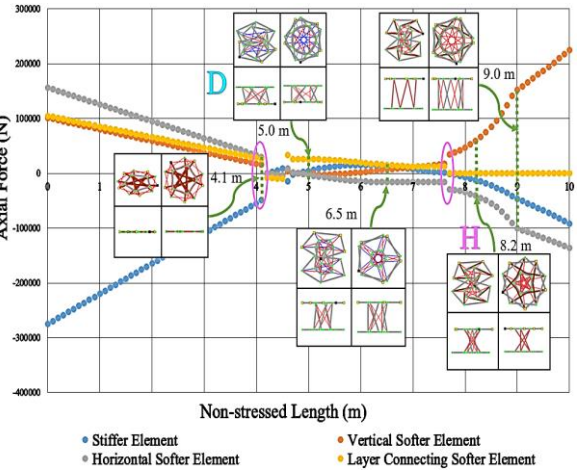


Figure 7: Incremental analysis for Group IV

The pattern drawn in figure 6 belongs to Group III where the two dimensional solution C of orange series and solution F of violet series are associated with each other after the snap through at 6.6 m. Similarly, solution D and solution H are formed in the same Group IV in which cyan series is found to be sandwiched between two snap through points at 4.1 m and 7.7 m of pink series as shown in figure 7. Group V in figure 8 indicates the consecutive pattern of solution G that deployed steadily along with the gradual increment of softer non-stressed length. The two dimensional equilibrium solution E of pink series is corresponding to Group VI where the path is deviated at 7.5 m, forming the solution I of grey series as depicted in figure 9. Therefore, in this analysis with the setting of proposed non-stressed lengths, total 6 groups can be summarized by tracing the paths of 9 color series resulted from 90 discrete equilibrium solutions. Moreover, the diversity of equilibrium shape formation is examined by the variation of setting different non-stressed lengths of softer element for the same primary unbalanced form of figure 1.

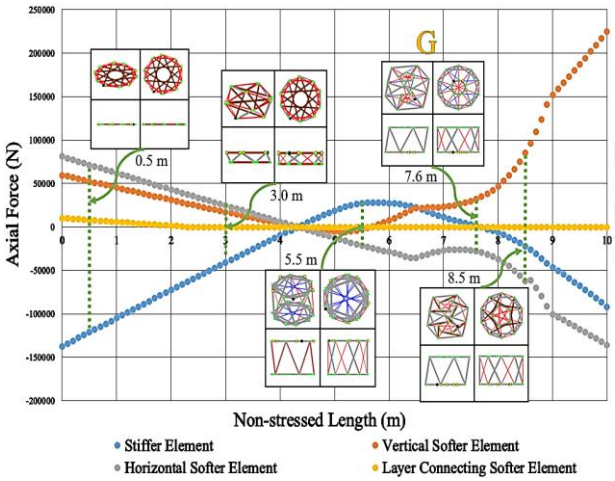


Figure 8: Incremental analysis for Group V

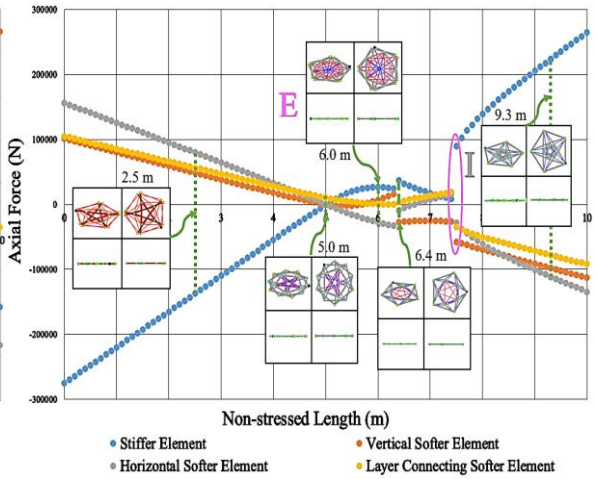


Figure 9: Incremental analysis for Group VI

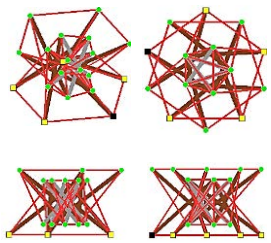
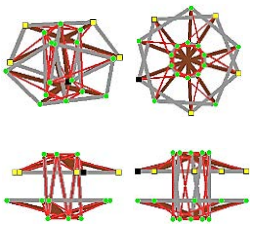
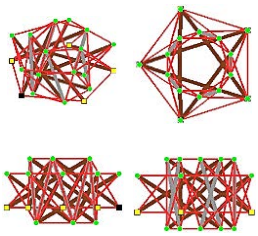
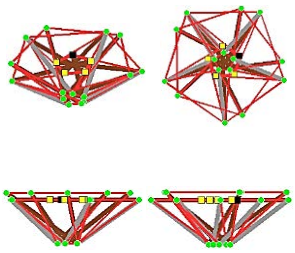
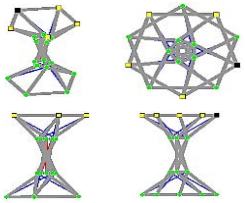
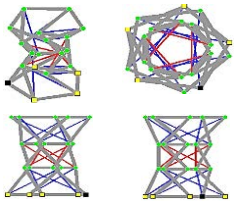
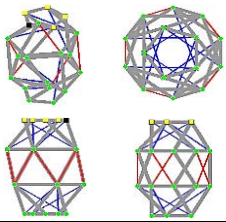
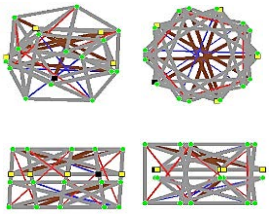
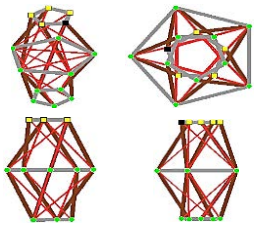
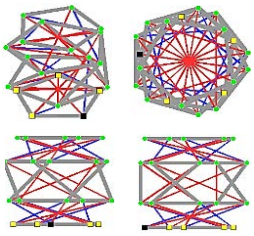
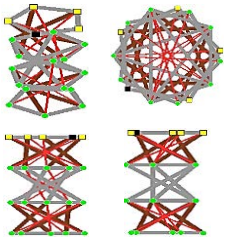
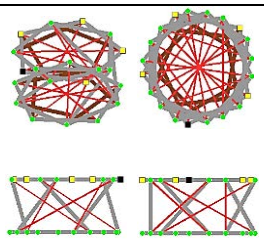
			
$l_{01} = 0.5$ m $l_{02} = 3.5$ m $l_{03} = 4.8$ m	$l_{01} = 2.0$ m $l_{02} = 6.0$ m $l_{03} = 4.8$ m	$l_{01} = 2.5$ m $l_{02} = 5.0$ m $l_{03} = 2.9$ m	$l_{01} = 4.0$ m $l_{02} = 6.0$ m $l_{03} = 9.0$ m
			
$l_{01} = 0.5$ m $l_{02} = 0.5$ m $l_{03} = 5.9$ m	$l_{01} = 1.5$ m $l_{02} = 1.0$ m $l_{03} = 3.5$ m	$l_{01} = 2.5$ m $l_{02} = 5.0$ m $l_{03} = 2.7$ m	$l_{01} = 4.0$ m $l_{02} = 6.0$ m $l_{03} = 5.1$ m
			
$l_{01} = 3.0$ m $l_{02} = 8.0$ m $l_{03} = 3.5$ m	$l_{01} = 4.5$ m $l_{02} = 8.5$ m $l_{03} = 4.4$ m	$l_{01} = 4.0$ m $l_{02} = 7.0$ m $l_{03} = 8.0$ m	$l_{01} = 6.9$ m $l_{02} = 6.9$ m $l_{03} = 7.1$ m

Figure 10: Results of one time analysis with multiple setting of non-stressed length

Figure 10 illustrates that various types of three dimensional equilibrium solutions can be expected from one time analysis by the combination of different multiple non-stressed lengths even for the same initial primary unbalanced configuration. By using the method of controlling the non-stressed length, the number of equilibrium solutions obtained is 3 times more than by the method which seeks the self-equilibrium solutions as the points with zero external forces on path finding process [9]. Therefore, the application of multiple non-stressed length makes us expect the higher possibility of obtaining equilibrium solutions in the shape analysis of tensegrity.

4. Conclusion

The form-finding of tensegrity is associated with the geometrical nonlinear analysis. Therefore, the tangent stiffness method for solving the geometrical nonlinear problems allows us to define many types of element force equation. Thus, it is a great advantage to apply “virtual” element force equations, and in this study, the concept of diversity is highlighted by the proposal of the equation with multiple non-stressed length. It is found that the discrete solutions resulted from one time

analysis of the proposed tensegrity model has its own unique tendency to form shapes according to the variation of the non-stressed length of softer element. In the incremental analysis, the correlated paths are observed in each pattern with the illustration of the example equilibrium solutions (A~I). During the analysis, some equilibrium solution series resemble plain shaped structures when the non-stressed length of softer element is close to that of stiffer element or getting too long near 10 m with the low potential energy as shown in figure 3. However, various types of three dimensional equilibrium solutions can be expected by controlling the non-stressed length with multiple setting as shown in figure 10. The proposed tensegrity models are simple but unique which will be in accordance with the fundamental concepts of tensegrity structures. Therefore, the analysis is able to find out numerous equilibrium solutions even under the same connectivity and give us much information about the unique tendency of shape formation. All in all, this analysis can explore a wider diversity of form-finding procedure of tensegrity structures.

References

[1] A.G. Tibert, S. Pellegrino, "Review of Form-finding Methods for Tensegrity Structures," *International Journal of Space Structures,* vol. 18, no. 4, pp. 209-223, 2003.

[2] H. Furuya, "Concept of deployable tensegrity structures in space application," *International Journal of Space Structures,* vol. 7, pp. 143-151, 1992.

[3] C. Paul, H. Lipson, F. Valero-Cuevas, "Design and control of tensegrity robots for locomotion," *IEEE Transaction on Robotics,* vol. 22, pp. 944-957, 2006.

[4] K. Linkwitz, "Form-finding by the "direct approach" and pertinent strategies for the conceptual design of prestressed and hanging structures," *International Journal of Space Structures,* vol. 14, no. 2, pp. 73-87, 1999.

[5] J.Y. Zhang, M. Ohsaki, "Adaptive force density method for form-finding problem of tensegrity structures," *International Journal of Solids and Structures,* vol. 43, no. 18-19, pp. 5658-5673, 2006.

[6] Li-Yuan Zhang, Yue Li, Yan-Ping Cao, Xi-Qiao Feng, "Stiffness Matrix Based Form-finding Method of Tensegrity Structures," *Engineering Structures,* vol. 58, pp. 36-48, January 2014.

[7] H. Obiya, "A study on accuracy and versatile of the tangent stiffness method by separation of element stiffness from geometrical stiffness (In Japanese)," Saga University, Japan, 1998.

[8] H. Obiya, S. Goto, K. Ijima, K. Koga, "Equilibrium analysis of plane structures by the tangent stiffness method," *International Colloquium Stability of Steel Structures,* vol. 2, pp. 305-312, 1995.

[9] H. Obiya, Z. M. Nizam, K. Ijima, N. Kawasaki, A. Matsuo, "A study on equilibrium shape of tensegrity structures with virtual stiffness through some numerical experiments," *Journal of Applied Mechanics JSCE,* vol. 15, pp. 45-56, 2012.

[10] C.K. Soe, Obiya H, Koga D, Nizam Z.M, Ijima K, "Potential function of element measurement for form-finding of wide sense tensegrity," in *IOP Conference Series: Earth and Environmental Science*, Langkawi, Malaysia, 2018.

Proceedings of the IASS Annual Symposium 2019 – Structural Membranes 2019
Form and Force
7 – 10 October 2019, Barcelona, Spain
C. Lázaro, K.-U. Bletzinger, E. Oñate (eds.)

Field tests, laboratory evaluation and modelling of slip joints

Ján BRODNIANSKY*, Tomáš KLAS[a], Prof. Ján BRODNIANSKY[a], Martin MAGURA[a], Jozef RECKÝ[a], Miroslav TILINGER[b]

* Slovak University of Technology in Bratislava, Faculty of Civil Engineering
Radlinského 11, 81005 Bratislava
jan_brodniansky@stuba.sk

[a] Slovak University of Technology in Bratislava, Faculty of Civil Engineering
[b] ELV PRODUKT a.s.

Abstract

Slip-joint connections are rarely used in engineering practice. The reasons for this are various, but it is apparent that the lack of design methods is an important one. Slip joint connection research is long lasting research that has been carried out in Department of Steel and Timber Structures at the Slovak University of Technology since 2007. Various problems have been investigated mainly for engineering praxis. Paper is divided in to three parts: Field tests of transmission line tower described in first part; Second part handles experimental and numerical analysis of slip-joint connection on rounded tubes; Third part is focused on the recent experimental and numerical analysis of slip-joint connection on 8-edged tube. All presented cases were verified by FEM modelling and these numerical results are compared to observations in situ or laboratory experiments. Nowadays appeared practical requirement of describing slip joint connection subjected to bending and torsional loads. Presented research is considered highly applicable in engineering praxis.

Keywords: Slip-joint, laboratory test, FEM model, electrical power masts

1. Introduction

Slip-joint connection is one of the less commonly used methods of assembling multi-segment conical towers. Despite many advantages, slip-joint connections are not so often used in engineering practice. The reasons of rare application are the lack of design methods. The most important parameter - the overlapping length is mentioned in some standards [1] by fixed ratio 1.5 multiple of the diameter. As the segments of this kind of towers are relatively slender in relation to their height, their sections fall into class 4 in majority of cases and it is thus necessary to consider the effect of buckling of the tower web when calculating. The overall calculation requires a more detailed analysis due to non-linear factors, such as inconstant cross-section, effects of friction, etc.

2. Field tests of transmission line tower

The presented analysis concerned a tower of 440 kV electrical transmission line. The towers material is steel S355, it has hex decagonal cross-sectional shape and is 41.40 m high. The structure was fixed to the anchoring platform. Steel cables were used for inducing the loads through steel cables and system of pulleys to hinges on the other end. The hinges were formed by connecting flat articles which hung from a pair of perpendicular portals. The unit construction form of the hinge enabled insertion of pulleys between the flat articles, making it easier to pilot and attach the cables in the horizontal direction. From the hinges, cables stretched down to the groove of the fixtures and attached to the hook of the manual pulley block. Afterwards, it is possible to further increase the loads to the ultimate state of the structure which causes a permanent plastic deformation in the critical spot (figure 1).

Copyright © 2019 by Ján BRODNIANSKY, Tomáš KLAS, Prof. Ján BRODNIANSKY, Martin MAGURA, Jozef RECKÝ, Miroslav TILINGER
Published by the International Association for Shell and Spatial Structures (IASS) with permission.



Figure 1: Test assembly of 440kV transmission line tower

The average diameter of the connection is 1.555 m. The length of the upper segment is 10.6 m, the length of the lower one is 9.6 m. Load is formed by the interaction of bending moment and axial force. Slip joint parameters for presented tower are: Diameter 1.555m; Conicity angle 1°; Web thickness 10mm; Friction coefficient between 0.1 to 0.5; Bending moment 3088,86kNm; Axial force 470,606kN. The FEM analysis focused primarily of comparing multiple variants of overlapping lengths (ranging from 1.0xD to 1.5xD) (figure 2, table 1). Design procedures of slip-joint connection are affected by standards [2], [3] and [4].

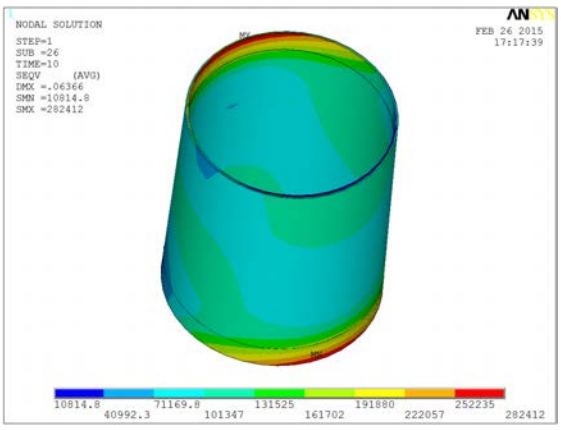


Figure 2: Von Mises stress in the slip joint connection

Table 1: Results of the analysis

Overlap	Friction	
	μ = 0.1	μ = 0.5
	Von Mises stress [MPa]	
1.0D = 1.555m	379.427	248.709
1.1D = 1.771m	326.738	215.381
1.2D = 1.866m	282.412	197.651
1.3D = 2.022m	251.046	174.863
1.4D = 2.177m	224.018	165.084
1.5D = 2.333m	209.873	144.589

The stress levels remain below the structure's characteristic stress (f_{yd} = 355 MPa) and even the buckling-reduced characteristic stress ($f_{yd,red}$ = 328 MPa) up to 1.1 multiple of the diameter, with higher friction coefficient even further. It is possible to assume that the economically reasonable overlapping length is between 1.1 and 1.3 multiple of the tower diameter depending on conditions the structure is in.

3. Experimental analysis of slip-joint connection on rounded tubes

Due to the spatial limits of the laboratory premises, it was necessary to test a smaller sample. The dimensions (the slenderness, in particular) were calculated based on the real structure and the load was adjusted to match the actual load levels. The sample was fixed into the loading frame and afterwards loaded by axial force (through a hydraulic press) and the bending moment (by deflecting the upper base) (figure 3 and figure 4). Simplified method of evaluation of slip joint connection is better described in [5] or [6]. Description of test samples can be found in table 2.



Figure 3: The experimental sample (left – before the loading, right – after the loading

Table 2: The test samples

Segment type	Pic.	Length	Upper diameter	Lower diameter
A – Upper segment	5	1.2m	0.131m	0.142m
B – Lower segment Overlap 1.5d	2	1.2m	0.126m	0.138m
C – Lower segment Overlap 1.2d	1	1.16m	0.126m	0.138m
D – Lower segment Overlap 1.0d	2	1.135m	0.126m	0.138m

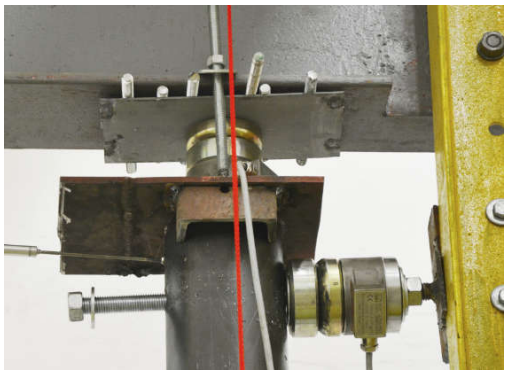


Figure 4: Deflection mechanism near the upper base of the test sample

The tangential stress in the web of the structure was the most important parameter measured by strain gauges HBM 1-LY6/120. Strain gauges were arranged as is shown in figure 5 left. Deflection measuring devices were applied in four locations – by the top base (figure 5 right), at the slip joint (to measure insertion of the lower segment into the upper one), and two more at the fixation point of the lower base.



Figure 5: Left: arrangement of strain gauges on slip joint connection; Right: top base defl. measuring device

3 loading phases were introduced:

Phase 0: Insertion phase determined value (13kN) was applied to achieve required overlapping lenght (table 3).

Phase 1: Centric compression, the axial force of previously determined value (13kN) was applied.

Phase 2: Bending, the upper base was deflected; the deflection was calculated based on the intended value of the bending moment. The deflection of the upper base was amounted to 60mm.

Phase 3: Combined load, where the axial force (13kN again) was applied on the structure bent in the previous phase.

Table 3: Achieved overlapping lengths

Test	Overlapping length	
No.1 Sample B	1.39d	191mm
No.2 Sample C	1.31d	180mm
No.3 Sample D	1.22d	167mm
No.4 Sample D	1.18d	162mm
No.5 Sample B	1.12d	153mm

Experimental results with numerical comparison are shown in table 4 (sample with overlapping length 1.4-multiple of the sample's diameter in this case 191mm). The friction coefficient was measured in the laboratory, its value equal to 0,342.

Table 4: Numerical comparison between experiment and FEM model

Phase	Tangential stress		
	Experiment	Numerical method	Discrepancy
Phase 1 - compression	8.35 MPa	10.47 MPa	20.2%
Phase 2 - bending	45.58 MPa	45.55 MPa	0.1%
Phase 3 - combined	49.03MPa	56.03 MPa	12.5%

All results from the experiment are showing that if the boundary conditions are well documented and respected and possible differences (such as the friction coefficient) are eliminated, the model can be considered accurate for designing common structures of this type. The important "flaw" of the experiment is the semi-rigid support, but it can be also considered acceptable, since in real conditions, the supports of the segments of towers (except for the bottom one) are not fixed but depend on the stiffness of the segment below them.

4. New approach in experimental analysis of slip-joint on 8-edged tube

In cooperation with company ELV PRODUKT first test sample for the calibration of testing methodology was procured. Sample is octagonal (8-edged tube) tube with web thickness of 3mm, both end plates have thickness 14mm. Height of the coupled sample is 4.041m (lower segment 2.209m; upper segment 2.210m), this means overlapping length of 0.378mm (figure 6). For loading it is used simple system of pulleys with steel cable (thickness 5mm) on one end anchored on the top of the sample and on another end to the mechanical pressure Testometric MN: 0500-02059 (figure 7). This device can introduce not only static load conditions, but it is possible to load sample by relatively short pulses and simulate dynamic actions. Overlapping length of the sample represents value in about 3.2d which can be considered not very effective, but this is only first stage of the test duration. In next steps will be cut of a slice of upper segment to ensure lower and lower overlapping length. In table 5 are displayed important dimensions of the test sample.

Table 5: Dimensions of the test sample

Sample part	Length	Web thickness	Lower diameter		Upper diameter	
			Inner*	Outer**	Inner*	Outer**
Lower segment	2.209m	3mm	0.118m	0.128m	0.100m	0.109m
Upper segment	2.210m	3mm	0.111m	0.120m	0.091m	0.099m
Whole sample	4.041m	-	-			
Overlap	0.378m	-	0.378m/0.118m = 3.2d			

*Inner – Inscribed circle; **Outer – Circumscribed circle

It is obvious that the upper segment should be inserted even lower into the lower segment This phenomenon is caused mainly due to the manufacturing imperfections, rounded edge configuration and the lack of the insertion phase (see chapter 3). First two mentioned reason cannot be influenced, but the third one can. Answer to the third one is, not to destroy overlapping part of the sample and to maintain possibility to open slip joint connection for the further treatment (slicing off bottom of the upper segment).

HBM spider8 system consisting from 4 units each has 8 inputs (32 inputs together) is used for measuring. 25 inputs are used as is shown in table 6. Inputs 1-7 are used for inductive displacement transducers; input 8 is used for load cell; inputs 9-25 are used for foil strain gauges. All of the used measuring device positions are displayed in figure 6. The test assembly is shown in figure 7.

Table 6: Measuring devices

No.	Mark	Device	Type of measurement
1.	I1	WA/300MM-L	Displacement [mm]
2.	I2	WA/100MM-L	Displacement [mm]
3.	I3	WA/100MM-L	Displacement [mm]
4.	I4	WA/100MM-L	Displacement [mm]
5.	I5	WA/100MM-L	Displacement [mm]
6.	IZ	WA/50MM-L	Displacement [mm]
7.	IO	WA/50MM-L	Displacement [mm]
8.	LC	S9M/50kN	Force [kN]
9.	TAKV H	1-XY91-6/120	Strain [μm/m]
10.	TAKV V	1-XY91-6/120	Strain [μm/m]
11.	TA30	1-LY11-6/120	Strain [μm/m]
12.	TLKV H	1-XY91-6/120	Strain [μm/m]
13.	TLKV V	1-XY91-6/120	Strain [μm/m]
14.	TL30	1-LY11-6/120	Strain [μm/m]
15.	TA1H	1-XY91-6/120	Strain [μm/m]
16.	TA1V	1-XY91-6/120	Strain [μm/m]
17.	TA2	1-LY11-6/120	Strain [μm/m]
18.	TA3	1-LY11-6/120	Strain [μm/m]
19.	TA4	1-LY11-6/120	Strain [μm/m]
20.	TA5	1-LY11-6/120	Strain [μm/m]
21.	TL1	1-LY11-6/120	Strain [μm/m]
22.	TL2	1-LY11-6/120	Strain [μm/m]
23.	TL3	1-LY11-6/120	Strain [μm/m]
24.	TL4	1-LY11-6/120	Strain [μm/m]
25.	TL5	1-LY11-6/120	Strain [μm/m]

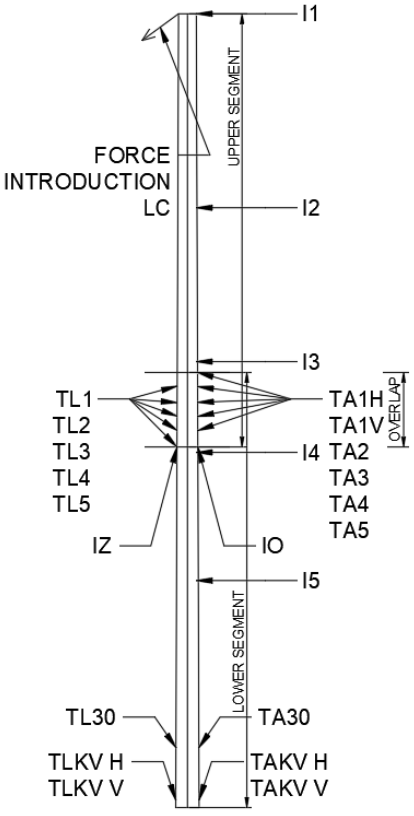


Figure 6: Simplified scheme of the position of measuring devices



Figure 7: Test assembly

First calibration tests were performed in a manner of setting up movement steps on the mechanical pressure Testometric MN: 0500-02059. At first, we choose steps 30mm; 60mm; 90mm; 120mm and

backwards (not going back to 0mm). This proved not to be satisfactory because of small stress in slip joint (according to both FEM model and measurements). The next chosen values of stepping were 60mm; 150mm; 210mm and backwards (not going back to 0mm). Presented stepping was repeated 50 times and after the last cycle reaches 0mm value. Some of the measured values are shown in table 7 to better visualize the course of the experiment.

Table 7: Measured values

Mech. Press. Displace. [mm]	Force LC [kN]	Anchoring stress TL30 [MPa]	Slip joint stress TA1H [MPa]	Slip joint stress TA1V [MPa]	Slip joint stress TL5 [MPa]	Disp. I1 [mm]
60	0.309	29.19	26.04	24,78	1.68	34.35
150	1.347	129.15	39.92	71,19	12.81	96.46
210	1.998	195.91	52.51	105,84	27.51	139.05

All stresses presented in table 7 are in good agreement with FEM model presented in figure 8 and 9 (Only vertical and horizontal stresses on upper segment in slip joint location are shown).

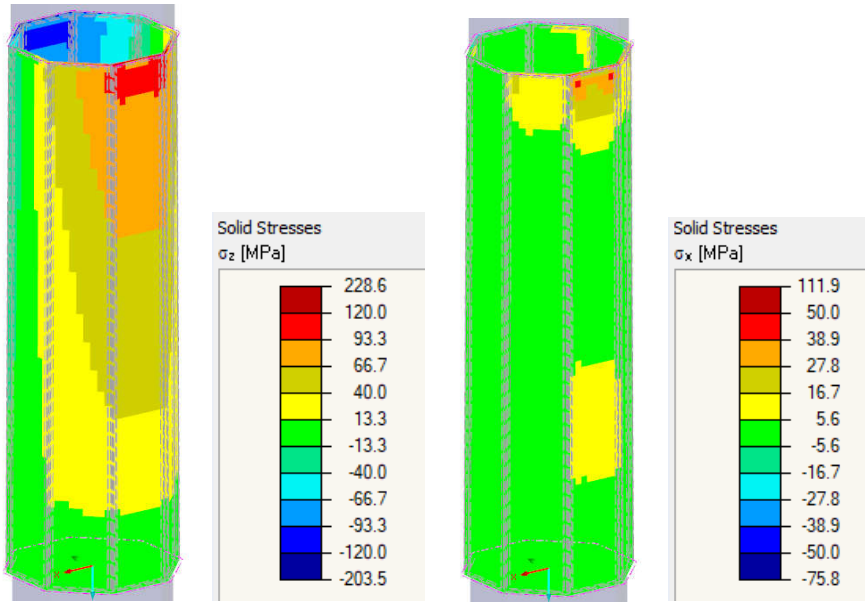


Figure 8: Left stresses in vertical direction; Right stresses in horizontal direction

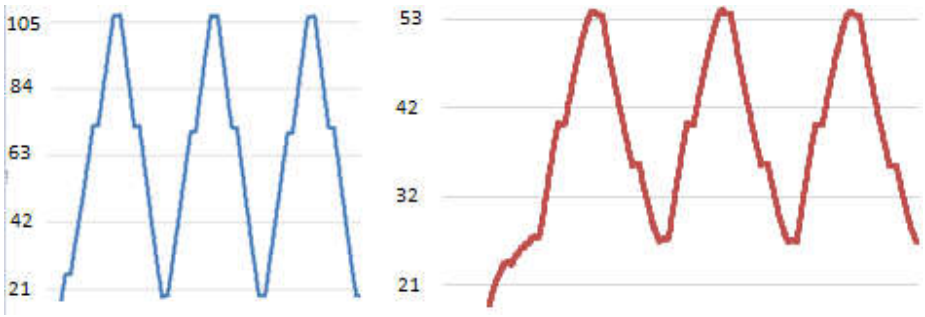


Figure 9: Left MPa values in vertical direction; Right MPa values in horizontal direction

Values shown in figure 9 are from the beginning of the test therefore there are measured little bit higher values as are shown in table 7. These measurements are proving right layout of measuring points and types of measured values.

5. Conclusion

The reduced overlapping length of the slip-joint connection equal to 1.2 multiple of the tower diameter safely withstands the least favourable loading conditions due to results from previous research shown in chapter 3. FEM-software results and the experiment proved that the commonly accepted empirical length (1.5 to 1.8 multiple of the tower) is conservative. The new approach in slip joint connection research on edged tubes presents great opportunity to enhance knowledge about such connections. First results are proving right movement in this research and the authors are looking forward to present more of the newly acquired findings in near future.

Acknowledgements

The authors would like to express thanks to the Grant agency of the Ministry of Education, Science, Research and Sports of the Slovak Republic for providing a grant from the research program VEGA Nr.1/0388/19 – Analysis and synthesis of the influence of the service conditions to line and thin walled structures. This article was created with the support of the Ministry of Education, Science, Research and Sport of the Slovak Republic within the Research and Development Operational Program for the project "University Science Park of STU Bratislava", ITMS:313021D243, co-funded by the European Regional Development Fund.

References

[1] ASCE/SEI 48-11, Design of Steel Transmission Pole Structures, Published by the American Society of Civil Engineers 2012

[2] STN EN 1993-3-1: Eurocode 3: Design of Steel Structures. Part 3-1: Towers, masts and chimneys. Towers and masts

[3] STN EN 50341-1-2006: Overhead electrical lines exceeding AC 45 kV. Part 1: General requirements. Common specifications.

[4] DNV-OS-J101: Design of offshore wind turbine structures.

[5] Botló, Michal - Magura, Martin - Brodniansky, Ján - Brodniansky, Ján. Numerical and experimental analysis of structural details of electrical transmission line towers. In IASS 2016: proceedings of the Annual Symposium. Spatial Structures in the 21st Century. September 26-30, 2016, Tokyo, Japan. Tokyo: The University of Tokyo, 2016

[6] Botló, Michal - Brodniansky, Ján. Simplified methodology of stress calculation in slip-joint connections. In SDSS ´2016: proceedings of the International Colloquim on Stability and Ductility of Steel Structures. Timisoara, Romania, 30. 5. - 1. 6. 2016. 1. vyd. [s.l.]: ECCS - European Convention for Constructional Steelwork, 2016

[7] Recký J., Teoretické a konštrukčné problémy oceľových stožiarov. Dissertation thesis, Bratislava, Slovakia, 2013.

[8] Botló M., Nasúvané spoje ohraňovaných stožiarov. Dissertation thesis, Bratislava, Slovakia, 2017

Proceedings of the IASS Annual Symposium 2019 – Structural Membranes 2019
Form and Force
7 – 10 October 2019, Barcelona, Spain
C. Lázaro, K.-U. Bletzinger, E. Oñate (eds.)

Finding Membrane Shells Subjected to Horizontal Body Forces with Radial Basis Functions

Yu-Chou CHIANG*, Andrew BORGART, Qingpeng LI[a]

* Faculty of Architecture and Built Environment, Delft University of Technology
Chiang.YuChou@gmail.com

[a] School of Architecture and Urban Planning, Nanjing University

Abstract

Membrane shells, which have minimized bending moments under certain load conditions, are regarded as ideal structural forms in terms of material efficiency. Most of the existing numerical form-finding methods are based on discretizing membranes into finite panels or funicular networks and focusing on gravitational loading only. In order to obtain smooth shells and to consider horizontal loads, this paper presents a method to find the equilibrium forms of the membrane shells by solving Pucher's equation. Radial base functions (RBFs) is utilized to represent stresses and shapes of the membranes, and a least square method is applied to find the controlling coefficients which allow the functions to fit the boundary conditions (e.g. zero stresses at the free edges) and the governing equation. When all the parameters are carefully chosen, the stress and shape functions can achieve sufficient accuracy. The presented method has been preliminarily implemented to find shells on a triangle ground plan incorporating horizontal loads. The form-found geometries are then analyzed by finite element models. The result confirms that the form-found shells have the stress distributions similar to the prescribed stresses.

Keywords: from finding, membrane shells, radial basis functions, Pucher's equation, funicular structures.

1. Introduction

The design of membrane shells is to contain stresses in the curved surface (force follows form) and to curve the surface following the embedded stresses (form follows forces). By carefully designing the stresses and the surfaces, membrane shell structures can elegantly span large area with minimal materials by membrane stresses (i.e. tension, compression, and in-plane shear stresses).

Although the shells are materially efficient structures, the complication of the shell theory prohibits them to be widely applied [1] (let alone the fabrication of the doubly curved surfaces). By the development of computational methods and techniques, numerical algorithms are able to analyze the statics of the shells by discretizing the continuous surfaces into finite elements [2] and sometimes reconstruct them back to smooth NURBS surfaces [3]. However, the design of smooth shells is still restricted to a few analytical solutions.

The aim of this paper is to utilize radial basis functions (RBFs), a numerical method developed in the 1990s, which can easily represent free-form C^{∞} smooth multivariate functions and facilitate scientists solving partial differential equations (PDEs)[4], [5]. Surprisingly, the method has not been applied for form-finding application, to the best of authors' knowledge. This paper investigates how to apply RBFs to represent both stress and shape functions and how to find an agreement between them by solving Pucher's equation. The investigation shows the RBFs are handy numerical design tools to even handle horizontal body forces and the singularity of the point-supported membrane shells.

Copyright © 2019 by Yu-Chou Chiang, Andrew Borgart, and Qingpeng Li.
Published by the International Association for Shell and Spatial Structures (IASS) with permission.

The outline of this paper is as follow. The first section introduces the features of membrane shells. The second section briefly explains how to apply RBFs to represent an arbitrary function and its differential operation. The third section focuses on the Pucher's equation and related boundary conditions. The fourth section proposes an overall workflow with a demonstration finding shapes of membrane shells on a triangular ground plane. The fifth section concludes the current finding and projects future works.

2. Basic Operations of Radial Basis Functions

Radial basis functions are used to represent a smooth multivariate function. An arbitrary function $f(\mathbf{x})$ can be approximated by a serious of radial basis functions $\phi(\|\mathbf{x}-\boldsymbol{\mu}_i\|;\rho_i)$ and polynomial terms $h(\mathbf{x})$ [4]:

$$f(\mathbf{x}) = \sum_{i=1}^{n} \lambda_i \phi(\|\mathbf{x}-\boldsymbol{\mu}_i\|;\rho_i) + h(\mathbf{x}) + \varepsilon\,, \tag{1}$$

in which $\mathbf{x}$ is the position of evaluation, λ_i are the magnitude coefficients of the RBFs, $\boldsymbol{\mu}_i$ are the source points, ρ_i are the shape parameter of the RBFs, and ε is the approximate error. By sufficient number of RBFs n, the equation (1) shall be able to deliver decent accuracy.

For a linear differential operator $\mathcal{D}[\cdot]$ acting on the function $f(\mathbf{x})$, the derivative equation would be

$$\mathcal{D}[f(\mathbf{x})] = \sum_{i=1}^{n} \lambda_i \cdot \mathcal{D}\left[\phi(\|\mathbf{x}-\boldsymbol{\mu}_i\|;\rho_i)\right] + \mathcal{D}[h(\mathbf{x})] + \varepsilon_{\mathcal{D}}\,. \tag{2}$$

which also can be presented in a matrix form:

$$\mathcal{D}[\mathbf{f}(\mathbf{x})] = \begin{bmatrix} \mathcal{D}[\boldsymbol{\Phi}(\mathbf{x})] & \mathcal{D}[\mathbf{H}(\mathbf{x})] \end{bmatrix} \begin{bmatrix} \boldsymbol{\lambda} \\ \mathbf{c} \end{bmatrix} + \boldsymbol{\varepsilon}_{\mathcal{D}}\,, \tag{2a}$$

in which $\boldsymbol{\lambda}$ are the magnitude coefficients of the radial basis functions, while $\mathbf{c}$ are the coefficients of the polynomial terms. The coefficients then can be regarded as the main arguments for minimizing the squared approximate errors. When the desired derivative values of the function ($\mathbf{g}_{xa}$) are provided at certain locations ($\mathbf{x}_a$), coefficient vectors can be provided by the weighted least square method:

$$\begin{bmatrix} \boldsymbol{\lambda} \\ \mathbf{c} \end{bmatrix} = \left(\mathbf{A}^T \mathbf{W}\, \mathbf{A}\right)^{-1} \mathbf{A}^T \mathbf{W}\, \mathbf{g}_{xa} \tag{3}$$

where $\mathbf{A}$ is defined by $\begin{bmatrix} \mathcal{D}[\boldsymbol{\Phi}(\mathbf{x})]\big|_{\mathbf{x}=\mathbf{x}_a} & \mathcal{D}[\mathbf{H}(\mathbf{x})]\big|_{\mathbf{x}=\mathbf{x}_a} \end{bmatrix}$, and $\mathbf{W}$ is the weight matrix.

Having the basic differential and the least-square operations of the RBFs in mind, the following sections state the specific differential operations should be concerned for designing a membrane shell.

3. Pucher's Equation and Boundary Conditions

The overall aim of designing membrane shells is to determine the equilibrium state of the membrane surface. Fortunately, the Airy stress function can describe the internal equilibrium of the 2D stress fields succinctly with a scalar function, and the C^0 continuation of the stress function guarantees the equilibrium in the two directions. The equilibrium stresses can be expressed as follow when body forces are also considered [6]:

$$\begin{aligned} \bar{N}_{11} &= \partial_{22} F - \int \bar{p}_1 dx_1, \\ \bar{N}_{12} &= -\partial_{12} F, \\ \bar{N}_{22} &= \partial_{11} F - \int \bar{p}_2 dx_2, \end{aligned} \tag{4}$$

in which $\bar{N}_{11}$ and $\bar{N}_{22}$ are normal stress in two directions, $\bar{N}_{12}$ is the in-plane shear stress, F is the Airy stress function, $\bar{p}_1$ and $\bar{p}_2$ are the body forces per unit area in related directions. ∂_{12} is the Euler's

notation for the mixed second partial derivative, meanwhile ∂_{11} and ∂_{22} are the derivatives with respect to the coordination 1 and 2.

While the Airy stress function guarantees the horizontal equilibrium, the equilibrium in z-direction is governed by the Pucher's equation [6]:

$$\bar{N}_{11}\cdot\partial_{11}z+2\bar{N}_{12}\cdot\partial_{12}z+\bar{N}_{22}\cdot\partial_{22}z=\bar{p}_1\cdot\partial_1 z+\bar{p}_2\cdot\partial_2 z-\bar{p}_z\,. \tag{5}$$

When the external loads $\bar{p}_1$, $\bar{p}_2$, and $\bar{p}_z$ are given, the designer only needs to find a set of the stress function $F(\mathbf{x})$ and shape function $z(\mathbf{x})$ that meet both of the equations (4) and (5).

Within the Pucher's equation, either the shape function $z(\mathbf{x})$ or the stress function $F(\mathbf{x})$ can be regarded as unknown, and others are assumed independent of the unknown functions. Explicitly, when the loads and the stresses are given, the shape function should be governed by

$$[(\partial_{22}F-\int\bar{p}_1dx_1)\cdot\partial_{11}-2\partial_{12}F\cdot\partial_{12}+(\partial_{11}F-\int\bar{p}_2dx_2)\cdot\partial_{22}-\bar{p}_1\cdot\partial_1-\bar{p}_2\cdot\partial_2]z=-\bar{p}_z\,, \tag{5a}$$

or in an abridged notation as $\mathcal{P}_z^{\mathcal{F}}[z]=-\bar{p}_z$, where $\mathcal{P}_z^{\mathcal{F}}[\cdot]$ is the differential operator acting on the shape function. In another way around, when the loads and the shape are given, the stress function should meets

$$[\partial_{11}z\cdot\partial_{22}-2\partial_{12}z\cdot\partial_{12}+\partial_{22}z\cdot\partial_{11}]F=\int\bar{p}_1dx_1\cdot\partial_{11}z+\int\bar{p}_2dx_2\cdot\partial_{22}z+\bar{p}_1\cdot\partial_1 z+\bar{p}_2\cdot\partial_2 z-\bar{p}_z\,, \tag{5b}$$

or in an abridged notation $\mathcal{P}_F^{\mathcal{Z}}[F]=-\bar{p}_z'$, where $\mathcal{P}_F^{\mathcal{Z}}[\cdot]$ is the differential operator action on the stress function while $-\bar{p}_z'$ is the summation of all the terms on the right-hand side.

Given the fact that the solution of the Airy stress function does not exist in the case of free-edges point-supported parabola membrane shell [1], it might also be possible that an arbitrarily given set of boundary conditions and stress function could not permit the existence of a shape function. In other words, the shape function and stress function should recursively be revised until they mutually agree.

3.2. Boundary Conditions of Stress Functions Subsections

The equilibriums in three directions within the domain are governed by equations (4) and (5). However, the stresses around the boundaries require extra attention. Stresses at the fully supported edges would have no constraints, given that all resultant forces that shell imposes can be balanced by resistance from the supports. In contrast, for free edges, there should have no normal stress transmitting from or towards the boundaries, have no shear stresses against the tangential direction, and have no unbalanced vertical loads. For other common boundary types and their constraints are listed in Table 1. The normal and tangential directions are shown in Figure 1.

In this paper, free-edge is the mainly considered boundary type. The related boundary conditions are

$$\begin{aligned}\bar{N}_{nn}&=0,\\ \bar{N}_{nt}&=0.\end{aligned} \tag{6}$$

Table 1 The boundary constraints on the functions.

Boundary types	Constraints on functions	
	$\bar{N}$	$\bar{p}_z$
Support	no constraint	no constraint
On diaphragm	$\bar{N}_{nn}=0$	no constraint
On columns	$\bar{N}_{nn}=0$, $\bar{N}_{nt}=0$	no constraint
Reinforced edge	$\bar{N}_{nn}=0$	$\bar{p}_z=$ self-weight
Free edge	$\bar{N}_{nn}=0$, $\bar{N}_{nt}=0$	$\bar{p}_z=$ self-weight

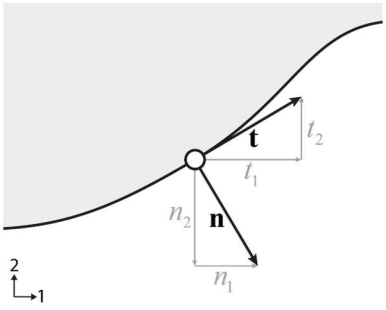


Figure 1 Directions at edges

When the normal vectors and the tangent vectors of the edges are expressed as $\begin{bmatrix} n_1 & n_2 \end{bmatrix}$ and $\begin{bmatrix} t_1 & t_2 \end{bmatrix} = \begin{bmatrix} -n_2 & n_1 \end{bmatrix}$, and equation (4) is incorporated, the conditions of the equation (6) become

$$\begin{aligned} \partial_{tt} F &= n_1^2 \int \bar{p}_1 dx_1 + n_2^2 \int \bar{p}_2 dx_2, \\ -\partial_{nt} F &= -n_1 n_2 \int \bar{p}_1 dx_1 + n_1 n_2 \int \bar{p}_2 dx_2. \end{aligned} \tag{7}$$

The final remark on the conditions of stress function is that only the second derivative, or curvature, of the stress function influence the Pucher's equation. In other words, the stress function can be homogenously elevated or sheered, and the stress field remains the same. Therefore, there are 3 degrees of freedom in the stress function, which regard the overall elevation and overall slops in two directions, shall be constrained in order to acquire a determined solution.

3.3. Boundary Condition of Shape Function

Designers may wish the shell be supported by few given locations. In mathematical terms, it means imposing the Dirichlet boundary condition in the shape function, which can be express as:

$$z(\mathbf{x}_s) = z_s \,, \tag{8}$$

where $\mathbf{x}_s$ are the location of the supports and z_s are the desired elevations of them.

4. Methodology and Application

Pucher's equation governs the equilibrium of the membrane shell, but it disregards compatibility conditions nor constitutive relation. These features make it a problem with non-unique solutions providing many degrees of freedom for structure designers.

To locate the converged solutions of the stress function and the shape function under the given loads in the Pucher's equation, this paper proposes a workflow of designing a membrane shell as follows:

1. Determine the ground plane. List the boundary conditions of the shell (supports, free edges).
2. Identify potential singular points and arrange the basis functions accordingly.

3a. Design initial shape.
4a. Find the corresponding stress function with the Pucher's equation.

3b. Design initial stress field.
4b. Find corresponding shape function with the Pucher's equation.

5. Revise stress function according to the shape, and revise shape according to the updated stress until two of them converged.

To explicitly show how to precede the design sequence, the sub-sections start with brief explanations that what type of RBF is chosen and the arrangement of them, and followed the implementation of RBFs to find the membrane shells.

4.1 Designing the ground-plane and arranging the source and calibration points for RBFs

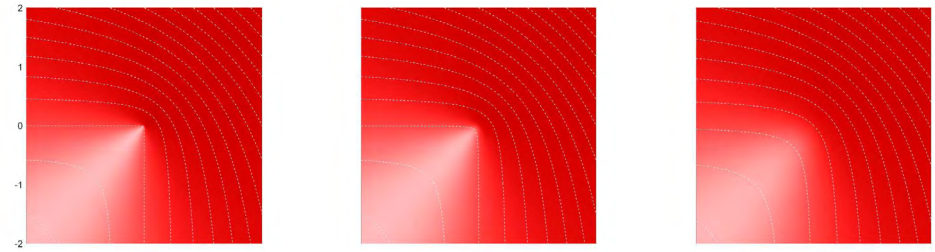
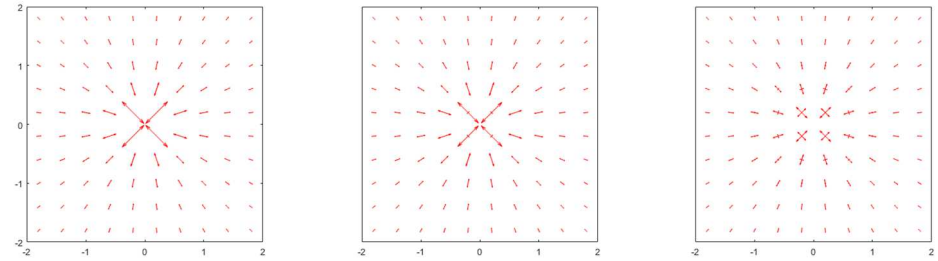
The demonstration focuses on a triangular-ground-plane points-supported shell. The supports are evenly distributed on a unit circle. The design of the ground plane leads to three free edges (boundary conditions for the stress function) and three grounded points (the Dirichlet boundary conditions for the shape function.) This subsection explains how the basis function $\phi(\cdot)$ is chosen and how the calibration points are arranged.

Suggested by Csonka [1], the curvature of the stress function $\partial_{nn} F(\mathbf{x})$ is extremely large as $\mathbf{x}$ on the edges approaches to the support points. Therefore, the RBFs should allow this singularity. To achieve such goal, the basis function $\phi(\cdot)$, scale parameters ρ_i and the centers of the sources $\boldsymbol{\mu}_i$ have to be nicely arranged. The chosen basis function is

$$\phi(\|\mathbf{x} - \boldsymbol{\mu}\|; \rho) = \sqrt{\|\mathbf{x} - \boldsymbol{\mu}\|^2 + \rho^2} \,, \tag{9}$$

which has a cone shape but with a blunt peak controlled by the scale parameter ρ. As ρ approaches to 0, the size of the blunt peak approaches to 0 thus the curvatures at the $\boldsymbol{\mu}$ approaches to infinity. Table 2 displays few basis functions with different scale parameters and their corresponding principle stresses calculated by equation (4). When there are multiple radial basis functions acting, their effects superpose each other, similar to static electric fields exerted by multiple charged objects.

Table 2 Radial basis functions with different scale parameters.

$F(\mathbf{x}) = \lambda\sqrt{\left\|\mathbf{x}-\boldsymbol{\mu}\right\|^2 + \rho^2} + c_1 x_1 + c_2 x_2$, where $\boldsymbol{\mu} = (0,0)$, $\lambda = c_1 = c_2 = 1$, and		
$\rho = 0.02$	$\rho = 0.1$	$\rho = 0.5$
Sress Function 		
Sress Field 		

Understanding these properties, a basis function right on each pointy support has to be arranged and assigned with relativity small scale parameter to enable the singularity. Consequently, the source points of stress function and shape function are intentionally disturbed on the support points along with other source points within and around the domain. The scale parameters are also set differently according to the location. The parameters are smaller when source points are closer to the support. The stress function and shape function can be represented by the RBFs as

$$F(\mathbf{x}) = \sum_{i=1}^{n} \lambda_{F_i} \phi_F(\left\|\mathbf{x}-\boldsymbol{\mu}_{F_i}\right\|; \rho_{F_i}) + h_F(\mathbf{x}) + \varepsilon_F, \tag{10}$$

$$z(\mathbf{x}) = \sum_{i=1}^{n} \lambda_{z_i} \phi_z(\left\|\mathbf{x}-\boldsymbol{\mu}_{z_i}\right\|; \rho_{z_i}) + h_z(\mathbf{x}) + \varepsilon_z, \tag{11}$$

which can also be expressed in matrix forms as

$$\mathbf{F}(\mathbf{x}) = \begin{bmatrix}\boldsymbol{\Phi}_F(\mathbf{x}) & \mathbf{H}_F(\mathbf{x})\end{bmatrix}\begin{bmatrix}\boldsymbol{\lambda}_F \\ \mathbf{c}_F\end{bmatrix} + \boldsymbol{\varepsilon}_F, \tag{10a}$$

$$\mathbf{z}(\mathbf{x}) = \begin{bmatrix}\boldsymbol{\Phi}_z(\mathbf{x}) & \mathbf{H}_z(\mathbf{x})\end{bmatrix}\begin{bmatrix}\boldsymbol{\lambda}_z \\ \mathbf{c}_z\end{bmatrix} + \boldsymbol{\varepsilon}_z. \tag{11a}$$

Other than source points, the calibration points are also indispensable. For the shape equation, it should meet the Pucher's equation (5a) at the calibration points in the domain $\mathbf{x}_d$ and the Dirichlet condition (8) at the support points $\mathbf{x}_s$. The overall conditions are

$$\begin{bmatrix} \mathcal{P}_z^{\mathcal{F}}\left[\mathbf{\Phi}_z(\mathbf{x}_d)\right] & \mathcal{P}_z^{\mathcal{F}}\left[\mathbf{H}_z(\mathbf{x}_d)\right] \\ \mathbf{\Phi}_z(\mathbf{x}_s) & \mathbf{H}_z(\mathbf{x}_s) \end{bmatrix} \begin{bmatrix} \boldsymbol{\lambda}_z \\ \mathbf{c}_z \end{bmatrix} = \begin{bmatrix} -\mathbf{p}_z \\ \mathbf{0} \end{bmatrix} - \begin{bmatrix} \boldsymbol{\varepsilon}_{\mathcal{P}z} \\ \boldsymbol{\varepsilon}_z \end{bmatrix}. \tag{12}$$

For the stress function, it should meet the Pucher's equation (5b) at the domain calibration points $\mathbf{x}_d$ and the free edge condition (7) at the calibration points on the edges $\mathbf{x}_e$. Along with the extra Dirichlet conditions to allow the stress function numerically determinate, all the conditions imposing in the stress function can be summarized by

$$\begin{bmatrix} \mathcal{P}_F^{\mathcal{Z}}\left[\mathbf{\Phi}_F(\mathbf{x}_d)\right] & \mathcal{P}_F^{\mathcal{Z}}\left[\mathbf{H}_F(\mathbf{x}_d)\right] \\ \partial_{tt}\mathbf{\Phi}_F(\mathbf{x}_e) & \partial_{tt}\mathbf{H}_F(\mathbf{x}_e) \\ -\partial_{nt}\mathbf{\Phi}_F(\mathbf{x}_e) & -\partial_{nt}\mathbf{H}_F(\mathbf{x}_e) \\ \mathbf{\Phi}_F(\mathbf{x}_s) & \mathbf{H}_F(\mathbf{x}_s) \end{bmatrix} \begin{bmatrix} \boldsymbol{\lambda}_F \\ \mathbf{c}_F \end{bmatrix} = \begin{bmatrix} -\mathbf{p}'_z \\ \mathbf{F}_{tt} \\ \mathbf{F}_{nt} \\ \mathbf{0} \end{bmatrix} - \begin{bmatrix} \boldsymbol{\varepsilon}_{\mathcal{P}F} \\ \boldsymbol{\varepsilon}_{Ftt} \\ \boldsymbol{\varepsilon}_{Fnt} \\ \boldsymbol{\varepsilon}_F \end{bmatrix}, \tag{13}$$

where $\mathbf{F}_{tt}$ is given by $n_1^2\int \bar{p}_1 dx_1 + n_2^2\int \bar{p}_2 dx_2$ and $\mathbf{F}_{nt}$ is $-n_1n_2\int \bar{p}_1 dx_1 + n_1n_2\int \bar{p}_2 dx_2$. Since the differential operators mutually depend on each other, iterations would be needed to obtain the agreement between the stress functions and shape functions. The following sub-sections with case studies show how to implement the workflow.

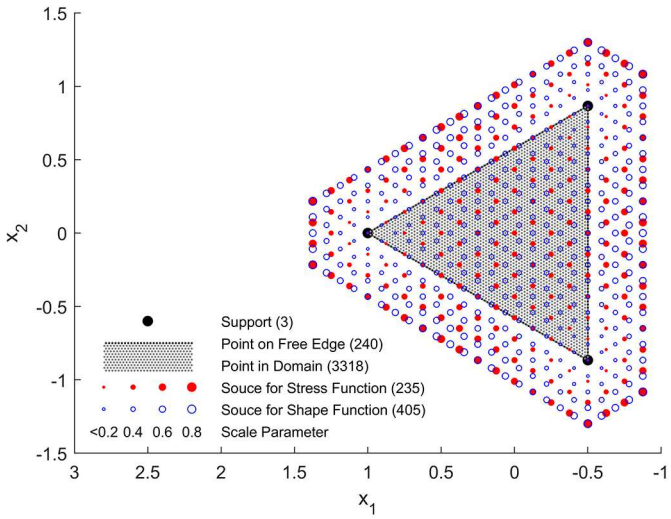


Figure 2 The distribution of all the points and their quantities (in the round brackets).

4.2. Case A: a Triangular Shell initiate from Parabola Shape Equations

The design process can either start with the stress function or the shape function. The first example shown is to initiate with a parabola shape function. By minimizing the errors in equation (13), one can derive the stress function to fit the parabola shape the most. Then, with the stress function, one can revise the shape function by minimizing the errors in equation (12). The alternating process may go forever until accuracy arrives at a certain satisfying level. The iteration process is shown in Figure 3a.

As suggested by Csonka [1], the free-edges conditions are not compatible with point-supported parabola membrane shells. As a result, the root-mean-square errors (RMSE) of the free-edge conditions initially are relatively high and drop dramatically after a few iterations while the shape has to deviate from the initial shape correspondingly. After 100 iterations, the shape function becomes another synclastic shape as shown in the first panel of Figure 4.

4.3. Case B: a Triangular Shell initiate from a Stress Function

In contrary to Case A, Case B opts to initiate the process from an analytical solution of the stress function from Csonka [1]. The initial input of the stress function goes as

$$F_{initial}(x_1, x_2) = \alpha_1 \frac{4}{3} \frac{L_0 \cdot L_1 \cdot L_2}{\alpha_2 \cdot L_0 \cdot L_1 \cdot L_2 + x_1^2 + x_2^2 - 1}, \tag{14}$$

where $L_n = \cos\left(\frac{2n\pi}{3}\right) x_1 + \sin\left(\frac{2n\pi}{3}\right) x_2 - \frac{1}{2}$, $\alpha_1 = \left.\frac{\partial F}{\partial n}\right|_{\text{at } L_n}$, and α_2 is a parameter influencing the peak of the stress function ($F_{initial}(0,0) = 4\alpha_1 / 3(\alpha_2 + 8)$). In this case, α_2 is set to be 12/5 for moderate upward edges in the final shape function. The RMS of the errors in the free edge conditions (i.e. ε_{Ftt} and ε_{Fnt}) in Case B are much smaller than their counterparts in Case A. The initial stress function, which fits the boundary conditions, may contribute to the low errors in the follow-up iterations.

4.4. Case C: Triangular Membrane Shells Considering Horizontal Load

As the previous two sub-sections demonstrate, the form-finding process can either starts with shape function or stress function. In this sub-section, the horizontal loads are introduced, which are set to be constant per projected area. The process of the iteration starts with the shape function found in Case B. Then the process proceeds with alternatively minimizing the errors in equation (13) and (12) as the process described in Case A. The major difference is that $\bar{p}_2$ is set to be -0.3 instead of 0. As a result, the converged shape function has no straight edges at the boundaries as equation (7) is asking the second derivatives to follow

$$\begin{aligned} \partial_{tt} F &= n_2^2 \bar{p}_2 x_2, \\ -\partial_{nt} F &= n_1 n_2 \bar{p}_2 x_2. \end{aligned} \tag{15}$$

The shifted stress function is shown in Figure 4.

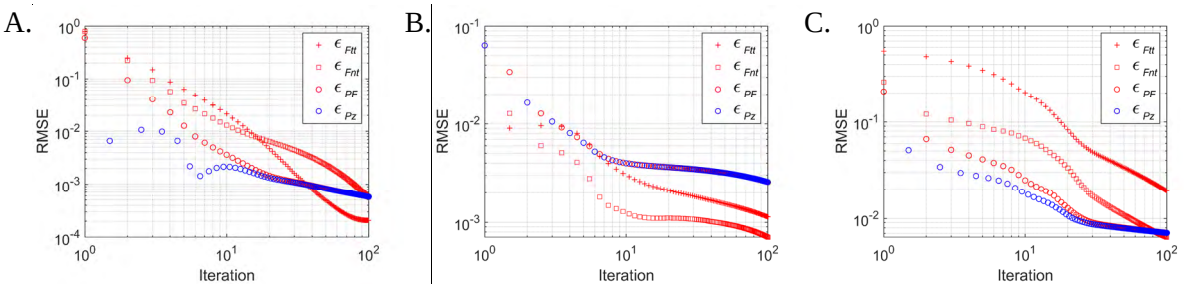


Figure 3 The mean squared errors during the iteration process of the three cases

5. Discussions and Conclusions

This paper has proposed the workflow of applying RBFs to solve Pucher's equation and implemented it on point-supported triangular-ground-plan shells with free-edge boundary conditions. Horizontal loads have been successfully integrated. FEM modeling has confirmed that the stresses distribution has similar patterns in the prescribe one.

Arrangement of RBFs is the most critical part. The arrangement works as an implicit filter excluding all the solutions within the left null spaces. The designer should foresee the potential solutions and arrange the RBFs accordingly.

For boarder application, the follow-up works are set to be implementing the proposed method to different ground plans and boundary conditions, such as oculus and reinforced edges. Load can also be revised to none homogenously distributed.

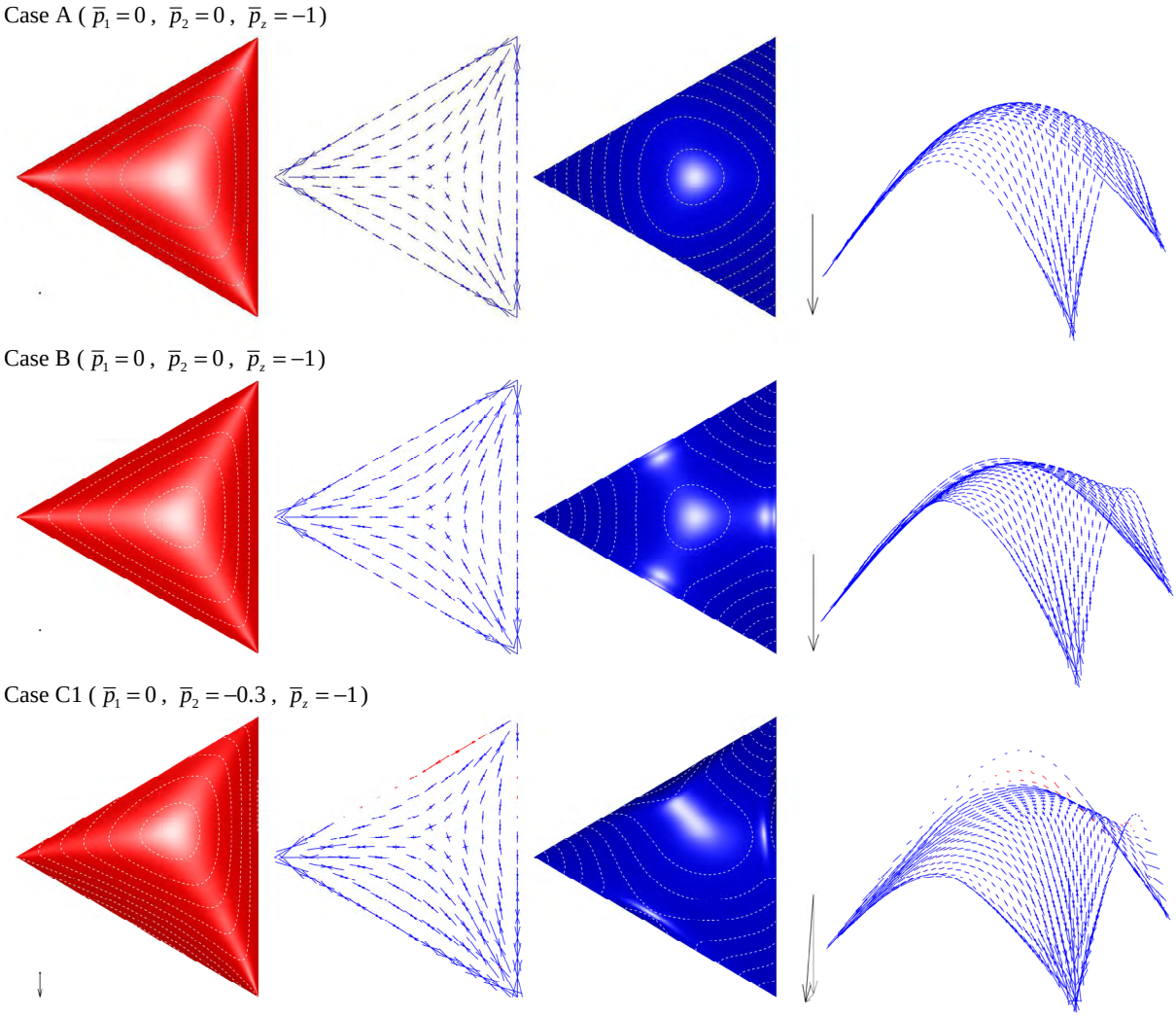


Figure 4 The converged solutions. First three columns are the top views of the stress function, stress field, shape function derived from the proposed method, and the last column is the stresses destitution calculated from FEM analysis. The back arrows suggest the directions of the loads.

References

[1] P. Csonka, *Theory and practice of membrane shells*. VDI Verlag, 1987.

[2] D. Veenendaal and P. Block, "An overview and comparison of structural form finding methods for general networks," *Int. J. Solids Struct.*, vol. 49, no. 26, pp. 3741–3753, 2012.

[3] A. Pugnale, T. M. Echenagucia, and M. Sassone, "Computational morphogenesis: Design of freeform surfaces," in *Shell Structures for Architecture: Form Finding and Optimization*, S. Adriaenssens, P. Block, D. Veenendaal, and C. Williams, Eds. New York: Routledge, 2014, pp. 225–236.

[4] M. D. Buhamann, *Radial Basis Functions*. Cambridge, 2003.

[5] C. Chen, Y. C. Hon, and R. A. Schaback, *Scientific computing with radial basis functions*. 2005.

[6] J. Heyman, *Equilibrium of shell structures*. Oxford: Oxford University Press, 1977.

Proceedings of the IASS Annual Symposium 2019 – Structural Membranes 2019
Form and Force
7 – 10 October 2019, Barcelona, Spain
C. Lázaro, K.-U. Bletzinger, E. Oñate (eds.)

Force Field Typological Design Strategies - A Data Centric Approach to Design

Robert OTANI*, Emil POULSEN, Sergey PIGACH

*Thornton Tomasetti
51 Madison Ave, New York, NY 10010
ROtani@thorntontomasetti.com

Abstract

This paper aims to present a design approach and software application that allows designers to explore thousands of design solutions to optimize the design process using precomputed solutions. The intelligence of the engineer would be integrated into the design solutions. Brown and Mueller [1] have researched similar approaches. The collaboration of Architects and Engineers in a typical building design begins with a dialog of the project brief, the programmatic needs, the desired building typology, a study of building precedents, and ultimately to a design exploration by the Architect and Engineer to meet the needs of the brief. In most instances the design process by the engineer includes a limited number of possible solutions based on the engineers' singular domain experience. The Force Field Typological design approach is one that can capture multitudes of engineers' experience into one application and at the control of the Architect.

Keywords: conceptual design, structural optimization, software development

1. Introduction

All building designs are a culmination of the design team's input into a design idea typically conceptualized by the Architect based on programmatic requirements and design brief set out by an Owner. The development of the design idea related to the building structure is a collaborative effort typically by the Architect and key structural engineering consultants and the process usually includes multiple iterations of design concepts. However, that collaboration is typically limited to the knowledge of the small team of engineers involved and since all projects are on a schedule, an engineer's input is also limited to the speed at which design concepts can be computed/analyzed into working structural typology.

The Force Field typology concept proposes a data centric approach to structural design where various structural typologies are pre-calculated by experienced structural engineers and depending on an Architect's design idea, a multitude of pre-calculated and conceptual level design solutions can be accessible to the Architect. Those design solutions would be mapped to a "force field" generated from a simple finite element analysis of only the resulting geometric and environmental parameters of the given project. The power of this data-centric approach is that it captures a collective intelligence into possible design solutions, allows the Architect to explore far more design options in a significantly shorter amount of time and allows the Engineer to only focus their expertise on design options that the Architect has already vetted eliminating the efforts required in exploring design options that are not used.

Copyright © 2019 by Robert OTANI, Emil POULSEN, and Sergey PIGACH
Published by the International Association for Shell and Spatial Structures (IASS) with permission.

2. Force Field Concept

The "force field" concept is the computational process in which a structural typology with inherent shear/moment/axial resisting capabilities are mapped to a pattern of the moments, shears, and axial forces generated from a particular structural element resulting from a simple finite element shell analysis. As an example, the Force Field of a roof structure with supports on 2 of the 4 sides of the roof and an aspect ratio (L/W) greater than 2 would generate a one-way force field of uni-directional internal forces. That force field can then be applied to a more complex typology of a pre-calculated one way beam system, a one way truss system, a continuous arch, or any other structural system that is predominantly capable of supporting a one way system with dependence on the type of support conditions and topology of the "field". Using the same roof example, a flat shell surface with a pin/roller (simple) support conditions will yield a consistent force field of shears and uni-directional moments in which case a one way beam or truss system with moment resisting capabilities will be the most appropriate structural typology that maps to the particular force field. With an arch-shaped roof topology and pin/pin support conditions, the predominant internal force field will be uni-directional moments and axial forces in which case a one way beam or truss system typology with both axial and moment resisting capabilities will computational mapped to inherent force field.

With today's computational capabilities, we are proposing this solution to be a web and cloud based software application where a simplified structural analysis will yield thousands of solutions whereby a structural or architectural design has the option of choosing as many possible solutions without any calculations and will allow a launching point for detailed design yet allow the designer far more choices at the outset of a project. The Force Field is created by a simple finite element analysis (FEA) Shell analysis.

2.1. Process: Step-by-step

As the objective of Force Field is to generate parametric structural systems with associated design spaces from conceptual input, the first step in this process is to provide a high level structural model. This typically consists of a surface geometry representing the structural element and boundary conditions. Optionally a loading diagram can be provided. If left unset, a default gravity loading will be applied onto the whole surface. See figure 1.

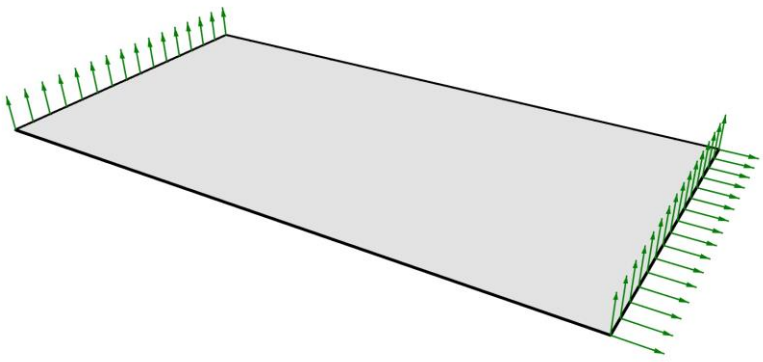


Figure 1: The input model consists of surface geometry and boundary conditions.

With the conceptual input, Force Field discretizes the surface into a mesh which then is used to build a finite shell element model. Generic elastic material properties and suitable thicknesses are applied to the

shell. The loading and support conditions are mapped appropriately to the shell FEA model. It is now able to run linear static analysis. See figure 2.

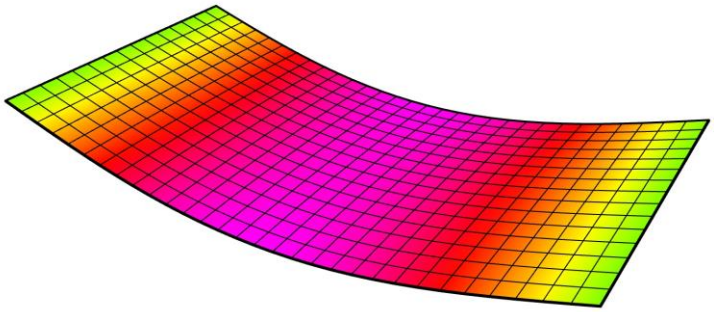


Figure 2: The output from the shell analysis.

Given the structural model and analysis result, Force Field can now begin to identify and classify its structural behavior and "understand" what type of structure it's dealing with. As shown in the example below, a rectangular surface with pinned supports along 2 opposing edges would be identified as a one-way slab. For this type of component, there are several structural topologies that would be suitable as designs. In the example below, the system will propose reinforce concrete, composite deck and truss. See figure 3.

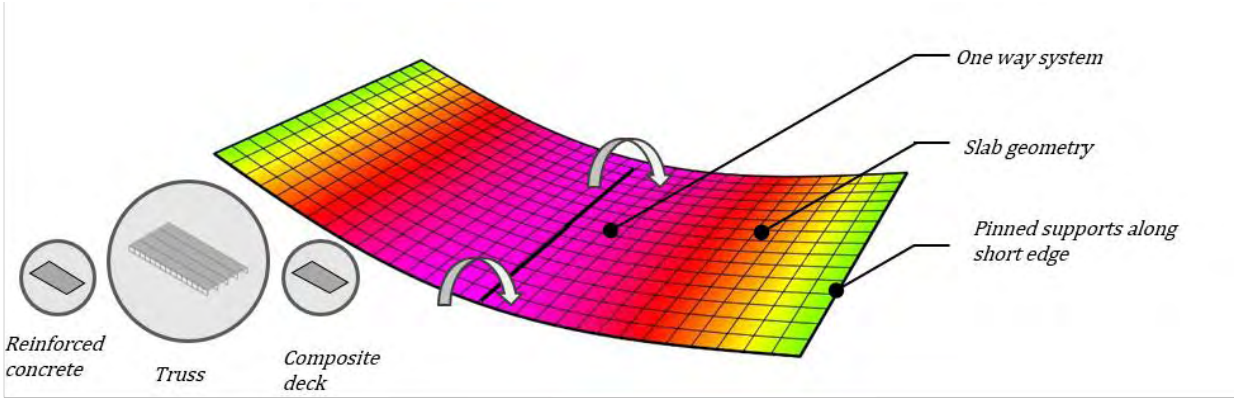


Figure 3: The classification of the system and results and recommendation of structural topology.

Given the options presented by Force Field, the user can now pick a preferred typology or group of typologies. For each design option there is a parametric model and an associated design space all with structural capacities that map to the generated force field. Each individual parametric model has input and output parameters presented through a comprehensive user interface. In the example of the one-way slab where a truss topology is selected, then depth, number of divisions, truss type would be input parameters, whereas maximum deflection, elastic energy and tonnage would be output parameters. See figure 4.

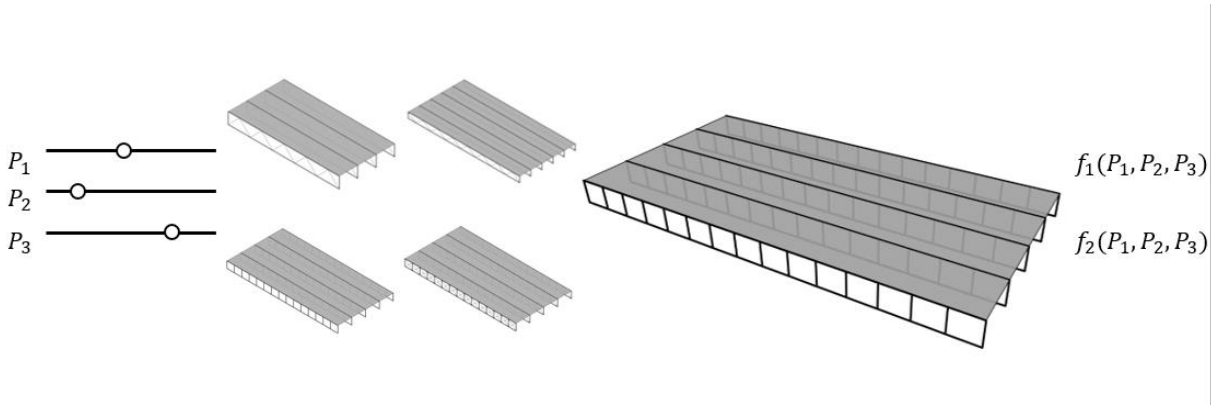


Figure 4: Each parametric system has a set parameter (left), where the permutation of these generates a model and additional numeric output (right).

With the parametric model now generated from the input, the system can now be used to browse and explore the design space. Furthermore, optimizations can be run with respect to a selection of input (P3) and outputs (*f*) to find permutations of the parameters producing desirable results.

$$Maximize\ f(P_3)\ subject\ to \begin{cases} P_1 = A \\ P_2 = B \end{cases}$$

The design space can also be explored using parallel coordinates using applications such as Design Explorer [2].



Figure 5: The data set can be explored using parallel coordinates using applications Design Explorer.

3. Implementation

In this section an implementation of the workflow described in section 2 will be presented. The prototype is built using *Swarm*, CORE studio Thornton Tomasetti's in-house system for remote solving - a software as a service (SaaS) solution.

In a 3D environment supported by Swarm, the user is required to provide the input geometry and the boundary conditions. By referencing the input data in the system, Swarm is able to parse it and pass it along to the backend service where the analysis and classification processes are run. See figure 6.

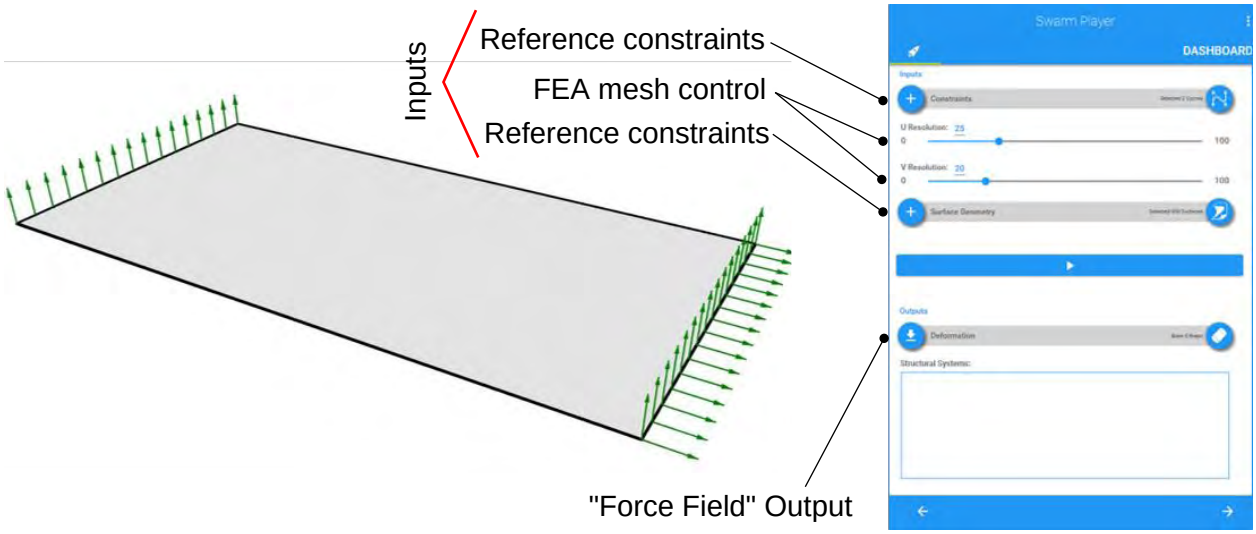


Figure 6: Reference model (right) with the Force field import page.

Once the backend is done computing, the results are sent back to the GUI. The results are mapped as a color gradient onto the input geometry to provide a better understanding of it's structural behavior. Additionally, a set of recommended typologies are presented as a list. See figure 7.

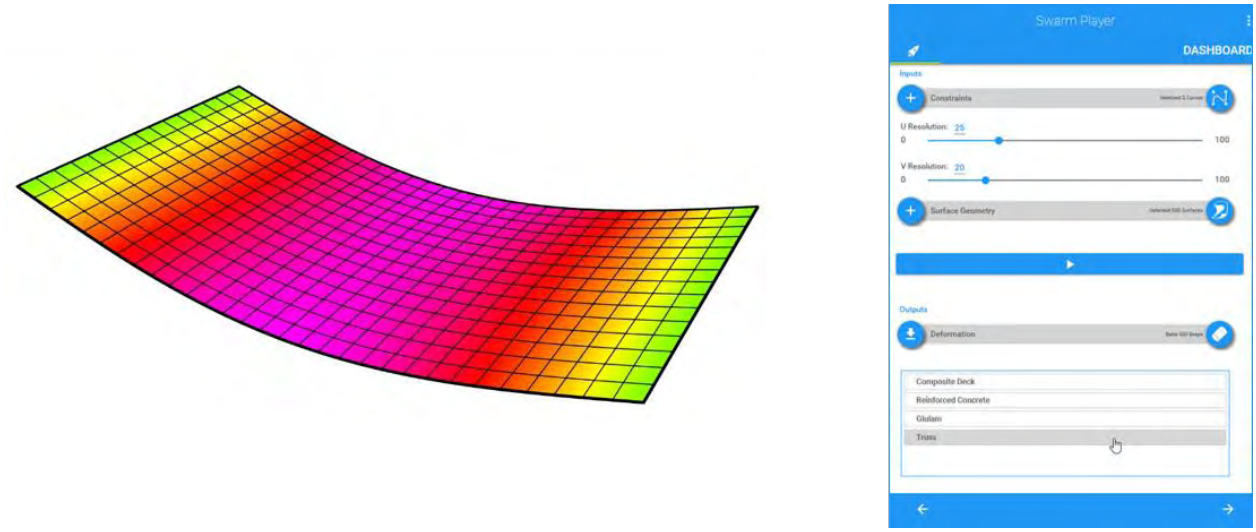


Figure 7. Analysis results of initial model and proposed systems.

By selecting one of the structural typology suggested by the system, the user is then presented with a dashboard where the parametric model can be utilized to explore the design space.

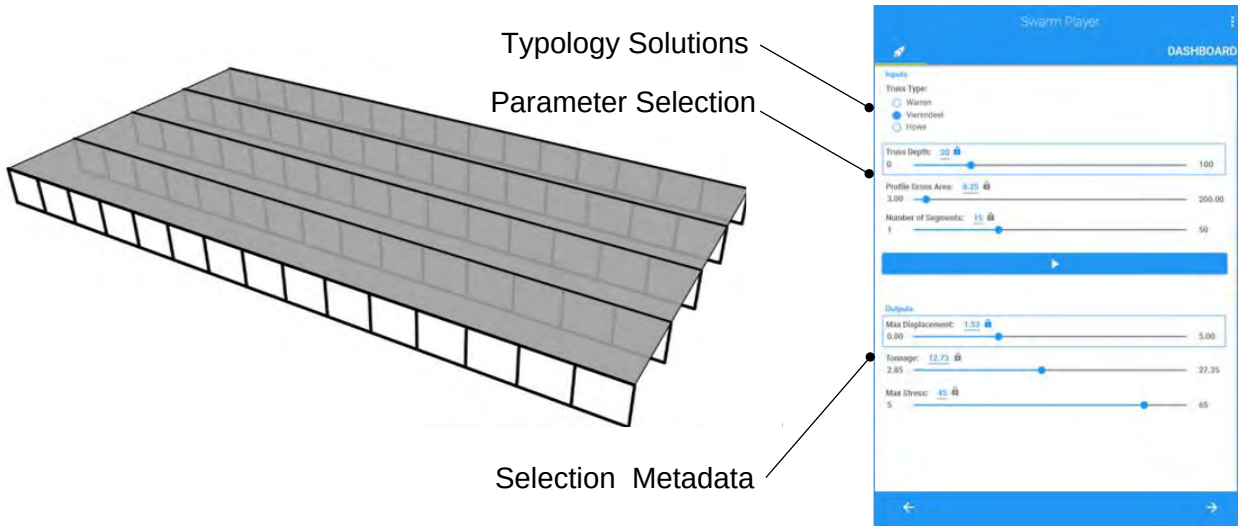


Figure 8: The parametric model generated by selecting the truss system in Figure 7.

4. Discussion and Future Opportunities

The Force Field approach is a big data approach for allowing architects, designers, and engineers the ability to find design solutions in a very short amount of time in addition to enabling an order-of-magnitude exploration of design options for a particular design concept. The crowd-sourcing of solutions from a multitude of experts into a database will allow a more intelligent "smart" solution set to mapping design solutions to a design concept while also enabling new design inspirations when a designer begins to learn the correlations between form/topology and structural typology solutions. Within those mapped solutions, a designer can then begin a detailed optimization process of material, weight, aesthetic, fabrication complexity, etc.

Future opportunities for increasing both the speed and intelligence of the Force Field approach would be to apply machine learning strategies per Reynolds et al. [3] for faster predictions of the structural mapping but also machine learning can allow predictions of hybridized solutions that are not in the original dataset.

5. Conclusion

The Force Field approach of mapping a catalogue of pre-computed structural typologies to a simple FEA simulation allows an elegant and efficient methodology in design space exploration and design optimization for both designers and engineers. This big data approach is made possible by modern high speed computing and cloud-based data storage capabilities and minimizes the repetitive and labor-intensive nature of current professional team-based practice whereby design solutions are significantly limited to a team or a single individual's engineering knowledge and time limitation of analytical feedback and fee limitations.

Acknowledgements

This concept of this paper was developed based upon the ideas and strategies proposed from the 2016 AEC Technology Hackathon event from a "Force Field" team consisting of Heath May and James Warton (HKS Line), Robert Otani, Daniel Segraves, and Emil Poulsen (Thornton Tomasetti) and Mark Rocha (HDR).

References

[1] N. Brown, C. Mueller, *Designing with data: moving beyond the design space catalog*, Acadia 2017

[2] "Design Explorer 2", *tt-acm.github.io*, 2018. [Online]. Available: http://tt-acm.github.io/DesignExplorer/. [Accessed: 14- Jun- 2019].

[3] D. Reynolds, K. Ghantous and R. Otani, "Performance Measures from Architectural Massing Using Machine Learning", in *Proceedings of the IASS Symposium*, Amsterdam, 2015.

Proceedings of the IASS Annual Symposium 2019 – Structural Membranes 2019
Form and Force
7 – 10 October 2019, Barcelona, Spain
C. Lázaro, K.-U. Bletzinger, E. Oñate (eds.)

Limit state approach for structurally informed design of shells composed of interlocking blocks

Elham MOUSAVIAN*, Claudia CASAPULLA

* Department of Structures for Engineering and Architecture, University of Napoli Federico II
Via Forno vecchio, 36, 80134 - Napoli, Italy
elham.mousavian@unina.it

Abstract

This work demonstrates an extension of limit analysis with concave model to design 3D assemblages of dry jointed interlocking rigid blocks with orthotropic sliding resistance. A digital framework is developed to design and analyse the structural feasibility of assemblages of interlocking blocks. The sliding resistance is defined as a function of the geometric properties of the interlocking interface. Adjusting the geometric parameters, designers can modify the infeasible models to be stable. The limit states are governed by two types of failure planes including dry joints and fracture strips between the locks and the main body of the block. These planes are merged and simplified to an orthotropic interface between two blocks. Then, the interface is abstracted to a number of point contact points distributed on lock centrelines, at which the stress resultants are computed by solving the equilibrium problem under proper sliding constraints. Applying this method, the limit conditions for several single layer shells with hexahedral units assembled with stack bond are illustrated.

Keywords: concave limit analysis, interlocking blocks, non-isotropic sliding resistance, structurally informed computer aided design.

1. Introduction

Limit analysis using point contact formulation (introduced by Livesley [1]) has been widely used to model the discrete nature of assemblages of rigid blocks, mainly for masonry structures. This model is less computationally expensive comparing to finite element [2] and discrete element methods [3], yet highly accurate to analyse the structural feasibility of rigid block assemblages. According to this formulation, the structural model consists of rigid bodies with failure planes (contact interfaces) as their boundaries, where internal forces are distributed on. The limit state formulation has been developed for the contact interfaces with infinite [4] and finite isotropic frictions [5, 6]. Still, modelling of contact interfaces with non-isotropic sliding resistance is an open problem.

Interlocking blocks with a number of locks on their faces keeping the blocks together can be considered as units with non-isotropic sliding resistance. As shown in [7-9] through experimental tests, the interlocking interfaces increase the block sliding resistance without adhesives during or after the construction [10]. This paper extends the Livesley's contact model to corrugated interlocking interfaces having rectangular cross section. The approach is extendable to other cross sections though. For such interface, the sliding resistance is different along and normal to the locks (orthotropic). The assemblage is subjected to any types of external forces and torques.

The extended contact formulation of the paper introduces the orthotropic sliding resistance as a function of the geometric parameters of interlocking interfaces and therefore considers this modelling as a structurally informed design problem. Interlocking blocks with customized shape can be manufactured

Copyright © 2019 by Elham Mousavian and Claudia Casapulla
Published by the International Association for Shell and Spatial Structures (IASS) with permission.

by advanced machines such as CNC mills. The key motivation of the paper is to provide a computationally efficient method to design structurally feasible assemblages, via tuning the geometric parameters of interlocking interfaces, beside exploring various geometries for the structure and its blocks with interfaces previously constrained to be normal to the flow of forces [11] or to satisfy isotropic frictional constraint [12].

The authors of this paper earlier introduced a convex or surface contact model for interlocking corrugated interfaces [13] of semi-circular arches. The convex model idealized the assemblage through finding the stress state at a single point on an interface. This paper extends Livesley's concave or point contact model, using several points to abstract the contact interfaces. This approach suits the non-isotropic nature of the interlocking interfaces better than the convex model. In the following first this concave contact model is introduced. Then, the design workflow and the results of the framework are demonstrated in Sections 3 and 4, respectively.

2. Concave contact model for interlocking blocks

As introduced above, the discrete structural model consists of rigid bodies with failure planes as their boundaries, where internal forces are distributed on. For an interlocking interface (Figure 1a), the failure planes are assumed to be the **dry joints** between two interlocking blocks (blue strips) together with the **fracture planes** at which each block might crack (red strips in Figure 1b). The main body of the block is assumed rigid enough so that other types of potential fracture planes are avoided.

The dry joints can only rock/separate when normal forces on them are in tension or slide along the direction parallel to the locks when violating the Coulomb's friction constraint. The fracture planes slide or twist when the shear or torsion yielding conditions are reached, respectively. To simplify the model of the stress state, these two types of strips are merged (Figure 1c). Extending the concave contact model introduced by [1] to an interlocking interface, the merged failure planes are abstracted to a number of points. For a structurally feasible model, the internal forces on these points satisfy the equilibrium conditions and a set of constraints preventing the failures described above. For such an interlocking interface, at each point, the normal component of the internal force r^n is in compression; the tangential component of internal forces along the locks r^{t1} satisfies the Coulomb's friction law and the tangential component of internal forces normal to the locks r^{t2} is less than the shear resistance at the point (Figure 1c).

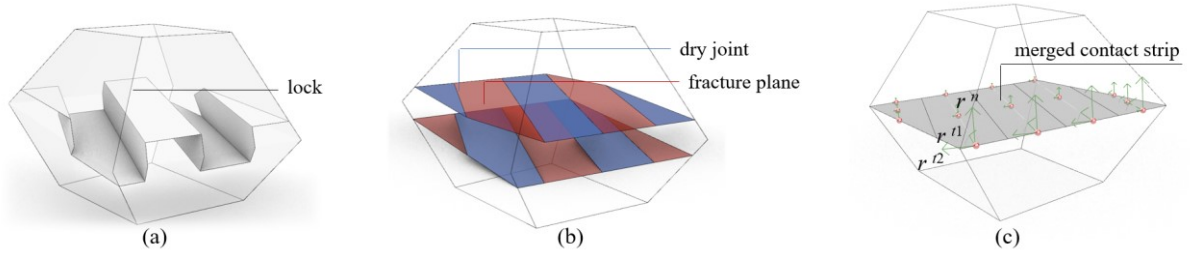


Figure 1: a) Two interlocking blocks kept together by the locks; b) dry joints (blue strips) and fracture planes (red strips), at which failure may occur; c) merged strip and point contacts distributed on their centrelines

To find the shear resistance at a point contact, first the lock is abstracted to its linear centreline, on which the tangential forces are distributed, uniformly or non-uniformly (Figures 2a,c). The lock is resistant when at each point along its length the force per unit length f_b is less than the shear resistance per unit length (yield force) $f_y = (\tau_k\, s)$ [13], where s is the lock thickness and τ_k is the material shear strength. In future work this resistance will be calibrated through experimental tests, similarly to what carried out in [14] for wooden interlocked pieces.

When the forces are distributed uniformly, the total shear resistance T_0 at the whole fracture plane between a lock and the main body of the block equals ($\tau_k\, sb$), where b is the lock length (Figures 2c,d). For a non-uniform distribution of the forces, the total shear resistance at the fracture plane T_r is lower than T_0 (Figures 2c,d), so that $f_b \leq f_y$. Based on that, the distribution of the tangential forces can be abstracted by a number of point loads along the lock centreline, under the constraint that their resultant is $\leq T_0$. Thus, the shear resistance at each point i on a lock centreline can be a portion of T_0 through a weight p_i, so that $\sum_{i=1}^{n} p_i = 1$.

A validation test is now introduced for two options of point distribution, involving the number of points and weighting rules. Option 1 presents two points at 1/6 distance to the end points of the centrelines (Figures 2e); the shear resistance at each point is $T_0/2$. Option 2 displays three points at the end points and the mid-point of the centrelines; the shear resistance at these points are shown in Figure 2f.

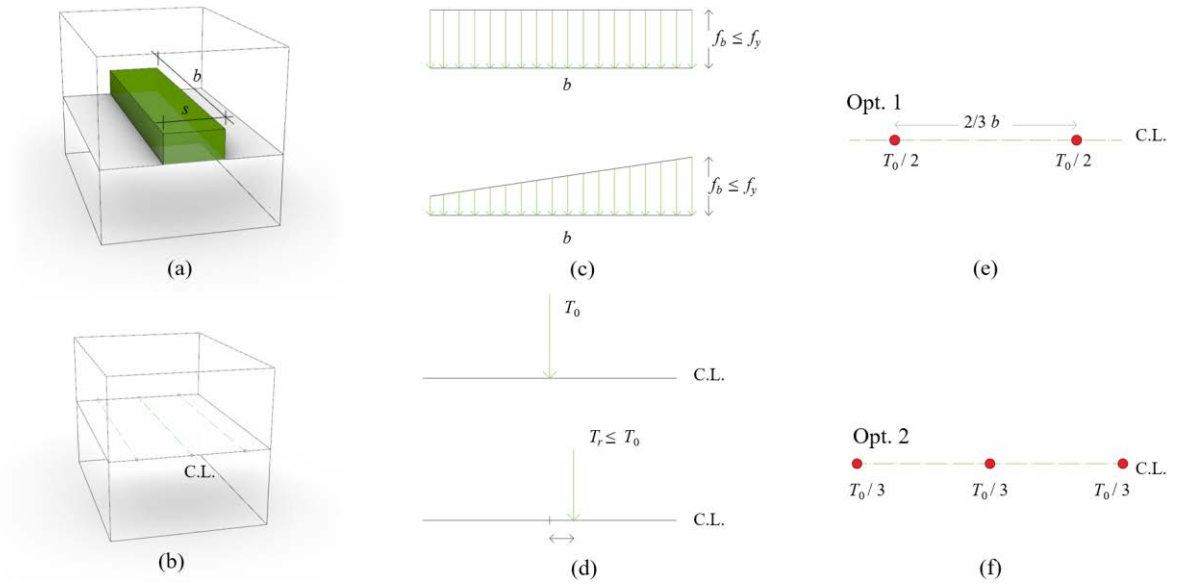


Figure 2: a) Generic lock; b) centrelines (C.L.) of the fracture planes between the locks and the main bodies of the blocks; c) uniform and non-uniform distributions of the tangential force on the lock centreline; d) limiting resultants of the two distributions; e) Option 1 and f) Option 2 for point distribution

The validation test is carried out to compare the sliding resistance obtained by these two options with the sliding resistance obtained by the literature convex formulation and experimental test [15] performed on two dry stacked tuff blocks subjected to different combinations of loading. For this comparison, only the interactions between torsion and tangential force are taken into consideration. These were executed by applying a lateral horizontal force with different eccentricities on the upper block, while the lower block was completely fixed.

The block dimensions and applied forces are reported in Figure 3a, while Figure 3b represents the configuration of point loads according to the point contact model Option 1, where T_0 at each lock is half of the total interface sliding resistance when pure tangential force is applied. Figure 3c shows different yield curves for the torsion-tangential force interaction related to: experimental results [15] (black dots); the convex method presented in [15] (dash red curve); the proposed Option 1 (blue dash-dot curve) and Option 2 (green continuous curve) for point distribution. While Option 1 provides conservative results, Option 2 shows a better agreement with the real behaviour of the interface.

Once defined the model of point distribution, the equilibrium problem under the limiting conditions is formulated as follows:

$$\begin{cases} C_{eq}.\vec{r} + \vec{E} = 0 \\ r_{i,j}^{n} \leq 0 \\ \left|r_{i,j}^{t1}\right| \leq \mu \left|r_{i,j}^{n}\right| \\ \left|r_{i,j}^{t2}\right| \leq p_{i,j}\, T_0 \end{cases} \quad \forall i \in \text{merged strip } j;\ \sum_{i=1} p_{i,j} = 1 \tag{1}$$

where C_{eq} is the coefficient matrix, $\vec{r}$ is a vector of all normal and tangential components of internal forces and $\vec{E}$ is a vector of all external forces *EF* and torques *ET*. In this framework, the external force vector always includes the block weight which is obtained through the block volume multiplied by density.

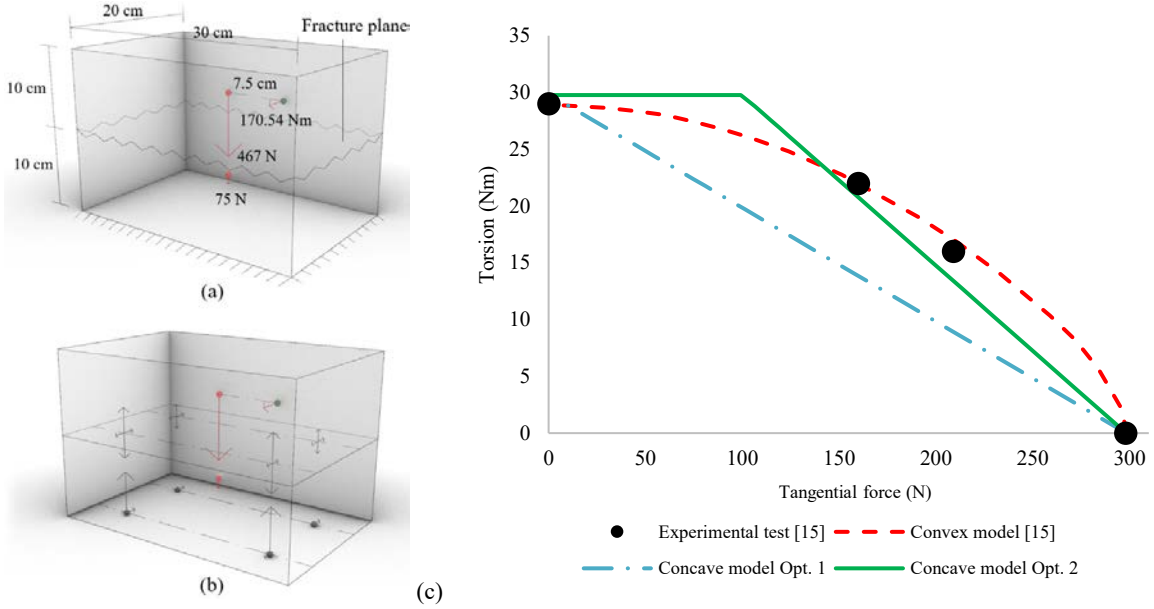


Figure 3: a) Block dimensions and one of the loading combinations on two dry stacked blocks experimentally investigated [15]; b) outline of internal forces using the point contact model-Option 1; c) compared results for torsion-shear interactions

3. Design process

This section introduces the design process including the proposed modelling and structural analysis procedure. The new computational framework for limit analysis of interlocking block assemblages presented in this paper is a plug-in for grasshopper editor which is developed using c# language. The plug-in consists of five grasshopper (GH) components for 1) modelling the rigid blocks and an assemblage of such blocks, 2) modelling the interlocking interfaces, 3) determining the boundary conditions, 4) determining the external forces and torques and 5) implementing the analysis of the designed model (grey boxes in Figure 4). Figure 4 displays the design workflow and each function of the GH components in detail. All the inputs marked by the pink lines can be modified parametrically during the shape exploration. Outputs are marked by the blue lines.

This workflow is designed to model and analyse a single layer assemblage of blocks with grid pattern, where the main body of the blocks are hexahedron units. The main body of each block must have flat faces. As shown in Figure 5, the gridlines are divided into two series *u* and *v*. The overall shell can be closed along a *v* gridline to build a ring and can be converged towards the shell apex and be closed along a *u* gridline to form a radial grid (Figure 5b).

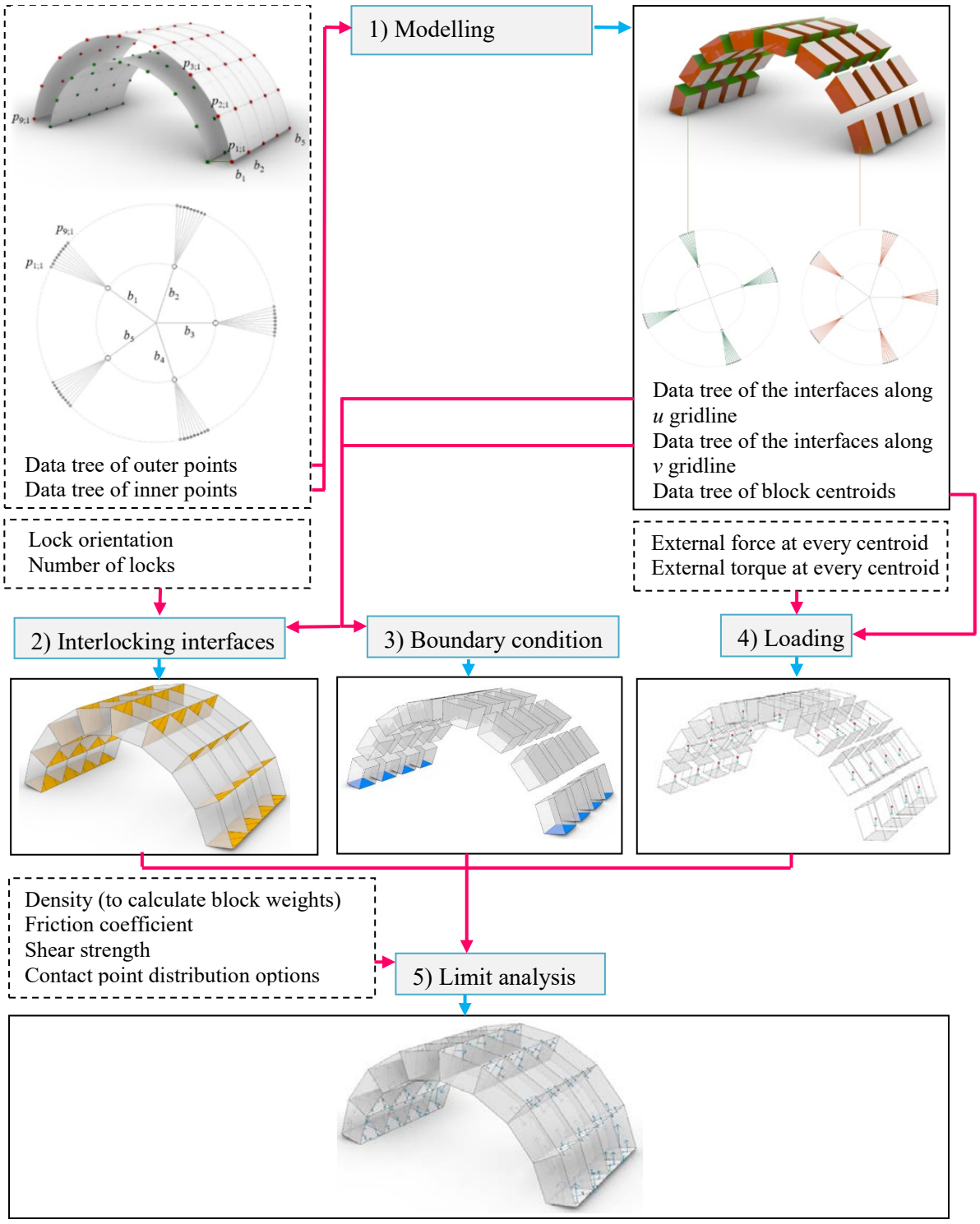


Figure 4: Design workflow

When the model is closed along a *v* gridline, the overlapped faces can be regarded as interfaces shared between two blocks. To use the coefficient matrix C_{eq} of Eq. (1) for such a model, a new set of constraints are added keeping the values of the internal forces on those overlapped faces equal in the opposite directions. When the closed surface is converged towards the upper side of the surface and is closed at

the last *u* gridline, a key unit is considered, and C_{eq} of Eq. (1) is updated by concatenating a row to it to equilibrate internal forces on the key unit.

In this workflow, the coordinate of the corners can be modified parametrically. Verifying the correctness of the assemblage topology and the flatness of the block faces during the initial modelling or the modification is beyond the framework of this paper and will be addressed in further works.

The linear system of Eq. (1) is solved by least square optimization using MATLAB's lsqlin method with linear equality and non-equality constraints. The implementation of the computational setup is validated through comparing the minimum thickness of a hemispherical dome with conventional blocks subjected to its own weight obtained by this framework with those obtained by [4, 16] (Figure 5c). The results specifically validate that the set-up is capable of analysing the closed surface converged towards the apex through the explained amendments on C_{eq} for the open surfaces.

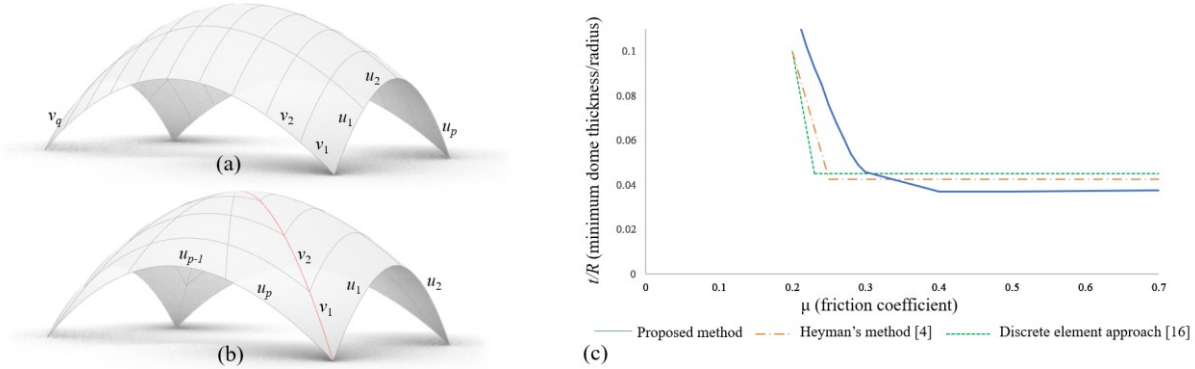


Figure 5: a) Normal grid (stacked) bonding pattern and b) radial grid bonding pattern; c) comparison of the thinnest hemispherical dome obtained by the proposed method and by [4, 16]

4. Results

Two examples are provided to study the interaction of: 1) orientation of locks and friction coefficient and 2) type of interfaces (conventional and interlocking) and friction coefficient.

Example 1. The first example is composed of three blocks (Figures 6a) with vertical interfaces between the blocks (yellow faces in Figures 6c,d). The assemblage is under the weight of the blocks whose density is 1 N/m^3. Two faces, represented in blue in Figure 6b, are the supports transferring the forces to the ground. The orientation of the locks on the vertical interfaces varies during the shape exploration (Table 1). Figures 6c,d show two models with the vertical and horizontal locks, respectively. The concave model Option 1 displayed in Figure 2 is selected for the analysis. The shear strength is 10 N/m^2. The number of locks at each interface is three.

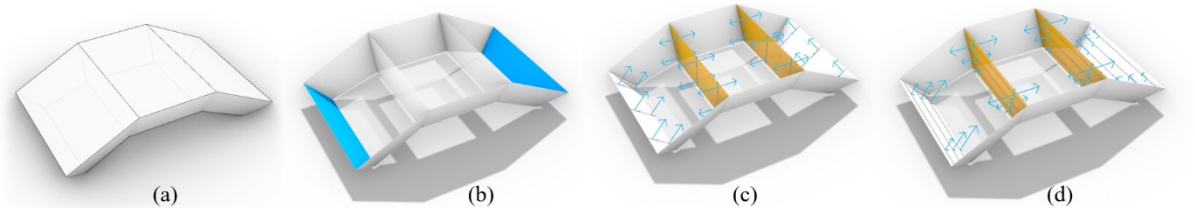


Figure 6: a) Input model; b) boundary conditions; c and d) models with vertical and horizontal locks

For the case with vertical locks, the tangential forces at the interlocking interfaces are along the locks, therefore the sliding resistance is only governed by the Coulomb's friction law. The case can resist against sliding when the friction coefficient is more than 0.3. For the case with horizontal locks, the tangential forces at the interlocking interfaces are normal to the locks. As a result, the sliding resistance is only governed by the shear resistance of the locks and the model is stable even with the friction

coefficient equal to 0. The minimum friction coefficient needed for stability of the models with different lock orientations is represented in Table 1.

Table 1: Minimum friction coefficient for different lock orientations

Orientation (degree)	0	10	20	30	40	50	60	70	80	90
minimum friction coefficient	0	0.05	0.11	0.15	0.19	0.23	0.26	0.28	0.29	0.3

Example 2. The second example is composed of sixteen blocks (Figure 7a), under their own weight, where density is determined 1 N/m^3 and supporting faces are represented in blue in Figure 7b. Two cases are studied: 1) all interfaces are conventional flat faces (Figure 7c); 2) the interfaces along *u* and *v* gridlines are interlocking faces (Figure 7d). Interfaces in one direction are modelled with three locks (at each interface) with the orientation of 0.8 radians with respect to the block edge, while the interfaces in the other direction have three locks as well, but orientation of 2 radians. Both concave model options were used for the analysis. The shear strength is 10 N/m^2.

Implementing concave model Options 1, the friction coefficient for the case with conventional blocks must be more than 0.23. Using concave model Option 2, this minimum value is reduced to 0.21. The computation time for Options 1 and 2 are 6.6 and 8.6 seconds, respectively, considering the larger number of points for Option 2. Whatever Option is implemented, the minimum friction coefficient for the case with the interlocking blocks is 0. This shows that when the shear strength is large enough, the model with interlocking interfaces can be stable with zero frictional resistance, while the minimum friction coefficient for such model with conventional flat interfaces is 0.23 or 0.21, depending on the model of point contact distribution.

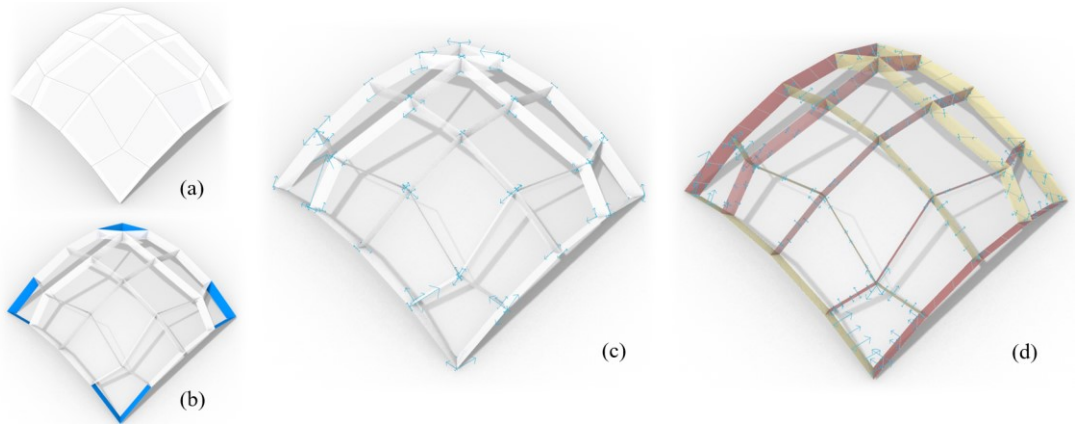


Figure 7: a) Input model; b) boundary conditions; cases with c) conventional blocks in two directions; and e) interlocking blocks in two directions analysed by concave model Option 1

4. Conclusion

The paper presents a digital framework for structurally-informed design of shells composed of interlocking blocks. The applied structural analysis method is an extension of the concave contact model to interlocking interfaces and the model is developed for corrugated interfaces with rectangular cross section. These can be idealized as interfaces with orthotropic sliding resistance, with components normal to and along the locks governed by lock shear strength and Coulomb's friction law, respectively. In the future the contact model can be extended to other geometries for the cross section.

The sliding resistance is defined as a function of geometric properties of the locks including their number and orientation. Therefore, the framework considers those properties as parameters which can be adjusted by the users to check the stability of the model. Material properties including the friction coefficient and shear strength are other variables which can be changed parametrically. In further works,

automated procedures will be developed which tunes the geometric properties to make an infeasible model feasible. Accordingly, the infeasibility caused by the violation of sliding constraints will be measured and minimized through adjusting the geometric parameters of interlocking interfaces.

Acknowledgements

This project has received funding from the European Union's Horizon 2020 research and innovation programme under the Marie Skłodowska-Curie Grant Agreement No. 791235.

References

[1] R.K. Livesley, "A computational model for the limit analysis of three-dimensional masonry structures," *Meccanica*, vol. 27(3), pp. 161-172, 1992.

[2] P.B. Lourenco, J.G. Rots, J. Blaauwendraad, "Two approaches for the analysis of masonry structures: micro and macro-modeling," *HERON*, vol. 40(4), 1995.

[3] B. Pantò, I. Caliò, P.B. Lourenço, "A 3D discrete macro-element for modelling the out-of-plane behaviour of infilled frame structures," *Engineering Structures*, vol. 175, pp. 371-385, 2018.

[4] J. Heyman, "The stone skeleton," *International Journal of solids and structures*, vol. 2(2), pp. 249-279, 1966.

[5] M. Gilbert, C. Casapulla, H.M. Ahmed, "Limit analysis of masonry block structures with non-associative frictional joints using linear programming," *Computers and structures*, vol. 84(13), pp. 873-887, 2006.

[6] V. Beatini, G. Royer-Carfagni, A. Tasora, "Modeling the shear failure of segmental arches," *International Journal of Solids and Structures*, vol. 158, pp. 21-39, 2019.

[7] Y. Z. Totoev, "Design Procedure for Semi Interlocking Masonry," *Journal of Civil Engineering and Architecture*, vol. 9, pp. 517-525, 2015.

[8] M. Sassu, A. Romanazzi, L. Giresini, W. Franco, C. Ferraresi, G. Quaglia, E. Orefice, "Production procedures and mechanical behaviour of interlocking stabilized compressed earth blocks (ISCEBs) manufactured using float ram 1.0 press," *Engineering Solid Mechanics*, vol. 6(2), pp. 89-104, 2018.

[9] H. Liu, P. Liu, K. Lin, and S. Zhao, "Cyclic behavior of mortarless brick joints with different interlocking shapes," *Materials*, vol. 9(3), pp. 166, 2016.

[10] A.V. Dyskin, E. Pasternak, Y. Estrin, "Mortarless structures based on topological interlocking," *Frontiers of Structural and Civil Engineering*, vol. 6(2), pp.1-10, 2012.

[11] M. Rippmann, *Funicular Shell Design: Geometric approaches to form finding and fabrication of discrete funicular structures*, Ph.D. dissertation, Dept. Architecture, ETH, Zurich, 2016.

[12] E.J.W. Whiting, *Design of structurally-sound masonry buildings using 3d static analysis*, Ph.D. thesis, MIT, Massachusetts, 2012.

[13] C. Casapulla, E. Mousavian, E. Zarghani, "A digital tool to design structurally feasible semi-circular masonry arches composed of interlocking blocks," *Computers & Structures*, in press.

[14] D. Fang, and C. Mueller, "Joinery connections in timber frames: analytical and experimental explorations of structural behavior," In *Proc. of International Association for Shell and Spatial Structures (IASS) Annual Symposia 2018, MIT, Boston, USA, July 16-20, 2018*, pp. 1-8.

[15] C. Casapulla, and F. Portioli, "Experimental and analytical investigation on the frictional contact behavior of 3D masonry block assemblages," *Construction and Building Materials*, vol. 78, pp.126-143, 2015.

[16] J. Simon, and K. Bagi, "Discrete element analysis of the minimum thickness of oval masonry domes," *International Journal of Architectural Heritage*, vol. 10(4), pp. 457-475, 2016.

Proceedings of the IASS Annual Symposium 2019 – Structural Membranes 2019
Form and Force
7 – 10 October 2019, Barcelona, Spain
C. Lázaro, K.-U. Bletzinger, E. Oñate (eds.)

Maintenance procedures and modelling of gas pipeline components

Ján BRODNIANSKY*, Martin MAGURA[a], Prof. Ján BRODNIANSKY[a]

*Slovak University of Technology in Bratislava, Faculty of Civil Engineering
Radlinského 11, 81005 Bratislava
jan_brodniansky@stuba.sk

[a] Slovak University of Technology in Bratislava, Faculty of Civil Engineering

Abstract

Regular diagnostic inspections on bridgings and other important gas pipeline components (compressor stations, road and rail underpasses, anchoring blocks) have been performed by the Department of Steel and Timber Structures since 1998 to ensure uninterrupted supply of natural gas. Paper presents these components (model cases): Bridging Sikenica and interaction bridging- 1st and 2nd transit line according to planned rectification works; Friction clamp ring on the newly built anchoring block near Sikenica bridging on the 1st transit line; Modelling of the landslide in real dimensions and its influence on pipeline. In presented article are shown various ways how to evaluate critical details by FEM modelling and verification of theoretical results by in-situ experimental measurements. Undergoing regular maintenance, the life of steel structures can be extended, and operational capability and safety can be ensured. All presented models are proving, that relatively difficult problems form engineering praxis can be solved.

Keywords: gas pipeline, FEM model, maintenance procedures, soil interaction

1. Introduction

Since 1998 regular diagnostic inspections on transit gas pipelines in Slovakia and its components (bridgings, compressor stations, road and rail underpasses, anchoring blocks) have been performed by Department of Steel and Timber Structures. This paper focuses on three typical problems which were solved by authors in recent time: Whole bridging Sikenica and interaction bridging- 1st and 2nd transit line according to planed rectification works; Friction clamp ring on newly built anchoring block near Sikenica bridging on 1st transit line in Slovakia (pipe diameter - DN1200), Modelling of the landslide in real dimensions and its influence on buried pipeline.

2. Rectification works on bridging Sikenica

Transit gas pipeline line no.1 TP-I. DN1200 and no.2 TP-II. DN1200 are overpassing river Sikenica on three hinge truss arch (figure 1). Pipeline bridge has span of 57318mm and camber of 7678mm. Structure is made of typified structural parts, made for bridge overpasses for transit gas pipelines (assembly PM-10-B). Pipelines has tendency to get closer in the middle of arch span, this phenomenon is occurring on all the gas pipeline bridgings in Slovakia. Spring supports under the pipelines are pressed to their maximum or there is no contact with pipeline and some of them are highly shifted from their original position (figure 2). Complex reconstruction and rectification of pipeline on bridging is proposed. All actual spring supports under the gas pipelines are proposed to be changed with new special designed telescopic spring supports. Transit line no.1 is proposed to be rectified to new position

Copyright © 2019 by Ján BRODNIANSKY, Martin MAGURA, Prof. Ján BRODNIANSKY
Published by the International Association for Shell and Spatial Structures (IASS) with permission.

(horizontal movement approx. 250mm from transit line no.2). New position of pipelines was designed for each of 12 crossbeams, two of them are shown in figures 3 and 4.



Figure 1: Bridging Sikenica



Figure 2: Original spring supports

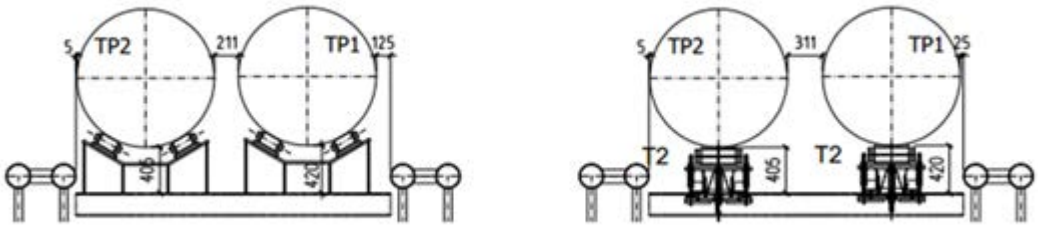


Figure 3: Crossbeam no.4; left – actual position; right – designed position

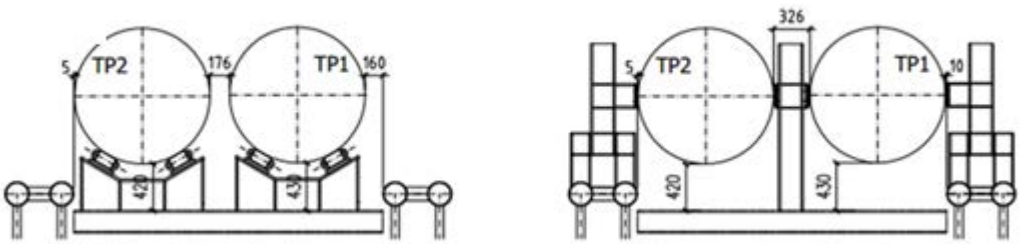


Figure 4: Crossbeam no.5; left – actual position; right – designed position with new guide beams

By rectification design on bridging Sikenica four separate models were done, each of these models represent different stage of rectification procedure. For modelling there were used only FEM beam elements but with different characteristics (only tension, only compression, sprig beam with definition of spring constant). Bridging with part of the underground lying pipelines was modelled to obtain reasonable results (figure 5). Soil parameters were considered according to [1].

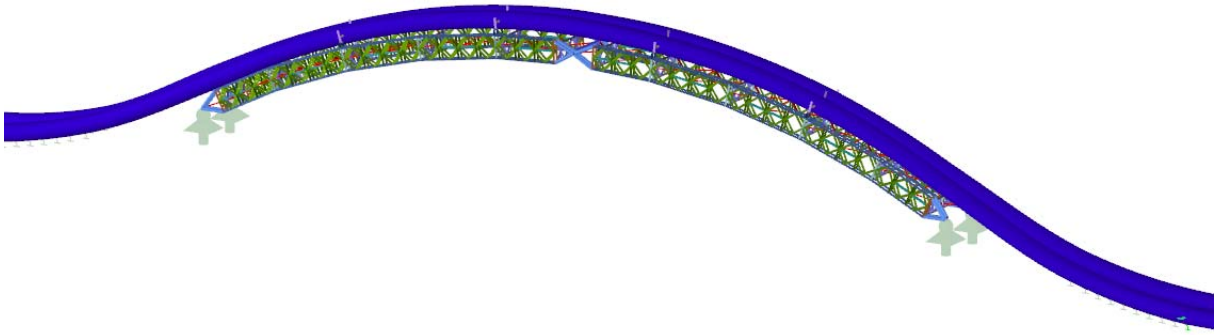


Figure 5: Modell of new position of pipelines on bridging Sikenica

Modelled construction phases:

Phase I. – Original position of pipelines on bridging (figure 6 left)

Phase II. – Horizontal rectification

Phase III. – Vertical rectification - newly mounted telescopic spring seats and newly mounted spacing beams between pipelines and on the edges of bridging

Phase IV. – New postilion of pipeline (figure 6 right)

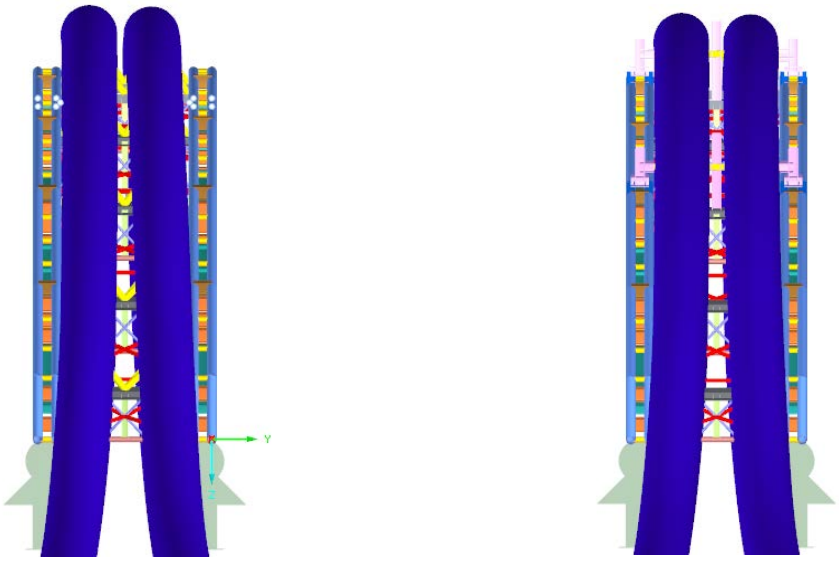


Figure 6: Front view of model, left original position of pipelines, right new position of pipelines

Assessment of all cross-sections on the structure was done. Whole calculation was done by means of STN EN standards, both bridging (material S235) and pipelines (material X60) are satisfactory. For the

control of real situation tensometric values was modelled phase II and phase III (phases during rectification works) and it was proved that stresses in pipelines do not overcome 20% of material strength of XC60 steel by vertical rectification and 5% of material strength of X60 steel by horizontal rectification.

3. Anchoring block and friction clamp ring near Sikenica bridging

In year 2017 arose requirement to rebuilt anchoring block near Sikenica bridging due to encountered corrosion on the pipeline in the old block. Main function of this structure is to transfer axial force from bridging's prefix into the ground environment and not to allow vertical displacement of the pipeline on the bridging. Situation and longitudinal section of new and old anchoring block is shown in figure 7 and 8.

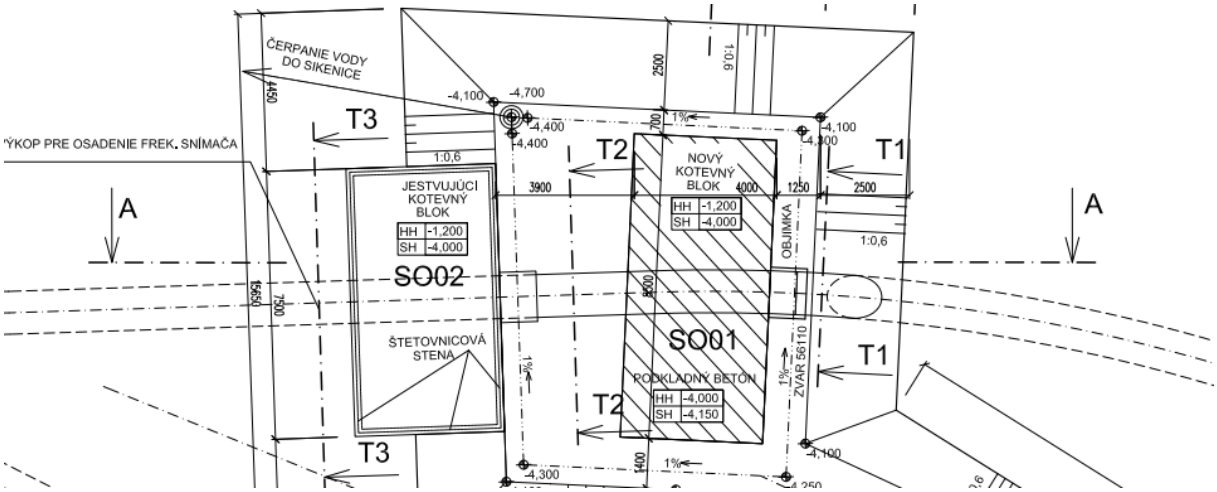


Figure 7: Situation of new and old anchoring block

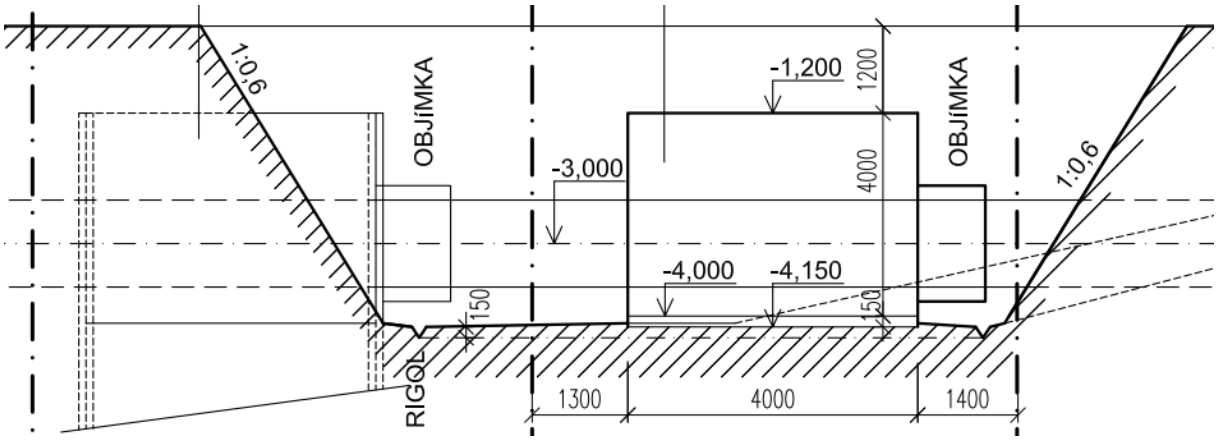


Figure 7: Longitudinal section of new and old anchoring block

Horizontal axial force from pipeline is transferred to the anchoring block through friction clamp ring (next in text FCR) consisting of four parts connected by bolts. FCR is leaning on the front of the anchoring block and it is necessary to assemble FCR right after sandblast cleaning of pipeline surface. Minimal prescribed inside pressure of gas in pipeline during mounting of FCR is 4,0MPa (standard operating pressure is between 6 – 7MPa). Design of FCR is made to enable the transfer of horizontal axial force by friction area FCR-pipe DN 1220.18.9 (diameter 1220 mm). All four parts of FCR are connected by 18pic M30 (10.9) bolts. Material of pipe is steel XC60 and material of FCR is S355.

Contact plates of FCR are from P20 (steel plate thickness 20 mm), triangular stiffeners are P20 and plate of bolt connection is P30. Contact plate width is 990 mm rounded with radius R=610 mm. Friction coefficient used of by the value 0,3 (in real interaction it will be higher). Mounted FCR is shown in figure 8 left.

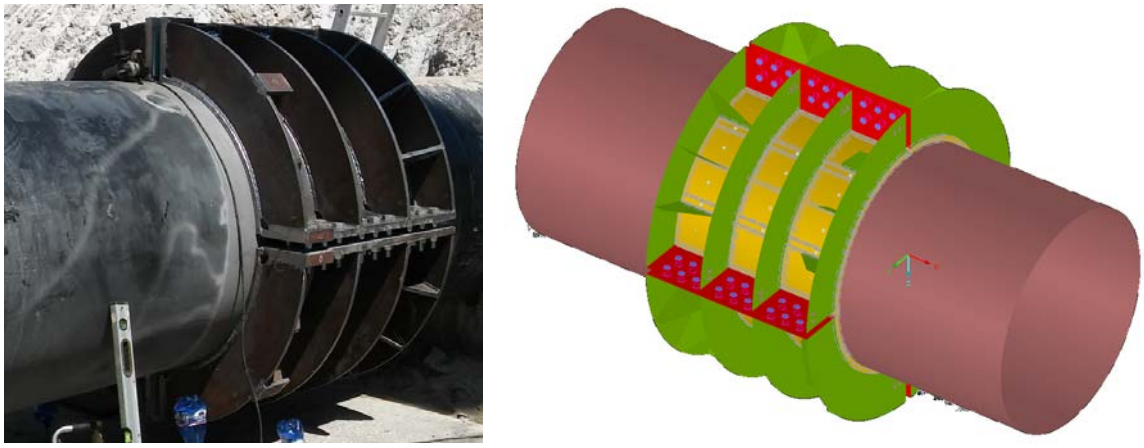


Figure 8: Left mounted friction clamp ring; Right FEM model of the friction clamp ring

Main aim of the whole FEM analysis was to predict FCR behaviour in interaction of inside pressure, bolt prestress [2] and friction. In presented FEM model there were used the following finite elements: Shell elements for pipe, FCR stiffeners, FCR frontal and central plates, plates with bolt connection; Volume elements for pipe in contact area, contact plate and contact zone between pipe and contact plate; Beam elements for bolts. (figure 8 right).

The most important results from modelling were internal forces in bolts due to internal prestress in pipeline and prestress of the bolts and combination of these loads. New Design of new FCR structure is more robust then FCR structures designed in the past, main reason is to enable better transfer of prestress forces (deformations of FCR bolt and stiffening plates are unwanted). As example there can be used the FCR mounted by internal gas pressure of 5MPa, minimum of 9 bolts on each connection is prestressed by force 200kN, gas pressure rises by 2MPa – this load combination can insure friction force of 3112kN.

Similar examples can be found in contribution of authors [3] and [4].

4. Gas pipeline – soil interaction by landslides

Gas-pipelines pass through different topographies. Their stress level is influenced not only by gas pressure, but also by the adjacent soil, the thickness of any covering layers and soil movements (sinking, landslides). The stress level may be unevenly spread over a pipe due to these effects. When evaluating the experimental measurements, errors may occur. The value of the resistance reserve of steel material can be adjusted by a detailed analysis of any loading. This reserve can be used in the assessments of a pipeline´s actual state or reconstructions. Results for the most common soil classes are shown in table 1.

Stresses induced by the internal pressure p

$$\sigma_{\varphi_p} = \frac{p.r}{t}; \qquad (1)$$

material strength of pipe X60 (f_y = 413,7MPa); ø 1220/15.9; internal pressure in pipe 7MPa; covering layer thickness 0,8m.

Table 1: Comparison of stresses

Soil class	F4 - stiff consistency	S4 - sand	G4 - gravel
Design value of material strength fy/γ_M [MPa]	296,43	296,43	296,43
Stress from internal pressure 7MPa (theory of elasticity) [MPa]	268,55	268,55	268,55
Reserve of stress Δs [MPa]	27,88	27,88	27,88
Stress from internal pressure 7MPa (FEM) [MPa]	244,55	249,06	249,21
Stress from bulk density (FEM) [MPa]	17,54	4,99	2,03
Stress from internal pressure + bulk density (FEM) [MPa]	259,73	253,14	250,40
Difference [MPa]	8,82	15,41	18,15
Reserve Δσ [MPa]	36,70	43,29	46,03

the effect of a landslide in the direction perpendicular to the axis of a pipe is shown as a working example. The modelled soil block was 1m thick, and the DN 1200 pipe had a wall thickness of 18.9mm. The internal gas pressure of 6.5MPa was simulated in the pipe (Fig 15). In the first model, the surrounding class F3 soil was homogeneous with the modulus of 12MPa and the specific gravity weight of 18kN/m3. In the second model, grade G3 gravel with a modulus of 70MPa was used. A section of pipe with the length of 120m was modeled. The middle part with the length of 100 meters lay in the lateral landslide with the value of 0.8m. The pipeline was anchored in the 10m long natural soil block. The load was specified as planar on one side of the soil block. Figure 9 shows that the maximum increase of tension in the pipe was at the joint from stable soil into the landslide section. The increment was approximately 299 MPa. The stress amounts to about 133 MPa in the middle of the landslide section (Fig. 9).

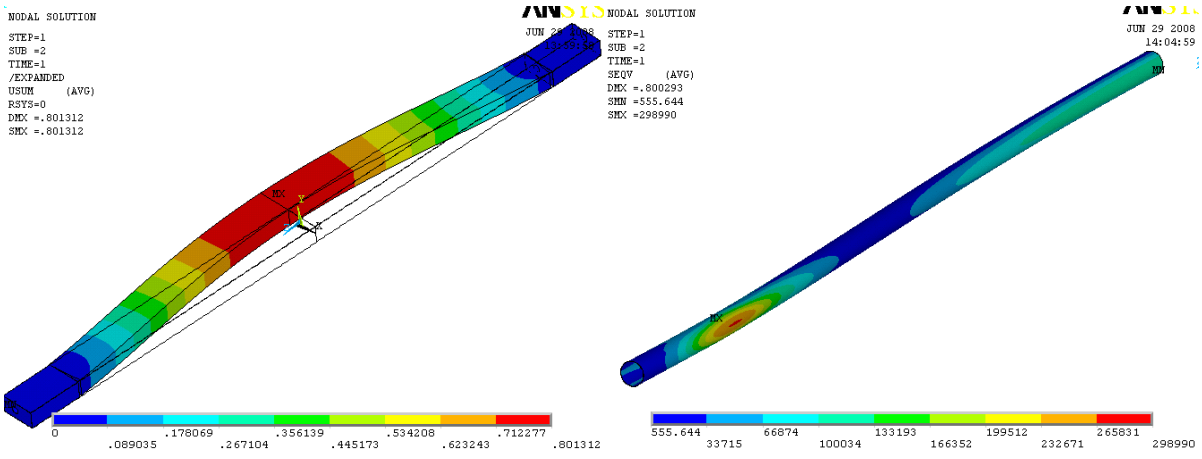


Figure 9: Left Global deformation of soil blocks and pipeline [m] - mirror view about symmetry; Right Stresses along the pipe by slide of length 100m [kPa]

At time of preparing this paper (May 2019) the construction of new gas pipeline connection has been already under construction. This pipeline is running from Polish border through eastern part of Slovakia to meet the main transit gas pipeline in the south east of Slovakia. The Department of Steel and Timber Structures namely authors of this paper were asked to determine the most suitable places in pipeline trajectory to mount long term measuring devices near land slide areas. Two locations were determined namely Hankovce (figure 10) and Zbojné (figure 11) (name was taken according to nearby villages).

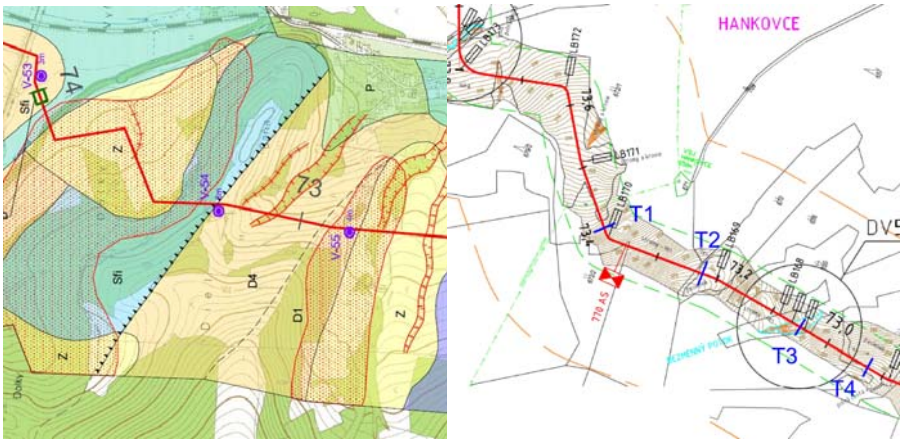


Figure 10: Location Hankovce; left land slide areas marked red; right position of measured cross section

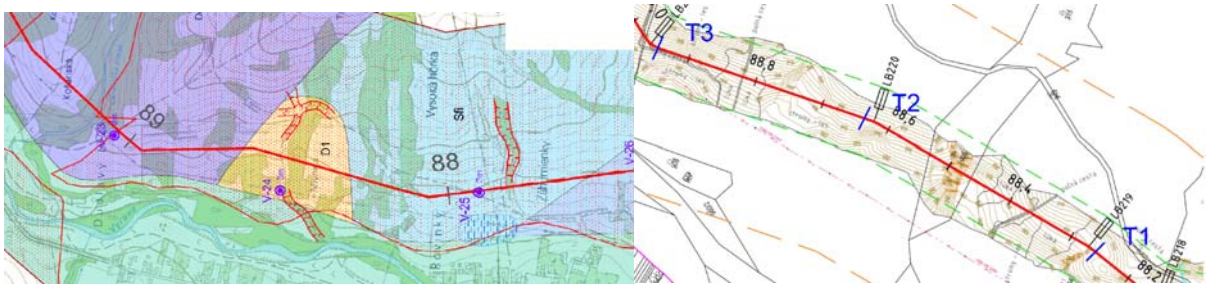


Figure 11: Location Zbojné; left land slide areas marked red; right position of measured cross section

In location Hankovce is necessayr to encounter with both lateral landslide (74-73km) and perpendicular landslide (73-72km). In location Zbojné is considered perpendicular landslide. For both locations simplified FEM models were made and values of estimated landslide movements were obtained. Position of the strain gauges in pipes cross-section are in figure 12 with type of designed gauge.

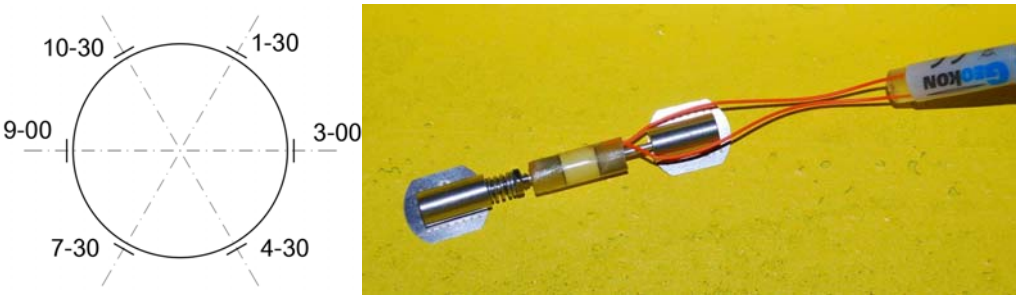


Figure 12: Left position of strain gauges in cross-section; Right designed strain gauge Geokon 4000

Estimated stress values from landslides conditions were the following: for location Hankovce i about 40MPa (37,8MPa) and for location Zbojne about 100MPa (99,2MPa). This means, that for selected

location, is highly recommended to measure possible landslide movements and consequent pipeline stresses see table 2. As is described in table 1 the real reserve (+bulk density) is higher and it is concluded that the pipeline is well designed in both locations.

Table 2: Simplified calculation of stress reserve for location Hankovce and Zbojná

Location	Hankovce	Zbojná
Design value of material strength fy/γ_M fy = 485MPa (steel L485ME) [MPa]	346,43	346,43
Pipe diameter/web thickness [mm]	1016/11.4	1016/13.5
Stress from internal pressure 7MPa (theory of elasticity) [MPa]	308,42	259,85
Reserve of stress Δs [MPa]	38,01	86,58

Measurements in locations Hankovce and Zbojné will by the first where it is possible to capture initial state of underground gas pipeline right after completion (this state was not able to achieve in other measurement points on transit gas pipeline because of commissioning age the main transit gas pipeline). Data transfer in this period should be intensive so the administrator of the gas pipeline should receive enough data of reliability and safety of the newly built transit system.

5. Conclusion

Presented paper describes three research tasks specified by Slovak transit gas pipeline administrator which were solved in recent time. Large FEM modelling was introduced to ensure safety and real structural behaviour of presented structural components, the FEM models were in good agreement with in-situ measurements. Each of the presented models is proving; that relatively difficult problems from engineering praxis can be solved. It can be stated that, operational capability and safety can be ensured by regular maintenance.

Acknowledgements

The authors would like to express thanks to the Grant agency of the Ministry of Education, Science, Research and Sports of the Slovak Republic for providing for a partly assistance a grant from the research program VEGA Nr.1/0388/19 – Analysis and synthesis of the influence of the service conditions to line and thin walled structures.

References

[1] Dický J., Mistríkova Z., Sumec J.: Pružnosť a plasticita v stavebníctve 2, Slovenská technická univerzita v Bratislave, 2006. ISBN 80-227-2515-3

[2] STN 73 1495: 2001 – Skrutkované trecie spoje oceľových konštrukcií (Bolted prestressed connections for steel structures)

[3] Brodniansky, J. - Magura, M. Repair Works, Experimental Resarch and Monitoring on Pipeline and Pipeline Bridges. In IASS - APCS 2012: From spatial structures to space structures.Seoul, Korea,21.-24.5.2012. Seoul: Korean Association for Spatial Structures, 2012

[4] Magura, M. - Brodniansky, J.: Structural analysis and of braking block sleeves on transit gaspipeline. In Procedia Engineering: Steel Structures and Bridge 2012. Czech and Slovak International Conference. Podbanské, SR, 26.-28. 9. 2012. Vol. 40 (2012), s.257-261. ISSN 1877-7058.

[5] Turček P., Hulla. J., Foundation Engineering, Bratislava: Jaga group, Slovakia, 2004

[6] STN 38 6410 Gas pipings and gas service pipes of high pressure, SUTN, Bratislava, Slovakia, 2009

Proceedings of the IASS Annual Symposium 2019 — Structural Membranes 2019
Form and Force
7—10 October 2019, Barcelona, Spain
C. Lázaro, K.-U. Bletzinger, E. Oñate (eds.)

Numerical modelling of masonry vaults with different brick pattern

Marco ALFORNO*, Chiara CALDERINI[a], Alessia MONACO[b], Fiammetta VENUTI[b]

* Politecnico di Torino, Department of Architecture and Design
viale Mattioli 39, 10125, Torino, Italy
marco.alforno@polito.it

[a] Universitá di Genova, Department of Civil, Chemical and Environmental Engineering
[b] Politecnico di Torino, Department of Architecture and Design

Abstract

Masonry vaults represent one of the most widespread types of horizontal structural elements in historical constructions. Vaults can be built according to different brick patterns, which, in historical building practices, were generally chosen for technical reasons. Brick pattern is expected to play an important role in the global behaviour of vaulted structures, but, despite the importance of this topic, its role on the mechanical behaviour of vaults has been investigated only by few authors. This study evaluates the influence of the masonry apparatus in barrel and cross vaults subjected to imposed displacements. The study is carried out through a numerical approach, considering micro finite element modelling. Results evidence that different brick patterns correspond to different structural stiffness and reaction forces. Moreover, barrel vaults are more sensitive than cross vaults to the orientation of the masonry apparatus.

Keywords: masonry vault, brick pattern, micro-modelling

1 Introduction

Historical buildings are very often characterised by the presence of masonry vaults. This horizontal structural element can be conceived starting from several geometrical configurations (e.g. barrel, cross, pavilion, etc) and each type of vault can be built according to different patterns of the masonry apparatus. The vault brick pattern derives from the historical building practice relative to a specific age and geographic area. As highlighted by Wendland [1], most often the choice of a certain masonry pattern was dictated by technical reasons, specifically by the possibility to build the vault without formwork. The principle was to build the vault with self-supporting courses that are stable through their shape by forming arches. This principle has been successfully applied to different vault typologies, as also testified by the building manuals published between the end of the eighteenth century and the beginning of the twentieth century (e.g., [2, 3]).
Brick pattern is expected to play a non negligible role in the global behaviour of vaulted structures. Baratta and Corbi [4] observe that a double curved surface, like a vault, is highly hyperstatic and the equilibrium is not uniquely determinated. Therefore, reading the masonry

Copyright © 2019 by Marco ALFORNO, Chiara CALDERINI, Alessia MONACO, Fiammetta VENUTI
Published by the International Association for Shell and Spatial Structures (IASS) with permission.

pattern can be a key to understand what equilibrium path would stresses follow. The cited authors compare two pavilion vaults with same geometry, but different orientation of the bed joints (in the first case parallel to the base perimeter, in the second case orthogonal). Starting from the assumption that the preferred equilibrium path for a vault is to have compression normal to the bed joints, the two different brick patterns result into different distribution of the horizontal thrust force along the perimeter. Foraboschi [5] further stresses the importance of the brick pattern in masonry domes, by comparing the Brunelleschi's dome in Santa Maria del Fiore in Florence and the Vasari's dome in Basilica della Madonna dell'Umiltá in Pistoia. The Vasari's dome was built in imitation of the Brunelleschi's dome, but Vasari adopted a different brick pattern: this choice caused cracks at the ribs (instead of in the webs) already during the dome construction, and the dome had to be reinforced immediately after its completion.
Despite the importance of this topic, a very limited number of scientific studies have been so far devoted to systematically investigate the effects of the brick pattern on the behaviour of masonry vaults. To our best knowledge, only three conference papers have been published about this issue [6, 7, 8]. Barbieri and Carloni [6] analysed a barrel vault by Finite Element Model, through a macro-modelling approach. The vault, subjected to dead load only, was modelled with shell elements and orthotropic linear elastic material properties. Five different orientations of the bed joints, represented by the angle α between the bed joints and the arch ring plane, were accounted for by rotating the element local axes. Comparison of the displacements in some reference nodes showed increasing stiffness of the vault for decreasing value of α: in particular, the lower stiffness was obtained for the most widespread pattern ($\alpha = 90°$). Calderini and Lagomarsino [7] proposed a micromechanical constitutive model of masonry – based on the homogenization theory - which specifically accounts for the brick pattern. This model, implemented in a finite element software, was applied to evaluate the influence of different masonry patterns on an ideal domed vault, subjected to dead load and a concentrated asymmetric load. The results of the non linear analyses showed different distribution of the stresses and different value of the collapse load depending on the adopted brick pattern. Finally, Romano and Grande [8] analysed the influence of the pattern on a barrel vault, modelled with both macro and micro-modelling approaches, subjected to both vertical and horizontal load. The results of the non linear analyses demonstrated once more that different masonry apparatus corresponds to different stiffness and collapse load.
The present study aims at making a step forward in understanding the effects of the brick

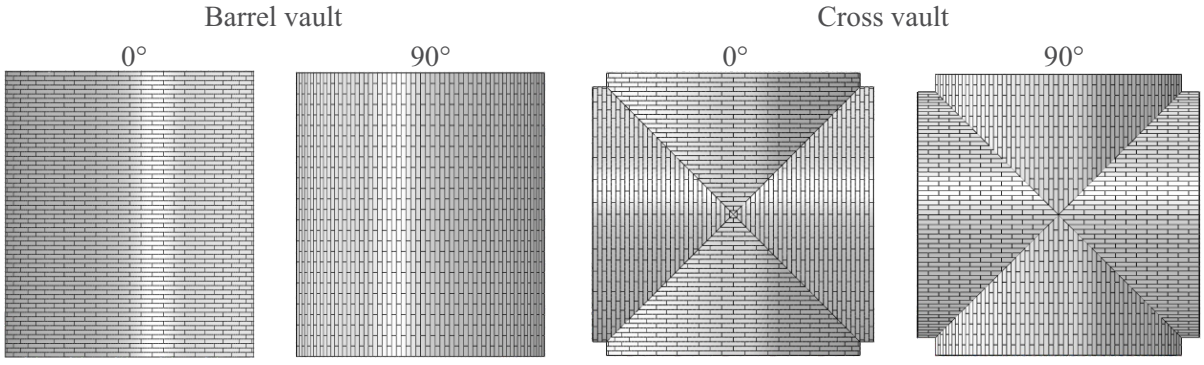


Figure 1: Vaults and brick patterns adopted as case studies

pattern on the behaviour of barrel and cross vaults under the action of vertical imposed displacements. The study is carried out through a computational approach by Finite Element Method (FEM), according to simplified micro-modelling approach. The paper develops as follows: first, the geometrical set up of the ideal vaults, adopted as case study, is described; then, the adopted structural modelling is described in details; subsequently, the results of the analyses are commented on; finally, conclusions and research perspectives are discussed.

2 Description of the case studies

The study focuses on barrel and cross masonry vaults. According to Wendland [1], barrel vaults can be built without formworks by positioning the planes of the bed joints in vertical or nearly vertical position, as in the case of the Nubian vault. A common solution in European vaults was to start the courses with a diagonal inclination. Bed joints parallel to the springing are also reported in manuals [3], but they require formworks.
Regarding cross vaults, they can be built without formworks through the intersection of four Nubian barrel vaults, where almost vertical arched courses are built starting from the surrounding walls. This solution was not very common in Europe, except for the Extremadura region in Spain. In the European tradition, the courses are most often orthogonal to the perimeter arches or to the diagonal arches.
The adopted case studies are a barrel vault and a cross vault made of brick blocks of typical dimension 6 x 12 x 24 cm. The barrel vault has a span of 3.1 m and a length of 3.5 m, while the cross vault has a square base of span 3.1 m. The geometrical set up of the cross vault reproduces in full scale the scale model tested in [9]. In this study, two different brick patterns are considered: a) bed joints orthogonal to the perimeter arches; b) bed joint parallel to the perimeter arches (Fig. 1).

3 Structural modelling

The study is carried out through numerical simulations according to simplified micro-modelling approach [10]: expanded blocks, each representing one brick whose dimensions are enlarged to include half the mortar thickness, are modelled as continuum elements, while the behaviour of the mortar joints and unit-mortar interfaces is lumped into average interface elements. The material of the blocks is isotropic and its properties comes from experimental tests on the masonry constituents.
Geometrical models have been generated with Rhinoceros [11]. Subsequently, the built geometry has been imported into Abaqus [12] for the generation of the mechanical model for the structural analyses.
The finite elements used for the bricks are linear hexahedra of 0.03 m size, while the blocks along the diagonal arches in the cross vault are modelled using first order tetrahedra of the same size. Finally, the abutments of the cross vault have been modelled with a larger mesh size (0.06 m size) using linear bricks. For the hexahedral elements the meshing technique is of structured type, while for the tetrahedral a free meshing algorithm has been adopted.
In most applications, when the simplified micro-modelling approach is used, the highly nonlinear behaviour of the mortar between the resisting blocks is modelled through interface elements or interaction properties [13, 14]. In this case, an analytical cohesive interaction has been defined between the surfaces of the bricks in contact, specifying the mechanical behaviour in both tangential and normal direction and, the latter, both in traction and compression. A damage

evolution law has been introduced for the cohesive tangential behaviour, which begins when a critical shear stress value is attained at the interface.
The analysis is performed assuming different boundary conditions in two different analysis steps. In the first step, the abutments of the vaults are all fixed so that the gravity load can be applied. The stress state of the vault at the end of the first analysis step is used as the initial configuration of the structure at the beginning of the second step of analysis. In the latter, the following boundary conditions have been applied:

- barrel vault: a differential vertical displacement is imposed along one of the spring lines: the magnitude of the displacement varies linearly at the two ring arches respectively;
- cross vault: a vertical displacement of equal magnitude is imposed in two of the four abutments.

In both kinds of vault a unilateral horizontal constraint is applied along the arch rings in order to avoid external overturning: this boundary condition is addressed to simulate the effect of adjacent vault or perimetral walls.

4 Model calibration

In order to properly calibrate the stiffness properties of the interface elements, the longitudinal opening mechanism of the cross vault, due to imposed horizontal displacement of two abutments, has been numerically simulated (Fig. 2). This load condition was experimentally tested in [9] on a 1:5 scale model made by 3D printed plastic blocks with dry joints with the same geometry of the case study described above.

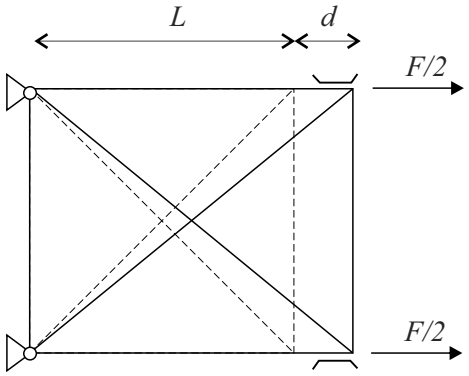


Figure 2: Structural scheme of the longitudinal opening test

The brick block elastic modulus has been set equal to 7500 MPa, the Poisson's ratio equal to 0.2 and the material density equal to 2700 kg/m^3. The value of the normal stiffness in compression has been set as the highest value assuring convergence of the analysis, based on the hypothesis of perfectly rigid contact in the normal direction. The normal stiffness in traction has been calibrated assuming that an almost instantaneous separation occurs when two surfaces initially in contact experience traction. On the contrary, the tangent stiffness value and the shear resistance have been estimated thanks to the availability of Shove tests performed on masonry walls of an historical building located in the province of Bologna (Fig. 3, courtesy of

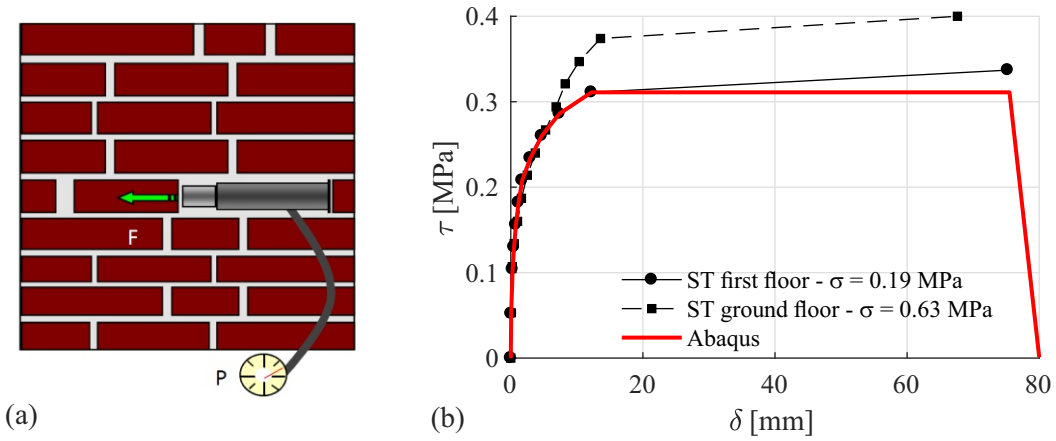


Figure 3: (a) Scheme of the Shove test, (b) measured $\tau - \delta$ diagrams at the ground and first floor and assumed $\tau - \delta$ diagram in the numerical model

prof. Paolo Napoli). The $\tau - \delta$ diagram obtained at the first floor has been retained in the numerical model, since the average compression stress in the vault is expected to be of the same order of magnitude as the one measured at the first floor.

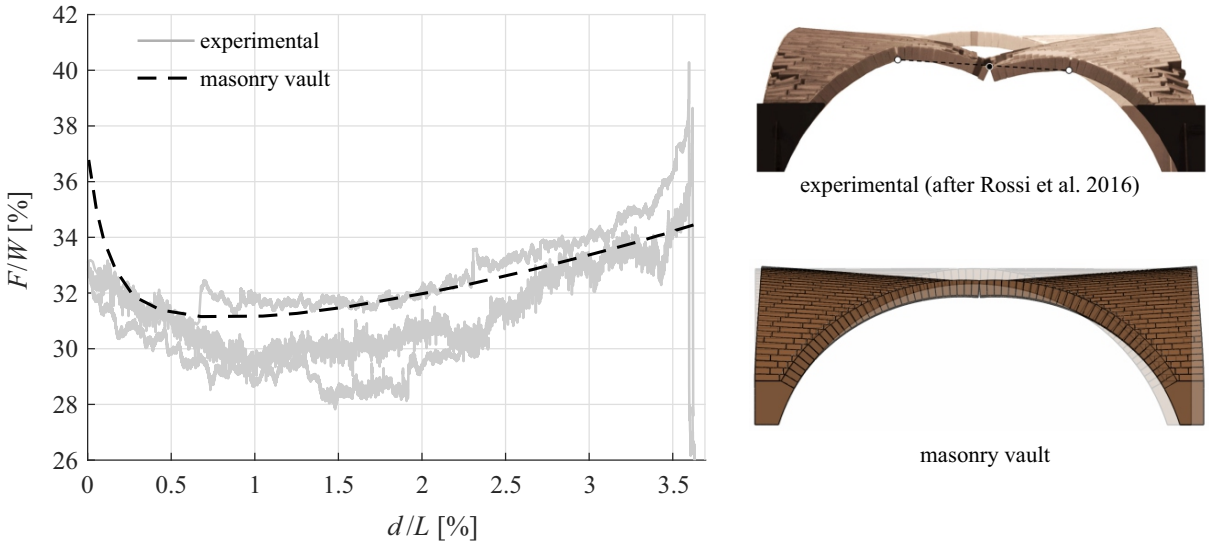


Figure 4: Comparison between force-displacement curves and deformed shapes from experimental tests and numerical simulations on scale model vault and full-scale masonry vault

Fig. 4 plots the comparison between the force-displacement curves obtained experimentally on the plastic model of the vault (grey envelope) and numerically on the full scale masonry vault. In order to compare the two curves, the resultant lateral reaction at the moving abutments F is scaled with respect to the vault self-weight W, while the lateral displacement d is scaled to the vault span L. The force-displacement curve obtained on the full-scale masonry vault is in good agreement with the experimental one. The simulated deformed shape (magnified of

20 %) shows a collapse mechanism that qualitatively agrees with the experimental one, even though the formation of the 3 hinges is not so evident. Therefore, the adopted interface model is retained in the following simulations.

5 Results

Figure 5 plots the load-displacement curves obtained for the two kinds of vault and the different brick patterns. For the barrel vault (Fig. 5a), the node with maximum displacement at the moving abutment is controlled. For the cross vault (Fig. 5b) the displacement of the node located in one of the moving abutment is monitored (red circle in Fig. 6). Both displacements are scaled with respect to the vault span. In both graphs the resultant of the vertical reaction forces at the moving abutments R_V is scaled with respect to the vault self weight W.

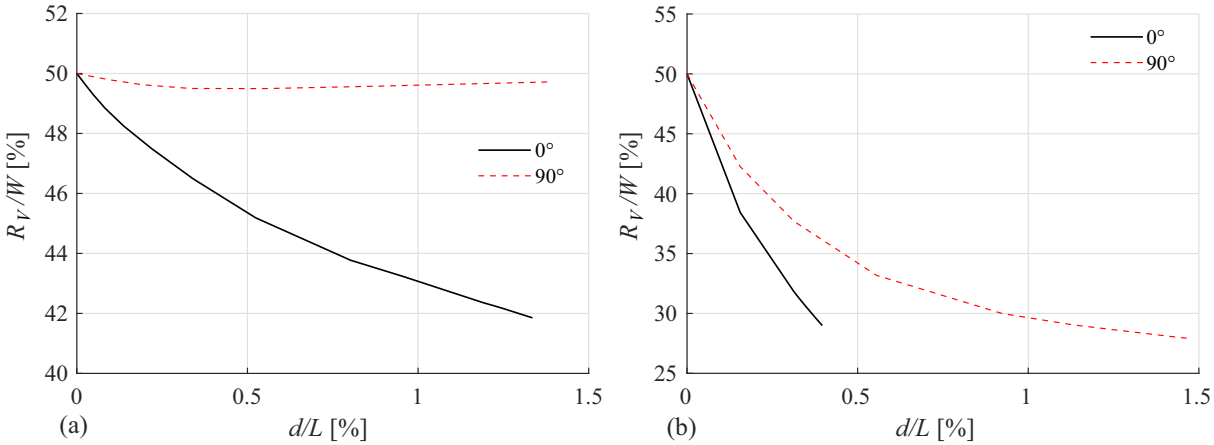


Figure 5: Load-displacement curves for barrel (a) and cross vaults (b)

The following considerations can be outlined. In both kinds of vault the change in brick pattern corresponds to a significant variation of the structural stiffness. The barrel vault is more sensitive to the bed joint orientation than the cross vault: the barrel vault with bed joints orthogonal to the arch rings exhibits an initial stiffness of about 85 % greater than the vault arranged with 0° pattern; conversely, the increase in initial stiffness is limited to 33 % in the cross vault.

Table 1: Horizontal to vertical reaction forces ratios

	Barrel		**Cross**	
Pattern	R_H/R_V [%]	$R_{H,ar}/R_V$ [%]	R_H/R_V [%]	$R_{H,ar}/R_V$ [%]
0°	77.31	23.30	13.82	57.48
90°	63.22	3.55	14.31	68.13

The higher sensitivity of the barrel vault to the brick pattern can also be observed by looking at Table 1, which reports the thrust forces at the abutments (R_H) as well as those orthogonal to the arch rings ($R_{H,ar}$) under self-weight, scaled with respect to the vertical reaction forces R_V. The variation in the reaction force ratios between the two patterns is much more pronounced in the case of the barrel vault, especially when $R_{H,ar}$ is considered. In particular, the value of $R_{H,ar}/R_V$ is more than six times higher in the 0° pattern: this result can be explained looking

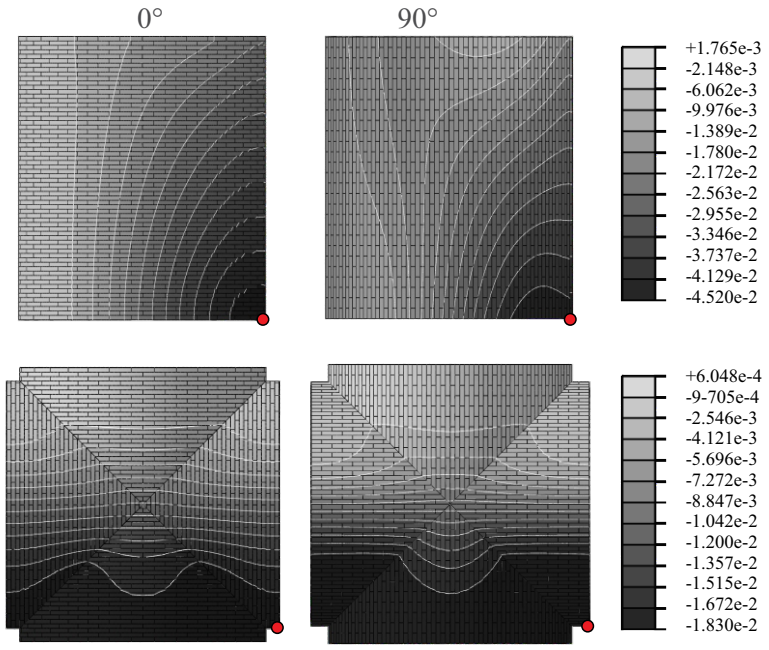


Figure 6: Contour plot of the vertical displacements corresponding to the last analysis step in the 0° pattern vault

at the barrel vault as a sequence of parallel independent arches, whose connection relies solely on the tensile strength of the bed joints, which is not efficient to prevent the normal separation of the arches, i.e. their out-of-plane movement.
Finally, the contour plots of the vertical displacements (Fig. 6) evidence that also contour lines are influenced by the orientation of the bed joints, and this effect is more pronounced in the barrel vault.

6 Conclusions

In this paper the influence of the masonry pattern on the static behaviour of barrel and cross vaults has been investigated. Computational simulations have been carried out through simplified micro-modelling approach. The arch rings have been constrained in order to avoid external overturning. Vertical displacements have been imposed at the abutments.
In general the orientation of the bed joints orthogonal to the perimeter arches resulted in stiffer structural behaviour. The barrel vault proved to be more sensitive to the orientation of the bed joints both in terms of initial stiffness and thrust forces at the abutments and orthogonal to the arch rings.
Future work will be addressed to extend the study to different patterns and vault geometries, by means of sensitivity analyses to the most relevant design parameters.

7 Acknowledgements

Alessia Monaco and Fiammetta Venuti wish to thank Politecnico di Torino for the financial support received in the form of Starting Grant for Young Researchers. Moreover, the authors wish to thank prof. Paolo Napoli for having provided experimental results of Shove tests on

historical masonry walls.

References

[1] D. Wendland, Traditional vault construction without formwork: Masonry pattern and vault shape in the historical technical literature and in experimental studies, International Journal of Architectural Heritage 1 (4) (2007) 311–365.

[2] J. C. Lassaulx, Beschreibung des Verfahrens bei Anfertigung leichter Gewölbeüber Kirchen und ähnlichen Räumen, Journal für die Baukunst 1 (4) (1829) 317–330.

[3] G. A. Breymann, Allgemeine Bau-Constructions-Lehre, mit besonderer Beziehung aufdas Hochbauwesen, Constructionen in Stein 1.

[4] A. Baratta, O. Corbi, The static behavior of historical vaults and cupolas, Journal of Heritage Conservation 32 (2012) 65–81.

[5] P. Foraboschi, Resisting system and failure modes of masonry domes, Engineering Failure Analysis 44 (2014) 315–337.

[6] A. Barbieri, C. Carloni, A. D. Tommaso, The static behavior of historical vaults and cupolas, in: Proceedings of the 4th International Conference on Arch Bridges ARCH 04, 2004.

[7] C. Calderini, S. Lagomarsino, The effect of the masonry pattern on the global behaviour of vaults, in: Proceedings of the 4th International Conference on Structural Analysis of Historical Constructions, 2004.

[8] A. Romano, E. Grande, Masonry barrel vaults: the influence of the pattern, in: Proceedings of the 14th World Conference on Earthquake Engineering, Beijing, 2008.

[9] M. Rossi, C. Calderini, S. Lagomarsino, Experimental testing of the seismic in-plane displacement capacity of masonry cross vaults through a scale model, Bulletin of Earthquake Engineering 14 (2016) 261–281.

[10] P. B. Lourenço, J. G. Rots, J. Blaauwendraad, Two approaches for the analysis of masonry structures - micro and macro-modeling, HERON 40 (4) (1995) 313–340.

[11] Rhinoceros User's Guide, v.5.4 (2018).

[12] Abaqus/CAE User's Manual (2019).

[13] G. Milani, M. Rossi, C. Calderini, S. Lagomarsino, Tilting plane tests on a small-scale masonry cross vault: Experimental results and numerical simulations through a heterogeneous approach, Engineering Structures 123 (2016) 300–312.

[14] A. Monaco, G. Minafó, C. Cucchiara, J. D'Anna, L. La Mendola, Finite element analysis of the out-of-plane behavior of frp strengthened masonry panels, Composites Part B 115 (2016) 188–202.

Proceedings of the IASS Annual Symposium 2019 – Structural Membranes 2019
Form and Force
7 – 10 October 2019, Barcelona, Spain
C. Lázaro, K.-U. Bletzinger, E. Oñate (eds.)

Numerical simulation and application of unloading clearance element method for temporary bracing of long-span orthogonal space truss structures

Hai-ying WAN*， Rui YUAN[a]， An-ying CHEN[b]

* School of Civil and Hydraulic Engineering, Hefei University of Technology
Hefei 230009, China
anyingchen@hfut.edu.cn

[a] School of Civil and Hydraulic Engineering, Hefei University of Technology
[b] School of Civil and Hydraulic Engineering, Hefei University of Technology

Abstract

The theoretical principle of unloaded clearance element method for temporary support construction of large span spatial structure is expounded. Taking the construction unloading of a four-point supported orthogonal steel truss structure with fixed ends as an example, the simulation and comparative analysis of the disassembly process using the gap element method, the equivalent rod end displacement method and the support seat displacement method are carried out.The numerical results are compared and analyzed,the change of internal force of structural members by gap element method is relatively gentle,it is more suitable for the analysis of orthogonal space truss. The gap element method is applied to the construction and unloading of a longitudinal 145m and transverse 83m span large-span orthogonal space truss structure.

Keywords: Temporary support, Construction, Unloading, Gap element method, Orthogonal space truss

1. Foreword

In recent years, with the continuous development of the national economy in China, long-span steel structures has been more and more widely applied, while in the construction of whose orthogonal space truss structure, temporary supports is usually necessary to be built up in advance during the installation phase and then removed according to the planned method and order after installation because temporary supports can not only provide a reliable operating platform for the high altitude installation of the main structure [1-5] , but reduce its internal force and deformation and enhance its safety and installation accuracy in the process of installation.

A very important problem is how to guarantee the safety of main structure and temporary support in the process of support removal of roof steel structure after installation. Such a removal is a process for structural system to transform and internal forces to redistribute, during which, the main structure is gradually transformed from partial being forced to completely forced, and the temporary support is gradually transformed from complete contact to to complete separation from the main structure

Copyright © 2019 by Haiying Wan
Published by the International Association for Shell and Spatial Structures (IASS) with permission.

gradually, that is to say, the temporary support gradually changes from loading to unloading with complicated internal force and displacement changes [6] . In order for the safety of such a removal, its accurate and reasonable numerical simulation analysis is necessary, and many simulations to the working principle and process of jack are available, and to whose defects, a new gap element method for a jack to simulate the temporary support was proposed in the paper to improve the accuracy, convenience and calculation efficiency of the support removal model.

2. Comparison of the principles of Common Simulation calculation methods

Bearing displacement method [7] is to replace temporary support with bearing in model calculation of support removal by applying vertical forced displacement to the bearing to simulate the process of a jack gradually falling till separating the main structure in the actual process of support removal, and which is called the Bearing Displacement Method and its calculation principle is shown in figure 1.

In unloading calculation, if the bearing reaction force of a certain step is tension, it is shown that the actual support removal process is progressed to the moment the actual support corresponding to the bearing has been unloading, at this time the bearing should be artificially deleted and the iterative calculation should be re-carried out. When all the bearings were deleted, the unloading was completed. The model calculation is simple, no need to establish temporary support in the calculation model of support removal process. However, this method can not simulate the actual jack how to separate the main structure temporarily, nor the compression or springback caused by internal force change of temporary support in the support removal.

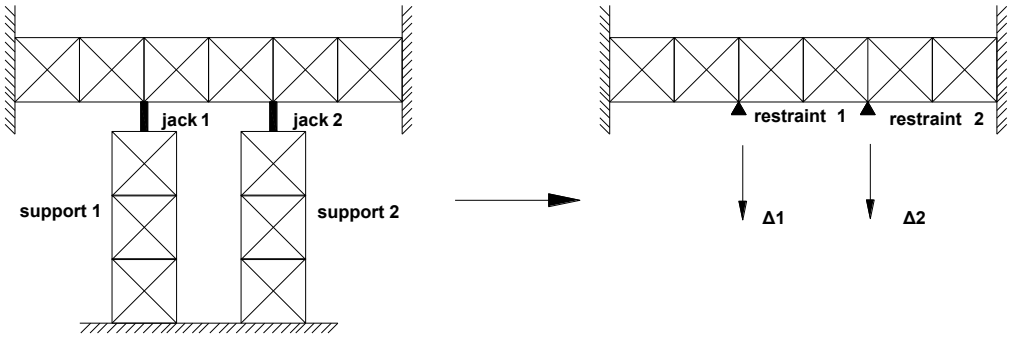


Fig. 1 Principle of bearing displacement method

Equivalent rod end displacement method [8] is to equivalent a temporary support to an elastic rod with the same axial linear stiffness, which can be stimulated with a unit that can only be compressed without tension when establishing support removal model calculation. The jack falling down(as shown in figure 2) was stimulated by applying vertical forced displacement to the elastic rod lower end bearing. This method can effectively simulate the compression or springback of the support caused by the change of axial compressive force in unloading, meanwhile, the unit characteristic of only compression without tension can accurately simulate the jack probable temporary separation from the main structure in the support removal. If at a stage of the support removal, the axial compression of all elastic rods is changed to 0, it indicates the complete support removal. However, this method can only simulate the independent, but not the conjoined temporary support, and the method does not establish the temporary support in the

calculation model of support removal, therefore, it is impossible to analyze and determine the safety of temporary support members in the whole process of support removal.

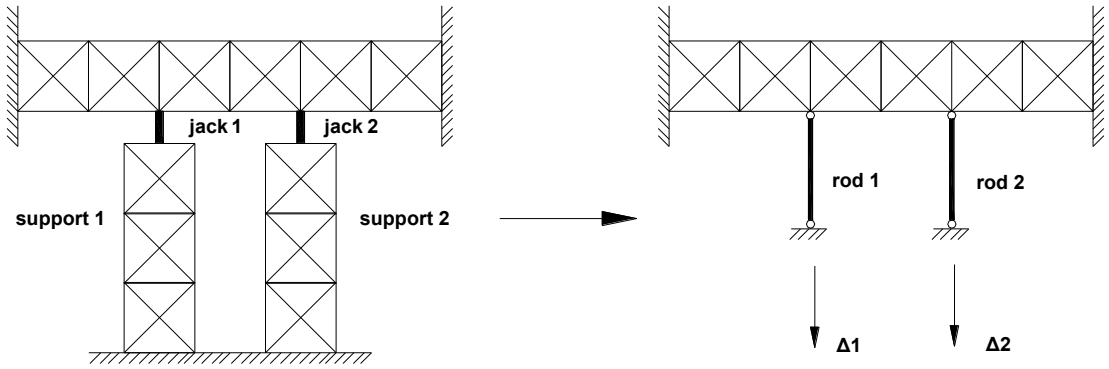


Fig. 2 Principle of equivalent rod bottom-end displacement method

3. Gap Element Method and Numerical Model

The principle of gap element method is as below:

In the model, to establish both the temporary support and the main structure, and between them to establish an analog jack only under compressive gap element. When calculation, by setting the gap displacement between the element and the main structure to simulate the jack unloading stroke, and such a gap displacement, if there is, means the jack separates the main structure. The displacement of upper node of a jack and that of the main structure connection node are independent each other, when the main structure completes the gap displacement set value, it moves downward and contacts with the gap element, the displacement of upper node of a jack and that of the main structure are coupling, with which to stimulate the separation and contact between the temporary support and main structure, the stiffness of the element is set to infinity without telescopic deformation so as to ensure the accuracy of the simulation.

Based on the working principle of gap element, the compression-only gap element in midas,the general finite element software, is used to simulate the jack. Only compression clearance unit is a two-node unit, one of the node on the main structure, the other is the endpoint of the jack , and only three lines in each node displacement degrees of freedom u^G_x and u^G_y and u^G_z, no rotational degree of freedom. Jack node coupling interval unit when in contact with the main structure of the axial displacement increment, that is $\Delta u^G_{Jx} = \Delta u^G_{Sx}$, Δu^G_{Jx} and Δu^G_{Sx} clearance unit respectively connected to the jack and the main structure nodes under the gap element local coordinate system x direction displacement increment. When the jack disconnects from the main structure, the displacement of the two nodes of the gap element is independent of each other, and the stiffness matrix of the gap element is set to zero, and the contribution to the stiffness of the overall structure is zero. This gap element can be used to simulate the contact and disconnection between the temporary support and the main structure.

1) When out of state,the stiffness matrix K^G of the gap element is zero, and there is node displacement u^G, but the unit strain and node force F^G are 0.

2）In the state of contact, the two endpoint displacement constraint equation for $\Delta u^G_{Jx} - \Delta u^G_{Sx} = 0$, the gap element stiffness matrix K^G and the control equation is:

$$\begin{pmatrix} c & 0 & 0 & -c & 0 & 0 \\ 0 & 0 & 0 & 0 & 0 & 0 \\ 0 & 0 & 0 & 0 & 0 & 0 \\ -c & 0 & 0 & c & 0 & 0 \\ 0 & 0 & 0 & 0 & 0 & 0 \\ 0 & 0 & 0 & 0 & 0 & 0 \end{pmatrix} \begin{pmatrix} \Delta u^G_{Jx} \\ \Delta u^G_{Jy} \\ \Delta u^G_{Jz} \\ \Delta u^G_{Sx} \\ \Delta u^G_{Sy} \\ \Delta u^G_{Sz} \end{pmatrix} = \begin{pmatrix} \Delta F^G_{Jx} \\ \Delta F^G_{Jy} \\ \Delta F^G_{Jz} \\ \Delta F^G_{Sx} \\ \Delta F^G_{Sy} \\ \Delta F^G_{Sz} \end{pmatrix}$$

After coordinate transformation, K^G is involved in the stiffness matrix of the whole structure in accordance with the principle of alignment.

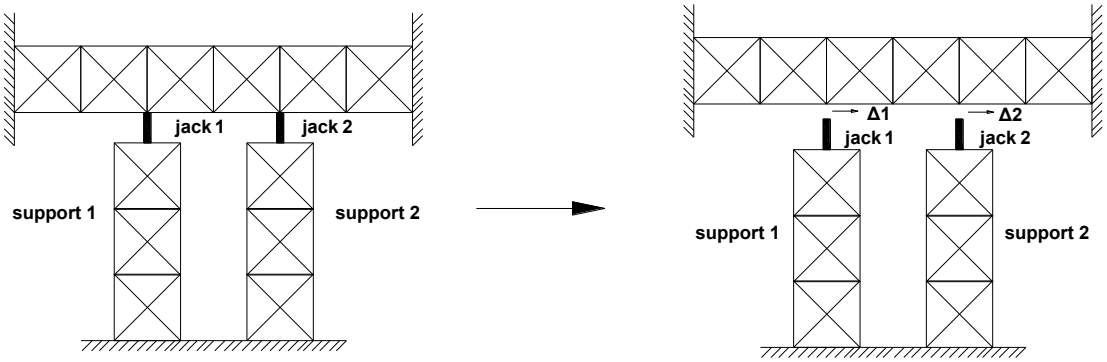


Fig. 3 principle of gap element method

Steps of numerical simulation of gap element method are as below:

1）Prepare reasonable unloading scheme.

2）According to the actual situation to establish the finite element model of the main structure and the lower supporting structure.

3）To connect the main structure and the lower supporting structure with the gap element, and simulate the gap element by compression-only gap element in midas, the stiffness is infinite, set the values of temporary support gaps according to the unloading scheme and conduct finite element calculation.

4）That to repeat step 3, modify gap value of gap element and conduct finite element calculation can result in the process of internal force development and deformation change of the main structure and temporary support in the process of support removal. Viewing the reaction force of the gap element in the post-processing can judge whether the main structure is separated from the temporary support, keeping unloading to finish until the reaction force of all gap elements is zero.

4. Numerical simulation analysis of calculating example

In this paper, the forced mechanism in unloading process of temporary support construction of long-span orthogonal spatial structure was studied to check the correctness of the support removal simulation with the example and simple analysis of the unloading construction of a both-ends-fixed and four-point-supported orthogonal steel truss structure.

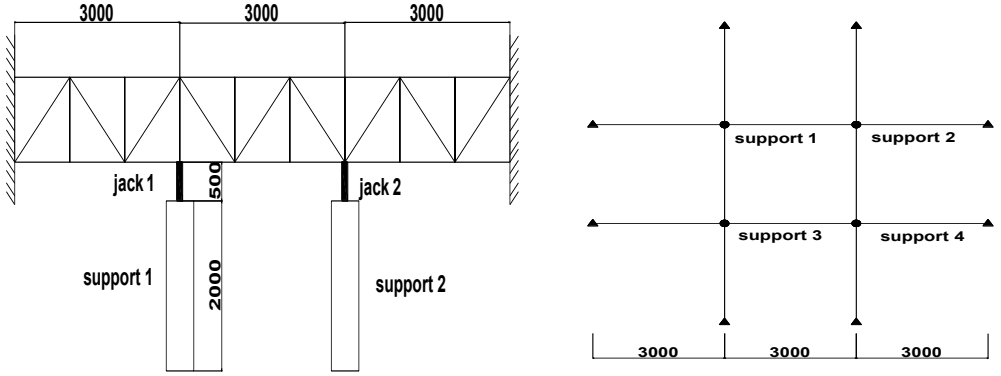


Fig. 4 schematic diagram of orthogonal truss

Based on Midas finite element software, the bearing displacement method, the equivalent rod end displacement method and gap element method are applied to simulate and analyze the support removal process of the structure. When modeling with the bearing displacement method, first to model the truss element and then the vertical bearing at the temporary support; when modeling with the equivalent rod end displacement method, first to model the truss element and then the compression-only elastic rod equivalent to the axial stiffness of supports 1, 2, 3, 4 at the temporary support node; when modeling with the gap element method, first to model the truss element and then the temporary support and gap element. The simulation calculation of support removal process adopts the unloading mode by steps and groups. According to jack general operation in practical engineering, the removal process was divided into 4 steps, each step was divided into 4 sub-steps and a total of 16 steps to complete. The 4 sub-steps were: jack 1 fell downward $U_1/4$→*jack 4* fell downward $U_4/4$→*jack 2* fell downward $U_2/4$→*jack 3* fell downward $U_3/4$, among them, U_1, U_2, U_3 and U_4 were the total vertical displacement of nodes of truss in contact with jacks when the unloading was completed. According to the calculation, it can be obtained U_1 = 21.3mm, U_2 = 21.8 mm, U_3 = 22.8 mm and U_4=22.2mm and the unloading process is shown in Table 1. The jack axial force obtained above and the displacement change at the support are shown in Fig. 5 ~ Fig. 12. The sub-steps I, 0 shown by x-axis in the figure represent the initial state of the structure; 16 represents the completed support removal; method 1 represents the bearing displacement method; method 2 represents the equivalent rod end displacement method and method 3 represents the gap element method.

Tabel 1 Displacement in every unloading step and substep

		displacement of jack 1	displacement of jack 2	displacement of jack 3	displacement of jack 4
stage 1	step 1	$0.25U_1$	0	0	0
	step 2	$0.25\ U_1$	0	0	$0.25U_4$
	step 3	$0.25\ U_1$	$0.25U_2$	0	$0.25U_4$
	step 4	$0.25\ U_1$	$0.25\ U_2$	$0.25\ U_3$	$0.25\ U_4$
stage 2	step 5	$0.5U_1$	$0.25U_2$	$0.25\ U_3$	$0.25\ U_4$
	step 6	$0.5U_1$	$0.25U_2$	$0.25\ U_3$	$0.5\ U_4$
	step 7	$0.5U_1$	$0.5U_2$	$0.25\ U_3$	$0.5\ U_4$

	step 8	$0.5U_1$	$0.5U_2$	$0.5\ U_3$	$0.5\ U_4$
stage 3	step 9	$0.75U_1$	$0.5U_2$	$0.5\ U_3$	$0.5\ U_4$
	step 10	$0.75U_1$	$0.5U_2$	$0.5\ U_3$	$0.75\ U_4$
	step 11	$0.75U_1$	$0.75U_2$	$0.5\ U_3$	$0.75\ U_4$
	step 12	$0.75U_1$	$0.75U_2$	$0.75\ U_3$	$0.75\ U_4$
stage 4	step 13	U_1	$0.75U_2$	$0.75\ U_3$	$0.75\ U_4$
	step 14	U_1	$0.75U_2$	$0.75\ U_3$	U_4
	step 15	U_1	U_2	$0.75\ U_3$	U_4
	step 16	U_1	U_2	U_3	U_4

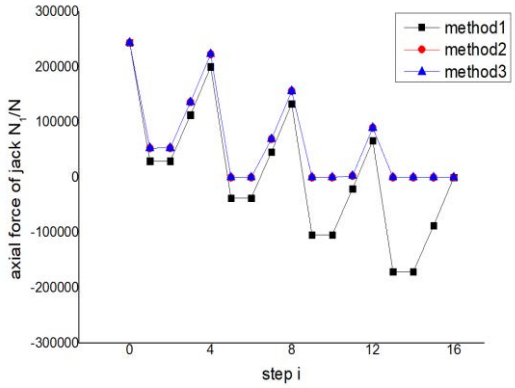


Fig. 5 axial force of the jack 1

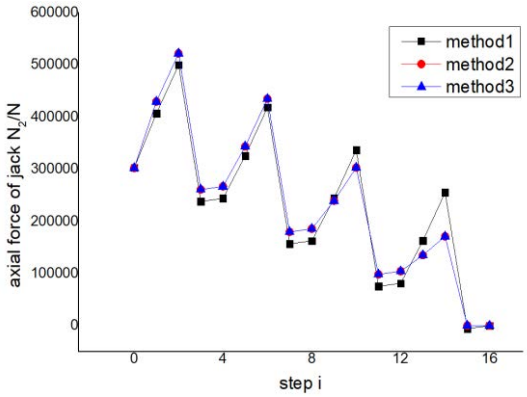


Fig. 6 axial force of the jack 2

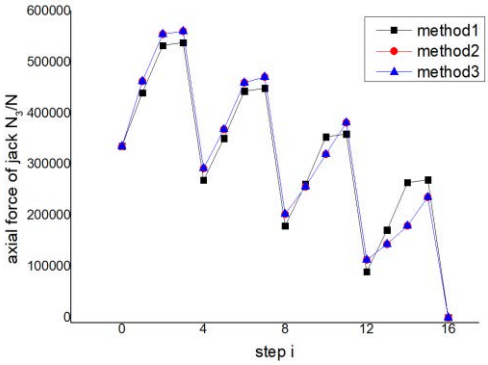


Fig. 7 axial force of the jack 3

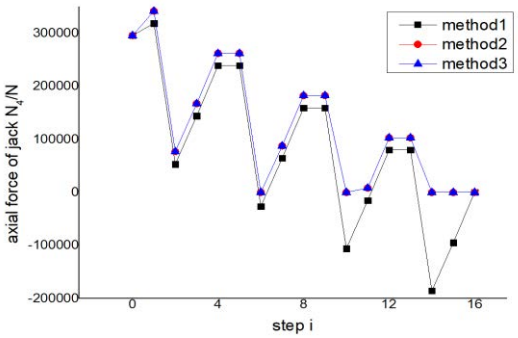


Fig. 8 axial force of the jack 4

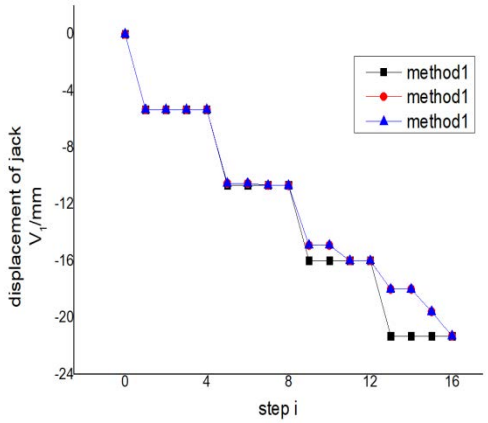


Fig. 9 displacement at support 1

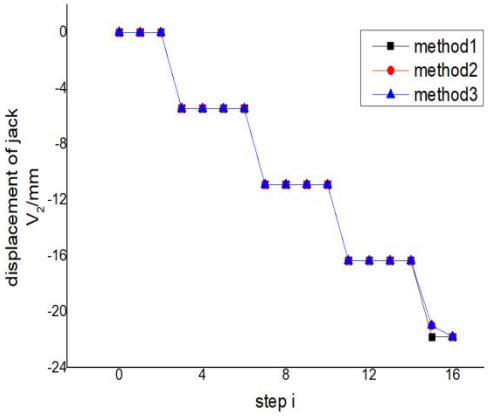


Fig. 10 displacement at support 2

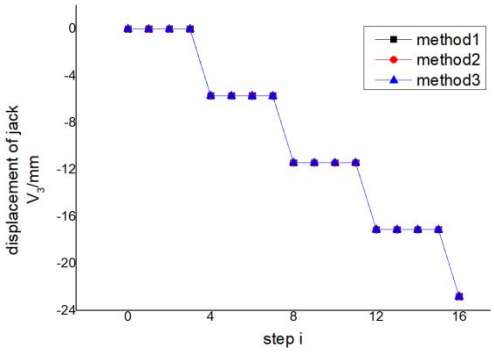


Fig. 11 displacement at support 3

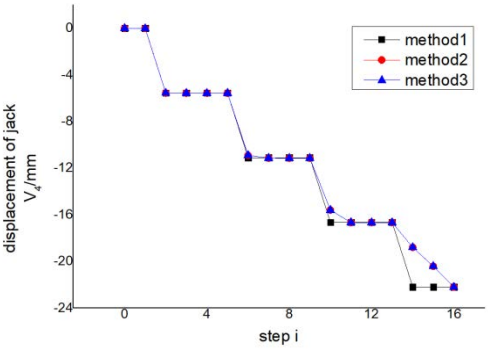


Fig. 12 displacement at support 4

From figure 5 to figure 8, the jack axial force obtained by three simulation methods shows the characteristics of oscillatory variation, for the equivalent rod end displacement method and the gap element method, the vibration amplitude decreases with the progress of support removal till it is completed that the axial force of the 4 jacks is 0, and the tow calculated results are very consistent; the calculated result of the bearing displacement method is very different from those of the former two that, the jack is in tensive axial force because some temporary supports were temporarily separated from the main structure when unloading by steps, which reflected in the numerical value is that the axial force of some jacks may be 0 before the support removal was completed shown as figures 5 and 8, which can be stimulate by equivalent rod end displacement method and gap element method but can not by the bearing displacement method and thus led to the improper result.

It can be seen from fig.9 to fig.12 that at the support, the node displacement is consistent with the unloading stroke by using the bearing displacement method, but that is generally slightly larger than the unloading stroke by equivalent rod end displacement method and gap element method because the jack moved down caused by forced temporary support deformation, which was accurately simulated in the actual support removal as fig.9 to fig.10 that at the support, node displacement is smaller than the unloading stroke, which was also caused by temporary separation of temporary support from main structure during steps of unloading.

In summary, the gap element method combines the advantages of equivalent rod end displacement method and bearing displacement method with accurate and feasible calculative results.

5. Engineering Application

Zhenjiang Evergrande Children World Convention and Exhibition Center locates in Zhenjiang Jurong City, Jiangsu Province, its profile appears in whirlpool as Figure 13 ~ 14, long as 145m and wide as 83m with one floor on the ground and partial interlayer. The roof, highest up to 32m and average height about 23 m, adopts long-span spatial steel structure system, the construction area is about 6453m^2. the spoke skylight is set in the middle of the roof inner ring beam, the compressive ring in the middle of skylight and the roof inner ring beam are rigid connection of 20 divergent box steel beams and secondary members. The skylight load is transmitted from inside by the radial steel beam to the roof inner ring beam outside. The inner ring beam and secondary members of the skylight ensure the stability of the structural plane. The complex structure under uneven force has brought great difficulties to site construction. In order for a smooth constructional progress, temporary support was set up under the larger span, so as to reduce the overhanging span on the one hand, on the other hand, to transform the structural force transmitted in vertical. A total of 32 temporary supports were planned in the construction scheme, and the layout and numbering are shown in figure 15.

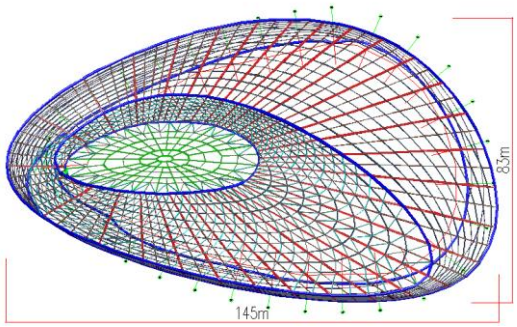


Fig.13 Top view

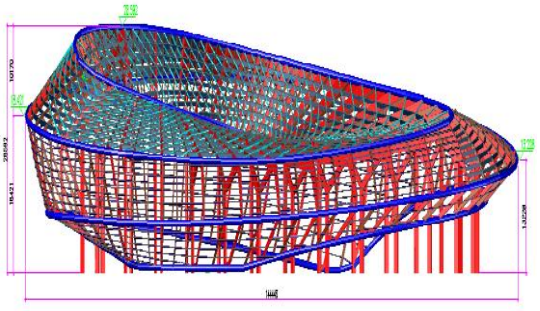


Fig.14 Front view

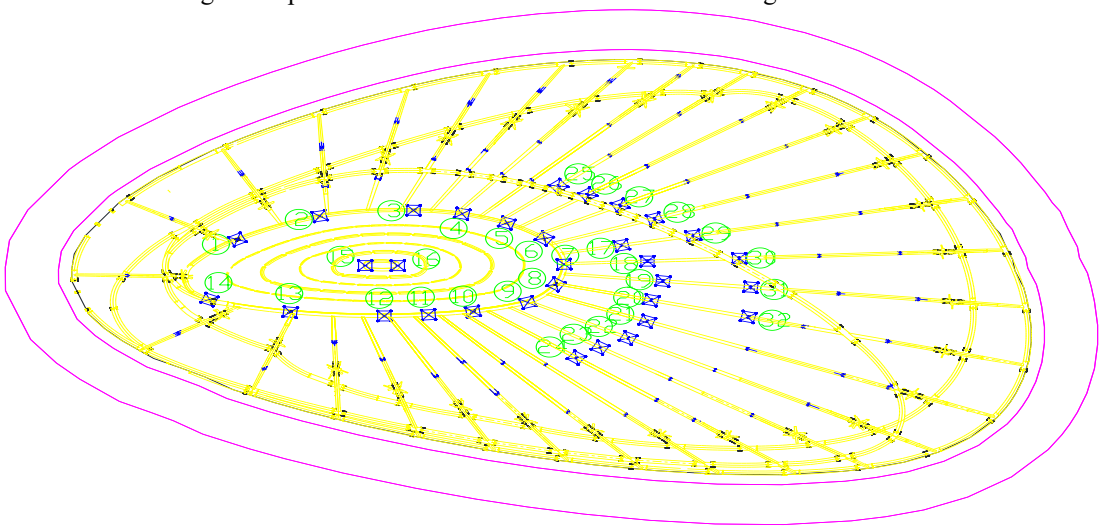


Fig. 15 Support layout

The structural system and internal force in unloading are different from the design state forlocal members easy to be too stressed and ultralimit deformed. The overhanging span of this structure is larger, problems of local strength and stability appeared more likely. Because of the structural particularity and larger temporary support loading, if unloading was in stages, part of the temporary supports may be excessive loaded to lead to their instability, and for long-span steel roof, synchronous unloading can make stress change more stable. Therefore, the synchronous unloading was adopted in this project in two schemes: one was synchronous equidistance unloading, or each temporary support upper jack retracted the same displacement at each stage at the same time; the other was synchronous equal proportional unloading that in each unloading stage to unload in proportion to the distance of the temporary support to the circle center, that was for the supporting point farther from the circle center to retract a larger displacement and for the nearer point a smaller displacement in each unloading stage, which can not only reduce the maximum reaction force of the temporary support, but allow the main structural stresses change more stable. Therefore, the synchronous equal proportional unloading was applied.

The unloading calculation of this project adopted the general finite element analysis and design software MIDAS with the load 1.2 times the weight of the finite element model itself. In unloading, the gap element method was applied to set the gap element between the temporary support and the main structure to stimulate jack unloading stroke. In unloading calculation, the two states of completed constructional installation(not unloaded) and unloaded(all supports removed) were calculated and compared first; based on whose whole structural stress distribution, displacement and support reaction to conduct the finite element simulated calculation of the whole unloading scheme and its stages; according to the structural stress, displacement deformation and support reaction force in each unloading stage, etc. to conduct the calculation and verification of the rationality of unloading scheme. Because of more temporary support points in the project, the unloading stroke of support 15, 19, 24 and 31(Table 2) and their support reaction force in the corresponding unloading process(figure 16) and node displacements(figure 17) were listed here only.

Table 2 supporting unloading schedule (unit: mm)

	displacement of support 15	displacement of support 19	displacement of support 24	displacement of support 31
step 1	15	20	15	20
step 2	30	40	30	40
step 3	45	60	45	60
step 4	60	80	60	80
step 5	75	100	75	100
step 6	85	115	85	110
step 7	95	130	95	120

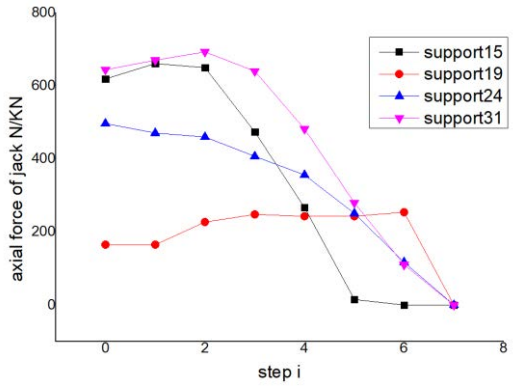


Fig. 16 supporting reaction

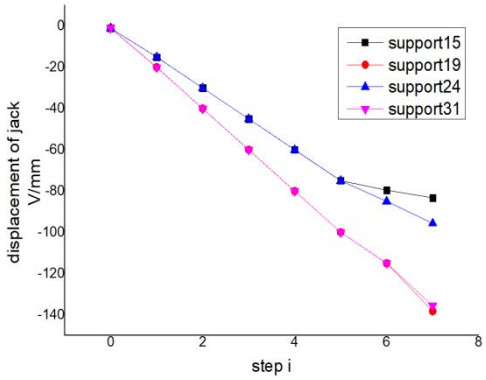


Fig. 17 node displacement

As shown in figure 16, according to the above unloading displacement control, each temporary support point gradually and regularly was out of work, and till stage 7 the unloading was completed, that was all the supports became out of work and separated from main structural supporting points with 0kN of the support reaction force without negative value appeared in unloading and the change trend accorded with the reality and the simulated results were accurate shown as figure 17 that, the displacement of the temporary support point increased gradually with the unloading stroke until it was stable; the node displacement value was slightly larger than that of the unloading stroke, that was, the support was forced and deformed; when the support was out of work- the reaction force was 0KN, the node displacement was stable and less than the set gap value-the unloading stroke, which indicated an accurate simulated results. The displacement and stress values of the whole structure have changed smoothly in unloading, the the model calculation was accurate, and the unloading scheme was reasonable.

6. Conclusion

1）A new numerical simulation method for support removal process is established: a compression-only gap element simulated jack is established between the temporary support and the main structure to simulate the jack unloading stroke.

2）Based on the four-point supported and both ends fixed orthogonal steel truss, the simulated support removal process by the gap element method, equivalent rod end displacement method and bearing displacement method has been compared and analyzed, which has indicated that the gap element method has been not only accurate in calculation, but convenient and feasible and more suitable for the analysis of support removal of orthogonal space truss.

3）Through the multi-scheme comparison and selection of unloading schemes for a practical project, the optimal selection of overall in-stage unloading in the same proportion method has been determined and applied for the engineering unloading, and which has been stimulated and analyzed with gap element method; the resulted structural stress, displacement deformation and support reaction force in each unloading stage have verified the rationality of unloading scheme and effectiveness of unloading method.

References

[1] WU Xiaoping, GAO Zhenfeng, LI Zixu(Shanghai Construction Group General Co., Shanghai 200050, China). The analysis of whole erection process for steel shell of National Grand Theatre. Joural of building structures, 2005, 26(05): 40-45.

[2] Guo Yanlin, Guo Yufei, Gao Wei, et al. Simulation analysis of steel structure roof falling process in national stadium [J]. Construction technology, 2006, 35(12):36-40.

[3] Chen Guodong, Ye Haowen. Dynamic analysis of roof lifting and dismantling process in guangzhou new gymnasium [J]. Architectural structure, 2002(1):53-57.

[4] Guo Xiaochuan, Qiu Liqiu, Luo Yongfeng, et al. Analysis and monitoring of unloading process of steel structure roof in yancheng stadium [J]. Structural engineer, 2013, 29(5):166-171.

[5] Guo Xiaocao, Luo Yongfeng, Shen Zuyan. Checking calculation of steel lattice shell pre-arching scheme and tracking analysis of construction process of the national center for the performing arts [C]// National academic seminar on modern structural engineering. 2004.

[6] Guo Xiaochuan, Qiu Liqiu, Luo Yongfeng, et al. Constraint equation method for simulation and analysis of steel structure stripping process of large-span roof [J]. Applied mathematics and mechanics, 2013, 34(9):986-994.

[7] Fan Zhong, Liu Xianming, Fan Xuewei, et al. Simulation calculation method for unloading process of long-span spatial structures [J]. Journal of architectural science and engineering, 2011, 28(4):19-25.

[8] Guo Yan-lin, Guo Yu-fei, Liu Xue-wu. Analysis method of falling frame of long-span steel structure roof [J]. Journal of architectural science and engineering, 2007, 24(1).

Proceedings of the IASS Annual Symposium 2019 – Structural Membranes 2019
Form and Force
7 – 10 October 2019, Barcelona, Spain
C. Lázaro, K.-U. Bletzinger, E. Oñate (eds.)

Some observations on bridges dynamic behaviour

Jan B. OBRĘBSKI*

*Retired full Professor, Faculty of Civil Engineering, Warsaw University of Technology
Al. Armii Ludowej 16, 00-637 Warsaw, Poland
Email: jobrebski@poczta.onet.pl

Abstract

The paper presents rather some conclusions from large investigations over dynamic behaviour of bridges under travelling loads. There, as basic tool was applied the *3D-Time Space Method* (**3D-TSM**) in edition proposed by present author. The method uses four-dimensional space, where besides of usual 3D space, the time is the fourth dimension. The bridge with simply supported steel girder is here modelled by means of theory for *thin-walled bars* (**TWB**s). In final calculations, solutions are obtained here on numerical way applying well known and simple *Finite Differences Method* (**FDM**). In consequence the task is brought to trivial determination of unknowns from set of linear algebraic equations. There, essential part of these equations is so called *dynamical stiffness matrix* (**DSM**). The last is additionally tested by *Uniform Criterion* (...) for evaluation of bridges *Critical States* (**CrS**).

Keywords: bridges, dynamic behaviour, critical states, critical velocity, critical length, uniform criterion, 3D-time-space method.

1. Introduction

Presented wide results of performed analyses for calculated numerous comparative examples concern of simply supported, one span steel bridge with thin-walled girder, having three closed circuits, figure 1. The compared bridges have lengths L=50, 60, 70, 80, 90, 100 m, and *cross-section* (**CS**) with dimensions 30×6m, defined in the figure 1b. The **CS** is inscribed into square mesh 6x6 m. Applied here 3D-TSM description for dynamical tasks gives some important possibilities for determination of: displacements of e.g. bridges or high-rise buildings; to show behaviour of structure in all considered time-moments (structure modes for positions of force P from 1 to 10 on the figure 1); *critical velocities* ($\mathbf{V_{cr}}$) of load(s) travelling over the bridge; or *critical length* ($\mathbf{L_{cr}}$) of bridge answering on traveling mass with given velocity. In the all mentioned cases, the bridge or high-rise buildings are treated as the large thin-walled bar. In general case it is possible to consider composite CSs.

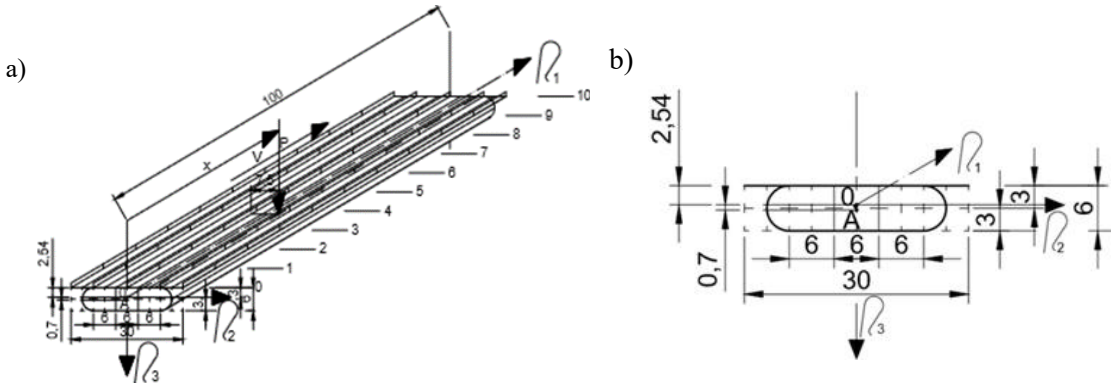


Figure 1: Axonometric view on bridge with moving load a) and shown cross-section of girder b, c). Visible force P and division of girder on 10 sections. Are shown centre of gravity and shearing centre.

Copyright © 2019 by Jan B. OBRĘBSKI
Published by the International Association for Shell and Spatial Structures (IASS) with permission.

2. Applied analysis

For dynamical analysis of bridges were used motion equations from theory of TWBs [6] implemented to four-dimensional space – 3D-TSM. The differential equations of motion by means of *Finite Differences* (**FD**) were transformed into global *Dynamical Stiffness Matrix* (**DSM**) of whole task.

In computer structural mechanics is well known global *Equilibrium Equation* (**EE**) in matrix form, expressing relation of displacements x to external forces Q:

$$Kx = Q \quad , \tag{1}$$

where, K - is *Stiffness Matrix* (**SM**) or **DSM,** x – are unknowns and Q - vector of loadings. Determination of unknowns from above equation can be done in some ways. There, among the others can be applied Cramer's method: $x_j = D_j / D$, where, $D = \Delta = det(K)$ is value of the main determinant of coefficients (or functions) of the matrix K. Determinant D_j is obtained replacing in D the j-th column by column of (loadings) free terms Q . So, the case, when

$$D = 0 \quad \text{means} \quad x_j \to \infty \qquad \text{and next} \qquad (D = 0) \to (GC = CrS) \quad . \tag{2}$$

So, it signalizes *Critical State* (**CrS**) or *Geometrical Changeability* (**GC**) of analysed structure. The matrix K in equation (1) can be composed on basis of any analytical theories or numerically by means of FD (see e.g. [7]), **FEM** or e.g. by *Difference-Matrix Equation Method* (**DMEM,** [5, 6]).

2.1. Used Equilibrium Equations

In theory of TWBs [6] are used four differential EE. It embraces the straight prismatic bars with any CSs homogenous, composite, open, closed and open-closed – with a few closed circuits etc. After special calculations and led step by step tests, now we can regarded the formulae derived for the theory of TWB as valid for any type prismatic composite straight bars with any type CSs. This theory [6] is constructed for first and second order, for static, dynamic, stability and dynamic-stability. There is possible taking into consideration interaction of the bar with surrounding medium, etc. Below, is omitted the first equation for longitudinal forces. Moreover, in considered tasks we have not bending in horizontal direction and therefore the second equation is neglected, too. Finally in tested tasks were used two independed equations (for vertical bending and torsion), only [10-13]:

$$\begin{aligned} &3) \quad \overline{E}\overline{I}_2 v_3^{IV} + \mu \ddot{v}_3 - \ddot{v}_3'' I_{2m} = q_3^w \quad , \\ &4) \quad \overline{E}\overline{I}_{\hat{\omega}} \Theta^{IV} - K_s \Theta'' + \ddot{\Theta}[I_{2m} + I_{3m} + \mu(\eta_{3A})^2] - \ddot{\Theta}'' I_{\hat{\omega}m} = m_1^w \quad . \end{aligned} \tag{3}$$

The above differential equations were formally transformed into *Finite Differences Operators* (**FDO**) (see [7]) to the following shape [13]:

Bending

$$\begin{aligned} 3) \quad & w_{t-1,i-1}K_1 + w_{t-1,i}K_2 + w_{t-1,i+1}K_1 + \\ & + w_{t,i-2} + w_{t,i-1}K_3 + w_{t,i}K_4 + w_{t,i+1}K_3 + w_{t,i+2} + \\ & + w_{t+1,i-1}K_1 + w_{t+1,i}K_2 + w_{t+1,i+1}K_1 = Q \quad , \end{aligned}$$

Torsion

$$\begin{aligned} 4) \quad & \Theta_{t-1,i-1}G_1 + \Theta_{t-1,i}G_2 + \Theta_{t-1,i+1}G_1 + \\ & + \Theta_{t,i-2} + \Theta_{t,i-1}G_3 + \Theta_{t,i}G_4 + \Theta_{t,i+1}G_3 + \Theta_{t,i+2} + \\ & + \Theta_{t+1,i-1}G_1 + \Theta_{t+1,i}G_2 + \Theta_{t+1,i+1}G_1 = S \quad . \end{aligned} \tag{4}$$

Symbols K_i and G_i means certain coefficients, [11, 12]. In both above equations three rows are describing three sequential time moments. The equations (4) are two independent FDO. There, the vertical deflections are denoted: $w = v_3$ and lower indices in brackets, separated by coma (t,i) – indicate actual point in time-3D space. The same point "i" of girder division (figure 1) in previous moment is denoted as (t-1,i) and for the next time moment as (t+1,i). Similarly, at time moment "t" previous points of girder division are denoted as (t,i-2), (t,i-1) and next sequential points as (t,i+1), (t,i+2). The torsion angles are denoted as "Θ".

2.2. Difference-Matrix Equation Method (DMEM)

It was the first theory elaborated by Obrębski [5, 6], oriented on static or dynamic analyses and synthesis of *Space Bar Structures* (**SBS**), with possible simplifications for plane bar-grids, shields and plates. It was oriented on application of numerical algorithms for some computer programs. Important advantage of this method with comparison to FEM (*Finite Element Method*) is much smoother, fluent manner of composition of global SM for whole SBS. There, equilibrium of one node is described by matrix type equation applying Boole's displacement operators.

2.3. Application of four-dimensional space: 3D-Time Space Method (3D-TSM)

Dynamical tasks can be solved for single bars in traditional - analytical way, what is well known in wide up to now literature, but can be also analysed by means of 3D-TSM what gives many new possibilities. There, solutions are led in the four-dimensional space. Here, traditional 3D space is extended on the fourth for time. The idea was developed by several authors and in Poland by Z. Kączkowski [3] and his co-workers. Certain step ahead was done in the doctor theses of R. Szmit (supervised by Obrębski, 2000), by dynamical analysis of tall buildings. There, were used four differential equations for TWB [6], transformed to FDO used in 3D-TSM. Simultaneously, the method was applied by its originator to masses (forces) travelling on bridges, plates, roads and airport landing belts. This paper is the next important step showing application of such description to dynamical stability of bridges under mowing loads. First time it was presented in [8] at 2004.

In the case of 3D-TSM, writing the equations (4), for all points „i" of the bar division, we obtain DSM, containing information about scheme of girder, its boundary conditions, velocities and positions of vehicle(s) on bridge for all discrete time moments, figure 2. In consequence the task is coming to solution of the two separate sets of linear algebraic equation type (1) (for bending and for torsion). They have band, symmetrical character. Moreover, in own program DGPST was used upper half band of K (see equation (1)), completed by column of "loadings" Q_i , figure 2.

It can be used on each node one equation 3) or 4), see (4). But when for each point of the girder are used two (d=2) or more equations, in such case are applied both equations type (4) (3 and 4). So, in the second case we say, that it is used **D**ifference-**M**atrix **E**quation **M**ethod (**DMEM** – description applied in computer program WDKM [5] for SBS), see figure 2. Space 3D-time from numerical point of view belongs to 2D tasks. There, we have equilibrium state of whole structure (1), taken together for all time moments (in the figure 2 for 9 moments).

Time m.	t=1	t=2	t=3	t=4	t=5	t=6	t=7	t=8	t=9	
t=1	K_r	V_r								Q_1
t=2	V_r	K_r	V_r							Q_2
t=3		V_r	K_r	V_r						Q_3
t=4			V_r	K_r	V_r					Q_4
t=5				V_r	K_r	V_r				Q_5
t=6					V_r	K_r	V_r			Q_6
t=7						V_r	K_r	V_r		Q_7
t=8							V_r	K_r	V_r	Q_8
t=9								V_r	K_r	Q_9

Figure 2. **DSM** equation (1) - K and terms Q for the bar, when p=10, p=9, T=9, by uniform motion. All sub-matrices have dimensions: K_r[9x9], V_r[9x9]. Here, the load is on bridge, only (case "bridge").

Here global matrix $\mathbf{K_G}$[G×G] as **DSM**, [12] has number of rows and columns equal G=N×T and T=number of considered time moments with time distance Δt , N=n×d, n=p-1= number of nodes (points of girder division), p - number of sections for girder division, d means number equations used for each node, e.g. one to four as equations (4). Each element of global **DSM -** is a traditional

stiffness matrix **K**[N×N] [10-13]. Moreover, boundary conditions for girder are taken into account traditionally [7] and for initial time $t=0$ (known or equal zero) and final –usually as „back" difference. Dependently on assumed sequence of unknowns in nodes, the shape of matrices K and K_G can be a little other [11].

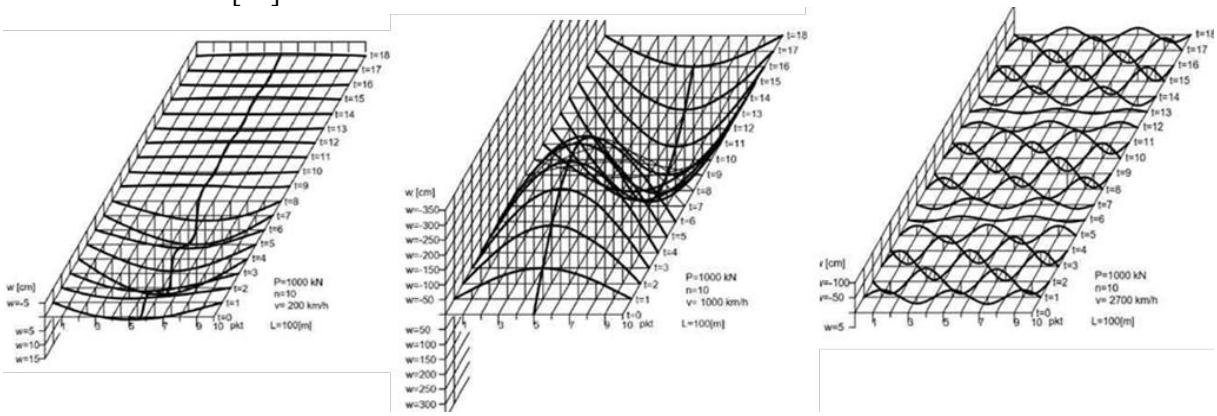


Figure 3. Calculated vertical displacements (deflections) for bridge with L=100 m, p=10, under travelling force P=1000kN with velocities 200km/h (up to 15 cm); with v=1000 km/h (up to 350 cm) and by 2700 km/h (up to 100 cm). Results are shown for T_z=18 (case "task"), when last 9 time moments force P is travelling behind bridge.

As the first natural application of equation (1) is determination of unknown x. In result we obtain deflections w or torsion angles Θ (see [14]) three examples of such calculations are given in the figure 3.

2.4. Uniform Criterion (UC)

The criterion represented by equations (2) can be here shown in a little extended form:

$$D = \Delta = det[K(P, \omega, v, a, m, M, d, t)] = 0 \ . \tag{5}$$

where symbolically: P –means any type combined external loading, ω - frequency of vibrations, v – velocity of travelling mass, a – loading acceleration, m – mass of structure (bridge, tall building), M - travelling mass, d – dumping, t - time. Next parameters, which it is difficult to show in formula 1, are: type of cross-section (full, thin-walled etc.), properties of used materials for composite CSs, location of materials in area of CS, structure boundary conditions, interaction of structure with surrounding media etc. The above list of parameters can be much longer. On multicriterial character of critical states of structures, presented in various tasks by worldwide literature, has turned attention Obrębski [8] (2004) in Cape Town and in Ithaca, USA [9] (2008). From that times, were started more systematic investigations influence of particular parameters and structure properties on its critical state.

Each change a sign of D means critical state. So, by application of UC – equation (5), a mathematic key-operation is comparison to zero main determinant of SM: $D = 0$ of the various types' tasks. The SM is denoted as K in fundamental EE (1) of matrix type. It can be composed as set of one or a few differential EEs (Euler, Vlasov [16], Nowacki [4], Kaliski [2], and Obrębski [6]) or by FD, FEM, DMEM in computer programs (e.g. Obrębski [5]). From mathematical point of view by numerical solutions (1) it is set of linear algebraic equations. It is important, that in all theories and computer algorithms applied in programs written by Obrębski, always was used the (1), only! As well for static, dynamic approaches with theory of first or second order, as with interactions of structure with surrounding media, big shearing forces etc., too.

Through years were tested by Obrębski some methods for determination of critical loadings. It were analytical, numerical and hybrid solutions, e.g. [5-7]. In the beginning was done test for single bars, applying DMEM implemented in computer program WDKM [5] and using FDM. Next, were done analytical tests on behaviour of dynamical stability of bar loaded by axial force and vibrating [6].

After it was verified CrS of bars under combined external loading with different boundary conditions and composite bars with some CSs: thin-walled, open, closed, full etc. At last, attention was turned on tall-buildings and bridges under loading travelling with some velocities (all summarized in [15]).

3. Tested bridges

The investigated almost real bridges have 6 lengths 50-100m (chapter 1). The considered CSs are not to the end real, for the reason omitting of reinforced plate over the girder, protecting steel girder against deformation by vehicles. Therefore, mass, rigidity and proper geometrical characteristics are smaller and girder is more feeble. In all tested tasks the bridges have scheme shown in the figure 1b, but thickness theirs walls assures static deflection of whole girder close to 1/1000 of their span (L). So the area of CS and the mass of the each bridge are another.

The girders have in both directions three traffic belts for cars and belt for bicycles and pedestrian. There, the one mass 20 or 100 t (approximated by 200 or 1000 kN) is travelling with uniform motion along the outward belt, with eccentricity 7.5 m, with velocities v= 50, 100, 200, 300, .. , 600 km/h (and in a few tasks v= 1200, 1500, 1800, 2100, 2400, 2700 km/h). Additionally there, were considered divisions of girder on: p=8 or 10 sections. The last permit on evaluation of influence of density division of girder on accuracy of calculated results by FDM and 3D-TSM.

The girders of bridges are simply supported, only. There are not considered dumping of interaction between travelling mass and girder. The smaller mass of bridge in relation to travelling masses permit on easier observation of critical states of bridge. Dimensions of calculated tasks are shown in table 1. Here, d – means number of degrees of freedom (used equations), "bridge" concern the task, when is analysed move of load along bridge, only (T) (case "bridge"). Contrary data in columns "task" shows parameters for case, when is investigated bridge behaviour under loading moving over girder and after leaving it and travelling further through next T time moments up to T_z (case "task").

Table 1: The essential parameters of comparative tasks in function of p – number of sections assumed for girder

Points	Nodes	DOF	dimension	Bridge			Task		
p	n=p-1	d	N=d×n	T=n	G=N×T	N_e=G×G	T_z=2×n	G_z=N×T_z	N_{ez}=G_z×G_z
8	7	1	7	7	49	2401	14	98	9604
10	9	1	9	9	81	6561	18	162	26244

4. Obtained results

The significant part of results was presented on previous conferences. So, in the papers [11, 12 and 13] were given wide lists of calculated of geometrical characteristics of CSs for analysed girders, coefficients K_i and G_i ,see (4) and values of Δ for particular DSMs.

At last in the paper [14] are shown diagrams of deflections (vertical displacements) and rotations of all calculated tasks. Moreover, were given graphs approximating the critical values of V_{cr} and L_{cr} for all tasks in variants for P=200 or 1000 kN, for considered velocities v=50 – 2700 km/h and for division of girder on p=8 or 10 sections. Now, are presented some comments and analysis of obtained results.

4.1. Critical velocities

On the basis of presented in the paper [14] diagrams of transversal displacements w and torsion angles Θ are formulated some more important following conclusions:

- As critical value of velocity is regarded point, where value of D=Δ – change its sign according to (2) or (5), in such case, deflections and/or torsion of bridge should be increasing to infinity.
- Up to velocity of 200 km/h values of deflections for all girders were rather similar to static ones.
- In the case, when v=50 km/h, deflections of bridge disappear just at the moment, when loading go out of the girder –at time moment T.

- But, in the case when loading is travelling with v=200 km/h or higher, after leaving of girder by travelling mass, small vibrations of bridge are observed up to last time moment T_z.
- The biggest unnormal values of transverse displacements were obtained for velocities: 900 km/h (2.5 m), 1000 km/h (3.5 m); and chaotic for 2700 km/h (1 m).
- Maximal, approximate calculated absolute deflections of bridge are shown in the Table 2.
- It is interesting, that by high velocities, the girder have tendency to lifting up.

Table 2: Calculated absolute values of bridge girder deflections by particular velocities of P=1000 kN

v [km/h]	0	50	100	200	300	400	500	600	700	800	900	1000	1100	1200	1500	1800	2100	2400	2700
w [cm]	10	10	10	15	30	25	35	25	30	20	250	350	25	15	15	30	35	15	100

Table 3: Critical velocities [km/h] for travelling force P=1000 kN; bridge, only

	p=10		p=8	
L=[m]	Bending	Torsion	Bending	Torsion
50	900	850		75,150
60	150, 420	150,440,830	150	75,240,440,830
70	240	150	250,850	75,150,430
80	70, 150,840	150,250,450,830	250,440	75,150,250
90	440,840	150,250,430,830	150,250,440	75,150,250,430,830
100	160,250,350,550,650,750, 850,1950,2120, 2550	75,150,250,750,85,11 50,1200,1640	870	75,150,250,320

Table 4: Critical velocities [km/h] for travelling force P=1000 kN; task

	p=10		p=8	
L=[m]	Bending	Torsion	Bending	Torsion
50	900		870	75,250
60	150,430,		150,440	150,410,820
70			150,840	150,830
80	150,430,		150,870	240,450,830
90	240,		150,430,880	240,440,820
100	150,250,350,450,550, 650,850,950,1150,1550	150, 350,780,930,1140, 1470,1540,2220,2540	240,880	250,430

Table 5: Critical velocities [km/h] for travelling force P=200 kN; bridge, only

	n=10		n=8	
L=[m]	Bending	Torsion	Bending	Torsion
50	850		870	75,250
60	150,430,830	150,430,830	150	75,250,440.820
70	250	150	250,870	75,150,440
80		150,250,440,820	250,430	75,150,250
90	75,250,430	150,250,450,820	150,250,430,870	75,150,250,450,830
100	150,850	150,250,440	180.250,430,870	75,150,250,440

Table 6: Critical velocities [km/h] for travelling force P=200 kN; task

	n=10		n=8	
L=[m]	Bending	Torsion	Bending	Torsion
50	150,250	150,820	150,250,450	440,830
60	150,430	150	150,450	150,430,830
70		820	250,880	150,830
80	150,430,870	440,820	250,880	250,440,830
90	150,870	250,440,820	150,450,880	250,440,830
100	420	250,820	75,880	

4.2. Critical lengths of bridge

There as critical length of girder by uniform motion of mass travelling with given velocity, is regarded such value L_{cr} resulting by $D=\Delta=0$ – change its sign. It is the other interpretation of results presented in the chapter 4.1. So, after analysis of some diagrams, can be formulated following conclusions. By small lengths of girder the problem of instability of bridge girder do not appears. So, for girders with the length L=50 m was not observed critical phenomena.

Table 7: Critical lengths L_{cr} [m] of bridge for travelling force P=1000 kN; bridge, only

	n=10		n=8	
v=[km/h]	Bending	Torsion	Bending	Torsion
50	75,84	54,95		
100	77,84	55		
200	54,63,97	55	56,65,85	55,64
300	54,75	75	55,85	75
600	65,78,84,95	94	65,75,85,95	66,85
1200	53,65,85,94	57,75,94	54,65,85	64,93

Table 8: Critical lengths L_{cr} [m] of bridge for travelling force P=1000 kN; task

	n=10		n=8	
v=[km/h]	Bending	Torsion	Bending	Torsion
50		53		95
100				54,95
200	55,65,76,85	64,95	55,65,75,95	75,94
300	55,65,76,94	64,84	55	55,94
600	84	66,75,85	65,84,95	66,75,93
1200	54,85	56,74,84	55,85,95	56,65,75

Table 9: Critical lengths L_{cr} [m] of bridge for travelling force P=200 kN; bridge, only

	n=10		n=8	
v=[km/h]	Bending	Torsion	Bending	Torsion
50				
100	85,95			
200	55,65,85	55	55,65,85	65
300	55,75,85	55,75	55,85	75
600	65,75,85	65	55,75,85	55,85
1200	54,64,75,85,95	54,75,95	65,85,95	65,95

Table 10: Critical lengths L_{cr} [m] of bridge for travelling force P=200 kN; task

	n=10		n=8	
v=[km/h]	Bending	Torsion	Bending	Torsion
50				
100			95	
200	65,75,95	65,	65,85	55,75
300	55,65,75,95	65,75,85,95	55,75,85	55,95
600	85	65,75,85,95	55,65,85,95	55,65,75
1200	75,85,95	55,75,85,95	55,85,95	55,65,75,95

5. Obtained results

The results presented above and in previous publications [8-15] permit to give general conclusion about efficacy of proposed innovative methods of calculation for dynamic behaviour of bridges and also tall buildings. It can be recommended. Many possible analyses of comparative calculations will be presented by oral presentation and probably in other, future papers.

6. Conclusions

The applied method of analysis is probably at all new approach to evaluation of bridges behaviour. It is very simple and can be performed even by easiest commercial program Excel, supported by other program calculating displacements. Here. As the last it was used own program named DGPST – giving deflections - w or rotations – Θ and value of main determinant of DSM (K_D). The accuracy of calculations increases when increase number p of girder division on sections. On the other hand such division should be not too dense. In analyzed examples it seems, that p=8 or 10 were quite enough.

The more information, pictures, diagrams and conclusions will be shown during oral presentation.

References

[1] O. Büttner, H. Stenker H.. *Metalleichtbauten, Volume 1, Ebene Raumstabwerke.* VEB Verlag für Bauwesen, Berlin, 1970, &. *Lekkie konstrukcje metalowe.* Arkady, Warsaw 1975.

[2] S. Kaliski, at all, *Vibrations and Waves* (In Polish – *Drgania i Fale*), PWN, Warsaw 1966.

[3] Z. Kączkowski, "The Method of Finite Space-Time Elements in Dynamics of Struct." *J.Techn. Physics*. **16**, nr 1, pp. 69-84, 1975.

[4] W. Nowacki, *Structural Mechanics* (In Polish – *Mechanika Budowli*), PWN, Warsaw, 1957.

[5] J.B. Obrebski, *Numerical Analysis and Synthesis of Large Structural Systems.* (In Polish - *Analiza i Synteza Numeryczna Wielkich Układów Konstrukcyjnych*). IBTP Reports 24/1979, (habilitation theses), Warsaw 1979.

[6] J.B. Obrębski, *Thin-Walled Elastic Straight Bars*" (In Polish - *Cienkościenne Sprężyste Pręty Proste*). 1991. Script WPW. Warsaw, pp.452 & 1999. 2-d Ed. OWPW. Warsaw pp.455.

[7] J.B. Obrębski, *Strength of Materials* (In Polish - *Wytrzymałość Materiałów*). Script PW, Micro-Publisher J.B. Obrębski Wydawnictwo Naukowe, Printed by AGAT, Warsaw 1997, pp. 238.

[8] J.B. Obrębski, "Examples of some parameters influence on bridges behaviour under moving loadings". 2-d Int.Conf. on *Struct.Eng., Mechanics and Computat*. *Cape Town, South Africa*, A.A.Balkema Publish. Leiden/ London/New York/ Philadelphia/ Singapore.Abs. vol. p.171, CD – pp. 859-864, 2004.

[9] J.B. Obrębski, "Multi parametrical instability of straight bars", *IASS-IACM 6th Int. Conf. on Computation of shell and spatial struct. Cornell University, Ithaca, USA,* 2008.

[10] J.B. Obrębski, "3D-Time Space in dynamical analysis of bridges". (In Polish - Czasoprzestrzeń w analizie dynamicznej mostów). *WAT, XXI Int. School CAD, Product.& Exploit., Jurata, 8-12.05.2017 Poland.*

[11] J.B. Obrębski, „Analysis of critical state for bridge in 3D-Time Space". (In Polish - Analiza stanów krytycznych mostu w czasoprzestrzeni), WAT, Pisz, Poland 2018.

[12] J.B. Obrębski, Analysis of critical state for bridge in 3D-Time Sp.DOI: https://doi.org/10.17814/mechanik .2018 .7.93 ; 2018 (see [11], too).

[13] J.B. Obrębski, „Analysis and forms of structures critical states", *LSCE-2018, Łódź, Poland*, pp. 76-86.

[14] J.B. Obrębski, „Analysis of bridge answer on loading thtoughfare" (In Polish – Analiza odpowiedzi mostu naprze jazd obciążenia). *Proceedings of the XXIII Miedzyn. szkoła CAD, wytwarzania i eksploatacji*, WAT, Pisz, Poland 13-17-05.2019, pp. 301-317.

[15] J.B. Obrębski, „Common criterion for structural critical states", *Proceedings of the 7-th Int. Conf. on Structural Engineering, Mechanics and Computation. Cape-Town, 2-4-09.2019, South Africa* (accepted for printing. Ref. No 108).

[16] W.Z. Vlasov, *Tonkostiennyje Uprugije Stierżni*. Moscow, Gosstrojizd. 1940 & 2-nd Ed.- Gos. Izd. Fiz.-Mat. Lit., 1959.

Proceedings of the IASS Annual Symposium 2019 – Structural Membranes 2019
Form and Force
7 – 10 October 2019, Barcelona, Spain
C. Lázaro, K.-U. Bletzinger, E. Oñate (eds.)

Stability analysis for an arch supported membranes roof

Dezső HEGYI*

* Associate professor
BME Dept. Mechanics, Materials and Structures
H-1111 Budapest, Műegyetem rkp. 3.
hegyi.dezso@szt.bme.hu

Abstract

To cover a large span area, a widely used solution is applying textile membrane supported by steel arches. To limit the weight of the arch, slender structural elements must be designed. While steel trusses effectively meet this goal, their loadbearing capacity is limited by stability resistance. As the trusses have large inertia in the plane of the arch, usually the out-of-plane buckling is the more dangerous. The out-of-plane buckling is a complex phenomenon as the membrane restricts the deformation of the arch resulting in an elastic embedded system with a highly nonlinear response. To get the equilibrium state of the structure Dynamic Relaxation Method is used with 8-node quadrilateral membrane elements [1]. The truss is modelled by straight rods. To get an appropriate model for the out-of-plane behavior of the truss the flanges of the truss are modelled by sub-trusses: four flange 3D trusses are used to represent the proper stiffness of the real bending resistance of a flange. This model fits smoothly into the highly nonlinear DRM algorithm of the membrane structure. In the equilibrium state of the structure the classical eigenvalue problem is solved [2] to obtain the critical multiplier of the actual load. The elastic and the geometric stiffness of the membrane and the truss elements, respectively, must be selected to safely withstand the destabilizing effects. The complex stability analysis of the joint system of the membrane and the steel truss gives the chance to get an optimal solution in terms of material usage.

Keywords: arch stability, membrane structure, eigenvalue problem, dynamic relaxation

1. Introduction

Membrane structures are frequently used as cost-effective solutions for large area covers. A steel arch is an adequate solution to support the membrane surface. Hollow tubes or hot rolled I beams can be used, and a truss is a good possibility, too. This paper focuses on a two-flange steel truss where the out-of-plane buckling behavior requires extra care.

Two-flange trusses have large stiffness along the strong axis and very small stiffness along the weak axis. The week axis is usually strengthened by additional bracings in traditional structural design. In the case of membrane structures there is no real possibility to apply bracing systems, but the membrane itself can serve as an elastic support against buckling.

The analysis of textile membranes is a highly nonlinear problem: large strains and large deformations belong to the equilibrium shape. The critical load can be determined only after the the equilibrium shape was obtained. In this paper the Dynamic Relaxation Method (DRM) is used to search the equilibrium configuration[1]. The algorithm used for the analysis is integrated with simple bar elements to represent compressed or tensioned line elements. There is no bended element in this

Copyright © 2019 by Dezső HEGYI
Published by the International Association for Shell and Spatial Structures (IASS) with permission.

software. To preserve the simplicity of the system, a truss model is applied to represent the moment resistant structural elements.

To evaluate the critical load of a structure with a certain load arrangement an eigenvalue problem is solved for [2]. Both the elastic stiffness and the geometric stiffness of the structure are necessary to determine the critical value. As membranes have ill-conditioned stiffness matrices, a special strategy is necessary to solve the eigenvalue problem.

2. The numerical model

The DRM method is used to find the equilibrium state of the structure. DRM is well-known as an effective and robust method for membrane analysis. For the membrane surface an 8-node quadrilateral element is used [1]. This is a complex element, which provide an accurate solution for the membrane analysis with moderate number of nodes. (The second order shape functions can describe the stress field with higher accuracy than linear elements at a rough nodal network.) This feature of the 8-node element is beneficial in the eigenvalue analysis in reducing the number of linear equations to be solved.

The truss structure supporting the membrane is made of tubes in the concept of this paper. In classical truss analysis all the bars of the truss meet in a hinged connection. This model gives adequate results usually but cannot indicate proper out of plane buckling behavior for the truss. Bended elements must be used to get a realistic value for the critical parameter of a certain load system.

The software used for this research works with 8-node surface elements, 3-node cable elements and 2-node truss elements. Only forces are handled and no moments. To get a bended beam element for the stability analysis one chance is to integrate a real moment resistant element and one chance is to use a truss model to built-up the bended elements.

The real bended beam element has six freedom for each node: three for translations and three for rotations. As we use the Total Lagrange strategy in the DRM, there is a difficulty to follow the twist deformation in the bended element. So we have three more degrees of freedom for each node of the bended elements and some additional difficulties arise to handle the twist deformation of the beams.

For the trust model of the beam a four-flange model can be a sufficient solution. In this model four extra nodes belong to each node of the beam. It means there are 12 additional degrees of freedom for each node of the bended element. Altogether 9 additional degrees of freedom belong to the truss model than in the usage of the real beam model, but no rotation freedom must be handle.

Although the bended beam model is more beneficial in the eigenvalue evaluation, there are some benefits of the truss model, too. It is easier to handle the twist deformations, there are just movements, no rotations (the mixed movements can make worse the condition number of the coefficient matrix of the linear equations), and it is easier to apply eccentricity for the beam-membrane connection.

Hence, the truss model is applied instead of the bended element model for the recent study.

2.1. The 8-node quadrilateral element

There is a very detailed paper about the 8-node quadrilateral element [1], so in this paper only a very short summary is presented. The element is based on the finite element formulation developed by Gosling for form-finding [3], and it is improved for nonlinear analysis in the paper by Hegyi [1].

Total Lagrange formulation is used, the stresses are calculated directly between the deformation-free and the actual state. The Biot stress tensor is used to determine the stresses on the actual state. This stress tensor fits to the engineering constitutive law, which is presented usually.

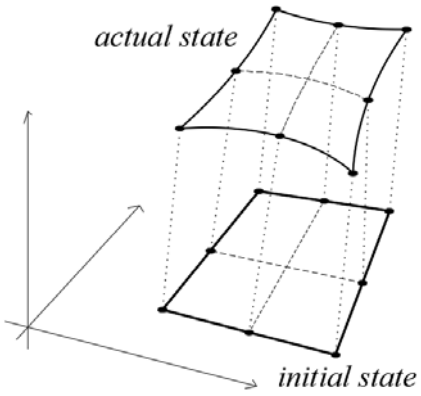


Figure 1: The 8-node quadrilateral element in the initial and actual state.

2.2. The truss model of the bended elements

The bended beam elements are modeled by a truss model. A four-flange truss is used to represent the bending and shear stiffness of the original beam.

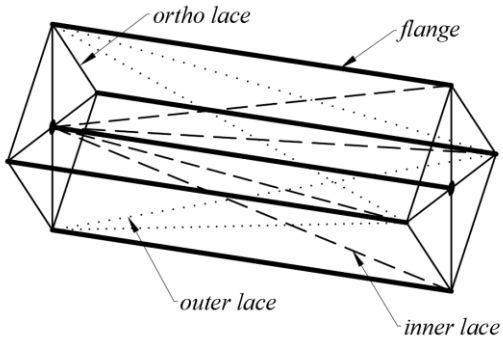


Figure 2: The truss model belongs to one unit of the beam element.

The evaluation of the bending stiffness is a simple transformation of the inertia of the original cross section to the inertia of the flanges:

$$I = 2A_f h^2, \tag{1}$$

where I is the inertia of the bended element, A_f is the area of the flange of the truss model and h is the half height of the truss. (The section is double symmetry, perhaps a tube.)

The evaluation of the shear stiffness is a more complex method. The basic formula for an N lace truss can be found in the web handbook [4]:

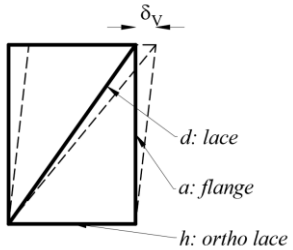


Figure 3: The shear deformation of an N-truss field.

$$\delta_V = \delta_d + \delta_h = \frac{d}{h}\frac{Vd}{EA_d}\frac{d}{h} + \frac{Vh}{EA_h}, \tag{2}$$

where δ_V is the shear deformation, the *d* and *h* lower index belongs to the lace and the ortho lace respectively. *V* is the shear-force *E* is the elastic modulus and *A* is the area of the cross sections. The shear stiffness belongs to the stiffness of the lace, but as we can see on equation (2), it depends on the sectional area of the ortho lace too. If the sectional area of the ortho lace has a considerable large area, this effect is not significant. The shear stiffness equation of a bended bar can be written like this:

$$\frac{V}{S_V} = \frac{\delta_V}{a} = \frac{1}{a}\left(\frac{d}{h}\frac{Vd}{EA_d}\frac{d}{h} + \frac{Vh}{EA_h}\right), \tag{3}$$

and the sectional area of the lace can be evaluated like this:

$$A_d = \frac{d^3}{h^2} / \left(\frac{Ea}{S_V} + \frac{h}{A_h}\right). \tag{4}$$

The recent truss model with the four-flange form a V-like lace system. The first idea is that the stiffness of the V is just the double of the N, and the evaluation of the equations derive for this result too. But the numerical verification of this idea shows, the stiffness of the V-like lace is larger than it must be. More deep study shows that the V-like lace lock the orthogonal component of the bending deformation of the beam element (Fig. 4.).

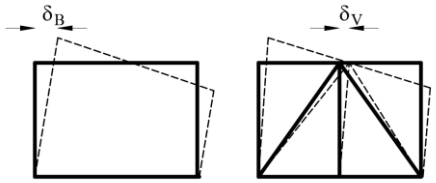


Figure 4: The orthogonal shift of a section with and without the V lace.

The V lace is connected to the neutral axis of the bended section, so there is no effect derived from the bending deformation on the elements subjected by the shear force. Only the shear deformation can be realized in such a configuration orthogonal to the axis of the structure. In the real bended elements, the orthogonal deformation can be obtained as the summary of the two kinds of deformation. A modification of eqs. (3) and (4) must be used. The orthogonal shift caused by the bending is

$$\frac{\delta_B}{a} = \frac{2\varepsilon a}{2h} = \frac{N}{EA_a}\frac{a}{h} = \frac{M}{hEA_a}\frac{a}{h} = \frac{Va}{hEA_a}\frac{a}{h} = \frac{Va^2}{EA_a h^2}, \tag{5}$$

where ε is the elongation of the flanges resulted from the bending moment on the element and the bending moment has differential relationship with the shear-force. The modified version of eq. (3) reads:

$$\frac{V}{S_V} + \frac{\delta_B}{a} = \frac{\delta_V}{a} = \frac{1}{a}\left(\frac{d}{h}\frac{Vd}{EA_d}\frac{d}{h} + \frac{Vh}{EA_h}\right), \tag{6}$$

and the final formulation evaluated from eqs. (5) and (6):

$$A_d = \frac{d^3}{h^2} / \left(\frac{Ea}{S_V} + \frac{h}{A_h} + \frac{a^3}{Ah^2}\right). \tag{7}$$

The torsional stiffness of the element can be evaluated in the same way, hence it is omitted in this paper.

3. The eigenvalue problem

3.1. The particularities of eigenvalue problem

The eigenvalue problem used to obtain the critical load level of the structure might be formulated as

$$\overline{\overline{K}}_E \cdot \bar{x} = \lambda \cdot \overline{\overline{K}}_G \cdot \bar{x}, \tag{8}$$

where $\overline{\overline{K}}_E$ is the elastic stiffness matrix, $\overline{\overline{K}}_G$ is the geometric stiffness matrix, $\bar{x}$ is the load vector and λ is the eigenvalue. The eigenvalue represents the critical load parameter. Traditionally eq. (8) is solved with the Cholesky decomposition based on reorganization:

$$\overline{\overline{K}}_G{}^{-1} \cdot \overline{\overline{K}}_E \cdot \bar{x} = \lambda \cdot \bar{x}. \tag{9}$$

Both the geometric and the deformation matrices are ill-conditioned, so the solver often has difficulties in obtaining the solution. According to the tests it is more advantageous to arrange the equation like this:

$$\frac{1}{\lambda} \cdot \bar{x} = \overline{\overline{K}}_E{}^{-1} \cdot \overline{\overline{K}}_G \cdot \bar{x}. \tag{10}$$

So that the result is the inverse of the eigenvalue, if we use a traditional solver.

As the membrane structure is very soft, large deformations occur. After these deformations there is a significant change in the elastic stiffness matrix, so we cannot use the stiffness matrix that belongs to the original state, the equilibrium state must be used to represent the actual behavior of the structure. If we solve eq. (8) for a traditional structure, the elastic stiffness belongs to the deformation-free state and the geometric stiffness belongs to the equilibrium state and the eigenvalues are positive if the load system can cause a stability failure. Here the elastic stiffness matrix belongs to the equilibrium state instead of the deformation-free state the context of the elastic and geometric stiffness is changed, and the results are negative.

After all the eigenvalues are negative invers of the parameters of the critical load.

3.2. The stiffness matrices

The elastic stiffness matrix can be evaluated by the general equation:

$$\overline{\overline{K}}_E = \int_A \overline{\overline{B}}_E{}^T \cdot \overline{\overline{D}} \cdot \overline{\overline{B}}_E, \tag{11}$$

where $\overline{\overline{B}}_E$ is the transformation matrix belongs to the elastic deformations of the structure and the $\overline{\overline{D}}$ matrix contain the constitutive law. The integral is written for the surface of the membrane or for the length of the line element. It is not necessary to use nonlinear transformation matrix, because we are not interested in the change between the deformation free state and the equilibrium state, but we are interested on the behavior of the equilibrium state.

The geometric stiffness matrix is the stiffness belongs to the stress in the structural elements [5]:

$$\overline{\overline{K}}_G = \int_A \overline{\overline{G}}^T \cdot \overline{\overline{\sigma}} \cdot \overline{\overline{G}}, \tag{12}$$

where $\overline{\overline{G}}$ is the so-called G matrix containing all the geometrical properties of the structure and $\overline{\overline{\sigma}}$ is the stress matrix belongs to the actual state. The G matrix looks like this:

$$\overline{\overline{G}} = \begin{bmatrix} \frac{\partial N_1}{\partial \xi} & \frac{\partial N_2}{\partial \xi} & \dots \\ \frac{\partial N_1}{\partial \eta} & \frac{\partial N_2}{\partial \eta} & \dots \end{bmatrix}, \tag{13}$$

where N_i is the shape function belongs to each node of the element and ξ, η are the surface coordinates

of the element (additional transformation is necessary from the surface to the global to get the stiffness in the global coordinate system). The stress matrix is a matrix filled with the stress values:

$$\bar{\bar{\sigma}} = \begin{bmatrix} \sigma_{\xi\xi} & \sigma_{\xi\eta} \\ \sigma_{\xi\eta} & \sigma_{\eta\eta} \end{bmatrix}, \tag{14}$$

Eqs. (11)-(14) are written for surface elements, the same formulations can be written for line elements, too.

3. A case study

3.1. The structure for analyses

A two-field arch supported membrane structure is used for the analysis. The arch on the middle is modelled like a realistic truss with a V-like lacing. The flanges are modeled with the bending resistance truss model described in sec. 2.2. The two arches on the two sides are enforced to deform just in the plane of the arch, no out-of-plane deformation to the arch. With this arch supports the buckling of the middle arch can be analyzed. The membrane is connected to the top flanges of the arches.

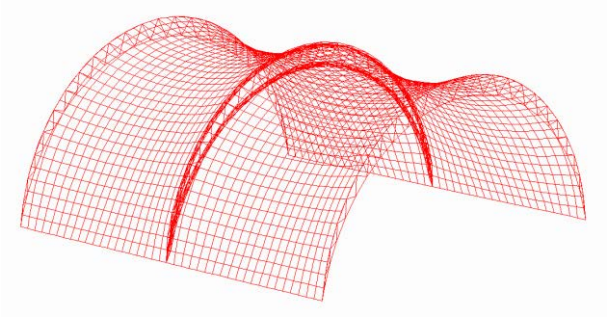


Figure 5: The arc supported structure of the analysis.

The span is 20 m, the distance between the arches is 10 m, the high of the arch is 9 m, the maximum distance between the flanges is 1 m at the middle. Tubes are used for the flanges of the arch with 250 mm outer diameter and 5 mm thickness, the laces are 50×3 mm tubes.

The half high of the truss model is 125 mm and the length of the flanges between two nodes are 1220 mm. The four-flange truss model of the 250×5 tube use solid circular sections: the flanges have 34.3 mm diameter, the laces have 17.2 mm diameter, and the orthogonal laces have 10 mm diameter. The elastic modulus of the steel is 210000 N/mm^2.

The textile membrane uses a mesh of 12×24 element for one field between two arches, the laces of the truss fit to the nodes of the 8-node quadrilaterals. The elastic stiffness is 10 N/mm for both the directions of the plane and the Poisson coefficient equals 0.3. The nodal error was 0.1 kN for the accepted equilibrium.

3.1. The critical load at different load levels

For the verification of the model a posteriori convergence test was carried out: different load levels were applied to the structure and the critical load level was determined for that set. The critical load values were applied on the structure to check if we really reach the critical load level or not.

According to Tab. 1 the critical load level is decreased a little bit as the load level is increased, but they are close to each other. One step over the critical load level is an instable state.

The first buckling shape belongs to the 2.0 kN/m^2 load can be seen in Fig. 7 in 1:100 scale. It is

identical to the real buckling shape in the postcritical state at load level 3.05 kN/m^2.

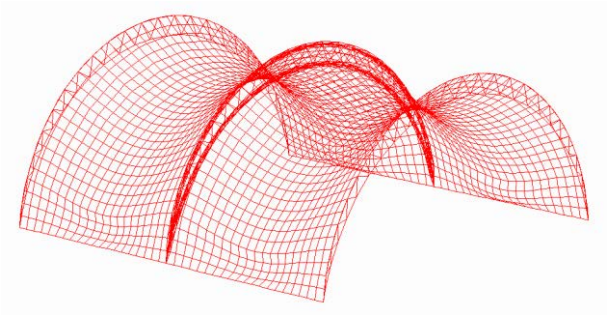


Figure 6: The structure under 2 kN/m2 distributed load.

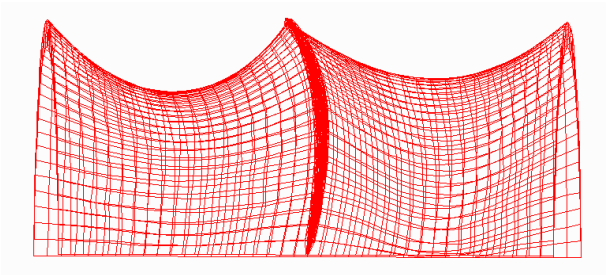


Figure 7: The first buckling shape belongs to the 2 kN/m2 distributed load (×100 scaled deformation).

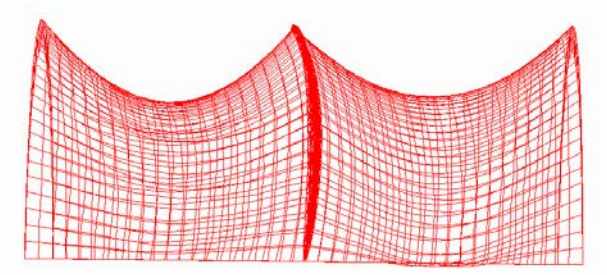


Figure 8: The shape belongs to the 3,05 kN/m2 distributed load (unstable).

Table 1: The critical force level

snow load [kN/m^2]	critical parameter	critical load [kN/m^2]
2.00	1.634	3.268
2.20	1.416	3.116
2.40	1.305	3.133
2.60	1.188	3.088
2.80	1.089	3.050
3.00	1.013	3.040
3.05	***0.287***	***0.876***

As we can see in Tab. 1 the critical load level determined by the eigenvalue is decreased while the load level is increased. This behavior require some more research. The larger stress in the textile

increases the geometric stiffness so that restrain capability again the buckling of the arch. In the same time the large deformation of the membrane changes the angle of the membrane at the connection to the arch. The steeper angle produces less stiffness in the direction perpendicular to the plane of the arch. It seams that the second effect is the stronger one in the case of the presented structure.

4. Conclusion

In the present paper a new method is described for the stability analysis of arch supported textile membranes. The arch is a two-flange steel truss. The buckling of the truss perpendicular to the plane of the arch is predictable. The textile membrane restrains against buckling the arch.

The eigenvalue problem is used to determine the critical parameter of the load. 8-node quadrilateral element is used for the membrane and a four-flange truss model is used to represent the flanges of the arch truss.

According to the case study the model represents a valid value for the critical parameter of the load. The buckling shape obtained from the eigen vector belongs to the smallest critical parameter is identical with the buckling shape of the postcritical state.

References

[1] D. Hegyi, I. Sajtos, Gy. Geiszter and K. Hincz, "Eight-node quadrilateral double-curved elenets ofr membrane analysis" *Comp & Struct*, vol. 84(31), pp. 2151-2158, 2006.

[2] O. C. Zienkiewich and R. L. Taylor, *The Finite Element Method.* Butterworth-Heinemann, 2000.

[3] P. D. Gosling, W. J. Lewis, "Optimal structural membranes – I. Formulation of curved quadrilateral element for surface definition" *Comp & Struct*, vol. 61, pp. 871-883, 1996.

[4] http://fgg-web.fgg.uni-lj.si/~/pmoze/esdep/master/wg07/l0600.htm

[5] O. C. Zienkiewich, *The Finite Element Method in Engineering Science*. McGraw-Hill. Maidenhead, 1971.

Proceedings of the IASS Annual Symposium 2019 – Structural Membranes 2019
Form and Force
7 – 10 October 2019, Barcelona, Spain
C. Lázaro, K.-U. Bletzinger, E. Oñate (eds.)

Stress evaluation of real shape of bi-valve shell by image-based finite element analysis

M. OGOSHI*, M TERANISHI[a], K ISHIKAWA[b], D. MATSUBARA[c]

*Dept. of Architecture & Civil Engineering, University of Fukui
3-9-1 Bunkyo, Fukui-shi, Fukui, 910-8507, Japan
ja190030@u-fukui.ac.jp

[a] Dept. of Nuclear Power & Energy Safety Engineering, University of Fukui
[b] Dept. of Architecture & Civil Engineering, University of Fukui
[c] Commercialization Support Dept. Engineering Validation Sector, Tokyo Metropolitan Industrial Technology Research Institute

Abstract

Biomimetics, which is the imitation of natural systems, models, and structures, has been applied in many fields. The external shapes of seashells are optimized in the natural environment to maintain the safety of their internal spaces. Thus, practical applications of seashells to shell structures are expected in architecture. It has been widely recognized that the geometric shapes of seashells can be depicted by simple mathematical formulations. However, the mechanical properties of seashells have not been revealed, although it is essential for the application of seashells to shell structures. In this study, the mechanical properties of a bi-valve shell are investigated through finite element analysis. Computed tomography (CT) images of the bi-valve shell are captured to obtain an accurate shape. The finite element model of the bi-valve shell is generated using CT images. The concentrations of the equivalent and first principal stresses are evaluated. In addition, the stress transfer mechanisms are investigated.

Keywords: bi-valve shell, image-based modeling, finite element analysis, CT scanning, biomimetics

1. Introduction

Shell structures have been widely recognized as effective structural systems owing to their light weight, high resistance, and elegance. Thus, they satisfy requirements of aesthetic design and structural safety simultaneously. The shell structure form used in structural design is an analytical curved surface such as a cylinder or a sphere and has the added advantage of being form-free. In natural environment, shell structures such as eggshells and seashells can be found, whose shapes are self-organized.

Many optimization methods and their applications have been proposed for creating effective shell structures from their economic and mechanical perspectives. The pioneering experimental approach for obtaining an optimized shell form is the hanging cloth model proposed by H. Isler [1], which was developed from Gaudi's hanging chain model used in the Sagrada Familia. The mechanical effectiveness of this model was investigated by three-dimensional (3D) scanning and finite element analysis [2]. Currently, the computational approach has been primarily used to optimize shell structures. This approach automatically provides an effective mechanical form [3] [4] [5] and new morphologies [5] [6]. In these optimization processes, however, the optimized shell structure, whose shape is the same as those of the self-organized natural objects such as seashells, has never been considered. The numerical conditions in the optimization process that differ from those of natural shell

Copyright © 2019 by Masaki Teranishi
Published by the International Association for Shell and Spatial Structures (IASS) with permission.

structures can thus only be assumed. It is extremely difficult to reproduce the natural condition accurately during optimization. However, we can learn the mechanical properties of natural shell structures using biomimetic techniques.

Biomimetics is the learning process from natural systems, models, and structures. Its applications can be useful in many fields for examining chemical products and machine devices etc. [8] [9] [10]. Architects and building designers have been inspired by nature for a long time and in a variety of ways. Most of them are visual or conceptual inspirations in architectural designs such as art deco and metabolism [11] [12] [13] [14] [15]. The natural ventilation system of the East gate center in Zimbabwe that is inspired by termite nest is an example application of a nature-based design [16]. In structural designs, examples of biomimetics include the tree-type support structure applied in Stuttgart airport, proposed by German architect Frei Otto [17]. The practical application of seashells to shell structures are expected as seashells exhibit long span with thin wall thickness resembling shell structures [18] [19]. Moreover, the shapes of seashells are self-organized in the aquatic environment subject to various forces. It is well known that the seashell shape can be modeled mathematically using an equiangular spiral, where only three or four parameters are required [20] [21]. Meanwhile, the mechanical properties of seashells have not been revealed.

In this study, the mechanical properties of seashells are evaluated to investigate their applicability to shell structures, where we focus on the bi-valve shell that allows us to assume the similarity of roofs for shell structures. To obtain the real shape of the bi-valve shell, microfocus X-ray computed tomography is used. An image-based finite element analysis of the bi-valve shell using computed tomography (CT) images is conducted. The concentrations of the equivalent stress and first principal stress are evaluated. Moreover, the stress transfer mechanism is investigated.

2. Experiment and methods

2.1. Specimen

The specimen used was one of a pair of bi-valve shells that allows us to assume the similarity to roofs for shell structures. The bi-valve shell was captured on a beach of Simane prefecture in Japan. To obtain the real shape of the specimen by reducing the artifact of the CT images, the smallest bi-valve shell obtainable was used. As shown in Fig. 1, the size of the specimen was approximately 4 mm × 4 mm × 2 mm. The bi-valve shell was identified as *Veneroida*.

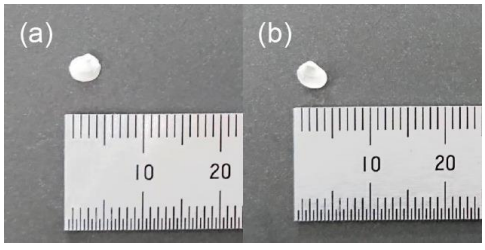


Fig. 1: Bi-valve shell used as specimen. (a) and (b) show plane images of front and back surfaces.

2.2. CT scanning of bi-valve shell

In biomimetic and biomaterial studies, X-ray computed tomography has been used to visualize the insides of structures and to measure their dimensions. To measure the bi-valve shell shape in detail, a CT scan of the bi-valve shell was performed using a microfocus X-ray computed tomography device, Skyscan 2211 manufactured by Bruker Corp. The specimen was set on a rotational stage as shown in Fig. 2; subsequently, the specimen was scanned in a 0.8° rotational step. The pixel size and slice pitch were 2.0 μm, and the size of each CT image was 4032 × 4032 × 4032 voxels. The intensity values of

the CT images that corresponded to the rate of X-ray absorption were obtained in 16-bit gray scale. The raw CT images included noise and pseudo-edges that could cause failed geometric measurements and instability for the image-based finite element analysis. To remove noise in the CT images and smoothen the bi-valve shell shape, 3D median and Gaussian filtering were performed. The processed CT images were used for the after-mentioned image-based finite element modeling.

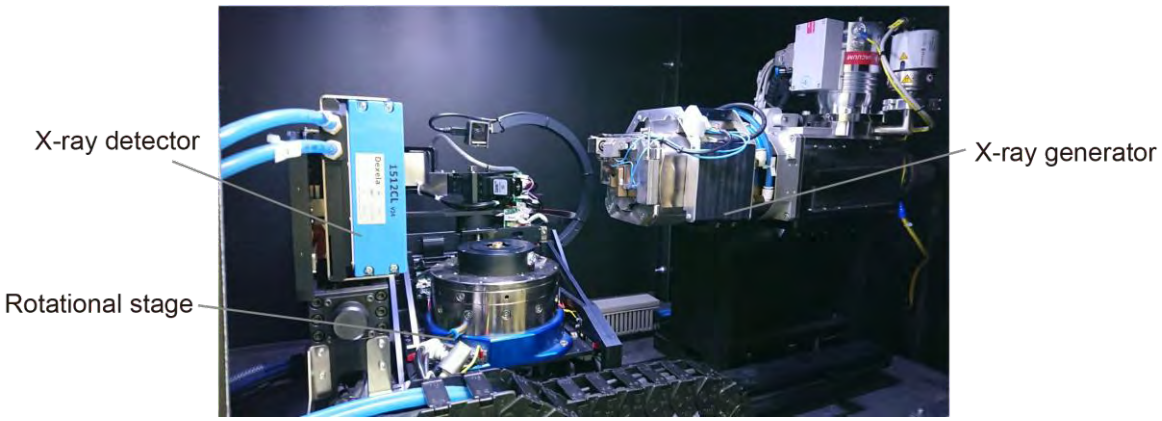


Fig. 2: Test apparatus for X-ray CT scanning of bi-valve shell.

2.3. Image-based finite element modeling

Fig. 3 shows the procedure of the image-based finite element modeling. The interface between the background and the interface of the bi-valve shell was recognized by the differences in the intensities of their CT images. The interface of the bi-valve shell was extracted by the interpolation of the intensity in the STL file format. Using the STL model of the bi-valve shell, a finite element mesh with a ten-node tetrahedron was generated, where the minimum mesh size was 0.001 μm, the number of nodes was 282,581, and the number of elements was 220,259. The bottom of the finite element model, which was the contact region of the bi-valve shell in the close state, was completely fixed by considering the mechanical symmetry of the pair of bi-valve shells. The boundary conditions may be stronger constraints compared with the bi-valve shells in the natural environment; however, these conditions were applied to stabilize the finite element analysis. To evaluate the resistance of the bi-valve shell to external forces, three types of numerical cases were performed in accordance with the direction of applied body force along the +x, +y, and –z axis. They were labelled cases X, Y, and Z respectively. The body force that acted on an element was a multiplication of the specific gravity by the element volume. The external force in case Z equaled to the self-weight of the bi-valve shell. The material properties of the bi-valve shell were assumed as those of plain concrete, where the Young modulus is 2.17×10^4 MPa, Poisson ratio is 0.2, and specific gravity is 24.0 kN/m^3. This is because few examples of the material properties of bi-valve shells have been presented and to determine it from mechanical testing is difficult. The elastic finite element analysis was performed under the numerical conditions above. In the image-based finite element modeling, the STL model was generated on the image-based structural analysis software VOXELCON, the finite element model was generated on the meshing software ANSYS ICEM CFD, and the finite element analysis was conducted on a parallel FEM system FrontISTR.

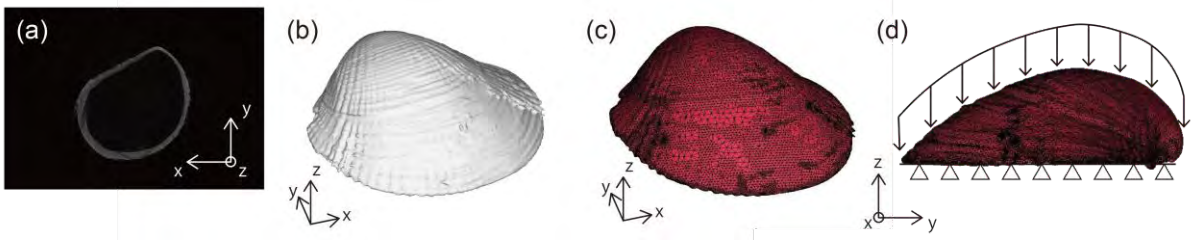


Fig. 3: Procedure of image-based finite element modeling. (a), (b), (c), and (d) show CT-image, STL model, meshed model, and boundary condition in finite element analysis.

3. Results

To present the stress evaluation of the bi-valve shell precisely and accurately, the front and back surfaces of the bi-valve shell are shown in Fig. 4. Additionally, this figure shows the thin and thick parts by two different colors. Fig. 5 shows the distribution of equivalent stress σ_{eq} on the bi-valve shell for cases X, Y, and Z. In this figure, the plan views of the front and back surfaces before and after deformation are represented. The results of the front surface show that the σ_{eq} concentrated on the commissure of the bi-valve shell in cases X and Y, while a low stress appeared on the commissure in case Z. The σ_{eq} concentration was observed on the growth ring, which was the boundary between the thin and thick parts. This is because the thickness of the bi-valve shell changes significantly on the growth ring. From the results of the back surface, the high σ_{eq} region ranged from the dorsal side to the ventral side in case X, whose direction was normal to the X axis. Similarly, the high σ_{eq} ranged from the posterior side to the anterior side in case Y. It is noteworthy that the σ_{eq} concentration was smaller on the back surface than it is on the front surface because of the smoothness of the back surface. In case Z, the σ_{eq} concentration occurred on the commissure; however, the value of σ_{eq} was lower than those in cases X and Y. Thus, the bi-valve shell resisted the horizontal force in the wide range of the back surface, and resistance-change part depended on the direction of the horizontal force. This implies that the bi-valve shell hindered the σ_{eq} from concentrating on the narrow part, which might cause a collapse of the structure. The deformed shapes show that the thin part, particularly in the vicinity of the growth ring, was primarily deformed, while the thick part was deformed slightly. Furthermore, the large deformation region corresponded to the high σ_{eq} region.

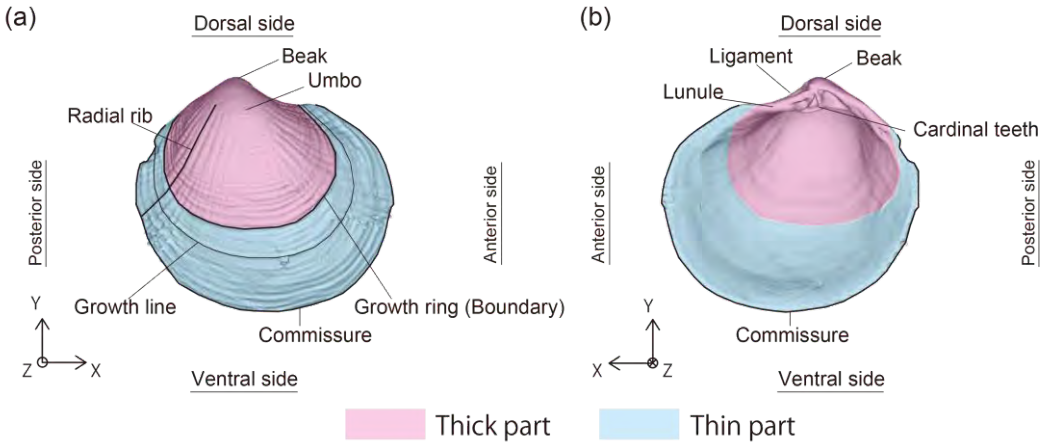


Fig. 4: Each part of bi-valve shell on (a) front and (b) back surfaces.

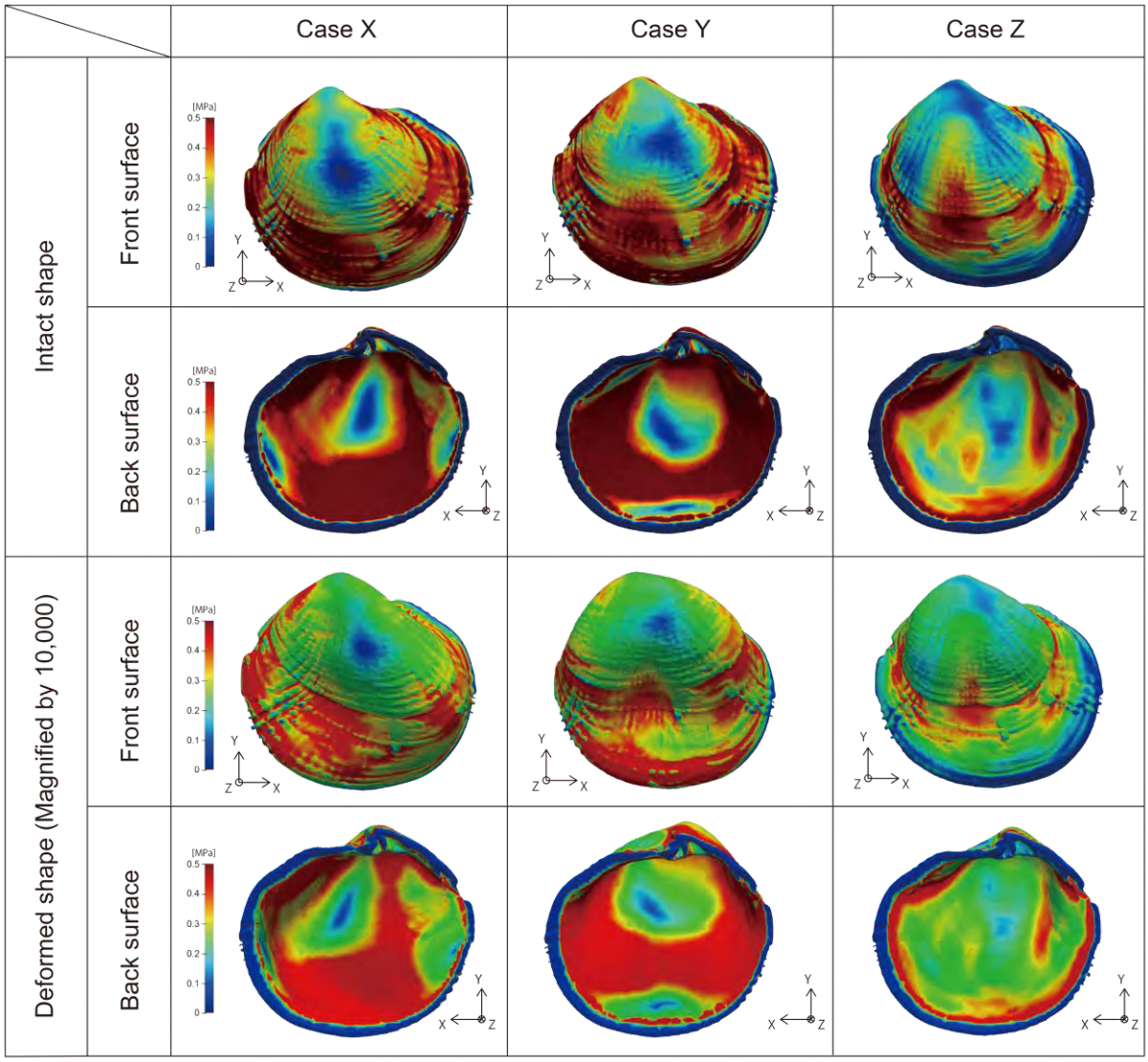


Fig. 5: Distribution of equivalent stresses in cases X, Y, and Z. Plan views of front and back surfaces are represented. Their deformed shapes magnified by 10,000 are shown.

To investigate the stress transfer mechanism of the bi-valve shell, the first principal stress σ_1, third principal stress σ_3, and their directions on the front and back surfaces are shown in Fig. 6. The length of the line in this figure is the absolute value of the first and third principal stresses. It can be observed from the results in case X that σ_1 is concentrated on the posterior side of the front surface, while σ_3 is concentrated on the anterior side. Similarly, in case Y, σ_1 is concentrated on the ventral side of the front surface while σ_3 is concentrated on the anterior side of the front surface. In case Z, the high compressive stress in σ_3 appeared on the front and back surfaces, while only a small tensile stress appeared in σ_1. The compressive stress was a tangent to the surface. This implies that the bi-valve shell resisted the external vertical force by the in-plain stiffness like arches. The results in cases Y and Z show that the high compressive stress in σ_3 on the front surface transferred from the umbo to the

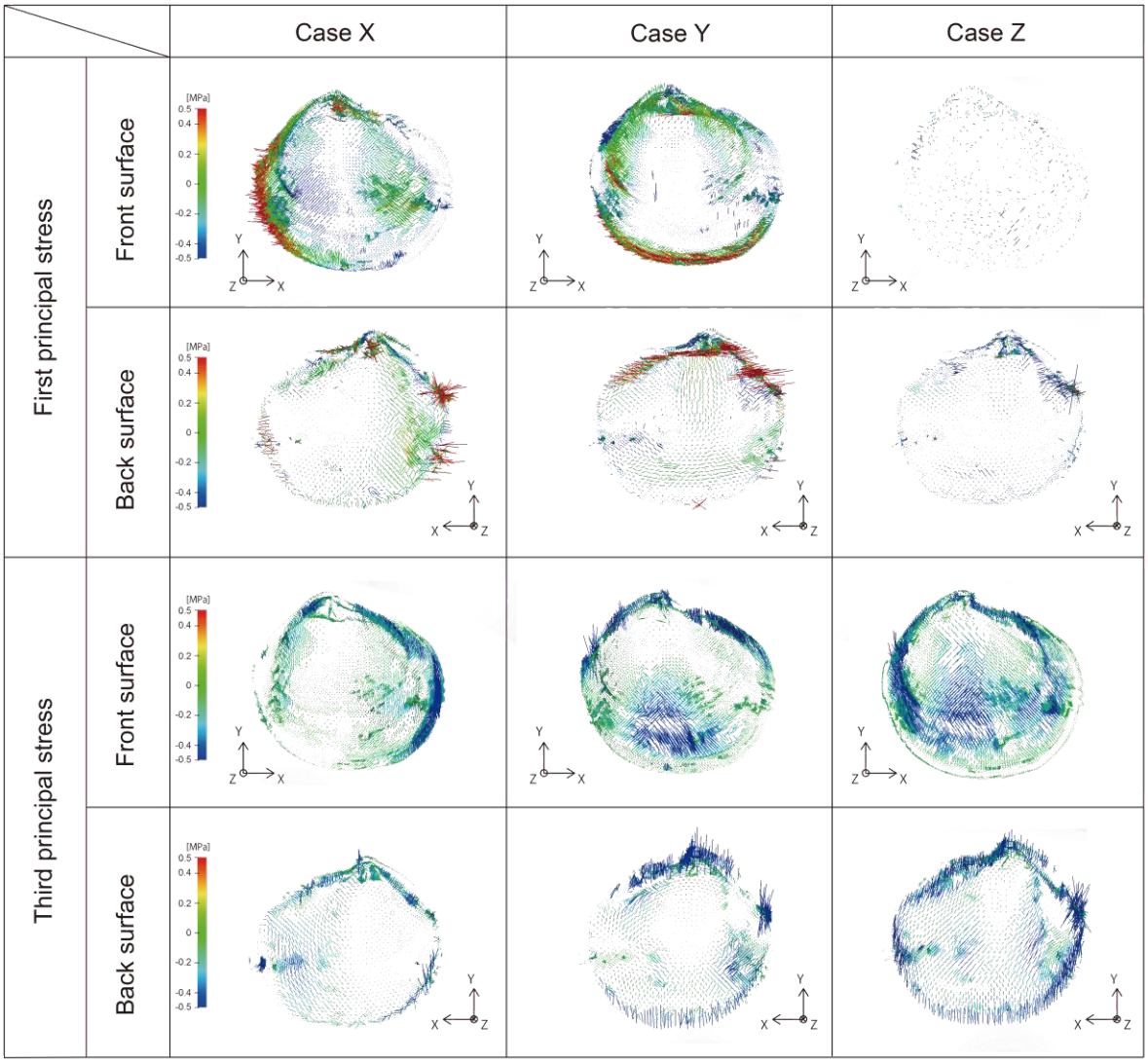


Fig. 6: Distribution of first and third principal stress and their direction in case (a) X, (b) Y, and (c) Z. The lengths of lines show the absolute values of the principal stress.

ventral side. The compressive stress was directed between the growth line and radial rib. To evaluate the tendency of the direction of the compressive stress quantitatively, the geometric properties of the bi-valve shell should be discussed in detail. Moreover, the mechanical and geometric properties are affected by the molluscous part inside the seashell; thus, further investigations are required.

4. Conclusion

In this study, the image-based finite element analysis of a bi-valve shell was performed to evaluate stress concentration. The conclusions of this study are summarized as follows:

1. The σ_{eq} concentration appeared on the front surface because of the surface roughness. In particular, σ_{eq} concentrated on the growth ring, which was the boundary between the thin and thick parts. Meanwhile, the σ_{eq} concentration was smaller on the back surface than it was on the front surface because of the smoothness of the back surface.

2. The bi-valve shell hindered σ_{eq} from concentrating on the narrow part by distributing the burden of the external force.
3. The thin part, particularly in the vicinity of the growth ring, was largely deformed, while the thick part was slightly deformed.
4. The bi-valve shell resisted the external vertical force by in-plain stiffnesses such as arches.

Our future works are listed as follows.

1. A bi-valve shell was employed as the specimen. The generality of the obtained results in this study should be verified using other specimens.
2. We qualitatively investigated the mechanical properties of the bi-valve shell through finite element analysis. To understand the mechanical properties quantitatively, the relationship between geometric and mechanical properties should be investigated.
3. In the finite element analysis, the boundary conditions were not sufficiently accurate to represent those of bi-valve shells in the natural condition. Thus, ocean currents, tides, and water pressures should be considered using computational fluid dynamics.
4. The external shape of bi-valve shells has evolved to protect the molluscous part through self-organization against external forces in the natural environment. Therefore, it is significant to investigate the relationship between the molluscous part and the distribution of stress.

Acknowledgements

This work was supported by the Nohmura Foundation for Membrane Structure's Technology.

References

[1] H. Isler, "New shapes for shells," *International Association for Shell Structures* (1960).

[2] A. Borgart, P. Eigenraam, "Scanning in 3D and analysing the models of Heinz Isler, the preliminary results," *IASS-APCS 2012: From spatial structures to space structures*, (2012).

[3] E. Ramm, "Nonlinear Analysis of Shells by Finite Elements: Shape finding methods of shells," *Springer*, pp. 269-283 (1992).

[4] K.-U. Bletzinger, E. Ramm, "Form finding of shells by structural optimization," *Engineering with computers*, Vol. 9, No. 1, pp. 27-35 (1993).

[5] H. Ohmori, K. Yamamoto, "Shape optimization of shell and spatial structure for specified stress distribution," *Memoirs-School of Engineering Nagoya University*, Vol. 50, pp. 1-32 (1998).

[6] M. Bischoff, "Modeling of shells with three-dimensional finite elements," *Proceedings of the 6th International Conference on Computation of Shell and Spatial Structures*, pp.28-31, (2008).

[7] A. Pugnale, M. Sassone, "Morphogenesis and structural optimization of shell structures with the aid of a genetic algorithm," *Journal of the International Association for Shell and Spatial Structures*, Vol. 48, No. 3, pp. 161-166 (2007).

[8] A. du Plessis, C. Broeckhoven, "Looking deep into nature: A review of micro-computed tomography in biomimicry," *Acta biomaterialia*, Vol.85, pp.27-40 (2018).

[9] J. Hwang, Y. Jeong, J. M. Park, K. H. Lee, J. W. Hong, J. Choi, "Biomimetics: forecasting the future of science, engineering, and medicine," *International journal of nanomedicine*, Vol. 10, pp. 5701-5713 (2015).

[10] J.F. Vincent, "Biomimetics—a review, Proceedings of the institution of mechanical engineers," *part H: Journal of Engineering in Medicine*, Vol. 223, No. 8, pp. 919-939 (2009).

[11] P. Gruber, "Biomimetics in architecture [Architekturbionik]." *Biomimetics--Materials*, Structures and Processes, Springer, pp. 127-148 (2011).

[12] J. F. Vincent, "Biomimetics in architectural design," *Intelligent Buildings International*, Vol. 8, No. 2, pp. 138-149 (2016).

[13] A. A. P. Kshirsagar, A. S. S. Malani, E. V. S. Tiware, "Biomimicry–Nature Inspired Building Structures," *International Journal of Engineering Research and Technology*, Vol. 10, No. 1, pp. 162-166 (2017).

[14] R. Oxman, "Morphogenesis in the theory and methodology of digital tectonics," *Journal of the International Association for Shell and Spatial Structures*, Vol. 51 No. 3 pp. 195-205 (2010).

[15] E. Stach, "Structural morphology and self-organization," *Journal of the International Association for Shell and Spatial Structures*, Vol. 51 No. 3, pp. 217-231 (2010).

[16] J. S. Turner, R.C. Soar, "Beyond biomimicry: What termites can tell us about realizing the living building. First International Conference on Industrialized," *Intelligent Construction at Loughborough University*, 2008.

[17] F. Otto, *Naturliche Konstruktionen*, 1982, Orion press (in Japanese).

[18] Edger. Stach, "Form-optimizing in biological structures—the morphology of seashells." *An Anthology of Structural Morphology*, World Scientific, pp. 173-187 (2009).

[19] T. Sasaki, *Malacology*, University of Tokyo Press (2013).

[20] D. M. Raup, "The geometry of coiling in gastropods," *Proceedings of the National Academy of Sciences of the United States of America*, Vol. 47, No. 4, pp. 602 -609 (1961).

[21] M. Cortie, "Models for mollusc shell shape," *South African Journal of Science*, Vol. 85, pp. 454-460 (1989).

Proceedings of the IASS Annual Symposium 2019 – Structural Membranes 2019
Form and Force
7 – 10 October 2019, Barcelona, Spain
C. Lázaro, K.-U. Bletzinger, E. Oñate (eds.)

Study of dynamic behavior in cylindrical shell coupled with fluid

Davidson de Oliveira FRANÇA JR*, Lineu José PEDROSO[a]

* Department of Civil Engineering and Environment of University of Brasília
Campus Darcy Ribeiro, Prédio SG-12, Brasília-DF, Brazil
davidson.francajunior@gmail.com

Abstract

In this work, are free vibration of an empty or filled with an inviscid and incompressible fluid cylindrical tank is presented. The tank is modeled by a cylindrical shell and the fluid represented by an acoustic cavity, in which the impulsive and convective modes (sloshing modes) were investigated. The approach is based on two methods: an energetic formulation implemented in MAPLE software to obtain impulsive modes and the finite element method through ANSYS software to evaluate impulsive and convective modes. The fluid-structure interaction (FSI) is done in terms of fluid continuity conditions and boundary conditions at the fluid-structure interface. To validate the analyzes, the values found with the analytical procedure and numerical discretization were compared with the experimental results found in the literature. The natural frequencies, impulsive mode shapes and convective (sloshing) mode shapes were studied. The comparative analytical, numerical and experimental results of the literature were satisfactory.

Keywords: Cylindrical Tank, Fluid-Structure Interaction, Impulsive Modes, Sloshing Modes.

1. Introduction

Cylindrical shells are characterized by an object with a curved surface, small thickness compared to its other dimensions, and usually made of solid material. Structural dynamic analysis of shells is complex because they have flexural and in-plane vibrations that act together. Many simultaneous factors influence the dynamic response of a cylindrical shell, like the type of material inside it (fluid or solid), the boundary conditions of the shell, the presence or lack of a ring support, the influence of the connection between the shell wall and the bottom and the lid, among others.

The study of free vibration in cylindrical shells has been receiving a lot of attention by many researchers for many years. Based on the classic works of Donnell [1], Flügge [2], Vlasov [3], Timoshenko and Woinowsky [4], Sanders [5], many other theories were developed and improved upon to simulate the dynamic behavior of a shell. Other analytical techniques differ from each other by the strains and curvatures assumed for the shell, as well as by the solution methods used in the problem. Leissa [6] presents the different classic theories mentioned and many simulation results.

Based on the classic theories, there was a big advance in the analytical studies towards the calculation of cylindrical shells vibration characteristics containing fluid, it is worth mentioning the works of Lakis e Paidoussis [7], where they present a theory to study partially or completely filled with liquid cylindrical shells free vibration using cylindrical finite elements in the solution of the Sanders equations. Haroun [8] presents theoretical and experimental investigations of the dynamic behavior of cylindrical tanks with elastic supports.

Gonçalves and Batista [9] applied the Rayleigh-Ritz method using the energy formulation and created a theoretical analysis method to determine the vibration characteristics of partially filled or submerged

Copyright © 2019 by Davidson de Oliveira França Júnior and Lineu José Pedroso
Published by the International Association for Shell and Spatial Structures (IASS) with permission.

cylindrical shells. Fernholz and Robinson [10], evaluated the free vibration in coupled cylindrical shells through the Donnell-Mushtari theory and the software NASTRAN.

Amabili and Dalpiaz [11], studied the free vibration of fully and partially filled circular cylindric tank theoretically and experimentally. Analytically, the shell was simulated by the Berry and Reissner theory and the fluid was modeled by the velocity potential function in the Laplace equation. França Júnior [12] evaluated the influence of the classic boundary conditions on the free vibration of coupled and uncoupled cylindric shells through analytical methods and numerical procedures. Ji et al. [13] developed an analytical method to calculate the free vibration characteristics of thick cylindrical shells filled with fluid. The fluid is modeled by the velocity potential incorporated in the shell wall by the impermeability condition.

In this article, the impulsive and convulsive modes (sloshing) in the vibration of a tank are investigated. The approach is based on an energetic formulation implemented in MAPLE software to evaluate the impulsive modes and the finite element method, through the ANSYS software, to study the impulsive and convective modes. The fluid-structure interaction is done in terms of fluid continuity conditions and boundary conditions at the fluid-structure interface. To validate the analyzes, the values found analytically and through the numerical discretization for the impulsive modes were compared with the experimental results obtained by Amabilli & Dalpiaz [11]. With the validated numerical modeling, the analyzes extended to sloshing modes of the tank. Therefore, the natural frequencies and mode shapes, with and without sloshing, of the tank are presented.

2. Analytical Formulation

The cylindrical shell is made of thin walls with length L, average radius R, radial angle ϕ and thickness h. The shell material is elastic with Young modulus E, Poisson coefficient μ and specific mass ρ. The displacement vector coordinates on the surface of the shell in the axial, circumferential and radial directions are u, v and w, respectively. Based on Flügge [2] linear theory, the shell strains and curvatures are given by:

$$\varepsilon_z{}^{(0)} = \frac{\partial u}{\partial z}; \quad \varepsilon_\emptyset{}^{(0)} = \frac{1}{R}\left(\frac{\partial v}{\partial \phi} + w\right);$$

$$\gamma_{z\phi}{}^{(0)} = \frac{\partial v}{\partial z} + \frac{1}{R}\frac{\partial u}{\partial \phi}; \quad \chi_z = \frac{\partial^2 w}{\partial z^2}; \tag{1}$$

$$\chi_\phi = -\frac{1}{R^2}\left(\frac{\partial^2 w}{\partial \phi^2} - \frac{\partial v}{\partial \phi}\right); \quad \chi_{z\phi} = -\frac{1}{R}\left(2\frac{\partial^2 w}{\partial z \partial \phi} - \frac{\partial v}{\partial z}\right)$$

where (0) is the superscript related to the average surface, ε_z and $\varepsilon_\emptyset$ represent the membrane and transverse strains, respectively, $\gamma_{z\phi}$ represent the distortions, χ_z e χ_ϕ represent the bending curvatures and $\chi_{z\phi}$ represent the torsional curvatures. The total strains are assumed to be the sum of the membrane and flexural strains. Thus, the strain in any point of the shell is given by:

$$\varepsilon_z = \varepsilon_z{}^0 + x\,\chi_z$$

$$\varepsilon_\emptyset = \varepsilon_\emptyset{}^0 + x\,\chi_\phi \tag{2}$$

$$\gamma_{z\phi} = \gamma_{z\phi}{}^0 + x\,\chi_{z\phi}$$

where x is the distance from a point in the shell to the average surface. The strains and stress are based on Hooke's Law, and can be expressed as:

$$\sigma_z = \frac{E}{1-\mu^2}\left(\varepsilon_z + \mu\varepsilon_\phi\right)$$

$$\sigma_\phi = \frac{E}{1-\mu^2}\left(\varepsilon_\phi + \mu\varepsilon_z\right) \tag{3}$$

$$\tau_{z\phi} = \frac{E}{2(1-\mu^2)}\gamma_{z\phi}$$

The equations of motion can be obtained by the Rayleigh-Ritz procedure using the Lagrange function (Γ), given by:

$$\Gamma = \mathrm{T} - \mathrm{U} \tag{4}$$

where T is the maximum kinetic energy and U is the maximum strain energy potential of the cylindrical shell. The strain energy potential and the kinetic energy, according to Brush e Almoroth [14], are given by:

$$U = \frac{1}{2}\int_{-\frac{h}{2}}^{\frac{h}{2}}\int_0^{2\pi}\int_0^L \left(\sigma_z\varepsilon_z + \sigma_\phi\varepsilon_\phi + \tau_{z\phi}\gamma_{z\phi}\right)dv \tag{5}$$

$$T = \frac{\rho R h}{2}\int_0^{2\pi}\int_0^L \left[\left(\frac{\partial u}{\partial t}\right)^2 + \left(\frac{\partial v}{\partial t}\right)^2 + \left(\frac{\partial w}{\partial t}\right)^2\right] dz d\phi \tag{6}$$

where *u*, *v* and *w* are, respectively, the longitudinal, circumferential and radial displacements and *t* is time. The equations for *u*, *v* and *w* displacements are given by:

$$u(z,\phi,t) = A\,u(z,\phi).e^{-j\omega t} \tag{7}$$

$$v(z,\phi,t) = B\,v(z,\phi).e^{-j\omega t} \tag{8}$$

$$w(z,\phi,t) = C\,w(z,\phi).e^{-j\omega t} \tag{9}$$

where *e* is the Euler's number, *u*(z, ϕ), *v*(z, ϕ) and *w*(z, ϕ) are the modal shapes (modes of vibration), $\mathrm{j} = \sqrt{-1}$ is the imaginary unit, *A*, *B*, and *C* are constants that represent the amplitude of the axial (*u*), circumferential (*v*) and radial (*w*) respectively and *ω* is the natural frequency of vibration. In the work, the beam mode and its respective transcendental equation coefficients for a simply supported beam presented by Blevins [15] are used. The Rayleigh-Ritz method applied to the Lagrange function is given by:

$$\frac{\partial \Gamma}{\partial \mathrm{A}} = 0$$

$$\frac{\partial \Gamma}{\partial B} = 0 \tag{10}$$

$$\frac{\partial \Gamma}{\partial \mathrm{C}} = 0$$

Thus, the system of three equations of motion is obtained. These equations can be written in a matrix format, with symmetrical terms, that leads to the following eigenvalues problem:

$$[\boldsymbol{K} - \omega^2 \boldsymbol{M}]\{X\} = \{0\} \tag{11}$$

Where $\{X\} = \{A \quad B \quad C\}^T$ is the eigenvector. The terms of the characteristic matrix $[\boldsymbol{C_{ij}}] = [\boldsymbol{K} - \omega^2 \boldsymbol{M}]$ consist in high complexity mathematical expressions, and the analytical computation of Det $[\boldsymbol{C_{ij}}] = 0$, which leads to the characteristic polynomial, and thus to the natural frequencies of the shell, becomes very hard and labor intensive. The problem has been solved using the MAPLE software.

2.1. Fluid-Structure Interaction

In the shell-cylindrical cavity fluid-structure interaction (coupled problem), two boundary conditions are present: the radial pressure at the shell surface is equal to the pressure on the cavity boundary, and the radial velocity at the shell surface is equal to the velocity on the acoustic cavity surface (impenetrability condition). Thus, as a simplification, the coupled shell modes of vibration are assumed to be equal to the structure modes of vibration in a vacuum.

Using the analytical method, the coupling of a simply supported cylindrical shell is done through an added fluid mass in the shell equation terms that correspond to the structure mass in the axial direction. The added mass equation for a partially or fully filled shell is presented by Gonçalves and Batista [9], given by:

$$\zeta = \left(\frac{\rho_f}{\rho}\right)\left(\frac{R}{h}\right)\left[\frac{H}{L} - \frac{sen\left(\frac{2m\pi H}{L}\right)}{2m\pi}\right]\left\{\frac{J_n(r_{\bar{i}})}{R\left[J'_n(r_{\bar{i}})\right]_{r=R}}\right\} \tag{12}$$

where ζ is the virtual added mass, ρ_f is the acoustic fluid density, $J'_n(r_{\bar{i}})$ is the Bessel function derivative. The added mass increases the inertial load in the shell radial direction. The shell displacements are bigger in the radial direction and including the added mass in this way yields more realistic results. The mass coupling is given by:

$$\left\{\begin{bmatrix} k_{1,1} & k_{1,2} & k_{1,3} \\ k_{2,1} & k_{2,2} & k_{2,3} \\ k_{3,1} & k_{3,2} & k_{3,3} \end{bmatrix} - \omega^2 \begin{bmatrix} m_{1,1} & m_{1,2} & m_{1,3} \\ m_{2,1} & m_{2,2} & m_{2,3} \\ m_{3,1} & m_{3,2} & m_{3,3} + \zeta \end{bmatrix}\right\}\begin{Bmatrix} A \\ B \\ C \end{Bmatrix} = \{0\} \tag{13}$$

3. Numerical Formulation

The numerical analysis (Figure 1) was done using Finite Elements Method through the software ANSYS. The element SHELL63 was used to model the tridimensional cylindrical shell and the element FLUID30 was used to model the acoustic cavity. The modules Block Lanczos and Unsymmetric were used to solve the eigenvalues and eigenvectors problem. The mesh independence analysis was done and can be checked in França Jr. [16]. The numerical formulation used in the simulations is based on the structure displacement and fluid pressure (U-P), given by:

$$\begin{bmatrix} \boldsymbol{M_s} & \boldsymbol{0} \\ \boldsymbol{\rho FS} & \boldsymbol{M_f} \end{bmatrix}\begin{Bmatrix} \ddot{U} \\ \ddot{P} \end{Bmatrix} + \begin{bmatrix} \boldsymbol{C_s} & \boldsymbol{0} \\ \boldsymbol{0} & \boldsymbol{C_f} \end{bmatrix}\begin{Bmatrix} \dot{U} \\ \dot{P} \end{Bmatrix} + \begin{bmatrix} \boldsymbol{K_s} & \boldsymbol{-FS} \\ \boldsymbol{0} & \boldsymbol{K_f} \end{bmatrix}\begin{Bmatrix} U \\ P \end{Bmatrix} = \begin{Bmatrix} F_E \\ 0 \end{Bmatrix} \tag{14}$$

where {Fe} is a force vector, {U} is the structure displacement vector, {P} is the fluid pressure vector, **Ms** is the structure mass matrix, **Ks** is the structure stiffness matrix, **Cs** is the structure damping matrix, $\mathbf{M_f}$ is the fluid mass matrix, $\mathbf{K_f}$ is the fluid stiffness matrix, $\mathbf{C_f}$ is the fluid damping matrix, **FS** is the fluid-structure coupling matrix. In the system above, if $\{F_E\}$=0, **Cs**=0 and $\mathbf{C_f}$=0, the dynamic response obtained corresponds to the coupled undamped free vibration problem.

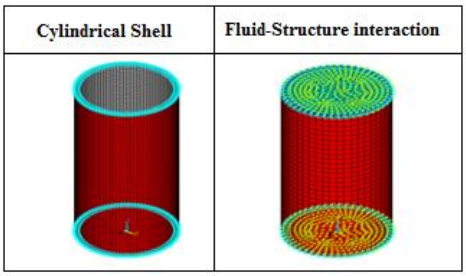


Figure 1: Numerical models.

4. Results

4.1. Impulsive modes

The first analysis is on the impulsive modes of tank in free vibration. The first six natural frequencies obtained through the analytical technique and the numerical method are presented and compared in Table 1. The index N represents the frequencies order, *m* is the number of longitudinal half waves, and *n* is the number of circumferential half waves. The lower natural frequencies are associated with the radial (w) modes of vibration.

Table 1: Comparisons of natural frequencies the cylindrical shell of impulsive modes the fluid.

N	*m*	*n*	$\omega_{i,m,n}$ (Hz) Analytical	$\omega_{i,m,n}$ (Hz) FEM	Diff. (%)	$\omega_{i,m,n}$ (Hz) Experiment	Diff. (%)
1	1	4	99,31	91,77	7,59	92,00	7,95
2	1	5	112,67	104,91	6,89	104,00	8,34
3	1	3	127,08	117,70	7,38	119,00	6,80
4	1	6	155,46	147,08	5,38	147,00	5,75
5	1	7	218,19	210,07	3,72	206,00	5,80

The coupled cylindrical shell analytical natural frequencies presented in Table 1 are satisfactory compared to the numerical results obtained with FEM using ANSYS and the experimental results. According to Lakis and Paidoussis (1971), the displacement amplitudes of a simply supported shell filled with liquid are smaller if compared to the empty shell due to the fluid influence. This behavior was observed herein, showing that the fluid presence reduces the natural frequencies and reproduce the same tendencies in the uncoupled shell. Figure 2 shows the impulsive modal shapes.

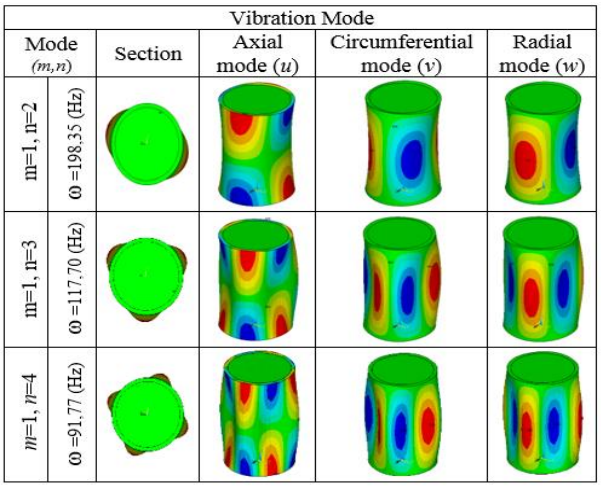


Figure 2: Natural frequencies and impulsive mode shapes of the tank.

4.2. Convective modes

The second analysis is on the sloshing modes of tank in free vibration. With the analysis validated for impulsive modes, a free surface condition was applied to the numerical model. The first five natural frequencies obtained through the numerical method are presented in Table 2. The index N represents the frequencies order.

Table 2: Natural frequencies for the sloshing modes the tank.

N	$\omega_{i,m,n}$ (Hz) FEM
1	1,62
2	2,10
3	2,48
4	2,81
5	2,82

The impulsive pressure corresponds to high frequency oscillations, while the convective corresponds to low frequency oscillations. However, there is always a coupling between the free surface sloshing fluctuations of the liquid and the structural deformations. Thus, during a dynamic action the first modes to be excited are the sloshing modes, then the impulsive coupled modes, structure modes and acoustic cavity modes. Therefore, it is indispensable to impose the condition of free surface. Figure 3 shows the sloshing modes.

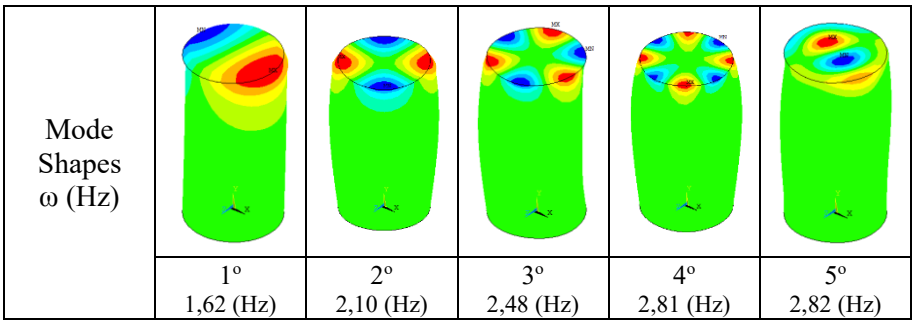


Figure 3: Natural frequencies and sloshing mode shapes of the tank.

When the excitation frequency is close to one of the natural frequencies of the sloshing liquid, large wave amplitudes can be generated. As a result, the hydrodynamic forces of sloshing waves affect the overall response of the tank and can cause damage to the top of the tank.

5. Conclusion

This work addressed the aspects of fluid-structure interaction in problems applied to the dynamic analysis of cylindrical tanks. The approach analytical, numerical and experiment was studied to investigate fully filled cylindrical shells free vibrations. In the problem study, the analytical technique based on the virtual added mass applied to the uncoupled shell formulation was satisfactory.

In the analysis of the impulsive modes, it was observed that despite having an influence in the system dynamic behavior, the fluid presence reproduced the characteristic structure dominant modes (same as the shell in a vacuum) in a significant range of frequencies analyzed. The convective modes (sloshing) corresponds to low-frequency oscillations, indispensable to dynamic analysis.

Thus, this work provides interesting results concerning the dynamic behavior of cylindrical shells

containing fluid, which is a problem of big interest to Industrial Engineering.

Acknowledgements

This study was financed in part by the Coordenação de Aperfeiçoamento de Pessoal de Nível Superior - Brasil (CAPES) - Finance Code 001. The authors also ackowledge the support from Grupo de Dinâmica e Fluido-Estrutura (GDFE) and University of Brasilia (UnB).

References

[1] Donnell, L. H. (1933): Stability oh thin walled tubes under torsion. *Inc. NACA Report*, No 479.

[2] Flugge, W. (1934). Statik und Dynamic der Schalen. Berlin, Julius Springer.

[3] Vlasov, V. S. (1951). Basic differential equations in general theory of elastic shells. *In: National Advisory Committee for Aeronautics. NACA-TM-1241*. Washington DC: US Government Printing Office.

[4] Timoshenko, S. & Woinowsky, K. S., (1959). Theory of plates and shells. Second Edition, United States, McGraw-Hill.

[5] Sanders, J. L., (1959). An improved first approximation theory of thin shells. In. NASA Report.

[6] Leissa, A. W. (1973): Vibration of Shells. *Technical Report NASA SP-288*, Washington, D. C. pp. 425.

[7] Lakis, A. A. & Paidoussis, M. P. (1971): Free vibration of cylindrical shells partially filled with liquid. *International Journal of Sound and Vibration*, pp. 1–15.

[8] Haroun, M.; (1983). Vibration Studies and Test of Liquid Storage Tanks. *In. Earthquake Engineering and Structural Dynamic*. p.179-206.

[9] Gonçalves, P. B. e Batista, R. C., (1986): Frequency Response of Cylindrical Shells Partially Submerge dor Filled with Liquid. *International Journal of Sound and Vibration*.

[10] Fernholz, C. M, Robinson, J. H. (1990): Fully-Coupled Fluid/Structure Vibration Analysis Using MSC/NASTRAN. *NASA technical memorandum 102857*.

[11] Amabili, M. & G. Dalpiaz, (1995): Breathing Vibrations of a horizontal circular cylindrical tank shells, partially filled with liquid. *International Journal of Vibration and Acoustics*, pp. 117–187.

[12] França Jr, D. O., Pedroso, L. J. e Mendes, N. B., (2017). Estudo de Vibrações Livres Desacopladas e Acopladas Fluido-Estrutura em Cascas Cilíndricas para Diferentes Condições de Contorno. *CILAMCE 2018 – XXXVIII Iberian Latin American Congress on Computational Methods in Engineering*, Florianópolis, SC, Brasil, 20 pp.

[13] Ji, M.; Inaba, K. & Triawan F. (2019). Vibration Characteristics of Cylindrical Shells Filled with Fluid Based on First-order Shell Theory. *Journal of Fluids and Structures*, Vol. 85, pp. 275–291.

[14] Brush, D. O.; Almroth, B. O. (1975): Buckling of Bars, Plates, and Shells. *New York: McGraw-Hill*. 379 pp.

[15] Blevins, R. D. (1979): Formulas for Natural Frequency and Mode Shape. *First Edition, Van Nostrand Renhoid Company*, New York, United States.

[16] França Jr, D. O. (2018): Estudo analítico-numérico em vibrações livres fluido-elásticas em cascas cilíndricas para diferentes condições de contorno. *Dissertação de Mestrado em Estruturas e Construção Civil. Publicação E.DM-003A/18, Departamento de Engenharia Civil e Ambiental, Universidade de Brasília*, Brasília, DF, 128 pp.

Proceedings of the IASS Annual Symposium 2019 – Structural Membranes 2019
Form and Force
7 – 10 October 2019, Barcelona, Spain
C. Lázaro, K.-U. Bletzinger, E. Oñate (eds.)

The role of rotational collapse mode and catenary-type thrust lines in the limit state analysis of masonry arches

Orsolya GÁSPÁR*, András Á. SIPOS[a], István SAJTOS[b]

*BME, Department of Mechanics, Materials and Structures
1111 Budapest, Muegyetem rkp. 3, Hungary
gaspar@szt.bme.hu

[a,b] BME, Department of Mechanics, Materials and Structures

Abstract

The result of a minimum thickness analysis of masonry arches based on the principle of thrust line is subject to loading, geometry and stereotomy (brick or stone laying pattern): if the latter is unknown, a range of minimum thickness values becomes available. Present paper applies the Heymanian assumptions regarding the material qualities, notably no-tension, infinite compression and no-sliding, and hence only a pure rotational collapse mode is considered. It is demonstrated that minimum thickness analysis based on the envelope of resultants results a bounding minimum thickness value and ultimately the rotational collapse mode of the arch selects whether it is a lower or an upper bound. It has been shown, that in case of self-load, the thrust line and envelope of resultants coincide for vertical stereotomy: it is denoted here as *catenary-type thrust line*. Next a simple, but effective algorithm is introduced which predicts the corresponding rotational collapse mechanism based on a simplified structural model and the geometric relation between catenary-type thrust line and the reference line of the arch. The applicable list of rotational failure modes for circular arches (found in the literature) subject to their geometry is analytically verified. It is also classified whether they result an upper-or lower bound minimum thickness in an analysis based on the catenary-type thrust line. The practical relevance of the study is illustrated by the revisited analysis of the dome of St. Peter's, Rome by Giovanni Poleni.

Keywords: masonry arch, catenary, thrust line, limit state analysis, rotational collapse mode, minimum thickness, stereotomy, function analysis, envelope of resultants

1. Introduction

The beginning of thrust line analysis of masonry structures (in the modern engineering sense) is marked by Giovanni Poleni's analysis [1] on the stability of the dome of St. Peter's in Rome. Considering that masonry primarily acts in compression, his study was based on Robert Hooke's principle regarding the ideal form of an arch. He compared the geometry of a proportionally loaded hanging chain to the (inverted) section of the dome. By proving, that the catenary would fit within the boundaries of the structure he concluded that the structure was safe, as the thrusting forces would be able to find their way to the supports. His study can be regarded as an early example of present-day minimum thickness analysis of masonry structures (based on limit state analysis as proposed by Heyman [2]), where the minimum thickness required to fully incorporate a thrust line corresponding to the loading is compared to the actual thickness of the structure.

Within the up-to-date framework of minimum thickness analysis however, the distinction between (weighted) catenary [3] and thrust line is important – the relation of the two is subject to *stereotomy* (assumed direction of sections, i.e brick-or stone laying pattern), whereas the envelope of resultants (on the difference to thrust lines see Moseley[4]) can be identified as weighted catenary for arbitrary loading

Copyright © 2019 by Orsolya Gáspár, András Á. Sipos and István Sajtos
Published by the International Association for Shell and Spatial Structures (IASS) with permission.

and geometry condition. Minimum thickness analysis relies on thrust lines. Note that different stereotomies result in different thrust lines (forming family of thrust lines) and hence different minimum thickness values for fixed geometry and loading [5]). It was shown by Milankovitch [6], that in case of self-load, vertical stereotomy results envelope of resultant (and hence the corresponding weighted catenary) and thrust line to coincide, which is labelled below as the catenary-type thrust line. Observing the geometry of the voussoirs on *Figure 1* it is evident, that the actual stereotomy of the dome St. Peter's is different, which would result in a different thrust line and a different minimum thickness value from the same assumed presets. Applying the Heymanian assumptions regarding material qualities this study demonstrates, that since the envelope of resultants bounds the family of thrust lines, an analysis at limit state based on the catenary type thrust line might lead to a bounding value of stereotomy-related minimum thicknesses – however, ultimately the rotational collapse mode of the arch determines, whether it is a lower(a)- or an upper bound(b) (if any, see Section 4). Hence in order to asses, whether Poleni's approach was on the safe side (case b), the rotational collapse mode of the arch has to be determined. Note, that in conjunction with the Heymaninan assumptions (notably no sliding) present study does not consider any other failure mode, for further reading on the subject authors refer to Aita[7].

A widely applicable method for determining a-priori to minimum thickness analysis the rotational collapse mechanism to the symmetrical arch of otherwise arbitrary geometry is (to the authors knowledge) missing. This paper proposes a simple algorithm based on the catenary type thrust line, that predicts the corresponding rotational failure mode of circular arches of constant thickness, subject to self-load. Results are verified by comparing them to the rigorous study of Nikolic [8], who identified the possible rotational collapse modes of circular arches based on an iterative procedure which minimized the thickness of the arch by adjusting the location of the thrust line. The applicability of the proposed algorithm to more general problems is shown in Section 4, when the rotational collapse mode of the dome of St. Peter's is determined, and it is demonstrated that it indeed leads to an upper bound minimum thickness value considering the catenary-type thrust line, hence a safe estimation.

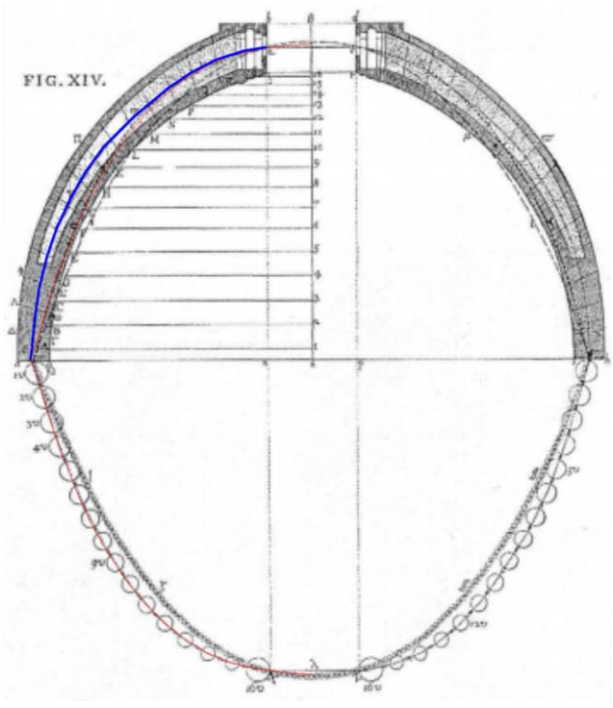


Figure 1. Cross section of the dome of St. Peters, Rome, Note, that *c(x)* (red dashed) is below *r(x)* (blue)

The rest of paper is organized as follows: Section 2 summarizes the goals of the research and describes the structural model applied. The catenary-type thrust line and its relation to other thrust lines is detailed in Section 3. Section 4 first verifies analytically, that the list of possible failure modes provided by Nikolic is complete, then the algorithm predicting the rotational failure mode of circular arches is presented. Rotational collapse modes are identified from those applicable, for which a minimum thickness analysis based on the catenary type thrust line result a lower or an upper bound thickness value. In Section 5 conclusions are drawn.

2. Research goals and modelling

While various studies of past and present aim at determining the *necessary number* of hinges for pure rotational mechanisms of symmetrical arches (5, or in case of pointed arches, 6), attempts to determine a-priori the actual corresponding rotational failure mode to otherwise arbitrary, symmetrical arch

geometry (the necessary starting point of minimum thickness analysis) are scarce. Nikolic's above cited recent study [8] is a partial exception: the failure mode is determined *during* the derivation of the minimum thickness value (based on the *envelope of resultants of the internal forces)*, which result a computationally demanding process. It is to highlighted, that his study offers an interesting new angle, as he demonstrates, that higher number of hinges (7) might formulate at the limit state concurrently than necessary, for special arch geometries. In accordance with the previous, introductory section, the following questions can be formulated:

- Can a simpler, illustrative tool be presented that defines the prospective rotational failure mode of arches prior to minimum thickness analysis, with possible extension to arbitrary arch geometry?

- Since different thrust lines result different minimum thickness values, how stereotomy affects the minimum thickness value obtained based on the envelope of resultants for the rotational collapse modes discussed?

- Was the list of corresponding failure modes provided by Nikolic complete: can it be proven analytically, that 7 is the upper bound number of hinges for circular arches as suggested by the results of Nikolic?

These problems are treated consecutively, based on the following modelling assumptions:

Only symmetrical arches are considered, the analysis is hence carried out on a half-arch and symmetry is accounted for in the constraints. The arch is represented by its axis (*r*), which is chosen to be the center line of the arch (*Figure 2*), parameterized with *x* in a fixed Cartesian system. The loading (self-weight) is assigned to *r(x)* and is distributed evenly according to arc length regardless of stereotomy (see [5] for a discussion on these latter two simplifications). Only twice differentiable (except for the top, e.g. pointed arches) concave functions are considered as *r(x)*. An internal force vector (**E**) and a section (*S*) are assigned for each point of the reference line. The direction of the section is characterized by the cut-angle to the vertical (β), the function $\beta(x)$ is the *stereotomy function* (corresponding to a continuous version of the classical terminology, where stereotomy refers to the stone laying pattern). Note, that an alternate, but related definition of the stereotomy function is possible as $\varphi(\alpha)$ *(Figure 2)*. The *thrust line* (*L*) is defined as the set of points of intersection between lines **E** and *S* (*see Figure 2*).

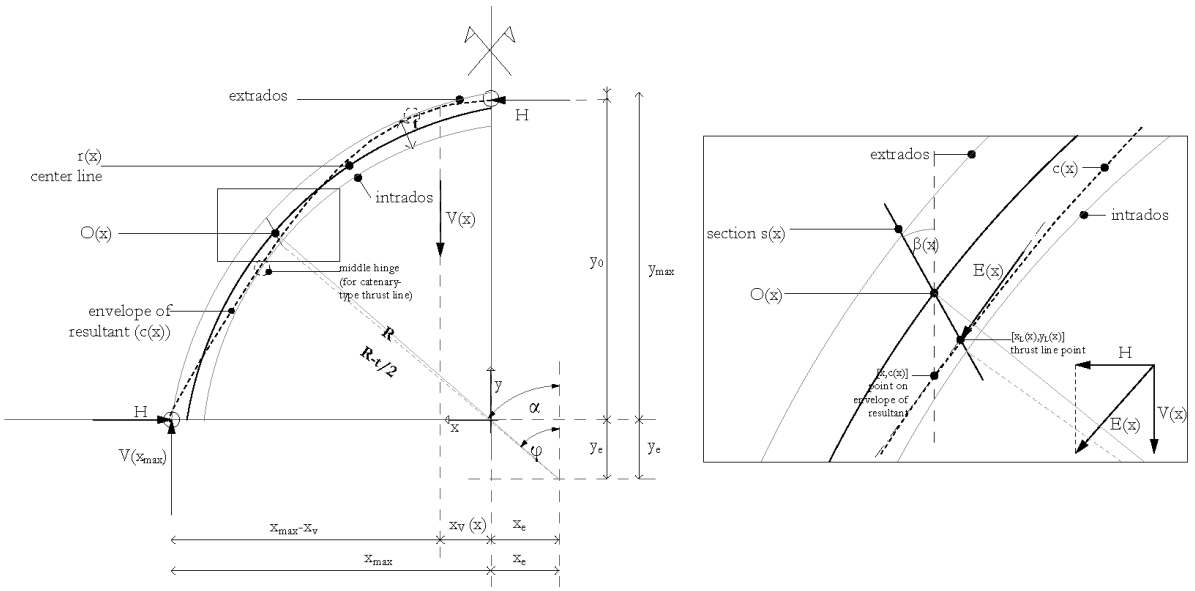


Figure 2. Equilibrium of the circular arch. φ denotes internal angle of intersection of *S* and intrados.

3. Catenary-type thrust line

Genrally speaking, a single minimum thickness value can result from multiple different, admissible stereotomies [5]. The various thrust lines resulting from those stereotomies for the same minimum thickness value form a *family of thrust lines*. Note that as opposed to the infinitely many admissible thrust line in the (amply thick) hyperstatic arch, the family of thrust lines emerge as the solution of a statically determinate problem – but a family also contains infinitely many members. *Figure 3* (top) demonstrates, that the family of thrust lines is always *bounded by the envelope of resultants*, as any thrust line point must lay on a resultant: It is shown below, that the envelope of resultants is a concave function in case of self-load which means, that should a thrust line 'cross' the envelope of resultant, at least one of its points could not lay on a resultant, contradicting its definition. Following the notation of *Figure 2*, the equation of the envelope of resultants (or the catenary-type thrust line) can be obtained based on the vanishing moment as:

$$c(x) = y_0 - \frac{\overbrace{V(x)}^{m(x)}}{H}\big(x - x_V(x)\big), \tag{1}$$

where y_0 denotes the y-intercept of H at the top, and x_v the x-coordinate of the center of mass. The concavity is more clearly illustrated by an alternate formulation:

$$c(x) = y_0 - \frac{\rho}{H}\iint_0^x s'(\eta)\, d\eta^2, \tag{2}$$

where

$$s'(\eta) = \sqrt{(1 + r'(\eta)^2} \tag{3}$$

is the arc length formula. Note that $V(x) = \rho \int_0^x s'(\eta) d\eta$, where ρ is the unit weight.

Reversing the problem-set up: based on the catenary-type thrust line, for specific rotational failure modes, it is possible to define a bounding value minimum thickness for arbitrary arch geometries, but as discussed before, the corresponding rotational collapse mode selects whether it is a lower or an upper bound. Two typical examples are illustrated in *Figure 3*, top: both correspond to a 5-hinge mechanism, but the left one is type (1) and the right one is type (2), respectively. Points of the thrust line should lay above or on the envelope of resultants, hence it is easy to see, that while for type (1) the envelope of resultant results an upper bound minimum thickness (other stereotomies would result thrust lines not even reaching the intrados), for type (2) the opposite is true, a lower bound is defined.

4. Rotational collapse modes of circular arches

Nikolic identifies 4-types of failure modes in his paper, see *Figure 6*. In addition to 5-hinge type (1) and (2) also 6-hinge and 7-hinge. Without further explanation, it is possible to map the admissible stereotomies for a single minimum thickness value for mechanisms 5-hinge type (1), (2) and 7-hinge (see *Figure 3*), based on the findings of [5]. These diagrams illustrate the necessity of the 5-hinge mechanisms leading to bounding values, whereas it can be deduced, that the 7-hinge type is a special case, which obtains a single minimum thickness value regardless of the stereotomy. The 6-hinge mechanism however requires further analysis in the future, for it does not result a hinge at the top, and hence represents an indeterminate (geometrically) problem for given *r(x)* functions, as opposed to the others. Creating a similar diagram of admissible stereotomies for it is therefore not straightforward.

In order to asses, if the list provided by Nikolic is complete, we show analytically, that at the limit state in a circular arch no more than 7 hinges might formulate simultaneously (note, that it is not investigated whether all hinges would be 'activated' during failure at this stage). We define a deviation function (*d(x)*) as the difference between the center line *r(x)* and the catenary-type thrust line *c(x)*:

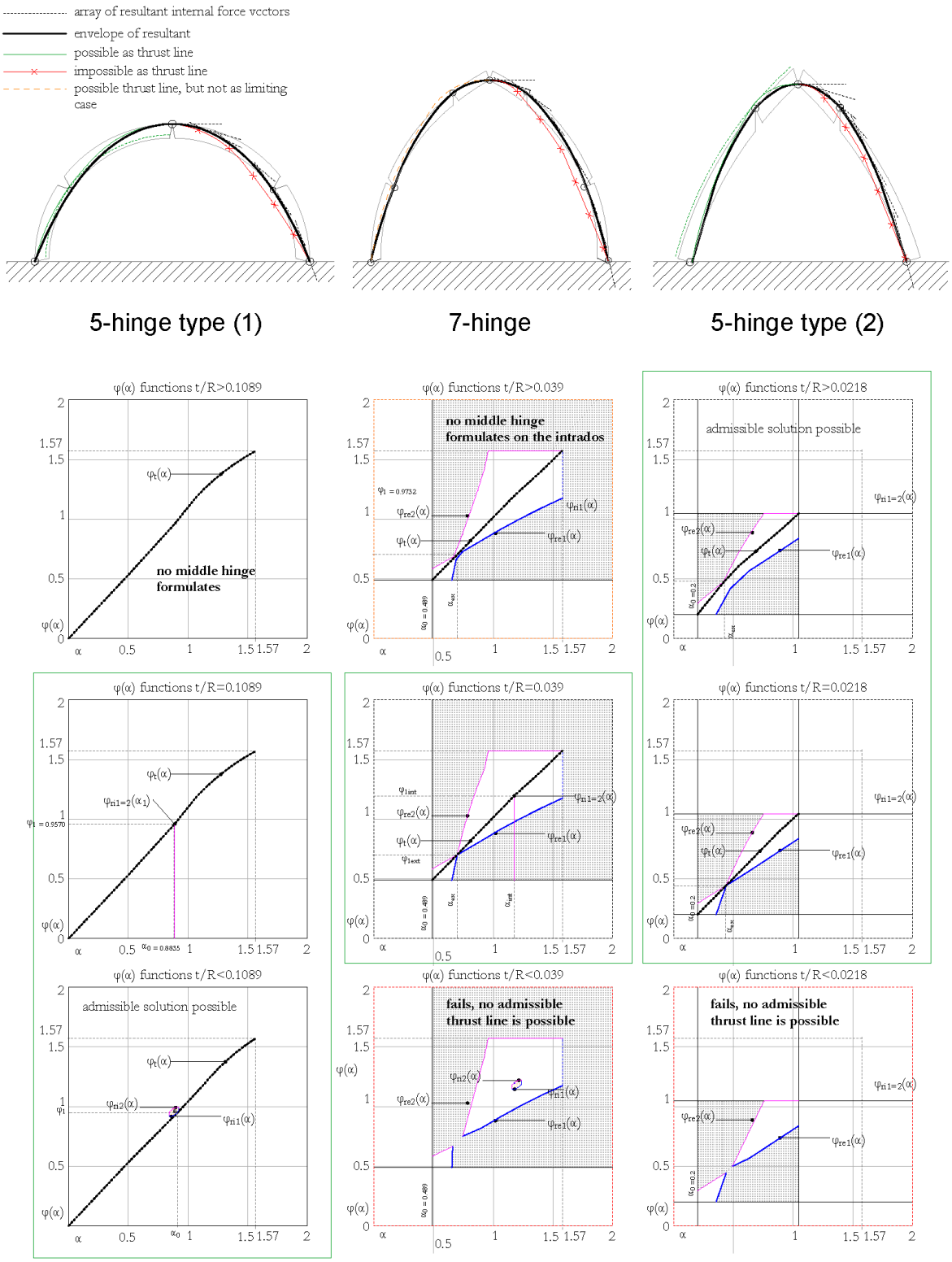


Figure 3. Top: Catenary-type thrust line (envelope of resultants) bounds the family of thrust lines.

Below: Effect of stereotomy on the minimum thickness value of circular arches derived considering the catenary-type thrust line for 5-hinge type(1), 7-hinge, and 5-hinge type(2) failure modes, for the derivation of the diagrams see [5]. The minimum thickness corresponding to the catenary type thrust line is shown in the middle, the effect of raising or reducing the thickness is depicted above and below, respectively. Green frame marks the admissible solutions.φ_t denotes the thrust line, φ_r is the function that bounds the admissible range

$$d(x) := r(x) - c(x). \tag{4}$$

Let n be a positive integer. If there are n local extrema of the deviation function (possible locations of the hinges), there must be (n-*1*) points of inflection between them. Hence, the number of hinges $k \leq 2*(n)+p$, where p is the number of hinges at the top and springing, for in general, they do not correspond to local extrema of $d(x)$ (see *Figure 4*). The number of inflection points is simply the number of points at which the second derivative vanishes, hence we aim to determine the zeros of the following equation:

$$d''(x) = r''(x) - c''(x) = 0. \tag{5}$$

The equation of the reference line for a pointed arch, made of unit circle,

$$r(x) = \sqrt{1 - (x + x_e)^2} - y_e, \tag{6}$$

where x_e and y_e denotes the shift of the vertical and horizontal symmetry line respectively from the axis of the circle (resulting pointed arches, see *Figure 2*). The general equation of the envelope of resultants is obtained in Eq 2. Note that we do not consider failure modes that does not produce hinges at the springings: for y_e can be any value in the range [0,1], otherwise the results would be redundant. Eq (5) can then be formulated as (based on the first and second derivatives of Eq (6)

$$-\frac{1}{\sqrt{1 - (x + x_e)^2}} \underbrace{\left(\frac{1 + \frac{\rho}{H} - \frac{\rho}{H}(x + x_e)^2}{1 - (x + x_e)^2} \right)}_{=0} = 0, \tag{7}$$

hence it follows that

$$x = \pm \underbrace{\sqrt{\frac{1 + \frac{\rho}{H}}{\frac{\rho}{H}}}}_{h} - x_e. \tag{8}$$

For x_e is a non-negative scalar, Eq (8) results maximum ***one positive root*** (n-*1*$\leq$*1*)for x. There are no positive roots, hence no points of inflection if $h < x_e$, which is the case for highly pointed arches. Hence $n \leq 2$. Now three cases can be distinguished (see *Figure 4*):

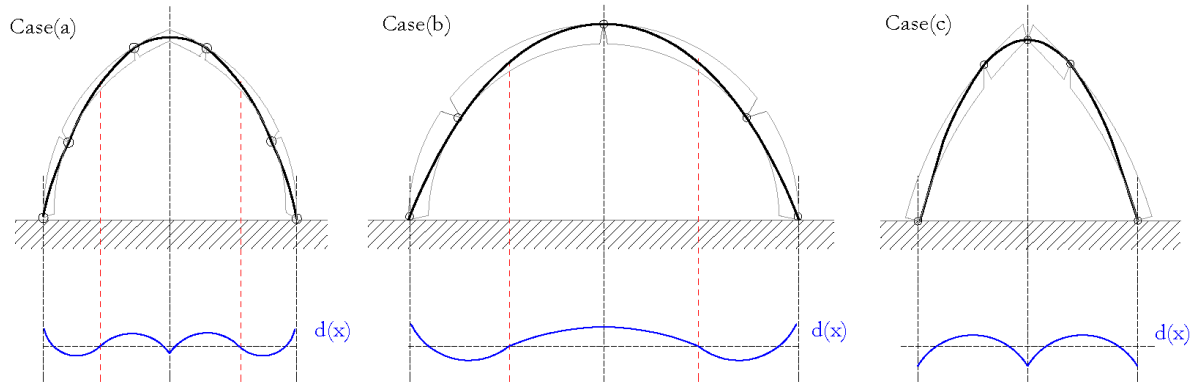


Figure 4. Number and location of inflection points on *d(x)* for circular arches, three cases

for Case (a), $n=2$, p=[2;3], $k \leq 2*2+3 = 7$. This proves, that in a circular, concave arch, a maximum of 7 hinge can formulate. Note, that the most typical arrangement of case (a) however is the 6-hinge

mechanism, when at the top the thrust line does not reach intrados. Case (b) should be treated as a special case of case (a): n=2, but one of the local maxima is located at the top, hence the formula for k modifies to k=2*n+p-1=5, (p=2) for the hinge at the top was counted twice. This leads to 5-hinge mechanism type (1). Case (c) is where n=1, p=3 k= 2*1+3=5, leading to 5-hinge mechanism type (2)

4.1. Numerical procedure for the prediction of the failure mode of circular arches of constant thickness

The prediction of the location of the plastic hinges is implemented in MATLAB, the schematic steps of the algorithm are summarized below, see *Figure 5* also. The procedure predicts the actual collapse mode by the analysis of the *d(x)* function (see previous section) of a circular arch. It accepts the *r(x)* function as input arch geometry. Note, that the initial, hyperstatic problem is substituted with a 3-hinge arch. Hinges are assigned to the reference line at the top and the springing, for their true location is not known a-priori the definition of the failure mode. This results an approximation, which is accounted for at the evaluation of the results by the feedback-parameter 'devhinge: ranging from 0 to 1, the larger devhinge is, the more reliable the result. Steps of the analysis are summarized on *Figure 5*. Based on the predicted failure mode, minimum thickness analysis is carried out (based on the catenary-type thrust line), selected results are shown on *Figure 6*.

Note, that the left branch of the algorithm offers an important insight, which is rather easily generalized for arbitrary geometry: if *c(x)* does not cross *r(x)* at all, the failure mode can be determined with certainty: should *d(x)* be positive, it is 5-hinge type (1), else type (2). For the case of the dome of St. Peter's (*Figure 1*): The relation of catenary-type thrust line (*c(x)*, red) and reference line (*r(x)*, blue) suggests a 5-hinge type (1) failure mode, for *d(x)* is positive. In this case, the minimum thickness analysis based on catenary-type thrust line results an upper bound, proving Poleni's intuition.

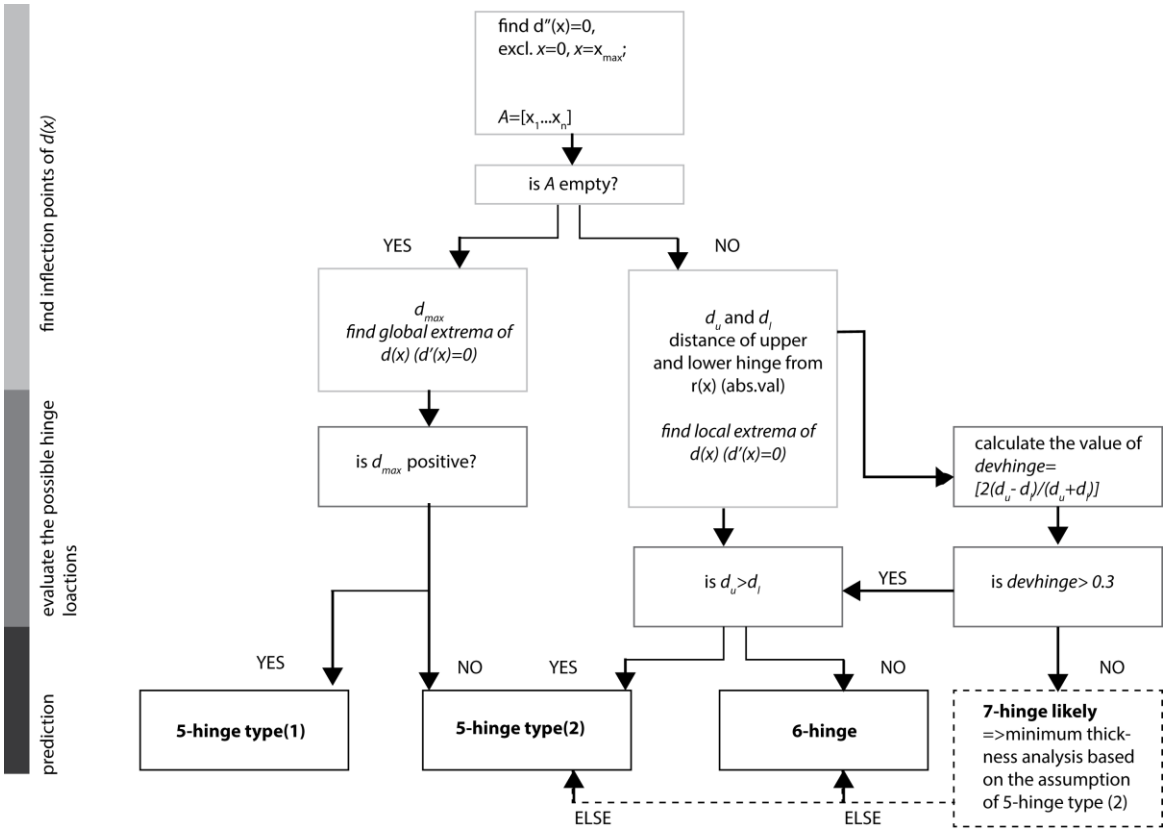


Figure 5. Function scheme of the proposed algorithm

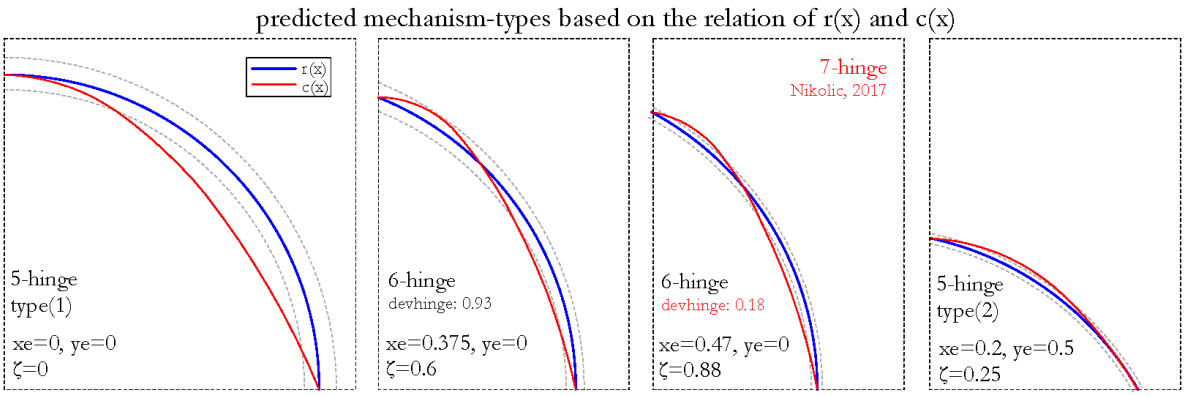


Figure 6. Hinge number and arrangement prediction –the derived results are in good agreement to those in [8]

5. Conclusion

Based on the Heymanian assumptions of limit state analysis this paper aims at determining the corresponding rotational failure mode of arches based on their geometry and loading (eminently self-weight). The previously [8] suggested applicable list of rotational failure modes is analytically verified for circular arches. A novel, simple numerical algorithm is presented that predicts the arrangement of hinges at the limit state based on the analysis of the deviation function (*d (x)*), which relates the reference line and the envelope of resultants (or catenary-type thrust line) of the arch. The results are verified against those present in [8]. It is highlighted, that minimum thickness analysis based on the catenary-type thrust lines leads to a bounding value minimum thickness, and the rotational failure mode is identified for which it results an upper bound. Potential of generalizing the method for arbitrary symmetrical arches was supported by revisiting Poleni's analysis of the dome of St. Peter's.

Acknowledgements

The research was supported by the NKFIH Grant 124859 and the FIKP grant of EMMI in the frame of BME FIKP-VÍZ.

References

[1] G. Poleni, *Historic Memories about the Great Dome of the Vatican Church*. Synoptic translation edited by Alessia Bianco. Rome: Aracne, 2015.

[2] J. Heyman, "The safety of masonry arches," *International Journal of Mechanical Sciences*, vol. 11(4), pp. 363-385, 1969.

[3] R. Osserman,. 2010. Mathematics of the Gateway Arch. *Notices of the AMS*, 57(2), 220-229.

[4] H. Moseley, On the theory of the arch. In: *The theory, practice and architecture of bridges*, ed. J. Weale.London: Architectural Library, 1843.

[5] O. Gáspár, A. A. Sipos, and I. Sajtos, "Effect of stereotomy on the lower bound value of minimum thickness of semi-circular masonry arches", *International Journal of Architectural Heritage* pp. 1-23., 2018.

[6] M. Milankovitch, Theorie der Druckkurven. *Zeitschrift für Mathematik und Physik* vol. 55, pp.1-27, 1907.

[7] D. Aita,R. Barsotti, S. Bennati, Looking at the collapse modes of circular and pointed masonry arches through the lens of Durand-Claye's stability area method. *Archive of Applied Mechanics*, pp. 1-18, 2019.

[8] D. Nikolić, "Thrust line analysis and the minimum thickness of pointed masonry arches", *Acta Mechanica,* vol. 6 (228), pp. 2219-2236, 2017.

Proceedings of the IASS Annual Symposium 2019 – Structural Membranes 2019
Form and Force
7 – 10 October 2019, Barcelona, Spain
C. Lázaro, K.-U. Bletzinger, E. Oñate (eds.)

A new approach to free form wooden shell structures using helical cuts

* Peer HALLER, * Marzia CALVARESE

*Technische Universität Dresden
Institute of Steel and Timber Construction
peer.haller@tu-dresden.de

Abstract

The paper gives a comprehensive review of wooden shell structures beginning from the twenties of the last century. It presents a typology by focussing on design aspects like shapes, textures, connections, executions and materials. Based on this typology advantages and disadvantages of different designs are being discussed.

The main emphasis lays on the design of an innovative free form wood structure that uses traditional joining techniques with compressed wood dowels instead of adhesives and metals.

This approach results from the research project "adhesive free timber buildings (AFTB)" financed by the European Commission within the Interreg framework.

The concept is part of AFTB and consists in cutting helical lamellas from a tree stem. In this way a stack of twisted boards can be bent in any direction to form a grid-like shell structure.

The form finding process of the structure begins with an artistic artwork from thin cardboard strips, digitalized by means of photogrammetry, then turned into a parametric model and scaled up thereafter. This parameterization has two objectives: The first is to retrieve the spatial target shape from a straight cylinder (stem); a deployment function is therefore introduced enabling the target spline to unfold progressively, so that it can be rectified. The second is to control the critical curvature which is limited by two factors: first the strength reduction across the grain due to the helical cut and second the mechanical stresses due to the subsequent bending of the twisted board into the spatial target shape. In this case a genetic algorithm in Python and Grasshopper is implemented, to determine the critical curvature.

In addition, bending tests on helical cut lumbers and connections are carried out. The minimum radius is compared with the critical radius and, if necessary, the shape may be adjusted and corrected. Final goal is the realization of an innovative demonstrator.

1. Introduction

In this research project, a target form has to be reached through the parameterization of the reference model and its subsequent monitoring to conduct eventual adjustments. In this way, the form finding principles are subverted and the concept of attaining the target-shape takes hold. The optimization process comes into play later, once the target form is reached.

The selected material is wood, which offers almost unlimited design potential. Wood is an aggregate of cells, it is a composite of a chemical complex of cellulose, hemicellulose and other ingredients, which are cemented together by a substance called lignin (a glue-like protein that holds the cellulose fibres together). Wood's lack of isotropy lies in that its strength properties varies along its different axes. It is strongest when loads induce stress parallel to grain, either in tension or compression. However, this

Copyright © 2019 by <substitute here the name(s) of the author(s) or individual(s) claiming copyright>
Published by the International Association for Shell and Spatial Structures (IASS) with permission.

circumstance is not always conceivable and loading perpendicular to grain may be accomplished in a satisfactory manner. [1]

The conceptual idea of the project originates from studies of design examples of structures having elements with irregular cross-section and, more specifically, helical. The most eloquent example is the proposal of "Groove", a pavilion designed by Innochain for Tallinn Architecture Biennale 2017 competition. The twisting, bifurcating elements have been tested and developed with physical prototypes as well as with a digital parametrization. The three-dimensional spaceframe-like structural scheme is organized as a self-supporting 'grove' of laminated timber elements which bifurcate and interconnect. [2]

The wooden element is helically cut and then bent in order to reach the target shape. The target form consists of several elements, each of which is subjected to individual analysis. The effect of cutting and bending is reproduced by means of a parametrization of each element constituting the overall design.

2. Overview of design parameters

2.1. Helical cut

Given that a proposal of this work concerns the attempt of bending a lumber that comes out from a helical cut (Figure 1), this paragraph is focused on the estimation of the reduction of stiffness in the lumber due to a cut which is not parallel to grain.



Figure 1: Helical cut of a lumber

Actual standards don't provide specific factors to establish the strength reduction of the helically cut wood. It is therefore taken into account the resistance reduction factor for a compressive stress for a given angle. According to DIN 1052: 2004-08, the resistance offered by a wooden beam subject to compressive stresses at an angle α comprised between $0° < \alpha < 90°$, should met the condition (1):

$$\frac{\sigma_{c,\alpha,d}}{k_{c,\alpha} \cdot f_{c,\alpha,d}} = 1 \tag{1}$$

Since the geometric definition of a helical cut presupposes the presence of two angles related to each other; both relations should be met (2):

$$\begin{aligned} k_{c,\alpha} &\geq \frac{\sigma_{c,\alpha,d}}{f_{c,\alpha,d}} \quad k_{t,\alpha} \geq \frac{\sigma_{t,\alpha,d}}{f_{c,\alpha,d}} \\ k_{c,\beta} &\geq \frac{\sigma_{c,\beta,d}}{f_{c,\beta,d}} \quad k_{c,\beta} \geq \frac{\sigma_{c,\beta,d}}{f_{c,\beta,d}} \end{aligned} \tag{2}$$

The wood transformation, as previously stated, is automated thanks to a collaborative robot (Robotmob) furnished by i-max pro, which is able to move on a track.

This robot should receive and implement information regarding the track to be conceived. This information will be provided after establishing the parametric model and its construction curves (which constitute the rails).

2.2 Wood bending

In harmony with its surrounding circumstances that directly affect its growth, timber is characterized by its substantial behavior, being possible to achieve a certain radius of curvature and getting back to form with the removal of constraints. The former property is known as flexibility, the latter as elasticity. [3] The steam bending of wood was already known in ancient Egypt. In the bending process developed by master carpenter Michael Thonet in the first half of 1900s, the lumber, heated up to 100° C, was stretched onto a shaped steel band so that it couldn't move longitudinally, causing it to buckle on the inside when bent. This technique made it possible to reach very small radii. The steel strip after bending also served as a mold for drying the bent timbers. [4]

When the thickness of the work-piece and the radius of curvature have a significant value, hot bending with supports should be performed. Supporting straps - usually made of mild, spring, or stainless steel - are indeed necessary to prevent fractures occurring on the elongated convex face.

Comparison of results of tests by adopting the hot bending techniques for beech woods are summarized in Table 1.

Table 1: Limiting Radii of Curvature of Beech species in Steam Bending (Air-dried steamed 25 mm thick)

Species		**R/S**	
Standard name	**Botanical name**	**Supported by a strap**	**Unsupported**
Beech, European (Danish)	*Fagus sylvatica*	**1,7**	**14,5**
Beech, European (Rumanian)	*Fagus sylvatica*	**1,6**	**16**

To estimate the value of endwise-compressibility e_c, as approximate index of bending quality, it is possible to calculate the radius of bending with an expectation that 50% of the bends will be successful. At the Forest Products Laboratory endwise-compressibility tests were carried out on 2-by 3-inch specimens steamed at atmospheric pressure for 40 minutes, with a moisture content of 25% to 30%. The specimens were placed between the plates of a hydraulic press and compressed until failure occurred. Table 2 gives endwise-compressibility values determined by this method. [4] Unfortunately, the Table doesn't provide a specific value for Beech wood.

Table 2: Average endwise compressibility value for different wood species

Species	**Average endwise-compressibility value (inch per inch)**
Red oak (Winsconsin)	0,354
Paper birch	0,287
Overcup oak (southern)	0,258
Winged elm	0,251
White oak (Ohio and Kentucky)	0,250
White oak (Winsconsin)	0,246
Yellow birch	see white oak (Winsconsin)
Sweetgum	0,172
Black willow	0,101
Eucalyptus (Chile)	0,071
Coigue (Chile)	0,057
Sitka spruce (1)	0,015
(1)approximate value	

In order to estimate the minimum bending radius at which successful bends can be expected in 50% of pieces per stock of a given thickness, the average endwise-compressibility value can be used in the following formula (3):

$$r = \frac{h(1 - e_c)}{e_t + e_c} \tag{3}$$

Where r is the radius of the form, h is the thickness of the piece, e_c is the compressive strain, just before failure, inch per inch, considered positive, e_t is the tensile strain associated with e_c, inch per inch, considered positive. Where an efficient strap and end blocks are used, e_t tends to zero. [5]

Assuming an average endwise-compressibility value (inch per inch) of about 0,3 for beech tree, this value can be used in the aforementioned formula (3). Having achieved factors that take into account the strength reduction due to the helical cut, a decrease experienced by the critical radius is observed (Figure 2).

The derived values can be used to verify whether parts of the target beam provide excessive curvature, in order to reparametrize the subdomain of the overall function and provide a new attainable form. This step can be easily monitored with parametric software, such as Grasshopper™, as successively reflected (see Paragraph 3).



Figure 2: Bending of a lumber subjected to helicoidal cut

2.3 Joints

In a project, joints are considered as structural elements, helping to withstand the loads and providing significant contribution against tension, compression, racking and sheer. Interlocking joints supply, through friction, a strength that is not entirely based on glue or bolts.

Wood joinery is thus one of the most common aspects of wood-working. Based on the project, a various number of joints in his arsenal arise from different types of wood joinery. The simplest method consists of merely gluing two pieces together, which means to entrust all the task of connective work to an adequate adhesive. Interlocking parts between pieces, like rabbets and dadoes, could on the other hand

contribute to the connection. Some joints fit together with a third wood member, which, depending on the adopted technique, may be called biscuit, spline or dowel. [6]

The present research project deals with designing connections between the various timber elements without the use of glue or metal elements. For this purpose, wooden bolts subject to pre-compression are used.

3. Design and digital reconstruction

The conceived form (the so-called Wolkenring), is realized through a cardboard scale model (Figure 3), which is then scanned for the purpose of a digital reconstruction, thanks to the use of the photogrammetrical survey (Figure 4).



Figure 3: Wolkenringe, Birgit Schuh

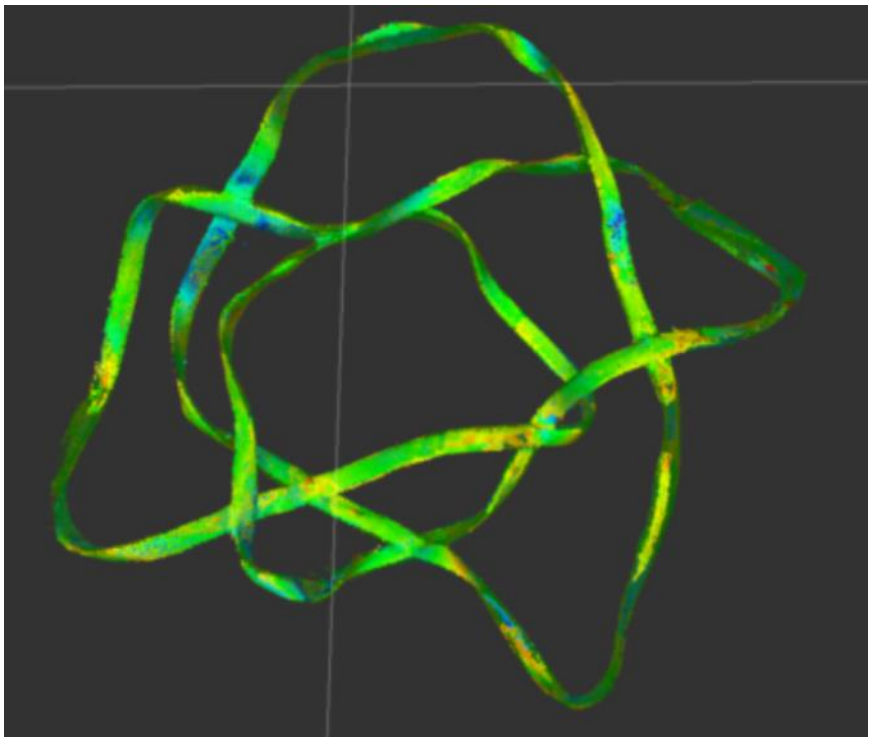


Figure 4: Cloud point obtained in Autodesk Recap

The edges of the ring-structures are rebuilt with lines, which are in addition reconnected by transversal segments, in order to establish the gravity centre of the local cross section (Figure 5).

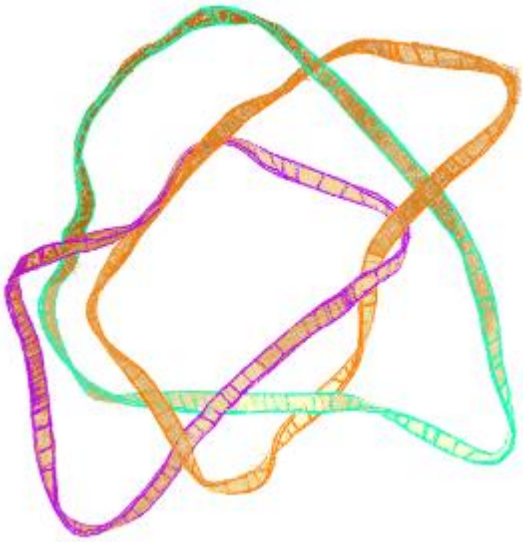


Figure 5: Reconstruction of border segments from the point cloud

These new inner points defined are then reconnected through third-degree Bézier splines, building the axial curved beams to which, after being split into defined subdomains, a local cross section has to be assigned.

3.1. Algorithm's development

The achieved Bézier splines are now ready to be read into the designed Grasshopper™ algorithm. For the sake of brevity, only the creation of the first segment is showed.

Every single Bézier curve is split into two pieces, so that the length of the entire beam is obtained and a straight element related to the target curve is reproduced. Each segment is oriented according to an arranged direction, that is given by the vector geared from the start to the end point.

It is now necessary to fix a start point where the linearized function (made up of the list of segments) can take place. This point is positioned in a mid-position, although this choice does not apply as a general rule, because disregarding the global form could be risky, in the interest of avoiding recursive points.

At this point, each element belonging to the whole function has to be divided into smaller pieces (Figure 6-a). The parameterization made up with Grasshopper allows to set a range slider which can be changed at any occurrence (adding or diminishing the number of divisions). The same splitting has to be done for the linearized curves, belonging to each portion and constituting a straight segment of the same length of the whole starting function.

The splitting is done – always by making possible the control of the number of partitions via sliders – in order to reconnect each corresponding point through lines of variable length.

Each line in turn has to be split (Figure 6-b) and each end point of the new small pieces is reconnected, so to obtain intermediate curves. The more the new intermediate curves are in close proximity with the original curves (the starting function or the linearized one), the more their length approximates the initial amount (Figure 6-c). This step allows to generate an animation of opening up of the starting function, also called the target curve (Figure 6-d).

The next step is to proceed with the attribution of mid-cross-sections, with a view to perform an uneven twisting trend. In the first place it is necessary to reparametrize the whole function and the intermediate curve itself, so that any point in the curve can be described by a parameter comprised in the interval $0 \leq x \leq 1$. The re-parameterization allows to describe a point on the generic starting function with a related point on the intermediate curve, that, in turn, degenerates on the linearized one.

More domains can be provided so that the cross-section orientation variability may be increased and, consequently, the subsequent randomized torsion, which is achieved through the aforementioned helical cut (Figure 6-e).

For each sub-domain a corresponding end cross-section with a given angle of orientation should be implemented; these sections constitute the halfway geometries distributed along the two rails (the curve itself and the linearized one), in order to build two related sweeps on their own respective rail (Figure 6-f, Figure 7).

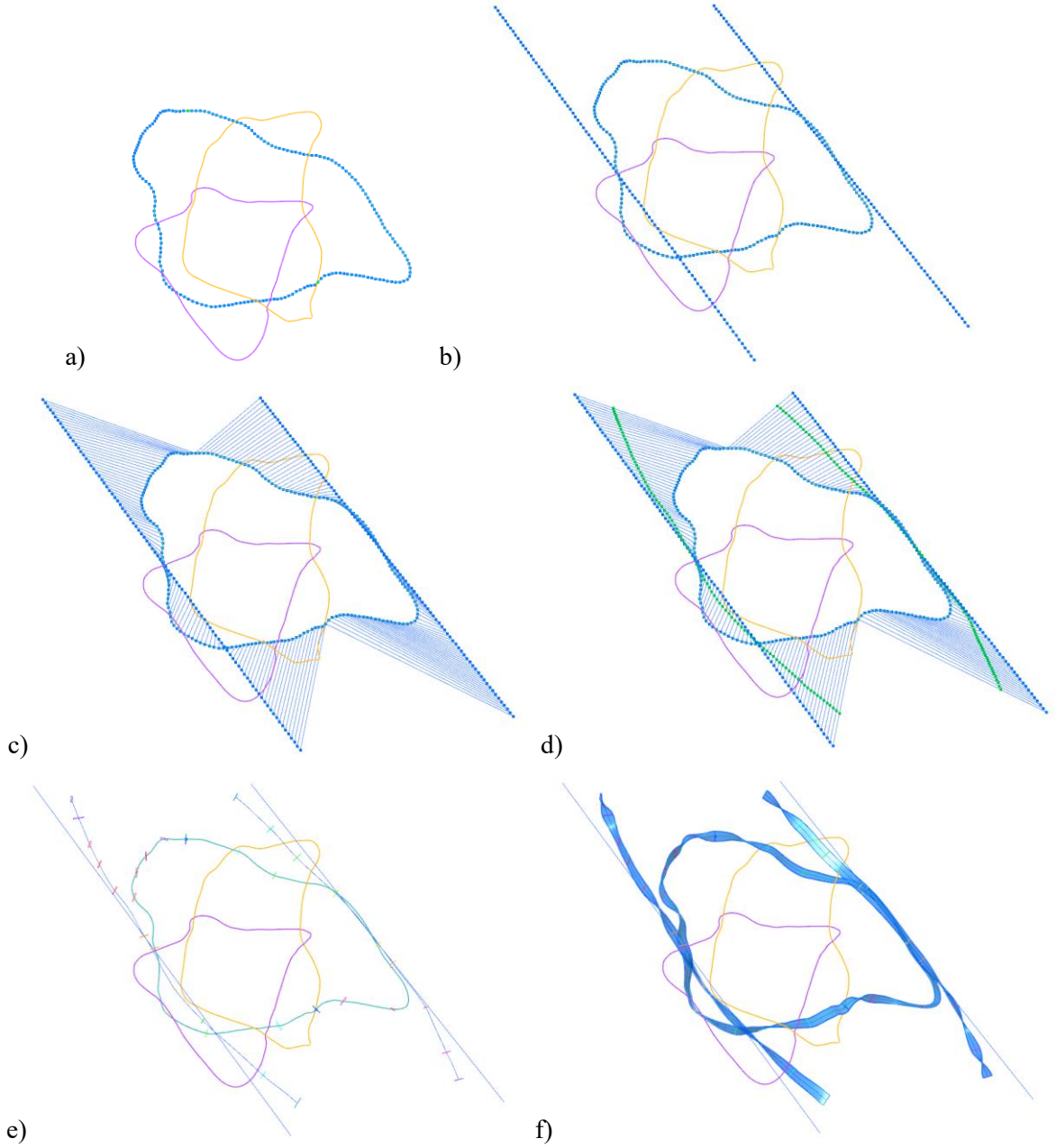


Figure 6: a) Split of the string into smaller pieces; b) Generation of two straight lines of equal length; c) Connection of the corresponding points; d) Construction of a simultaneous curve that reproduces the deployment of the half-string; e) Allocation of the cross-section at the end of each sub-domain; f) Generation of the 3D-Model (one-rail-sweep)

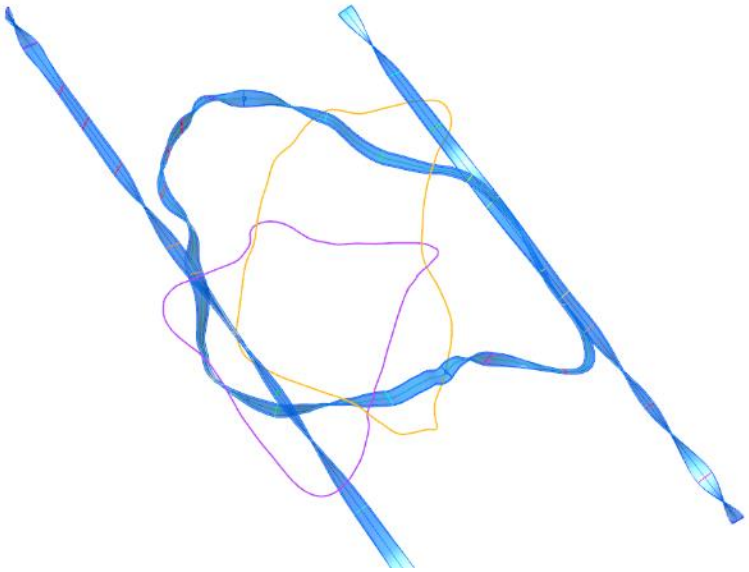


Figure 7: Final outcome by reference to the target open-up straight line

This approach may also allow the control of the cross section of the trunk, from which the original shape is sawed off (Figure 8).

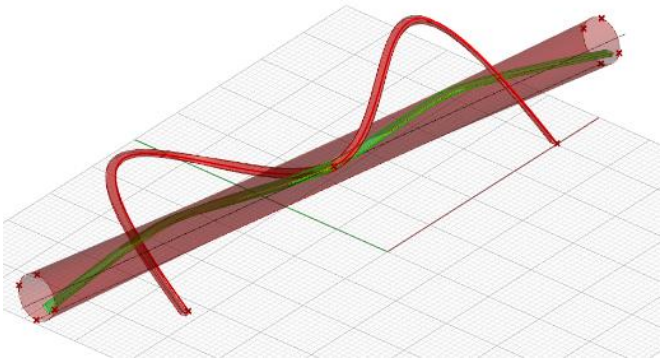


Figure 8: Generic function modelled in Rhinoceros. Step 7: trunk´s diameter correlation

The final product has to be monitored with a view to prevent an exceeding of the limit value for critical radius and thus for curvature.

In order to find out the minimal fitness function experienced by the examined curve, Galapagos genetic algorithm is adopted. In a genetic algorithm, a population of candidate solutions to an optimization problem (where "to optimize" means, in this case, the individuation of the lowest value) is evolved toward better solutions. The Genome function is assigned to the slider controlling the parameter t describing a generic point on the curve and the fitness function is given to the corresponding resulting radius. Is therefore detected each critical point along any ring of the whole structure and an eventual reduction of curvature is foreseen.

Small pieces tests are hence carried out, checking whether the bending can be performed or a reduction of the radius is needed.

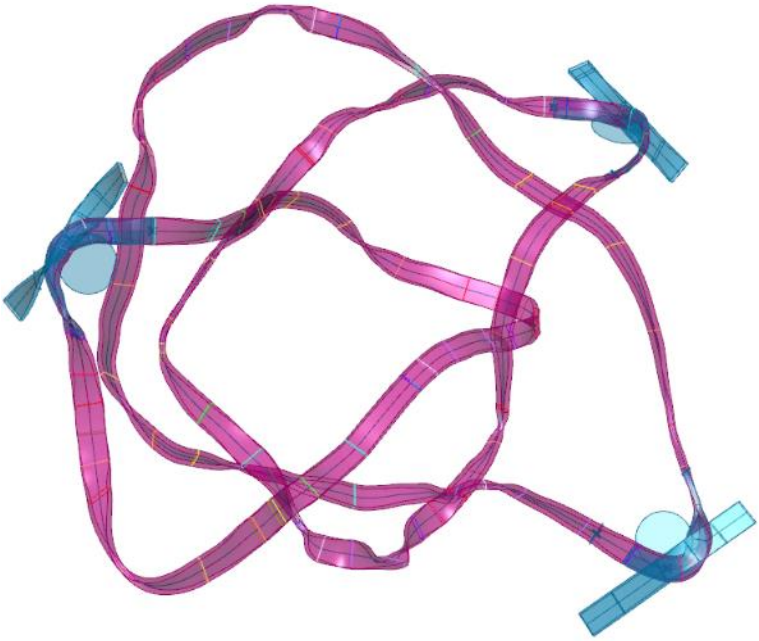


Figure 9: 3m-lenght elements with maximal curvature are grossed up and linearized

The design algorithm is also tested in a small 3d printed model beginning with the straight pieces and then proceeding with the bending.

After preparing of the substructure to control and facilitate the curvature to be achieved (Figure 10), an hot-bending of the thermoplastic pieces is provided.



Figure 10: Printed result

4. Full-scale model

The elements resulting from the algotithm described in Paragraph 3.1 are then imported as separate data to i-max pro robot, that perform the helical milling to full-scale elements. The bending phase is carried out at a subsequent stage, where achieving the target curvature and thus the target form is the final purpose. In this context it shall be investigated whether the minimum radius does not lead to failure of the test pieces.

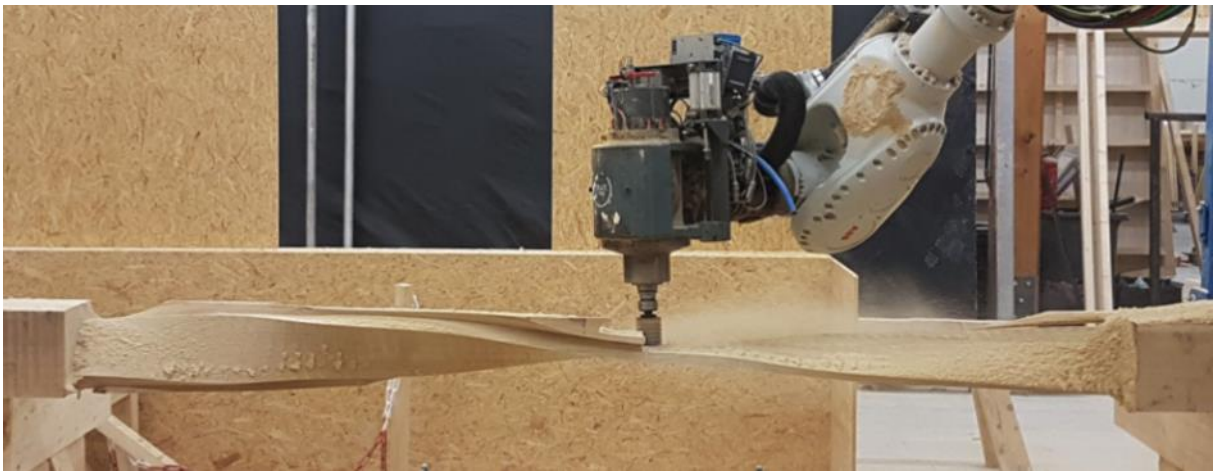


Figure 11: helical cut of a full-scale timber element

Bending tests on helical cut lumbers will be carried out, for the purpose of comparing the minimum radius with the critical radius and, if necessary, adjusting and correcting the target shape.

5. Conclusion

The present work shows an innovative purpose of designing a pioneering timber structure, by taking advantage of experienced tests, material limits and norms, and the multilateral development offered by a parameterization.

The demonstrator planned will showcase the use of adhesive free products in an innovative wood structure and is full-size adhesive free laminated timber structure. The demonstrator will be monitored for ten years after the project with the data to update and strengthen the design guidelines developed during project.

The development of the script, in order to obtain a deployment line, which constitutes the departure point for the information to be furnished to the robot, in charge of either cutting or milling the trunk following a random helical direction. The resulting lumber shall be subsequently bent in accordance with the target form to be achieved. A concrete acknowledgment of the script is made with a 3D-Printing process, which shows, tangibly, if the algorithm operates in a proper manner.

The final product has to be monitored in order to avoid an exceeding of the limit value for critical radius and thus for maximum curvature. In this respect, thanks to the use of a genetic algorithm, minimum radius values shall be detected and, secondarily, tests will be conducted for these specific portions of structure, since results for lumbers, subject to this special cut, which is not parallel to grain (which implies a reduction of strength), and then to a bent, are still not available in the literature.

References

[1] *Wood structural design data*, American Forest & Paper Association, 1986 Edition with 1992 Revisions

[2] http://innochain.net/tallinn-architecture-biennale-2017-folly-competition/

[3] *Bent Timber Ships and Universal Wood Bending Machinery: Two Prize Medals Awarded at the International Exhibition*, Philadelphia, 1876

[4] Barbara Glasner, Stephan Ott: *Wonder Wood: Holz in Design, Architektur und Kunst*, Walter de Gruyter, 30 gen 2013

[5] Agriculture Handbook No. 125, *Bending Solid Wood to form*, U.S. Department of Agriculture, Forest Service, Packaging Research Division, 1957

[6] Creative Publishing Editors, *Black and Decker The Complete Guide to Basic Woodworking: Skills and Projects Every Woodworker Needs*, Quarto Publishing Group USA, 2005, 304 pages

Proceedings of the IASS Annual Symposium 2019 – Structural Membranes 2019
Form and Force
7 – 10 October 2019, Barcelona, Spain
C. Lázaro, K.-U. Bletzinger, E. Oñate (eds.)

Architectural ceramics influenced by structured materials

Dana SAEZ*, Juan MUSTO*, Martin TRAUTZ*

*RWTH Aachen University, Faculty of Architecture, Chair of Structures and Structural Design
Schinkelstraße 1, 52062 Aachen, Germany
saez@trako.arch.rwth-aachen.de

Abstract

The possibility of using digital processes to develop and deploy individual, prototypical and shape-optimized structures motivates architects to explore the use of Additive Manufacturing (AM) and its formal and structural capabilities. Although the AM with materials like polymers and concrete have been intensively explored, these results cannot be directly transferred to other traditional contruction materials like ceramics because of a different physical behavior. This paper proposes to explore formal and mechanical properties of ceramics in order to improve its structural performance for innovative applications in architecture. Furthermore, structurally efficient cellular configurations are investigated due to its resource performance. Case-studies are presented in order to re-interpret them in analog 3D-printed structures, so called 'structured materials' in nature (namely honeycomb-like, foam-like, sandwich panels). After the analysis of the case-studies, the methodology involves computational models in order to achieve a family of customized possible design solutions. With the digital workflow this research attempts to optimize the final designs by reducing material and weight, while increasing structural integrity.

Keywords: conceptual design, morphology, optimization, digital fabricarion, aditive manufacturing, architectural ceramics, structured materials.

1. Introduction

1.1 Potential of additively produced ceramic components

In general, Additive Manufacturing (AM) techniques allows the production of customized solutions for specific design requirements. Since we understand that this particular feature has a great industrial potential, we decided to explore the application of AM tools with a traditional building material, in our case, ceramics. In an ongoing collaboration with the Chair of Artistic Design at RWTH [4], we organized a Seminar [5] where we explore AM with ceramics, more specifically Fused Deposition Modeling (FDM) [6]. This time, the 3D-printing technique we used is not actually 'fused' because of the use of ceramics as printing material, but, as well as FDM materials (e.g. PLA, ABS), the main constrain is the one-way or single deposition.

AM redefines the use of ceramics in architecture itself. It allows multi-functional applications for new uses and functions of this versatile material, while enhancing free-form geometries, flexible interlocking and new performative and structural characteristics. In other words, AM enables processes and production of ceramics in a new way facilitating the designer to forego the use of standardized modular systems. That is why, one of the goals of our Seminar [5] is to design load-bearing column modules which embrace the variability of the material within the deposition process. Considering the structural behavior, computational approach or even fabrication issues, these approximations will be presented under the Methodology description (see 3.1, 3.2).

Copyright © 2019 by Dana SAEZ, Juan MUSTO, Martin TRAUTZ
Published by the International Association for Shell and Spatial Structures (IASS) with permission.

1.2 Current issue with ceramics AM

The main issue about implementing ceramics as a deposition material within the AM techniques is that this material is formally and performatively limited. One of the distinctive characteristics of ceramics is its shrinkage rate which is highly influenced by the design-shape (d1> d2, d3) and fabrication (liquid- or plastic-stage) [1]. This special feature influences the structure in such a way that it is exposed to multi-axial stresses and deformations depending, among others, on the manufacturing process.

Another limitation regarding the production is the manufacturing-time itself. In order to achieve cost-effective ceramic modular fabrication, we explored different designs by reducing the amount of material (e.g. avoiding the use of the so-called support structures) and time-consuming fabrication steps (e.g. avoiding unnecessary traveling paths).

1.3 Possible solutions to optimize ceramics in AM processes

We understand the importance of using Computational Models to understand the geometry during the design process but also, especially for the case of ceramics, it is necessary to further experiment with the material itself. For that purpose, an empirical trial phase was necessary in order to explore the actual mechanical characteristics of ceramics during the fabrication process. As an outcome of this phase, we define a set of rules defining specific formal material configurations in order to forego support structures. The fact that we decided to avoid the use of support structures during the fabrication process, allows alternative formal opportunities inherent by one hand, to the nature of the extrusion and by another hand to the mechanical properties of ceramics itself.

This paper explores the interaction between the bionic-inspired-design of cellular structures [3] and AM in the context of architectural ceramics. We understand this design strategy as an opportunity to reduce the amount of material in the final piece. On this regard, we understand that structurally efficient cellular configurations are smart as they consume less resources [2]. Case-studies are presented in order to re-interpret them in analog 3D-printed structures, so called 'structured materials' in nature (namely honeycomb-like, foam-like, sandwich panels) [7].

2. Objectives

The aim of this research is to design and manufacture load-bearing clay structures using AM techniques (in our case, extruded clay deposition). That is why we decided to analyze the relationship between structural performance and manufacturing resources: time, material, cost, etc.

For that purpose, we proposed to design, manufacture and setup a series of load-bearing column modules. The reason why we decided to produce modules and not a complete column regards on the fabrication equipment provided by the Chair of Artistic Design at RWTH [4]. In this case, a Delta WASP 2040 which limited our maximal printable volume to ⌀ 200 x h 400 mm.

3. Methodology

3.1 Computational models in design processes

With the integration of computational models and AM techniques we can obtain customized designs influenced by physical and formal constrains, by one hand of the AM tool and by another hand, the material itself, in our case: ceramics.

Digital tools allow novel design solutions by combining different parameter relations in the design process. Digital mechanical simulations are more complex in the case of ceramics since a lot of different factors during its manufacturing can significantly affect the mechanical properties (see 3.2 ceramics mechanical properties). For that reason, we were only capable to use computational workflows to analyze only the geometry in order to compensate anticipated deformations (geometrical analysis independent from material properties). Through the use of computational models (Rhinoceros, Grasshopper, Karamba) the designs were simulated in order to improve the structural performance of

the modules. Here it is important to mention that the optimal solution in terms of structural performance was not always the optimal solution regarding ceramic deposition techniques. Other influencing factors play a main role here, depending on the special material properties and the implemented AM technology.

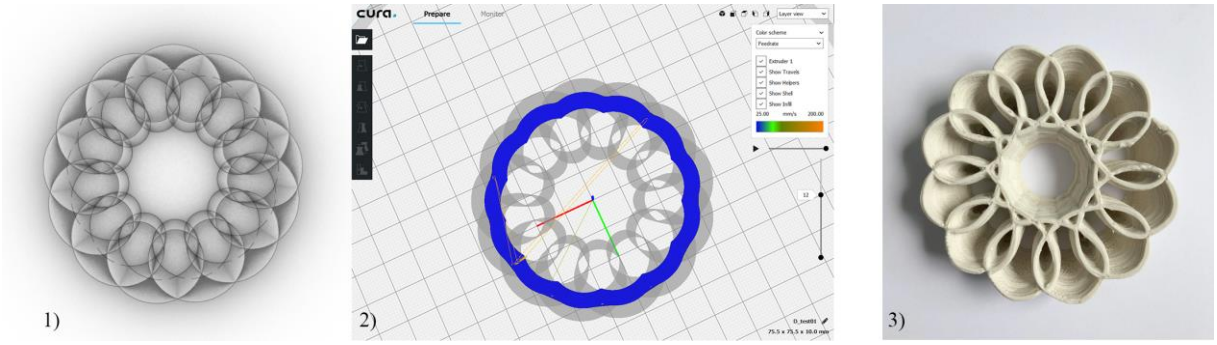


Figure 1: Test 01, Curve walls and intersection (1) Digital geometry after simulation (2) Toolpath analysis and layer preview with slicing software *Cura* (3) 3D-printed model after sintering process.

3.2 Compression reinforcements in nature

We have been working with three different structured materials: Honey-comb-like structures, foam-like structures and sandwich panels. We developed a series of biomimetic digital models looking for the most efficient solution to create material efficient ceramic structures. After a case-study analysis, we implemented computational models in order to achieve a family of customized possible design solutions. Through the digital workflow we attempted to optimize the final designs by reducing material and weight, while increasing structural integrity.

3.3 Case-studies in nature and its application in the digital workflow

We propose the use of parametric modelling tools to solve optimization problems and sort or filter relevant criteria. Since we decided to work with case-studies, namely material formations in nature (Honey-comb-like structures, foam-like structures and sandwich panels), we propose to develop a series of biomimetic digital models looking for the most efficient solution to efficiently create ceramic building components.

This part of the research aims to explore the use of algorithms with the help of Rhinoceros 6, Grasshopper and Karamba in order to produce a series of load-bearing column modules. This workflow allowed us to work with families of possible solutions and catalogues, in order to compare the different designs, analyze them and finally select the most efficient in terms of form, material, load bearing capacity and manufacturing.

4. Materials

4.1 Understanding ceramic materials in AM

All minerals on material-science terms are ceramics [7]. When talking about ceramics, we refer to refractory, inorganic and nonmetallic materials. We can divide them in traditional clay products, e.g. silicate glass, and advanced ceramics, e.g. carbides (SiC), pure oxides (Al_2O_3), nitrides (Si_3N_4), non-silicate glasses, etc. They are harder and stiffer than steel, better heat and corrosion resistant than metals or polymers, less dense than most metals and alloys, and their raw materials are plentiful and inexpensive [8].

4.2 The role of ceramics in architecture

Ceramic materials display a wide range of properties which facilitate their use in many different product areas [8]: aerospace, consumer uses, automotive, medical (bio ceramics), military, communications and other where we can include the construction industry (bricks, cement, membranes).

Traditional use of ceramics in architecture is mostly in the form of as masonry modular units which are traditionally mass-produced. When we talk about masonry, we refer to brittle, load-bearing, discrete elements (see 3.2 ceramics mechanical properties).

In addition to its formal expression, regarding some of its functional applications we can also mention thermal and acoustic isolation.

4.3 Ceramics mechanical properties

We can classify physical properties of ceramics in: Thermal, Optical, Mechanical and Electrical, we can mention e.g. heat capacity and low heat conductance, corrosion resistance, electrical insulation, semi conductive, non-magnetic and magnetic, hard and strong, brittle, etc.

In the microstructure, these properties are strongly affected by the ceramic bonding mechanisms and its internal structure. We can find two different kind of bonding in ceramics: ionic, btw. metallic and non-metallic, large difference in their electro magnitudes – electron transfer, high melting point since bonds are strong and non-directional, and covalent, non-metallic with small electronegativity differences – electron transfer. Here it is important to take into account that melting points increase both by ionic or covalent predominance, rather than no kind of bonding predominance at all.

Regarding the internal structure of ceramics, we can distinguish: crystalline ceramics, characterized by a lattice point occupied by atoms and ions (short-range order), arranged by a regularly repeating pattern in 3 dimensions (long-range order) and amorphous ceramics (Glazes) [9]. From now on, in purpose of this research, we are only going to refer to crystalline ceramics.

We are especially interested in the analysis of mechanical properties: how the material responds to forces, loads and impacts.

Material Classification: Ceramics							
Material composition		**Microstructural bonding**		**Internal structure**		**Structural behavior**	
Inorganic		**Crystalline** (one or more crystals)		**Homogeneous**		**Ductile** (Break with advanced notice)	
Mineral	●	Anisotropic	●	Substance related		Ideal for structural materials	
Metallic		Brittle	●	similar		**Brittle** (Break without advanced notice)	
Organic		**Amorphous** (non-crystal lattice)		One-component		Sudden failure (unfavorable)	●
		Isotropic	●	**Non-homogeneous**			
		Tough/Brittle	●	Fiber-based			
		Micellar		different			
		Anisotropic		+ than one component	●		
		Tension Resistance					

Figure 2: Material classification for Ceramics.

We decided to stablish a material classification for Ceramics based on the 'Basics for material properties' [10]. As we stayed before, all minerals on material-science terms are ceramics [7] and according to its material composition we can say that ceramic is a natural inorganic material.

According to its microstructural bonding, we can talk about crystalline or amorphous ceramics. In our case we work only with crystalline ceramics which are anisotropic (different properties in different special directions) and brittle (cleavage fracture). The material brittleness represents a big limitation: it has the tendency to fail suddenly with little plastic deformation.

Regarding its internal structure, we understand ceramic as a non-homogeneous material since it has an atomic composition with more than one compound. According to its fracture behavior, we can define ceramic as a brittle material: its ability to deform is limited as well as its fracture strength.

After this first analytic classification of ceramics we can define intrinsic advantages and disadvantages of the material. As advantages we can mention: high elastic stiffness, high strength (specially under compressive load), good chemical resistance and high temperature resistance (crystalline ceramics). As we mentioned before, the huge disadvantage of ceramics is its blittable condition. Also, brittle behavior is caused by the type of bond. This can be problematic not only in use but also in the manufacture of the ceramic building-components. The crack propagation determines the material strength. The crack propagation in ceramics is caused by the type of bond and the manufacture process. Because the size of the initial cracks is stochastically distributed, statistic methods are required to analyze the strength of ceramics [9].

The theoretical strength of a material is the tensile stress that could be needed to break the bonds between atoms in a perfect solid and pull the object apart. But ceramics contain micro-structured bonds and manufacture flaws that make them significantly weaker than the ideal strength. Any flaw, pore, crack or inclusion, results in stress concentration, which amplifies the applied stress. Pores also reduces the cross-sectional area over which a load is applied. Thus, denser, less porous materials are generally stronger. The smaller the grain size the better the mechanical properties [8].

4.4 Ceramics manufacture.

Since ceramics manufacturing has a great impact in the final fracture strength of the produced objects, we decided to focus on the proceeding criteria. First, it is important to understand that the different individual steps differ depending on the ceramic material: crystalline or amorphous. As we work with crystalline ceramics, among the standard manufacturing processes we can mention: sintering (without external load), hot pressure and hot isostatic pression (superimposed uniaxial or hydrostatic stresses). Under the point 3. Methodology we already described the use of AM with ceramics which implies of course a sintering manufacture process.

For the purpose of this research, we divided the sintering process into five different steps: raw material selection, mixture, consolidation, drying and sintering.

Under the raw material selection (dry powders) we can find different materials regarding traditional or advanced ceramics. In our case, we use traditional ceramics which involves the use of various forms of clay powders. The particle size and purity affect the structure and properties (e.g. fracture strength) of the final product. The strength is proportionally inverted to the grain size (diameter < 1 μm).

Dry powders are difficult to shape, that is why, during the mixture step, processing additives (water, polymers, etc.) are implemented in order to improve its plasticity. For our research we developed a special ceramic recipe where the only chemical binder is water (see 'Clay body for AM').

The consolidation stage implies forming the ceramic mixture into a specific shape. The material needs to be in a plastic stage, so it can be formed. Here we can find traditional hand or industrialized techniques. Under the industrialized techniques we can mention: Extrusion, Injection, Dry pressing, slip casting, being extrusion one of great importance since it is involved in the depositing AM.

During the buildup (consolidation stage) tension stresses will differ according to different form and size of the piece. Round shapes are perfectly suited as they are able to absorb tension more informally than rectangular forms, flat pieces and tiles. Corners, abrupt changes in the direction of a form, and sudden changes in wall thickness all negatively affect the desired distribution of stresses resulting in an uneven buildup of tension within the piece. As the wall thickness and size of a piece increases, the chance of tension buildup as well [1].

In the drying stage, we can find the shrinkage and reabsorption phenomena. The shrinkage depends on the plasticity of the clay body composition, for example, a clay body with ultra-fine minerals will shrink more since it has strong bonds, a denser body which difficult the transport of water towards the surface. The shrinkage amount determines as well the fracture strength of the piece. During the drying stage, drying stresses are produced. High stresses will cause a piece to crack. Drying crack resistance is very

difficult to determine since it increases if the plasticity of the material is neither too high nor too low. Sometimes additives like e.g. cellulose are added to the mixture in order to increase its strength.

Parallelly to the shrinkage effect we also find water reabsorption during the drying stage. A piece that has been fully dried and is then returned to a humid atmosphere will attract water into its pores. This last effect causes an expansion on the piece allowing distortion and/or cracks.

Finally, in the sintering stage, the high temperatures (between 800°C and 1800°C) cause densification and vitrification giving strength and other properties to the material. Ceramic particles coalesce to form a continuous solid network and pores (in the micro-structure) are eliminated.

The Figure 3 sketches a sintering process during consolidation, material diffuses to the contact area between the particles, driven by the energy gained in reducing the surface. The contact areas round off and become larger. One consequence od this process is that the component shrinks by as much as 30% to 40% (this means a reduction of the length of the component in each direction of about 10% to 15%) [9].

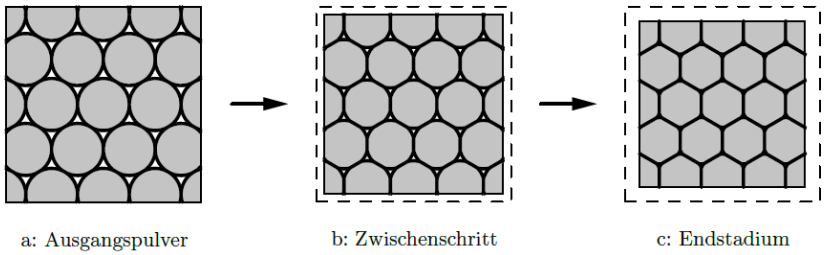


Figure 3: (a) Microstructure of raw materials, (b) consolidation and (c) sintered product [9]. We can name also mixture between (a) and (b) drying between (b) and (c).

Also, the porosity plays a big role in the sintering process. It is determined by the amount of the interconnected open pores. The sintered strength is proportionally related to its porosity. Increasing the firing temperature will reduce porosity and will reduce fracture strength (up to vitrification point) [1].

4.5 Clay body for AM

To sum up we can stay that in ceramics directed atomic bonds and complex crystal structures cause no plastic deformation, also known as *cleavage fracture*. It is the most dangerous form of fracture, which is classified as a brittle trans granular fracture by separation across well-defined crystallographic planes [9] See Fig. 1, Structural behavior.

Because of the crack sensitivity of ceramics, even small defects during the manufacturing process (e.g. bonding, consolidation) can determine the strength – the pre-cracks formed during manufacturing are thus crucial for the mechanical behavior. That is why the theoretical strength of a perfect ceramic piece without any defects is technically irrelevant.

We understand that, to minimize the manufacturing defects, we should have high control over the plasticity and shrinkage of the clay mixture. However, the 3D-Printer developer recommends the use of a mixture based on porcelain and alcohol. But, as described in the material properties charts of our clay powder provider [10], dry to fired shrinkage percentage in porcelain bodies can oscillate between 10,2% to 12%. This high shrinkage percentage difficult the control over the manufacturing process. Also, the use of alcohol as a processing additive is not recommended in ceramics, since it evaporates faster than water and accelerates the drying process increasing the cracks emergence. For those reasons, we decided to develop our own clay body recipe based on water and earthen-ware in order to determine an optimal plasticity for AM.

We developed a recipe with good packing density which showed positive results during the 3D-printing tests. The provider properties chart points out a dry to fired shrinkage of 7% and a strength of 7,2 N/mm²

(plastic extruded tests) but since we can't determine the amount of water added to the provider's tests, further tests are necessary to determine if this is positive in the case of our developed clay body as well.

Chamotte	Firing Range °C	DS%	Water absorption %			Firing Shrinkage %			Thermal expansion (20-500°C)		
			(1040°C)	(1100°C)	(1200°C)	(1040°C)	(1100°C)	(1200°C)	(1040°C)	(1100°C)	(1200°C)
-	-	4,3	-	-	0,3	-	-	7,0	-	-	6,8

Figure 4: material properties chart based on our clay powder provider tests [13]

4.6 Material weight and geometry influence

Different factors such as material weight and geometry have great influence in the final object. These are expressed as a result of the forces on the matter, in our case: ceramics. Unexpected or non-preconceived emergencies are experienced in the final object as a consequence of both, the material properties (which affect the geometry) and the digital manufacturing process.

After a thorough analysis of the 3D-printed objects we can identify specific emergences linked to the use of ceramics in AM fabrication processes. Among others, we experienced a shrinkage pattern on the bottom layers in all the pieces. It is a direct consequence on this specific digital manufacturing procedure, since the first layers of deposited ceramics are dried faster than the following layers.

5. Pre-Conditions

After the analysis of the first series of experiments, we were able to stablish a series of specific material and manufacturing parameters: clay plasticity, material shrinkage percentage, air pressure, nozzle diameter, maximal printable area. At the same time, we could define some digitally defined parameters like: flow rate, tool path, printing speed. Is important to emphasize here that all these parameters work together as project constrains or pre-conditions during the design process. These parameters conditionate the final outcome of the designed object.

6. Conclusions & further research

As an outcome after our first series of experiments we can attempt some conclusions regarding the application of AM techniques in load-bearing clay structures where we focused on the interdependency between structural performance and manufacturing resources.

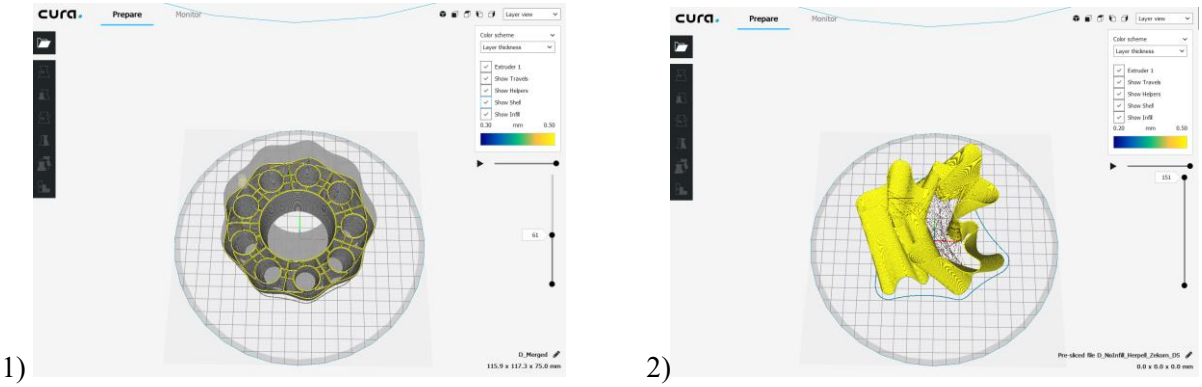


Figure 5: Strategies to reduce traveling time (1) with infill structure (2) without infill structure.

Regarding the fabrication time, we developed an efficient way to 3D-print reducing traveling time (the toolpath from one deposition point to another). In some cases, we designed the infill structure in order to increase load-bearing capabilities and, at the same time, to ensure less traveling time. In other cases, we decreased the time traveling by designing modules without infill structure, with a continuous

toolpath. Here, we had to improve the load-bearing capabilities with other resources like e.g. folding the walls of the objects (Figure 5).

After an empirical trial phase, we found out that we needed a deeply understanding of ceramics´ mechanical properties. These studies helped us to understand ceramics in the context of AM, as deposition material. That is why we decided to avoid the use of support structures challenging the formal capabilities of both, material and manufacturing. Here we found out that parallel to the e.g. maximal printable volume, also the printable angles played an important role in order to avoid overhangs. It is important to mention that, in the case of ceramic AM, the optimal solution for performative structures, not always is the best solution for AM techniques and specially for ceramics. We understand it as a heuristic process involving all the before mentioned constrains (form, material, load-bearing capacity and manufacturing) as input information within the design project.

As a future research, it would be necessary to focus on the on-site construction of the columns, which type of bonds, joints and interlocking are more accurate to this type of digitally manufactured construction elements. Here it would be interesting to consider not only the file-to-factory specificity but also, the in-situ production of the blocks avoiding transport and storage costs.

With respect to sustainability within the fabrication process of ceramics, nevertheless it is less novice than another construction products in the construction industry. Since ceramic involve a large amount of every during the sintering process, we can say that we still have a pending account with the environment. Further research would be necessary in order to determine how to reduce que carbon footprint during the ceramic AM process.

References

[1] A. Reijnders. European Ceramic Work Centre. *The ceramic process. A manual and source of inspiration for ceramic art and design.* University of Pennsylvania Press. Philadelphia, 2007.

[2] M. Trautz, *Growth and Construction in nature as a pradigm and process for innovative technical sollutions.* Proceedings of ADICT Conference, Ed.: DWI – Leibnitz-Institut für Interaktive Materialien e.V., Aachen, 2015.

[3] M. Hensel, A. Menges and M. Weinstock, *Emergence: Morphogenetic Design Strategies.* AD Vol 74 N°3, Wiley Academy, London, 2004.

[4] Collaboration between the Chair of Structures and Structural Design (Univ.-Prof. Dr.-Ing. Martin Trautz) and the Chair of Artistic Design (Univ.-Prof.-Dipl.-Ing. Thomas Schmitz) at the Faculty of Architecture, RWTH-Aachen.

[5] We Clay! Lightweight Structures, Seminar organized by Associated Researchers M. Sc. Dana Sáez (Chair of Structures and Structural Design) and M. Sc. Christina Klug (Chair of Artistic Design) at the Faculty of Architecture, RWTH-Aachen, Summer Term, 2019.

[6] ASTM International, Designation: F2792 – 12a, *Additive Manufacturing Technologies1,2*, West Conshohocken, 2019.

[7] L. Gibson, M. Ashby, B: Harley, *Cellular Materials in Nature and Medicine.* Cambridge University Press. Cambridge, 2010.

[8] P. Block, C. Gengnagel, S. Peters, Faustformel, Tragwerksentwurf. Deutsche Verlags-Anstalt, Münche, 2013.

[9] Rösler J., Harders H., Bäker M., Mechanisches Verhalten der Werkstoffe, 5. aktualisierte und erweiterte Auflage, Springer, Wiesbaden, 2016.

[10] Sibelco Deutschland GmbH, Technical Data, www. Sibelco.eu, Ransbach-Baumbach, 2015.

Proceedings of the IASS Annual Symposium 2019 – Structural Membranes 2019
Form and Force
7 – 10 October 2019, Barcelona, Spain
C. Lázaro, K.-U. Bletzinger, E. Oñate (eds.)

Creative rational design of free form buildings and their constructions roofed with transformed corrugated steel sheeting

Jacek ABRAMCZYK, Aleksandra PROKOPSKA

Rzeszow University of Technology, Department of Architectural Design and Engineering Graphics
Al. Powstańców Warszawy 12, bud.V, pok VD-37, Rzeszów, 35-959, podkarpackie, Poland
jacabram@prz.edu.pl

Abstract

The possibilities of using an author's method for creative searching for unconventional forms and rational geometric and structural solutions of individual parts of these forms is analyzed. In the process of geometrical and static-strength shaping of such forms, three basic steps of the above search related to: innovative forms and unusual static-strength work of the transformed folded shells, shaping unconventional general forms of the buildings, and the forms of structural systems intended for the examined free forms have been distiguished. The presented results of the analysis provide the innovative and holistic insight into interdisciplinary issues related to the possibilities of shaping the investigated free forms and their computational simplified and accurate models. The proposed simplified models can be employed for engineering developments and the accurate ones can be used for scientific research.

Keywords: building free forms, transformed corrugated shell roofs, steel structural systems, creative rational design, conceptual design, thin-walled folded sheeting, parametric architectural design, static-strength shaping.

1. Introduction

Shaping of unconventional free forms of buildings roofed with shells made up of nominally flat, thin-walled folded sheets transformed into spatial forms requires many interdisciplinary problems and is determined by several non-linear changes of geometrical and mechanical properties of transformed sheeting. The purpose of the transformations is to achieve shell roofs characterized by an attractive spatial form resulting from the variation in the inclination of subsequent folds in a shell to a horizontal building base plane. The diversified slopes of the shell folds and roof eaves allow further increase of the attractiveness and consistency of the entire building. This is achieved by inclination of elevation walls and edges to the vertical as well as definition of the appropriate proportions between elements of roof, façade and construction of the building designed.

The transformations are performed as a result of spreading flat folded sheets, connected with each other by their longitudinal edges into one strip, on two skew directrices, so that the transverse edges of the folds pass along the directions of these directrices, Figure 1. Since both two directrices supporting the transverse edges of the transformed shell are mutually skew lines, each of the subsequent folds in such a transformed roof shell contracts at its central area and extends at its both transverse ends in the manner specific for thin-walled folds. In addition, the skew directrices cause the fact that the degree of the shape changes and supporting conditions are different for the subsequent folds of each shell roof.

What is a very important effect of the transformations are the fold's width increments, values of which depend on the degree of the shape transformations, including the twist of each shell fold around its longitudinal axis. The twist degree of the fold affects the level of its initial effort, which should be

Copyright © 2019 by Aleksandra Prokopska and Jacek Abramczyk
Published by the International Association for Shell and Spatial Structures (IASS) with permission.

limited due to the necessity to maintain the capacity for bearing the live load appearing at the service step of buildings. Because of the nature of the fold's shape changes and relatively small fold's width changes related to the big transformations and mutual displacements of the subsequent folds in a shell, the increments must be calculated precisely [1]. This, however, requires the development of unconventional methods based on the results of laboratory tests on the shape transformations of folded sheets of different profiles.

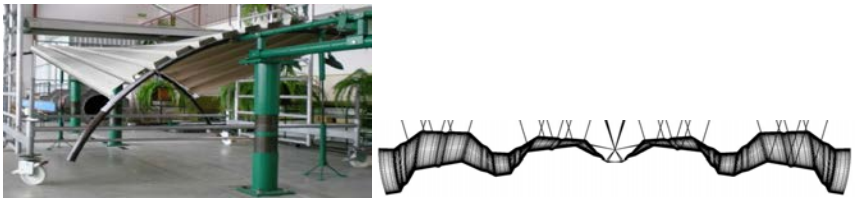


Figure 1: Shape transformations of thin-walled folded steel shells: twisted and bent experimental shell sheeting and a computational folded model of an experimental steel sheet

For research purposes, thin-walled folded models of transformed shells based on an accurate description of the geometrical and static-strength properties of the sheets tested in laboratory conditions are created [2], Figure 1. For engineering purposes, however, the sufficient modeling accuracy can be obtained by means of simplified smooth models created as regular warped surfaces [3-4].

2. Critical analysis

Geometrical and static-strength shaping of thin-walled folded cylindrical shells has been relatively well recognized and described, *inter alia* in the works by El-Atrouzy and Abdel-Sayed. In such shell sheeting, the folds are transversally bent and sheared, so their bending and shear stiffness is increased in comparison with flat folded roofs.

The geometrical and static-strength shaping of thin-walled folded parabolic-hyperbolic shells, called hypars, was performed by such researchers including Winter, Fisher, Edger and Resinger [5], Gergely, Banavalkar and Parker [6], Brayan and Davis [7]. Petcu and Gioncu have used their numerical program for shaping hyperbolic paraboloids of this type [8]. Each hypar is shaped as a central sector of right hyperbolic paraboloid or one-fourth of the sector. Each right hyperbolic paraboloid is characterized by the existence of two straight lines, called rulings, contained in this hyperbolic paraboloid, which are perpendicular to each other. Additionally, in order to obtain different roof forms, the aforementioned quadrants are set together in various configurations.

The aforementioned researchers investigated shallow hyperbolic paraboloid shells characterized by relatively small curvature, which resulted from the way they accomplished the shape transformations, assembly techniques and fixing of the transformed sheets into the roof directrices as well as adjusting the longitudinal fold's axes to the selected positions of rulings of an arbitrary hyperbolic paraboloid. The models created by means of the methods proposed by these researchers have lead to unjustified high stresses appearing in the fold's flanges and webs, which radically limits the maximum permissible transformation degree of shell folds. The well-known conventional methods for shaping smooth shells were implemented by the aforementioned researches, which also increases the initial stresses occurring in the walls of the transformed folds.

Unlike the above-mentioned researchers, Reichhart [9] has proposed an innovative concept of shaping corrugated transformed shells of the considered type and do not affect unnecessary big pre-stresses. It consists in the fact that it is not the longitudinal axes of all shell folds that should be adapted to the positions of some rulings selected in advance at an arbitrary hyperbolic paraboloid. The Reichhart's method is useful and relatively accurate for engineering developments only in the cases when the axes

of all folds in the transformed shell are perpendicular to the adopted directrices or close to perpendicular [3]. This results from the way of the modeling of subsequent folds in a shell by means of the central sectors of right hyperbolic paraboloids. He did not define the sufficient number of quantities describing the shape of a shell fold in the case when its longitudinal axis is not perpendicular to directrices. What further reduces the modeling accuracy of the Reichhart method is the adoption of the lack of cooperation between two adjacent folds in a shell and the calculation of these folds as independent beams, whose static-strength work can be described by conventional methods following the theory of the first order. The method is not suitable for scientific purposes.

3. The aim

The main aim of the article is to analyze the possibilities of creative and rational shaping of the unconventional architectural free forms of buildings and the steel structural systems intended for these forms based on the authors' methods [1-4]. The basic assumption is that the aforementioned free forms are covered with thin-walled folded steel roofs transformed into shell forms, and flat façades made up of glass panels.

The methodology adopted to achieve the above purpose consists in distinguishing, in the process of shaping the considered type of buildings, three basic steps accomplishing the possibilities of: a) creative searching for the unconventional and attractive forms of buildings and their elements, b) rational solving of the emerging diverse problems and constraints related to static-strength work of the structural systems of the buildings. The creative search for unconventional forms of buildings is carried out with the help of parametric descriptions, algorithms based on these descriptions, and their computer implementations, especially in the computer programs used for parametric shaping of geometrical free forms like the Rhino/Grasshopper and AutoCAD programs. In the choice of rational solutions, the static-strength work of all members of a building structural system is analyzed by means of accurate computer models created in the ADINA and Robot programs. These members are the transformed steel sheet's folds and individual elements of the structural system.

4. The concept and the range

The algorithm of shaping the considered free forms of buildings roofed with the transformed corrugated shells was divided into three basic steps. At each of these steps a detailed analysis of the possibility of a creative searching for diversified rational solutions is accomplished.

In the first step of the algorithm, the possibilities and limitations appearing during the process of forming thin-walled folded steel roofs transformed into shell forms are analyzed. As an example of the analysis, the selected research results related to the experimental tests [2,9] and accurate thin-walled computer models [2-3] used by the authors for scientific purposes as well as simplified smooth surface models used for engineering purposes are presented [1,10].

In the second step of the algorithm, the possibilities of a creative shaping of unconventional general forms of buildings covered with transformed roofs are analyzed. An initial model of any free form building can be adopted as a specific reference tetrahedron [1-4]. The possibilities of changes in positions of the planes, straight lines and points representing all walls, edges and vertices of a cuboid can be analyzed in order to tilt them out of the mutual parallel positions and obtain the reference tetrahedrons. These action allows for a relatively simple parameterization of all activities and objects created at this step and makes it possible to shape creatively interesting and attractive building forms.

In the third step of the algorithm, the structural rationality of the searched geometrical forms of buildings and the static schemes adopted for the structural systems dedicated to these forms are analyzed in view of the various slope of the eaves and folds of the roof shells as well as elevation walls and edges to a horizontal plane. For this purpose, the stiff eaves frames, their rigid joints to oblique posts and connections of these posts with the foundation are analyzed.

5. Transformed corrugated shell steel roofs

Because of small torsional stiffness of thin-walled folded sheets, an arrangement of a strip of the sheets, connected to each other with their longitudinal edges, on two mutually skew directrices makes important changes in its general shape under its own weight. The strip changes from a nominally flat form into shell shape and adapts itself to the shape and mutual position of the directrices. The directrices decide on the supporting conditions diversified for the subsequent folds of the roof shell. The rationality of using the above transformations is accomplished by means of the condition that the contraction of each fold of the transformed shell appears halfway at the length of the fold. Such a situation takes place when a freedom of the fold's transversal width increments is ensured during the transformation. These transformations are called effective by Abramczyk [3], because they allow to obtain big deformations of cross-sections and walls of the transformed folds, big mutual displacements of these folds, and the initial effort of these folds resulting from the initial transformations is small.

Effective transformations allow to obtain interdependent relationships between the supporting conditions of each shell fold, including the degree of the twist angle of the fold, and its geometrical and mechanical properties. A nonlinear relation between the relative width increments b_{wr} of shell folds belonging to different profiles, at its transverse end and the measure of the fold's unit twist angle α_j is shown in Figure 2. The line named Serie1 refers to a sheet TR50 x 0,75 x 8,0 whose profile's height is of 50 mm, thickness is of 0.75 mm and fold's length is of 8.0 m. Serie2 refers to the sheet T55 x 0.88 x 6,2 whose profile has the height of 55 mm, thickness is of 0.88 mm and fold's length is of 6.2 m. The descriptions of other curves at this diagram have the same meaning.

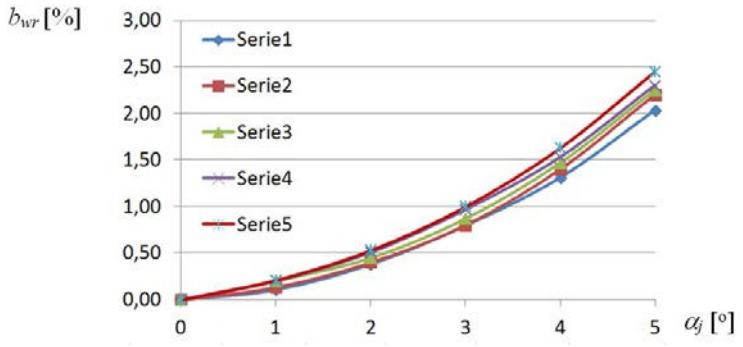


Figure 2: Nonlinear relations between b_{wr} relative width increments of fold's crosswise ends and α_j unit angle obtained for various profiles of a shell fold: Serie1 - TR50 x 0.75 x 8,0m; Serie2 – T55 x 0.88 x 6.2m; Serie3 – TR85 x 0.75 x 5,0m; Serie4 – TR136 x 0.88 x 6.0m; Serie5 – T160 x 0.75 x 6.6m

Total twist angle α of a shell fold is defined as the angle of twist of the opposite transverse fold's ends passing compatible with the directrices of a shell. The unit twist angle α_j is defined as the total twist angle α divided by the fold's length. The relative b_{wr} width increments of any shell fold are defined as the quotient of its absolute b_w width after transformation to the width b_0 before the transformation. The relative width increments are taken into account in order to precisely study the obtained relationships and make the analyses independent of the number and width of the folds in the examined sheets.

Figure 3 also shows a non-linear relationship between normal stresses acting in the fold's walls in directions perpendicular to the longitudinal axes of shell folds and the unit twist angle of the folds. The above diagrams show that effective transformations cause non-linear relationships between supporting conditions and the geometrical and mechanical properties of shell folds. From these and analogous diagrams achieved by the author follows the fact that it is possible to read the proper values of the quantities required in the process of designing the transformed corrugated shells. The rationality of the effective transformations results from the possibility of seeking for the smallest possible initial effort caused by these transformations in all shell folds.

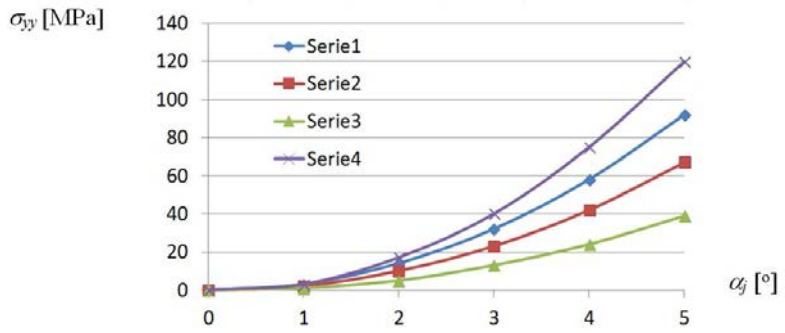


Figure 3: Relations between σ_{yy} normal stresses acting orthogonally to longitudinal axes and α_j unit angle of numerically transformed sheets of the following profiles: Series 1 - TR50 x 0.75 x 6.2 m; Series 2 – TR60 x 0.75 x 6.2 m; Series 3 – TR130 x 0.75 x 6.2 m; Series 4 – TR85 x 0.75 x 5.0 m

Small flexural transverse stiffness of thin-walled folds and its insignificant influence on the fold's effort allow for a significant increase in the diversity of free forms of the transformed roofs, and thus for a creative shaping of different warped shell roofs. A method for shaping simplified, smooth shell models of the transformed corrugated roofs, was developed and implemented by the authors in the Rhino/Grasshopper computer program intended for parametric geometrical shaping. The program can be successfully used to determine the diversified arrangement of the supporting points of the subsequent folds belonging to the transformed shell along roof directrices, diversified lengths of the fold's supporting lines and the length of the roof directrices.

Points D_{e1}, D_{e2}, D_{f1} and D_{f2} are intermediate points selected in the three dimensional space to define e_g and f_g directrices of the upper roof shell surface Ω_g. Points D_{g1}, D_{g2}, D_{g3} and D_{g4} are the end points of the directrices. Coordinates of the above points are the input of the authors' application of the Rhino-Grasshopper program to create the directrices. The coordinates of the aforementioned points of the general free form presented in Figure 4 are given in Table 1 in millimeters. The model of the above roof shall was determined using the innovative application built by the author in the Rhino/Grasshopper program [1].

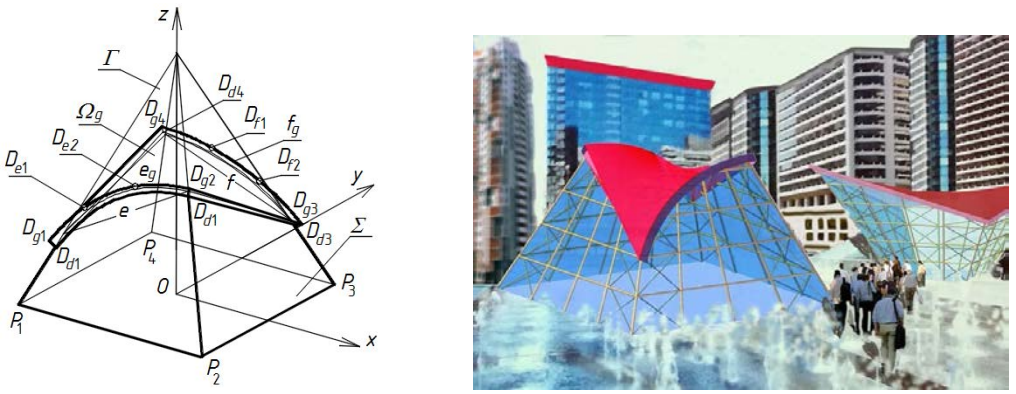


Figure 4: A simplified model and an architectural free form of a building

Table 1: Coordinates of the selected points used for creating the free form shown in Figure 4

Vertex	X-coordinate	Y-coordinate	Z-coordinate
P_1	-10000.0	-10000.0	0.0
P_2	10000.0	-10000.0	0.0
P_3	10000. 0	10000.0	0.0

P_4	-10000.0	10000.0	0.0
$S_1 = S_2 = H_1 = H_2 = H_3 = H_4$	0.0	0.0	23333.3
D_{g1}	-8011.4	-7977.4	5988.8
D_{g2}	5009.9	-4885.4	13203.5
D_{g3}	8011.4	7977.4	5988.8
D_{g4}	-5009.9	4885.4	13203.5
D_{e1}	-5349.2	-6561.3	9293.0
D_{e2}	-413.5	-5291.2	12256.5
D_{f1}	413.5	5291.2	12256.5
D_{f2}	5349.2	6561.3	9293.0

6. Unconventional building free forms roofed with transformed corrugated shells

A detailed parametric description of such created free forms [1] allows the implementation of the above algorithm in the AutoCAD and Rhino\Grasshopper computer programs to support the design process. Possible various types of the diversified reference tetrahedrons, Figure 5, also support the creative search for attractive architectural free forms of buildings [11]. A few methods of combining complete free forms into one complex free form structure roofed with complex structures of many smooth shells is presented in the other authors' publications [2,4].

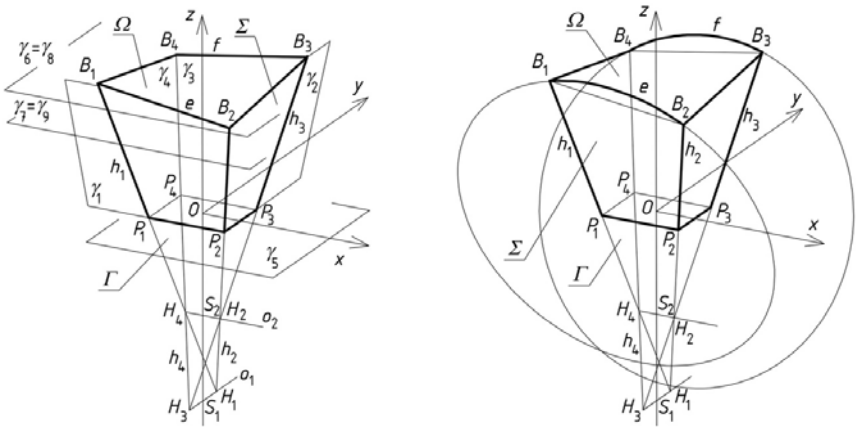


Figure 5: Two simplified models of the same free form building roofed with transformed warped shells supported by straight directrices and curved directrices

Four flat quadrangles Σ and one sector Ω of a warped surface, shown in Figure 6, create an unconventional building free form. Two curved roof directrices can limit two of the aforementioned four quadrangles modeling two opposite elevation gable walls.

Creativity of searching for attractive individual building free forms manifests in: a) adopting appropriate proportions between the parameters describing the dimensions of individual building elements such as roof and façades [1,11], b) adopting appropriate proportions between the parameters describing the slope of selected individual roof elements and façades, such as shell folds, eaves and side edges of the façade [1,11], c) unconventional shape and position of the roof directrices relative to the façade walls [3].

Rationality of shaping the general free form shapes consists in: a) the use of a symmetry and asymmetry, which can lead to simplifications in the determination of the reference tetrahedrons, repeatability and unification of the geometric and mechanical properties of several elements belonging to roof, façade and structural system, b) the adoption of flat roof directrices contained in gable walls or, in the case of spatial directrices, the definition of their positions relative to the tetrahedron's gable

walls, c) the limitation of the transformation degree of all shell roof folds by checking and controlling their supporting conditions defined by the shape and mutual position of the directrices.

7. Steel structural systems for the unconventional free form buildings

Rationality of the structural systems intended for the examined free forms, roofed with transformed folded shells can manifest in ensuring their proper stiffness, stability, strength, durability and static schemes. The implementation of the above postulate is associated with the adoption of specific parts of these structural systems as follows: a) a rigid frame passing around the designed building in accordance with the inclination of the individual segments of the oblique roof's eaves and directrices, Figure 6, b) rigid joints of poles with a foundation or eaves frame. In addition, it is necessary to analyze: a) the possibility of replacing some simple individual members with complex elements, such as multi-branches posts and spatial roof girders, b) the impact of adopting different static schemes for the examined structural systems.

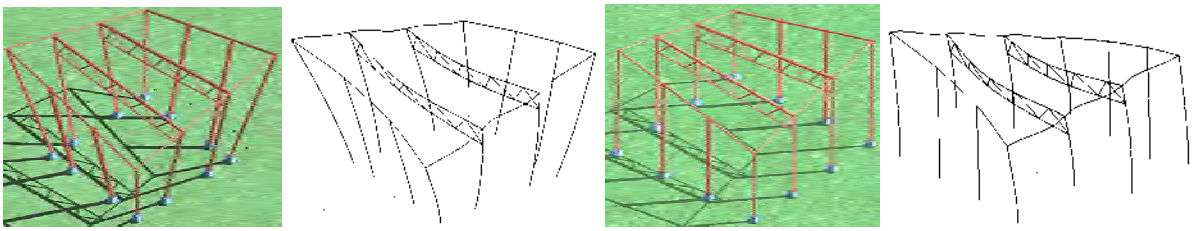


Figure 6: Models of two U1 and U2 structural systems intended for the support of identical shell roofs and their 1st mode shapes

Two from among the several structural systems analyzed by the authors and intended for the considered free forms are presented in the Figure 6. The first one named U1 is created by means of oblique columns, and the other named U2 created by means of vertical columns. Both systems are made of identical hollow sections of cross-sections adapted to the type of the member employed. Both systems have been subjected to the similar configurations of vertical and horizontal loads typical for the investigated buildings.

The performed analyzes show that the inclination of elevation walls to the vertical at the angle equal to 15^{o} significantly affects the cross-section effort rate of almost all structural elements, and the difference for the cases of U1 and U2 systems is about 10 to 30%. The radical difference in the effective stresses of U1 and U2 occurs only in the upper spar flange of the vertical truss near its connection to the higher intermediate pillar and are five times higher for U1 than for U2. Both systems evidence similar general stability, the first mode shapes, Figure 6, and critical load multiplier of about 6 in the Robot program and about 7.5 in the ADINA program.

The creativity in shaping specific forms of the structural systems intended for the examined free forms manifests in the fact that: a) the form can be taken into account as a part of either an elevation pattern observed from the outside of the building or the fittings of the building attracting its interior view, b) a parameterization of a description referred to the shape and static-strength work of the structural system and implementations of the description in graphical computer programs can support the designer in the process of searching for attractive building free forms.

8. Conclusions

To achieve a lot of creativity in shaping the examined free forms of buildings, the following main variables should be investigated: a) proportions between the dimensions of their basic elements, such as the width and height of the façade walls and roof shell, b) ratios between the slope of eaves and folds of their shell roofs and the inclination of the walls and edges of their façade to the vertical, c)

parameters defining curvature and position of their roof directrices, d) parameters describing the shape and position of their structural systems in relation to the position of façades and roofs.

The rationality of the adopted solutions related to shaping of the examined unconventional forms of buildings and their structural systems consists in: a) using symmetry and asymmetry in defining their elements, including the shell roof directrices, façade walls and edges and members, b) simplifying the definition of: straight lines and planes representing façade edges and walls, curves representing roof directrices and static schemes of structural systems, c) effective using the geometrical and mechanical properties of the folded sheets to limit the value of the pre-stresses of the roof shell sheeting resulting from the shape elastic transformations of its folds, d) adjusting the forms of the structural systems to the shapes of building free forms.

The holistic process of shaping the building free forms covered with transformed roof shell sheeting and supported by specific structural systems is presented in the article by means of a few examples. The authors' method for shaping simplified, smooth models of the transformed corrugated roof shells can be employed in several cases. However, it requires further accurate tests related to the correctness and accuracy of modeling of civil engineering thin-walled shells. The method of defining structural systems intended for the examined free forms is so far a preliminary version that requires further analyses and laboratory tests.

References

[1] J. Abramczyk and A. Prokopska, "Responsive Parametric Building Free Forms Determined by Their Elastically Transformed Steel Shell Roofs Sheeting," *Buildingss*, 9, 46, 2019.

[2] J. Abramczyk and A. Prokopska, "Shape Transformations of Plane Folded Sheets for Shell Roofing," *IOP Conf. Ser.: Mater. Sci. Eng.* 471 082064, 2019.

[3] J. Abramczyk, *Shell Free forms of Buildings Roofed with Transformed Corrugated Sheeting. Monograph*. Rzeszow: Publishing House of Rzeszow University of Technology, 2017.

[4] J. Abramczyk, "Transformed Shell Roof Structures as the Main Determinant in Creative Shaping Building Free Forms Sensitive to Man-Made and Natural Environments," *Buildingss*, 9(3), 74, 2019.

[5] H. Egger, M. Fischer and F. Resinger, "Hyperschale aus Profilblechen," *Der Stahlbau*, vol. 12, pp. 353–361, 1971.

[6] P. Gergely, P. V. Banavalkar and J. E. Parker, "The analysis and behavior of thin-steel hyperbolic paraboloid shells," *A Research Project Sponsored by the America Iron and Steel Institute*, Report 338, New York, Sep. 1971.

[7] E. R. Bryan and J. M. Davis, *Manual of stressed skin diaphragm design.* London, Granada,1982.

[8] D. Gioncu and V. Petcu, "Corrugated hypar structures," in *Proceedings of the I International Conference on Lightweight Structures in Civil Engineering, Warsaw, Poland, December 5, 1995,* J.B. Obrębski Ed., 1995. pp. 637-644.

[9] A. Reichhart, *Geometrical and structural shaping building shells made up of transformed flat folded sheets*. *Monograph*. Rzeszow: Publishing House of Rzeszow University of Technology, 2002.

[10] A. Prokopska, "Creativity Method applied in Architectural Spatial cubic Form Case of the Ronchamp Chapel of Le Corbusier," *Journal of Transdisciplinary Systems Science,* vol. 12, pp. 49-57, 2007.

[11] J. Abramczyk, "Parametric shaping of consistent architectural forms for buildings roofed with corrugated shell sheeting," *Journal of Architecture Civil Engineering and Environment,* vol. 10, pp. 5-18, March 2017.

Proceedings of the IASS Annual Symposium 2019 – Structural Membranes 2019
Form and Force
7 – 10 October 2019, Barcelona, Spain
C. Lázaro, K.-U. Bletzinger, E. Oñate (eds.)

Study on Membrane Roof Schemes of Annular Crossed Cable-truss Structure

Suduo XUE*, Jian LU[b], Xiongyan LI[c], Renjie LIU[d]

*College of Civil and Architecture Engineering, Beijing University of Technology
100 Ping Le Yuan, Chaoyang District, Beijing 100124, China,sdxue@bjut.edu.cn

[b]College of Civil and Architecture Engineering, Beijing University of Technology, lujian2020@126.com
[c]College of Civil and Architecture Engineering, Beijing University of Technology,xiongy2006@126.com
[d]School of Civil Engineering, Yantai University,xiongy2006@126.com

Abstract

Based on Annular Crossed Cable-truss Structure(ACCTS) model with diameter of 17.15m， the type of membrane roof was firstly studied. Two schemes of membrane roofs, cable-supported membrane roof and skeleton supported membrane roof, were proposed. The form-finding analysis of two types of membrane roof structure was carried out. By comparative study, the strengths and weaknesses of two schemes were given, and the feasibility of skeleton membrane roof was demonstrated. Secondly, skeleton membrane roof was studied by collaborative form-finding and non-collaborative form-finding. The form-finding method being suitable for the structure was given. Finally, load analysis of membrane and non-membrane roof structure were carried out. The results showed skeleton membrane roof had strength to resist to external loads. The studied content has promoted the application of annular crossed cable-truss structure in practical engineering.

Keywords: Annular Crossed Cable-truss Structure (ACCTS); membrane roof; form-finding; load analysis; parametric analysis; film-covering effects

1. Introduction

Annular crossed cable-truss structure (ACCTS) is a new type tension cable-truss structure system proposed by the Spatial Structure Center of Beijing University of Technology. The feature of ACCTS is a spatial structure formed by a series of crossed and waved plane cable-truss frame[1,2]. ACCTS is evolved from the spoke cable-truss structure[3], but its collapse-resistant performance is significantly higher than that of the spoke cable-truss structure[4,5]. For ACCTS, Xue et al. have carried out form-finding analysis[1], static analysis[5], parameterized analysis[5], construction forming analysis[6], collapse resistance performance[4,5]. The feasibility of the structure has been demonstrated, and some important conclusions have been obtained. The theoretical basis for studying the film-covering effects of ACCTS under film-covering effects has been given.

Based on research achievement of research group, membrane roof structure is added to ACCTS to consider its integral structural effects. Firstly, according to the characteristics of ACCTS, cable-supported membrane roof and skeleton-supported roof are proposed. Cable-supported membrane roof refers to a triangular or quadrilateral substructure formed by directly utilizing the upper radial cable section of ACCTS, and the membrane is laid on the substructure, shown in Figure 1. Skeleton-supported roof refers to the upper radial cable components using the circular crossed cable structure, and adds a rigid arch-shaped secondary structure on the upper radial cable components, and then lays membrane on the existing structure and the arched-shaped secondary structure, shown in Figure 2. The feasibility and advantages of skeleton-supported roof are

Copyright © 2019 by the authors.
Published by the International Association for Shell and Spatial Structures (IASS) with permission.

demonstrated through comparative analysis. Secondly, skeleton membrane roof is studied by collaborative form-finding and non-collaborative form-finding. According to the comparative analysis results, the form-finding method being suitable for membrane roof structure of ACCTS is given. Meanwhile, load analysis of membrane roof are carried out. Finally, summarize the research content of paper.

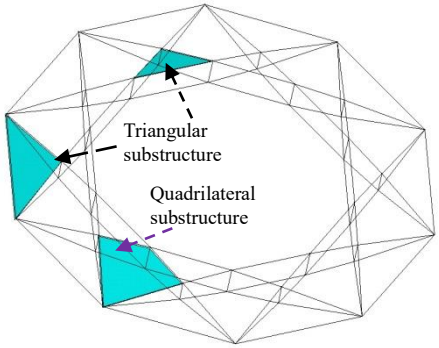


Figure 1. Cable-supported membrane roof

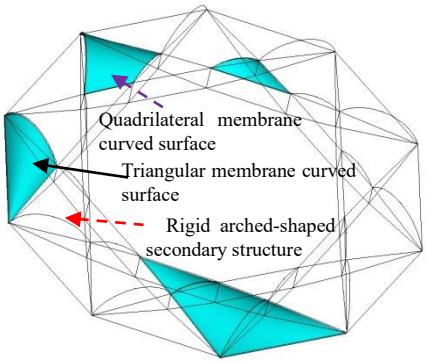
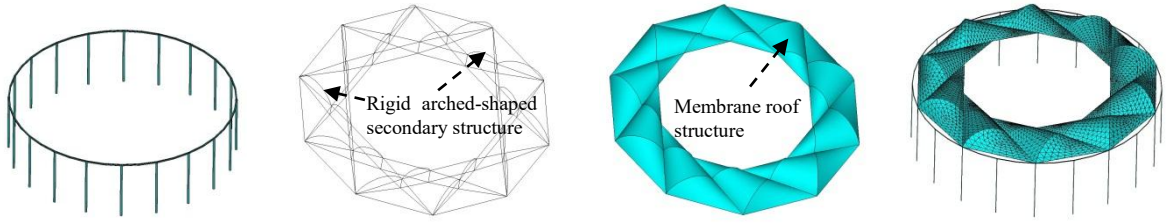


Figure 2. Skeleton-supported membrane roof

2. Schemes of Membrane Roof Structure

2.1. Membrane roof schemes of ACCTS

Annular Crossed Cable-truss Structure model with diameter of 17.15m is used as cable-supported structure, and cable-supported structure is the cable- supported system, which is formed by 10 crossed and waved plane cable trusses, shown as Figure 3. Due to the features of cable truss by itself, ACCTS naturally forms a structure with a certain slope. So, two types of membrane roof schemes are proposed: cable-supported membrane roof and skeleton-supported membrane roof. Mainly study from whether the shape of membrane roof is beautiful and good for drainage, whether applied membrane pretension meets the requirements of Code, the scope of membrane pretension after form-finding, and the influence of membrane pretension on membrane roof and its substructure are studied. The structure from and size of ACCTS is the same as that of the literature [6]. The cross-section characteristics and material properties of membrane and arched-shaped substructure are shown in Table 1. The structure is analyzed by large-scale general finite element software ANSYS. Cables adopt



(a) Ring beam and support column (b) ACCTS and arched substructure (c) Membrane roof structure (d) Integral FEM model

Figure 3. Annular crossed cable truss—membrane roof structure and integral model

LINK10 number. Struts adopt LINK8 number. Arched-shaped substructures adopt BEAM4. Compression ring beam and support column adopt BEAM188. Membranes adopt SHELL41. During calculation, considering the rigidity of ring beam and support column is very large, assume that almost no deformation occurs. So the action of ring beam and support column is not considered, and the boundary of ACCTS is set as rigid

connection.

As the model consists of 10 plane cable trusses with same specification (shown in Figure 1 and Figure 2), each truss is symmetrical about centerline, so half plane truss is taken for analysis (shown in Figure 4). The feasible pre-stress distribution of structure is obtained by using node equilibrium method and results are shown in Table 2.

Table 1: Material parameter of membrane roof structure of ACCTS

Material type	Element type	Size (mm)	Cross-section ($mm\times mm$)	Elastic modulus (MPa)	Poisson ratio	Yield strength (MPa)	Density (N/m^3)
Cable	LINK10	Φ10	59.69	1.38×10^5	0.3	1330	7850
Strut	LINK8	P38×3.5	379.15	2.06×10^5	0.3	315	7850
Secondary structure	BEAM4	P48×5.0	675.442	2.06×10^5	0.3	315	7850
Membrane	SHELL41	1.0	—	3.0×10^2	0.3	5.0/0.5	1500

Table 2: Feasible pre-stress distribution unit: kN

Element number	Cable						Strut	
	SS1	SS2	SS3	XS1	XS2	XS3	B1	B2
Internal force	4.650	4.659	4.719	6.845	6.798	6.797	-0.827	-0.818

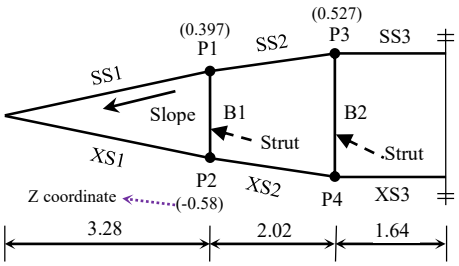


Figure 4: Half span planar cable-truss frame

2.2 Comparison of two membrane roof schemes

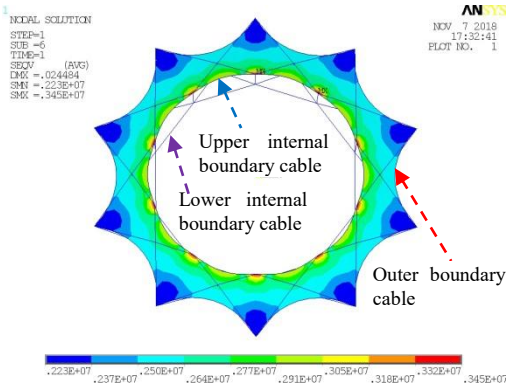
In order to consider the interaction between ACCTS and upper membrane structure, collaborative form-finding method is used to find the shape of integral structure. Cables and membranes are fully deformed by small elastic modulus method to obtain a reasonable membrane shape. In ANSYS finite element software, the pretension of structure is considered by applying initial strain to cable and applying initial temperature to membrane. In two schemes, the internal forces of outer boundary cables are 4.81kN, and the others are shown in Table 2. The initial pretension applied on the membrane is 2.02MPa.

2.2.1 Cable-supported membrane roof scheme

In cable-supported membrane roof, there are 20 triangular substructures and 10 quadrilateral substructures, and accord with《Technical Specification for Membrane Structure》[7]: The span of a single piece of membrane should not exceed 15m, and coverage area should not exceed 400m^2.

Through collaborative form-finding of cable-supported membrane roof, the integral stress diagram of membrane roof is obtained, shown in Figure 5. The stresses range of membrane roof model are 2.23~3.45MPa (mostly in the range of 2.5~2.7MPa), and the maximum displacements are 2.45cm. It is easy to get the shape

of membrane roof because plane projection can be established first and then coordinates of key points can be raised. However, when the initial pretension applied to membrane surface is large, it has large influence on the deformation and internal force of outer boundary cable and upper inner boundary cable (shown in Figure 5), and sometimes the slope of drainage requirement is not suitable (the slope should not be lower than 1:10). In cable-supported membrane roof, it can be seen from the analysis that structure deformation is large, and the calculation is not easy to converge when initial pretension applied to membrane is greater than 2.3*MPa*.



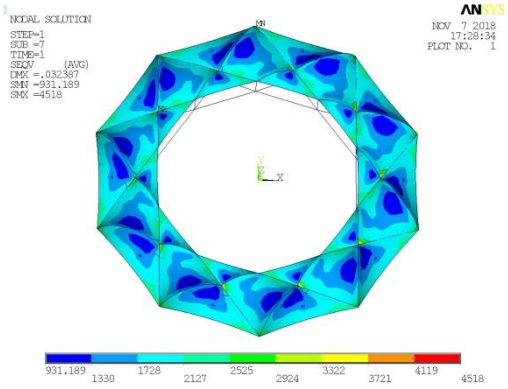


Figure 5: Integral stress diagram of cable-supported membrane roof Figure 6. Integral stress diagram of skeleton-supported membrane roof

2.2.2 Skeleton-supported membrane roof scheme

Skeleton-supported membrane roof is another scheme formed by adding rigid arched-shaped secondary structure on the basis of cable-supported membrane roof (shown in Figure 2 and figure 3b). In skeleton-supported membrane roof, there are 20 arched-shaped secondary structures, 20 triangular substructures and 10 quadrilateral substructures, and accord with《Technical Specification for Membrane Structure》[7]: The span of a single piece of membrane should not exceed 15m, and coverage area should not exceed 400m^2. When membrane structure is involved, because ACCTS has been tensioned and arched-shaped substructure has been installed, skeleton-supported membrane roof needs to be form-finding based on existing cable-arch support structure, which requires that there is no iterative operation during form-finding of membrane structure. After accurate modeling, repeated debugging and pretension calculation, we have found the shape that meets the architectural and structural requirements.

Table 3: Comparison of two membrane schemes

Scheme type	Pre-stress distribution	Structural deformation	Secondary structure	Substructure type	Membrane structure shape	Drainage capacity
Cable-supported membrane roof	uniform	Obvious	No	Two types	Single	General
Skeleton-supported membrane roof	uniform	Not obvious	Arch secondary structure	Two types	Variable	Better

Through collaborative form-finding of skeleton-supported membrane roof, the integral stress diagram of membrane roof is obtained, shown in Figure 6. The stress range of membrane roof model is 0.93~4.52*MPa* (mostly in the range of 1.7~2.1*MPa*), and the maximum displacement is 3.2*cm*.

2.2.3 Comparative results of two schemes

It can be seen from chapter 2.2.1 and 2.2.2 that although initial pre-stress applied to membrane is same, the form-finding results of two membrane roof schemes are significantly different. The quantitative and qualitative comparison results of two schemes are shown in Table 3.

(1) In cable-supported membrane roof scheme, there is no arched-shaped secondary structure, which will save cost. However, due to structure being used to find slope, when the shape of structure is within a reasonable range, the minimum slope requirement of membrane structure is usually not satisfied. In the skeleton-supported membrane roof, arched-shaped secondary structure is used as part of the support of the membrane structure. Although the cost is increased, the arch height of arch substructure can be set arbitrarily, which can easily meet minimum slope requirements of membrane structure. In addition, from inside to outside, skeleton-supported membrane roof is as same as the waves, magnificent and graceful in shape. It not only has the agility and elegance of membrane, but also has the stiffness and uprightness of arch (shown in Figure 3c~d).

(2) In cable-supported membrane roof, the curvature of the membrane surface is smaller because the membrane material is directly laid on the triangular or quadrilateral substructure formed by the upper radial cables. When small modulus of elasticity is used for form-finding, membrane structure will be fully deformed to obtain a reasonable geometric shape, so it has a great impact on internal and external boundary cables (shown in Figure 5). In skeleton-supported membrane roof, due to the existence of arch substructure, the membrane surface has a large curvature, so the influence on the boundary cable is relatively small.

(3) In cable-supported membrane roof, the stress of membrane mainly is in the range of 2.5~2.7*MPa*. In skeleton-supported membrane roof, the stress of membrane mainly is in the range of 1.7~2.1*MPa*. Because the initial pretension applied to membrane surface is 2.02*MPa*, the skeleton membrane roof is closer to actual situation.

3 Influence of form-finding method on the integral structure

Through the comparative study of two schemes, it is found that skeleton membrane roof scheme is more suitable for ACCTS. On the basis of skeleton membrane roof, the influence of form-finding method on the ACCTS is studied from two different angles of non-collaborative and collaborative form-finding. Non-collaborative form-finding means that form-finding is firstly carried out on the membrane roof to obtain constraint reaction of each constraint on the lower part of membrane roof, and then apply constraint reaction force to ACCTS. Collaborative form-finding means that form-finding is firstly carried out, then ACCTS is introduced to integral structure, and then calculation is carried out. The initial pretension actually applied to membrane roof is 3.6*MPa*.

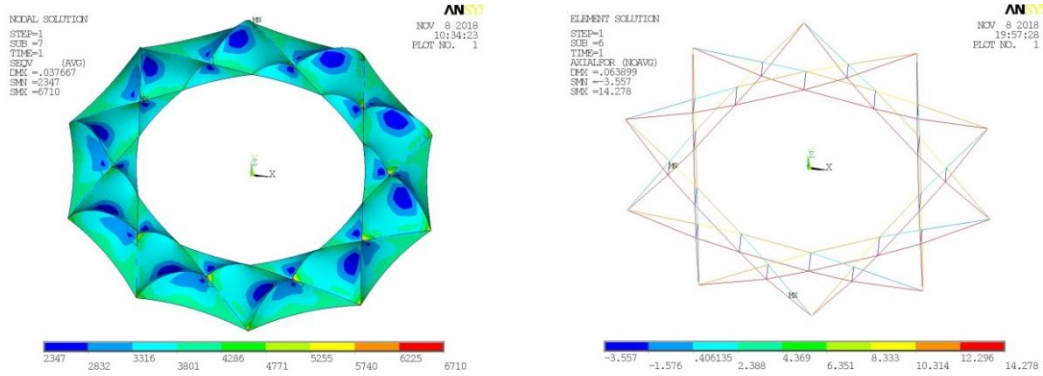
3.1 Non-collaborative form-finding analysis

According to the non-collaborative form-finding process, the stress cloud diagram of membrane roof is shown in Figure 7a, the stress cloud diagram of ACCTS is shown in Figure 7b. From Figure 7, it can be seen that the stress range of membrane roof is 2.35~6.71*MPa* (mostly in the range of 3.32~3.80*MPa*). The stress distribution is relative uniform, and its maximum displacement is 3.7*cm*. In ACCTS, the maximum pressure stress of cables is 14.28*kN*, and the maximum stress of struts is 3.56*MPa*, and the maximum of ACCTS is 6.39*cm*.

3.2 Collaborative form-finding analysis

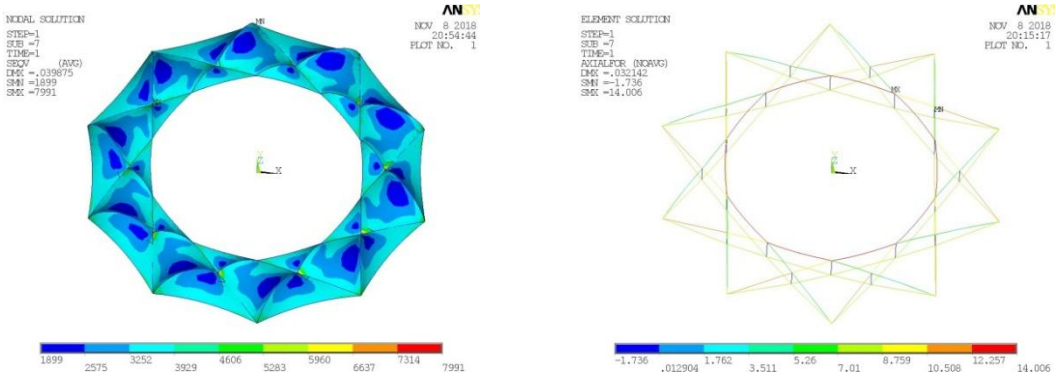
According to the collaborative form-finding process, the stress cloud diagram of membrane roof is shown in Figure 8a, the stress cloud diagram of ACCTS is shown in Figure 8b. From Figure 8, it can be seen that the

stress range of membrane roof is 1.89~7.99*MPa* (mostly in the range of 2.58~3.90*MPa*). The stress distribution is relative uniform, and its maximum displacement is 3.99*cm*. In ACCTS, the maximum stress of cables is 14.01*kN*, and the maximum pressure stress of struts is 1.74*MPa*, and the maximum of structure is 3.21*cm*.



(a) Stress cloud diagram of membrane roof (b) Stress cloud diagram of ACCTS

Figure 7: Stress cloud diagram of membrane roof and ACCTS



(b) Stress cloud diagram of membrane roof (b) Stress cloud diagram of ACCTS

Figure 8: Stress cloud diagram of membrane roof and ACCTS

Table 4: Comparison of non-collaborative and collaborative form-finding computational results

Form-finding method	Membrane roof structure		ACCTS		
	Stress range (mostly Stress range) (*MPa*)	Maximum Displacement (*mm*)	Maximum internal force of cable (*kN*)	Maximum pressure forces of strut (*kN*)	Maximum displacement (*cm*)
Non-collaborative from-finding	2.35~6.71 (3.32~3.80)	3.7	14.28	-3.56	6.39
Collaborative from-finding	1.89~7.99 (2.58~3.90)	3.99	14.01	-1.74	3.21

3.3 Comparison of two form-finding methods

From chapter 3.1 and 3.2, it can be seen that although structure model and initial pretension applied to membrane roof is same, the results of two form-finding methods are significantly different. The comparison

results of two form-finding methods are shown in Table 4.

From Table 4, it can be seen that non-collaborative and collaborative form-finding analysis methods have different effects on internal forces and displacements of structure. And two form-finding methods have no significant influence on stress distribution range and displacement of membrane roof, but have a great influence on the internal force and displacement of lower ACCTS. Therefore, collaborative form-finding method should be adopted in the design of membrane roof structure.

4 Load analysis

Under the action of dead load and live load, considering the combined external load size of 0.6kN/m2, the internal force response of structure is analyzed in three work conditions. Meanwhile, consider the response of membrane roof structure under full span and half span loads. Internal forces and displacements of structure under different conditions are shown in Table 5.

Case 1: under the pretension of membrane roof

Case 2: under pretension and dead load

Case 3: under pretension, dead load and living load

Table 5: maximum internal force and displacement of structural members under different situations

Load case	Case 1	Case 2	Case 3
SS1/*kN*	5.062	6.344	8.273
SS2/*kN*	5.659	7.121	9.268
SS3/*kN*	13.409	15.562	18.789
XS1/*kN*	8.537	7.120	5.253
XS2/*kN*	8.407	7.020	5.190
XS3/*kN*	8.401	7.001	5.160
B1/*kN*	-1.736	-1.354	-0.906
B2/*kN*	-1.360	-1.186	-0.926
Max displacement of ACCTS/*mm*	32.1	44.9	79.2
Membrane stress /*MPa*	2.57~3.25	2.62~3.28	2.78~3.40
Max displacement of membrane /*mm*	39.8	53.8	61.3

Under case 1~3, membrane stress is positive, that is, there is no winkle on membrane. At the same time, from case 1~3, it can be seen that internal forces of upper radial cables of ACCTS increase gradually, and internal forces of lower radial cables decrease gradually. That is to say, the relaxation of pre-stress occurs in the ACCTS under external loads, which should be paid more attention. Meanwhile, under case1~3, membrane stress is mostly in the range of 2.78~3.40MPa (suitable for 《Technical Specification for Membrane Structure 》[7]: membrane stress should be in the range of 1~4MPa) . Maximum displacement of membrane is 61.3mm (tolerable value [σ]=l/200=85.8mm). Maximum displacement of ACCTS is 61.3mm (according with tolerable value [σ]=l/200=85.8mm).

5 Conclusions

Based on ANSYS finite element software， roof type, form-finding method, load analysis, parametric analysis, dynamic feature analysis and film-covering effects have been analyzed. The main content and results are as follows:

(1) Two schemes of skeleton membrane roof and cable-supported roof are proposed for ACCTS. The good and

bad points of two schemes are compared and analyzed from these aspects that include the substructure of supported membrane, uniformity of membrane prestress, structure deformation and drainage capacity, and the feasibility of skeleton membrane roof scheme is further demonstrated.

(2) By non-collaborative and collaborative form-finding analysis of skeleton membrane roof, it can be concluded that the influence of two form-finding methods on structure is different. So, collaborative form-finding method should be adopted in the design of membrane roof.

(3) It can be seen by load analysis of structure that skeleton membrane roof structure has good performance to resist external load.

Acknowledgement

Thanks for the support of the National Science Foundation of China (51778017), the National Science Foundation of Beijing (8172011), the Key Laboratory Urban Security and Disaster Engineering of Ministry of Education in Beijing University of Technology.

References

[1] LIU Ren-jie, XUE Su-duo, LI Xiong-yan. Dynamic response analysis under local break of cable or rod in the annular crossed cable-truss structure[J]. industrial buildings, 2015,45(01):32-35.

[2] Renjie Liu, Suduo Xue, Xiongyan Li, et al. Formulas for The Derivation of Node Coordinates of AnnularCrossed Cable-truss Structure in A Pre-stressed State[J]，Journal of International Assoc iation for Shell and Spatial Structures,4(55),pp 223-228,2014/12/1.

[3] Guo Yanlin, Wang Kun, Tian Guangyu, et al. Research on key structural design problems of the Bao'an Stadium[J]. Journal ofBuilding Structures, 2013,34(05):1-10.

[4] Renjie Liu, Suduo Xue, Xiongyan Li, et al. Preventing disproportionate displacements in an annular crossed cable-truss structure[J]. International Journal of Steel Structures, 2017, 32(1): 3-10.

[5] LIU Ren-jie, XUE Su-duo, LI Xiong-yan. Static behavior analysis for annular crossed cable-truss structures[J]. spatial structure, 2014,20(01):89-96.

[6] LIU Renjie, LI Xiongyan, XUE Suduo, et al. Numerical and experimental research on annular crossed cable-truss structure under cable rupture[J]，EARTHQUAKE ENGINEERING AND ENGINEERING VIBRATION. 2017, 16(3):557-569.

[7] Technical Specification for Membrane Structure《JGJ257-2012》[S]. Beijing: china building industry press, 2008.

Proceedings of the IASS Annual Symposium 2019 – Structural Membranes 2019
Form and Force
7 – 10 October 2019, Barcelona, Spain
C. Lázaro, K.-U. Bletzinger, E. Oñate (eds.)

A Study on Shape Determination Method and Operation Experiment of Inspection Guide Frame to Avoid Obstacle in Tunnel

Fumihiro INOUE*, Soonsu KWON [a], Momoe TERATA[a], Satoru NAKAMURA[b], Yoshitaka YANAGIHARA[b]

* Shonan Institute of Technology
1-1-25 Tsujidou-Nishikaigan, Fujisawa, Kanagawa, 251-8511, Japan
inoue@mech.shonon-it.ac.jp

[a] Shonan Institute of Technology
[b] Institute of Technology, Tokyu Construction Co. Ltd

Abstract

To progress the automated inspection and maintenance of inner wall health of tunnel, the advanced inspection system with restricting the traffic regulation was developed. The IGF(Inspection Guide Frame) was constructed on adaptable arch structure using several VGTs mechanism. By controlling the lengths of the extendable members, it was possible to create various truss shapes. Detacting the obstacle shape and location in tunnel by LRF(Laser Range Finder), the shape that the obstacles like a speed plate, blower and side lights were avoided was able to simulate by motion analysis. As a shape adaptation of the guide frame, the inverse analysis method and mathematical interpolation method were applied. The angle of each frame was reversely analyzed according to the shape of the obstacle and the actuator of the frame was controlled simultaneously. These results were recognized by scale model guide flame . In this paper, the basic structure of the guide frame, the shape determination method, the obstacle exploration method and the experimental result of the IGF structure applying the real guide frame

Keywords: Automated Inspection system, Guide Frame, Shape Adaptation, Variable Geometry Truss, Obstacle Detection, Tunnel Inspection

1. Introduction

Most of infrastructures for civil engineering structures such as highway roads, bridges, tunnels constructed around the urban region in high-growth era of 1970-1990 begun to reach the life, and it has been the time when large-scale repair and renewal, rebuilding were demanded. Since these structures are difficult to renovate after completion, it is necessary to grasp the progress of deterioration by periodic inspection and to maintain and manage such as repair and renewal based on future prediction. Especially, with the collapse accident of the high way tunnel generated some time ago in Japan, the inspection of the superannuated tunnel was requested.

Generally, in the periodic inspection of the road tunnel, a maintenance engineer approached the wall by using mobile elevating work platform as much as possible and by restricting the traffic regulation and the engineers detected the deteriorated wall parts by sighting and hammering sound. To progress the automated inspection and maintenance of inner wall of tunnel, some advanced methods were adopted in the SIP program in Japan of the theme of "Maintenance

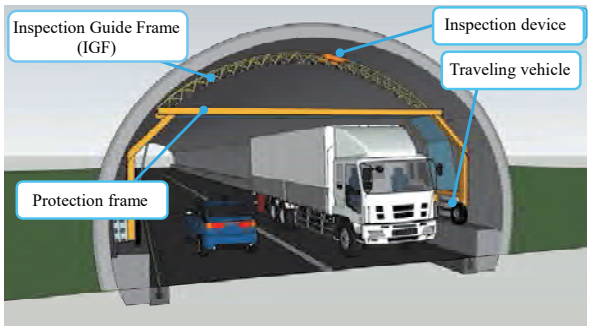


Fig. 1 Traveling vehicle with IGF for tunnel inspection

Copyright © 2019 by F. Inoue, Shonan Institute of Technology in Japan.
Published by the International Association for Shell and Spatial Structures (IASS) with permission.

and management robot". In our proposal of this theme, the inspection system was developed applying the variable guide frame to evade the obstacle in the tunnel without restriction of the traffic regulation as indicating in Fig. 1. In this inspection system, this guide frame was installed on the protection frame with travelling unit. When this unit moved along the tunnel, the guide frame should avoid the obstacles such as traffic plate, lamp and discharged ducts in the tunnel. The shape of this guide frame changing flexibly, the frame was able to pass these obstacles in the tunnel easily [1], [2],[3].

In this paper, the outline of tunnel wall inspection applied guide frame, the finding of convex obstacles using 3 dimension LRF of the high-resolution evaluation, shape adaptation method of guide frame by analysis and experiment, are explained in detail.

2. Obstacle Detection Method in Tunnel

Since the positions and shapes of the various obstacles existing in the tunnel are described on the construction drawing of the tunnel, it is possible to change the shape of the frame so as to avoid obstacles. However, the guide frame being on the traveling vehicle, it is necessary to accurately measure the relative distance between the protection frame and the obstacle. Also, because the movement error of the traveling vehicle is actually included, the obstacle search was carried out on the traveling vehicle. In this chapter, LRF measurement system, analysis method of the shape and position of the obstacle, and its measurement results were verified.

2.1 Measurement System Using Laser Rang Finder

As the traveling vehicle on which the guide frame is installed moves along the inner wall of the tunnel, obstacles protruding from the inner wall near the ceiling may come into contact with the guide frame. Here, as shown in Fig.2, two kind of the LRF was installed at the center surface of the protection frame part. LRF-1 is used to measure obstacles of short distance (6 m or less) with high accuracy, and LMS-2 is used to measure the whole area including obstacles at long distances (30 m or less), as shown in Fig. 3. The specification of LRF-1 and LRF-2 are indicated in Table 1. We connected the LRF to the pan unit and constructed the 3-dimenstinal measurement system giving its inclination angle θ_2 to the plane measurement area angle θ_1 of LRF as indicated in Fig. 4-(a). In this case, if the distance to an obstacle measured by the reflection time of the laser is l, its coordinates (x, y, z) can be expressed.

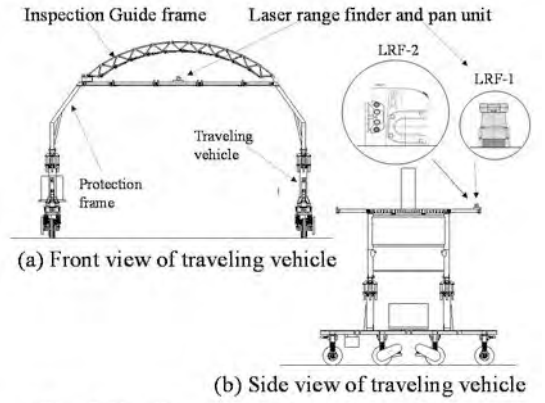


Fig. 2 Configuration of traveling vehicle



(a) LRF-1 and pan unit (b) LRF-2 and pan unit

Fig.3 LRFs installed on the traveling vehicle

Table 1 Specification of LRF1 and LRF-2

Type	LRF-1	LRF-2
Model Number	UTM-30LX	SICK-LMS511
Light Source	1 = 870 nm	1 = 870 nm
Measureable Area	270 deg	190 deg
Accuracy	1-10 m	10-30 m
Angular Resolution	0.25 deg	0.166 or 0.25 deg
Scantime	25 ms	10-11.3 ms
Pan unit resolution	0.5 deg	0.5 deg

$$x = l \cdot \cos\theta_2 \cdot \cos\theta_1$$
$$y = l \cdot \cos\theta_2 \cdot \sin\theta_1$$
$$z = l \cdot \sin\theta_2$$

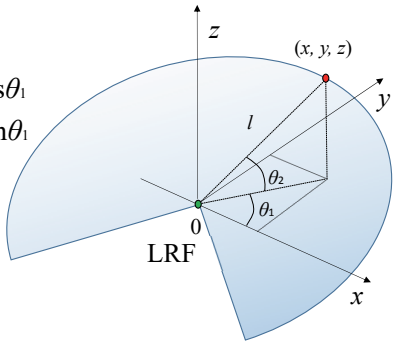


Fig. 4 Measurement system using 3-dimenstinal LRF

2.2 Position Analysis Method of Obstacles

In order to determine the position of the obstacle in the cross-sectional of tunnel, the center position of the obstacle was analyzed assuming that the shape of the obstacle was a circle from the contour of the point group. By assuming that the obstacle was circular even if it was rectangular, the contour of the obstacle was estimated on the safe side. Fig. 5 shows the analysis flow for estimating the position and shape of the obstacle.

①: First of all, scanned the inside of the tunnel with LRF and derived and recorded the laser reflection point. However, since the laser reflection points from the inner wall of the tunnel were geometrically known, their reflection points were deleted. As a result, the shape of the obstacle ahead of the truck was extracted.②: We classified the start position and the end position where the laser reflection point of the obstacle was recorded and extracted the edge of the obstacle.③: The center position of the circle was estimated using the Constant Distance Method (CDM) [4] and the Least Squares Method (LSM) [5], assuming that the point group constituting the edge was an arc of a circle. ④: Finally, we confirmed the range that the shape change of the guide frame avoids with an extra margin against obstacles.

By repeating the above process, the shape and forward position of the obstacle to be avoided by the guide frame are determined.

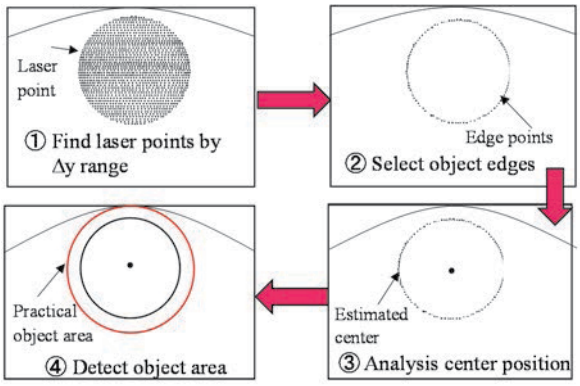


Fig.5 Analysis flow for estimating the position and shape of the obstacle by 3D LRF

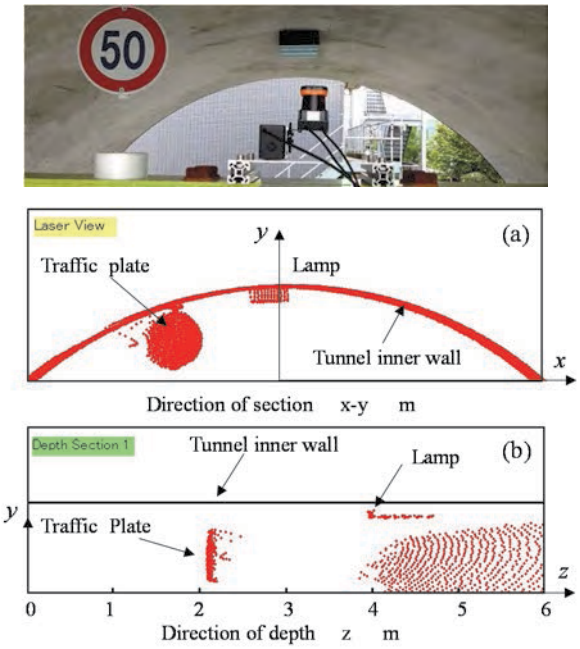


Fig.6 Obstacles state and positions measured by LRF-1

2.3 Measurement Result of Obstacle

2.3.1 Short Distance Measurement by LRF-1

In short distance measurement using LRF-1, it is necessary to determine the position with an obstacle with high accuracy. Using the real simulated tunnel constructed for the experiment, the obstacles attached to the inner wall of tunnel was measured by LRF-1. Fig. 6 shows the state of the obstacle measured. In the x - y plane (Fig. 6- (a)), the shape including the traffic signs and the contours of the ceiling lamp in the tunnel is better captured by comparing to the actual picture. In the depth direction z-y plane (Fig.6- (b)), the position of traffic plate and the lamp could be estimated from the portion where the reflection points of the laser are densely concentrated, and it was confirmed that the position was also nearly accurate. In the calculated center position based on the obstacle data in the x - y plane was described in reference [6].

2.3.2 Long Distance Measurement by LRF-2

In order to confirm the long distance measurement using LMS-2, the obstacle was searched using actual tunnel. The radius of the tunnel was about 6 m, and LRF-2 was installed at a point of 90 degrees from the horizontal plane was performed at a resolution angle of 0.5 degrees, and the laser reflection distance in the tunnel was acquired. Fig. 7 shows the measurement situation in the tunnel.

The lamp protrudes at regular intervals on the side of the ceiling surface of the tunnel, which is expected to become an obstacle when passing through the guide frame. Fig. 8 shows the measurement situation of the obstacle on the x-y plane seen in the entire cross section of the tunnel. When observing on the x-y plane, the obstacles overlap, so it is difficult to determine the exact shape of each obstacle.

As described above, by combining the two LRFs methods, it was possible to detect the approximate position and shape of the obstacle at a long distance, and the accurate position and shape at short distance.



Fig.7 Obstacles in the tunnel and LRF-2

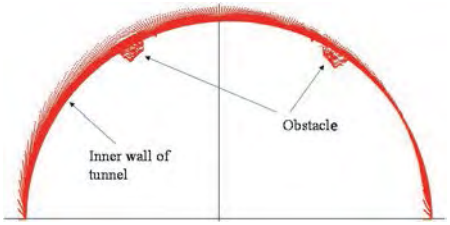


Fig.8 Measurement result of the obstacle on the x-y plane by LRF

3. Shape detestation of Inspection Guide Frame

In chapter 2, we explain the development of the guide frame which can avoid obstacles (lighting lamp, display board, etc.) by using a variable guide frame adaptable to the tunnel shape. In order to create a complicated guide frame shape, the shape of guide frame was simulated by mathematical method, and the possibility of guide frame was verified using real guide frame experimentally.

3.1. Basic Structure of IGF

The proposed IGF was constructed on several VGT (Variable Geometry Truss) elements. This VGT was very simple truss structure composed of extendable members, fixed members and hinges, as showing in Fig. 9. By controlling the lengths of the extendable members, it was possible to create various truss shapes. When extendable members are extended simultaneously as indicated in Fig.10, the VGT structure was changed like a spring stretching from (a) to (b). When the extendable members are extended alternately, the structure was changed to a circular shape (c) Moreover, when they are extended optionally and their length were controlled, the structure could be changed into any intended shape (d).

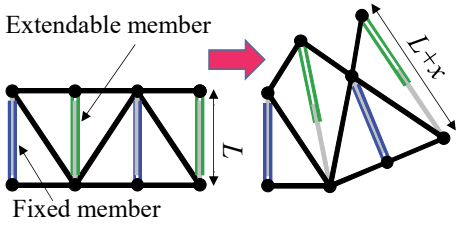


Fig. 9 Basic structure of VGT

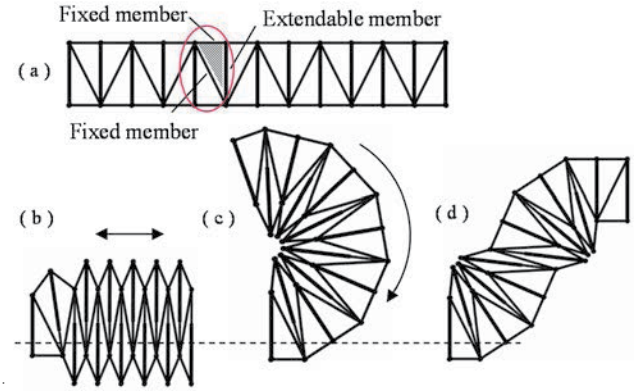


Fig. 10 Example of shape change of VGT strycture

In case of VGF, the basic shape of guide frame was assumed to be an arch structure and its two edges were supported on the protection frame. Though the guide frame was changed flexibly by VGTs shape, the shape was limited by upper side of tunnel wall and traffic space area. So, to avoid projecting obstacle in the tunnel space, it was necessary to correspond to the shape of the guide frame close to the section shape of the obstacle as much as possible. Knowing the obstacle location and shape from the drawing map before inspection, the shape of obstacles as speed plate, blower and side lights were able to simulate by motion analysis. In an actual measurement, the shapes of obstacle were detected by the data of LRF continually.

3.2 Structure of Inspection Guide Frame

3.2.1. Basic Equation and Shape of Frame

As analysing the arch structure composed of VGT, the whole of guide frame was assumed to be a cantilever structure as indicated. The frame can replace a robot manipulator combining two fixed-length members in series. When the supported edge of frame was $q(x_0, y_0)$, the top $q(x, y)$ of the x, y co-ordinates of the frame combined with n (n≧2) VGT sets was given by Eq. (1) and Eq.(2) using each hinge angle θ_j.(j=1, 2, 3, · ·n),

$$q(x,n) = l_0 \cdot \sum_{k=1}^{n} \cos\left\{\sum_{j=1}^{k} \theta_j\right\} \quad (1) \qquad q(y,n) = l_0 \cdot \sum_{k=1}^{n} \sin\left\{\sum_{j=1}^{k} \theta_j\right\} \quad (2)$$

Where, l_0 was the length of diagonal member of the frame. To transform the shape of arch frame, some hinge positions on the frame only had to change in proportion to target shape. However, for an intended frame shape fixed by equations (1) and (2), it was quite difficult to solve these equations analytically and to decide the angle because the frame was a very highly redundant. In this case, inverse kinematics analysis was applied [7], [8]. Considering a temporal change of the whole of the frame, the top edge modifying the original point by inverse analysis to all VGT angle velocity $\dot{\theta}_i$, the shape change was absorbed according to the arch.

$$\dot{\theta}_i = J^{-1} \cdot \dot{q}_i(x,y) \quad (3)$$

Where, J^{-1} indicates inverse Jacobean Matrix (2×n). However J^{-1} isn't necessarily decided because $\boldsymbol{J}$ is not a regular system in n>2. In this case, the suitable matrix such a pseudoinvesre matrix $\boldsymbol{J}^{\#}$ was generally inducedinstead of $\boldsymbol{J}^{-1}$**.** Iterating such modification of shape changes, the shape of original arch was able to carve partially to extent in which the obstacle could be evaded.

3.2.2. Shape Change of VGF Avoiding Obstacles

Applying an inverse analysis in the previous chapter 3.2.1, the shape of the frame that avoided the obstacle was analyzed. First of all, a virtual obstacle was positioned on the perpendicular line of the obstacle. The position of a virtual obstacle was gradually lowered, and the frame shape was changed so that surroundings of the obstacle should not come in contact with the frame.

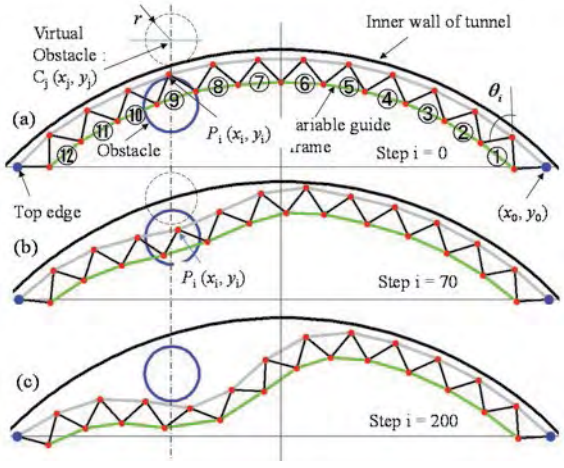


Fig. 11 Shape simulation of IGF by inverse analysis



Fig. 13 Shape control of IGF in model tunnel

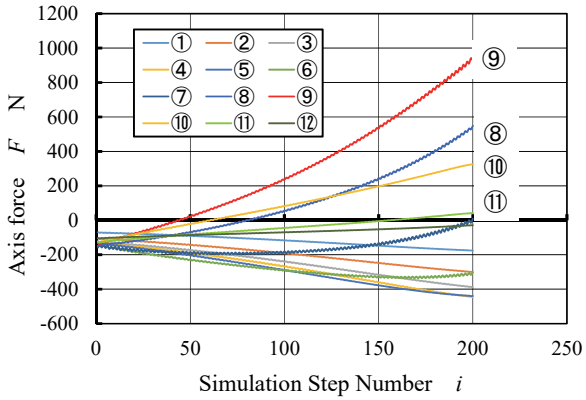


Fig.12 Axial force acting on each actuator with change of guide frame

Fig.11-(a)～(d) show the shape change of the arch frame by simulation results. Introducing an inverse analysis to avoid the obstacle, first of all, a virtual obstacle was positioned on the perpendicular line of the obstacle as shown in Fig12-(a). The position of a virtual obstacle was gradually lowered, and the frame shape was changed so that surroundings of the obstacle should not come in contact with the frame. As showing the Fig.11-(b) and (c), the arch frame was indicated to change like avoiding the obstacle. Finally, a virtual obstacle came in succession at the position of a real obstacle, and the shape of a final arch frame was decided. Fig.12 shows the axial force acting on each actuator with change of guide frame. Before the shape of the guide frame changed, weak compressive force was applied to each actuator. When the shape of the guide frame became a curved shape avoiding the obstacle, large tensiloe force was exerted on the actuators ⑧ to⑪, but the allowable load was sufficiently satisfied. The advantage is that there is no concern about buckling force, as it is a tensile force. Fig.13 shows the result of experiment in actual model tunnel using variable guide frame. With the real arch frame of 6 m in length, similar shape was able to be also achieved by referring to the simulation result very shout times.

3.3. Frame Analysis by Spline Function

In order for the guide frame to avoid obstacles, it is necessary to predict the final shape of the guide frame avoiding obstacles. In this section, the shape of the guide frame was analyzed using a Spline interpolation method and its effectiveness of the method was considered.

3.3.1 Shape Analysis by Spline Interpolation

To the initial guide frame shape, the overall shapes for obstacles were mathematically combined by the spline interpolation f avoiding unction. Spline interpolation is a method of combining arbitrary shapes with polynomials to form a continuous shape. Assuming a function that interpolates the section (x_j, x_{j+1})the piecewise polynomial $S_j(x)$ is expressed by the Equation (4).

$$S_j(x) = a_j(x-x_j)^3 + b_j(x-x_j)^2 + c_j(x-x_j) + d_j \quad (j = 0,1,2\cdots) \qquad (4)$$

In order for this cubic equation to be a smooth curve, it is assumed that the value of the first derivative and the second derivative of $S_j(x)$ are equal, and the value of the second derivative at the start point x_0 and the end poin x_n is 0. By applying the above conditions to each equation for several interpolation points, the coefficient of function a_j, b_j, c_j, d_j was calculated, and the function by the spline interpolation was decided. Here, each coefficient was determined as follows;

$$a_j = \frac{S_j''(x_{j+1}) - S_j''(x_j)}{6(x_{j+1}-x_j)} \qquad (5) \qquad \text{›}_j = S_j''(x_j)/2 \qquad (6)$$

$$c_j = \frac{y_{j+1}-y_j}{(x_{j+1}-x_j)} - \frac{(x_{j+1}-x_j)(2S''(x_j)+S''(x_{j+1})}{6} \qquad (7) \qquad d_j = y_j \qquad (8)$$

3.3.2 Estimation of IGF Shape Avoiding Obstacles

Using the method in the previous section, several interpolation points (x_j, y_j) were determined so as to avoid obstacles, and the constants of the piecewise function were calculated using equation (9). Here, arbitrary six points (including both end points) that avoid obstacles are selected for the shape of the upper chord of the guide frame, and the shape of the new guide frame is analyzed. By constructing easy system that can select representative points by touching the tablet screen, we were able to visually show the position to avoid obstacles. Several examples are shown below.

(1) Example of side obstacle 1

The shape of a circular obstacle suspended from the left side of the tunnel ceiling overlapped the guide frame as shown in Fig.14-(a). We selected 6 optimum interpolation points to avoid obstacles and analyzed the shape of the upper chord by spline interpolation. As shown in Fig. 14-(b), the obtained spline curve is a smooth shape that continuously connects five regions sandwiching selected points, and is connected at the start and end points while avoiding obstacles. The shape of the guide frame was

suitable

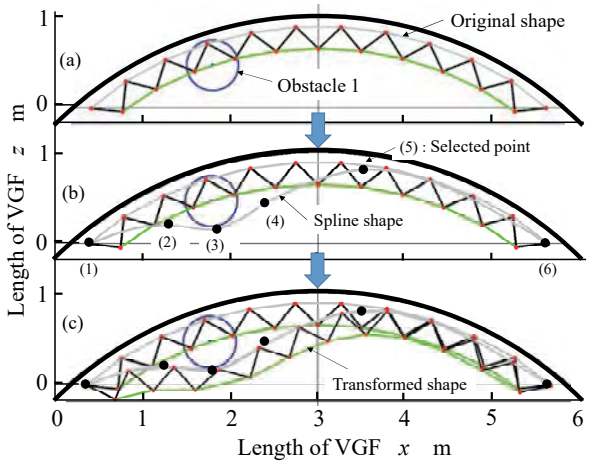


Fig.14 Shape decision of spline function for obstacle 1

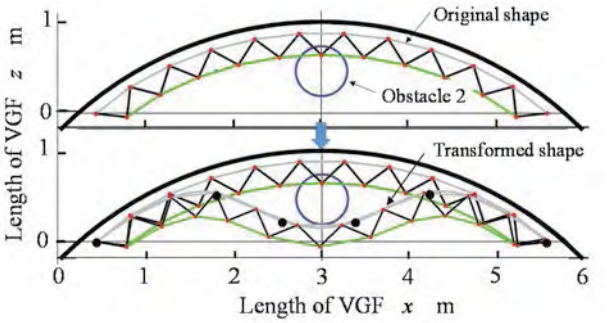


Fig.15 Shape decision of spline function for obstacle 2

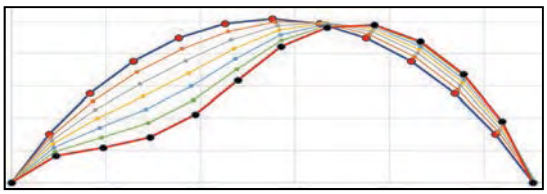


Fig16 Shape control of guide frame for obstacle 2

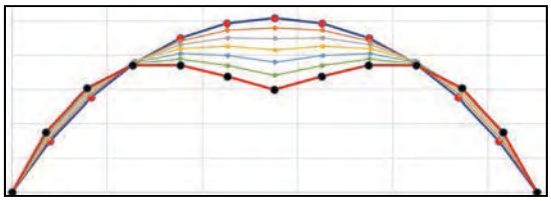
for fitting because there are no discontinuities or parts with a large polar fraction.
The new guide frame was reproduced by configuring the guide frame to conform to the shape of the obtained upper chord member as shown in Fig.14-(c). However, although the total length of the guide frame of the new shape is slightly different from the original shape, the shape is optimized by proportional distribution, but since there is almost no significant change in shape, the obstacle can be sufficiently avoided. Based on the above analysis results, the shape of the actual guide frame was observed in Fig.11. It was verified experimentally that the shape of the guide frame analyzed by spline interpolation was a shape that could smoothly obstruct obstacles.

(2) Example of center obstacle 2

In this case, the shape of the guide frame was analysed assuming an obstacle such as a discharge fan at the center of the tunnel as shown in Fig.15-(a). As showing inFig.15-(b), the interpolation points placing symmetrically at the bottom arc of a circular obstacle, it was possible to determine the shape of the guide frame for avoiding any obstacle. The shape of the actual guide frame was transformed using data analyzed. The experimental situation is shown in Fig.16. The guide frame was shaped to avoid obstacles, and it was confirmed that there was sufficient margin for structural mechanics. From the above results, by using Spline interpolation method, it was possible to determine the shape of the guide frame for avoiding any obstacle.



(a) Shape change of VGF for obstacle 1 at each step .



(b) Shape change of VGF for obstacle 2 at each step .

Fig.17 Shape decision of VGF to avoid obstacle

3.3.2 Movement of transformed IGF

Since the shape after deformation by spline interpolation method was decided, the deformation process from the initial state was examined. The length change of each actuator was divided by the target time to determine the moving speed of the actuator. Fig.17 shows the analysis example of the shape change of the guide frame for obstacle at each step. It confirmed that it changed smoothly from the initial stage

to the final shape. Thus, by applying the spline interpolation method, it is possible to easily determine the shape, and to change the shape of the guide frame to the desired shape.

5. Conclusion

The tunnel ceiling area which was an obstacle of the guide frame was searched using two kind of LRF. LMS-1 was used to measure obstacles of short distance with high accuracy, and LMS-2 is used to measure the whole area including obstacles at long distances. Next, we proposed a method to analyzed the shape of the guide frame by inverse analysis and spline interpolation in order to create complicated frame shape avoiding arbitrary obstacles on the tunnel ceiling surface. In the case of using spline interpolation method, since the function classification can be divided according to the shape of the obstacle, complicated obstacles can be dealt with. Applying the spline interpolation method, it is possible to easily determine the shape, and to change the shape of the guide frame to the desired shape.

In the future, we will establish the control method to continuously change the shape of the guide frame from the obstacle search in the tunnel, and to apply it to the actual inspection system.

Acknowledgements

Finally, the author thanks all who supported the development of the movable arch structure and its accompanying external panel. Further, this work was supported by Council for Science, Technology and Innovation, "Cross-ministerial Strategic Innovation Promotion Program (SIP), Infrastructure Maintenance, Renovation, and Management". (Funding agency: NEDO)

References

[1] Inoue F, Nakamura S, "Development of Variable Guide Frame to Inspect Inner Wall Tunnel", Proceedingsof the 6th International Conference on AdvanceMechatronics (ICAM2015), Tokyo, Japan, PP. 284-285,2010..

[2] Fujii H, Yamashita A and Asama H, "Defect Detection with Estimation of Material Condition Using Ensemble Learning for Hammering Test", Proceedings of the 20 16 IEEE International Conference on Robotics and Automation, pp.847-3854 , Stockholm (Sweden), 2016.

[3] Inoue F, "Shape Control of Variable Guide Frame for Tunnel Wall Inspection", Proceeding of T 34th International Symposium on Automation and Robotics in Construction (ISARC 2017),Taipei, Taiwan, pp.675-682, 2009.5.

[4] Tamura H, Sasaki T, Hashimoto H and Inoue F, "Circle Fitting Based Position Measurement System Using Laser Range Finder in Construction Fields," 2010 IEEE/RSJ Intl. Conf. on Intelligent Robots and Systems, pp.209–214, 2010.

[5] Chernov N, Lesort C, "Least Square Fitting of Circles", Journal of Mathematical Imaging and Vision, Vol. 23, pp. 239-251, 2005.

[6] Inoue F, Sasaki T, Huang X and Hashimoto H, "A Study on Position Measurement System Using Laser Range Finder and Its Application for Construction Work", Journal of Robotics and Mechatronics, Vol. 26, No.1, pp. 226-234, 2012.

[7] Inoue F, "A Study on Adaptive Structure Applying Variable Geometry Truss (Mechanism of Movable Arch Roof with External Panel)"Journal of Robotics and Mechatronics, Vol. 21, No.2, pp.172-178, 2009.

[8] Inoue F, "A Study on Optimum Shapes and Motion of Movable Arch Structure By Variable Geometry Truss", Proceeding of The 9th Asian Pacific Conference on Shell and Spatial Structures (APCS2009) , Nagoya, Japan, pp.121-128, 2009.5.

Proceedings of the IASS Annual Symposium 2019 – Structural Membranes 2019
Form and Force
7 – 10 October 2019, Barcelona, Spain
C. Lázaro, K.-U. Bletzinger, E. Oñate (eds.)

Comparative Structural Evaluation and Analysis of Modular Deployable Structures of Expandable Frames

Mauricio SOTO-RUBIO*, Cody JEW

*University of Calgary. School of Architecture, Planning and Landscape
2500 University Drive NW. Calgary, AB T2N 1N4
Mauricio.sotorubio@ucalgary.ca

Abstract

This paper studies multiple geometries commonly used in modular deployable structures of expandable frames and compares their structural performance under similar conditions including loads, spans, and materials. The structures are then ranked according to maximum stress and axial forces. The study presents an evident-based system to evaluate the relative structural performance of structural systems commonly used in the design of deployable structures, helping to determine their adequacy for different applications.

Keywords: Deployable Structures, Collapsible Structures, Scissor Structures, Pantographic Structures, Lightweight Structures, Modular Structures, Structural Analysis

1. Introduction

Deployable structures of expandable frames, commonly known as scissor or pantographic structures, are collapsible assemblies that can be easily expanded to activate a space or contracted into a compact, transportable configuration. Due to their inherent flexibility and versatility, they can be used for a wide variety of purposes such as temporary shelters, travelling medical centers, exhibition spaces, pop-up installations, etc. The geometric rules that govern the design of deployable structures of expandable frames have been extensively documented. Architects and researchers such as Felix Escrig (Escrig, 2012), Sergio Peregrino, and Charis J. Gantes (Gantes, Connor, Logcher, & Rosenfeld, 1989) have catalogued the morphology of these type of structures and described the geometric requirements for them to fold and unfold. Other architects such as Niels De Temmerman (De Temmerman, 2007), Carlos Henrique Hernandez (Hernandez, 1987), Juan Perez Valcarcel (Valcárcel & Escrig, 1992), have also developed innovative solutions based on this technology and documented their findings in numerous academic journals. However, the relative structural performance of these modular designs has never been compared in a single study. The extensive number of geometrical alternatives and the lack of evidence-based information regarding their general structural behaviour presents a challenge to new designers looking for the most efficient design for a specific set of conditions. This study represents an attempt to evaluate the structural performance of different geometries of deployable structures of expandable frames. By comparing the structural behaviour of standard designs and classify them according to maximum stress, stability, and maximum axial forces, the paper will produce evidence-based guidelines that will allow future design professionals to determine the adequacy of different configurations for deployable structures.

2. Methodology

The methodology used for this study consists in the following steps. First, a representative sample of modular geometries was selected from existing academic literature. This selection does not include ad-hoc designs and it is not intended to be complete or all encompassing. However, the selection is wide

Copyright © 2019 by Mauricio SOTO-RUBIO, Cody JEW
Published by the International Association for Shell and Spatial Structures (IASS) with permission.

enough to include the most commonly used geometries in deployable structures of expandable frames. Second, standard tensile fabric structures were designed to fit every modular structure. The forms used were not minimal surfaces, which is what is normally required for tensile fabric structures. However, the shapes used were consistent enough to helped determine tributary areas and the forces acting on the connecting points to the scissor structure, which included dead, wind, and snow loads. The value of these loads were determined according to the 2010 National Building Code of Canada and applied using the computer program SAP 2000 to determine the maximum compressive and tensile forces for each geometry. Finally, the largest steel cross section required was applied to all 9 structures, and the program was ran again to determine individual stress distribution and maximum deflections for all structures.

2. Geometries

There are many geometric possibilities for the design of modular structures of deployable frames. The following geometries represent the main categories or types found in existing academic literature. The structures are first divided according to their general shape: Vault, Dome or Pendentive. Secondly, the structures are arranged according to whether their system lines are parallel to one another (Translational) or meet radially on a central point (Polar). Finally, the structures are organized according to how many deployable frames make up their system: 2-Way, which forms a square or rectangular grid on the structure, or 3-Way, which forms a triangular grid on the structure.

The following 9 separate geometries were tested and analyzed in this study. All these structures were dimensioned to span 15 meters, cover approximately 225m2, and were composed of structural elements of similar lengths.

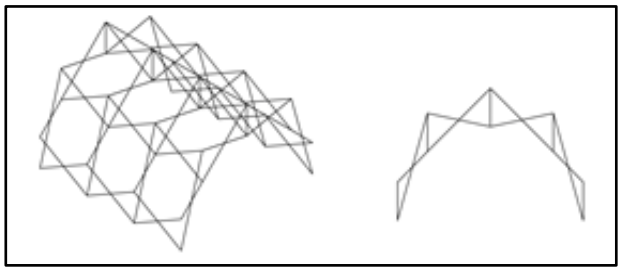


Fig. 1: Vault – Translational – 2 Way

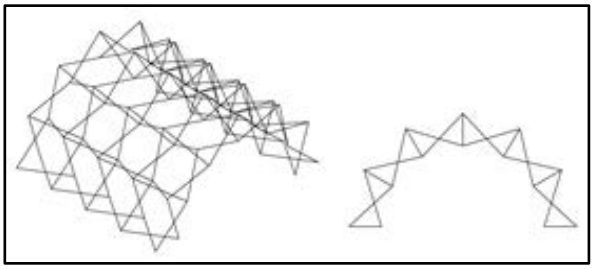


Fig. 2: Vault – Polar – 2 Way

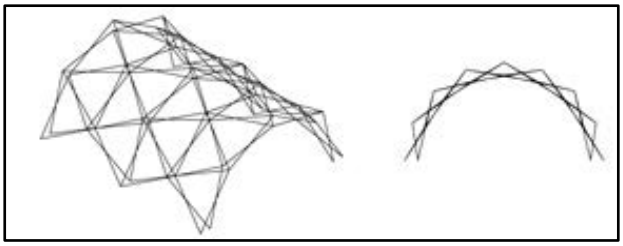


Fig. 3: Vault – Polar – 3 Way -– Type 1

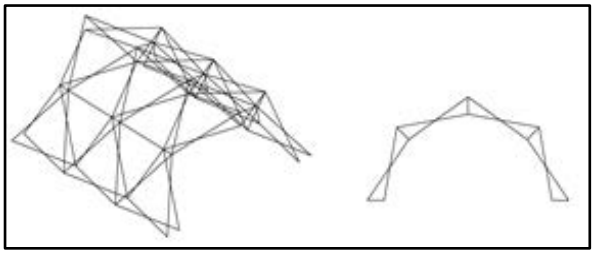


Fig. 4: Vault – Polar – 3 Way – Type 2

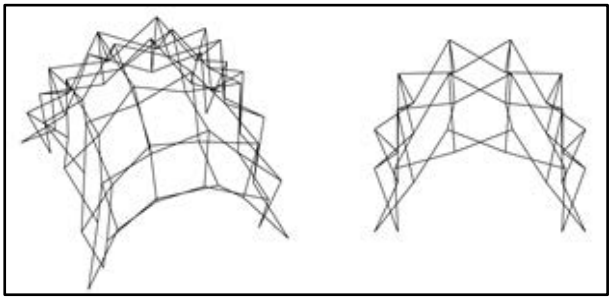


Fig. 5: Pendentive – Polar – 2 Way

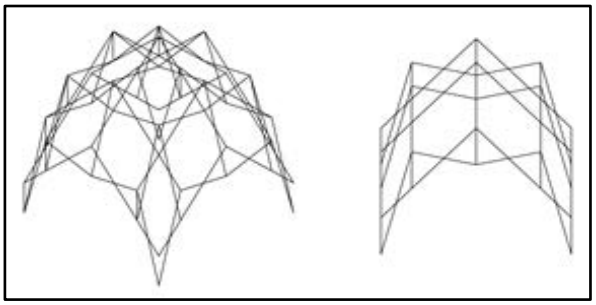


Fig. 6: Pendentive – Translational – 2 Way

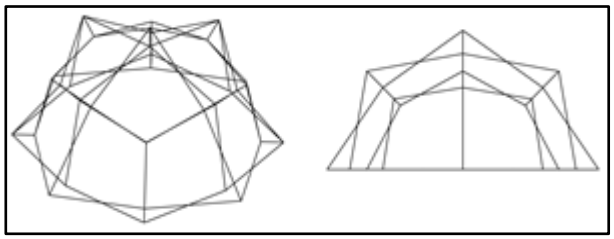


Fig. 7: Dome – Polar – 2 Way

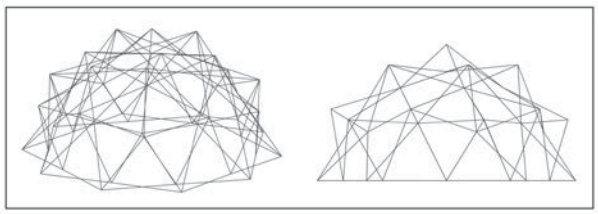


Fig. 8: Dome – Geodesic

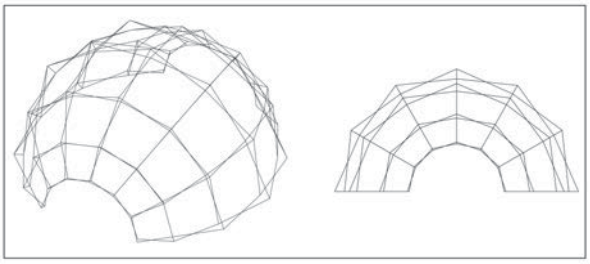


Fig. 9: Dome – Polar – Parallels and *Meridians*

3. Loads

The applied loads were designed to comply with the National Building Code of Canada 2010. The structures were tested in SAP 2000 to record stresses based on a controlled set of loads including dead, wind, and snow loads.

Load Resistance Factored Design (LRFD), also referred to as Limit State Design (LSD) was used instead of Allowable Stress Design (ASD). This is due to ASD being deterministic and therefore more suited for detailed structural analysis. Also, building codes based on LSD (such as the NBCC) implicitly define the appropriate level of reliability since the factors are determined using probability of failure. Thus, LSD results in a more consistently designed structure where all elements have the same probability of failure, which may be better suited to practical engineering applications.

A normal importance factor value of 1.0 was chosen because all types of structure are currently not covered by the code. For example, the analyzed structural systems have low density and small size, consisting of HSS members less than eight inches per side. This type of infrastructure is not as deadly as traditional projects which consists of concrete, rebar, piping, lighting, walls, and floors. In the event of collapse, these deployable structures would be easier to evacuate, having a maximum width of 20 meters in the longitudinal direction and only having fabric inside the structure in a hangar-like formation. Also, we have considered these structures to be temporary in nature and to be deployed for only weeks at the time.

A fabric roof was estimated to be attached to connection joints inside the structure to decrease the work required to assemble the structure as well as the amount of fabric needed. The area of the fabric would be much greater compared to that of the members, therefore the loading conditions were calculated with respect to the fabric. Loads were applied at the points where fabric would be attached, therefore distributing the loads experienced due to the fabric through tributary areas. The attachment of fabric at certain nodes would cause areas of flatness; there areas were numbered for ease of calculation, with the lowest number representing area at the top of the structure and increasing numbers until the ground level was reached. Free body diagrams were drawn and used to solve for tributary loads and to account for all applied forces. Dead loads included not only the weight of the members (ASTM A992 Fy50 – HSS4x4x1/2), but also the weight of the fabric as well as its average pre-stress. The fabric selected demonstrated sufficient strength and durability while maintaining a low weight. That being, Polyester (Precontraint 402) with a weight of 0.49 kg/m2 and a maximum tensile strength of 2.2 kN/5 cm. A pre-

stress of 1 kN was applied to each joint where the fabric would be attached as an over-conservative approximation for preliminary analysis.

It is important to mention that all geometries were designed and evaluated without diagonal bracing elements. These bars or cables are required to be installed after deployment in all 2-Way modules in order to guarantee their lateral stability.

1 in 50 year events were used for both snow loads and wind pressures, as stipulated by the NBCC. These loads were considered critical to best observe the performance of each geometry. The loads were applied on the structures according to the following tributary areas:

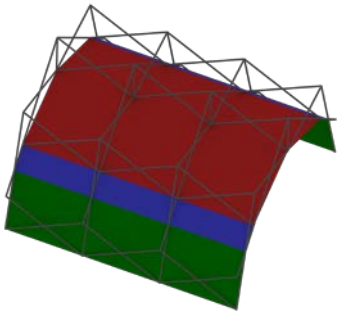


Fig.11 Vault – Trans - 2 Way Type

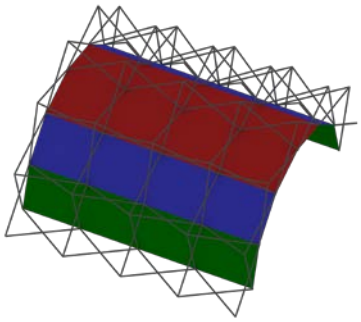


Fig. 12: Vault – Polar – 2 Way

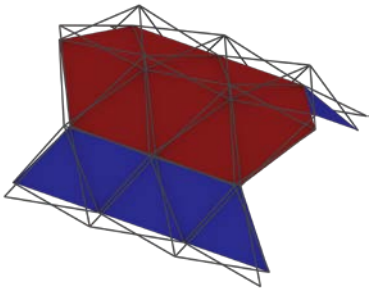


Fig. 13: Vault – Polar – 3 Way -

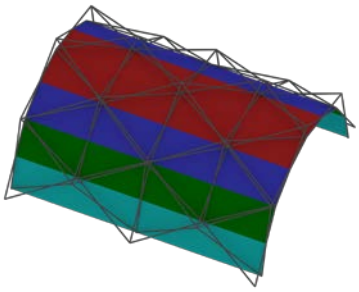


Fig. 14: Vault–Polar–3 Way-Type 2

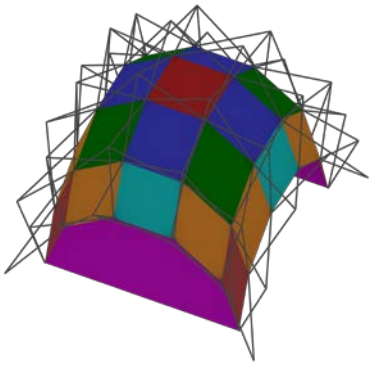


Fig. 15: Pendentive–Polar–2 Way

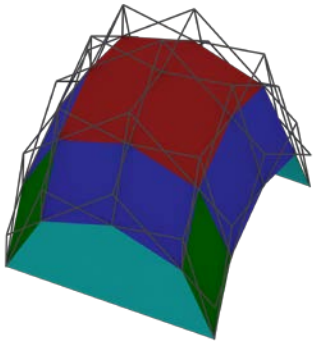


Fig.16: Pendentive–Translational–2 Way

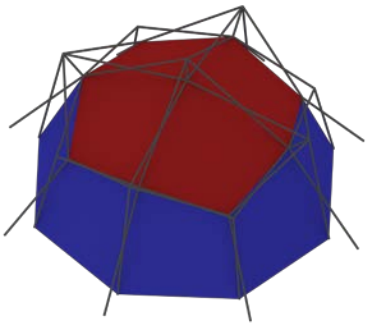


Fig. 17: Dome–Polar–2 Way

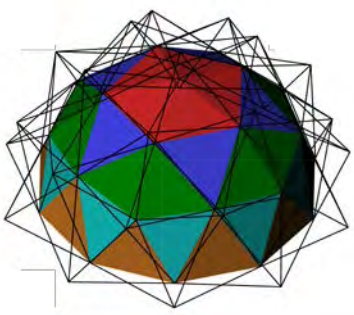


Fig. 18: Dome–Geodesic

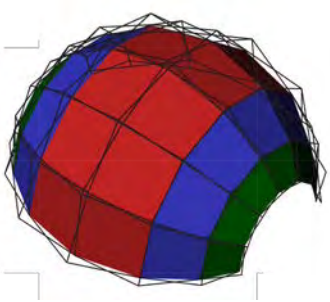


Fig. 19: Dome–Polar–Parallels and Meridians

The following equations were used to determine loads.

3.1. Snow

$$S = IS[SS(CbCwCSCa)+Sr] \quad (1)$$

Where:

IS = importance factor for snow load = 1.0

Ss = 1-in-50 year ground snow load, in KPa = 3.6 (found in Banff, Alberta. This is the largest value of the province)

Cb= basic roof snow load factor = 0.8, for small roofs

Cw= wind exposure factor = 1.0

Cs= slope factor

Ca= shape factor = 1.0,

Sr= 1-in-50 year associated rain load, in KPa, not greater than Ss (CbCwCsCa) = 0.3 or Ss (CbCwCsCa)

3.2. Wind

$$p = IwqCeCgCp \quad \text{for external}$$

$$pi=IwqCeCgiCpi \quad \text{for internal}$$

Where:

p = specified external pressure, or suction, acting statically and in a direction normal to the surface

pi = specified internal pressure, or suction, acting statically and in a direction normal to the surface

Iw= Importance factor for wind load = 1.0

q = reference velocity pressure, in KPa = 1.01 (found in Cowley, Alberta. This is the largest value of the province)

Ce = exposure factor = 0.9 for open, level terrain with scattered obstructions

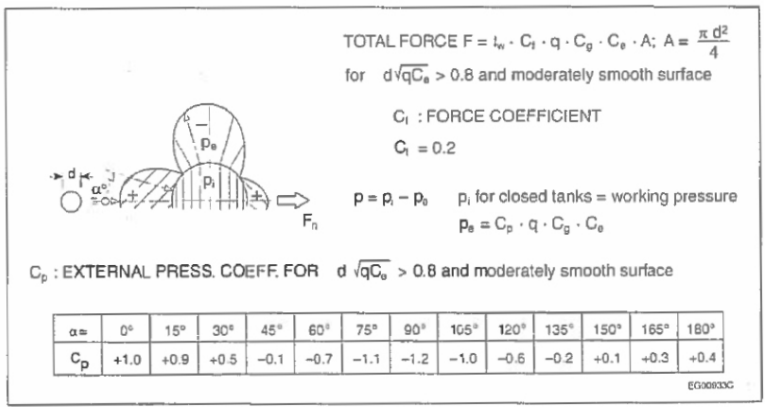
Cg = gust effect factor = 2.5 for small elements (to be conservative)

Cgi = internal gust effect factor = 2.0

Cp = external pressure coefficient

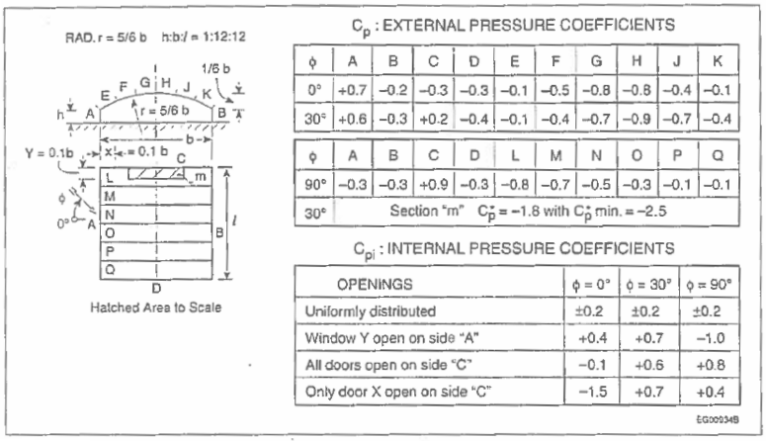
Cpi = internal pressure coefficient

The sphere (found in Part 4 of Division B of NBCC 2010) and hangar (found in Part 4 of Division B of NBCC 2010) simplification figures and tables from the NBCC commentary were used to calculate wind pressures for preliminary analysis (see tables 1 and 2). The dome geometry was the only one where the sphere approximation was used while the rest were considered as hangars and the fabric was arranged in a hangar-like configuration. The internal pressure, Cpi was taken as uniformly distributed for the dome and as all doors open on one side for the rest of the geometries in order to approximate a hangar-like structure.



α=	0°	15°	30°	45°	60°	75°	90°	105°	120°	135°	150°	165°	180°
C_p	+1.0	+0.9	+0.5	−0.1	−0.7	−1.1	−1.2	−1.0	−0.6	−0.2	+0.1	+0.3	+0.4

Table 1: Sphere Simplification Shart Found in Part 4 of Division B of NBCC 2010



ϕ	A	B	C	D	E	F	G	H	J	K
0°	+0.7	−0.2	−0.3	−0.3	−0.1	−0.5	−0.8	−0.8	−0.4	−0.1
30°	+0.6	−0.3	+0.2	−0.4	−0.1	−0.4	−0.7	−0.9	−0.7	−0.4

ϕ	A	B	C	D	L	M	N	O	P	Q
90°	−0.3	−0.3	+0.9	−0.3	−0.8	−0.7	−0.5	−0.3	−0.1	−0.1
30°	Section "m" $C_p^* = -1.8$ with C_p^* min. = −2.5									

OPENINGS	ϕ = 0°	ϕ = 30°	ϕ = 90°
Uniformly distributed	±0.2	±0.2	±0.2
Window Y open on side "A"	+0.4	+0.7	−1.0
All doors open on side "C"	−0.1	+0.6	+0.8
Only door X open on side "C"	−1.5	+0.7	+0.4

Table 2: Hangar Simplification Shart Found in Part 4 of Division B of NBCC 2010

The wind loads applied were at 0, 30, and 90 degrees with respect to one longitudinal side of the structure, with load combinations applied to snow and wind at each of the degrees. The combinations of varying degrees and environmental loads are listed below.

3.3. Load Combinations

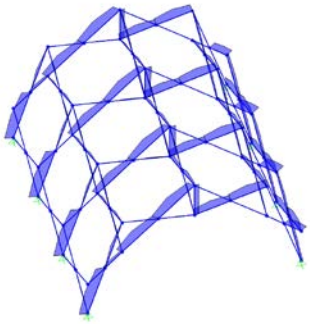
Wind Direction	0 degrees	30 degrees	90 degrees
Load Combination with Snow as Principal Load	1.25D+1.5S+0.4W	1.25D+1.5S+0.4W	1.25D+1.5S+0.4W
Load Combination with Wind as Principal Load	1.25D+0.5S+1.4W	1.25D+0.5S+1.4W	1.25D+0.5S+1.4W

Table 3: Load Combinations

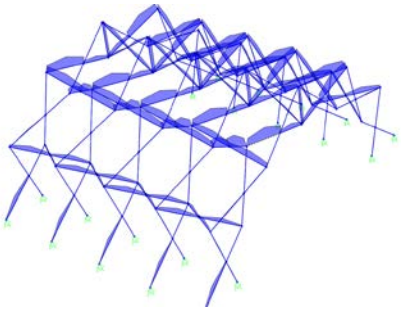
For the final structural analysis, the load combination with snow as principal factor and 30 degrees wind direction was selected.

3. Results

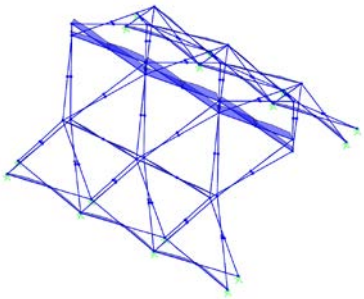
The information below shows the location and magnitude of the maximum stress forces, both in tension and compression, in every structure according to the loads previously described.



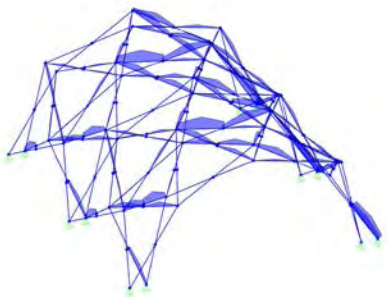
Vault–Translational–2 Way
Max Tension = 14,056.34 KN/m2
Max Comp. = -34,487.43 KN/m2



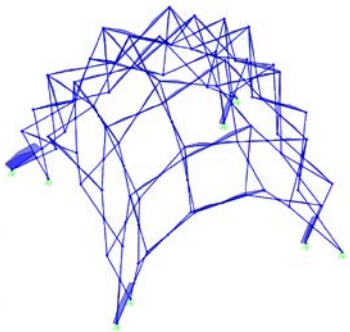
Vault–Polar–2 Way
Max Tension = 11,846.86 KN/m2
Max Comp. = -17,278.75 KN/m2



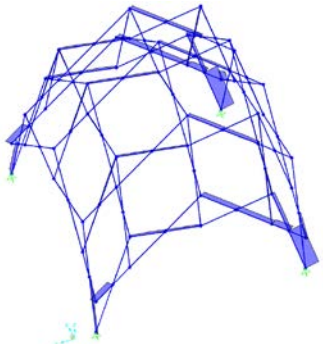
Vault–Polar–3 Way –– Type 1
Max Tension = 36,391.41 KN/m2
Max Comp. = -29,848.99 KN/m2



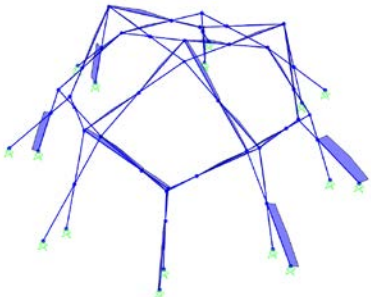
Vault–Polar–3 Way – Type 2
Max Tension = 11,958.75 KN/m2
Max Comp. = -21,721.96 KN/m2



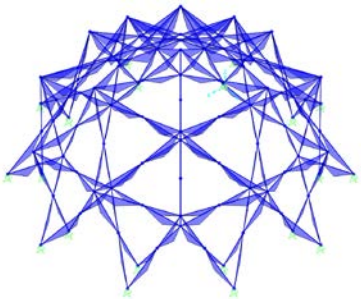
Pendentive – Polar – 2 Way
Max Tension = 19,292.21 KN/m2
Max Comp. = (-28,600.84 KN/m2)



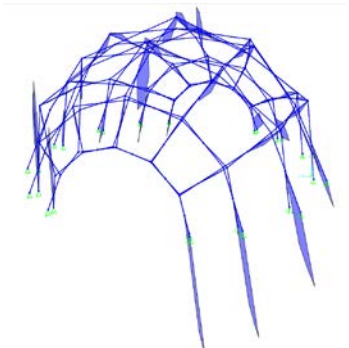
Pendentive–Translational–2 Way
Max Tension = 93,594.52 KN/m2
Max Comp. = -116,613.62 KN/m2



Dome–Polar–2 Way
Max Tension = 24,557.79 KN/m2
Max Comp. = -31,518.88 KN/m2



Dome–Geodesic
Max Tension = 29,960.13 KN/m2
Max Comp. = -19,097.61KN/m2



Dome–Polar–Parallels & Meridians
Max Tension = 12,579.8 KN/m2
Max Comp. = -53,668.92 KN/m2

4. Conclusions

The following lessons can be learned from this study:

1. As expected, maximum compression and tension stresses in vault configurations accumulates on one side of the scissor-like elements according to the direction of the wind. However, under the exact same loading conditions, span, and sectional and material properties, translational variations can be 2 times less efficient than polar configurations.
2. Maximum stresses on pendentive structures tend to accumulate at their bases. Under exactly the same loading conditions, span, and material and sectional properties, translational variations can be up to 4 times less efficient than polar configurations.
3. Regarding dome structures, geometries that follow a parallels and meridians configurations seem less efficient that simple 2-way structures. Geodesic configurations are extremely efficient and exhibit relatively low and equally distributed stresses throughout the structure.

The selection of a particular geometry of a modular deployable structure of expandable frames for a particular application must include a variety of project specific factors including the proposed programmatic activities for the module, site location and conditions, availability of materials and building expertise, installation procedures, etc. However, one of the main reasons for using lightweight deployable structures is to capitalize on their inherent lightness and flexibility. Therefore, a high level of structural performance and efficiency is key. The goal of this study is to produce evidence-based guidelines that allow future design professionals to compare and contrast the structural performance of different geometric alternatives and determine their adequacy for a specific application.

References

[1] De Temmerman, N. (2007). *Design and Analysis of Deployable Bar Structures for Mobile Architectural Applications* (Doctor in Engineering). Vrije Universiteit Brussel, Brussel.

[2] Escrig, F. (2012). *Modular, Ligero, Transformable. un paseo por la arquitectura ligera móvil*. Spain: Universidad de Sevilla. Secretariado de publicaciones.

[3] Gantes, C. J., Connor, J. J., Logcher, R. D., & Rosenfeld, Y. (1989). Structural analysis and design of deployable structures. *Computers & Structures*, *32*(3), 661–669. https://doi.org/10.1016/0045-7949(89)90354-4

[4] Hernandez, C. (1987). *Deployable Structures* (Master is Science in Architecture Studies). Massachusetts Institute of Technology, Cambridge.

[5] Valcárcel, J. P., & Escrig, F. (1992). Expandable Triangular Cylindrical Vaults. *Actas Del Congreso Internacional Sobre Los Métodos Numéricos En Ingeniería y Ciencias Aplicadas*, *1*, 327–336. Chile.

Proceedings of the IASS Annual Symposium 2019 – Structural Membranes 2019
Form and Force
7 – 10 October 2019, Barcelona, Spain
C. Lázaro, K.-U. Bletzinger, E. Oñate (eds.)

Design requirements for maximum compactness in deployable structures

Cristina RAMOS-JAIME*, José SÁNCHEZ-SÁNCHEZ[a]

*[a] University of Seville
Reina Mercedes 2, 41012 Seville, Spain
ramosjaime@us.es

Abstract

This paper presents the essential design requirements for the development of deployable structures in order to: ensure a proper functioning during the folding-unfolding process, as well as at the final stages; achieve the maximum compactness possible in the folded position; prevent possible local failures that can trigger the collapse of the whole assembly. The different types of modules are described, and the advantages and limitations of foldable strings composed by the addition of equal units are exposed. The transformation of any generic curve into a deployable string results of higher interest for the creation of new geometries. The method of the ellipse has been proven as an effective technique to achieve this aim, and, in this research, it is generalized and automated to transform a generic surface into a deployable grid. A collection of digital parametric tools has been developed, and this paper contains the scripts to test the fulfillment maximum compactness condition and to detect localized fold-over failures.

Keywords: spatial structures, deployable grids, transformable systems, kinetic mechanisms, scissor-like-elements, parametric design, automatization, digital tools.

1. Introduction

This paper is part of the research that is being developed and compiled in the doctoral thesis *Parametric Design and Digital Fabrication of Deployable Structures based on Scissors-like-Elements and Quadrangular Patterns* by the author of this manuscript. The main aim of the work is to develop and automate a geometrical method to transform any surface into a deployable grid based on families of scissors-like-element strings arranged in two directions.

SLE modules are composed by two rods connected by an articulated joint. These units can be linked by the endpoints of their bars composing straight and curved foldable strings. The combination of strings in two, three or more directions allows to generate spatial deployable grids, capable of cover large spans when expanded and that can be folded in compact bundles for storage or transportation. This feature makes them ideal for applications such: emergency shelters, that require a quick and easy assembly and delivery of large number of units; temporary or nomadic architecture, which implies transport and reutilization in different locations; or space installations, as satellites or antennas, which require lightness and transport within an extremely limited space.

This research continues and expands the studies developed by Félix Escrig and José Sánchez, professors at the University of Seville in Spain, in spatial deployable structures based on quadrangular patterns [2,3,4]. The development of deployable grids based on SLE modules with straight rods has been broadly studied by several researchers [5,7,10,11]. However, it doesn't exist yet a general standardized method to transform a generic surface into a foldable grid.

Copyright © 2019 by Cristina Ramos Jaime
Published by the International Association for Shell and Spatial Structures (IASS) with permission.

The work developed by Luis Sánchez-Cuenca, professor at the University of Girona in Spain, is the closest one to achieve this aim, through the generation of translational foldable grids based on two generic perpendicular curves [8,9]. Sánchez-Cuenca applies an original technique to construct the SLE strings on a predefined directrix through a set of identical and tangent ellipses. The result is a foldable string with parallel axes, constant thickness, and equal length in all half-scissors, what automatically guarantees the fulfillment of the condition for a maximum compactness at the folded position.

The typology of translational foldable grids has been also explored by Travis Langbecker, professor at the University of Queensland in Australia [6], and Niels de Temmerman at the Vrije Universiteit Brussel [1].

The graphical method of the ellipse offers great possibilities in the creation of new deployable geometries and it cannot stay limited to translational surfaces with constant thickness. It is used as one of the starting points of this research and it is generalized, establishing the method of the ellipsoid, and automatized, using Grasshopper, for the development of new types of deployable grids.

This paper introduces the main design requirements for the development of spatial deployable grids, ensuring the correct functioning of the structure during the folding/unfolding process, as well as at its final closed/open position. It also presents two digital tools: to test the fulfillment of the maximum compactness condition, and to detect possible risks of local fold-over failure. Both scripts can be applied to any predesigned spatial deployable grid.

2. Connectivity conditions for a maximum compactness at the folded stage

2.1. Connections between modules

The minimum unit in deployable structures is the scissor-like element (SLE). It is composed by two rods connected by an internal articulated joint, which can be located at their midpoint or eccentric to them, resulting in bar-segments of equal or different length respectively.

The modules connect one another by the endpoints of their rods, creating straight or curved deployable strings. If the unit is composed by bar-segments of equal length at each side of the internal joint, the connection between scissors can only generate straight lines. Curved strings are achieved when the bar-segments have different dimensions and, if the module has angular symmetry, the curvature of the string will be constant.

Figure 1 shows the different SLE typologies and some examples of deployable strings composed by the addition of identical units. In the diagram, the dashed line represents the directrix polyline on which the central nodes rest. The modules and strings at the left column (cases 1,3,5,7) have constant thickness, that is to say, the distance between the upper and lower layer remains the same at any time; while the examples shown at the right column (cases 2,4,6,8) have variable thickness.

In cases 1 and 2 the axes of the unit (virtual lines connecting upper and lower external nodes) are parallel between them and, at the same time, perpendicular to the directrix polyline, generating modules with equal length segments at each side of the internal joint only connectable in a straight line. In example 1 the internal joint is centred, and all the rod-segments have equal length; in example 2 the node is eccentric allowing to vary the thickness of the string. The deployable strings 3 and 4 are also composed by units with parallel axis but, in this case, oblique to the directrix polyline. The connection of flipped units can generate sloped and zig-zag strings. The cases 5 to 8 are modules with radial axes, which allow to create single and double curvature deployable strings. If the units have angular symmetry (cases 5 and 6), the curvature of the string will be constant; otherwise, we will achieve assemblies with variable curvature (cases 7 and 8).

In strings composed by the addition of identical modules, the correct functioning of the structure during the deployment process, and the maximum compactness at its folded stage are guaranteed. However, the type of curves that they allow to generate are limited, and the design process to create spatial deployable surfaces usually requires of complex strings formed by different type of units and based on predefined guidelines. That is the reason why it is more interesting to learn how to subdivide any generic curve into a collection of modules, rather than compose strings by the addition of them.

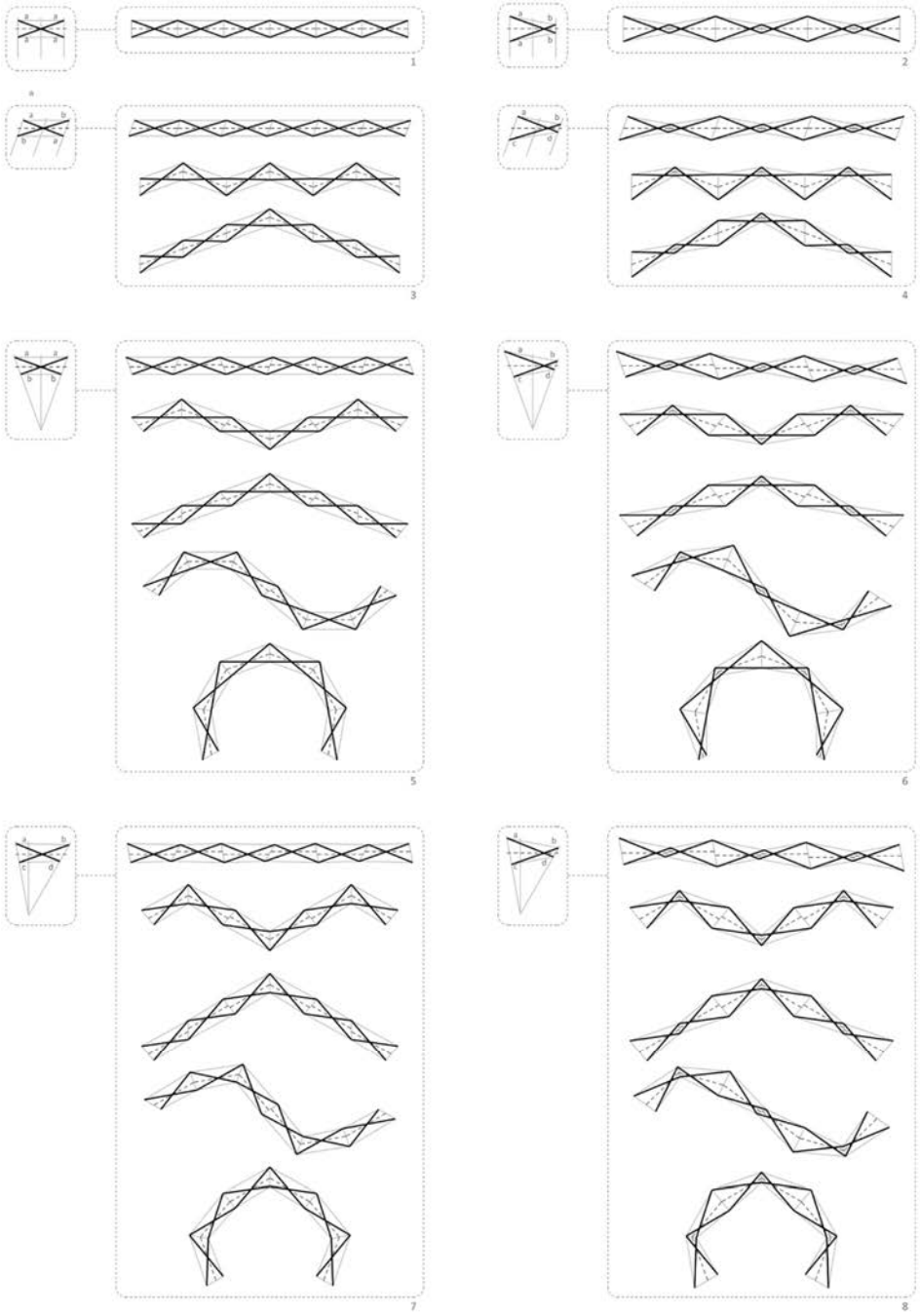


Figure 1: Deployable strings composed by the addition of identical units

The transformation of a generic curve into a deployable string requires a previous study of the connectivity constraints between SLE in order to ensure the correct functioning of the assembly during the deployment process, as well as at its final folded and unfolded positions.

The essential requirement to achieve a maximum compactness at the folded stage, that is to say, that all the bars are vertical and parallel between them minimizing the volume of the bundle, is that the length of the half-scissors that connect to the same pair of external nodes must be a constant value (1).

$$L1+L2 = L3+L4 \tag{1}$$

If this condition is not met, the module with the shortest half-scissor will be properly folded at the final stage, while the second unit won't be able to close completely, resulting in a reduction of the compactness degree, not just of the string but of the whole grid (figure2).

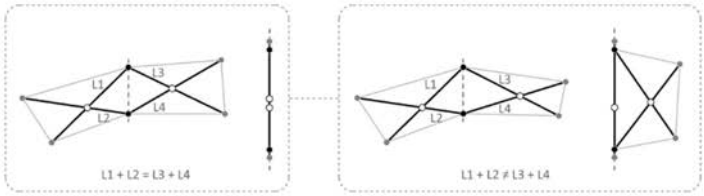


Figure 2: Essential requirement for a maximum compactness at the folded stage.

Figure 3 illustrates different connectivity configurations between SLE, meeting, all of them, the condition of maximum compactness. The example 1 is a generic case, in which all the bar-segments have different lengths, however both units are capable of completely fold together by satisfying equation (1). An ideal scenario is that in which the bar-segments are symmetric with respect to the virtual axis of connection: L1=L3 and L2=L4, and the internal joints of both units are coincident at the folded position (case 2).

In spatial deployable grids the SLE strings are usually arranged perpendicular to the surface, defining the thickness of the structure, and a vertical folding is of the units is desired in order to achieve a compact bundle. However, if for any design reason the modules are required to fold horizontally (for example, in the case of deployable towers where the units are stacked one of the top of each other instead of being laterally connected; spatial grids in which the SLE strings are arranged in parallel to the surface instead of perpendicular to it; or any deployable structure designed to be folded in a ring shape instead of in a compact bundle) the condition for a maximum compactness must be met at each side of the virtual horizontal axis that connects the internal joints of the units (2) (case 3).

$$L1+L3 = L2+L4 \tag{2}$$

An ideal case is that in which the bar-segments are symmetric with respect to the virtual horizontal axis and the external nodes are coincident at the folded stage (case 4).

In order to achieve a deployable grid capable to fold in both directions, it must satisfy equations (1) and (2) simultaneously (case5). Therefore, the relationship between bar-segments is established with equation (3).

$$L1=L4 \; ; \; L2=L3 \tag{3}$$

The ideal scenario is that in which all the bar-segments are equal L1=L2=L3=L4, in the way that, when folded in vertical the internal joints are coincident, and when folded in horizontal the external nodes are coincident (case 6). If, in addition to this, the internal joint is located at the mid-point of the bars, then the compact bundle will also have the minimum height possible. In the case of a vertical folding, that minimum height corresponds to the length of the bar, and for an horizontal folding to twice that dimension (case 7).

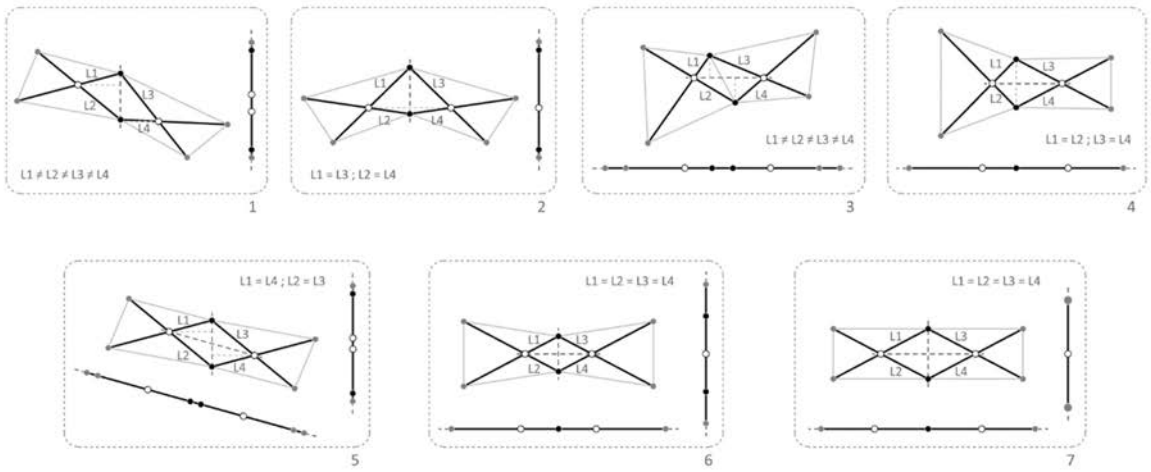


Figure 3: Connectivity between modules

The connections between units in which the internal or the external joints are coincident at the folded position; those which allow a maximum compactness in both directions; or even achieve the minimum height for the compact bundle, are all particular cases. They are perfect in its functioning and for the construction of simple strings and surfaces, but, at the same time, they can be limiting for the development of new deployable geometries.

In order to create a general method to transform any generic curve or surface into a deployable string or grid, we must select only those requirements that are essential, in the way the initial conditions at the early stages of the design are not excessively restrictive for the creative process.

This research focusses in the development of spatial deployable grids with SLE strings arranged perpendicular to the surface, that fold vertically in compact bundles. Therefore, the only mandatory requirement for a maximum compactness at the closed position is equation (1).

2.2. Transformation of a generic curve into a deployable string. The method of the ellipsoid.

The simplest graphic method to guarantee the satisfaction of condition (1) is to construct the modules based on the guideline of an ellipse, in the way that: the external nodes are coincident with the focal points, and the internal nodes rest on the elliptic curve (figure 4). By definition, and ellipse is a planar curve based on two fixed focal points, such that for all the points on the curve the sum of the two distances to the foci is constant. This intrinsic condition ensures an equal length for all half-scissors constructed within the same ellipse, fulfilling automatically the maximum compactness condition (1).

Therefore, we can construct a deployable string based on any generic guideline by drawing a collection of tangent ellipses in the way that: the centres of the ellipses are located on the directrix; the focal points define the external nodes of the string; and the tangency points between ellipses establish the internal joint of the units. The ellipses can be of equal or different sizes, creating strings with constant or variable thickness.

The method of the ellipse was originally proposed by Luis Sánchez-Cuenca, professor at the University of Girona, in 1996 [8,9], applying it to the construction of SLE strings based on modules with parallel axes and constant thickness for the generation of deployable grids based on translational surfaces.

This research expands, generalizes and automates the ellipse method, applying it to the construction of SLE strings composed by modules with parallel, perpendicular or radial axes, with constant or variable thickness. They can be based on any generic curve: open or closed; planar or spatial; with

constant or variable curvature. And those strings can be used to generate deployable grids based on any generic surface.

The method of the ellipsoid for the development of three-dimensional deployable grids is established, creating groups of half-scissors in the way that: the SLEs connect one another by their external joints, which are coincident with the focal points of the ellipsoid; and all the internal joints rest on the elliptic surface. Thus, the assembly meets automatically the maximum compactness condition, as the length of all half-scissors within the same ellipsoid remains constant (figure 4).

The groups of half-scissors can be composed by any number, generating grids of two, three or more directions. The ellipsoids can be of equal or different sizes, leading to structures with constant or variable thickness respectively. The fact of working in three dimensions allows to create deployable strings that don't necessarily need to be planar, because the axis of the ellipsoid can act as a hinge, modifying the horizontal angle between modules and allowing to create spatial deployable strings. Each surface typology requires a specific technique to arrange the collection of tangent ellipsoids in order to construct compatible and connectable deployable strings.

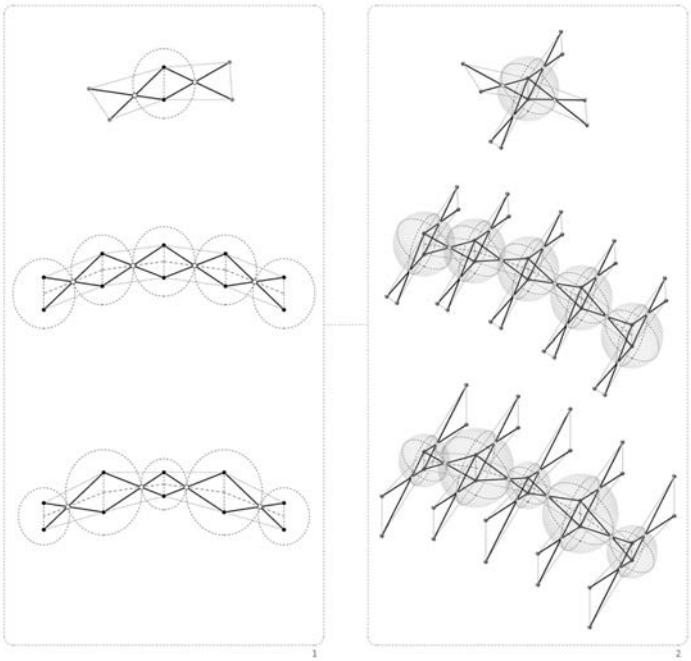


Figure 4: Method of the ellipse and ellipsoid

2.3. Digital tool for testing maximum compactness.

Once the design of the grid has been generated, it is necessary to proof that it actually satisfies the maximum compactness condition at each pair of external nodes (1). For this purpose, a digital parametric tool, applicable to any spatial deployable grid based on SLE strings arranged in two directions, has been developed with the following inputs and outputs:

- Inputs: directrix deployable strings; generatrix deployable strings; axes of the grid (virtual line that connects upper and lower external nodes)
- Outputs: half-scissors grouped by external node; list of lengths of the half-scissors at each external node; list of boolean values indicating if the maximum compactness condition is satisfied at each external node; colour diagram of the grid for visual verification.

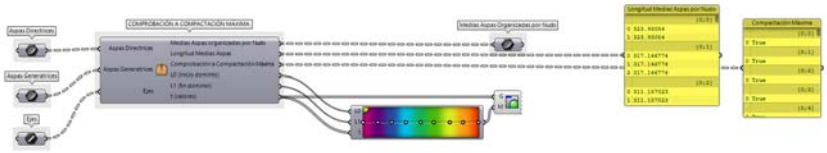


Figure 5: Script for testing maximum compactness

Geometric construction:

1. The intersection between each pair of rods that compose the units is calculated, obtaining the location of the internal joint. That point is used to split each one of the bars in two parts, achieving four segments per unit. The segments are grouped by pairs at each side of the internal joint, creating two half-scissors that connect to different and adjacent external nodes.
2. The half-scissors are classified based on their location on the grid as internal, edge or corner elements.
3. Steps 1 and 2 are performed for directrices and generatrices independently, and it is now when all half-scissors are combined and grouped based on the type of extreme node they connect to. In that way, nodes located in the interior of the grid will be composed by groups of 4 half-scissors, edge nodes will have 3 half-scissors, and corner nodes just 2 of them.
4. The groups of half-scissors are reorganized following the original order of the nodes on the grid.
5. The length of the half-scissors is calculated, and a comparative analysis is performed within each group in order to evaluate if they satisfy the condition of maximum compactness. If all the groups of half-scissors meet equation (1), the whole grid will be able to fold properly as a compact bundle.

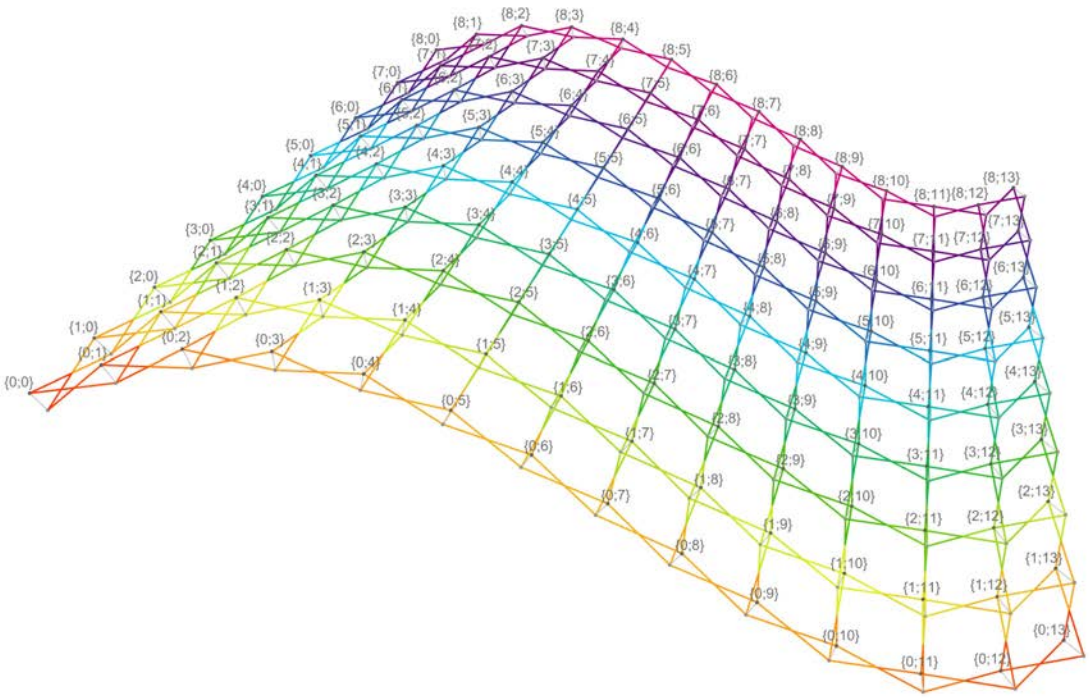


Figure 6: Colour diagram based on the length of the half-scissors (output script I)

COMPROBACIÓN A COMPACTACIÓN MÁXIMA (Longitudes Medias Aspas en mm)													
{0;0}	{0;1}	{0;2}	{0;3}	{0;4}	{0;5}	{0;6}	{0;7}	{0;8}	{0;9}	{0;10}	{0;11}	{0;12}	{0;13}
-	-	-	-	-	-	-	-	-	-	-	-	-	-
323.930540	317.146774	311.157023	305.838598	301.396702	298.246345	296.645903	296.628731	298.197687	301.364616	306.131040	312.155801	317.343070	-
323.930540	317.146774	311.157023	305.838598	301.396701	298.246345	296.645904	296.628731	298.197686	301.364617	306.131041	312.155802	317.343070	321.699045
-	317.146774	311.157023	305.838598	301.396702	298.246345	296.645903	296.628731	298.197687	301.364616	306.131040	312.155801	317.343070	321.699044
{1;0}	{1;1}	{1;2}	{1;3}	{1;4}	{1;5}	{1;6}	{1;7}	{1;8}	{1;9}	{1;10}	{1;11}	{1;12}	{1;13}
301.147581	294.840937	289.272462	284.328098	280.198612	277.269829	275.781952	275.765987	277.224593	280.168784	284.599972	290.200994	295.023427	299.073034
301.147581	294.840937	289.272462	284.328098	280.198613	277.269830	275.781951	275.765987	277.224593	280.168783	284.599971	290.200994	295.023427	-
301.147581	294.840937	289.272462	284.328098	280.198612	277.269829	275.781952	275.765987	277.224593	280.168784	284.599972	290.200994	295.023427	299.073034
-	294.840937	289.272462	284.328098	280.198613	277.269830	275.781951	275.765987	277.224593	280.168783	284.599971	290.200994	295.023427	299.073033
{2;0}	{2;1}	{2;2}	{2;3}	{2;4}	{2;5}	{2;6}	{2;7}	{2;8}	{2;9}	{2;10}	{2;11}	{2;12}	{2;13}
279.967013	274.103933	268.927105	264.330492	260.491445	257.768651	256.385421	256.370579	257.726597	260.463715	264.583244	269.790331	274.273588	278.038375
279.967013	274.103933	268.927105	264.330492	260.491445	257.768652	256.385420	256.370579	257.726597	260.463714	264.583244	269.790330	274.273588	-
279.967013	274.103933	268.927105	264.330492	260.491445	257.768651	256.385421	256.370579	257.726597	260.463715	264.583244	269.790331	274.273588	278.038375
-	274.103933	268.927105	264.330492	260.491445	257.768652	256.385420	256.370579	257.726597	260.463714	264.583244	269.790330	274.273588	278.038374
{3;0}	{3;1}	{3;2}	{3;3}	{3;4}	{3;5}	{3;6}	{3;7}	{3;8}	{3;9}	{3;10}	{3;11}	{3;12}	{3;13}
260.276135	254.825422	250.012695	245.739375	242.170339	239.639047	238.353103	238.339305	239.599951	242.144559	245.974350	250.815207	254.983144	258.483143
260.276135	254.825422	250.012695	245.739375	242.170339	239.639048	238.353103	238.339305	239.599951	242.144558	245.974350	250.815207	254.983144	-
260.276135	254.825422	250.012695	245.739375	242.170339	239.639047	238.353103	238.339305	239.599951	242.144559	245.974350	250.815207	254.983144	258.483143
-	254.825422	250.012695	245.739375	242.170339	239.639048	238.353103	238.339305	239.599951	242.144558	245.974350	250.815207	254.983144	258.483142
{4;0}	{4;1}	{4;2}	{4;3}	{4;4}	{4;5}	{4;6}	{4;7}	{4;8}	{4;9}	{4;10}	{4;11}	{4;12}	{4;13}
241.970172	236.902823	232.428589	228.455824	225.137808	222.784550	221.589050	221.576222	222.748203	225.113842	228.674273	233.174659	237.049453	240.303287
241.970172	236.902823	232.428590	228.455824	225.137809	222.784550	221.589049	221.576222	222.748203	225.113841	228.674272	233.174659	237.049453	-
241.970172	236.902823	232.428589	228.455824	225.137808	222.784550	221.589050	221.576222	222.748203	225.113842	228.674273	233.174659	237.049453	240.303287
-	236.902823	232.428590	228.455824	225.137809	222.784550	221.589049	221.576222	222.748203	225.113841	228.674272	233.174659	237.049453	240.303286
{5;0}	{5;1}	{5;2}	{5;3}	{5;4}	{5;5}	{5;6}	{5;7}	{5;8}	{5;9}	{5;10}	{5;11}	{5;12}	{5;13}
224.951720	220.240772	216.081224	212.387874	209.303224	207.115477	206.004060	205.992135	207.081687	209.280943	212.590959	216.774820	220.377089	223.402071
224.951720	220.240772	216.081224	212.387874	209.303225	207.115478	206.004060	205.992134	207.081687	209.280943	212.590959	216.774820	220.377089	-
224.951720	220.240772	216.081224	212.387874	209.303224	207.115477	206.004060	205.992135	207.081687	209.280943	212.590959	216.774820	220.377089	223.402071
-	220.240772	216.081224	212.387874	209.303225	207.115478	206.004060	205.992134	207.081687	209.280943	212.590959	216.774820	220.377089	223.402071
{6;0}	{6;1}	{6;2}	{6;3}	{6;4}	{6;5}	{6;6}	{6;7}	{6;8}	{6;9}	{6;10}	{6;11}	{6;12}	{6;13}
209.130224	204.750611	200.883615	197.450030	194.582332	192.548455	191.515207	191.504120	192.517041	194.561618	197.638831	201.528429	204.877340	207.689567
209.130224	204.750611	200.883616	197.450030	194.582332	192.548456	191.515207	191.504120	192.517041	194.561617	197.638830	201.528429	204.877340	-
209.130224	204.750611	200.883615	197.450030	194.582332	192.548455	191.515207	191.504120	192.517041	194.561618	197.638831	201.528429	204.877340	207.689567
-	204.750611	200.883616	197.450030	194.582332	192.548456	191.515207	191.504120	192.517041	194.561617	197.638830	201.528429	204.877340	207.689566
{7;0}	{7;1}	{7;2}	{7;3}	{7;4}	{7;5}	{7;6}	{7;7}	{7;8}	{7;9}	{7;10}	{7;11}	{7;12}	{7;13}
194.421499	190.349917	186.754898	183.562806	180.896802	179.005973	178.045397	178.035090	178.976769	180.877545	183.738329	187.354360	190.467733	193.082167
194.421499	190.349917	186.754898	183.562806	180.896802	179.005974	178.045396	178.035090	178.976769	180.877544	183.738328	187.354360	190.467733	-
194.421499	190.349917	186.754898	183.562806	180.896802	179.005973	178.045397	178.035090	178.976769	180.877545	183.738329	187.354360	190.467733	193.082167
-	190.349917	186.754898	183.562806	180.896802	179.005974	178.045396	178.035090	178.976769	180.877544	183.738328	187.354360	190.467733	193.082167
{8;0}	{8;1}	{8;2}	{8;3}	{8;4}	{8;5}	{8;6}	{8;7}	{8;8}	{8;9}	{8;10}	{8;11}	{8;12}	{8;13}
180.747281	176.962064	173.619894	170.652311	168.173814	166.415973	165.522956	165.513374	166.388822	168.155911	170.815488	174.177194	177.071594	179.502148
180.747281	176.962064	173.619894	170.652311	168.173814	166.415973	165.522956	165.513374	166.388823	168.155911	170.815488	174.177194	177.071594	-
-	-	-	-	-	-	-	-	-	-	-	-	-	-
-	176.962064	173.619894	170.652311	168.173814	166.415973	165.522956	165.513374	166.388823	168.155911	170.815488	174.177194	177.071594	179.502147

Table 1: Length of the half-scissors (output script I)

Figure 6 and table 1 illustrate an example of the results obtained by applying the script to a spatial deployable grid constructed based on the design requirements defined in this work. The diagram, as well as the values show that the structures satisfies the maximum compactness condition at each one of the nodes.

3. The fold-over angle as limitation and optimization in the design.

3.1. Maximum angle between bars

The second design requirement that must be considered in the generation of deployable grids is that the angle between bars that connect to the same upper or lower external node must be always smaller than 180°. A fold-over angle in a single node of the grid can trigger the collapse of the whole structure.

Deployable strings and grids are design at their final unfolded position, stage in which the angle rod-axis is the maximum of the whole deployment process, representing the worst-case scenario and, therefore, the best one to critically test the correct functioning of the structure.

Figure 7 illustrates three connectivity cases between SLE at three different stages of deployment. In example 1, the angle between rods that connect to the same external node is below 180°, and during the folding process the angle gets progressively smaller till it is reduced to 0° at the final closed position, thus, the modules fold properly. In example 3 the angle between bars connected to the lower node is greater than 180° so, during the folding process the external nodes get closer to each other, and the angle increases progressively achieving a value of 360° at the closed position. The modules fold in the wrong direction, which can cause that adjacent units can neither fold properly, and ultimately causing the collapse of the whole structure.

Example 2 shows the limit case, in which the angle between bars is equal to 180°, during the folding process two different scenarios can happen: the external nodes might slide away from each other, increasing the distance between them and, therefore the modules will fold properly as in case 1; or the external nodes might get closer to each other causing a fold-over failure with a result similar to case 3. The correct functioning of the structure will depend on the location and value of the forces applied to fold the grid, as well as on the angular tolerances used in the design of the adjacent units.

In order to guarantee a proper folding process, it is necessary to ensure that the maximum angle between bars that connect to the same external node is always slightly smaller than 180°. A single degree of difference allows to guide the SLE in the proper folding direction, avoiding the collapse.

The design of deployable grids at their unfolded position based on the limit angle between bars (or, it would be better to say, one degree below the limit angle) can be considered as an optimization technique, in which using the same bar lengths, the largest span possible is achieved.

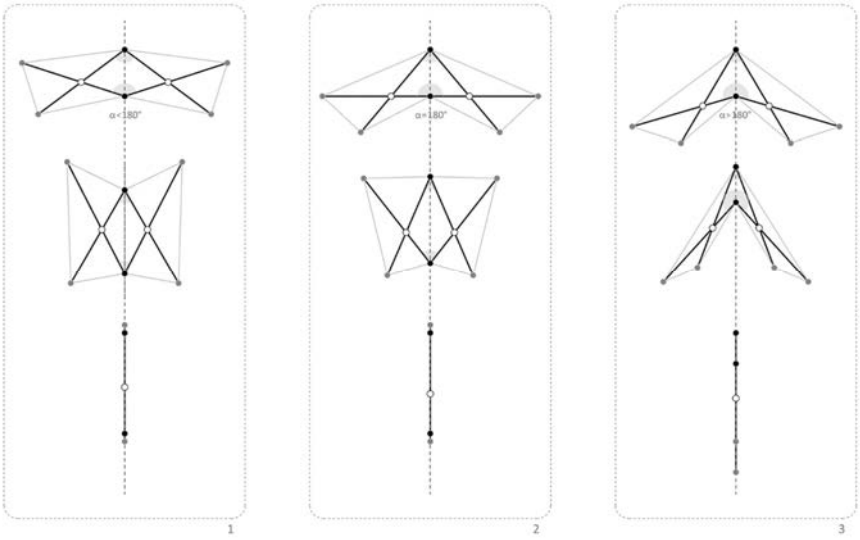


Figure 7: Connection between SLE below the limit angle; at their limit position; and under fold-over failure

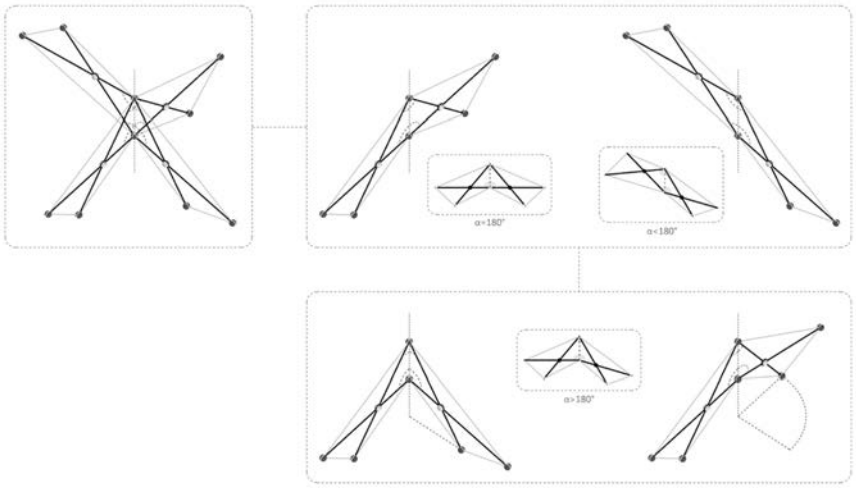


Figure 8: Fold-over failure in three dimensions

It must be taken into account that, in a spatial deployable grid, the fold-over failure can happen for any pair of SLE that meet at the same common node and, therefore, is not enough to check the angle between bars within the same string, but also for all possible combinations of SLE taken in groups of two half-scissors. Figure 8 shows a graphical example: the first diagram represents the connection between four units that share the same pair of external nodes, that might be part of a bigger grid with strings arranged in two different directions. If we separate the two strings, we can see that the first one has been designed in such a way that the angle between bars connected to the lower node is close to the limit, while in the second string the angle is clearly smaller than 180°. So, is there a risk of fold-over failure? In the first instance we may think that there is no risk, because the limit angle is not overpassed in either of the two directions. However, if we select one SLE from each string and we rotate it around the axis, it can be clearly observed that the sum of the angles at the bottom node is greater than 180° and, therefore we can deduce that the grid will collapse due a fold-over failure at this specific node.

It can be established that, for a group of bars that connect to the same node, if any of them is forming an angle greater than 90° with respect to the virtual hinge axis, there might be risk of fold-over failure. This is the reason why the test must be done for all pairs of SLE, independently of the string they belong to. A local failure in a single node is enough to trigger the collapse of the whole structure.

3.2. Digital tool to detect risk of fold-over failure

In order to check that there is no risk of fold-over failure at any node of the grid, a script has been developed with the following inputs and outputs (figure 9):

- Inputs: half-scissors grouped by node (output script I); axes of the grid (virtual line that connects upper and lower external nodes)
- Outputs: list of angles rod-axis grouped by node; list of boolean values indicating if there is risk of fold-over failure; colour diagram for visual detection.

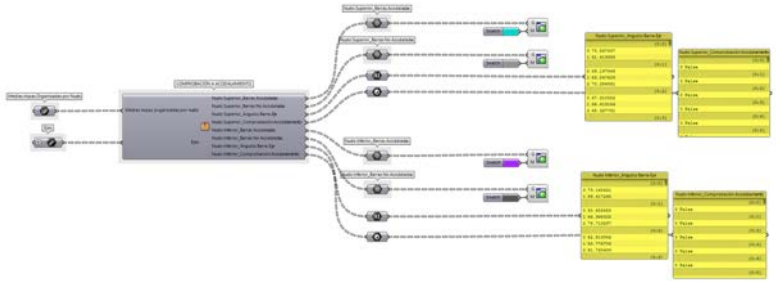


Figure 9: Script for testing risk of fold-over failure

Geometric construction:

1. The half-scissors are organized in groups surrounding each pair of external nodes. The first step is to explode the polyline that defines each one of the half-scissors, achieving two separated segments. Then, two sub-collections are created by grouping together the segments that connect to the upper node, and those connecting to the lower node.
2. Within those sub-groups, the angle that each bar forms with respect to the axis (virtual line that connects upper and lower node) is measured.
3. For each node, all possible combination of angles taken by pairs are summed and evaluated. The nodes are classified as “fold-over” and “non fold-over”, depending if the result of the maximum angular value is smaller, or equal or greater than 180°. Those nodes with risk of fold-over failure, as well as their associated bar-segments, are marked with colour at the grid diagram.

Figure 10 and table 2 illustrate an example of the results obtained when applying the script to a spatial deployable grid. The first diagram shows that there is risk of fold-over failure in some of the upper (blue) and lower (purple) nodes. Those areas with pronounced curvature are more susceptible of having this type of issue. The possibility of detecting and visualizing the problem in real time allows to solve it by slightly modifying the parameter that controls the thickness of the grid or the number of subdivisions on the digital parametric model. The second diagram shows the same structure after increasing a bit its thickness, demonstrating the utility and effectiveness of the tool to reduce or eliminate possible risk of local failures. The data on table 2 correspond to this second diagram.

The fact of modifying, even slightly, the original design of the structure, might imply an alteration in the length of the bars and, therefore, another test to proof that the grid stills satisfying the condition of maximum compactness would be required. As the digital parametric model is simultaneously connected to scripts I and II, any modification on the geometry of the grid is automatically reflected in the diagrams and tables of both testing tools. In that way, we just need to take a look to the updated results of script I to verify that the grid stills fulfilling the maximum compactness condition.

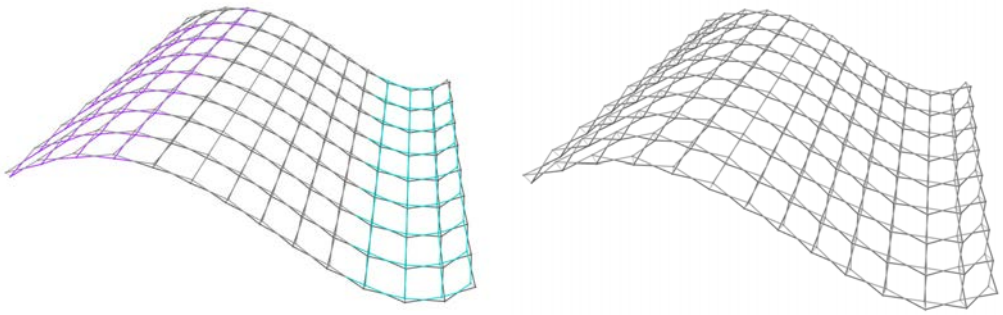


Figure 10: Colour diagram for visual detection of fold-over failure (output script II)

COMPROBACIÓN A ACODALAMIENTO EN NUDOS SUPERIORES (Ángulo Barra-Eje en grados)												
{0;0}	{0;1}	{0;2}	{0;3}	{0;4}	{0;5}	{0;6}	{0;7}	{0;8}	{0;9}	{0;10}	{0;11}	{0;12}	{0;13}
-	-	-	-	-	-	-	-	-	-	-	-	-	-
70.84	69.20	67.31	66.97	68.56	70.90	72.73	74.45	76.23	79.32	85.21	90.60	85.26	-
61.41	63.55	66.42	69.82	72.74	74.36	74.91	74.94	74.93	75.43	77.48	83.12	90.57	94.46
-	70.28	68.33	66.91	67.33	69.51	71.60	73.44	75.01	77.20	80.97	88.07	89.38	82.80
{1;0}	{1;1}	{1;2}	{1;3}	{1;4}	{1;5}	{1;6}	{1;7}	{1;8}	{1;9}	{1;10}	{1;11}	{1;12}	{1;13}
89.42	86.99	83.78	80.11	77.13	75.53	75.01	74.99	75.00	74.49	72.39	66.72	60.20	57.06
70.84	69.20	67.31	66.97	68.56	70.90	72.73	74.45	76.23	79.32	85.21	90.60	85.26	-
61.41	63.55	66.42	69.82	72.74	74.36	74.91	74.94	74.93	75.43	77.48	83.12	90.57	94.46
-	70.28	68.33	66.91	67.33	69.51	71.60	73.44	75.01	77.20	80.97	88.07	89.38	82.80
{2;0}	{2;1}	{2;2}	{2;3}	{2;4}	{2;5}	{2;6}	{2;7}	{2;8}	{2;9}	{2;10}	{2;11}	{2;12}	{2;13}
89.42	86.99	83.78	80.11	77.13	75.53	75.01	74.99	75.00	74.49	72.39	66.72	60.20	57.06
70.84	69.20	67.31	66.97	68.56	70.90	72.73	74.45	76.23	79.32	85.21	90.60	85.26	-
61.41	63.55	66.42	69.82	72.74	74.36	74.91	74.94	74.93	75.43	77.48	83.12	90.57	94.46
-	70.28	68.33	66.91	67.33	69.51	71.60	73.44	75.01	77.20	80.97	88.07	89.38	82.80
{3;0}	{3;1}	{3;2}	{3;3}	{3;4}	{3;5}	{3;6}	{3;7}	{3;8}	{3;9}	{3;10}	{3;11}	{3;12}	{3;13}
89.42	86.99	83.78	80.11	77.13	75.53	75.01	74.99	75.00	74.49	72.39	66.72	60.20	57.06
70.84	69.20	67.31	66.97	68.56	70.90	72.73	74.45	76.23	79.32	85.21	90.60	85.26	-
61.41	63.55	66.42	69.82	72.74	74.36	74.91	74.94	74.93	75.43	77.48	83.12	90.57	94.46
-	70.28	68.33	66.91	67.33	69.51	71.60	73.44	75.01	77.20	80.97	88.07	89.38	82.80
{4;0}	{4;1}	{4;2}	{4;3}	{4;4}	{4;5}	{4;6}	{4;7}	{4;8}	{4;9}	{4;10}	{4;11}	{4;12}	{4;13}
89.42	86.99	83.78	80.11	77.13	75.53	75.01	74.99	75.00	74.49	72.39	66.72	60.20	57.06
70.84	69.20	67.31	66.97	68.56	70.90	72.73	74.45	76.23	79.32	85.21	90.60	85.26	-
61.41	63.55	66.42	69.82	72.74	74.36	74.91	74.94	74.93	75.43	77.48	83.12	90.57	94.46
-	70.28	68.33	66.91	67.33	69.51	71.60	73.44	75.01	77.20	80.97	88.07	89.38	82.80
{5;0}	{5;1}	{5;2}	{5;3}	{5;4}	{5;5}	{5;6}	{5;7}	{5;8}	{5;9}	{5;10}	{5;11}	{5;12}	{5;13}
89.42	86.99	83.78	80.11	77.13	75.53	75.01	74.99	75.00	74.49	72.39	66.72	60.20	57.06
70.84	69.20	67.31	66.97	68.56	70.90	72.73	74.45	76.23	79.32	85.21	90.60	85.26	-
61.41	63.55	66.42	69.82	72.74	74.36	74.91	74.94	74.93	75.43	77.48	83.12	90.57	94.46
-	70.28	68.33	66.91	67.33	69.51	71.60	73.44	75.01	77.20	80.97	88.07	89.38	82.80
{6;0}	{6;1}	{6;2}	{6;3}	{6;4}	{6;5}	{6;6}	{6;7}	{6;8}	{6;9}	{6;10}	{6;11}	{6;12}	{6;13}
89.42	86.99	83.78	80.11	77.13	75.53	75.01	74.99	75.00	74.49	72.39	66.72	60.20	57.06
70.84	69.20	67.31	66.97	68.56	70.90	72.73	74.45	76.23	79.32	85.21	90.60	85.26	-
61.41	63.55	66.42	69.82	72.74	74.36	74.91	74.94	74.93	75.43	77.48	83.12	90.57	94.46
-	70.28	68.33	66.91	67.33	69.51	71.60	73.44	75.01	77.20	80.97	88.07	89.38	82.80
{7;0}	{7;1}	{7;2}	{7;3}	{7;4}	{7;5}	{7;6}	{7;7}	{7;8}	{7;9}	{7;10}	{7;11}	{7;12}	{7;13}
89.42	86.99	83.78	80.11	77.13	75.53	75.01	74.99	75.00	74.49	72.39	66.72	60.20	57.06
70.84	69.20	67.31	66.97	68.56	70.90	72.73	74.45	76.23	79.32	85.21	90.60	85.26	-
61.41	63.55	66.42	69.82	72.74	74.36	74.91	74.94	74.93	75.43	77.48	83.12	90.57	94.46
-	70.28	68.33	66.91	67.33	69.51	71.60	73.44	75.01	77.20	80.97	88.07	89.38	82.80
{8;0}	{8;1}	{8;2}	{8;3}	{8;4}	{8;5}	{8;6}	{8;7}	{8;8}	{8;9}	{8;10}	{8;11}	{8;12}	{8;13}
89.42	86.99	83.78	80.11	77.13	75.53	75.01	74.99	75.00	74.49	72.39	66.72	60.20	57.06
70.84	69.20	67.31	66.97	68.56	70.90	72.73	74.45	76.23	79.32	85.21	90.60	85.26	-
-	-	-	-	-	-	-	-	-	-	-	-	-	-
-	70.28	68.33	66.91	67.33	69.51	71.60	73.44	75.01	77.20	80.97	88.07	89.38	82.80

COMPROBACIÓN A ACODALAMIENTO EN NUDOS INFERIORES (Ángulo Barra-Eje en grados)												
{0;0}	{0;1}	{0;2}	{0;3}	{0;4}	{0;5}	{0;6}	{0;7}	{0;8}	{0;9}	{0;10}	{0;11}	{0;12}	{0;13}
-	-	-	-	-	-	-	-	-	-	-	-	-	-
79.16	80.86	82.81	83.15	81.47	79.07	77.21	75.48	73.71	70.69	65.10	60.02	64.92	-
89.42	86.99	83.78	80.11	77.13	75.53	75.01	74.99	75.00	74.49	72.39	66.72	60.20	57.06
-	79.71	81.73	83.21	82.79	80.53	78.38	76.50	74.92	72.74	69.04	62.23	61.24	67.38
{1;0}	{1;1}	{1;2}	{1;3}	{1;4}	{1;5}	{1;6}	{1;7}	{1;8}	{1;9}	{1;10}	{1;11}	{1;12}	{1;13}
61.41	63.55	66.42	69.82	72.74	74.36	74.91	74.94	74.93	75.43	77.48	83.12	90.57	94.46
79.16	80.86	82.81	83.15	81.47	79.07	77.21	75.48	73.71	70.69	65.10	60.02	64.92	-
89.42	86.99	83.78	80.11	77.13	75.53	75.01	74.99	75.00	74.49	72.39	66.72	60.20	57.06
-	79.71	81.73	83.21	82.79	80.53	78.38	76.50	74.92	72.74	69.04	62.23	61.24	67.38
{2;0}	{2;1}	{2;2}	{2;3}	{2;4}	{2;5}	{2;6}	{2;7}	{2;8}	{2;9}	{2;10}	{2;11}	{2;12}	{2;13}
61.41	63.55	66.42	69.82	72.74	74.36	74.91	74.94	74.93	75.43	77.48	83.12	90.57	94.46
79.16	80.86	82.81	83.15	81.47	79.07	77.21	75.48	73.71	70.69	65.10	60.02	64.92	-
89.42	86.99	83.78	80.11	77.13	75.53	75.01	74.99	75.00	74.49	72.39	66.72	60.20	57.06
-	79.71	81.73	83.21	82.79	80.53	78.38	76.50	74.92	72.74	69.04	62.23	61.24	67.38
{3;0}	{3;1}	{3;2}	{3;3}	{3;4}	{3;5}	{3;6}	{3;7}	{3;8}	{3;9}	{3;10}	{3;11}	{3;12}	{3;13}
61.41	63.55	66.42	69.82	72.74	74.36	74.91	74.94	74.93	75.43	77.48	83.12	90.57	94.46
79.16	80.86	82.81	83.15	81.47	79.07	77.21	75.48	73.71	70.69	65.10	60.02	64.92	-
89.42	86.99	83.78	80.11	77.13	75.53	75.01	74.99	75.00	74.49	72.39	66.72	60.20	57.06
-	79.71	81.73	83.21	82.79	80.53	78.38	76.50	74.92	72.74	69.04	62.23	61.24	67.38
{4;0}	{4;1}	{4;2}	{4;3}	{4;4}	{4;5}	{4;6}	{4;7}	{4;8}	{4;9}	{4;10}	{4;11}	{4;12}	{4;13}
61.41	63.55	66.42	69.82	72.74	74.36	74.91	74.94	74.93	75.43	77.48	83.12	90.57	94.46
79.16	80.86	82.81	83.15	81.47	79.07	77.21	75.48	73.71	70.69	65.10	60.02	64.92	-
89.42	86.99	83.78	80.11	77.13	75.53	75.01	74.99	75.00	74.49	72.39	66.72	60.20	57.06
-	79.71	81.73	83.21	82.79	80.53	78.38	76.50	74.92	72.74	69.04	62.23	61.24	67.38
{5;0}	{5;1}	{5;2}	{5;3}	{5;4}	{5;5}	{5;6}	{5;7}	{5;8}	{5;9}	{5;10}	{5;11}	{5;12}	{5;13}
61.41	63.55	66.42	69.82	72.74	74.36	74.91	74.94	74.93	75.43	77.48	83.12	90.57	94.46
79.16	80.86	82.81	83.15	81.47	79.07	77.21	75.48	73.71	70.69	65.10	60.02	64.92	-
89.42	86.99	83.78	80.11	77.13	75.53	75.01	74.99	75.00	74.49	72.39	66.72	60.20	57.06
-	79.71	81.73	83.21	82.79	80.53	78.38	76.50	74.92	72.74	69.04	62.23	61.24	67.38
{6;0}	{6;1}	{6;2}	{6;3}	{6;4}	{6;5}	{6;6}	{6;7}	{6;8}	{6;9}	{6;10}	{6;11}	{6;12}	{6;13}
61.41	63.55	66.42	69.82	72.74	74.36	74.91	74.94	74.93	75.43	77.48	83.12	90.57	94.46
79.16	80.86	82.81	83.15	81.47	79.07	77.21	75.48	73.71	70.69	65.10	60.02	64.92	-
89.42	86.99	83.78	80.11	77.13	75.53	75.01	74.99	75.00	74.49	72.39	66.72	60.20	57.06
-	79.71	81.73	83.21	82.79	80.53	78.38	76.50	74.92	72.74	69.04	62.23	61.24	67.38
{7;0}	{7;1}	{7;2}	{7;3}	{7;4}	{7;5}	{7;6}	{7;7}	{7;8}	{7;9}	{7;10}	{7;11}	{7;12}	{7;13}
61.41	63.55	66.42	69.82	72.74	74.36	74.91	74.94	74.93	75.43	77.48	83.12	90.57	94.46
79.16	80.86	82.81	83.15	81.47	79.07	77.21	75.48	73.71	70.69	65.10	60.02	64.92	-
89.42	86.99	83.78	80.11	77.13	75.53	75.01	74.99	75.00	74.49	72.39	66.72	60.20	57.06
-	79.71	81.73	83.21	82.79	80.53	78.38	76.50	74.92	72.74	69.04	62.23	61.24	67.38
{8;0}	{8;1}	{8;2}	{8;3}	{8;4}	{8;5}	{8;6}	{8;7}	{8;8}	{8;9}	{8;10}	{8;11}	{8;12}	{8;13}
61.41	63.55	66.42	69.82	72.74	74.36	74.91	74.94	74.93	75.43	77.48	83.12	90.57	94.46
79.16	80.86	82.81	83.15	81.47	79.07	77.21	75.48	73.71	70.69	65.10	60.02	64.92	-
-	-	-	-	-	-	-	-	-	-	-	-	-	-
-	79.71	81.73	83.21	82.79	80.53	78.38	76.50	74.92	72.74	69.04	62.23	61.24	67.38

Table 2: Angles in upper and lower nodes (output script II)

4. Conclusions

As a conclusion, it can be established that the essential design requirements to create a spatial deployable grid ensuring its correct functioning during the folding process, as well as at its final open and closed positions are that: the grid must satisfy the condition of maximum compactness, meaning that the length of all half-scissors that connect to the same pair of external nodes must be constant; and the grid cannot have subassemblies with risk of fold-over failure, that is to say, the sum by pairs of angles bar-axis at each node of the grid must be smaller than 180°.

The thickness of the grid can be constant or variable. It is usually desirable to have a constant thickness, but it is not essential for the proper functioning of the assembly, and the viability of keeping fixed the distance between the upper and lower nodes along the grid will depend on the geometric properties of the surface, and on the constrains imposed by the collection of strings displayed in the other direction of the grid.

The length of the half-scissors can be constant or variable along the string. A constant value is not essential for the correct functioning of the grid, moreover, its only possible for particular cases: in deployable strings with parallel axes and constant thickness; and in strings with radial axes based on constant curvature directrices.

In this research the method of the ellipsoid has been proven as an efficient technique for the development of spatial deployable structures, allowing to transform a generic curve or surface into a foldable string or grid. A digital parametric tool that automates this method has been developed and used to create the structural models shown in figures 6 and 10.

The scripts I and II, presented in this paper, have been proven as effective tools for testing the fulfillment of the maximum compactness condition and to detect possible risk of fold-over failure, for any predesigned spatial deployable grid.

References

[1] N. De Temmerman, *Design and Analysis of Deployable Bars Structures for Mobile Architectural Applications*. Vrije Universiteit Brussel. PhD thesis, 2007.

[2] F. Escrig, *Modular, Ligero, Transformable. Un paseo por la Arquitectura Ligera Móvil*. Sevilla, 2012.

[3] F. Escrig, J. Sánchez-Sánchez, and J. P. Valcárcel, "Two Way Deployable Spherical Grids," *International Journal of Space Structures*, vol. 11, n.1&2, pp. 257–274, 1996.

[4] F. Escrig and J.P. Valcárcel, "Geometry of Expandable Space Structures". *International Journal of Space Structures,* 8 (1&2), pp. 71–84, 1993.

[5] C.J. Gantes, *Deployable Structures: Analysis and Design*. 2001.

[6] T. Langbecker and F. Albermani, "Foldable Positive and Negative Curvature Structures: Geometric Design and Structural Response", *Journal of the International Association for Shell and Spatial Structures*, vol 41, n.134, pp. 147-161, 2000.

[7] E. Pérez Piñero, *Estructura Reticular Estérea Plegable*. Patent: ES-266.801, 1961

[8] L. Sánchez-Cuenca, "Medium Size Deployable Structures," in *Proceedings of the IASS Symposium 2008*, p.058, 2008

[9] L. Sánchez-Cuenca, "Geometry for 'X' Expandable Structures," in *Conceptual Design of Structures. Proceedings of the IASS Symposium 1996*, vol. 2, pp. 937–944, 1996.

[10] Z. You and S. Pellegrino, S. "Foldable Bar Structures". *International Journal of Solids and Structures.*, vol. 34, no. 15, pp. 1825–1847, 1997.

[11] T.R. Zeigler, *Collapsible Self-Supporting Structure*. Patent: US-3.968.808. 1976

Proceedings of the IASS Annual Symposium 2019 – Structural Membranes 2019
Form and Force
7 – 10 October 2019, Barcelona, Spain
C. Lázaro, K.-U. Bletzinger, E. Oñate (eds.)

Distributed *Pneu* Elements for Surface Kinetics

Vera PARLAC

School of Architecture
New Jersey Institute of Technology
University Heights, Newark, New Jersey 07102 USA
parlac@njit.edu

Abstract

The presented project is a part of a larger body of an ongoing design research that investigates the potential for kinetic and responsive architectural skin systems to influence the use of space and users' behavior. The project explores the integration of custom-made soft robotic muscles into a component-based surface. The result of this project is a prototype of a light modular system capable of kinetic response to external stimuli such as occupancy or atmospheric conditions. The project focuses on kinetics of architectural surfaces and tectonics that integrate stasis and motion. It investigates the potential for a 'programmable' architectural modular system that simultaneously addresses stability, dynamics and adaptability of a material system. The project is informed by a history of pneumatic structures, the technology of soft robotics, and a kit-of-parts design strategy.

Keywords: Kinetic surface, responsive architecture, dynamic material systems, morphology of kinetic surface, soft robotics, pneumatic structures.

1. Introduction

In the Introduction of his 1970's book *Kinetic Architecture* William Zuk, an engineer, architect and educator at the University of Virginia, speculates about changes in design approach necessary to envision architecture capable of kinematic movement [1]. He suggests that new construction techniques, materials and technologies would have to be established. But, at the same time, Zuk predicts that even though kinetic architecture will require a more mechanistic and technological approach through the use of sensing technologies, new materials and embedded computation, it may also usher a new kind of relationship between the human body and space. According to him social relationships as well as personal sense of space and enclosure would be challenged. Associations between a dynamic body and dynamic space could provide a context where organization of human activities and experiences becomes more sensitive and responsive to changing needs, form, and phenomena.

The project presented here looks for an alternative relationship between body and space. It uses soft pneumatic muscles as a form of actuation, seeks seamless transition between hard and soft elements of the modular system and tries to imagine new realities in which we can build responsive building skins that more intimately relate to the human body.

In particular the project explores the capacity of *pneu* structures to produce a kinetic effect in architectural surfaces. Being delineated by an elastic membrane the *pneu* structure responds to the change of pressure by changing its mass and can cause considerable physical transformation of the structure. In soft robotics, the pneu-like capacity is used to design robots that move or handle fragile objects by manipulating the inflation and deflation patterns. The research by Harvard's Biodesign Lab

Copyright © 2019 by Vera Parlac
Published by the International Association for Shell and Spatial Structures (IASS) with permission.

and soft robot fabrication techniques, described by Andrew D. Marchese et al. [2], provided a starting point for the initial studies of *pneu* elements in this project. Other relevant studies that informed the project were related to the movement of soft actuators and their motion patterns [3], and the complexity of this movement [4]. The capacity of soft robotic components to affect larger structures in which they are incorporated is of key importance for this project since this capacity is used to produce kinetic effects in a larger modular construct and utilized to produce many different configurations. This research demonstrates the possibility to move parts of the aggregated modular structure by inflating and deflating integrated soft components (*pneu*).

The project attempts to address two challenges present in designing dynamic and adaptive surfaces: actuation system and surface tectonics. Therefore, on one hand, it explores a capacity of pneu structures to induce kinetic movement, and on the other, it articulates a component-based tectonic assembly that can integrate such movement. The main premise of the project is that integration of elastic inflatable pneumatic components into a component-based structure will influence the structure dynamically and support a variety of movements (Figure 1).



Figure 1. Active pneumatic muscles move part of the structure [Vera Parlac]

2. Background

Inflatable or pneumatic structures have been used in architecture primarily for their lightness in relation to the structural span. One of the first fully inflatable structures was a radome developed by Walter Bird in late 1940s. But between 1940s and 1970s these structures underwent a significant evolution and their use quickly grew beyond that of shelters for equipment or supplies. In 1960s and 1970s they were used in a variety of experimental projects in architecture, from the Fuji Group Pavilion, designed by Yutaka Murata for the 1970 World Expo in Osaka, to experiments by Coop Himmelb(l)au, Archigram, and Haus-Rucker-Co created at the scale of a human body. Inflatable structures offered a potential to design soft, transformable spaces with new formal (and dynamic) qualities. This new kind of architectural spaces operated as an extension of the immediate body space. Coop Himmelb(l)au's Villa Rosa, for example, even allowed for a change in volume by inflation. These mobile and mostly temporary structures were acknowledging the transformational potential of inflatable form. They brought into architecture the notions of a dynamic, changeable and soft space with boundaries no longer defined exclusively by rigid material enclosures.

Today researchers are experimenting with smaller scale inflatables that could be integrated into architectural surfaces and components i.e. into tectonics of a material system itself. Current experiments with elastic inflatable elements influenced by soft robotics are suggesting new trajectories in exploring dynamic spatial boundaries. The projects such as *The PneumaKnit* by Sean Ahlquist, McGee and Sharmin [5] and *Modular Pneu-Façade System* by Daekwon Park and Martin Bechthold [6] are integrating inflatable elements to add new functionalities of dynamics or sensing to the architectural surface. *The PneumaKnit* is concerned with motion and dynamic articulation of inflatable components. This is achieved by using knitted constraints that regulate expansion of the actuator and direction of its motion. The emphasis is on the material structure of the knitted constraint, which, through a variable density of its weaves, produces the surface transformation when actuators are inflated. This work is concerned not only with the actuator itself; equally important is its constricting surface. The material integration between the inflatable and knitted elements is a step forward in

rethinking the material assembly in which constituent parts are dynamic, and perform synergistically as one material system. The *Modular Pneu-Façade System* is imagined as "a dynamic pneumatic interface, which can be used in building applications including responsive façade, ceiling, floor and interior screen, etc." [6]. This layer of soft inflatable elements that can be integrated into a building's skin to make them transformable and active is sensitive to human touch. Its surface utilizes capacitive sensors and conductive gel, which make it conductive to touch. Both of these projects deal with a challenging question of how to integrate an active layer into an architectural assembly and speculate about architectural surface capable of interfacing information, dynamics and a user.

3. Methods

The *Soft Kinetics* project brings together two strategies for designing adaptive architectural skins. One is concerned with the combinatorial variability of a light structure built by aggregating small self-similar components. The other one focuses on the integration and distribution of pneumatic muscles within an aggregated structure. The proposed system reflects a deep interest in the development of a component-based material system whose properties range from rigid/stable (self-supporting) to pliable/active (dynamic). To achieve these variable properties particular emphasis was placed on the system's morphology that emerged by integrating self-similar rigid and pliable components with pneumatic muscles. This process produced a 'programmable' surface that can open, close or alter its basic form.

3.1. Light Modular Structure

The light modular structure is built using self-similar elements with a non-orthogonal alignment. It is aggregated through slot-friction connections and can be organized in a number of different configurations. The configuration of the construct is governed by the requirements for stability (self-support) and kinetics; both of these criteria are equally important to support dynamic transformations. Stability is achieved in two ways: by interlocking the components through simple slot-friction connections, and by the patterns of aggregation. The kinetic behavior is enabled by a system of pneumatic muscles, their full integration with the patterns of aggregation, and the capacity of the modular structure to allow for disruptions in pattern continuity without compromising the construct's stability. The redundancy of connections and elements provides a structural resiliency.

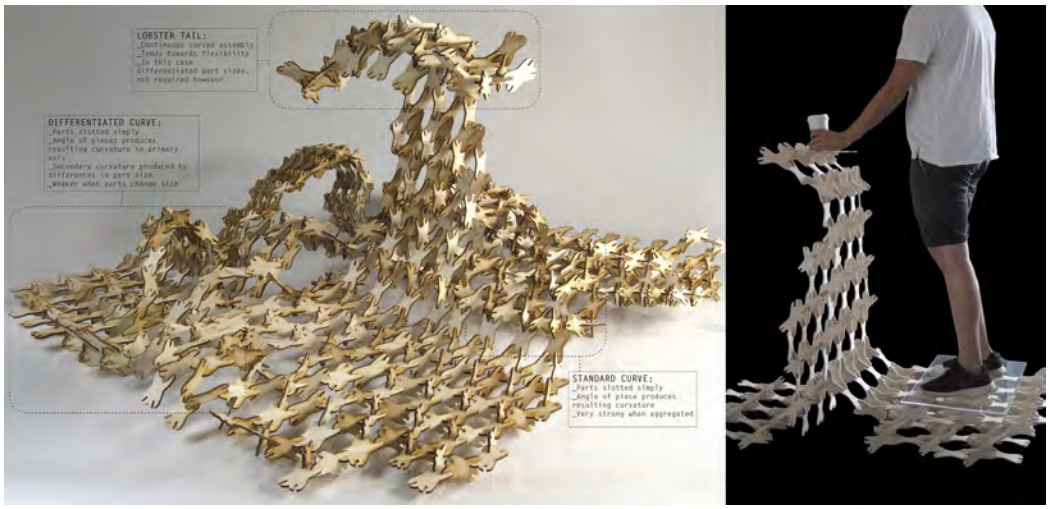


Figure 2. Rigid and pliant configuration; Integration of bendable component [Vera Parlac]

By utilizing a kit-of-parts design strategy the structure can be built in a variety of configurations and adapted to a variety of spaces. Due to the self-similar unit shape and the standardized connection between the units, there is a great combinatorial potential for a structure assembly. On a more local

scale, however, the combinatorial potential is driven by the assembly pattern that is contingent on the shape of the unit and the angle of its connections. Following the assembly pattern, two main configuration trajectories emerged: rigid (self-supporting) and pliant (flexible) (Figure 2).

Individual components can form any number of permutations, but discrete assemblies, used to govern the form of a larger construct, were generated to support change in functionality, directionality and form. These discrete assemblies were then combined into larger formations and their tectonic and spatial capacities examined. However, the system itself remains open and able to adjust to a variety of spatial/contextual conditions as well as to support part replacement. In this way, recalibration of the construct can be maintained since its parts could be reconfigured in a variety of ways (Figure 3).

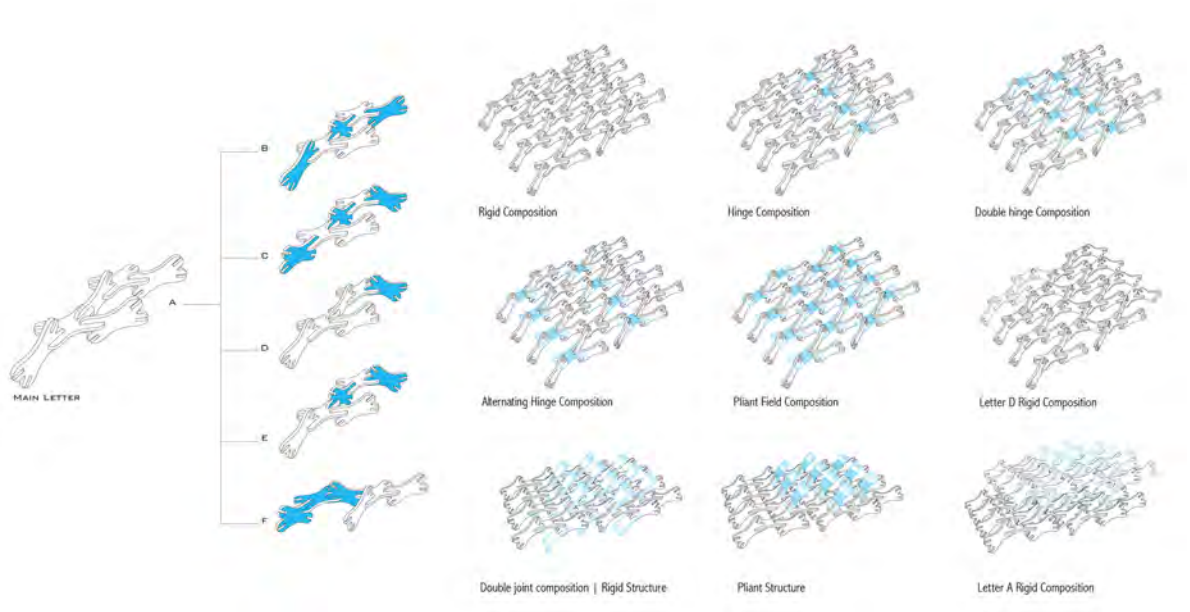


Figure 3. Combinatorial Potential [Vera Parlac]

The component shape was chosen for its capacity to produce a significant number of different combinations while maintaining the pattern that generates rigid and pliant versions. These configurations were then modeled digitally and tested physically for their behaviour. The tests resulted in a design of a new bendable component that was positioned adjacent to pneumatic muscles to facilitated bending of the regions surrounding the muscles. Ultimately, the modular structure can negotiate a change in direction (straight, angled, curved), change in thickness by smoothly transitioning from single to multiple layers (from a surface to a three-dimensional construct) and change in structural capacity (from self-supporting to bendable).

3.2. Pneumatic Muscles

The movement of pneumatic muscles depends on the flexibility of the elastic material, and the volume of internal chambers and their geometry [3]. Andrew Marchese et al [2] list three soft robot morphologies differentiated by their internal channel structure: ribbed, cylindrical, and pleated. The soft body (actuation system) of the *Soft Kinetics* project is developed using a ribbed morphology but its internal channels are produced using two different techniques: the lost wax casting, and a combination of the lamination casting and the soft lithography fabrication method. As a result, two types of muscles are produced: the central channel muscles (S, B, and V) and the distributed channel muscle (M) (Figure 5). The fabrication technique is important in achieving consistent properties of the muscles as they get reproduced; it plays an important role in achieving consistent elasticity and inner channel geometry.

The behavior of designed pneumatic muscles was explored through prototyping and iterative design and their performance observed as they were activated within a modular structure. The central channel muscles produced using the lost wax technique were resilient and durable (by not being cast in laminated fashion). Compared to the distributed channel muscle it achieved significant bending. In general the lost wax technique allows for a great variety of cavity forms since the muscle was made as a solid body and was designed that way, not in layers. The proposed central channel muscles underwent several modifications to achieve maximum bending after inflation.

The muscles were conceived as modular elements of the structure and as such could be integrated into the structure interchangeably; two muscles (S and V) were designed to integrate into the assembly grid pattern while the other two (B and M) to nest within the voids of the grid. In terms of their behavior, the central channel type muscles (S, B, V) act as linear actuators while the distributed channel muscle (M) acts as a folding hinge (Figure 5).

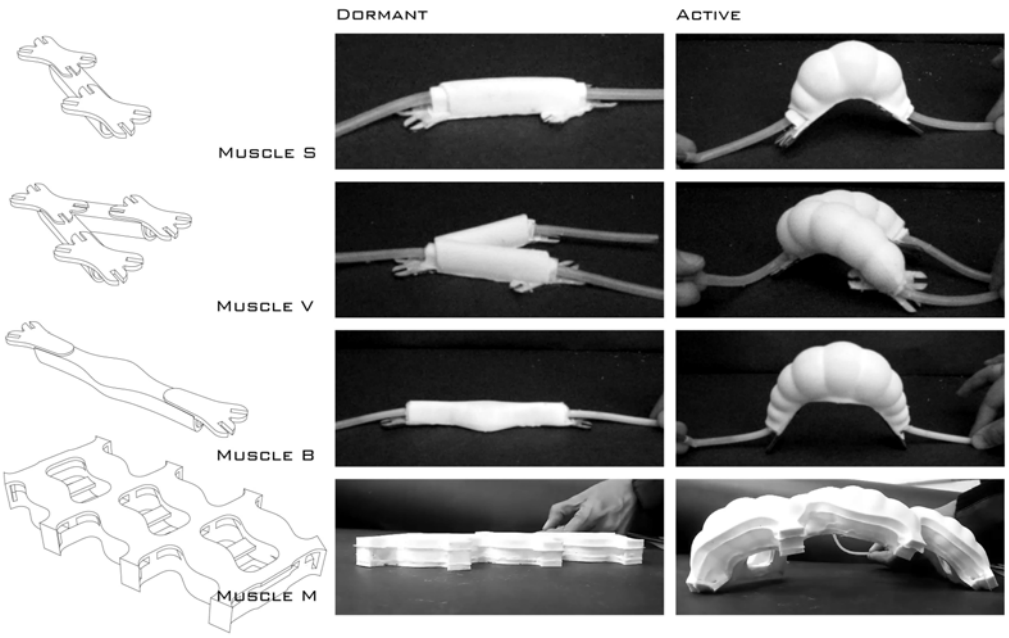


Figure 5. Muscle types and their performance [Vera Parlac]

The muscle morphology and geometry were designed to balance the wall thickness and the volume of air channels. These two different types of muscles required different approaches to mold production. The central channel muscle molds were CNC milled, while the distributed channel mold was produced by layering laser-cut acrylic material. Both muscle types were made from silicon rubber. To direct their motion, one side was fabric-reinforced. Soft elastomer pneumatic muscles are capable of continuous deformation but the challenge is to isolate a particular bending movement within its length [5]. For that reason, the pneumatic muscles used in this project were short and compliant with the grid pattern of the modular structure (Figure 5); their length and cluster organization, however, will be further explored in the next phase of the project, to produce asymmetrical shifts within the fabric of the modular structure.

3.3. Integration and Prototypes

The “soft” body of pneumatic muscles could easily be integrated with the “hard” body of the light modular structure. The connection was achieved by embedding the modular component within the central channel muscles or by weaving the components through the openings in the distributed channel muscle. (Figure 6).

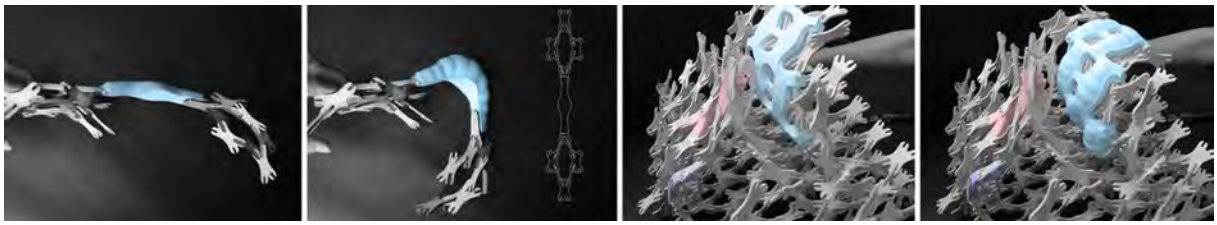


Figure 6. Testing the connection and movement of the muscle; dormant and active muscles [Vera Parlac]

The central channel muscles integrate into the hard body of the structure by a slip joint, just like any other modular component of the system. Therefore, the soft pneumatic muscles could be positioned to displace the "hard" parts of the modular structure, working as an active connective tissue, while the overall assembly pattern was maintained. This strategy allows muscles to be asymmetrically distributed throughout the structure, concentrated in some areas, or placed sporadically in others. This is seen as a very promising direction that will be further explored in the next phase of the project. For example, larger segments of the modular structure could be dynamically altered to open and close apertures of varying sizes and shapes (Figure 7).

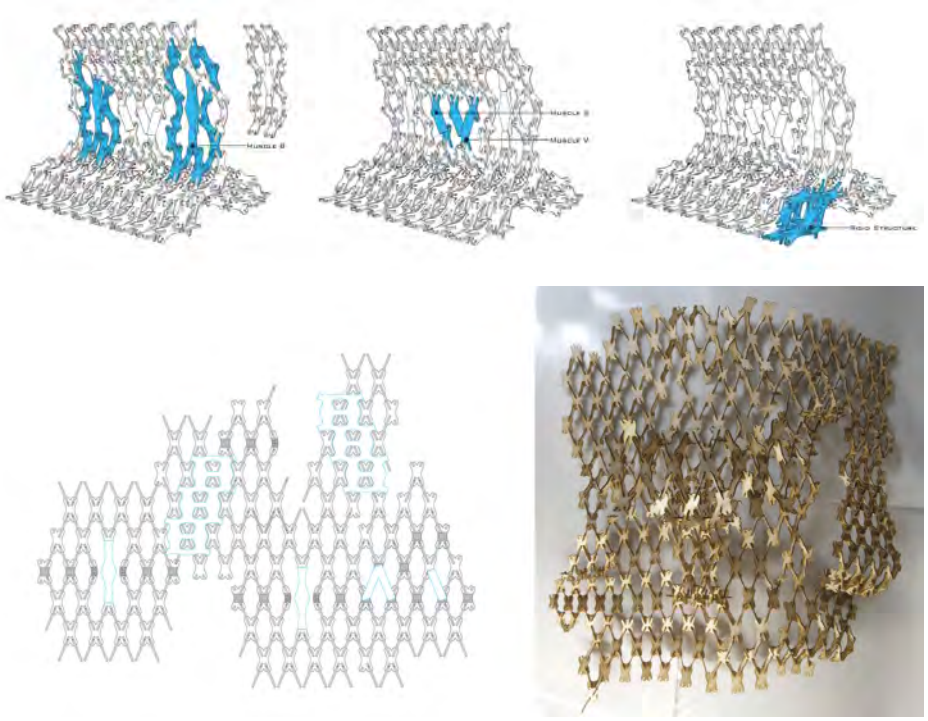


Figure 7. Illustration of muscle integration, assembly pattern and surface deformation [Vera Parlac]

Several small prototypes were constructed to test various ways and combinations of muscle integration. It is in the prototypes that the clustering of muscles was explored. The clusters, consisting of three to five pneumatic muscles, were inflated in sequence. Solenoid valves controlled the inflation and deflation pattern (supply and exhaust) and their work was regulated through an Arduino microcontroller. The rate and duration of valve opening and closing was set to allow all linked muscles to inflate in a sequence; the pressure was controlled through a sensor to prevent over-inflation and damage to the muscles. Muscles linked in a cluster worked as a group, affecting dynamically a designated region of the structure. The work of the "soft" body could be controlled through proximity sensors to reveal a clear view out or in, or could be regulated by light sensors to serve as a functioning shading device (Figure 8).

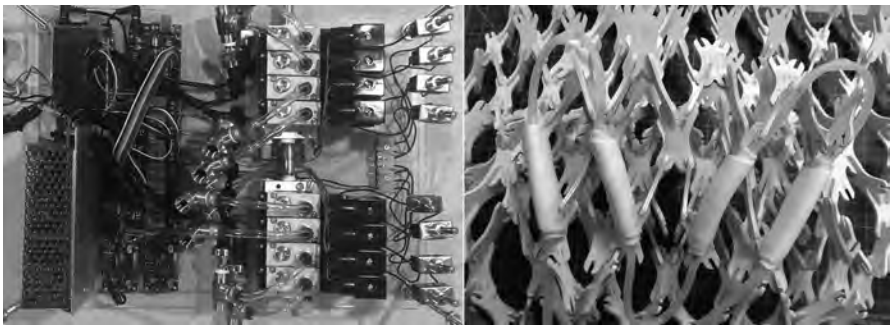


Figure 8. Solenoid valves board and pneumatic muscles cluster [Vera Parlac]

4. Discussion and Conclusion

This paper proposes a novel approach for constructing kinetic surfaces. Self-similar modular components can create a variety of surface/structure configurations while integration of soft robotic elements into a component-based surface has a potential to eliminate mechanical actuators and reduce a presence of other mechanical components within dynamic architectural assemblies.

A study of the surface configurations shows that by using the same modular components the aggregation patterns can form rigid (self-supporting) or pliant (flexible) regions of the structure. This insures the stability of the aggregation while creating a possibility for integration of dynamic regions. The smooth transition between the rigid and dynamic regions of the structure is an important aspect of the structure and it is mediated by bendable components that connect the pneumatic muscles with modular components that make up the structure. The system allows for a large number of configurations where self-supporting regions, providing structural stability, while other parts permit different levels of movement without compromising the structural integrity. The *Soft Kinetics* project weaves together soft (pneumatic muscles), hard (self-supporting) and pliable (dynamic) elements to create a material system that can behave dynamically. This variation in performance is achieved by a variable density of the assembly pattern and its extensive combinatorial capacity.

The design of pneumatic muscles builds on projects such as the *Adaptive Pneumatic Frameworks* and the *Modular Pneu-Façade System*, and strives to seamlessly integrate them into a modular system that follows the same aggregation pattern. Their geometry fits into the overall structural pattern of the construct making a smooth transition between self-supporting and dynamic regions possible.

The main motivation for the development of this system of soft actuation is to produce a uniform material system that can be built in a variety of configurations and to reduce a presence of complex mechanical systems.

The weight of the structure is an important factor; therefore more research is required to define the materiality of the modular structure as well as durability and weight of the embedded pneumatic components. Current composite structure is made of plywood; but the use of aluminum or plastic will be explored in future iterations.

The current study examined behavior of small clusters of actuators but their distribution and density (within a larger structure) need further study to fully understand the potential of this system to move larger regions of a structure. New computational tools for simulation of complex non-elastic behavior will be employed to quickly test alternative designs. Future research will also focus on the design of alternative aggregation patterns to further experiment with the range and amplitude of motions.

Integration of pneumatic muscles into a modular component based surface opens up wide filed of opportunities for design of lightweight, variable and dynamic surfaces that can serve as adaptable building skins or self supporting small scale structures. Due to its modularity and versatility this

system could be built to fit into variety of spatial configurations while also enabling dynamic activation of its parts.

When the infrastructure for space organization is not only concerned with the traditional logic of the constructed environment but is informed by the logics of thermodynamic behaviors, a new notion of order and organization of space could be achieved that would increase organizational complexity, introduce emergence, and possibly result in the design of open systems [7]. Energetically or kinetically active boundary has a level of agency and can, through its variability, attract, dispel or disperse users within spaces. It might unfold additional otherwise hidden layers of usable space or attract gathering of people by its coolness or heat (Figure 9). By responding to information from the environment, responsive boundary can serve as an effective interface between the users and their surroundings.

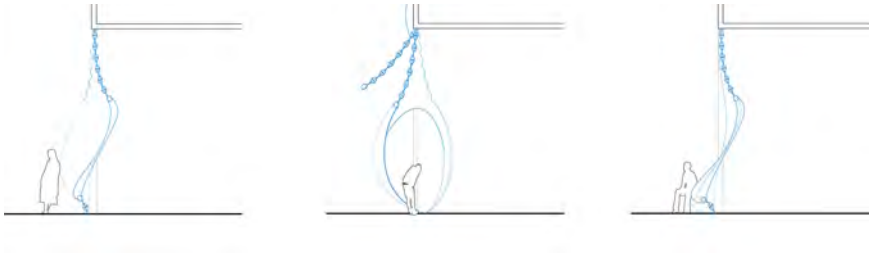


Figure 9: Kinetically active responsive building skin [Vera Parlac]

Acknowledgements

Parts of this paper are adapted from two texts published in Proceedings of the 2019 ACSA Annual Meeting and 2019 ARCC Conference Proceedings. The contribution of the previous conference organizers and committees is hereby gratefully acknowledged.

References

[1] W. Zuk, Roger H. Clark, *Kinetic Architecture*, New York: Von Nostrand Reinhold Company, 1970.

[2] A.D. Marchese, Robert K. Katzschmann and Daniela Rus, "A Recipe for Soft Fluidic Elastomer Robots." *Soft Robotics*, vol. 2, pp. 7-25, March 2015.

[3] J. Bishop-Moser, G. Krishnan, C. Kim, and S. Kota, "Design of soft robotic actuators using fluid-filled fiber-reinforced elastomeric enclosures in parallel combinations," in *2012 IEEE/RSJ International Conference on Intelligent Robots and Systems (IROS)*, IEEE, pp. 4264-4269.

[4] F. Connolly, C. J. Walsh and K. Bertoldi, "Using Analytical Modeling to Design Customized Fiber-Reinforced Soft Actuators." in *Society of Engineering Science 53rd Annual Technical Meeting* (SES 2016).

[5] S. Ahlquist, Sean, W. McGee and S. Sharmin, "PneumaKnit: Actuated Architectures Through Wale- and Course-Wise Tubular Knit-Constrained Pneumatic Systems," in *ACADIA 2017:Discliplines and Disruptions, Proceedings of the 37th Annual Conference of the Association for Computer Aided Design in Architecture*, Cambridge, Massachusetts, November 2-4, 2017, T. Nagakura Ed., Cambridge: ACADIA, pp. 38-51.

[6] D. Park, M. Bechthold, "Designing Biologically-Inspired Smart Building Systems: Processes and Guidelines," *International Journal of Architectural Computing* vol. 11 (4), pp. 437-464, 2013, doi:10.1260/1478-0771.11.4.437.

[7] A. Pavé, A. 2006. "Biological and Ecological Systems Hierarchical Organization", in Hierarchy in Natural and Social Sciences, D. Pumain Ed., New York: Springer-Verlag, pp. 39-70, 2006.

Proceedings of the IASS Annual Symposium 2019 – Structural Membranes 2019
Form and Force
7 – 10 October 2019, Barcelona, Spain
C. Lázaro, K.-U. Bletzinger, E. Oñate (eds.)

Energy-efficient actuator placement for a convertible bending-active structure

Paul MARKER*, Lisa STAMMEN, Achim BLEICHER

*Brandenburg University of Technology Cottbus - Senftenberg, Chair of Hybrid Structures - Structural Concrete
Konrad-Wachsmann-Allee 2, 03046 Cottbus, Germany
paul.marker@b-tu.de

Abstract

The requirements on load-bearing structures regarding their multifunctionality and adaptability are steadily growing [1] and the significance of resource- and energy-saving measures is increasing. In order to derive a method for the generation of energy-efficient active structures, in this paper procedures of the principles of lightweight construction are combined with those of bending-activity and optimal actuator placement. This approach was applied to the example of a bending-active pavilion. The principles of lightweight construction aim to create structures with the maximum possible structural stiffness at the minimum mass. Less mass also leads to a reduction of the energy required to actuate the structure. Bending-active structures are based on the principle of large elastic deformations. As with springs, it is thus possible to store energy in the form of elastic deformation in the structure and use it for transformations. Another decisive influence on the total energy balance of an active structure is associated with its actuator placement. An attempt was made to generate a structure that meets the described multiple requirements. The results obtained are presented in this paper.

Keywords: convertible, hybrid, lightweight, bending-active, energy-efficient, actuator placement, optimisation

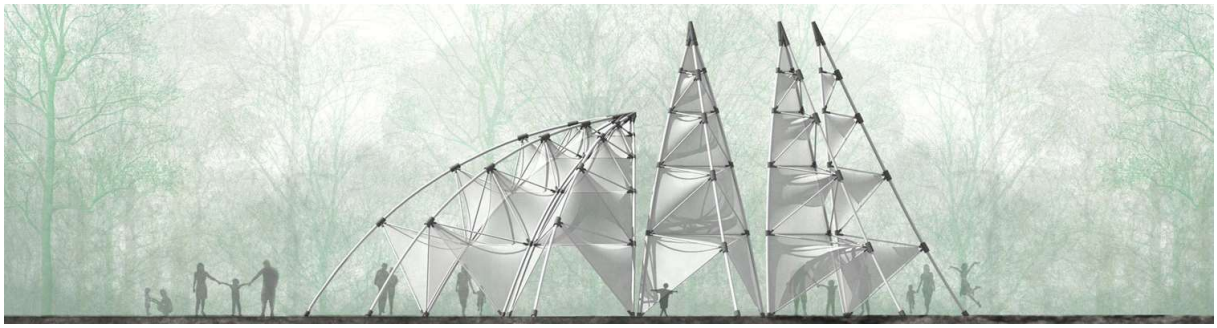


Figure 1 : Initial design of a convertible pavilion with sliding joints and actuation at the supports [2]

1. Introduction

Combining bending activity with the principles of lightweight construction efficient bending-active structures like "Bending-Active Textile Hybrids" (BAHS) can be designed; with regard to adaptive structures, a high application potential has been identified for kinetic bending-active structures [3]. These can use the elastic strain energy stored in the structure for transformation processes cf. compliant mechanisms [4], [5]. Research on the analysis of bending-active structures can be found in [6], [7], or [8] for instance. In addition to the possibility of achieving a higher structural stiffness for bending-active structures, another advantage is that for the actuation of a lighter structure less energy

Copyright © 2019 by Paul MARKER, Lisa STAMMEN, Achim BLEICHER
Published by the International Association for Shell and Spatial Structures (IASS) with permission.

is required. An optimal actuator placement can contribute to save even more energy, which is why this should already be determined in the design process. An optimal actuator placement is investigated for example in the field of active vibration control [9], [10], load path control [11], [12], [13] and minimum whole-life energy design [14].
In the scope of this paper an approach is presented, which tries to combine the mentioned concepts using the example of a convertible bending-active pavilion. In the digital design process, a hybrid structure consisting of bending elements and a kinematic truss, was derived from results of structural optimisation. In order to facilitate the transformation, sliding joints were integrated. By means of dynamic relaxation, the large deformation analyses for the different transformation states were performed, which could be verified with FEM and a small-scale convertible prototype. In order to investigate the potential of integrated actuators, the sliding joints were fixed and all rods were considered as possible actuators. A complete analysis of all possibilities for the placement of a maximum of eight actuators was performed due to large computation time. Subsequently, solutions for concepts of integrated actuation with minimal energy requirements were found. To shorten the computation time, an improved search algorithm was implemented. The solutions represent energy efficient alternatives for the initial design, in which the actuation is realised with actuation at the supports. An overview about the investigations is illustrated in the following Figure 2.

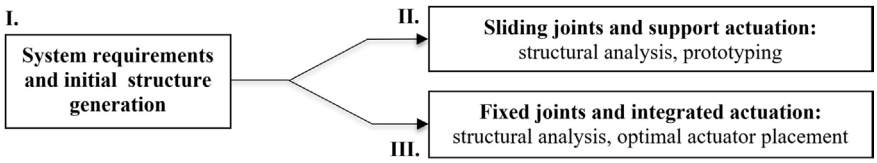


Figure 2 : Overview of the methodology presented in this paper

2. System requirements and initial structure generation (I.)

2.1 System requirements:

In the beginning, a transforming design space and the associated boundary conditions were defined. For the generation of the structure presented here, the goal was to create a dome-shaped transformable pavilion. Thus, free standing radially arranged segments were to be created, each with a cantilevering static system, with boundary conditions at the bottom. Constraint for the subsequent large deformation analysis is the proper closure of the structure as shown in Figure 3.

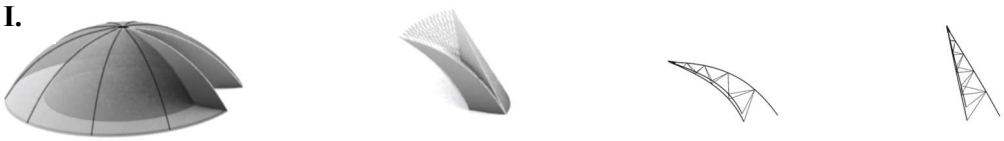


Figure 3 : dome-shape, transforming design space segment, derived two truss girder segments

2.2 Initial structure generation:

In order to generate a structure that is as material-efficient as possible, the principles of lightweight construction can be used. This is especially important to counteract the influence of the dimension effect and therefore essential if larger spans should be realised. Preliminary inspiring investigations on the open and the closed state of one segment of the design space (cf. Figure 3), were carried out by topology optimisation using ANSYS [15]. For a line load, there were different resulting topologies for the two states, which however, showed similarities. While the arrangement of the webs changed dependent on the state, the investigations always resulted in outer main chords. Inspired by that two truss girders tapered from the support to the top (cf. Figure 3, right) were derived. These structures for the different states each describe independent structures that cannot be transformed into each other

without intervention. In order to enable the transformation of the structure, large elastic bending deformations have to be allowed and a compromise between the principles of lightweight construction and those of bending-active structures has to be achieved. To make this possible, two variants were analysed, one with sliding joints (II.) and the other with integrated actuation (III.).

3. Sliding joints and support actuation (II.)

3.1 Compromising the principles of lightweight construction and active-bending

The following approach was to modify the static system of the structure by designing the rear joints (cf. D II in Figure 4) of the truss girder as sliding joints. Thus, it is possible to use bending-active component behaviour to reach the other states of transformation. This inevitably leads to a contradiction with the originally derived structures as the large bending stresses conflict with the approach of creating lightweight structures in which the cross-sections are fully utilised.

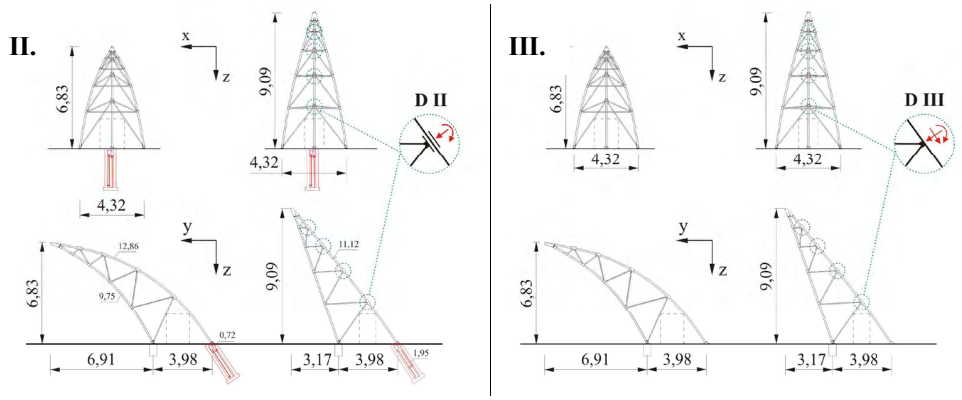


Figure 4 : II. Initial structure with sliding joints (D II) and support actuation (red), (left side)
III. Initial structure with fixed joints (D III) and internal actuation, (right side)

3.2 Structural analysis and prototyping

In the context of the present investigations the large deformation analysis was conducted using the software Kangaroo [16] (cf. Figure 5 a)), which uses the method of dynamic relaxation. These results could be validated with the FEM software SOFiSTiK [17] (cf. Figure 5 b)) on the one hand and with a convertible small-scale prototype (cf. Figure 5 c),d)) on the other. Both the dead load and a support displacement oriented in the direction of the rear chord were applied to the structure in the open state (cf. Figure 4, II, right side). In order to ensure the curved bending geometry of the structure, the supports were modelled as fixed. As cross sections, tubes (GFRP) with a diameter of 10 cm with a wall thickness of 3.5 mm were selected for the chords, and a diameter of 5 cm with a wall thickness of 3.5 mm for the webs. In Kangaroo [16] the sliding joints were implemented on the nodes of the rear chord using geometric constraints, whereas couplings with local alignment were used in SOFiSTiK [17]. This variant (II) of the structure has the special characteristic that the curved target geometry can be achieved with only one actuator, effecting a support displacement.

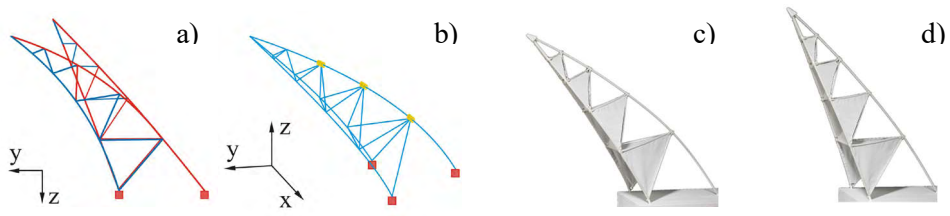


Figure 5: Large deformation analysis with: Kangaroo a); SOFiSTiK b); convertible prototype (scale 1:10) c), d)

4. Fixed joints and integrated actuation (III.)

4.1 Actuation concept & efficiency analysis

For the investigations in this chapter, the joints (cf. D III in Figure 4) and supports were regarded as fixed. Each of the 35 rods has the same cross section and was considered as a potential actuator which is modelled as strain load. The corresponding numbering, which the following analyses refer to, is depicted in Figure 6 (right). As the main goal is to achieve an energy-efficient actuation, the regarded objectives were primarily the transformation of the node at the top of the structure in the desired y-direction u_y and the minimisation of the energy Π necessary therefore. The ratio of the two criterions is implemented as target criterion as shown in the following formula.

$$f_1 = \frac{u_y}{\Pi} \tag{1}$$

The calculation of the considered deformation energy Π and their parts Π_N and Π_M that are resulting from axial respectively bending stresses is shown in the following formula (2). Wherein A_0 is the initial cross sectional area, l_0 the initial length, E the Young's modulus, ε the strain and κ the curvature of the beam.

$$\Pi = \Pi_N + \Pi_M = \frac{1}{2}\int_{l_0} E \cdot A_0 \cdot \varepsilon^2 \, dx + \frac{1}{2}\int_{l_0} EI_0 \cdot \kappa^2 \, dx \tag{2}$$

As result of the evaluation of the two parts of this energy, it became obvious that the amount of elastically stored energy due to bending is much higher than that resulting from normal stresses. The analyses were performed for single actuators (ch. 4.2) as well as for combinations of actuators (ch. 4.3) using Karamba3D [18]. The results were visualised and evaluated with MATLAB [19].

4.2 Analyses of single actuators

In a first analysis, each rod is considered both as single compression and single tension actuator. In the following Figure 6 (left), the comparison of the different positions as compression actuators with an elongation of 100 mm is shown as example.

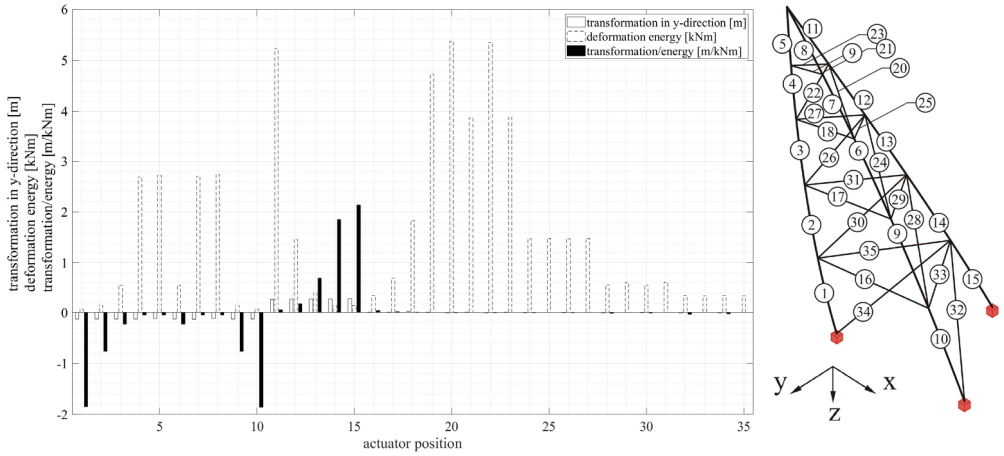


Figure 6: Individual evaluation of the actuators as compression actuators for an elongation of 100 mm and numbering of actuator positions

It clearly can be seen that the actuator positions 13 to 15 located on the rear chord offer the most efficient solutions according to the criterion shown in formula (1).

In a following analysis, we investigated the influence of a variable elongation for all 35 rods. The following Figure 7 depicts the results for the actuator positions 1 to 15 located at the chords in the space of objectives as example.

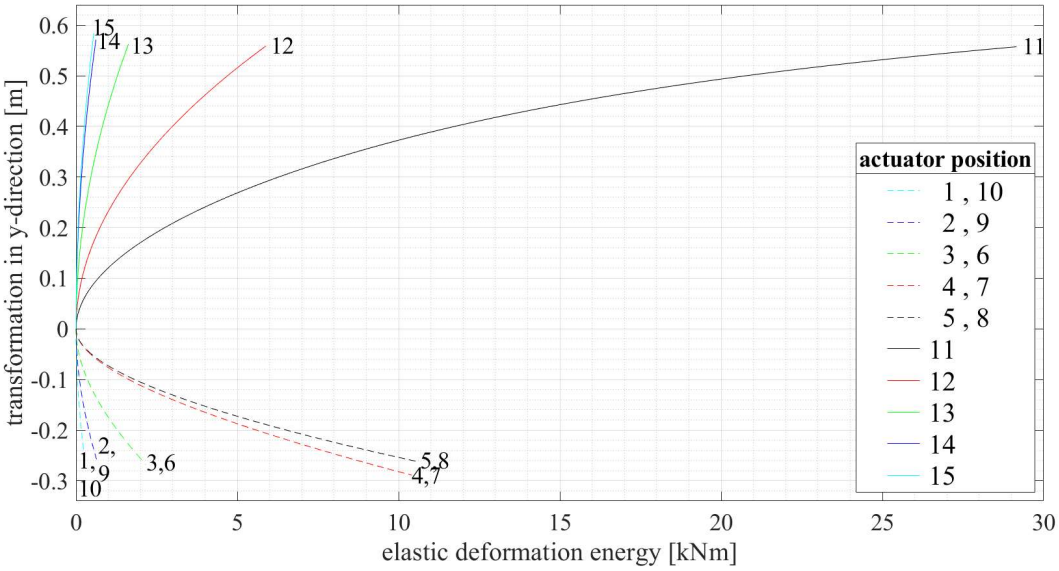


Figure 7: Individual evaluation of the actuators as compression actuators for an elongation of 0 - 200 mm

This diagram also points out that the positions 13 to 15 are the preferable ones regarding the development of their efficiency as the other gradients are decreasing while they show a linear correlation. In addition, the graphs show that there are many actuator positions (dotted lines) that are not appropriate for compression actuators because they result in a transformation into the opposite direction. Performing these investigations for tension actuators lead to 1 and 10 as well as 2 and 9 as the most efficient actuators.

4.3 Combination of actuators

In the following step, optimal combinations of actuators and their placement were investigated for the given structure. The sets examined were differently partitioned into tension and compression actuators and consist of up to eight actuators. This amount was limited due to the rising computational effort. Furthermore, the choice of eight actuators allows to reduce the elongation of each actuator necessary to reach the desired transformation and a smoother curvature of the whole structure.

In general the resulting number of possibilities of combinations can be calculated by the following combinatorial formula (3), wherein n_{rod} is the number of rods that are possible actuator positions and n_{act} is the number of actuators chosen out of them.

$$\binom{n_{rod}}{n_{act}} = \frac{n_{rod}!}{n_{act}! \cdot (n_{rod} - n_{act})!} \tag{3}$$

If different actuators (concerning the amount of actuation or kind of actuator) are to be placed, the combinatorial formula (6) has to be modified to the following formula (4).

$$\frac{n_{rod}!}{(n_{rod} - n_{act})!} \tag{4}$$

As a result, the following Figure 8 (left) depicts the rising number of possible combinations calculated by formula (3) and (4) in dependence of the amount of actuators chosen.

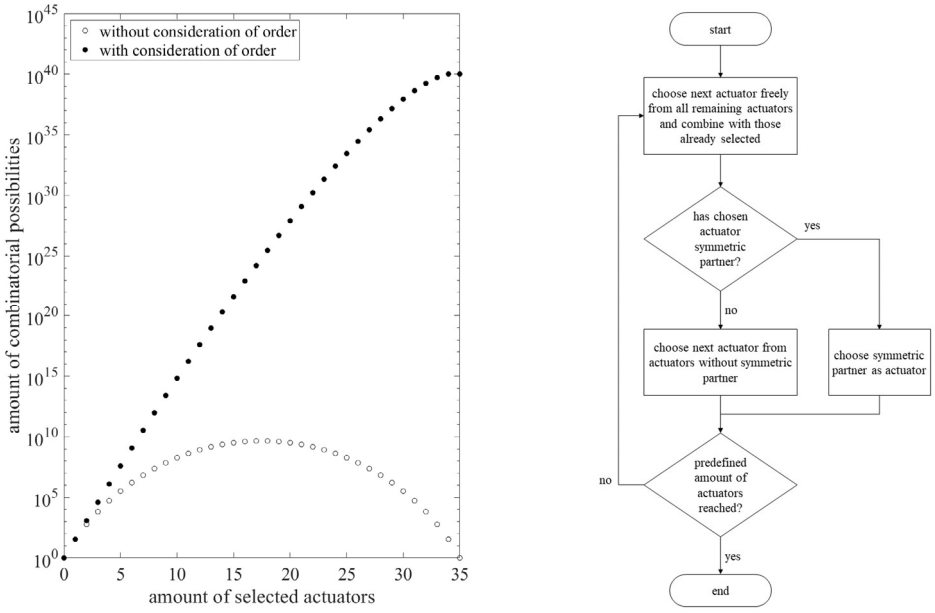


Figure 8: Number of possibilities for the actuator placement (left) and flow chart for the generation of the combination under symmetry condition (right)

In Figure 8 (left) it clearly can be seen that there is a huge effort to perform finite element analyses for all possibilities, even for a small number of chosen actuators. For this reason and due to the desired closing of the segments to a dome shaped pavilion (cf. Figure 3), a condition of symmetry was implemented in the algorithm that calculates all possible combinations for a specified amount of actuators to be chosen as depicted in the flow chart in Figure 8 (right). Consequently, for the placement of an actuator set consisting of four tension and four compression actuators 237048 placements are possible. This combination was chosen to enable a comparison with the later introduced improved search algorithm. The following Figure 9 depicts the results for the full amount of this possibilities in the two-dimensional space of target criterions and the structure with the chosen efficient set of actuators (compression = red, tension = blue), which offers the maximum possible transformation and was also the result of the improved search algorithm.

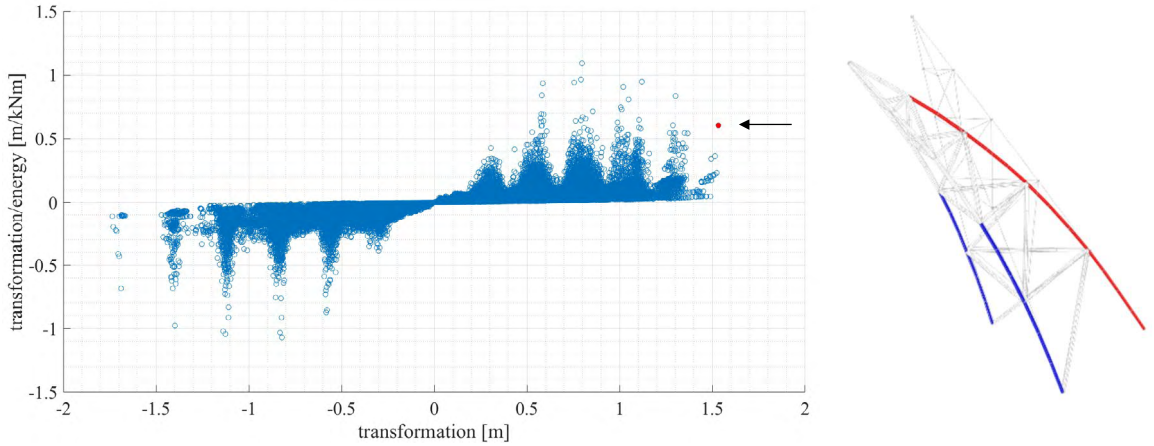


Figure 9: Solution space for all 237048 possible combinations of 4 tension and 4 compression actuators in the two-dimensional space of the target criteria (left) and corresponding chosen solution (right)

Since the calculation of the total solution space for eight actuators resulted in a very large computation time, an improved search algorithm was implemented to accelerate this for further calculations. The algorithm is depicted in the following Figure 10. In every search depth, all remaining possible actuators that have not been chosen in a previous step are evaluated (black bold arrows) as both compression (red) and tension actuator (blue) in combination with the actuators already chosen. This neglects the possible effect that a formerly chosen actuator becomes inefficient due to one chosen in a later step (dashed grey lines). This assumption reduces the amount of necessary evaluations in the first step by nearly 5000 evaluations. As a result, a significant benefit in computation time could be reached, reducing it to less than 0.005% without obtaining much more inefficient solutions. The solution found (cf. in Figure 9 right) is 99.989% optimal compared to the most efficient one in Figure 9 (left). The stepwise process of the algorithm for choosing that optimal solution according to the following weighted sum criterion in formula (5) can also be seen in Figure 11.

$$f_3 = 0.7 \cdot u_y + 0.3 \cdot \Pi \tag{5}$$

Another advantage of this method is that the algorithm can be aborted in any depth and later continued to generate solutions with a greater amount of actuators as the solution in each step is a partial solution of that one with more steps respectively actuators.

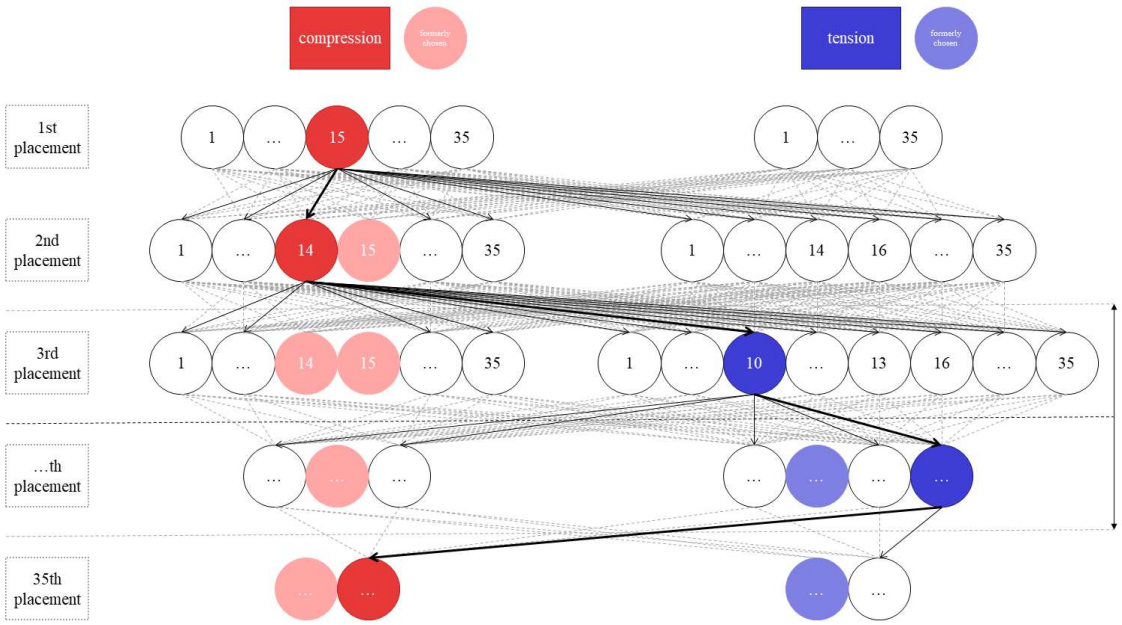


Figure 10: Improved search algorithm for the determination of an optimal solution

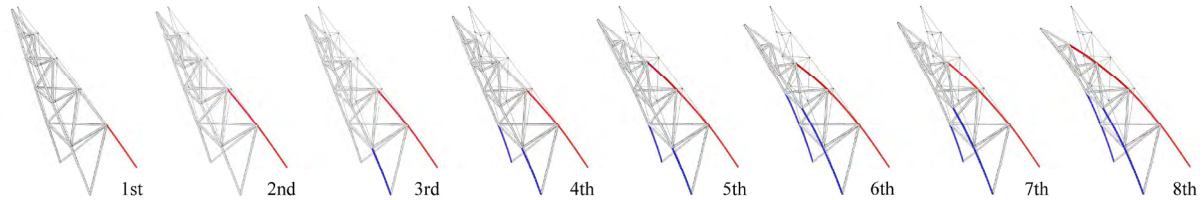


Figure 11: Process of optimal choice for the placement of eight actuators according to the weighted sum criterion

5. Summary and conclusion

Two variants of a convertible bending active structure could be generated, whose transformation is based on elastic component behaviour and can be transformed to various stable states. Therefore, a compromise between the principles of lightweight construction and those of bending activity could be reached. It was investigated that a similar transformation shape of the structure can be achieved by both variants with sliding joints and actuation by support displacement (II.) as well as with fixed joints and integrated actuators (III.). Furthermore, a method was implemented which allows an optimal actuator placement in the design process. As the current state of investigations only regards the deformation energy, further investigations could consider other forms of energy like kinetic energy for instance. A more precise modelling of the actuation should take into account the real actuator stiffness and its influence on the structural behaviour. If the actuators were modelled as hydraulic cylinders and thus not be exposed to bending, a polygonal deformation figure would result which stores less elastic energy. More detailed investigations on the optimal utilisation of large bending deflections in relation to energy-efficient actuation will follow. A further question concerns the weighting of material- and energy efficiency and hence between the principles of lightweight construction and bending activity.

References

[1] M. Schlaich, "Aktive und wandelbare Ingenieurbauten," *Stahlbau*, vol. 73, no. 12, Dec. 2004.
[2] A. Schneider, "Design, analysis and detailing of a convertible bending active structure," M.S. thesis, Chair of Hybrid Structures - Structural Concrete, BTU Cottbus - Senftenberg, 2018.
[3] J. Lienhard and C. Gengnagel, "Recent developments in bending-active structures," in *Proc. of the IASS Ann. Symp. 2018 "Creativity in structural design",* Boston, 2018.
[4] L. L. Howell, S. P. Magleby, and B. M. Olsen, Eds., *Handbook of compliant mechanisms*. Chichester, West Sussex, United Kingdom ; Hoboken: John Wiley & Sons, Inc, 2013.
[5] L. Zentner, *Nachgiebige Mechanismen*. München: De Gruyter Oldenbourg, 2014.
[6] G. Quinn et al., "Calibrated and Interactive Modelling of Form-Active Hybrid Structures," in *Proc. of the IASS Ann. Symp. 2016 "Spatial Structures in the 21st Century",* Tokyo, 2016.
[7] A. M. Bauer, P. Längst, G. Quinn, C. Gengnagel, and K.-U. Bletzinger, "Exploring Software Approaches for the Design and Simulation of Bending Active Systems," in *Proc. of the IASS Ann. Symp. 2018 "Creativity in structural design",* Boston, 2018.
[8] J. Lienhard, "Bending-Active Structures," Ph.D. thesis, Universität Stuttgart, 2014.
[9] A. Bleicher, "Aktive Schwingungskontrolle einer Spannbandbrücke mit pneumatischen Aktuatoren," Ph.D. thesis, Technische Universität Berlin, 2011.
[10] M. Heidingsfeld, P. Rapp, M. Bohm, and O. Sawodny, "Gramian-based actuator placement with spillover reduction for active damping of adaptive structures," in *2017 IEEE International Conference on Advanced Intelligent Mechatronics (AIM),* Munich, Germany, 2017.
[11] A. P. Reksowardojo, G. Senatore, and I. F. C. Smith, "A new method to design structures that adapt to loads via large shape changes," in *Proc. of the IASS Ann. Symp. 2018 "Creativity in structural design",* Boston, 2018.
[12] P. Teuffel, "Entwerfen adaptiver Strukturen," Ph.D. thesis, Universität Stuttgart, 2005.
[13] J. L. Wagner *et al.*, "On steady-state disturbance compensability for actuator placement in adaptive structures," *Automatisierungstechnik,* vol. 66, no. 8, Aug. 2018.
[14] G. Senatore, P. Duffour, and P. Winslow, "Synthesis of minimum energy adaptive structures," *Struct. Multidiscip. Optim.,* Mar. 2019.
[15] *ANSYS Workbench 19.2.* ANSYS Inc., 2018.
[16] Daniel Piker, *Kangaroo.* 2017.
[17] *SOFiSTiK 2018.* SOFiSTiK AG, 2018.
[18] Clemens Preisinger, *Karamba3D 1.3.1.* 2018.
[19] *MATLAB R2018b.* MathWorks, 2018.

Proceedings of the IASS Annual Symposium 2019 – Structural Membranes 2019
Form and Force
7 – 10 October 2019, Barcelona, Spain
C. Lázaro, K.-U. Bletzinger, E. Oñate (eds.)

Expandable origami for architectural applications: layers of ORIGAMI-SCISSOR hinged deployable structures

Esther RIVAS-ADROVER

Department of Architecture, University of Cambridge
1-5 Scroope Terrace, Trumpington Street, Cambridge, CB2 1PX, U.K.
er460@cam.ac.uk

Abstract

Origami and scissor-hinged had been different types of deployable structures out of many others that exist. The author of this research unified both types and made a diamond origami-scissor hinged pattern, and therefore created a new hybrid type of deployable structure. Origami-scissor hinged patterns are lattice expandable origami structures that can fold and unfold as the thick origami, and expand and contract as a scissor structure; this therefore provides an extra degree of freedom to the thick origami. This paper tests the geometric compatibility of several possibilities of thicknesses of the scissor pantographic layers of the origami-scissor hinged pattern. The purpose of this research is to ascertain what are the geometric constraints and allowances in the design of the layers of origami-scissor hinged deployable structures, and to investigate whether an origami-scissor hinged pattern can be done with an overall reduction in thickness, which would allow a more efficient ratio of stowed to deployed configuration. This new technology has potential applications for mobile or transformable architecture, aerospace, robotics, industrial design and kinetic art.

Keywords: Deployable, transformable, expandable, thick origami, architecture, scissor-hinged, pantograph, geometry.

1. Introduction

The diamond origami-scissor hinged pattern unified origami and scissor hinged deployable structures, which had so far remained separate types within the field [1]; this signified the birth of a hybrid new type of deployable structure: origami-scissor hinged, invented by Rivas-Adrover [2]. This was achieved by applying the 'form generation method of relative ratios' (FGMORR) for 2-bar scissor-hinged structures by Rivas-Adrover [3] to the 'origami of thick panels' by Chen et al. [4].

Advances have been made in zero thickness (paper model) such as the symmetry based method that allows modifications in origami design by Sareh [5]. However, in order to build origami in large scales for architecture and engineering applications, a rigidity and thickness of the material is required. Applications of thick origami include space applications such as the solar array designed by BYU which is inspired on the origami flasher pattern by Zirbel et al. [6].

Various methods have been suggested in order to make thick origami using its zero-thickness kinematic model by De Temmerman et al. [7], Edmondson et al. [8], Hoberman [9] and Tachi [10]. 'Origami of thick panels' by Chen, Peng and You [4] demonstrates that origami of thick panels can be

Copyright © 2019 by Esther Rivas-Adrover
Published by the International Association for Shell and Spatial Structures (IASS) with permission.

devised by mechanism theory alone, and propose a method that can be extended and generalized to different types of origami.

Scissor-hinged deployable structures are made by units of bars joined by a pivot. While a single scissor mechanism is relatively simple, its replication to create large structures that can expand and contract is highly complex. Scissor-hinged projects include the transportable pavilion for exhibitions by Pérez Piñero [11], the swimming pool cover in Seville by Escrig, Valcárcel and Sanchez [12], and the Iris Dome by Hoberman [13]. Recent advancements on scissor grids include the research by Roovers and De Temmerman on grids done with polar and translational units [14] and [15].

2. Form generation method of relative ratios (FGMORR)

Scissor hinged surfaces have been made by replicating scissor units to make grids that make triangles or squares. The 'form generation method of relative ratios' (FGMORR) [3] can be applied to an indefinite number of combinations of lines, and therefore allows for potentially infinite scissor structures to be made with optimum deployment; this therefore opens a significant space for innovation.

The fundamental principle of the FGMORR is that in any given combination of lines, a ratio for a scissor unit (or various ratios for different sizes of scissor units with equal angles of motion) can be found, that distributed throughout the segments and subsegments results in geometrically compatible scissor hinged structure, as long as the following conditions are satisfied: the combinations of lines must intersect so that it can be translated in pantographs that intersect and join at the end nodes; the combination of lines is interpreted as a plan view; all the scissor units of all different ratios, must have equal angles of motion; the relative position of the scissor units in space must also remain constant and proportional throughout the deployment; the different ratios allow for scissor units with bars of different lengths (with equal angles of motion), and the smaller bars have to be at least half or longer than the bars of the first ratio to allow a good mobility of the structure; all the different ratios for different lengths of bars must mirror another scissor unit of the same ratio, by doing this the geometric deployability constrain defined by Escrig is guaranteed [16]. These conditions can be satisfied when using translational scissor units. This method enables for the scissor structure to be made with the minimum number possible of different sizes of bars, as well as achieving an optimum expansion and contraction.

The premise that the method can be applied to any given combination of lines was tested by applying it to a pattern derived from the geometry of the Alhambra in Granada, and resulted in the proposal of the Alhambra transportable pavilion in Cambridge Market Square [17].

3. ORIGAMI-SCISSOR hinged deployable structures

The diamond origami-scissor hinged structure [2] made by applying the 'form generation method of relative ratios' (FGMORR) [3] to the origami of thick panels [4]. This is done with two bar scissor hinged translational units. The origami panels are translated in virtual lattice thicknesses that can expand and contract while retaining the angles of the origami intact. Where in the diamond thick origami, one triangulated face would be made of two panels, in the diamond origami-scissor structure one triangulated face is made of 77 bars and 124 nodes. The diamond origami-scissor prototype was made of six triangulated faces. This prototype is made of 744 nodes and 462 bars (with six different types of bars). The prototype is structurally stable and it is kinematically compatible without any deformation of parts. While the diamond origami of thick panels has one degree of freedom, the origami-scissor structure has two degrees of freedom.

The origami-scissor hinged geometry method was also applied to the waterbomb origami of thick panels where the theoretical model was also geometrically compatible, and it also provides an extra degree of freedom to its thick origami counterpart [18]. Research indicates that this method could be extended and generalized to other types of thick origami patterns.

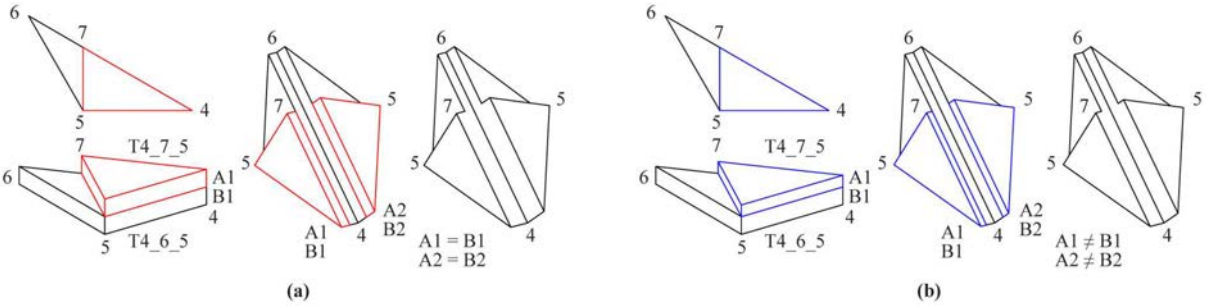


Figure 1: Thicknesses of the diamond origami panels. (a) Panels of equal thicknesses; (b) panels of different thicknesses.

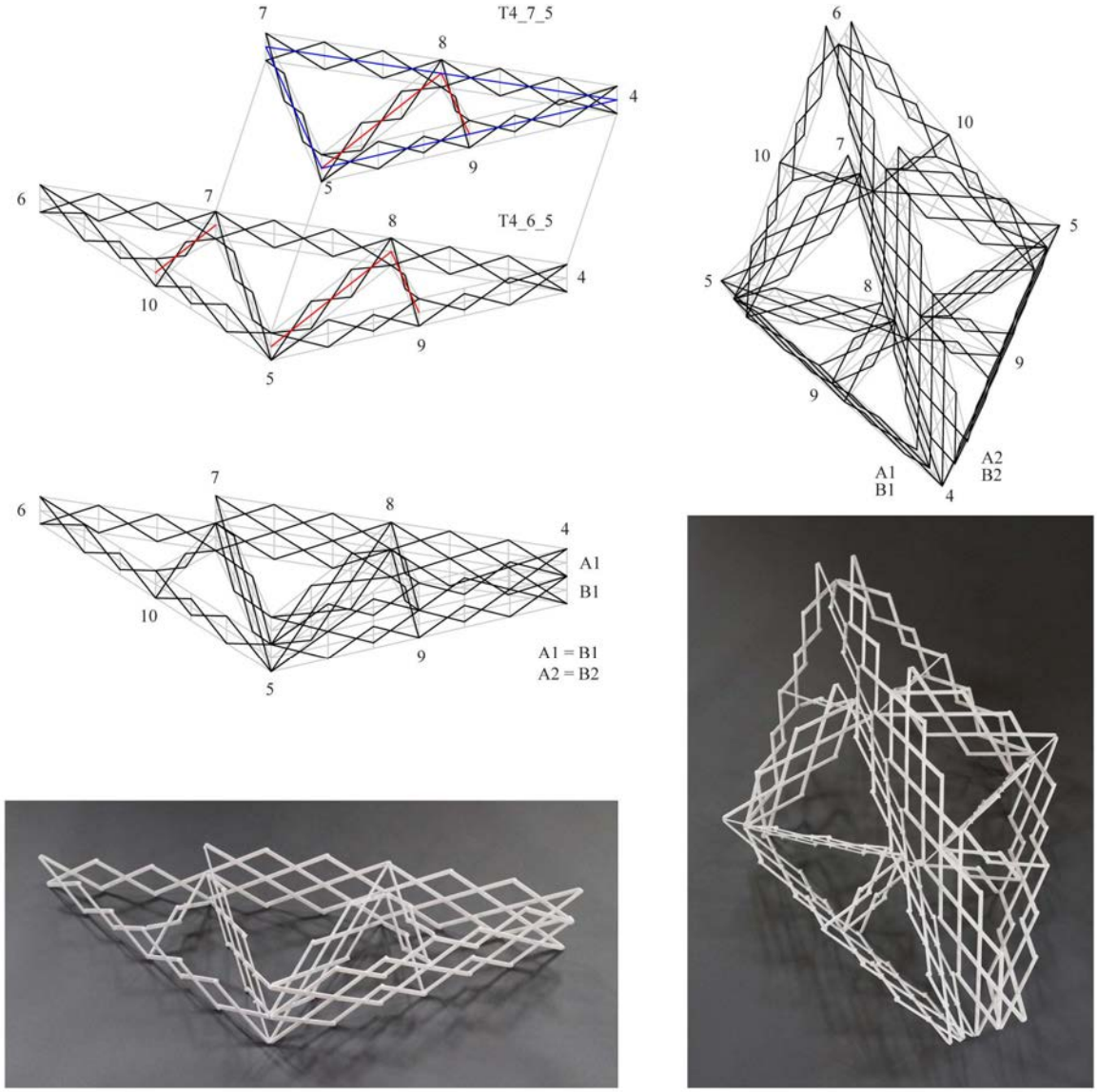


Figure 2: Diamond origami-scissor hinged structure made with panels of equal thicknesses (thickness A is equal to that of B). Theoretical model and built prototype.

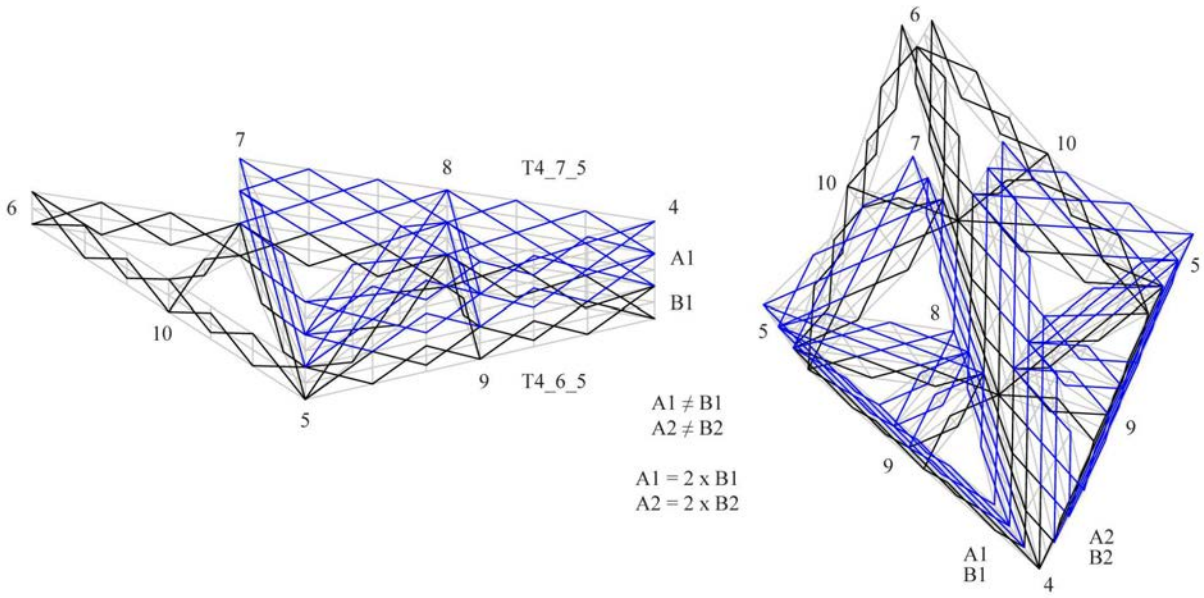


Figure 3: Diamond origami-scissor hinged structure made with panels of different proportional thicknesses. Thickness A is twice that of B.

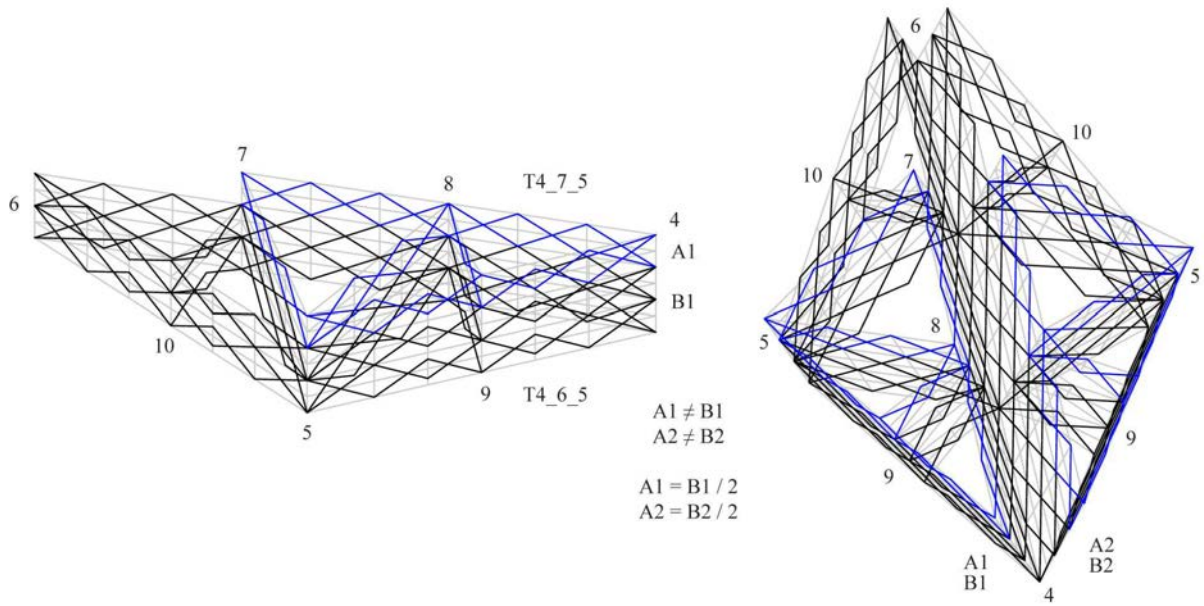


Figure 4: Diamond origami-scissor hinged structure made with panels of different proportional thicknesses. Thickness A is half that of B.

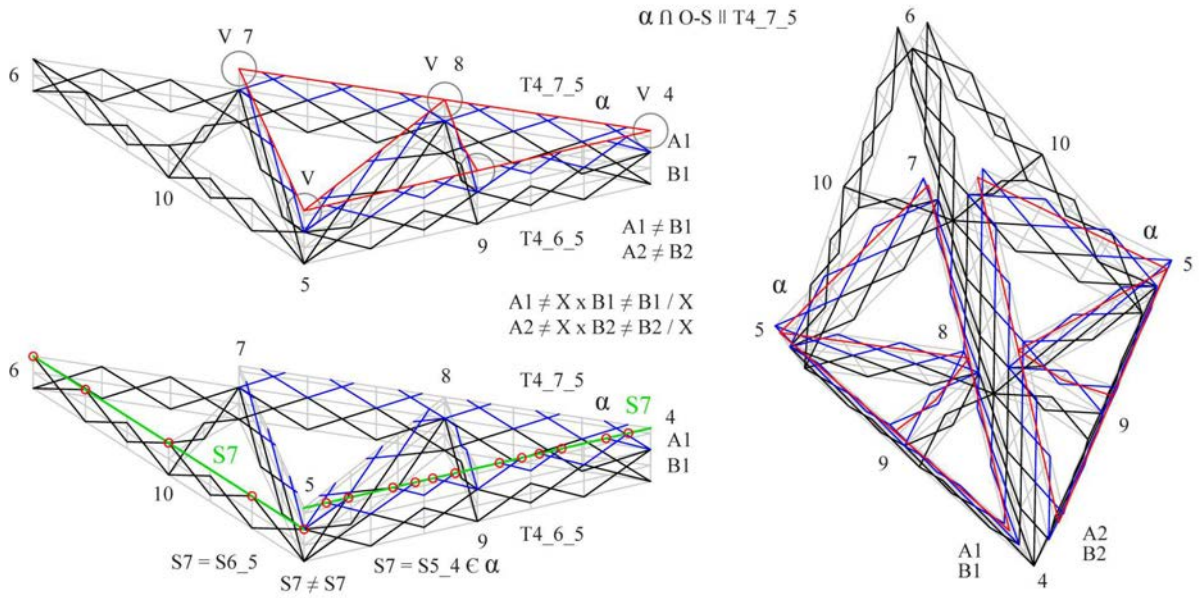


Figure 5: Diamond origami-scissor hinged structure made with different non-proportional thicknesses. Intersecting plane alpha.

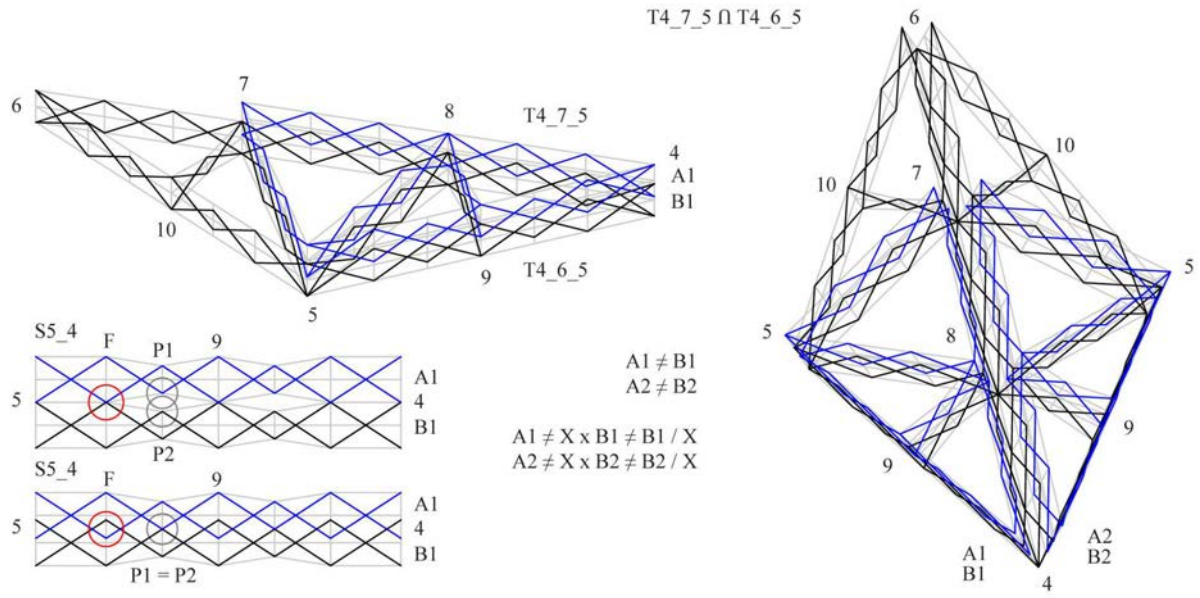


Figure 6: Diamond origami-scissor hinged structure made with different non-proportional thicknesses. Interweaving layers of scissor hinged pantographs.

4. Thicknesses of origami-scissor hinged layers

The diamond origami-scissor structure was made of two panels of equal thicknesses superimposed; this facilitated placing one triangle of pantographs on top of another, where both triangles were made of equal sizes of scissor units. The following research will test whether the method could be extended to origami of thick panels made with different thicknesses, therefore with different lengths of bars for the scissor pantographs.

The thicknesses of the origami panels will dictate the relative lengths of the bars of the scissor units to make the pantographs; therefore, a determination of its precise geometry is required in order to unify thick origami and scissors. The geometry consequence of applying mechanism theory to origami of thick panels, is that in some origami types, if certain ratios of thicknesses of panels apply, the origami type could be made with various options of thicknesses. For instance, in the case of the diamond origami of thick panels, each triangulated face is made of two thicknesses: A1 and B1, which are dictated by triangles T4_7_5 and T4_6_5. This mirrors another identical triangulated face made with: A2 and B2 (Figure 1). If the thicknesses of the diamond origami pattern made with thick panels comply with the following geometry conditions, the thick origami will have a fluid deployment:

$$\begin{aligned} &A1 + B1 = A2 + B2 \\ &A1 = A2 \\ &B1 = B2 \end{aligned} \qquad (1)$$

However, as long as the above conditions are satisfied, the panels A and B may or may not be of equal thicknesses:

$$\begin{aligned} &A1 = B1 \\ &A2 = B2 \end{aligned} \qquad (2) \qquad\qquad \begin{aligned} &A1 \neq B1 \\ &A2 \neq B2 \end{aligned} \qquad (3)$$

The option of equal thicknesses of panels expressed in (2) is represented in Figure 1 (a). The option with different thicknesses panels expressed in (3) is represented in Figure 1 (b). The following is an investigation of three main possibilities of thicknesses of panels made with pantographs for the diamond origami-scissor hinged pattern: equal thicknesses, different proportional thicknesses and different non-proportional thicknesses. This aims to determine the form generation capabilities of the origami-scissor hinged geometry method, which could then be applied to other origami patterns.

4.1. Equal thicknesses

Figure 2 represents the option used to build the diamond origami of thick panels where A and B have equal thicknesses and correspond to equations (2) and Figure 2 (a). Wherever possible this will be the preferred option, as equal thicknesses translates in equal lengths of bars in the different layers of pantographs that can therefore be joined at the nodes. Therefore, instead of building the pantographs as separate layers, the bars are extended throughout the different layers and joined as a trellis for structural stability and efficiency during assembly.

4.2. Different proportional thicknesses

Where different thicknesses are used (3) that are proportional, the layers of scissor pantographs can be arranged that have equal length of bars and can therefore be replicated using the same principles described in the previous option. Figure 3 displays an option where thickness A is twice that of B (4), and Figure 4 represents an option where the thickness A is half of B (5):

$$\begin{aligned} &A1 = 2 \times B1 \\ &A2 = 2 \times B2 \end{aligned} \qquad (4) \qquad\qquad \begin{aligned} &A1 = B1 / 2 \\ &A2 = B2 / 2 \end{aligned} \qquad (5)$$

Although both options are geometrically compatible, it is important to consider that in scenario (4) illustrated in Figure 3, triangle T5_6_7 is half of T4_7_5 and would be susceptible to considerable pressure during unfolding and the structure would have to be designed to withstand this. Therefore option (5) represented in Figure 4 would be structurally more stable.

4.3. Different non-proportional thicknesses

Two options are here investigated for origami of thick panels made with scissor pantographs with different non-proportional thicknesses, both of which satisfy:

$$A1 \neq X \times B1 \neq B1 / X$$
$$A2 \neq X \times B2 \neq B2 / X \quad (6)$$

4.3.1. Intersecting plane

By intersecting a plane α through the top layer A1 of the origami- scissor diamond structure parallel to T4_7_5 through a non-proportional plane, one obtains two different and not proportional thicknesses, as expressed in (6) and illustrated in Figure 5. As the plane cuts through the scissor pantographs, single bars are left throughout the length of the edge and nodes V are lost in vertices 4, 9, 5, 7 and 8, therefore the nodes along the segment S7 defined by pantograph S6_5 do not match the nodes along its counterpart segment S7 defined by S5_4 pantograph. This case study therefore highlights the condition for adjoining scissor pantographs to make creases: the adjoining pantographs must not only have the same length, but have the same morphology and bilateral symmetry so that they are geometrically compatible and can be joined at the end nodes.

4.3.2. Interweaving layers of scissor pantographs

Another option to achieve an origami-scissor structure made with different non-proportional thicknesses (6), is to interweave the layers of scissor pantographs. Figure 6 displays how triangle T4_7_5 (thickness A1) is lowered down interweaving T4_6_5 (thickness B1), by doing this both segments S7 (7) remain intact and will be able to be joined to generate the origami scissor structure. In this instance, points P1 and P2 have been aligned so that the bars at these nodes can be made of continuous bars. Where F was previously a single node where the bars of thickness A1 and B1 would coincide, now there are four nodes closely placed, creating shorter bars. These shorter bars could have an impact on the mobility of the structure and would require the design of specific ratio of thickness versus length in order to be viable.

5. Conclusions

Origami-scissor hinged deployable structures [2] [18], built with layers of pantographs, can fold and unfold as the origami of thick panels [4], and simultaneously expand and contract retaining the geometry and the relative angles of the thick origami intact. This paper illustrates a study that tests the geometric compatibility of different possibilities of morphology of origami-scissor hinged layers. If various layers are used, it is preferable to use layers of equal thicknesses as it was done with the diamond origami-scissor hinged pattern [2]. If different thicknesses of layers are used, they can be fully geometrically compatible if they are proportional. A fundamental condition so that they are geometrically compatible in the creases is that the pantographs must have equal morphology and bilateral symmetry; this allows for the different origami faces to be joined at the end nodes.

An interesting option is that of interweaving pantographs. This scenario illustrates how in this instance it would be possible to achieve a geometrically compatible diamond origami-scissor hinged pattern with interweaved layers of pantographs. Therefore, if certain ratios of thickness versus length of bars have been accounted for, interweaving pantographic layers can decrease the overall thickness of the structure, increase is structural strength and allow for new geometric and morphological design possibilities.

References

[1] E. Rivas-Adrover, *Deployable Structures*, Laurence King Publishing, London, 2015.

[2] E. Rivas-Adrover, "A New Hybrid Type of Deployable Structure: ORIGAMI-SCISSOR Hinged", *Journal of the International Association for Shell and Spatial Structures*, Vol. 59 No.3, n. 197, pp. 183-190, September, 2018.

[3] E. Rivas-Adrover," Classification Of Geometry For Deployable Structures Used For Innovation: Design Of New Surfaces With Scissor 2 Bar, And Form Generation Method Of Relative Ratios", *International Journal of Computational Methods and Experimental Measurements*, Vol. 5, No. 4, pp. 464–474, 2017.

[4] Y. Chen, R. Peng, Z. You, "Origami of thick panels", *Science*, Vol. 349, No. 6246, pp. 396-400, 2015.

[5] P. Sareh, "Symmetric descendants of the miura-ori", *University of Cambridge*, U.K., 2014.

[6] S. A. Zirbel, R. J. Lang, M. W. Thomson, D. A. Sigel, P. E. Walkemeyer, B. P. Trease, S. P. Magleby and L. L. Howell, "Accommodating Thickness in Origami-Based Deployable Arrays", *Journal of Mechanical Design*, Vol. 135, Issue 11, 2013.

[7] N. De Temmerman, M. Mollaert, T. Van Mele, L.De Laet, "Design and Analysis of a Foldable Mobile Shelter System", *Int. J. Space Structures*, Vol. 22, pp. 161-168, 2007.

[8] B. J. Edmondson et al., "An offset panel technique for thick rigidity foldable origami", *ASME Int. Design Engineering Technical Conferences 2014*, Buffalo, NY.

[9] C.S. Hoberman, U.S. Patent No. 4,780,344, 1988.

[10] T. Tachi, Rigid-Foldable Thick Origami, *Origami 5*, Eds. P. Wang-Iverson, R. J. Lang, M. Yim, A K Peters/CRC Press, 2011, pp. 253-264.

[11] F. Escrig, "Pabellón Transportable para exposiciones, 1964", *Arquitectura Transformable*, Eds. F. Candela, E. Pérez Piñero, S. Calatrava, F. Escrig, J. P. Valcárcel, Escuela Técnica Superior de Arquitectura: Sevilla, 1993, pp. 21-22, 1964, 1993.

[12] F. Escrig, J.P. Valcárcel, J. Sánchez, "Deployable cover on a swimming pool in Seville", *Journal of the International Association for Shell and Spatial Structures*, Vol. 37, No. 120, pp. 39-70, 1996.

[13] C. Hoberman, Expanding Sphere 1988–92 and Iris Dome 1990–94, *Archaeology of the Digital*, Ed. G. Lynn, Canadian Centre for Architecture and Sternberg Press, Montreal, 2013.

[14] K. Roovers, N. De Temmerman, "Deployable scissor grids consisting of translational units", International Journal of Solids and Structures 121 pp 45-61, 2017.

[15] K. Roovers, N. De Temmerman, "Geometric design of deployable scissor grids consisting of generalized polar units", Journal of the International Association for Shell and Spatial Structures, Vol. 58, No. 3, pp. 227-238, 2017.

[16] F. Escrig, "Expandable Space Structures". *Int. J. Space Structures*, Vol. 11, No. 1&2, pp. 257-274, 1996.

[17] Rivas-Adrover, Esther, "Transforming Architecture Made With Scissor Hinged Deployable Structures: Alhambra Pavilions in Cambridge Market Square", *The 5th International Conference on Architecture and Built Environment S.ARCH held in Venice, Italy, 2018,* Get It Published, 04.055, pp. 760-770.

[18] Rivas-Adrover, Esther, "ORIGAMI-SCISSOR Hinged Geometry Method", *Origami7, The proceedings from the 7th International Meeting on Origami in Science, Mathematics, and Education held in Oxford UK, 2018*, Volume Three: Engineering One, Ed. J. Lang, Bolitho and You, Tarquin, pp 779-793.

Proceedings of the IASS Annual Symposium 2019 – Structural Membranes 2019
Form and Force
7 – 10 October 2019, Barcelona, Spain
C. Lázaro, K.-U. Bletzinger, E. Oñate (eds.)

Experimental and Analytical Investigation of the Spin-Valence Kirigami Space Frame

Julien SAHUC*, Gordana M. HERNING*, Emily BAKER[a]

* Massachusetts Institute of Technology
77 Massachusetts Avenue, MIT Room 1-163
Cambridge, MA 02139, USA
gherning@mit.edu
jsahuc@mit.edu

[a] University of Arkansas, Fay Jones School of Architecture + Design, Fayetteville, AR, USA

Abstract

Spin-Valence is a pattern-logic that transforms a flat sheet of material into a structural space frame. Through cut patterns, spin-folds and encoded connections, a single layer effectively becomes two layers connected via triangulated legs. Unlike most space frame systems, this method is not a series of connected members, but one single sheet, cut and folded (kirigami), and reconnected to itself [1]. This work presents experimental tests conducted on steel versions of square Spin-Valence units and multi-unit assemblies to evaluate their structural behavior and capacity. Test results are compared with analytical predictions to propose a performance-oriented design framework relating geometric variables of the frame elements to the stiffness and strength of potential assembly configurations.

Keywords: kirigami, space frame, deployable structure, physical testing, structural capacity, buckling

1. Introduction

A set of patterns that, when cut into a sheet of material, allow it to be folded into a geometric arrangement of mutually supporting structural units was developed and termed Spin-Valence. These imaginative kirigami space frames are promising for a variety of applications at multiple scales, including architectural-scale structures. The original square version of Spin-Valence was refined through heuristic design iterations that proceeded in search of performative efficiency of the sysetm as a double-layer space frame. In order to deploy the system, a Spin-Valence pattern is cut into a sheet of material, and the central hub of each unit is allowed to spin-fold out of the primary surface, resulting in two offset surfaces continuously connected by the triangulating legs that surround each hub. The patternisation of the system was guided by physical insight about the ensuing forms, gained both through structured play *and* qualitative assessments of stiffness (Baker [1, 2]). Previously studied patterns include triangular shapes and elements of uniform width. Through design iterations, certain legs were transformed into single plates shaped with slight convex curvature and the widest section at mid-height, and others into latticed angle-shaped elements formed from curved plates, both of which connect the curved elements in the parallel top and bottom surfaces, as seen in Figure 1. By deploying multiple units, and welding adjacent corners of unit hubs, a space frame is created without complex detailing and assembly of discrete elements and joints.

Copyright © 2019 by Julien Sahuc, Gordana M. Herning, and Emily Baker
Published by the International Association for Shell and Spatial Structures (IASS) with permission.

Spin-Valence converts a continuous sheet of steel into a double-layer spatial structure, aiming to simultaneously achieve lightweight transparency and a span that is large relative to its depth. Its cut patterns influence cross-sectional properties of elements, joint geometry, ease of unit and frame deployment, and connectivity between the units upon lifting and rotating of the unit hubs.

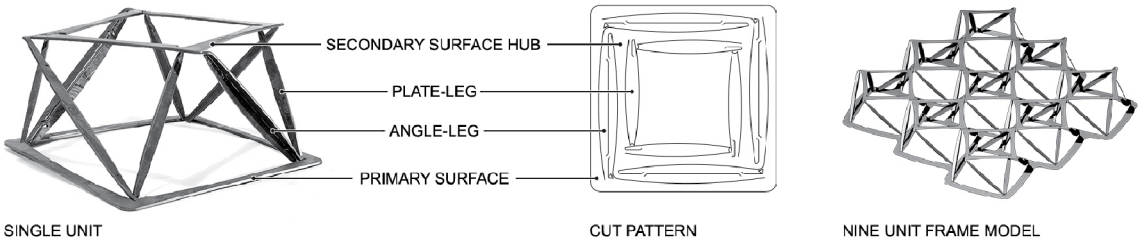


Figure 1: Single unit and multi-unit assembly of the Spin-Valence kirigami space frame

This paper presents the structural characterization of the square Spin-Valence space frame based on experimental testing and theoretical calculations employed to analyze component behavior and to propose a preliminary parametric study of the influence of geometry on behavior of the frame. In the multi-unit frame, strength and stiffness gains due to structural triangulation are investigated, and the overall behavior is analyzed to identify optimal solutions for strengthening the form through geometry. As the frame is further analyzed for potential use in flat spanning systems (e.g., as a wall or a roof), curved vaults, and gable frames, understanding the relationship between geometry, support conditions, force paths, element capacities, global and local behaviors, and buildability is needed to characterize its performance variants for multiple applications.

2. Emergence of space frames and kirigami structures

Spatial structures are composed of linear or surface elements arranged into geometric patterns that enhance the stiffness of the system while enabling large spans and lightness through efficient use of material. Inseparable from an essential function to transmit forces to the supports, an aesthetic vision for a space frame implies refinement of structure that is usually open to views, and may define the building enclosure and interior shading patterns that follow the path of sunlight.

Historic works from the 19th century mark early developments of space frames, and express structural mechanics enabled by innovative geometric patterns and the advent of iron and steel that were combined with more traditional wood elements. The roof structure of the Crystal Palace in London, an architectural icon designed by Joseph Paxton, was a synthesis of construction skill and speed through prefabrication, reduction of bending moments through geometry, and design optimized by the use of pre-tensioned timber and iron elements (Addis [3]). The principle of tetrahedral frames used by Alexander Graham Bell to achieve lightness in kites heralded the now familiar geometry of modern-day space structures (Bell [4]). In the early 20th century, Buckminster Fuller, Stéphane Du Chateau, and Konrad Wachsmann were among the leading investigators of space frames, whose use significantly increased with the introduction of the MERO system of tubular elements joined at ball-shaped nodes, which was developed by Max Mengeringhausen.

Space frames present a possibility to be quickly deployed and dismounted, taking a wide range of forms, module patterns, and element shapes. Hanaor and Levy [5] classified deployable spatial structures according to their morphological and kinematics characteristics and their purpose as “temporary structures”, or when access to “inaccessible or remote places” is needed. Indeed, spatial structures can be designed to meet immediate needs for temporary occasions (such as exhibitions, cultural events, or athletic competitions), when a natural catastrophe like an earthquake, or a flood, happens, or as transportable civic or military shelters.

The novel kirigami-inspired space frame typology is created by CNC cutting of sheet material, in this case steel, into an assembly of manually deployable units, which form triangulated elements when the hubs are rotated and welded at the secondary surface, benefitting from interconnected modules through improved global stiffness and load carrying capacity. A single unit of the Spin-Valence frame consists of four plate-legs and four angle-legs linking two parallel surfaces, concentric square shapes (Figure 1). The multi-unit frame module is composed of 9 units such that plate-legs occur only around the perimeter, while triangulation of the interior angle-legs serves to improve the stiffness of the frame. Experimental and analytical evaluation of the component and frame strength is presented in the next two sections. This is followed by a summary of findings including design considerations for distributing the available steel sheet material to optimize geometry such that the elements driving the deformation can better respond to the load demand.

3. Experimental testing of single units, frames, and columns

The sequence of testing began with single units, followed by the frame deployment and testing, and concluding with tests aiming to validate the analytically calculated critical buckling strength of individual diagonal legs.

3.1 Compression test and deployment of the single unit

The displacement-controlled loading was conducted using a Baldwin test frame with a 267 kN load cell. A steel plate 25.4 cm x 25.4 cm x 1.9 cm was positioned on the top surface of the unit to distribute the load to the four joints, as seen in Figure 2.

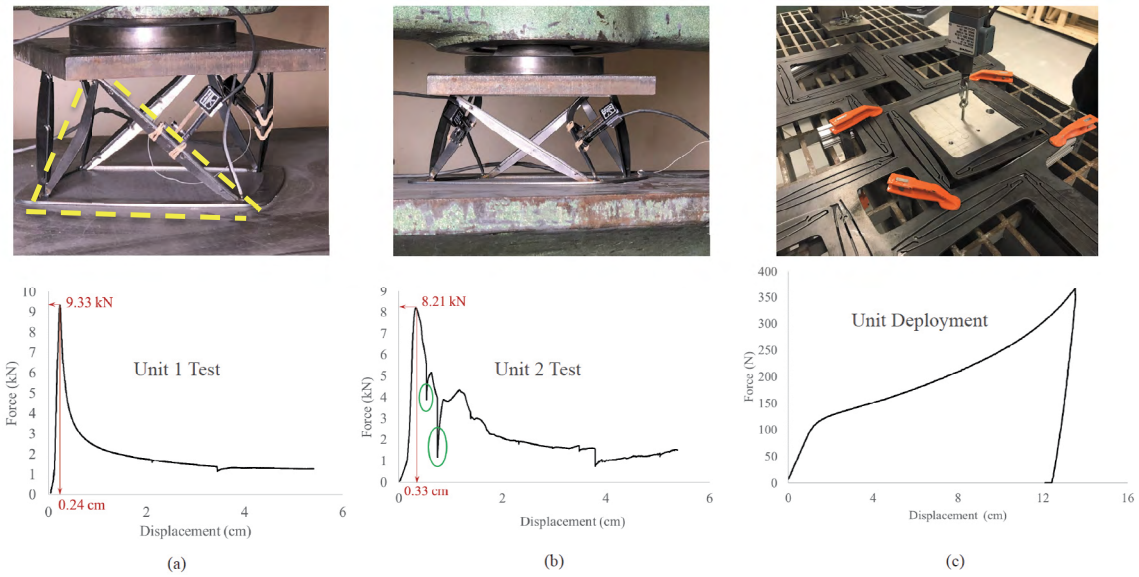


Figure 2: (a) and (b) Compression tests of frame units. (c) Unit deployment

The loading plate thickness was selected so that its bending deflection was negligible, and distortion of results was not a concern. Two diagonal legs in Unit 1 were angle-legs with three connections joining the leg plates, and two angle-legs had four connections between the plates. The remaining four legs were single-plate diagonals. In Unit 2, all angle-legs had two connections.

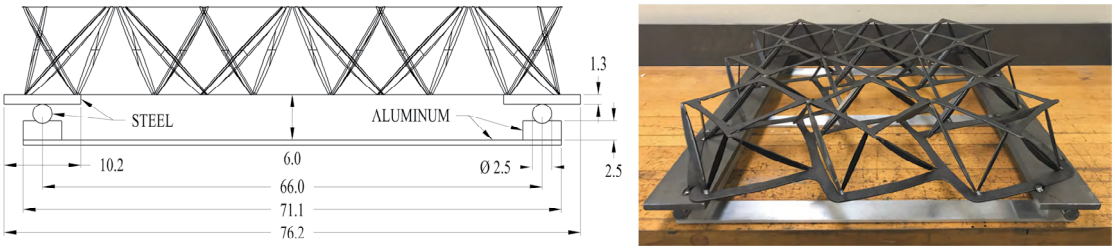
Buckling of the single-plate legs determined the capacity of both units. The ultimate bearing capacity of Unit 1 was 9.33 kN when the displacement of the load cell reached 0.24 cm. The bearing capacity of the Unit 2 was 8.21 kN at the displacement of 0.33 cm. The encircled points on the load-displacement curve in Figure 2 indicate fractures of leg joints consistent with the loss of load-carrying capacity.

In both tests, deformation of the angle-legs was not perceptible or measurable by the use of strain sensors. In the test of Unit 2, strain sensor data was inconclusive, since the point of buckling was located near the three-quarter point of the leg height, while the sensor was placed at mid-height. This indicates a potential difference in the rotational restraint between the top and the bottom of the leg, which may be related to initial imperfections, crack initiation, or plastification during the folding of the legs such that the welded end of the leg provides a greater level of fixity relative to the folded end.

Unit deployment using a plate attached to a crankshaft mechanism indicated a reduction in the initial resistance of the legs being raised from a flat position in the steel sheet once the top surface rose to approximately 1.2 cm above the primary one, allowing larger rotation at the ends of the legs and easier upward movement of the hub. At that point the rotation of the top surface became more apparent, and lifting continued with combined axial load in the legs and twisting at the end fillets.

3.2 Compression test of the multi-unit frame

An aluminum frame was built to support the multi-unit frame in the compression test, and to provide continuous simple support along two edges. The supporting frame was made of two 76.2 cm long aluminum bars linked at their ends and at midpoint by three aluminum cross-bars of the same length. Steel rods having 2.5 cm diameter and 76.2 cm length were centered on a groove machined in the supporting aluminum bars as shown in Figure 3. These rods allowed small rotation of the space frame at the supports. The bottom of the space frame was tack-welded to two rectangular steel plates with length equal to that of the rods, on which they were bearing.



(a) (b)

Figure 3: (a) Elevation of the experimental setup. (b) Frame with welded joints facing up.

In the first experiment, the welded connections between the units faced up, opposite of their orientation in the second test (Figure 4). In both cases the plate described in the previous section was used to distribute the applied point load to the top surface of the central unit. Deformation of the diagonal legs of the frame was negligible, as seen in the individual unit tests, and the strain measured by two sensors confirmed this observation. In both frame tests, elements in the surface facing up buckled as a result of compression forces. In multiple locations of the frame shown in Figure 3b and Figure 4a the bottom surface elements were the first to exhibit plastic deformation. Their bending was initiated by the adjoining diagonal legs that were in tension (Figure 4b).

Comparison of the load-displacement relationships in Figure 5 shows essentially equal ultimate load capacity and initial stiffness for the two tested orientations of the frame. The ultimate loads equaled 5.3 kN and 5.4 kN for the frame with unit welds facing up, and the welds facing down, respectively. The initial elastic stiffness of the frame with the latter orientation was slightly larger. It is seen that subjecting the welded connections between the units to tension (when they face down) leads to sudden loss of weld integrity and slight reduction in load bearing capacity that is followed by redistribution of forces until the ultimate load of the frame is reached. At the point when displacement of 6.4 cm was reached, the bottom of the frame made contact with the base, therefore the increased load resistance beyond this point should not be taken into account.

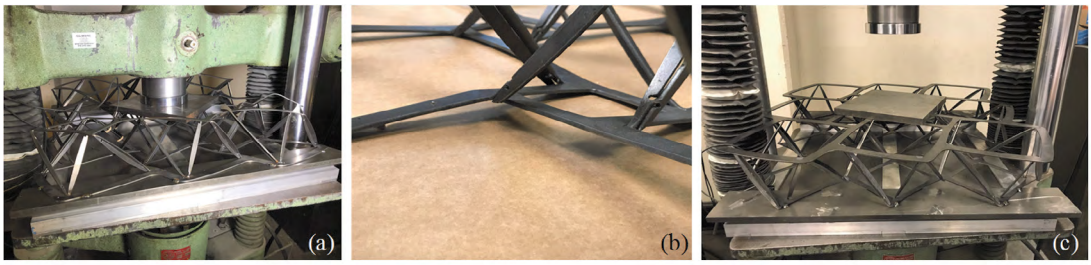


Figure 4: (a) Testing of the frame with welded unit connections facing up.
(b) Bending in the element of the primary surface. (c) Frame with welded unit connections facing down.

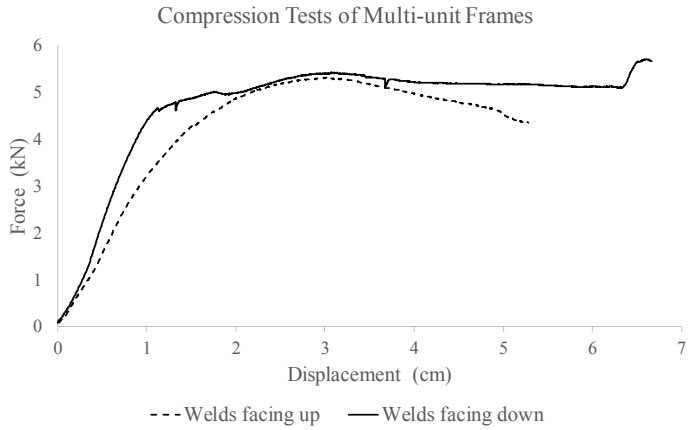


Figure 5: Variation of load-displacement relationship due to orientation of the multi-unit frames

3.3 Testing of diagonal legs

As noted earlier, two types of diagonal legs in the frame include plate-legs and angle-legs (Figure 6). Twelve diagonals, including 4 each of the plate-legs and angle-legs with 2 connectors plus 2 each of the angles with 3 and 4 connectors, were tested under axial compression as shown in Figure 6d. The end connectors between the plates in the angles were at the same location in all angles, and any intermediate connectors are positioned to create equal unbraced portions of the plates. In these tests, both angle legs received load at the loading plates, which is not the case in the frame. Separation of the legs at the end fillets is seen in Figure 2c and Figure 6b, which show how the primary legs are connected to the parallel surfaces, while the secondary legs are attached to the primary ones via plate connectors. Both plates contribute to the strength of the legs, however an increased load resistance could be achieved by engaging both plates into the load path at the ends of the angle-legs.

The plate-legs buckled at mid-height, while the angle-legs bent about their weakest point, where the width of the section is the smallest. The load values at buckling in the plate-legs ranged from 3.3 kN to 4.7 kN with the average load equal to 4.1 kN. The average values of the buckling load in the angle-legs with 2, 3, and 4 connectors were 2.97 kN, 2.3 kN, and 1.9 kN, respectively. As seen in the next section, a quadratic relationship between the length of a leg and the buckling load confirms that, generally speaking, longer columns with larger sectional properties may buckle at lower loads than shorter columns with smaller sectional properties. Experimental results show that decreasing the slenderness ratio of the angle-legs by increasing the number of plate connectors may lead to a lower (instead of a theoretically anticipated higher) buckling capacity. This may be caused by initial out-of-straightness introduced in the angle-columns with 3 and 4 connectors through additional clamping and folding. Moreover, a slightly larger angle between the plates leads to a reduced moment of inertia of the section, thereby lowering the buckling load.

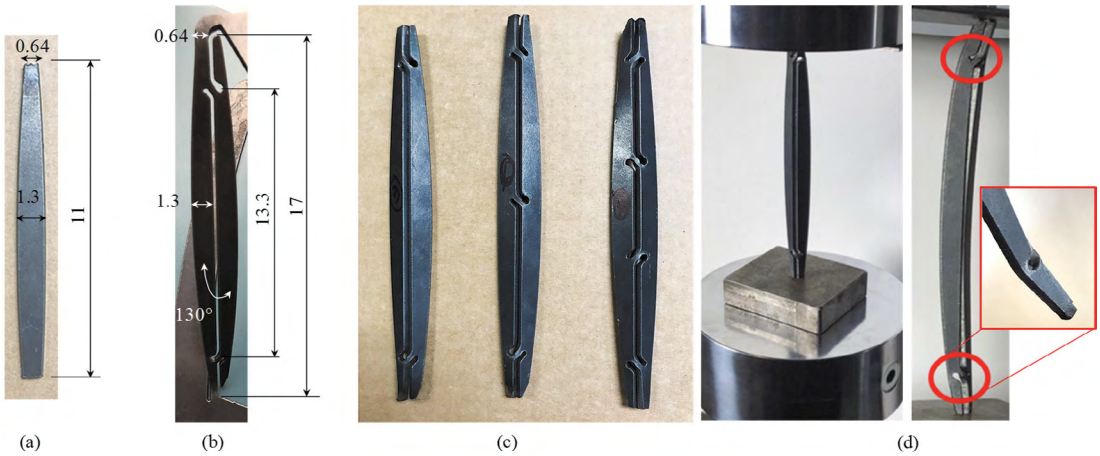


Figure 6: (a) Typical plate-leg (dimensions shown are in *cm*). (b) Typical angle-leg in the frame. (c) Angle-legs with varied number of connectors between plates. (d) Compression test of an angle-leg.

4. Analysis of frame components

Elements in the parallel surfaces of the frame were cut with a concave curvature reducing the section width at mid-point, while the convex curvature of the legs led to the widest section at their mid-height. Shape effects on column capacity for various geometric configurations and support conditions have been studied since antiquity (e.g., Penrose [6], Keller [7], Timoshenko and Gere [8], Thompson *et al.* [9], Ruocco *et al.* [10], and Atanackovic and Glavardanov [11]), affirming the benefit of increasing the moment of inertia of a section in areas where critical load effects are expected, in order to achieve optimal structural behavior *and* reduced use of material. In this frame, element length and steel sheet thickness will significantly impact the critical buckling strength of axial elements, and the axial capacity can be further improved by using angle-shaped sections instead of the single plates.

4.1. Analysis of diagonal legs

While the experimentally observed continuity of deformation at the joints of elements that underwent buckling provides evidence of semi-rigid connections (i.e., between idealized pin connections that are typical in trusses, and rigid moment resisting joints), pinned supports were assumed throughout to simplify calculations aiming to evaluate the effects of element geometry.

The AISC provisions [12] specify column strength when inelastic buckling (due to the presence of residual stresses in the material or column slenderness) governs its behavior. The Euler critical buckling load, $P_{cr} = \pi^2 EI/L^2$ (where Young's modulus E ≈ 200 GPa, I equals moment of inertia for the cross section, and L is the unbraced length of the element), equals 2.8 kN when uniform width of 0.64 cm and 12 gauge steel sheet are assumed for the leg shown in Figure 6a. This value is 26% greater than the strength according to the AISC [12] standard, indicating that inelastic buckling controls. For the 1.3 cm wide leg, the AISC specification leads to P_{cr} = 3.1 kN. Taking into account the convex curvature of plate-legs, the Euler theory adapted to tapered columns according to Zhang et al. [13] results in P_{cr} = 3.7 kN, and the modification according to Lubliner and Papadopoulos [14] suggests P_{cr}=9 kN. Critical buckling load is doubled if 10-gauge instead of the 12-gauge steel sheet is considered, leading to a 29% increase of plate thickness. Analysis of the effects of incremental angle variation from 90^0 to 130^0 between the plates of an angle-leg (with 12-gauge plates of uniform 1 cm width) showed nonlinearly decreasing P_{cr} values from 3 kN to 2.4 kN (AISC [12]).

To evaluate effects of multiple connections between the plates of angle-legs, modified slenderness ratios for built-up columns were calculated according to the AISC specifications [12]. Based on the 12-gauge

steel sheet, the leg dimensions shown in Figure 6, and the angle between plates of 135^0, P_{cr} equals 3 kN, 6.7 kN and 7.8 kN, when 2, 3, and 4 connections are created between the plates of angle-legs, respectively. These results are consistent with an increased axial strength as a result of reduced element slenderness by the addition of connections between the plates of the angle-leg.

4.2. Analysis of a frame unit

The frame unit shown in Figure 1 can be analyzed as a small space truss. Element forces are determined using equations of equilibrium and any method of structural analysis for determinate trusses. With 8 joints in the truss, there are 24 available equations of static equilibrium, which are sufficient to determine axial forces in 16 elements and 8 support reactions. For various combinations of vertical and horizontal point loads applied at the nodes, resulting distribution of element forces leads to conclusions about the required element strength.

However, by inspection of the geometry in Figure 1 and Figure 6, it is seen that, in response to a vertical point load applied at a top node, axial force in the nearly vertical plate-leg (that is inclined at a 75^0 angle with respect to the primary surface) is approximately 1.75 times larger than that in the angle-leg (which assumes a 45^0 angle with the horizontal plane). The triangle formed by these two legs and the element connecting them at the base is outlined by a dashed line in Figure 2a. Therefore, providing a shape with larger sectional properties in place of the plate-legs would increase the buckling load of the unit.

5. Concluding remarks and future directions

The dominant modes of deformation in the frame were (1) element bending within the primary surface due to the tensile forces in the adjoining legs, and (2) element buckling in the secondary surface hub. Based on the deformed shapes, the onset of buckling in the secondary hub may be delayed by considering a cutting pattern that would increase the sectional properties in the hub elements, while maintaining a sufficient strength of the angle-legs. Due to the load path in the angle-legs that indirectly include the secondary plate of the angle, steel material may be redirected to the hub elements where buckling was observed. If the ultimate frame compression load equal to 5.4 kN were distributed as an equivalent uniform load over the multi-unit area, its value would be approximately 11 kN/m^2. In a future study, the frame stiffness and strength under uniform load, as well as support conditions including a fixed support along one edge, continuously supported perimeter, and uniformly spaced point supports through branching columns may be considered. Current work to further develop the analytical model that approximates frame behavior by two perpendicular trusses intersecting at the central unit should be compared and calibrated with numerical analyses conducted in the related study by Sherrow-Groves and Baker [15].

Variation of the moment diagram along the span could guide development of future cutting patterns. For example, the variable depth of the frame (i.e., the distance between the parallel surfaces) may gradually follow the shape of the moment diagram, so that the parallel surfaces are farthest apart in the region of the maximum moment, thereby reducing the compression forces in the surface elements and their susceptibility to buckling. Employing curvature in the overall form of the frame is another strategy that can be used effectively to increase the stiffness of the structure while maintaining its lightness and ability to span large distances.

Acknowledgements

The authors thank Stephen Rudolph (MIT) for his contributions in devising the experimental tests, Grace Melcher (MIT), Nick Sherrow-Groves (ARUP), and Edmund Harriss (University of Arkansas).

References

[1] E. Baker, "Spin-Valence: Kirigami Space Frame," *Proceedings of the IASS Symposium 2018, Boston, July 16-20, 2018, C. Mueller, S. Addriaenssens Eds.*, 2018, pp. 1–7.

[2] E. Baker, "Search for a rooted aesthetic: Study in Spin-Valence," in *Fabricate 2014: Negotiating Design and Making,* Gramazio, Kohler, & Langenberg, Eds. London: UCL Press, pp. 128-135, 2014.

[3] B. Addis, "The Crystal Palace and its place in structural history," *International Journal of Space Structures*, vol. 21, pp. 3-19, Mar. 2006.

[4] A. Bell, "The tetrahedral principle in kite structure," *National Geographic Magazine*, vol. 14, no. 6, pp. 219-251, Jun. 1903.

[5] A. Hanaor and R. Levy, "Evaluation of deployable structures for space enclosures," *International Journal of Space Structures*, vol. 16, pp. 211–229, 2001.

[6] F. Penrose, *An Investigation of the Principles of Athenian Architecture.* London, Macmillan, 1888.

[7] J. Keller, "The shape of the strongest column." *Archive for Rational Mechanics and Analysis,* vol. 5, pp. 275-285, 1960.

[8] S. Timoshenko and J. Gere, *Theory of Elastic Stability*. New York: McGraw Hill, 1961.

[9] P. Thompson, G. Papadopoulou and E. Vassiliou, "The origins of entasis: Illusion, aesthetics or engineering?," *Spatial Vision*, vol. 20, pp. 531–543, (2007).

[10] E. Ruocco, C.M. Wang, H. Zhang and N. Challamel, "An approximate model for optimizing Bernoulli columns against buckling," *Engineering Structures*, vol. 141, pp. 316-327, 2017.

[11] T. Atanackovic and V. Glavardanov, "Optimal shape of a heavy compressed column," *Structural and Multidisciplinary Optimization*, vol. 28, pp. 388–396, 2004.

[12] AISC, *Steel Construction Manual* (15th ed.). Chicago, IL: American Institute of Steel Construction, 2017.

[13] B. Zhang, Y. Guo and C. Dou, "Ultimate bearing capacity of asymmetrically double tapered steel columns with tubular cross-section," *Journal of Constructional Steel Research*, vol. 89, pp. 52–62, 2013.

[14] J. Lubliner and P. Papadopoulos, *Introduction to Solid Mechanics – An Integrated Approach*. (2nd ed.). Cham, Switzerland: Springer International Publishing, 2017.

[15] N. Sherrow-Groves and E. Baker, "Structural finite-element analysis of the steel kirigami frame to characterize global behavior", paper abstract accepted for the *Proceedings of the International Association for Shell and Spatial Structures (IASS) Symposium*, Barcelona, Spain, 2019.

Proceedings of the IASS Annual Symposium 2019 – Structural Membranes 2019
Form and Force
7 – 10 October 2019, Barcelona, Spain
C. Lázaro, K.-U. Bletzinger, E. Oñate (eds.)

Load and constructional experiments on beam-shape string crescent structure with pretension cables fitted to the neutral surface

Akira TANAKA*

*Lecturer, Department of Industrial Information Tsukuba University of Technology, Japan
Amakubo 4-3-15, Tsukuba City, Ibaraki, 305-8520 Japan
Email akira@a.tsukuba-tech.ac.jp

Abstract

String Crescent Structure (SCS) [1] is Reuse System, and this is kinetic structure that can change the structural shape without replacement members. The author has already worked the load experiments of the column SCS and had confirmed the stability and the prestress effect. The pretension cable of SCS fitted to the neutral surface or the upper chord. As a result, two kind of SCS are able to get. In this paper, the experimental subject is narrowed down to SCS with the pretension cables that set to neutral surface. At first, the constructional experiment was worked. The chains are used for the lower chord of SCS. The method of control to length of the lower chord is to shift the fixing position of the chain, and makes it easy to control the structural shape of SCS without replacement members. This method inevitably change contact positions between C-members. As a result, the change in the stress distribution of each members of SCS occurs. At next, the load experiments were worked to verity the change in this stress distribution and the stability & PS effect of beam-shape SCS. For this experiment, SCS with 7 unit of C-members was used.

Keywords: Reuse System, Kinetic System, String Crescent Structure, constructional experiment, load experiment, PS effect,

1. Introduction

1-1 Structure and Assembly In 21st century, global environmental issues were highlighted. In order to address this challenge, the technical developments are tried in various field. These themes in the field of architectural and civil engineering include “Long-lived building”, “Reuse of member” and “Recycle of material”. In this paper, the research object is temporary structure that is easy to reuse. The existing reuse systems are mainly controlled by the structural form (Figure 1a). At first, the structural form is decided. At next, the assembly shape is decided. This assembly may be difficult to reuse in different structural forms. As a result, if the demand for this same structural form as the reuse system decreases, these assemblies are no use or store. At worst, these assemblies are recycle or disposal. This means that this system can not have enough reuse performance. These examples are introduced as follow. Air-support structure is the light structure without rigid members. This is the structure that is inflated by the inflation blower, and “Building” and “Removal” are easy. These characteristic are suitable for temporary space. But, even if this curved surface shape and scale want to be changed, the membrane after the removal are difficult of the reparting and re-cutting. Truss structure is the light structure with the rigid members. If this system is designed on the premise of reuse, that can be easily the dismantlement/assembling. Therefore this structure is suitable for temporary space too. However, as for the change of this structure form and scale, the change of the assembly shape and the joining angle isn’t avoided, and the reprocessing assemblies is essential. In future, the reuse system must be controlled by the assembly form (Figure 1b). This reuse system is able to change the structural form without the replacement/reprocessing assembly. This reuse system is named “Flexibility Reuse System”.

Copyright © 2019 by Akira TANAKA
Published by the International Association for Shell and Spatial Structures (IASS) with permission.

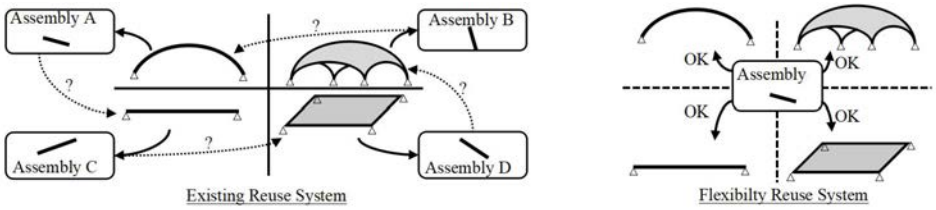


Figure 1: Comparison of Existing Reuse System and Flexibility Reuse System

1-2 Flexibility Reuse System The design target of Flexibility Reuse System is coexistence with "Following ability of various structural form" and "Reuse performance". The assembly type that can make Flexibility Reuse System are two types (Figure 2a). The primary type is the line-shape assembly (ex. bar) with the pin. This permits the rotation of the ends. The pin with different positions and numbers lead to a various assemblies. Examples of these assemblies are the rink type with pin set up both ends, and the scissors type with the pin the pivot as well as the ends.

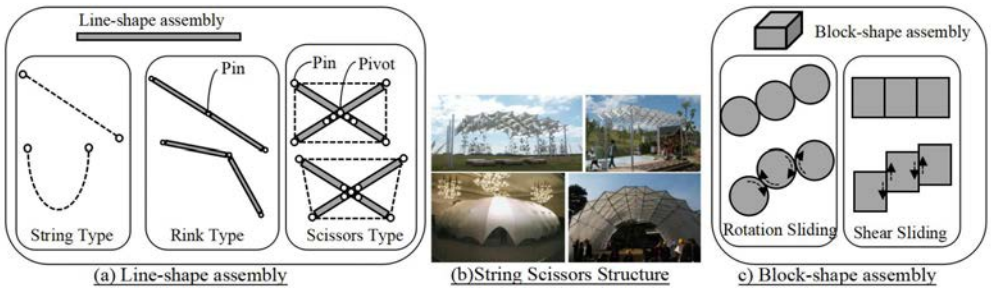


Figure 2: Classification of Line-shape assembly

The scissors type is known to have make "Construction / Dismantlement" fast and easy. However, this isn't known to have the characteristic as Flexibility Reuse System. The moving of pivot position can make "Various structural form" without the replacement bars. An example of this is String Scissors Structure (Figure 2b). This is the stable Scissors Structure with the strings. It is confirmed that SSS has the reuse performance and the following ability of Various structural shape [2].

The second type is the block-shape assembly (Figure 2c). The contact-joint that set between the blocks. This contact-joint permits the sliding between the contact surface. The difference shape of block make the several sliding type. For example, this sliding deformation is the shear sliding between flat contact surfaces and the rotation sliding between curved contact surfaces. There is no such instance that the block for Flexibility Reuse System is proposed.

1-3 The block-shape assembly The base shapes of block are Hexahedron and Cylinder (Figure 3). The sliding between the contact surfaces of Hexahedron lead to change the center distance between the assemblies. In contrast, the sliding between the contact surfaces of Cylinders doesn't change the center distance. The unchanged center distance facilitates placement of the block's connector. Cylinder can follow the structural shape change, and is applicable to Kinetic System like Sudare. But this contact area is very small, and causes the stress concentration.

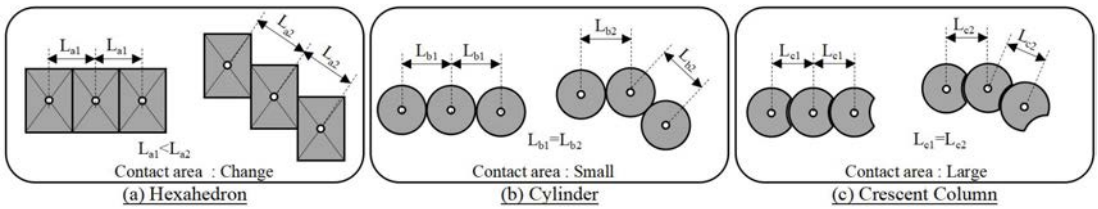


Figure 3: Center distance and Contact area

This solution is to use Crescent Column that can get the large contact area. Crescent Column can have the center distance that doesn't change like Cylinder. However the sliding type of both is different. All Cylinders that contact with each other rotate freely. The contact surface between Crescent Columns

doesn't rotate on the concave side but rotates on the convex side. Throughout the following paper, the structure with Crescent Columns will be explained.

2 From Crescent System to SCS

2-1 Crescent System Crescent Column became the assembly of Kinetic System, and the connect members are installed between the center distance. The repetition of this works forms Kinetic System like snake (Figure 4a).

2-2 Design of C-member Crescent Column has the cross-section like bone to get to both lightweight and rigidity. This Crescent Column is named Crescent member (C-member) (Figure 6b). The through hole is used to joint of the connect members. The role of Side Portion is the joint between C-members. The shape of Side Portion is the curved surface. As a result, a non-standard joint is necessary. To prevent this, two Flat Portions are designed to fit shop-bought joint.



Figure 4: Crescent System

2-3 SCS The condition of stabilization of Crescent System is to prevent the rotation sliding between C-members. One of this method is to insert the lower chord between C-members. Crescent System with the lower chord become String Crescent Structure (SCS). But, this alone can not gave SCS enough stability. The pretension cable (PC) is required to ensure further stability. The different arrangements of PC form two types of SCS (Figure 5).

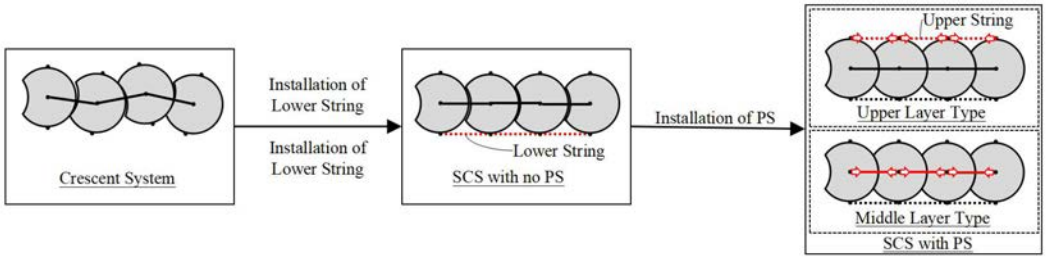


Figure 5: From Crescent System to SCS

The first of these is Upper Layer Type that PC are placed on the upper layer. When changing the structural shape, replacement of PC isn't avoided. As a result, the waste members and carry-in members are produced. The second is Middle Layer Type that PC are placed on the neutral surface. The structural shape change doesn't lead to replacement of PC. As a result, the waste members and carry-in members decrease. This paper, pick up only Middle Layer Type, the several experiments have been conducted. These contents and purpose are follow.

[Construction experiment] It is confirmed that SCS have both "Following ability of various structural shape" and "Reuse performance".

[Prestress experiment] It is confirmed that the different install point of Prestress (PS) affect the structural behavior of the whole SCS.

[Load experiment] It is confirmed that the different condition (Structural shape and PS) affect the structural behavior of SCS under load.

3 Construction experiment by the small model

3-1 Experiment model The low chord of SCS is either the rod, the strand cable or the chain. SCS is expected to have the ruse performance. For this reason, SCS must have the function that can change the structural shape without the replacement assembly. This condition is compatible with the chain. Compared to the strand cable, the chain have the advantage of requiring no clasp, and is easy compatible for Reuse System (Figure 6b). PC near the neutral surface is the strand cable. This is passed through the eye nuts (Figure 6d) that are set at the through hole of C-members, is fixed by the eye bot (Figure 6c) that install on both ends of SCS. The clamp for the strand cable isn't set to the eye nuts except for both ends of SCS. Because these clamps reduce the performance of Construction / Dismantlement for temporary space. The method of PS is only the tightening both the end eye bolts. SCS that is used the construction experiment is connected on 16 C-members. The purpose of this experiment is the confirmation that SCS have "Following ability of various structural form", "Reuse performance" and "Structural stability" without the replacement assemblies.

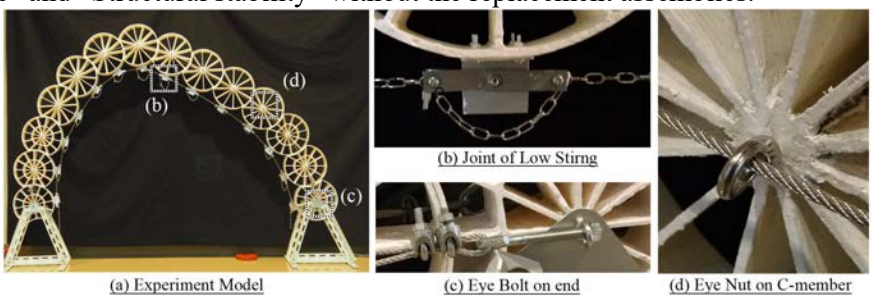


Figure 6: SCS for Construction experiment

3-2 Experiment result When SCS was coil up the direction in which the string slack, it changed to the coil shape like "Sdare". The process of uncoil to the line shape is shown Figure7. SCS could be uncoiled until the low chord occur the tension.



Figure 7 : From coil shape to uncoil shape

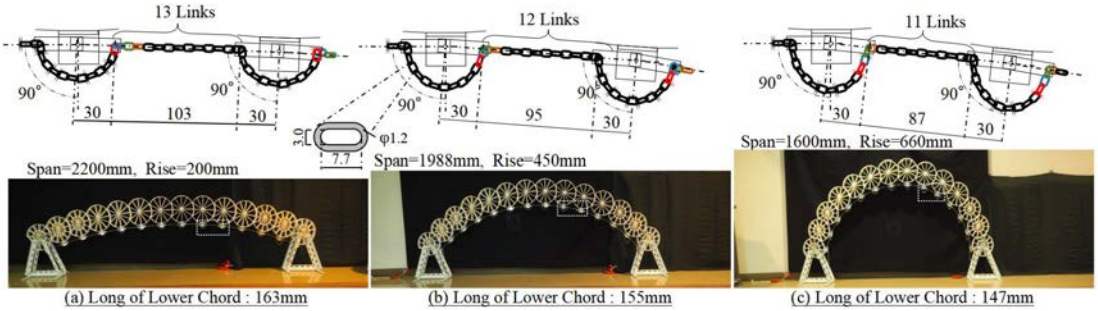


Figure 8 : Result of Construction Experiment

When the joint position of chain moved, the rise span ratio of SCS was change (Figure 8). This demonstrated the maintaining stability and Reuse performance.

4 Prestress experiment

4-1 Experiment model The experimental model is shown in Figure 9. SCS that 7 C-members is connected was used. Both of Beam and Arch were used to compare differences in structural behavior. "3 Construction Experiment by the small model" explained that the low string was the chain. But the low string for the experiments is the stainless-steel bar. Because a strain gauge is difficult to cement

on the chain. When the experiment model changes to the different shape (Beam or Arch), the replacement assemblies are only different length low strings. PC is the strand cable that is picked up 3 chapter. The conditions of PS are shown in Figure 9c. The pretension point is either the right end of PC or the left that. Because it is estimated that the choice of the pretension point lead to different structural behavior of SCS. This reason is that the section-cross of C-member is asymmetric shape. The PS experiments are conducted to confirm the validity of this estimate. The measuring points are shown in Figure 9e.

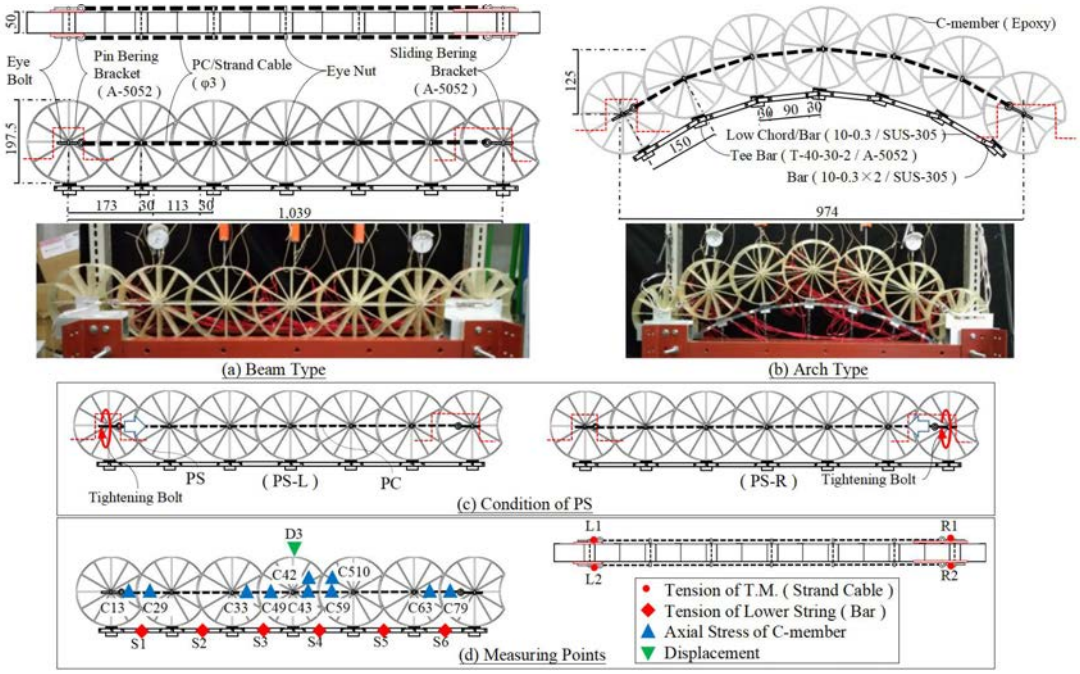


Figure 9 : Experiment Model

4-2 Experiment result Change in the tension stress of PC is shown in Figure 10. The measuring points (L1~R2) are shown in Figure 9d. PS under each step is 2N. If the pretension point was only the left end, the tension stress of the right end was about 50% of the left end (Figure 10a). If this is the right end, the difference between the tension stress at the both ends was small (Figure 10c). Therefore, the different PS points affect the tension condition of PC. However, the choice of the structural shape (Beam or Arch) don't affect this tension condition(Figure 10ac,10bd).

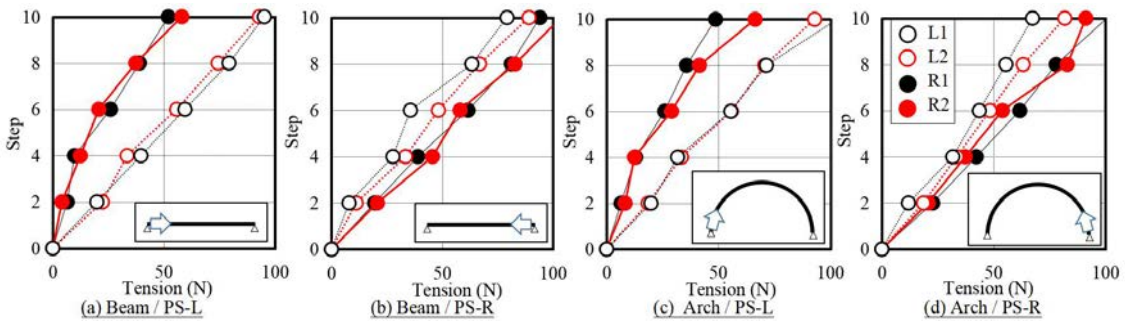


Figure 10 : Change in tension stress of PC

Change in the axial stress of the low chord is shown in Figure 11. The measuring points (S1~S6) are shown in Figure 9d. The compression occurred the right side of low chord. The small tension stress occurred at the left chord of Beam. In this contrast, the small compression occurred at it of Arch. These cause is the rotation sliding behavior, and will be explained in Chapter 6.

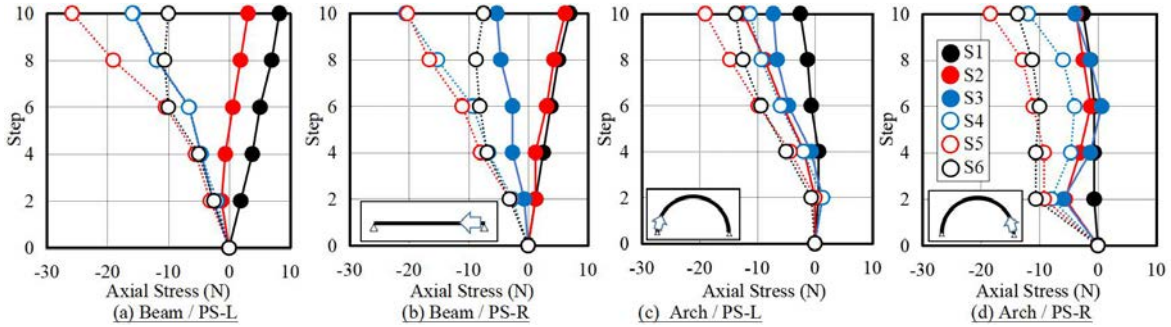


Figure 11 : Change in axial stress of Low chard

5 Load experiment

5-1 Experiment model The experiment model is based on the model that is picked up Figure 9. The condition of PS is PS/R. Load condition is shown in Table 1. This experiment purpose is to confirm PS effect.

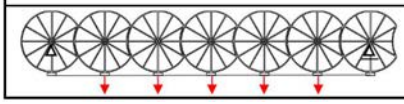
Load Point	Maximun Load (N)	PS (N)
	Tota of Maximun Load P_{max} = 200 Maximun Load per a point = 70	PS= 0 or 30 or 60

Table 1 : Load Condition

5-2-1 Load-Displacement of D3 In case of Beam, the sliding deformation of SCS without PS occurred. PS effect is to prevent this deformation and improve the stability of SCS (Figure12a). However, when the quantity of PS exceeded 30N, the stiffness of SCS didn't increase. In case of Arch, when the quantity of PS change from 0N to 30N, the displacement decreased. However, when that change from 30N to 60N, that didn't decrease so much.

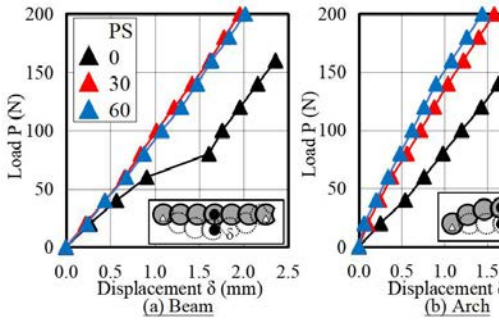


Figure 12 : Load-Displacement of D3

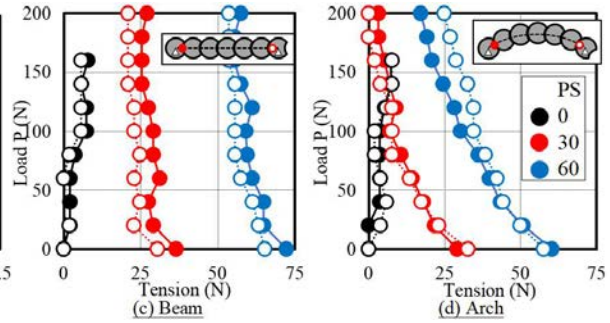


Figure 13 : Load-tension stress of PC

5-2-2 Load-Tension of PC In case of Beam, the increasing load doesn't change the quantity of the tension stress of PC (Figure13a). In case of Arch, that reduce the tension stress of PC with PS, and the load that occurred the slackness of PC increased with the increasing PS (Figure13b). The cause of both different structural behaviors is the difference in the resistant mechanisms. In case of Beam, the neutral surface and PC are at the same position, and the axial stress of PC didn't change. In case of Arch, the compression occurred in the axial cross section including PC. If the quantity of PS is 0N, regardless of the structure shape, the small tension stress occur under the load exceeding 10N. This cause will be explained in Chapter 6.

5-2-3 Load-Tension force of low chord In case of Beam, the increasing PS reduced the generation tension stress of S3 and S4, but doesn't reduced that of S1, S2 and S6 (Figure14a). In case of Arch, All low strings had PS effects that the generation tension stress decrease (Figure14b).

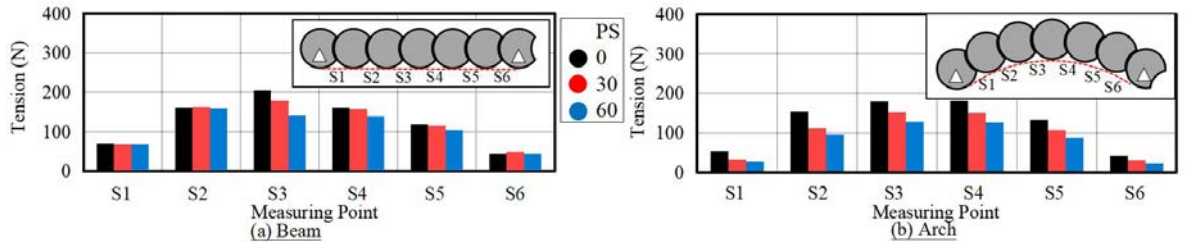


Figure 14 : Load-Tension of Low Chord under P=160N

5-2-4 Load-Strain of C-member In case of Beam, the measuring point that occurred the maximum compression strain was C510, and this was not reduced despite increasing PS (Figure 15a). As the measuring point near neutral surface in C-member moves from left to right, the direction of strain shifted from compression to tension (Figure 16a). In case of Arch, the measuring point that occurred the maximum compression strain was C59, this was not reduced like Beam too (Figure 15b). The compression strain occurs at all measuring point near neutral surface in C-member (Figure 16b). These cause will be explained in Chapter 6.

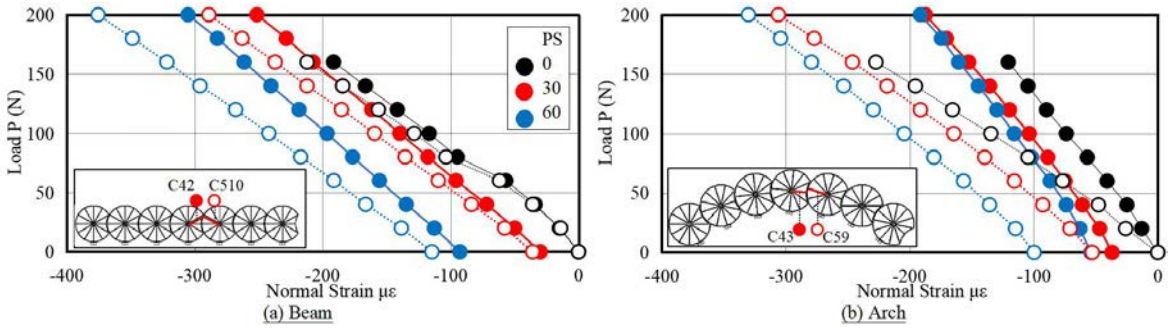


Figure 15 : Load - Maximum Normal Strain of C-member

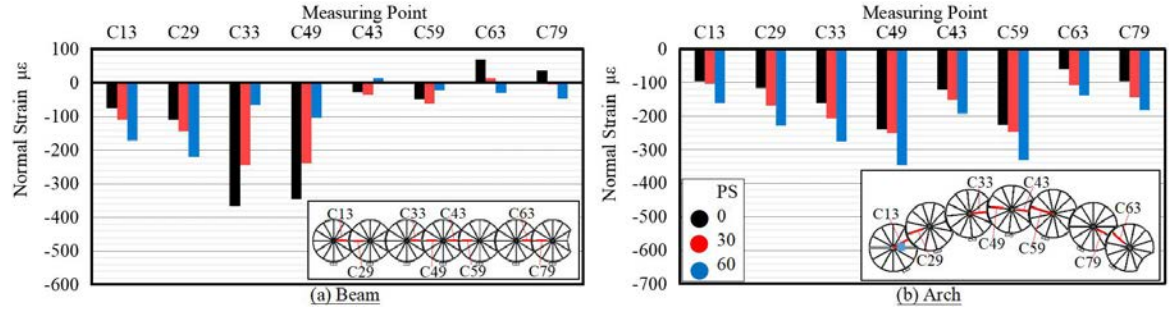


Figure 16 : Normal Strain Sate of C-member under "P=160N"

6 Estimation of Structural behavior by rotation sliding

Through two experiments, it was confirmed that the asymmetric structural behavior of SCS occurs. The different pretension points (PS-L or PS-R) generate the different tension condition of PC. This cause are shown Figure 17a. [PS-L] "1 Contact" become "(2) Rotation Center", and C-menbers hug each other. At this times, "4 Rotation Sliding" doesn't occur, PC mismatch the compression line. As a result, different "(3) Contact Forces" are generated for PC and C-member, and "6 Tension" becomes uneven. [PS-R] "(4) Rotation Sliding" between C-members occur. As a result, PC match the compression line and "6 Tension" becomes uniform.

Figure 17b shows the cause of the asymmetrical stress condition that picked up in Figure13, 14 and 16. "4 Tension" as resistance of the whole structure is generated. At the same times, "4 Resistance" to "3 Rotation" and "5 Tension" occurred the left side of SCS. On the other hand, "5 Tension" doesn't occur

the right side of that. Because "4 Resistance" to "3 Rotation" doesn't function. As a result, an asymmetric tension condition that shown in Figure14 occurs. "6 Tension" occur to prevent the progress of separation between C-members. This is related to the graph in Figure13 that the tension stress under PS=0 has increased. The relationship between Figure11 and Figure17 has not been elucidated yet. In the future, the experimental data must be analyzed in detail.

The case of the asymmetric strain condition that is showed in Figure16 will be explained the follow. "4 Resistance" doesn't function between C-members of the right side of SCS, and the separation occurs between C-members. As a result, it is difficult for the compression stain of C-member to occur in near the neutral surface.

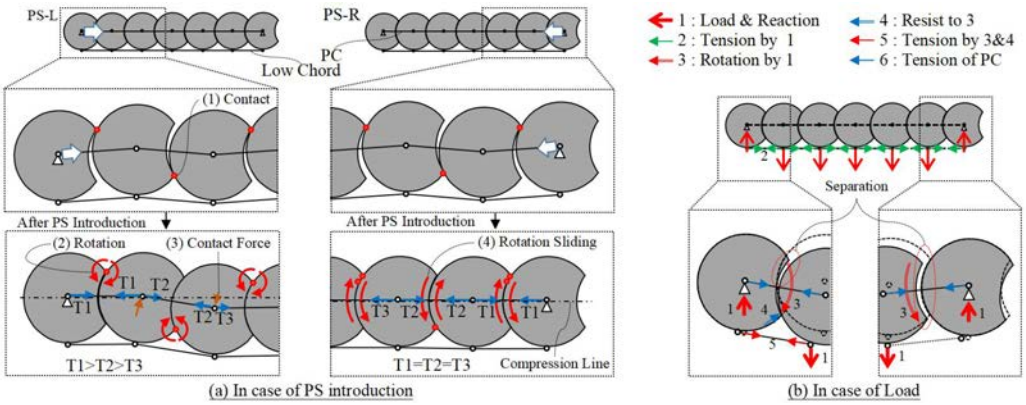


Figure 17 : Structural behavior by Rotation sliding

7 Conclusion

Three experiments provided the following insights.

(1) SCS is useful for Flexibility Reuse System that doesn't require the replacement assemblies.

(2) Arch is easier to apply to SCS than Beam that the asymmetric structural behavior occur

(3) PS effect is to prevent the rotation sliding and to reduce the tension stress of the lower chord. However, excessive PS that lead to increasing stress of C-members isn't necessarily the best.

(4) The tension stress of PC doesn't change when PC overlaps with the neutral surface of Beam. And this deceases when PC overlaps with the compression line of Arch.

(5) The relationship between part of the experimental results and the rotation sliding isn't understood. Therefore, the experimental date must be analyzed in more detail.

References

[1] A. Tanaka and M. Saitoh, "Proposal of String Crescent Structure - About concept and structural characteristic for String Crescent Structure -", *Proceeding of 12th Asian Pacific Conference on Shell & Spatial Structure (APCS2018)*, *Penang, Malaysia*, October 29-30, 2018, pp. 579-589.

[2] [2] Akira TANAKA and Masao SAITOH, et al, STRUCTURAL BEHAVIOUR OF VAUT ROOF UNDER WIND LOADS CONSIDERING CONSTRUCTION, *in Journal of Structural and Construction Engineering (Transactions of AIJ), No. 611*, pp. 95-102, 2007. 1

Proceedings of the IASS Annual Symposium 2019 – Structural Membranes 2019
Form and Force
7 – 10 October 2019, Barcelona, Spain
C. Lázaro, K.-U. Bletzinger, E. Oñate (eds.)

Our world in a line: Deploying the reality

Carlos J. GARCÍA-MORA*, Jose SÁNCHEZ-SÁNCHEZ[a]

*Ph. D candidate, Department of Structural Engineering and Land Engineering
Seville University, Av. de la Reina Mercedes, 2, 41012 Sevilla, España
architeengineering@gmail.com

[a]Professor, Department of Structural Engineering and Land Engineering
Seville University, Av. de la Reina Mercedes, 2, 41012 Sevilla, España
josess@us.es

Abstract

Numerous authors have tried to design a lot of deployable geometries with straight scissors like cilinders, spheres, cubes, etc… since this type of structures began to have a real application in the Engineering and the Architecture. However, other more complex geometries (Composed surfaces or organic shapes) have been always more difficult to design as deployable surfaces with straight scissors because the final structure has a behaviour of a rigid structure instead of the behaviour of a mechanism (Or it hasn't a full deployment process). These limits in the design of this type of structures have already disappeared due to the development of the theorems that govern any kind of deployable structure of straight scissors. In this paper, a brief summary of the theory for the design of this type of structures in curves and surfaces will be shown. This information will be accompanied by the current methods of design and with 3 practical applications: Two Pavilions of the Sagrada Familia of Barcelona and his main facade (Facade of the Glory) will be designed as deployable. Likewise, an exposition in the symposium with the built models will be done (One of the Pavilion and the Facade of the Glory, this last one will depend of the available time). Consequently, in this paper also will be developed the automatization of these models and the needed electronic.

Keywords: Deployable structure, scissor structure, transformable structure, linkage mechanism, Ellipse, Ellipsoid

1. Introduction

The geometric compatibility of a deployable structure of straight scissor was developed by Félix Escrig Pallares [1] in 1985 with Eq. (1) (Figure 1). Later, Luis Sanchez Cuenca discovered in 1996 that this equation can be satisfied in any scissor with the use of ellipsoids in the design of this type of structures [2] (Figure 1) and in 2007, Niels de Temmerman wrote in his PhD the basic math to understand this design process based on the use of ellipsoids.

$$k_1 + k_2 = k_3 + k_4 \tag{1}$$

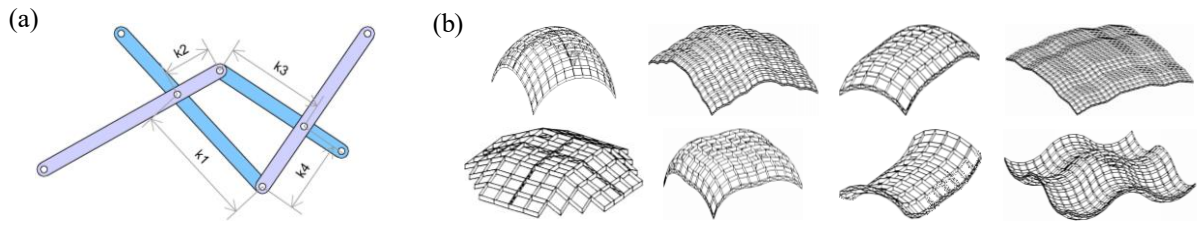


Figure 1: (a) Graphic representation of Eq. (1) (b) Deployable surfaces designed by Luis Sanchez Cuenca

Copyright © 2019 by Carlos J. García - Mora and Jose Sánchez - Sánchez
Published by the International Association for Shell and Spatial Structures (IASS) with permission.

However, the study of Temmerman was not widespread because its study can be used only in geometries with certain design conditions. Also, its method only gives a random point where the geometric convergence is satisfied (If we want to get another point we have to apply the method again) [3]. The ideal situation would be to obtain the set of points of the space that satisfy Eq. (1) and that guarantee the compatibility of the structure in any phase of its deployment.

As the authors of this paper demonstrated in the universal Theory for the deployable structures of straight scissors, this convergence will be satisfied in a surface that has a triaxial hyperboloid shape (When the axes of the ellipsoids are parallel) and a nonstandard shape (When the axes of the ellipsoids aren`t parallel). Also, this Theory allows to put the scissors with respect to the surface that we want to design as deployable, for example, all superior joints of the scissors can belong to the surface that we want to design as deployable.

2. Universal theory for deployable structures of straight scissors

The deployment with straight scissors in any geometry can be divided in two sections: Application to a curve and application to a surface

2.1. Application to a curve

There are two ways to design deployable a curve regardless of its shape: Using directly the convergence equation in the plane (Eq. (2) y Eq. (3)) or using the geometric interpretation of this equation.

$$x_c = \frac{c_1 \cdot \left[\begin{matrix}(d \cdot sin\,\gamma)^2 + (l^2 - c_2^2) \cdot (sin\,\alpha)^2 + \\ +2 \cdot d \cdot l \cdot sin\,\gamma \cdot sin\,\alpha\end{matrix}\right]}{c_1 \cdot (d \cdot sin\,\gamma + l \cdot sin\,\alpha) + c_2 \cdot d \cdot sin(\alpha + \gamma)} \;;\; y_c = \frac{c_1 \cdot \left[\begin{matrix}c_2^2 \cdot sin(2 \cdot \alpha) + 2 \cdot c_1 \cdot c_2 \cdot sin\,\alpha + d^2 \cdot sin(2 \cdot \gamma) + \\ +2 \cdot d \cdot l \cdot sin(\alpha - \gamma) - l^2 \cdot sin(2 \cdot \alpha)\end{matrix}\right]}{2 \cdot c_1 \cdot (d \cdot sin\,\gamma + l \cdot sin\,\alpha) + 2 \cdot c_2 \cdot d \cdot sin(\alpha + \gamma)} \quad (2)$$

$$\forall (x_c, y_c) \in \left(\frac{x_c}{b_1}\right)^2 + \left(\frac{y_c}{a_1}\right)^2 = 1 \quad (3)$$

The geometric meaning of each parameter that is in the convergence equation in the plane can be observed in Figure 2.

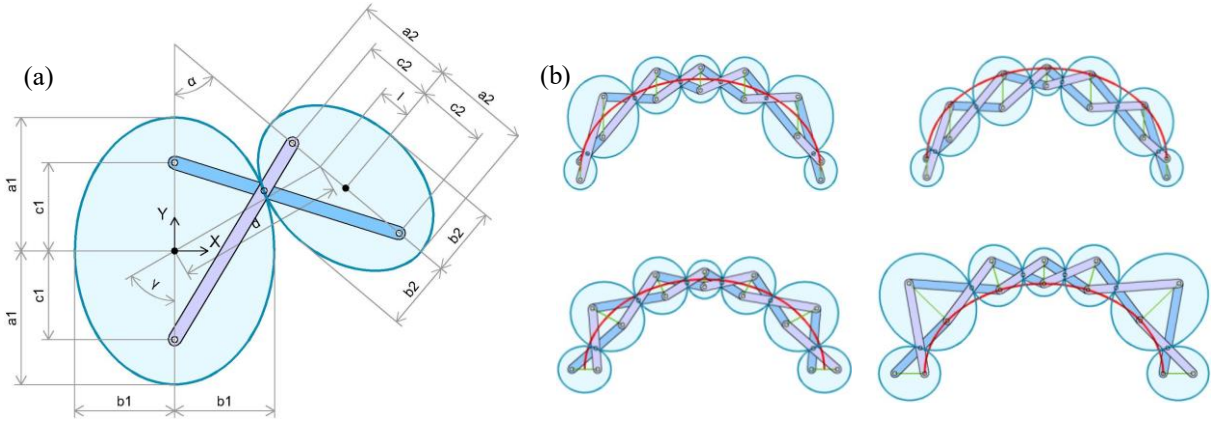


Figure 2: (a) Parameters between the initial ellipse (Ellipse 1) and the final ellipse (Ellipse 2) (b) Deployable design of a curve using different values of α and l. Up and left: $\alpha = 0$ y $l = 0$; Up and right: $\alpha \neq 0$ y $l = c_2$; Down and left: : $\alpha \neq 0$ y $l = 0$; Down and right: $\alpha \neq 0$ y $l = c_2$

Consequently, this equation works using the following parameters:

- Input parameters: a_1, b_1, c_1

- Parameters that can be controlled by the designer: d, γ, l

- Output parameters: c_2

Then, if we have an ellipse in the plane (Ellipse with parameters a_1, b_1 y c_1) and if we replace the position of any point in Eq. (2) y Eq. (3) (The position of this point is determined by "d" and "γ" and this point can't be an inner point of the ellipse), the value of c_2 for this point that satisfy Eq. (1) in any phase of the deployment will be obtained. With the c_2 value, the a_2 value is calculated with the semisuma of the focal distances of the ellipse 2. The b_2 value is obtained using the Pitagoras triangle. The third parameter that can control the designer is the "l" parameter, this parameter allows the control of the relative position of the scissors with respect to the curve that we want to design as deployable. The most important cases of this variable are:

- If $l = -c_2$, the superior joints of the scissors will belong to the curve that we want to design as deployable.

- If $l = 0$, the middle point of the distance between the two extremes of the obtained scissor will belong to the curve that we want to design as deployable.

- If $l = c_2$, the inferior joints of the scissors will belong to the curve that we want to design as deployable.

The second way to design a deployable curve is with the geometric interpretation of Eq. (2) and Eq. (3). If in these equations some variables changes are done, we will obtain from Eq. (4), to Eq. (7).

$$\left(\frac{y - f_1}{f_2}\right)^2 + \left(\frac{x}{f_3}\right)^2 = 1 \tag{4}$$

$$f_1(Si\ \alpha \neq 0) = -\frac{h \cdot u^2 + c_1 \cdot u - h \cdot v - h \cdot v^2}{(1+v)^2 - u^2} \quad y \quad f_1(Si\ \alpha = 0) = l \tag{5}$$

$$f_2(Si\ \alpha \neq 0) = \left[\frac{a_1}{(1+v)^2 - u^2}\right] \cdot \left[1 + v + \frac{u \cdot h}{c_1}\right] \quad y \quad f_2(Si\ \alpha \neq 0) = a_1 \cdot \left(1 + \frac{c_2}{c_1}\right) \tag{6}$$

$$f_3(Si\ \alpha \neq 0) = \left[\frac{b_1}{(1+v)^2 - u^2}\right] \cdot \left[1 + v + \frac{u \cdot h}{c_1}\right] \quad y \quad f_3(Si\ \alpha \neq 0) = b_1 \cdot \left(1 + \frac{c_2}{c_1}\right) \tag{7}$$

As we can see, Eq. (4) is the equation of an ellipse (Semi-major axis with a f_2 value and Semi-minor axis with a f_3 value) that is moved in the direction of its axis with a f_1 value. Likewise, the "u" and "v" parameters are using in this equation where $u = c_2/n$ y $v = l/n$. Also, "n" will be the distance between the point of the curve where we will put the following scissor and the cross point between the axis of both ellipses (The initial ellipse and the final ellipse). "h" will be the distance between this cross point and the inferior focus of the initial ellipse. Consequently, the control parameters will be "u" and "v" (If $\alpha \neq 0$) and c_2 and "l" (If $\alpha = 0$). If we give a value to "u" or to c_2 we will obtain an ellipse where all of their points will have a scissor with this "u" or c_2 value. The cross point between this ellipse and the curve that we want to design as deployable will give us a point that belongs to this curve with the desired "u" (If $\alpha \neq 0$) or c_2 (If $\alpha = 0$) value. Niels de Temmerman used in his PhD [4] the geometric method but he only developed the case with $\alpha = 0$ and $l = 0$, that means, he did not develop a method that would consider all possible cases.

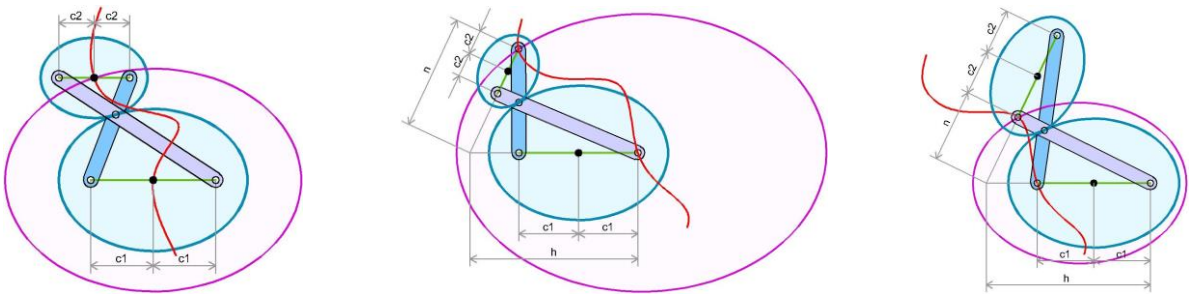


Figure 3: From left to right: $\alpha = 0$ y $l = 0$; $\alpha \neq 0$ y $l = -c_2$; $\alpha \neq 0$ y $l = c_2$. The ellipse of magenta color is the obtained ellipse for a u ($\alpha \neq 0$) or a c2 ($\alpha = 0$) value and with a v ($\alpha \neq 0$) or l ($\alpha = 0$) value given by the designer

2.2. Application to a surface

The goal will be to find the set of the points of the space that satisfy simultaneously Eq. (1) and the geometric convergence between two ellipsoids in the space. After some calculus are done, we can obtain that this set of points in the space from only one ellipsoid has the equation Eq. (8)

$$\left(\frac{z-f_1}{f_2}\right)^2+\left(\frac{x}{f_3}\right)^2+\left(\frac{y}{f_3}\right)^2=1 \tag{8}$$

Eq. (8) is the equation of another ellipsoid with a circular revolution and that is moved in the direction of its axis (f_1, f_2 y f_3 have already been defined previously). Then, if we give values to the "u" parameter, we can obtain a family of ellipsoids where each one will have an associated "u" value. On the other hand, the "v" parameter will be used for the relative position of the scissor (Figure 4).

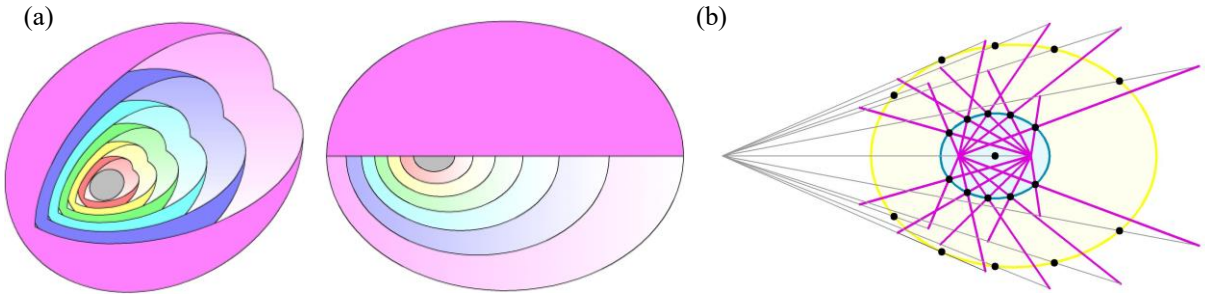


Figure 4: (a) Family of ellipsoids that is obtained changing the "u" value (The ellipsoid with gray color is the initial ellipsoid) (b) Geometric convergence for a concrete value of "u"

However, the Figure 4 only represents the geometric convergence from an isolated ellipsoid. If we want to find the simultaneous convergence from two ellipsoids in the space, we can use two methods: The exact method and the approximate methods.

2.2.1. Exact method

The exact method determines the analytic equation of the points that satisfy Eq. (1) simultaneously from two ellipsoids in the space. This equation only can be obtained if $\alpha = 0$ and the shape of the surface of this equation is a triaxial Hyperboloid (Hyperboloid with an elliptic revolution): Eq. (9)

$$\left[\frac{x-d_1}{d_2}\right]^2-\left[\frac{y}{d_3}\right]^2-\left[\frac{z-d_4}{d_5}\right]^2=1 \tag{9}$$

The equations of d_1, d_2, d_3, d_4 y d_5 aren't in this paper because they are too big.

2.2.2. Approximate methods.

The approximate methods are used because the analytic equation of the points that satisfy Eq. (1) simultaneously from two ellipsoids in the space can`t be obtained for $\alpha \neq 0$. The first of these methods is known as "Numeric method" where we must obtain 6 points from the intersection between ellipsoids with the same "u" value (These "u" values are random). When we have these 6 points we solve the determinant of Eq. (10) to get the polynomial of Eq. (10) and using several algebraic transformation we can obtain Eq. (9).

$$\begin{vmatrix} x^2 & y^2 & z^2 & x\cdot z & x & z & 1 \\ x_1^2 & y_1^2 & z_1^2 & x_1\cdot z_1 & x_1 & z_1 & 1 \\ x_2^2 & y_2^2 & z_2^2 & x_2\cdot z_2 & x_2 & z_2 & 1 \\ x_3^2 & y_3^2 & z_3^2 & x_3\cdot z_3 & x_3 & z_3 & 1 \\ x_4^2 & y_4^2 & z_4^2 & x_4\cdot z_4 & x_4 & z_4 & 1 \\ x_5^2 & y_5^2 & z_5^2 & x_5\cdot z_5 & x_5 & z_5 & 1 \\ x_6^2 & y_6^2 & z_6^2 & x_6\cdot z_6 & x_6 & z_6 & 1 \end{vmatrix} = k_1\cdot x^2+k_2\cdot y^2+k_3\cdot z^2+k_4\cdot x\cdot z+k_5\cdot x+k_6\cdot z-k_7 \tag{10}$$

The second approximate method is known as "Geometric method" where we obtain a set of ellipses from the intersection between ellipsoids with the same "u" value. After that, the searched surface is obtained with a loft through these ellipses (Figure 5). The advantages of this method are that it is very easy to automate and that the designer can control the resolution of the obtained surface. The disadvantage of this method is that we need to calculate the minimum "u" value (Tangency between two ellipsoids and mínimum growth of the surface) and the maximum "u" value (Maximum growth of the surface). This problem has been already solved by the authors of this paper for all possible combinations (Figure 5).

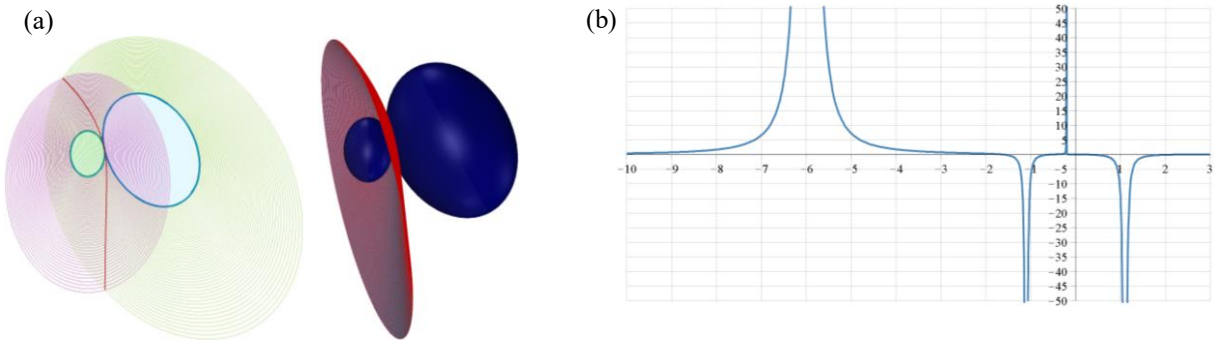


Figure 5: Surface of geometric convergence (Surface with red lines) that is obtained with the geometric method (b) Graphic of the minimum u value for two ellipsoids that aren't crossed and tangent

3. Examples of deployable structures that have been designed using this Theory

3.1. Lemniscata

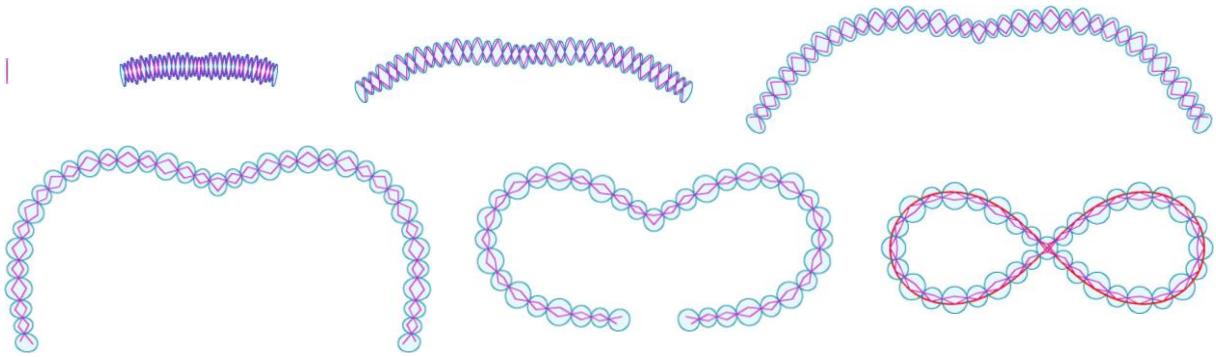


Figure 6: Deployment of the Lemniscara curve. Start: Up and left. Final: Down and right

3.2. Los Manantiales Restaurant (Xochimilco, México)

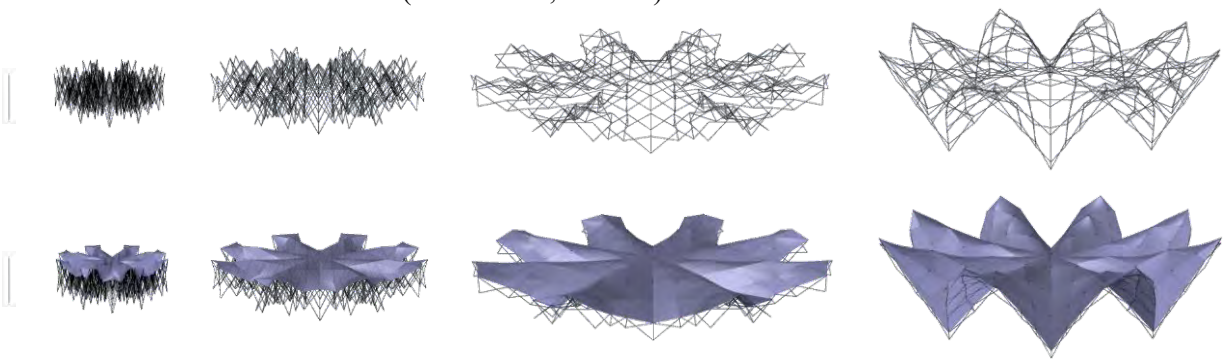


Figure 7: Deployment of the Manantiales Restaurant. Up: Wireframe model. Down: Textil model

4. Example 1 of the Sagrada Familia: Pavilion A and Pavilion B

The first parts of the Sagrada Familia that are going to be designed as deployable are its two extreme Pavilions (Figure 8). The fold process of both Pavilions has only one degree of freedom during the process of deployment and in his final position, that means, these Pavilions haven't a behavior of a crazy mechanism.

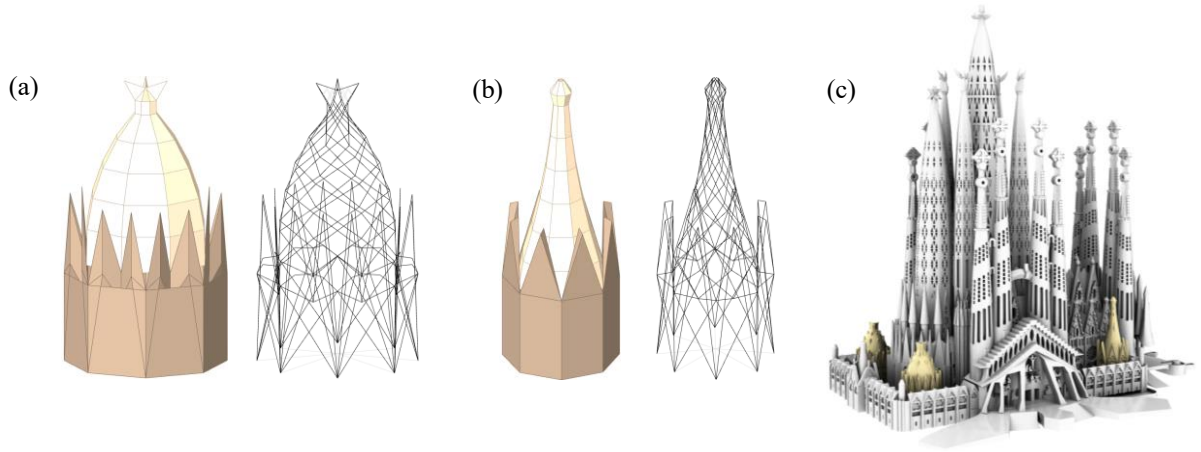
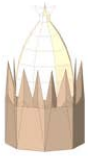


Figure 8: (a) Perspective with textil and wireframe perspective of the A Pavilion (b) Perspective with textil and wireframe perspective of the B Pavilion (c) Ubication of the Pavilion A and of the Pavilion B in the Sagrada Familia

Table 1: Deployment process of the Pavilions. The wireframe model is the model with scissors. The textil model is the same than the wireframe model but with the textil. The ellipsoid model represents the evolution of the ellipsoids of each scissor during the deployment process

	Pavilion A			Pavilion B		
Deployment percentage	Wireframe model	Textil mode	Ellipsoid model	Wireframe model	Textil mode	Ellipsoid model
0%						
33%						
66%						
100%						

5. Example 2 of the Sagrada Familia: Facade of the Glory

The last part of the Sagrada Familia that is going to be designed as deployable is his main facade. As in the previous case, the design of this facade has only one degree of freedom (Figure 9).

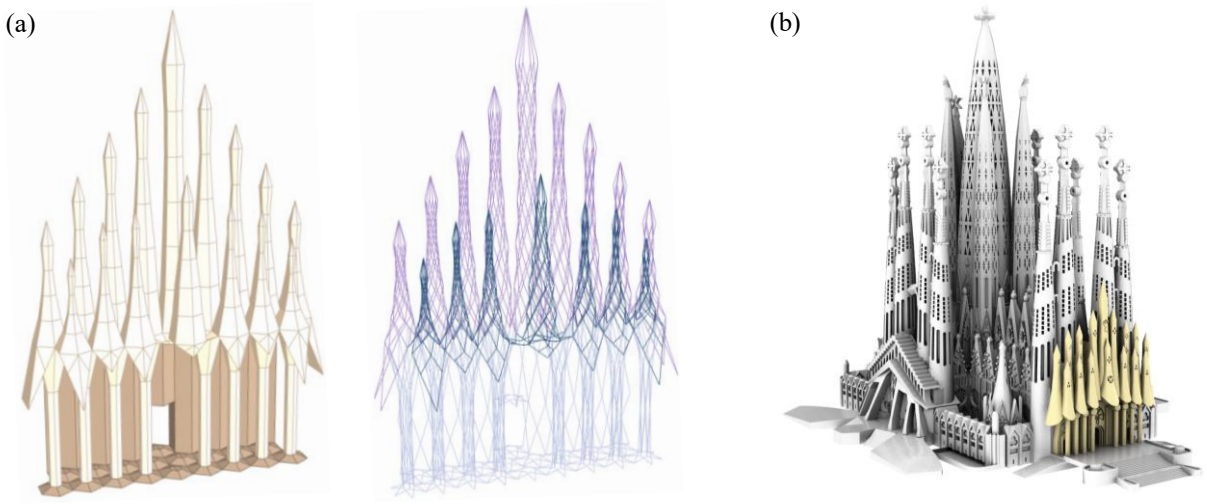
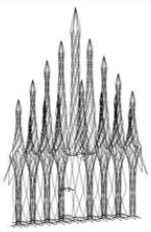
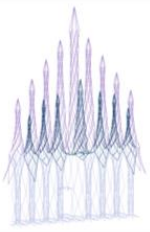
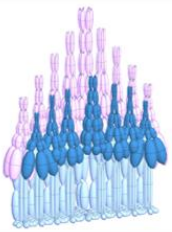


Figure 9: Perspective with textil and wireframe perspective of the Facade of the Glory (b) Ubication of the Facade of the Glory in the Sagrada Familia

Table 2: Deployment process of the Facade of the Glory. The wireframe model is the model with scissors. The textil model is the same than the wireframe model but with the textil. The ellipsoid model represents the evolution of the ellipsoids of each scissor during the deployment process

Deployment percentage	Wireframe model (Black and White)	Wireframe model (Color parts)	Textil mode	Ellipsoid model
0%				
50%				
100%				

6. Construction of the models

This section shows the automatic system and the PCB that has been designed to automate the deployment of the Pavilion B and the Facade of the Glory during the exposition (The Facade of the Glory will depend of the available time) (Figure 10). This machine will allow to deploy the structure when the public want or in time periods.

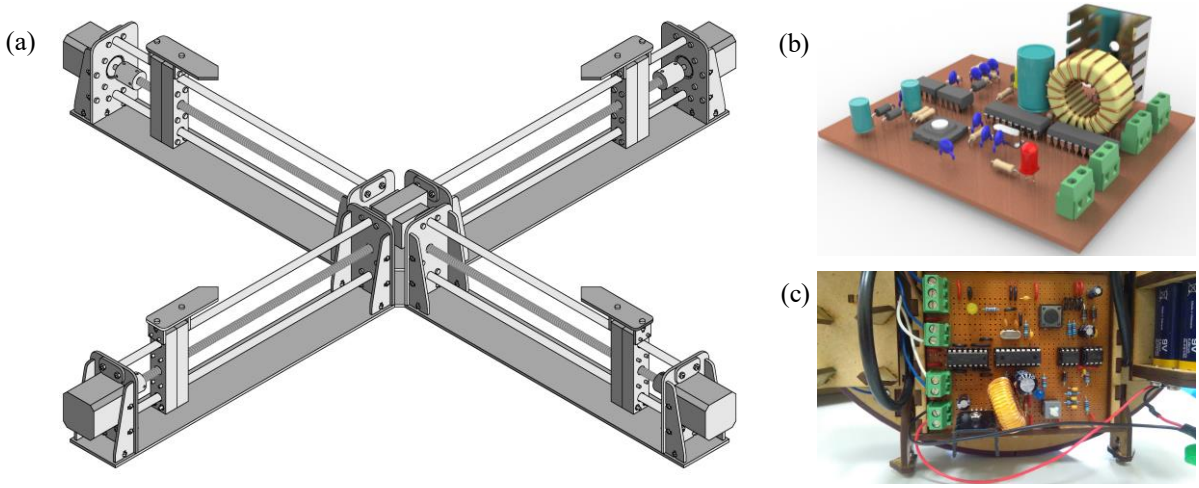


Figure 10: (a) Linear displacement system that is controlled by stepper motors (b) Render of the PCB that has been designed for the control of the deployable structure (c) Built PCB

7. Conclusion: submission of contributions

In this paper a brief summary of the Theory that unifies all methods to design deployable structures of straight scissors has been exposed. To demonstrate the utility of this Theory, some examples of the Sagrada Familia of Barcelona have been designed as deployable. Consequently, all types of geometries can be designed as a deployable structure with straight scissors like the Sydney Opera or the National Stadium of Beijing because this Theory considers all possible cases and using its theorems we can guarantee the geometric convergence during the deployment process (These theorems have not been developed in this paper). Likewise, this research opens the door to deployable structures with straight scissors with a huge rigidity (Around the 70% of the rigidity of a structure with the same design but with welded joints). This situation allows the design of structures with a huge resistance against the wind and the earthquake solving one of the main problems of this type of structures

8. Acknowledgements

This research did not receive any specific grant from funding agencies.

9. References

[1] ESCRIG, F. & P. VARCÁRCEL. “Introducción a la geometría de Estructuras Desplegables de Barras”. Boletín Académico de la ETSA de la Coruña, n1 3, 1986. Pp. 48-57. La Coruña. ISSN 0213-3474

[2] L. Sánchez - Cuenca, Geometric models for expandable structures (1996) MARAS 96. Sevilla

[3] K. Roovers, N. De Temmerman, "Geometric design of deployable scissor grids consisting of generalized polar unit", Journal of the International Association for Shell and Spatial Structures, vol. 58, Sept. 2017.

[4] N. De Temmerman, Design and analysis of deployable bar structures for mobile architectural applications (2007), Vrije Universiteit Brussel

Proceedings of the IASS Annual Symposium 2019 – Structural Membranes 2019
Form and Force
7 – 10 October 2019, Barcelona, Spain
C. Lázaro, K.-U. Bletzinger, E. Oñate (eds.)

Structural finite-element analysis of steel kirigami space frame to characterize global behavior

Nick SHERROW-GROVES*, Emily BAKER[a]

* Arup
560 Mission St., Suite 700,
San Francisco, CA, 94105, USA
nick.sherrow-groves@arup.com

[a] University of Arkansas, Fay Jones School of Architecture + Design, Fayetteville, AR, USA

Abstract

This paper builds on the work done by Baker to develop a structural system using a single sheet of CNC plasma cut steel, folded and reconnected to itself to form a double-layer space frame [1] [2]. This system is called "Spin-Valence." The process of creation of this system was entirely physical – no computer modeling was performed. The current work aims to address this lack by characterizing the structural behavior of the Spin Valence via finite element modeling. This is accomplished through the creation and analysis of three models: 1. A model representing the deployment of an individual cell, to establish the deployed geometry of a single cell and determine the degree of residual plastic strain this deployment produces; 2. A model replicating the testing conditions of physical tests performed by Sahuc and Herning on a 3-unit by 3-unit sample [3], to calibrate the model to real-world results; 3. A 6-unit by 12-unit model using reasonable material properties and support conditions, to establish allowable loads and stiffness values for a larger panel in closer-to-real-world conditions. The result of this analysis indicate that the system is viable for use in some real-world use-cases, but that the ductility of the system is highly configuration-dependent. Some improvements are suggested to increase strength and ductility.

Keywords: space frame, steel structure, structural design, structural analysis, FEM, kirigami, origami, folded structure

1. Introduction

This paper builds on the work done by Baker to develop a structural system using a single sheet of CNC plasma cut steel, folded and reconnected to itself to form a double-layer space frame [1]. The process of creating this system, called Spin Valence, involved the iterative improvement of physical test models. Improvement was characterized through qualitative observation of model characteristics such as internal stability and overall system stiffness. This process was integral to the development of the final form, but also totally separate from any computational analysis. Though the system could have been created in no other way, the lack of analytical modeling makes it more difficult to extend the current system to possible new uses or to rapidly evaluate the effect of changes to material or geometric properties.

Copyright © 2019 by Nick SHERROW-GROVES, Emily BAKER
Published by the International Association for Shell and Spatial Structures (IASS) with permission.

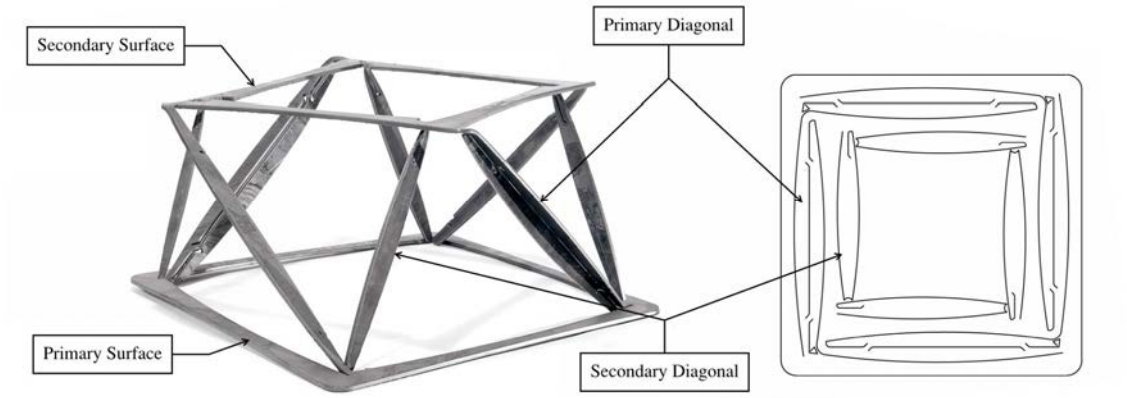


Figure 1.1: A single Spin-Valence cell, left, and the associated cut pattern in the steel sheet, right, including identifying labels for the associated components

The current work aims to address this issue by characterizing the structural behavior of the Spin Valence system via finite element modeling.

The first model constructed is of a single Spin-Valence cell like the one shown in Figure 2.1. This model is deployed in a similar manner to the physical model, in order to determine the form of the bent portion of the primary diagonal. This form is difficult to assess via non-modeling means, as it depends on the inelastic deformation of the steel as the cell is pushed through. In addition, this model is used to assess the extent of work-hardening in the primary diagonals, for incorporation into later models.

The second model constructed is of a set of 9 units arranged in a 3x3 grid. The grid is supported on two sides by roller supports, and loaded via an imposed displacement on the central unit. This is the same configuration used in physical testing by Sahuc and Herning [3]. The purpose of this model is to allow calibration of the numerical model to actual test results and to determine the primary characteristics of the system that govern its behavior.

The third and final model constructed is of a set of 72 units arranged in a 6x12 grid. This is meant to simulate how the Spin-Valence system might be used in a real-world application, as a façade element or a piece of structural art. The system is supported by roller supports at ¼ points along its long axis and loaded first via an imposed displacement on the secondary surface, and then by a distributed force. Using this model, allowable working loads may be determined at associated performance states.

2. General Model Setup

2.1. Modeling Software

Geometry was defined in Rhinoceros v6, meshed in Hypermesh v13.0, and analyzed in LS-DYNA v10.0.

2.2. Material Properties

For all models, the MAT_PLASTIC_KINEMATIC material model was used. This model assumes bi-linear behavior. The material model was not configured to degrade or fail, and therefore allows infinite plastic strain after the yield point. Unless noted otherwise, the following values were used to define the material model.

An important note: The material used in the samples by Sahuc and Herning is relatively ill-defined. It was purchased in bulk from a supplier that did not provide material certifications. Based on common practice in the United States, it is likely ASTM A1008 commercial sheet steel (i.e. grade CS), which has

a yield strength anywhere from 140 to 275 MPa (20 to 40 ksi). A value of 228 MPa (33 ksi) was assumed in the model, as Grade 33 sheet steel is a common structural grade. Further discussion of the effect of material grade on the model can be seen below.

Note that the density of the material was increased by a factor of 1000 to limit dynamic effects in the model. This density change will have no effect since no dynamic behavior is expected and no gravity loads were applied.

Table 2-1: Typical material properties for steel material during modeling

Yield Stress	Elastic Modulus	Post-Yield Modulus	Density	Poisson's Ratio
228 MPa (33 ksi)	205 GPa (29000 ksi)	205 MPa (29 ksi)	7850000 kg/m^3 (490000 lb/ft^3)	0.3

2.3. Element Formulation

Unless otherwise noted, the element formulation is based on the Belytschko-Tsay shell element with 6 integration points through the thickness. The thickness of the element is 2.78mm (12-gauge).

3. Deployment Model

Geometry of the 2-dimensions cut pattern was provided by Baker. After input into LS-DYNA, the central panel of the meshed model was then pushed and rotated upwards with a prescribed motion defined by Baker, based on the required geometric transformation to tessellate this unit with following units: 113.5mm upward while rotating 0.28 degrees counterclockwise. In this model, the primary surface was held in place with nodal pin connections.

The results of this model allow for two things: First, defining the geometric form of the ends of each primary diagonal after it has been bent into shape, and second, assessing the extent and degree of plastic strain in those same elements.

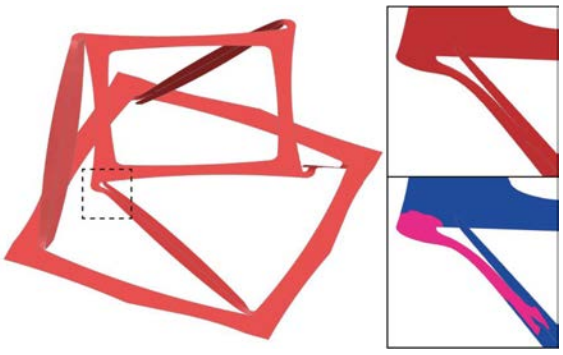


Figure 3.1: Deployed cell, showing deployed shape of top of primary diagonal (top right) and extent of plastic strain (bottom right)

The bent portions of the primary diagonal were incorporated into the geometry of multi-cell models. The extent of plastic strain suggests portions of the cell that may have experienced strain hardening during the deployment process. Since the PLASTIC_KINEMATIC material model does not explicitly allow for strain hardening, the extents of plastic strain are likely somewhat smaller than are shown here, but this model provides an adequate estimate for future modeling.

4. 3x3 Unit Model

4.1. Geometry

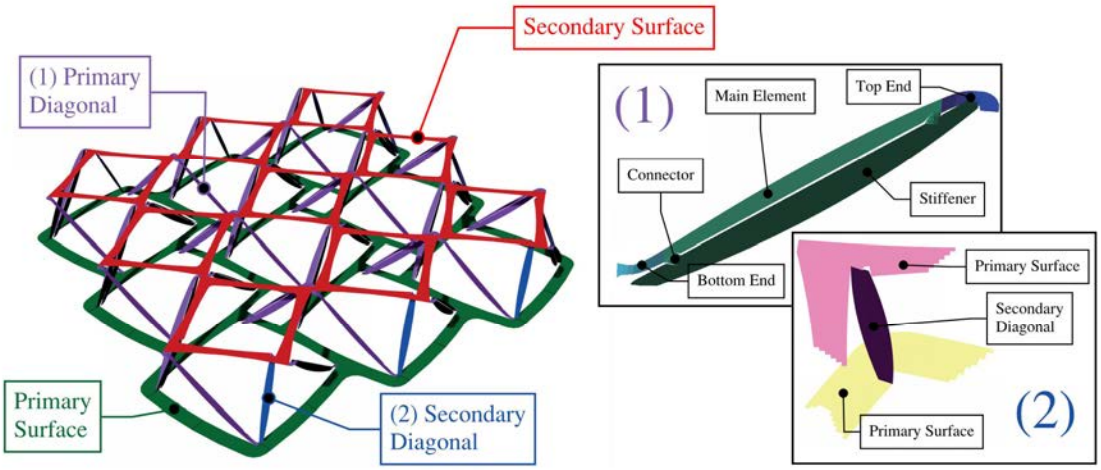


Figure 4.1: The overall view of the 3x3 unit model, identifying the primary and secondary surfaces and diagonals and their component parts. Note that the secondary diagonals only occur at the edge of the structure.

The general geometry of the 3x3 unit follows the geometry of the unit tested by Sahuc and Herning [3], with a total of (9) units supported by (4) primary diagonals each. In addition, stiffening secondary diagonals have been added around the exterior, (3) per side for a total of (12). These secondary diagonals are provided to resist the return of the system to its unfolded state. The entire 3x3 unit is 753mm square and 119mm high.

4.1.1.Primary Diagonal

As mentioned above, the curvature of the top of each primary diagonal was incorporated into the 3x3 unit model, based on the geometry of the deployed section. In addition, the stiffener on each primary diagonal was folded to a 90° angle, relative to the main element of the diagonal. The stiffener and the main element were connected with a curved quadrilateral surface fitted such that it connects on its straight face with the stiffener and the main element.

Based on the results from the deployed model, the curved top and bottom portions of the main element were split into their own parts, to reflect the fact that these portions likely have separate material properties from the rest of the structure.

4.1.2.Secondary Diagonal

The secondary diagonals were not included in the deployed model, and as such were modeled more simply, connected along an edge at the top and bottom with a discontinuous angle.

4.2. Boundary Conditions

The test setup used by Sahuc and Herning was designed to provide vertical support on two sides of the structure, allowing these supports to rotate along one axis. In addition, the structure was spot-welded to the supports to provide resistance to shear slipping. The loading was provided by a steel plate pressing

Copyright © 2019 by <substitute here the name(s) of the author(s) or individual(s) claiming copyright>
Published by the International Association for Shell and Spatial Structures (IASS) with permission.

downward on the central portion of the structure. Notably, this steel plate extends beyond the extents of the central portion, thus preventing the upward motion of the primary diagonals.

The numerical model was constructed to simulate these boundary and loading conditions. Nodal rigid bodies were applied to the outside edges of the primary surface of the model, and allowed to rotate around the global Y-axis. A nodal rigid body was also created for the central portion of the secondary surface, to simulate the loading surface.

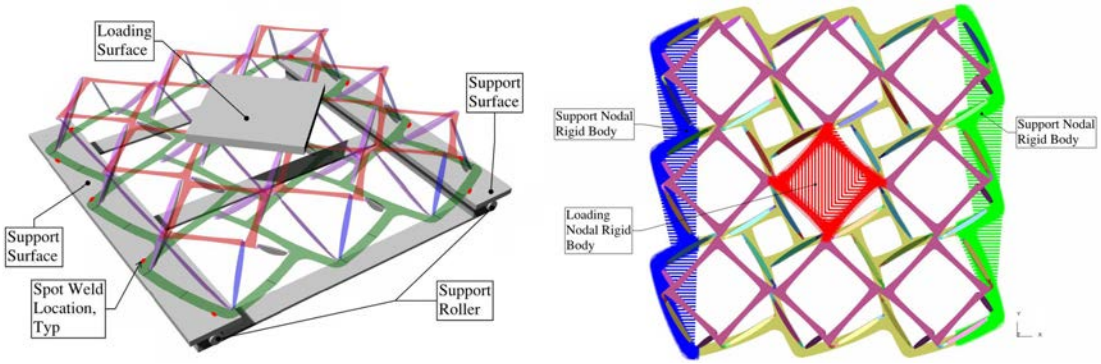


Figure 4.2: Test setup for Sahuc and Herning (left) and model boundary conditions (right)

4.3. Loading

Loading for this model was an applied downward (-Z) displacement of 70mm, applied over 15 seconds.

4.4. Effects on Model Behavior

The goal of this model is to simulate as closely as possible the force-displacement behavior of the tested physical model. This behavior was influenced most by the following factors:

1. Material properties of model elements
2. Self-contact between model elements

Each of these factors will be discussed in the following sections.

4.4.1.Material Properties of Model Elements

As discussed in section 4 above, the deployment of each unit results in strain-hardening at each end of each primary diagonal. Because the material model does not explicitly account for strain hardening, this was approximated by increasing the yield strength of the material for the top and bottom portion of the primary diagonal to the tensile strength for the assumed material. Because ASTM A1008 CS steel does not have a stated ultimate stress, A1008 SS Gr. 33 steel was assumed, which has a tensile strength of 331 MPa (48 ksi).

Using these proportions, material properties were varied to determine the closest conformance with experimental results. A material 1.2 times stronger than A1008 SS Gr. 33 was found to have the closest conformance.

4.4.2.Self-Contact Between Model Elements

An important part of the behavior of the frame depends on the interaction of the primary diagonals with the primary and secondary surfaces. These occur in in two ways. For the interaction with the primary surface, the bottom portion of the primary diagonal deforms such that the bottom surface presses against the primary surface. This allows the main element in the primary diagonal to form a stiff load path in axial bearing. In both the physical testing and the numerical model, this load path persists until the end of the test, and can thus be considered a ductile form of failure.

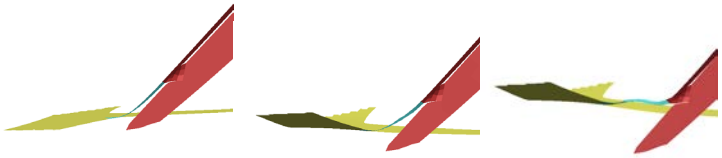


Figure 4.3: Behavior of lower portion of primary diagonal, showing initial position (left), bending during compression of the primary diagonal (center) and buckling of the lower portion to rest on the primary surface below (right)

The contact between the secondary surface and the primary diagonals is less reliable – it involves the tab on the top of the primary diagonal stiffener slipping past the edge of the secondary surface. It adds significant capacity to the structure, but this contact does not persist, and at points during the test these components will slip past each other. This results in sudden losses of stiffness and can be considered a non-ductile failure.

4.5. Results

Based on the parametric studies in the previous section, the criteria for the final numerical model are as determined below.

Table 4-1: Criteria for final numerical model

Typical Yield Strength	Yield Strength at Primary Diagonal Ends	Contact Surfaces
273 MPa (39.6 ksi)	397 MPa (57.6 ksi)	All

The force-displacement curve for the numerical model with these criteria is shown below.

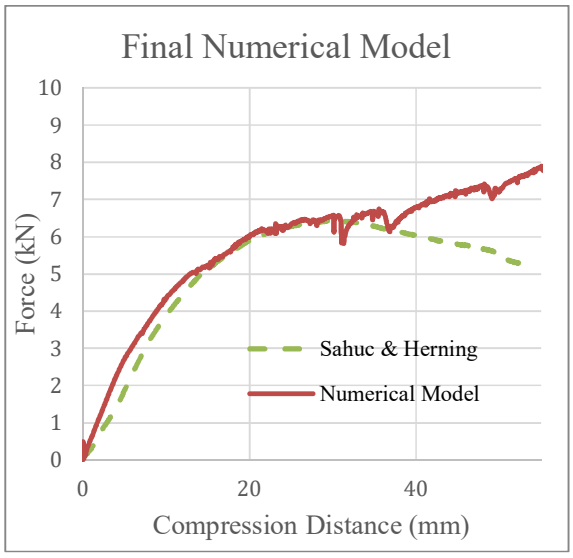


Figure 4.4: Force-Displacement curve for the final numerical mode.

The conformance is closest in the initial stages of pressure, and diverges after the peak strength in the physical test model. This is likely explained by the following:

1. The physical model displayed non-ductile cracking in some of the welds attaching the deployed modules together, which may explain the strength degradation after the peak force. Material degradation and welding were not modeled in the numerical model, so the numerical model did not display the same negative stiffness at high displacements.
2. The numerical model was loaded with a nodal rigid body, which sees every reversal in force, resulting in a more jagged curve. The plate loading the experimental model did not see these reversals as it was not positively attached to the structure.

The behavior of the 3x3 module before ~30mm in compression distance can be characterized by the following phases (See Figure 5.5):

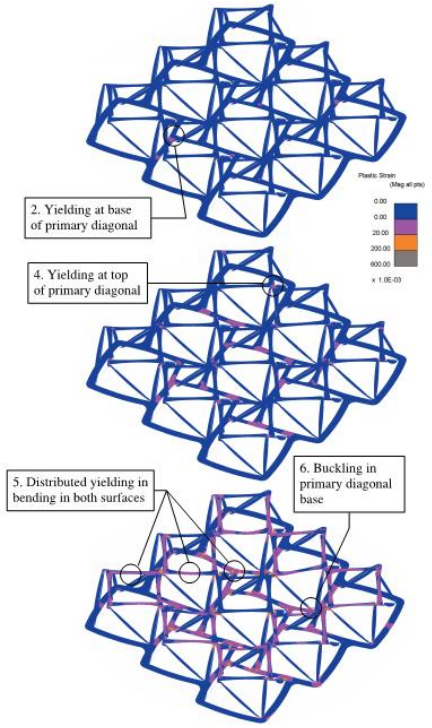


Figure 4.5: Behavior of the 3x3 cell

1. 0mm to ~4mm: Elastic range
2. **~4mm, 2.2kN:** First yielding occurs at the base of the primary diagonals
3. ~4mm to 8mm: Yielding spreads through the primary surface as it yields in bending at the base of the primary diagonals
4. **~9mm, 4.0kN:** First yielding occurs in the secondary surface, at the top of the primary diagonals
5. ~8mm to 30mm: Yielding continues to spread in both surfaces, resulting in high bending deformation
6. **~30mm, 6.5kN:** Buckling occurs in the base of one primary diagonal
7. >30mm: Numerical model diverges from experimental results

These results show that the Spin-Valence system in this configuration is highly ductile, with significant displacement capacity and force resistance beyond the linear zone. However, the extensive yielding that occurs in the material and the highly indeterminate nature of the structure mean that full usage of this capacity may be impractical, and design may be conservatively limited to the linear zone.

5. 6x12 Unit Model

The model was then expanded to 6x12 units, with the goal of identifying behavior of a system that would more closely resemble a real-life use-case for this system. As such, the material properties were pegged to the design values for ASTM A1008 SS Gr. 33 steel, which is a conservative lower bound for strength. In addition, since it is a low-ductility resistance mechanism (See section 5.4.2), the contact between the primary diagonals and the secondary surface was omitted.

The overall dimensions of the assembly were 2852mm x 1453mm x 119mm, supported at quarter points by 50mm-wide supports, modeled as nodal rigid bodies. The secondary surface was loaded with a pressure increasing from 0 to 70kPa (1460psf) over 15s and then held for 10s. Distributed over the total area of the unit, this is equivalent to 10.4kPa (218psf). This is meant to simulate real-world loading conditions, through wind, live, or other distributed loading.

The behavior of the structure under this load is linear up until the point at which the top portions of the primary diagonals buckle over the supports, where the axial load in the primary diagonals is highest. After this buckling event, the stiffness of the system markedly decreases, and during the portion of the test where load is sustained, the model continues to deflect. This indicates that the post-buckling stiffness

Copyright © 2019 by <substitute here the name(s) of the author(s) or individual(s) claiming copyright>
Published by the International Association for Shell and Spatial Structures (IASS) with permission.

of the system is very low. As such, any design usage of this configuration should remain in the zone of linear behavior.

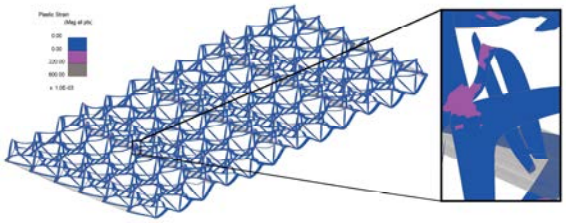


Figure 5.1: Deflection of the 6x12 model (left), and a view of the buckling failure of the primary diagonal (right)

Based on this assumption, the following design capacities and stiffness can be determined. Note that these assume a safety factor of 2. These capacities are sufficient for typical wind loading in a façade use-case, but not for gravity loading, which requires greater redundancy and higher capacities.

Table 5-1: Design properties for 6x12 Spin-Valence configuration, supported at ¼ points

Total Allowable Load	Allowable Pressure	Equivalent Distributed Load	Stiffness at Center of Span
6.3 kN (1.4 kips)	10 kPa (210 psf)	1.5 kPa (32 psf)	0.79 kPa/mm (420 psf/in)

6. Conclusions and Recommendations

- The ends of the primary diagonals will be strain-hardened by the deployment procedure, which is key to the behavior of the unit as a whole. As these portions of the structure see the most plastic deformation, this hardening behavior merits further study to ensure that brittle failures do not occur.
- Post-buckling contact of the ends of the primary diagonals with the primary and secondary surfaces results in significant additional strength and stiffness in the system, but these interactions are not reliable. If the unit could be changed to force this contact and ensure that it remained at high deformation, significant gains in strength and stiffness could be achieved.
- The Spin-Valence system can be highly ductile, but this ductility is configuration-dependent. High through-thickness shear (such as over supports) without secondary diagonals results in non-ductile "pop-through" behavior as the ends of primary diagonals buckle. This may be ameliorated by adding additional braces at support locations or moving the connecting elements on each primary diagonal closer to the end of the stiffener so as to reduce the buckling length of the main element.
- The system should be sufficiently strong for typical façade or art installation uses. To avoid non-ductile buckling behavior, large panels should be designed to remain in the linear range.

References

[1] E. Baker, "Spin-Valence: Kirigami Space Frame," in *Proceedings of the International Association for Shell and Spatial Structures (IASS) Symposium*, Cambridge, MA, 2018.

[2] J. Sahuc, G. Herning and E. Baker, "Experimental and Analytical Investigation of the Spin-Valence Kirigami Space Frame," in *Proceedings of the International Association for Shell and Spatial Structures (IASS) Symposium*, Barcelona, Spain, 2019.

[3] E. Baker, "Search for a Rooted Aesthetic: Study in Spin-Valence," in *Fabricate: Negotiating Design & Making*, Zurich, Switzerland, 2014.

Proceedings of the IASS Annual Symposium 2019 – Structural Membranes 2019
Form and Force
7 – 10 October 2019, Barcelona, Spain
C. Lázaro, K.-U. Bletzinger, E. Oñate (eds.)

Structural optimisation of a bistable deployable scissor module

Liesbeth I.W. ARNOUTS*, Thierry J. MASSART[a], Niels DE TEMMERMAN[b], Péter Z. BERKE[a]

*Structural and Material Computational Mechanics, BATir Department, Université libre de Bruxelles (ULB)
50, avenue Franklin Roosevelt, 1050 Brussels, Belgium
larnouts@ulb.ac.be

[a] Structural and Material Computational Mechanics, BATir Department, Université libre de Bruxelles (ULB)
[b] VUB Architectural Engineering, Vrije Universiteit Brussel (VUB)

Abstract

Bistable deployable scissor structures can be designed to be transportable and can easily be transformed between two stable states, the compact and the deployed state, offering a huge volume expansion. In the deployed state they instantaneously reach structural stability as a consequence of an intended snap-through behaviour during transformation, generated by designed geometric incompatibilities. The design of such structures is ideally based on the duality of taking into account both their nonlinear transformation phase, as well as their service state in the deployed configuration, with opposing requirements. During transformation the peak force – and snap-through magnitude – needs to be minimized to obtain an easily transformable structure, while in the deployed state the stiffness of the structure should be high enough to allow sustaining gravity loads – requiring a high snap-through magnitude. In this contribution the computational design based on these opposing trends is formulated as a multi-objective optimisation approach. The feasibility of the proposed computational optimisation approach is demonstrated on the example of a bistable module.

Keywords: structural engineering, non-linear computational mechanics, deployable structures, scissor structures, bistable structures, multi-objective optimisation

1. Introduction

Scissor structures consist of beams connected by hinges. They can be designed to be transportable and can easily be transformed between two stable states, the compact and the deployed state, resulting in a huge volume expansion. In the deployed configuration they instantaneously offer some structural stability as a consequence of an intended snap-through behaviour during transformation, generated by designed geometric incompatibilities. The transformation of bistable scissor structures, first studied computationally by Gantes [1], is highly non-linear due to the large displacements and rotations and their bistable nature. Hence, such scissor structures should ideally be based upon the duality of taking into account both their nonlinear transformation phase as well as their service state in the deployed configuration, with opposing requirements. During transformation the peak force – and snap-through magnitude – needs to be minimized to obtain an easily transformable structure, while in the deployed state, the stiffness of the structure should be high enough to allow sustaining gravity loads – which can be showed to require a high snap-through magnitude. Because of this complex structural behaviour, the formulation of any simplified rigorous and automated design methodology is hindered, and consequently existing applications of the bistable scissor concept are rare in civil engineering.

In the past, several researchers in the field of mechanism-type scissor structures (without snap-through, otherwise called foldable) have successfully used optimisation methods [2-6]. All of these efforts were aimed at optimizing the deployed configuration through linear structural analyses. The optimisation of

Copyright © 2019 by Liesbeth I.W. ARNOUTS, Thierry J. MASSART, Niels DE TEMMERMAN, Péter Z. BERKE.
Published by the International Association for Shell and Spatial Structures (IASS) with permission.

bistable scissor structures, taking into account geometric non-linearities during transformation, was attempted by Gantes [7] by using genetic algorithms to minimise the weight, by varying the cross-sectional dimensions and material properties using penalty functions for the stress and displacement constraints, leading to a single optimal design. The proposed approach resulting in a single optimal design didn't allow the designer to make choices based on preferences related for instance to the desired aesthetics or morphologic parameters of the structure.

In this contribution, the computational design based on a multi-objective optimisation approach is proposed as design concept and its feasibility is demonstrated using an example of a single bistable module. The objectives are the minimisation of the peak force during transformation, as well as of the deflection in the deployed state of a bistable module as a function of the geometry and the cross-sections of the beams. The originality of this contribution is the proposal of a multi-objective optimisation concept for bistable scissor structures, obtaining a Pareto front with several optimal solutions based on the transformation as well as on the structural response in the deployed configuration.

2. Optimisation problem statement

2.1. Geometry and structural response

The considered structure is a square flat polygonal bistable deployable scissor module of 0.7x0.7 m and a height of 23 cm (Fig. 1). During transformation, the inner beams of the module bend elastically while the outer elements remain straight. The lower corner points are considered to be fixed in the vertical direction, while the upper corner points are subjected to a horizontal load in the diagonal direction, as shown in Fig. 1.

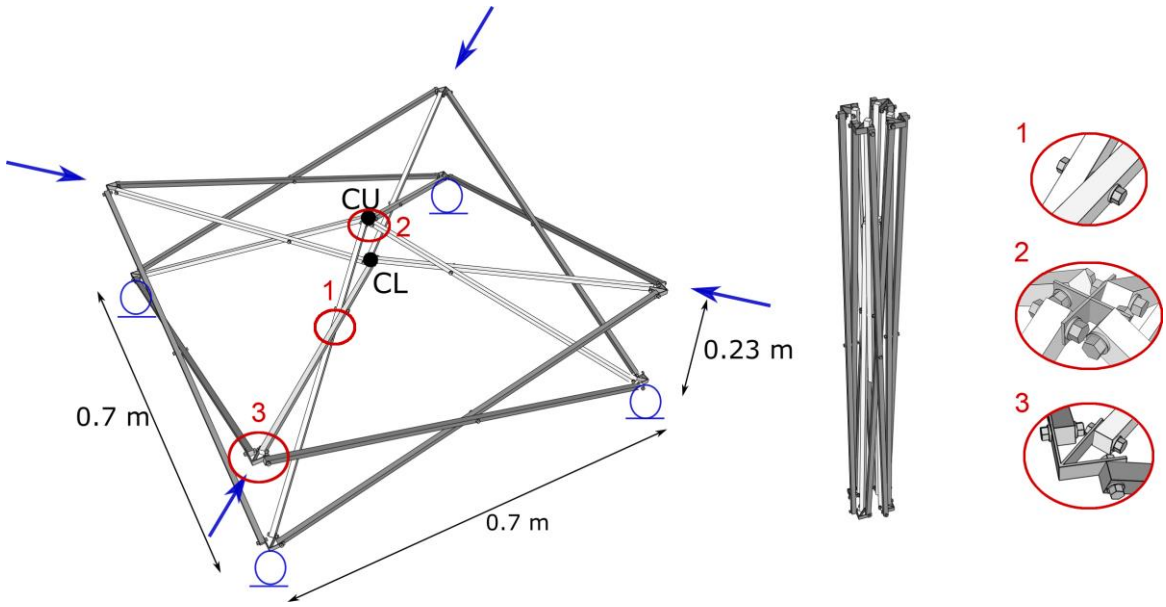


Figure 1: A square bistable scissor module in the deployed configuration with the applied loads and boundary conditions (left) and in the folded configuration (middle) and a detail of the different connections (right).

In general, the load displacement curve of bistable scissor structures is similar to Fig. 2. Point A corresponds to the initial deployed configuration. Due to geometric incompatibilities, an increasing force is required to fold the structure. The peak load is reached at point B, followed by a snap-through from B to D. The required load becomes negative (the applied load changes direction) from C to E, which implies that the structure would 'snap' dynamically to point E without a restraining force. After point D, the bent beams become straight again. Point E can be considered as the final folded configuration. To fold the structure further, an increasing load would be needed. When gravity is

considered in the considered setup, the curve shifts upwards, which might result in a curve defined in the positive force range only (dashed line in Fig. 2). This would imply that the structure would unfold by itself from the folded to the deployed state due to its self-weight, a situation that should be avoided.

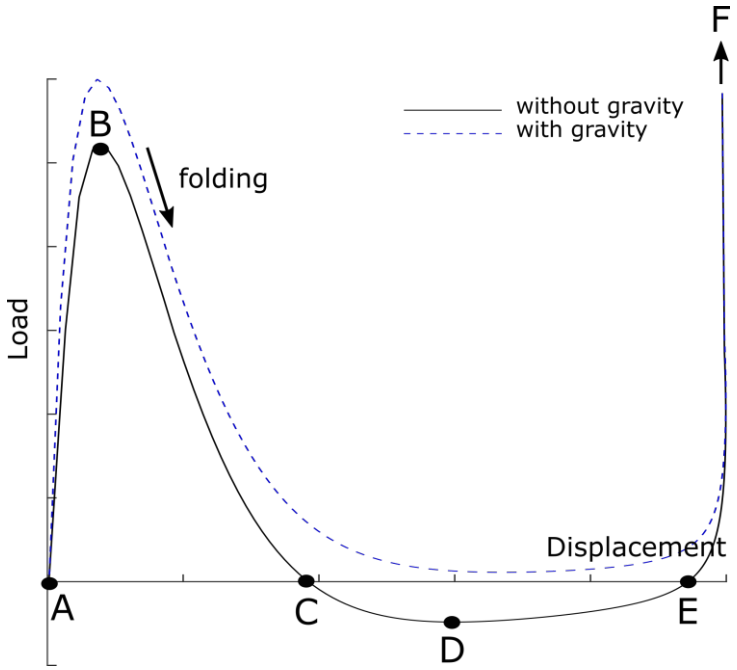


Figure 2: Schematic load-displacement curve of a bistable scissor structure with and without considering gravity.

The main design criteria to consider, define opposing trends in the non-linear problem: (1) point D must be negative to resist against spontaneous unfolding due to self-weight, (2) point B should be as low as possible to ensure an easy transformation, (3) the gradient between A and B should be as high as possible because it is related to the structural stiffness in the deployed state. It can be shown computationally that criterion (2) is opposed to (1)-(3), the former requirement striving for high stiffness, while the latter ones aim for low stiffness of the structural elements.

2.2 Objectives and constraints

The objectives of the structural optimisation are to minimize the peak load required for the transformation and the deflection of the structure in the deployed configuration. The peak load is deduced from the load-displacement curve which is obtained from the computational analysis of the transformation phase. The deflection is obtained from a linear analysis of the deployed configuration under gravity loads. It is measured as the highest vertical deflection under self-weight.

The considered constraints are:

1. The maximum stress, both during transformation and in the deployed state, has to be below the material yield limit;
2. The maximum deflection in the deployed state has to be lower than the span of the structure divided by 100, according to [5];
3. The local buckling of each element has to be avoided (formula from Eurocode 9);
4. The minimum load during transformation has to be negative.

2.3 Design variables

To obtain a lightweight structure, hollow rectangular cross sections are chosen. The height of the upper centre point of the module (point CU on Fig. 1) and the cross-sectional dimensions are variables in the

optimisation process, while the height of the lower centre point (point CL on Fig. 1) and the hub size (where the beams are connected) are dependent variables. The hub size (connections 2 and 3 in Fig. 1) changes according to the cross sections of the beams to allow their sound connection. In total, seven continuous design variables are defined (Table 1): the width, height and thickness of two groups of cross sections: the inner beams (which bend during transformation) and the outer beams (which remain straight). The seventh variable is a geometrical parameter being the height of the module in the centre (the height of the upper centre point) relative to the height between the lower and upper corners which is 23 cm. The lower centre point is constrained to be located above the lower corner points and it has to be below an upper limit chosen so that the structure can be folded using horizontal forces in the corner points. Aluminium (Young's modulus 70 GPa, Poisson's ration 0.35, density 2700 kg/m³, yield strength 200 MPa) is used for all of the beams.

Table 1: Upper and lower bounds for the design variables, considering 2 sets of cross sections.

	Lower limit	**Upper limit**
Cross-section width (x2)	0.01 m	0.05 m
Cross-section height (x2)	0.01 m	0.05 m
Cross-section thickness (x2)	0.002 m	0.005 m
h/H (height in the centre)	0.4	1.3

2.4 Mathematical formulation of the problem

To find optimal solutions that combine a low peak force during transformation with a low deflection in the deployed state, the following optimisation problem has to be solved:

$$\min_x f_i(x_p) \quad i = 1,2 \tag{1}$$
$$subject\ to: g_j(x_p) \leq 0 \quad j = 1, \dots, n$$
$$x_p \in X_p \quad p = 1, \dots, m$$

where x_p is the vector of design variables ($x_1 \dots x_7$) (Table 1), X_p the set of x_p, $f_i(x_p)$ the objective functions (peak load and maximum deflection) and $g_j(x_p)$ the (in)equality constraints. Neither $f_i(x_p)$ nor $g_j(x_p)$ are known, therefore they are sampled point-wise, running non-linear FE simulations for each set of variables. A genetic algorithm is used to solve computationally Eq. (1).

3. Optimisation methodology

3.1 Multi-objective evolutionary algorithm

Evolutionary algorithms are inspired by nature and use a series of iterations to obtain converging approximate solutions of the optimisation problem. These methods can result in several non-dominated optimal solutions (a Pareto front) from which the designer can choose the desired solution. NSGA-II is a popular method for multi-objective optimisation problems in civil engineering [5] and is the approach used in this work. An initial population N of 100 individuals is chosen randomly from which each individual is associated with a different design parameter set. An offspring population is created by applying the usual crossover (probability 0.9) and mutation (probability 0.1) operators by randomly picking parents from the parent population. The parent population P_t and its offspring population Q_t both have N members. The best N members are chosen from the combined population $R_t = P_t \cup Q_t$ which is sorted according to non-domination levels and the procedure is repeated until convergence is reached.

3.2 Geometric design

To define the geometry of the structure, the 3D modelling software Rhinoceros® and its parametric design plug-in Grasshopper® are used. As input parameters, the overall dimensions, the height of the centre points (CU and CL in Fig. 1), the spacing in between the beam midlines of each scissor (the two beams in a scissor-like element do not lie in the same plane, as can be seen in connection 1 in Fig. 1) and the hub size are used. As output, the wireframe design i.e. the beam lengths and the position of the nodes is obtained [8].

3.3 Structural analysis

Abaqus is used for the FE analysis of the non-linear transformation phase [9] as well as for the linear analysis of the deployed configuration under self-weight. 2-noded beam elements discretize the structural members and the connections are simulated with the Abaqus connector type 'hinge'. Four beam finite elements are used to model the semi-length of each beam, which was verified to be converged. The hubs are represented as a rigid grid of small beam elements.

3.4 Combination of different tools

To couple the structural analysis with the optimisation algorithm, a framework is used in which MatLab is combined with Grasshopper, Abaqus and Python (Fig. 3). First, the NSGA-II algorithm, written in MatLab, generates the initial population and sends the design variables for each individual to Grasshopper, in which the geometry is updated parametrically, and input files are written for Abaqus. Then, finite element computations are performed. The output of these FE analyses is accessed using a Python script and the constraints are calculated. The objectives and constraints are sent back to MatLab in which the optimisation algorithm evaluates the objective functions and creates a new population.

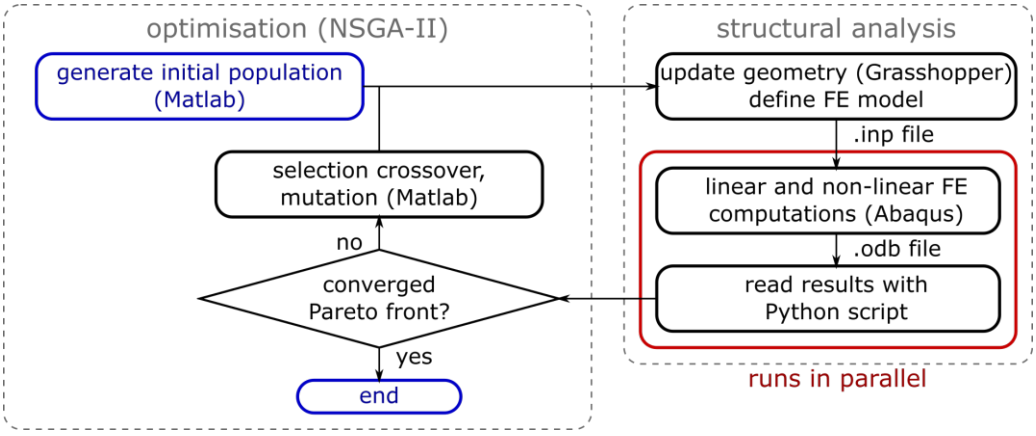


Figure 3: Flowchart of the computational approach.

4. Example of the optimisation of a single module

The evolution of the Pareto front throughout the optimisation process of a single bistable module is plotted in Fig. 4. After 5 generations, only a few structures are found that are a solution to the optimisation problem. This is due to the limiting constraints as well as the defined range for the design variables. Once a few solutions are found, the optimisation algorithm quickly finds other solutions by crossover and mutation. After 10 generations, already 20 solutions are part of the Pareto front. This number of solutions on the Pareto front increases throughout the generations until it reaches 100. In this example of the optimisation of a single module, it took 130 generations to obtain a converged Pareto front. The computational time for 130 generations, and thus for 1 linear and 1 non-linear FE simulation for 13,000 individuals, was around 16 hours using a personal laptop (2.9 GHz processor and 32 GB RAM).

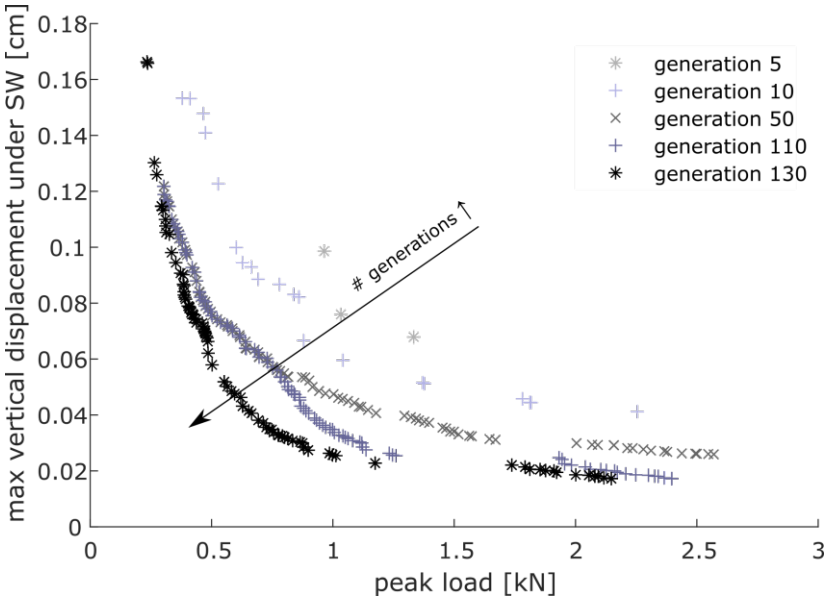


Figure 4: Evolution of the Pareto front throughout the optimisation process.

The final Pareto front is shown in Fig. 5. Three of the optimal solutions are shown i.e. the solution with the highest deflection (0.166 cm) and lowest peak load (0.234 kN), the solution with the lowest deflection (0.017 cm) and highest peak load (2.148 kN), and a solution in the middle of the Pareto front, i.e. a deflection of 0.023 cm and a peak load of 1.174 kN. By looking at these three solutions, it becomes clear how the design variables, i.e. the cross-sectional dimensions and the geometry, evolve on the Pareto front. The width of the cross section of the outer beams (the upper cross section on Fig. 5) is always as low as possible (1 cm), while the height of the outer beams is lower for low peak loads (1.59 cm) and higher for high peak loads (2.43 cm). The width and the height for the inner beams are as low as possible (around 1 cm) for all the solutions on the Pareto front and the height in the centre is for all the solutions approximately the same as the height in the corners.

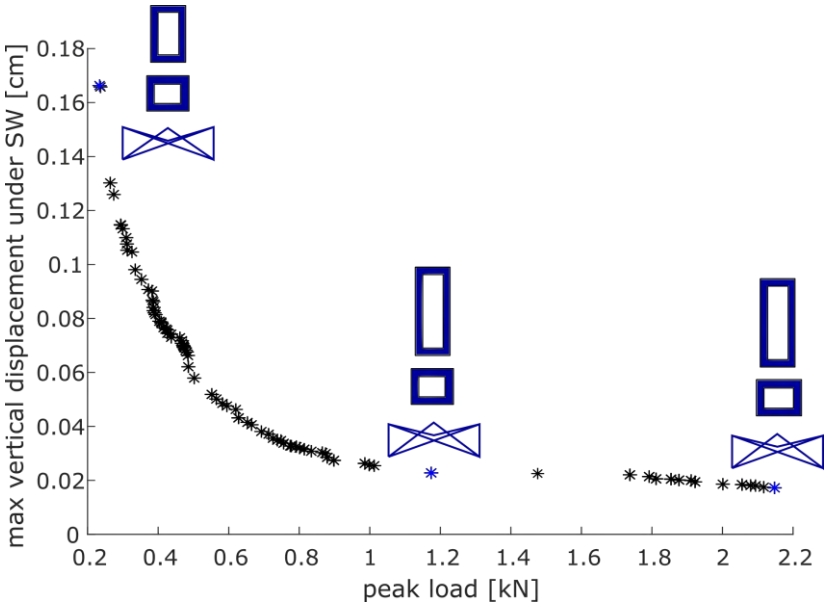


Figure 5: Pareto front and the design variables (from top to bottom: cross section of the outer beams, cross section of the inner beams and structural geometry) for three solutions.

In this example, the outer beams have the lowest width and thickness, while the inner beams have the lowest height possible (i.e. reaching their design bounds set in Table 1). A lower height for the inner beams corresponds to a decreased stiffness of the inner beams (which bend during transformation) against in-plane bending, leading to a decrease in the peak load. For the height of the upper centre point, values of around 1 are found for the parameter h/H, which corresponds to a height in the centre of the module which is approximately the same as the height in the corners of the module. The higher the upper centre point, the more pronounced the snap-through becomes, which increases the structural stiffness in the deployed state, but also leads to a higher peak load during transformation.

5. Conclusions and outlook

Bistable scissor structures should be lightweight, easy to deploy and provide enough stiffness in the deployed configuration to sustain their self-weight and potentially small external loads. To find acceptable compromises between these conflicting requirements, an optimisation methodology is proposed in which the peak force during deployment as well as the deflection in the deployed state are minimized, taking into account stress, deflection and buckling constraints. The proposed optimisation approach results in a Pareto front, i.e. several non-dominated solutions, illustrated in this contribution on the example of a single bistable module. This optimisation methodology was shown to be a feasible approach and can the basis of a rigorous design procedure, which will be developed in the future and validated on several real-life examples and shapes with real application potential such as domes and arches.

Acknowledgements

This work was supported by a Research Fellow (ASP – Aspirant) fellowship of the Fund for Scientific Research – FNRS (F.R.S.-FNRS) (Grant No. FC 23469).

References

[1] C.J. Gantes, J.J. Connor, R.D. Logcher and Y. Rosenfeld, “Structural Analysis and Design of Deployable Structures”, *Computers and Structures*, vol. 32, pp. 661-669, 1989.

[2] A. Kaveh and S. Talatahari, “A particle swarm ant colony optimization for truss structures with discrete variables”, *Journal of Constructional Steel Research*, vol. 65, pp. 1558-1568, 2009.

[3] A.P. Thrall, S. Adriaenssens, I. Paya-Zaforteza and T.P. Zoli, “Linkage-based movable bridges: Design methodology and three novel forms”, Engineering Structures, vol. 37, pp. 214-223, 2012.

[4] L. Alegria Mira, A.P. Thrall and N. De Temmerman, “The universal scissor component: Optimization of a reconfigurable component for deployable scissor structures”, *Engineering Optimization*, vol. 48, pp. 317-333, 2015.

[5] A. Koumar, T. Tysmans, R. Filomeno Coelho and N. De Temmerman, “An Automated Structural Optimisation Methodology for Scissor Structures Using a Genetic Algorithm”, *Applied Computational Intelligence and Soft Computing*, 2017.

[6] M. Salar, M.R. Ghasemi and B. Dizangian, “Practical optimization of deployable and scissor-like structures using a fast GA method”, *Frontiers of Structural and Civil Engineering*, 2018.

[7] C.J. Gantes, P.G. Georgiou and V.K. Koumousis, “Optimum design of deployable structures using genetic algorithms”, *Transactions on the Built Environment*, vol. 35, pp. 255-264, 1998.

[8] L.I.W. Arnouts, T.J. Massart, N. De Temmerman and P.Z. Berke, “Computational design of bistable deployable scissor structures: trends and challenges”, Journal of the International Association for Shell and Spatial Structures, vol. 199, 2019.

[9] L.I.W. Arnouts, T.J. Massart, N. De Temmerman and P.Z. Berke, “Computational modelling of the transformation of bistable scissor structures with geometrical imperfections”, Engineering Structures, vol. 177, pp. 409-420, 2018.

Proceedings of the IASS Annual Symposium 2019 – Structural Membranes 2019
Form and Force
7 – 10 October 2019, Barcelona, Spain
C. Lázaro, K.-U. Bletzinger, E. Oñate (eds.)

The Development of Space Flexible Deployable Structure Technology

Huang WEI*

* Beijing Institute of Space Mechanics & Electricity
No.104 of Youyi road, Beijing 100094
Huangwei1977@139.com

Abstract

In this paper, the space flexible deployable structure technology was introduced briefly. The current development status of three types of space flexible deployable structures were described including the space tether system, the space inflatable structure and the deployable membrane structure. For the space tether system, missions which had been carried out or proposed were summarized. These missions include the Gemini-11 in 1966 to the T-Rex in 2010. The author considers that the space tethers will be more widely applied in the future. For example, the electrodynamic tether has noteworthy application prospect because the problems of space debris are aggravating. For the space inflatable structure, some projects were introduced such as the IAE, the ARISE, the Transhab and so on. Specially, the first space inflatable structure executed in China, an inflatable gravity gradient bar with three meters in length was described. For the deployable membrane structure, the typical applications such as the sunshade film of JWST and the solar sail in FASTSAT satellite were introduced. In fact, with the launch of the first satellite DFH-1 of China in 1970, a deployable membrane structure which was called the observation body was successfully tested and met the requirement of being visible by human on the ground. In addition, the key technologies of space flexible deployable structure were generalized briefly. The author thinks that the most important key technologies include deployment methods, folding technique, flexible materials, simulation and testing techniques.

Keywords: flexible deployable structure, space tether system, inflatable deployment structure, membrane structure.

1. Introduction

The space flexible deployable structure is manufactured by flexible materials, can be folded to small volume at launch time, and can be deployed to work at orbit. There are mainly three types of space flexible deployable structures including the space tether system, the space inflatable structure and the deployable membrane structure. The space flexible deployable structure has been studied for more than sixty years. Back in the 1950s, the earliest space flexible deployable structure was put forward as the inflatable balloon antenna by Goodyear.Inc in American. In China, the first space flexible deployable structure is a deployable observable device which was developed by Beijing institute of space mechanics & electricity and was launched with the Dongfanghong-1 satellite on April 24, 1970.

Because of its low weight and foldability, the space flexible deployable structure has got many attentions from space agencies for decades. But it has not become a mainstream spacecraft structure type because of the gross technical difficulties and lacking of urgent needs. But the situation is changing. With the developments of space technology, more large size spacecraft are in demands. The contradiction between larger dimension and limited space and launch weight has become increasingly

Copyright © 2019 by Huang WEI
Published by the International Association for Shell and Spatial Structures (IASS) with permission.

obvious. In this case, the space flexible deployable structure definitely will become one of main technological means of future spacecraft.

2. State-of-the art

2.1 Space tether system

The earliest space tether system concept was proposed by famous Konstantin Tsiolkovsky in1895. Tsiolkovsky imagined that the transportation link between the earth and the space can be built through tether system and the man-made gravity can be generated through resolving a tether linked with the space station, etc. In the past decades, some countries have carried out a lot of study and implemented dozens of space tether system on-orbit tests, as table 1 shows[1].

Table 1: The summary of on-orbit space tethers

No.	Mission and Country	Orbit	Launch Year	Tether lenth(m)	Unfolded length(m)
1	GEMINI-11 (USA)	LEO	1966	36	36
2	GEMINI-12 (USA)	LEO	1966	36	36
3	TPE-1 (USA/Japan)	Suborbital	1980	400	38
4	TPE-2 (USA/Japan)	Suborbital	1981	400	103
5	CHARGE-1(TPE-3) (USA/Japan)	Suborbital	1983	418	418
6	CHARGE-2(TPE- (USA/Japan)	Suborbital	1984	426	426
7	OEDIPUS-A (USA/Canada)	Suborbital	1989	958	958
8	CHARGE-2B (USA/Japan)	Suborbital	1992	426	426
9	TSS-1 (USA/Italian)	LEO	1992	20000	268
10	SEDS-1 (USA)	LEO	1993	20000	20000
11	PMG (USA)	LEO	1993	500	500
12	SEDS-2 (USA)	LEO	1994	20000	20000
13	OEDIPUS-C (USA/Canada)	Suborbital	1995	1174	1174
14	TSS-1R (USA)	LEO	1996	19700	19700
15	TiPS (USA)	LEO	1996	4000	4000
16	YES (Russian/Europe)	LEO	1997	35000	-
17	ATEx (USA)	LEO	1998	6050	22
18	PICOSAT1.0 (USA)	LEO	2000	30	30
19	PICOSAT1.1 (USA)	LEO	2000	30	30
20	ProSEDS (USA)	LEO	2003（mission was canceled）	15000	-

No.	Mission and Country	Orbit	Launch Year	Tether lenth(m)	Unfolded length(m)
21	YES2 (Russian/Europe)	LEO	2007	31700	29000
22	T-REX (USA/Japan)	Suborbital	2010	300	300

In General, the space tether system has a good prospect of development and application. But the real engineering application hasn't been mature except some simple application such as mooring the astronauts conducting space walk from the capsule. One reason is the difficulty of space tether induced by its high flexibility, its nonlinear dynamic problems. In addition, the application needs are not urgent because the current space applications are still based on ordinary satellites.

With the space environment is becoming increasingly prominent, the space debris has become a serious problem. The space tether especially the electrodynamic tether is facing good opportunity of dealing the space debris problem. An insulated conducting tether, terminated at the ends by plasma contactors, can be used as an electromagnetic decelerator. A decelerating force is generated on the spacecraft/tether system when current is fed into the tether against the emf induced in it by the geomagnetic field. A deorbiting device called Terminator Tether which aimed to avoid the small satellite to become space debris after operating life was developed by NASA. The research analysis conclusion indicated that Terminator Tether which occupy 2% weight of satellite can make satellite operating at 400km with 50 ° orbit inclination deorbit within two weeks, make satellite operating at 850km with 50 ° orbit inclination deorbit within three months, make satellite operating at 1400km with 50 ° orbit inclination deorbit within one year[2]~[3].

2.2 Space inflatable structure

Space inflatable structure can be folded into small volume and can be inflated to the work state after lunched to the operating obit. Through rigidization method, the inflatable structure need no gas compensation and can work long time.

Because of its low weight, low cost, high packing efficiency and high deployment reliability, various space inflatable structures have been researched and developed for decades such as the Goodyear antennas in the early 1960s, the Echo Balloon series from the late 1950s to the early 1960s, the Contraves antennas and sunshades in the late 1970s to the middle 1980s, the latest Biglow inflatable space station modules, and so on. In summary, the space inflatable structures are considered for many applications including inflatable antennas, inflatable capsules, inflatable sun arrays, etc[4~5].

The inflatable antenna experiment (IAE) launched in 1996 by space shuttle was an important demonstration of space inflatable structure technology. The inflatable structure comprised two parts: the 14m diameter inflatable reflector assembly and the torus/strut supporting structure. The experiment was successfully flown and demonstrated the robustness and surface precision of this new, unique, and low cost inflatable structure[6].



Figure 1: The inflation deployment process of IAE

After IAE program, the inflatable antenna named ARISE was developed and a prototype with diameter 25m was manufactured. Some ground tests was conducted in American. In Europe, ESA also developed some inflatable antennas and manufactured and tested series of prototype models with diameter from 3.5 meters to 12 meters[7].

Besides inflatable antenna, the inflatable space capsule has been focused from 1990s because it has broad application expectations in space stations, lunar bases, Mars bases, etc. A typical program is the Transhab habitation module developed by NASA. The Transhab module's inflated dimension was 9.1m in length and 7.6m in diameter. The whole structure was mainly made by Kevlar material. A new-style inflatable lunar base module was proposed by ILC Dover. Inc. The module was 3.65m in diameter and was supported by eight landing legs. Multiple modules can be connected each other by smaller airlock to form a larger lunar base. Actually, the real application of inflatable space capsule in orbit was Bigelow's space station module.

In China, the first verified space inflatable structure program in orbit was an inflatable gravity gradient boom (IGGB) developed by Beijing Institute of Space Mechanics & Electricity and Harbin Institute of Technology. IGGB was one part of the Chinese satellite XY-1 launched on May 28, 2013. The gravity gradient boom was used in attitude and orbit control system of the small satellite. A boom with stretched length of 3m acted as both the gravity gradient boom of the satellite and a space experiment of IGGB to testify the space inflatable structure functions. The results of IGGB space experiment indicated that its functions and performance can meet the requirements of XY-1[8].

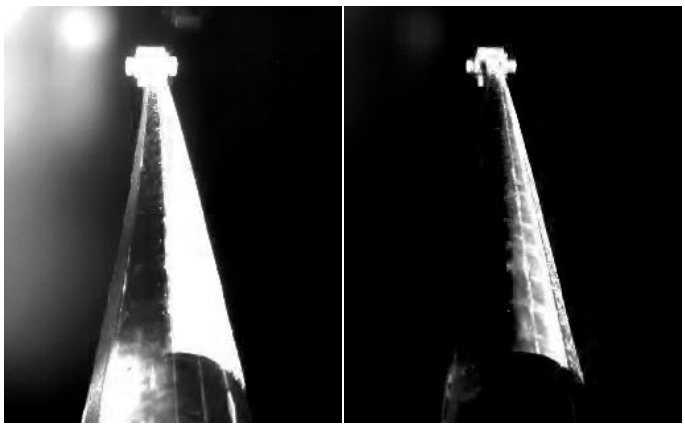


Figure 2: Pictures of IGGB in orbit taken by onboard small camera

2.3 Space deployable membrane structure

The space deployable membrane structure generally has a large area of membrane supported by expandable booms or torus. The expandable function may implemented by inflatable structures, collapsible and deployable rigid structures, or elastic rods. The typical applications of space deployable membrane structure are sunshades and solar sails, etc[9].

JamesWebb space telescope (JWST) has a sunshield membrane assembly which is about 20m long and 15m wide made of five layers polyimide material. The sunshield membrane can protect the telescope from sunshine and make sure the telescope works in appropriate temperature. The sunshield membrane is illustrated below.



Figure 3: Picture of JWST's sunshield membrane assembly

The solar sail called NanaSail-D on NASA's FASTSAT satellite unfolded successfully in an orbit about 650 km above the earth in November, 2011. The solar sail membrane coated with aluminum film is about 10 square meters in area and just 2 micron in thickness. NanaSail-D worked 240 days in orbit and was the first successful solar sail program.

In fact, when China launched the first man-made satellite DFH-1 on April 24 of 1970, a deployable membrane structure which was called the observation body was mounted on the third stage of CZ-1 launch vehicle. The observation body was unfolded through spinning the stage and formed a sphere with 4 meters diameter by the centrifugal force. It achieved a brightness of second to third magnitude star and was visible by people on the ground. The observation body was mainly composed by membrane, bag, pulley block and stretchable mechanism. The membrane was made of polyimide material coated with aluminum[10].

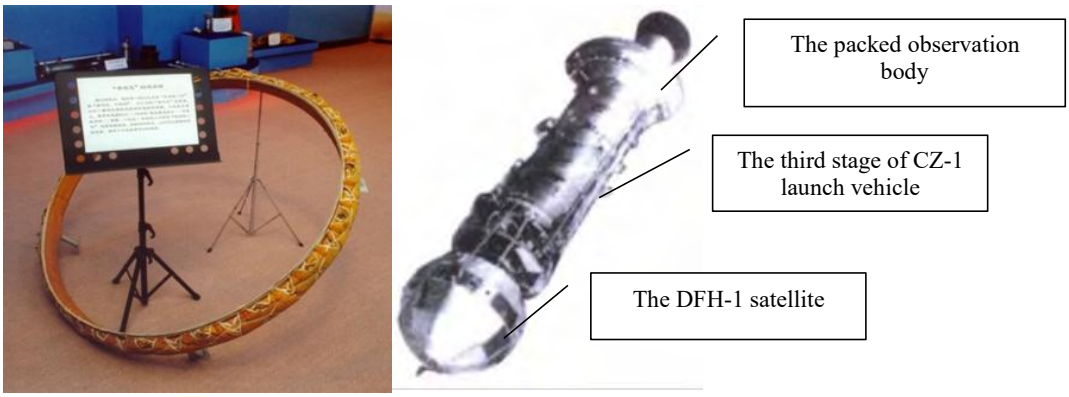


Figure 4: The assembly of DFH-1, CZ-1 third stage and the observation body

3. The key technologies

3.1 Deployment technology

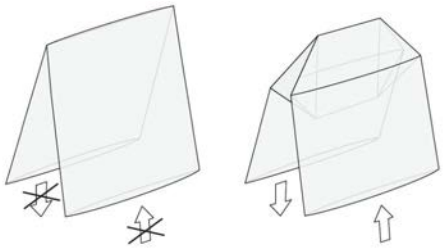
For space flexible deployable structures, high fidelity of deployment is essential. Deployment method becomes more complex with the bigger structure dimension. There are various deployment methods including ejection deployment, inflation deployment, elastic mechanism deployment, spin deployment, and so on. Each method has its own strength and weakness. So it is very important to choose a proper deployment method according to the needs of the space mission.

3.2 Folding technology

(1) Folding technology for thin walled booms

For inflatable or flexible thin walled booms, some folding techniques were developed including coiling and wrapping method, z-folding method, Origami folding method, and conical folding method, etc. The advantage of coiling and wrapping method include that it is simple and easy to execute and the folding efficiency is high. This method is to first flatten the uninflated boom, before rolling it into a coil or wrapping it around a hub like the usual tapeline.

The z-folding method is one of most frequently used for inflatable cylindrical booms. It has a very simple folding pattern. This method is to flatten the uninflated boom at first, then simply fold the boom back and forth at regularly spaced intervals at discrete lines or hinges. Like the coiling and wrapping method, the z-folding method also has a disadvantage that the airflow is restricted and the trapped residual gas is hardly expelled from the booms. The modification to z-folding method was proposed by some researchers. The method is to replace the single fold line with a number of additional folds that provide a small opening between the folded sections of the boom; see Fig.8. Experiments showed the modification has favorable effects on the smoother inflation pressure and flow rate with more uniform deployment process.



（Left）standard z-folding （Right）modified z-folding

Figure 5: The sketch of standard z-folding and modified z-folding method

In recent years, a number of origami folding methods have become a research hotspot in space flexible deployable structure field. Based on different patterns, the origami folding methods mainly include Yoshimura method, Bellows method, Miura method, Helically triangulated method, Waterboom method, Kresling method and so on. Unlike the z-folding method to fold the whole boom with the same crease, origami folding method need not flatten the boom at first and will induce different crease for the different surfaces. So origami folding method has advantage on preventing the exits of residual gas and more efficient inflation effect.

The conical folding method is to introduce a slight taper, a conical boom is formed, which can be inverted and everted at regular interval, to form a compact telescopic stowage configuration. A mandrel can be placed at the narrow end of the conical boom to improve the straightness of deployment. The disadvantage is that the boom elongation is resisted by friction. So the boom outside surface must be smooth enough[11].

(2) Folding technology for membrane structure

The key of membrane structure folding technology is the design of the fold pattern. For a flat membrane, the mainly used fold patterns include spin deployment fold pattern, leaf-in fold pattern, leaf-out fold pattern, Miura-ori fold pattern, and so on. The spin deployment fold pattern method is to drive the membrane to full shape through revolving as the name suggests. For the other methods, the driving force mostly can be acted on the four corners of the membrane, so the whole structure is deployed along the diagonal directions.

For a cylindrical surface membrane, the folding methods for thin walled booms can be adapted. For a parabolic membrane, through changing the design of fold pattern angle based on the flat plane

membrane fold method, the package and deployment can be achieved. For example, showed by fig.9, a parabolic membrane structure which was folded through specific fold pattern can be inflated into the acquired shape. But, for such parabolic membrane structure, some circumjacent constraints must be designed carefully in prevent of the structure being inflated to become sphere instead of parabolic shape in need[12].

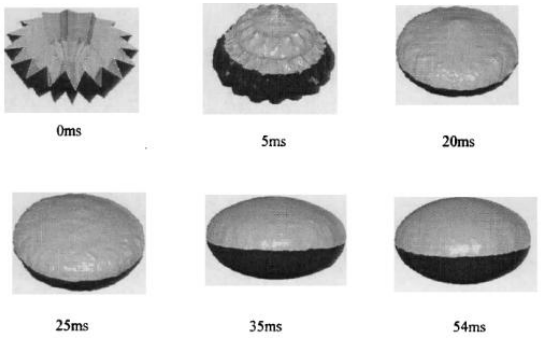


Figure9: The sketch of deployment of a parabolic membrane

3.3 The space flexible deployable structure materials

As for the space flexible deployable structure, the frequently-used membrane materials include polyimide film, polyvinyl fluoride film, metallic film, etc. The frequently-used fiber materials include PBO, Kevlar, Vectran, aluminium oxide fiber, polyimide fiber, etc. We need to choose the proper material according to the space structure ' s operating orbit, working features and technical requirements.

Commonly speaking, for the inflatable structure, the skin is constructed by multilayer flexible composite material including mainly the airtight liner, the enhancement layer, shielding layer, thermal protecting layer, etc. The function and typical materials of these layers are listed in the following table. Different components of multilayer flexible composite material will be chosen for the specific mission.

Table 2: The common space inflatable structure multilayer flexible composite material

Function Layer	**Function**	**Material**
Airtight liner	Preventing the gas leakage	Polyurethane(PU),Polythene(HD),Ethylene -vinyl alcohol copolymer(EVOH), polyimide(PI), aluminum foil…
Enhancement layer	Bearing the pressure load	Kevlar，Vectran, PBO, PE…
Shielding layer	Shielding space debris impact and space radiation	Polyester, Polythene, Kevlar…
thermal protecting layer	Heat proofing and thermal insulation	aluminium oxide fiber, aerogel, asbestos fiber…

Many space inflatable structures need to be rigidized to maintain its shape and assure its function for its whole life. So the material rigidization technology is important. The rigidization methods in development include thermal heating, ultraviolet radiation, inflated gas reaction, hydro-gel rigidization, aluminum laminate, foam injection, shape memory materials, and so on.

3.4 Simulation and testing technology

The deployment of space flexible structure is a complex dynamic process. It comes down the nonlinear dynamic problem of the large deformation of highly flexible structure. Furthermore, for the space inflatable structure, the fluid-structure couple problem in the large displacement situation is involved. At present, the mostly used dynamic simulation model for the space tether system is

multiple mass point connection calculation model. The tether system is simplified to series of mass points, and the connection between points is set by spring-damping system. The key problem of this model is dividing the continuous rope into the proper number of discrete mass points.

For the inflatable structure, many researchers have studied the simulation theory and technology and different methods have been developed such as multi rigid body dynamics method, finite element method based on control volume, arbitrary Lagrangian-Euler fluid-solid coupling method.

For the accurate numerical simulation is very difficult, the experiment is necessary and need more attention. The key of experiment for space flexible deployment structure is the simulation of microgravity environment. The developed microgravity simulation experiment methods include free-falling weightlessness method, buoyancy balance method, air bearing platform simulator method, over hanging test, etc.

4. Conclusions

Flexible deployable structure is an important development direction of realization of light spacecraft and has a huge potential for applications in spacecraft because of the low weight, low storage volume, diversity, and reliability of deployment. The applications of flexible deployable structure include space tether system, space habitats, inflatable antennas and reflectors, inflatable support structures, huge membrane solar concentrators, solar sails, and so on. In order to develop the space flexible structure, some key technologies must be mastered such as the folding and deployment technology, the flexible materials suitable for the space environment, the numerical simulation and microgravity experiment technology.

Acknowledgements

This article got the help of Cao xu and Cai jianguo.

References

[1] Cao Xibing, Zhang Jinxiu, *Dynamics of tethered satellite systems*. Beijing: National Defence Industry Press, 2015. (in Chinese)

[2] Wang changing, Zhen guanghua, *Introduction to space tether system motion dynamics and control*. Beijing: Science Press, 2013. (in Chinese).

[3] Kong Xianren, Xu Dafu, "The research overview of space tether system", *Spacecraft Environment Engineering,* 2010.27（6）：775-783.

[4] C.Sickinger, E. Breitbach, "Ultra-lightweight deployable space structures" in *4th International Conference on Thin-Walled Structures. Loughborough， England. 2004,*6.

[5] Clem A L， Smith S W， Main J A, "A pressurized deployment model for inflatable space structures". *AIAA-2000-1808*, 2000.

[6] Anthony P. Ewing, Jason M. Back, Branwen M. Schuettpelz,etc. "JamesWeb Space Telescope Sunshield Membrane Assembly". *AIAA-2009-2156*, 2009.

[7] Hiroshi Furuya，Yasutaka Satou, "Deployment and Retraction Mechanisms for Spinning Solar Sail Membrane" in *49th AIAA/ASME/ASCE/AHS/ASC Structures， Structural Dynamics， and Materials Conference, Schaumburg.2008,4.*

[8] Cao Xu, Wang Weizhi, Zhang Hongwei, etc. "Development and Space Experiment of a New Inflatable Gravity Gradient Boom". *Spacecraft Recovery & Remote Sensing,* 2014(35):20-27.

[9] Christopher H.M. Jenkins, *Gossamer Spacecraft: Membrane and Inflatable Structures Technology for Space Application* . AIAA, Inc, 2001.

[10] Lin Xinyou, "A new star appeared in space". *Space Industry Management,* 2005(5):13-14.

[11] Mark Schenk, Andrew D.Viquerat, Keith A.Seffen,etc. "Review of Inflatable Booms for Deployable Space Structures: Packing and Rigidization". *Journal of Spacecraft and Rockets,* 2014(51):762-778.

[12] Miura, K. "Method of packaging and deployable of large membrane in space" in *31st IAF Congress，Tokyo，Japan.1980,9.*

Proceedings of the IASS Annual Symposium 2019 – Structural Membranes 2019
Form and Force
7 – 10 October 2019, Barcelona, Spain
C. Lázaro, K.-U. Bletzinger, E. Oñate (eds.)

A Prefabricated UHPC Shell Pedestrian Bridge

Ahmet TOPBAS*, F. Omur TULEN, Muhammed MARASLI [a], Beni KOHEN

*ATTEC
Muhurdar Karakolu Sok. 28/2 Moda 34710 Istanbul Turkey
topbas@ateknik.design

[a] Fibrobeton
Erturk Sok. Uzka İş Merkezi N:11 Kavacık 34810 Istanbul Turkey
Muhammed@fibrobeton.com.tr

Abstract

This article is about research and development for a UHPC shell bridge. The bridge is developed to be site-assembled from prefabricated shell and deck parts. Thereby, a "Dry," field-connected, concrete shell assembly is being achieved. The parametrization of the form and the structural design, materials engineering, prototype production, testing, and method development will be presented and discussed in the paper. The study is made to develop a fast, economic, elegant, and sustainable bridge solution. It is mostly developed for the need in remote areas and countryside anywhere around the world, where valley and road crossings can be achieved with minimum preparation prior to bridge assembly and, where it is hard to bring local resources at the location.

1. Introduction

Prefabrication and site-assembled elements are the commonly used methods in the GFRC and UHPC industries. These materials produce elements which are always more slender, lighter-weight, and stronger compared to traditionally precast concrete elements. It is customary to use these materials in architectural cladding of walls and ceilings, since they can be strong and slender at the same time, but also they are more complicated to produce, therefore more expensive per the cubic meter to be used in a massive manner such as in structural systems. We are exploring methods and designs to use these materials for structural applications, but in manners which are very suitable to the nature of these materials and the construction techniques commonly used specific to them. We can both improve structural efficiency and elegance, along with the techniques and applicability areas of these materials following this path.

2. Inspirations

Our first inspiration came from design and academia. Geometric, structural and materials exploration by colleagues who either [2] used GFRC concrete shell bridges either as their prototypes, or made a summary of shell bridge experience around the world and a new steel specimen bridge [1] based on similar thoughts. Secondly, we were encouraged by our own design and fabrication experiences for innovative and large GFRC and UHPC cladding and canopy elements. Figure 1 shows long canopy precast UHPC elements that we bolt-assembled on site in Africa, which have been fabricated in the Fibrobeton shop in Duzce, near Izmit, Turkey.

Copyright © 2019 by Ahmet TOPBAS, F. Omur TULEN, Muhammed MARASLI, Beni KOHEN
Published by the International Association for Shell and Spatial Structures (IASS) with permission.



Figure 1: UHPC Canopy module bolted to a concrete shear wall on site.

Other accumulated GFRC experiences also include daring structural applications such as shown in Figure 2 for the Arter Contemporary Art Museum in Istanbul facade cladding, where zig-zagging 8cm thick elements were standing upright as 6m cantilevers or spanning 10m by 10m spans with only the assistance of 5cm steel zig-zag tubular back-up posts. Innovative approaches in design, fabrication and detailing allowed these experiences, and now we can take this experience to one step further by utilizing these so-called 'cladding' materials in a very efficient, but purely structural manner.

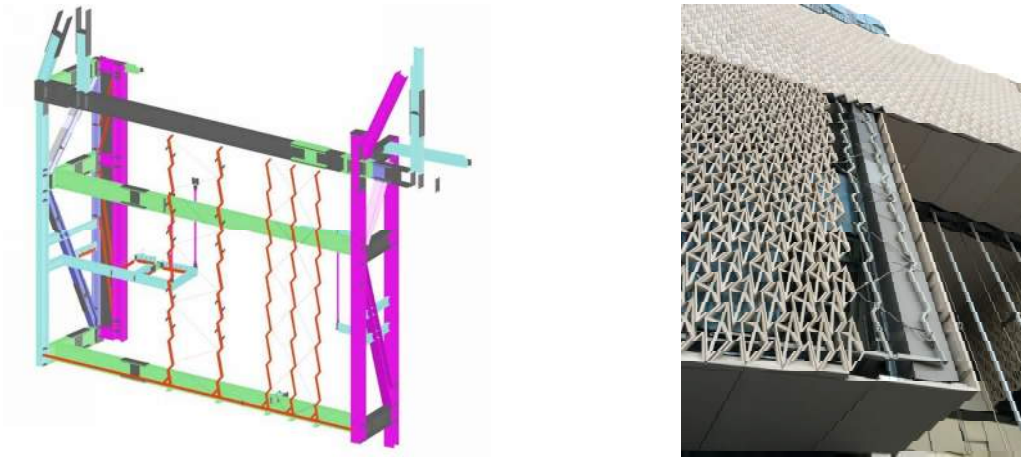
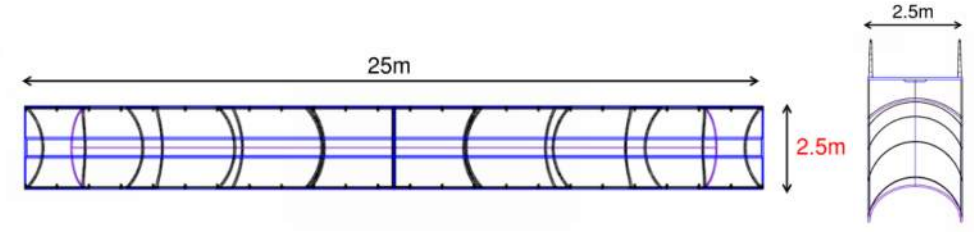


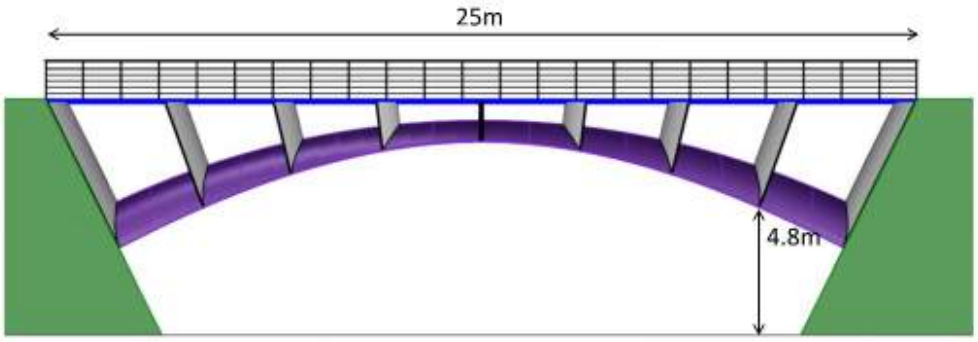
Figure 2: Zig-zag slender steel columns compositely working to support GFRC slender façade panels

3. The Concept

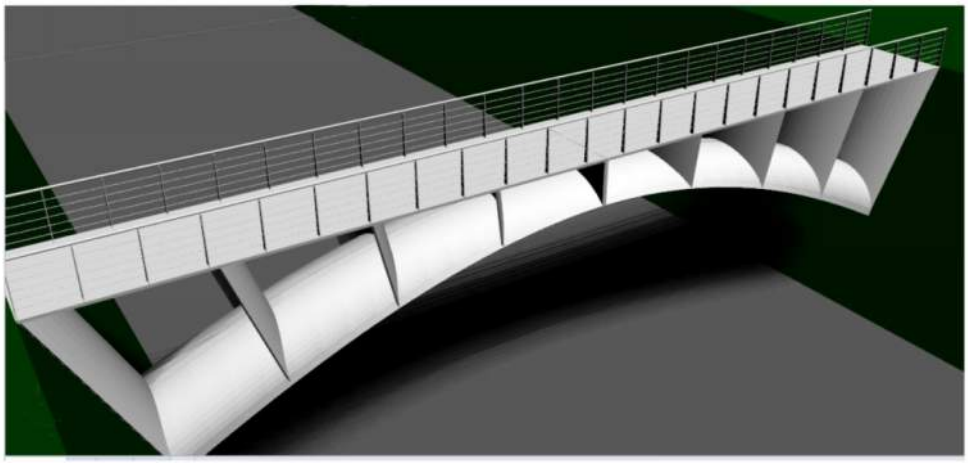
Figure 3 shows the plan, section, and 3D views of the bridge concept. The bolted field connections were studied schematic planning of assembly



a) b)



c)



d)

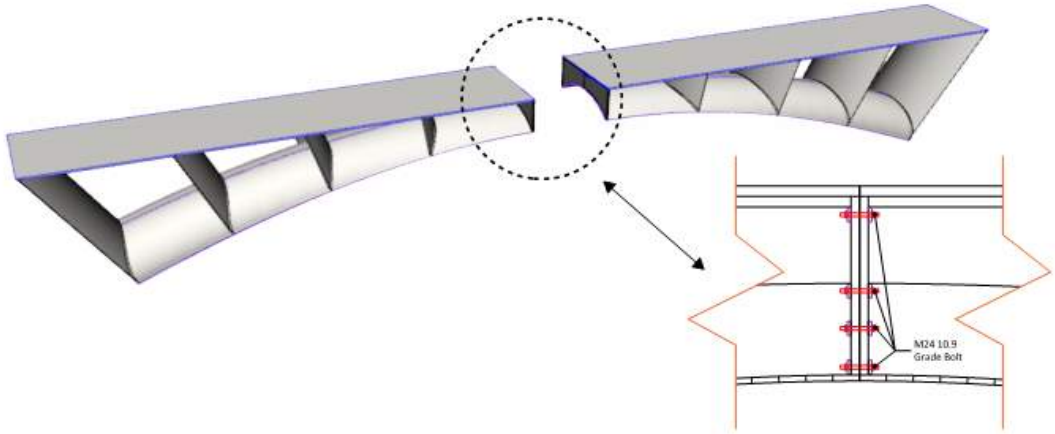


Figure 3a, 3b, 3c, 3d,3e: Plans, section, 3D Views and connection detail of Precast-Site Assembled Bridge

4. Form Finding

When writing this article, we have assumed basic curvatures from experience and similar constructions to achieve slenderness and very possible curvatures. The total weight of the materials and their cost was a constraint we needed to achieve. 20tons of concrete weight was targeted for cost, and we achieved it with our geometry and structural scheme. We are building mockups based on this form, so we can also simultaneously study prefabrication and erection scenarios simultaneously along with the form finding. This way a multi-task operation is possible in a faster and more efficient way. So, a further form finding study is underway for seeing whether it is possible to optimize the transverse curve heights Hc_1 (see figure 4) of the bottom arch, and the curve heights of the vertical Hc_2 wall panels. The Ha_1 arch height is also being studied based on multiple location applications where the valley can be less deep or the road height requirements differ in different geographies. But most importantly the arch height optimization will also bring further strength and slenderness to the total system.

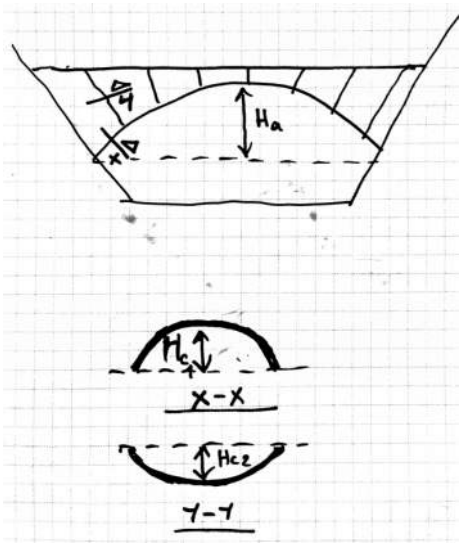


Figure 4: Sketch drawing of bridge showing the form finding parameters of study

4. The Analysis

We have investigated this slender construction including the non-linear buckling affects and the p-delta secondary affects in a FEM. As a very slender structure spanning 25m with only 5cm thickness, the buckling was obviously very critical. The curvature of the bottom arch brought us a huge advantage against the in plane and transverse buckling modes. In figure 5, we can observe the various buckling modal shapes that we investigated, and seemed in the most critical locations.

According to general foot bridge loading, 5kN/m^2 Live load, 1.5 kN/m^2 additional dead load and 1 kN/m^2 additional load for reflecting other effects (snow, sand etc.) are loaded to the bridge and nonlinear buckling analysis are performed according to these loads. ±20 temperature loads are effected as well.

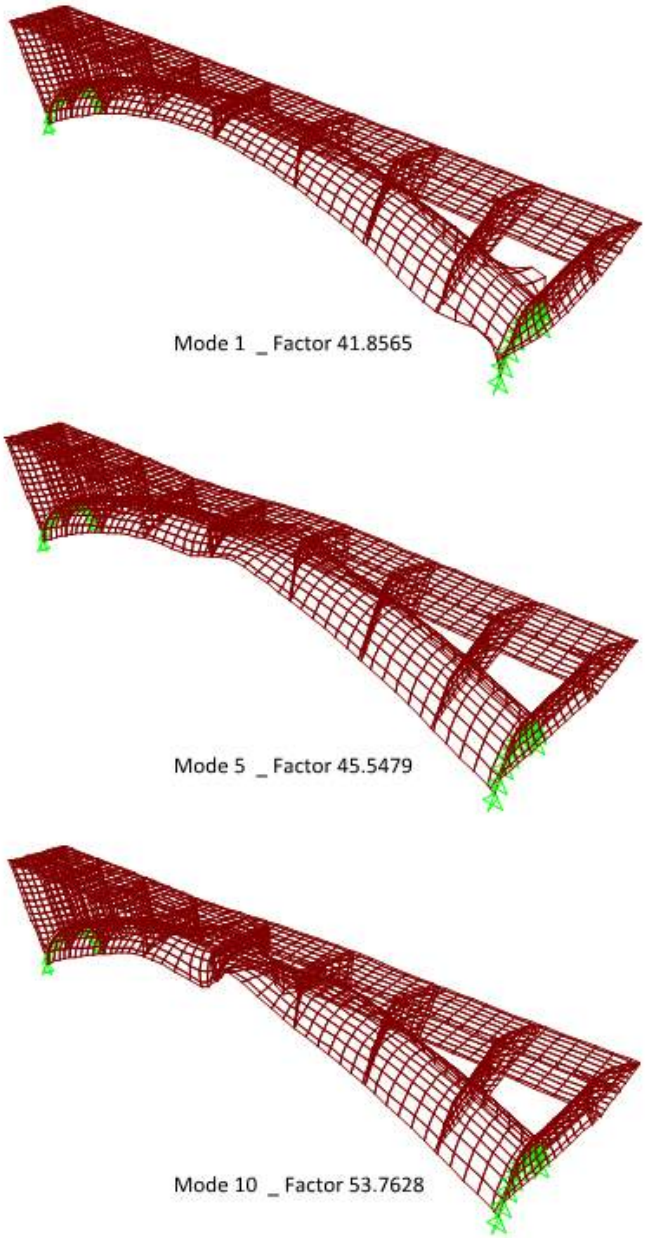


Figure 5: Buckling Factors of Shell Bridge

Also in figure 6 graph plotted for showing relationship between buckling factor and UHPC plate thickness, it can be observed that the curved nature of the plates brings around three times more strength for the same thickness.

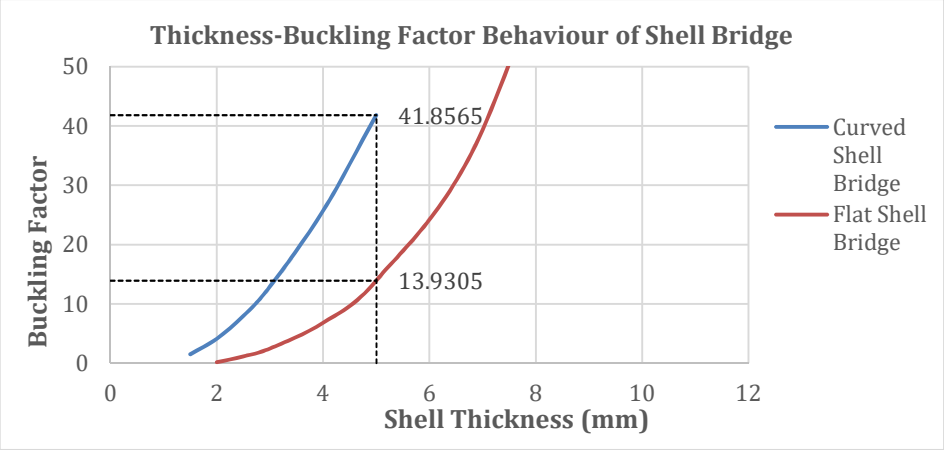


Figure 6: Shell thickness-buckling factor graph

Regarding to FEM analysis, it is seen that displacement of bridge stays under L/1000 limitation (see figure 7). Fundamental frequency is 5.64 Hz and bigger than 5 Hz (AASTHO-Guide for design of pedestrian bridges). So Vibration problems under walking excitation are not expected.

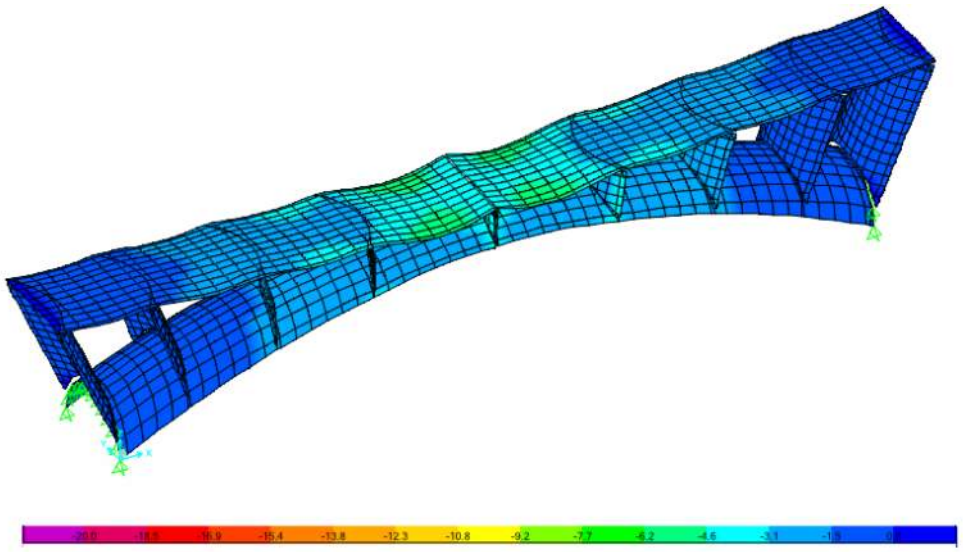


Figure 7: Displacement result of bridge(D+LL)

5. The Scaled Model

We have worked on two physical models to study form, prefabrication, material testing, and strength testing. The middle field bolted connection was particularly of interest to both the design and the fabrication teams. With this joint, it is possible to bring the bridge on site with only two pieces and the assembly can be made even above flowing traffic, or with just very minimal disruption. The Figure 8 shows the 1/50 scale digitally printed model. This model was studied for general form and geometry above the road and the valley. There is a second 1/5 scale model being planned at the time of writing this article. This will be made with the UHPC material which to be used in the full scale, but in 1.5 to 2cm thickness. We will load test this model along with studying the middle bolted connection while actually working with concrete.



Figure 8: The prefab construction sequencing study with the 1/50 scale model

6. The Test

Before the testing of the 1/5 physical model in the factory for vertical loads, suitable UHPC mix samples are studied and 70mm x140mm samples are prepared for testing (see Figure 9). Figure 10 shows stress-strain graph of the cylinder sample under testing and the compression test results with around 140 Mpa

average strength. The fibers that will be used in the mix could be poly-fibers or stainless steel. We are at the moment testing both options to see which material would be best fit for the particular project.



Figure 9: Test Samples

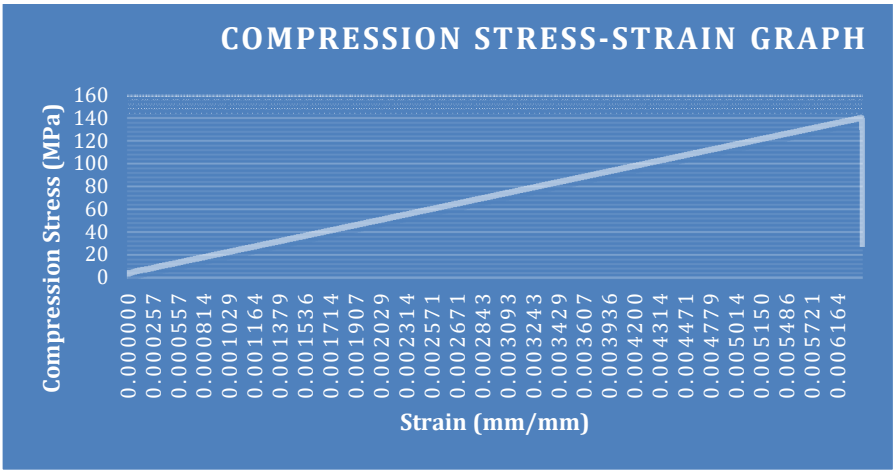


Figure 10: Compression stress-strain graph of sample

7. The Next Steps

A protype UHPC prefabricated bridge was modeled as a sustainable and elegant solution for a particular problem that is valid for all parts of the world. The design and testing will be investigated further by solid FEM modeling of site bolted connection between two bridge parts before test phase. A 1/5 scaled model will be load tested in the Fibrobeton factory and results are compared with FEM analysis. Furthermore a full scale prototype is also being planned to be built based on the outcome of small scale and design explorations. Form finding with a more precise parametrization is also underway and this might change some of the geometric constants of the bridge shape. The full scale model is planned to be built after the form finding precision study.

References

[1] Mike Schlaich, "Shell Bridges – A New Specimen Made of Stainless Steel," *Journal of IASS*, Vol. 59, pp. 215-224, 2019.

[2] Juan P. Osman-Letelier, Arndt Goldack, Mike Schlaich, Daniel Lordick, Jakob Grave "Shape Optimization of Concrete Shells with Ruled Surface Geometry Using Line Geometry," in *Interfaces: Architecture, Engineering, Science, Proceedings of the IASS Annual Symposium 2017*, Hamburg, Germany, September 25-28, 2017

Proceedings of the IASS Annual Symposium 2019 – Structural Membranes 2019
Form and Force
7 – 10 October 2019, Barcelona, Spain
C. Lázaro, K.-U. Bletzinger, E. Oñate (eds.)

Design of a free-form single-layer lattice shell connecting ten building

Jian ZHOU*, Yanpeng LI,YaoKang ZHANG, Hongjun WANG, XiaoTian YANG, Jiahun CHUI

*East China Architectural Design & Research Institute Co., Ltd.,
151Hankou Road, Shanghai, China
Jian_zhou@ecadi.com

Abstract

This paper is to introduce the structure design of a single-layer aluminum latticed shell supported by ten high-rise buildings, including structural conception, form-finding, mesh generation, wind load and temperature load determination, and global analysis of the structure. A method based on the minimum strain energy theory is adopted in form-finding using Grasshopper parametric analysis program, Mesh generation is based on the principle of force flow direction under gravity and is determined among several possible regular layout modes. There is a technical difficulty on wind tunnel test, owing to the undersized member section at uncladding area, wind load was determined through numerical simulation combined with wind tunnel test on partial models. The huge temperature effect on the 600-meter continuous length structure was declined by controlling structural closure temperature, choosing appropriate layout of member density and inclination angle of inclined column.

Keywords: single-layer latticed shell, form-finding; free-form, wind load on uncladded structure, grid optimization

1. Project summary

This paper is to introduce a single-layered aluminum latticed shell that was overall supported by an architectural complex which was consisted of ten buildings. The shell was approximately 600 meter long and 150 meter wide. Those buildings" were 80-meter-high reinforced concrete tower with frame-shear wall system, and the space interval between buildings ranged from 50 to 100 meters. Around 20% to 30% of the shell was covered by solar panels that would supply electric energy to the complex, whereas rest structure grid remained uncladded. Certain member surface was decorated by LED light bar, enabling varied light effect to roof. The project is located at Xingqiao Town, Songjiang District, sitting next to the G60 expressway. It would be the symbolic image of south gateway to Shanghai central area. Its perspective rendering was shown in Figure 1.



Figure 1: Perspective rendering



Figure 2: the design sketch of „cloud top" image

Copyright © 2019 by Jian Zhou, Yanpeng Li
Published by the International Association for Shell and Spatial Structures (IASS) with permission.

2. Structural concept

Architects‟ design concept was „cloud top‟, hoping to achieve the effect being similar to the clouds floating on roof, as shown in Figure 2. As a result, the structure appearance should be in the rolling pattern of clouds that was achieved by single-layer grid structural form in the shape of crest and trough wave. Member height was restricted within 550 millimeters to highlight the lightness and transparency of the structure. In order to reduce structure span as well as the effect from roof to lower construction, the single-layered lattice structure was pin connected with lower tower structure by outward tilted Y-shaped column.

The largest span of this structure was 100 meters and the greatest member height was 550 millimeters, resulting in the span to height ratio reaching 180. This would be impossible to achieve in reality if relying simply on the bending resistance of material itself; instead, the optimization of structure configuration was required on an axial-force-dominant structure that could fully utilize the strength of total section. There were two structure concept options. One was to set roof top as trough. Structure span could be achieved by arching effect and members would be mostly in compression. The other was to set roof top as crest. Structure span could be achieved by catenary action and members would be mainly in tension. The height of this project was restricted in 100 meters, with the evaluation of lower structure in 80 meters and that of mechanical penthouse top in 85 meters, as presented in Figure 3; nevertheless, the lowest roof height for option one needed to be higher than the evaluation of 85 meters, leading to the maximum available rise being 15 meters and a comparatively small angle between Y-shaped column and lattice structure. Comparatively, for option two, the lowest roof height could be controlled by big roof evaluation (80 meters), which meant that the rise could be 20 meters, resulting in an appropriate angle between Y-shaped column and lattice structure. As the outward tilted column could further decrease the span of small roof, option two was adopted, as seen in Figure 4.

Aluminum alloy was selected due to the following two reasons. Firstly, the roof truss was an uncladded structure in high-altitude, where would be highly dangerous for human to walk on. However, aluminum alloy barely required anti-corrosion maintenance, which would largely reduce potential risk for maintenance staff. Secondly, the main vertical load of roof truss was mostly equal to its self-weight, whereas the specific mass of aluminum alloy was merely 1/3 of that of steel. Aluminum alloy structure could release maximal burdens to lower structure from higher part.

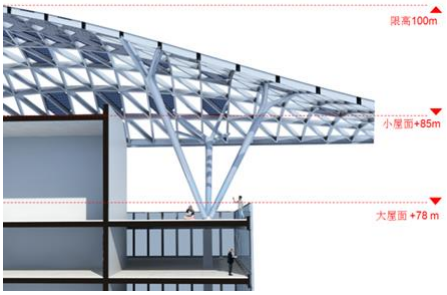


Figure 3: the sketch of architectural height limit

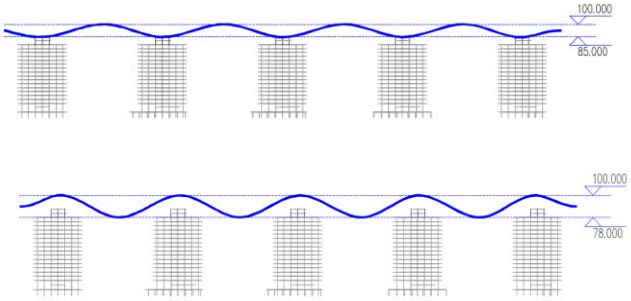


Figure 4: typical structural vertical section

3. Construction of structural morphology

3.1 The principle of structural morphology

Structural morphology could be comprehended in two aspects. To begin with, structural appearance was presented in structure form. Throughout design process, structure form was to meet the requirements of architectural application, novelty and artistry. What‟s more, structure condition meant structural performance under load conditions. A well designed structure format was contributed by appropriate internal force distribution and simple load path. As a free surface in roof structure, its reasonability on surface shape could not only enhance architectural expression, but also assist to resist

external loads; therefore, the method of structure form finding could provide an optimized mechanical behavior for the given architectural restriction.

The configuration of roof truss was based on the principle of minimum strain energy under gravity. Strain energy is the integral of strain energy density to volume[1].

$$C = \int c\, dV \tag{3.1}$$

where c is the strain energy density, which could be defined in below equation:

$$c = \frac{1}{2}\sigma\varepsilon = \frac{\sigma^2}{2E} = \frac{f_y^2}{2E}\lambda^2 \tag{3.2}$$

In the equation, σ is stress， ε is strain and λ is stress ratio.

Therefore, equation (3.1) could be derived into following equation:

$$C = \frac{f_y^2}{2E}\int \lambda\, dV \tag{3.3}$$

As expressed from above equations, strain energy could represent the relationship between stress ratio and steel consumption. For the same theoretical material consumption, the smaller strain energy consumed in the structure, the lower stress ratio was; also, for a given stress ratio, the smaller strain energy consumed, the lower theoretical material consumption required.

3.2 Method of structural morphology

The structural morphology of this project was obtained based on Grasshopper, a plug-in developed by Rhinoceros software platform who equipped the feature of visualized node programming. 'Visualized programming' is a brand new program method, which enables programmers to apply those restrictions provided by program itself to set up interfaces. 'Node programming' is to encapsulation command as functional node, forming a logic script procedure through the reference operation among joints. The programming measurement of modularization emphasizes on the data connection among program sections, enabling structure designers easily handle complicated connections within structural models [2].

Considering the specific characteristics of roof structure, the concept idea of curved surface was explained below:

1. To define a series of controlled point. Those points were located evenly in the range of curved plan, with x and y coordinate as fixed value and z coordinate as variation within a defined range. The variation ranged between restricted architecture elevations and provided a controlled architectural surface.

2. Set restrains to the curved plan. Based on architectural requirements and column positions, the curvature border was restrained as straight and the curvature was restrained at column top.

3. Mesh those curved plans. Gravity load was applied and strain energy was obtained through analysis.

4. Target optimization on minimum strain energy. Z-coordinate of controlled points on curved plan was set to be optimized variables. Iterative computation was conducted by applying genetic algorithm to achieve the most reasonable curvature in stress aspect.

5. Fine adjustment was preceded based on architectural appearance requirement on cloud shape to eventually achieve both high efficiency on load transfer and architectural aesthetic requirement in cloud-shaped curvature.

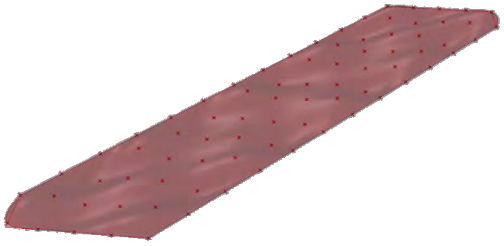


Figure 5:Construct curved plan through controlled points

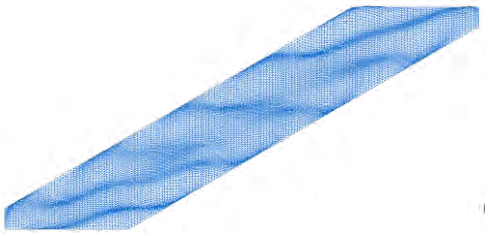


Figure 6: structural geometry model constructed based on above curved plan

3.3 Comparison on the configuration under different restrain conditions

During the stage of comparison and selection on aesthetic appearance, according to architectural requirement, a set of curved plan was modeled with changed restrain position, along with rise and boundary condition; eventually, the basic layout of curvature form was developed.

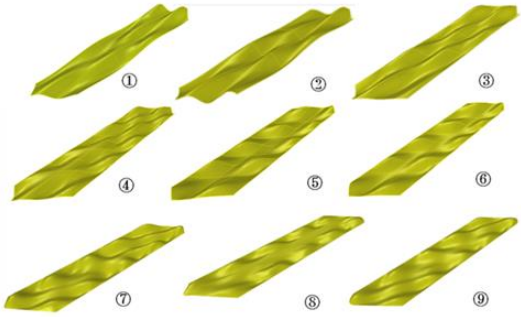
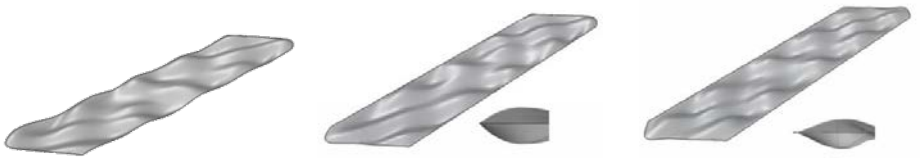


Figure 7: the development of curvature form-finding

From the basic layout, considering different requirements from architects, three types of free surface were obtained from structure program.

Table 1. Boundary condition

	Boundary condition
Curve 1	Rise was controlled within 18 meters. Boundary condition was set as free in restrain. Column top was pin connected.
Curve 2	Rise was controlled within 18 meters. Boundary was forced to be straight. Column top was pin connected.
Curve 3	Rise was controlled within 18 meters. Boundary was forced to be straight. Edge region was transformed smoothly. Column top was pin connected.



Curve 1 Curve 2 Curve 3

Figure 8: the comparison of curved plans and corresponding numerical models

From above three curved plans, structure engineers constructed numerical models, analyzed and compared the deflection, theoretical material consumption and overall stability factor for each one, which results were listed in the following table. As could be told from table, the more restrain in

construction, the larger theoretical steel consumption and lower stability factor. Hence, form-finding procedure was to research the balance between aesthetic appearance and structural performance. Eventually, Curve 2 was selected to be target curvature after considering both architectural effect and structural performance.

Table 2: the comparison on structural performance of each curve

	Curve 1	Curve 2	Curve 3
Strain energy	13666	15380	17082
Maximum deflection under dead load (mm)	416	482	660
Theoretical material consumption (t)	2307	2329	2899
Overall stability factor	6.41	6.26	3.12

3.4 The inner force analysis of curved plan

Principle stress analysis was conducted based on the final targeted curvature, which was shown below. As illustrated from analysis result, the plan was divided explicitly into tension region, compression region and bending region. Specifically, the members at troughs, spanning between buildings, were in catenary action, those at roof top were in compression due to arch action, and column top areas were bending transition regions. Axial strain energy was 7075 (46%) and bending strain was 8306 (54%). In this model, strain energy was obtained based on uniform surface assumption; whereas in reality, member layout was seldom completely uniformed, which could result in the slight difference in strain energy value. However, by comparing the effect on density of grid layout, it turned out that the difference was comparatively small. Therefore, the analysis result could be quite accurate as guideline for structural design. In later design stage, grid would be aligned with principle stress direction; appropriate member would be designed from region to region to fully perform material property due to the layout of force characteristics.

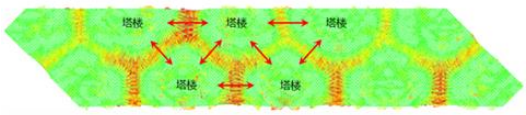


Figure 9: principle stress analysis of curved plan

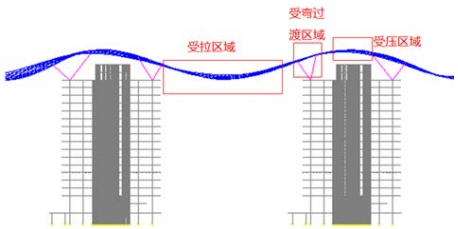


Figure 10: transition element under different load condition

4. Wind load evaluation

Wind load was the dominant action for roof structure design. Wind load relates not only to meteorological information, but also to roof form, member layout, grid size and several other factors. Therefore, the determination of its value would require wind engineering research measurements.

Over 70% of roof top was uncovered and was in the form of structural member only. Undersized member cross section would bring technical difficulty for wind tunnel test and numerical wind-tunnel simulation. For example, for the pressure testing model in wind tunnel, at least 1/15 reduced size was needed to measure pressure from simulated minimum member size. On the other hand, for numerical analysis simulation, the size of grid unit in structure and wind field depended on members' cross-section size. After meshing entire structure and wind environment, at least approximately 160-million-grid quantity was developed, which was over computation capability, being inaccuracy in numerical simulation and being impossible to check. As a solution, the wind load in this project was obtained from overall numerical simulation through simplified grid before being corrected based on the wind tunnel experiment result on force measurement through partial models.

According to the scale of wind tunnel, one third length of east end was selected as experiment object to conduct 1:150 scale wind tunnel tests. Under 16 wind directions, total reactions at support for each roof piece could be obtained. Figure 11 illustrated the numbering of roof pieces truss and Figure 12 presented the actual wind tunnel model.

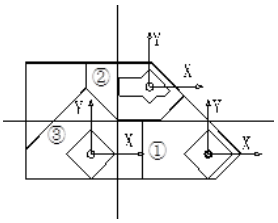


Figure 11: roof pieces

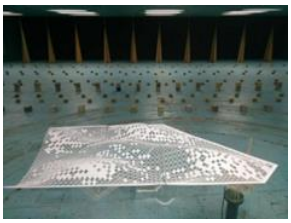


Figure 12: wind tunnel test

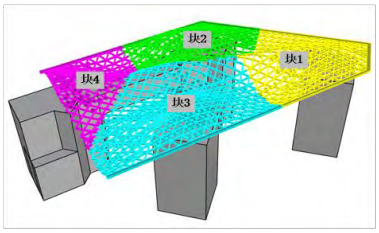


Figure 13: wind tunnel test model and division

In the following step, same region was elected to conduct numerical wind tunnel for comparison purpose. During the modeling procedure, merge three 3mx3m grids to a 9mx9m grid to effectively decrease grid quantity. Meanwhile, total reactions of roof at support could be accessed under 8 wind directions, whose results would be compared with the ones from wind tunnel test.

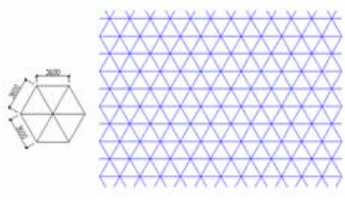
After comparing numerical wind tunnel value with experiment wind tunnel at majority wind angle, both results show almost the same regularity, indicating that numerical wind tunnel could simulate the actual load condition correctly. Also, comparison proved that numerical values were mostly greater than those tested ones; therefore, actual computation value could be taken from numerical results without reduction. Normally, for cladding roof, wind load is mainly presented in vertical suction and pressure, with comparatively small lateral wind. However, as there is no cladding for this roof structure, lateral wind value becomes comparatively large, being even greater than vertical wind load at critical wind direction. Hence, the resistance of lateral wind on roof and lower structure should be enlarged in structure design.

After contrasting, analyzing and verifying the correctness of numerical wind tunnel and corresponding correction factor, the numerical wind tunnel model was conducted for whole roof truss. While computation, the nodal reactions at each node for eight wind angles were exported and applied as load case to numerical models.

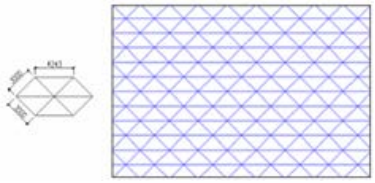
5. Structure optimization

5.1 Grid optimization

The layout of roof grid was aligned based on the principle stress flow direction. After comparing several possible regularized layouts that are in the same permeability ratio, the model of equilateral triangle grid in the size of 3.6mx3.6m and the one of right triangle grid in the size of 3mx3m were chosen to contrast the maximum displacement, material consumption and overall stability factor under dead load. Grid illustration was sketched in Figure 14 and comparison results were listed in Table 3.



Equilateral triangle grid



Right triangle grid

Figure 14: grid illustration

Table 3: the comparison of structure performance for different grid types

	Equilateral triangle grid	Right triangle grid
maximum displacement under dead load (mm)	483	365
material consumption (t)	5151	3471
overall stability factor	3.14	7.99

Table 3 proved that the structural performance of right triangle grid was obviously superior to that of equilateral angle because principle stress direction was in right angle that was resulted from the staggered arrangement in south and north lines at lower concrete elements (see Figure 10). Hence, right angle grid was selected, with the size meeting the requirements of both permeability and member slenderness ratio.

5.2 Temperature effect optimization

The thermal expansion coefficient of aluminum alloy was around twice that of steel. As this structure was uncladded, aluminum alloy member was exposed and would be highly affected by temperature. In addition, the continuous length of roof truss (600 meters) made temperature imposing a large influence to structure itself and members at lower levels. Therefore, how to control the temperature effect of roof truss became another question to be solved.

Figure 15 presented the axial force contour diagram of roof truss member under the load case of rising temperature. As could be told from the figure, the main temperature effect was centralized in the middle region of roof truss in long direction. Comparing with the axial force contour diagram under vertical loads, the stress in this part was smaller, which meant that those members in long direction were redundant. Hence, all these longitudinal members in middle range could be abandoned and those every second longitudinal members in the end 1/3 area was eliminated. Revised structure layout was shown Figure 16, whose maximum floor reaction under rising temperature was decreased from 6243KN to 3464KN.

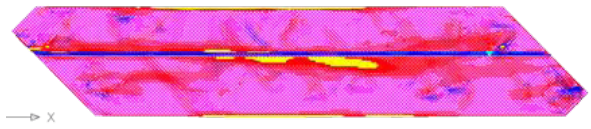


Figure 15: axial force cloud diagram of roof under the load case of rising temperature

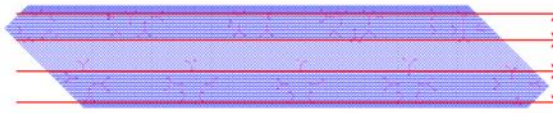


Figure 16: illustration of reduced grid

For the roof structure with reduced member quantity, the axial load contour figure under the load case of rising temperature was presented in Figure 17. The maximum axial load was along the major direction, and the wind load on this section was greater, leading to a higher demand on member strength. Hence, those aluminum alloy members were replaced with high strength steel to reduce both member size and temperature effect. After the replacement, the maximum floor reaction under rising temperature could be further reduced from 3464KN to 2628KN.

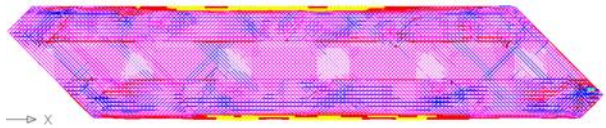


Figure 17: the axial load contour diagram of roof under rising temperature

Besides above two measurements, the inclination angle of inclined column was adjusted based on the critical reactions of specific temperature load cases. Temperature effect could be reduced by sacrificing structure stiffness. Meanwhile, closure temperature of structure should be restricted, ensuring members warming less than 50℃ and cooling less than 30℃.

6. Conclusion

(1) Single-layered structural configuration was selected to achieve maximum structure rise. Considering the elevation limit of structure, roof top was designed as crest and the region between buildings were designed as trough. Supported column was in Y shape, inclining outward to decrease roof span at most.

(2) The construction of configuration was founded on the minimum strain energy principle under gravity load. The height of controlled point was achieved by changed parameter. The iterative analysis was performed to determine the most efficient load transition to satisfy architecture required curved surface.

(3) Numerical simulation was combined with wind tunnel test on partial pressure-tested model to determine the value of wind load.

(4) The layout of member grid was designed based on the idea of principle stress flow under gravity. Right triangle along with one-way diagonal grid was selected to meet the requirements of both ventilation rate and member slenderness ratio.

(5) Temperature effect imposed large influence to roof structure and members at lower floor levels. By controlling structural closure temperature, appropriate layout of member density, inclination angle of inclined column and other methods, the adverse impact of temperature effect could be declined.

References

[1] Cui Changyu, Yan Hui, "Amorphosis technique for curved-surface structures of arbitrary geometries-Height adjusting method and its engineering applications", *[J].China civil engineering journal,* 2006, 39(12): 1-6.

[2] Zeng Xudong, Wang Dachuan, Chen Hui. "Rhinoceros & Grasshopper parametric modeling[M]". *Wuhan: Huazhong University of Science and Technology Press,*2011.

Proceedings of the IASS Annual Symposium 2019 – Structural Membranes 2019
Form and Force
7 – 10 October 2019, Barcelona, Spain
C. Lázaro, K.-U. Bletzinger, E. Oñate (eds.)

Kinetic umbrellas for coastal defense applications

Shengzhe WANG*, Maria GARLOCK, Branko GLISIC

*Department of Civil and Environmental Engineering
Princeton University, Princeton, NJ 08544, United States
shengzhe@princeton.edu

Abstract

Inspired by architect-engineer Félix Candela, we present an innovative structural system consisting of four-sided hyperbolic paraboloid (hypar) umbrellas as hard countermeasures against nearshore hazards. The umbrellas line the coast and remain upright during normal operation, providing shade and shelter along the waterfront while not limiting visibility and access to the shore. A hinge at the hypar-column interface enables tilting such that the panels can transition into a physical barrier against surge induced coastal inundation during imminent hazard scenarios. A decoupled numerical scheme constituting smoothed particle hydrodynamics (SPH) and the finite element method (FEM) was implemented to simulate hydrostatic inundation on the frontal surface of a tilted umbrella as a proof-of-concept. In assuming concrete construction, the study successfully illustrated the applicability of deployable hypar shells as coastal armor from a structural engineering perspective. This work ultimately demonstrates the feasibility of decoupled SPH-FEM methods in modeling fluid-structure interaction involving hypar forms, while establishing a foundation for their analysis and design for coastal hazard adaptation.

Keywords: smoothed particle hydrodynamics, finite element method, hypar shell, coastal hazard adaptation

1. Introduction

This paper introduces an innovative concept in the form of deployable four-sided hyperbolic paraboloid (hypar) shells as an alternative to traditional forms of coastal armor against surge-induced coastal inundation. Adapted from the works of Félix Candela [1], the proposal seeks to formalize the amalgamation between structural art and coastal hazard engineering. Commonly referred as "umbrellas", such structures arise from the merger of four straight-edged quadrants derived from a hypar manifold exhibiting negative gaussian curvature (Figure 1a and b). Since Candela's initial experimentation in the early 1950s, architecture embodying the four-sided hypar has graced the roofs of public facilities across the Americas. In addition to the popular four-sided form, eight and even twelve-sided renditions were realized, as exemplified via the roofs of Metro Candelaria in Mexico City. However, such forms were demonstrated to experience increased stresses and deflections relative to their more modest four-sided counterparts [2]. For a detailed architectural account of Candela's many works involving the hypar umbrella, the reader is referred to Garlock and Billington [3].

In this study, the typical concept of a four-sided hypar roof structure is modified to incorporate a hinge at the vertex, allowing the umbrella to tilt from its initial upright position (Figure 1c). When simultaneously deployed in a row, the panels effectively act as a physical barrier to coastal inundation during surge or extreme flood events (Figure 1d). This dynamic mechanism introduces an element of flexibility into coastal hazard adaptation strategies not demonstrated by classical shoreline armoring initiatives [4]. The kinetic panels are intended to remain in their upright position during normal operation, providing shade and shelter along the waterfront while not limiting access to the shore. The deployment of this defense system through its transition into a conventional seawall is only initiated

Copyright © 2019 by Wang, Garlock, Glisic
Published by the International Association for Shell and Spatial Structures (IASS) with permission.

during imminent hazard scenarios. This seamless conversion between structural art and coastal armor effectively pays homage to the tradition of rationalism implemented in the context of modern landscape architecture.

Evidently, the feasibility of such a system needs to be evaluated via considering fluid-structure interaction (FSI) in the hydrostatic and hydrodynamic regime. Hence, the primary objective of this paper is to develop and explore the numerical tools necessary for such assessments. A decoupled numerical scheme constituting smoothed particle hydrodynamics (SPH) and the finite element method (FEM) was proposed to assess the structural response to fluid accumulation in the hydrostatic regime. A proof-of-concept study was carried out assessing the capabilities of a typical deployed hypar in resisting hydrostatic inundation from a structural engineering perspective. Through this process, the practical feasibility of hyperbolic paraboloid shells and their analysis via SPH-FEM methods in the context of coastal armoring solutions are explored. The scope of the research is limited to hydrostatic and gravity loading, while hydrodynamic considerations will be addressed in future work.

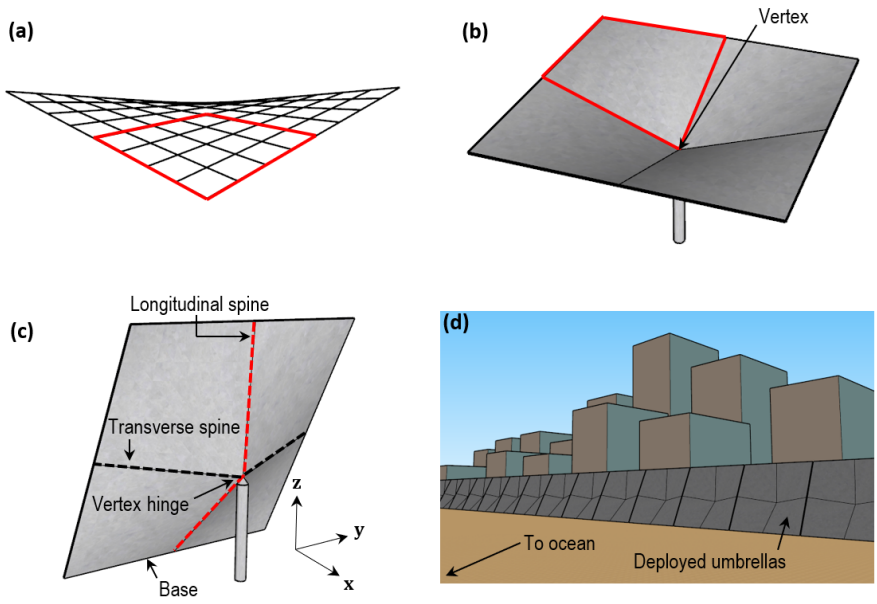


Figure 1: Quadrant of panel extracted from hypar manifold (a) to create the form of a four-sided umbrella in upright (b) and deployed configuration with location of hinge indicated (c). Concept of a typical deployed panel system in an urban waterfront setting also illustrated (d)

2. Implementation of SPH-FEM scheme

A doubly symmetric squarely projected hypar 105 mm thick along the spine, exhibiting sides of 8 m and rise 1.92 m with the vertex hinge 3 m above ground level (height of supporting column) was modeled via the SPH-FEM scheme. The hypar geometry was inspired by Candela's 1953 experimentation at Las Aduanas, albeit with an increased panel thickness and rise at the vertex [3]. The open source CUDA-enabled SPH solver DualSPHysics [5] was implemented for the spatial discretization of hydrostatic fluid forces acting upon the panel. This facilitates the subsequent determination of reaction forces and shell bending moments via the Open System for Earthquake Engineering Simulation (OpenSees) open source FEM solver [6].

2.1. Smoothed particle hydrodynamics

SPH is a mesh-free Lagrangian particle method commonly adopted for the simulation of FSI involving free surface fluid behavior [7]. The fluid continuum was represented as a set of discrete particles, each exhibiting physical properties including position, velocity, density, and pressure. Such quantities for

any given particle are computed via the integral interpolant of adjacent particles within its support domain. The extent to which each nearby particle influences a given property is dependent upon the interparticle distance, to which the quintic kernel by Wendland [8] was adopted to represent this contribution. The determination of fluid forces results from changes in the velocity field stipulated by the conservation of linear momentum. This was implemented via the popular artificial viscosity scheme developed by Monaghan [9]. Additionally, changes in the fluid density were determined by adopting a weakly compressible approach such that Batchelor's equation of state may be implemented to determine the pressure-density relationship [10]. By determining the acceleration of boundary particles constituting the frontal surface of the deployed panel, the spatial distribution of fluid forces ($\boldsymbol{f}_s^w$) imposed upon the hypar at any given timestep can be computed via:

$$\boldsymbol{f}_s^w = -m_b \sum_{i=1}^{K_s} \frac{d\boldsymbol{v}_i}{dt} \tag{1}$$

where $\boldsymbol{v}_i$ is the velocity of boundary particle i and m_b denotes its mass. K_s represents the total number of particles forming the impacted surface over which $\boldsymbol{f}_s^w$ acts. In this work, dynamic boundary conditions proposed by Crespo *et al.* [11] were adopted where boundary particles exert a repulsive force on adjacent fluid particles. All boundary particles exhibit the same equations of continuity and state as their fluid counterparts but are fixed in position. The repulsive force is generated by an increase in pressure as the distance between boundary and fluid particles fall within the kernel threshold, effectively preventing fluid penetration.

The SPH computational domain in this study consists of a box 6 m long in **x**, 8 m wide in **y**, and 10 m tall in **z** (Figure 2). The frontal side of the tilted panel in contact with the fluid was discretized into a collection of quadrilaterals (referred as "cells") with 36 cells constituting each panel quadrant (based on an optimization study). The height of fluid inundation (h_w) was 5.6 m, equal to 75% of the total effective height of the deployed panel. A total 15 seconds of physical time was simulated in order to provide sufficient time for initial particle oscillations to dampen. The **x**, **y**, and **z** components of the total hydrostatic force $\boldsymbol{f}_s^w$ acting on each cell was subsequently determined via the time averaging of fluid forces over the final 7.5 seconds of the simulation. Time-stepping was conducted via the computationally efficient Verlet algorithm [12] with each time step determined according to the Courant-Friedrichs-Lewy condition [13]. The simulation was performed within DualSPHysics utilizing a NVIDIA GeForce GTX 1060 GPU.

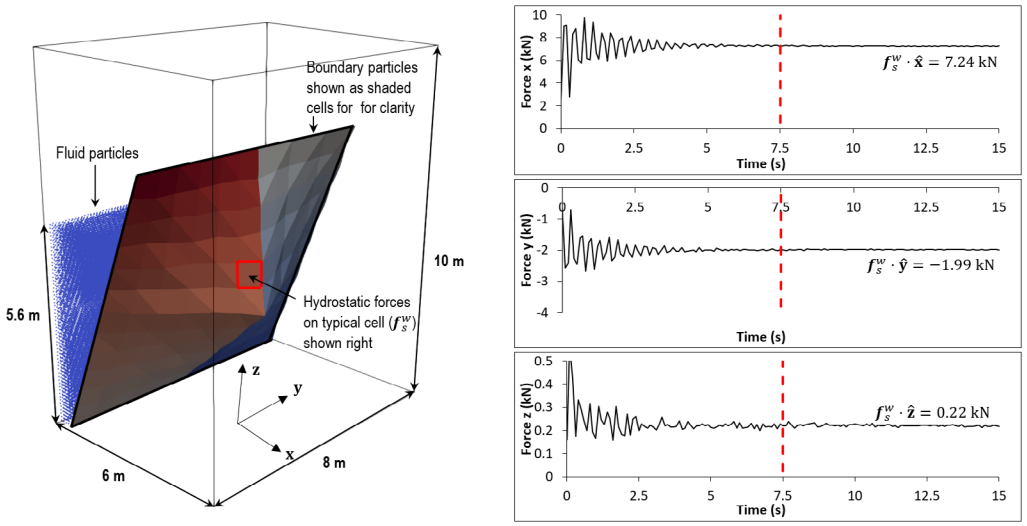


Figure 2: Illustration of SPH computational domain for deployed hypar discretized into 144 cells (with 36 cells per quadrant) and the determination of time averaged hydrostatic force components acting on a typical cell

2.2. Finite element modeling

The computation of hydrostatic demands via SPH subsequently enables the determination of shell stresses and reaction forces at the vertex via finite element analysis. OpenSees was implemented for evaluation of the structural response in which the hypar continuum was modeled via eight-node hexahedral stabilized single-point integration brick elements (*SSPbrick*), eliminating the potential for volumetric or shear locking [14]. Each SPH cell was represented using four brick element "sets" (Figure 3a and b) with each set composed of 10 element layers. This effectively results in the specification of 10 integration points (located at the centroid of each element) through the panel thickness (t_s). The individual cartesian components of the hydrostatic force on each SPH cell $\boldsymbol{f}_s^w$ was subsequently applied to the center node on the frontal surface of each four-element set constituting a given cell. Due to symmetry of the panel about the **xz** plane, only half of the hypar extending in the positive **y** ordinate was modeled. As such, nodes forming the longitudinal spine were translationally constrained in the **y** direction, effectively restricting rotation about **z**. The implementation of this boundary constraint was shown to be applicable for the modeling of symmetrical hypar shells as demonstrated by Levine [15]. Furthermore, the vertex node was free to translate only in **x** (reflecting a flexible column) while all nodes at the base were fully translationally constrained about the neutral axis, permitting only rotation about **y** (Figure 3c).

For the determination of panel self-weight, each brick element was discretized into eight sectors with the volume of each sector approximated via computation of the minimum volume encapsulating the interpolated coordinates of its eight corner positions using the convex hull algorithm. The total computed volume of the panel arising from the global summation of all sector volumes was then compared against the true theoretical hypar volume. This enabled the determination of a global volume correction factor, which was applied to the self-weight force vector assigned to the eight corner nodes of each brick element. Mechanical properties of the panel material matching that of typical structural concrete were adopted with density $\rho_s = 2400\ \mathrm{kg/m^3}$, Poisson's ratio $\nu = 0.15$, and Young's modulus $E = 30000$ MPa. Implementation of the *ElasticIsotropic* OpenSees material thus results in panel behavior constrained entirely within the elastic regime.

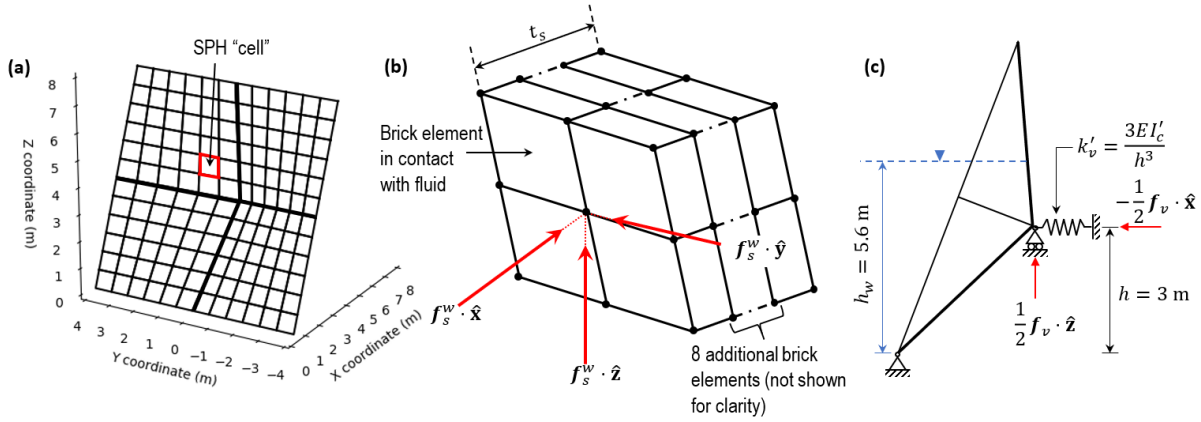


Figure 3: Discretization of SPH cells implemented in DualSPHysics (a) into OpenSees brick elements with four element sets per cell (b) with the application of hydrostatic force vectors shown. Idealized boundary conditions at the vertex and base implemented within OpenSees also illustrated (c)

3. Proof-of-concept

The structural feasibility of the hypar geometry modeled via the decoupled SPH-FEM numerical scheme was subsequently assessed. The objective is to provide preliminary justification for the viability of such structures as hard countermeasures against coastal inundation up to 5.6 m. This height was observed to conservatively capture the extent of inundation expected from storm surges and storm

tides impacting the eastern United States Seaboard [16]. A 500 mm square reinforced concrete column was adopted to support the hypar. The dimensions are such that slenderness effects may be neglected per ACI 318-14 [17]. Structural concrete with compressive strength (f_c') 40 MPa was implemented for the column and panel, incorporating A706 Grade 80 reinforcing steel. The yield and ultimate strength of G80 reinforcement were taken as 552 and 689 MPa respectively, while the strain at onset of strain hardening and the ultimate tensile strain were respectively 0.0074 and 0.0954 [18]. Longitudinal reinforcement within the column consisted of eight #7 bars evenly positioned around the perimeter confined with #4 stirrups at 200 mm spacing. The hypar shell was reinforced with a mesh of #4 bars spaced at approximately 170 mm in the longitudinal and transverse direction located about the neutral axis of the cross-section. To account for the column, a linear spring with stiffness $k_v' = 3EI_c'/h^3$ was implemented at the vertex hinge, to which I_c' represents half the second moment of area of the square column cross-section (Figure 3c). This allows for the determination of axial, shear, and moment demands associated with the column. The panel capacity was assessed in terms of the bending moment demand associated with hydrostatic loading acting on the frontal surface. The bending moment per unit width along the local **u** and **v** ordinates pertaining to the deployed panel (Figure 4), respectively denoted M_u and M_v, were determined for each element set by integrating the Cauchy stress resolved along **u** and **v** at each of the 10 integration points through the thickness.

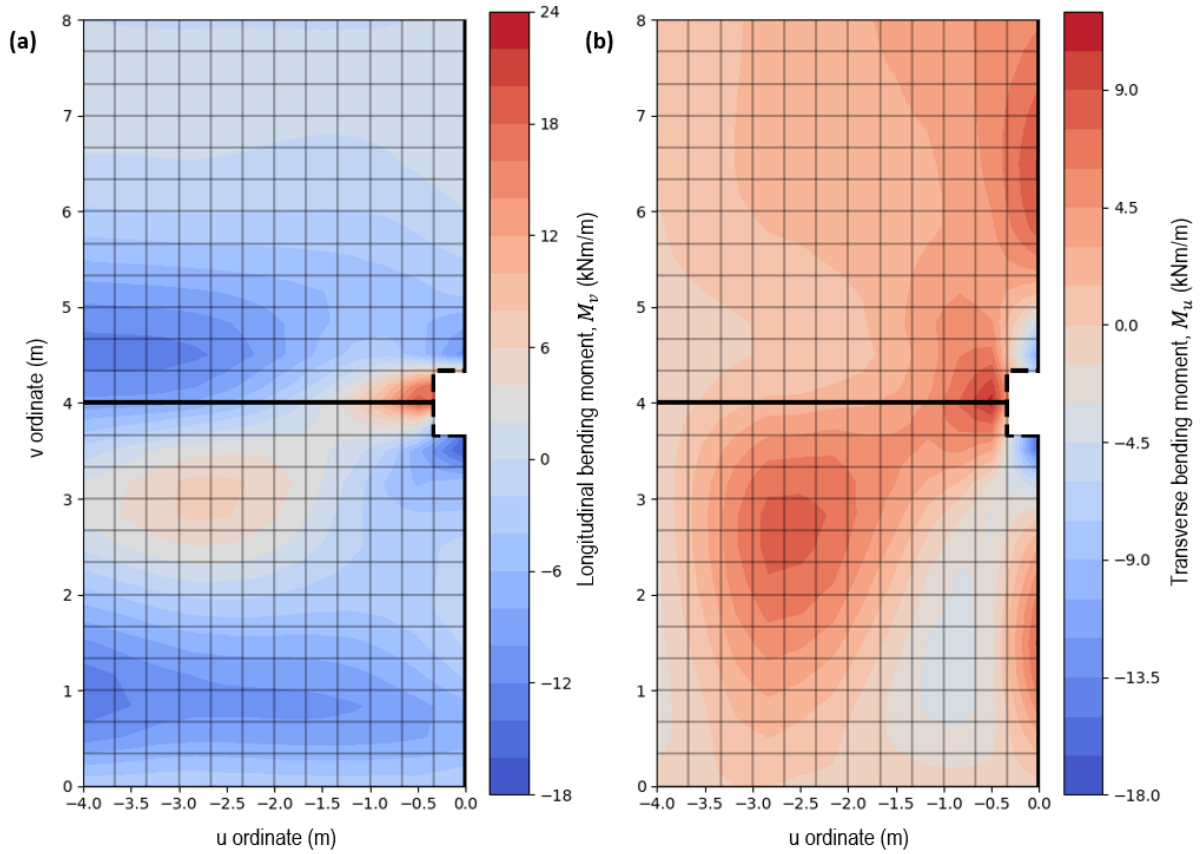


Figure 4: Longitudinal (a) and transverse (b) spatial bending moment distribution for the proof-of-concept study. Note that positive values of M_u and M_v reflect tension on the frontal surface in contact with the fluid.

Figure 4 illustrates the bending moment distribution of the panel along both the transverse (**u**) and longitudinal (**v**) ordinates. Note that the spatial moment distribution computed via OpenSees was independently verified using the commercial finite element software SAP2000 via Mindlin-Reissner shell approximations. Moments associated with the area immediately adjacent to the vertex node

(enclosed by dashed lines in Figure 4) were ignored since the boundary condition does not account for the tributary area associated with the vertex hinge and will be highly overestimated at this location. The design and detailing of the hinging mechanism will be investigated as part of future research and is beyond the scope of this paper.

The maximum bending moment averaged over one meter ($\bar{M}_p^*$) was subsequently determined to be 14 kNm/m from Figure 4. In addition, the axial ($N_c^* = \boldsymbol{f}_v \cdot \hat{\mathbf{z}}$), shear ($V_c^* = -\boldsymbol{f}_v \cdot \hat{\mathbf{x}}$), and moment ($M_c^* = V_c^* h$) demands attributed to the column were 1013 kN, 47 kN, and 141 kNm respectively. The nonlinear sectional analysis program for reinforced concrete, Response-2000 [19], was utilized to determine the theoretical capacities of the hypar shell and supporting column via the trilinear moment-curvature relationship characteristic of reinforced concrete. The layout of reinforcement within the 500 mm square concrete column and a 1-meter segment of the 105 mm thick panel as previously described are illustrated in Figure 5a and b respectively. The yield moment of the concrete column and hypar shell were subsequently computed to be 494 kNm and 18.6 kNm/m respectively, exceeding their respective moment demands of 141 kNm and 14 kNm/m (Figure 5). Hence, the detailing of structural members adopted for the proof-of-concept study proved adequate for the hydrostatic forces exerted on the deployed hypar. The conceptual feasibility of such structures for use as coastal armor against storm surge inundation in terms of a simplified hydrostatic situation is therefore demonstrated.

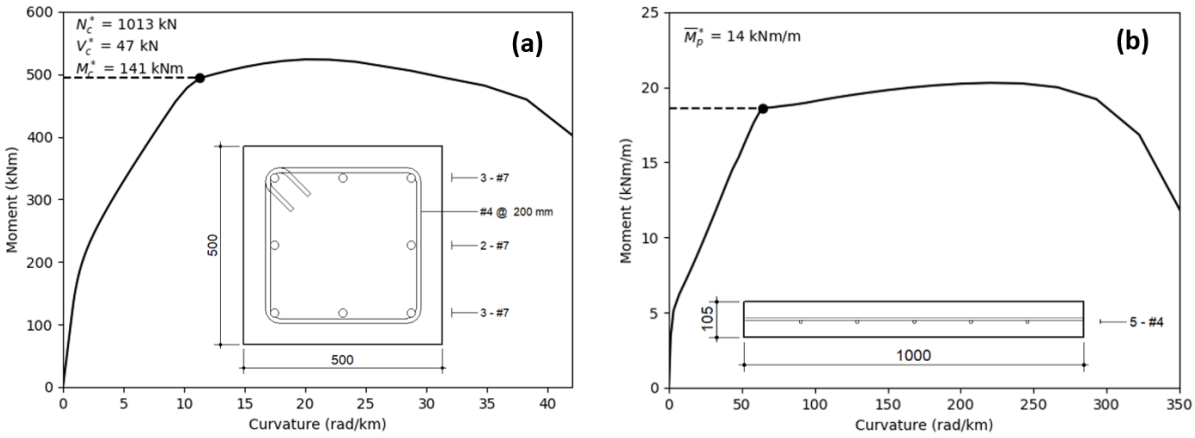


Figure 5: Moment-curvature relationship with yield capacity indicated for reinforced concrete column (a) and hypar panel segment (b) adopted for the proof-of-concept

4. Conclusions

An adaptable solution to coastal armoring against nearshore hazards in the form of deployable hyperbolic paraboloid shells was introduced, enhancing the flexibility of traditional coastal hazard adaptation strategies. A decoupled numerical scheme constituting smoothed particle hydrodynamics and the finite element method for the simulation of fluid-structure interaction within an entirely open source computing environment was developed. A proof-of-concept study was implemented to assess the performance of such systems within a structural engineering context. Preliminary designs of the panel and support column were evaluated, to which its feasibility in resisting hydrostatic inundation characteristic of extreme surge events along the United States' east coast were successfully demonstrated. The ability of SPH methods to accurately simulate complex wave and coastal phenomena can therefore be integrated with complex hypar forms described via FEM models to obtain detailed panel behavior across a wide range of loading and geometric scenarios. This work effectively establishes a theoretical foundation for the analysis and design of dynamic hypar shells for coastal defense applications.

Acknowledgements

Funding for this research was partially sponsored by Princeton University through the "Project X" grant.

References

[1] F. Candela, "Structural applications of hyperbolic paraboloidical shells," *J. Am. Concr. Inst.*, vol. 51, no. 1, pp. 397–416, 1955.
[2] A. Levine and M. E. M. Garlock, "Structural comparison of Candela's 4-sided and 8-sided concrete umbrellas," in *Proceedings of the IASS Symposium*, MIT, Boston, USA, 2018.
[3] M. E. M. Garlock and D. P. Billington, *Felix Candela: Engineer, Builder, Structural Artist*. Princeton, NJ 08544: Princeton University Art Museum, 2008.
[4] D. P. Horn, "Chapter 6 - Storm surge warning, mitigation, and adaptation," in *Coastal and Marine Hazards, Risks, and Disasters*, 2015.
[5] A. J. C. Crespo *et al.*, "DualSPHysics: open-source parallel CFD solver based on smoothed particle hydrodynamics (SPH)," *Comput. Phys. Commun.*, vol. 187, pp. 204–216, 2015.
[6] S. Mazzoni, F. McKenna, M. H. Scott, and G. L. Fenves, "OpenSees command language manual." 2006.
[7] M. B. Liu and G. R. Liu, "Smoothed particle hydrodynamics (SPH): an overview and recent developments," *Arch. Comput. Methods Eng.*, vol. 17, pp. 25–76, 2010.
[8] H. Wendland, "Piecewise polynomial, positive definite and compactly supported radial functions of minimal degree," *Adv. Comput. Math.*, vol. 4, pp. 389–396, 1995.
[9] J. J. Monaghan, "Smoothed particle hydrodynamics," *Annu. Rev. Astron. Astrophys.*, vol. 30, pp. 543–574, 1992.
[10] G. K. Batchelor, *An introduction to fluid dynamics*. Cambridge Mathematical Library, 2000.
[11] A. J. C. Crespo, M. Gomez-Gesteira, and R. A. Dalrymple, "Boundary conditions generated by dynamic particles in SPH methods," *CMC - Tech Sci. Press*, vol. 5, no. 3, pp. 173–184, 2007.
[12] L. Verlet, "Computer 'experiments' on classical fluids. I. Thermodynamical properties of Lennard-Jones Molecules," *Phys. Rev.*, vol. 159, no. 1, pp. 98–103, 1967.
[13] J. J. Monaghan and A. Kos, "Solitary waves on a Cretan beach," *J. Waterw. Port Coast. Ocean Eng.*, vol. 125, pp. 145–155, 1999.
[14] C. McGann, P. Arduino, and P. Mackenzie-Helnwein, "SSPbrick Element - OpenSeesWiki." [Online]. Available: http://opensees.berkeley.edu/wiki/index.php/SSPbrick_Element. [Accessed: 17-Oct-2018].
[15] A. Levine, "A structural analysis and comparison of Felix Candela's 4-sided and 8-sided concrete umbrellas," M.S. Thesis, Princeton University, 2018.
[16] H. F. Needham, B. D. Keim, and D. Sathiaraj, "A review of tropical cyclone-generated storm surges: Global data sources, observations, and impacts," *Rev. Geophys.*, vol. 53, pp. 545–591, 2015.
[17] American Concrete Institute, "Building code requirements for structural concrete (ACI 318-14)," 2014.
[18] D. Overby, M. Kowalsky, and R. Seracino, "A706 Grade 80 reinforcement for seismic applications," Constructed Facilities Laboratory, NC State University, 2015.
[19] E. Bentz and M. P. Collins, "Response-2000 user manual," Department of Civil Engineering, University of Toronto, 2001.

Proceedings of the IASS Annual Symposium 2019 – Structural Membranes 2019
Form and Force
7 – 10 October 2019, Barcelona, Spain
C. Lázaro, K.-U. Bletzinger, E. Oñate (eds.)

Multi-Objective Optimization of a Concrete Shell

Viktoria HENRIKSSON*[,a], Scott LOMAX[a], James N. RICHARDSON[a]

[a]Thornton Tomasetti, Inc.
51 Madison Avenue, New York, NY 10010, USA
*VHenriksson@ThorntonTomasetti.com

Abstract

In this paper the design of a perforated free-form concrete shell structure is discussed, demonstrating the practical implementation of form-finding and optimization in a real-world design. This project is designed as an architecturally expressive building with undulating, exposed material across several levels, housing interior and exterior living spaces. As one of the most significant features of the project, the upper surface of the building is envisioned as a perforated concrete shell, which is the focus of this paper. This surface is supported at the center of the shell, housing a swimming pool, and touches down at four locations at the perimeter. A form-finding procedure, respecting the design intent of the shell was carried out, demonstrating the material-savings that can be achieved with minimal visual impact on the design. The topology of the shell perforations is controlled by a multi-objective optimization algorithm, minimizing mass and deflection to determine the size and distribution of the perforations on the shell surface. This iterative algorithm is constrained by maximum peak stresses for the envelope load combinations and architectural considerations. Options for visualizing the optimization problem are presented at the end of this paper.

Keywords: conceptual design, form-finding, optimization, concrete shells, genetic algorithms, multi-objective

1. Introduction

Villamar is a new luxury residential project located at the west coast of Mexico. The project is designed to be an iconic building with an undulating form of exposed concrete with several levels, housing interior and exterior living spaces.



Figure 1: Overview rendering of design intent, Image courtesy Fernando Romero Enterprise

The investigation detailed in this document focusses on the upper level, forming the roof of the building, which also supports a swimming pool, and is accessible by the occupants as an outdoor deck space.

Copyright © 2019 by Viktoria Henriksson, Scott Lomax, James Richardson
Published by the International Association for Shell and Spatial Structures (IASS) with permission.

The geometry has been developed through a form-finding exercise balancing architectural requirements, efficiency of structural form and constructability. The openings (perforations) in the shell are required to allow light into the space below, while at the same time reducing the weight of the shell and improve structural performance. The architect was interested in the clustering of perforations, demonstrating the location of areas of low stress, while at the same time limiting deflections to maintain the desired form of the shell.

2. Design assumptions

The structure has been divided into the following four major structural portions (described in the sections below) depending on their support conditions and spanning requirements. The main focus of this paper is the top, perforated concrete shell seen in bottom right image.

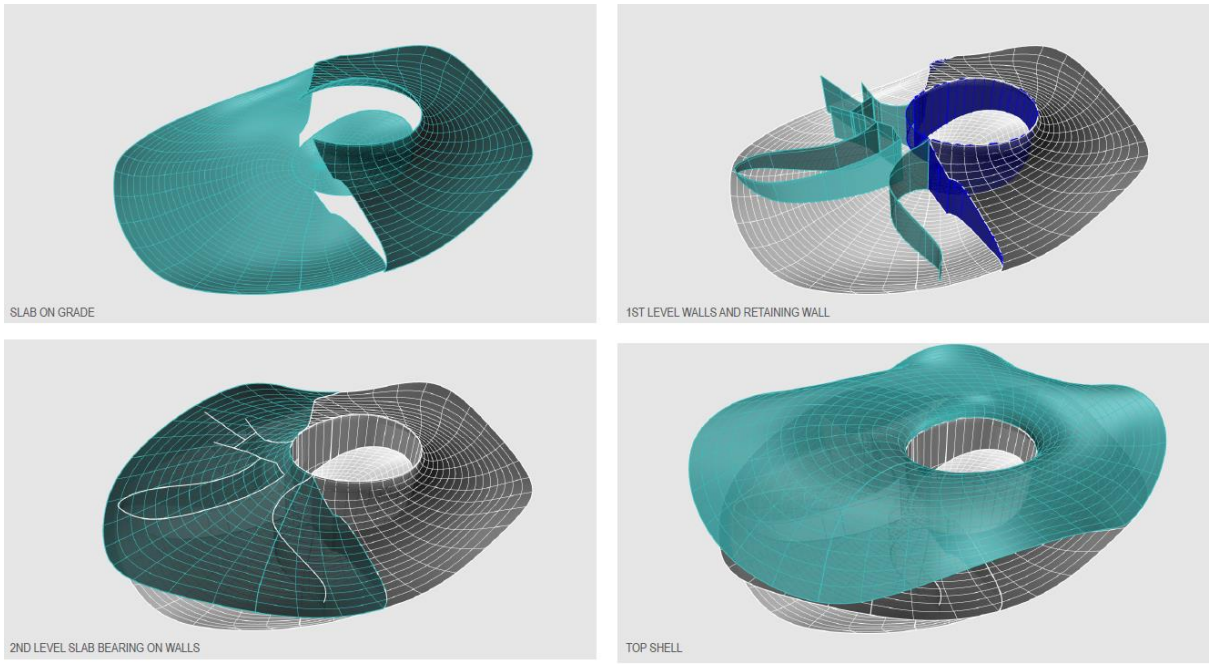


Figure 2: Structural Delineation concept overview

The lower slab is foreseen as a slab on grade as it rests directly on the earth and can be most efficiently supported and formed in this way. The grade is cut back and laterally supported by retaining walls. A portion of the second level slab will be supported directly on grade, while the remainder spans short distances between supporting walls, between levels one and two. The top shell is assumed to be separated from the 2nd level slab, only connecting to each other at a pinned connection at 4 touch-down points as well as at the central circular "funnel". Several material options were considered, however, cast-in-place concrete, in combination with sprayed shotcrete was decided on as the material that best suited the project.

2.1. Design Loading

During these early phases of the design, ASCE 7-10 Minimum Design Loads for Buildings and Other Structures was used to generate loads and combination [1]. This resulted in an uplift or downward acting wind load of 1.2 kN/m^2 as well as roof live loads of 1.9 kN/m^2 that were studied both as a distributed and in unbalanced load patterns. Additionally a super imposed dead load of 1.4 kN/m^2 was added to account for concrete topping and MEP. For every code-prescribed load combination, the concrete was designed according to ACI 318-11 Building Code Requirements for Structural Concrete [2].

2.2. Initial Structural Review

The initial form (provided by the architect) was analyzed as a monolithic concrete shell using finite element software. In this preliminary analysis, the concrete is assumed to have a homogenous thickness of 250 mm and any large stress peaks are resolved by local steel reinforcement. With gravity loads applied, the finite element analysis indicates no major stress concentrations. Highest stresses are notes over the supports and at the free spanning north-west edge of the building. All finite element analysis in this phase are performed on a single layer mesh (representing the middle of the shell) with uniform thickness.

From this first study, it is clear that the long spanning free edge at north-west edge of the top shell is experiencing the largest deformations. The figure below shows the required concrete thickness and reinforcement for four zones, determined according to [2].

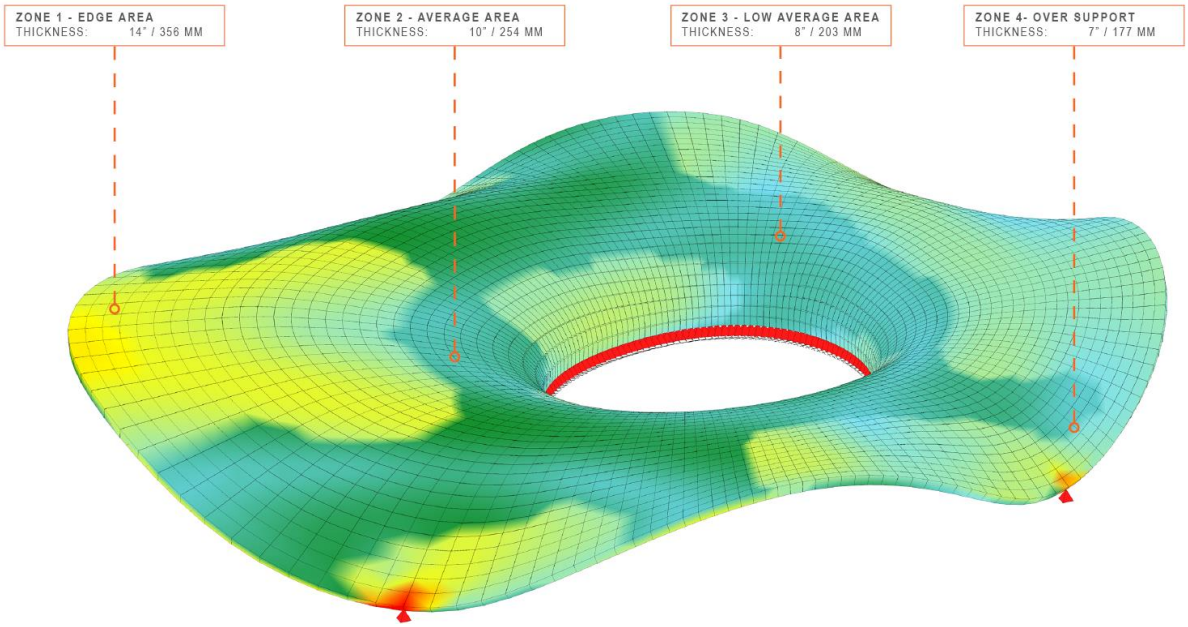


Figure 3 Concrete thickness requirements for four studied zones of the initial form

3. Form-finding

Using Dynamic Relaxation [3], a form-finding study was performed on the initial shell form. Uniform distributed load was assumed to be the dominant force in the form-finding exercise. Based on discussions with the architects, the following boundary conditions were to be kept fixed during the (partial) form-finding exercise:

- Boundary edge shall be kept similar to the initial design
- Supports at touch-down points (outer edge) shall be assumed pinned and appear as minimal as possible
- Minimal change of the form compared to initial design intent

With the above mentioned conditions, the form is partially form-found. During the form-finding study, the design team was faced with many design options where trade-offs between structural performance and deviation from initial design intent had to be considered. The options stem from the need to set initial parameters within the form-finding process, leading to a large number of possible form-found solutions. The design team, together with the architect, evaluated and filtered the various options at this stage to select a suitable overall geometry, both structurally and aesthetically.

The color plot diagrams below show the distance between the initial and final form-found mesh. The plot below demonstrates which areas of the final form have a larger discrepancy with the original form. In the selected form-found model, the maximum distance in the red zones are almost 1 meter, and less than 0.5 m in the yellow areas, however this was judged to be acceptable by the design team.

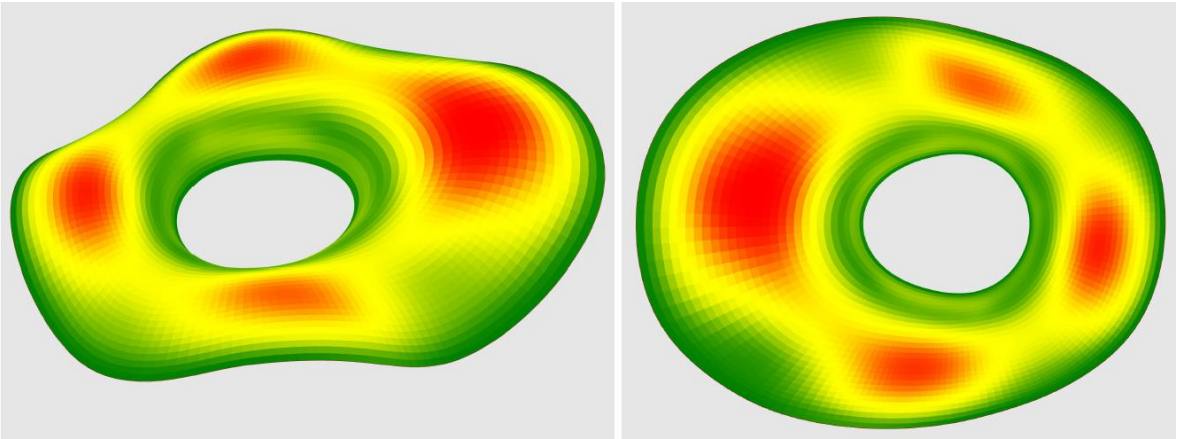


Figure 4 Color plot indicating distance between the initial and form-found options

3.1. Structural Performance

The same four zones that were previously studied for the initial form were studied for the partially form-found model, the results are shown in the figure below.

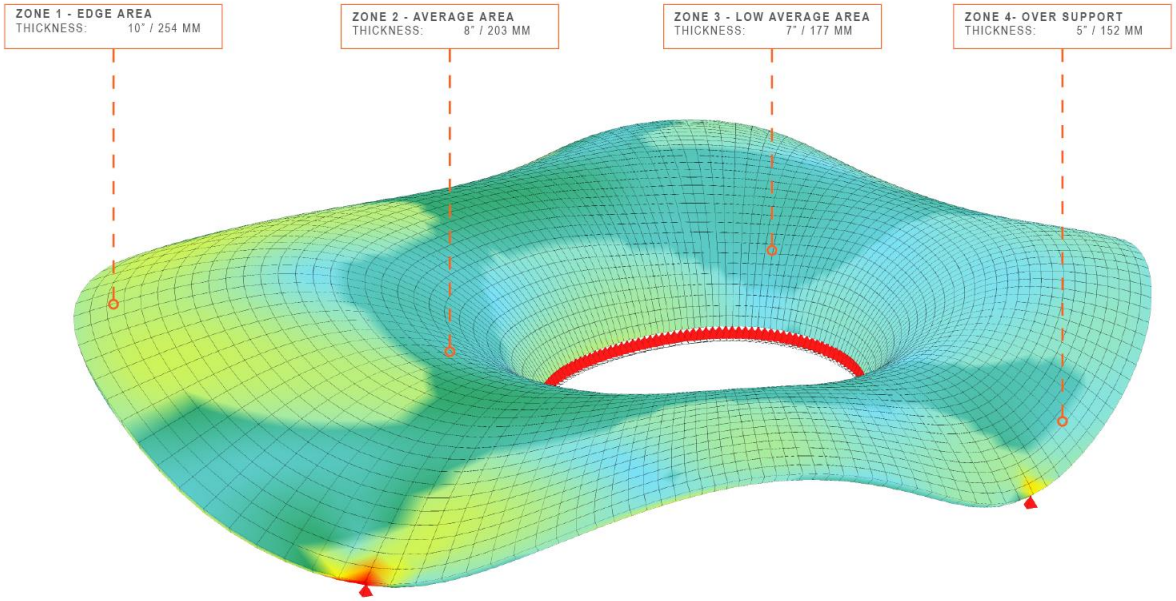


Figure 5 Concrete thickness requirements for four studied zones of the form-found option

The two studied forms (initial and form-found) were both analyzed for all code prescribed load combinations [1]. In this way an overall saving of material and therefore cost could be evaluated for the two real-world design options.

Table 1: Comparison of concrete thickness of initial and partially form-found option in four selected areas.

Zone	1 - Edge area	2 - Average area	3 - Low average area	4 - Over support	Average
Initial form (mm)	356 mm	254 mm	203 mm	177 mm	248 mm
Partially form-found (mm)	254 mm	203 mm	177 mm	127 mm	191 mm
% Thickness Reduction	29%	20%	13%	29%	23%

The table above shows a break-down of the concrete shell thicknesses required at the four studied zones, through a design compliant with ACI 318 [2]. Note that the thickness mentioned above includes a 2" (50.8mm) concrete cover required for corrosion protection of steel reinforcement. A reduction of up to 29% (average 23%) can be noted between the initial form and partially form-found option.

4. Concrete Perforations

The initial design of the top shell proposes perforations of various sizes and distribution across the shell to allow for improved daylight access and a dynamic pattern. Since the overall structural efficiency will depend on the placement and amount of perforations, an optimization study was set up to find and evaluate a best-fit solution.



Figure 6 Design intent - perforations over the four touch down locations

The architectural intent was to place the perforations in four clusters over the shell touch down locations. These locations are also areas of high stress and it was clear that the perforations would affect the structural performance of the shell. Architecturally, there was a desire to maintain a cluster-like perforation language as shown above, with perforation gradients within particular zones.

4.1. Initial Perforation Studies

An initial structural analysis was performed on a single layer mesh, representing the center of the top shell according to the design intent. Three cases were compared, in order to study the structural impact of perforations on the global performance.

Stress concentrations and a 15% increase in deflections can be noted for large size openings, while smaller size perforations induced minimal structural impact compared to the initial form.

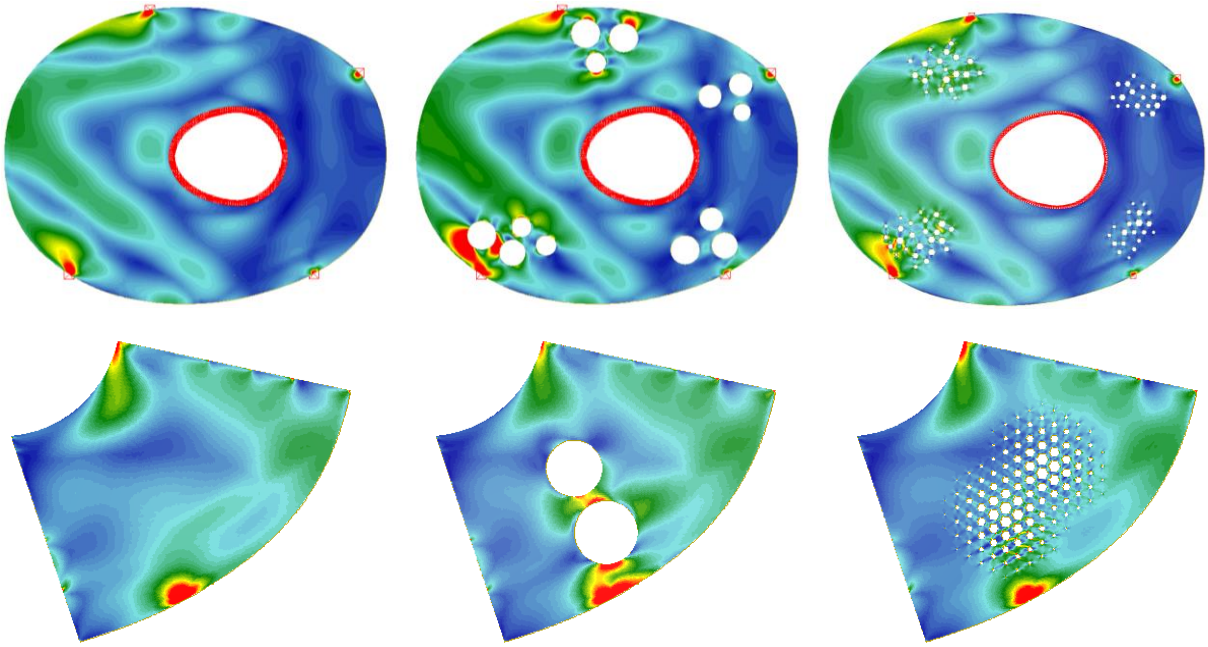


Figure 7 Overview of initial perforation studies. Sizes and locations of perforations are varied to study overall performance and stress concentrations

The larger structural openings were also contrary to the overall architectural vision for the project. Openings with a maximum diameter of 0.3 m were selected for structural and aesthetic reasons.

4.2. Perforation Optimization

In order to find and study the best-fit solution, the size and location of the shell perforations were controlled by a multi-objective optimization algorithm, minimizing mass and deflection to determine the distribution on the shell surface. The central aim of the optimization routine is to search for a set of best-tradeoff solutions, according to multiple objective functions, so-called fitness functions [4]. This project, as most other real design problems, had multiple competing objectives leading to a set of Pareto Optimal solutions. Furthermore, constraints were placed on the clustering of the perforations, by parameterization of the perforations using a geometric encoding for location of cluster on the shell, size of cluster and size of perforation. To compare these solutions, a Pareto front can be graphed. The form-found shape in the previous step was used as the basis form, however a genetic algorithm optimization could have been combined with the form-finding of the overall form. This approach is similar to the coupled form-finding/topology optimization approach in [5]. The following three objectives have been considered for the shell topology optimization:

$min(\sum M_i)$	Minimize total mass	(1)
$min(\delta_{max})$	Minimize maximum deformation	(2)

In addition to the objectives listed above, the following constrains need to be fulfilled for the optimization process to generate a solution.

$\sigma_{max} < 30\ MPa$	Maximum principal stress below threshold	(4)
$d \leq 0.3\ m$	Diameter of perforations limited to 0.3 m	(5)
$\Phi \leq 4\ m$	Perforation group diameter limited to 4 m	(6)

4.3. Results

As mentioned previously, the solution space results in many different options which the designer needs to evaluate to determine which of the solutions is desired. The set of Pareto-optimal solutions which results from the optimization process can be seen in the figure below. This set of best trade-off solutions allows the design team to evaluate competing objectives and select the most desirable from these solutions by weighting these and other criteria (such as aesthetic appeal).

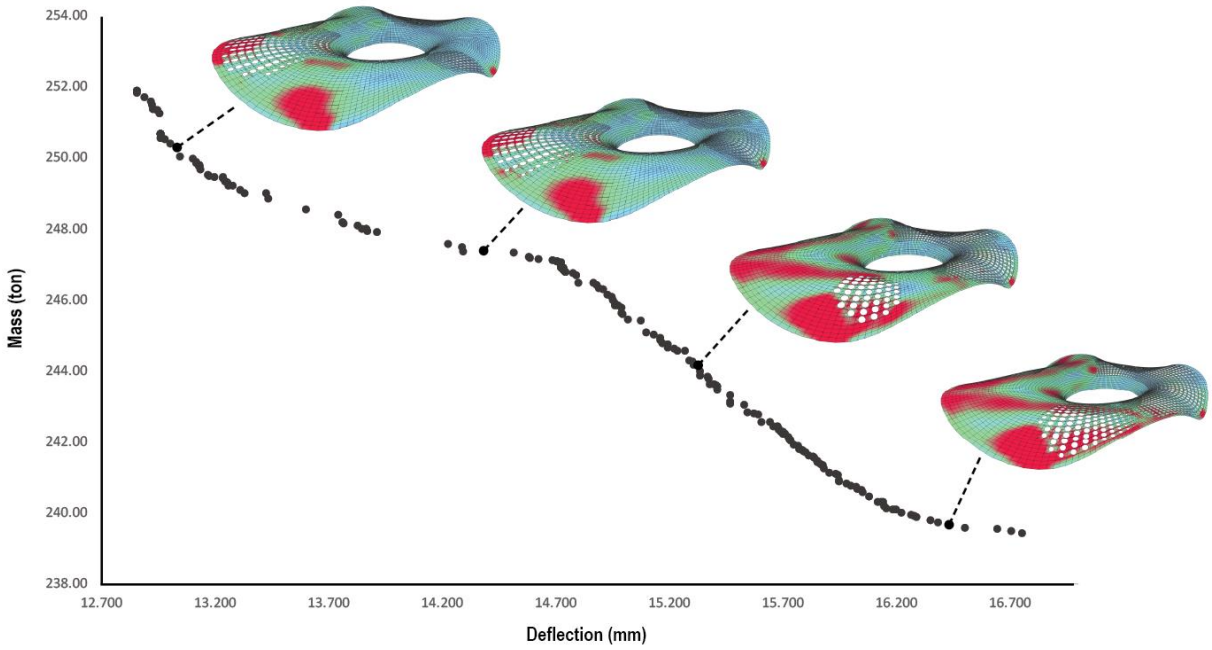


Figure 8 Pareto front of the solutions to the mass and deflection minimization multi-objective problems

Verification of convergence was performed with multiple initial genetic parameters. For a population size of 250 individuals with 200 generations suitable agreement was reached between multiple compared runs of the same problem. Below are two examples of Pareto-Optimal solutions taken from the Pareto Front in the figure above.

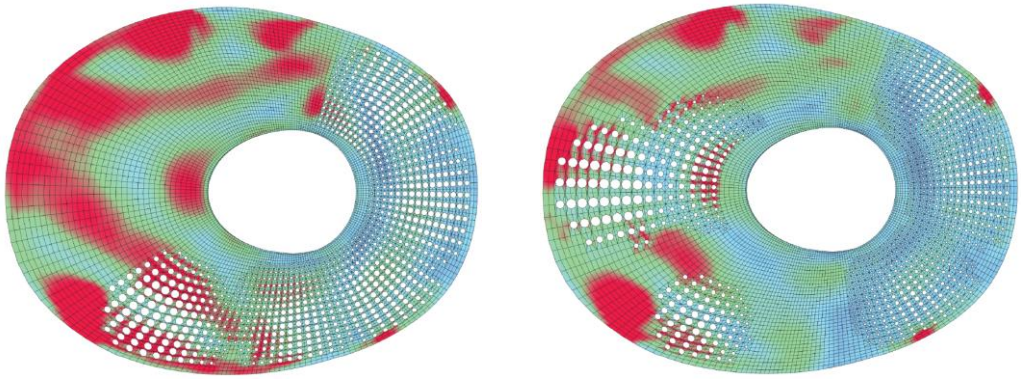


Figure 9 Two of the design solutions from the design space

Evaluating best trade-off design solutions can further be performance a parallel coordinates plot. The visualization tool Design Explorer, developed at Thornton Tomasetti was used for this purpose [6]. The result is a user-friendly representation of the various solutions for selection by the end user. This approach encourages simple and intuitive decision-making. Each solution is associated with a set of performance values that can be sorted, filtered and neglected based on the design intent.

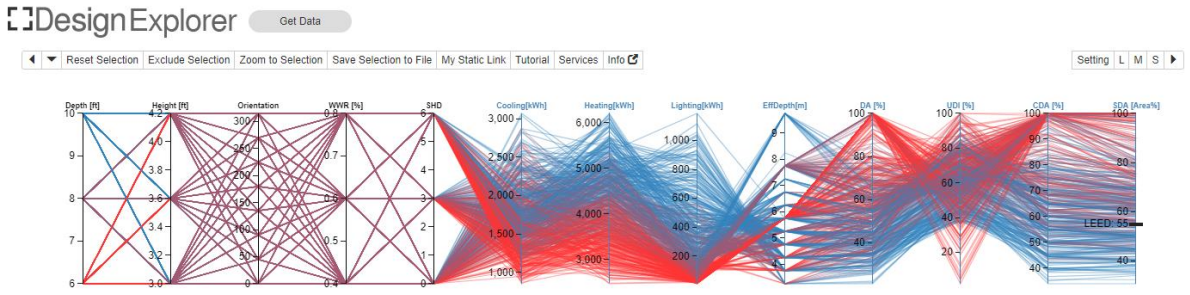


Figure 10 Parallel coordinate plot of all solutions found in the optimization search

Conclusions

Computational software are making it easier and faster to generate many different design solutions. The approach in this paper offers solutions to find and evaluate design options through a multi-objective optimization approach. While only one loading case and two objectives (mass and deflections) were considered in this study, the designer may wish to consider any number of loading cases and/or objectives. Genetic algorithms can easily be adapted to consider other objectives and constrains and this ability is one of the key factors in the decision to implement them in this study. In this paper, a form-finding through dynamic relaxation was performed in a first phase, while the perforation study was applied thereafter. This two-phase approach could easily be combined into one optimization process, where the perforations of the concrete also would influence the overall shape of the structure, however this is subject for future investigations. In doing so, a real-world project team in early stage design is able to make a number of important design choices. The design team is able to filter out inefficient, undesirable solutions and is presented with a series of best trade-off solutions to the design problem from which to select "equivalent" options.

Constructability is an extremely important criteria to take into account in this project, given the constraints on the project site. In the next phase, constructability could be an additional criteria to add to the optimization procedure, to ensure practical, structurally performative, and aesthetically pleasing solutions for construction.

Acknowledgements

The authors would like to thank Fernando Romero and Fernando Romero Enterprise (FR-EE).

References

[1] American Society of Civil Engineers. (2010). *Minimum Design Loads for Buildings and Other Structures.* Reston: ASCE.

[2] American Concrete Institute. (2011). *Building Code Requirements for Structural Concrete (ACI 318-11).* Farmington Hills: ACI.

[3] Day, A. S. (1965, vol 219). An Introduction to Dynamic Relaxation. *The Engineer*, pp. 218-221.

[4] R. Filomeno Chelho, T. M. (2014). Genetic Algorithms for Structural Design. In S. Adriaenssens, P. Block, D. Veenedaal, & C. Williams, *Shell Structures for Architecture* (pp. 290-294). New York: Routledge.

[5] J. N. Richardson, S. A. (2013). Coupled form-finding and Grid Optimization approach for Single Layer Grid Shells. *Engineering Strucures, vol. 52*, 230-239.

[6] Thornton Tomasetti. (2019, May 28). *Design Explorer 2*. Retrieved from https://tt-acm.github.io: https://tt-acm.github.io/DesignExplorer/

Proceedings of the IASS Annual Symposium 2019 – Structural Membranes 2019
Form and Force
7 – 10 October 2019, Barcelona, Spain
C. Lázaro, K.-U. Bletzinger, E. Oñate (eds.)

Structural design of the new Sørlandets Kunstmuseum, Kristiansand – Rehabilitation of 1930s concrete silos

Alejandro CLEMENTE*, Alberto ORDIÑANA, Gaute MO, Mario RANDO, Manuel SÁNCHEZ-SOLIS

*Degree of Freedom
C/ Colon 18 5B, Valencia (Spain) 46804
a.clemente@dofengineers.com

Abstract

Degree of Freedom as structural engineers, in collaboration with main consultants Rambøll and contractor Kruse-Smith, with architects Mestres Wåge Arquitectes, BAX Studio, and Mendoza Partida are currently working on the revised preliminary design for the new Sørlandets Kunstmuseum in Odderøya, Kristiansand. The museum will be centered around the structure of the original grain silos on the proposed site, which were constructed in separate blocks in 1935 and 1939. The new building has three volumes; an eight-storey central part based on the existing silos, a new four-storey structure to the west replacing the original extension and a new five-storey annex building to the east. The architectural proposal is to create an impressive, open exhibition area, the Silo Hall, by demolishing extensively the cylindrical silos below level 5. There will also be a new glass-walled restaurant space, that replicates the silo geometry located on the top floor. The existing silo walls are 150mm thick with an inner diameter of 4.4m. Original drawings show the older silos have only a central layer of reinforcement whereas the 1939 silos have two reinforcement layers. The silos are supported on reinforced concrete columns at ground floor transferring directly to rock, or to rectangular RC piles founded at a variable depth of up to 10m. Major structural challenges include the demolition, repair and strengthening of the silos and the creation of new "super columns" based on the remaining parts of the silo walls. In addition, due to the proximity of the site to the sea, the existing foundations' capacity, in contact with saltwater, is unknown and the silo building will be underpinned with new foundations.

Keywords: Rehabilitation, Reinforced concrete, Silo structure, membranes.

1. Description of the project. Architectural vision

The Kunstsilo project is a rehabilitation and transformation of the old grain silos located at Odderøya in Kristiansand (Norway) into a contemporary art museum. The original silos, designed in 1935, have an architectural and patrimonial value, but are currently in decay and will not survive without a new use. The building is located today next to the Kilden Performing Arts Centre and is to become a part of Kristiansand´s new cultural quarter with strong regional ambitions.

1.1. Existing building

The existing silo construction can be divided in three parts according to the time of their construction: original silos from 1935, silos extension from 1939 and annex north extension from 1996. The main volume is formed by the old battery of 3x10 reinforced concrete silos, with a height of 38m, an interior diameter of 4.40m per cylinder and a thickness of the concrete walls of 150mm.

Copyright © 2019 by Alejandro CLEMENTE, Alberto ORDIÑANA, Gaute MO, Mario RANDO, Manuel SÁNCHEZ-SOLIS
Published by the International Association for Shell and Spatial Structures (IASS) with permission.

The silos are supported on reinforced concrete columns at the first floor to provide access under the silos. There is an expansion joint between the 1935 and 1939 buildings. The annex building facing towards the sea (west side), and the existing north extension, will be demolished for the new project.

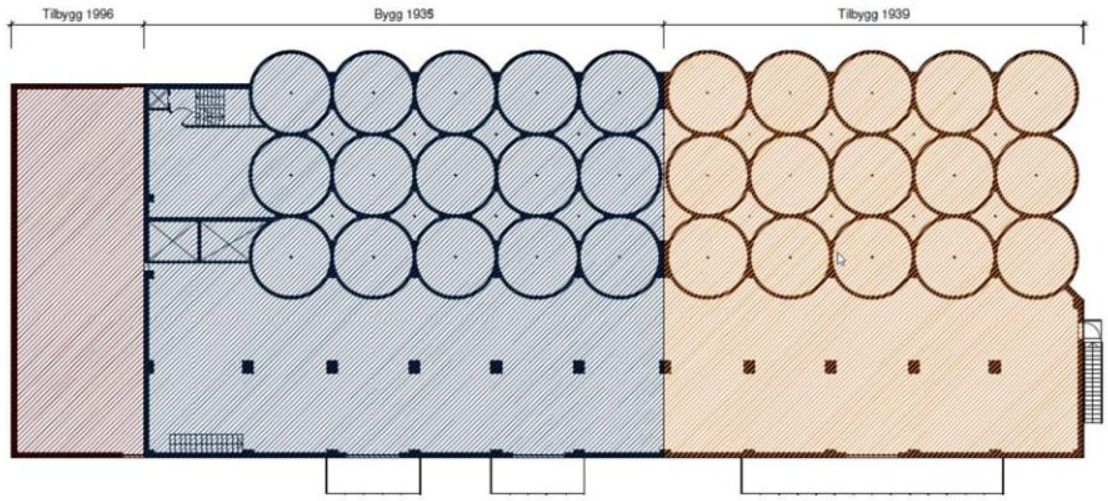


Figure 1: Plan of the existing silos built over different years.

1.2. Architectural vision. New Building

The new project proposal by architects Mestres Wåge, BAX studio and Mendoza Partida was chosen as the competition winner due to its simple and powerful strategy for the redesign of the silo in accordance with its new function. By making some cuts into the interior of the silos a monumental volume is opened up to create an impressive exhibition area that gives the future museum a strong and unique character.

The new building will consist of three volumes: the central part occupied by the silos, the volume at the west side and the new annex building at the east side.

The biggest impact on the structure from the architectural proposal is the large exhibition area (silo hall) that requires the demolition of most of the cylindrical silos from level 5 downwards to create a large open exhibition space. The exhibition floors are to have large spans without columns. The following images illustrate the new building proposal.



Figure 2: Renderings of the renovated building as projected. Internal longitudinal cut and external view.

2. Study of alternatives for the structural system

During the concept design process different alternatives were studied for the support of the silos structure following aspects such as reliability, redundancy, compatible with construction sequence or respect of the architectural requirements.

2.1. Alternative 1: Silos acting as a deep beam

The concept behind this option is to make the silos to work as a deep transfer beam. This is to assume, and to analyse the possibility that, once the silos bottom has been cut, the remaining part will act as vertical diaphragm that would be able to transfer the loads to the super columns (silos left without being cut). This option takes benefit from the stiffness of the silos structure, but to act as a proper deep beam, horizontal diaphragms are to be introduced at the top and bottom of the silos. To do so, strategically located radial steel structures are envisaged, to be placed at top and bottom of the silos, as well as concrete diaphragms within the rhomboid shaped spaces available between the silos.

2.2. Alternative 2: Two-Level-Transfer Structures

This option is conceptually based on hanging the silos from stiff trusses located at roof level. These trusses will transfer the load towards the perimeter, where new embedded concrete columns will be provided in the space available between silos. These new columns dimensions will be defined not to compromise the silos outline aesthetics.

A second transfer structure is provided at level 5using large RC beams spanning between super columns (silos not demolished) taking the loads from the new embedded perimeter columns. The super columns will include those silos that are not cut at fifth floor (although they will be partially demolished) strengthened by a new concrete outer layer. This will increase their stiffness against buckling, as well taking the heavy point loads from the concrete RC transfer beams.

2.3. Alternative 3: Roof steel transfer structure

The structural principles of this solution are based on providing all the transfer structure at roof level. This solution would propose a system of spatial transfer trusses that would take the load of the silos to the super columns that would start at roof level. However, the stiffness of this structure is much lower than the silos which leads to an inefficient system. Therefore, no further analysis was developed.

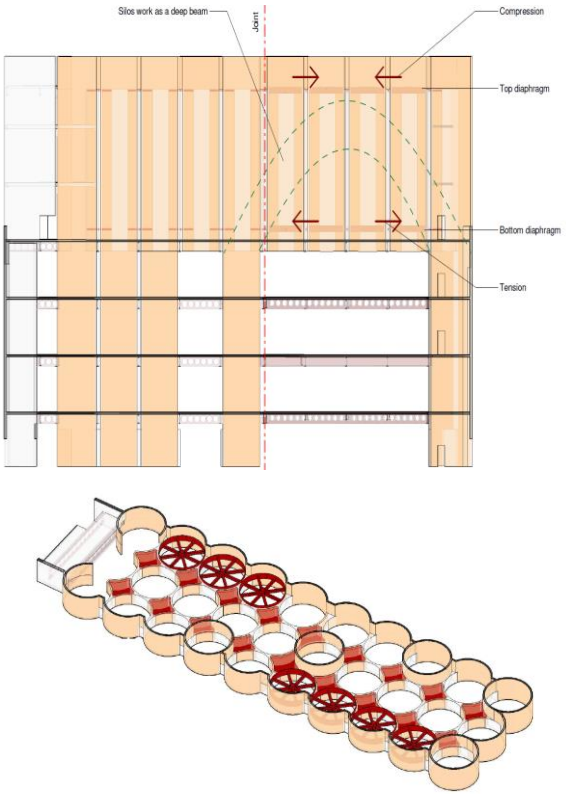
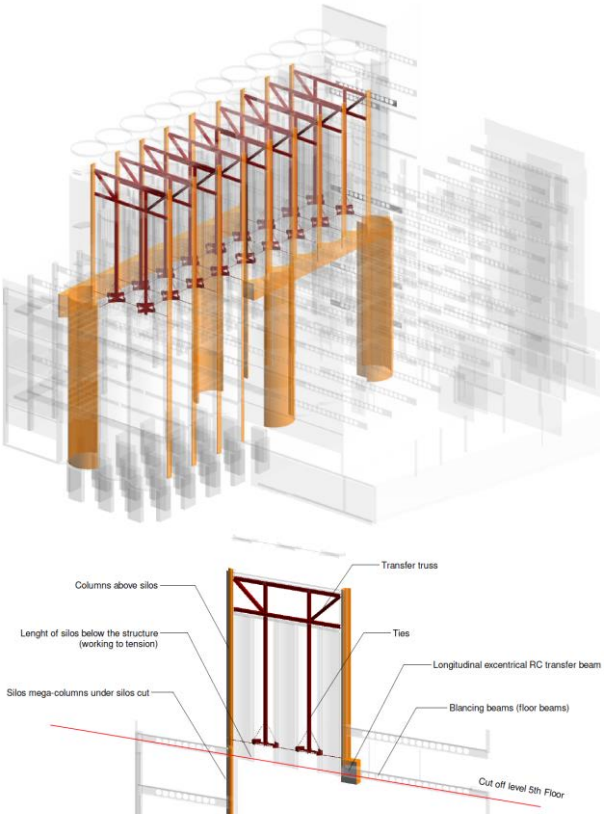
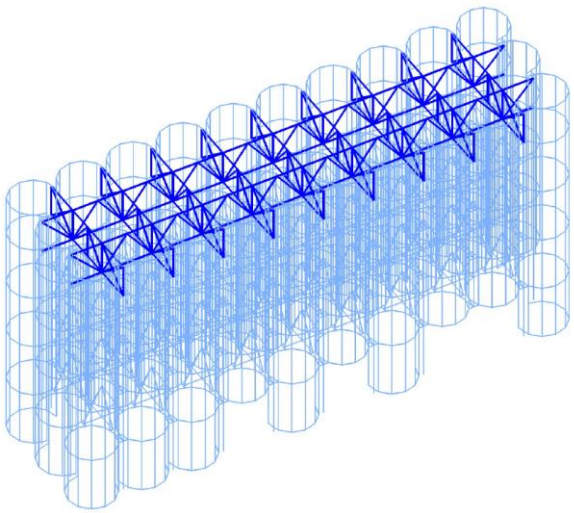
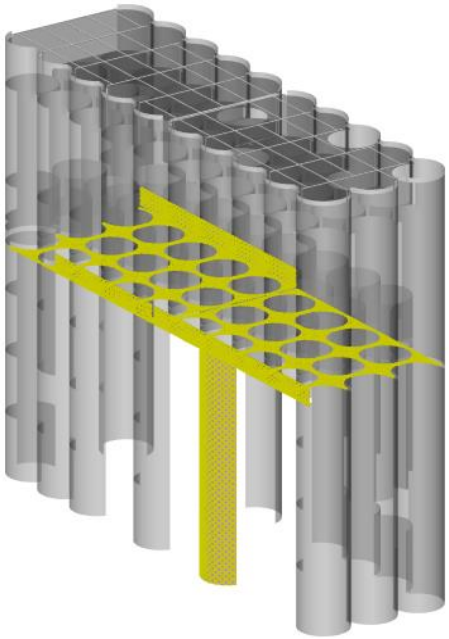
2.4. Alternative 4: Additional half silo acting as a new support and diaphragm at cut level

This option is conceptually based on the silos as the main structural system. To provide stability, it is proposed to add an extra support from that conceived by the architects. Furthermore, the cut level is reinforced by adding a diaphragm which connects all silos while keeps the holes visible from below. The lateral RC beams are placed to ensure a collaborative vertical behaviour.

The final solution is based on keeping the joint between silos disconnected. Therefore, there are two separate structures with different behaviour. The 1939 silos have a much more flexible response.

Several additional analyses were performed with different alternatives for the joint. However, the design team established a premise to try to minimise the impact on the existing structure. That is the reason why alternative 4 was the preferred one for all the disciplines involved.

Table 1: Structural systems analysed at the alternatives study

Alternative 1: Silos acting as a deep beam	Alternative 2: Two-Level-Transfer Structures
	
Alternative 3: Roof steel transfer structure	Alternative 4: Additional support and diaphragm
	

3. Structural Concept

The joint between the 1935 and 1939 silo blocks is kept as a structural joint in the rehabilitated building above ground, separating thus into two separate structures as shown in the figure below. Each of those structures would then consist of a part which is purely singular, the rehabilitated silos, i.e. structures conceived as silos that will now be driven to work very differently, and the standard buildings to the east and west. All will rest on foundations to be built while maintaining the stability of the existing silo structures.

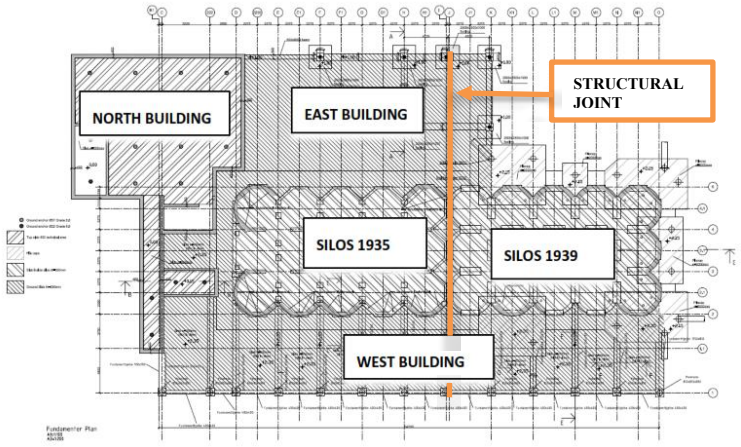


Figure 3: Plan distribution of different buildings at the renovation project.

3.1. Silos Buildings –Two independent structures separated by the existing joint.

The concept is based on creating a deep transfer beam with the silos above the cut level.

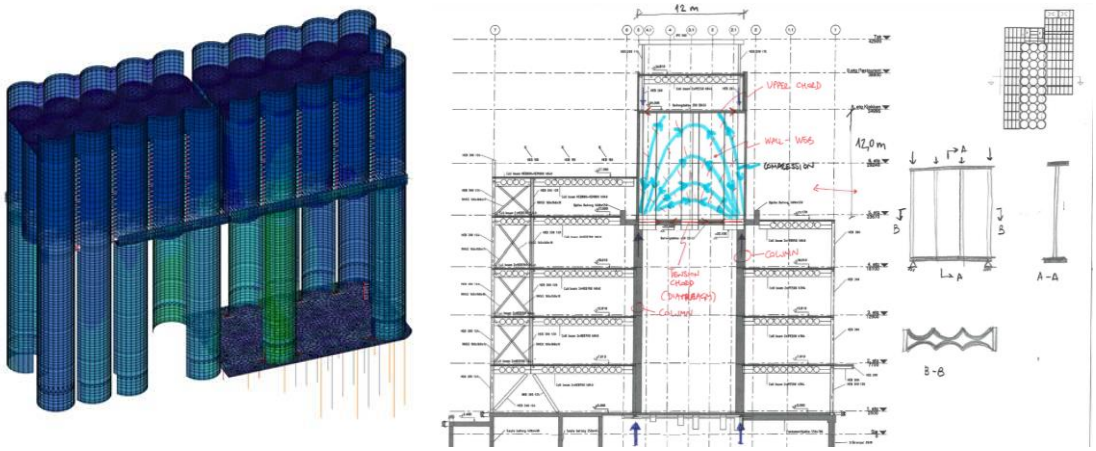


Figure 4: Structural scheme in a transverse cut of silos, and F.E.M. view.

This is to assume, and to analyse, the possibility that, once the bottom of the silos has been cut, the remaining part will act as vertical diaphragm, able to transfer the loads to the supercolumns (silos left without being cut). This benefits from the stiffness of the silos structure, but in order to act as a proper deep beam, horizontal diaphragms are to be introduced at the top and bottom of the silos. The deep transfer beam built adjacent to the silos and the new diaphragms at cut level and top level will span between super columns, which are the silos that are not cut at 5th floor (+22.1). These columns are partially demolished, so in order to prevent them from buckling due to their reduced thickness

(150mm), as well as to guarantee that they can take the additional loads, they will be strengthened with an additional outer concrete layer attached to the existing one and increasing its overall thickness.

Two beams must be executed at the same slab level in order to support the cut silos which do not reach foundation level and therefore have no support. The solution of adding a new silo-column to foundation allows that the row nearest to the expansion joint can work as a cantilever, avoiding that the new beams must be supported at the edge of the 1935 silos.

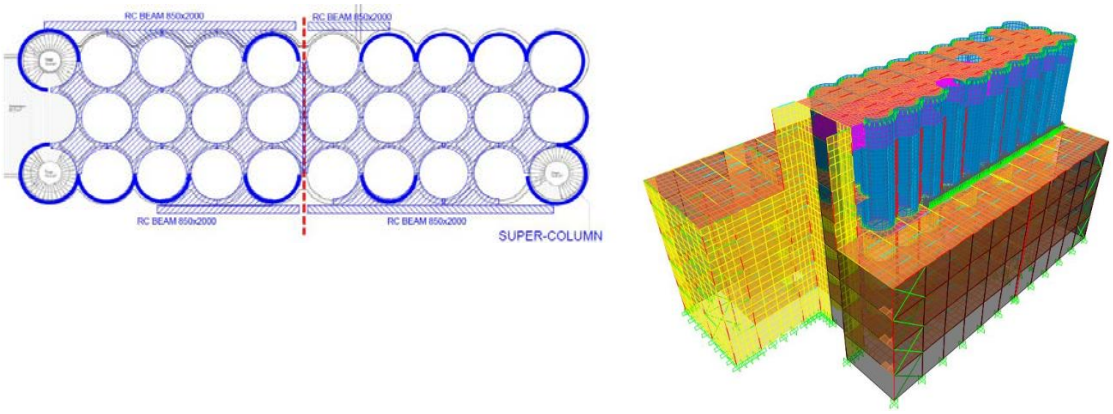


Figure 5: Plan of the diaphragm slab and F.E.M. view.

3.2. Adjacent Buildings – Two standard buildings connected to their respective silo

In this case, the structure is more conventional, and will be governed by the long spans, as well as the necessity to provide a lateral bracing stability system to mitigate the impact of the wind loads on the silos structure. In order to provide the required spans without columns at the exhibition areas, a system of composite metal deck spanning between long span cellular beams has been designed. The holes of the cellular beams will allow for passing the conducts for services.

3.3. Foundation – A common foundation for all buildings

The foundations of the East and North buildings consist of a basement slab at the underground level and isolated footings for the areas outside the basement. Both foundations bear at the same level, directly onto rock or onto filling layers where the rock bed is lower. The basement slab is tied down with ground anchors to withstand the ground water pressure. In relation to the silo foundations, the existing foundations from 1935 are strip footings bearing directly to rock and will now be enlarged and strengthened. The 1939 foundations consist of columns that are not found reliable and are disregarded in the project. As a result, the foundation is executed by means of steel core piles and inclined/vertical steel bored piles. The foundation of the new West building is also steel bored piles.

4. Construction sequence

One of the key factors for the success of the project is to develop a construction sequence that establishes the correct order to execute the demolition and reinforcement works without compromising the stability of the remaining silos. The final sequence has been carefully planned and discussed with the future Contractor (Kruse Smith) to guarantee the viability of the different phases.

A detailed analysis has been performed of the structure during the different construction phases: A FEM Model simulating the different erection and demolition stages has been implemented and the structure has been verified at the end of the different construction stages, as well as for the final building configuration. The following are the main phases of the construction:

4.1. Phase 1: Demolition of the auxiliary buildings around the silos.

This phase includes the demolition of the light steel structures on top of the silos, the demolition of the six storey annex building, made of reinforced concrete, located to the west of the silos and the demolition of the stair communication core located to the north. The idea is to leave standing only the old silo constructions, which are self-supporting structures.

4.2. Phase 2: Preparation works and rehabilitation of the existing silos.

It is necessary to open up some holes in the concrete slab at the top of the silos in order to allow the placement of auxiliary steel platforms that will be suspended inside the silo cylinders by means of steel cables. These platforms can be moved up and down to inspect and rehabilitate the interior of the silo walls. The rehabilitation of the existing silos consists of a combination of mechanical repair of the damaged concrete and the electrochemical re-alkalization of the interior part of the silos to halt the corrosion of the steel in the carbonated concrete. The mechanical repair will be done both inside and outside of the walls and it will include the removal of loose concrete, filling of damaged areas with mortar and the repair of all the cracks larger than 0.8mm width.

4.3. Phase 3: Reinforcement of existing foundations and execution of new foundations.

This phase includes the reinforcement of the existing direct foundations to rock of the 1935 silo walls by means of their enlargement with new pad foundation, tied to the existing ones. This way the additional loads at the remaining silo walls will be transferred safely to the sound rock below. The 1939 silos have deeper foundations with variable length RC concrete columns to the rock. New small diameter steel core piles can be installed inside the silo walls with small machinery and large diameter steel tube piles can be installed outside the remaining silo walls (super-columns) to transfer the additional loads. Large pile caps will be cast connecting the interior piles to the remaining silo walls and the large diameter exterior steel piles. A new ground floor concrete slab will be cast to connect and tie all the interior elements inside the silos.

4.4. Phase 4: Reinforcement of the existing silo construction.

All remaining silos below +22,10 m (cut level), which support the silos above the cutting level (super-columns), shall be reinforced from outside with a minimum of 200mm concrete with a double reinforcement layer.

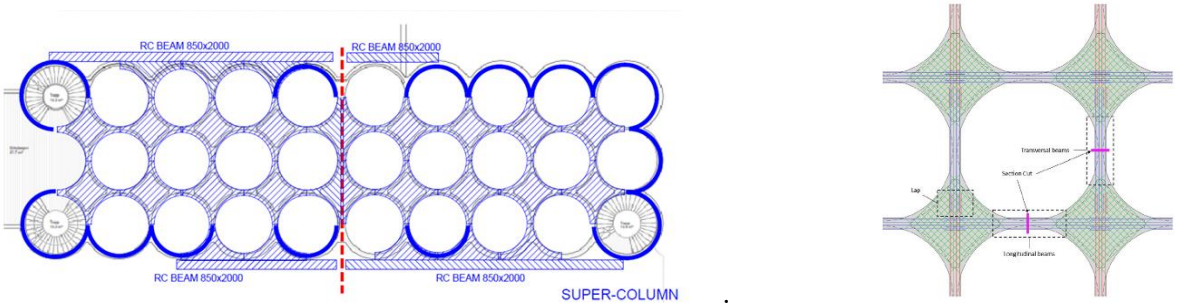


Figure 6: Plan of the diaphragm slab at cut level.

A diaphragm of reinforced concrete 450mm deep will be executed directly above the cutting level (+22.50m) to tie the base of the silos and to support them. This diaphragm has also circular openings aligned with the interior silo walls to respect the architects design, but an orthogonal grid of beams 350mm wide will be executed to transfer the forces in two directions. Local cuts will be done at the existing walls to cast the new diaphragm. There are two powerful lateral RC beams to distribute the loads to the remaining super-columns below. Exterior silos over 22,10m (cut level) shall be also reinforced to withstand the tension forces.

4.5. Phase 5: Demolition of existing silo walls below the cut level.

When all the reinforcement works have been executed, it will be safe to proceed carefully to the cut and demolish the silo walls.

Only new reinforced external walls will be maintained. Demolitions will start from the cut level progressing downwards to the ground level. Subphases for the demolitions have been carefully planned, with a maximum of six cylinders affected per stage. The works will start at the south, starting with exterior walls to permit the access to the interior rhomboidal walls. In total 17 demolition subphases have been planned.

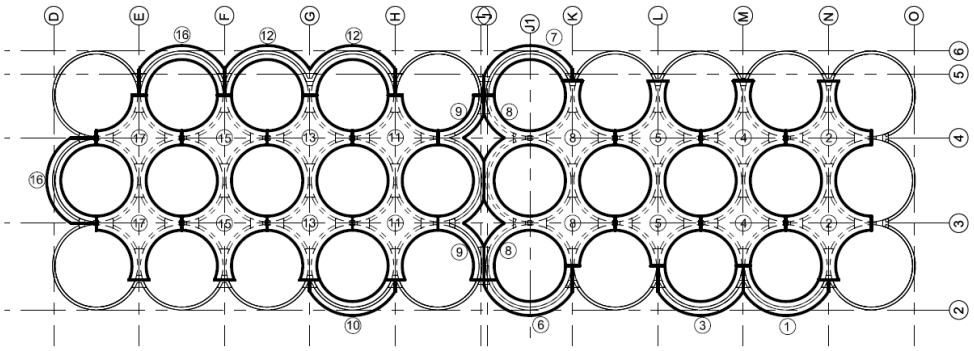


Figure 7: Demolition sequence below the cut level.

4.6. Phase 6: Execution of new buildings around the remaining silos.

After finishing the demolition of the concrete silo walls, the works to erect the new annex buildings at west and east of the silos can start.

The structural system of the new buildings consists of steel columns placed at the façade alignments that support large span steel cellular beams and composite slabs. Where necessary cross bracing elements have been designed to guarantee the horizontal stability.

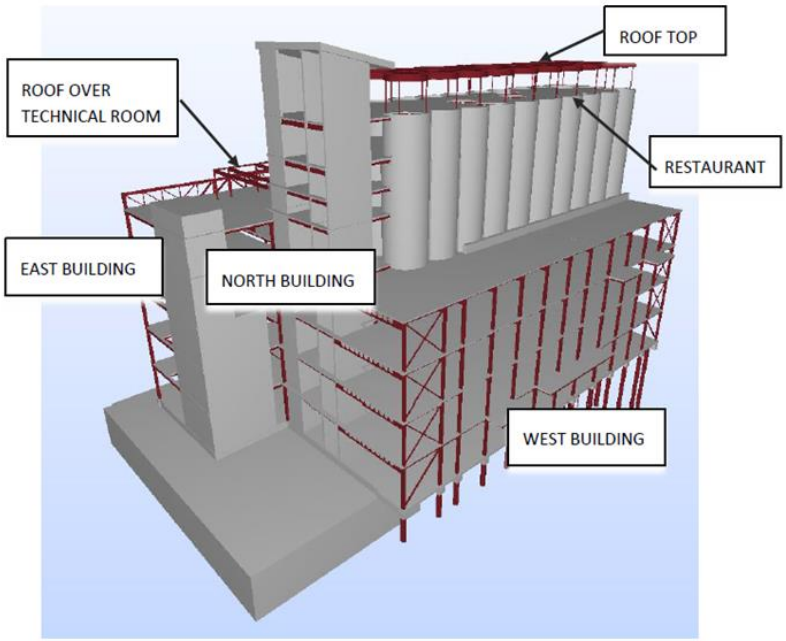


Figure 8: Buildings around the silos construction.

Proceedings of the IASS Annual Symposium 2019 – Structural Membranes 2019
Form and Force
7 – 10 October 2019, Barcelona, Spain
C. Lázaro, K.-U. Bletzinger, E. Oñate (eds.)

Structural optimisation and rationalisation of the BUGA fibre composite dome

Bas RONGEN*, Valentin KOSLOWSKI, Marta GIL PÉREZ, Jan KNIPPERS

* Institute of Building Structures and Structural Design (ITKE)
University of Stuttgart
b.rongen@itke.uni-stuttgart.de

Abstract

A Pavilion, manufactured using core-less fibre wound (CFW) reinforced polymers was exhibited in the Bundesgartenschau 2019 (BUGA) in Heilbronn from the 17th of April until the 6th of October 2019. The load bearing structure of this Pavilion is the latest endeavour, developed as a collaborative effort of the ICD and ITKE institutes at the University of Stuttgart. The goal of the research is to design and engineer lightweight and high-performance building components. A previous structure with the same manufacturing methodology was exhibited in 2016 at the Victoria and Albert Museum in London. The structural system of the pavilion was a dome structure covered by a transparent Ethylene tetrafluoroethylene (ETFE) membrane with steel ridge and edge cables. The structural typology was such that maximum bending moments appear at the nodes, leading to maximum forces at the connections. The dome structure was made of 60 components, each hollow in section and bone-like in shape. Due to the membrane nature of the ETFE skin, loads were unequally distributed over the dome. This paper will describe how the shape of the dome was structurally optimised in order to reduce design forces in the components as the main objective, while rationalizing the 60 different components in manageable geometries for fabrication.

Keywords: FRP, Dome, Optimization, Rationalization, prefabricated shell, form finding, modular system, digital workflow, robotic fabrication

1. Introduction

The Bundesgartenschau (BUGA) fibre pavilion, was a lightweight shell structure made out of 60 core-less fibre wound (CFW) components in carbon and glass fibre reinforced polymers. The global geometry of the pavilion was a dome in which each member was a hollow bone-shaped component. On the component level, CFW allows for tailored placing of material, taking into account the flow of forces. In the pavilion, all the components were connected to form a doubly-curved shell structure, allowing the use of material with great efficiency. In this paper first a context is established on related works with the CFW fabrication system, and afterwards the construction system of the BUGA fibre pavilion will be introduced. Finally, the focus of this paper will be on how the global geometry was structurally optimised in a manner that was easy to manufacture.

2. Context and Related Work

The Institute for Computational Design and Construction (ICD) and the Institute for Building Structures and Structural Design (ITKE) designed several structures using the CFW fabrication system. For the purpose of this paper the most relevant work is the Elytra Pavilion designed for the Victoria and Albert Museum in London [1]. In core-less filament winding (CFW), a robotic arm places fibres impregnated in epoxy resin from point to point. During the manufacturing process a shape gradually emerges and

Copyright © 2019 by Bas Rongen, Valentin Koslowski, Marta Gil Pérez, and Jan Knippers
Published by the International Association for Shell and Spatial Structures (IASS) with permission.

fibres can be placed according to the flow of forces [2, 3]. For the Elytra Pavilion the geometry was a horizontal tessellation of hexagonal modules which had a bottom and top chord, working in tensions and compression. Modules closer to the columns that received higher loads gradually received additional fibre reinforcement. The Elytra Pavilion was one of the predecessors that had to undergo structural testing to prove structural safety and reliability [1].

3. Construction System

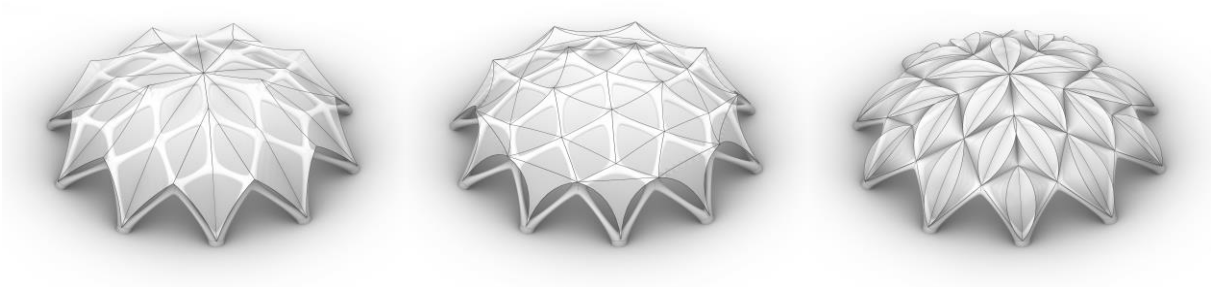
The brief given by the BUGA was the design of a dome with a transparent skin for the BUGA in Heilbronn, starting in April 2019. Structurally, the dome spanned larger than 22m and is 6.8m in height, as shown in Figure 1 (right). The dome consisted out of 60 prefabricated CFRP components that were assembled on site.



Figure 1: Left, Photograph of the BUGA Fibre Pavilion © ICD/ITKE; Right, Top view drawing © ICD/ITKE

3.1 Membrane

In Figure 1 (left) a skin protecting the interior against rain can be seen. In order to create this membrane, several options for the cable supporting grid were investigated during the design phase. A selection of three options is shown in Figure 2 below.



1) Radial Grid 2) Tangential Grid 3) Arches

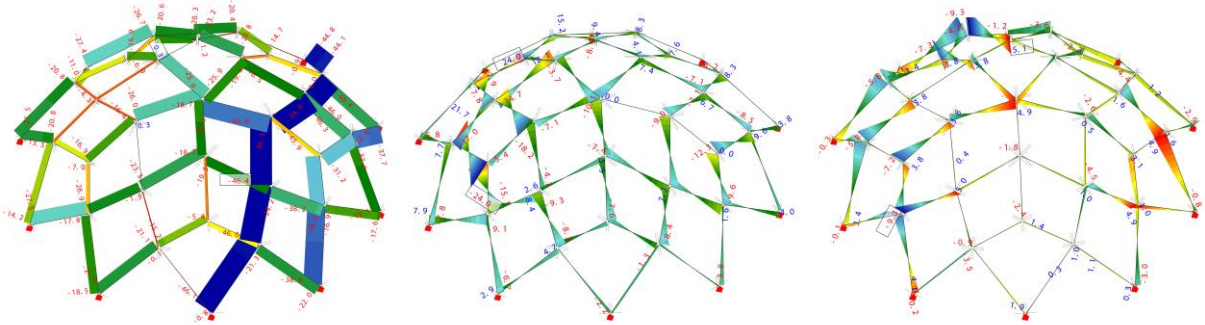
Figure 2: ETFE membrane supporting structure, design variants

The radial cable grid (option 1) was considered optimal, because it reduced the complexities in detailing and pre-stressing. In the final design, pre-stress was applied both at the top of the dome and at its foundations. The transparent membrane in-between the steel ridge cables was materialized in Ethylene tetrafluoroethylene (ETFE).

3.2 Structural Typology of the Fibre Composite

In the BUGA Fibre Pavilion, each line segment of the geometrical topology was realised as a hollow FRP tube. Each component is bone-like in shape, manufactured with the CFW technique, using the materials carbon fibre and glass fibre. The components are connected at the nodes using custom manufactured steel pieces. The topology of the BUGA Fibre Pavilion defined by the designers, is dominated by the use of quadrilaterals. The edges of the quadrilaterals (quad-grid) are executed as structural members. A quad-grid as in this design can be stabilised in three ways: it must either be braced using a cable grid, triangulated with additional members, or the grid members must act in bending. However, triangulation or a bracing grid for the design were deemed undesirable and therefore, all components were subjected to bending moments at nodes of the quad-grid.

The overall topology of a quad-grid in combination with the discrete punctual load-induction at the nodes leads to maximum bending moments at the components ends. For this particular geometry this means that maximum forces can arise locally at the joints due to the combination of normal forces with bending moments.



Normal Force [kN] | In-Plane Bending Moments [kNm] | Out-of-Plane Moments [kNm]

Figure 3: Force plots from Finite Element Program for wind load case

In Figure 3 above, the structural action of the dome is visualized, unequal compression forces appear in the components, as well as in-plane bending moments and out-of-plane bending moments.

3.3 FRP Components and Structural Testing

The design was made out of 60 carbon fibre reinforced composite components, each weighing approximately 70 kg. The overall dome can be divided in 5 identical pieces that repeat around the central axis. In order to improve manufacturing, a rationalisation was performed in order to minimize the amount of unique parts.

The structural use of Continuous Filament Wound (CFW) CFRP in this particular geometrical configuration was not tested thus far. Moreover, no Eurocode for Fiber-reinforced polymer (FRP) structures that can support the design in the approval process was yet developed. Hence, the building system had to undergo structural testing to prove its structural safety according to German regulations (Zustimmung im Einzelfall). In the testing procedure, the components were tested with a material safety factor of 3. Therefore, reducing the design forces within the components as much as possible was crucial for the feasibility of the project.

4. Optimisation & Rationalisation of the Global Geometry

A manually subdivided dome in CAD in order to come to equal elements did not give satisfactory results in terms of repeatable geometries. An iterative geometrical rationalisation of the different component geometries was therefore required. The geometrical rationalisation clustered the geometrical parameters of the components in groups, while reducing forces in the composite structure.

4.1 Abstraction

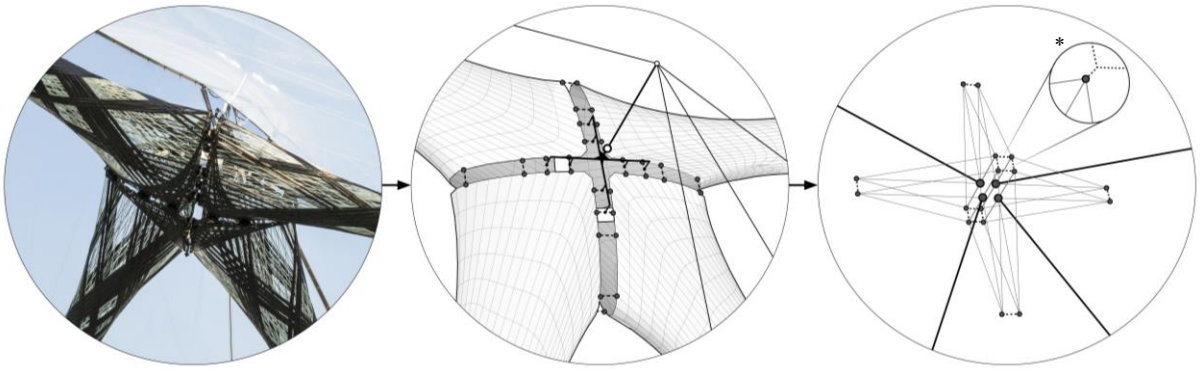


Figure 4: Abstraction of component geometries towards simplified FE approach
(* = Zoom-in of modelling approach)

The hollow tube components were abstracted to form a simplified wireframe representation, with special attention required at to the nodes. Figure 4 shows the abstraction steps taken with special focus on the nodal geometry. From the simplified model geometrical data could be extracted to serve as input for a finite element model for a structural evaluation, and as evaluation on reoccurring geometries.

4.2 Geometrical Boundary Conditions

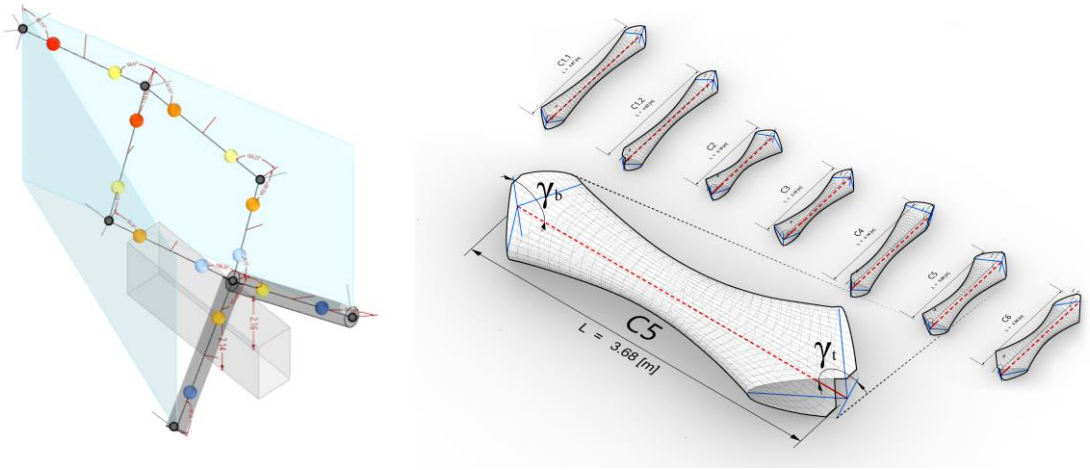
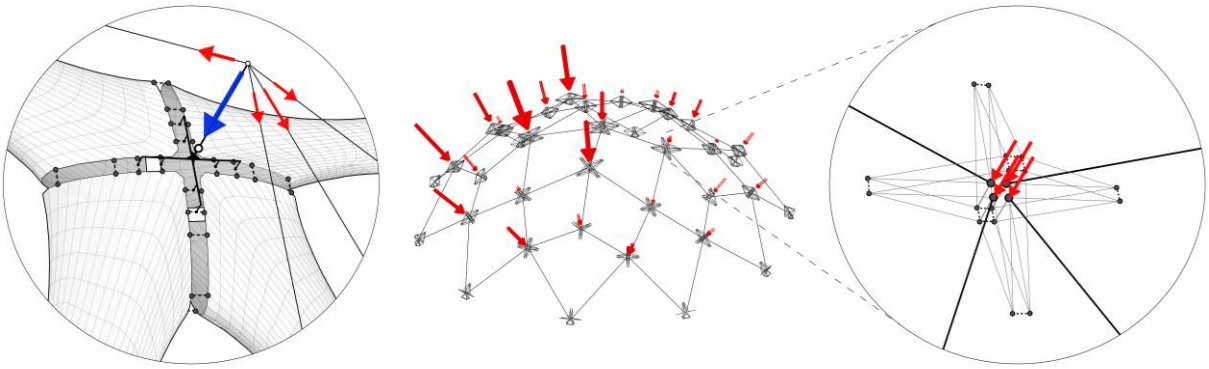


Figure 5: Left, 1/10th of the Global Geometry; Right, Component geometries, structural axis in red and frame inclinations in blue

Due to symmetry, the geometrical freedom was limited to 7 different members instead of 60, which can be seen in Figure 5 (left). These 7 members, representing 1/10th of the dome were geometrically parametrized and used to construct the full dome for a structural evaluation. In Figure 5 (right) two gamma angles that drove the geometrical rationalisation, γ_b and γ_t are indicated. On both Gamma angles a clustering was performed in order to sort these in different groups. During the process a height restriction was included for the entrance as well, in order not to conflict with building regulations.

4.3 Loads



Cable forces (red) leading to compression pole forces (blue)

Simplified global model with sectional forces applied in red

Local application of loads on the simplified building node

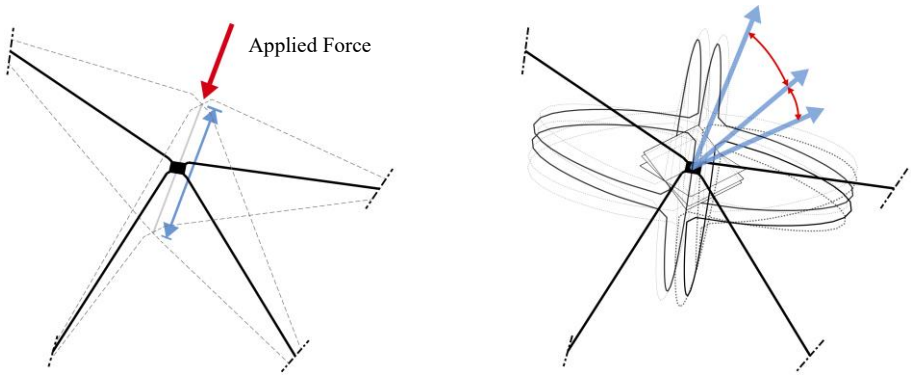
Figure 6: Force transfer from Geometrical Nonlinear model with membrane to simplified optimisation model

Loads are extracted by making a structural cut at the membrane supports in a geometric nonlinear finite element (FE) model. The membrane supports were modelled as trusses for the membrane height points and as beams for the low points. These elements can be seen as interface elements for load transfer from the cable structure into the composite structure. Previously mentioned structural cut allowed for a separate simplified linear geometrical FE model, without the inclusion of the geometric nonlinear membrane. The "interface" forces were extracted for more than 60 load cases.

The extracted "interface" forces were applied as external forces on the simplified finite element model. Figure 6 shows how the forces are abstracted and transferred to the simplified FE model.

For the geometrical optimisation the assumption was made that the amplitude and characteristics of the forces would not change significantly. This assumption was based on two reasons: the membrane & cable network topology did not change, and the shape of the dome was limited in moving in the XY-plane, which limits the rearrangement of membrane/cable spans and therefore limits changes in loads.

4.4 Degrees of Freedom



Translational Degree of Freedom

Rotational Degree of Freedom

Figure 7: Degrees of Freedom Per Node

In the parametric model of 1/10th of the dome every node possessed two principle degrees of freedom (Figure 7). The first degree of freedom (DOF) was in perpendicular direction of reference sphere of the dome geometry. In addition, every node had a construction plane, which allowed the node to rotate in space. The rotation of the construction plane was required in order to achieve the rationalized geometry.

4.5 Object Function

The optimisation was performed in a two-step approach. First, by finding a geometry that structurally performs better than the initial geometry within geometrical bounds. Secondly the "structural "better"" shape was approximated with a separate rationalisation algorithm within a set of predetermined geometrical bounds. The rationalisation of the geometry relied on sorting of the occurring Gamma angles, and dividing these into groups. A midrange was defined per angle group. Subsequently the amplitude from the midrange (error) of each group was minimized to fall under a particular threshold value. The optimisation was performed using genetic algorithms inside the grasshopper software environment. For the simplified FE model Karamba3D was used. Custom weighting functions were applied in order to steer the algorithm. A penalty function was used for example in case the design would collide with the entrance clearance that was required (as depicted in Figure 5).

5 Results

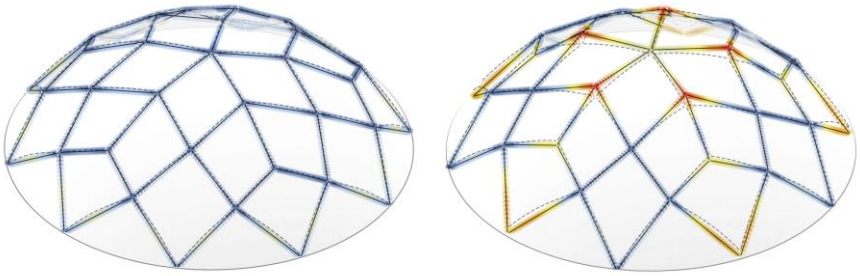
As a result of the optimisation, design forces in the connections were reduced by 27%. At the same time geometrical complexity was reduced from 14 different gamma angles to 6. The system lengths of the membrane supports were reduced due to the change in geometry. This reduction in system length meant that the steel cross-sections for these elements could be reduced in size.

Table 1 summarizes the options from the optimisation process. It was discovered that rationalisation in two groups was not possible as the pavilion would become inaccessible.

Table 1: Design options, comparison of geometrical data and structural performance

Properties	Co-Spherical (Initial Design)	Co-Spherical Rationalized	Improved Structural Performance	Final Design
Amount of angle groups	-	3	-	6
Normal force connection	36.8 [kN]	35.4 [kN]	23.2 [kN]	26.7 [kN]
Connection performance	100%	96%	63%	73%
Angle deviation	0.4˚ (6 groups)	0.19˚ (3 groups)	1.04˚ (6 groups)	0.15˚ (6 groups)
Angles range	94.18˚ <> 104.14˚	91.60˚ <> 110.72˚	91.60˚ <> 110.72˚	85.78˚ <> 109.63˚
Note	Un-rationalized	-Not accessible -Angle deviation to big	Un-rationalized	-

Loads are not equally distributed over the spherical surface, due to the topology of the cable network. As an effect of this the improved geometry tends to detach from the reference sphere in order to more effectively align towards the load induction points. Figure 8 shows the difference between the initial and final design in relation to their reference spheres.



Initial Design Final Design

Figure 8: Comparison of Initial and Final Design in relation to a reference sphere

6 Recommendation

The CFW fabrication method allows for the production of component geometries with negative Gaussian curvature. It is noticed, however, that zones with almost zero Gaussian curvature pose a possible weak point in the structure for two reasons: shell action is low because of limited curvature leaving it prone for local buckling, and during manufacturing fibres "are not wound tightly together", leading to a case where the formwork (fibre anchor pins) fills up faster.

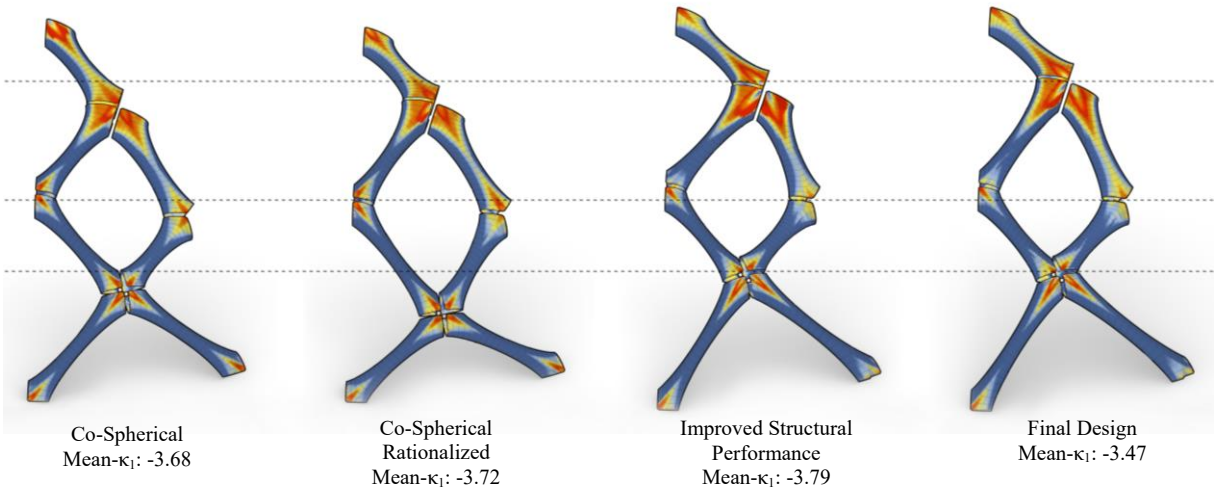


Figure 9: Geometrical options Gaussian curvature, mapped for κ_1 between: [-2.5 (blue) < > 0 (red)]; including mean principal Gaussian curvature (κ_1) computed per geometry

In Figure 9 an assessment on principle Gaussian curvature is performed, for four design options that were developed as part of the optimisation process. From Figure 10, it can be concluded that there exist zones with almost no curvature at the nodes. These zones became larger (mean-κ_1 decreases) as the design process informed by the optimisation developed. The decrease of Gaussian curvature was because the geometry detached from the reference sphere.

This absence of curvature is undesirable as it might negatively influence the individual stability of each component. Therefore, for future designs, it is recommended to evaluate the principle Gaussian curvatures of component designs early on in the conceptual phase. If local regions of zero principle Gaussian curvature are detected, then this can still be corrected before components are prototyped and/or manufactured.

Conclusion

The BUGA Fibre Pavilion showcases the potential for geometric flexibility and high structural performance of coreless fibre wound (CFW) structures in carbon and glass fibre reinforced polymers.

In the design of the pavilion, the building system allows for adapting its geometry towards predominating load paths whilst keeping the geometry easy to manufacture. The geometric flexibility of the building system allows for reduced maximum forces, overall decrease in material use, simplified structural testing, and consequently, a lower overall risk for the project.

The BUGA Fibre Pavilion showcases the potential of structural optimisation during the design development. The project also shows that constraints of manufacturing should be taken into account, in order not to "over optimise" for structural performance and neglect ease of manufacturing. In this project a hypothetical reduction of forces of 37% could have been achieved, however with the manufacturer a compromise was made. It was decided to go for 27% of force reduction with a manufacturing process which is less complex.

Without the right soft skills and digital toolsets, designing an innovative dome structure like this is an impossible challenge. A building as novel as the BUGA Fibre Pavilion raises many new challenges, some of the most important being: data handling, data transfer, clear communication and division of responsibilities.

Acknowledgements

The work presented in this paper was partially funded by the State of Baden-Wuerttemberg, the University of Stuttgart, EFRE European Union, GETTYLAB and DFG German Research Foundation. The authors would like to express their gratitude towards their fellow investigators, Prof. Achim Menges, Serban Bodea, Niccolò Dambrosio, Monika Goebel, Christoph Zechmeister of the Institute for Computational Design and Construction (ICD), University of Stuttgart. The authors would also like thank their project partners FibR GmbH and PFEIFER GmbH and the Bundesgartenschau Heilbronn 2019 GmbH.

References

1. J. Knippers, V. Koslowski, J. Solly and T. Fildhuth, "Modular coreless filament winding for lightweight systems in architecture" *CICE 2016 8th International Conference on Fibre-Reinforced Polymer (FRP),* Dec. 2016.
2. S. Parascho, J. Knippers, M. Dörstelmann, M. Prado, and A. Menges, "Modular Fibrous Morphologies: Computational Design, Simulation and Fabrication of Differentiated Fibre Composite Building Components", *Advances in Architectural Geometry 2014*, pp. 29–45, 2014.
3. F. Waimer, R. La Magna and J. Knippers, "Integrative numerical techniques for fibre reinforced polymers – forming process and analysis of differentiated anisotropy" *Journal of the International Association for Shell and Spatial Structures*, vol. 54, pp. 301-309, Dec. 2013.

Proceedings of the IASS Annual Symposium 2019 – Structural Membranes 2019
Form and Force
7 – 10 October 2019, Barcelona, Spain
C. Lázaro, K.-U. Bletzinger, E. Oñate (eds.)

Subaru Nursery School with the 3D curved roof structurally optimized by sensitivity analysis

Eisuke MITSUDA*, Kazuhiro EBATA[a]

*Professor, Faculty of Design and Architecture, Kyoto Institute of Technology, Dr.Eng.
Matsugasaki, Sakyo-ku, Kyoto 606-8585 JAPAN
mitsuda@kit.ac.jp

[a] Director, Mitsuda Structural Consultants Co. Ltd., M. Eng.

Abstract

Subaru Nursery School is built on a site in the suburb of Fukuoka. This building has about 1,200 square meter total floor areas and has one story. Authors are structural engineer of this building. The structural and architectural characteristic of this building is the shape of the roof. The greater part of this roof is made with general flat RC slab. The thickness of the slab is 180[mm] and it was decided by the cantilever length of the eaves and the size of the classrooms. On the other hand, the maximum wide of the assembly hall is 15[m]. Of course, the flat slab with 180[mm] thickness can't cover the hall. And then, we did the shape design by sensitivity analysis to minimize the structural strain energy. The shape of the roof changed to the 3D curved surface. In this analysis, we modify the shape (Z coordinate of the nodes) only above and vicinity of the assembly hall. In addition to this, we restrict the Z coordinate of the end-line of the hall not to modify, we got the horizontal ribbon windows at the corner of the hall. As a result, we could design the lovely roof that is mainly flat and partially undulating with the same thickness RC slab. The architecture merges into the surrounding landscape.

Keywords: structural design, form finding, optimization, sensitivity analysis, concrete shell, effect of partial application of complex design, cost of formwork, architecture as a continuous body

1. Introduction

Recently, the number of buildings with free curved roofs (or slabs) made of concrete has increased. Some of them are very famous as a beautiful architecture, but they are not common at all. Because of the difficulty of making formwork, the total amount of them is still few. There are several types of formwork, for example, truss-wall method, combination of normal formwork system and bending plywood, pile up the soil and dig it, cutting-steel-plate and steel mesh, and so on. Adding them, research & development for new other systems are going on. But every curved formwork is still too



Figure 1: formwork of truss-wall method in fabricator



Figure 2: formwork with bending plywood at site

Copyright © 2019 by Eisuke MITSUDA and Kazuhiro EBATA
Published by the International Association for Shell and Spatial Structures (IASS) with permission.

expensive. And the height of the wall which separates the inside and outside of the building under the free curved shell roof is not constant. Therefore, in many cases, the building with free curved shell roof loses easily on a cost in the one with normal flat roof before discussing about the beauty and the charming point of the architecture. In this paper, we show the successful project in which the free curved shell roof is applied partially to the space where the shell is needed.

2. Outline of the building and the whole structural planning

Subaru Nursery School is built on a site in the suburb of Fukuoka. This building has about 1,200 square meter total floor areas and has one story. Authors are structural engineer of this building. Architect of this building is Ryuji Fujimura / RFA and Shunji Hayashida / CFA. Ryuji Fujimura is one of the most famous promising young architect in JAPAN and his keyword for design is “architecture as a continuous body”.

This building is classified in RC wall construction. To resist eathquakes, walls should be located in a good balance.

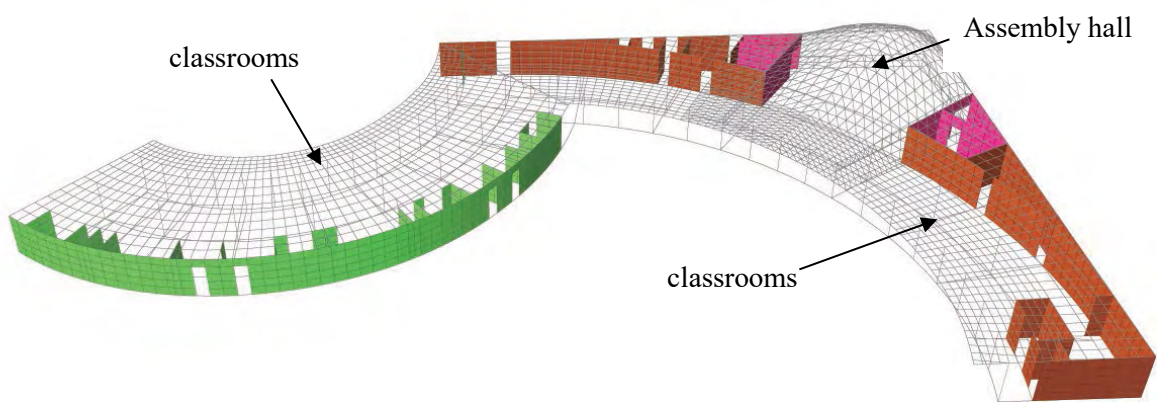


Figure 3: whole FEM model for structural analysis

The structural and architectural characteristic of this building is the shape of the roof. The greater part of this roof is made with general flat RC slab. The thickness of the slab is 180[mm] and it was decided by the length of the eaves and the size of the classrooms. On the other hand, the maximum wide of the assembly hall is 15[m]. Of course, the flat slab with 180[mm] thickness can’t cover the assembly hall. And, we apply 3D curved surface to the roof as a shell structure. This is convenient for the assembly hall which requires higher ceiling height. In this project, we use computational morphogenesis to determine the shape of the shell roof above and vicinity of the assembly hall. (I will explain it in detail later.) As a result, we could design the lovely roof that is mainly flat and partially undulating with the same thickness RC slab.



Figure 4: bird view of the Subaru Nursery School

3. Partial application of form finding by sensitivity analysis

3.1. Outline of partial model

In this project, we made a full FEM model as a whole model to evaluate the stress of the shell and thrust force, and to execute a form finding program we extract the partial roof FEM model from that whole model. In this partial model, walls, columns and beams are converted to the supporting points.

3.2. boundary conditions and the setting of design variables

Fig.5 shows the boundary conditions on the partial model. Supporting point on the wall can support the vertical force and in-plane direction force (and can't support out-of-plane direction force). Fig.6 shows the setting of design variables. Nodes in modifiable area can be updated their Z-coordinates. For example, the points on the wall around the assembly hall can be updated, but the points on the exterior skin at the corner of the assembly hall can't be updated. These un-updated points which is on the unmodifiable line keep horizontal line and lead the upper-side frame of the consecutive ribbon window. Therefore, we can adopt the normal window sash which doesn't cost.

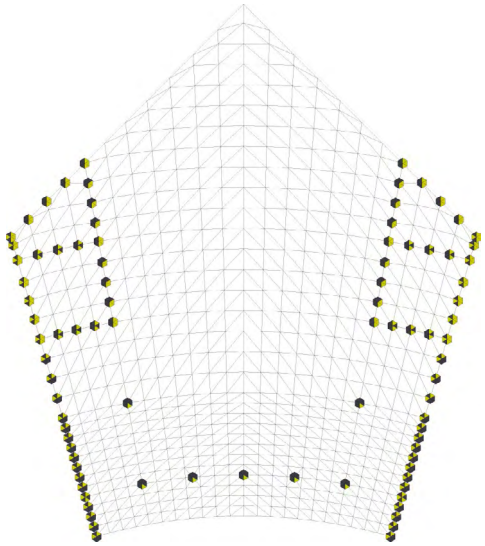


Figure 5: supporting point

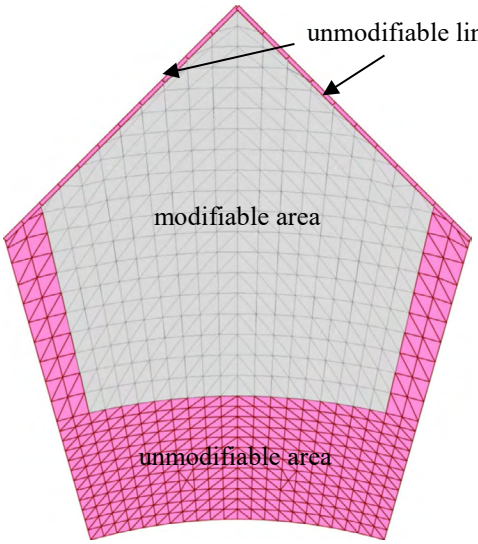


Figure 6: grouping of nodes

3.3. form finding by sensitivity analysis

We did the computational morphogenesis by sensitivity analysis to minimize the structural strain energy. In this analysis, we calculate the sensitivity coefficient to all the modifiable nodes to determine the amount of change of Z-coordinate of modifiable nodes. Through the calculation, the shape of the roof evolutionary changed to the 3D curved surface. Fig.7 shows the evolutinary process from the initial shape to the last shape. The color shows the deformation under vertical load. In initial shape, large deformation and large bending moment occurs, and we couldn't design in such a situation. To reduce the deformation, the center of the slab go up step by step. The higher the top of the slab, the smaller the bending moment. This means that the RC slab is evolutionary changing to the shell step by step.

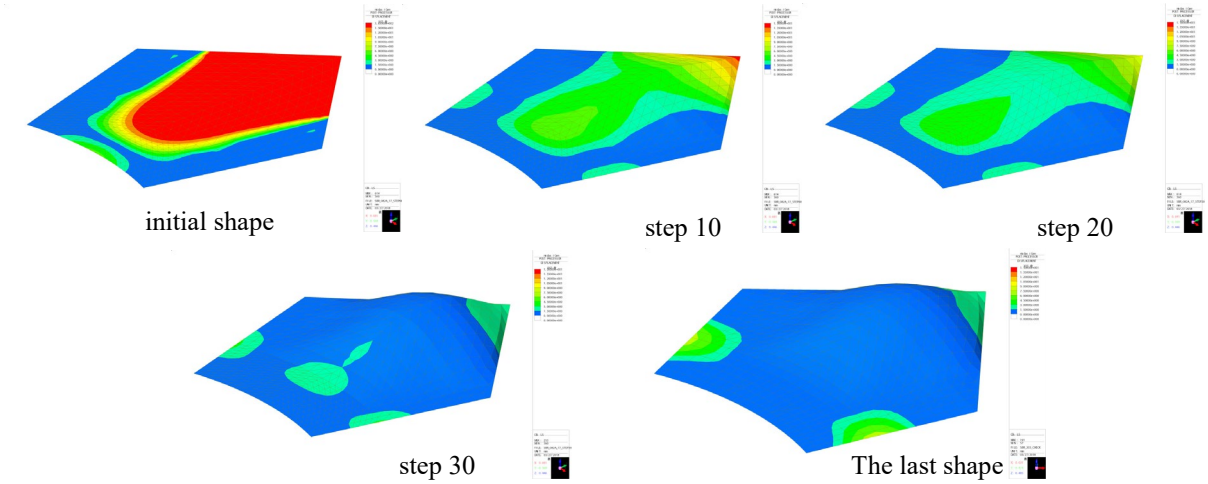


Figure 7: evolutionary process of the roof



Figure 8: external appearance of ribbon window



Figure 9: interior view of the assembly hall

4. formwork and bar arrangement at the site

Fig.10 shows the formwork for curved surface at the site. These formwork were made like furniture, and set on a scaffold whose level is measured exactly. Fig.11 shows the bar arrangement at the site. After setting the formwork, reinforcement bars are put on the curved formwork. In this project, the size of the reinforcement bar of the roof is D13 which doesn't need pre-bending.



Figure 10: formwork of the shell



Figure 11: bar-arrangement of the shell

Fig. 12 shows other characteristic bar arrangement. Inside the wall, there are diagonal reinforcement bar. These bars are put to resist the thrust force from the shell roof.




Figure 12: diagonal reinforcement bars put in the centre of wall to resist the thrust force

5. Observation about the cost of formwork

Table 1 shows the unit cost of formwork and Table 2 shows the comparison of the cost of formwork among the three cases which are in case of this project, in case of flat roof only and curved roof only. We can see the increasement of the cost from the case of flat roof only. If we design all the roof curved only, total cost increase so much. By considering the ratio of the area of flat roof and curved one, we could suppress the increasement of the cost.

Table 1: unit cost of framework

unit cost	
flat roof	curved roof
4.3	30.2

Table 2: comparison of framework cost among the ratio of flat and curved

	area	cost of flat roof	cost of curved roof	total cost
flat roof	1,045	4,494		
curved roof	368		11,114	15,607
flat roof only	1,413	6,076		
(no curved roof)	0		0	6,076
(no flat roof)	0	0		
curved roof only	1,413		42,673	42,673

6. Conclusion

In this project, we solve the individual problems and integrated them as below;

1) By using the shell structure, we could cover the assembly hall with 15[m] span by 180[mm] thickness slab.
2) To decide the shape of 3D curved roof, we did the form finding by sensitivity analysis.
3) In ordinary, using shell structure is expensive. But, in this project, we use the curved structure partially, we could suppress the increasement of the total cost.
4) Partial application means the difference of the system. In fact, above the assembly hall is shell structure and the other part is normal flat slab. But, to equalize the thickness of each slabs 180[mm], we could design this building as integrated structure.

As a result, we could design the lovely shaped roof that is mainly flat and partially undulating with the same thickness RC slab, and realize the architect's keyword "architecture as a continuous body". The architecture merges into the surrounding landscape.

References

[1] K. Ebata, C. Cui, M. Sasaki, "Creation of Free-formed Shell by Sensitivity Analysis (Application to Structural Design)", Summaries of technical papers of Annual Meeting, Architectural Institute of Japan, pp.269-270, 2003.

[2] M. Sasaki, *FLUX STRUCTURE*, TOTO publisher, 2005.

[3] R. Fujimura, *The form of Knowledge -The Prototype of Architectural Thinking and Its Application-*, TOTO publisher, 2018.

Proceedings of the IASS Annual Symposium 2019 – Structural Membranes 2019
Form and Force
7 – 10 October 2019, Barcelona, Spain
C. Lázaro, K.-U. Bletzinger, E. Oñate (eds.)

The Large Scale Wooden Structure Composed with the Replaceable Small Units

Ikuya HANAOKA*, Naoki ASOU*, Atsunari HANAI*, Kensuke HOTTA[a]

*Takenaka Corporation
1-13, 4-chome, Hommachi, Chuo-ku, Osaka, Japan.
Email hanaoka.ikuya@takenaka.co.jp

[a]Keio Univeristy

Abstract

The oldest wooden structure that exists now is the 'Horyuji temple' in Nara prefecture in Japan. It was built in the 7th century. The reason why the temple existed over 1300 years is because each element of the wooden structure was able to be replaced individually according to each of their damages. Our aim was to adapt this concept to a large modern architecture to realize a large scale wood structure. The building footprint is 40m×40m and the floor plate is designed without columns. The floor plate is composed by three dimensional curves as the deformation of the HP shell form. The floor and the surrounding structures are composed with multiple layers of elements that are able to be replaced individually according to their future damages. The surrounding structure is designed not only against the vertical load but also against the horizontal load by earthquake and the joineries were designed using dry drift pins to realize the replacement.

Keywords: wooden structure, computational design, form finding, optimization, shell structure, earthquake design, large span.

1. Introduction

The traditional Japanese buildings have been built with wood that utilized domestic timber. Many of the Japanese buildings were made of wood and forests are maintained to through the cycle "plant → grow → use". However, in Japan, a large number of people were killed by having a fire from a wooden building that collapsed and due to the 1923 Kanto earthquake that struck Tokyo. After the earthquake, wooden constructions except small scale houses were prohibited over a long period of time.The restriction against the wood structure has decreased the demand for timber and accordingly, the numbers of workers in forest have declined. The shrinking industry of the forestry has caused the condition that the forests are not being utilized even though they cover two-thirds of the land area in Japan.

As the global movement, utilization of the forests to decrease carbon and to recycle resource, was incorporated into CO2 reduction scenarios at COP21. To realize the low carbon society and to vitalize economy of the regional districts in Japan, some part of the building cord was revised to make a large-scale wooden construction possible. Therefore, by utilizing the lightness and ease of manufacturing, which is the merit of wooden construction, we will be able to realize an optimal form of construction,.

Furthermore, our attempt was to make the construction to be sustainable for the long period of time. The oldest wooden structure that exists now is the 'Horyuji temple' in Nara prefecture in Japan that was built in the 7th century. The reason why the temple existed over 1300 years is because each element of the wooden structure was able to be replaced individually according to each of their

Copyright © 2019 by Ikuya HANAOKA, Naoki ASOU, Atsunari HANAI, Kensuke HOTTA
Published by the International Association for Shell and Spatial Structures (IASS) with permission.

damages. Our proposal is a construction that is large but combined with small elements that make it possible to replace it.

2. Structural design concept

Our aim was to design the structure which elements are all wood-based materials that are able to be replaced after completion. Also to have rich space compared to small housings, we aimed to create a pillar-free space of 40m x 40m. The building image is as shown in the figure 1. The section is as shown in figure 2.



Figure 1: The building image

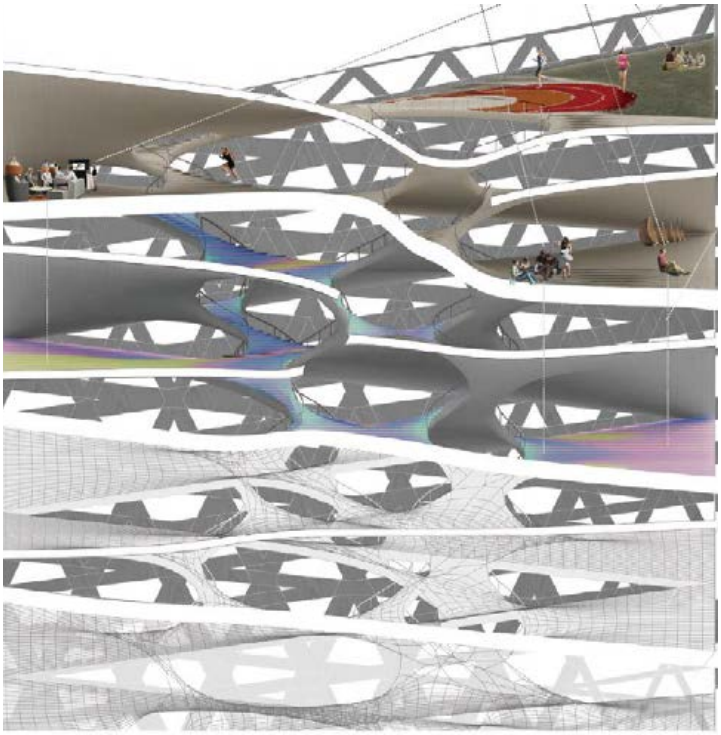


Figure 2: Section

3. Structural planning

The composition of the outer frame is show in the figure 3 and the slab in figure 4. By making the slab of each floor into the HP shell shape, a pillar-free space of 40m x 40m is realized. The slab is a composite of CLT plate and laminated wood.with the thickness of 600 mm. Horizontal force and vertical force will be borne by the outer frame. In order to enhance horizontal rigidity, the shell frame is made of diagonal members. By making the vertical member in a diagonal possition, it becomes possible to treat horizontal force with axial force, and it is possible to reduce the bending moment generated in the vertical member. The angle of the diagonal member of the shell frame was the angle that minimizes the vertical deformation and horizontal deformation due to the external force, and a parametric study was performed to determine the optimum angle.The inter-layer deformation angle is about 5.0 × 10 -4 (rad), and the vertical displacement of the slab is about 30 mm at maximum, for earthquake motion with ground acceleration of about 100 gal. The in-plane shear force of the slab due to the horizontal force is axially transmitted to the shell frame by tilting the HP shell-shaped slab to the angle of the diagonal members of the shell frame.

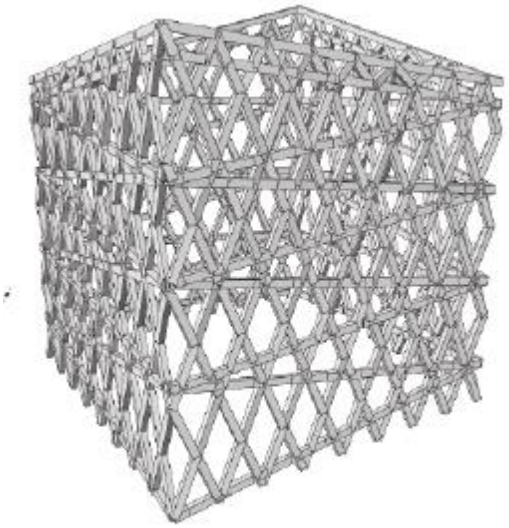


Figure 3: Compositoin of the outer frame

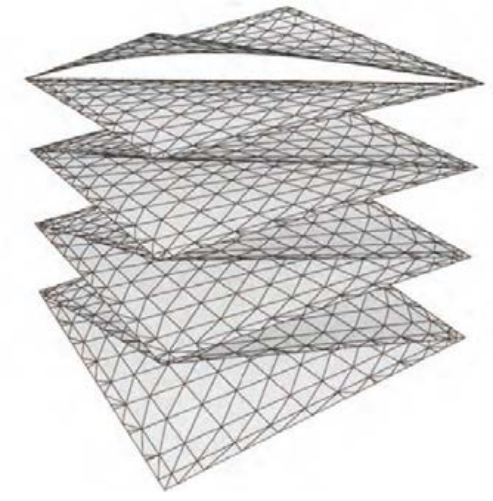


Figure 4: Compositoin of the slab

4. The outer frame configuration

The shape of the shell frame is basically composed of X-shaped pieces. Each piece has a five-layer structure that can cope with joining of members from three directions. The horizontal member is an X-shaped configuration with a three-layer structure of laminated members with a width of 200 mm and a height of 800 mm. In order to clamp three horizontal members at the intersection of X-shaped horizontal members, a diamond shaped wedge is fitted and a drift pin is disposed around the periphery. As a vertical member, a laminated member with a width of 300 mm and a height of 800 mm is inserted between three horizontal members. Vertical and horizontal members are tightened by the drift pin as shown in the figure 5. By changing the length of each laminated material in each piece, the joint position of each laminated material becomes non-identical, and it is possible to disperse the deterioration of the structural performance due to the joint. If it is necessary to replace a certain member by using a horizontal member with a three-layer structure and a vertical member with a two-layer structure, the remaining members can support the building, allowing repair work while using the building

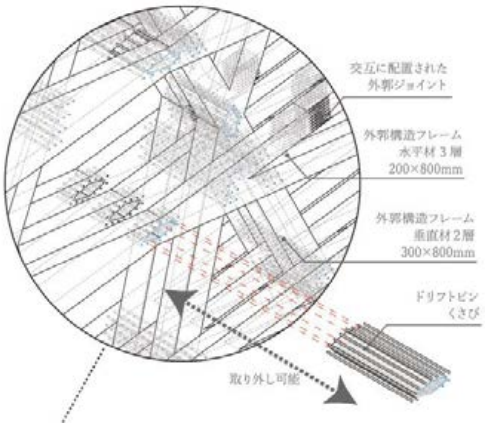


Figure 5: Detail of the frame

5. The slab configuration

The detail of the slab is shown in the figure 6.

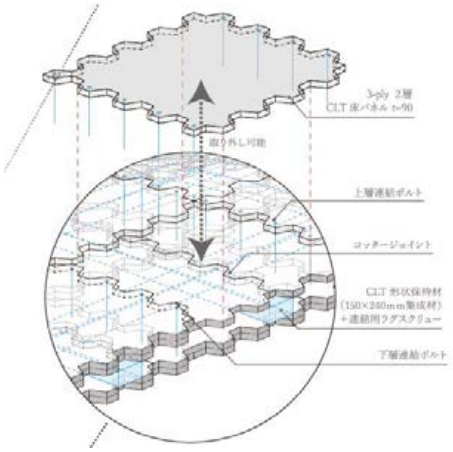


Figure 6: Detail of the slab

The CLT version hits the upper and lower chords in the composite cross section. The upper chord material and the lower chord material have a two-layer structure of a CLT plate having a thickness of 90 mm, and the strong axis direction and the weak axis direction are arranged 90 degrees different in the vertical direction. The upper and lower CLT versions are connected by screws. Because CLT version is also removable, the piece of CLT version is about 1 m in size, with one side that can be carried by human (about 400 N). Adjacent CLT plates are joined by fitting a cotter in which the end of the piece is processed into a concavo-convex shape. The in-plane shear force of the CLT slab is transmitted by engagement of the uneven cotter. In order to disperse the deterioration of the structural performance due to the bonding of the CLT plate, the upper and lower CLT plates of the two-layer structure are not provided at the same position. Tighten the upper and lower chords of the CLT plate and the connection material of the laminated material (width 150 mm, height 240 mm) by screws so that they are integrated as a composite cross section.

6. Overview

We believe that it is possible to realize a low carbon society and vitalize regional districts by utilizing wood for structure not only for small housings but also for large architecture. By building wooden buildings in the city with the latest wooden technology, we can realize a sustainable society connecting forests and towns, promoting the circulation of the forestry and economy that connects the city and the regional destrict.

Proceedings of the IASS Annual Symposium 2019 – Structural Membranes 2019
Form and Force
7 – 10 October 2019, Barcelona, Spain
C. Lázaro, K.-U. Bletzinger, E. Oñate (eds.)

Design, analysis and construction of a bending-active tensile hybrid structure

Evy L. M. SLABBINCK *, Seiichi SUZUKI[a], Anja MADER[a], Florian A. JONAS[a], Jan KNIPPERS[a]

*Institute of Building Structures and Structural Design (ITKE)
Faculty of Urban Planning, University of Stuttgart, Germany, Keplerstrasse 11, 70174 Stuttgart, Germany
evylauraslabbinck@gmail.com

[a] Institute of Building Structures and Structural Design (ITKE), University of Stuttgart, Germany

Abstract

This paper examines the design, simulation and construction of a bending-active tensile hybrid structure, designed as cantilevered roof, part of the 'ITECH Research Demonstrator 2017-18', a collaborative project between ITKE and ICD. The hybrid structure, which will be referred to as 'pringle' for the continuation of this paper, investigates the complex reciprocal interaction between bending and torsion in a plate and pure tension in two surface elements, their interdependence in the simulation process and advantage during construction.

Keywords: form-finding, hybrid structure, bending-active, composites, membrane structures

1. Introduction

The so-called 'pringle' was part of the latest collaboration (ITECH Research Demonstrator 2017-18) between the Institute of Building Structures and Structural design (ITKE) and the Institute for Computational Design and Construction (ICD), both part of the University of Stuttgart. The project, that was an outcome of the design-and-build studio of the ITECH Masters Programme, was built on the Stadtmitte Campus of the University in October 2018. The 'pringle' was the static part of the adaptable bending-active structure and was designed as a lightweight spatial roof. The structure itself was a local bending-active tensile hybrid, which was self-stressed-equilibrated, as defined by Slabbinck *et al.* [1] and thus resolves the forces, to keep the bending-active plate in bending and torsion, within the system itself.



Figure 1: (From left to right) Finished pringle; and 'ITECH Research Demonstrator 2017-18' [*Photograph by Burggraf / Reichert*]

Copyright © 2019 by Slabbinck E., Suzuki S., Mader A., Jonas F., Knippers J., ITKE, University of Stuttgart
Published by the International Association for Shell and Spatial Structures (IASS) with permission.

2. Background and context

The aesthetic and material qualities of bending-active tensile hybrid structures has intrigued architects and engineers over the past decades. These structures refer to coupled systems of tensile form- and bending-active components in which stiffness was gained through reciprocal stress dependency and elastic deformations of parental systems [2]. Concrete, prestress in membranes was introduced through the elastic deformation of bending-active components whose shape was in turn controlled by the deformation of membranes. Such hybrid constructions commonly refer to structures that integrate slender elastic beams with prestressed membranes, but the dimensionality of the bending-active components may not be limited to linear elements as described in La Magna [3]. The integration of elastic bent elements within prestressed membranes permits to design a self-tensioned solution. Moreover, the great advantage is that complex free-form geometries can be created from simple and planar components. However, the task of designing such hybrid constructs was not trivial due to the unpredictability of their geometry, and requires a shape optimization process called form-finding.

3. Integrative design concept

The local hybrid structure (pringle) was designed to fit a primary structure (ITECH Research Demonstrator 2017-18) that was conceived from a complex aggregation of elastically bent CFRP (carbon fiber reinforced polymers) plates. The primary structure was shaped from five different types of plate morphologies and composed of two self-equilibrated assemblies for defining a space with adaptable levels of enclosure. The completed 'pringle' has a span of approx. 4.2 m, a width of 3 m and a height of 1 m. The magnitude of prestress was related to the geometry and scale of the membranes and was preferred to be between 0.2 and 1 kN/m. This structure was designed as a doubly-curved element composed of an initially straight GFRP (glass fiber reinforced polymer) plate with slim constant rectangular cross-section that was first bent into a closed ring and then twisted for coupling two structural PTFE-GF (polytetrafluoroethylene coated glass fiber) membranes to the corresponding upper and lower edges of the plate. In doing so, both membranes didn´t require to be mechanically prestressed with edge cables, which was a desirable condition for facilitating the erection process, and enabled the use of GF-continuity for the whole structure including the connections. When twisting the closed ring, a state of over-torsion needs to be created in order to connect the edges of both membranes to a set of fixed points that were uniformly distributed along the ring. Consequently, the bending and torsion of the plate was used as a mechanism to prestress the membranes during construction, to avoid loss of prestress after a certain timeframe, to generate structural stiffness, and to fit the overall designed shape of the primary structure. The final doubly-curved geometry of the structure was then solely held in shape by the prestress of both membranes, which avoids the plate deforming back to a ring-shape. This condition permits to design a self-stressed-equilibrated system in which the stresses introduced on the membranes through the elastic deformation of the plate were internally solved with null reaction forces acting on the primary structure. The amount and direction of torsion and bending induced on the plate was in direct relation with the required curvature and prestress to withstand external loading and to have a rigid overall equilibrium shape. This was because the amount of double curvature induced on membranes by the elastic deformation of the plate constituted the fundamental mechanism to withstand external loads since their stiffness for bending and compression was almost neglectable. Both membranes fall into the typology of "barrel vaults" as their edges are continuously clamped. The top membrane has the main prestress direction in the sagging curvature direction and the bottom membrane in the hogging curvature direction, wherefore the upper and lower membrane can take the selected forces caused by downward and uplift wind. In addition to its structural capabilities, the geometry was conceptually designed to address functional and aesthetical criteria. The asymmetric prestress direction in both membranes generated an elliptical shape in top view and a curved shape in both lateral views, which creates multiple spatial experiences from different viewpoints.

4. Material design and testing

Quadraxial glass fiber fabric (EQX 1200, 1210 g/m²) in combination with an epoxy was used to fabricate the GFRP loop. The epoxy resin RIMR 135 (EPIKOTE Resin MGS RIMR 135) was chosen, as this forms a comparably flexible thermoset with an elongation at break of 8-12 % [4]. With the curing agent RIMR 1366 (EPIKURE Curing Agent MGS RIMH 1366) the resin has a long pot life of 210 minutes and cures at room temperature within 24 hours [4]. In combination with a low viscosity these properties make it especially suitable for large-scale bending-active structures fabricated in a manual process and the later material connection of the membrane to the GFRP. The used membrane was a typical woven glass fiber fabric coated with PTFE to ensure material consistency and show the potential of a continuous material transition from a stiff plate to membrane. The advantages here of using a PTFE-coated glass fiber fabric was a relatively low level of creep, which could avoid re-tensioning, having a non-sticky surface to avoid dirt build-up, and being a relative stiff material, which reduces the deflections of the membrane under external loading [5]. For connection of the membrane to the plate, a 12.5 cm wide band of uncoated glass fiber was welded to the coated fabric (7234 AF, KASTILO). The PTFE shows brownish color that changes to white under the influence of UV light after several weeks.

Even though the membrane material has a non-linear biaxial stress-strain behavior, a uniaxial tensile test was conducted to get initial results. To measure potential creep of the membrane at the given load level, a cyclic load test of 50 mm wide membrane stripes was conducted. In four cycles the load was varied from an estimated prestress state (25 N; 0.5 kN/m) to a maximum load possibly occurring during its life-time of 500 N (10 kN/m), which for every cycle was applied three times in a row (testing speed: 10 mm/min, Zwick/ROELL universal testing machine, clamping length: 200 mm, distance displacement sensors: 100 mm, pre-force: 5 N). Between the cycles, the load was held at the estimated prestress of the membrane for one hour. The mean strain remaining at prestress level after the four load cycles was 2.6 ± 0.1 %. For the three specimen tested no increase in the maximum membrane strain was measured over the number of cycles. The mean strain of all cycles at 500 N for all three samples was 4.4 ± 0.1 %.

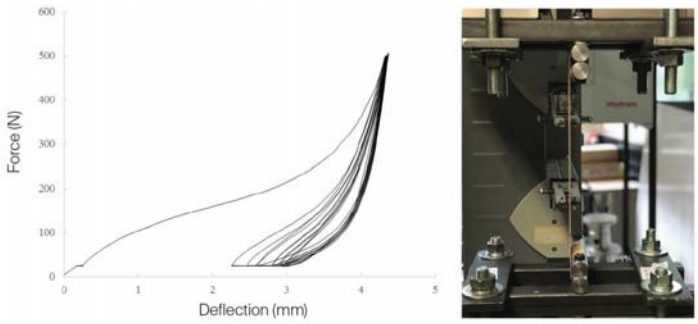


Figure 2: Cyclic load-test of the PTFE coated glass fiber membrane

In order to test the material connection between the GFRP and the membrane close to the later occurring loads, a GFRP plate in the estimated thickness of the later GFRP ring (approx. 10 mm) was fabricated and the edges sanded to form a smooth edge with a constant radius. The membrane with the weld-connected uncoated glass fiber fabric was then laminated to it. Beforehand the GFRP plate surface was sanded and cleaned using isopropanol. The membrane was positioned in such a way that the laminated connection ends 20 mm before the GFRP plate edge to avoid brittle resined fibers in that region and ensure that the flexible membrane curves around the rounded plate edge in order to avoid fiber breakage. After letting the resin cure for 24 hours at room temperature, to the free end of the coated membrane a load of 250 N was applied perpendicular to the GFRP plate orientation, following the later direction of prestress and loading. Due to the lack of sample material, no test series determining the exact failure load with an appropriate specimen number was possible to conduct. However, in the above described prototype test, the load applied to the 50 mm wide sample was 10 times higher than the expected

membrane prestress of 0.5 kN/m. After 7 days in this position, placed in a workshop environment including mild vibrations and moderate wind loads, no damage was visible at the specimen. Also a small mockup with a diameter of 1.8 m was built to learn how the material interacts with the geometry.

The Young's modulus of the GFRP was measured by a three-point bending test according to DIN EN ISO 14125. In a conservative approach, a fiber orientation in the outermost fiber layer perpendicular to the bending direction of the tested plate was chosen to get the lowest possibly occurring stiffness and strength used for the subsequent calculations. For the test, the distance of supports was 400 mm, the testing speed 5 mm/min and a sample width and thickness of 150 mm and 15 mm respectively. For the GFRP a Young's modulus of 13.5 ± 0.1 GPa and a strength of 330 ± 2 MPa were measured. In addition, prototypes of the integrated connection's threads were tested for the calculated maximum bending moments and were able to bear them.

5. Structural design methodology

Due to the strong reciprocal interaction between both types of structural elements, i.e. the bending-active plate and the two membranes, the structural behavior of the pringle was highly complex and required a simultaneous iterative nonlinear form-finding process. This interaction together with the observed material property variations, membrane orientation, prestress direction, and custom bond connections have a great influence on the simulation results and the overall behavior of the structure. The resulting 3D shape was developed through a multistep computational workflow in which each construction step was parametrically modeled in CAD software Rhinoceros-Grasshopper (Rhinoceros 3D© - Grasshopper©), and numerically form-found and analyzed with the commercial Finite Element Modeling (FEM) software Sofistik (SOFiSTiK AG©). Design iterations (e.g. form-finding and structural-mechanical analysis) needed to be rapidly as it was intertwined with the parallel design of the primary structure. Easy bidirectional transfer of data between Grasshopper and Sofistik where achieved by using an in-house ITKE-plugin so that results from one software could be used in the other to generate the next step in the analysis and modeling process. Because of this parametric workflow there was a smooth collaboration between the different expert student teams and allowed working on different aspects and scales of the structure. Simulation of the bending-active plates in FEM software, utilizes third-order-theory calculations, where for every iteration step, a new equilibrium was calculated on the actual updated deformed shape. "*The Elastic Cable Approach*" [2] was applied to simulate controlled and gradually the large elastic deformations. Similar use of the geometrical non-linear FE analysis was used for simulating the tensile elements, which was defined as a continuum analysis [5].

The bending of the initially straight 12-meter-long plate (using plane elements) into a circular ring was modeled in by applying a bending moment at both ends. The bending stresses were compared with straightforward hand calculations. In a second step, torsion was applied to obtain the desired elliptical shape. Torsion of the plate was used as a design driver, described in paragraph 3, and led also to the advantage of gaining geometrical stiffness [6]. The thickness of the plate was defined by utilizing it to 50 % of the maximum tensile and shear strength, and to 60 % in the over-torsion state during construction, while keeping the normal forces in the modeling cables and the reaction forces in the supports in an acceptable limit.

The mesh of the membrane was generated in Grasshopper, based on form-found geometry of the GFRP plate in FEM. This implied working on a polygonal boundary with a pre-defined number of fixed vertices; therefore, the mesh was generated through a relaxation technique in order to match this predefined discretization of the boundary. To do this, an initial planar quad mesh was constructed with the same number of naked vertices than those of the pre-given discrete boundary. By mapping in a sorted sequence the corresponding vertices on both discrete geometries, the naked boundary of the planar quad mesh was pulled towards the geometry of the pre-given boundary. Then, the internal edges of the quad-mesh were relaxed as a cable-net system to create a structured quad mesh fitting the elliptical doubly

curved geometry of the boundary. This input of the mesh in Sofistik was defined as a three-dimensional initial system, and was restricted by hinge supports all along the boundary. The initial form-finding step of the simulation was using a temporary reduced stiffness, so the strains don't lead to a stress modification [7]. Afterwards, a second calculation was done where the stiffness was set to its normal stiffness. To keep the required elliptical shape, an asymmetric prestress was needed, the applied prestress in the main direction was 0.5 kN/m (warp), and 0.2 kN/m in the secondary direction (weft). The additional local stiffening of the cutting pattern seams was not taken into consideration.

To assure that the correct 3D-geometry of the plate was used for the precise cutting pattern, the plate was scanned with a panorama laser scanner (Faro Focus3D 120). Because of the elastic property-form relationship differences between the achieved and initial simulated configuration of the structural system occurred. The membrane simulation was remodeled based on the measured data to include any effects of deviations. The two types of structural elements were brought together to form-find the structure as a whole. The spring-back effect of the plate was brought in relation with the stress values of the membrane. These results were used for the design iterations of the primary structure and the load analysis of the pringle itself. The load analysis under external loading uses the following available European Standards: "Eurocode for wind actions" (BS EN 1991-1-4:2005) and "Temporary structures – Tents – Safety" (BS EN 13782:2005). The structure was designed to be erected for a few months during summer and therefore no snow load was considered. The aim of the membrane analysis was to control the deflections so that no ponding or wrinkling of the membrane occurs, neither collision with other structural elements. The wind analysis was conducted on two separate levels. First, a uniform uplifting wind load of 1 kN/m² perpendicular to the lower membrane surface was applied, and similar a downward wind loading on the top membrane. Second, a reduced wind load according to the EC-zones with sucking and pushing wind force was applied to assess the local characteristic values where the sign changes. As the hybrid simulation was complex, the anisotropic prestress solutions were unknown as described by Gosling *et al.* [5], the material properties were less well defined and no wind tunnel testing for this complex form was available, the simulation and stress asses required significant engineering deliberation. After the form-finding of the membrane, the geometry was exported to CAD as part of the parametric workflow, where the geodesic lines were generated. The 3D cutting areas were then loaded back into Sofistik for developing into a 2D plane in respect of (de)compensation, creep and prestress. The compensation factor was experimentally defined, cf. paragraph 4, while a reduced factor was used in the weft direction. The most outer elements of the pattern were decompensated as it was nearly impossible to tangentially stress them.

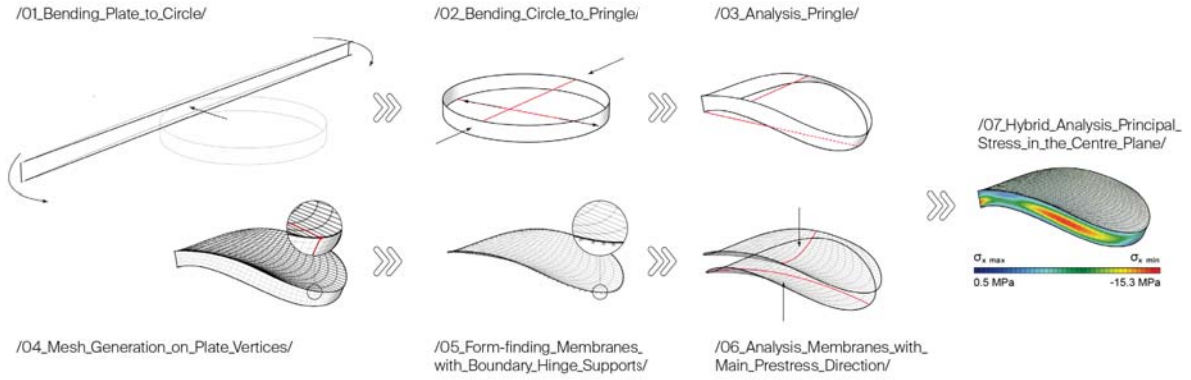


Figure 3: Overview structural design methodology

6. Fabrication

A 12 m long flat plate with a thickness of 11 mm and width of 35 cm was produced in a hand-lamination process from 12 layers of the quadraxial glass fiber fabric, leaving 50 cm of the glass fiber fabric at both sides unimpregnated. A vacuum of 100 mbar was applied to get rid of excess resin. In a second step, the

plate was bent into a circle, the two edges fixed and the overlapping unresined glass textiles were fitted together with ply-wise varying location and angle of the meeting edges and impregnated with the same process as for the rest of the plate. After curing and loosening of all external fixations a perfectly circular round glass fiber ring was achieved. Composite screws were embedded for construction purpose and to later connect to the primary structure.

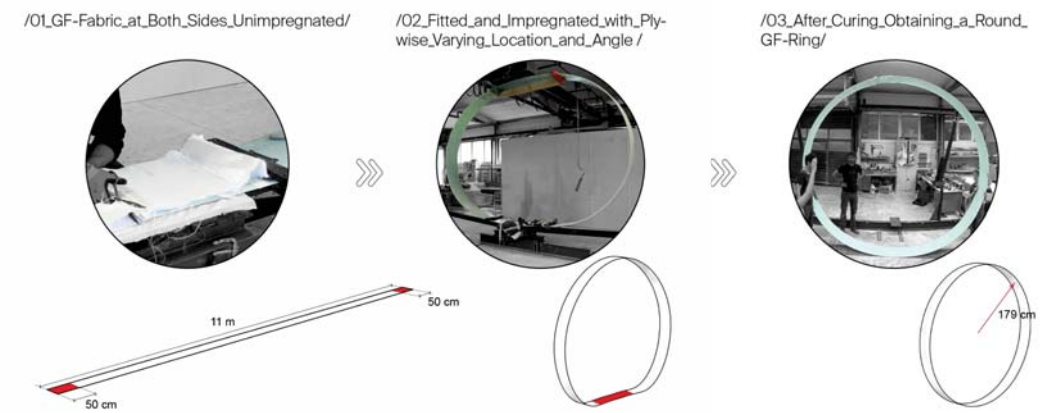


Figure 4: Overview plate fabrication process

The cutting pattern of the top membrane existed out of 12 pieces, and the bottom one of 8. The seam line was aligned with the warp direction of the fabric, the direction of the main prestress and the main principles curvatures. In consequence both membranes are relative to each other oppositely oriented. Onto the boundary of the PTFE-GF membrane, a piece of uncoated GF was attached and as well PTFE-GF-flaps (two per membrane strip), for construction purposes. The membrane was welded together with a high frequency welding machine, due to the complexity of the already 3D formed membrane, the additional flaps and GF-strip were welded by hand.

7. Construction

To achieve the target geometry of the composite structural elements, different construction phases and stress states have to be passed through. The process of connecting the membrane to the plate-ring leads to the intended shape changes of both load-bearing elements.

In the first step the ring with circular shape was put into a custom made jig to twist it into an elliptical shape (a first time for surveying and a second time for the construction several weeks later). Due to an inclination change of two lever arms of the jig, the ring was torsioned and bent (step 1) to later prestress the first layer of membrane through a spring back effect. The membrane was put upon the edge of the elliptically bent ring (step 2). To establish the planned pretension situation, temporary flaps were pulled piecewise outwards beyond the ring edge with tension belts against composite screws or hooks on the lower ring edge. The ends of the membrane flaps were reinforced by clamping in between a pair of CFRP blocks, which were bolted together and provided a whole to attach a tension strap. The ends of the fabric in the secondary prestress direction were pulled with a cable winch in the first round of tensioning. Every tension strap was gradually tensioned in a clockwise fashion until the membrane established its targeted prestress state. As it was not possible to conduct a biaxial test of the material, the elongation of the membrane was observed during installation, and the amount of tensioning was modified to the local status. In the next step (step 3), the membrane was adhesively connected (laminated) through the unimpregnated GF textile (0|90). The mounting sequence was: release of one temporary flap, pulling and laminating of the GF-textile, and reattachment (tension force) of the temporary flap. This process was repeated to bond every final flap section in the manner of a back-step method with periods of resin hardening to ensure maintaining the correct pre-shape and the connection between the first membrane and the ring. To allow the second over-torsioned state for the bottom

membrane, the plate with the top membrane needed to be released from the jig arms (step 4). To avoid this single membrane taking all spring-back forces, the plate was partially restricted with tension straps. After that the last two flaps where the jig was mounted were bonded. The component was not flipped over but readjusted and mounted again to the jig, with torsioning the ring in opposite spin to achieve a second spring back effect for prestressing the second membrane later (step 5).

For installation of the second membrane, steps 3 and 4 where planned to be repeated, but the top membrane failed during prestressing the temporary flaps due to partially ripping of the laminated 0|90 fabric parallel to the rim edge. Through the piecewise mounting sequence relative forces parallel to the ring edge unfavorable for the used uncoated 0|90 GF-textile occurred. While during the analysis shear stresses and strains were checked, the installation introduced shear strains into the system. Using a soft coating that provides tear resistance would be a solution, but prevents us from laminating the GF onto the plate. The GF-textile was impregnated with resin and became stiff and brittle. To improve the construction, the textile fiber direction should be rotated, reinforced by a second layer, or impregnated with additional fibers with an 45° angle between the plate edge and membrane. To nevertheless achieve the planned bending-active tensile structure a cable net (consisting of 3 longitudinal and 5 transversal steel cables with 5 mm diameter) instead of the second membrane were mounted. This led to a different appearance as one side was not a closed surface any more, but was in terms of load-carrying action a comparable solution. With repetition of step 4 prestress to both sides of the ring was established and the structure of planned shape and targeted resistance could be achieved.



Figure 5: Overview pringle – top membrane construction process (step 1-5)

8. Results and Conclusion

A local bending-active tensile hybrid structure was designed, analyzed, fabricated and constructed; and demonstrated that a self-stressed-equilibrated system out of a continuous material can achieve a lightweight performative structural solution. Conventional constructions, which transfer the tensile forces of the membrane to the ground can lead to massive connections and support cables. This has an influence to the economical and visual quality of the structure. An integrated system as presented where the reaction forces are resolved within the system itself possesses potential to contribute to alternative solutions. The membrane showed a high prestress level, a secure membrane-plate connection and a stiffness gratifying serviceability demands, i.e. there was no visible deformation during a load test with a point load of 600 N (no horizontal constraint). The pringle finally was not integrated in the 'ITECH Research Demonstrator 2017-18' due to a plate failure of the primary structure, instead a non-structural replica was constructed and placed. As there is no post-stressing system available, e.g. turnbuckles, the system is relying on the ongoing spring back effect of the GFRP plate. Research on the long-term fatigue and the plastic deformations of the GFRP plate, and the creep of the membrane within this system should be further investigated.

Acknowledgements

The 'ITECH Research Demonstrator 2017-18' is a joint project of the Institute for Computational Design and Construction (ICD, Prof. Achim Menges) and the Institute of Building Structures and Structural Design (ITKE, Prof. Jan Knippers) at the University of Stuttgart. The authors would like to thank their colleagues and volunteers: Oliver Bucklin, Lauren Vasey, Marion Lutz, Leyla Kyjánek Yunis, Behrooz Tahanzadeh, Michael Preisack, Maria Yablonina, Larissa Born, Daniel Reist, Daniel Sonntag, Bas Rongen, Boris Brozovic, Annette Smitt (IIGS institute) and James Solly. This project was in collaboration with the Institute for Textile and Fiber Technologies Denkendorf (ITFT, Prof. Götz T. Gresser), and received great support and/or funding from SGL Technologies GmbH, Sofistik AG, Kastilo Technische Gewebe GmbH, LORD sensing MicroStrain, S-form Kunststofftechnik, Fiber Method, Saertex GmbH & Co. KG, Hexion Inc., Lange+Ritter GmbH, R&G Faserverbundwerkstoffe GmbH, and Institute of Textile Technology and Process Engineering (DITF).

The presented research was conducted on the intersection between research and teaching together with students of the ITECH Masters Programme. The authors would like to express their gratitude towards everybody that collaborated on the design and development of the pringle: Elaine Bonavia, Brad Elsbury, Samuel Leder, and Sabīne Vecvagare; and the other students, i.e. Rasha Alshami, Xun Li, Mathias Maierhofer, Israel Luna Miño, Marie Razzhivina, Jacob Russo, Hosna Shayani, Valentina Soana, Ramon Weber, and Jacob Zindroski, who contributed to the work as part of two consecutive design and fabrication studios. Additional contributions by: Lidia Atanasova, Sven Baur, Ludwig Ebert, and Eric Fuertas.

The work presented in this article was partially funded by the European Union's Horizon 2020 research and innovation programme under the Marie Sklodowska-Curie grant agreement No 642877, and by the German Research Foundation (DFG) as part of the Transregional Research Centre (SFB/Transregio) 141 'Biological Design and Integrative Structures'.

References

[1] E. L.M. Slabbinck, S. Suzuki, J. J. Solly, A. Mader and J. Knippers, "Conceptual framework for analyzing and designing bending-active tensile hybrid structures," in *Interfaces: architecture, engineering, science: Proceedings of the IASS Annual Symposium 2017*, Hamburg, Germany, September 25-28, 2017, A. Bögle and M. Grohmann Ed., 2017.

[2] J. Lienhard and J. Knippers, "Bending-active textile hybrids," in *Journal of the International Association for Shell and Spatial Structures (J. IASS)*, vol. 56 (2015), no. 1, pp. 37-48, March 2015

[3] R. La Magna, "Bending-Active Plates. Strategies for the Induction of Curvature through the Means of Elastic Bending of Plate-based Structures," *Stuttgart: Universität Stuttgart Inst. f. Tragkonstr. (Forschungsberichte aus dem Institut für Tragkonstruktionen und konstruktives Entwerfen der Universität Stuttgart, 43),* 2017.

[4] Lange+Ritter GmbH, "Verstärkt im Einsatz," *Produktkatalog*, Gerlingen, 2019/2020.

[5] P. D. Gosling, B. N. Bridgens, A. Albrecht, H. Alpermann, A. Angeleri, M. Barnes, N. Bartle, R. Canobbio, F. Dieringer, S. Gellin, W.J. Lewis, N. Mageau, R. Mahadevan, J-M. Marion, P. Marsden, E. Milligan, Y.P. Phang, K. Sahlin, B. Stimpfle, O. Suire and J. Uhlemann, "Analysis and design of membrane structures: Results of a round robin exercise," in *Engineering Structures*, vol. 48, pp. 313-328, March 2013.

[6] E. L.M. Slabbinck, A. Körner and J. Knippers, "Torsion as a design driver in plate-bending-active tensile structures," in: *Proceedings of the IASS Annual Symposium (IASS)*, Hamburg, Germany, September 25-28, 2017.

[7] SOFiSTiK AG ©, "ASE, General Static Analysis of Finite Element Structures," *Sofistik manual Version 27.11*, pp. 2-68, Oberschleissheim, 2013.

Proceedings of the IASS Annual Symposium 2019 – Structural Membranes 2019
Form and Force
7 – 10 October 2019, Barcelona, Spain
C. Lázaro, K.-U. Bletzinger, E. Oñate (eds.)

Experimental investigation of beams under coupled bending and torsion

Nicolas MONTAGNE[a]*, Cyril DOUTHE[a], Olivier BAVEREL[a,b], Corentin FIVET[c]

* [a] Laboratoire Navier, UMR 8205, Ecole des Ponts, IFSTTAR, CNRS, UPE, France, nicolas.montagne@enpc.fr
[b] Laboratoire GSA, ENS Architecture Paris Malaquais, France
[c] EPFL, ENAC, Structural Xploration Lab, Passage du Cardinal 13b CH-1700 Fribourg

Abstract

The design of doubly-curved systems called for innovative modelling techniques to evaluate the final geometry of the structure. They can simulate the behaviour of beams under large displacements. Even though it is never analysed, the deformation path is can be critical in such complex configurations. This paper analyses the potential of digital technologies to investigate the behaviour of beams under bending-torsion coupling in large deformation. In a first part, we will present the setup for an experiment, based on the use of robotic arms. The versatility of robotic arms allows to access complex configurations or loading paths, while controlling the test either in displacements or in forces. In a second part, an enhanced photogrammetry procedure is introduced. The aim is to retrieve the geometry of the beam even in the case of complex 3D shapes. The acquisition yields a point cloud representation of the beam. Finally, we propose a workflow to make the interaction with robotic arm, simple and efficient. The novel experimental setup aims at making possible the study of beams with complex form, under ever more complex force.

Keywords: Large Deformation, Robotic, Photogrammetry,

1. Introduction

Active-bending structures are a family of systems built from elastically deformed rods. For example, an elastic gridshell is made of continuous bars assembled on the ground to form a grid. This initial grid is then bent to a target shape and braced to fix the geometry. In the last few decades, active-bending systems have become very popular for their capacity to develop complex doubly-curved shapes. They can be found in various context, from temporary doubly-curved roof structures [1], to structural demonstrators with an innovative use of materials [2], and art pieces where elastically bent bars interact with tensile membranes [3].

The common factor in active-bending structures is the large deformation of its members responsible for the stiffness of the final form. In their deformed configuration, the beams are subject to all kind off stresses, essentially bending, but also torsion due to couplings effects and to connections between them [4]. It induces a pre-stress state in the structure. Therefore, it is necessary to account for the material properties in the design and form-finding process of a bending-active structure. In order to allow for large deformation of the beam, the material must have high elastic strain and a high limit stress. Yet, leaving aside the strength requirements of these structures, the mechanical properties also impacts the stable shape. The curvature of a beam depends on its bending stiffness. The interdependence of form, force and materiality is very strong in active-bending structures which calls for a thorough understanding of the behaviour of beams.

Many recent researches have been led on how to model these structures and get the geometry in static equilibrium. Common algorithms tend to have heavy convergence problems due to the large rotations

Copyright © 2019 by N. Montagne, C. Douthe, O. Baverel and C. Fivet
Published by the International Association for Shell and Spatial Structures (IASS) with permission.

and displacements, and can become very expensive in terms of computational time. A very popular method to form-find these structures is the dynamic relaxation method combined with the use of a discrete element model. Since the 3 degree-of-freedom element proposed by Adriaenssens et al. [5], more complete formulations have been proposed [4],[6][7],[8]. The aim is to model as best as possible the structural behaviour of the beams and of the connections to obtain a precise evaluation of the final shape. However, in these methods, very little attention is given on the actual erection process. During this phase, the members are subject to complex deformation paths which are the origin of strong non-linearity and potential instability [9]. For such deformations, it is necessary to account for second order effect, like beam-length variation.

The accuracy of the different formulations is only being tested through the design of pavilions. Experimentally, little has been done to study the behaviour of beams under large deformations following complex deformation paths. The lack of experimental results in this domain can be explained by two reasons. On the one hand, the principal difficulty is to prescribe 3D deformation paths. Commonly, experimental setups are able to work in-plane, using either an imposed force or displacement. They often focus on evaluating the characteristic for one stress only, leaving aside any coupling effects. Therefore, they are not able to replicate the peculiar situations found in active bending structures. On the other hand, to get a hold of the beam behaviour, one wants to have access to the displacements in the deformed configuration. To measure displacements along one axis, tools like linear variable differential transformers (LVDT) or laser sensors are capable of very precise assessment. When it comes to 3D deformations, contactless measurement techniques are preferred. A popular method is digital image correlation (DIC). However, for large deformations, large decorrelation between images occurs, preventing the algorithm from evaluating the displacements properly. Acquiring the geometry of a deformed beam is a complex matter in the case of large displacements because of the wide range of shapes accessible. Thus, even though the theoretical backgrounds of the proposed discrete element formulations are reliable – e.g. Saint-Venant, Kirchhoff – few experiments have assessed the models.

This paper analyses the potential of digital and robotics technologies to investigate the behaviour of beams under bending-torsion couplings and large deformations. In a first part, a robotic control of the experiment will be examined. The positioning flexibility and accuracy is placed at the service of the experiment. In a second part, an improved photogrammetry procedure is presented for a full-field geometry measurement of a 3D deformed beam. Finally, a software solution is presented to overcome the difficulties introduced by the use of robotic arms.

2. A robotized experiment

As for the experiment, it is typically desired to examine the behaviour of a single slender beam by imposing conditions at its ends, either in displacements or in force. With these conditions, already a vast number of problems and configurations can be tested.

2.1. Motivation

Previously, we have seen that complex deformation paths could not be followed with the currently available setup. To allow for such experiments, we propose to introduce robotic arms in the process. Several reasons motivate this choice:

- Accuracy: A robotic arm is controlled by a series of servomotors. A feedback of the angular position of each of the axis of the robot is available thanks to rotatory encoders. This system gives industrial robots the capacity to position any tool fixed at its end with a submillimetre precision. In the case of the ABB IRB120, the positioning accuracy is about 0.02 mm, when the orientation precision is about 0.005° on each axis. This experimental measure was evaluated with a weight of 1.1kg at the arm end. It is important to understand that when several positions are prescribed, there isn't any propagation of the error on the position. Each target of the robot is calculated with respect to the robot coordinate system and not to the previous position.

- Automation: The motion of an industrial robot is controlled via programming. One solution is to give a set of successive positions to be reached, called targets, while specifying the type of movement to be achieved in-between. Another way, is to provide a curve, called the path, to be followed by the end of the robotic arm. The automation of the movement comes as a benefit, and not as a constraint. Firstly, the experiment can be conducted without much supervision and intervention. More importantly, once the path of the tool is defined, the experiment can be repeated easily by relaunching the program.
- Flexibility: A 6 axis robotic arm gives access to many positions. Each axis has a range of movement of at least 180°. Thus, the limiting factor of these robots is their reach. In addition to the position, the speed and the acceleration of the motion can be dictated or bounded.
- Adaptability: The robot has the capacity to host various tools, as long as it can be wired up to the wrist of the robot. For example, in the last few years, many companies and laboratories have been starting to pour concrete using robots [10]. The ITKE in Stuttgart has been building several pavilions using robotic fabrication. In [11], timber beams of a reciprocal structure were robotically manufactured using a milling head on a 6-axis robotic. Recently, [12] used a laser doppler vibrometer fixed on an industrial robot to perform full-field velocity measurements.

2.2. Principle of robotic monitoring of complex path

For the purpose of large deformation experiments, the versatility in position and in use of 6 axis robotic arms can be used to perform complex path using an adapted tool to hold one end of the beam, with the other fixed in place. During such experiment, the beam is deformed progressively by either controlling the displacements along a programmed path or by dictating the force applied. Thanks to the rotatory encoders it is possible to get a precise estimation of the position of the robot's wrist.

However, by default, there is no force measurement embedded in the robot. To have an evaluation of the stress, a force sensor has been installed at the end of the robotic arm. Fixed on large 6-axis robots (ABB IRB6620), the force sensor is able to measure forces up to 1500 N applied in any direction with a precision of 0.5N, and to measure all three moments up to 240 N.m with a precision of 0.1 N.m. The force sensor is also connected to the robot's motion controllers, enabling the control of the robot according to the measured force and to cancel the effect of the sensor's weight when the force is monitored.

Thus, with the force sensor coupled to the robot, we are able to dictate the position while measuring the force, or apply a given force while monitoring the position of the tool. With this robotic setup, a great variety of new tests can be conducted, with reliable information acquisition.

2.3. Experimental validation

In order to demonstrate the validity of the described setup, we present a case study. In this experiment, we want to study the torsional buckling of a beam, which includes instability, out-of-plane deformations and large displacements. The setup involves a beam fixed at one end and loaded by a robotic arm at the other end. To foster the apparition of torsional buckling, a thin-walled bar is used and loaded in the strong bending axis. The beam is a 3-meters long steel IPE80. Because the control in force of the experiment was not yet available, for security reasons, the displacement at the end was dictated and the force monitored.

The finite element software suite Abaqus has been used to dimension the test. The aim is to find a deformation path of the beam when the load is progressively increased and to ensure that the maximal force measurable by the sensor is not reached. The mechanical modelling of beam instabilities requires the introduction of initial geometrical defects. The path and the force found with the analysis are strongly dependent on the initial imperfection. Thus, the deformation path imposed to the beams may not be the one that would have been followed with a force controlled essay. Analyses were consequently run, in order to get a post-evaluation of the initial out-of-straightness.

The initial geometrical defect was evaluated with respect to the first torsional buckling mode of the beam. The mode has been normalized in order to have a 1 mm default at the loaded end of the beam. A visual estimation of the out-of-straightness evaluates the imperfections at no more than 20 mm at the end of the beam. Thank to simulations on Abaqus, it was found that the best fitting force-displacement curve corresponded to a beam with a 40 mm default (Figure 2). Thus, even though the visual defect isn't large, the experiment allowed to identify that the beam behaved with an equivalent defect of 40 mm. Reverse engineering of equivalent imperfections for stability analysis is thus one open problem that could be addressed with this kind of robotic experiment.



Figure 1: Torsional buckling

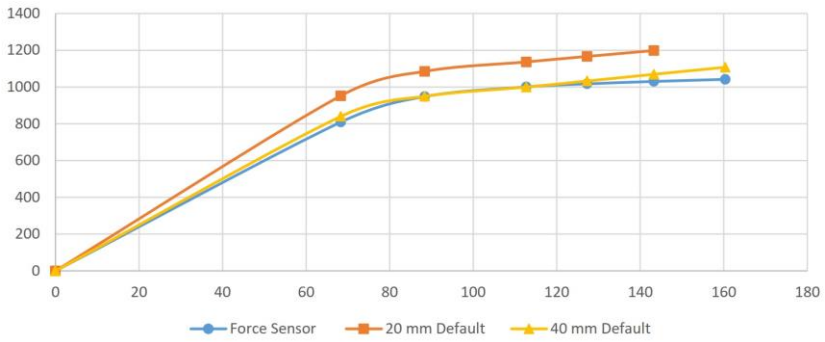


Figure 2: Force(N) - Displacement(mm) curve of the experiment and simulation

3. Robotized Photogrammetry

In the presented experiment, material properties of the tested beam can be retrieved with information on forces and displacements at one single point. However, for an increasing number of identification techniques based on the redundancy of measures, full-field displacement measurement is required. If so, additional dispositions should be used to evaluate the 3D deformed geometry.

3.1. Photogrammetry for large displacements

The measure of large out-of-plane deformation, as of 3D deformed shape in general, is complex. The most popular technique involves the digital image correlation (DIC). In this method, a fixed camera captures the motion of the beam being deformed. Having a fixed camera and tracking the beam in each image allows to evaluate the successive positions of the beam. In order to measure out-of-plane displacements at least two cameras are needed. Still, large decorrelation between images may occur when the displacement of the beam is too large, preventing the software from evaluating the actual deformation.

A popular tool, also based on numerical image correlation is photogrammetry. It refers to every measuring technique that allows to model a 3D space using only 2D images [13]. Contrarily to DIC which uses a fixed camera to capture several configurations of a moving element, photogrammetry analyses a fixed configuration of an element using a moving camera. Pictures are taken all around the studied object and a numerical 3D point cloud is produced after post treatment. Because the camera is not bound to a single position, this technique allows to rebuild almost every shape. Photogrammetry allows to accommodate the large displacements and is able to rebuild very complex configuration. The point cloud model produce after analysing the pictures yields the measure of the beam 3D displacement.

3.2. Robotic contributions to the photogrammetric process

Since the 19th century, the photogrammetric analysis process has evolved a lot thanks to the creation of dedicated tools. In the middle of the 20th century, the analysis needed a qualified personnel to be carried out and was time consuming. With the apparition of computers and thanks to their increasing calculation capacity, the photogrammetric process has been simplified and is also much more precise than what it used to be [14]. The parameters of the camera (optical settings, position and orientation in space) are

found automatically thanks to feature detection algorithms [15], bundle adjustment methods (Levenberg-Marquardt) and optical distortion models (Fraser). However, some steps in the process could not be improved. Taking the pictures for the analysis is time consuming. But more importantly, the model produced at the end is in a relative scale. The point cloud model is built using pictures whose size is counted in pixels and not meters. Solutions involving GPS localisation can be found for aerial photogrammetry. For human scale acquisition, like the reconstruction of the shape of a deformed beam, more precision is needed.

The idea here, is to fix a digital camera on a robotic arm and to adapt the photogrammetric study to this setup. The flexibility of the robot is again at the service of the large deformation experiment. Thanks to the wide range of positions available to the robotic arm, pictures can be taken all around the studied object, even in case of complex shape.

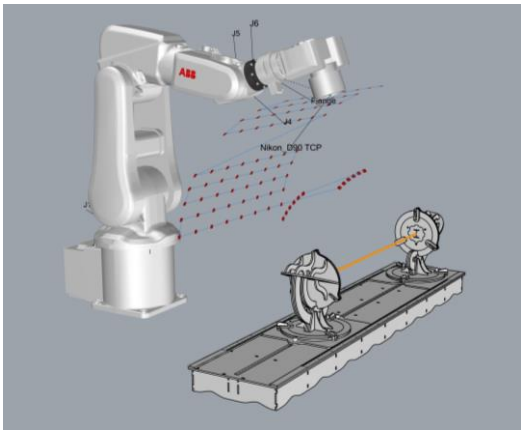


Figure 3: Simulation of the experiment

With the proposed setup, the acquisition process becomes fully automated. The robotic arm is given a list of positions and orientations from where the pictures have to be taken. The camera and the motion of the robotic arm need to be synchronized: once in position, a picture is captured then the robot moves to the next point. The coordinates from where the pictures are taken are then given as an input for the photogrammetry analysis. During the post-treatment of the images, the input positions define a scale for the 3D point cloud, in a similar way as interpreting the GPS information. Furthermore, it is possible to skip the research for the parameters of the camera, which is a delicate step of the analysis. The positioning accuracy of the robot provides the exact orientations for every pictures in space. Therefore, this setup allows for an improved and more robust procedure for the reconstruction of a scene while using photogrammetry.

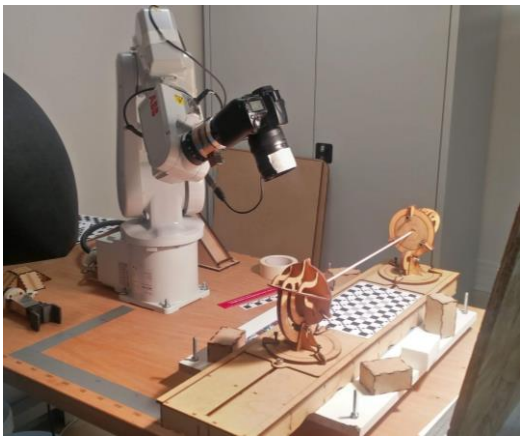


Figure 4: Robotized photogrammetry setup

3.3. Case study

In order to evaluate the proposed system, a slender element with imposed boundary conditions is studied. We want to get a full-field measurement of the position of the beam thanks to the point cloud. For practical purposes, the experiment had to be led on objects with reduced dimensions. The beam has a constant 1.5x4.5 mm cross-section and is 600mm long. It is fixed on a laser-cut support to manage the boundary condition accurately. A commercial camera is fixed at the end of an IRB120 (Figure 4).

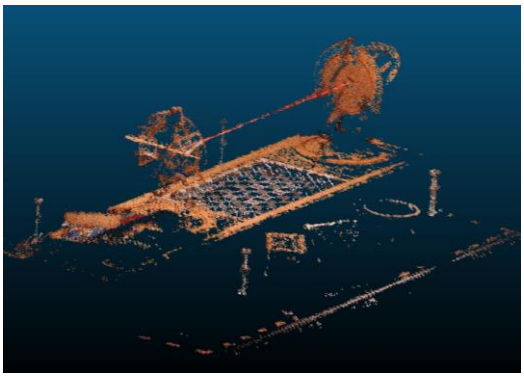


Figure 5: Point cloud of the experiment

The photogrammetry study has been conducted with MicMac, a software solution developed by the French National Institute of Geography [16]. The proposed setup allows to simplify and to speed-up the analysis. However, the quality of the point cloud (Figure 5) was not as good

as expected. The beam was rebuilt with a precision of ±3 mm, which is not enough in comparison with its dimension.

It was identified that the calibration process of the camera had to be improved to get accurate results. Indeed, the information obtained from the robot is the position of its wrist, when the optical centre of the camera is required for the photogrammetric software. The orientation of the optic centre with respect to wrist of the robot corresponds to a rigid body transformation of each position. This problem of homogeneous transformation of the form AX=BX has been raised and solved in many different ways in Euclidian space or quaternions [17],[18]. For photogrammetry, a very precise calibration is needed in position and in orientation. To get such demanding accuracy, dedicated tools are necessary.

4. Workflow

In the previous sections, solutions introducing industrial robots were presented to answer the need, on the one hand to apply elaborate 3D loading paths to the beam, and on the other and to measure complex deformed geometries. However, the use of a robotic arm implies a specific workflow. To overcome this concern, a software solution has been developed. It makes use of a virtual experimental setup, upstream of the essay, to model the path and the manage the interaction with the robot.

4.1. Virtual experimental model

The use of industrial robots constrains the user to program the robotic arm ahead of the experiment. To help the user design the experiment and define the path followed by the arm, a virtual experimental setup [12] is modelled. To do so, we have chosen to work with the CAO software Rhino3D and its parametric design interface called Grasshopper3D. The aim is to create a virtual representation of the robot's working environment (Figure 6). The model must include the geometry of different objects:

- The measuring tool, defining the spatial occupancy, as well as the lever arm between the end of the arm and the tool control point;
- The measured object, used to create targets to be reached by the tool control point;
- The robotic arm, needed to evaluate the accessibility of the targets;
- The reference objects, helping the positioning of the measured object with respect to the robot.
- The environment objects, i.e. all objects that are in the robot's reach, and can be a potential source of collision;

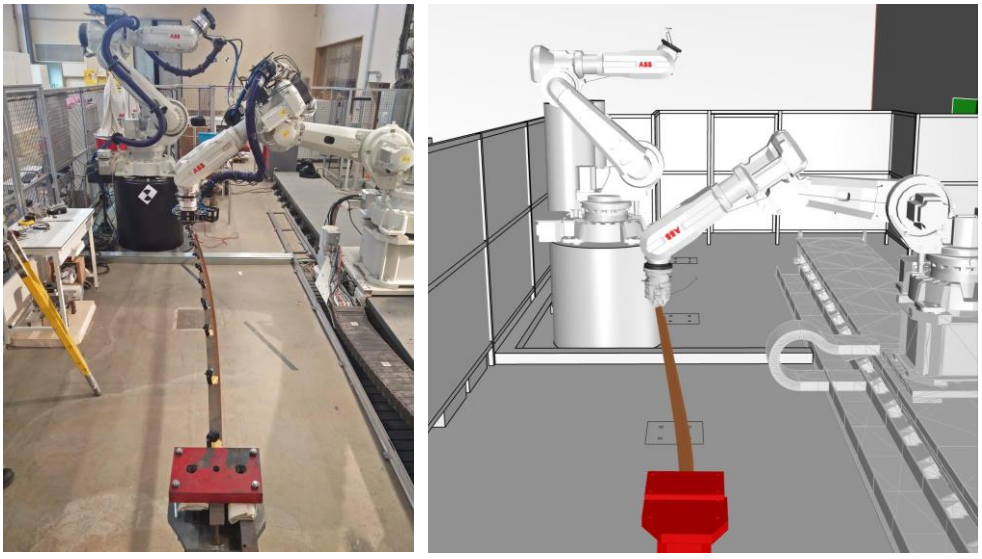


Figure 6: Virtual experimental setup

From the virtual experimental situation, the list of positions for the arm is defined. The strength of this step lies in the ability to parametrize the path in Grasshopper3D. It is possible that the wanted position, does not fit the limitations of the robotic arm. Thus, when a target cannot be reached by the robot, it will be necessary to take a step back. Therefore, the definition of the trajectory of the robots should rely on the position, the form of the measured object, and eventual other parameters. The definition of the set of points is thereby an iterative process (Figure 7).

4.2. Robot management

From the list of positions defined in the parametric software, we want to verify their accessibility and the motion of the arm in-between which is done using HAL-Robotics software. This Grasshopper3D plug-in manages and predicts the motion of the robots. It can predict whether or not the robotic arm is capable of reaching the position, and also allows to give constraints on the motion, like speed, acceleration or spatial restrictions. The whole movement of the robotic arm between the positions is simulated and previewed. Thus, thanks to the virtual experimental setup, collisions between the tool, the robot and its environment can be easily avoided.

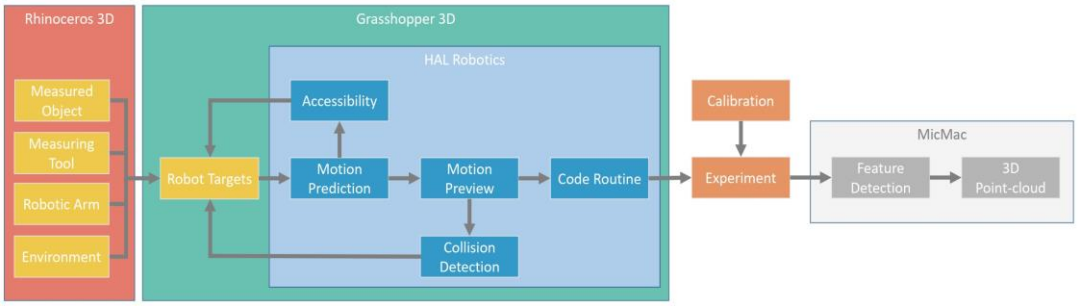


Figure 7: Proposed workflow for the design of the experiment

Once all the targets are reachable by the arm, HAL-Robotics generates the instructions for the movement of the robot in the form of a code. The code is written in a specific programming language depending on the brand of the robot used. The communication between the computer and the robot controller can be directly configured in the plug-in to export the code directly.

The combination of a coarse model of the object, of parametric design of the position in Grasshopper3D and of the simulated robotic cell using HAL Robotics, is extremely powerful. Thanks to parametric design, the object studied can be moved in space to accommodate accessibility issues and the list of positions, the analysis of the targets by HAL, and the code generation will be automatically updated. A clever parametrisation allows for a quick adaptive solutions and makes the design phase of the experiment extremely efficient.

4.3. Preparing the actual experiment.

Before running the experiment, the real setup has to be calibrated in order to match as best as possible the virtual experiment model. The measured object has to be positioned relatively to the robot, using the reference objects. For some experiment, like the robotized photogrammetry, an accurate positioning of the object is not essential, the principal requirement is for the object to be in the area of sharp focus of the camera. In many case a precise visual calibration can be sufficient. However, for procedure like the milling of a wooden object, great precision may be necessary [11].

Conclusion

This paper presents a novel and promising methodology to study the behaviour of beams under coupled bending and torsion. The introduction of industrial 6 axes robotic arm improves the range of possibilities in terms of large deformation experiments. Using only one setup, objects with a wide variety of shapes

and sizes can be measured. To overcome the difficulties introduced by the uses of the robots, a software solution has been presented which rely on the use of a virtual experimental setup.

Acknowledgements

The authors would like to thank researchers of the MATIS (IGN) for their help with photogrammetry, HAL Robotics and the Build'In platform for their assistance on the robotic aspects.

References

[1] O. Baverel, J.-F. Caron, F. Tayeb, and L. du Peloux de Saint Romain, 'Gridshells in Composite Materials: Construction of a 300 m2 Forum for the Solidays' Festival in Paris', *Structural Engineering International*, vol. 22, no. 3, pp. 408–414, 2012.

[2] S. Colabella, B. D'Amico, E. Hoxha, and C. Fivet, 'Structural Design with Reclaimed Materials: an Elastic Gridshell out of Skis', in *International Association for Shell and Spatial Structures*, Hamburg, 2017, p. 10.

[3] J. Lienhard, H. Alpermann, C. Gengnagel, and J. Knippers, 'Active Bending, a Review on Structures where Bending is Used as a Self-Formation Process', *International Journal of Space Structures*, vol. 28, no. 3–4, pp. 187–196, 2013.

[4] L. Du Peloux, F. Tayeb, B. Lefevre, O. Baverel, and J.-F. Caron, 'Formulation of a 4-DoF torsion/bending element for the formfinding of elastic gridshells', in *International Association for Shell and Spatial Structures*, Amsterdam, 2015, p. 16.

[5] S. M. L. Adriaenssens, M. R. Barnes, and C. Williams, 'A new analytic and numerical basis for the form-finding and analysis of spline and gridshell structures', *Computing Developments in Civil and Structural Engineering*, pp. 83–91, 1999.

[6] M. R. Barnes, S. M. L. Adriaenssens, and M. Krupka, 'A novel torsion/bending element for dynamic relaxation modeling', *Computers & Structures*, vol. 119, pp. 60–67, 2013.

[7] B. D'Amico, A. Kermani, and H. Zhang, 'A form finding method for post formed timber grid shell structures', presented at the World Conference On Timber Engineering, Quebec, 2014, p. 6.

[8] J. Bessini, C. Lázaro, and S. Monleón, 'A form-finding method based on the geometrically exact rod model for bending-active structures', *Engineering Structures*, vol. 152, pp. 549–558, 2017.

[9] S. Timoshenko and J. Gere, *Theory of Elastic Stability*, 2nd ed. McGraw-Hill Book Company, 1936.

[10] R. Duballet, O. Baverel, and J. Dirrenberger, 'Design of Space Truss Based Insulating Walls for Robotic Fabrication in Concrete', presented at the Humanizing Digital Reality, 2017, pp. 453–461.

[11] C. Douthe *et al.*, 'Design and construction of a shell-nexorade hybrid timber structure', in *International Association for Shell and Spatial Structures*, Boston, 2018.

[12] P. Margerit, 'Wide-band characterization of the heterogeneous viscoelastic and anisotropic dynamical behavior of structures. Application to the piano soundboard. (in french)', PhD thesis, Université Paris-Est, 2018, Chapter 3.

[13] R. Martin and R. Challine, *Photogrammétrie*, Eyrolles. 1973.

[14] M. Kasser and Y. Egels, *Photogrammétrie numérique*, Lavoisier., vol. 1. 2001.

[15] D. G. Lowe, 'Distinctive Image Features from Scale-Invariant Keypoints', *International Journal of Computer Vision*, vol. 60, no. 2, pp. 91–110, 2004.

[16] IGN MicMac: http://logiciels.ign.fr/?-Micmac,3-.

[17] Y. C. Shiu and S. Ahmad, 'Calibration of wrist-mounted robotic sensors by solving homogeneous transform equations of the form AX=XB', *IEEE Transactions on Robotics and Automation*, vol. 5, no. 1, pp. 16–29, 1989.

[18] F. C. Park and B. J. Martin, 'Robot sensor calibration: solving AX=XB on the Euclidean group', *IEEE Transactions on Robotics and Automation*, vol. 10, no. 5, pp. 717–721, 1994.

Proceedings of the IASS Annual Symposium 2019 – Structural Membranes 2019
Form and Force
7 – 10 October 2019, Barcelona, Spain
C. Lázaro, K.-U. Bletzinger, E. Oñate (eds.)

G-shells: Flat collapsible geodesic mechanisms for gridshells

Enrique SORIANO*, Ramon SASTRE*, Dionis BOIXADER[b]

*CODA / LiTA BarcelonaTech
ETSAV C/Pere Serra 1 08173 Sant Cugat del Vallès. Barcelona. Spain
enrique.soriano@upc.edu

[a] ETS d'Arquitectura del Vallès BarcelonaTech

Abstract

We present G-shells, a new strategy for deployable elastic gridshells developed from an initially flat and compact geodesic mechanism. The one-degree of freedom mechanism evolves from its initially flat state into a geodesic net corresponding to some smooth doubly-curved surface. The construction is based on straight, flat planks, and simple coplanar joints. As the geodesic mechanism deploys, it provides a smooth transition across a characteristic family of surfaces. By reversing the path, the mechanism may be returned to its initial state, and thus collapse. Our approach opens new possibilities for the prefabrication, transport and erection of gridshells.

Keywords: geodesic gridshell, gridshell, bending-active, deployable structures

1. Introduction

The construction of complex curved shapes with timber planks has a long tradition. Starting from a flat, straight state, a plank can twist and bend out of their plane but cannot be stretched or bent in their own plane. The neutral fiber of the plank has a vanishing geodesic curvature over any surface it is tangent to, and we can assimilate the plank's neutral fiber trajectory to a geodesic curve of such surface. Construction with timber planks has been employed for hulls and shells across history taming the plank geometric constraints, and therefore geodesic nets have been intuitively used for a long time.

In the last century, geodesic nets were used to optimize construction in fields ranging from airframes to civil shells. J.Natterer's ribbed shell new design was based on the plank layering geometry [1] which was further developed with the advent of computational methods [2]. More recently, the works from [3] and [4] independently described alternative generation methods of geodesic nets simply connected by bolts for the efficient generation of shells or industrial custom chassis.

As bending-active structure, elastically bending geodesic nets, made from initially planar and straight coupled elements, benefit from the prestress stiffening effect and could potentially have a kinetic behaviour. However, the previously depicted geodesic nets are built by individual three dimensional plank placement. We present a geodesic mechanism that have the advantage of creating custom surfaces but employing a kinetic expansion. It's a hybrid compliant mechanism which bases the transformation of the structure in a combination of the free rotation of elements at hinges and the elastic deformation of lath elements.

Copyright © 2019 by <substitute here the name(s) of the author(s) or individual(s) claiming copyright>
Published by the International Association for Shell and Spatial Structures (IASS) with permission.

2. Genesis

2.1. Emergence of behaviour in physical models

Inspired by the work of Pirazzi and Weinand [3], we had the chance to build a timber gridshell for hosting a student parliament, the Almond pavilion [1], which intended to prove the feasibility of multilayered geodesic gridshell by simple means. Instead, it provided an interesting type of deployable mechanism which emerged in the scale model [5]. When unconstrained at boundaries, the scale model which was composed of thin laths simply connected by bolts at specific distances, collapsed into a compact and flat structure (fig.2b). Reducing both geodesic and normal curvature and torsion was a way of straightening all laths and achieving this lower energetical state. Surprisingly, it achieved a planar state for which it had not been designed in the first place. Moreover, the building system of wide laths and simple bolts forced the grid to approximate a geodesic net at any time of the deployment by changing the local curvature.



Figure 2: Almond pavilion (2012) a.Built structure b.Transformation of scale model from flat to curved

From the flat compact state, we firstly observed that the intersections laid in curved fashion, although this was repeatable without any surface curvature on deployment (fig. 6). Secondly, we observed that planks were not parallel and were smoothly changing the angle which finally seemed to be key in the emergence of the behaviour. From these observations we built several models, initially symmetrical, producing corrugated gridshells yet some exhibited smooth anticlastic or synclastic curvature (fig. 3).



Figure 3: Anticlastic G-Shell

2.2. Early G-Shell implementation in anticlastic models: Focaccia and Neula

As soon as we had the opportunity for a design commission at a larger scale, we built Focaccia (fig. 4) in 2014 as the assembly of several anticlastic hypar-like G-shells (fig. 3) at the edge of their twisting side planks. We simply built all the laths of a hypar from a plywood board, with almost no waste. The board was *expanding* around 3.4 times almost effortless since there is almost no bending and there is mainly twisting. The G-shell proved to gain stiffness by the torsional effect, and it packed efficiently for transport. Nevertheless, there were two inconveniences in this anticlastic case: the plank's twist was making the connection to change the angle along the plank; dividing a surface in geodesic net patches do not warranty the lath continuity.



Figure 4: Focaccia Pavilion (2014). Assembly of several anticlastic G-shells. [Photo: Andrés Flajszer]

Later on the same year, we had the opportunity of building a similar structure at a larger scale. We then used the same anticlastic model, yet denser. We assembled a large plank mat on site, made out of connected short plywood planks with a smooth phenolic coating providing frictionless coplanar joints. We then used a crane to lift a rectangular frame that vertically pulled four symmetrical points to their final horizontal position. It initially had a side component that helped the angle change in the mechanism which was rapidly open. The attachment to the ground was the sole bracing of the grid.



Figure 5: Neula Pavilion (2014). Deployment of large scale anticlastic G-shell. [Photo: Andrés Flajszer]

2.3. Early G-Shell implementation in sinclastic models: Labsis shell

For the commission to cover a scenario, we decided to build a sinclastic model, having better insight with grid generation(section 4.1). The design consisted of a compact trimmed diamond shape that once deployed would allow both sides to rest on horizontal planks serving as base for foundations. The bracing consisted solely in a single axis in the middle, which had to be based on the scale model measurements since the simulations were not robust enough.

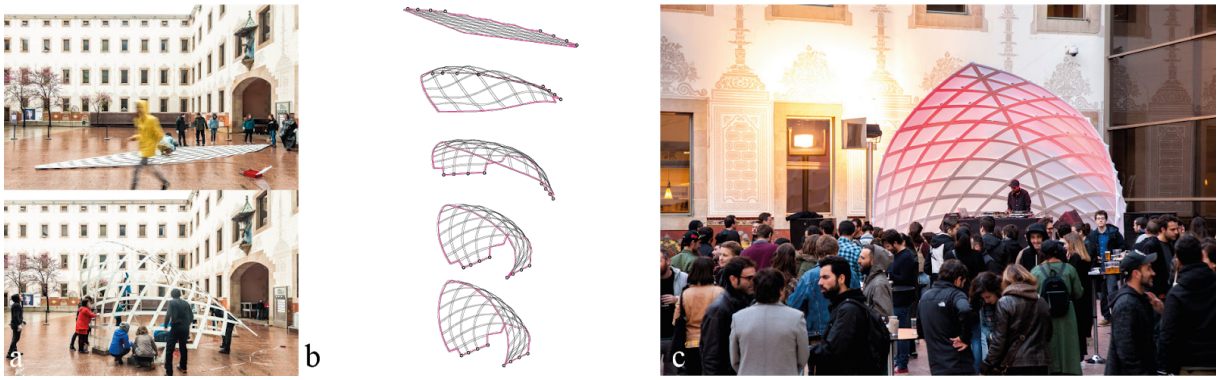


Figure 6: Labsis stage (2016) a. Deployment of the flat mat. b. Simulation c. Final stage [Photo:Andrés Flajszer]

The assembly process was the same as previously: get planks in size, bore holes, assemble the flat mat, although it differed in the erection. In the sinclastic case, there is mainly normal bending in the planks and lot of energy involved especially in the pre-buckled initial state. Therefore, it was fully buckled and erected by pushing from under without any mechanical help since it was very lightweight, as planks were 5x100 mm in section, while being helped by pulling laterally to unfold the scissor effect.

3 G-Shells

Very recently Peneta et al. [6] presented a mathematical analysis for these deployable beam structures , which they named X-hsells, a term that encompasses a more general kind of structures than that of this paper, because their study considers framing for all sort of beams. Since we have focussed specifically on plank based gridshells, and therefore we restrict ourselves to geodesic approximation, we propose to refer to our own range of structures as G-Shells, being a subclass of the more general X-shells. Our artifacts are based on planks of simple rectangular sections.

3.1 Hybrid compliant plank mechanism

The deployability of flat mats consisting in two families of beams which are "pinned", such as the chebyshev nets traditionally used in the gridshell tradition, is allowed by the unrestrained change in the local angle the two families of beams form, thus producing a curvature change when subjected to external actions. Among this *pantograph* mechanism group, we can include the special type of geodesic mechanism [7], restricted to beam sections with an order of magnitude higher in the width than in height, where the change of curvature is intrinsic to the surface by means of local angle change but producing only twist and normal bending. Laths avoid bending in their strong axis, so the phenomenon of side buckling effect translates all motion to normal curvature and torsion of the curves. Among this group, we can find the special case of G-shell, where they can have and exotic state of being flat and compact without overlapping of the laths.

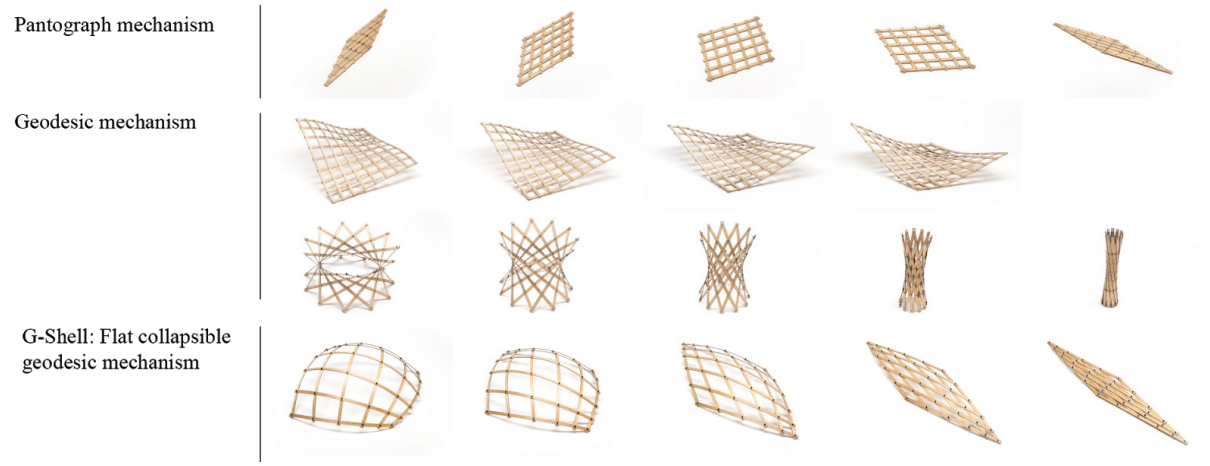


Figure 7: Flat collapsible Geodesic Mechanism or G-Shell

3.2 Double quad mechanism

From a tangible perspective, the smallest lath configuration where the phenomenon happens is two connected rhombus by two continuous sides forming a *double quad mechanism* or DQM. If we analyze one small lath by freeing one of its vertex, operating the mechanism by changing the angle at any vertex produces a global angle change and ultimately an excess or defect of the original distance,

thus a buckling on the piece itself or on the lateral ones. The incompatibility of deformation produces the side buckling of the long laths. This difference is not linear and can even change sign during the transformation.

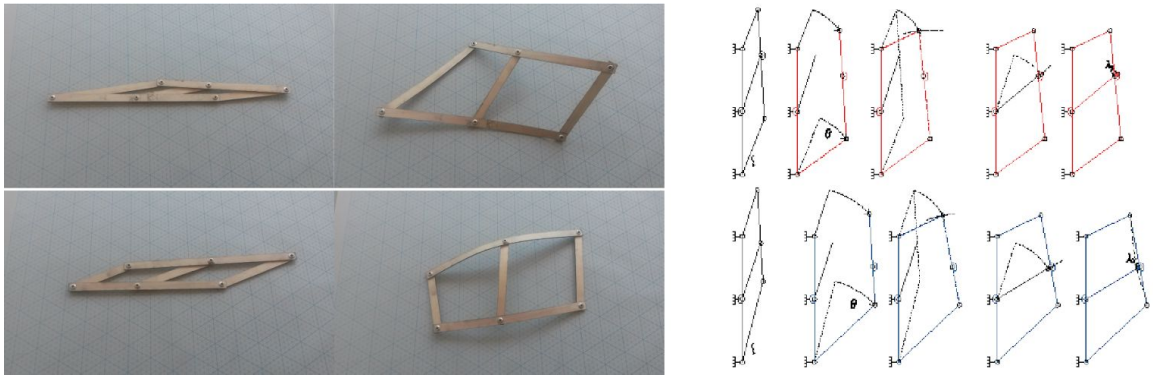


Figure 8: Double quad mechanism

4. Bottom up: from flat grid to curvature

The first approach is to directly draw a compatible G-Shell grid, which ensures planarity at compact state, but the form of the operated mechanism has to be predicted by analysis or simulation.

4.1 Grid generations

We can draw planar oblique two-way grids, with several initialization methods. This instantiation feature will be reciprocally a property from the other methods (fig. 9). Firstly, we can define a curve where a row of intersections of the grid will lay. Secondly, we can generate a family of curves which are all tangent to their envelope curve. Finally, we can apply a rotation and a translation function to any given line.

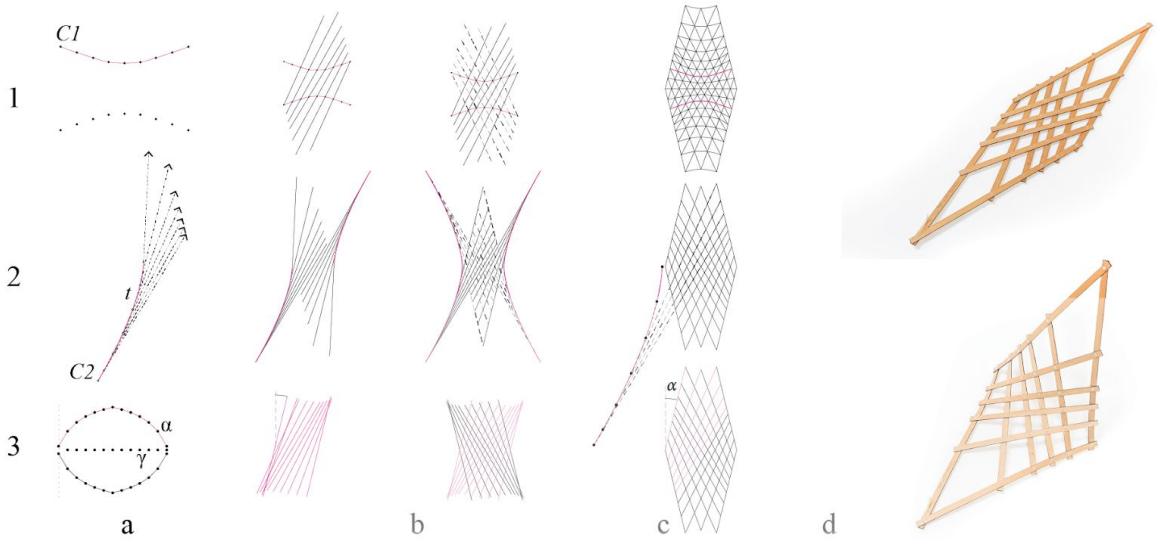


Figure 9: G-shell flat grid generation. a.Initialization b.Overlap c.Flat G-mesh d.Physical model

These inputs have no glimpse on the final curvature output. We observe that most of the grids produce internal corrugations and a combination of curvatures, which indeed can be beneficial for certain shell

design and requires a specific research. Nevertheless, we notice that method 3, applying smooth functions tend to produce smooth curvatures.

4.2 Simulation of mechanism in DR

We use the dynamic relaxation method using Kangaroo2 [8] by implementing two strategies. The simulation goals have to ensure that planks are inextensible and cannot bend out of their plane and that the normal vector of crossing geodesics are the same, or that both planks are coplanar at that point. Our first approach is to treat the plank as a coarse triangular mesh with hinge stiffness. At the intersection we enforce the coplanarity of the five vertices defined by the two rails meeting. Moreover we enforce a loose coplanarity of a cluster of 12 closest points around the intersection. Secondly, we implement the discrete geodesic model as described in [9], by simply forcing opposite angles to be equal in the geodesic mesh at every vertex. At the sides, we reproduce the same definition as it really happens in the physical models, by adding a small member.

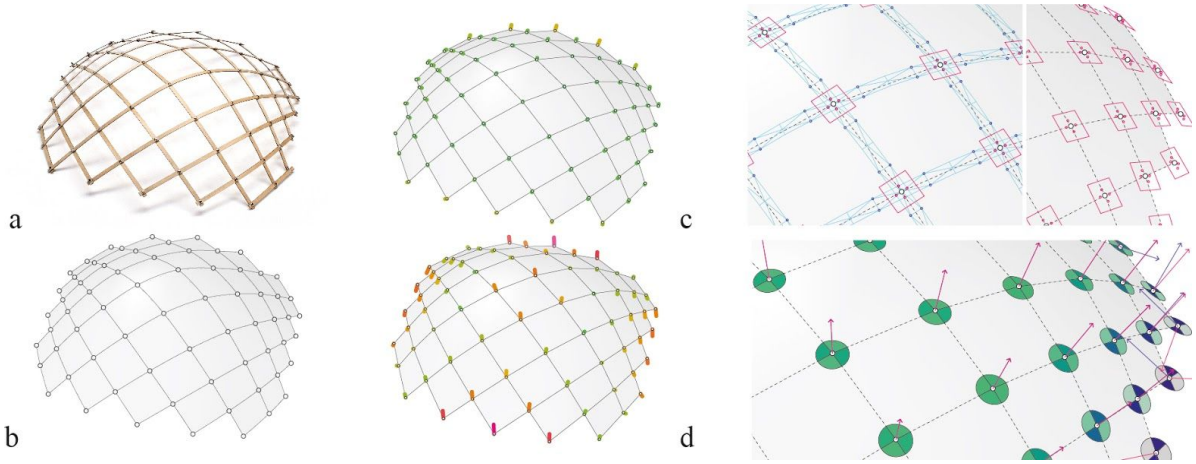


Figure 10: a.Physical Model b.Scan model c. Triangular mesh plank approach (divergence and detail) d. Discrete geodesics approach (divergence and detail)

5. Top Down: from target surface to flat grid

We propose secondly a method to approximate a G-Shell to a given target custom surface (i.e. parabolic dishes, funicular forms, small patches of a larger surface). Moreover given the target surface is known, we can produce as many offsets as needed.

5.1 Flattenize. Simulation in DR and minimization

Given a discrete geodesic net approximating the surface, we can collapse the grid by using the dynamic relaxation solver Kangaroo2, to minimize the curvature and preserve the length. Using an EMO (evolutionary multiobjective optimization) we can iteratively vary the geodesic net parameters to minimize the errors. A simple discrete 3DOF rod model is enough to minimize the geodesic curvature since curves are forced to be all coplanar and normal and geodesic curvature are the same. The length to be preserved is not from the discrete segment lengths but from the continuous curve fragments. Moreover, it's critical to preserve a plank distance between plank axis otherwise they would not be able to be assembled. This can be done by introducing a length dimension in the main diagonal or introducing a collision-aware goal. Additionally, to facilitate the convergence we can pull points to horizontal plane, and keep the points in the symmetry axis to be fixed in the same plane.

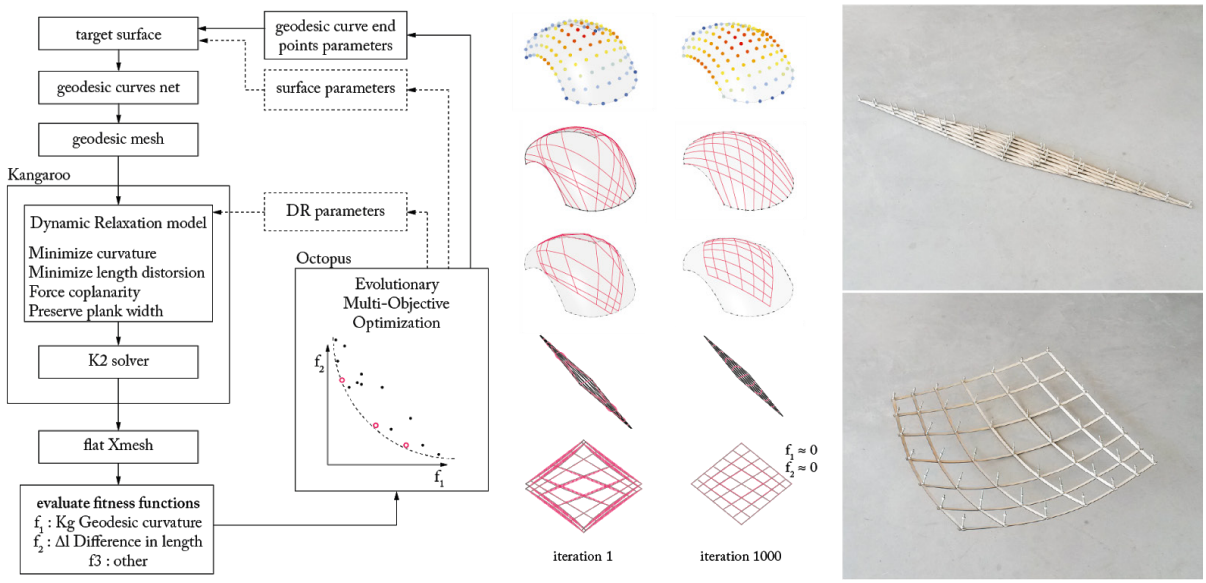


Figure 11: *Flattenize* algorithm

5.2 Multi-layered G-shell

The limitation of G-shells can be the small structural thickness of the planks, thus we propose a method for increasing the layers, while preserving on each of them the geodesic and collapsibility properties. The main benefit for the *top down* approach is that knowing the target surface we can easily create offset surfaces, with the restrictions that a topological equivalent G-shell laying on it has to share the normal vector of each equivalent vertex on both surfaces. We use an extended version of the *flattenize* algorithm, including the *vector normals divergence* as an extra fitness (fig.12).

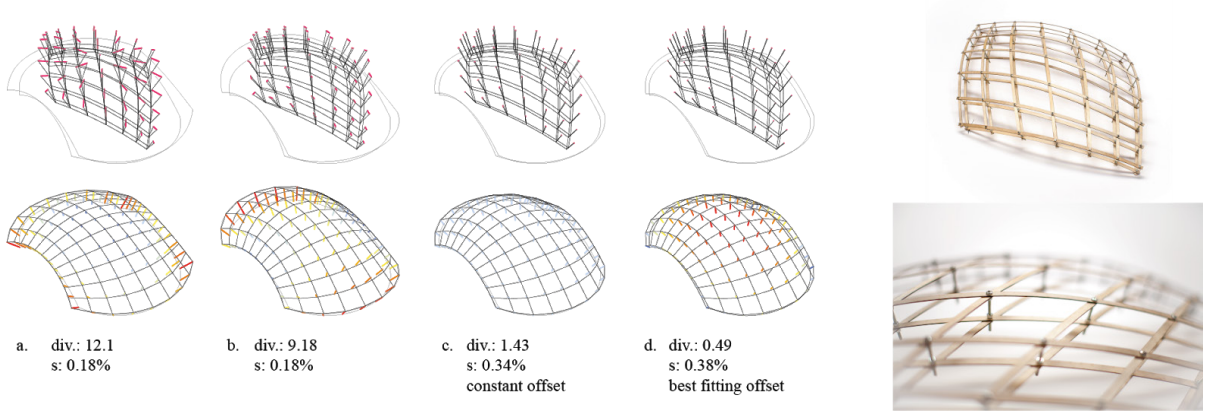


Figure 12: Offset Flattenize fitnesses

The first observation is that we need non constant offset, otherwise we lose the collapsing properties. The second observation, in the symmetric models we study, is that for sinclastic surfaces the mechanism is collapsing in a bent arched mat, whereas for anticlastic surface, it is collapsing flat (fig.13).

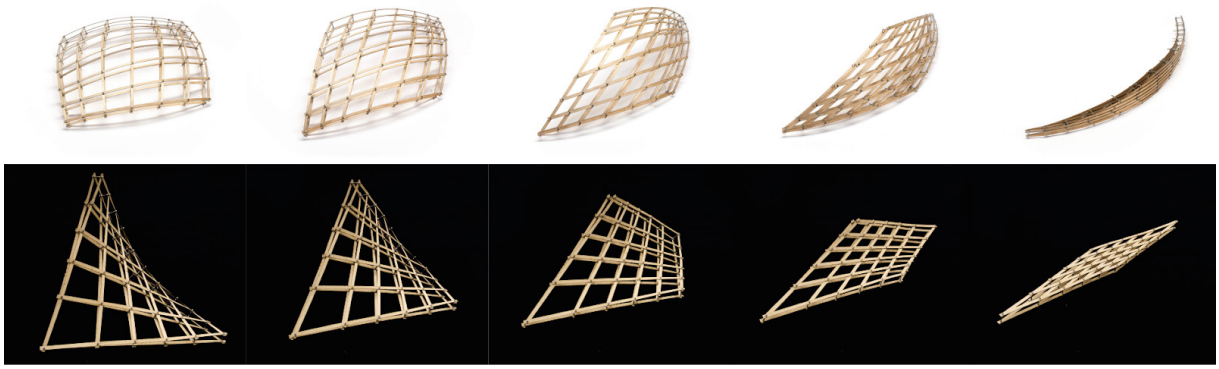


Figure 13: offset

6. Conclusions

The existence of special flat states in curved geodesic mechanisms is not mathematically proven, yet we can empirically confirm the construction interest in the transportation and deployability efficiency. We may continue in the mathematical understanding of the phenomenon. Further research may also assess the structural behaviour of single and multilayered G-shells, the deployable activation for large scale sinclastic shells and explore the instrumentalization of emergent corrugation of the G-shells.

Acknowledgement

This research has been conducted under an FPI-UPC predoctoral grant from BarcelonaTech. Special thanks to Pep Tornabell, Gerard Bertomeu, research trainee Anna Rizou and Andrés Flajszer. Also thanks to Dragos Naicu, Chris Williams and Daniel Piker for their generous support and feedback.

References

[1] E.Soriano,"Low-Tech Geodesic Gridshell:Almond Pavilion"ArchiDoct_vol4_iss2 02 Feb. 2017

[2] K.Kensek, J.Leuppi, D.Anoble, "Plank lines of ribbed timber shell structures". In Acadia 2000: Eternity, Infinity and Virtuality in Architecture, 261–266.

[3] C.Pirazzi, Y.Weinand, "Geodesic lines on free-form surfaces-Optimized Grids for Timber Rib Shells". *World Conference on Timber Engineering*, vol. 7

[4] R.J.Lind, "Variably-curved, meshed thin shells: geometry, mechanics and fabrication" ProQuest.

[5] E. Soriano, P.Tornabell, R.Sastre, D.Boixader "Surface curvature transformation of oblique planks grid" Poster session at AAG 2014 London, September 18 2014.

[6] J.Panetta, M.Konaković-luković, F.Isvoranu, E.Bouleau, M.Pauly, "X-Shells: A New Class of Deployable Beam Structures" ACM Transactions on Graphics (Proceedings of SIGGRAPH)

[7] E.Soriano, C.Williams, "Surface mechanism with two sets of geodesic laths" Nov. 2015 http://people.bath.ac.uk/abscjkw/DoubleGeodesicLathMechanism/

[8] D.Piker,"Kangaroo: form finding with computational physics"Architectural Design83(2) 136-137

[9] M. Rabinovich, T.Hoffmann, O. Sorkine-Hornung, "Discrete Geodesic Nets for Modeling Developable Surfaces". ArXiv, abs/1707.08360

Proceedings of the IASS Annual Symposium 2019 – Structural Membranes 2019
Form and Force
7 – 10 October 2019, Barcelona, Spain
C. Lázaro, K.-U. Bletzinger, E. Oñate (eds.)

Lightweight curved surface structures composed of bending-active plate units

Yi-Hsuan TU*, Ting-Yun KOU, Chia-Chia LI

* Department of Architecture, National Cheng Kung University
#1 University Road, Tainan, Taiwan
yhtu@mail.ncku.edu.tw

Abstract

This paper presents a method for fabricating reversible curved surface plate units through active bending. The original flat plates were bent and self-stabilized by inserting braces into precut parallel slits in the plates. The units can be easily assembled into a modular structure and disassembled to be transported or stored in their flat form. The curvature of the units can be controlled by adjusting the length and the spacing of the slits. The deformation of the bent units were simulated using a geometrically nonlinear analysis in SAP2000 and compared with measured results from both small-scale and full-size models. It was found that the bending deformation was proportional to the ratio of the slit spacing to the plate width as well as the ratio of the brace depth to the slit length. An empirical function between the bent angle and the slit dimension factors for symmetric rectangular units was derived. Two lightweight structures, including a catenary arch that spanned 4.2 m and a geodesic dome with a diameter of 3.45 m, were built using 3 mm plywood units. 1/5-scale models were used to study the stability of the structures. The initial attempt to construct the catenary arch was unsuccessful due to the scale effect. The design was modified by adding out-of-plane stiffeners. It was found that the scale effect may be reduced by changing the geometry of the structure. A geodesic dome was then developed with reciprocally connected units. It was assembled multiple times at different sites.

Keywords: bending-active, lightweight structure, plate, modular structure, self-stabilized

1. Introduction

Active bending is a simple method that can be used to produce curved elements. As reviewed by Lienhard et al. [1], it is a widely recognized technique for buildings using traditional materials such as softwood, bamboo, and reed. It was reintroduced as an economic way to construct curved structures in the last century. One of the best-known examples is the gridshell structure developed by Frei Otto for the Multihalle Mannheim. Form-finding was a major problem in building bending-active structures at that time due to a lack of computational tools. In recent years, the interest in bending-active structures has been growing because of the advance in numerical analysis techniques. The Research Pavilion ICD/ITKE 2010 [2] demonstrated an integrated approach to constructing a bending-active structure with planar strips of plywood. The geometry was precisely controlled by using a finite element simulation (FEM). Recent case studies by Schleicher et al. [3] showed how the design process for bending-active structures greatly benefits from computer simulation tools. New materials with high strength and bending capacity, such as fiber-reinforced polymer (FRP), also aid the use of active bending in various forms. Nicholas and Tamke [4] built three bending-active structures at different scales with FRP strips and poles. They also introduced an FEM simulation to the design process and concluded that the digital tools used for this process should be calibrated through real material behavior.

Thin plates and sheets, usually made of plywood or plastic, are often used as bending-active elements

Copyright © 2019 by Yi-Hsuan TU, Ting-Yun KOU, and Chia-Chia LI
Published by the International Association for Shell and Spatial Structures (IASS) with permission.

because of advantages including the fact that they are lightweight and efficient to construct. Schleicher and La Magna [5] proposed a methodology to convert flat plate elements into desired curved shapes and reviewed three built cases. In the largest built case, a cross-connected double layers design was used to improve the load resistance. Lienhard and Knippers [6] studied the scale effect that limits the dimensions of bending-active structures. The effect cannot be easily compensated for by increasing the elastic stiffness as is the case in other structural systems since the thicknesses of bending-active elements are limited by the material strength and the bending curvature. Takahashi et al. [7] further explored the subject through an analytical approach. They proposed that combining tension elements and bending-active plates can improve the stability and widen the applicable scale range.

While most bending-active structures are formed with elements bent on site, Brancart et al. [8] developed a reciprocal structure system composed of pre-fabricated bending-active units to simplify the assembly process. The double-layered units were actively bent by clamping the end points of two plywood members of different lengths. The full-sized built prototype of a reciprocal dome showed the great potential for the use of active bending in portable structures.

This paper presents a curved surface structural system that consists of pre-bent plate units. The development of the system was aimed to maximize the structural material efficiency and to minimize the labor necessary for construction. To validate the system, two full-sized structures, including a catenary arch and a geodesic dome, were built using 3mm plywood plates.

2. Bending-active plate unit

The original concept for the unit came from a design task that required building a spanning structure from a sheet of paper and minimizing the amount of material used. It was found that instead of directly bending a paper strip by applying compression at both ends, inserting a brace into precut slits on the paper and forcing out-of-plane deformation could keep it bent in a self-stabilized state. Figure 1 shows how the basic unit was formed.

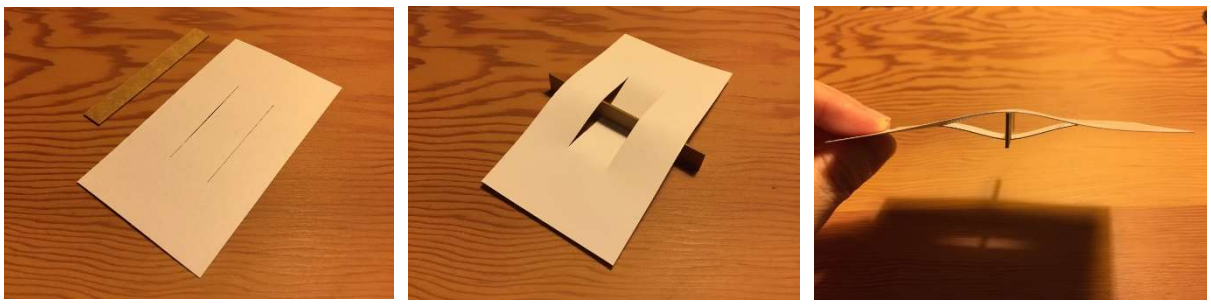


Figure 1: Formation of the self-stabilized bending-active plate unit

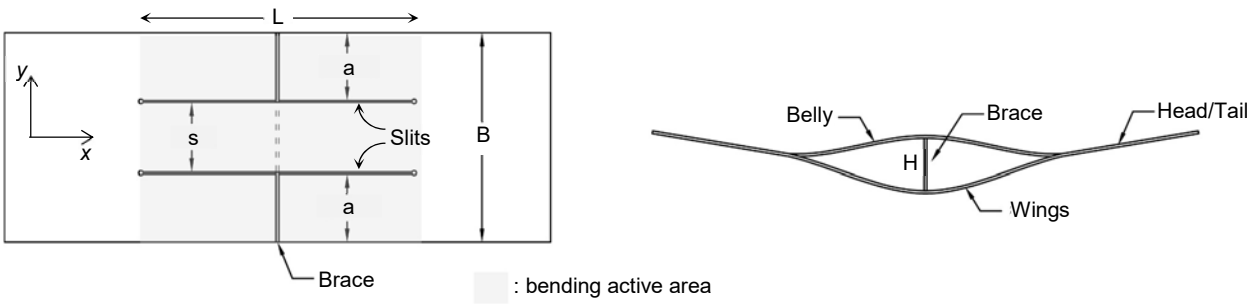


Figure 2: The plan and the elevation of the self-stabilized bending-active plate unit

Figure 2 shows the plan and the elevation of a regular unit with parallel slits, where the active bending stress only occurred in the slit area, including the "belly" and the "wings." The non-slit areas, i.e. the

"head" or "tail," were not directly affected by the active bending and remained flat in the longitudinal direction (x). However, the shear force couples transferred from the belly to the wings slightly curved the head/tail areas in the transverse direction (y).

The effects of the geometric factors on the bent angle of the unit were firstly studied using plastic sheets. Figure 3 shows one of the examples. The studied factors included the brace height (H), the slit spacing (s), the slit length (L), the plate width (B), the ratio of the slit spacing to the plate width (R = s/B), and the number of slits. The bent angle refers to the reference angle between the head and the tail of a bent unit, as illustrated in Figure 4(a). It was found that when the other factors were controlled, the bent angle increased as the brace height increased or the slit length decreased. The bent angle was not solely determined by the slit spacing or the plate width but was rather dependent on the slit width ratio R. When R was equal to 0.5, the bent angle was nearly zero. The bent angle increased regardless of whether R became smaller or larger than 0.5, but the bent directions were reversed. The same tendency was obtained when the slit numbers were increased as long as the slit width ratio was kept constant.

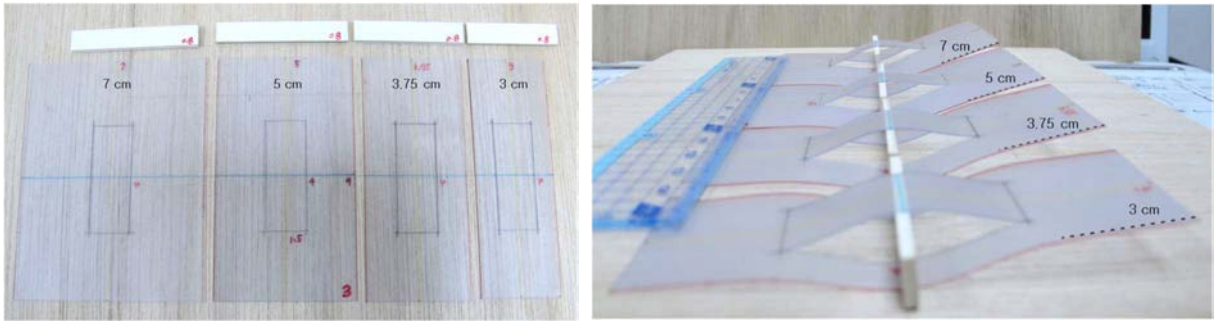
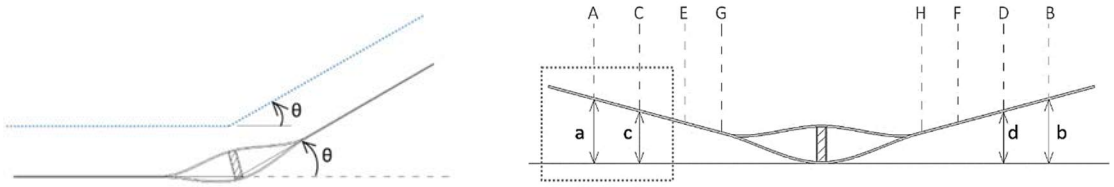
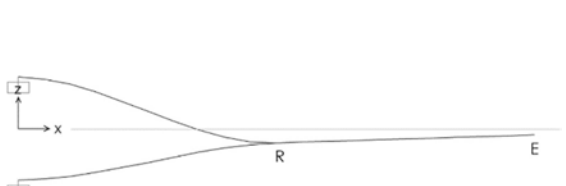


Figure 3: The differences in the bent angle for units with fixed slit spacing and changes in plate width

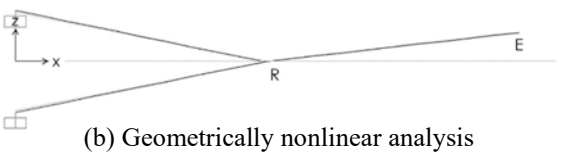


(a) Definition of the bent angle (b) Measurement of the bent angle

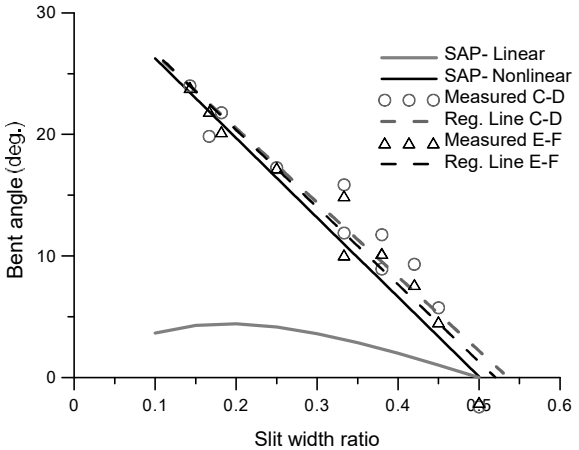
Figure 4: The definition of the bent angle and how it was measured from a full-sized unit



(a) Linear analysis



(b) Geometrically nonlinear analysis



(c) Relationships between bent angle and slit width ratio

Figure 5: Comparisons of the measured bent angles and the simulations using 2D models

The preliminary research by Li [9] used simplified 2D frame models with SAP 2000 to simulate the deformation of rectangular units with symmetric and parallel slits with different spacing. The analytical bent angles were compared with those measured from full-sized 3mm plywood units (600mm 900mm). The bent angles of the plywood units were converted from measured displacements at different positions, as shown in Figure 4(b). Figure 5 shows the comparisons between the measured results and the analytical results fir two modes: an ordinary linear analysis and a geometrically nonlinear analysis. Good agreement was found between the geometrically nonlinear analysis (solid black line) and the regression lines (dotted lines) for the measured results from different positions. They all showed a linear correlation between the bent angle and the slit width ratio R, while the analytical result (solid gray line) that did not include geometric nonlinearity exhibited obvious errors. Figure 5(c) suggests that there should be an absolute upper limit of the bent angle when the slit width ratio decreases to zero. However, a realistic upper limit must be determined in accordance with the allowable material strength when the slit width ratio becomes too small.

In the subsequent analyses by Kou [10], SAP 2000 2D frame models were used to study the effects of self-weight, elastic modulus, plate thickness, plate width, slit length, and brace height on the bent angle. It was found that the bent angle varied slightly due to the deflection of the head/tail caused by self-weight, and this effect decreased when the elastic modulus increased. When the self-weight was neglected, the bent angle was independent of the elastic modulus. The increase in plate thickness slightly decreased the bent angle, and this effect became less obvious as the slit width ratio increased. Similar to the effect of the plate width, the bent angle depended on the slit depth ratio (H/L) rather than solely on the brace height H or the slit length L. As shown in Figure 6, a linear relationship was found between the bent angle and the slit depth ratio. An empirical function summarizing the above findings is proposed in Eq.(1). It can be used to approximately estimate the bent angle θ (in degrees) from given slit dimensions for a regular unit when the self-weight is neglected.

$$\theta = 326 \times \frac{H}{L}(0.5 - R) \tag{1}$$

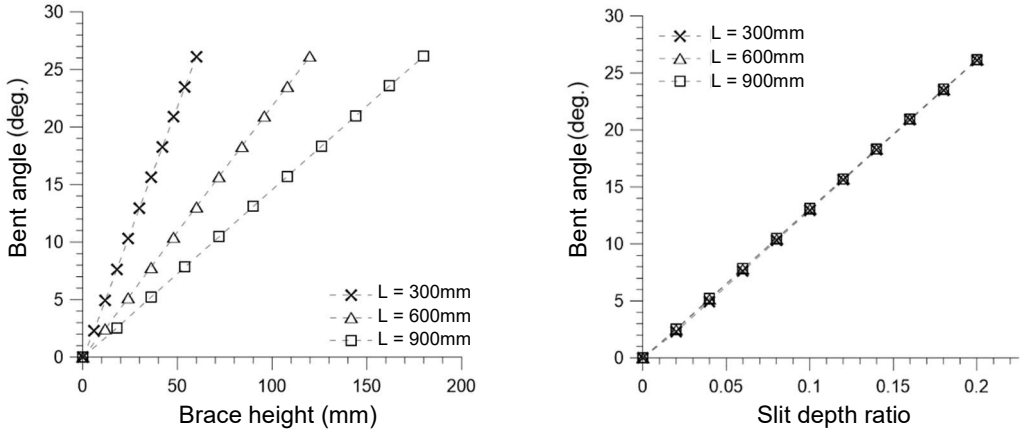
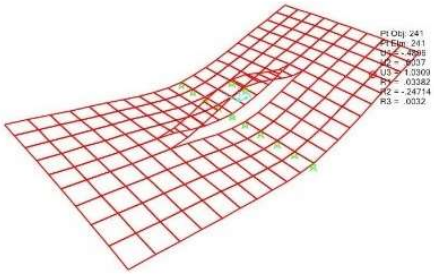
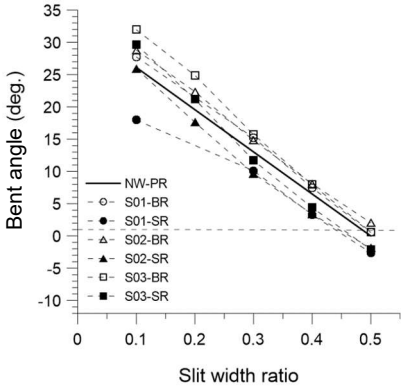


Figure 6: Relationship between the bent angle and the brace height

3D models using shell elements in SAP 2000 were compared with the results of 2D models, as shown in Figure 7. The solid line in Figure 7(b) came from the 2D models, and the dotted lines were from the 3D models with meshes of different densities. Varying degrees of difference were found due to the transverse bending caused by the shear transfer between the belly and the wings, as mentioned earlier. This transverse bending was expected to be more obvious when the unit shape and slit layout became irregular. Several irregular patterns were studied using 3D shell simulations. Figure 8 shows one of the results when the slit width ratio = 0.5. The differences between 3D and 2D simulations increased with the irregularity of the unit shape and slit layout, as expected.

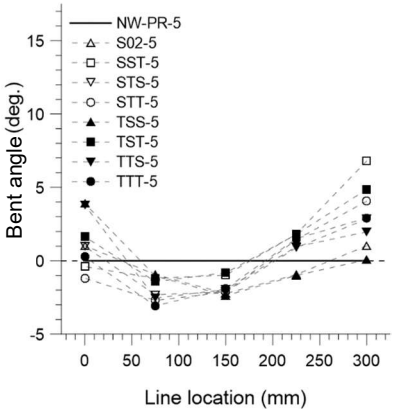


(a) 3D shell model (S02)



(b) Comparison between results from the 3D and 2D models

Figure 7: 3D shell analytical model and a comparison with 2D models



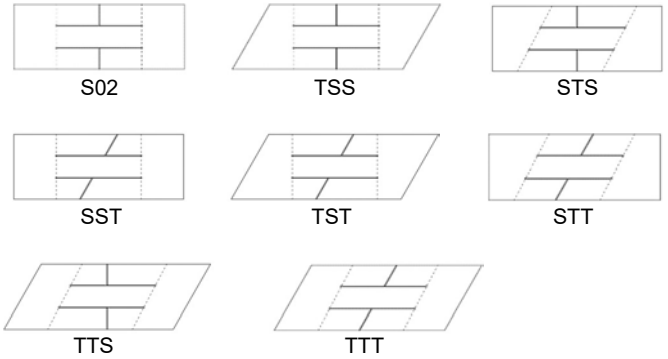


Figure 8: Simulated bending deformation along the transverse sections of irregular units

The 3D simulations were verified with 1/5 and full-scale models. The 1/5-scale models of the patterns shown in Figure 8 were made with plastic sheet. The longitudinal deformations were captured using a photo scanner. Figure 9 shows good agreement between the scanned photo with the dotted white lines emphasizing the real deformations and the red lines generated by SAP 2000 simulations. Full-scaled models of a regular unit and two irregular units were made of 3 mm plywood plates. The deformations were captured using a 3D scanner, as shown in Figure 10. The comparisons also showed good agreement between the real and simulated deformations.

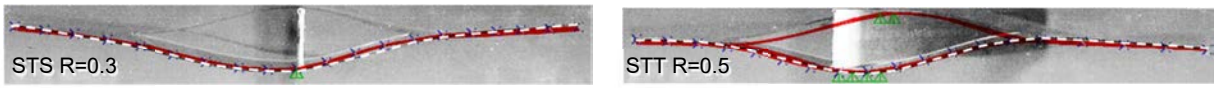


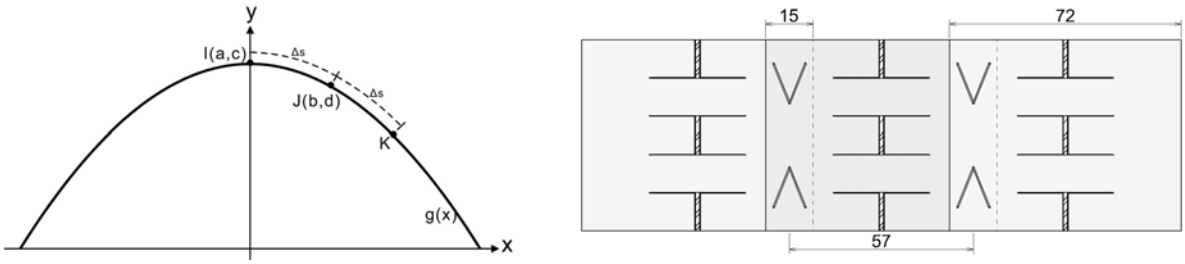
Figure 9: Comparison between the simulated deformation using 3D models and the 1/5 scale physical models



Figure 10: Comparison between the simulated deformation using 3D models and the full-scale physical models

3. Catenary arch composed of bending-active plate units

A catenary arch formed by connecting the heads and the tails of the bending-active plate units was proposed to study the use of this system. As shown in Figure 11, the catenary curve was divided into segments, and the required bent angle of each segment was determined by the slopes of the tangent lines at the dividing points. The units were made of 3 mm plywood plates. The initial proposal for the connection of the units involved overlapping of the head/tail plates of the adjacent units and fixing the overlapped area with cable ties. However, the first attempt to build the arch was unsuccessful. It appeared that the connecting areas were too thin to sustain the P-delta effect, and the structure became unstable when the number of connected units increased. This was not found in the linear structural analysis prior to construction. A subsequent geometrically nonlinear analysis confirmed the occurrence of the instability, as shown in Figure 12. The design was then modified. Stiffeners that were also used as connecting plates were added between adjacent units. Figure 13 shows the final result that was 1.7m high and spanned 4.2m.



(a) Segmenting the catenary (b) Overlapping the plate units (unit: cm)

Figure 11: Composing a catenary arch with bending-active plate units

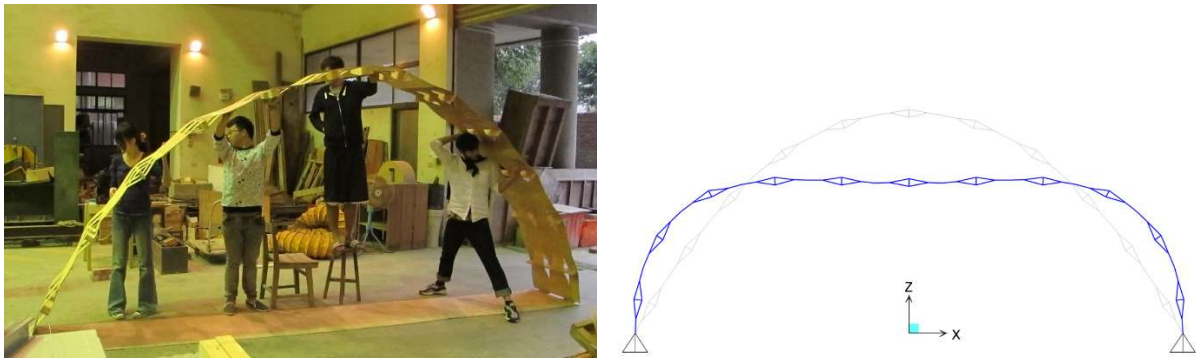


Figure 12: The first version of the catenary arch and the simulation using a geometric nonlinear analysis



Figure 13: The final version of the catenary arch built in 2014

4. Geodesic dome with reciprocally connected units

The scale effect was considered to be responsible for the instability of the first catenary arch. The subsequent research was then aimed toward enhancing the stability of the system. 1/5-scale models were used to study the structural composition. A reciprocal composition using the brace of a unit as the connecting plate of the crossing units was developed, as shown in Figure 14. The composition enabled a two-way connecting pattern suitable for spatial structures. A geodesic dome composed of 130 units of four main types was proposed. The 1/5-scale model confirmed that the stability was obviously improved because it was an undevelopable surface. The full-sized structure was 3.1 m high with a diameter of 3.45 m. It was assembled and disassembled twice in the laboratory to allow detailed adjustments. Then, the parts were transported and assembled in an indoor space for a 6-week exhibition. Finally, it was constructed again at an outdoor site and was left there for approximately 4 months to study its long-term behavior, as shown in Figure 15. The height and width of the dome were measured regularly to monitor deformation. Severe creep deformation was found because the plywood plates were exposed to humidity. Some braces in the bottom layer units were found to be torqued or separated from the units because of shear and compressive stress under long-term loading. The creep aggravated the failure at the bottom units and eventually collapsed the structure. A comparison between the linear and geometrically nonlinear analyses using simplified frame elements, as shown in Figure 16, confirmed that the geometric nonlinearity was not obvious in this structure. It also explained the stress distribution corresponding with the observed failure under long-term loading.

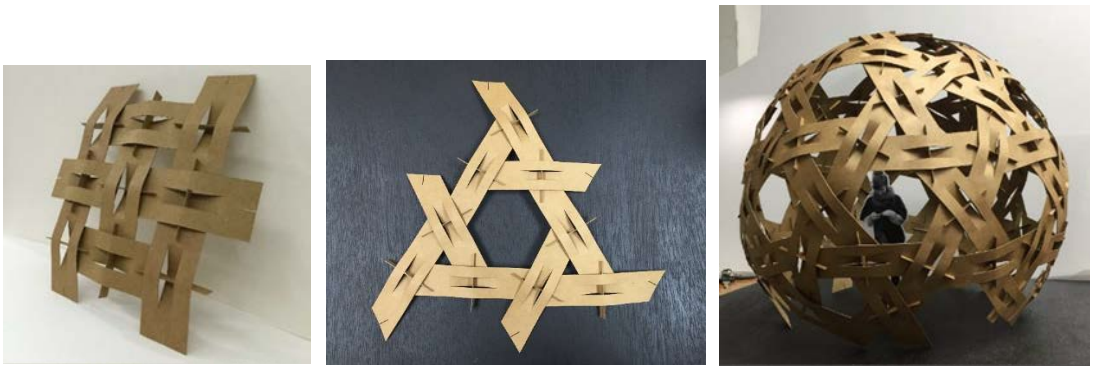


Figure 14: Reciprocally connected units and the 1/5-scale model of the geodesic dome

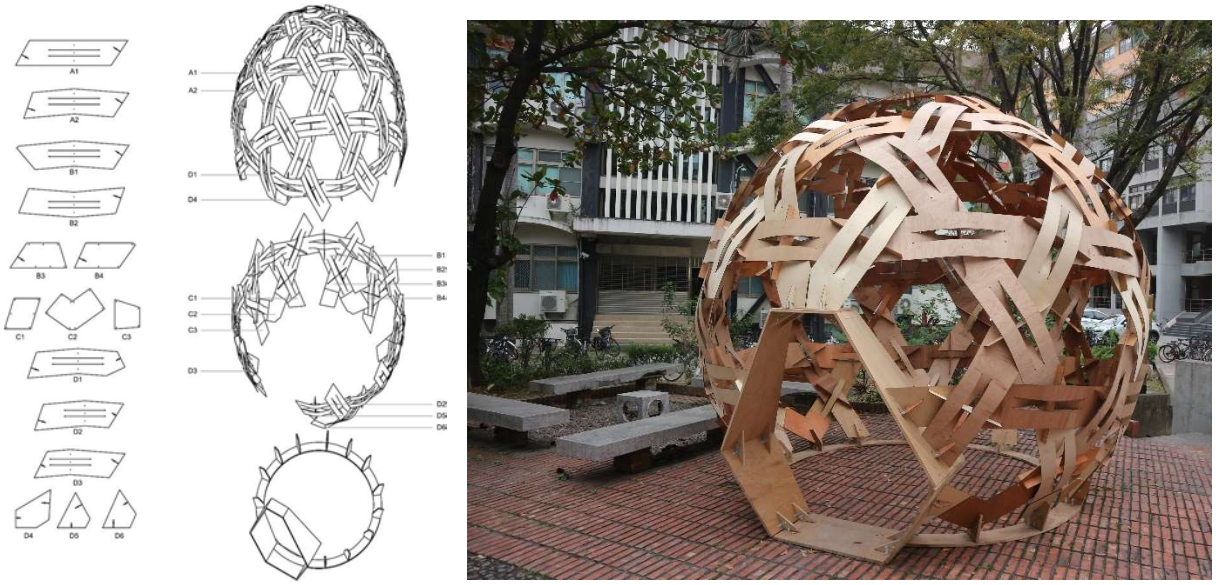
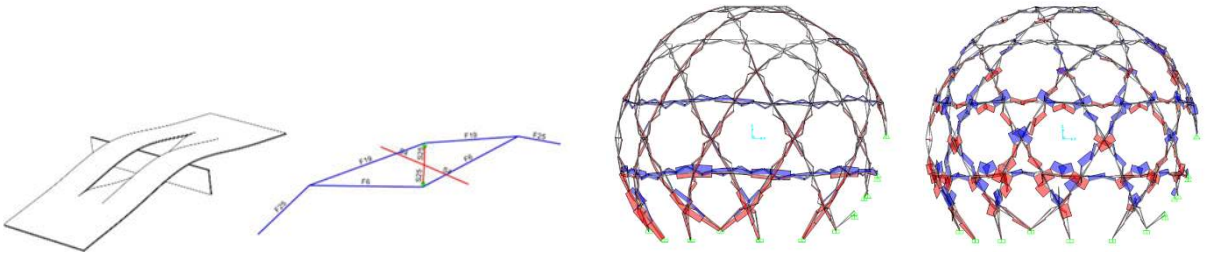


Figure 15: The full-sized geodesic dome



(a) Simplified frame element model (b) Axial force (c) Shear force

Figure 16: Simplified analytical model of the geodesic dome in SAP 2000

4. Conclusions

A lightweight structural system was proposed, where active bending was used to fabricate curved surface plate units. The self-stabilized units were easy to assemble. The geodesic dome presented in this paper was constructed manually by two individuals in one day without formworks or scaffolds. The curvature of the unit could be simply estimated using the proposed empirical equation or could be precisely simulated using 3D analytical models. The 3 mm plywood plates used in the presented structures had good workability, but the material strength and elastic modulus were unsatisfactory. Further studies of the material and the construction details will be needed when the system is applied to large-scale structures.

References

[1] J. Lienhard, H. Alpermann, C. Gengnagel, and J. Knippers, "Active bending, a review on structures where bending is used as a self-formation process," *International Journal of Space Structures*, vol. 28, no. 3&4, pp. 187-196, 2013.

[2] J. Lienhard, S. Schleicher, and J. Knippers, "Bending-active structures – research pavilion ICD/ITKE," *Proceedings of the IABSE-IASS Symposium*, London, UK, 2011.

[3] S. Schleicher, A. Rastetter, R. La Magna, A. Schönbrunner, N. Haberbosch, and J. Knippers, "Form-finding and design potentials of bending-active plate structures," in *Modelling Behaviour*, edited by M. Ramsgaard Thomsen, M. Tamke, C., Gengnagel, B. Faircloth, F. Scheurer., Berlin: Springer., pp. 53-64, 2015.

[4] P. Nicholas and M. Tamke, "Computational strategies for the architectural design of bending active structures," *International Journal of Space Structures*, vol. 28, no. 3&4, pp. 215-228, 2013.

[5] S. Schleicher, and R. La Magna, "Bending-active plates: form-finding and form-conversion," *Posthuman Frontiers: Data, Designers, and Cognitive Machines*, pp. 260-269, 2016.

[6] J. Lienhard and J. Knippers, "Considerations on the scaling of bending-active structures," *International Journal of Space Structures*, vol. 28, no. 3&4, pp. 137-147, 2013.

[7] K. Takahashi, A. Körner, V. Koslowski, and J. Knippers, "Scale effect in bending-active plates and a novel concept for elastic kinetic roof systems," *Proceedings of the IASS Annual Symposium 2016*, September 26-30, Tokyo, Japan, 2016.

[8] S. Brancart, O. Popovic Larsen, L. De Laet, and N. De Temmerman, "Bending-active reciprocal structures based on equilateral polyhedral geometries," *Proceedings of the IASS Annual Symposium 2017*, September 25-28, Hamburg, Germany, 2017.

[9] C.C. Li, "Lightweight curved surface structure using plywood sheets," *Master Thesis*, National Cheng Kung University, Tainan, Taiwan, 2014.

[10] T.Y. Kou, "A spatial structure using slit curved surface system," *Master Thesis*, National Cheng Kung University, Tainan, Taiwan, 2017.

Proceedings of the IASS Annual Symposium 2019 – Structural Membranes 2019
Form and Force
7 – 10 October 2019, Barcelona, Spain
C. Lázaro, K.-U. Bletzinger, E. Oñate (eds.)

MOBIUS Pavilion: A Double-Layer Grid Shell Combined with Ice Based on Bending-active Weaving Structure

Weixin HUANG*, Yueqi SUN, Jingyan ZHOU, Huiyin PAN

*School of Architecture, Tsinghua University

S400C, School of Architecture, Tsinghua University, Beijing,

China, 100084 huangwx@tsinghua.edu.cn

Abstract

Bending-active weaving structure made of Fiber Reinforced Polymer (FRP) rods is a reliable approach to the substantiation of free-form geometry. This paper presents the design and construction process of an architectural scale self-standing grid shell, the geometrical prototype of which is the Mobius strip. Coherent to the features of Mobius strip, the loop-like structure twisted all along the way with high curvature, which challenged both the design and assembly session. For the first time a double-layer weaving pattern was adopted by our team to utilize the synergy of two layers of bending rods and thus to improve the structure's performance.

Keywords: bending-active, grid shell, weaving structure, double-layer, free-form construction, Mobius strip

1. Introduction

Bending-active weaving structure made of Fiber Reinforced Polymer (FRP) rods is a reliable approach to the substantiation of free-form geometries [1]. Such structural system in previous researches has the following merits: a relatively wide range of organic geometries can be realized due to the flexibility of weaving system; the structure simulation is highly integrated into the form-finding process; and the assembly procedure is convenient and accurate without complicated 3D positioning works [2].

There are also other approaches to the construction of free-form grid shells. Sophisticated large-scale gird shells are commonly made up of masonry units, or interconnecting rigid materials, for example, steel, the construction of which is usually expensive and time-consuming. In a smaller scale, elastic material, bamboo or timber, for instance, are widely employed. However, the material performance of which is not as good as fiber reinforced polymer rods. Besides, in the field of ice structure, inflated molds are frequently used to shape a shell structure made of fiber-reinforced ice. It can be built in a quite large scale up to 30 meters high, yet the feature of the inflated mold prevents the gird shape from becoming complicated and organic ones.

Though the bending-active weaving structure system has its own advantages over other approaches mentioned in the literature review, due to the overall stiffness as well as joint strength, previous works usually adopted vaulted shapes to enhance the structure's stability [3]. Thus the available range of initial geometry was topologically constrained, and the spatial scale of the structure was also limited.

So in this research, we were going to explore approaches to constructing a larger scale grid shell of more topological complexity based on bending-active weaving structure. And through this project, our team were hoping to ameliorate the generic algorithm of form-finding and structural simulation [4] and to optimize the assembly procedure, thus to expand the application range and the scale of

Copyright © 2019 by Weixin HUANG, Yueqi SUN, Jingyan ZHOU, Huiyin PAN
Published by the International Association for Shell and Spatial Structures (IASS) with permission.

the bending-active weaving structure system. The structure was also combined with ice, by spraying water on the surface of the rods to form ice shell and rime [5].

2. Design and analysis approaches

2.1. Prototype

The geometrical prototype of the grid shell pavilion was the Mobius strip, which demonstrated both structural elegance and typological complexity. Coherent to the features of Mobius strip, the loop-like structure twisted all along the way with high curvature. As for the scale, the body of the gird shell encompassed over an area of 10x10m with its highest point of 4 meters including a relatively long-span cantilevered part served as an entrance for people. The convoluted form logic and the relatively larger scale compared with former projects challenged both the design and assembly session [6].

The structural simulation process gets involved at the very early stage of the design, right after the raw concept is established. We found that the original shape could hardly stand on itself when employed our previous weaving structure system because of two main problems: firstly, the cantilevered part would be sinking too low to allow people passing through; and secondly, the overall stiffness of the structure was not strong enough to bear the wind load or other external disturbance.

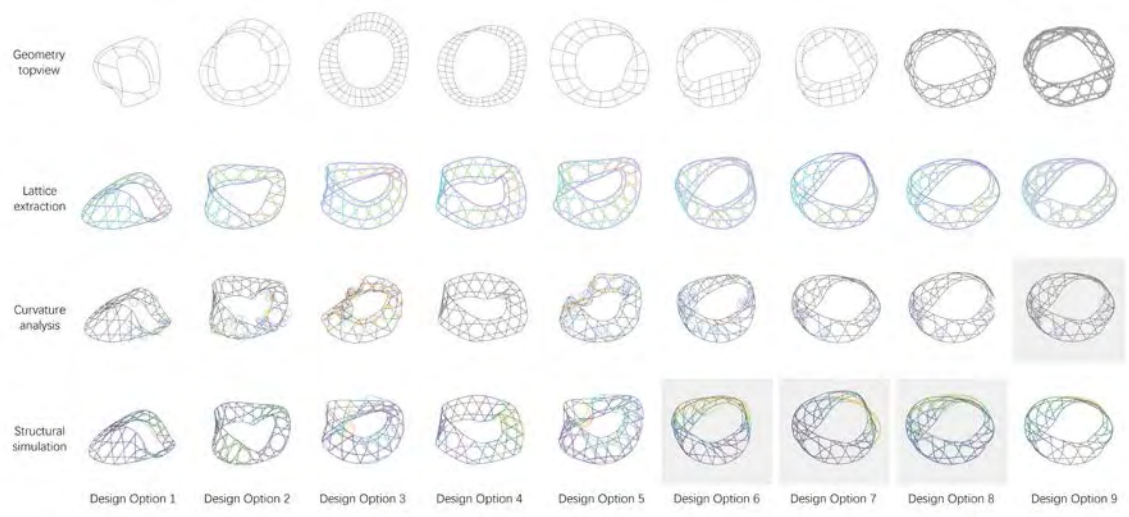


Figure 1: Prototype assuming procedure, using Kangaroo

2.2. Structure Optimizing

To solve the aforementioned problems, for the first time a double-layer weaving pattern was adopted by our team to utilize the synergy of two layers of bending rods, and thus to improve the structure's performance. Also, we fine-tuned the shape of particular parts of the structure to avoid huge shear forces or deformation on specific area. The optimizing process including both digital simulation and hand model making. On one hand, we set up the grasshopper algorithm to conveniently adjust the original surface of Mobius strip including the twisting tendency, partial curvature, and the strip's width at certain position. And we coded the double-layer rods generating program as well as making the simulation analysis program suitable for such structures. On the other hand, we learned lessons from weaving hand models: it helped us to figure out some common features for a robust self-standing structure regardless of particular shapes and also to verify the digital simulation results generated by the revised algorithm.

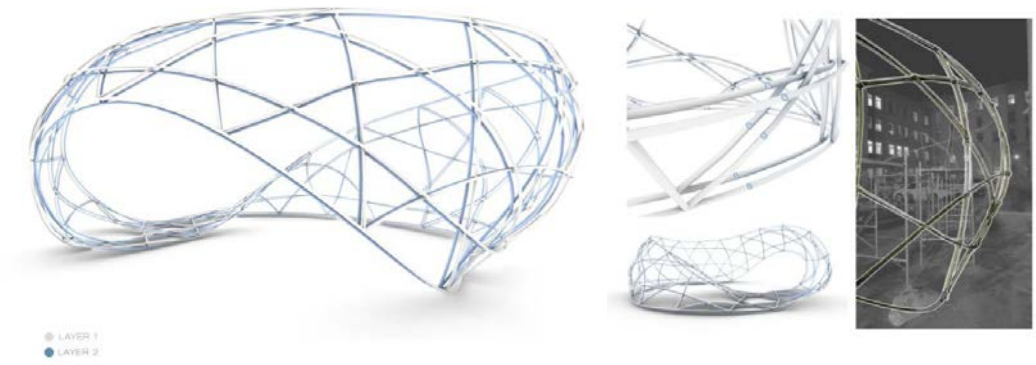


Figure 2: Double-Layer structure system

During the simulation analysis, we found that the stiffness of a double-layer structure improved obviously, and the maximum deformation decreased to nearly 1/6 compared to the same shape made of one-layer structure with doubled rod diameter. Thus we successfully controlled the theoretic value of the deformation of the cantilevered part into less than 12 centimeters, and provided enough stiffness to resist the wind load and other external forces. Thenceforth, we were able to anticipate the final state of the FRP rods after deformation, and what we should do then was simply to adjust the input structure to make sure that the output final shape is acceptable.

2.3 Assembly process and joint design

After the final shape was confirmed, the design of assembly was also a significant part of the pavilion design. The double-layer weaving pattern added difficulties to the assembly: two rods in different layer had different length due to bending - inner rods were a little bit shorter than the outer ones due to bending. So we had to generate two sets of labels of rods and intersection nodes, and give clear instruction of their overlapping and intersecting relationships. We also designed a new type of joints consisting of two steel panels and four rotary sockets fixed by bolts to tolerate possible manufacturing errors of rods as well as to provide enough joint strength since under such scale the bending force of rods could be considerably huge.

3. On-site assembly

One of the advantages of bending-active structure is that it doesn't need to build accurate molds when assembling, nor does the fixation or precast foundation on the ground since it is self-standing. However, the time for on-site manufacture and assembly was limited in 6 days, and the average temperature on site was about -15ºC, both of which brought us some problems to be surmounted.

In the first two days, we cut the GFRP rods and labeled them referring to the length and node positions generated by Grasshopper, which accelerated the following assembly procedure. Then we combined the short rods into long ones with 10cm steel pipes serving as reinforced joints.



Figure 3: Connecting GFRP rods by steel pipe and adhesive

In the next two days, we came across some of problems when assembling the rest of the rods to the outer ring one after another. For example, the inner rods and the outer ones could not match each other due to the measurement error, which led to the dislocation of the node positions. Iron wires were used to fix the adjacent rods, so that the nodes can be correctly organized. Another problem was that, although the FRP rods were flexible, they were too stiff for workers to bend manually at some specific parts where with high curvature. To solve this problem, three pairs of tension puller were placed to help bend the rods to their position and proper arc shape.

For decoration, we attached LED stripes on both layers of the rods on the last day. In order to show the only surface composing the Mobius, which is the most notable feature of it, we designed an electric circuit that could have yellow light as well as blue. In addition, we made ice shell over rods to make the appearance of the structure more attractive. Rods were covered with paper of high absorption and then became easily attached by ice. We spray Pykrete, a frozen composite material made of 14% sawdust or paper pulp and 86% ice [5] onto the Mobius, and it could freeze well at low temperature at night.



Figure 4: Construction process of the double layered Mobius strip



Figure 5: LED assembly on the finished structure

The time Schedule of on-site assembly can be arranged in six days respectively as shown below:

- Day 1: prepare the rods, cut and label.
- Day 2: process the rods, and connect.
- Day 3: prepare for outdoor work, mark the site and position the outer ring.
- Day 4: assemble the rods.

- Day 5: continue assembling the rods.
- Day 6: attach the LED stripes and make ice shell over rods.



Figure 6: Mobius View at Night

4. Discussion

The completed grid shell was 3D scanned in order to measure the structural deformation, and to verify the structural simulation algorithm. The point cloud of the completed model was generated by the 3D laser scanner. When comparing the point cloud to the original design, we found that all the deformations were in an acceptable range, and the deformation tendencies in certain position were successfully anticipated before. And we also input the finished model into the structural simulation program, finding that the deformation was almost negligible, which meant the finished structure itself was stable and structurally reasonable.

We also optimized assembly procedure. First, it saved us plenty of time that two groups were working at the same time from the opposite direction of weaving process. And an assembly plan was designed in advance that directed us to construct in order. Also the real-time adjustment against the electronic model was necessary during the construction process. For instance, we chose 3mm iron wire to bind nodes instead of the commonly used metal binding belt, due to the size and geometric characteristics of Mobius. Therefore, the joint reliability was greatly increased by using the technology of binding iron wire which was commonly used in the construction process. And lessons were learned for future projects.

As for the ice part, because the complicated assembly process lasted six days, we only had one night left for ice shell construction, we did not make sufficient preparation for how to combine ice with rods. Actually, ice and FRP rods may work together to improve the structural performance of the pavilion. The scheme we chose in this project was more a kind of decoration, and does not affect the inner force characteristics of the structure itself, which ensures the visual effect, and avoids the potential risks caused by ice melting and breaking. In our future project, we will explore the possibility of synergistic effect of ice shell and bending-active structure.

5. Conclusion

The completion of the pavilion proved the possibility of building a typologically complex grid shell in a large scale based on bending-active weaving structure.

The double-layer structure we adopted for the first time obviously improved the structural performance of a weaving structure, though it required a more carefully assembling procedure. And the new type of joints made of steel were able to tolerate possible manufacturing errors of rods as well as to provide enough joint strength.

And more generally, we ameliorated the generic algorithm of form-finding and structural simulation for free- from geometries, thus expanded the application range and scale of the weaving structure system. It can be expected that bending-active weaving structure will have a broad application prospect in future architectural projects.

Acknowledgements

The authors gratefully acknowledge the financial support provided by the National Natural Science Foundation of China (NSFC) (Project No. 51278263) and the Harbin Institute of Technology, China.

References

[1] W.HUANG, "A Weaving Structure for Design & Construction of Organic Geometry," *Proceedings of the IASS Annual Symposium 2017,* Hamburg, Germany, 25-28th September, 2017.

[2] W. X. HUANG, "Digital Design and Construction of a Weaving Structure," *The 8th International Conference on Fibre-Reinforced Polymer (FRP) Composites in Civil Engineering (CICE 2016),* Hong Kong, 2016.12.

[3] J. Lienhard, H. Alpermann, C. Gengnagel, J. Knippers, “Active Bending, A Review on Structures where Bending is used as a Self-Formation Process”, *International Journal of Space Structures,* Vol. 28 · No. 3 & 4, pp. 187-196, 2013

[4] M. R. Barnes, “Form finding and analysis of tension structures by dynamic relaxation”, *International Journal of Space Structures,* 14(2), pp.89-104. 1999

[5] A. Pronk, "Design and construct of the 30.5 meter Flamenco Ice Tower.," *Symposium conducted at the meeting of the IASS Annual Symposium 2018,* Boston, USA.

Proceedings of the IASS Annual Symposium 2019 – Structural Membranes 2019
Form and Force
7 – 10 October 2019, Barcelona, Spain
C. Lázaro, K.-U. Bletzinger, E. Oñate (eds.)

Numerical Analysis of a Hybrid Bending-Active Gridshell

Ioanna ANASTASIADOU*, Marios C. PHOCAS

* Department of Architecture, University of Cyprus
Kallipoleos St. 75, 1678 Nicosia, Cyprus
mcphocas@ucy.ac.cy

Abstract

Elastic gridshells were incepted in the 1960s and popularized by the work of Frei Otto, especially through the famous Mannheim Multihalle in the early 1970s. Since then, a number of researchers have dealt with the systems' materiality, constructability and applicability, driven by respective advantages in their production, transportation, erection and construction. Adaptive architecture has also triggered the interest of many architects and structural engineers, aiming at an optimized static performance and reconfigurable spatial systems that can adapt to functional or structural requirements. Along these lines, the current paper examines the design and analysis of a hybrid bending-active gridshell that consists of an array of elastic strips interconnected through a secondary system of struts and cable segments. The proposed gridshell has a span of 9.6 m and a length of 10 m. The three-stage development of the gridshell includes the planar deformation of the bending-active members, the erection of the system and its external loading. The analysis examines three different materials for the bending-active members. The numerical investigation of the system is conducted through a progressive form-finding and load-deformation Finite-Element Analysis (FEA). The analysis provides insight to the efficiency of the proposed hybrid bending-active gridshell in terms of deployability, transformability and operability, highlighting the structural and architectural potentials in achieving lightweight, adaptive structures.

Keywords: Bending-active gridshells, Hybrid structures, Form-finding, Load-deformation behavior, Finite-Element Analysis.

1. Introduction

The utilization of transformations at structural level, has shown high potential over the last years in achieving efficient, lightweight, adaptive systems. Active-bending principles enable reconfigurable, transformable structural systems through the inherent ability of the elastic members to provide different morphological transitions while they are able to return to their initial straight geometry (Brancart, De Laet and De Temmerman [1]). Adaptive spatial structural systems may emerge by utilizing reversible elastic deformations of bending-active members integrated with secondary actuation and control components to achieve active shape control. In this respect, effective spatial free-form shapes emerge by utilizing bending-active principles in gridshell structures. Gridshells refer to shell structures consisting of a grid rather than a solid surface, but with respective shape and strength abilities. Elastic gridshells obtain their geometry through the elastic bending of their initially straight continuous profiles (Hernández [2]) and are primarily characterized by means of the materiality and erection method applied. By utilizing the bending flexibility of the members, the grid is elastically deformed to reach its target form and then stabilized. Elastic gridshells present a wide variety in terms of surface geometry, grid configuration and materiality, while their initially flat and regular grid is beneficial in terms of constructability and configurability due to its planar initial geometry, standard connection nodes and profiles (Du Peloux [3]).

Copyright © 2019 by Ioanna ANASTASIADOU and Marios C. PHOCAS
Published by the International Association for Shell and Spatial Structures (IASS) with permission.

The main structural aspects in the design process of elastic gridshells are the system geometry, the level of residual stresses and stiffness (Hernández [2]). The geometry of gridshells depends on the curvature of the elastic members, having a significant impact on its structural performance. The erection phase can be characterized as the major load case for an elastic gridshell (Quinn and Gengnagel [4]). During erection, tight curvatures result to higher residual stresses induced in the elastic members. Bending stresses have to be monitored, in order to avoid breakages or plastic deformations of the elastic members during erection and ensure an adequate bearing capacity against external loads. The spatial curvature of the gridshell along with the materiality and cross-section properties of the elastic members mainly determine the system stiffness. By extension, respective structural requirements refer to the system stability and level of allowable material stresses. For static bending-active structures appropriate materials have a ratio of maximum elastic bending stress to Young's Modulus, $\sigma_{M/Rd}/E > 2.5$, while for elastic kinetic systems, the respective ratio is $\sigma_{M/Rd}/E > 10$ due to the additional requirement for fatigue control (Lienhard [5]). In this frame, wood, Glass Fibre-Reinforced Polymer, GFRP, and Natural Fibre-Reinforced Polymer Composites, NFRP, are suitable materials for bending-active structures.

Excessive research in the field of elastic gridshells has been conducted since the late 50s by Frei Otto, who investigated lightweight shells that obtain their shape using the Hookean principle of inverting a hanging net (Liddell [6]). The research conducted by Frei Otto lead to the design and construction of the Mannheim Multihalle in the mid 70s. The 9000 m^2 curved roof with a span of 60 x 60 m, constructed in timber laths of 5 cm thickness, revealed the potential of utilizing bending principles in larger scale structures. Since then, a number of elastic gridshells has been realized, following different erection techniques and materiality. Representative examples of timber elastic gridshells are the Weald and Downland Gridshell with a span of 50 x 16 m (Kelly *et al.* [7]), and the Savill Garden Gridshell with a span of 28 x 98 m (Harris, Haskins and Roynon [8]). In parallel, recent researches focus on the potential of composite materials in the field due to their large permissible strain and high stiffness. Their application was investigated in built prototypes constructed with GFRP rods, such as the Flying Dome Installation (Hernández, Baverel and Gengnagel [9]) and the Faraday Pavilion (Nicholas, Hernández and Gengnagel [10]), while the construction of the ephemeral cathedral of Creteil in France (Du Peloux *et al.* [11]) proved the applicability of composite materials in elastic gridshells with larger span. In search for the most appropriate materials, GFRP and NFRP present a similar forming ability to that of wood, but are favorable in terms of stiffness. The high initial price of composite materials balances the high maintenance cost of wood, while in environmental terms, wood is preferable due to the environmental impact of composite materials (Kotelnikova *et al.* [12]).

In dealing with the aforementioned aspects of materiality, erectability and structural performance of bending-active structures, the current paper examines the behavior of a hybrid bending-active gridshell, assigned to three different materials, namely polytetrafluorethylene, PTFE, plywood and GFRP. The analysis gives insight to the gridshell behavior during the form-finding process and under external loading. Initial related investigations conducted by the authors in (Anastasiadou, Alexandrou and Phocas [13]) refer to a hybrid system series of two continuous elastic strips of PTFE interconnected through a secondary system of struts and cable segments along the system span. The analysis results gave insight to respective configurational and load-deformation interdependencies of the hybrid system and its individual components that also comprise the main elements of the gridshell investigated in the current paper.

2. Hybrid Gridshell

2.1 Deployment and erection

The proposed bending-active gridshell consists of pairs of elastic strips, positioned with their strong axis aligned perpendicular to the ground. The elastic members are interconnected at constant distances through strut elements and cable segments. The deployment of the gridshell is handled through auxiliary contracting cables connecting the supports. The cables' length reduction induces bending to the elastic

members, providing the deployment of the gridshell. The resulting deployed grid has overall dimensions on its flat form of 12.4 x 10 m and 22 support points at the ends. The supports at the first edge of the elastic members enable displacements on the y-axis, while the supports at the second edge enable displacements on both, x and y-axis. A corner support is anchored to the ground, in order for the structure to remain stable. Cable segments connecting the upper and lower edges of the struts are applied, once the structure has obtained its form-found shape. The erected structure has a span of 9.6 m and a length of 10 m (Fig. 1).

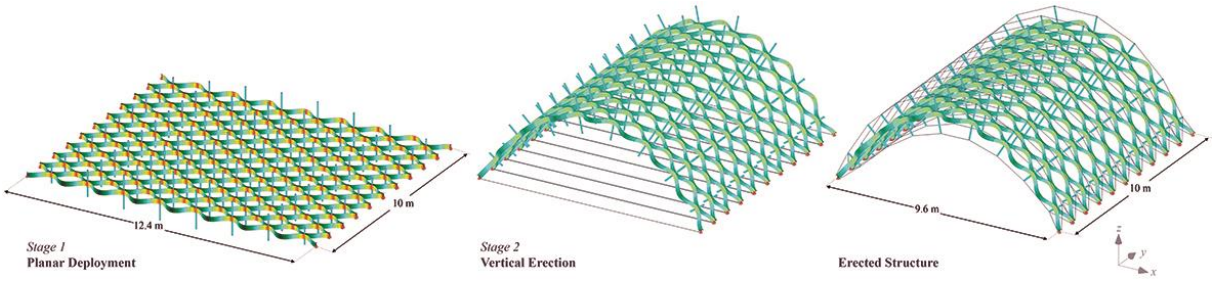


Figure 1: Analysis stages

2.2 Materials

The analysis examines three different materials for the bending-active members that fall under the categories of polymers, wood and composites, namely PTFE, plywood and GFRP. The mechanical properties of the materials used in FEA are presented in Table 1. The elastic members have a height of 200 mm and a thickness of 8 mm. The cables have 10 mm diameter and are assigned to prestressing steel Y1770 of 195 GPa elastic modulus and 1520 MPa yield strength. The struts consist of steel hollow sections of 60 mm diameter and wall thickness of 5 mm. The struts' height varies from 70 to 160 cm, successively increasing from the first segment up to midspan.

Table 1: Mechanical properties of PTFE, Plywood and GFRP, used in FEA

	Elastic Modulus, E	Yield Strength, $\sigma_{M/Rd}$	$\sigma_{M/Rd}/E$
PTFE	2.5	48	19.2
Plywood	5.5	60	10.9
GFRP	30	500	16.7

3. Numerical Analysis

The structural behavior of the hybrid gridshell was investigated with the FEA software SOFiSTiK®. The geometry of the system was defined in McNeel Rhinoceros program and exported to SOFiSTiK's main database. The elastic members were modeled as structural surfaces, while all other structural members, as beam elements. Each elastic member mesh has 80 divisions in the longitudinal direction and two divisions in the transverse direction, resulting into 160 quadrilateral elements, in order to increase the accuracy level of the analysis. Bending of the structure was simulated by taking into consideration both, the external forces and internal material stresses. The system simulations are based on the third-order theory, considering nonlinear geometrical effects and large displacements. The SOFiLOAD module was used for the definition of loads, while ASE was used as the general static analysis solver. SOFiLOAD and ASE were handled through the alternative text input tool, TEDDY. The analysis follows an incremental induction of bending deformations, where inner stresses of the material developed in each step are stored in the model.

The numerical analysis of the proposed hybrid gridshell was conducted for the three abovementioned materials of the elastic members. The gridshell is examined in its form-finding process and under external loading, acting on the middle upper points of the struts. The respective point loads derive from

a uniform distribution of respective vertical and horizontal loads of 1 kN/m². The external loads have been applied on the gridshell in 10 incremental load steps.

3.1 Erection stage

Material differentiation does not affect morphological aspects of the gridshell, since in all three analysis cases the overall static height of the erected structure reaches approximately 3.48 m at midspan, with the respective span to height ratio been equal to 2.75 (Table 2). With a PTFE material, the maximum axial force N_{xx} of the elastic members develops at the support points of the structure, reaching a maximum value of 7.22 kN/m. Elastic members assigned to plywood and GFRP, develop maximum axial force N_{xx} at the connecting areas with the struts, with maximum values of 10.8 and 84.6 kN/m respectively. The elastic members of PTFE, plywood and GFRP material, exhibit maximum respective axial force values N_{yy} of 7.41, 11.1 and 58.2 kN/m. The maximum bending moments M_{xx} develop at midspan, while the maximum bending moments M_{yy} are uniformly developed along the structure in all material cases. The maximum stress of the elastic members reaches values of 39.6, 54.5 and 436 MPa, corresponding to a stress utilization of 82.5, 90.8 and 87.2 % of the respective material's yield strength (Fig. 2). In the cases of PTFE and plywood, maximum stresses of the elastic members develop at midspan, while in the case of GFRP, they are uniformly developed along the structure.

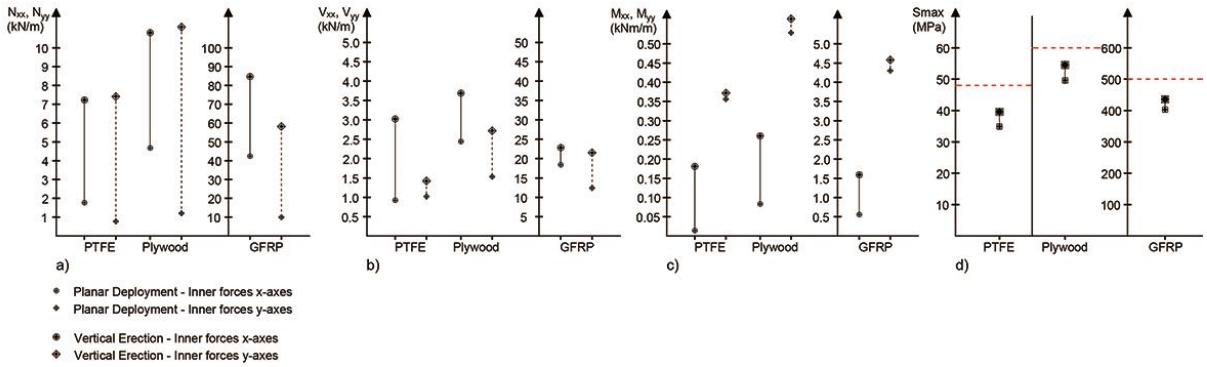


Figure 2: Numerical analysis results in vertical erection stage. Maximum a) Axial force, b) Shear force, c) Bending moment, d) Stress

3.2 Vertical load-deformation behavior

Under vertical loading, elastic members assigned to GFRP clearly demonstrate their ability to increase the load-bearing capacity of the structure, since the maximum deformations at midspan amount to only 5 mm. The respective deformations increase by 960 and 620 %, amounting to 53 and 36 mm, when elastic members are assigned to PTFE and plywood respectively (Table 2). With a PTFE material, the maximum axial force N_{xx} of the elastic members presents a decrease of 26 % under vertical loading, compared to the erected stage. Contrariwise, elastic members assigned to plywood and GFRP present higher axial force N_{xx}, by 6.5 and 2.5 % respectively. The maximum axial force N_{yy} records values of 7.00, 12.2 and 56.5 kN/m for each elastic members' material selection, i.e. PTFE, plywood and GFRP. The shear forces V_{xx} and V_{yy} decrease under vertical loading, when the elastic members are assigned to plywood and GFRP. In the case of plywood, the shear forces reach maximum values of 3.42 and 2.06 kN/m, which correspond to a decrease of 7.3 and 24.3 % compared to the respective values in the erection stage. In the case of GFRP, the shear forces reach maximum values of 22.6 and 20.6 kN/m, presenting a respective decrease of 0.9 and 4.2 %. With an elastic members material selection of PTFE, the shear force V_{xx} has a decrease of 7.3 %, reaching a maximum value of 2.80 kN/m. In contrary, the shear force V_{yy} has an increase of 1.4 %, reaching a value of 1.44 kN/m. In all material selection cases, the maximum bending moments M_{xx} and M_{yy} decrease by 3.9, 3.1 and 0.6 % and 9.4, 5.3 and 0.9 %, for a PTFE, plywood and GFRP elastic members' material selection respectively. Similarly to the erection stage, the maximum bending moments M_{xx} develop at midspan, while the maximum bending moments

M_{yy} develop in the connecting areas of the elastic members with the struts. The maximum stresses present a decrease of 6.3, 4.4 and 1.0 % compared to the erection stage, corresponding to a stress utilization of 77.3, 86.8 and 86.3 % (Fig. 3). In the cases of PTFE and plywood, maximum stresses of the elastic members develop at midspan, while in the case of GFRP, they are uniformly developed along the structure. The maximum axial force N_c of the cables develops in the cable segments connecting the lower edges of the central struts. The maximum value develops when elastic members are assigned to GFRP, and amounts to 0.6 kN. When it comes to PTFE and plywood, the respective value decreases by 16.7%.

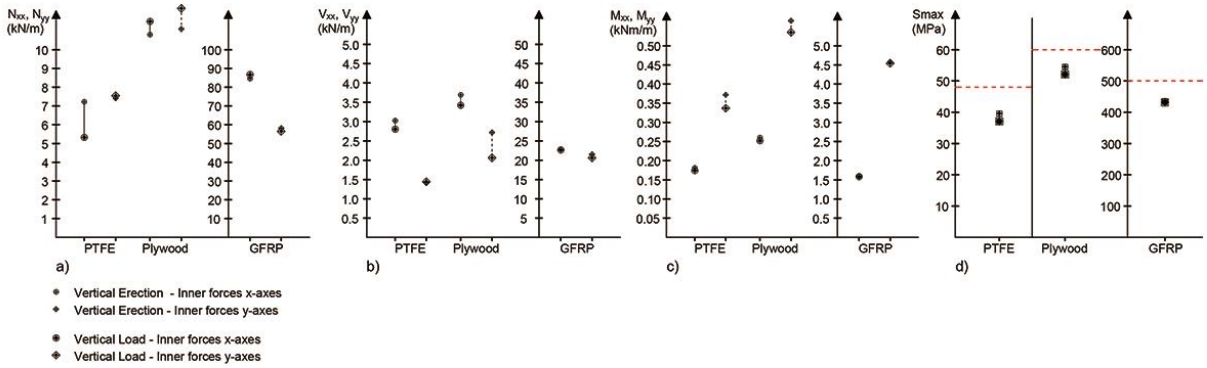


Figure 3: Numerical analysis results in vertical loading stage. Maximum a) Axial force, b) Shear force, c) Bending moment, d) Stress

3.3 Horizontal load-deformation behavior

Similarly to the vertical loading stage, under horizontal loading, the structure presents minor vertical and horizontal deformations at midspan, when assigning GFRP to the elastic members. The maximum vertical deformation amounts to only 1 mm while the horizontal deformation amounts to 7 mm. With PTFE for the elastic members, the vertical deformation increases by 2200 %, amounting to 23 mm, while the horizontal deformation increases by 557 %, amounting to 46 mm. When the elastic members are assigned to plywood, they present vertical and horizontal deformations at midspan of 13 and 44 mm respectively, increased by 1200 and 529 % compared to the ones with GFRP (Table 2). Horizontal loading induces higher axial forces N_{xx} and N_{yy} in the elastic members. The respective values amount to 9.62, 12.6 and 88.3 kN/m and 11.0, 12.3 and 58.9 kN/m, for each respective material. These values correspond to an increase of 33, 17 and 4.4 % of the axial force N_{xx}, and 48, 11 and 1.2 % of the axial force N_{yy}, compared to the erection stage. When assigned to PTFE and plywood, the elastic members exhibit a decrease in the maximum shear force V_{xx} by 2.0 and 2.17 %, while the maximum shear force V_{yy} increases by 43 and 9.2 %, compared to the erection stage. With a GFRP material selection, the maximum shear forces V_{xx} and V_{yy} preserve their maximum values developed in the erection stage. The elastic members exhibit a maximum value of 0.18, 0.26 and 1.6 kNm/m in bending moment M_{xx} and 0.41, 0.60 and 4.6 kNm/m in bending moment M_{yy}, for each respective material. Under horizontal loading, the material's stress utilization reaches 82.3, 94 and 86.9 % of the respective yield strength limit, with values of 39.5, 56.4 and 434.3 MPa (Fig. 4). In the cases of PTFE and plywood, maximum stresses of the elastic members develop in the area close to the supports, on the loading-ward side, while in the case of GFRP, they develop in the connection areas of the struts at midspan. In all material cases, the maximum cables axial force N_c develops in the cable segments connecting the lower edges of the first and second strut in span direction, with the respective maximum values been equal to 0.5, 0.6 and 0.64 kN.

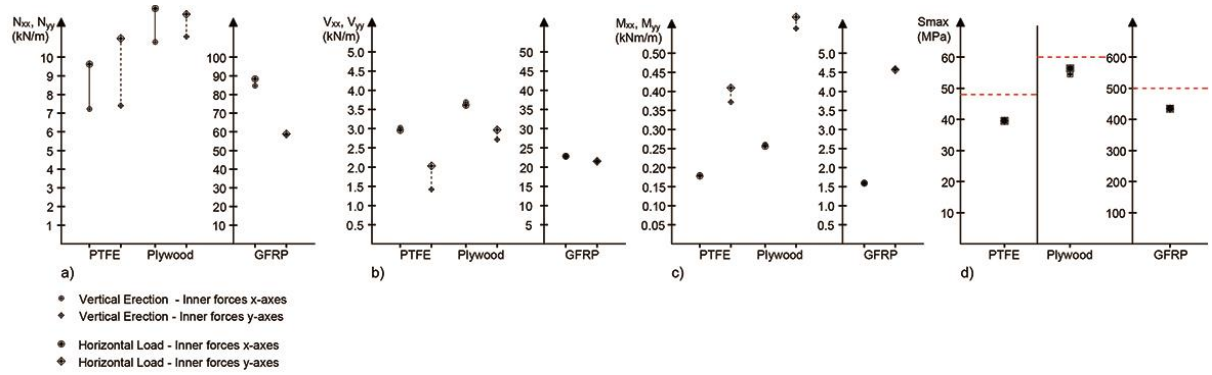


Figure 4: Numerical analysis results in horizontal loading stage. Maximum a) Axial force, b) Shear force, c) Bending moment, d) Stress

3.4 Combined load-deformation behavior

Under combined action of vertical and horizontal loading, the maximum vertical deformation at midspan amounts to 47, 31 and 4 mm, whereas the maximum horizontal deformation amounts to 36, 30 and 5 mm, for an elastic members' material selection of PTFE, plywood and GFRP respectively (Table 2). Axial forces N_{xx} and N_{yy} recorded in the elastic members assigned to PTFE reach 7.25 and 7.77 kN/m, which are by 0.42 and 4.9 % higher compared to ones developed in the erection stage. The respective values recorded with plywood also present an increase of 17.6 and 10.8 %, with maximum values of 12.7 and 12.3 kN/m. Elastic members assigned to GFRP have maximum axial forces N_{xx} and N_{yy} of 88.1 and 56.9 kN/m, corresponding to an increase of 4.1 % and a decrease of 2.2 %, compared to the ones developed in the erection stage. The maximum shear force V_{xx} records maximum values of 2.83, 3.45 and 22.6 kN/m, while the maximum shear force V_{yy}, 1.51, 2.16 and 20.6 kN/m, for each respective material. In all cases, the maximum bending moments M_{xx} and M_{yy} decrease compared to the erection stage. The maximum bending moment M_{xx} reaches respective values of 0.175, 0.252 and 1.58 kNm/m, whereas the maximum bending moment M_{yy}, 0.353, 0.537 and 4.54 kNm/m. These values correspond to a decrease of 3.31, 3.08, 0.63 % and 5.11, 4.96, 0.87 % respectively. Compared to the erection stage, the maximum elastic members stresses decrease by 6.1, 4.4 and 1.1 %, obtaining values of 37.2, 52.1 and 431 MPa (Fig. 5). In the cases of PTFE and plywood, maximum stresses of the elastic members develop at midspan, while in the case of GFRP, they develop in the connection areas of the struts at midspan. The respective cables maximum axial force N_c values amount to 0.15, 0.16 and 0.19 kN.

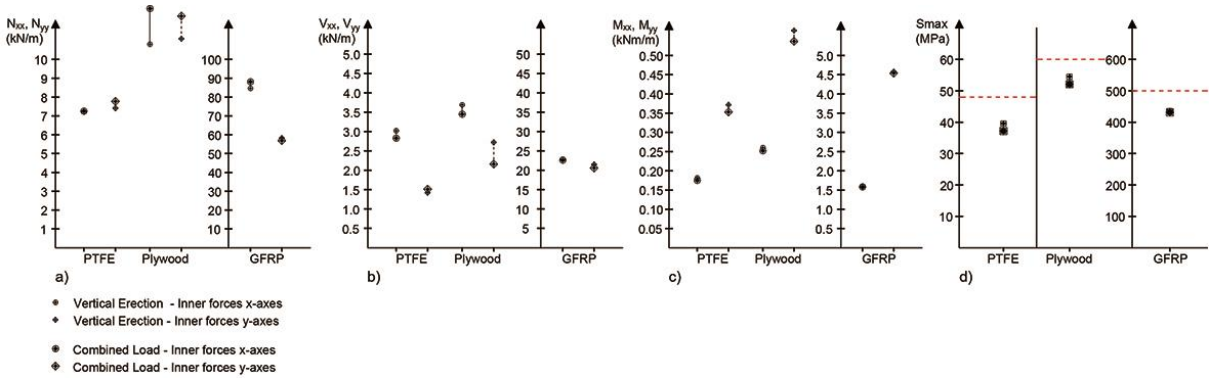


Figure 5: Numerical analysis results in combined loading stage. Maximum a) Axial force, b) Shear force, c) Bending moment, d) Stress

Table 2: Gridshell deformations in erection, vertical, horizontal and combined loading stages of analysis.

Stage of Analysis	**PTFE**			**Plywood**			**GFRP**		
	h [mm]	U(z) [mm]	U(x) [mm]	h [mm]	U(z) [mm]	U(x) [mm]	h [mm]	U(z) [mm]	U(x) [mm]
Vertical Erection	3486	-	-	3476	-	-	3478	-	-
Vertical Load	3433	53	-	3440	36	-	3473	5	-
Horizontal Load	3463	23	46	3463	13	44	3477	1	7
Combined Load	3439	47	36	3445	31	30	3474	4	5

4. Conclusions

The present paper investigates a hybrid bending-active gridshell. The gridshell consists of interconnected elastic strips placed with their strong axis vertically. The elastic strips are interconnected with strut elements and cable segments along the span direction. The investigation focuses on the form-finding and load-deformation behavior of the gridshell. The static analysis follows a three-stage development, including the planar deployment of the elastic strips, the vertical erection of the gridshell and its external vertical and horizontal loading. The analysis examines three different materials for the bending-active members, namely PTFE, plywood and GFRP. The form-found configuration of the proposed gridshell reaches similar span to height ratios, regardless of the material assigned to the elastic members. In all analysis cases, the elastic members do not override the yield strength limit of the material. A maximum stress utilization is recorded with a plywood selection and amounts to 94 % of the material's yield strength limit. Most favorable results in terms of load-deformation behavior of the structure are obtained with GFRP, since the maximum deformations at midspan are significantly reduced, when compared with the ones recorded with PTFE and plywood. Future work includes investigation of the load-deformation behavior of the gridshell in different configurations and its post-stiffening capacity, involving simulations and experimental testing of small-scale prototypes.

References

[1] S. Brancart, L. De Laet and N. De Temmerman, "Transformable active bending: Elastic deformation as component transformation in transformable structures", in *Shells, membranes and spatial structures: Footprints: Proceedings of the IASS-SLTE 2014 Symposium*, Brasilia, Brazil, 2014, pp. 1-8.

[2] E.L. Hernández, *Design and optimisation of elastic gridshells, Ph.D. Thesis*, Berlin University of the Arts (UdK), 2015.

[3] L. Du Peloux, *Modeling of bending-torsion couplings in active-bending structures. Application to the design of elastic gridshells, Ph.D. Thesis*, École des Ponts Paris Tech, 2017.

[4] G. Quinn and C. Gengnagel, "A review of elastic grid shells, their erection methods and the potential use of pneumatic formwork" in *Mobile and Rapidly Assembled Structures IV: 4th International Conference on Mobile, Adaptable and Rapidly Assembled Structures MARAS2014*, Ostend, Belgium, Vol. 136, 2014, pp. 129–143.

[5] J. Lienhard, *Bending-active structures: Form-finding strategies using elastic deformation in static and kinetic systems and the structural potentials therein, Ph.D. Thesis*, University of Stuttgart, 2014.

[6] I. Liddell, "Frei Otto and the development of gridshells", *Case Studies in Structural Engineering*, Vol. 4, pp. 39-49, 2015.

[7] O.J. Kelly, R.J.L. Harris, M.G.T. Dickson and J.A Rowe, "Construction of the Downland gridshell", *The Structural Engineer*, Vol. 79, No. 17, pp. 25–33, 2001.

[8] R. Harris, S. Haskins and J. Roynon, "The Savill Garden gridshell: Design and construction", *The Structural Engineer*, Vol. 86, No. 17, pp. 27–34, 2008.

[9] E.L. Hernández, O. Baverel and C. Gengnagel, "On the design and construction of elastic gridshells with irregular meshes", *International Journal of Space Structures*, Vol. 28, No. 3–4, pp. 161–174, 2013.

[10] P. Nicholas, E.L. Hernández and C. Gengnagel, "The Faraday Pavilion: Activating bending in the design and analysis of an elastic gridshell", in *SimAUD '13 Proceedings of the Symposium on Simulation for Architecture & Urban Design*, No. 21, 2013, pp. 15-22.

[11] L. Du Peloux, F. Tayeb, J.F. Caron and O. Baverel, "The ephemeral Cathedral of Créteil : A 350 m² lightweight gridshell structure made of 2 kilometers of GFRP tubes", in *Innovations in Construction: CIGOS, Cachan, France*, 2015.

[12] N. Kotelnikova-Weiler, C. Douthe, E.L. Hernández, O. Baverel, C. Gengnagel and J.F Caron, "Materials for actively-bent structures", *International Journal of Space Structures*, Vol. 28, pp. 229-240, 2013.

[13] I. Anastasiadou, K. Alexandrou and M.C. Phocas, "Deformation control of hybrid bending-active structures by multiple cables", in *Creativity in Structural Design: Proceedings of the IASS Annual Symposium 2018, Boston, U.S.A., 16.07-20.07.2018*, C. Müller and S. Adriaenssens Eds., 2018, pp. 1-8.

Proceedings of the IASS Annual Symposium 2019 – Structural Membranes 2019
Form and Force
7 – 10 October 2019, Barcelona, Spain
C. Lázaro, K.-U. Bletzinger, E. Oñate (eds.)

Point load Actuated Adaptive Gridshells: Methods for initial design and modeling

Elaine BONAVIA [a]*, Sabine VECVAGARE** [a], Axel KÖRNER[a], Dylan WOOD[b], Jan KNIPPERS[a],

[a] Institute for Building Structures and Structural Design (ITKE), Faculty of Architecture and Urban Planning, Universität Stuttgart, Keplerstrasse 11, 70174 Stuttgart, Germany
[b] Institute for Computational Design and Construction, Architecture Department, Universität Stuttgart, Keplerstrasse 11, 70174 Stuttgart, Germany

*ebonavia2@gmail.com ** sabinevecvagare@gmail.com

Abstract

This paper presents a series of physical and digital experiments concerning the design of multiple state adaptive gridshells actuated by strategically applied point loads. A gridshell made of bending active rods is actuated through the placement of weights (point loads) at different positions on the grid. This results in an adaptive structure that is capable of transforming into multiple states of equilibrium. Such an approach may be useful as a form of temporary architecture that is able to change itself significantly to suit users' spatial demands. Building upon the topic of lightweight, material based adaptive architecture, the presented research explores the untapped capabilities of elastic gridshells beyond their well-known expediency during the construction process. This research establishes an understanding of the design methods necessary to control elastic deformation for the purpose of shape change for desired architectural outcomes.

Keywords: elastic gridshells, adaptive architecture, multiple equilibrium states, point-load actuation, bending-active, form finding

1. Introduction

1.1 Contextualization

Physically adaptive architecture beyond roofs, openings or facades is an uncommon occurrence in engineering and architecture due to the greater complexity that the design and implementation entails, which also increases the overall costs. In addition to these constraints, the resulting architectural forms and spatial changes are generally limited and often only able to produce discrete or predefined states. Such a result is exemplified in projects such as 'The Shed' in New York or 'Sharifi-ha House' in Tehran [1], [2]. This research has stemmed from the ambition to address adaptive architecture through a material based, lightweight approach to achieve more significant variation in geometry. In other words, to explore an adaptive system which could produce multiple states of equilibrium.

Recently, it has become evident that the approach of pairing material elasticity with adaptivity can be achieved through the use of active bending [3]. Using a material such as GFRP which has high strength and high flexural rigidity allows the use of more geometric states that emerge from the non-linear behavior of the material. Keeping the potential for architectural scale in mind, it must be noted that elastic gridshells are *"the only application of active bending where large span efficient structures are possible"* [3].

Elastic gridshells have traditionally been used for the ease with which they can be constructed on site. Once erected, the gridshell is usually locked into shape immediately (by constraining the joints and

Copyright © 2019 by Elaine BONAVIA, Sabine VECVAGARE, Axel KÖRNER, Dylan WOOD, Jan KNIPPERS
Published by the International Association for Shell and Spatial Structures (IASS) with permission.

supports) and secured into a static form that corresponds with the intended design, preventing any additional transformation. However, the gridshell is self-stable even in the unlocked state. Thus, when striving for more variation in form and geometric reconfiguration, an unrestrained elastic gridshell is a highly effective system able to achieve a wide range of forms and architectural variation.

The proposed adaptive gridshell is actuated by interchangeable point loads which are placed at differing intersection points. As a result, two more parameters that further reinforce the aim to generate shape change are introduced: freedom in the actuator location and variation in weight magnitude. Additionally, this approach can be achieved in a variety of simple ways, such as hanging weights. Unlike typical control mechanisms which tend to limit the design possibilities, this greatly expands the design space for adaptive states.

1.2 Aim of the Research

This research aims to present the unique advantages that unrestrained elastic gridshells can offer to the field of adaptive architecture. Through this system, multiple equilibrium states are achieved when coupled with a flexible actuation strategy of weights that can vary their magnitude and location. The research demonstrates that adaptive design has much to gain from the careful consideration of the structural system, material system and actuation system. It shows that customised adaptivity can be designed by careful consideration of those parameters. The initial design methods and experimentation with such a system are presented on a symmetrical, synclastic gridshell through a series of physical prototypes and form finding simulations. These identify the important control parameters necessary for geometric change and strategic elastic deformation. The research is concluded in a discussion of the further potential of the system.

2. Methods

2.1. Physical Setup

Two physical models of a gridshell dome measuring 1.3m (l) x 1.3m (b) x 0.8m (h) were set up to test the adaptive gridshell concept. The gridshell is comprised of flexible GFRP rods (2mm in diameter) arranged in a 5x5 grid along orthogonal axes and connected together by freely rotating 3D printed joints. Glass fibre was chosen for its greater flexibility and a rod cross section was preferred to eliminate torsion induced failures. The point load actuator is a detachable, adjustable weight which was hooked from node to node. The weights were incrementally added in steps of 170g (0.17N) although in certain cases this amount was halved to allow for smaller increments. The degrees of freedom of the support condition have great influence in the adaptive behaviour of the gridshell. Therefore, two different physical models were built, one with fully restrained supports (G0) and one with fully rotational supports (G180) were tested with several actuator combinations.

2.2. Digital Setup

Due to the large number of possible outcomes and parameters involved, a digital model was set up to obtain quantifiable data for comparison between the loaded states. The plugins Kangaroo2 and K2 Engineering were used with Grasshopper due to the software's suitability in dealing with large deformations through dynamic relaxation [4]. The GFRP material properties were included through K2 Engineering which was set up specifically to simulate calibrated structural behaviour [5]. This plug-in allowed for the monitoring of bending moments, axial stresses and reaction forces, which was used to stay within the material limit or evaluate certain behaviours such as stiffening under load. Additional analysis tools were developed to track the curvature, vertical displacement and quad angles of the resultant geometry, allowing more insight on the processes of form generation through this method of targeted loading. This digital model was calibrated to match with the physical model through iterative loadings and comparison of the resulting displacements (Fig. 2.02)

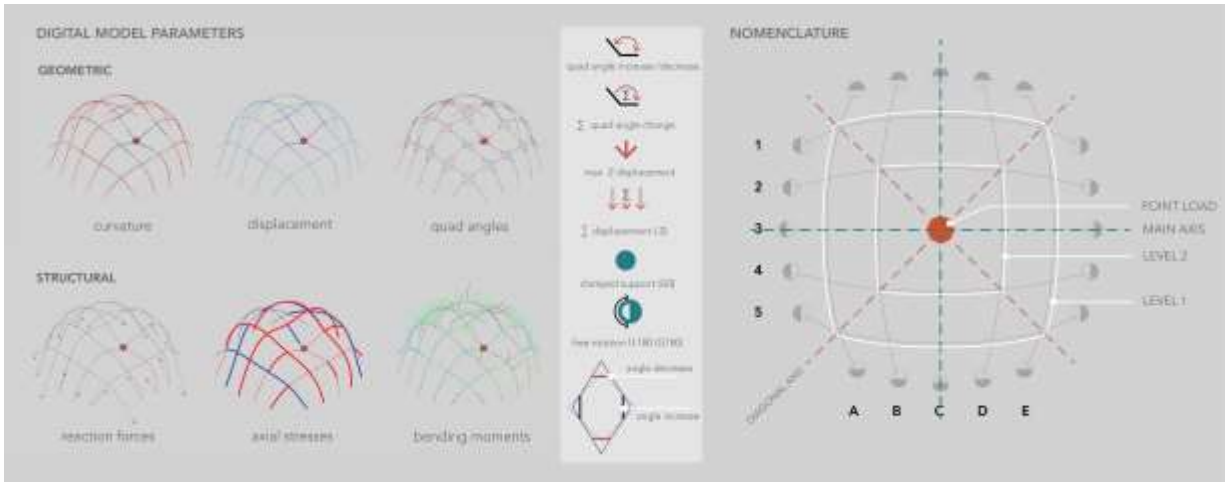


Figure 2.01: Graphical nomenclature and overview of parameters

A graphical nomenclature (Figure 2.01) was established to indicate displacement, curvature, quad angle changes and actuator locations on the gridshell.

2.3 Load Distribution

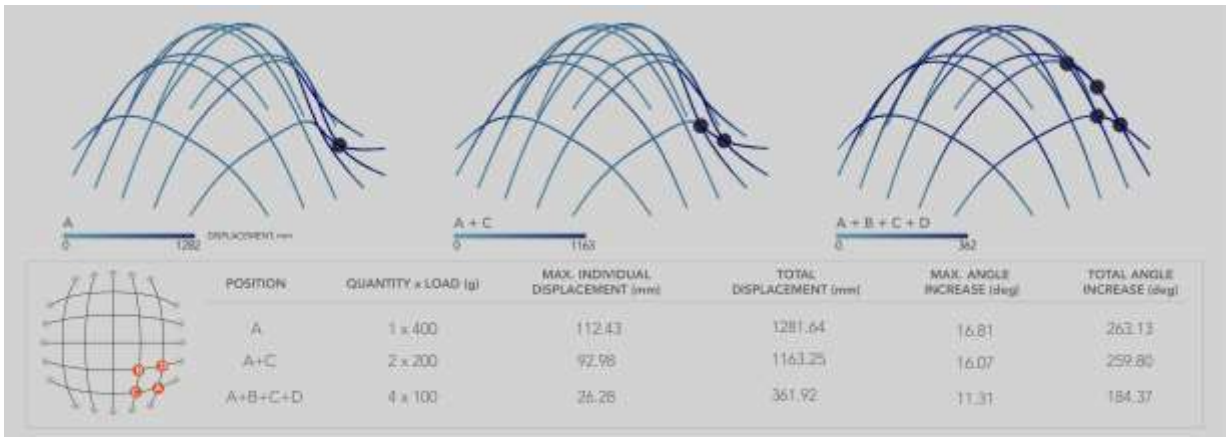


Figure 2.02: Effect of load distribution on the adaptive gridshell

As this research aimed to produce geometric change with the least number of possible actuators, the effect of load distribution on an unrestrained gridshell of type G180 was checked through initial simulations. As expected, a distributed load of 4x100g caused less vertical displacement and less rotations in the quads than a concentrated load of 1x400g. This result was consistent on all four positions A, B, C and D. For one case of 2x200g, the results obtained were almost identical to 1x400g. (Figure 2.02) Thus, single or coupled point loads were subsequently used for this research.

3. Point Load investigations

3.1 Physical Catalog of States

A series of loading conditions were set up on the aforementioned physical models G0 and G180. These allowed for quick observations of the gridshell behaviour when loaded incrementally, or with a traveling load. All images are showing a moment when the gridshell is at rest, after the weight has been placed on a specific joint and the setup is in equilibrium. A selection of some of the more interesting geometries

are presented in this paper, although the full catalogue is far more extensive. Figure 3.01 shows an increasing point load in the same position on G180 and a constant load of 6.8N on G0 circulating at level 2 intersection points. Figure 3.02 shows how dual loads on G180 and G0 produced very different states.

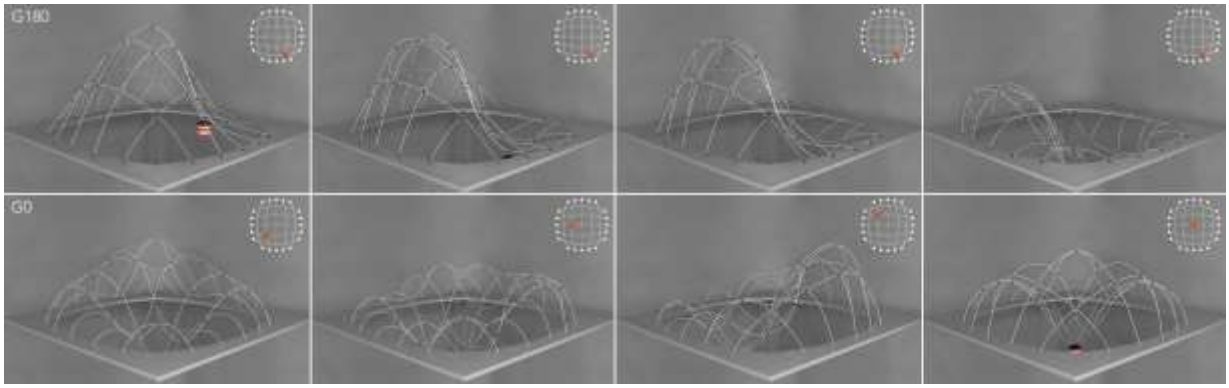


Figure 3.01: G180 loaded with increasing load and G0 loaded with circulating point load.

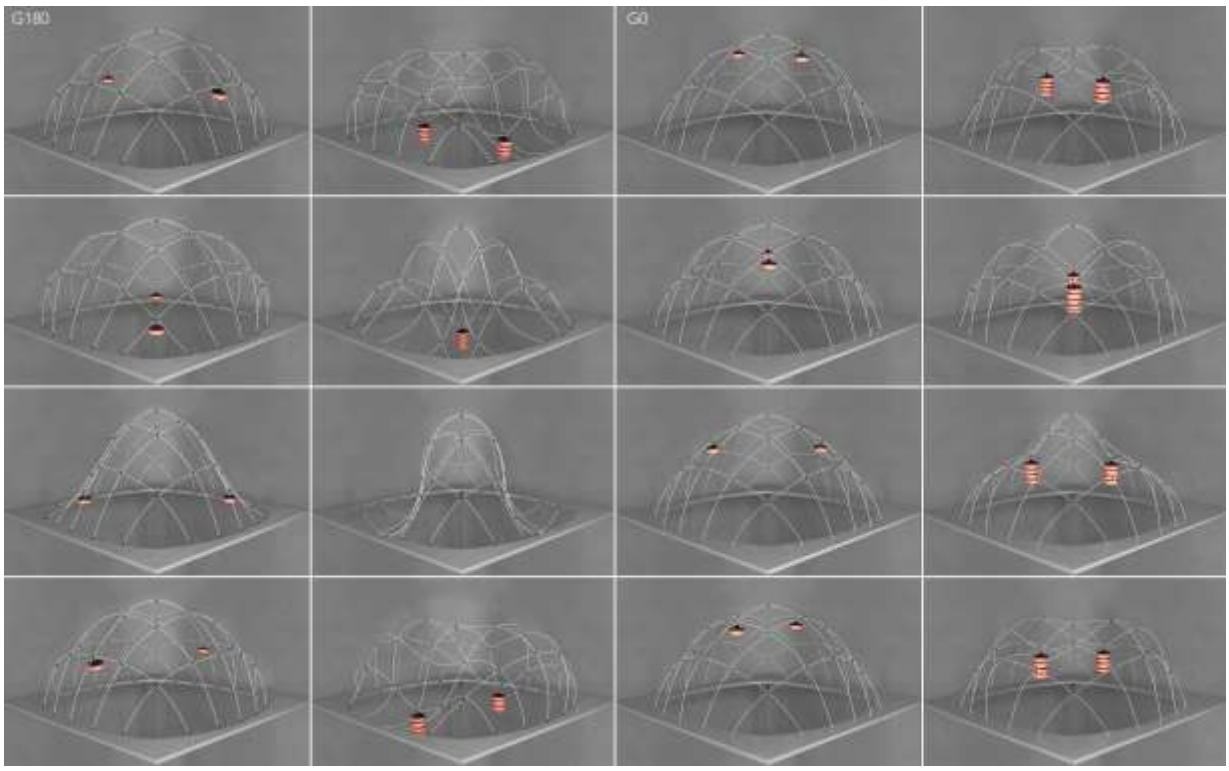


Figure 3.02: Gridshell G0 and G180 loaded with 1 or 4 loads on main and diagonal axes.

3.2 System Overview

Since each gridshell rod is bent into an arch, the weight actuator is a negative Z vector causing displacement and negative bending moments in the elements. As the weight is transferred from one point to another, the curvature of the gridshell changes with it and shape change occurs through the rearrangement of positive and negative curvatures. Applying a point load on a stiffened gridshell eventually causes local buckling, however in this case the rotational freedom at the joints allows for shape change to occur first. The quads expand in either of the two diagonal directions, and the laths

twist along their longitudinal axis, resulting in the differentiated grids. For certain loading configurations, the gridshell can result in two different geometries with the same loading configuration because of the dual symmetry in the initial geometry. The supports have no translational freedom.

3.4 Adaptive Gridshell with Single Point Loads

The aim was to determine where and how to place loads for the maximum amount of deformation and shape change. The main factors that influence the resulting geometry are the allowable rotations at the supports, the proximity of the load to the supports and the location of the load with respect to the main axes. The supports have a major influence on the way the deformation occurs. By definition, G0 is stiffer than G180 and requires more load to achieve the same amount of displacement. When comparing both gridshells, the quad rotations behave differently and these affect the overall shape of the deformed geometry and therefore its architectural potential.

Load proximity to Main Axes – both G0 and G180: placing the load off the main axes produces more vertical displacement in the gridshell. Placing the load on the main axes produces less overall rotation in the quads – this is because the laths on the main axes are simply bent prior to loading while the laths off the main axes are already torsioned out of plane. Adding a point load on these laths accentuates this torsion in addition to bending. (Figure 3.03)

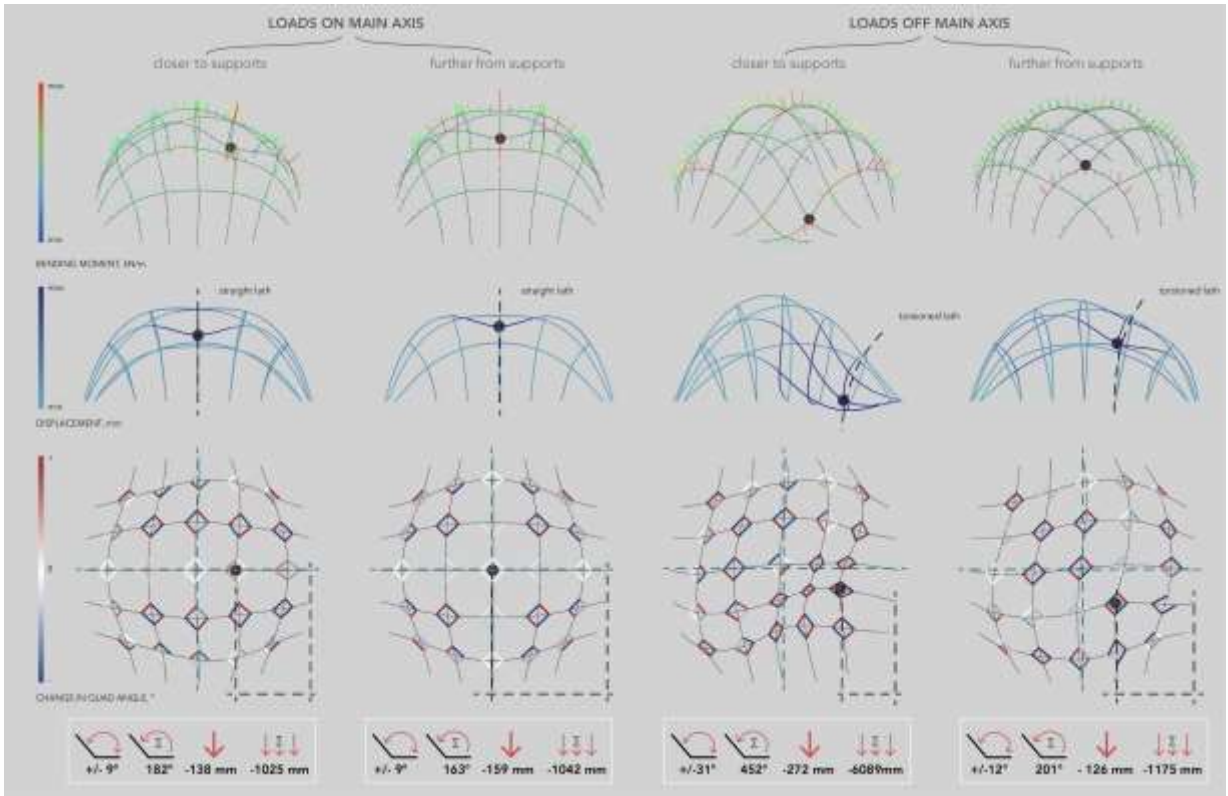


Figure 3.03: Loads on and off the main axes on G180

Load proximity to supports – G0: a load further away from the supports is more effective and induces higher displacement. A load near the supports enhances the existing positive curvature which is generally very high already, thus placing a limitation on the displacement. G0 gridshell is much stiffer near the supports than towards the centre.

G180: a load further away is less effective than a load at the supports. A load located far enough from the supports increases the positive curvature causing the gridshell to become stiffer and thus able to take more loads. Figure 3.04 also shows the displacements reflected by the quad rotations.

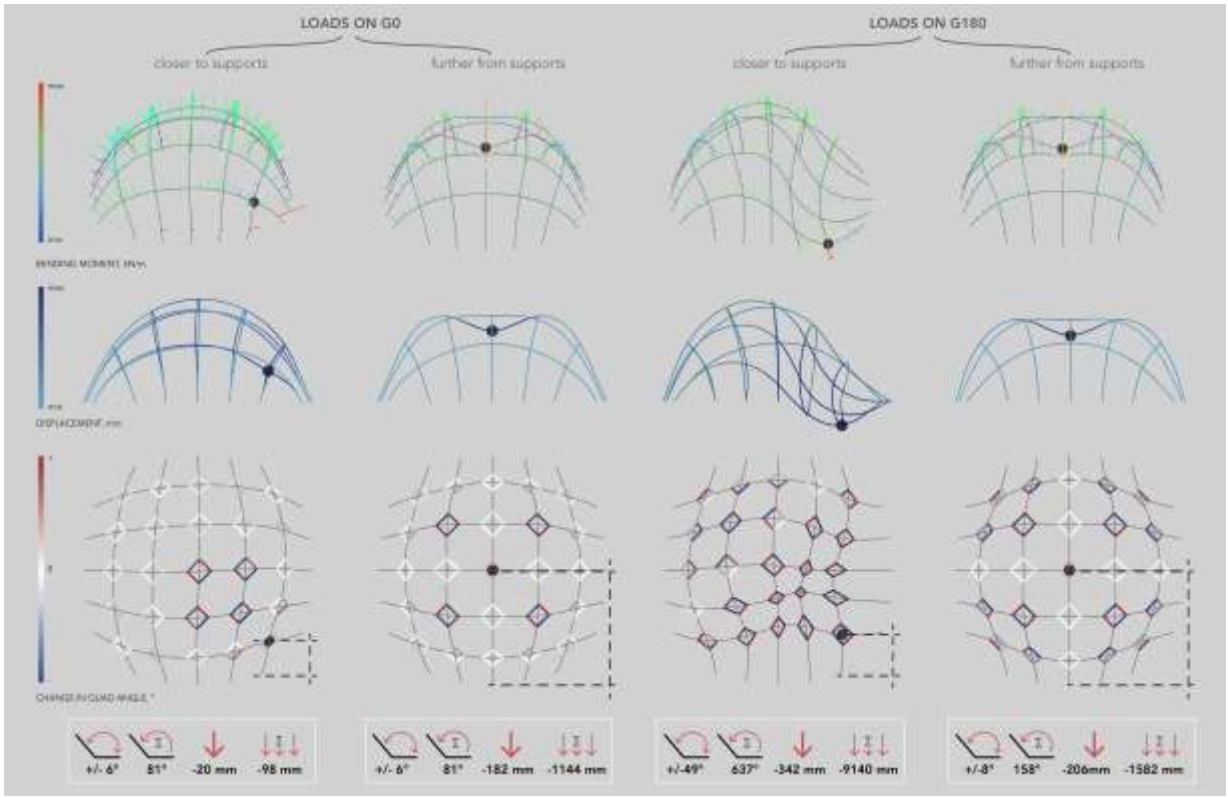


Figure 3.04: G180 and G0 gridshells when loaded further and closer to the supports.

3.5 Adaptive Gridshell with Dual Point Loads

For dual point loads, the same relations (loads to supports, loads to main axes) apply, along with the relation of the loads to each other. Since G180 gridshell is more flexible and susceptible to rotations, it was used for simulations with two loads. The relationship between the two loads greatly influences the geometric outcome and the effects are most noticeable through observation of the quad rotations. Two loads can either complement or block each other, respectively leading to a higher change in quad angle or no change whatsoever. Two loads on the same rod block each other's rotations, leading to less deformation while two loads eccentric from each other allow for more rotations and therefore deformation. (Figure 3.05)

Main Axis loads: loads on the same rod should be closer together so that eventually the negative bending moments can be superimposed together to achieve more deformation. If their position on the gridshell is asymmetric, more deformation occurs., their impact on the displacement is less.

Diagonal Axis loads: In this case, the deformation effect is greater when these loads are further apart. As they get closer, their effect on the quad rotation diminishes.

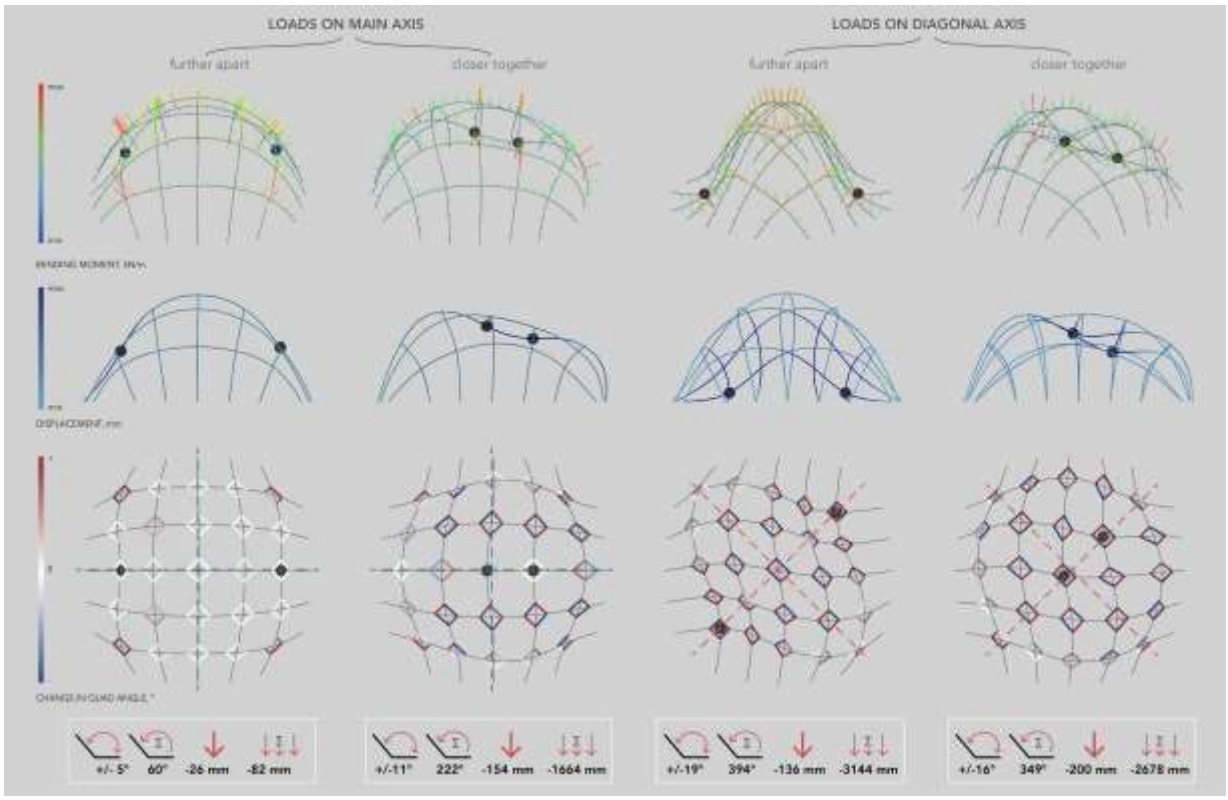


Figure 3.05: G180 loaded with eccentric and non- eccentric loads closer or further apart.

3.6 Results

When loads are placed on the gridshell, the resulting geometry is a negotiation between the presented factors. With G0, the stiff boundary maintains overall stability and displacements are always higher if the point loads are further from the supports. Total inversion can never completely occur and the gridshell is always able to resume its initial state after the load is removed. This can be an advantage however larger load magnitudes are required to achieve effective deformations. The effectiveness of loading G180 is highlighted through its relation with the main axes. If the load is off the main axes and closer to the supports, the more effective it is for the deformation and shape change. This is because both bending and rotations are contributing to the resulting movement. Form variation is much more effective; however, risk of inversion and loss of stability is bigger, influencing the sequence in which point loads should be placed. The stiffening effect becomes important in this scenario – the gridshell can be given a temporary stiffened state if loads cannot be placed simultaneously. The supports have an overarching influence in both G0 and G180.

4. Conclusion and Discussion

The proposed concept of point load actuated, unrestrained gridshells demonstrates the potential of this unconventional system to provide variation in adaptive states. The support conditions, the position of the point loads and the initial grid geometry are all main factors to be considered in the design of the adaptive gridshell. The quad angle variation is a determining factor in the amount of shape change that occurs besides local vertical displacement. This is because it is the main factor that accentuates torsion in the individual rods and therefore causes change in the overall double curvature of the gridshell.

Although this is to be investigated further, the system has great potential to be upscaled and further developed with a variety of tools. The point loads can be controlled by a computationally driven system that utilises human interaction as a design driver for adaptivity.

Acknowledgements

The research was realized as a master thesis in the framework of the Integrative Technologies and Architectural Design Research M.Sc. program (ITECH) at the University of Stuttgart, led by the Institute of Building Structures and Structural Design (itke) and the Institute of Computational Design and Construction (ICD).

References

[1] Diller Scofidio + Renfro, Rockwell Group. The Shed. 2019, Hudson Yards, Manhattan, New York City, Website: https://dsrny.com/project/the-shed , last consulted on May 30, 2019.

[2] NextOffice–Alireza Taghaboni. Sharifi-ha House. 2013, Tehran, Iran. Website: http://nextoffice.ir/#!/project/sharifi-ha-house/ , last consulted on May 30, 2019.

[3] Lienhard and C. Gengnagel, "Recent Developments in Bending-Active Structures," *Proceedings of IASS Annual Symposia, IASS 2018 Boston Symposium: Active bending: New hybrids,* pp. 1-8(8), Aug. 2018.

[4] Piker, Daniel. (2011) Kangaroo Physics for Grasshopper. Live Physics engine for interactive simulation, form-finding, optimization and constraint solving. Rhinoceros Plug-in Website; https://www.food4rhino.com/app/kangaroo-physics, last consulted on May 30, 2019.

[5] Brandt, Cecilie. (2016) Calibrated Modelling of Form-Active Structures. Master Thesis at DTU. Cecilie Brandt Olsen, Website; http://www.ceciliebrandt.com/wp-content/uploads/2016/11/Calibrated_Modelling_CBO.pdf, last consulted on May 30, 2019.

Proceedings of the IASS Annual Symposium 2019 – Structural Membranes 2019
Form and Force
7 – 10 October 2019, Barcelona, Spain
C. Lázaro, K.-U. Bletzinger, E. Oñate (eds.)

χ-Shell, a new spatial deployable lattice compared to traditional reticulated shells

Etienne BOULEAU*, Florin ISVORANU[a], Julian PANETTA[a], Mark PAULY[a]

*Ingeni SA - Genève
Pont-neuf 12 – 1227 Carouge CH
etienne.bouleau@ingeni.ch

[a] Computer Graphics and Geometry Laboratory, EPFL

Abstract

The χ-Shells is a new kind of deployable reticulated shells that has features comparable to other traditional shells. Its deployment uses the mechanical properties of a beam grid to generate a three-dimensional shape. This new generation of reticulated shells differs in its typology, but its structural performance and construction process have points in common with other types of shells made in the past. We present the fundamental characteristics of this new generation of shells, comparing it to other existing families with criteria related to materials, span, self weight, load capacity, slenderness, construction process and joint detailing. The development of this technology is accompanied by small-scale physical models that validate the principle of deployment, and a full-scale pavilion to discuss constructive and static aspects.

Keywords: Deployable structure, grid-shells, scissors grid mechanism, reticulated shells.

1. χ-Shell concept

1.1. Definition

χ-Shells are a new class of deployable structure composed of ribbed linear elements connected together by hinges. The spacing between the hinges varies along each rib, creating a regular, but non-uniform pattern. The configuration of the χ-Shell ribs can be constructed and transported in a flat and compact state, then deployed into a double-curved spatial configuration, and finally used as a roof structure. The design of its ribs generates an elastic mechanism with only one degree of movement in the plane, which requires an expansion force to be activated. In theory, thanks to the property of the mechanism, the deployment can be actuated by pushing or pulling two opposite nodes of a quadrangle. In practice, because the actuating force depends on the return spring effect and the friction of the hinges, the actuation of several specific nodes reduces high local stresses and ensures uniform deployment.

1.1. Physical models

To apply the χ-Shell principle to surfaces with positive and negative curvature, we built two models, the first with hyperbolic geometry and the second with spherical geometry. The hyperboloid is composed of two crossed layers of nine straight ribs, and each rib is a 10 mm x 10 mm x 1 mm aluminum profile connected by a rivet that also serves as a pivot. The spherical model consists of two crossed layers of twelve identical straight flat ribs of 10 mm and 1 mm thick.

On both models, the deployment induces deformations and stresses in the ribs, the hyperboloid ribs only undergo torsion without bending, while the spherical ribs only undergo bending without torsion. The

Copyright © 2019 by Etienne BOULEAU, Florin ISVORANU, Julian PANETTA and Mark PAULY
Published by the International Association for Shell and Spatial Structures (IASS) with permission.

cross-section of the ribs (angle for the hyperboloid and flat for the sphere) was chosen so that the ribs follow the deformations induced by the deployment while generating a minimum of parasitic stresses against this deployment.

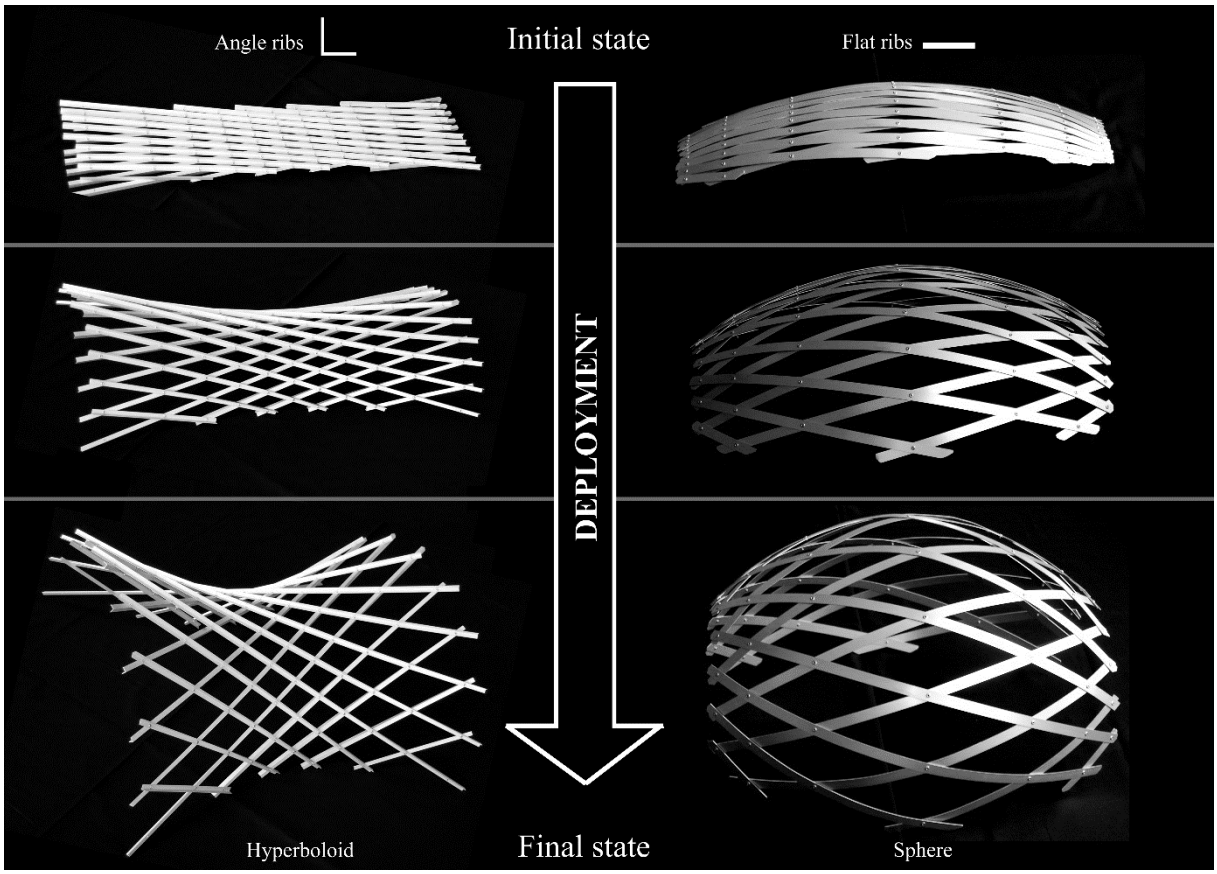


Figure 1: Left, one-meter long hyperboloid models. Right, one meter long spherical models where the flatness at the initial state is disturbed by collisions between the ribs.

The most important conclusion of these two models is that deployment leads to a single final geometry regardless of the nodes where the actuation is applied and the accuracy of the actuation. The deployment is robust in the sense that the actuation process can be completely independent of a geometric control process.

1.3. Shell like behavior

As mentioned above, deployment induces deformations and stresses in the ribs, which means that the actuation must counter a spring back effect, so that once deployment is achieved, the geometry must be locked. On the two previous models, the friction between the ribs at each node was sufficient to counter the spring back and lock the geometry, but other technical solutions must be devised on larger projects such as additional bars or ties, or even using a coating to reinforce the rib quads.

Once the geometry is locked, the χ-Shell becomes a solid unit independent of edge conditions and supports. In contrast to grid-shells where the support and edge conditions act strongly to maintain the geometry, the deployed shape of the χ-Shell is maintained by the rib pattern itself, once locked. The χ-Shell has no constraint at the boundary, which gives more freedom for shape design.

2. Structural typology

χ-Shells belong to the typology of deployable structures, but in terms of their structural properties and design process, a deployed χ-Shell could be linked to the diagrid family, as an irregular sequence of two diagonal generators, and could also be linked to the lattice shell family, as a variable quad pattern. As explained above, an χ-Shell differs from a grid-shell in terms of boundary conditions and design process (see also Panetta and al. [8]), but they have in common that the deformations induced at the ribs depend on the deployed configuration.

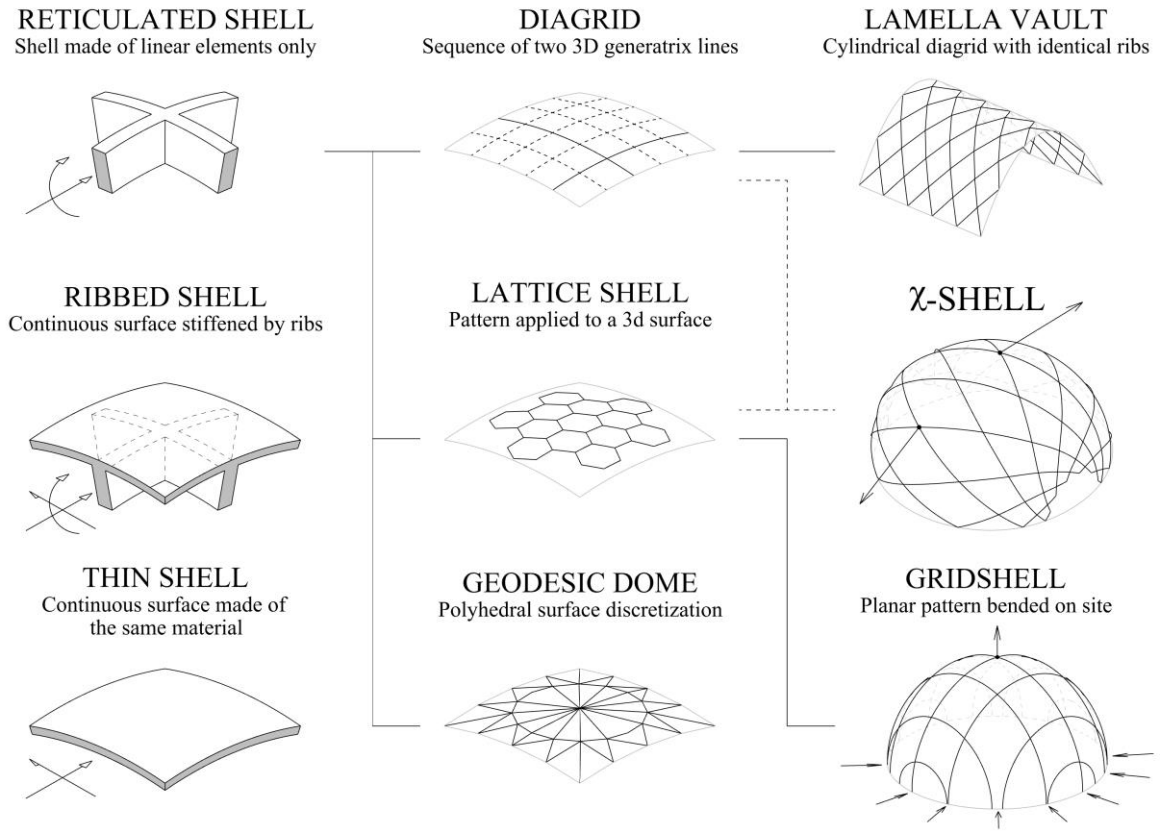


Figure 2: Diagram of shell families

As techniques progressed, new families of reticulated shells developed. Metal machining has favored the development of geodesic domes, new cement formulations have allowed the development of concrete shells, photogrammetry and digital tools have allowed the development of grid-shells. As shown on Fig. 3, until 1990 the development of shells was manifested by increasingly large spans. From the 2000s their geometries became more and more varied.

In this context, the future development of χ-Shells depends on architectural utility, performance, and economic reliability. We assume that their potential lies in short-span roof structures, for the main reason that their principal advantage is the rapid deployment on site. If the dimensions of the project require on-site assembly, on-site time increases and the use of a lifting device may be necessary, which limits the relevance of rapid deployment.

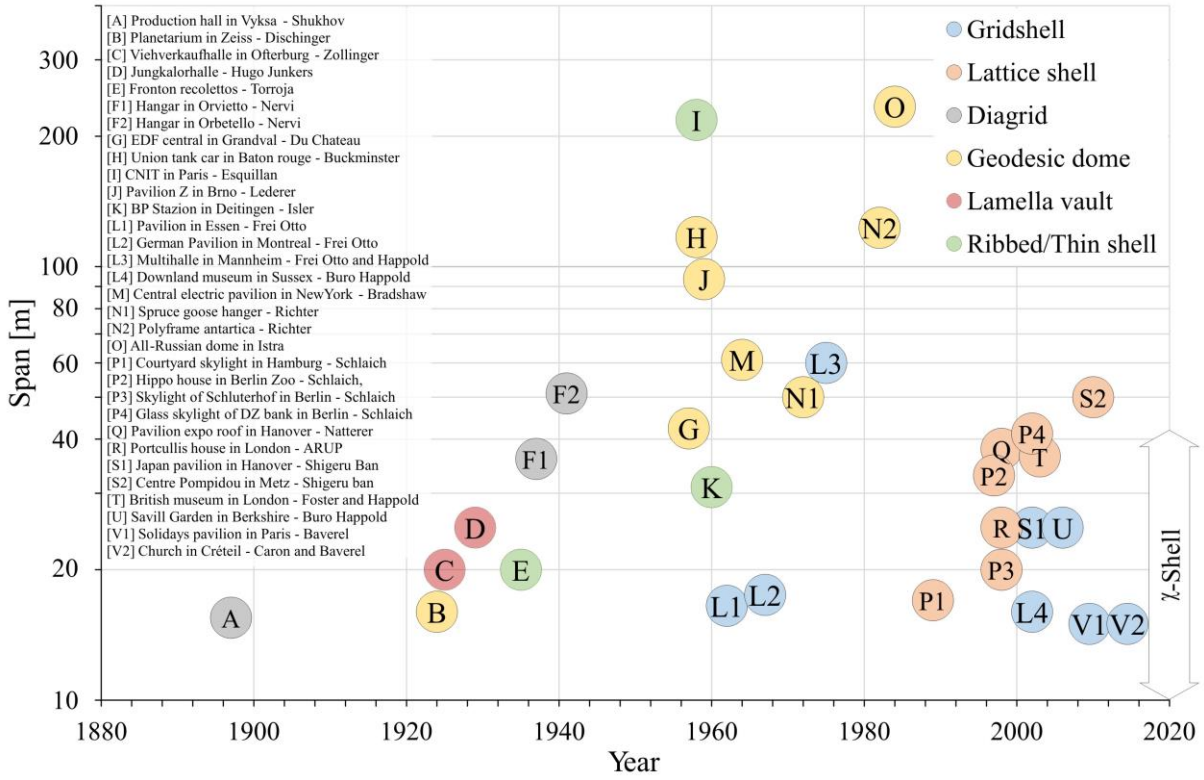
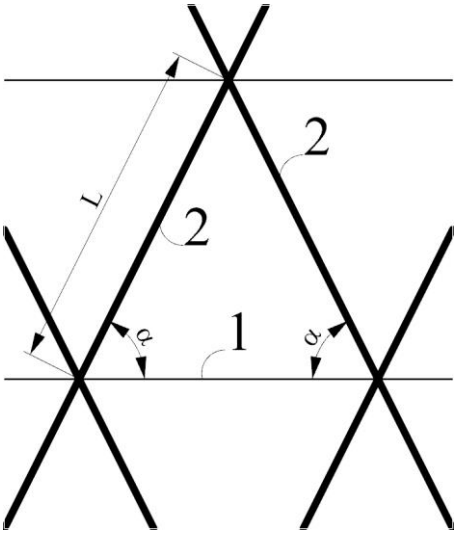


Figure 3: Few examples of shell by topology along time and span.

3. Performance

The assessment of the shell performance is based on two main criteria: relative capacity and slenderness. The first is related to the quantity of material used and the second to its relative size. To have an objective comparison with these two criteria, we estimate the equivalent using a method initiated by Wright [1] and extended here for a variable mesh geometry:



$$t'^2_x = \frac{24 I_1 \sin\alpha}{\sqrt{3} A_1}\left(1 + \frac{I_2}{I_1}\cos^3 \propto\right)\left(1 - \nu_x \nu_y\right) \quad (1)$$

$$t'^2_y = \frac{6 I_2}{A_2 \cos\alpha}\left(1 + \frac{A_2}{A_1}\cos^3 \propto\right)\left(1 - \nu_x \nu_y\right) \quad (2)$$

$$E'_x = \frac{A_1 E}{L t'_x \sin \propto} \quad (3) \qquad E'_y = \frac{2 A_2 E \sin^3 \propto}{L t'_y \left(1 + \frac{A_2}{A_1}\cos^3 \propto\right)} \quad (4)$$

$$\nu_y = \frac{\cos \propto}{2 \sin^2 \propto} \quad (5) \qquad \nu_x = \frac{2 A_2 \cos^2 \propto \sin^2 \propto}{A_1 + A_2 \cos^3 \propto} \quad (6)$$

$$p_c = 0{,}4 \frac{E' t'^2}{R^2} \quad (7)$$

Where E, A, I, L and R are respectively the elastic modulus, the area cross section, the inertia, the length and the radius of the rib elements, and t', E' and pc are respectively the effective thickness, the effective

modulus and the critical radial pressure. According to Mesnil and al [7], the buckling capacity of grid-shells must be reduced by 10%, due to the pre-bending stress, this reduction was applied to the concerned projects.

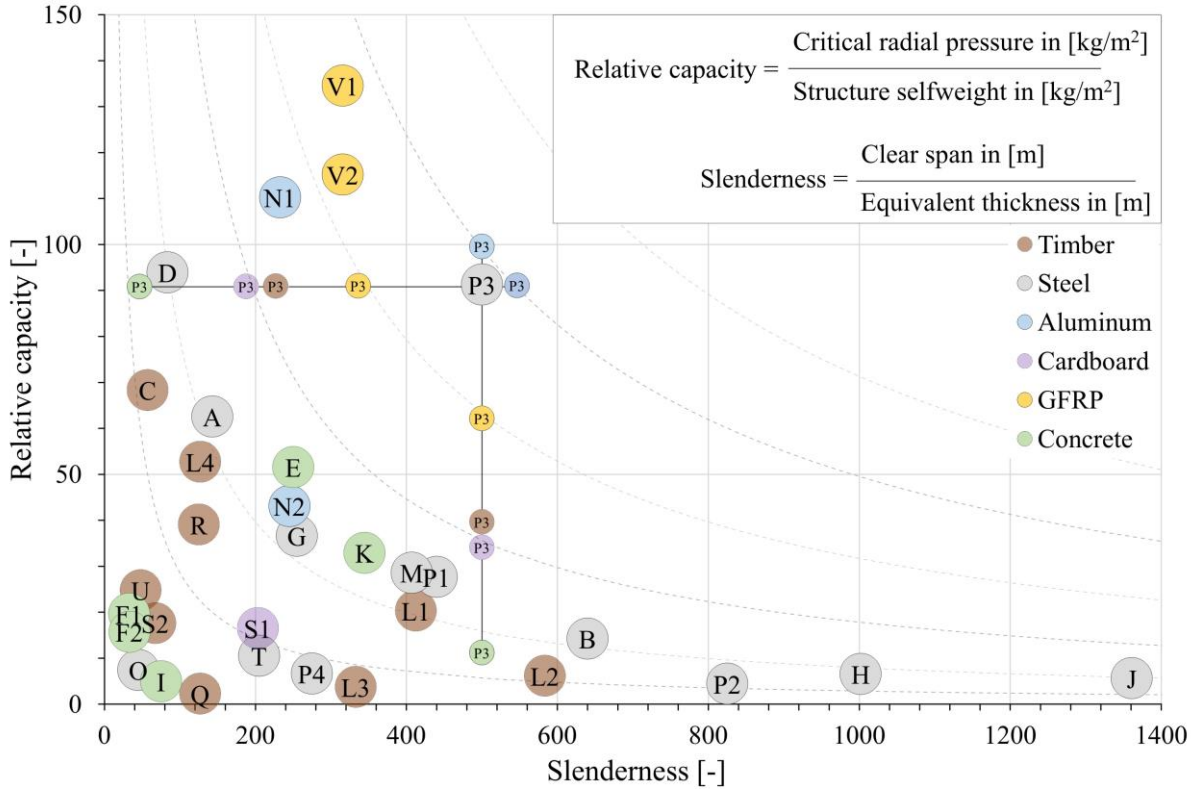


Figure 4: Diagram for shell examples comparison with the relative capacity and the slenderness. The dashed grey lines show the direction where the project tags move when the section property (A, I) change.

For all projects, the relative capacity evolves inversely to slenderness and vice versa. To increase the load capacity without changing the weight, it is necessary to increase the inertia and therefore reduce the slenderness. However, when one criterion is weak, its effect on the other is marginal. The risk of great slenderness with insufficient capacity is buckling instability as occurs for the project (J) - Pavilion Z in Brno which collapsed in 1963.

Changing the property of the material on a project such as (P3) leads to a variation in the relative capacity while maintaining the invariant slenderness. As shown in Fig. 4, if (P3) were made of aluminium instead of steel, the relative capacity would have increased by 9%, and if (P3) were made of GFRP its relative capacity would have decreased by 32%. In addition, with constant relative capacity, the variation in slenderness leads to the same order of material performance.

In general, the material modifies the performance of the shell, in order of importance: Aluminium, Steel, GFRP, Timber, Cardboard and last Concrete. For both criteria, it appears that the better the modulus/density (E/D) ratio of the material, the better the performance.

Obviously, an χ-Shell needs an elastic material, because of the deformation induced at the ribs, but if the modulus is high, the stress induced by deployment would increase proportionally, so it is important to have a material with a long range of elasticity but not necessarily a high modulus E.

4. Construction process

Each reticulated shell has its own specific construction process, but we can distinguish three main types that are related to how geometry is managed during construction.

- Cast on mould: the geometry is nowhere in the shell elements and is entirely given by an associated temporary object which is both a mould and a support, which makes it difficult to remove afterward. This is the main type for thin concrete shells, masonry vaults, composite boat hulls, etc.
- Bricks stacking: the object is cut into small pieces for transport and assembly, then reassembled on site. The geometry is given by the elements themselves and the way they are subdivided. The accuracy of the final shape depends on the tolerances between elements, the assembly sets and the movements during the assembly sequence.
- Shaped on site: the elements are elastically shaped on site to obtain the spatial geometry, then anchored or fixed together to maintain this geometry. The accuracy of the geometry is difficult to manage due to the large number of parameters that influence this shaping. There is a trade-off between the need for rigidity to resist and the ease of shaping.

Each method presents particular difficulties that should not be underestimated in order to carry out the project correctly. Indeed, the Russian Istra dome (O) collapsed in 1984 due to a lack of geometric survey during construction, and several wooden ribs in the Mannheim Multihalle broke during lifting and had to be replaced.

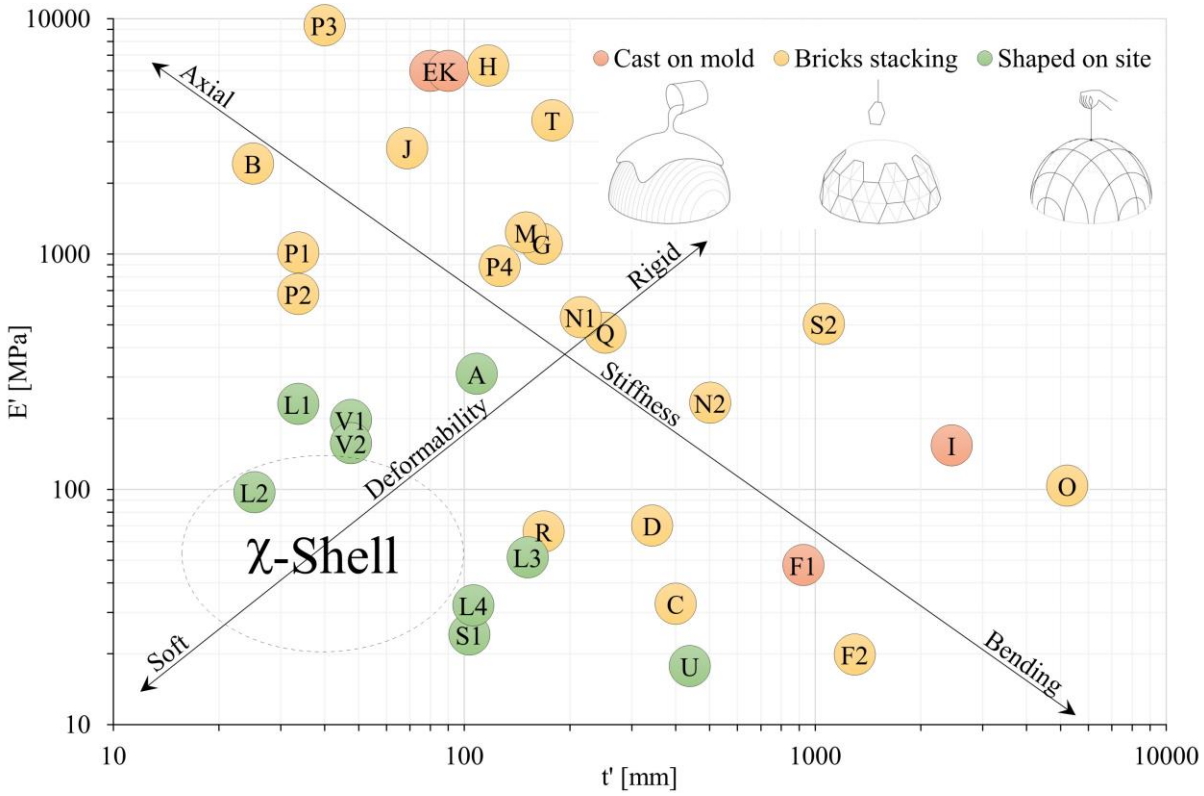


Figure 5: graph plotting the effective modulus E' with the effective thickness t'.

The χ-Shell belongs to the last type of construction process because the rib elements are bent or twisted in place to create the spatial shape, so the design consists of a compromise between the deformability of the ribs to deploy into a precise shape and the final stiffness to withstand once deployed.

The Wright method introduces the effective modulus of elasticity E' and the effective thickness t' which are related to the rigidity of an equivalent thin shell. As shown on fig. 5, projects that are shaped on site are those that combine a low E' value and a low t' value, therefore they require a high curvature to have an acceptable critical pressure. Usually, the bending strength requirement is determined by the local or global buckling requirement, which imposes a minimum thickness. The axial strength requirement could then be obtained by changing the density of the mesh or its axial section.

As with grid-shells, the χ-Shell design process is iterative. First, the need for strength defines a specific cross section of the rib, then the cross section of the ribs must allow deployment to achieve the desired geometry.

When the deformation of the ribs is torsional only, the need for buckling resistance is not in competition with the need for deployment. However, even for the hyperboloid model shown above, the irregular pattern implies an increase in the dimensions of the grid on the edge, which affects the effective module and reduces the loading capacity.

5. Joint detailing

Usually, the design of joint details comes after engineering calculations, but some joint details reflect the difficulties encountered during the design process and sometimes provide an opportunity to improve shell performance.

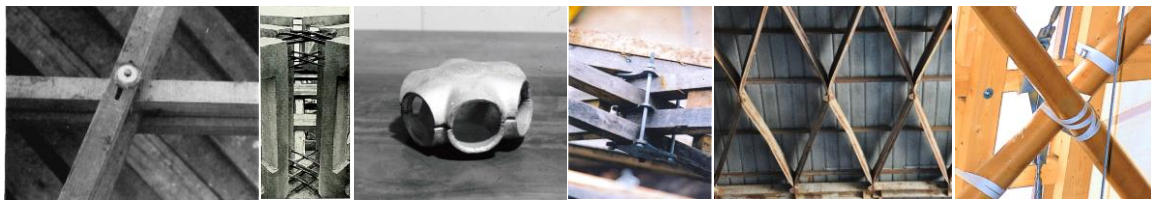


Figure 6: Few examples of joining, from left to right: Mannheim multihalle, Orbetello's hangar, Grandval Roof, Downland Museum, Oberschleißheim hangar, Hanover's Japan pavilion.

As shown on fig. 6, the slots in the Mannheim ribs allow sufficient sliding to limit stresses in the wooden ribs during lifting, on-site casting of connections between Orbetello's prefabricated beams eliminates differences in tolerance between each element, the prefabricated steel knot by Du Chateau makes repetition of detail affordable, the Junker joint system transmits bending stresses throughout the diagonal ribs, even the Japanese Pavilion nodes in Hanover is a solution to avoid drilling and weakening the cardboard pipes.

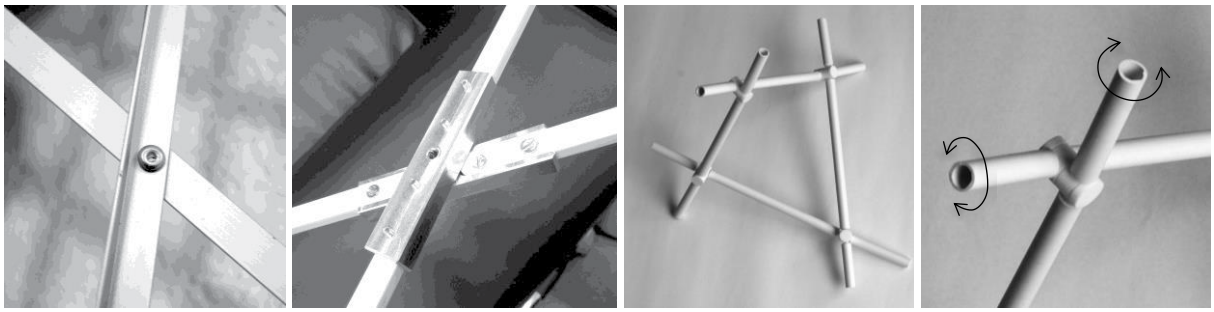


Figure 7: Few possibilities of rib joining for χ-Shell, from left to right: rib connected with a rivet, rib connected to a precast aluminum hinge, tubular rib connected with a 3D printed hinge, view of the 3d printed hinge with released rotation.

For an χ-Shell, the joints must transfer axial forces, bending and torsion moments and allow a rotational movement in the plane between the ribs. In the case of physical models, a single rivet between two ribs is sufficient, but for a larger project a more sophisticated joint that reduces friction between the ribs is required.

For the hyperboloid and other shapes where there is mainly torsion during deployment, it is even possible to design a node that does not transfer torsion, see fig.7. This will allow the use of a more rigid ribbed cross section like a tube without any disadvantages in terms of deployment.

Conclusion

The χ-Shell is completely new, it combines the performance of a reticulated shell with the advantage of a deployable mechanism. The scope of this technology is vast and it still needs to be further developed on several practical and technical aspects, such as joints, bracing and covering. The link between geometry and structure is so close that each project must have its own development, in terms of rib pattern, material, rib cross-section, assembly design and actuation system. The construction of the pavilion planned as part of the WG21 exhibition is an opportunity to show a concrete application of the χ-Shell on real scale, and to discuss the potential of the design method we have developed.

References

[1] D.T. Wright, "Membrane Forces and Buckling in Reticulated Shells," *Journal of the Structural Division*," vol. 91, Issue 1, pp. 173-201, 1965.

[2] S. E. Forman, J. W. Hutchinson, "Buckling of reticulated shell structures" *Int. J. Solids Structures*, Vol 6, pp 909-932, 1970.

[3] E. Happold, W. I. Lidell, "Timber lattice roof for the Mannheim Bundesgartenschau" *The structural Engineer*, No. 3, vol 53, pp 99-135, March 1975.

[4] M. Beckh, R. Barthel, "The First Doubly Curved Gridshell Structure - Shukhovs Building for the Plate Rolling Workshop in Vyksa" *Proceedings of the Third International Congress on Construction History*, Cottbus, May 2009.

[5] N. Kotelnikova-Weiler, C. Douthe, E. Lafuente Hernandez, O. Baverel, C. Gengnagel and J-F Caron, "Materials for actively-bent structures" *International Journal of Space Structures*, Vol. 28 pp 229-240, 2013.

[6] G. Quinn, C. Gengnagel, "A review of elastic grid shells, their erection methods and the potential use of pneumatic formwork" *Mobile and Rapidly Assembled Structures IV*, pp 129-143, 2014.

[7] R. Mesnil, J. Ochsendorf and C. Douthe, "Stability of Pseudo-Funicular Elastic Grid Shells" *International Journal of Space Structures* Vol. 30 No. 1, 2015

[8] J. Panetta, M. Konakovic-Lukovic, F. Isvoranu, E. Bouleau, M. Pauly, "X-Shells: A new class of deployable beam structures." *ACM Transactions on Graphics*, Vol 38, No 4, 2019.

Proceedings of the IASS Annual Symposium 2019 – Structural Membranes 2019
Form and Force
7 – 10 October 2019, Barcelona, Spain
C. Lázaro, K.-U. Bletzinger, E. Oñate (eds.)

From Utilizing Material to Listening to What "Material Speaks"

Norihide IMAGAWA*

* Surgical Architect / Director of TIS&PARTNERS. Co., Ltd.
Honorary Professor of Tokyo Denki University
Eiko Bldg. 3F, 1-54, Jimbocyo, Kanda, Chiyoda-ku, Tokyo, 101-0051 JAPAN
Email: norihide.imagawa@gmail.com

Abstract

For the 60th anniversary of IASS, I would like to introduce a designing method for innovative ideas, which I developed through structural designing in last 50 years. I named the method as Material Speaks Design. While conventional methods have designed frameworks in space by focusing on characteristics particular to each material [mechanical characteristics] to utilize them, Material Speaks Design, focusing on energy [J: joule] particular to each material used, enables to compare frameworks in space with different originality, variety, and regionality beyond time and place. To understand the former, I use two functions and diagram. The first function represents the structural design recognition. This Function has seven evaluations on the left side: material, frame, load, joint, cost, durability and construction, and on the right side are natural condition, social environment, client's demand and designs to date. This function can be used to evaluate whether the four target items on the right side are equal to or more than seven items on the left side. The second function is for the skeleton energy function of material and space. This function defines how much each material works on the skeleton of the space. This Structural Energy of Material and Space Function makes possible to compare efficiency of framework in space between different building structures, and moreover, CO2 emission efficiency until completion of the building beyond material, space, time and place. This means The Eiffel Tower made of cast-iron and wrought iron, burnt down The Crystal Palace of cast-iron, wrought iron, glass and wood, Villa Savoye of concrete, and "Silver Pavilion" Ginkakuji Temple of wood, all located in different parts of the world can be compared. Another example, when Villa Savoye, originally built in suburban Paris with few earthquakes, is planned in a country with frequent earthquakes, reaction of framework in space and material efficiency can be compared. This new function depends on $E=mc^2$. This method is based on the 2,500 projects I realized in 25 countries in 50 years.

Keywords : Material speaks, structure design epistemology, tensegrity, serendipity, gravity, earthquake, typhoon, joint, art, Nature of Structure, net playground equipment

Copyright © 2019 by Norihide IMAGAWA
Published by the International Association for Shell and Spatial Structures (IASS) with permission.

1. Introduction

For the 60th Symposium, I would like to recollect the field of architectural structure, which has been developed focusing on technical design. 20 years ago, I presented Special Topics "Architecture & Engineering Concepts: Structural Design Binding Material and Space" in IASS 1999 Symposium in Madrid. Since then, I have been studying the relationship between structural design of materials and space and society through construction documents. Today I will present about framework of wood and space as part of the achievements of my study. In its 60 years of history, IASS has undergone significant growth; its innovative activities led through designs brought by serendipity, are now accessible throughout the world.

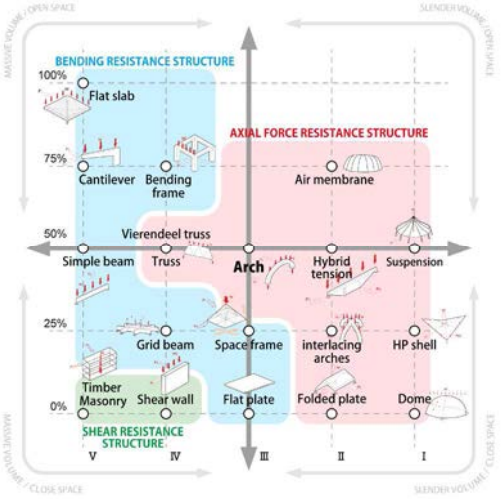


Figure 1: Space and Skeleton Design Recognition

2. From "Material and Space" to "Material and Society": What Connected with Materials by Design

Through IASS's studies about relationships between material and design, theory and practice, new material and its system, etc., stunning innovations has been achieved and provided variety of benefits around the globe. However, if we pause now to look back what IASS's research progress brought to our everyday nature and society on the earth where we continue living, we will find that it is too complicated for the general public other than professionals despite its preciousness and great impact upon our society.

After I made presentation in IASS 1999 Symposium in Madrid, I have realized approx. 2,500 projects in 25 countries utilizing materials available at each site. These projects are based on the concept design as "structure connecting material and space", which I presented 20 years ago in "Steel Building Material and Space."

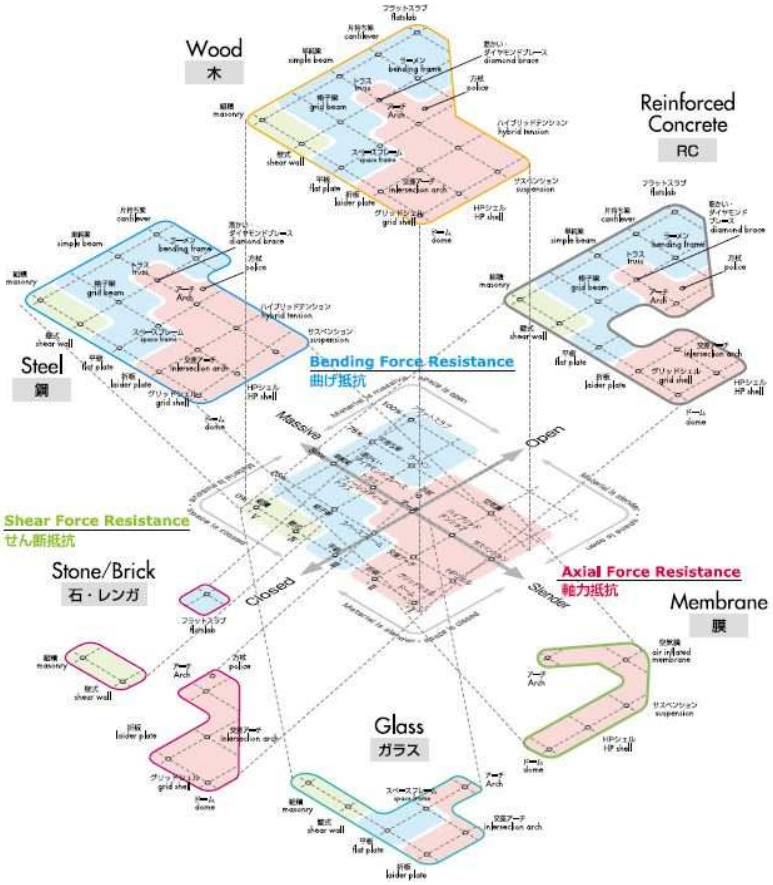


Figure 2: Material and Space Skeleton Design Recognition

I named this concept as Epistemological Design Theory (EDT) and frequently use it. This is a design concept function and of course numerical analysis is impossible with it. What can be understood concisely by designer, client and society using this function is that the result of design on the left-hand side surpasses the 4 factors on the right-hand side; requirements by each society such as safety and durability. This is neither spoken nor written language, but a kind of “Non-verbal Information design” using function and figure.

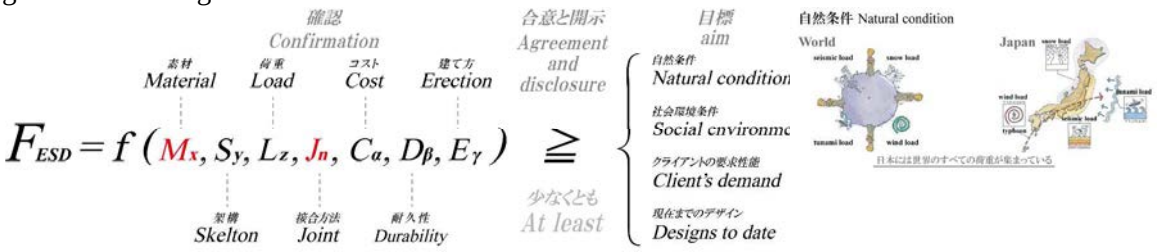


Figure 3: "EDT" Epistemological Structural Design of Material and Space

Until now, approx. 2,500 projects in 25 countries have been realized based on the concept of EDT. The projects include residence, office, gymnasium, music hall, monument, geothermal power plant, folly, playground equipment, tea-ceremony room, macaroni, mobile art gallery, grave, arts with ideas of "Tensegrity" by Kenneth Snelson. The materials include stone, wood, iron, cast steel, stainless, copper, aluminum, reinforced concrete, nylon, glass (SiO2+CO2), etc. To realize the projects, varieties of structure of different materials have been used. Thus, even projects done by myself alone, space realized there are hugely diversified. To compare and classify the huge variety of projects "concisely and clearly" and "broadly and carefully-considered," Material Speaks Theory (MST) has been established. Today I will introduce this MST.

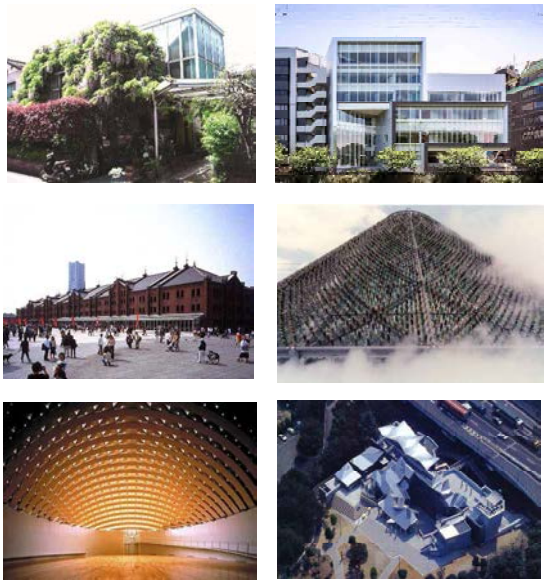




Figure 4: Projects That Have Realized Various Structures with Various

3. Visualization of Energy of Material

I would like to take this opportunity to discuss the significance to personify each material and ask them what framework they want to be used in, and design based on what they tell. This is also an information theory which describes work done by the material using workload and amount of energy per unit volume, 1m3, of the material.

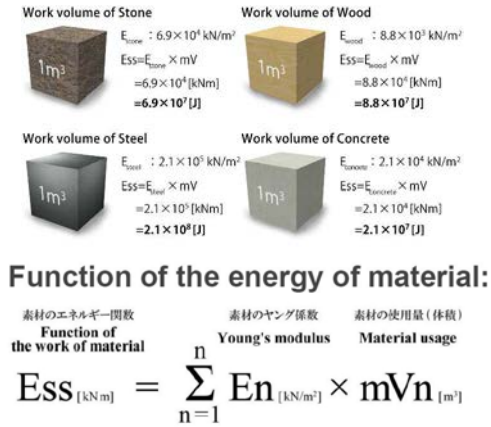


Figure 5: Structural Energy of Material and Space Function

In MST, volume (sV), total floor area (tS), building are (gS), maximum height (Hmax), and maximum span (Lmax) of space and CO2 emission efficiency (Ce) of the framework in space can be visualized by using amount of energy of material per 1m3 (ESS).

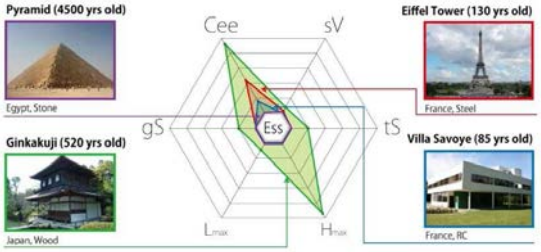


Figure 6: i. Buildings Built in Different Materials, Times and Spaces

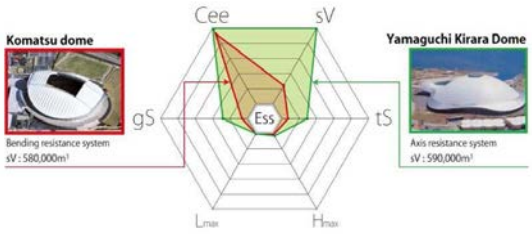


Figure 7: ii. 2 Structural Systems Built with the Same Materials andSimilar Amount of Spatial Volume

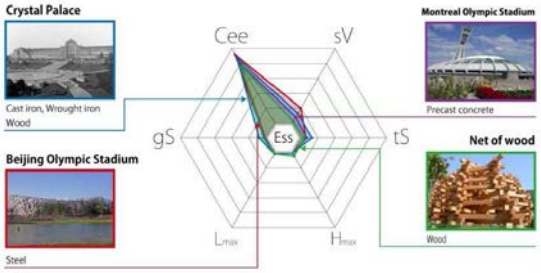


Figure 8: iii. Comparison with Symbolic Modern Architecture

4. Material Speaks Theory

For existing projects, by multiplying material (m) and volume of framework (V) to find [mV:m3] and then dividing known value of the project by this [mV], 6 material efficiency indexes per unit volume (1m3) as volume (sV:m3), total floor area (tS:m2), building area (gS:m2), maximum height (Hmax:m), maximum span (Lmax:m) of space, and CO2 emission efficiency (Ce:kg-CO2/m3) can be calculated. Hexagon diagram with these 6 indexes gives comparison of space done with 1m3 of the material at a glance. I named this series of process as "Non-Verbal Material Speaks Theory" and often use that as well.

*I will discuss the role of structural design in society in the future.

Amount of energy as the very core of MST utilizes the fact that E=mc2 and mESS (workload of material) are equivalent when evaluated in joule.

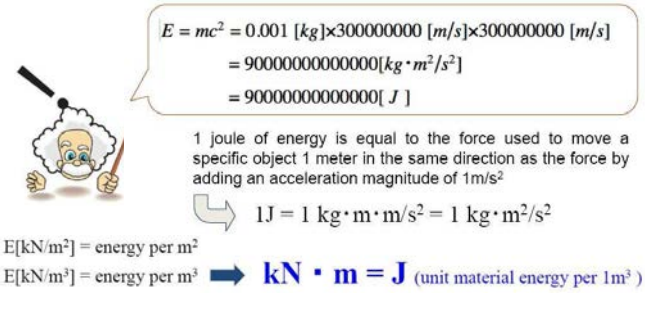


Figure 9: Diagram of Epistemological Structural Design of Material and Space

1.Masonry structure
2.Simple beam structure
3.Bending flame structure
4.Hybrid Vierendeel beamstructure
5.Grid beam structure
6.Brace structure
7.Japanese nuki structure
8.Flat slab structure
9.Hybrid arch structure
10.Space frame structure
11.Hybrid tension structure
12.Hybrid suspension structure
13.3 way hybrid tension structure
14.HP shear wall structure
15.Wooden grid shell roof structure
16.Folded plate structure
17.2 way hybrid truss domestructure
18.Shear wall structure

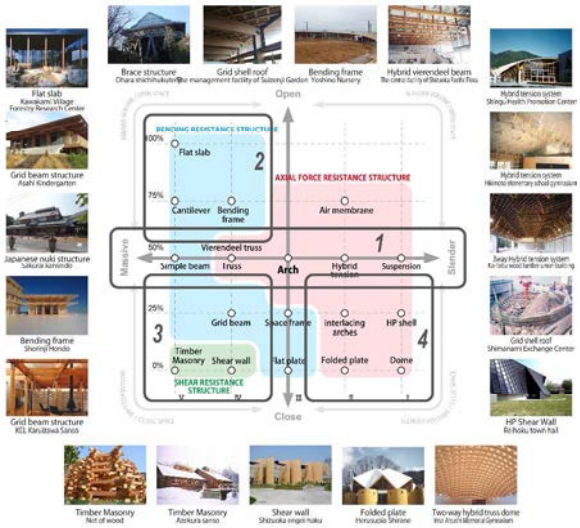


Figure 10: Analysis of 18 Types of Structure in Space Made of Wood

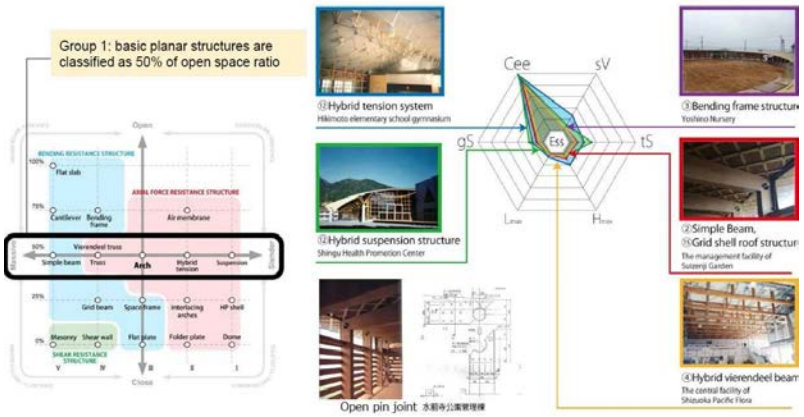


Figure 11: Analysis of 18 Types of Structure in Space Made of Wood
Group 1: Basic Planar Structures Are Classified as 50% of Open Space Ratio

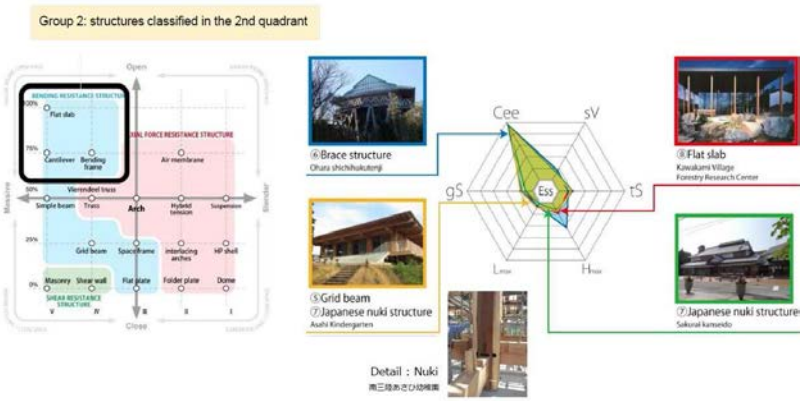


Figure 12: Analysis of 18 Types of Structure in Space Made of Wood
Group 2: Structures Classified in the 2nd Quadrant

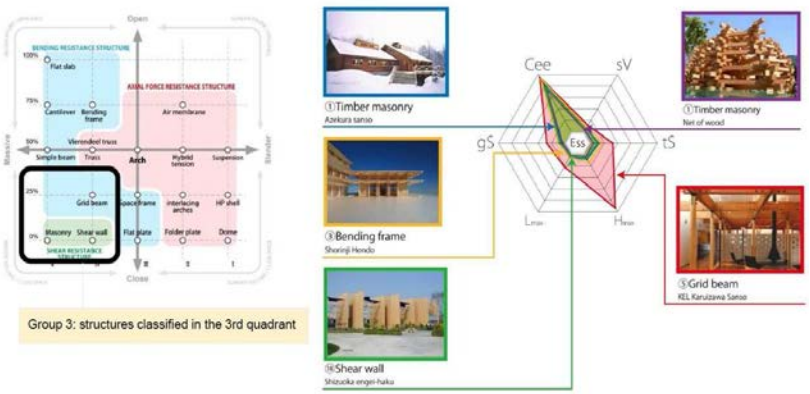


Figure 13: Analysis of 18 Types of Structure in Space Made of Wood
Group 3: Structures Classified in the 3rd Quadrant

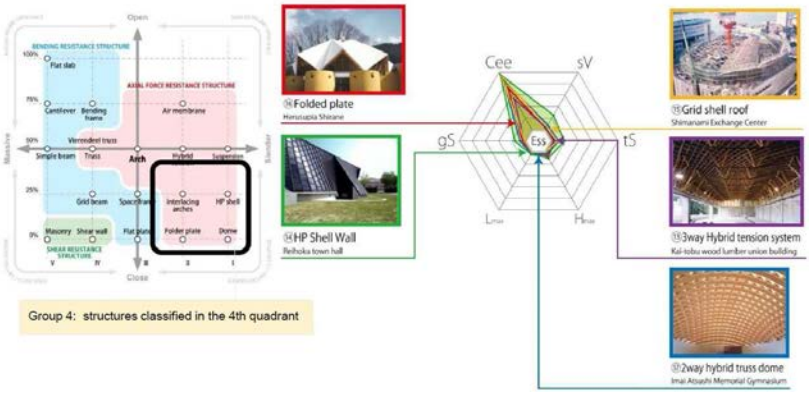


Figure 14: Analysis of 18 Types of Structure in Space Made of Wood
Group 3: Structures Classified in the 3rd QuadrantGroup 4: structures classified in the 4th

5. Discussion

The main features of Material Speaks Theory are as follows.

1. spaces made of different materials can be compared

2. spaces in different time can be compared

3. spaces using different basic framework can be compared

4. framework that reduces CO2 can be predicted

For example, a new structure can be born from a chemical formula “SiO2+α+Co2.”



Figure 15: UIA 2011 Chidren’s Garden

References

[1] Norihide Imagawa, *Material Speaks*, 2018, Inoueshoin , Japan

[2] Albert Einstein, *Special relativity* , 1905

Proceedings of the IASS Annual Symposium 2019 – Structural Membranes 2019
Form and Force
7 – 10 October 2019, Barcelona, Spain
C. Lázaro, K.-U. Bletzinger, E. Oñate (eds.)

Next Generation Residential High-Rise: Evaluating and comparing the Global Warming Potential of different structural systems and materials

Michael BUDIG, Oliver HECKMANN, Markus HUDERT*, Amanda Qi Boon NG

* Singapore University of Technology and Design
8 Somapah Road, Singapore 487372
markus_hudert@sutd.edu.sg

Abstract

The research project "Next Generation Residential High-Rise" aims at reducing the environmental impact of future housing developments in high-density urban environments. The main goal of the research is the development of a software tool that evaluates the consequences of early and intermediate design decisions for the *Global Warming Potential* (GWP) of buildings. Based on modular floorplan layouts with a systemic division into a permanent support and a flexible infill system [1, 2], this tool will help to determine the interdepending material ratios of alternative load-bearing systems and the respectively required infill components. As an integral component, it also considers the impact of alterations within the infill system during a building's service lifetime. The increasingly heterogeneous nature and the rapidly changing demands of society have led to a broad multiplicity of ideas on possible housing forms [3], which in general require a higher degree of flexibility. As they have the potential of increasing the service lifetime of a building, facilitating alterations will thus become more important. The final version of the software tool will also provide insights on long-term costs and possible financial benefits. This paper focuses on the role of materials and structural systems in the geographical context of Southeast Asia, and here with a focus on Singapore. It presents the results of two preliminary *LCA*-based studies, each of which compares the *GWP* of three construction variants of a notional case-study building. The paper also elaborates on how the software tool will facilitate the evaluation of decisions regarding materiality and structural systems in the future.

Keywords: Environmental impact of building structures, Global Warming Potential (GWP) of construction materials and structural systems, Life Cycle Assessment (LCA), simplified Building Information Modelling (BIM), Southeast Asian specific Life Cycle Inventory (LCI), LCA Visualization, quantifying flexibility in building construction.

1. Introduction

Largely driven by the need to decrease the environmental impact of buildings, timber is nowadays an established construction material and a serious alternative to concrete or steel in Europe and Northern America. In addition to applications in small and medium sized office and residential buildings, there also seems to be an ongoing competition for the tallest timber high-rise, pushing the boundaries of what is technically possible with wood based construction materials. In Southeast Asia and in Asia in general, it would be crucial to reduce the environmental impact of new residential high-rise buildings, large quantities of which will be required in order to cope with the rapidly growing population and the high density in this largely urbanized area. One step in that direction would be to build with lower-impact materials and to increase the use of renewable resources. In this geographical region, however, the 'rise' or 'renaissance' of timber has just begun. Among other things, this might be due to some of the basic conditions, which are quite different from those in Europe or Northern America: an insufficient amount

Copyright © 2019 by Michael Budig, Oliver Heckmann, Markus Hudert, Amanda Qi Boon Ng
Published by the International Association for Shell and Spatial Structures (IASS) with permission.

of sustainable forestry, the lack of locally or regionally produced materials and components, a high level of air moisture, and other difficulties, such as termites.

In order to underline the improvements that could be achieved by increasing the use of wood as a construction material in Southeast Asia, the authors carried out two studies, each of which compares the *GWP* of three different construction variants of a notional case-study building. The focus of these studies is on the structural elements, which typically have a bigger impact on the life cycle energy balance than other elements, such as surface and inner components [4]. Whereas it is foreseeable that choosing timber will lead to better results, it is less foreseeable how big the difference between the results for the different variants would be. In addition to that, this paper will also discuss the general advantages and disadvantages of each of the structural system in each of the three variants. A specific structural system can have an impact on the flexibility and adaptability of floorplan layouts and the infill system. While shear wall systems are space enclosing and would thus require less material investment to accommodate alterations, they might also offer less flexibility. Frame structures, on the other hand, might allow for higher levels of flexibility, but also require a larger amount of infill components to meet spatial requirements, with a subsequent impact on material investments and consequently environmental performance. Both the construction system and the choice of the construction material have implications for the overall weight of the building, which in turn determines the size of the foundations.

2. The impact of material choices

In Singapore, most residential buildings are currently built in concrete. Due to its relatively high environmental impact, the use of concrete becomes increasingly problematic. One option to reduce the environmental impact of concrete, specifically in Singapore, would be to import it from neighboring countries such as Malaysia [5]. However, given that practically everything is imported to Singapore, all building materials would benefit from shorter routes of transport. In principle, this is a desirable future development, but it does not solve the general challenges related to using concrete. One of these challenges is the re-usability of concrete, which typically involves down cycling. Yet another challenge is the increasing scarcity of sand, which is one of the main components of concrete [6]. Reducing the overall amount of concrete in a building leads to smaller foundations, due to the reduced deadweight of the structure. This reduction could be achieved either by high-performance concrete or by replacing concrete with lighter materials. Whereas the use of high-performance concrete could increase the resulting floor area and thus add economic value to the building, wood has the advantage of being approximately five times lighter than concrete. This could lead to considerable savings, even when taking into account that a higher material quantity is needed due to the lower loadbearing capacity of wood. The reduced deadweight would lead to savings in the construction of the foundations. More importantly, recent research has shown that using wood instead of reinforced concrete can lead to a 34 to 84 % lower climate change impact [7].

Although there are numerous reasons to reduce the use of concrete, there are also some concerns regarding wood and timber based products in Southeast Asia. Possible reasons for this are mentioned in the introduction. In order to make concessions to these reservations and to dispel doubts, timber based construction materials should be introduced in an incremental manner. The initial focus of this research is hence on hybrid building structures.

Regarding one of the here presented variants, *hybrid* means that every second floor slab – as well as the loadbearing walls – consist of concrete. The floor plates and division walls in-between would be made of *Cross Laminated Timber* (CLT). The second hybrid variant is based on the *Cree* construction system [8], which involves glulam columns and composite floor slabs made of glulam beams and a concrete deck. All of the here presented variants have to deal with the procedure of concrete pouring to a certain degree, as it is necessary for the foundations. Building the first floor in concrete as well could be a measure against termites.

3. The impact of structural systems

Each of the two studies compares three different construction variants, which also involve different structural systems (see Figure 3). Two variants use a shear wall system. The third variant, which makes reference to the *Cree* construction system, involves columns as principal structural elements along one of the facades. Additional options for future studies would be frame construction – both in concrete and in timber – as well as a timber-only shear wall structure. Although the studies' focus is the environmental impact of the structural system and the materials, related and affected aspects are addressed as well.

3.1. Variant 1: Concrete-only shear walls

In most scenarios, a shear wall system requires more material than a skeleton frame system. However, exceptions to this are possible, depending on the height of the building as well as the seismic activities in the site-adjacent region. One of the advantages of a shear wall system is that it requires less infill and façade elements. The erection of a shear wall system in concrete requires formwork and leads to comparatively long building processes, due to the curing time of the concrete, and increased traffic, as the concrete needs to be delivered to the site. This variant serves as benchmark for the other two.

3.2. Variant 2: Concrete shear walls and timber infills

In this hybrid variant, every second floor slab as well as the shear walls consist of concrete. The floor slabs and division walls in-between consist of *CLT*. The dimensions of the remaining concrete walls would increase as the *CLT* elements will take on different positions over time and only carry themselves. The buckling length of the walls would double, unless countermeasures, like for example introducing a tie beam, are taken. Nevertheless, this approach would accelerate the construction process as approximately half of the building would be prefabricated. Moreover, among the three variants discussed in this paper, this would be the only one that facilitates the option of easily converting normal into duplex apartments and vice versa.

3.3. Variant 3: *Cree*-inspired

Similar to frame construction, the *Cree* approach probably consumes less material on the structural level, compared to a shear wall system. The material composition is determined by the system. The building would involve a high degree of prefabrication, with exception, for example, of the concrete cores. In comparison with the other two variants, this variant should have the shortest erection time. Prefabrication also facilitates disassembly procedures at the end of the buildings' service lifetime.

In addition to shear wall and frame structures, future studies will also examine modular volumetric construction, or *PPVC*, as this approach is referred to in Singapore. This construction method seems to be gaining interest in Asia and beyond. Typically, the modules either are made of concrete or incorporate a steel frame [9]. One recent example is the *T30 Hotel* with 30 stories [10] in Changsha, China. The *Clement Canopy* is another example in Singapore with 40 stories, made of concrete modules. In *PPVC* buildings, the modules are typically arranged around a concrete core that incorporates staircases and elevators. Moreover, this core also contributes to the structural stability of the building. In Central and Northern Europe, modular volumetric construction is gaining momentum as well. The difference is, however, that these modules are often made of wood. Consisting of six stories of stacked modules, the *Woodie* dormitory in Hamburg is currently the highest *PPVC* building in wood known to the authors.

4. Preliminary comparative studies of *GWP*

Two *LCA*-based studies were carried out in order to clarify the impact of different materials on the *GWP* of a building's loadbearing structure. The first variant uses a concrete shear wall system. The second variant is based on a shear wall system that combines concrete with *CLT* floor and wall elements. The third variant is an adaption of the *Cree* construction system.

For both studies, the *LCA* system boundary is set to cradle-to-gate, assessing the embodied environmental impact of each of three unit models. The boundary corresponds to raw material production, inbound transportation and manufacturing. Installation, use, and maintenance phases are not considered, and transportation of materials to construction site are not considered either. The impact category *Global Warming Potential* (GWP) is used as the environmental factor for the *LCA* comparison, using characterization factors from fifth assessment of the *Intergovernmental Panel on Climate Change* (IPCC). In the first study, the *LCI* values originate from the *Athena* software package, whereas the second study uses *LCI* data from the *Quartz Project* [11].

As mentioned previously, it is foreseeable that choosing timber will lead to better results. What is less foreseeable is how big the difference between the results for the different variants would be. Moreover, the two studies pursue different approaches. It will be interesting to see if and how this affects their respective outcomes. The results of these two studies will also serve as benchmark for results obtained with the software tool, once it is fully operational.

4.1. First preliminary study

A first comparison of above described variants was carried out in a preliminary study, using the *Athena Impact Estimator for Buildings* and the included *LCI* data. The input parameters were the volumetric and material values for the floor slabs, the cores, shear walls, columns and beams. The material quantities of the entire building were used as input. The results were recently presented at the *Future Habitation Symposium* at the *National Design Centre in Singapore*.

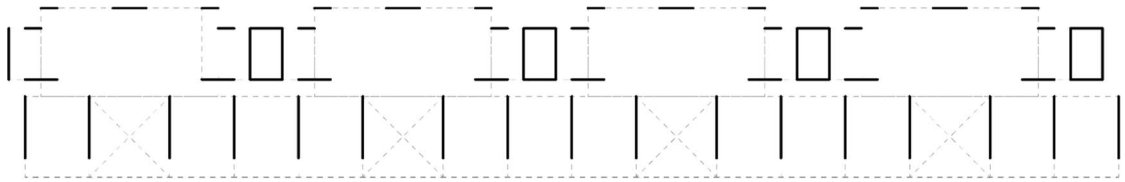


Figure 1. Floorplan of the notional 18-story building for the first *LCA*-based study.

With 547,000 *kg* CO_2 *eq*, the full concrete shear wall building had the highest *GWP*, confirming earlier assumptions. The result for the *Cree* inspired solution was 349,000 *kg* CO_2 *eq*. The hybrid variant with *CLT* floor and wall elements resulted in 283,000 *kg* CO_2 *eq*.

The results show that shifting from a pure concrete shear wall system towards a hybrid solution can lead to an important reduction in the *GWP*. The hybrid variant with timber walls and floor slabs led to a reduction of 48.26 %. The *Cree* inspired variant had a 36.2 % lower *GWP*. These figures do not yet take into account the savings in the foundations.

Some limitations need to be considered regarding the results of this early study. Firstly, *Athena* is a 'black box.' The *LCI* data and calculation method are not accessible. Secondly, the *3D* models from which the material quantities originate are simplified models and might need further refinement. The structural dimensioning of the timber and concrete components would need to be verified in all variants. The general structural performance of the *Cree* inspired variant would need verification as well. The effort and time required for carrying out this study showed how beneficial a simplified 'shoe-box'-based tool would be for designers and other stakeholders.

4.2. Refined preliminary study

The second study moves a step closer to what the research aims to achieve, which is a unit based configuration and evaluation tool that includes a preliminary dimensioning of a building's structural components. Instead of comparing the totality of three different configurations of an 18-story building,

this study only compares the material quantities of one unit, which in this case corresponds to an apartment for a nuclear family. The footprints of the three unit models have an area of about 232 m^2 and 235 m^2, and a floor-to-floor height of 3 m. The floor-to-floor height, floor area footprint and plan layout of all three-unit models are almost identical and are thus considered comparable.

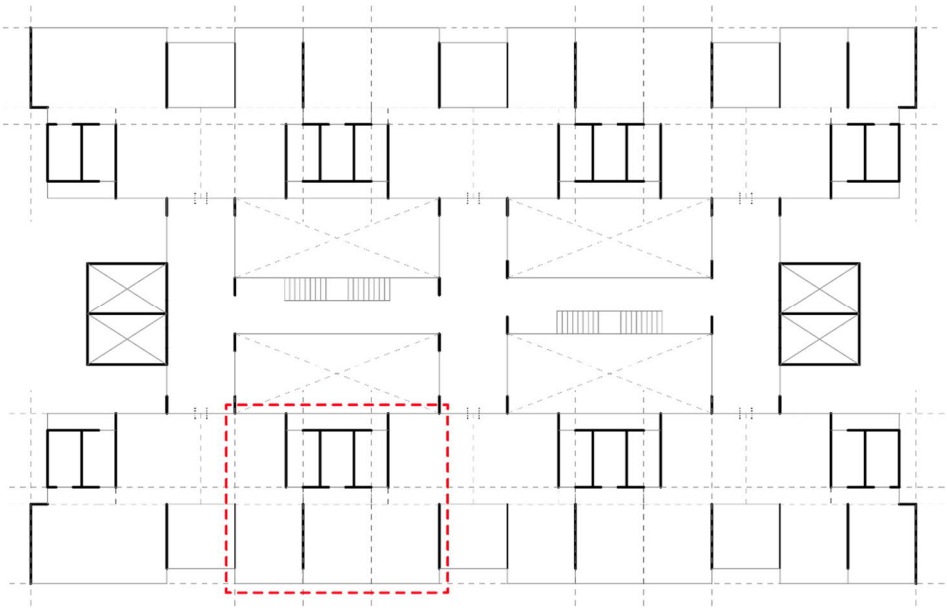


Figure 2. Floorplan of the notional building used in the second study. The red dotted rectangle indicates the unit module, which corresponds to the size of a nuclear family apartment.

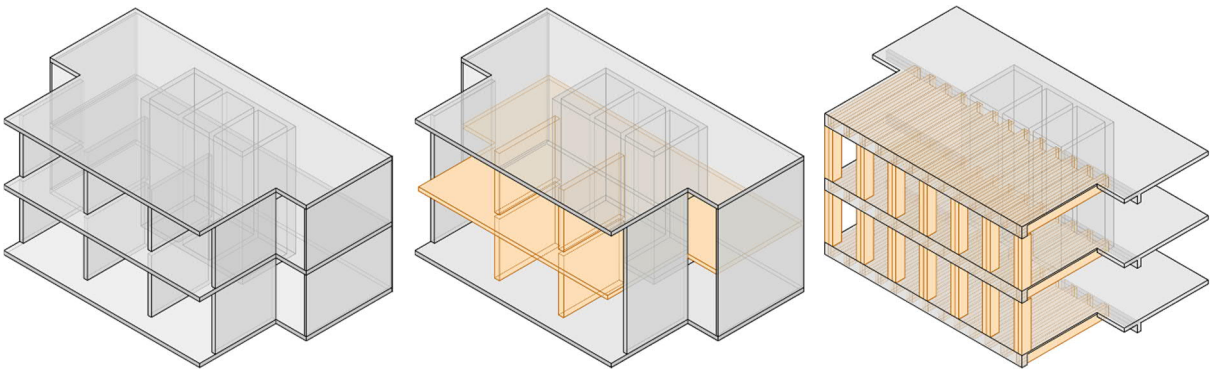


Figure 3. From left to right: unit module of concrete-only (Variant 1), concrete and timber (Variant 2), and *Cree* inspired system (Variant 3) respectively.

For this study, a spreadsheet-based *Life Cycle Inventory* (LCI) was established based on the *Quartz Common Product Database* [11], in which geographical boundary and production steps are modelled under *US* conditions. Transport related carbon emissions for importing the materials to Singapore are modelled according to the 2012 Guidelines of the United Kingdom's *Department for Environment, Food and Rural Affairs* (Defra) and the *Department for Energy and Climate Change* (DECC) Greenhouse Gas Conversation Factors for Company Reporting. *GWP* emission conversion factors taken from the guideline are multiplied with weight distance via shipping of the cargo. *CLT* and *glulam* are assumed to be shipped from Austria [12] and cement from Japan [5]. The assumed mode of shipping was based on an averaged sized general cargo with an average loading of 60 %. Moreover, the second

study also uses more detailed geometrical models, based on a preliminary dimensioning of the structural members. In contrast to the first study, the calculation of the *GWP* is carried out within a *Grasshopper*™ definition, set up by the authors. The full concrete shear wall system remains the system with the highest environmental impact of 94,118 *kg CO_2 eq*. The *Cree* inspired solution and the hybrid shear wall systems have significantly lower results:

- Full concrete system: 94,118 *kg CO_2 eq*
- *Cree* inspired 33,371 *kg CO_2 eq* (35.5 %)
- *CLT* concrete hybrid system: 56,036 *kg CO_2 eq* (59.5 %)

To facilitate the comparability of the two studies, the building model in the first study can be divided into 24 unit models of similar dimensions and layout with that of the second study. The concrete shear wall system, hybrid timber and concrete shear wall system and *Cree* inspired system in the first study had a deviation of 75.8 %, 79.0 % and 56.4 % respectively. As the dimensioning is preliminary, it is highly probable that more precise structural calculations would lead to different results. The general tendency of the results, which underline the positive impact of using more wood, is expected to remain unchanged.

5. Simplifying the assessment of material choices at early design stages

As mentioned earlier, the main goal of the research is the development of a software tool that evaluates the consequences of early and intermediate design decisions for the *GWP* of buildings and thus internalizes and facilitates such calculations. In this context, the results of the above-described studies will also serve as benchmark for results obtained with the software tool, once it is fully operational. The tool could either be conceived as a stand-alone software, as an online platform, a plugin for existing software environments, or a combination of these options. The software will provide a combination of configuration, generation and evaluation functionalities. In order to support the evaluation of early stage design decisions, it is crucial to find the right balance between ease of use and the complexity of information handled in the background. The software is hence based on a parametric set-up, which allows for digitally generating, modifying and evaluating an entire building by interacting only with a small part of it, the so-called 'shoe-box' model.

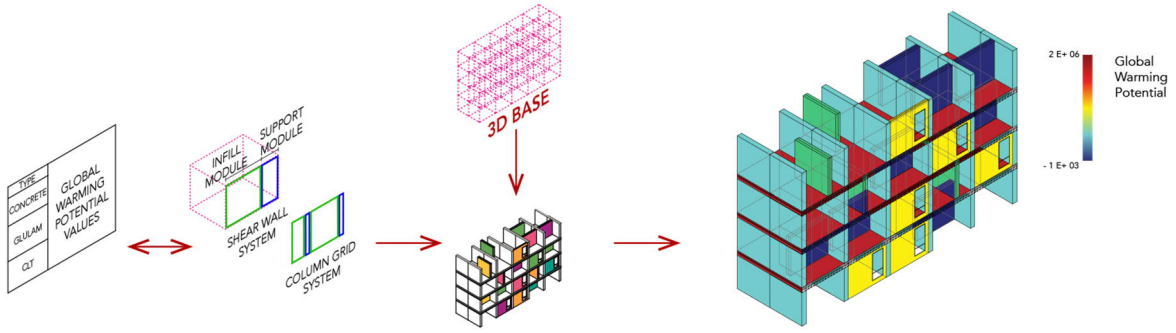


Figure 4. The workflow diagram, from left to right: *LCI* database, simplified parametric 'shoe-box' model, correlation with overall choice of hybrid system, and the visualization of results.

Being a central component of the user interface, the 'shoe-box' model is essentially a simplified three-dimensional representation of the primary unit-cell – or cells – of the overall building. In other words, it represents a repetitive unit of a standard floor level, including both support- and infill components [1]. The assumption would be that residential and office buildings typically involve a repetition of such cells, and that any modulation of the characteristics of a single cell could be scaled up to extract data on the entire building.

Changes in the unit cell affect the overall building and vice versa. Within the 'shoe-box' model, the user can for example modify the ratio between infill and support system, as well as the width, depth and height of the rooms. Moreover, the user can assign different materials or material combinations to predefined components such as fixed walls, partition walls, façade components and others. The material options are linked to a *LCI* database, which enables an immediate *LCA*-based visualization based on the decisions made. Some design decisions, and here especially the one concerning the structural system, should be made on a global level and would then affect the range of design options within the 'shoe-box' model. Other global inputs would provide information on the height of the building, respectively the number of stories. This information would then enable the preliminary and software-embedded dimensioning of the structural members, which would in turn increase the precision of the *LCA*-based evaluation results.

The authors are currently evaluating different options regarding the boundary definition of the 'shoe-box.' One option would be to align this boundary with the most typical type or types of rooms. In this case, the data for other parts of the building, such as circulation areas, cores and bathrooms, would be added by using percental reference values from existing projects. Alternatively, in order to directly include the above-mentioned parts of the building, the boundary of the 'shoe-box' would exceed the room cells and span over the whole width of the floorplan. The latter option would also facilitate the partitioning of the building into a *PPVC* compatible grid. A final decision on how to define the perimeter of the 'shoe-box' has yet to be made.

6. Summary and conclusion

This paper introduces the research project "Next Generation Residential High-Rise" as well as the motivation and goals that drive this research. The research proposes a novel approach towards the evaluation of early stage design decisions and their consequences regarding the environmental impact of a building. In this context, the paper presents the results of two comparative *LCA*-based studies that identify the environmental impact of different construction materials and material combinations. Moreover, this paper provides non-local experts with a better understanding of the special situation regarding sustainable construction in Southeast Asia. It identifies the benefits of increasing the use of wood in Southeast Asia and suggests a strategy on how to achieve this. Future research will focus on solving and implementing the aspects listed in section five and on moving closer to a beta version of the software tool.

Acknowledgements

The research project "Next Generation High-Rise" is funded by the *SUTD-MIT International Design Centre* (Project No. IDG21800103, Principal Investigators: Assistant Professor Michael Budig, *ASD* / *SUTD*, Assistant Professor Oliver Heckmann, *ASD* / *SUTD*; Research Fellow: Dr. Markus Hudert; Research Assistants: Amanda Ng Qi Boon (M.Arch), Tee Zhi Tian; Collaborators: Assistant Professor Lynette Cheah, *ESD* / *SUTD*, Colin Yip, Arup Singapore; Mentor: Professor Richard de Neufville, *MIT*). The authors would like thank Abhishek Goswami of Arup Singapore for his support with the preliminary dimensioning of the structural members.

References

[1] N. J. Habraken, Supports: an Alternative to Mass Housing, Urban International Press, UK, Edited by Jonathan Teicher, 1999. Edited reprint of the 1972 English edition.

[2] O. Heckmann, M. Budig, A. Ng. "Next Generic Residential High-Rise - Flexible Housing Typologies and their Social and Environmental Sustainability," CIB World Building Congress 2019, Hong Kong, China, 2019.

[3] O. Heckmann, F. Schneider, with E. Zapel. Floor Plan Manual Housing, Fifth, revised and expanded edition, Birkhäuser, Basel, 2017.

[4] A. Takano, S. K. Pal, M. Kuittinen, K. Alanne, M. Hughes, S. Winter. "The effect of material selection on life cycle energy balance: A case study on a hypothetical building model in Finland." Building and Environment 89 (2015) pp. 192-202, 2015.

[5] A. P. Gursel, C. Ostertag, 2016. "Impact of Singapore's Importers on Life-cycle Assessment of Concrete." Journal of Cleaner Production, 118, 140-50. (10.1016/j.jclepro.2016.01.051)

[6] UNEP 2019. Sand and sustainability: Finding new solutions for environmental governance of global sand resources. GRID-Geneva, United Nations Environment Programme, Geneva, Switzerland.

[7] J. L. Skullestad, R. A. Bohne, J. Lohne. "High-Rise Timber Buildings as a Climate Change Mitigation Measure - A Comparative LCA of Structural System Alternatives." Proceedings of the SBE conference 2016, Tallinn Helsinki.

[8] Cree by Rhomberg: https://www.creebyrhomberg.com, accessed on 01.04.2019

[9] Building and Construction Authority (BCA), Design for Manufacturing and Assembly (DfMA) Prefabricated Prefinished Volumetric Construction, Singapore, 2017.

[10] S. Mills, D. Grove, M. Egan, "Breaking the Pre-Fabricated Ceiling: Challenging the limits for Modular High-Rise," in Global Interchanges: Resurgance of the Skyscraper City, CTBUH conference proceedings, 2015.

[11] The Quartz Project, Quartz Common Product Database: http://quartzproject.org/, 2015, accessed on 14.06.2019.

[12] Building and Construction Authority (BCA), Design for Manufacturing and Assembly (DfMA) Mass Engineered Timber, Singapore, pp. 49-50, 2018.

Proceedings of the IASS Annual Symposium 2019 – Structural Membranes 2019
Form and Force
7 – 10 October 2019, Barcelona, Spain
C. Lázaro, K.-U. Bletzinger, E. Oñate (eds.)

On the Ecology of Climate & Structures

J. CHRIST, J. FERNANDOY-BAK[a], J. FIEBIG[a], H. KOSS[a]

*DTU Civil Engineering, Brovej 118, 2800 Kgs. Lyngby
julch@byg.dtu.dk

[a] DTU Civil Engineering, Brovej 118, 2800 Kgs. Lyngby

Abstract

The paper discusses various aspects of the interrelation between climate and structures as part of the biosphere's ecosystem. Structural design is hereby understood as a subsystem of humanity, seen as a biological organism, and the climate, as part of the organism's abiotic environment. Possibilities within recent advancements in digitalization and automation to adopt structural design to climatic loading conditions and to mitigate the effect of the manufacturing of structures on the climate are presented as core disciplines of the research group 'Climate&Structures' and are placed within the ecosystem's interrelations. These disciplines are: observation and simulation of climatic loading phenomena (icing, snow- and wind loading), adaption of structures to these with parametric multi-objective and topology optimization, and realization of these structures with additive manufacturing with circular and recycled construction materials.

Keywords: ecological structures, climate, climatic loading, wind load, snow load, icing, parametric multi-objective optimization, topology optimization, constructional 3D-printing, biologically based concrete composites

1. Introduction

Ecology, a science evolving from biology, describes the interrelation of organisms with their biotic and abiotic environment [1]. The investigated body within an ecological unit is thereby the ecosystem and includes the interaction of its biological, physical and chemical components [2]. This relation exists and is subjected to investigation at different scales: from Petri-dish bacteria cultures to our planetary biosphere [3]. On the example of the largest anthropogenic affected ecosystem, humans affect their environment by changing available resources in their physical, chemical and biological state [2]. In the same way, humans in turn are affected by other living components of the ecosystem and by the availability of non-living resources and physical states in nature. An ecosystem is often misunderstood as a community, limited to a field in ecology describing the interrelation of living biotic components (plants animals, microbes, etc.). By the definitions introduced above, a full view of an ecosystem includes as well numerous abiotic factors like climate, soil, and general energy and material consumption [1][4].

In fields, such as ecological economics [5], ecological agriculture, or ecological building [1], the objective is to adopt the respective human systems (economics, industry, etc.) to be co-existent in symbiosis [6] (or mutualism [7]) with their environment. Consequently, these disciplines are a subsystem of the human organism within the ecosystem [5] of our own biosphere. The term 'ecological building' describes this role for the field of Civil Engineering and is explained in Daniels [1]. Focusing on a specific part of this field, the paper describes the interrelation of the load carrying structure (design and construction) as a subsystem of the human organism, with the climate as its abiotic environment. Conceptual relations are laid out by mapping interdependencies between climate and structures. Furthermore, strategies and methodologies are presented to understand, quantify and influence the

Copyright © 2019 by J. Christ, J. Fernandoy-Bak, J. Fiebig, H. Koss
Published by the International Association for Shell and Spatial Structures (IASS) with permission.

ecological processes and are presented as part of the core disciplines of the research group 'Climate&Structures' at DTU Civil Engineering.

1.2. Climate and structures – A concept of interrelation

Throughout the history of humankind, structures were erected to create shelter from weather and environmental impacts, starting by using locally available materials. Structural geometry and concepts of the load carrying system were adapted and optimized through trial-and-error and systematic experimentation. Available resources were refined, material properties enhanced, and design methods improved, leading gradually to optimized structures within the associated ecosystem.

With the advent of globalization and industrialization, the supply chain for raw materials changed significantly and with that the advancement in architecture, design and structural performance. Construction materials, like concrete and steel, were produced from large-scale centralized industrial branches, affecting the environment by heavy resourcing of raw materials and changing its chemical state [8]. Such, not only standing in the direct interrelation with its local ecosystem, but rather affecting the biosphere and global climate, marking hence the era of the Anthropocene.

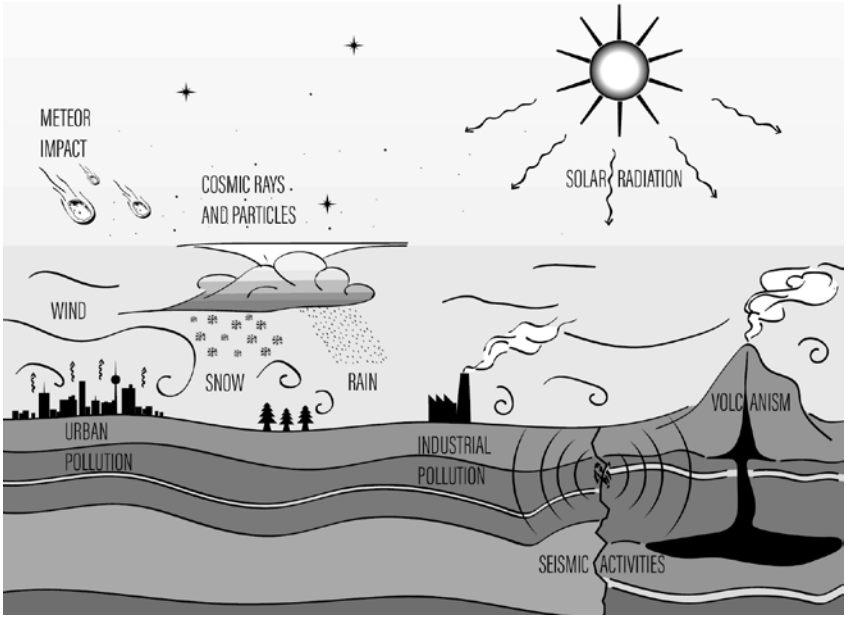


Figure 1: Aspects of climate-structures interrelation, including direct load impacts and long-term exposures of structures and humans within the built environment.

Figure 1 illustrates some of the main natural and anthropogenic elements in the ecology of natural environment, climate, structures and humans in the built environment. Structures are designed to withstand the impact from natural forces such as wind, snow, ice and earthquakes and are subjected to deterioration by climate impact like temperature, humidity and solar radiation. The climate in turn is affected by the manufacturing process of structures, e.g. through the herewith connected particle- and greenhouse gas emission, and through the expansion of urban land (e.g. surface albedo change). As described by the International Panel on Climate Change (IPCC), CO_2-emissions are one of the key drivers in climate change [10], for which the construction sector plays a major role [8], [11], [12] - Cement production alone is responsible for around 4% of the world's fossil fuel emissions [13]. The material use in structural building components has therefore a direct influence on the climate and the change of its physical state. The drivers of climate change derive from anthropogenic sources of aerosols and greenhouse gases like other fossil fuel consuming industries and of natural origin like volcanism, solar radiation flux, impacts from cosmic rays and particles [9] or even extraterrestrial objects, etc. [10]

some of which are still under discussion (Figure 1). Other natural- but not climate related boundary conditions include soil and seismic activities. These conditions influence the choice for material, manufacturing technology, design of structural components and transportation and consequently the extent of associated emissions. Figure 2 illustrates the circular dependency of climatic boundary conditions, choice of resources and building technology, associated impact on environment and climate.

1.2. Ecological structures

Centralization of material resourcing and the establishment of ubiquitous architectural and engineering standards are increasing the construction industry's economical efficiency and safety. Construction materials are produced by large-scale industry branches and transported to construction sites, making it simple to apply proven and time-efficient structural designs. However, the same set of designs is used for all types of geographical highly diverse regions, giving less priority to the exploitation of local raw materials and customized designs. In this respect, current building practice has a significant impact on climate and environment caused by unnecessary greenhouse gas emission, resource consumption [11], and waste production.

As part of the UN-Sustainable Development goals [14], expressed by the EU-Commission [15] and the IPCC [10], sustainable solutions for mitigating climate change are needed. Therefore, awareness of an overuse of resources is also increasing in the construction sector, causing a call for more efficient technologies [16]. Recent advancements towards digitalization and automation could enable a high degree of structural customization for local climatic loading and resource availability. Technologies, such as advanced load simulation techniques, structural optimization methods, free form construction techniques, and novel material alternatives could increase the effectiveness of the industry [11] in terms of its ecological mutualism by rendering safe structures with minimal use of local materials.

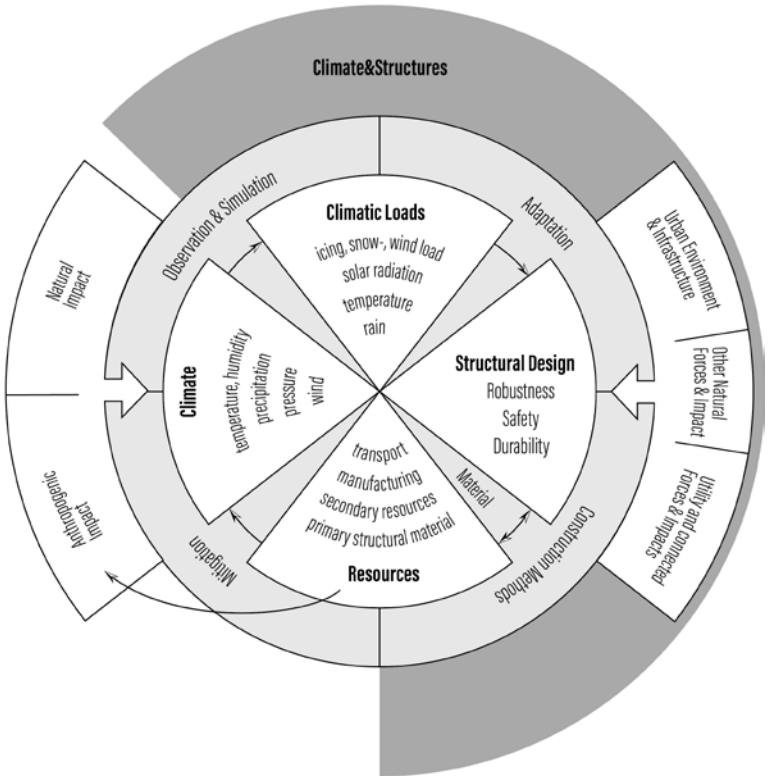


Figure 2: Illustration of circular dependency of climatic boundary conditions, resulting climatic loading, choice of resources and building technology, and the associated impact on environment and climate.

The central strategy of the research group 'Climate&Structures' is to contribute to sustainable advancements in the technological aspects of the circular interdependency between climate and structures. To this end, the research work focuses on three main areas: 1) observation and simulation of loading processes (physical states of the climate action), 2) response, deterioration and adaptation of structural designs to climate and environmental loads, and 3) advancement of material science and construction methods to render ecological structures with optimized performance.

2. Climatic loads

In structural engineering, climatic loads are extreme impacts resulting from the fluctuating state of the Earth's climate system in general or of processes in the Earth's atmospheric in particular. They are considered as single events such as extreme storms (e.g. hurricanes, extratropical cyclones) to ensure structural safety or as long-term processes to ensure durability. When planning development projects in urban areas not only the safe and durable design of the building or structure in question is of importance. With a trend to a high level of global urbanization, the effect of the local microclimate on human well-being has increasingly gained attention. A resourceful and climate conscious design of both, the built (structures and buildings) and urban (space between buildings) environment is indispensable to ensure sustainable urban planning [17].

2.1. Wind

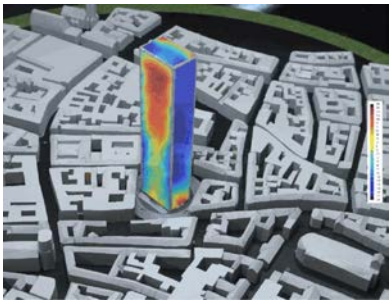
Few other forces have so universally shaped the diverse terrains and waters of the earth. Few other phenomena have exerted such profound influence on the history of humankind, on the way we live and how we build and where [18]. Being one of the principal forces in structural engineering, wind loads are determined by two main factors: the local climate and the shape of the object exposed to the wind. With the latter, the architectural form language plays a significant role for the loading the structure or building has to sustain throughout its lifetime. Hence, the load-carrying system on the inside and the outside shape of the building skin are key elements of any structural optimization process.

Wind loading is a fluctuating process governed by the aerodynamic behavior of the building, structure or structural element. To identify the extreme characteristic used for structural design, a large quantity of data is usually required and obtained through simulations with experimental or numerical models. Main challenge in these simulations is the accurate reflection of the turbulent atmospheric boundary-layer (ABL) in the lower part of the Earth's atmosphere. A mismatch in the turbulent structure and velocity distribution has a significant influence on the safety [19] or lifetime prediction of the structure designed with the data obtained through simulation. Wind tunnel testing (Figure 3a) is a proven and reliable method to investigate the complex wind loading process and allows amassing a large amount of data for reliable statistical analysis and probabilistic modelling of the structural response. On the other hand, a disadvantage of wind tunnel model is limit of shape variability. Depending on the type of model, a shape-load optimization has to done manually, i.e. through stepwise variation of the model shape (force balance models). Here, the numerical simulation provides the possibility of an automated process, linking aerodynamic optimization of the outer shape with a topology optimization of the load carrying structure. The present state-of-the-art of numerical simulation software and computational power puts some limits to a reliable and reasonably fast application. Current research effort within the group 'Climate&Structures' aims on numerical modelling strategies of sufficient accuracy and acceptable computation time [20], [21].

2.2. Icing

Icing of structures is part of phenomena occurring under cold climate conditions starting just under 0°C. The type of icing and magnitude of its effect on structural and aerodynamic loading is a function of temperature, wind speed and precipitation. All types have in common that the precipitating water is still liquid at the instant of impact on the object's surface and solidifies gradually in the subsequent thermodynamic process. Air temperature, wind speed, droplet size (median volume diameter), liquid

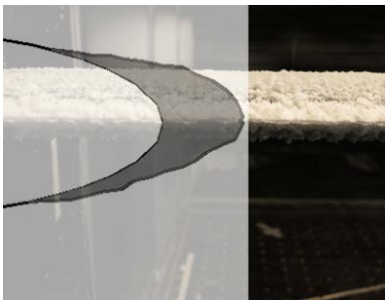
water content (LWC) in air, object's surface and core temperature, thermal conductivity, geometric shape and surface roughness determine the ice accretion process and with that the quantity of additional mass on the object and the alteration of the object's geometry, i.e. its aerodynamic performance. The phenomenon of atmospheric icing on structural elements is the observable manifestation of a complex thermodynamic process which is best studied by recreating the governing climatic and structural boundary conditions as true-to-life as possible. For this reason, the 'Climate&Structures' group uses a climatic wind tunnel (CWT) jointly developed and operated with the Department of Hydro- and Aerodynamics of FORCE Technology [22]. Amongst other, in-cloud icing on structural bridge cables [23] and wind turbine wings are investigated. The wind tunnel allows using prototype samples of cables and wing section are studies at reduced scale compared as validation data to numerical icing simulations [24] (Figure 3b,c). Apart from additional mass and increase of aerodynamic resistance amplifying static loads or reducing energy production, ice accretion also bears a risk of aerodynamic instabilities such as galloping or flutter. Both can lead to large-amplitude vibrations reducing significantly structural lifespan and/or lead to structural failure. With respect to structural ecology, controlling and reducing the driving mechanisms behind aerodynamic instabilities for extreme and changing climate conditions allows minimizing maintenance and material consumption. The CWT is part of a wind tunnel network at DTU including test facilities at the Departments of Civil and Mechanical Engineering and of Wind Energy.



a) Wind tunnel study of surface pressure on a high-rise building in urban terrain for comparison with numerical simulation.



b) Study in climatic wind tunnel of ice accretion on structural bridge cable and its effect on overall aerodynamic performance and instability [25]



c) Icing study on an airfoil to specify the geometric characteristic of the ice layer at leading edge and the change of aerodynamic force coefficients during icing process.

Figure 3: Examples for investigations of wind actions on civil engineering structures under different climatic conditions.

2.3. Snow

With respect to structural loading snow is a considerable factor in cold climates, which in extreme cases exceeds the carrying capacity of roofs and, as in Arctic regions, can remain for months on the structure leading to densification and water penetration. Long-term penetration leads to mold growth deteriorating the integrity of the mostly wooden load carrying system and contaminating the indoor climate. The research group on 'Climate&Structures' looks at the relation of architectural design of Arctic residential buildings and snow accumulation on and around the buildings. The former address snow loading events whereas the latter focuses on the usability of buildings and their accessibility to formulate guidelines and recommendation for Arctic architecture and urban planning. Especially for Arctic regions, an increase of the annual mean temperature may lead to an increase of snow and wind event frequency and intensity. To investigate the mechanics of wind-driven snow accumulation the small closed-circuit boundary-layer wind tunnel at DTU Civil Engineering is fitted with a seeding mechanism of substitutional material. For validation of model-scale tests, a reference cube was installed in Nuuk (Greenland) with simultaneous monitoring of climatic conditions and snow accumulation throughout, up to now, two winter seasons.

3. Climatic structural design

Structures today are conceived from experience, mathematical description of mechanical behavior, experimental and numerical modelling, and are a result of a complex interaction of economical-, building performance- and infrastructural optimization. Automation and digitalization will possibly lower the dependency on large industrial manufacturing infrastructure and create structural customization for specific local climatic and loading condition (Section 2). It will thereby decrease resource consumption and increase the sustainability account of the construction sector. The interface between local loading conditions (climatic, natural forces, function, dead weight) and the construction material (primary material consumption, transport, manufacturing, waste) is the structural design (Figure 2). 'Climate&Structures' aims on the creation of climate-oriented structural designs, i.e. resource conscious structures that use a minimum of material to withstand extreme local climatic loading conditions using parametric and topology optimization tools.

3.1. Topology optimization

Structural optimization in terms of topology optimization can minimize the material use for a maximized structural performance within a given domain. A computational algorithm places material within a space of finite volumes at the location of high strain energy according to the given loading boundary conditions. To design structural components with this tool, a set of detailed loading conditions is required to prevent over- and under-dimensioning of the structure. 'Climate&Structures' uses topology optimization to create high performance structures for fluctuating loading impacts, obtained from wind tunnel simulations (Section 2.1). In Fernandoy-Bak, et al. [26], a vault-shaped structure was optimized (Figure 4-a) to withstand the stochastic loading process of wind-induced surface pressures. The turbulent structure of the simulated ABL-flow is visualized in Figure 4-b. First results indicate a common solution of the topology optimization for all loading instants [26]. This in turn could lead to a full stochastic topology optimization of the load carrying system for extreme climate impacts. Placing even inferior material strategically where it serves best structural safety and durability, will lead to a significant reduction of material consumption (Figure 2).

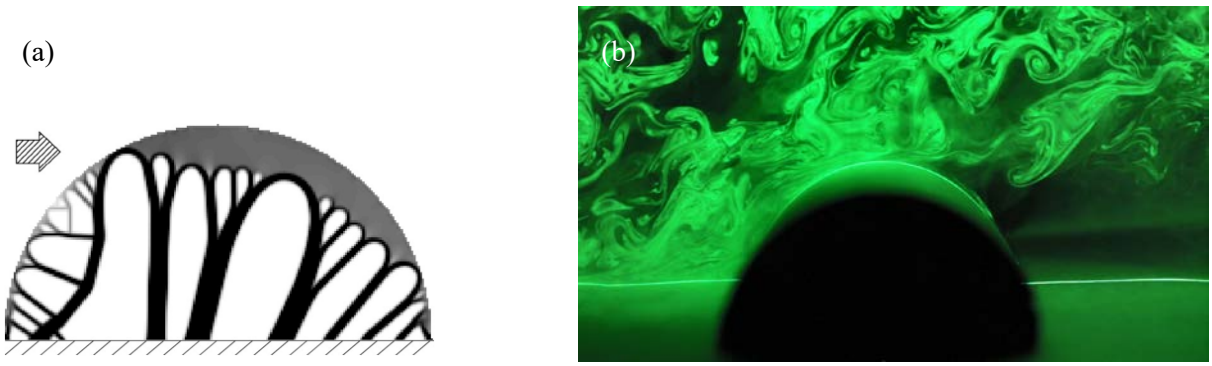


Figure 4: (a) Result from structural optimization (topology optimization) for wind loading scenarios [26], (b) visualization of turbulent flow over model in wind tunnel (flow from left to right).

3.2. Parametric multi-objective-optimization

'Climate&Structures' uses parametric design tools to optimize the performance of structural components. Through the inclusion of various performance objectives, the optimization process can consider not only material minimization of the structure as in Section 3.1, but include also e.g. manufacturing- and architectural boundary conditions. In Fernandoy-Bak, et al. [26], a frame-supported membrane structure has been parametrically designed for the use as an Antarctic research station. The structure was dimensioned to withstand extreme climatic loading conditions, to be transported to remote sites and assembled without mechanical help. The optimization scheme has therefore been adopted to

the objectives of reaching a minimal number of structural components with limited dimensions and to create structures, being light in weight. Some of the outcomes are shown in Figure 5.

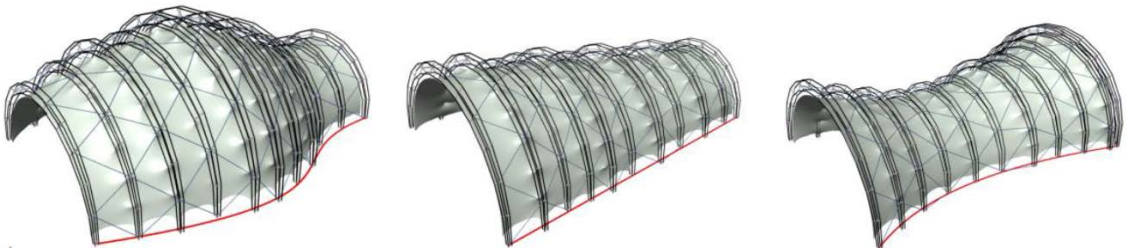


Figure 5: Frame-supported membrane structure, designed with multi-objective-optimization to withstand climatic loading impact and to fit several architectural boundary conditions. *Image:* [26].

Multi-objective optimizations with parametric tools give therefore the possibility, to design structural representations of climatic loading impacts, and at the same time respecting boundaries of manufacturing technologies, material resourcing, and architecture. Hence, representing the interface of all technological aspects (dark grey) in Figure 2.

4. Construction methods and resources

Computational optimized biomimetic structural design is a highly advanced field [27], pathing the way to create more sustainable and resource conscious constructions. However, the mostly biomorphic and freely shaped structural designs (Figure 4 - a) have a large draw-back in conventional manufacturing due to intensive use of non-standard molding and manufacturing shapes. Recent advancements in additive manufacturing (AM) [28] show possibilities in computer numerical controlled production without formwork and little waste material. The most advanced technology in constructional AM is 3D-printing of concrete using cementitious composites as a filament for construction. Judging the State-of-Art, designs manufactured by using this technology show a high potential for reaching construction-site-readiness in near future. Using cementitious filament allows relying on proven properties regarding performance as building material, but implies as well disadvantages such as lack of tensional strength, long setting times and environmental impact.

Novel construction methods and the associated material choices are the link between optimized structural designs, resource consumption feeding into the impact on the global climate (Figure 1). The aim of 'Climate&Structures' is to advance construction methods using materials, that enable the realization of the complex and optimized geometries presented in Section 3.

4.1. Additive manufacturing

The group explores possibilities of applying and advancing layered, extrusion-based constructional 3D-printing. The up to date, rather limited free form construction techniques, show difficulties in printing overhanging geometries needed for the realization of structures as shown in Figure 4. Climate&Structures focuses on the advancement of the filament's performance in terms of hardening characteristics, early age material strength, printed induced dead load and increasing tensional strengths by attempting and introducing novel choices of extruded materials [29].

4.2. Use of secondary resources

Filaments for constructional 3D-printing can be taken from secondary resources of local industry branches as attempted before (e.g. in Guan [30]). These could deliver solutions to waste problems and increase reuse possibilities of secondary resources in constructions through modern construction technologies.

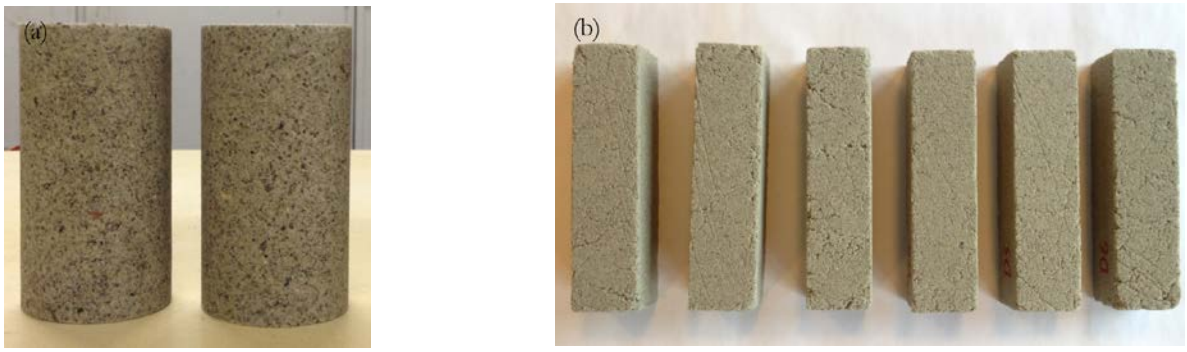


Figure 6: (a), (b) Concrete composite samples with biologically based binding materials, envisaged as filament for constructional 3D-printing. *Image:* [29].

Local resourcing from waste products reducing or even avoiding long transportation ways and production infrastructures is thereby one of the group's core ideas. The approach aims on the use of basic biological secondary materials connected with the food industry. The reuse of these materials could decrease emission and waste products due to lower production temperatures and recycle/reuse possibilities [29], falling in line with the EU's bioeconomic strategy [31]. Current research shows that use of secondary materials from food industry (biologically gels) as bio-based binding material for concrete (Figure 6) has a high potential for advanced applicability as filament in constructional 3D-printing [29].

5. Discussion

The discussed methodologies and technological fields of the research group 'Climate&Structures' have been presented and placed within the interrelation of climate and structural design (Figure 2). Being part of the biosphere's ecosystem, the interrelation between climate and structures is described by defining the structural design as a subsystem of humanity, seen as a natural organism, and the climate as its abiotic environment. The research group's activities are placed within the technological aspects of this interdependence. In this context, the observation and simulation of climatic conditions (snow-, ice-, wind loading) allow for detailed understanding and description of the associated loading processes. With the application of this information in structural design (topology optimization, parametric multi-objective optimization), structures can be adopted to different climates, dependent on geographical regions and to changing boundary conditions. Key approach is herein the close link between manufacturing methods (additive manufacturing), the "free form" (topology) optimization of structures and the use of novel circular materials (secondary resources) in these manufacturing technologies to mitigate climate change (Figure 2).

Overall, the work conducted by the 'Climate&Structures' research group seeks to improve existing and develop new technologies for ecological designs of buildings, structures and built environment by exploring advanced digitalization and automation methods. To succeed with this endeavor, the work depends on collaboration with other research groups and sections within the department, institutes at DTU and other universities and with partners from industry. Thoughtful consideration of human made structures within the boundaries of rapidly advancing technology and a changing climate is, considering the scale of the construction sector's pollutants and emissions, one of the most important of our time.

Acknowledgements

The research of the 'Climate&Structures' group is currently funded by grant (00023307) from VILLUM FONDEN (VILLUM Experiment), the Ingeniør Kaptain Aage Nielsens Familienfond, Rambøll A/S, Danish Research Foundation, RealDania, Estate Owner's Investment Font, VSL, FORCE Technology and DTU's Department for Civil Engineering.

References

[1] K. Daniels, J. Stoll, and L. Ilg, *Technology of Ecological Building*. Birkhäuser Verlag, 1997.

[2] P. Calow, "E," in *The Encyclopedia of Ecology & Environmental Management*, Blackwell Science Ltd., 1998, pp. 209–264.

[3] A. J. Willis, "The Ecosystem: An Evolving Concept Viewed Historically," *Source Funct. Ecol.*, vol. 11, no. 2, pp. 268–271, 1997.

[4] P. Calow, "C," in *The Encyclopedia of Ecology & Environmental Management*, Blackwell Science Ltd., 1998, pp. 107–169.

[5] R. Goodland, "Inegration of Economy and Ecology," *Ecol. Econ.*, vol. 2, pp. 343–359, 1990.

[6] P. Calow, "S," in *The Encyclopedia of Ecology & Environmental Management*, Blackwell Science Ltd., 1998, pp. 652–738.

[7] P. Calow, "M," in *The Encyclopedia of Ecology & Environmental Management*, Blackwell Science Ltd., 1998, pp. 420–467.

[8] L. Huang, G. Krigsvoll, F. Johansen, Y. Liu, and X. Zhang, "Carbon emission of global construction sector," *Renew. Sustain. Energy Rev.*, vol. 81, no. June 2016, pp. 1906–1916, 2018.

[9] Svensmark, H., Friis-Christenssen, E., "Variation of cosmic ray flux and global cloud coverage - A missing link in solar-climate relationships", J. of Atmospheric and Solar-Terrestrial Physics, Vol.59 No.11, 1997, pp. 1225-1232

[10] T. F. Stocker *et al.*, "IPCC - Summary for Policymakers," Cambridge, United Kingdom and New York, NY, USA, 2013.

[11] S. C. C. R. and A. R. Philipp Gerbert, "Shaping the Future of Construction A Breakthrough in Mindset and Technology," *World Econ. Forum*, no. May, pp. 1–64, 2016.

[12] D. G. Dhavale and J. Sarkis, "Greenhouse gas emissions in the construction industry : An analysis and evaluation of a concrete supply chain," vol. 167, 2017.

[13] R. M. Andrew, "Global CO 2 emissions from cement production , 1928 – 2017," pp. 2213–2239, 2018.

[14] UNDP, *UN -Sustainable Development Goals 2030*. .

[15] G. Amanatidis, "European policies on climate and energy towards 2020, 2030 and 2050," 2019.

[16] S. Castagnino, C. Rothballer, and P. Gebert, "What's the future of the construction industry?," *World Economic Forum (WEF)*, 2016. [Online]. Available: https://www.weforum.org/agenda/2016/04/building-in-the-fourth-industrial-revolution/. [Accessed: 14-Jun-2019].

[17] Koss, H.H. "Understanding urban environments and developing methods for sustainable urban design". In preparation for publication in *Journal Building and Environment*, 2019

[18] J. DeBlieu, "Wind - How the Flow of Air Has Shaped Life, Myth, and the Land ", *Open Road Distribution*, 2nd Ed. 2015

[19] H.H. Koss, "Influence of the natural wind simulation on the prognosis of overload risk of industrial low-rise structures" *Doctoral thesis, Ruhr-University of Bochum, Faculty for Civil Engineering*, Germany, 2001 (German language)

[20] M.S. Thordal, J.C. Bennetsen, H.H. Koss, "Review for practical application of CFD for the determination of wind load on high-rise buildings" *Journal of Wind Engineering and Industrial Aerodynamics*, 2019, Vol. 186, pp. 155-168

[21] H.H. Koss, L. Jørgensen, P. Jørgensen, N.G. Jørgensen, M.K. Rasmussen, "Benchmark for self-accreditation", in Proc. *European-African Conference on Wind Engineeing (EACWE)*, Liege, 2017

[22] C.T. Georgakis, H.H. Koss and F. Ricciardelli, 2009, "Design Specifications for a Novel Climatic Wind Tunnel for the Testing of Structural Cable*s"*. Proceedings *8th International Symposium on Cable Dynamics*, Paris, France

[23] H.H. Koss, J.F. Henningsen, I. Olsen, 2013, "Influence of Icing on Bridge Cable Aerodynamics", In: *15th International Workshop on Atmospheric Icing of Structure*s, St. John's, Newfoundland and Labrador, Canada

[24] C. Son, H.H. Koss, T. Kim. "Development of 3D icing simulation code for wind turbines". Proc. of *International Workshop on Atmospheric Icing of Structures (IWAIS)*, Reykjavik, Iceland, June 23-28 2019

[25] H.H. Koss, "Investigating the influence of cold climate conditions on structural dynamics". Proc. of *International RILEM Conference on Materials, Systems and Structures in Civil Engineering*, 22-24 August 2016

[26] J. Fernandoy-bak, J. Christ, P. Shepherd, and H. Koss, "Cases of Lightweight Structures for Polar Areas," 2017.

[27] J. F. Dynowski *et al.*, *Evolution of Lightweight Structures*. Springer Dordrecht Heidelberg New York London, 2015.

[28] P. Shakor, S. Nejadi, G. Paul, and S. Malek, "Review of Emerging Additive Manufacturing Technologies in 3D Printing of Cementitious Materials in the Construction Industry," vol. 4, no. January, 2019.

[29] J. Christ, H. Koss, and L. M. Ottosen, "A concrete composite from biologically based binders and mineral aggregates for constructional 3D-printing," in *2nd International Conference of Sustainable Building Materials*, 2019.

[30] G. Heng, A. Ting, Y. Wei, D. Tay, Y. Qian, and M. Jen, "Utilization of recycled glass for 3D concrete printing : rheological and mechanical properties," *J. Mater. Cycles Waste Manag.*, vol. 0, no. 0, p. 0, 2019.

[31] European Commission, *A sustainable Bioeconomy for Europe: strengthening the connection between economy, society and the environment*. 2018.

Proceedings of the IASS Annual Symposium 2019 – Structural Membranes 2019
Form and Force
7 – 10 October 2019, Barcelona, Spain
C. Lázaro, K.-U. Bletzinger, E. Oñate (eds.)

Optimized structure for Ice Stupa - architecture that supports nature to resist climate change

Sourabh MAHESHWARY*, Felix RASPALL[a], Simant VERMA[b]

Singapore University of Technology and Design
8 Somapah Road, Singapore, 487372
ar.sourabh25@gmail.com
[b] Ice Stupa Team, simantverma94@gmail.com

Abstract

Natural life and human populations in high-altitude arid regions like Leh-Ladakh depend solely upon streams from natural glacial meltwater. Due to climate change, population growth, modernization and sudden surge in tourism, water scarcity becomes a pressing challenge. This led to local innovators to develop the technique of artificial ice reservoirs. Ice Stupas are a type of ice reservoirs, created by freezing the stream water vertically on a structure in the form of huge ice towers or cones of 30 to 50 m height that look very similar to the local sacred mud structures called Stupa or Chorten. The stupa requires an initial base structure usually a dome for shape and stability. To tackle the difficulties faced by previous designs and make construction faster and more suitable, we introduced precise and reliable technology of 3D printing in amalgamation with local material. To test this, we built a prototype with locals using 3D printed joints and regional timber. This paper presents the structural and construction design, design process, the production of components, and on-site construction, and discusses the limitations and opportunities of ice stupa structures.

Keywords: Artificial Ice Reservoirs / Ice Stupa / Geodesic Dome / 3D Printing / Climate Change / Drought / Ladakh / Himalaya

1. Introduction

Glacierized mountains are often referred to as our world's water towers because glaciers have twofold benefits: a) they store water over time, and b:) they help regulate seasonal streamflow by releasing runoff during dry seasons when societies are starved of water [1]. One of these water towers, the Hindu Kush Himalayas stores the largest volume of snow and ice deposits outside the two north and south poles. They are also the source of 10 major rivers which provide food, energy and ecosystem services to up to 1.3 billion people [2] [3].

Ladakh dwelled in the northern extremity of India, seizes a unique niche: physiographically, climatically and culturally. Located in the leeward side of the Himalayas, it does not receive any summer monsoon and the annual rainfall is less than 70 mm, making it one of the world's highest cold deserts. Temperatures drop to minus 45 °C in winters and hover between 10-30 °C during summer. The region is snow-clad for almost 7–8 months, the remaining being the only agriculturally productive months in the year [4]. Unfortunately, like numerous rural areas across India, agriculture is the predominant livelihood which solely depends on glacier meltwater [5].

Copyright © 2019 by Sourabh MAHESHWARY, Felix RASPALL, Simant VERMA
Published by the International Association for Shell and Spatial Structures (IASS) with permission.

However, in the face of global warming, most Himalayan glaciers have been retreating. The IPCC Fourth Assessment Report (IPCC 2007a [6]; 2007b [7]) states that there is a high measure of confidence that in the coming decades' many glaciers in the region will retreat, while smaller glaciers may disappear altogether. Under such situations, even small change in glacial volume and snow cover are severe for the functioning of meltwater-dependent mountain agriculture.[8]

In order to adapt and mitigate the impacts of global and climatic changes, the region is experimenting with new techniques blend of traditional knowledge and modern science. The approach is centered around water management to sustain the livelihoods in harsh environs [4]. The Food and Agriculture Organization of the United Nations (2008) classifies Ladakhi agriculture among the possible "Globally Important Agricultural Heritage Systems", defined as "remarkable land use systems and landscapes which are rich in globally significant biological diversity evolving from the coadaptation of a community with its environment and its needs and aspirations for sustainable development".

One such technique is building artificial ice reservoirs, which stores water in the form of ice during winters and releases in the form of water supply in summers. Planar ice reservoirs are the most widespread type, acting as a frozen lake. The main drawback was that the flat surface has a highly exposed area to direct sunlight which increases the melting rate and reduces the life of the reservoir, also it demanded to be at a certain altitude which creates difficulty in maintaining it. To tackle these challenges, Sonam Wangchuk and students from SECMOL experimented with conical shaped ice reservoirs which are termed as Ice Stupa. In the proposed design, water droplets are made to fall on a dome-like structure from a height to form ice crystals.

Previous designs of structures are difficult to build, mainly due to the usage of primitive methods of construction with lack of blueprints, which lead to uncertainties and excessive material consumption. Moreover, replicating the structure was always challenging due to the lack of modularity in design.

We leverage precision and fast emulation capabilities of computer-aided modelling and 3D printing to propose an optimized design. The design considers extreme terrains and climate conditions of such regions. Hence it has been proposed as plug and play modules which ease on-site assembly, even by a non-expert local resident. The structure was designed as the modules of the elongated pentagonal pyramid of which all the vertices or nodes were 3D printed which hosted locally available barks of a willow tree. This module can be assembled at the base station and transported to higher altitudes for final assembly into a geodesic dome.

To test this, we built a first functional Ice Stupa 2.0 in Gangalas, Ladakh with local Ice Stupa team.

2. Background

2.1 Artificial Ice Reservoirs

Artificial ice reservoirs are also known as artificial glaciers and the process is often referred as glacier seeding. It is a grafting technique to freeze and hold water in the form of ice, received due to the melting of natural glaciers. The lifecycle of individual artificial glaciers varies according to the size of the natural glacier that feeds the artificial glacier, anticipated rainfall or snowfall, and overall temperature variation across seasons. Unlike many climate geoengineering experiments, these glaciers are physical structures that, once built, can be dismantled and effectively erased.[9]

2.2 Ice Stupa

Ice Stupas are created by freezing the stream water vertically on a structure in the form of huge ice towers or cones of 30 to 50 m height that look very similar to the local sacred mud structures called Stupa or Chorten. This method requires no pump or external pressure to freeze the water but rather adapts to the environment. It immediately turns into ice due to wind chill factor and cold winter, by the

time it falls to the ground [10]. Because of the shape of the stupa, less surface area is exposed to the wind and sun than there would be with a glacial field [9].

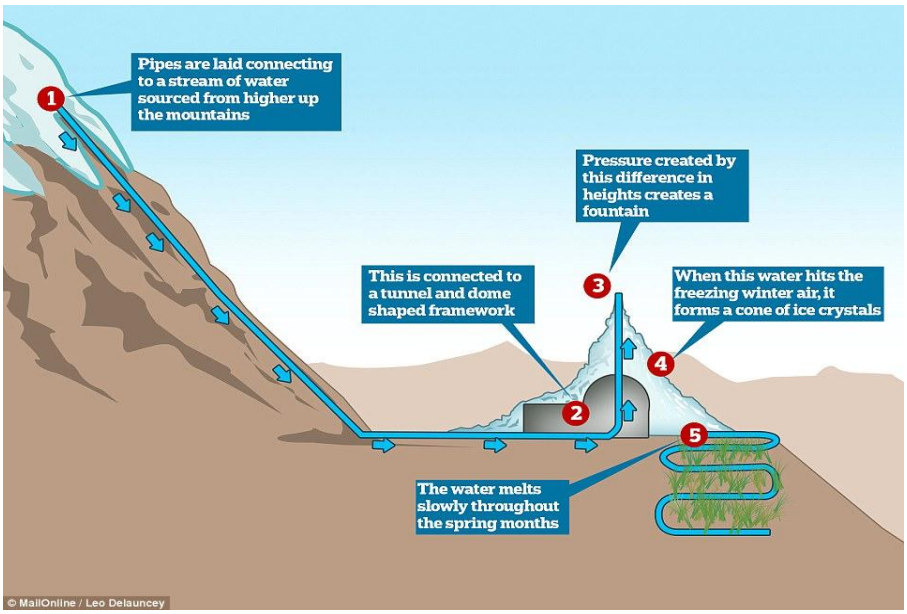


Figure 1: This is a typical process of an Ice Stupa [credits: © MailOnline / Leo Delauncey]

The process of designing an Ice stupa can broadly be divided into 4 parts: a) site selection, b) water supply, c) designing and erecting the structure and d) headworks. Each part has its own challenges and limitations, but this paper focuses on the supporting structure which is usually a geodesic dome (for structural stability and conical shape).

Selecting a site is based on the availability of water supply, slope and terrain, minimum exposure to sunlight and preferred location. Once the site is selected, the high-density plastic pipes are laid, usually buried in the earth to prevent freezing, to divert water by gravity from the upper stream area to the site, using the hydraulic head, produced by the altitudinal difference between intake and outflow. A narrower vertical pipe is erected in the center of the dome with a sprinkler fixed on top spraying out a fountain of water due to hydrostatic pressure [8].

The ground or site is plastered with clay to reduce its permeability and to prevent rapid seepage during the melting phase in spring. The base structure of stupa is usually a dome-like to give the stupa its initial structural stability and initiates the conical form. Branches of sea buckthorn and barbed wire are laid around the structure to provide additional surfaces for ice aggregation [8]. Once the ice formation occurs, i.e., at least after a couple of layers are formed, the ice becomes a monolithic structure which is strong enough to take its own weight like an igloo.

The structure also provisions for an arched tunnel attached to it. This tunnel allows access to the internal chamber of the stupa, where services for the pipe takes place mainly defrosting, adjusting the height or changing/tweaking the sprinkler.

Till now the construction was done using primitive methods such as randomly stacked sea buckthorn twigs onto the dome, which were not handy. There was no particular way to construct the dome or organized system to easily understand and replicate with minimum error. This led to uncertainties and excessive material consumption which challenged the stability, replicability and maintenance of the structure. This labor-intensive way stretched the working time in harsh conditions and had a lesser probability of lasting throughout the seasons.

2.3 Additive Manufacturing

Joints and connectors are among the most critical components that affect the overall assemblies and systems. This is because these components are often the most complex element in an assembly with respect to geometry, functional requirements, and details [11].

Additive Manufacturing (AM) colloquially known as 3D printing is the technology that builds 3D objects by adding layer-upon-layer of material. The range of material can vary from plastic, metal, concrete and many more. AM has been making rapid progress through recent years, overcoming limitations of speed, resolution, type of materials, and diversification of application fields. AM technologies can be easily customized to create complex geometries without additional costs and wastes during production is also less compared to subtractive manufacturing [11]. AM are well-established technologies and has been validated as a promising future in architecture [12].

3. Design

We introduce the concept of integrating new technologies with local resources and hence propose a new design, Ice-Stupa 2.0, which encapsulates computer-aided modelling and 3D printing with locally available timber. Computer-aided modelling was used to optimize the design of the nodes by reducing the excess material and guide precise locations for screws to hold the timber. The idea behind using 3D printing was to resolve complex issues at the joints and connections which demanded customization and precision. 3D printing also gave the flexibility to produce locally.

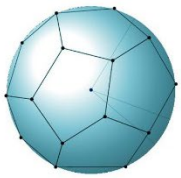


Fig. 2.1 Polyhedron



Fig. 2.2 Regular pentagonal dodecahedron



Fig. 2.3 Six module dodecahedron

Figure 2.1 credits: https://math.stackexchange.com/users/62024/herman-jaramillo
Figure 2.2 credits: https://en.wikipedia.org/wiki/Regular_dodecahedron#/media/File:Dodecahedron.jpg

The design of the proposed dome consists of a polyhedron with edges formed by linear willow trunks. The regular pentagonal dodecahedron, being a platonic solid, was chosen and split into half for a stable dome structure consisting of 6 pentagons. To further reinforce the stability and strength of the structure, each pentagon of an edge length of 2m formed an elongated pyramid module as shown in figure 3.1-4.

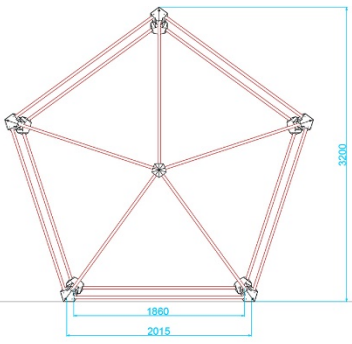


Fig.3.1 PLAN

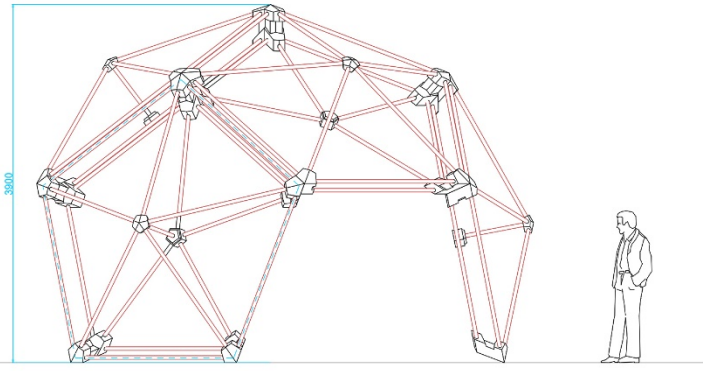


Fig.3.2 ELEVATIONAL VIEW

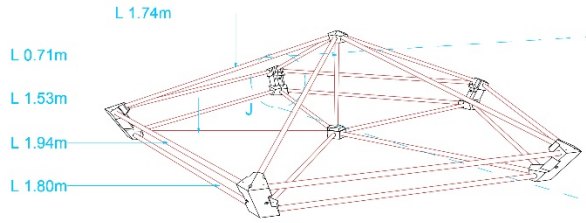


Fig.3.3 VIEW SHOWING ONE MODULE

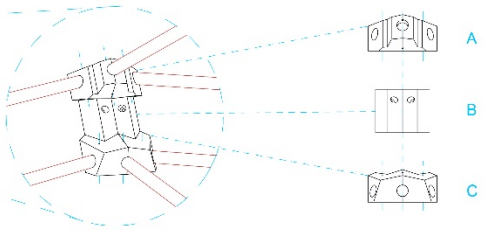


Fig.3.4 DETAIL J

Each module consisted of 7 3D printed nodes (5 at the vertices and 2 in the center), and 21 sticks of 5 different lengths (10 in the lower level, 10 in the upper level and remaining 1 connected both the centers) as shown in Fig 3.3. These modules can be easily transported (either pre-assembled or in parts) to the site and quickly assembled together to form the dome, thus minimizing the time spent in harsh conditions on site. This kind of modularity made manufacturing and prototyping easier and organized.

4. Prototyping

4.1. Site

The Site was chosen in Gangalas, Ladakh which is situated 33 km north of Leh district at the altitude of approximately 4000 mt, after discussing with Ice Stupa team. The site is located at the foothill and is surrounded by the mountains, with minimum direct exposure to the sun as the mountains create a vertical backdrop in the south.



Figure 04: Site- Gangalas (34º12'46"N 77º36'36"E)

4.2. Water supply

The site rests on a sloppy terrain which ran an existing system of artificial pond and canal, receiving meltwater from the glaciers. A 300-meter long 75mm pipeline was laid from the artificial pond going

downhill to a rockfall. Glacial meltwater was to be sprinkled from this point to the dome below unlike the usual way of sprinkling through the stupa. The pipeline was fully covered with insulation of sleeping bags, in order to protect them from the cold and prevent freezing.

4.3 3D Printing of the nodes

Polylactic Acid (PLA), a bio-based plastic material was used for the 3D prints. All the vertices nodes were divided into 3 parts A, B, C as shown in Fig 3.4. due to the limited build volume of the 3D printers. The three parts were joined together by a single threaded M6 rod passing through the central axis with a nut at the ends. As a whole, the project consisted of 5 (vertices nodes) * 3 (parts) * 6 (modules) + 2 (center nodes) * 6 (module) = 102 printed parts. On average, each print took 20 hours with 30-40% infill in addition to a failure rate of approx. 10%. All the nodes were printed at the Singapore University of Technology, Singapore using 7 printers on an average, running continuously for 3 weeks. Later these prints were couriered to the site location in India.

4.4. Assembly of the dome

For this prototype, these modules were assembled directly at the site. This was decided to limit risk factors as this was the first prototype and the roads were unpaved with sloppy terrain which would further increase the risk of damaging the pre-assembled modules. Assembly of structure can be enumerated as followings steps:



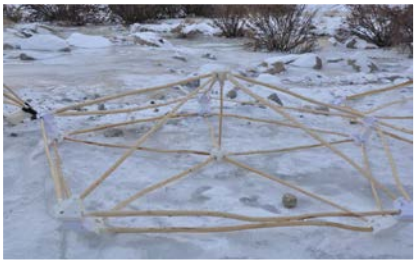
Step 1: transport to site



Step 2: sharpen the edges of sticks



Step 3: place parts on marked site



Step 4: drill the sticks to the nodes



Step 5: join the modules together



Step 6: fix the net

Once all the 6 pentagonal modules were prepared, they were attached together by a nut and bolt connection via 3D printed nodes. After assembling the structure, it was secured to the dry-stone stacks (foundation) for each of the 5 nodes touching the ground with heavy stones. The stacks also helped to level the uneven ground for the dome to sit upon. Then the structure was covered with a green colored fine-textured net. The purpose of this cloth was to further breakdown the water droplets and make the freezing process faster.

5. Results

The structure took about 20 hours to be built and spread across 4 days with a 6-member team working on an average. This included measuring and cutting the sticks to the required length, sharpening the ends, transportation and travel time to the site, marking and preparing the modules, assembling them

together, building dry stack foundations, and finally attaching the structure to the foundation and laying the cloth-net onto it. Some of the aspects to look in detail are as follows:

Assembly strategies: Although the whole assembly was much faster and neat relative to the previous design. It could be improved further in following aspects - a) the orientation of the dome led single module to face the direct pressure of falling water, leading to failure in the first trial and hence required extra reinforcements; b) assembly of modules in rough and sloppy terrain, prevented it to reach desired accuracy level; c) due to rough handling of the modules, the modules were detached and misaligned and resulted in using zip-ties in addition to nuts and bolts; and d) it would have cut the time at least by half if the sticks were sharpened before and alternatively one fourth if modules were pre-assembled at a base station. These aspects can be addressed with a more flexible design, especially if aiming for universal design, additionally with better planning and more equipment on site location.

3D printing: The potential of 3D printing could be explored in depth by customizing every node with respect to its function and location and not limited to repetition. Different methods and material of 3D printing shall be explored for faster and better-quality prints.

The structure was expected to grow up to about 25m but the water reaching the artificial pond reduced (due to water in the channel freezing), because of which siphoning stopped and so the water inside the pipeline froze. Hence, the final measured height was approximated to 15m. This was approximated because it was inaccessible to measure and snow covering increased inaccuracy. Finally, it withstood the harsh winter conditions and is now withstanding the summer and facilitating melting of the ice and snow formation into the water supply. After its purpose is served, the structure will be disassembled into pentagonal modules and possibly reused for another winter.



Fig. 5.1: complete structure



Fig. 5.2: water sprinkling on structure



Fig. 5.3: covered in ice and snow

6. Conclusions and Future work

Ice Stupas are emerging as technique for reserving ice flow and facilitating local adaptation in response to climate change. practically, they are challenging to build due to complexities arising out of difficult terrains, limited resources and unskilled labors at the construction sites. We demonstrate how technologies such as CAD and CAM can give a control over usage of material by standardizing the joints and lengths of the sticks and still flexible enough to use raw timber. Our research also demonstrates how introduction of modular design organized and speed up the assembly process leading to less time spent on the site in harsh conditions. Ice stupa 2.0 shows a way how easy and effective is to coherently involve and indulge with local and hence bridge the gap between traditional knowledge and necessities.

The proactive exploitation of design, technology and contextual awareness has led to frugal innovations across the whole process which ultimately developed into a unique integrated solution. Apart from improving designs for optimal ice capping, the study can be referred to and used across many areas such as construction and manufacturing technologies, deployable structures, landscape elements and opens new possibilities of integrating architecture to solve practical needs.

We identify shape optimization, structural adaptation to extreme site, integration of pipe services, margin of error for 3D prints and inaccuracies in cut to length timber as key challenges in the current design. Flexible designs and optimized structures would be explored, designed, deployed and evaluated in coming winters.

Acknowledgements

This would not have been possible without the Ice stupa team: Stanzin Norboo, Yasin Ahmad, Padma Rigzen, Angchuk Norboo, Rigzen Mingyur and Sonam Dorjay. Heartfelt thanks to AIRLAB for aiding the project. We would like to thank Jay Prakash and Khushbu Maheshwary for their immense support.

References

[1] Mark Carey, Olivia C. Molden, Mattias Borg Rasmussen, M Jackson, Anne W. Nolin & Bryan G. Mark (2017) Impacts of Glacier Recession and Declining Meltwater on Mountain Societies, Annals of the American Association of Geographers, 107:2, 350-359, DOI:10.1080/24694452.2016.1243039

[2] Eriksson, Mats & Xu, Jianchu & Shrestha, Arun & Ananda Vaidya, Ramesh & Nepal, Santosh & Sandström, Klas. (2009). The Changing Himalayas: Impact of Climate Change on Water Resources and Livelihoods in the Greater Himalayas.

[3] Samjwal Ratna Bajracharya, Sudan Bikash Maharjan, Finu Shrestha, Wanqin Guo, Shiyin Liu, Walter Immerzeel & Basanta Shrestha (2015) The glaciers of the Hindu Kush Himalayas: current status and observed changes from the 1980s to 2010, International Journal of Water Resources Development, 31:2, 161-173, DOI: 10.1080/07900627.2015.1005731

[4] Shaheen, F. A. 2016. The art of glacier grafting: innovative water harvesting techniques in Ladakh. IWMI-Tata Water Policy Research Highlight, 8. 8p.

[5] Ladakh Autonomous Hill Development Council, Leh - District Statistical Handbook Leh – 2016-17, chapter 3, page 15. https://leh.nic.in/document-category/statistical-report/

[6] IPCC (2007a) Climate Change 2007: The Physical Science Basis. Contribution of Working Group I to the Fourth Assessment Report of the Intergovernmental Panel on Climate Change [Solomon, S; Qin, D; Manning, M; Chen, Z; Marquis, M; Averyt, KB; Tignor, M; Miller, HL (eds)]. Cambridge and New York: Cambridge University Press

[7] IPCC (2007b) Climate Change 2007: Impacts, Adaptation and Vulnerability. Contribution of Working Group II to the Fourth Assessment Report of the Intergovernmental Panel on Climate Change [Parry, ML; Canziani, OF; Palutikof, JP; van der Linden, PJ; Hanson, CE (eds)]. Cambridge: Cambridge University Press

[8] Marcus Nüsser, Juliane Dame, Benjamin Kraus, Ravi Baghe, Susanne Schmidt, Socio-hydrology of "artificial glaciers" in Ladakh, India: assessing adaptive strategies in a changing cryosphere, Regional Environmental Change, https://doi.org/10.1007/s10113-018-1372-0

[9] Carey Clouse (2014) Learning from artificial glaciers in the Himalaya: design for climate change through low-tech infrastructural devices, Journal of Landscape Architecture, 9:3, 6-19, DOI: 10.1080/18626033.2014.968411

[10] Artificial Glaciers of Ladakh, http://icestupa.org/

[11] Junho Chun, Juhun Lee, Daekwon Park (2018) TOPO-JOINT, Proceedings of the 23rd International Conference on Computer-Aided Architectural Design Research in Asia (CAADRIA 2018), 205-214.

[12] Felix Raspall, Carlos Banon (2018) 3D Printing Architecture: Towards Functional Space Frames, Proceedings of the 23rd International Conference on Computer-Aided Architectural Design Research in Asia (CAADRIA 2018), 215-224.

Proceedings of the IASS Annual Symposium 2019 – Structural Membranes 2019
Form and Force
7 – 10 October 2019, Barcelona, Spain
C. Lázaro, K.-U. Bletzinger, E. Oñate (eds.)

Performative shading structures for public spaces applied in San Andrés Cholula, México

Edwin GONZALEZ*, Doris A. CHI, Eduardo GUTIERREZ, Renato VALDIVIA

* Department of Architecture, Universidad de las Américas Puebla
Ex-Hacienda Santa Catarina Martir s/n
edwin.gonzalez@udlap.mx
doris.chi@udlap.mx
eduardo.gutierrez@udlap.mx
renato.valdiviabo@udlap.mx

Abstract

Cholula, a sacred city, is located at a latitude of 19°N, in the State of Puebla, México. It has been a historical focus point since the beginning of the 12th century B.C. There is a diversity of esplanades and parks in Cholula surrounded by local history, commerce and civil architecture. They are part of a complex system of public spaces. Most of them present a lack of shadowed areas although they are necessary to provide comfort and wellness, particularly during the steamy months of summer. This work aims to design shading structures that protect open public spaces from the sun during the day that also serve aesthetic purposes; at night, they can be closed to enjoy the view to the sky. The shading structures are designed with a methodology that couples parametric architecture and sustainable technology with the local sun trajectory by using specialized climate-based software and simulation tools. The case study is the public space named Square of the Seven Cultures where a performative shading structure is planned. Hence, parametric design is used to propose a light structure that adapts to different sun trajectories throughout the year. Rhinoceros, Grasshopper and other advanced simulation tools are implemented to conceptualize the geometry and the structure, with the support of plug-ins for exploring mathematical shapes, paneling, structures and parametric finite element programs.

Keywords: Parametric design, public spaces, shadow simulation, optimization, evolutionary solution.

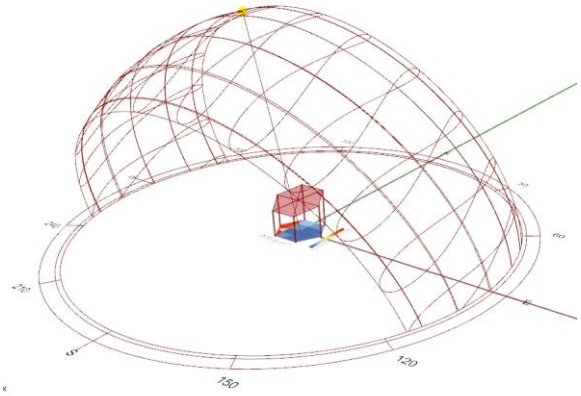


Figure 1: Sun-path diagram and calculation of solar radiation.

Copyright © 2019 by Edwin GONZALEZ, Doris A. CHI, Eduardo GUTIERREZ, Renato VALDIVIA
Published by the International Association for Shell and Spatial Structures (IASS) with permission.

1. Introduction

Public space is the structuring element of the urban fabric. It is a key element to the city as it articulates its life not only in a morphological sense but also and most importantly in a socio-cultural way. Thus, public space should have a variety of features to accomplish its purpose. It must be secure, inclusive and comfortable [1].

One of the most important ones is comfort. Among the things that give this particular feature to public space is shadow, it is not casual that since the beginnings of urbanization, shadow has had a primary importance in the use of public space, mainly due to climatic reason but in time, it got sophisticated and has become a powerful feature in public space.

In the pre-hispanic history in Mexico, the public places were in some cases destined to trade. Tianguis started as a point of social-commercial exchange, where people could sell handmade products, food, among other products. Commonly, the plaza had a circular morphology. All stands where placed around this circle, so they could concentrate more people.

Currently, the municipalities of San Andres Cholula and San Pedro Cholula have the distinction of Magical Towns, which represents a greater income of visitors. Their history is marked by thousand-year-old culture, the pyramid considered the largest in its base and the Sanctuary of the Virgin of the Remedies at its peak are presented as a tourist attraction for the area.

In Cholula, the plazas are a stall as audience, where they are always sitting ten or twelve people, who are judges and punishers of all cases that take place in the market. There are other people in the plaza who walk continuously among the people, looking that every negotiation is measured.

An attractive variant that the Cholulas are their public spaces that although they represent considerable areas, their design and quality are poor. An example is the areas destined to rest, where the design is modulated and easy to fabricate, but much of the year does not generate the comfort that is sought in this type of structure. Many times, they are separated which prevents a coexistence between people.

In the world from the second half of the twentieth century and with an economic crisis caused by the Second World War, light proposals arise from structures capable of being built in a shorter time and with few materials. The textile-based structures built by Frei Otto become options in low-cost, easy-to-build public spaces, used to this day.

2. Description of the existing structures.

For this paper, the case study is the Plaza of the Seven Cultures. It is located next to the regional Museum of Cholula and it has great views to the east and south faces of the Great Pyramid, with the Iglesia de Nuestra Señora de los Remedios sanctuary on top. The city is divided into two, San Andrés and San Pedro Cholula. Historically, both sides have been dissatisfied with political decisions and society has been split in two for some years.



Figure 2: Plaza of Seven Cultures

In the Plaza, it can be observed two different types of structures designed for resting. The structures in the square are manufactured with metallic materials with measurements and commercial sections (square section and channels). However, the shadows projected under the structures are almost nonexistent, so they are not useful to provide user comfort. These structures were analyzed on site and through digitally simulations by using parametric design tools, such as Rhinoceros 6, Grasshopper, Ladybug and Galapagos.

Parametric design is the generation of geometry from the definition of a family of initial parameters chosen by the designer and the proposal of the formal relations they keep with each other. Rhinoceros 6 [2] can create, edit, analyze, document, render, animate, and translate NURBS curves, surfaces, and solids, point clouds, and polygon meshes. There are no limits on complexity, degree, or size beyond those of your hardware. Grasshopper is a graphical algorithm editor tightly integrated with Rhino's 3-D modeling tools. Ladybug tools analyze standard weather data in Grasshopper [3].

3. Methodology

The proposed methodology consists of two main phases. The first one is focused on analyzing the shadows projection of the structures that already exist in the square. The second phase develops a new geometry for the shadings that can be adaptive to the sun angles variability. The aim is to optimize the shadows projection under the structures to improve user comfort.

The existing structures and the new proposals were modelled in Rhinoceros. Then, the global irradiance and the sun-paths diagrams were both calculated by using Ladybug, an open source computer application that supports environmental design. It connects Rhinoceros interface to several validated simulation engines, such as Radiance and EnergyPlus. The weather file used was the EPW for Puebla, Mexico. A horizontal plane placed at the ground level, under the main structures, was used for the irradiation calculations.

To further illustrate the performance differences between the existing structure and the proposal, the following specific instances were chosen: June 22nd and December 22nd, both at 8 h, 13 h and 17 h. These instances allowed comparing results for the maximum and minimum solar altitudes, as well as for the longest and shortest days of the year. An additional day was also analyzed since it was the visit day to the site, that is, April 26th. This last instance allowed comparing simulation results again the actual performance of the existing structure.

3.1. Modeling existing structures.

Measured drawings and 3D models of the existing shading structure were constructed with Rhinoceros. The model data was then imported into Grasshopper to analyze the solar radiation that hits the horizontal plane and to make 3D sun-path diagrams through Ladybug tool. These last diagrams were then compared to the photographs taken on the site to test the software capabilities.

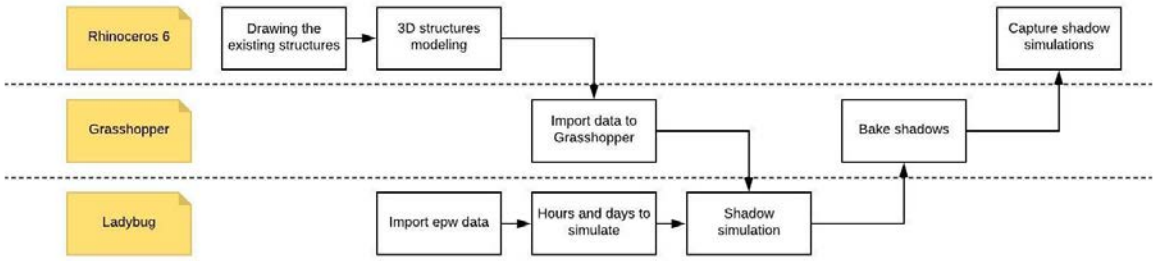


Figure 3: Workflow for irradiation simulations and sun-path diagrams construction of the existing structures.

3.2. Modeling of the proposed structure.

After observing the shading performance from the site photographs and simulation results, the necessity of a new geometry for the shadings was confirmed. Thus, an adaptive structure was designed to minimize solar radiation under it. It consisted of six triangular screens forming a hexagon. The module shape was chosen since it can be easily adapted to cover greater areas. Every triangle was able to rotate axially from 0° to 270°. The rotation axis of every triangle coincided with every side of the hexagon. A radius of 2.40 m and a height of 3.00 m were established for the hexagonal structure. These measures were proposed based on modular materials in Mexico.

Added to the triangular screen axial rotation (V1), two other design variables were considered in order to optimize the performance of the shading structure. The hexagonal panel was able to be tilted from 0° (horizontal) to 35° (V2). Moreover, the orientation of the structure was changed from 0° (North) to 360° clockwise (V3). The range of values of the three variables was set with a step size of 1° between each sequence value.

Table 1: Ranges for the three variables.

RANGES	V1-Screen axial rotation	V1-Panel inclination	V3-Plan orientation
Minimum	0°	0°	0°
Maximum	270	35°	360°

A base case (*f*) of the design proposal was simulated with the minimum value (0°) for the three variables. Then, a Grasshopper component named Galapagos, was run aiming to minimize the solar irradiance falling on the horizontal measurement plane. Galapagos is an app of Grasshopper that attempt to maximize or minimize fitness. Several computer simulations were run to analyze and compare different shading configurations in order to search for an optimal solution. These simulations were carried out in two steps with a different selection of parameters:

(a) Optimization of both the screen axial rotation of every triangular screen and the panel inclination.
(b) Optimization of the three design variables, that is to say, the screen axial rotation, the panel inclination and the plan orientation.

After running all simulations, the best configuration that minimizes the solar irradiation at every specific instance studied was identified. Here, it was assumed the capability of the shading structure to be adaptive and reach the values of the optimal configurations. Therefore, sun-path diagrams were made with Ladybug considering the optimal values. Finally, comparisons of the shadowing projections between the base case and the optimal solutions were constructed.

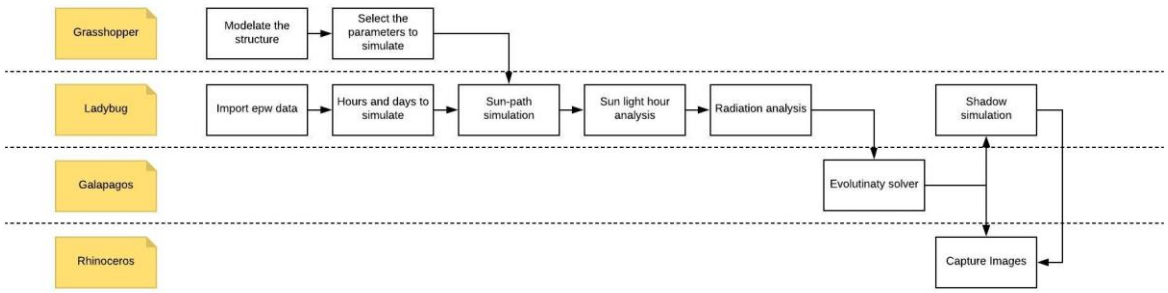


Figure 4: Workflow for optimization of parameters.

4. Results

4.1. Shadow simulation of the existing structures.

The first set of results is showed in Figure 5. Here, photographs that were taken on the Square of the Seven Cultures are compared against the images resulted from Ladybug simulations for two different structures already existing on the site. For both cases, the time chosen corresponds to April 26th at 8 h, 13 h and 17 h. From the comparison, it can be noticed that the sun-path diagrams constructed with the simulation tool get results very close to the real sun position. Besides, the shadows look pretty similar to those from the photos taken on site.

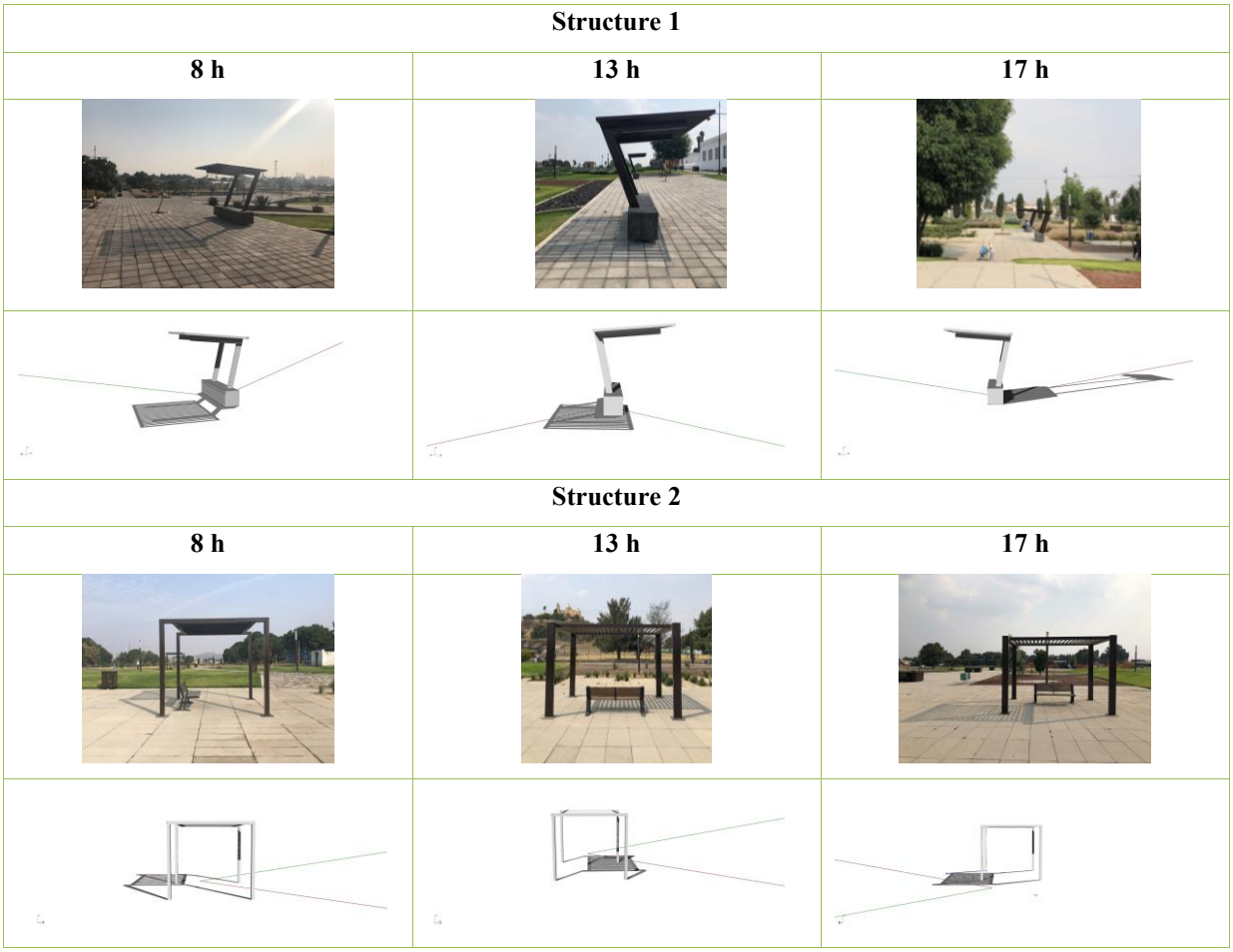


Figure 5: Comparison of shadows projections for two existing structures on the site.

4.2. Shadow simulations of the proposed structure.

The second set of results correspond to the adaptive design proposed for the shadowing structure. Table 2 summarizes the global radiation results (Kwh/m^2 × e^{-6}) for each set configuration (*f, a* and *b*) previously described in Section 3.2. From simulations, it can be observed that the optimizations through the two algorithms were successful since they get reductions of the total irradiation under the structures. This is attributed to the movable panels that were linked and adapted to the actual sun trajectory. Furthermore, Figure 6 and 7 show the simulation results for the specific instances studied

during summer and winter, respectively. Once again, a considerably reduction of the incident radiation under the structures is reached.

Table 2: Total radiation from simulations

Day/hour	**8 h**			**13 h**			**17 h**		
	f	*a*	*b*	*f*	*a*	*b*	*f*	*a*	*b*
22 jun Kwh/m2(e-6)	5.17	3.72	3.11	3.84	3.05	3.73	2.66	1.95	2.01
22 dec Kwh/m2(e-6)	2.90	2.12	1.93	8.52	5.48	5.77	3.56	2.67	2.19

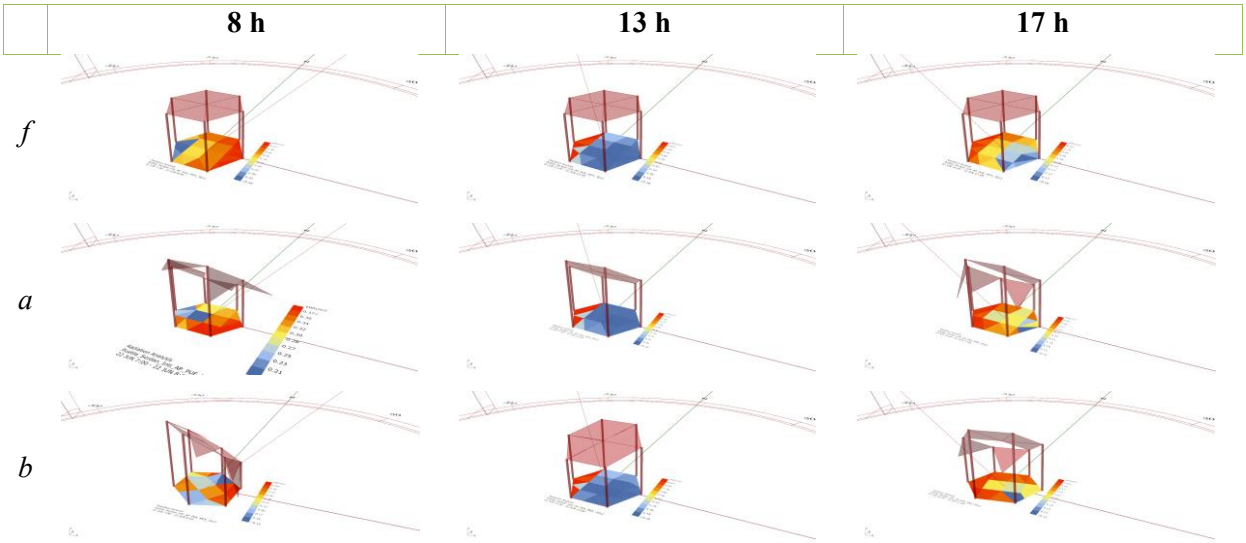


Figure 6: Comparison of global irradiances obtained for several instances during June 22nd.

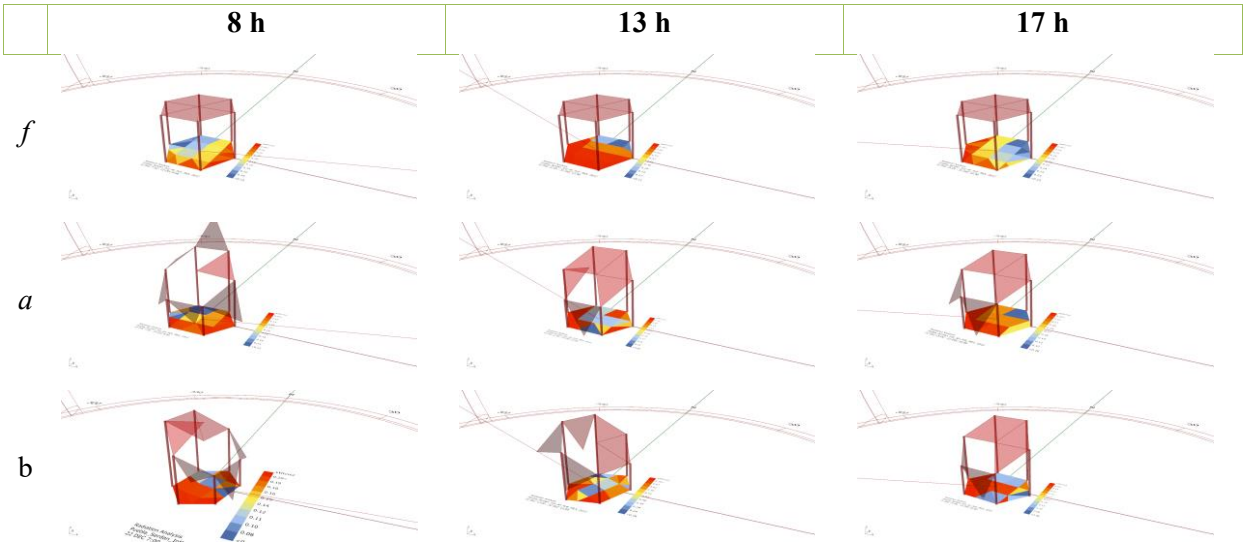


Figure 7: Comparison of global irradiances obtained for several instances during December 22nd.

From the above analysis, the best configurations that block the largest amount of solar radiation falling on the ground under the structure were selected and further analyzed. Figure 8 compares the shadowing projections made from the best configurations against those made from the base case (*f*). Every optimal configuration was constructed with a specific set of the optimal values recorded for every instance. The aim was to get the largest possible shadowed area under the structure. As it can be observed, the adaptive structures clearly optimized the shadowed area.

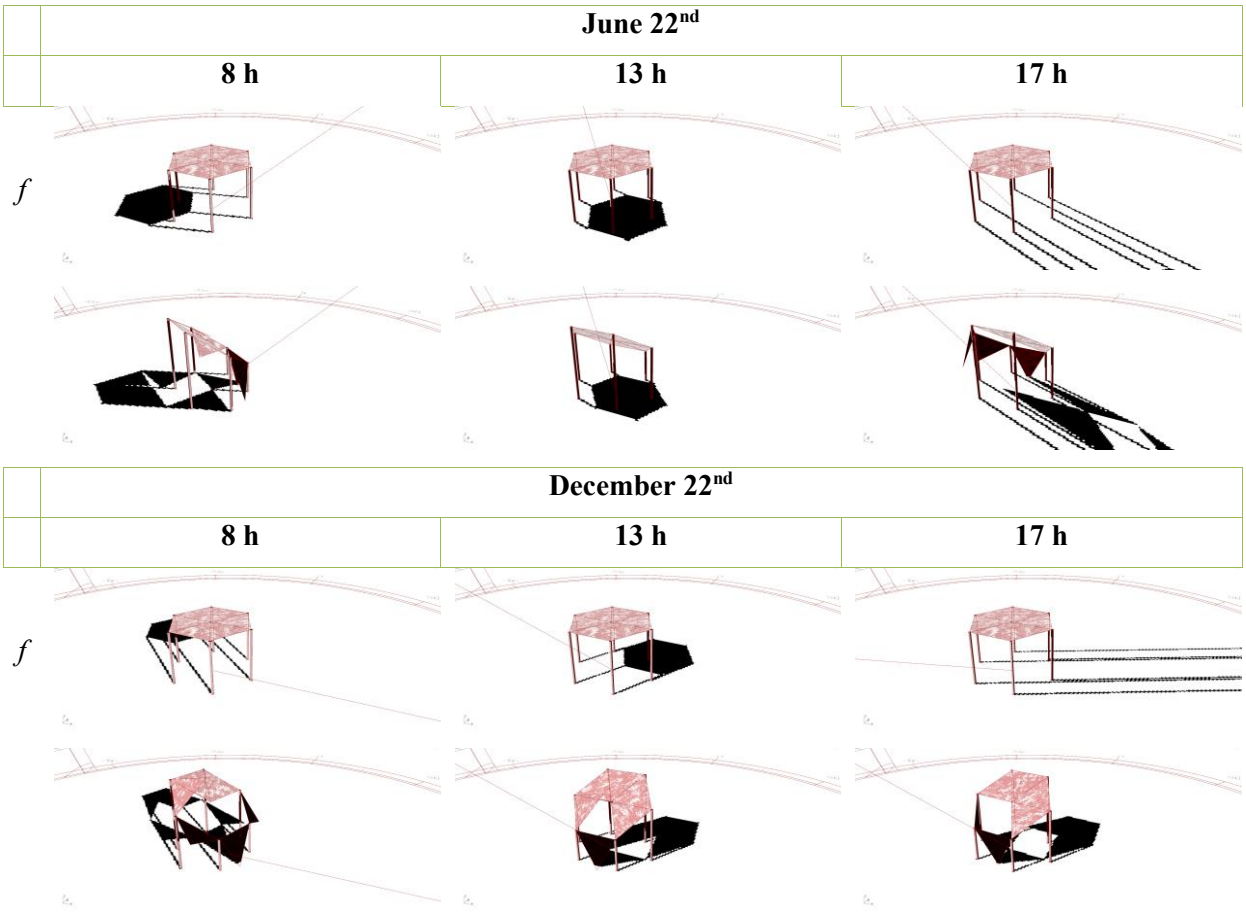


Figure 8: Comparison of shadows projections performed for the base case (*f*) against those for the proposal adapted to different angles and positions.

To show an example of the optimization, the particular position that was configured for the specific instance of December 22nd, at 13 h, is presented in Figure 9. The graph corresponds to the optimal values that were obtained from the set b of the simulation parameters (See Section 3.2). Since every triangular panel can be rotated independently of each other, the shadowed area under the structures is formed closer to it. Thus, the occupants can benefit from these areas and improve their comfort in public spaces. With this movable position, a 5.77 KWh/m^2 x e^{-6} radiation was obtained under the structure. That means a reduction of 2.75 KWh/m^2 x e^{-6} radiation.

V1-Screen axial rotation	V1-Panel inclination	V3-Plan orientation
35°	Panel 1 – 15° Panel 2 – 2° Panel 3, 4, 5 y 6 – 0°	143°

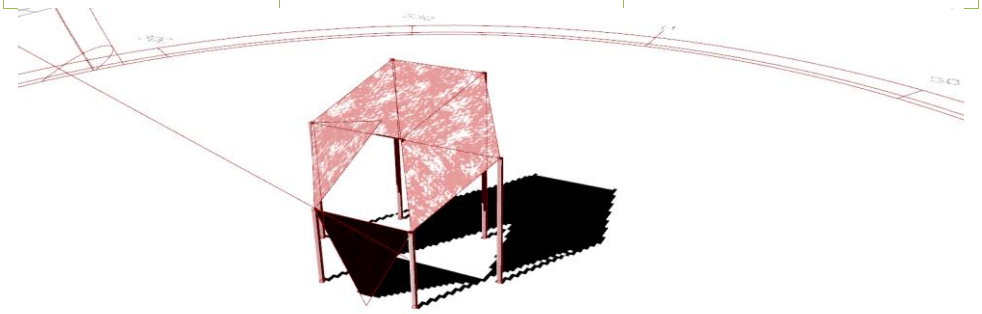


Figure 9: Set of optimal values for December 22nd at 13 h.

4. Conclusion

This paper has presented the implementation of the parametric design to improve the performance of shading structures located in the Plaza of the Seven Cultures in Cholula, Mexico. From the visit to the site, it was observed that the existing structures were not well designed since they do not provide either shade or comfort. Therefore, a new design was proposed to enhance the performance of the shadings.

From simulation results, it was noticed that a fixed structure is not a solution at all to provide shade to the areas under it. Fixed structures only provide shadowing at specific moments, which in most cases do not coincide with the occupancy hours. In contrast, movable structures can be adapted to the environmental conditions. This work shows how two different algorithms can predict the sun trajectory and adapt the angle rotations, the screen tilts and the orientation of the shading structures in order to reduce the total irradiation and to improve the provision of shade.

From the findings here presented, it can be concluded that the use of advanced simulation software and parametric algorithms is a powerful tool that allows modeling performative complex systems and analyzing their performance. Thus, these tools are important to be implemented during the initial stages of design projects. A wider study currently ongoing is aiming to improve building performance within urban contexts through the use of parametric design and different environmental simulation tools.

References

[1] J. Borja and Z. Muxí, “El espacio público: ciudad y ciudadanía,” 2003.

[2] G. Di Marco, *Simplified Complexity. Método para el modelado NURBS avanzado con Rhinoceros.* Le Pensour, 2017.

[3] M. Sadeghipour, M. Pak, A. Smith, and Gordon Gill Architecture, “Ladybug: A parametric environmental plugin for Grasshopper to help designers create an environmentally-conscious design,” in *13th Conference of International Building Performance Association*, 2013, pp. 26–28.

Proceedings of the IASS Annual Symposium 2019 – Structural Membranes 2019
Form and Force
7 – 10 October 2019, Barcelona, Spain
C. Lázaro, K.-U. Bletzinger, E. Oñate (eds.)

The ideal ETFE fenestration: The influence of material properties on the thermal performance

Jan CREMERS*, David MIRBACH*, Heiko LIEBHART*, Hannes MARX*, Oliver HAJEK*

*Hochschule für Technik Stuttgart
Schellingstraße 24, 70174 Stuttgart
heiko.liebhart@hft-stuttgart.de

Abstract

The obvious benefits of ETFE – constructions opposed to glass, regarding weight, and flexibility, have generally to be traded in by inferior properties and options regarding thermal behavior. In this paper we present a general overview on the current development and recent activities at HFT Stuttgart in the context of ETFE cushion research. The main emphasis is put on the numerical simulation of the heat transfer and energy consumption of buildings with various ETFE roof, façade or fenestration constructions. Starting from theoretical considerations on the thermal behavior of ETFE cushions, we embark on the quest to explore the most suitable methods for modelling of said thermal behavior of ETFE cushion constructions. We compare various methods of modelling and evaluate the calculations with regard to the reproduction of experimental data. We will elaborate on the influence of various methods for altering the thermal and visual properties of the material, like surface treatment, electrochromic or physical shading mechanisms and sheet configuration, on the energy consumption of hypothetical buildings in terms of heating and cooling loads. Numerical simulations will be shown, in order to shed some light on the expectable energetic efficiency of said measures, which are investigated within the course of several research projects at HFT Stuttgart (Follow-e, Flex-G, FMESG). The outcomes of these research activities will ideally put ETFE cushions further on par with commercially available glass fenestration systems in terms of thermal efficiency.

Keywords: ETFE, Flex-G, Follow-e, FMESG, radiative properties, dynamic building simulation, optimization algorithm

1. Introduction

The interconnecting topic of the various investigations presented within this article is the influence of the radiative properties of the material on the thermal behavior of ETFE fenestration elements with the goal of increasing thermal performance of the building. On this quest for the ideal ETFE fenestration the quantification of the influence of the proposed measures is done by means of numerical dynamic building simulation. The tool used for the numerical simulation is the TRNSYS simulation suite.

The structure of this paper is as follows: In Section 2 we will set up the foundations for the investigations with some general considerations starting from fundamental basic principles regarding radiative and thermal properties and requirements of fenestration systems. From there we will tackle the peculiarities of the thermal phenomena and the proper numerical modelling of ETFE-cushions. In Section 3 we will illustrate the impact of different methods of modelling with regard to accounting for the aforementioned phenomena on the thermal condition of a building. The numerical results are contrasted with available measurements of an experimental setup [1]. In Section 4 we will then introduce some possible solutions which have been investigated within the scope of several scientific projects at HFT Stuttgart during recent years.

Copyright © 2019 by Jan Cremers, David Mirbach, Heiko Liebhart, Hannes Marx, Oliver Hajek
Published by the International Association for Shell and Spatial Structures (IASS) with permission.

2. Characteristics of the ideal fenestration element

The expectations towards transparent elements of the building envelope can be categorized into optical properties on the one hand and thermal characteristics on the other. On the optical part the fenestration element is mostly expected to be sufficiently transparent in the visual spectrum, enabling the occupants a free view to the outside and providing sufficient daylight illuminance whilst preventing irritating glare. From the thermal perspective the expectations toward fenestration elements are similar to those toward opaque elements of the building envelope e.g. walls and roofs. The elements are expected to provide heat retention during periods of low outside temperature on the one hand and heat protection during periods of high outside temperature on the other hand, without blocking solar energy influx entirely [2].

The radiative flux from the sun, impinging on the surface of earth, is depicted in Figure 1 in terms of spectral irradiance of the AM1.5 spectrum [3] alongside the luminosity function representing the spectral sensitivity of human visual perception of brightness V(λ) [4] and the calculated blackbody radiation emitted at a temperature of T = 300 K.

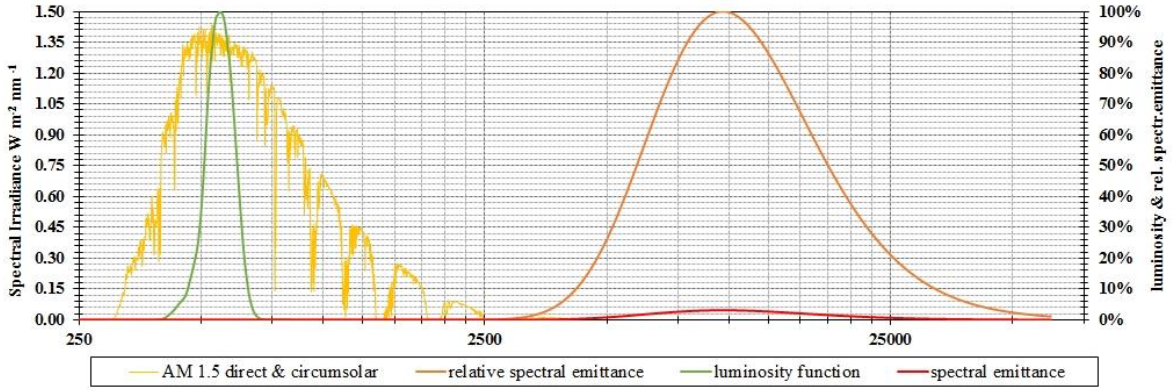


Figure 1: Spectrum of solar irradiation, luminosity function and thermal blackbody radiation

The relative amounts of energy carried in the different spectral intervals of solar radiation are listed below in Table 1.

Table 1: Relative contributions from different spectral regions to overall solar energy influx

	UV (280 - 380nm)	Vis (380 - 780nm)	IR (780 - 2500nm)	IR komplett (780 - 4000nm)	IR (2500 - 4000nm)
Direct+Circ	2.29%	52.06%	44.78%	45.65%	0.87%

The ideal radiative properties (transmission, reflection and absorption) of a fenestration element in order to fulfill the desired abilities of heat retention, heat protection and visual transparency are illustrated in Figure 2.

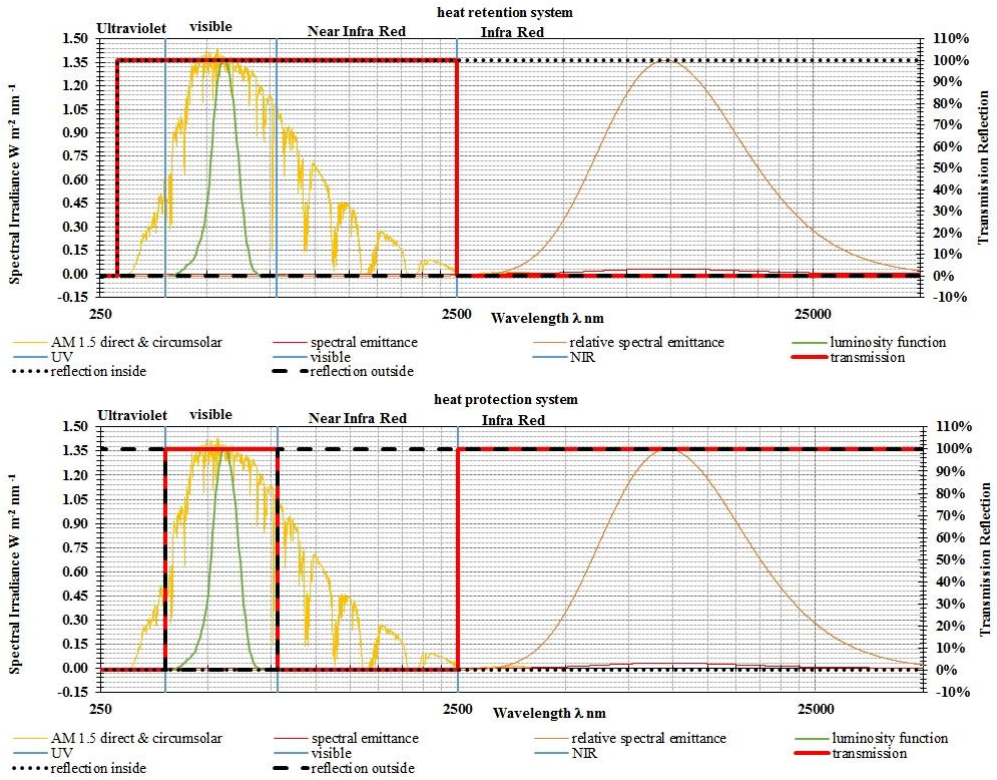


Figure 2: Radiative properties in terms of transmission and reflection for heat retention (top) and heat protection (bottom) of an ideal fenestration element

In Figure 2 there are two principal cases displayed which need to be distinguished. On the one hand, there is the situation where heat retention is desired (top) on the other hand (bottom) there is the scenario of heat protection.

In the scenario of heat retention the prevention of the decrease of the inside temperature below a comfortable limit is desired, in order to minimize heating energy demand. A high transmission in the solar range and a high reflectance inwards in the infrared (i.e. a high inward emission coefficient) would be required to prevent heat radiation from exiting through the fenestration while still collecting energy from the incoming solar radiation. The transmission in the visual part of spectrum should still be modifiable to prevent glare.

On the other hand in the scenario of heat protection the goal is to limit the increase of inside temperature past a comfortable value by preventing energy flux into the building in order to minimize the cooling energy demand. A low or adaptable transmission and high reflectance in the overall spectral range would be desirable in a way to maximize the prevention of solar radiative heat flux from entering the building while still providing adequate amounts of daylight illumination for the inhabitants.

The ideal solution to fully satisfy all the requirements of all of these scenarios would require a highly dynamic way to adapt the radiative properties of the fenestration element to changing climatic boundary conditions in real-time. Dynamic solutions in order to fulfill these demands do already exist in various forms ranging from mechanical shading devices to different coatings and built in shading mechanism and are commonly applied to conventional glass fenestration elements [5]. The conversion of such solutions to ETFE fenestration elements is mostly not ad hoc possible. Static solutions, configured to satisfy the specific needs according to the prevailing climatic boundary conditions, are still able to establish an improvement of the overall thermal performance of the fenestration element.

Three different, both static and dynamic, approaches to reach the goal of improving the thermal situation in the building by means of modification of the radiative properties of ETFE-cushions have been investigated at HFT Stuttgart and will be introduced in Section 4.

Our weapon of choice for investigating questions of the thermal behavior of buildings with respect to variation of the radiative properties of the fenestration is the dynamical numerical simulation of the building with TRNSYS. The quality of the results of numerical simulations in terms of accuracy and comparability to experimental physical data depends strongly on the method of modelling of the physical phenomena. Furthermore the realizable level of sophistication of the method of modelling always manifests as a trade off in terms of computational workload and acceptable accuracy.

In the specific case of modelling the thermal behavior of ETFE cushions some peculiarities need to be addressed. The occurring physical phenomena inside an ETFE cushion element differ significantly from the phenomena inside a regular multi pane glass window. Some of the occurring phenomena inside a cushion fenestration element are schematically depicted in Figure 3.

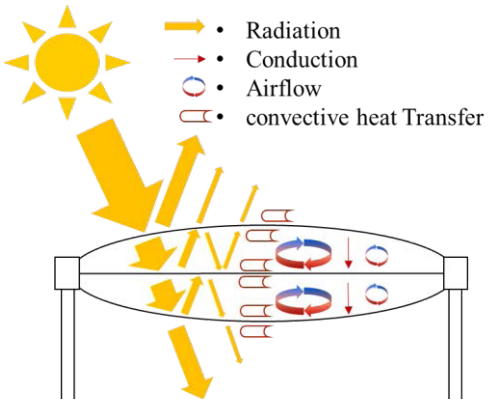


Figure 3: Some relevant thermal phenomena inside ETFE cushion elements

The probably most prominent and influential phenomenon is the establishment of steady airflow conditions within the cushion driven by the temperature difference of the surfaces, affecting convective heat flow within the cushion. The flow conditions within ETFE cushion have been investigated repeatedly [6][7] but general consensus on an applicable integration of the phenomena into the modelling for building simulation is not available so far. The straightforward method of coupling numerical CFD and building simulations is prohibitive in terms of computational workload for simulation of large timespans. In a rigorous implementation each time step of the building simulation would require several coupled iterations of converged CFD simulations. The common treatment of the convective heat transfer is by modeling of the thermal behavior via convective heat transfer coefficients. These coefficients can either be assumed to be reasonable fixed values or adaptive values calculated depending on surface temperature difference and wind speed. The use of adaptive coefficients is a brief part of the investigation within this work.

The influence of optical effects of the cushion and the employed shading mechanism on the heat flux is assumed to be considerably less susceptible to the modeling method, since the shading configuration in the discussed cases is mostly homogenous. The common treatment is conducted via angular resolved coefficients for transmission, absorption and reflection, regularly derived from spectral data of the glazing and shading material in the fenestration. A rigorous numerical treatment by means of a spectrally resolved ray tracing algorithm might be desirable in certain cases where geometric effects cannot be sufficiently modeled via overall optical coefficients. Investigations employing ray tracing procedures have been conducted by Flor et al. [8] but will not be discussed in this work. The influence of the shading mechanism on the illumination of the inside of the building is treated with the implemented DAYSIM ray tracing routines in TRNSYS.

3. Numerical Modelling of ETFE cushion

The investigation on the influence of different methods of modelling the effects relevant for the thermal behavior of ETFE cushion fenestration element was conducted on a building model derived from the experimental set up of preceding work of Kaufmann et al. within the Project OPTIMA [1]. The experimental set up of the OPTIMA project was equipped with a set of sensors to conduct measurements of parameters like temperature, illuminance, heat flux. A sketch of the model and the positions of the installed sensors is shown in the left part of Figure 4.

For the numerical building simulation with TRNSYS a geometrical model was designed with the Trnsys3d Plugin in SketchUp. The schematics of the geometrical model are shown in the right section of Figure 4.

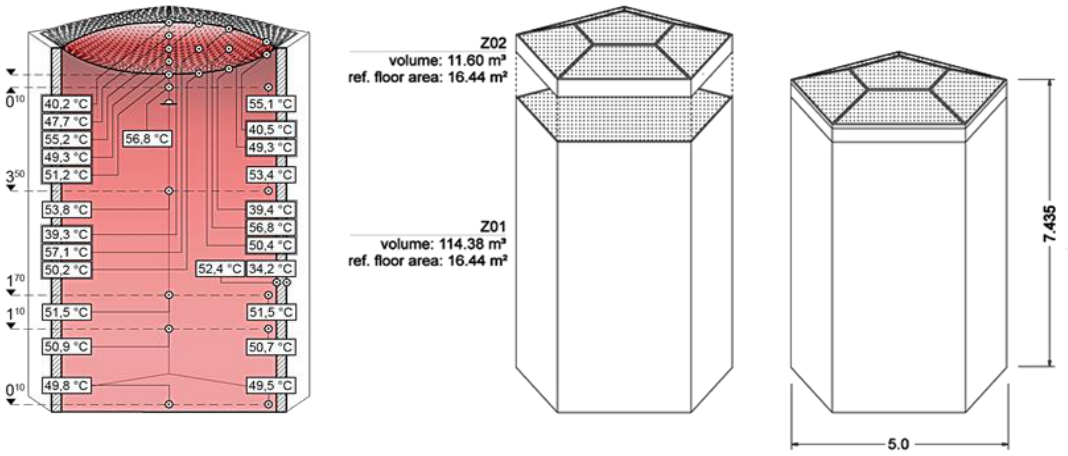


Figure 4: Sketch of the experimental set up with instrumentation (left) and 3D-model for the building simulation

The design of the geometrical model is differing in some aspects compared to the experimental set up due to the constraints of the TRNSYS simulation suite. Explicitly the surfaces of the cushion layers in the geometrical model are forced to deviate from the actual curved free form configuration of the experimental set up. The curved free form surface of the outside layer of the cushion of the experimental set up is approximated by a set of plane trapezoid and a central pentagonal polygon construction in the geometrical model due to the constraints of TRNSYS in treating free form surfaces. The curved free form surface of the lower layer of the cushion of the actual set up is constructed as a single plane surface in the geometrical model since the detailed radiation model in TRNSYS requires a concave configuration of the enveloping planes. The configuration of the airspace within the cushion by means of distance between the layers is designed to match the volume of the airspace of the cushion in the experimental set up.

The numerical building simulation was done with weather data provided from a weather station close to the location of the actual experimental set up. The derived measurement data of the experimental set up was generously provided by researchers from Fraunhofer IBP for comparison. Simulations have been conducted with a variation in the sets of certain modelling parameters, namely the convective heat transfer coefficient. The different sets of parameter configuration are displayed in Table 2.

Table 2: Parameter sets of convective heat transfer coefficients

	case I	case II	case III
qconv_in	11 kJ/h m² K	internal calculation	internal calculation
qconv_out	64 kJ/hm²K	64 kJ/hm²K	dynamic wind speed

The influence of the different ways of accounting for the convective heat transfer is evaluated by the average deviation of the calculated and measured values for the temperature in the cushion. The results in terms of temperature deviation are illustrated in Figure 5.

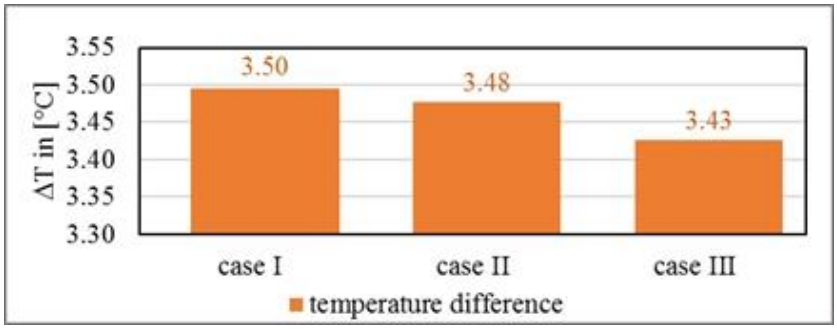


Figure 5: Average temperature deviation between measurements from IBP and simulation at HFT

The displayed values for temperature deviation are the arithmetic mean values of the absolute differences between calculated and measured temperature in the cushion for the time span of one year. A clear albeit small impact of the different ways of treating the convective heat transfer can be seen in the graphical representation. A reduction of the temperature difference can be noted with increasing complexity of the modeling from case I with fixed coefficient to case II with adaptive coefficients (internal calculation) and case III with adaptive coefficients (internal calculation) additionally taking wind effects into account. A general recommendation deduced from the calculation is to prefer modelling the thermal behavior of the cushion with a multilayer model and additionally accounting for effects of wind and airflow by means of adaptive convective heat transfer coefficients instead of using a single layer model with fixed convective heat transfer coefficients.

4. Scientific Projects at HFT Stuttgart

In this section we will give an overview to the recent scientific activity at Hochschule für Technik Stuttgart within three research projects, namely FMESG, Follow-e2 and FLEX-G, addressing the issue of shading capability of ETE cushions. The three projects share the common goal to improve the thermal behavior of ETFE cushion elements via the modification of the optical specifications of the material. We will give a brief introduction to each Project and an overview to some of the results where available.

All three project are part of government funded research programms carried out by cooperative research groups consisting of a number of partners with both academic and industrial background.

4.1 FMESG: Functionalized membrane structures for energy-efficient retrofitting of buildings

The project "FMESG" was a research project funded by the German Federal Ministry for Economic Affairs and Energy, succesfully completed within its project term on 30.09.2018. The aim of the project was the development of novel concepts for optimizing membranes with respect to architectural concepts and properties related to building physics in order to increase the energy efficiency in buildings. This includes especially the thermal and otpical enhancement of membrane constructions by combining membranes with other materials, such as glass fiber webs or aerogels. The main focus was on the improvement of energy and resource efficiency of new and existing buildings. The part of the project which will be emphasized within this article is the development of a static solution for partial shading analogous to a miniature sawtooth roof configuration [9].

A shading solution for the integration within ETFE cushions was developed and investigated at HFT within the scope of FMESG. Analogous to the sawtooth roof principle of limiting solar heat gain inside a building while still allowing light to enter the building through the roof to provide sufficient

natural illumination by blocking direct light in a range of angles, a threedimensional shaped foil was designed [10]. A sketch, displaying the underlying considerations (left and right) and the finished product (center) is shown in Figure 6.

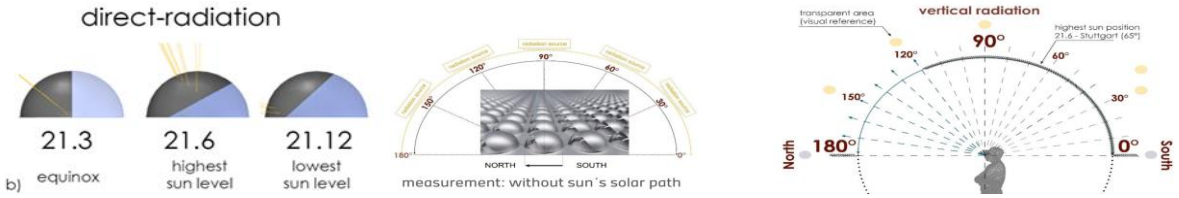


Figure 6: General considerations about incident angel (left and right) and final product (center)[11].

The influence of this method of shading was investigated with numerical simulations of a building in atrium configuration with TRNSYS. The geometrical model of the building is shown in Figure 7.

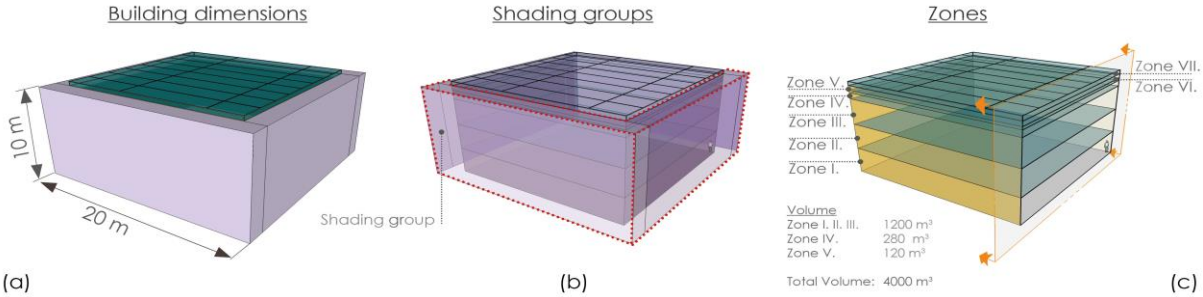


Figure 7: Geometrical model for the numerical investigation of a building in atrium configuration. (a) building dimensions, (b) shading groups, (c) internal zones

In the simulation the 3D-shaped and printed foil is integrated as middle layer into a three layer ETFE cushion. The comparison of some results of the numerical simulation with regard to relative energy demand are displayed in Figure 8.

The reference case for the comparison is the initial design of the 3D-shaped foil denoted as FMESG_Original. The overall relative energy demand of the final design denoted as FMESG_Optimiert is reduced compared to other shading solutions. This reduction in the overall energy demand is caused by a reduction in cooling energy demand while the heating energy demand does increase with the implementation of each shading solution.

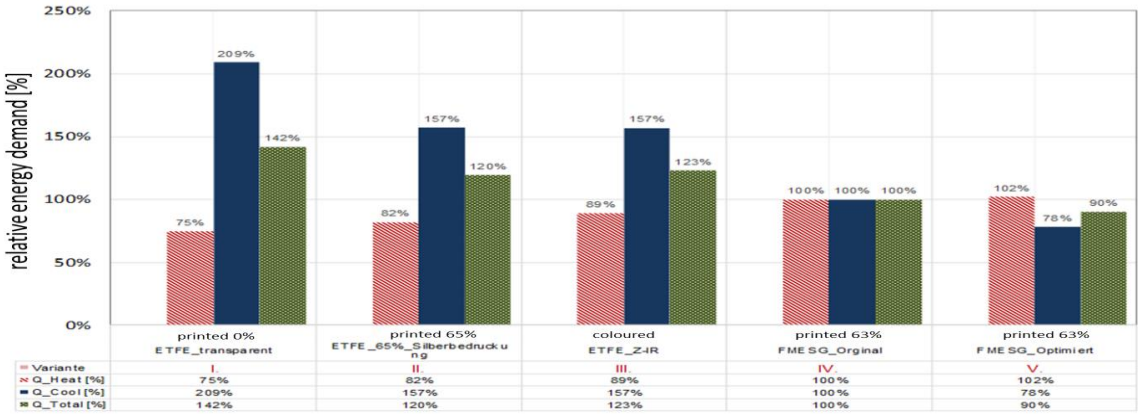


Figure 8: Influence of the shading solution with regard to energy demand in comparison with available printed foils as shading solutions [12].

Detailed information about the research is documented in the final report of the Project [12].

4.2 Follow-e2: Energy-saving functional coating of polymer materials for foil architecture

The project "Follow-e2" is funded by the German Federal Ministry of Education and Research. It started on March 01, 2017 and will end on August 31, 2019. Subject of the project is the refinement of transparent polymer films for use in architectural applications by vacuum deposition processes and rotogravure coating. An improvement of energy efficiency, sun protection and thermal comfort of film-based buildings e.g. by modifying emission characteristics of the surfaces is the goal of these measures. The project examines the manufacturing process from processing of the coated ETFE films to the actual cushions and up to the final installation on site, focusses on the development of coating systems according to these requirements and on the presentation of a repair system. Furthermore, a product portfolio for different building types, user scenarios and climate zones will be developed. Dynamic building simulations are used to compare the potential of functional coated foils with well-established products regarding energy savings. The architectural integration of typical assembly situations is regarded as well as constructional details.

The focus of the investigations done by HFT within the project lies on modelling the influence of the coated surfaces in ETFE fenestration elements on the energy demand within the building by numerical simulations. The two principle configurations for the application as heat retention and sun protection which have been investigated are depicted in Figure 9.

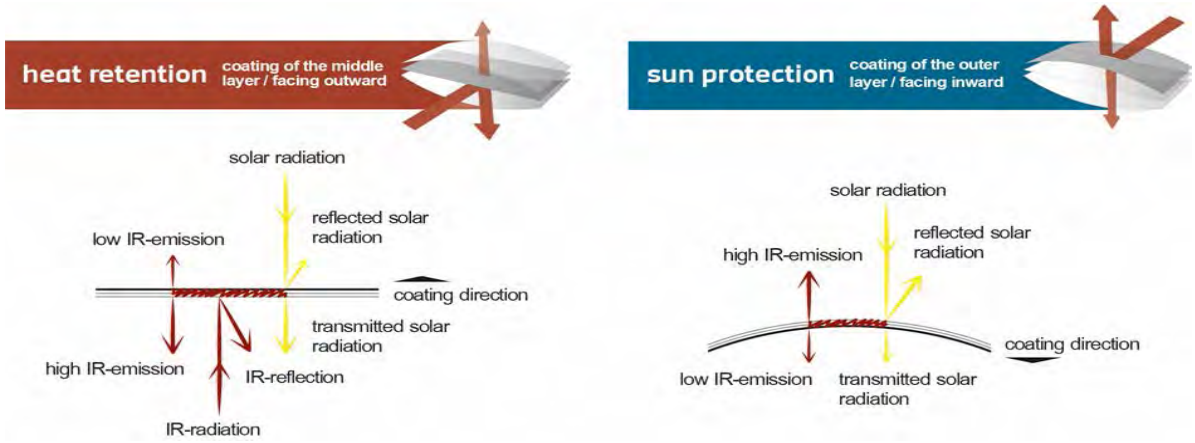


Figure 9: Principle sketch of heat transport for heat retention and sun protection configuration

The numerical simulations corresponding to these two cases were conducted with TRNSYS employing the building model introduced in section 2 equipped with a three layer ETFE cushion. The results of the simulation with regard to potential energy saving are given in Figure 10.

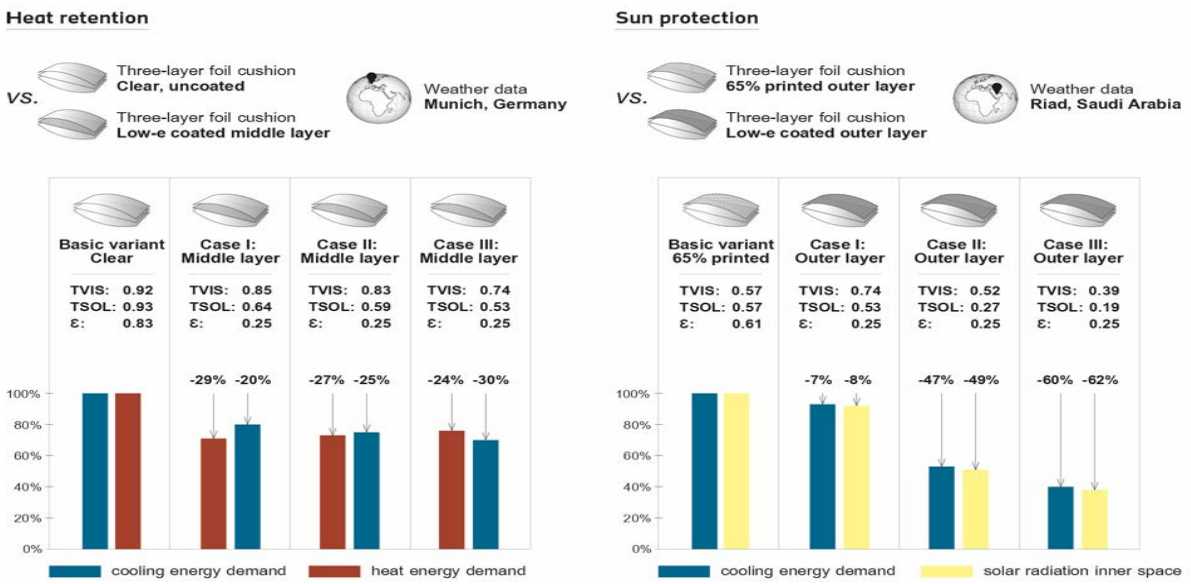


Figure 10: Relative energy saving potential determined by thermal simulations.

The simulation results show that the object of research low emission coated ETFE foil, in its application as a heat retention- as well as sun protection solution, can certainly offer energetic saving potentials.

For the energetic optimum of a heat retention solution, the transmissivity in the solar spectral range should be as high as possible. So the heating energy demand can be significantly compensated by solar heat gains. Conversely, the transmissivity as well as the emissivity in the long-wave IR-B and IR-C spectral range should be as low as possible in order to reduce the long-wave heat radiation through the building envelope surface or into the air chambers of the foil cushion adjacent to the outside air.

For the energetic optimum as a sun protection solution, it is important to keep the solar transmissivity as low as possible. The low-e film layer, which functions as a full-surface sun protection on the outer layer (low-e facing inward), has the advantage, in addition to the reduction of cooling energy demand, that the visual transmission is high and the view is therefore not disturbed significantly. Since transparent sun protection coatings with high color neutrality offer a high market potential, this property will be crucial in application.

4.3 FLEX-G: Smart buildings through innovative membrane roofs and façades

The cooperative research project FLEX-G started on June 1st, 2017 funded by the German Federal Ministry for Economic Affairs and Energy. Goal of the research project is to investigate technologies for manufacturing of translucent and transparent membrane roof and façade elements with integrated optoelectronic components. The focus lies on a switchable total energy transmittance, the so-called solar heat gain factor and on flexible solar cell integration to significantly contribute to both energy saving and power generation in buildings. One of the tasks of HFT Stuttgart in this Project is to investigate the effect of dynamic electrochromic shading solutions on the energy demand of buildings via numerical simulations.

The numerical simulations were conducted with TRNSYS on a number of different buildings and different electrochromic shading systems employing additional numerical tools like GenOpt for Optimization of the switching algorithm. For the sake of brevity only one building model and one shading system will be discussed here. The geometrical model used for building simulation introduced here is a generic box with dimensions of 3m x 3m x 3m equipped with a three layer ETFE cushion construction roof shown in Figure 11.

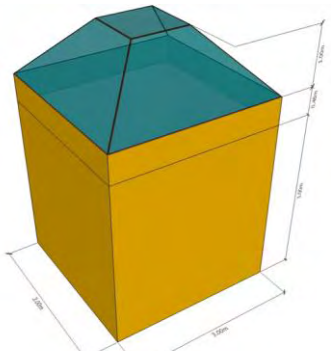


Figure 11: geometrical model of generic building model for the numerical simulation

Scheduled internal loads were implemented from occupants, devices, artificial lighting and natural air change. Heating and cooling were set up to provide a comfortable temperature range between 21°C and 26°C. A genetic optimization algorithm was employed to find the optimal shading parameters for minimal total energy demand and the optimal switching parameters for the electrochromic shading devices.

A schematic flow chart of the interaction of the employed numerical tools is given in Figure 12.

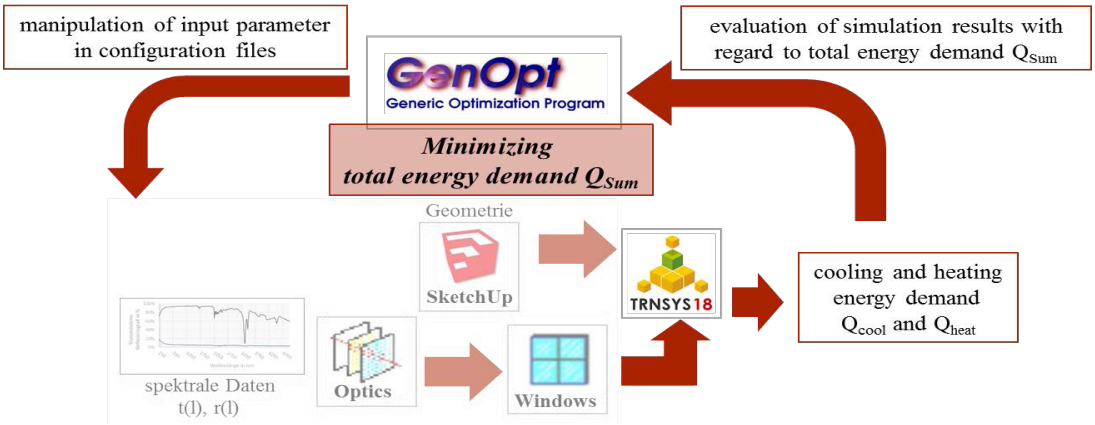


Figure 12: Flow chart of the numerical tools used for optimization

The optimization algorithm was coupled to the building simulation process with customized scripts to automatize and provide further flexibility in the optimization process. The results of a converged optimization calculation with optized switching parameters for each month for the generic building with the weather data from Stuttgart are shown in Figure 13.

The electrochromic shading system in the displayed calculation is a commercially available product from the german manufacturer ECONTROL on glass. The optical data for the simulation was generated from spectroscopic data provided by the manufacturer.

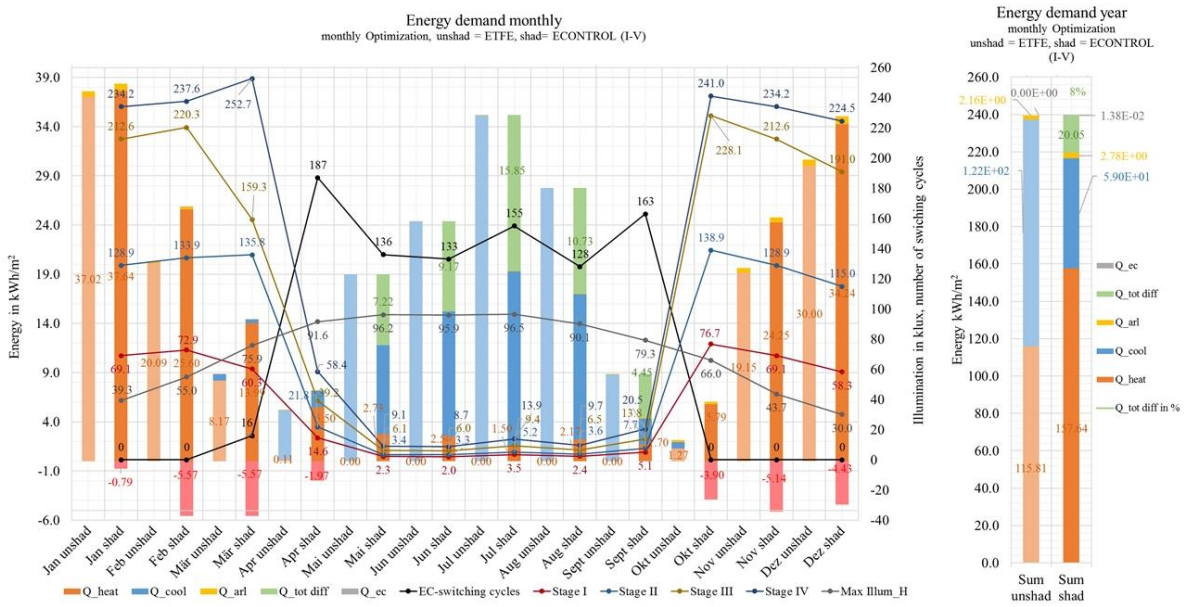


Figure 13: Results of optimization calculations of switchable electrochromic shading system with regard to energy demand in comparison with unshaded simulation

The overall yearly energy demand is reduced by 8%. The main source for the obtained reduction is a decrease in cooling energy demand during the hot timeperiods which is unfortunately partly compensated by an increased heating energy demand during cold timeperiods.

Calculations with a theoretical shading system yielded a potential reduction in energy demand by about 37% which seems to be the upper limit in the climatic situation in Stuttgart. Further investigations with different electrochromic shading systems on PET yielded a reduction in total energy demand of around 22%. The research on the translation of this technology to direct application on ETFE is not yet completed but calculations of first prototypical samples hint at a promising realization of the technology in applications for ETFE fenestration elements.

5. Conclusion

In the present work some general characteristics of the modeling of thermal behavior of ETFE fenestration elements were discussed to shed some light on the influences of modelling methods on the quality of numerical simulations and give solutions for the improvement of ETFE cushions toward an ideal fenestration system. The relationship between the degree of sophistication of the modelling of the thermal effect in terms of convective heat transfer and the quality of numerical results in terms of difference of calculated and measured temperature were shown. A principal feasibility of improvement of ETFE fenestration elements was shown within the validity of numerical investigations for three exemplary research projects dealing with the topic of static and dynamic modification of optical properties of ETFE material.

Acknowledgements

The authors would like to thank Mr. A. Kaufmann of Fraunhofer IBP for providing the measurement data of the experimental set up.

The projects "FMESG" *(funding reference 03ET1309F)* and "FLEX-G" *(funding reference 03ET1470A)* are funded by the German Federal Ministry for Economic Affairs and Energy (BMWI).

The project "Follow-e2" *(funding reference 03ET1468E)* is funded by the German Federal Ministry of Education and Research (BMBF).

Supported by:
Federal Ministry for Economic Affairs and Energy
Federal Ministry of Education and Research
on the basis of a decision by the German Bundestag

References

[1] A. Kaufmann, C. Mitterer, *Membrane im Bau - bauphysikalische Optimierung und neue Einsatzbereiche Kurztitel: OptiMA*, Fraunhofer IBP Selbstverlag, 2007.

[2] J. Cremers (Ed.), *Building Openings Construction Manual. Windows, Vents, Exterior Doors,* München: Detail, 2016.

[3] *ASTM G173-03*, *Standard Tables for Reference Solar Spectral Irradiances: Direct Normal and Hemispherical on 37° Tilted Surface*, ASTM International, West Conshohocken, PA, 2012.

[4] J. J. Vos, "Colorimetric and photometric properties of a 2-deg fundamental observer", *Color Research and Application*, vol. 3, pp. 125-128, 1978.

[5] M. Casini (Ed.), *Smart Buildings*, Woodhead Publishing, 2016.

[6] F. Antretter, *Thermal Transfer through Membrane Cushions Analyzed by Computational Fluid Dynamics*, FHG-IPB, Holzkirchen, 2008.

[7] J. Hu, W. Chen, Z. Qiu, B. Zhao, J. Zhou, Y. Qu, "Thermal performances of ETFE cushion roof integrated amorphous silicon photovoltaic", *Energy Conversion and Management*, vol. 106, pp. 1201-1211, 2015.

[8] J.-F. Flor, D. Liu, Y. Sun, P. Beccarelli, J. Chilton, Y. Wu, "Optical aspects and energy performance of switchable ethylene-tetrafluoroethylene (ETFE) foil cushions", *Applied Energy*, vol. 229, pp 335-351, 2018.

[9] J. Cremers, H. Marx, "Improved Daylight Comfort by a New 3D-Foil That Allows to Trade off Solar Gains and Light Individually", in *Proceedings Structural Membranes 2017, Munich, Germany, October 09-11, 2017* pp.133-140.

[10] J. Cremers, H. Marx, "Assessment of building physical aspects of a new angular selective 3d-prototype foil (ETFE)", *in Proceedings of TensiNet Symposium 2019, Milano, Italy, June 03-05, 2019,* pp. 592-601.

[11] J. Cremers, H. Marx, "3D-ETFE: Development and evaluation of a new printed and spatially transformed foil improving shading, light quality, thermal comfort and energy demand for membrane cushion structures", *Energy Procedia*, vol. 122, pp. 115–120, 2017.

[12] .H. Marx, *FMESG: 'Functionalised membrane structures for energy-efficient retrofitting of buildings', Partial project: Building physics and architectural concepts*, Final report, Stuttgart 2018.

Proceedings of the IASS Annual Symposium 2019 - Structural Membranes 2019
Form and Force
7-10 October 2019, Barcelona, Spain
C. Lázaro, K.-U. Bletzinger, E. Oñate (eds.)

A comparative study on the optimisation-based form-finding of tensile membrane structures

Allan L. MARBANIANG[a], Subhrajit DUTTA[b], Siddhartha GHOSH[a*]

[a] Structural Safety, Risk & Reliability Lab, Dept. of Civil Engineering,
Indian Institute of Technology Bombay, Mumbai, India

[b] Dept. of Civil Engineering, National Institute of Technology Silchar, Silchar, India

[*] Corresponding author, *sghosh@civil.iitb.ac.in*

Abstract

Form-finding of tensile membrane structures (TMS) is an inverse problem in mechanics, wherein the (primary) form/shape of a structure needs to be found based on the applied loads and boundary conditions. Several numerical methods have been developed and employed for the form-finding of TMS. However, some important characteristics of such algorithms, such as robustness and computation cost, – needs to be investigated further for arriving at an efficient form-finding solution. In this study, the form-finding of TMS is formulated as an area minimisation problem. Two nature-based heuristic algorithms, (i) particle swarm optimisation (PSO) and (ii) ant colony optimisation (ACO), are used to solve this optimisation problem. Form-finding solutions obtained using these heuristic algorithms are compared with the results from the well-known dynamic relaxation (DR) algorithm, in terms of the important algorithm efficiency characteristics mentioned earlier. The proposed methods are tested on two common TMS types. Both the heuristic methods proposed are found to be similarly efficient as DR.

Keywords: tensile membrane, form-finding, heuristic algorithm, dynamic relaxation, optimisation.

1 Introduction

The attractive nature of lightweight and efficient systems makes tensile membrane structures (TMS) an appealing solution for roofing different types of structures. The shape that gives TMS its stability is not known beforehand and requires what is known as *form-finding*. This procedure involves finding the initial equilibrium shape for a particular set of prestress forces and boundary conditions. It is recommended that in the stable shape of TMS, the applied prestress should be constant throughout the surface, resulting in a minimal shape. This attribute reduces the occurrence of wrinkles and local stress concentrations. However, minimal shapes are not attainable for all boundary conditions. Certain boundary conditions do not allow the formation of a minimal surface and may result in a neck off [1]. Physical methods like soap films can be used to model minimal shapes. The soap film models are ideal minimal surface solutions obtained by minimising the surface area [2]. Over the last few decades, computational methods have become more popular than physical methods due to their accuracy, low cost, and

Copyright © 2019 by Allan L. Marbaniang, Subhrajit Dutta & Siddhartha Ghosh
Published by the International Association for Shell and Spatial Structures (IASS) with permission.

flexibility to include different analysis methods. Veenendaal and Block [3] gave an overall comparison of different types of computational methods within the same computational framework for unloaded self stressed nets. The different methods were categorized into stiffness matrix methods [4, 5], geometric stiffness methods [6, 7] and dynamic equilibrium methods [8]. Some of the most popular methods used today are the force density method, transient stiffness method and dynamic relaxation (DR) method [2].
Bletzinger and Ramm [7] showed that for minimal shapes having isotropic prestress, the minimum (potential) energy state corresponds to a minimal surface area. Minimal shapes were also found by minimizing the area functional formulated as an optimisation problem [9, 10]. A large number of optimisation methods are available, which can be classified as being gradient based or non-gradient based. Most of the non-gradient heuristic methods – for example genetic algorithm [11], particle swarm optimisation (PSO) [12] or ant colony optimisation (ACO) [13] – are inspired by natural processes that have evolved successfully over time. A section of these heuristic methods is dependent on the "social interaction" within the population, such as PSO and ACO. These methods have shown to be flexible and successful at solving different types of optimisation problems that are multi-modal and having different types of constraints.
The objective of this paper is to formulate the form-finding procedure for a minimal surface as an area minimisation problem, which inherently minimises the potential energy for a minimal surface. Two heuristic methods, PSO and $\text{ACO}_{\mathbb{R}}$ (this is the extension of ACO to a continuous design space) are used to minimise the area functional for different common TMS shapes, and are compared with DR. Finally, comments on the efficiency and robustness of the methods are made.

2 Form-finding methodology

2.1 Formulation

The membrane surface is discretised using constant-strain triangular elements that are capable of accurately modelling the membrane fabric and its behaviour [2]. Finding a minimal shape for a given mesh topology corresponds to the minimum area of the discretising triangles between neighbouring points/nodes [9], and can be formulated as

$$\underset{\mathbf{x}}{\text{minimise}}\ A(\mathbf{x}) = \sum_{e=1}^{E} A_e \tag{1}$$

where, the objective function is the total surface area $A(\mathbf{x})$ of E elements, A_e is the area of element e, and the design variable $\mathbf{x}$ is the vector of all the free nodal coordinates in the global coordinate system (X, Y, Z). The problem is to find a solution for $\mathbf{x}$ which minimises the area ($\text{argmin}\ A(\mathbf{x})$) for a given surface topology constrained to a predefined boundary support and configuration in space. The heuristic optimisers, PSO and $\text{ACO}_{\mathbb{R}}$ are used to solve this optimisation problem. The area of each triangular element having side lengths l_i, $i = 1, 2, 3$, is found using Heron's equation:

$$A_e = \sqrt{s(s - l_1)(s - l_2)(s - l_3)} \tag{2}$$

where s is the semi-perimeter, $s = (l_1 + l_2 + l_3)/2$.
The residual force R_i at the ith node is found from the side forces contributed by all the connected elements. The side force along the ith side of an element for a minimal surface can

be found as [1]

$$T_i = \frac{\sigma l_i t}{2 \tan \alpha_i} \qquad i = 1, 2, 3 \tag{3}$$

where σ is the target prestress, t is the thickness and α_i is the angle between the other two sides.

2.2 Particle swarm optimisation

PSO is based on groups of swarms in nature like flocks of birds. A swarm consists of particles, with each particle capable of taking a position in the design space and forming a solution. Each particle contains the knowledge of the best global solution (*gbest*), ($\mathbf{p}_k^g$), found by the swarm, and the best position (*pbest*), ($\mathbf{p}_k$), found at the kth iteration. An update to the position of the ith particle at iteration $k+1$ is obtained by a velocity vector $\mathbf{v}$:

$$\mathbf{x}_{k+1}^i = \mathbf{x}_k^i + \mathbf{v}_{k+1}^i \Delta t \tag{4}$$

$$\mathbf{v}_{k+1}^i = w\mathbf{v}_k^i + c_1 r_1 \frac{(\mathbf{p}_k^i - \mathbf{x}_k^i)}{\Delta t} + c_2 r_2 \frac{(\mathbf{p}_k^g - \mathbf{x}_k^i)}{\Delta t} \tag{5}$$

where, $\mathbf{x}_{k+1}^i$ and $\mathbf{x}_k^i$ are the updated and current positions, $\mathbf{v}_{k+1}^i$ and $\mathbf{v}_k^i$ are the updated and current velocities, w is the inertia weight parameter which can be constant or varying linearly, c_1 and c_2 are the "cognitive" and "social" parameters, r_1 and r_2 are random numbers between 0 and 1 ($r_1, r_2 \sim \mathcal{U}(0,1)$), Δt is the time step, $\mathbf{p}_k^i$ is the current best position of particle i and $\mathbf{p}_k^g$ is the current best position of the whole swarm. Each particle is influenced by the importance given to the information gathered by itself (c_1 and $\mathbf{p}_k$) and the whole swarm (c_2 and $\mathbf{p}_k^g$). A schematic diagram of the method between the iterations k and $k+1$ is shown in Figure 1.

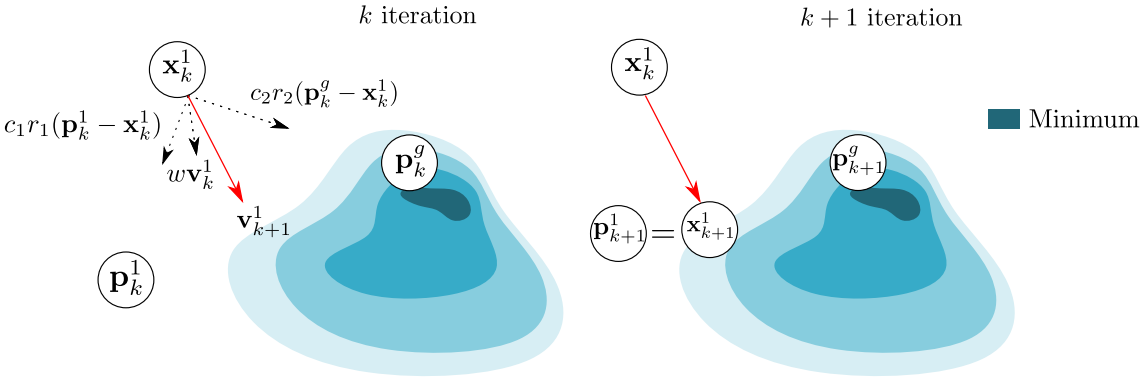


Figure 1: Schematic of PSO between iterations k and $k+1$, for particle $\mathbf{x}^1$

2.3 Ant colony optimisation

ACO derives its inspiration from how ants find the best path to a food source by leaving "pheromone trails". Increasing the pheromone levels of a trail increases the probability of it being chosen. An "evaporation phase" then reduces the pheromone levels in all the trails to promote exploration. ACO was extended to continuous domains ($\text{ACO}_{\mathbb{R}}$) by replacing discrete probability distributions with probability density functions (PDFs). Different solutions are stored in a solution archive S of size k (Figure 2). The pheromone updating and evaporation are performed by ranking all the different solutions in S and removing the worst solutions after

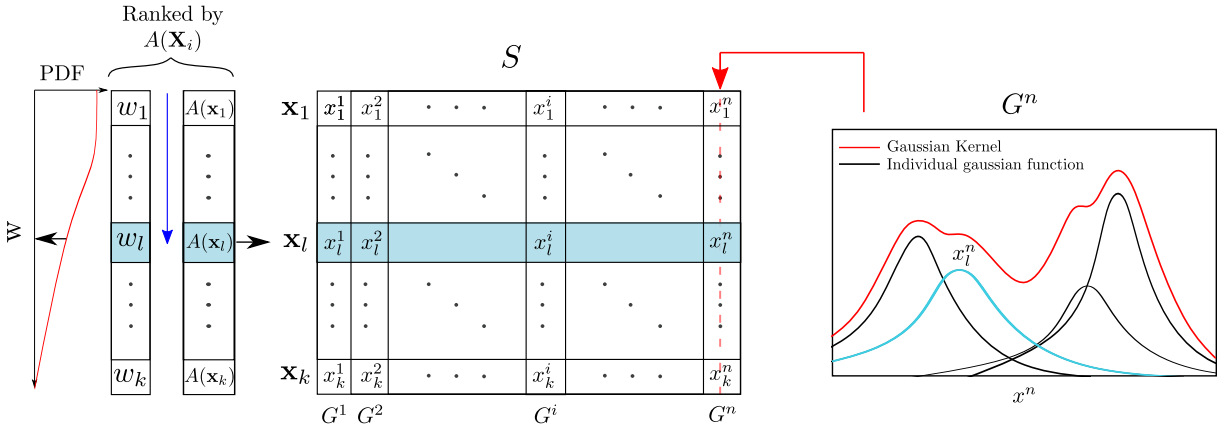


Figure 2: Schematic of $\text{ACO}_{\mathbb{R}}$ with solution archive S and sampling process

every iteration. Each solution $\mathbf{x}_l$ has an associated weight w_l based on the fitness of the objective function $A(\mathbf{x}_l)$, given as

$$w_l = \frac{1}{qk\sqrt{2\pi}} \exp\left[-\frac{(l-1)^2}{2(qk)^2}\right] \tag{6}$$

where, q is a parameter that controls the exploration of different solutions. When q is small, the best ranked solutions are preferred. Each design variable, over multiple solutions, is described by a Gaussian kernel G^i comprising of separate Gaussian functions (g_l^i):

$$G^i(x) = \sum_{l=1}^{k} w_l g_l^i(x) = \sum_{l=1}^{k} w_l \frac{1}{\sigma_l^i\sqrt{2\pi}} \exp\left[-\frac{(x_l^i - \mu_l^i)^2}{2(\sigma_l^i)^2}\right] \qquad i = 1, ..., n \tag{7}$$

In the first stage, an ant chooses a solution $\mathbf{x}_l$ from the solution archive based on its rank and subsequent probability of selection. In the next phase, for the ant based construction of each design variable x_l^i, an ant samples a value from the Gaussian kernel. This sampling is based on the mean μ_l^i and the standard deviation σ_l^i at each construction stage. For all the solutions, the values of each variable x_l^i in the solution archive becomes the value of μ_l^i. The σ_l^i for each variable is found from the average distance of the chosen solution $\mathbf{x}_l$ from the other solutions:

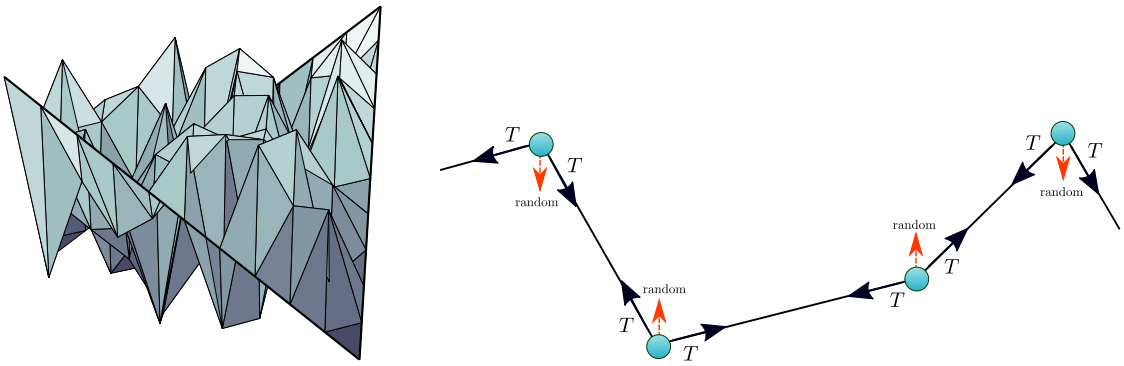
$$\sigma_l^i = \xi \sum_{e=1}^{k} \frac{|x_e^i - x_l^i|}{k-1} \tag{8}$$

where ξ has an evaporating effect and it controls how quickly the algorithm converges. A larger value leads to slower convergence and greater exploration. An iteration is completed when all the ants have constructed a feasible solution. The number of ants (N) add their solution to the solution archive, which further gets ranked, sorted and trimmed.

2.4 Dynamic relaxation method

DR is a popular method where the structural system oscillates towards its equilibrium state (under damping) until the residuals at all the nodes are close to zero. The mass used for the nodes are pseudo in nature while the damping can be viscous or kinetic. The equation of motion of an undamped system for the ith node along direction $j = (X, Y, Z)$ at time t is

$$R_{ij}^t = M_{ij}\dot{v}_{ij}^t \tag{9}$$



(a) (b)

Figure 3: (a) Geometric noise; (b) Random search in the direction of residual

where, R_{ij}^t is the residual force, due to external and member forces, M_{ij} is the assumed nodal lumped mass and $\dot{v}_{ij}^t$ is the acceleration. Using a central difference scheme for $\dot{v}_{ij}^t$, the updated velocity v_{ij}^t and geometry x_{ij}^t in the next time increment are given as

$$v_{ij}{}^{t+\Delta t/2} = v_{ij}{}^{t-\Delta t/2} + \frac{R_{ij}^t \Delta t}{M_{ij}} \tag{10}$$

$$x_{ij}{}^{t+\Delta t} = x_{ij}{}^{t} + \Delta t \cdot v_{ij}{}^{t+\Delta t/2} \tag{11}$$

where x_{ij}^t and $x_{ij}^{t+\Delta t}$ are the current and updated position of the nodes and Δt is the assumed time step. Kinetic damping is applied to the system to dampen the system towards its equilibrium.

2.5 Approach for heuristic optimisation-based form-finding

In DR, the position of each node x_{ij} is updated, depending on the value and direction of v_{ij} and R_{ij}. This, performed iteratively over the whole system, minimises the residual forces at all the nodes. While using the heuristic methods for minimising the total surface area, each free node is a design variable having a design space within the range of the fixed boundaries. This causes a considerable amount of geometric noise as the heuristic method randomly generates displacements for each free node. This can lead to non-convergence as shown in Figure 3(a). This issue is avoided by using the direction of R_{ij} as a basis of guiding the random displacements. Both PSO and $\text{ACO}_{\mathbb{R}}$ – while updating or sampling a value for a design variable – do so only in the direction of the residual as seen in Figure 3(b). This implementation for both the methods, however, is not similar due to the difference in their basic methodology. In PSO, the particles are used to find the best displacement in the direction of the residual from a reference geometry, which gets updated over iterations. In $\text{ACO}_{\mathbb{R}}$, each variable construction within a solution in the archive does so in the direction of the residual corresponding to that solution.

3 Study problems and parameters

A case study is performed on two different membrane shapes that are frame supported. The first example is a "Scherk" surface whose analytical expression for the minimal surface is given as [2]

$$z = \frac{1}{k}[\ln(\cos ky) - \ln(\cos kx)] + c \tag{12}$$

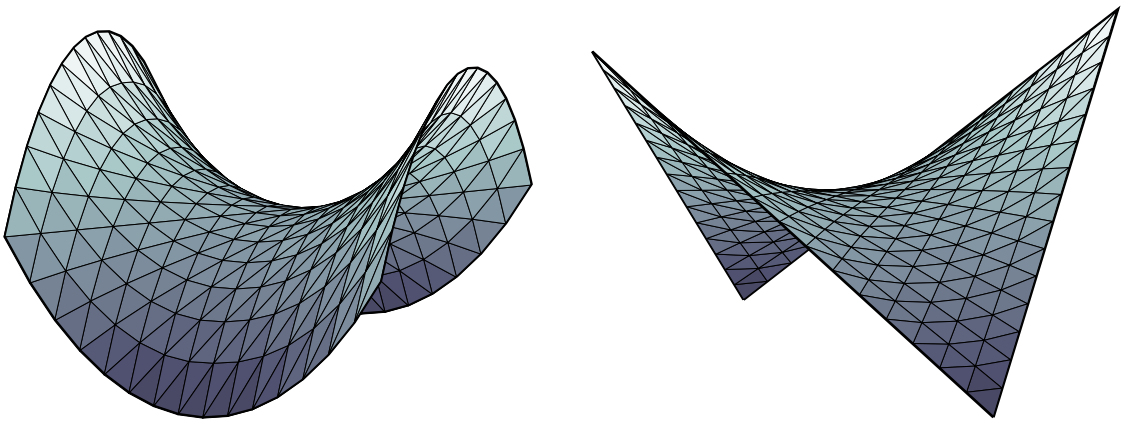
where the assumed values for x and y are in the range [-0.8, 0.8]. k and c are taken equal to 1 and 0, respectively. The nodes on the perimeter (outer boundary) are firstly found using the expression and constrained in all directions, while the inner nodes are free to move. The second example is performed with another frame supported structure, simply denoted as "saddle", with width and length taken as 6 m. The height of both the high points relative to the lower vertices is 2 m. Both TMS shapes have a have an uniformly applied initial prestress of 3 kN/m along the surface. Form-finding for both TMS are performed using PSO, $\text{ACO}_{\mathbb{R}}$ and DR.
In PSO, the values of c_1 and c_2 are taken as 2 and 1, respectively. A linear varying weight is used with $w_{\min} = 0.4$ and $w_{\max} = 0.9$. In $\text{ACO}_{\mathbb{R}}$, since correlation is not considered, the archive size need not be larger than the number of divisions [13]. The optimum parameter values used are selected using an experimental design, with the final adopted values of $q = 0.001$, $\xi = 0.6$, $k = 20$ and $N = 1$. In DR, the main parameters available are the time step, initial shape and mass. The damping used is kinetic in nature with $\Delta t = 1$ and mass, $M_{i(x,y,z)} = \max(M_{ix}, M_{iy}, M_{iz})$. The mass is found from the stiffness at the ith node contributed by the surrounding triangular elements [1]. The free nodes are initially placed at the mid-height for both the examples.
Convergence for the heuristic methods is achieved when the incremental change in the total area remains less than 0.001% for 25 successive iterations. The optimisation convergence criterion is based on preliminary comparisons with the (robustness of the) heuristic solution for the chosen parameters. The stopping criterion for DR is the (absolute) residual force values being less than a tolerance value of 0.001.

4 Results

The form-finding results from PSO and $\text{ACO}_{\mathbb{R}}$ are presented, following the methodology explained in the previous sections. Sample final form-found shapes for the Scherk and the saddle surface are shown in Figure 4. The Scherk surface allows for a check on the accuracy of the methods using Equation 12. Comparing the difference in the Z coordinate with the analytical solution, PSO and $\text{ACO}_{\mathbb{R}}$ showed a maximum error of 0.179% and 0.183% respectively.
The heuristic methods are also compared with DR in terms of their efficiency. On the basis of the area, a comparison on the computational time among all three methods is given in Figure 5. It can be seen that heuristic methods are slower than DR for the Scherk surface, while for the saddle $\text{ACO}_{\mathbb{R}}$ is able to converge to a minimal area faster followed by PSO and DR, respectively. DR however, converges with lower final residual forces. It can also be seen that both the heuristic methods perform satisfactorily when compared to DR in terms of solution accuracy. The maximum nodal residuals from all the nodes after form-finding using the heuristic methods are presented in Table 1. The final residual forces obtained are however, higher than the usual tolerance limit (0.001 kN), which may be improved by incorporating the residual as a constraint to the objective function and improving the local search strategies near the optimal point.

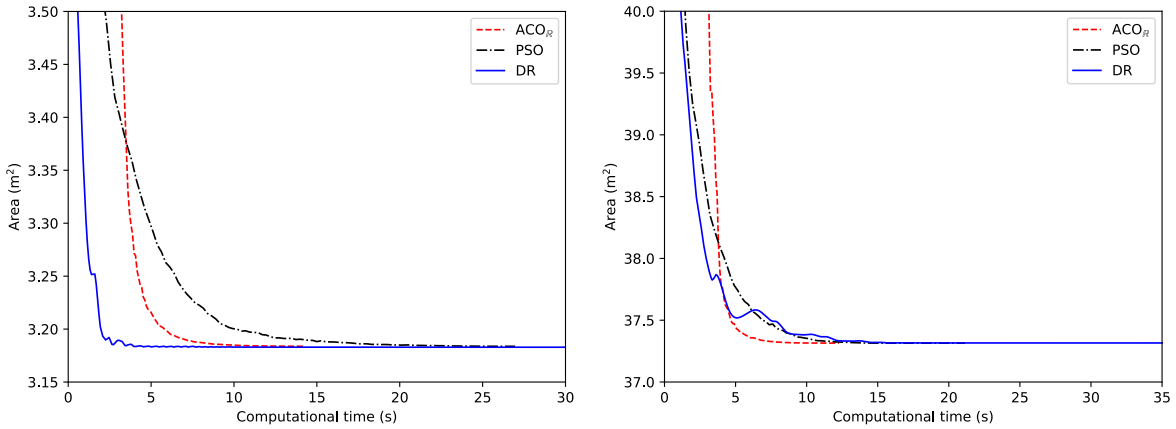
Table 1: Maximum residual force using heuristic methods

	Scherk		saddle	
	PSO	$\text{ACO}_{\mathbb{R}}$	PSO	$\text{ACO}_{\mathbb{R}}$
R_x (kN)	0.053	0.054	0.060	0.058
R_y (kN)	0.055	0.055	0.060	0.058
R_z (kN)	0.005	0.005	0.070	0.063



(a) (b)

Figure 4: Final shapes for (a) the Scherk surface (based on PSO) and (b) the saddle surface (based on $ACO_{\mathbb{R}}$)



(a) (b)

Figure 5: Area vs. computational time plot for (a) the Scherk surface and (b) the saddle surface

5 Conclusions

In this paper, the form-finding of a TMS is formulated as a stochastic optimisation problem where the total surface area is minimised. Two heuristic methods, namely PSO and $ACO_{\mathbb{R}}$ are used to find the minimal area of two frame supported TMS, discretised using triangular elements. Improvement to the heuristic methods is made by using the direction of the residuals to guide the random movements. Both the methods are compared with DR showing a satisfactory speed in convergence for both structures indicating their robustness. It is found that even though the minimal area is reached, the maximum nodal residual forces are higher than the usually adopted tolerance limit. This may be improved by using the residual as a constraint indicating a scope for enhancing the method.

This is a work in progress on the application of heuristic optimisation algorithms for the form-finding of TMS. The proposed approach also needs to be tested for other common TMS shapes, including cable supported TMS. Reducing the number of design variables by adopting some parameterised function or NURBS can also be an area for improvement.

References

[1] B. H. V. Topping and P. Iványi, *Computer Aided Design of Cable Membrane Structures*. Saxe-Coburg Publications, 2007.

[2] W. J. Lewis, *Tension Structures - Form and Behaviour*. London: Thomas Telford Publishing, 2003.

[3] D. Veenendaal and P. Block, "An overview and comparison of structural form finding methods for general networks," *International Journal of Solids and Structures*, vol. 49, no. 26, pp. 3741–3753, 2012.

[4] J. H. Argyris, T. Angelopoulos, and B. Bichat, "A general method for the shape finding of lightweight tension structures," *Computer Methods in Applied Mechanics and Engineering*, vol. 3, no. 1, pp. 135–149, 1974.

[5] B. Tabarrok and Z. Qin, "Nonlinear analysis of tension structures," *Computers and Structures*, vol. 45, no. 5, pp. 973–984, 1992.

[6] H. J. Schek, "The force density method for form finding and computation of general networks," *Computer Methods in Applied Mechanics and Engineering*, vol. 3, no. 1, pp. 115–134, 1974.

[7] K.-U. Bletzinger and E. Ramm, "A general finite element approach to the form finding of tensile structures by the updated reference strategy," *International Journal of Space structures*, vol. 14, no. 2, pp. 131–145, 1999.

[8] M. R. Barnes, "Form finding and analysis of tension structures by dynamic relaxation," *International Journal of Space Structures*, vol. 14, no. 2, pp. 89–104, 1999.

[9] L. Gründig, "Minimal surfaces for finding forms of structural membranes," *Computers and Structures*, vol. 30, no. 3, pp. 679 – 683, 1988.

[10] M. Shimoda and K. Yamane, "A numerical form-finding method for the minimal surface of membrane structures," *Structural and Multidisciplinary Optimization*, vol. 51, no. 2, pp. 333–345, 2015.

[11] D.E. Goldberg, *Genetic Algorithms in Search, Optimization and Machine Learning*. Boston: Addison-Wesley Longman Publishing Co., Inc., 1989.

[12] J. Kennedy and R. Eberhart, "Particle swarm optimization," in *Proceedings of ICNN'95 - International Conference on Neural Networks*, vol. 4, pp. 1942 – 1948, Nov. 1995.

[13] K. Socha and M. Dorigo, "Ant colony optimization for continuous domains," *European Journal of Operational Research*, vol. 185, pp. 1155–1173, 2008.

Proceedings of the IASS Annual Symposium 2019 – Structural Membranes 2019
Form and Force
7 – 10 October 2019, Barcelona, Spain
C. Lázaro, K.-U. Bletzinger, E. Oñate (eds.)

A new form-finding method for shell structures based on BESO algorithm

Xin YAN[a,b], Ding Wen BAO[a], Kun CAI[a], Yu Fang ZHOU[b,c], Yi Min XIE[a,d,*]

[a,*] Centre for Innovative Structures and Materials, School of Engineering, RMIT University, Melbourne, 3001, Australia
mike.xie@rmit.edu.au
[b] Centre of Architecture Research and Design, University of Chinese Academy of Sciences, Beijing, 100190, China
[c] School of Architecture, Central Academy of Fine Arts Beijing, 100102, China
[d] XIE Archi-Structure Design, Shanghai, 200092, China

Abstract

Due to high efficiency and elegant geometry, shell structures are widely used in architectural and structural designs. This paper presents a new numerical form-finding method for the design of shell structures based on the bi-directional evolutionary structural optimization (BESO) algorithm. This technique can perform topology optimization to find new forms of shell structures with high structural performance, elegant geometries, and other features that are of interest to architects and engineers. Diverse designs from the optimization process as a result of using different parameters in BESO are also discussed. Finally, the innovative results produced by the BESO method are compared with a well-known shell structure, the Palazzetto dello Sport, designed by Nervi.

Keywords: BESO, shell structure, topology optimization, form-finding

1. Introduction

With the fast development of computational technics, shell structure with complex geometry has made an appeal to architects because of its characteristic of high structural efficiency and more elegant shape potentials. Many engineers and architects have engaged into researches of shell form-finding methods, e.g. force density method [1] , thrust network analysis [2], dynamic analysis [3], particle spring system [4] and so on. Instead of concerning the continuum shell surface, topology optimization method pays more attention to topology relationship of shell surface, which means that the functional cavities, e.g. windows and air outlets, can be considered as well as structural performance in the form-finding process. And the result is not only a beautiful pattern but also a structural design diagram for us to clarify where the frameworks should be denser and thicker or vice versa.

The aim of topology optimization is to find a form with the maximal structural performance under a certain constraints. Several topology optimization methods have been developed over the past three decades, such as evolutionary structural optimization (ESO) and bi-directional evolutionary structural optimization (BESO) [5,6], the homogenization method [7,8], the solid isotropic material with penalization (SIMP) method [9,10] and the level-set method [11,12]. There was one recent study which applied the homogenization method and obtained interesting topologies of shell domes [13]. In the present work, we develop a new form-finding method for shell structures based on the BESO algorithm by taking advantage of its simplicity and effectiveness.

Copyright © 2019 by Xin YAN, Ding Wen BAO, Kun CAI, Yu Fang ZHOU, Yi Min XIE
Published by the International Association for Shell and Spatial Structures (IASS) with permission.

2. Methodology

To realize the shell structure design, BESO method is introduced to optimize the shell structurally. In the BESO method, the basic problem can be described mathematically as follows:

$$\min C(\boldsymbol{X}) = \frac{1}{2}\boldsymbol{U}^T\boldsymbol{K}\boldsymbol{U} = \frac{1}{2}\sum_{i=1}^{N} x_i^p \boldsymbol{u}_i^T \boldsymbol{k}_i \boldsymbol{u}_i \tag{1}$$

$$\text{Subject to: } V(\boldsymbol{X}) = \sum_{i=1}^{N} x_i v_i \le V^* \tag{2}$$

in which C, $\boldsymbol{U}$, $\boldsymbol{K}$, V^* are the objective function (compliance), displacement vector, global stiffness matrix and the objective volumn, respectively. The terms v_i, x_i, $\boldsymbol{k}_i$ and $\boldsymbol{u}_i$ are the volumn, design variable, stiffness matrix and nodal displacement vector for i th element. Particularly, it's necessary to point out that there are two alternative values for x_i in BESO, which are 1 for solid element or prescribed value x_{min} for void element.

For stiffness optimization, the sensitivity α_i for i th element, which is the criterion for desgin variable x_i, can be calculated as the gradient of compliance with respect to the design variable [14],

$$\frac{\partial C(\boldsymbol{X})}{\partial x_i} = -\frac{1}{2} p x_i^{p-1} \boldsymbol{u}_i^T \boldsymbol{k}_i \boldsymbol{u}_i \tag{3}$$

$$\alpha_i = -\frac{1}{p}\frac{\partial C}{\partial x_i} = \begin{cases} \dfrac{1}{2}\boldsymbol{u}_i^T \boldsymbol{k}_i \boldsymbol{u}_i & \text{when } x_i = 1 \\ \dfrac{x_{\min}^{p-1}}{2}\boldsymbol{u}_i^T \boldsymbol{k}_i \boldsymbol{u}_i & \text{when } x_i = x_{\min} \end{cases} \tag{4}$$

And when the penalty coefficient p tends to infinity, the sensitivity number α_i becomes the one in hard-kill BESO method[14],

$$\alpha_i = -\frac{1}{p}\frac{\partial C}{\partial x_i} = \begin{cases} \dfrac{1}{2}\boldsymbol{u}_i^T \boldsymbol{k}_i \boldsymbol{u}_i & \text{when } x_i = 1 \\ 0 & \text{when } x_i = x_{\min} = 0 \end{cases} \tag{5}$$

The above sensitivity is usually modified to solve the mesh-dependent problem [15,16], using a filtering scheme:

$$\widetilde{\alpha}_i = \frac{\sum_{j=1}^{N} w_{ij}\alpha_j}{\sum_{j=1}^{N} w_{ij}} \tag{6}$$

$$w_{ij} = \max(0, r_f - d_{ij}) \tag{7}$$

in which d_{ij} is the distance between the center of the j th element and the i th element and r_f, α_j is the filter radius and the original sensitivity of the j th element.

To achieve a convergent solution, another historical average of $\overline{\alpha}_i$ in different iterations is introduced [17]:

$$\overline{\alpha}_i = \frac{\widetilde{\alpha}_i^{(n)} + \widetilde{\alpha}_i^{(n-1)}}{2} \tag{8}$$

In the BESO method, the element sensitivities are ranked in each iteration to determine a threshold with target volumn of next iteration, $V^{(n)}$, which is defined based on the current volumn $V^{(n-1)}$ and the evolutionary ratio δ.

$$V^{(n)} = V^{(n-1)}(1-\delta) \tag{9}$$

The threshold can be used to evaluate if the element shall be changed in a such way that if one solid element's sensitivity is lower than the threshold, its design variable will be switch from 1 to x_{min}, and the design variable of a void element will be changed from x_{min} to 1 as well if its sensitivity is higher than the threshold.

3. Shell form-finding based on BESO method

In this work, a shell structure composed of shell elements is introduced (Fig. 1). The objective of the problem is to find the optimal topology of the structure withstanding its self-weight. The whole structure's radius in the xy plane is 30 m, and the distance from the top point to xy plane is 4.5 m. The thickness of shell element is 0.3 m. The following material properies are assumed: Young's modulus 200 GPa, Poisson's ratio 0.3 and the desity 7800 kg/m^3. Considering symmetric geometry and boundary conditions of the structure, only a one-eighth part with an angle of 45° is analysed, and 3 points at the bottom boundary are fixed (Fig. 1). The total number of mesh nodes and elements are 16,396 and 32,230, respectively.

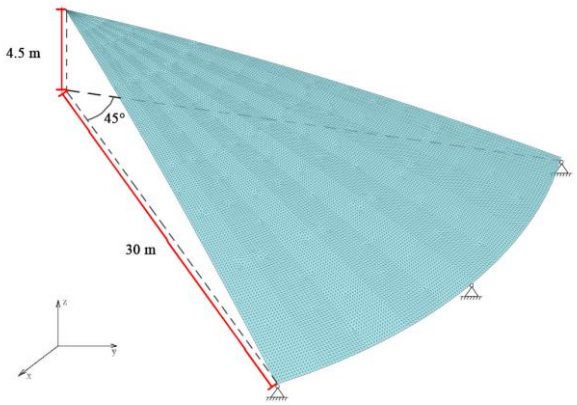


Figure 1: The shell model and boundary condition

To achieve diverse designs from the topology optimization process, several controlled trials with different BESO parameters are set up. The parameters for BESO algorithm are as evolution ratio (*ER*) = 6%, 4%, 2%, filter radius (*FR*) of 30 mm (3 times of the element size) and volume fraction (*VF*) = 30%. The results are given below (Figs. 2-4).

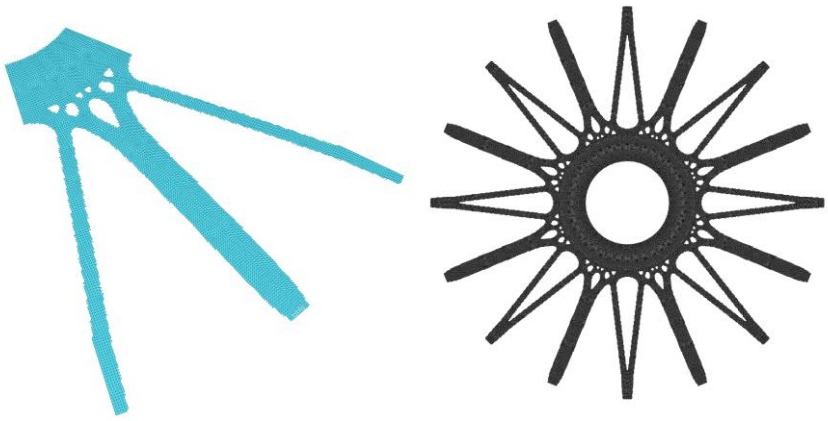


Figure 2: The BESO result of shell structure under self-weight load (*ER* =6%, *FR* =30 mm, *VF* =30%)

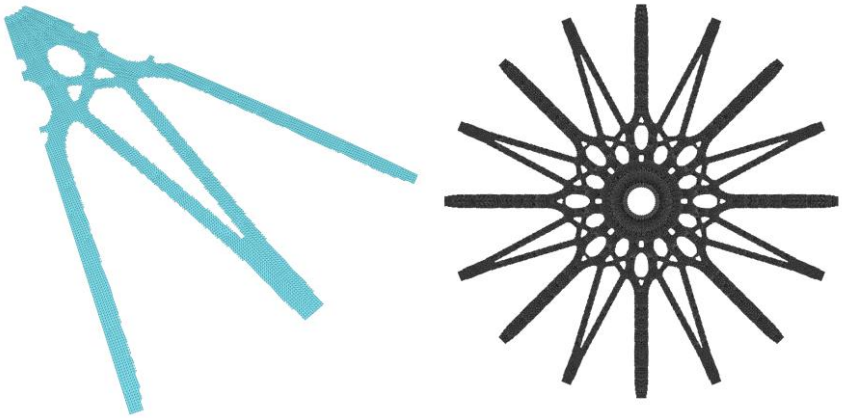


Figure 3: The BESO result of shell structure under self-weight load (*ER* =4%, *FR* =30 mm, *VF* =30%)

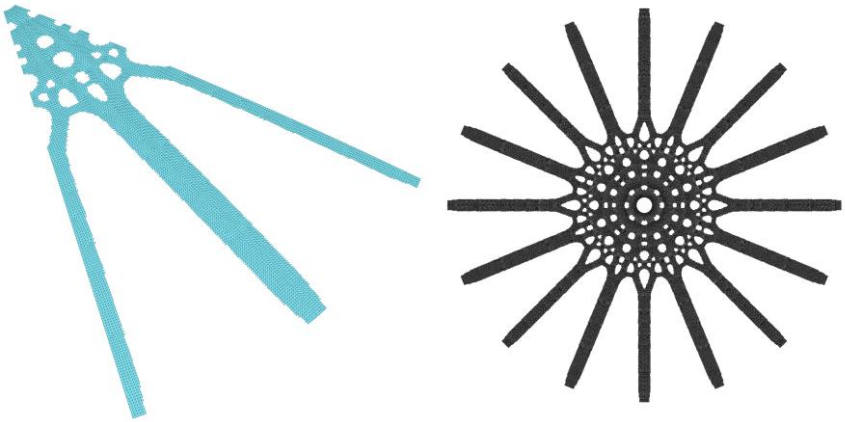


Figure 4: The BESO result of shell structure under self-weight load (*ER* =2%, *FR* =30 mm, *VF* =30%)

From the above BESO results, although the forms vary slightly, the differences of structural stiffness among them are just within 0.4%, which means all of the structures share the almost same structural perfomance.

4. A numerical example compared with Palazzetto dello Sport

The Palazzetto dello Sport, designed by Pier Luigi Nervi and Annibale Vitellozzi [18], is a concrete shell characterized by its sixty-meter diameter, 36 Y-shape struts and the elegant interior ribbings with Michell truss pattern (Fig. 5). In this part, self-weight and torsion are mainly taken into consideration in the BESO process for the reason that they are the main load cases for shell structures.

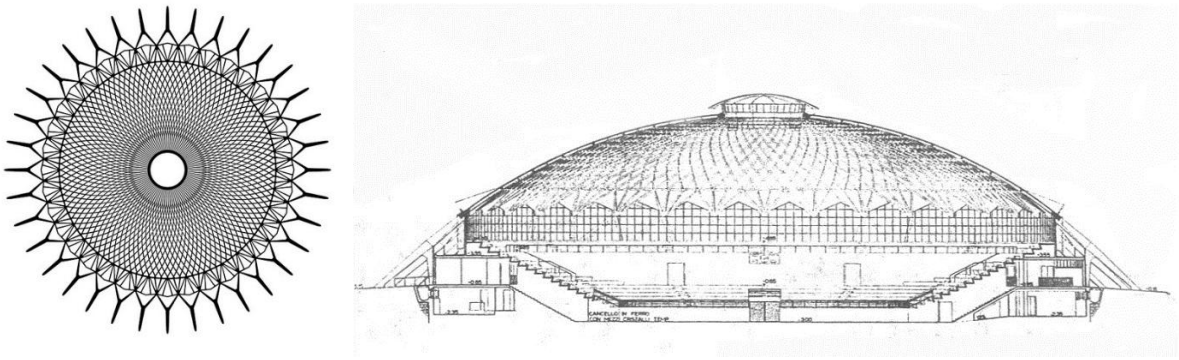


Figure 5: The design drawings of Palazzetto dello Sport

(Picture source: http://www.archidiap.com/opera/palazzetto-dello-sport/)

From the BESO result of the model with the only load of self-weight in z direction, the Y-shape struts and central hole with the similar size as Nervi's design are also generated in BESO result (Fig. 6). In Nervi's design, the strucutres between the interior ribbings (the red line in Fig. 6) and the bottom supports (the blue line in Fig. 6) are redesigned as a transitional structure to amplify the number of fixed points from 36 to 108.

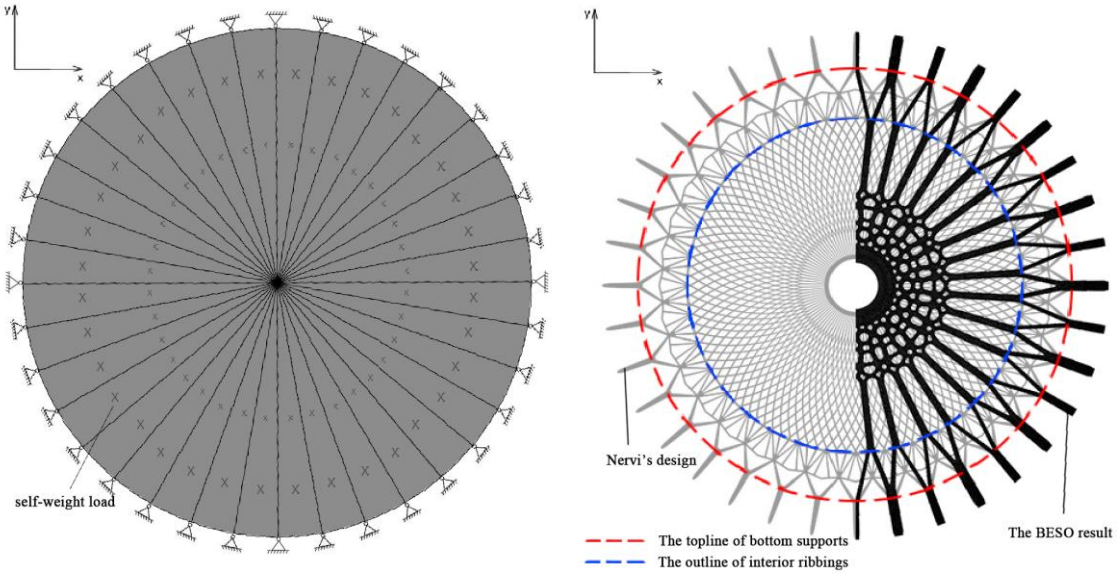


Figure 6: The original design condition and the BESO result of shell structure under self-weight

However, there is a significant difference of the interior ribbings' pattern between Nervi's design and the BESO result. This is because that the load of torsion has not been introduced. Another calculation is implented on the central part (Fig. 7). The load is a torsion on the boundary of the top hole. The number of fixed points and the volume fraction for BESO are set as 36 and 40% respectively becuse of the

limitation of element number in FEA. It is clearly seen that the optimized design from the BESO method has a similar pattern to Nervi's design.

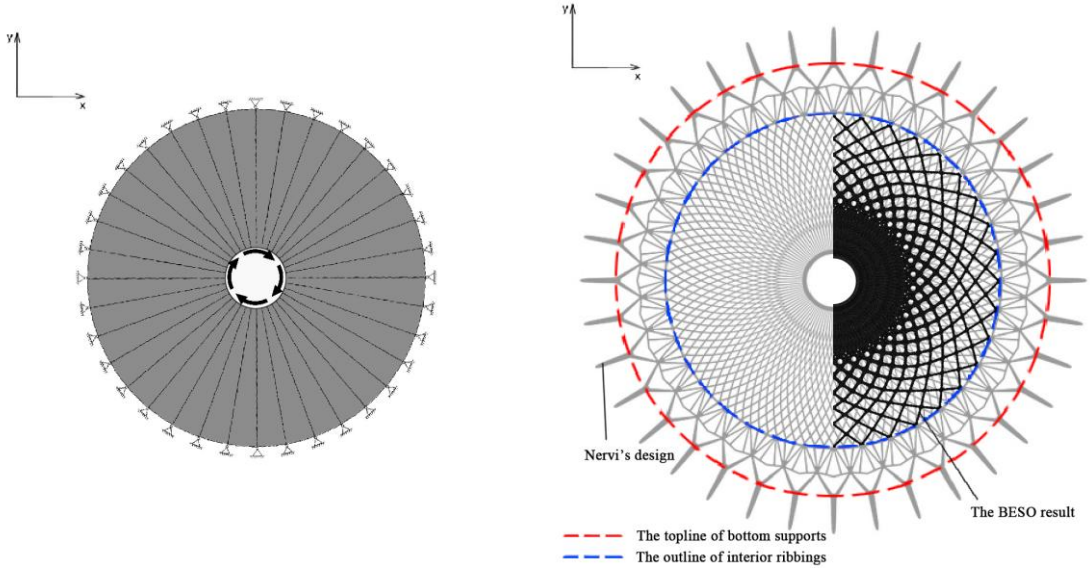


Figure 7: The original design condition and the BESO result of shell structure under torsional load

Furthermore, a new structure for this model can be obtained with BESO to exert these two load cases at the same time. The relative weight for these two load cases are set equally. The BESO parameters are evolution ratio (*ER*) =2%, filter radius (*FR*) of 30 mm (3 times of the element size), volume fraction (*VF*) = 40%.

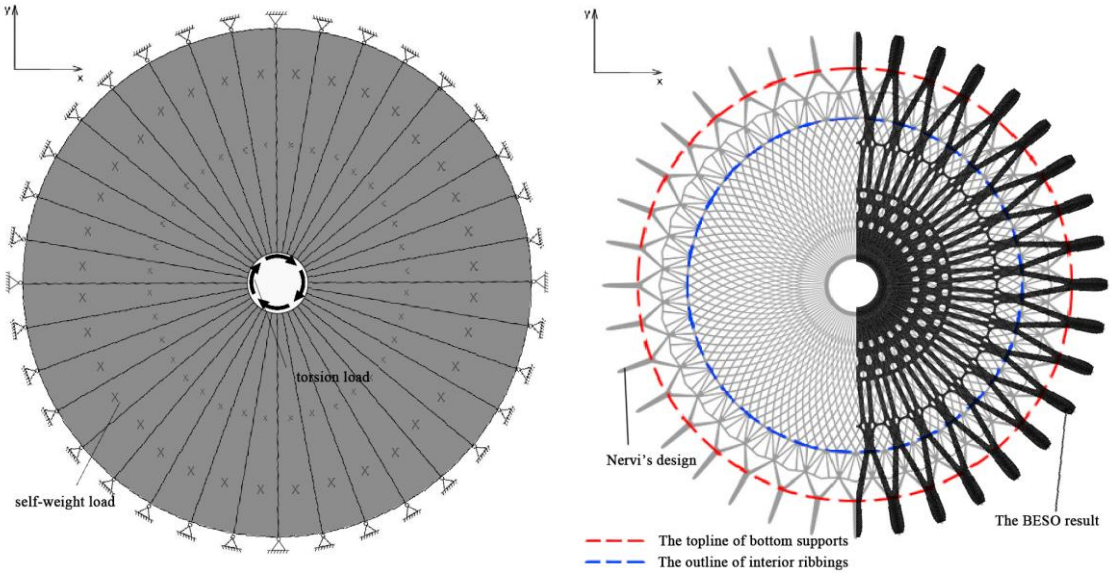


Figure 8: The original design condition and the BESO result of shell structure with multiple load cases

5. Conclusion

Most traditional form-finding methods for shell structures usually focus on shape rather than topology optimization. In this work, a new BESO method is developed to help engineers and architects to perform conceptual design of shells with complex geometries and high structural performance. Using this

method, it is also possible to obtain diverse designs of shell structures with similar structural performance. Different BESO parameters and different loading conditions are effective tools for form-finding in the early stage of the conceptual design, and designer could get many inspirations from these results. It is worth noting that the form-finding method developed in this study can be applied to structures other than shells.

Acknowledgements

The authors would like to thank several colleagues whose support helped fulfill the research project described in this paper:

Mr Yulin Xiong and Mr Yunzhen He (Centre for Innovative Structures and Materials, RMIT)

References

[1] H. J. Schek, "The force density method for form finding and computation of general networks," *Computer Methods in Applied Mechanics and Engineering*, vol. 3, no. 1, pp. 115–134, 1974.

[2] P. Block and J. Ochesendorf, "Thrust network analysis: A new methodology for 3D equillibrium," *Journal of the International Association for Shell and Spatial Structures*, vol. 48, no. 155, pp. 1–7, 2007.

[3] M. R. Barnes, S. Adriaenssens, and M. Krupka, "A novel torsion/bending element for dynamic relaxation modeling," *Computers & Structures*, vol. 119, pp. 60–67, 2013.

[4] A. Kilian and J. Ochsendorf, "Particle-Spring Systems for Structural Form Finding," *Journal of the International Association for Shell and Spatial Structures*, vol. 148, no. 2, p. 77, 2005.

[5] Y. M. Xie and G. P. Steven, "A simple evolutionary procedure for structural optimization," *Compurers & Structures*, vol. 49, no. 5, pp. 885–896, 1993.

[6] X. Huang and Y. M. Xie, *Evolutionary Topology Optimization of Continuum Structures, Methods and Applications*. Chichester: Wiley, 2010.

[7] G. Carotenuto, L. Nicolais, B. Martorana, and P. Perlo, "Optimal shape design as a material distribution problem," *Structural Optimization*, vol. 28, no. 12, pp. 384–388, 2003.

[8] Martin Philip Bendsoe and Noboru Kikuchi, "Generating optimal topologies in structural design using a homogenization method," *Computer Methods in Applied Mechanics and Engineering*, vol. 71, pp. 197–224, 1988.

[9] M. P. Bendsøe and O. Sigmund, *Topology Optimization: Theory, Methods, and Applications.* Berlin: Springer, 2003.

[10] M. P. Bendsøe and O. Sigmund, "Material interpolation schemes in topology optimization," *Archive of Applied Mechanics*, vol. 69, no. 9–10, pp. 635–654, 1999.

[11] S. Y. Wang, K. M. Lim, B. C. Khoo, and M. Y. Wang, "An extended level set method for shape and topology optimization," *Journal of Computational Physics*, vol. 221, no. 1, pp. 395–421, 2007.

[12] M. Yulin and W. Xiaoming, "A level set method for structural topology optimization and its applications," *Advances in Engineering software*, vol. 35, no. 7, pp. 415–441, 2004.

[13] S. Adriaenssens, P. Block, D. Veenendaal and C. Williams (eds.), *Shell Structures for Architecture: Form Finding and Optimization*. London: Routledge, 2014.

[14] X. Huang and Y. M. Xie, "A further review of ESO type methods for topology optimization," *Structural and Multidisciplinary Optimization*, vol. 41, no. 5, pp. 671–683, 2010.

[15] O. Sigmund and J. Petersson, "Numerical instabilities in topology optimization: A survey on procedures dealing with checkerboards, mesh-dependencies and local minima," *Structural Optimization*, vol. 16, no. 1, pp. 68–75, 1998.

[16] O. Sigmund, "Morphology-based black and white filters for topology optimization," *Structural and Multidisciplinary Optimization*, vol. 33, no. 4–5, pp. 401–424, 2007.

[17] X. Huang and Y. M. Xie, "Convergent and mesh-independent solutions for the bi-directional evolutionary structural optimization method," *Finite Elements in Analysis and Design*, vol. 43, no. 14, pp. 1039–1049, 2007.

[18] T. Iori and S. Poretti, "Pier Luigi Nervi's works for the 1960 Rome Olympics," *Actas del Cuarto Congreso Nacional de Historia de la Construcción*, pp. 27–29, 2005.

Proceedings of the IASS Annual Symposium 2019 - Structural Membranes 2019
Form and Force
7-10 October 2019, Barcelona, Spain
C. Lázaro, K.-U. Bletzinger, E. Oñate (eds.)

An Extended Linear Procedure for Constrained Form Finding

E. ŠAMEC*, K. FRESL[a], P. GIDAK[a]

*[a]Faculty of Civil Engineering, University of Zagreb
26 Kačićeva Street, Zagreb, Croatia
esamec@grad.hr

Abstract

The execution time of the form finding algorithm plays a key role in the performance of the interactive form finding tool. Therefore, enhanced by the idea of establishing an algorithm that would answer the need for fast calculation, the paper presents the extension of iterative application of the force density method, originally used for design and internal force evaluation of tensile structures. Preserving the benefits of the initial linear procedure, the presented extension focuses on both the acceleration of the method and the greater influence on the appearance of the final solution in the form finding problems with design constraints. In order to achieve a reduction in the number of iteration steps, and consequently a reduction in the execution time, tolerance optimisation for solving the system of equilibrium equations in each iteration step is introduced. For more control over the structures geometry, in addition to force and length constraints from the initial setup of the algorithm, the ability to assign unstrained lengths of elements is enabled. Form finding of several cable nets is conducted in order to compare the performance of the proposed procedure against the original method, and to show the potential of using unstrained length constraints in influencing the final geometry of the structure.

Keywords: constrained form finding, constrained force density method, iterative methods, tolerance optimisation, time comparison, system of linear equations, cable-nets, unstrained length constraint

1 Introduction

In the past, form finding was not possible without using physical models, and today it cannot be imagined without using advanced computational tools. The physical model enables an intuitive design process through interactive shape exploration, and if the same experience wants to be created in the form finding tool, real-time interventions on the structures geometry are necessary. In order to develop such an interactive tool, the execution time of the implemented algorithm needs to be minimal. The number of potential algorithms to be used is quite vast, but despite numerous literature on the form finding methods, the existing comparisons are not straightforward and few sources compare the actual performance (CPU time). The reason is certainly different nomenclature, mathematical structure and notation used for each method. In [1] by using the newly developed generic method, the CPU time for ten different methods is compared for form finding of minimal-length nets, whereby geometric methods seem to be superior to stiffness and dynamic methods. The category of geometric methods is based on the

Copyright © 2019 by Šamec E., Fresl K.and Gidak P.
Published by the International Association for Shell and Spatial Structures (IASS) with permission.

force density method (FDM), where the concept of force density, as a ratio of one static and one geometric magnitude, has arisen from formal manipulation of the mathematical expression [2]. The introduction of force densities into the system of nonlinear equilibrium equations results in an easily solvable linear system. Besides respecting the restrictions imposed by static equilibrium and boundary conditions, the shape of the form active structure needs to satisfy some additional architectural and fabrication constraints. It is difficult to select the distribution of force densities that will comply with all aesthetic, functional, and structural requirements. Therefore, in order to find a satisfactory shape, a compromise has to be made between the geometry and the forces by using constrained form finding. The constrained form finding demands extension to nonlinear FDM. By using nonlinear FDM, some structural requirements can be satisfied in a systematic way: attainment of the prescribed force values in selected elements, attainment of prescribed lengths of elements in equilibrium configuration, and attainment of prescribed unstrained lengths of elements. If the obtained system of equations is nonlinear, one typically tries to solve this system incrementally, most commonly by using the Newton-Krylov methods [3]. In [4] it is shown how the Newton-Krylov methods, when implemented in the programme code, have slow convergence for more complicated examples, which can be explained by the saddle shape problem. In order to avoid the nonlinear system of equations, but still attain the prescribed constraints in the elements, alternatively iterative application of linear FDM can be used (Iterated FDM). For constrained form finding, when FDM is iteratively applied, the equation system is solved multiple times and therefore, the standard algorithm needs to be accelerated in order to address the necessary speed requirements.
In the paper, the development and programming implementation of extended Iterated FDM is presented, enhanced by the idea of establishing a linear procedure for constrained form finding that would answer the need for a quick realisation in the future interactive tool. The shown extension of the initial method is focused on the acceleration of the method in section 3, while enabling more influence on the final geometry of structure in section 4. In section 5, form finding of several cable nets is conducted in order to compare the performance of the proposed procedure against the original method. Also, the possibilities of influencing the final geometry using unstrained length constraints are shown.

2 Iterated FDM - Prior Work

As indicated in [5], when it comes to constrained form finding, the linear procedure can be preserved and force constraints can be partially or completely fulfilled by applying linear FDM iteratively and changing the distribution of force density values in each iteration step. In [6] the same principle is used, for each iteration step the force density coefficients are recalculated using the force values from the previous iteration as shown in line 10 in Algorithm 1 (blue lines denote extensions to the existing algorithm presented in Section 4.). Conveniently adapted coefficients lead the calculation towards the geometry which fulfils imposed force constraints. In [4], the described procedure is extended in order to attain prescribed lengths of elements. Target element length, and respectively target distance of nodes i and j in the equilibrium configuration can be attained in the same way as in case of the forces, by recalculating the force density coefficients in each step according to the expression from line 11. It is evident that the length constraint and the force constraint cannot be assigned for the same element. However, it is possible to assign an approximate force value and then, after a few iteration steps, switch over to obtaining the length. The iteration is terminated when the conditions from line 8, assigned for different groups of cables, are satisfied. The proposed framework shows some advantages: unlike other

Algorithm 1 Inexact Iterated FDM algorithm

Require: net topology, supports, $\mathbf{q}^{(0)}$, $\bar{\mathbf{S}}$, $\bar{\boldsymbol{\ell}}$, $\bar{\boldsymbol{\ell}}_{\mathbf{0}}$, τ_S, τ_ℓ, τ_{eq}, $n_{\max}$

Ensure: $[\,\mathbf{x}^{(k)}\ \mathbf{y}^{(k)}\ \mathbf{z}^{(k)}\,]$ { nodal coordinates }

$k \leftarrow 0$

form $\mathbf{A}^{(0)}$ and $[\,\mathbf{x}_{\text{f}}^{(0)}\ \mathbf{y}_{\text{f}}^{(0)}\ \mathbf{z}_{\text{f}}^{(0)}\,]$ with $\mathbf{q}^{(0)}$

solve $\mathbf{A}^{(0)}\,[\,\mathbf{x}^{(0)}\ \mathbf{y}^{(0)}\ \mathbf{z}^{(0)}\,] = [\,\mathbf{x}_{\text{f}}^{(0)}\ \mathbf{y}_{\text{f}}^{(0)}\ \mathbf{z}_{\text{f}}^{(0)}\,]$ with tolerance τ_{eq}

calculate $\boldsymbol{\ell}^{(0)}$, $\boldsymbol{\ell}_{\mathbf{0}}{}^{(0)}$ and $\mathbf{S}^{(0)}$

calculate $e_S^{(0)}$, $e_\ell^{(0)}$ and $e_{\ell_0}^{(0)}$

$\gamma_S \leftarrow \tau_{\text{eq}}(1-\sqrt{\tau_S})/\tau_S^2$

$\gamma_\ell \leftarrow \tau_{\text{eq}}(1-\sqrt{\tau_\ell})/\tau_\ell^2$

while $\left(\left(e_S^{(k)} > \tau_S\right) \vee \left(e_\ell^{(k)} > \tau_\ell\right) \vee \left(e_{\ell_0}^{(k)} > \tau_\ell\right)\right) \wedge \left(k \le n_{\max}\right)$ **do**

  $k \leftarrow k+1$

  $q_{i,j}^{(k)} \leftarrow q_{i,j}^{(k-1)}\,\bar{S}_{i,j}/S_{i,j}^{(k-1)}$ for $(i,j) : \bar{S}_{i,j} \in \bar{\mathbf{S}}$

  $q_{i,j}^{(k)} \leftarrow q_{i,j}^{(k-1)}\,\ell_{i,j}^{(k-1)}/\bar{\ell}_{i,j}$ for $(i,j) : \bar{\ell}_{i,j} \in \bar{\boldsymbol{\ell}}$

  $q_{i,j}^{(k)} \leftarrow A_{i,j}E_{i,j}S_{i,j}^{(k-1)}/(A_{i,j}E_{i,j}+S_{i,j}^{(k-1)})\bar{\ell}_{0;i,j}$ for $(i,j) : \bar{\ell}_{0;i,j} \in \bar{\boldsymbol{\ell}}_{\mathbf{0}}$

  form $\mathbf{A}^{(k)}$ and $[\,\mathbf{x}_{\text{f}}^{(k)}\ \mathbf{y}_{\text{f}}^{(k)}\ \mathbf{z}_{\text{f}}^{(k)}\,]$ with $\mathbf{q}^{(k)}$

  $\tau_S^{(k)} \leftarrow \min\left\{\gamma_S\left(e_S^{(k-1)}\right)^2,\ \eta\left(e_S^{(k-1)}\right)^3/\left(e_S^{(k-2)}\right)^2\right\}$

  $\tau_\ell^{(k)} \leftarrow \min\left\{\gamma_\ell\left(e_\ell^{(k-1)}\right)^2,\ \eta\left(e_\ell^{(k-1)}\right)^3/\left(e_\ell^{(k-2)}\right)^2\right\}$

  $\tau_{\ell_0}^{(k)} \leftarrow \min\left\{\gamma_\ell\left(e_{\ell_0}^{(k-1)}\right)^2,\ \eta\left(e_{\ell_0}^{(k-1)}\right)^3/\left(e_{\ell_0}^{(k-2)}\right)^2\right\}$

  $\tau^{(k)} \leftarrow \min\left\{\tau^{(k)},\ \max\left\{\tau_S^{(k)},\tau_\ell^{(k)},\tau_{\ell_0}^{(k)},\tau_{\text{eq}}\right\}\right\}$

  solve $\mathbf{A}^{(k)}\,[\,\mathbf{x}\ \mathbf{y}\ \mathbf{z}\,] = [\,\mathbf{x}_{\text{f}}^{(k)}\ \mathbf{y}_{\text{f}}^{(k)}\ \mathbf{z}_{\text{f}}^{(k)}\,]$ with tolerance $\tau^{(k)}$

  calculate $\boldsymbol{\ell}^{(k)}$, $\boldsymbol{\ell}_{\mathbf{0}}{}^{(k)}$ and $\mathbf{S}^{(k)}$

  calculate $e_S^{(k)}$, $e_\ell^{(k)}$ and $e_{\ell_0}^{(k)}$

end while

$q_{i,j}^{(k)}$ – force density coefficient in k-th step, $\mathbf{q}^{(k)}$ – vector of force density coefficients
$S_{i,j}^{(k-1)}$, $l_{i,j}^{(k-1)}$, $l_{0;i,j}^{(k-1)}$ – obtained force, length and unstrained length value from previous step
$\bar{S}_{i,j}$, $\bar{\ell}_{i,j}$, $\bar{\ell}_{0;i,j}$ – target force, length and unstrained length value
τ_s, τ_ℓ – prescribed force and length tolerances
τ_{eq} – tolerance providing final equilibrium configuration
$e_s^{(k)}$, $e_\ell^{(k)}$, $e_{\ell_0}^{(k)}$ – force, length and unstrained length error
n_{max} – maximum number of outer loop steps, η – constant providing additional control

iterative procedures, it converges toward the required solution through a set of equilibrium configurations, the specified element lengths are obtained without introducing Lagrange multipliers, and the first approximation of the solution need not be assumed.

3 Inexact Iterated FDM - Accelerating the Procedure

The proposed procedure from [4] sometimes demands time-consuming calculations, and can therefore be inappropriate for intended interactive work. Hence, the goal is to reduce the number of iteration steps necessary to solve the equation system, and consequently reduce the execution time. Hereafter, the possibility for accelerating Iterated FDM, noticed by the authors, is presented.

If the computed force values or element lengths in a certain iteration step of Iterated FDM are far from the required ones, it makes sense to solve the equation system only approximately, and with less accuracy the further away they are. Therefore, in [7] Inexact Iterated FDM was presented with the aim to accelerate the procedure by optimising the accuracy for system solving (inner loop) in every iteration step of Iterated FDM (outer loop). Inspired by the Inexact Newton method, the procedure gradually decreases the tolerance from relatively loose initial tolerance towards specified tight tolerance which provides the final equilibrium configuration. Algorithm 1 shows a simple pseudocode, where tolerance optimisation is conducted according to optimisation rules in lines 14 and 15. To calculate the "optimal" tolerance for a certain step of iteration, the optimisation rule uses tolerance values contained in the criteria for the outer loop termination and takes into account the reduction rate of force and length errors by considering the ratio of these values in two consecutive steps, similar as in [8]. The tolerance in the k–th step should not be smaller than the tolerance in the final step, and since the convergence of the outer loop can be nonuniform, it should be verified that the obtained tolerance in the current step is equal to or smaller than the tolerance of the previous step. Therefore, the additional rule in row 17 is introduced. In that way, the excessively fast increase in accuracy is prevented, but the accuracy is still high enough not to compromise the convergence of the iterative process. The new procedure inherits the beneficial features of the original scheme, however, it should be noted that since the equation system is solved only approximately in nearly all steps, the obtained configurations, except those in the last steps, are not in equilibrium.

The numerical examples presented in [7] have shown the beneficial influence of tolerance optimisation upon a number of iteration steps needed to solve the system of equations. In this paper, in order to confirm that the reduction of iteration steps brings actual reduction in the execution time, in addition to counting the number of steps, the CPU time will be measured as well.

4 Unstrained Element Lengths

Besides the acceleration of the method, the paper is focused on the ability to assign unstrained element lengths, in addition to force and length constraints from the initial setup of the algorithm. In that way, the demand for more possibilities to control the final geometry of the structure can be addressed. Although new fabrication technologies question the standard building practice (for example irregular cable-nets are investigated in order to achieve a more equal force distribution, and to expand the design space [9]), for now, from a constructional point of view, a uniform mesh in an unstrained state is still the preferred cable arrangement. An equidistant mesh enables easy mounting, therefore, for fabrication purposes, the prescription of constant unstrained lengths is necessary [10].

For the derivation of the additional constraint, a relation between force, strained and unstrained length of the element is required [2]. Assuming the linear Hookes law of elasticity, which describes the material relationship between force and element elongation, the relation between strained and unstrained lengths is

$$\ell_{i,j} = \frac{A_{i,j}E_{i,j} + S_{i,j}}{A_{i,j}E_{i,j}}\,\ell_{0;i,j}, \tag{1}$$

where $E_{i,j}$ is the modulus of elasticity and $A_{i,j}$ is the cross–sectional area of the element $\{i,j\}$. The unstrained length constraints can be introduced in the computation by means of Lagrange multipliers (the system of nonlinear equations is obtained). However, when implemented in programme code, the procedure shows a slow convergence for more complicated examples. It is already mentioned that the slow convergence can be explained by the fact that this is a saddle point problem [4]. To avoid using Lagrange multipliers, Iterated FDM (with or without acceleration) can be extended to enable the assignment of unstrained length constraint, since it has already proven to be successful in form finding of minimal-length nets and in the assignment of force and length constraints.
The expression for the force density coefficient from line 11 in Algorithm 1 can also be written as $q_{i,j}^{(k)} = S_{i,j}^{(k-1)}/\bar{\ell}_{i,j}$ and by using the expression for the element length from (1) we obtain:

$$q_{i,j}^{(k)} \;=\; \frac{A_{i,j}E_{i,j}S_{i,j}^{(k-1)}}{(A_{i,j}E_{i,j} + S_{i,j}^{(k-1)})\,\bar{\ell}_{0;i,j}}\,. \tag{2}$$

By increasing the value of stiffness we are striving towards $\bar{\ell}_{0;i,j} = \bar{\ell}_{i,j}$ and unstrained length constraint becomes the length constraint from Section 2. The implementation of this additional constraint in the existing Algorithm 1 is marked in blue color.

5 Case Studies

The performance of the extended procedure is evaluated through three characteristic examples by comparing the number of iteration steps and the execution time against the existing method. The original version of Iterated FDM uses the conjugate gradient method (CG) as the solver in each step of the outer loop. For comparison, in addition to CG, a direct solver - the Cholesky decomposition is used. The genuine programme code developed in [7], containing extensions presented in this paper, is implemented in the programming language C++.
The first net is spread over a ground–plan area $[a,a]^2$. All cables have fixed nodes (supports) at both ends, and their height is given by the expression $z = a\,\ln(\cos(x/a)/\cos(y/a))$. For two families of 23 cables the uniform distribution of force values along the cables i.e. minimal net is sought (Figure 1). The second net has nine supports, eight on the edges and one inner high point. The ridge and valley cables are stretched between the high point and the edge supports (Figure 2). The lengths of edge cable elements, as well as the lengths of elements of the ridge and valley cables are specified. In the rest of the cables force values are specified. The third example is a high point net with an internal loop, illustrated by Figure 3. The net is spread over a square ground-plan area with four corner supports and one inner high point support. In this case, the form finding procedure with force constraints on the inner cables and length constraints for the elements of the edge cables and the loop shows sliding of the cables. The cables are sliding around the loop, which is expected since element lengths strive to minimum. Cable sliding in the numerical model can be restricted by using unstrained length constraints since the elongation of the cable elements can be controlled by stiffness. The value of

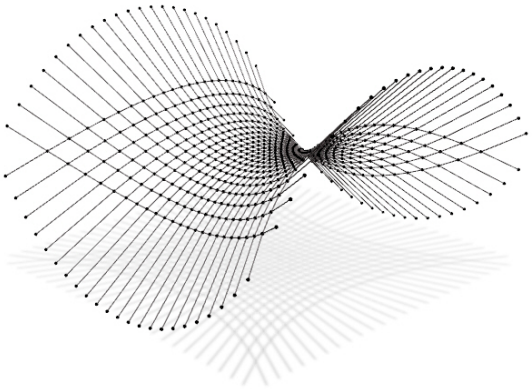


Figure 1: Net with "rigid" supports

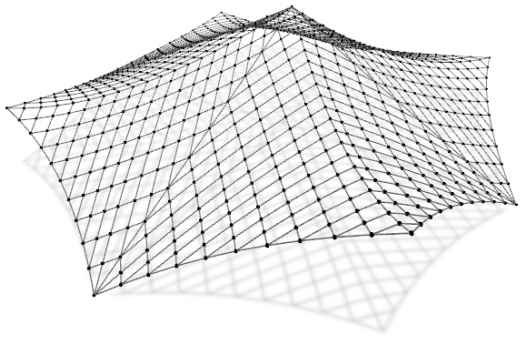


Figure 2: Net over octagon

Table 1: Net characteristics

	Free nodes	Elements	Force constr.	Length constr.	Unstrained length constr.	τ_S	τ_ℓ	τ_{eq}
Net 1	529	1 104	1 104	–	–	10^{-4}	–	10^{-7}
Net 2	832	1 720	1 520	200	–	10^{-4}	10^{-3}	10^{-7}
Net 3.1	208	422	–	52	370	10^{-4}	10^{-4}	10^{-7}
Net 3.2	208	422	322	52	48	10^{-3}	10^{-3}	10^{-6}

"stiffness" does not have to correspond to real cable stiffness, rather it serves as an additional control parameter. Besides preventing cable sliding, the goal is to keep the distribution of the prestressing force quite uniform. By assigning unstrained lengths to the inner elements and force constraints to the elements in contact with the edges, it is possible to take into account both the uniform force distribution and the equidistant cable layout. However, when using this approach for certain cable nets, especially the ones with edge cables, intolerable angle changes of elements connected to the edge cable can occur. Hence, force distribution and net deformation in this example are compared in two different design approaches. In the first design approach, unstrained length constraints are assigned to all internal elements in order to obtain an equidistant net. In the second design approach, unstrained lengths are assigned locally (according to the scheme on Figure 3), while for the rest of the elements of inner cables, force constraints are assigned in order to control the force distribution. The main characteristics of cable nets are summarized in Table 1. The constant in tolerance optimisation is $\eta = 0.025$ and the value of $E_{i,j}A_{i,j}$ is defined as 100 for all cables. The comparison of the obtained numbers of steps in outer and inner loops, as well as the corresponding execution time for Iterated FDM (using the Cholesky decomposition and CG) and Inexact Iterated FDM (using CG with tolerance optimisation (ICG)) are given in Table 2.

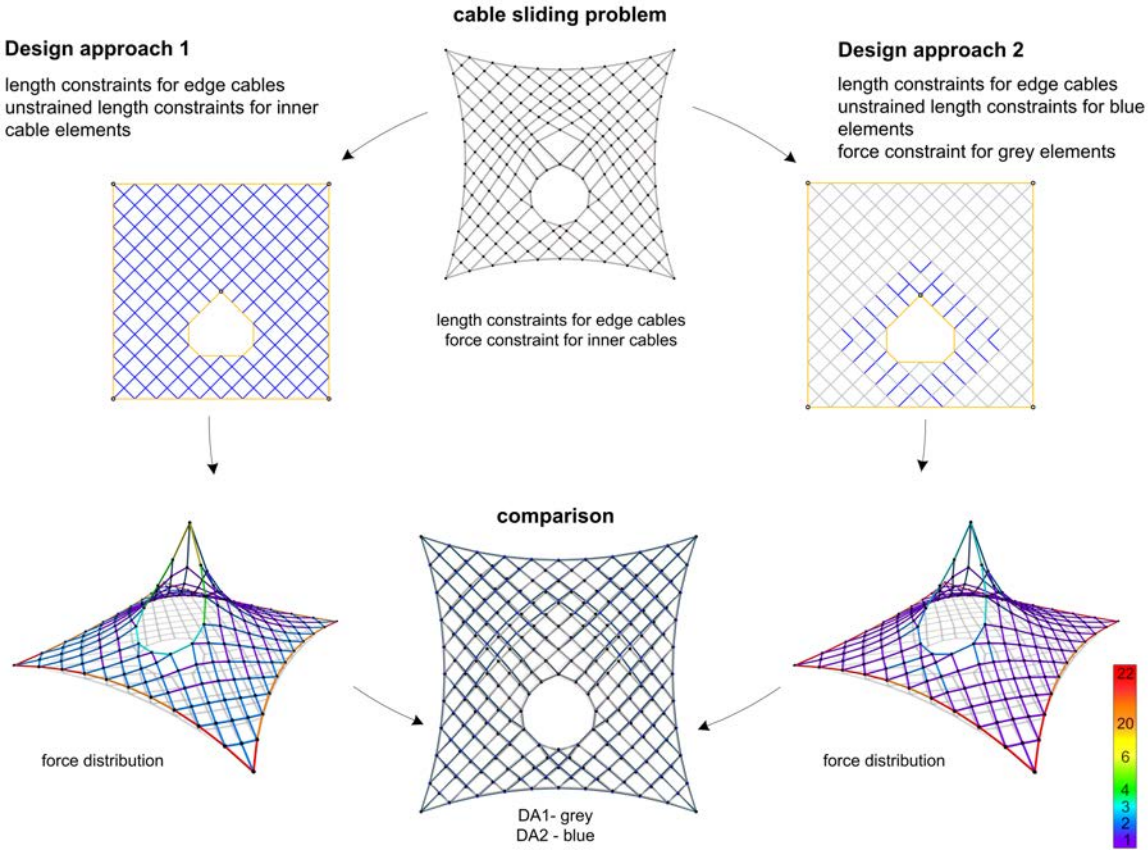


Figure 3: Two design approaches to form finding of high point cable-net using unstrained length constraints

Table 2: Comparison of the number of steps in outer and inner loops and the execution time (in ms) for Iterated and Inexact Iterated FDM

	Net 1			Net 2			Net 3.1			Net 3.2		
	outer	inner	time	outer	inner	time	outer	inner	time	outer	inner	time
LL^T	576	–	576.2	296	–	690.9	305	–	113.2	3 473	–	1 381.3
CG	576	34 506	396.4	298	24 748	574.7	305	17 239	81.5	3 414	46 115	469.6
ICG	576	18 681	258.1	261	6 741	306.9	300	5 806	43.1	3 438	20 349	378.8

6 Concluding Remarks

By comparing the execution time for the initial and the extended procedure in four presented case studies it has been shown that the usage of tolerance optimisation in the extended algorithm can bring satisfying reduction in the execution time. If tolerance is optimised, further time reduction can only be expected from the solver itself. Therefore, instead of CG, IRM - the new iterative solver with a symmetric positive definitive matrix, is considered to be used in future research. The solver is proposed by the project [11], and for its detailed description and programming

implementation one can refer to [12] and [13]. In addition to acceleration, in the final example it was shown that by enabling the assignment of unstrained length constraint, the algorithm gives the possibility to cope with cable sliding, and by combining force and unstrained length constraints in the inner cable elements, a satisfactory shape can be obtained both regarding uniform force distribution and deformation of the net.

7 Acknowledgements

This work was supported by the Croatian Science Foundation under the project IP-2014-09-2899.

References

[1] D. Veenendaal. *Design and form finding of flexibly formed shell structures*. PhD thesis, Zurich, March 2017.

[2] H.J. Schek. The force density method for form finding and computation of general networks. *Computer Methods in Applied Mechanics and Engineering*, 3(1):115–134, 1974.

[3] C. T. Kelley. *Iterative Methods for Linear and Nonlinear Equations*. Society for Industrial and Applied Mathematics, 1995.

[4] K. Fresl, P. Gidak, and R. Vrančić. Generalized minimal nets in form finding of prestressed cable nets. *Građevinar*, 65(8):707–720, 2013.

[5] J. Dvornik and D. Lazarević. Prestressed flexible cable and fabric structures. *Građevinar*, 47(4):185–199, 1995.

[6] B. Maurin and R. Motro. Investigation of minimal forms with conjugate gradient method. *International Journal of Solids and Structures*, 38(14):2387–2399, 2001.

[7] E. Šamec, K. Fresl, and M. Baniček. Increasing efficiency of iterative application of the force density method. *Građevinar*, 69(12):1075–1084, 2017.

[8] S.C. Eisenstat and H.F. Walker. Choosing the forcing terms in an inexact Newton method. *SIAM Journal on Scientific Computing*, 17(1):16–32, 1996.

[9] P. A. G. S. Giachini, B. Al Bahar, J. J. Solly, E. L. M. Slabbinick, and J. Knippers. Irregular cable-nets: exploring irregularity as a driver for form and structure. In *Proceedings of the 2017 IASS Symposium*, Hamburg, Germany, September 2528 2017.

[10] G. Tibert. *Numerical Analyses of Cable Roof Structures*. PhD thesis, Stockholm, 1999.

[11] Novel, Efficient Iterative Procedure for the Structural Analysis - Generalisation of Modern Methods. https://www.grad.unizg.hr/yoda. Accessed: 2019-05-30.

[12] J. Dvornik, D. Lazarević, A. Jaguljnjak Lazarević, and M. Demšić. The iterated ritz method: Basis, implementation and further development. *Coupled Systems Mechanics*, 7(6):755–774, 2018.

[13] J. Dvornik, D. Lazarević, A. Jaguljnjak Lazarević, and M. Demšić. Non-recursive equivalent of the conjugate gradient method without the need to restart. *Advances in Civil Engineering*, 2019:5, 2019.

Proceedings of the IASS Annual Symposium 2019 – Structural Membranes 2019
Form and Force
7 – 10 October 2019, Barcelona, Spain
C. Lázaro, K.-U. Bletzinger, E. Oñate (eds.)

Topology optimization of structural frames formulated as MISOCP. Comparison between branch-and-cut method and meta-heuristic approach

Shinnosuke FUJITA*
* The University of Kitakyushu
N337 1-1 Hibikino, Wakamatsu-ku, Kitakyushu, Fukuoka 808-0135, Japan
s-fujita@kitakyu-u.ac.jp

Abstract

It is known that the topology optimization (TopOpt) problem of frame structures can be formulated as a mixed-integer second-order cone programming problem (MISOCP), when the compliance is minimized and the cross-section of each member is chosen from a set of predetermined candidates [1]. An MISOCP problem can be solved globally with a branch-and-cut method (B&C). Previous studies have demonstrated the effectiveness of TopOpt by MISOCP for the simple stiffness maximization problem of medium-sized frame structures [2]. On the other hand, as another method of solving TopOpt, there is a meta-heuristic approach, which is general approach to obtain solution of optimization problem with discrete design variables [3] [4]. The meta-heuristic method is a very versatile method. In recent years, algorithms based on meta-heuristics have been implemented as components such as Rhino/GH and are widely used not only in frame TopOpt but also various computational design approach. However, in general, it takes a lot of computation time in order to obtain a good solution and there is no guarantee that the obtained solution is a global optimal solution. In this paper, Mixed-integer distributed ant colony optimization method (MIDACO) [5] is used as the algorithm for solving MISOCP heuristically. By comparing the results of the B&C and the MIDACO to various analytical models, the computational cost required to obtain a good solution in the vicinity of the global optimum solution by using meta-heuristic approach is quantitatively evaluated.

Keywords: topology optimization, ground structure method, meta-heuristic approach

1 Introduction

When deal with steel structures, TopOpt problem of the structural frame is a discrete variable problem in which the cross section is selected from the standardized section list. There are two types of solution strategies for such problems, theoretical methods and heuristic methods. The branch and cut method (B&C) is a typical method of the former. B&C has the advantage that the global optimality of the solution is guaranteed, but applying it to a conventional TopOpt problem formulated as a mixed integer linear programming problem (MIP), huge computational cost is required. However, it is also possible to formulate the TopOpt problem of frame structures as a MISOCP. When MISOCP is solved by B&C, it is comfirmed from recent researches that the calculation cost can be reduced because the continuous relaxation problem of MISOCP bacomes a SOCP and can be solved efficiently by the primal-dual Interior point method.
On the other hand, there are many algorithms for the latter method, Either method can be applied without depending on the discreteness of the objective function or the design variable. Because of its versatility, it is widely used as a component of Rhino/grasshopper, but there is no guarantee that the obtained solution is a global optimal solution.

Copyright © 2019 by Shinnosuke FUJITA
Published by the International Association for Shell and Spatial Structures (IASS) with permission.

In this research, the TopOpt problem of frame structures is solved by both theoretical and heuristic methods and the results are compared. The theoretical method is defined as solving the TopOpt problem of frame structures treated as MISOCP by using B&C. MIDACO is used as a heuristic algorithm. At first, the global optimal solution is found by B&C for several analysis cases. Then, the same analysis cases are treated by MIDACO. by comparing the required computational time to converge on the global optimum solution each other, the computational efficiency of theoretical and heuristic methods are compared.

2 Formulation of mixed-integer second-order cone programming problem

Consider a 2D frame structures with n nodes, m elements, and D degrees of freedom for node displacement. According to the previous study for the ground structure of the 2D frame with external nodal load $\boldsymbol{p} \in \mathbb{R}^D$, compliance minimization TopOpt with some constraints of non-mechanical performances in which the optimal sections are selected from the list of the combinations of the member cross-section performances can be formulated as follows:

$$\text{minimize} \quad \sum_{e=1}^{m}\sum_{l=1}^{3} 2w_{el} \tag{1a}$$

$$\text{subject to} \quad w_{e1} + a_e \geq \left\| \begin{bmatrix} w_{e1} - a_e \\ q_{e1}\sqrt{\dfrac{2l_e}{E}} \end{bmatrix} \right\|, \quad e = 1, \cdots, m \tag{1b}$$

$$w_{e2} + I_e \geq \left\| \begin{bmatrix} w_{e2} - I_e \\ q_{e2}\sqrt{\dfrac{6l_e}{E}} \end{bmatrix} \right\|, \quad e = 1, \cdots, m \tag{1c}$$

$$w_{e3} + I_e \geq \left\| \begin{bmatrix} w_{e3} - I_e \\ q_{e3}\sqrt{\dfrac{2l_e}{E}} \end{bmatrix} \right\|, \quad e = 1, \cdots, m \tag{1d}$$

$$\boldsymbol{p} = \sum_{e=1}^{m}\sum_{l=1}^{3} q_{el}\boldsymbol{b}_{el} \tag{1e}$$

$$\sum_{e=1}^{m} l_e a_e \leq \bar{V} \tag{1f}$$

$$a_e = \sum_{j=1}^{r} \bar{a}_j t_{ej}, \quad e = 1, \cdots, m \tag{1g}$$

$$I_e = \sum_{j=1}^{r} \bar{I}_j t_{ej}, \quad e = 1, \cdots, m \tag{1h}$$

$$\sum_{j=1}^{r} t_{ej} \leq 1, \quad e = 1, \cdots, m \tag{1i}$$

$$t_{ej} \in \{0, 1\}, \quad e = 1, \cdots, m, \quad j = 1, \cdots, r \tag{1j}$$

$$\sum_{j=1}^{r} t_{\alpha j} + \sum_{j=1}^{r} t_{\beta j} \leq 1, \quad \begin{matrix} \alpha = C_{k1}, \quad \beta = C_{k2} \\ k = 1, \cdots, x \end{matrix} \tag{1k}$$

$$z_i = \sum_{e \in S(i)} a_e, \quad i = 1, \cdots, n \tag{1l}$$

$$z_i \leq \frac{\bar{V}}{l_{\min}} \cdot s_i, \quad i = 1, \cdots, n \tag{1m}$$

$$\sum_{i=1}^{n} s_i \leq \bar{n} \tag{1n}$$

$$s_i \in \{0, 1\}, \quad i = 1, \cdots, n \tag{1o}$$

$$\sum_{j=1}^{r} t_{\gamma j} + \sum_{j=1}^{r} t_{\zeta j} \leq 1, \quad \begin{matrix} \gamma = B_{k1}, \quad \zeta = B_{k2} \\ k = 1, \cdots, y \end{matrix} \tag{1p}$$

where, E, a_e, I_e, and l_e are Young's modulus, section area, second moment of area, and length of member e, respectively. $\{(\bar{a}_1, \bar{I}_1), \cdots, (\bar{a}_r, \bar{I}_r)\}$ is the list of the combinations of the member cross-section performances and t_{ej} is a 0-1 variable for selection of member section from the list. $\boldsymbol{p} \in \mathbb{R}^n$ and $\boldsymbol{b}_{el} \in \mathbb{R}^D$ are external force vector and constant vector, respectively. z_i is the sum of the cross-sectional areas of the members connected to the node i. s_i is a 0-1 variable used to indicate the existence of node i. The design variable of the problem (1) is t_{ej}, q_{el}, w_{el}, and s_i. In the optimal solution, q_{e1}, q_{e2}, and q_{e3} are internal forces about axial, shear, and bending, respectively, w_{e1}, w_{e2}, and w_{e3} are complementary strain energies for axial, shear, and bending, respectively, and $\sum_{e=1}^{m}\sum_{l=1}^{3} 2w_{el}$ is consistent with compliance.

Unlike a conventional approach, overlapping members in a ground structure are not removed in this paper in order to consider the constraints on lengths and/or joints of members (Fig.1).

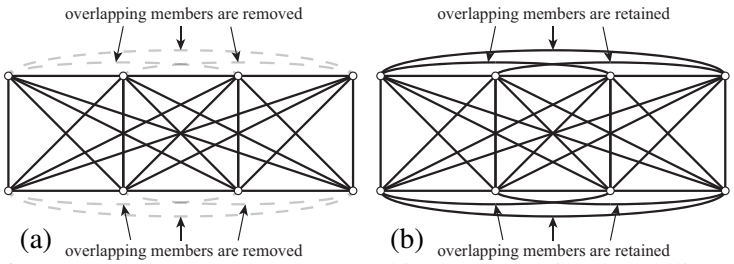


Figure 1: Examples of ground structure. (a) The one used in the conventional compliance minimization; and (b) the one for optimization under the constraint on the number of nodes.

By removing members with lengths that exceed the specified value $\bar{L}$ from the ground structure involving the overlapping members, upper bounds for member lengths are considered in the problem (1).

Overlapping and intersection of members can be avoided by constraint (1k). x is the number of pairs of overlapping or intersecting members and $(C_{11}, C_{12}), \cdots, (C_{x1}, C_{x2})$ are pairs of member indexes of overlapping or intersecting members.

Due to constraints (1l)〜(1o), the optimal frame is composed of $\bar{n}$ or fewer nodes. In these constraints, a set of indexes of members connected to node i is defined as $S(i) \subseteq \{1, \cdots, m\}$ $(i = 1, \cdots, n)$ (In the example of Fig.2, $S(i) = \{2, 4, 5, 11, 12\}$).

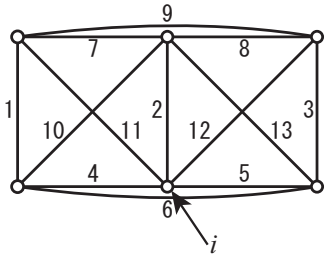


Figure 2: Node i and its surrounding members

Finally, the constraint (1p) forces all joint angles to be larger than or equal to the lower limit value $\bar{\theta}$. y is the number of pairs of members connected at an angle less than $\bar{\theta}$ and $(B_{11}, B_{12}), \cdots, (B_{y1}, B_{y2})$ are pairs of member indexes connected at an angle less than $\bar{\theta}$.

3 Optimization problem for MIDACO

$$\text{minimize} \quad \boldsymbol{p}^\top \boldsymbol{u}(\boldsymbol{t}) \tag{2a}$$

$$\text{subject to} \quad \sum_{e=1}^{m} l_e a_e(\boldsymbol{t}) \leq \bar{V} \tag{2b}$$

$$\sum_{j=1}^{r} t_{ej} \leq 1, \quad e = 1, \cdots, m \tag{2c}$$

$$t_{ej} \in \{0, 1\}, \quad e = 1, \cdots, m, \quad j = 1, \cdots, r \tag{2d}$$

$$\sum_{j=1}^{r} t_{\alpha j} + \sum_{j=1}^{r} t_{\beta j} \leq 1, \quad \begin{array}{l} \alpha = C_{k1}, \quad \beta = C_{k2} \\ k = 1, \cdots, x \end{array} \tag{2e}$$

$$\sum_{i=1}^{n} s_i(\boldsymbol{t}) \leq \bar{n} \tag{2f}$$

$$\sum_{j=1}^{r} t_{\gamma j} + \sum_{j=1}^{r} t_{\zeta j} \leq 1, \quad \begin{array}{l} \gamma = B_{k1}, \quad \zeta = B_{k2} \\ k = 1, \cdots, y \end{array} \tag{2g}$$

where, $\boldsymbol{u} \in \mathbb{R}^n$ is the nodal displacement vector and $\boldsymbol{t} \in \mathbb{R}^{m \times r}$ is the vector which has t_{ej} as the components.
This problem is equivalent to problem (1) except design variables are reduced to $\boldsymbol{t}$ only. In each iteration of the optimization calculation, a_e, I_e, s_i, and $\boldsymbol{u}$ are calculated as follows:

$$a_e = \sum_{j=1}^{r} \bar{a}_j t_{ej}, \quad e = 1, \cdots, m \tag{3}$$

$$I_e = \sum_{j=1}^{r} \bar{I}_j t_{ej}, \quad e = 1, \cdots, m \tag{4}$$

$$s_i = \begin{cases} 1 & \text{if} \quad z_i \neq 0 \\ 0 & \text{otherwise} \end{cases}, \quad i = 1, \cdots, n \tag{5}$$

$$\boldsymbol{K}\boldsymbol{u} = \boldsymbol{p} \tag{6}$$

where, $\boldsymbol{K}$ is the global stiffness matrix which is the function of E, a_e, and I_e. To avoid the matrix becomes singular, sufficiently small positive stiffness is given to the e-th member when $\sum_{j=1}^{r} t_{ej} = 0$ (i.e. there is no member).

4 Numerical examples

Two equivalent optimization problems (1) & (2) are solved in B&C and MIDACO, respectively. In each numerical examples, Young's modulus and Poison's ratio are setted to $E = 210$ GPa and $\nu = 0.3$, respectively. Length limit $\bar{L}$ is setted to 12 m, which is usual transportation limit size of trailer. To prevent the members from connecting at extremely sharp angles, the lower limit of joint angles is setted to $\bar{\theta} = 30^\circ$ in constraints (1p) and (2g). For the sake of simplicity, the cross-section of the member to be selected is limited to a hollow cylinder with external radius R_j and internal radius r_j. Suppose that the

ratio of r_j to R_j, denoted $c \in]0, 1[$, is fixed, i.e., $r_j = cR_j$. Then the set of jth section performance is calculated by the following equations:

$$\bar{a}_j = \pi(1 - c^2)R_j^2, \quad \bar{I}_j = \frac{\pi}{4}(1 - c^4)R_j^4 \tag{7}$$

Additionally, $\bar{I}_j$ is expressed by the following equation as a function of $\bar{a}_j$:

$$\bar{I}_j = \bar{\gamma}\bar{a}_j^2, \quad \bar{\gamma} = \frac{1}{4\pi}\frac{1 + c^2}{1 - c^2} \tag{8}$$

In this paper, we set $c = 0.9$ while the upper limit of the volume is set to $\bar{V} = 2.0$ m^3, and the optimization is performed for the following two cases (all units are m^2):

$$\begin{array}{ll} \text{Case 1}: & \{\bar{a}_1, \bar{a}_2\} = \{0.001, 0.002\} \quad (r = 2) \\ \text{Case 2}: & \{\bar{a}_1, \bar{a}_2, \bar{a}_3, \bar{a}_4\} = \{0.001, 0.002, 0.003, 0.004\} \quad (r = 4) \end{array} \tag{9}$$

In this paper, cantilever ground structure with a tip load as shown in Fig. 3 is considered. Note that this ground structure has overlapping members and members whose length exceeds $\bar{L}$ have been removed in advance. In order to make it easy to consider the results, the nodes are numbered 1–15. The total number of members of the ground structure is 72.

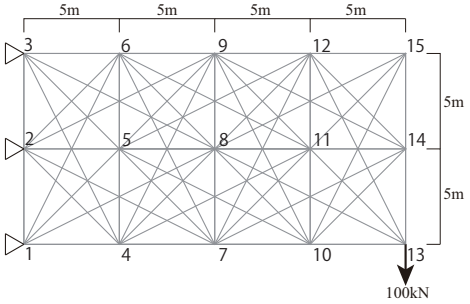


Figure 3: Model 1: Cantilever ground structure with a tip load

For the problem (1), MOSEK ver. 8.1.0 [6] was used as the B&C solver. For the problem (2), MIDACO ver.6.0 [5] was used as the heuristic solver. Computation was carried out on two 3.2 GHz Intel Xeon E5-2667 v4 processors with 256GB RAM. In each cases, the node limit constraint of $\bar{n} = 7, 6, 5, 4$ is iteratively carried out. In this numerical experiment, the optimal calculation is stopped in one day(86,400 seconds) for the heuristic solver.

Optimization results of case 1 & 2 are shown in Fig. 4 and 5, respectively. In each figures, 7-(1)∼4-(1) show the optimal topology of problem (1) solved by B&C while $\bar{n}$ is setted to 7, 6, 5, and 4. Note that these all solutions are mathematically guaranteed to be global optimal. On the other hand, figures 7-(2) ∼4-(2) show the optimal topology of problem (1) solved by MIDACO while $\bar{n}$ is setted to 7, 6, 5, and 4. Note that these all solutions are not guaranteed to be global optimal.

According to the optimization results of case 1, it can be comfirmed that all optimal solutions by MIDACO are finally converged to the same solutions by B&C (i.e. global optimal solutions). However, if problem (2) is solved by MIDACO, it takes several thousands to tens of thousands of seconds to converge to a global optimal solution. Problem (1) solved by B&C is converged to the optimal solution in a few tens of seconds, so it can be comfirmed that the computational cost of solving problem (2) by MIDACO is much greater than solving problem (1) by B&C.

According to the optimization results of case 2, it can be comfirmed that all optimal solutions by MIDACO except for $\bar{n} = 4$ could no be converged to global optimal solutions in one day. On the other

hand, if problem (1) is solved by B&C, global optimimal solutions can be obtained in tens to hundreds of seconds.

From the above results, it can be concluded that solving problem (1) by B&C is more effective than solving problem (2) by MIDACO in TopOpt of frame structures with compliance as the objective function.

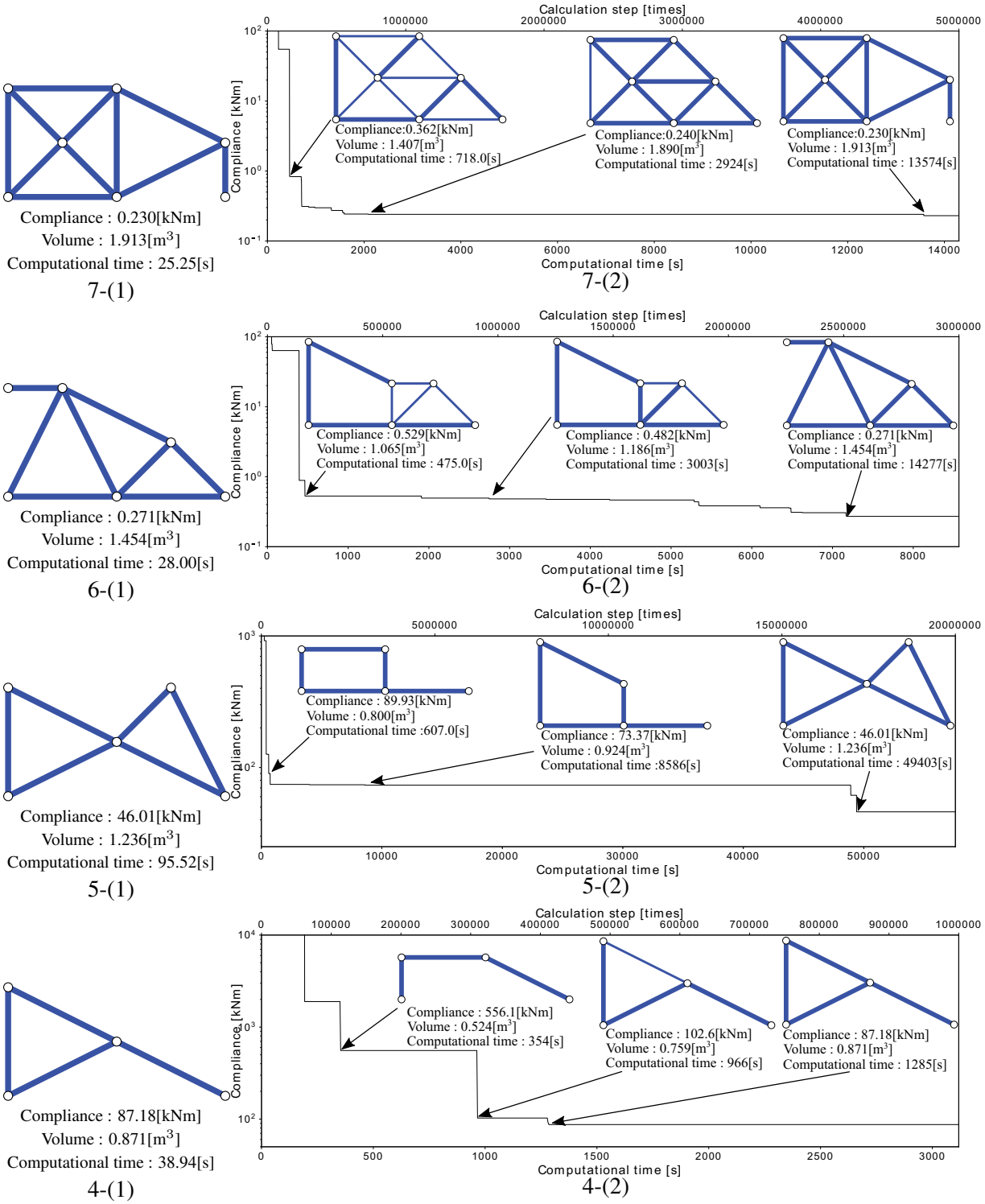


Figure 4: Optimal result of Case 1

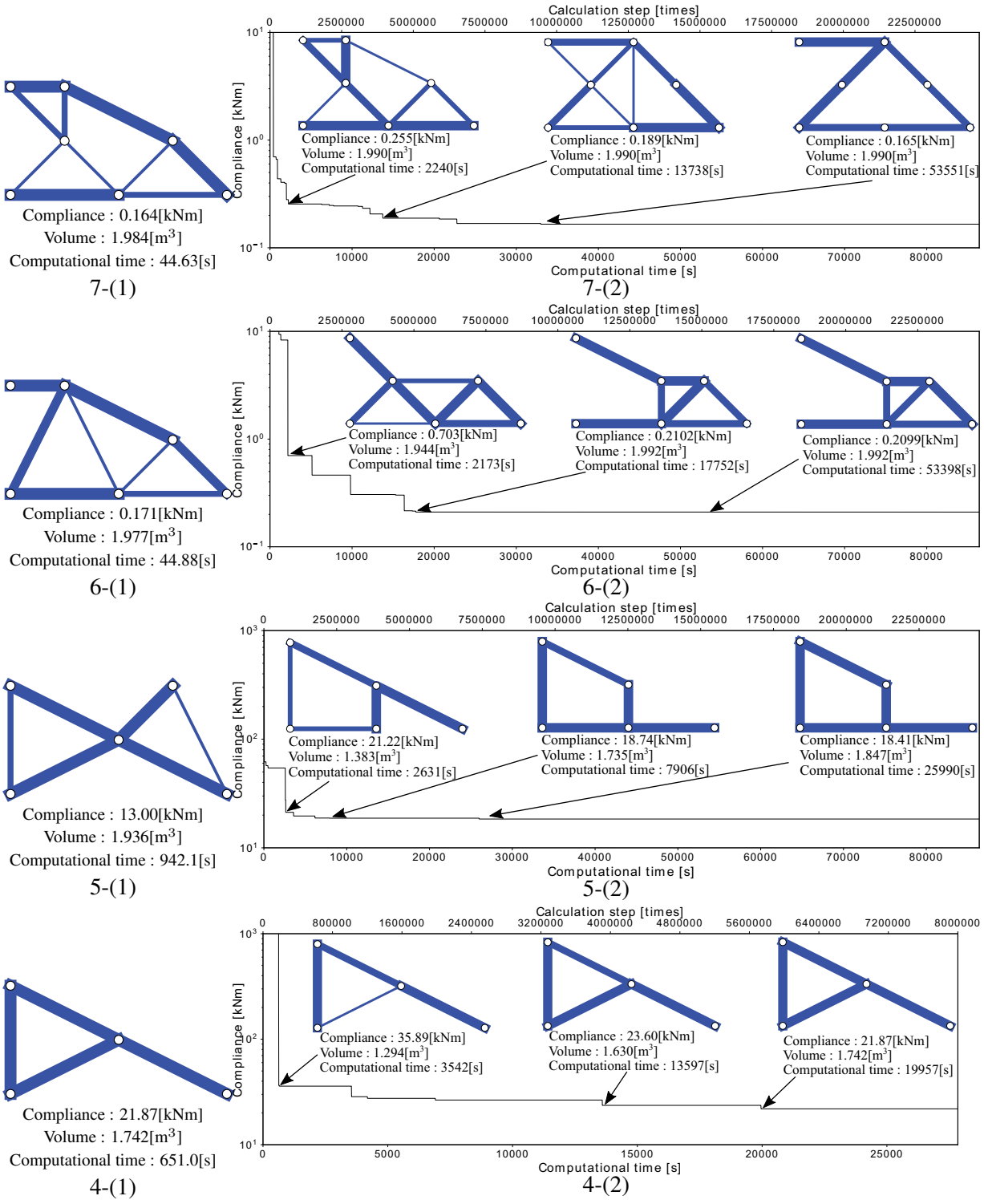


Figure 5: Optimal result of Case 2

5 Conclution

In this paper, we compared the difference between optimization results by theoretical method and heuristic method for TopOpt problem of frame structures considering constructability. As a result, it was shown that solving such TopOpt problem formulated as MISOCP with B&C is more advantageous in terms of computational cost than using heuristics (specifically, MIDACO in this paper). However, the former approach is less versatile and less extensible. With MIDACO, although it takes time to calculate, case 1 with a small problem size could obtain global optimal solutions. Even in case 2, it was possible to obtain good solutions. If the objective function is not compliance, it is difficult to formulate such TopOpt problem as MISOCP. In such a case, if you use MIDACO, you can obtain a global optimal solution or its neighboring solution if the problem size is the comparable to what is treated in this paper.

References

[1] Y. Kanno. Mixed-integer second-order cone programming for global optimization of compliance of frame structure with discrete design variables. *Structural and Multidisciplinary Optimization*, 54:301–316, 2016.

[2] S. Fujita and Y. Kanno. Topology optimization of three-dimensional frame structures using mixed-integer second-order cone programming. *Journal of Structural and Construction Engineering (Transactions of AIJ)*, 82(732):193–201, 2017. (in Japanerse).

[3] P. Hajela and E. Lee. Genetic algorithms in truss topological optimization. *International Journal of Solids and Structures*, 32:3341–3357, 1995.

[4] M. Kociecki and H. Adeli. Two-phase genetic algorithm for topology optimization of free-form steel space-frame roof "structures with complex curvatures". *Engineering Applications of Artificial Intelligence*, 32:218–227, 2014.

[5] M. Schlueter, S. O. Erb, M. Gerdts, S. Kemble, and J. J. Ruckmann. Midaco on minlp space applications. *Advances in Space Research*, 51:1116–1131, 2013.

[6] E. D. Andersen, C. Roos, and T. Terlaky. On implementing a primal-dual interior-point method for conic quadratic optimization. *Mathematical Programming*, 95:249–277, 2003.

Proceedings of the IASS Annual Symposium 2019 – Structural Membranes 2019
Form and Force
7 – 10 October 2019, Barcelona, Spain
C. Lázaro, K.-U. Bletzinger, E. Oñate (eds.)

How to obtain diverse and efficient structural designs through topology optimization

Yi Min XIE*[,a,b], Kai YANG[a], Yunzhen HE[a], Zi-Long ZHAO[a], Kun CAI[a]

*[, a] Centre for Innovative Structures and Materials, School of Engineering, RMIT University, Melbourne, 3001, Australia
mike.xie@rmit.edu.au

[b] XIE Archi-Structure Design, Shanghai, 200092, China

Abstract

Topology optimization techniques are widely used to maximize the performance or minimize the weight of a structure through optimally distributing its material within a prescribed design domain. However, existing optimization techniques usually produce a single optimal solution for a given set of loading and boundary conditions. In architectural design, it is highly desirable to obtain multiple design options which possess not only high structural performance but also distinctly different shapes and forms. Here we present three simple and effective strategies for achieving diverse and competitive structural designs, including (i) penalizing precedent designs, (ii) using constraints as design drivers, and (iii) introducing randomness into structural models. These strategies are successfully applied in the computational morphogenesis of a variety of structures. The results demonstrate that the developed methodology is capable of providing the designer with structurally efficient and topologically different solutions. The structural performance of alternative designs is only slightly lower than that of the optimal design. This methodology holds great potential for practical applications in architecture and engineering. The examples shown in this study are based on the bi-directional evolutionary structural optimization (BESO) technique. However, the proposed strategies are general and would be applicable to other commonly used topology optimization techniques.

Keywords: topology optimization, diverse and competitive structural designs, BESO

1. Introduction

Over the past few decades, topology optimization has been developed as an effective tool for architects and engineers to search for the optimal design. Different topology optimization methods, such as the homogenization method [1, 2], the solid isotropic material with penalization (SIMP) method [2, 3], the level set method [4, 5] and the bi-directional evolutionary structural optimization (BESO) method [6-8] have been used widely in multiple disciplines [9-12]. The structural design in many architectural and engineering projects was based on the BESO method [13-15]. According to the structural contribution of each element, the BESO method gradually removes inefficient elements from the structure and adds elements to the most needed areas.

Although topology optimization has provided the designer with inspirations, existing optimization techniques do not allow the designer to play an active role in the form-finding process. In practice, architects usually desire to have more control or influence on the optimization process, so that they can choose a better conceptual design according to their artistic intuitions or functional requirements. Conventional optimization methods usually aim to create a single optimal solution which can minimize or maximize the objective function [16, 17] subject to various constraints [18, 19]. Many researchers tried to obtain diverse solutions by employing the multi-objective problems with the

Copyright © 2019 by Yi Min XIE, Kai YANG, Yunzhen HE, Zi-Long ZHAO, Kun CAI
Published by the International Association for Shell and Spatial Structures (IASS) with permission.

application of different weights on objective responses [20, 21]. However, there is still a lack of an efficient method which can generate diverse and competitive designs for a single-objective optimization problem. On the basis of the SIMP method, Wang et al. added several graphic diversity constraints to find multiple solutions and applied this technique to several 2D cases [22]. Further research is required for more practical engineering applications.

Here, we present three strategies to achieving diverse and competitive designs. The first strategy is to penalize the precedent designs. The second strategy uses constraints as design drivers to create diverse solutions [23]. In the third strategy, by adding some random factors into the form-finding process, designers can obtain multiple random designs. The effectiveness of these strategies is verified by a series of numerical examples. Further discussions on the first two strategies can be found in [24].

2. Topology optimization formulation

In this study, we consider the compliance minimization problem as examples. The single-objective topology optimization problem of compliance minimization can be written as:

$$\min C(\boldsymbol{X}) = \frac{1}{2}\boldsymbol{U}^T\boldsymbol{K}\boldsymbol{U} = \frac{1}{2}\sum_{i=1}^{N} x_i^p \boldsymbol{u}_i^T \boldsymbol{k}_i \boldsymbol{u}_i \tag{1}$$

$$\text{Subject to: } V(\boldsymbol{X}) = \sum_{i=1}^{N} x_i v_i \le V^* \tag{2}$$

where C is the structural compliance and $\boldsymbol{X}=\{x_i\}$ is vector of the design variable (i=1,2,…, N). x_i =1 or x_{min} indicates the presence or absence of element i, respectively. N is the total number of elements. $\boldsymbol{U}$ and $\boldsymbol{K}$ are the displacement vector and global stiffness matrix, respectively. p is the penalty exponent [25], which is usually set as 3. $\boldsymbol{u}_i$ and $\boldsymbol{k}_i$ are the nodal displacement vector and stiffness matrix of element i, respectively. V is the total material volume and v_i is the volume of element i. V^* is the target volume of V.

The gradient of the compliance C with regard to the design variable x_i is obtained by employing the adjoint method [7]:

$$\frac{\partial C(\boldsymbol{X})}{\partial x_i} = -\frac{1}{2} p x_i^{p-1} \boldsymbol{u}_i^T \boldsymbol{k}_i \boldsymbol{u}_i \tag{3}$$

$$\alpha_i = -\frac{1}{p}\frac{\partial C}{\partial x_i} = \begin{cases} \dfrac{1}{2}\boldsymbol{u}_i^T \boldsymbol{k}_i \boldsymbol{u}_i & \text{when } x_i = 1 \\ \dfrac{x_{\min}^{p-1}}{2}\boldsymbol{u}_i^T \boldsymbol{k}_i \boldsymbol{u}_i & \text{when } x_i = x_{\min} \end{cases} \tag{4}$$

In order to avoid numerical instabilities such as checkerboard and mesh-dependency, the raw sensitivities defined in Eq.(4) need to be smoothed by using the following filtering technique [26, 27]:

$$\tilde{\alpha}_i = \frac{\sum_{j=1}^{N} w_{ij}\alpha_j}{\sum_{j=1}^{N} w_{ij}} \tag{5}$$

$$w_{ij} = \max(0, r_f - d_{ij}) \tag{6}$$

where the linear weight factor w_{ij} is independent of the elemental sensitivities and can be pre-calculated before the optimization process. r_f is the filter radius and d_{ij} is the distance between the centroids of elements i and j. The smoothed elemental sensitivity $\tilde{\alpha}_i$ is averaged with its value in previous step in order to achieve a stable and convergent solution [6]:

$$\overline{\alpha}_i = \frac{\tilde{\alpha}_i^{(n)} + \tilde{\alpha}_i^{(n-1)}}{2} \tag{7}$$

where $\tilde{\alpha}_i^{(n)}$ and $\tilde{\alpha}_i^{(n\text{-}1)}$ are the smoothed sensitivities of element i in the nth and (n-1)th iterations, respectively. During the optimization, the material volume $V^{(n)}$ is gradually decreased as:

$$V^{(n)} = V^{(n-1)}(1-\delta) \tag{8}$$

where the evolutionary ratio δ is set as 0.02 for all examples in this study.

3. Strategies for achieving diverse and competitive structural designs

3.1. Penalizing precedent designs

We present two different methods to create diverse and competitive designs based on penalizing a certain number of the solid elements of the previously optimized designs. In the first method, in order to create topologically different designs without significantly sacrificing the structural performance, we penalize a prescribed percentage of the least efficient element in the initial optimized (IO) design which is obtained by the normal BESO process. By setting a different penalty percentage, we can achieve a series of new designs. Figure 1 shows the IO design (Figure 1b) and a subsequent optimized (SO) design (Figure 1c) obtained from the same design model (Figure 1a). The penalty percentage of the solid element is set as 100% in this example and the structural compliance of SO design is only 10% higher than that of the IO design.

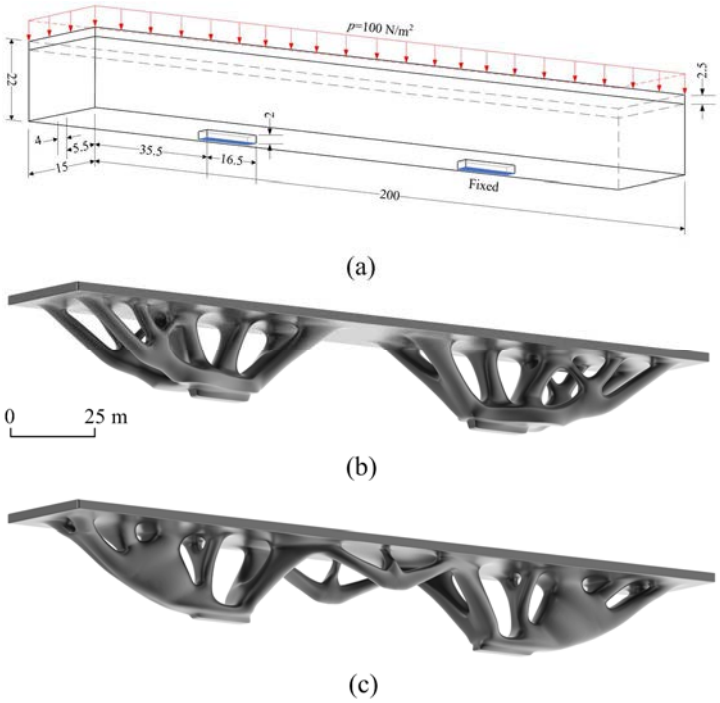


Figure 1: A new design generated by penalizing the initial optimized design

It is interesting to note that a magnificent structure very similar to the IO design has been constructed at the Qatar National Convention Centre, which was designed by renowned architect Arata Isozaki and his team using the extended evolutionary structural optimization (XESO) method [28, 29]. The SO design would provide an innovative and elegant alternative structural form for a project which might have similar or identical loading and boundary conditions.

In the second method, all of the precedent designs are included in the penalization process to search for new design shapes. A certain percentage of the least efficient element in each precedent design is considered to be penalized during the current design cycle, so all the least efficient elements in the previous designs will less likely reappear in the new design. Figure 2 shows the IO design (Figure 2b) and two SO designs (Figure 2c and 2d). The penalty percentage is set as 10% for creating the two SO designs. The two arches of the bridge have distinctly different arrangements in the three designs. They are all structurally efficient and aesthetically pleasing. These bridges could be used under different traffic conditions as their lanes change from the middle (Figure 2b) to the two sides (Figure 2d). The structural compliances of these two SO designs are only 3% higher than that of the IO design, in spite of the significant differences in topologies.

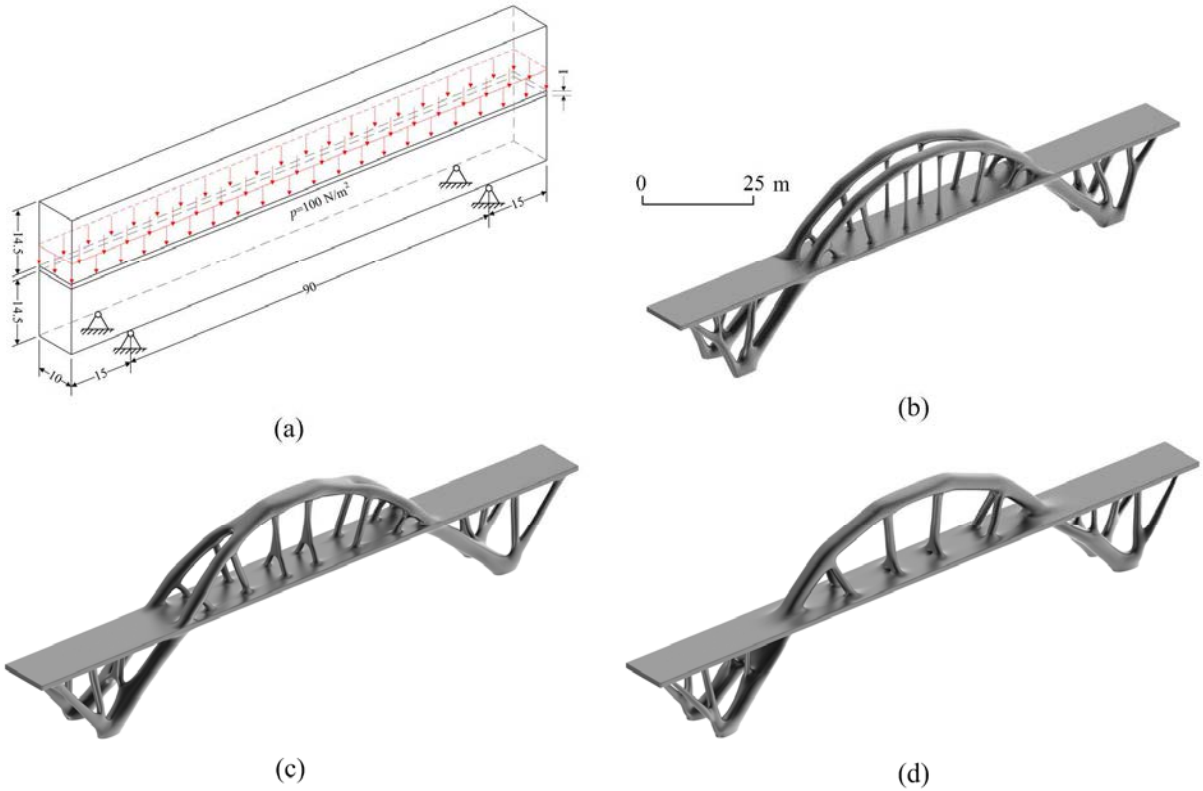


Figure 2: New designs generated by penalizing all the precedent designs

3.2. Using constraints as design drivers

Manufacturing constraints need to be considered in structural design. These constraints can also be used as design drivers [23]. By slightly changing the design domain, we can achieve diverse designs which satisfy the functional requirements. For example, the initial optimized design of the beam bridge example is demonstrated in Figure 3b. Although this design might be the most ideal structural form in this case, it may deviate significantly from the functional requirements because most bridges should allow traffic to pass through below the deck. As shown in Figure 3a (lower graph), by setting a small gap as non-designable, a new bridge form (Figure 3c) is generated.

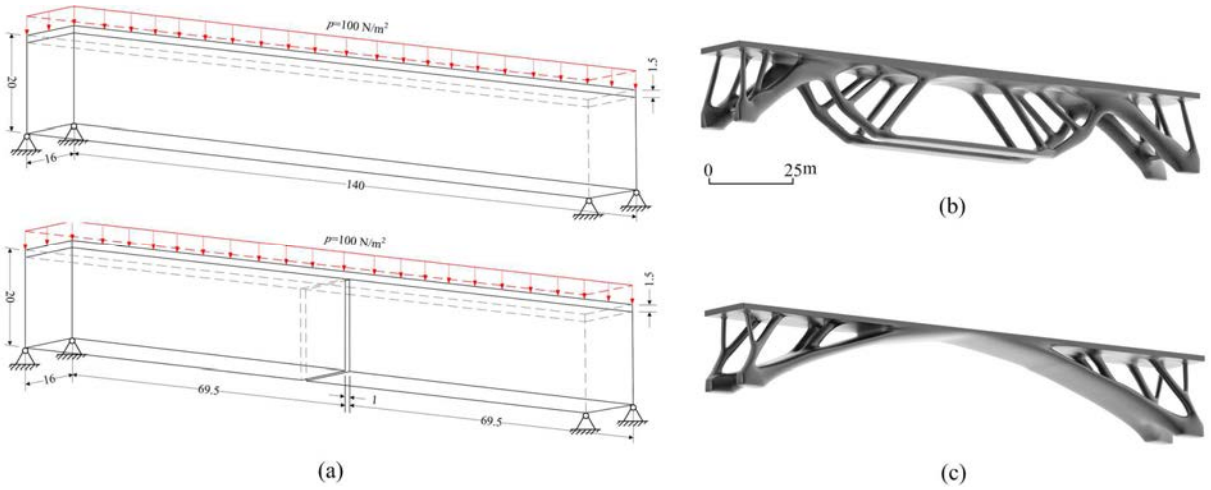


Figure 3: A new design generated by altering the design domain

In addition to altering the design domain, unsymmetrical designs can be obtained in a symmetrical optimization problem by imposing unsymmetrical constraints. Figure 4a and Figure 4b show the cantilever beam example and the symmetrical optimized design, respectively. In Figure 4c and Figure 4d, the elemental sensitivity of the lower half of the cantilever beam is penalized by 0.6 and 0.7, respectively. The compliances of the optimized structures only increase 2% (Figure 4c) and 4% (Figure 4d), respectively.

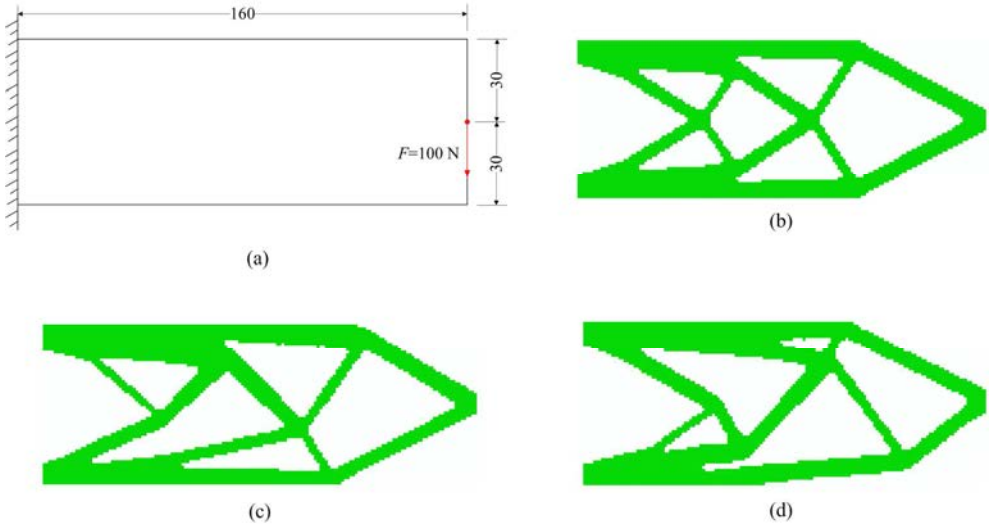


Figure 4: New designs generated by penalizing the sub-region

3.3. Introducing randomness into structural models

Based on the previous structural forms or designers' own experience, multiple diverse and competitive designs can be achieved by the above approaches. Unlike these two approaches, the third approach can search for every possible solution for the designer and can also maintain a high structural performance. By randomly penalizing each element, multiple random designs can be obtained. It is important to mention that through this technique, the designer might get a distinctly different structural form every time when they restart the whole optimization process. As shown in Figure 5, this method is able to achieve different random solutions. By penalizing each element using a random penalty coefficient ranging from 0.85 to 1.15, two subsequent competitive designs are obtained by running the

optimization process twice. However, it is interesting and essential to note that sometimes we can even achieve asymmetric designs which have lower compliance than the symmetry initial optimized design like what Daniel and Alexey found in their research [30]. The compliance value of each subsequent optimized design (Figure 5c and 5d) is 1% lower than that of the initial optimized design (Figure 5b).

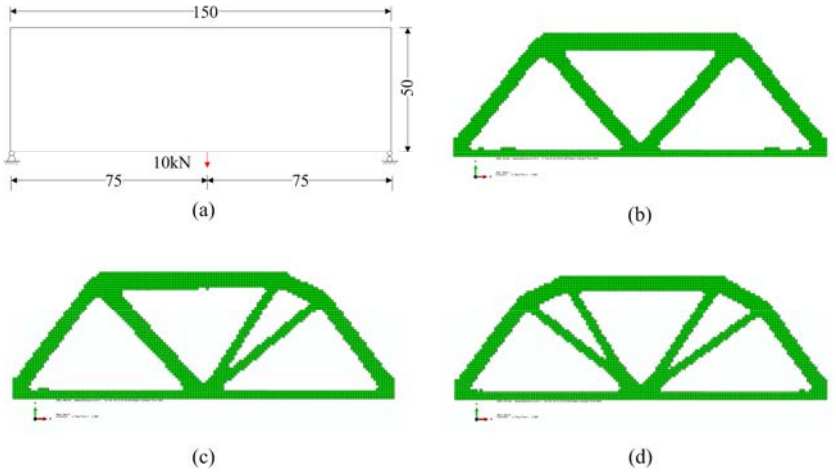


Figure 5: New designs generated by randomly penalizing each element

In order to stabilize the form-finding process, the sensitivity number is averaged with its historical value [6]. The BESO algorithm is history-dependent, where the new sensitivity number includes the sensitivity information in all previous iterations. It is suggested that BESO should start from the full design, as sometimes BESO starting from an initial guess design may converge to a local optimum [7]. However, when concerning the diverse and competitive designs, this feature turns out to be a really effective way to explore alternative structural designs. By employing this feature, we can start the optimization process from a random initial design and different competitive solutions can be obtained. As shown in Figure 6, a few elements are set as void in the initial design. Because of the randomness of the initial conditions, we can achieve different random solutions. In comparison to the initial optimized design (Figure 6a), the compliance of the design in Figure 6b is only 4% higher and the compliance of the design in Figure 6c is even 3% lower.

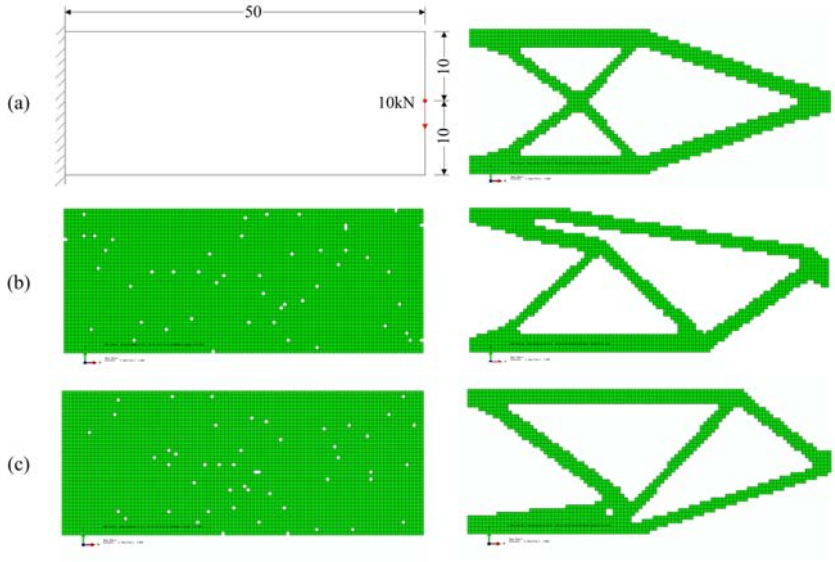


Figure 6: New designs generated by setting random initial conditions

4. Conclusions

Traditional topology optimization techniques are aimed at finding the single optimal solution under given conditions (e.g., loading and boundary conditions). In this work, we have presented three simple and effective approaches to create alternative designs. These approaches are readily implemented by engineers and architects for practical applications. The first strategies takes advantage of the information of the precedent designs, while the second strategy uses constraints as design drivers. The structural performance of the subsequent designs can be controlled by the level of penalty on precedent designs. Constraints have the potential to be the driving force to create new structural forms and it is practically useful when the functional requirements need to be considered in the design, e.g., rooms or columns in the building. In addition to changing the design result by altering the penalty level or design constraints, we can achieve a series of random designs through introducing randomness into our design model. Designers can choose their preferable designs from multiple structurally efficient solutions. It is worth noting that the proposed strategies are applicable to other commonly used topology optimization techniques, although examples shown in this study are based on the BESO technique.

Acknowledgements

This research was financially supported by the Australian Research Council (DP160101400) and the National Natural Science Foundation of China (51778283).

References

[1] M. P. Bendsøe and N. Kikuchi, "Generating optimal topologies in structural design using a homogenization method," *Computer Methods in Applied Mechanics and Engineering*, vol. 71, no. 2, pp. 197-224, 1988.

[2] M. P. Bendsøe, "Optimal shape design as a material distribution problem," *Structural Optimization*, vol. 1, no. 4, pp. 193-202, 1989.

[3] M. P. Bendsøe and O. Sigmund, *Optimization of Structural Topology, Shape, and Material*. Springer, 1995.

[4] M. Y. Wang, X. Wang, and D. Guo, "A level set method for structural topology optimization," *Computer Methods in Applied Mechanics and Engineering*, vol. 192, no. 1-2, pp. 227-246, 2003.

[5] G. Allaire, F. Jouve, and A.-M. Toader, "Structural optimization using sensitivity analysis and a level-set method," *Journal of Computational Physics*, vol. 194, no. 1, pp. 363-393, 2004.

[6] X. Huang and Y. M. Xie, "Convergent and mesh-independent solutions for the bi-directional evolutionary structural optimization method," *Finite Elements in Analysis and Design*, vol. 43, no. 14, pp. 1039-1049, 2007.

[7] X. Huang and Y. M. Xie, *Evolutionary Topology Optimization of Continuum Structures: Methods and Applications*. Chichester: Wiley, 2010.

[8] Y. M. Xie and G. P. Steven, *Evolutionary Structural Optimization.* London: Springer, 1997.

[9] B. Hassani and E. Hinton, *Homogenization and Structural Topology Optimization: Theory, Practice and Software*. London: Springer, 1999.

[10] N. P. van Dijk, K. Maute, M. Langelaar, and F. van Keulen, "Level-set methods for structural topology optimization: a review," *Structural and Multidisciplinary Optimization*, vol. 48, no. 3, pp. 437-472, 2013.

[11] J.-H. Zhu, W.-H. Zhang, and L. Xia, "Topology optimization in aircraft and aerospace structures design," *Archives of Computational Methods in Engineering*, vol. 23, no. 4, pp. 595-622, 2016.

[12] M. Cavazzuti, A. Baldini, E. Bertocchi, D. Costi, E. Torricelli, and P. Moruzzi, "High performance automotive chassis design: a topology optimization based approach," *Structural and Multidisciplinary Optimization*, vol. 44, no. 1, pp. 45-56, 2011.

[13] J. D. Deaton and R. V. Grandhi, "A survey of structural and multidisciplinary continuum topology optimization: post 2000," *Structural and Multidisciplinary Optimization*, vol. 49, no. 1, pp. 1-38, 2014.

[14] L. Xia, Q. Xia, X. Huang, and Y. M. Xie, "Bi-directional evolutionary structural optimization on advanced structures and materials: a comprehensive review," *Archives of Computational Methods in Engineering*, vol. 25, no. 2, pp. 437-478, 2018.

[15] Z.-L. Zhao, S. Zhou, X.-Q. Feng, and Y. M. Xie, "On the internal architecture of emergent plants," *Journal of the Mechanics and Physics of Solids*, vol. 119, pp. 224-239, 2018.

[16] O. Sigmund, "On the design of compliant mechanisms using topology optimization," *Journal of Structural Mechanics*, vol. 25, no. 4, pp. 493-524, 1997.

[17] A. P. Seyranian, E. Lund, and N. Olhoff, "Multiple eigenvalues in structural optimization problems," *Structural Optimization*, vol. 8, no. 4, pp. 207-227, 1994.

[18] G. Cheng and Z. Jiang, "Study on topology optimization with stress constraints," *Engineering Optimization*, vol. 20, no. 2, pp. 129-148, 1992.

[19] G. Cheng and X. Guo, "ε-relaxed approach in structural topology optimization," *Structural Optimization*, vol. 13, no. 4, pp. 258-266, 1997.

[20] Y. Chen, S. Zhou, and Q. Li, "Multiobjective topology optimization for finite periodic structures," *Computers & Structures*, vol. 88, no. 11-12, pp. 806-811, 2010.

[21] J. Deng, J. Yan, and G. Cheng, "Multi-objective concurrent topology optimization of thermoelastic structures composed of homogeneous porous material," *Structural and Multidisciplinary Optimization*, vol. 47, no. 4, pp. 583-597, 2013.

[22] B. Wang, Y. Zhou, Y. Zhou, S. Xu, and B. Niu, "Diverse competitive design for topology optimization," *Structural and Multidisciplinary Optimization*, vol. 57, no. 2, pp. 891-902, 2018.

[23] A. Kilian, *Design Exploration through Bidirectional Modeling of Constraints*, Doctoral thesis, MIT, 2006.

[23] K. Yang, Z.-L. Zhao, Y. He, S. Zhou, Q. Zhou, W. Huang and Y. M. Xie, "Simple and effective strategies for achieving diverse and competitive structural designs," *Extreme Mechanics Letters*, vol. 30, 100481, 2019.

[24] M. P. Bendsøe and O. Sigmund, *Topology Optimization: Theory, Methods and Applications.* Berlin: Springer, 2003.

[25] O. Sigmund and J. Petersson, "Numerical instabilities in topology optimization: a survey on procedures dealing with checkerboards, mesh-dependencies and local minima," *Structural Optimization*, vol. 16, no. 1, pp. 68-75, 1998.

[26] B. Bourdin, "Filters in topology optimization," *International Journal for Numerical Methods in Engineering*, vol. 50, no. 9, pp. 2143-2158, 2001.

[27] C. Cui, H. Ohmori, and M. Sasaki, "Computational morphogenesis of 3D structures by extended ESO method," *Journal of the International Association for Shell and Spatial Structures*, vol. 44, no. 1, pp. 51-61, 2003.

[28] J. Burry and M. Burry, *The New Mathematics of Architecture*. New York: Thames & Hudson, 2010.

[29] D. A. White and A. Voronin, "A computational study of symmetry and well-posedness of structural topology optimization," *Structural and Multidisciplinary Optimization*, vol. 59, no. 3, pp. 759-766, 2019.

Proceedings of the IASS Annual Symposium 2019 – Structural Membranes 2019
Form and Force
7 – 10 October 2019, Barcelona, Spain
C. Lázaro, K.-U. Bletzinger, E. Oñate (eds.)

Hybrid connection distribution optimization of precast concrete frames using GA-based method

Bowen JIANG[a], Xiao LAI[a], Bin DU[a], Zheng HE*, Guohui HUANG[b], Feng PAN[c]

* State Key Laboratory of Coastal and Offshore Engineering, Dalian University of Technology, Dalian, China
Email: hezheng@dlut.edu.cn

[a] Dalian University of Technology, Dalian, China
[b] China Machinery International Engineering Design & Research Institute Co., Ltd, Changsha, China
[c] Shanghai Construction No.5 (Group) Co., Ltd, Shanghai, China

Abstract

Previous researches in improving the seismic performance of prefabricated structures have mostly focused on proposing new forms of connections and joints. But it usually takes a long period of time from the research to the use in practice. The cost could usually be another constraint. This paper presents an optimization method considering hybrid connections distribution of precast concrete frames for the earthquake design. The optimization process aims to find a reasonable arrangement of different types of connections to improve the seismic performance and save the cost of precast concrete frames. A niched master-slave genetic algorithm is used for the optimization and Sap2000 is used for the finite element analysis. The mode decomposition method is used for the earthquake action analysis. Parameters related to the structural stiffness such as the lateral stiffness ratio and the inter-story drift are considered as constraints. And a multi-stage cost is considered as the objective. The result reveals that the optimized structure reduces the connection cost to a great extent and exhibits a more reasonable deformation form under frequent earthquakes compared to those with traditional connection forms.

Keywords: structural optimization, precast concrete frame, genetic algorithm, hybrid connections, earthquake design

1. Introduction

More and more researchers have introduced optimization methods into the structural design field. In terms of prefabricated structures, Andam [1] used the Rosenbrock algorithm to implement the optimization of precast concrete structures. The cost model consists of fabrication, haulage, foundation, cladding and erection costs. Catallo [2] uses the genetic algorithm and fuzzy theory to deal with the anti-optimization problem considering structural reliability. Augusto [3] uses genetic algorithms to optimize the cost of the prefabricated concrete floor in the process of manufacture, transportation, and assembly. Yepes [4] proposes a hybrid glowworm swarm algorithm to solve the cost and CO_2 emission optimization problem of precast concrete road bridges. Most of precast concrete structural optimization problems use geometry parameters or the size of components as variables, and few researchers consider the distribution of connections. The seismic performance of the prefabricated structure is directly related to connection forms. When the whole structure adopts the connection form with poor rigidity, it is easy to cause a large increase in the lateral displacement of the structure and even an unreasonable brittle failure mode under the strong lateral load. But the use of high-strength and high-stiffness joints such as welded steel plate joints [5] will result in higher engineering costs.

The genetic algorithm was first proposed by Holland [6] according to Darwin's theory of evolution. After decades of development, it has been widely used in structural optimization problems. Okasha [7]

Copyright © 2019 by Bowen Jiang, Xiao Lai, Bin Du, Zheng He, Guohui Huang, Feng Pan
Published by the International Association for Shell and Spatial Structures (IASS) with permission.

uses the genetic algorithm to perform a structural maintenance optimization considering reliability, redundancy and life-cycle costs of the system. Garg [8] uses the hybrid genetic algorithm to deal with the structural cost optimization problem, which shows the applicability of the genetic algorithm to engineering problems. In this paper, A GA-based method is used to deal with the hybrid connection distribution optimization problem. The optimization algorithm is used to search the mixed distribution form of connections in the frame structure in order to obtain the reasonable deformation of the structure under the earthquake action and control the construction cost effectively. This method does not require the extensive use of high-strength materials or additional supports, but rather controls the performance of the structure by connections themselves. Compared with size optimization problems, it can be more flexible to control the stiffness distribution because the component grouping is not necessary for this process. The effect of this method is ultimately illustrated by an optimization design process for a high-rise frame structure.

2. Hybrid connection distribution optimization model

The performance of the prefabricated structure can be flexibly controlled by the hybrid arrangement of connections within the structure. For a relatively complex structure, it is often difficult to obtain an optimal design by relying solely on the designers' experience to control the connection distribution artificially. It makes sense to realize the optimization design by means of optimization algorithms and the computing power of modern computers. To this end, it is necessary to establish an optimization model firstly.

2.1. Precast concrete frame connection forms

Due to the different ability of joints to transmit the bending moment, shearing force, etc., the performance of the overall structure will ultimately be affected by the form of joints. In this optimization problem, four common connection forms with different rotation stiffness and manufacturing costs are adopted. Distribution of these four kinds of connections will directly affect the response of the structure under load. The first type of connections connects components by welding steel pipes or plates that are embedded in columns into those of beams. This connection type is well developed and close to a rigid connection. The second type of connections connects steel plates that are embedded in components by high-strength bolts. According to Choi *et al*. [9], the connection has high strength and stiffness but is still a typical semi-rigid connection. The third kind inserts billets into columns and connects beams and columns by steel pins and angle steel. Compared with the welded steel plate connection, the connection doesn't contain large-area steel in beams and columns. The stiffness is lower than the two kinds mentioned before, but it is still a semi-rigid connection. The last connection form is the commonly used pinned connection form in engineering. This kind of joints connects beams to corbels with pins and continuous steel bar. A great number of researchers studied the performance of this kind of connections by experiments and numerical simulations [10-12]. Results show that their strength and stiffness are weaker than general connections. But the connection has the advantage of lower price.

2.2. Cost model

The traditional structural optimization process targets the total weight of the structure. This kind of evaluation method has an acceptable accuracy when the structure is relatively simple and component forms are not diversified. However, for prefabricated structures with kinds of complicated forms of connections, designers need to consider the cost with more aspects which include machining and installation of materials and components. Although these connections account for a lower proportion of total weight in structures, the cost of production and processing constitutes a non-negligible part of the total cost according to the research by Hamchaoui [13]. Secondly, the on-site splicing processes of different connection forms are also different. Nizar [14] considered a series of costs such as materials, workshop labor costs, installation labor costs and construction costs in his research of the steel frame

section optimization. The result proved the rationality of adopting this multi-stage cost assessment approach for prefabricated structures.

Reinforcements and the size of concrete components do not change during the optimization process and only the change of connection forms has an influence on the total cost. The cost of connections can be divided into material, processing and installation costs. The total cost is formed by the superposition of those three kinds. The cost of materials can be calculated by the quantity and quality of materials and components. For finished products on the market, costs could be directly calculated with the price. The processing cost of materials includes costs of cutting, drilling, milling, welding, etc. of steel. Usually, the total processing cost is calculated according to the type of machinery that is used in the processing process and man-hours consumed. The cost of the on-site assembly is mainly determined by the on-site steel plate welding, bolting, and anchoring. It can be calculated by the type of workers and required working hours.

2.3. Optimization problem description and expression

In order to obtain a reasonable stiffness distribution and the minimum cost of the structure, this optimization problem takes manufacturing, processing and assembly costs of connections as optimization objectives and the limits of the inter-story drift ratio, lateral stiffness ratio as constraints. The optimization expressions are as follows:

$$\min \ C = C_1 + C_2 + C_3 \tag{1}$$

$$s.t.\ \Delta u_i / h_i < \delta_{iu} \quad i = 1,2,...,n \tag{2}$$

$$\gamma_1 = \frac{V_i \Delta_{i+1}}{V_{i+1} \Delta_i} \geq 0.7 \quad i = 1,2,...,n \tag{3}$$

$$\gamma_2 = \frac{3V_i / \Delta_i}{(V_{i+1} / \Delta_{i+1} + V_{i+2} / \Delta_{i+2} + V_{i+3} / \Delta_{i+3})} \geq 0.8 \quad i = 1,2,...,n \tag{4}$$

In formula (1), the total price C consists of three parts. C1, C2, C3 represent material, processing and installation costs respectively. The optimization process takes steps towards the minimum cost of all connections.

In formula (2), Δu_i represents the inter-story drift of the i^{th} story, h_i represents the story height, δ_{iu} is the limit of inter-story drift ratio stipulated by codes and n is the total number of stories of the structure;

In formula (3) and (4), V_i, V_{i+1}, V_{i+2}, and V_{i+3} represent the seismic shearing force of the i^{th}, $i+1^{th}$, $i+2^{th,}$ and $i+3^{th}$ floor respectively. Δi, $\Delta i+1$, $\Delta i+2$, $\Delta i+3$ represent the inter-story drift of the i^{th}, $i+1^{th}$, $i+2^{th}$ and $i+3^{th}$ floor under seismic action. Experimental studies show that the lateral stiffness ratio of a story to its upper adjacent story and the average value of the upper three adjacent stories should not be less than 0.7 and 0.8 respectively. Otherwise, irregularities of the vertical stiffness distribution may occur which may lead to unreasonable forms of damages under large earthquakes.

3. Handling of discrete optimization problems

In the optimization process, positions of connections are at the end of beams and the optimization problem takes the type of the connection at each position as the variable. These variables are a series of discrete variables and the genetic algorithm is used to solve this problem. The penalty function method is used for constraints handling. The parallel strategy and niched scheme are adopted to improve the ability of the genetic algorithm to handle complex engineering problems.

3.1. Master-slave parallel genetic algorithm

Goldberg [15] gave a detailed introduction to genetic algorithms in his book. Traditional genetic algorithms have strong applicability when dealing with simple discrete variable optimization problems. For specific engineering problems, in order to avoid excessive search time due to more optimization variables and larger search spaces, it is necessary to use the acceleration technology to increase the speed of the algorithm. The master-slave parallelization and multi-population strategy are two commonly used acceleration strategies. The multi-population acceleration strategy divides the original population into a certain number of sub-populations. Studies indicated that the average fitness value of individuals in sub-populations will show a faster growth rate [16]. Although the multi-population genetic algorithm has become one of the most popular acceleration strategies so far, there are still problems such as the determination of rational migrations that have not been completely solved. The master-slave parallel strategy is a purer acceleration strategy. The master stores the population and is responsible for the crossover, mutation and other operations between individuals while slaves are only responsible for assessing individuals' fitness. The algorithm is equivalent to the simple genetic algorithm, but it fully calls computer threads and greatly increases the calculation speed.

3.3. Constraints handling

The genetic algorithm-based optimization method can only deal with unconstrained optimization problems. For constrained problems, constraints need to be handled. Among these handling techniques, the penalty function method, special representations and operators, repair algorithms, etc. are commonly used [17]. In this optimization process, a dynamic penalty function method is used. Individuals are punished according to the degree of constraint violations and the generation number. In order to integrate constraint inequalities into the objective function, all inequalities need to be standardized. The standardized constraint functions are as follows:

$$g_{1,i} = \Delta u_i / h_i - \delta_{iu} \quad i = 1,2,...,n \tag{5}$$

$$g_{2,i} = 0.7 - \frac{V_i \Delta_{i+1}}{V_{i+1} \Delta_i} \quad i = 1,2,...,n \tag{6}$$

$$g_{3,i} = 0.8 - \frac{3V_i / \Delta_i}{(V_{i+1} / \Delta_{i+1} + V_{i+2} / \Delta_{i+2} + V_{i+3} / \Delta_{i+3})} \quad i = 1,2,...,n \tag{7}$$

The new objective function takes constraint violations of individuals into account:

$$F = C + r_k \sum_{j=1}^{3} (g_{j,i})^2 u_i \tag{8}$$

Where,

$$u_i = \begin{cases} 1, & g_{j,i} > 0 \\ 0, & g_{j,i} \le 0 \end{cases} \tag{9}$$

r_k is a positive number that grows with iterations. Penalties at the beginning of iterations are relatively small, which allow the retention of individuals that are not too far away from boundaries. This is reasonable at the beginning of the optimization, which allows individuals to approach the optimal solution from the unfeasible domain and increases the initial search space so that the algorithm has a greater probability of convergence to the global optimum. In the later stage of the optimization process, the gradual increase of r_k causes individuals who violate constraints to be attached with larger objective function values, which accelerates the movement of individuals outside the feasible domain. In this paper, r_k increases exponentially. Considering that the inter-story drift constraint violation is relatively

small, an amplification factor of 10^8 will be used to balance its contribution to the objective value with other constraints.

3.3. Optimization procedure

The hybrid connection distribution optimization process is based on the master-slave parallel genetic algorithm. The optimization process consists of several steps, i.e. 1) Establish a gene decoding rule to map an individual's genes into variables including connection types and positions; 2) Use a random generator to generate an initial population of 50; 3) Import individuals' information into the finite element analysis unit and assign them to different computer threads for finite element analysis and calculation. And then displacement, shearing force, and other information are output; 4) Complete fitness calculation in each slave and store the value as a part of individual information; 5) Return all individuals to the master and sort the individuals by their fitness values, then store the maximum fitness value of individuals, select 8 elite individuals, exclude individuals with similar genetic compositions and lower fitness values by the crowding strategy; 6) Elite individuals perform crossover and mutation operations according to the probability. Retained elite individuals and their offspring make up a new population with 24 individuals; 7) Return to step 3 and enter the next generation of the algorithm. When the best individual is not updated in multiple generations, the algorithm is considered to have converged. The exclusion-based elite selection mechanism [18] in step 5 is a common strategy of the niche technology to ensure the diversity of the population. The crowding factor is designed to exclude a certain number of similar individuals. The degree of similarity between genes of individuals can be measured by hamming distance.

4. Design case

A twenty-story, three-bay design example is used to illustrate the specific process of optimizing the connection distribution with the niched master-slave genetic algorithm. In this case, the concrete strength grade is C40. The column size is estimated by the axial pressure ratio and is not lower than the limit of the 400 mm. The beam height is initially estimated by the span, and the width is not higher than 2/3 of the column width. Under this principle, structural components are divided into four groups marked as 1, 2, 3 and 4. The dimensions are 500 mm × 500 mm, 450 mm × 450 mm, 400 mm × 400 mm, and 250 mm × 500 mm.

In this paper, the lateral load calculated by the vibration mode decomposition method is considered. According to the Chinese code for seismic design [19], the horizontal seismic influence coefficient is 0.16 under an 8-degree earthquake. The site characteristic period is 0.4s. Columns are considered to be continuous in the vertical direction and connections are uniformly located at the end of beams. The cost of materials is based on the market price of Chinese mainland, including 5800 ¥/t for steel, 365¥/m^3 for concrete and 10~20¥/ for bolts. The processing cost is estimated according to the type of machines hired and working hours. The cost of installation is determined based on installation hours. It should be noted that it is still difficult to obtain a completely accurate estimation. The processing cost is affected by various factors such as the processing accuracy, geographic location and component form, but it can usually be roughly estimated according to the size or volume of components to be processed. As the size and complexity of components increase, processing costs will also increase. According to above principles, the cost generated in the entire structure construction process of the four kinds of connections is shown in Table 1.

The optimization history of the master-slave genetic algorithm using niche scheme is shown in Figure 7. Before 25 generations, the optimal individuals often appear outside the constraint boundary and objective values are often several orders of magnitude higher than those of individuals in the later stage. But it is necessary to reserve these individuals in the initial stage of optimization. After 25 generations, optimal individuals have all entered the feasible region and moved towards the optimal solution. Fitness values do not change after about 275 generations and the connection distribution result is shown in Figure 6. The statistical result of the connection distribution of each floor is shown in Fig. 5. It can be

seen that the distribution of various connections is not completely uniform and symmetrical, but still exhibits a certain rule. Rigid connections with larger rotational stiffness are distributed more in middle and lower positions of the structure, and pinned connections with almost negligible stiffness are mainly concentrated in the upper part of the structure. From the perspective of the algorithm, the optimization process will push individuals to be closer to the constraint boundary. In order to achieve this, the stiffness required on each floor is different. The genetic algorithm retains the connection distribution form that meets requirements and has the smallest objective value during the optimization process. What's more, since the added seismic action is unidirectional, connections of different kinds exhibit an asymmetrical distribution. In addition, when the whole frame adopts the same kind of connections, the overall structure exhibits the shearing deformation and shear deformations of lower stories are larger than upper stories. The optimization process makes the structure a bending-shearing deformation form with relatively uniform deformations, which requires that the lower structure has a relatively large rigidity and the upper structure a relatively lower rigidity due to the difference of horizontal seismic shearing force.

Table 1: Connection cost (¥)

Connection type	Cost estimation			
	Material cost	Processing cost	Installation cost	Total cost
Welded steel plate connection(C1)	3083.6	5149.5	515.8	8748.9
Steel bolt connection(C2)	2576.8	3298.3	349.1	6224.2
Billet connection(C3)	1104.8	1237.3	218.3	2560.4
Steel pin connection(C4)	525.8	\	215.7	741.5

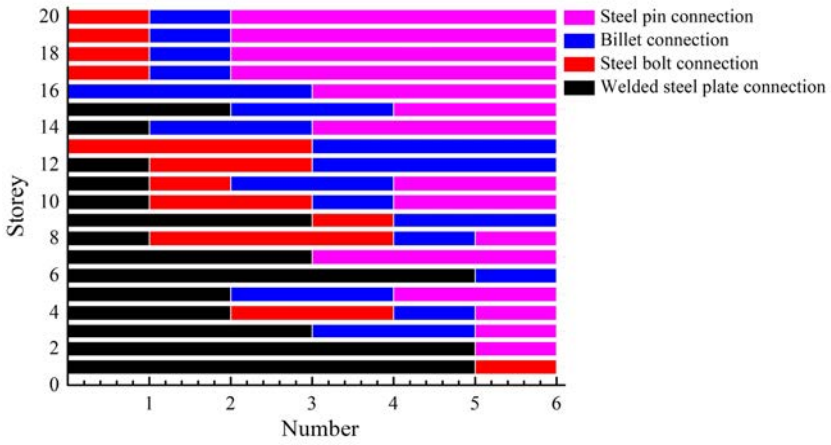


Figure 5: Distribution of different types of connections along the floors

The displacement responses of structures with different types of connections are shown in Fig. 8. Compared with traditional connection forms, the structure with hybrid connections exhibits a more reasonable bending-shearing deformation. There are no relatively weak parts and the deformation ability of each component can be fully utilized. In addition, compared with the bolt connection form which costs 0.747 million yuan, hybrid connections only costs 0.506 million yuan with a decrease of the max inter-story displacement by 51%. Compared with welded steel plate connections which cost 1.050 million yuan, hybrid connections save the cost by nearly a half. Although billet connections only cost 0.307 million yuan but its max inter-story displacement is far from the limit. As a result, the optimized structure could save the construction cost and improve the structural deformation form at the same time, which is also a goal pursued by engineers.

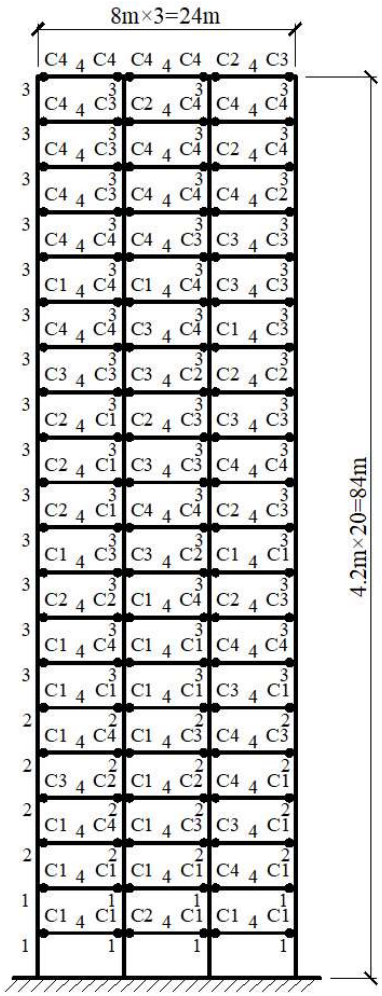


Figure 6: Connection distribution result

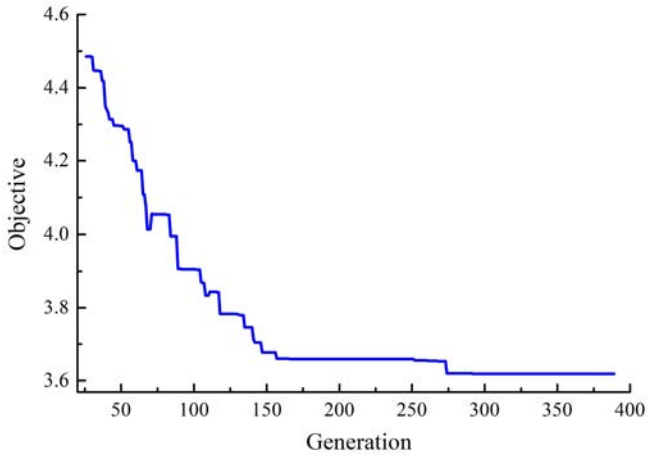


Figure 7: The optimization process

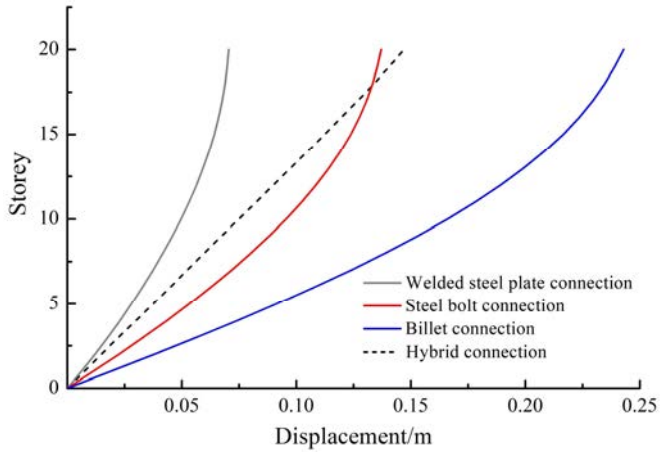


Figure 8: Displacement response of structures with different connections

5. Conclusions

According to the above optimization results, the following conclusions can be drawn: 1) The structural deformation with hybrid connections is different from the shearing deformation of traditional frame structures. It shows a bending-shearing deformation form and a relatively uniform distribution of inter-story displacement. 2) There are more connections with high rotation stiffness in the lower part of the structure and more connections with low rotation stiffness in the upper part. The distribution of these connections allows the structure to meet the requirements for stiffness at different heights, improving the efficiency of connections and components used and suppressing adverse failure modes. This deformation form is produced without additional rigid components such as supports or shear walls, which also provides a new idea for the designing of prefabricated structures with reasonable deformation forms. 3) Compared with traditional semi-rigid connections, structures with hybrid connections achieve a significant reduction in engineering construction costs without sacrificing significant mechanical properties. It also provides a significant improvement in displacement control. Therefore, the hybrid connection strategy allows engineers to get high-performance, low-cost prefabricated structures with the help of optimization methods.

Acknowledgements

This research is financially supported by the Natural Science Foundation of China (Grant No. 51878123) and the Fundamental Research Funds for the Central Universities (Grant No. DUT19G208).

References

[1] K. A. Andam and J. Knapton, "Optimum cost design of precast concrete framed structures," Eng. Optim., vol. 5, no. 1, pp. 41–49, 1980.

[2] L. Catallo, "Genetic anti-optimization for reliability structural assessment of precast concrete structures," Comput. Struct., vol. 82, no. 13–14, pp. 1053–1065, 2004.

[3] T. Augusto, K. Mounir, and A. M. C. Melo, "A cost optimization-based design of precast concrete floors using genetic algorithms," Autom. Constr., vol. 22, pp. 348–356, 2012.

[4] V. Yepes, J. V Mart\'\i, and T. Garc\'\ia-Segura, "Cost and CO2 emission optimization of precast--prestressed concrete U-beam road bridges by a hybrid glowworm swarm algorithm," Autom. Constr., vol. 49, pp. 123–134, 2015.

[5] K. S. Elliott and C. Jolly, Multi-storey precast concrete framed structures. Wiley, 2013.

[6] J. H. Holland, "Genetic algorithms," Sci. Am., vol. 267, no. 1, pp. 66–73, 1992.

[7] N. M. Okasha and D. M. Frangopol, "Lifetime-oriented multi-objective optimization of structural maintenance considering system reliability, redundancy and life-cycle cost using GA," Struct. Saf., vol. 31, no. 6, pp. 460–474, 2009.

[8] H. Garg, "A hybrid PSO-GA algorithm for constrained optimization problems," Appl. Math. Comput., vol. 274, pp. 292–305, 2016.

[9] H.-K. Choi, Y.-C. Choi, and C.-S. Choi, "Development and testing of precast concrete beam-to-column connections," Eng. Struct., vol. 56, pp. 1820–1835, 2013.

[10] E. A. B. Aguiar, E. K. Bellucio, and M. K. El Debs, "Behaviour of grouted dowels used in precast concrete connections," Struct. Concr., vol. 13, no. 2, pp. 84–94, 2012.

[11] M. K. El Debs, A. M. Miotto, and A. L. H. C. El Debs, "Analysis of a semi-rigid connection for precast concrete," Proc. Inst. Civ. Eng. Build., vol. 163, no. 1, pp. 41–51, 2010.

[12] K. S. Elliott, G. Davies, M. Ferreira, H. Gorgun, and A. A. Mahdi, "Can precast concrete structures be designed as semi-rigid frames? Pt. 1: the experimental evidence.," Struct. Eng., vol. 81, no. 16, pp. 14–27, 2003.

[13] M. Hamchaoui, "Conception économique des assemblages en Construction Métallique," Chambéry, 1997.

[14] N. B. H. Ali, M. Sellami, A.-F. Cutting-Decelle, and J.-C. Mangin, "Multi-stage production cost optimization of semi-rigid steel frames using genetic algorithms," Eng. Struct., vol. 31, no. 11, pp. 2766–2778, 2009.

[15] D. E. Goldberg, "Genetic Algorithms in Search. Optimization and Machine Learning, 1989, Addi-son-Wesley," Reading, MA.

[16] P. Grosso, "Computer simulations of genetic adaptation: Parallel subcomponent interaction in multilocus model," Ph. D. Diss. Univ. Michigan, 1985.

[17] C. A. C. Coello, "Theoretical and numerical constraint-handling techniques used with evolutionary algorithms: a survey of the state of the art," Comput. Methods Appl. Mech. Eng., vol. 191, no. 11–12, pp. 1245–1287, 2002.

[18] S. W. Mahfoud, "Niching methods for genetic algorithms," Citeseer, 1995.

[19] Ministry of Housing and Urban-Rural Development of the People's Republic of China, GB 50011-2010, Code for Seismic Design of Buildings, China Architecture & Building Press, Beijing, 2010.

Proceedings of the IASS Annual Symposium 2019 – Structural Membranes 2019
Form and Force
7 – 10 October 2019, Barcelona, Spain
C. Lázaro, K.-U. Bletzinger, E. Oñate (eds.)

Layout optimization of elasto-plastic dampers for perimeter steel braced frames based on Generalized Response Spectrum Analysis

Yuki TERAZAWA* and Toru TAKEUCHI[a]

*Assistant professor, Department of Architecture and Building Engineering, Tokyo Institute of Technology
2-12-1-M1-29 Ookayama, Meguro-ku, Tokyo 158-84.40, Japan
terazawa.y.aa@m.titech.ac.jp

[a]Professor, Department of Architecture and Building Engineering, Tokyo Institute of Technology

Abstract

This paper presents the damper layout optimization of elasto-plastic dampers, such as buckling restrained braces (BRBs), for steel braced tubes to analyze the effective member configuration for various objective functions. The author's proposed generalized RSA-based optimal damper design strategy is adopted in this study.

Keywords: response spectrum analysis, non-proportional damped system, complex stiffness, elasto-plastic damper, layout optimization

1. Introduction

It is growing common to employ energy-dissipation devices because numerous structures are recently required continuous use even after large earthquakes. Elasto-plastic dampers, such as buckling-restrained braces (BRBs), particularly act as fuses to prevent member buckling of axial members, and are hence widely used. The challenge is to determine a set of discrete locations where a limited number of dampers would be most effective, and in practice, designers tend to rely on time-consuming trial-and-error studies using non-linear response history analysis (NLRHA) except for building systems that are easily translated into lumped mass models. In constraint, the authors proposed a generalized response spectrum analysis (GRSA) for highly indeterminate 3-D structures considering both viscous and elasto-plastic damping (Terazawa et al. [1]). As GRSA requires few computational resources compared with NLRHA, it can be used for genetic optimization studies and the authors demonstrated the efficiency of the proposed RSA-based optimal damper design strategy in the previous work (Terazawa et al. [2]). However, the author's application study was limited to single-span lattice tower, and there are still few optimization studies of elasto-plastic dampers under seismic loads. Moreover, the appropriate settings of damper optimization problems considering practical design criteria are still unknown. Therefore this paper presents the layout optimization studies of elasto-plastic dampers for the multi-spans braced tubes shown in Figure 2 to analyze the effective member arrangements with the various objective functions and various layout operations.

2. Methodology

The proposed GRSA-based optimal damper design strategy is briefly explained. Figure 1 shows the schematic image. The core of the proposed strategy is to iteratively conduct a complex eigenvalue analysis and RSA, a process reffered to GRSA. In this design strategy, an optimization algorithm and the GRSA exchange data with each other through simple scripting. Furthermore, these computations are parallel processed on HPC servers. As GRSA constitutes the novel contribution, optimization algorithms are used as pure tools. With the exception of some numerical libraries, the entire source

Copyright © 2019 by Yuki Terazawa and Toru Takeuchi
Published by the International Association for Shell and Spatial Structures (IASS) with permission.

code of the GRSA was written by the first author. Python scripts were used for the data exchange and parallel processing. Python module (DEAP 1.1.0) was used as an optimization tool. TSUBAME 3.0 (28 processors per node) at Tokyo Institute of Technology was used instead of running the optimization on the cloud-based HPC servers. In GRSA, elasto-plastic dampers are modeled as complex stiffness elements (which can simulate displacement-dependent damping.) The modified CQC method for real symmetric damped systems including viscous damping (Sinha and Igusa et al [4]) was extended to complex assymetric damped systems including both complex stiffness and viscous damping, and is iteratively conducted. The detailed procedure is described in the author's papers (Terazawa et al. [1], [2] and [3]).

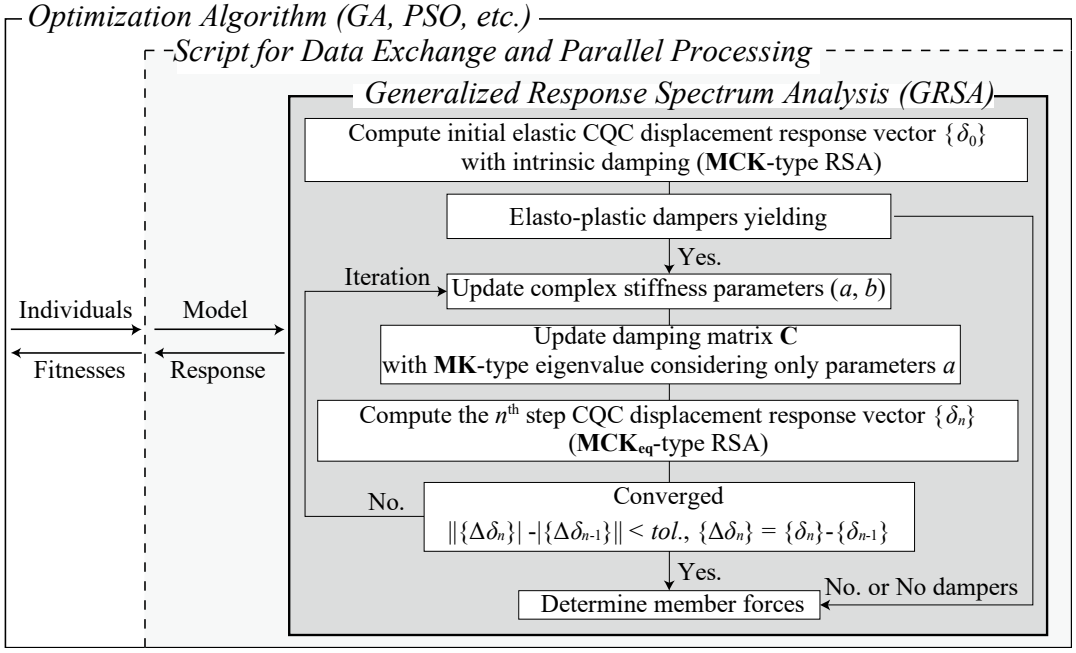


Figure 1: The optimal damper design routine based on GRSA

3. Target Structure and Optimization Problems

Figure 2 shows a schematic of the numerical model in this chapter. The target building is a steel braced tube so that aseismic diagonal members are arranged along the outer periphery of the building. This type of building system is selected because various diagonal member layouts (which are not dependent on the constraint of the architectural design and service equipment) can be designed in this structure. The plane frame extracted from the 3-D model indicated by the dotted line in Figure 2 is adopted, and is designed using the Japanese building code-based ductile design criteria with a base shear ratio C_0 (= 1.0), considering the corresponding dead load as a concentric perimeter braced frame (hereinafter referred to as "CBF"). The member specifications are listed in Table 1. Figure 3 shows the dominant modes. Diagonal members significantly affect the natural period because the bare frame was designed only for the vertical load. As shown in Figure 4, while the horizontal stiffness of the CBF is high and SDRs less than approximately 1/200 rad, the maximum DCR of the whole structure plotted in gray in Figure 4 is greater than 1.0. On the other hand, the maximum SDR of the whole structure in the bare frame model (hereinafter referred to as the "Frame") is greater than 1/50 rad. The CBF has the above mentioned characteristics, is defined as the initial structure, and is adopted for the member layout optimization.

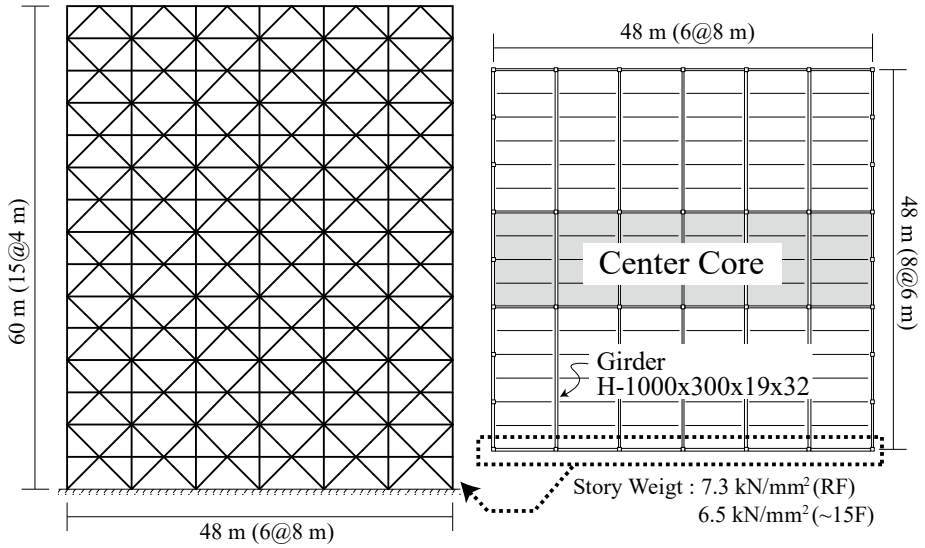


Figure 2: Numerical model schematic of the braced tube

Table 1: Initial member specification

Story	Column SHS (BCP325)	M_{pc} (kNm)	Girder Wide flange (SS400)	M_{pg} (kNm)	M_{pg}/M_{pc}	Brace CHS (STK540)	D/t	Rank
15	500×25	2,490	H-500×300×12×22	895	0.36	ϕ267.4×6.6	41	BC
14	500×25	2,490	H-500×300×12×22	895	0.36	ϕ267.4×6.6	41	BC
13	500×25	2,490	H-500×300×12×22	895	0.36	ϕ267.4×6.6	41	BC
12	500×25	2,490	H-500×300×16×22	945	0.38	ϕ267.4×8.0	33	BC
11	500×25	2,490	H-500×300×16×22	945	0.38	ϕ267.4×8.0	33	BC
10	500×28	2,717	H-500×300×16×22	945	0.35	ϕ267.4×8.0	33	BC
9	500×28	2,717	H-500×300×16×22	945	0.35	ϕ267.4×9.3	29	BC
8	500×28	2,717	H-500×300×16×22	945	0.35	ϕ267.4×9.3	29	BC
7	500×28	2,717	H-500×300×16×22	945	0.35	ϕ267.4×9.3	29	BC
6	500×28	2,717	H-500×300×16×25	1,034	0.38	ϕ318.5×10.3	31	BB
5	500×28	2,717	H-500×300×16×25	1,034	0.38	ϕ318.5×10.3	31	BB
4	500×28	2,717	H-500×300×16×25	1,034	0.38	ϕ318.5×10.3	31	BB
3	500×28	2,717	H-500×300×16×25	1,034	0.38	ϕ318.5×12.7	25	BB
2	500×28	2,717	H-500×300×16×25	1,034	0.38	ϕ318.5×12.7	25	BB
1	500×32	2,993	H-500×300×16×28	1,126	0.38	ϕ318.5×12.7	25	BB

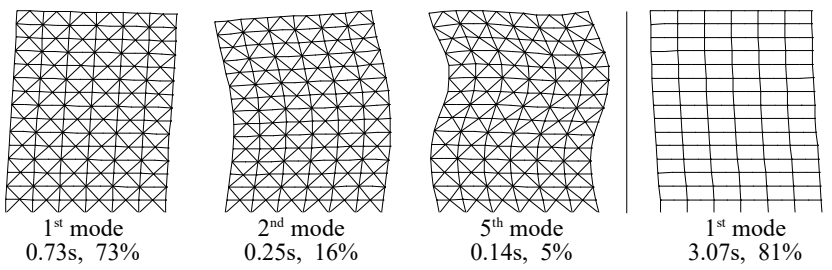


Figure 3: Dominant modes (natural period, mass ratio)

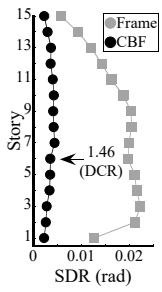
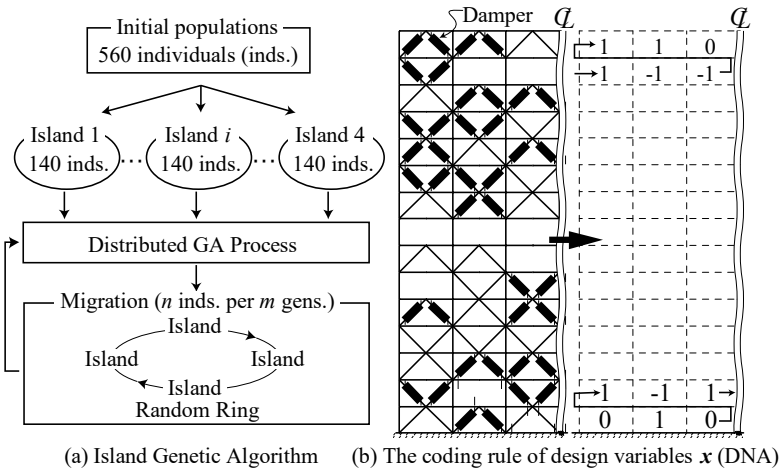


Figure 4: Initial response (El Centro)

The island genetic algorithm is adopted in the optimization calculation. Figure 5 presents the optimization schematic. In the island genetic algorithm, the initial population is separated into partial populations (corresponding to islands), and each island is distributed to a GA process. The islands exchange superior solutions with each other to keep the diversity of solution and prevent local convergence. In addition to the standard process, a large mutation combined with elitism is applied to this optimization, where the mutation ratio is forcibly increased if the fitness-based standard deviation converges. The crossing and mutation are evenly applied to each story, bay, or genetic locus in a DNA code, as shown in Figure 5 (b). The other details are summarized in Table 2.

In addition to three types of DNA operations for the 180 CBs (including "BRB replacement", "CB removal", and "no change"), the column members in the first story are also replaced by BRBs (hereinafter referred to as "BRC replacement"). The chevron configuration for diagonal members and a symmetrical layout are considered for the coding of the DNA vector, $\boldsymbol{x}$, as shown in Figure 5 (b). The number of each diagonal-member-based operation is constrained to 60, which corresponds to the equal condition for the optimization problem including the abovementioned three operations (Section 4.3). However, for the optimization problems including BRC replacements (Section 4.4 and 4.5), the number of arranged BRBs is constrained to 62, which includes at least two columns replaced with BRBs. In Section 4.4 and 4.5, the numbers of BRBs introduced as diagonal members or columns are not separated so that the design solutions are searched evenly and all first story columns are either replaced with BRBs or not. BRC replacement in which only the column on the center line is replaced with a BRB is also allowed. The degree of $\boldsymbol{x}$ is 45 (Section 4.2 and 4.3) or 49 (Section 4.4 and 4.5). The BRB size is defined as 250 kN with a section of 1,111 mm^2. The BRC size is defined as 5,000 kN with a section of 22,222 mm^2.

In this study, the single-objective function is the maximum SDR of the whole structure (hereinafter referred to as "SDR"), the maximum buckling demand capacity ratio of the whole structure (hereinafter referred to as "DCR"), the SDR with a penalty of DCRs or the standard deviation of SDRs (hereinafter referred to as S.D.) with a penalty of DCRs. As shown in Figure 4, three types of spectrally matched input ground motions are considered. As mentioned previously, in this study 16 types of optimization problems are prepared by the four types of operations (including BRB replacement in Section 4.1, BRB replacement + CB removal in Section 4.2, BRB replacement + BRC replacement in Section 4.3, and BRB replacement + CB removal + BRC replacement in Section 4.4), and four types of objective functions are considered. The optimization problem matrix is summarized in Table 4. Note that the seismic response to El Centro, which is generally similar to the average response, is shown in Figures 7 to 10.



(a) Island Genetic Algorithm (b) The coding rule of design variables $\boldsymbol{x}$ (DNA)

Figure 5: Optimization schematic of Island Genetic Algorithm

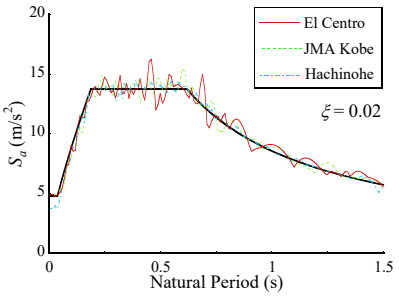


Figure 6: Response spectra

Table 2: Parameter list of the Island Genetic Algorithm

Selection	Crossing (Rate)	Mutate (Rate)	Migration
Tournament (3 inds.)	Uniform (60%)	Shuffle Index (1%)	Random Ring (2 inds., 6 gens.)

Table 3: Parameter list of Island Genetic Algorithm

Section	DNA Operation	Minimize Response of	Subject to the number of
4.1	BRB replaclement	SDR, DCR, SDR with a penalty*1 or S.D. with a penalty*1 *1: DCR < 1.0	BRB (60)
4.2	BRB replaclement + CB removal		BRB (60), CB (60) and Removed CB (60)
4.3	BRB replaclement + BRC replacement		BRB+BRC (62)
4.4	BRB replaclement + CB removal + BRC replacemnt		BRB+BRC (62), CB (60) and Removed CB (60)

4. Analysis of Optimization Results

4.1 Optimal diagonal member layout trends with the BRB replacement

The optimal diagonal member layout trend to minimize the SDR or DCR with only BRB replacement is analyzed first. As shown in Figures 7 (a) and 7 (b), the member layout with i) BRBs almost uniformly arranged along the story height direction are selected for the step to minimize the SDR, and ii) BRBs intensively arranged along the spanwise direction in the continuum stories are selected for the step to minimize the DCR. While the optimal member layout trend, with a centralized BRB arrangement, is efficient for preventing member buckling and similar to the results for the single-span lattice tower (Terazawa et al. [2]); for multi-span buildings, it is suggested that there is a clear difference when optimizing the SDR or DCR. BRB replacement has response reduction and fuse effects, but also has the horizontal stiffness reduction effect from the initial CBF condition. According to this trade-off relationship for the BRB replacement, it is assumed that i) a uniform BRB arrangement along the story height should be selected for the optimal diagonal member layout to minimize the SDR because the horizontal story stiffness distribution (including the equivalent BRB stiffness) is uniform, and ii) the concentrated BRB arrangement along the spanwise direction in the continuum stories should be selected as the optimal solution because these soft stories using the BRB replacement have a response reduction effect similar to seismic isolation. It should be noted that the BRBs are arranged on the outside of each story with the relatively high BRB equivalent stiffness when minimizing the SDR because the story drift in each bay is not uniform owing to the dominant modes, including over bending similar to a multi-story shear wall, as shown in Figure 3. This is the dynamic characteristic of the CBF skin structure.

Nevertheless, the uniform BRB arrangement along the story height for minimizing the SDR reduces the SDRs to 1/200 rad, however the member buckling is not eliminated yet and the concentrated BRB arrangement along the spanwise direction for minimizing the DCR creates the side effect that the larger story drifts are concentrated in the BRB arranged stories. This suggests that these optimization problems produce design solutions that are over optimized for each objective function. Although an efficient technique is to employ a multi-objective optimization, the single-objective optimization with a penalty is purposely adopted in this study. The motivation is that the single-objective optimization for minimizing a specific seismic response type under a penalty is a straightforward approach for the design step prioritization of reducing each response under the design criteria. In this study, the DCR was defined as the penalty (DCRs < 1.0) for the target structure. Figure 7 (c) shows the optimal

diagonal member layout for minimizing the SDR with a penalty of DCRs, and Figure 7 (d) shows the optimal diagonal member layout for minimizing the S.D. with a penalty of DCRs. For both optimization problems, the concentrated BRB layouts along the spanwise direction are distributed in the story height direction for the uniformity of each story drift, and this trend is clearer for the optimization problem that minimizes the S.D. with a penalty of DCRs. The deformation concentration localized in the continuum stories are mitigated although the maximum SDR increases.

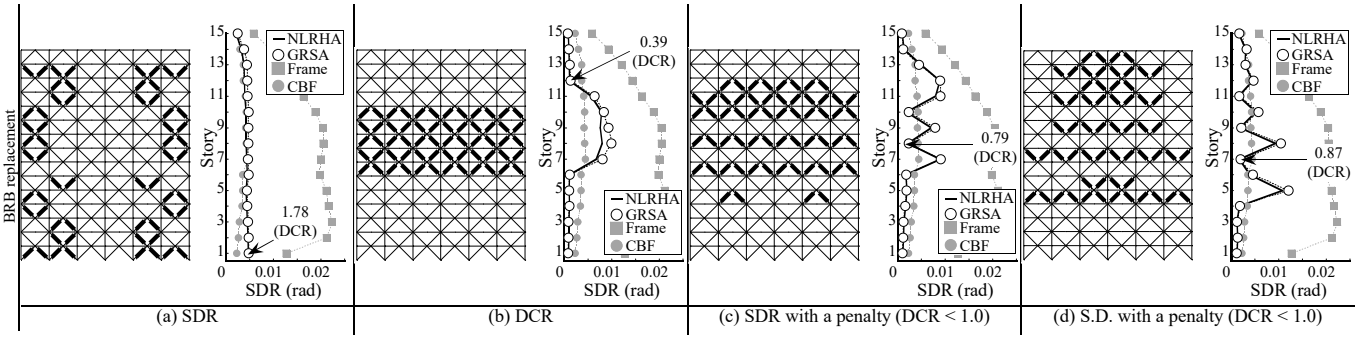


Figure 7: Layout optimization results (Operation: BRB replacement, ex. Response to El Centro)

4.2 Optimal diagonal member layout trends including the CB removal

The optimal diagonal member layout trends including the CB removal are analyzed here. Although the cost efficiency is not included in the objective functions of this study, removing the CBs contributes to a reduction in the amount of steel. As shown in Figure 8 (a), while the uniform BRB arrangement along the story height is selected as the optimal design solution for minimizing the SDR, the BRBs are arranged in the inside of each story, which is different from the optimization problem utilizing only the BRB replacement. It is assumed that the reason for this is that the inside BRB arrangement used for obtaining a large yielding deformation and additional damping effects of the BRBs is more efficient, compared with the outside BRB arrangement used for obtaining a high equivalent stiffness of the BRBs. However, member buckling is not completely eliminated, even when CB removal (the DCR becomes zero in this position) is considered. As shown in Figure 8 (b), the diagonal member layout with CBs in the lower stories replaced with BRBs or removed is selected as the optimal solution for minimizing the DCR, however a large deformation is also localized in the lower stories. On the other hand, as shown in Figures 8 (c) and 8 (d), the optimization problems that consider the penalty of DCRs produce reasonable design solutions that reduce the story drift and eliminate member buckling. In particular, for the optimal diagonal member layout that minimizes the S.D. with a penalty of DCRs, the localization of the story drifts is uniformly mitigated as a result. It is assumed that the reason for this is that the horizontal story stiffness distribution is made uniform by both the concentrated BRB replacement and concentrated CB removal in a story.

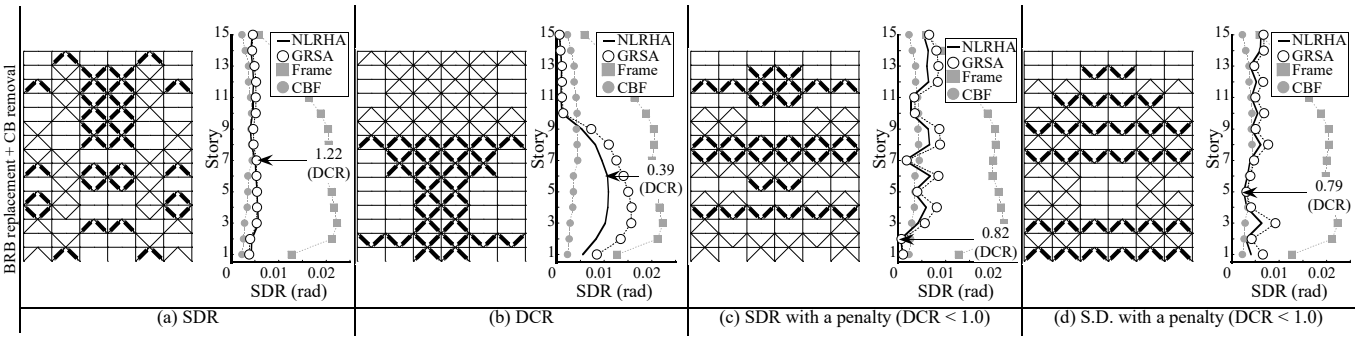


Figure 8: Layout optimization results (Operation: BRB replacement + CB removal, ex. Response to El Centro)

4.3 Optimal member layout trends including the BRC replacement of the first story

The optimal diagonal member layout trends, including the BRC replacement of the first story (positively utilizing the over bending response of the whole structure), are analyzed here. Note that the proposed brace-type complex stiffness (Terazawa et al. [2]) is also applicable for the axial force member as for the BRC. A structure with BRCs is sometimes called a "Spine Frame (Chen et al. [5])." As shown in Figure 9 (a), for the simple optimization problem of minimizing the SDR, the BRBs are arranged in the upper stories where the story drift response is generally small and elasto-plastic dampers cannot experience large yielding deformations. This therefore suggests that the BRBs in the upper stories are wasted as elasto-plastic dampers. As shown in Figure 9 (b), for the simple optimization of minimizing the DCR, the BRBs are intensively arranged in the lower stories, compared with that of Section 4.1, because the first story drift response is increased by allowing BRC replacement. On the other hand, as shown in Figures 9 (c) and 9 (d), for the optimization problem of minimizing the SDR with a penalty of DCRs or the S.D. with a penalty of DCRs, the concentrated BRB layouts along the spanwise direction (efficient for minimizing the DCRs) is not selected. Instead the uniform BRB arrangement along the story height (efficient for minimizing the SDR) between two rocking spine frames is selected as the optimal member layouts, which is clearly different from the cases of Section 4.1 and 4.2. This is because the diagonal member buckling in a design solution belonging to the uniform BRB arrangement is eliminated by utilizing the over bending response of the whole structure.

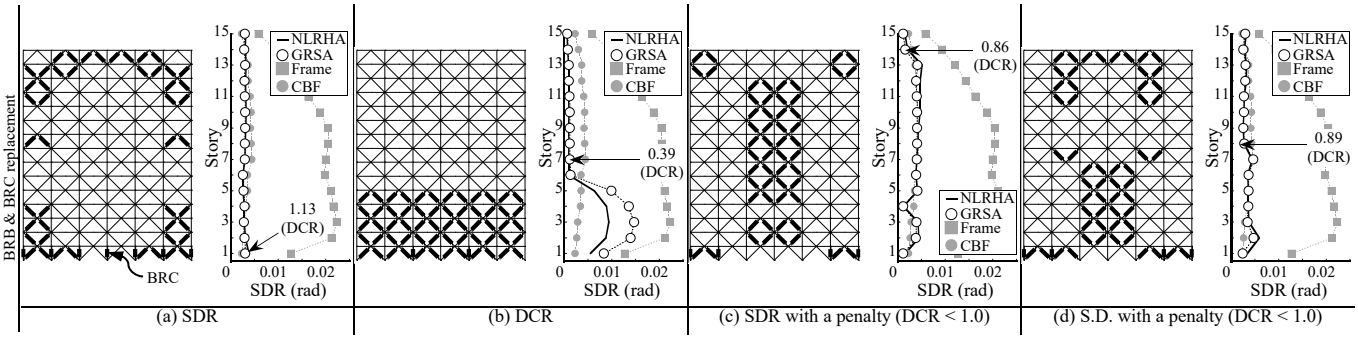


Figure 9: Layout optimization results (Operation: BRB & BRC replacement, ex. Response to El Centro)

4.4 Optimal member layout trends including the CB removal and the BRC replacement of the first story

The optimal member layout trends allowing all operations are analyzed here. It is easy to eliminate member buckling by employing CB removal and BRC replacement of the first story. As shown in Figure 10 (a), even for the simple optimization problem of minimizing the SDR, member buckling is eliminated, which means that the optimization problem of minimizing the SDR with a penalty of DCRs is unnecessary. The layout trend of the BRBs arranged on the inside of each story for obtaining a large additional damping effect is clearer, compared with the optimal member layout that includes only CB removal shown in Figure 8 (a). As shown in Figure 10 (b), the optimal member layout for minimizing the DCR is similar to the optimal member layout that includes only the CB removal shown in Figure 8 (b). As shown in Figure 10 (c), for the optimization problem of minimizing the S.D. with a penalty of DCRs, the member layout in which some BRBs are arranged in the upper stories, as for the result in Section 4.2, is selected as the optimal member layout. It should be noted that the GRSA response evaluation of the individuals (with the BRBs intensively arranged in a story or CBs intensively removed from a story) has a conservative error of approximately 30% because the nonlinearity of these story responses is generally strong according to the stiffness reduction and high damper-to-moment-frame stiffness ratio, as shown in Figures 7 to 10.

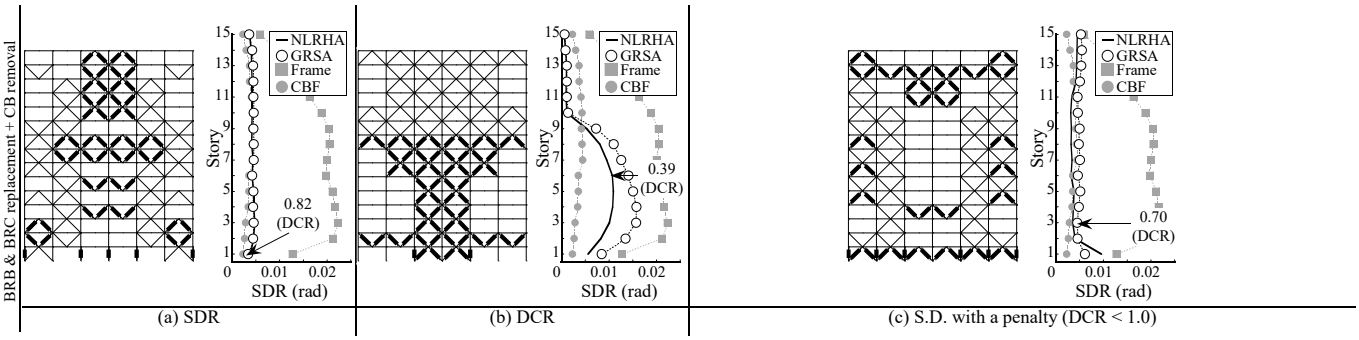


Figure 10: Layout optimization results (Operation: BRB & BRC replacement + CB removal, ex. Response to El Centro)

5. Conclusion

This paper presented the GRSA-based damper layout optimization of elasto-plastic dampers for perimeter steel braced frames. According to the results, for a perimeter braced frame including buckling braces, the simple single-objective optimization of minimizing a specific response does not necessarily produce the optimal design solution satisfying both design criteria of the displacement response and member buckling demand. For those cases, the single-objective optimization with a penalty of the buckling demand capacity ratio or the single-objective optimization considering the additional member layout operation (including the BRC replacement of the columns) successfully provided practical solutions. On the other hand, from this study, it proved that the proposed GRSA-based optimal damper design stratedy can produce various design options. The authors is planning to distribute the optimization routine as an open source module.

Acknowledgements

This work was supported by a Grant-in-Aid from the Japan Society for the Promotion of Science Fellowships (No. 16J04303). A campus supercomputer (TSUBAME 3.0 at Tokyo Institute of Technology, in service since 2017) was used to perform the optimizations.

References

[1] Y. Terazawa and T. Takeuchi, “Generalized Response Spectrum Analysis for Strucutres with Dampers,” Earthquake Spectra, Vol. 34, No. 3, pp. 1459-1479, 2018.8

[2] Y. Terazawa and T. Takeuchi, “Elasto-plastic Damper Optimization Routine for Lattice Towers Based on Generalized Response Spectrum Analysis,” Journal of the IASS, Vol. 59, No. 4, pp. 243-250, 2018.12

[3] Y. Terazawa and T. Takeuchi, “Optimal Damper Design Strategy For Braced Structures Based on Generalized Response Spectrum Analysis,” Journal of Structural and Construction Engineering (Transactions of AIJ), Vol.83, No.74.2, pp.1689-1699, 2018.11 (in Japanese)

[4] R. Sinha and T. Igusa “CQC and SRSS methods for non-classically damped structures,” Earthquake Engineering & Structural Dynamics, Vol. 24, pp. 615-619, 1995.

[5] Chen, X., Takeuchi, T. and Matsui R. “Simplified design procedure for controlled spine frames with energy-dissipating members,” Journal of Constructional Steel Research, Vol.135, pp.242-252, 2017.

Proceedings of the IASS Annual Symposium 2019 – Structural Membranes 2019
Form and Force
7 – 10 October 2019, Barcelona, Spain
C. Lázaro, K.-U. Bletzinger, E. Oñate (eds.)

Machine Hallucinations

A comprehensive interrogation of Neural Networks as Architecture Design

Matias DEL CAMPO *, Alexandra CARLSON[a] , Sandra MANNINGER[b]

*Taubman College of Architecture and Urban Planning, University of Michigan
2000 Bonisteel Boulevard, Ann Arbor, MI 48109, USA
mdelc@umich.edu

[a] Michigan Robotics, University of Michigan
[c] Taubman College of Architecture and Urban Planning, University of Michigan

Abstract

Artificial Neural networks have become ubiquitous across disciplines due to their high performance in modeling the real world to execute complex tasks in the wild. This paper presents a computational design approach that uses the learned, internal representations of deep vision neural networks to invoke stylistic edits in both 2D objects (images) and 3D objects (meshes). The proposed technique unshelves ideas of style and interrogates this architectural position in the light of 21st century toolsets and production environments. Neural Networks, a branch of the research on Artificial Intelligence, serves as the main driving force in the exploration of novel design trajectories that evoke questions of agency, style and perception in a posthuman architecture design ecology.

Keywords: Artificial Intelligence, Generative Adversarial Networks, Computational Design, Hallucinations, Dreaming, Style Transfer,

Copyright © 2019 by Matias del Campo, Alexandra Carlson & Sandra Manninger
Published by the International Association for Shell and Spatial Structures (IASS) with permission.

1 Introduction

The main aim of this paper is to demonstrate and interrogate a design technique based on Deep Learning. This paper primary focus is to discuss aspects of 2D to 3D style and shape transfer techniques. The paper describes the motivation to explore design methodologies embedded in a posthuman architecture design ecology, although the technique itself can be expanded to any area of creativity such as product design, writing and music. The paper examines the meaning of agency in a world where decision making processes are defined by human/machine collaborations. Taking cues from the language used by experts in AI such as Hallucinations, Dreaming, Style Transfer and Vision (see glossary), the paper strives to clarify the position and role of Artificial Intelligence in the discipline of Architecture. There are two main paths of inquiry: the technical expertise necessary to train neural networks successfully to obtain comprehensive results in pragmatic problems, such as plan optimization, structural optimization and the consumption of material. All of which can be described as tamed problems, dealing primarily with engineering problems. Artificial Intelligence (AI) however allows to explore the wicked part of architectural design pertaining to aspects of morphological studies, Style and mood.

Traditionally, the architecture education contains a large portion of learning through images. Architecture students browse through thousands of pictures during their education, from books, lectures, blogs and Instagram accounts, learning the nature of architecture through the ages in the process. Similar to other fields, such as diagnostics in medicine or the memorizing of text in the law education, it is primarily a learning through the absorption of visual stimuli. In a similar fashion to the beforementioned fields, Architecture is experiencing a profound change in the nature of analyzing and assessing the respective approaches for design tasks. The efficacy of neural networks to emulate and surpass the performance of biological vision systems on certain tasks makes them a unique computational tool for generating novel design techniques. For example, neural network architectures achieve higher-than-human performance on image classification[1], suggesting that these algorithms extract better visual representations of objects than humans for this task. Considering this it might be possible for a Neural Network to understand, for example, a specific architectural style such as Gothic, Baroque or Renaissance in a far more sophisticated way, and with higher expertise than a human could – provided the database of images and tags is big enough. Wither it could form thoughts such as Rudolf Wittkower[2],(Fig.1) or the Antithesis to it, is a different story.

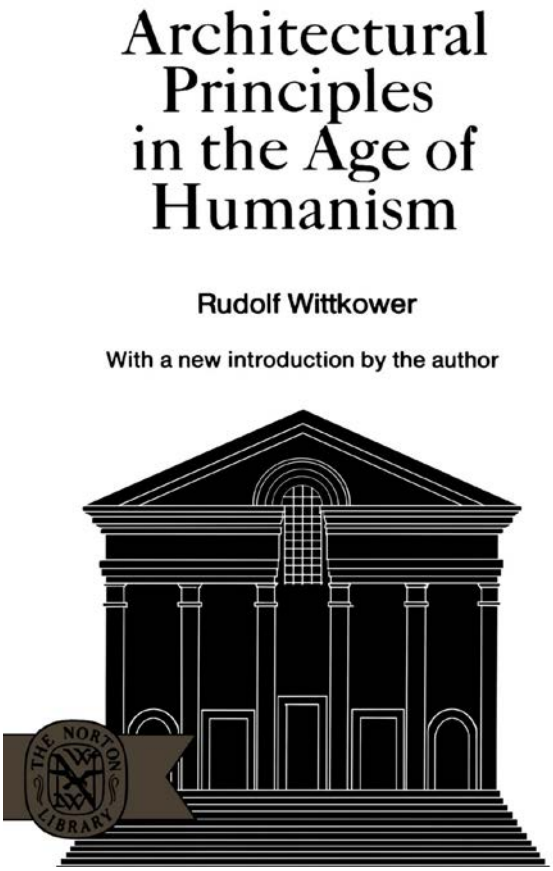


Figure 1: Rudolf Wittkower, Architectural Principles in the Age of Humanism.

We can use the learned features of such networks to achieve novel representations of form for standard architectural motifs. For example, what is the set of features learned for 'arches' by a neural network? Are there specific patterns to arches that the human visual system disregards when it performs classification that a neural network utilizes? The learned visual representations of neural networks could capture new ways of 'seeing' and understanding building structure and aesthetics. Thus, in this paper, we use the learned representations of Convolutional Neural Networks (CNNs) to invoke edits to both 2D objects (images) and 3D objects (polymeshes) in an effort to transform and potentially remove the constraints of the human visual system on the design process.

The proof of concept project - presented for the first time in this paper- is the Robot Garden (Fig.2) currently under construction. The Robot Garden is designed as a future test ground for bipedal and quadrupedal robots. Part of the challenge consisted in designing various ground conditions and complexities that robots have to overcome. In order to achieve this, and also to include a Neural Network component in the design process we designed a methodology that would involve satellite images of the site and a particular training set to dream features on this image. These features consisted of architectural elements derived from a sprawling dataset trained to recognize architectural features such as arches, architraves, columns, mullions, mouldings, rustications and many more. This allows to generate a synthetic ecology present somewhere between the natural and the artificial. The resulting digital model serves on the one side as the template for the construction, on the other it serves the purpose of simulating and preparing the test of robots in the garden. The garden itself is executed in natural material providing various different terrains such as grass, gravel, stone, sand, water and has topographical features such as waves, inclinations, pits etc. to emulate difficult terrain. Though the garden is made of natural materials, there is a contrast between the natural landscape features adjacent to the Robot Garden, and the Robot Garden itself which flirts with an intentional artificiality – operating within the realm of a synthetic ecology, befitting the origin of robots as an artificial progeny. In the following the authors would like to explain the background of this approach, in particular explaining the computational methods used in Neural Networks.

2 Background

A neural network is a neurobiologically-inspired computing system comprised of groups, called layers, of simple, highly interconnected processing elements, called neurons. Input information flows through a neural network in a feed-forward, hierarchical manner: each node in a neural network receives input from neurons in the preceding layer, but not neurons within its own layer. It transforms

this input into a new representation, and then passes it to the neurons it is connected to in the proceeding layer.
Mathematically, this transformation is defined as follows: a neuron calculates a weighted sum of its inputs and applies a threshold onto this value via a nonlinear function to determine if it has been 'activated' given its input. This output, i.e. the neuron's state of activation, is then sent to neurons it is connected to in the following layer. The thresholding operation effectively filters out specific information from being sent to the next layer, allowing for different features in the input to be extracted by each neuron. Because each layer operates on the activations of the previous layer, neurons can also extract/detect groups of input features depending on the values of weights used to calculate their activation.

Thus, how neurons are connected between layers controls how input information is transformed through the network. This connectivity structure varies based upon the application. The most widely used neural network structure for a wide range of visual tasks, including facial recognition, pedestrian detection, and image generation, is the convolutional neural network (CNN).

The neuron in a CNN processes the information about a location (x,y) in its input. It calculates its activation by applying a 2D convolutional kernel to the pixel information at its spatial location, and thresholds the value with a nonlinear function. This convolution kernel is slid over the entire 2D input (the same kernel is applied at each neuron's location) to create a 2D activation map. The value of an element within the activation map indicates the presence and magnitude of a particular visual pattern, called a 'feature', at a specific location in the input. Depending on the values of the weights of the convolution kernel, different 2D spatial patterns of pixels can be detected and thus extracted by the CNN.
Each layer can have multiple convolutional kernels, so the output of a single CNN layer is a 3D activation volume of stacked activation maps. Conceptually, a CNN layer transforms its input by decomposing it into the set of spatially-varying visual features captured by the layer's convolutional kernels.

Increasingly complex spatial patterns/features can be extracted by each proceeding layer. For example, a convolutional kernel A in the first layer of a CNN may have weight values that cause it to detect the presence of patterns that resemble diagonal lines within the input image, and a second convolutional kernel B in the same layer may detect groups of pixels that look like horizontal lines. A convolutional kernel C in layer 2 operates on the activation maps from convolutional kernel A and kernel B from the first layer, so it could activate in the presence of patterns that resemble line intersections, which would require the activation of both convolutional kernel A and convolutional kernel B in the same neuron/spatial location in the first layer. As a result, at the final layers of the network, neurons will have weights that activate to the semantic content of the image (as opposed to pixel values), complex structures, such as written digits (Fig.3).

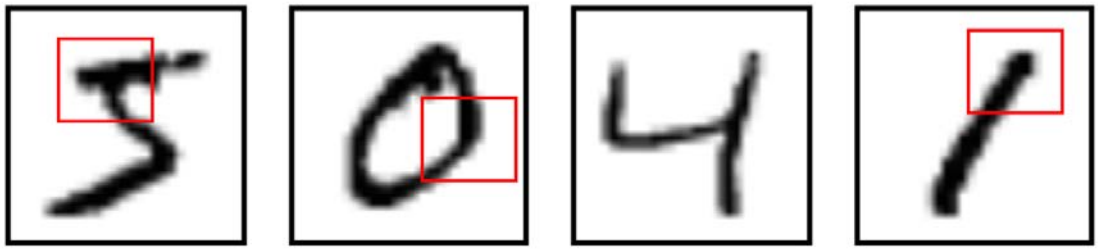


Figure 2 In the visual task of number recognition, a neural network may learn to associate only curve features with the class 0, where as for the class 1, it may learn only vertical line features, where as for 5 it needs to

additionally learn the spatial relationships between lines (intersections) to correctly predict the class. Neurons across all layers need to activate in specific patterns in order for the network to predict one class vs. another.

2.1 Learning Architectural Features

The weights of each convolutional kernel (and thus which visual features are extracted from the input) need to be learned from data. A popular learning paradigm is a training procedure called supervised learning. In this training scheme, a large number of different (image, label) pairs are presented repeatedly to the network with the goal of teaching the network to perform a specific visual task. For example, in image classification, an image would be paired with a label that describes elements of its semantic content, such as 'arch', "fountain" or 'column'.

For each image input to the CNN, the network uses its current set of weights to process relevant visual information, which is transformed at the final layer into a prediction of the input image label. For example, in image classification, a neuron in the output layer would activate/detect if all the visual features associated with a particular class are present in the input image. In a winner-takes-all fashion, the neuron in the output layer with the highest activation would be considered as the class prediction of the network.
An error (also referred to as loss) is then calculated on this predicted label based on how close it is to the ground truth label of the input image. Multivariate differentiation (specifically the chain rule for partial derivatives) is used to calculate the gradient of this error with respect to the network's weights. Conceptually, the gradient of the error represents how much each weight parameter contributed to the network's prediction, and thus its error. The values of the weights are then changed based upon the magnitude of their gradient, with the objective that on the next iteration, the updated weight values will yield a more accurate prediction. This process is referred to as backpropagation, because the error is literally being passed backwards through the network layers to learn better visual features.

This procedure is performed for many iterations, repeatedly feeding in randomly sampled image-label pairs from the dataset until the network achieves the highest possible prediction accuracy. The labels act as a supervisory signal that guides the network to process, extract and transform visual information into a representation that maximizes the network performance on the desired task. For example, in image classification, the network decomposes images into visual features that maximally differentiate the visual appearance between classes, which makes grouping images into a class easy. The class 'column' may have features associated with vertical lines and/or ones that capture standard column material, like marble texture. Examples of learned feature sets for particular classes are shown in Fig.4.

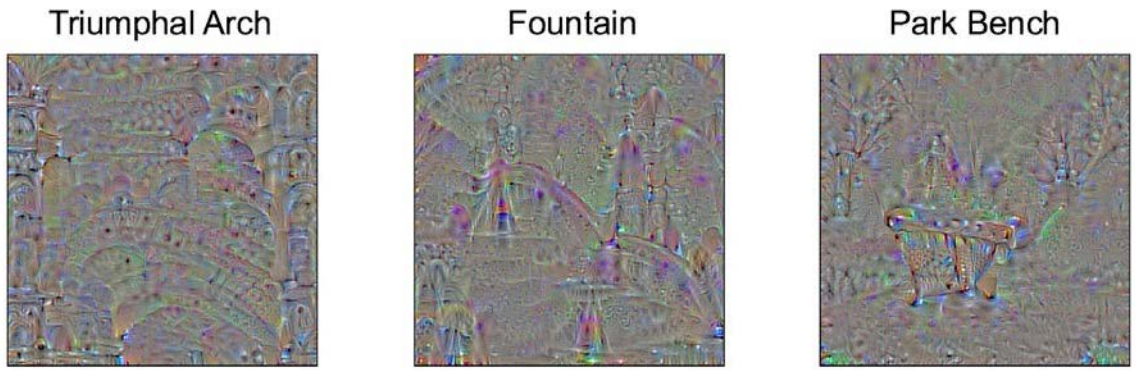


Figure 3: Series of iterations of the CNN in regards of columns, or marble.

Applying a visualization technique similar to google deep dream, we can visualize the spatial/visual features that maximally activate a particular class for a network trained on image classification (the method is discussed in more detail in the methods). The above images were generated from a CNN trained upon the ImageNet dataset, which is over a million images and is labeled for over 1600 classes, which includes 'triumphal arch', 'fountain', and 'park bench'. It is the dataset that 'best approximates' the real world due to its sheer size.

2.2 Fountains, Figures and Features – or how to confuse an AI

However, outside of the error function, there are no constraints upon what visual features the network actually learns from the data. There is no way to know what the weights end up being at the end of the training procedure, and these values can change depending on a variety of factors, including the mathematical form of the error/loss, how many training iterations are completed, how many layers are in the network, how many neurons per layer, how many convolutional kernels per layer, the amount of image data and variability of images. The salient feature information captured by the weights is hugely dependent upon the visual information that is contained within the training data. In a sense, the training dataset defines the CNN's notion of the 'world', and encounter difficulties when given information that falls outside of it.

For example, if the CNN from Fig.4 was only shown images of tiered fountains with vertical water spouts to learn the 'fountain' class, it may not be able to accurately identify dry fountains or wall fountains, because it has associated the vertical 'spout' or 'water feature' as being necessary for a fountain to occur. As can be seen in Figure 4, there is more spatial information than just a 'vertical spout' that the CNN has learned as discriminative features for the fountain class. Compare this to Figure 5, which is a visualization of the learned features for the 'fountain' class from the same CNN network that has been trained upon a different, smaller dataset for a smaller set of other classes, specifically the set 'fountain', 'stairs', 'cinderblock', 'ditch', 'stepping stone', and 'boulder'.

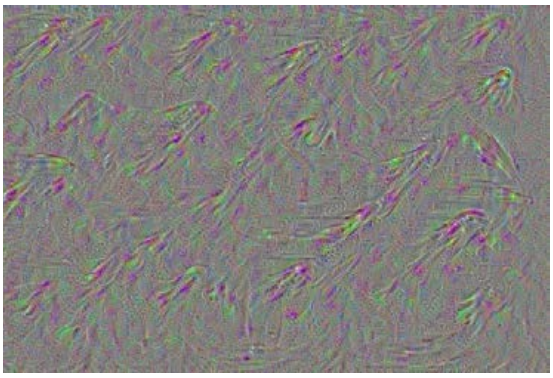


Figure 4: Here is an example of the same CNN as in Fig.4, but trained on a much smaller dataset with a significantly smaller number of classes. We see that the primary feature learned for the fountain class appears to be based on water, which suggests that either (1) the dataset had few to no examples of dry fountains, and/or (2) that the other classes did not have water features, so this was the primary differentiating visual pattern between 'fountain' and the other classes (and thus the only patter the CNN needed to learn to classify a fountain).

The visual features learned by the network are also dependent upon the chosen task. For example, in the instance of image classification, visual features for a given class would be learned that differentiate

it from other chosen classes, which can be seen upon comparing the differences in the visualized classes in both Figures 4 and 5.

Ultimately, while it is understood how a single neuron processes information, given the large number of parameters and nonlinearities that comprise a single network as well as the dependence upon the training data, it is difficult to tease apart how the neurons collectively function upon images to achieve a prediction. This results in the 'black box' nature of neural networks; we cannot guarantee what is learned or how its learned. In contrast for example to a human architect who can rely on his/her education, and the many images ingested throughout his/her career as well as an inherent sensibility towards design. If and how sensibility, for example, can be part of this process is yet to be seen. This means that, in the specification/definition of both task and dataset, practitioners of neural networks can guide what and how the neural network algorithm processes information about the world.

3 Methods - or: What it means to be a Pixel

Visual tasks can be extended to 3D by redefining what it means to be a pixel. Naively, a third dimension can be added to an image pixel to create a voxel to represent a discretized 3D space. However, the additional spatial dimension creates a huge computational burden as a result of the increased input size and intermediate network representation sizes, which ultimately renders 3D vision/perception infeasible for many vision problems. Other commonly used representations for modeling objects in the 3D world are depth maps, point clouds and polygon meshes (see Fig.6). The choice of input data representation (specifically, the information it contains) will directly impact the features learned by the neural network. There are pros and cons of each type of data format in this regard. For example, while point clouds are much sparser and thus take up much less computer memory than voxels, they do not capture a sense of a 'face' or 'surface', and therefore editing techniques involving lighting or texture manipulation, such as style transfer, cannot be easily applied to this input[3].

While the majority of neural networks have been developed to process 2D visual information in the form of images, their structure can be extended to operate upon these different 3D representations of the world. These deep learning approaches fall into two groups: neural networks that project a 3D object into a 2D representation (and then perform the task using standard 2D approaches, such as convolutional neural networks), and the second are neural networks whose connectivity structure has been modified directly to operate on 3D information.



Figure 5: One or the first attempts of a 2D to 3D Style transfer on the Robot Garden project. The method of simply creating a depth map shader for a 3D model resulting in a noisy, albeit interesting, result.

Applying the techniques of the first group of algorithms, 2D image editing methods/techniques can be used to make aesthetic changes to 3D objects based upon the learned representations of neural networks trained on 2D image data.
Two of these methods, which are used in this paper, are 2D deep dreaming, a method popularized by Google, and neural style transfer[4].

Deep dreaming is an image editing algorithm that was originally developed as a tool to visualize the image features learned by a neuron, a layer of neurons, or the features that are associated with a particular class (e.g., dogs).

Neural style transfer is an image editing technique whose objective is to alter a given input image so that it captures the style of a second, 'style guide' image without altering the original content, i.e., the original geometric/spatial structure.

In practice, is difficult to apply editing methods in 3D because they require a dense, connected surface to manipulate, which rules out many 3D representations. For example, point clouds have no sense of connected structure or surface, and thus cannot contain 3D texture information to edit. While voxels contain more connectivity information in the sense that they distinguish free space from unknown space, they also lack smooth surface information that is necessary for modeling 3D texture and style features. These techniques can be applied to 2D representations of 3D data, like depth map images, but there isn't a way to model how the 2D manipulations manifest in the 3D nature of the object.

Object meshes are a happy medium between point clouds and voxels: they are computationally more efficient than voxels but have enough visual information about surfaces that can be manipulated with interesting aesthetic edits.

Currently, the Neural 3D Mesh Renderer[5] is the only method that allows for easy object editing based upon neural style transfer and dreaming. It is a differentiable rendering/rasterizer algorithm that can be used as an input layer with CNNs and other forms of 2D neural networks. This framework effectively

yields a mapping function (the fusion of the differentiable renderer and neural networks) between the 3D polygon mesh and 2D image representation of objects. The Neural 3D Mesh Renderer network is differentiable so the gradients of an image can be taken with respect to the vertices and surfaces of the input mesh. Thus, the same principles/formulations guiding the aforementioned 2D dreaming and 2D style transfer techniques can be used to perform image editing on the surfaces of 3D objects.

The project ***Robot Garden (Fig.8)***, makes extensive use of the described technique. The provided site was analyzed using a set of satellite images as a basis. The given shape of the site was cut out of the satellite images to create a set of pictures to create 2D to 3D Neural mesh rendering. In an attempt to have a Neural Network dream or hallucinate architectural features on the site, it was trained using an extensive library of images of features such as columns, stairs, fountains etc. Surprisingly the resulting images represent a novel view to these archaic architectural features. The hybrid nature of the resulting meshes do not show the features in full clarity but are rather the hallucinogenic dream of a machine trying to see these features in the landscape.



Figure 6: The lens-shaped site of the Robot Garden in a current satellite image. Various satellite images, of different age, were used in the design process as basis of a 2D to 3D Style transfer.

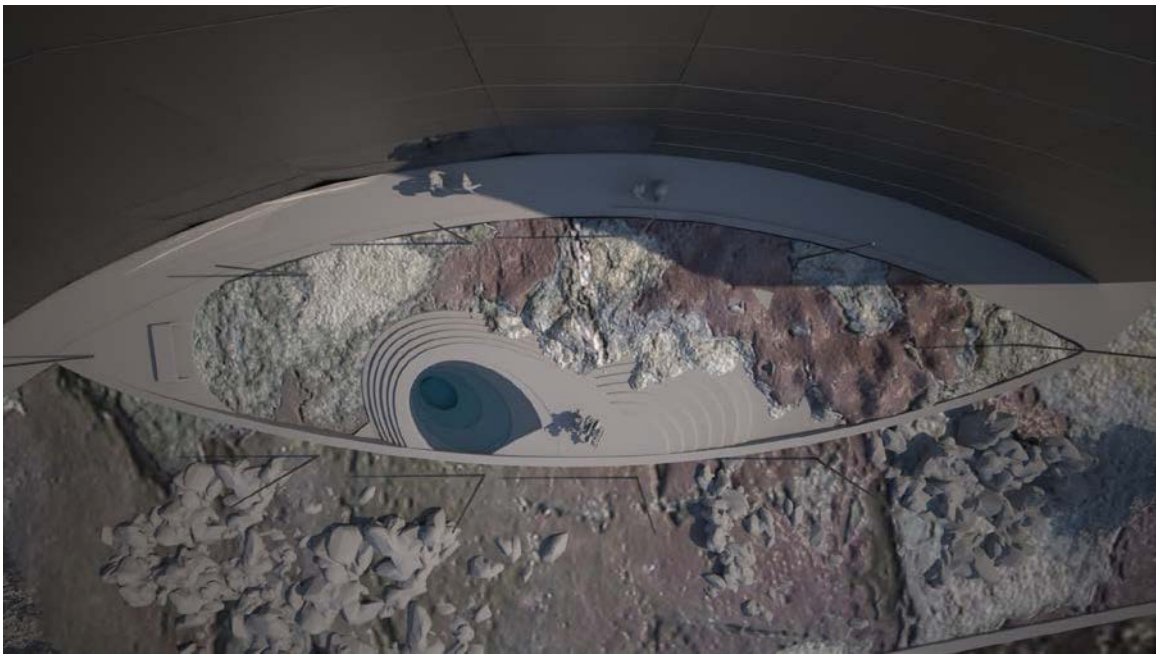


Figure 7: Current top view of the Robot Garden, with the current version of the features dreamed on the site. Minor things were implemented manually, such as the position of the poles holding sensors for tests with robots, and a platform (left of image) to hold a control desk.

4 Conclusion – Machines hallucinating Architecture

In conclusion it can be stated that the Project Robot Garden serves as a first successful attempt to use machine hallucinations, based on architectural imagery, as the basis for a building project. Construction for this project began in May 2019. The main task of the design process presented in this paper was to analyze and explore how current techniques in AI applications can be utilized in architecture design. On a technical level it can be stated that there are shading/lighting/perspective/geometric cues that exist in images that contain 3D information, however it is unclear if 2D CNNs have a sense of a 3D model captured in their weights/learned representations. Therefore using 2D image editing methods in 3D are not easily interpretable in terms of what features are being transferred and how 2D features are projected into the 3D space. Future work would be to generate fully 3D pipelines that allow us to explore design modifications in the purely 3D realm. On the other side this project only barely skims the surface of the possibilities, in terms of speculating about possible applications in the discipline. Provided proper training CNN's and Generative Adversarial Networks could learn how to dream urban scapes in landscapes – serving as the basis for urban design. Or they can be used in projects of cultural preservation, in that they dream how to complete the restoration of historic buildings, or they can be used to optimize the planning of housing projects by learning to compare thousands and thousands of housing plans. The opportunities are remarkable, and possibly will generate a completely new paradigm as of how to approach architecture design. In terms of disciplinary implementations, the project contributes to the discussion of style in the 21st century. Borrowing from the conversations of Gottfried Semper[6] about the nature of style it can be stated that style has turned into a posthuman quality, where artificial players contribute to the discussion by analyzing and proposing ideas for a cultural discussion with an ever increasing speed. If robots can dream of gothic cathedrals, humans need to renegotiate their position in a contemporary design ecology.

Glossary – Mathematical Supplementary

We provide the mathematical formulation for the different 2D to 3D image editing methods in this section. Each of the following descriptions treats a neural network as a function whose parameters/weights map the input space of images to the output space of labels, or into the activation/feature space of a given network substructure, e.g. a layer or neuron. Additionally, when the term *error* is used, we are referring to calculating the euclidean distance between two quantities. This is denoted by $| \dots |^2$ in the following equations and definitions.

2D to 3D Style Transfer

Using the learned representations of a pretrained image classification neural network, VGG-16, we can define a training objective that is based upon the spatial features, or 'content features' of the input 3D mesh, which we assign the name m^c and the 2D 'style features' of the second, user-provided guide image, which we assign x_s.
To make the shape of the generated mesh, m, similar to that of m^c, the 3D content loss can be defined as:

$$\ell(m|m^c) = \sum_{v_i, v_i^c \in m, m^c} |v_i - v_i^c|^2 \qquad (1)$$

Where v_i is the set of vertices for the manipulated mesh m and v_i^c is the set of vertices for the original content mesh m^c.
The style loss is defined to be the same in the 2D image case using the rendered/rasterized image that is output from the 3D Neural mesh renderer:

$$\ell(m|x_s, \phi) = |M(f_s(R(m, \phi))) - M(f_s(x_s))|_F^2 \qquad (2)$$

Where R is the 3D neural renderer function that projects the 3D mesh m to a rasterized 2D image, ϕ is the viewing angle at which to rasterize m, f_s is the pretrained VGG-16 network (used as a function) that projects the rasterized image into the feature space/representation of a specific network layer, and M is the Gram matrix function, which acts as a metric of style. The feature layers of the VGG-16 network used were *conv1_2*, *conv2_3*, *conv3_3*, and *conv4_3*. These two losses are summed to make the final objective, which is minimized via backpropagation to make the output mesh object.

2D to 3D vertex optimization

This method is similar to style transfer, but instead of using the learned feature representations to manipulate the mesh, the training method minimizes the error between the input mesh rasterized into a silhouette image and a user-provided guide silhouette image, $x_{silhouette}$. To rasterize a silhouette image from a mesh, the 3D neural mesh renderer is paired with a neural network that generates a silhouette image from the output of the mesh renderer. The training objective is to minimize the difference between the rendered silhouette image and the reference/guide silhouette image via backpropagation:

$$\ell(m|x_{silhouette}) = |R(m|\phi) - x_{silhouette}|^2 \quad (3)$$

3D Deep Dreaming

Deep dreaming, whether it is applied in 2D or 3D, is a visualization technique that allows us to qualitatively determine what visual features a given substructure of the network has learned. Conceptually, it makes assumptions similar to the grandmother cell hypothesis in Neuroscience: there is one neuron that is trained to be the detector for the face of a grandmother. Thus, this process of deep dreaming is more like hallucinating or pareidolia; the network is emphasizing vague pixel patterns in the image if those patterns resemble something that the neuron has learned to detect. In essence, we are seeing what the network is 'seeing' in the image.

To achieve deep dreaming, the training objective is to maximize the activation of a specific neuron, layer, or class by changing the values of the input image pixel intensities over many iterations. In 3D, the same objective is used to manipulated the vertices of a mesh object. Let *f(x)* be the GoogleLeNet pretrained neural network as a function that outputs an activation/feature map for the input image *x* at the specified neuron. The 3D neural mesh renderer is used to transform the mesh *m* into an image, which is then fed into GoogleLeNet to produce an activation map for the chosen neuron. A neuron in layer *inception_4* from GoogLeNet was used for all of the mesh manipulation.
The training objective for 3D deep dreaming to be optimized is

$$\ell(m) = -|f(R(m,\phi))|_F^2 \quad (4)$$

where $R(m,\phi)$ is the rasterized image given the input mesh and viewing angle and *f* is the GoogleLeNet pretrained network that projects an image into the representation of the specified neuron.

References

[1] Simonyan, Karen, and Andrew Zisserman. "Very deep convolutional networks for large-scale image recognition." arXiv preprint arXiv:1409.1556 (2014).

[2] Wittkower, Rudolf. "Architectural Principles in the Age of Humanism." W. W. Norton & Company, New York, 1971M. A. Crisfield, *Non-linear Finite Element Analysis of Solids and Structures. Volume 2: Advanced Topics*. (2nd ed.). New York: Wiley, 1997.

[3] Simonyan, Karen, Andrea Vedaldi, and Andrew Zisserman. "Deep inside convolutional networks: Visualising image classification models and saliency maps." arXiv preprint arXiv:1312.6034 (2013).

[4] Gatys, Leon A., Alexander S. Ecker, and Matthias Bethge. "A neural algorithm of artistic style." arXiv preprint arXiv:1508.06576 (2015).

[5] Kato, Hiroharu, Yoshitaka Ushiku, and Tatsuya Harada. "Neural 3d mesh renderer." Proceedings of the IEEE Conference on Computer Vision and Pattern Recognition.

[6] Semper, Gottfried, Der Stil in den Technischen und Tektonischnen Künsten oder praktische Ästhetik: Ein Handbuch für techniker, Künstler und Kunstfreunde (Band 1): die textile Kunst für sich betrachtet und in Beziehung zur Baukunst. Verlag für Kunst und Wissenschaft Frankfurt am Main, 1860, P.13

Proceedings of the IASS Annual Symposium 2019 – Structural Membranes 2019
Form and Force
7 – 10 October 2019, Barcelona, Spain
C. Lázaro, K.-U. Bletzinger, E. Oñate (eds.)

Multi-objective optimization of non-rigid stratospheric airship

Tian-E LI*, Xiao-Ying SUN[a], Yue WU[a]

* College of Civil Engineering, Taiyuan University of Technology, 030024 Taiyuan, China
No. 79 Yingze West Street, Taiyuan City, Shanxi Province
woshitiane@126.com

[a] Key Lab of Structures Dynamic Behavior and Control of the Ministry of Education, Harbin Institute of Technology, 150090 Harbin, China

Abstract

Multi-objective optimization of a non-rigid stratospheric airship envelope based on Pareto genetic algorithm is systematically introduced. The simplified Finite Element Model (FEM) of the airship envelope considering aerodynamic forces and static forces is built and Finite Element Analysis (FEA) is conducted. Based on the FEA, multi-objective optimization of the airship envelope is implemented using Pareto genetic algorithm. During the optimization process, the expression of aerodynamic drag force coefficient $C_{D,V}$ of the research airship envelope, which represents the aerodynamic objective, is given out based on the CFD (Computational Fluid Dynamics) simulations. In addition, all the structural objectives including weight, stress and deformation of the envelope are obtained based on the FEA, which has higher accuracy than directly using empirical equations. To intuitively track the convergence of the optimization process, a convergence index is proposed. In a single optimization run, Pareto optimal set can be obtained.

Keywords: Decision making, Finite Element Analysis, Multi-objective optimization, Non-rigid stratospheric airship, Pareto

1. Introduction

Stratospheric airship is a type of "lighter-than-air" aircraft equipped with propulsion and control system. With the advantages of long-endurance and station-keeping, stratospheric airship has become one of the most promising research topics in the aviation field [1]. Non-rigid airship with lighter weight and greater ability to achieve large volume is the preferred structure for stratospheric airship [2].

Hovering endurance, load capacity together with structural mechanical properties are the key indicators to evaluate the performance of a stratospheric airship. So, it is necessary to conduct multi-objective optimization considering aerodynamic drag force reduction, structural weight reduction and mechanical properties improvement.

The principal component of an airship is the envelope, which is usually a rotating body [3]. In the past decades, many researches and developments have been in progress on envelope optimization. In earlier research, optimizations with an objective of minimizing the aerodynamic drag force were performed [3-5]. Because having no consideration of the structural characteristics, the optimal results diverge from the actual situation. Then, many optimization investigations were carried out considering structural characteristics [6]. Most of these studies converted multiple objective functions to a composite single-objective function and only an optimal solution corresponding to the defined weights can be obtained in a single run. In fact, multi-objective optimization problem should correspond to a set of compromise solutions, which is known as Pareto optimal set. Therefore, the Pareto genetic

Copyright © 2019 by Tian-E Li, Xiao-Ying Sun, Yue Wu
Published by the International Association for Shell and Spatial Structures (IASS) with permission.

algorithm which can obtain the Pareto set in a single run is a better method for multi-objective optimization problems.

The present study attempts to address the optimization problem of a non-rigid stratospheric airship based on Pareto genetic algorithm. The rest of this paper is arranged as follows: Section 2 builds the FEM of the airship envelope and conducts FEA for the reference airship model. Section 3 presents the multi-objective optimization of the research airship. Conclusions are drawn in Section 4.

2. Finite element analysis (FEA)

2.1. Finite element model (FEM)

When performing static analysis of an airship in flight, constraints are needed to prevent its motions: completely fixed the tail cone and allowed the degree of freedom in the X direction of the nose cone. The nose and tail region are set as rigid bodies to simulate the nose cone and tail cone (Figure 1).

The reference airship model has a length of 60.8 m and a diameter of 13.78 m, corresponding to the slenderness ratio λ_0=4.38. SHELL181 elements and triangle FEM grids are used for meshing. For FEM of the reference model, the maximum size and minimum size of the elements is 1.5m and 0.24m, respectively, corresponding to about 12.0 thousand elements. The size of elements and airship model will be varied in proportion to the slenderness ratio λ during the optimization process.

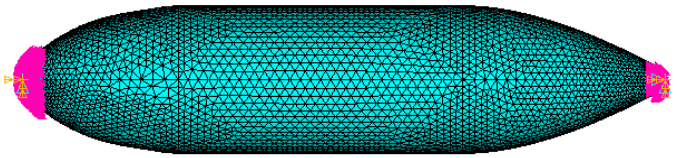


Figure 1: Finite element model of the airship envelope

2.2. Load cases

During the optimization process, only the airship envelope is analyzed. From the perspective of force category, the envelope is subjected to static forces and aerodynamic forces. The static forces include differential pressure, buoyancy, structure self-weight and payload. Aerodynamic forces represent wind loads. Among them, differential pressure and buoyancy correspond to the overpressure loads. Weight and payload are collectively classified into gravity loads.

2.2.1. Overpressure loads

Figure 2 displays the working principle of the non-rigid airships' lift force. The pressure shows a gradient distribution: both the internal and external pressure decrease with the increase of the section height, and the decrease degree is proportional to the gas density.

Pressure of any point of the envelope can be calculated according to the following formula [7]:

$$P = \Delta P + \left(\rho_{a\text{-}H} - \rho_{\text{He-}H}\right) g h' \tag{1}$$

$$h' = y + R \tag{2}$$

where h' represents the height from the lowest point of the largest cross section of the envelope. y and R are respectively the ordinate value of the point and the maximum radius of the envelope. ΔP is the differential pressure of the lowest point of the largest cross section of the envelope, which is calculated refer to literatures [8-9]. For the reference airship, the value of ΔP is set as 600Pa ($\Delta P \geq$509.91Pa).

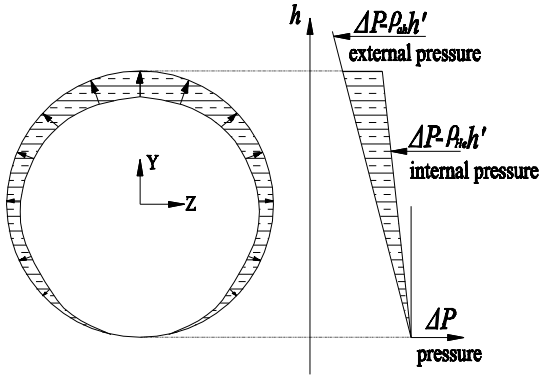


Figure 2: Schematic diagram of the airship envelope overpressure

2.2.2. Gravity loads

The major structural components of a non-rigid airship are envelope, fins, suspension system, nose cone and tail cone. To reduce computational cost, only the airship envelope is considered during the optimization process. The effect of other components is simplified according to their characteristics. The envelope mass is considered in form of distributed load, and the mass of other components is converted to a concentrated force acting on the corresponding position.

According to the equilibrium of vertical forces, net lift force L_J balances with total mass of airship structure m_s and payload m_p. Aglietti et al. [10] proposed the estimated formula of the m_s=1.33m_f=1.33$S_f\rho_f$, where S_f is envelope area, ρ_f is surface density of envelope material. For the reference airship model, m_p=39.1kg, S_f=2278.2m^2, ρ_f=155.5g/m^2, material thickness t=0.2mm; the buoyancy at the working height B=$V\rho_{a\text{-}H}$=6846×0.0889=608.61kg; L_J=B-m_{He}=608.61-98.40=510.21kg; m_f=354.22kg and the mass of other components m'=m_s-m_f=116.89kg.

According to the equilibrium of moments about the center of buoyancy at horizontal condition, the effect of other components is arranged, as shown in Figure 3. The mass of each component and its action point from the center of buoyancy are listed in Table 1.

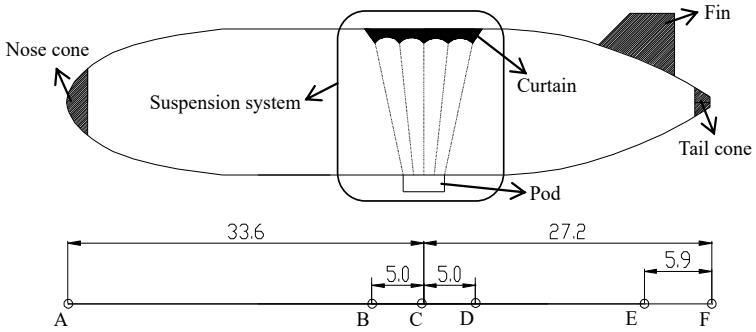


Figure 3: Location of each component

A - starting point; B - starting point of the curtain; C - center of buoyancy; D - ending point of the curtain; E - center of mass of fins; F - ending point

Table 1: The mass of each component and its action point

	Mass (kg)	Distance (m)		Mass (kg)	Distance (m)
Nose cone	40.61	33.6	Tail cone	35.6	27.2
Suspension system	22.08	----	Fins	18.6	21.3

2.2.3. Wind loads

Mean wind pressure coefficient of the partition is adopted to simplify the wind loads. The airship envelope is divided into n partitions according to the pressure distribution characteristics, and mean wind pressure coefficient of the nth partition is given by:

$$C_{p,n} = \frac{\sum_i C_{pi} A_i}{A_n} \tag{3}$$

where n is the number of partitions, A_i is affiliated area of the ith measuring point, A_n is area of the nth partition, i=1,2,…,m, and m is the number of measuring points of the nth partition. C_{pi} is pressure coefficient of the ith measuring point which is obtained based on the experiments of wind pressure measurement on the 1/30-scale airship model [11].

According to the pressure distribution characteristics of the envelope, eight partitions are divided along the hull (Figure 4). Partitions A and H are further divided into five equal parts due to the greater curvature. The position and mean wind pressure coefficient of each partition are listed in Table 2.

During the FEA, the mean wind pressure coefficient is converted to the nodal load F_k=0.5$\rho U^2 A'_k C_{p,n}$, where A'_k is the affiliated area of the kth node, $C_{p,n}$ is mean wind pressure coefficient of the nth partition, ρ=0.0889kg/m^3 is air density and U=20m/s is the velocity.

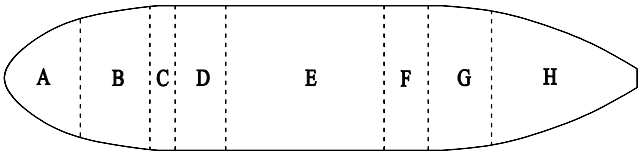


Figure 4: Schematic diagram of the airship envelope division

Table 2: Mean wind pressure coefficient of each partition

	A	B	C	D	E	F	G	H
x/L	0-0.12	0.12-0.23	0.23-0.27	0.27-0.35	0.35-0.60	0.60-0.67	0.67-0.77	0.77-1.0
$C_{p,n}$	[0.98,-0.25]	-0.28	-0.35	-0.15	-0.10	-0.16	-0.32	[-0.30, 0.36]

2.3. Finite element analysis (FEA)

The essence of multi-objective optimization analysis is the structural analysis with variable parameters. Take the reference airship model as an example to investigate the mechanical properties.

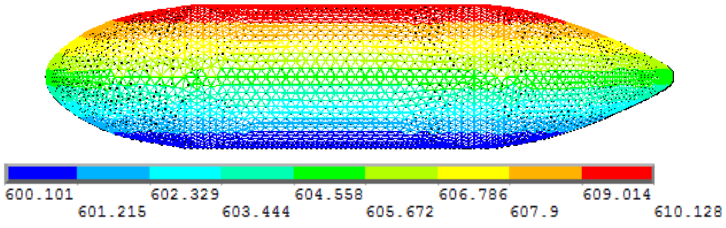


Figure 5: Schematic diagram of the airship envelope under pressure load

Firstly, the gradient pressure load P, which is used for maintaining the shape, is applied, as shown in Figure 5. Figure 6 and Figure 7 display the stress and displacement contour graph. It is obvious that the maximum equivalent stress (18.47MPa) appears in the middle cylindrical section. The maximum displacement appears around the top of the head and the middle connected region.

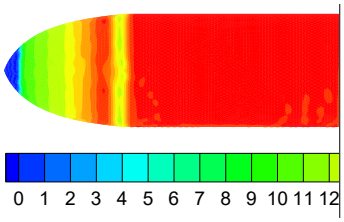


Figure 6: Stress contour graph of the airship envelope under pressure load (MPa)

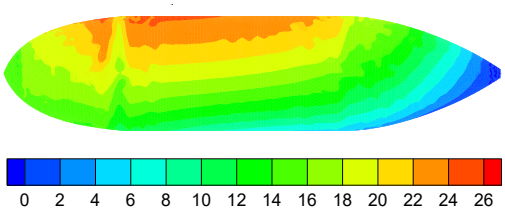


Figure 7: Displacement contour graph of the airship envelope under pressure load (mm)

Figure 8 presents the stress contour graph of the airship envelope under all the loads. It is found that the maximum equivalent stress is 18.55MPa, which is slightly larger than the value under pressure. This indicates that the stress state under the gradient pressure load P is the main design references.

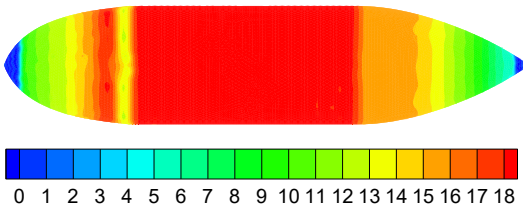
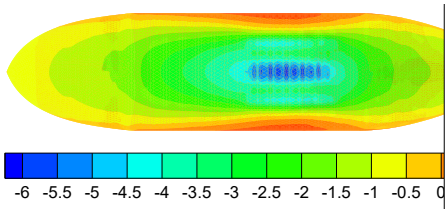
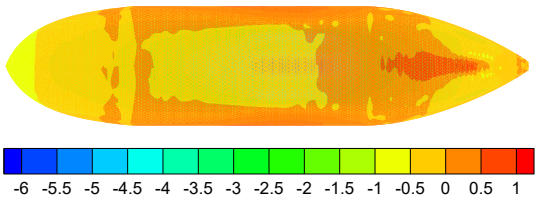


Figure 8: Stress contour graph of the airship envelope under all loads (MPa)

Figure 9 shows the displacement contour graph relative to overpressure state. The maximum displacement appears around the connected region of the suspender cable and the hull. The scale of modern stratospheric airship can be up to 200m with thousands of kilograms payload, which is far greater than the design value 39.1kg of the reference airship whose length is 60.8m. Therefore, the connected region of the suspender cable and the hull should be paid special attention.



a) Top view



b) Bottom view

Figure 9: Relative displacement contour of the airship envelope graph under all loads (mm)

3. Multi-objective optimization

3.1. Optimization model

3.1.1. Objectives

Four optimization objectives are considered: aerodynamic drag force coefficient $C_{D,V}$, volume of the airship envelope material, maximum stress of the airship envelope and maximum deformation of the airship envelope.

Formula of the $C_{D,V}$ eliminates the need for running CFD simulation each time when the envelope shape is altered. Refer to the expression of $C_{D,V}$ given by Hoerner [8], which has been widely used for axisymmetric streamline bodies, and based on the CFD simulation data [11], the $C_{D,V}$ of the reference envelope is finally written as:

$$C_{D,V}(\lambda, \mathrm{Re}) = \frac{0.135\lambda^{1.627} + 20.981\lambda^{-2.696} - 0.418\lambda^{0.929}}{Re^{0.133}} \tag{4}$$

The *Re* varies from [0.25E6, 1.25E7] corresponding to the velocity of 6~30m/s, and the slenderness ratio λ varies from [4.0-5.0].

The objective function is expressed as min $\{f_1, f_2, f_3, f_4\}$, f_1 represents the aerodynamic drag force coefficient $C_{D,V}$ calculated by Eq. (4). The other three objectives are introduced as follow: the volume of the envelope material, which reflects the envelope mass, is set as the second optimization objective. The maximum stress of the envelope is set as the third optimization objective to reflect the structural strength. The maximum deformation of the envelope is set as the forth optimization objective. During the optimization process, all the structural objectives $\{f_2, f_3, f_4\}$ are extracted real-time based on the software platform which has higher accuracy than the value directly using estimated formula.

3.1.2. Variables

All the objectives are directly influenced by its shape. So, the slenderness ratio λ is set as one variable. The differential pressure of the lowest point of the largest cross section of the envelope ΔP, which influence the mechanical properties, is set as the other variable. The range of λ is [4.0-5.0], and the range of ΔP is [550-650].

3.1.3. Constraints

Generally, the volume of the airship envelope V is determined during the preliminary design base on the working height and load capacity [8]. So, V is set as constant during the optimization process. To ensure that the structure is not damaged, the maximum stress of the envelope should not exceed the material limit stress value, which is assumed as $250\times10^6 \mathrm{N/m^2}$.

3.2. Optimization

The integrated algorithm SPEA-SRCC (Strength Pareto Evolutionary Algorithm-Spearman Rank Correlation Coefficient) is used. In the algorithm, the optimization variables also are worked as samples of sensitivity analysis, and the consequent sensitivity result is used to guide the optimization process by changing the evolutionary parameters (p_c and p_m). Variables with low sensitivity are assigned with low evolutionary parameters corresponding to smaller opportunity in following genetic evolution, which can effectively accelerate the optimization process. The details of SRCC-SPEA refer to the corresponding literature [12]. The evolutionary parameters are presented in Table 3.

Table 3: The evolutionary parameters

Number of each generation	Number of external population	Max generation	Cross probability p_c	Mutation probability p_m
60	60	60	0.40	0.02

In order to intuitively evaluate the convergence of optimization process with more objectives, a convergence index K_n is defined:

$$K_n = \sum (K_{1n} + K_{2n} + \ldots + K_{in}) \tag{5}$$

where $K_{in} = \overline{f_{in}} / f_{i0}$, $\overline{f_{in}}$ is the average value of the ith objective of all the Pareto solutions corresponding to the nth generation. f_{i0} is the value of the ith objective of the reference airship, i=1, 2, 3…, m, m represents the number of objectives.

Calculate the index K of each generation and draw the convergence curve, as shown in Figure 10. The curve shows fluctuation in the first few generations, and then the index K gradually decreases with the

increase of evolution generations. After 45 generations, the trend of the curve achieves stability. This article takes the result of the 60th generation.

Figure 11 shows the optimal variables corresponding to the Pareto set. The star symbol represents the reference value. It is found that the Pareto set mainly concentrates in the smaller pressure range: 550Pa~600Pa. For the Pareto set, no one solution can be considered to be better than any other [13]. Designer can select the final solution from the Pareto set according to the actual specific requirements.

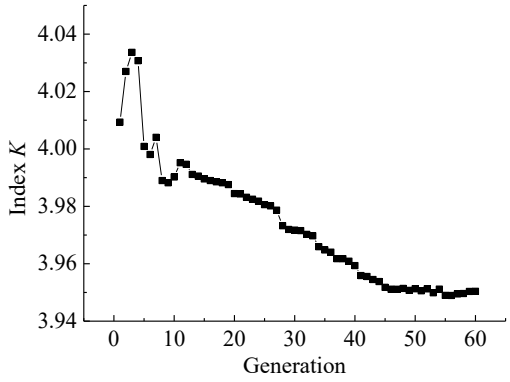


Figure 10: Convergence process of optimization

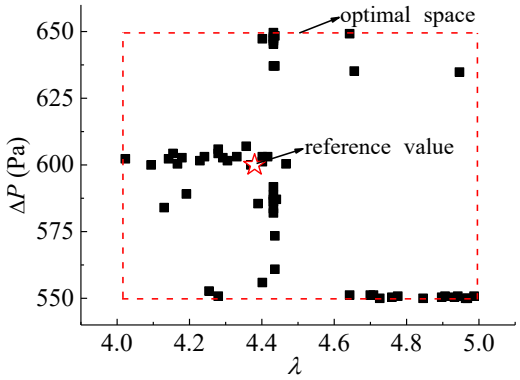


Figure 11: Optimal variables corresponding to the Pareto set

The sensitivity of the optimization variables can also be obtained based on the SRCC-SPEA, as listed in Table 4. Theoretically, variable ΔP has no influence on the aerodynamic drag force coefficient (f_1) and volume of the material (f_2). The results show that SRCC of ΔP with f_1 is 0.01 and the SRCC of ΔP with f_2 is 0.02, whose corresponding normalized sensitivities are 1.18% and 1.99%, respectively. Compared with the sensitivities of λ which are 98.82% and 98.01%, the error degree is considered to be acceptable. Table 4 shows that the influence of ΔP on objective f_3 is greater than that of objective f_4. And smaller ΔP corresponds to the smaller f_3. This is why ΔP of the Pareto optimal set approaches smaller value, as shown in Figure 11.

Table 4: SRCC and normalized parameter sensitivity

variables	SRCC				Sensitivity (%)			
	f_1	f_2	f_3	f_4	f_1	f_2	f_3	f_4
λ	0.89	1.00	0.37	0.22	98.82	98.01	27.99	53.85
ΔP	0.01	0.02	0.94	0.19	1.18	1.99	72.0	46.15

4. Conclusion

The main conclusions can be summarized as follows. 1) The FEA of the reference airship envelope indicates that the connected region between the suspender cable and the hull corresponding to the maximum deformation which should be paid special attention in the design process; 2) A convergence index is defined to intuitively evaluate the convergence of optimization process with more objectives; 3) The optimization results show that the Pareto optimal set concentrates in the smaller pressure range which can be explained by the parameters sensitivity: the influence of ΔP on maximum stress is greater than that of maximum deformation.

Acknowledgements

The authors gratefully acknowledge financial supports from National Natural Science Foundation of China (Grant Nos. 51678192 and 51808374).

References

[1] Q. Liu, YC. Yang and YX. Cui, et al, "Thermal performance of stratospheric airship with photovoltaic array," *Advances in Space Research*, Vol. 59, pp. 1486-1501, Mar. 2017.

[2] YW. Li, M. Nahon and I. Sharf. "Airship dynamics modeling: A literature review," *Progress in Aerospace Sciences*, Vol. 47, pp. 217-239, Apr. 2011.

[3] V. Nejati and K. Matsuuchi, "Aerodynamics design and genetic algorithms for optimization of airship bodies," *Bulletin of the JSME*, Vol. 46, pp. 610-617, Nov. 2003.

[4] XL. Wang and XX. Shan, "Shape Optimization of Stratosphere Airship," *Journal of Aircraft*, Vol. 43, pp. 283-287, Jan-Feb. 2006.

[5] MI. Alam and RS. Pant, "Surrogate Based Shape Optimization of Airship Envelopes," in *24th AIAA Aerodynamic Decelerator Systems Technology Conference*, Denver, Colorado, 2017.

[6] X. Zhang and AW. Zhang, "Shape Optimization of airship based on constrained particle swarm optimization," *Journal of Information & Computational Science*, Vol. 10, pp.5849-5857, Dec. 2013.

[7] JB. Xi, *Nonlinear finite element analysis of airship envelope*. Xi-an: Northwestern Polytechnical University, 2006.

[8] GA. Khoury, *Airship Technology*. Cambridge: Cambridge University Press, 1999.

[9] P. Gan, *Experiment research on deformation behaviour of inflated membrane structure under suspending loading*. Shanghai: Shanghai Jiao Tong University, 2012.

[10] GS. Aglietti, T. Markvart and RA. Tatnall, et al, "Aerostat for electrical power generation: concept feasibility," *Proceedings of the Institution of Mechanical Engineers, Part G: Journal of Aerospace Engineering*, Vol. 222, pp: 29-39, Jan. 2008.

[11] XX. Sun, TE. Li and Lin GC, et al, "A study on the aerodynamic characteristics of a stratospheric airship in its entire flight envelope," *Proceedings of the Institution of Mechanical Engineers, Part G: Journal of Aerospace Engineering*, vol. 232, pp. 902-921, Aug. 2017.

[12] TE. Li, XX. Sun and ZZ. Lu, et al, "A Novel Multiobjective Optimization Method Based on Sensitivity Analysis," *Mathematical Problems in Engineering*, Vol. 2016, pp: 1-12, Sep. 2016.

[13] C. Lücken, B. Barán and C. Brizuela, "A survey on multi-objective evolutionary algorithms for many-objective problems," *Computational Optimization and Applications*, Vol. 58, pp. 707-756, Jul. 2014.

Proceedings of the IASS Annual Symposium 2019 – Structural Membranes 2019
Form and Force
7 – 10 October 2019, Barcelona, Spain
C. Lázaro, K.-U. Bletzinger, E. Oñate (eds.)

Numerical and practical experiments for maximally stiff structure under tensile loading based on the topology optimization theory and the FEM

Takahiko KURAHASHI*, Kenta YOSHIHARA[a], Masanari KOBAYASHI[b]

* Department of Mechanical Engineering, Nagaoka University of Technology
1603-1 Kamitomioka-machi, Nagaoka-shi, Niigata 940-2188, Japan
kurahashi@mech.nagaokaut.ac.jp

[a] Department of Mechanical Engineering, Nagaoka University of Technology
[b] Oiles Cooperation

Abstract

In this study, we present topology optimization analysis for tensile test model. In topology optimization, we investigated the filtering effect for the sensitivity of Lagrange function. Next, the optimized model is fabricated by 3D printer, and tensile test is carried out by changing the thickness of specimen in optimized model.

Keywords: Topology optimization, Tensile test, Filtering technique

1. Introduction

In this study, numerical studies for a maximally stiff structure based on the topology optimization theory, i.e., the density method and the adjoint variable method, and the finite element method (FEM) are carried out [1], and the result of some actual tensile tests for the optimized structure is shown. Although papers related to research on the topology optimization and experiments can be seen [2], it is difficult to find research papers that have considered the weight reduction based on the topology optimization and experiments. Therefore, in this study, the specimens for tensile testing are made using 3D printer, and the thickness of the optimized model is also investigated, assuming the displacement of the optimized model to be the same as that of the initial model.

2. Formulation for topology optimization

The performance function is defined by the total strain energy as shown in Eq. (1).

$$J = \frac{1}{2}\{F\}^T \{U\} = \frac{1}{2}\{U\}^T [K]\{U\} \tag{1}$$

Here, $\{F\}$ and $\{U\}$ indicate the external force and the displacement vectors, respectively. The matrix $[K]$ means the stiffness matrix, and this matrix is derived by the FEM. The problem is to find the maximally stiff structure so as to minimize the performance function J. The finite element equation, i.e., $\{F\}=[K]\{U\}$, is the constraint condition for the performance function, and it is necessary to consider that this problem is minimization problem with constraint condition. Therefore, the Lagrange multiplier method is introduced in the formation, and the Lagrange function J^* is obtained as shown in Eq. (2). The vector $\{\lambda\}$ represents the adjoint variable vector.

Copyright © 2019 by Takahiko KURAHASHI, Kenta YOSHIHARA, Masanari KOBAYASHI
Published by the International Association for Shell and Spatial Structures (IASS) with permission.

$$J^* = \frac{1}{2}\left(\{F\}^T\{U\} + \{\lambda\}^T([K]\{U\} - \{F\})\right) \tag{2}$$

The first variation of the Lagrange function is calculated to obtain the stationary condition. Consequently, the adjoint equation, i.e., the equation of the adjoint variable, is obtained as the self-adjoint form, and the vector $\{\lambda\}$ can be expressed by minus displacement vector, i.e., $-\{U\}$. In addition, the Young's modulus E is expressed as the function of the design variable ρ, and is defined by $E = (E_0\text{-}E_{\min})\rho^p + E_{\min}$. The design parameter ρ represents the non-dimensional density parameter, and the parameters $E_{\min}$, E_0 and p indicate the numerical stability parameter, the Young's modulus and the penalty parameter, respectively. Finally, the gradient of the Lagrange function with respect to design parameter ρ is obtained as Eq. (3).

$$\frac{\partial J^*}{\partial \rho} = \frac{1}{2}\{\lambda\}^T \frac{\partial [K]}{\partial \rho}\{U\} = -\frac{1}{2}\{U\}^T \frac{\partial [K]}{\partial \rho}\{U\} \tag{3}$$

It is known that if the gradient shown in Eq. (3) is directly applied to shape update, the shape including the checker board pattern is obtained. Therefore, in this study, the filtering treatment shown in Eq. (4) is employed [3]. The weighting parameter w is given by Eq. (5), and R indicates the filtering radius. The parameter M represents the number of element in the radius R. The coordinate (x_i, y_i) indicates the center of the radius R, and the coordinate (x_j, y_j) means the coordinate in the radius R. The design parameter ρ is updated by the optimal criteria method using the gradient shown in Eq. (4).

$$\overline{\frac{\partial J^*}{\partial \rho_i}} = \frac{1}{\rho_i \sum_{j\in M_i} w(x_j,y_j)} \sum_{j\in M_i} w(x_j, y_j)\rho_j \frac{\partial J^*}{\partial \rho_i} \tag{4}$$

$$w(x_j, y_j) = R - \sqrt{(x_j - x_i)^2 + (y_j - y_i)^2} \tag{5}$$

3. Numerical and practical experiments

In this study, the topology optimization analysis is performed for tensile loading model in two dimensions. After that, the practical tensile test is carried out by changing the thickness of optimized structure, and we investigate possibility of the material reduction from initial model.

The computational model is shown in Fig.1. Considering the symmetry of the specimen, numerical experiment is performed for 1/4 model. The finite element mesh and boundary conditions are shown in Fig.2. Numerical experiments are carried out by changing the filtering radius R. Results are shown in Fig.3, and left, middle and right figures are results in case of R =0.75mm, R =1.50mm, R =2.50mm, respectively. It is found that the shape is clear in case that R is given by small value.

Next, specimen was fabricated for the optimized model in case of R =0.75mm by changing the thickness of specimen (See Fig.4), and tensile test was carried out for each model. The thickness in cases A-D is 2.12mm, 2.03mm, 1.95mm, 1.90mm, respectively. The relationship between load and displacement is shown in Fig.5. From this result, it is seen that the displacement curve in case D is in good agreement with that of initial model. The mass of initial model is 3.1g, and that of case D is 2.9g. Therefore, comparing with initial model, 10% material reduction could be achieved by using the optimized model in case D.

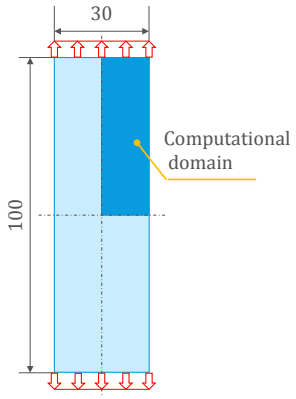


Figure 1: Computational model.

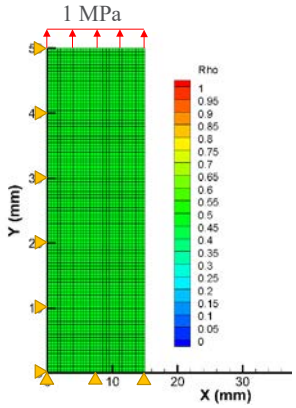


Figure 2: Finite element mesh and boundary conditions. (1/4 model)

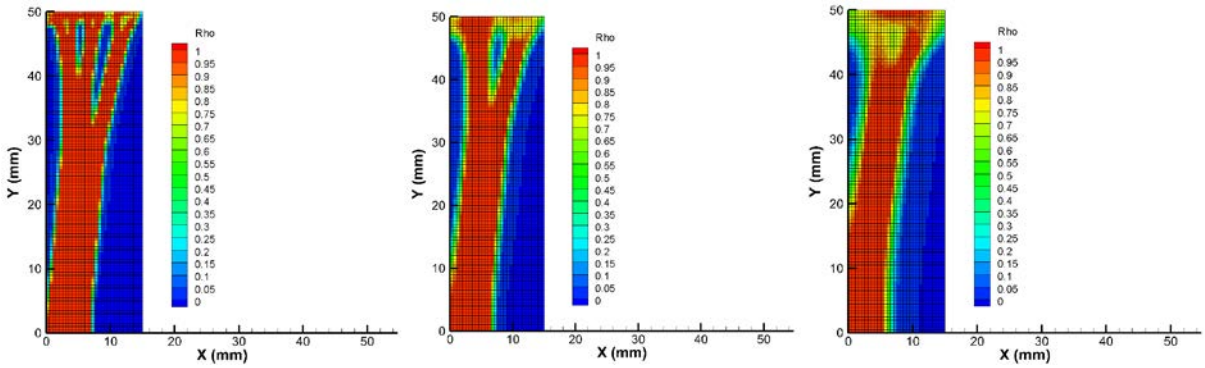


Figure 3: Comparison of optimized structures, i.e., density distribution, in each filtering radius "*R*". (Left *R* =0.75mm, Middle *R* =1.50mm, Right *R* =2.50mm) This is the result of 1/4 model in tensile loading test. 1MPa is acting on upper surface, and the symmetric surface is set on lines of *x*=0mm and *y*=0mm.

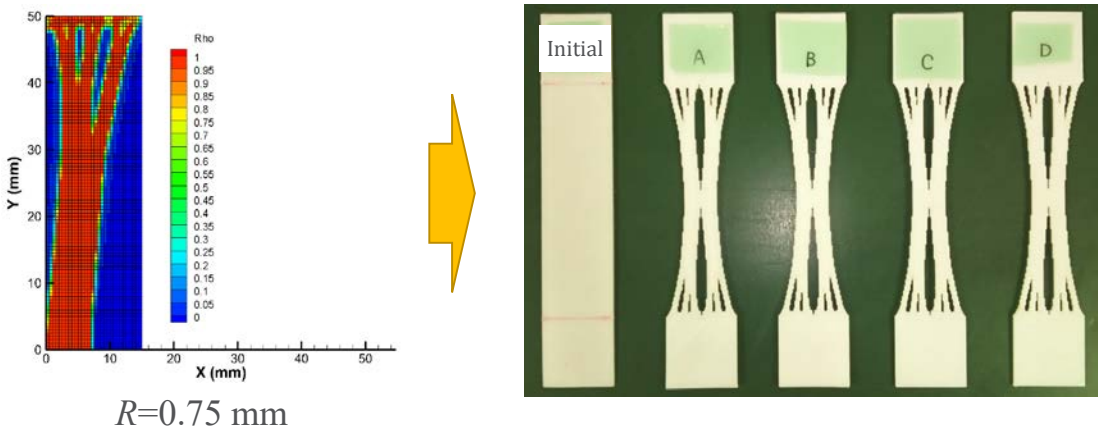


Figure 4: Fabrication of specimens based on result in case of *R*=0.75 by 3D printer. (Thickness and mass : Initial model (1.06mm, 3.1g), A(2.12mm, 3.1g), B(2.03mm, 3.0g), C(1.95mm, 3.9g), D(1.90mm, 2.8g))

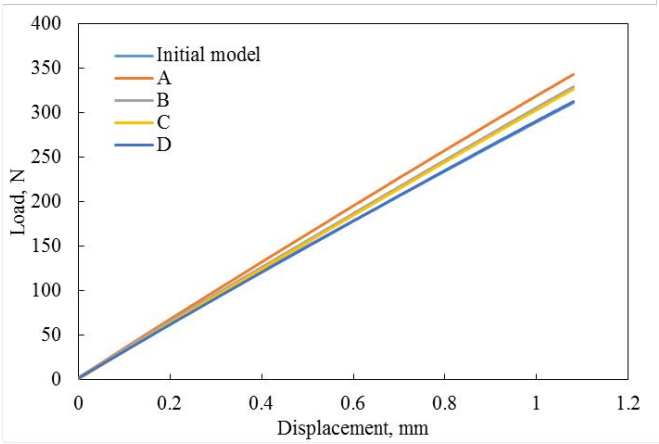


Figure 5: Result of tensile test. In case D, the displacement curve is in good agreement with that of initial model. The mass of initial model is 3.1g, and that of case D is 2.9g. Therefore, 10% material reduction could be achieved.

4. Conclusions

In this study, numerical studies for a maximally stiff structure based on the topology optimization theory, i.e., the density method and the adjoint variable method, and the FEM were carried. In addition, a practical tensile test was also carried out on the optimized model. It was found that the displacement of the optimized model was smaller than that of the initial model under the same loading conditions.

Acknowledgements

This work was supported by a Grant-in-Aid for Scientific Research (c) Grant No. 18K03897. The topology optimization analysis was carried out using the supercomputer system at Kyushu University's Institute for Information Technology. We wish to thank all the persons for assisted us in this study.

References

[1] S. Nishiwaki, K. Izui and N. Kikuchi, "Topology optimization (in Japanese)", Maruzen, Tokyo, 2013.

[2] Y. Saadlaoui, J. L.Milan, J. M. Rossi and P. Chabrand, "Topology optimization and additive manufacturing: Comparison of conception methods using industrial codes", *J. Manuf. Syst.*, Vol.43 2017, pp.178–186.

[3] O. Sigmud, "On the design of compliant mechanisms using topology optimization", *Mech. Struct. Mach*., Vol. 25, 1997, pp.493-524.

Proceedings of the IASS Annual Symposium 2019 – Structural Membranes 2019
Form and Force
7 – 10 October 2019, Barcelona, Spain
C. Lázaro, K.-U. Bletzinger, E. Oñate (eds.)

Optimization of grid patterns for single-layer latticed domes

M. TERANISHI*, S. AN[a], K. ISHIKAWA[a]

*Dept. of Nuclear Power & Energy Safety Engineering, University of Fukui
3-9-1 Bunkyo, Fukui-shi, Fukui, 910-8507, Japan
masaki_t@u-fukui.ac.jp

[a]Dept. of Architecture & Civil Engineering, University of Fukui

Abstract

Recently, several types of optimized single-layer latticed domes have been proposed by various research groups. A few of these domes are considered effective from a mechanical viewpoint and are applied in practice. However, the optimization processes proposed by these studies lead to a few transformations in the inner space of the dome, which may cause loss of structural functionality and aesthetics intended by the designer. In this study, the optimization of grid patterns for single-layer latticed domes are conducted under geometrical constraints that preserve the inner space of the dome during the optimization process. In this optimization process, the safety factors that prevent shell buckling and member buckling, which may cause the structure to collapse, are employed as objective functions. In addition, a few geometrical objective functions are proposed to grasp the geometrical characteristics of the grid pattern of the single-layer latticed dome. The effects of each of these objective functions and the interaction between the optimized grid patterns are also investigated.

Keywords: single-layer latticed shell, optimization, grid pattern, member buckling, shell buckling

1. Introduction

A latticed shell is an effective structure in terms of mechanics and aesthetics. In particular, single-layer latticed domes, which are mainly used in sports halls and music halls, enable the construction of large aesthetical spaces using slender members and an arranged grid pattern. However, during the design process, the single-layer latticed dome requires safety against buckling because it may initiate the collapse of the structure. This is because the out-of-plane stiffness is extremely lower than the in-plane stiffness in single-layer latticed domes.

Many optimization methods have been proposed to obtain an effective form of truss structure with a high resistance to buckling [1] [2] [3] [4]. Ogawa et al. optimized the linear buckling loading factor for single-layer latticed domes and used the member grouping technique to improve the construction efficiency [1]. In this optimization method, the form of the single-layer latticed dome was controlled by the Bézier surface to obtain a smooth surface with a few design variables; however, the inner space of the optimized form of the single-layer latticed dome was changed from that of the initial dome during the optimization process. This change in the optimization process may result in the loss of structural functionality and aesthetics intended by the designer.

Some methods that can optimize single-layer latticed domes without the loss of inner space or external form have also been proposed. Ohsaki et al. proposed the practical optimization method of minimizing the structural volume under constraints of stress and buckling loads using the building code of steel structures in Japan [4]. In this method, the design variables employed the cross-sectional geometry of members, which was independent of the inner space of the dome. Therefore, the inner space of the dome was preserved during the optimization. Carbas et al. conducted the optimization of single-layer latticed

Copyright © 2019 by Masaki Teranishi
Published by the International Association for Shell and Spatial Structures (IASS) with permission.

domes using a harmonic search algorithm. In this method, the height of the crown, total number of rings, and the tubular sections are considered the design variables [5]. Thus, the method enables the optimization of grid pattern of the latticed dome with a few design variables under the geometrical constraints of its rings and crowns. Therefore, these members retain their spherical shape during the optimization process. However, such strong geometrical constraints reduce the variations of the optimized grid pattern, which may hinder the process of discovering improved grid patterns.

Single-layer latticed domes with braces can be classified as Schwedler, network, lamella, and diamatic domes based on their grid patterns, which are derived empirically [6]. Conventional grid patterns are arranged using certain geometrical rules, which can be generated automatically by formex algebra [7] [8]. However, their mechanical properties have not been revealed, even though the buckling load and member yielding of the single-layer latticed domes are highly depend on their grid patterns. Thus, it is important to understand the mechanical properties of grid patterns in single-layer latticed domes so that an improved pattern can be discovered.

In this study, the optimization of a grid pattern for single-layer latticed domes is conducted under certain geometrical constraints that preserve the inner space of the dome during the optimization process. The parameters of the optimization are the number of members and a half-open-angle. In this optimization process, two types of geometrical objective functions and three types of mechanical objective functions are employed. The geometrical and mechanical properties of optimized grid patterns and their interactions are investigated.

2. Optimization problems and assumptions

2.1. Diamatic dome by Formian

As the after-mentioned optimization problems of the grid pattern of a single-layer latticed dome are non-convex ones, the optimal solution highly depends on the initial value of nodal coordinates. To evaluate the optimal solution quantitatively, the initial shape of a single-layer latticed dome is constructed using the programing language Formian, which is based on formex algebra [7] [8]. This algorithm can generate a single-layer latticed dome with various grid patterns unambiguously. The diamatic dome was considered for the initial shape of the dome during the optimization process, as it is a commonly used efficient dome type. Fig. 1 shows the diamatic dome generated by Formian, in which o is the origin of the dome; s is the dome span; θ is the half-open angle; h is the dome rise; m is the number of members on meridian, which is equal to the number of rings; and n is the number of sectors. A sector is a part of the diamatic dome, and the entire dome is created by assembling the sectors, as shown in Fig. 1(b).

Single-layer latticed domes parameterized by m, n, and θ as numerical cases are considered for this study. The number of members m on the meridian and the number of sectors n both ranged from 4–7. The half-open angle θ was set to 20°, 30°, 45°, or 60° for various domes. The span of the dome s was fixed at 45.0 m. Thus, the number of single-layer latticed domes utilized in the numerical case was estimated as 64. The members were connected rigidly. The cross section of the members depicted a circular tube with an external radius of 69.9 mm and a thickness of 4.5 mm. Pinned support was applied in the perimeter of the dome. The grade of steel adopted was SN400, in which Young's modulus was 205,000 N/mm^2, Poisson's ratio was 0.3, and the specific gravity was 7.80 g/cm^3. The permanent load, which was the self-weight of the members, was applied at each node in vertical direction. Note that the connection of members and the number of nodes remained constant during the optimization.

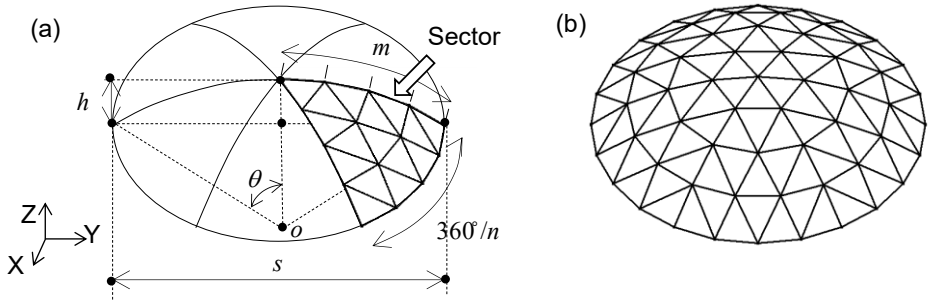


Fig. 1(a) Diamatic dome generated by Formian (m = 4 and n = 6). (b) The entire dome generated by assembling six sectors.

2.2. Objective functions and geometrical constraints

The mechanical and geometrical characteristics of grid patterns of single-layer latticed domes were investigated through the optimization of grid patterns by minimizing some objective functions under geometrical constraints. Let **U** denote the vector of the design variable. It is defined as follows:

$$\mathbf{U} = \left(x_1, y_1, z_1, x_2, y_2, z_2 \cdots x_N, y_N, z_N\right), \tag{1}$$

where x_i, y_i, and z_i are the coordinate values of the i-th node on the Cartesian coordinate system, and N is the number of nodes in the structure. Note that the cross-sectional properties of the members are not included in the design variables and all the member sections are equal.

Two types of geometrical objective functions and three types of mechanical objective functions were employed in the optimization process. The uniformity of the member length was considered to evaluate the aesthetics and construction efficiency of the structure. The standard deviation of the member length δ is defined as

$$\delta = \frac{1}{M}\sum_{i=1}^{M}\left(L_{ave} - L_i\right)^2 \ , \tag{2}$$

$$L_{ave} = \frac{1}{M}\sum_{i=1}^{M} L_i \ , \tag{3}$$

where L_i is length of the i-th member, L_{ave} is the average length of the member, and M is the number of members in the structure. The total structural volume, which is frequently applied to evaluate the economic efficiency and total structural weight, is defined as

$$V = A\sum_{i=1}^{M} L_i \ , \tag{4}$$

where A is the cross-sectional area of a member. This value is equal for all members. The safety factor which prevents member buckling should be considered particularly for single-layer domes with a high rise-span ratio. The members have been interconnected by pin-joint for simplicity of calculation of the member buckling factor. Then the safety factor λ_i against the member buckling load factor for the i-th member is defined as

$$\lambda_i = \frac{P_i^{cr}}{P_i} = \frac{\pi^2 EI}{L_i^2 P_i} \ , \tag{5}$$

where P_i is the axial force of i-th member, P_i^{cr} is the member buckling load of the i-th member, E is Young's modulus, and I is the second moment of area. Moreover, the minimum member buckling load for all members is defined as

$$\lambda_{\min} = \min\left\{\lambda_1, \lambda_2, \cdots, \lambda_M\right\}. \tag{6}$$

The safety factor which prevents shell buckling should be considered particularly for single-layer latticed domes with a small rise-span ratio. If the geometrical nonlinearity before buckling is minimal, the shell buckling can be estimated using the linear buckling analysis. By solving the following eigenvalue problem, the incremental i-th order eigenvalue μ_i is obtained as the linear buckling load factor.

$$\left[\mathbf{K}_E + \mu_i \mathbf{K}_G\right]\mathbf{\Phi}_i = \mathbf{0}, \tag{7}$$

where $\mathbf{K}_E$ is the linear stiffness matrix, $\mathbf{K}_G$ is the geometrical stiffness matrix, and $\mathbf{\Phi}_i$ is i-th order eigenvector. The lowest linear buckling load factor $\mu_{\min}$ for all eigenvalues is defined as

$$\mu_{\min} = \min\left\{\mu_1, \mu_2, \cdots, \mu_F\right\}, \tag{8}$$

where F is the number of degrees of freedom in the structure. The maximum absolute value of normal stress in the axial direction for the i-th member is defined as σ_i to evaluate the member yielding. The minimum value of $\sigma_{\min}$ for all members is defined as

$$\sigma_{\min} = \min\left\{\sigma_1, \sigma_2, \cdots, \sigma_M\right\}. \tag{9}$$

The two types of geometrical objective functions are defined as Eq. (2) and Eq. (4), and the three types of mechanical objective functions are defined as Eq. (6), Eq. (8), and Eq. (9).

It is noted that preserving the inner space of the single-layer latticed dome in the optimization process is significant to maintain the structural functionality and aesthetics intended by the designer. To fulfil this demand, two types of geometrical constraints were simultaneously applied during the optimization process. The coordinate of the i-th node is constrained geometrically, as defined in the following equation, to retain the nodes on the surface of the dome:

$$x_i^2 + y_i^2 + z_i^2 = R^2, \tag{10}$$

where R is radius of the dome. Moreover, to prevent members from intersecting, the movement of each node is constrained from $-L_{ave}/2$ of initial dome to $+L_{ave}/2$, as defined by the following equation:

$$\begin{aligned} &x_{i0} - 0.5L_{ave} \le x_i \le x_{i0} + 0.5L_{ave} \\ &y_{i0} - 0.5L_{ave} \le y_i \le y_{i0} + 0.5L_{ave} \\ &z_{i0} - 0.5L_{ave} \le z_i \le z_{i0} + 0.5L_{ave} \end{aligned}, \tag{11}$$

where x_{i0}, y_{i0}, and z_{i0} are the coordinate values of the i-th node of initial dome. Using the objective functions and geometrical constraints, the optimization problems are formulated as follows:

$$\begin{aligned} &\text{Minimize } \delta \text{ or } V \text{ or } 1/\lambda_{\min} \text{ or } 1/\mu_{\min} \text{ or } \sigma_{\min}, \\ &\text{Subject to } x_i^2 + y_i^2 + z_i^2 = R^2 \\ &\qquad x_{i0} - 0.5L_{ave} \le x_i \le x_{i0} + 0.5L_{ave} \\ &\qquad y_{i0} - 0.5L_{ave} \le y_i \le y_{i0} + 0.5L_{ave} \\ &\qquad z_{i0} - 0.5L_{ave} \le z_i \le z_{i0} + 0.5L_{ave} \end{aligned}. \tag{12}$$

The optimization problems were labeled Opts.1, 2, 3, 4, and 5 in accordance with the objective functions δ, V, $1/\lambda_{\min}$, $1/\mu_{\min}$, and $\sigma_{\min}$. The optimization problems were solved in the aforementioned 64 single-

layer latticed domes. The Optimization Toolbox software from MATLAB was employed to optimize, in which sequential quadratic programming was used as the optimization algorithm.

3. Optimization results

Fig. 2 shows the plan views of initial domes and the optimized ones obtained after each optimization problem. In this figure, the dome with $m = 5$, $n = 4$, and $\theta = 60°$, is treated as the standard form of the dome. The first to fourth rows shown in this figure demonstrate the effect of n on the optimized form. The fifth and sixth rows demonstrate the effect of m and θ. The columns in this figure show the optimized domes with different objective functions. The optimized domes in Opt. 2 can be classified roughly according to the value of n. All the nodes of optimized domes with $n = 4$ and $n = 5$ move toward the top of the dome, while all the nodes of domes with $n = 6$ and $n = 7$ move from the top to the peripheral of the domes. The optimized domes in Opt. 1 and Opt. 2 can also be classified roughly based on n, where the nodes of optimized domes on meridian with $n = 4$ move marginally, while the nodes of domes on meridian with $n = 5$, $n = 6$, and $n = 7$ move from the top to the peripheral of the domes significantly. In contrast, in Opt. 4, the radius of rings in the optimized dome is extended. Moreover, the extension of the radius of rings and moving of nodes on the meridian occur simultaneously to optimize domes in Opt. 3. Note that the optimized domes in Opt. 1, 2, 3, and 4 retain their symmetrical patterns around the top of the dome, while the optimized dome in Opt. 5 demonstrates an irregular pattern. Moreover, it can be observed that the optimized grid pattern in each optimization problem has changed marginally according to the parameters m and θ. This implies that the number of sectors n is significant in determining the optimized grid pattern in a single-layer latticed dome.

To evaluate the variation of the value of objective functions due to optimization, the relative difference $(\ )^r$ between the value of a parameter before and after the optimization is defined as follows:

$$(\ )^r = \frac{(\ )^a - (\ )^b}{(\ )^b} \times 100[\%], \tag{13}$$

where $(\ )^b$ and $(\ )^a$ are the values of the objective function $(\ )$ before and after the optimization process, respectively. Table 1 lists the average and standard deviation of the relative values with respect to each optimization problem. The result shows that the value of V improves marginally in all the cases, where the average and standard deviation of V^r are minimal. This implies that the total volume of the structure is insensitive to the optimization of grid patterns. The relative values of geometrical objective functions in Opt. 2, 4, and 5 are scattered throughout a wider range compared to those in Opt. 1 and 3. The optimized domes in Opt. 1 and 3 vary in accordance with the geometrical rules of the optimization process. Moreover, Opt. 1 and 3 improve not only the values of the objective function but also the values of other functions. They may also worsen the values of the other functions marginally. However, the values of objective functions improve in Opt. 2 and 5, while those of other functions worsen extremely. It is evident from these results that Opt. 1 and 3 are promising optimization problems from mechanical and geometrical viewpoints. Moreover, Opt. 1 and Opt. 3 can be combined effectively, as they are complementary to $1/\lambda_{\min}$ and $\sigma_{\min}$.

Figs. 3 and 4 show the effect of the number of sectors n on the relative values of functions in Opt. 1 and 3, respectively. In Opt. 1, the relative value of $1/\lambda_{\min}$ is less than 10%, when $n = 6$ or $n = 7$, and the relative value of $1/\lambda_{\min}$ is more than 10%, when $n = 4$ or $n = 5$. However, in Opt. 3, the relative value of $\sigma_{\min}$ is less than 10%, when $n = 4$ or $n = 5$, and the relative value of $\sigma_{\min}$ is more than 10%, when $n = 6$ or $n = 7$. Thus, Opt. 1 and Opt. 3 are effective, when $n = 6$ or $n = 7$ and $n = 4$ or $n = 5$, respectively.

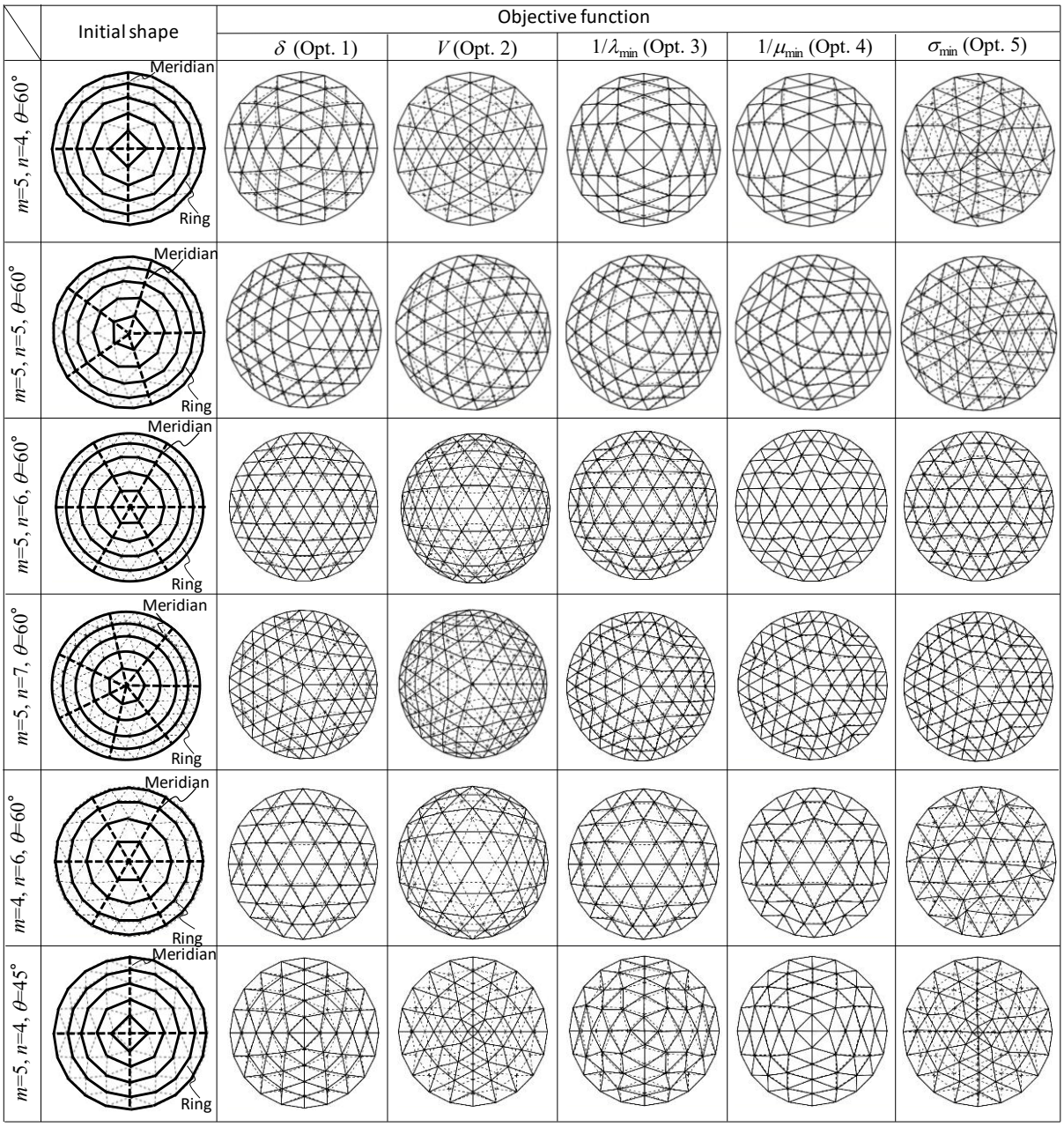


Fig. 2 Plan view of the initial and optimized domes after minimizing δ, V, $1/\lambda_{\min}$, $1/\mu_{\min}$, and $\sigma_{\min}$. The bold lines, bold dotted lines, and thin dotted lines in the initial domes represent the ring, meridian, and brace of the dome, respectively. The dotted lines and solid lines in the optimized domes represent the members of the dome before and after the optimization, respectively.

Table 1 Average and standard deviation of relative values of objective functions in each optimization problem.

		Objective functions				
		δ (Opt. 1)	V (Opt. 2)	$1/\lambda_{min}$ (Opt. 3)	$1/\mu_{min}$ (Opt. 4)	σ_{min} (Opt. 5)
δ^r (%)	Ave.	-25.3	49.2	1.0	4.7	27.4
	S. D.	5.1	32.7	6.9	22.6	35.2
V^r (%)	Ave.	-1.4	-2.7	-0.1	-0.4	-0.5
	S. D.	0.4	1.2	0.3	0.5	0.7
$1/\lambda^r_{min}$ (%)	Ave.	7.7	75.3	-9.3	17.8	47.8
	S. D.	8.0	41.1	3.4	53.3	37.9
$1/\mu^r_{min}$ (%)	Ave.	-0.9	30.0	-2.1	-7.0	12.7
	S. D.	7.3	26.2	2.0	2.6	15.3
σ^r_{min} (%)	Ave.	-2.9	5.7	5.7	11.5	-25.0
	S. D.	7.5	22.6	4.4	18.3	14.4

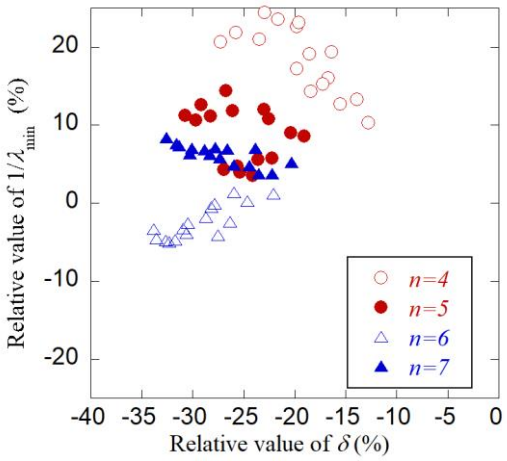


Fig. 3 Relationship between the relative values of δ and $1/\lambda_{min}$ in Opt. 1.

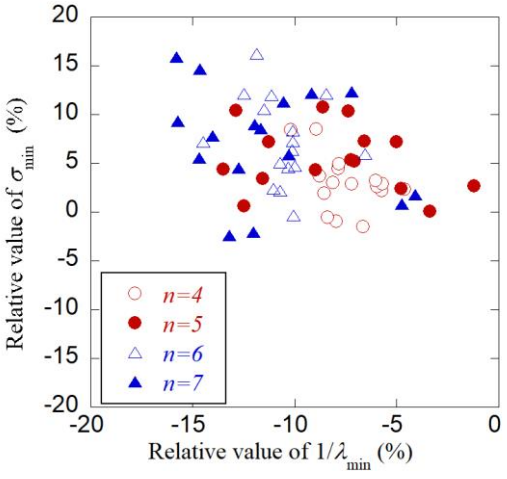


Fig. 4 Relationship between the relative values of $1/\lambda_{min}$ and σ_{min} in Opt. 3.

4. Conclusions

In this study, the optimization of grid patterns in single-layer latticed domes was conducted against five types of objective functions under geometrical constraints. The conclusions of this study are summarized as follows:

1) The total volume of the structure varied marginally after the optimization of the grid pattern.
2) The grid pattern of the optimized dome highly depended on the number of sectors n, while it was influenced slightly by the number of rings m and half-open angle θ.
3) Optimization against $1/\lambda_{\min}$ buckling was observed to be effective, as it improved $1/\lambda_{\min}$ and $1/\mu_{\min}$ simultaneously and worsened $\sigma_{\min}$ marginally. In the optimization against δ, $1/\mu_{\min}$ and $\sigma_{\min}$ improved simultaneously, while $1/\lambda_{\min}$ worsened marginally. Thus, it was assumed that they could be combined effectively, as they were complementary against $1/\lambda_{\min}$ and $\sigma_{\min}$.
4) Optimizations against δ and $1/\lambda_{\min}$ were observed to effective, when $n = 6$ or $n = 7$ and $n = 4$ or $n = 5$, respectively.

In this study, only limited number of initial dome shapes, joint of members, boundary conditions, and loading conditions were considered. Therefore, further parametric studies are required. The sensitivity of imperfection for optimized domes, which significantly influences the shell buckling load of single-layer latticed domes, should also be investigated using the geometrical nonlinear elasto-plastic finite element analysis for practical utilization.

Acknowledgements

This work was supported by Nohmura Foundation for Membrane Structure's Technology.

References

[1] T. Ogawa, M. Ohsaki, R. Tateishi, "Shape optimization of single-layer latticed shells for maximum linear buckling loads and uniform member lengths," *J. Struct. Constr. Eng.*, AIJ, Vol. 68, No. 570, pp. 129-136, 2003 (in Japanese).

[2] M. Ohsaki, "Design sensitivity analysis and optimization for nonlinear buckling of finite-dimensional elastic conservative structures," *Computer methods in applied mechanics and engineering*, Vol. 194, No. 30-33, pp. 3331-3358, 2005.

[3] Y. Takiuchi, S. Kato, S. Nakazawa, "Buckling maximization of single layer free-form reticulated shells, " *J. Struct. Constr. Eng., AIJ*, Vol. 82, No. 733, pp. 441-450, 2017 (in Japanese).

[4] M. Ohsaki, T. Ogawa, "Code-Based Design Optimization of Single-Layer Latticed Dome," J*ournal of the International Association for Shell and Spatial Structures*, Vol. 49, No. 1, pp. 49-55, 2008.

[5] S. Çarbaş, M. P. Saka, "Optimum topology design of various geometrically nonlinear latticed domes using improved harmony search method," *Structural and Multidisciplinary Optimization*, Vol. 45, No. 3, pp. 377-399, 2012.

[6] S. R. Malek, "The effect of geometry and topology on the mechanics of grid shells," *Massachusetts Institute of Technology*, 2012.

[7] H. Nooshin, P. Disney, "Formex configuration processing I.," *International journal of space structures*, Vol. 15, No. 1, pp. 1-56, 2000.

[8] H. Nooshin, P. Disney, "Formex configuration processing II.," *International journal of space structures*, Vol. 16, No. 1, pp. 1-56, 2001.

Proceedings of the IASS Annual Symposium 2019 – Structural Membranes 2019
Form and Force
7 – 10 October 2019, Barcelona, Spain
C. Lázaro, K.-U. Bletzinger, E. Oñate (eds.)

Prediction of minimum weight design of 3D steel frame structure from decomposition into 2D frames

Yuki ASAKAWA*, Makoto YAMAKAWA[a]

*Department of Architecture, Tokyo University of Science, Japan
6-3-1 Niijuku, Katsushika-ku, Tokyo 125-8585, Japan
Email Address: 4119501@ed.tus.ac.jp

[a] Department of Architecture, Tokyo University of Science, Japan

Abstract

This paper presents a prediction method of minimum weight design of a 3D steel frame structure by decomposition into and composition from 2D frames. An optimum design problem is set up as a minimum weight design problem whose design variables takes the cross-sectional dimensions. We investigate the influence of the constraints of cross-sectional dimensions to minimum structural volume and the initial value dependences by random multi-start method. From the results of numerical examples, we can decrease dispersion of the solutions by the approach and hence we can improve predictability of the solutions. Finally, we show that the decomposition into 2D frames and composition from optimum solutions have a good correspondence to the optimum solution of 3D frame under certain conditions.

Keywords: minimum weight design, optimal design, steel frame, decision support, constraints control

1. Introduction

Recent increase in computing power enables us to solve realistic, large and complex structural design optimization problems[1]. Various structural optimization methods were developed in the 1970s, where optimality criteria approaches[2] were mainly used. Recently, even in structural design, mathematical programming approach[3] has been becoming most important and regarded as a sophisticated computational optimization technique. It can handle a large number of various constraints and/or cost functions about structural and requirements[4].

It is mainstream to use FEA software in practical structural design. The software is basically used for check of the structural indices of a given structure. Such software could only indirectly assist designers and/or engineers to determine the structural system, material, member cross-sections and so on. Structural design still largely depends on the designer's experience and intuition. Some of them propose rationalization of the conventional design by structural optimization[5]. There are may studies that treat the minimum weight design of a 3D frame structure[6]. The structural optimization can suggest member cross-sections with appropriate member grouping. It also enables to control the structural performance, e.g., the safety factor to the allowable stress, the deformation quantity, bearing capacity of the structure. Furthermore, we can grasp its qualitative characteristics and easily compare efficiency of the different designs. As one of such studies, prediction of the minimum weight design of a 3D frame structure based on decomposition into and composition from 2D frames[7]. In the study, cross-sectional areas has been only considered as design variables.

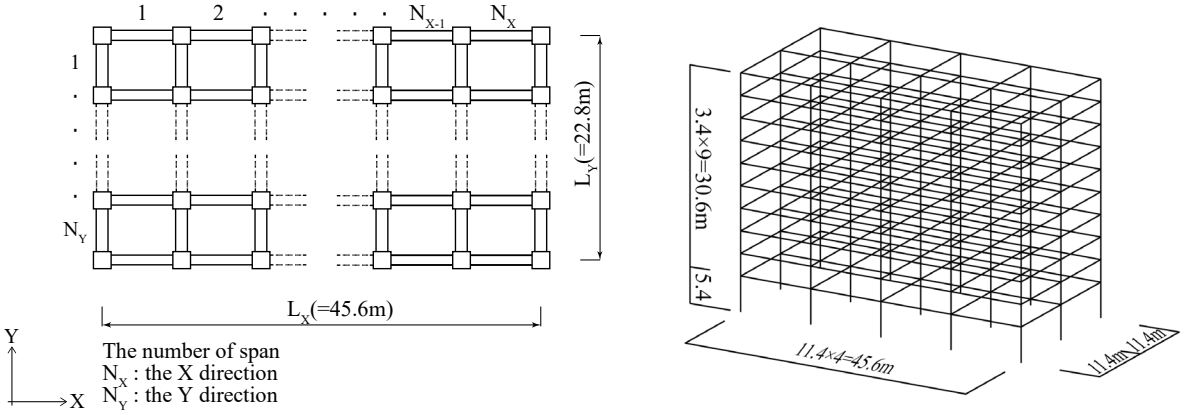
In the presenting approach, we decompose a 3D frame structure into 2D frames, then solve the corresponding minimum weight design problems. Finally, the solutions are composed to predict the minimum weight design of the original 3D frame. Computational cost of structural optimization of the

Copyright © 2019 by Yuki ASAKAWA, Makoto YAMAKAWA
Published by the International Association for Shell and Spatial Structures (IASS) with permission.

decomposed 2D frames is much lower than that of the 3D frame. Main difference from existing research[7] is the formulation of design variables. In earlier research on minimum weight design of steel frames, cross-sectional areas are treated as design variables. In contrast with this, we treat cross-sectional dimensions as design variables. This approach has disadvantage, where we must handle many design variables when compared with earlier studies. However, the approach is necessary for treatment of practical constraints and hence for realistic design solutions. We study applicability and predictability of the approach to the minimum weight design problem of 3D frame structures. In particular, we investigate prediction accuracy of the decomposition and composition framework, the initial value dependence on the solution, and control method to decrease the dependence.

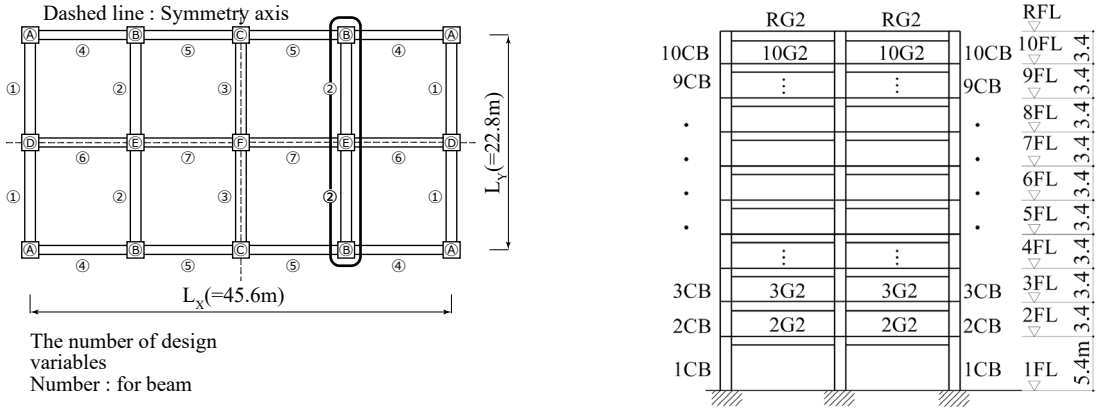
2. Three-dimensional steel frame model

Let us first define a 3D steel frame structure. The design model, which is shown in [7], is a 10-story steel frame structure with a first-floor height of 5.4 m and other floor heights are 3.4 m. The outline of the floor is fixed to the rectangle of $L_x = 45.6$ m $\times$ $L_y = 22.8$ m. The floor plan of the structure and an example of entire analysis model is shown in Figure 1. The spans are divided into N_x and N_y in the X-direction and Y-direction, respectively. With considering symmetry, member sections are grouped for each axis. Figure 2 shows an example of decomposed 2D frame and grouping of member sections in the floor plan. Thus, we decompose the 3D frame into 2D frames.



(a) Floor plan (b) An example of entire analysis model

Figure 1. 3D frame structure



(a) Floor plan (b) Decomposed 2D frame

Figure 2. An example of decomposed frame and member sections

3. Decomposed minimum weight design problem

3.1. Design condition

The floor load per unit area for long-term loading is 11.8 kN/m^2 and given as uniformly distributed load acting on the beam. The seismic shear force is calculated by Building Standard Law of Japan [8] (BSLJ) as shown in Table 1. The base of the first floor is fixed, and the foundation beam is not considered. It is assumed that the slab is rigid enough to transfer horizontal loads (Rigid floor assumption). The 3D steel frame shown in Fig. 1 is targeted, and the models of X and Y structures decomposed from it are analyzed. The vertical load is proportional to the width of the floor area, and the horizontal load is proportional to the floor width and length.

Table 1. The horizontal load

story	1F	2F	3F	4F	5F	6F	7F	8F	9F	10F
horizontal force (kN)	530.2	642.9	864.4	1059.4	1263.2	1507.2	1752.2	2046.2	2460.8	4172.8

3.2. Problem formulation

In our study the cross-sectional dimensions are taken as design variables. H-shaped cross-sections are used for the beams, and their height H_i (mm), flange width B_i (mm), web thickness tw_j (mm) and flange thickness tf_j (mm) $(i=1,\cdots,n_s; j=1,\cdots,n_G)$, where n_s is the number of layer and n_G is the number of cross-section of beam. Square hollow structural sections (HSS) are used for the columns, and their height D_k (mm) and thickness t_k (mm) $(k=1,\cdots,n_C)$, where n_C is the number of cross-section of column. Let $\mathbf{x}$ denote the vector of the design variable composed of cross-sectional dimensions. For steel types, use SN400 for beams and BCP 325 for columns. The objective functions $V(\mathbf{x})$ is formulated as the sum of the structural volume as

$$V(\mathbf{x}) = \sum_{i=1}^{n_m} A_i L_i \tag{1}$$

where A_i denotes the cross-sectional area of the members in the i th group, L_i is the total length of the members in i th group and n_m is the number of member. Additionally, the upper bounds are usually given for the response displacements and stresses against static loads based on BSLJ. As shown in Table2, we consider five types of constraints including practical construction constraints, lower and upper bounds for the cross-sectional dimension, stress ratio, inter-story direction angle, width-thickness ratio and central deflection, and they are formulate as $\mathbf{g}(\mathbf{x}) \le \mathbf{0}$, where $\mathbf{g}$ is assumed to be an implicit function of $\mathbf{x}$ after eliminating the state variables. Hence, the optimization problem for minimizing the objective function, the total structural volume $V(\mathbf{x})$, is formulated as a standard Non-Liner Problem (NLP):

$$\left.\begin{array}{ll} \text{find} & \mathbf{x} = \left\{ \begin{array}{l} H_i, B_i, tw_j, tf_j, D_k, t_k, \\ \qquad i=1,...,n_s; j=1,...,n_G; k=1,...,n_c \end{array} \right\} \\ \text{to minmize} & V(\mathbf{x}) = \sum_{i=1}^{n_m} A_i L_i \\ \text{subject to} & \mathbf{g}(\mathbf{x}) \le \mathbf{0} \end{array}\right\} \tag{2}$$

Table 2. Constraints

<table>
<tr><td colspan="3">Lower and Upper dimension</td></tr>
<tr><td>Beam</td><td colspan="2">Column</td></tr>
<tr><td>Height
$100 \le H_i \le 900$
$H_{i+1} \le H_i \quad (i = 1, \cdots, n_s - 1)$
Flange width
$100 \le B_i \le 400 \quad (i = 1, \cdots, n_s)$
Web and flange thickness
$6 \le tw_j, tf_j \le 36 \quad (j = 1, \cdots, n_G)$</td><td colspan="2">Height
$300 \le D_k \le 800$
$D_k^{i+1} \le D_k^i \quad (i = 1, ..., n_s; k = 1, ...n_C)$
Thickness
$13 \le t_k \le 36 \quad (k = 1, \cdots, n_C)$</td></tr>
<tr><td colspan="3">Width-thickness ratio</td></tr>
<tr><td>Beam</td><td colspan="2">Column</td></tr>
<tr><td>Web plate
$H_i / t_w \le 60\sqrt{235 / F}$
Flange plate
$B_i / 2 \Big/ t_f \le 11\sqrt{235 / F}$</td><td colspan="2">Plate
$D_k \Big/ t_k \le 33\sqrt{235 \Big/ F}$</td></tr>
<tr><td>Stress ratio</td><td>Inter-story deflection angle</td><td>Central deflection</td></tr>
<tr><td>Long and short term load
$\left\lvert \frac{M_y}{Z_y f_b} \right\rvert + \left\lvert \frac{N}{A f_c} \right\rvert \le 1$</td><td>Short term load each floor
$\delta / h \le 1 / 200$</td><td>Long term load
$d / l_b \le 1 / 300$</td></tr>
</table>

F is design strength, M_y is strong-axis bending moment , N is axial force, Z_y is strong-axis section modulus, A is cross-sectional area, f_b is allowable bending unit stress, f_c is allowable compressive unit stress, δ is inter-story deflection, h is floor height, d is beam central deflection, l_b is length of stiffener.

4. Prediction of minimum weight

4.1. Optimal solution properties of 2D frame

For 2D frame of Y-axis structure, the interior point method is used as optimization method and five cases of initial solutions at random are given. The maximum value of the standard deviation of all the models is $0.46\,\mathrm{m}^3$, and the initial value dependence is not large when compared with the total volume. Relationship between optimum structural volume and span length is shown in Figure 4 for floor width of 11.4m, 7.6m and 5.7m. As shown in Figure 4, the structural volume also increases with the increase in span length or floor width, and the regression equations of structural volume are approximated as

$$V(l_x, l_y) = 4.574 + 0.4682 l_z - 0.383 l_y + 0.04073 {l_y}^2 + 0.02239 l_x l_y \tag{3}$$

where $l_x = L_x / N_x$ is the floor width in the x-axis direction, l_y is the span length in the y-axis direction and R is correlation coefficient. As shown in Eq.(7), the correlation coefficient R becomes 0.95, and it is a curved surface where a liner relationship between structural volume and floor width and a well-correlated quadratic curve convex downward in the direction of span length hold. In the optimal solution obtained from five cases with different initial solutions, comparing the cross-sectional areas and dimensions of each member, the cross-sectional area, column and beam webs are almost same, while the width plate and thickness of the beam flanges differ as shown in Figure 5.

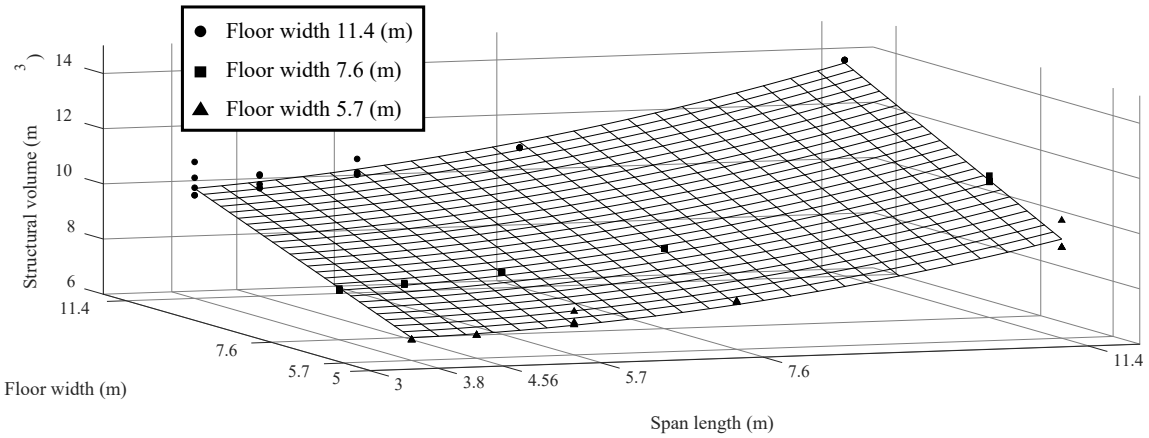
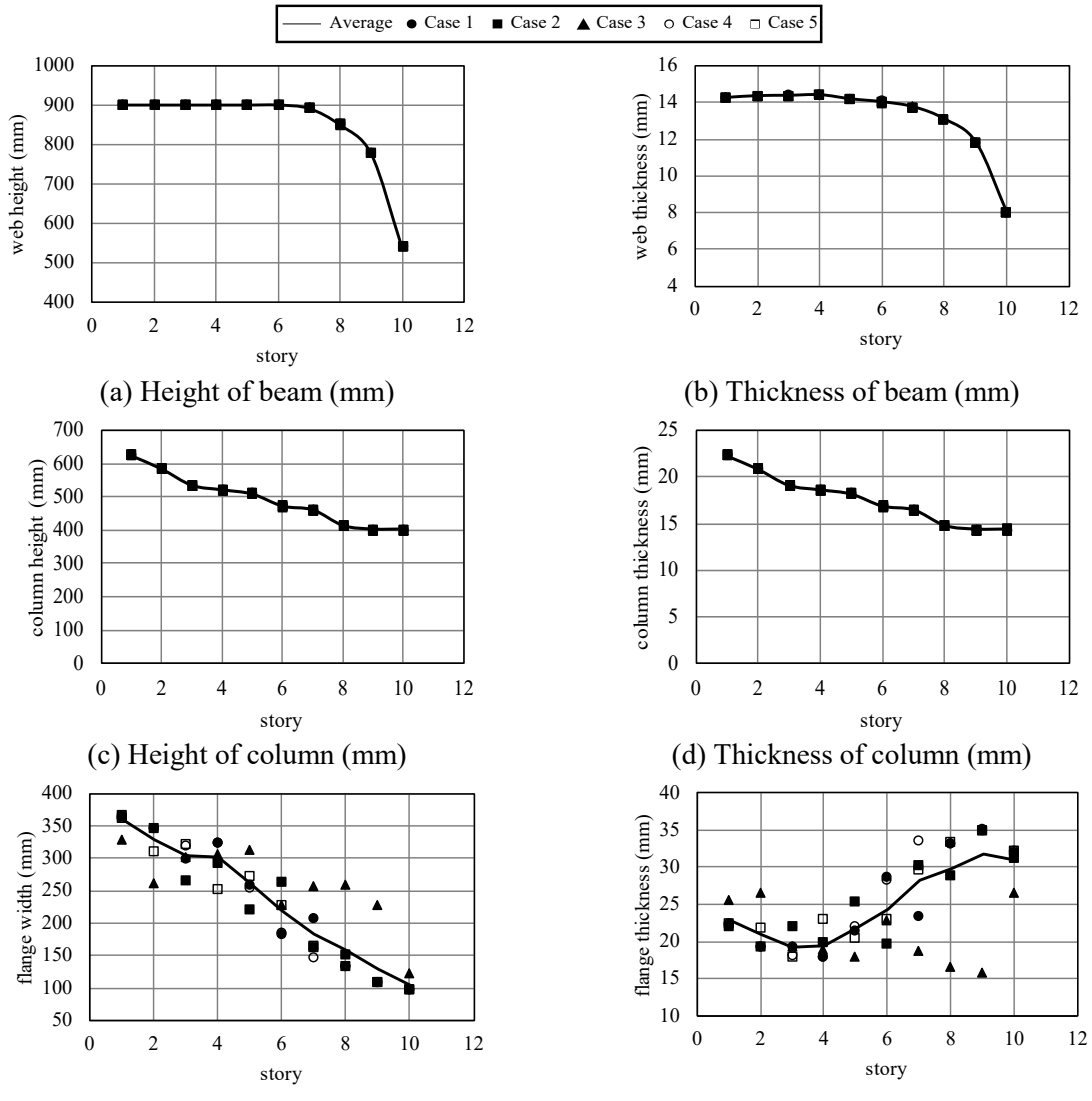


Figure 4. Relation between optimum structural volume and span length



(a) Height of beam (mm)

(b) Thickness of beam (mm)

(c) Height of column (mm)

(d) Thickness of column (mm)

(e) Width of beam (mm)

(f) Thickness of column (mm)

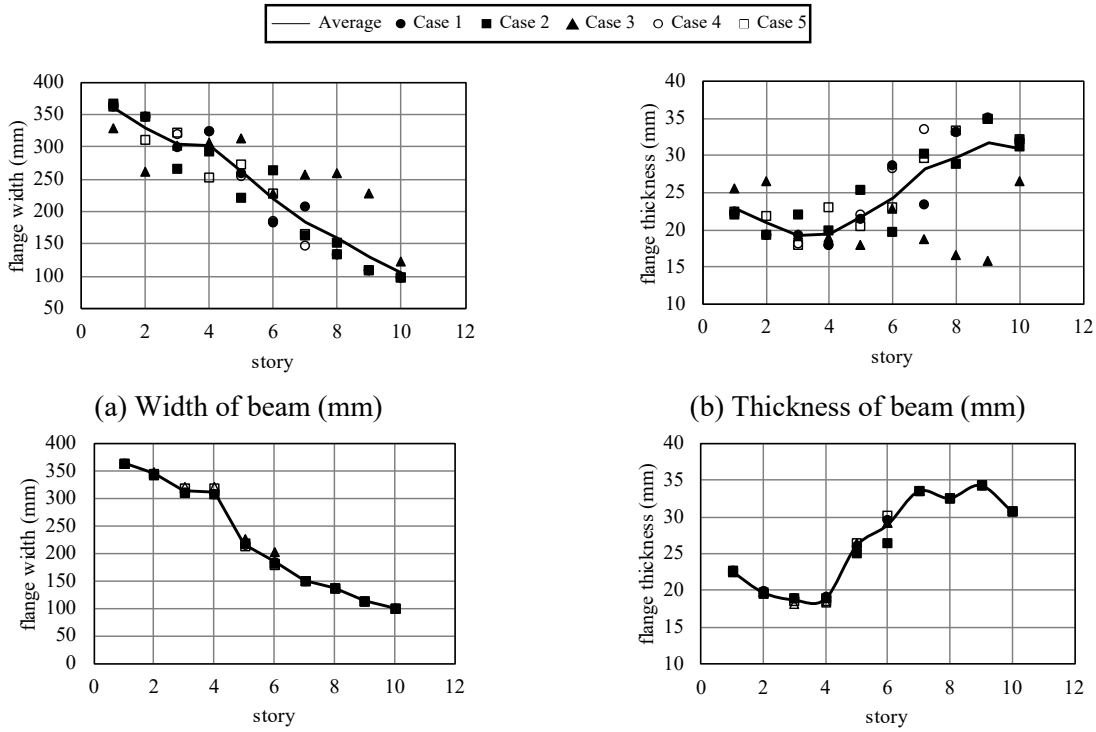
Figure 5. Cross-sectional dimension distribution

4.2. Comparative study of optimum solutions by size constraints

In this study, we propose that the upper and lower story constraint of the beam width are introduced as a method to control the variation of cross-sectional dimensions. It is formulated as

$$B_{i+1} \le B_i \quad (i = 1, \cdots, n_s - 1) \tag{4}$$

where B_i is the width of beam in i th group and n_s is the number of layer. With Eq. (7) added to the constraints, the distribution of the beam width in the case of analysis under the same condition is shown in Figure 6, and the standard deviation and the maximum difference are shown in Table 3. As shown in Figure 6 and Table 3, it is found that the variation in cross-sectional dimensions can be controlled, and the standard deviation and the maximum difference are decreased by introducing the beam width constraint. When we consider with or without the constraint in the analysis for the 2D frames, the change in optimum structural volume is shown in Table 4. The difference with or without the constraint is at most 3.2%, and it is considered that the addition of constraints does not substantially affect the optimum structural volume as shown in Table 4.



(a) Width of beam (mm) (b) Thickness of beam (mm)

(c) Width of beam (mm) (d) Thickness of beam (mm)

Figure 6. Cross-sectional dimension variation with or without constraint

Table3. The standard deviation and maximum difference of the flange

(a) The thickness of beam

The flange thickness	Story constraint	2FL	3FL	4FL	5FL	6FL	7FL	8FL	9FL	10FL	RFL
Standard deviation	With	0.06	0.12	0.29	0.36	0.49	1.30	0.02	0.02	0.02	0.02
	Without	1.22	2.65	1.34	1.70	2.32	3.23	5.44	6.08	7.10	2.05
Maximum difference	With	0.09	0.24	0.47	0.55	0.91	2.48	0.04	0.03	0.03	0.04
	Without	2.71	5.58	2.75	3.55	3.88	4.69	9.48	13.12	15.89	4.52

(b) The width of column

The flange width	Story constraint	2FL	3FL	4FL	5FL	6FL	7FL	8FL	9FL	10FL	RFL
Standard deviation	With	0.64	1.81	4.92	5.92	4.06	8.57	0.10	0.08	0.06	0.07
	Without	13.35	31.92	18.90	23.82	28.78	27.75	39.47	45.99	44.31	8.84
Maximum difference	With	1.11	3.60	7.89	9.18	7.58	16.55	0.19	0.13	0.10	0.13
	Without	29.69	65.41	37.63	48.02	52.60	45.86	75.72	101.66	99.08	19.77

Table 3. The change of optimum structural volume with or without of the constraint

Span ($N_X \times N_Y$)		4×2	4×3	4×4	4×5	4×6	6×2	6×3	6×4	6×5	6×6
Optimum solution(m^3)	ON	13.83	11.06	10.42	10.14	10.16	10.97	8.91	8.25	7.95	7.81
	OFF	13.66	11.02	10.29	10.18	10.03	10.83	8.90	8.24	8.10	7.99
Ratio(%)		101.24	100.32	101.21	99.54	101.30	101.29	100.02	100.16	98.10	97.80

Span ($N_X \times N_Y$)		8×2	8×3	8×4	8×5	8×6
Optimum solution(m^3)	ON	9.49	7.73	7.22	6.85	6.76
	OFF	9.19	7.72	7.05	6.89	6.75
Ratio(%)		103.18	100.02	102.34	99.30	100.06

4.3. Optimal solution comparison of 2D and 3 frame model

We compare the optimum structural volume using the design solutions in which the optimal solution of 2D frame model in both X and Y directions is placed on each structural frame of the 3D steel frame and the optimal solution obtained from the structural optimization of the 3D frame. In addition, column cross-sectional dimensions of the optimal solutions are calculated in two cases: the average value of each structure and the maximum value. It was confirmed that the difference of the ratio was less than 5%, and the optimal solution of 2D frame and the optimal solution of 3D frame had a good correspondence as in the conclusion of reference [1].

Table 4. Comparison of optimum structural volume

$N_X \times N_Y$ 3D frame sturacture	4×2			4×3		
	3D	2D		3D	2D	
		Average	Max		Average	Max
Structural Volume (m^3)	110.0	107.0	112.0	102.1	97.0	97.8
Ratio (%)	100	97.3	101.8	100	95.1	95.8

5. Conclusion

It is proposed that prediction of the minimum weight design of a 3D frame structure based on decomposition into and composition from 2D frames. In this paper, we treat cross-sectional dimensions as design variables, investigate the characteristics of the optimum solutions and verified prediction accuracy of the minimum weight of the 3D frame. The results are as follows:

1. Although 2D frame structures have a low dependence on initial solution in the structural volume, variations in flange width and thickness for beam are seen.
2. By considering the upper and lower story constraint of the flange width, the initial solution dependency is significantly reduced, and the variations can be decreased.
3. The difference in the ratio between the prediction structural volume from decomposition into and composition from the 2D frames and the minimum volume of the 3D frame structure is less than 5% and hence the minimum structural volume of the 3D frame structure can be accurately predicted by decomposition and composition framework.

Acknowledgements

This work was partially supported by JSPS KAKENHI Grant Number 18K04444.

References

[1] M. Ohsaki, Optimization of Finite Dimensional Structures, CRC Press, 2017.

[2] N. S. Khot, L. Berke, V. B. Venkayya, "Comparison of optimality criteria algorithms for minimum weight design of Structures", *AIAA Journal*, Vol. 17, No. 2.

[3] M. W. Dobbs, L. P. Felton, "Optimization of truss geometry", *Journal of structural division*, Vol. 95, pp. 2105-2118, 1969.

[4] S. R. Labanda, M. Stolpe, "Benchmarking optimization solvers for structural topology optimization", *Struct Multidisc Optim*, pp. 527-547, 2015. 5.

[5] K. Ikago, M. Yamakawa, K, Uetani, "Structural design based on a numerical design method and sensitivity analysis of optimum designs of buildings", *Journal of structural engineering*, *the Architectural Institute of Japan*, No.599, pp. 87-94, 2006(in Japanese).

[6] C. P. Rubin, H. Aircraft, E. Segundo, Calif, "Minimum weight design of complex structures subject to a frequency constraint", 2012. 5.

[7] Y. Lee, S. Yoshitomi, and K. Uetani, "A study on structural planning using the characteristics of the optimal solutions for plane steel frame models", *Journal of structural engineering, the Architectural Institute of Japan*, vol. 50B, pp. 215-220, 2004 (in Japanese).

[8] The Building Center of Japan, *The Building Standard Law of Japan*, 2016

Proceedings of the IASS Annual Symposium 2019 – Structural Membranes 2019
Form and Force
7 – 10 October 2019, Barcelona, Spain
C. Lázaro, K.-U. Bletzinger, E. Oñate (eds.)

Rationalization of layout optimization result by updating discretization of the design domain

Qingpeng LI*, Paul SHEPHERD[a], Matthew GILBERT[b], Linwei HE[b]

* Department of Architecture & Civil Engineering, University of Bath, Bath BA2 7AY, UK
hitssrclqp@gmail.com

[a] Department of Architecture & Civil Engineering, University of Bath
[b] Department of Civil and Structural Engineering, University of Sheffield

Abstract

Truss layout optimization provides a means of identifying the global optimal arrangement of truss bars capable of transmitting a given load or loads to defined support points within a defined design domain. However, the solutions obtained are generally complex and lead to structures with far too many members to be practical, especially when fine discretization of the design domain is employed. In this paper, a heuristic approach to the practical rationalization of optimal layouts is proposed, based on the observation that fan-like segments of bicycle-wheel structures often appear in multiple places in an optimal layout, with a central 'hub' joint of high valence linking through 'spokes' to a curved 'rim'. In this proposed method, the global optimum layout of a given problem is first obtained, and joints that are not used in the optimal truss are removed from the design domain. Subsequently, 'hub' joints of high valence are identified, as are the 'rim' joints they are connected to. A new discretization of the design domain is then produced, which reduces the density of joints in the curved 'rim'. A second layout optimization is then conducted to generate a more rational and buildable truss, with only a small increase in structural weight compared to the global optimal. Using two case-studies, the effectiveness and the efficiency of the proposed approach is validated.

Keywords: Rationalization, layout optimization, optimal layout, discretization, design domain

1. Introduction

Truss layout optimization provides a computationally efficient means of identifying the global optimal arrangement of truss bars capable of transmitting a given load or loads to defined support points within a design domain. Among others, 'ground structure' based layout optimization methods are used widely. The 'ground structure' layout optimization procedure was first proposed by Dorn et al. [1]. More recently, Gilbert and Tyas [2] made it more efficient by proposing an adaptive 'member adding' algorithm, which means that much larger scale layout optimization problems can be solved. Based on the proposed method, a Grasshopper plugin was subsequently developed to make the procedure accessible to those in practice [3].

The solutions obtained are provably globally optimal, but are generally complex and lead to structures with far too many members to be practical, especially when a fine discretization of the design domain is employed. Others have made good progress in employing integer programming methods to address some of these issues [4][5], but these techniques are computationally expensive and therefore not capable of tackling very large problems. Therefore, an efficient post-processing rationalization method, which can consider practical constraints and is suitable for computationally larger problems, is needed urgently.

Copyright © 2019 by Qingpeng LI, Paul SHEPHERD, Matthew GILBERT and Linwei HE.
Published by the International Association for Shell and Spatial Structures (IASS) with permission.

From the authors' experience of applying these techniques to many case-studies, they have observed that fan-like segments of bicycle-wheel structures often appear in multiple places in an optimal layout, with a central 'hub' joint of high valence linking through 'spokes' to a curved 'rim'. Based on this interesting observation, a heuristic approach to the practical rationalization of optimal layouts is proposed.

2. Methodology

In this section, the layout optimization method of truss structures and the resulting Grasshopper plugin are briefly introduced. Subsequently, the rationalization method for optimal layouts, which updates the discretization of the design domain is proposed.

2.1. Layout Optimization Method and the Grasshopper Plug-in

The standard layout optimization process involves four steps, as shown in Figure 1. Firstly the design domain, load and support conditions are specified, Figure 1(a). Secondly, the design domain is discretized using nodes, Figure 1(b). Thirdly, these nodes are interconnected with all potential members to create a 'ground structure', Figure 1(c). This 'ground structure' normally contains a vast number of potential structural forms, even with medium number of nodes (e.g., 100∼1000 nodes).

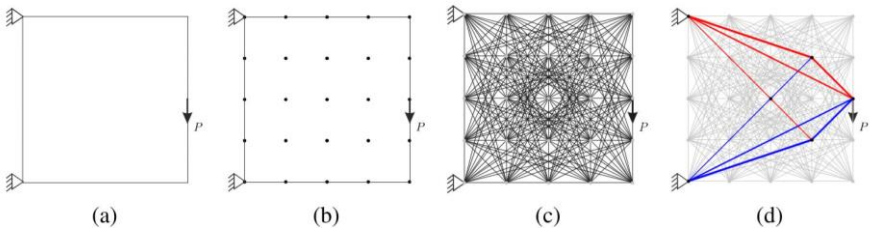


Figure 1: Steps in layout optimization: (a) specify design domain, loads and supports; (b) discretize domain using nodes; (c) interconnect nodes with potential truss members; (d) use optimization to identify the optimal structural layout.

The most efficient structural layout is then identified (Figure 1(d)) by solving the optimization problem below:

$$\begin{aligned} &\underset{\mathbf{a},\mathbf{q}}{\text{Minimize}} \quad V = \mathbf{l}^{\mathrm{T}}\mathbf{a} \\ &\text{Subject to} \\ &\qquad \left.\begin{aligned} &\mathbf{B}\mathbf{q}^{(k)} = \mathbf{f}^{(k)} \\ &\mathbf{q}^{(k)} \geq -\sigma^{-}\mathbf{a} \\ &\mathbf{q}^{(k)} \leq \sigma^{+}\mathbf{a} \end{aligned}\right\} \text{for } k = 1, 2, ..., p \\ &\qquad \mathbf{a} \geq \mathbf{0}, \end{aligned} \tag{1}$$

where, V is the structural volume, $\mathbf{a} = [a_1, a_2, ..., a_m]^{\mathrm{T}}$ is a vector containing member cross-sectional areas, with m denoting the number of members. $\mathbf{l} = [l_1, l_2, ..., l_m]^{\mathrm{T}}$ is a vector of member lengths. $\boldsymbol{B}$ is a 2n×m equilibrium matrix comprising direction cosines, with n denoting the number of nodes. k is the load case identifier and p is the number of load cases. $\mathbf{q}^{(k)}$ and $\mathbf{f}^{(k)}$ are vectors containing the internal member forces and the external forces in the k^{th} load case, respectively. σ^{+} and σ^{-} are limiting tensile and compressive stresses respectively.

Using this 'ground structure' approach, the number of members increases with the square of the number of nodes, which leads to very large-scale optimization problems. Fortunately, problem (1) is a linear programming (LP) problem that can be solved very efficiently via modern LP solvers utilizing an interior-point method, e.g., MOSEK. Moreover, an adaptive solution scheme can be adopted [2] to decompose the problem into a number of sub-problems that can be tackled relatively easily.

Based on the proposed approach by Gilbert and Tyas [2], a conceptual design optimization tool [5] was developed for Rhinoceros-Grasshopper [6]. Figure 2 shows an example of the components in use, where they can be grouped into the following types:

1) Geometry Definition. The geometry of the design domain is defined using standard Grasshopper components so as to provide a parametric workflow. Users are free to define a design space in terms of lines, polygons, NURBS surfaces and complex BReps. The geometry is then meshed to faces and vertices as input for the design domain. A number of bespoke components have been provided to aid this process for layout optimization.

2) Design Domain. A number of components are then used to assign material properties such as tensile and compressive strength, Young's modulus, Passion's ratio, and material density. The support and load conditions need to be defined.

3) Layout Optimization. This component performs the layout optimization and provides diagnostic information on the time and number of iterations needed to solve. The volume of material required by the structure is also reported.

4) Visualization of solutions. A component is provided to visually present the resulting members, joint positions, internal forces and cross-sectional areas.

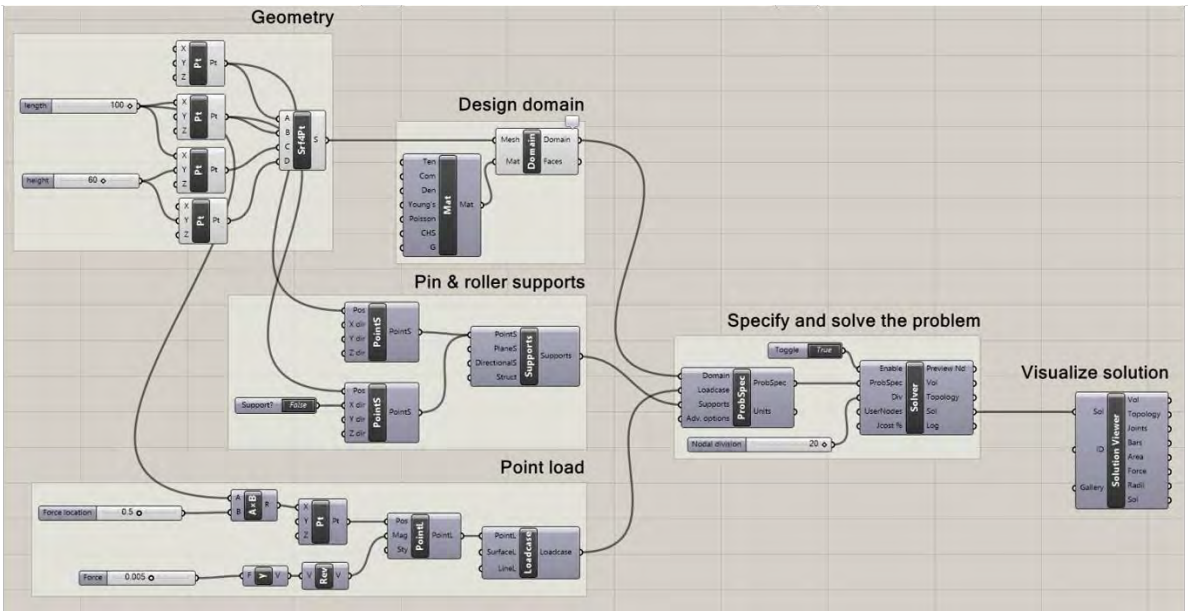
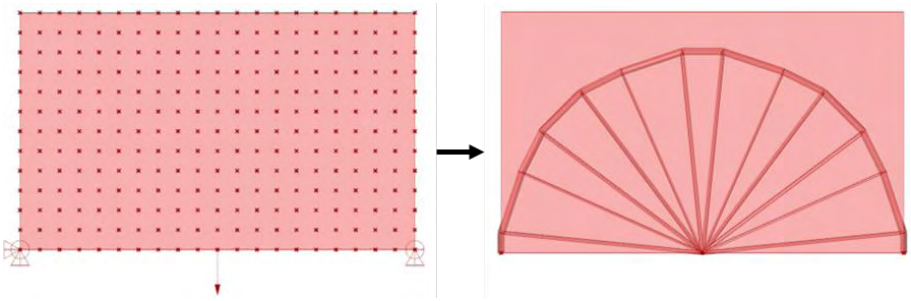


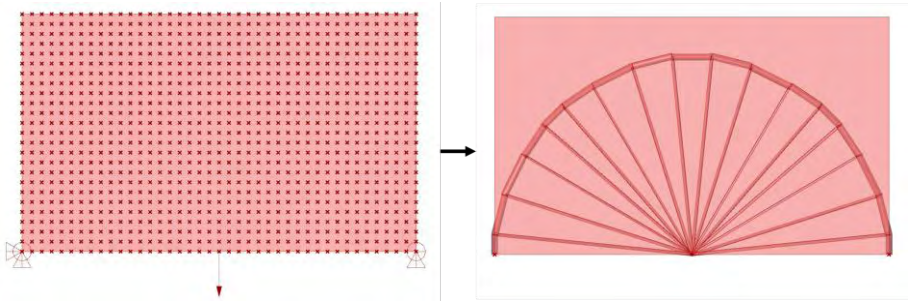
Figure 2: The Grasshopper layout optimization plugin.

2.2. The Rationalization Method

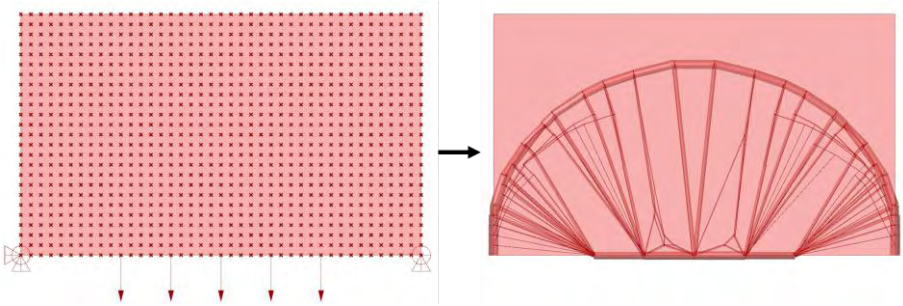
Figure 3(a) shows the optimal layout of a simply supported truss under one concentrated load. It can be observed that there appear fan-like segments of bicycle-wheel structures in the optimal layout, with a central 'hub' joint of high valence linking through 'spokes' to a curved 'rim'. Moreover, the resulting truss structure would be too complex to build, since too many members are linked to the same central joint, which would not be practical to manufacture. When a finer discretization of the design domain is employed, as in Figure 3(b), the number of 'spoke' members increases further, and when the concentrated load is distributed over multiple joints, as in Figure 3(c), the manufacturing complexity of the optimal solution become even more prohibitive.



(a) The simply supported truss under one concentrated load with a coarse mesh.



(b) The simply supported truss under one concentrated load with a finer mesh.



(c) A simply supported truss under five equally-spaced concentrated loads.

Figure 3: Numerical examples.

Base on the observations above, a rationalization approach have been developed. As the optimal layout of the truss can represent the load path of the applied load within the given design domain (ignoring multiple load cases for now), the basic assumption is that a rational and buildable truss exists close to the unbuildable optimal layout. By considering simplifications of the optimal layout, a practical truss using a sub-set of joints from the optimal layout is found. Thus the goal of the rationalization approach becomes a sensible selection of joints from the optimal layout. Considering the main contribution to complexity of the optimal layout results from the fan-like segments of bicycle-wheel structures, then a rationalization approach that reduces the density of the joints used in the curved 'rim' seems a sensible first step.

A numerical example, which is of a simply supported truss under three concentrated loads, is chosen here to describe the rationalization approach:

1) The optimal layout of the truss is obtained by conducting layout optimization within the given design domain using the Grasshopper plugin, shown in Figure 4. For later benchmarking, the structural volume of this optimal layout is 1239500 units^3.

2) Joints which are not used in the optimal layout are removed from the design domain.

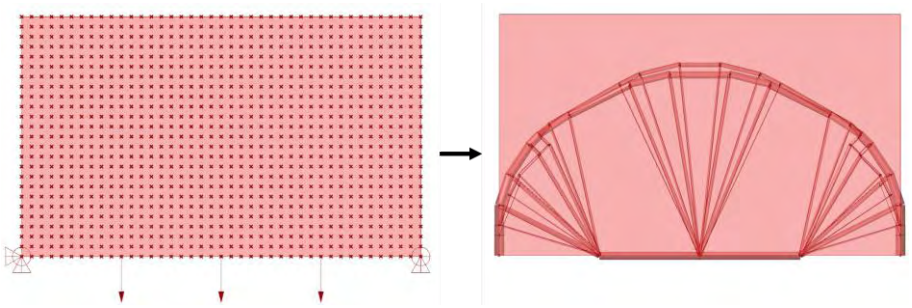


Figure 4: 1st layout optimization.

3) Potential 'hubs', which denote joints with high valence, are identified by counting the number of bars connected to each joint. Figure 5 shows three 'hub' joints identified in the optimal layout, which are joints where the concentrated loads are applied.

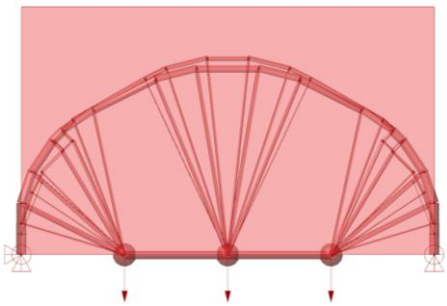


Figure 5: Three identified 'hub' joints.

4) Joints and relevant bars which are connected to each potential 'hub' are ordered by the angle they wind around the 'hub', for example Figure 6 shows in green the fifth connected joint/bar of the first 'hub' joint. Note that this angle ordering works well for 2D problems, using the best-fit plane as a coordinate system, but a different approach is needed to order the members in 3D.

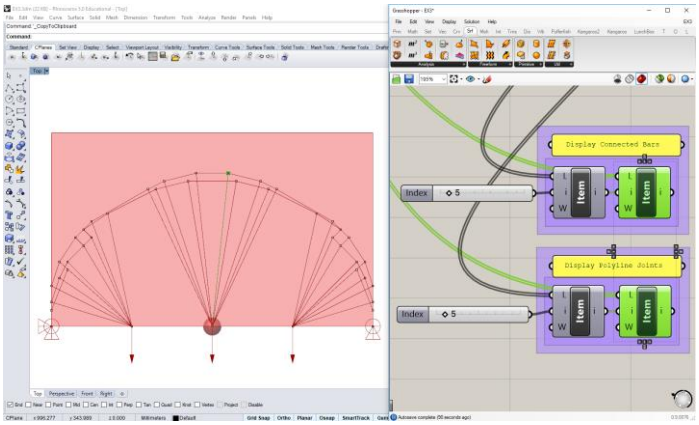


Figure 6: Fifth connected joint and bar of the first 'hub' joint.

5) A sub-set of connected joints and bars is created for each 'hub' joint, in which lengths of the bars within each group only differ from the length of the previous by ±10%. In this way, a smooth 'rim' is identified, ignoring 'spokes' which are of a very different length to their neighbours, indicating they might be part of a different 'rim' or of another sub-structure altogether.

6) For each 'hub' joint, a polyline is constructed, linking its 'rim' joints together. The polyline is smoothed using standard Grasshopper 'smooth' and 'rebuild' components. If the connected joints form more than one candidate polyline, the geometrically shortest polyline is chosen, representing an arc-like segment of the bicycle wheel. For example, Figure 7 shows the shortest polyline of the central 'hub', where the two connected joints at the ends of the two horizontal members have not been included.

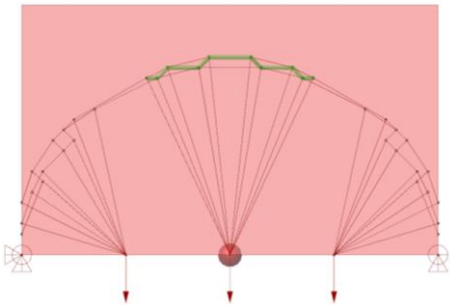


Figure 7: The shortest polyline of the first 'hub' joint.

7) The curved 'rim' polylines are then sub-divided into equal-length segments, resulting in several new joints. This provides a new (more rationalized) discretization of the design domain, as shown in green in Figure 8.

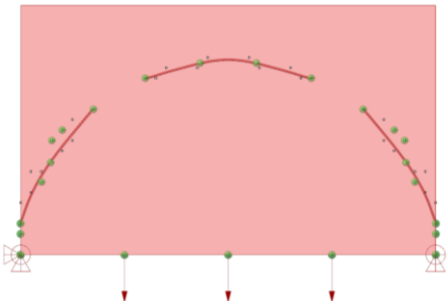


Figure 8: New mesh of the design domain.

8) A second layout optimization is then performed using the new design domain discretization. Figure 9 shows a more rational and buildable truss structure is obtained. Its structural volume is 1258900 units³, only 1.57% larger than the volume of the original optimal layout shown in Figure 4.

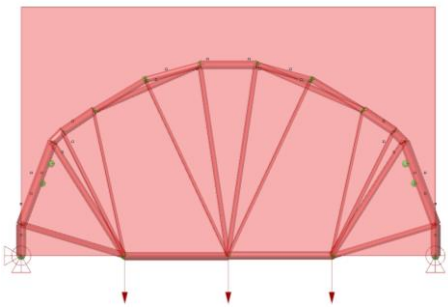


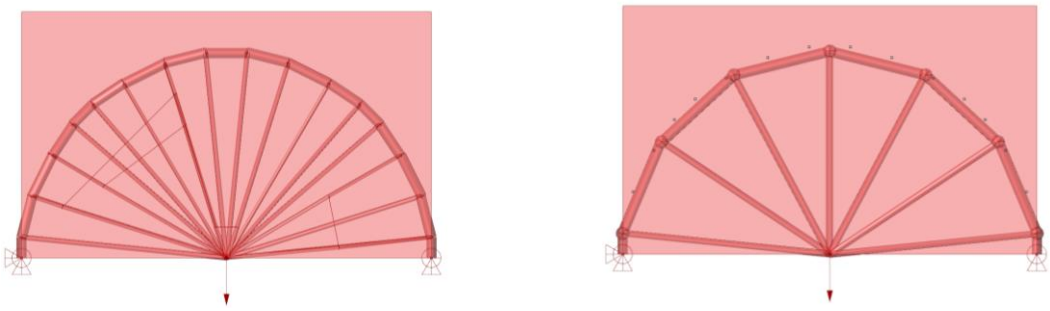
Figure 9: The simpler optimal layout.

Using these eight steps, more rational and buildable trusses can be quickly obtained, with an acceptably small increase in structural weight compared to the global optimal. In this example, it can also be seen that a circular-arc 'rim' appears around the central 'hub', whilst non-circular, curved 'rims' appear around the other two potential 'hubs'.

3. Examples

In this section, two further case-studies are illustrated to validate the effectiveness of the proposed rationalization approach.

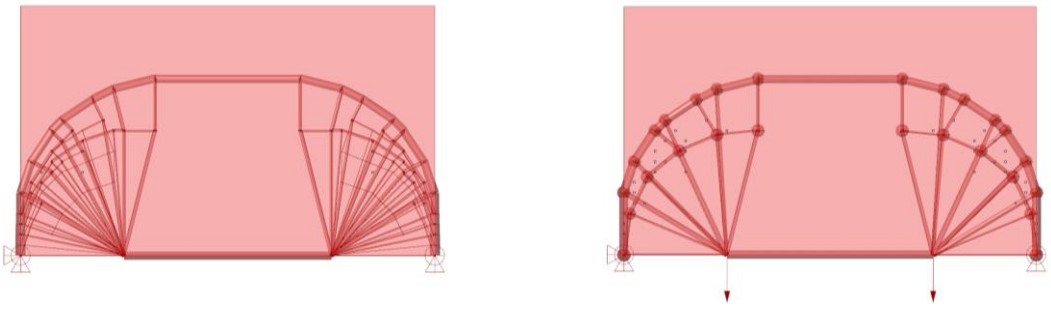
The first example is a simply supported truss under one concentrated load. Shown in Figure 10, it can be seen that one 'hub' joint is identified, and after rationalization, the circular-arc 'rim' is maintained around it. By using the proposed rationalization approach, the structural volume of the rationalized optimal layout is 1602900 units^3, which is just 1.57% larger than its original optimal volume of 1578200 units^3).



(a) The original optimal layout. (b) The rationalized optimal layout.

Figure 10: The simpler optimal layout.

The second example is a simply supported truss under two concentrated loads. Shown in Figure 11, it can be seen that two potential centres are identified, and circular-arc 'rims' appear around them. By using the proposed rationalization approach, the structural volume of the rationalized optimal layout is increased from 1169600 units^3 to 1174000, an increase of only 0.38%.



(a) The original optimal layout. (b) The rationalized optimal layout.

Figure 11: The simpler optimal layout.

4. Conclusions

By updating and simplifying the discretization of the design domain, a heuristic approach to the practical rationalization of optimal layouts is proposed. This approach is a post-processing procedure,

which can consider practical constraints and is independent of the layout optimization algorithm used. It produces simplified layouts that are more practical from a fabrication point of view with only a small penalty in terms of increased material use. Moreover, by reducing the density of the joints within the design domain, the computational overhead of this post-processing step is small. However, there are still some limitations of the current rationalization approach. For example, so far, only 2D problems have been studied, and only for a single load case. Heuristics for post-processing of more general truss structures therefore remains the subject of ongoing work by the authors.

5. Acknowledgements

This research was supported by the EPSRC, under grants EP/N023269/1 and EP/N023471/1.

References

[1] W.S. Dorn, R.E. Gomory, H.J. Greenberg. "Automatic design of optimal structures", *Journal de M`ecanique*, vol. 3, pp.25-52, 1964.

[2] M. Gilbert and A. Tyas, "Layout optimization of large-scale pin-jointed frames", *Engineering Computations*, vol. 20, iss. 8, pp.1044-1064, 2003.

[3] L. He, M. Gilbert, P. Shepherd, J. Ye, A. Koronaki, H.E. Fairclough, B. Davison, A. Tyas, J. Gondzio, A.G. Weldeyesus. "A new conceptual design optimization tool for frame structures", in *Creativity in Structural Design: Proceedings of the IASS Annual Symposium 2018*, MIT, Boston, USA, July 16-20, 2018, C. Mueller and S. Adriaenssens Ed.

[4] H. Fairclough, M. Gilbert, C. Thirion and A. Tyas, "Balancing complexity and structural efficiency in the design of optimal trusses", in *Creativity in Structural Design: Proceedings of the IASS Annual Symposium 2018*, MIT, Boston, USA, July 16-20, 2018, C. Mueller and S. Adriaenssens Ed.

[5] L. He and M. Gilbert, "Rationalization of trusses generated via layout optimization", *Structural and Multidisciplinary Optimization*, vol. 52, iss. 4, pp. 677–694, 2015.

[6] McNeel R. Grasshopper generative modeling for Rhino. Computer software (2011b), http://www.grasshopper3d.com. 2010.

Proceedings of the IASS Annual Symposium 2019 - Structural Membranes 2019
Form and Force
7-10 October 2019, Barcelona, Spain
C. Lázaro, K.-U. Bletzinger, E. Oñate (eds.)

Rule-based topology finding of patterns towards multi-objective structural design

Robin OVAL[*a,b], **Romain MESNIL**[a], **Tom VAN MELE**[b], **Philippe BLOCK**[b], **Olivier BAVEREL**[a]

[*] robin.oval@enpc.fr

[a] Laboratoire Navier, UMR 8205, École des Ponts des Ponts, IFSTTAR, CNRS, UPE, Champs-sur-Marne, France
[b] ETH Zurich, Institute of Technology in Architecture, Block Research Group, Zurich, Switzerland

Abstract

Design of patterns involves meeting multiple objectives regarding architecture, engineering and construction. Form finding allows to explore the geometrical design space defined by the topology of the pattern, and to optimise a geometry to meet these objectives. This research introduces rule-based topology finding for the exploration of singularities in quad-based mesh patterns by introducing a strip grammar. This grammar allows to generate and combine multiple topologies, and therefore, multiple geometrical design spaces with qualitatively different parameters. Applying rules to create hybrid topologies based on single-objective topologies that are heuristically or algorithmically generated, allows to explore hybrid geometrical design spaces in order to meet trade-offs between multiple design objectives. This research opens a new family of rule-based topology-optimisation methods that allow to tackle multiple objectives that can relate to statics as well as fabrication, construction and other design aspects.

Keywords: conceptual design, structural design, rule-based design, surface structures, patterns, topology, singularities, topology finding, form finding, multi-objective.

1 Introduction

Discrete shell-like structures consist of the assembly of structure and cladding elements, like beams and panels for gridshells or voussoirs for vaults. Designing these patterns relates to structural, fabrication and construction efficiency, and therefore to cost and sustainability. The geometry of curved surface structures can be designed using diverse geometrical exploration algorithms to achieve feasible and affordable structures. However, the topology of the pattern controls its geometry. Indeed, the geometrical design parameters are defined by the topology, which constrains the exploration of the geometrical design space, which may not contain suitable or efficient designs. Exploring different topologies allows to break this limitation and to explore a more general topological design space, by exploring multiple parametric geometrical design spaces.

Copyright ©2019 by R. OVAL, R. MESNIL, T. VAN MELE, P. BLOCK, O. BAVEREL
Published by the International Association for Shell and Spatial Structures (IASS) with permission.

1.1 Challenges for topological design of patterns

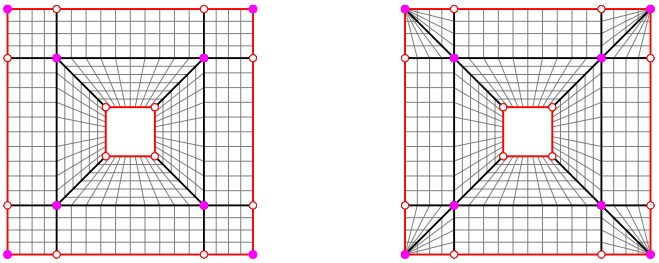
Design of patterns can face different levels of obstacles if a flexible topological design approach is not enabled. Full design opportunities are missed when the designer is forced to:

- resort to a classic quad-mesh grid relevant for very regular design problems only;
- spend time in a tedious project-specific procedure without automation process;
- algorithmically optimise the topology for a single, specific requirement; or,
- stick to a static topology all along the design process, while design objectives evolve.

Addressing these challenges would provide the opportunity to perform structural design with a dynamic topology to explore different geometrical design spaces. Such a flexibility would allow finding trade-offs between multiple, evolving, project-specific objectives regarding diverse architectural, engineering and construction aspects, like structural efficiency and fabrication affordability.

1.2 Approach to topology finding of patterns

Topological design necessitates a different approach than geometrical design. Unlike geometry, topology is not controlled by continuous-valued parameters, but topological modifications can be performed using a grammar of rules, which are designed per application. Shape grammars were introduced in Stiny and Gips [1] and evolved into functional and structural grammars (Mueller [2]) to include non-geometrical data related to structures, with multiple applications including a triangular mesh grammar for geodesic domes in Shea and Cagan [3].
Topology finding of patterns focuses on the generation and exploration of coarse quad meshes, as in Figure 1, that encode the data regarding the singularities in quad-based mesh patterns (Oval *et al.* [4]). The singularities are the mesh vertices with an irregular valency, i.e. different from four, or three on the boundary. High-valency pole points, a specific type of singularities adjacent to triangles, are integrated via pseudo-quads, which are geometrically like triangles but topologically like quads with a zero-length edge a the pole location, as in Figure 1b. The singularities constitute the core topological data, from which density and geometry are managed separately. Their exploration allows to yield a large variety of different topological design as the ones shown in Figure 2 from Oval *et al.* [5].



(a) Coarse quad mesh (b) Coarse pseudo-quad mesh

Figure 1: Coarse quad and pseudo-quad meshes, with boundaries in red, encoding the data regarding singularities, in pink, independently from density and from geometry.

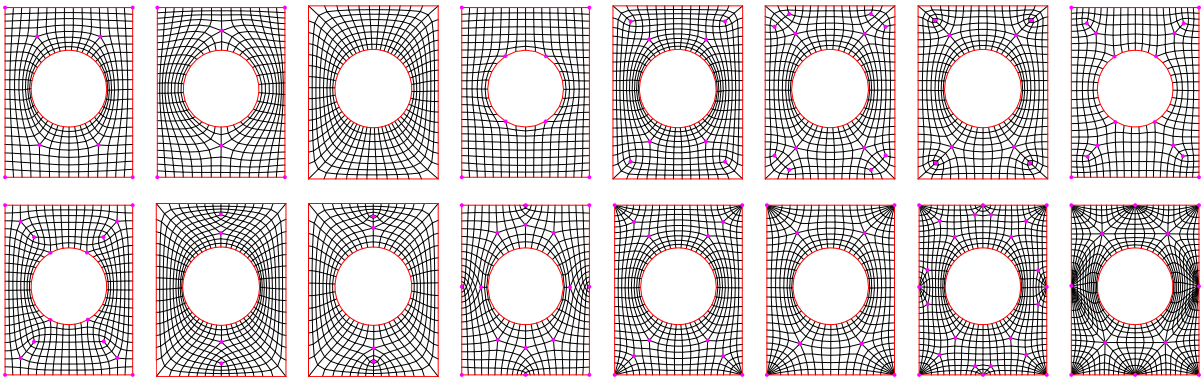


Figure 2: Topological exploration of quad-mesh patterns, with singularities highlighted in pink, for the British Museum courtyard roof from Oval *et al.* [5].

1.3 Contributions

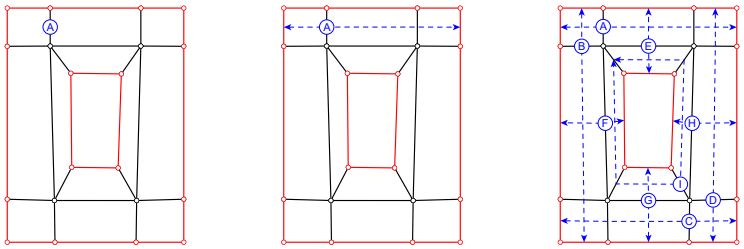
This paper introduces rule-based topology finding of quad-based mesh patterns as a means for topological exploration and structural design of patterns. The focus is set on quad meshes because they can directly describe a large variety of patterns or be converted into triangular or other polygonal meshes. This design approach enables new strategies to meet multiple objectives from statics, as well as fabrication or construction.
Section 2 develops a low-level grammar for topological exploration of coarse quad meshes based on two reciprocal rules to add and delete strips of quad faces. Generating, changing and combining topologies allows to explore multiple geometrical design spaces beyond parametric design.
Section 3 applies rule-based topology finding to the exploration of multiple topologies, aiming at finding trade-offs between multiple objectives through the generation of hybrid topologies, based on heuristically or algorithmically generated topologies for specific objectives.

2 Design grammar for the singularities in quad-mesh patterns

The design space of quad-mesh singularities is a topological space. Contrary to geometrical spaces, topological spaces do not have a metric based on continuous-valued parameters, which allow to describe and organise designs. Therefore, a rule-based approach is developed for the exploration of the singularity design space.
As opposed to a high-level grammar, as in Oval et al. [5], a low-level grammar allows comprehensive exploration of the design space with a limited number of rules. A low-level grammar consisting of adding and deleting vertices, edges or faces, for instance, can yield any type of polygonal mesh. To restrain rule-based generation to quad meshes, the low-level grammar is based on the strip structure in quad meshes, which will be introduced next.

2.1 Quad-mesh strip structure

Quad meshes have a specific structure made of strips of quad faces, which general meshes do not have, introduced in Oval *et al.* [4]. The strips in a quad mesh are collected as a list of edges by collecting edges across adjacent quad faces, as shown in Figure 3.

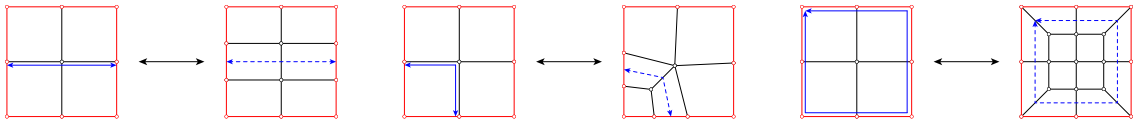


(a) Pop edge (b) Collect strip (c) Repeat

Figure 3: Collecting the face strip structure in blue in a quad mesh, with boundaries in red.

2.2 Strip addition and deletion rules

Any quad mesh can be transformed into another one with the same shape topology, i.e. the same Euler's characteristic and the same number of boundaries, by combining these fundamental strip elements. Therefore, the low-level grammar consists of two reciprocal addition and deletion rules applied to strips of quad faces (Oval *et al.* [4]). The addition rule inserts a strip along a polyedge and the deletion rule collapses a strip into a polyedge, as shown in Figure 4 for different polyedge and strip inputs. Polyedges and strips can have repeated elements, allowing overlapping and crossing. Pole points are included by converting the quad face extremity of a strip into a pseudo-quad. Combining addition and deletion rules allows to perform topological exploration of the singularity design space, as illustrated in Figure 5.



(a) (b) (c)

Figure 4: Reciprocal addition and deletion rules of strips, shown as dashed blue polylines with their corresponding polyedges as blue continuous polylines.

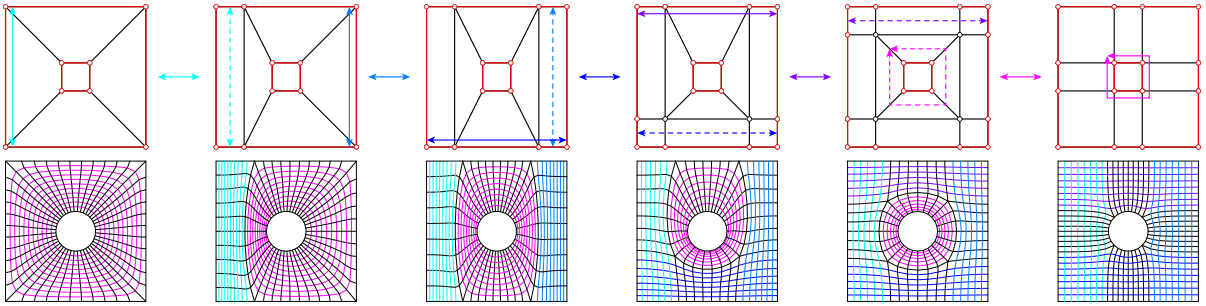


Figure 5: Combining strip rules. Reciprocal addition and deletion rules are represented in the same colour with polyedges as continuous polylines and strips as dashed polylines.

2.3 Combining topologies and their parametric design spaces

The introduced low-level grammar of strip rules allows to explore qualitatively different geometrical design spaces, whose parameters are defined by the topology. This approach can be applied to any geometrical approach, such as funicular form finding using Thrust Network Analysis (Block and Ochsendorf [6]). In Figure 6, funicular – or compression-only – shapes are explored by creasing smooth shapes along their respective pattern, concentrating the initially quasi-constant thrust distribution along specific strip polyedges. Topology A allows to add orthogonal creases to the smooth funicular shape. Multiple creases can be added but only of the same type, as constrained by the topology. Adding new strips allows to form new types of creases, as in topologies B and C with O- and U-shaped creases, respectively. The richness for topological exploration is as great as the number of combinations of strips to add. The strip rules can be enumerated separately and combined, as topology D is combining the rules that yield topologies B and C, allowing to form both O-shaped and U-shaped creases in the funicular shape. Enhancing geometrical exploration with topological exploration enables a design approach beyond only form finding.

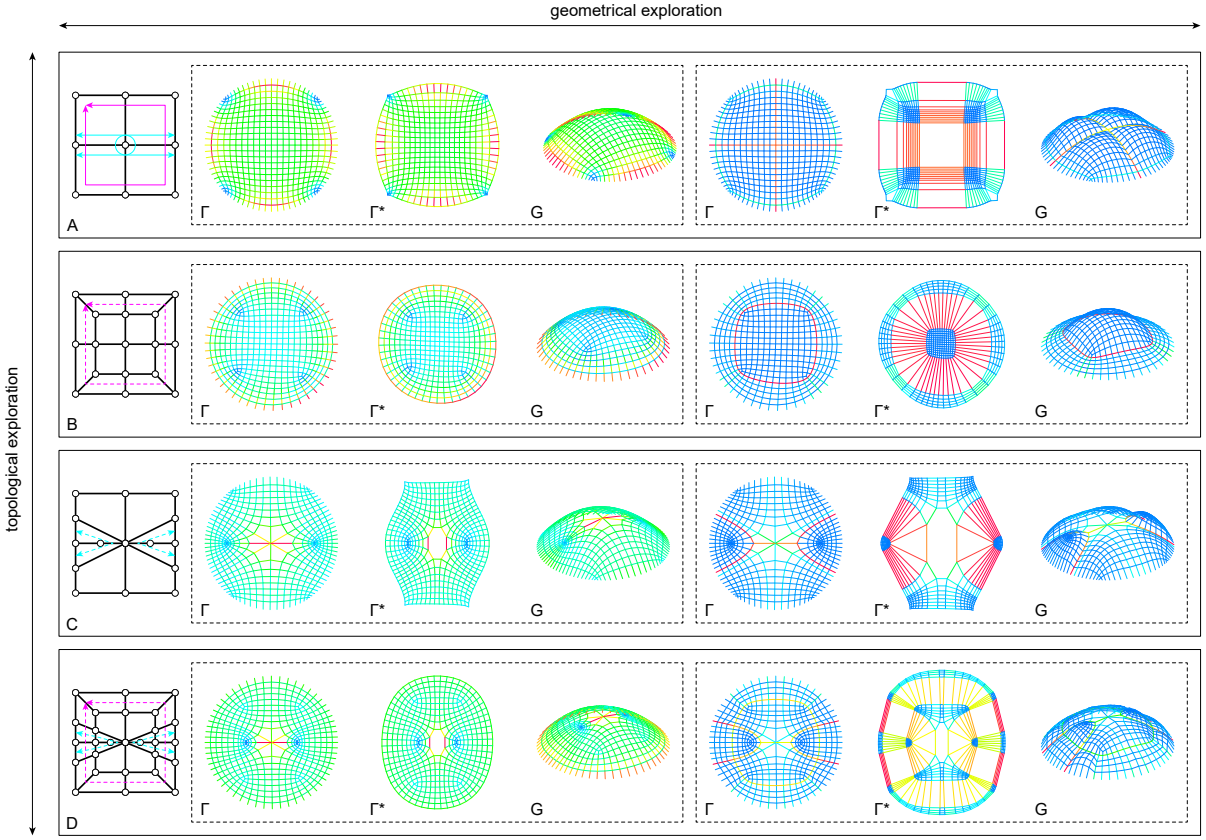


Figure 6: Exploring multiple geometrical design spaces via topological exploration of coarse quad meshes by enumerating and combining strip addition rules. The funicular shapes G derive from the form and force diagrams Γ and Γ*.

3 Application for multi-objective structural design

Rule-based topology finding of quad-mesh patterns using the presented grammar provides an exploration means to search topologies to find trade-offs between multiple requirements, starting from heuristically or algorithmically generated topologies. Hybrid topologies can be generated through the application of rules that combine the strip of the input topologies.
This concept is applied to mapping gridshell quad structures on a pillow-like shape, with a square boundary and pinned at its four corners only. The span is 10m for a rise of 2 m. The clamped, steel S235 beams have RO 114.3/4 tubular cross sections. The free-edge cross section are made around a 100 times stiffer for local stability using RO 457.2/6.3 cross sections [7].
The coarse quad meshes are densified based on a target number of faces equal to 500, constraining the strips to have the same density parameter. Surface mapping and relaxation is performed with Laplacian smoothing.

3.1 Combining objective-oriented heuristic topologies

In Figure 7, the three topologies A, B and C are generated based on heuristic rules to meet different design objectives: topology A provides geometrical regularity to ease fabrication; topology B, with four poles, provides a high number of paths towards the four corners; and, topology C, with one pole, provides a high number of paths from the surface's centre. These poles stem from interpretation of statics considerations, here the location of supports or loads. The strips of each of the three topologies are combined using addition rules to generate the four new hybrid topologies AB, AC, BC and ABC.

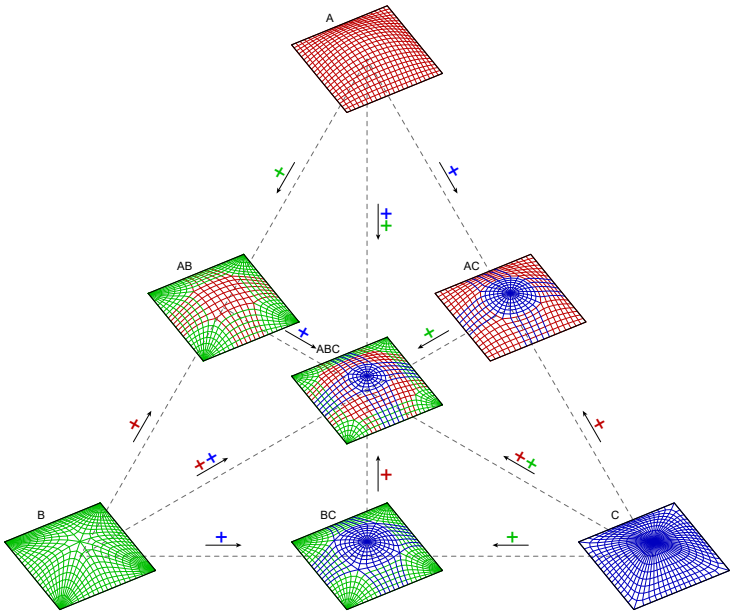


Figure 7: Rule-based topological combination of three heuristic topologies A, B, C into hybrid topologies with different strip structures. Common strips are highlighted using the same colour.

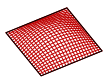
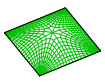
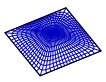
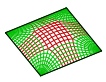
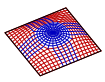
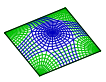
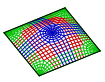
The seven designs are assessed according to three performance metrics to be minimised: the strain energy for a uniform downward surface load E_{srf}; the strain energy for a central point

load E_{pt}; and, a measure of edge length disparity L, in Equation 1. The first two metrics relate to structural efficiency, using a FEA linear elastic model, and the third one relates to fabrication ease.

$$L = (l_{max} - l_{min})/l_{total}. \tag{1}$$

The relative performances, normalised by the maximum value, are displayed along with the rank in Table 1. The lower the value or the rank, the more efficient the design. The numerical results confirm the relevance of the proposed heuristics for this design problem: adding poles at the support corners induce generally stiffer structures; adding a pole at the point load location induce stiffer structures against this specific load case; however adding poles induce strong distortions in the edge lengths. None of the designs is optimal for all the performance metrics, and each features a different trade-off. It belongs to the designer to select the most relevant one regarding the project specificity.

Table 1: Performance metrics to minimise, with ranks between parentheses.

							
$\overline{E_{srf}}$ [-]	0.77 (6)	0.44 (3)	0.56 (5)	0.43 (2)	1 (7)	0.41 (1)	0.51 (4)
$\overline{E_{pt}}$ [-]	1 (7)	0.63 (4)	0.29 (1)	0.95 (6)	0.66 (5)	0.32 (2)	0.57 (3)
$\overline{L}$ [-]	0.07 (1)	0.96 (6)	1.00 (7)	0.77 (5)	0.40 (2)	0.79 (4)	0.61 (3)

3.2 Interpolating objective-informed topologies

In Figure 8, instead of being heuristically designed, the initial topologies are generated informed by the principal stress lines at the medial surface. Two different downwards surface loading are considered: a symmetrical one applied all over the surface and an asymmetrical one applied on the right half only. Two patterns are generated with the singularities of the two cross fields. Then, strip grammar rules are applied to go from one topology to the other, interpolating hybrid topologies that act as a rule-based topological gradient. Due to its combinatorial nature, for n rules to apply between two – or more – topologies, 2^n combinations of rules exist to generate hybrid topologies with different strip structures. Here, only 12 of the $2^7 = 128$ are displayed, at different rule-based topological distances or similarities between the input topologies.
Nervi-like ribbed structures based on principal stress lines [8] can be revisited, enhanced by topological exploration of hybrid pattern topologies between multiple loading conditions. Structural performance optimisation necessitates to take into account the density and geometry design spaces as well, combining both topology finding and optimisation.

Conclusion

Rule-based topology finding has been introduced for topological exploration of the singularities in quad-based patterns to explore multiple geometrical design spaces in order to meet trade-offs between multiple objectives for the design of structures. The topological design space is explored using a low-level grammar that applies addition and deletion of strips of quad faces, which modifies the singularities and poles in quad meshes. Topological exploration using these rules allows

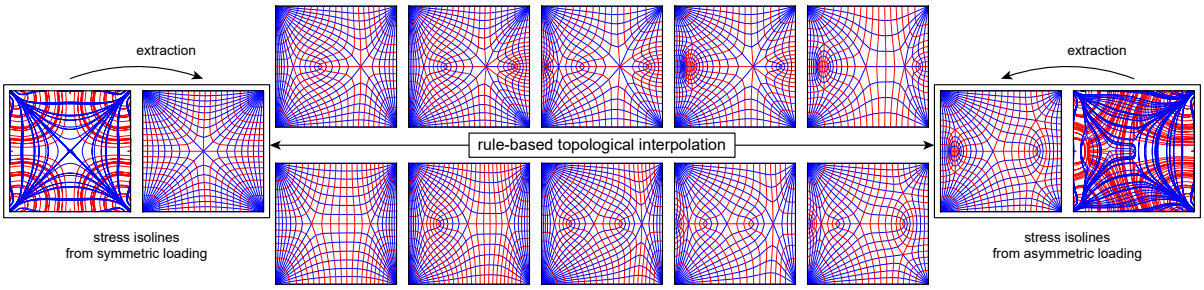


Figure 8: Interpolating hybrid topologies in a topological gradient between topologies derived from principal stress lines for different load cases.

to generate and combine different parametric design spaces for the purpose of geometrical exploration and optimisation. Yielding hybrid topologies and geometrical design spaces, based on heuristically or algorithmically generated topologies meant to meet specific objectives, allows the designer to find trade-offs between multiple objectives. This approach is complementary with existing design and analysis algorithms that are embedded in parametric design environments, providing form finding and performance evaluation for instance.
The challenges for topological design are answered: any topology, including advanced ones, can be generated; their generation is instantaneous, thanks to the direct application of topological rules; multiple objectives of different natures can be addressed, thanks to its complementarity; and, the topology can evolve during the design process. This approach opens to a new opportunity to perform rule-based topology optimisation, including multiple objectives, which can relate to statics as well as fabrication, construction and other design aspects.

References

[1] G. Stiny and J. Gips, "Shape grammars and the generative specification of painting and sculpture", in *Proceedings of the CIFIP 1971*, 1971.

[2] C. T. Mueller, *Computational exploration of the structural design space*, PhD thesis, Massachusetts Institute of Technology, 2014.

[3] K. Shea and J. Cagan, "Innovative dome design: applying geodesic patterns with shape annealing", *AI EDAM*, 11(5):379–394, 1997.

[4] R. Oval, M. Rippmann, R. Mesnil, T. Van Mele, O. Baverel and P. Block, "Feature-based topology finding of patterns for shell structures", *AIC*, 103:185–201, 2019.

[5] R. Oval, M. Rippmann, R. Mesnil, T. Van Mele, O. Baverel and P. Block, "Topology finding of structural patterns", in *AAG 2018*, Klein Publishing GmbH (Ltd.), 2018.

[6] P. Block and J. Ochsendorf, "Thrust Network Analysis: a new methodology for three-dimensional equilibrium", *Journal of the IASS*, 48(3):167–173, 2007.

[7] F. Venuti and L. Bruno, "Influence of in-plane and out-of-plane stiffness on the stability of free-edge gridshells: A parametric analysis", *Thin-Walled Structures*, 131:755–68.

[8] A. B. Halpern, D. P. Billington and S. Adriaenssens, "The ribbed floor slab systems of Pier Luigi Nervi", *Journal of the IASS*, 54(3):127–136, 2013.

Proceedings of the IASS Annual Symposium 2019 – Structural Membranes 2019
Form and Force
7 – 10 October 2019, Barcelona, Spain
C. Lázaro, K.-U. Bletzinger, E. Oñate (eds.)

Shape optimization of braced frames for tall timber buildings

Koliann MAM [a,c], Cyril DOUTHE [a], Robert LE ROY [a,b], François CONSIGNY [c]

[a] Laboratoire Navier, Ecole des Ponts ParisTech, UMR 8205, IFSTTAR, CNRS
6-8 Av. B. Pascal, 77455 MLV Cedex 2
koliann.mam@enpc.fr
[b] Laboratoire GSA (Géométrie, Structure, Architecture), ENSA Paris Malaquais,
75272 Paris Cedex 06, France
[c] Elioth (Egis Concept), SAS, 4 rue Dolorès Ibarruri, 93188 Montreuil, France

Abstract

With the recent development of timber as a viable structural material for high-rise structures, glulam braced frames have been recently introduced in lateral load-resisting system of timber buildings. Based on a simple shape optimization problem of a braced frame, this paper explores one of the specificity of timber structures: the influence of semi-rigid connections on their overall structural behavior and design. To this end, a simple linear relationship between connection stiffness and capacity is introduced in the shape optimization process and design of a discrete braced frame subject to lateral drift constraint under wind load. The problem is solved by a COBYLA optimization method, combined with Optimality Criteria member sizing techniques. Solutions are then evaluated and compared with classical steel/concrete type design.

Keywords: timber structure, high-rise building, structural optimization, semi-rigid connection, optimality criteria

1. Introduction

Wood has recently (re)emerged as a sustainable construction material for high-rise structures, leading to a global race towards the world's tallest timber building [1–3]. This fast development fosters today an extensive review of structural systems and constructive principles suited to the material's specific properties and design process. While steel and concrete has shaped city's landscape for more than a century, timber cannot stand for a pure substitute, but has to find its own structural and architectural expression [4]. While first generation of timber buildings were mainly CLT cellular walled systems, recent design proposal use glulam braced frames acting as one of the lateral load-resisting system of the building: Treet (49 m, Bergen, Norway, 2015), Mjøstårnet (89 m, Brumunddal, Norway 2019), 25 King (47 m, Brisbane, Australia 2018).

1.1 Braced frame optimization

Numerous attempts have been made to use topology optimization techniques for the design of lateral bracing systems for steel and concrete high-rise buildings. Depending on the type of structure, two classes of topology optimization can be distinguished [5]. For discrete structures, the optimum topology or layout design problem consists in determining the optimum number, positions, size, and mutual connectivity of the structural members. For continuum structures, it aims to find the optimal density distribution of material in a fixed domain.

In the case of continuum topology optimization for bracing layout applications, a multistory frame is generally modeled by discrete steel elements with an underlying continuum mesh. The density of each element serves as the design variable for the topology optimization problem of the bracing layout generally under global stiffness or compliance constraints, but also for other objectives, including

Copyright © 2019 by K. Mam, C. Douthe, R. Le Roy, F. Consigny
Published by the International Association for Shell and Spatial Structures (IASS) with permission.

eigenfrequency, buckling, etc. To solve this problem, many techniques have been developed. Mijar *et al.* [6] introduced a formulation based on classical Voigt and Reuss mixing rules and a *Sequential Linear Programming* (SLP) method was used to optimize the topology problem. Liang proposed an *Evolutionary Structural Optimization* (ESO) approach, with a performance index based on strain energy density [7], improved later on by Baldock [8] with a *Bi-directional* ESO (BESO) allowing material that was removed early in the evolutionary process to be replaced later if advantageous, and introducing constraints on patterns aesthetics (repeatability, symmetry, etc.). Using a *Solid Isotropic Material with Penalization* (SIMP) optimization approach, Stromberg *et al.* [9] explored the impact of including the beam elements of the existing frame in the analysis. For comparison of numerical results, the optimal geometry of a braced frame is analytically derived, with energy-based method presented in Baker [10] used for member sizing. This problem acts as a guideline for the research presented in this paper. This discrete/continuum framework was extended by Beghini *et al.* [11] with the simultaneous sizing of the discrete frame elements during the continuum topology optimization procedure.

Despite the interest and efficiency of the aforementioned techniques, the interpretation of continuum solutions into feasible (discrete) design is not always an easy thing for designers. To tackle this issue, and rationalize final solutions, discrete topology optimization with ruled-based approaches have been explored [12] [13].

1.2 Connections in timber engineering

Joints are generally a critical factor in the design of timber structures: their strength can dictate the strength of the structure, their stiffness influences global deformations and member size can be determined by characteristics of the connector [14–16].

This notion has long been recognized by carpenters and timber engineers, but the risks and potential consequences on structures were mainly neglected, or rather accepted for traditional wooden construction. The development of engineered wood and improvements of manufacturing processes in the last century, made possible the construction of complex timber structures, with larger dimensions and high-strength elements [17]. While Eurocode 5 (EC5) [18] methods (principally based on the Yield Analysis Theory proposed by Johansen [19]) are adequate for many applications, it is nevertheless clear for practitioners that they become insufficient to address the current challenges of modern complex timber engineering, especially those related to tall building design.

1.3 Paper organization

In the next section (section 2), we present the shape optimization process and design of a discrete braced frame subject to a tip displacement constraint under wind load. This problem is solved by a two-level optimization scheme, using at low-level both FSD (*Fully Stressed Design)* and a rigorously derived OC (*Optimality Criteria*) techniques for *size optimization* ; and a COBYLA (*Constrained Optimization by Linear Approximation*) method to solve the global *shape optimization* problem of the defined timber frame. Results are then illustrated in section 3, with a particular emphasis on the influence of timber connection stiffness on the global structural response of the structure. Finally, in section 4, some conclusions are drawn on the application of the proposed methodology in view of tall timber building design.

2. Braced frame problem and shape optimization methodology

We study the optimal geometry – and sizing – of a braced frame structure part of the lateral system of a high-rise building subject to wind loading shown in Figure 1 and previously described by Stromberg *et al.* [9]. The frame has an overall height H and a half-width B and is composed of N bracing modules along the height. The top-height of the ith bracing module is given as z_{2i} and the height of the diagonals intersection as z_{2i-1}. Each timber member is supposed to have a square cross-section A_i and dowel-type

joints at both end Figure 1c. Node locations z_i and cross-sectional area A_i are the design variables of the shape + size optimization problem.

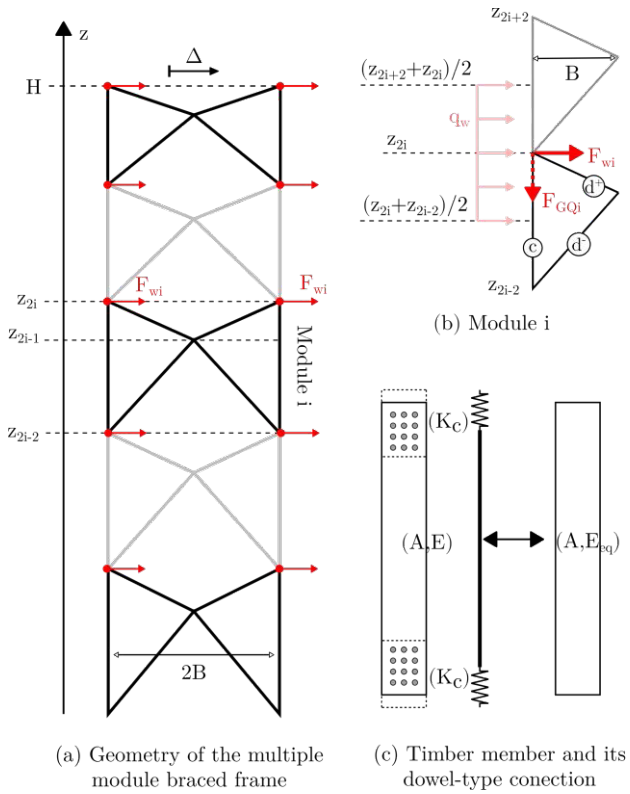


Figure 1 : Geometry and notation of the multiple modules braced frame optimization problem.

In lateral system design for high-rise structures, multiple structural objectives can be considered, mainly, overall drift, compliance, period and buckling. Each objective relates to a different aspect of the design, but they all can affect the topological layout of the structural system and the sizing of the members. In the present work, the structure is subject to an overall drift constraint under wind load, with a limit of displacement at the top of the structure set to $H/500$. Depending on the model, strength requirements – for ultimate limit state load combinations – is considered, in order to study the impact on member sizing and optimal layout of the frame.

Wind load profiles are generally represented by a power or logarithmic law, describing the increase of wind velocity with height. However, not to introduce unnecessary complexity, a uniform wind load distribution q_w is used. As illustrated in Figure 1b, wind load is distributed to the nodes of the frame, with equivalent lateral forces acting at the top of each module $F_{W,i}$.

We finally define distributed gravity loadings q_G and q_Q acting only on vertical elements, which accounts for the portion of dead (G) and live loads (Q) applied on the floors of the building and transferred to the columns of the frame.

2.1 Connection sizing

On initial examination for design stage, the relationship between stiffness and load-bearing capacity can be modeled by a simple linear relationship. The stiffness of a connection depends on:

$$K_i^{ULS} = c_1 F_{U,d,i} \tag{2-1}$$

$$F_{U,d,i} = \max_j \left[F_{U,i}^{(j)} / k_{mod}^{(ULSj)} \right] \quad (2\text{-}2)$$

- $F_{U,d,i}$ – Design tensile/compressive force. Design forces calculation takes into account the modification factor $k_{mod}^{(ULS,j)}$ of each ULS load combinations using the equation
- c_1 – The slope of the linear regression model. A sensitivity analysis on this parameter will be conducted in section 3.

2.2 Overall design and optimization process

The overall optimization process is solved by a two-level optimization routine: at a low-level, for a fixed geometry, size optimization techniques are used to find the optimal material distribution in the frame given the strength and drift requirements. Then a more general optimization method is used to solve the global shape optimization problem of the timber frame (see Figure 2).

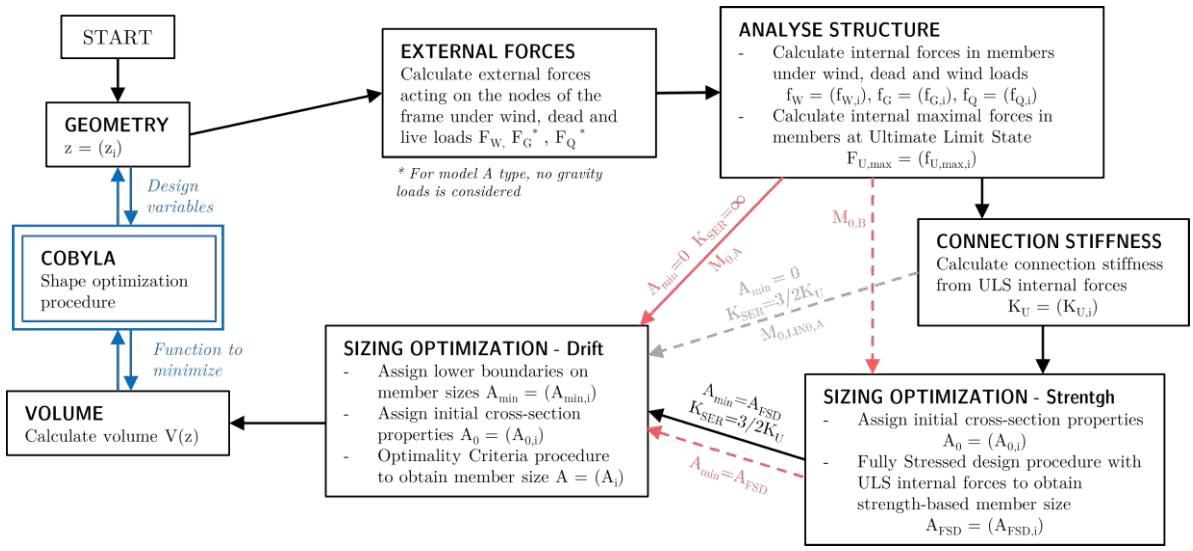


Figure 2 : Optimization process

For a given geometry of the frame, internal forces in members are first calculated for wind (W), dead (G) and live (Q) loads. In accordance with the previously described methodology, the stiffness of end joints K_i are then estimated. A classic Fully Stressed Design (FSD) [20] technique with a stress-ratio resizing rule is used to obtain the minimum sizing of each member A_i^{FSD} of the frame under ULS load combinations to satisfy EC5 strength requirements. For buckling length calculations, we suppose that members are stabilized at each floor.

Sizing optimization for top-displacement constraint under wind load is then performed using a rigorously derived Optimality Criteria (OC) method as presented in [21]. The previously calculated strength-based cross-sectional area A_i^{FSD} act as lower size bounds on the design variables.

Finally, the global shape optimization problem to minimize the volume of timber material is solved using a *Constrained Optimization by Linear Approximation* (COBYLA). COBYLA is a derivative-free algorithm which constructs successive linear approximations of the objective and constraint functions by interpolation at the vertices of a simplex and optimizes these approximations in a trust region at each step [22]. The overall design and optimization process is summarized in Figure 2 and have been implemented in SciPy [23], a Python based ecosystem.

3. Results: influence of semi-rigid connections

To assess the impact of connection stiffness and strength requirements on the optimization of a braced frame for top drift constraint, various models are studied and presented in Table 1. In models "A", no gravity loads and no strength requirements are considered for member sizing. In models "B", gravity loads are introduced and strength requirements at ULS are taken into account for member sizing optimization. "0" indicates that the stiffness of timber joints are not considered, while "K" indicates that the semi-rigid behavior is included in the frame analysis. "LIN" indicates that the simplified linear relation for timber connection stiffness (1) is used.

Load combinations and modification factor considered under ULS design are presented as follows, where G, W, and Q are dead load, wind load, and live load respectively:

$$\begin{aligned} ULS0 &= (1.35G, k_{mod} = 0.6) = ULS.G \\ ULS1 &= (1.35G + 1.5Q, k_{mod} = 0.8) = ULS.GQ \\ ULS2 &= (1.35G + 1.5W + 1.05Q, k_{mod} = 1.1) = ULS.GWQ \end{aligned} \quad (1)$$

Model	Connection Stiffness*	Member Sizing	Gravity loads
$M_{0,A}$	$K_{U,i} = \infty$	Overall Stiffness Optimization	No
$M_{K,LIN0,A}$	$K_{U,i} = c_1 F_{U,d,i}$ **		
$M_{0,B}$	$K_{U,i} = \infty$	Overall Stiffness Optimization + ULS(G+GQ+GWQ) strength	Yes
$M_{K,LIN0,B}$	$K_{U,i} = c_1 F_{U,d,i}$ **		

* $K_{U,i}$ indicates the connection stiffness at ULS and is calculated from ULS internal forces in members $F_{U,i}$. Connection stiffness at SLS is given by the relation $K_{SER,i} = 3/2K_{U,i}$

Table 1 : Notation and description of the different models used for the optimization of the braced frame. Influence of connection stiffness and member sizing criteria.

3.1 Single module frame

The analysis is first conducted for a single module braced frame subject to a point load at the top. As analytically and numerically described by Stromberg *et al.* [9], without any consideration of joint stiffness, strength requirements and gravity loads, the optimal geometry of the single module – i.e. that minimizes the tip deflection of the frame – is defined by a height ratio z/H of 0.75.

For the following numerical example, we assume that $c_1 = 0.65\ m^{-1}$ and that drift constraint is set to $H/500$. Figure 3 shows the optimal brace work point as a function of the aspect ratio H/B, for different values of the frame's half width B. For model $M_{0,A}$, the results confirm that the optimal bracing work point for minimal tip deflection is located at 75% of the height of the module regardless of the aspect ratio. According to the figure, for high and medium value of the aspect ratio ($H/B > 2$), the optimum geometry for model $M_{K,LIN0,A}$ depends very little on the aspect ratio of the frame. It can be noted that the connection stiffness leads to a marginal increase of optimum work point ratio, which becomes almost negligible as width increases. We also notice that for aspect ratio under 2 (*i.e.* when the height of the module is lower than its width), the optimal intersection of the cross-brace significantly moves upward.

Note that as expected, the loss of stiffness due to doweled connections in model $M_{K,LIN0,A}$ is compensated by members with larger cross-section, leading to a greater volume of timber used in the frame than in model $M_{0,A}$.

Strength requirements on members could influence this optimum, and particularly as columns are generally to be sized for gravity loads. This impact is assessed by introducing a dead load N applied to the columns, and by considering strength requirements under the different ULS load combinations. Figure 4 shows the optimum geometry (z_{opt}/H) versus $(N/(FH/B)$ which represents a ratio between

an indicator of the axial force in the columns due to bending under the horizontal load F, and the axial force caused by the gravity load N. Results are calculated for $B = 6\,m$ and different values of the aspect ratio H/B. For small values of the $(N/(FH/B)$ ratio the optimum work point ratio remains close to 0.75 (strictly equal for model $M_{0,A}$), as the design of the frame, and particularly column sizing, is controlled by lateral drift requirements. Above a certain threshold value of $(N/(FH/B)$ ratio, a significant change of behavior is observed, and the optimum work point significantly moves down. Strength requirements starts to control columns sizing. Therefore, the column area is higher than the optimal area. As strength-based size increases with N, the bending rigidity of the frame increases and the displacement becomes mainly due to axial deformation of the diagonals, in other words due to shear deformation of the frame. For very large value of $(N/(FH/B)$ ratio the problem can be reduced to a pure-shear beam problem in which the optimum intersection of the cross-brace is located at 50% of the module height.

As might be expected, introducing semi-rigid connections results in a slightly higher break point in model $M_{K,LIN0,B}$ than in $M_{0,B}$. Finally, it should be noted from Figure 4 that, in the same way, the larger the aspect ratio H/B, the larger the range in which design is controlled by stiffness is extended.

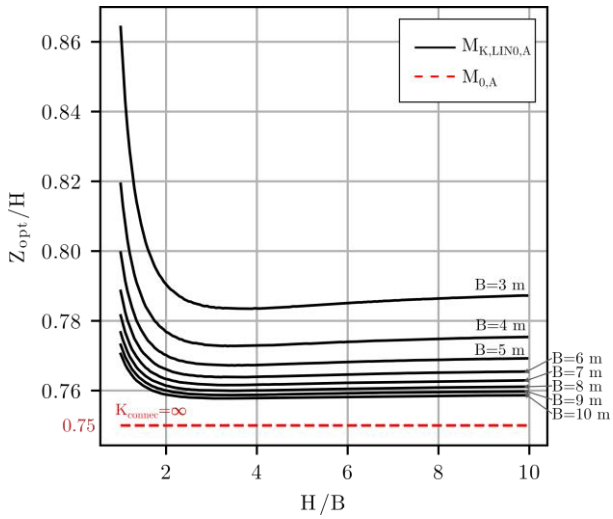


Figure 3 : Single module frame stiffness optimization under wind load only (Models A). Brace work point z/H vs. aspect ratio H/B for different values of frame half-width B

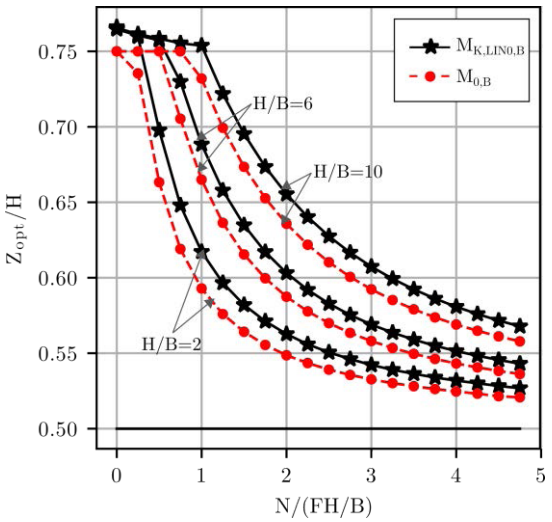


Figure 4 : Single module frame stiffness optimization with strength constraints under gravity and wind loads (Models B). Brace work point z/H vs. aspect ratio $N/(FH/B)$ for different values of frame aspect ratio H/B with B = 6 m

3.2 Multiple modules frame

Analysis is now generalized to a braced frame with multiple modules and multiple point loads along the height, as previously described in Section 2. The following parameters are used to illustrate a typical high-rise case study: the height is $H = 80\,m$, the width $2B = 12\,m$, the number of floors $N_{floor} = 25$, the wind load distribution $q_w = 10\,kN/m$, the axial forces per floor in the column due to dead loads $F_{floor,G} = 60\,kN$, and due to live loads $F_{floor,Q} = 22.5\,kN$. We assume for the stiffness behavior model that $c_1 = 0.65\,m^{-1}$ (model $M_{K,LIN0,B}$) in equation (1). A sensitivity analysis on this parameter is conducted assuming $c_1 = 1\,m^{-1}$ (model $M_{K,LIN1,B}$) and $c_1 = 0.45\,m^{-1}$ (model $M_{K,LIN2,B}$).

The results of the shape optimization problem for the different models with a varying number of modules are illustrated in, with the plot of volume versus the number of modules. A detailed analysis of the solutions for the 5 modules case and models $M_{0,A}$ and $M_{K,LIN0,B}$ is presented in Figure 6. For each

solution, this figure shows: the displacement due to each module, each element type (columns or diagonals) and connections; the utilization ratio of the members for the ULS load combinations described in equation (3); and the equivalent Young's modulus ratio E_{eq}/E defined as follows:

$$E_{eq,i}/E = \frac{1}{1+2^{EA_i}/_{K_{SER,i}L_i}} \tag{2}$$

The loss of stiffness due to doweled connections can be approached by considering an equivalent Young's modulus E_{eq} for each timber member as illustrated in Figure 1c.

3.2.1 Volume of timber

As already noted in the single module case, considering connection stiffness leads to a significant increase in the volume of the optimal timber frame compared to model $M_{0,A}$ (see Figure 5), all the more as the slope c_1 of the linear model for connection stiffness is low. Figure 6 illustrates that the ratio of tip displacement due to the semi-rigid behavior of timber connections is far from being negligible.

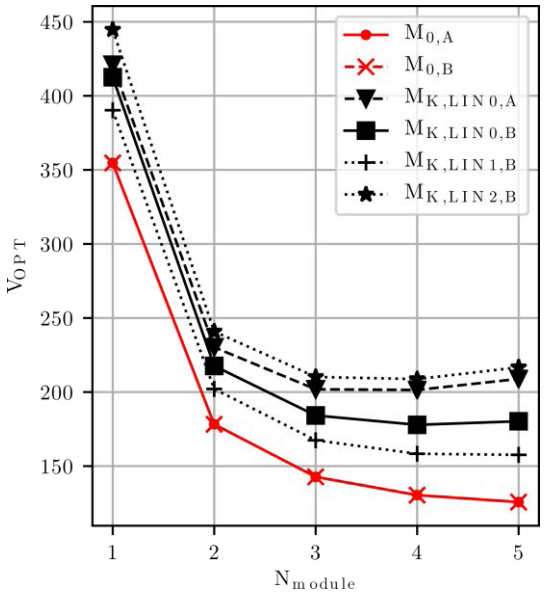


Figure 5 : Plot of volume versus number of modules.

3.2.2 Optimum geometry

From a geometric point of view, overall, connection stiffness has little effect on the relative work point ratio of each module (height of the intersection of the diagonals on the total height of the module), and remains close to 0.75, which generalizes the observation already made for the single module problem. However, two exceptions are worth mentioning and will be analyzed in the next paragraphs.

The main difference introduced by connection semi-rigid behavior in optimal solutions lies in the distribution of modules along the height. For model $M_{0,A}$, modules are equally distributed in height, and optimal bracing point ratio is 0.75. Looking at the detailed analysis of $M_{0,A}$ solutions in Figure 6, we note that the portion of tip displacement due to each modules decrease along the height. Therefore, we can assume that the most efficient way to increase the overall stiffness of a multiple module frame structure is to increase the relative stiffness of the lower modules. When connection stiffness behavior is taken into account, the optimum distribution deviates from the equally distributed solutions, and modules height consecutively decreases. This unequal distribution is more pronounced as the coefficient c_1 of the linear stiffness regression model decreases.

Optimal solutions tend to maximize the equivalent Young's modulus ratio E_{eq}/E of timber members defined in equation (4), and in particular those of columns, as they accounts here for the major part of tip displacement (see Figure 6). According to equation (4), for a given cross-sectional area, the equivalent Young's modulus ratio is higher as the length of the member increases. This observation, combined with the one previously made on the interest to maximize stiffness of the lower modules, explains the observed distribution for the model with connection stiffness.

Note that this behavior leads to top modules with low aspect-ratio. If the aspect ratio falls under a certain threshold value (more or less under the square aspect ratio), the single module analysis has shown that the optimum work point rapidly moves upwards as aspect ratio decreases. This explains why for model $M_{K,LIN0,A}$ and $N = 5$ (see Figure 6), top module presents a K bracing shape.

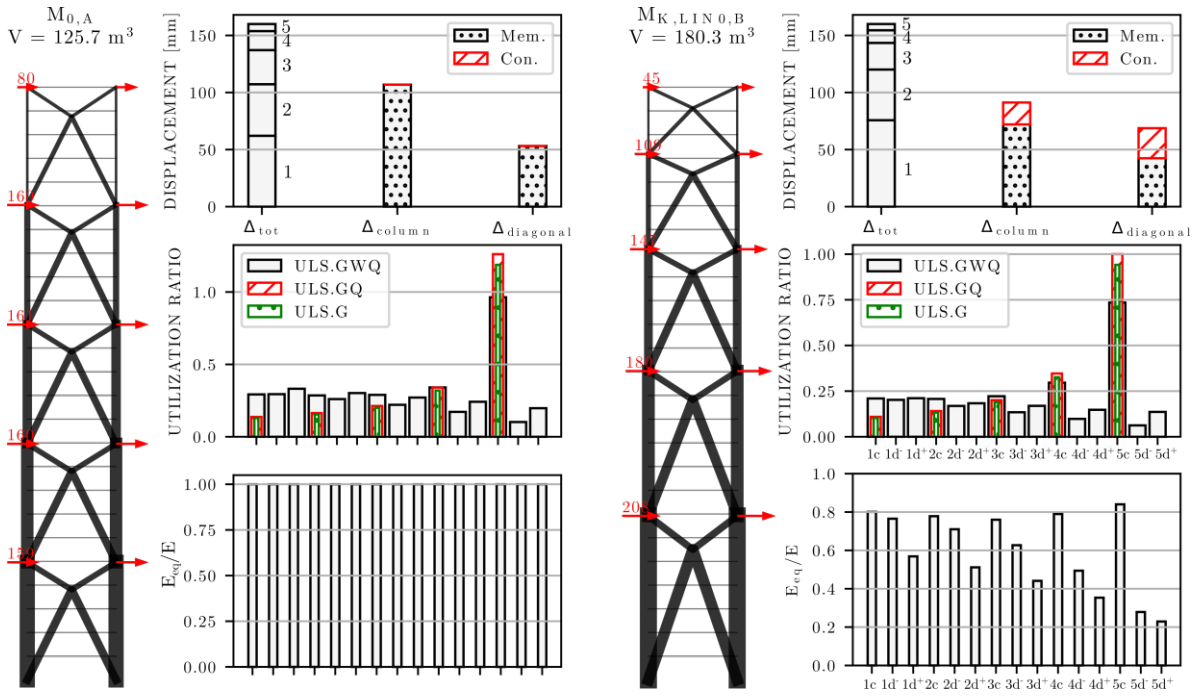


Figure 6 : Shape optimization of a braced frame with 4 and 5 modules. Analysis of optimum geometry and sizing for models $M_{0,A}$ and $M_{K,LIN0,B}$. *NB: cross-sectional areas are relative*

3.2.3 Influence of strength requirements

In this example, design and especially member sizing is controlled by overall stiffness. Overall, timber members are under-stressed, except maybe for the columns of the higher module. In particular in the case $N = 5$, the cross-sectional area of higher columns is controlled by strength requirements at ULS. With regards to the influence of strength requirements on optimal geometry observed in the single module frame (see Figure 4), the work point ratio of these modules is lower than 0.75, especially for model $M_{K,LIN0,B}$ for which the aspect ratio of the higher module is relatively small.

4. Conclusions

This paper presents the shape optimization of a timber braced frame with dowel-type joints, subject to an overall drift constraint and strength requirements under wind and gravity loads. The main objective of this work is to highlight the impact of joint flexibility on the optimum solution of a truss like structure. The influence of connections in timber engineering, whether in terms of structural behavior or

constructability cannot be overlooked. The development of simplified methodologies that takes into account this specificity remains one of the challenges for structural exploration in design phase.

The main results coming from this research, and presented in section 3, can be summarized as follows:

- When design is controlled by stiffness constraints, the optimal work point of a braced frame module is located near 75% of its height.
- When strength requirements starts to control the sizing of columns, the optimal intersection of the diagonals moves down, and converges towards 50% for columns with infinite stiffness.
- The introduction of semi-rigid connections has little influence on the optimum work point ratio of the modules, but leads inevitably to a significant increase of the timber volume. This seems to suggest that the number of connections should be reduced to limit the loss of stiffness due to connections in timber structures.
- For a given cross-sectional area, equivalent Young's modulus ratio increases with length. This remark suggests to foster longer members, in line with the previous observation to reduce the number of connections.
- The introduction of semi-rigid connections influences the optimal distribution of modules height, from an equally distributed solution (*i.e.* all the modules have the same height) towards a solution with consecutives modules with decreasing height.

References

[1] R.M. Foster, M.H. Ramage, and T. Reynolds, "Rethinking CTBUH height criteria in the context of tall timber.," *CTBUH Journal*. vol. 2017, no. 4, pp. 28–33, 2017.

[2] I. Kuzmanovska, E. Gasparri, D.T. Monne, and M. Aitchison, "Tall Timber Buildings : Emerging Trends and Typologies.," In: *World Conference on Timber Engineering 2018*. , Seoul, Corea (2018).

[3] M.H. Ramage, H. Burridge, M. Busse-Wicher, et al., "The wood from the trees: The use of timber in construction.," *Renewable and Sustainable Energy Reviews*. vol. 68, no. October 2015, pp. 333–359, 2017.

[4] P. Fleming, S. Smith, and M. Ramage, "Measuring-up in timber: a critical perspective on mid- and high-rise timber building design.," *Architectural Research Quarterly*. vol. 18, no. 01, pp. 20–30, 2014.

[5] M.P. Bendsøe and O. Sigmund, *Topology Optimization*. *Springer Berlin Heidelberg*, Berlin, Heidelberg, 2004.

[6] A.R. Mijar, C.C. Swan, J.S. Arora, and I. Kosaka, "Continuum Topology Optimization for Concept Design of Frame Bracing Systems.," *Journal of Structural Engineering*. vol. 124, no. 5, pp. 541–550, 1998.

[7] Q.Q. Liang, Y.M. Xie, and G.P. Steven, "Optimal Topology Design of Bracing Systems for Multistory Steel Frames.," *Journal of Structural Engineering*. vol. 126, no. 7, pp. 823–829, 2000.

[8] R. Baldock, "Structural Optimisation in Building Design Practice," (2007).

[9] L.L. Stromberg, A. Beghini, W.F. Baker, and G.H. Paulino, "Topology optimization for braced frames: Combining continuum and beam/column elements.," *Engineering Structures*. vol. 37, pp. 106–124, 2012.

[10] W.F. Baker, "Energy-Based Design of Lateral Systems.," *Structural Engineering International*. vol. 2, no. 2, pp. 99–102, 1992.

[11] L.L. Beghini, A. Beghini, W.F. Baker, and G.H. Paulino, "Integrated Discrete/Continuum Topology Optimization Framework for Stiffness or Global Stability of High-Rise Buildings.," *Journal of Structural Engineering*. vol. 141, no. 8, p. 04014207, 2015.

[12] R. Kicinger, T. Arciszewski, and K. DeJong, "Evolutionary Design of Steel Structures in Tall Buildings.," *Journal of Computing in Civil Engineering*. vol. 19, no. 3, pp. 223–238, 2005.

[13] R. Baldock and K. Shea, "Structural Topology Optimization of Braced Steel Frameworks Using Genetic Programming Robert.," In: I.F.C. Smith, Ed. *Intelligent Computing in Engineering and Architecture, EG-ICE 2006, LNAI 4200*. pp. 54–61. *Springer Berlin Heidelberg*, Berlin, Heidelberg (2006).

[14] R.J. Leichti, R.A. Hyde, M.L. French, and S.G. Camillos, "The continuum of connection rigidity in timber structures.," *Wood and Fiber Science*. vol. 32, no. 1, pp. 11–19, 2000.

[15] D.I. Masse and J.J. Salinas, "Analysis of timber trusses using semi-rigid joints.," *Canadian Agricultural Engineering*. no. May 1987, pp. 111–124, 1987.

[16] K.A. Malo, R.B. Abrahamsen, and M.A. Bjertnæs, "Some structural design issues of the 14-storey timber framed building 'Treet' in Norway,." *European Journal of Wood and Wood Products*. vol. 74, no. 3, pp. 407–424, 2016.

[17] R. Lemaître, *Works on Different Numerical modelling Approach to Predict the Load Distribution in Timber Joints. European COST Action FP1402 - Basis of structural timber design - from research to standards*., 2018.

[18] European Committee for Standardization (CEN), "Eurocode 5: Design of timber structures - Part 1-1: General - Common rules and rules for buildings," (2004).

[19] K.W. Johansen, "Theory of Timber Connections.," *IABSE: International Association of Bridge and Structural Engineering*. vol. 9, pp. 249–262, 1949.

[20] R. Razani, "Behavior of fully stressed design of structures and its relationshipto minimum-weight design.," *AIAA Journal*. vol. 3, no. 12, pp. 2262–2268, 1965.

[21] C.-M. Chan, "Optimal lateral stiffness design of tall buildings of mixed steel and concrete construction.," *The Structural Design of Tall Buildings*. vol. 10, no. 3, pp. 155–177, 2001.

[22] M.J.D. Powell, "A Direct Search Optimization Method That Models the Objective and Constraint Functions by Linear Interpolation.," In: *Advances in Optimization and Numerical Analysis*. pp. 51–67. *Springer Netherlands*, Dordrecht (1994).

[23] E. Jones, T. Oliphant, and P. Peterson, "SciPy: Open Source Scientific Tools for Python," http://www.scipy.org/, (2001).

Proceedings of the IASS Annual Symposium 2019 – Structural Membranes 2019
Form and Force
7 – 10 October 2019, Barcelona, Spain
C. Lázaro, K.-U. Bletzinger, E. Oñate (eds.)

Structural Optimization of frames or lattices with beam elements

Ioannis N. TSIPTSIS[*a], Kai-Uwe BLETZINGER[a]

*a Technical University of Munich
Arcisstraße 21, D-80333 München
mrtsip@hotmail.com

Abstract

In the present research paper, the structural optimization problem is studied for various structural unit cell structural arrangements, namely square bi-linear 4-noded elements with two translational degrees of freedom, truss unit cells of two different bracings and framed unit cell with Euler-Bernoulli (EB) or Timoshenko (TS) beam elements. The Cowper shear coefficient formula for solid cross sections and the assumption of shear frames have been considered. The minimization of the compliance is performed with both Optimality Criteria approach and the Method of Moving Asymptotes. Comparisons between bar, EB and TS unit-cell configurations have been performed in order to study the influence of shear during optimization of lattice structures and frames. This is the first step towards investigating the influence of higher order phenomena, such as warping (secondary shear deformation effect), in the analysis of these structural arrangements. Moreover, the Ground Structure method has been employed to formulate truss-like configurations and compare the optimized structure derived by both Sequential Linear Programming and Particle Swarm Optimizer, which belongs to metaheuristic methods.

Keywords: structural optimization, optimality criteria, method of moving asymptotes, unit cells, lattices, frames, shear, warping, compliance.

1. Introduction

Recent advances in materials (i.e. composite materials) and manufacturing methods have enabled superior performance of engineering products and structures with minimized material or weight. However, adopting new materials and scaling up manufacturing processes presents many challenges and is not always cost effective; hence new manufacturing processes are necessary to reduce both time-to-market and cost. To this end, unlike traditional manufacturing methods, Additive Manufacturing (AM) or 3D (three-dimensional) printing, which is still in its early stages, can produce parts with complex geometrical features and high performance without significantly increasing fabrication time and cost. This technology has been increasingly used not only in academic research but also in industrial applications and healthcare engineering [1]. However, 3D printing processes are currently limited mostly to small objects while the interest in applying the technology to large-scale structures, such as buildings, is increasing. Low fabrication cost of structures with variable material distribution and/or complex geometry can be achieved by AM, since materials are joined together layer by layer. This advantageous procedure widely broadens the application field of design models and provides the chance to further improve the performance of various structural arrangements. However, this technology creates the need for new design methods that maximize the performance through the optimized synthesis of shapes, sizes, and material distributions subjected to multiple constraints (i.e. limits for cost, volume, weight, stresses, stiffness etc.). Therefore, a new design field called structural optimization has been initiated and developed mainly in the latest decades [2-3]. Today, the research in this field is very intense and several companies related to construction or transportation have been active in the implementation of optimized elements.

Copyright © 2019 by Ioannis N. TSIPTSIS, Kai-Uwe BLETZINGER
Published by the International Association for Shell and Spatial Structures (IASS) with permission.

Structural optimization offers a number of opportunities with the so-called topology optimization been the most fundamental one. The topology optimization has become a rapidly growing research field and within a few years divided into a number of different subfields. Various approaches for solving problems of topology optimization have been reported in literature regarding both the treatment of the material and the optimization of the objective function [4]. Regarding the material, numerical homogenization method [5] and Solid Isotropic with Material Penalization (SIMP) procedure [6] have been adopted in most papers in the literature. However, the former method has mainly been employed for cellular with unit cells, functionally graded and/or composite materials in order to determine their effective micro- and macroscopic properties (e.g. elasticity tensor of a periodic composite material) via the Finite Element Analysis (FEA) [7]. Lately, a voxel model obtained by a lattice frame has been developed to facilitate the procedure which can be quite complex in the 3D case [8]. The use of discrete elements (bars or beams) for the discretization of 3D unit cells can result in computationally more efficient arrangements than those with continuum unit cells. The SIMP or power-law approach has been employed in the majority of research contributions due to its simplicity and the lack of manufacturing means for microstructures during the previous decades. With the advent of 3D printing, the homogenization method has been lately reconsidered for the design of cellular structures with a regular grid. A mixed formulation consisting of the homogenization and the power-law approaches has been developed to design conforming lattice structures and has shown quite promising results comparing to traditional SIMP [9]. However, the use of SIMP is quite simple and well-defined for gradient-based (GB) optimizers, which are ideal for continuous design variables. Regarding the optimization solver, the most common approaches that have been studied and employed in practice are the following: Sequential Linear Programming (SLP) for linear problems [10] or linearized sub-problems [11], Sequential Quadratic Programming (SQP) [11-12], the Method of Moving Asymptotes (MMA) [13] and Optimality Criteria (OC) [2, 4]. Even though OC approach is historically older than sequential approximation methods and MMA, it is still being studied and employed in topology optimization software due to its computational efficiency with respect to time and required memory [14]. However, OC cannot be used for the optimization of any structural problem and handle any type of objective function or any number of constraints as it is the case for the nonlinear SQP and MMA. Recently, much research has also been done on metaheuristic methods, which have succeeded to decrease the compliance or other objective functions in comparison with the previous optimizers. Structural optimization problems are usually cumbersome and include both continuous and discrete design variables. Thus, metaheuristic methods tend to perform better since there is no need for gradient information and good performance with respect to the search for global optima [15].

As mentioned previously, structural optimization includes both continuous and discrete design variables, thus leading to two main categories, namely truss (or frame)-based approach (discrete topology optimization) [16] and density-based approach (continuum topology optimization) [17]. Truss/Frame models are typical in most studies for optimal design of lightweight cellular materials that can be identified by optimizing the geometric parameters of a predefined lattice-type structural arrangement (ground structure [18]). The Finite element Method (FEM) with bars or Timoshenko (TS) or Euler-Bernoulli (EB) beam elements has mainly been employed in previous research works to model different patterns of lattices for the calculation of their stiffness [19-21]. In most of these studies, only circular, compact or hollow, cross sections of beams have been considered in simulations. Other research efforts propose models that do not follow a lattice-type pattern either in 2D or 3D space employing novel algorithms with springs [22] or truss models but still remaining restricted to specific load cases, boundary conditions and materials. In the frame-like parts of a model, a mesh of beams connected at nodes is usually initially defined in a predetermined area where the mesh can either be formulated for the whole domain, such as a spatial framed structure (instead of a truss with bars under tension and compression only), or it is based on unit cells (i.e. in lattices). The optimization problem is formulated in order to minimize the compliance or the structural weight of the beam-like arrangement subjected to stiffness, volume, density, cross sectional and/or other constraints. These constraints account for a number of design objectives (i.e. maximum stress, displacements etc.). Starting from a dense mesh of

beam members for a unit cell or a spatial frame, topology optimization seeks the most important elements of the problem in order to define the best connectivity by removing those with insignificant contribution and resize the cross section of the most efficient ones [23]. Different cross section shapes need to be investigated with respect to structural efficiency through limitations in the set of constraints and be compared to corresponding configurations with circular cross sections. Their shape is expected to affect the final arrangements and volume of beams, particularly for large-scale problems. Additionally, aesthetics criteria have been integrated in the procedure by optimizing the shape of the whole structure. For example, the envelope of a lattice is described by curved surfaces or in the case of a frame by curved lines allowing for smooth geometries and flexible design. For this purpose, Isogeometic Analysis (IGA) tools (B-splines and Nonuniform Rational B-Splines- NURBS) have been employed to describe the envelope's shape. In this case, shape optimization consists of finding the optimal position of the control points which are employed to describe the curved surfaces or curves of the model [23-24]. Results have resembled a 2D/3D lattice or framed structure with evident variations in beam properties. The stiffness matrices (local and global) of each design have been derived employing IGA combined with the FEM to model the deformations of all unit cells of the lattice or frame elements. IGA can also be employed in combination with the Boundary Element Method (BEM). It is estimated that in this case the accuracy and the computational effort will be improved comparing to FEM, as its previous applications indicated [25]. Towards, developing a unified framework of exact modeling, analysis and optimization, the IGA tools have been used to evaluate the sensitivities during the optimization of both framed (1D) and panel (2D/3D) structures [26-28]. However, this is not within the scope of this effort. In order to allow for more general loading (axial, flexural, torsional and/or distortional) and boundary conditions contrary to the traditional EB or TS beam models, Advanced Beam Elements either straight or curved have been developed [25]. These elements account for cross-sectional warping and/or distortion (higher-order phenomena) as well as Poisson ratio effects, which vary along the length of the beam exponentially. They can be integrated to model the aforementioned unit cells or the spatial frame. Different patterns of unit cells can be studied and compared with a cubic grid of circular cross sections, which is considered as the reference configuration.

In the density-based approach, the appropriate material density is determined in a set of small elements the design domain is split into. This method is commonly used with the Solid Isotropic with Material Penalization (SIMP) procedure in order to account for continuous values of density Material [6]. Other material interpolation schemes have also been proposed in the literature [29-30]. However, these models are usually accompanied with numerical defects, such as the checkerboard problem, which have been mostly encountered using methods of high computational cost. Filtering schemes have been employed to eliminate these defects [4, 31]. Additionally, linear Finite Elements, which account for the majority of the computational cost in large-scale topology, have usually been employed. Even though beam-like arrangements can also be employed for the discretization of volume and surface parts of the model, these regions of material are optimized with the aid of the density-based approach with solid and plate discretization elements in order to reflect realistic configurations where lattices or spatial frames are connected to solids and plates (i.e. mechanical parts which provide lifting forces in aircrafts, buildings with beams, columns, walls, slabs etc.). This optimization method is employed in the majority of commercial software packages as being the most mature and popular. The constitutive parameters, which define the stiffness of each element, are chosen as design parameters, and in this way elements containing solid material get a finite stiffness value while void elements get a null one. In other words, it is determined whether an element should contain material or not. Particularly, the optimization is performed in a loop until a stopping criterion with respect to density parameter is satisfied and the optimum material distribution is found. In practice, the material in the density distribution is either void or solid, which means that a 0-1 solution is sought. Therefore, the convergence to intermediate values between 0 and 1 is then penalized using the SIMP method, which is the most well-known. A slightly modified version of the SIMP method can be used in order to obtain mesh-independent, discrete and manufacturable solutions. GB optimization is usually performed using the OC or MMA. Density distributions employed in topology optimization are voxel-based models and their values are used to

scale voxel stiffness values in the models employed during the optimization process. The vast majority of topology optimizers employ traditional FEM, which results in excessive computational effort for geometrically complex large-scale objects. In addition to this, linear shape functions are still employed (linear Finite Elements) and, thus, the degrees of freedom (dofs) are significantly increased. p-FEM (p is the polynomial order) has been developed to compensate for these disadvantages by increasing the order of the employed polynomials. Higher-order B-splines and NURBS have been integrated in FEM for the same purpose and compared to traditional FEM and p-FEM with respect to computational cost. Moreover, a fictitious domain method can be investigated as a promising alternative [25], since it is suitable for models based on voxels. In addition to these, stress-constraint optimization problems have also investigated, since the description of stress fields is highly benefited from higher-order basis functions. Finally, static condensation of the stiffness matrix with respect to internal higher deformation modes can also be employed to further reduce the computational cost of topology optimization.

Within this research effort, several optimizers and structural arrangements have been studied and compared. OC and MMA have mainly been employed to optimize either square bi-linear 4-node element models [4] or truss/frame ones. Comparisons between bar, EB and TS unit-cell configurations have been performed in order to study the influence of shear during optimization of lattice structures and frames. This is the first step towards investigating the influence of higher order phenomena, such as warping (secondary shear deformation effect), in the analysis of these structural arrangements. Moreover, the ground structure method [16] has been employed to formulate bar-like configurations and compare the optimized structure derived both by SLP and Particle Swarm Optimizer (PSO), which belongs to metaheuristic methods [23].

2. Statement of the problem

In the present effort, the topology optimization problem described in [4] and formulated for square bi-linear 4-noded elements with two translational dofs and 8 by 8 stiffness matrices (as mentioned in [4]), has also been formulated in this effort for truss and framed unit cell arrangements of the same volume fraction. The shapes shown in Fig. 1 have been employed as unit cells. Both EB and TS (employing the shear coefficient for solid circular cross section) beams have been employed for the framed unit cell, which is analyzed as shear frame in order to derive its local stiffness matrix. The end rotations have been taken into account in the derivation of elements' stiffness matrices but finally have been condensed. The minimization of the compliance is considered.

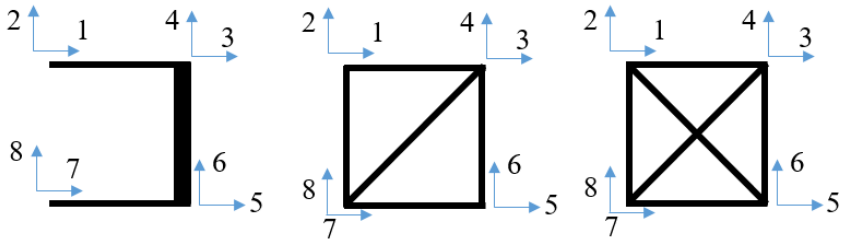


Figure 1: Unit Cells employed: EB or TS frame (on the left) and two trusses with one or two diagonals.

In order to allow for a more flexible arrangement of bars in the structural domain, the ground structure of unstructured mesh developed in [16] has been employed for the optimization of truss arrangements in 2D. However, instead of the plastic analysis and nodal equilibrium matrix, the stiffness matrix has been derived in order to perform an elastic analysis of the truss. In this formulation, beams elements have not been introduced yet. The minimization of the truss volume is considered in this formulation and size (bar cross section) optimization is also performed.

3. Numerical Implementation

Both OC (as described in [4]) and MMA have been employed for the unit cell formulations together with penalization. Truss and 2D Frame analysis toolboxes in MATLAB have been employed [32-33]. Regarding the ground structure method and the unstructured mesh, the MATLAB code developed in [16] has been employed but for the elastic analysis of the 2D truss. SLP and SQP have been used in order to optimize the volume in this case.

4. Results and Conclusions

Initially, the simply supported method studied also in [4] is optimized with various solvers as shown in the graph of Fig. 2 (obj: OC with square bi-linear 4-noded elements, MMA obj: MMA with square bi-linear 4-noded elements, OC Truss obj: OC with truss unit cell of one diagonal, Beam Frame Obj: OC with TS beam unit cell and MMA Frame obj: MMA with TS beam unit cell). The modulus of elasticity is equal to unity for simplicity and comparison reasons. In order to obtain a similar starting compliance, around 4 times more material has been employed for the truss unit cell with the X bracing (Fig. 1).

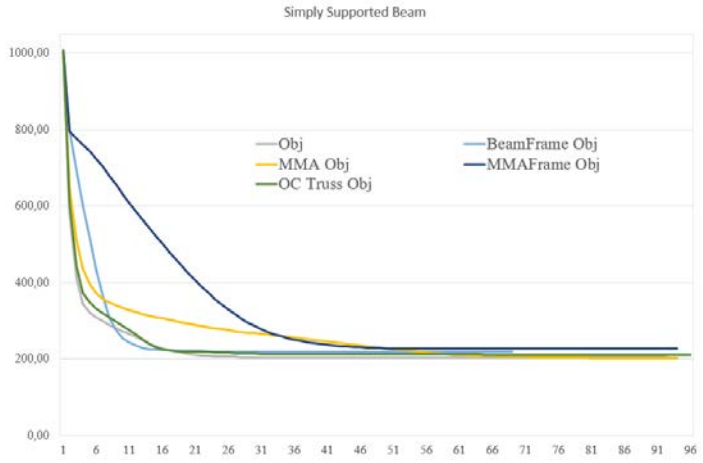


Figure 2: History of compliance for different structural arrangements employing both OC and MMA.

Secondly, the compliance minimization problem has been studied for a simply supported and cantilever beam (Fig. 3). Framed unit cells both with EB and TS beam elements have been employed with OC for

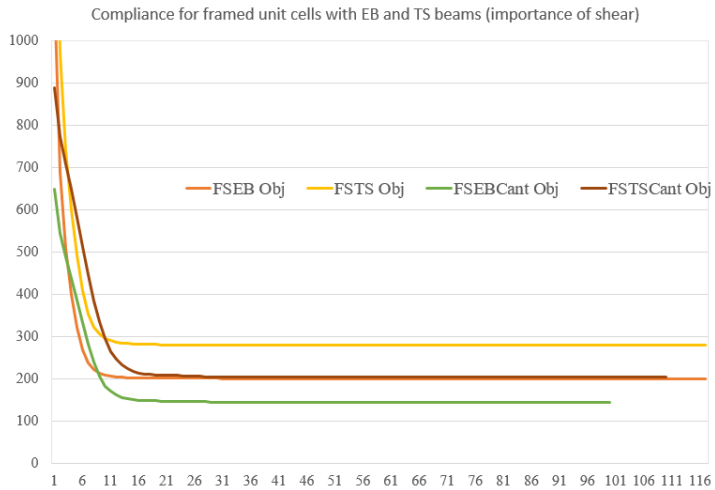


Figure 3: History of compliance for different structural arrangements employing both EB and TS unit cells (Cant stands for cantilever)

this purpose (Fig. 3). Almost 30% higher compliance is obtained for the TS unit cell indicating the importance of shear for both boundary conditions of the beam.

Thirdly, various structural arrangements and optimizers have been employed to minimize the compliance of both simply supported and cantilever beam for realistic values of the modulus of elasticity (E=2000 for the frame and shell unit cells or E=20000 for the truss unit cells). Results have been compiled in the graph shown in Fig. 4 (when MMA is not mentioned in the name of the curve presented in the figure, it means that the OC optimizer has been employed). In this case, the difference raised between the EB and TS arrangements is almost 20%. The MMA is easier to implement with framed unit cells and its parameters seem to be less susceptible to changes, even though it needs more iterations to reach the optimum comparing to OC solver. The X-braced truss as unit cell leads to a material save of around 14% comparing to the other truss configuration (Fig. 1) due to the increase in the cross sectional areas obtained for similar minimum compliance.

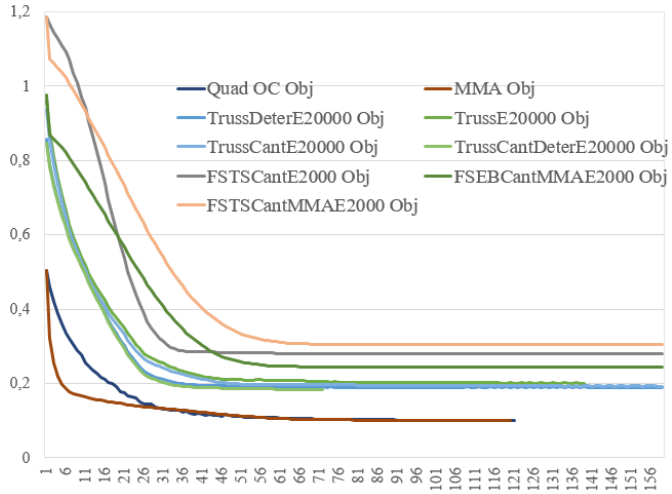


Figure 4: History of compliance for different structural arrangements of more realistic elastic modulus (values are shown) employing OC and MMA (TrussDeter stands for determinate truss and describes the truss unit cell with one diagonal and Cant stands for cantilever, while these are not mentioned when the truss has two diagonals and the beam is simply supported, respectively)

Finally, when employing the unstructured mesh solver with SLP, a decrease of around 20% is achieved in the minimum compliance for the truss arrangements solved for elastic analysis (similarly to the plastic analysis in [16]) compared to the structured mesh used in OC or MMA. This is mainly attributed to the flexibility of the unstructured mesh which broadens the search domain of the solver. When comparing to the PSO for the tower with linear chords described in [23] and starting from a similar initial mesh, it is observed that even for a high level of connectivity between the bars the minimum derived by the PSO cannot be reached. However, further investigation is needed regarding the rest of the parameters employed. It is also worth noting that in the case of SQP the algorithm becomes much slower due to the calculation of the Hessian matrices.

References

[1] L.E. Murr, "Frontiers of 3D Printing/Additive Manufacturing: from Human Organs to Aircraft Fabrication," *Journal of Materials Science & Technology*, vol. 32, pp. 987-995, Oct. 2016.

[2] M. Ohsaki, *Optimization of finite dimensional structures*. CRC Press, Boca Raton: Taylor & Francis Group, 2010.

[3] M.P. Bendsøe and O. Sigmund, *Topology optimization: theory, methods, and applications*. Berlin: Springer, 2003.

[4] O. Sigmund, "A 99 line topology optimization code written in Matlab", *Structural and Multidisciplinary Optimization*, vol. 21, pp 120-127, 2001.

[5] E. Andreassen and C.S. Andreasen, "How to determine composite material properties using numerical homogenization," *Computational Materials Science*, vol. 83, pp. 488-495, Feb. 2014.

[6] M.P. Bendsøe, "Optimal shape design as a material distribution problem," *Structural Optimization*, vol. 1, pp. 193-202, Dec. 1989.

[7] G.H. Paulino, E.C. Nelli Silva and C.H. Le, "Optimal design of periodic functionally graded composites with prescribed properties," *Structural and Multidisciplinary Optimization*, vol. 38, pp. 469-489, Jun. 2009.

[8] G. Dong, Y. Tang and Y.F. Zhao, "A 149 Line Homogenization Code for Three-Dimensional Cellular Materials Written in MATLAB," *Journal of Engineering Materials and Technology*, vol. 141, 011005, Jan. 2019.

[9] J. Wu, W. Wang and X. Gao, "Design and Optimization of Conforming Lattice Structures," *https://arxiv.org/abs/1905.02902*, May 2019.

[10] R.M. Freund, *Truss Design and Convex Optimization*. Massachusetts Institute of Technology, Apr. 2004.

[11] J. Schwarz, T. Chen, K. Shea and T. Stankovic, "Efficient size and shape optimization of truss structures subject to stress and local buckling constraints using sequential linear programming," *Structural and Multidisciplinary Optimization*, vol. 58, pp. 171-184, Jan. 2018.

[12] R. Arora, A. Jacobson, T.R. Langlois, Y. Huang, C. Mueller, W. Matusik, A. Shamir, K. Singh and D.I.W. Levin, "Volumetric Michell Trusses for Parametric Design & Fabrication," in *Proceedings of SCF '19, Pittsburgh, PA, USA, June 16-18, 2019*, Association for Computing Machinery, New York, USA, 2019.

[13] K. Svanberg, "The Method of Moving Asymptotes - A new method for structural optimization," *International Journal for Numerical Methods in Engineering*, vol. 24, pp. 359-373, Feb. 1987.

[14] K. Liu and A. Tovar, "An efficient 3D topology optimization code written in Matlab," *Structural and Multidisciplinary Optimization*, vol. 50, pp. 1175-1196, Jun. 2014.

[15] A.E. Charalampakis, "Comparison of metaheuristic algorithms for size optimization of trusses", *in Proceedings of 11th HSTAM International Congress on Mechanics, Athens, May 27-30, 2016*, Athens, Greece, 2016.

[16] T. Zegard and G.H. Paulino, "GRAND-Ground structure based topology optimization for arbitrary 2D domains using MATLAB," *Structural and Multidisciplinary Optimization*, vol. 50, pp. 861-882, Jun. 2014.

[17] C. Talischi, G.H. Paulino, A. Pereira and I.F.M. Menezes, "PolyTop: a Matlab implementation of a general topology optimization framework using unstructured polygonal finite element meshes," *Structural and Multidisciplinary Optimization*, vol. 45, pp. 329-357, Jan. 2012.

[18] S.Engelbrecht, L. Folgar, D.W. Rosen, G. Schulberger and J. Williams, "Cellular structures for optimal performance," in *Proceedings of SFF Symposium, Austin, Texas, August 3-5, 2009*, University of Texas, 2009. pp.831-842.

[19] A. Asadpoure and L. Valdevit, "Topology optimization of lightweight periodic lattices under simultaneous compressive and shear stiffness constraints," *International Journal of Solids and Structures*, vol. 60-61, pp. 1-16, Feb. 2015.

[20] M.C. Messner, "Optimal lattice-structured materials," *Journal of the Mechanics and Physics of Solids*, vol. 96, pp. 162-183, Nov. 2016.

[21] D. Rosen, S. Johnston, M. Reed and H. Wang, "Design of general lattice structures for lightweight and compliance applications," in *Proceedings of Rapid Manufacturing Conference, Loughborough University, July 5-6, 2006*.

[22] A. Nadal, H. Cifre, J. Pavóna and Ó. Liébana, "Material use optimization in 3D printing through a physical simulation algorithm," *Automation in Construction*, vol. 78, pp. 24-33, Feb. 2017.

[23] I.N. Tsiptsis, L. Liimatainen, J. Niiranen and T. Kotnik, "Structural optimization employing isogeometric tools in Particle Swarm Optimizer," *Journal of Building Engineering*, vol. 24, 100761, Apr. 2019.

[24] J. Felkner, E. Chatzi and T. Kotnik, "Interactive truss design using Particle Swarm Optimization and NURBS curves," *Journal of Building Engineering*, vol. 4, pp. 60-74, Dec. 2015.

[25] I.N. Tsiptsis and E.J. Sapountzakis, "Generalized warping and distortional analysis of curved beams with isogeometric methods," *Computers and Structures*, vol. 191, pp. 33-50, Oct. 2017.

[26] X. Qian, "Full analytical sensitivities in NURBS based isogeometric shape optimization," *Computer Methods in Applied Mechanics and Engineering*, vol. 199, pp. 2059-2071, Mar. 2010.

[27] M.J. Choi and S. Cho, "Isogeometric configuration design optimization of shape memory polymer curved beam structures for extremal negative Poisson's ratio," *Structural and Multidisciplinary Optimization*, vol. 58, pp. 1861-1883, Sep. 2018.

[28] P. Hao, X. Yuan, C. Liu, B. Wang, H. Liu, G. Li and F. Niu, "An integrated framework of exact modeling, isogeometric analysis and optimization for variable-stiffness composite panels," *Computer Methods in Applied Mechanics and Engineering*, vol. 339, pp. 205-238, May 2018.

[29] M.P. Bendsøe and O. Sigmund, "Material interpolation schemes in topology optimization," *Applied Mechanics*, vol. 69, pp. 635-654, May 1999.

[30] Y.C. Chan, K. Shintani and W. Chen, "Robust topology optimization of multi-material lattice structures under material and load uncertainties," *Frontiers of Mechanical Engineering*, vol. 14, 141-152, Jun. 2019.

[31] B. Shiye and Z. Jiejiang, "Topology Optimization Design of 3D Continuum Structure with Reserved Hole Based on Variable Density Method," *Journal of Engineering Science and Technology Review*, vol. 9, pp. 121-128, May 2016.

[32] Truss Analysis toolbox: https://se.mathworks.com/matlabcentral/fileexchange/38044-truss-analysis

[33] 2D Frame Analysis toolbox: https://se.mathworks.com/matlabcentral/fileexchange/49996-2d-frame-analysis

Proceedings of the IASS Annual Symposium 2019 – Structural Membranes 2019
Form and Force
7 – 10 October 2019, Barcelona, Spain
C. Lázaro, K.-U. Bletzinger, E. Oñate (eds.)

Tendon Geometry Optimization Using Path Integrals

Jack LEHRECKE*, Juan P. OSMAN-LETELIER[a], Mike SCHLAICH[a]

*TU Berlin
Gustav-Meyer-Allee 25, 13355 Berlin
jacklehrecke@gmail.com

[a] TU Berlin

Abstract

The implementation of post-tensioned elements in concrete structures offers a multitude of benefits with regards to the overall structural behavior, with the efficacy of the applied tendons depending heavily on their geometry. However, the derivation of an optimal tendon geometry for a given structure is nontrivial, requiring engineering experience or the use of complex and often computationally demanding methodologies, e.g. the use of topology optimization strategies. This paper aims to investigate the possibility for optimizing tendon geometries using a path integral based objective function developed at the TU Berlin. For this purpose, the mathematical background is first presented to illustrate the proposed concept. Beginning with a tendon geometry optimization of a simply supported beam and progressing to more complex systems, a generalized approach for doubly curved spatial structures will be presented.

Keywords: concrete shells, prestressing, post-tensioning, tendon geometry, optimization

1. Introduction

The prestressing of concrete beams, slabs and shells can compress areas which would otherwise experience tension under certain loads. The permanent internal stress condition induced by pre- or post-tensioning (PRT and PT) considerably reduces the risk of crack development, resulting in an improved structural performance of the system over the course of its lifespan. Prestressing thus increases the stiffness of the system, allowing for the minimization of the necessary cross-section while fulfilling Serviceability Limit State (SLS) requirements. Furthermore, displacements due to bending can be counteracted with prestressing, especially with the use of post-tensioned curved tendons.

There are various computational methodologies typically used for the derivation of optimal tendon geometries. Using linear programming and assuming an elastic response, Kirsch [1] successfully optimized the tendon cross-section, geometry, and initial stress magnitude for a series of concrete beams. More recently, Eurviriyanukul and Askes [2] demonstrated the feasibility of utilizing the equilibration of configurational forces to derive the optimal tendon layouts for concrete structures subjected to in plane stresses. An interesting alternative approach was investigated by Amir and Shakour [3], in which they performed a topology optimization to simultaneously find an optimal mass distribution for the concrete along with the corresponding tendon geometries for a simply supported prestressed beam under various loading conditions. The application of a topology optimization to derive efficient tendon layout schemes has also been recently applied to PT concrete slabs in tandem with a force density method, effectively delivering three-dimensional optimized tendon geometries for floor systems with various boundary conditions [4], [5].

These methodologies are all capable of delivering optimal tendon geometries, effectively reducing overall material costs and improving the long-term structural behavior of the given system. However, each approach mentioned above implements an iterative optimization algorithm, with each step

Copyright © 2019 by Jack Lehrecke, Juan Pablo Osman-Letelier and Mike Schlaich
Published by the International Association for Shell and Spatial Structures (IASS) with permission.

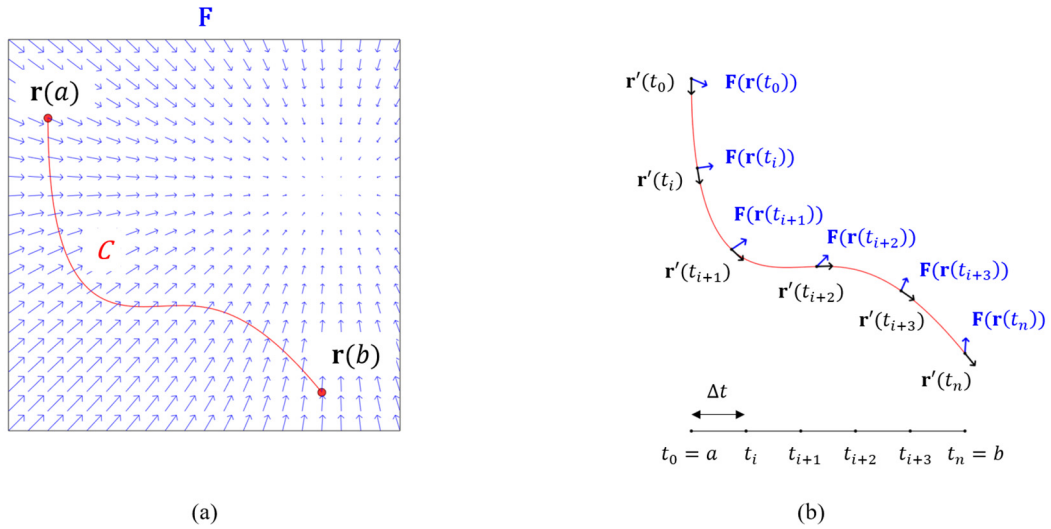
requiring a structural analysis of the given system. While the overall efficiency of the optimization can be compensated, for example, through the implementation of gradient-based algorithms, the required computational effort increases exponentially with the complexity of the structure and the total degrees of freedom of the discretized system. The methodology introduced in this paper aims to investigate the possibility of performing a tendon geometry optimization using only a single structural analysis, greatly reducing the overall computational effort.

2. Path integrals

The basis for the proposed methodology involves calculating a form of path integral along a series of curves representative of the tendon geometry. A brief introduction of the underlying mathematical theory is, therefore, necessary for a derivation of the strategy outlined in this paper. For an arbitrary vector field $\mathbf{F}: U \to \mathbb{R}^n, U \subseteq \mathbb{R}^n$, the path integral along a piecewise smooth curve $C \subset U$, in the direction of $\mathbf{r}$ is defined as [6]:

$$\int_C \mathbf{F}(\mathbf{r}) \cdot d\mathbf{r} = \int_a^b \mathbf{F}(\mathbf{r}(t)) \cdot \mathbf{r}'(t) dt \tag{1}$$

Here, $\mathbf{r}: [a, b] \to U$ is the bijective parameterization of the curve C, such that $\mathbf{r}(a)$ and $\mathbf{r}(b)$ denote the endpoints of the curve as seen in Figure 1(a).



(a) (b)

Figure 1: (a) Curve C and vector field $\mathbf{F}$ (b) discretized approach to calculating the path integral

As the general methodology introduced in the next section relies on a finite-element-based structural analysis, a discretized variant of the path integral equation seen above is necessary. This can be achieved by dividing the given parameter interval $[a, b]$ into n segments of equal length and evaluating the dot product between the tangent of the curve at the resulting points and the corresponding field vector. By then summing the products of the resulting dot product values with the uniform parameter interval $\Delta t = (b - a)/n$, a discrete variant of the path integral described by eq. (1) is obtained:

$$\int_C \mathbf{F}(\mathbf{r}) \cdot d\mathbf{r} \approx \sum_{i=0}^{n} \mathbf{F}(\mathbf{r}(t_i)) \cdot \mathbf{r}'(t_i) \Delta t \tag{2}$$

By then taking the limit of the resulting sum as the parameter interval approaches zero, an exact solution equivalent to the continuous path integral can be calculated using the mean value theorem [6]:

$$\lim_{n \to \infty} \sum_{i=0}^{n} \mathbf{F}(\mathbf{r}(t_i^*)) \cdot \mathbf{r}'(t_i^*) \Delta t = \int_a^b \mathbf{F}(\mathbf{r}(t)) \cdot \mathbf{r}'(t) dt, \; t_i^* \in]t_i, t_{i+1}[\tag{3}$$

As seen in Figure 1(b), a and b correspond to t_0 and t_n respectively, with the absolute value of the resultant integral independent of the direction of the parameterization. However, it is important to note that a reversal of the orientation of the parameterization (i.e. $t_0 = b, t_n = a$) results in a sign change for the resulting integral.

3. Objective function derivation

Path integrals are commonly implemented to calculate the work exerted by a force field on a particle travelling along a given trajectory. As the total work is dependent on the magnitude of the force and the relative direction of the field along the given trajectory, a maximal path integral value corresponds to a curve whose trajectory runs parallel to the field through the largest forces. If a vector field describing the direction and magnitude of the principal tensile stress in the concrete under a given load is selected for analysis, then a tendon whose geometry corresponds to a curve with a maximal path integral value in said field should then also pass parallelly through the largest tensile stresses. This allows for an optimal influence of the tendon on the given stress field, as prestressing forces introduced tangentially along this curve directly counteract the largest tensile stresses. As the general objective when implementing prestressed elements is to minimize the remaining tensile stresses within the concrete under a given load, this maximal influence of the tendon is highly desirable.

To reformulate the path integral equation presented in the previous section for implementation as the objective function for the proposed optimization, the following assumptions are made. For a given structure inhabiting the n-dimensional Euclidian space U, let $\mathbf{F}$ represent a smooth vector field of the principal tensile stresses induced by a given load such that $\mathbf{F}: U \to \mathbb{R}^n, U \subset \mathbb{R}^n$ (n = 2 or 3). Let $\mathbf{r}: [a, b] \to U$ then be a parametric representation of the curve C, describing the geometry of a given tendon. Normalizing the derivative of $\mathbf{r}(t)$ then yields the unit vector function $\mathbf{T}(t) = \mathbf{r}'(t)/\|\mathbf{r}'(t)\|$, which describes the tangent vector of the tendon geometry at any given point along the curve C. Assuming a constant prestressing force p, the magnitude and direction of the stress exerted by the tendon can be expressed by the vector function $\mathbf{p}(t) = \mathrm{p}\mathbf{T}(t)$. The influence of the tendon at any point along its geometry is then dependent on the direction of the constant prestressing force as expressed by $\mathbf{T}(t)$ and the corresponding magnitude and relative direction of the principal tensile stress field. Calculating the path integral with respect to $\mathbf{T}(t)$ in the field $\mathbf{F}$ then yields a single value indicative of the cumulative influence of the tendon in the given field. If we then define ψ as the following, the application of the absolute value ensures that the resulting path integral is independent of relative senses of the unit tangent vectors and corresponding field vectors:

$$\psi = \int_a^b |\mathbf{F}(\mathbf{r}(t)) \cdot \mathbf{T}(t)| dt \approx \sum_{i=0}^{n} |\mathbf{F}(\mathbf{r}(t_i)) \cdot \mathbf{T}(t_i)| \Delta t \tag{4}$$

By setting $-\psi$ as the given objective for minimization, the resulting optimization should then effectively converge on a solution in which the given geometry allows for an optimal influence of the tendon on the surrounding principal tensile stress field:

$$f = -\psi \tag{5}$$

This concept is illustrated in Figure 2, in which a simply supported beam under a uniform load is considered. Here, the beam is analyzed as a two-dimensional plate with the resulting principal tensile stress field $\mathbf{F}$ flowing lengthwise along the beam and increasing in magnitude from the bending axis to the outer edge, with the largest stress values occurring at the midspan. The tendon geometry represented by the curve C is then divided into n discrete components and the normalized tangential vector and corresponding field vector are displayed for each node as seen in Figure 2(b). The dot product of these two vectors is then calculated at each node and plotted with respect to the parameter t, with the area under the resulting curve equivalent to the path integral ψ as seen in Figure 2(c). Here, the correlation between the influence of the tendon and the angle between the tangential vector and corresponding field vector is clearly displayed, with an optimal tendon geometry corresponding to a curve that runs parallel

to the flow of principal stress. Furthermore, the efficacy of the tendon is also dependent on the magnitude of the surrounding field vectors, with the influence of the given tendon maximized when the curve passes through regions of maximal tensile stress. An optimal tendon geometry as defined by a minimum value of eq. (5), and corresponding maximum path integral ψ, is then achieved with a curve that most closely matches the flow of the largest principal tensile stress vectors in the field **F**.

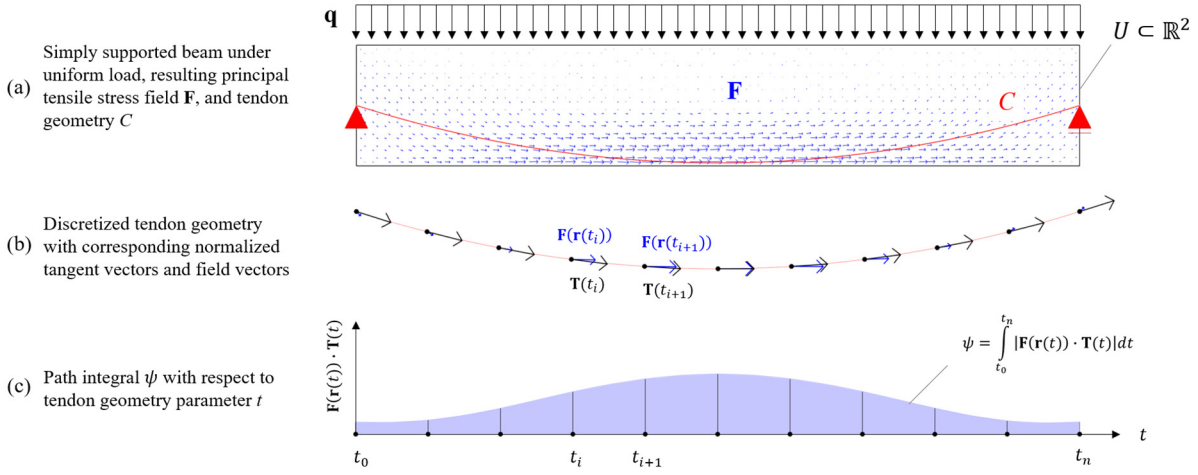


Figure 2: Path integral computation for a parabolic tendon in a simply supported beam under a uniform load

4. Methodology

To implement the objective function derived in the previous section, a multiphase iterative strategy is applied. In the initial structural analysis phase, the geometry, boundary conditions, and loads are defined. The system is then discretized and analyzed using finite element (FE) software, which returns the principal stress vectors for each individual element under the applied load. The principal stress vectors representing compression are then filtered out, leaving a purely tensile vector field **F**, which is then saved and exported to the design model. It is important to note, that this initial structural analysis is only conducted once, with the same vector field being used for the remainder of the iterative process.

In the design model, the tendon geometry C is parameterized to be dependent on a given design vector **s**. For the examples investigated in this work, the implemented design vectors are comprised of a series of parametrically defined control points, through which a NURBS-curve (Non-Uniform Rational Basis Spline) is generated to define the given tendon geometry. The generated curve is then exported to the analysis model for the calculation of the path integral.

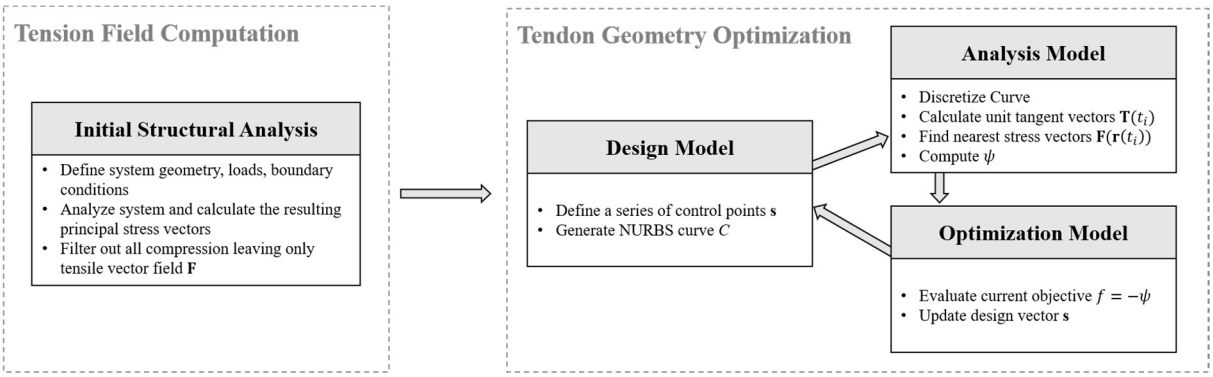


Figure 3: Generalized tendon geometry optimization methodology

The analysis model then provides the required path integral value for the objective function (eq. (5)) using the following algorithm:

1. Divide the tendon geometry curve *C* into *n* discrete components
2. Evaluate $\mathbf{r}(t_i)$ at each node and calculate the unit tangent vectors $\mathbf{T}(t_i)$
3. For each node, search **F** for the closest principal stress vector in *U* providing $\mathbf{F}(\mathbf{r}(t_i))$
   - If no tensile stress vectors exist within a predefined radius of the node, then: $\mathbf{F}(\mathbf{r}(t_i)) = \mathbf{0}$
4. Compute the path integral $\psi = \sum_{i=0}^{n} |\mathbf{F}(\mathbf{r}(t_i)) \cdot \mathbf{T}(t_i)| \Delta t$

The objective $f = -\psi$ is then calculated and exported to the optimization model for evaluation. For the examples investigated in this work, a simple genetic algorithm was applied to evaluate the standard single objective optimization problem:

$$\begin{aligned} &\text{min} && f(\mathbf{s}, \psi) = -\psi && \mathbf{s} \in \mathbb{R}^l \\ &\text{subject to} && g_i(\mathbf{s}, \psi) \geq 0 && i = \{1, \dots l^g\} \\ & && h_j(\mathbf{s}, \psi) = 0 && j = \{1, \dots l^h\} \end{aligned}$$

with the objective function *f*, design vector **s**, number of design variables l, path integral ψ, and constraint functions *g* and *h*. Here, the constraint functions allow for the requirement that certain geometric conditions are fulfilled throughout the optimization, such as a minimum concrete cover depth or maximum allowable curvature of the tendon. Based on the performance of the current solution with respect to the objective function, the optimization model then updates the design vector **s**, and the iterative process starts anew from the design model phase as displayed in Figure 3. This process then repeats itself until a convergence upon an optimal solution is obtained.

5. Applied examples

5.1. Beams

To demonstrate the proposed methodology, the simply supported beam under a uniform load introduced in section 3 is evaluated for optimization. To achieve this, a NURBS-curve representing the given tendon geometry is parameterized to be dependent on a set of five control points as seen in Figure 4(a).

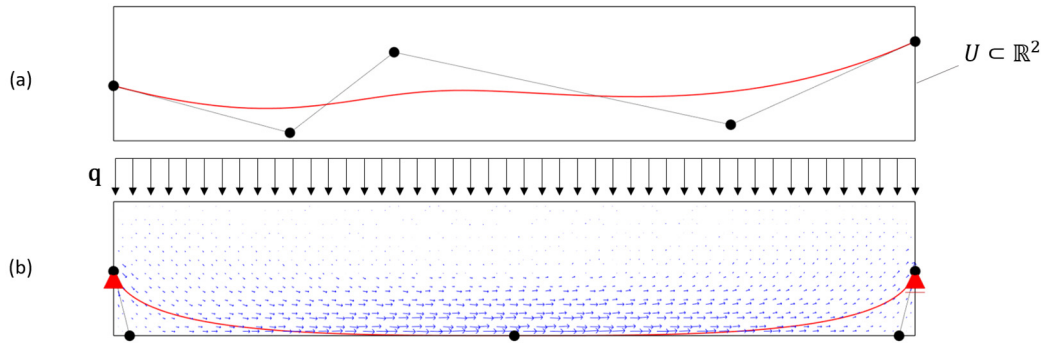
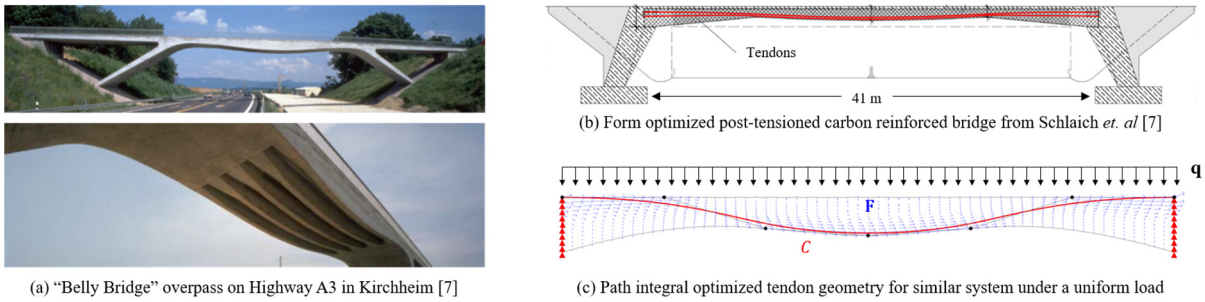


Figure 4: (a) NURBS-curve generated through a series of control points (b) optimized tendon geometry

The series of coordinate values used to define these control points are then the design variables for the given problem. Here, the two outer points are required to lie on the vertical free edges of the structure, thus ensuring that the resultant tendon spans the entire width of the beam. The vertical coordinate of these outer points as well as both spatial coordinates for the three remaining inner points are then parametrically defined, with the respective bounds spanning the entirety of the space *U*. Discretizing the resultant curve and implementing the iterative methodology described in the previous section, an optimal solution is converged upon as displayed in Figure 4(b).

The optimal curve provided by the applied methodology deviates slightly from the parabolic geometry typically implemented for simply supported beams under a uniform load. Through an increased curvature of the tendon near the supports, the optimal curve is effectively able to intersect a larger portion of the maximal stress vectors at the lower edge of the beam, while maintaining a trajectory that runs parallel to the surrounding stress field along the entire length of the curve. It is important to note, that the optimal geometry delivered by the optimization is heavily dependent on the parameterization of the curve, with an alternative method of spline generation or number of control points resulting in a dissimilar design space and corresponding optimal geometry. Furthermore, for the examples presented in this work, cover depth requirements were not implemented, with the resulting curves free to traverse the entirety of the given structural surface.

To demonstrate the flexibility of the path integral approach, a "Belly Bridge" girder with a non-uniform cross-section is investigated and compared to results provided by an optimization carried out by Schlaich *et al.* [7] as seen in Figure 5. Here, the cross-section of the beam is designed to mirror the magnitude of the bending moment induced by a uniform load, with an increased height at the supports and midspan where the largest negative and positive bending actions occur respectively. The resulting principal tensile stress field then flows along the length of the beam, with the largest vectors occurring first at the upper extremity of the cross-section near the supports and migrating to the lower edge at the midspan due to the change in sign of the bending moment.



(a) "Belly Bridge" overpass on Highway A3 in Kirchheim [7]

(b) Form optimized post-tensioned carbon reinforced bridge from Schlaich *et. al* [7]

(c) Path integral optimized tendon geometry for similar system under a uniform load

Figure 5: Path integral optimization applied to variable cross-section beam

Again, a NURBS-curve representative of the tendon trajectory is generated through a set of control points and optimized with respect to a maximization of the path integral, with the resultant optimal geometry displayed in Figure 5(c). The optimized trajectory intersects the largest tensile vectors in both the upper and lower extremities of the beam, while also remaining parallel to the flow of stress along the entire length of the curve, closely mirroring the optimized layout derived by Schlaich *et al.* [7] for a similar system as seen in Figure 5(b).

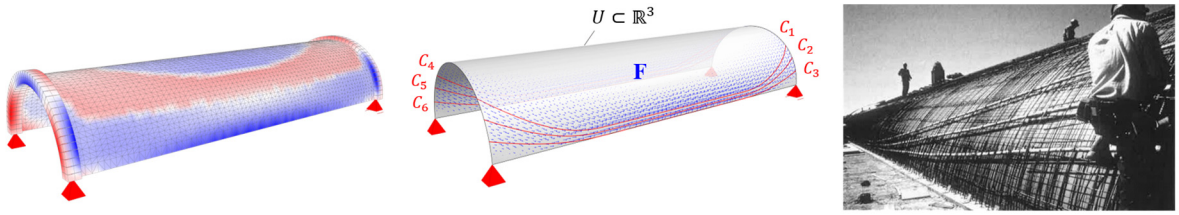
5.2. Barrel vault shell

The application of the proposed methodology is by no means limited to beams, with an implementation for thin shell structures requiring no modifications to the general theory. Furthermore, it becomes possible to simultaneously optimize multiple tendon geometries for a given structure by simply adjusting the objective function:

$$f = -\sum_{i=1}^{m} \psi_i \tag{6}$$

where ψ_i denotes the path integral along the curve C_i and m denotes the total number of tendons, effectively maximizing the combined influence of the tendons on the surrounding field. Figure 6 displays this concept applied to a thin barrel vault structure based on the system implemented for the Kimbell Art Museum in Fort Worth, Texas [8]. Due to the curvature of the shell, the available design space U now exists in three dimensions, with the resulting vector field inhabiting the two-dimensional manifold of the surface describing the shell midplane. For the examples considered in this paper, the

shells are assumed to be relatively thin, requiring the tendons to be implemented in the midplane of the shell and thus precluding them from counteracting local bending actions through an eccentricity between their geometry and the local bending axis. The tendon trajectories are generated exactly as before, with a series of parametrically defined control points governing the NURBS-curves describing their geometry. The curves are then subjected to the optimization methodology described in section 4 and evaluated with regards to eq. (6). Here, six curves were implemented, and the objective function was supplemented with a constraint equation requiring a minimum spacing between the tendons, yielding the optimal geometry displayed in Figure 6(b). Again, the path integral methodology delivers an optimal tendon layout similar to that of the actual structure as seen in Figure 6(c).



(a) FE structural model of Kimbell Museum vault and stress distribution under dead load

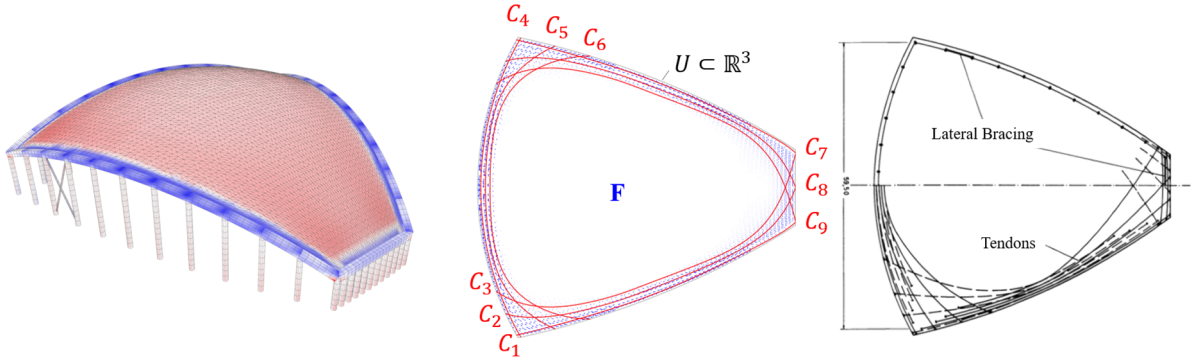
(b) Resultant principal tensile stress field in shell midplane and optimized tendon geometry

(c) Tendon layout applied for actual structure [8]

Figure 6: Path integral optimization applied to Kimbell Museum barrel vault

5.3. Truncated dome shell

To further demonstrate the robustness of the path integral methodology for generalized application, the Auditorium Maximum at the University of Hamburg is considered. The structure is comprised of a doubly curved truncated dome supported about its periphery by a series of thin columns as seen in Figure 7(a). Due to the reduced horizontal stiffness provided by the columns to the shell, the resulting hoop stress leads to a flow of tension about the shell perimeter, requiring the implementation of prestressed tendons [9].



(a) FE structural model of Auditorium Maximum and stress distribution under dead load

(b) Resultant principal tensile stress field in shell midplane and optimized tendon geometry

(c) Geometry and tendon layout applied for actual structure [9]

Figure 7: Path integral optimization applied to Auditorium Maximum in Hamburg

A total of nine curves are parameterized and input into the optimization cycle, with a similar constraint to the previous example requiring a minimum spacing between tendons travelling in a similar direction. Furthermore, an additional constraint is defined requiring that the end points of each curve lie on opposing edges of the shell surface. With these restraints, the path integral approach is able to provide a logical and constructionally feasible layout for the tendons, with the resulting optimized geometry remarkably similar to the layout implemented in the actual structure as seen in Figure 7(b) and (c) respectively. This application of a constrained optimization highlights another advantage offered by the path integral approach, with the methodology able to comfortably deliver a conditionalized optimum. This is highly convenient for practical applications, as this allows for the derivation of an optimal

geometry that fulfills a series of constructionally dictated geometric constraints, such as fixed anchor positions, minimum anchor spacing, maximum tendon curvature, and minimum concrete cover depth.

6. Conclusions and outlook

The use of a path integral based approach to inform the choice of PT tendon geometry shows significant potential for future development. The examples investigated in this paper demonstrate the flexibility of this approach and its potential for implementation with a variety of structural forms. Because of the single structural analysis phase, the efficiency with which the path integral approach can deliver an informed result makes it ideal for application during any stage of the design process. Additionally, the ability to define the tendon geometry with parameterized NURBS-curves and other freeform splines allows for a great freedom with respect to the available design space. Implementing a path integral optimization with a series of geometric constraints also allows for the derivation of conditionalized optimal geometries. The exploitation of this geometric freedom to generate curves following the flow of the largest principal tensile stress vectors represents an efficient union between the classical concept of "form follows force" and modern computational modelling capabilities.

While the examples investigated in this paper were restricted to 2-D stress fields occupying either a flat surface (beams) or curved manifold (shells), the proposed methodology could also potentially be extended upon for implementation in three dimensions. An interesting avenue for future research could entail the use of volume elements to analyze a slab system, yielding a three-dimensional principal tensile stress field. The tendon geometries could then be defined as a series of 3-D parametric curves inhabiting the volume defined by the given slab and the path integral optimization would be carried out normally, attempting to maximize the influence of the tendons on the given stress field.

References

[1] U. Kirsch, "Optimized prestressing by linear programming," *International Journal for Numerical Methods in Engineering,* vol. 7, no. 2, pp. 125-136, 1973.

[2] S. Eurviriyanukul and H. Askes, "The equilibration of configurational forces in the tendon layout optimisation of pre-stressed concrete beams," *Computers and Structures,* vol. 88, no. 23, pp. 1412-1418, 2010.

[3] O. Amir and E. Shakour, "Simultaneous shape and topology optimization of prestressed concrete beams," *Structural and Multidisciplinary Optimization,* vol. 57, no. 5, pp. 1831-1843, 2018.

[4] R. M. Avelino, D. Shook, A. Beghini, E. Long and M. Sarkisian, "Efficient flat-slab post-tensioning layouts guided by Topology Optimization," in *Proceedings of the IASS Symposium 2018: Creativity in Structural Design*, MIT, Boston, USA, July 16-20, 2018.

[5] M. Hymans, M. Sarkisian, E. Long, F. Mola, E. Mola and D. Shook, "Optimization of post-tensioned concrete floor slabs," in *Proceedings of the IASS Symposium 2018: Creativity in Structural Design*, MIT, Boston, USA, July 16-20, 2018.

[6] V. Alvarado A. and J. Leiva V., Cálculo Integral en $\mathbb{R}^n$, Valdivia: Universidad Austral de Chile, Facultad de Ciencias, Instituto de Matemáticas, 2006.

[7] M. Schlaich, A. Apitz and A. Goldack, "Form optimized CFRP reinforced and post-tensioned integral concrete bridge using precast girders," in *40th IABSE Symposium: Tomorrow's Megastructures*, Nantes, France, September 19-21, 2018.

[8] A. Komendant, Contemporary Concrete Structures, R.E. Krieger Publishing Company, 1977.

[9] J. Joedicke, Schalenbau, Stuttgart: Karl Krämer Verlag, 1962.

Proceedings of the IASS Annual Symposium 2019 – Structural Membranes 2019
Form and Force
7 – 10 October 2019, Barcelona, Spain
C. Lázaro, K.-U. Bletzinger, E. Oñate (eds.)

Topology Optimization in architectural spaces: From logical to rational design domains

Samir AL-AZRI *, Ingrid PAOLETTI [a], Justine NOULIN [b]

* Politecnico Di Milano
Via Ponzio, 31, Milano - Italy
samir.alazri@polimi.it

[a] ingrid.paoletti@polimi.it

[b] Mines'Alès
6 Avenue de Clavières, 30100 Alès - France
Justine.noulin@mines-ales.org

Abstract

The research conducted on the applications of Topology Optimization (TO) in the architectural field is limited. This paper proposes an alternative process and investigates the significance of assigning the right design and non-design domain in the TO process and its effects on the optimization results. The existing approach relies on defining the design domains in areas that are usually allocated for structural elements. This research challenges the norm of where structure is allocated to evaluate the results against the criteria of minimizing material. The study investigates the idea of interpreting the design domains in a more rational perspective, using an anthropometric approach to create efficient spaces with minimum material use. The methodology involves modelling a spatial structure that evaluate scenarios with different design domains, using the SIMP method. The research is part of the Material Balance Research group projects in Politecnico di Milano, where a case study is conducted on a roof canopy in an attraction park in Orlando to investigate the results on a practical project. The study illustrates the impact of assigning the right design domain on the optimization process, not only on the performative and material distribution, but in terms of meeting design criteria and creating usable spaces. It also reexamines the idea of optimization and highlights the concept of an optimized design not necessarily being the best design.

Keywords: topology optimization, metal spatial structures, Isovist

1. Introduction

The building industry is a major part of the climate change debate as cement accounts for a significant share of global CO2 emission, while steel has around 26% of its production used in buildings [1]. Regardless of material choice, architects and engineers are continuously challenged to provide solutions that minimize the amount of material, cost of fabrication and operation. Material efficient design is a broadly researched area that aims to reduce the impact of climate change while meeting the demand of a rapid growth in global population.

The pursuit of minimizing the amount of material in construction precedes our present-day environmental dilemma. The processes of optimization and form finding have been explored for over a century, providing many opportunities of reassessing our approach to building design. Topology

Copyright © 2019 by Samir AL-AZRI, Ingrid PAOLETTI, Justine NOULIN
Published by the International Association for Shell and Spatial Structures (IASS) with permission.

Optimization (TO) is one of the many heavily researched processes today, producing a variety of techniques including SIMP [2] and BESOS [3].

Nevertheless, the research conducted on the applications of Topology (TO) in the architectural field is limited making its integration into the design practice slow and restricted to a handful of projects. There are two main challenges hindering the integration process; computing power and design variation. The GPU based tool by Bialkowski [4] and the diverse structural designs by Yang *et.al* [5] attempt to resolve these obstacles. However, architects would require more than fast processing and a variation of design options to choose from. The current state with TO is still regarded as a black box solution where only experienced structural engineers can predict the outcome of the design. TO would be widely more accepted if it allowed for more design control allowing the designer to comprehend the design decisions being made. It would also be more accepted if other design objectives are integrated into the design process.

This paper attempts to address this topic through a case study that examines the effects of different design domains on the outcome of a TO process. The aim is to explore a methodology of utilizing the optimization process to enhance the architectural use of spaces. Anthropomorphic criteria in the form of visual objectives (Isovist) is used as a measure for the fitness of the design.

2. Background

2.1. Topology Optimization

The goal of topology optimization is to find the best distribution of material given a set of constraints. It assumes a solid block of material for a start where material is removed (and added in some cases) to minimize or maximize an optimization objective such as mass, displacement, or compliance while satisfying a set of constraints including maximum stress or displacement.

From a mathematical point of view, optimization involves searching for the critical point of the function that describes the problem. To reach the maximal or minimal solution, it is necessary to define a mathematical function which depends on the design variables. An optimization problem could be a maximization, as in the case of structural stiffness, or minimization, as in the case of production cost. Nevertheless, there is no admissible solution which decreases one of its parameters without increasing one of the other objective functions, usually resulting in a Pareto front.

Optimization problems can be divided into two categories depending on whether the variables are continuous or discrete. Solving TO problems in a discrete sense is done by discretizing the design domain into finite elements. The material densities inside these elements are then treated as the problem variables. In this case material density of '1' indicates the presence of material, while '0' indicates an absence of material. It's a binary method which involves using finite elements and utilizing an algorithm (usually evolutionary) to converge to a solution. The other method is modelling the densities with continuous variables. The material densities can now also attain values between '1' and '0'. Gradient based algorithms that handle large amounts of continuous variables and multiple constraints are used. The material properties must be modelled in a continuous setting.

A topology optimization problem can be written in the general form of an optimization problem as:

$$\begin{aligned} \underset{x}{\text{minimize}} \quad & F = F(\mathbf{u}(\rho), \rho) = \int_{\Omega} f(\mathbf{u}(\rho), \rho) \mathrm{d}V \\ \text{subject to} \quad & G_0(\rho) = \int_{\Omega} \rho \mathrm{d}V - V_0 \leq 0 \\ & G_j(\mathbf{u}(\rho), \rho) \leq 0 \text{ with } j = 1, \ldots, m \end{aligned} \tag{1}$$

The problem statement includes an objective function $F(u(\rho), \rho)$. This function represents the quantity that is being minimized for best performance. The most common objective function is compliance, where minimizing compliance leads to maximizing the stiffness of a structure. It also includes the material distribution as a problem variable. This is described by the density of the material at each location ρ. The design space is denoted with Ω, which indicates the allowable volume within which the design can exist. Finally, constraints $G_j(u(\rho), \rho)$ as a characteristic that the solution must satisfy.

2.2. Applications in Architecture

Topology optimization is a widely applied method for creating high-performance structural and mechanical designs in automotive, naval and aeronautic industries. Within the construction industry, this technique provides an outlook for enabling substantial reductions in material consumption and structural design innovation, indicating a significant potential for lowering the environmental impact of construction. Several architects attempted adopting the generative process of TO as a concept for their projects. The most successful, and by far the largest, is the design of the Qatar National Convention Centre by Arata Isozaki who was recently awarded the Pritzker Prize 2019. He is a pioneer in using evolutionary algorithms and had several proposals in Spain and Italy that were previously not fortunate enough to be realized [6].

Arup adopted a smaller scale investigation with TO in 3D printing a steel joint entirely from maraging steel. The material reduction achieved was up to 75% in some nodes showing great potential in using TO with additive manufacturing [7]. Besides the previously discussed design challenges, the main inhibitor for larger scale implementation is the difficulty of fabricating such complex forms. Envisioning a faster and more cost-effective implementation of additive manufacturing in the future, TO has the potential to be a leading design methodology. Additive manufacturing and other robotic fabrication techniques including hotwire cutting have been the focal of TO research recently and can be seen in the works of Yuan *el. at* [8], Feringa *el. at* [9], and Søndergaard *el. at* [10].

Topology optimization has also been applied in other design elements, most notably by Zaha Code. They have researched applications of TO extensively while conducting workshops and designing installations. Collaborating with educational institutes and software developers, they have investigated the innovative application of TO, producing everything from a single chair to a shell structure [11]. Examples of topological optimization as standalone elements are numerous. The challenge remains in its incorporation into the standard design workflow and producing it at a large scale in a cost-effective manner.

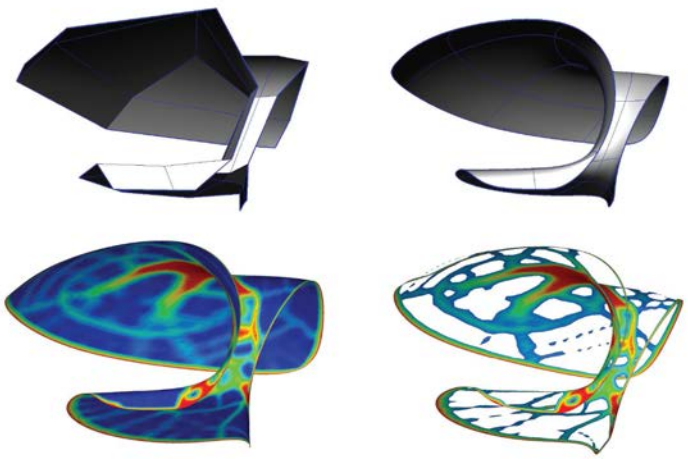


Figure 1: Volu Pavilion TO simulation - Zaha Hadid in collaboration with Altair

3. Methodology

3.1. Case Study

The case study adopted for this paper is a steel roof canopy that is part of the TRON Lightcycle Power Run attraction in Orlando. The attraction is a coaster-style ride that reaches a speed of up to 97 km/h. The canopy structure covers the entire Tron attraction without being the main supporting structure. It spans 116 meters at the longest side and has a maximum height of over 30 meters. The structural frame of the canopy is made of steel with concrete foundations. The roof is covered with ethylene tetrafluoroethylene (ETFE), that are installed with lighting for visual effects when the coaster passes by. The aim is to redesign the steel canopy using TO and identify a way of generating the structure without drastically covering the panels of ETFE and blocking the effects. This strategy is relevant in this case but could also serve the designer while considering the views from the surrounding spaces being designed with TO.

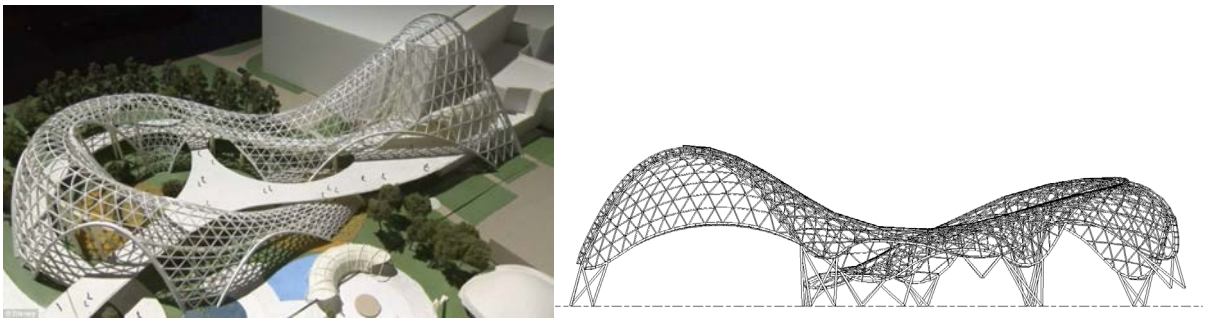


Figure 2: Tron Lightcycle Power Run model and elevation

3.2. Tools and Algorithms

The initial tests were run with Optistruct [12], a TO tool by Altair, which uses the SIMP (Solid Isotropic Material with Penalization) method. The results proved the most accurate with the tool handling large numbers of finite elements. However, many issues were highlighted pertaining to its reduced modelling capabilities and its interoperability with NURBS modelling tools. This was a critical point as the aim of the study is to handle the design domains and use other objectives as variables for further optimization.

Subsequently, the two chosen tools were TOpos [4] and Ameba [13] which are based on SIMP and BESO (Bi-directional Evolutionary Structural Optimization) respectively. TOpos is a tool developed to leverage on the speed of the GPU to reduce computation time. Ameba on the other hand, is an evolutionary based optimisation process that runs on the cloud. Upon testing both tools for applicability to this study, Topos was chosen as the preferred tool. This was mainly due to the limited finite elements which were being analysed. The Author was only able to use a maximum of 70,000 elements with Ameba, while TOpos allowed for up to 200,000. For the scale of the given project, more elements were required to render accurate results. Hence the SIMP method through TOpos was used.

3.3. Design domains

A design domain in TO is the area to be analyzed by the finite element model and where material is to be removed or added. During the initial phase of assigning boundary conditions, it is possible to assign any part of the design domain as a non-design domain. Depending on how the problem is set up, this could be an area with no material from the beginning, or an area that will always have material. This assigning of design and non-design domains affects the outcome of the optimization as suggested by Bendose [2]. It is worth noting that assigning the right domains will also affect the amount of material at the end of the optimization process. Hence it is crucial to assign the design domain only in the areas that cover the design. All loads and material properties are kept constant for all simulations, and only design domains and support conditions are variables.

The main design domain for the project was assigned by creating a bounding volume that started at the roof of the attraction. The steel frames were interpolated to produce a NURB surface that was then used to calculate the highest point of the canopy. This surface was then subdivided into 3 smaller strips which were assigned as the load areas. Leaving the entire surface area as a load domain would result in excessive material that would cover the ETFE panels. Instead the 3 strips act as the main structural elements with the assumption that a secondary structure would in place to frame the ETFE as it would be difficult to mount them on the new structure.

Three different main scenarios were proposed to vary the different domains. The first was the introduction of various openings in the domains with different sizes and locations(Figure 3). The openings were assigned to areas that exhibited high material density after the first simulation. The second scenario involved altering the number and location of supports in various configuration to draw their effects on the design process. Finally, a scenario with a combination of both openings and different support conditions were simulated to analyze their combined effect.

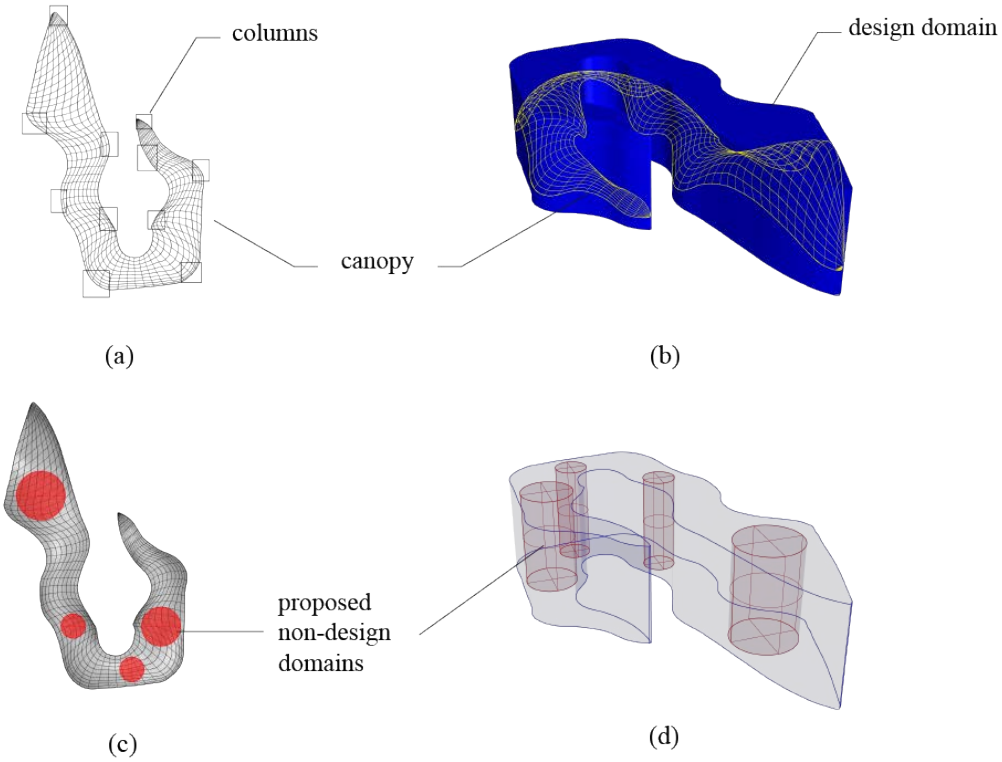


Figure 3: (a) canopy plan with columns. (b) design domain of canopy. (c) location of non-design domain. (d) perspective of non-design domains

3.4. Isovist

Setting up the optimization process to minimize the material is a logical approach that only serves the structural performance. Architectural design is a multifaceted discipline where other objectives play an important role and the user of the space should be at the center of the design intent. To rationalize the TO process, an Isovist analysis is used to investigate the performance of the designed canopy in relation to anthropomorphic visual aspects. An Isovist is a volume of space that describes the visibility from a certain position by creating vectors from that position to the furthest vantage point [14]. Surfaces are then created from the collection of vectors to create the volume. The optimized structure acts as an obstacle that creates many vantage points that block the view behind it. Hence the larger the Isovist volume the better the visibility from a given point.

Two positions were selected for the Isovist analysis which coincide with the entrances to the canopy structure (Figure 4). The viewing angles were set to 120 degrees vertical and horizontal at a viewpoint height of 1.7 meters. These positions would define the experience of the user as they enter the structure and see the lighting effect of the ETFE panels mounted on the roof canopy. Each TO scenario produced would be analyzed for the Isovist volume from these two points. This analysis would provide insight on how the TO structures performs in terms of other objectives other than structural performance.

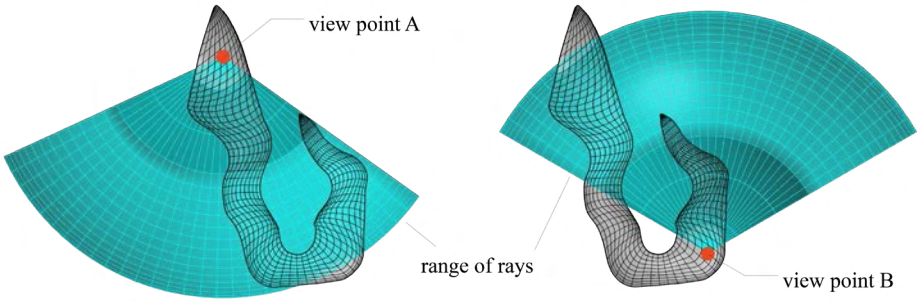


Figure 4: Location of viewpoints and range of rays to vantage point

4. Results

Several optimization processes were run for the different scenarios producing structures with relatively varying compositions, most notably with regards to the branching between the load surfaces. The most uniform result was produced from the flat roof which consisted of two load surfaces at the bottom rail of the structure. The branching was smoother which is expected since the load is transferred in a linear direction. This reinforces the fact that the load positioning is the main factor is forming the overall shape of the structure. In terms of material reduction and Isovist volume, no significant change is justified to change the roof from a shell like to a flat roof.

The number of supports and their locations were also important in shaping the overall form of the structure. It was determined that the supports are design decisions from the early phase of the design since the overall curvature of the roof can be adjusted accordingly. Allocating supports in areas where the roof was at the highest point of an arch resulted in many branch-like columns that had to extend to undesired parts of the structure. These elements were problematic when they crossed the viewpoints and resulted in poor visibility. The non-design domains should hence be expanded to cover the footpaths up to a certain height. In terms of material reduction, no significant change is worth considering.

The most substantial single contributor to the reduction of material is the addition of openings that act as non-design domain that will have no material. This is expected as the smaller the design domain the less material is available for the structure. However, it is worth noting that only the size (or overall volume) of the non-design domains reduced the material while their position did not vary the amount of material. The Isovist volume was also reduced as was expected as there is less material to block the rays from the viewpoint.

Finally, the combination of both varying support conditions and openings for non-design domain were analyzed. These were the most favorable results in terms of material reduction and Isovist volume. The observation worth noting is that the design with the most reduced material (four columns with four openings from 10 to 20-meter diameter cylinders) did not produce the smallest Isovist volume. A more rigorous investigation with more viewpoints should be conducted to confirm the hypothesis that the optimized solution of reducing material might not always be the best design when considering other variables. A multi-objective optimization process in the future would be a promising methodology for tackling such design problems.

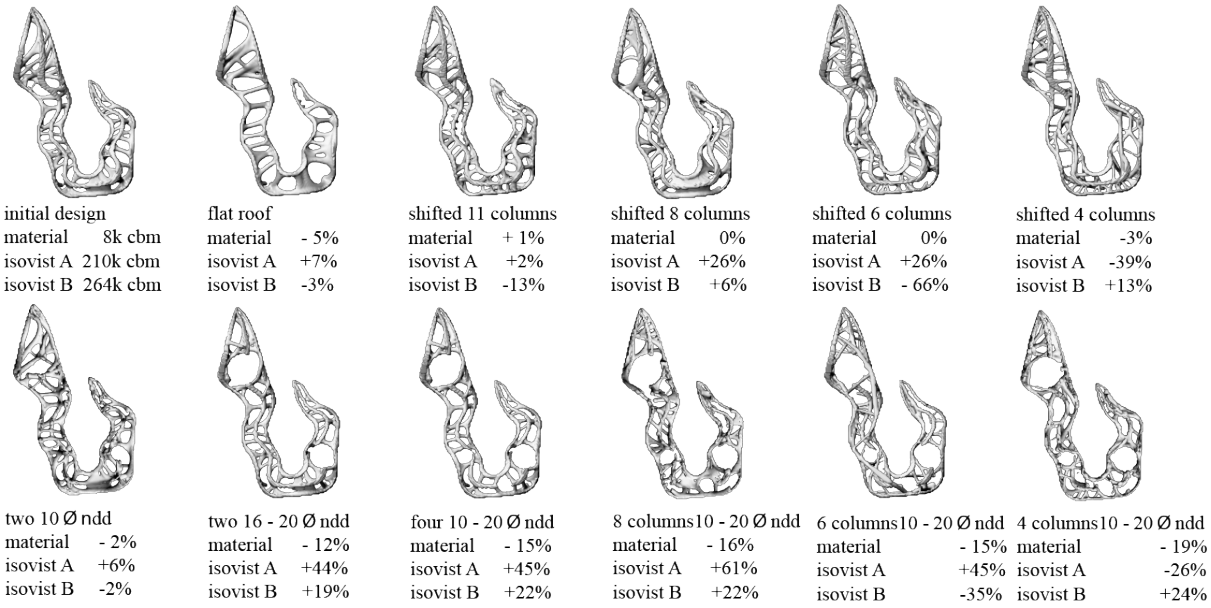


Figure 5: a sample of TO results obtained with various non-design domains (ndd) and support conditions

5. Conclusion

This paper conducted a study on the effects of various non-design domains and support conditions on the results of TO processes. Isovist was used as a variable to analyze the new structures in terms of their anthropomorphic value and suitability for the users of the space. The case study used was a roof canopy of the TRON Lightcycle Power Run attraction in Orlando. The results showed that size of the non-design domains was decisive in reducing the amount of material. However, this reduction did not always translate into a better user experience as the Isovist volume was at times higher. The decisions of assigning the design and non-design domains needs to be more rational and inclusive of other design variables the architect sees fit. The concept of optimization is only valid for the one objective and the potential of faster computing powers in the future can provide opportunities for an optimization process that is more comprehensive.

6. Further Studies

Exploring a multi-objective optimization process for topologies is promising for future studies. A more relevant study for the time being is the modelling of design and non-design domains. Difficulties were encountered in this study in assigning complex shapes as design domains. All TO tools explored only accepted ruled surfaces for the geometry input. The meshing that feeds the finite element model did not accept any other form of surfaces. For a more creative generative process, the designer should have the freedom of using complex forms. It was established that the design domains are decisive in producing the results of TO. Hence a more advanced modelling process for integration into TO tools would be beneficial for this stage and would allow architects to explore more creative solutions.

Acknowledgements

This research is conducted as part of the Material Balance Research group at the Politecnico di Milano.

References

[1] N. D. Lagaros, "The environmental and economic impact of structural optimization," *Structural and Multidisciplinary Optimization,* vol. 58, no. 4, p. 1751–1768 , 2018.

[2] M. P. S. O. Bendsoe, *Topology Optimization Theory, Methods, and Applications*, Springer, 2004.

[3] X. H. Y. M. Xie, *Evolutionary Topology Optimization of Continuum Structures: Methods and Applications,* John Wiley & Sons, Ltd, 2010.

[4] Bialkowski, S. "tOpos GPGPU Accelerated Structural Optimisation Utility for Architects." *eCAADe 35* (pp. 679 - 688). Rome: eCAADe : Faculty of Civil and Industrial Engineering, Sapienza University of Rome, 2017.

[5] Kai Yang, Z.-L. Z. "Simple and effective strategies for achieving diverse and competitive." *Extreme Mechanics Letters*, 100481. 2019

[6] Bialkowski, S. "Structural Optimisation Methods as a New Toolset for Architects." *eCAADe 35* (pp. 255 - 264). eCAADe: Oulu School of Architecture, University of Oulu, cop. 2016.

[7] Donofrio, M. "Topology Optimization and Advanced Manufacturing as a Means for the Design of Sustainable Building Components." *Procedia Engineering 145*, 638 – 645 . 2016

[8] PHILIP F. YUAN, Z. "FORM FINDING FOR 3D PRINTED PEDESTRIAN BRIDGES." *International Conference of the Association for Computer-Aided Architectural (CAADRIA) Volume 1* (pp. 225-234). Hong Kong: CAADRIA. 2018

[9] Jelle Feringa, A. S. (2012). "Design and Fabrication of Topologically Optimized". *eCAADe Digital Physicality* (pp. 485 - 490). Prague: eCAADe. 2012

[10] Asbjørn Søndergaard, O. A. "TOPOLOGY OPTIMIZATION AND DIGITAL ASSEMBLY OF ADVANCED SPACE-FRAME STRUCTURES." *ACADIA Adaptive Architecture* (pp. 367 - 378). Ontario: ACADIA. 2013

[11] Hadid, Z. *Zaha Code*. Retrieved from Zaha Hadid Education: http://www.zha-code-education.org/. June 2019

[12] Altair. *Optistruct*. Retrieved from Altair: https://www.altair.com/optistruct/. June 2019

[13] Technologies, X. *Ameba*. Retrieved from Topology Optimisation Based on BESO: https://ameba.xieym.com/. June 2019

[14] Benedikt, M. "To Take Hold of Space: Isovists and Isovist Fields." *Environment and Planning B: Planning and Design, Volume: 6 issue: 1*, 47-65. 1979

Proceedings of the IASS Annual Symposium 2019 – Structural Membranes 2019
Form and Force
7 – 10 October 2019, Barcelona, Spain
C. Lázaro, K.-U. Bletzinger, E. Oñate (eds.)

Topology Optimization of Free Formed Shells using Improved ESO

Koki OTANI*, Koichi KAMIMURA[a], Shinya MATSUMOTO[b], Daiji FUJII[b]

* Graduate School of Systems Engineering, Kindai university,
1, Takaya Umenobe, Higashi-hiroshima, Hiroshima, 739-2116, Japan
Kokiotani03@gmail.com

[a] Kinoshita Structural Engineers
[b] Faculty of Engineering, Kindai university

Abstract

D. Fujii et al. [1] proposed the topology optimization method using voxel finite element method for morphogenesis of continuum shell structures. In this method, unnecessary elements are gradually removed from the fixed design domain (rectangular parallelepiped divided by voxels) to obtain the optimal morphology. And, Improved Evolutionary Structural Optimization (IESO) method [2-4] is used for removing the elements in the optimization process. Also, the external force is uniformly applied as body force (inertial force) over the entire design domain. In the proposed method, the morphology of shell structure is obtained in which are simultaneously optimized. In the previous paper [1], we verified the effectiveness of this method with basic examples such as hemispherical shell and cylindrical shell. In this paper, we verify that this method can create various morphologies of shell structures by showing the several numerical examples.

Keywords: Topology optimization, ESO method, Computational Morphogenesis, Continuum shell structures, Voxel finite element method

1. Introduction

In recent years, concrete shells with various morphologies have been constructed due to the increase in strength, weight reduction, and diversification of reinforcement by new materials. However, since such concrete shell structure is treated as a continuum, more advanced analysis techniques such as the finite element method are required. Therefore, it is not easy to find the optimal morphology for free-form shell structures. From such a background, in the design of shell structures, introduction of shape optimization technology is in progress. However, the methods for simultaneously optimizing the shape, topology and thickness have not been developed yet.

For such problems, D. Fujii et al. [1] proposed the method in which the shape, topology and thickness of continuum shell structures are simultaneously optimized. In this method, unnecessary elements are gradually removed from the fixed design domain (rectangular parallelepiped divided by voxels) to obtain the optimal morphology. And, Improved Evolutionary Structural Optimization (IESO) method [2-4] is used for removing the elements in the optimization process. Also, the external force is uniformly applied as body force (inertial force) over the entire design domain. In IESO method, the strain energy of element is used as the sensitivity coefficient, and the number of elements to be removed in each step is determined by the threshold value used in ref.[5].

In the previous paper [1], we verified the effectiveness of this method with basic examples such as hemispherical shell and cylindrical shell. In this paper, we verify that this method can create various morphologies of shells by showing the several numerical examples.

Copyright © 2019 by Koki OTANI, Koichi KAMIMURA, Shinya MATSUMOTO, Daiji FUJII
Published by the International Association for Shell and Spatial Structures (IASS) with permission.

2. Improved Evolutionary Structural Optimization Procedure

In IESO method, the design domain is divided in the same eight-node brick elements (voxels) as shown in Figure 1, and in the optimization process, for solid element, it will be removed if the sensitivity coefficient (strain energy) is less than the threshold value X_{cr}. That is,

$$\rho_i = 0 \quad \text{if} \quad \alpha_i < X_{cr} \qquad ;i = 1,\cdots,N_L \tag{1}$$

where, ρ_i is the material density (1 for solid, 0 for void) of *i*-th element, α_i is the sensitivity coefficient of *i*-th element, N_L is the total number of solid elements (not void).

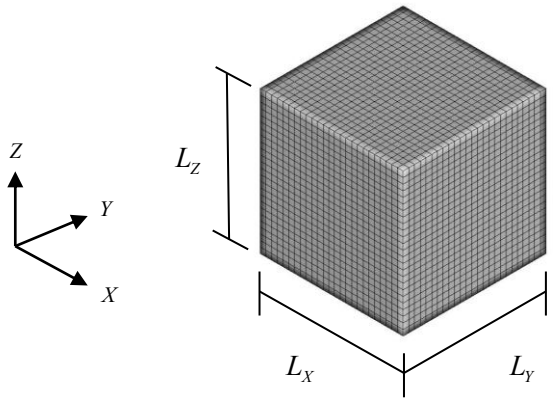


Figure 1: Design domain in analysis

In this method, the sensitivity coefficient is calculated in the same manner as BESO [6]. The threshold value X_{cr} is obtained from the equation proposed in extended ESO [5]. It is shown as follows,

$$X_{cr} = \alpha_{av} - \eta \cdot \phi \tag{2}$$

where, α_{av} is the average value of sensitivity coefficient, ϕ is the standard deviation of sensitivity coefficient, that is,

$$\alpha_{av} = \frac{1}{N_L}\sum_{i=1}^{N_L}\alpha_i \qquad \phi = \sqrt{\sum_{i=1}^{N_L}\left(\alpha_i - \alpha_{av}\right)^2 \Big/ N_L} \tag{3}$$

and η is a control parameter.

In this method, the evolutionary volume ratio (reduction ratio) is given as input data, and this control parameter η is determined automatically in the program so as to satisfy the given reduction ratio approximately [4]. If λ is the reduction ratio given as input data, the number of reduction elements in *k*-th step of the optimization process is given by follow equation.

$$N_R^{(k)} = \begin{cases} \lambda N_L^{(k-1)} & \text{if} \quad \left(1-\lambda\right)N_L^{(k-1)} \geq \bar{N}_L \\ N_L^{(k-1)} - \bar{N}_L & \text{if} \quad \left(1-\lambda\right)N_L^{(k-1)} < \bar{N}_L \end{cases} \tag{4}$$

Where, $N_R^{(k)}$ is the number of reduction elements in *k*-th step, $N_L^{(k-1)}$ is the number of solid elements in $(k-1)$ th step, $\bar{N}_L$ is the lower limit number of elements (viz. the number of elements of target volume). In IESO, $\boldsymbol{\eta}^{(k)}$ (the control parameter in *k*-th step) is determined in the program to bring the actual number of reduction elements ($\tilde{N}_R$) close to $N_R^{(k)}$.

In this program, it is necessary to input the size of design domain (L_X, L_Y, L_Z), the number of divisions (n_X, n_Y, n_Z), Young's modulus, Poisson's ratio, boundary conditions, loading conditions (see Fig.1). Also, as the optimization parameters, it is necessary to input the influence radius $r_{\min}$ defined by [6], $\bar{N}_L$ in Eq.(4) and the reduction ratio λ in Eq.(4). Where, in this program, b_r is used instead of $r_{\min}$ (where, $r_{\min} = b_r \cdot l_X$ and $l_X = L_X / n_X$), and $\bar{V}_r$ is used instead of $\bar{N}_L$ (where, $\bar{V}_r = \bar{N}_L / (n_X \cdot n_Y \cdot n_Z)$).

In the analysis of shell structures, the external force is uniformly applied as body force (inertial force) over the entire design domain. In this case, the shape and size of all voxels are equal, and therefore, the body force of each element is replaced by the following nodal forces.

$$\begin{aligned} f_{Xj}^{(i)} &= (1/8) \cdot \rho_i \cdot \gamma \cdot (l_X \cdot l_Y \cdot l_Z) \cdot g_X \\ f_{Yj}^{(i)} &= (1/8) \cdot \rho_i \cdot \gamma \cdot (l_X \cdot l_Y \cdot l_Z) \cdot g_Y \qquad (j = 1, \cdots, 8) \\ f_{Zj}^{(i)} &= (1/8) \cdot \rho_i \cdot \gamma \cdot (l_X \cdot l_Y \cdot l_Z) \cdot g_Z \end{aligned} \tag{5}$$

Where, γ is the unit volume weight, $(l_X \cdot l_Y \cdot l_Z)$ is the volume of the voxel ($l_Y = L_Y / n_Y$, $l_Z = L_Z / n_Z$), and g_X, g_Y, g_Z are the acceleration of X, Y, Z direction.

In the following numerical examples, the nodal forces in Eq.(5) apply to all voxels in the design domain. In addition, in the analysis applying the body force, ρ_i is set to 0.001 if $\rho_i = 0$ in Eq.(1), because the isolated elements (voxels with $\rho_i = 1$) often appear in the optimization process.

3. Numerical examples

3.1. Example 1

As an analysis model, the fixed design domain of 50 × 50 × 25 voxel division shown in Figure 2 is used. Analysis parameters are Poisson's ratio v= 0.3, Young's modulus E = 21000 (N / mm^2).

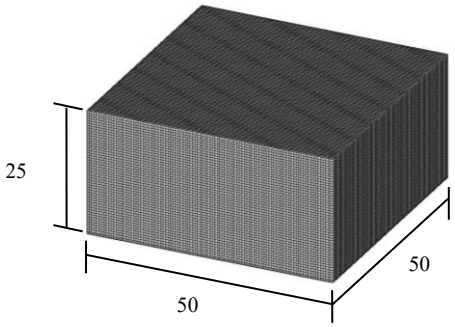
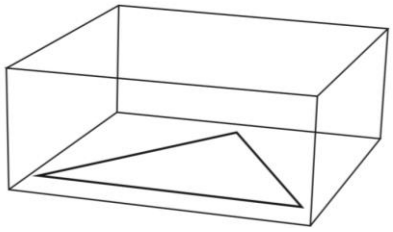


Figure 2: Fixed design domain for Example 1

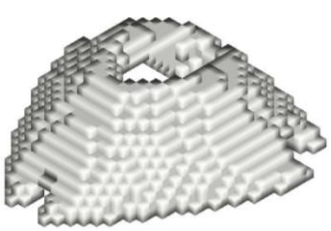
Figures 3 to 6 show the results of topology optimization by the proposed method when the support condition of the shell structure is a triangle, a square, a pentagon, and a hexagon. Where, the optimization parameters $(\bar{V}_r, \lambda, b_r)$ are shown in each figure. In these figures, (a1) to (a4) show the fixed design domain with boundary condition, (b1) to (b4) show a view from diagonally above, (c1) to (c4) show a view from above, (d1) to (d4) show a view from below. In the analysis of Fig. 4 and 6, the symmetry of the x and y axes is taken into account, and in the analysis of Fig. 3 and 5, the symmetry of the y axes is taken into account.

From these figures, it can be seen that shell morphologies, in which shape, topology and thickness are simultaneously optimized, can be obtained for any boundary shape. Also, it can be seen that all

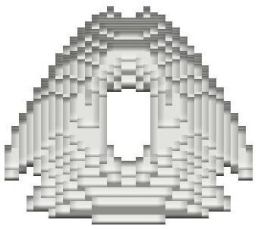
morphologies have a hole at the top. Such results can be used effectively at the stage of deciding the design concept.



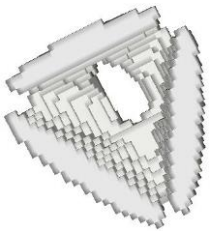
(a1): Fixed design domain with triangle boundary condition



(b1):External view

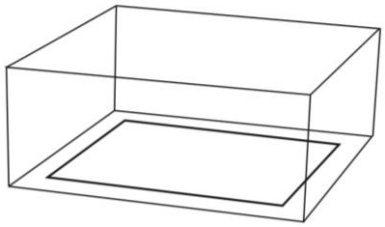


(c1):Top view

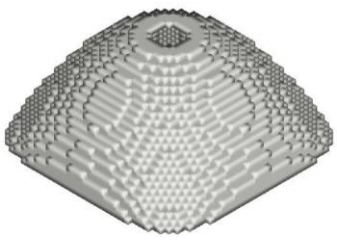


(d1):Bottom view

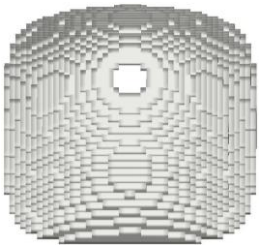
Figure 3: Analysis result （$\bar{V}_r = 0.05,\quad \lambda$=0.05,$\quad b_r = 1$）



(a2): Fixed design domain with square boundary condition



(b2):External view

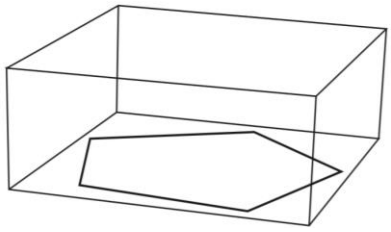


(c2):Top view

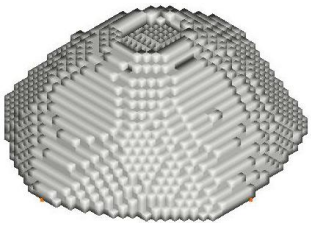


(d2):Bottom view

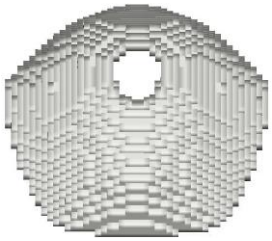
Figure 4: Analysis result （$\bar{V}_r = 0.15,\quad \lambda$=0.05,$\quad b_r = 1$）



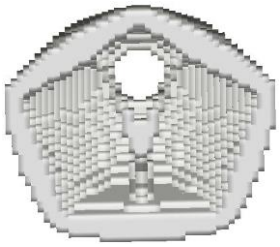
(a3): Fixed design domain with pentagon boundary condition



(b3):External view

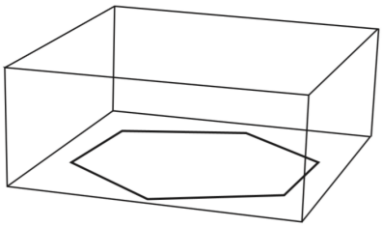


(c3):Top view

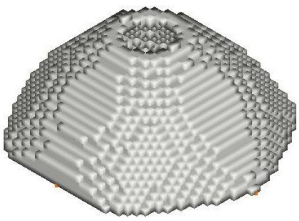


(d3):Bottom view

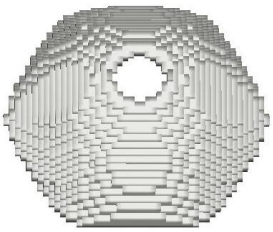
Figure 5: Analysis result（$\bar{V}_r = 0.15,\quad \lambda$=0.05,$\quad b_r = 1$）



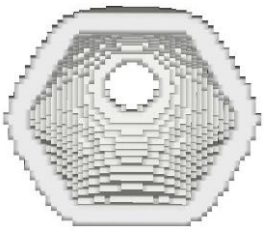
(a4): Fixed design domain with hexagon boundary condition



(b4):External view



(c4):Top view

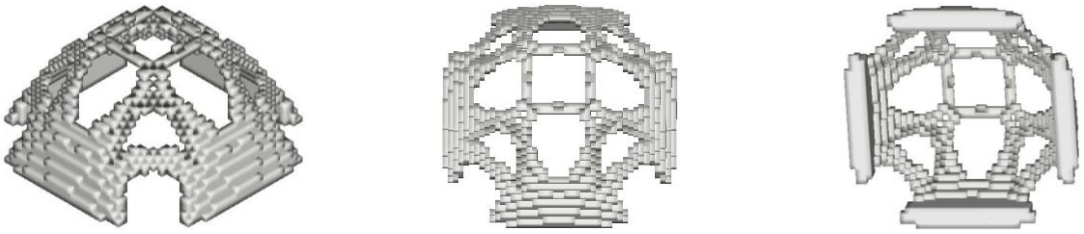


(d4):Bottom view

Figure 6: Analysis result（$\bar{V}_r = 0.10,\quad \lambda$=0.10,$\quad b_r = 1$）

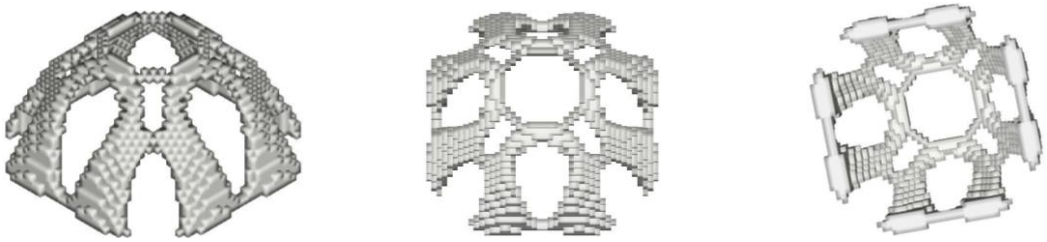
Fig.7, 8 and Fig.9, 10 show the analysis results when the value of $\bar{V}_r$ is lower than the analysis in Fig.4 and Fig.6. Also, in Fig. 7,9 and Fig. 8,10, the value of λ is changed.

From these figures, it can be seen that various morphologies of shell can be obtained by varying the parameters of the optimization.



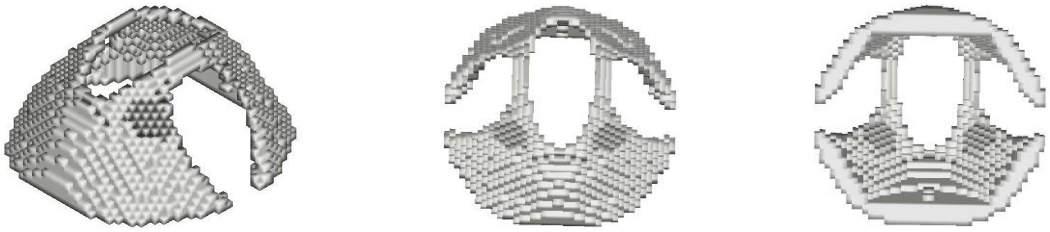
(b5):External view (c5):Top view (d5):Bottom view

Figure 7: Analysis result in the case of square boundary （$\bar{V}_r = 0.05$, λ=0.05, $b_r = 1$）



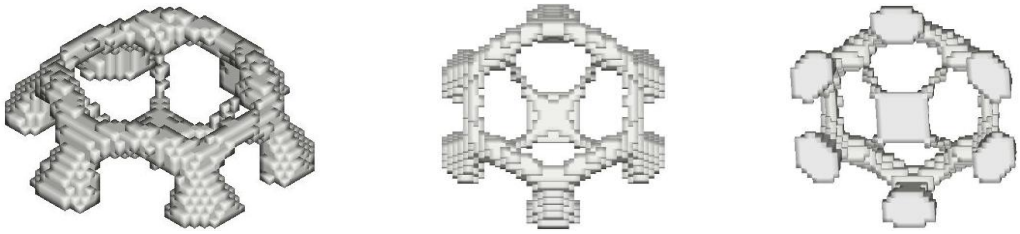
(b6):External view (c6):Top view (d6):Bottom view

Figure 8: Analysis result in the case of square boundary （$\bar{V}_r = 0.05$, λ=0.10, $b_r = 1$）



(b7):External view (c7):Top view (d7):Bottom view

Figure 9: Analysis result in the case of hexagon boundary （$\bar{V}_r = 0.15$, λ=0.05, $b_r = 1$）



(b8):External view (c8):Top view (d8):Bottom view

Figure 10: Analysis result in the case of hexagon boundary （$\bar{V}_r = 0.05$, λ=0.01, $b_r = 5$）

3.2. Example 2

Next, an application example is shown. This example that we designed as an idea competition. We proposed a break space. We set up one entrance and made plans to catch the people. In addition, we set up a top light on the extension line of the entrance and planned the light to be felt even from the outside. Fig.11 shows the morphogenesis process by the proposed method. Fig.12 is the plan. Fig.13 is the west side elevation. Fig.14 is the cross section. Fig.15 is the image perspective. From these figures, it can be seen that a purposeful shell morphology can be created according to the boundary condition and spatial condition using the proposed method.

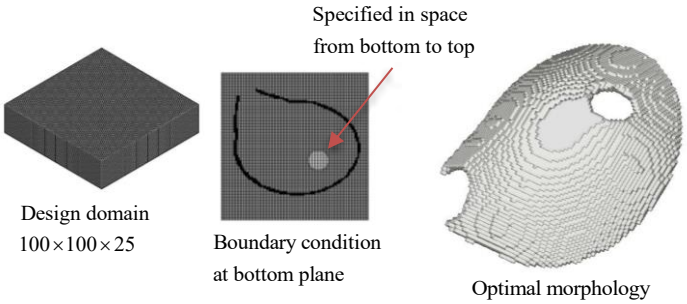


Figure 11: Morphogenesis process by the proposed method

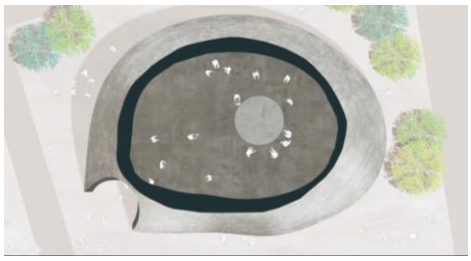


Figure 12: Plan



Figure 13: West side elevation



Figure 14: Cross section



Figure15: Image perspective

4. Conclusion

In this paper, we verified that the proposed method (IESO method) can create various morphologies of shells by showing the several numerical examples. As the results, the following knowledges were obtained.

(1) It was shown that various shell morphologies in which shape, topology and thickness are simultaneously optimized can be obtained for any boundary shape.

(2) It was shown that various shell morphologies can be created by controlling the target volume ratio and removal rate.

(3) It was shown that the proposed method can be used effectively by the work of the design competition.

From the above, it can be verified that the proposed method can be used effectively at the stage of deciding the design concept of shell structure such as a concrete shell.

References

[1] Koichi Kamimura, Shinya Matsumoto and Daiji Fujii : "Computational morphogenesis of continuum shell structures using Improved ESO method", Proceedings of the IASS Annual Symposium 2017, Monday, September 25 - Thursday, September 28, 2017, Hamburg

[2] Yohei Niiuchi, Shinya Matsumoto, Daiji Fujii : Topology optimization of 3D structures using Improved ESO method, J. Struct. Constr. Eng., AIJ (in Japanese), Vol.81, No.723, 851-858, May, 2016.5.

[3] Yohei Niiuchi, Shinya Matsumoto, Daiji Fujii : Topology optimization of 3D structure using improved ESO method, Proceedings of the IASS Annual Symposium 2016, Tokyo .

[4] Yohei Niiuchi, Shinya Matsumoto, Daiji Fujii : Computational morphogenesis of building structures using IESO method - Natural shape of buildings which resist vertical and seismic load, J. Struct. Constr. Eng., AIJ (in Japanese), Vol.82, No.731, 97-103, Jan., 2017.

[5] Hiroshi Ohmori and Chang Yu CHI : Structural form creation by Extended ESO method - Application to adaptive structures and shells -, J. Struct. Constr. Eng., AIJ (in Japanese), No.552, 109-116, Feb., 2002.

[6] X. Huang, Y. M. Xie : Convergent and mesh-independent solutions for the bi-directional evolutionary structural optimization method, Finite Elements in Analysis and Design 43 (2007) 1039-1049.

[7] Mutsuro Sasaki : Flux Structure, Toto Publishers, Jan., 2005.

[8] Ruben Ansola, Javier Canales, Jose A. Tarrago, John Rasmussen : A integrated approach for shape and topology optimization of shell structures, Computers and Structures 80 (2002) 449-458

[9] Pilseong Kang, Sung-Kie Youn : Isogeometric topology optimization of shell structures using trimmed NURBS surfaces, Finite Elements in Analysis and Design 120 (2016) 18-40k.

[10] H. Ohmori, T. Kimura and A. Maene : Computational Morphogenesis of Free Form Shells, Proceedings of the IASS Symposium 2009 Valencia, CD-ROM, Abstracts pp.158-159, 2009.

[11] Y. M. Xie, G. P. Steven : Evolutionary Structural Optimization, Springer, 1997Crisfield M.A., Non-linear Finite Element Analysis of Solids and Structures. Volume 2: Advanced Topic*s*. (2nd ed.), Wiley, 1997.

[12] C. Cui, H. Ohmori and M. Sasaki : Computational morphogenesis by extended ESO method – Extension for three-dimensional structures -, J. Struct. Constr. Eng., AIJ (in Japanese), No.576, 79-86, Feb., 2004.

[13] Daiji Fujii, Ryo Okabe, Masatoshi Manabe : Topology optimization of 3D structures using CA-ESO Method and voxel finite element method, J. Struct. Constr. Eng., AIJ (in Japanese), Vol.79, No.703, 1279-1286, Sep., 2014.

Proceedings of the IASS Annual Symposium 2019—Structural Membranes 2019
Form and Force
7–10 October 2019, Barcelona, Spain
C. Lázaro, K.-U. Bletzinger, E. Oñate (eds.)

Unified treatment of some different fabrication-cost functions in truss topology optimization

Yoshihiro KANNO [*], **Makoto OHSAKI** [a], **James K. GUEST** [b]

[*] Mathematics and Informatics Center, The University of Tokyo
Hongo 7-3-1, Tokyo 113-8656, Japan
E-mail: kanno@mist.i.u-tokyo.ac.jp

[a] Department of Architecture and Architectural Engineering, Kyoto University
[b] Department of Civil Engineering, Johns Hopkins University

Abstract

This paper presents a unified formulation of the fabrication costs, or the cost of nodes (connections), in truss topology optimization. This formulation is readily incorporated into an existing mixed-integer programming approach to compliance optimization with self-weight load. We perform preliminary numerical experiments to show how the optimal topology depends on different cost functions.

Keywords: Truss topology optimization, fabrication cost, mixed-integer programming, global optimization.

1 Introduction

The fabrication costs of structures can be significantly influenced by design decisions made during early stages of the design process. Therefore, it is of great importance to incorporate the fabrication cost into structural optimization. For truss topology optimization based on the ground structure approach, recent work has proposed including the fabrication cost into the problem formulation by assuming that this cost is proportional either to the number of members (bars) or to the number of nodes (connections) [1, 9, 10].

The number of existing members and the number of existing nodes are not differentiable with respect to the design variables (the member cross-sectional areas). This is the major difficulty in incorporating such a cost function into truss topology optimization, because nonsmoothness of the cost function forbids direct application of a gradient-based optimization method. As a remedy, Asadpoure *et al.* [1] proposed to make use of a regularized Heaviside function. Similarly, Torii *et al.* [10] used a negative power function. Kanno and Fujita [7] proposed an approach based on the alternating direction method of multipliers (ADMM). More heuristic manners for taking the truss design complexity into account can be found in, e.g., He and Gilbert [4] and the references therein.

In this paper, we introduce the ℓ_p-norm constraint on a vector consisting of the degrees of nodes to deal with some different fabrication-cost functions in a unified manner. Here, the degree of a node is defined

Copyright © 2019 by Yoshihiro Kanno, Makoto Ohsaki, and James K. Guest
Published by the International Association for Shell and Spatial Structures (IASS) with permission.

as the number of members connected to the node. The presented formulation includes the cost functions proportional to the number of members [1] and the number of nodes [7, 9, 10] as two particular cases. Another interesting case is that the cost of a node is assumed to increase dramatically as the degree of a node increases. Although such a cost function seems to be realistic, to the best of the authors' knowledge it cannot be found in literature on truss topology optimization.

We incorporate the presented formulation in a straightforward manner into a *mixed-integer second-order cone programming* (MISOCP) approach to truss topology optimization considering the self-weight load [8]. We present numerical examples to illustrate how the difference in the fabrication-cost function affects optimal truss designs.

2 Degree of node and topology of truss

Following the conventional ground structure approach, consider an initial truss having m candidate members, n nodes, and d degrees of freedom of the nodal displacements. Let $x_1, \ldots, x_m$ denote the member cross-sectional areas, which are the design variables to be optimized. The conventional compliance minimization problem is written as

$$\begin{aligned} &\text{minimize} && \pi(\boldsymbol{x}) && \text{(1a)}\\ &\text{subject to} && \boldsymbol{l}^\top \boldsymbol{x} \le \bar{V}, && \text{(1b)} \end{aligned}$$

where $\pi(\boldsymbol{x})$ is the compliance of the truss, l_i $(i = 1, \ldots, m)$ is the undeformed member length, and $\bar{V}$ is the specified upper bound for the structural volume. To avoid presence of extremely thin and thick members, we consider the constraints

$$x_e \in \{0\} \cup [x_{\min}, x_{\max}], \quad e = 1, \ldots, m, \tag{2}$$

where $x_{\min}$ and $x_{\max}$ are the specified lower and upper bounds, respectively, of member cross-sectional areas.

As for an external load, consider the sum of a fixed load and member self-weight loads. A ground structure includes, in general, some overlapping members, but we prohibit the presence of overlapping members in a final truss design. It is known that the compliance minimization problem with this setting can be recast as an MISOCP problem [8]. This MISOCP formulation uses binary design variables t_e $(e = 1, \ldots, m)$ satisfying

$$\begin{aligned} t_e = 0 \quad &\Leftrightarrow \quad x_e = 0, && \text{(3a)}\\ t_e = 1 \quad &\Leftrightarrow \quad x_e \in [x_{\min}, x_{\max}]. && \text{(3b)} \end{aligned}$$

Namely, vector $\boldsymbol{t}$ represents the truss topology.

Let δ_v denote the degree of node v $(v = 1, \ldots, n)$. To describe the relation between $\boldsymbol{\delta}$ and $\boldsymbol{t}$, it is convenient to use the incidence matrix of an undirected graph. Consider a corresponding relation between the structural elements and the graph elements, where a member and a node of the ground structure are regarded as an edge and a vertex of an undirected graph, respectively. The incidence matrix $B = (B_{ve}) \in \mathbb{R}^{n \times m}$ of this graph is defined by [3]

$$B_{ve} = \begin{cases} 1 & \text{if node } v \text{ is connected to member } e, \\ 0 & \text{otherwise.} \end{cases} \tag{4}$$

Then we readily see that the relation

$$\boldsymbol{\delta} = B\boldsymbol{t} \tag{5}$$

holds.

3 Cost of nodes

Let $\phi : \mathbb{Z}_{\geq 0} \to \mathbb{R}$ denote the cost function of a node. It is natural to assume that $\phi(0) = 0$ and $\phi(\delta_v) > 0$ ($\delta_v = 1, 2, \dots$). Moreover, for any $\delta_v = 1, 2, \dots$, we assume that ϕ satisfies one of the following four properties:

(i) $\phi(\delta_v + 1) - \phi(\delta_v) = 0$.

(ii) $\phi(\delta_v + 1) - \phi(\delta_v) = \phi(\delta_v) - \phi(\delta_v - 1)$.

(iii) $\phi(\delta_v + 1) - \phi(\delta_v) > \phi(\delta_v) - \phi(\delta_v - 1)$.

(iv) $(\phi(\delta_v + 1) - \phi(\delta_v))/(\phi(\delta_v) - \phi(\delta_v - 1)) \to \infty$.

As illustrated in Figure 1a, property (i) means that the cost is irrelevant to the degree of a node. This cost model has been often used in literature [7, 9, 10]. Figure 1b depicts property (ii). This model can be found in Asadpoure *et al.* [1]. The cost is assumed to be proportional to the degree, i.e., $\phi(\delta_v) = a\delta_v$ with a positive constant a. In several practical situations, it is more realistic to assume that the cost of a node dramatically increases as its degree increases. Property (iii) covers such situations, as illustrated in Figure 1c. For example, $\phi(\delta_v) = a\delta_v^r$ with $r > 1$ satisfies property (iii). Property (iv) corresponds to the extreme case of property (iii), and highly prohibits use of a node with a large degree: It concerns only the nodes with the largest degree in a truss design.

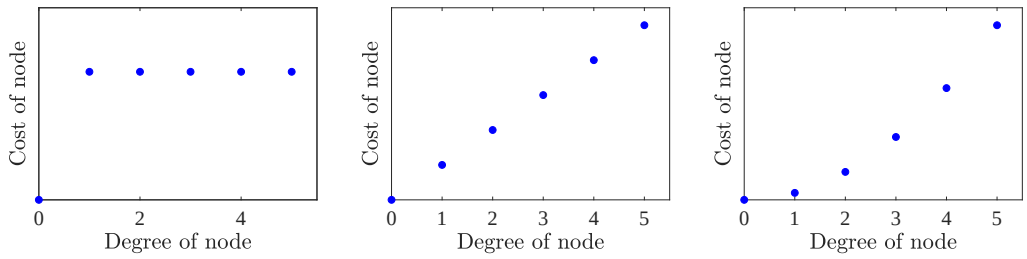


Figure 1: Cost functions of a node.

Assume that the costs of a support node and a free node are same if they have the same degree. The total cost of nodes in each case is evaluated as follows.

(i) The total cost of nodes is proportional to the number of nodes used in a truss design, i.e., the number of nonzero entries of $\boldsymbol{\delta}$, denoted $\|\boldsymbol{\delta}\|_0$. Although $\|\boldsymbol{\delta}\|_0$ is *not* a proper norm, it is often called the ℓ_0-norm of $\boldsymbol{\delta}$.

(ii) The total cost of nodes is proportional to the ℓ_1-norm of $\boldsymbol{\delta}$, i.e., $\|\boldsymbol{\delta}\|_1 = |\delta_1| + \cdots + |\delta_n|$. It is worth noting that (5) and the definition of B imply $\|\boldsymbol{\delta}\|_1 = 2\|\boldsymbol{t}\|_1$, and hence the total cost is proportional also to the number of members.

(iii) Assume that $\phi(\delta_v) = a\delta_v^2$, where $a > 0$ is a constant. Then the total cost is proportional to the square of the ℓ_2-norm of $\boldsymbol{\delta}$, i.e., $\|\boldsymbol{\delta}\|_2^2 = \delta_1^2 + \cdots + \delta_n^2$.

(iv) The total cost of nodes is a monotone function of the ℓ_∞-norm of $\boldsymbol{\delta}$, i.e., $\|\boldsymbol{\delta}\|_\infty = \max\{|\delta_1|, \ldots, |\delta_n|\}$.

4 Mixed-integer programming formulation

From the observation made in section 3, we can see that the upper bound constraint on the cost of nodes is written as

$$\|\boldsymbol{\delta}\|_p \leq \bar{c} \tag{6}$$

with $p = 0$, 1, 2, or ∞ and constant $\bar{c} > 0$. Our preliminary numerical experiments suggest that handling constraint (6) directly within the framework of *mixed-integer programming* (MIP) is not efficient. Specifically, when $\bar{c}$ is small, a MIP solver spends huge computational time even for small-scale problem instances. This is because, for a small value of $\bar{c}$, the optimization problem has only few feasible solutions, and hence a solver has to explore a vast number of branch-and-bound nodes before finding the first feasible solution.

As a remedy, we use the ℓ_1-exact penalty function

$$\rho \max\{\|\boldsymbol{\delta}\|_p - \bar{c}, 0\} = \min_y \{\rho y \mid y \geq \|\boldsymbol{\delta}\|_p - \bar{c},\ y \geq 0\} \tag{7}$$

with a sufficiently large penalty parameter $\rho > 0$, instead of using constraint (6). In the formulation with this penalty function, the number of feasible solutions does not depend on $\bar{c}$. Therefore, it is likely that this formulation is more suited for application of a MIP solver. In practice, we add constraint

$$\|\boldsymbol{\delta}\|_p \leq y + \bar{c}, \tag{8}$$

$$y \geq 0 \tag{9}$$

to the MISOCP formulation in Kanno and Yamada [8], and add ρy to the objective function. The resulting problem is still an MISOCP problem, because we can treat constraint (8) within the framework of MISOCP as follows.

(i) $p = 0$: Analogous to Kanno and Fujita [7, section 3.2] and Kanno [6].

(ii) $p = 1$: (8) is reduced to a linear inequality constraint $\displaystyle\sum_{v=1}^{n} \delta_v \leq y + \bar{c}$.

(iii) $p = 2$: (8) is a second-order cone constraint.

(iv) $p = \infty$: (8) is reduced to linear inequality constraints $\delta_v \leq y + \bar{c}$ $(v = 1, \ldots, n)$.

Remark 1. It is known that, for any rational number $p \in (1, \infty)$, a constraint in the form (8) can be represented as some second-order cone constraints [2, section 3.3.1]. Therefore, any cost function in the form $\phi(\delta_v) = a\delta_v^p$ with rational $p \in (1, \infty)$ can be handled within the framework of MISOCP. ■

5 Numerical examples

The numerical examples presented in this section were computed on a 2.2 GHz Intel Core i7 processor with 8 GB RAM. We solved MISOCP problems with CPLEX ver. 12.8.0 [5]. We set parameters of CPLEX as follows. The `MIQCP strategy` parameter was two (linear programming relaxations were solved), the integrality tolerance and the relative MIP gap tolerance were 0, and the `MIP emphasis` was `BESTBOUND` (a branch-and-bound strategy emphasizing to improving the best bound value was adopted). The penalty parameter was $\rho = 10^3$. The Young's modulus and the mass density were 200 GPa and 7800 kg/m^3, respectively.

Consider the problem instance outlined in Figure 2, which shows a ground structure and fixed external load. The nodes are aligned on a 1 m $\times$ 1 m grid. This ground structure has $n = 15$ nodes and $m = 105$ members (i.e., every pair of two nodes is connected by a single member). We apply a downward vertical force of 50 kN at the bottom rightmost node, and set $x_{\max} = 2500\,\mathrm{mm}^2$ and $x_{\min} = 200\,\mathrm{mm}^2$. The upper bound for the structural volume is $\bar{V} = 1.6 \times 10^7\,\mathrm{mm}^3$.

Figure 3 shows the obtained solution for the problem without considering the cost of nodes, where the width of each member is proportional to its cross-sectional area. For the problems with the constraint on the cost of nodes, the solutions obtained by CPLEX for $p = 0$, 1, 2, and ∞ are collected in Figures 4, 5, 6,

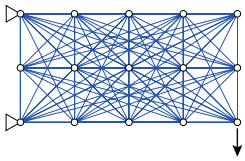


Figure 2: Problem setting of numerical examples.

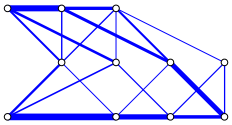
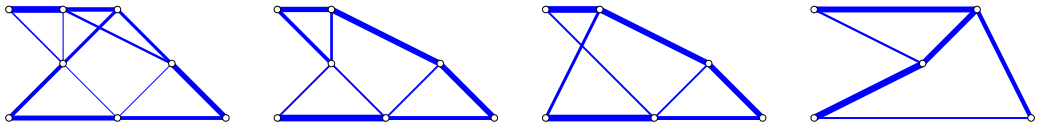
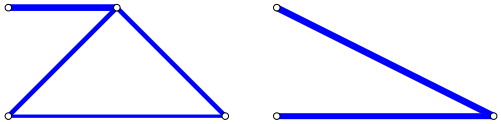


Figure 3: The obtained solution without considering the cost of nodes. $\|\boldsymbol{\delta}\|_0 = 11$, $\|\boldsymbol{\delta}\|_1 = 42$, $\|\boldsymbol{\delta}\|_2 = \sqrt{166}$ and $\|\boldsymbol{\delta}\|_\infty = 5$.

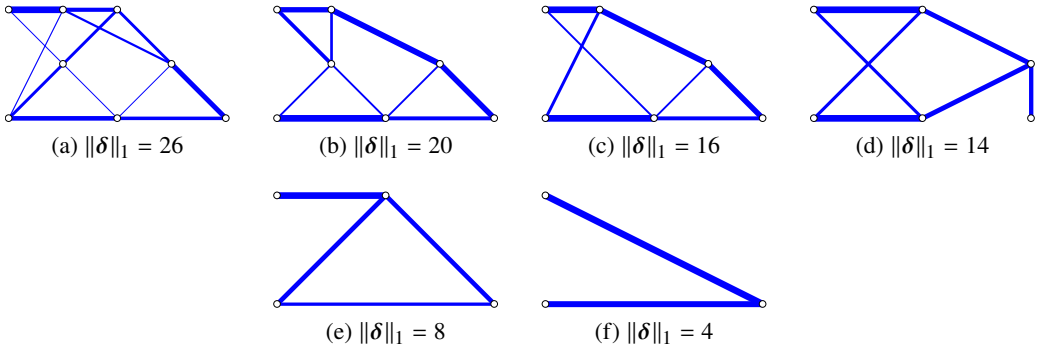


(a) $\|\boldsymbol{\delta}\|_0 = 8$ (b) $\|\boldsymbol{\delta}\|_0 = 7$ (c) $\|\boldsymbol{\delta}\|_0 = 6$ (d) $\|\boldsymbol{\delta}\|_0 = 5$



(e) $\|\boldsymbol{\delta}\|_0 = 4$ (f) $\|\boldsymbol{\delta}\|_0 = 3$

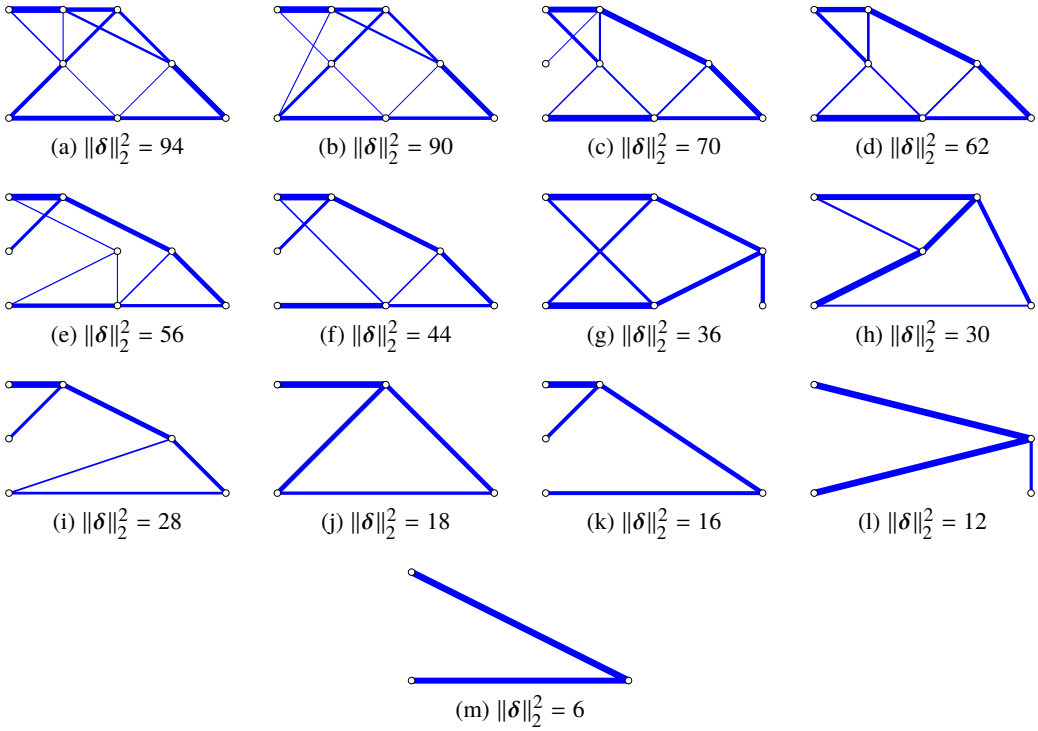
Figure 4: The obtained solutions with $p = 0$.



(a) $\|\boldsymbol{\delta}\|_1 = 26$ (b) $\|\boldsymbol{\delta}\|_1 = 20$ (c) $\|\boldsymbol{\delta}\|_1 = 16$ (d) $\|\boldsymbol{\delta}\|_1 = 14$

(e) $\|\boldsymbol{\delta}\|_1 = 8$ (f) $\|\boldsymbol{\delta}\|_1 = 4$

Figure 5: The obtained solutions with $p = 1$.



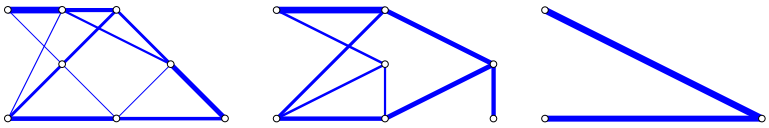
(a) $\|\boldsymbol{\delta}\|_2^2 = 94$ (b) $\|\boldsymbol{\delta}\|_2^2 = 90$ (c) $\|\boldsymbol{\delta}\|_2^2 = 70$ (d) $\|\boldsymbol{\delta}\|_2^2 = 62$

(e) $\|\boldsymbol{\delta}\|_2^2 = 56$ (f) $\|\boldsymbol{\delta}\|_2^2 = 44$ (g) $\|\boldsymbol{\delta}\|_2^2 = 36$ (h) $\|\boldsymbol{\delta}\|_2^2 = 30$

(i) $\|\boldsymbol{\delta}\|_2^2 = 28$ (j) $\|\boldsymbol{\delta}\|_2^2 = 18$ (k) $\|\boldsymbol{\delta}\|_2^2 = 16$ (l) $\|\boldsymbol{\delta}\|_2^2 = 12$

(m) $\|\boldsymbol{\delta}\|_2^2 = 6$

Figure 6: The obtained solutions with $p = 2$.



(a) $\|\boldsymbol{\delta}\|_\infty = 4$ (b) $\|\boldsymbol{\delta}\|_\infty = 3$ (c) $\|\boldsymbol{\delta}\|_\infty = 2$

Figure 7: The obtained solutions with $p = \infty$.

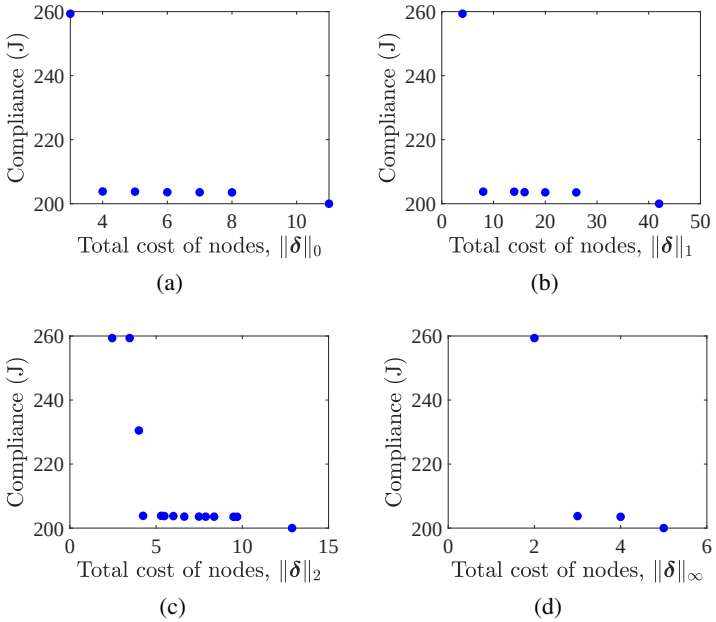


Figure 8: Variation of the compliance with respect to the cost of nodes.

and 7, respectively.[*1] We found these solutions with varying the value of $\bar{c}$. Figure 8 shows the variation of the compliance with respect to the cost of nodes. Here, the smallest compliance value corresponds to the solution shown in Figure 2, i.e., the solution without considering the cost of nodes. We can observe in Figure 8 that the cost of nodes can often be reduced at the expense of only small increase of the compliance. In contrast, the solutions shown in Figure 6k, Figure 6l, and Figure 6m have relatively large values of the compliance, as observed in Figure 8c.

Difference in the results for different cost functions is observed, for example, as follows. The solutions in Figure 4a and Figure 5a have the same number of nodes. Since the ℓ_0-norm does not take the nodal degrees into account, the Figure 4a has one node with degree five. This node is replaced with a node with degree four in Figure 5a. Thus, the sum of the degrees of nodes is reduced by adopting the ℓ_1-norm. Next, consider the solutions in Figure 5c and Figure 6f, both of which have $\|\boldsymbol{\delta}\|_1 = 16$. We see that one node with degree two in Figure 5c is divided into two nodes with degree one in Figure 6f. Thus, use of the ℓ_2-norm decreases the number of nodes with relatively large degrees, although this may possibly yield increase in the number of nodes. A similar observation can be made for the solutions in Figure 5b and Figure 6e. With the ℓ_∞-norm, the number of nodes is not taken into account. Accordingly, the solutions in Figure 7a and Figure 7b have relatively large numbers of nodes.

6 Conclusions

In this paper, we have shown that several cost functions of nodes in truss topology optimization can be expressed as a unified form of a norm constraint on the vector of the degrees of nodes. We have shown that this constraint can be incorporated into a global optimization approach based on MISOCP. In the

[*1] In Figure 5d, the bottom rightmost node is counted so that it has one degree. However, this node does not connect members. In the present formulation, no distinction between such a free node with degree one and a pin-support with degree one (e.g., the left nodes in Figure 5f) is made.

numerical examples, we have observed how the difference in the nodal cost function affects optimal truss designs.

Acknowledgments This research is partly supported by SPIRITS program of Kyoto University.

References

[1] A. Asadpoure, J. K. Guest and L. Valdevit, "Incorporating fabrication cost into topology optimization of discrete structures and lattices," *Structural and Multidisciplinary Optimization*, vol. 51, pp. 385–396, 2015.

[2] A. Ben-Tal and A. Nemirovski, *Lectures on Modern Convex Optimization: Analysis, Algorithms, and Engineering Applications*. SIAM: Philadelphia, 2001.

[3] R. Diestel, *Graph Theory (3rd ed.)*. Springer-Verlag: Heidelberg, 2005.

[4] L. He and M. Gilbert, "Rationalization of trusses generated via layout optimization," *Structural and Multidisciplinary Optimization*, vol. 52, pp. 677–694, 2015.

[5] IBM Knowledge Center, *IBM ILOG CPLEX Optimization Studio Documentation*. `http://www.ibm.com/support/knowledgecenter/` (Accessed January 2019).

[6] Y. Kanno, "Mixed-integer second-order cone programming for truss topology optimization with self-weight load and limitation on number of nodes," *IEEE International Conference on Industrial Engineering and Engineering Management (IEEE IEEM2017)*, pp. 1009–1012, Singapore, December 10–13, 2017.

[7] Y. Kanno and S. Fujita, "Alternating direction method of multipliers for truss topology optimization with limited number of nodes: a cardinality-constrained second-order cone programming approach," *Optimization and Engineering*, vol. 19, pp. 327–358, 2018.

[8] Y. Kanno and H. Yamada, "A note on truss topology optimization under self-weight load: mixed-integer second-order cone programming approach," *Structural and Multidisciplinary Optimization*, vol. 56, pp. 221–226, 2017.

[9] M. Ohsaki, "Genetic algorithm for topology optimization of trusses," *Computers and Structures*, vol. 57, pp. 219–225, 1995.

[10] A. J. Torii, R. H. Lopez and L. F. F. Miguel, "Design complexity control in truss optimization," *Structural and Multidisciplinary Optimization*, vol. 54, pp. 289–299, 2016.

Proceedings of the IASS Annual Symposium 2019 – Structural Membranes 2019
Form and Force
7 – 10 October 2019, Barcelona, Spain
C. Lázaro, K.-U. Bletzinger, E. Oñate (eds.)

Continuum form and force diagrams in NURBS-based shell form-finding

Masaaki MIKI *, Toby MITCHELL, William BAKER

*Skidmore, Owing and Merrill
SKIDMORE, OWINGS & MERRILL LLP
224 SOUTH MICHIGAN AVENUE
CHICAGO, IL 60604
masaaki.miki@som.com

Abstract

This paper introduces force diagrams represented by a set of NURBS surfaces. A NURBS-based computational form-finding method that utilizes Airy stress functions for continuum shell form-finding was presented at SIGGRAPH 2015 [1]. The Airy stress function also has been explored for form-finding and analysis of discrete 2D trusses, with the discrete version shown to be a subset of the continuum stress function [2]. In 2D graphic statics, the connection between form and force diagrams and the Airy function is well-understood [3,4]. However, continuum form-finding methods, though it includes the Airy function, currently lacks force diagrams. As multiple methods that manipulate force, or reciprocal, diagrams have already proven successful in the discrete case [5], force diagrams in the NURBS-based methods have a large potential to establish a user-friendly interactive interface to manipulate continuum shell form while maintaining equilibrium. This paper explains what continuum force diagrams are, and by picking up the famous Xochimilco restaurant of Felix Candela, an isogeometric form-finding analysis using NURBS force diagrams is explained.

Keywords: NURBS, isogeometric analysis, form-finding, Graphic Statics, form diagram, Candela

1. Introduction

In 2015, an Airy stress function-based shell form-finding that utilizes NURBS surfaces and curves as finite elements has been presented at SIGGRAPH 2015 [1]. This method represents an Airy stress function as a piecewise smooth continuous surface. For a smooth area, the second derivatives of the surface are used as the components of stress tensors, whereas a "jump" of the first derivatives are used as an axial force on an edge where two smooth surfaces intersect.

The method employs a second-order conic optimization method to obtain a desired stress function suitable for shell form-finding. Also, the authors pointed out that it is hard to manipulate parameters directly, and the authors attempted to indirectly manipulate the parameters by changing the lower and upper bounds set to the parameters. Therefore, although the method itself was interesting, it is a bit hard to argue the proposed method is easy to use for everyone.

In the method, the stress tensor computation part can be easily replaced by another method such as a method using a force diagram, and the rest of the process remains the same. Such a continuous force diagram maybe represented by a set of NURBS surfaces.

On the other hand, in Graphic Statics, a pair of two line-networks, a force and form diagram, is constructed. Some authors have pointed out [3, 6] that once a force and form diagram are constructed, one can construct a polyhedron whose projection is the form diagram while the lines in the force diagram

Copyright © 2019 by Masaaki MIKI, Toby MITCHELL, William BAKER
Published by the International Association for Shell and Spatial Structures (IASS) with permission.

defines the adjacencies of the cells in the polyhedron. This polyhedron is a discrete version of Airy stress function found in continuum mechanics theory.

The Airy stress functions define stress fields. Hence, an interactive control of stress fields during a shell form-finding process by manipulating an Airy stress function seems a promising idea. However, because the stress tensor is the second derivatives of the stress function, even minor changes in Airy stress function results in a large change in the shell form. A control of stress fields via a force diagram will be less sensitive, because stress tensors are the first derivatives of the force diagrams.

Having those as its background, this paper focuses on continuous force diagrams, clarifies what it is, and introduces a NURBS based form-finding process using a continuous force diagram.

2. Normal Vectors of Airy stress functions

A good starting point to discuss a continuous force diagram is the normal vectors of Airy stress functions. An example of a pair of form and force diagram is shown in Fig. 1. Both are line-networks and a cell in a form diagram is mapped to a point in a force diagram, while a cell in a force diagram is mapped to a point in a form diagram. In addition to these, a line in a form diagram is mapped to a line in a force diagram and those two lines are always perpendicular to each other. When a pair of form and force diagrams are given, one can construct a planar-faced polyhedron whose planar projection is the form diagram and whose face normal vectors locate the points of the force diagram as shown in Fig. 2.

More specifically, if a plane of a face is expressed as

$$ax + by + c = z,$$

a point in the force diagram that corresponds to a cell in the form diagram that gives a planar projection of the face is located at (a,b). On the other hand, a "normalized" normal vector of the face is

$$N = \begin{bmatrix} a \\ b \\ -1 \end{bmatrix}.$$

Note that this normal vector is "normalized" in that its Z-component is "flattened" to -1.

Imagine you have a point on a form diagram. Even if you move the point around on the form diagram, the point (a,b) stays at where it is in the force diagram unless you drag the point out of the cell because the normal vector doesn't change. When the point crossed a border of the cell, the point (a,b) jumps to a new point as the new face in the polyhedron has a different normal vector. This jump is seen as a line connecting two points in the force diagram as shown in Fig. 3.

This view, to see a force diagram as the normal vectors of an Airy stress polyhedron, gives us a way to find out what are force diagrams in a continuous mechanics context, because both smooth and piecewise smooth stress functions have normal vectors.

Given an Airy stress function $z = f(x, y)$, the normal vectors can be computed by $N = \begin{bmatrix} \frac{\partial f}{\partial x} & \frac{\partial f}{\partial y} & -1 \end{bmatrix}^T$. In this paper, we will show that $(X, Y) = \left(\frac{\partial f}{\partial x}, \frac{\partial f}{\partial y}\right)$ is the force diagram in the continuum mechanics context in a later section.

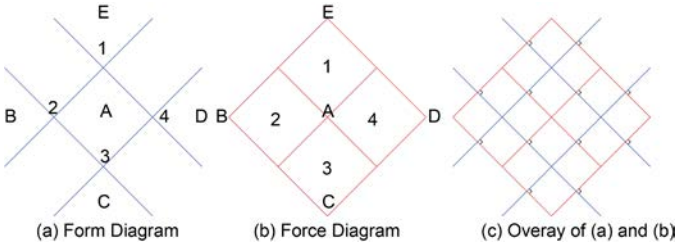


Figure 1: an example of form and force diagrams

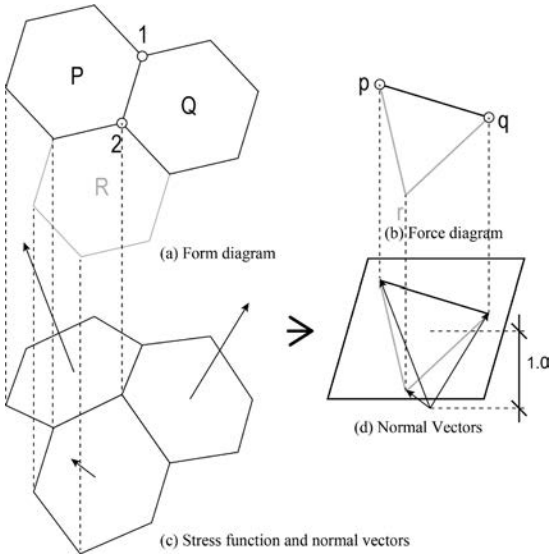


Figure 2: Stress function and face normal vectors

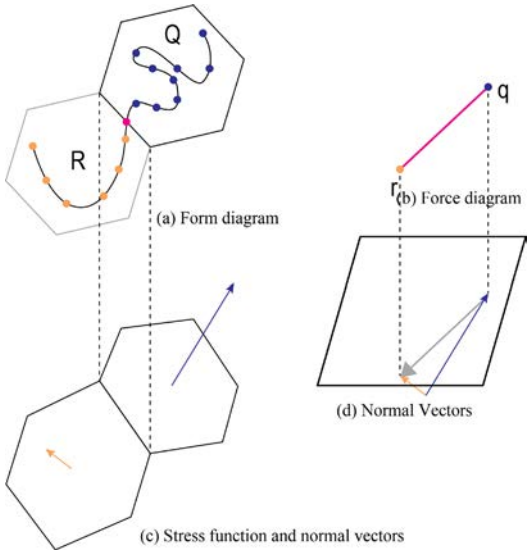


Figure 3: Mapping through normal vectors

3. Continuous Airy stress function

Given an Airy stress function, $z = f(x, y)$, a stress tensor can be computed as

$$S = \begin{bmatrix} S_{xx} & S_{xy} \\ S_{yx} & S_{yy} \end{bmatrix} = \begin{bmatrix} \dfrac{\partial^2 f}{\partial y \partial y} & -\dfrac{\partial^2 f}{\partial y \partial x} \\ -\dfrac{\partial^2 f}{\partial x \partial y} & \dfrac{\partial^2 f}{\partial x \partial x} \end{bmatrix}.$$

This type of stress tensor always satisfies the self-equilibrium equations;

$$\frac{\partial S_{xx}}{\partial x} + \frac{\partial S_{xy}}{\partial y} = \frac{\partial f}{\partial x \partial y \partial y} - \frac{\partial f}{\partial y \partial x \partial y} = 0,$$

$$\frac{\partial S_{xy}}{\partial x} + \frac{\partial S_{yy}}{\partial y} = \frac{\partial f}{\partial x \partial x \partial y} - \frac{\partial f}{\partial y \partial x \partial x} = 0.$$

These equations always give zeros because the order of partial differentiation can be swapped, i.e. $\frac{\partial^2}{\partial x \partial y} = \frac{\partial^2}{\partial y \partial x}$. Now, let us derive normal vectors of a surface defined by $z = f(x, y)$. Let us restrict normal vectors to vectors whose z-components are -1. Such a vector $(X, Y, -1)$ can be computed by

$$X = \frac{\partial f}{\partial x}, Y = \frac{\partial f}{\partial y}.$$

Fig. 4 shows how (x,y), a form diagram, is mapped to (X,Y), a force diagram, by taking a stress function introduced in [10] as an example.

Those functions X, Y have a significant property

$$\frac{\partial X}{\partial y} = \frac{\partial Y}{\partial x}.$$

This property is the only necessary property to make the self-equilibrium equations to be satisfied. In fact, if a stress tensor is computed by

$$S = \begin{bmatrix} S_{xx} & S_{xy} \\ S_{yx} & S_{yy} \end{bmatrix} = \begin{bmatrix} \dfrac{\partial Y}{\partial y} & -\dfrac{\partial X}{\partial y} \\ -\dfrac{\partial Y}{\partial x} & \dfrac{\partial X}{\partial x} \end{bmatrix},$$

the self-equilibrium equations give zeros as follows.

$$\frac{\partial S_{xx}}{\partial x} + \frac{\partial S_{xy}}{\partial y} = \frac{\partial Y}{\partial x \partial y} - \frac{\partial X}{\partial y \partial y} = 0,$$
$$\frac{\partial S_{xy}}{\partial x} + \frac{\partial S_{yy}}{\partial y} = \frac{\partial Y}{\partial x \partial x} - \frac{\partial X}{\partial y \partial x} = 0.$$

This indicates that any functions X, Y that has $\frac{\partial X}{\partial y} = \frac{\partial Y}{\partial x}$ as a property can yield a stress field satisfies the self-equilibrium equations. At this point, Airy stress functions can be eliminated from the discussion.

3. Deformation gradient

Let us start with an arbitrary pair of (X,Y) such that $\frac{\partial X}{\partial y} = \frac{\partial Y}{\partial x}$. Let us define a deformation gradient tensor

$$F = \begin{bmatrix} \dfrac{\partial X}{\partial x} & \dfrac{\partial Y}{\partial x} \\ \dfrac{\partial X}{\partial y} & \dfrac{\partial Y}{\partial y} \end{bmatrix} = \begin{bmatrix} F_{xx} & F_{yx} \\ F_{xy} & F_{yy} \end{bmatrix}.$$

The condition $\frac{\partial X}{\partial y} = \frac{\partial Y}{\partial x}$ means the deformation gradient F is symmetric, which is interpreted to be free of rotation. Let us introduce a new set of parameters θ^1, θ^2. Using those parameters, two parametric surfaces $[x(\theta^1, \theta^2), y(\theta^1, \theta^2)]^T$ and $[X(\theta^1, \theta^2), Y(\theta^1, \theta^2)]^T$ can be defined. Fig. 4 shows an example of parametric surfaces that are form and force diagrams. These two surfaces are apparently different, but base vectors are parallel (no rotation) between those two surfaces.

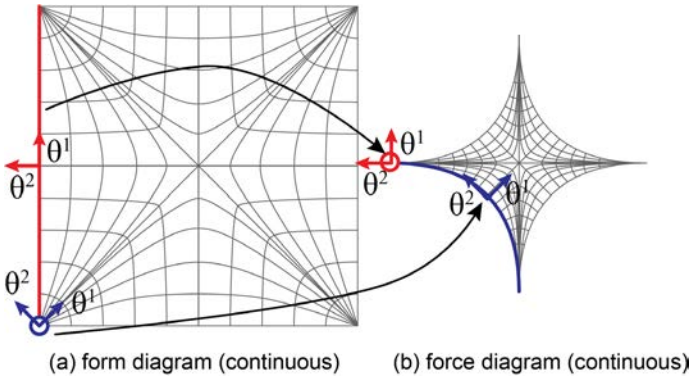


Figure 4: continuous form and force diagrams

Now, it seems fair to claim that **a pair of continuous form and force diagrams is a pair of parametric surfaces whose deformation gradient defined between them is symmetric.** The form and force diagrams are not necessarily parameterized by (θ^1, θ^2), but let us keep this setting because it helps discussion, and it is essential for visualization and computation. With (θ^1, θ^2), a deformation gradient can be computed by

$$\frac{\partial X_j}{\partial x_i} = \frac{\partial X_j}{\partial \theta^\alpha} \frac{\partial \theta^\alpha}{\partial x_i} = \boldsymbol{g}_\alpha \otimes \boldsymbol{G}^\alpha \ ,$$

where Einstein's summation convention was used, and $\boldsymbol{g}_\alpha$ is a set of base vectors of the force diagram and $\boldsymbol{G}^\alpha$ is a set of dual base vectors of a form diagram. The symbol $\otimes$ is called dyad, but to obtain $\frac{\partial x_j}{\partial x_i}$, it is interpreted to $[a \quad b]^T[c \quad d] = 2x2\ matrix$. This is a common notation of deformation gradient used in continuum mechanics and in Finite Element analysis formulations [7].

From a deformation gradient computed from form and force diagrams, a stress tensor can be computed by

$$S = \begin{bmatrix} F_{yy} & -F_{xy} \\ -F_{yx} & F_{xx} \end{bmatrix}.$$

4. Candela Shell

The biggest question is where/how a pair of continuous force and form diagrams can be found. So far, the authors do not have a clear answer. However, the authors have found one particular case that works.

Fig. 5 shows a pair of discrete force and form diagram that produces a form of shell resembles Candela's famous Xotimilco restaurant. In the figure, the area needed for computation of 1/6 of the shell form is indicated by a dashed red curve.

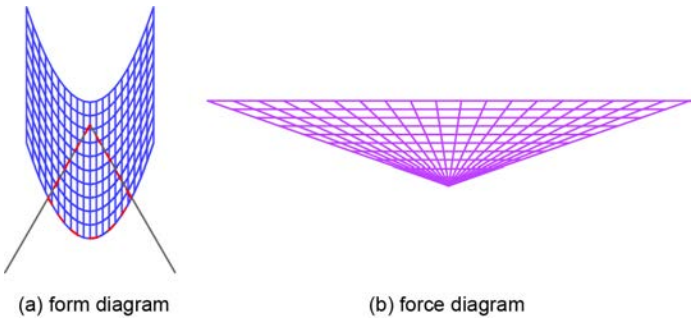


Figure 5: a pair of force and form diagram

Fig. 6 shows an Airy stress function computed based on these diagrams. For the sake of computing Candela shell, the stress function is trimmed and radially repeated six times. From this Airy stress function, by taking adjacency information from the stress function, the entire force diagram can be identified as shown in Fig. 7. From both form and force diagrams, the force densities on all the lines can be identified and a form-finding result, shown in Fig. 8, is obtained [8].

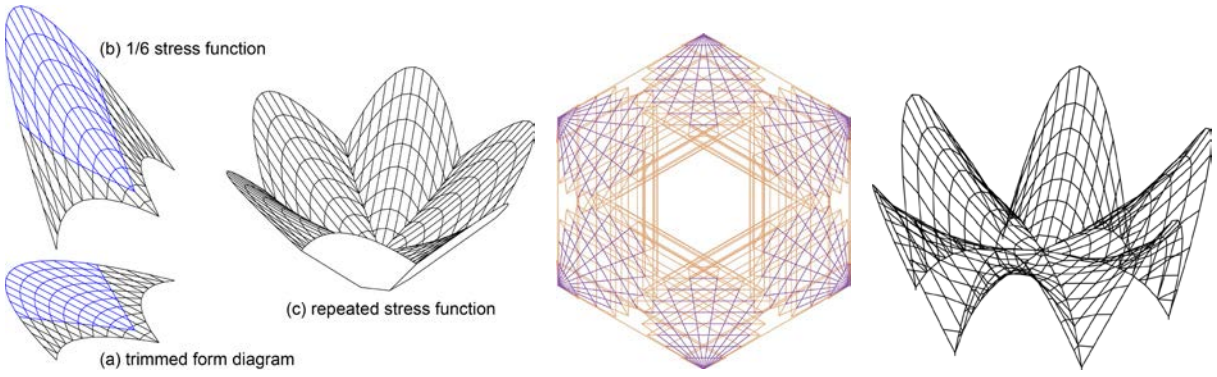


Figure 6: construction of stress function Figure 7: overall force diagram Figure 8: a Force Density method result

The basic idea is to use the points in the form and force diagrams as control points of NURBS surfaces. Fig. 9 and 10 show two NURBS surfaces that are generated by this idea. The authors used a Rhino command to perform this and the dimension of the surfaces was set to 3. As is shown in Fig. 11, dX/dy-

dY/dx is around 1.0E-15, which is regarded to be zero considering the machine precision, in most areas except two bands observed on the left and right ends. In these two bands, dX/dy-dY/dx is around 1.0E-05, hence, the area that excluded these two bands is claimed to be truly a force diagram. The area needed for the form-finding of Candela shell is also shown in the same figure, and the area does not intersect the area that is not a force diagram.

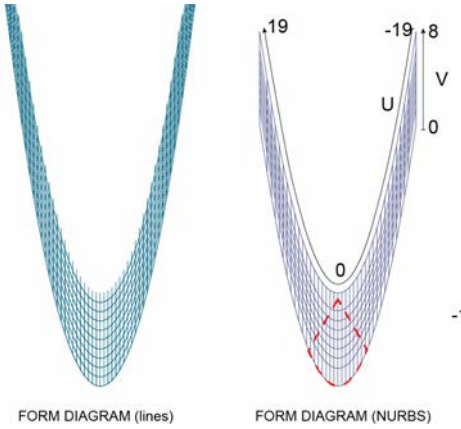


Figure 9: a NURBS surface (right) obtained by turning the point grid in a form diagram (left) to control points

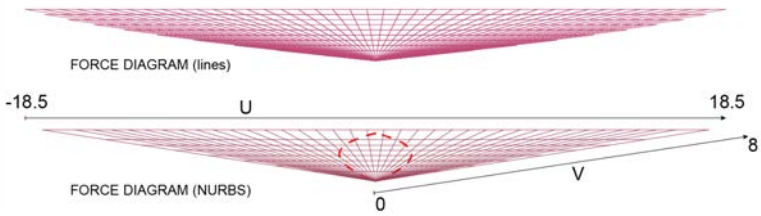


Figure 10: a NURBS surface (bottom) obtained by turning the point grid in a force diagram (top) to control points

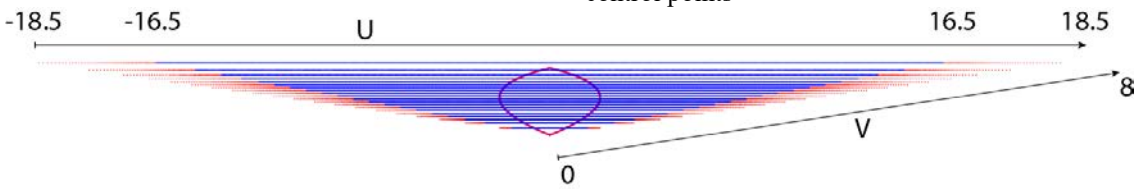
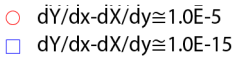


Figure 11: blue: area satisfies the form-force diagram relation, red: area does not satisfy the form-force diagram relation



In this way, a complete continuous force and form diagrams can be obtained by trimming and repeating the surfaces as shown in Fig. 12.

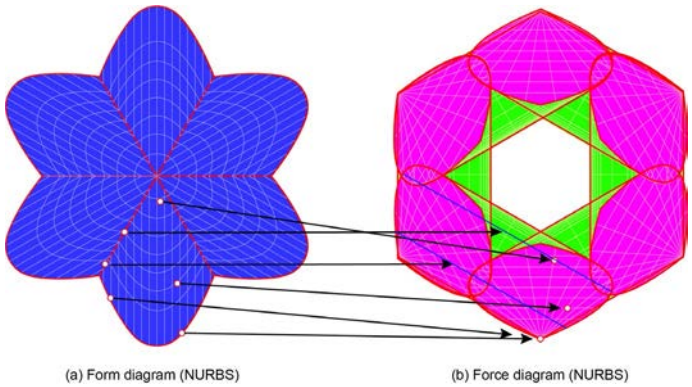


Figure 12: continuous form and force diagrams, left: 6 NURBS surfaces that represent a continuous form diagram, right: 12 NURBS surfaces that represent a continuous force diagram.

To proceed to a form-finding process, the NURBS surfaces in the form diagram need to share the control points at their intersections. However, the surfaces of the form diagram shown in Fig. 11 do not, because they are trimmed surfaces. Hence, practically, the form diagram needs to be re-parameterized into untrimmed surfaces. Fig. 13 shows a re-parameterized form diagram that gives the same geometry as the original form diagram.

The stress tensor components S^{ij} on the re-parameterized form diagram can be computed by

$$S^{ij} = \left(\boldsymbol{E}^i\right)^T S \boldsymbol{E}^j,$$

where $\boldsymbol{E}^1, \boldsymbol{E}^2$ are base vectors of the form diagram computed with the new parameters.

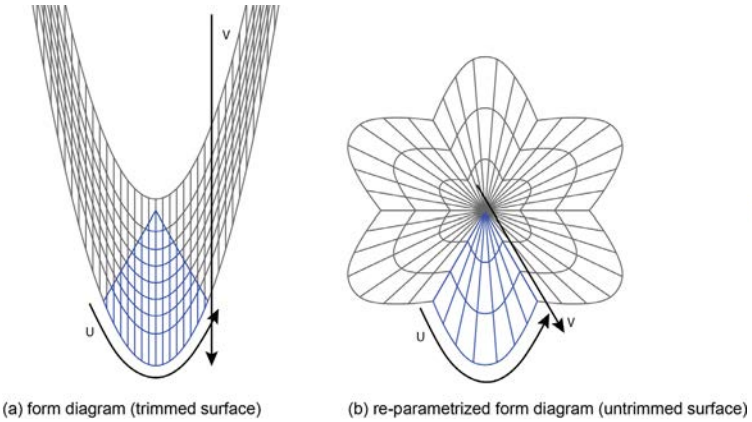


Figure 13: re-parametrization of the form diagram

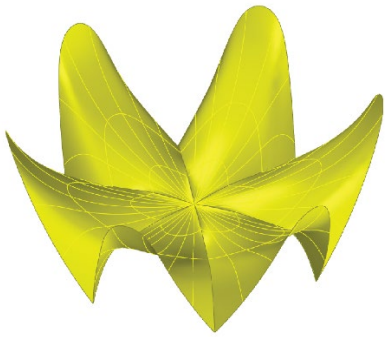


Figure 14: a form-finding result

5. Shell-form finding

A strain energy of a membrane material can be expressed as

$$E = \int S^{ij} g_{ij} \sqrt{\det \bar{g}_{\alpha\beta}}\, d\theta^1 d\theta^2$$

where S^{ij} is a 2nd PK stress tensor, g_{ij} is the first fundamental form on the deformed configuration, and $\bar{g}_{\alpha\beta}$ is the first fundamental form on the reference configuration, i.e., the form diagram. In an elastic material, in the form-finding approach discussed in this paper, this tensor is regarded as a constant value computed from a force diagram. The force diagram introduced in the previous section had jumps between NURBS surfaces that correspond to surfaces adjacent in the form diagram. The length of this jump will also be used as a stress tensor set to the curves that are intersections between adjacent surfaces in the form diagram. The strain energy of this curve is computed by

$$E = \int n^{11} g_{11} \sqrt{\det \bar{g}_{11}}\, d\theta^1.$$

If the length of this jump is L, then $\bar{n}^{11} = L/\sqrt{\det \bar{g}_{11}}$.

Summing up all the strain energies of the surfaces and curves and apply a numerical integration, the total energy is approximately computed by

$$E = \sum_{\text{I:integrating points}} \bar{w}_{\text{I}} \bar{S}^{ij} g_{ij} \sqrt{\det \bar{g}_{\alpha\beta}} + \sum_{\text{I:integrating points}} \bar{w}_{\text{I}} \bar{n}^{11} g_{11} \sqrt{\det \bar{g}_{11}},$$

where $\bar{w}_{\text{I}}$ is a weight coefficient of an integrating point. Because g_{ij} is quadratic in x, y and z coordinates of the control points, the total energy is also quadratic and thus, the system equation takes the same form as the Force Density method [8];

$$\boldsymbol{D}_c \boldsymbol{x}_c = \boldsymbol{p} - \boldsymbol{D}_f \boldsymbol{x}_f,$$

For more detail, see the Force Density method [8]. Also, note that it has already been pointed out that specifying 2nd PK stress tensors as constant values gives a membrane version of the Force Density method [9].

If the stress tensors are computed from a proper force diagram, the x and y coordinatea of the control points in the solution should be exactly same to those in the form diagram. There are small errors, but this is rooted to the numerical integration. Because x, y and z are independent in this linear system, how much ever vertical forces are applied to the system, it does not affect to the x and y coordinates. Fig. 14 was obtained by this approach.

6. Discussions and remarks

Few remarks are listed below.

1. In this paper, a special case was introduced that turning point grids to control points of NURBS surfaces give a continuous pair of force and form diagrams. However, in general, this is not expected.

2. Even if NURBS surfaces whose control points are force and form diagrams are not truly continuous force and form diagrams, they should already be very close to a perfect pair. Hence, an optimization process starting from those NURBS surface as a good initial guess should be further studied.

3. The Re-parameterization of a trimmed form diagram does not give exactly the same shape as the original trimmed surface. This issue needs to be carefully examined.

8. Conclusions

Starting from an idea that a force diagram is essentially a map of normal vectors of an Airy stress function, discrete force diagrams were generalized to continuous force diagrams. A NURBS-based form finding process using a continuous force diagram was also discussed. A particular case which simply converting point grids to NURBS surfaces work was discussed. However, this case is only a special case and methods to obtain true pair of continuous force and form diagrams need to be further discussed.

References

[1] M. Miki, T. Igarashi. and P. Block, Paramertic Self-supporting Surfaces via Direct Computation of Airy Stress Functions, ACM Transactions on Graphics (TOG), vol. 34, no. 4, 2015.

[2] A. Mazurek, J. Carrion, A. Beghini, WF. Baker, Minimum weight single span bridge obtained using graphics statics, Amsterdam: Future Visions IASS, 2015

[3] T. Mitchell, WF. Baker, A. McRobie, A. Mazurek, Mechanisms and states pf self-stress of planar trusses using graphic statics, part I: the fundamental theorem of linear algebra and the Airy stress function, International Journal of Space Structures, 2016; 31, pp 85-101

[4] C. Hartz, A. Mazurek, M. Miki, T. Zegard, T. Mitchell, WF. Baker, The applications of 2D and 3D Graphic Statics in Design, International Journal of Space Structures, 2018, vol. 59, No. 4, pp 235-242

[5] M. Rippmann , L. Lachauer . and P. Block, RhinoVAULT - Interactive Vault Design,International Journal of Space Structures,27(4): 219-230,2012

[6] E. Vouga, M. Höbinger, J. Wallner, H. Pottmann, Design of self-supporting surfaces. ACM Transactions on Graphics (TOG), vol. 34, no 4, 2012.

[7] K.-U. Bletzinger, R. Wuchner, F. Daoud, N. Camprubi, (2005). Computational methods for form finding and optimization of shells and membranes. *Computer Methods in Applied Mechanics and Engineering*, *194*(30–33), 3438–3452

[8] H. J. Schek, (1974). The force density method for form finding and computation of general networks. *Computer Methods in Applied Mechanics and Engineering*, *3*(1), 115–134.

[9] R. M. O. Pauletti, P. M. Pimenta, (2008). The natural force density method for the shape finding of taut structures. *Computer Methods in Applied Mechanics and Engineering*, *197*(49–50), 4419–4428.

Proceedings of the IASS Annual Symposium 2019 – Structural Membranes 2019
Form and Force
7 – 10 October 2019, Barcelona, Spain
C. Lázaro, K.-U. Bletzinger, E. Oñate (eds.)

Superposed functions as Airy stress functions for form-finding of funicular shell structures

Austin F. DEVIN*, Masaaki MIKI [a], Demi FANG [a], Jonathan BARANOWSKI [a], Jingwen WANG [b], William F. BAKER [a]

*, [a] Skidmore, Owings & Merrill LLP
224 S Michigan Ave, Chicago, IL 60605, USA
[b] Skidmore, Owings & Merrill LLP
14 Wall Street, NY 10005, USA
austin.devin@som.com

Abstract

The design and optimization of funicular compression-only shells can be enabled by Airy stress functions. A method to superpose elementary mathematical functions into Airy stress functions to enable improved designer feedback relating to optimization of funicular compression-only shells is presented, determining stress functions directly [1]. This paper aims to broaden the design freedom allowed by utilizing Airy stress functions, thus alleviating the major cited limitation of this approach [2]. A library of mathematical functions is established, wherein each function is assigned a variety of parameters and weights. This paper will describe a procedure to superpose mathematical functions into new Airy stress functions for broader diversity of compression-only forms created using Airy stress functions.

Keywords: Airy stress function, funicular shells, self-supporting surfaces, form-finding

1. Introduction

A shell or self-supporting surface can support its self-weight by purely compressive membrane action. A structure of this form does not exhibit bending which is advantageous for compressive only structures, such as masonry or reinforced concrete shells which result in structurally elegant and efficient forms [3]. An improperly formed shell, however, requires a combination of membrane action, bending and twisting moments and normal shear forces to maintain equilibrium [1]. Therefore, a method of form-finding to accurately create shapes that exhibit pure shell behavior is especially beneficial to both engineers and architects. Graphics statics is one historical method to manipulate both the form and force diagrams [4]–[6]. Like this, form-finding utilizing Airy stress functions provides opportunity to shape both in the form and force domains [7].

Several authors have presented computational methods for the form-finding of self-supporting surfaces, including Vouga [8], Panozzo [9], Liu [10], de Goes [11] and Tang [12]. These methods are based on Thrust Network Analysis (TNA) or discrete Airy potential polyhedral by Fraternali [13]. TNA is a practical graphical method for calculating the range of lower-bound equilibrium solutions of compression-only systems, however this method is suited primarily to 2 dimensional cases. These methods define surfaces as triangulated meshes, such meshes cannot handle continuous parametric surfaces without discretization.

The Airy stress function method as presented in previous work [7], simultaneously applies the theory to parametric surfaces directly and the discrete theory to the edges of parametric patches. Airy stress functions are simply described as that the Hodge dual of a Hessian of an arbitrary scalar valued function can be a stress field that satisfies a self-equilibrium condition [14]. This method is typically called iso-

Copyright © 2019 by A Devin, M Miki, D Fang, J Baranowski, J Wang, W Baker & Skidmore, Owings & Merrill LLP. Published by the International Association for Shell and Spatial Structures (IASS) with permission.

geometric analysis [15], [16]. Both input and output geometries are represented by NURBS, which enables a precise and smooth control of form-finding without requiring discretization. Combining discrete and continuous theories, plenty of compelling dualities are observed in this method. Such dualities uniquely transform geometric conditions to mechanics conditions is more realistic than struggling with mechanicals conditions directly.

Utilizing Airy stress functions as a form-finding tool has been demonstrated to be a very powerful tool in architectural form and space [7]. However, one limitation of this method is that it is difficult to control the form as minute manipulation of the Airy stress function can result in drastic changes to the geometric form of the structure. This paper presents a method of superposing two or more mathematical equations to create an Airy stress function. This combination of equations can then be manipulated by the user using range of variables thus, allowing an enhanced method of creating compelling vault surfaces, utilizing the previously described Airy stress functions in a curvilinear coordinate system.

2. Methodology

2.1. Implementation of Airy stress function

When boundary edges are supported, an Airy stress function can be any function with no limitation nor constraint. A simple way to approximate such a surface is by a set of triangle elements. Usually, when the domain is subdivided into triangle elements, one integrating point is placed at the center of each element. The strain tensor is constant over the triangle. The stress tensor also remains constant because it is a function of a strain tensor.

In the current work, one integrating point per triangle element is assumed. Though outside the scope of this work, more generally it should be ensured that there are a enough integrating points per element by examining the form of the function.

When a 2nd Piola-Kirchhoff stress tensor is given as $\bar{S}^{ij}$, the total strain energy of a membrane material is given by

$$E = \sum_{triangles} \int \bar{S}^{ij} g_{ij} \sqrt{det \bar{g}_{\alpha\beta}} d\theta^1 d\theta^2$$

where Einstein's summation convention is used and, $d\theta^1 d\theta^2$ are coordinate parameters given to the triangle domain, $\bar{g}_{\alpha\beta}$ is the first fundamental form of reference configuration, i.e., a planar projection of the stress function, g_{ij} is the first fundamental form of a deformed configuration.

A principle of virtual work is given by

$$\delta E = \sum_{triangles} \int \bar{S}^{ij} \delta g_{ij} \sqrt{det \bar{g}_{\alpha\beta}} d\theta^1 d\theta^2 = \sum_{triangles} \int \bar{S}^{ij} D_{ij} \delta x \sqrt{det \bar{g}_{\alpha\beta}} d\theta^1 d\theta^2$$

This leads to the same form as the Force Density method [1], i.e.,$D_c x_c = -D_f x_f + p$ where x_c is a vector packing x, y and z coordinates of the free nodes, x_f of the supported nodes, D_c and D_f to be submatrices of the full system matrix and p is a nodal force vector that have non-zero components on the z-components only. Note that it has already been pointed out that specifying a 2nd-PK stress tensor in a membrane system gives a membrane version of the Force Density method [2].

While the condition of supported boundary edges does not limit the functions to be used, the solution exhibits instabilities when the function is anticlastic (Figure 1). Thus, considering regions of the functions that are synclastic are of interest and perhaps more useful.



Figure 1: (a) A synclastic force diagram generates a smooth solution, while (b) an anticlastic force diagram can create instabilities in the solution.

To implement this approach, a Grasshopper component was created using C#, which accepts an input of a closed polyline defining the boundary extents of the surface to be created. Following the methods described above, the Airy stress function and resultant geometry are output as geometric meshes in Rhino. An example of the components and result and geometries is shown in Figure 2.

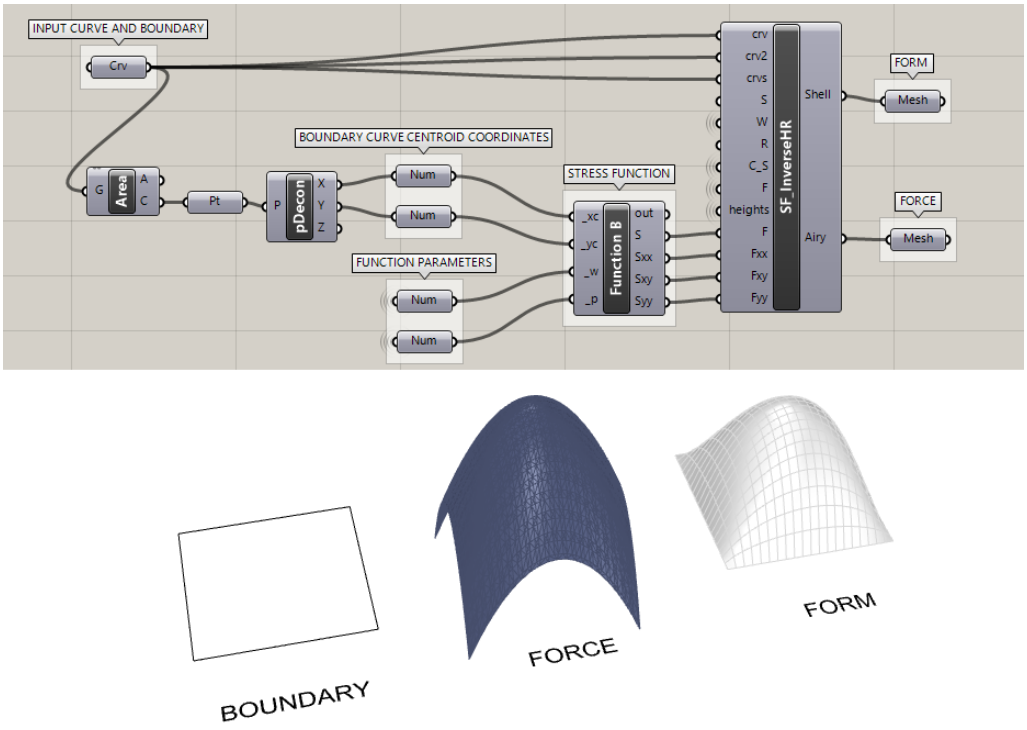


Figure 2: Grasshopper workflow for creating the Airy stress function and resultant geometry.

2.2. Library of elementary mathematical functions

A preliminary library of elementary mathematical functions was defined with the goal of superposing functions to provide a diverse set of solutions. The selected functions studied are summarized in Figure 3.

	FUNCTION	EXAMPLE z(x,y) $-5 \le x \le 5$ $-5 \le y \le 5$	SOLUTION TO EXAMPLE	Symmetry characteristics	Parameter constraints
A	See Williams [1]			Rotational symmetry	None
B1	$z_{B1}(x,y) = -(x^2 + y^2)^p$			Rotational symmetry	$0.75 \le p \le 1.5$
B2	$z_{B2}(x,y) = -(x^{2n} + y^{2n})^{\frac{u}{n}}$			Rotational symmetry	$1 \le n \le 7$ $0.9 \le u \le 1.1$
C	$z_C(x,y) = \sin\left(a\left(x - \frac{2\pi}{4a}\right)\right) + \cos\left(b\left(y - \frac{2\pi}{2b}\right)\right)$			Symmetric about x=0 and y=0	$-0.25 \le a \le 0.25$ $-0.25 \le b \le 0.25$
D1	$z_{D1}(x,y) = \frac{(x-j)(y-j)}{\left((x-m)+(y-m)\right)^2}$			Symmetric about y=x	$-50 \le j \le -8$ $2j \le m \le j$
D2	$z_{D2}(x,y) = \frac{(ax-j)(y-j)}{\left(b(x-m)+(y-m)\right)^2}$			Asymmetric	$-0.5 \le a \le 3$ $0.25 \le b \le 1$ $-50 \le j \le -8$ $2j \le m \le j$

Figure 3: Preliminary library of elementary mathematical functions. (The origin (x,y) = (0,0) is defined at the centroid of the input boundary curve).

With the exception of Function A, each function has a set of parameters associated with it. For any function $z(x, y)$, these parameters were constrained in order to limit the function to synclastic regions that would result in smooth forms or solutions. These constraints are summarized in the last column of Figure 3 and are specific to the selected domain of x and y.

2.3. Superposition of mathematical functions

In addition to the parameters in the table, each function can have a weight contribution, which is inversely related with the height of the solution. Superposition expands the diversity of stress functions to be considered as the library of functions can be mixed with varying weights to achieve a variety of different forms.

3. Discussion of results

Figure 4 illustrates the variety of forms available for each function in the library by varying the parameters associated with each function.

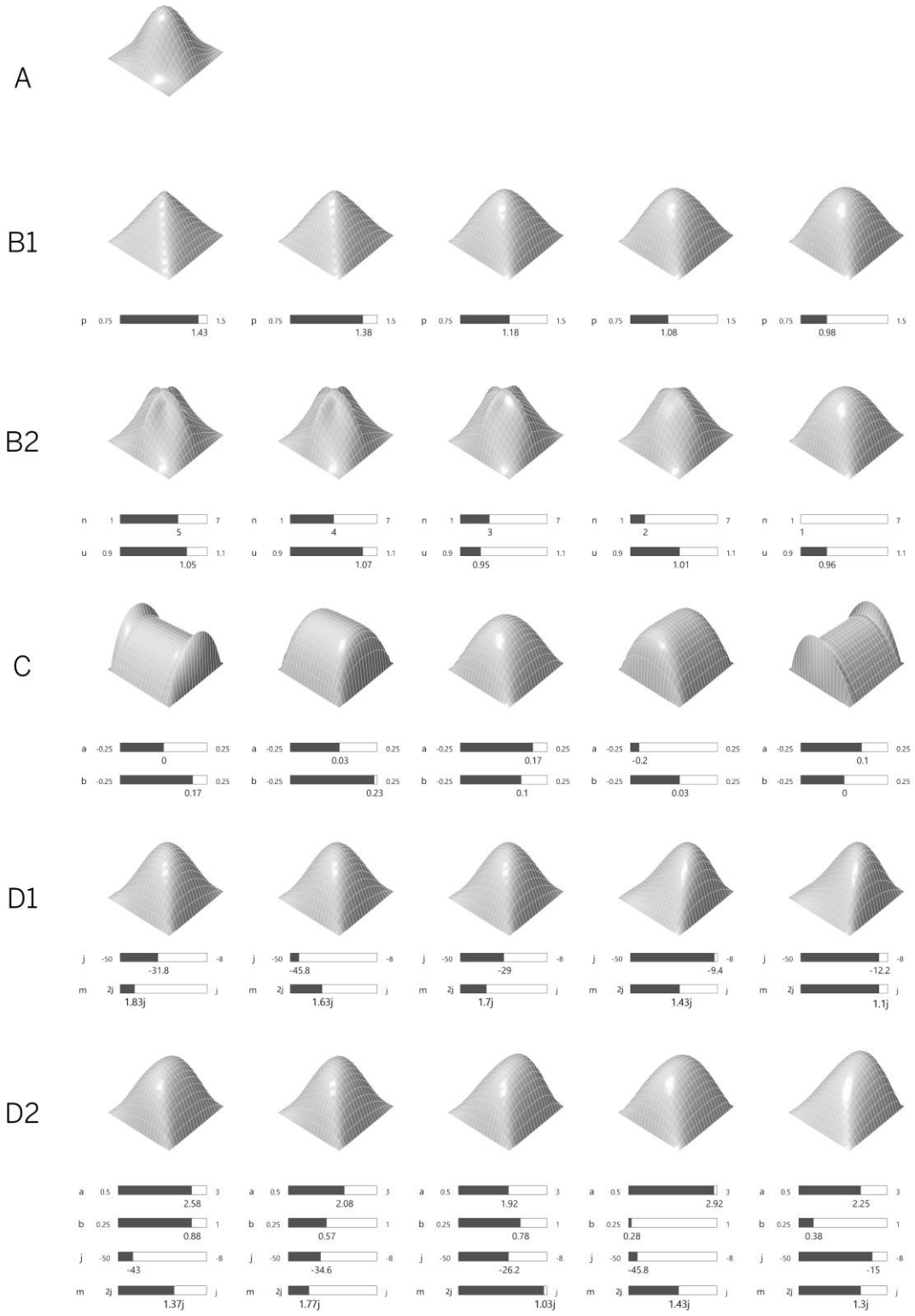


Figure 4: Summary of resultant geometry as created from the mathematical functions.

Figure 5 demonstrates how superposition of weighted functions in the library can result in diverse forms by varying the contributions of each function. For clarity, parameters associated with each function are held fixed and only the contribution of each function to the final geometry is varied.

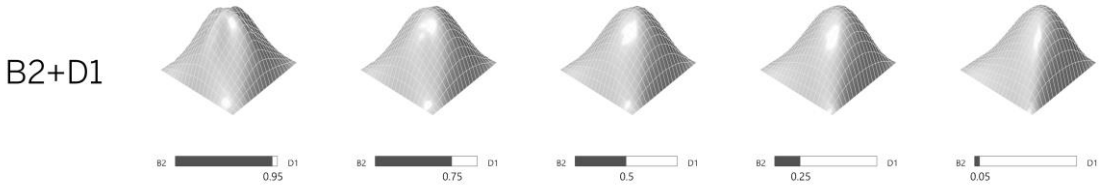


Figure 5: Example of how varying weights of each function can change the resultant geometry.

Figure 6 demonstrates how the same function can be applied to different boundary curves to achieve diverse appearances. For clarity, parameters associated with each function are held fixed.

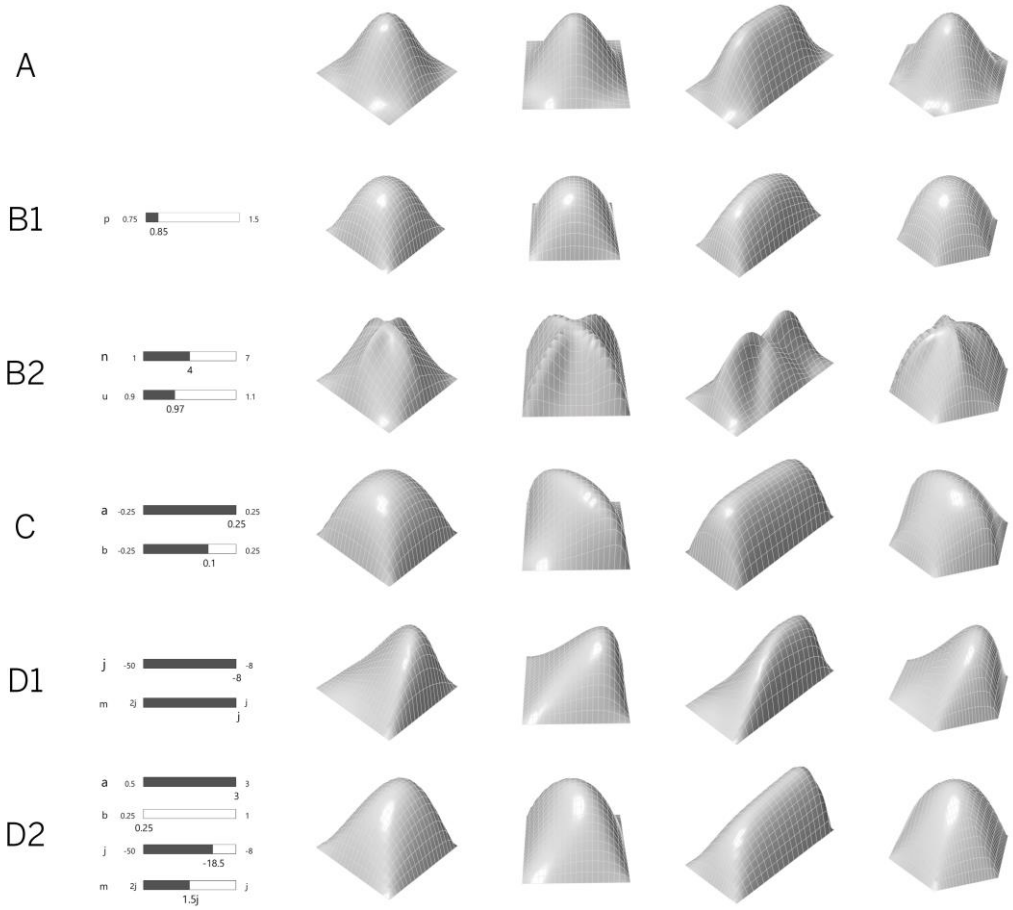


Figure 6: Examples of possible resultant geometries from different initial boundary extents.

3.1. Form-finding applications

The variety of forms available by varying 1) parameters of each function, 2) weight contributions of each function, and 3) input boundary curves were demonstrated. The diverse design space made available by varying these parameters can be harnessed for form-finding: a given target surface

supported at its boundary, a superposition of functions can be manipulated to match the target surface as closely as possible.

An initial form-finding study is constructed as follows: a target surface is established, and a collection of functions is selected for form-finding. It is important to select functions with parameter bounds that are diverse enough to have solutions that can come close to the target surface. For example, the solution to the superposed functions should achieve a similar height as the target surface or have similar symmetrical properties to the target surface.

The superposition of functions is constructed as follows:

$$z(x,y) = \frac{1}{w_{super}} \sum \frac{z_{function}(x,y)}{w_{function}}$$

where $z_{function}$ is a function in the selected library, $w_{function}$ describes the relative contribution of the function's solution, and w_{super} adjusts the overall height of the solution to the superposed function. To avoid redundancy in the design space, it is recommended that $w_{function}$ is constrained such that $\sum w_{function} = k$ where k is some constant. Note that relative contribution of functions ($w_{function}$) is here defined as the relative contribution of solution height in the final solution to the superposed function. The coefficients of each function are thus the inverses of $w_{function}$.

The mesh points of the solution to superposed functions is projected onto the target surface in the z-direction. The objective of the optimization is the sum of squares of the distances between mesh points and the target surface points. Variables for optimization include 1) the parameters of each function selected for superposition, 2) the relative contributions of each function ($w_{function}$), and 3) the overall weight of the superposed function (w_{super}).

As an example demonstration, rotationally symmetric target surfaces are first selected. Symmetric functions A, B2, and C are selected to make up the library for superposition form-finding. The superposed function is thus:

$$z(x,y) = \frac{1}{w_{super}} \left(\frac{z_A(x,y)}{w_A} + \frac{z_{B2}(x,y)}{w_{B2}} + \frac{z_C(x,y)}{w_C} \right) \; where \; w_A + w_{B2} + w_C = 1$$

The constraints on parameters for each function are summarized in the last column of Figure 3. Form-finding results for three different target surfaces are summarized in Figure 7. The single-objective optimization was executed in Grasshopper using Radical with the LN_COBYLA algorithm [17]–[19].

Among the three target surfaces, the form-found surfaces varied in relative weights of library functions A and B2, demonstrating some usefulness of the diversity enabled by superposing functions. The contribution of function C in each form-found solution is very weak (< 0.01). This may be attributed to function C being symmetric in 2 axes rather than being rotationally symmetric, leading to the optimization to favor the rotationally symmetric functions A and B2.

In all three target surfaces studied, the greatest discrepancy between the two surfaces was at the peak of the form. The selected library of functions and selected parameter constraints may not have been sufficiently diverse to capture the flat-top characteristics of the target surfaces. This topic will require further research and a broader range of functions may be required to achieve such forms.

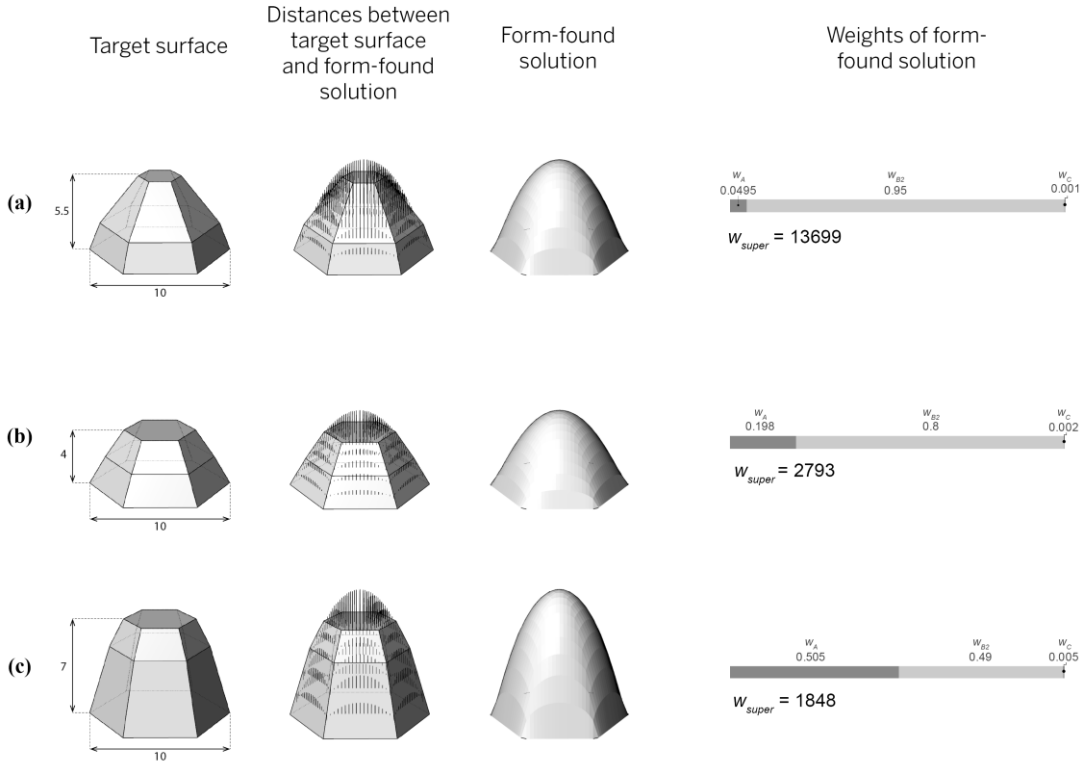


Figure 7: Examples of form-finding applications of superposition of mathematical functions as Airy stress functions.

4. Conclusions

This paper presents preliminary results from exploring a superposition approach to expanding the diversity of compression-only surfaces supported along their boundaries. The approach utilizes the superposition of elementary mathematical functions to control Airy stress functions and could potentially improve the practicality of utilizing Airy stress functions as a form-finding tool for self-supporting structures.

Initial results are promising, and further exploration of mathematical functions shall certainly provide an even broader ability to manipulate Airy stress functions to create efficient and compelling structural geometries. Currently the method presented has several advantages, but also some limitations that will require some further investigation to overcome.

This method is advantageous over previous presented methods since it provides a greater freedom to the designer, allowing one to divert from single solutions. As a result, a broader range of forms can be explored, presenting the designer with a design space rather than a limited geometry for a given boundary condition and load case.

Current limitations include finding bounds for where the function is synclastic in order to find applicable (smooth) solutions. In addition, currently this approach is limited to forms where all nodes along the boundary are supported. Controlling support points shall be further investigated in the future.

In addition to presenting the method of superposition of mathematical functions as Airy stress function, this method was applied to form-finding of a target surface. The results of this exploration were promising, and it is understood that with a broader selection of functions, a large range of surfaces could be defined utilizing this method.

References

[1] C. J. K. Williams, "The Generation of a Class of Structural Forms for Vaults and Sails," *Struct. Eng.*, vol. 68, no. 12, pp. 231–235, 1990.

[2] M. Miki, T. Igarashi, and P Block, "Parametric self-supporting surfaces via direct computation of airy stress functions," *ACM Trans. Graph.*, vol. 34, no. 4, 2015.

[3] G.-S. Athanasopoulos, M. Akbarzadeh, and A. Mcrobie, "Graphic Statics: Constrained form finding for parallel system of forces using Corsican sum," in *Proceedings of the IASS Symposium 2018 Creativity in Structural Design*, 2018.

[4] W. F. Baker, "Structural Innovation: Combining Classic Theories with New Technologies," *NASCC Proc.*, pp. 1–21, 2013.

[5] W. F. Baker, L. L. Beghini, A. Mazurek, J. Carrion, and A. Beghini, "Maxwell's reciprocal diagrams and discrete Michell frames," *Struct. Multidiscip. Optim.*, vol. 48, no. 2, pp. 267–277, 2013.

[6] L. L. Beghini, J. Carrion, A. Beghini, A. Mazurek, and W. F. Baker, "Structural optimization using graphic statics," *Struct. Multidiscip. Optim.*, vol. 49, no. 3, pp. 351–366, Mar. 2014.

[7] M. Miki, T. Igarashi, and P Block, "Parametric self-supporting surfaces via direct computation of Airy stress functions," *ACM Trans. Graph.*, vol. 34, no. 4, 2015.

[8] E. Vouga and H. Höbinger, M, J Wallner, Pottmann, "Design of self-supporting surfaces," *ACM Trans. Graph.*, vol. 31, no. 4, 2012.

[9] D. Panozzo, P. Block, O. S.-H.-A. T. On, and U. 2013, "Designing unreinforced masonry models," *ACM Trans. Graph.*, vol. 32, no. 4, 2013.

[10] T. Liu and Z. He, "The resilience performance classification of latticed shell structures and the primary research of the evaluation system," in *Proceedings of the IASS Annual Symposium 2017 - Interfaces: architecture.engineering.science*, 2017.

[11] F. De Goes, P. Alliez, H. Owhadi, and M. D. On, "On the equilibrium of simplicial masonry structures," *ACM Trans. Graph.*, vol. 32, no. 4, 2013.

[12] C. Tang, X. Sun, and J. W. Gomes, "Form-finding with polyhedral meshes made simple," in *ACM Transactions on Graphics, Association for Computing Machinery, 2013, Proceedings of SIGGRAPH 32 (4). hal-00826280*.

[13] F. Fraternali, M. Angelillo, and A. Fortunato, "A lumped stress method for plane elastic problems and the discrete-continuum approximation," *Int. J. Solids Struct.*, vol. 39, pp. 6211–6240, 2002.

[14] M. Miki, T. Igarashi, and P. Block, "Direct application of Airy stress functions to NURBS patches for computing compression shells," *Proc. Int. Assoc. Shell Spat. Struct.*, vol. 17, no. August, pp. 1–9, 2015.

[15] T. Hughes, J. Cottrell, and Y. Bazilevs, "Isogeometric analysis: CAD, finite elements, NURBS, exact geometry and mesh refinement," *Comput. Methods Appl. Mech. Eng.*, vol. 194, no. 39–41, pp. 4135–4195, 2005.

[16] M. Scott *et al.*, "Isogeometric boundary element analysis using unstructured T-splines," *Elsevier*.

[17] N. Brown and C. Mueller, "The effect of performance feedback and optimization on the conceptual design process," in *Proceedings of the IASS Annual Symposium 2016 "Spatial Structures in the 21st Century,"* 2016.

[18] N. Brown and C. Mueller, "Designing With Data: Moving Beyond The Design Space Catalog," *ACADIA*, 2017.

[19] N. Brown, J. Felipe, R. Danhaive, V. Jusiega, A. Nimrick, and C. Mueller, *Design Space Exploration*. Digitial Structures, 2019.

FORM and FORCE

Proceedings of the IASS Annual Symposium 2019 — Structural Membranes 2019
Form and Force
7—10 October 2019, Barcelona, Spain
C. Lázaro, K.-U. Bletzinger, E. Oñate (eds.)

Ultimate Force Boundary of Trusses

Caigui Jiang[*,a]

[*] King Abdullah University of Science and Technology
Thuwal, KSA
caigui.jiang@kaust.edu.sa

[a] ICSI/UC Berkeley

Abstract

In this paper, we introduce an effective way of limit analysis on the bearing capacity of given trusses. To illustrate the maximum external forces that a truss can carry on different directions, we propose the concept of ultimate force boundary (UFB) which is usually a closed polygon for a 2D truss and a closed polygonal mesh for a 3D truss. We prove that UFB is convex, and we introduce an efficient algorithm to compute the precise UFB based on its convexity. UFB can be used as direct visualization of bearing capacity of trusses and also provides insight of reducing the complexity of continuous boundary condition in truss optimization.

Keywords: trusses, optimization, ultimate force boundary, linear programming, limit analysis, cutting line, cutting plane.

1 Introduction

Trusses as fundamental structures have been studied in the field of civil engineering for decades. Recently, more attention has been paid to truss optimization in the community of computer graphics as the development of digital fabrication and geometric modeling such as research works in [1, 2, 3]. For a given truss, one of the important concern is the bearing capacity of truss when external forces are applied. To illustrate the maximum external forces that a truss can carry along different directions, we propose the concept of *ultimate force boundary*, UFB for short. We first set the joint where the external force applied as the origin. The maximum affordable external force along an arbitrary direction can be represented as a vertex on the boundary. UFB is a collection of all possible external force vectors which form a closed curve in 2D and a closed surface in 3D. Because of discreteness of trusses, more precisely, UFB is a closed polygon for a 2D truss and a closed polygonal mesh for a 3D truss. The region enclosed by the boundary represents all the affordable forces for a given truss. UFB can be used as a direct illustration of the bearing capacity of a truss, and more importantly, it provides an easy way to access the information of the maximum affordable force for any possible external force direction.

In the following chapters, we will first provide a formulation of finding the maximum external force along a given direction and provide a rough method of estimating UFB for given trusses. Then we will analysis the properties of UFB and provide an algorithm which can generate an exact ultimate force boundary.

Copyright © 2019 by Caigui Jiang
Published by the International Association for Shell and Spatial Structures (IASS) with permission.

2 Plastic Limit Analysis

2.1 A Simple Example

We first look at a simple 2D example, as shown in Fig.1(a), a truss connected by two bars i and j. Each bar has one end fixed as supporting point (red) and another end connected at the joint p. The bars can afford compression(-) and tension(+) along axial directions. Assume the limited compression and tension in bar i is $-\mathbf{F}_i$ and $\mathbf{F}_i$, and in bar j is $-\mathbf{F}_j$ and $\mathbf{F}_j$. We would like to know the bearing capacity of the truss when an external force is applied at the pin-joint p. The truss can afford an external force if the force can be decomposed into two forces along bar i and j and less than their limits. Then the solution of bearing capacity boundary is simply defined by a parallelogram with four vertices $\mathbf{F}_i + \mathbf{F}_j$, $\mathbf{F}_i - \mathbf{F}_j$, $-\mathbf{F}_i - \mathbf{F}_j$, and $-\mathbf{F}_i + \mathbf{F}_j$. Any external force within the parallelogram is affordable for the truss in Fig.1(a). Here the affordable force region bounded by the boundary is shown in yellow. In Fig.1(b), one more supporting bar k is connected at the joint p and its limited internal force range is $-\mathbf{F}_k$ and $\mathbf{F}_k$ shown in blue. The new ultimate force boundary in Fig.1(d) is the outline of region when moving the parallelogram by vector $-\mathbf{F}_k$ and $\mathbf{F}_k$ illustrated in Fig.1(c). This simple example provides a basic sense of the ultimate bearing capacity boundary and a simple way of calculation. However, when the truss gets complex, the analysis and calculation of the bearing capacity region are not straightforward.

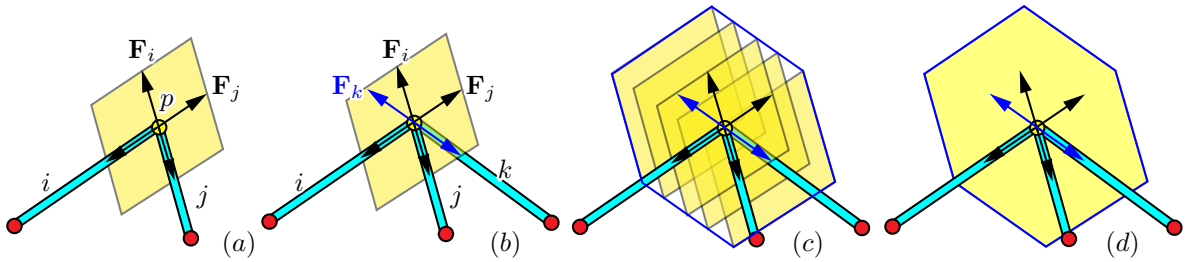


Figure 1: A simple example of ultimate force boundary.

2.2 LP Formulation

The LP formulation has been used commonly in truss optimization, such as the *ground structure method* (GSM) mentioned in [4], and methods used for truss limit analysis such in [5] and [6]. Given an external force direction and detailed information of a truss, such as its joint positions, connectivity, and cross-sections of bars, we can formulate the problem of finding the maximum force magnitude along this external force by a linear programming as shown below,

$$\begin{aligned}
&\underset{\lambda,\mathbf{s}}{\text{minimize}} && -\lambda, && && (1)\\
&\text{subject to} && \mathbf{B}^T\mathbf{s} = -\lambda\mathbf{f}, && && (1a)\\
& && \sigma_C a_i + s_i \geq 0, && i = 1,\ldots,|E| && (1b)\\
& && \sigma_T a_i - s_i \geq 0, && i = 1,\ldots,|E| && (1c)
\end{aligned}$$

where $\mathbf{B}^T$ is the nodal equilibrium matrix, built from the directional cosines of the bars. a_i is the cross-section area of the i-th bar, and s_i is its internal force. $\mathbf{s}$ is a vector with the internal forces for all bars and $|E|$ is the number of bars. $\mathbf{f}$ is a unit vector of the external force. Here we assume there is only one external force, and λ is its magnitude. The problem formulation

used in this paper is based on the plastic analysis. σ_C and σ_T are stress limits in tension and compression, which are constant values when the material of bars is determined. The limited force the i-th bar can afford is $\sigma_C a_i$ in compression and $\sigma_T a_i$ in tension. As formulated in the constraints, the internal forces of each bar should be within its limit. Solving this LP problem, we can easily find the maximum affordable external force for any given direction.
This formulation as a building block itself doesn't provide a direct computation of the bearing capacity boundary. This means for each given external force direction, to find its maximum bearing force, we need to solve this LP problem once. It may be not efficient because the number of possible directions could be infinitely many. However, we can still use this formulation to estimated a rough bearing capacity boundary when we sample a limited number of external force directions. For instance, we sample the external force directions along a unit circle for the 2D case and along a unit sphere for the 3D case. One example is shown in Fig. 2. The upper row is for a 2D truss, and the lower one is for a 3D truss. From left to right, (a1) and (a2) show the input trusses with given joint positions, topologies and cross-sections of bars, the trusses are supported at the red joints and external forces are applied at the blue joints, (b1) and (b2) illustrate different sampled external force directions, (c1) and (c2) show the maximum magnitude of external forces that the given trusses can afford, and (d1) and (d2) show the color coding of the magnitude, here the magnitude increases from blue to red. Note that the boundary curve of 2D shape in (d1) and the surface of 3D shape in (d2) are the so-called ultimate bearing capacity curve and surface which are convex polygon and polygonal mesh respectively. However, the results from this kind of sampling method only provide a limited number of vertices on UFB which is a rough limit analysis.

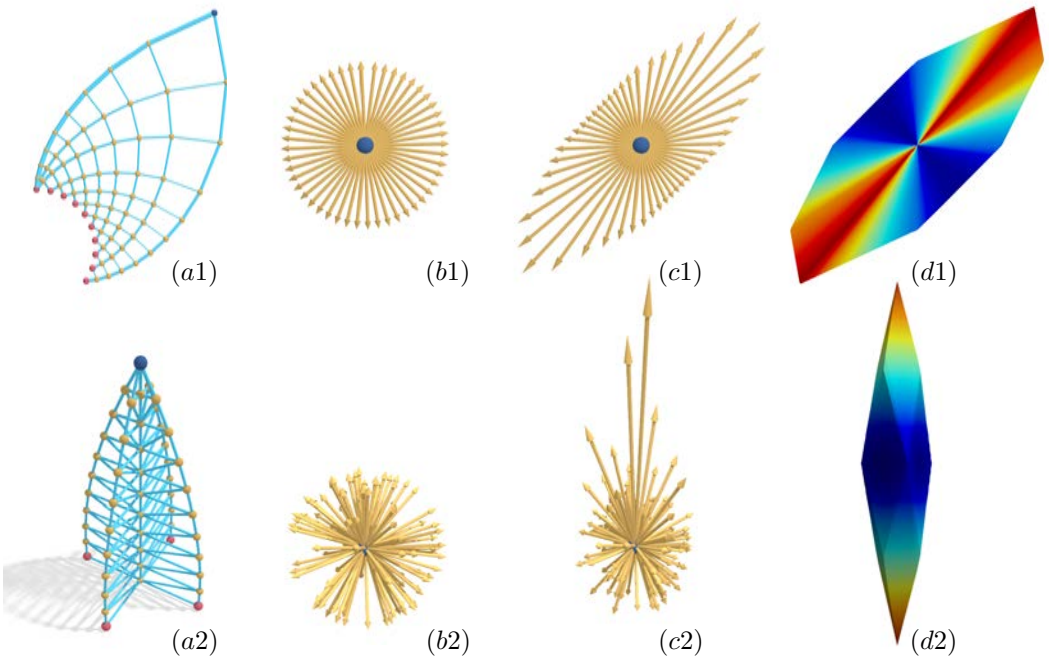


Figure 2: A rough limit analysis of given trusses.

To estimate the exact bearing capacity boundary, in the next chapters, we will first analyze the properties of the boundary and provide an efficient algorithm of computing the bearing capacity

boundary using the properties and the basic formulation in Eq. 1.

3 Properties of UFB

In the following, we first provide some properties of the ultimate force boundary and prove these properties briefly. These properties can be used to find the exact force bearing capacity boundary for 2D and 3D trusses.

Property I *Ultimate force boundary is convex.*

This property can also be described as if a truss can bear the external forces $\mathbf{F}_1$ and $\mathbf{F}_2$, it can always bear an external force $\mathbf{F}_3 = \delta\mathbf{F}_1 + (1-\delta)\mathbf{F}_2$, where $0 \leq \delta \leq 1$. Assume $\mathbf{F}_1 = \lambda_1\mathbf{f}_1$ and $\mathbf{F}_2 = \lambda_2\mathbf{f}_2$, where $\mathbf{f}_1$, $\mathbf{f}_2$ are unit vectors and λ_1, λ_2 are force magnitudes as shown in Fig. 3 left. To prove the convexity of ultimate force boundary, we take a look at the constraint part of Eq. 1. As $\mathbf{F}_1$ and $\mathbf{F}_2$ are affordable external forces, we can always obtain the internal forces $\mathbf{s}_1$ and $\mathbf{s}_2$, such that the following constraints are satisfied.

$$\begin{aligned} &B^T\mathbf{s}_1 = -\lambda_1\mathbf{f}_1 = -\mathbf{F}_1, \\ &-\sigma_C\mathbf{a} \leq \mathbf{s}_1 \leq \sigma_T\mathbf{a}. \end{aligned} \quad \textit{and} \quad \begin{aligned} &B^T\mathbf{s}_2 = -\lambda_2\mathbf{f}_2 = -\mathbf{F}_2, \\ &-\sigma_C\mathbf{a} \leq \mathbf{s}_2 \leq \sigma_T\mathbf{a}. \end{aligned}$$

Then, we have

$$\begin{aligned} B^T(\delta\mathbf{s}_1 + (1-\delta)\mathbf{s}_2) = -(\delta\mathbf{F}_1 + (1-\delta)\mathbf{F}_2)) = -\mathbf{F}_3, \\ -\sigma_C\mathbf{a} \leq (\delta\mathbf{s}_1 + (1-\delta)\mathbf{s}_2) \leq \sigma_T\mathbf{a}. \end{aligned}$$

The above formulation means we can always find the internal forces $\mathbf{s}_3 = \delta\mathbf{s}_1 + (1-\delta)\mathbf{s}_2$ which satisfy the constrain in Eq. 1 when the external force is $\mathbf{F}_3 = \delta\mathbf{F}_1 + (1-\delta)\mathbf{F}_2$. Assume $\mathbf{f}_3$ and λ_3 are the unit direction and magnitude of $\mathbf{F}_3$. When the external force direction $\mathbf{f} = \mathbf{f}_3$, the above formulation also means $(\lambda_3, \mathbf{s}_3)$ is in the feasible region of the LP formulation with $\mathbf{f}_3$ as the external force. Then solving the LP problem can always lead to an optima $\lambda_3^* \geq \lambda_3$. This means the maximum external force along $\mathbf{f}_3$ is

$$\mathbf{F}_3^* = \lambda_3^*\mathbf{f}_3 \geq \lambda_3\mathbf{f}_3 = \mathbf{F}_3 = \delta\mathbf{F}_1 + (1-\delta)\mathbf{F}_2 \tag{2}$$

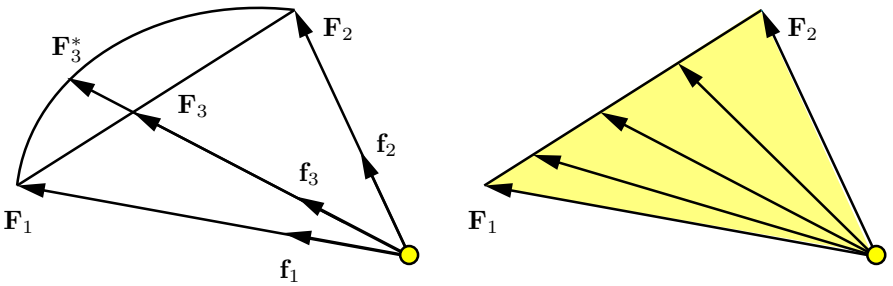


Figure 3: Convexity of UFB.

Similarly in 3D, we can prove if a truss can afford external forces $\mathbf{F}_1$, $\mathbf{F}_2$ and $\mathbf{F}_3$, the truss can always afford an external forces which is the linear interpolation of these three vertices.

According to the definition of ultimate force boundary and observations in Fig. 1 and 2. UFB is a polygon in 2D and a polygonal mesh in 3D which is enclosed by a limited number of lines or planes. We call such lines and planes as *cutting lines* and *cutting planes*. The following property can be used as a tool to find the cutting lines and planes.

Property II *For a 2D truss, if three vertices* $\mathbf{F}_1$, $\mathbf{F}_2$ *and* $\mathbf{F}_3$ *are on the ultimate force boundary and lie on a common line, then this line is a cutting line of the ultimate force boundary.*
This property also means the affordable force region is bounded by the line connected by $\mathbf{F}_1$ and $\mathbf{F}_2$, or the line segment $\mathbf{F}_1\mathbf{F}_2$ is a part of the ultimate force boundary. As show in Fig. 4, the maximum affordable forces $\mathbf{F}_1$, $\mathbf{F}_2$ and $\mathbf{F}_3$ are collinear. For an arbitrary direction $\mathbf{f}_4$ between force vectors $\mathbf{F}_1$ and $\mathbf{F}_2$, its maximum affordable force $\mathbf{F}_4$ can only be the case in Fig.4 (c). For the other cases, we can simply find the concavity of $\mathbf{F}_1\mathbf{F}_3\mathbf{F}_4$ in Fig. 4(a) and $\mathbf{F}_3\mathbf{F}_4\mathbf{F}_2$ in Fig. 4(b) is conflict with Property I.

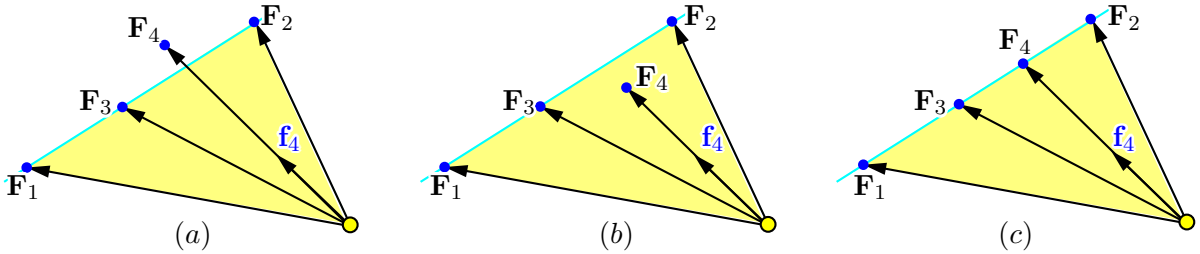


Figure 4: Cutting line for finding UFB of 2D trusses.

Similarly for 3D trusses, if a linear interpolation of three vertices $\mathbf{F}_1$, $\mathbf{F}_2$, and $\mathbf{F}_3$ on the ultimate force boundary is also on the boundary, the plane defined by $\mathbf{F}_1$, $\mathbf{F}_2$, and $\mathbf{F}_3$ is a cutting plane of ultimate force boundary as shown in Fig. 5.

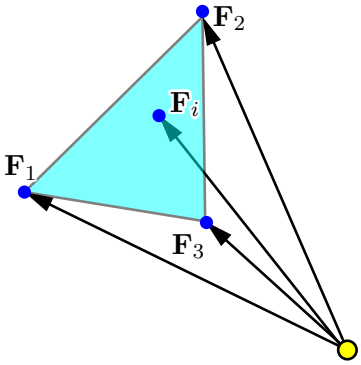


Figure 5: Cutting plane for finding UFB of 3D trusses.

4 Our Algorithm

Based on the properties mentioned in the last chapter. We propose an efficient algorithm of computing the bearing capacity boundary for given trusses.

4.1 Calculating of Cutting Line and Plane

Given an external force direction $\mathbf{f}_i$, the formulation in Section 2.2 tells us how to compute its maximum affordable force $\mathbf{F}_i$. After that, we would like to know how to calculate the boundary line or plane (3D) passing through $\mathbf{F}_i$, here we also call them cutting line or plane. To calculate the cutting line or plane, we estimate the maximum external forces of its several neighboring directions such as the ones with an angle of θ between $\mathbf{f}_i$ for the 2D case shown in Fig. 6 (a). Then we check whether the neighboring maximum external forces are collinear. If the case is at least three neighboring maximum external forces lie on a common line, as shown in Fig. 6 (a), then this common line (cyan) is the cutting line. Otherwise, in the case shown in Fig. 6 (b), we need to narrow down the neighboring searching directions further and check whether the cutting line or plane can be found. Usually, a cutting line or plane can be achieved within a few iterations as shown in Fig. 6 (c) and (d). Similar idea of cutting plane has been investigated in the solutions of mixed integer programming such as in [7].

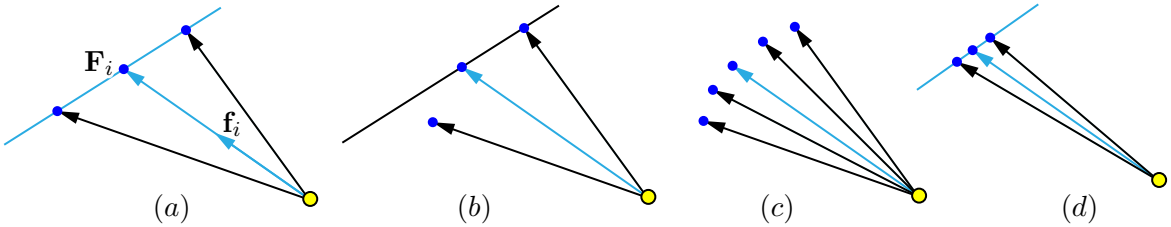


Figure 6: Procedure of finding cutting line.

4.2 Calculating of UFB

The calculating of cutting line or cutting plane in the previous sub-section is the basic building block. Here we illustrate the workflow of our algorithm in the 2D case shown in Fig.7, the calculating of boundary for 3D is similar. As shown in Fig.7 (a), we initially calculate the maximum external forces along with axis directions and estimate their cutting lines using the method described before. Then we obtain intersections (red) of neighboring cutting lines shown in Fig.7 (b). For each intersection vertex, we can use the formulation in Section 2.2 to check whether this vertex is located on the ultimate force boundary. If it's true, we mark this vertex as blue and continue the checkup of the next intersection vertex. If it's false, we calculate the maximum affordable force along the direction pointed to this vertex from the origin, and also its cutting line as shown in Fig.7 (c). New intersection vertices will be added to the checking list as the new cutting line intersects with the region enclosed by the previous cutting lines. The procedure continues until all the intersection vertices are marked as blue. The resulting polygon is the ultimate force boundary. For 3D truss, the basic idea is the same. We first sample some direction and estimate the maximum affordable force and their cutting planes. Further, the region is refined by finding possible cutting planes related to the directions pointed to the intersection vertices.

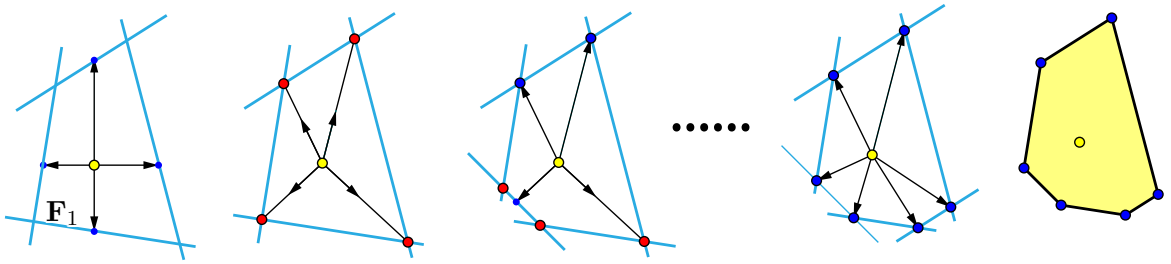


Figure 7: Basic workflow of the algorithm.

5 Applications

Our method provides an efficient way of calculating the exact ultimate force boundary which can be used as direct visualization of the bearing capacity of given trusses. For example, for the supporting truss for a dome shown in Fig.8 (a), we calculate its exact UFB when external forces applied at the top vertex of the truss using the algorithm introduced in the last chapter. The UFB is shown in Fig. 8 (b). Here, we assume $\sigma_C = \sigma_T$ and all the bars have the same cross-sections.

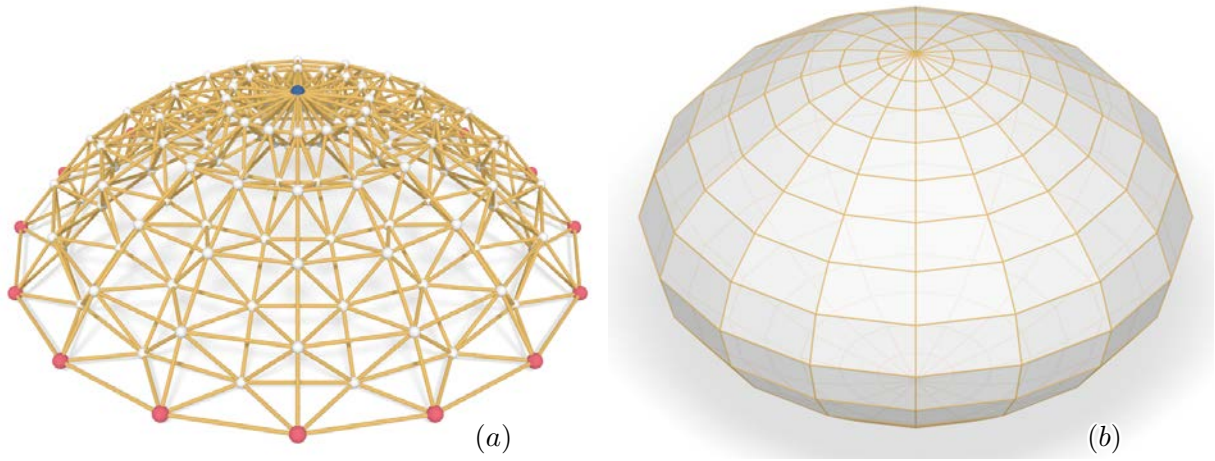


Figure 8: Left is a supporting truss. Right is the ultimate force boundary when external force applied at the top vertex (blue) of the truss.

Further, the idea used in our paper could also be used in other scenarios, such as truss optimization for dynamic external forces. For example, as shown in Fig. 9, the external forces from a hanging pendulum at the top joint change dynamically. It's challenging to incorporate infinitely many external forces in the truss optimization such as minimizing the total material consumption of truss using the traditional method such as GSM. Instead, we can consider the maximum affordable forces of several directions because of the convexity of the ultimate force boundary. For example, if the truss can afford the three external force shown in Fig.9 (c), it can always afford any external force from the pendulum shown in Fig.9 (b) because the possible external force region (gray) is covered by the affordable force region formed by three external forces. In this example, the boundary condition of external forces could be simplified dramatically. The truss optimization can be formulated as a linear programming problem as

$$
\begin{aligned}
\underset{a_i, s_i^k}{\text{minimize}} \quad & \sum_{i=1}^{|E|} l_i a_i, & \\
\text{subject to} \quad & \mathbf{B}^T \mathbf{s}^1 = -\mathbf{F}_1, & \\
& \sigma_C a_i + s_i^1 \geq 0, & i = 1, \ldots, |E| \\
& \sigma_T a_i - s_i^1 \geq 0, & i = 1, \ldots, |E| \\
& \mathbf{B}^T \mathbf{s}^2 = -\mathbf{F}_2, & \\
& \sigma_C a_i + s_i^2 \geq 0, & i = 1, \ldots, |E| \\
& \sigma_T a_i - s_i^2 \geq 0, & i = 1, \ldots, |E| \\
& \mathbf{B}^T \mathbf{s}^3 = -\mathbf{F}_3, & \\
& \sigma_C a_i + s_i^3 \geq 0, & i = 1, \ldots, |E| \\
& \sigma_T a_i - s_i^3 \geq 0, & i = 1, \ldots, |E|
\end{aligned}
$$

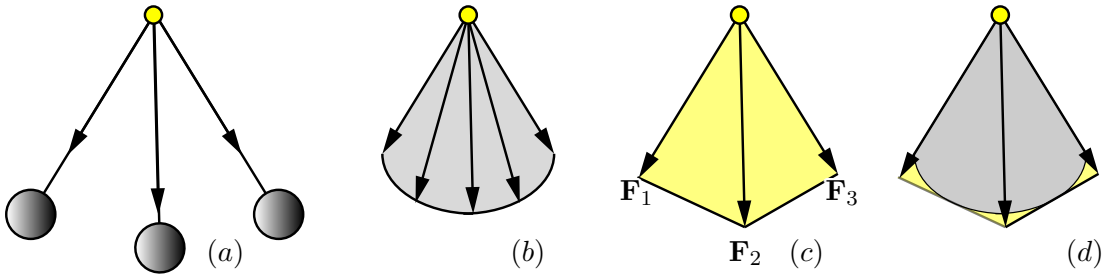


Figure 9: Dynamic external forces from a pendulum.

6 Conclusions and Future Work

We present an efficient approach to calculate the ultimate force boundary for 2D and 3D trusses. We prove that UFB is convex, and this convexity is useful for truss optimization when the external forces are continuous and dynamic. In the future, we would like to incorporate the other aspects of truss optimization such as geometry and topology, which may provide more degree of freedom for lightweight truss design. We also interested in the cases of multiple external forces applied simultaneously.

7 Acknowledgements

This research was supported by the Visual Computing Center (VCC) at KAUST. The author would like to thank Helmut Pottmann, Peter Wonka and Chi-Han Peng for discussions.

References

[1] J. Smith, J. Hodgins, I. Oppenheim and A. Witkin, "Creating models of truss structures with optimization," *ACM Transactions on Graphics (TOG)*, 21, no.3 (2002): pp. 295-301.

[2] C. Jiang, C. Tang, H.P. Seidel and P. Wonka, "Design and volume optimization of space structures," *ACM Transactions on Graphics (TOG)*, 36, no.4 (2017): 159.

[3] W. Wang, T. Yang, Z, Yang, L. Liu, X. Tong, W. Tong, J. Deng, F. Chen and X. Liu, "Cost-effective Printing of 3D Objects with Skin-Frame Structures," *ACM Transactions on Graphics (TOG)*, 32, no.5 (2013): 177.

[4] T. Zegard and G.H. Paulino, "GRAND—Ground structure based topology optimization for arbitrary 2D domains using MATLAB," *Structural and Multidisciplinary Optimization*, 50, no.5 (2014): pp. 861-882.

[5] E. Anderheggen and H. Knöpfel, "Finite element limit analysis using linear programming," *International Journal of Solids and Structures*, 8, no.12 (1972): pp. 1413-1431.

[6] K.D. Andersen and E. Christiansen, "Limit analysis with the dual affine scaling algorithm," *Journal of computational and Applied Mathematics*, 59, no.2 (1995): pp. 233-243.

[7] H. Marchand, A. Martin, R. Weismantel and L. Wolsey, "Cutting planes in integer and mixed integer programming," *Discrete Applied Mathematics*, 123, no.1-3 (2002): 397-446.

Proceedings of the IASS Annual Symposium 2019 — Structural Membranes 2019
Form and Force
7—10 October 2019, Barcelona, Spain
C. Lázaro, K.-U. Bletzinger, E. Oñate (eds.)

Concept and cable-tensioning optimization of post-tensioned shells made of structural glass

Francesco LACCONE*, Luigi MALOMO[a], Maurizio FROLI[b], Paolo CIGNONI[a], Nico PIETRONI[c,a]

* ISTI - CNR and DESTEC - University of Pisa; via Giuseppe Moruzzi 1, 56124 Pisa, Italy
francesco.laccone@isti.cnr.it; francesco.laccone@destec.unipi.it
[a] ISTI - CNR
[b] DESTEC - University of Pisa
[c] University of Technology Sidney

Abstract

Shells made of structural glass are charming objects from both the aesthetics and the engineering point of view. However, they pose two significant challenges: the first one is to assure adequate safety and redundancy concerning possible global collapse; the second one is to guarantee the economy for replacing collapsed components. To address both requirements, this research explores a novel concept where triangular panels of structural glass are both post-tensioned and reinforced to create 3D free-form systems. Hence, the filigree steel truss, made of edges reinforcements, is sized in performance-based perspective to bear at least the weight of all panels in the occurrence of simultaneous cracks (worst-case scenario). The panels are post-tensioned using a set of edge-aligned cables that add beneficial compressive stress on the surface. The cable placement and pre-loads are optimized to minimize the tensile stress acting on the shell and match the manufacturing constraints. These shells optimize material usage by providing not only a transparent and fascinating building separation but also load-bearing capabilities. Visual and structural lightness are improved to grid shell competitors.

Keywords: conceptual design, glass structures, thin shell, fail-safe, reinforcement, post-tensioning, cables, optimization.

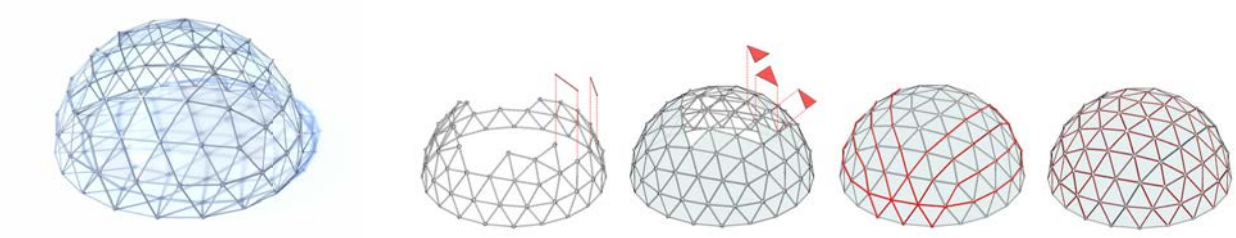


Figure 1: Semi-sphere geometry: impression and assembly procedure (skeleton assembly; panels lying; post-tensioning; edge sealant).

Copyright © 2019 by Francesco LACCONE, Luigi MALOMO, Maurizio FROLI, Paolo CIGNONI, Nico PIETRONI
Published by the International Association for Shell and Spatial Structures (IASS) with permission.

1 Introduction

Glass is nowadays the most common employed building material for structures, façades, and envelopes that requires a high degree of transparency. Usually, transparent shells are realized as grid shells, in which the grid bearing steel structure is optimized to support large and complex shapes, and the glass is used as cladding [1]. Nevertheless, a recent trend is to maximize the immaterial appearance of the structure and to leave the load bearing function to glass [2]. For shells, a few exemplars are representing a niche category that uses glass as a primary load-bearing material.

Glass-steel systems can be divided into two main categories, depending on their static behavior:

1. Strut-and-tie or tensegrity behavior is founded on a nodal force transfer that activates strut zones along glass panels edges, while the steel profiles - if present - act as ties. In return, the nodes are high-stressed zones and need special design and assembly care. The adopted panels are usually triangular or braced quads. The static response of these structures is akin to grid shells. Examples of these structures are the post-tensioned dome at *Weltbild Verlag* building in Augsburg [3] and the *Maximilianmuseum* roof [4].
2. Shell behaviour is akin to continuous shells, i.e the surface offers a continuous global resistance. The linear joining system enables an uninterrupted transfer of loads between the panel edges. Consequently, it reduces stress concentrations and increases the efficiency of the glass panels. In this case, polygonal panels (usually quads or hexagons) might be preferred to triangles as they offer major redundancy, due to a larger number of edges. Examples of these structures are the Delft dome [5], Blandini's dome [6] and Plate shell structures [7],

Strut-and-tie structures are more diffuse, hence they have been extensively tested, including for failure scenarios such as the complete collapse of panels. On the other hand, shell structures possess more local redundancy: if a single panel is weakened by a crack, the membrane behavior distributes the load on alternative paths. However, the complete collapse of single or multiple panels appears not managed.

Generally, glass structures adopt additional safety layers to avoid dangerous brittle failures. Apart from tempering and lamination, these additional support can be provided by mechanical collaboration with other materials.

Glass and steel collaboration is particularly fruitful and is used to realize mono-dimensional elements (such as beams and columns) or simple bi-dimensional elements (arches, domes, barrel vaults, shear walls). Similarly to rebars in Reinforced Concrete (RC) structures, reinforced glass elements [8] use steel as a ductile material to carry tensile loads. Steel reinforcement sustains the shards of glass from falling and offers redundancy in case the cracking of glass. At the same time, it increases the overall ductility of the structure.

An additional improvement might be provided if steel (bars, cables, strands etc.), as in post-tensioned concrete, is used to install a pre-compression regime on the glass [9].

The present work pursues the Strut-and-tie approach and develops the research of Froli [10, 11] on TVT post-tensioned glass beams. The objective is to realize shells using glass as primary bearing material expanding the possibilities for larger spans or free form geometries, and achieving aesthetic quality (more transparency) and structural efficiency.

The structural concept for these shells is linked to a more general framework that also includes dual layer structures [12]. Optimized in-plane cables are employed to compress glass, conferring it an apparent traction resistance. Conversely, Todisco *et al.* [13] optimize external cables post-

tensioning but in out-of-plane configuration to achieve funicularity in non-funicular structures via Graphic Statics.
The design of these structures [14] is automatically derived through a bespoke statics-aware algorithm which is able to manage, among other constraints, the optimal post-tensioning load provided by a set of edge-aligned cables [15]. The concept and the algorithm are presented in the next section. Several examples are analysed and discussed to validate this approach and to provide quantitative information.

2 Reinforced and post-tensioned glass shells

2.1 Conceptual design

This research explores a novel structural concept where glass is both post-tensioned and reinforced (fig. 1). These structures addresses two important requirements. The first one is to assure adequate safety and redundancy concerning possible global collapse adopting a Fail-Safe Design [2]. The second one is to avoid damages, especially on the glass, or at least to guarantee a cheap and easy replacing of collapsed components, following the Damage Avoidance Design (DAD) principles [16]. The glass surface is split into triangular panels with rounded corners, clamped into dry mono-lateral steel nodes equipped with spacers. The nodes are a fundamental component of the system because they also merge the reinforcement bars and post-tensioning cables. Other DAD features, such as energy dissipation and post-event serviceability, were already observed in TVTs experimental tests and are expected in the present shells.
The reinforcement bars are located at all edge of panels (fig. 2). Hence they form a triangulated truss (skeleton) that can be sized to withstand at least the weight of the panels. This expedient enhances the redundancy with respect to the Worst Case Scenario (WCS) in which all panels are considered cracked and so only a dead load.

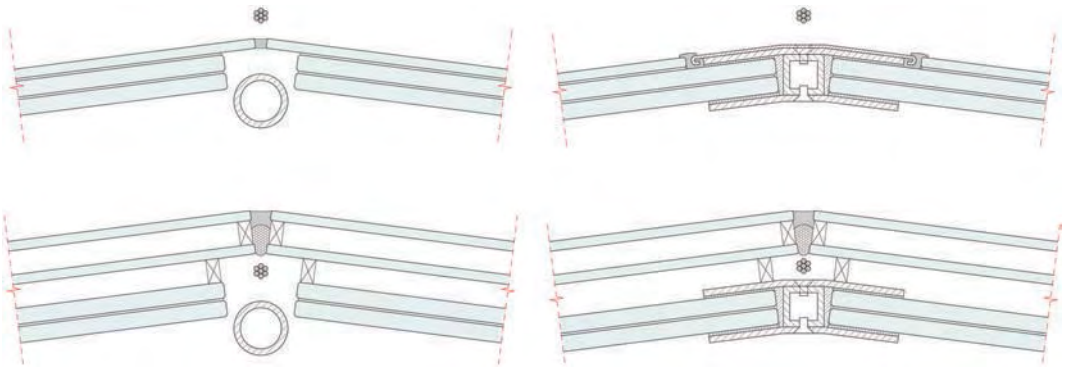
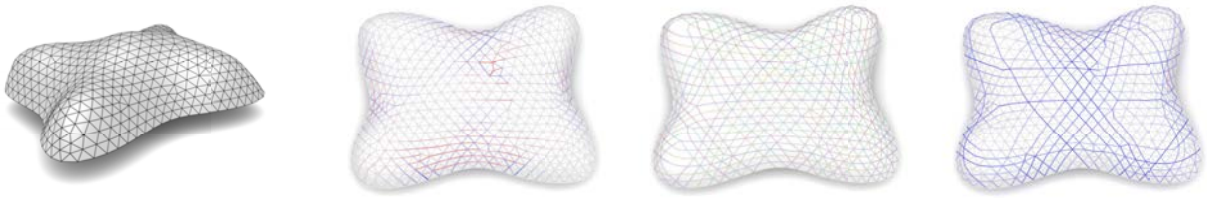


Figure 2: Edge detail with structural laminated glass package, hollow rod as reinforcement (without and with mutual restraint) and spiral cable: (top) with sacrificial glass layer; (bottom) with IGU

2.2 Morphogenesis and optimization

Since all triangular edges are reinforced, post-tensioning forces can be exerted by cables along dedicated paths, that is only where the glass must be compressed. The equilibrium of the hybrid structure is guaranteed since the reinforcement can sustain tensile forces, and simultaneously, glass can escape positive stresses because the panel corner can detach from the nodal cap. The skeleton of reinforcements realizes a self-supporting structure, which can be effectively used in



(a) (b) (c) (d)

Figure 3: Morphogenesis pipeline: (a) regular remeshing of the input surface; (b) SLS stress on the linear truss model subject to an external load (red compression, blue tension); (c) set of candidate cables; (d) resulting stress on the truss model after the optimization with selected cables and pre-loads.

the assembly phase.
This optimization is formulated as a mixed integer quadratic problem, whose basic assumptions are thin shell theory, linearity and negligible loss of pre-load. Input data of the problem are a membrane or quasi-membrane surfaces and their boundary supports.
The pipeline includes the following steps (refer to fig. 3):

- Surface triangular meshing, to build a quasi-isotropic panel tassellation (fig. 3(a));
- Generation of a linear truss model, where each edge stiffness includes the contribution of both glass and the bar, and computation of stress caused by SLS uniformly distributed load (fig. 3(b));
- Generation of a large set of cables by joining subsequent mesh edges (forming angles not smaller than 40°) until a border is hit or a loop is formed (fig. 3(c));
- Individual solutions of the truss subject to each cable loading;
- Superimposition of effect and selection of an optimal subset of cables with appropriate pre-loads such that the overall tensile stress is minimized (fig. 3(d)).

Additional constraints are imposed to limit the maximum truss compression and the maximum cable pre-load. This workflow has been implemented in Matlab [17] and C++ environment, in particular using the VCG Library. Several case studies analyzed show an almost complete null of tension stress on the equivalent truss model and an impressive increase of the buckling multiplier with respect to the non-post-tensioned shell.
All case studies use triangular laminated heat-strengthened glass panes ($8+8mm$ with $1.52mm$ PVB interlayer) and reinforcement bars (hollow steel profile) of $33.7mm$ outer diameter and $4mm$ thickness. The target edge of the mesh is $1m$. Cables have steel $15mm$ in diameter.

3 Design exploration

Some of the case studies previously optimized in [15] are analyzed by means of global nonlinear analyses in the FEM package Straus7 [18] and discussed. These tests are not meant to be exhaustive of all phenomena, but only to catch the shells global performance. The modeling phase has been supported by the TVT state of the art [19], especially for the calibration of contacts.
For each case, the extracted results are: (i) axial forces and stress field in the post-tensioning phase (in order to check if glass effectively undergoes compression stresses in the assembly); (ii) axial forces and stress field at SLS; (iii) axial forces and stress field at the ULS; (iv) redundancy rate R. The latter quantity is obtained as the ratio between the safety factors for the ULS load combination of the structure SF_{hyb} over the safety factor in the WCS SF_{WCS}. The WCS

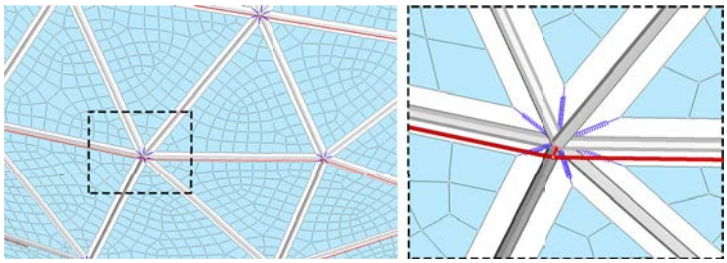


Figure 4: Modelling of the node and merging elements adopted for the FEM analysis

Table 1: Metrics and analysis results on different models (see fig. 5)

Name	Nodes	Panels	Size (m)	Rods	Cables	Buck.mult. λ	$SF_{hyb}/SF_{WCS} = R$
Vault	506	931	19.1x20.3x6.9	1436	59	14.69	3.12/1.65=1.46
Simplilium	582	1090	25.7x24.2x6.3	1671	48	15.22	5.58/3.14=2.57
Calla	557	1036	20.8x16.0x8.6	1593	56	17.91	3.85/1.54=2.50
Bean	429	796	21.7x16.7x5.7	1224	38	19.12	5.88/3.14=1.87

scenario is simulated in a separate model where the plates are substituted with load patches, non-structural elements for area load distribution.

3.1 FE modelling

Nonlinear static analyses are performed to take into account mono-lateral connections (contact non-linearities), shrinkage in the post-tensioning phase and geometric nonlinearities. However, since these analyses already involve a considerable number of variables, material non-linearities have been neglected. Characteristic values are adopted for materials.
The cable pre-load is applied through tension-only elements simultaneously with the dead load. The dead load G_1 is automatically computed from the element property definition, moreover, an additional uniformly-distributed vertical $Q_k = 1.00kN/m^2$ loading acting on the panels (in the direction of gravity, i.e. snow loading) is superimposed.
Steel reinforcements are modeled as beams, however, both bending and torsion are negligible. Steel nodes where rods merge are dimensionless nodes, with the additional effect of augmenting the slenderness of the rods, ignoring the node encumbrance (fig. 4). The glass-to-steel link is a spring with axial capacity (to resist deformations along its axis), lateral (for all lateral movements) and twist resistance (about its axis). The bending constraint that in real cases, is given by the steel caps is not included. The modeling of panel moreover suggests that peak stresses that may arise in the tip closeness because of force concentration. Stress verification is meaningless in this phase and are demanded to successive detailing design. Monolithic plate elements are used for glass panes and are re-meshed with an eight-node quadrilateral FE (Quad8). The cables are modeled as tension-only segments, which nodes are assumed to be coupled to the frame nodes. In the current analysis border conditions for all models are pin joints and correspond to their boundary vertices.

3.2 Results and discussion

The results of nonlinear analyses are shown in tab. 1 and in figs. 5 and 6. The main objective is achieved since all optimized cases manifest low tensile stresses on panels and low positive axial

forces on rods at SLS even in the nonlinear model. Glass pre-compression is diffuse and uniform in the assembly phase, while from the SLS phase, de-compression spreads and high stresses are located in adjacency to post-tensioned edges (principal stress σ_{22} reported in grey scale in fig. 5). In all cases, the safety factors result $SF_{hyb} \geq 3.00$ and $SF_{WCS} \geq 1.00$, with a redundancy always larger than unitary $R \geq 1.00$. For an effective comparison of both the design scenario, the full ULS load is considered. The comparison of axial forces can be then considered as a comparison between the present structures and grid shells in terms of steel utilization and stress map. In this regard, the spectrum of axial forces is very reduced with the center of distribution on negative values, while on the WCS side a larger and scattered range of values can be noted.
Grid shells are principal competitors of the shells here investigated. Effective criteria cannot be based on the steel resistance, because it would penalize grid shells. Instead, the two structures can be compared if they both have the same buckling multiplier. So, for each case study the cross-section properties of the grid shell are varied (among those present in commercial catalogs) to match the value of the buckling multiplier λ (ref. tab. 1). Using hollow steel beams in grid shells, both the outer diameter and thickness can be tuned. Usually, for comparable performances, the diameter should be doubled, and the total weight is also roughly doubled. The overall transparency of the structure will be inevitably affected by the new size of the beam. Instead, with solid steel beams, the cross-section is more compact, but however bigger and, even worse, the total weight of the steel will be roughly quintupled.

4 Conclusion

Transparent shells can be realized as piecewise assembly of structural glass triangular panels both reinforced with unbonded steel rods and post-tensioned by cables. The specific concept proposed provides safe highly-transparent structures with broad applicability, also in the context of free form architecture.
The structural safety can be deemed appropriate since the panel is mostly compressed at the SLS, and the structure is uniformly and diffusely loaded. A high redundancy with respect to the WCS is stated within the investigated case studies.
These structures might fit the target category of the intermediate-spanned thin-shell structures, in which grid shells are the principal competitors. Making use of structural glass demonstrates advantages in terms of both visual and structural lightness.

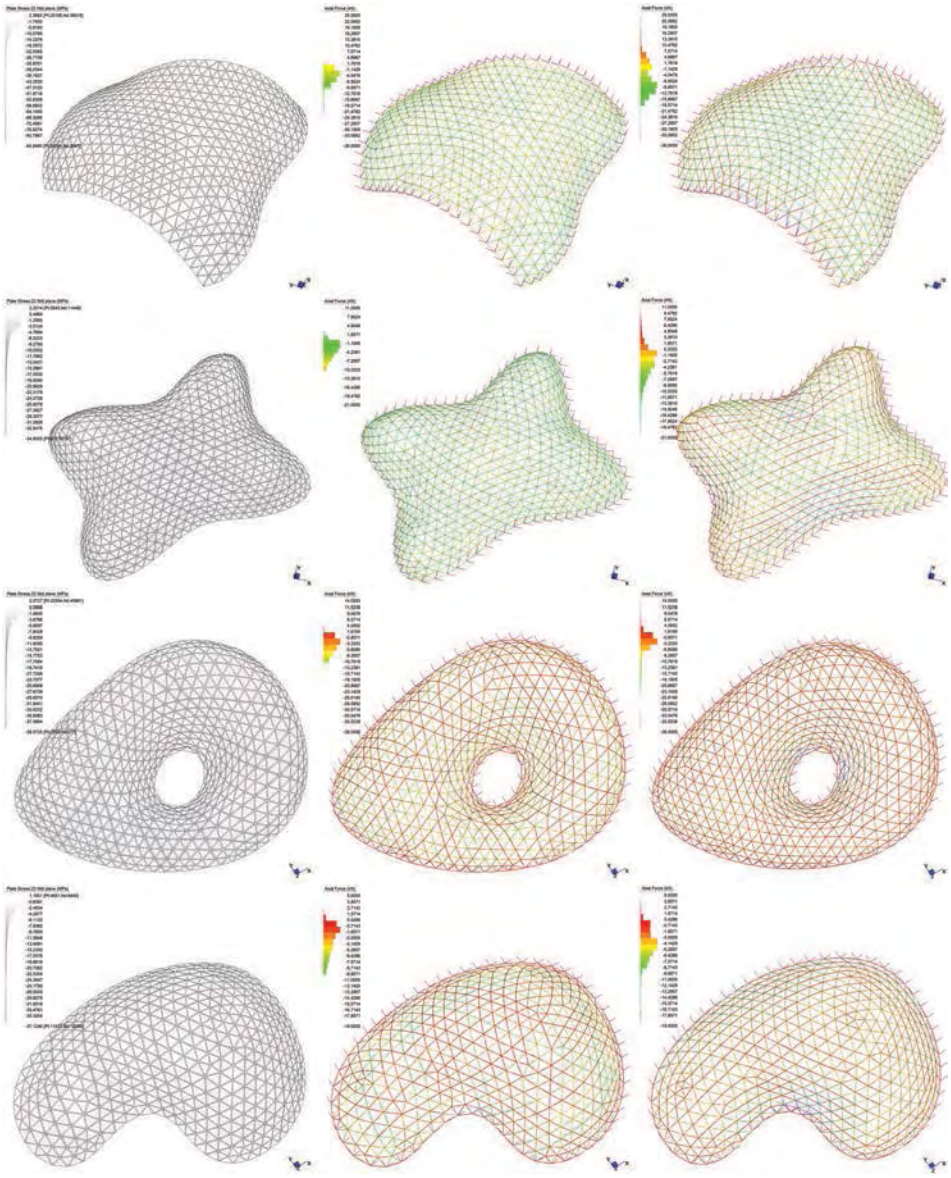


Figure 5: Results of non-linear analyses on Vault, Simplilium, Calla and Bean case studies: (left) glass σ_{22} at SLS; (center) truss axial forces at the ULS; (right) axial forces in the WCS (glass cracked)

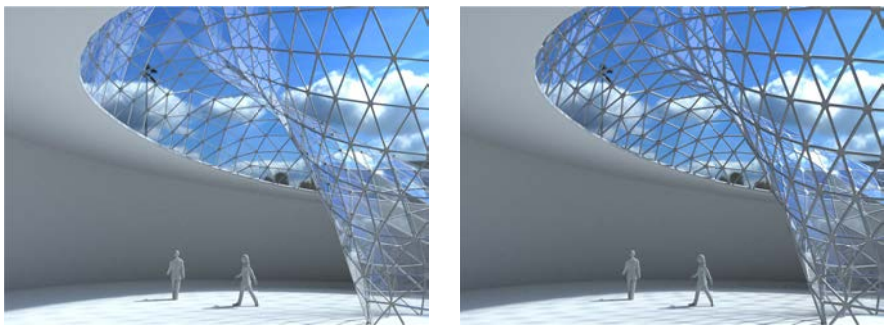


Figure 6: Visual comparison (Calla case study) between the present glass shell (left)) and a classical grid shell with same tessellation and comparable buckling factor (right). Hollow steel beams of 63.5mm outer diameter and 4mm thickness are used for the grid shell (double section size and weight).

References

[1] S. Adriaenssens, P. Block, D. Veenendaal, and C. Williams, *Shell structures for architecture: form finding and optimization*, Routledge, 2014.

[2] M. Haldimann, A. Luible, and M. Overend, *Structural use of glass*, volume 10, Iabse, 2008.

[3] J. Wurm, *Glass Structures, Design and Construction of Self-supporting Skin*, Birkhäuser, Berlin (Germany), 2007.

[4] J. J. Ludwig, and H.-U. Weiler, "Tragstrukturen aus Glas am Beispiel einer Ganzglastonne-Schalenkonstruktion ohne tragende Stahlunterkonstruktion am Maximilianmuseum in Augsburg," *Bautechnik*, 77(4), pp. 246-249, 2000.

[5] F. A. Veer, J. Wurm, and G. J. Hobbelman, "The design, construction and validation of a structural glass dome," *Proceedings of the Glass Processing Days*, Poster, 12, vol. 12, 2003.

[6] Blandini, L. 2005. *Structural use of adhesives in glass shells*, PhD thesis, Institut für Leichtbau Entwerfen und Konstruieren (ILEK), Universit'at Stuttgart.

[7] Bagger, A. 2010. *Plate shell structures of glass: Studies leading to guidelines for structural design* PhD thesis, Technical University of Denmark (DTU).

[8] K. Martens, R. Caspeele, and J. Belis, "Development of composite glass beams - a review," *Engineering Structures*, 101, pp. 1-15, 2015.

[9] K. Martens, R. Caspeele, and J. Belis, "Development of reinforced and posttensioned glass beams: review of experimental research," *Journal of Structural Engineering*, 142(5):04015173, 2015.

[10] M. Froli, and L. Lani, "Glass Tensegrity Trusses," *Structural Engineering International*, 20.4, pp. 436-441, 2010. doi:10.2749/101686610793557564

[11] M. Froli, and V. Mamone, "A 12 meter long segmented, post-tensioned steel-glass beam (TVT Gamma)," *Challenging Glass 4 & COST Action TU0905 Final Conference*, pp. 243-251, 2014.

[12] M. Froli, and F. Laccone, "Static concept for long span and high-rise glass structures," *Journal of Architectural Engineering*, 24.1, 04017030, 2018. doi:10.1061/(ASCE)AE.1943-5568.0000285

[13] L. Todisco, C. Fivet, H. Corres-Peiretti, and C. Mueller, "Design and exploration of externally post-tensioned structures using graphic statics," *Journal of the International Association for shell and Spatial Structures*, 56(4), pp.249-258, 2015.

[14] F. Laccone, *Reinforced and post-tensioned structural glass shells: Concept, morphogenesis and analysis*, PhD thesis, University of Pisa, 2019.

[15] F. Laccone, L. Malomo, M. Froli, P. Cignoni, N. Pietroni, "Automatic Design of Cable-Tensioned Glass Shells," *Computer Graphics Forum*. In press (2019)

[16] J. B. Mander, and C.-T. Cheng, *Seismic resistance of bridge piers based on damage avoidance design*, Technical Report Technical Report NCEER-97-0014, University at Buffalo, State University of New York, 1997.

[17] MATLAB version R2018a, The MathWorks Inc., Natick, Massachusetts, 2018.

[18] G+D Computing 2005. *Straus7 User's Manual*.

[19] M. Froli, and F. Laccone, and D. Maesano, "The TVT Glass Pavilion: Theoretical Study on a Highly Transparent Building Made with Long-Spanned TVT Portals Braced with Hybrid Glass-Steel Panels," *Buildings*, 7(2):50, 2017. doi:10.3390/buildings7020050

Proceedings of the IASS Annual Symposium 2019 – Structural Membranes 2019
Form and Force
7 – 10 October 2019, Barcelona, Spain
C. Lázaro, K.-U. Bletzinger, E. Oñate (eds.)

Exploratory numerical investigation on Aluminum reinforced PVB-laminated glass beam

Dejun ZHANG[a], Suwen CHEN[b]*

[a] College of Civil Engineering, Tongji University, Shanghai, P.R.China

[b*] State Key Laboratory for Disaster Reduction in Civil Engineering, Tongji University, Shanghai, P.R.China
Swchen@tongji.edu.cn

Abstract

Recently, reinforcement technology is introduced into structural glass beam design creating reinforced glass beam (RG beam). Although many pioneering experimental studies have demonstrated the technical superior, such structures frequently exhibited premature failure modes due to the adhesive detachment and glass brittleness. Numerical methods are in need for RG beam bond-slip behavior analyses and strength prediction. In this paper, a numerical model is proposed to analyze RG beam mechanical behavior. Based on previous experimental studies, the in-plane bending performance of newly invented Aluminum-reinforced glass beam (ARG beam) is validated by means of a simplified but focused 2D numerical model for quasi-static loading. Adhesive detachment behavior is simulated in the numerical model by using cohesive zone model (CZM) and 'killing element method'. Besides, the PVB interlayer effect is blended into the 'brittle cracking' module for glass elements in a subtle way. Effect of mesh size, adhesive fracture energy and adhesive thickness were analyzed.

Keywords: Reinforced glass, Aluminum, Experiment, Numerical investigation, Ultimate strength

1. Introduction

In recent years, full glass structures prevail in many major cities owing to the aesthetic reason. As one of the key components in full glass structure, glass beam or glass rib is designed to sustain vertical load from glass roof plates. Compared with traditional steel beam and cable in glass structure, glass beam possesses significant higher transparency and better visual effect. However, glass beam commonly has a low in-plane bending resistance due to its relative brittle failure behavior. Therefore, reinforced glass beam (RG beam) typology, in which glass plates are retrofitted by gluing reinforcement of other material, has been widely adopted for strengthening concept of ordinary glass beam [1]. Previous experimental investigations [2] have found that reinforced glass beams (in which the glass type was annealed float glass) not only possessed higher ultimate strength and in-plane deformation capacity, but also exhibited safer post-crack mechanical behavior compared to unreinforced glass beams. When overloading, the glass pane in reinforced glass beam would crack, nevertheless, the crack propagation will be limited and may not directly spread to compressive edge of the beam because the reinforcement, acting as a crack bridge, can dissipate glass fracture energy by deformation [3]. The reinforced glass beams exhibited multiple kinds of failure modes and tended to fail prematurely due to debonding, shear tension fracture or lateral buckling. The uncertainty of failure behavior mainly caused by the adhesive bond-slip behavior, glass initial defects.

Aiming to offer an insight into the potential and criticalities of reinforced glass beam concept, numerical methods were commonly applied in failure process investigations. Since glass compressive strength is much higher than the tensile strength [4], similar to concrete or ceramic material, a sequentially linear elastic analysis (SLA) technique [5] was firstly developed for RG beam analysis in which the

Copyright © 2019 by Dejun ZHANG, Suwen CHEN
Published by the International Association for Shell and Spatial Structures (IASS) with permission.

reinforcements were simplified as truss elements and embedded into glass elements. Analogously, "concrete damage plasticity" (CDP) model was also taken advantage in post-tensioned glass beam failure simulation previously [6]. The inherent 'brittle cracking' module in Abaqus [7], which is also applied in this paper, was implemented in two-sided reinforced laminated glass beams investigation[8]. Ulteriorly, to similate the glass-reinforcement interfacial influence, the a linear elastic constitutive law was implemented for adhesive layer in numerical research by Bedon et al.[6] so that the effect of post-tensioning could be properly reproduced. These models, however, ignored the influences of adhesive softening and detachment behaviors, and these behaviors were observed in previous researches [3, 9] but also in this paper. Similarly, the adhesive softening and detachment behaviors also existed in FRP-reinforced concrete field. Khan et al. [10] validated a simple but focused numerical model in which the Cohesive Zone Model (CZM) with discrete elements were assigned to concrete-FRP interfacial adhesive layer so as to indicate closeness to actual conditions.

This paper presents an exploratory numerical investigation on Aluminum-reinforced glass beam (ARG beam) with focus on the modelling of PVB-laminated glass and adhesive layer failure behavior. The influence of adhesive strength, glass element post-crack behavior and element sizes on results were analyzed and discussed. Besides, models with optimum parameters were compared with experimental data. Finally, an analytical model based on the crack-induced intermediate debonding failure mode is developed aiming to provide a tentive ultimate strength prediction method.

2. Numerical modelling

2.1. Specimen description

As the reinforcement technology have been introduced into structural glass beam design, this key component in full glass structure obtains effective and aesthetic solution. Crucially, nevertheless, compared to reinforced concrete beam, the reinforcement in RG beam is adhesively bonded to glass pane and expose to the air. Therefore, the reinforcement material is required to be aesthetic and anti-corrosive. Aluminum is one kind of the architectural material have beautiful metallic luster and high corrosion resistance as well as light weight. In this paper, an aluminum-reinforced glass beam concept is presented, in which the high-strength 6061-T6 Aluminum alloy bar is applied.

The ARG beam specimen composed of PVB (polyvinyl butyral) laminated annealed float glass plane, Aluminum alloy bar, steel anchorage plate and two types of industrial adhesives applied in the interface, as Figure 2 shown. Since the Aluminum bar only dominated a small amount of cross-sectional area, it had limited influence on the overall aesthetic and transparency. Figure 1 presents the detailed specimen dimension as well as the loading configuration. Specially, in the actual tests, a 6-point lateral support condition was applied to effectively prevent lateral instability. Therefore, the lateral buckling behavior could be neglected so that the 2D numerical model could be used to validate test results. As Figure 1 illustrated, the beam was 150 mm high and 1400 mm long. The glass web measuring 20.76×140 mm composed of 10 mm-thick two annealed floated glass layers and one 0.76 mm-thick PVB interlayer. The Aluminum reinforcement measured 20×10 mm in cross-section. Delu® GB368 industrial adhesive was applied to the interface between aluminum bar and glass plane tensile edge. Theoretically, the thickness of GB368 adhesive layer was about 0.1mm according to the instructions given by the manufacture. Since previous research [11] on FRP-reinforced concrete beam had shown that the interfacial shear stresses close to the beam end were significantly larger than the mid-span interfacial area, the anchorage of the reinforcement at the beam end is strengthened by adhesively bonding the steel anchorage plates (see Figure 1(a)) , measuring 2×25×100 mm each and using Leaftop ® 9903 Acrylic Adhesive. The specimen was 4-point in-plane bending loaded as Figure 1 loading configuration. To ensure the distribution of concerntrated forces to larger area, load introduction points were modelled by 30 mm long rigid surface which corresponded to the test setup.

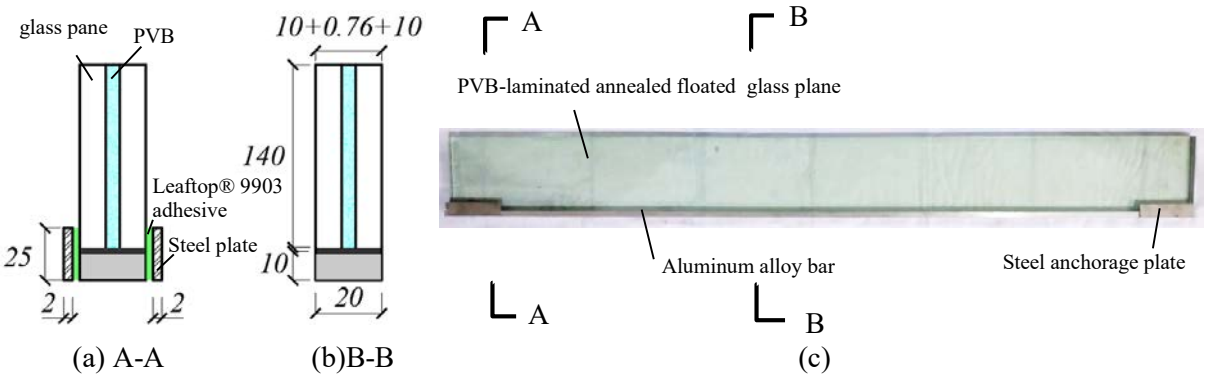


Figure 1: Specimen of Aluminum-reinforced glass beam: A-A (a), B-B section (b) and actual specimen(c)

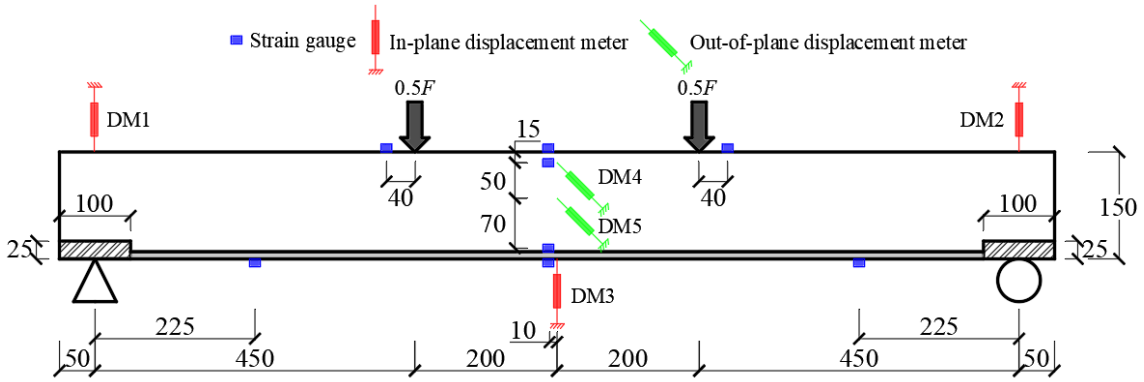


Figure 2: Geometry and loading configuration of Aluminum reinforced glass beam (ARG beam) specimen

2.2. Simplified 2D material model for laminated glass

In previous researches [6, 12, 13], laminated glass beam components were commonly modelled by 3D solid elements so that the glass layers and interlayers could be separately modelled and assigned material properties. However, the interlayer thickness was usually less than 1 mm, furthermore, the Poisson's ratio of interlayer material was close to 0.5. Therefore, the direct modelling of interlayer material in finite element model would cause high-frequency noise and relatively low computational efficiency in Abaqus/Explicit analyses[7]. On the other hand, PVB interlayer compressive behavior remained unknown but had to be defined in 3D modelling. To address these issues, interlayer material were integrated into the tensile behavior of glass material properties in a tricky way so that the 2D glass elements would have residual strength and stiffness after the glass element reaching its original critical fracture energy. Then, the glass material tensile behavior herein could be express as stacking up pure glass and PVB interlayer each weighted by the thickness. Pure glass was described as isotropic and linear elastic brittle material properties. The elastic modulus E_g = 72000 MPa, Poisson's ratio υ = 0.2 and characteristic tensile stress f_{gt} = 45 MPa were defined based on the recommendation of the Chinese code JGJ 102-2003[14] and the European Guidance[4]. To describe the failure of glass elements, the ABAQUS® built-in '*brittle cracking*' module along with '*brittle shear'* and '*brittle failure'* sub-options based on the smeared crack theory was applied. The element crack initiation is dominated by the initial direct cracking stress f_t and the post-crack behavior is described by the aforementioned two sub-options. In previous numerical research [13, 15], the '*GFI*' type in '*brittle failure'* sub-option was often used to

define the fracture energy G_f . However, in this paper, the '*Strain*' type was applied so that the PVB interlayer behavior could be taken into consideration. As the '*brittle cracking*' module was a smeared crack model, the critical cracking strains were determined based on the mesh geometry. The crack strain ε was substituted for crack opening displacement w according to Equation 1 proposed by Louter[5] :

$$\varepsilon = \frac{w}{h_{cbw}} = \frac{w}{\sqrt{A_{element}}} \tag{1}$$

Where h_{cbw} denotes crack band width which related to the side-length of cracked element and $A_{element}$ is the area of single element(seeFigure 3) .

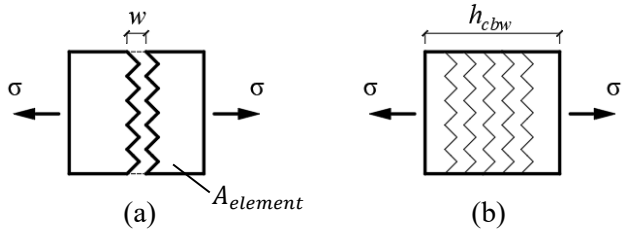


Figure 3: Schematic representation of a crack for a (a) discrete crack and; (b) smeared crack [5]

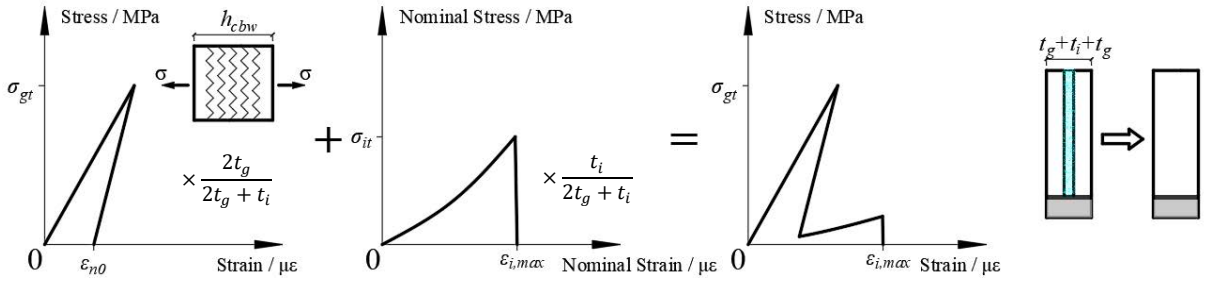


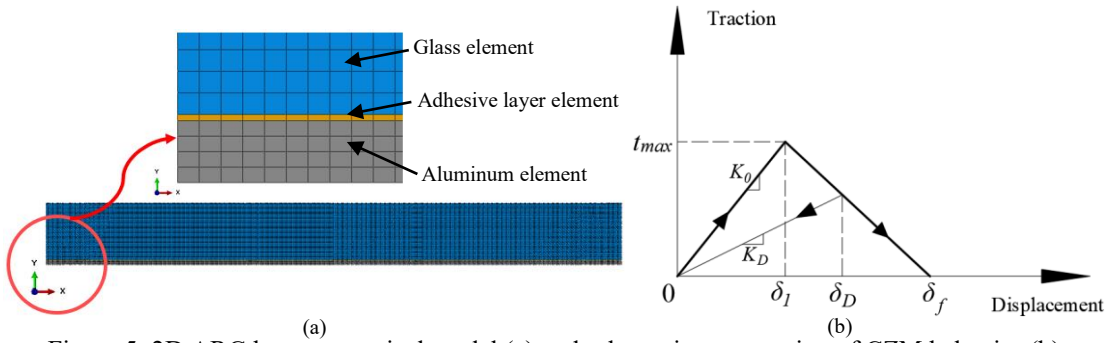
Figure 4: Composite tensile behavior for PVB-laminated glass component in-plane loading in 2D modelling

At the cracking moment of laminated glass, PVB interlayer bridged the crack gap and inhibited the crack opening as well as propagation by instant high-strain-rate tensile deformation. Yet, there was little research on the actual strain rate and deformation magnitude of PVB interlayer at the laminated glass cracking moment. Former numerical research [8] determined the glass maximum crack opening strain $e_{max}^{ck} = 0.001$. After reaching this strain, the glass element was assumed to completely lose aggregate interlock and the PVB interlayer deformation strain rate started to fall. Although in actual tests PVB would deform until it was teared after unstable glass crack opening completed, the deform strain rate became small and the stresses were negligible. Therefore, the PVB interlayer deformation contribution was limited to $\varepsilon_{i,max} = e_{max}^{ck} = 0.001$ and the strain rate was postulated 100 s^{-1}. Based on the above assumption, the glass pane and PVB interlayer tensile behavior could be merged as Figure 4 illustrated. The glass tensile behavior was transferred to smeared crack expression according to the element geometry (see Figure 4(a)), which indicated that glass element sizes affect the determination of crack opening strain ε_{n0}. Subsequently, composite tensile behavior was obtained by adding PVB tensile behavior multiplied by its thickness weighted coefficient $w_{PVB} = \frac{t_i}{2t_g+t_i}$ to glass tensile behavior which also multiplied by thickness weighted coefficient $w_{PVB} = \frac{2t_g}{2t_g+t_i}$. In this way, the PVB interlayer positive action was taken into consideration within 2D glass element.

2.3. Cohesive zone model for adhesive layer

Adhesive layer (see Figure 5(a)) material behavior was the key point of numerical modelling herein. A bi-linear Cohesive Zone Model (CZM) along with traction-separation behavior was applied for adhesive layer. Maximum nominal stress criterion used for damage initiation which could be represented as Equation 2. Correspondingly, the adhesive element statue could be divided into 3 stages. The first stage was linear elastic stage governed by the normal and tangential traction behavior separately. After normal or tangential traction reaching user-defined maximum nominal stress, the damage initialed and the element stiffness declined linearly as illustrated in Figure 5(b). After maximun nominal stress exceeding the ultimate displacement δ_f, both the cohesive element tractions of all direction and stiffnesses reduced to zreo resulting in the final element deletion and fracture eneregy dissapation $G_f = \frac{1}{2} t_{max} \delta_f$.

$$\max\left\{\frac{\langle t_n \rangle}{t_n^0}, \frac{t_s}{t_s^0}, \frac{t_t}{t_t^0}\right\} = 1 \tag{2}$$



(a) (b)

Figure 5: 2D ARG beam numerical model (a) and schematic presentation of CZM behavior (b)

2.4. Aluminum reinforcement material model

A 6061-T6 type Aluminum alloy bar was attached to the tensile edge of each specimen. According to the previous experimental research, 6061-T6 Aluminum alloy was modelled with isotropic, bi-linear elastic-plastic model. The initial yield stress of this model was 245 MPa while the ultimate strength was 265 MPa with elongation 8%. The properties of all test material are listed in Table 1.

Table 1: Material properties of numerical model

Material	f_y (Mpa)	f_u (Mpa)	E (Mpa)	G (Mpa)	G_f (J/m^2)	υ	γ_g (kN/m^3)
Glass	-	45	72000	-	-	0.23	25.6
Aluminum	245	265	68000	-	-	0.3	28
End-section adhesive	-	46	1080	480	$G_{f1} = 3$, $G_{f2} = 4.5$	-	10
Mid-section adhesive	-	23	900	300	0.7	-	10

2.5. Numerical method

The overall model was simulated by 2D plane stress approach through ABAQUS/Explicit solver in order to improve the computational efficiency and avoid out-of-plane Euler instability in numerical nonlinear analysis. Besides, owing to the highly brittle crack opening behavior of glass, explicit dynamic approach was applied herein instead of static approach. Forasmuch, 4-node bilinear plane stress quadrilateral reduced-integration (CPS4R) elements were used for glass web and Aluminum reinforcement to control the hourglass phenomena in explicit analysis. Discrete elements, specifically 4-node two-dimensional cohesive (COH2D4) elements were staked between glass and Aluminum bar surfaces.

Table 2: Overview of parameters of numerical models

Variation	Model	h_{cbw} (mm)	$G_{f\text{-}end}$ (J/mm^2)	t_a (mm)
Reference	BPNL3-10-30	3.5	3	0.1
Mesh size h_{cbw}	BPNL7-10-30	7	3	0.1
End-section adhesive fracture energy $G_{f\text{-}end}$	BPNL3-10-45	3.5	4.5	0.1
Adhesive thickness t_a	BPNL3-5-30	3.5	3	0.05

Owing to the application of steel anchorage plate as illustrated in Figure 1(a) at end-section, adhesive material properties at steel-plate-applied section (end section) were enhanced in numerical model. The adhesive thickness and the steel-plate-applied section adhesive fracture energy were uncertain in the experimental research, aforesmuch, these factors were varied to investigate their effect to find the optimal parameters fitting experimental result. The glass element size were also altered to analyze the mesh effect as illustrated in Table 2 numerical example explanation.

3. Numerical result and discussion

3.1. Validation with test results

In numerical model, monotonic 4-point bending was performed by displacement-control loading system as Figure 1(c) illustrated, with the loading rate at 2 mm/s until the flexural crack reached the compressive edge. Energy balance was monitored throughout the overall analyses, so that the inertial effect could be assessed in the explicit analyses. Owing to the extremely large requirement of increment numbers (>300000) in quasi-static ABAQUS/Explicit analyses, double precision executable was applied in each simulation. Figure 6 presents the test results compared to the Reference numerical result. As shown, the obtained numerical result is in good agreement with three test results. Besides, the numerical crack pattern was close to the test result. During actual testing it was found that final failure of test specimens was caused by the propagation of crack-induced adhesive layer detachment. Both of their cracks were mainly located at pure-bending section. In addition, at the end of beam there was glass cracks exist when final failure happened due to the sudden debonding. However, the numerical load-deflection plot does not perfectly fitted the test results. Some test specimens exhibited obviously higher strengths than numerical result, which might account for mesh size effect, underestimation of adhesive layer fracture energy or overestimation of adhesive layer thickness. The degrees of these effects are uncertain so far, and forasmuch, parametric analyses are conducted to learn relative influence levels of these effects.

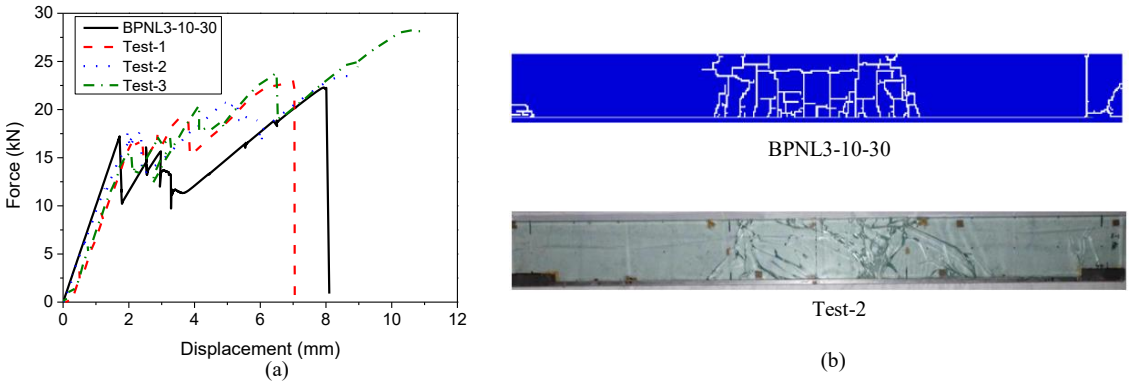


Figure 6: Load–displacement plots(a) and crack patterns at final failure (b) of numerical and test results

3.2. Parametric analyses

Since the smeared crack model was sensitive to element size, BPNL7-10-30 with 7 mm mesh size was compared to Reference model of smaller size (3.5 mm). The initial crack loads and the ultimate strengths

of two numerical similations were almost the same, while the BPNL7-10-30 possessed slightly higher ultimate deflection (≈8.7 mm) compared to the reference model (≈8.1 mm). Therefore, the mesh size had limited influence on the numerical result. In terms of end-section adhesive fracture energy. As Figure 1(c) shown, extra steel anchorage plates were bonded to the end section to enhance the Aluminum reinforcement anchorage at the end of beam. Correspondently in 2D simulation, the steel plates were not modelled and instead, the strength and fracture energy of end-section adhesive element was increased compared to the mid-span section. However, the fracture energy of end-section adhesive was uncertain because the Leaftop® adhesive (see Figure 1(a)) supplier did not provide enough detailed information. As Figure 7(b) presents, ultimate strength of model BPNL3-10-45 was 27.02 KN which was clearly larger than reference model (22.29 KN) . So, the end-section fracture energy had great effect on the ARG beam post-crack behavior, indicating the significances of steel anchorage plate. Adhesive thickness mainly influence the initial stiffness of adhesive layer. Owing that the maximum adhesive gap filling ability herein was less than 0.1 mm (less than 0.1 % beam height), it was tough to precisely measure the adhesive thickness along the beam. Besides, the effect of adhesive thickness on detachment was uncertain. Two adhesive thicknesses (0.1 mm and 0.05 mm) were compared herein. As Figure 7(c) presented, the reference model load-displacement curve almost overlapped the model with 0.05 mm adhesive thickness. As for the fracture pattern, model with 0.05 mm thickness exhibited slightly more cracks. In conclusion, the adhesive thickness in numerical simulations had negligible affect on the numerical results.

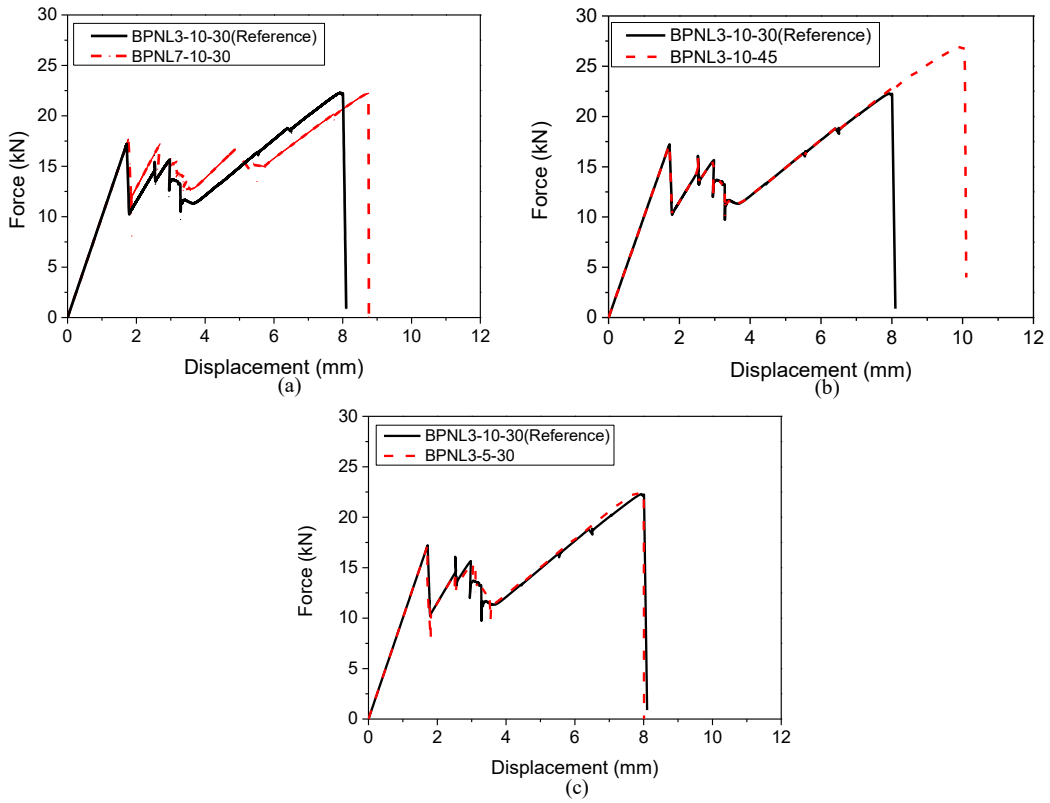


Figure 7: Effects of element size (a), end-section adhesive $G_{f\text{-}end}$ (b) and adhesive thickness t_a (c)

4. Conclusions

This paper mainly presented an effective 2D numerical approach to analyzed structural response of Aluminum-reinforced PVB laminated glass beam. Firstly, in the numerical modelling the PVB positive action was blended into the glass elements and a CZM law with traction-separation behavior was applied to adhesive layer. Subsequently, the models were validated with previous test results. Finally, the effects

of mesh size, end-section adhesive fracture energy and adhesive thickness were analyzed by comparing different explicit numerical simulation results.

Generally, the Abaqus explicit solver provided reasonable numerical results in terms of macro responses and fracture behavior. From the parametric investigations, it could be concluded that the mesh sizes and the adhesive thickness have limited influence on the numerical results while the end-section adhesive fracture energy have significant effect on the ultimate strength and deformation capacity. Therefore, it demonstrated the steel anchorage plate had positive effect on enhancing the structural behavior of ARG beam herein. The response and fracture pattern of numerical result are in good agreement with test result, proofing the effectiveness of numerical model.

References

[1] Bos FP. Safety concepts in structural glass engineering: towards an integrated approach: Technische Universiteit Delft; 2009.
[2] Martens K, Caspeele R, Belis J. Development of Reinforced and Posttensioned Glass Beams: Review of Experimental Research. Journal of Structural Engineering. 2016;142:23.
[3] Louter P. Adhesively bonded reinforced glass beams. HERON-ENGLISH EDITION-. 2007;52:31.
[4] Feldmann M, Kasper R, Abeln B, Cruz P, Belis J, Beyer J et al. Guidance for European Structural Design of Glass Components. Publications Office of the European Union. 2014:1-196.
[5] Louter PC. Fragile yet ductile: structural aspects of reinforced glass beams: Technische Universiteit Delft; 2011.
[6] Bedon C, Louter C. Finite-element analysis of post-tensioned SG-laminated glass beams with mechanically anchored tendons. Glass Structures & Engineering. 2016;1:39-59.
[7] Simulia. ABAQUS v. 6.12 computer software and online documentation. Providence, RI, USA: Dassault Systems; 2012.
[8] Martens K, Caspeele R, Belis J. Numerical investigation of two-sided reinforced laminated glass beams in statically indeterminate systems. Glass Structures & Engineering. 2016;1:417-31.
[9] Correia JR, Valarinho L, Branco FA. Post-cracking strength and ductility of glass–GFRP composite beams. Composite Structures. 2011;93:2299-309.
[10] Khan MA, El-Rimawi J, Silberschmidt VV. Relative behaviour of premature failures in adhesively plated RC beam using controllable and existing parameters. Composite Structures. 2017;180:75-87.
[11] Abdelouahed T. Improved theoretical solution for interfacial stresses in concrete beams strengthened with FRP plate. International Journal of solids and Structures. 2006;43:4154-74.
[12] Amadio C, Bedon C. Buckling of laminated glass elements in out-of-plane bending. Engineering Structures. 2010;32:3780-8.
[13] Bedon C, Louter C. Exploratory numerical analysis of SG-laminated reinforced glass beam experiments. Engineering Structures. 2014;75:457-68.
[14] PRC MoCot. JGJ 102-2003. Technical code for glass curtain wall engineering. Beijing: China Architecture & Building Press; 2005.
[15] Kozłowski M, Kadela M, Hulimka J. Numerical Investigation of Structural Behaviour of Timber-Glass Composite Beams. Procedia Engineering. 2016;161:990-1000.

Proceedings of the IASS Annual Symposium 2019 – Structural Membranes 2019
Form and Force
7 – 10 October 2019, Barcelona, Spain
C. Lázaro, K.-U. Bletzinger, E. Oñate (eds.)

Thin glass in membrane-like structures - applications, modelling and testing

Timon PETERS*, Simon JASCHKE, Jens SCHNEIDER

*Technische Universität Darmstadt, Institute of Structural Mechanics and Design ISM+D
Franziska-Braun-Straße 3, 64287 Darmstadt, Germany
peters@ismd.tu-darmstadt.de

Abstract

With the recent advances in development of thin glass for consumer electronics, and improved glass prestressing technologies, it is now possible to create structures where the glass withstands significant cold bending (elastic bending without heating). This is not limited to uniaxial bending, but can also comprise biaxial deformation where the glass is acting as a stiff membrane. While there are a lot of potential applications, like bendable façade elements, cable net structures with form-following glass, thin glass pneus and cold-bent laminates, another important factor is testing of thin glass. High deformation and membrane stress prevent currently used testing methods like the four-point bending test and the double ring bending test from working with thin glass. This paper first gives an introduction to thin glass, then shows examples for the aforementioned applications of thin glass in architecture and explains how we proceeded in executing some of the designs. Finally, it addresses the problems with testing of thin glass and explains our solutions to these challenges.

Keywords: spatial structures, membrane structures, thin glass, glass design, material testing, conceptual design, form finding, optimization, glass membranes

1. Introduction

1.1. What is “thin glass”?

The differentiation between “thin” and “regular” glass requires more than just the definition of a thickness limit. It usually depends on the application and mechanical properties of the whole system. This means that a glass pane will usually be seen as “thin” when its mechanical behavior becomes significantly different from that of a thick, stiff plate, thus complicating the prediction, calculation or simulation of its characteristics. This can comprise effects such as large deflections, membrane stress, local or global buckling and sensitivity to vibrations.

For products intended to be used in the construction industry, which usually have dimensions in the order of one or more meters, the thickness limit between “thin” and “regular” glass can be narrowed down to a range of about 2 to 3 millimeters for most applications.

These differences in behavior allow for applications that wouldn't be possible with thick glass panes. One of these applications is (significant) cold bending. This means bending the glass without heating it up to the softening point. The glass is then either held in the desired shape by lamination of several glass layers using a polymer interlayer or by clamping/gluing it to a support/frame system. Also, cold bending allows for the use as a flexible element (e.g. a hinge).

Copyright © 2019 by Timon Peters, Simon Jaschke and Jens Schneider
Published by the International Association for Shell and Spatial Structures (IASS) with permission.

1.2 Products

Besides "regular" float glass for window panes, which can also be produced in thicknesses far below the standard thickness of 4 to 19mm (e.g. Asahi SPOOL™, a 50µm float glass), a wide variety of specialized thin glass products made by gravity-fed "down-draw" processes (e.g. Schott D263®T, available from 30µm to 1.1mm) is currently available on the market. In the down-draw-process, the glass flows out of a channel or elongated nozzle and is pulled flat and cooled in mid-air, resulting in a much higher surface quality. This makes it suitable for precision electronics and optics applications, most of which can be found in the consumer electronics industry. The high demand for new high-performance products has boosted glass research within the last decades. Products like Corning Gorilla® glass (introduced in 2007), which according to the manufacturer can be found on ¾ of all smartphone screens, have therefore revolutionized the glass industry.

Improved material properties and prestressing methods also allow for modern thin glass to be exposed to much higher stress than most standard float glass products. One example for a much-used process that can significantly increase the performance of glass products is chemical prestressing, a process leading to a high bending and tensile strength and very good scratch resistance. In this process, the glass is immersed in a bath of molten alkaline salts (usually potassium nitrate) for several hours. Since the glass contains sodium, the high temperatures cause the ion concentrations to equalize. The bigger ions then create a compression zone with a pressure of up to 1GPa in the glass surface (Fig. 1).

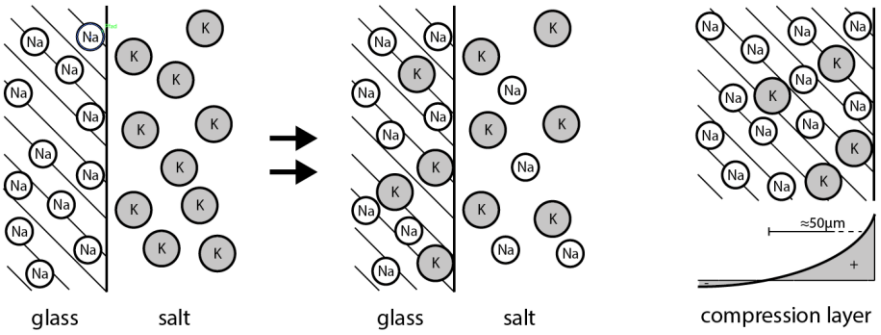


Figure 1: Chemical prestressing using a potassium salt

Common applications for thin glass are scratch-resistant display covers, micro-optics, sensors and semiconductor substrates (wafers). It is also used in biology, chemistry and medicine.

In construction, the only current large-scale application for thin glass is in standard flat windows, where it serves as a lighter inner layer for insulated glass units (IGUs). Many other applications have been suggested and tested, some of which will be presented hereafter.

1.3. Mechanical Properties

As mentioned before, a big difference between "regular" thick glass and thin glass can be found in the mechanical properties. First of all, the low bending stiffness allows thin glass to be bent significantly without the need to heat the material to a temperature above the softening point. As an example, a 2mm fully toughened glass pane can be bent to a radius of less than one meter without exceeding the stress limits given by the glass codes (e.g. the German DIN 18008). For uniaxial bending, the relation between bending radius and surface stress can be expressed by:

$$\sigma = \frac{E\,t}{2\,r\,(1-\nu^2)} \tag{1}$$

σ = stress

E = Young's Modulus

t = thickness

r = radius

ν = Poisson's ratio

For the edges, the formula simplifies to:

$$\sigma = \frac{E\,t}{2\,r} \tag{2}$$

Another difference between the different thicknesses is that while, for biaxial bending, thicker glass can usually be calculated as a plate (Kichhoff plate theory: Δ Δw=p/K), the membrane stresses in thin glass become so high that they can't be ignored anymore. Besides making calculations much more complicated, this can also cause problems when trying to determine the surface strength of the glass. A solution to this problem is shown in the last chapter of this paper.

2. Applications

2.1. Cold-bent laminates

Cold bending describes the act of forcing the glass into a specific shape without permanently deforming the glass itself. Unlike hot-bent glass that is made by heating it to a temperature above the softening point where the glass becomes permanently deformed, cold-bent glass will spring back into its original flat shape if no outside forces are being applied. These forces can be created by clamping or gluing the glass to supports, e.g. a frame. Alternatively, multiple layers of glass can be laminated to each other using a polymer interlayer (e.g. polyvinyl butyral, or the stiffer ionoplast SentryGlas® foils).

An obvious application for laminated cold-bent glass is the creation of complex window geometries, e.g. panes with a non-constant curvature that can't be created inside a modern flexible prestressing oven. The shape of cold-bent laminates might therefore also be optimized to yield a stiffer, yet much lighter window element.

Compared to hot-bent glass, cold bending has a few big advantages. The first is that unless the desired shape just has a single, small curvature that can be created inside a prestressing oven, a lot of expensive specialized equipment is needed for hot bending, e.g. a large oven and heat-resistant moulds. Another advantage is the surface flatness which can be very hard to control during hot bending. The flatness of cold-bent glass is much easier to control due to the fact that it is made from flat glass that is bent by outside forces, so the shape follows the applied bending moment. Still, hot bending glass outside a prestressing oven might sometimes be preferred when it comes to creating larger double curvatures, since cold bending only works for large single and small double curvatures.

There are two methods of producing a cold-bent laminate, both of which have been previously used at our institute:

The first method is to laminate the glass inside a mould. The advantage of this process is that only one production step is required. The laminate layers are stacked, put inside a vacuum bag and then pressed into the mould. The unit is then autoclaved at about 140°C to 160°C, which works fine with most wooden moulds, so in most cases no expensive materials are required. Afterwards the glass laminate needs to cool down before it can be taken out of the mould.

However, a downside of this method is that while it only consists of one step, the moulds take up a lot of space inside the autoclave. For some ovens, they might not even fit inside. Also, the cooling process takes a lot longer if the mould prevents heat flow.

Therefore, the second method might in many cases be the more useful: The glass is first laminated flat as it would be done with any laminated safety glass used in architecture, and then brought to a different oven where it is heated again and pressed into the mould. This allows for a much better use of the

autoclave. Also, the second step does not need any special process parameters or equipment. The finished laminates only need to be heated to about 120°C and pressed into the mould using weights or spring clamps. This can even happen inside a simple heated box.

The limits of this second method are that the bending radius can usually not be as small as with the one step lamination, since too much viscous flow of the softened interlayer causes it to lose its constant thickness, and since delamination may occur on the edges.

2.2. Flexible Façade Elements

The real advantage of thin glass comes into play when it is used in applications where its flexibility allows for moveable, bendable and adaptive structures. Two main concepts exist here: the glass can either be bent actively to change its shape, or the flexibility can be used to adapt to outside loads.

2.2.1. The Rolling Window

A good example for the application of flexible cold bending is the "rolling window" created by our institute for the "glass technology live" exhibition at glasstec fair 2018 in Düsseldorf, Germany.

The "rolling window" is a frameless window element with a mechanical system that curves the glass outwards. The system is attached to the inside of the glass, creating a flat and elegant façade that enables a high light permeability. Due to the single-edge bearing, the expense for material and installation is highly reduced, and the element can be quickly replaced. The mechanics are based on flexible, motor-driven shafts that expand or contract, creating an axial force along the inner glass surface. This force is then transferred into a bending moment leading to a constant curvature.



Figure 2: Rollable window prototype at glasstec 2018

The window element is mainly intended for application in secondary layer façade systems (due to the lack of thermal insulation). Besides the use as regular windows, the glass can be coated to act as a shading, as a visual shield, or as a carrier for photovoltaics (which may be semi-transparent). Nanocoating the surface to change the transparency with different bending radii might also be possible.

The critical point when designing such a window is fixing the mechanical parts to the glass surface. While the 1mm thick chemically prestressed glass used for this window could theoretically be rolled upwards by more than 180° without exceeding strength limits, the adhesive has to transfer high forces while still allowing deformation.

To fix a point support to flexible glass, an adhesive that is both strong and flexible is needed. It has to be able to stick to the glass and still transfer forces when the pane is being bent, so it needs to withstand large deformations without delaminating or breaking. After ruling out most adhesives, the performance of two different bonding materials were investigated: acrylic UV-resin and structural silicone (Dow ® TSSA, which is being studied extensively at our institute).

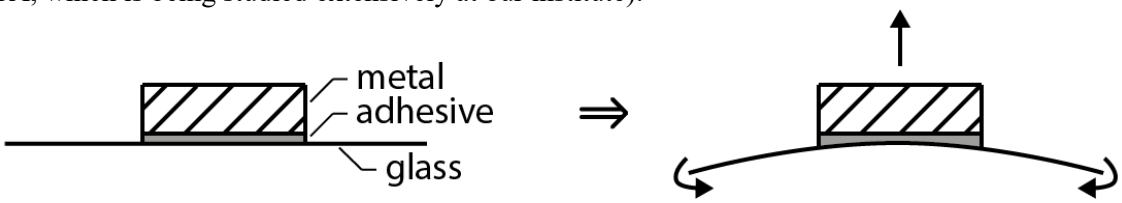


Figure 3: Point fixings for the mechanical opening system

The advantage of UV adhesives is that the material combination is not limited to materials with a similar thermal expansion or to heat-resistant materials. The adhesive can be applied on site during installation, allowing for better tolerance control, and it only needs UV light to cure. After hardening, most acrylic UV adhesives stay flexible enough to allow for (at least small) deformations.

In contrast to that, structural silicone adhesive needs to "baked" to the glass in an autoclave oven. Not only does this take a lot longer, it also strongly limits the material choice for the supports/fixings. First of all, the materials need to be able to withstand curing temperatures of around 150°C, which already excludes most polymers. Also, for larger adhesive surfaces, the thermal expansion coefficients cannot differ too much from the thermal expansion coefficient of glass, otherwise stresses and deformations would strongly limit the size of adhesive surfaces. Yet, an advantage of structural silicone is the generally much better structural performance, allowing for higher forces to be transferred. Also, the mechanical properties are known much better and the material usually gives better optical results.

2.2.2. Thin glass cable net structure

Inspired by the Munich Olympic Park roof structure created by Frei Otto for the Olympic Games in 1972, an attempt was made to create a flexible cable net structure using thin glass as form-following cover. A special focus was on the connections of the glass to the cables. The glass needs to be connected continuously to the cables in order to enable a weatherproof and rain-impermeable roof structure as well as involving the glass in the load transfer.

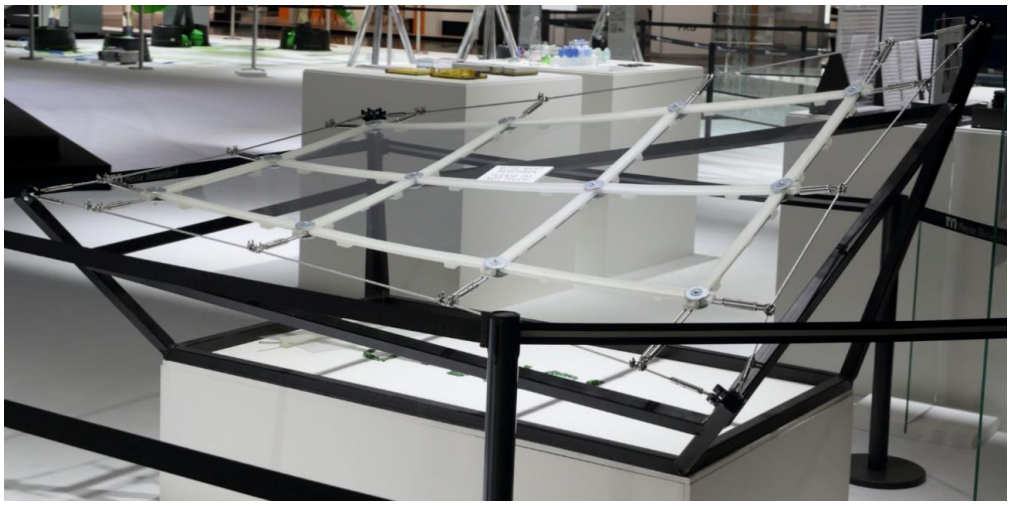


Figure 4: Cable net structure at glasstec 2018

In order to achieve a stable and efficient surface, to use as a reference cable network, a hyperbolic paraboloid was given as a starting geometry. Then the model was filled with boundary conditions like the stiffness of the support springs, maximum allowed prestress for the cables, and loads. With this, the surface was optimized with the grasshopper add-on "K2-Engineering" according to the "force-density-method" by both reducing the differential forces at each knot as well as finding the coordinates of the knots at which the network is in equilibrium. The force-density q is defined as the ratio of force (F) to length (l): $q=(A/l)$; $\sigma=(F/l)$. After a stable configuration was found, the geometry was exported to other software for further calculations. The model was used to find the stiffness of the system in different load situations, the resulting deformation, and the general behavior of the structure under asymmetric load. From this, the curvature, the change of curvature during different kind of load situations as well as the stiffness was extracted to do more detailed finite-element studies on glass and connections.

Expecting a geometrically linear behavior for the thin glass would lead to incorrect results. The deformations are so high, compared to the thickness of the "plate", that geometrically non-linear effects had to be considered. As [1] shows, there is a specific limit of stability after which the glass does no longer follow the Kirchhoff-Love prediction of a hyperbolic paraboloid shape but instead will find its energetic minimum in a "buckled configuration" (Fig. 5). This phenomenon leads to a problem that, if using point supports, two neighboring glass edges will not automatically follow one common curve which is necessary to ensure a continuous structure with a smooth curvature. It can be shown that a linear support of the edges increases the limit at which the indifferent state of the plate occurs. However, at the same time, the local stress will often increase.

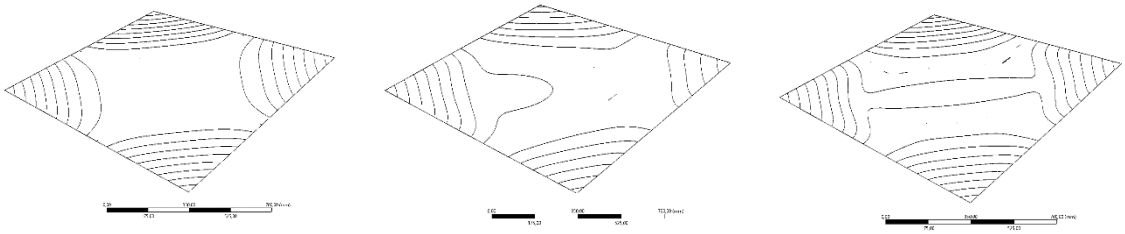


Figure 5: Point supported glass plate with increasing deformation (from left to right) causing an indifferent state during deformation process (middle), leading to a stable state with different curvatures in the diagonals $\kappa_1 \neq \kappa_2$

For a continuous support, a clamping bar was created. From the first sketches to 3D-printed prototypes and a functional model, different problems had to be solved. The structure should resist all weather situations, the clamps should bear the stress coming from the biaxial bending as well as from external loads, and both assembling without difficulties and a non-destructive disassembly should be made possible. A module was created which is clamped between the glass and onto the cables using bolts.

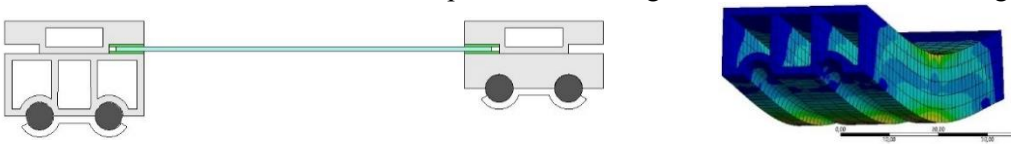


Figure 6: Left: clamping system: different heights of the modules for the different cable axes were designed to have the same resulting stiffness; Right: FE analysis

To get the equivalent stiffness for further calculations and to analyze the behavior of the bar under load, different geometries were created and calculated in ANSYS, some of which were later as well confirmed in physical tests. From this analysis the quality of the design was assessed, and then tested in the cable net. To ensure the impermeability of the system, thin strips of elastomer were taped to the glass edges before assembly. By clamping the glass between the upper and the lower part of the clamping bar, no water will permeate trough the structure.

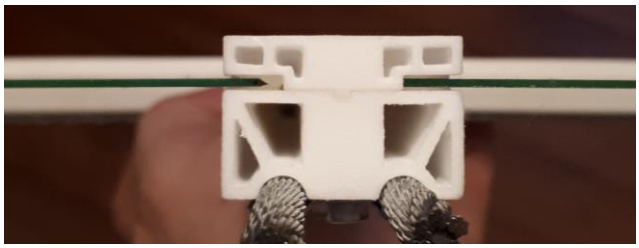


Figure 7: Protoype of clamping bar with thin glass

2.2.3. Thin glass pneus

Another type of flexible façade or roof element is the "glass pneu", a lightweight double or triple glazing where core pressure is changed to vary the elements stiffness by activating membrane effects.

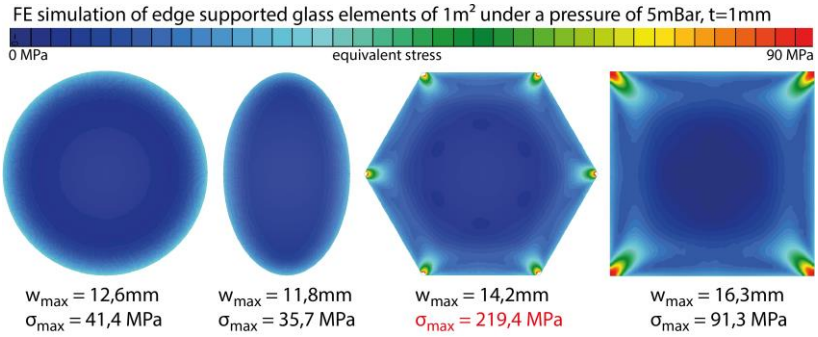


Figure 8: Stress in inflated glass elements for some basic shapes

Since the glass shows a membrane-like geometrically non-linear behavior under large deformation, it stiffens up rapidly the more it gets inflated. This then allows to create structures where the deformation of the glass becomes much lower than it would be with flat panels.

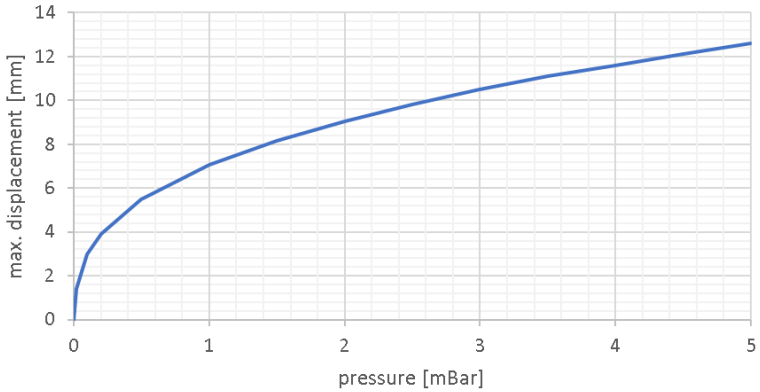


Figure 9: Stiffening of the element due to membrane stresses for a 1m², 1mm thick, round thin glass pneu

Of course, due to the higher stiffness, the glass pneus will not look as pillow-like as textile membrane pneus, but this may in many cases be an advantage, either esthetically, or when space constraints limit the volume of the elements.

Shape optimization showed that large inner angles of the pneu surface lead to very high local stress concentrations. Therefore, if multiple elements are to be joined in a regular pattern, a triangular or square configuration might be better than a hexagonal (as shown in Fig. 8 for simple shapes).

3. Testing

3.1. Edge strength measurement

In the standard four-point bending test, thin glass will undergo such large deformations that it will simply slide from its supports. This could be compensated by decreasing the specimen's length, which would unfortunately decrease the significance of the results. Therefore, a testing setup that can deal with large deformations had to be built. The solution was quite simple: the machine clamps the pane at both ends and applies a bending moment that forces the glass into a constant radius (which, in our case, can get as low as a few millimetres for testing ultra-thin glass). Rotation and bending moment are measured.



Figure 10: Uniaxial bending test with a 250mm long, 1mm thick chemically prestressed glass plate

3.2. Surface strength measurement

In the double-ring bending test, as with the glass pneus from chapter 2.2.3, membrane stresses cause the glass to undergo a geometrically non-linear deformation and therefore have a non-uniform stress distribution below the testing ring, which would not be the case for thicker glass (see [3]). A way to compensate this is by using air pressure to apply part of the load. A testing setup is currently being optimized that uses a small vacuum chamber below the support ring. The vacuum partly compensates the membrane stresses to yield a better, more uniform stress distribution.

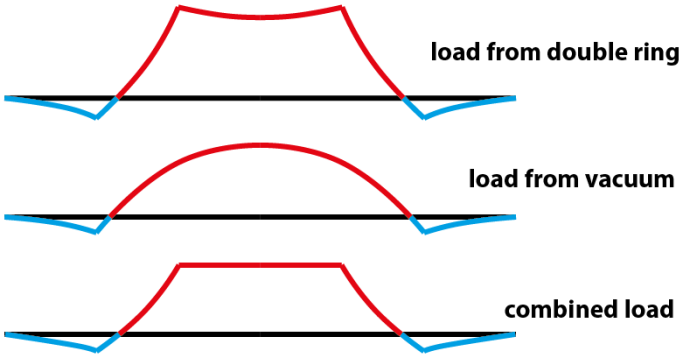


Figure 11: radial tensile stress at the underside of a square thin glass plate under different load types, from FE.

References

[1] L. Galuppi, S. Massimiani, and G. Royer Carfagni, "Buckling phenomena in double curved cold-bent glass". In: *International Journal of Non-Linear Mechanics 64*. 2014

[2] P. Singer, "Die Berechnung von Minimalflächen, Seifenblasen, Membrane und Pneus aus geodätischer Sicht", Institut für Anwendungen der Geodäsie im Bauwesen, Stuttgart 1995

[3] J. Schneider, J. Neugebauer, M. Schuster and T. Peters, "Cold-bent thin glass laminates for architectural applications: Computational design and material modeling". In: *Proceedings IASS* (Hamburg, Germany) 2017

Proceedings of the IASS Annual Symposium 2019 – Structural Membranes 2019
Form and Force
7 – 10 October 2019, Barcelona, Spain
C. Lázaro, K.-U. Bletzinger, E. Oñate (eds.)

Prototyping with Ultra-Thin Glass

Sophie PENNETIER*, Josephine STODDARD [a]

* Enclos Advanced Technology Studio
1035 S Grand Ave, Los Angeles, CA 90015
spennetier@enclos.com

[a] University of Southern California
850 Bloom Walk, Los Angeles, CA 90089
jfstodda@usc.edu

Abstract

Capitalizing on recent developments of an ultra-thin glass sculpture [1] and a pavilion [2],[3] further research was conducted on glass connections, glass cutting and lamination. This article focusses on the calibration and validation of the protyping methods. The results documented herein include cutting with waterjet CNC equipment, laser cutter and mechanical cutting wheel testing performed in Boston in 2018 and 2019. Support methods, materials, machine equipment and parameters are discussed. Each viable sample has been subsequently bent to rupture to assess impact of edge finish on ultimate glass strength.

Keywords: Ultra-thin Glass, Cold Bending, Curved Glass, Structural Glass, Sculpture

1. Introduction

Ultra-thin glass comprises glass below 1-2mm in thickness. As such, it is very flexible. For example, ultra-thin glass of 0.1mm thickness will bend similarly to a regular sheet of paper, which is also typically 0.1mm thick. Ultra-thin glass is either produced by "Draw Down" [1] or "Fusion Draw" [2]. These processes, developed in the 60's, consist of stretching the glass vertically before rolling it up in spools. Ultra-thin glass typically comes in spools 1.3m wide, in length of 300m. The main suppliers are Corning, AGC and Schott. Unless otherwise specified, the ultra-thin glass product used for this research is Willow Glass by Corning. It is made of alkali-free borosilicate manufactured in 0.1 and 0.2mm thicknesses. In the current market, applications for ultra-thin glass include automotive interior glass, consumer electronics, LCD display technologies, electric wafers and interior architectural glass. In most applications the glass is mounted to a substrate. For instance, interior architectural applications with small thermal loads allow for bonding to material of dissimilar Coefficient of Thermal Expansion (CTE) such as aluminum or wood fiberboard (MDF). It is essential to laminate the glass to ensure post-breakage redundancy for its use in the build environment, as it breaks in large shards, similar to annealed glass.

The potentials of ultra-thin glass in facades include light weight dual skins, retrofitting, curved facades, or Insulated Glass Units (IGU) with multiple cavities. Furthermore, the potential of using glass material that comes in spools of 300m is unfathomable.

Cold bending glass is a process of deforming glass elastically at room temperature, in opposition to hot bending which involves slumping glass at high temperature. The shape of cold bent glass needs to be maintained by connections: if the connecting elements are removed, the glass springs back, completely regaining its original flatness. Many projects use cold bent glass panels, such as the IAC Headquarters in New York, the Strasbourg Railway Station, or the One Blackfriars tower in London. For each of these

Copyright © 2019 by Sophie PENNETIER, Josephine STODDARD
Published by the International Association for Shell and Spatial Structures (IASS) with permission.

projects the components retaining the glass, whether it is the supporting structure, the interlayer ensuring shear transfer, or the seal of the IGU frame, must be designed to sustain high spring-back forces which depend on the stiffness of the bent glass system. Due to its thinness, flat ultra-thin glass has very little stiffness, so it results in very low spring-back forces when cold bent. Furthermore, curving glass augments geometrical stiffness which enhances serviceability.

The research topics discussed herein were inspired by the advancements in ultra-thin glass research attributed to Pennetier's sculpture project in 2017 [3]. The sculpture is 700mm high and 750 x 750mm in plan. It showcased an iterative analysis of geometry and internal forces can result in a rigid free form design and a process scalable to the build environment. It combined six (6) non-laminated 0.2mm glass panels, connected by means of 3D printed PLA V-shaped profiles. The glass was supplied by Coresix, a glass manufacturer located in Virginia (USA) masters of cutting ultra-thin glass. The V profiles were printed in 250mm lengths on parallel printers, an economical approach to produce the connections (further discussed in section 3). While these materials were adequate for prototyping and research on the glass itself, a few lessons were drawn from this project: The connections of the disjointed V sub-profiles created soft hinging locations where the glass broke (Fig.2). Furthermore, the adhesive used to connect the glass to the V profiles was chosen for its rotation capacity combined with immediate bonding capacity but did not perform well as the adhesive creeped under long term load and high temperatures in storage through the summer. Further lessons learned are discussed throughout this paper.

The primary goal of this research is to explore solutions accessible to students and designers for prototyping ultra-thin glass systems for architectural applications. These explorations cannot compare to the extensive research and development from major glass manufacturers. However, very little of their great knowledge has yet diffused into the facade industry.



Figure 1,2,3: Glass Sculpture June 2017 (left) and October 2017 (middle),
USC Master Thesis J. Stoddard Pavilion Model (right)

The research presented here is twofold: manufacturing and design. The manufacturing aspect of this research was greatly helped by Enclos colleagues, available equipment and materials, as well as our residency at the Autodesk Boston Build Space, where multiple pieces of equipment was accessible, as well as the valuable support from the Build Space team. In the following sections, advances in ultra-thin glass cutting are documented, including the use of waterjet (1.1), laser cutter (1.2) and scribing wheel tooling (1.3). Multiple cut specimens were submitted to bending to assess bending strength, which depends on edge condition (1.4). Secondly, the developments in lamination (2) and connections (3) are discussed. Lastly, the work of USC Master student Josephine Stoddard [4] in collaboration with Enclos is presented, including design development of a pavilion, its geometry, innovative detailing, structural analysis and prototyping (4) which addressed the second aspect of this twofold research project.

2. Glass cutting

Glass manufacturers using ultra-thin glass for consumer electronics or interior wall panel applications use either scribing or laser cutting technologies. Scribing consists of scoring the surface of the glass with a small diamond wheel and mechanically breaking it. This technique is used by Coresix for the applications mentioned above, for thicknesses down to 0.05mm (although typically between 0.1 and 0.7mm). A scribing wheel is mounted onto a router, which can translate in both X and Y directions, with an additional Z rotation to keep the wheel parallel to the scribing contour. The scribing contour can be either straight or curved, with a curvature radius to as tight as 0.025mm [5]. Theoretically, this technology allows for panels which are virtually as large as the spools themselves (1.3x300m).

Alternatively, Corning produces a laser cutter, CLT 500X [6] which has an accuracy of less than 0.005mm (per 200mm). The laser cutter can cut pieces up to 450 x 660mm, for glass from 0.05 to 6mm in thickness. The cutting contours may be curved, straight, perpendicular or angled lines, as well as holes and slots.

Finding affordable and easily accessible tools is key for façade designers and architects exploring the potential of ultra-thin glass. This section covers three technologies: waterjet, laser and scribing. It is worth noting that the research was performed using Willow Glass, which behaves like an annealed glass product [3] and therefore can be cut without shattering in small fragments like tempered glass. It does not require further chemical tempering either, which would greatly restrict prototyping for the size and locations of baths.



Figure 4,5,6: Corning CLT500X (left, middle), Coresix router (right)

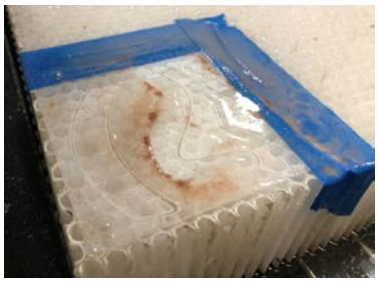
2.1. Waterjet cutting

The use of a waterjet to cut glass is quite common when glass is in the range of 2-20mm. The team tested cutting ultra-thin glass with a 5-axis CNC waterjet available at the Boston Build Space, which other teams have successfully used to cut glass as little as 2mm in thickness. The waterjet fluid is purely water with a small amount of abrasive mixed in. Each trial piece was taped to a rigid plastic honeycomb structure (see Figure 7 and 8).

The first trial pieces were non-laminated, 0.1mm, and would either fail to cut or completely shatter. Upon lamination of two 0.1mm sheets of glass (see separate section on lamination) the trial was, in some sense successful since it didn't completely shatter. The cutting contours were single curved and double curved (S shaped). However, the rough edge condition still wasn't satisfactory (see Figures 9,10, 11). At this point in the project, the other cutting methods were already giving better results, so the waterjet cutting research was discontinued. Further areas of research should investigate thicker laminates of ultra-thin glass, alternative interlayer materials, different abrasive mixes and densities, and other supporting materials.




Figure 7,8: Waterjet at Boston Build Space



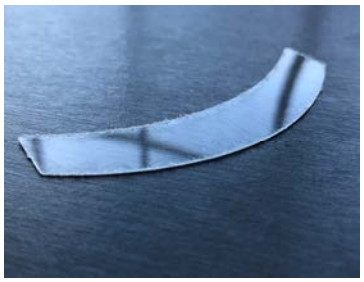


Figure 9,10,11: Waterjet cut laminated 0.1+0.1mm specimens

2.2. Laser cutting

With the goal of developing a widely available cutting methodology, our team explored the use of tabletop laser cutters generally available in multiple architects or designers' offices. These laser cutters are most often used to cut PET, acrylic and thin MDF boards for architectural models or signage.

The Boston Build Space has four Epilog Fusion40 CO2 120 watts Laser Cutters, with a cutting plane bed of 1000x710mm. The team successfully cut 0.1 and 0.2mm non-laminated glass without shattering and we fine-tuned the following parameters to get the best the edge quality: speed, power and frequency of the laser. Plastic and steel backing materials were tested, as well as having no backing material, cutting directly on waffle support. The plastic support proved to be the best option, as it was less reflective than the steel support and leading to a better edge condition. The absence of material did not result in a satisfactory edge condition. The best results were obtained by using a 3mm thick clear plastic backing: in fact, smoke from colored plastic would color the glass itself and be very hard to remove. Perfect flatness of the 3mm thick backing is crucial to ensure an accurate focal point of the laser. Optimum results combined a low speed, low power and high frequency laser setup.

Each laser pass would remove material, as the ultra-thin glass will burn. The cutting contour width would be approximately 0.5-1mm wide with the optimum parameters. It is worth noting that laser cutters are equipped with a ventilation system which evacuates the smoke of glass and plastic.

When cutting through free edges, small "ears" were observed (see Fig. 13), especially at the start of the cut at the free edge of the glass. Adding tape to secure the edges did not resolved the problem. Straight, single curved, doubly curved (S-shaped) and circles were successfully testing. Good results were also observed cutting one laminated sample (see section 1.4). The team couldn't tune the laser cutter to obtain a scored vent in order to subsequently mechanically break it.

Each laser cut specimen was submitted to a bending test (see section 1.4). Given the rough edge quality, some of the samples were polished with fine sanding paper before test. Although laser cut pieces did not perform as well as scribed pieces it is still considered a promising alley to produce cut ultra-thin

glass pieces for prototyping. Future research should include laser cutting of ticker laminates, alternate interlayer materials and other support materials.

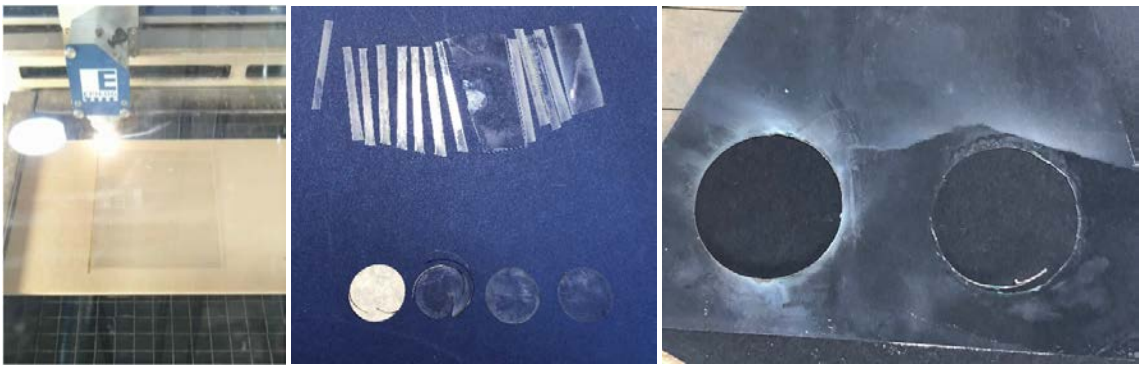


Figure 12, 13, 14: Straight and curved cuts with laser cutter

2.3. Scribing

Scribing consist of scoring glass with a diamond wheel in order to create a vent, before the glass is manually broken along the vent. This technique has been mastered by Coresix and was used for cutting the 0.2m glass panels of the 2017 sculpture project. Standard glass cutting wheels used for thicker glass were too rough for the ultra-thin glass and resulted in uncontrolled breakage. While procuring the adequate diamond wheel is more expensive than standard laser cutters; so far it produced the best results.

Figures 15 and 16 show manual cuts obtained using a diamond wheel. Straight, single curved, doubly curved (S-shaped) and free-form contours were successfully tested on a thick MDF office desk support or a stiff cutting mat. Manually handling the wheel is limited to small size samples and is not a very forgivable method as the pressure and angle of the wheel are crucial to ensure a smooth continuous cut. At the time of publication of this article, the team is exploring mounting the wheel onto a router.

Straight pieces were subjected to a bending test (see section 1.4) to compare this technique to laser cutting.

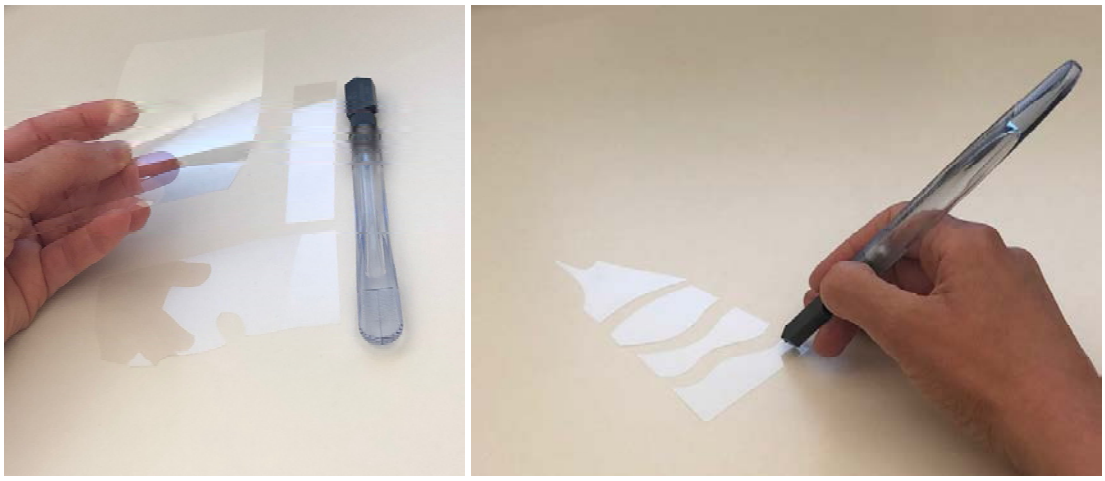


Figure 15,16: Scribing straight and curved cuts with diamond wheel

2.4. Structural testing

Glass strength is a function of the distributions of material flaws and their propensity to grow and is primarily affected by the edge roughness. While being innovative (and quite open-minded) in the process of researching accessible means to cut ultra-thin glass, the team is overly aware that glass cutting technology needs to be optimized to preserve or at least maximize the strength of glass panels. The latter is especially important since the product, here Willow Glass, has a relatively low bending strength. As documented in [3], Corning glass specifies a design value of 40 MPa. While non weathered ultra-thin glass proved to have a safety factor of 3-4, the authors recommend using larger safety factors where ultra-thin glass is to be used for a flexible application. As a matter of fact, glass manufacturers label the "compression" surface on the glass sheets after cut, which corresponds to the surface facing the inside of the spool, whereas the exterior surface is stored in tension.

Several specimens were produced and tested, for each of the cutting methods aforementioned. The specimen sizes were 0.1x20x100mm. All types are listed below and illustrated in Fig.17, from left to right:

A - Laser cut (4)
B - Laser cut manually sanded (3)
C - Scribed Enclos (2)
D - Scribed Coresix (7)

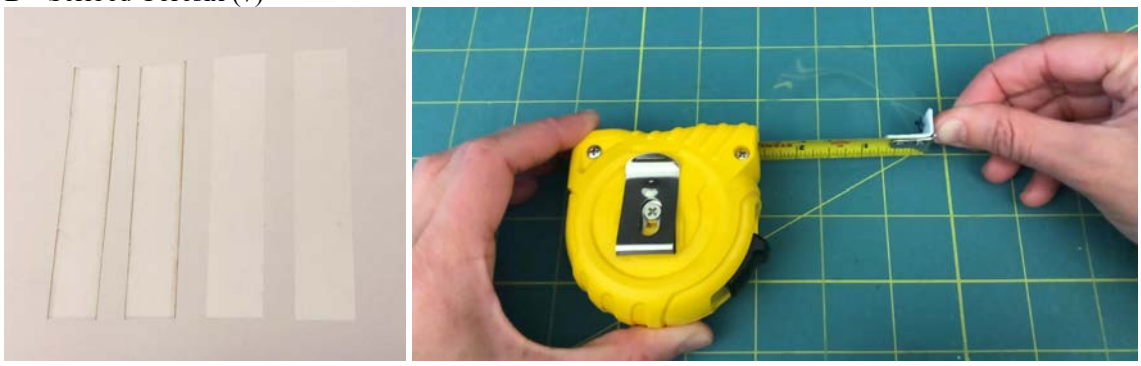


Figure 17,18: Bending strips specimens A, B, C and D.

A total of 16 specimens were tested, which is not a significant sample population, but offers enough insights on the order of magnitude of the relative capacity of the glass elements. The samples were placed on a system that slid at one end and were fixed at the other (see Figure 18). Where necessary, a thin sheet of foam spacer was placed to avoid glass contact with metal and prevent a failure at the short edge. No specimen broke at the short edge; they all broke at approximately mid-length of the long edge, as expected. Some samples experienced further breakage after slipping out of the testing support, but upon review of the videos of each test and review of the sample pieces, it was confirmed that they all broke at approximately mid-length of the long edge.

The bending radius of the deformed shape (first parabolic then circular) was monitored then normalized to the index D and summarized in Fig.19 and 20. The bending capacity of samples type A was 47% of index D. Specimens of type B and C were respectively 48% and 97% of index D.

The results were relatively scattered, which might be due to multiple parameters, not isolated by the time of this publication: storage of glass and possible weathering or scratching due to handling, cutting method variability, testing setup and measurement method. While all samples for each family type were produced from one single sheet of glass each (totaling four source sheets total, for the four sample types), the distribution of flaws could vary across the surface. While the testing setup and measurement method was the same for all samples, some minimal out of plane rotation of the support could lead to

dissimilarity in the results. The results were more scattered for the series E than the other series, which can be explained by handling specific to this set, but also the fact that these samples were subject to multiple loading before tests, which could have induced fatigue in the glass flaws. Another parameter not isolated at this point is whether the samples were bent on the "compression" side or "tension" side of the product.

The edge polishing of the samples did not show a significant improvement, which remains of the order of magnitude of the measurement itself. The method of polishing, the grit grade (50), the orientation of the polishing (which is known by architectural glass designers) did not seem to soften the edge defaults produced by laser cutting. In either case, the laser cut samples were far from optimal, with a bending radius, and therefore bending capacity, half of those for samples C and D.

The scribed samples (C, D) were bent at radii of approx. 23mm. This value compared to the 90mm value recommended by Corning provides a safety factor of 3.9 in average, or 3.5 to 4.7 for the extreme cases. The authors do not recommend designing for less than the value recommended by Corning (90mm) as the effects of handling, weathering or stress fatigue are not quantified at this point.

In conclusion, the laser cutting methodology, while providing results half of other techniques remain a viable, consistent and affordable cutting technique for early stages of prototyping. The scribing technique, while much lesser economical provided the best results for prototyping and production. Future research should address weathering of ultra-thin glass, edge treatment, stress fatigue, testing apparatus refinement, metrology.

	Specimen	Count	Radius	Min	Max	%
A	Laser cut	4	47.7	45.8 (-4%)	51.0 (+7%)	47%
B	Laser cut polished	3	46.6	45.8 (-3%)	48.7 (+3%)	48%
C	Scribed (Enclos)	2	23.3	22.5 (-3%)	24.0 (+3%)	97%
D	Scribed (Coresix)	7	22.5	19.0 (-16%)	26.0 (+16%)	100%

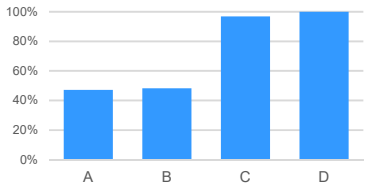


Figure 19,20: Bending test specimens list and relative bending radius (mm)

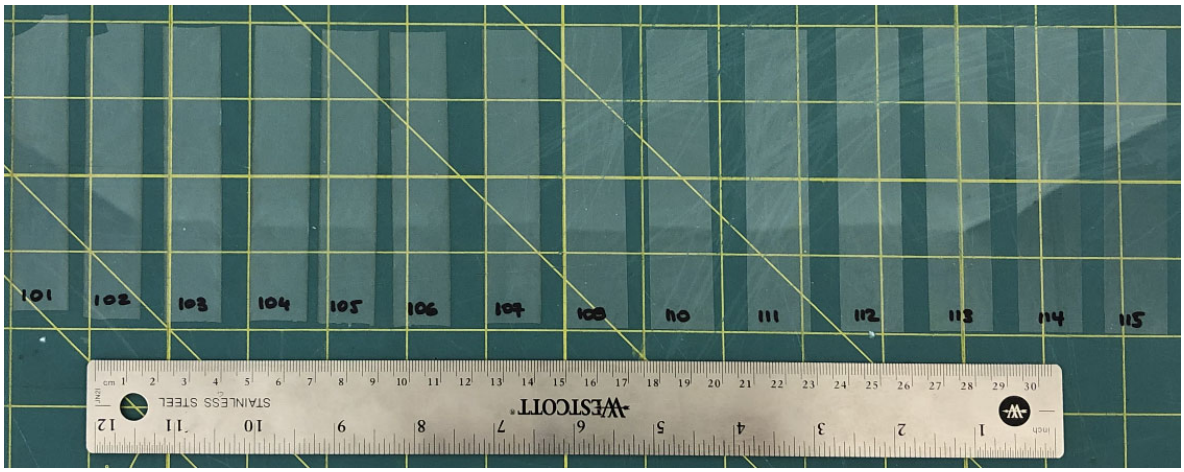


Figure 21: Bending test specimens before test

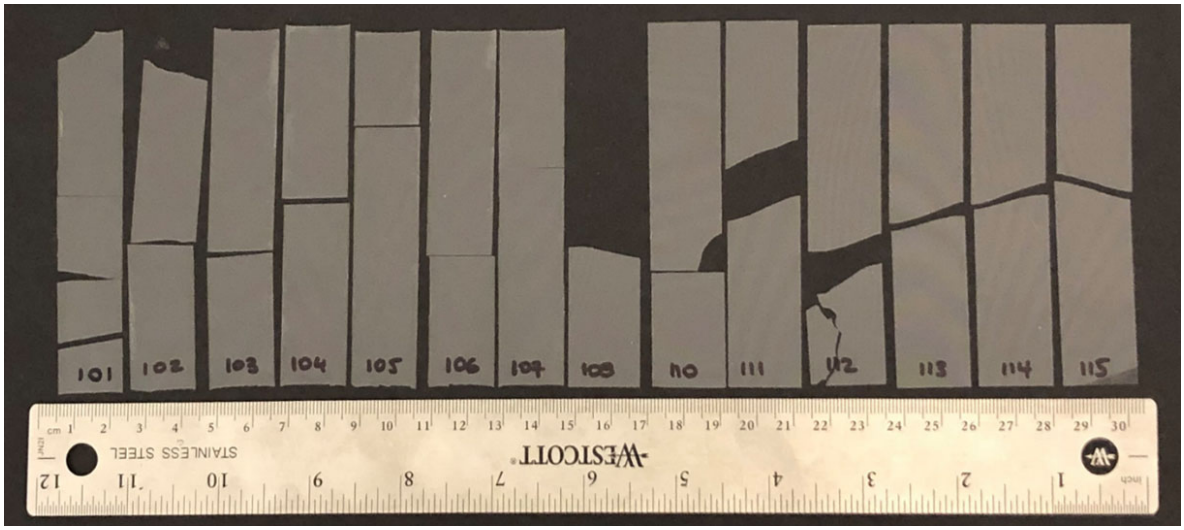


Figure 22: Bending test specimens after test

3. Referencing literature

Safety glass is comprised of tempered and/or laminated glass. As previously documented [3], Willow Glass behaves like an annealed product which breaks into large shards and requires lamination. Lamination enables retention of the glass fragments, should the panel come to break. Typically, safety glass in buildings is laminated with PVB, EVA or SGP interlayer. However, these films are much thicker than the ultra-thin glass itself, and SGP would typically be stiffer than the ultra-thin glass itself. As the context of this research is to use the flexible nature of ultra-thin glass, another thinner interlayer was investigated. We used a 1 mil (0.025mm) high quality, optically clear PET film, coated on both sides with a pressure sensitive, permanent solvent acrylic adhesive, both of which are protected by a clear PET release liner. The film and adhesive are using the finest optical clarity components and offer excellent UV stability.

The laminated specimen size was 0.1 x 100 x 20 mm, using two (2) glass specimens cut by Coresix, and one sheet of interlayer. Figures 21 and 22 depict the application of two-sided film on the glass strip at the time, before the laminate is pressed through a laminator roll at room temperature.

The glass laminate was manually bent (Figure 25). One lite broke at a radius close to 25mm, then the second broke shortly after. A hinge was formed at the break, the interlayer kept pieces together and no shards flew out of the glass laminate.

Whereas PET proved to be adequate to procure retention of the shards after breakage of small glass pieces, it is unlikely adequate for composite action for its very low E modulus and is extremely sensitive to temperature and creeps under permanent loads.

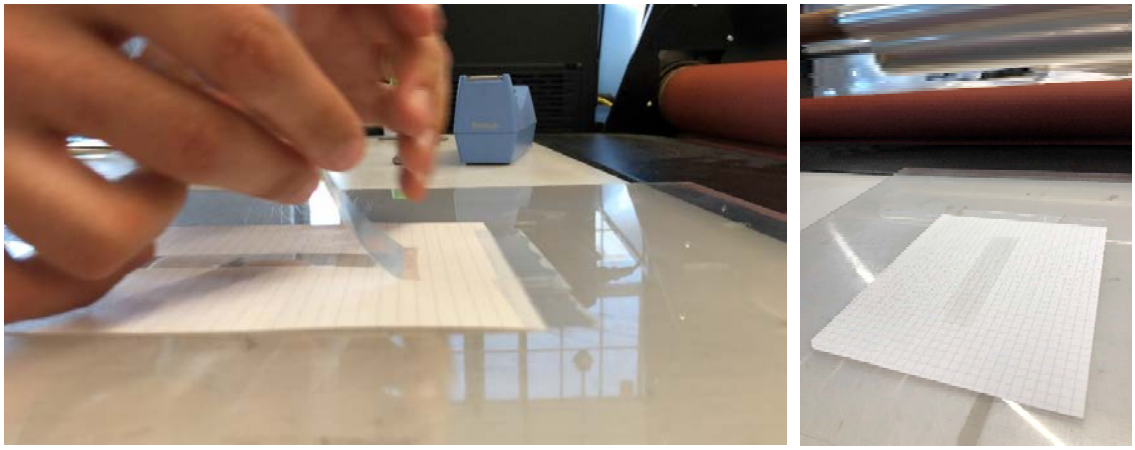


Figure 23,24: Pression Lamination @ Autodesk Build Space



Figure 25: Bending of laminated specimen

4. Connections

The ultra-thin glass panels of the 2017 sculpture project were interconnected by means of free-form sweeping V profiles, following helicoidal curves. At that scale, the V profiles could not have been fabricated from a single strip bent in its middle, because of the crease or opening occurring along the piece. It could be fabricated out of two (2) curved strips of material joined along one edge. Various fabrication options were investigated, such as CNC cutting metal sheets and welding. Given the free-form non-repetitive geometry of the sculpture, the cutting contours couldn't be perfectly nested and resulted in large material yield. Additionally, the strips would need to be spatially curved, either plastically or elastically which didn't suit well the free-form nature of the project. The plastic approach was disregarded because no economical technique matched the free-form nature of the geometry. Elastic forming results in spring-back forces which would require continuous or multiple pass welds which was both timely and costly. In either case, welding could not be automatized. These aspects greatly impacted the fabrication cost and due to budget constraints, the use of metals was discarded for the sculpture project in 2017. Further explorations on metals connectors are documented below.



Figure 26, 27: From left to right: Manually formed aluminum angle, Autodesk Boston Tube Bender, Twisted profile (Enclos supplier)

3D printing was deemed appropriate for the 2017 sculpture, subject to limited loads and is also appropriate for tabletop scale prototyping. However, at the scale of building façade systems, stainless or aluminum are definitively the strongest, most durable and optimal materials. The sweeping V profiles were 3D printed using clear PLA filament. Time and budget constraints resulted in choosing small printers which limited the maximum size of the part to 250mm. The pieces were jointed with adhesive, creating a discontinuity in stiffness. The sculpture was built in June 2017 and stored for a few months over the summer. During that time, the adhesive parts creeped, and the connection profiles hinged at the connections, which overstressed the glass (Fig. 2). Learning from it, alternate materials and equipment were investigated.

The Boston Build space has a large BigRep printer in residence, which has a 1x1x1m print bed. The team performed PLA prints trials for the pavilion project (Fig. 29). The free-form sweeping V profiles, which did not have a single flat surface, required support material during printing. Unlike several small printers, the BigRep printer does not offer a solvable support option, as the dissolution bath would need to be over 1 cubic meter. While 3D printing is a promising prototyping approach, it is worth noting that the absence of dissimilar support and print material requires intensive post-processing of the parts, which did not represent a valid fast prototyping option nor matched the pavilion project schedule.



Figure 28, 29: 3D printed curved V profiles (Pennetier sculpture + Boston Build Space collaboration with Enclos and BigRep)

Stemming back from the lessons learned on the sculpture, consisted in using more repetitive shapes were investigated, that nest well on a sheet. Although this drastically restricts the design, the result is much more promising and allows for automatization (Fig. 30).



Figure 30: Welded curved aluminum V profile (undisclosed Enclos subcontractor)

5. Pavilion Design + Connections

While team Enclos performed research on cutting and laminating ultra-thin glass through the residency at the Boston Build Space and capitalizing on internal knowledge and external suppliers, Josephine Stoddard wrote a thesis for the USC Building Sciences Master program on the topic: "Concepts for Working with Ultra-Thin Glass in Elastic Bending: Typological Development and Emergent Technology". The thesis documented precedent projects, material properties, design of a pavilion with bending active ultra-thin glass, numerical analysis of the ultra-thin glass pavilion structure and the elaboration of a physical scaled model. The scaled model was made of PET sheets, 3D printed connectors, wood mast and stainless cables connected to a stiff MDF platform. It was 850mm tall and 1200x1200mm wide (Fig. 31,32,33).

Whereas some steps capitalized on the development of the 2017 sculpture, such as geometry rationalization principals or most of the connections, the pavilion design also carved several innovative ideas. The designer was keen on reusing tensile architecture typology and elements, where glass panels would wrap around a central mast, stabilized by cables, like multiple boat sails.

While connections between glass ribs would be detailed as sweeping V's like in the sculpture, the design used channels to reinforce straight edges. These straight edges profiles were introduced not only to connect the glass edge to the tension cables in order to limit the glass edge deflections but also to protect naked edges from the public which would be able to walk around the full-scale pavilion. The straight edge pieces would run along the tension cable and connect to it with a spiraling secondary rigging (Fig. 36).

The PET was cold bent on the 3D printed supports and adhered with hot glue gun. The subparts were jointed to one another in a large preassembly (Fig.34). The sails assembly was subsequently propped off the tension cable by a small truss (Fig.35). Ultimately, the tension in the cables was adjusted and the cables locked.

Not only did this research propose innovative detailing ideas, not all reflected in the pavilion project, but it also well documented the strenuous iterative design process and prototyping process as it impacts the scale of the model and project schedule.

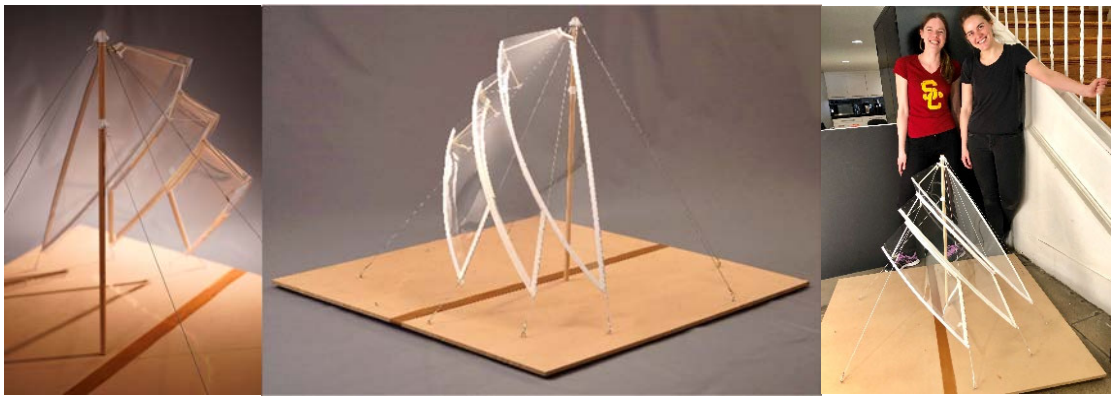


Figure 31,32,33: USC Master Student Josephine Stoddard scaled model (left, center);
Scaled model and humans for scale (right)



Figure 34,35,36: USC Master Student Josephine Stoddard model details

6. Conclusion and future works



The present research was approached on two aspects: manufacturing and design, as these are inextricable.

This article demonstrates that low cost tools, accessible to a large pool of students and design professionals, are available for the prototyping of ultra-thin glass elements. While professional waterjet and industrial laser cutting equipment are not accessible to all designers, two viable techniques are proposed: table-top laser cutting and manual scribing with a diamond wheel. At this point, the manual scribing gave the best immediate results but is hard to scale up, even for prototyping table-top models. Multiple findings on lamination and connections have been presented, providing guidance for economical prototyping.

As for the design, the 2017 sculpture project set forth a concept for design and analysis. The 2018-2019 USC Master thesis provided an excellent documentation for the current state of the research, and a successful demonstration that a very determined Building Science student from the USC Architecture School, with limited structural engineering or glass knowledge can yet become a local expert in designing with ultra-thin glass.

The research identified plethora of further ultra-thin glass research topics: weathering, edge treatment, stress fatigue, testing apparatus refinement, metrology, etc. Other topics to be addressed are connections, structural, chemical and thermal compatibility of adhesives, numerical analysis, glare and optics. These topics are sine qua non for the implementation of ultra-thin glass in the build environment.

Ultra-thin glass has a great potential in the build environment for its light weight, durability and its optical quality. Yet there are still many outstanding questions to be answered regarding the detailing and scalability of ultra-thin glass panels. The authors hope that sharing their prototyping ideas will inspire other designers to explore designing and prototyping with ultra-thin glass.

Acknowledgements

The authors are grateful to Enclos for the research and development funding, design and manufacturing input, rendering images. USC Master Student Josephine Stoddard was essential to keep the ultra-thin design research alive and well documented. The Autodesk Boston Build Space team and neighboring residents offered time and equipment to support this research (eg. Lumi inc for the laminator and BigRep 3D printer).

References

[1] https://www.us.schott.com/advanced_optics/english/capabilities/down-draw-process.html (accessed 4/30/2019)

[2] https://www.cmog.org/article/long-road-success-fusion-draw-glass (accessed 4/30/2019)

[3] *Shaping ultra-thin glass,* Pennetier, Bowers, Evain, GPD 2017

[4] *Concepts for Working with Ultra-Thin Glass in Elastic Bending: Typological Development and Emergent Technology*, Josephine Stoddard, University of Southern California school of Architecture, 2019

[5] https://coresix.com/services/cutting (accessed 4/30/2019)

[6] https://www.corning.com/worldwide/en/products/advanced-optics/product-materials/laser-technologies/clt-500x.html (accessed 4/30/2019)

Proceedings of the IASS Annual Symposium 2019 – Structural Membranes 2019
Form and Force
7 – 10 October 2019, Barcelona, Spain
C. Lázaro, K.-U. Bletzinger, E. Oñate (eds.)

From foam to form – the peculiar first free-form shell of Heinz Isler

Matthias BECKH*, Giulia BOLLER

*ETH Zurich, Institute of Technology in Architecture (ITA), Chair of Structural Design
Stefano-Franscini-Platz 1, 8093 Zurich (CH)
beckh@arch.ethz.ch

Abstract

The paper focuses on the first free-form project of the eminent Swiss engineer Heinz Isler, which was based on the so-called expansion or flow-form method [1]. Isler used this method early in his career before he moved on to use the more labor-intensive and intricate yet structurally better suited hanging models to generate the form of his free-form structures. The flow-form method is based on a fluid foam made of polyurethane, which slowly expands through a rectangular matrix while it hardens. The resulting surface geometry of the hardened PU foam can then be measured and used as a basis to determine the final geometry of the shell. Interestingly, this method was not mentioned during his seminal presentation at the founding congress of the IASS 1959 in Madrid [2], where he famously introduced three different approaches to seek the geometry of free-form shells structures: the hanging cloth, the freely shaped hill, and the inflated rubber membrane. The paper traces the first experiments with polyurethane foam and the first realized project conceived by Isler by means of this method: the Migros supermarket in Bellinzona (1964).

Keywords: Concrete Shells, Free-Form, Flow-Form, Expansion-Form, Experiment, Polyurethane, Heinz Isler

1. Moving towards free-form shells

In the year 1962, Heinz Isler started to work on the design of the Wyss garden center in Zuchwil near to Solothurn. The expressive shell structure, which is resting only on its four corners, is often referred to as Isler´s first "free-form" shell structure. At a closer look, however, it turns out that the geometry was not developed by means of one of the form-finding procedures that he had famously championed for at the IASS founding conference in Madrid. In fact, the shell surface of the garden center is based on a translation surface, with a first generatrix, a spherical segment with a radius of 14.40m, being moved along a second spherical segment (r = 17.50m). The resulting surface geometry therefore belongs exactly to the group of mathematically defined shapes that he had denounced in Madrid.

2. The first foam experiments

About at the same time as the proiect for Wyss, Isler had started to experiment with polyurethane foam models. Plenty of undated models from the gta archive of ETH Zurich suggest that this method must have intrigued Isler quite a lot. Most likely, he was fascinated by the variety of unexpected und surprising shapes that could be created by letting different mixtures of the two-component material expand. Apart from that, experiments with this methods could be done quite swiftly as the surface hardens so quickly – a significant advantage over models made of gypsum or other moist materials that required a much longer time to set. The expansion process could be controlled by the mixture itself (Isler

Copyright © 2019 by Matthias BECKH, Giulia BOLLER
Published by the International Association for Shell and Spatial Structures (IASS) with permission.

usually used mixtures that expanded with a ratio of 1:30 in volume), and the surrounding in which the expansion process took place. Typically, this was done during the initial studies within wooden boxes of 10x10x10cm. The friction along the wooden walls inhibited the expansion at the perimeter method, particularly at the corners. In the next step, Isler studied the so-found shapes by slicing the foam models and measured their geometry and surface curvatures.



Figure 1: Undated polyurethane testing model, early 1960s [gta Archive]



Figure 2: Undated polyurethane testing model, early 1960s [gta Archive]

3. Migros supermarked in Bellinzona (1964)

In 1964, the flow-form method was used for the first time to conceive the geometry of a shell structure: the domed Migros supermarket in Bellinzona. Similar to the Wyss shell, the design brief called for a shell structure over a square footprint with spans of approx. 31.30m between the supports in either direction. An initial sketch shows the spatial requirements with strict constraints for the heights at the perimeter and at the apex. Early conceptual sketches by Isler show that he tried to find fitting geometries based on spherical segments or ellipsoids. But the geometric constraints could not be fulfilled with this approach. Photographs from the archive as well as his notes and sketches show that he undertook a variety of experiments with the flow-form method, carefully altering the mixtures and boundary conditions in order to find a form that would suit best the architectural brief – with a steep inclination at the support and a rather low curvature towards the apex of the shell.

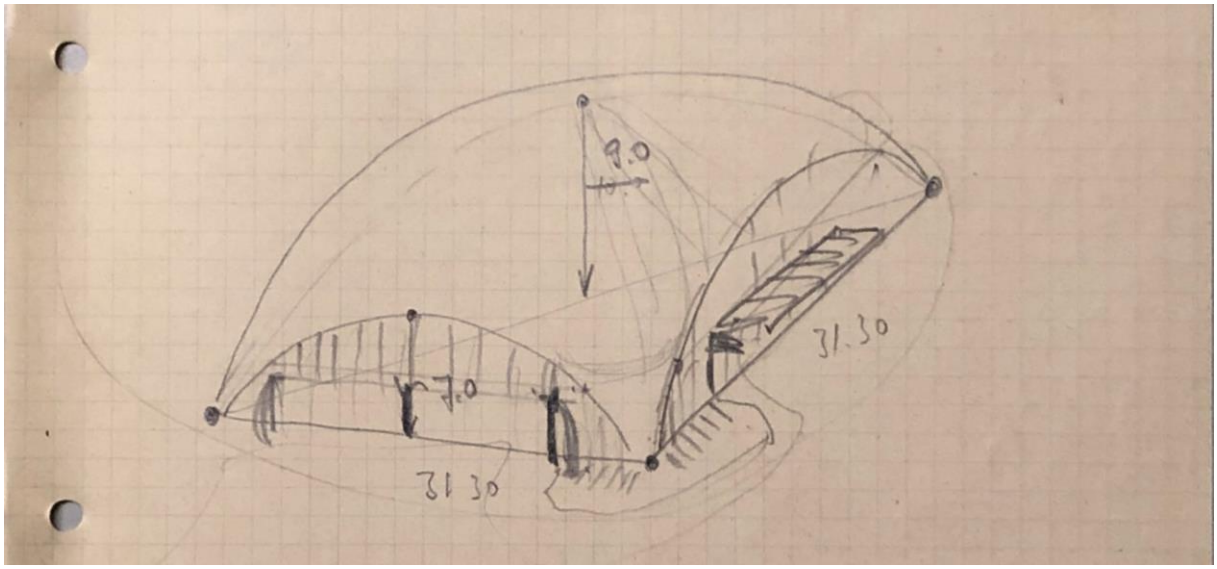


Figure 3: Sketch with the geometric constraints of the Bellinzona shell, 1964 [gta Archive]



Figure 4: Polyurethane model in 10cm/10cm/10cm box during preliminary design [gta Archive]



Figure 5: Photographs of polyurethane studying models in 1:100 [gta Archive]

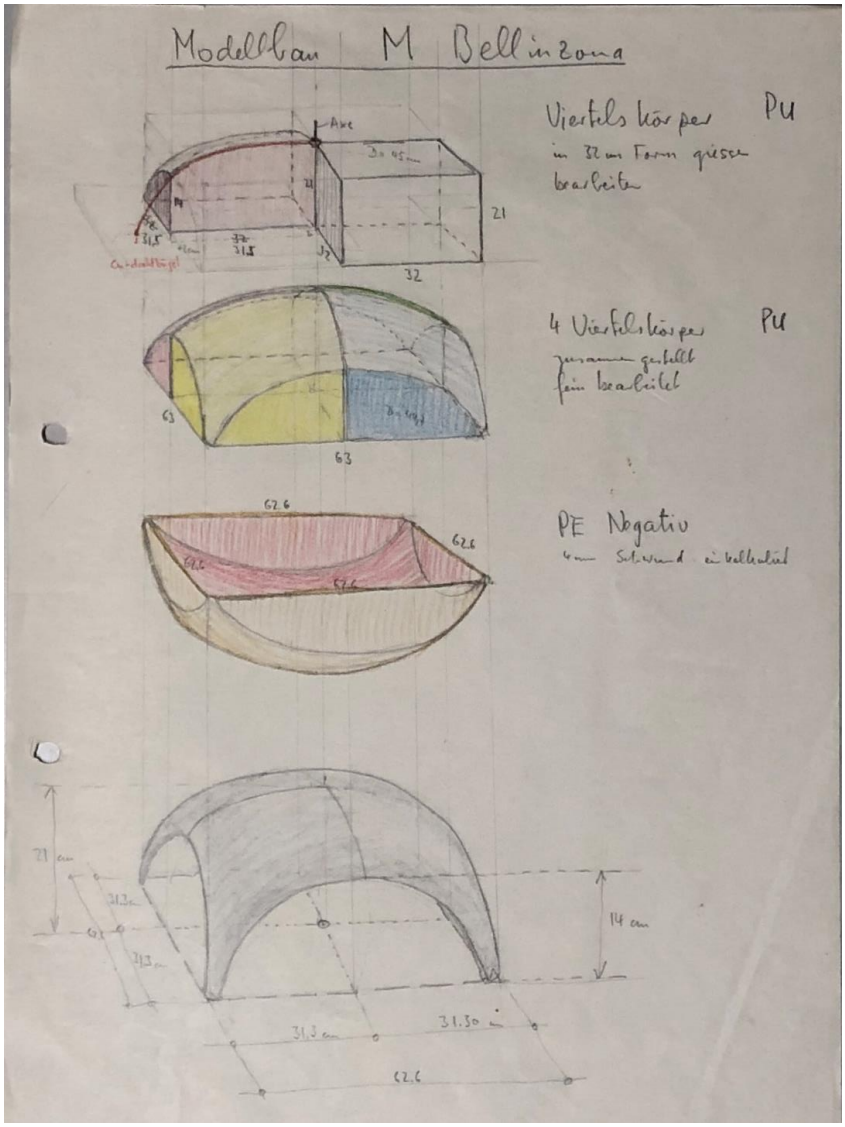


Figure 6: Sketch showing the making of the 1:50 model [gta Archive]

The flow-form experiments were first carried out within 10cm/10cm/10cm wooden boxes, and later in boxes made in the scale of 1:100. After a best fitting form to suit the spatial requirements was finally found, a replica was made in the scale of 1:50, which was carved out of PU cubes. A negative cast taken from this replica served then as the basis to produce representational models as well as structural models made of polyester.

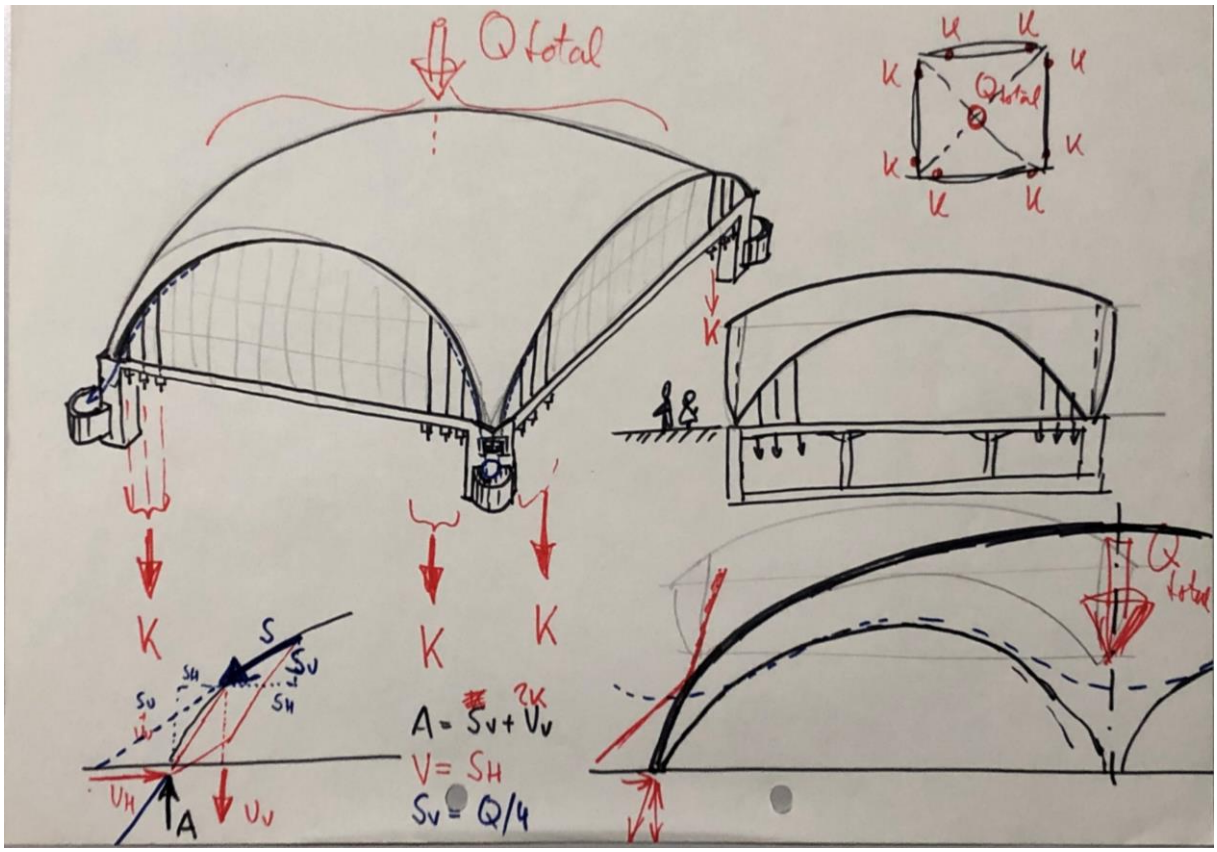


Figure 7: Sketch of the shell showing the function of the vertical tendons at the corners [gta Archive]



Figure 8: Structural model made of polyester with wires representing the prestressing elements [gta Archive]



Figure 8: Construction of the shell in 1964 [gta Archive]

Isler was well aware that the developed shell geometry was far from ideal in terms of its structural behavior, as it differs significantly from a funicular shell. In order to improve the force flow next to the supports, vertical tendons divert the horizontal thrust from the upper part of the shell into the steep abutments (compare figure 7 and 8). These pre-stressing elements were integrated into the façade plane. The construction of the shell started in mid-1964 and was finished in the same year.

4. Conclusion

The shell for the Migros supermarket in Bellinzona is the first realized shell with a shape that was generated with the so called flow-form method. Even though shell geometries derived from this method a far from structurally ideal shell shapes, the flow-form method had its own advantages: the quickly setting polyurethane foam allowed to approach given architectural constraints by means of the chosen polyurethane mixture and the boundary conditions. The autonomous process of the expanding foam provided geometries followed physical laws – albeit not structural ones - and provided even surfaces and smooth transitions. Moreover, the quickly hardened surface of the foam allowed to cast polyester models in order to test the structural qualities of the newly found shape.

Although Isler was well aware of the inherent structural deficiencies of the flow-form method, he used it for a variety of other free-form shell structures in the following years: most notably the Kilcher factory in Recherswil (1965) and the Florélites garden centers (1965) out of Paris.

References

[1] J. Chilton, *Heinz Isler. The Engineer's Contribution to Contemporary Architecture*, Thomas Telford Ltd., 2000, pp. 66-67.

[2] H. Isler, "New Shapes for Shells", in *Bulletin of the International Association for Shell Structures [1959]*, IASS, 1960, paper C-3.

[3] H. Isler, "New Shapes for Shells – Twenty Years After", in *Bulletin of the International Association for Shell and Spatial Structures*, IASS, 1979, vol. 71/72.

Proceedings of the IASS Annual Symposium 2019 – Structural Membranes 2019
Form and Force
7 – 10 October 2019, Barcelona, Spain
C. Lázaro, K.-U. Bletzinger, E. Oñate (eds.)

Interaction between architecture and structures designed by Waclaw Zalewski

Sabina KUC*, Waldemar BOBER[a]

* Cracow University of Technology
31-155 Krakow, Warszawska 24
skuc@pk.edu.pl

[a] University of Science and Technology Wroclaw

Abstract
Waclaw Zalewski was the author of a unique set of structural solutions that significantly contributed to designing building massings. These solutions always took into account the specific architectural conditions of buildings. His completed projects show a surprising diversity of form and perfect harmony with their surroundings. They are also characterized by a very good technological compatibility that demonstrates a deep practical knowledge in the use of structural materials. When designing buildings, Zalewski employed structural analysis and model studies. His conceptual proposals of structural systems feature many creative solutions, many of which are hidden in the massings of the building and are not visible to an external observer. The paper contains analyses of the forms of structural systems of less-known buildings, whose designs were influenced by Wacław Zalewski's proposals. The methods of shaping the structures designed by Zalewski were based on the latest achievements of world researchers in this field at the time and always led to their practical implementation. This procedure can also be observed in the presented topic of the application of elements with static schemes incorporating the cantilever beam in construction. This article is a review and contains a general description of studies related to its topic.

Keywords: architecture, construction, Waclaw Zalewski,

1. Introduction
Development of architecture was always directly connected with the development of civilization. Despite constant progress, nowadays there are buildings and structures that are still considered to be milestones of human thinking, design, planning and construction. Architecture has been shaping and leading individuals and communities to innovation and urbanization for thousands of years—from the simplest of buildings to the stunning structures of the 21st century. Quite often, those structures, buildings and concepts were ahead of their time. Waclaw Zalewski's structural system proposals were not only filling in architectural space but also giving it a highly individual character. He had comprehensive knowledge of construction materials that helped him with ease design complex architectural spaces. In his conceptual proposals, he used custom solutions, that resulted in a range of well recognizable works and avoided commonly-used schematic structures. This work is not aberrant nor extravagant. The projects are characterized by justified decisions, made on the basis of thorough analyses of design problems in connection with in-depth knowledge and many years of practical experience. Through his work one can see his unparalleled engineering intuition, which enabled him to pick an optimal solution for certain space. Waclaw Zalewski well combined efficient use of building materials and effective technologies with the aesthetic qualities of his designs.

Copyright © 2019 by Sabina Kuc, Waldemar Bober
Published by the International Association for Shell and Spatial Structures (IASS) with permission.

2. A product of the blending of architecture and structural engineering—the *Spodek* in Katowice

First of all, what are structure and architecture? There are two main approaches to their significance. One stresses the role of architecture, while the other—that of structure. There is a third way—in which the structure is the architecture. It blends them together, without implying the dominance of one over the other [1].

In the third case, the structural engineer and the architect are one and the same. The good example here can be the artistic vision of Santiago Calatrava- one famous designer who blends the two: engineering and architectural knowledge. Even though Wacław Zalewski was not an architect himself, yet his work—the structural systems he designed—directly determined the shape of architecture. In our opinion, such blend of extraordinary vision of one person is visible in the case of the *Spodek* building in Katowice. Zalewski was not only the author of the structural elements which determined its architecture but also of the structural elements which were created and intended to be that architecture.

History of architecture mostly focuses on the achievements of architects itself, and quite often omit the names of structural engineers. It is assumed that the architect supervises, approves and becomes the owner of their work and sometimes even the whole project. Sometimes, the structural engineer's contribution is appreciated, and their name is written next to the architect's name. What is to be done when it is the structural engineer who actually creates the architecture? What is to be done when the structural and architectural design proposal of a structure bears the mark of innovation and the author's work is a significant or even key contribution to the architectural characteristics of the building? In such a case, the authorship should be attributed to them and credit should be given where it is due. This is also accurate in the case of Wacław Zalewski [2], [3] and his life works, which were the result of a consistent creative path along which the *Spodek* was but one of the first steps.



Figure 1: The Spodek in Katowice - contemporary view [photo by Sabina Kuc]

Since the opening of *Spodek* in May 1971, it instantly became the most important symbol of the city and the entire region, and one of the most recognizable buildings in the whole country. Its' architecture consists of all iconic attributes. It has a distinct, visually attractive shape and an innovative design. It stands out from the background formed by the surrounding buildings. Moreover, its shape and design have been an inspiration for architects and civil engineers in Poland for years, however, *Spodek* cannot be copied and are one of its kind. The *Spodek* attracts crowds of tourists and

various visitors, evoking positive emotions and associations, and it is one of the most important elements of the region's identity. The building is known not only for its unique structure but also for its characteristic and distinct architecture.

One of its main features was its *tensegrity roof structure* [4]. Structures gain a unique character because of their spatial character. This was the case of the *Spodek*, for which Zalewski proposed a shape in the form of a flattened, inverted cone with suspended audience stands [1]. This a little extravagant in shape and technically advanced form was the deciding factor in the team's victory in the competition, as this was the most characteristic out of the presented works matching in its spirit the vision of the developing city of Katowice. The *Spodek* was going to, shortly, become the architectural symbol of this city.

The team that was to design a Sports and Recreation Arena in Katowice, called *Spodek*, was selected through an architectural competition in 1959. It was won by a team from Warsaw, including: architects Maciej Gintowt, Maciej Krasiński and civil engineers: Wacław Zalewski [5], Andrzej Żurawski and Aleksander Włodarz [6] (employees of the Biuro Studiów i Projektów Typowych Budownictwa Przemysłowego—Typical Industrial Construction Study and Design Bureau in English).





Figure 2, 3: The Spodek in Katowice, construction view [7, Wacław Zalewski, Shaping Structure, Wolk Gallery, MIT School of Architecture and Planning, exhibition presented at Politechnika Wrocławska, image by Waldemar Bober]

The conceptual design of the *Spodek* was changed during construction [8]. Initially, the building was designed for the Park of Culture and Recreation in Chorzów (Silesia), but eventually, the location was changed. After the authors finished the design of the building, it got well-deserved recognition and, therefore, a new, more representative site was chosen—in the centre of Katowice. The placement decision determines not only the architectural perception of the building but also its architectural and structural principles. The new site and its conditions determined the need to formulate a new vision of the building's foundations. The foundations were designed in the form of an immense reinforced concrete basin with different construction elements to support it [5], [8]. The structure became the architecture underground.

Tensegrity roofs are a case in which structure is architecture. Wacław Zalewski had been the first to use this type of structure, for which he did not receive appropriate recognition and structural engineers who used tensegrity roofs many years later were labelled as the precursors of their use. "Zalewski began the dome before Fuller filed his patent for the ansuspension dome and completed it before Fuller's patent was granted; this was twenty-six years before David Geiger's first tensegrity domes, which were thought to have been the first-ever built." [5]. Wacław Zalewski, as one of the best Polish structural engineers, was a true asset of the *Spodek* design team and his engineering vision became the architecture of this building. The Team shaped a structure which was going to become architecture. The unique tensegrity roof constitutes the architecture of *Spodek.*

Zalewski—the lead designer of the structural system, was moved away from the design and construction of the project [9], [6]. After he moved abroad, the communist government wanted to erase his contributions to the creation of the *Spodek*. That was the reason why there was no information about Zalewski's contributions or the fact that he was a part of the original team that had won the competition for the design of the *Spodek* for such a long time. Later, whe Wacław Zalewski had relocated abroad, the team continued to work without him and made some changes to the overall conceptual design. However, the overarching idea remained the same. [6], [8], [9]. The *Spodek* is a good example when the greatest emphasis is put on the achievements of the architects and the contribution of the structural engineers are mentioned very rarely. Would the *Spodek* look the same without the contribution of Wacław Zalewski? Due to the fact that the main part of this building's architecture is its structure, its creator—a structural engineer—should receive adequate recognition.

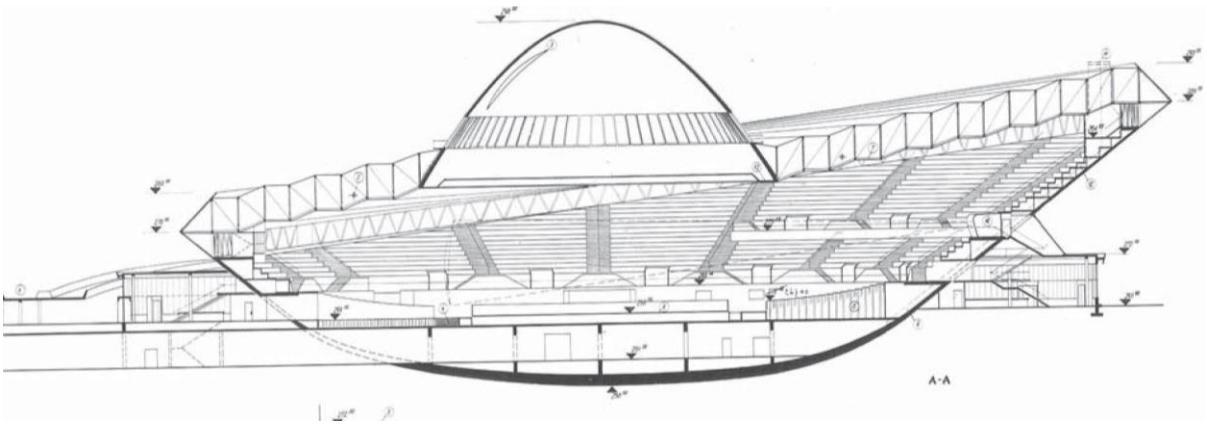


Figure 4: The Spodek in Katowice, structural view [7, Wacław Zalewski, Shaping Structure, Wolk Gallery, MIT School of Architecture and Planning, exhibition presented at Politechnika Wrocławska, image by Waldemar Bober]

The *Spodek* is one of the first buildings in the world to be built in the *tensegrity system* (a structural system in which elements under tension and compression are reciprocally balanced). The steel structure of the dome, weighing almost 300 tons, is connected to an external, likewise steel plate with 120 ropes, which provided the basis for the structure of the roof. This causes the building to resemble a UFO that has landed.

The *Spodek* stands on a large, concrete foundation basin, supported by 40 piles capable of self-adjusting as they protect the foundation from ground movements caused by mining damage. The *Spodek*'s foundation supports 120 steel ribs that support its roof, which has a span of 126 meters. This unusual structural scheme, which features a domed roof "suspended" from steel ropes, made it easier to design the building's structural system. In contrast to how it looks from a distance, the *Spodek* is not circular—its cover has the shape of a circle inscribed in an ellipse. Although similar buildings usually have a circular plan, the *Spodek* was planned as a multi-purpose hall from the beginning—so the layout of the stage and the spectator stands had to be quite flexible. Many events such as sports competitions, concerts, shows and mass gatherings take place here.

3. Leipzig fair pavilion

The roof of the Leipzig Trade Fair entrance pavilion is a saddle structure discretized with the use of a curvilinear triangle surface [11]. Its internal divisions consisting of right-angled triangles are designed according to the pattern of the Sierpinski triangle. The outer triangles are fitted with a rib system. The empty triangle in the middle of the roof structure may serve as a skylight. The layout of right-angled triangles creates a contrast between the massive structural fields and the empty inner one. The fields filled with parallel elements give the impression of a gridshell. A key component that adds a finishing touch to the structure, contrasting with its overall geometry, is the membrane shell located in the central part of the ceiling. The triangles forming the shell of the pavilion can be prefabricated, which allows for the extension of the structure beyond the presented design. Two-way curvature and deviation of external arcs from the vertical plane have a significant influence on the stiffness of the shell structure. It is easy to fill in the triangular shapes on the surface of the shell with flat materials.

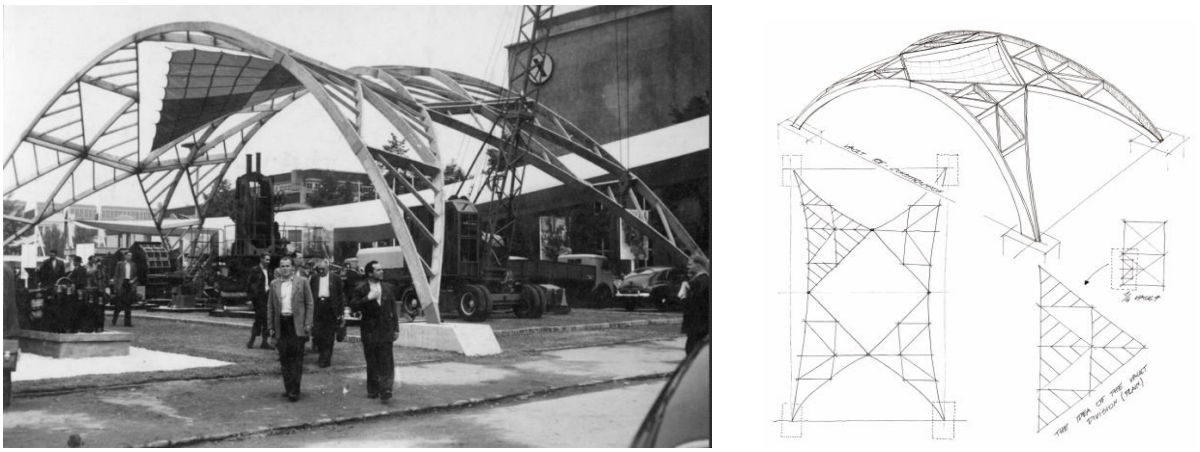


Figure 5: Leipzig International Fair Pavillon a. (12, Photo from private archive of Prof. Waclaw Zalewski), b. (Drawing by J. Onyszkiewicz) [11]

4. Roof grid of an industrial hall

Lightweight reinforced concrete mesh as a roof structure is an excellent alternative to steel or timber solutions for the same roof geometry [11]. It also meets the basic requirement for the use of non-flammable materials. The small cross-section of the grid elements creates the impression of closed-profile steel members. These small elements can be obtained by using a specific structural scheme and computational method capable of transferring the forces exerted by external loads on the structural members. The structural module has a connection in the tangential part of the keystone, placed at two points. The number of such connections depends on the imperfect nature of the prefabricated rigid elements. Assembling elements with more joints may turn out to be much more challenging. The placement of connections between the ribs of prefabricated elements results in a symmetrical load that is evenly distributed over all four ribs. Bending the diagonal support branches approximates the properties of the structural arch.

The innovative solution was also designed for the lower support area of the prefabricated elements. As the edge of the adjacent hall did not carry any linear loads along the roof, tension beams were introduced to transfer most of the loads to the support points in the columns of the existing structure. The upper points of the branches are connected by a rigid beam which, together with the branches, is an approximation of a compressed arc. This bar system constitutes a discrete graphic form of the "Flow of Forces" method used for flat shielding. By minimising the cross-sections of the main beams, bending in the support areas is reduced, creating a system that transmits compression forces to the support point. The roof construction module, made up of two prefabricated elements, had to be assembled on site, as temporary supports could not be placed on the floor of the hall. After assembly, the module was connected between the support points by means of steel rod ties. The 12.8-ton module was lifted with a crane by means of intermediate beams. A prefabricated seamless skylight is located in the main part of the prefabricated roof modules. The use of prefabricated concrete elements reduced the range of connections in the roofing area. Unfortunately, the shortage of material resulted in the fact that the roof surface was covered with pressed corrugated cement and asbestos plates. Today, it is possible to use such advanced materials as transparent covers or organic glass panels. In modern roof designs for hall buildings, it is possible to use the structural system described above in repeatable systems with separate suspended roofs, as shown in Figure 6a.

5. Conceptual proposal of a multi-storey building with an open ground floor space

Although Zalewski's proposal for a 30-storey building has never been built, it is worth mentioning given its immense potential [11]. The main load-bearing structure of this multi-storey building was to be based on a pyramid made up of diagonal columns converging at the mid-height of the building. This layout of the building structure was intended to reduce the bending effect caused by horizontal loads. In this case, the horizontal load can be equated with the wind load acting on the structure at approximately this position (at the mid-point of its height) as a resultant force. The load-bearing solid hidden inside the building provides support for the structural walls that hold each storey of the building. The columns of the main body made of two perpendicularly positioned reinforced concrete walls would guarantee a large open space inside the building. Such a cross-section of the columns allows for their installation in load-bearing walls on each floor. Simultaneously, the expanded walls of the main section of the column support the grids of load-bearing slabs. These grids may have an abutment that ends close to the external walls. The rigidness of the cantilever ends can be increased by connecting each floor with rods that would act as hangers. This increases the reliability of the slabs. In addition, the slabs connected vertically by bars form a spatially complex system in which exceptional loads are distributed over small areas.

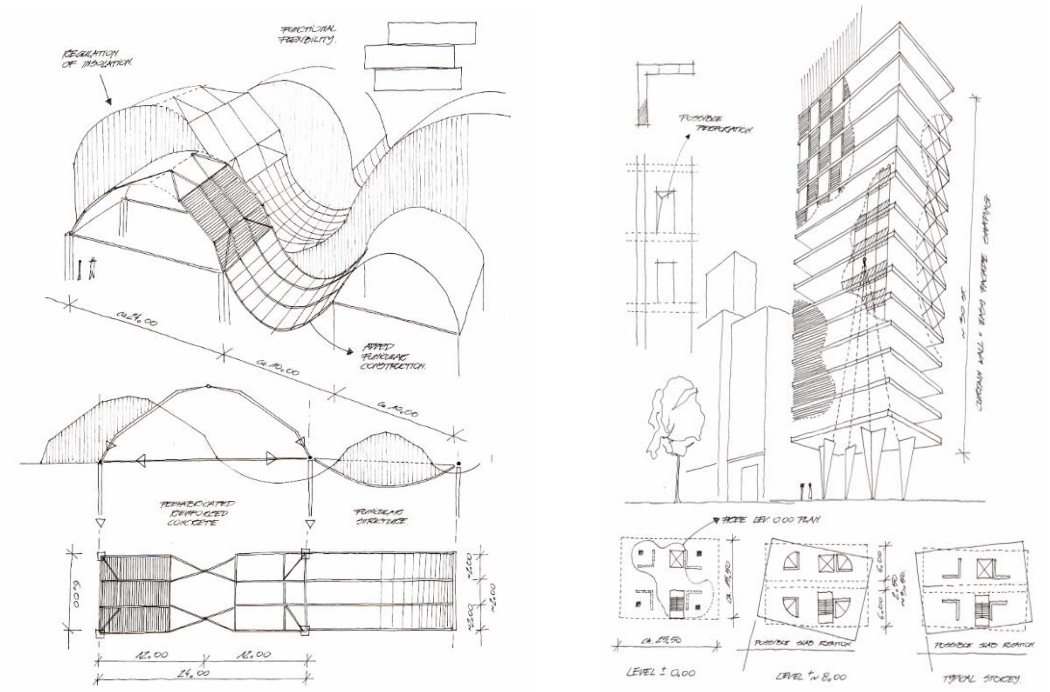


Figure 6: a .Arrangement of roof structures in an industrial space. b. The impact of the support system on the massing of the tall building. (Drawing by J. Onyszkiewicz) [11]

Diagonal distribution of the main structural columns on the ground floor would result in the reduction of the bending effect and an axial transfer of compression force. Taking into account the durability of the material in the 1950s, Zalewski estimated the cross-section of column bases at 0.8 x 0.8 m. The open space in front of the facility allows the axis of sight to remain at the street level and provides unrestricted pedestrian traffic, which is an important feature of the design. The necessary vertical circulation shafts could be installed in a light, glazed structure to provide maximum transparency in front of the building. Zalewski implemented the idea of open space in the first four floors of an office building built in Gdansk (PL). There, however, the main load-bearing system of the building was based on two reinforced concrete cores, which is a typical solution found in high-rise structures. The architect's idea to introduce mega-structures to high-risers was applied in the 1970s.

6. Conclusions

The structural system solutions proposed by Wacław Zalewski presented in this paper have made a significant contribution to the progress in shaping the blocks of buildings that perform various functions. The technologies used in this design in an original way exploit the potential of construction materials. The results of structural analysis can serve as an excellent training material for architects. The examples analysed in the present study allow to confirm the synergy effect achieved by Zalewski in the application of well-known design tools. The contribution of the intuitive factor to making design decisions on the basis of in-depth knowledge of materials and structural systems statics should be emphasized. Despite far-reaching changes in building technology over the last several decades, most of Zalewski's pioneering ideas remain valid. Zalewski's works demonstrate the aesthetic load of sophisticated structural systems, along with the fact that by prominently exposing them, or even designing the entire form of the building around them, can yield remarkable artistic results.

References

[1] S. Kuc, “The construction and the architecture. The vision of Professor Wacław Zalewski. The example of “Spodek” in Katowice, Poland”, *Creativity in Structural Design : proceedings of the IASS Symposium 2018, MIT, Boston, USA, July 16-20, 2018*, Sigrid Adriaenssens, Caitlin Mueller Ed., International Association for Shell and Spatial Structures, 2018, IASS2018_FullPaper_531.pdf.

[2] E. Allen and W. Zalewski, Form and Forces, Designing efficient expressive structures, John Wiley & Sons, Hoboken 2010.

[3] S. Kuś, "O konstrukcjach Profesora Wacława Zalewskiego" (On the Structures of Professor Wacław Zalewski), Inżynieria i Budownictwo (Engineering and Construction), vol.2, 1997.

[4] A. G. Tibert and S. Pellegrino, "Review of Form-Finding Methods for Tensegrity Structures," International Journal of Space Structures, vol. 26, no. 3, pp. 241-255, 2011.

[5] T. Robbin, Engineering a New Architecture, Yale University Press,1996.

[6] A. Żórawski, "Ewolucja projektu konstrukcyjnego Wojewódzkiej Hali Widowiskowo-sportowej w Katowicach" (Evolution of the structural design of the Sport and Recreation Arena in Katowice), Inżynieria i Budownictwo (Engineering and Construction), vol.10, 1969.

[7] Wacław Zalewski, Shaping Structure, Wolk Gallery, MIT School of Architecture and Planning, E. Allen, Visiting Professor of Architecture and Building Technology Exhibit Direction, 2006, katalog wystawy (exhibition catalogue).

[8] M. Pelczarski, "O kształtowaniu konstrukcji dachu katowickiej hali Spodka. Rozważania z wywiadów z Profesorem Wacławem Zalewskim, About shaping the structure of Katowice Spodek-arena roof. Consideration from interviews with Professor Wacław Zalewski", Architectus, vol.2(34), pp. 69-82, 2013.

[9] J. Zamorowski, "Specyfika konstrukcji Hali Widowiskowo-Sportowej– Spodek w Katowicach" (Specification of the construction of the Sports and Entertainment Arena - Spodek in Katowice), Zeszyty Naukowe Politechniki Rzeszowskiej, Budownictwo i Inżynieria Środowiska (Building and Environmental Engineering), 2011, vol. 58, pp. 422–432.

[10] S. Kuś, "Śp. Prof. dr inż. Wacław Zalewski, dr h.c. Politechniki Warszawskiej (1917-2016)", Inżynieria i Budownictwo (Engineering and Construction), vol. 3, 2017, [online] Available at: http://www.inzynieriaibudownictwo.pl [Accessed April 04, 2018].

[11] W. Bober and J. Onyszkiewicz, “Geometric modeling of solids for structural systems”, *Creativity in Structural Design : proceedings of the IASS Symposium 2018, MIT, Boston, USA, July 16-20, 2018,* Sigrid Adriaenssens, Caitlin Mueller Ed., International Association for Shell and Spatial Structures, 2018, IASS2018_FullPaper_278.pdf.

[12] Private archiv of Professor Wacław Zalewski.

Proceedings of the IASS Annual Symposium 2019 – Structural Membranes 2019
Form and Force
7 – 10 October 2019, Barcelona, Spain
C. Lázaro, K.-U. Bletzinger, E. Oñate (eds.)

Pioneers cantilever concrete shells / Del Río, Gollo, Nervi, Torroja, Zulueta

Pepa CASSINELLO

Director of Eduardo Torroja Foundation
c/ Serrano Galvache 4, Madrid 28033, Spain
p.cassinello.p@gmail.com, director@fundacioneduardotorroja.org

Abstract

On IASS 60th anniversary, this paper wants to contribute to remember a small relevant part of the large and fascinating history that motivated its foundation in 1959. Thin reinforced concrete shells are one of the most admired milestones of international Modernist history and an unforgettable conquest in structural design. The second decade of the twentieth century witnessed the beginning of what might be termed the '*Concrete Shells Adventure*', in which engineers and architects joined forces, bound like links in the same chain forged in pursuit of the most *effective, naked and slender structural form*. Undoubtedly the greatest feats were the large and slender concrete shells as well as those built in cantilever. In fact, the shells that fly over the space, not only have a great difficulty of design but also a special and disturbing attractive. In this paper we are going to go through a few of the pioneer cantilever concrete shells designed by some of the most relevant authors in different countries; Emilio Giovani Gollo, Eduardo Torroja, Pier Luigi Nervi, Ildefonso Sánchez del Río and Guillermo González Zuleta.

Keywords: concrete shell, cantilevered structures, conceptual design, slender forms, construction process.

1. Introduction

In 2019 we are celebrating IASS' 60th anniversary. It is time to remember what IASS means and celebrate its international continuity over time.

The *International Association for Shell and Spatial Structures* was born in the year 1959 under the name *International Association for Shell Structures*, when the fascinating "*Concrete Shells Adventure*" had reached its peak internationally. It was from the second decade of the 20th century when this formal and technological adventure was born. Engineers and architects joined forces, bound like links in the same chain forged in pursuit of the most *effective, naked and slender concrete structural form.* They strove to conquer the new freedom of shape and size afforded by reinforced concrete, very much in keeping with the new outlook that gave rise to Modernism in that same decade. It was a very special moment of change in the history of architecture, engineering and its structural forms. A long history of which we can only remember here its important *raison d'être* and why this adventure continues under another name.

The formal and technological conquest of Modernism's thin concrete shells is inseparable from the history of the development of reinforced and prestressed concrete, although that does not mean it necessarily had to be so. Humanity's ingenuity drove its birth, development and *raison d'être*. It´s a fact that at the end of the 19th century a large variety of concrete patents had already emerged, as well as companies engaged in construction with this new material and Portland cement factories. The first vaults and reinforced concrete domes were built using these patents, among others those of; Monier,

Copyright © 2019 by Pepa Cassinello
Published by the International Association for Shell and Spatial Structures (IASS) with permission.

Henebique, Schlüter and Habrich [1]. They were the precedents of the thin concrete shells. To the rhythm of the development of the reinforced and prestressed concrete, the thick concrete vault and domes became shell structures which were evolving, becoming bigger, thinner and slender.

By way of curious prophecy, although scantly slender and limited in size, the earliest reinforced concrete works were shells: the small reinforced cement flower pots devised by French gardener Joseph Monier in 1849, or the boat designed by Joseph-Louis Lambot between 1848 and 1855. The change of scale, like all others recorded throughout history, spawned any number of problems, attesting, once again, to the seldom recognised but disturbing truth in platitudes about the 'weakness of giants' [2]. After a long period of experimentation and analysis in different countries, the problems arising around the change of scale in each specific geometry were controlled. As a result, reinforced and prestressed concrete could be used to build new spatial forms spanning over 200 m between bearings, comfortably exceeding the 40-some metres possible with historic masonry or the 60 m with shells made of reinforced masonry. Although the geometries differed, the maximum span achieved with ancient masonry, the 43 m diameter dome over Agrippa's Pantheon in Rome, was to progress into the 218 m between bearings in the reinforced concrete shell – double sheet- that roofs the CNIT outside Paris (1956-1958).

By 1959, a large number of relevant shell structures had already been built in most of the countries by relevant pioneers, among many others; Frank Dischinger, Ulrich Finsterwalder, Eugene Freyssinet, Eduardo Torroja, Pier Luigi Nervi, Robert Maillart, Peter Pasternak, Boris M. Iofant, Fernand Aimond, Boris F. Matari, Giorgio Baroni Albert Caquot, Andre Paduart, Nicolas Esquillan, Auguste Perret, Mario Salvadori, Anton Tedesco, Bernard Laffaille, Ove Arup, Eero Saarinen, Yoshikatsu Tsuboi, Kenzo Tange, Félix Candela, Arseniusz Romanowicz, Heinz Hossdorf, Jorg Schlaich. This year 1959, an international symposium entitled 'International Colloquium on Non-traditional Thin Shell Construction' was held at Madrid's Institute for Construction and Cement Engineering. Further to a proposal put forward by Eduardo Torroja, *International Association for Shell Structures* – IASS- was founded. The time had come to pool the achievements of the decades-old thin shell adventure. At that time shell structures were frequently used all over the world. It was necessary to share and disseminate the achievements and have an international forum for the exchange of knowledge. The 100-plus specialists taking part in the symposium hailed from Argentina, Brazil, Belgium, Ceylon, Denmark, England, Finland, France, Germany, Italy, Japan, Netherlands, Norway, Poland, Portugal, Spain, Sweden, Switzerland and Uruguay. Membership on the first IASS committee was as follows: President, Eduardo Torroja (Spain); Vice-Presidents, A.L. Parme (U.S.A.) and W. Olszak (Poland); members: A. Aas Jackobsen (Norway), A.L.L. Baker (United KIngdom), N. Esquillan (France), A.M. Haas (Netherlands), R.S. Jenkins (United Kingdom), K.W. Johansen (Denmark), F. Levi (Italy), O.D. Oniashvill (U.S.S.R.), A. Paduart (Belgium), H. Rüle (German D.R.), W.Zerna (F.R. of Germany); Secretary, Florencio del Pozo (Spain).

At the end of the nineteen sixties, thin concrete shells had ceased to be the lead actors on stage. Their place had been gradually taken by other lightweight, large span and spatial structures made with other materials. It was a very wise decision that in 1970, under the presidency of Aren M. Haas, the International Association for Shell Structures, decided to change its name to the *International Association for Shell and Spatial Structures* (retaining its acronym, IASS). From that time on, the IASS has engaged in activities involving all manner of spatial structures rather than just concrete shells, which continued to be built more or less sporadically through the end of the nineteen seventies, when they practically disappeared. This change was the reason why the IASS continues to live leading innovation in the field of space structures [3].

Undoubtedly it is time to celebrate the 60th anniversary of the IASS in which it has gathered the most important pioneers in the history of the conquest of new structures; first concrete shells, then lightweight and soon to come an endless adventure lived internationally without recognizing borders.

2. Pioneers Cantilever Concrete Shells

Throughout history, humans have used cantilevered structures in their buildings, even with material such as stone, which has low flexural strength. Suffice it to remember here the stone balcony that crowns the Trajan's Column in Rome (113 AC) from which the whole city could be seen. It is a fact that the extensive historical heritage of architecture and civil engineering contains a lot of different cantilevered structures that now come to our memory, fundamentally constructed of wood given its natural flexural resistance. But what allowed man to build large cantilever structures was the discovery of new materials with high flexural strength and rigidity, such as iron and reinforced and prestressed concrete.

The largest cantilever structures which man has built of iron and concrete have been fundamentally in civil engineering works. Certainly, the bridges and viaducts have achieved the greatest flights during their construction process named "system of successive cantilevers". One of the first was the Forth Bridge built in Scotland in 1882-1890 with metal structure. It was the world record with a length of more than half a kilometer. Nowadays, thanks to this system of successive cantilevers, bridges of more than 300 meters have been built. This fact points out the relevant importance of knowing how to fly although when these bridges are finished you can´t see that its sections, finally joined, were cantilevered. On the other hand, although it was unfortunately demolished, there was a spectacular example of architectural cantilevered reinforced concrete structure. It was the famous "Arrow" built in 1958 in the Brussels International Exhibition by the Belgian civil engineer Andre Paduart, who was IASS President from 1961 to 1971. A reinforced concrete cantilever beam with a flight of 80 meters which was balanced by a reinforced concrete shell dome. An audacious and unforgettable cantilever reinforced concrete structure [4].

It is a fact that the appearance of the first shell structures of reinforced concrete in the second decade of the 20th century opened up new possibilities of "flying". Undoubtedly the thin and slender concrete shells that flies in space, not only have a great difficulty of design but also a special and disturbing attractive. For this reason, we are going to remember now some pioneers cantilever concrete shell built as canopies on spectator grandstands in racetracks, football or baseball fields. These are roofs that require large flights to cover the spectators without the visual interruption that constitutes the existence of supports. The pioneer master concrete shells had to sharpen their ingenuity to fly when still reinforced and prestressed concrete were in full development.



Figure 1: The Royal Turf Club in Bangkok 1922 (Eduardo Torroja´s Archive)

One of the first precedent was the Royal Turf Club in Bangkok, Thailand, which was inaugurated in 1922 (Figure 1). It was designed by the Italian engineer Emilio Giovani Gollo (1873-1925) representative of the Hennebique patent. The building is formed by a longitudinal central body of double height covered with a set of cylindrical shells of reinforced concrete placed transversely, and two longitudinal canopies of 8 meters long (apparent flight), which are also formed by a continuous sequence of cylindrical concrete shells. The shells are hung from the pillars of the central building. In this way the set is balanced.

These reinforced concrete shells were not cantilevering from the structural point of view because they were leaning on one end and hanging the other. However, they were formally perceived as such from their intrados. An ingenious and pioneer design in which there are no pillars that interrupt the view of horse races from the stands. The concrete shell roof seems to fly over the people who are under it even though it is hanging.

How the cantilevered shells were designed during the "*Concrete Shells Adventure*"?. It is well known that the cantilever structures are highly based on torque moment and rotational equilibrium. Loads, whether dead or live, on the cantilever section must be balanced out. They have to be rigid, so the easer way to get rigid shells it is to used a set of ribs-beams. This is the reason why most of the firsts cantilever concrete shells were designed with depth ribs.

In 1929 Pier Luigi Nervi (1871-1979), one of the most relevant protagonists of the '*Concrete Shells Adventure*', designed his famous Florence Football Stadium "Giovanni Berta" [5], which was inaugurated in 1932. It is a cantilever concrete shell masterpiece, a pioneer building of modernity architecture, and an icon worldwide (Figure 2).



Figure 2: Florence Football Stadium 1932 (Eduardo Torroja´s Archive)

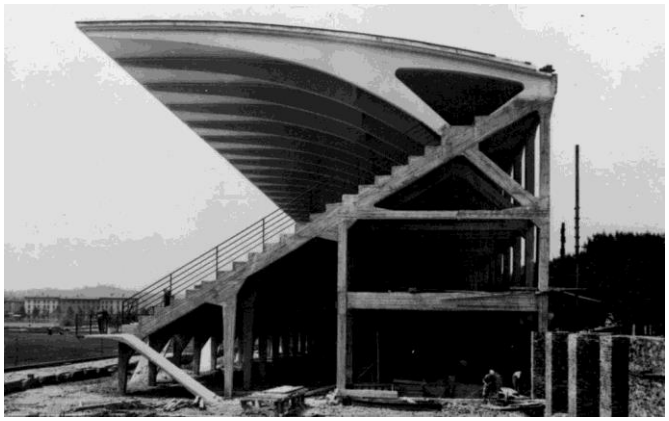


Figure 3: Florence Football Stadium. Under construction (Eduardo Torroja´s Archive)

The structure of the grandstand and its cantilever roof form an ingenious resistant unity. It was made of reinforced concrete with a scenography image of resounding and nudity modernity. Its roof is a pioneer cantilever ribbed shell. It consists in a set of 23 concrete modules formed by 8 pillars of different height in which 2 inclined beams and 2 cantilever curved ribs support. These cantilever ribs have an aerodynamic shape with 22 m long and 17 m of flight, and a light sheet of ceramic material that supports on them. The curved ribs have a shocking geometric shape that serves to balance the structural set by

the large inclined foot which crosses the inclined beam to the back pillar. In this way, the grandstands act as a buttress resisting the overturning-moment. The inclined beam starts from the head of the same pillar (Figure 3). The transverse bracing of the cantilever curved ribs is formed by small curved ridge reinforced concrete ribs between two main ribs. They are located just when their flight start (Figure 4).



Figure 4: Transverse bracing of the cantilever concrete shell (Eduardo Torroja´s Archive)

All the structural elements form an ingenious resistant unit which has not only an optimal structural behavior, use of material and process of construction, but also the naked modernity image with Pier Luigi Nervi designed it. The structural shapes are molded with special detail. The striking geometry of its resistant form is cut out in the air allowing its visual perception. These are the keys of the magistral Pier Luigi Nervi´s works which have always resulted as pioneer, rational and beauty [6].

In 1932 the Oviedo Stadium (Spain) was also inaugurated (Figure 5). The structure of the pioneer blancher and its cantilever reinforced concrete shell roof were designed by the Spanish engineer Ildefonso Sánchez del Río. It was a cantilever ribbed shell formed by a set of reinforced concrete cantilever frames separated 3 meters from their axes.



Figure 5: Oviedo Stadium. Spain (Fundación Juanelo Turriano)

One of the most original aspects of these frames was that their horizontal cantilever was not curved, it was of variable flat section with 14 meters of flight (Figure 6) and 1 meter wide. The transverse bracing of the frames and their roof was guaranteed by the structure of the inclined bleachers. Unfortunately, this stadium was damaged during the Spanish Civil War and some years later it was demolished. Before that the Oviedo Stadium was named “Sánchez del Río Stadium”.

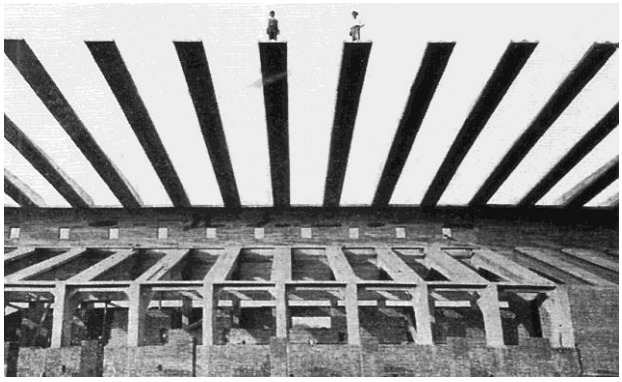


Figure 6: Oviedo Stadium under construction (Fundación Juanelo Turriano)

Ildefonso Sánchez del Río used in this occasion one of his usual own design system which consisted of a set of ribs on which screwed light domed prefabricated fibrocement plates. In this way he optimized the weight and the cost of the roof. From 1925 he used this system to build many concrete umbrellas as in the Ciaño music kiosk with 7 meters of flight. His legacy is not well known despite the fact that he built a lot of innovative concrete shell structures, including the largest concrete shell umbrella ever built (40 m diameter / 3,5 cm thick), and the Sport Palace in Oviedo (100 m span) [7].

Another important cantilever ribbed shell was built in 1947 by the Colombian engineer Guillermo González Zuleta (1916-1995) built, in Cartagena de Indias, the Estadio Eleven de Noviembre, known as the "Colombian Baseball Temple" (Fig. 7) [8]. The reinforced concrete laminar cover has a flight of 19 m over the spectator bleachers. It is a ribbed sheet that is formed by eight ribs in the shape of a parabola, separated from each other by 10.75 m and resting on two columns. The ribs are braced together by thick transverse beams. On the ribs, a reinforced concrete membrane formed by a grid of ribs 8 cm thick was executed. The empty spaces between this network of ribs have a thickness of 5 cm. Zulueta designed a special construction process for these empty spaces, consisting of the use of small wooden coffers as formwork. A system of lightening of the blade.



Figure 7: Colombian Baseball Temple. Cartagena de Indias, Colombia (J. Galindo, C. Salazar, L. Hernando)

Another way to design slender cantilevered concrete roof was to use folded plates. These were the easiest to build, for in essence the formwork and reinforcement are planar. Structurally, as in corrugated shells, the rim is built up (amplitude of the fold) to absorb bending without thickening the shell, a cost-effective solution to stabilize and stiffen the element as a whole. Many folded plates were built with different geometries and sizes. Among many other; 1956 Workers' University Tarragona by Eduardo Torroja, 1958 the UNESCO building by Marcel Breuer, Pier Luigi Nervi and Bernard Fehrfus ,1968 Groenendael hippodrome Belgium by Andre Paduart.

In 1934 the Spanish civil engineer Eduardo Torroja, founder and first president of the IASS, started to build the structure of the Zarzuela Racecourse at Madrid. One of his most iconic masterpieces internationally. The cantilever reinforced concrete shell that covers the stands is a thin and continuous sheet without ribs or folds. Appears on the bleachers like a fine wavy fabric that floats in the air (Figure 8). An attractive feat that could only be carried out by one of the protagonists of the pioneer development of reinforced concrete and the '*Concrete Shells Adventure*'.



Figure 8: Cantilever concrete shell. Zarzuela Racecourse, Madrid, Spain (Fundación Eduardo Torroja)

The Zarzuela Racecourse has three blanchers, with the two outer 60 m long structures flanking a 30 m long centre stand. Each unit consists in transverse portal frames spaced at 5.00 m. These structures carry the intersecting (two-lobed) vaults that both roof the betting halls below and support the grandstands and their 12.75 m cantilevered thin shell roofing system. A threaded steel tie positioned at the rear provides the balance for these bold structural forms. It is like a big Calder´s sculpture. When the wind blows you can see its slight movement in its articulated props on the pillars (Figure 9). The cantilevered roof, which features two nearly hyperboloid sectors, projects outward 12.80 m. It measures 5 cm thick at the outer edge and 14 cm over the support.

In this case Torroja conducted a test on a full-scale physical model. That approach verified not only structural behaviour, but at the same time the complex construction process of this innovative structural cantilever form [9] [10].

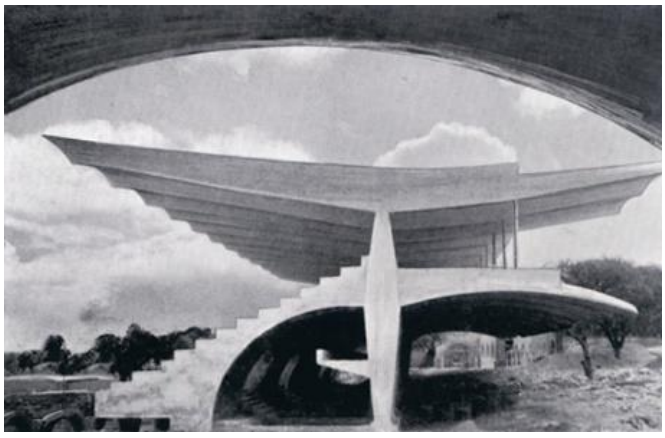


Figure 9: Zarzuela Racecourse under construction (Fundación Eduardo Toroja)

Its conspicuously modernist language and innovative structural form merited its inclusion in the book *Art and Artist*, along with sculptures by Henry Moore, Ernest Mundt and Alberto Giacometti, as well as paintings by Paul Klee, among others [11].

3. Conclusion

As we said at the beginning, thin reinforced concrete shells are one of the most admired milestones of international Modernist history and an unforgettable conquest in structural design. And, undoubtedly the shells that fly over the space, not only have a great difficulty of design but also a special and disturbing attractive. We only have talked here about a very few of them which were built during the first half of the twentieth century.

In any case, it is a fact that the most pioneer cantilever concrete shells were built with depth ribs which usually were unit to the pillars forming a structural frame. In the case of the canopies on spectator grandstands in racetracks, football or baseball fields, the blanchers were usually used as a buttress to get the balance of the structure. But every specific work is different, because as Eduardo Torroja said:

The laws that guide our thoughts toward the conception of a new solution remain unknown to us. Undoubtedly our imagination is constrained, guided, and attracted by a complex pattern of knowledge, feeling, ideas, and desires previously experienced [11].

References

[1] P. Christophe, "Le béton armé et ses applications". Annales des Travaux Publics de Belgique. 1899

[2] P. Cassinello, ". Félix Candela Centenary". *International context of the thin concrete shells*, p.p 61-110. Edition Fundación Juanelo Turriano. Madrid, Spain. 2010.

[3] J.F. Abel and other authors, "The IASS 50th Jubilee Book/Fifty Years of Progress for Shell and Spatial Structures". Publisher: International Association for shell and spatial structures. 2011

[4] A. Paduart and J. Van Doosselaere, "Design and Construction of the Civil Engineering Arrow at Brussels International Exhibition". Dans: Journal of te American Concrete Institute, v.57, n.7, p.p 51-72. 1960

[5] P.L. Nervi, "Structures", p.p 17-28. F.W. Dodge Corporation, New York, USA. 1956

[6] T. Iori, "Pier Luigi Nervi". Edition: Motta, Italy 2009

[7] P. Cassinello, "Ildefonso Sánchez del Río Pisón/ El Ingenio de un legado". *Las cubiertas de Sánchez del Río en el contexto internacional de la arquitectura Moderna*, p.p 93-149. Edition: Fundación Juanelo Turriano, Madrid, Spain 2011

[8] J. Galindo, C. Salazar, L. Hernando, "Laminate roofing in reinforced ceramic: contributions by the engineer Guillermo González Zuleta (Colombia, 1947-1962)". Journal Informes de la Construcción. vol 70, 551, e270. Edition: Instituto de Ciencias de la Construcción Eduardo Torroja. Madrid, Spain 2018

[9] E. Torroja, "The Structures of Eduardo Torroja" Edittion F.W. Dodge Corporation, New York. 1958

[10] P. Cassinello, "Museo Eduardo Torroja Museum". Edition Fundación Eduardo Torroja, Madrid Spain, 2016. Book translated into; English, French, German, Italian, Japan, and Portuguese.

[11] E. Torroja, "Art and Artist", *Notes on Structural Expresion*, p.p 219-228.University of California Press, Berkeley and Los Angeles, USA, 1956

Revisiting the "*M Stadium*" Project by Luigi Moretti: A Forgotten Model of Parametric Architecture

Piermaria CAPONI*, Fabio CUTRONI[a], Landolf RHODE-BARBARIGOS[b]

*University of Rome La Sapienza
Department of Civil Engineering, Environmental, Architecture, Via Eudossiana 18, 00184 Roma
piermaria.caponi@uniroma1.it
[b] University of Miami, Department of Civil, Architecture and Environmental Engineering

Abstract

Nowadays the term parametric modeling refers to a computer-aided design process where digital representation and interactive computation allow designers to have complete freedom on their designs' form and sometimes behavior. However, the term historically did not reflect such a freedom. In his article entitled "*Structure comme Forme*" published in 1953 on the "*United States Lines Paris Review*" [1] Italian architect *Luigi Moretti (1907-1973)* defined it as: *[…]"The enumeration of the parameters, scientific research, the quantitative mathematical analysis of these parameters, these form a task to be tackled a priori by the new architecture in every case. There will thus be born that architecture I have long demanded, and to which I gave the name parametric. Its ineluctable geometrical character, the rigorous interconnection of its forms, the absolute freedom of phantasy itself which can spring up where equations cannot fix their own roots all this will give it a crystal splendor."[…]* According to Moretti, parametric architecture is thus expressed through mathematics and the exploration of parametric equations [2]. Therefore, this study revisits Moretti's work on the IRMOU's "M Soccer Stadium" project, designed for the XII Triennale Exposition of Milan in 1960, in order to examine his mathematical form-finding approach to architecture. The mathematically generated shape of the *"M Stadium"* based on "*iso-visibility curves"* is recreated and explored through three-dimensional CAD modeling. The mathematical relationship that drives the design of the stadium analyzed and the influence of its parameters is further investigated using current graphical techniques.

Introduction

The architecture and engineering theories developed by *Luigi Walter Moretti (1907-1973)* derive from his specific cultural humanist background that is linked to the Italian historical context as well as the post-war construction period. His goal was to create science-based architectural paradigms that address the debate of the technological age. Therefore, his research was followed by a new architectural language definition. It is in such cultural and socio-economic contexts that the work of architect Moretti has to be analyzed constituting combining research practice and theory. Moretti assimilated knowledge in sciences, arts and architecture from his father, who was a Belgian architect engineer. Moretti's interest in applied mathematics and modern science motivated him to develop a novel framework based on the combination of the mathematic and architecture (Rostagni, 2008 [3]). He affirmed more than once that his peculiar approach was inspired by *"groups theory"* enunciated by *Évariste Galois (1811-1832)*. After World War II, he returned to Rome and founded the magazine *«Spazio»* in 1950 published until 1953. The magazine can be considered as his personal manifesto reflecting an opportunity of interaction between arts, from architecture



Figure 1: XII Triennale Exposition of Milan in 1960, M Stadium and N Stadium Physical Model; Palazzo dell'Arte, Sept. Oct. 1960. Curated by the IRMOU (Istituto Nazionale di Ricerca Matematica e Operativa per l'Urbanistica).
"su concessione del Ministero per i Beni e le attività culturali"; (Archivio centrale dello Stato, (2019, N.A.), acs_mor_progetti_198_foto_03051.

to sculpture, painting and science theories through technological features. It is, in the sixth publication of *«Spazio»* (dec.1951/jan1952) that Moretti first exposed an extensive theory on Parametric Architecture. This theory was also presented in English and French on the *«United States Lines Paris Review»* later in 1954.

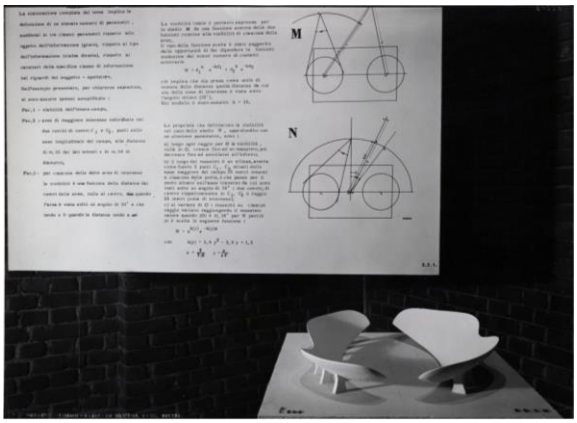


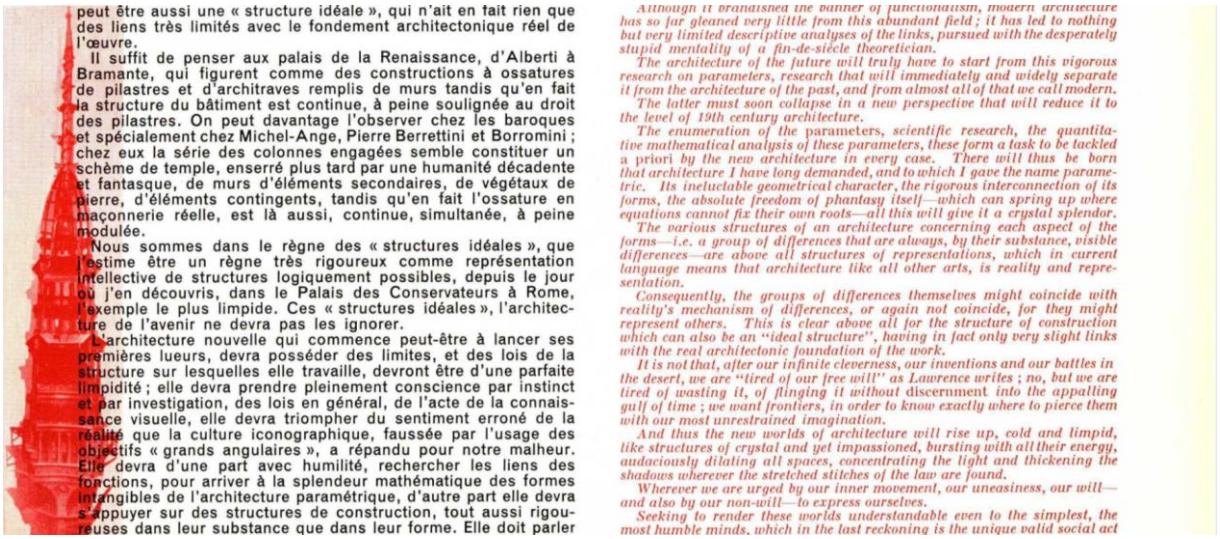
Figure 2: Moretti M stadium design in "Palazzo dell'Arte, Sept. Oct., 1960. Curated by the IRMOU (Istituto Nazionale di Ricerca Matematica e Operativa per l'Urbanistica). "su concessione del Ministero per i Beni e le attività culturali"; (Archivio centrale dello Stato, (2019, N.A.), acs_mor_progetti_198_foto_03065.

Moretti's theory aligns with the activities of the "*National Institute for Mathematical and Operative Research for Urbanism – IRMOU"* 1957. Moretti along with several scientists, worked on this foundation on parametric theory operative aspects (Esposito De Vita, 2009 [4]). First, they focused on urban design. Their objective was to moderate subjectivity by modelling planning through mathematical parametric equations. Another application they worked on was design, as Moretti had theoretically illustrated years before. The Vice-president of IRMOU's group, the mathematician *Bruno de Finetti (1906-1985),* had the key note in the group's success. His collaboration with Moretti resulted in a series of stadium design conceived for the exhibition "XII Milan Triennale" in 1960 (Fig. 1) (Fig. 2), that were presented in the *"Parametric Architecture Manifesto"*.

Moretti remained attached to the parametric architecture concept he improved during his professional activities. (1951-1960) (Viati Navone, 2012 [5]), (Reichlin, 2010 [6]), (Bucci, 2000 [7]). In 1958, he was involved into the Olympic Village project and construction for the XVII Olympic Games scheduled for 1960 in Rome. A decade later, he designed the Stock Exchange Tower of Montreal, (Tour de la Bourse 1964 Montreal, Canada) (Sheppard, 2008 [8]) and the Watergate complex in Washington (1963 and 1971, United States of America). In addition, he conducted a remarkable project based on parametric architecture theory for the two thousand-seat underground car park under Villa Borghese in Rome, which was inaugurated in 1973. Moretti's belief on parametric architecture can also be found in another important project designed in Fiuggi, the new Bonifacio VIII Spa thermal complex 1972.

Parametric Architecture Theory: A New Paradigm of Design

Nowadays the debate on parametric modelling derives from a co-optation of the mathematical meaning into a digital domain, identifying a new architectural *"style"* represented by coding-based models. However, in a brief historical note attributable to an article entitled *"Structure comme Forme"* (published in 1954 on the *«United States Lines Paris Review»)* Moretti wrote: (Fig. 3) *[...] The Architecture of the future will truly have to start from this vigorous research on the parameters, research that will immediately and widely separate it from the architecture of the past, and from almost all of that we call modern. The latter must soon collapse in a new perspective that will reduce it to the level of 19th century architecture. The enumeration of the parameters, scientific research, the quantitative mathematical analysis of these parameters, these form a task to be tackled a priori by the new architecture in every case. There will thus be born that architecture I have long demanded, and to which I gave the name parametric. Its ineluctable geometrical character, the rigorous interconnection of its forms, the absolute freedom of phantasy itself which can spring up where equations cannot fix their own roots all this will give it a crystal splendor. The various structures of an architecture concerning each aspect of the forms a group of differences that are always, by their substance, visible differences are above all structures of representations, which in current language means that architecture, like all other arts, is reality and representation. [...]* (Moretti, 1954 [9]). The origin of the note documented above is associated to the article intitled *"Struttura come Forma",* that Moretti wrote on his *«Spazio 6»* magazine. As matter of fact the parametric architecture theory was introduced years earlier (Moretti, 1951 [10]).



peut être aussi une « structure idéale », qui n'ait en fait rien que des liens très limités avec le fondement architectonique réel de l'œuvre.

Il suffit de penser aux palais de la Renaissance, d'Alberti à Bramante, qui figurent comme des constructions à ossatures de pilastres et d'architraves remplis de murs tandis qu'en fait la structure du bâtiment est continue, à peine soulignée au droit des pilastres. On peut davantage l'observer chez les baroques et spécialement chez Michel-Ange, Pierre Berrettini et Borromini ; chez eux la série des colonnes engagées semble constituer un schème de temple, enserré plus tard par une humanité décadente et fantasque, de murs d'éléments secondaires, de végétaux de pierre, d'éléments contingents, tandis qu'en fait l'ossature en maçonnerie réelle, est là aussi, continue, simultanée, à peine modulée.

Nous sommes dans le règne des « structures idéales », que j'estime être un règne très rigoureux comme représentation intellective de structures logiquement possibles, depuis le jour où j'en découvris, dans le Palais des Conservateurs à Rome, l'exemple le plus limpide. Ces « structures idéales », l'architecture de l'avenir ne devra pas les ignorer.

L'architecture nouvelle qui commence peut-être à lancer ses premières lueurs, devra posséder des limites, et des lois de la structure sur lesquelles elle travaille, devront être d'une parfaite limpidité ; elle devra prendre pleinement conscience par instinct et par investigation, des lois en général, de l'acte de la connaissance visuelle, elle devra triompher du sentiment erroné de la réalité que la culture iconographique, faussée par l'usage des objectifs « grands angulaires », a répandu pour notre malheur. Elle devra d'une part avec humilité, rechercher les liens des fonctions, pour arriver à la splendeur mathématique des formes intangibles de l'architecture paramétrique, d'autre part elle devra s'appuyer sur des structures de construction, tout aussi rigoureuses dans leur substance que dans leur forme. Elle doit parler

Although it brandished the banner of functionalism, modern architecture has so far gleaned very little from this abundant field ; it has led to nothing but very limited descriptive analyses of the links, pursued with the desperately stupid mentality of a fin-de-siècle theoretician.

The architecture of the future will truly have to start from this vigorous research on parameters, research that will immediately and widely separate it from the architecture of the past, and from almost all of that we call modern.

The latter must soon collapse in a new perspective that will reduce it to the level of 19th century architecture.

The enumeration of the parameters, scientific research, the quantitative mathematical analysis of these parameters, these form a task to be tackled a priori by the new architecture in every case. There will thus be born that architecture I have long demanded, and to which I gave the name parametric. Its ineluctable geometrical character, the rigorous interconnection of its forms, the absolute freedom of phantasy itself—which can spring up where equations cannot fix their own roots—all this will give it a crystal splendor.

The various structures of an architecture concerning each aspect of the forms—i.e. a group of differences that are always, by their substance, visible differences—are above all structures of representations, which in current language means that architecture like all other arts, is reality and representation.

Consequently, the groups of differences themselves might coincide with reality's mechanism of differences, or again not coincide, for they might represent others. This is clear above all for the structure of construction which can also be an "ideal structure", having in fact only very slight links with the real architectonic foundation of the work.

It is not that, after our infinite cleverness, our inventions and our battles in the desert, we are "tired of our free will" as Lawrence writes ; no, but we are tired of wasting it, of flinging it without discernment into the appalling gulf of time ; we want frontiers, in order to know exactly where to pierce them with our most unrestrained imagination.

And thus the new worlds of architecture will rise up, cold and limpid, like structures of crystal and yet impassioned, bursting with all their energy, audaciously dilating all spaces, concentrating the light and thickening the shadows wherever the stretched stitches of the law are found.

Wherever we are urged by our inner movement, our uneasiness, our will—and also by our non-will—to express ourselves.

Seeking to render these worlds understandable even to the simplest, the most humble minds, which in the last reckoning is the unique valid social act

Figure 3: Structure as Form group's theory analogy, by L. Moretti. United States Lines Paris Review, presented by Marcel Coudeyre, Luigi Moretti, "Structure comme forme" (Structure as Form), published in French and English, 1954. The New York Public Library, NY 10018 United States

The parametric architecture theory describes the design process in terms of mathematical relationships. Mathematical relationships are analyzed in a parametric form, described by Moretti himself as *"structure"*. Thus, these associations are his source of both inspiration and aesthetic exploration. This engaged Moretti to establish rules of quantitative parameters related to the equation, leading to the architectural creation. Thus, his work reflects thus a primary form of dialectic form finding with the form being defined by a mathematical equation with a multitude of parameters. These parameters and their interconnections are settled starting from qualitative analysis of the architectural scheme with the solution of the parametric equation being form demanded. Moretti's awareness incites us to pay attention to the fact that the parametric architecture theory derived from the need to clarify the architectural design process. It is the overcoming and discouraging plethora of forms presented to us by the traditional architectural language that is overwhelming us, moreover now that is supported by an iconographic culture. For this reason, an intuition should lead us to reject as many as possible *"free form"*, design as self-referential (Moretti, 1951 [11]). In other words, if the designer establishes a mathematical expression based on quantitative parameters and their reciprocal concatenations (such as the qualities of materials), the concept will be clearly indicated by the solution. From this point of view, the solution forces the designer to explore with scientific rigor its form and its alternatives as minimal design oscillations of the concept itself. If the parameters are numerous and hardly definable, the *"simplified"* parametric equation can only indicate an approximate form. Consequentially, additional steps are required to define the *"structure"* in order to have a complete form definition. The *"structure"* has its own proper meaning assumed from a mathematical logic perspective, related to a set of relations based on Évariste Galois group's theory analogy (Moretti, 1954 [9]). A new design with architectural aesthetic paradigm emerged from those complex relationships among parameters constituted by the *"structure of the form"* and underlined by pure relationships (Imperiale, 2018 [12]).

IRMOU's work on parametric architecture theory is known from the XII Milan Triennale 1960, where Moretti in collaboration with Sergio Bertuglia, Anna Cuzzer, Giovanni Cordella and other professionals presented an architectural form design for sports facilities through several physical models. It is important to notice that the design scope was to optimize the form of the stadium by defining the spectators' seats through the consideration of their visibility to selected field areas. Based on this concept, five parametric equations were created and presented in the exhibition with several physical models. Furthermore, the inputs of the parametric equation, analyzed trough the assistance of an IBM 610 Auto Point computer, allowed the visitors to compute in real time parameters' values and generate different bi-dimensional geometries of soccer stadium in order to validate the theory. A swimming pool and a tennis stadium models were also presented in order to demonstrate the versatility of this dialectic design process.

IRMOU: 12ª Triennale di Milano 1960: The "M Stadium" Project

In order to understand Moretti's work, it is important to clearly enunciate the parametric architecture principles and illustrate the analytical process. The aim of this section is to explore, through three-dimensional modeling and current graphical techniques, the mathematically generated *"M Stadium"* form. The stadium form is based on *"iso-visibility area"* generation, thus the scope of this work is to analyze the parametric equation that governs the design. Moreover, as deduced during the study, the parametric architecture methodology has been summarized into three main steps, clearly reported and the mathematical equation is enunciated in synthesis as following:

i. Typology definition;
ii. Parameters definition;
iii. Analytical description;

Visual perception research was employed to identify the critical areas associated to stadium's typology as well to affected activities, as illustrated in the schematized photogrammetry survey analysis (Typology definition) (Fig. 4). Once the visual perception is identified, as main theme of the stadium form design, leads to determining the optimal viewing angle, which is approximately 35° in mutual definition from spectator's seats distance to main interest's areas centers (Parameter definition). This geometrical study is illustrated in the original drawing (Fig. 5). The parameters taken into account in the analytical description are shown in the (Fig. 6), that addresses visual path of the field. The main areas of interest are represented by two circles with 50 meters diameter centers. C_1 and C_2 indicate the circles overlapping on the playground field. These centers are positioned on the longitudinal axis of the soccer playground, (110 per 60 m rectangular section) at 15 meters of distance from the smaller sides. (Fig. 6)

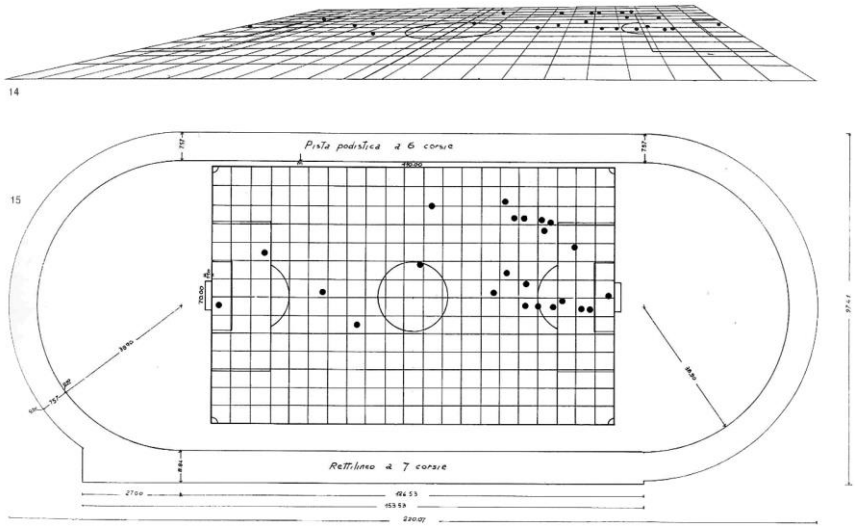


Figure 4: Moebius Unità della cultura: Architettura Urbanistica Arte, 14. Transport of the photogram on a perspective, 15. Transport of the photogram on an azimuth reticle.

The circles represent the main area of interest. For each of these areas, the visibility is based on a distance function $d_i = \mathrm{C}_i P$. The visibility in the centers of the areas C_1, C_2 is considered (0). The visibility is considered at its maximum when the area itself is seen under an angle of 35°. Consequently, if the distance tends to (∞), the viewing tends to (0) instead. (Analytical relationship description).

The visibility for the *"M Stadium"* is expressed by the mathematical function $W = d_1^k\,(e^{-kd}) + d_2^k\,(e^{-kd})$ *«Moebius Unità della cultura: Architettura Urbanistica Arte»* (Moretti 1971 [13]).The function is the sum of two parametric equation combining the visibility of the two circles (Fig. 7)

The physical prototype showed at the exhibition, is reconstructed here using a three-dimensional model. Starting from several measurements deducted in the picture, the reciprocal distance from P point to C_1, C_2 circumference' centers generates the *"Iso visibility curves"* diagram (Fig. 5). The distance between the *i* center and point *p* that generate the *"Iso - visibility curves"*:

$$d_i = \mathrm{C}_i P$$

$$P(x,y); \quad C_1(a,b); \quad C_2(c,d);$$

$$d_1 = \mathrm{C}_1\mathrm{P} = \sqrt{(x-a)^2 + (y-b)^2}$$

$$d_2 = \mathrm{C}_2\mathrm{P} = \sqrt{(x-c)^2 + (y-d)^2}$$

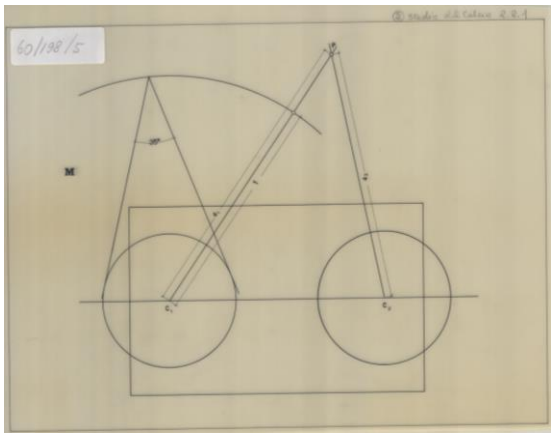


Figure 5: Original Drawing from; *"su concessione del Ministero per i Beni e le attività culturali"; (Archivio centrale dello Stato, (2019, N.A.), acs_mor_progetti_60_198_es_05.*

The parametric equations established for the areas are given by:

$$W1 = d_1^k\,(e^{-kd_1}); \qquad W2 = d_2^k\,(e^{-kd_2}); \qquad K_i \neq 0$$

with their sum being the *"M Stadium"* equation:

$$W = d_1^k\,(e^{-kd}) + d_2^k\,(e^{-kd}) =$$

$$(e^{-d_1k-d_2k})(d_1^k\,e^{d_2k} + e^{d_1k}d_2^k)$$

The described *"Iso - visibility Areas"* of *"M Stadium"* are the projections on the horizontal plan of the shape's curve described by the integral (Fig. 7).

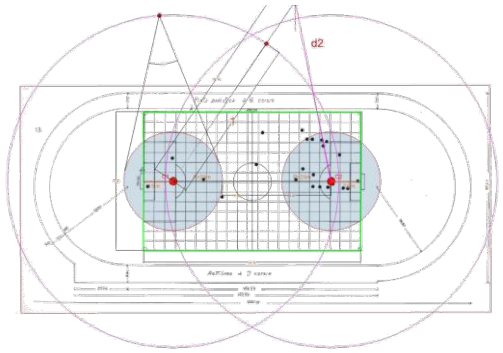


Figure 6: Transport of the photograph on an azimuthal plan superimposed on geometrical Cad based design. The cad design clearly and graphically explicit the distance between the i centers and the point p, generating the iso-visibility main curve of 35 degree

$$\frac{\partial}{\partial d_1}(d_1^k\,e^{-(kd_1)} + d_2^k\,e^{-(kd_2)}) = (d_1\text{-}1)kd_1^{k-1}\,e^{-(kd_1)}$$

$$\int \left(d_1^k\,e^{-(kd_1)} + d_2^k\,e^{-(kd_2)}\right)\boldsymbol{d}\,d_1$$

$$= d_1 d_2^k\,e^{-(d_2k)} - \frac{d_1^k(d_1k)^{-k}\Gamma(k+1,\,kd_1)}{k} + Constant$$

The explicit K's formula describes the logarithmic trend of the surfaces in space, assumed as:

$$d_1 \neq 0, \qquad d_2 \neq 0, \qquad Re(K) > 0, \qquad d_1 - \log(d_1) - d_2 + \log(d_2) \neq 0$$

$$K = \frac{i(2\pi n + \pi)}{d_1 - \log(d_1) - d_2 + \log(d_2)}, \quad n \in Z$$

Geometrical CAD based design is superimposed on azimuthal plane photograph (Fig. 6). The CAD design graphically illustrates the distance between the *i* centers and the point *p* that generates the iso-visibility curve at 35 degree.

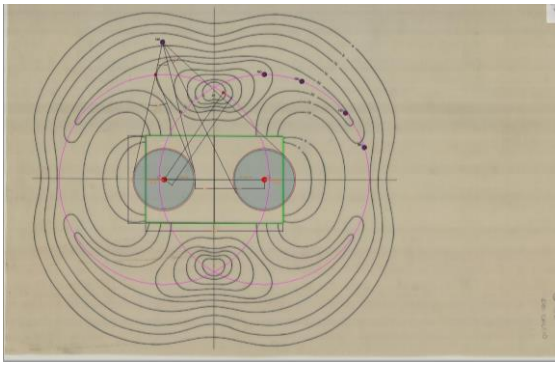


Figure 7: Original Drawing of projected Iso-Visibility areas on horizontal plan created by the parametric equation W. Geometrical overlapping CAD based design on level curves (4 - 41 progression). "su concessione del Ministero per i Beni e le attività culturali"; (Archivio centrale dello Stato, (2019, N.A.), acs_mor_progetti_60_198_es_07

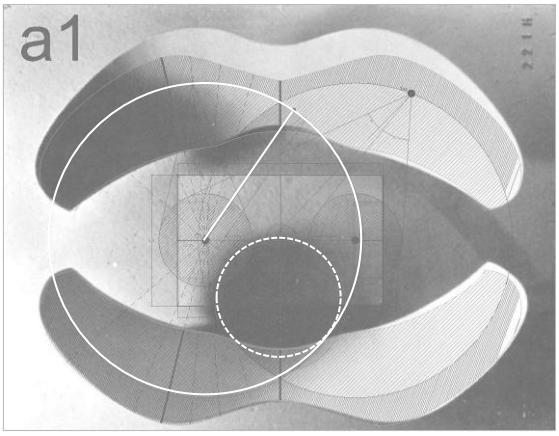


Figure 8: M stadium prototype's photo from on an azimuthal plan at distance of 1m. It has been superimposed by geometrical Cad based design. The geometrical design, that generates the iso-visibility curve at 35 degree, is overlapping in order to rebuild the symmetry of the model without focus distance distortion of the picture taken. The original photo has been taken from «Moebius Unità della cultura: Architettura Urbanistica Arte» 1971/72, Stadium M model.)

In order to verify the geometrical design assumptions made (Fig. 6), the azimuth photo of M stadium prototype, from XII Triennale Milan Exhibition, was combined by CAD design itself. The design has been calibrated on the photo, that has been taken from a point distance deducted and re-aligned, to determine the exact projection on horizontal plan of the measures, as showed by the design symmetry (Fig. 8). The dashed circle visualizes the imprint of the photography focus, which has been estimated approximately at 1 meter from the object. Through this comparison we assume that the proposed design validates Moretti's model

In order to reproduce the M stadium a combined framework was enstablished (Fig. 9). The mathematical equation was explored and integrated into CAD software. The equation has small values on the Z axis compared with other values on the x, y axes. Therefore re-scaling is required in order to achieve the correct three-dimensional representation of the spacial surface developed (Fig. 10-11). This process is necessary for overlapping the surface on original drawings made by Moretti, as shown in the following figures. Furthermore, the parametric model has been reproduced through graphic algorithm process for investigate the impact's values of the equation parameters (a, b, c, d, k) in the spacial shape mathematically generated. In fact, to reproduce exactly the M stadium form several software have been combined together (.dxf) as showed by the scheme (Fig. 9).

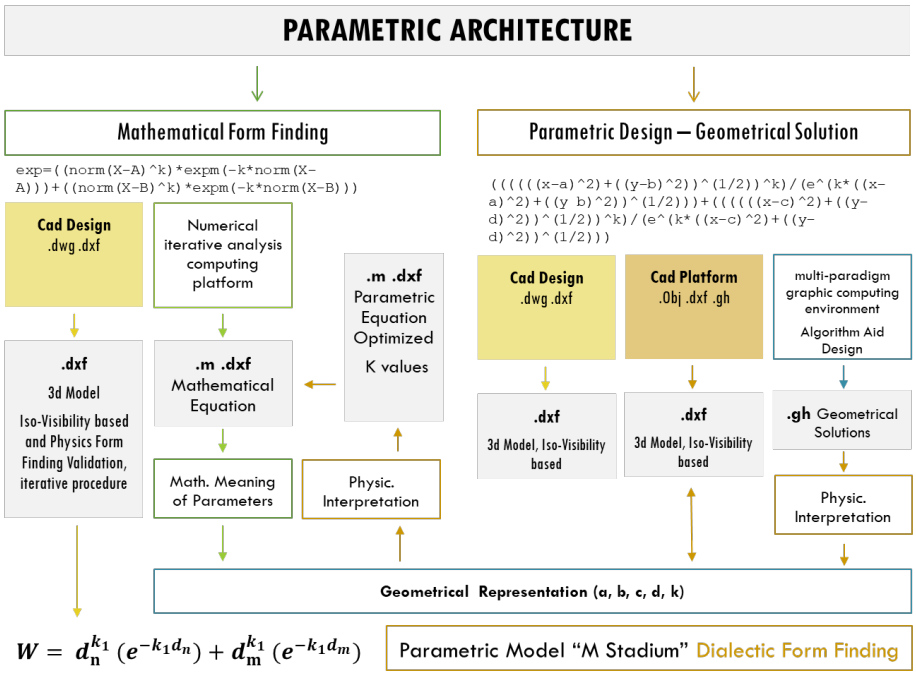


Figure 9: Framework-Workflow developed to study the "M Stadium" Project, IRMOU 12ª Triennale di Milano 1960 and to integrate structural concepts based on geometry design solutions. Iterative process for manipulating the parameters values of the equation.

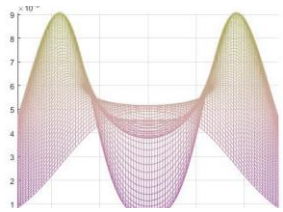


Figure 10: bi-dimensional representation on frontal elevation, curvatures value K=10

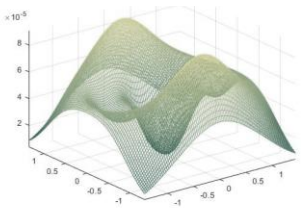


Figure 11: Three-dimensional representation Curvature values K=10

A framework has been developed to represent the form without approximations that could misrephesent the scientific rigor of the proposed method. Therefore, the shape and the K values has been adopted as per the Moretti's statement and the form is conceptually matching it (Fig. 12).

1_The image on the top is based on prototype's photo from on an azimuthal plan at distance of 1m. It has been superimposed by geometrical Cad design as showed on the right. The geometrical design, that has generated the iso-visibility curves, has been designed by on the model shape projection of the mesh itself. The mesh has been designed exactly how it has been described by the W equation;

2_W Parametric Equation three-dimensional represented by the spatial mesh has a curvature value K=10. The "mesh" model has been sectioned by a plan at 4.00 curve level, as showed on the right image, that represents the 0.00 altitude point of the Stadium, the quote of the playground. The entire form of the stadium is the part upon of the plan itself till the last curve level;

3_Bi-dimensional original Drawing of projected Iso-Visibility areas on *horizontal plan created by the parametric equation* W. *Geometrical overlapping CAD based design on level curves (4 - 41 progression) (right)*

4_Transport of the photograph on an azimuthal plane superimposed on geometrical Cad based design. The cad graphically designs the distance between the i centers and the point p, generating the iso-visibility main curve of 35 degree

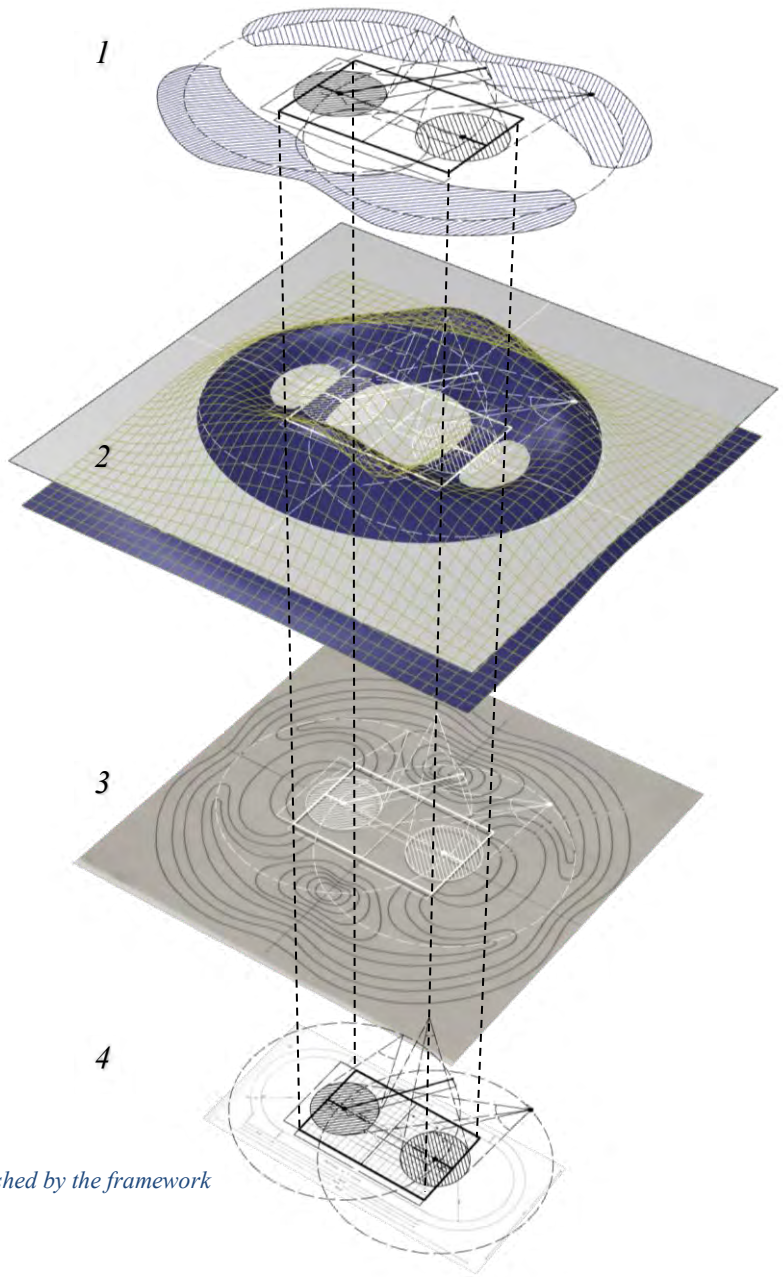


Figure 12: M stadium form design process established by the framework

IRMOU: Revisiting the Dialectic Form Finding Method of "M Stadium" Project

In order to explore how parametric architecture can integrate structural considerations, geometry principles of curves theory involving the theory of surfaces, are investigated. From an architectural and engineering point of view, this theory takes into consideration stiffness and weight, which are often considered as key criteria for evaluate the structural components. The structural interpretation of the stadium can be defined by two parallel curved surfaces. The thickness of the form *h* is the perpendicular segment between each other is assumed as surface of reference as showed in the images. The *W* equation established is based on the principle that once the parameters are fixed (a, b, c, d, K) for the summed function, their interconnection allows the shape's investigation trough an iterative process by parameters' value manipulation. The alternatives geometrical shapes generated are implicitly indicated by the process concept and scientifically deducted as minimal oscillation of the form itself. Therefore, new parameter values allow an approximation towards specific the geometrical-structural *"physic*

interpretation" of the form (Fig. 13). This form obtained through this manipulation is the benchmark for future structural verification and specification. The geometrical shape conventional CAD designed, as illustrated in the framework-workflow (Fig. 9), takes into consideration the following assumptions for the analysis process:

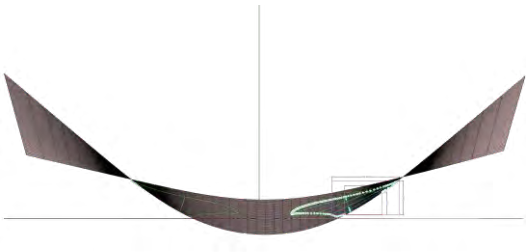


Figure 13: Qualitative modeling and simulation of the Reengineered shape, curvatures control trough algorithms and K's value establishment

i. Geometrical analysis of the architectural design towards single surface curvature developable (Fig. 14);
ii. Computer aided design for mathematical mesh/surfaces generation and reshaping form to finalize the structural concept through mesh density from A to B alternative (Fig. 14);
iii. Qualitative modeling and simulation of the reengineered shape, curvatures control trough algorithms and K's value establishment (Fig. 15)

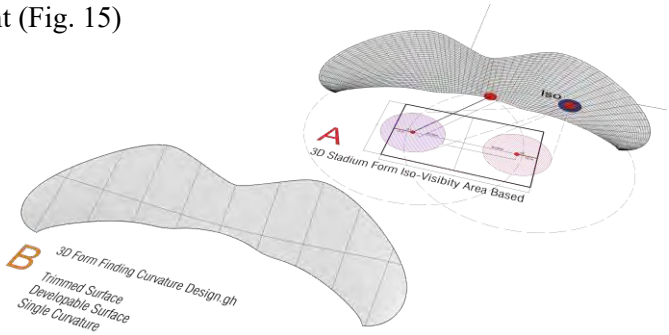


Figure 14: Geometrical analysis of the Architectural design Iso Visibility based, A; Single spatial surface curvature developable B; On the bottom, Algorithms design computing for mathematical mesh/surfaces generation. Form Re-shaping to finalize the structural concept through mesh density from A to B alternatives.

The form is reproduced through the computer aided design in order to manipulate the geometrical form of the stadium and the mesh density as shown in below. The mesh is ascribable to radial geometry in terms of pure architectural free-form surface (Fig. 14, A). The spatial surface generated and presented has been explored with graphical design computing, as show by framework-workflow developed to study the "M Stadium" project. Thus, the mathematical mesh/surface generated has been utilized to re-shaping and finalize the structural concept through a developable single spatial surface curvature, illustrated in the same image below (Fig. 14, B). In other words, an alternative form has been found as iso-visibility geometry based, from *A* toward *B*. This obtained form is the benchmark to structural features validation. The elaboration occurred through three-dimensional model developed with several cad platform to support design explorations for performance-oriented design. Parametric modeling allows representing geometric entities having with editable attributes, and relationships, *"structure",* by means of associations. In other words, the parametric architecture process theorized by Moretti is adequate to be performed through current graphical technique. The attributes can be expressed by independent values, which act as input to the model. The associations allow for elaborating inputs among related geometric entities. Several solutions of the model have been generated respecting the consistency of pre-established relations among geometric entities, as much as been respected the iso-visibility performance. The stadium form is now superimposed to spatial surface, as show in the image below (Fig. 15), that prompt a new curvature ratio. Consequently, the K value can be modified due to take into consideration also the structural concept shown by the spatial surface shape. Geometric features can thus be automatically repeated in order to customize the variations of the form. The elements can be modelled while guaranteeing pre-established constraints and geometric relations (Fig. 16). In this way is probable to reaffirm what has been said at the beginning: ... *the concept's form should conduct us to assume with scientific rigor the form or its alternatives as minimal designing oscillations in the concept itself*

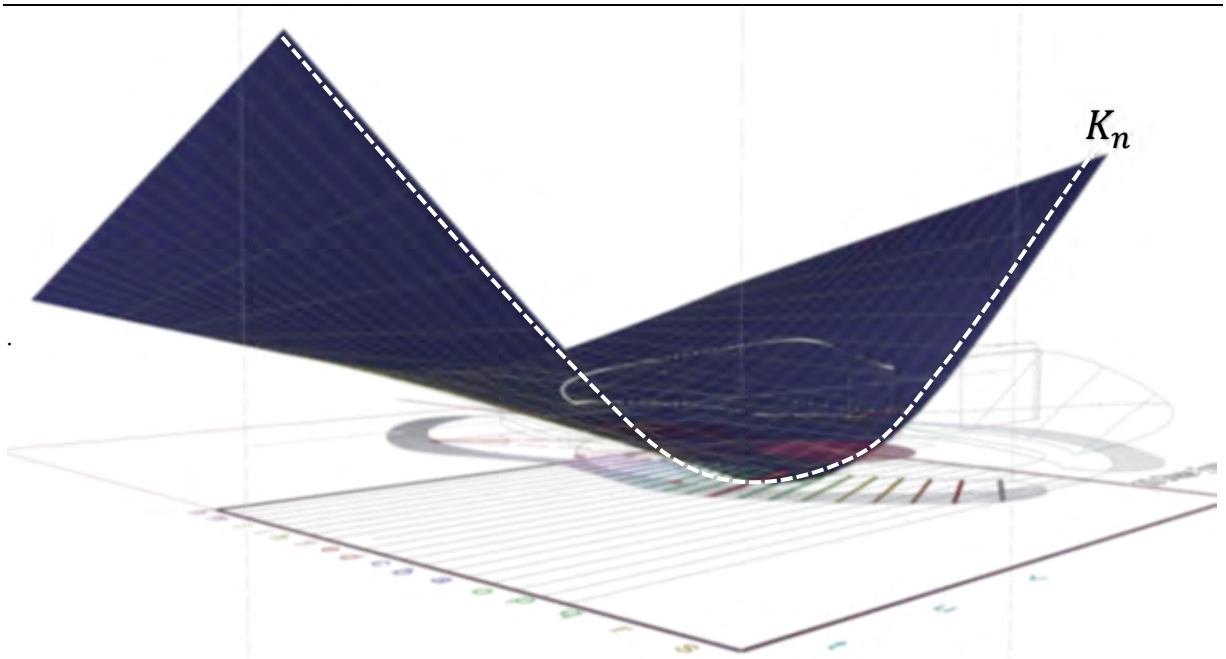


Figure 15: Qualitative modeling and simulation of the reengineered shape, curvatures control trough algorithms and K's value establishment; .gh file is used to support design explorations for performance-oriented design, in which interdisciplinary performance evaluations are integrated in the early phase of the process. This graphic algorithm has been developed for spatial surface design variation in order to looking for a new K value.

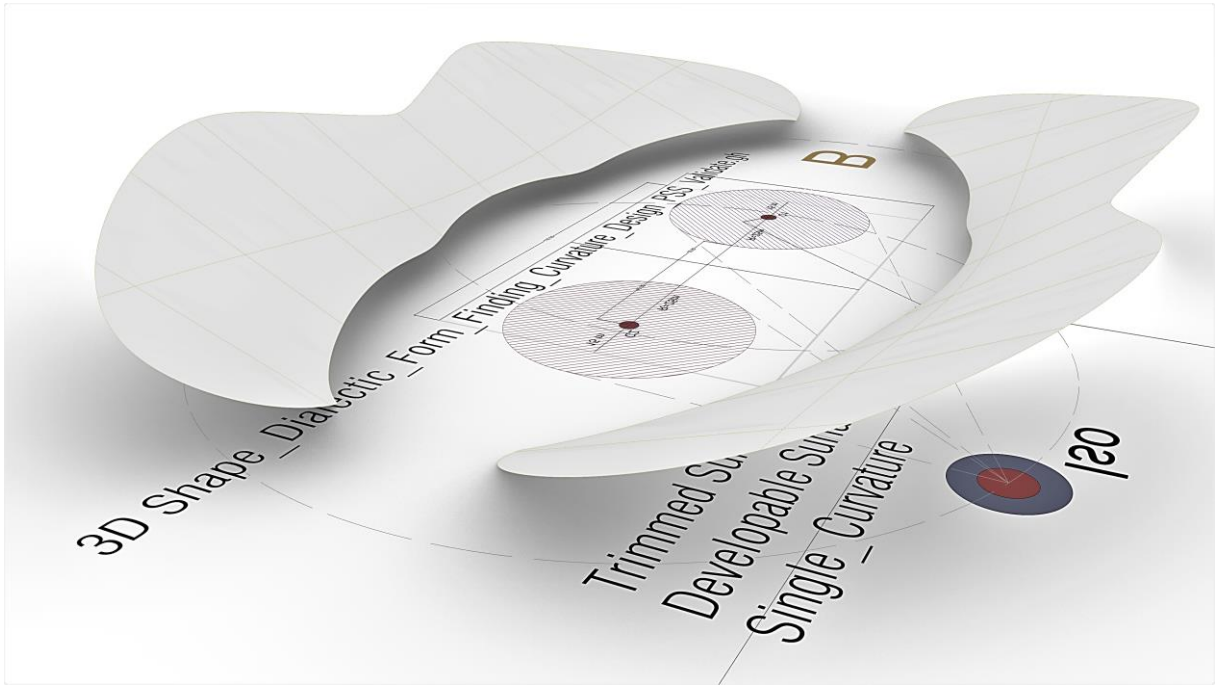


*Figure 16: "**M** Stadium", three-dimensional dialectic form finding* $\mathrm{Ne}\boldsymbol{W} = d_n^{k_n}\,(e^{-k_1 d_n}) + d_m^{k_n}\,(e^{-k_1 d_m})$

Discussion

The XII Milan Triennale exhibition has reviewed by Architect *Bruno Zevi (1918 - 2000)* in his publication *« L'architettura: Cronache e Storia »* 1960, where he argues about Parametric Architecture Manifesto as follow: *[…] Everything that serves to give us distance from empiricism and rationalization in design should be applauded. Especially in a moment like the current one in which the characteristic of the (working methods) of the majority of Italian architects is careless […] a parametric method encompasses the tools, procedures and objectives, but to what end? For these questions, electronic brains are barely useful, brains are needed. If parametric architecture is not to remain a brilliant intellectual exercise, it is indispensable that research is sustained by a high moral inspiration. For now, the idea surprises and fascinates us; tomorrow, it may convince […]* (Zevi 1960 [14]) Moretti itself

during his speech at the "Technology and ecological problem" conference 1972, seems to answer indirectly to Bruno Zevi: *[...] The authentic humanism, in ancient civilization, in its rebirth, was precisely the synthesis and integral thought between the abstract thought, the empiricism, the fantasy in the logical or illogical chains that implemented them, for this reason that humanism in the modern world, is Bacon, Alberti, Vinci, Galileo and last splendid Leibniz. [...]* (de Finetti 2008 [15])

Perhaps, the ethical question remains open for discussion from this point of view if we attribute to the architecture practice an eschatological scope and humanistic intent. However, the parametric architecture theory revisited and combined with current form finding methods, establishes an integrated approach between architectural and engineering purposes. In fact, as illustrated before, the visual-related design aspects have been considered with other architectural constrains under a more specific geometrical-structural performance control. Therefore, it represents an integrate wide-reaching and pertinent method to be adopted as performance-based framework for architectural and structural morphology research. This integrated method is particularly useful for clarifying the design purpose, for analyzing the technical boundary condition, for achieving specific objectives and for solving the design problem into a more pragmatic project scheme at the early stage of design. Once the parametric equation has been scientifically investigated and co-educated through graphic algorithmic procedures, it allows us to evaluate several form alternatives. In fact, it has been virtually modelled and dynamically simulated through powerful CAD investigation instruments in order to validate the complex geometry into a tridimensional space and the iso-visibility areas that were graphically manipulated. Additionally, the core of these early stage design qualitative analysis leads us to assess the design alternatives among the architectural and geometrical-structural forms, providing us a range of compromising solutions that have been explored during the K values investigation. In conclusion, even if in the past decade the project has been supported by powerful computer-based design mediums, it is essential to have a deeper design expertise and thoughtful instrument understanding to customize it. On the other hand, we require a more sophisticated intellectual approach forward the architectural and engineering demand. This *"Forgotten Model of Parametric Architecture*" could be a benchmark to interrogate and stimulate the creative process again. The importance of this method is also pointed to establish and prove a collaborative procedure. Specifically, a framework able to trigger creative design with engineering performance modeling to inspire innovative design solution and augment the project reliability.

References

[1] "United States Lines Paris Review, Presented by Marcel Coudeyre."
[2] C. Beguinot, G. Esposito, and Fondazione Aldo Della Rocca, *Luigi Moretti e la Fondazione della Rocca: urbanistica e ricerca operativa*. Roma: Progetto, 2009.
[3] "Rostagni C., Luigi Moretti 1907 1973, Electa, 2008, 74-92."
[4] "Esposito De Vita G., Luigi Moretti e la Fondazione della Rocca Urbanistica e Ricerca Operativa, Fondazione della Rocca, 2009."
[5] "Viati Navone A., The Architect Luigi Moretti from Rationalism to Informalism, Archivio del Moderno, Università della Svizzera italiana, 2012."
[6] "Reichlin B., Tedeschi L., Luigi Moretti, Razionalismo e trasgressività tra barocco e inf."
[7] "Bucci F., Muzzalani M., Luigi Moretti. Opere e scritti. Electa, Milano, 2000."
[8] "Sheppard A., Luigi Moretti A Testimony, McGill University, 2008."
[9] "United States Lines Paris Review, Presented by Marcel Coudeyre, Luigi Moretti, 'Structure comme forme' (Structure as Form), published in French and English, 1954. The New York Public Library, NY, United States."
[10] "Moretti L., Spazio 6, Struttura come Forma, 1951, 110."
[11] "Moretti L., Spazio 6, Struttura come Forma, 1951."
[12] "Imperiale A., An Other Aesthetic Moretti's Parametric Architecture, 2018."
[13] "Moretti L., Moebius Unità della cultura: Architettura Urbanistica Arte, Ricerca matematica in architettura e urbanisica, 1971."
[14] "Zevi B., L'Architettura Cronache e Storie, Cervelli elettronici No macchine calcolatrici, 1960."
[15] "de Finetti F., Bruno de Finetti e Luigi Moretti, Editore Controluce, 2008."

Proceedings of the IASS Annual Symposium 2019 – Structural Membranes 2019
Form and Force
7 – 10 October 2019, Barcelona, Spain
C. Lázaro, K.-U. Bletzinger, E. Oñate (eds.)

The Concrete Shell of the Engineers Center in the state of Zulia, Maracaibo, Venezuela, analyzed with parametric tools

Edwin GONZALEZ*, Astrid PETZOLD, Francisco MUSTIELES[a], Giancarlo DI MARCO[b].

Department of Architecture, Universidad de las Américas Puebla
Ex-Hacienda Santa Catarina Martir s/n, San Andrés Cholula, Puebla.
edwin.gonzalez@udlap.mx
astrid.petzold@udlap.mx
[a] Department of Art, Design and Architecture, Universidad Iberoamericana Puebla, Blvd. del Niño Poblano 1901, Reserva Territorial Atlixcayotl, Puebla.
francisco.mustieles@iberopuebla.mx
[b] Centro de Diseño, Cine y Televisión, Av. Constituyentes 455, Col. América, CDMX
gdimarco@centro.edu.mx

Abstract

The decade of the 60's in Venezuela speaks of a society with a firm will of modernizing even though there was inequity in it. A society that not only entered the peak of world oil production, but also in a stage of accelerated professionalization to direct the public institutions and the growing professional practice of architecture and urbanism, to accompany that modernization. For the project of the construction of the Engineers Center of Zulia State (CIDEZ, 1962-1965) [1], known as the oil state, and in the second largest city of the country, Maracaibo, Candela is summoned once again, not only for his completion of Playa Azul Beach Club, but also because he had already built, in the same city of Maracaibo, and in association with Miguel Casas Armengol (architect), the headquarters of the Medical Association Centre of Zulia State (1960-1963), and where he had also carried out several other projects and works. This document, concerning specifically the Engineers Center, will show elements and constructive details of the structural plan sent by Félix Candela, to later go on to analyze the structure of the concrete shell using advanced NURBS modeling techniques with Rhinoceros [2], and parametric design with Grasshopper. Force simulation and finite element analysis tools will be used along with shape search techniques for design simulations to generate the geometry and compare the results under normal design conditions with the concrete shell.

Keywords: Concrete shells, light structures, Cubiertas Ala, parametric design, NURBS, finite elements.



Figure 1: Engineers Center, Maracaibo, Venezuela (Source: Photos by Carlos Marval).

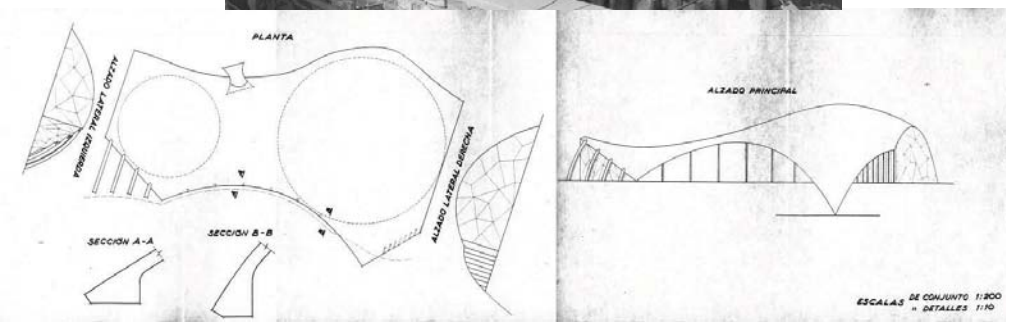
Copyright © 2019 by Edwin GONZALEZ, Astrid PETZOLD, Francisco MUSTIELES, Giancarlo DI MARCO.
Published by the International Association for Shell and Spatial Structures (IASS) with permission.

1. Introduction

There is no study on the structures of hyperbolic paraboloids in Venezuela, to locate in it the work of Felix Candela, of *Cubiertas Ala* and his subsequent followers. However, it should be noted that in 1954, before the beginning of the epistolary relations registered in the Avery Library, the Venezuelan architect Fruto Vivas (1928) had won a contest, being at the time an architecture student at the Central University of Venezuela, for the design of Club Táchira in Caracas.

Vivas requested that the Spaniard Eduardo Torroja be contracted as engineer of the work, who both together, designed the project, which was completed in 1957. In this project two double curved laminated roofs were contemplated: one designed and calculated by Eduardo Torroja, in concrete, a conoid, called by the authors *"La cascada",* and another designed by Fruto Vivas and calculated by Eduardo Torroja, in a metallic structure of trusses, called by Vivas *"El rancho",* covered on both sides with wood, which generate a cone shaped parabolic membrane. It is the latter, the only one that was built (figures 2).





La Cascada: Photograph of the reduced model tested, and plan and elevation (Instituto Eduardo Torroja).





El Rancho: Photograph of the metal structure of trusses by Fruto Vivas y Eduardo Torroja.
Source: Club Táchira. Photos by Jito D´Queen.

Figures 2: Caracas Club Táchira (1954-1957) by Fruto Vivas and Eduardo Torroja.

The epistolary analysis reveals that the first hyperbolic parabolic structure built by Candela in Venezuela was that of an "umbrella" (12mx12m); in fact, it was Guillermo Shelley who proposed it to Candela in February 1956, so that "it could serve as both propaganda and cost analysis; in order to do it, he would need me to send him the calculations and structural plans, design of forms, concrete proportions, etc.". 18 days later, Candela sent Shelley "plans for the construction of the test umbrella".

A little over a week later, Shelley asks Candela: "For the test umbrella, using normal cement, what time does it recommend to unzip?" In that same 1956 letter, Shelley talks to Candela about a very likely first contracted project in Venezuela: "Attached is a plan of a project of a group of apartments on the northern central coast (Litoral), to cover the area of the dining room, bar and ballroom with paraboloids in the indicated schematic form. We await your instructions". This project would be completed in 1957. Candela's work took off with a firm foot in Venezuela. Loomis (1999: 13) will further qualify these structures, both the work of Torroja and Candela, as a formal avant-garde plastic.

2. Engineers Center

In 1962, Felix Candela and Alvaro Coto made a first project for the so-called Maracaibo's Auditorium that would be located in what would be the headquarters of the new building of the College of Engineers designed by Jorge Castillo; this cover was projected with four hyperbolic paraboloids joined by mullions and supported in 4 points (figure 3).

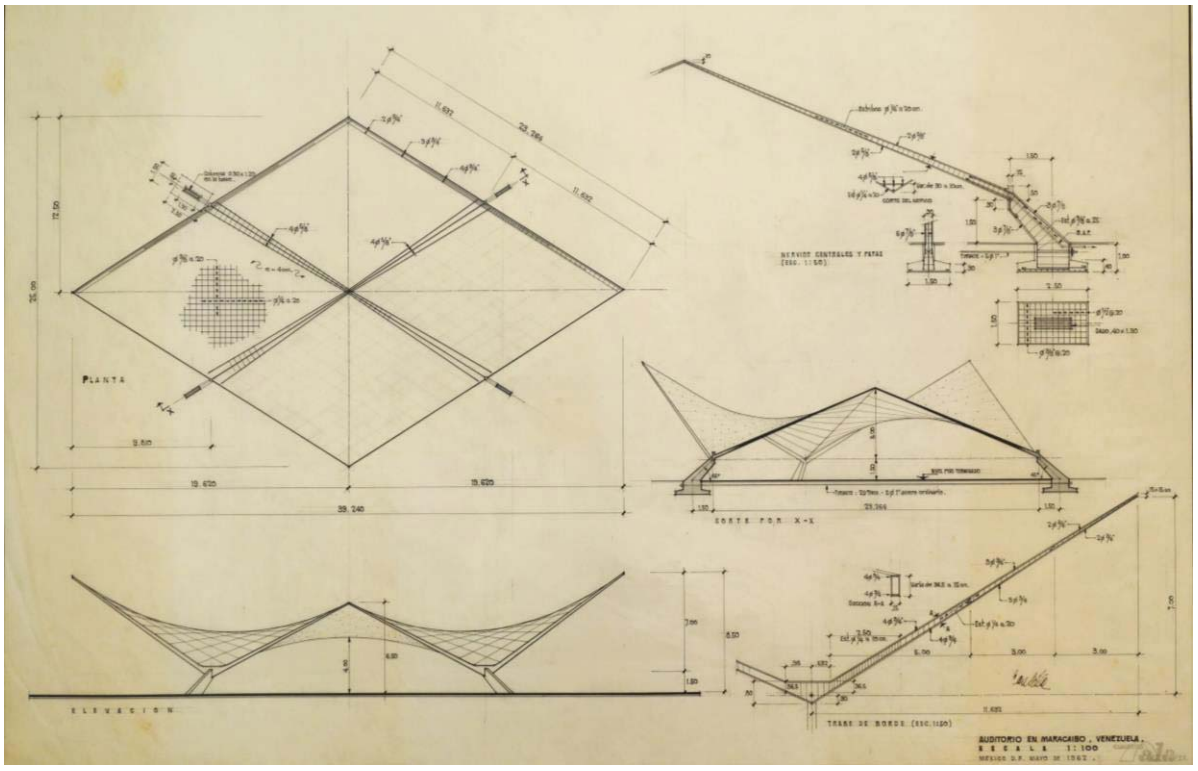


Figure 3: Elevation and plan of Maracaibo's Auditorium (Source: Avery Library).

The final project (1963) required of Candela for the CIDEZ, is that of a cover (concrete shell) for a multiple use space (open auditorium, ballroom, court, etc.). The concrete shell proposed and subsequently built forms a hexagon on the plain, a geometry composed of the union of three hyperbolic paraboloids supported by three reinforced concrete beams (figure 4).



Figure 4: Engineers Center, Maracaibo, Venezuela (Source: Photos by Carlos Marval).

3. Structural project and geometry

Of the various geometric proposals solved by Félix Candela stand out those made by four hyperbolic paraboloids for the formation of umbrellas, widely used mainly in the construction of markets and gas stations in Mexico, to which are added saddle-shaped shells in different sections and scales for the construction of churches or the renowned Restaurant Los Manantiales. For this proposal, and after the first project for the Auditorium of the Engineers Center, Félix Candela and Álvaro Coto changes the geometry to be constructed with three hyperbolic paraboloids joined by mullions and supported in 3 points.

The proposal and construction of the concrete shell for the new proposal of Auditorium at the Engineers Center of Maracaibo forms a polygon with six sides. Four sides have a length of 13,598 m and two sides of approximately 12,702 m, four internal angles of 126.01° and two internal angles 107.98°, which breaks with the regularity of the hexagon with six sides and six equal internal angles. This geometry of six sides with two different measures breaks with the style of the proposals in plant that Félix Candela usually calculated. The geometrical proposal has in the union of the three hyperbolic paraboloids a series of mullions with a variable aperture of 20 cm to 60 cm, the three hyperbolic paraboloids in their mullions are joined by concrete beams (figure 5).

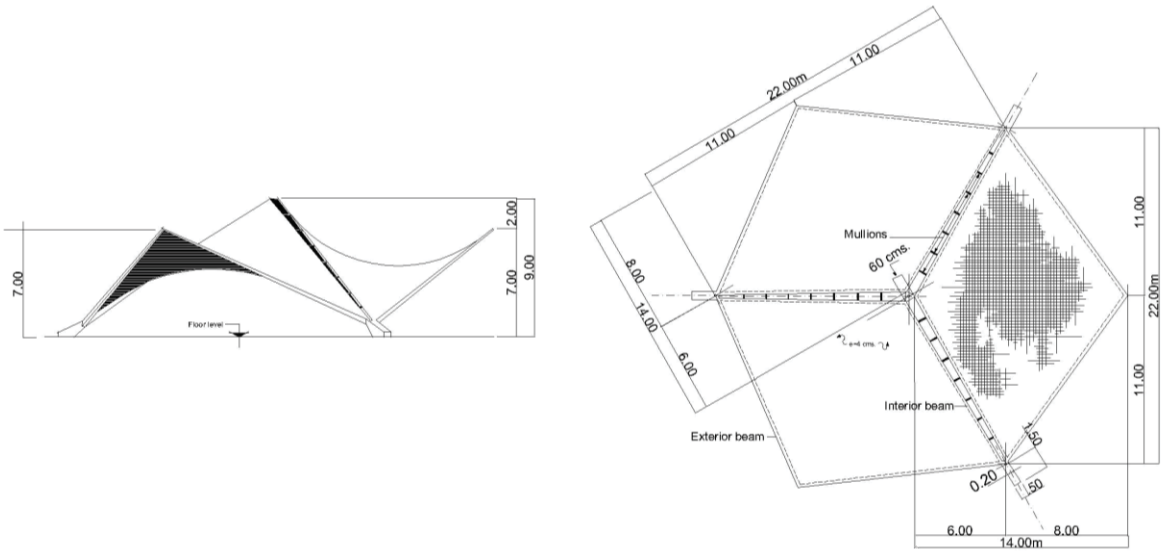


Figure 5: Elevation and plan (Source: Being Avery Library).

4. Constructive and structural system

4.1 Foundation

Félix Candela solves the foundation with three isolated footings of reinforced concrete. Each footing measures 2.00 m x 2.00 m with a variable high from 15 cm to 25 cm, in the direction of the long side of the footing was used bars of ½" at each 17 cm and in the direction of the short side was used bars of 5/8"at each 9.5 cm. The column has a section of 1.00 m x 0.50 m, reinforced with 10 bars of 1" and stirrups of 3/8" at each 20 cm.

Each footing and column are joined by three tensioned ties to 20 tons each, each tie is drowned in the column of the footing and are joined in the center of the plant formed by the structure, this tie prevents the shell to be opened by the thrusts of forces produced mainly by dead charges and gravitational forces. Each footing will be buried 85 cm from the finished floor level.

4.2 Concrete Shell

The reinforced concrete shell has a variable thickness of 4 to 8 cm with a general assembly with rods of 3/8 "to 20 cm in both directions. The greater thickness of 8 cm of the shell part of the center of the structure and is lightened towards the ends.

Two different types of concrete beam support each of the three hyperbolic paraboloids. The first type of beam goes from the center of the shell to the column of the insulated footings. This beam has a section of 15 cm of base, a variable high of 30 to 50 cm with an assembly of four bars and beam hangers of ¼" at each 20 cm. The second type of beam goes along the perimeter of the shell with an irregular section. This beam has a section of 20 cm of base and a variable high of 10 to 30 cm with armed also variable. In its highest high of the section, it is assembled by eight bars of ½" and ¼" beam hangers at each 20 cm, changing in its minimum cant to an assembly of four bars ½" and ¼" beam hangers at each 20 cm (figure 6).

The three hyperbolic paraboloids that make up the complete structure are joined by small concrete beams between their internal type beams to prevent each hyperbolic paraboloid from working independently from external forces. Each mullion has a section of 10 cm x 10 cm armed with four bars of 3/8 "and beam hangers of ¼".

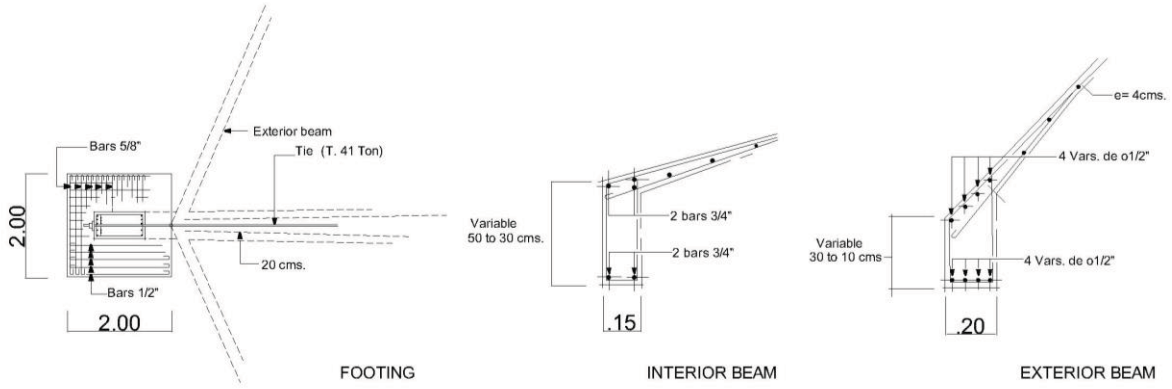


Figure 6: Structure details (Source: Being Avery Library).

5. Simulation of structural behavior

The process begins with the analysis of the structural plans and the layout of the plant in Autocad, afterwards the modeling of the surface of the hyperbolic paraboloids and beams with Rhinoceros 6 is performed. Finally, the structural behavior is simulated in the app Karamba 3D once the data is inserted in Grasshopper.

Rhinoceros 6 can create, edit, analyze, document, render, animate, and translate NURBS curves, surfaces, and solids, point clouds, and polygon meshes. There are no limits on complexity, degree, or size beyond those of your hardware. Grasshopper is a graphical algorithm editor tightly integrated with Rhino's 3-D modeling tools. Karamba3D is a parametric structural engineering tool, which provides accurate analysis of spatial trusses, frames and shells [4] (figure 7).

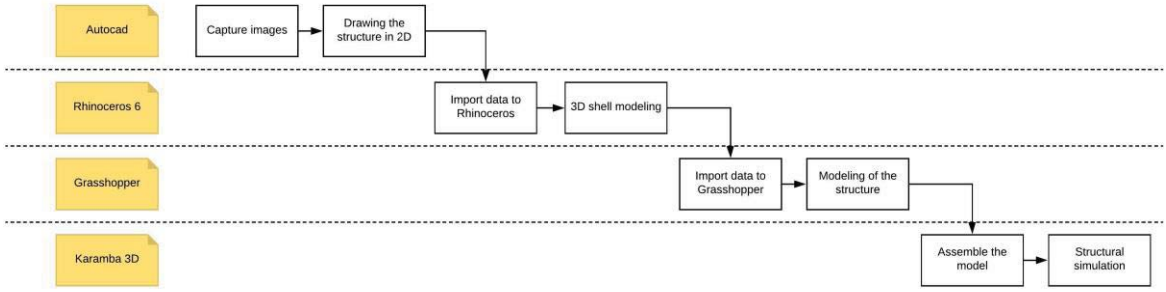


Figure 7: Modeling workflow.

5.1 Modeling of the concrete shell

The modeling of the structure in Grasshopper was facilitated by modeling the geometry in Rhinoceros, importing the data by means of a container of surfaces and later reparametrizing the geometry in the grasshopper. Then, the surface becomes a mesh, an important characteristic for the realization of the structural behavior simulation with Karamba 3D.

In the modeling process, it was determined to work the simulation with a thickness of 4 cm in the concrete shell, although in the extremes grow the section up to 8 cm. It is also determined to divide the exterior and interior concrete beams into 3 sections, this with the intention of simulating the variable height section of the beams. In the outer beam, it is modeled with the sections 30 x 20 cm, 20 x 20 cm and 10 x 20 cm. In the inner beam is modeled with sections of 50 x 15 cm, 40 x 15 cm and 30 x 15 cm.

5.2 Simulation with Karamba 3D

Once the modeling of the structure is done, each of the geometries is converted into structural elements divided into two types: the concrete shell and the concrete beams including the mullions. Later the model is assembled. For the first data collection, shell beams will be separated.

In the simulation of the beams, a greater concentration of axial stresses is observed at the ends, the joining of the supports with the concrete shell standing out. A large number of axial forces are also concentrated in the upper mullions. The maximum bending moments in kNm are simulated in all the elements applying all the existing loads, having the highest value of the cross sections in My and Mz between 4.22 and 100.21 kNm, where the values of the bending moments are calculated with N number of points as long of the elements. The maximum shear force in kN is simulated in all elements applying all existing loads, having the highest value of the cross sections in Vy and Vz between 0.08 and 238.05 kN, where the values of the shears forces are calculated with N number of points a long of the elements (figure 8).

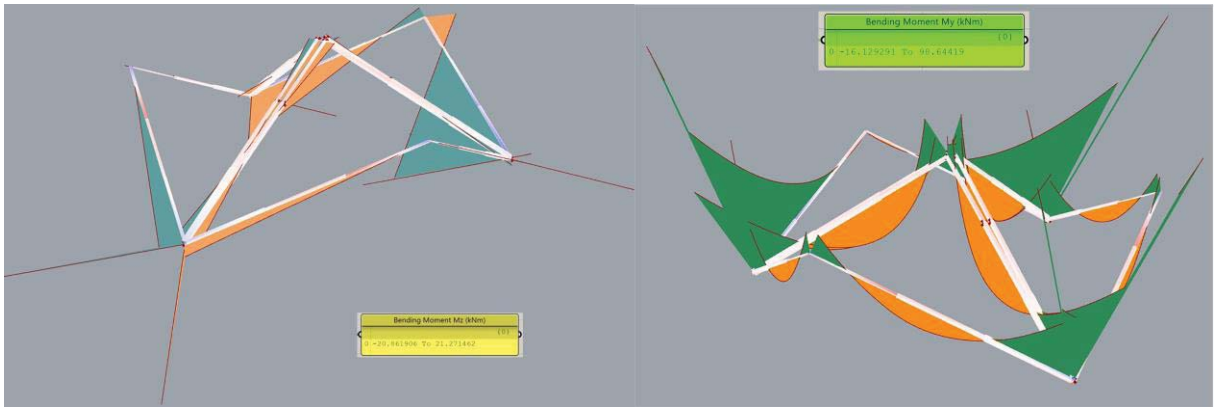


Figure 8: Bending moment diagrams of the concrete beams (Mz and My).

In the simulation of the shell, a greater concentration of axial forces is observed in the supports with the edge beams and in the center of the shell due to the deflections. The bending moment on cross section X causes normal stresses in local X-direction of all shell elements with values between -1.46 to 0.95 kNm/m. The bending moment on cross section Y causes normal stresses in local Y-direction of all shell elements with values between -2.48 to 1.24 kNm/m. Distributed normal forces are negative in case of compression. Positive bending moments result in tension on the upper side of a shell. Transverse shear force on cross section X of all shell elements has values between -5.53 to 5.53 kNm. Transverse shear force on cross section Y of all shell elements has values between -6.01 to 3.60 kNm.

In the simulation of the structure contemplating concrete shell and concrete beams, an approximate mass of 72,356.72 kg is obtained and a maximum deflection of approximately 30.33 cm. The mullions absorb axial loads that allow the stabilization of the structure increased its maximum deflection approximated to 43.70 cm, which would cause that the majority of the axial forces were to traction. The edge or perimeter beam to be removed in the simulation decreases the maximum deflection to 29.79 cm, but increasing the axial forces in compression to the center of each of the shells (figure 9).

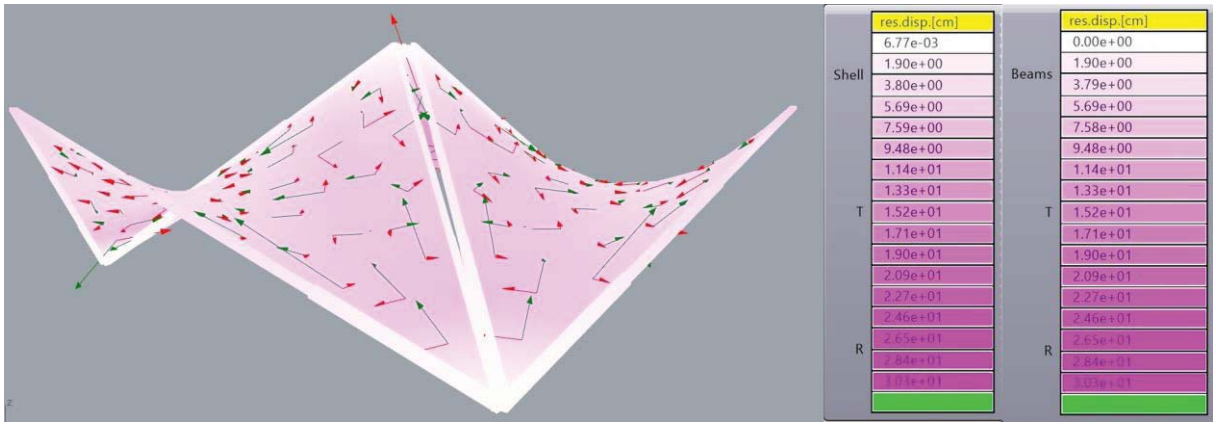


Figure 9: Displacements of the shell and beams, and principal stresses on the shell.

5. Conclusion.

In the second half of the twentieth century, a concrete shell construction boom continues and, with the influence of European builders such as Eduardo Torroja, Heinz Isler, among others, will transfer an influence to Latin America. Influence that the same exiled Spaniards after the war would share their ideas and knowledge, being Felix Candela one of the most representative.

The influence of Felix Candela would move throughout Latin America being Mexico and Venezuela the countries where more structures would calculate and build. Outstanding structures such as the Church of La Medalla Milagrosa in Mexico or the roof for the factory of the Volkswagen in Venezuela.

In Venezuela the Concrete Shell for the Center of Engineers in Zulia stands out as a structure composed of three hyperbolic paraboloids, something unusual in the works of Felix Candela. In its proposal it solves the structure by placing beams and central beams that support the three shells, the central beams are joined by the mullions.

In the simulation of the structural behavior it can be observed that the edge beams did not benefit to reduce the deformations or axial loads on the shells, so they would not be necessary to stabilize the structure, the deformations of the structure are mainly concentrated on the shell. It is with the central beams where the deformations are reduce. The mullions have an important function in the stabilization of the structure by preventing the three concrete shells from separating, without the mullions the structure would collapse in its supports when concentrating most bending moment and shear stresses.

Acknowledgements

Avery Library de Columbia University, New York.

References

[1] *Drawings and Archives* de la Avery Library de Columbia University, New York, EEUU.

[2] G. Di Marco, "Simplified Complexity, Método para el modelado NURBS avanzado con Rhinoceros", *Le Penseur*, 2017.

[3] Loomis, John A. (1999), *Revolution of Forms. Cuba's Forgotten Art Schools*, Nueva York, Princeton Architectural Press.

[4] Preisinger, Clemens, "Linking Structure and Parametric Design", in *Architectural Design 83.2, 201,* p.p 110-113.

Files consulted.

Drawings and Archives de la Avery Library de Columbia University, New York.

Félix & Dorothy Candela Archive, Princeton University.

Coto Asenjo Files, family Coto Villarroel.

Shelley Torres Files, family Shelley Herrera.

Photo credits.

Club Táchira. Jito D´Queen.

Instituto Eduardo Torroja.

Carlos Marval.

Proceedings of the IASS Annual Symposium 2019 – Structural Membranes 2019
Form and Force
7 – 10 October 2019, Barcelona, Spain
C. Lázaro, K.-U. Bletzinger, E. Oñate (eds.)

Design and fabrication of a mesh reinforced membrane inflatable deployable reflector and its shape stability

Qiang TAO[a], Changguo WANG[*b], Huifeng TAN[b]

[*b] National Key Laboratory of Science and Technology for National Defence on Advanced Composites in Special Environments, Harbin Institute of Technology
2 Yikuang Street, Nan Gang District, Harbin, China
wangcg@hit.edu.cn

[a] Center for Composite Materials and Structures, Harbin Institute of Technology

Abstract

Maintaining shape accuracy of reflector is the key point of deployable antennas. Inspired by MRM, a mesh reinforced membrane inflatable deployable reflector was proposed. A MRM inflatable deployable reflector (focal length to diameter ratio F/D=0.8, Diameter=3.0m) was designed and fabricated. The shape accuracy testing of membrane reflector was conducted by the Video-Simultaneous Triangulation and Resection System. RMS value of the geometric configuration between the fabricated membrane reflector and designed membrane reflector was used to evaluate the shape accuracy. The results revealed that the MRM reflector performed higher shape accuracy than the pure membrane reflector. Also, the characteristics of the pressure expansion and the deformability against the external load were studied via the experiments and numerical simulations. The experimental results showed that the reinforced mesh greatly improved the shape stability of the inflatable membrane structure. The simulation results showed good agreement with experimental results.

Keywords: mesh reinforced membrane, deployable reflector, shape stability, design, fabrication.

1. Introduction

Maintaining shape stability and increasing the deformability against the external load are essential for application of inflated structure. Researchers make different attempts about these. Yoo et al. [1] and Wang [2] studied the wrinkling control of inflated beams using using SMA wires by experimental and numerical studies. SMA wires have achieved good effects on the shape and wrinkling controls of membrane structures [3, 4]. In addition, several novel applications such as carbon-reinforced isogrid inflatable booms [5], pumpkin balloons [6], and inflatable habitat reinforced by woven fabric webbings [7] may guide us to control the wrinkles and enhance the deformability against the external load of inflated beams by adding the mesh on the surface. Tao et al. [8] proposed a novel concept of mesh reinforced membrane (MRM), and applied MRM to inflatable beam. The experimental results showed that MRM greatly improved the deformability against the external load of inflatable beam.

Shape accuracy of reflector is the key point of deployable antennas. Inspired by MRM, a mesh reinfored membrane inflatable deployable reflector was proposed. It mainly includes membrane reflector, mirror reflector, reinforced mesh and edge ring, among which the membrane reflector is the main functional layer; the reinforced mesh is designed to improve the shape stability of reflector and can be optimized to meet different performance requirements.

In this paper, a novel concept of mesh reinforced membrane (MRM) inflatable deployable reflector was proposed at first. In the following, the MRM inflatable deployable reflector structure was design.

Copyright © 2019 by Qiang Tao, Changguo Wang, Huifeng Tan
Published by the International Association for Shell and Spatial Structures (IASS) with permission.

Then, the fabrication process of MRM reflector structure was introduced. And a MRM inflatable deployable reflector (focal length to diameter ratio F/D=0.8, Diameter=3.0m) was fabricated. The shape accuracy testing of MRM reflector was conducted by the Video-Simultaneous Triangulation and Resection System (V-STARS), and the deformability against the external load was tested. At last, a finite element model was established, and the characteristics of the pressure expansion and the deformability against the external load were studied.

2. Concept and design of MRM reflector

2.1. Concept

The conceptual diagram of a lens-type mesh reinforced membrane inflatable deployable antenna reflector was shown in Figure 1. The MRM reflector mainly included the membrane reflector, the mirror reflector, the reinforced mesh and the edge ring. The membrane reflector was the main functional layer. The reinforced mesh was designed to improve the shape stability of reflector and can be optimized to meet different performance requirements. The purpose of the mirror reflector layer was to form an inflatable cavity with the membrane reflector layer for inflation and expansion. The reinforced mesh layer was attached to the membrane reflector, which can be optimized by the mesh type to meet different performance requirements. The edge ring wan designed to smooth the distribution of the edge force flow, restrain the wrinkles and warpage of the reflector edge when the reflector was unfolded.

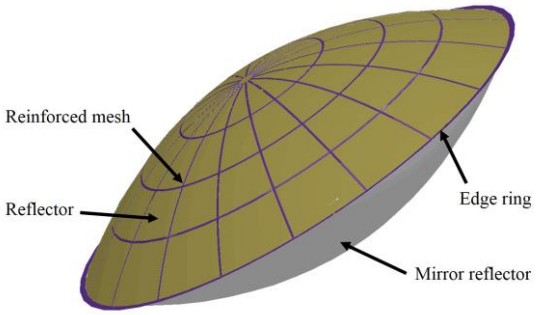


Figure 1: Concept and design of mesh reinforced inflatable deployable reflector

2.2. Design of MRM reflector

The key point of design of MRM reflector is the design of the reinforcement mesh structure. In order to confirm the optimal choice of the mesh type, the finite element models of cylindrical shell comprised of different mesh types was established, and buckling analysis was conducted. The load-carrying efficiency was defined to evaluate the buckling behavior of different mesh structures. The results was shown in Figure 2 as follow.

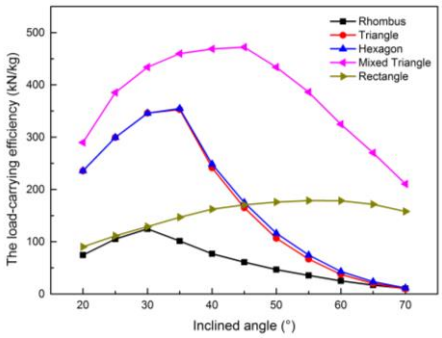


Figure 2: The effect of inclined angle on load-carrying efficiency of different mesh structures

According to the results in Figure 2, the mixed triangle mesh structure performed the highest load-carrying efficiency. So the optimal choice of mesh type of MRM reflector will be the mixed triangle.

3. Fabrication of MRM reflector

The fabrication process of MRM reflector mainly inclued six steps: the fabrication of pure membrane reflector, laying the radial reinforcement strips, laying the circumferential reinforcement strips, laying the helical reinforcement strips, coating resin and curing. A MRM inflatable deployable reflector (focal length to diameter ratio F/D=0.8, Diameter=3.0m) was fabricated. The fabrication process was shown in Figure 3.

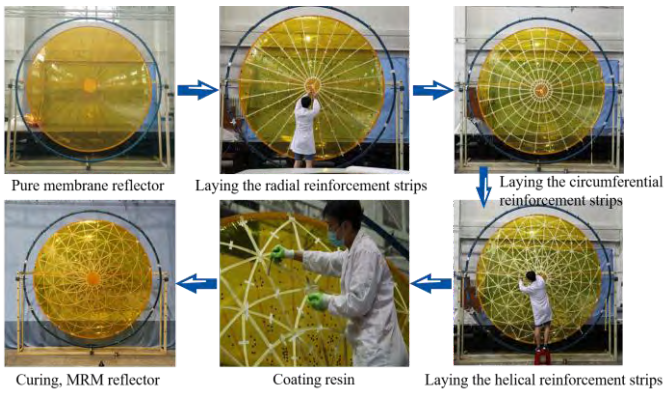


Figure 3: The fabrication process of MRM reflector

The material of pure membrane reflector was polyimide membrane, which thickness is 25μm. The Kevlar strips were selected to form the mesh structure. And the resin was shape memory epoxy resin, which glass transition temperature is 78°C.

4. Experiments

4.1. The shape accuracy testing

The shape accuracy testing of membrane reflector was conducted by the Video-Simultaneous Triangulation and Resection System (V-STARS). RMS value of the geometric configuration between the fabricated membrane reflector and designed membrane reflector was used to evaluate the shape accuracy. As shown in Figure 4, the results revealed that the MRM reflector performed higher shape accuracy than the pure membrane reflector. The mesh is helpful to improve the shape accuracy of membrane reflector.

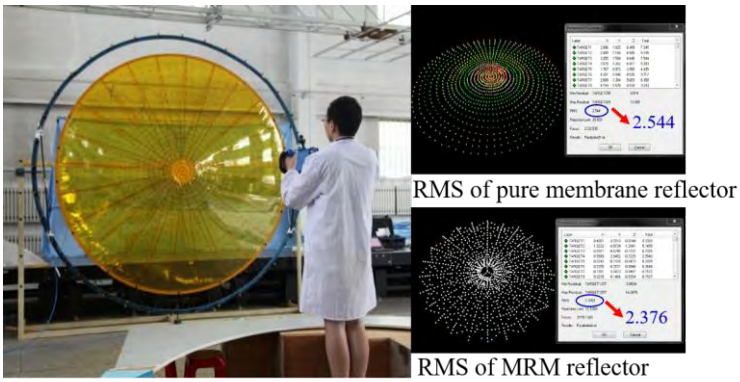


Figure 4: The shape accuracy testing of pure membrane reflector and MRM reflector

4.2. The testing of deformability against the external load

The compression experiments of MRM reflector was carried out to evaluate the deformability against the external load. The edge of the MRM reflector was fixed on a circle metal frame; a concentrated tip compressed load was applied at the center of the MRM reflector. The deflection at the center was captured by Leica Total Station; the internal pressure of the MRM reflector was monitored by a digital monometer. The layouts of compression experiments were shown in Figure 5.

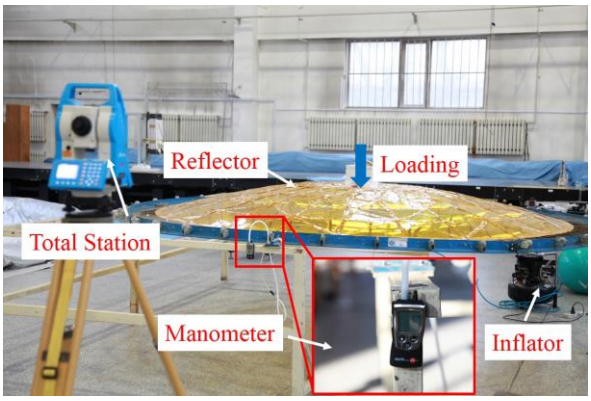


Figure 5: Layouts of bending experiments

5. Finite element modeling

In the modeling, the ABAQUS S4R shell element with reduced integration was selected as it is efficient and well-suited for linear and non-linear problems of curved thin shell deformations with large displacements, large rotations and finite membrane strains.

As the reflector is rotational symmetry, One-twelfth model was selected to analyze for time saving and computing costs. The analytical model was shown in Figure 6. The edge of reflector is all constrained. At the center of the reflector, a concentrated tip compressed load was applied. Mesh element size was 15mm. The loads were introduced in two steps. In the first step, the reflector was inflated by applying an internal pressure p which is 60Pa in these cases. Then, a tip compressed load F was applied at the center of reflector.

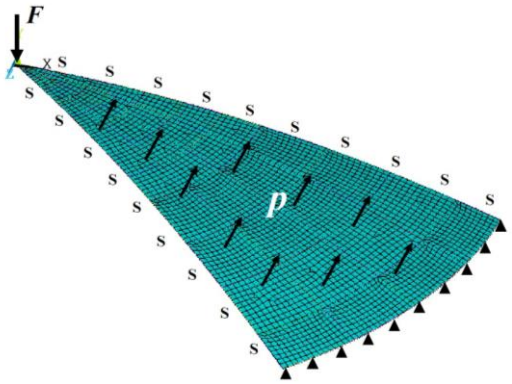


Figure 6: The FE model for membrane reflector

The characteristics of the pressure expansion and displacements in the Y direction of inflatable reflectors were depicted in Figure 7. The two reflectors performed a vastly different pattern. For MRM reflector, the bulging effect induced by discrete feature of mesh structure appeared during the process of inflating. Also, the failure mode for two reflectors were similar, which both collapsed at the center of the reflectors.

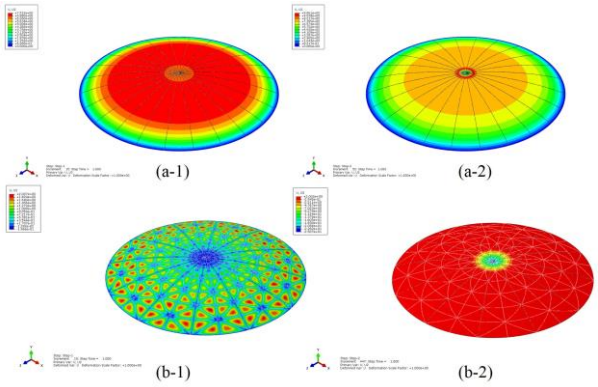


Figure 7: Configurations after inflating and displacements in the Y direction of inflatable reflectors:

(a) Pure membrane reflector; (b) MRM reflector

6. Discussion

Figure 8-9 showed the load-displacement curves of pure membrane and MRM reflectors with p=60Pa. The modeling results curves showed similar trend to the experimental results curves. Seen from Figure 8, the critical buckling load tested by experiment for pure membrane reflector was 1.72N, while 1.87N for modeling result. The critical buckling load error between experimental result and modeling result was 8.72%.

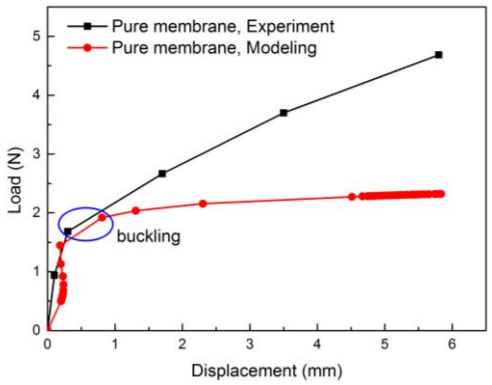


Figure 8: Experimental and modeling load-displacement curves of pure membrane reflector

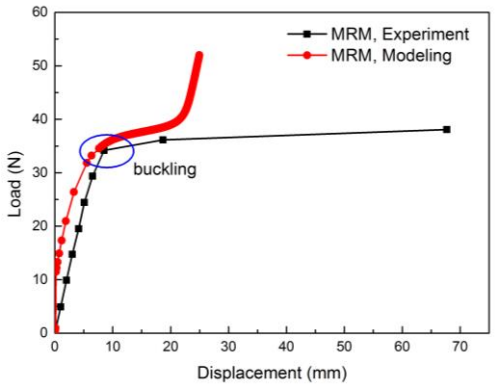


Figure 9: Experimental and modeling load-displacement curves of MRM reflector

Seen from Figure 9, the critical buckling load tested by experiment for MRM reflector was 33.91N, while 35.87N for modeling result. The critical buckling load error between experimental result and modeling result was 5.78%. Also, the critical buckling load tested by experiment for MRM reflector was improved by 18.72 times more than the critical buckling load tested by experiment for pure membrane reflector. However, mesh will inevitably increase structure weight. Therefore define the specific load calculated from the following equation to evaluate the deformability against the external load of MRM reflector.

$$\eta = \frac{Load(\mathrm{N})}{Weight(\mathrm{N})} \tag{1}$$

According the equation (1), the specific critical buckling load for MRM reflector was 1.50N, while 0.92N for pure membrane reflector. And the specific critical buckling load for MRM reflector was improved by 63.04% than the specific critical buckling load for pure membrane reflector.

7. Conclusions

A novel concept of mesh reinfored membrane (MRM) inflatable deployable reflector was proposed in this paper. The MRM inflatable deployable reflector (focal length to diameter ratio F/D=0.8, Diameter=3.0m) was designed and fabricated. The shape accuracy and the deformability against the external load was studied by experiments. Also, the characteristics of the pressure expansion and the deformability against the external load were studied via the numerical simulations. Several important conclusions can be drawn as follows.

(a) The MRM reflector performed higher shape accuracy than the pure membrane reflector.

(b) The experimental results showed that the reinforced mesh greatly improved the shape stability of the inflatable membrane reflector. The modeling results showed good agreement with the experimental results.

(c) The specific critical buckling load for MRM reflector was improved by 63.04% than the specific critical buckling load for pure membrane reflector.

(d) MRM is an effective way to improve the shape accuracy and shape stability of the inflatable membrane structure.

Acknowledgements

The authors gratefully acknowledge financial supports from National Natural Science Foundation of China, 11572099; Natural Science Foundation of Heilongjiang Province of China, A2015002; the Fundamental Research Funds for the Central Universities, HIT.MKSTISP.2016 29. The Aeronautical Science Foundation of China, 2016ZA77001.

References

[1] E.J. Yoo, J.H. Roh, J.H. Han. Wrinkling control of inflatable booms using shape memory alloy wires. *Smart Materials and Structures*, vol. 16, pp. 340-348, 2007.

[2] C.G. Wang, HF Tan. Experimental and numerical studies on wrinkling control of an inflated beam using SMA wires. *Smart Materials and Structures*, vol. 19, pp. 1-9, 2010.

[3] I. Lee, J.H. Roh, E.J. Yoo, J.H. Han, S.M. Yang. Configuration control of aerospace structures with smart materials. *Journal of Advanced Science*, vol. 18, pp. 1-5, 2006.

[4] F. Peng, Y.R. Hu, A. Ng. Testing of membrane space structure shape control using genetic algorithm. *Journal of Spacecraft and Rockets*, vol. 43, pp. 788-793, 2006.

[5] R.E. Allred, A.E. Hoyt. UV Rigidizable carbon-reinforced isogrid inflatable booms, In: *Proceedings of the 43rd AIAA/ASME/ASCE/AHS/ASC Structures, Structural Dynamics, and Materials Conference*, Denver, Colorado AIAA, 2002, pp. 1-11.

[6] M. Pagitz, S. Pellegrino. Buckling pressure of pumpkin balloons. *International Journal of Solids and Structures*, vol. 44, pp. 6963-6986, 2007.

[7] W.S. Kenner, T.C. Jones, W.R. Doggett. Long Term Displacement Data of Woven Fabric Webbings under Constant Load for Inflatable Structures, *55th AIAA/ASME/ASCE/AHS/ASC Structures, Structural Dynamics, and Materials Conference*, Maryland, 2014, pp. 1-30.

[8] Q. Tao, C. G. Wang, Z. M. Xue, Z. M. Xie, H. F. Tan. "Wrinkling and collapse of mesh reinforced membrane inflated beam under bending", *Acta Astronautica*. vol. 128, pp. 551-559, 2016.

Proceedings of the IASS Annual Symposium 2019 – Structural Membranes 2019
Form and Force
7 – 10 October 2019, Barcelona, Spain
C. Lázaro, K.-U. Bletzinger, E. Oñate (eds.)

Development for Comprehensive Health Monitoring System for a New Air-supported Membrane Structure Hall

Wujun CHEN*, Yue YIN, Jianhui HU, Bing ZHAO

* Space Structure Research Center, Department of Civil Engineering, Shanghai Jiao Tong University
Room A302, Ruth Mulan Chu Chao Building, 800 Dongchuan Road, Shanghai, China
Email: cwj@sjtu.edu.cn

Abstract

Air-supported membrane structure hall has been widely used in large-span structures in recent years due to its prior properties including low-weight, convenient installation and authentic appearance. Unlike steel and concrete structures, membrane structures are more vulnerable to harsh external environment and catastrophic failure from structural vibration. Moreover, heat preservation and insulation property of the pneumatic membrane structure hall tends to be affected by surrounding environment in virtue of the limited thickness of its membrane facades. Hence, a comprehensive health monitoring system was developed to carry out a thorough measurement of the air-supported membrane structure hall. Such monitoring system was composed of four parts, which were sensor sub-system, data collection sub-system, data communication & memory sub-system, and alarm & data analysis sub-system, respectively. In this measurement lasting for 1~2 years, data involving thermal environment and structural behaviors were detected at key positions on external or internal surface of the air hall. All the data gathered was stored in a server by special data cables and then uploaded to web storage for ease of accessing using network. Alarm sub-system would be activated once the feature parameters exceeded its threshold, then these data would be extracted and further analyzed. The comprehensive health monitoring system presented in this paper can help understand the dynamic properties of pneumatic structures under wind loads and the thermal environment in a relatively long period. Besides, analysis of structural and thermal behaviors can be used to improve internal pressure control methods and air conditioning management schemes to maintain a good health of pneumatic membrane structures.

Keywords: health monitoring system, air-supported membrane structures, dynamic properties, thermal environment

1. Introduction

Over recent decades health monitoring system is widely applied in civil engineering in order to eliminate potentially structural risks of buildings. Health monitoring technology of constructions incorporates large amount of technologies from different fields including engineering, materials science, mechanics, data collection and analysis, satellite positioning, as well as computer science [1]. Using approaches of noninvasive measurement, parameters related to structural properties can be measured, such as internal force, deformation and strain. Then data processing and analysis are conducted to evaluate whether the building is in a good health in terms of service life, structural stability and reliability during the operation stage (even the construction stage) of building. All the assessment metrics of the building can serve for alarm and responses to help people reduce or even avoid structural damage. Nowadays, health monitoring system is mainly used in multi-purpose facility [2], skyscrapers [3], historic landmarks [4], large-span bridges [5,6]. However, the usage of such system is uncommon in the field of membrane structure and no precedent is found in pneumatic membrane structures.

Copyright © 2019 by Wujun CHEN, Yue YIN, Jianhui HU, Bing ZHAO
Published by the International Association for Shell and Spatial Structures (IASS) with permission.

As a vital branch of novel space structures, pneumatic structures can be categorized into three basic forms: air-supported (insufflated), inflated and aspired structure [7]. Air-supported membrane structure has been widespread owning to its excellent features of low-weight, fast installation, easy dismantling, semi-translucence, as well as authentic appearance. Hence, it has arrested considerable attention of structural engineers to use such kind of structural form to construct large-span stadium, storage buildings, as well as factory buildings. Air-supported membrane structures are typically consisted of flexible membrane facades and cable systems. Membrane facades are fixed at the ring beam or the ground beam of building. A pneumatic system inflates interior space of the whole structure with external air to provide pre-stress to the membrane. Cable systems are installed outside to enhance integral rigidity of the structures.

Given the widespread application of air-supported membrane structures, a number of researchers have investigated its properties from different aspects. Qing *et al.* [8] studied deflation behaviors of air-supported membrane structure under normal and emergency deflation condition. On-site tests of vertical displacement, pressure variation and pumping air flow were recorded, and then a numerical model was proposed to illustrate the deflation process. Pauletti and Oliveira [7] adopted different numerical models to examine stress and displacement distribution of the air-supported membrane structure with adherent or non-adherent reinforced cables. Structural properties under transversal and longitudinal wind loads were also explored in this research. Suo *et al.* [9] performed site survey and measurement in a typical winter day to investigate thermal-physical behavior and energy-performance of air-supported membranes for sports halls Numerical simulation was carried out as an auxiliary approach to assess internal thermal environment and energy loses. Zrim *et al.* [10] used daylight factors to examine illumination levels and light distribution inside an air-supported membrane structure. DAYSIM program was applied to calculate daylight factors to help predict other cases with various color patterns and different material properties.

The research to date commonly focused on the properties of air-supported membrane structures in a temporary time, but there is very little scientific understanding of its long-term performance. Although some research has examined the structural behaviors under wind loads by numerical analysis, no convincing studies based on experimental data have been reported. Unlike steel and concrete structures, membrane structures are more vulnerable to harsh external environment and catastrophic failure from structural vibration. In general, internal pressure is monitored in almost all the air-supported membrane structure in order to adjust the pressure value in response to external environmental load. However, current pressure regulation is based on several preset operating modes which are not accurate enough to make corresponding reaction according to different load conditions. Therefore, it is necessary to understand the dynamic properties of the air-supported structure in a long term to optimize its pressure control method, so that the pneumatic system can be actively adjusted in response to the level of wind loads. In addition, internal thermal environment inside membrane structure tends to be influenced by surrounding environment given the limited thickness of membrane facades. Therefore, it is worthy to pay attention to long-term thermal physical behaviors in order to improve energy performance of the air-supported structure.

This paper proposes a comprehensive health monitoring system for air-supported membrane structure to record data involving its structural and thermal physical behaviors. Firstly, a complete design is introduced, including components of the system, as well as the operation mechanism. Then a detailed installation process of the monitoring system is demonstrated. Finally, some measured results are presented to show how the monitoring system works. Long-term dynamic properties and thermal performance of air-supported membrane can be further analyzed based on the collected data.

2. Design and installation

2.1. Air-supported Membrane Structure Hall in SJTU

The comprehensive health monitoring system is installed at SJTU pneumatic sports hall, a new air-supported membrane structure built in 2019. It occupies 5700m^2 and lies in the north of Minhang campus of Shanghai Jiao Tong University from north to south direction. As shown in Figure 1, it has dimensions of 142m long, 38m wide, and 15m high. A highway and several dormitory buildings lie to the east and west of the hall, respectively. The air-supported membrane structure is a cable-membrane structure with design life of 15 to 20 years. Double-layer Brite PVF membrane is used to form the facades of the hall, on which sliding cable net system with PE skins are adherent. Positioned at the middle part of the top membrane roof, there is a transparent daylighting zone covering less than 15% of the total area. The other parts of the top membrane facades are equipped with 50mm thick glass wool blankets which are sealed by aluminum foil on both sides. Internal pressure of the air-supported membrane structure is set to 250Pa and its maximum value is 500Pa.



Figure 1. Top view of SJTU pneumatic sports hall

2.2 Design principles

The comprehensive health monitoring system is installed at the sports hall mentioned above to monitor its structural health and internal thermal environment. In general, two principles are primarily considered when design the health monitoring system: function and cost. First, the requirement for measuring target parameters related to structural health ought to be satisfied. Secondly, both the scale and the component devices of monitoring system are determined according to the upper limit of investment. In addition, the health monitoring system proposed in this paper is required to operate for a long period of 1 to 2 years. Therefore, the durability and long-term stability of each component of the monitoring system need to be taken into account.

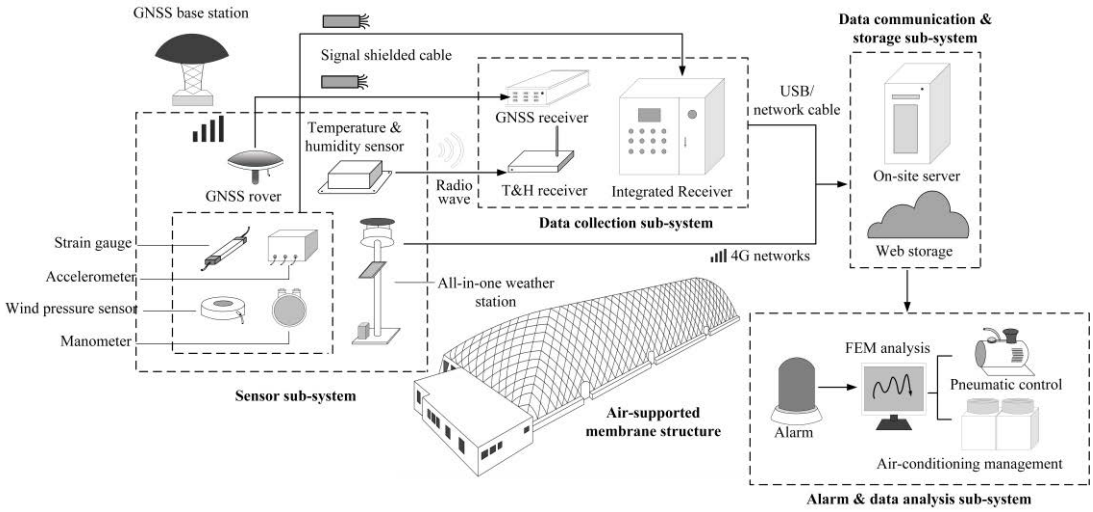


Figure 2. Diagram of the comprehensive health monitoring system

2.3 Design of sub-systems

A comprehensive health monitoring system is classified in terms of functions into four components as presented in Figure 2: (1) sensor sub-system, (2) data collection sub-system, (3) data communication & memory sub-system, and (4) alarm & data analysis sub-system. The former three sub-systems are installed at the air-supported membrane structures. They have characteristics of complex framework, simple flow-process and automatic operation using sensors and network technology. Operation of alarm & data analysis sub-system needs analyzing data manually and conducting finite element simulations assisted by high-performance computers. Thus, it has a relatively simple framework and complex operating procedures.

2.3.1 Sensor sub-system

On the basis of functional requirements of monitoring structural and thermal behaviors, the sensor sub-system is consisted of different sorts of instruments as following: accelerometer, GNSS (Global Navigation Satellite System) receiver, wind pressure sensor, strain gauge, manometer, and temperature & humidity sensor. Accelerometer, GNSS receiver and wind pressure sensor are applied to measure acceleration, displacement and surficial wind pressure of the membrane facades, respectively. All these data are essential to analyze dynamic properties of the sports hall. Strain gauge is used to record the strain variation of the sliding cable to judge the force consistence of the colinear cable. Interior temperature and humidity are measured by temperature & humidity sensor in order to study the thermal-physical behaviors in long term. Moreover, an all-in-one weather station adjacent to the hall is installed to collect weather data containing wind direction, velocity, air temperature, humidity and rain fall, which can reflect the change of surrounding environment.

Table 1 gives some essential descriptions of the sensors adopted in the sub-system. Instruments selected are required to be highly accurate and be able to detect low-frequency signal. Power supply and battery capacity are two primary factors to be considered beside of measuring precision when setting sampling rate of each sensor. Signal cables can also realize the funtion of wire in the sensor, including accelerometer, GNSS (Global Navigation Satellite System) receiver, wind pressure sensor, strain gauge, manometer. Temperature & humidity sensor is powered by lithium battery. Photovoltaics in the all-in - one weather station can supply power for this device. Sampling rate of each sensor is therefore set to be 1Hz except the temperature & humidity sensor and weather station since weather will not change dramatically in short time. Sampling period of them is 10 minutes and 3minutes, respectively.

Table 1 Specification of sensors

Category	Range	Accuracy	Sampling frequency or period
Accelerometer	0.5~8000 Hz	0.0005 g	1Hz
GNSS Rover	-	1cm	1Hz
Wind pressure sensor	-3~3kPa	0.5%	1Hz
Strain gauge	±1500με	1με	1Hz
Temperature & humidity sensor	-40~85℃&0~99.9%	±0.2℃&±2%	10min
Manometer	0~1000Pa	0.5%	1Hz
All-in-one weather station	-	-	3min

2.3.2 Data collection sub-system

Signal collected by the sensors are conveyed to the corresponding receivers via signal cables, radio waves or networks. In data collection sub-system, networks and radio waves are used to transmit signals form temperature & humidity sensor and weather station to their receivers, and shield cables are adopted in the rest of sensors. It is necessary to point that GNSS receivers contains three parts which are rover, signal receiver and base station. In particularly, GNSS rovers are installed on the membrane facades, and signal receivers are components of data collection sub-system. The base station used in this project

lies at the campus which is 2 kilometers far from the sports hall. GNSS rover receives RTK data bag form the base station via 4G networks and then sends them to signal receiver by the shield cable. Receivers in data collection sub-system are divided into three main classes according to the patterns of data acquisition. Acceleration, wind pressure, internal pressure and cable strain are integrated into one receiver while the rest signals are collected by independent receiver. The version of integrated receiver is EY221, while GNSS signal receiver and temperature & humidity receiver is M300mini and RE-78-M485, respectively.

2.3.3 Data communication & memory sub-system

The all-in-one could automatically upload the weather data to web storage by a built-in network unit. The rest of data is stored in the on-site high-performance server. EY221, M300mini and RE-78-M485 receivers are connected with the serve via networking cable, RS-232 cable and USB cable, respectively. All the data collected is uploaded to web storage for ease of remote processing.

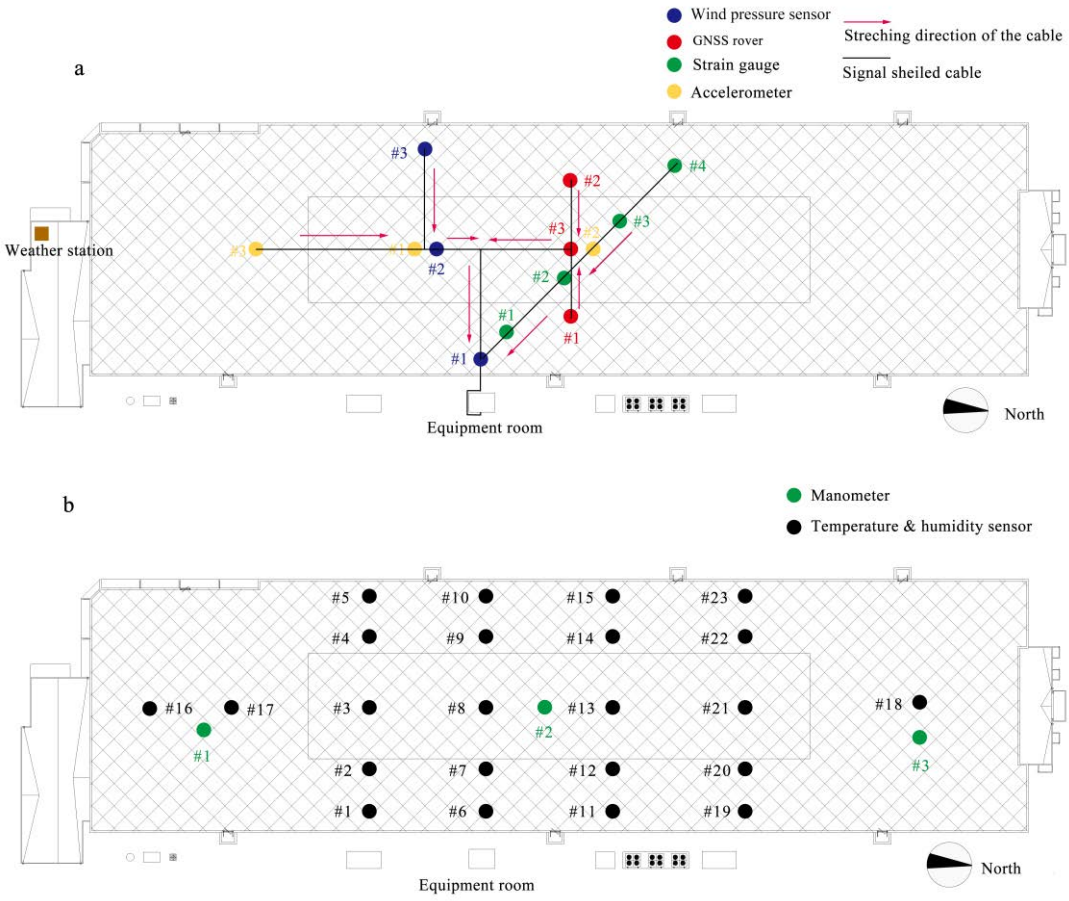


Figure 3. Layout of the sensors

a, Layout of the sensors and signal shield cables outside the membrane facades. b, Layout of temperature & humidity sensors and Manometers

2.3.4 Alarm & data analysis sub-system

In this sub-system, alarm would be activated once internal pressure is out of the range of pre-setting threshold, which indicates that wind loads are so severe that effective measures ought to be taken by adjusting pneumatic control system. In addition, temperature inside the sports hall is monitored all the

time, especially during days with extreme weather. Precise numerical model of the air-supported membrane structures is established to analyze dynamic properties and thermal behaviors based on the data measured. In this way, a real-time method of controlling the internal pressure could be proposed. Control program can be developed based on this method to allow air fans in pneumatic control system adjust the air flow automatically to maintain proper internal pressure for air-supported structures. Besides, study on thermal behaviors based on statistic results is beneficial to air conditioning management in terms of energy saving.

2.4 Installation of sensors

2.4.1 Layout of sensors

Figure 3 presents the layout of sensors. All the sensors are installed at exterior space of the sports hall except temperature & humidity sensors and manometers. Temperature & humidity sensors are arranged evenly to cover the whole membrane inside the building. Specifically, there are just three temperature & humidity sensors arranged at the edged zone in longitudinal direction, but at the middle zone the amount of them is 20. These sensors are distributed symmetrically in the transversal direction. As Figure 3a presents, one sensor fixed along the middle axis of the hall on top, and two sensors are positioned on the both sides respectively at the height of 5m and 9.5m. Three manometers are positioned at the point of trisection in the direction of length of the hall.

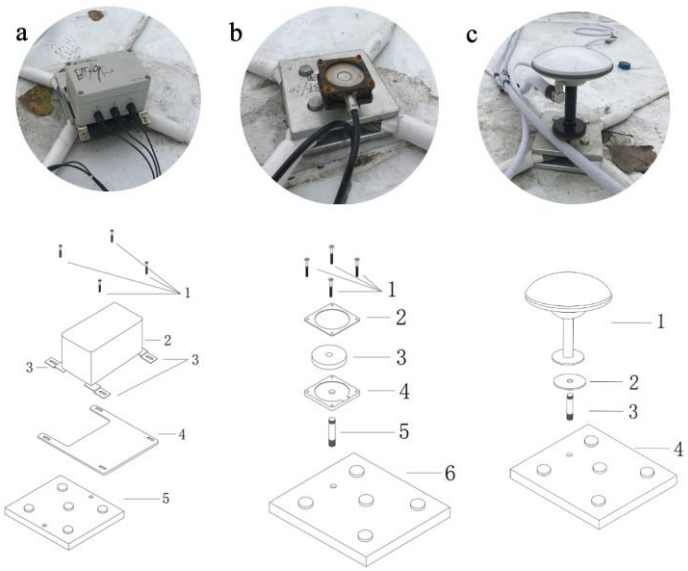


Figure 4. Installation of accelerometer, wind pressure sensor and GNSS rover

a, Installation of accelerometer, 1-screws, 2-accelerometer, 3-angle plate, 4-U-shaped connector, 5-connection plate with screw thread. b, Installation of wind pressure sensor, 1-screws, 3-wind pressure sensor, 2,4,5-connector (2-upper plate cover, 4-lower plate with central groove, 5-strut with screw thread), 6-connection plate with screw thread. c, Installation of GNSS rover, 1-GNSS rover, 2,3-connector (2-circualr plate, 3- strut with screw thread), 4- connection plate.

The weather station is fixed on the roof of the south wing of the hall to obtain more irradiance for solar cell. Other sensors are mainly installed at southeast zone of the external membrane considering prevailing wind direction in Shanghai. Three wind pressure sensors and three GNSS rovers are symmetric with respect to the middle axis in longitudinal direction. Three accelerometers are installed at the middle axis. Four strain gauges are equidistantly distributed along a sliding cable.

All the signal cables are spread out in order on the membrane, and then are bindle together into a bunch that stretch to the equipment room adjacent to the hall. Specifically, both data collection and data communication & memory sub-system are positioned at the equipment room.

2.4.2 Installation methods

Outer protective covering is required to make all the sensors and signal cables impervious to water. Given the difficulty of installing sensors on the membrane surface, special connectors are designed to allow sensors to be fixed on the connection plates in the cable system. All of the connectors are made of steel with anti-corrosion covering. As Figure 4 shows, screw threads are cut inside the connection plates in order to hold sensor and its connector together by screws. The shape of connector is defined in consistence with the sensor fixed. For example, the shape accelerometer's connector is in the form of a U (Figure 4a). The connector of GNSS rover is a circular plate, while the wind pressure sensor is fastened by a rectangular plate with a central circular groove (Figure 4b, 4c).

Specifically, an upper plate cover with four screw threads is used to fix the wind pressure sensor at the groove of lower plate. A magnet sucker connects the GNSS rover and its steel connector firmly. Four angle plates are installed at corners of the accelerometer to hold the sensor and the U-shaped plate by screws.

3. Operation of the system

All of the signals could be detected, and no errors occurs in data communication and storage up to now (July, 2019). But no valuable data has been acquired to monitor dynamic response under heavy wind load since the strong wind such as storm, hurricane and typhoon does not occur in Shanghai. Graphical user interfaces of data collection program are shown in Figure 5. Besides, file format of the data upload to the web storage is ".txt" or ".xlsx" for ease of remote loading and processing. In general, the comprehensive health monitoring system operates smoothly.



Figure 5. Graphical user interfaces of data collection program

4. Conclusions

Air-supported membrane structure hall has been widely used in large-span structures in recent years due to its prior properties including low-weight, easy installation and authentic appearance. Unlike steel and concrete structures, membrane structures are more vulnerable to harsh external environment and catastrophic failure from structural vibration. Internal pressure is monitored in almost all the air-supported membrane structure in order to adjust the value of the pressure in response to external environmental load. However, current pressure regulation in air-supported structure is based on several preset operating modes which are not accurate enough to reflect real conditions. In addition, it is also necessary to monitor other parameters that reflect the dynamic properties and internal thermal environment to maintain comprehensive health of the membrane structure.

In this paper, a comprehensive health monitoring system for a new air-supported membrane structure hall is developed. This system is consisted of four sub-systems, including sensor sub-system, data collection sub-system, data communication & memory sub-system, and alarm & data analysis sub-system. In sensor sub-system, three accelerometers, three wind pressure sensors, three GNSS rovers, three manometers and four strain gauges are used to measure the acceleration, wind pressure, membrane

displacement, internal pressure and cable strain, respectively. 23 wireless temperature & humidity sensors are used to gather data of internal temperature and humidity of the hall. Meteorological station is set near the hall to record weather data, providing reference for structural performance and thermal environment analysis. Besides, the data collected is transmitted via signal cable connected to receivers or wireless technology. All of the data is stored in an on-site serve with high performance, and then uploaded to the web storage.

Analysis of long-term monitoring data is definitely helpful for maintaining a good health for a new air-supported membrane structure hall: (1) Dynamic properties under different environment conditions could be obtained, which is beneficial to design a completely active pressure control system for air-supported membrane structure to resist external load in time. (2) Study of thermal environment in the membrane hall is useful for ventilation organization and air conditioning management, which can effectively promote energy efficiency (3) Analysis of structural and thermal behaviors can be used to improve structural analysis methodology and design theory of membrane structures.

Acknowledgements

This work was supported by National Natural Science Foundation of China (Nos.51278299, 51708345). We thank Qin Wang, Yongliang Guo, and Xiao Liu from the Shenzhen Broadwell Environment Technology Co., Ltd. for assistance with installation of the system; and infrastructure division and department of physical education for allowing access to install the system and monitor the sports hall.

References

[1] C.R Farrar and K. Worden. "An introduction to structural health monitoring," *Philosophical Transactions of the Royal Society A: Mathematical, Physical and Engineering Sciences*, 365(1851), pp.303-315, 2006,

[2] L. Ren, C.L Yuan, H.N Li, *et al.* "Structural health monitoring system developed for Dalian stadium," *International Journal of Structural Stability and Dynamics*, 16(04), pp.1640018, 2016.

[3] Y.Q. Ni, Y. Xia, W.Y. Liao, *et al.* "Technology innovation in developing the structural health monitoring system for Guangzhou New TV Tower," *Structural Control and Health Monitoring: The Official Journal of the International Association for Structural Control and Monitoring and of the European Association for the Control of Structures*, 16(1), pp.73-98, 2009.

[4] P. Clemente, "Structural health monitoring of historical heritage in Italy: some relevant experiences," *Journal of Civil Structural Health Monitoring*, 6(1), pp.83-106, 2016.

[5] Y. Zhou and L. Sun, "A comprehensive study of the thermal response of a long-span cable-stayed bridge: From monitoring phenomena to underlying mechanisms," *Mechanical Systems and Signal Processing*, 124, pp.330-348, 2019.

[6] M.M. Alamdari, T. Rakotoarivelo, and N.L.D. Khoa, "A spectral-based clustering for structural health monitoring of the Sydney Harbour Bridge," *Mechanical Systems and Signal Processing*, 87, pp.384-400, 2017.

[7] Pauletti and R.M.D. Oliveira, "Some issues on the design and analysis of pneumatic structures," *International Journal of Structural Engineering*, 1.3-4, pp.217-240, 2010.

[8] Q. Qing, S. Shen, and J. Gong, "Deflation behavior and related safety assessment of an air-supported membrane structure," *Thin-Walled Structures,* 129, pp.225-236, 2018.

[9] H. Suo, Hua, A. Angelotti, and A. Zanelli. "Thermal-physical behavior and energy performance of air-supported membranes for sports halls: a comparison among traditional and advanced building envelopes," *Energy and Buildings*, 109, pp.35-46, 2015.

[10] Zrim, Grega, *et al.* "Light distribution in air-supported pneumatic structures: Comparison of experimental and computer calculated daylight factors," *Building and Environment*, 119, pp.110-127, 2017.

Proceedings of the IASS Annual Symposium 2019 – Structural Membranes 2019
Form and Force
7 – 10 October 2019, Barcelona, Spain
C. Lázaro, K.-U. Bletzinger, E. Oñate (eds.)

Pedestrian evacuation in an air-supported membrane structure under emergency

Jin GAO[a], Qiang QING[a], Guozhi QIU[a*]

[a*] Department of Civil Engineering, Shanghai Jiao Tong University
No. 800 Dong Chuan Road Shanghai, 200240, China
qiugz@sjtu.edu.cn
[a] Department of Civil Engineering, Shanghai Jiao Tong University

Abstract

Air-supported structure may suffer from danger of deflation caused by the opening of exit or failure of inflation system, which is significant for pedestrians′ evacuation under emergency. Evacuation efficiency will be affected when the height of membrane is lower than the pedestrian in a building during the dynamic deflation process, which mainly occurs near the boundary of the air-supported membrane structure. An evacuation model in the air-supported structure subjected to emergency deflation is built in the software maritimeExodus. This paper proposes a method to consider the effect of the changing membrane profile on evacuation time during dynamic deflation process, since it determines pedestrians′ travel speed. Simulation results show that pedestrians′ evacuation time in a structure without deflation is much less than in a deflating membrane structure. An interesting phenomenon is also found that the depression of membrane increases evacuation time by slowing down pedestrians′ speed and altering their moving direction. This work is expected to give some advice in the designing of air-supported membrane structures, and the evacuation model will be further used to predict pedestrians′ evacuation route and total evacuation time in a deflating air-supported membrane structures under emergency.

Keywords: air-supported membrane structure, dynamic deflation process, pedestrian evacuation, maritime Exodus.

1. Introduction

With the development of social economy and the progress of building technology, building structure becomes more and more complex. Recently, a growing number of buildings with large span and space are emerging, such as the air-supported membrane structure, which is usually used in gymnasium, airport terminal, conference and exhibition center, etc. Accidents usually occurs in these places when a great number of people gather inside there, which can easily cause massive deaths and injuries without proper evacuation. For example, in 1985, a fire broke out rapidly at the outdoor stadium in Bradford, England that lasted seven hours, which resulted in 52 deaths and more than 200 injuries. In 2005, a large fire broke out in a theatre in Beni Suviv caused by an actor knocking down a candle accidentally, which led to 30 people dying and 35 people injuring. In 2006, Yemen's western governorate Ibb stadium suffered a serious stampede accident, with 150,000 spectators flocked at the exit simultaneously, which caused 51 deaths and 238 people injuries, etc. These safety accidents arouse much attention from society, so pedestrian safe evacuation from space structures is a crucial issue to research.

So far most researches focus on pedestrian evacuation dynamics in ordinary buildings, like classrooms [1–3], dormitories [4], schools [5,6], etc. However, air-supported membrane structure, as a significant

Copyright © 2019 by Jin GAO, Jinghai GONG, Qiang QING, Guozhi QIU
Published by the International Association for Shell and Spatial Structures (IASS) with permission.

building type, has received less attention. To bridge this gap, this paper pays attention to pedestrians′ evacuation in an air-supported membrane structure. When an emergency occurs in an air-supported membrane structure, with the opening of the escape exits or the failure of inflation system, it will produce indoor and outdoor residual pressure difference, and the height of membrane will descend. If the height of membrane is lower than the pedestrians in the building, pedestrians′ evacuation efficiency will be affected, which mainly occurs near the boundary area of the air-supported membrane structure. Qiang Q et al [7,8] proposed a simplified calculation method for deflation of an air-supported membrane structure under emergency evacuation conditions and they conducted a deflation experiment on an air-supported membrane structure of the Yi Zhuang Badminton Hall in Beijing, obtaining the normal operating air loss and calculating the deflation time for emergency evacuation in international units according to the Air-supported structures. However, they did not further research how the deflation process affects pedestrians′ evacuation behavior and efficiency.

Based on the study of Qiang Q et al, this paper presents a method to consider the impact of the deflation process of a membrane structure on pedestrians′ evacuation efficiency by building an evacuation model in maritimeExodus. The deflation data of the membrane structure is imported to the evacuation model as a type of hazards that determines travel speed of pedestrians. This work bridges the gap between pedestrian evacuation dynamics and the dynamic deflation process of air-supported membrane structures, which is expected to give more advices in the designing of membrane structures by considering pedestrians′ safety evacuation time accurately, and the evacuation model will be further used to predict pedestrians′ evacuation route and total evacuation time in air-supported membrane structures under emergency to guide their evacuation.

The rest of this paper is organized as follows: Section 2 introduces the methodology to research pedestrians′ evacuation in a deflating membrane structure. The simulation scenario, results and further comparison and discussions are presented in Section 3. Conclusions drawn from the study are summarized in Section 4.

2. Methodology

To investigate pedestrian evacuation dynamics in an air-supported membrane structure, a deflation model of the membrane structure is built by employing *SMCAD* developed by Gong [9]. *SMCAD* is an analysis and design software for cable and membrane structure that is first developed by the second author in 2003. Evacuation model is built by maritimeExodus, which is a suite of software tools designed to simulate the evacuation and movement of large numbers of individuals within complex structures. However, maritime Exodus can only simulate pedestrian evacuation in the normal evacuation situation or hazardous condition, like fire or smoke, which has not considered the impact of the deflation of the membrane structure on pedestrian evacuation efficiency.

This paper proposes a method to import the deflation data of a membrane structure into evacuation model. The deflation process is regarded as a type of hazard during pedestrians′ evacuation in the evacuation model. According to the theory manual of maritimeExodus [10], the hazard usually decreases the evacuation efficiency by slowing down individual′s speed (see Eq.(1)) or changing pedestrian′s direction.

$$v = v_{ini} \times d \tag{1}$$

Here, v represents individual′s travel speed, v_{ini} indicates the initial travel speed of a pedestrian. d is a degradation factor of velocity.

In maritimeExodus, pedestrian′s travel speed is mainly affected by smoke concentration when fire broke in an evacuation area [11]. The theory manual provides the relationship between smoke concentration and velocity degradation factor, as shown in Table 1 (a).

Table 1: The value of velocity degradation factor (d)

(a) Relationship between smoke concentration and d

Smoke concentration ($1/m$)	d
0-0.1	1.0
0.2	0.92
0.3	0.76
0.4	0.57
0.5	0.36
>0.5	0.36*

(b) Relationship between membrane height and d

Membrane height h (m)	d
$h \geq 1.8$	1.0
$1.5 \leq h < 1.8$	0.92
$1.0 \leq h < 1.5$	0.76
$0.5 \leq h < 1$	0.57
$h \leq 0.5$	0.36*

*if a pedestrian is forced to crawl and the travel speed will dependent upon the pedestrian′s crawl rate rather than upon the walk rate.

According to Table 1 (a), this paper assumes that the degradation factor d and the height of the membrane subjects to the relationships in Table 1 (b). Pedestrian′s travel speed will be reduced when the height of membrane is lower than the height of pedestrian in an air-supported structure during the dynamic deflation process. With the descending of the membrane structure, individual′s travel speed will be smaller. When the height of the structure is lower than 0.5 m, pedestrian′s speed will keep at 0.36 m/s, which means the pedestrian is forced to crawl in the membrane structure.

Deflation process of the membrane is equivalently transformed to smoke concentration in the evacuation model based on Table 1. During the simulation procedure, maritimeExodus defines the hazard as Eq. (2):

$$Hazard = initial\ hazard + m \times t^p \tag{3}$$

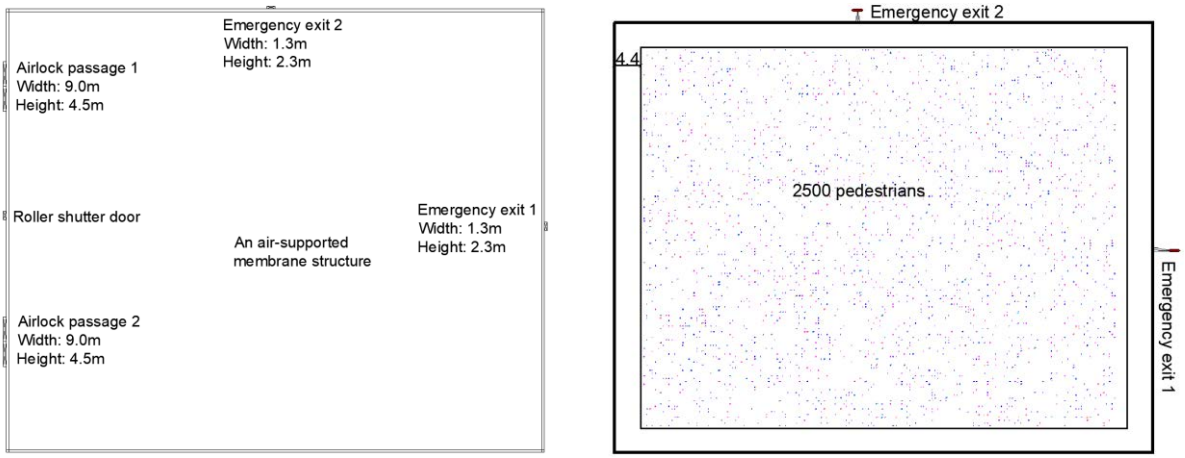
Here, m is the gradient, t is the simulation time and p is the power [13]. The deflation data can be imported into maritimeExodus by Eq.(3) or a user-define step function according the displacement of the membrane in the deflation model.

Following sections examine the effect of the depression of the height of membrane on evacuation efficiency. Pedestrian′s evacuation time (T) is used to assess the evacuation efficiency, which is composed of pedestrian′s response time (T_{res}) and travel time (T_{tra}) [12]. Response time is the duration it takes for people to react to the situation that begins upon initial notification (e.g. alarm) of an emergency and ends when the pedestrian has accepted the situation and begins to move towards an emergency exit. Individual travel time is the duration incurred by an individual in moving from its starting location to reach the emergency exit.

3. Simulation and results

3.1. Evacuation scenario

The studied structure is semi-cylindrical, the designed dimension is 97 m long, and 32 m tall under the inflation pressure of 200 Pa, the deflation behavior of which was researched by Qiang Q in Ref. [8] by both experiment tests and numerical simulations for the safety of occupants. One revolving door and two airlock passages are equipped to provide easy access for pedestrians, and two emergency gate for emergency evacuation. The position and size of each exit are shown in Figure 1 (a).



(a) Layout and position of exits (b) Distribution of 2500 pedestrians and boundary area

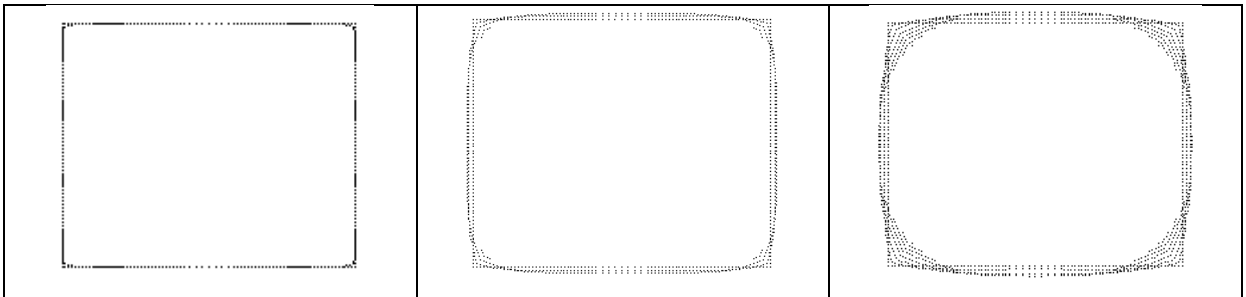
Figure 1: Test schematic layout of the air-supported structure

Before the deflation of the structure, the height of boundary area of the membrane structure is lower than 2.0 m. So 2500 pedestrians are distributed at central area randomly in the building in the evacuation model as shown in Figure 1 (b).

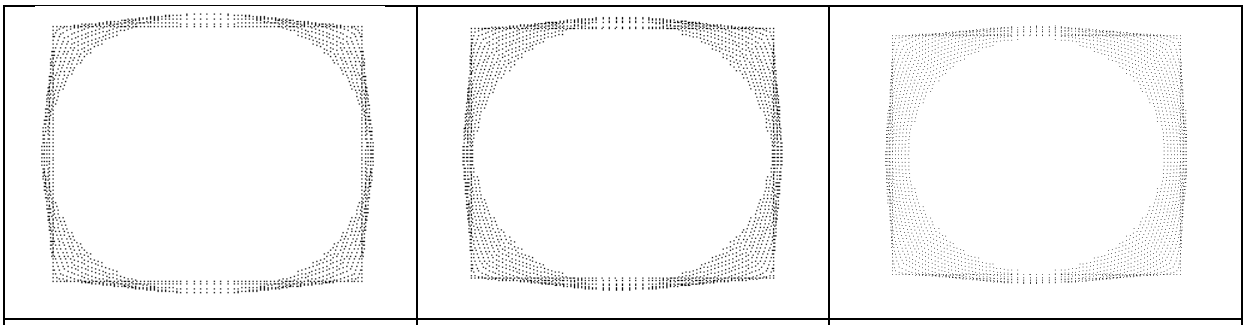
According to Ref. [8], three experiment tests were conducted: one normal deflation test and two emergency deflation tests. This paper intends to research pedestrian evacuation under emergency, so we employ the second deflation test in Ref. [8] to investigate the impact of the dynamic deflation process on pedestrian′s travel speed and evacuation time. In this experiment test, one venting hole (4.5 m wide × 1.27 m tall) was opened designedly to produce distinct air leakage during deflation. Therefore, in the evacuation model, it is assumed that only two emergency gates are opening for pedestrians′ evacuation, the area of these two doors is 5.98 m^2, which is similar to the leakage area in the experiment.

3.2. Results and discussions

In the deflation model, total deflation time is about 42 min. Figure 2 shows the deflation process and the shadow zones represent the area that the height of membrane is lower than 2.0 m. It is obviously that the lower area is gradually expanding over time.



(a) 0 min	(b) 8 min	(c) 16 min



(d) 25 min | (e) 33 min | (f) 42 min

Figure 2: Lower area (height < 2.0 m) in the deflating structure at typical time

To research the impact of the effect of the deflation process of the structure, the lower area near the emergency exits in the air-supported membrane structure is considered as a hazard zone in the evacuation model in maritimeExodus as shown in Figure 3. The deflation data is imported into the evacuation model by a user-define step function according the displacement of the membrane in the deflation model (see Figure 4 (a)), and the hazard is divided into four stages. At each stage, the mean height is calculated based on the deflation data of the hazard zones. And the corresponding smoke concentration level in the maritimeExodus can be got according to Table 1. Figure 4 (b) shows the hazard edit dialog box in the software.

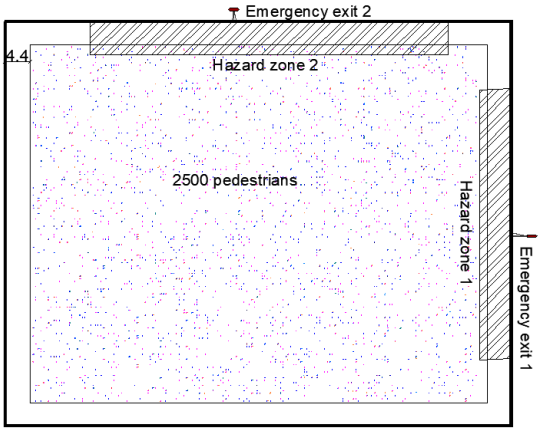
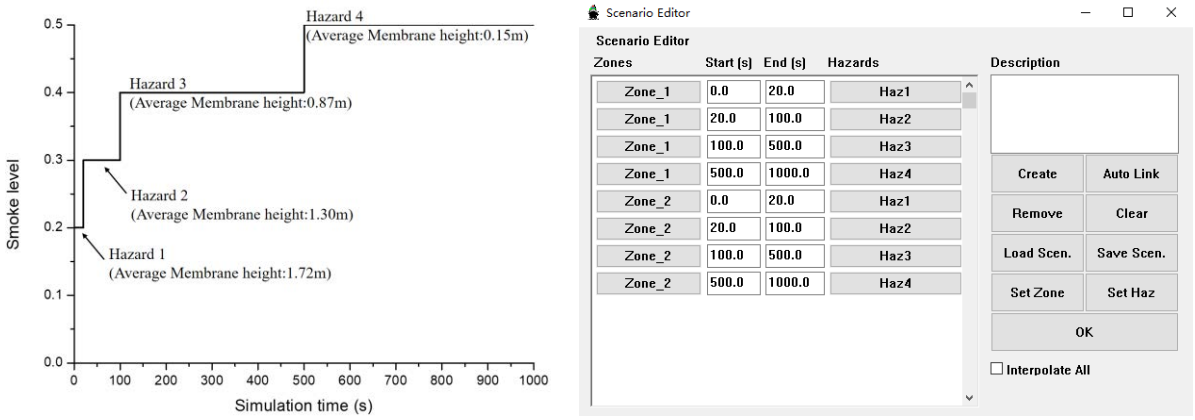


Figure 3: Layout of hazard zone in the evacuation model



(a) A user-define step function of deflation hazard (b) Hazard edit dialog box in maritimeExodus

Figure 4: Defining hazards using a step function

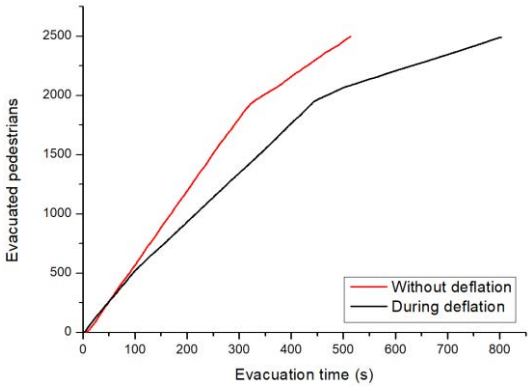


Figure 5: Simulation curves of the evacuated pedestrians against evacuation time <s>

Figure 5 shows the simulation curves of evacuated pedestrians against evacuation time <s> in two different situations. It is obviosly that it cost about 800 s for pedestrians to elapse from the deflating membrane structure via two emergency gates, almost twice the evacuation time of the situation that without deflation, which is about 500 s. Relationship between evacuation time and the number of pedestrians is further studied as shown in Figure 6. With the increment of the number of pedestrians, evacuation time increases almost linearly. It is also found that pedestrians cost much more evacuation time in the deflating membrane than in the membrane without deflation. And the effect of the delation process on the evacuation time will be lessend with the decreasing of the number of pedestrians. This is because when pedestrian density is lower, evacuation time becomes less, during which only small displacement occurred in the boundary of membrane profile, so the descending of the membrane has little impact on the pedestrians′ travel speed.

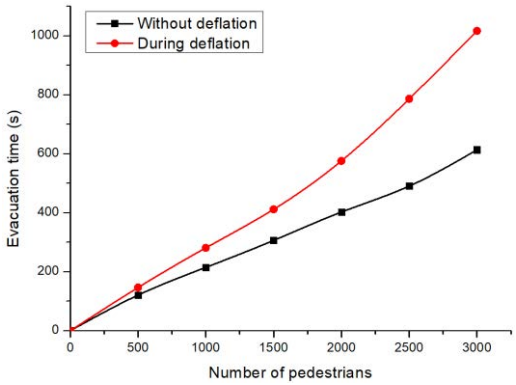


Figure 7: Simulation curves of evacuation time <s> against the number of pedestrians in the membrane

4. Conclusion

This paper proposes a method to simulate pedestrian evacuation in a deflating air-supported membrane structure. The deflation process is seemed as a type of hazard and is imported into the evacuation model in maritimeExodus to research the pedestrian evacuation dynamics under emergency. Simulation results show that the deflation of the membrane has an adverse impact on pedestrian′s evacuation efficiency that mainly depends on the crowd density and pedestrian′s position and speed. When pedestrians approach the boundary area of the membrane, the height of the which is usually lower than pedestrian, which will increase the evacuation time by slowing down pedestrian′s travel speed. So it is essential to set up construction measures near the boundary in a membrane structure (see Figure 8) to guarantee that the deflation of the membrane has little impact on pedestrians′ evacuation efficiency.

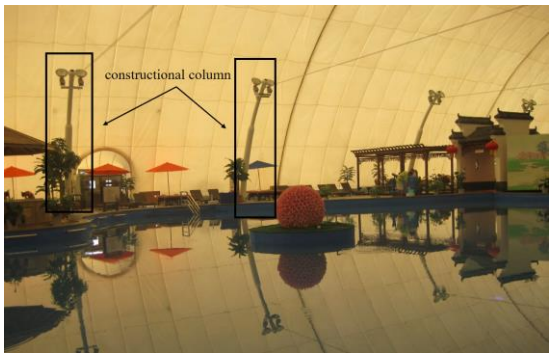


Figure 8: Construction measures in a membrane structure: constructional column

This work can be applied in the designing of the air-supported membrane structure and planning rational evacuation route for pedestrians under emergency. In the future, we will further conduct some experiments to test and verify the relationship between membrane height and velocity degradation factor.

Acknowledgements

This paper is supported by the Ministry of Industry and Information Technology project "Research on Emergency and Escape Technology for Large Living Quarters of Offshore Platforms" (MIIT [2016] No. 546). The authors deeply appreciate its supports.

References

[1] Zhang J, Song W and Xu X "Experiment and multi-grid modeling of evacuation from a classroom" *Phys. A Stat. Mech. its Appl.* vol. 387, pp 5901–9, 2008

[2] Kong-Jin Z and Li-Zhong Y "The effects of exit position and internal layout of classroom on evacuation efficiency" *Acta Phys. Sin.* vol. 59, pp 7701–7, 2010

[3] Chen L, Tang T-Q, Huang H-J and Song Z "Elementary students' evacuation route choice in a classroom: A questionnaire-based method" *Phys. A Stat. Mech. its Appl.* vol. 492, pp 1066–74, 2018

[4] Lei W, Li A, Gao R, Zhou N, Mei S and Tian Z "Experimental study and numerical simulation of evacuation from a dormitory" *Phys. A Stat. Mech. its Appl.* vol. 391, pp 5189–96, 2012

[5] Poulos A, Tocornal F, de la Llera J C and Mitrani-Reiser J "Validation of an agent-based building evacuation model with a school drill" *Transp. Res. Part C Emerg. Technol.* vol. 97, pp 82–95, 2018

[6] Vásquez A, Marinkovic K, Bernales M, León J, González J and Castro S "Children's views on evacuation drills and school preparedness: Mapping experiences and unfolding perspectives" *Int. J. Disaster Risk Reduct.* vol. 28, pp 165–75, 2018

[7] Qiang Q, Jinghai G and Zhongli L "Simplified calculation method for deflation of an air-supported membrane structure under emergency evacuation conditions" *Build. Struct.* vol. 43 pp 96–92, 2013

[8] Qiang Q, Shen S and Gong J "Deflation behavior and related safety assessment of an air-supported membrane structure" *Thin-Walled Struct.* vol. 129, pp 225–36, 2018

[9] Jinghai G, *SMCAD User's Manual, 4.0 ed* . China: Shanghai, 2012

[10] E.R.Galea, P.J.Lawrence, L.filippidis, D.balckshields, D.Cooney and G.Sharp, *maritimeExodus v5.1 Theory Manual*. UK: London, 2014

[11] E.R.Galea, P.J.Lawrence, L.filippidis, D.balckshields, D.Cooney and G.Sharp, *maritimeExodus v5.1 Application Manual.* UK: London, 2014

[12] International Maritime Organization, *MSC/Circ.1533-2016. Revised guidelines on evacuation analysis for new and existing passenger ships,* 2016

[13] GALEA E R, LAWRENCE P J, FILIPPIDIS L, BLACKSHIELDS D, COONEY D and SHARP G *maritimeEXODUS v5.1 User Guide*. UK: London, 2016

Proceedings of the IASS Annual Symposium 2019 – Structural Membranes 2019
Form and Force
7 – 10 October 2019, Barcelona, Spain
C. Lázaro, K.-U. Bletzinger, E. Oñate (eds.)

PNEULASTICS, pneumatically activated differentiated stretchable membranes

Anna RIZOU*, Enrique SORIANO[a], Ramon SASTRE[a]

*Universitat Politécnica de Catalunya
Aragó 247, 08007, Barcelona, Spain
anna.rizou23@gmail.com

[a] CODA / LiTA BarcelonaTech

Abstract

The object of this research is the design of *pneulastics*, initially flat, pneumatically activated stretchable membranes with areas of differentiated thickness- and therefore elasticity- that respond with a different expansion rate and create complex tension conditions on their surface when sealed and pneumatically inflated. Previous work [1],[2],[4] has already shown interest in the analysis and acquisition of control over the geometry of inflatable structures, by introducing tension conditions upon the uniform pressure stresses, by means of additional third members other than air and membrane that raise the complexity of the structure. Other precedents [3] manage to embody constraints in pneumatic activation, laying emphasis on the activation itself rather than the final shape. *Pneulastics* introduce the integration of active material strategies in order to encode the differentiated activation into one single skin. With a series of physical experimentations that confirm the initial hypothesis, that *pneulastics* can provide a wide range of doubly curved shapes, we empirically decipher and describe material behaviour into digital simulation. Starting with a target shape input, our design method translates curvature and topology into flat membrane configuration that may lead upon inflation to the best approximation of the initial shape.

Keywords: pneumatic activation, inflatable structures, elasticity, auxetic material, target shape approximation

1. Introduction

Pneulastics attempt to produce complex geometries of double curvatures, both convex and concave in one single skin, out of the pneumatic activation of initially flat elastic membranes. Based on the hypothesis that stretchable membranes of differentiated cross sections (and therefore elasticity rates) across their surface may distend to consequently differentiated extents when sealed and inflated, we try to extend the capacity in form-finding of inflatable structures that tend to adapt to spherical shapes due to the uniform stresses applied vertically on the surface of plain, non-expandable membranes.

A complex tension-compression system is developed between areas of the same surface that distend to non-linearly different extents due to the different modulus of elasticity and thickness when forced by the same differential of pressure. Thicker zones act as compression borders for their neighbouring thinner ones, and on that very condition form emerges.

The aim is the control over pneumatic activation so as to map elasticity and thickness onto flat uninflated elements, thus inverting the inflation process. This controlled deformation has to remain

Copyright © 2019 by Anna RIZOU, Enrique SORIANO, Ramon SASTRE
Published by the International Association for Shell and Spatial Structures (IASS)with permission.

within the limits of tolerance of the membrane, in order to be reversible, avoid failure or plastic deformation and maintain the flat original configuration when air pressure is no longer provided.

The reinforced zones replace external tensor elements, seen often as cables, in large span pneumatic structures. Surface stresses are accumulated on the reinforced thicker zones, which by definition have higher tolerance to tension. This integrated, compact skin solution eliminates the need for developing complex tensor nodes. In natural systems, performance variation and multifunctionality are often achieved with one single material, where active properties are inherent, as opposed to manmade ones with their distinct parts and multiple materials.

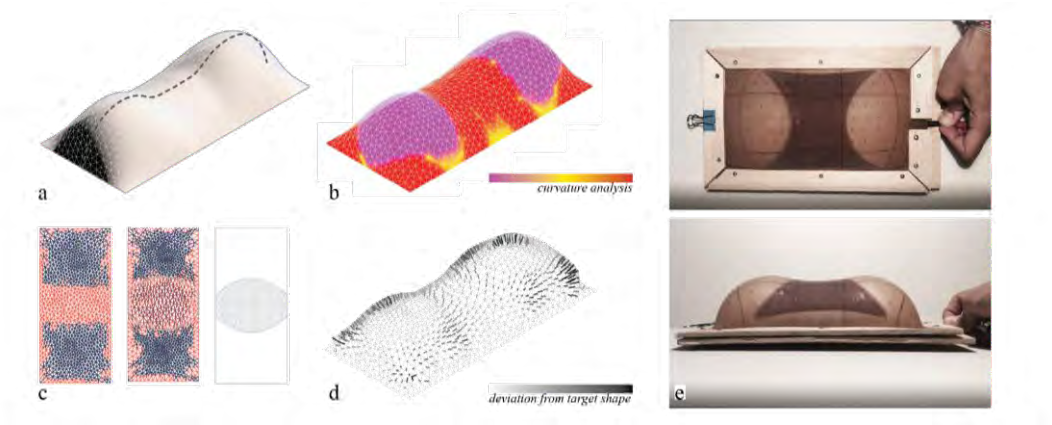


Figure 1: Pneulastics design routine: doubly curved shell as an input is discretized (a), and curvature analysis (b) isfollowed by a dynamic relaxation to a flat mesh (c), where the members of extreme negative curvature rates are marked as thick zones. Digital simulation and physical model (d & e) approximate the original form.

There is also an important simplification in the physical production of flat membranes, replacing cutting patterns of inelastic fabrics and cable-stiffening third members by a tool that translates topology into case specific local thickness of a flat membrane, that when inflated transforms into a tensile doubly curved surface. Elastic surface materials have the capacity to increase their surface up to several times their initial measure, when bi-directionally distended under tension forces. We could therefore provide a space-saving solution for the production of membranes of very large surfaces, that when fabricated only occupy a flat, relatively small and manageable footprint.

Finally, in terms of structural behaviour, given that they act as pre-stressed surfaces, pneulastic membranes demonstrate better performance against external loads, like wind, having developed very larger surface stresses that resist negative deformation due to compression stresses.

Even when pressure differential conditions constitute the interior of pneulastics inappropriate for inhabiting, their pneumatically derived form can be employed as formwork for shell structures. Comparing catenary to pneumatic forms, the catenary only ensures that the shell will endure compressive forces rather that tensile, formed by the self-weight of the cast material, supported at its ends, without accounting for bending and torsion moments.On the other hand, the pneumatic form, being the result of an outward pressure with vector forces that act upon the normal of the surface and change direction during inflation, achieves equilibrium combating wind forces.

When it comes to pneulastics as falsework, Quin and Gengnagel's ongoing research[7] with experimental measurements and FEM analysis both show that the method of pneumatically erecting a strained gridshell is feasible and more practical for simple shell shapes and curvatures, compared to the ‘lift up’ and ‘push up’ erection methods.

2. State of the art_ Current Related Work

Over the past years, there has been an increased interest in the analysis and acquisition of control over the geometry found by pneumatic activation in membrane structures. The challenge lies in defying the natural tendency of inflatables towards synclastic curvatures, as well as in the approximation of target geometries that are predetermined rather than form-found. Equally popular are the developments in the field of soft robotics, where the adjustment of pressure activates elastic elbows.

Typical methods used to achieve target geometries frequently include the use of third external elements as tensor constraints and modulations. These are met either as seams of a discretized cut pattern [1], secondary skins [2,4] or most commonly, external cables that restrain the growth of the membrane in specific "low" points[3]. In the case of elastic skins, additive manufacturing has been employed as a stiffening means [5], having material itself become the rigid condition on the zones dictated by the toolpath. However, most of these efforts focus on closed shapes with initial "resting"configurations that come from a complex mold and resemble the target[6], rather than start as planar shapes that would prove ergonomical in large architectural applications.

Our role in this evolutive thought is to integrate active material strategies and digital fabrication methods in order to embody this differentiated activation into one single multi-capable skin that initially lies flat, maintain the forementioned advantages of elastic inflatable structures in lightness, transportability, load bearing capacities and economic value, and also shorten the fabrication and assembly procedures.

3. Research Hypothesis

3.1. Bottom-up

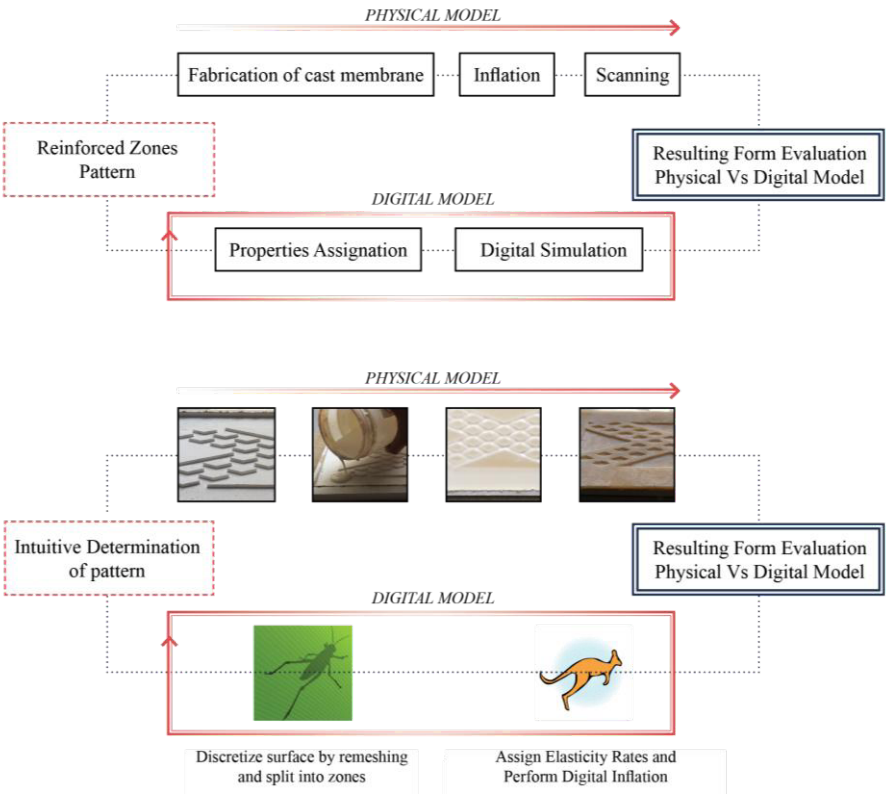


Figure 2: Intuitive bottom-up workflow and loop.

This approach includes the comparison of physical with their corresponding digital models of membranes with differentiated elasticity rates on their surface, under pneumatic activation. A first series of experiments was led by pure curiosity and the very initial binary hypothesis that on the border of the transition between two thicknesses, form and therefore negative curvature would emerge.

Material investigations and parallel digital simulations, proved the potential of reproducing the behavior of inflated cast latex membranes. With the help of Grasshopper plugin and Kangaroo by Daniel Piker, we have assigned differentiated stiffening conditions to the members of our interest. For this purpose, we have employed a plain discretized mesh with each of its elements having an assigned elasticity rate (which is translated into a freedom to deform) related to its local stiffening conditions.

Rubberlike materials have non-monotonic pressure-radius characteristic, and do not deform according to Hooke's law. However, the combination of different elasticity rates on one single surface subjected to inflation constitutes a very complex tension-compression model, which we did not hope to mathematically describe in this research.

3.1.1. Qualitative

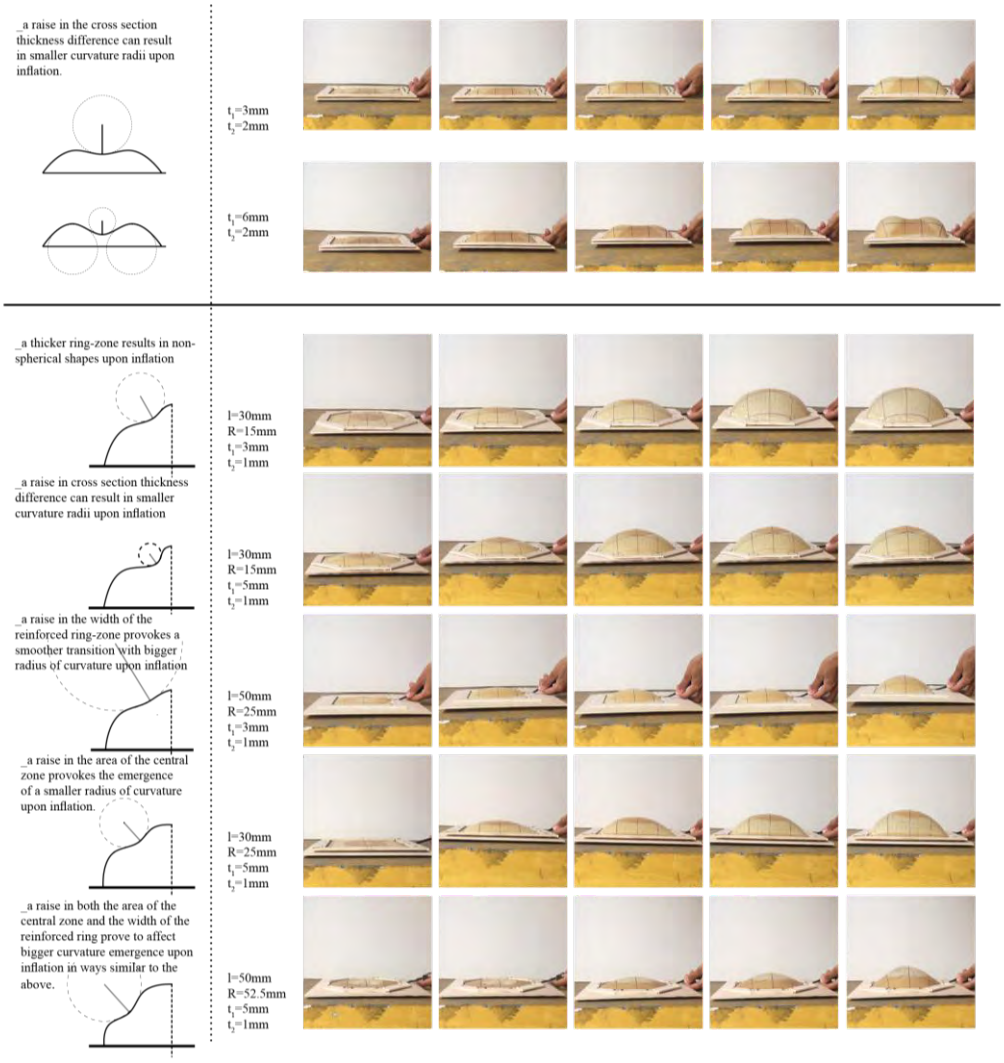


Figure 3: Quantitative hypothesis stated and checked upon with physical models of variable properties.

After getting familiar with the general principles of pneulastics'function, we asked ourselves a series of qualitative questions, to be answered by a series of material experiments:
How can a difference in thickness of the same shape perform?
How can a difference in the width of a zone affect curvature rates?

Comparing this property variation in two different configurations [Figure 3], we came to the following conclusions:

A. A transversal thickened zone can act as a tensor upon inflation, converting surface to linear stresses and transfering them to the perimetrical anchoring.
B. A thickened zone/patch may disrupt constant spherical curvature.Headings for third-level subsections, if needed, are 11pt italic [Style: Heading 3] and are numbered as shown in this example. Please do not use any further levels of subsections.

3.1.2. Quantitative

In order to describe more convincingly the pneumatic activation of pneulastics, we proceeded to a series of digital models for calibration and comparison to photogrammetric measurements of a physical inflated model. The aim of this step is to aproximate the elastic deformation seen in the latex membrane, fine-tune the representation of the differentiated inflation digitally and set a more accurate rule for our simulations.

Observing that a binary definition of stiffness (elastic-non elastic) is not realistic, we proceed to consider a functionally *graded object* depending on the distance of the boundary condition between two thicknesses. [Figure 4]

A comparative study of the results, compared to annotated points on the physical surface and their digital correspondants helped us evaluate the best simulation of the pneumatic deformation.

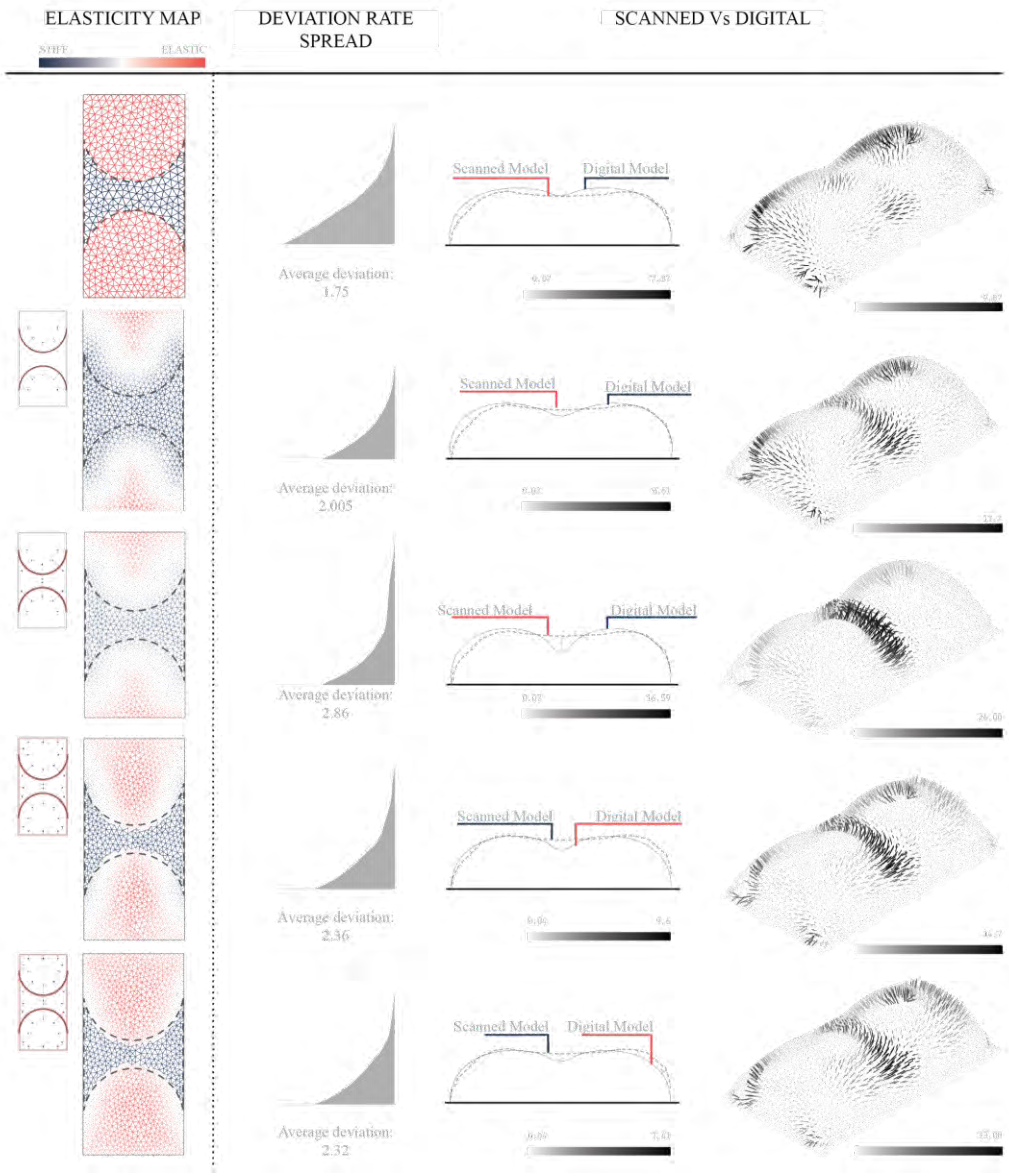


Figure 4: Gradient maps of elasticity and corresponding digital model compared to the scanned physical model.

3.2. Top Down

This approach aims to algorithmically automate the translation of an inflated geometry into a pattern for the fabrication of a differentiated cross-section, expandable membrane. It is a final step in the trajectory of our investigation that fully depends on the experimental findings that were presented.

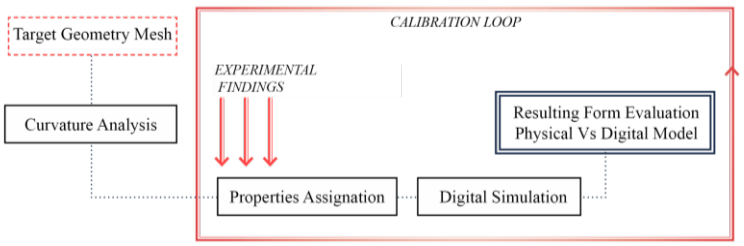


Figure 5: Systematic top down inversion of inflation process and loop.

3.2.1. Curvature-based Relaxation

A first approach starts with the mapping of the target shape on a flat configuration. A curvature analysis combined with the experimental quantitative findings of previous steps helped us redistribute the zones of elasticity on the plane.

The method begins with a curvature analysis of the mesh that is taken as an input, followed by a mapping of the distended form to a flat configuration, according to an inverted expansion mockup, that takes into account the differentiated properties of the zones marked by curvature. Here we can reverse the quantitative relations we found on the previous step.

The loop is closed with the evaluation of the digital simulation results, that may either be approximating satisfactorily the given target geometry, or not, in which case we shall return to the mapping phase and manipulate according to the error we detected the properties thickness and width of reinforced zone [Figure 6].

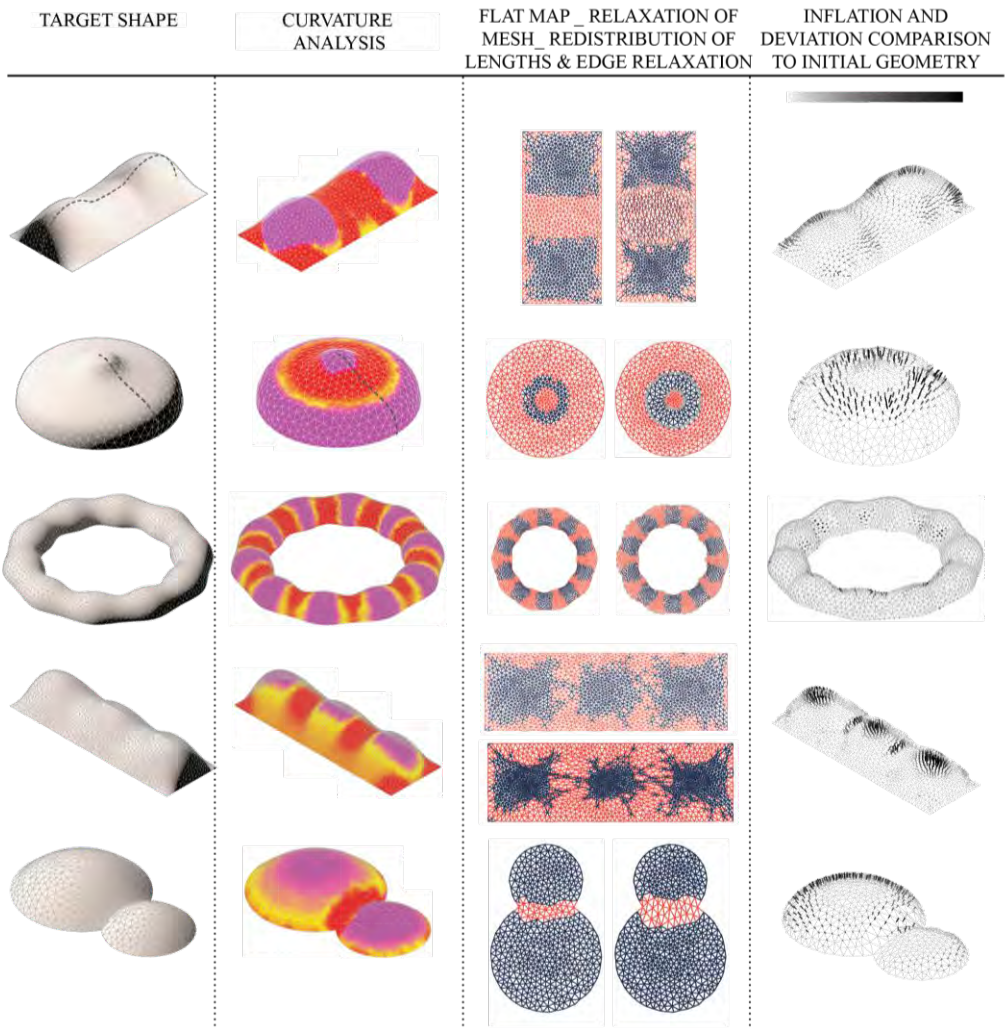


Figure 6: Method 1 applied to a series of shell shapes. These are analysed by curvature, then relaxed into a flat map, with their discrete members separated in patches. A second relaxation redistributes lengths of elastic and stiff zones, and a digital inflation will prove whether the estimation has been accurate.

3.2.2. Curvature-adaptive Remeshing

On a second hypothesis, we proceed to a curvature-adaptive remeshing of the target geometry, so that the zones of bigger stiffness are more densely populated, and therefore, when the flat mesh is relaxed, the thicker areas occupy a larger percentage of the membrane area.

Even though we find a lot of potential in this option, the current tool provided by Daniel Piker's Kangaroo cannot embody on no account the complexity of the gradient of growth that we have been trying to describe. The remeshing process includes all areas of tighter curvature, including the positive ones, and is therefore not satisfying the goals we pursue [Figure 7].

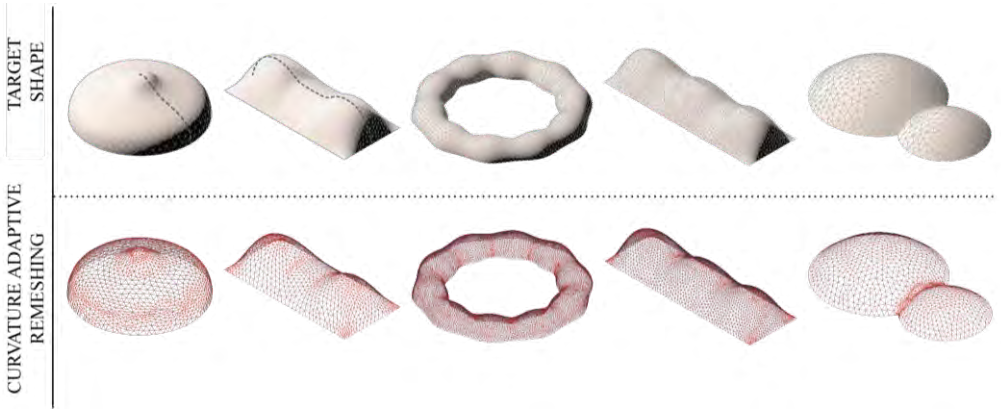


Figure 7: Curvature-adaptive remeshing raises mesh density in both positive and negative extreme rates of curvature, and therefore does not help in defining thick zone discrete members.

4. Conclusion _Results & Further Research

Our initial hypothesis was confirmed and the capacity of elastic membranes of differentiated thickness in adapting to complex geometries upon inflation was demonstrated. We have observed and quantified behaviours, until reaching a certain control over the differentiated inflation conditions and have inverted the inflation process in the format of an algorithm, in order to come up with the flat configuration of the un-distended surface that would lead to a given target shape approximation.

Transversal thickened zones act as tensors, transferring stress loads to the base, converting them from surface to linear and allowing for negative curvature capacity. Punctual zones allow for disruption and steering of the continuous spherical tendency.

This research has focused on the potential of combined elasticity/stiffness properties on a single expandable membrane, from an experimental design point of view, and has intentionally ignored the calculation of the non-linear growth of the membrane surface upon inflation, proceeding to a qualitative description of their behaviour.

We have proposed two methods for the inversion of the inflation, one of which has managed to provide us with satisfactory results-approximations of pneulastics' behaviour, while the other, based on curvature-adaptive remeshing, did not prove effective given the digital tools available at the moment. However, we consider it worth investigating and do not discard its further development.

Given the scope of architectural purposes, we have focused on shell structures and therefore open shapes. A more thorough exploration of the potential of pneulastics would require answers to the following questions: What is the design space for pneulastics? Which curvature rates can be encoded in thickness patterns? The range of feasibility for shapes that can be satisfactorily approximated by pneulastics would have to be defined.

When scaling up to architectural applications, big thickness ranges are not usual in membrane structures. We would therefore need consultation on material and fabrication alternatives that maintain the principle of embedding stiffness in one non-fragile single body, via density or other. We would also opt for a more efficient, digitally controlled and space-saving fabrication method, like an additive deposition of the elastic membrane material.

Even though the pressure differential levels required for the pneumatic activation of pneulastics are prohibitive for habitable spaces on earth conditions, the growing interest for space exploration and speculation on viability on other planets constitute pneulastics extremely relevant for pressurized spaces in conditions where external conditions of lower pressure and internal pressure don't cancel each other.

References

[1] Ayres, Phil & Vestartas, Petras & Thomsen, Mette. (2018). *Enlisting Clustering and Graph-Traversal Methods for Cutting Pattern and Net Topology Design in Pneumatic Hybrids,* 10.1007/978-981-10-6611-5_25

[2] Baranovskaya, Yuliya, Prado, Marshall, Dörstelmann, Moritz and Menges, Achim, *Knitflatable Architecture - Pneumatically Activated Preprogrammed Knitted Textiles*, Complexity & Simplicity - Proceedings of the 34th eCAADe Conference - Volume 1, University of Oulu, Oulu, Finland, 22-26 August 2016, pp. 571-580.

[3] Paul Poinet, Ehsan Baharlou, Tobias Schwinn, Achim Menges, *Adaptive Pneumatic Shell Structures: Feedback-driven robotic stiffening of inflated extensible membranes and further rigidification for architectural applications*, Complexity & Simplicity - Proceedings of the 34th eCAADe Conference - Volume1, University of Oulu, Oulu, Finland, 22-26 August 2016, pp. 549-558.

[4] Konaković-Luković, Mina, Panetta, Julian, Crane, Keenan and Pauly, Mark, *Rapid Deployment of Curved Surfaces via Programmable Auxetics*, Advances in Architectural Geometry 2018, pp.94-111.

[5] Bjorn Sparrman, Shokofeh Darbari, Rami Rustom, Maggie Hughes, Schendy Kernizan, Jared Laucks, Skylar Tibbits(Self Assembly Lab), Sophie Richter, Akos Stegmar (BMW), *Liquid Printed Pneumatics*,

[6] Mélina Skouras , Bernhard Thomaszewski , Bernd Bickel , Markus Gross, *Computational Design of Rubber Balloons*, Computer Graphics Forum, v.31 n.2pt4, p.835-844, May 2012.

[7] Quinn Gregory, 2018, *Pneumatic erection of elastic gridshells: design, simulation & realisation.*

Proceedings of the IASS Annual Symposium 2019 – Structural Membranes 2019
Form and Force
7 – 10 October 2019, Barcelona, Spain
C. Lázaro, K.-U. Bletzinger, E. Oñate (eds.)

Structural behavior of circular air cushion considering variation of internal pressure and material plasticization

Masaya KAWABATA*

*Associate professor, Yokohama National University
79-5 Tokiwadai, Hodogaya, Yokohama, Japan
kawabata-masaya-gx@ynu.jp

Abstract

In order to establish three dimensional curved surface fabrication technique by stretching plane film, this paper discusses the elastic-plastic characteristic of air cushion using ETFE film and its evaluation method. Air cushion has a small air volume and duct diameter, and the internal pressure is likely to change with changes in external force, temperature, air pressure. Elasto-plastic deformation of spherical film, state change of sealed circular air cushion and influence of initial rise ratio and air flow system are examined in this paper.

Keywords: plastic, shrink, true stress, true strain, equivalent strain, relaxation, yield stress

1. Introduction

An air cushion (double air film structure having a lens type cross section) is a bag-shaped film whose internal pressure is increased, and is often used for a film structure using an ETFE (ethylene-tetrafluoroethylene copolymer resin) film. ETFE film is excellent in transparency and weatherability, and has been used in large stadiums and roofs and exterior walls of large buildings. The film is lower in strength and rigidity than the membrane material in which the woven fabric is coated with a resin, and causes a large plastic strain above the yield point. In addition, it is essential in design to properly consider film specific properties, such as creep and relaxation become significant at stress levels 1/2 to 2/3 or more of the yield point. The allowable state of ETFE film in the cushion method is 1.2 times the first reference strength (corresponding to the initial yield stress at the reference value based on the stress at 2.5% strain). This is that ETFE film exhibits stable behavior with strain hardening even at a stress level exceeding the yield stress, and even if plastic strain is caused, the air cushion has a small effect with some increase in the rise, plasticization and It is considered that due to the increase of the rise, the existing stress of the film becomes flattered.

Since membrane materials and films have little bending stiffness or shearing stiffness in the out-of-plane direction, they will deform along the load distribution when they are subjected to external force. In particular, the air dome (air-supported membrane structure roof) has a roof that is balanced by the effective pressure of the membrane (the pressure difference between the internal air pressure and the external atmospheric pressure and the applied pressure due to wind pressure and snow) and membrane stress. When a film surface with curvature is deformed in the left-right antisymmetric mode, it may be in a state close to no elongation deformation without stress change. Therefore, it is general to make the internal pressure higher than that of the air dome in order to prevent excessive deformation and fluttering at the time of storm and to not lower the film surface at the time of snow accumulation. In addition, in FEM analysis, if wrinkling occurs in a relatively wide range of the analysis region, the ranks of the stiffness matrix will be insufficient and it will be difficult to obtain a convergent solution. Wrinkling is

Copyright © 2019 by Masaya KAWABATA
Published by the International Association for Shell and Spatial Structures (IASS) with permission.

a phenomenon in which the strain in the direction of minimum principal stress becomes negative to cause wrinkles or loosening on the film surface, and the condition in which the initial tension is zero is particularly called tension loss. In order to avoid such numerically unstable conditions, it is necessary to increase the initial tension in advance for the air dome by raising the internal pressure during storm and snowfall.

The air cushion has a small air space because the pressurized space and the architectural space are separated, and it is easy to ensure airtightness. Therefore, it is also possible to use a closed type in which the air does not have to be constantly supplied. However, in actual design, there are many cases where the blower is operated at all times to maintain the internal pressure from the viewpoint of measures against air leakage. A typical air cushion has a small air volume and duct diameter, and the internal pressure is likely to change with changes in external force, temperature, air pressure. In particular, during a storm, the volume change speed of the cushion with respect to the dynamic wind pressure exceeds the moving speed of air passing through the duct, and the internal pressure fluctuates greatly. In Japan where severe load conditions such as wind storms and snow cover etc., it is particularly important to design an air cushion taking into consideration these effects appropriately.

The air cushion exhibits a complex behavior with strong nonlinearity of load-displacement relationship and displacement-internal pressure relationship. Therefore, it is essential to grasp the characteristics by experiments and analysis, but it is difficult to measure the film stress directly by experiments. FEM analysis can predict behavior in detail if modeling is appropriate. However, it is not easy to decipher the relationship between structural behavior and various factors such as stress transfer between upper and lower membranes via contained air, internal pressure fluctuation with changes in physical quantity, and plasticity of the film. The movement of air through the air duct is a situation where model assumptions are difficult and the designer's judgment is lacking.

2. Elasto-plastic deformation of spherical film

As shown in Fig. 1, a spherical film with a radius of curvature R0, rise h0, and thickness t0 in the unstrained state is deformed by receiving an internal pressure (differential pressure) p and the radius of curvature R, rise h, film thickness t, tensile stress? It is assumed that it becomes a spherical surface (equal tension curved surface). When the spherical membrane fixed to the outer periphery is deformed by the internal pressure, the film surface after deformation is not spherical, but here, it is formulated to be regarded as maintaining the spherical shape for simplification. When the membrane is an isotropic elasto-plastic body, the equilibrium equation of internal pressure and membrane tension, the stress-strain relationship of the membrane, and the condition formula for adaptation of strain are as follows.

$$\sigma = \frac{pR}{2t} \tag{1}$$

$$\sigma = \frac{E}{1-\nu}\varepsilon \tag{2}$$

$$R = \frac{L^2 + 4h^2}{8h} \tag{3}$$

Defining strain using nominal strain,

$$\varepsilon = \frac{R\theta}{R_0\theta_0} - 1 \tag{4}$$

It becomes. Defining the strain by using logarithmic strain, considering that the film after plasticization causes large strain,

$$\varepsilon_1 = \int d\varepsilon = \log\frac{l}{l_0} = \log\frac{R\theta}{R_0\theta_0} \qquad (5)$$

It becomes. In the case of the nominal strain, the film thickness of the denominator in the equation (1) uses a nominal stress which is constant t0 regardless of deformation, and in the case of the logarithmic strain, a true stress taking into consideration changes in the film thickness t is used.

The validity of the elasto-plastic analysis using spherical air film model is verified by comparison with pressure experiment of circular flat film. In the experiment, a 200 m ETFE film is attached to a 1 m diameter (0.95 m internal length) circular ring as shown in Fig. 2, and pressure and pressure reduction are performed stepwise in the out-of-plane direction, and vertical displacement in the center Measure The curved surface after deformation is assumed to be a sphere, and the stress and strain after deformation are obtained from equations (1) to (4). The definition of strain and stress uses logarithmic strain and true stress. Table 1 shows the analysis specifications. The strain and stress at uniaxial tension corresponding to the first and second yield points are (1.875%, 15 MPa) and (15.875%, 29 MPa), respectively. These are converted from nominal strain and nominal stress obtained by uniaxial tension test of ETFE film into logarithmic strain and true stress. The strain rate at pressure increase / decrease is in the range of 5 to 30% / min. Figure 3 shows the relationship between pressure and vertical displacement, stress, and strain at the center of the film surface. The analysis also shows the curves when unloaded at a rise ratio of 0.10, 0.15, 0.20. After yielding, the experimental curve is greatly curved, and the difference with the analysis is large. In particular, the curvature of the stress-strain curve is large in the region where the stress at unloading is less than or equal to half of the stress at reversal, at around the yield point at the time of loading, at the time of reversal from loading to unloading. This is considered to be the influence of the viscosity of the ETFE film, and microscopically, it is considered to be a change in the entangled state of polymer chains constituting the resin. Although there remains a problem in modeling material behavior including viscosity, in the analysis, the internal pressure-displacement relationship of the experiment is enveloped with good accuracy, and the stiffness at each rise ratio can be appropriately evaluated. Therefore, elasto-plastic analysis can be said to be effective for predicting film behavior.

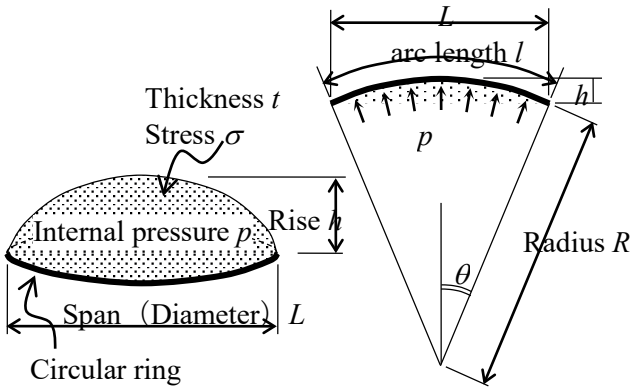


Fig.1 Shape of spherical membrane and pressure



Fig.2 Inflation experiment of plane film fixed on circular boundary

Table1 Analysis properties

Span	L	950	[mm]
Thickness	t	0.2	[mm]
Young's modulus	E	800	[N/mm^2]
Poisson's ratio	v	0.44	
Yield stress （1st）	Y_1	15	[N/mm^2]
Work hardening coefficient （1st）	H'_1	100	[N/mm^2]
Yield stress （2nd）	Y_2	29	[N/mm^2]
Work hardening coefficient （2nd）	H'_2	50	[N/mm^2]

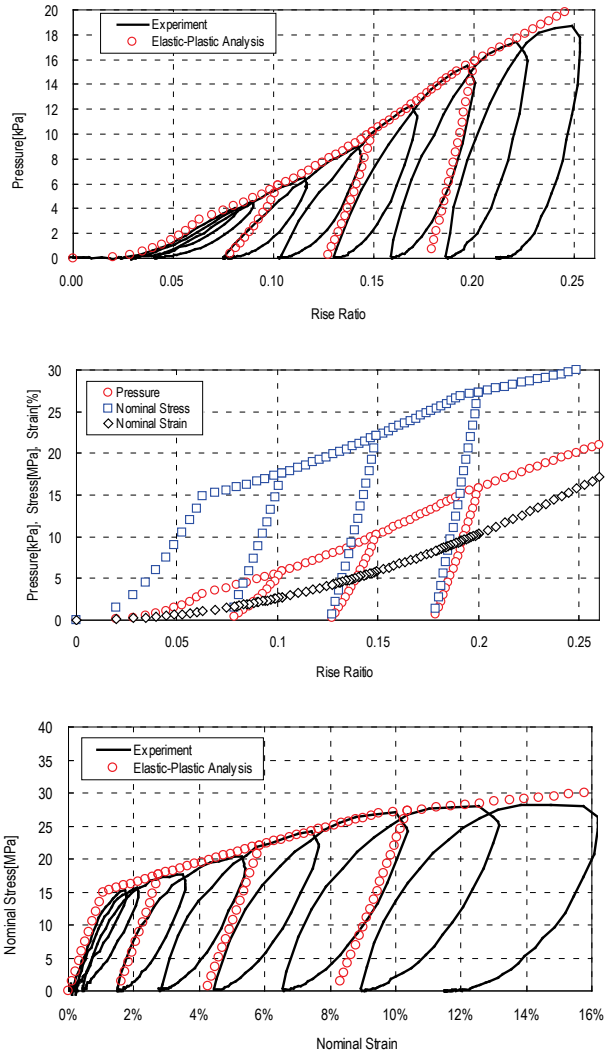


Fig.3 State change of circular film subjected to out-of-plane pressure

3. A Study on State Change of Sealed Circular Air Cushion

In order to verify the validity of the theoretical formula derived in the previous chapter, we compare it with the applied load experiment of the air cushion. In the experiment, after attaching an air cushion to the jig shown in Fig. 2 and setting a predetermined internal pressure and rise ratio, positive and negative pressure is applied to one side of the air cushion by changing the pressure in the chamber. Air cushions are of low rise type (initial rise ratio is about 0.03 to 0.04) in which the flat film is pressed within the elastic range and plastic deformation is applied to the film with internal pressure to cause residual deformation of about 0.1 rise ratio. There are 2 ways. Figures 6 and 7 show the results for the initial internal pressure of 600 Pa. The relationships of deformation, internal pressure and stress to applied pressure are matched with relatively good accuracy in the range where the absolute value of applied pressure is approximately twice or less of the initial internal pressure.

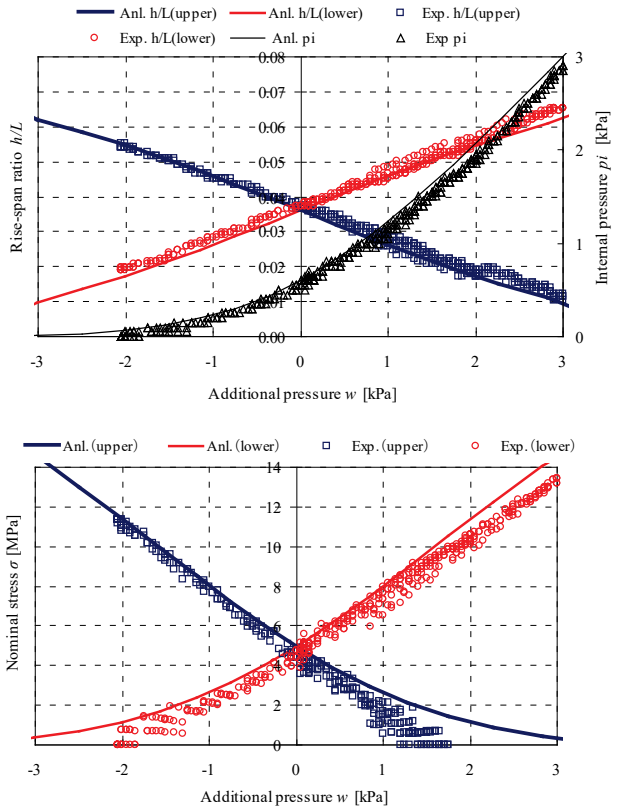


Fig.4 State change of air cushion subject to additional pressure
(Initial rise ratio 0.04, Initial internal pressure 600Pa)

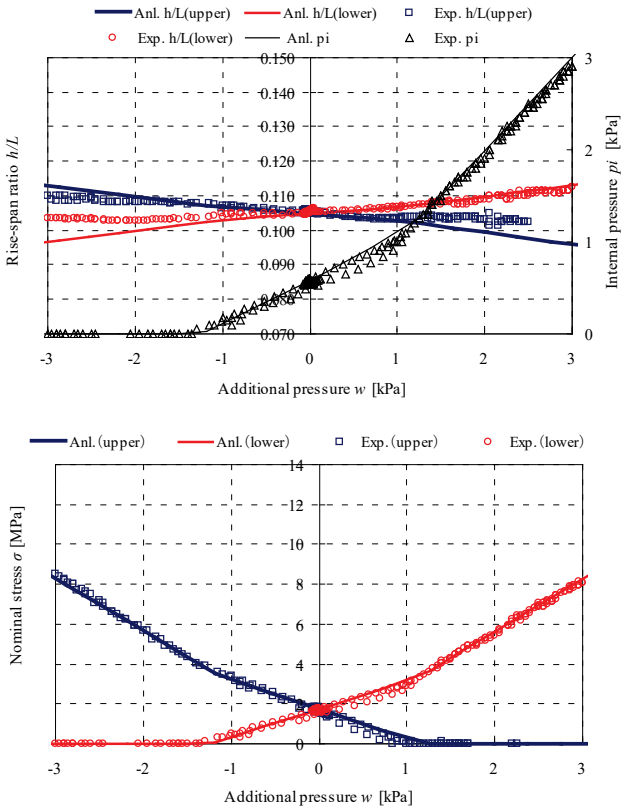


Fig.5 State change of air cushion subject to additional pressure
(Initial rise ratio 0.105, Initial internal pressure 600Pa)

Since a model with an initial rise ratio of 0.04 is flat at zero applied pressure, tension does not disappear in the theoretical solution, but in the experiment, the film viscosity causes residual strain in the film immediately after unloading, and residual strain disappears with the passage of time It began to. The model has a large shape change and is unlikely to cause tension loss. The model with an initial rise ratio of 0.105 has rise at zero applied pressure, so it is difficult to change its shape, but tension loss occurs. Since the film surface shape after tension loss is indeterminate, the rise ratio in the experiment fluctuates up and down. However, the rise ratio of the opposite film surface is in good agreement with the experiment and analysis, and no significant change in stiffness occurs with the loss of tension. The same result was obtained when the initial internal pressure was 300 Pa. From the above, it can be said that the theoretical formula in the previous section can accurately evaluate the behavior of a circular air cushion.

4. Influence of initial rise ratio and air flow system

Figure 6 compares the effects of the difference between the closed type and the constant pressure type, and the initial rise ratio, for an air cushion with an initial internal pressure of 500 Pa. In the constant pressure type, only the upper film side is shown because the sag and film stress on the lower film side do not change. The closed type has a smaller change in shape than the constant pressure type because the internal pressure changes in the direction to offset the effect of the applied pressure. In the constant pressure type, when a positive pressure of 500 Pa, which is equal to the initial internal pressure, acts, the effective pressure on the upper membrane side becomes zero, and the rigidity disappears. In the closed type, the upper membrane or the lower membrane loses tension when the absolute value of the applied pressure reaches about twice the initial internal pressure. As the influence of the internal pressure fluctuation of the closed type on the membrane stress, the tension increase on the lower side of the

positive applied pressure and the upper side tension on the negative applied pressure is concerned, but the amount of change is smaller than that of the constant pressure type. As the initial rise ratio is small 0.05, the initial stress is higher than in the case of 0.1, so the film reaches the yield stress with a small applied pressure. If the film yields, the rigidity decreases and the deformation increases, but if the rise is allowed to increase, the curvature of the air cushion increases, which is structurally advantageous.

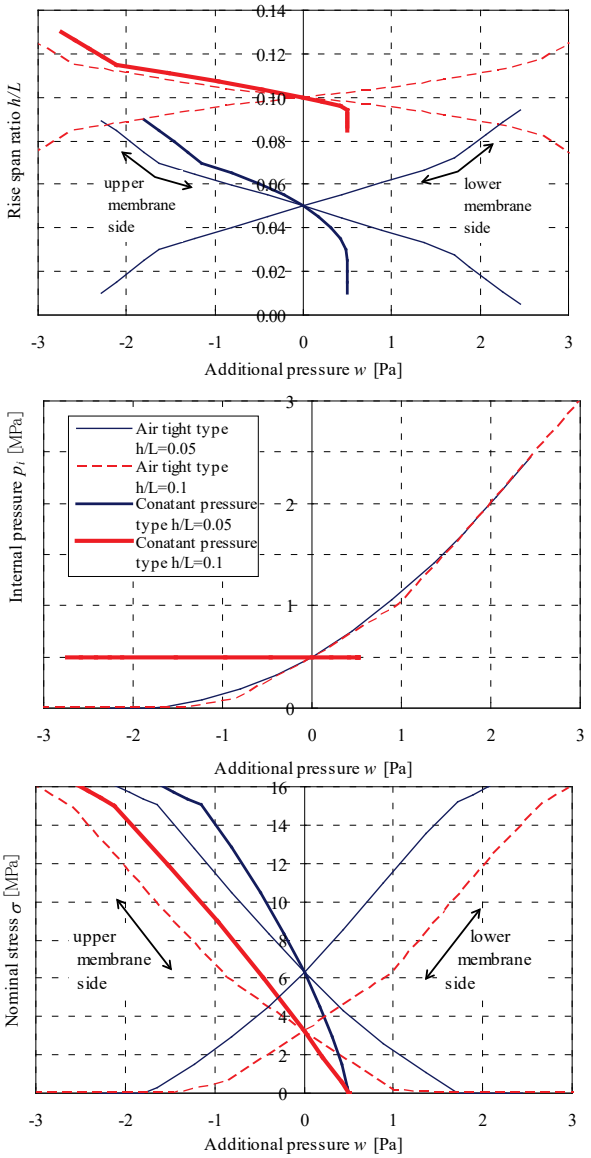


Fig.6 State change of air cushion subject to additional pressure
Effect of pressure type and rise ratio（closed type, constant pressure type, initial internal pressure 0.5kPa）

5. Conclusion: submission of contributions

Elastic-plastic analysis is applicable to calculate the stress and deformation of ETFE film uder the increasing load. Elasto-plastic deformation of spherical film, state change of sealed circular air cushion and influence of initial rise ratio and air flow system are examined.

References

[1] Coelho M., Roehla D. and Bletzingerb K.U., Numerical simulation of burst-test of an ETFE membrane, in *IASS-SLTE 2014*. *Shells, Membranes and Spatial Structures: Footprints*, Reyolando M.L.R.F. BRASIL and Ruy M.O. PAULETTI (eds.), 2014

[2] Chen W., Zhao B., SONG H. and CAI J., Experimental study of ETFE cushion-inflated form-developing through flat-patterning, in *IASS-SLTE 2014*. *Shells, Membranes and Spatial Structures: Footprints*, Reyolando M.L.R.F. BRASIL and Ruy M.O. PAULETTI (eds.), 2014

[3] Jeong E. and Kawabata M., An Experimental and Analytical Study on High Strength of ETFE Film by Stretch Fabrication, in *IASS 2015*. *Future Visions*, 2014

Proceedings of the IASS Annual Symposium 2019 – Structural Membranes 2019
Form and Force
7 – 10 October 2019, Barcelona, Spain
C. Lázaro, K.-U. Bletzinger, E. Oñate (eds.)

Deformation Analysis and Processing Stability Assessment for Fabric Specimens with Local Defects or Seams Based on Inflatable Bulging Test

Y.Z. SHEN, T. MA, G.C. LIN, H.F. TAN*

* National Key Laboratory of Science and Technology for National Defence on Advanced Composites in Special Environments, Harbin Institute of Technology, China
Harbin, Heilongjiang Province 150000, China
* Corresponding author, Email: tanhf@hit.edu.cn

Abstract

Local defects and seams of fabric materials have a certain effect on the performance of inflatable structures, especially in the inflatable deformation. This paper focuses on the analysis of inflatable surface deformation for the fabric materials with local defects and seams, as well as the assessment of the processing stability. The several fabric specimens with seams or local defects are designed and processed, including the fabric specimen with single seam, cross-shaped seam, local defect and gripper. Based on the inflatable bulging test, the fabric specimens are simulated as the inflatable states. The digital image correlation (DIC) technology is introduced. The surface deformations for each fabric specimen are calculated by the correlation algorithm under inflatable pressures, including the out-of-plane displacement and the full field principal strains. The finite element and formula method are utilized for verifying the accuracy of the test data. The processing stability of seams is assessed with the surface deformations for fabric specimens. The relationship between the surface deformation for the gripper and the inflatable pressure or the tensile load is obtained. According to the test results for the surface deformations, the local enhancement of the structural strength for the gripper to improve the tensile capacity.

Keywords: fabric specimens, inflatable bulging test, local defects and seams, surface deformations, processing stability assessment.

1. Introduction

The inflatable structure is generally formed by cutting pieces. To construct inflatable structures, air-tight lap seams to join pieces are formed through use of a heat seaming process. At the same time, the surfaces of the inflatable structure introduce some grip structures for controlling the position. Inevitably, the overall integrity of the structure depends on the quality of the seams. Local defects, seams and grip structures for fabric materials have a certain effect on the performance of inflatable structures, especially in the inflatable deformation. The assessment of processing stability becomes particularly important for evaluation of inflatable structures. A battery of tensile tests was conducted on different geosynthetics to assess the effects of seam type, puncture, and clamping techniques on strain distributions using image analysis techniques [1,2]. The UV-Visible Reflectometry and Thermography as potential NDE methods was assessed for assessing the quality of such seams in structures comprised of composite laminate fabric panels [3]. It can be seen that some scholars have carried out research on the quality assessment of seams under the tensile test combined with image processing technology and the thermographic method. At present, the assessment of the quality for seams under inflatable bulging state is relatively small.

Copyright © 2019 by Y.Z. Shen, T. Ma, G.C. Lin, H.F. Tan
Published by the International Association for Shell and Spatial Structures (IASS) with permission.

A bulge test for a circular fabric sheet is performed for obtaining the strain fields by digital image correlation (DIC) [4]. In-plane shear performance for F-12 aramid fabric was investigated by DIC [5]. A three-dimensional DIC system for deformation measurement in experimental mechanics has been developed, which can give both in-plane and out-of-plane displacement/strain fields [6,7]. Characterization of nonlinear properties for composite materials was obtained by using digital image correlation and finite element analysis [8-10]. As can be seen from the above studies, DIC system has proven to be a powerful non-contact technique for measuring 3D displacement/strain fields on any 3D object.

The several fabric specimens with seams or local defects are designed and processed, including the fabric specimen with single seam, cross-shaped seam, local defect and gripper. Based on the inflatable bulging test, the fabric specimens are simulated as the inflatable states. DIC technology is introduced. The surface deformations for each fabric specimen are calculated by the correlation algorithm under inflatable pressures, including the displacements and strains. The finite element and formula method are utilized for verifying the accuracy of the test data. This paper focuses on the analysis of inflatable surface deformation for the fabric materials with local defects and seams, as well as the assessment of processing stability.

2. Circular fabric specimen and gripper

The several fabric specimens with seams or local defects are designed and processed, including the circular fabric specimens and the gripper. The circular fabric specimens include the fabric specimen with single seam, cross-shaped seam, and local defect. The fabric specimen with single seam is made by two semi-circular fabric specimens. A certain width of fabric tape is used for bonding. A seam is formed. Another certain width of fabric tape is used for bonding along the vertical direction. Then this is the fabric specimen with cross-shaped seam. The fabric specimen with local defect indicates that the fabric is skewed along the weft direction. This phenomenon is named as skewing. The shape of the gripper is an isosceles trapezoid. The gripper structure passes through the gap of the skin material and is bonded to the back of the skin material. The inflatable pressures are applied for the circular fabric specimens. The inflatable pressures and tensile loads are applied for the skin of the gripper. Figure 1 is the physical map for the circular fabric specimens and the gripper. Table 1 is the material parameters for the circular fabric specimens and the gripper.

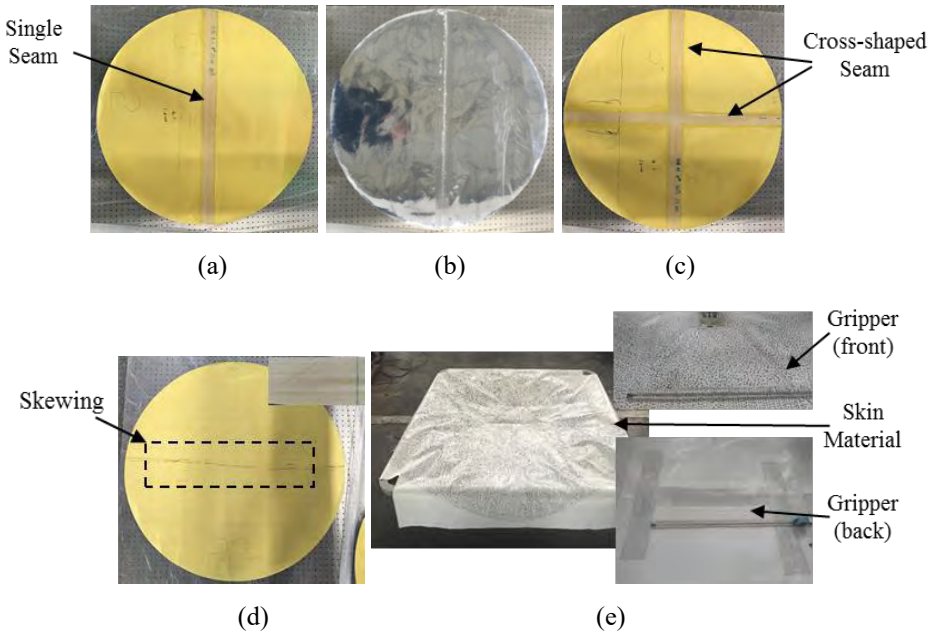


Figure 1: The physical map for the circular fabric specimens and the gripper

Table 1: The material parameters for the circular fabric specimens and the gripper

Name	Circular Fabric Specimen	Gripper
Elastic Modulus (MPa)	9,897 (warp) 11,480 (weft)	3,000(σ<50MPa) 10,000(σ>50MPa)
Poisson's Ratio	0.3	0.3
Thickness(mm)	0.177	0.177

3. Inflatable bulging test

The inflatable bulging devices are used to carry out the inflatable bulging test for the circular fabric specimens and the gripper. The inflatable state of the fabric specimens is simulated. Combined with DIC technology, the surface deformation test for the fabric specimens is carried out. The surface deformation distributions are obtained.

3.1. Inflatable bulging device

Two inflatable bulging devices are designed. One is a column barrel. The column barrel is composed of the cylinder body, the bottom cover and the annular cover. The annular cover can be connected to the bottom cover by the bolts. In order to ensure the sealing of this inflatable bulging device, a circular groove is provided between the bottom cover and the annular cover. The rubber ring can be placed. This inflatable bulging device can provide the inflatable pressure to the circular fabric specimens. Another inflatable bulging device consists of two parts. Part one consists of ground anchor, main body, cover plate and press plate. The gripper is placed between the main body and the cover plate. The other part consists of wire rope, fixed pulley and motor. The motor is connected to the end of the wire rope. This inflatable bulging device can apply the inflatable pressure and tensile loads to the gripper. Figure 2 is the inflatable bulging devices.



(a) (b)

Figure 2: The inflatable bulging devices

3.2. Inflatable bulging test

Combined with DIC technology and the inflatable bulging test, the surface deformations of the circular fabric specimens under the inflatable pressures and the surface deformations of the gripper under the inflatable pressures and the tensile loads are obtained. DIC technology is an algorithm that compares image-related points to calculate the surface displacement and strain distribution. DIC generally refers to a class of non-contacting methods that acquire images of an object in digital form and perform image analysis to extract sensor-plane motions that can be converted into full-field measurements on the corresponding object [11]. The inflatable bulging test mainly includes preliminary preparation, speckle making, erection and commissioning of DIC system, calibration of

DIC system, collection of speckle image information and data processing. Figure 3 is the flow chart of the inflatable bulging test.

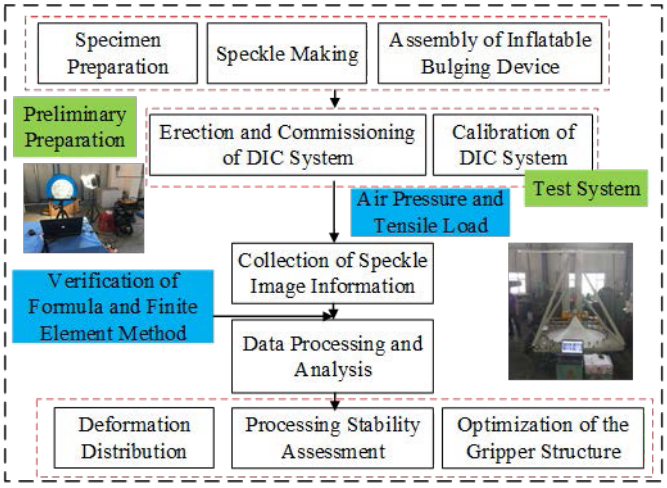


Figure 3: The flow chart of the inflatable bulging test

4. Results and discussions

4.1. Accuracy verification

The accuracy of the test data for the surface deformations is verified firstly. According to the Strain Energy Theory and the Cartesian Theorem, X. Xiao [12] derived deflection formula of the circular fabric film under the inflatable pressure. The deflection formula is described as:

$$w_{\max} = a \cdot \sqrt[3]{\frac{1.45Pa}{Et} \cdot \frac{1-\upsilon^2}{2.08+4\upsilon-1.2\upsilon^2}} \tag{1}$$

where w_{max} is the maximum deflection value, a is the effective radius of the circular fabric film, t is the thickness of the fabric material, E is the elastic modulus of the fabric material, v is the Poisson's ratio of the fabric material, and P is the inflatable pressure. The elastic modulus E takes the average value of the warp and weft directions for the circular fabric specimens. The circular normal fabric specimen is indicated that the specimen without seams or defects. Table 2 is the comparison results between the test values of the out-of-plane displacements for the circular normal fabric specimen and the values of the deflection formula. The out-of-plane displacement is named as w.

The finite element method is used to simulate the deformation for the gripper. The finite element results of the deformation for the gripper are compared with the test data. Table 3 is the comparison results of test data of the out-of-plane displacements for the gripper.

Table 2: The comparison results of test data of the out-of-plane displacements for the circular normal fabric specimen

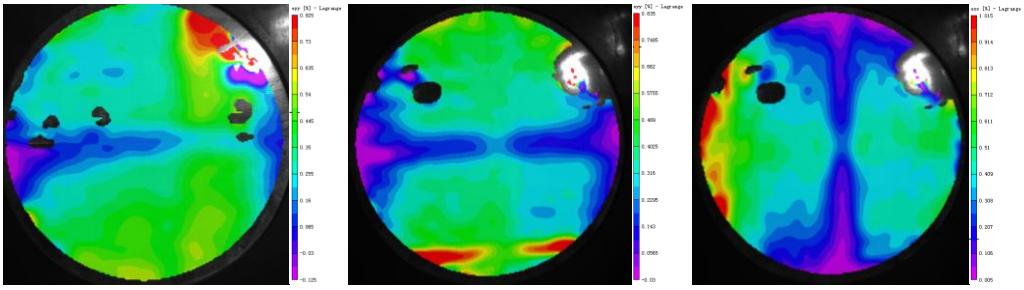
Internal Pressure (kPa)	Test Value w (mm)	Formula Value w (mm)	Relative Deviation (%)
0.4	14.21	12.65	12.29
1.0	18.38	17.17	7.05
5.0	31.42	29.36	6.98
7.0	35.58	32.85	8.31

Table 3: The comparison results of test data of the out-of-plane displacements for the gripper

Tensile Angle(°)	Internal Pressure(kPa)	Tensile Load(kN)	Test Value *w* (mm)	Finite Element Value *w* (mm)	Relative Deviation(%)
56.40	0.2	8.0	117.20	126.00	6.98
42.79	1.0	5.0	79.31	69.48	14.15
35.88	2.0	5.1	60.50	55.17	9.66

4.2. Processing stability assessment for circular fabric specimens

Figure 4 shows the eyy and exx strain clouds for the circular fabric specimen with single seam and cross-shaped seam under 15kPa inflatable pressure. The eyy and exx strains are the in-plane strain. e1 is named as the principal strain. It can be seen that the strains for the circular fabric specimen with single seam are asymmetrical along the seam direction. The strain value on the left side is less than that at the corresponding position on the right side. The circular fabric specimen with cross-shaped seam show better symmetry in both exx and eyy strain clouds. This indicates that the bonding process of the circular fabric specimen with single seam is unstable. And the bonding process of the fabric specimen with cross-shaped seam is better. Figure 5 shows the eyy and e1 strain clouds for the circular fabric specimen with local defect under 15kPa inflatable pressure. The strain values of the defective portion are relatively larger. The surface for the defective portion is relatively to be destroyed firstly. The results indicate that DIC technology is highly effective in determining the strains distributions within inflatable bulging test for the fabric specimens. And the processing stability for the fabric specimens can be assessed quickly by the test results.



(a) (b) (c)

Figure 4: The strain clouds for the circular fabric specimens: a) single seam, eyy cloud, b) cross-shaped seam, eyy cloud, and c) cross-shaped seam, exx cloud

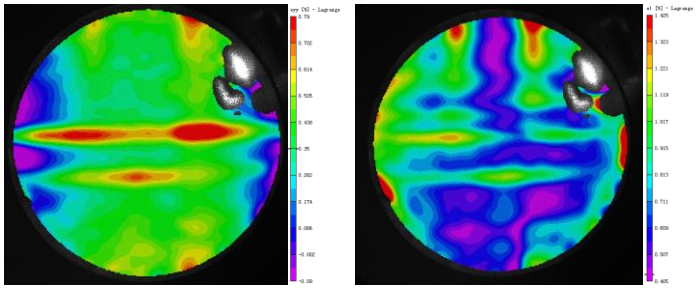


Figure 5: The strain clouds for the circular fabric specimen with local defect: a) eyy cloud, and b) e1 cloud

4.3. Enhancement of structural strength for gripper

When the inflatable structure is in the state of inflatable pressure, the gripper is applied tensile load for controlling it. During the process of the inflatable bulging test, the surface strains of the gripper are tested under multiple initial internal pressures and tensile loads. The relationship between the tensile

load, the initial internal pressure and the deformation of the gripper is obtained. During the same tensile angle, Figure 6 shows the curve between the deformations of the gripper and the tensile load under different initial internal pressures. It can be seen that the smaller the initial internal pressure, the larger the value of the maximum out-of-plane displacement and the principal strain of the gripper. When the tensile load is lower, the initial internal pressure has little effect on the principal strain. When the tensile load is higher, the out-of-plane deformation and the principal strain changes linearly. Figure 7 shows the relationship between the maximum principal strain and the tensile load for the gripper under the different initial internal pressures. When the initial internal pressure of the skin material is lower, the larger the tensile angle within a certain range the smaller the value for the principal strain. When the initial internal pressure of the skin material is higher, the tensile angle within a certain range has less influence on the value for the principal strain.

At the same time, the gripper is broken when the tensile load is applied to a certain value. The tear appears at both ends of the gripper and expands along the direction of the seam. Figure 8 is the breaking map for the gripper. It can be seen from the strain clouds that the strain extreme value appears at both ends of the gripper. Therefore, the strength enhancement on both ends of the gripper is the most effective solution. The reinforcement bands are attached to both ends of the gripper. Figure 9 shows the strain clouds of the simulation results before and after enhancement by the finite element method. The simulation results show that the maximum stress value is reduced by 22%. Based on the inflatable bulging test and DIC technology, the relationship between the tensile load for the gripper and the internal pressure is obtained. The most effective solution for improving the structural strength of the gripper is proposed.

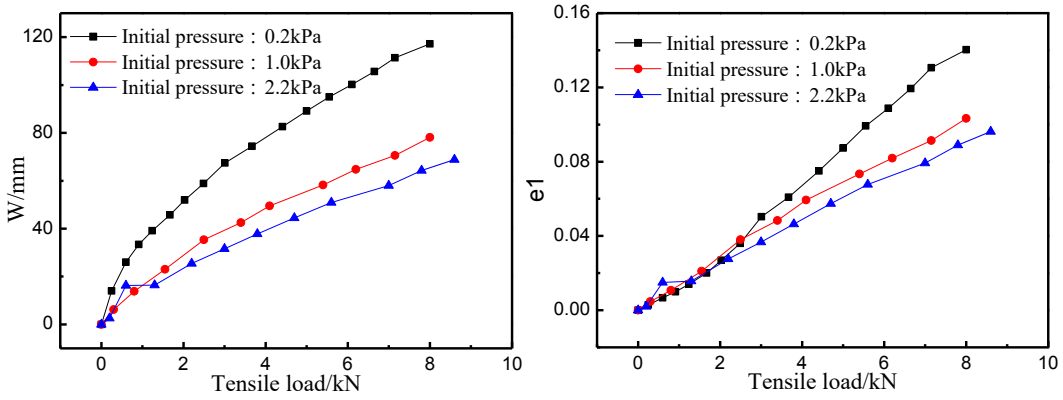
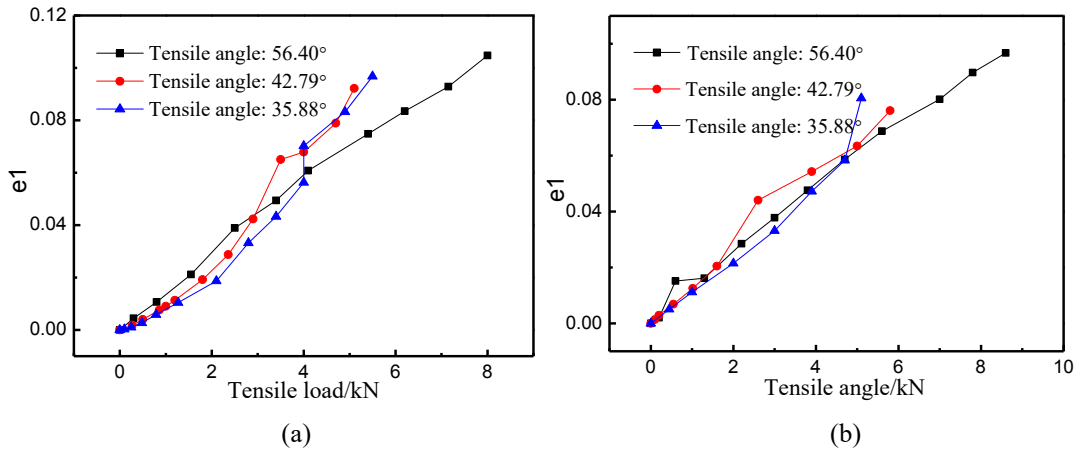
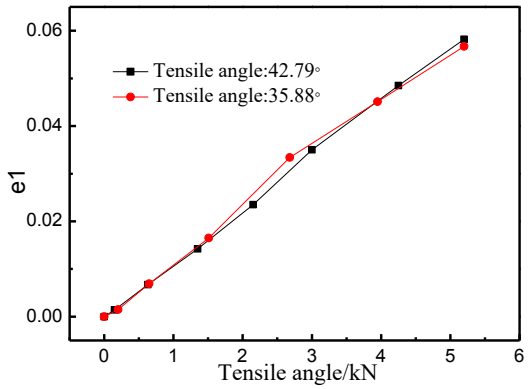


Figure 6: The curves between the deformations of the gripper and the tensile load under 56.40° tensile angle: a) maximum value of out-of-plane displacement, and b) maximum value of principal strain





(c)

Figure 7: The curves between the maximum value of the principal strain and the tensile load for the gripper under the different initial internal pressures: a) 1kPa, b) 2kPa, and c)3kPa

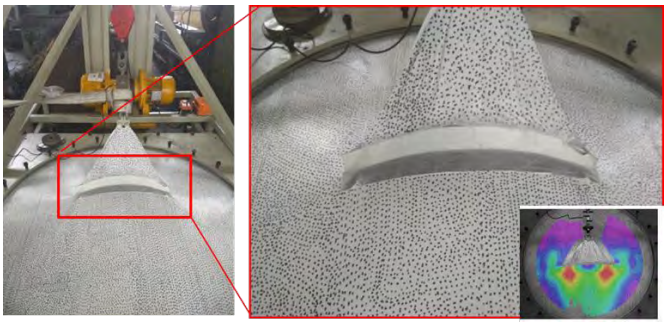
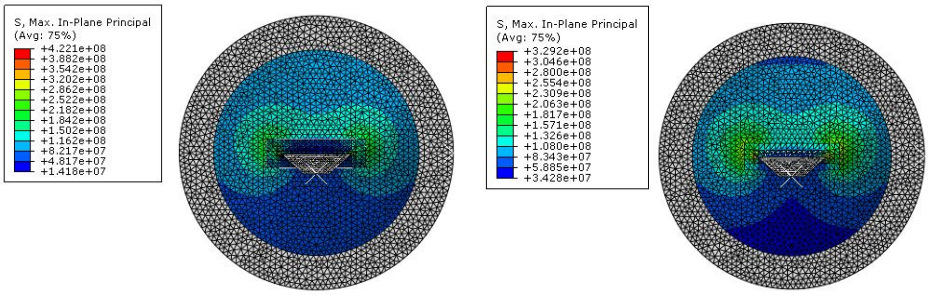


Figure 8: The breaking map for the gripper



(a) (b)

Figure 9: The stress clouds for the gripper: a) before enhancement, and b) after enhancement

5. Conclusion

Inflatable surface deformations for the fabric materials with local defects and seams are analyzed, as well as the assessment of processing stability. The several fabric specimens with seams or local defects are designed and processed, including the fabric specimen with single seam, cross-shaped seam, local defect and gripper. Based on the inflatable bulging test, the fabric specimens are simulated as the inflatable states. The DIC technology is introduced. The surface deformations for each fabric specimen are calculated by the correlation algorithm under inflatable pressures, including the out-of-plane displacement and the full field principal strains. The finite element and formula method are utilized for verifying the accuracy of the test data.

The surface deformations for the circular fabric specimens are obtained. The results indicate that DIC technology is highly effective in determining the strains distributions within inflatable bulging test for

the fabric specimens. And the processing stability for the fabric specimens can be assessed quickly by the test results.

Based on the inflatable bulging test and DIC technology, the relationship between the tensile load for the gripper and the internal pressure is obtained. The most effective solution for improving the structural strength of the gripper is proposed.

Acknowledgements

The authors gratefully acknowledge support from the Foundation for Innovative Research Groups of the National Natural Science Foundation of China (Grant No. 11421091) and the Fundamental Research Funds for the Central Universities (Grant NO.HIT.MKSTISP.2016 09).

References

[1] M. Guler, M. E. Kutay and A. H. Aydilek, "Evaluation of Strain Distribution in Geotextiles Using Image Analysis," *Geo-Frontiers Congress*, 2005.

[2] M. E. Kutay, M. Guler, and A. H. Aydilek, "Analysis of Factors Affecting Strain Distribution in Geosynthetics," *Journal of Geotechnical and Geoenvironmental Engineering*, vol. 132, pp. 1-11, January, 2006.

[3] E. C. Johnson, D. N. Patel, C. J. Panetta, O. Esquivel, and Y. M. Kim, "NDE of lap seams in composite laminate fabric structures," *13th International Symposium on Nondestructive Characterization of Materials*, Le Mans, France, May. 2013, pp. 20-24.

[4] X.L. Luo, H.F. Tan, G.C. Lin and Y. Lian, "Strain Field Measurements Using Digital Photogrammetry for Large Inflatable Structures," *Experimental Techniques*, vol. 41, pp. 453-462, 2017.

[5] X.L. Luo, H.F. Tan and G.C. Lin, "Experimental investigation of in-plane shear performance for F-12 aramid fabric," *Acta Materiae Compositae Sinica*, vol. 35, pp. 591-598, 2018.

[6] O. Jean-Jose, "3-D computer vision in experimental mechanics," *Optics and Lasers in Engineering*, vol. 47, pp. 282-291, 2009.

[7] Z. Z. Tang, J. Liang, Z. Z. Xiao, C. Guo, H. Hu, "Three-dimensional digital image correlation system for deformation measurement in experimental mechanics," *Optical Engineering*, vol. 49, pp. 103601, 2010.

[8] A. Makeev, Y. He, P. Carpentier, B. Shonkwiler, "A method for measurement of multiple constitutive properties for composite materials," *Composites Part A: Applied Science and Manufacturing*, vol. 43, pp. 2199-29210, 2012.

[9] A. Makeev, P. Carpentier, B. Shonkwiler, "Methods to measure interlaminar tensile modulus of composites," *Composites Part A: Applied Science and Manufacturing*, vol. 56, pp. 256-261, 2014.

[10] Y. He, A. Makeev, B. Shonkwiler, "Characterization of nonlinear shear properties for composite materials using digital image correlation and finite element analysis," *Composites Science and Technology*, vol. 73, pp. 64-71, 2012.

[11] M.A. Sutton, J.H. Yan, V. Tiwari, et al, "The effect of out-of-plane motion on 2D and 3D digital image correlation measurements," *Optics and Lasers in Engineering*, vol. 46, pp. 746-757, 2008.

[12] X. Xiao, A. Long, H. Lin, et al, "Large deformation modelling of tight woven fabric under high air pressure," *Journal of Engineered Fibers & Fabrics*, vol. 10, pp. 63-74, 2015.

Proceedings of the IASS Annual Symposium 2019 – Structural Membranes 2019
Form and Force
7 – 10 October 2019, Barcelona, Spain
C. Lázaro, K.-U. Bletzinger, E. Oñate (eds.)

Experiment of bi-axial creep of fabric membranes under cyclic temperature and its formulation of constitutive equation based on Fabric Lattice Model

Tatsuya YOSHINO[a], Shiro KATO*

* Emeritus Professor, Toyohashi University of Technology,
Hibarigaoka, Tempaku, Toyohashi, 441-8580, Japan
kato-shiro@tg.commufa.jp

[a] Engineering division, Taiyo Kogyo Corporation, 532-0012, Japan

Abstract

With an aim at application to FEM analysis under cyclic temperature environments, first the present study proposes, on a basis of fabric lattice model, new constitutive equations of PTFE material under creep and relaxation, and second presents new experimental results for bi-axial stress ranges from small to large regions considering fracture deformation together investigating relaxation and creep. Especially, from a view point of visco-elastic characteristics of PTFE under bi-axial stresses with environmentally changing temperature in time, experiments are conducted for creep of several different stress ratios to observe creep deformations under a temperature change. Finally, the results based on constitutive equations are compared with the experimental ones, and the validity of the equations is proven, and the applicability in FEM analysis in terms of incremental steps is confirmed

Keywords: PTFE membrane materials, constitutive equations, FEM, biaxial creep test,

1. Introduction

Exact information of material properties of PTFE is indispensable to realize safe and precise manufacturing and in-site construction. The visco-elastic characteristic is one of the key factors, due to which stresses induced in-site are lost depending on time process after completion. The phenomenon should be carefully treated, otherwise leading to some damage. Few researches have been performed so far except for the experiments by Minami et al. [1,2]. They conducted creep experiments of one week in the case of both uni-axial stress and bi-axial stresses under a constant temperature. On the other hand, the present authors performed experiments for relaxation [3] under repeated loading using bi-axial test equipment, and found stress drop after each repetition is moderately small compared with the previous one meaning that depending an increased cycle the ratio of stress drop doe to relaxation is reduced step by step. And also the present authors have developed a constitutive equation based on a fabric lattice model [3-5], with which they tried a simulation to see if the equation is valid or not and have confirmed that the proposed constitutive equation can simulate rather well. However, the studies [3-5], the temperature environments during experiments was constant, not variable, and they did not focus the effects due to temperature change.

With a background mentioned above, the present authors have recently performed a series of experiments of PTFE material under bi-axial stresses accompanied with temperature change, and have grasped their material characteristics. By reflecting the experimental results together with former ones, the material constants for the fabric lattice model [5] are reorganized here. Moreover, the present study shows not only a new set of material constants especially for viscous coefficient for elements in the

Copyright © 2019 by Tatsuya YOSHINO, Shiro KATO
Published by the International Association for Shell and Spatial Structures (IASS) with permission.

Fabric Lattice model but also the validity and preciseness of the constitutive equations are proven based on experimental results.

2. Fabric Lattice Model

The Fabric Lattice Model (FLM) has been validated as one type of constitutive equations of PTFE through the studies [3-5]. The physical components are shown in Figure1, and a set of line elements are applied for the formulation as A, AA, A for the warp, B, BB, B for the fill (weft), C and D for the coating between yarns, E and F for the coating under shear, and V (struts) for crimp interchanging. The fundamental theories of the Model is referred to the papers [3-5]. With respect to their static hysteresis rules, they are respectively shown in Figure 4.1 to Figure 4.5.

For the line elements, the present authors have applied 6-elements Voigt model [4] hitherto, and the present study adopts a generalized model composed also of 6 elements shown in Figure 2.6 for coating materials of C, D and V excluding warp and fill. The material constants are later explained.

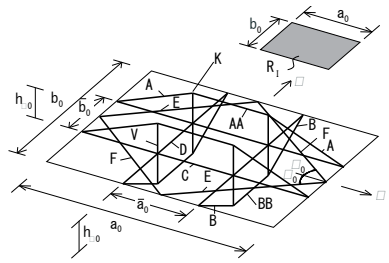


Figure 1.1 Fabric Lattice Model

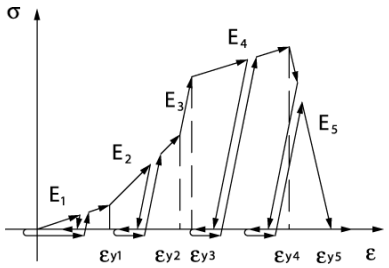


Figure 1.2 Warp and weft (elements A, AA, B and BB)

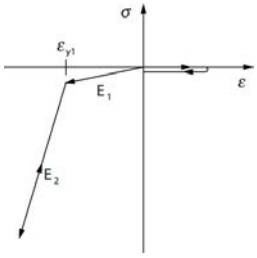


Figure 1.3 Struts (elements V)

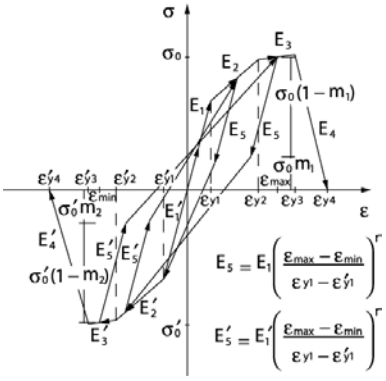


Figure 1.4 Coating materials (elements C, D, E, F)

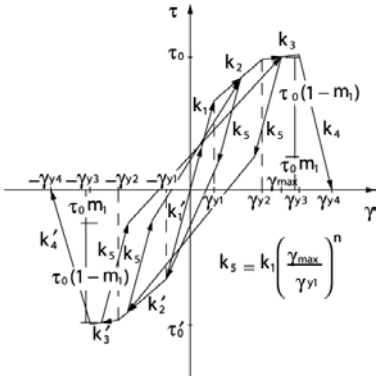


Figure 1.5 Coating material between yarns (elements R_1)

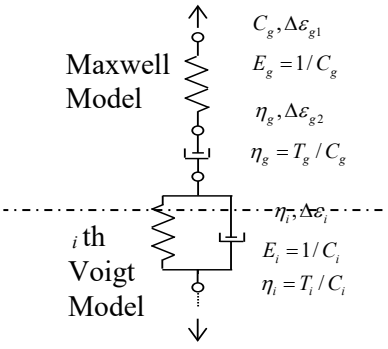


Figure 1.6 Generalized Voigt model for elements C,D and V

3. Experiment for Creep under Bi-Axial Stress and Temperature Change

The present authors conducted experiments of bi-axial creep as well as bi-axial relaxation so far, however, they reflected that the temperature control during experiments were not so exact for precise results because the experiments were processed under a room temperature not controlled, and they felt that the results might have been subject to fluctuation of temperature to some extent. And the authors have recently set up a new experimental equipment for creep and relaxation, and have conducted again experiments of PTFE under bi-axial under a strict control.

3.1. Experiment of creep for a stress ratio of 1:1 under a constant temperature

As the first experiment using a new equipment, bi-axial test with a stress ratio 1:1 is performed under a constant temperature of 20.4 C° during one week to check if some difference would appear from the previous results under the same temperature. The new condition is given in Table 1. The results are

included and shown together in Figures 3.1 and 3.2 marked with Exp-W for warp and Exp-F for fill, and compared with the previous ones marked with Exp-W (1m) and Exp-F (1m) which were performed previously for one month. No clear difference is found between the present and previous ones, showing that the previous results are admitted fine..

3.2. Experiment of creep for a stress ratio of 1:1 under cyclic temperature change

Second, experiments are conducted under a cyclic temperature change with a stress ratio of 1:1, from 2.6 C^0 to 20.4C^o, with seven cycles in one week, and the temperature is cyclically varied as shown in Figure 2. The results marked with (1w, 20-2) in Figures 3.1 and 3.2 are those from experiments of creep for stress ratio of 1:1 under a test condition in Table 1.

Just after the loading applied, some difference of 1% is found between the present two loadings; a constant temperature (1w, 20) and cyclic temperature (1w, 20-2), however, they are almost same each other with a same creep strain. This error is judged within a permissible threshold of fluctuation of PTFE material itself and a testing procedure.

During the new experiment of seven days, merely 0.1% difference is found in strain magnitude, evaluated after seven days, between the two results under a constant temperature and temperature change of 17.8C^o. Judging from the difference between the two results for creep, one under a constant temperature and one under a cyclic temperature, the effects due to temperature change may be negligibly small. One of the reasons may be that the deformation of creep due to temperature change is rather small than that due to plasticity. However, judging from Figures 5.1 to 5.6 for relaxation later shown, the reduction in stress due to temperature change is rather large compared with initial stress value. For example, the experiments in a room temperature, not controlled for room temperature, shows that the difference in stress reduction changes by about 0.5kN/m, this value being not so small compared with initial stress.

Table 1 Test conditions

width	100mm
chuck distance	200mm
gauge length	24mm
max stress	3 and 5kN/m
stress ratio	1:1
chuck speed	Loading / 2sec.
creep time	7days (1 w)
temperature	20.4 ℃ (20) (only 1:1)
	20.4 and 2.6 ℃ (20-2) 7 cycles, 12 hours for each cycle (Figure 3.1.1)

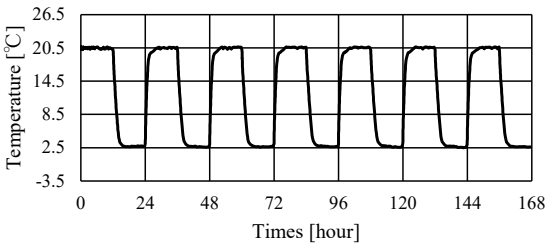


Figure 2 Temperature history

3.3. Experiment of creep for stress ratio of 1:0 and 0:1 under cyclic temperature change

Figures 3.3 and 3.4 are the results under uni-axial stress, respectively, for 3 kN/m and 5 kN/m under a cyclic temperature change.The stress is applied to yarns. Due to uni-axial stress, the deformation of yarns are larger than those under bi-axial streses of equal stress intensity in both directions. From Figure 3.4 for a stress ratio of 1:0 in the case of 5.0 kN/m for the maximum stress, some amount of discrepancy is found between the two results of Exp-W(1w, 20-2) and Exp-W(1m), while a relatively fine agrrement is found between Exp-W(1w, 20-2) and Exp-W(1m) in the case of 3.0 kN/m for the maximum stress. The difference due to stress intencity with a uni-axial large stress in the warp may appear in the magintude of creep strain.

Figures 3.5 and 3.6 are the results under uni-axial stress, respectively, for 3 kN/m and 5 kN/m under a cyclic temperature change.The stress is applied to fills. A tendecy is also found, as anticipated, that the strains are much larger than tthose under a uni-axial stress in the warp drection.

3.4. Experiment for bi-axial stresses and relaxation of one month

The previous experiment are shown for bi-axial stress in Figures 4.1 to 4.4, for shear in Figure 4.5, also for relaxation in Figures 5.1 to 5.6. Also the results for relaxation under repeated stresses are shown in Figures 6.1 and 6.2. The data are also applied here to identify the material constants for FLM..

4. Material Constants of Composing Elements and Numerical Simulation

4.1. Identification of material constants of Fabric Lattice Model

Reflecting the recent experiments excluding fractured data, material constants of the Fabric Lattice Model are reformulated, but by try and error, in consideration of both of strain-to-stress relationships and stress or strain-to-time relationships. The results of identification are given in Table 2 to 4.

Table 2: Parameter of length [mm] identified

a_0=1.38	b_0=1.00	$\overline{a}_0$ =0.152	$\overline{b}_0$ =0.149	$h_{\varepsilon 0}$ =0.459	h_{n0} =0.333

Table 3 Material properties identified: dimensions and constants identified for Fabric Lattice Model

elements		A,AA	B,BB	C		D		E,F		V
A_0	(mm^2)	0.16/2	0.16/2	0.40/2		0.40/2		0.14		0.25/2
E_1, E'_1	(kN/mm)	0.981	0.981	27.5	33.3	29.9	50.5	5.00	5.00	0.0031
E_2, E'_2	(kN/mm)	4.903	58.8	13.2	13.7	3.9	14.7	2.94	2.94	29.9
E_3, E'_3	(kN/mm)	515	280	4.71	7.85	0.98	3.92	0.001	0.001	31.4
E_4, E'_4	(kN/mm)	0.001	0.001	-294	-294	-9.81	-9.81	-9.81	-9.81	-
E_5, E'_5	(kN/mm)	-392	-392	-		-		-		-
ε_{y1}, ε'_{y1}	(%)	0.001	1.01	0.5	-0.06	0.4	-0.35	0.2	-0.2	-15
ε_{y2}, ε'_{y2}	(%)	0.012	1.9	90	-1.6	7.3	-90	3	-3	-37
ε_{y3}, ε'_{y3}	(%)	3.30	4.17	100	-6	100	-100	100	100	-
ε_{y4}, ε'_{y4}	(%)	4.11	5.18	-		-		-		-
n	-	-	-	0.0		0.0		0.0		-
m_1	-	-	-	0.07		0.08		0.4		-
m_2	-	-	-	0.5		0.5		0.4		-

Table 4 Visco-elastic constants from test identified

	T_g sec	C_1 mm^2/kN	T_1 sec	C_2 mm^2/kN	T_2 sec	C_3 mm^2/kN	T_3 sec	C_4 mm^2/kN	T_4 sec	C_5 mm^2/kN	T_5 sec
C	1E+10	8E-06	1	9E-06	10	1E-05	100	1E-07	1000	2E-05	10000
D	1E+10	6E-06	1	6E-06	10	2E-05	100	1E-07	1000	6E-05	10000
V	5E+10	0.0001	1000	0.0003	100000	-	-	-	-	-	-

4.2 Numerical simulations

The results based on the re-identified constants for FLM, a set of simulation are performed for comparison with experiments. They are shown for creep experiment in Figures 3.1 to 3.6, for bi-axial test in Figures 4.1 to 4.4, for shear test in Figure 4.5, for relaxation test in Figures 5.1 to 6.2.

With respect to simulations of creep strains in Figures 3.1 to 3.6, relatively agreeable simulations are obtained in the cases of the new expreiments, except for the previous strains for 1 month. The difference from 1 month may be due to some experimental fluctuations of the previous experiments, or may be due to fluctuation of the tested materials useed for the previous experiments. The issue will be a study targent in future.

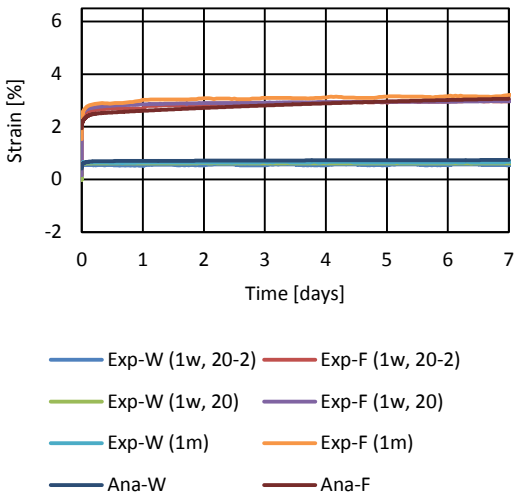


Figure 3.1 Time-strain relationships; maxuimum stress of 3:3 kN/m

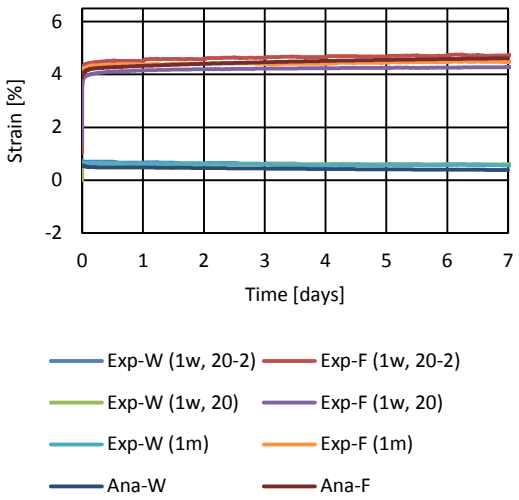


Figure 3.2 Time-strain relationships; maxuimum stress of 5:5 kN/m

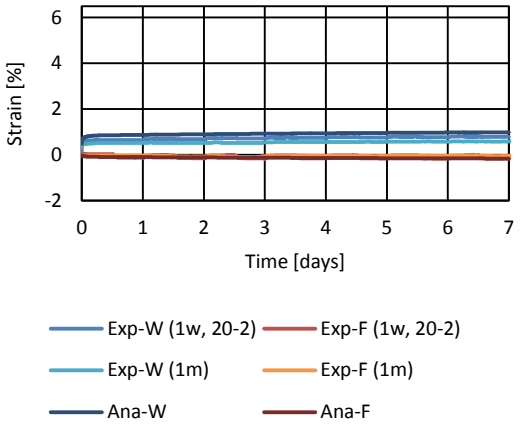


Figure 3.3 Time-Strain relationships; maximum stress of 3:0 kN/m

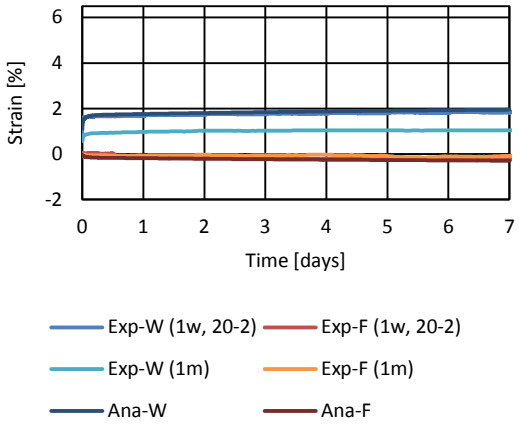


Figure 3.4 Time-Strain relationships; maximum stress of 5:0 kN/m

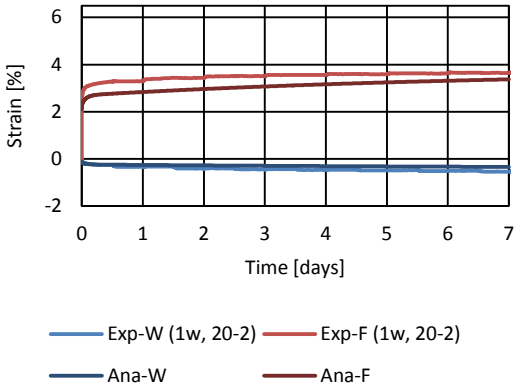


Figure 3.5 Time-Strain relationships; maximum stress of 0:3 kN/m

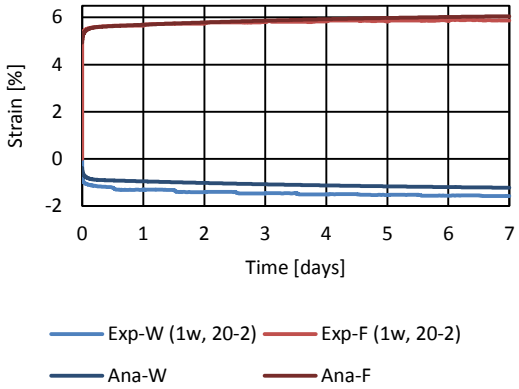


Figure 3.6 Time-Strain relationships; maximum stress of 0:5 kN/m

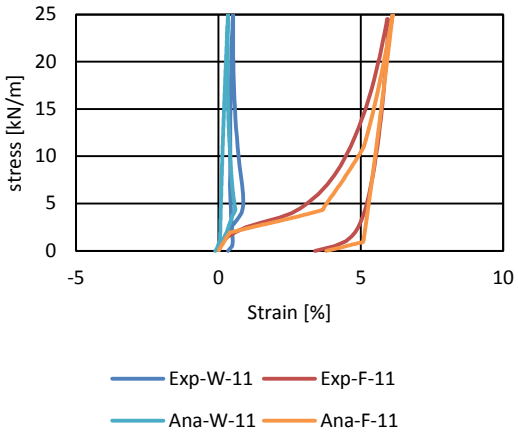


Figure 4.1 Stress-Strain relationships; maximum stress 25:25 kN/m

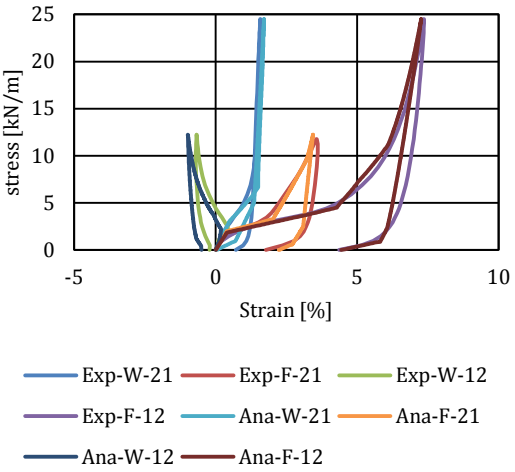


Figure 4.2 Stress-Strain relationships; maximum stress 25:12.5 and 12.5:25 kN/m

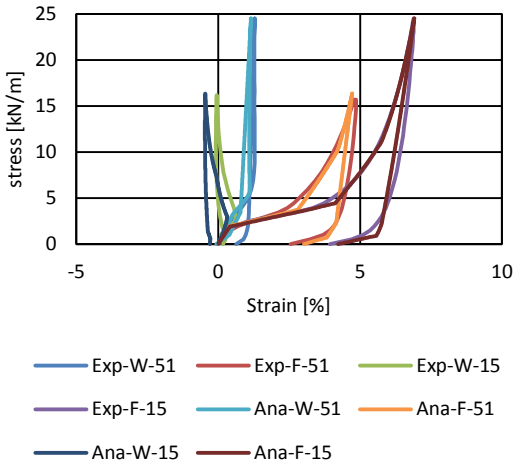


Figure 4.3 Stress-Strain relationships; maximum stress 25:16.7 and 16.7:25 kN/m

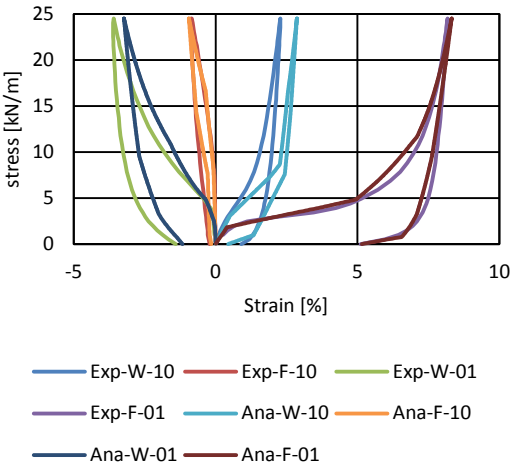


Figure 4.4 Stress-Strain relationships; maximum stress 25:0 and 0:25 kN/m

With respect to the static cyclic loading tests, a fine agrrement between analysis and experiment is obtained in any stress ratio, irrespective of the stress magnitude, as shown in Figures 4.1 to 4.4. For shear stress-strain relationships under cyclic loading, also a fine agreement is obtained shown in Figure 4.5.

As for relaxation of stresses after one step loading shown in Figures 5.1 to 5.6, a tendency for relaxation is evaliated to some extent, however, some discrepacy still remains to be solved. Especially, in the cases for bi-axial stresses, the accuracy of prediction for relatively high stress like 3 kN/m are rather low. The disagrement may one target in fututre.

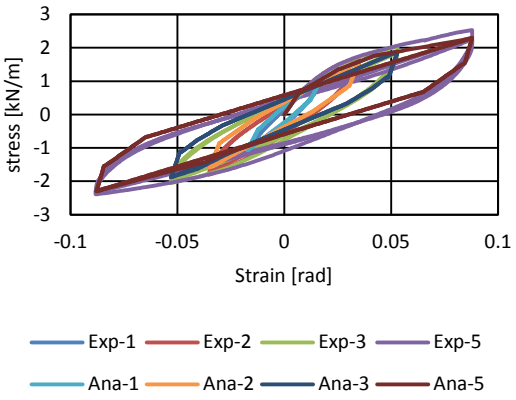


Figure 4.5 Shear stress-shear strain relationships
Shear angle $\pm 1, 2, 3, 5$deg.

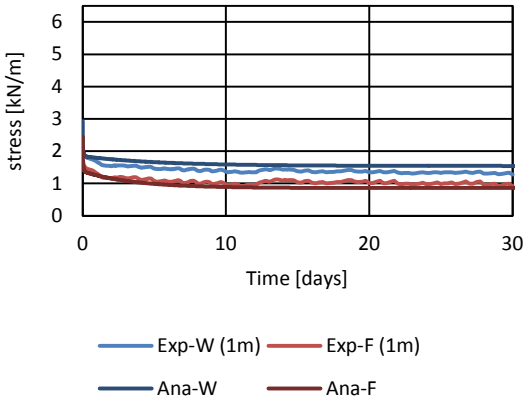


Figure 5.1 Time-Stress relationships; Maximum stress (3:3kN/m)

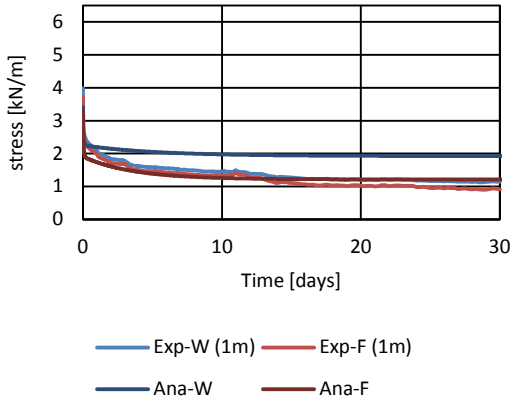


Figure 5.2 Time-Stress relationships; Maximum stress (5:5kN/m)

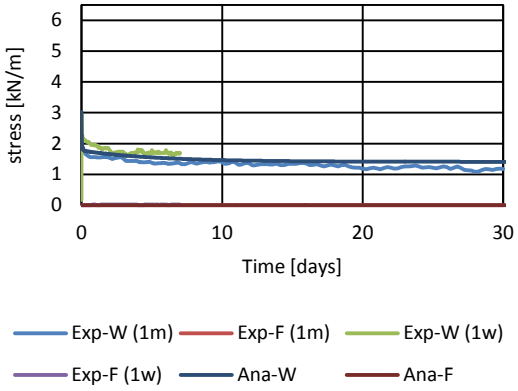


Figure 5.3 Time-Stress relationships; Maximum stress (3:0kN/m)

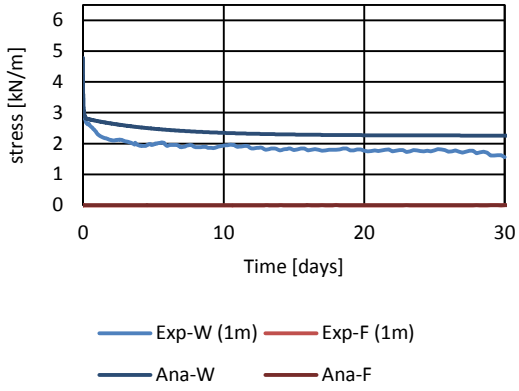


Figure 5.4 Time-Stress relationships; Maximum stress (5:0kN/m)

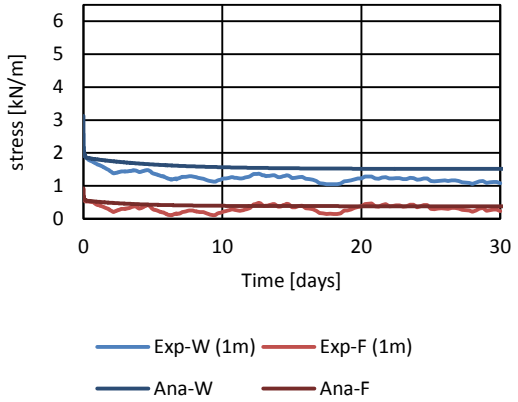


Figure 5.5 Time-Stress relationships; Maximum stress (3:1.5kN/m)

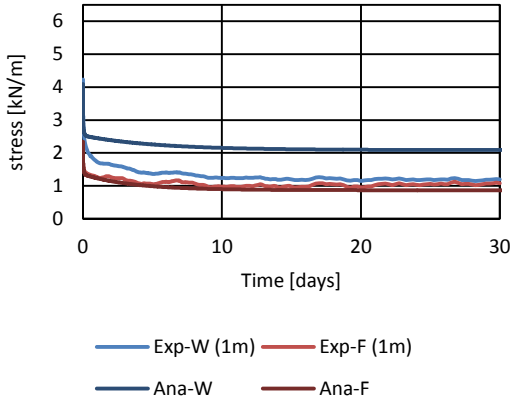


Figure 5.6 Time-Stress relationships; Maximum stress (5:2.5kN/m)]

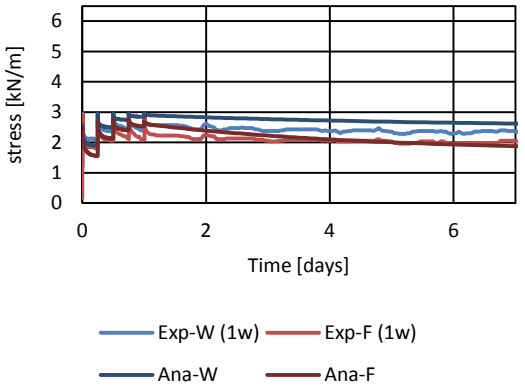


Figure 6.1 Time-Stress relationships
[Repeated Maximum stress (3:3kN/m)]

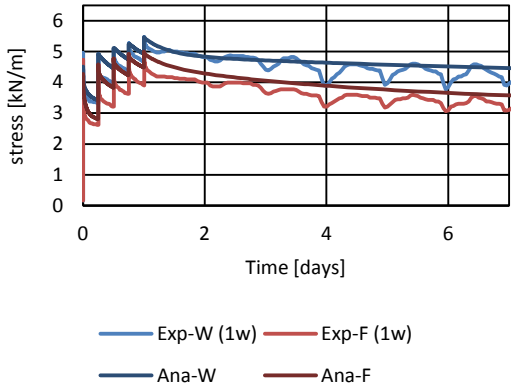


Figure 6.2 Time-Stress relationships
[Repeated Maximum stress (5:5kN/m)]

5. Conclusions

The authors present a set of new experimental results for creep and relaxation as well as experimental data for static but cyclic loading. Based on the new data, re-identification of material constants applied for Fabric Lattice Model. A set of simulations have been conducted in the study to prove the validity and applicability of the re-identified material constants together with the Fabric Lattice Model for membrane structures.

As for creep deformation as well as static strains, it is confirmed that the constitutive equations based on the re-identified material constants predict a fine stress-strain relationship for PTFE materials under various stress strain rates.

Although a relatively fine agreement is confirmed between analysis and experiment, a fact is still found and may suggest that more refinement be required to evaluate stress release due to relaxation after a long duration.

References

[1] H. Minami, T. Taga, H. Toyoda and S. Segawa : Experimental Studies on Stress Relaxation and Creep Properties on Uniaxial and Biaxial Stress Conditions of a PTFE-coated glass fiber fabric, 10 years of progress in shell and spatial structures, *30 anniversary of IASS, Madrid 1989, September 11-15 1989*, Volume 2, 1989

[2] H. Minami, C Yamamoto, S. Segawa and Y. Kono : A Method for Estimation of Relaxed Stress and Creep in Membrane Structure, *Proceedings of the LSA98, Sydney, October 5-9 1998*, pp. 848-855

[3] S. Kato, T. Yoshino, H. Minami, Formulation of constitutive equations for fabric membranes based on the concept of fabric lattice model, *Engineering Structures 21,* 1999, pp. 691-708

[4] S. Kato, H. Minami, S. Segawa, T. Yoshino, Experimental and analytical study on viscoelasto-plastic characteristics of PTFE-coated Glass Fiber Fabric under cyclic loadings, *Proceedings of the Lightweight Structures in Architecture, Engineering and Construction IASS/IEAust/LSAA International Congress, Sydney, Australia, 1998*, pp. 800-806

[5] S Kato, T Yoshino: Simulation for Introducing Tensions into Curved Membranes Considering Both of the Cutting Pattern Method and Visco-Elasto-Plastic Characteristics of the Fabrics, *International Symposium on Theory, Design and Realization of Shell and Spatial Structures, Nagoya, Japan, TP046, October 9-13, 2001*, pp. 178-179

Proceedings of the IASS Annual Symposium 2019 – Structural Membranes 2019
Form and Force
7 – 10 October 2019, Barcelona, Spain
C. Lázaro, K.-U. Bletzinger, E. Oñate (eds.)

Experimental studies on tear failure of PVC coated fabric

Han BAO*, Minger WU, Xubo ZHANG, Fuling GUAN[a]

Department of Structural Engineering, Tongji University
1239 Siping Road, Shanghai 200092, China
Email: 1610215@tongji.edu.cn

[a] College of Civil Engineering, Zhejiang University

Abstract:

The uniaxial central tearing performance of a kind of PVC coated polyester fiber membrane commonly used in membrane structure was experimentally studied in detail. Firstly, the effect of the combination of the crack orientation and the number of yarns cut off on tearing property of this membrane material was investigated, resulting in the conclusion that these two variables can be replaced by initial equivalent crack length and this key parameter has great influence on tearing strength of coated fabrics. Then, the evolution of strain and displacement fields in the whole process of tearing was measured by a non-contact digital speckle measurement method. It can be found that the maximum strain almost always concentrates in the del-zone at the crack tip and the number of cutting-off yarns and whether the specimen is in warp or weft direction affected the strain field distribution greatly. This paper provides a reference for the study of tear resistance of building membrane materials.

Keywords: Membrane structure, the uniaxial central tearing, initial equivalent crack length, the strain field

1. Introduction

Membrane structure is light in weight and rich in morphological changes. With the extensive application of membrane materials in building structures such as stadiums, transportation facilities, shopping and exhibition centers, tear damage as one of the main failure modes occurs from time to time [1].

Membrane materials are easy to cause local damage, including broken wires, cracks, creases, damage caused by external flying objects and so on, in the process of manufacture, transportation, installation and use. The damage on membrane surface may propagate due to strong wind and snow before repair, even directly leading to overall structural collapse. Therefore, the research on tear strength of membrane materials has always been a hot issue in the field of membrane structures.

As a widely used membrane material, PVC coated polyester fiber membrane is a typical composite material which can be regarded as orthotropic in structural mechanics analysis [2]. It is interwoven by warp and weft yarns which provide main tensile strength and the PVC coated on both sides can transmits shear force and provide protection for the yarns. In view of the

Copyright © 2019 by Han BAO, Minger WU, Xubo ZHANG, Fuling GUAN
Published by the International Association for Shell and Spatial Structures (IASS) with permission.

complex structure of this coated fabric, the factors affecting its tearing behavior is more complex than steel, including the tensile strength and breaking elongation of yarns, the friction between yarns, the fabric structure, the role of coatings and other factors.

At present, the commonly used testing methods for measuring tearing strength of coated fabrics are trapezoidal [3] and tongue tearing method [4]. Because the tearing mode of the former is simple and the results are consistent [5], it is adopted by Chinese code [6]. In fact, the tearing damage in the actual membrane structure is closer to the central tearing method [7], but this method is only adopted by few codes around world, such as FAAP-8110-2 [8]. Therefore, it is necessary to further study the central tearing method in order to evaluate the tearing resistance of coated fabric membrane more reasonably.

In this paper, a kind of PVC coated polyester fiber membrane for building is studied in detail by uniaxial central tearing test. The difference of tearing resistance in warp and weft directions and the relation between tearing strength and initial equivalent crack length are investigated. The strain field distribution on the membrane surface especially near the crack tip is measured for the first time by non-contact equipment, and the result for load bearing capacity of each yarn is obtained in the tests.

2. Experimental program

2.1. Specimens and test set-up

In this paper, a domestic and commonly used PVC coated polyester fiber membrane was tested. The thickness is 0.823 mm and the tensile strength was 5440 N/5cm in warp direction and 4911 N/5 cm in weft direction through a uniaxial test. The uniaxial tension stress-strain curves are shown in figure 1. Weft yarns have lower tensile strength and higher strain at break than warp yarns.

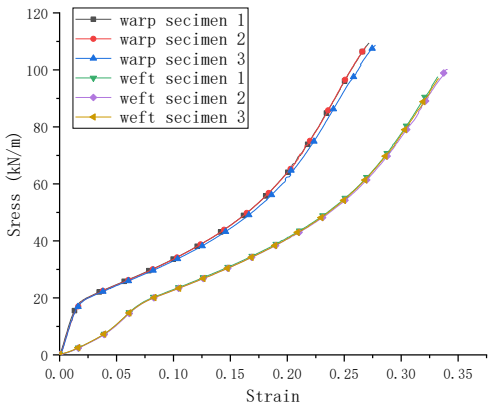


Figure 1: Stress-strain curve of uniaxial tension

The fabrication of uniaxial center tear specimens refers to FAA-8110-2 [8]. The measuring length of the specimen is set to 76.2 mm. In view of the limitation of the fixture of uniaxial stretching machine (figure 2(b)), the width of the specimen is set to 70 mm. The total length of the specimen is set to 700 mm. The clamping length of the two ends is 40 mm. All specimens are cut along the warp and weft yarn direction, and the cutting should be carried out carefully as far as possible along the middle of two adjacent groups of yarns. In this way, there should

be no loss of fiber yarns on both sides of the specimen, see figure 2(a). The test equipment is universal testing machine CMT4204, and the tension speed is 2 mm/min, so as to ensure static loading. The displacement data are obtained by clamping the extensometer at both ends of the measuring length of the specimen (figure 2(b)).



(a) tear specimen (mm) (b) testing machine (c) DIC equipment

Figure 2: Test set-up

In order to obtain the displacement and strain field distribution of specimens during tests, a three-dimensional digital speckle dynamic strain measurement and analysis system was used. The system uses digital image correlation method DIC (Digital Image Association), see Figure 2 (c), combined with binocular stereo vision technology. Two high-speed cameras are used to acquire speckle images at each deformation stage of the object in real time, and image correlation algorithm is used to stereo match the deformed points on the surface of the object, and the three-dimensional coordinates of the matched points are reconstructed. By smoothing the displacement field data and visualizing the deformation information, the full-field strain measurement can be carried out quickly, accurately, real-time and non-contact.

2.2. Test procedure

In the process of test, the number of yarns is used, instead of the usual international unit length, because this can avoid the single yarn being partially cut off to the greatest extent, so as to ensure the stability of the test results. The test layout is shown in table 1. The research parameters include the initial number of cutting-off yarns n_c and the initial crack orientation θ, which represents the angle between the crack section and the width direction. And $2a$ indicates the macro crack length on the membrane surface when there are n_c yarns are cut off. Therefore, warp specimens can be represented by warp-θ-n_c and weft specimens are weft-θ-n_c. The total yarns count in width range are 44 in warp specimens and 45 in weft specimens, therefore warp-0-4 and weft-0-5 have the same number of intact yarns and this correspondence is also valid for other specimens.

3. Results and discussions

3.1 Tearing process

Taking specimens warp-0-6 and warp-60-6 as examples, the tearing process can be roughly divided into three stages:

Table 1: Layout of the uniaxial central tearing tests

	Initial Crack Length $2a$ (mm)	Initial Crack Orientation θ (degree)	Number of Cutting-off Yarns n_c	Total Yarns Count in Width Range	Width of Specimen (mm)
warp-60-2	6.36	60	2	44	69.96
warp-60-6	19.08	60	6	44	69.96
warp-0-4	6.36	0	4	44	69.96
warp-0-6	9.54	0	6	44	69.96
warp-0-12	19.08	0	12	44	69.96
weft-60-3	9.36	60	3	45	70.2
weft-60-7	21.84	60	7	45	70.2
weft-0-5	7.80	0	5	45	70.2
weft-0-7	10.92	0	7	45	70.2
weft-0-13	20.28	0	13	45	70.2

1) Initial loading stage: when specimens begin to bear external load, the yarns in the drawing direction begins to be stretched gradually from crimp to straight, and the crack changes from initial closed state to ellipse, see figure 3(a) and 3(b).

2) Del-zone formation stage: with the increase of load, the warp yarns near the crack tip is greatly deformed, stripped from the coating, and then stretched to form an approximate triangle area, which can be called the del-zone, see figure 3(c).

3) The crack propagation and failure stage: due to the further increase of load, the first yarn in the del-zone breaks suddenly when it reaches the elongation at break. After that, the specimens show two main failure modes:

- Brutal failure: after the first yarn breaks, the crack expands rapidly, the whole specimen is destroyed instantaneously, and the falling section of stress-displacement can be hardly recorded by the universal testing machine.
- Progressive failure: the tear propagation occurs alternately at both ends of the crack, the yarns are unloaded instantaneously after breaking. At the same time, the stress redistribution is completed rapidly, and new del-zones are formed continuously, so that the specimen can continue to bear the load, and the stress-displacement curve has a long descending section, with a zigzag fluctuation.

From the tearing failure of warp-60-6 (figure 3(e) and 3(f)), we can see that no matter what the initial crack orientation is, the direction of del-zone evolution and tear propagation are always perpendicular to the direction of external load. This phenomenon caused by the plain weaving structure of membrane material is quite different from the fracture of steel.

From figure 4, it can be found that the external load at the moment of the crack propagation is also the peak load the specimen can bear, therefore, we take this threshold force when crack start to propagate as the tear strength σ_c of the uniaxial central tearing.

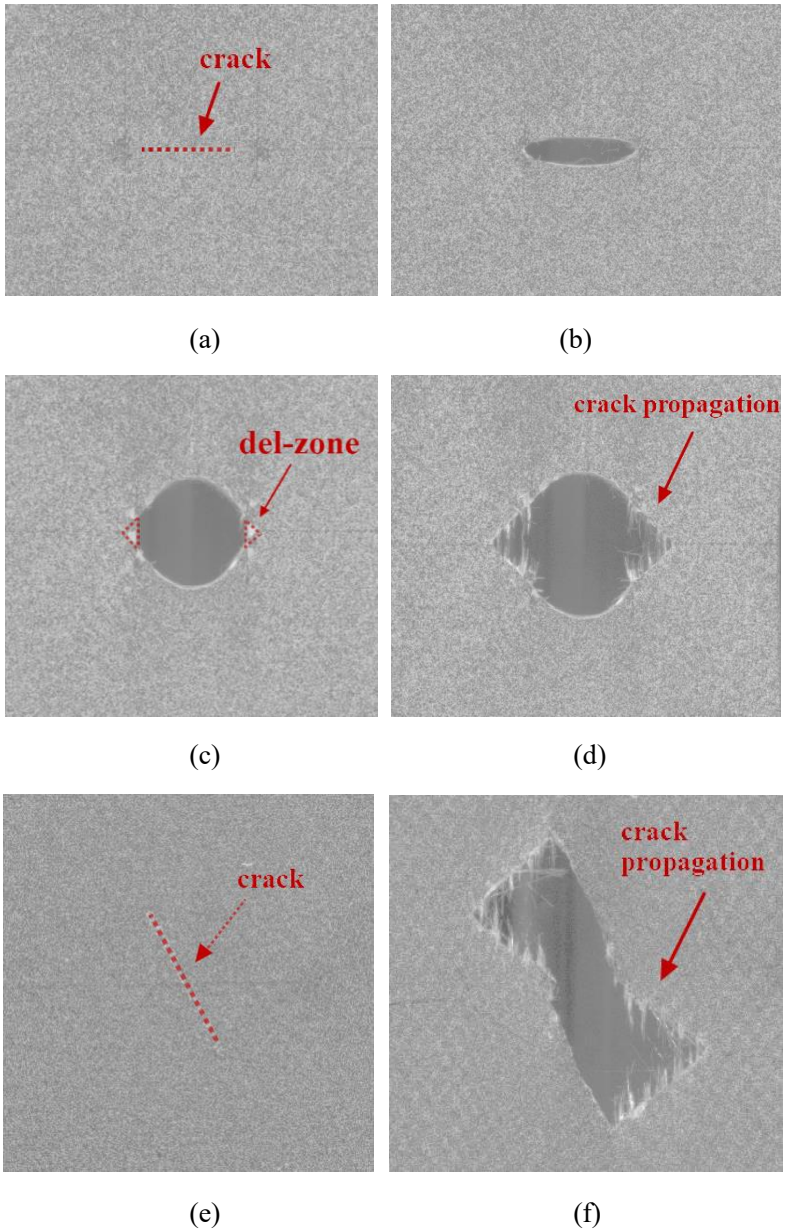


Figure 3: Tearing process of the uniaxial central tear specimen

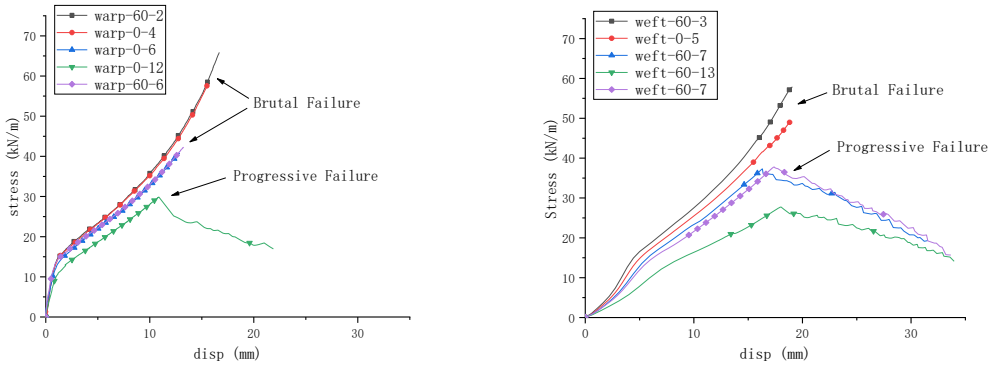
3.2 Verification of initial equivalent crack length

Many studies [7] have shown that oblique and horizontal cracks can be equivalent to each other when the number of cutting-off yarns is the same regardless of the orientation of the initial crack. In order to verify the applicability of this conclusion to the PVC fabrics in this paper, specimens warp-60-6 and warp-0-6, weft-60-7 and weft-0-7 were compared. Obviously, they have the same number of cutting-off yarns respectively. From figure 4 and table 3, we can see that their stress-displacement curves are very close, and the differences of their tear strength are 1.4% in warp specimens and 1.6% in weft specimens. This good coincidence implies that we can replace the two variables of initial crack length $2a$ and initial crack orientation θ with only one variable, which is initial equivalent crack length, in following researches.

3.3 Initial equivalent crack length influence

The test results of uniaxial central tear specimens in warp and weft directions are summarized in figure 4, in which the stress is defined as the external load divided by the width of the specimen. The tension curves of uniaxial central tearing specimens in figure 4 and of the specimens without crack in figure 1 have similar non-linear characteristics, including yield section in warp specimens and upper concave segments in weft ones. Obviously, the tensile strength of fabrics decreased significantly after yarns cutting. Specifically, When 2, 4, 6 and 12 yarns were cut off in warp specimens, the strength of the material decreased by 39.8%, 48%, 62.2% and 72.6% respectively, while when 3, 5, 7 and 13 yarns were cut off in weft specimens, the strength decrement are 41.9%, 49.2%, 61.6% and 71.7% respectively. Since the sharp decrease due to cracks as we can see may lead to irreparable damage for structures, we should pay enough attention to the capacity of fabrics to resist tearing.

Figure 4 also implies that, on the whole, as more and more yarns are cut off, the tensile stiffness of the fabrics decreases gradually, and this decrement is more obvious in weft specimens. To be specific, the stress-displacement curves of warp-60-2, warp-0-4 and warp-0-6 almost coincide and show typical features of brutal failure, while the curve of warp-0-12 is obviously different with lower stiffness and has a long descending section which represents progressive failure. While in weft specimens, the stiffness decreases continuously with the increase of the number of cutting-off yarns, and when this number ranges from 5 to 7, the failure mode changes form brutal to progressive.



(a) warp specimens (b) weft specimes

Figure 4: Stress-displacement curves of uniaxial central tearing tests

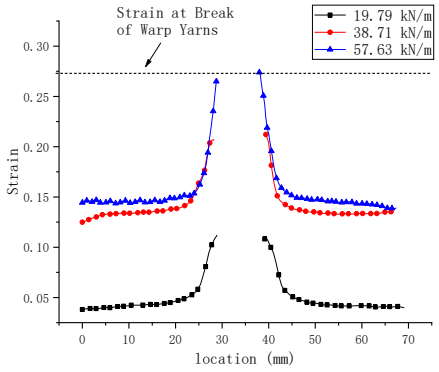
3.4 Strain field distribution

Distribution of strain and displacement during the whole tearing process of this coated fabrics was measured by DIC equipment. Figure 5(a) shows the strain field of specimen warp-0-6 across the section of the crack when the external load are 19.79 kN/m, 38.71kN/m and 57.63kN/m. We can see that the strain begins to concentrate in the del-zone at the beginning of tension, however, when away from the crack tip, strain drops rapidly. With the increase of load, the difference between the strain near the tip and in distant location becomes larger and larger.

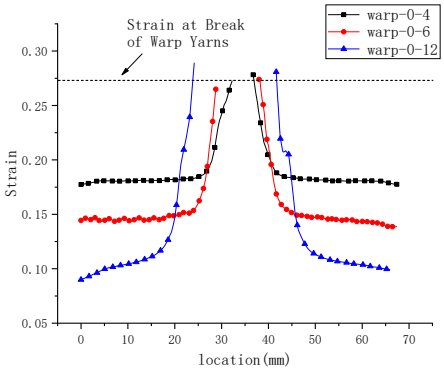
Figure 5(b)(c) display the strain distribution with the change of cutting-off yarns number at the moment of propagation. As we can see, no matter how many yarns are cut off, the warp

specimens begin to tear when the strain of the tip yarn reaches its breaking strain (0.273). However, the weft specimens begin to tear when the tip yarn strain is slightly lower than its breaking strain (0.336) since this ultimate strain of weft yarns achieved from uniaxial tensile test include the fake part caused by initial crimps. As when we cut off more yarns, we can find the difference of strain between the yarns near and far from the crack tip will increase significantly which, in other words, means the number of cutting-off yarns influence greatly on the strain distribution. Few yarns we cut off, more uniform the strain field will be, and more load-carrying capacity of specimens can be achieved.

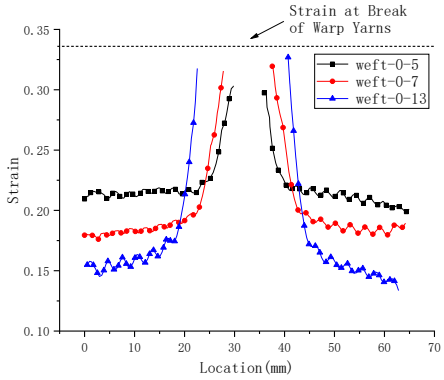
Figure 5(d) shows the difference of strain field between warp and weft specimens which have the same number of intact yarns at the moment of crack propagation. The strain of weft specimens is obviously larger than that of warp specimens, while the shapes of their strain fields are very similar.



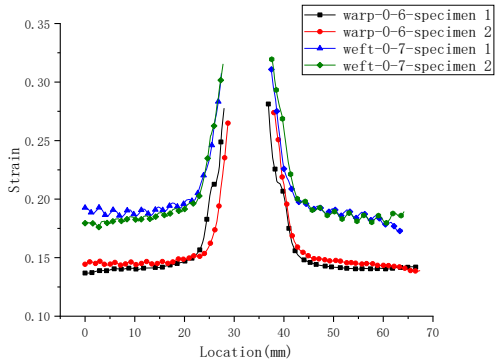
(a) warp-0-6



(b) warp specimens



(c) weft specimens



(d) warp & weft specimens

Figure 5: Strain distribution of specimens in tearing test

4. Conclusions

In this paper, the tearing property of a kind of PVC coated polyester fiber membrane was studied in detail by uniaxial central tearing test and the strain distribution in the whole process of tearing was measured by non-contact digital speckle measurement method, resulting in the following conclusions:

1) The direction of del-zone evolution and tear propagation are always perpendicular to the direction of external load regardless of the change of initial crack orientations.

2) Initial crack length and initial crack orientation can be combined with one variable of initial equivalent crack length.

3) During the whole tearing process, strains almost always concentrate in the del-zone, and when the first intact yarn in this zone reaches the strain at break in warp specimens or slightly less than the break strain in weft specimens, the crack starts to propagate.

4) As the number of cutting-off yarns increase, the strain distribution changes greatly and the failure modes will transform between progressive failure and brutal failure, and it is more and more difficult for yarns far from crack to exert their load-bearing capacity.

Acknowledgements

This work was funded by the National Science Foundation of China through the research project No. 51778458.

References

[1] Umezawa, Ryozo, and Takuya Agari. "Report of snow damage of Kumagaya Dome." *Proceedings of IASS Annual Symposia*. Vol. 2016. No. 5. International Association for Shell and Spatial Structures (IASS), 2016.

[2] Li, Yang. "Study and applications on mechanical properties of membrane materials and structures." *Shanghai, Tongji University* (2007).

[3] Chu, Cai-yuan. "A study of tearing properties of membrane coated fabrics." *Journal of China Textile University (English Edition)* 4 (1991).

[4] Scelzo, W. A., S. Backer, and M. C. Boyce. "Mechanistic role of yarn and fabric structure in determining tear resistance of woven cloth: part I: understanding tongue tear." *Textile research journal* 64.5 (1994): 291-304.

[5] YI, Hong-lei, Xin Ding, and Shou-hui CHEN. "Study on Tear Testing Method and Rupture Mechanism of Architectural Membrane Materials [J]." *Journal of Donghua University (Natural Science)* 4 (2006).

[6] DG/TJ08-2019-2007. Technical specification for inspection of membrane structures.

[7] Bigaud, D., C. Szostkiewicz, and P. Hamelin. "Tearing analysis for textile reinforced soft composites under mono-axial and bi-axial tensile stresses." *Composite Structures* 62.2 (2003): 129-137.

[8] FAA-P-8110-2-1995 Airship Design Criteria (USA Department of Transportation)

Proceedings of the IASS Annual Symposium 2019 – Structural Membranes 2019
Form and Force
7 – 10 October 2019, Barcelona, Spain
C. Lázaro, K.-U. Bletzinger, E. Oñate (eds.)

Study on mechanical properties of coated biaxial warp knitted fabrics

Bin YANG, Zeliang YU*

* Tongji University
No.1239, Siping Road, Shanghai, China.
1732529@tongji.edu.cn

Abstract

In recent years, coated fabrics have become the major material used in membrane structures. Scholars have conducted a series of researches on mechanical properties of coated woven fabrics, however, there are few studies focusing on coated knitted fabrics which are generally used in pneumatic structures. In this paper, the mechanical properties of coated biaxial warp knitted fabrics (CBWKF) are investigated. First, the CBWKF's base layer is observed and the unique design of warp knitted polyester and stitch structure is described. Then the uniaxial tensile and tearing strength of warp and weft CBWKF samples are tested, since there is no crimp interchange between yarns, the initial stress-strain curve is linear which is different from coated woven fabrics. The creep elongation is also tested under 24 hour's sustained uniaxial load. To further investigate the mechanical properties of CBWKF, the Membrane Structures Association of Japan (MSAJ) standard testing method for elastic constants of membrane materials is adopted, and the stress-strain curves under five different biaxial load ratios are analyzed. Finally the elastic constants and Poisson's ratio are calculated using least square method based on linear orthotropic assumption, and three-dimensional strain surfaces are plotted. Results show that the strain surfaces fit well with test data, which means the linear orthotropic constitutive equation can make a good representation of CBWKF's biaxial tensile stress-strain relationship.

Keywords: mechanical property, coated biaxial warp knitted fabrics, orthotropic assumption

1. Introduction

With the wide application of membrane structures, the type and performance of membrane materials have also been further developed, and coated woven fabrics account for the majority of membrane materials. In recent years, coated knitted fabrics are also used in pneumatic structures and researches have been made to investigate its mechanical properties.

Yixi Luo *et al.* [1][2] have conducted a series of research on biaxial knitted coated fabrics, they present the tensile and tearing strength under uniaxial load in seven in-plane directions and give the conclusion that the biaxial knitted coated fabrics show strong orthotropic behavior, but the mechanical properties under multi-axial show isotropic behavior. Jianwen Chen *et al*. [3][4] present a new equation to estimate Poisson's ratio for coated biaxial warp knitted fabrics under bias tensile loading by testing the uniaxial behavior in seven directions of 0º, 15º, 30º, 45º, 60º, 75º, and 90º. T.D. Dinh *et al.* [5] investigate the mechanical behavior of knitted fabrics by numerical method and using representative unit cells analyze the tensile and tearing strength. Results show that the predicted mechanical behavior of knitted fabrics are in good agreement with the corresponding experimental data. In addition, some scholars [6]-[8] also investigate the mechanical properties of coated multi-axial warp knitted fabrics under uniaxial or multi-axial tensile test.

Copyright © 2019 by Bin Yang and Zeliang Yu
Published by the International Association for Shell and Spatial Structures (IASS) with permission.

In this paper, the comprehensive and detailed study on coated biaxial warp knitted fabrics are presented. Tensile strength and elongation, trapezoid-shaped tearing strength and creep elongation are tested under uniaxial load, and the stress-strain curves are analyzed and compared to coated woven fabrics. Then the Membrane Structures Association of Japan (MSAJ) standard testing method [9] for elastic constants of membrane materials is adopted for biaxial test. Three-dimensional strain surfaces are plotted by linear orthotropic constitutive model and fit well with tested biaxial stress-strain data.

2. Experiment and analysis

2.1 Materials

In this paper, the mechanical properties of coated biaxial warp knitted fabrics (CBWKF) produced by Seaman Corporation are investigated, and the coated fabric consists of architectural colored exterior PVDF layer and the white interior PVC layer as is shown in Figure 1. Figure 2 shows the base layer of warp knitted fabrics, compared to ordinary plain woven fabrics, the warp and weft yarns of knitted fabric are connected by the loop stitches, thus the yarns are parallel to each other and no crimp exists in yarns. Some of the specifications are listed in Table 1.

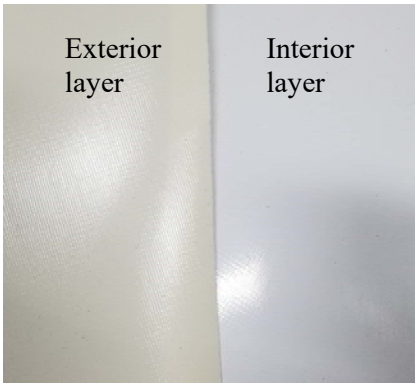


Figure 1: Appearance of CBWKF material

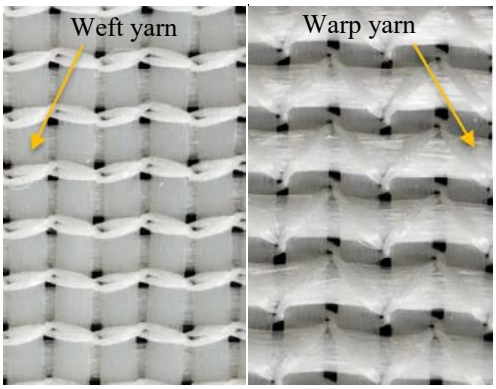


Figure 2: Base fabric layer

Table 1: Specifications of the CBWKF material

Base fabric type	Base fabric weight	Finished coated weight	Weave density (ends/inch)	Thickness
Polyester	254 g/m^2	949 g/m^2	19×21	0.88mm

2.2 Uniaxial tensile and tearing test

The uniaxial tensile and tearing tests were carried out on the base of Chinese Technical specification for inspection of membrane structures [10], and the standard strip size of tensile and tearing specimen are shown in Figure 3 and Figure 4 respectively. The universal testing machine was adopted for the test shown in Figure 5 and Figure 6, and the constant loading speed was 100mm/min. Five specimens were tested for warp and weft directions to obtain the average tensile and tearing strength, and test results are listed in Table 2.

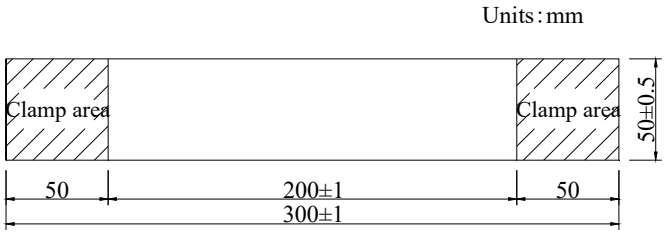


Figure 3: Tensile test specimen size

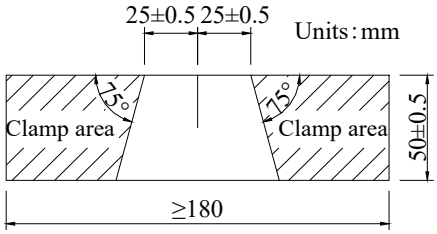


Figure 4: Trapezoid-shaped specimen



Figure 5: Tensile test

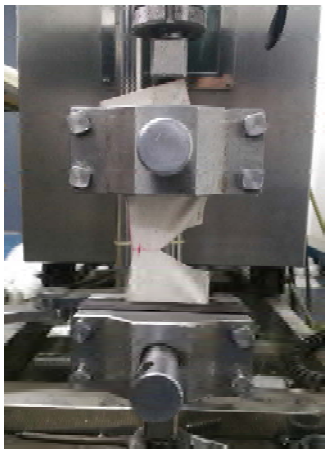


Figure 6: Tearing test

Table 2: Results of tensile and tearing strength

Direction	Tensile strength	Elongation	Tearing strength
Warp	4236 N/50mm	22.3%	593 N
Weft	4073 N/50mm	31.0%	823 N

The stress-strain curve of CBWKF material of uniaxial tensile test is shown in Figure 7. As can be seen, the stress-strain relation is different from typical coated woven fabrics. For coated woven fabric material, due to the warp and weft yarns are cross-woven, there is crimp interchange during the initial stretching, resulting in a non-linear stress-strain relationship with small rigidity. However, for the CBWKF material, it can be seen from chapter 2.1 that the warp and weft yarns are arranged in parallel and no crimp exists, so that the warp and weft yarns can directly bear the external load during the initial stretching. Therefore, the initial tensile modulus is only related to the yarn itself and coating material and exhibits linear features.

The load-displacement curve of tearing test is shown in Figure 8. For the trapezoid-shaped tearing test, the longitudinal yarn around the crack part of the specimen will stretch and form a tear triangle region under external tensile loading. With load increase, the yarn in tear triangle region which exceeds the elongation at break will first crack and the load-displacement curve will reach the first peak point, and finally the tearing strength is determined by averaging five peak load. As can be seen from Figure 8, the tearing strength in weft direction is more than warp direction. Due to the weft yarns have a larger stretching ratio than warp yarns, and thus more yarns are involved in the load bearing process which will lead to higher tearing strength.

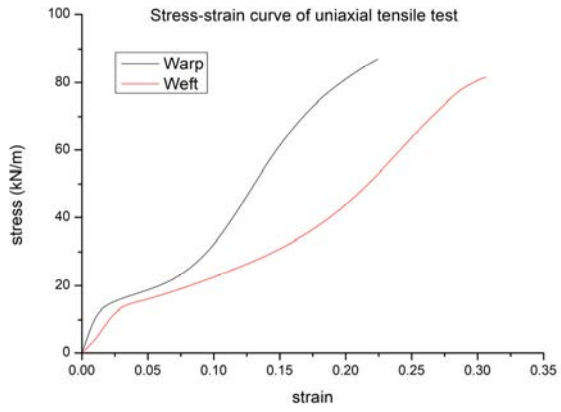


Figure 7: Stress-strain curve of uniaxial tensile test

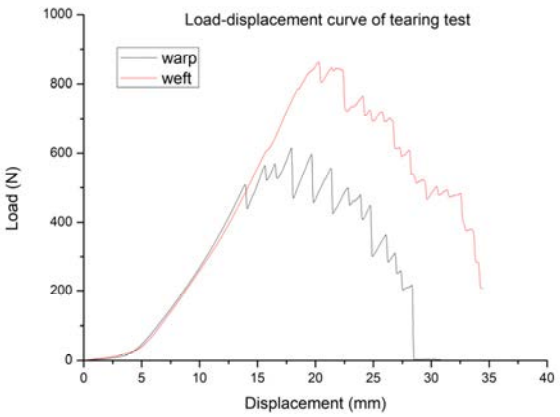


Figure 8: Load-displacement curve of tearing test

2.3 creep test

The creep test specimen size is the same as uniaxial tensile test as shown in Figure 3 and five specimens are tested in both warp and weft directions. First, the specimen was loaded to 1/4 tensile strength, then maintain the constant tension level for 24 hours. During this process, the displacement between two clamping ends will slowly increase and creep elongation can be calculated by equation (1).

$$\varepsilon_c = \frac{L_2 - L_1}{200} \times 100\% \tag{1}$$

Where L_1 represents the length between two clamping ends when the 1/4 tensile strength was first applied, L_2 represents the length between two clamping ends after sustained load for 24 hours. The creep history is shown in Figure 9 and Figure 10 and results show the creep elongations are 1.9% and 3.8% in warp and weft directions respectively. From the perspective of the entire creep loading process, the rapid change in displacement is in the first 100 minutes, after that the creep is slow down and almost remains constant. The ratio of creep elongation to elastic elongation is also calculated by equation (2), and the ratio is 23% in warp direction and 31% in weft direction which means the impact of creep must be considered in structural design, especially the cutting pattern analysis.

$$\rho_c = \frac{L_2 - L_1}{L_1} \times 100\% \tag{2}$$

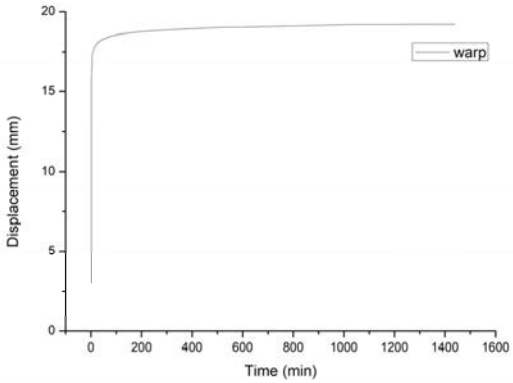


Figure 9: Creep history in warp direction

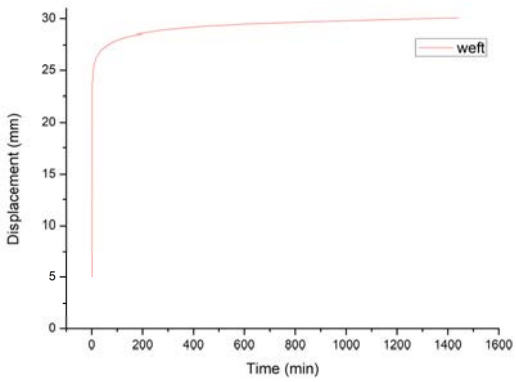


Figure 10: Creep history in weft direction

2.4 biaxial test

Membrane Structures Association of Japan (MSAJ) proposed a detailed test procedure in evaluating the elastic constant under biaxial loading. Standard biaxial test procedure is described in Figure 11, and the stress-strain data of five specified load ratios (warp: weft) including 1:1, 2:1, 1:2, 1:0 and 0:1 are recorded. As can be seen, three times 1:1 biaxial loading procedure should be completed in order to remove the residual strains before each specified load ratio is performed. The maximum load range is up to 1/4 tensile strength (minimum tensile strength in warp and weft direction) with a standard tensile rate of 2-4mm/min.

Three CBWKF material specimens were tested under MSAJ biaxial test procedure. The test machine and specimen size are shown in Figure 12 and Figure 13, as is shown, the self-developed biaxial tensile testing machine is adopted and the strain are measured by Digital Image Correlation instrument. Stress-strain data are selected per 1kN/m under five load ratios for calculation.

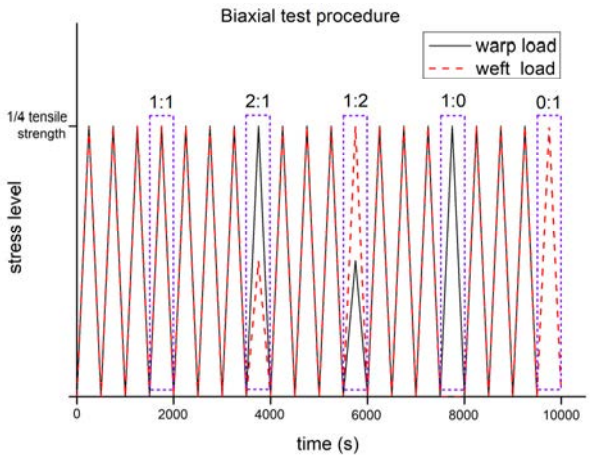


Figure 11: Biaxial test procedure

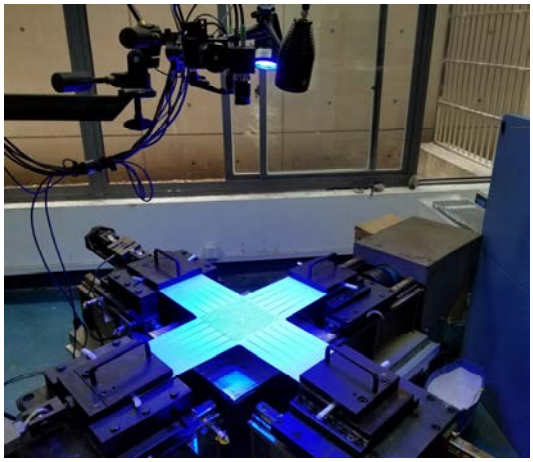


Figure 12: Test instruments

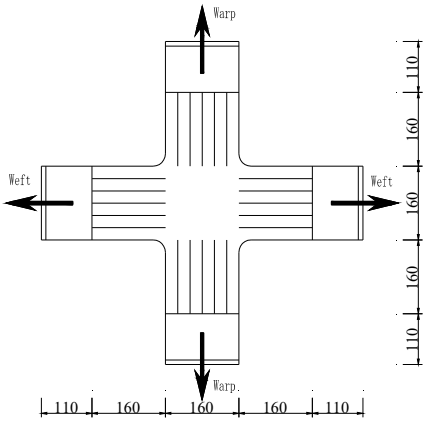


Figure 13: Biaxial test specimen

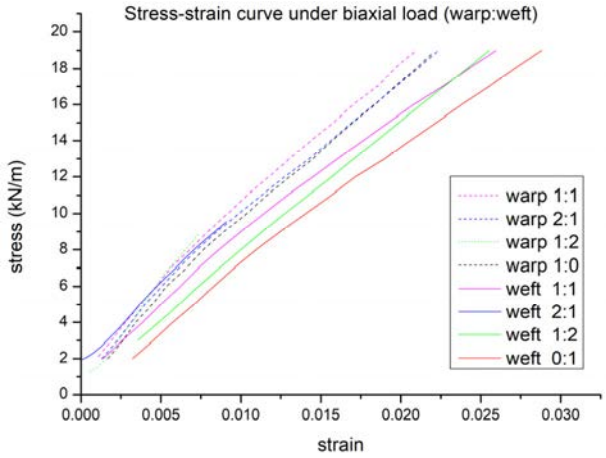


Figure 14: Stress-strain curve under biaxial load

For coated woven fabrics, crimp interchange is the interaction between orthogonal warp and weft yarns which leads to fundamentally non-linear stress–strain behavior [11]. Under biaxial load, the ratio of the applied loads will determine the equilibrium configuration of the crimp, and this balancing of the crimp results in a highly variable Poisson's ratio. However, the stress-strain curves of CBWKF are basically linear under five different biaxial load ratios shown in Figure 14, and even in the less loaded direction of 1:2 and 2:1 load ratios, the curve has no negative strain or nonlinear part which is different from the biaxial test results of coated woven fabrics.

Researchers usually assume the coated fabrics as linear orthotropic materials and the stress-strain relationship can be expressed as equation (3) and (4). In the equation, x represents warp direction, y represents weft direction. With the stress-strain data of five specified load ratio (weft data for the 1:0 load ratio and warp data for the 0:1 load ratio are disregard) measured by biaxial test, MSAJ suggests that elastic constants and Poisson's ratio can be determined by Least-squares method of minimizing strain. The calculated elastic modulus and Poisson's ratio are listed in Table 3, and the average Poisson's ratios are only 0.10 in warp direction and 0.09 in weft direction which are smaller than coated woven fabrics.

To further investigate the suitability of orthotropic assumption in the CBWKF material, warp and weft strain surface are plotted and shown in Figure 15. As can be seen, both strain surfaces fit well with test data and the total squared strain error is 0.012. Results show the CBWKF material conform to the linear orthotropic assumption, and the constitutive equation can well describe its biaxial mechanical behavior.

$$\begin{bmatrix}\varepsilon_x\\ \varepsilon_y\end{bmatrix} = \begin{bmatrix}\frac{1}{E_x} & -\frac{v_{yx}}{E_y}\\ -\frac{v_{xy}}{E_x} & \frac{1}{E_y}\end{bmatrix} \cdot \begin{bmatrix}\sigma_x\\ \sigma_y\end{bmatrix} \tag{3}$$

$$\frac{v_{yx}}{E_y} = \frac{v_{xy}}{E_x} \tag{4}$$

Table 3: Elastic modulus and Poisson's ratio of CBWKF material

Specimen	E_x	E_x	v_{xy}	v_{yx}
1	848	692	0.15	0.12
2	825	736	0.07	0.07
3	898	735	0.08	0.07
Average value	857	721	0.10	0.09

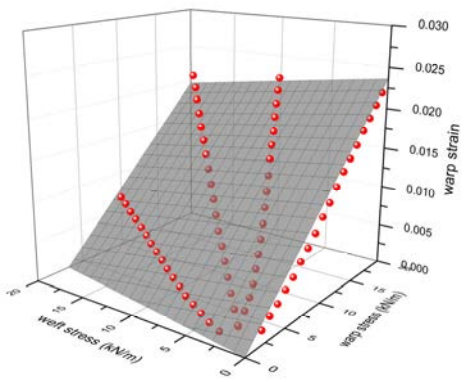
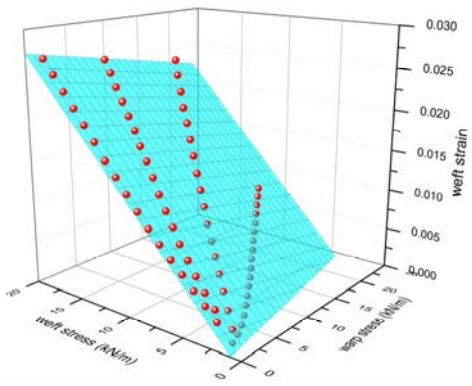


Figure 15: (a) Warp strain surface



(b) Weft strain surface

3. Conclusion

In this paper, the mechanical properties of coated biaxial warp knitted fabrics are investigated and the following conclusions can be drawn:

(1) Under uniaxial tensile test, the initial stress-strain curves of coated woven fabrics are nonlinear due to the crimp interchange between warp and weft yarns. However, the initial stress-strain curves of CBWKF materials are both linear in two directions due to its special base layer structure.

(2)The ratio of creep elongation to elastic elongation is 23% in warp direction and 31% in weft direction, which means the impact of creep must be considered in structural design, especially the cutting pattern analysis.

(3) Under biaxial tensile test, the stress-strain curves of five different load ratios are analyzed and elastic modulus and Poisson's ratio are calculated. The conformity of the 3D strain surfaces with experimental stress-strain data proves the applicability of the linear orthotropic assumption and provides good guidance for engineering design.

References

[1] Yixi Luo, Hu Hong and Raul Fangueiro, "Tensile and tearing properties of bi-axial warp knitted coated fabrics," *AUTEX Research Journal*, Vol. 8, pp. 17-20, 2008.

[2] Yixi Luo and Hu Hong, "Mechanical Properties of PVC Coated Bi-Axial Warp Knitted Fabric with and without Initial Cracks under Multi-Axial Tensile Loads." *Composite Structures*, no. 4, pp. 536-542, 2009.

[3] Jianwen Chen, Han Zhou, Bing Zhao, Wujun Chen, Mingyang Wang and Zhihong Xu, "A New Theoretical Equation to Estimate Poisson's Ratio for Coated Bi-axial Warp Knitted Fabrics under Bias Tensile Loading," *Fibers and Polymers*, vol. 19, no. 12, pp. 2631-2641, 2018.

[4] Jianwen Chen, Han Zhou, Wujun Chen, MingyangWang, Bing Zhao and Weiwei Sun, "Full-strain range characteristics of the Poisson's ratio for coated biaxial warp-knitted fabrics under bias tensile loading," *Textile Research Journal*, vol. 89, no. 10, pp. 1997-2009, 2018.

[5] T.D. Dinh, O. Weeger, S. Kaijima and S.-K. Yeung, "Prediction of mechanical properties of knitted fabrics under tensile and shear loading: Mesoscale analysis using representative unit cells and its validation," *Composites Part B: Engineering*, vol. 148, pp. 81-92, 2018.

[6] Zhe Gao, Gaoming Jiang, Pibo Ma, Qi Zhang and Ailan Wan, "Tear properties and meso-scale mechanism of multi-axial warp-knitted fabric from various architectures: Studied by photography," *Fibers and Polymers*, vol. 14, no. 11, pp. 1953-1963, 2013.

[7] Lingxiao Jing, Nangkuo Guo, Haiyan Xu, Jinhua Jiang, Tonghua Zhang and Nanliang Chen, "Tensile characteristics of flexible PU-coated multi-axial warp-knitted fabrics," *Journal of Industrial Textiles*, vol. 47, no. 1, pp. 38-56, 2016.

[8] H. Kong, A.P. Mouritz and R. Paton, "Tensile extension properties and deformation mechanisms of multiaxial non-crimp fabrics," *Composite Structures*, vol. 66, no. 1-4, pp. 249-259, 2004.

[9] B.N. Bridgens and P.D. Gosling, "Interpretation of results from the MSAJ 'Testing Method for Elastic Constants of Membrane Materials'." In *Tensinet Symposium 2010, Sofia, Bulgaria,* September 49-57.

[10] *Technical specification for inspection of membrane structures (DG/TJ08-2019-2007)*, Shanghai China, 2007. (In Chinese)

[11] B.N. Bridgens, P.D. Gosling and M.J.S. Birchall, "Membrane material behaviour: Concepts, practice & developments," *The Structural Engineer*, Vol. 82, pp. 28–33, 2004.

Proceedings of the IASS Annual Symposium 2019 – Structural Membranes 2019
Form and Force
7 – 10 October 2019, Barcelona, Spain
C. Lázaro, K.-U. Bletzinger, E. Oñate (eds.)

Using a nonlinear thermo-viscoelastic constitutive model for the design and analysis of ETFE structures

Adrian CABELLO*, Adam C. BOWN

Tensys Ltd
1 St Swithins Yard, Walcot Street, Bath, BA1 5BG, UK
adrian.cabello@tensys.com
adam.bown@tensys.com

Abstract

A nonlinear, time dependent thermo-viscoelastic material model has been developed at Caltech [1] to represent thin polyethylene based films, typically used as the shell for high altitude balloons. This material model has been implemented in the aerospace industry for several years in support of the design and analysis of stratospheric balloons. Viscoelastic material models have already been successfully applied in a finite element (FE) environment [2] for modelling of such balloons. Ethylene tetrafluoroethylene (ETFE) is fluorine-based plastic which also shows a significant time-dependent and temperature-dependent response under load. The Caltech material model can therefore be factored and calibrated in order to be used for the design and analysis of ETFE films. In doing this a more precise and controlled analysis of this type of structures can be achieved. The most remarkable advantage of having such a complete tool is how the design process gets simplified on one hand but at the same time better understood and more accurate. This gained precision may be critical for some extreme cases, as will be exemplified in this paper. This comprehensive approach can also dispense the designer with some of the factors currently required to account for biaxial stress, temperature variation and long-term effects. A yield locus can be also defined [3] to aid in the design and analysis tasks.

Keywords: ETFE, polyethylene film, LLDPE, tensile structures, non-linear material, thermo-viscoelastic model

1. Introduction

ETFE (ethylene-tetrafluoroethylene) has excellent chemical, thermal and electrical properties yet it is mainly because of its lightness, transparency, low flammability and its mechanical properties that is has become a major player in the construction industry. Among the mechanical properties that should be mentioned are strength and toughness, leading this last one to a great tear resistance, which is always welcome on tensile structures. Other features, derived from the chemical stability, are its anti-adhesive property that makes it a self-cleaning product and the fact that it doesn't become brittle when aging [4]. Since it is a copolymer synthesised with ethylene (C_2H_4) and tetrafluoroethylene (C_2F_4), it has advantageous properties that can be found on both, also well-known materials, polytetrafluoroethylene (PTFE) and polyethylene (PE) [5, 6]

The first work where ETFE was used as part of a permanent structure was in 1982 on Arnhem Burger Botanical Garden in the Netherlands. Since then it has been successfully used in many other occasions, in some cases as part of renown landmarks such as the Eden Project and National Space Centre in England, the Water Cube in China, the Allianz Arena in Germany, etc. Since its use is not declining but rising and becoming highly competitive against other translucent materials such as glass,

Copyright © 2019 by Adrian CABELLO, Adam C. BOWN
Published by the International Association for Shell and Spatial Structures (IASS) with permission.

it would be beneficial to have a complete understanding, characterisation and normalisation of the material and how to design with it. The benefits of doing that will be further explained under title 1.2

1.1. Estate of the art

The work of engineers like Moritz [7], Schiemann [8] and Galliot [6] is always considered a solid reference when dealing with the current characterisation of ETFE. They already underlined the strong time, temperature and stress rate-dependence of the material.

More recent studies have focused on specific aspects like creep [9], behavior at low temperatures [10], viscous properties [11], uniaxial deformation [5], cyclic mechanical properties [12] or burst [13], among others.

In terms of design approaches, the most agreed method recommends to remain in the elastic regime. This is what the Tensinet guideline [4] and the Prospect for European Guidance [14] advise. An example of this approach can be found in the work of Ströbel [15]. Conversely, some authors encourage designers to exceed the yield point in a controlled manner [16, 17] but this is of course a sensitive approach not suitable for some structures, for example single skin flat ETFE structures.

It can be shown below [fig. 1] two examples of simplified stress-strain curves at different temperatures, from the Tensinet guideline, where the first yield point can be identified at ε = 1.7%.

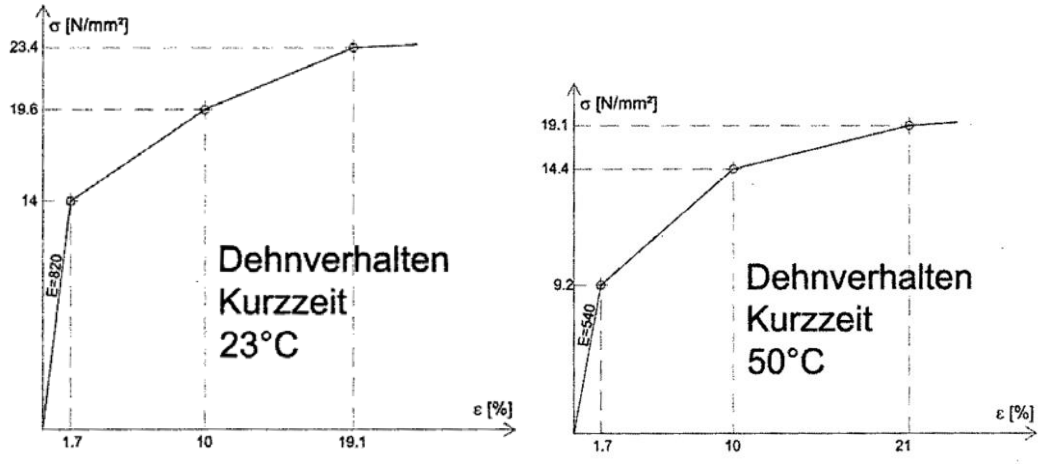


Figure 1: Stress-strain curves of ETFE at 23°C and 50°C, unknown load rate [4]

Different attempts have been made to capture the non-linearity of the material. For example, the work of Jeong [18] expounds a visco-plastic constitutive equation that accounts for variations in strain rate but not dependent on the temperature. Authors like Coelho [19] have worked on an elasto-viscoplastic material model accounting for variations in viscosity at different temperatures, although this study shows limitations in the applicability of the model beyond yielding onset for a broad range of temperatures.

1.2. Need of a comprehensive characterisation

The previous paragraph gives just a glance on the number of individual efforts undertaken to understand, define and predict the structural performance of ETFE.

Nonetheless, available information is very scattered and there is a significant variability in the results [5, 9], leading to inconsistencies. A clear example of that is the yield stress, which is not the same depending on the source.

It is still missing a comprehensive and systematic characterisation. It perfectly may be the case it has to go hand in hand with a normalisation of the chemical composition and manufacturing process, as it has happened with other construction materials.

Such a characterisation should ideally be undertaken by one entity alone (university or laboratory) and should include uniaxial tests at different strain rates and temperatures, in both machine direction (MD) and transversal direction (TD), until breakage; other set of uniaxial tests to study film recovery and define a yield criterion (which will be an agreed residual strain after certain time) [3]; biaxial tests at different MD:TD ratios; creep tests and shear tests. From each of the above, a minimum of 5 samples should provide a reasonable average.

Among the benefits of a complete characterisation would be: the possibility of exploring reliably any stress state of the structure for any given time, temperature or history of loads, using realistic loading profiles and avoiding reliance on close values on a chart for stiffness, max. stresses, max. prestrain, etc. This simplifies the analysis and gives not only freedom but also confidence to the designer because it provides full control over his/her structure. It will also avoid the use of conservative knockdown A-factors [4] for temperature variation (1.2), biaxial stress (1.4) or long-term effects (1.8).

It is particularly noteworthy the case of the stiffness of the material, for which the Tensinet guideline gives only two values: 405 MPa for long-term loading (slow strain rate) and 900 (alternatively 810) MPa for short-term loading (fast strain rate). This is deemed by the authors insufficient for a proper modelling of an ETFE structure.

On the absence of such a characterisation this paper explains how one has been generated numerically, based on readily available data and an existing visco-elastic material model, to emphasise the advantages this laboratory effort would lead to, especially from the designers' point of view. It is worth insisting it is not the purpose of this study to characterise accurately ETFE for the whole range of working temperatures and strain rates but to underline the importance of it and, for certain critical scenarios explored through worked examples, the urgency of it.

2. The case of the Polyethylene film

The big effort described under previous title has been done in the case of polyethylene film, namely on Linear Low-Density Polyethylene (LLDPE). This material is the base of the Strato-Film (SF420) [25, 26], used on stratospheric balloons, subjected to severe weather conditions. A complete, systematic and consistent set of tests have been done to characterise this film [1] and then feed a numerical model that has been successfully used for several years.

LLDPE shows also a visco-elastic behaviour hugely dependant on temperature and strain-rate [fig.2]

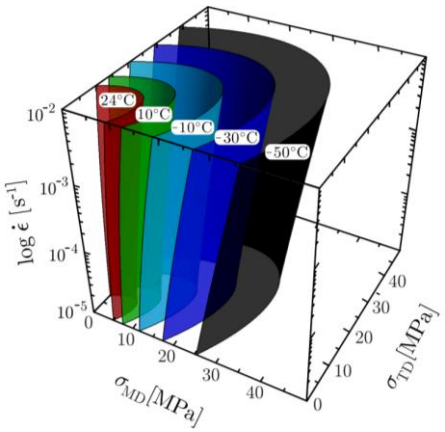


Figure 2: Three-dimensional representation of LLDPE film yield surfaces in principal stress coordinates [3]

2.1. The free-volume model

A nonlinear viscoelastic equation was firstly derived from thermo-dynamic principles by Schapery [20]. Rand et al. [21] showed that the material model developed by Schapery could be applied to the balloons' film. Wakefield [22] implemented it on the dynamic relaxation environment. This model had though some limitations because it didn't account for volumetric changes; it was adequate for small strains. Li et al. [23] combined a linear viscoelastic model based on experimentally derived master curves with the free-volume theory, leading to a model suitable for small and large strains. Bosi [1] extended the validity of this model to a wider range of operational conditions.

The model from Bosi and Li, developed at Caltech under Dr. Pellegrino's mentorship, uses the next creep compliance matrix:

$$\boldsymbol{D}(t) = \begin{bmatrix} D_{11}(t) & D_{12}(t) & D_{13}(t) & 0 \\ D_{12}(t) & D_{22}(t) & D_{23}(t) & 0 \\ D_{13}(t) & D_{23}(t) & 0 & 0 \\ 0 & 0 & 0 & D_{66}(t) \end{bmatrix} \quad \text{(Eq. 1)}$$

where indices 1 and 2 are the in-plane axes, representing MD and TD, 3 is the out-of-plane axis and 6 is shear. Each compliance term $D_{ij}(t)$ in Eq. (1) is represented by a sum of exponential functions called Prony Series:

$$D_{ij}(t) = D_{ij,0} + \sum_{k=1}^{n} D_{ij,k}\left(1 - e^{-t/\tau_k}\right) \quad \text{(Eq. 2)}$$

In Eq. 2, t is time, $D_{ij,0}$ is the Elastic Compliance for t=0, $D_{ij,k}$ are the Prony coefficients and τ_k is the retardation time corresponding to the k-th element. The second term of the equation is called Transient Compliance. Prony coefficients were obtained experimentally (data obtained from the characterisation tests), together with other factors required for the free-volume model. This model, as opposed to the one from Rand, is able to utilise a time-stepping analysis where the strain history of the laded material is passed through from one time step to the next. This approach allows the accurate modelling of time dependant behaviour. The Caltech model is therefore typically used in conjunction with a time dependant load profile, which has to be defined as part of any analysis.

2.2. Factorisation of the model

This model has been implemented in the Dynamic Relaxation solver by Wakefield [32, 33], incorporating the ability to factor it to represent other viscoelastic films of similar nature to SF420. This factoring technique, has been successfully implemented on some alternative films, having been calibrated against physical tests undertaken on said films.

Four factors have been used: one controls the stiffness of the elastic compliance (Eq. 2), two more factors modify the overall MD and TD stiffness and a fourth factor affects the non-linear strain-hardening modulus. The factors are called, in order: v_{kE}, v_{k1}, v_{k2} and v_{NL}

3. Modelling ETFE

The ideal choice would be to undertake a complete set of tests as described on chapter 1.2 and then to obtain all the Prony coefficients and free-volume factors to calibrate the thermo-viscoelastic model used to model LLDPE films. Since there isn't such a consistent set of tests, the same factoring technique described on chapter 2.2 will be used to obtain a numerical characterisation for ETFE.

First, it is chosen a set of reliable uniaxial tests of which raw data is ready accessible; in this case it is project related test data undertaken on Asahi Glass Fluon ETFE ffilm, which is suitable because tests were performed for MD and TD, at different temperatures. After that, factors will be applied to the

thermo-viscoelastic model to achieve a reasonably close curve fit of those uniaxial tests. Biaxial and shear stiffnesses, together with behaviour at different strain rates is inferred from this factorisation. It generates a numerical characterisation of the material that should be cross-checked against tests addressing those properties, if possible, although based on previous experiences the results should be reasonably close. This is the reason why the characterisation generated cannot be considered definitive and will be used only to identify potential scenarios where the use of this viscoelastic model would be helpful (chapter 4). Any firm conclusion would need the complete characterisation.

The next image [fig. 3] shows the comparison of stress-strain curves from real uniaxial tests (grey lines) against curves generated from the viscoelastic model once factored. Tested samples were 100mm long and one of the ends was pulled at 250mm/min, leading to a strain rate $\dot{\varepsilon}$ = 4.167 %/s; therefore, model was fitted at this strain rate too. Factors used are: v_{kE}=0.6, v_{k1}=1.4, v_{k2}=1.4 and v_{NL} varying linearly from 1.65 at 0°C to 0.85 at 50°C. During a typical analysis in the FE environment, v_{NL} is linearly interpolated at intermediate temperatures if needed. In addition, the film temperature had to be artificially shifted to achieve a good curve-fit, so that $T_{ETFE\ model} = T_{seed\ model}$ - 30°C. Curve fitness is deemed suitable up to strains ε = 6% approximately. Beyond this point the numerical prediction deviates from the real tests.

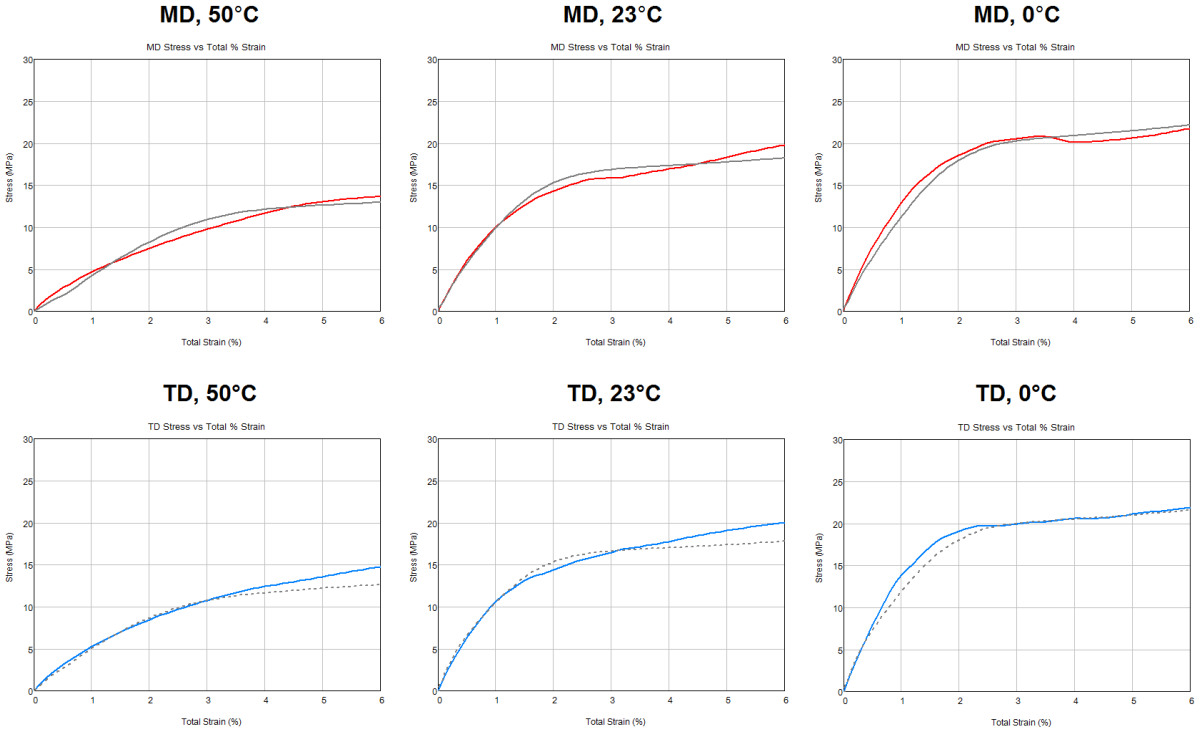


Figure 3: ETFE Uniaxial stress-strain curves for different temperatures and different pulling direction (MD on top, TD on bottom). Grey curves correspond to physical tests and coloured ones to the numerical model. Strain rate is 4.167 %/s.

Note that in the case of 0°C there wasn't a physical test available from the same batch of material so its curves have been extrapolated based on a different source (Asahi Glass [24], figure 4) so that

$$\left(\sigma_{0C,i}(\varepsilon_i)\Big/\sigma_{23C,i}(\varepsilon_i)\right)_{figure\ 3} = \left(\sigma_{0C,i}(\varepsilon_i)\Big/\sigma_{23C,i}(\varepsilon_i)\right)_{figure\ 4} \quad ; \quad \forall\varepsilon_i \in (0\% - 6\%) \qquad \text{(Eq. 3)}$$

It is worth taking the chance again to emphasise the importance of undertaking a complete set of physical tests to characterise properly ETFE under all working conditions, as explained on chapter 1.2

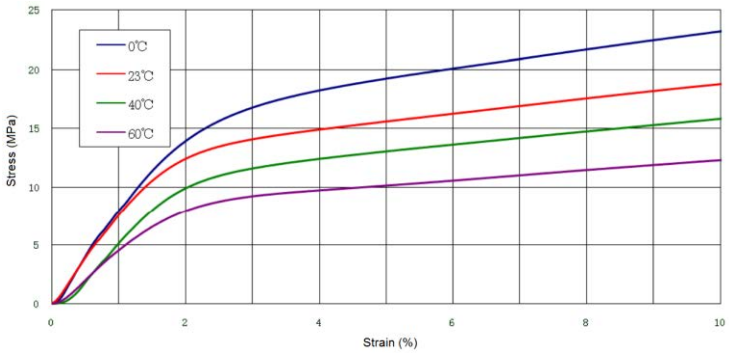


Figure 4: ETFE Stress-strain curves at different temperatures from Asahi Glass [24]

The next images [fig. 5a, fig. 5b] show a broad comparison between uniaxial stress-strain curves from the numerically generated characterisation for ETFE and the seed material SF420 (unfactored). These figures give also an insight on the impact temperature and strain rate have on these viscoelastic materials. Note SF420 is a film conceived to work at temperatures ranging between room and -60°C; this is why the original model shows a poor performance at 50°C. The differences between the two sets of graphs (left/right) are a result of the factorisation process.

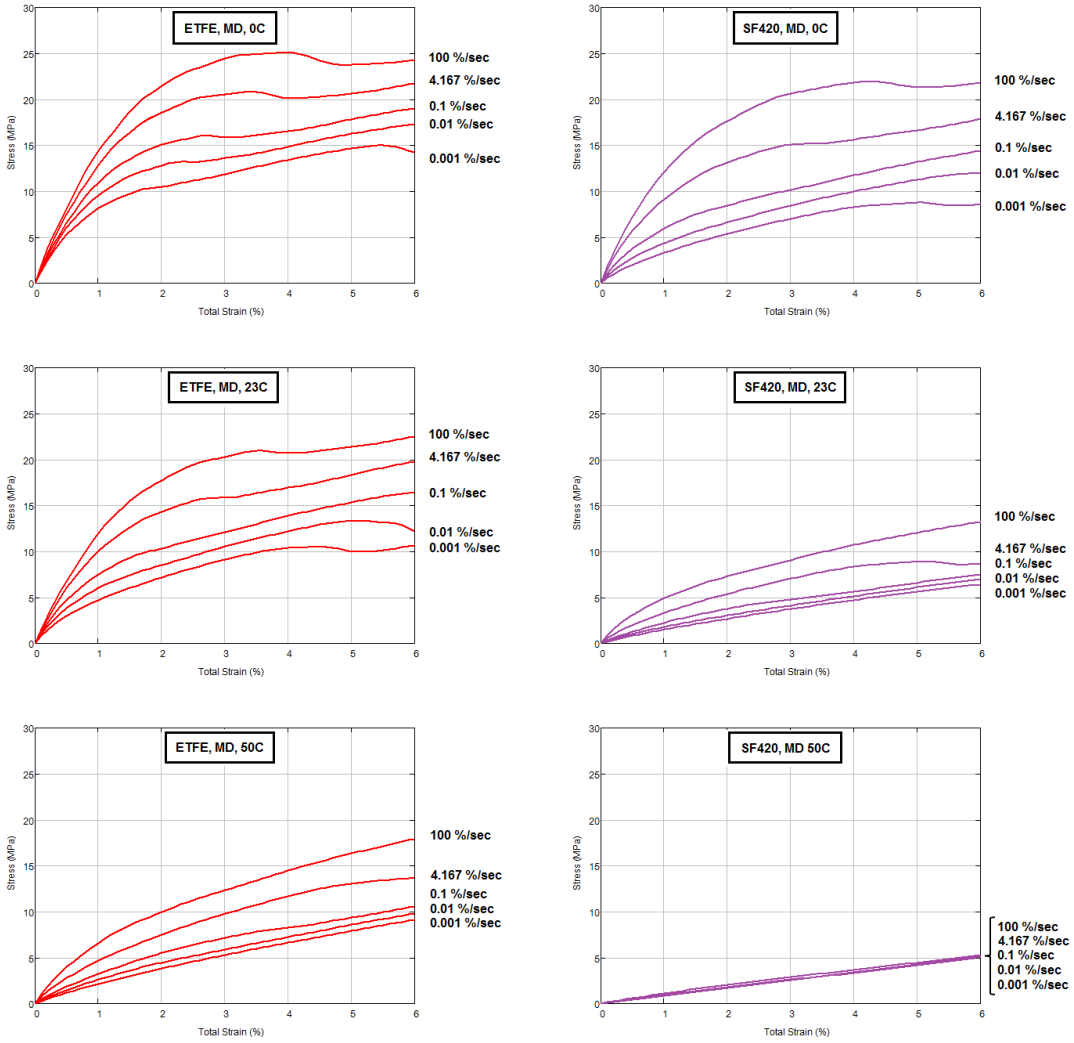


Figure 5a: MD Stress-strain curves for ETFE (left) and SF420 (right) at different temperatures and strain rates

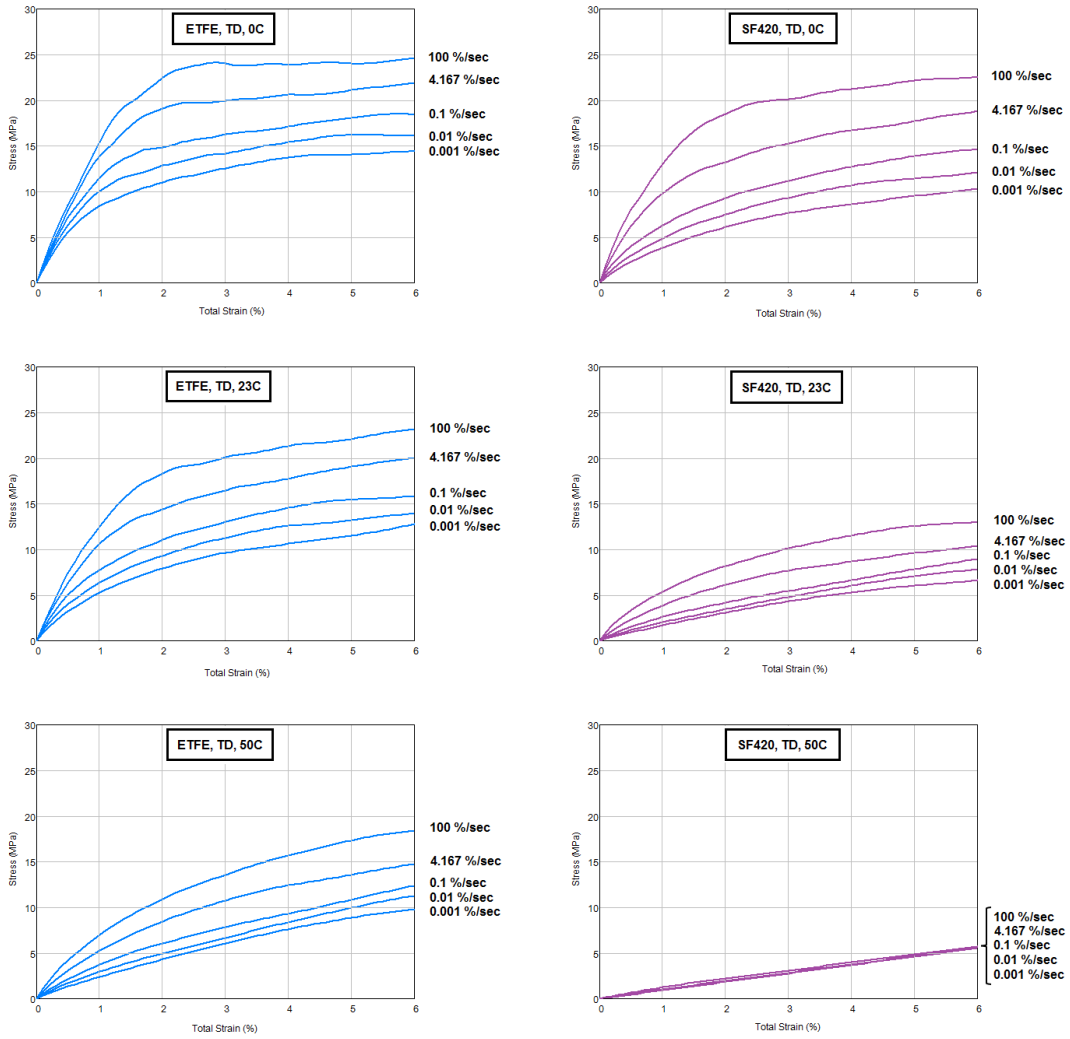


Figure 5b: TD Stress-strain curves for ETFE (left) and SF420 (right) at different temperatures and strain rates

ETFE is prone to creep under load. This effect cannot be neglected since it will limit the maximum service prestress and the permanent loads the structure can withstand. The Tensinet Guideline gives some directions on creep values to be used for design. As per other material properties, creep depends hugely on the manufacturer/chemical composition of the film considered, according to Charbonneau [9]. The material model should then be carefully calibrated against creep tests from samples extracted from the same batch of material used for the rest of tests involved in the characterisation. In the absence of suitable tests, figure 6 shows the strains due to creep as a result of the factors chosen for the aforementioned numerical characterisation. In that example, constant stress is maintained in TD for 14 hours. It can be observed that when a stress of 12 MPa is applied, the curve shows the onset of tertiary creep.

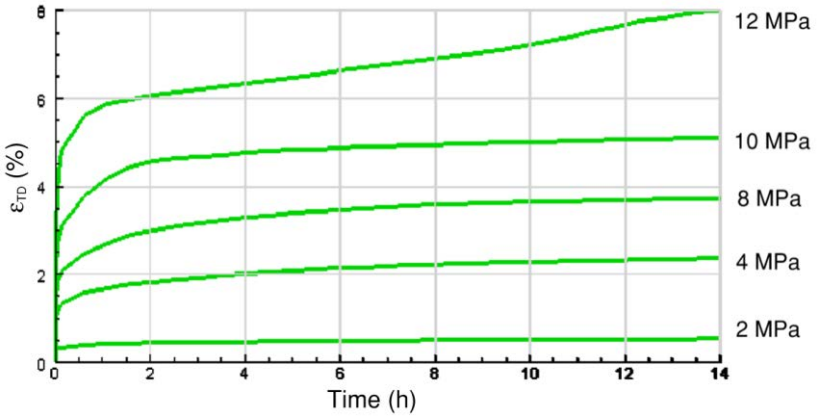


Figure 6: Strain-time curves from creep tests at different constant stresses applied on the numerical model for ETFE. Orientation = TD; room temperature.

Thermal expansion is not linear either. In the case of LLDPE, thermal expansion coefficient is different for different temperatures and different for each main direction. In that instance polynomial curves are defined to represent this coefficient. In the case of ETFE, given the lack of studies on this matter, a constant coefficient equal to 0.0001 is assumed in the modelling, for both directions.

4. Worked examples

A complete characterisation of ETFE and a proper implementation in the FE environment is not only a useful tool that simplifies design and prevents reliance on given assumptions but it may also be of paramount importance, if not critical, in some cases where choosing the right stiffness is needed or where creep effects have an impact in the design.

Three worked examples have been prepared to illustrate these scenarios. In them, the same FE model will be fed and run with elastic properties and with the viscoelastic model for ETFE. Results will be compared. When creating the linear elastic models, mechanical properties recommended by the Tensinet Guideline [table 1] are used:

Table 1: Mechanical properties for linear elastic analysis

	Axial stiffness		Shear stiffness	Poisson ratio
	E_{MD}	E_{TD}	G	ν
	[N/mm^2]	[N/mm^2]	[N/mm^2]	[-]
Short term loading	900	900	335	0.33
Long term loading	405	405	335	0.33

The film considered is 250 microns thick and density of the material is 1750 kg/m^3.

The worked examples are done based on the finite element mesh shown on figure 7. It is a square model fixed all around its perimeter, comprising 40x40=1600 constant strain triangular elements. Dimensions of the model will change depending on the exercise.

In-house software inTens is used in the analyses. It is a Dynamic Relaxation solver [22] able to work with either linear or thermo-viscoelastic non-linear materials. Geometric nonlinearity is inherently accounted for.

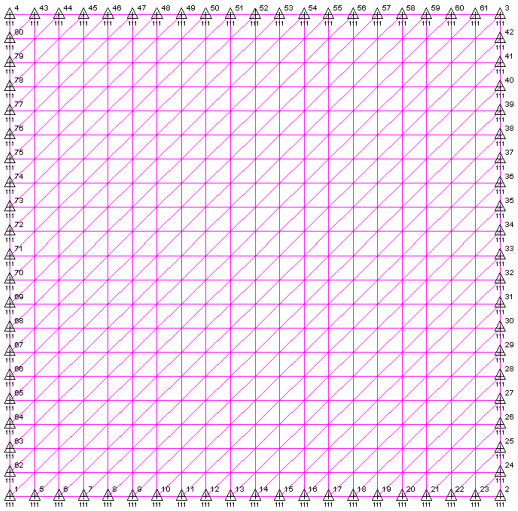


Figure 7: base mesh used on the FE models for the examples, supported on fixed edges.

4.1. Example 1: studying yielding

This exercise presents a scenario where a structure is satisfactorily designed to withstand a wind load at ambient conditions but as soon as temperature increases, it yields under the same load. It is considered a maximum temperature equal to 50°C because it is a common design value on hot countries.

An ETFE cushion with dimensions 3x3m^2 is designed to withstand a 3-second wind gust which reaches a peak value of -1.7 KPa (suction). The 3 seconds gust is a common design value used, for instance, in the ASCE code [27]. It is assumed the internal pressure of the cushion doesn't contribute during this event. Three models are required for this exercise:

- An elastic model at room temperature (Model A); Young's modulus taken is 900 MPa. The load is applied statically. The Tensinet Guideline recommends to take as admissible stress for SLS some figure between 12 and 15 MPa. As it can be seen on figure 9, the cushion reaches 13.5 MPa.
- Two non-linear models where the stiffness varies according to the viscoelastic constitutive equation. A loading profile is prepared for this model, shown in figure 8. Temperature is kept constant, equal to 23°C for the first nonlinear model (B) and then increased to 50°C on a second nonlinear model (C).

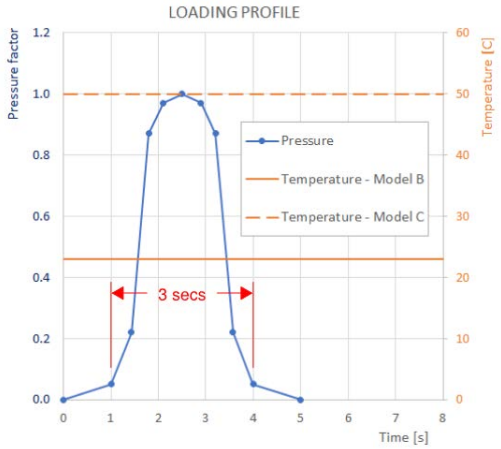


Figure 8: loading profile for a 3-seconds gust reaching -1.7 KPa at constant temperature

Stresses and strains for the three models are shown on figures 9a and 9b. It has been chosen for models B and C the instant of maximum load, i.e. second 2.5.

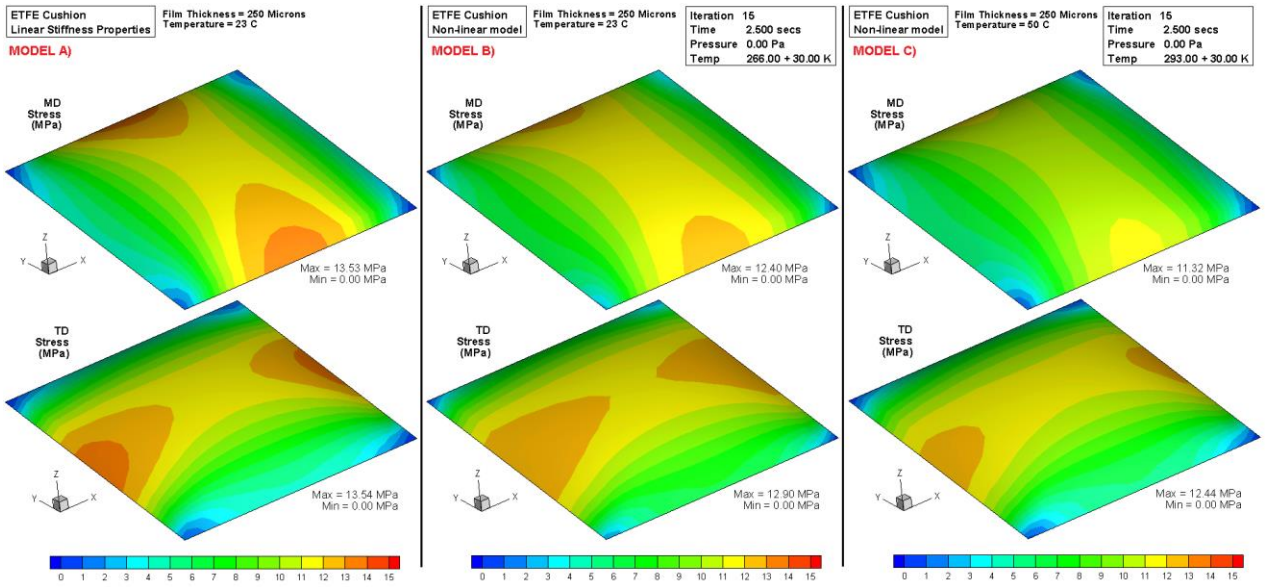


Figure 9a: MD stresses (top) and TD stresses (bottom) on three models. From left to right: elastic model at 23°C, non-linear model at 23°C and non-linear model at 50°C

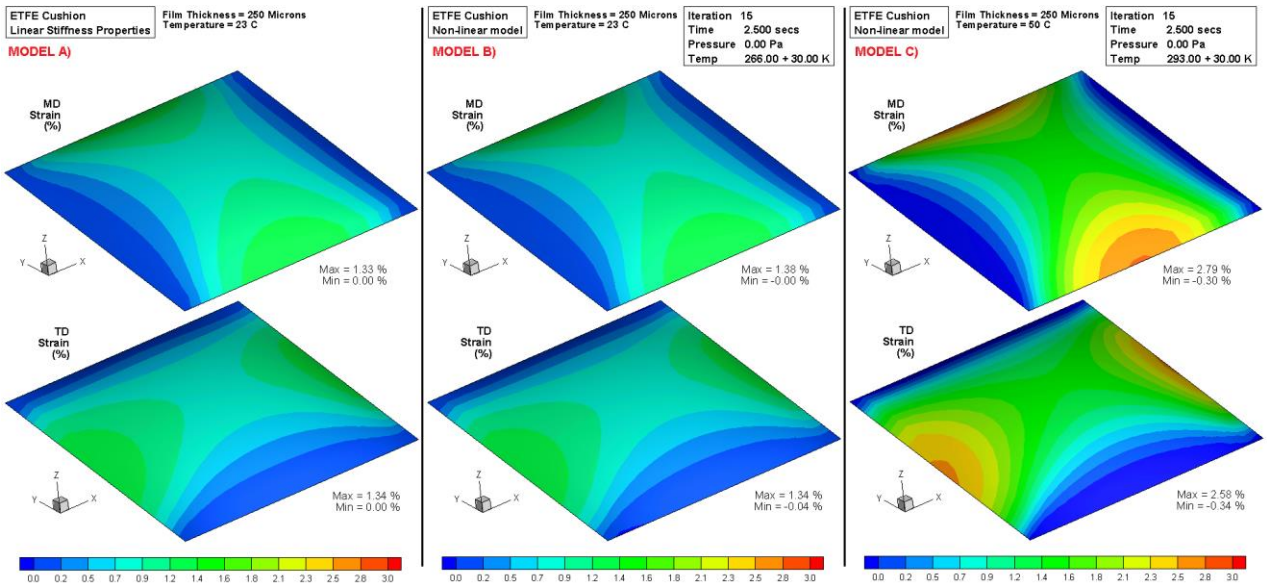


Figure 9a: MD strains (top) and TD strains (bottom) on three models. From left to right: Model A: elastic model at 23°C, Model B: non-linear model at 23°C, Model C: non-linear model at 50°C

When models A and B are compared, stresses are similar and strains almost identical. Maximum stresses are slightly lower on model B because the stiffness provided for model A, for short-term loads, is only an indicative value that matches a certain strain rate and temperature from the broad spectrum of responses of the ETFE. In this case, it seems the stiffness for model A is slightly high for this strain rate in particular, but still valid. Nonetheless this stiffness is not valid for higher temperature.

The strain rate shown by model B, where maximum strains are reached, is about 2.7%/s. With this last value and the temperature, the uniaxial stress-strain curves can be plotted [fig. 10]

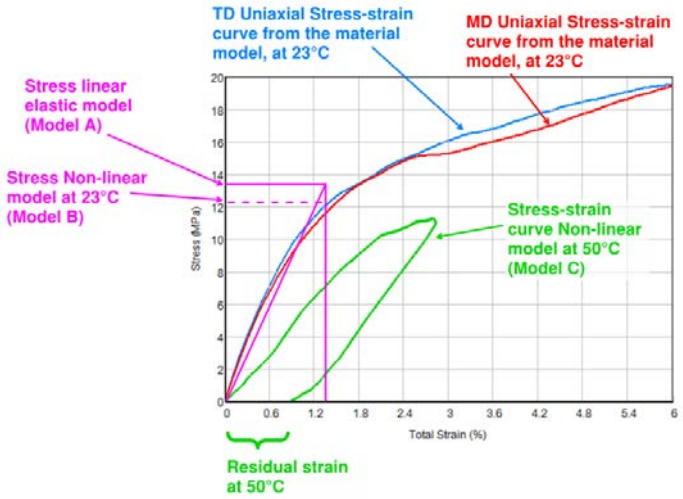


Figure 10: Red and Blue: MD and TD uniaxial stress-strain curves generated by the numerical model for ETFE, at 23°C and $\dot{\varepsilon}$ =2.7%/s. Pink: Stresses predicted by the linear elastic model and those shown by the non-linear model at 23°C. Green: stress-strain curve at location of max. strain, on the non-linear model at 50°C.

Figure 10 shows uniaxial curves for MD and TD, generated by the numerical model for ETFE. Maximum stresses on models A and B are also shown for reference because they take place on the sides of the cushion, where behavior is closer to uniaxial than to biaxial. In the case of model A, max. MD stress is equal to the max. TD stress. In the case of model B they are similar and, for simplicity, only one line (dashed) is shown. It is plotted, in addition, the MD stress-strain curve for model C, where strains are maximum. In this last green curve it can be clearly seen the softening of the material due to the increment of temperature, the lack of validity of the linear stiffness for short term loads and the fact that film has yielded if the yield point is considered to be at ε=1.7% as per figure 1. Finally, this curve shows the residual strains after unloading.

The yield locus [3] for a range of temperatures, strain rates and stress states is one of the outcomes of the characterisation proposed on chapter 1.2. It should be based on an agreed residual strain, once stable after the recovery period.

4.2. Example 2: studying ponding

This exercise has been chosen to illustrate an example where a design can be unsafe if the wrong stiffness is taken and ponding occurs. Ponding has to be prevented not only for aesthetic but for safety reasons because the pond can become unstable, collecting very large amounts of water before bursting. Non-linear stability of accumulations of water is out of the scope of this study but it can be assessed in inTens too [28].

It is chosen a single flat sheet of ETFE film 3x3 m^2, inclined by 15 degrees. Prestress chosen is 3 MPa (MD/TD) at room temperature, staying within the limits recommended by the Tensinet Guideline. The structure will be subjected to a uniform heavy snow load equal to 0.95 KPa and maximum stresses are to remain below 15.5 MPa, as suggested for long-term loading at cold temperature. It will be shown a comparison between a linear-elastic design leading to satisfactory results, where allowable stress is not exceeded and ponding is not happening, against a non-linear analysis where some accumulation of water will result:

- Model A is the elastic model, using long-term stiffness properties from table 1. Load is applied statically.

- Model B uses the viscoelastic definition for ETFE. It has been defined a load profile [fig. 11] more complex than in Example 1 to represent accurately what the structure will experience and, in doing so, demonstrate the capabilities of the viscoelastic model. This figure plots also in parallel the history of stresses and strains at the location where they are maximum (see also figure 12 for reference).

Regarding the load profile for model B, firstly, the prestress is achieved by placing in the metal frame a pattern slightly smaller than the frame dimensions so that after some period of relaxation the stresses get stable enough. This relaxation period (Zone 1) is taken as 1 day and, at the end of it, prestress is to be approximately 3 MPa in both directions. From this moment commences the second period (Zone 2) where temperature drops to zero degrees in 5 hours and it starts snowing at a rate of around 12mm/hr, taking 25 hours to reach 0.95 KPa. Last period (Zone 3) assumes snow is not been removed and is characterised by the creep and redistribution of stresses (this explains why the maximum stress drops also during this period). It is in zone 3 where models A and B can be compared since both represent the same.

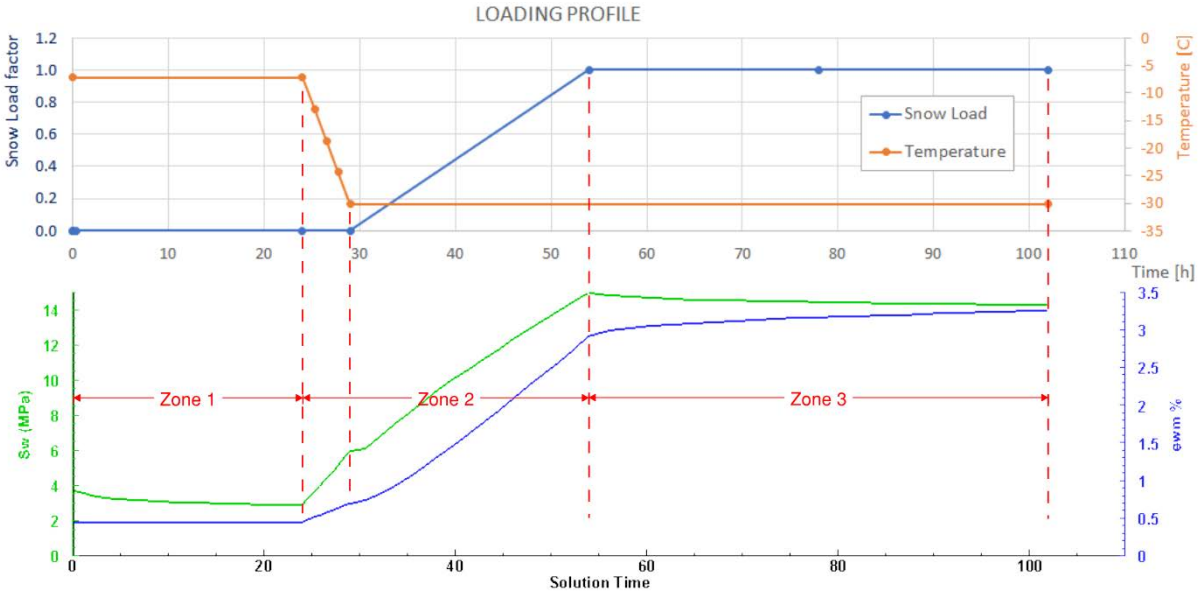


Figure 11: Loading profile for model B (top)
and parallel history of MD stresses/strains at location of the structure where they are maximum (bottom).

The next figure shows a comparison of stresses and strains between models A and B at the beginning of Zone 3 (hour 54)

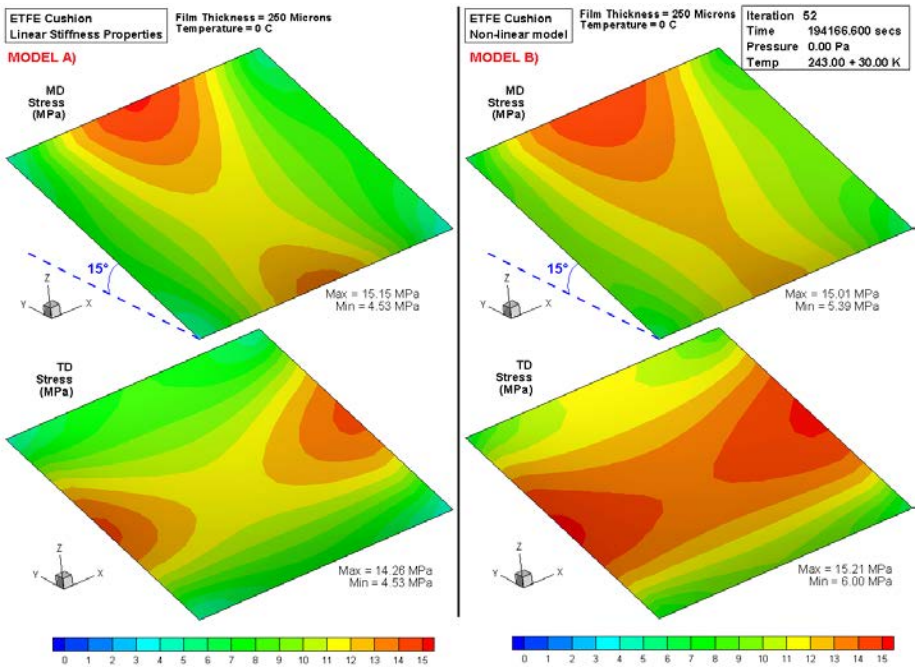


Figure 12: MD stresses (top) and TD stresses (bottom) on two models. From left to right: elastic model at 0°C and non-linear model at 0°C

Both models show maximum stresses are in the order of 15 MPa, what suggests the stiffness for the elastic model is not misguided. However, distribution of MD stress is slightly different and TD stress in model A is lower than in model B.

It is after some hours, if the snow is not removed and the film creeps under load, that a small pond of melted snow can be formed. The next image shows the onset of ponding after more than 24 hours, on model B, which is not apparent on model A.

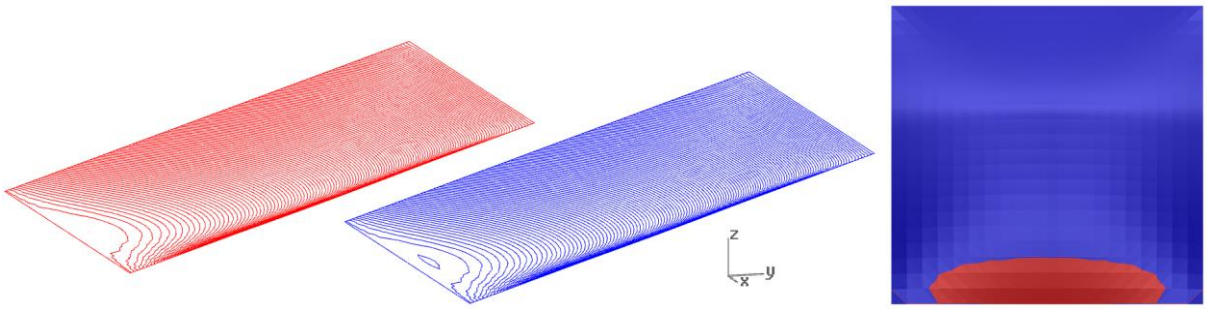


Figure 13: Contour lines every z=7mm on model A (left) and model B (centre). Right: Top view of an overlay of models A and B; red colour shows where model B is deeper than A and vice versa.

4.3. Example 3: studying wrinkling

It is a common problem on some ETFE structures that while they present a smooth surface, perfectly tensioned in all directions, after installation, they become wrinkly over time. This may not pose necessarily a hazard on terms of structural safety but it is certainly aesthetically unpleasant. Wrinkles can appear as a result of deformations on the fixed boundaries or underestimation of the permanent or temporary loads applied directly on the membrane. The second scenario will be investigated with an example.

It will be considered an ill-conceived structure subjected to a severe yet realistic 8.3 minutes wind storm simulated numerically. The same base mesh as per the other examples is used but, in this case, dimensions are 3.5x3.5 m^2 and edges are warped so that a hyperbolic paraboloid shape is generated when form-finding. Prestress is set equal to 3 MPa. It can be argued a lower prestress would help to move the permanent stress away from the yield stress but some prestress is definitely needed to avoid large dynamic amplification of the wind loads due to flutter.

The wind load w is based on a mean wind velocity v_m plus a turbulent component v':

$$w = \frac{1}{2}\rho\, V^2(z,t) \qquad \text{(Eq. 4)}$$

where

$$V(z,t) = v_m(z) + v'(z,t) \qquad \text{(Eq. 5)}$$

The mean wind velocity v_m is calculated according to the Eurocode EN 1991-1-4, obtained from the parameters listed on table 2. The pressure coefficient for suction C_p = -0.8 is estimated uniform based on an average value from those given for hypar structures on the European Design Guide for Tensile Surface Structures [29].

Table 2: Parameters used to calculate the mean wind velocity

Basic wind velocity	v_b	=	28	[m/s]	*Air density*	ρ	=	1.25	[kg/m^3]
Terrain category		=	0	[-]	*Pressure coefficient*	C_p	=	-0.8	[-]
Roughness length	z_0	=	0.003	[m]	*Terrain factor*	k_r	=	0.156	[-]
Minimum heigth	z_{min}	=	1	[m]	*Roughness factor*	$c_r(z)$	=	1.374	[-]
Height above ground	z	=	20	[m]	*Orography factor*	$c_o(z)$	=	1.15	[-]
Roughness length for category II	$z_{0,II}$	=	0.05	[m]	*Mean wind velocity*	$v_m(z)$	=	44.24	[m/s]

The fluctuating component of the wind v' (z, t) is calculated from Shinozuka and Jan [30, 31]:

$$v'(z,t) = \sqrt{2}\sum_{j=1}^{N}\sqrt{S_u(z,n_j)\Delta n}\,\cos(2\pi n_j t + \phi_j) \qquad \text{(Eq. 6)}$$

where n_j is the wind frequency, N the number of discrete frequencies, Δn is the frequency step, t is the time and ϕ is the phase angle varying randomly between 0 and 2π. It has been taken Solari's power spectral density function to keep consistency with the Eurocode. The wind simulation takes 500 seconds, considering a frequency range from 0 to 10 Hz and 600 discrete frequencies. Time step is 0.05 seconds. This simulation corresponds to the blue curve plotted on figure 14. However, this simulation has been simplified to save computational time by reducing the number of inputs still preserving the fluctuating nature of the wind, respecting the shape of the turbulent peaks. This can be achieved by using a time step equal to 0.5 s (orange curve on figure 14) but if it is further increased then the peaks smooth down and the simulations is not a proper representation of a real wind.

Another 100 seconds have been added, in the load profile for the FE analysis, before the 500-seconds wind simulation. During these first 100 seconds the wind pressure is increased monotonically until reaching the pressure corresponding to the mean wind velocity. The maximum turbulent peak v' = 6.07 m/s takes place at second 330 (second 430 on the FE analysis) and leads to a wind pressure on the structure equal to 1.58 KPa.

The structure is small enough to presume a coherence function is not needed.

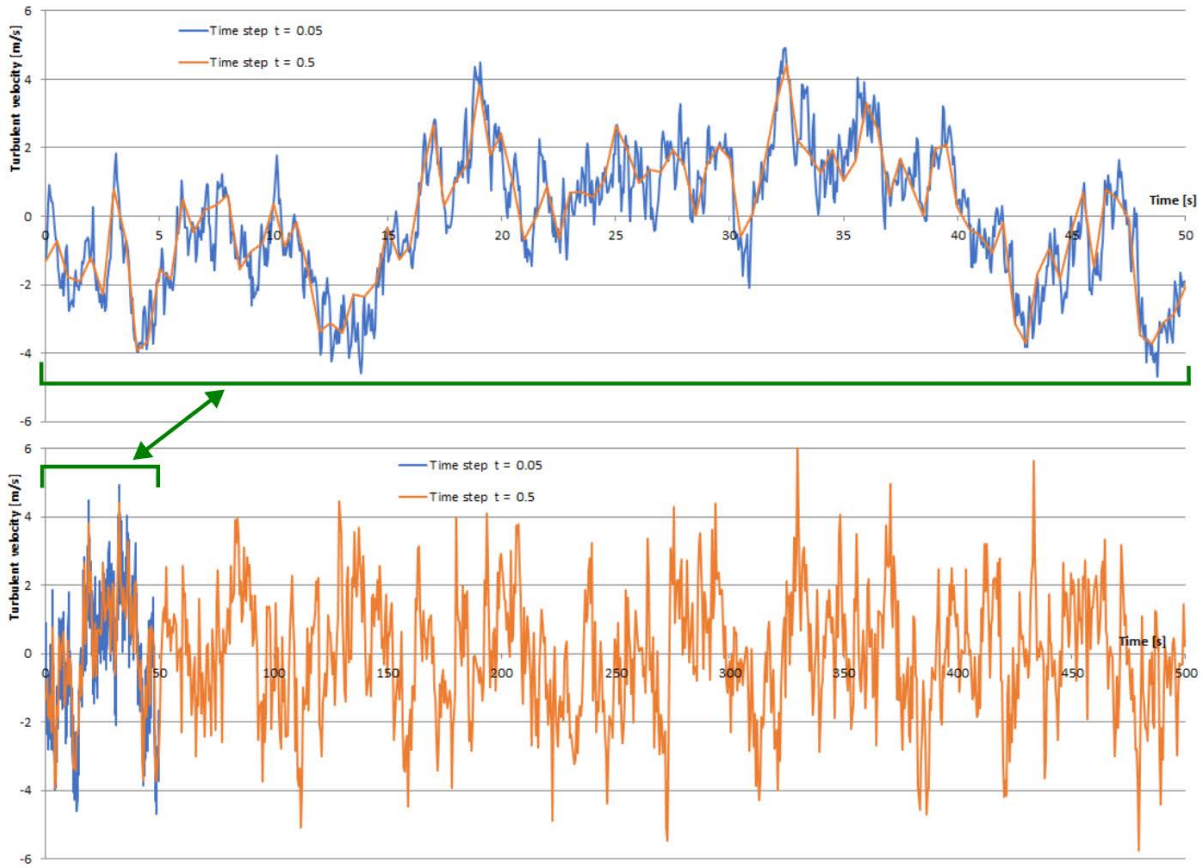


Figure 14: Wind simulation during 50 seconds (top) and 500 seconds (bottom).
Time step = 0.5s is eventually used on Example 3

The hypar single sheet of ETFE has been form-found to achieve the intended prestress and then has been exposed to the wind simulation, keeping temperature constant equal to 23°C. Figure 15 shows the contour of maximum stresses at second 430.

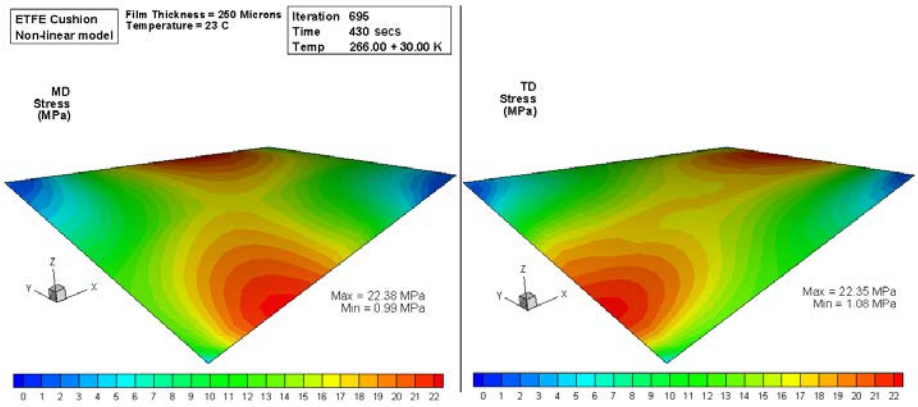


Figure 15: Stress contours for MD (left) and TD (right) at point in time where maximum stress is reached.

Two plots have been created probing on the node where stresses reach the maximum value [fig. 16]. It can be noticed the stresses are too high and the film yields and creeps significantly. The trend curve on the right-hand side plot resembles a typical creep curve. Residual strains can be seen on the left-hand side plot.

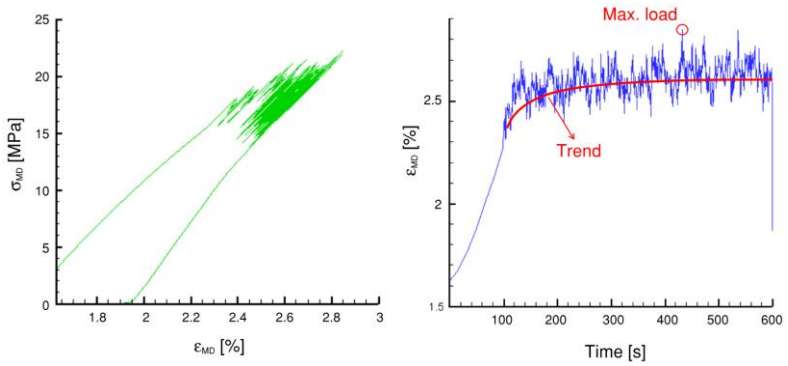


Figure 16: Plots obtained at the point where stresses reach maximum value (refer to fig. 15).
Left: Stress-strain curve showing the cyclic loading. Right: Strain-time curve.

From a visual point of view, all this translates into macroscopic wrinkles in the surface that can be seen by the public. Figure 17 shows the difference between the aspect of the hypar just after being installed, where prestress is uniform in the main directions, as a result of a proper form-finding and patterning, against the same structure after being subjected to the heavy wind load, when no external load is applied. Figure 18 confirms this slackness is related to a loss of prestress; it has almost disappeared.

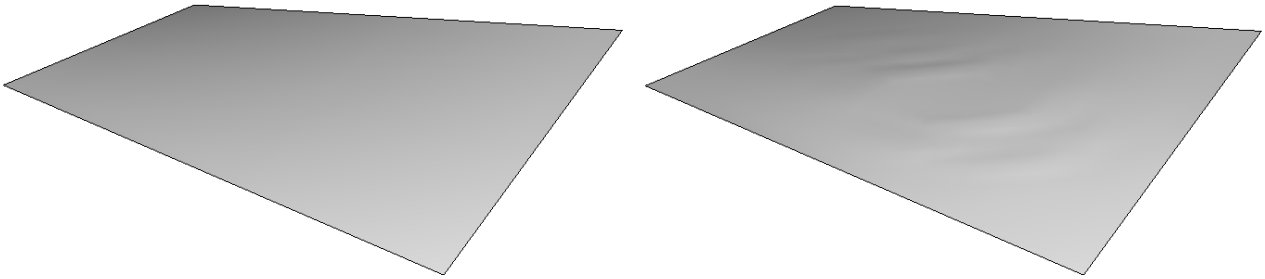


Figure 17: shaded view of the structure before (left) and after (right) the wind storm.

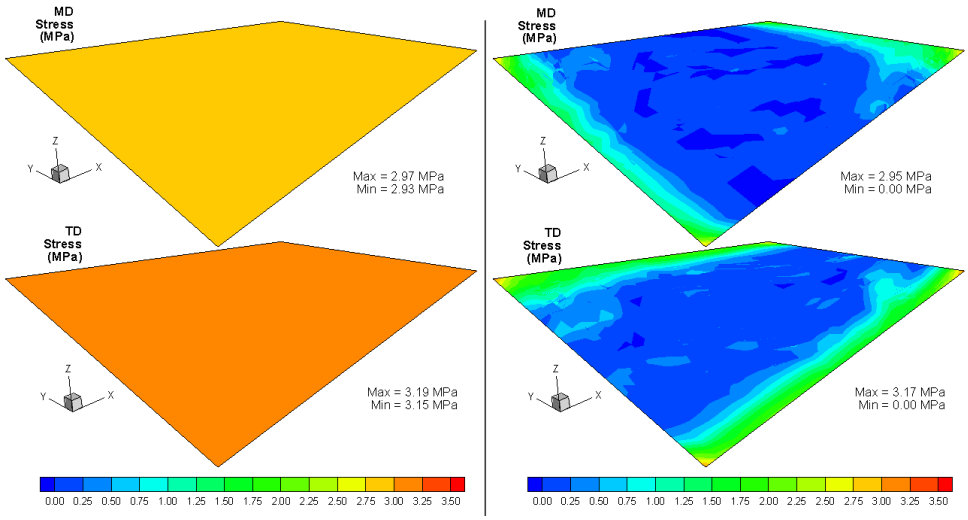


Figure 18: prestress before (left) and after (right) the wind storm.
Top figures are MD stress; bottom figures are TD stress

5. Conclusions

A complete, comprehensive characterisation of ETFE is still a pending task that is worth pursuing not only because it would provide a better understanding of the material but because it would enable the development of a constitutive model that would considerably improve the design and analysis process of structures of this typology. This exercise should be the outcome of a complete number of experiments enough to consistently quantify all mechanical properties of the material. Among the advantages of accounting for such a characterisation would be simplifying the analysis yet gaining control and accuracy over it.

Given the success of the thermo-viscoelastic model for LLDPE films in the aerospace industry, this paper propose, as a first attempt, the direct calibration of this type of model for the case of ETFE films from a series or physical test. In the absence of that effort and given the lack of a comprehensive characterisation at hand to perform this calibration, this paper proposes as an alternative the factorisation of the thermo-viscoelastic model for LLDPE so that it performs as ETFE.

Finally, to demonstrate the usefulness of undertaking this characterisation task and the utility of using the free-volume model from Caltech, this paper presents a number of examples analysed by a DR solver where a factored of the viscoelastic model, able to behave as ETFE does, is implemented. These examples underline the importance of the correct modelling of ETFE, highlighting the relevance of temperature, creep and loading rate, and flagging up some scenarios where basic assumptions can lead to unsafe designs.

References

[1] F. Bosi, S. Pellegrino, "Nonlinear thermomechanical response and constitutive modeling of viscoelastic polyethylene membranes", *Mechanics of Materials*, vol. 117, pp 9-21, 2018.

[2] D. Wakefield, "Non-linear viscoelastic analysis and design of Super-pressure Balloons: stress, strain and stability", *AIAA Balloon Systems Conference*, 2009.

[3] F. Bosi, S. Pellegrino, "Molecular based temperature and strain rate dependent yield criterion for anisotropic elastomeric thin films", *Polymer*, vol. 125, pp 144-153, 2017.

[4] ETFE working group, "Design Recommendations for ETFE foil structures", *Tensinet*, 2013.

[5] D.S.A. De Focatiis, L. Gubler "Uniaxial deformation and orientation of ethylene-tetrafluoro-ethylene films" *Polymer Testing,* 32:1423-35, 2013.

[6] C. Galliot, R.H. Luchsinger "Uniaxial and biaxial mechanical properties of ETFE foils" *Polymer Testin*g, 30:356-65, 2011.

[7] K. Moritz "ETFE-Folie als Tragverhalten". PhD Thesis, *Technische Universitat Munchen*, 2007.

[8] L. Schiemann "Tragverhalten von ETFE-Folien unter biaxialer Beanspruchung". PhD Thesis, *Technische Universitat Munchen*, 2009.

[9] L. Charbonneau "Time-Dependent Tensile Properties of ETFE Foils" Master Thesis, *University of Waterloo, Canada,* 2011.

[10] B. Zhao "Mechanical properties and structural performance of ETFE (ethylene-tetrafluoro-ethylene) cushion structures at low temperatures" *Engineering Structures*, vol. 136, pp 420-429, 2017.

[11] T. Yoshino, S. Kato "Viscous characteristics of ETFE film sheet under equal biaxial tensions" *Procedia Engineering*, vol. 155, pp 442–451, 2016.

[12] J. Hu, et al. "Uniaxial cyclic tensile mechanical properties of ethylene tetrafluoroethylene (ETFE) foils" *Construction and Building Materials*, vol. 63, pp 311–319, 2014.

[13] M. Coelho, et al. "Numerical simulation of burst-test of an ETFE membrane", *Proceedings of the IASS-SLTE 2014 Symposium Shells and Spatial Structures: Footprints,* 2014.

[14] Various authors, "Prospect for European Guidance for the Structural Design of Tensile Membrane Structures" *Publications Office of the European Union*, 2016.

[15] D. Ströbel "Holistic Calculation of (Multi)-Chambered ETFE-Cushions". Technet GmbH, *Tensinet Istambul Symposium*, 2013.

[16] R. Blum et al. "On the mechanical behaviour of ETFE-films: Elastic range, yielding conditions, break determined by different test methods and the influence of the results on the analysis of ETFE-structures" *Procedia Engineering*, vol 155, pp 496 – 506, 2016.

[17] M. Wu et al. "Tensile property of ETFE foil after viscoplastic-forming process" *Proceedings of the IASS-SLTE 2014 Symposium Shells and Spatial Structures: Footprints*, 2014.

[18] E.S. Jeong "Visco-Plastic Constitutive Equation of ETFE Film" *IABSE/IASS Symposium Report,* 2011.

[19] M. Coelho "Elasto-viscoplastic material model considering large strains for ETFE-foils" *VII International Conference on Textile Composites and inflatable structures,* 2015.

[20] R.A. Schapery "On the characterization of nonlinear viscoelastic materials" *SPE Symposium on Design of Experiments and Data Analysis in Plastics Engineering*, 1969.

[21] J.L. Rand et al "Nonlinear behaviour of Linear Low-Density Polyethylene", *Polymer Engineering and Science*, vol. 36 No 8, 1996.

[22] D. Wakefield "Non-linear Viscoelastic Analysis and the design of Super-Pressure Balloons: Stress, Strain and Stability" *AIAA Balloon Systems Conference*, 2009.

[23] J. Li et al "Thermoviscoelastic models for polyethylene thin films". *Mechanics of Time-Dependent Materials,* vol. 20, pp 13-43, 2016.

[24] Asahi Glass Co, "Fluon ETFE film. Technical data", *AGC*, 2014.

[25] J.L. Rand "An improved constitutive equation for SF420 Part I: the master curve," *Report by Winzen Engineering Inc*., 2008.

[26] J.L. Rand "An improved constitutive equation for SF420 Part II: the biaxial behaviour," *Report by Winzen Engineering Inc.*, 2008.

[27] Various authors "ASCE 7-05 Minimum Design Loads for Buildings and Other Structures", *American Society of Civil Engineers,* 2006.

[28] A. Bown et al "Beyond static analysis: Investigation of membrane structure performance using time stepping, transient and progressive analyses" *Procedia Engineering,* vol. 155, pp 313-322, 2016.

[29] B. Forster, M. Mollaert "European Design Guide for Tensile Surface Structures" *Tensinet,* 2004.

[30] M. Shinozuka, C. Jan "Digital Simulation of random processes and its applications", *Journal of Sound and Vibration*, vol. 25, pp 111-128, 1972.

[31] R. Soltys et al "Study of local turbulent wind characteristics and wind velocity simulations" *Building Research Journal*, vol 60, pp 31-50, 2012.

[32] D. Wakefield, A. Bown "Non-Linear Analysis of the NASA Super Pressure Balloons: Implementation of a Large Strain Material Model", *AIAA Journal*, 2015.

[33] D. Wakefield, A. Bown "Non-Linear Analysis of the NASA Super Pressure Balloons: Whole Flight Simulations", *AIAA Journal*, 2017.

Proceedings of the IASS Annual Symposium 2019 – Structural Membranes 2019
Form and Force
7 – 10 October 2019, Barcelona, Spain
C. Lázaro, K.-U. Bletzinger, E. Oñate (eds.)

Viscous characteristics near the initial yield stress of ETFE film sheet under biaxial tension and temperature change

Tatsuya YOSHINO[a], Shiro KATO*

* Engineering Division, Taiyo Kogyo, Japan
4-8-4 Kikawahigashi, Yodogawa-ku, Osaka, 532-0012, Japan
yt003051@mb.taiyokogyo.co.jp

[a] Toyohashi University of Technology, Japan

Abstract

In this paper, our target is to grasp the elongation characteristics of ETFE films, based on which to understand the behavior of ETFE film membrane structures by using FEM analysis. We focus on visco-elastic characteristics under temperature changes in a biaxial tension state using both experiments and numerical analyses. First, biaxial creep tests under a repeated temperature change for stress intensity of 10, 12, 14MPa are performed. Tested results are shown for time-creep relationships including the nonlinearities of plasticity. Second, the tested results are compared with those based on a set of numerical simulations using the proposed constitutive equations. Finally, the validity and applicability of the proposed constitutive equations are confirmed.

Keywords: membrane structures, ETFE film, polymeric material, visco-elasticity, linear expansion coefficient, constitutive equation, time-temperature superposition principle

1. Introduction

In order to design and construct membrane structures using ETFE film, it is importatnt to understand their material properties.

Among researches which focus viscosity of ETFE film, in addition to a research carried out by the present authors, researches have been conducted by Moriyama and Kawabata [1,2], Jeong and Kawabata [3], Wu [4], Galliot and Luchsinger [5], and Li and Wu [6]. The researches mentioned have investigated either the viscous characteristics or the effects due to change of temperature environments on constitutive equations of FEM. However, none of them has extended their consideration to the general constitutive equations for visco-elastic-olastic behavior including the effects of a temperature change.

The present authors [7] carried out previously both biaxial tension tests and shearing tests of ETFE film under a condition of a fixed temperature based on MSAJ Standards [8,9]. In the studies, (1) with respect to five stress ratios, a set of biaxial tensile tests were conducted, and the relationship between equivalent stress and equivalent plastic strain was identified. From the results, regardless of any stress ratio, the curves obtained as relationships between equivalent stress and equivalent plastic strain were proved consistent. (2) It was confirmed in the study that the yield stress as well as stress after breaking down can be expressed in terms of streess-strain relationships, which are formulated as newly proposed elastic-plastic constitutive equations. (3) Also tests for an interbnal pressure on a membrane under a fixed temperature proved that the material behaviour can be expressed sufficiently with high accuracy by the proposed elastic-plastic constitutive equations.

Moreover, in the reference [10], the proposed incremental nonlinear visco-elasticity constitutive equations regarding a uniaxial tension field has been extended in te reference [11,12] to a biaxial tension

Copyright © 2019 by Tatsuya YOSHINO, Shiro KATO
Published by the International Association for Shell and Spatial Structures (IASS) with permission.

field, and the extension has been confirmed accurate. In the extension, the constitutive equations have been formulated in an incremental form on a basis of integration on FEM, which can include the effects of the three conditions of elapsed time, stress change and temperature change. Regarding to the temperature change on the viscosity component, a formulation using time-temperature superposition principle has been evaluated, however, expansion and contraction due to temperature change has not been included in the formulation so far.

In the literatures [14,15], for the purpose of expressing the strain accompanied by the temperature change, the thermal strain was added to the constitutive laws using the linear expansion coefficient. In order to confirm the validity of the constitutive laws, a biaxial creep test with temperature change is considered in the present paper. The maximum stress is set 6 and 8 MPa.

In the present paper,

(1) Similary to the previous paper, a biaxial creep test under a temperature change is carried out, with a restriction that the maximum stress is set 10, 12 and 14MPa.
(2) Application of the proposed constitutive laws with identified material constants is perfomed, and a simulation of biaxial creep test accompanied with temperature change is conducted. Then, based on the comparison betwwen the laws and simulation simulation, proof are validity are concluded.

2. Formulation of incremental constitutive equations for ETFE film

2.1. Incremental constitutive equations extended to biaxial stresses

The generalized Voight model in Figure 2.1.1 is applied for incremental constitutive equations. In order to formulate the biaxial stress condition, variables related to Maxwell elements and Voigt elements are divided into deviatoric components and volumetric components. Divided variables are shown in Table 2.1.1.

Incremental constitutive equations are shown by Eqs.(2.1). In details, the formulation of constitutive equations is found in the previous paper [14].

$$\Delta\sigma = \Delta\sigma' + \Delta\sigma_m = \frac{2\Delta\varepsilon'}{\overline{C}_G(t)} + \frac{3\Delta\varepsilon_m}{\overline{C}_K(t)} - \frac{\Delta\varepsilon_\alpha{}'}{\overline{C}_G(t)} - \frac{\Delta\varepsilon_{\alpha m}}{\overline{C}_K(t)} - \frac{\Delta\varepsilon^\theta}{\overline{C}_K(t)} \tag{2.1}$$

where

$$\begin{aligned}
\Delta\varepsilon' &= \frac{1}{2}\left(C_G + \frac{\Delta t}{2\eta_G}\right)\Delta\sigma' + \sum_i \frac{C_{Gi}}{2}\left\{1 - \left[1 - \exp\left(-\frac{\Delta t}{T_{Gi}}\right)\right]\frac{T_{Gi}}{\Delta t}\right\}\Delta\sigma' \\
&\quad + \frac{\Delta t}{2\eta_G}\sigma'(t) + \sum_i \frac{C_{Gi}}{2}\left[1 - \exp\left(-\frac{\Delta t}{T_{Gi}}\right)\right]\sigma'(t) - \sum_i \left[1 - \exp\left(-\frac{\Delta t}{T_{Gi}}\right)\right]\varepsilon'_i(t) \qquad (2.2) \\
\Delta\varepsilon_a{}' &= \frac{\Delta t}{\eta_G}\sigma'(t) + \sum_i C_{Gi}\left[1 - \exp\left(-\frac{\Delta t}{T_{Gi}}\right)\right]\sigma'(t) - 2\sum_i \left[1 - \exp\left(-\frac{\Delta t}{T_{Gi}}\right)\right]\varepsilon'_i(t) \\
\Delta\varepsilon_m &= \frac{1}{2}\left(C_K + \frac{\Delta t}{3\eta_K}\right)\Delta\sigma_m + \sum_i \frac{C_{Ki}}{3}\left\{1 - \left[1 - \exp\left(-\frac{\Delta t}{T_{Ki}}\right)\right]\frac{T_{Ki}}{\Delta t}\right\}\Delta\sigma_m \\
&\quad + \frac{\Delta t}{3\eta_K}\sigma_m(t) + \sum_i \frac{C_{Ki}}{3}\left[1 - \exp\left(-\frac{\Delta t}{T_{Ki}}\right)\right]\sigma_m(t) - \sum_i \left[1 - \exp\left(-\frac{\Delta t}{T_{Ki}}\right)\right]\varepsilon_{mi}(t) \qquad (2.3) \\
\Delta\varepsilon_{am} &= \frac{\Delta t}{\eta_K}\sigma_m(t) + \sum_i C_{Ki}\left[1 - \exp\left(-\frac{\Delta t}{T_{Ki}}\right)\right]\sigma_m(t) - 3\sum_i \left[1 - \exp\left(-\frac{\Delta t}{T_{Ki}}\right)\right]\varepsilon_{mi}(t)
\end{aligned}$$

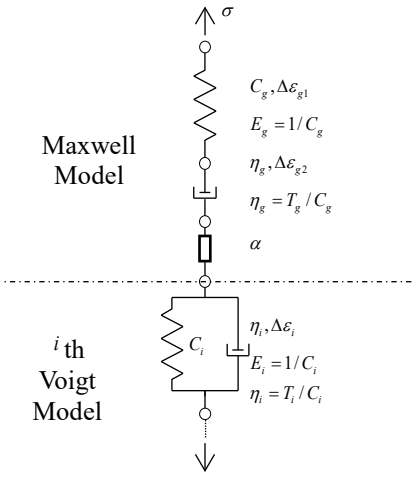


Figure 2.1.1 generalized Voigt model

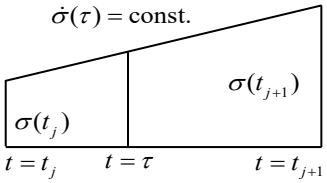


Figure 2.1.2 Linear variation of stress during a time increment Δt step

Table 2.1.1 Variables of the constitutive equations of biaxial tension

Item	Variable
For Maxwell model	Suffix g
For Voigt model	Suffix i
Time increment	Δt
Temperature increment	ΔT
stress increment	$\Delta\sigma', \Delta\sigma_m$
Visco-elastic strain increment	$\Delta\varepsilon^{el}$
Incremental strain for Maxwell element	$\Delta\varepsilon'_{g1}$, $\Delta\varepsilon_{mg1}$, $\Delta\varepsilon'_{g2}$, $\Delta\varepsilon_{mg2}$
Incremental strain for voigt element i	$\Delta\varepsilon'_i$, $\Delta\varepsilon_{mi}$
Compliance of elastic spring element	C_{Gg}, C_{Kg}, C_{Gi}, C_{Ki}
Viscosity	η_{Gg}, η_{Kg}, η_{Gi}, η_{Ki}
Relaxation and retardation time	$T_g = T_{Gg} = T_{Kg}$, $T_i = T_{Gi} = T_{Ki}$
Coefficient of linear expansion	$\alpha(T)$

$$\overline{C}_G(t) = C_{Gg} + \frac{\Delta t}{2\eta_G} + \sum_i C_{Gi}\left\{1 - \left[1 - \exp\left(-\frac{\Delta t}{T_{Gi}}\right)\right]\frac{T_{Gi}}{\Delta t}\right\}$$
$$\overline{C}_K(t) = C_{Kg} + \frac{\Delta t}{2\eta_K} + \sum_i C_{Ki}\left\{1 - \left[1 - \exp\left(-\frac{\Delta t}{T_{Ki}}\right)\right]\frac{T_{Ki}}{\Delta t}\right\} \tag{2.4}$$

Depending on strain level of ETFE Film, creep strains show nonlinearity. Accordingly, the relation between linear strain vector $\{\varepsilon^{el}\}$ and nonlinear strain vector $\{\varepsilon^{nl}\}$ is expressed in the following equations with nonlinear visco-elastic coefficient, $\beta(\overline{\sigma})$.

The nonlinear visco-elastic strain increment vector $\{\Delta\varepsilon^{nl}{}_{j+1}\}$ is expressed as follows;

$$\begin{aligned}\{\Delta\varepsilon^{nl}{}_{j+1}\} &= \{\varepsilon^{nl}{}_{j+1}\} - \{\varepsilon^{nl}{}_{j}\} \\ &= \left\langle \beta(\overline{\sigma}_{j+1}) - \beta(\overline{\sigma}_j)\right\rangle\left\langle \{\varepsilon^{el}{}_j\} - \{\varepsilon^{\theta}{}_j\}\right\rangle + \beta(\overline{\sigma}_{j+1})\left\langle \{\varepsilon^{el}{}_{j+1}\} - \{\varepsilon^{\theta}{}_{j+1}\}\right\rangle + \{\varepsilon^{\theta}{}_{j+1}\}\end{aligned} \tag{2.5}$$

where $\beta(\overline{\sigma})$ is a nonlinear visco-elastic coefficient

$$\beta(\overline{\sigma}_i) = B_4\overline{\sigma}_i^{\,4} + B_3\overline{\sigma}_i^{\,3} + B_2\overline{\sigma}_i^{\,2} + B_1\overline{\sigma}_i + B_0 \tag{2.6}$$
$$\overline{\sigma} = \left(\sigma_x^{\,2} - \sigma_x\sigma_y + \sigma_y^{\,2} + 3\tau_{xy}^{\,2}\right)^{1/2} \tag{2.7}$$

From the above, we can obtain the nonlinear visco-elastic strain increment vector $\{\Delta\varepsilon^{nl}{}_{j+1}\}$ by using the nonlinear visco-elastic coefficient $\beta(\sigma)$. In this paper, $\beta(\sigma) = 1$ to simplify the problem.

The shift factor a_T is also expressed by Eq.(2.8) with activation energy ΔH.

$$\log_{10} a_T(T) = \frac{1}{2.303}\frac{\Delta H}{R}\left(\frac{1}{T}-\frac{1}{T_0}\right) \tag{2.8}$$

where $R = 8.314\times10^{-3}\,kJ/(mol\cdot K)$ is applied.

3. Constants to be applied in the incremental model constitutive equations

The following several parameters, being the same values as in the previous paper, are used; creep compliance of ETFE, activation energy ΔH , coefficient of linear expansion $\alpha(T)$.

Creep compliances are shown in Table 3.1.1 on a basis of C_g=4.14E-04 [mm^2/N]. Activation energy ΔH of ETFE is shown in Table 3.2.1 and Figure 3.2.1. The values are to be utilized later in the present analysis.

Coefficient of linear expansion $\alpha(T)$ of Eq,(3.1) is used.

$$\alpha(T) = (-2.057\times10^{-8}T^4 + 3.289\times10^{-5}T^4 - 1.847\times10^{-2}T^2 + 4.443T - 379.6)\times\overline{\alpha} \tag{3.1}$$

Table 3.1.1 Retardation time T_i [sec] and compliance C_i [mm^2/N]

i	T_i	C_i	i	T_i	C_i	i	T_i	C_i
1	9.13E+13	9.12E-04	10	9.35E+06	1.72E-05	19	9.57E-01	1.25E-05
2	3.65E+12	2.37E-04	11	1.87E+06	2.69E-04	20	1.91E-01	6.04E-05
3	7.30E+11	6.65E-04	12	3.74E+05	4.70E-05	21	7.66E-03	1.66E-05
4	1.46E+11	2.65E-04	13	7.48E+04	1.98E-04	22	1.53E-03	8.20E-07
5	2.92E+10	1.07E-03	14	1.50E+04	2.22E-05	23	3.06E-04	1.48E-04
6	5.84E+09	1.54E-04	15	2.99E+03	1.35E-04	24	1.23E-05	1.92E-05
7	1.17E+09	7.95E-04	16	5.98E+02	3.49E-05	25	2.45E-06	5.54E-05
8	2.34E+08	1.21E-04	17	1.20E+02	1.28E-04	26	4.90E-07	7.44E-06
9	4.67E+07	4.61E-04	18	4.79E+00	6.30E-05			

Table 3.2.1 Activation energy[1,2]

temperature T [°C]	activation energy ΔH [kJ/(mol K)]
$T <$ 40	113.707
40 $< T <$ 90	342.261
90 $< T$	447.237

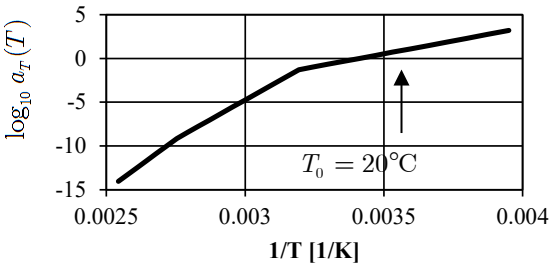


Figure 3.2.1 Relationship between inverse of temperature T and shift factor represented in $\log_{10} a_T(T)$ with reference temperature T_0 of 20°C

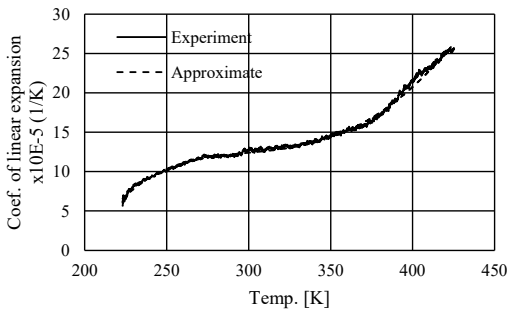


Figure 3.3.1 Coefficient of linear expansion $\alpha(T)$

Table 4.1.1 Biaxial Creep Test Conditions

Film thickness	250μm
Width	100mm
Chuck distance	200mm
Gauge length	24mm
Max Stress	10, 12, 14MPa
Stress Ratio	1:1, 2:1, 1:2, 5:1, 1:5, 1:0, 0:1
Chuck Speed	Loading / 2sec.
Creep Time	7days
Temperature	20.4 and 2.6 ℃ 7 cycles, each 12hours (Figure 4.1.2)

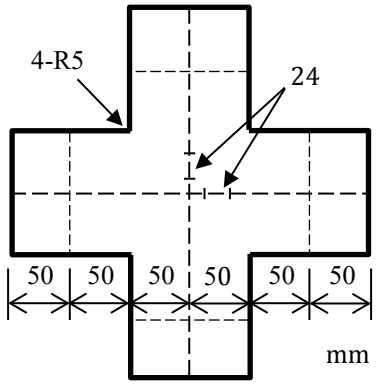


Figure 4.1.1 Shape of test specimen

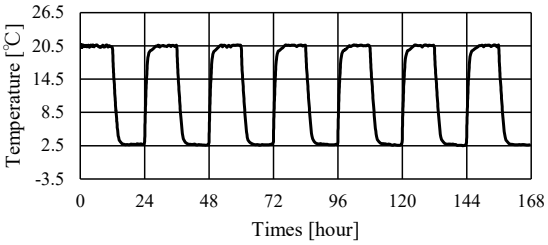


Figure 4.1.2 Temperature history

4. Biaxial creep characteristics of ETFE film under temperature change

4.1. Biaxial creep tests

Biaxial creep tests are performed. The shape of test specimen, temperature history and biaxial creep test conditions are shown in Figures 4.1.1, 4.1.2 and Table 4.1.1. Experimental results are shown in Figure 4.1.3. Phenomenon can be seen that a temperature strain of about 0.3% occurs due to a temperature change of 18 ℃. In creep test results, the temperature strains are small than the other strains.
Creep compliance is calculated from the test results. The strain after one week is shown in Fig. 4.1.3 and 4.1.4 for the stress ratio 1: 0 and 1: 1. The creep compliance ratio J/J0 is determined from the following equation and is shown in Figures 4.1.5 and 4.1.6. Here, stress ratio 1:0 assumes J0 = 0.144 [%] and stress ratio 1:0 assumes J0 = 0.072 [%].

$$J / J_0 = (\varepsilon / \sigma) / J_0 \tag{4.1}$$

From these results, it was found that creep compliance needs to be different for each stress ratio. However, no good method has been found at the moment. Therefore, in this paper, nonlinear viscoelastic coefficients $\overline{\beta}\left(\overline{\sigma_j}\right)$ obtained from the stress ratio 1: 0 are used.

$$\overline{\beta}\left(\overline{\sigma_j}\right) = 9\text{E-}05\overline{\sigma_j}^4 - 0.0039\overline{\sigma_j}^2 + 1.0 \tag{4.1}$$

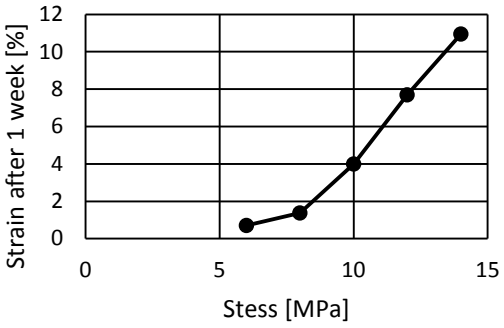


Figure 4.1.3 Strain after 1 week;
Stress ratio 1:0

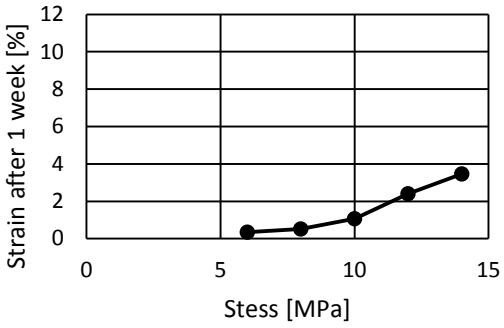


Figure 4.1.4 Strain after 1 week;
Stress ratio 1:1

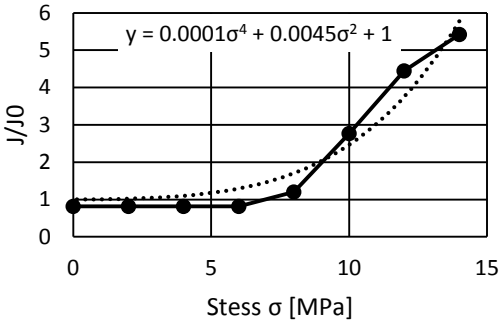


Figure 4.1.5 J/J0 after 1 week;
Stress ratio 1:0, J0=0.144%

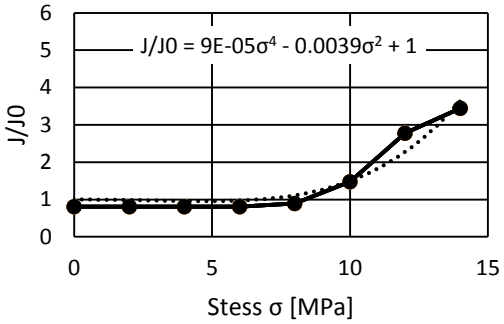


Figure 4.1.6 J/J0 after 1 week
Stress ratio 1:1, J0=0.072%

4.2. Numerical simulation

The results of numerical simulation for biaxial creep test are shown in Figure 4.2.1. The results confirm that the creep characteristic as a tendency is accurately expressed by the proposed constitutive equations. In particular, by adopting nonlinear viscoelastic coefficients for the stress ratio 1:1, it can be confirmed that the experimental results can be accurately expressed for the stress ratios 1:1. But, other stress ratio results have differences in strain between experiment and numerical analysis.

It is found that the proposed equation of nonlinear viscoelastic coefficient does not show good value.

5. Conclusions

The present study presents biaxial creep tests under a temperature change together with the constitutive equations for numerical simulation, then through comparison the validity is confirmed. In future, identification of nonlinear viscoelastic coefficients will be carried out through consideration of biaxial effectt. Implementation of creep tests which include large range of stress levels as well as proposition of the constitutive equation will be developed.

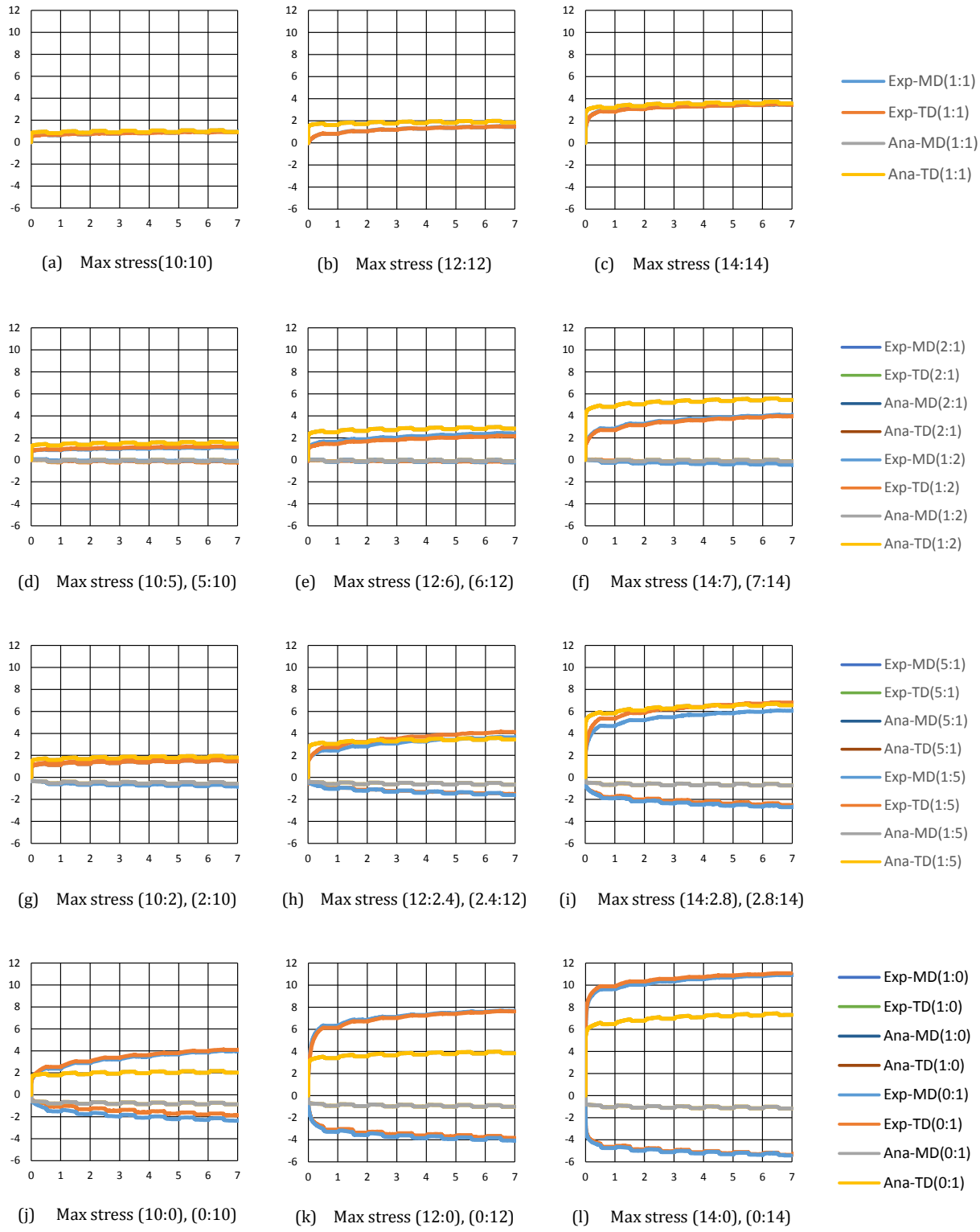


Figure 4.2.1 Creep strain of creep test and estimated results
(Ana : Analytical results, Exp : Experimental results, X-axis : Times [day], Y-axis : Strain[%])

References

[1] Kawabata K., Moriyama F.: Study on viscoelastic characteristics and structural response of film membrane structures, *Proc. of the IASS-APCS 2006 International Symposium*, MB01.150-151, 2006.10

[2] Moriyama F.: Study on Viscoelastic Behavior of ETFE Film Pneumatic Structure, *PhD Thesis*, Yokohama National University, Japan, 2006.3 (In Japanese)

[3] Eul-Seok JEONG, Masaya KAWABATA : Visco-Plastic Constitutive Equation of ETFE Film - Examination on the Stress Strain relationships of Uniaxial and Biaxial Tensile Deformation, *IABSE-IASS 2011 Symposium Proceedings*, Ref. No. 0799, 2011.9

[4] Wu M., Li Y. : Revised finite element formulation for membrane creep analysis, *Proc. of the IASS-SLTE 2014*, Paper No. 209, 2014

[5] Galliot C, Luchsinger RH. : Uniaxial and biaxial mechanical properties of ETFE foils, *Polymer Testing* 30(4), 356-365, 2011

[6] Li Y., Wu M., Wang H. : biaxial creep tests of ETFE foil, *Proc. of the IASS-SLTE 2014*, Paper No. 136, 2014

[7] Yoshino T., Segawa S., Oda K.: Material characteristics of ETFE film under bi-axial tension and stress-displacement analysis considering the elasto-plastic characteristics, *Research Report on Membrane Structures 2004*, 18, 31-39, 2005.2 (In Japanese)

[8] Testing method for elastic constants of membrane materials, *Standard of Membrane Structures Association of Japan MSAJ/M-02-1995*, 1995

[9] Testing method for in-plane shear stiffness of membrane materials, *Standard of Membrane Structures Association of Japan MSAJ/M-01-1993*, 1993

[10] Tatsuya Yoshino, Shiro Kato : Formulation of non-linear incremental constitutive equation of ETFE film structure considering the dependence on temperature change, *IASS 2013 Symposium*, Paper ID 1331, 2013.9

[11] Tatsuya YOSHINO, Shiro KATO : Viscous characteristics of ETFE film sheet under biaxial tensions, *Proc. of IASS Symposium 2015*, No. IASS2015-419518, 2015.8

[12] Tatsuya YOSHINO, Shiro KATO : Viscous characteristics of ETFE film sheet under equal biaxial tensions, *TENSINET - COST TU1303 International Symposium 2016*, Procedia Engineering, Volume 155, Pages 442-451, 2016.9

[13] Tatsuya YOSHINO, Shiro KATO : Viscous characteristics of ETFE film sheet under temperature change, *VIII International Conference on Textile Composites and Inflatable Structures STRUCTURAL MEMBRANES 2017*, pp. 253-264, 2017.10

[14] Tatsuya YOSHINO, Shiro KATO : Viscous characteristics of ETFE film sheet under temperature change in biaxial tensions, *Proceedings of the IASS Symposium 2018, Boston, USA, July 16-20, 2018*

Proceedings of the IASS Annual Symposium 2019 – Structural Membranes 2019
Form and Force
7 – 10 October 2019, Barcelona, Spain
C. Lázaro, K.-U. Bletzinger, E. Oñate (eds.)

Weathering influence on the mechanical properties of PVC-coated polyester fabrics with special emphasis on irradiance control

Hastia ASADI *, Jörg UHLEMANN*, Natalie STRANGHÖNER*

*University of Duisburg-Essen, Institute for Metal and Lightweight Structures, Universitätsstr. 15, 45141 Essen, Germany, hastia.asadi@uni-due.de

Abstract

Weathering resistance assessment of membrane material is very important while studying the durability of membrane structures. However, until now only few studies have been focused on it. The first objective of this paper is to show the importance of coating (both main and top coating) on the weathering resistance of PVC-coated polyester fabrics by using an artificial accelerated weathering chamber. The quantitative degradation rates for PVC-coated and uncoated polyester fabrics are compared using a standardized artificial weathering procedure. The outcome illustrates the quantitative protection potential of the coating system against weathering. The second objective is to determine the influence of different amounts of irradiance on the degradation of uncoated woven polyester material while the final radiant energy is the same. Increasing the amount of irradiance on PES-PVC fabrics while the degradation mode for mechanical properties is the same as during natural outdoor weathering can provide a suitable accelerating approach of artificial weathering. These tests were carried out on uncoated polyester fabrics in order to study the effect directly on the load bearing component of the composite PES-PVC.

Keywords: PES-PVC fabric, weathering, artificial accelerated weathering, UV irradiance, photo degradation, tensile strength.

1. Introduction

Architectural fabrics degrade through different environmental stress factors including UV radiation, heat, moisture and so on, which are collectively known as weathering. Each one of these factors causes weathering degradation, individually or in combination. In principle, weathering resistance assessment of materials can be carried out by natural or artificial weathering tests. On the one hand, unfortunately, natural weathering tests are very slow and need several years to lead to significant degradation of the material. On the other hand, new architectural fabrics need performance data before they can enter the market. For this reason, accelerated exposure strategies are required. It should be noticed that among atmospheric environmental factors, the UV irradiation of the sunlight is the main parameter in service performance of polyester and PVC materials [1].

“Polyester-PVC” fabrics consist of a woven base polyester (PES) fabric stabilized and protected by PVC-coatings on both sides. The PVC coating contains additives that include UV stabilizers, fire retardants, colouring and fungicidal agents. In fact, polyester yarn is mainly bright or semi bright which makes it sensitive to UV and also polyester is in the group of ester organic material which is sensitive to hydrolysis. The PVC barrier protects the yarns. For avoiding wicking, sometimes low wick polyester yarns are used which are made hydrophobic. PVC (polyvinylchloride) coating is used as paste. PVC is made of either suspension or emulsion and plasticizers. Plasticizers might be phthalates, phosphates, chlorinated or other ester products which are susceptible to migrate to the surface of the fabric [2]. Actually, the PVC coating is the “prime” or “main” coating. This prime coat itself is in turn protected

Copyright © 2019 by Hastia Asadi, Jörg Uhlemann, Natalie Stranghöner
Published by the International Association for Shell and Spatial Structures (IASS) with permission.

by a top coat while both main and top coat under normal use condition can erode and even disappear. The disappearance of the top coat exposes the PVC directly to aggressive impacts. In vinyl coated fabrics there are three top finishes including liquid acrylic and PVDF (polyvinylidene fluoride) and PVF film. In a technical report of DuPont [3], a series of artificial weathering tests on seven commercially available fabrics at different exposure time periods were reported. By comparing the changes of thickness, colour and glossiness of three different top coatings it was concluded that PVF films are more durable. In this study, liquid acrylic and PVDF coatings were depleted after artificial weathering equals to 5 years of south Florida exposure at the angle of 45 degrees to the horizon. In this report, the "south Florida exposure" is represented by an exposure of 1200 kilojoules over one year at an angle of 45 degrees to the horizon; no information are given regarding temperature as well as duration and amount of humidity. It might be added at this stage that "Florida exposure" is often used in various studies, but it is nowhere specified, so that each study has its own "Florida exposure definition" not clearly specified in the publications. Herewith, it is nearly impossible to assess the influence of Florida exposure especially comparing different studies. Additionally, a TiO_2 (titanium dioxide) primer can improve the weathering resistance as well [4] although it causes post-photo reaction in dark cycles [5]. In Table 1 a list of artificial weathering research works on PES-PVC fabrics is shown. According to this table, different accelerated weathering test methods are used for weathering simulation. For this reason, there are big discrepancies in the results [6] that arises the following two questions: Which accelerated weathering test methods describes the reality better? Is there any possibility to unify them in a way to achieve a satisfying simulation of statistical models of effects of natural weathering?

Table 1: Various specifications of accelerated aging, state of the art

Authors	Year	Standard	Test cycle
Hiroshi Toyoda et al. [7]	1994	JIS B 7754[8]	Xenon arc lamp 6.5 kw, panel temperature = 63 °C ± 3 K, Relative humidity (RH) = 65 % ± 20 %, spray cycle = 18 min., total test time: 5000 hours
Hiroshi Toyoda, Kenji Motohashi [9]	2005	-	Xenon-arc source and open-flame sunshine carbon-arc lamp with 180 W/m^2, 41 W/m^2 and 75 W/m^2 at 300-400 nm, black panel temperature = 63 °C ± 3 K, RH = 50 % ± 5 %, duration of spraying = 18 min., dry interval between spraying = 102 min.
Zhaorong Chen, Qilin Zhang and Wanli Xue [10]	2013	DG/TJ08-2019-2007 [11]	Irradiation = 800 W/m^2, temperature = 63 °C, RH = 50 % and rainfall time/time without rain =18 min./102 min.
Luís São Joãoa, Raquel Carvalhob and Raul Fangueiroa [12]	2016	AATCC Test Method 186-2001 [13]	Fluorescent lamp with a wavelength of 340 nm, corresponding to UVA light. UVA exposure cycle = 16 hours with a temperature of 50 °C, followed by a water "pulverization" at 50 ºC
Xudong Yang et al. [5]	2016	ASTM G53-88 [14]	Four fluorescent UVB-313 lamps, temperature between 25 °C and 30 °C and a working cycle of 22 h continuous light exposure, followed by 2 h water spray
Yingying Zhang and Mingyue Zhang [15]	2017	EN ISO 4892-2 [16]	Xenon lamp SN-300, the irradiation intensity is 872 W/m^2, temperature = 63 ºC, RH = 50 %, and the rain/dry cycle is 18 min./102 min.

The correlation of the results between artificial accelerated and natural weathering is crucial to predict the service life of materials. Mostly, the establishment of the correlation is based on the "reciprocity law". Bunsen and Roscoe [18] proved by their experiments that all photochemical reaction mechanisms are not dependent on radiant intensity (I) and exposure time (t), but related to the product of them, known as total absorbed energy, which means that with the same total absorbed energy (It = constant) the photo responses do not change. This hypothesis was later known as the reciprocity law [19]. After the publication of Bunsen and Roscoe some scientists observed reciprocity law failures in their experiments (e. g. [20]) until finally the astronomer Schwarzschild [21] proposed a modification for this law. This is given as I^pt = constant or It^p = constant, where p is the "Schwarzschild coefficient" and depends on material and experimental conditions. Yang et al. [22], did a research on photo-oxidation kinetics of PVC-coated membrane material under three different UV radiation intensities while the yellowness index and UV spectrum were analysed to trace the degradation products (conjugated double bonds). They observed, Schwarzschild's law with p = 0.7 had a good correlation under various radiation intensities. They continued their research on PVC-coated membrane material to establish a correlation between two light sources (UVA-340 and UVB-313) and three different UV intensities [23]. Tensile properties of the samples were measured and Fourier-transform infrared spectroscopy (FTIR) and ultraviolate-visible spectrometry were used to analyse the chemical change of the material. Finally, they proposed: $I^{1.112}$ t = constant, for different UV radiation in UVB-313 lamps, and $(\alpha I)^{1.22}$t = constant, for correlation of both UVA-340 and UVB-313 lamps where α is the effective UV radiation coefficient (ratio of effective UV radiation to total UV radiation). Finally, in 2016 [5] this team focused on PVC-coated membrane material under both artificial and outdoor weathering conditions where the cumulative UV radiation energy was the same. Here, both tensile strength and whiteness index were measured for specimens with different tensile stresses (0 %, 5 %, 10 % and 20 % of the breaking strength). Under the assumption of equivalent aging degradation between artificial and natural weathering results, p was estimated 0.87 and 0.96 for whiteness index and breaking strength retention, respectively.
On this basis, it is the aim of the present contribution to compare:

(1) tensile strength changes of artificially accelerated pure polyester and PVC-coated polyester fabrics type II at different weathering periods and
(2) the photo-oxidation reaction results under three different UV irradiance intensities with the same cumulative UV radiation energy for recognizing if the original reciprocity law could be applied for the prediction of service life of pure polyester and PVC-coated polyester fabrics type III.

Both experimental studies were carried out in the Essen Laboratory for Lightweight Structures (ELLF) at the Institute for Metal and Lightweight Structures of the University of Duisburg-Essen.

2. Materials and methods

2.1. General

In this contribution, two experimental series were carried out to assess (1) weathering degradation of coated and uncoated fabrics under the same artificial weathering conditions (combination of UV+temperature+humidity) at different time periods, and (2) the applicability of the reciprocity law with considering three different UV irradiance intensities while the cumulative UV radiation energy is the same. The second test procedure was artificial weathering with only combination of UV+temperature. In fact, the photo degradation process is always influenced by these two parameters together.

2.2. Materials

The mechanical properties of coated fabrics depend on the properties of the substrate (yarns), coating formulation, coating technique and processing conditions during the coating [24]. For this reason, in this paper for assessing the influence of the aforementioned parameters, coated and uncoated polyester fabrics were used for artificial weathering tests.

For the comparison of strength degradations of coated and uncoated fabrics, pure woven polyester and PVC-coated polyester fabrics type II were analysed. For the analysis of the UV irradiance intensity impact, pure woven polyester and PVC-coated polyester fabrics type III were utilized. The specifications of the aforementioned materials are shown in Table 2. It should be mentioned that all materials were given from the same material producer while the first two ones had the same batch number. PES-PVC type II and III have light brown and white colour, respectively whereas uncoated fabrics in both types are white. The type classification is according to the JRC Science and Policy Report [25]. For the present contribution, the usage of the two different types of PES-PVC fabrics is due to availability.

Table 2: Specification of PES/PVC membrane material

Material	Weave pattern	Yarn	Mass [g/m^2]	Main coating	Top coating	Primer
PES-PVC type II	Panama 2/2	PES low wick	900	PVC	PVDF	TiO_2
PES type II	Panama 2/2	PES low wick	-	-	-	-
PES-PVC type III	Panama 2/2	PES low wick	1050	PVC	PVDF	TiO_2
PES type III	Panama 2/2	PES low wick	-	-	-	-

2.3. Methods

As it is mentioned before, in the first experiment, an artificial weathering test with a combination of UV+temperature+humidity was carried out. The parameters were set according to exposure mode 1 of EN ISO 4892-3 [26]. The exposure mode 1 consists of 8 hours radiation of UVA-340 lamps with 0.76 W/m^2 at 340 nm at 60 °C ± 3 K and 4 hours condensation at 50 °C ± 3 K. By considering 12 hours for each cycle and 250 cycles as proposed for coated fabrics in EN 15619 [22], the overall test duration is equal to 3000 hours. As the study of João et al. [12] showed that 3 months (2160 h) of artificial weathering did not lead to any significant changes of the tensile strength of PES-PVC fabrics, in the presented study, weathering periods were assumed not only as 3000 hours but also 6000 hours with the same specifications of exposure mode 1.

In the second experiment, a combination of UV+temperature was utilized to survey the photo degradation process. In this way, the exposure cycles include only the use of UVA-340 lamps with three different irradiances, namely 0.76 W/m^2, 0.9 W/m^2 and 1.2 W/m^2 at 340 nm while the temperature is fixed at 60 °C ± 3 K. Utilizing irradiances more than 1.2 W/m^2 with UV-fluorescent lamps turned out to be not economical because the lamps broke very fast after only a few hours. Time periods of each test were calculated in a way that the cumulative UV radiation energy was the same under different UV intensities. This is shown in Table 3. In both test procedures, the weathering chamber is a QUV/spray accelerated weathering tester. The mechanical performance has been assessed using a CRE tensile testing machine according to EN ISO 1421 [28].

Table 3: Cumulative UV radiation under different UV intensities and time periods

Aging time [h]	UV irradiance [W/m^2 at 340 nm]	Cumulative energy [KJ/m^2]
720	0.76	1969.9
608	0.9	1969.9
456	1.2	1969.9

3. Results and discussions

3.1. Comparison of strength degradation of coated and uncoated fabrics

There are three specific regions in stress-strain curves of both woven coated and uncoated fabrics including inter-fiber friction, decrimping, and yarn extension regions [29], [30], see Figure 1. This general trend remains almost unchanged in PES-PVC specimens during all tested weathering time periods and in PES fabric with up to 480 hours of weathering in both warp and weft directions, see Figure 1. After 480 hours, the behaviour of the uncoated woven PES fabric is changing significantly: the decrimping region disappears, i. e. the degraded tensile strength is reached and filaments break before the yarns decrimp and become strained. These three aforementioned regions are not recognizable for 3000 hours and 4684 hours of weathering in both directions for uncoated polyester type II. It should be noticed that the given stress-strain curves represent mean values of three tested specimens. Zooms depict a limited range of strains (0 % to 12 %) for scrutinizing the behaviour of the longer weathered specimens.

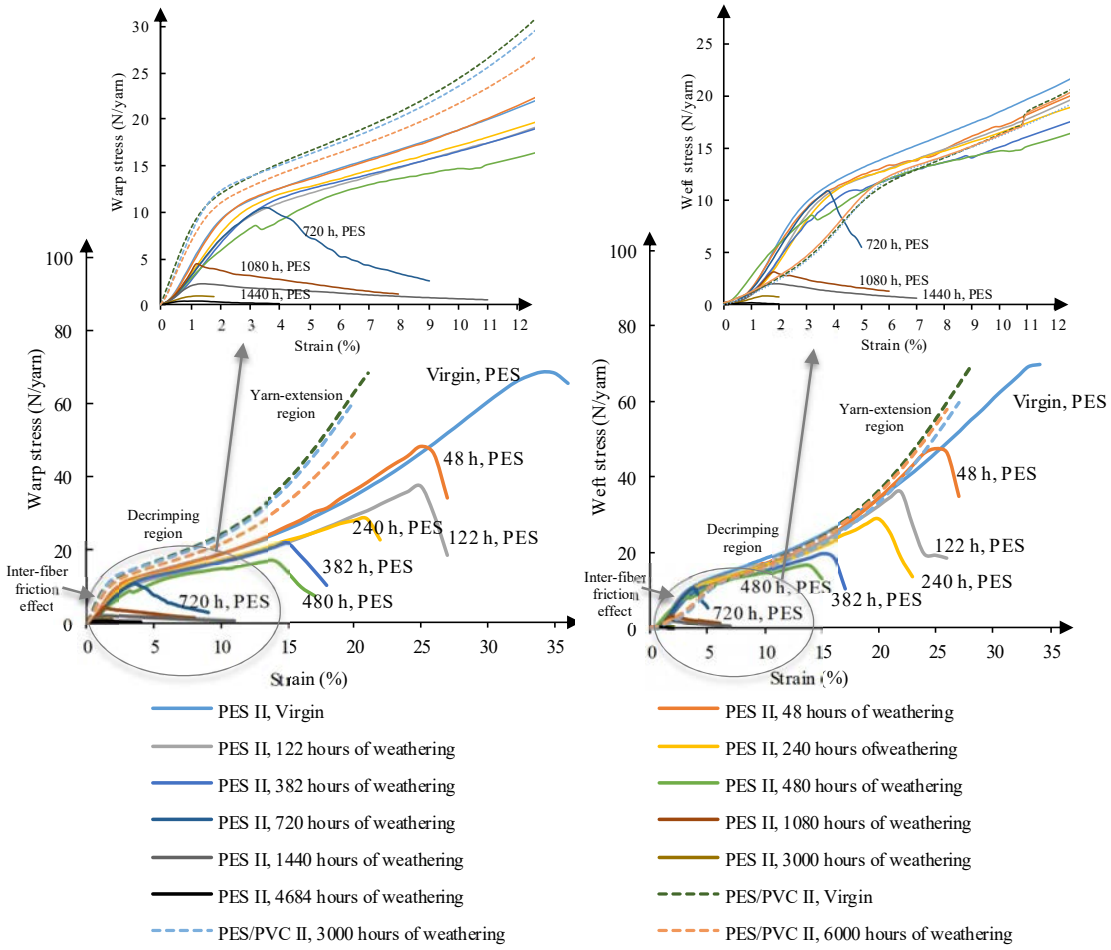


Figure 1: Mean stress-strain curves of non-coated and PVC-coated polyester fabrics type II under different aging time

Figure 2 illustrates the mean residual tensile strength of three single tests after different periods of weathering. According to this figure, a decreasing trend is governing the charts that shows with the passage of time weathering causes negative changes in tensile strength of both materials, coated and

uncoated fabric. But these unfavourable changes are far bigger in uncoated fabrics than in the coated ones. For example, during 3000 hours of weathering, the tensile strength of the coated PES fabric decreases about 5 % in warp and 13 % in weft direction while the uncoated PES fabric decreases about 99 % in both warp and weft directions. This shows the quantitative protection potential of the coating system against weathering.

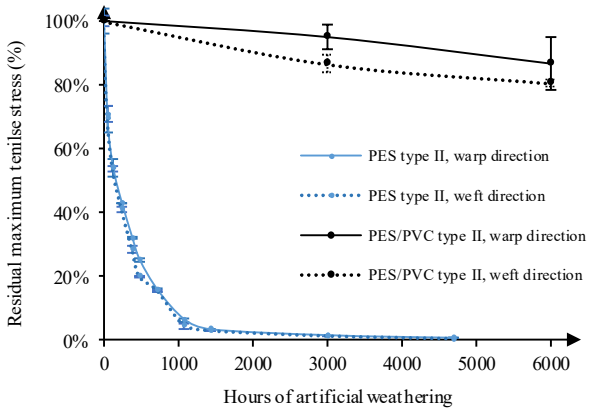


Figure 2: Residual maximum tensile stress of non-coated and PVC-coated polyester fabrics type II under different aging time

3.2. Investigations into the applicability of the reciprocity law in photo degradation

Figure 3 and 4 depict stress-strain curves of virgin and artificially weathered fabrics under different UV intensities while the UV degrading energy is the same. Mean stress-strain curves based on five single tests each are documented. Based on Figure 4, for non-coated polyester fabrics type III the applied energy of 1969.9 KJ/m^2 is very aggressive and causes a break far earlier than the virgin material. Nevertheless, this amount of energy does not lead to a significant change in PES-PVC type III fabrics (see Figure 3). Generally, by considering this amount of energy, the stress-strain behaviour of both weathered materials does not change by varying the amount of irradiance.

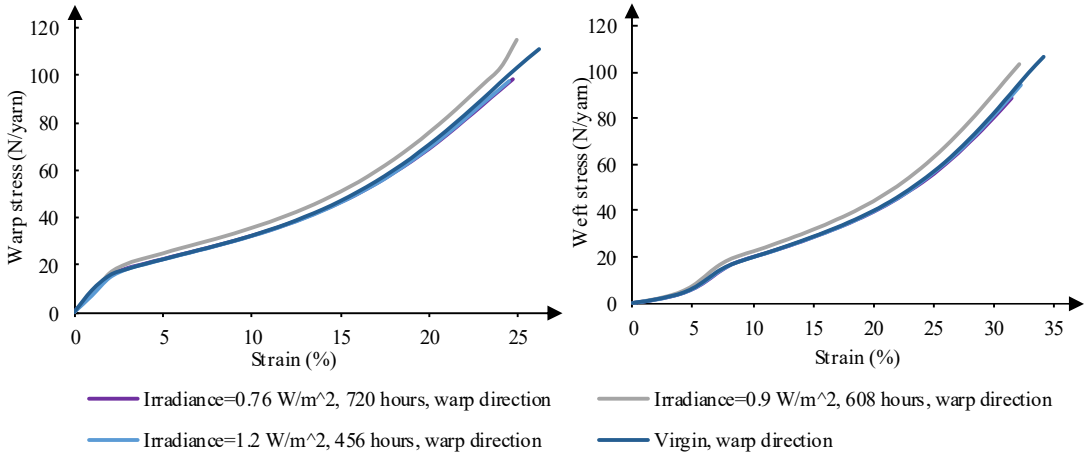


Figure 3: Mean stress-strain curves of PES-PVC type III under different irradiances with the same cumulative energy

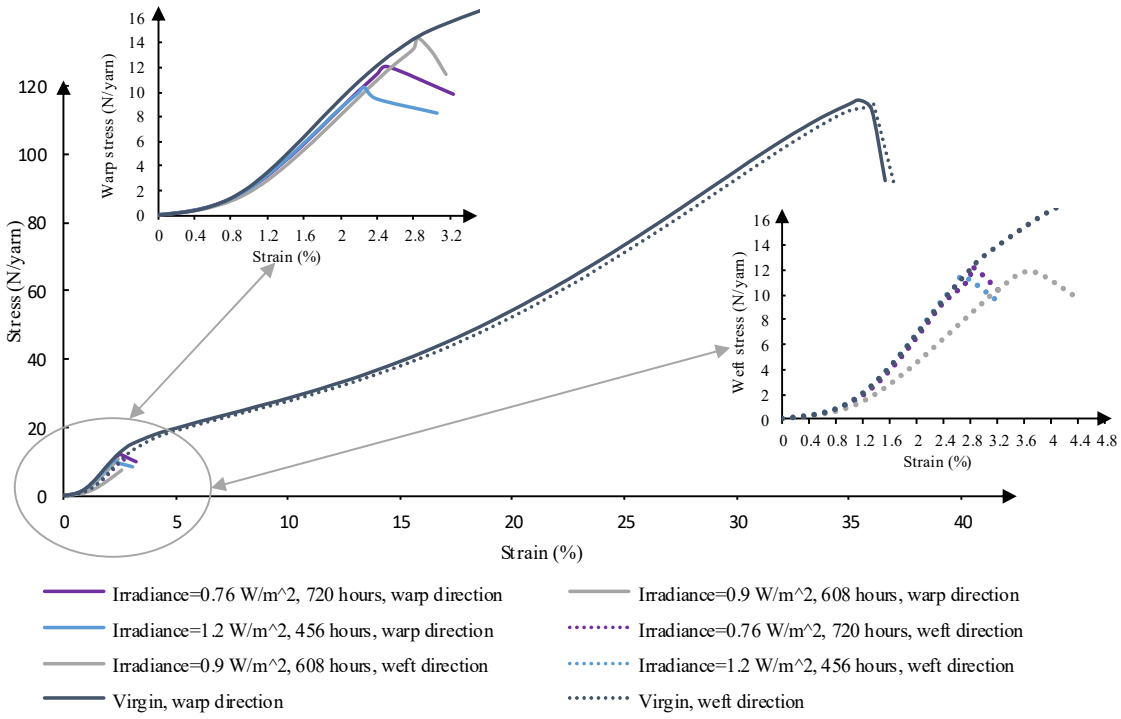


Figure 4: Mean stress-strain curves of non-coated polyester fabrics type III under different irradiances with the same cumulative energy

If the tested materials would follow the original reciprocity law then graphs in Figure 5 should be linear and parallel to the abscissa. In contrast, nonlinear graphs are observed which express that the reached maximum stresses of both coated and uncoated polyester fabrics type III change with varied irradiance while the cumulative energy is the same. Due to this behaviour, more research is required to obtain a Schwarzschild modification of the reciprocity law for the investigated materials.

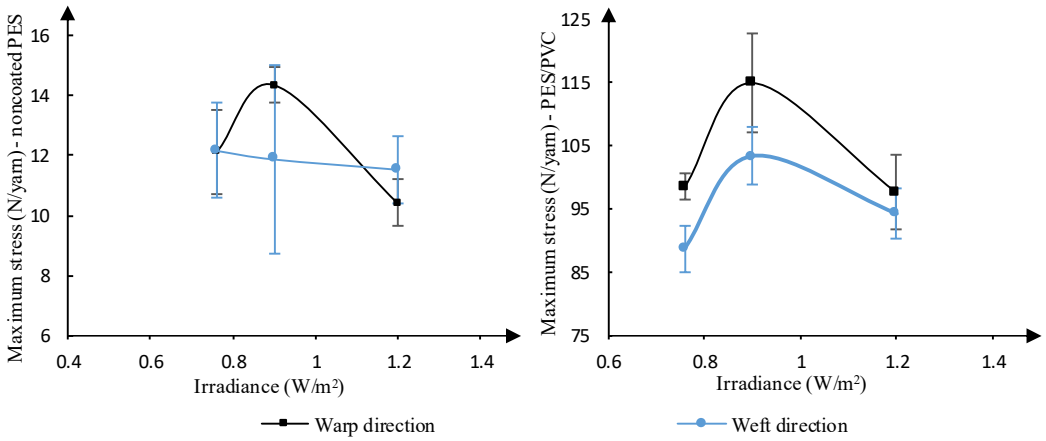


Figure 5: Maximum reached tensile stress of non-coated (left) and PVC-coated (right) polyester fabrics type III under different irradiances with the same cumulative energy

4. Conclusion

This paper presents a study regarding the aging degradation of uncoated and PVC-coated polyester fabrics under combination of UV+temperature+humidity with the help of an accelerated weathering chamber. Additionally, the influence of UV irradiance on the tensile strength of both fabrics was assessed while the total cumulative energy was constant. Taking advantages of these test results, following conclusions are obtained:

(1) It can be confirmed that in PES-PVC fabrics, polyester yarns do not have any considerable resistance against environmental degradation and only the main and top coating provides this resistance during the weathering of these polymers.

(2) In PES-PVC fabrics, the decrease of the tensile strength (photo-oxidation reaction rate) does not obey the original reciprocity law. Further research is needed to develop a Schwarzschild modification equation.

References

[1] R. Benavides et al., "Different thermo-oxidative degradation routes in poly(vinyl chloride)," *Polymer Degradation and Stability*, vol. 73, pp. 417-423, Dec. 2001, cited in [5].

[2] R. Blum, H. Bögner, G. Némoz, *Material properties and testing*, in: B. Forster and M. Mollaert (eds.), *European design guide for tensile surface structures*. TensiNet, 2004.

[3] Du PONT, *A comparative study: architectural fabric top finish performance,* Du Pont™ Tedlar® PVF films

[4] H.A. Razak, C.S. Chue, and H. Toyoda, "Weatherability of coated fabrics as roofing material in tropical environment," *Building and Environment*, vol. 73, no.1, pp. 87-92, 2004.

[5] X. Yang, et al., "Relationship between physical and mechanical properties of accelerated weathering and outdoor weathering of PVC-coated membrane material under tensile stress," *Journal of industrial textiles,* vol. 47, no. 2, pp. 197-210, 2017.

[6] J. Uhlemann, H. Asadi, and N. Stranghöner, "A survey on strength deterioration of Polyester-PVC fabrics," *in Interfaces: architecture. engineering. science: Proceedings of the IASS Annual Symposium 2017, Hamburg, Germany, September 25 - 28, 2017*, A. Bögle, M. Grohmann (Eds.), pp. 1-10.

[7] H. Toyoda et al., "Weatherability of Membrane Structure Materials as Determined by their Exposure Conditions," *J.Stage*, vol. 50, no. 10, pp. 484-488, 1994.

[8] JIS B 7754: 1991-03-01, Light-exposure and light-and-water-exposure apparatus (xenon-arc lamp type).

[9] H. Toyoda, and K. Motohashi, "The Evaluation Method for Weatherability of Membrane Materials for Architectural Membrane Structures," *10DBMC International Conference on Durability of Building Materials and Components, Lyon, France, April 17-20, 2005.*

[10] Z.h. Chen, Q. Zhang, and W. Xue, "Experimental research on Mechanical Properties of PVC Membrane After Aging," *in: Beyond the Limits of Man: Proceedings of the IASS Annual Symposium 2013, Wroclaw, Poland, 2013*, pp. 1-5.

[11] DG/TJ08-2019-2007, Technical specification for inspection of membrane structures, Shanghai.

[12] L.S. João., R. Carvalho and R. Fangueiro, "A Study on the Durability of Textile Membranes for Architectural Purposes," *Procedia Engineering*, 2016; vol. 155, pp. 230-237, 2016.

[13] AATCC Test Method 186-2001, Weather resistance: UV light and moisture exposure.

[14] ASTM G53-88, Practice for operating light- and water-exposure apparatus (Fluorescent UV-Condensation Type) for exposure of nonmetallic materials.

[15] Y. Zhang, and M. Zhang, "Aging properties of polyvinylidenefluoride-coated polyester used in tension membrane structure: effect of loading protocol and environment," *Advances in material and engineering*, vol. 2017, pp.1-10, 2017.

[16] EN ISO 4892-2:2018, Plastics – Methods of exposure to laboratory light sources – Part 2: Xenon-arc lamps (ISO 4892-2:2013).

[17] J.W. Martin, J.W. Chin, and T. Nguyen, "Reciprocity law experiments in polymeric photodegradation: a critical review," *Progress in Organic Coatings,* vol. 47, pp. 292-311, 2003.

[18] R.W. Bunsen and H.E. Roscoe, "Photochemische Untersuchungen," *Ann. Phys*, vol. 2, no. 108, pp. 193, 1859 cited in [17].

[19] R. Latarjet, "Etude expérimentale de la loi de réciprocité dans I'effect biologique primaire des radiations," *CR Acad. Sci.,* vol. 218, pp. 294, 1940, cited in [17].

[20] W.W. de Abney, "Chemical action and exposure," *Photogr. J*, vol. 18, pp. 753, 1893, cited in [17].

[21] K. Schwarzschild, "On the law of reciprocity for bromide of silver gelatin, *Astrophys. J*, vol. 11, pp. 89, 1900.

[22] X. Yang, Y. Yan, and W. Q, "Photo-oxidation of PVC-coated membrane material," *Advanced material research*, vol. 650, pp. 238-244, 2013.

[23] X. Yang et al., "Photo-oxidation of PVC-coated membrane material under different light sources," *Asian journal of chemistry,* vol. 26, no. 17, pp. 5777-5782, 2014.

[24] A.K. Sen, *Coated textiles: principles and applications*, 2nd ed., CRC Press, 2007 cited in [15].

[25] N. Stranghöner, J. Uhlemann et al., *Prospect for European Guidance for the Structural Design of Tensile Membrane Structures*, Luxembourg: Publication Office of the European Union, 2016.

[26] EN ISO 4892-3:2016, Plastics - Methods of exposure to laboratory light sources - Part 3: Fluorescent UV lamps (ISO 4892-3:2016).

[27] EN 15619:2014, Rubber or plastic coated fabrics - Safety of temporary structures (tents) - Specification for coated fabrics intended for tents and related structures.

[28] EN ISO 1421:2016, Rubber- or plastics-coated fabrics – Determination of tensile strength and elongation at break (ISO 1421:2016).

[29] J.J. Lin, "Prediction of elastic properties of plain weave fabric using geometrical modelling," *Woven Fabric Engineering,* chapter 7, 2010.

[30] B.N. Bridgens, and P.D. Gosling, "A Predictive Fabric Model for Membrane Structure Design," *Textile Composites and Inflatable Structures II,* Springer Netherlands, vol. 8, pp. 35–50, 2008.

Proceedings of the IASS Annual Symposium 2019 - Structural Membranes 2019
Form and Force
7-10 October 2019, Barcelona, Spain
C. Lázaro, K.-U. Bletzinger, E. Oñate (eds.)

Architecture from textiles in motion

Erica HÖRTEBORN*, Malgorzata A. ZBOINSKA*, Delia DUMITRESCU[a], Chris WILLIAMS*, Benjamin FELBRICH[b]

* Chalmers University of Technology, Göteborg, Sweden. erica.horteborn@chalmers.se

[a] The Swedish School of Textiles, University of Borås. [b] University of Stuttgart.

Abstract

Wind is one important concern when it comes to its impact on textile structures within architecture. One method to limit wind-caused displacements is to heavily pre-stress the structures. We discuss an alternative approach, in which wind is seen as a positive design parameter for architectural textiles. We explore how one could work with the shape and internal structure of the textile to design architectural structures which become kinetic volumes when airflow is applied. The implications of such a design approach are formulated based on a two-day workshop at the conference Advances in Architectural Geometry (AAG) 2018. The explorations embraced digital and physical simulations of textile behaviors arising from the presence of wind. Smart textiles, whose structures can be changed using heat, were employed to explore how the geometrical expressions of textiles under wind load can be affected through local internal textile property changes. The ambition was to investigate the possibility of dynamically altering the 3-dimensionality of the textiles by reshaping them in real-time using airflow. The main conclusion from the workshop is that the dialogue between the digital and physical simulations seems to play an important role in supporting and enhancing the process of designing the geometrical expressions of textiles subjected to dynamic influence. A combination of the digital and the physical design tools enables the creation of a unique workflow to generate architectural design typologies that would have been difficult to develop if such complementary design tools have not been employed.

Keywords: Textile architecture, architectural form design, digital wind and textile simulation, physical wind simulation, research workshop

1 Introduction

Textiles as design materials in architecture are considered formless. One of the key properties of textiles is their flexibility as they move, bend and adapt to external forces. In tensile architecture, textiles are designed to follow a pre-designed shape, with coated woven fabrics stretched until the resulting shape is virtually stiff; this to avoid deformation by wind. But what happens if we allow movement in the textile? What if wind becomes a design variable that decides upon the expression of a textile architectural form?

As a building material textiles are starting to gain more interest in architecture [5]. The possi-

Copyright © 2019 by Erica Hörteborn, Malgorzata A. Zboinska, Delia Dumitrescu, Chris Williams, Benjamin Felbrich
Published by the International Association for Shell and Spatial Structures (IASS) with permission.

bility of creating seemingly endless variations of textiles with different behaviours and functionalities is very appealing from a design perspective. Similarly appealing is their great potential of becoming a more sustainable choice for architecture - an easily-transported and lightweight material that can be made from a range of different yarns, including recycled and recyclable textile fibres, wood and other organic materials.

1.1 Textile architecture

The textile architecture that we see today embraces mainly tensile structures made from a hybrid combination of polyester membranes and steel cables, pioneered by Frei Otto in projects including the Dance Pavilion at the Federal Garden Exhibition 1957 [7], the German Pavilion Expo 67 and the Munich Olympic Stadium 1972. These types of structures are designed to only work in tension, which makes them very efficient structurally, enabling them to span large distances with little material. At the same time, they are designed to remain static. Furthermore, in terms of geometric expression, these structures are bound to an anticlastic surface typology only. Exceptions can also be found, however. They include the non-tensile use of textiles, in designs in which the softness of the material in combination with the movement of air was embraced as an aesthetic quality. Example projects include the Book House by Olga Sanina and Marcelo Dantas (2012) and the COS X installation at Milan 2015 by Snarkitecture. In the first case, the textile was designed to hang so that it is free to move with the slightest breeze. In the second example, the textile is loosely draped from the ceiling so that airflow caused by people walking through the space can move the respective textile strips. Both projects are more or less temporary structures, and the lightness and flexibility of their textile components are of great advantage not only for creating an ephemeral atmosphere of a building, but also for practical reasons, such as ease of packaging, transport and mounting.

1.1.1 Wind simulations of textile behaviours

Allowing the textile structures to move with and adapt to the can will efficiently lower the wind loads, but opens up for new challenges. Wind loads on structures in the scale of buildings are usually evaluated in either wind-tunnel tests or in computational fluid dynamics (CFD) simulations. For textile structures, it is especially difficult to accurately simulate interactions with wind. Researchers have been able to accurately simulate this behavior of the flapping of a flag in steady wind, in 2D and 3D, in reasent years, making use of the immersed boundary (IB) method [6]. However, especially the simulation in 3D still remains a challenge [10] and consumes high amounts of computational resources . These complications mainly result from the fact that the mass of the air in the boundary layer around the structure is significantly higher than the mass of the textile, thus large deformations occur, especially in the case of loose fabric. [8]. The motion of the fabric mirrors the vortices and turbulence of the wind which makes it difficult for the traditional mesh-based CFD analyses to handle the analysis. The deformations cause the mesh model of the textile and air around it to get tangled up if it is not rebuilt often enough. Re-meshing the model requires considerable computing power, making these calculations less applicable for early-stage design and iterative design processes. However, as exact load calculations are rarely of interest in these early design phases, other less precise simulation methods capable of real-time computation seem more relevant for that purpose. Specifically, the physically based animation (PBA), a field of research in computer graphics, game-engine development and movie animation, offers useful techniques. Here, a set

of particles is simulated to act under the influence of various physical forces and constraints. These constraints range from external forces imposed onto the system from outside, such as gravity and wind, to internal forces that interconnected particles exert on one another, such as spring forces, shape retaining forces or triangular force connections. Additional constraints incorporate collision detection or the definition of immobile particles (anchors).

PBA solvers typically aim at resolving the Newton-based law of forces that the multitude of constraints exert on each individual particle as efficiently as possible, without trading-off too much accuracy. Currently, the popular approaches include position-based dynamics (PBD) [9] and the more recent projective dynamics (PD) [1]. PBD, due to its simplicity and robustness, is widely applied in game engines, such as Nvidia® PhysX™, Havok Cloth™, and Bullet. Maya® nCloth makes use of the PBD paradigm in a 3D modelling environment. PD, on the other hand, is a state-of-the-art technique for geometry processing and constraint-based modelling. Its C++ implementation Shape-Op [2] and especially its descendent Kangaroo, a plugin for McNeel's Rhinoceros® and Grasshopper®, gained popularity among architects and designers for its modular goal-based design, robustness and generality.

Another game-engine called Nvidia Flex combines a very efficient GPU-based implementation of PBD with fluid particle simulation by means of smoothed particle hydrodynamics (SPH) and thus offers a unified platform for simulating a wide range of particle properties. It is accessible to the .Net environment through the platform FlexCLI and available as a Grasshopper® plugin called FlexHopper (figure 1), both of which were developed by one of the authors. With FlexHopper, the simulation of high resolution textiles is possible through the definition of an ordered particle set, spring and triangle constraints, a wind force, anchors and arbitrary additional constraints. FlexCLI and FlexHopper can be found open-source in a Github repository [4].

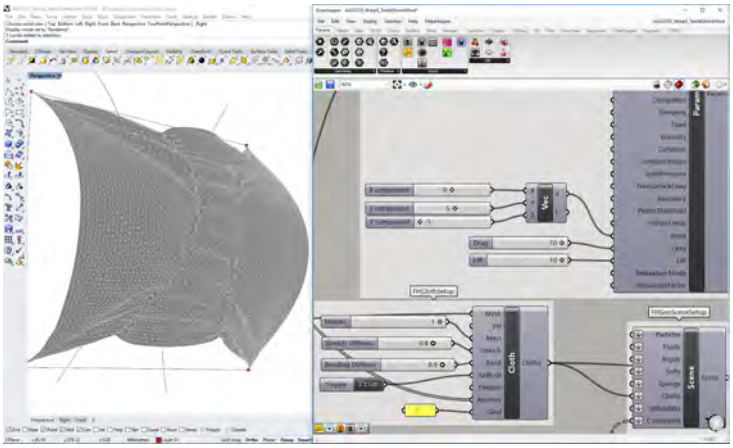


Figure 1: A GPU-based simulation engine, Flexhopper, used in the research workshop.

As mentioned earlier, yet another tool to comprehend the behavior of a large-scale textile system is a downsized model in a wind-tunnel. The discrepancies between this approximation and the actual behavior of fabric architecture mainly arise from the issue of scaling the material system (thickness of the textile and connections, material properties and strength) and the scaling of Reynolds number. Furthermore, the directionality and unpredictability of wind gusts can be

problematic. Despite that, the physical simulations are usefull and relevant, especially for early-stage design of textile architecture, as they provide visual feedback for at least some of the textile behaviors, which from the standpoint of aesthetic explorations is a virtue.

2 Aim of the study

In light of the presented background, our main aim was to generate initial insights on the relevance of using a combination of digital and physical wind simulations in early-stage exploratory design of textile facades. The aesthetic expression of the textiles in our study was informed by two interrelated factors: the internal structure of the textile, intentionally altered across the textile piece to achieve varied wind deformations and therefore varied aesthetic effects, and the action of airflow, transforming the geometrical shapes of textile facade elements in real time. On the one hand, our focus was to explore how the internal structure of textiles can affect their behaviour and geometric expression when in movement. On the other, to evaluate the usefulness of a range of design aids for exploring the design alternatives for such textile architecture in movement, ranging from digital simulations of aesthetic expressions and behaviours to physical models set in motion by moving air.

3 Research design

A workshop involving architectural designers with different levels of design experience and computational competence was chosen as a vehicle for generating the research insights on the subject of designing textile architectural elements informed by airflow and wind.

The research setup in the workshop assumed the development of textile facade concepts using digital simulations and physical models. The processes were executed in 4 groups of 2-3 designers. The digital workflows embraced 3D modelling and parametric design of facade concepts and the simulation of their thermal shrinkage and deformations caused by wind. The physical workflows embraced creating models of facade concepts, generated by first changing the textile structures using heat, applied using various methods, and then by exposing the models to airflow influence using a dedicated fan.

3.1 Workflow

The first day of the workshop embraced introductions to the state of the art in textile architecture design, the fundamentals of textile design and knitting and digital wind simulations. After these introductions, the participants explored the principles of simulating textile shrinkage and wind deformation, by working with an example file and a code in which the parameters of the textile and airflow could be altered. After this hands-on trial session, the participants were given smaller textile samples to test different heating techniques, get a basic understanding of the material behavior and explore different heat application patterns on textiles.

On the second day, each group of designers developed their final concepts and models of textile facades informed by airflow. The output embraced video-animations showing selected digital simulations of textile behaviors and bigger textile pieces, representing the design proposals.

For this study, two simulation tools were used; The earlier described Flexhopper and a custom program, written in a Java-based textual programming platform, Processing. The program was relatively simple, fast and platform-independent, but had less intuative modelling and interaction

options, as it is text textbased scripting. It treated the fabric as a grid using 3 node quadratic B spline elements to calculate the forces due to the bending stiffness of the fabric, which is important in controlling how the fabric drapes. Having found the forces, the equations of motion are integrated using the Verlet algorithm[11], which is essentially the dynamic version of dynamic relaxation which, despite its name, is used for static problems. The script can be found at: http://www.archeng.se/tools/.

3.2 The heat-induced textile typologies

The yarns of our textiles were Trevira CS PEMOTEX® and COMFIL® PET [3]. Both have thermoplastic properties; they exhibit both a shrinkage and stiffening behavior. However, their behavior and end-expression are not identical. Trevira CS PEMOTEX® shrinks 40% at a temperature of 100 °C but changes occur at a temperature above 70 °C. So variations in temperature affect the density and elasticity of the textile surface. After shrinkage, the textile surface is still flexible (Figure 2). The COMFIL® PET starts to change at 130 °C, its melting point is at 235 °C and the shrinkage effect is more dramatic (between 40-60% depending on the temperature). Variations in temperature affect the density and elasticity of the textile, which becomes rigid after heat treatment (Figure 2). Furthermore for both types of yarns the textile expression is dependent on the number of threads.

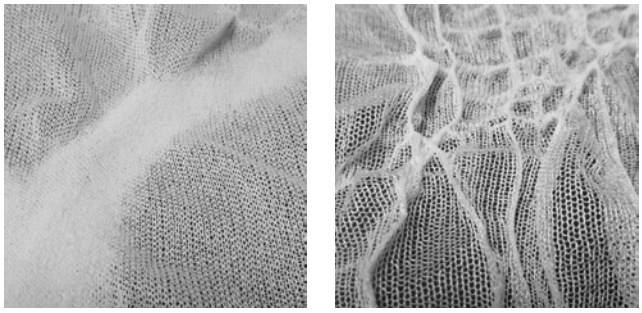


Figure 2: The textiles used and examples of modifications. Left: Trevira CS PEMOTEX®, interlock knitted with 2 yarns. Right: COMFIL® PET, single jersey knitted with 1 tread.

For the workshop, the textile structures were knitted in single bed as Single Jersey and as Interlock. The Single Jersey structure is elastic in both x and y direction, while the Interlock is less elastic in the y direction. Both structures were produced in the same flat knitting machine in gauge 10/inch with the same stitch length but with 1 and 2 threads. The reason was to provide material structures with varying form and weight which would affect their aesthetic expression when airflow was applied.

The heating techniques used, to alter the textile structures, in the workshop were: blowing warm air with a hairdryer, ironing on the flat and using the edges and tip of an iron to "draw" points and fine lines. In Figure 2, the textile on the left is modified with a hairdryer and the one on the right is modified using an iron.

Upon the completion of heat changes, the textile pieces (50x200 cm) were point-mounted onto a 2x2 m wooden frame. The airflow was generated using a Trotec® TTW 45000 Wind Machine, with an air flow rate of 12 650 l/s (45 600 m^3/h) and a maximum air pressure of 70 Pa. The airflow was applied as a frontal force to shape the textile pieces.

4 Results

The two different digital simulation methods seem to have led the participants to work in with their respective designs in different ways. The groups that worked with Flexhopper tended to explore variations of one design. This was probably caused by the intuitiveness of the graphical interfaces of the visual programming environment Grasshopper/Flexhopper and of Rhinoceros 3D. Owing to these, the users could instantly see in the 3D model the effects of applying changes to parameters affecting heat shrinkage pattern proportions within the same design. The groups working with the Processing code, on the other hand, tended to explore several different heat shrinkage designs. This was probably caused by the fact that alterations of heat patterns could only be done by using bitmap image brightness value remapping. Therefore, different images representing different heat patterns were explored. Figure 3 is showing a comparison between a digital simulation, made in Flexhopper, and a textile sample, with the same pattern and wind applied. Figure 4 is showing a comparison between a digital simulation from the Processing program and a physical model, both having the same geometric pattern.

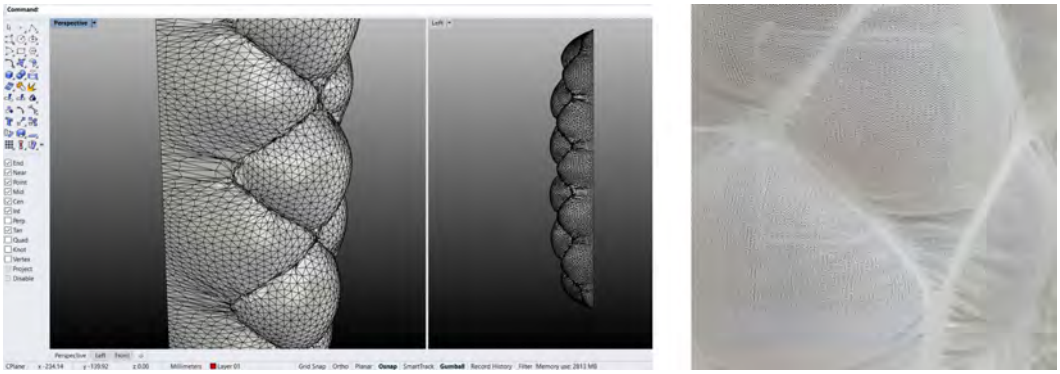


Figure 3: Comparison between a flexhopper simulation and a textile, with the same curve pattern, in wind.

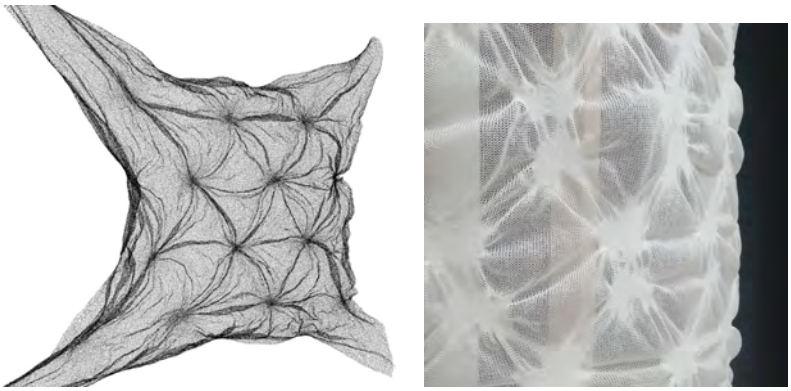


Figure 4: Comparison between a simulation made with the processing program and a textile, with the same repeated geometric (chesterfield) pattern, in wind.

The modification possibilities of the textiles seem to have mimicked the ease with which it was possible to modify the digital models, with the number of produced physical models similar to the number of digital ones. Some examples of the variations of patterns of physical models can

be seen in figure 5.

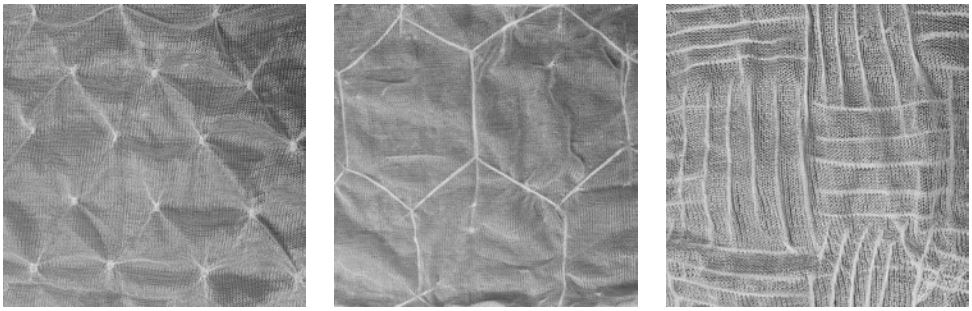


Figure 5: Explorations of geometric geometric heat patterns in the Single Jersey COMFIL® PET textile. Design team: Mathias Bernhard, Oldouz Moslemian and Hiroyuki Tachikawa

The produced textile samples can be divided into three typologies; organic irregular patterns, tubes, repeated regular geometric pattern. The final models of 3D textile volumes that the wind shapes the textiles into can be seen in figure 6.



Figure 6: The final result from the workshop: modified textiles mounted on the frame, with wind applied

5 Conclusion

While it is difficult to make completely accurate digital simulations of wind and textiles, an important conclusion from our study is that even less accurate simulations are still inspiring and useful for the purpose of the conceptual architectural design process. The design tool strategy investigated in this workshop has proven effective for trying out and communicating different cross-disciplinary design concepts by linking textile and architectural design. The physical models enable meaningful explorations of different geometrical patterns of heat-changed textile zones in relation to the applied wind directions, gives an understanding of the material behavior and further inform their digital translation into new form-generative processes. The

explorations of the different design variables such as textile form, wind intensity or direction, would however be less fruitful and more time consuming to explore if only physical models were employed in concept development. For this reason, it can be concluded that physical and digital models have equal importance in the conceptual design phase. They complement each-other, providing a broad overview of the material behaviors and the aesthetic consequences arising from their fine-tuning.

6 Acknowledgements

This research was financially supported by Chalmers University of Technology Foundation. We thank participants at the workshop during AAG2018; David Andreen, Matthew Ault, Mathias Bernhard, Malin Borgny, Constantinos Gregoriou, Nikoletta Karastathi, Joanna Maria Lesna, Oldouz Moslemian, Hiroyuki Tachikawa, Linda Wallander. The materials used in the workshop were developed by The Smart Textiles Design lab at the Swedish School of Textiles and produced in collaboration with the knitting technician Kristian Rödby.

References

[1] S. Bouaziz et al. "Projective Dynamics: Fusing Constraint Projections for Fast Simulation". In: *ACM Trans. Graph.* 33.4 (July 2014), 154:1–154:11. DOI: 10.1145/2601097.2601116. URL: http://doi.acm.org/10.1145/2601097.2601116.

[2] M. Deuss et al. "ShapeOp—A Robust and Extensible Geometric Modelling Paradigm". In: *Modelling Behaviour: Design Modelling Symposium 2015*. Ed. by M. R. Thomsen et al. Cham: Springer International Publishing, 2015, pp. 505–515. DOI: 10.1007/978-3-319-24208-8_42. URL: https://doi.org/10.1007/978-3-319-24208-8_42.

[3] D. Dumitrescu et al. "Smart textiles as raw materials for design". In: *Proceedings Shape Shifting* (Apr. 2014). Auckland, New Zeeland.

[4] B. Felbrich. *FlexCLI*. https://github.com/HeinzBenjamin/FlexCLI. 2019.

[5] M. Garcia. "Prologue for a history and theory of architextiles". In: *Architectural design* 76.6 (2006), pp. 12–20.

[6] W.-X. Huang and F.-B. Tian. "Recent trends and progresses in the immersed boundary method". In: *Proceedings of the Institution of Mechanical Engineers, Part C: Journal of Mechanical Engineering Science* 0.0 (0), p. 0954406219842606. DOI: 10.1177/0954406219842606. URL: https://doi.org/10.1177/0954406219842606.

[7] K.-M. Koch, K. J. Habermann, and B. Forster. *Membrane structures: innovative building with film and fabric*. Prestel Publishing, 2004.

[8] L. Mabon and C. Williams. "Wind generated waves on fabric structures". In: *Institute of mathematics and its applications conference series*. Vol. 69. 1999, pp. 119–126.

[9] M. Müller et al. "Position Based Dynamics". In: *J. Vis. Comun. Image Represent.* 18.2 (Apr. 2007), pp. 109–118. DOI: 10.1016/j.jvcir.2007.01.005. URL: http://dx.doi.org/10.1016/j.jvcir.2007.01.005.

[10] M. J. Shelley and J. Zhang. "Flapping and bending bodies interacting with fluid flows". In: *Annual Review of Fluid Mechanics* 43 (2011), pp. 449–465.

[11] L. Verlet. "Computer "experiments" on classical fluids. I. Thermodynamical properties of Lennard-Jones molecules". In: *Physical review* 159.1 (1967), pp. 98–103. DOI: 10.1103/PhysRev.159.98.

Proceedings of the IASS Annual Symposium 2019 – Structural Membranes 2019
Form and Force
7 – 10 October 2019, Barcelona, Spain
C. Lázaro, K.-U. Bletzinger, E. Oñate (eds.)

Smart Wraps

Dipl. Ing. Architect Katja BERNERT*

* Low & Bonar GmbH, Germany
Rheinstr. 11, 41836 Hückelhoven
Katja.Bernert@LowandBonar.com

Abstract

Fabric façades are now much more than just a textile wrap for a building. Of course one can still highlight the merits of fabric meshes as lightweight materials: they are apt to wrap buildings at a fraction of the material need for other aesthetical enclosures as stone or aluminum façades. Savings in weight, hence sub construction and material consumption are smart in terms of sustainability. Smartness nowadays has to be much more than that. Today it is more to do with adaptivity. Almost all building types need to provide for a maximum of adaptivity when it comes to their ground floor flexibility. Hence they need to be wrapped into a façade with a maximum of adaptivity. About 15 years ago, distinction in textile façades meant for example XXL prints – that was to do with extravagance rather than adaptivity. Actual smartness is only evolving now: at the end of this development the fabric mesh will be the matrix for all sorts of applications – ranging from leading electricity through its veins to supplying lighting as in a vast LED screen. In its first part the paper will give a brief introductory input regarding the interrelation between material science and design of smart fabrics. Focus of the second part are recent material developments and their input for actual projects. Showing a variety of today's applications will lead to a conclusion where future research in the field of smart composites will be heading.

Keywords: Fabric Façades, Smart Wraps, Matrix, Material Developments, Case Studies



Fig. 1 extravagance rather than adaptivity: printed mesh

Copyright © 2019 by Katja Bernert
Published by the International Association for Shell and Spatial Structures (IASS) with permission.

1. Introduction

Fabric façades play a minor role in urban street views. Their part in shaping the city is still very small. As stone or aluminum claddings fabrics are mostly used for optical reasons. Their functionality is hence limited to providing for a cover of other –probably less presentable- building skins. The building's climatic wrap is conventionally done with the four main building materials: stone, glass, wood or metal. People involved in textile architecture have an interest in promoting fabrics as fifth building material. The few samples of fabric building wraps show that textiles can provide for a building skin at a fraction of the material which is needed for a stone cladding for example.

Stone, glass, wood and metal as building materials evolved over hundreds of years. The only function of an ancient stone building was to shelter the inhabitants. Nowadays bricks and concrete are much more sophisticated than the initial natural stones. When it comes to fabric or –more generally- soft skins used as building material the question is why the millennia of development were missed in the first place. Talking about tensile architecture the Indian tipi or the Bedouin tent are often cited samples for historic –or even ancient- building skins. It is obvious that at least the last centenaries were missed out in order to develop the fabrics properties along with the other four building materials. Whereas glass evolved over hundreds of years to what we now know as high tech glass façades, fabrics have to make up for a huge gap in their development in order to keep pace.

Smartness and adaptivity are now a must for building wraps. Fabric façades have the enormous advantage of being perfectly equipped for adopting this challenge. Developments in this direction are done on a push and pull basis. On the one hand it is the input of architects and designers that strive for innovative solutions for their building skins and hence pull the industry. On the other hand it is the industry itself which pushes the material development forward in order to provide for solutions that are easily applicable by the market.

One of the main players within the fabrics' evolution process are the material developers of the internationally operating weaving and coating industry. They work together with universities and textile institutions on the one hand and architects and manufacturers on the other – the latter being their direct customers.

2. What is smart?

2.1. Smartness in material science

Smart phones are omnipresent in today's life. Using them almost constantly does not make it easier to answer the question what smartness really means. According to the phone analogy one possible answer is that smart is everything that facilitates processes. Our smart phones enable actions that used to take a lot of time – only a couple of years ago. Taken into the material world smartness could hence mean that a smart material is able to solve complex specifications at one glance and in one form. That is to say that smartness in material science has a spatial and a temporal notion.



Fig. 2 Façade example, stone shelter

It took a couple of strong men and a day to build a brick wall two hundred years ago. This wall fulfilled the function as a shelter. It limited the output of climate for the people living within this sheltering wall. It is now a question of a couple of hours and a machine to build a wall. And because we have been so smart to invent these machines we are no longer confident with the wall only serving *one* means: the shelter. We expect the wall to protect us not only against the cold of winter. It has to keep out the warmth in summer. It has to protect us against harming radiation. At the same time it needs to let through the vital wireless communication. We want the wall at least to provide for a screen for the projections of our non-verbal communication. It is only a question of time that projection feels antiquated and nothing but self-emitting walls will surround us. We already live in smart homes that link all our smart devices with the smart materials – enabled by our smart ideas. Following this line smartness in material science means providing for multifunctionality. Smart wraps are hence building skins that are not mere climatic façades but provide for many other functions at the same time.

2.2. Smartness in textiles

For the manufacturer of coated fabrics it is primarily vital to find a definition for smartness in textiles. It is easy enough to incorporate various functions into one fabric. Already the Indian tipis which are usually linked to early tensile architecture provided for more than a mere shelter.



Fig. 3 Façade example, Sioux Tipi

These tents protected against sun and rain, provided for ventilation and chimney. They mirrored the inhabitant's status. These functions taken alone could hint at a smart development behind the material. Nonetheless society nowadays is driven by technical advances. Therefore smart textiles have to provide for more than a combination of various functions. Smartness in textiles hence involves features as electricity, light, energy harvesting. Smartness -as striven for in today's fabric material science- has to involve conductors.

3. Who is developing smart wraps?

3.1. The lab approach: PUSH

Most of the globally operating coaters and weavers have a portfolio which includes a number of other performance materials apart from the main coated fabric part. Hence the local research and development (R&D) teams try to find synergies when it comes to new, innovative materials. The easiest approach is to find combinations of properties of existing materials that are matched together in a new way: a new façade material for example is a combination of an agricultural fabric with the properties of a print material.

Often it is much more innovative to work on a more abstract level: thinking outside the box, beyond the properties of *existing* materials. The cooperation between the industry's rather pragmatic thinking R&D departments and university institutes can be very fruitful for these ends. Experience has shown that the scientific approach is far more open-minded than the down-to-earth method that mirrors the daily work of quality control within the company.

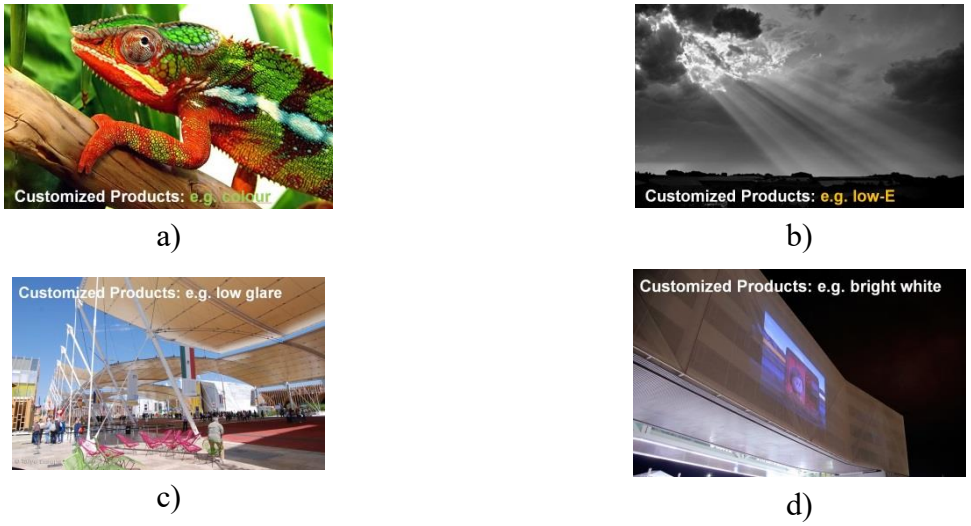
3.2. New products created by product management

One advantage of a globally operating weaving and coating company is a wide spread portfolio. There is an enormous variety of different products. These products have different properties. The properties can be mixed and matched.



Fig. 4 typical stock of a weaver and coater

There is a team of product managers dealing with necessary alterations wherever a customer needs a specific solution. Given hundreds of stock items, altered by colour, energy emissivity and many other properties, means an uncountable number of possible custom made products. A product of the textile architecture range could easily be combined with a colour of a truck tarpaulin – a modification which often takes place in the daily business. This of course is rather a modification than a proper invention. In Most cases there is no actual smartness involved in this daily process – smartness at least in the way described above. Taking into account that this is only a very basic task of a product manager and that there are many more possibilities of modifications that come not only one by one but sometimes all at the same time there is a number of complex tasks that involve many different parties. According to a definition of smartness that concentrates on a combination of different functions and properties the product manager only rarely becomes the inventor of a smart material. As it is common sense that smartness in textile wraps has to be more than the combination of various functions there needs to be more to invention of really smart fabrics.



a) b) c) d)

Fig. 5a), b), c) and d) pictures of possible customization

3.3. The project-wise approach: PULL

Whereas the process mentioned before often fits into the frame of a standardized stage gate process, the inventive work needed for most textile architecture projects is in most cases much more complex. That of course does not make it smart in itself. It is only the amount of time and therefore money which distinguishes project-wise inventions from the day to day business. As the textile part of a construction almost always comes last, the financial constraints of the owner do not allow for a time and cost intensive search. That is why the inventive work of the coater – sometimes in collaboration with the manufacturer- is vital for a successful output.

It is becoming more and more common to be facing smart necessities within these customer triggered material development processes. The architect does not want to have a mere textile cover for a building. Adaptivity demands the simultaneous use of state of the art LED-

techniques in order to transform the textile wrap into a huge screen. Of course there is more to smart wraps than for example a film projection onto a mesh membrane.



Fig. 6 office building in Esmeraldas, Ecuador

4. Smartness as joint venture

4.1. Material combination

In most of today's application it is the fabric façade *in combination* with other materials providing for different –at best: smart- functions. The most crucial function which a fabric –as roof or as façade material- is still *not* able to fulfil properly on its own is insulating a building. That is the main reason why most of the fabric façades are multilayered systems. Strictly speaking the fabric façade is often not much more than an optical gimmick. The same is the case with any stone or aluminum covers. A multifunctional façade system is a compilation of multiple layers that –in most cases- are each providing for only *one* functionality.

Adaptivity in the example shown above meant moving the fabric screen to the one or the other side in order to cover-up the windows or let the views pass through without obstacle.

In most cases fabric façades are used as curtain-wall facing with air space. Smartness is hence limited to providing for a clever way of spreading the light. The sun-shading effect is the most important function of today's fabric façades. Here again adaptivity is limited to making whole parts of the façade move. Hence it is the structural system which reacts to climatic alterations rather than the fabric itself.



Fig. 7 fabric façade panel in La Rochelle

In the case of a fabric façade of an office building in Esmeraldas, Ecuador, adaptivity of the façade was even not necessary: the sun radiation is extremely high and as the office spaces are only used during the day. Here the constant sun shading effect of the fabric façade is absolutely beneficial for the Indoor Environmental Quality (IEQ) [1].



Fig. 8 office building in Esmeraldas, Ecuador

This example shows another advantage of fabric façades: the location of the offices, directly on the beach of the Pacific Ocean, would make it almost impossible to open windows individually if there was not the sun- and simultaneously wind-shielding screen in front of the climatic façade. Though these two properties are not smart in terms of adaptivity, they are still adding to a clever usage of fabric façades. There is yet a third property which underlines the multifunctionality of fabric façades. Whereas the people working in the offices can easily look through the fabric from inside, it is almost impossible to peek through from the other direction. This is the only functionality that is adaptive: during the day the fabric screen blocks peeks from the outside world into the inner office spaces.



Fig. 9 office building in Esmeraldas, Ecuador

At night this function is reversed: if the inner spaces are lit, the open area within the fabric mesh becomes more evident than the woven material itself and therefore allows outsiders to look into the building. The department of building technology at the RWTH in Aachen provides for an ample scientific research into this topic. They joint up with the opticians of the same university's medical institute in order to find out more about the different grades of transparency: how the mesh's geometry must be altered in order to vary the visual shielding effect. They developed new, experimental procedures for the evaluation of fabric façades. The research in this field was starting point for students' work elaborating on possible measures of adaptivity within the fabric material itself [2]. Part of the students' projects was to evaluate the adaptivity along the processes that were experimentally developed before.

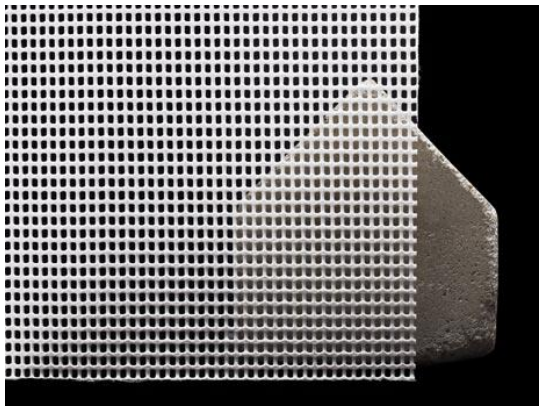


Fig. 10 visibility and transparency

4.2. Smart wraps in building refurbishments

It is obvious that a combination of different materials is necessary especially when it comes to improving existing façades. Usually the old building skin will stay on – possibly ripped off its used-up or damaged parts. In northern European refurbishments the primary goal is to enhance the façade's insulating property. Clear enough that this function is only rarely provided for by fabrics. Yet again the textile wrap is degraded to a mere optical device. Smartness could significantly enhance the chances for fabrics as a "one go" wrap in refurbishments. If the textile was not only able to fresh up the building's optical appearance

but to insulate it properly at the same time, many more fabric façades would pop-up in the cities.

4.3. Textile as matrix

At the moment we see various approaches in integrating either LED's or conductors into the fabric. The weak point of these kinds of applications is the predefinition of functions. Usually the setting for one use automatically excludes other options. Thinking ahead the textile grid itself is the matrix and integrates numerous functions like the circuit board of a computer. This way the matrix stays flexible all through its lifetime – even flexible enough to change functionalities easily.



Fig. 11 Circuit poard of a computer as sample for the textile matrix

5. An analogue textile matrix

5.1. The template

One template for using the textile grid as a matrix is called "Valmex Systems". It is a coated fabric that integrates tube-like bags. These bags can be woven into the fabric either in warp or in weft direction. The most common application is with a filling of LED light strips. Apart from that there are numerous more possibilities: the fabric adapts to the user's needs. This is the analogue application of the fabric as a matrix for not pre-specified uses. It obviously is a very basic answer to the question of adaptivity or smartness.

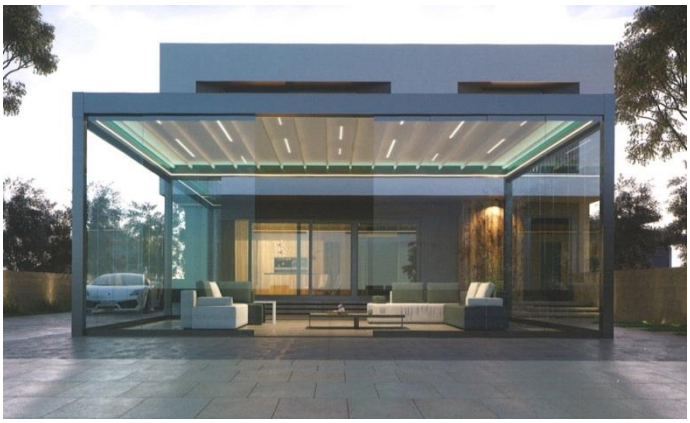
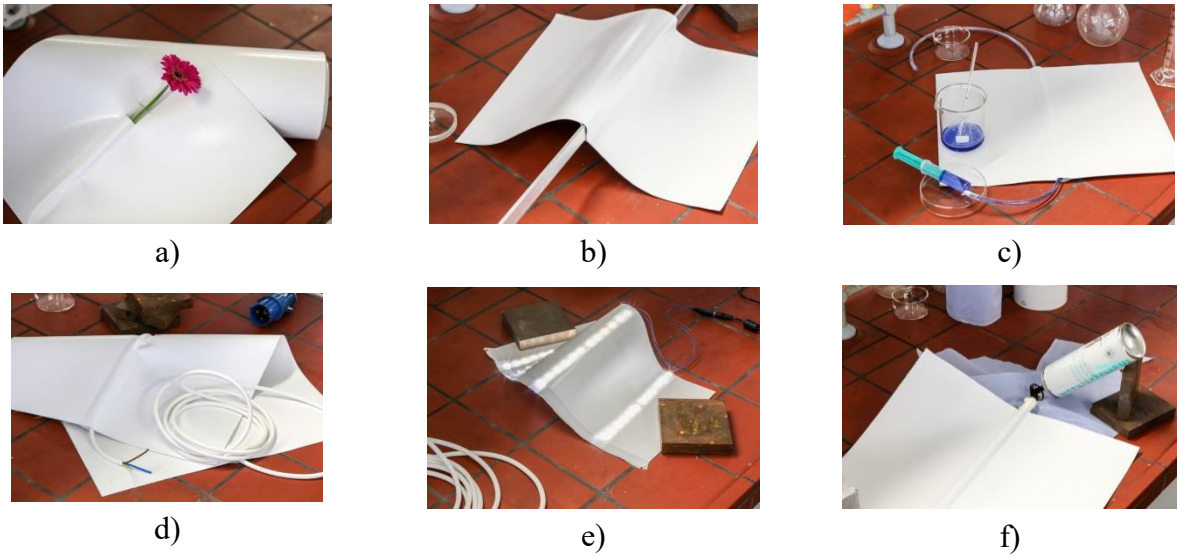


Fig. 12 Fabric example: pergola with integrated LED's



a) b) c)

d) e) f)

Fig. 12a), b), c), d), e) and f) pictures of possible applications

5.2. The analogue matrix as example for the smart main board version

Nonetheless it is an obvious hint on what the textile industry and its customers are heading for: at the end of this itinerary the textile grid itself is the circuit board. At the moment the tubes in the pocket membrane primarily need to be opened, secondly need to be filled with whatever ingredient suitable for the respective solution and last but not least: the tubes, respectively fillings need to be interconnected in order to work as a whole.

Compared to the circuit board of a computer this seems to be a last century process. For the inventors in the coating industry it serves as a blueprint for what is the aim of a more abstract approach. The analogue matrix as example of what is needed on a significantly smaller scale: the tubes which are now around 40 cm apart will then be the conductors that are directly woven into the fabric – one next to the other. The result is a grid of conductors that are flexible to be interconnected in whichever direction and fashion.

In consequence smart fabrics insert yet another player to the textile industry. The supplier of the fabric will not only be weaver and coater. The coating industry will need experts for smartness within their R&D departments. Whereas nowadays it is mainly chemical and textile engineers collaborating in the laboratories there will be a strong need for IT knowledge in the future. The next step in the creation of a textile structure is the form finding and engineering. Here as well the influence of information technics will be crucial. The most important additional player will be in the team of the manufacturer: only the interconnection of the textile matrix with its environment will make it really smart. Hence it is obvious that the coating industry alone is not able to bring smartness into the world of fabrics. Once more, cooperation between these parties and architects/designers will be vital for bringing forward the idea of smartness in fabrics.

5.3. The analogue matrix as simulation tool for smart wraps

Regarding the analogue matrix as blueprint of a woven multifunctional and interconnected fabric, the biggest challenge is to close the scaling gap. In principle it is clear that the integrated bags of the tube-fabric correspond to the filaments of the multifunctional, smart fabric. Whereas the tubes need to be filled with a third material providing for the function it is the filament itself within the smart fabric that can be activated for different functionalities.

Textile façade materials mainly consist of fabric meshes, that is to say grids or scrims. When used for example for stadia façades where wind tunnel testing is essential within building permission processes it is very difficult to simulate the fabric's open area. Whereas the 1:1 mesh consists of around 70 % material and 30 % open area it is almost impossible to scale down the open area –and mostly its effect on wind movements- scaled down to 1:200 for example. Scaling down functionalities as insulating fills from the size of a pocket membrane to a microscopic size will be equally challenging. Additionally the analogue matrix shows a completely different behaviour when it comes to form finding for example. The normal procedure to look for a three dimensional shape of a fabric façade would be to do computational form finding – or even to take alternative materials like lycra or even soap. The latter is perfectly suitable for giving a first impression of the wrap's shape. Because of the built-in tubes the pocket membrane is far stiffer than a normal membrane. Within a smart fabric the filaments take over the functionalities and stiffening pockets are not needed any longer. At best the smart wrap would behave like a normal textile wrap – not even revealing its additional functions.

From the material developers' point of view the analogue matrix can still be a precursor to the matrix fabric which is smart in itself. From the designer's viewpoint and particularly when it comes to the engineer's approach, new experimental procedures must be developed that are apt to simulate the smart effect of the building's skin.

6. Conclusion

Smart fabrics will not be on the market overnight. We see various approaches, of which the analogous matrix called "Valmex Systems" is one example, a first step. Self-illuminating curtain fabrics for indoor uses are another step in the direction of using the fabric itself as a smart matrix – open for all sorts of applications, not limited in flexibility or indoor uses.

The necessary invention work will be done by experts in all different companies. It will often be triggered by the above described project-wise approach. At the same time, there will be scientific approaches. At best these two strands will join-up within the development process.

If at the same time there are experts within all players of the industry able to collaborate on these issues the textile industry will eventually end up with real smartness in textiles.

Cooperation between the above described parties and the ones interested in these inventions – that is to say architects and designers, respectively their customers - will be vital for bringing the idea of smartness in fabrics forward.

At the moment the idea of smart wraps for building is still on a rather abstract level. The few examples are the result of elaborate, individual development processes. Standardization is generally not very far in Textile Architecture – let alone its application for smart wraps.

Finally all involved parties have to remember Frei Otto's saying about all intentions within the built environment: »The secret, I think, of the future is not doing too much. All architects have the tendency to do too much.« [3] Regarding fabric skins this means that there is no correlation between the number of functions and the degree of smartness. Simply speaking, a smart wrap can still be a mere sun shading/wind shielding/blinding building device. The mere concentration on minimal material consumption is sometimes just smart enough.

Notes

[1]according to the US American recommendation of the "Sustainable Facilities Tool", Online document, published by the National Institute of Building Science within the "Whole building design guide", https://www.wbdg.org/, accessed 6 August 2018

[2]this topic is discussed in detail in a paper for the same conference by Jan Serode, M.Sc. Architekt, RWTH Aachen

[3]Frei Otto quotation found in ILEK publication of 2015: The lightness of being

Figures

Niggemeyer Bildproduktion, photographer of picture 1

Rachel Marlene Williams, photographer of picture 2, published under the Creative Commons Attribution-Share Alike 4.0 International license: structure was built in 1933 by the Civilian Conservation Corps. It is located in Lincoln County, Oregon in the Cape Perpetua National Scenic Area.

Karl Bodmer (1809-1893), painter of picture 3, Sioux tipi, Watercolor on paper by Karl Bodmer from his travel to the U.S. 1832-1834

Figure 4, Low & Bonar GmbH's stock

Figure 5a and 5b taken from Low & Bonar ppt presentation, part on customization

Figure 5c, Decumano at the World Exhibition in Milan 2015, photographer Taiyo Europe

Figure 5d, Flopec office building in Esmeraldas, Ecuador, photographer Preysi, Ecuador

Figure 6, Flopec office building in Esmeraldas, Ecuador, photographer Preysi, Ecuador

Figure 7, fabric façade panel in La Rochelle, Low & Bonar TF400 project

Figure 8, Flopec office building in Esmeraldas, Ecuador, photographer Preysi, Ecuador

Figure 9, Flopec office building in Esmeraldas, Ecuador, photographer Preysi, Ecuador

Figure 10, Valmex TF400 sample, photographer raumProbe, Stuttgart

Raimond Spekking, author of Picture 11, ZyXEL ZyAIR B-2000 - printed circuit board, via Wikimedia Commons

Figure 12, Fabric example: pergola with integrated LED's, ® by SunTech, customer of Low & Bonar GmbH

Figures 12a-12f, laboratory test samples of Valmex Systems at Low & Bonar GmbH

References

[1] Mollaert, M., Dimova, S., Pinto, A., Denton (2016). JRC Science and Policy Report: Prospect for European Guidance for Structural Design of Tensile Membrane Structures

[2] van Uffelen, Ch. (2013). Creating Shade: Design, Construction, Technology

[3] Krüger, S. (2009), Textile Architecture: Textile Architektur

Proceedings of the IASS Annual Symposium 2019 – Structural Membranes 2019
Form and Force
7 – 10 October 2019, Barcelona, Spain
C. Lázaro, K.-U. Bletzinger, E. Oñate (eds.)

An enhanced modal pushover analysis procedure for seismic evaluation of single-layer latticed shell structures

Yang QU*, Yongfeng LUO, Qinglong HUANG, Zhaochen ZHU

*Department of Structural Engineering, Tongji University
1239, Siping Road, Shanghai, China
quyang_phd@tongji.edu.cn

Abstract

Nonlinear static analysis procedures on seismic assessment are mainly studied and retrofitted specific to frame buildings. This fact hinders the application of such methods on the widely-adopted latticed shell structures featured with strong geometrical nonlinearity and multi-dimensional coupling. This paper proposes a novel enhanced modal pushover analysis procedure aiming at giving a better consideration of the multi-dimensional coupling effects associated with single-layer latticed shells. Within this proposal, modal stiffness is derived to describe the nonlinearity using overall loads and displacements, based on which an equivalent single-degree-of-freedom system is established as well as the capacity curve derived in *A-D* format. Then by the aid of capacity spectrum method or response history analysis method, the overall responses are obtained. The novelty of this proposal is to conquer the drawback of conventional pushover method that the capacity curve is described resorting to base shear and roof displacement. Seismic responses of a spherical single-layer latticed shell are calculated by means of the proposed procedure. The results demonstrates that the nodal displacements, element stresses, as well as the yielding members, are estimated accurately.

Keywords: seismic evaluation, pushover analysis, nonlinear response, single-layer latticed shell, modal stiffness.

1. Introduction

Seismic assessment of structures has drawn much attention of researchers and engineers, while the main scope of associated studies focuses more on that of frame buildings, instead of spatial latticed shells. Loosely speaking, the core issues that distinguish the spatial latticed shell from other forms of structure lie in: (i) complexity of nonlinear properties, and (ii) multi-dimensional coupling effect.

Much work has been mainly concentrated on the stability analysis and buckling path tracking [1-3], to give a better understanding of nonlinearity and failure mechanism of a latticed shell. While little attention has been paid to suitable simplified methods such as capacity spectrum method (CSM) or static pushover procedure, instead of the time-consuming response history analysis (RHA) method. Since proposed by Chopra and Goel [4], modal pushover analysis (MPA) method has achieved rapid development along with continuous modifications [5-6]. But in fact, some important problems remains unsettled for MPA method applied to the single-layer latticed shell structure. Since the significant multi-dimensional coupling effect is ignored in the conventional MPA method [7], the description of capacity curve given by the base shear and roof displacement is inapplicable for a latticed structure.

In view of these facts, by means of the nonlinear pushover analysis, modal stiffness is derived to describe the structural nonlinearity. A novel equivalent single-degree-of-freedom (ESDF) system is then generated as well as its capacity curve derived in terms of *A-D* format. Thus, the modal seismic demand is figured out, and finally, the overall responses are obtained. The accuracy of the procedure is investigated by applying it to a typical single-layer latticed shell and the results attest its feasibility.

Copyright © 2019 by Yang QU, Yongfeng LUO, Qinglong HUANG, Zhaochen ZHU
Published by the International Association for Shell and Spatial Structures (IASS) with permission.

2. Theoretical background

2.1. Establishment of the nonlinear ESDF system

The nonlinear differential equations governing the displacement responses of a multi-degree-of-freedom (MDF) system with N nodes and $6N$ degrees (e.g. a single-layer latticed shell), under earthquake ground motions $\ddot{u}_g(t)$, are shown by Eq. (1):

$$\boldsymbol{M}\ddot{\boldsymbol{u}}(t)+\boldsymbol{C}\dot{\boldsymbol{u}}(t)+\boldsymbol{F}_s(t)=-\boldsymbol{M}\boldsymbol{l}\ddot{u}_g(t) \tag{1}$$

where $\boldsymbol{u}(t)$ is the displacement vector defined as $\boldsymbol{u}(t)=(\boldsymbol{u}_x(t),\boldsymbol{u}_y(t),\boldsymbol{u}_z(t),\boldsymbol{u}_{rotx}(t),\boldsymbol{u}_{roty}(t),\boldsymbol{u}_{rotz}(t))^{\mathrm{T}}$; $\boldsymbol{M}$, a diagonal mass matrix of order $6N$, includes submatrix $\boldsymbol{m}$ associated with translational degrees-of-freedom (DOFs), and $\boldsymbol{I}_o$ with rotational DOFs; $\boldsymbol{C}$ is the classical damping matrix of the system; $\boldsymbol{l}$ is the influenced vector with each x-lateral element equal to unity and the others equal to zero. $\boldsymbol{F}_s(t)$ is the nonlinear restoring force, depending on the history of loading and displacements.

According to the conventional MPA method, displacements of the inelastic system can be expanded approximately in terms of the natural vibration modes of the corresponding linear system, as given below:

$$\boldsymbol{u}(t)=\sum_{l=1}^{6N}\boldsymbol{\phi}_l q_l(t) \tag{2}$$

where $\boldsymbol{\phi}_l$ and $q_l(t)$ are the l^{th} vibration mode vector and coordinates.

Substituting Eq. (2) into Eq. (1), pre-multiplying by $\boldsymbol{\phi}_n^{\mathrm{T}}$, and considering the mass- and classical damping-orthogonality property of modes could uncouple the governing equations as follows:

$$M_n\ddot{q}_n(t)+2M_n\zeta_n\omega_n\dot{q}_n(t)+\frac{\boldsymbol{\phi}_n^{\mathrm{T}}\boldsymbol{F}_s(t)}{\boldsymbol{\phi}_n^{\mathrm{T}}\boldsymbol{\phi}_n}=-L_n\ddot{u}_g(t),\ n=1,2,...,6N \tag{3}$$

in which ω_n and ζ_n is the circular frequency and damping ratio of the n^{th} mode, M_n, C_n, L_n are the properties of the system, interpreted by:

$$M_n=\frac{\boldsymbol{\phi}_n^{\mathrm{T}}\boldsymbol{M}\boldsymbol{\phi}_n}{\boldsymbol{\phi}_n^{\mathrm{T}}\boldsymbol{\phi}_n},\ C_n=\frac{\boldsymbol{\phi}_n^{\mathrm{T}}\boldsymbol{C}\boldsymbol{\phi}_n}{\boldsymbol{\phi}_n^{\mathrm{T}}\boldsymbol{\phi}_n}=2M_n\zeta_n\omega_n,\ L_n=\frac{\boldsymbol{\phi}_n^{\mathrm{T}}\boldsymbol{M}\boldsymbol{l}}{\boldsymbol{\phi}_n^{\mathrm{T}}\boldsymbol{\phi}_n} \tag{4}$$

For n^{th} mode, $q_n(t)$ can be calculated by $q_n(t)=\Gamma_n D_n(t)$, where Γ_n and $D_n(t)$ is the modal participation factor and modal displacement of the n^{th} mode. By substituting $q_n(t)=\Gamma_n D_n(t)$ into Eq. (3) and considering $\Gamma_n=L_n/M_n$, the n^{th} dynamic equation could be derived with $D_n(t)$ as independent variable:

$$\ddot{D}_n(t)+2\zeta_n\omega_n\dot{D}_n(t)+\frac{\boldsymbol{\phi}_n^{\mathrm{T}}\boldsymbol{F}_s(t)}{\boldsymbol{\phi}_n^{\mathrm{T}}\boldsymbol{\phi}_n L_n}=-\ddot{u}_g(t) \tag{5}$$

Further, the pseudo acceleration of n^{th}-mode ESDF could be defined by Eq. (6):

$$A_n(t)=\frac{\boldsymbol{\phi}_n^{\mathrm{T}}\boldsymbol{F}_s(t)}{\boldsymbol{\phi}_n^{\mathrm{T}}\boldsymbol{\phi}_n L_n} \tag{6}$$

which represents the influence of the nonlinear restoring force $\boldsymbol{F}_s(t)$ on $D_n(t)$. Note that for linear system, that is $A_n(t)=\omega_n^2 D_n(t)$. Hence, the dynamic equation is finally expressed as:

$$\ddot{D}_n(t)+2\zeta_n\omega_n\dot{D}_n(t)+A_n(t)=-\ddot{u}_g(t) \tag{7}$$

Given above, an ESDF system with vibration properties—mass M_n, damping ratio ζ_n, natural frequency ω_n, and displacement response D_n—same as those of the n^{th} mode of the original system, is established, subjected to $\ddot{u}_g(t)$. According to Eq. (7), provided that the A_n-D_n relationship is given, then the modal displacement D_n could be figured out by the well-known CSM or RHA method.

2.2. Modal stiffness

Governed by Eq. (7), modal displacement of the n^{th}-mode ESDF system contributes to the overall displacements. In this sense, the seismic performance of n^{th}-mode ESDF is of great significance to not only the modal responses, but also the overall responses. In order to capture the nonlinear behaviors of the modal ESDF system, modal pushover analysis is employed.

In linear pushover analysis of the MDF system, the relationship between pushover load $\boldsymbol{P}$ and displacement $\boldsymbol{u}$ is generally built by Eq. (8):

$$\boldsymbol{P} = \boldsymbol{K}\boldsymbol{u} \tag{8}$$

where $\boldsymbol{K}$ is elastic stiffness matrix.

During the pushing process, the pushover load resisted by the n^{th} mode and the displacement caused on the n^{th} mode could be expressed by the projections of $\boldsymbol{P}$ and $\boldsymbol{u}$ on the mode vector as Eq. (9):

$$p_n^* = \frac{\boldsymbol{\phi}_n^{\mathrm{T}}\boldsymbol{P}}{\|\boldsymbol{\phi}_n\|}, u_n^* = \frac{\boldsymbol{\phi}_n^{\mathrm{T}}\boldsymbol{u}}{\|\boldsymbol{\phi}_n\|} \tag{9}$$

in which p_n^* and u_n^* are the projections of $\boldsymbol{P}$ and $\boldsymbol{u}$ on the n^{th} mode vector.

Thus, the modal stiffness in linear range is defined as:

$$k_n^* = \frac{p_n^*}{u_n^*} = \frac{\boldsymbol{\phi}_n^{\mathrm{T}}\boldsymbol{P}}{\boldsymbol{\phi}_n^{\mathrm{T}}\boldsymbol{u}} = \frac{\boldsymbol{\phi}_n^{\mathrm{T}}\boldsymbol{K}\boldsymbol{u}}{\boldsymbol{\phi}_n^{\mathrm{T}}\boldsymbol{u}} \tag{10}$$

In nonlinear range, the relationship between p_n^* and u_n^* is usually described by an incremental equilibrium equation at a generic iteration step i, as follows:

$$\Delta\boldsymbol{P}_i = \boldsymbol{K}_{\mathrm{T},i}\Delta\boldsymbol{u}_i \tag{11}$$

in which $\boldsymbol{K}_{\mathrm{T},i}$ is the tangent stiffness matrix at step i.

In a similar manner, the projections of incremental pushover load and displacement are:

$$\Delta p_{n,i}^* = \frac{\boldsymbol{\phi}_n^{\mathrm{T}}\Delta\boldsymbol{P}_i}{\|\boldsymbol{\phi}_n\|}, \Delta u_{n,i}^* = \frac{\boldsymbol{\phi}_n^{\mathrm{T}}\Delta\boldsymbol{u}_i}{\|\boldsymbol{\phi}_n\|} \tag{12}$$

Thus, the modal stiffness in nonlinear range is defined as:

$$k_{n,i}^* = \frac{\Delta p_{n,i}^*}{\Delta u_{n,i}^*} = \frac{\boldsymbol{\phi}_n^{\mathrm{T}}\Delta\boldsymbol{P}_i}{\boldsymbol{\phi}_n^{\mathrm{T}}\Delta\boldsymbol{u}_i} = \frac{\boldsymbol{\phi}_n^{\mathrm{T}}\boldsymbol{K}_{\mathrm{T},i}\Delta\boldsymbol{u}_i}{\boldsymbol{\phi}_n^{\mathrm{T}}\Delta\boldsymbol{u}_i} \tag{13}$$

Seeing the definition formula of both linear and nonlinear modal stiffness in Eq. (10) and (13), k^* could reflect the overall tangent stiffness matrix and retain the same dimension as that of $\boldsymbol{K}$. More importantly, using k^* to describe the nonlinear characteristics could take into account the overall responses of structure and avoid the one-sided dependence on simple responses of any specific node or element, which is distinct from the conventional MPA method using top node displacement and base shear. Based on the $\boldsymbol{P}$ and $\boldsymbol{u}$ directly outputted from pushover analysis database, k^* could be easily obtained according to Eq. (10) for linear range and Eq. (13) for nonlinear range.

2.3. Capacity curve of the ESDF system

Modal pushover analyses is conducted for the MDF system, in order to obtain modal ESDF systems and the A_n-D_n relationships by the aid of k^*. For n^{th}-mode ESDF system, the displacement response $\boldsymbol{u}_n(t)$ and restoring force $\boldsymbol{F}_{sn}(t)$ in linear range are calculated by Eq. (14) and (15):

$$\boldsymbol{u}_n(t) = \boldsymbol{\phi}_n\Gamma_n D_n(t) \tag{14}$$

$$\boldsymbol{F}_{sn}(t) = \boldsymbol{K}_{\mathrm{T}}\boldsymbol{u}_n(t) = \boldsymbol{K}_{\mathrm{T}}\boldsymbol{\phi}_n\Gamma_n D_n(t) = \omega_n^2\Gamma_n D_n(t)\boldsymbol{M}\boldsymbol{\phi}_n \tag{15}$$

Thereby, the pushover load is obtained through Eq. (16):

$$\boldsymbol{F}_n = \chi \boldsymbol{M}\boldsymbol{\phi}_n \tag{16}$$

where χ is the pushover load factor. Note that since the multi-dimensional responses are coupled inevitably, the pushover load should be exerted as following pattern:

$$\boldsymbol{F}_n = \chi \boldsymbol{M}\boldsymbol{\phi}_n = \chi \left(\boldsymbol{m}\boldsymbol{\phi}_{n,x}, \boldsymbol{m}\boldsymbol{\phi}_{n,y}, \boldsymbol{m}\boldsymbol{\phi}_{n,z}, \boldsymbol{I}_o\boldsymbol{\phi}_{n,rotx}, \boldsymbol{I}_o\boldsymbol{\phi}_{n,roty}, \boldsymbol{I}_o\boldsymbol{\phi}_{n,rotz} \right)^{\mathrm{T}} \tag{17}$$

Under the pushover load pattern, the displacement of MDF would behave as:

$$\boldsymbol{u}_n = \boldsymbol{\phi}_n \Gamma_n D_n \tag{18}$$

Further for the n^{th}-mode ESDF system, the stiffness k_n is derived as follows:

$$k_n = \frac{M_n A_n}{D_n} = \omega_n^{\,2} M_n = \frac{\boldsymbol{\phi}_n^{\mathrm{T}} \boldsymbol{K}\boldsymbol{\phi}_n}{\boldsymbol{\phi}_n^{\mathrm{T}}\boldsymbol{\phi}_n} = \frac{\boldsymbol{\phi}_n^{\mathrm{T}} \boldsymbol{K}\boldsymbol{u}_n}{\boldsymbol{\phi}_n^{\mathrm{T}}\boldsymbol{u}_n} = k_n^* \tag{19}$$

which shows that in linear range, the stiffness of n^{th}-mode ESDF is exactly equal to the k_n^* proposed. Therefore, the pseudo acceleration A_n and modal displacement D_n could be computed successively as:

$$A_n = \frac{\boldsymbol{\phi}_n^{\mathrm{T}} \boldsymbol{F}_n}{\boldsymbol{\phi}_n^{\mathrm{T}}\boldsymbol{\phi}_n L_n} = \frac{\chi}{\Gamma_n}, \; D_n = \frac{A_n}{\omega_n^{\,2}} = \frac{\chi}{\omega_n^{\,2}\Gamma_n} \tag{20}$$

In nonlinear range of MDF, despite the fact that vibration modes are actually coupled and differ from those in linear range upon yielding, the mode vectors in inelastic stage are approximated to be constant and accordant with those in elastic stage, leading to Eq. (17) acceptable in nonlinear range as well. Similarly, the stiffness of n^{th}-mode ESDF at i^{th} step could be derived as:

$$k_{n,i} = \frac{M_n \Delta A_{n,i}}{\Delta D_{n,i}} = \frac{M_n \boldsymbol{\phi}_n^{\mathrm{T}} \Delta \boldsymbol{F}_{n,i}}{\boldsymbol{\phi}_n^{\mathrm{T}} \cdot \boldsymbol{\phi}_n L_n \Delta D_{n,i}} = \frac{\boldsymbol{\phi}_n^{\mathrm{T}} \Delta \boldsymbol{F}_{n,i}}{\boldsymbol{\phi}_n^{\mathrm{T}} \cdot \boldsymbol{\phi}_n \Gamma_n \Delta D_{n,i}} = \frac{\boldsymbol{\phi}_n^{\mathrm{T}} \Delta \boldsymbol{F}_{n,i}}{\boldsymbol{\phi}_n^{\mathrm{T}} \Delta \boldsymbol{u}_{n,i}} = k_{n,i}^* \tag{21}$$

Eq. (23) shows that in nonlinear range, the stiffness of n^{th}-mode ESDF is also exactly equal to the modal stiffness proposed. Thus, the incremental pseudo acceleration $\Delta A_{n,i}$ and modal displacement $\Delta D_{n,i}$ could be obtained as below:

$$\Delta A_{n,i} = \frac{\boldsymbol{\phi}_n^{\mathrm{T}} \Delta \boldsymbol{F}_{n,i}}{\boldsymbol{\phi}_n^{\mathrm{T}}\boldsymbol{\phi}_n L_n} = \frac{\Delta \chi_i}{\Gamma_n}, \; \Delta D_{n,i} = \frac{M_n \Delta A_{n,i}}{k^*_{n,i}} = \frac{M_n \Delta \chi_i}{\Gamma_n k^*_{n,i}} \tag{22}$$

As a consequence, on the basis of k_n^*, the displacement and pseudo acceleration of n^{th}-mode ESDF are obtained so as to depict the A_n-D_n relationship curve, which is the so-called capacity curve, and then the ESDF is generated accordingly. Meanwhile, the modal stiffness could be employed as a key intermediate link in converting dynamic solving into static pushover analysis, free from arbitrary selection of reference node and taking into account the coupled multi-dimensional responses. Besides, the modal stiffness helps to observe the intricate variation process and trend of deformation resistibility capacity of the ESDF, so that nonlinear performance of a mode is able to be predicted more conveniently. By means of the capacity curve, the modal displacement D_n could be figured out by the well-known CSM or RHA method. Finally, the overall responses are acquired combining the response of each dominant mode using multi-mode combination rules. Hereby, a modal-stiffness-based pushover analysis (MSPA) procedure is established as thus.

2.4. Step-by-step guideline of the MSPA procedure

In this section, a step-by-step guideline of the MSPA procedure is elaborated as below:

***Step* 1**: Create the structural model.

***Step* 2**: Carry out modal analysis to obtain the natural frequencies ω_n and mode shape vectors $\boldsymbol{\phi}_n$.

***Step* 3**: Determine the dominant vibration modes based on the modal analysis database.

***Step* 4**: For the dominant mode n, conduct the modal pushover analysis up to the model failure.

***Step* 5**: Through the analysis, monitor the variation process of modal stiffness. Accordingly, depict the nonlinear capacity curve of n^{th} mode. In this way, the n^{th}-mode ESDF system is established.

***Step* 7**: By means of the well-known CSM or RHA method, figure out the n^{th}-mode responses.

***Step* 8**: Repeat *Step* 4-7 for as many modes as required for adequate precision.

***Step* 9**: By utilizing one of the well-established rules of mode superposition, calculate the maximum values of overall dynamic responses. Since latticed shell structures are characterized with closely spaced vibration modes, the CQC rule is highly recommended for combining the modal responses.

3. Structural model and ground motions

3.1. The model considered

The structural model herein is a Kiewitt-6 spherical latticed shell, which is commonly designed as exhibition and conference halls, as shown in Figure 1. All the structural members are made of steel pipes, and the radial members are ϕ140×5, the others are ϕ121×4. In regard to the supports, the shell is pinned along perimeters and rigidly connected at each joint. To consider the full-span uniform loads with value of 1.5 kN/m^2 on the shell, a set of lumped mass is adopted and imposed on each node. Both the material nonlinearity and geometrical nonlinearity are taken into considered. As for the material properties, the bilinear kinematic hardening model is utilized for structural elements, with yielding strength f_y = 235 MPa, Young-modulus $E = 2.06\times10^5$ MPa, tangent modulus $E_T = 8.0\times10^2$ MPa, and Poisson's ratio v = 0.3. The Rayleigh damping is adopted with a damping ratio of ζ = 0.02. All the modeling and solving processes are conducted in ANSYS program and MATLAB platform.

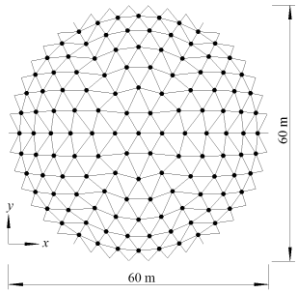


Figure 1: Structural layout of the latticed shell

3.2. Dynamic properties

According to the modal analysis database, the fundamental vibrating mode of the shell hold the largest effective mass ratio of 66.1%, whose mode shape is exhibited in Figure 2. With effective mass ratio of the mode over 65%, it is reasonable to predict that the fundamental modal response are supposed to dominate the overall seismic responses. Such a prediction would be validated by the numerical examples displayed in subsequent sections.

On the fundamental modes, pushover analysis was carried out and the stiffness k^* was monitored, as portrayed in Figure 2. Then, the fundamental modal ESDF system was established, along with the capacity curves in terms of k^*-D and A-D relationships exhibited in Figure 2.

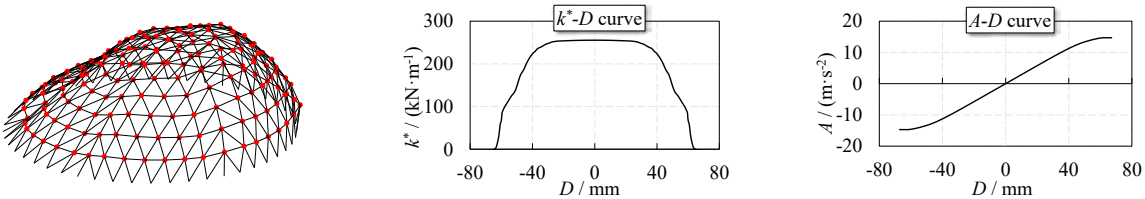


Figure 2: Dynamic properties of the shell considered

3.3. Ground motion inputs

The ground motion inputs are provided by K-net database on NIED. To validate the feasibility of MSPA for both short and long predominant periods of sites, the data set consists of eight records on firm sites (FS1~FS8) and another eight records on soft sites (SS1~SS8), which belongs to six different strong earthquake incidents in the last fifteen years, with magnitudes greater than 6.5. The acceleration spectra of ground motion records are exhibited in Figure 3, with accelerations at fundamental period amplified as 1.0 *g*. Due to limited space, detailed informations of the records are not listed.

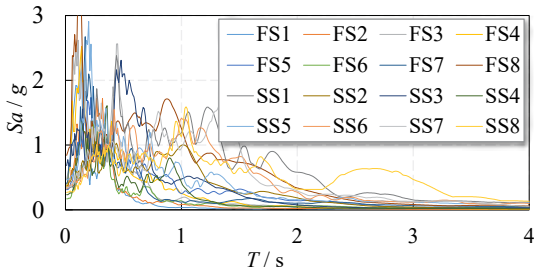


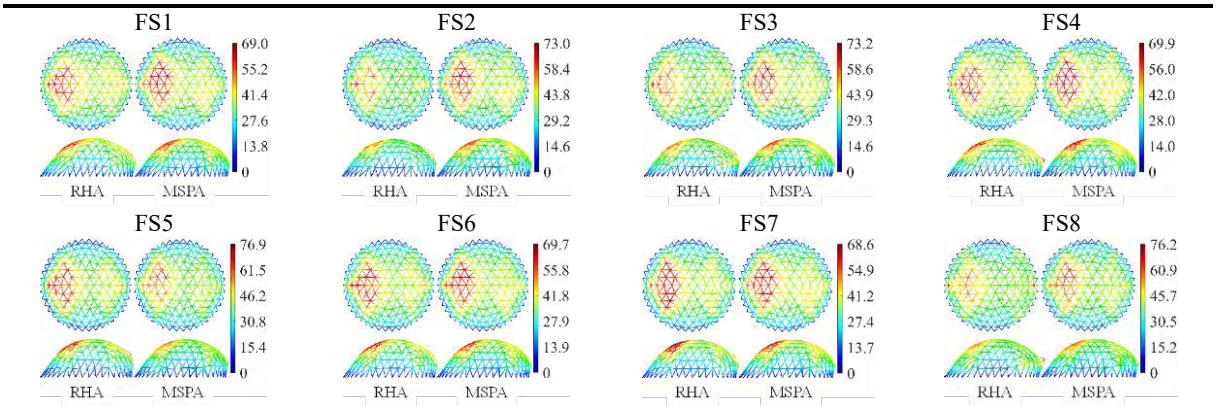
Figure 3: Acceleration spectra of ground motion inputs

4. Comparative study for MSPA procedure

4.1. Nodal displacements estimation

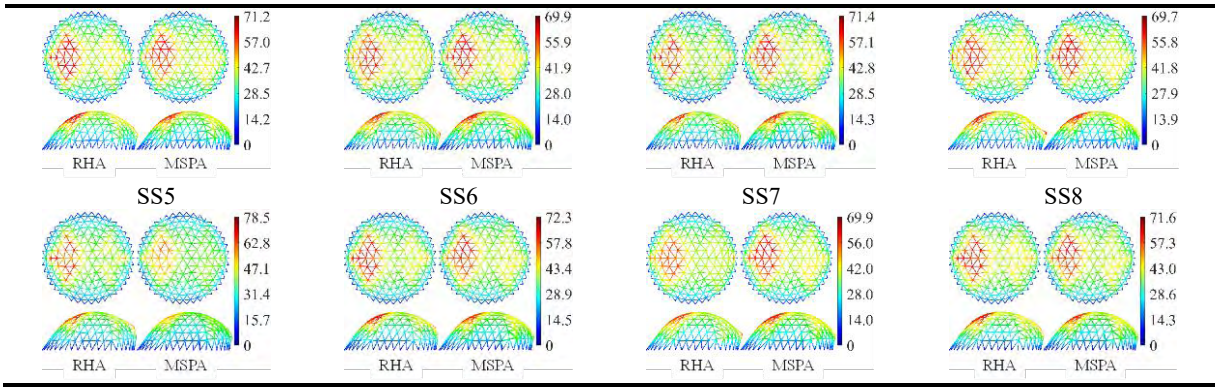
Generally for pushover analysis, computational accuracy depends highly on whether the structural deformation pattern and amplitude could be predicted exactly. Naturally, nodal displacements at the target points were extracted, as displayed visually in Figure 4. As shown, the deformation patterns are in approximate accord with the fundamental mode shape as expected. To be more detailed, those nodes reaching maximum displacements mainly distribute at the left part of the shell.

Comparing the results in each case helps to observe a favorable agreement between MSPA and RHA methods, which demonstrates in most cases, the two set of displacements are consistent in not only the overall profiles but also the corresponding values. The errors of most results are less than 15%, which reveals that nonlinear behaviors of the models are described correctly by the aid of modal stiffness. To be more specific, the nodes with large displacements always feature high accuracy, whereas the nodes with unfavorable errors seem not so dangerous. Such acceptable errors on the safe side no doubt improve the reliability of the MSPA procedure.



(a) firm sites

SS1 SS2 SS3 SS4

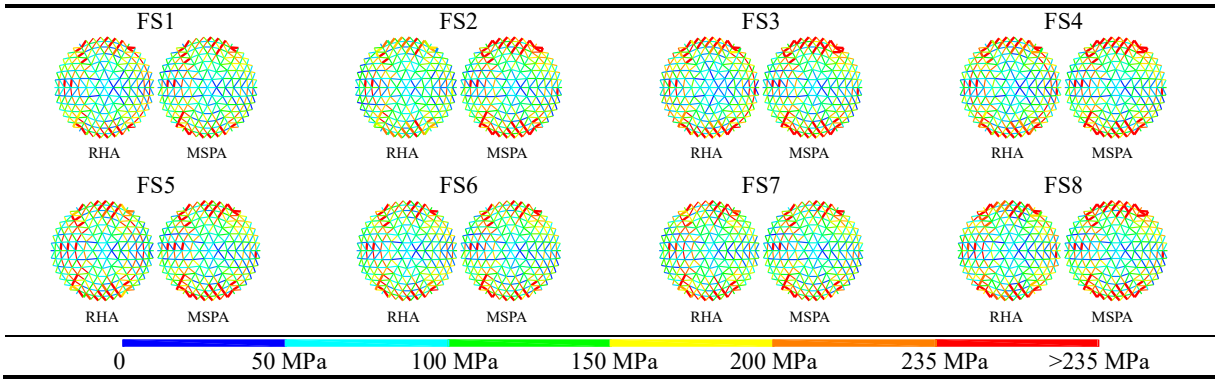


(b) soft sites

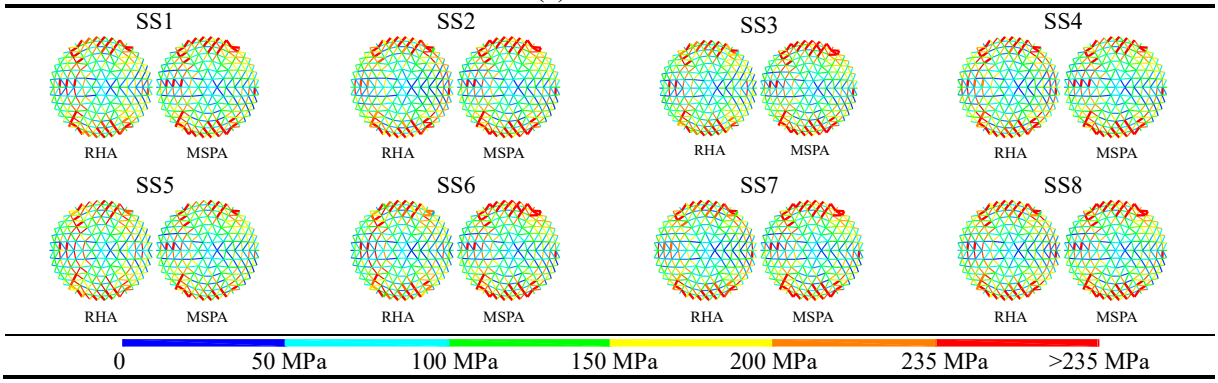
Figure 4: Comparison of nodal displacements calculated by RHA and MSPA methods

4.2. Element stresses estimation

Stress responses are also the responses of interest for seismic evaluation, given in a same manner in Figure 5, where the element stress means the maximum stress value of all the integrating points in the element. Generally, stress states of most elements are quite uniform in tendency and magnitude especially the distributions of high-stress areas estimated by the two methods, attesting the correctness of the pushover load pattern. The discrepancies are acceptable because the majority of element stresses are analyzed accurately with errors below 20%. The elements with large stress errors mainly locate in low-stress areas. Better still, focusing on the red lines, member yielding predicted by MSPA procedure was largely validated by RHA method. However, more significant dispersions of stresses could be recognized herein, in comparison to those of displacements. This is because element stress responses might be affected by higher order modes, especially the modes associated with localized effects.



(a) firm sites



(b) soft sites

Figure 5: Comparison of element stresses calculated by RHA and MSPA methods

5. Conclusion

Based on the modal stiffness derived herein, an enhanced modal pushover analysis procedure was proposed for evaluating seismic performance of the single-layer latticed shell, taking the un-ignorable multi-dimensional response coupling effect into account, which could not be reflected only by base shear and roof displacement. According to the results compared with that by RHA, the appropriateness of MSPA was examined and the following conclusions were drawn:

(1) The MSPA proposed avoids the dependence on the base shear and roof displacement for describing the capacity curve, which is the drawback of conventional MPA method.

(2) Whether on firm sites or soft sites, the calculating results of responses are quite precise in nodal displacements and element stresses, with errors of most cases below 20%. Besides, yielding members are predicted accurately by the MSPA procedure.

(3) The MSPA procedure is able to be extended to seismic performance evaluation of other forms of latticed shells and easy to be programmed.

Acknowledgements

The present work has been conducted with the financial support from the Chinese National Natural Science Foundation (Project designation: 51378379). Acknowledgement from the first author would be sent to Miss Chen Ji for her being supported all the time.

References

[1] Z.C. Zhu, Y.F. Luo and Y. Xiang, "Global stability analysis of spatial structures based on Eigen-stiffness and structural Eigen-curve," *Journal of Constructional Steel Research*, vol. 141, pp. 226-240, 2015.

[2] G.B. Nie, X.D. Zhi, F. Fan and J.W. Dai, "Seismic performance evaluation of single-layer reticulated dome and its fragility analysis," *Journal of Constructional Steel Research*, vol. 100, pp. 176-182, 2014.

[3] X.D. Zhi, F. Fan and S.Z. Shen, "Elasto-plastic instability of single-layer reticulated shells under dynamic actions," *Thin-Walled Structures*, vol. 48, pp. 837-845, 2010.

[4] A.K. Chopra and R.K. Goel, "A modal pushover analysis procedure for estimating seismic demands for buildings," *Earthquake Engineering and Structural Dynamics*, vol. 31, pp.561-582, 2002.

[5] M. Poursha, F. Khoshnoudian and A.S Moghadam, "A consecutive modal pushover procedure for estimating the seismic demands of tall buildings," *Engineering Structures*, vol. 31, pp. 591-599, 2009.

[6] Y. Xiang, Y.F. Luo, X.N. Guo, Z. Xiong,Z.Y. Shen, "A linearized approach for the seismic response analysis of flexible cable net structures," *Soil Dynamic and Earthquake Engineering*, vol. 88, pp. 92-108, 2016.

[7] Y. Xiang, Y.F. Luo and Z.Y. Shen, "An extended modal pushover procedure for estimating the in-plane seismic responses of latticed arches," *Soil Dynamic and Earthquake Engineering*, vol. 93, pp. 42-60, 2017.

Proceedings of the IASS Annual Symposium 2019 – Structural Membranes 2019
Form and Force
7 – 10 October 2019, Barcelona, Spain
C. Lázaro, K.-U. Bletzinger, E. Oñate (eds.)

Analysis of anti-collapse performance of the multi-scale model of terminal building under blast loads

Zaigen MU*, Yuqing YANG, Yali CHEN

*University of Science and Technology Beijing, Beijing 100083, China
E-mail: zgmu@ces.ustb.edu.cn

Abstract

According to the characteristics of the terminal structure and the effect of blast loads, this paper reasonably determines the possible parts under blast loads of the anti-explosive key components of the long-span spatial steel structure. Through the study of the relationship among blast equivalent, blast distance and damage degree of structural members, the damage of key components and their adjacent components is determined. The multi-scale model was used to measure the collapse resistance of the terminal structure under blast loads. The analysis results show that the damage degree of the box-shaped steel column is mainly related to the blasting distance and the explosive equivalent. The deformation of the blasting surface is much larger than that of the back blasting surface. The damage degree of the oblique members is closely related to the incident angle of the explosion shock wave. In the multi-scale model, the shell element can be used to accurately simulate the damage of the component under blast loading. Due to the large redundancy of the vertical members of the long-span spatial steel structure, the residual bearing capacity still has a certain residual bearing capacity after the explosion, which can effectively suppress the development of the deformation.

Keywords: Long-span structure, blast loads, anti-collapse performance, multi-scale model, finite element analysis

1. Introduction

With the rapid development of economy, long-span structures are widely used in all kinds of public buildings. Anti-collapse performance of long-span structures has been paid more attention, such as Pengshan Gymnasium[1], Meijiang Convention and Exhibition Center in Tianjin[2], Guangzhounan Railway Station [3] and so on. Long-span structures are complex structures with large span, and structures have important social functions as important public facilities. Safety and reliability of long-span structures not only maintain the safety of people but also have a significant international and domestic impact. Therefore, it has also become a key target to prevent terrorist attacks, and the risk of continuous collapse cannot be ignored.

Scholars have done a lot of research on the collapse resistance of structural members and the whole structure. Li and Shi[4-5] used the finite element analysis software LS-DYNA to study the dynamic response and failure mode of reinforced concrete columns under blast loads and put forward the corresponding macro model. According to the reflection pressure curve of the building surface under the action of blast equivalent and distance, the damage degree of reinforced concrete columns under blast loads was numerically studied[6]. Gong et al.[7] numerically simulated the damage process and failure mechanism of reinforced concrete columns under close-in explosion, considering the fluid-solid coupling interaction among explosive, air and structure. Moreover, the difference of blast impact load of reinforced concrete columns in different reflection zones was analyzed. Li et al.[8] studied the

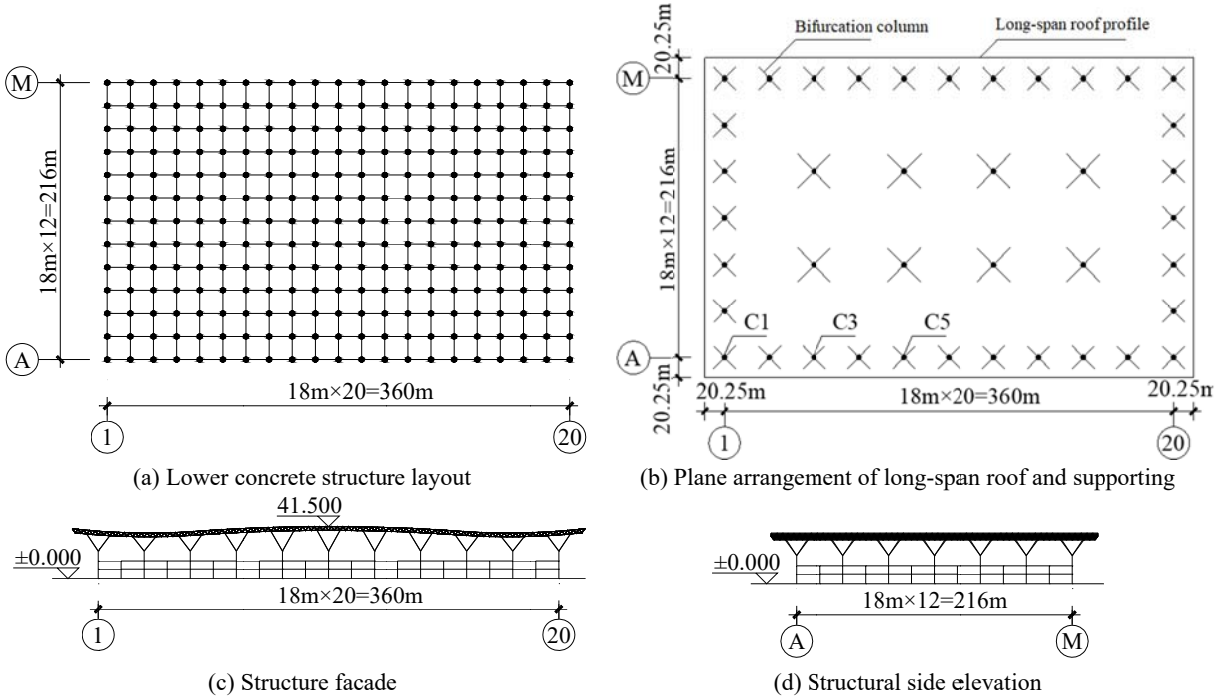
Copyright © 2019 by Zaigen MU, Yuqing YANG, Yali CHEN
Published by the International Association for Shell and Spatial Structures (IASS) with permission.

influence of strain rate and damage accumulation effect on steel. The dynamic response and failure mode of steel column and plane steel frame under blast loads were analyzed. Yi and He[9-10] used mechanical jacks to replace the middle columns on the ground floor and carried out the collapse test of the reinforced concrete plane frame. Ding et al.[11] studied the dynamic response and collapse mode of four kinds of plate grid structures with different column arrangement under outdoor blast loads.

There are many factors affecting the anti-collapse performance of terminal under blast loads. As China has not yet formally promulgated the design code for blast-proof design of civil buildings, the method of removing components is widely used in the analysis of anti-collapse performance of terminal structures[12-13]. This method is mainly based on the sensitivity of the internal force, deformation or energy of the structure to the failure of the members. The key components that may lead to continuous collapse were determined [14-15]. In this paper, according to the characteristics of the terminal structures and the risk degree of the possible explosion, the parts of the key anti-explosion components of the long-span steel structure were reasonably determined. The relationship among blast equivalent, blast distance and damage degree of the structural members were studied. The damage of key components and their adjacent components were preliminarily determined. Furthermore, the multi-scale models[16] were used to simulate the seriously damaged components, and the collapse resistance of the terminal structure under blast loads was investigated.

2. General situation of terminal structure

The lower two floors of the terminal building were reinforced concrete frame structure, and the size of column net was 18m × 18m. The secondary beams (section sizes were 400mm × 900 mm) were arranged in both directions, and the spacing was 4.5 m × 4.5 m. The height of the first floor was 6.5 m, the height of the second floor was 7.5 m, and the thickness of the floor was 150 mm. The inner column spacing of upper steel structure was 72 m and the side column spacing was 36 m. The long-span roof was a tetragonal conical reticulated shell, the projection size of the grid plane was 4.5 m × 4.5 m, and the thickness of the reticulated shell was 3.0 m. The structural arrangements are shown in Figure 1, and the section specifications of the main structural components are shown in Table 1.



(a) Lower concrete structure layout

(b) Plane arrangement of long-span roof and supporting

(c) Structure facade

(d) Structural side elevation

Figure 1: Structural layout of the terminal

Table 1: Section specification of main structural members

Location	Section /mm	Material	Remarks
Concrete frame column (supporting roof)	Side span:□1200×1200;Other:□1600×1600	C50	Concrete member
Concrete frame column (unsupported roof)	Side span:D1100×1100;Other:D1200×1200	C50	Concrete member
Concrete frame beam	Side span:900×1400;Other:900×1200	C40	Concrete member
Supporting roof steel pipe column	Side column C3:□1100×1100×35 Middle column:□1500×1500×45	Q345B	Welded straight seam tube
Supporting roof incline brace	Side span:D500×20;D550×20;Other:D750×30	Q345B	Welded straight seam tube
Reticulated shell lower chord bar	D95×5;D121×6;D152×10;D245×16	Q345B	Hot rolled seamless tube
Reticulated shell upper chord bar	D102×6;D108×6;D203×12;D203×14	Q345B	Hot rolled seamless tube
Reticulated shell web bar	D95×5;D121×6;D152×8;D203×14; D245×14	Q345B	Hot rolled seamless tube

3. Blast damage analysis of key components

3.1. Analysis of blast damage parameters of steel columns

In the long-span structure of the terminal, the cross-section of the box column was 1100mm × 1100 mm×35mm. The material was Q345B with 345 MPa yield force. Shell element S4R was used for simulate the box column, and the mesh size was 100mm × 100mm. In order to simulate the actual stress characteristics of the box column, the bottom of the column was fixed. The axial pressure 3000 kN (0.046 axial compression ratio) was applied to the top of the column.

According to the characteristics of the van, the height of the blast center to the third floor was 2.0 m. The calculated blast distance R (the vertical distance between the blast center and the surface of the box column), TNT equivalent W and the corresponding proportional distance Z are shown in Table 2.

The analysis results of box column damage caused by blast distance and TNT equivalent are shown in Table 3. It can be seen from Table 3 that under the blast action of car bomb TNT equivalent, except for the case where the blast distance is close or the TNT equivalent is large, the vertical deformation of other components is very small.

Obvious depression occurs in the corresponding part of the box column to the blast center. The deformation of the blasting surface is much larger than that of the back-blast surface, and the deformation near the blast center is very concentrated which the panel is seriously sunken. The larger the TNT equivalent and the closer the distance, the greater the proportion of residual deformation. All the components have entered yield and obvious plastic strain has appeared. The maximum plastic strain of three of them exceeds 0.1, which indicates that the damage of the components is very serious.

Table 2: Blast distance R, TNT equivalent W and corresponding proportional distance Z /m/kg1/3

Blast distance R /m	TNT equivalent W /kg			
	500	1000	2000	4000
4.0	0.504	0.400	0.317	0.252
6.0	0.756	0.600	0.476	0.378
8.0	1.008	0.800	0.635	0.504

Table 3: Calculation results of box-shaped columns for different blasting distances R and TNT equivalents W

TNT equivalent /kg	Blast distance /m	Vertical deformation w /m	Transverse deformation δ_{max} /m	Plastic strain ε_p	Axial transverse deformation δ /m	Relative deflection δ/h	Damage degree
500	4.0	0.0020	0.1150	0.0225	0.0131	1/608	Mild
	6.0	0.0018	0.0449	0.0067	0.0079	1/1002	Mild
	8.0	0.0020	0.0261	0.0023	0.0056	1/1419	Mild
1000	4.0	0.0043	0.2564	0.0522	0.0252	1/317	Mild
	6.0	0.0021	0.1112	0.0216	0.0144	1/554	Mild
	8.0	0.0016	0.0558	0.0093	0.0098	1/816	Mild
2000	4.0	0.0169	0.5618	0.1004	0.0552	1/145	Moderate
	6.0	0.0049	0.2532	0.0557	0.0265	1/302	Mild
	8.0	0.0026	0.1359	0.0274	0.0173	1/461	Mild
4000	4.0	0.1097	1.1124	0.1595	0.1968	1/40	Damage
	6.0	0.0192	0.5727	0.1160	0.0592	1/135	Moderate
	8.0	0.0075	0.3089	0.0733	0.0317	1/251	Mild

Under the action of blast loads, the overall bending of the box column is remarkable, and the relationship between the relative deflection and the proportional distance of the box member is shown in Figure 2. Taking the central axis of the side column as the reference, the relative deflection of the member increases gradually with the decrease of the proportional distance. The relative deflection of two members exceeds 1/200, reaching the degree of moderate damage. And the relative deflection of one member exceeds 1/45, beyond the limit of serious damage.

Under the action of blast distance 4m and TNT equivalent 4000kg, the vertical deformation and lateral deformation time history curve, failure mode and plastic strain distribution of the box column are shown in Figure 3.

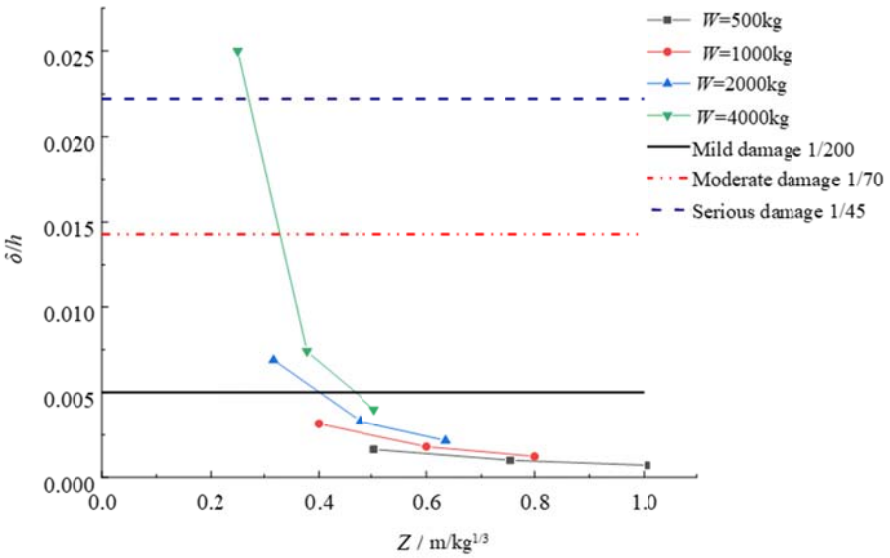
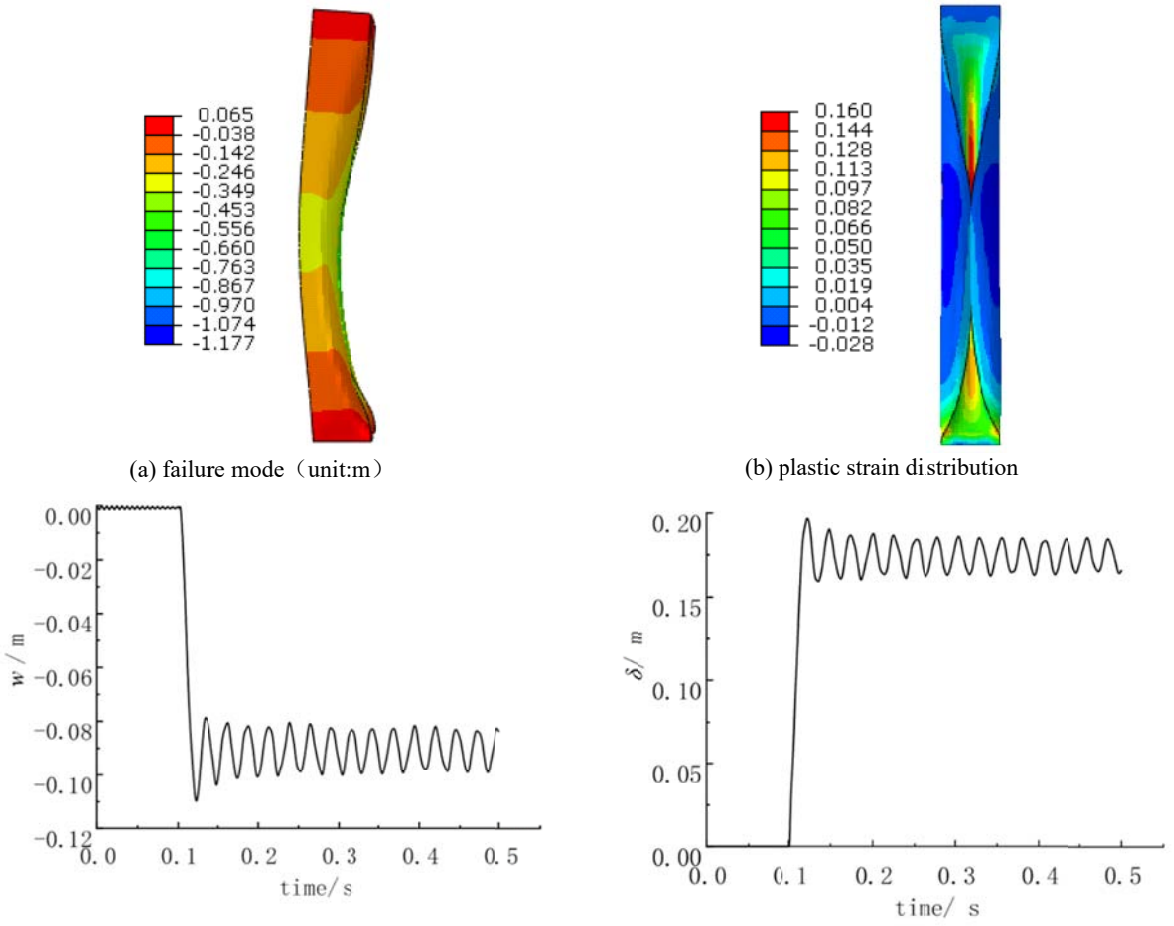


Figure 2: Relationship between relative deflection and proportional distance of box-shaped columns



(a) failure mode（unit:m）

(b) plastic strain distribution

(c) vertical deformation time history curve

(d) lateral deformation time history curve

Figure 3: Damage of box-shaped columns under blast distance 4m, TNT equivalent 4000kg

4. Analysis of collapse resistance of multi-scale model structures

4.1. Computational assumption

For the terminal structure, the range of direct damage caused by blast loads is very small. In order to accurately simulate the influence of blast loads on the terminal structure, the multi-scale model is used to directly analyze the collapse resistance of the whole structure under the action of blast distance 4m and TNT equivalent 4000 kg. The multi-scale finite element analysis of the structure, that is, different types of elements are used to simulate different parts of the structure. In this paper, the shell element is used to simulate the box columns and inclined brace adjacent to the blast center. The other components are simulated by beam element or pipe element. Multi-scale model has many advantages, such as accurately simulating the boundary conditions of the key components, considering the simultaneous damage of multiple components near the blast center, moreover, investigating the influence of residual bearing capacity of damaged members after the blast on the collapse resistance of the structure. Multi-scale model compared with the overall calculation model with solid element or shell element, calculation efficiency is greatly improved. Multi-scale model of the blast center near the side column C3 is shown in Figure 4.

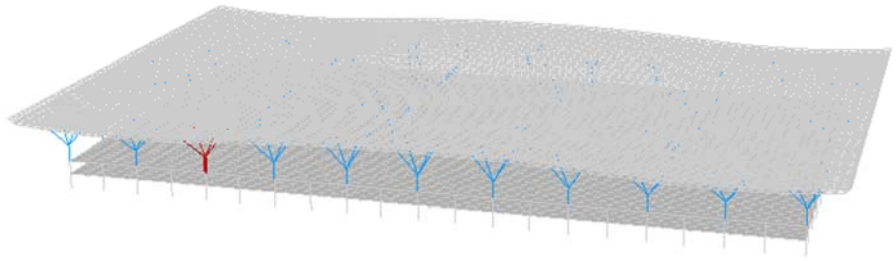
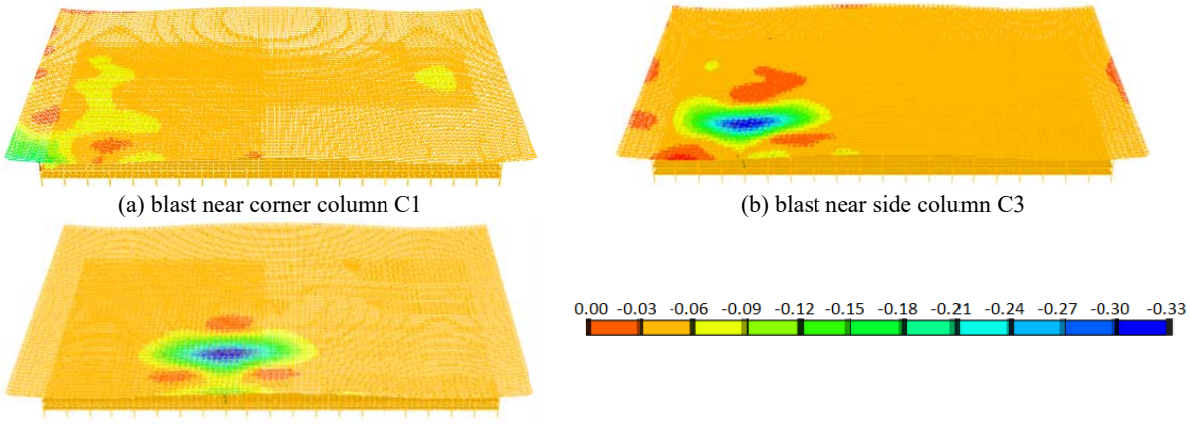


Figure 4: Multi-scale model for the explosion adjacent to column C3

4.2. Structural deformation analysis

At TNT equivalent 4000kg and blast distance 4m, the overall deformation of the roof with difference blast centers is shown in Figure 5. The deformation of the roof is mainly concentrated in the vicinity of the blast damage component, and the displacement response of the direct blast area is much smaller than that of the non-direct blast area. The results show that the continuous collapse of the long-span spatial structure under blast loads is local and weakly transitive. When blast near corner column C1, the maximum vertical displacement of roof suspension is 0.33m. When blast near side column C3, the maximum vertical displacement of roof edge is 0.28m. And when blast near side middle column C5, the maximum vertical displacement of roof edge is 0.25m.



(a) blast near corner column C1

(b) blast near side column C3

(c) blast near side middle column C5

Figure 5: Deformation of the structure after the key components damaged（unite: m）

The time history curve of the maximum vertical deformation of the reticulated shell under blast loads is shown in Figure 6. After the damage of the adjacent members of the blast center, the initial deformation speed of the roof is faster, then the oscillation amplitude of the vertical deformation gradually becomes smaller, indicating that the structure tends to be stable and there is no continuous collapse.

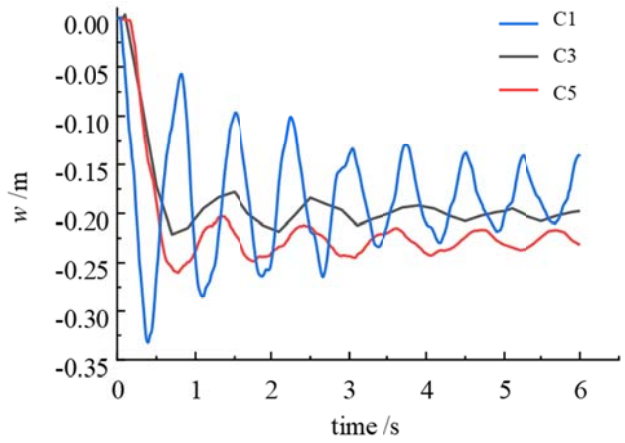


Figure 6: Maximum vertical deformation curves of roof after damage of key components of multi-scale model

5. Conclusion

(1) The damage degree of the box column is mainly related to the blast distance and TNT equivalent, and the deformation of the blasting surface is much larger than that of the back-blasting surface.

(2) The middle point of the inclined brace is far away from the blast center; therefore, the damage degree is not only related to the blast distance and TNT equivalent but also closely related to the incident angle of the blast shock wave. However, there is little difference between the deformation of the blast surface and the back-blasting surface.

(3) Through the multi-scale model method, the shell element can be used to accurately simulate the damage of the component under blast loads, and the beam element or pipe element can be used to simulate the non-adjacent members, in this way, the calculation efficiency can be greatly improved.

(4) The vertical bearing members of the long-span structure have large redundancy. The vertical member still has a certain residual bearing capacity after the blast, which can effectively inhibit the development of deformation.

Acknowledgements

This work was supported by the National Natural Science Foundation of China (grant No. 51578064) and the Natural Science Foundation of Beijing (grant No. 8172031).

References

[1] Y. F. Zhu, J. G. Feng, J. G. Cai, et al. “Analysis on progressive collapse resistance of truss string structure of Meijiang Exhibition Center”, *Journal of Building Structures*. vol. 34, no. 3, pp. 45-53, 2013.

[2] C. G. Liu, L. Y. Chen, Q. W. Su. “Research on the progressive collapse resistance performance of pengshan gymnasium”, *Steel Construction*. vol. 30, no. 11, pp. 1-5, 2015.

[3] J. G. Cai, F. L. Wang, J. Feng, et al. “Progressive collapse analysis of cable-arch structures of the New Guangzhou Railway Station”, *Journal of Building Structures*. vol. 31, no. 7, pp. 103-109, 2010.

[4] Y. C. Shi, Z. X. Li. “Dynamic responses and failure modes of RC columns under blast loading”, *Journal of Building Structures*. vol. 29, no. 4, pp. 112-117, 2008.

[5] Z. X. Li, Z. F. He, Y. C. Shi, et al. "Macro model for dynamic analysis of reinforced concrete columns under blast loading", *Engineering Mechanics*. vol. 32, no. 9, pp. 76-83, 2015.

[6] S. Yan, D. Wang, L. Zhang, J. Sun. "Damage analysis for RC column under explosive loads", *Engineering Mechanics*. vol. 25, no. s1, pp. 90-93, 2008.

[7] S. F. Gong, Q. Xia, W. L. Jin. "Investigation on damage mechanism of RC column under close-in explosion", *Journal of Zhejiang University*, vol. 45, no. 8, pp. 1405-1410, 2011.

[8] Z. X. Li, Z. X. Liu, Y. Ding. "Dynamic responses and failure modes of steel structures under blast loading", *Journal of building structure*. vol. 29, no. 4, pp. 106-111, 2008.

[9] Yi Weijian, He Qingfeng, Xiao Yan. "Collapse performance of RC frame structure", *Journal of Building Structures*, vol. 28, no. 5, pp. 104-109, 2007.

[10] Q. F. He, C. Zhou, W. J. Yi. "Numerical Simulation on Collapse Behavior of RC Frames with a Column Removal under Blast Loads", *Journal of Hunan University*, vol. 43, no. 11, pp. 61-67, 2016.

[11] Y. Ding, M. Wang, Z. X. Li. "Numerical analysis of the damage and collapse process of planar lattice structures under blast loads", *China Civil Engineering Journal*, vol. 43, no. s, pp. 34-41, 2010.

[12] G. P. Zhao, K. J. Xiao, Y. Feng, et al. "Progressive collapse analysis on large span steel structure of Chengdu Shuangliu International Airport T2 Terminal Building", *Building Structure*, vol. 40, no. 9, pp. 27-30, 2010.

[13] W. N. Shu, Z. Y. Zhu, Y. Qi, at el. "Design and research on terminal building of Beijing New Airport", *Building Structure*, vol. 46, no. 17, pp. 1-7, 2016.

[14] P. C. Pandey, S. V. Barai. "Structural sensitivity as a measure of redundancy", *Journal of Structural Engineering*, ASCE, vol. 123, no. 3, pp. 360-364, 1997.

[15] J. G. Cai, F. L. Wang, J. Zhang, et al. "Discussion on the progressive collapse analysis of long-span space structure", *Engineering Mechanics*, vol. 29, no. 3, pp. 143-149, 2012.

[16] X. Z. Lu, L. P. Ye, Z. W. Miao, et al. *Elasto-Plastic Analysis of Buildings Against Earthquake: Theory, Model and Implementation on ABAQUS, MSC.MARC and SAP2000*. Beijing: China Architecture and Building Press, 2009.

Proceedings of the IASS Annual Symposium 2019 – Structural Membranes 2019
Form and Force
7 – 10 October 2019, Barcelona, Spain
C. Lázaro, K.-U. Bletzinger, E. Oñate (eds.)

Nonlinear effects under compression-flexion combination for sleeveless space frame connection systems and validation of linear superposition for resistance verification

Josu GOÑI*[a], Ruben FERNANDEZ[a], Mikel MONASTERIO[a], Aurelio GARCIA[a], Zak KOSTURA[b]

*[a] LANIK I, S.A.
Mundaiz 8, 20012, San Sebastián, Spain
jgoni@lanik.com

[b] PE. Associate, Arup, New York, NY, USA, Zak.Kostura@arup.com

Abstract

In general, it is admitted to consider biarticulated elements when we simulate space frame structures, which implies that elements just transmit axial forces and there is no flexion through the nodes. Of course, for this consideration to be correct, loads and constraints must be applied in the center of the nodes, and this is how the great majority of space frames are calculated. However, this is a simplification of the reality: There can be moments in space frame nodes due to different events (eccentricities, hyperstaticity with substructure), and these moments cannot always be considered insignificant. This is the case of Mexico's New International Airport's space frame and many other particular cases. Focusing on the ORTZ as an example of a sleeveless space frame connection system, the linear superposition of axil and moment efforts when evaluating the resistance the of space frame's connection bolts can only be admitted if the behavior of the node under combination of compression and flexion is linear until reaching design limits, and this is not something that can be taken for granted. In this research, FEM has been used to simulate and analyze under different considerations the nonlinear behavior of ORTZ connection system under combination of flexion and compression. It is concluded that in all cases the instability of the node appears once the design loads are largely exceeded, so the linear superposition of axil and flexion for checking a bolt's section can be admitted.

Keywords: space frame, ORTZ, buckling, connection system, sleeveless, nonlinear

1. Introduction

As it is well known, space frames have been designed for decades considering its elements working as biarticulated bars. This means that only axil efforts are transmitted through the bars and the static equilibrium is reached at each node without being necessary to withstand any bending moment.

This simplification is generally accepted because loads and supports are generally applied to the center of the nodes and because of the lower bending stiffness of each bolted connection in comparation with the bending stiffness of the whole space frame structure. Nevertheless, this assumption is indeed a simplification of the real behavior of the structure. Bending moments can appear in the space frame`s nodes as a consequence of diverse events, and therefore we should ask ourselves whether these moments can be disregarded or not.

In the case of Mexico's New International Airport's space frame, this issue was relevant in the design of the space frame connections and ARUP took always into account that the selected constructive space frame system had to guarantee the stability of the nodes when the combination of flexion and compression appeared.

Copyright © 2019 by Josu GOÑI, Ruben FERNANDEZ, Mikel MONASTERIO, Aurelio GARCIA, Zak KOSTURA
Published by the International Association for Shell and Spatial Structures (IASS) with permission.

The initial design of Mexico's New International Airport's space frame included connections using sleeves and bolts, and it was proved by ARUP that the stability of nodes was guaranteed. When the ORTZ system was suggested for the execution of this project, it was questioned if a sleeveless space frame bolted system as the ORTZ system was going to be able to keep the nodes stable against local buckling when moments and compression efforts where combined.

This paper shows how LANIK proved by means of nonlinear FEM simulations that the ORTZ system is stiff enough to avoid the unstable rotation of the nodes in combination of compression and flexion.

2. Bending moment in space frame nodes

There are two main cases where moments can appear in space frame's nodes.

2.1. Eccentric pin joints

Connections of space frames are supposed to be applied to the center of the spheres, but this is not always so. In fact, many times the substructure or the support joints are located some centimeters over the center of the sphere. If a shear effort is transmitted trough this joint, then a bending effort appears in the sphere and this must be withstood by the bolts of the space frame members.

This effort is easy to obtain as the shear effort has to be multiplied by the distance from the center of the sphere and the eccentric pin joint.

2.2. Embedded connections between space frame and substructure

There are again two possible scenarios in the case of embedded connections:

2.2.1. non self-supporting substructure

This can be the case of a non-braced substructure which needs the nodes to stabilize some rotational degrees of freedom. In these cases, as the previous one, the calculation of the moment is quite easy because there is a high level of isostaticity and can be obtained by means of a simple multiplication

2.2.2. self-supporting substructure

When the substructure is braced enough or gantries are used for the substructure to be stable, and at the same time, the connections to the space frame nodes are embedded, the space frame and the substructure work simultaneously against turns of the substructure. This means that rotations appear in the spheres, and therefore bending moments. The value of this bending moments depends though on the ratio of stiffness against the turn of the sphere between the substructure and the space frame connections.

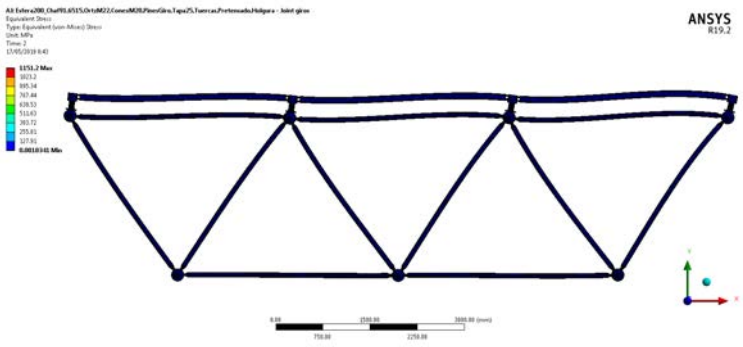


Figure 1: self-supporting substructure embedded to the space frame nodes with tangential effort

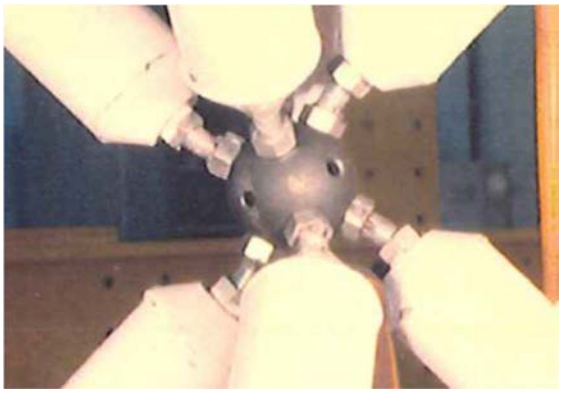
It is very difficult to simulate with enough accuracy this hiperstatic behavior because of the vast amount of different bolt combinations at nodes and the complex and sometimes nonlinear behavior of the

substructure. This is why generally, if the substructure is self-supporting and therefore the space frame's nodes do not need to stabilize the substructure, moments at nodes are considered negligible.

Nevertheless, in the case of Mexico's New International Airport's space frame (from now on, NAIM), ARUP made the needed simulations to obtain these bending moment efforts.

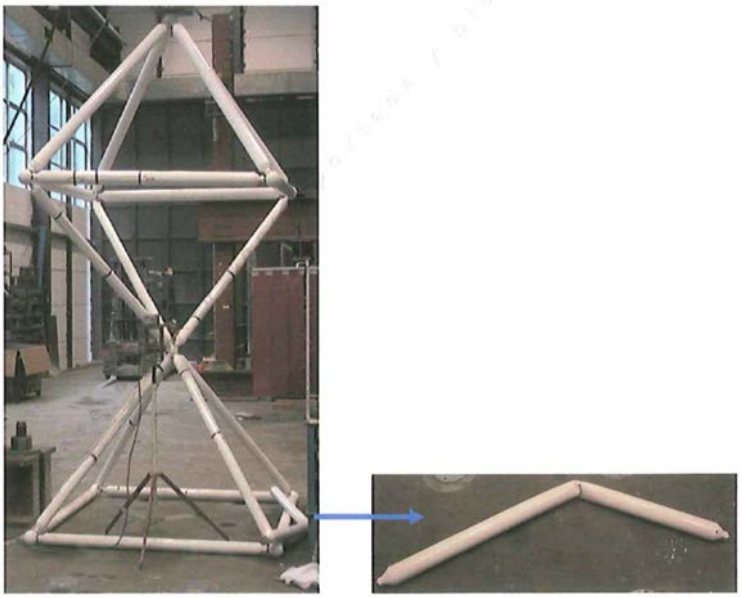
3. Nodal buckling

The risk of nodal buckling is something well known and checked for decades. This phenomenon can appear when many compression loads appear simultaneously at a node. If the bolted joints are not stiff enough against the rotation of the sphere, the node could rotate and generate an eccentricity with a non-stable progress.



Figures 2: Nodal buckling with NUCLOS space frame sleeveless system

ORTZ sleeveless space frame system has been tested in the past to verify this phenomenon does not appear before member buckling with some test samples as shown below:



Figures 3 and 4: ORTZ test sample to promote a controlled full compression at a node and member buckling

However, these tests did not take into account that an extra bending moment applied to the sphere could promote a rotation that could accelerate the nodal buckling.

4. ORTZ system description

Custom-designed bolts are inserted through conical fittings. These dual-threaded bolts consist of a solid cylinder bisected by a conical truncated surface spirally grooved in the opposite direction of the main body of the bolt which is of greater diameter. As part of the bar assembly, the portion of lesser diameter fits into the node openings. This two-way thread allows for double tightening using a single-directional twisting motion. This makes it possible to tighten the bolt in relation to the spherical node, as well as to the tubular bar by means of the two nuts situated on the portion of the bolt of greater diameter. The main purpose for this nut-nut combination is to create a blocking system by means of a tightening and back-tightening effect. Furthermore, in its final position, the nut-nut combination ensures constant tightness and preempts the eventual loosening of the union due to vibration from happening.

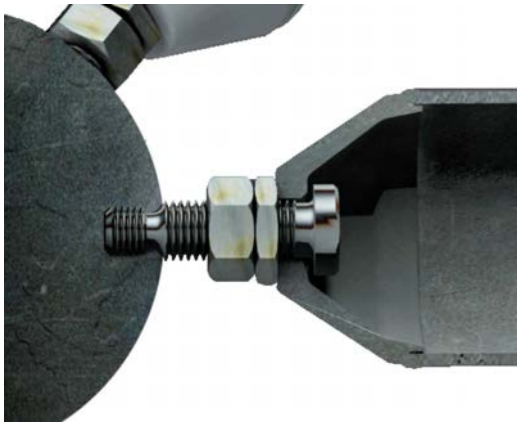


Figure 5: ORTZ system

This technology allows the dual-threaded bolt to retract towards the interior of the tubular bar. This action permits the easy assembly and disassembly of any intervening tubular bar without modifying the relative positions of its two interconnected spherical nodes. This is possible even when the nodes are in their definitive position. The advantages of this retractable bolt are the increased flexibility in the assembly process and the ease in maintenance and replacement of damaged tubular bars.

5. FEM analysis description

The objective of this simulation is to check the behavior of the ORTZ connection subjected simultaneously to compression and a bending moment.

5.1. Geometric configuration

The analysis performed consists of two bars facing each other and connected by a sphere, which simulates a configuration of an upper layer. The bars have been simulated as constituted by the tube and two terminals.

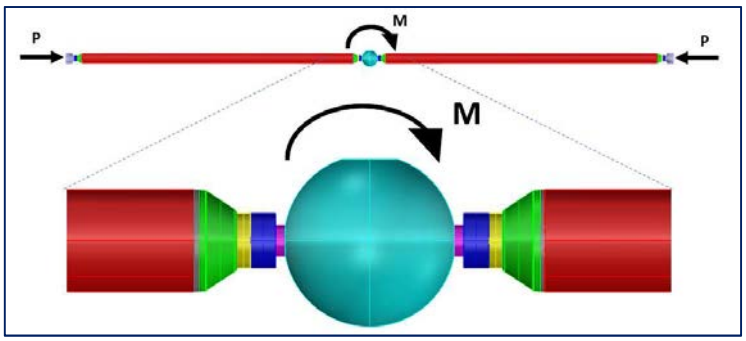


Figure 6: FEM model configuration

Two cases have been analyzed, one with a metric 16 and the other with a metric 22. The smallest metrics of the system have been selected, since they will be the most affected by the bending stress caused by the enclosure. In the case of NAIM, the bending efforts were equal in all the knots of the upper layer of the spatial frame and therefore, with the same efforts, the smaller screws were more affected than the larger ones.

This paper shows the result of one of these two cases:

- Sphere: 150 mm (diameter)
- Tube: 88.9 x 2.6 mm (diameter x thickness)
- Screws: 22 mm (metric)

5.2. Boundary conditions

The sphere is restricted in the directions perpendicular to the load, allowing the rotation in the direction of the moment.

The compression load is applied at both ends of the bars. The two terminals that constitute these ends are simulated. The loads are applied to the terminals as if they were applied to the center of spheres, so this axil effort is transferred by the screws of the ends of the bars. In these ends, the movements in the local Z and Y directions are restricted, allowing movement only in the X axis (parallel to bars).

5.3. Load cases

Five cases are analyzed:

A. Flexible ORTZ bar. Bending moment: 1066 N·m and an increasing axial effort. The first case analyzed considers the flexibility of the bars subjected to compression. A constant bending moment is applied to the sphere (the one calculated to be transmitted from the substructure to the space frame's nodes in the case of NAIM). The axial effort increases over the bars' buckling design limit.

B. Rigid ORTZ bar. Bending moment: 1066 N·m and an increasing axial effort. In this second case, bars with infinite stiffness are considered, so that the behavior of the screws can be seen independently of the buckling behavior of the bars. This is not a real case, but it helps to understand the model. The moment introduced in the sphere is equal to case A.

C. Rigid ORTZ bar. Bending moment (x4): 4264 N·m and an increasing axial effort. In order to check if the bending moment increase strongly affects the stability of the node, the nominal bending is multiplied by 4.

D. Flexible Ortz bar. Constant Axil (next to design limit) and an increasing moment. An opposite case, with a constant compression close to the bars' buckling limit increasing the bending moment progressively.

E. Flexible welded rod. Bending moment: 1066 N·m and an increasing axial effort. Same as case A, but with the bars welded to the central sphere, instead of with an Ortz connection.

In order to analyze the results obtained, they have been compared with the compressive design limit loads of the analyzed bars. The simulated bars have a length of 2500 mm. This is shown in Table 1.

Table 1. Buckling resistance of tubular bars subjected to compression. According to AISC 360-10, LRFD

Diameter (mm)	Thickness (mm)	Fy (MPa)	Section (mm2)	Turning radius (mm)	Length (mm)	kL/r	Fe (N/mm2)	Fcr (N/mm2)	Compression limit (kN)
88.9	2.6	240	704.91	30.53	2500	81.90	294.29	170.60	**108.23**

6. FEM analysis results

All the simulations are geometrically nonlinear. The result obtained for the five study cases are:

6.1. Case A. Flexible ORTZ bar. Bending moment: 1066 N·m and increasing axial effort

Figure 7 shows the scaled deformation of the bar at the moment just after buckling.

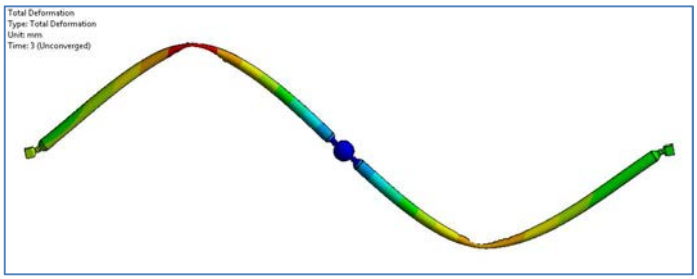


Figure 7: scaled deformation of case A just after buckling

Figure 8 shows the increase in the rotation produced in the sphere, due to the increase in compression of the bars that reach that sphere. The instability is produced by buckling of the bars, while the Ortz terminal assembly and the sphere receiving the bending moment do not suffer the rotation that produces the failure.

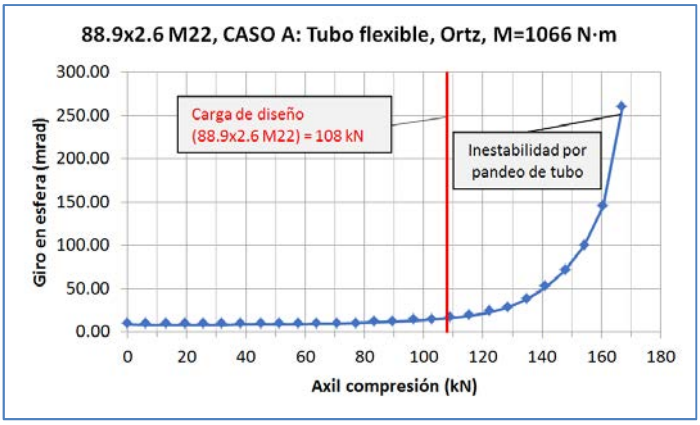


Figure 8: Case A. Evolution of the turnover produced in the sphere due to a compression increase.

6.2. Case B. Rigid ORTZ bar. Bending moment: 1066 N·m and increasing axial effort.

This case is thought to promote the failure at the node avoiding the bar to buckle by means of an increase of their stiffness. This case is not real, but it helps to know how far the nodal buckling from the bar's buckling is.

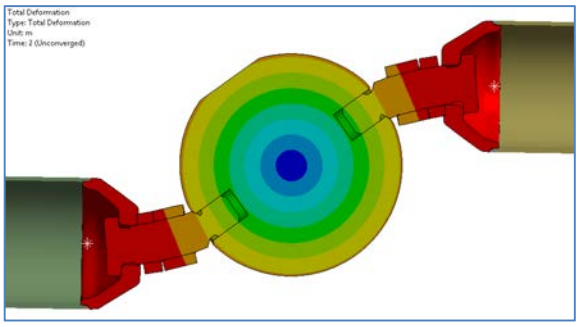


Figure 9: deformation of case B just after buckling. Node detail

Nodal bucking happens once the compression has been increased more than ten times over the bar buckling design limit. This means the bars would have buckled much before reaching this compression load.

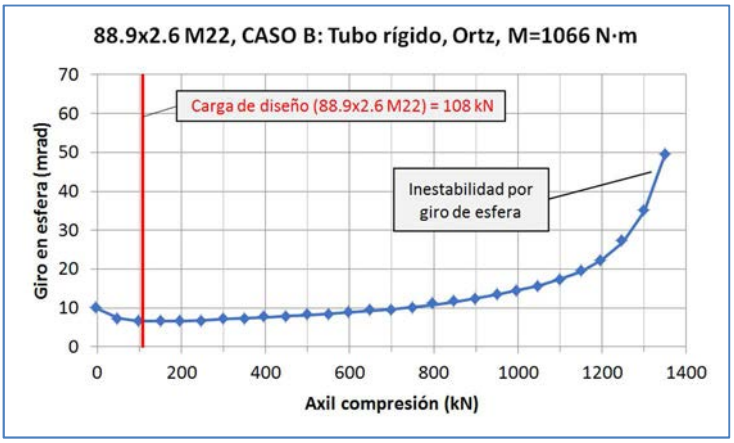


Figure 10: Case B. Evolution of the turnover produced in the sphere due to a compression increase.

6.3. Case C. Rigid ORTZ bar. Bending moment (x4): 4264 N·m and increasing axial

This increase of the moment continues producing an instability due to excessive rotation of the sphere with values much higher than the design load of the tube studied.

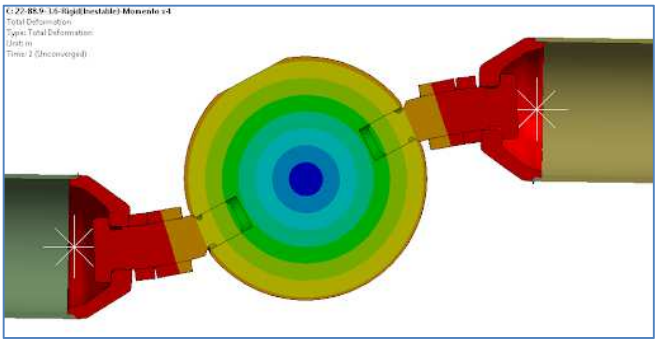


Figure 11: deformation of case C just after buckling. Node detail

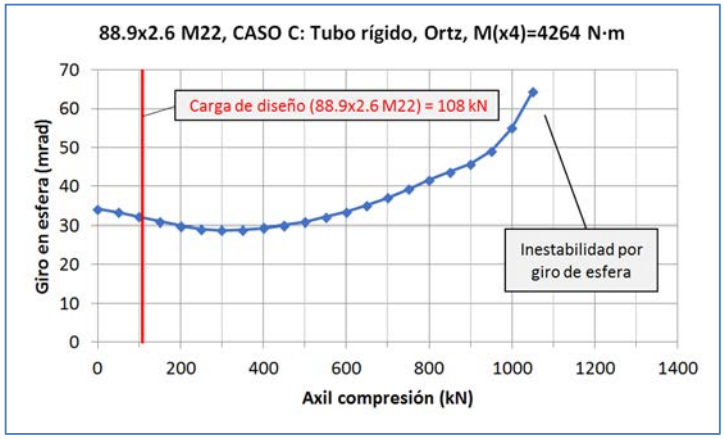


Figure 12: Case C. Evolution of the turnover produced in the sphere due to a compression increase.

With this study case C, it can be checked that the bending load applied is not critical, since a load four times bigger still doesn't trigger nodal buckling.

6.4. Case D. Flexible Ortz bar. Constant Axil (next to design limit) and increasing moment.

The analysis of this case concludes that no unstable phenomenon happens with the increase of the bending moment, but a linear proportional rotation does.

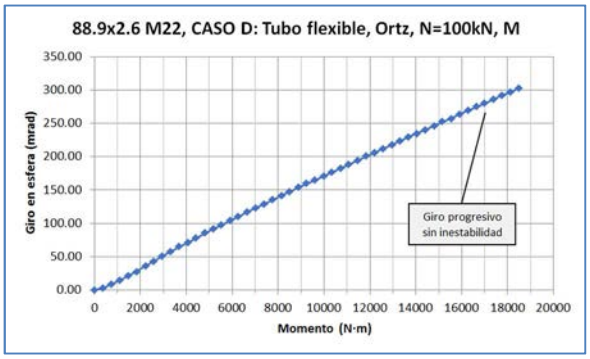


Figure 13: Case D. Evolution of the turnover produced in the sphere due to a bending increase.

6.5. Case E. Flexible welded rod. Bending moment: 1066 N·m and increasing axial effort

This analysis confirms that the bending elasticity at the node doesn't affect the buckling failure limit.

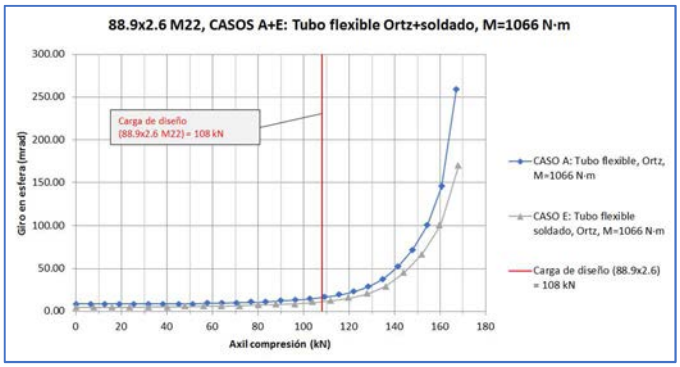


Figure 14: Comparison of the turnover produced in the sphere in cases A and E.

7. Conclusions

The failure due to instability of the node occurs at load values much higher than the failure due to buckling of the bar.

It is impossible to reproduce the effect of node instability in a real physical test (member bucking would occur first).

Linear superposition of axil and flexion for checking bolt's section can be admitted.

References

[1] J. Goñi and L. Irisarri, "Elastic-plastic behaviour of the SLO node for the second order calculation of the safety factor against global buckling in single layer structure", *IASS Symposium*, Wroclaw, Poland, 2013.

[2] Z. Kostura, M.C.J. Clark, J.R. Olson, "Design of a 500,000m^2 Iconic Roof for the New International Airport for Mexico City", *IASS Symposium,* Boston, 2018

[3] Z. Kostura, M.C.J. Clark, J.R. Olson, "Necessity and Invention: Leveraging a Megaproject to Advance the use of Computational Design", *IABSE Symposium*, Guimarães, Portugal, 2019

Proceedings of the IASS Annual Symposium 2019 – Structural Membranes 2019
Form and Force
7 – 10 October 2019, Barcelona, Spain
C. Lázaro, K.-U. Bletzinger, E. Oñate (eds.)

Damping characteristics of aluminum alloy cylindrical latticed shell

Shuyu GAO*, Xiaonong GUO, Xiaoqun LUO, Jindong ZHANG

*Department of Structural Engineering, Tongji University
No.1239 Siping Road, Yangpu District, Shanghai, China
1910004@tongji.edu.cn

Abstract

In order to give a specific damping ratio value of aluminum alloy latticed shells, the field measurement was carried out on an aluminum alloy cylindrical latticed shell with a planar dimension of 40m×36m and a height of 3.9m. A total number of 19 kinds of load cases were designed. Subsequently, 380 damped free vibration acceleration responses of the joints were collected. Then using analytical modal decomposition (AMD) and Hilbert transform, the natural frequency and modal damping ratio of the structure can be obtained. Based on the statistical analysis of the obtained data, the damping ratio for such aluminum alloy cylindrical latticed shells was suggested as 4%. Besides, a finite element model of the measured structure was established using the suggested damping ratio. And the nodal dynamic responses given by numerical analysis show good consistency with test results. Consequently, the damping ratio given in the paper could be applied in dynamic response analysis and engineering design of cylindrical latticed shells with aluminum alloy gusset (AAG) joints.

Keywords: cylindrical latticed shell, aluminum alloy gusset joints, analytical modal decomposition, modal identification, damping ratio.

1. Introduction

In recent years, thousands of aluminum alloy structures have been built in China, most of which belong to long-span spatial structures [1]. And single-layer latticed shell is the most common form among them. Besides, the membrane force is dominant in shell structures. Generally, this latticed shell is composed of three-dimensional grids with H-section members and gusset joints [2]. As for the mechanical characteristics of aluminum alloy gusset (AAG) joints, numerous scholars have carried out relevant researches on the failure mechanism, stiffness and load-bearing capacity of AAG joints[3]- [9]. Based on the achieved results, researches on the static bearing capacity of aluminum alloy latticed shells tends to be perfect [10][11].

However, studies on damping characteristics of latticed shells with AAG joints [12] is relatively insufficient compared to steel reticulated shells. In this paper, the field measurement was carried out on a cylindrical latticed shell with AAG joints (see Figure 1) to provide more references for practical engineering. By collecting the damped free vibration response of measuring points under jump excitation, modal parameter identification for acceleration response could be performed. After deriving the natural frequencies and modal damping ratios of various orders, the average damping ratio of the shell with AAG joints was calculated successively. Moreover, a finite element (FE) model of the measured shell was established using the obtained damping ratio. And the nodal acceleration responses given by numerical analysis show good consistency with test results. It is indicated that the measured damping ratio could be applied in dynamic response analysis and engineering design of cylindrical latticed shells with (AAG) joints.

Copyright © 2019 by Shuyu GAO, Xiaonong GUO, Xiaoqun LUO, Jindong ZHANG
Published by the International Association for Shell and Spatial Structures (IASS) with permission.

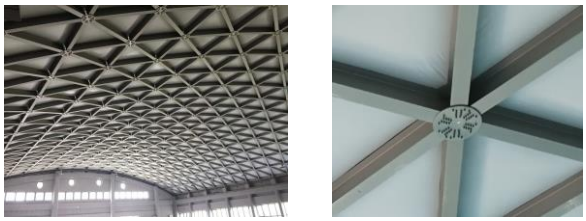


Figure 1: The measured cylindrical latticed shell with gusset joints

2. Modal parameter identification

2.1. Analytical modal decomposition

Empirical mode decomposition (EMD) and Hilbert-Huang (HHT) transform [13] are unable to decompose a signal with closely spaced frequency components and narrowband signals, also difficult to separate intermittent fluctuations. In view of these, a new analytical mode decomposition (AMD) theorem [14] was developed to cope with the above challenges. Its principle and calculation can be explained as follows.

Suppose that a signal $x(t)$ consists of a series of n single-frequency signals $x_i(t)$ (i=1, 2,…, n) whose frequency ω_i are mutually exclusive ($0 \le \omega_1 < \omega_{b1} < \omega_2 < \omega_{b2} \ldots < \omega_i < \omega_{bi} < \omega_{i+1} \ldots \omega_{n-1} < \omega_{b(n-1)} < \omega_n$). That is,

$$x(t) = \sum_{i=1}^{n} x_i(t) \tag{1}$$

Here, ω_{bi} (i=1, 2,…, n-1) represent n-1 bisecting frequencies. Thus, each signal has a narrow bandwidth and can be determined as follows:

$$x_i = s_i - s_{i-1}, \ldots, x_n = x(t) - s_{n-1} \tag{2}$$

$$s_i(t) = \sin(\omega_{bi}t) H[x(t)\cos(\omega_{bi}t)] - \cos(\omega_{bi}t) H[x(t)\sin(\omega_{bi}t)] \quad (i = 2,3,\cdots,n-1) \tag{3}$$

where $s_0(t)$=0, and H[*] represents the Hilbert transform of the function inside the bracket.

2.2. Modal parameters identification

Similar to HHT method, the instantaneous amplitude A_j(t) and phase angle θ_j(t) of jth decomposed mode can be described from:

$$x_j(t) + iH[x_j(t)] = A_j(t) e^{-i\theta_j(t)} \tag{4}$$

If the structure is subjected to an impulsive load, the instantaneous frequency and damping ratio can be detected using the method in [15]：

$$\omega_j = \frac{d(\theta_j(t))}{dt} \quad \text{and} \quad \xi_j = \frac{d[\ln(A_j(t)]}{\omega_j dt} \tag{5}$$

3. Test program

3.1. The measured cylindrical latticed shell

The single-layer cylindrical latticed shell with AAG joints measured in this article has a planar dimension of 40m×36m and a height of 3.9m, as depicted in Figure 1. All the members are made of extruded H-section aluminum, the cross-section of which is H280mm×160mm×8mm×10mm.

3.2. Test scheme

The vertical impulsive load was applied to the shell by tester's jump excitation, while the horizontal impulsive load by hammering. The acceleration responses of the shell was obtained by two method: (1) single-point excitation, multi-point data collection, and (2) two-point excitation, multi-point data collection. The vertical vibration is dominant in the shell because of its small rise-span ratio. After completing modal analysis carried out by ANSYS, the measuring points were arranged at places where the deformation is larger in former 6 vibration modes. The arrangement of data collection and excitation points is shown in Figure 2. And the first 6 natural frequencies and corresponding test schemes are listed in Table 1, where A1-A7 represent vertical excitation, B1-B2 mean horizontal excitation and 1-10 are the numbers of accelerometers. The name pattern of the test scheme is excitation point-1st collection point – 2nd collection point. For example, A3-4-6 means that the excitation point is A3, the collection points is No.4 and No.6. Moreover, 19 kinds of load cases were designed. And the excitation points are stimulated 10 times under each load case.

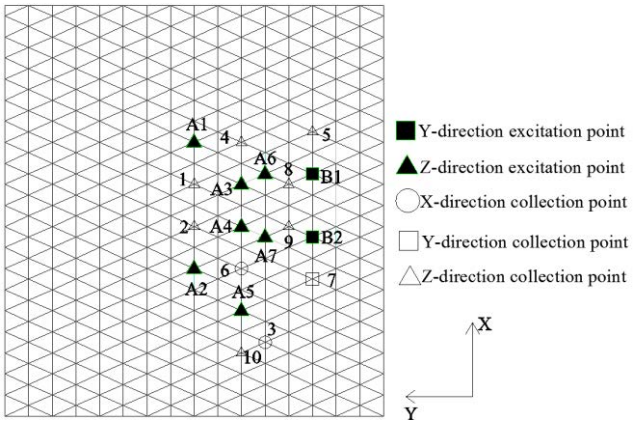


Figure 2: The arrangement of data collection and excitation points

Table 1: Test scheme

Mode order	Natural frequency	Test scheme
1	3.78	A3-4-6, A4-4-6, A2A5-2-3, A3A4-4-6
2	4.42	A1-1-2, A2-2-3, A1A2-1-3
3	5.73	A6-8-9, A7-8-9, A6A7-8-9
4	5.82	B1-4-5, A5-3-10, B1A3-4-5
5	7.54	A5-2-3, B2-6-7, A5A7-9-10
6	7.61	A3-1-2, B1B2-5-7, A4A7-6-9

4. Results of modal parameters identification

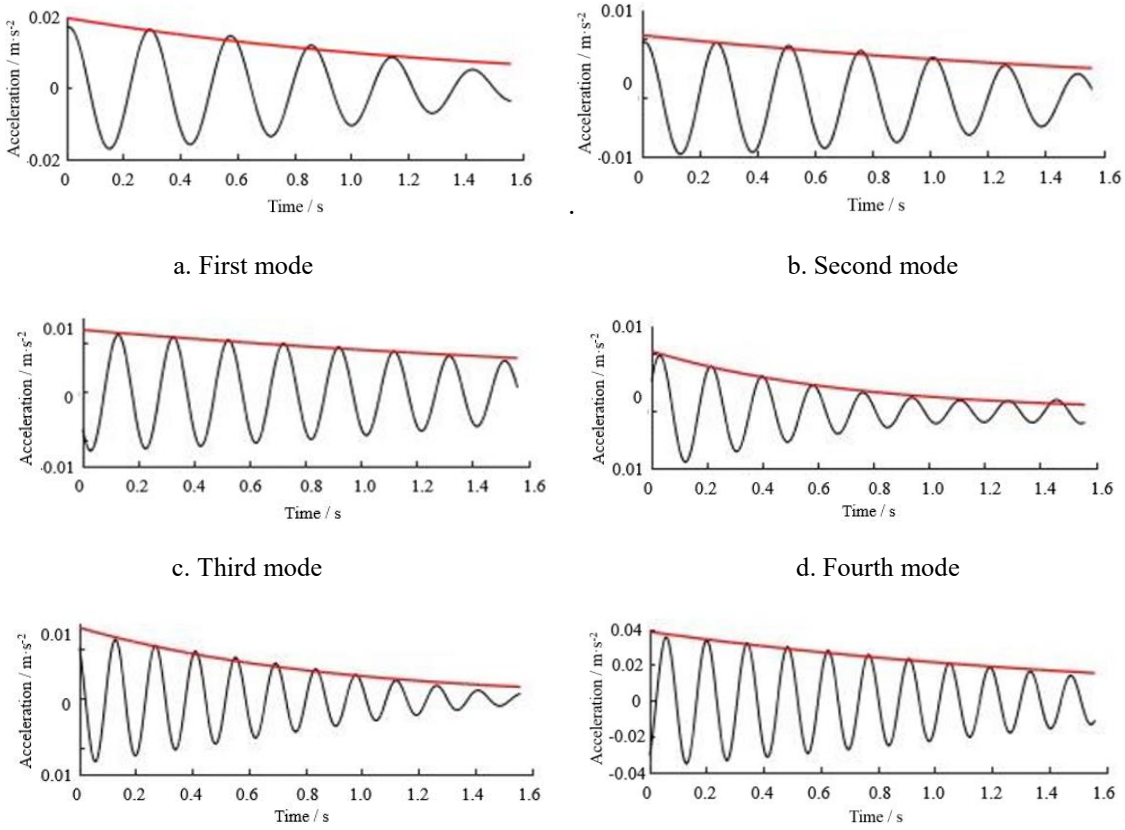
For this test, a total of 380 damped free vibration acceleration responses of the joints were collected under 190 jump excitations. The first 6 vibration modes of structure were studied in this article. Processing each collected acceleration response by AMD method and Hilbert transform, the modal parameters of first 6 modes can be derived.

Taking test scheme A1-2 as an example, the process and results of the acceleration-time curve obtained at No.2 collection point are discussed. Using AMD method, Figure 3 illustrates the damped free vibration curves of the first 6 modes of the shell, also the fitting curves of their instantaneous amplitude. f. Sixth mode

Figure 4 shows the power spectral density (PSD)-frequency curves of the first 6 modes.

Then the 380 acceleration-time curves are decomposed in the same way. Statistical analysis was conducted on the modal identification results of these 380 curves. Figure 5 shows the scatter plot and

average value of natural frequencies of 380 curves. The frequency histograms of identified modal damping ratio were illustrated in Figure 6. It is indicated that the discreteness of natural frequencies of each mode is very small. Consequently, the average value was taken as the damping ratio.

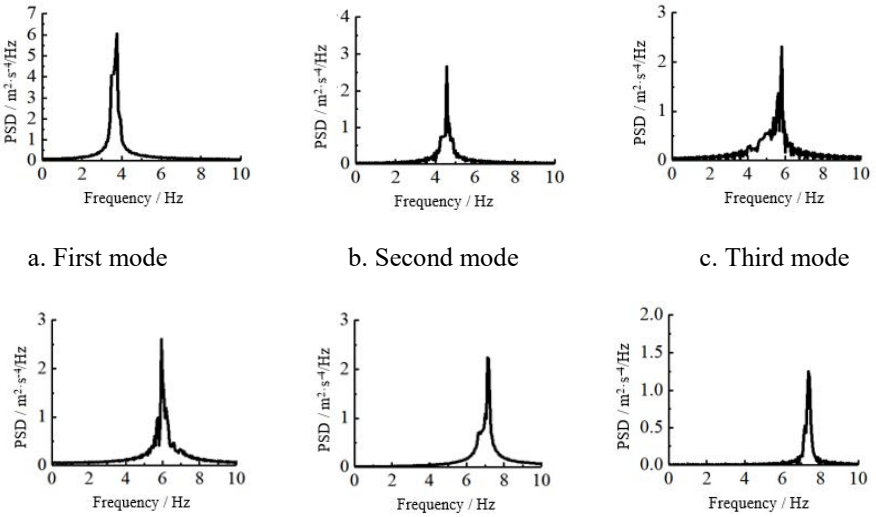


a. First mode b. Second mode

c. Third mode d. Fourth mode

e. Fifth mode f. Sixth mode

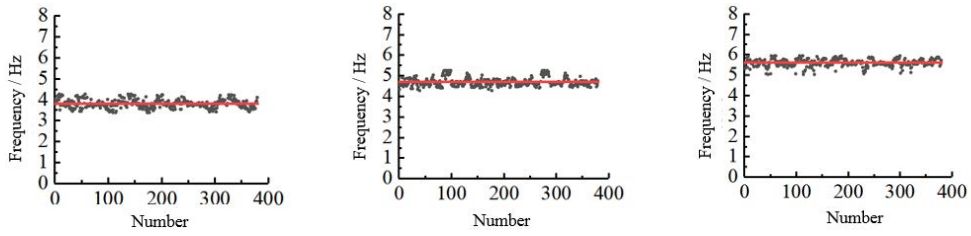
Figure 3: Acceleration-time curve of first 6 modes



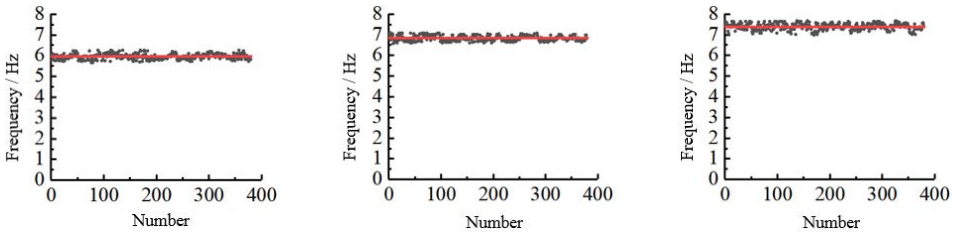
a. First mode b. Second mode c. Third mode

d. Fourth mode e. Fifth mode f. Sixth mode

Figure 4: PSD-frequency curves of first 6 modes

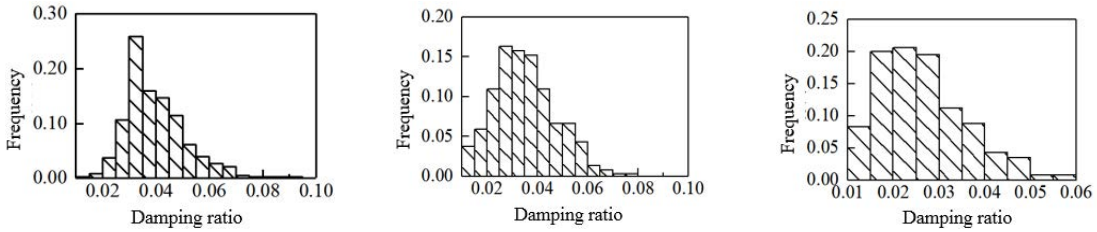


a. First mode b. Second mode c. Third mode

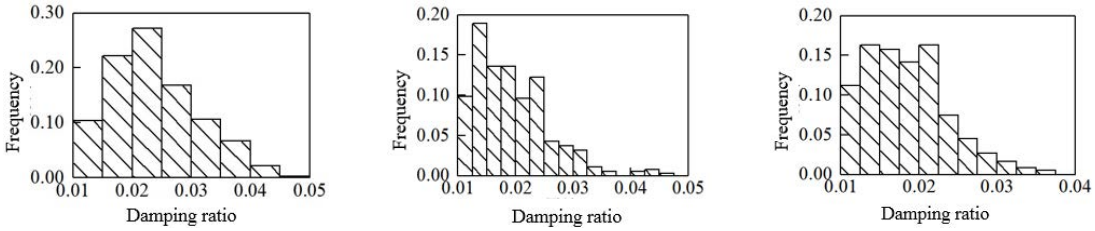


d. Fourth mode e. Fifth mode f. Sixth mode

Figure 5: Statistics of natural frequencies



a. First mode b. Second mode c. Third mode



d. Fourth mode e. Fifth mode f. Sixth mode

Figure 6: Frequency histogram of damping ratio

Table 2: The results of modal analysis

Mode order	Damping ratio/%	Natural frenquency / Hz		Error/%
		Test	FE	
1	3.99	3.79	3.78	0.26%
2	3.49	4.68	4.42	5.56%
3	2.59	5.59	5.73	2.50%
4	2.32	5.94	5.82	2.02%
5	1.97	6.92	7.54	8.96%
6	2.05	7.38	7.61	3.12%

The results of modal parameters identification were listed in Table.2. It was indicated that the error between the natural frequency of the FE model and the measured results is less than 10%. Therefore, the above FE model can simulate the dynamic characteristics accurately.

5. Verification of the FE model

Rayleigh damping was adopted in the FE model to simulate the damping characteristics of the structure. The Rayleigh damping coefficients are calculated as formula (6) to verify the rationality of the measured damping ratios above.

$$\alpha=\frac{2\omega_i\omega_j(\xi_i\omega_j-\xi_j\omega_i)}{\omega_j^2-\omega_i^2} \quad \text{and} \quad \beta=\frac{2(\xi_j\omega_j-\xi_i\omega_i)}{\omega_j^2-\omega_i^2} \tag{6}$$

where ω_i and ω_i are the natural frequencies of any two modes, ξ_i and ξ_i are the corresponding damping ratios. Two kinds FE models were established adopting two different Rayleigh damping.

1) First FE model used modal damping ratio. For modal damping ratio using in the first FE model, the ξ_1 and ξ_2 are 3.99% and 3.49% as listed in Table 2. According to formula (6), its Rayleigh damping ratio is: α=1.613 and β= 0.00052.

2) Second FE models adopted constant damping ratio. The constant damping ratio was usually used in practical engineering. It was assumed that the damping ratios of each mode are equal to that of 1st mode. Here, the ξ_1 and ξ_2 are all 3.99%. Then, its Rayleigh damping ratio is: α=1.647 and β= 0.00083.

Figure 7 compares the acceleration response curves of scheme A3-4 obtained from test results and FE analyses. It can be concluded that the peak values and trends of the curves are considerably close to each other. And so are the curves under the other load cases.

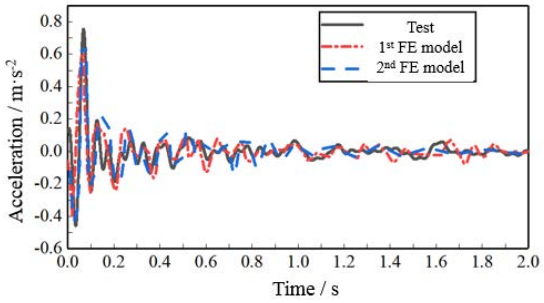


Figure 7: Comparison of test result an FE analysis

Besides, the correlation coeefficient was used to evaluate the relationship between the simulated curves and the measured curves. It can be determined by:

$$r(X,Y)=\frac{Cov(X,Y)}{\sqrt{Var[X]Var[Y]}} \tag{7}$$

where $Cov(*)$ means covariance and $Var(*)$ represents variance. Table 3 shows the correlation coefficents between the measured results and FE simulations under all the test shcemes as listed in Table1, where $r(X,Y)$ is the correlation coefficient of the measured result and first FE simulation, and $r(X,Y)$ is the correlation coefficient of the measured result and second FE simulation. As shown in Table 3, all the correlation coefficients are in the range of 0.65-0.9, most of which are around 0.8. FE simulations can precisely reflect the dynamic characteristics of the measured shell. As a result, the suggested damping ratio is applicable in the practical engineering.

Table 3: Correlation coefficients between measured results and FE simulations

Test scheme	*r(X,Y)*	*r(X,Z)*	Test scheme	*r(X,Y)*	*r(X,Z)*
A3-4	0.712	0.683	A3-6	0.683	0.802
A4-4	0.703	0.713	A4-6	0.723	0.861
A2A5-2	0.663	0.851	A2A5-3	0.832	0.782
A3A4-4	0.693	0.772	A3A4-6	0.812	0.663
A1-1	0.792	0.822	A1-2	0.792	0.772
A2-2	0.762	0.683	A2-3	0.881	0.723
A1A2-1	0.792	0.812	A1A2-3	0.802	0.842
A6-8	0.782	0.663	A6-9	0.663	0.802
A7-8	0.792	0.842	A7-9	0.752	0.871
A6A7-8	0.752	0.871	A6A7-9	0.703	0.871
B1-4	0.762	0.693	B1-5	0.842	0.762
A5-3	0.822	0.822	A5-10	0.851	0.703
B1A3-4	0.861	0.812	B1A3-5	0.792	0.772
A5-2	0.713	0.733	A5-3	0.842	0.782
B2-6	0.773	0.881	B2-7	0.802	0.733
A5A7-9	0.743	0.752	A5A7-10	0.861	0.802
A3-1	0.762	0.812	A3-2	0.863	0.861
B1B2-5	0.693	0.881	B1B2-7	0.752	0.842
A4A7-6	0.832	0.743	A4A7-9	0.832	0.673

6. Conclusions

The field measurement was carried out on an aluminum alloy cylindrical latticed shell with a planar dimension of 40m×36m and a height of 3.9m. A total of 380 damped free vibration acceleration responses of the joints were collected under 190 jump excitations. The main conclusions can be drawn as follows:

(1) Using AMD method and Hilbert transform to process these 380 curves, the natural frequencies and damping ratios of the first 6 modes can be obtained. The discreteness of the above identified parameters is very small. Consequently, the average value was taken as the final results.

(2) FE models were established to verify the rationality of the measured damping ratios. The ANSYS FE analyses results can precisely simulate the dynamic characteristics of the measured shell. Therefore, the suggested damping ratio is applicable in the practical engineering.

(3) The measured damping ratio of the 1st mode of the cylindrical latticed shell can express the energy dissipation of the structure. The damping ratio of all these cylindrical latticed shells with AAG joints is suggested to be 4%.

References

[1] L. Yang, S. Wei and Q. Zhang, "Aluminum reticulated spatial structures: state of the art and key issues," *Journal of Building Structures*, vol.34, pp. 1-19+60, Feb. 2013.

[2] Z. Shen, X. Guo and Y. Li, "State-of-the-arts of research on aluminum alloy structures," *Journal of Building Structures*, vol.28, pp. 100-109, June. 2007.

[3] X. Guo, X. Zhe, Y. Luo, L. Qiu and J. Liu, "Experimental investigation on the semi-rigid behaviour of aluminium alloy gusset joints," T*hin-Walled Structures*, vol.87, pp. 30-40, Feb. 2015.

[4] X. Guo, X. Zhe, Y. Luo, H. Xu and S. Liang, "Block tearing and local buckling of aluminum alloy gusset joint plates," *KSCE Journal of Civil Engineering*, vol.20, pp. 820-831, Mar. 2015.

[5] X. Guo, S. Zhu, X. Liu and L. Liu, "Experimental study on hysteretic behavior of aluminum alloy gusset joints," *Thin-Walled Structures*, vol.131, pp. 883-901, Oct. 2018.

[6] X. Guo, L. Qiu, Y. Luo and B. Zheng, "Experimental research on the bending capacity of aluminum alloy gusset joints," *Journal of Hunan University(Natural Sciences)*, vol. 41, pp. 47-53, Apr. 2014.

[7] X. Guo, X. Zhe, Y. Luo and H. Xu, "Experimental research on load-bearing behavior of aluminum alloy gusset joint," *Journal of Tongji University(Natural Science)*, vol. 42, pp. 1024-1030, Jul. 2014.

[8] X. Guo, X. Zhe, Y. Luo, H. Xu and L. Qiu, "Theoretical study on bending stiffness of aluminum alloy gusset joint," *Journal of Building Structures*, vol. 35, pp. 144-150, Oct. 2014.

[9] X. Zhe, X. Guo, Y. Luo and H. Xu, "Numerical analysis of aluminium alloy gusset joints subjected to bending moment and axial force," *Engineering Structures*, vol. 152, pp. 1-13, Dec. 2017.

[10] X. Zhe, X. Guo, Y. Luo and S. Zhu, "Elasto-plastic stability of single-layer reticulated shells with aluminium alloy gusset joints," *Thin-Walled Structures*, vol. 115, pp. 163-175, June. 2017.

[11] X. Zhe, X. Guo, Y. Luo and H. Xu, "Influence of joint stiffness on stability of latticed shells with aluminum alloy gusset joints," *Journal of Tianjin University(Science and Technology)*, vol. 48, pp. 39-45, Jul. 2015.

[12] X. Guo, L. Wang, Y. Xiang Y and *et.al*, "Experimental study on the damping property of aluminum alloy latticed shells with gusset joints," *Journal of Vibration and Shock*, vol. 35, pp. 34-39, Oct. 2016.

[13] N. Huang, Z. Shen, S. Long and *et al*. "The empirical mode decomposition and the Hilbert spectrum for nonlinear and non-stationary time series analysis," *Proceedings of the royal Society A*, vol. 454, pp. 903-995, Mar. 1998.

[14] G. Chen and Z. Wang, "A signal decomposition theorem with Hilbert transform and its application to narrowband time series with closely spaced frequency components," *Mechanical Systems and Signal Processing*, vol. 28, pp. 258-279, Apr. 2012.

[15] J. Yang, Y. Lei and *et al*, "System identification of linear structures based on Hilbert–Huang spectral analysis. Part I: Normal modes," *Earthquake Engineering & Structural Dynamics* vol.32, pp. 1533-1554, Oct. 2010.

Proceedings of the IASS Annual Symposium 2019 — Structural Membranes 2019
Form and Force
7—10 October 2019, Barcelona, Spain
C. Lázaro, K.-U. Bletzinger, E. Oñate (eds.)

Effects of geometrical factors on the buckling behaviour of free-edge single-layer gridshells

Fiammetta VENUTI*

* Politecnico di Torino, Department of Architecture and Design
viale Mattioli 39, 10125, Torino, Italy
fiammetta.venuti@polito.it

Abstract

Gridshells are form-resistant lightweight structures usually designed to cover large spans. Stability studies on gridshell domes are usually carried out by referring to structures with a horizontal spring-plane and rigid supports, while gridshells with free edges have seldom been sistematically studied, despite they represent the majority of built gridshells. This study aims at investigating the effects of geometrical factors on the stability of free-edge single-layer gridshells. In particular, two geometrical factors are considered: i. the orientation of the free edge with respect to the grid main directions, to study the effects of anisotropy; ii. the location of the free edge, to study the influence of the ratio between the gridshell and free-edge spans. The parametric study is carried out through numerical simulations on an ideal single-layer free-edge steel gridshell, with different grid topologies. Results are discussed in terms of both load factors and buckling shapes, evaluated through linear buckling analysis and geometrically and materially non linear analysis.

Keywords: single-layer gridshell, free-edge, anisotropy, stability

1 Introduction

Gridshells are lightweight form-resistant structures designed to cover large spans and to ideally bear loads by means of in-plane internal forces. Being mainly subjected to compressive stresses, gridshell structures are highly prone to buckling phenomena. Since the catastrophic collapse of



(a) (b) (c)

Figure 1: Examples of built free-edge gridshells: (a) Multihalle in Mannheim [1], (b) Hippo House [2], (c) Cabot Circus [3]

Copyright © 2019 by Fiammetta VENUTI
Published by the International Association for Shell and Spatial Structures (IASS) with permission.

the Bucharest Exhibition Hall dome in 1963, a lot of research has been devoted to the buckling behaviour of these kind of structures (for a review see e.g. [4, 5]).
In most cases, the studies on gridshell stability have been carried out by referring to gridshells with horizontal spring-plane and rigid supports. Surprisingly, gridshells of this kind represent a minority and are limited to research pavilions (e.g. [6]) - horizontally constrained at the ground level - or roofs - rigidly constrained along their perimeter to the underlying structure (e.g.[7]). In the majority of built gridshells, the gridshell reference surface has been trimmed due to functional or architectural reasons, giving rise to free-edges at the intersection between the reference geometry and the trimming surface. Outstanding examples of this kind are illustrated in Figure 1. Despite the current design practice, "this kind of elastic boundary has not been extensively investigated, and studies are needed in each design to know how and if the supports improve the buckling resistance" [5].
A first attempt to systematically study the stability of free-edge gridshells has been performed by Venuti and Bruno [8]. They studied the effects of the flexural stiffness of the elastic boundaries and of the in-plane shear stiffness of the gridshell on an ideal hybrid single-layer steel gridshell dome. The results of the study showed that, depending on the ratio between stiffness of the boundary and in-plane stiffness of the gridshell, the structural buckling behaviour could be free-edge driven or shell-driven.
This paper aims at investigating the influence of some geometrical factors on the buckling behaviour of free-edge gridshells. Specifically, their stability is expected to also depend on the orientation of the boundary structure with respect to the grid main directions and on its location (i.e. on the ratio between the free-edge and the gridshell spans).
The paper develops through the following sections: in Section 2, the parametric study is described in terms of geometrical and structural set ups and kind of structural analyses adopted to evaluate the buckling behaviour; in Section 3, the results are illustrated and commented on; finally, conclusions are summarised in 4.

2 Analysis set-up

2.1 Reference gridshell structure

The reference geometry of the investigated free-edge single-layer gridshell is a paraboloid, having a parabola as both the directrix and generatrix (red and blue curves in Fig. 2a). The considered free-edge dome is obtained by trimming the complete dome with a vertical plane Ω passing through the origin of the reference system and rotated of an angle $\theta = 0°$ with respect to the $y - z$ plane. The obtained half dome is, therefore, bounded by a vertical parabolic arch with span length L=30 m and span to rise ratio L/f=8.
Gridshells having different grid topology are considered: i. quadrangular (Q); ii. hybrid (H), where the quad meshes are stiffened by bracing cables [7]; iii. triangular (T), where the original quad mesh is triangularised by the addition of diagonal elements with the same cross section as the straight ones.
The main grid is composed of steel beams with solid quadrilateral cross section of area equal to $2.5e-3$ m^2, while the bracing cables have a circular cross section with area equal to $1.6e-4$ m^2 and prestress of 100 MPa [9]. The boundary arch has a solid quadrilateral cross section, whose moment of inertia is 100 times greater than the grid beam one: this, according to the study in [8], should assure a shell-driven buckling behaviour.
The dead load g of structural steel members and of 20 mm-thick glass glazing is set equal to 0.5

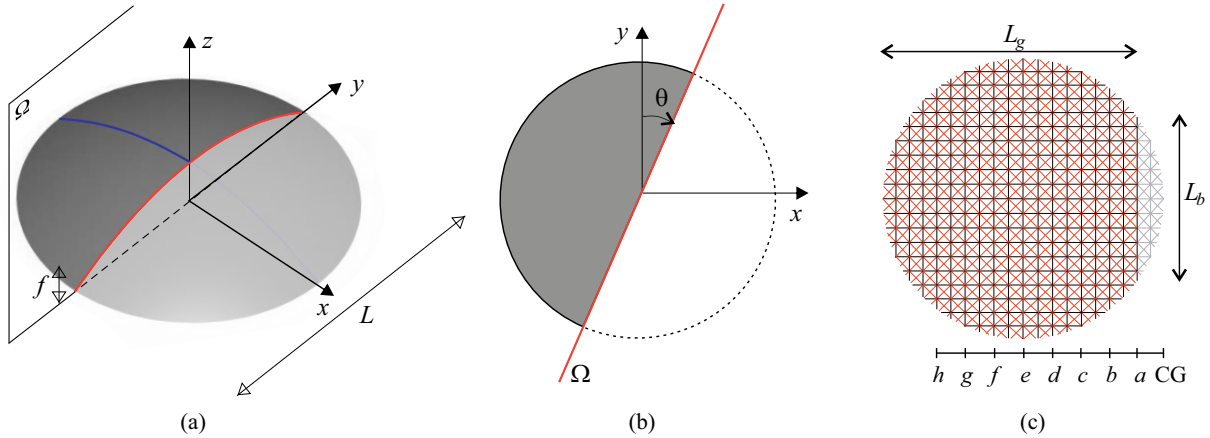


Figure 2: Reference geometry (a), free-edge orientation (b) and free-edge location (c)

KN/m^2. A uniform load case $q = 1.3g + 1.5s$ is applied to the structure, where s=0.75 kN/m^2 is the snow load. The resultant p-th nodal load is defined as $Q_p = \int_A q da$, being A the tributary area of the p-th node.
The structure is modelled by means of the finite element software ANSYS® v19.2. Both the grid elements and the boundary arch are modelled by BEAM188 finite element, while cables are modelled by 3D tension-only trusses with circular cross section (LINK180 finite element). The whole structure is assumed to be hinged at the boundaries, while the joints between steel bars are modelled as rigid, as usually done in the literature [9, 10].
The constitutive model of the steel is linear elastic - perfect plastic, with a yield strength equal to f_y=355 MPa, Young's modulus $E = 2.1e + 5$ MPa and Poisson's ratio ν=0.3.

2.2 Parametric analyses

Differently from continuous shells, gridshells are characterised by an intrinsic global anisotropy, given by the fact that the discrete grid intersects its boundaries (either rigid or elastic) with orientations that can differ from those of the main grid directions. The effects of this anisotropy on the buckling behaviour are explored in a first parametric analysis by changing the relative orientation between the grid direction and the free-edge. Four different orientations of the Ω plane are considered, corresponding to angle θ of 0°, 15°, 30° and 45° (Fig. 2b). Since the adopted mesh pattern is expected to play a crucial role, all the three grid topologies mentioned in the previous section are explored for each value of θ.
A second parametric analysis is addressed to evaluate the influence of the free-edge location on the buckling behaviour. In this case, the free parameter is the ratio $L_r = L_b/L_g$ between the boundary structure and gridshell spans, where L_g is measured normally to L_b (Fig. 2c). The considered free-edge locations are labelled from a to h in Figure 2c. Besides free-edge gridshells, also the complete gridshell (CG) is analysed for reference. In this study, only the hybrid gridshell is taken into account.
It should be pointed out that, among the considered design parameters (i.e. θ, grid pattern and L_r), the designer is expected to have the highest freedom of choice on the first two, since the ratio L_r is often imposed by the design constraints.
In both parametric studies, Linear Buckling Analysis (LBA) and Geometrically and Materially

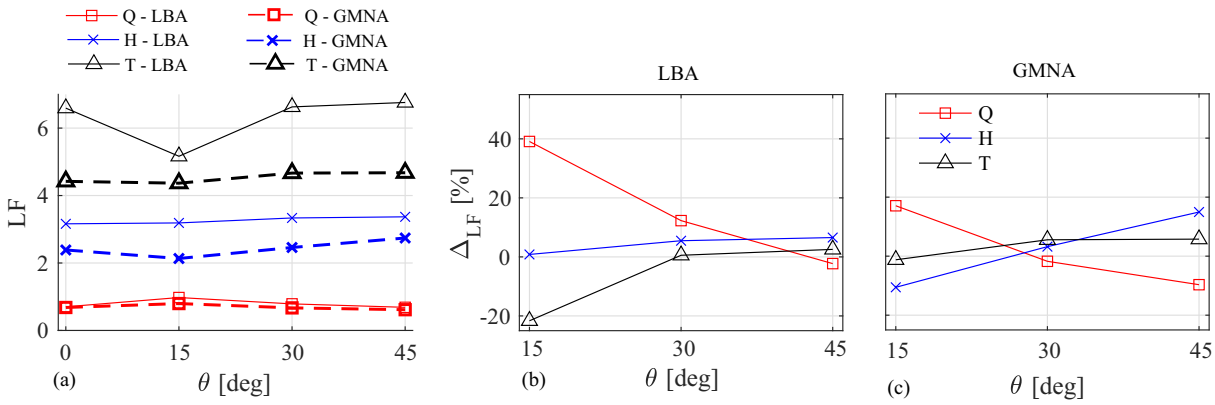


Figure 3: Load Factors (a) and their percentage variation ΔLF obtained from (b) LBA and (c) GMNA

Nonlinear Analysis (GMNA) are performed. Despite the well-known influence of geometrical imperfections on the stability of gridshells, herein only the perfect geometry is considered to better interpret the influence of the selected parameters. The results of the numerical simulations are compared in terms of Load Factors (LFs) and buckling shapes. In general, the LF can be defined as the ratio between the buckling load and the reference load as defined in the previous section. Within GMNA, the LF is the load multiplier corresponding to the limit point in the load-displacement curve.

3 Results

3.1 Free-edge orientation

Figure 3a illustrates the LFs as a function of θ, obtained from each structural analysis for each gridshell layout. Some expected trends are confirmed: the linear buckling load is higher than the elastic-plastic buckling load [5]; for each structural analysis and θ, the LFs are increasingly higher from Q to H to T gridshell, due to increasing stiffness of the mesh.
Looking at the percentage variation of the load factor with respect to the reference configuration $\theta = 0°$, $\Delta\text{LF} = (\text{LF}_i - \text{LF}_0)/\text{LF}_0$, $i = 15, 30, 45$ (Fig. 3b-c), it can be observed that the degree of sensitivity to θ strongly depends on the grid pattern. The Q pattern, that can be defined as orthotropic [11], is the most sensitive, with LF variations that can reach 40%. On the contrary, the influence of the free-edge orientation is almost negligible on the H (with LBA) and T gridshells (with GMNA), which mostly resemble the behaviour of an isotropic shell.
A deeper insight into the influence of θ on the gridshell mechanical behaviour is provided for GMNA. The buckling shapes illustrated in Figure 4 show a significant change in the collapse shape when the free-edge is not aligned with the grid. The most significant effect of the rotation of the boundary structure is to induce non-symmetrical collapse shapes. Moreover, when the boundary structure is aligned with the grid direction, the node with maximum displacement (red circle) is usually located near the rigid boundary, while it moves in proximity of the free edge for $\theta \neq 0°$ (from "shell-driven" to "boundary-driven" collapse [8]).
The concept of Structural Eigen-stiffness (SES), introduced by Zhu et al. [12] can help in the mechanical reading of the obtained results. The Eigen-stiffness k^* is a scalar quantity that provides a measure of the global structural stiffness. The advantage of computing SES is that it

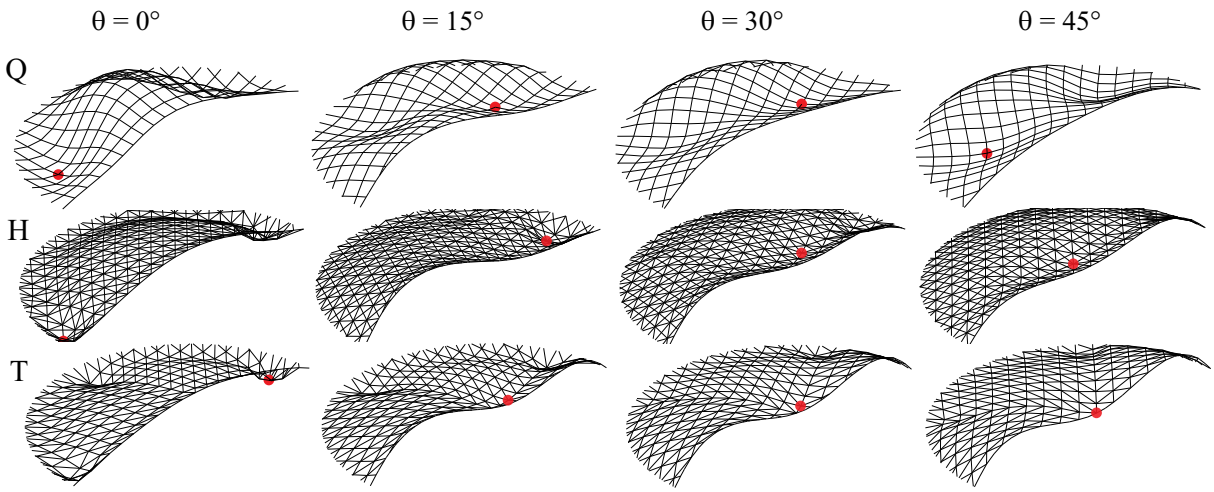


Figure 4: Buckling shapes (displacements normalised to 2m)

does not rely on a specific nodal displacement, but it takes into account the displacements of all nodes. Considering the j-th iteration step of a non linear structural analysis, $k_j^* = \Delta p_j^* / \Delta u_j^*$, where Δu_j^* and Δp_j^* are the incremental Eigen-displacement and incremental work, respectively (see [12] for further details on the basic theory). In particular, the following two metrics will be taken into account: i. the tangent Eigen-stiffness at the origin k_{T}^*, which is a measure of the original structural stiffness; ii. the Eigen-stiffness ratio $k_{\mathrm{r}}^* = k_{\mathrm{T}}^* / k_{\mathrm{S}}^*$, where $k_{\mathrm{S}}^* = p_u^* / u_u^*$ is the secant Eigen-stiffness, which is a measure of the mean SES from the initial to the ultimate state. In other words, the Eigen-stiffness ratio, whose value ranges between 0 and 1, allows to evaluate the amount of non linear effects, i.e. of softening, before buckling.
Figure 5a plots the tangent Eigen-stiffness versus θ for each grid pattern. As expected, T gridshells have the highest global stiffness, while Q gridshells the lowest one; for all grid patterns, the initial global stiffness significantly decreases when the boundary structure is rotated with respect to the grid main directions; the Q gridshell displays the highest reduction of the initial stiffness for $\theta \neq 0°$ (around 95%). The decrease in the original stiffness does not always correspond to a decrease in LF. To investigate a possible relation between LFs and softening before buckling, Figure 5b plots the Eigen-stiffness ratio (solid lines) and LFs (dashed lines) versus θ. The Figure evidences a proportionality between the trends of the two parameters: this proportionality is direct for the Q gridshell, which undergoes the highest softening, and inverse for T and H patterns, which have the highest value of k_{r}^*.
For isotropic gridshells the preferred orientation seems to coincide with $\theta = 0°$. Different orientations can slightly increase the load factor, but this can imply an increase in softening, i.e. unacceptable ultimate displacements. For orthotropic gridshells, the best orientation should be carefully evaluated by considering the best compromise between, on one hand, the increase in LF and the decrease in softening and, on the other hand, the significant reduction of the initial structural stiffness.

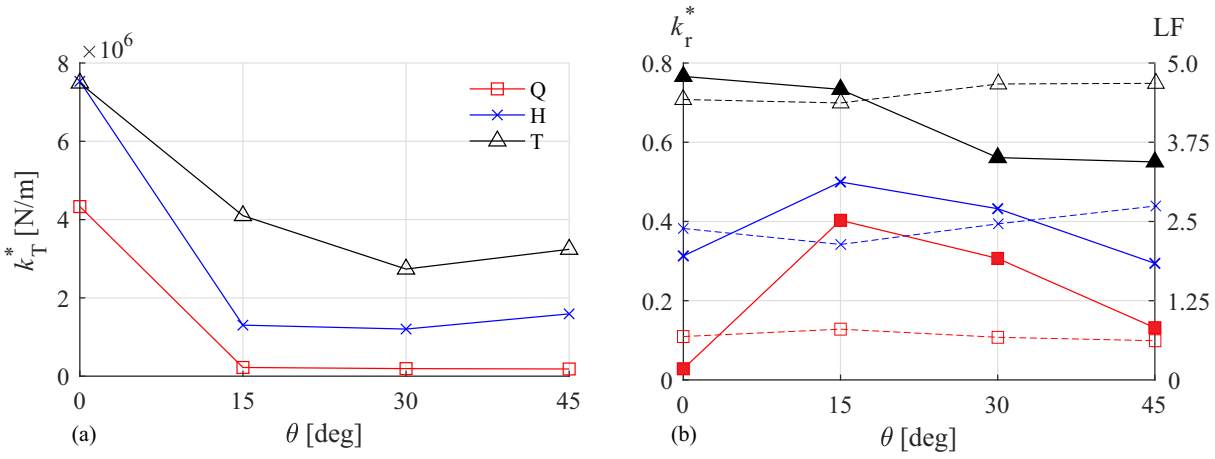


Figure 5: Tangent Eigen-Stiffness (a), Eigen-stiffness ratio (solid lines) and LFs (dashed lines) versus θ

3.2 Free-edge location

The results of the second parametric study are summarised in Figure 6, where both the LFs and the buckling shapes obtained through LBA and GMNA are plotted for each location of the boundary structure and for the complete gridshell. The buckling shapes are normalised with respect to the maximum displacement and the dimension of the filled circles is proportional to the normalised nodal displacement.

Both kinds of analysis provide a similar trend of LF versus L_r, even though the range of variation is higher for GMNA: the LF decreases for L_r approaching 2 (which corresponds to half the complete gridshell) and subsequently increases for higher values of L_r. The variation in LF is strictly related to a modification in the way the gridshell buckles, which can be observed quite clearly looking at the buckling shapes. In fact, passing from the a to h geometrical configuration, the maximum displacements, which are initially located near the centre of the boundary structure, progressively move towards the nodes adjacent to both the boundary arch and the spring curve with a progressive involvement of a higher number of internal nodes. This is a consequency of the change in the relative overall stiffness of the boundary structure and of the gridshell, which is particularly clear if we compare the gridshell configurations having the same free-edge geometry (d and f, c and g, b and h): for each of these couples, the highest LF belongs to the configuration characterised by lower L_g (i.e. the smallest gridshell).

4 Conclusions

This paper aimed at investigating the influence of some geometrical factors on the stability of free-edge single-layer gridshells. Two parametric studies have been carried out on a reference perfect gridshell structure in order to highlight the effects of the free-edge orientation θ with respect to the grid main directions and of the free-edge to gridshell span ratio L_r on the buckling behaviour. In the first study, three different grid patterns have been analysed, while in the second only the hybrid pattern has been taken into account.

The results of both parametric studies highlight the significant influence of geometry on the buckling behaviour of free-edge gridshells, due to the strong relation between geometry and relative stiffness of the boundary to gridshell structure. The first parametric study shows that

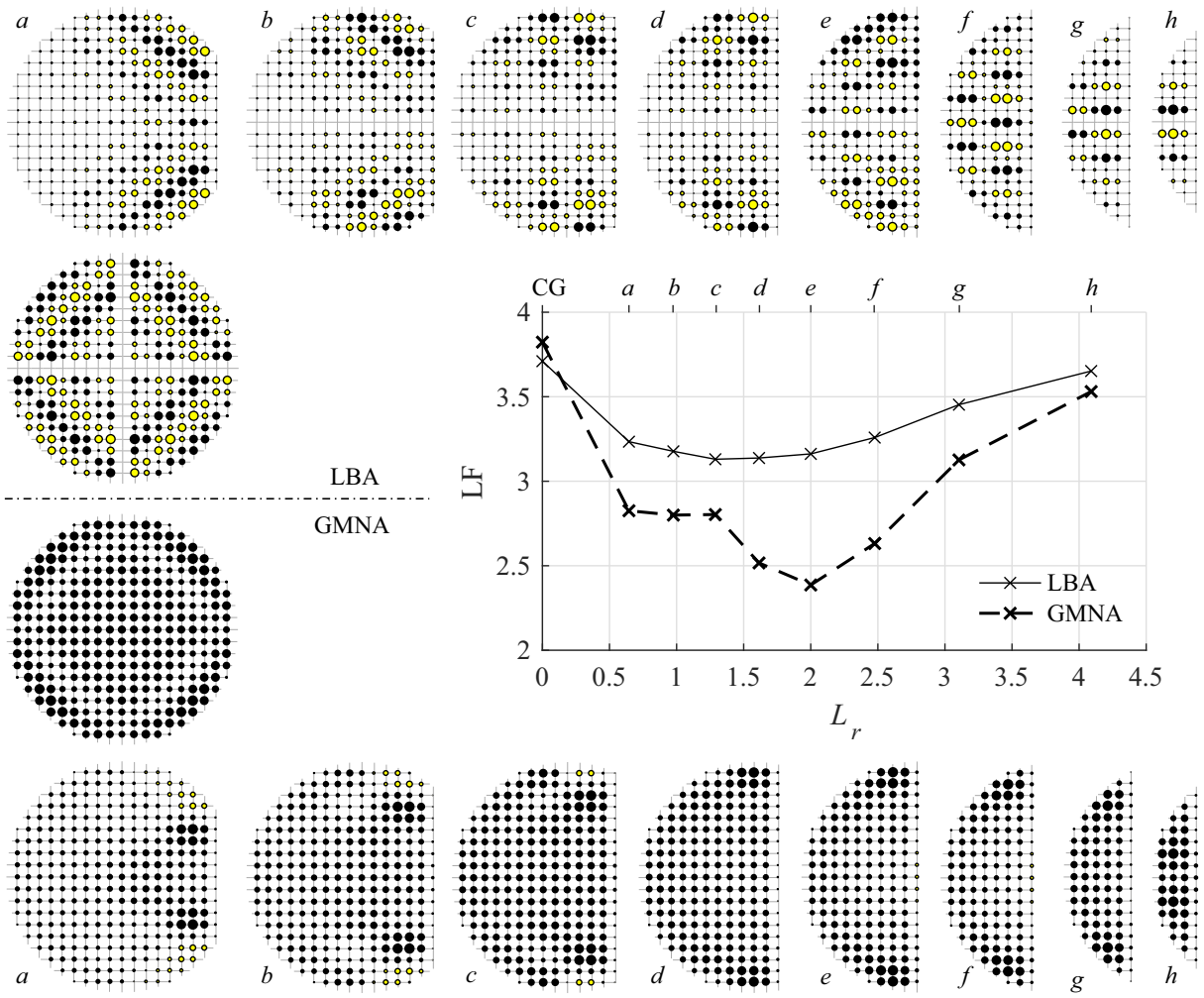


Figure 6: Load factors and buckling shapes with LBA and GMNA (black circle = downward; yellow circle = upward

Q grishells (classified as orthotropic), whose buckling load is mainly influenced by the in-plane shear stiffness, are the most sensitive to variation of the angle θ, both in terms of LF, of global structural stiffness and of softening before buckling. The opposite holds for isotropic gridshells. The second parametric study, despite the fact that the designer is expected to have less freedom of choice on L_r, evidences the strong relation between L_r and the buckling behaviour, since different L_r values correspond to different ratio between the boundary and gridshell stiffness. The lowest LF correspond to L_r near 2.

These results suggest the need, in the design phase of a free-edge gridshell, to explore different design solutions in order to identify the one corresponding to the most satisfying buckling behaviour. In the case of more complex geometries than the one herein analysed, e.g. free-form gridshells with multiple free-edges, this aim could be achieved by means of structural and topological optimisation [13, 14].

5 Acknowledgements

The author wishes to thank Politecnico di Torino, for the financial support received in the form of Starting Grant for Young Researchers (Grant 59_ ATEN_ RSG17VEF).

References

[1] E. Happold, W. Liddell, Timber lattice roof for the Mannheim Bundesgartenschau, The Structural Engineer 53 (3) (1975) 99–135.

[2] J. Schlaich, H. Schober, Glass roof for the Hippo House at the Berlin Zoo, Structural Engineering International 7 (4) (1997) 252–254.

[3] H. Schober, S. Justi, Cabot Circus, Bristol - Ebene Viereckknetze für freigeformte glasdächer, Stahlbau 81 (Supplement S1) (2012) 28–42.

[4] V. Gioncu, Buckling of reticulated shells: State-of-the-art, International Journal of Space Structures 10 (1) (1995) 1–46.

[5] IASS WG 8 for Metal Spatial Structures, (Draft) Guide to buckling load evaluation of metal reticulated roof structures, Tech. rep., International Association for Shell and Spatial Structures (2014).

[6] I. Liddell, Frei otto and the development of gridshells, Case Studies in Structural Engineering 4 (2015) 39–49.

[7] J. Schlaich, H. Schober, Glass-covered grid-shells, Structural Engineering International 6 (2) (1996) 88–90.

[8] F. Venuti, L. Bruno, Influence of in-plane and out-of-plane stiffness on the stability of free-edge gridshells: A parametric analysis, Thin-Walled Structures 131 (2018) 755–768.

[9] T. Bulenda, J. Knippers, Stability of grid shells, Computer & Structures 79 (2001) 1161–1174.

[10] F. Fan, Z. Cao, S. Shen, Elasto-plastic stability of single-layer reticulated shells, Thin-Walled Structures 48 (2010) 827–836.

[11] R. Mesnil, C. Douthe, O. Baverel, B. Léger, Linear buckling of quadrangular and kagome gridshells: A comparative assessment, Engineering Structures 132 (2017) 337–348.

[12] Z.-C. Zhu, Y.-F. Luo, Y. Xiang, Global stability analysis of spatial structures based on Eigen-stiffness and structural Eigen-curve, Journal of Constructional Steel Research 141 (2018) 226–240.

[13] P. Winslow, S. Pellegrino, S. Sharma, Multi-objective optimization of free-form grid structures, Structural and Multidisciplinary Optimization 40 (2010) 257–269.

[14] R. Oval, M. Rippmann, R. Mesnil, T. V. Mele, O. Baverel, P. Block, Feature-based topology finding of patterns for shell structures, Automation in Construction 103 (2019) 185–201.

Proceedings of the IASS Annual Symposium 2019 – Structural Membranes 2019
Form and Force
7 – 10 October 2019, Barcelona, Spain
C. Lázaro, K.-U. Bletzinger, E. Oñate (eds.)

Experimental research on anti-uplift three-dimensional seismic isolation bearing

Xiongyan LI[a], Shuanzhu LIANG[b], Suduo XUE[c],

[a]College of Civil and Architecture Engineering, Beijing University of Technology
100 Ping Le Yuan, Chaoyang District, Beijing 100124, China , xiongy2006@126.com
[b]College of Civil and Architecture Engineering, Beijing University of Technology,lszbjut@126.com
[c]College of Civil and Architecture Engineering, Beijing University of Technology, sdxue@bjut.edu.cn

Abstract

The long-span spatial structure is flexible, and the damping ratio of the structure is relatively strong under horizontal and vertical earthquakes, and the uplift force exists at the support. To satisfy the application of seismic isolation of such buildings, the paper proposes an anti-uplift three-dimensional bearing. The bearing is composed of a high damping rubber bearing and an upper disc spring device in series. The horizontal and vertical mechanical properties of the test were studied. In the horizontal direction, the test focuses on the hysteretic behavior of the bearing under simple harmonic excitation, and investigates the influence of shear strain and loading frequency on its horizontal mechanical properties. In the vertical direction, the equivalent stiffness and equivalent damping ratio of the bearing were tested as well. Experimental research was carried out to investigate the effects of different loading amplitudes and different loading frequencies on their vertical hysteresis performance. The results show that the composite isolation bearing has good hysteresis performance in both horizontal and vertical directions. The horizontal equivalent damping ratio is between 12.48% and 14.77%, which decreases with the increase of shear strain, it increases with the loading frequency; the vertical equivalent damping ratio is from 6.67% to 17.76%, vertical loading frequency makes minor effect on it.

Keywords: three-dimensional seismic isolation; Hysteresis test; equivalent damping ratio; equivalent stiffness

1. Introduction

The large-span spatial structure is widely used in large public buildings because of its many advantages such as lightweight, fast construction speed and diverse shapes. Large-span spatial structure, due to the large flexibility of the span structure, the complex structure of vibration characteristics is a three-dimensional seismic response [1,2,3], the horizontal shear force at the support is large and there is an uplift force; the isolation support for such buildings Should have anti-pull three-dimensional isolation.

In recent years, many scholars have been conducted related research on three-dimensional composite isolation bearings. Xiong Shishu et al [4] proposed a three-dimensional isolation bearing (3DB) for lead-core rubber disc springs, and installed a 3D three-dimensional base isolation for one building. Multi-layer seismic simulation analysis of the five-story frame structure shows that the seismic response of the structure with 3DB isolation support can be reduced by 50%. Li Xiongyan [5] developed a friction-disc three-dimensional composite isolation bearing for the isolation of large-span hangar structures, and conducted a shaking-table experiment on its mechanical properties. The research suggests that the support is horizontal and vertical both provide greater damping and good isolation. A.Parvin [6] was a combination of coil spring and liquid damper and applied it to the theoretical analysis of the vertical isolation effect of the bridge structure.In this paper, a three-dimensional composite anti-extraction isolation bearing is made for large-span structural isolation.

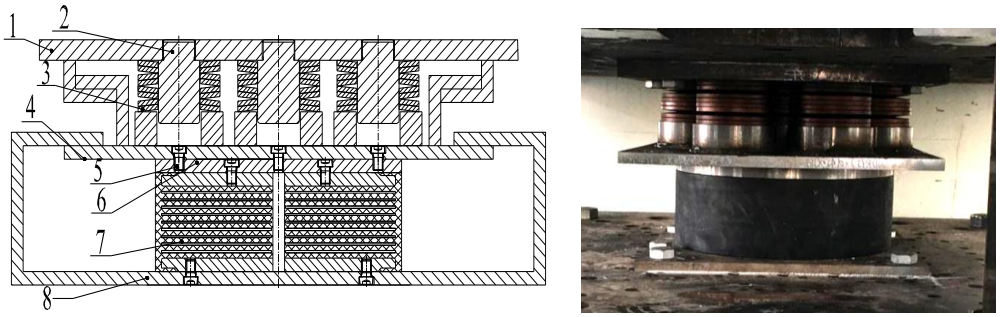
2.Test introduction

2.1. Introduction of test pieces

Copyright © 2019 by Xiongyan LI, Shuanzhu LIANG, Suduo XUE
Published by the International Association for Shell and Spatial Structures (IASS) with permission.

As showed in Figure 1, the three-dimensional composite anti-extraction isolation support is composed of a horizontal isolation system and a vertical isolation system in series. The horizontal isolation system utilized high-damping rubber bearing, which shares strong energy-consuming ability, can significantly extend the structural period to reduce the structural seismic response, and it also offer good reset function, and the vertical setting of the disc spring group changes the vertical stiffness provides damping through the friction between the disc springs, thus reducing the vertical seismic response of the structure.

The horizontal allowable design shear deformation of the test support is 80mm, the vertical design displacement is 10mm, the ultimate displacement is 12.67mm, the vertical design bearing capacity is 1400kN, and the vertical design tensile force is 1000kN. The height of the high damping rubber bearing is 400mm. The exact parameters are shown in Table 1. The vertical isolation device consists of 7 sets of disc springs in parallel, each set of 12 pieces (2 pieces stacked, 4 sets of matching), single piece The relevant parameters of the disc spring are given in table 2.



1. Pull-out member 1 2. Disc spring internal guide rod 3. Disc spring 4. Pull-out member 2 5. Connecting bolt 6. Connecting plate 7. Support body 8. Lower cover

Fig 1: Pull-out type three-dimensional isolation bearing sectional view

Tab 1: High damping rubber bearing basic parameters

Diameter /mm	Single layer rubber thickness /mm	Number of layers of rubber	Stiffening plate thickness /mm	Number of steel layers	Shear modulus G/MPa	Rubber hardness	First shape factor (S_1)	Second shape factor (S_2)
400	8	10	3	9	1.0	60	12.5	5

Tab 2: The base parameters of disk spring

Outer diameter /mm	Inner diameter /mm	Thickness /mm	Ultimate displacement /mm	Free height /mm	Bearing capacity /kN
140	72	8	3.2	11.2	85.3

2.2 Experimental equipment and test

Bearing device As showed in Figure 2, rubber bearing shear tester can provide vertical force of 10000kN, vertical stroke of 1000mm, vertical no-load rate of 0~200mm/min, through four fibers set at four corners. The displacement meter measures the perpendicular displacement. The average value of the four displacement meter reading is taken during data processing. The horizontal direction provides 2100kN horizontal force. The horizontal stroke is 800mm, and the horizontal direction no-load rate is 0~100mm/s. The force sensor and built-in cable displacement meter automatically collect horizontal direction experimental data.

The bearing test consists of two parts: the horizontal and vertical isolation of the support. The horizontal isolation performance test mainly investigates the influence of horizontal shear strain and horizontal loading frequency on its performance. The vertical isolation test mainly investigates the influence of loading amplitude and loading frequency on its mechanical properties.



Fig 2: The loading device

2.3 Finite Element Analysis of Anti-uplift Device

The ABAQUS is used to carry out the finite element analysis of the anti-uplift device of the bearing under the design load, and the reliability of the anti-drawing device is investigated to ensure that the bearing does not suffer from tensile damage during normal use.

Liu Wenguang, Han Qiang et al. proposed a double stiffness calculation model based on the tensile test of the rubber bearing, based on the tensile stress-strain curve of the rubber bearing, and gave the evaluation of the tensile properties of the rubber bearing. 3G evaluation criteria, Liu Wenguang pointed out that the maximum tensile stress in the design of rubber isolation bearing is controlled within 3G, and the tensile strain does not exceed 10%, which can ensure the isolation structure is in a safe state.

The three-dimensional isolation bearing designed in this paper, the horizontal thickness of the rubber layer of the high damping rubber bearing of the horizontal isolation device is 80mm, the total thickness of the 10% rubber layer is 8mm; the vertical displacement of the anti-pulling device and the high damping rubber bearing is less than 8mm, can ensure that the rubber support is not pulled.

Figure 3-6 displays the analysis results of the anti-pulling device under different working conditions. It can be seen from Fig. 5 that the maximum stress of the anti-drawing device is 305.3 MPa when the bearing is offset by 80mm under the condition of the shearing and shearing. Yield strength of Q345 grade steel is in the safe range; the maximum displacement of the anti-pull device is 7.36mm less than 8mm, and the high damping rubber bearing is in an elastic state. It indicates that the anti-extraction has sufficient safety reserves to ensure that the support is pulled in a harmless state.

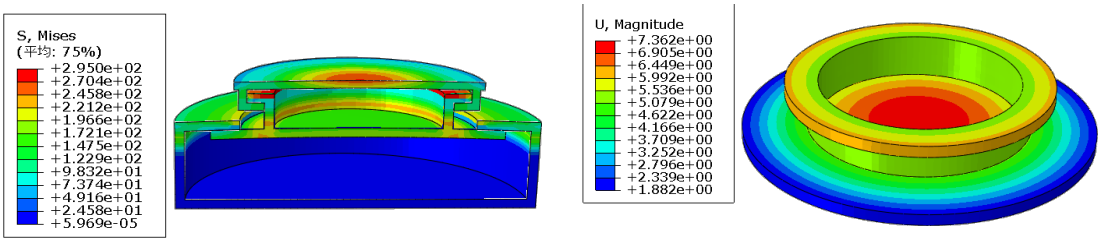


Fig.3 Stress and displacement cloud diagram of the device under axial force

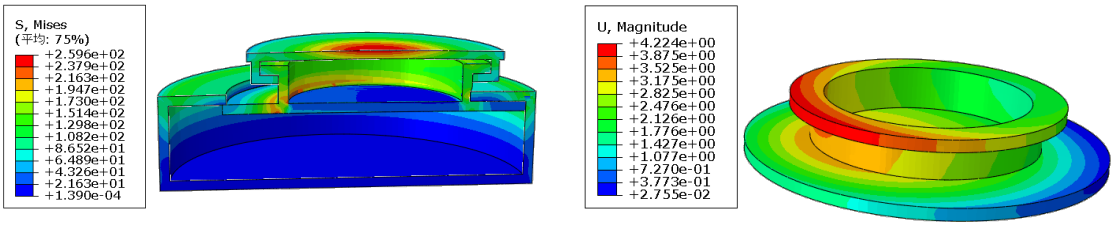


Fig.4 Stress and displacement cloud diagram of the device under eccentric 80mm tension

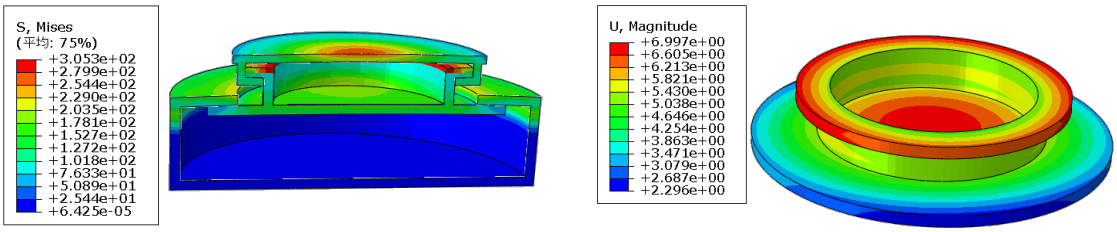


Fig.5 Stress and displacement cloud diagram of the device under axial shearing

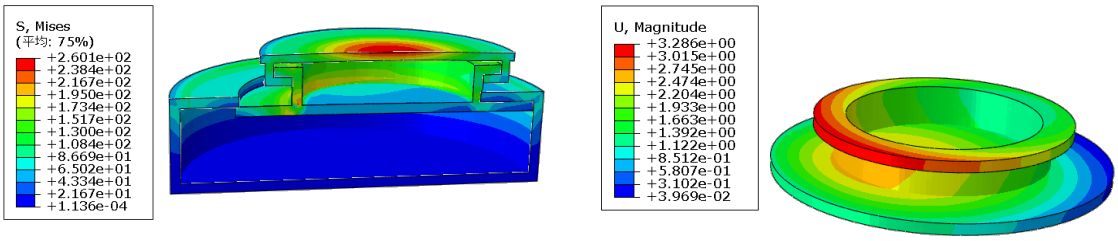


Fig 6: Stress and displacement cloud diagram of the device under eccentric 80mm shearing

3.Seismic isolation performance in horzintal direction

3.1 Influence of Shear Strain on Horizontal Isolation Performance of Bearings

In order to study the influence of shear strain on the horizontal isolation performance of the bearing, the three-dimensional composite anti-extracting isolation bearing was subjected to compression shear test using the "single shear test method". The vertical pressure was 900kN and the horizontal frequency was 0.05. Hz sinusoidal load, horizontal loading is controlled by displacement.The design shear strain γ_0 is 0.75, 1.0, 1.25 times, and the three-cycle reciprocating cycle is applied. The test conditions are given in table 3. The test piece was placed on the loading system before the test, and the pre-compression was performed three times after the alignment, and the pre-pressure was taken in order to be 300 kN.

Figure 7 shows the hysteresis curve of the bearing under different shear strain conditions. The hysteresis curve shows good double nonlinearity, and the reverse curve appears on the loading curve. During the reverse loading process, the curve begins to recover sharply. Small, the curve is usually gentle after the shear strain is reduced,

the recovery deformation is gradually accelerated, and the recovery deformation hysteresis occurs. With the increase of shear strain, the hysteresis curve is more rounded, which indicates that the three-dimensional isolation bearing still has certain energy dissipation capacity and stable mechanical properties under the condition of large deformation.

Tab 3: Horizontal isolation performance test condition

Research content	Working condition	Loading method	Vertical pressure/kN	Loading frequency/Hz	Horizontal displacement/mm
Different shear strain	1	Three cycles	900	0.05	60
	2	Three cycles	900	0.05	80
	3	Three cycles	900	0.05	100
Different loading frequency	4	Three cycles	900	0.05	80
	5	Three cycles	900	0.1	80
	6	Three cycles	900	0.2	80

Tab 4: Calculation results of horizontal equivalent stiffness and equivalent damping ratio

Research content	Different shear strain			Different load frequency		
Working condition	1	2	3	4	5	6
Horizontal equivalent stiffness (kN·mm^{-1})	1.27	1.22	1.21	1.22	1.24	1.26
Equivalent damping ratio（%）	14.72	13.65	12.48	13.65	14.08	14.77

Table 4 shows the calculation results of the equivalent damping ratio of equivalent stiffness of bearings under different working conditions. It can be observed in Fig. 8 that as the shear strain increases, the horizontal equivalent stiffness of the bearing decreases. This is because as the shear strain of the bearing increases. The area of the core compression zone of the support decreases. The rubber away from the core compression zone becomes less constrained. It can be seen from Fig. 9 that the horizontal equivalent damping ratio of the support decreases with the increase of the shear strain, because the increase of the elastic strain energy caused by the stiffness of the support is greater than the increase of the hysteresis curve of the support. Faster.

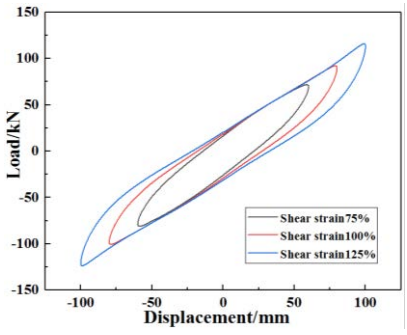


Fig 7: Hysteresis curve of bearing under different shear strains

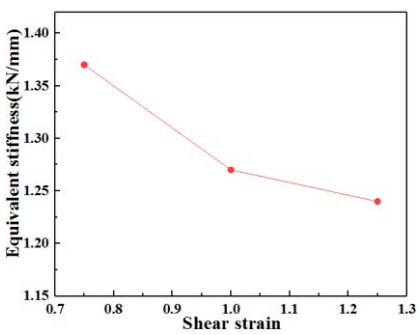


Fig 8: Horizontal equivalent stiffness changes with shear strain

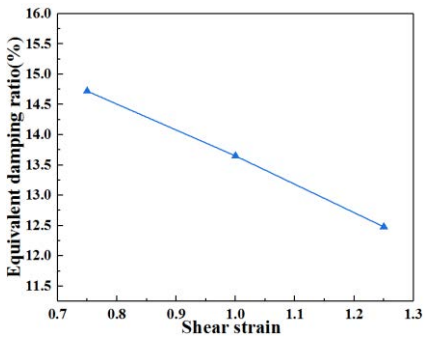


Fig 9: Horizontal equivalent damping ratio changes with shear strain

3.2 Influence of horizontal loading frequency

The rubber material is a motion-related material. Different loading frequency has a definite influence on the horizontal isolation performance of the bearing. For this reason, the load frequency score test is carried out on the bearing, and the pressure of 900kN is applied vertically, and the frequency applied in the horizontal

direction is 0.02Hz. The sinusoidal load of 0.1Hz and 0.2Hz is controlled by the displacement in horizontal loading, and the shear strain of the bearing is taken as 100% (see Table 3 for test conditions).

Fig 10 is a hysteresis curve measured by the test. The curve shows that the hysteresis curve of support tends to be full as the loading frequency increases, showing a good double nonlinearity. The calculation results of the equivalent stiffness equivalent damping ratio of the bearing are shown in Table 4. It can be observed in Figure 11 that the horizontal equivalent stiffness is stable with the increase of the loading frequency, and the increasing amplitude is small. The horizontal equivalent damping ratio of the support of Figure 12 increases as the loading frequency increases.

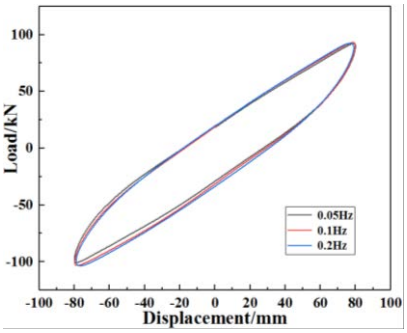


Fig 10: Hysteresis curve of bearing at different loading frequencies

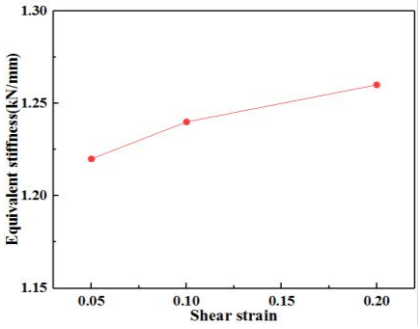


Fig 11: Horizontal equivalent stiffness loading frequency change

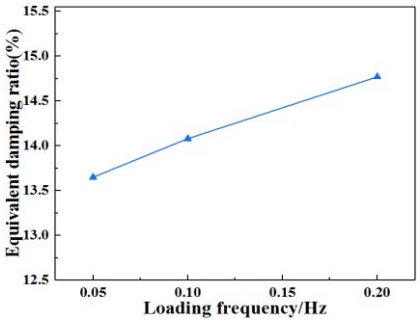


Fig 12:Horizontal equivalent damping ratio change of loading frequency

4. Seismic isolation performance in horzintal direction

4.1 Influence of loading amplitude

The influence of different loading amplitude on the vertical isolation performance of the bearing, the preload of 700kN is applied vertically in the bearing, and the vertical load is applied to the bearing at a loading frequency of 0.02Hz. The loading amplitude is 100kN, 200kN and 300kN. The vertical load is monitored by force, and the three-cycle reciprocating cycle is applied. The third equivalent hysteresis curve is utilized to calculate calculate the vertical equivalent stiffness and the equivalent damping ratio of the support. The test conditions are given in table 5.

Figure 13 shows the vertical hysteresis curve of the bearing under different loading amplitudes. It can be seen that as the loading amplitude increases, the hysteresis curve of the bearing tends to be full and the hysteresis loop area increases significantly. The energy dissipation capacity of the support increases with the increase of the load amplitude; in addition, the hysteresis curve of the support has obvious asymmetry, because the vertical damping of the support mainly comes from between the disc springs. Friction force, as the pressure increases during the loading process, the contact area between the disc spring pieces increases the frictional damping, so that the hysteresis curve tends to be full; the friction between the disc spring pieces during the unloading process With decreasing, the frictional damping between the discs becomes smaller, making the hysteresis curve tend to be narrow.

Calculated values of vertical equivalent stiffness and equivalent damping ratio are shown in Table 6. Figures 14 and 15 show the variation trend of vertical equivalent stiffness and equivalent damping ratio of the bearing under different loading amplitude conditions. It can be observed in Figures 14 and 15 that due to the variable stiffness characteristics of the disc spring, the vertical equivalent stiffness of the support decreases with the increase of the load amplitude; the equivalent damping ratio of the support follows the loading amplitude. The increase is inclined to increase first and then decrease.

Tab 5: Vertical isolation performance test conditions

Research content	Working condition	Loading method	Vertical preload /kN	Loading frequency /Hz	Loading amplitude / kN
Loading amplitude is differen	1	Three cycles	700	0.02	100
	2	Three cycles	700	0.02	200
	3	Three cycles	700	0.02	300
Different loading frequency	4	Three cycles	700	0.02	200
	5	Three cycles	700	0.1	200
	6	Three cycles	700	0.2	200

Tab 6: Calculation results of vertical equivalent stiffness and equivalent damping ratio of bearing

Research content	Different load amplitude			Different loading frequency		
Working condition	1	2	3	4	5	6
Vertical equivalent stiffness (kN·mm^{-1})	318.93	188.21	149.77	189.80	190.90	191.53
Equivalent damping ratio（%）	6.67	16.94	14.44	16.87	17.21	17.76

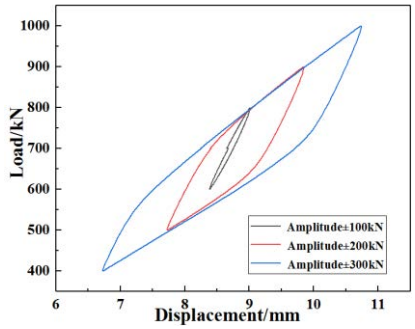


Fig 13: Hysteresis curve of bearing under different loading amplitudes

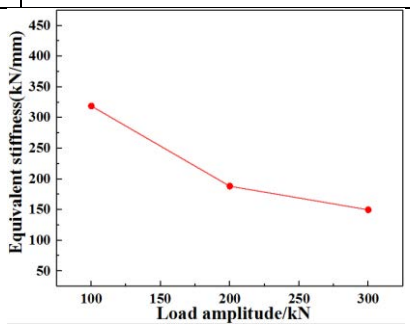


Fig 14: Vertical equivalent stiffness as a function of loading amplitude

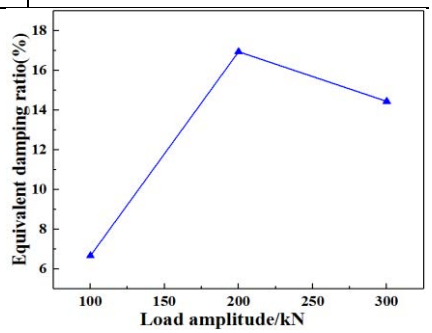


Fig 15: Vertical equivalent damping ratio as a function of loading amplitude

4.2 Loading frequency effects

In order to consider the influence of loading frequency on the vertical isolation performance of the bearing, a pre-stress of 700kN is applied to the vertical direction of the bearing, and the triangular load is applied vertically to the bearing at the loading frequency of 0.02Hz, 0.1Hz and 0.2Hz, and the amplitude is loaded. 200kN, the vertical loading is controlled by force, and the test conditions are shown in Table 5.

Figure 16 displays the vertical hysteresis curve of the bearing at different loading frequencies. It can be seen that as the loading frequency of the bearing increases, the hysteresis curve of the bearing tends to be packed and the energy consumption of the bearing increases. Calculated values of vertical equivalent stiffness and equivalent damping ratio are shown in Table 6. Figures 17 and 18 show the variation trend of the vertical equivalent stiffness and the equivalent damping ratio of the bearing. It can be seen that the vertical equivalent stiffness of the support varies little with the increase of the loading frequency; the equivalent damping ratio increases with the increase of the loading frequency, which is due to the increase of the loading frequency, the disc spring The frictional damping between them becomes large.

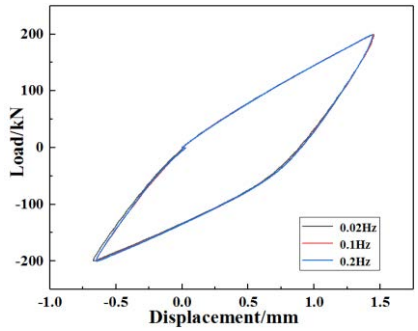


Fig 16 Hysteresis curve of bearing at different loading frequencies

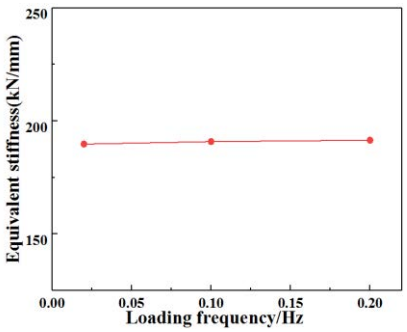


Fig 17 Vertical equivalent stiffness as a function of loading frequency

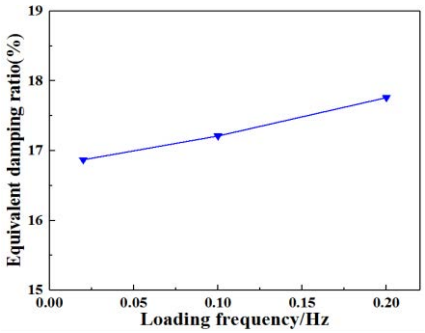


Fig 18 Vertical equivalent damping ratio of loading frequency

5. Conclusion

(1) The finite element simulation results show that the anti-drawing device has a strong safety reserve and can effectively ensure that the rubber bearing is in the elastic range.

(2) The hysteresis curve of the three-dimensional bearing measured by the test is smooth and stable, indicating that the three-dimensional bearing has stable horizontal and vertical mechanical properties; the three-dimensional bearing shows strong horizontal and vertical recovery ability during trial and error.

(3) The horizontal equivalent stiffness of the three-dimensional composite isolation bearing is about 1.22N•mm-1, the horizontal equivalent damping ratio is about 13.50%; the vertical equivalent stiffness is about 190.90N•mm-1, vertical damping The ratio is about 16.94%; it indicates that the three-dimensional composite support has strong energy dissipation capacity in both horizontal and vertical directions, which can effectively reduce the horizontal seismic force and vertical seismic force of the structure, and can realize the function of three-dimensional isolation.

Acknowledgements

The authors gratefully acknowledge the support from the National Key Research and Development Plan of China (Grant No. 2016YFC0701103).

References

[1] Zayas V A, Low S S, Mahin S A. The FPS earthquake resisting system. *California: University of California at Berkeley*, 1987.

[2] WANG, J. Q., DING, Y. G, LI, D. W., "Study on restoring force model of friction pendulum isolator," *Sichuan Building Science*, Vol.33, No.3, pp. 25-27, 2007.

[3] XUE, S. D., PAN, K. J., LI, X. Y., "The experimental research on mechanical property of vertical uplift-resistant friction pendulum bearing support," *China civil engineering journal*, Vol.45, No.2, pp. 6-10, 2012.

[4] XIONG,S.S, TANG, J. S,LIANG B. Flat Torsional-Vertical Seismic Response Analysis of 3D Isolated Buildings with 3DB [J]. *Earthquake resistance and reinforcement of engineering,* 2004,10(5),pp.17—22.

[5] LI,X.Y. Research on friction-spring three-dimensional composite isolation bearing and its application in large-span hangar [D].*Beijing: Beijing University of Technology*, 2008.

[6] A Parvin and Z Ma. The Use of Helical Spring and Fluid Damper Isolation Systems for Bridge Structures Subjected to Vertical Ground Acceleration, *Electronic Journal of Structural Engineering*, 2001, No.2:pp,98—110.

Proceedings of the IASS Annual Symposium 2019 – Structural Membranes 2019
Form and Force
7 – 10 October 2019, Barcelona, Spain
C. Lázaro, K.-U. Bletzinger, E. Oñate (eds.)

Free vibration characteristic of single-layer spherical aluminium alloy latticed shells

Li WANG*, Xiaonong GUO, Shuyu GAO, Qiang ZENG

*Department of Structural Engineering, Tongji University
No.1239 Siping Road, Yangpu District, Shanghai, China
1810025@tongji.edu.cn

Abstract

With the wide application and rapid development of the aluminum alloy structure in China, the insufficiency of study on its dynamic characteristic becomes increasingly prominent. Moreover, the free vibration characteristic is the research foundation of its dynamic characteristic. In order to study the free vibration characteristic of Kiewitt-6 and Kiewitt-8 (K6 and K8) aluminum alloy single-layer spherical latticed shells with gusset joints, large amount of finite element (FE) analysis was carried out using ANSYS. In the established models, various parameters including rise-span ratio, span, roof load, span-thickness ratio, grid density and support boundary conditions were considered. Based on the FE results, the formula to estimate the fundamental frequency of single-layer spherical latticed shells was derived, without considering the effects of joint stiffness. Subsequently, by introducing the amplification factor, the formula of the fundamental frequency of aluminum alloy shells with gusset joints was proposed. Finally, the proposed formulae were validated against the experimental values of an actual shell. The theoretical values agreed well with the test results, indicating the proposed formulae had good accuracy.

Keywords: aluminum alloy, gusset joint, single-layer spherical latticed shell, free vibration characteristic, joint stiffness.

1. Introduction

Compared with traditional structures, the single-layer spherical aluminium alloy latticed shells offer attractive appearance, material savings, reasonable stress, convenient construction and favorable durability. Therefore, such shells have been widely used in spatial structures recently [1] - [2].

The aluminium alloy gusset (AAG) joint is one of the major joint systems in the single-layer spherical aluminium alloy latticed shells. It is composed by I-shaped aluminum alloy bars, which are joined together in the nodes and connected to a couple of circular gusset plates by means of bolted connection. The practical implementations have stimulated a series of investigations in static mechanical properties. Guo [3] - [9] carried out the experimental and numerical research on the AAG joint. Consequently, the failure modes of the AAG joint were summarized and a four-linear model of bending stiffness of joint was proposed. Xu [10] analyzed the hysteretic behavior of the AAG joint under out-of-plane cyclic loading conditions. It is found that the hysteretic curve was stable but not so plump. Liu [11] clarified the effects of joint stiffness on the static stability of aluminum alloy single-layer latticed shell with the AAG joint. It is indicated that the joint semi-rigidity would reduce the global stability bearing capacity.

As for the dynamic properties of the shell, Guo [12] investigated the damping of aluminium alloy single-layer latticed shell with the AAG joint, and suggested the damping ratio ξ=3.3%. Besides, few literatures have studied the dynamic characteristics of single-layer latticed shell with the AAG joint.

Obviously, to reveal the dynamic properties, it is necessary to start with the free vibration characteristic. In this paper, large number of single-layer spherical aluminium alloy latticed shell models were analyzed

Copyright © 2019 by Li Wang, Xiaonong Guo, Shuyu Gao, Qiang Zeng
Published by the International Association for Shell and Spatial Structures (IASS) with permission.

with FE software ANSYS. Firstly, the influences of various parameters were explored. Secondly, formula to estimate the fundamental frequency of single-layer spherical latticed shells were derived, without considering the effects of joint stiffness. Subsequently, by introducing the amplification factor, the formula of the fundamental frequency of aluminum alloy shells with the AAG joint was proposed. Finally, the proposed formulae were validated against the experimental values of an actual shell.

2. Free vibration characteristic without considering the joint stiffness

2.1. Numerical model

Beam188 was selected to simulate the I-shaped beam. The mechanical properties were shown in Table 1. The uniform mass of roof was simplified to the lumped mass of the joint. The contribution of the roof slab to the stiffness of the whole structure was ignored.

Table 1 Material properties of the structure

Material	Yield strength	Young's modulus	Poisson's ratio	Volume weight
6061-T6	240 MPa	70 GPa	0.3	2.65×10^4 N/m^3

Table 2 Parameter analysis scheme

Span L (m)	30, 35, 40, 45, 50, 55, 60, 65, 70, 75, 80, 85, 90, 95, 100, 105, 110, 115, 120
Rise-span ratio f/L (m/m)	1/2, 1/3, 1/4, 1/5, 1/6, 1/7, 1/10, 1/13, 1/16
Roof load p (kN/m^2)	0.4, 0.8, 1.2, 1.6, 2.0
Bar section	①, ②, ③, ④, ⑤
Grid size	3m~6m
Boundary condition	hinged, fixed

A total of 342000 shell models were established. The parameter analysis scheme was tabulated in Table 2. The extruded I-shaped aluminum alloy bars were applied, with these five cross-sections: ① H250×150×6×12mm, ② H300×150×8×12mm, ③ H350×175×10×14mm, ④ H400×200×12×14mm, ⑤ H500×200×12×16mm. The grid size refers to the length of the main rib members of each ring.

2.2. Numerical results and discussions

2.2.1. Influence of rise-span ratio

When the rise-span ratio was 1/3, the first three vibration modes were antisymmetric modes with mainly horizontal deformation, as shown in Figure 1. However, when the rise-span ratio was 1/7, the first two vibration modes were antisymmetric modes with mainly vertical deformation, and the third mode was a symmetrical mode with mainly vertical deformation, as revealed in Figure 2.

The fundamental frequency of reticulated shells increased firstly and then decreased with the rise of the rise-span ratio, as described in Figure 3. There was an optimum rise-span ratio which maximized the fundamental frequency, and the optimum rise-span ratio was about 1/4.

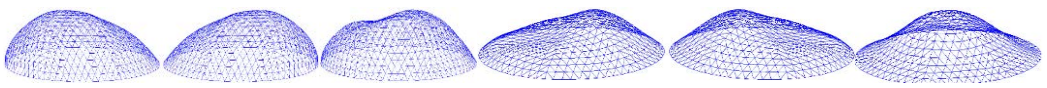


Figure 1: Vibration modes of the shell (f/L =1/3)

Figure 2: Vibration modes of the shell (f/L =1/7)

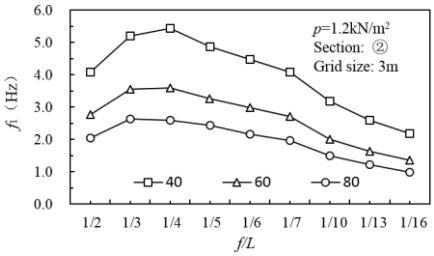
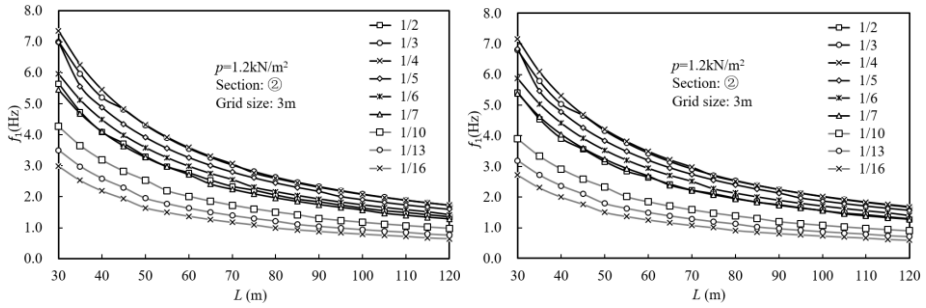


Figure 3: Fundamental frequency vs rise-span ratio

2.2.2. Influence of span

As the span went up, the fundamental frequency of reticulated shells decreased and gradually tended to be flat, as plotted in Figure 4. Meanwhile, the increase of span would reduce the stiffness of the shell in both vertical and horizontal directions.

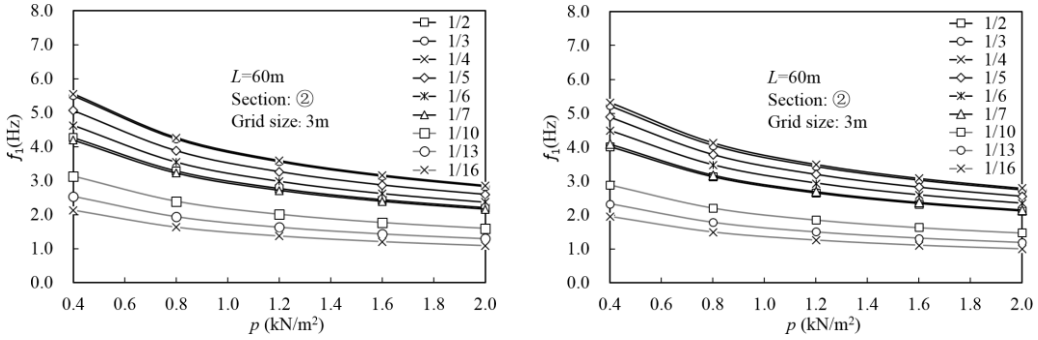


K6 K8

Figure 4: Fundamental frequency vs span

2.2.3. Influence of roof load

In the practical project, the roof load of the latticed shell was transmitted to the joints by purlin mainly. Therefore, the surface load can be equivalent to the lumped mass of the related joints according to the static equivalent principle. The frequencies dropped with the increase of roof load, as signified in Figure 5. This is because the increase of load was equivalent to the increase of mass.



K6 K8

Figure 5: Fundamental frequency vs roof load

2.2.4. Influence of span-thickness ratio

The dimensionless parameter β was used to express the span-thickness ratio. If the arc length going through the apex and two supports on the spherical surface is s, and the radius of gyration around the

strong axis of the bar section is i_x, the span-thickness ratio is $\beta=s/i_x$.The frequencies of the latticed shell sank with the rise of the span-thickness ratio, as shown in Figure 6.

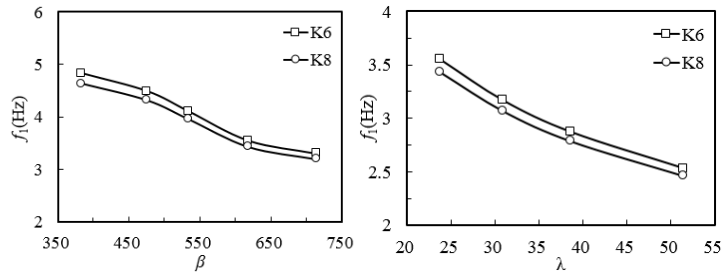


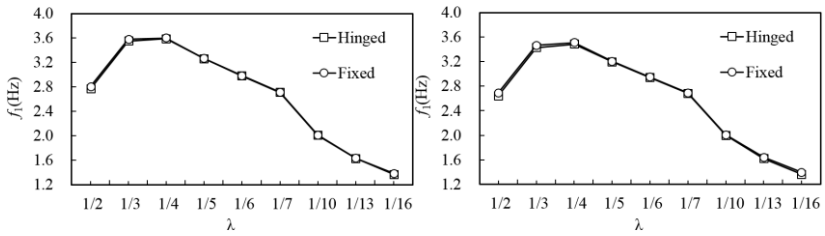
Figure 6: Fundamental frequency vs span-thickness ratio Figure 7: Fundamental frequency vs grid density

2.2.5. Influence of grid density

The dimensionless parameter λ was adopted to express the grid density. If the length of the main rib is l, the dimensionless parameter $\lambda=l/i_x$. The frequencies of the reticulated shell decreased with the increase of λ (in Figure 7). Because the larger λ meant the lower stiffness, leading to lower natural frequencies.

2.2.6. Influence of boundary condition

The shell with hinged and fixed boundary condition were analyzed in Figure 8. Generally speaking, the fundamental frequencies of shells with two types of boundary were basically the same. It is indicated that the different supports play a minor role in the fundamental frequencies of shells.



K6 K8

Figure 8: Fundamental frequency vs boundary conditions

3. Fundamental frequency formula without considering the joint stiffness

According to the fundamental frequencies of continuous shell [13], the estimation formula was proposed:

$$f_1=kL^a M^b \lambda^c \beta^d \sqrt{E/70000} \quad (1)$$

Where f_1 is the first natural frequency, L is the span of spherical latticed shell, M is the equivalent uniform mass of roof (including roof load and dead-weight of shell), λ is the dimensionless parameter of grid density, β is the dimensionless parameter of span-thickness ratio, E is the elastic modulus of aluminium alloy, and *a, b, c, d, k* are all fitting coefficients.

On the basis of the parameter analysis above, the coefficients in formula (1) were fitted. The results of were listed in Table 3 and Table 4, respectively.

Table 3 Values of fundamental frequency coefficients of K6 shells

	1/2	1/3	1/4	1/5	1/6	1/7	1/10	1/13	1/16	Average
k	25496.93	29715.60	29891.54	29565.97	28422.64	27112.95	23413.69	20866.39	19497.64	--
a	-0.739	-0.740	-0.740	-0.738	-0.738	-0.738	-0.737	-0.736	-0.736	-0.738

b	-0.515	-0.512	-0.511	-0.512	-0.513	-0.513	-0.513	-0.512	-0.512	-0.513
c	-0.500	-0.502	-0.502	-0.500	-0.500	-0.500	-0.503	-0.504	-0.506	-0.503
d	-0.291	-0.287	-0.292	-0.306	-0.318	-0.327	-0.348	-0.365	-0.381	--

Table 4 Values of fundamental frequency coefficients of K8 shells

	1/2	1/3	1/4	1/5	1/6	1/7	1/10	1/13	1/16	Average
k	26399.41	31075.59	31211.38	29975.97	28520.73	27109.55	23495.65	21362.66	20625.78	--
a	-0.739	-0.739	-0.738	-0.738	-0.738	-0.737	-0.736	-0.736	-0.739	-0.738
b	-0.517	-0.514	-0.514	-0.514	-0.514	-0.514	-0.514	-0.513	-0.513	-0.513
c	-0.505	-0.501	-0.501	-0.502	-0.501	-0.502	-0.504	-0.506	-0.508	-0.503
d	-0.296	-0.296	-0.300	-0.308	-0.317	-0.326	-0.347	-0.365	-0.384	--

The discreteness of fitting coefficients *a, b,* and *c* is very small. In addition, the mean values of K6 and K8 shells are quite close. Therefore, the mean values in Table 3 and Table 4 are unified in last column. However, *k* and *d* vary greatly with the rise-span ratio. Hence, cubic polynomials were selected to fit.

For K6 latticed shells,

$$k_6 = 439524\left(\frac{f}{L}\right)^3 - 534626\left(\frac{f}{L}\right)^2 + 189504\frac{f}{L} + 9479 \tag{2}$$

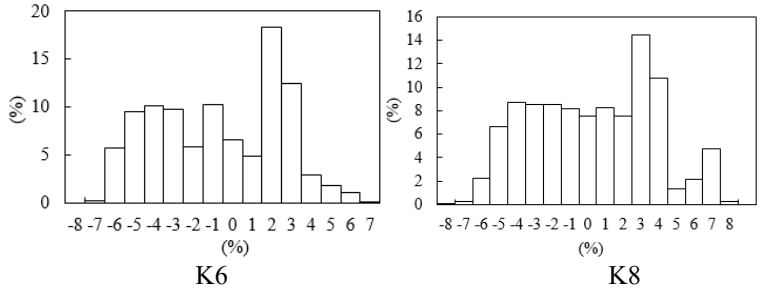
$$d_6 = 2.162\left(\frac{f}{L}\right)^3 - 2.764\left(\frac{f}{L}\right)^2 + 1.138\frac{f}{L} - 0.439 \tag{3}$$

For K8 latticed shells,

$$k_8 = 214660\left(\frac{f}{L}\right)^3 - 351440\left(\frac{f}{L}\right)^2 + 150653\frac{f}{L} + 12081 \tag{4}$$

$$d_8 = 3.497\left(\frac{f}{L}\right)^3 - 3.803\left(\frac{f}{L}\right)^2 + 1.335\frac{f}{L} - 0.449 \tag{5}$$

Figure 9 describes the error distribution between the fundamental frequency estimation formula and FE results. The horizontal axis represents the error, and the vertical axis denotes the percentage of shells in the error interval. The estimation errors of 34200 reticulated shells are all less than 10%, and the most are even less than 5%. It is implied that the proposed estimation formula provides high accuracy.



K6 K8

Figure 9: Error distribution

The appropriate rise-span ratio was selected initially. Then *k* and *d* can be calculated according to formula (2) ~ (5), and *a, b, c* can be obtained from Table 3 or Table 4. Finally, the fundamental frequency of latticed shells can be estimated from formula (1).

4. Fundamental frequency considering the joint stiffness

In reference [5], the stiffness of aluminium alloy gusset joint was studied, and a four-linear model of bending stiffness of joint was proposed. The M-ϕ curve goes through four phases: the bolt fixed phase, the bolt slipping phase, the hole wall bearing phase and the failure phase. Owing to the large size of the plates, the actual rotational stiffness of the joint is greater than the bending stiffness of the bar before the bolt slipping. Therefore the gusset joint presents certain super-rigidity.

Under frequent earthquake, the bolt slipping hardly ever occurs. The fundamental frequency increases due to the super-rigidity. As a result, the seismic response is enlarged. It is necessary to consider the effects of joint stiffness on the natural frequencies of latticed shells. The fundamental frequency amplification factor η was introduced to take the effect of joint super-rigidity into account.

The FE models of reticulated shell considering the joint stiffness were established. The model consisted of a rigid panel zone, a non-linear stiffness spring and a bar. The panel zone was simulated by Beam188 with infinite elastic modulus; the spring by Combin39; and the bar by Beam188.

The natural frequencies of mentioned 34200 latticed shells were obtained. Obviously, the most important influence of η is l/R. Figure 10 summaries the variation of η with l/R for the 34200 shells.

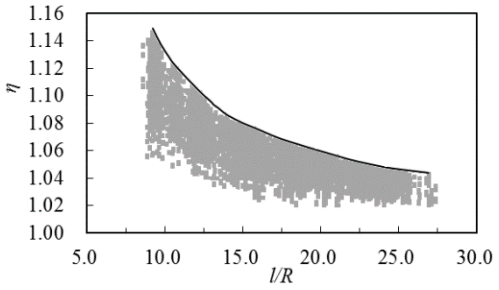


Figure 10: Distribution of amplification coefficient η

It can be observed that η presents strip distribution, ranging from 1.02 to 1.14. And η decreases with the increase of l/R. The upper limit of data was chosen to fit safely, and the formula is as follows:

$$\eta=1.011+0.652/\left(l/R\right)+5.610/\left(l/R\right)^2 \tag{6}$$

5. Case study

In order to verify the availability of the formula, the natural frequencies of an aluminium alloy latticed shell were measured by hammering method in reference [12]. The shell for testing was shown in Figure 11 and the detailed joint was shown in Figure 12. According to reference [12], the measured fundamental frequency of the shell was 17Hz, and that of the FE model was 16.375Hz. The proposed formula was verified by this latticed shell as follows.



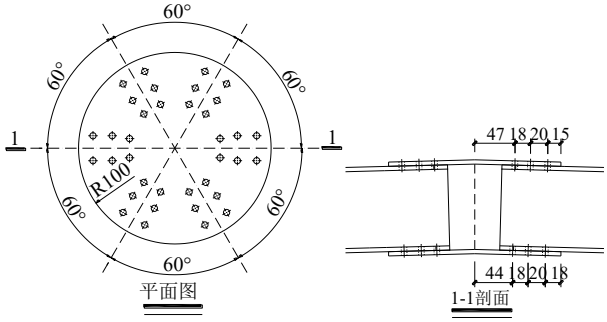


Figure 11: The aluminum alloy latticed shell used for the test Figure 12: Aluminum alloy gusset joints

The known condition:

Type: K6;

Span: L=8m

Rise: f=0.5m

Rise-span ratio: f/L=1/16

Equivalent uniform mass of roof (including dead-weight): M=41.2kg/m^2

Bar section： H100×50×4×5 mm

Elastic modulus： E=65364MPa

Arc length of main rib: s=8080mm

Length of main rib： l=808mm

Gusset radius of main rib: R=100mm

Radius of gyration of bar section： i_x=39.94mm

Fundamental frequency formula without considering the joint stiffness:

Dimensionless parameter of grid density: $\lambda = l / i_x$=20.23

Dimensionless parameter of span-thickness ratio: $\beta = s / i_x$=202.3

According to formula (2), k_6： k_6=19342

According to formula (3), d_6： d_6= -0.378

According to Table 3, a_6： a_6= -0.738

According to Table 3, b_6： b_6= -0.512

According to Table 3, c_6： c_6= -0.502

The above parameters can be substituted in formula (1)： f_1= 17.78Hz

Fundamental frequency considering the joint stiffness:

l/R of main rib： l/R= 8.0

Frequency amplification factor according to formula (6)： η=1.18>1.14，take 1.14

Fundamental frequency considering the joint stiffness: f_1=17.78×1.14=20.27Hz

From the above process, the measured fundamental frequency of the shell is 17Hz and that of the FE model is 16.375Hz. The fundamental frequency calculated by the proposed formula is 17.78Hz without considering the joint stiffness, 4.5% error from the measured value. When the effects of joint stiffness were taken into account, the fundamental frequency calculated by the proposed formula is 20.27 Hz, 19.2% larger than the measured value. There may be the following reasons: 1) the upper limit is adopted in fitting formula (6). When l/R = 8.0, η = 1.14, according to formula (6). However, according to the result of the FE model considering the joint stiffness, η = 1.05; 2) the test is limited by measuring means and the accuracy of measuring instruments; 3) the test shell was manually installed, so the pretension force of bolt might be not enough.

6. Conclusion

The research results indicate the following:

(1) The rise-span ratio, span, roof load, span-thickness ratio and grid density are the main factors influencing the fundamental frequency of single-layer spherical latticed shells. The shells with larger rise-span ratio demonstrate horizontal low-order vibration modes mostly, while those with lower rise-span ratio show vertical low-order vibration modes mainly.

(2) Without considering the joint stiffness, the fundamental frequency of aluminum alloy latticed shell can be estimated by the proposed formula.

(3) When the stiffness of gusset joints is taken into account, the fundamental frequency of latticed shell will increase, and the amplification factor can be captured by the modifier formula.

Acknowledgements

The authors gratefully acknowledge the financial support provided by Natural Science Foundation of China under Grant No. 51478335.

References

[1] L. Yang, S. Wei, and Q. Zhang, "Aluminum reticulated spatial structures: state of the art and key issues," *Journal of Building Structures*, vol. 34, pp. 1-19, 2013.

[2] Z. Shen, X. Guo, and Y. Li, "State-of-the-arts of research on aluminum alloy structures," *Journal of Building Structures*, vol. 28, pp. 100-109, 2007.

[3] X. Guo, Z. Xiong, and Y. Luo, "Initial bending stiffness of aluminum alloy gusset joint,"*Journal of Tongji University: Natural Science*, vol. 43, pp. 47-53, 2015.

[4] X. Guo, Z. Xiong, and Y. Luo, "Experimental research on the load-bearing behavior of aluminum alloy ausset joint," *Journal of Tongji University: Natural Science*, vol. 42, pp. 1024-1030, 2014.

[5] X. Guo, Z. Xiong, and Y. Luo, "Theoretical study on bending stiffness of aluminum alloy gusset joint," *Journal of building engineering*, vol. 35, pp. 144-150, 2014.

[6] X. Guo, Z. Xiong, and Y. Luo, "The Design Method and Detailed Requirements of Bearing Capacity of Aluminum Alloy Gusset Joint," *Journal of Tongji University: Natural Science*, vol. 43, pp. 47-53, 2015.

[7] X. Guo, Z. Xiong, and Y. Luo, "Experimental Investigation on the Semi-rigid Behaviour of Aluminium Alloy Gusset Joints" *Thin-Walled Structures*, vol. 87, pp. 30-40, 2015.

[8] X. Guo, Z. Xiong, and Y. Luo, "Application of the Component Method to Aluminium Alloy Gusset Joints" *Advances in Structural Engineering*, vol. 18, pp. 1931-1946, 2015.

[9] X. Guo, Z. Xiong, and Y. Luo, "Block Tearing and Local Buckling of Aluminum Alloy Gusset Joint Plates" *KSCE Journal of Civil Engineering*, vol. 20, pp. 820-831, 2016.

[10] S. Xu, Z. Chen, and X. Wang, "Hysteretic Out-Of –Plane Behavior of the Temcor Joint," *Thin-Walled Structures*, vol. 94, pp. 585-592, 2015.

[11] H. Liu, Y. Ding, and Z. Chen, "Static Stability Behavior of Aluminum Alloy Single-Layer Spherical Latticed Shell Structure with Temcor Joints," *Thin-Walled Structures*, vol. 120, pp. 355-365, 2017.

[12] X. Guo, L. Wang, and Y. Xiang, "Experimental Study on Damping Property of Aluminum Alloy Latticed Shell with Gusset Joints," *Journal of Vibration and Shock*, vol. 35, pp. 34-39, 2016.

[13] Y. Xing and B. Liu (Eds.), *Exact Solutions of Free Vibrations of Plates and Shells*, Science Press, 2015.

Proceedings of the IASS Annual Symposium 2019 – Structural Membranes 2019
Form and Force
7 – 10 October 2019, Barcelona, Spain
C. Lázaro, K.-U. Bletzinger, E. Oñate (eds.)

Linear Buckling Analysis Considering No-Compression Property of Metal Grid Shells Stiffened by Tension Braces

Kenji YAMAMOTO *, Hayato UTEBI[a]

* Department of Architecture and Building Engineering, Tokai University
4-1-1 Kitakaname, Hiratsuka City, Kanagawa, Japan
kyamamoto@tokai-u.jp

[a] Former Graduate Student of Tokai University

Abstract

In order to analyze the buckling behavior of lattice shells which are stiffened by cables or slender braces without pre-tension, it is necessary to take no-compression property of braces into consideration. In this paper, an innovative method of linear buckling analysis considering no-compression property of braces is proposed. Moreover, in order to examine about the validity of the proposed method, the results by the proposed method are compared with the results by the nonlinear buckling analysis with the geometrical nonlinearity and the material nonlinearity to express no-compression property of braces. Through the result, it is shown that the buckling behaviors of lattice shells stiffened by the tension braces is predictable by the proposed method well.

Keywords: linear buckling analysis, nonlinear buckling analysis, no-compression property, tension brace, grid shell.

1. Introduction

The flat roof of a general chevron frame such as a factory and gymnasium is usually stiffened with tension braces as shown in Fig. 1(a). On the other hand, the roof of a single layer lattice shell with double curvature is usually constructed by arranging steel members in triangular shapes as shown in Fig. 1(b). There is also two-way grid shell roof stiffened with braces as in Fig.1(c), but in this case the braces are usually pretensioned ([1]-[5]). In contrast to the flat roof, the shell roof stiffened by braces without pre-tension has hardly been built so far. The reason would be that it is difficult to grasp the buckling behavior of the shell roof. Although the rigidity of the brace with pre-tension is constant until the tension is released, the rigidity of the brace without pre-tension changes according to the deformation.

In the shell roof as shown in Fig. 1(c), the joint is simple and low cost compared with Fig.1(b), but when introducing the pre-tension into the braces, the strategy of tension introduction and the measurement of tension are required. If sufficient stiffening effect can be obtained without pre-tension, the construction cost could be greatly reduced.



(a) (b) (c)

Figure 1: Types of steel frame roof

Copyright © 2019 by Kenji Yamamoto and Hayato Utebi
Published by the International Association for Shell and Spatial Structures (IASS) with permission.

When analyzing the buckling behavior of a reticulated shell stiffened by tension braces that have large slenderness ratio and no pre-tension, it is necessary to consider the no-compression property of the braces into the analysis. Since the tensile and compressive states of the braces would change before and after the buckling, it is difficult to predict the buckling behavior by using ordinary linear buckling analysis. Therefore, it is necessary to use the material and geometrical nonlinear buckling analysis in which the no-compression property of braces is modeled as the material nonlinearity and the equilibrium path is traced by the iterative calculation. Such analysis would be complicated and it is not easy to verify the validity of the results obtained.

If it is possible to consider the no-compression property of braces into the linear buckling analysis, it would be useful because an approximate value of the buckling load could be obtained with small computational work in trial and error on the structural design process. Also, it could be used for verification of the results by the nonlinear buckling analysis.

In this paper, we propose a linear buckling analysis method considering the no-compression property applicable to grid shells stiffened by tension braces without pretension. The results by the proposed method are compared with the results by the material and geometrical nonlinear buckling analysis, and the validity of the proposed method is shown.

2. Nonlinear buckling analysis of grid shell stiffened by tension braces

The buckling behaviors of metal grid shells stiffened by braces without pre-tension are not well known. Therefore, we first carried out the nonlinear buckling analysis to investigate the buckling behavior of such a grid shell in detail. The analysis model is shown in Fig. 2. It has an EP curved surface shape of 8 m in height and 40 m in span. The grid members are assumed to be steel pipes of ϕ 165.2 × 4.5, and the diagonal braces are assumed to be round steel bars of ϕ 16. For both the grid members and the braces, the Young's modulus is 205 GPa and the Poisson's ratio is 0.3. However, the Young's modulus of the braces in the compression direction is set to be zero to express the no-compression property. The support condition is pinned support for the whole circumference of the shell. The external force is given as nodal concentrated forces corresponding to an equally distributed load of 1.0 kN/m^2.

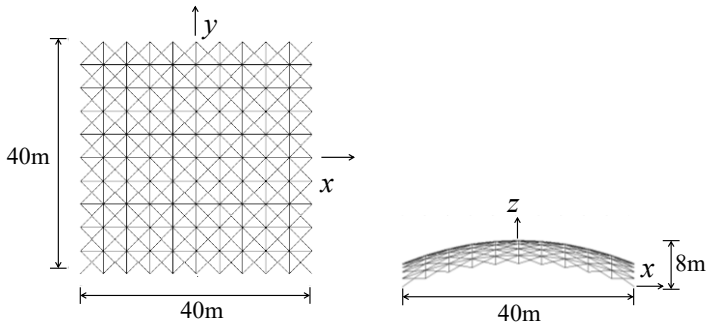


Figure 2: Model for analysis

The results of nonlinear buckling analysis are shown below. The relationship between the vertical displacement of the top node and the load factor is shown in Fig. 3. Two 'x' marks in the figure indicate the bifurcation point first appearing on the fundamental equilibrium path, and the buckling point that first appeared on the bifurcation path from the bifurcation point, respectively. The broken line denotes the fundamental equilibrium path, and the solid line denotes the bifurcation path from the first bifurcation point. The relationship between the minimum eigenvalue of the tangential stiffness matrix and load factor is shown in Fig. 4. The axial force distribution diagram of the braces and the buckling mode at the bifurcation point are shown in Fig. 5 (a) and (b). However, at the bifurcation point, since all the braces are compressed and have no axial force, actually no axial force is drawn in Fig. 5 (a). We confirmed that the buckling mode of Fig. 5(b) is the same as the first buckling mode of the grid shell without the braces. It is found that the braces do not contribute to the stiffness of the

shell on the fundamental path.

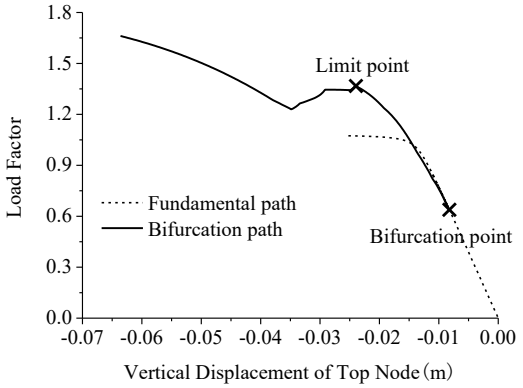


Figure 3: Relation between load and displacement

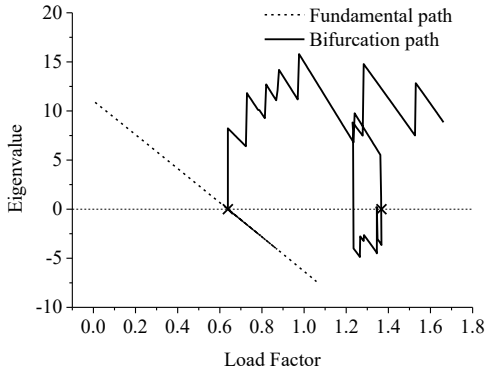
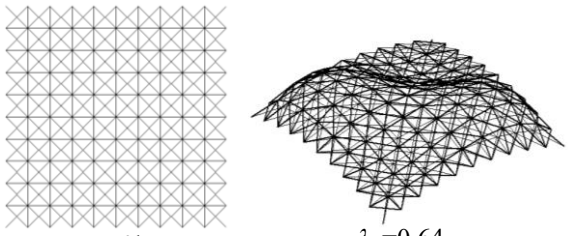
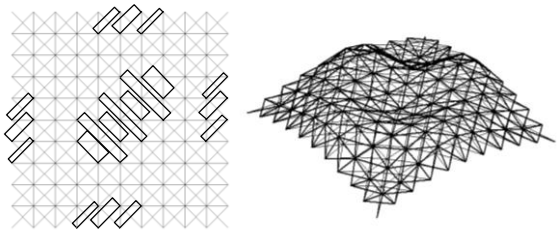


Figure 4: Relation between load and eigenvalue



(a) Axial force diagram of braces (b) Buckling mode

Figure 5: Axial force diagram and buckling mode on bifurcation point



(a) Axial force diagram of braces (b) Buckling mode

Figure 6: Axial force diagram and buckling mode on bifurcation point

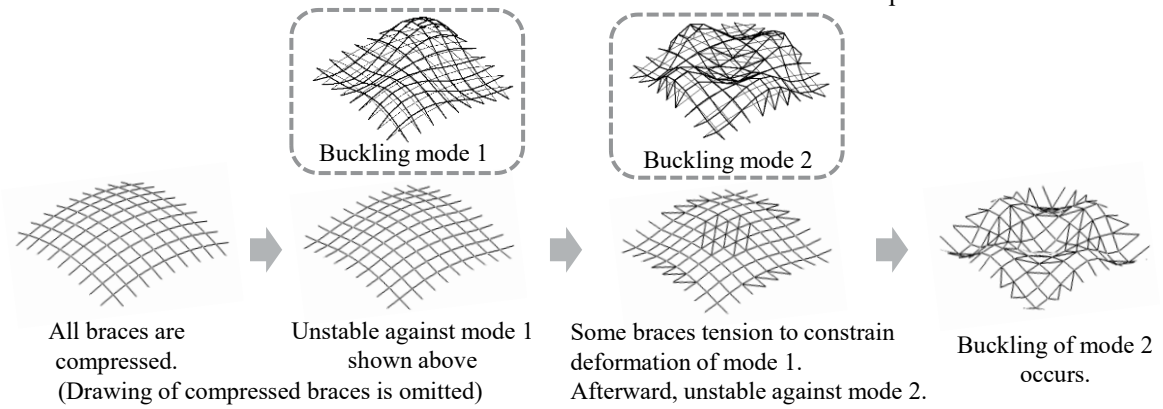


Figure 7: Buckling behavior of reticulated shell stiffened by tension braces (deformation 100 times)

Looking at the behavior of the shell after the bifurcation in Fig. 3, the load increases while maintaining the gradient of the fundamental path. Because tension forces are generated in some braces after the bifurcation and the braces restrain the deformation of the buckling mode. This is the reason that the eigenvalue fluctuates up and down after the bifurcation in Fig. 4. From the viewpoint of numerical analysis theory the first 'x' mark is judged to be a buckling point, but in practice the deformation of the buckling mode is restrained by the tension braces and the buckling does not occur.

The bifurcation path reaches the limit point when the load factor is 1.37, and the negative gradient appears beyond the point. Fig. 6 (a) and (b) show the axial force distribution diagram of the braces and the buckling mode at the limit point, respectively. It is shown that tension forces are generated in

the some braces at the limit point.

A schematic diagram of the buckling behavior of the shell is shown in Fig.7. Fig.3 is underestimated the judgement of the bifurcation point as the buckling strength of the shell, because the stiffening effect of the braces is ignored. Therefore, the limit point appearing after the bifurcation point should be judged as the buckling strength of the shell. The buckling strength is about twice that of the bifurcation point.

In this section, the buckling behavior of the grid shell stiffened by tension braces was investigated in detail using the nonlinear buckling analysis. In the following, we would consider a method of evaluating the limit point appearing after the bifurcation by the linear buckling analysis considering the no-compression property of the braces. The method simplifies the nonlinear buckling behavior described above and is useful for deeply understanding the buckling behavior.

3. Linear buckling analysis considering no-compression property

In general, equilibrium equations and incremental equilibrium equations considering geometric nonlinearity are represented by Eq. (1) and Eq. (2),

$$\mathbf{q}(\mathbf{d}) - \lambda \mathbf{f} = \mathbf{0} \tag{1}$$

$$\mathbf{K}_T(\mathbf{d})\Delta\mathbf{d} - \Delta\lambda \mathbf{f} = \mathbf{0} \tag{2}$$

where $\mathbf{q}$ is the internal force vector, $\mathbf{d}$ is the displacement vector, λ is the load factor, $\mathbf{f}$ is the external force mode, $\mathbf{K}_T$ is the tangential stiffness matrix, $\Delta\mathbf{d}$ is the incremental displacement vector, and $\Delta\lambda$ the incremental load factor. $\mathbf{q}$ and $\mathbf{K}_T$ are nonlinear functions of $\mathbf{d}$. The tangent stiffness matrix is expressed as

$$\mathbf{K}_T = \mathbf{K}_L + \mathbf{K}_D(\mathbf{d}) + \mathbf{K}_G(\mathbf{q}) \tag{3}$$

$\mathbf{K}_L$ is the linear stiffness matrix, $\mathbf{K}_D$ is the large displacement stiffness matrix, and $\mathbf{K}_G$ is the geometric stiffness matrix.

In the linear buckling analysis, $\mathbf{K}_D = \mathbf{O}$ is assumed and the internal force vector $\mathbf{q}_0 = \mathbf{K}_L\mathbf{d}_0$ obtained by solving the linear stress analysis $\mathbf{K}_L\mathbf{d}_0 - \mathbf{f} = \mathbf{0}$ when applying external force mode $\mathbf{f}$ is used, and the tangential stiffness matrix is approximated as follows.

$$\mathbf{K}_T = \mathbf{K}_L + \lambda \mathbf{K}_G(\mathbf{q}_0) \tag{4}$$

Since $\mathbf{K}_T$ is singular at the buckling point, the linear buckling load factor can be obtained by solving the minimum eigenvalue of the following eigenvalue problem.

$$\left[\mathbf{K}_L + \lambda_i \mathbf{K}_G(\mathbf{q}_0)\right]\boldsymbol{\phi}_i = \mathbf{0} \tag{5}$$

where λ_i is the i-th linear buckling load factor, and $\boldsymbol{\phi}_i$ is the i-th buckling mode.

Now, the no-compression property of the braces is taken into the two linear stiffness matricies. The one is $\mathbf{K}_L$ on the linear stress analysis for obtaining $\mathbf{q}_0$, and the another one is $\mathbf{K}_L$ in the Eq. (5). These $\mathbf{K}_L$ are constructed by removing the stiffness of the braces compressed under the external force mode $\mathbf{f}$. Therefore, the linear buckling load obtained by Eq. (5) approximates the first bifurcation point appearing on the fundermental path of the above-described nonlinear buckling analysis.

Next, we consider to evaluate the second buckling point that appears on the bifurcation path, where the stiffness is increased by turning the compression on the braces into the tension after the first buckling. First, the equilibrium equation of Eq. (1) and the incremental equilibrium equation of Eq. (2) are approximated as follows to correspond to the linear buckling analysis of Eq. (5).

$$\left[\mathbf{K}_L + \lambda \mathbf{K}_G(\mathbf{q}_0)\right]\mathbf{d} - \lambda \mathbf{f} = \mathbf{0} \tag{6}$$

$$\left[\mathbf{K}_L + \lambda \mathbf{K}_G(\mathbf{q}_0)\right]\Delta\mathbf{d} - \Delta\lambda\left\{\mathbf{f} - \mathbf{K}_G(\mathbf{q}_0)\mathbf{d}\right\} = \mathbf{0} \tag{7}$$

Please note that the incremental form of Eq. (6) is equal to Eq. (7) and that the tangent stiffness matrix of Eq. (7) is equal to Eq. (4).

After buckling in the first buckling mode obtained by the linear buckling analysis of Eq.(5), tension force would be generated in some compressed braces, and the stiffness of the braces is added to the stiffness of the grid shell. It is assumed that the displacement after the first buckling could be approximately expressed by the linear sum of $\mathbf{d}_0$ and $\boldsymbol{\phi}_1$ as

$$\mathbf{d} = \xi\mathbf{d}_0 + \eta\boldsymbol{\phi}_1 \tag{8}$$

where ξ and η are weighting coefficients of $\mathbf{d}_0$ and $\boldsymbol{\phi}_1$. The deformation changes from the distribution of the mode $\boldsymbol{\phi}_1$ on the fundamental path to the distribution of Eq. (8) on the bifurcation path. As the result, some braces change from compression to tension, and the stiffness of the grid shell is increased. This added stiffness is denoted by $\mathbf{K}_B$. Whether the braces are tensioned or compressed is determined by the balance of ξ and η, and the specific magnitudes of ξ and η are not necessary. Therefore, $\mathbf{K}_B$ could be expressed as a function of η/ξ, i.e. $\mathbf{K}_B = \mathbf{K}_B(\eta/\xi)$.

The equilibrium equation and the incremental equilibrium equation on the bifurcation path are approximated by equations (9) and (10).

$$\left[\mathbf{K}_L + \mathbf{K}_B(\eta/\xi) + \lambda \mathbf{K}_G(\mathbf{q}_0)\right]\mathbf{d} - \lambda\mathbf{f} = \mathbf{0} \tag{9}$$

$$\left[\mathbf{K}_L + \mathbf{K}_B(\eta/\xi) + \lambda \mathbf{K}_G(\mathbf{q}_0)\right]\Delta\mathbf{d} - \Delta\lambda\left\{\mathbf{f} - \mathbf{K}_G(\mathbf{q}_0)\mathbf{d}\right\} = \mathbf{0} \tag{10}$$

In the above equations, it is assumed that the influence of the large displacement stiffness and the geometric stiffness of the braces is small, and could be neglected. The buckling point appearing on the bifurcation path is obtained by solving the below eigenvalue problem, since the tangential stiffness matrix becomes singular.

$$\left[\mathbf{K}_L + \mathbf{K}_B(\eta/\xi) + \lambda_i^* \mathbf{K}_G(\mathbf{q}_0)\right]\boldsymbol{\phi}_i^* = \mathbf{0} \tag{11}$$

The superscript * of λ_i^* and $\boldsymbol{\phi}_i^*$ is attached to distinguish them from the linear buckling analysis of Eq. (5). Here, assuming that the buckling modes do not change even after the stiffness of the braces $\mathbf{K}_B$ is added, λ_i^* can be obtained as

$$\lambda_i^* = \lambda_i - \frac{\boldsymbol{\phi}_i^T \mathbf{K}_B(\eta/\xi)\boldsymbol{\phi}_i}{\boldsymbol{\phi}_i^T \mathbf{K}_G(\mathbf{q}_0)\boldsymbol{\phi}_i}, \quad (i = 1,...,N). \tag{12}$$

The minimum value $\lambda_{\min}^*$ in the above equation expresses the second buckling load factor appearing on the bifurcation path.

Eqs. (11) and (12) could not be evaluated unless $\mathbf{K}_B$, i.e. the value of η/ξ at the buckling point is known. This value could be obtained from Eq. (9). Eq. (8) is substituted into Eq. (9), and it would be organized by multiplying by $\boldsymbol{\phi}_1^T$ from the left. At that time, we assume that $\boldsymbol{\phi}_1$ is mode of bifurcation point type, not limit point type. In this case, there are the following relations.

$$\boldsymbol{\phi}_1^T \mathbf{K}_L \mathbf{d}_0 = 0, \quad \boldsymbol{\phi}_1^T \mathbf{K}_G \mathbf{d}_0 = 0, \quad \boldsymbol{\phi}_1^T \mathbf{f} = 0 \tag{13}$$

Therefore, we obtain

$$\boldsymbol{\phi}_1^T\left[\mathbf{K}_L + \mathbf{K}_B(\eta/\xi) + \lambda \mathbf{K}_G(\mathbf{q}_0)\right]\boldsymbol{\phi}_1\eta + \boldsymbol{\phi}_1^T \mathbf{K}_B(\eta/\xi)\mathbf{d}_0\xi = 0 \tag{14}$$

Furthermore, the above equation could be rearranged as follows.

$$\frac{\eta}{\xi}+\frac{\boldsymbol{\phi}_1^T\mathbf{K}_B(\eta/\xi)\mathbf{d}_0}{\boldsymbol{\phi}_1^T\left[\mathbf{K}_L+\mathbf{K}_B(\eta/\xi)+\lambda\mathbf{K}_G(\mathbf{q}_0)\right]\boldsymbol{\phi}_1}=0 \quad (15)$$

η/ξ and λ simultaneously satisfying Eqs. (12) and (15) are obtained as follows. In order to intuitively handle the magnitude of η/ξ, it is expressed by multiplying the norm ratio of $\mathbf{d}_0$ and $\boldsymbol{\phi}_1$ by a coefficient α.

$$\frac{\eta}{\xi}=\alpha\sqrt{\frac{\mathbf{d}_0^T\mathbf{d}_0}{\boldsymbol{\phi}_1^T\boldsymbol{\phi}_1}} \quad (16)$$

α is regarded as a new parameter instead of η/ξ.
Eqs. (12) and (15) could be transformed as

$$\lambda_{\min}^{*}=\min_{i=1,\ldots,N}\left(\lambda_i-\frac{\boldsymbol{\phi}_i^T\mathbf{K}_B(\alpha)\boldsymbol{\phi}_i}{\boldsymbol{\phi}_i^T\mathbf{K}_G(\mathbf{q}_0)\boldsymbol{\phi}_i}\right) \quad (17)$$

$$E(\alpha)=\left|\alpha\sqrt{\frac{\mathbf{d}_0^T\mathbf{d}_0}{\boldsymbol{\phi}_1^T\boldsymbol{\phi}_1}}+\frac{\boldsymbol{\phi}_1^T\mathbf{K}_B(\alpha)\mathbf{d}_0}{\boldsymbol{\phi}_1^T\left[\mathbf{K}_L+\mathbf{K}_B(a)+\lambda_{\min}^{*}\mathbf{K}_G(\mathbf{q}_0)\right]\boldsymbol{\phi}_1}\right|=0 \quad (18)$$

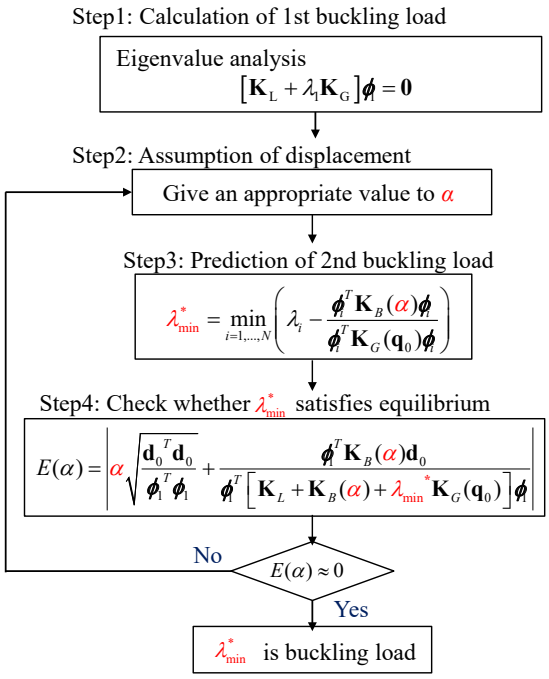


Figure 8: Computational flow

Now, we assign arbitrary α to Eq. (17) and obtain the minimum buckling load factor $\lambda_{\min}^{*}$. Further substituting $\lambda_{\min}^{*}$ and α into Eq. (18), if $E(\alpha)\approx 0$, $\lambda_{\min}^{*}$ would approximate the buckling load factor on the bifurcation path of the nonlinear buckling analysis.

The Computational flow of the proposed method is shown in Figure 8. In the calculations, eigenvalue analysis is performed only once, and the calculations are relatively easy. However, the value of α must be determined by trial and error. In this paper, we analyzed the range of α from 0 to 1 by 0.01 and regarded $\lambda_{\min}^{*}$ as the buckling load factor when $E(\alpha)$ is the closest to zero. It is assumed that $\boldsymbol{\phi}_1$ is a bifurcation point type buckling when deriving Eq. (18), so it should be noted that this method could not be applied to the first buckling of the limit point type.

4. Numerical analysis example

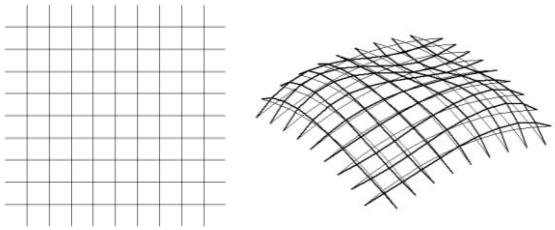
In order to investigate the validity of the above mentioned proposed method, the same model as shown in Section 2 is analyzed by the proposed method. As another example, a dome model is also analyzed.

4.1. Analysis of grid shell

The grid shell shown in Section 2 is analyzed by the proposed method. The result of the eigenvalue analysis of Eq. (5), which corresponds to the first buckling point on the fundamental path, is shown. The positions of the braces in tension and the buckling mode are shown in Figs. 9 (a) and 9 (b), respectively. As can be seen from Fig. 9 (a), there is no brace in tension. As shown in Fig. 9 (b), the buckling load factor is 0.67. Comparing Figs. 9 (a) and (b) with Figs. 6 (a) and (b), they are in good agreement.

Next, to calculate the buckling load corresponding to the buckling point on the bifurcation path, the calculations of Eqs. (17) and (18) are performed. The relationship between $E(\alpha)$ and α is shown in Fig. 10, and the relationship between $\lambda_{\min}^{*}$ and α is shown in Fig. 11. From Fig. 10, $E(\alpha)\approx 0$ when $\alpha=0.46$, and $\lambda_{\min}^{*}=1.45$ when $\alpha=0.46$ from Fig. 11. The positions of the braces in tension and the buckling mode when $\alpha=0.46$ are shown in Figs. 12 (a) and 11 (b). The braces in tension are indicated

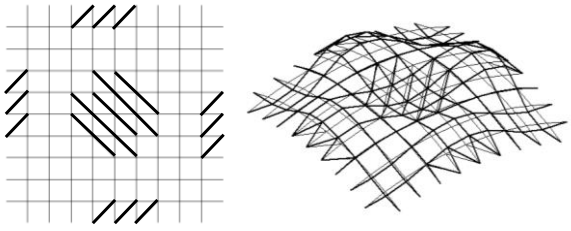
by bold lines in Fig. 12 (a). Comparing Figs. 12 (a) and (b) with Figs. 5 (a) and (b), they are in good agreement. In Fig. 13, the buckling load factor by the proposed method is added as a horizontal line on the equilibrium curve diagram by the nonlinear buckling analysis.



λ_1=0.67

(a) Positions of braces in tension (b) Buckling mode

Figure 9: Result of eigenvalue analysis of Eq. (5)



λ_{min}^*=1.45

(a) Positions of braces in tension (b) Buckling mode

Figure 12: Result of linear buckling analysis considering no-compression property

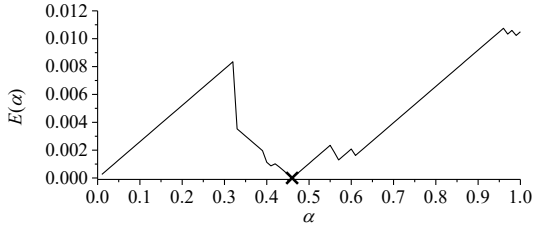


Figure 10: Relation between $E(\alpha)$ and α

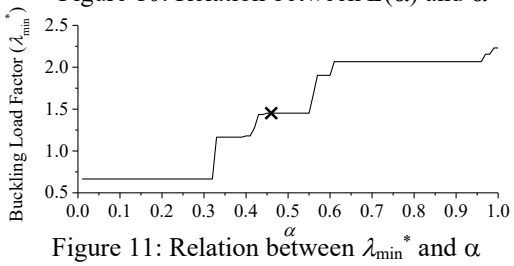


Figure 11: Relation between λ_{min}^* and α

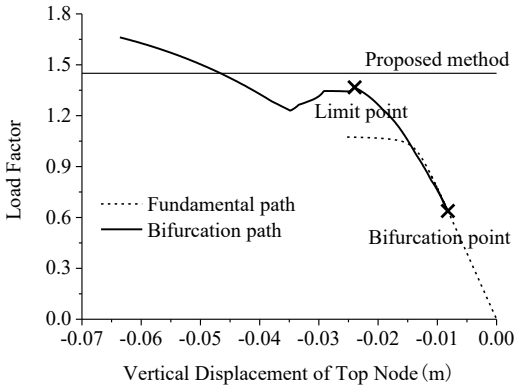
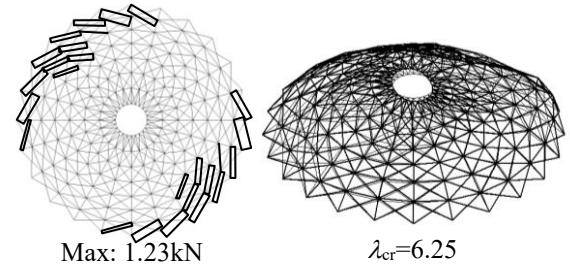


Figure 13: Relation between load and displacement

4.2. Analysis of ribbed dome

In addition to the above grid shell, we applied the proposed method to a ribbed dome stiffened with slender braces as another example. The dome shape is a sphere of 8 m in height and 40 m in span, and the members are the same as the above grid shells. The support condition is pinned support and the load is an equally distributed load of 1.0 kN/m^2. Although omitted the detailed analysis results owing to space limitations, the buckling load and mode of the second buckling point of the nonlinear buckling analysis and the proposed method agreed well (See Fig. 14).



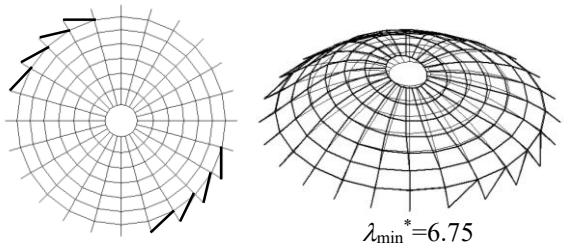
Max: 1.23kN

(a1)Axial force diagram of braces

λ_{cr}=6.25

(a2) Buckling mode

(a)Nonlinear bukling analysis



(b1) Positions of braces in tension

λ_{min}^*=6.75

(b2) Buckling mode

(b)Proposed method

Figure 14: Numerical analysis example of ribbed dome

5. Summury

There has been little discussion about buckling behavior of reticulated shells stiffened by slender braces without pre-tension. The reason would be that it is difficult to grasp the buckling behavior because the brace changes the rigidity according to deformation.

In this paper, the nonlinear buckling analysis of several grid shells stiffened by the braces without pre-tension was performed, and the part of the stiffening effect was shown. And to clarify the complex buckling behavior and to easily predict the buckling strength without using the nonlinear buckling analysis, we proposed a new method considering the no-compression property of the braces into the linear buckling analysis.

Two models, the EP grid shell and ribbed dome, were analyzed using the proposed method, and the results were compared with the results of the nonlinear buckling analysis. The results of both were in good correspondence, and the validity of the proposed method was confirmed. Since there are only a few analysis models in this paper, it is necessary to increase the numerical examples to further prove the validity of the proposed method.

Since grid shells like that shown in this paper are ordinary stiffened with the braces after construction of the grid members, the initial stress by its own weight is generated in the grid members, but not in the braces. This influence is not taken into consideration and it is a future task. In addition, the load in this paper is assumed to be only equally distributed loads, and the applicability of the proposed method to uneven loads also needs to be investigated.

The proposed method could be expected to be applied and developed for buckling analysis of various structures including members with different rigidity depending on the direction of deformation.

References

[1] J. Schlaich and H. Schober, “Glass-covered Lightweight Spatial Structures”, *Proceedings of IASS-ASCE International Symposium*, pp.1-27, 1994

[2] T. Kanayama and Y. Hangai, “Hybrid Single-layer Lattice Shell Using Supplementary Parts and a Design Method for Buckling Laod” , *J. Struct. Constr. Eng.*, AIJ, No. 522, pp.79-86, 1999 (in Japanese)

[3] S. Kushima, M. Fujimoto and K. Imai, "Numerical Results on Buckling Behaviors of Single Layer Two-way Grid Dome with Tension Members," *J. Struct. Constr. Eng*., AIJ, No.617, pp.121-128, 2007. (in Japanese)

[4] T. Yamashita and S. Kato, “Apprecation of Buckling Characteristics of Braced Single-layer Two-way Grid Shells Based on Continuum Analogy”, *Journal of Structural Engineering*, AIJ, Vol.54B, pp.331-336, 2008 (in Japanese)

[5] S. Kato, N. Yoshida and S. Nakazawa, “Buckling Strength of Two-way Single-layer Lattice Domes Stiffened by Diagonal Braces”, *J. Struct. Constr. Eng.*, AIJ, No. 676, pp.891-898, 2012 (in Japanese)

Proceedings of the IASS Annual Symposium 2019 – Structural Membranes 2019
Form and Force
7 – 10 October 2019, Barcelona, Spain
C. Lázaro, K.-U. Bletzinger, E. Oñate (eds.)

Structural aluminium nodes in free form reticulated structures - geometric variables and manufacturing constraints

Steinar H. DYVIK*, Bendik MANUM, Marcin LUCZKOWSKI [a]

* Norwegian University of Science and Technology (NTNU), Department of Architecture and Technology, Alfred Getz vei 3, 7491 Trondheim, Norway
steinar.dyvik@ntnu.no

[a] Norwegian University of Science and Technology (NTNU), Department of Structural Engineering, Trondheim, Norway

Abstract

This paper discusses and describes the geometry and manufacturing of nodes in free form reticulated shell structures. Reticulated shells are commonly produced with steel nodes, providing new design solutions aluminium has different manufacturing constraints. The paper presents manufacturing methods for mass customized aluminium nodes and discusses the future potential of aluminium as a structural material for free form shells and spatial structures. The node's relation to the global shape, the grid division and the design choices is presented. Based on this, the future potential of aluminium nodes in free form reticulated shells is discussed.

Keywords: Reticulated Shell, Grid Shell, Aluminium, Fabrication, Node, Free Form Structures

1. Introduction

The geometry of shell and spatial structural surfaces are typically described by analytical geometries or generated with form finding based on physical models or numerical methods. A more general description of such surfaces, that does not exclude form finding or shape optimization, are free form surfaces, that could be described as a NURBS-surface or as a mesh representation. A common way to define a geometrical model for a shell surface is to divide the surface into a network-topology, or gridshell, also known as a reticulated structure. The nodes of reticulated structures are structural elements that normally transfer beam forces, but also handle geometric complexity [1]. This paper part of a PhD project working with aluminium nodes for reticulated shells structures and this paper aims to describe relevant perspectives around the design of aluminium nodes. With digital design tools, complex geometrical shapes for nodes can quite easily be designed and evaluated. The node has however a large architectural and aesthetic potential beyond the practical design and this is discussed in Section 2.1.

With respect to the fabrication, the nodes are either repeated or customized. When repeated, the overall structure is made from one or few identical nodes that can be mass-produced. The nodes will then typically cater for a limited number of angles and rotations between bars, and the design options of the global shape is limited to structures like barrel-vaults and geodesic domes. On the contrary, a customized node should allow for every node to be different and enable free-form structures. Reticulated shells shapes and the conventional node types are further described in Section 2.2 to 2.4.

Compared to steel, aluminium has different manufacturing constraints and benefits. Aluminium is generally formable, malleable, softer to machine, extrudable and suitable for casting. These manufacturing features can provide new design options for corrosion resistant light weight structures. Section 3.1 and 3.2 includes characteristics of aluminium as a structural material and describes aluminium manufacturing methods.

Copyright © 2019 by Steinar Hillersøy Dyvik, Bendik Manum, Marcin Luczkowski
Published by the International Association for Shell and Spatial Structures (IASS) with permission.

2. Background

2.1 The potential of the node

With the help of a digital parametric model, complex node geometry can be designed, prepared for fabrication and evaluated for structural feasibility [2]. It is possible to establish an algorithm that generates all the nodes, or details, in a reticulated shell. Parametric, or object-oriented detailing defines variables and constraints to define the geometry of the detail [3]. This method collects many similar nodes in one detail type and lets variables control the final geometry. In a reticulated shell, these are typically the valence (the number of connecting members), node angles, the function, like a support, and possibly the forces in the node. For the final appearance of such a detail it could be hard to imagine the exact outcome. It could therefore be hard for the designer to ensure that the result is not only functional but also aesthetically pleasing. A good parametric detail should be good-looking in all variations.

When detailing elements in any structure, one can talk about two approaches, namely abstract and articulated detailing[4]. An abstract detail does not consist of a visible object, but rather diminishes the transition. An articulated detail creates an architectural element in the junction instead. Either way, the detail would solve its practical or aesthetical concerns, however it could be argued that the potential to create a narrative with the detail are larger when the detail is articulated. Reticulated shell structures are also designed with either an abstract or articulated approach. The detail is in some cases completely covered by plates, and in other cases it clearly shows the transition between the elements.

Ford[4] argues that parametric modelling enables and encourages seamless abstract detailing. This might be true, but it is not the only truth. Another interesting and appealing potential lays in the articulation of details, which parametric modelling also enables. When designing seamless envelopes or assemblies, the parametric model might need to involve sub-components with internal and external data references that could be rather complex. In the capital C project in Amsterdam, the engineers Octatube emphasises that they succeeded to hide the nodes and make a *node-free* connection that look more elegant with parametric design tools [5]. In the case of reticulated shells articulating the detail could be simpler than not to. From the architectural point of view, node designs that transition between two elements in a smooth and precise manner are preferred. Other visual design goals are listed in table 1.

Table 1.Aesthetic design goals for nodes in reticulated shells

Node-free connection design (Abstract detail)	Junction between node and member (Articulated detail)	Smooth node surface without visible bolts or rivets	Same dimensions where node and member meet	Light / heavy appearance

2.2 Global shapes for reticulated shells

Most reticulated shells have a global shape derived from the geodesic dome, spherical cap or barrel vault. This is to enable mass production of one or more elements. These “simpler” shapes can be beautiful architectural pieces, as opposed to more industrial applications they usually accommodate however, for architects and designers to be able to solve more complex situations allowing for free form can be crucial. Enabling free form for shell structures are important to gain more options regarding site specific design, whether it is to form a roof over an existing street or related to existing structures, to blend into a landscape, to adjust the shape towards a view or other qualities, or to make just the right sculptural shape. In addition to the architectural arguments, a shell structure is dependent on a structural shape defined by some kind of form finding or structural optimization to be functional. A desired shape for reticulated shells could therefore be defined as a *free form site specific structurally optimized shape*.

2.3 Grid division

In addition to the global shape, the grid division plays a large role in both how the structure works, how it appears visually and how the node geometry turns out. Figure 1 shows a simple node and its element angles in relation to some global shapes with different grid divisions. The most common are variations

of quadrangular or triangular grids, but any grid topology is in theory possible. While triangular networks are geometrically stiffer and by default offers planar surfaces for cladding, quad networks offer fewer members connecting in each node and less material use. Much research is put into the rationalization of free form surfaces and the discretization of reticulated shells. Methods for fabrication aware discretisation include planar quad meshes and conical meshes, ensuring that nodes are torsion free and that the faces for the panels are planar [6]. By constructing the grid following the asymptotic curves on a surface, one can make developable members. The asymptotic curves on a minimal surface can also provide members in the principal direction that intersect each other orthogonally [7].

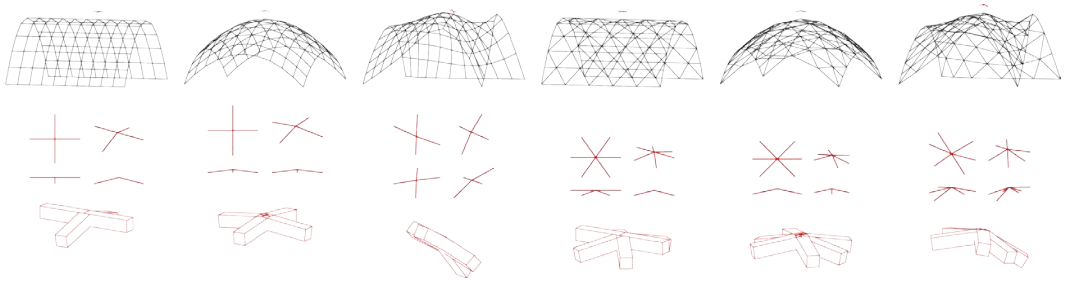


Figure 1. Some global shapes for reticulated shells with a characteristic node for quadrangular and triangular grid division. Top: Barrel Vault (x^2+y), Mathematical Shell (x^2+y^2) and "Free form shell". Mid: Node-member centrelines. Bottom: Node-members illustrated with rectangular cross sections

2.4 Types of nodes and influences on its geometry

Nodes in reticulated shells are usually manufactured with high precision steel manufacturing and lower tolerances than on typical steel projects. The function of the node is not only load transfer, but also to handle geometric complexity. The dimension of the node can span from small space frame connections of 40mm in diameter to large castings of 1000mm in diameter, however the typical reticulated shell node connects to a member between 100 and 500mm in height, and the dimensions are thereafter.

The nodes of reticulated shells and space frames typically constitute from 20-30% and up to 50% of the total weight of a steel structure. Because of the precise manufacturing and the large weight contribution, nodes are one of the most important factors affecting the final economy of a reticulated shell. A typical node in a steel gridshell carries about 2-3m^2 of the roof [8]. The member lengths in a reticulated timber shell is often longer and taller than in steel, causing larger roof areas per node.

Table 2. Taxonomy of node systems for single layer reticulated shells

Customization		**Fabrication**		**Connection type**		**Connection method**		**Connection direction**		**Node parts**	
Repeated	Customized	Proprietary	Purpose made	End-Face	Splice	Bolted	Welded	Vertical	Horizontal	One part	Multiple parts

Design of the node in a reticulated shell is influenced by many factors. Complex nodes would have larger deviation in horizontal angles (U), vertical angles (V) and twist angles (W), which is a direct result of the surface curvature (κ) and the grid configuration. The horizontal angle is mainly influenced by the grid configuration and the vertical angle mainly by the curvature. The twist angle is dependent on both [1].

There are two categories for nodes in reticulated shells: the purpose-made joint and the proprietary joint. Based on the connection method, Stephan et al describes several types of proprietary splice and end-face joints for single layer reticulated shells [1]. A further collection of nodes and types are described by Lan [8]. Including the node types for types of reticulated shells with multiple layers, such as space frames, Lan reports that over 250 different node types are suggested or used worldwide. Some examples of purpose made joints are described in [2], [9] and [10].

The node type and how it is manufactured plays an important role in which angles, shapes and forces that can be accommodated for. Typical types of nodes for single layer reticulated shells are described in Table 2 and Figure 2. The node geometry often originates from a general shape like a sphere, cylinder, disk, prism or plate. It can also be cast or forged in a specific shape, cut from thick plate or the connection could be "nodeless". Metal to metal connectors can be both end-face connected, and splice connected with both horizontal and vertical splices. Designs where the nodes are wrapped by a hollow section or the members are connected with in a gusset plate is also found. Metal to timber connectors are usually end-face connected with threaded rods, however, splice connection with vertical splices connected with bolts or glue are also common. Some examples where the nodes encloses the member also exist.

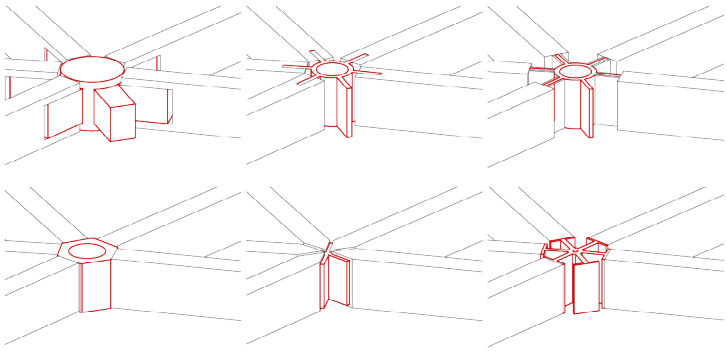


Figure 2. Variations of splice connected nodes (top) and end face connected nodes (bottom)

2.5 Other shells and nodes

The definition of a reticulated shell can be expanded to also include any kind of shell or shell-like structure discretized into members to form a grid. Kinematic or post formed gridshells are constructed from flat members and shaped into place [11]. The connection between the elements are usually done seamlessly with a finger or lap joint, and they overlap at the node. Nodes are usually identical and either a plate with four surrounding bolts or simply a central bolt. Bending and torsion of the members both enables and limits the shape. A special case of reticulated structures called nexorades, or reciprocal structures, is characterized by a non-hierarchical structural system where the member ends connects along the edge of another member rather than at a high-valence node [12]. In the case of nexorades, the connection detail is often abstract with timber members joined with a barely visible lap or tenon/mortise connection, or with a rotation free "scaffolding" connection. Shells constructed from plate elements have recently become more popular in the form of timber or CLT [13,14] and glass [15], and would also need special care to the connection detail. Manufacturing the connections of the structures mentioned in this paragraph are much related to the work but not in the scope of this paper.

2.6 Novel and bespoke node designs

New computational design methods has provided new design solutions in addition to the known node designs. Topology optimization is a design and optimization method that enables the designer to predefine loads, supports and a design space. By dividing the design space into voxels, three-dimensional pixels, the optimization removes material that does not contribute to load transfer in the given load case. The main challenge is however often how to manufacture the result, which usually is done with additive manufacturing. The topology-optimized solution must also be redrawn or refined both to make it more manufacturable and to handle different load cases. Topology optimization can also be used to optimize the layout for the global shape for better load distribution [16,17] which in turn could be interpreted as the network topology for a reticulated shell. With additive manufacturing, topology optimized nodes have been made in steel for several cases [18–20]. Additive manufacturing has also recently used for various custom-made splice connection for timber [21] and aluminium [18] members. Another project shows a free form façade node in aluminium [22] adapted to window profiles.

Another novel approach for bespoke node designs was done with 3D printed sand moulds for metal casting. A design studio at ETH Zurich used cast aluminium nodes in a free form grid topology to connect hollow aluminium tubes [16]. The translation from 3D-model via sand printing to casting were investigated, and several node designs were proposed. The study concludes that 3D printing sand moulds for casting provides design freedom for space frames in a much cheaper way than direct metal printing.

3. Reticulated shells with aluminium nodes

Reticulated structures are most commonly produced with steel nodes and connecting steel members, both for in the case of repeated or customized nodes. Aluminium systems often consist of several sub-assemblies rather than one or few complex objects solving the whole. Aluminium shells are durable and suitable for corrosive environments, the low-self weight favours transportation and cast, extruded and formed elements favours mass production. Kaiser aluminium domes started production and erection of aluminium domes in the 1950s [24]. The system was based on a geodesic dome geometry, ensuring repetition of elements. Brake formed diamond panels of 10 different types function as structure and cladding. They connected at a cast hub and were braced with struts crossing the short side. Several other aluminium systems exists for simpler global shapes like barrel vaults and various geodesic domes, including Temcor Rollwell, BACO Triodetic, Tuball Octatruss and Alutruss. The systems are most common in industrial cases in corrosive environments, but such roofs are used for many other purposes.

Table 3. Characteristics of aluminium relevant to structural use of aluminium. Data from [25,26]

Characteristic	**Comment**
High strength to weight ratio (depends on alloy).	Gives weight reduction that can compensate for high costs. Can provide savings in erection and construction. Lower self-weight on the structure.
Many fabrication methods	Formable, machinable, extrudable, castable and malleable, and most processes are easier than with steel.
Recyclable	High residual value and low energy needed for recycling compared to raw production
Corrosion resistant	Lowers maintenance costs.
Many surface finishes	Can be rough or polished finished, painted and anodized, and take ornamental patterns.
High thermal conductivity	Similar issues as steel. Can cause thermal bridges in building construction.
Yield strength close to ultimate tensile strength combined with lower plastic deformation	Can cause lower safety margins for construction compared to steel.
High thermal expansion	Dimension changes with temperature change must be handled in design
High carbon footprint	High power usage in raw production gives aluminium a high global warming potential
About 1/3rd of the E-module compared to steel	Demands larger construction height and more material for an equivalent aluminium solution
Sensitive to high temperatures (200-400 degrees)	Structural applications demands fire protection through passive or active systems.
High material cost compared to steel	Aluminium is normally more costly, however partly compensated with weight savings, but should benefit from other characteristics too.

Aluminium nodes usually connect to aluminium members but could in theory connect to other materials such as timber or composites A purpose-made cast joint for the IBM Travelling pavilion in 1970 connects to timber members through glued finger joints. Timber member are interesting for several reasons; it has a large potential in articulation of the detail, it combines two light-weight materials and

precise timber is either way produced through a subtractive fabrication process. Then it is almost indifferent whether elements are customized or equal, and putting parts of the complexity in the timber can therefore be rational [27]. In the Norwegian context, it also provides strong roots to local industry.

3.1 Aluminium characteristics

Table 3 shows the characteristics of aluminium relevant to structural design. The most interesting characteristics are those who are unique to aluminium compared to other materials. Low self-weight of the structure is most relevant when this is a dominant load, which is not the case for large external load such as snow and wind. However, using less material in a structure is by definition an environmentally friendly solution that can reduce the need of foundations and the transportation and erection costs. Aluminium shells has reported structural weights down to around 20kg/m^2 [25], which is lower than recently developed light weight timber plate shells scoring between 35 and 60kg/m^2 [13]. Complex building shapes can be hard to maintain and could benefit from an aluminium construction which is generally corrosion resistant. With proper design for disassembly, the aluminium used in construction can easily be reused and re-melted for another purpose. The many fabrication methods are favourable to steel since aluminium is softer and has a lower melting point. Fabrication methods are further described in the next section.

Table 4. Summary of fabrication methods for aluminium

Pre-fabrication:				
Ingot casting, Sheet rolling, Plate rolling				
Casting	**Printing**	**Joining**	**Forming**	**Subtractive**
Investment Cast	Direct Metal Laser Sintering	Welding	Bending	CNC Cutting
Injection Moulding	Selective Laser Melting	Adhesive bonding	Rolling	Saw Cutting
Die Cast	Ultrasonic Additive Manufacturing	Bolting	Spinning	Drilling (Hole Making)
Permanent Mould Cast	Electron-beam Additive manufacturing	Riveting	Stamping	Turning
Continuous Casting	Binder Jetting		Forging	Machining (Milling)
Sand casting	Hybrid metal extrusion & bonding		Extrusion	Wire EDM Cutting
Patternless cast			Drawing	
3D-printed sand cast			Sheet forming	
Post-Fabrication:				
Heat Treatment, Anodizing, Painting, Powder Coating, Sand Blasting, Bead Blasting, Polishing				

3.2 Aluminium fabrication methods

Aluminium is castable, printable, formable, malleable and machinable. The formability and the suitable fabrication, as well as the structural capacity and other characteristics are directly related to the aluminium alloys, although, this paper discusses fabrication of aluminium without specific focus on the alloys. For machined or mass-produced cast products in aluminium, the precision could be very high, while for some procedures, like sand casting, the precision is generally lower and must be compensated for in the design. Table 4 shows an overview of fabrication methods available for aluminium. As this paper focuses on free form global shapes for reticulated shells, the most relevant procedures, or combinations of procedures are those suitable for customization and individualization of the nodes.

3D printing is especially relevant for manufacturing customized and complex node designs however, state of the art metal printing are too slow and expensive to compete with other techniques. A conventional way to produce aluminium nodes would be to cut the outline of the node from a thick plate

using wire EDM, and machine the final precision with a multi-axis CNC mill. Other conventional procedures would start with an extruded section that is cut into shape, or a cast pieces that are machined to precision. Customized cast nodes can also be produced through sand casting or investment casting. Recent development in 3D printing has also provided new procedures for casting, also called Rapid Casting [28]. Both investment casting and sand casting are possible with the help of 3D printing, but at various dimensions and precision. A successful procedure of patternless casting for custom nodes was described in Section 2.6, that includes direct 3D printing of moulds with sand binder jetting. Another interesting and little explored procedure in this context, that could produce fast and precise results, but with some more geometrical limitations, is patternless casting with CNC milling of the form [29].

4. Conclusion

With new digital design and manufacturing tools, it is now possible to design and manufacture complex geometries for nodes in reticulated shells. More development is currently needed for 3D printing to be competitive, but patternless casting through 3D printing or CNC milling seems like advantageous procedures for the future of customized node designs in aluminium. Another approach could be to use digital tools to cluster similar nodes and mass produce rough shapes through forging or casting, and then, with a minimized material waste, mill the final precision. Aluminium as a formable, recyclable, lightweight and corrosion resistance material has many characteristics relevant to design of nodes in reticulated shells.

The main contribution of the paper is the mapping of geometric variables and constraints related to any node design and how the characteristics of aluminium and aluminium manufacturing relate to the design of nodes. Based on this paper, work will be followed up in the PhD project "Design of free form reticulated shell structures with aluminium nodes". The authors have particular interest in developing aluminium nodes connecting to timber members, and the project will study the following: How can manufacturing constraints for different processes inform the design of aluminium nodes? How can a customized reticulated shell node in aluminium be manufactured? How can aluminium nodes connect to timber members?

References

[1] Stephan S, Sánchez-Alvarez J, Knebel K. RETICULATED STRUCTURES ON FREE-FORM SURFACES 2004:15.
[2] Knippers J, Helbig T. Recent Developments in the Design of Glazed Grid Shells. International Journal of Space Structures 2009;24:111–26. doi:10.1260/026635109789043205.
[3] Shelden DR. Information, Complexity and the Detail. Architectural Design 2014;84:92–7. doi:10.1002/ad.1786.
[4] Ford E. The Grand Work of Fiction: The Detail as Narrative. Architectural Design 2014;84:26–35. doi:10.1002/ad.1778.
[5] Octatube. Parametric design 2019. /en_GB/system-item/systemitem/23-parametric-design.html (accessed May 29, 2019).
[6] Pottmann H, Wallner J. The focal geometry of circular and conical meshes. Advances in Computational Mathematics 2008;29:249–68. doi:10.1007/s10444-007-9045-4.
[7] Schling E. Repetitive Structures. Technical University of Munich, 2018. doi:10.14459/2018md1449869.
[8] Lan TT. Space frame structures. In: Wai-Fab C, editor. Structural engineering handbook, CRC Press LLC; 1999.
[9] RABAGLIATI, J, HUBER C, LINKE D. BALANCING COMPLEXITY AND SIMPLICITY. Fabricate 2014 - Negotiating Design & Making, 2017.
[10] Harris R, Gusinde B, Roynon J. DESIGN AND CONSTRUCTION OF THE PODS SPORTS ACADEMY, SCUNTHORPE, ENGLAND n.d.:9.

[11] Mork JH, Dyvik SH, Manum B. INTRODUCING THE SEGMENT LATH - A SIMPLIFIED MODULAR TIMBER GRIDSHELL BUILT IN TRONDHEIM NORWAY n.d.:8.
[12] Baverel O, Larsen OP. A Review of Woven Structures with Focus on Reciprocal Systems - Nexorades. International Journal of Space Structures 2011;26:281–8. doi:10.1260/0266-3511.26.4.281.
[13] Bechert S, Groenewolt A, Krieg OD, Menges A. Structural Performance of Construction Systems for Segmented Timber Shell Structures 2018:10.
[14] Robeller C, Konakovic M, Dedijer M, Pauly M, Weinand Y. A Double-Layered Timber Plate Shell Computational Methods for Assembly, Prefabrication, and Structural Design. Zurich: Vdf Hochschulverlag Ag an Der Eth Zurich; 2016.
[15] Bagger A, Danmarks Tekniske Universitet, DTU Byg. Plate shell structures of glass: studies leading to guidelines for structural design : Ph. D. Thesis. Lyngby: DTU Civil Engineering, Technical University of Denmark; 2010.
[16] Bhooshan S. Parametric design thinking: A case-study of practice-embedded architectural research. Design Studies 2017;52:115–43. doi:10.1016/j.destud.2017.05.003.
[17] Adriaenssens S, Block P, Veenendaal D, Williams C. Shell structures for architecture: form finding and optimization. Routledge; 2014.
[18] Crolla K, Williams N, Muehlbauer M, Burry J. SMARTNODES PAVILION Towards Custom-optimized Nodes Applications in Construction, The Association for Computer-Aided Architectural Design Research in Asia (CAADRIA),; 2017, p. 467–77.
[19] Galjaard S, Hofman S, Perry N, Ren S. Optimizing Structural Building Elements in Metal by using Additive Manufacturing 2015:13.
[20] Seifi H, Rezaee Javan A, Xu S, Zhao Y, Xie YM. Design optimization and additive manufacturing of nodes in gridshell structures. Engineering Structures 2018;160:161–70. doi:10.1016/j.engstruct.2018.01.036.
[21] Dyvik SH, Luczkowski M, Mork JH, Rønnquist A, Manum B. Design of freeform gridshell structures – Simplifying the parametric workflow, 2019, p. 8.
[22] Strauß H. AM Envelope / The potential of Additive Manufacturing for façade construction. Delft University of Technology, Faculty of Architecture, Architectural Engineering + Technology department; 2013.
[23] Meibodi MA, Giesecke R, Dillenburger B. 3D printing sand molds for casting bespoke metal connections. Digital metal: Additive manufacturing for cast metal joints in architecture. In: Haeusler MH, Schnabel MA, Fukuda T, editors. Intelligent & Informed: Proceedings of the 24th International Conference of the Association for Computer-Aided Architectural Design Research in Asia (CAADRIA 2019), vol. 1, 2019, p. 133–42.
[24] Kaiser. The Kaiser aluminum dome : general information. 1957.
[25] Mazzolani FM. Competing issues for aluminium alloys in structural engineering. Progress in Structural Engineering and Materials 2004;6:185–96. doi:10.1002/pse.178.
[26] Thaulow C, Valberg H. Produktutvikling med Aluminium. TMM4140 Plastisk deformasjon og brudd, Trondheim: NTNU; 2014, p. 46.
[27] Schwinn T. Manufacturing Perspectives: Tobias Schwinn in Conversation with Holzbau Amann and Müllerblaustein. Advancing Wood Architecture – A Computational Approach, Oxford: Routledge; 2016, p. 185–98.
[28] Chhabra M, Singh R. Rapid casting solutions: a review. Rapid Prototyping Journal 2011;17:328–50. doi:10.1108/13552541111156469.
[29] Rodríguez A, Lacalle LNL de, Calleja A, Fernández A, Lamikiz A. Maximal reduction of steps for iron casting one-of-a-kind parts. Journal of Cleaner Production 2012;24:48–55. doi:https://doi.org/10.1016/j.jclepro.2011.11.054.

Proceedings of the IASS Annual Symposium 2019 – Structural Membranes 2019
Form and Force
7 – 10 October 2019, Barcelona, Spain
C. Lázaro, K.-U. Bletzinger, E. Oñate (eds.)

Shaking table test on the failure of OLF1000 by considering the dynamic coupling effect of transmission lines

Jun GONG*, Xundong ZHI[a], Feng FAN[b]

*1. Key Lab of Structure Dynamic Behavior and Control of the Ministry of Education, Harbin Institute of Technology, Harbin, 150090, China
2. Key Lab of Smart Prevention and Mitigation of Civil Engineering Disasters of Ministry of Industry and Information Technology, Harbin Institute of Technology, Harbin, 150090, China
202 Haihe Rd., Nangang District, Harbin 150090, China
Email: gongjun_hit@163.com

[a] zhixudong@hit.edu.cn
[b] fanf@hit.edu.cn

Abstract

To investigate the influence of the dynamic coupling effect (DCE) on the failure of 1000-kV outgoing line frame (OLF1000) subjected to real strong earthquakes, a reduced-scale experiment was performed on a shaking table. The transmission lines were simulated by the massless springs with dynamic stiffnesses. The numerical recurrence of the experiment was carried out in the finite element software and the results obtained by the experimental and numerical recurrence matched very well. The collapse analysis of OLF1000 was conducted by FEM. The research results significantly indicate that the DCE between the transmission lines and OLF1000 is very strong. It obviously reduces the seismic responses of OLF1000 under small earthquakes, accelerates the development of the existed damage of OLF1000 under strong earthquakes and apparently reduces the ultimate bearing capacity of OLF1000.

Keywords: Dynamic coupling effect, 1000-kV outgoing frame, shaking table test, collapse analysis, failure mechanism

1. Introduction

Long-span frames (LSFs) play a significant role in supporting electrical equipment, transmission lines and insulation terminals in substations and exhibit complicated seismic responses under earthquakes based on earthquake damage data[1, 2]. These could be due to the influence of the dynamic coupling effect (DCE) of transmission lines on the collapse of LSFs under earthquakes, which is a critical matter of concern.

Over past years, many scholars have studied the DCE between the transmission lines and structures[3]. Irvine proposed a method for static and dynamic analysis of cable vibration. Where the dynamic characteristics of cables with fixed ends were deduced under the conditions of considering the cable stiffness[4]. Ozono and Maeda investigated the in-plane dynamic interaction between a tower and conductors with varying support stiffness and proposed a representation of the mechanism of the in-plane free vibration of transmission line systems[5]. Ghobarah, et al. analyzed the effect of multiple support excitations on the response of overhead power transmission lines. It was found that the wave propagation velocity has a substantial effect on the system response[6]. Filiatrant and Stearns investigated experimentally the dynamic interaction between components of electrical substation equipment interconnected by flexible conductors. It was concluded that low interaction between the interconnected equipment due to a large slack and/or low intensity ground motion whereas high

Copyright © 2019 by Jun GONG, Xundong ZHI, Feng FAN
Published by the International Association for Shell and Spatial Structures (IASS) with permission.

interaction between interconnected equipment due to a small slack and/or high intensity ground motion[7].

Efforts have been made to study the collapse of space truss structures under strong earthquakes. Wang, et al. proposed a progressive collapse analytical procedure for the transmission tower-line system based on the finite element method. The collapse analysis could provide collapse mode and vulnerable points for use in seismic performance and retrofit evaluation of structure[8]. Tian, et al. studied the simulation of progressive collapse of a power transmission tower-line system subjected to extremely strong earthquakes. The results showed that the effect of multi-component seismic excitations should be taken into account in simulation of progressive collapse of the transmission tower[9]. Zheng and Fan investigated the progressive collapse of space truss structures during earthquakes based on a physical theory hysteretic model. The analytical results demonstrated that the selection of the fracture criterion for the bar members significantly affects the calculation of the collapse of the space truss structure under seismic loading[10].

The abovementioned researches focused on seismic analysis of transmission towers. Compared with transmission towers, LSFs deserved more attention from the perspective of seismic collapse analysis due to very limited research, particularly collapse test, has been completed for LSFs. This paper performs a shaking table test on the progressive collapse of a 1000-kV outgoing line frame (OLF1000, a type of LSF) by considering the DCE of transmission lines. Transmission lines are simulated by massless springs based on the dynamic stiffness. The damage mechanism is conducted to obtain the frangible position of an OLF1000, and the collapse analysis is carried out to investigate the influence of the DCE on the OLF1000 under strong earthquakes. This research, especially experimental research, helps engineers to understand the genuine behavior of the OLF1000 subjected to strong earthquakes.

2. Experimental and finite element model (FE model)

2.1. Prototype

A typical OLF1000 in an Ultra High Voltage (UHV) substation in Shandong Province, China, was selected. This engineering was designed for the seismic hazard having a probability of exceedance of 10% in 50 years. The OLF1000 has the configuration with a height of 57 m, a span of 153 m, three equal section beams at the elevation of 41 m and four variable cross-section columns, as shown in Figure 1. The members are made of Q345B steel tubes and connected by bolted connections. Six transmission lines are supported by the OLF1000 and terminal tower. The transmission lines having a sag-span ratio of 1/12 are LGJ-500/35 with the properties listed in Table 1. The insulation terminals have a length of 9.44 m and a linear density of 91.9 kg/m and the hardware has a weight of 650kg.

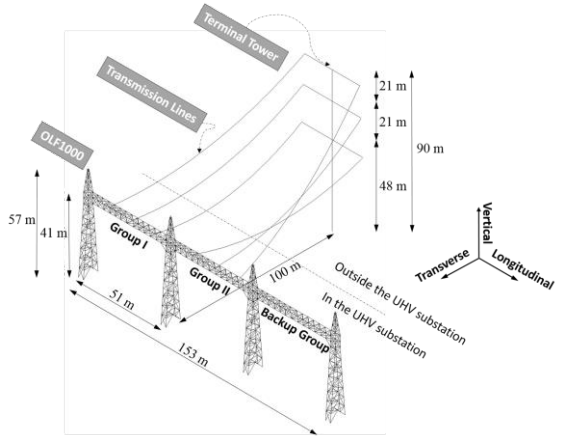


Figure 1: Prototype of OLF1000

Table 1 Properties of transmission lines

Designation	LGJ-500/35
Outside diameter (mm)	30
Modulus of elasticity (GPa)	63
Cross-section area (mm^2)	531
Mass per unit length (kg/km)	1642
Rated tensile strength (kN)	119.5

2.2. Experimental model

The experimental model was tested at the laboratory of Harbin Institute of Technology. A one-span reduced-scale model with a scale factor of 1/15 was adopted to develop this experiment due to the 1-DOF (horizontal direction) shaking table having a size of 4 m ×3 m.

The OLF1000 model was designed with scale factors determined based on the artificial mass law[11].The extra artificial mass, determined by equation (1), was distributed on 160 joints. Each steel welded ball having a mass of 2.4 kg and diameter of 83 mm was used to connect steel tube members by welded connections. Five kinds of section size (i.e., Φ10×2 mm, Φ10×1 mm, Φ8×2 mm, Φ6×2 mm and Φ6×1 mm) were selected in this experiment.

$$m_a = m_p S_L^2 - m_m \tag{1}$$

where m_p and m_m are the total masses of the one-span prototype and model, respectively; S_L is the scale factor of length.

The transmission lines are simulated by the massless springs based on the equivalent dynamic stiffness, determined by equation (2). The scale factors of the stiffness S_K and horizontal tension S_H are expressed by equations (3) and (4), where S_E is the scale factor of E. The insulation terminals and hardware are modeled as steel rods with a diameter of 10 mm and a lumped mass of 2.9 kg, respectively, owing to the mass of nonstructural elements defined in the general similitude law[11].

$$K = \frac{1}{1 + \frac{1}{12}\lambda^2} \frac{EA}{L_e} (1 + \eta) \tag{2}$$

where λ^2 *i*s the cable structure parameter, L_e is the equivalent span, η is the cable dynamic efficiency, E and A are the modulus of elasticity and the area of the section, respectively.

$$S_K = S_E S_L \tag{3}$$

$$S_H = S_E S_L^2 \tag{4}$$

The theodolite, laser level and total station were used in the construction and installation of the OLF1000 model whereas an electronic dynamometer and Vernier caliper were used to make spring models. The experimental model was completely constructed, as shown in Figure 2.

2.3. FE model

To accurately reconstruct the experimental model in the ABAQUS software, four significant factors were considered in the modeling, which include that (i) the basic characteristic tests were conducted to determine the properties of steel tubes (i.e., the modulus of elasticity of 206.5 GPa, the yield strength of 303.2 MPa, the ultimate strength of 429 MPa and the yield strain of 0.001 467); (ii) the damage accumulation subroutine of the steel tube was compiled based on the secondary development of ABAQUS; (iii) the measured coordinates of the welded ball by the total station were applied and (iv) variables including the diameter and thickness of the steel tube and the diameter of the welded ball were taken into account as random factors. The FE model was established as shown in Figure 3. Note that the measured shaking table displacement-time history data were used as the input load in the numerical simulation.

3. Test plan

To investigate the damage mechanism of the OLF1000 by considering the DCE under a real strong earthquake, the TAFT seismic record was selected as the input excitation. Moreover, the white noise with an amplitude of 0.04 g was used to detect the completeness of the experimental model after each excitation by sweeping the frequency.

The IMC data acquisition instrument was used to collect structural responses including acceleration, displacement and strain. The instrumentations were arranged as shown in Figure 4. All the accelerometers and displacement sensors were installed along the transverse direction, and strain gauges with large strain responses are marked in Figure 4.

4. Analysis of experimental and numerical results

4.1. DCE of transmission lines

Figure 5 illustrates the seismic responses of experimental models without and with the DCE under the excitation of TAFT when PGA = 0.172 g. As shown, the DCE significantly reduced the seismic responses of the OLF1000 with the maximum reduction of 21.2% and the average reduction of 10.7%, listed in Table 2. This indicates that the DCE of transmission lines are beneficial to the OLF1000 under small earthquakes.

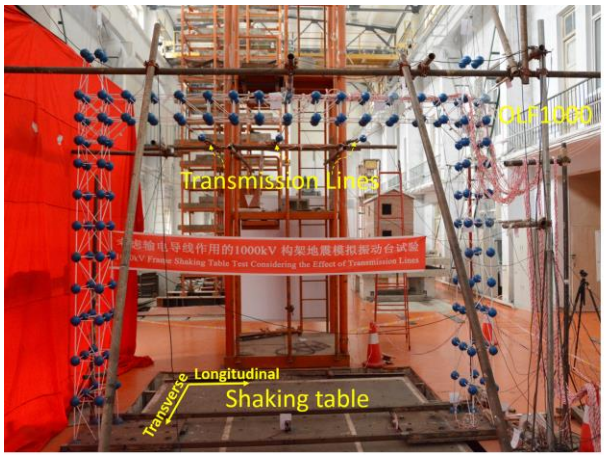


Figure 2: Experimental model

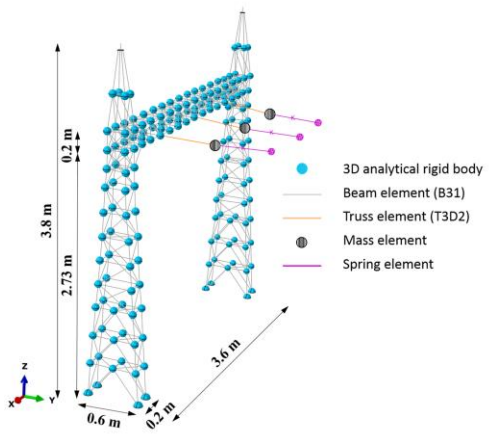


Figure 3: FE model

Table 2: Reduction of seismic responses (%)

D2	D3	D4	D5	D6	S1
12.7	9.0	10.7	12.0	10.8	6.5
A2	A3	A4	A5	A6	S4
3.6	12.9	20.3	11.8	18.2	21.2

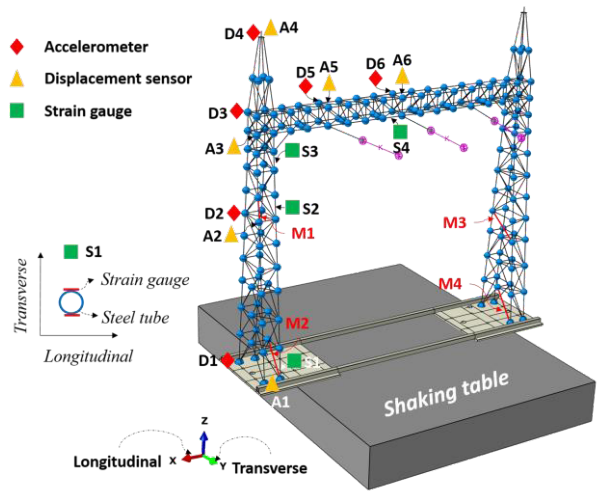


Figure 4: Instrumentations of the experimental model

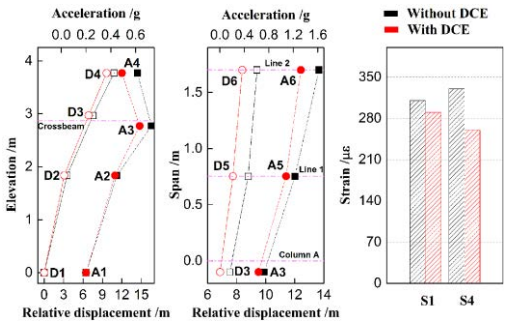
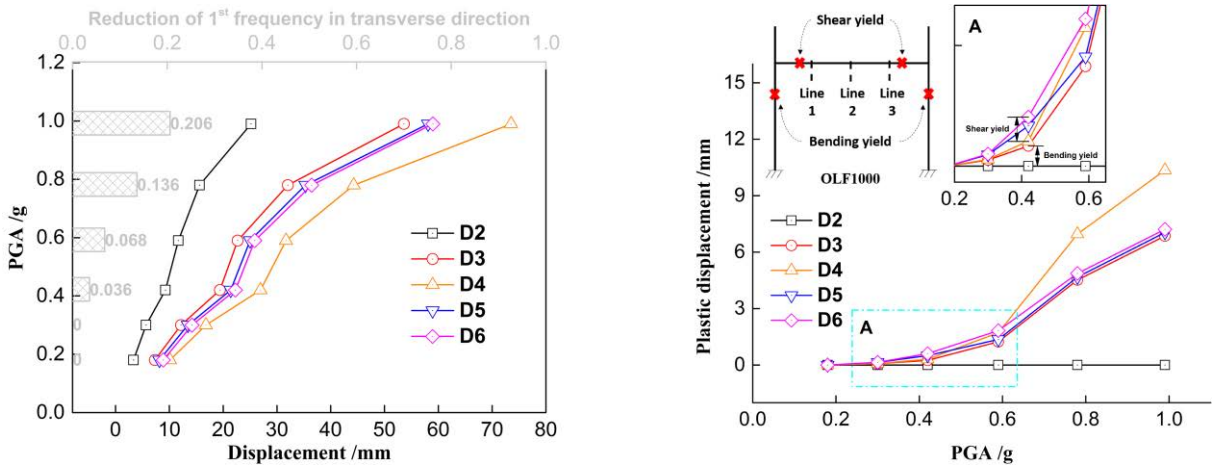


Figure 5: Seismic responses of experimental models without and with the DCE

4.2. Damage mechanism of OLF1000 by considering DCE

Based on the experimental phenomena, the suspended system including transmission lines, hardware and insulation terminals vibrated strongly by a wide margin under strong earthquakes. It significantly indicates that the DCE between the transmission lines and OLF1000 is very strong.

Figure 6 illustrates the change of structural displacements with the increase in intensities of seismic excitations. As shown in Figure 6(a), the displacements increase nonlinearly, the integral stiffness of OLF1000 reduces and fundamental frequency decreases with the increase in intensities. Specially, when PGA = 0.99 g, the maximum displacement of the top of Column A (D4) reaches 70.2 mm (1/54 H, H is the height of Column A), the 1st frequency in transverse direction reduces 20.6%, and the OLF1000 damaged seriously. Thereafter, the acquisition instrument is dismantled. Figure 6(b) shows that plastic displacements of D3–D6 significantly increase when PGA > 0.3 g whereas D2 has none plastic displacement for all tested PGAs. It greatly indicates that members with severe yield deformation are above the height where D2 displacement sensor locates. Besides, members at the middle of columns exhibit bending yield deformation whereas members at both sides of the crossbeam deform due to shear yield. Moreover, the bending yield develops further but the shear yield do not with the increase in PGA, which resulted that D3, D5 and D6 have very close plastic displacements (6.86 mm, 7.04 mm and 7.21 mm respectively), D4 has the maximum plastic displacement of 10.36 mm and the OLF1000 inclines to the suspended side in the transverse direction. Figure 7 lists some damaged members, marked in Figure 4, when PGA = 0.78 g.



(a) Total displacement (b) Plastic displacement

Figure 6: Complete displacement-loading curves

Figure 8 compares the results obtained by the experimental and numerical investigation. As shown, the complete loading-displacement curves and displacement-time history curves match very well. Moreover, according to Figure 7, the deformation of members in the finite element software, ABAQUS, is basically consistent with that in the test. These illustrate the correctness of the FE model and the validity of the modeling method.

4.3. Collapse analysis of OLF1000

According to the reliable FE model, the collapse analysis for NONSS and SS12 was developed in ABAQUS, where NONSS and SS12 represent the OLF1000 models without and with transmission lines having a sag-span ratio of 1/12. The incremental dynamic analysis method (IDA) was used and TAFT was selected as the excitation in this section.

Figure 9 illustrates that the two models exhibit distinct complete loading-displacement curves and displacement-time history curves due to the DCE. As shown, the bearing capacity of SS12 is reduced

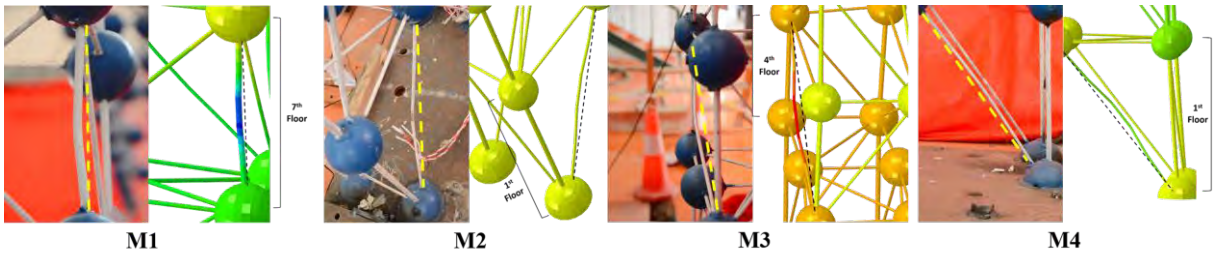
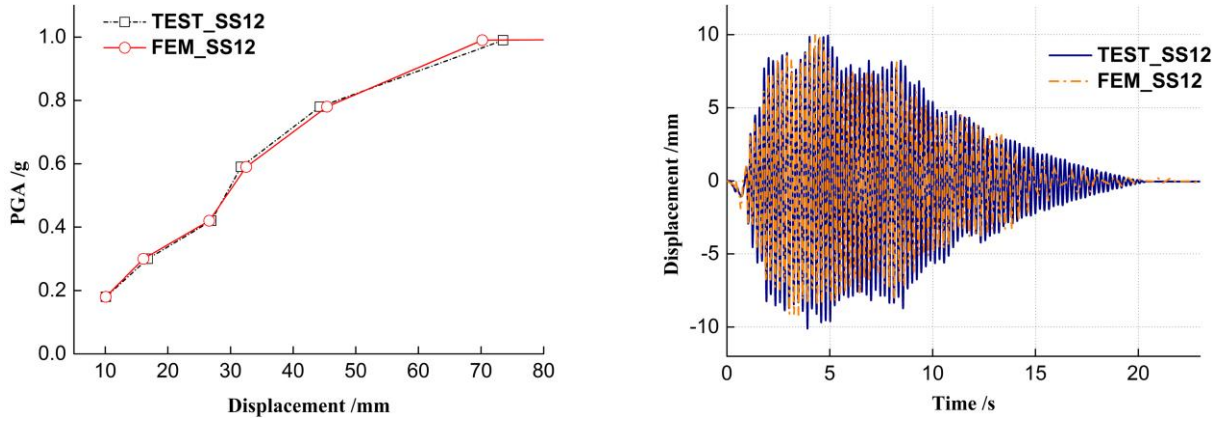
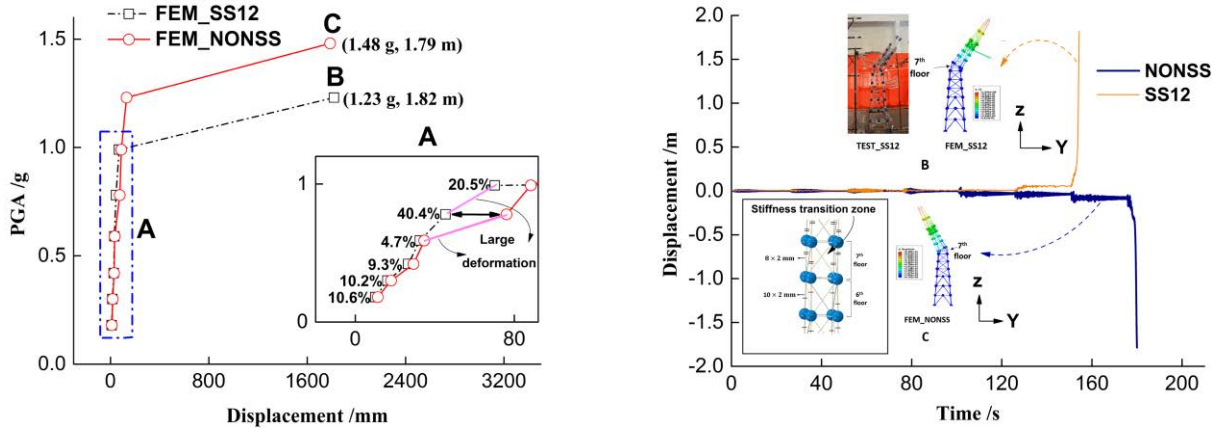


Figure 7: Damage in members when PGA = 0.78g in the test and numerical simulation



(a) Complete loading-displacement curves (b) Displacement-time history curves when PGA = 0.18 g

Figure 8: Comparison of results of D4 obtained by the test and FEM.



(a) Complete loading-displacement curve (b) Displacement-time history curves for all PGAs

Figure 9: Collapse analysis for NONSS and SS12 by FEM under TAFT

The PGAs, selected to excite the numerical models, include 0.18 g, 0.30 g, 0.42 g, 0.59 g, 0.78 g, 0.99 g, 1.23 g and 1.48 g, and the duration of each record having a PGA is 25.00 s.

by 15.8% compared with that of NONSS. Besides, before the collapse of SS12, the maximum displacement of D4 of SS12 is less than that of NONSS when PGA $\leqslant$ 0.99 g and the reduction is maintained at about 10% when PGA < 0.42 g. Moreover, NONSS has obviously large deformation due to only serious bending yield in columns when PGA = 0.78 g whereas SS12 dose due to serious bending yield in columns and slight shear yield in crossbeam when PGA = 0.99 g. However, the collapse of SS12 happens when PGA = 1.23 g whereas PGA = 1.46 g for NONSS. Furthermore, the maximum collapse displacements of NONSS and SS12 are about 1.8 m, and the failure zones of

NONSS and SS12 are located at the 7th floor of columns. NONSS and SS12 overturns to the directions of –Y and +Y, respectively, shown in Figure 9(b).

The reasons for the above phenomena are as follows: when the OLF1000 remains elastic under small earthquakes, the influence of the DCE on the seismic responses of OLF1000 remains constant. Besides, with the increase in PGA, NONSS preceded SS12 in yielding damage owing to the reduction of responses caused by the DCE. The failure zone is located at the 7th floor due to this floor is the stiffness transition zone, shown in Figure 9(b). Additionally, the additional dynamic tensions from the suspended system accelerate the development of the existed damage of SS12. It has contributed to the lower bearing capacity of SS12 compared with that of NONSS and different collapse directions.

5. Conclusion: submission of contributions

This study investigated experimentally and numerically the influence of the DCE of transmission lines on the failure of OLF1000 under real strong earthquakes. The transmission lines were simulated by massless springs based on the dynamic stiffness. The numerical recurrence of the experiment was carried out in the finite element software and the results obtained by the experimental and numerical recurrence matched very well. The collapse analysis of OLF1000 was conducted by FEM. The following significant conclusions were drawn:

- The DCE significantly reduces the seismic responses of the OLF1000 with the approximate reduction of 10% when OLF1000 remains elastic under small earthquakes.
- Members at the middle of columns exhibit bending yield deformation whereas members at both sides of the crossbeam deform due to shear yield. The bending yield develops further but the shear yield d0 not with the increase in PGA.
- The DCE accelerates the development of the existed damage of OLF1000, reduces the ultimate bearing capacity by 15.8% and affects the collapse direction of OLF1000.

Acknowledgements

The present work was conducted with financial support from the Chinese National Natural Science Foundation (Project designations: 51525802 and 51778183).

References

[1] J. Eidinger, "Wenchuan Earthquake Impact to Power Systems," in Technical council on lifeline earthquake engineering conference 2009, Oakland, California, U.S., June 28-1 July, A. Tang and S. Warner Ed., 2009. pp. 1359-1370.

[2] M. Shinozuka, "The Hanshin-Awaji Earthquake of January 17, 1995: Performance of Lifelines," National Center for Earthquake Engineering Research, State Univ. New York, Buffalo, Rech. Rep. NCEER-95-0015, 1995.

[3] L. Tian, R. S. Ma, F. Zhu, and Z. Xu, "Seismic research progress of high voltage transmission tower-line system," WORLD EARTHQUAKE ENGINEERING, vol.30, pp. 87-95, 2014 [in Chinese].

[4] H. M. Irvine, Cable structures. Cambridge, MA: MIT press, 1981.

[5] S. Ozono and J. Maeda, "In-plane dynamic interaction between a tower and conductors at lower frequencies," Engineering Structures, vol. 14, pp. 210-216, 1992.

[6] A. Ghobarah, T. Aziz, and M. El-Attar, "Response of transmission lines to multiple support excitation," Engineering Structures, vol. 18, pp. 936-946, 1996.

[7] A. Filiatrault and C. Stearns, "Seismic response of electrical substation equipment interconnected by flexible conductors," Journal of Structural Engineering, vol. 130, pp. 769-778, 2004.

[8] W. Wang, H. Li, and L. Tian, "Progressive collapse analysis of transmission tower-line system under earthquake," Advanced Steel Construction, vol. 9, pp. 161-172, 2013.

[9] L. Tian, R. S. Ma, H. N. Li, and Y. Wang, "Progressive collapse of power transmission tower-line system under extremely strong earthquake excitations," International Journal of Structural Stability and Dynamics, vol. 16, p. 1550030, 2016.

[10] H. D. Zheng and J. Fan, "Analysis of the progressive collapse of space truss structures during earthquakes based on a physical theory hysteretic model," Thin-Walled Structures, vol. 123, pp. 70-81, 2018.

[11] M. Z. Zhang, "Study on similitude laws for shaking table tests," EARTHQUAKE ENGINEERING AND ENGINEERING VIBRATION, vol. 17, pp. 52-58, 1997 [in Chinese].

Proceedings of the IASS Annual Symposium 2019 – Structural Membranes 2019
Form and Force
7 – 10 October 2019, Barcelona, Spain
C. Lázaro, K.-U. Bletzinger, E. Oñate (eds.)

Spatial System Sampling Method for Calculating Joint Positions of Existing Spatial Structures

Xu YANG*, Yongfeng LUO [a], Jun LIU[b]

* Department of Structural Engineering, Tongji University
1239, Siping Road, Shanghai, China
1610196@tongji.edu.cn

Abstract

According to randomness and inherent correlation of joint position deviations of existing spatial structures, a spatial system sampling (SSS) method is proposed to calculate all joint positions and to reckon the geometric shapes in this paper. Based on the distribution pattern of structure joints and spatial sampling theory, sampling principles and an approach to calculating minimum sample size in the SSS are presented. On account of the theory of testing hypothesis of non-independent samples under normal population, a statistical inference method considering sample correlation is presented, which can infer the probabilistic distributions of the joint position deviations by inversion of partial coordinate information. Finally, a procedure for constructing the existing structural numerical model with prior accuracy is proposed. A single layer reticulated shell structure was designed and set up. In view of the testing data of the joint positions, a variety of numerical modeling methods are used to construct the computation model of the structure. By carrying out comparative analysis of the ultimate bearing capacity of each computation model, it proves that the joint positions calculated by the SSS is closer to the actual structure.

Keywords: joint position deviation, system sampling, correlation coefficient, statistical inference.

1. Introduction

In the process of inspection and safety evaluation of existing structures, obtaining accurate and comprehensive data of structural configuration is necessary, especially for lattice shell structures which are sensitive to geometric imperfections. The Chinese detection code [1] notes that the model used in safety evaluation of existing structures shall be two-dimensional or three-dimensional models established according to the actual condition of the structures. However, architectural ornaments and cost of testing make it difficult to measure the coordinate information of all joints of a structure. Sampling measurement methods are then often used in inspection of existing structures, but the data obtained by sampling measurement is incomplete, which make it an important problem that calculating all joint positions of existing spatial through the incomplete information.

As for this problem, J. Liu *et al* [2] proposed a method of reckoning nodal position of existing grid shell structures based on surface interpolation, J. Wu *et al* [3] brought up inversion algorithm for the geometric imperfection distribution of existing reticulated structures, YF. Luo and J. Liu [4] suggested a stochastic deviation method of reckoning geometric shapes of existing spatial structures. The first two methods do not take into account the influence of sample selection, and cannot guide the determination of the sample positions in the actual project. The third method is based on simple random sampling, which cannot consider the correlation between samples.

The sampling method should be based on the distribution characteristics of the deviations of the existing spatial structure joints. G. Tang *et al* [5] and XC. Liu *et al* [6] carried out statistical analysis on the joint

Copyright © 2019 by Xu YANG, Yongfeng LUO, Jun LIU
Published by the International Association for Shell and Spatial Structures (IASS) with permission.

position deviations of several actual structures, and verified that the position deviations of joints subject to normal distribution. In addition, GB. Chen *et al* [7] analyzed the joint position deviations of a single layer reticulated shell in Shenyang, and found that the partial deviation of the nodes showed obvious regional correlation. And SY. Chao and JP. Yan [8] pointed out that for non-independent samples, applying statistical inference methods based on simple random samples will lead to erroneous results.

Different from simple random sampling, the spatial sampling method mentioned in JF. Wang *et al*[9] can consider the correlation of samples. K. Wu and YX. Liu [10] proposed a hypothesis test method on non-independent samples. Based on the above references, this paper suggests a spatial system sampling (SSS) method for calculating joint positions of existing spatial structures.

2. Correlation analysis of joint position deviation

2.1. Random field theory

Let U_i denotes position deviation value at the ith joint of the existing spatial structure, where i rands from 1 to N, and N represemts the total number of joints. Then the deviation value of the entire spatial structure joints constitute a discrete random field, which is recorded as $F(\boldsymbol{u})=\{U_1,U_2, \ldots ,U_N\}$, where $\boldsymbol{u} = \{\boldsymbol{u}_1,\boldsymbol{u}_2, \ldots ,\boldsymbol{u}_N\}$, $\boldsymbol{u}_i$ indicates the position coordinates of the ith joint in the random field. E. Vanmarcke *et al* [11] mentioned that the distribution features of the points in the random field are usually described by characteristic parameter (such as mean, covariance, and correlation coefficient). For an existing spatial structure without obvious deformation, we can assume the random field is weakly homogeneous, therefore, $\mu_1 = \mu_2 ,..., = \mu_N = \mu$, where $\mu(\boldsymbol{u})$ represents the mean function of each joint position deviation and μ is a constant, and the correlation function of any two joint position deviation values can be expressed as[8]:

$$\rho(\boldsymbol{u}_i, \boldsymbol{u}_j) = \rho(|\boldsymbol{u}_i - \boldsymbol{u}_j|) \tag{1}$$

in which $\rho(\boldsymbol{u}_i, \boldsymbol{u}_j)$ represents the correlation coefficient between $U_x$and U_y, and $|\boldsymbol{u}_i,-\boldsymbol{u}_j|$ represents the distand between the joint i and joint j.

The correlation function can describe the linear correlation of any two joint position deviations. Common correlation functions for random field include gaussian correlation function, linear correlation function, and exponential correlation function, as mentioned in E. Vanmarcke [12]. Wherein, the exponential correlation function can be expressed as:

$$\rho(\boldsymbol{u}_i, \boldsymbol{u}_j) = \exp\left(-\frac{|\boldsymbol{u}_i - \boldsymbol{u}_j|}{l}\right) \tag{2}$$

in which l is a scaling parameter. And Figure 1 schematically shows the three typical correlation models.

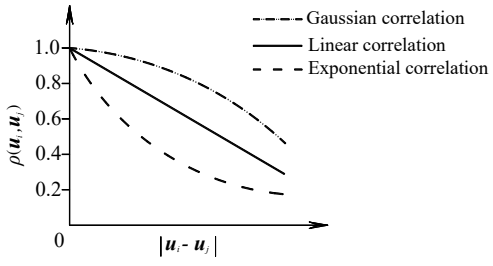


Figure 1: Typical correlation function of random field

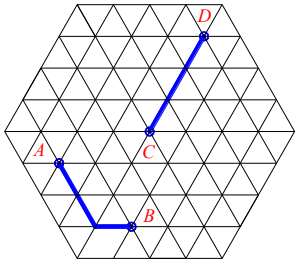


Figure 2: Minimum number of members between two joints

If the lengths of connecting members between joints are approximately same, the number of the connecting members can represent the distance between nodes. Then the Equation (2) simplifies to

$$\rho(\boldsymbol{u}_i, \boldsymbol{u}_j) = \rho(m) \tag{3}$$

in which m represents the minimum number of members between two joints. As show in Figure 2, joint A, B, C, and D respectively form a joint pair, and in these two joint pairs, the minimum number of members between joints is three.

2.2. Fitting of the correlation function

The correlation analysis of the joint position deviations of existing spatial structure should be based on the correlation function, which can be fitted as follows.

First, we randomly choose t pairs of joints which are connected by m members, where m is a set integer. The position deviations of these joints are represented by $[(x_1, y_1), (x_2, y_2), \ldots, (x_t, y_t)]$, in which (x_i, y_i) represents the deviations of the two joints of the ith pair. As mentioned in E. Kreyszig [13], the correlation coefficient ρ is calculated as

$$\rho = \frac{s_{xy}}{s_x s_y} \tag{4}$$

in which s_{xy} represents covariance function of x and y, s_x and s_y are the standard deviation function of x and y. Then, a set of correlation coefficients corresponding to different connecting munbers will be obtained, which can be plotted as a scatter plot. A appropriate correlation function can be selected to fit the trend of the scatter plot. Taking the exponential correlation function as an example, the fitting formula can be expresed as:

$$\rho = a_0 \cdot e^{-m/l} \tag{5}$$

in which a_0 and l are undetermined parameters. Finally, through nonlinear regression of the calculated ρ and m , we will get a fitting formula of the correlation function. This fitting formula quantitatively describes the correlation between any two mensured joints.

3. Spatial system sampling method

Space system sampling method is based on classical system sampling method, which aims to evenly distribute the sample points in the spatial structure. The sampling process consists of three parts. First, sample interval is determined according to the sample size and the distribution form of structure joints. Then, an initial sample point can be randomly selected. Finally, taking the initial sample point as the center, the remaining sample points are selected according to the sample interval.

3.1 Sample distribution pattern

The sampling distribution pattern is the key of sampling, which can be determined in accordance with grid forms of spatial structures. For a spatial structure in which the grid is a quadrilateral, such as intersecting lattice truss system, square pyramid system, lamella grid system, etc. We can sample equidistantly in the horizontal and vertical directions of the initial sample point with reference to Figure 3a. For a spatial structure in which the grid is a triangle, such as triangular pyramid system, spherical latticed shell, cylindrical latticed shell, hyperbolic paraboloid latticed shell, etc. We can sample according to the specific distribution pattern of the grid as shown in Figure 3b. It has to ensure that the adjacent sample points are kept at the same interval, and the other sample points are equally spread from the initial sample points until new sample points can no longer be selected within sample interval.

In addition, for triangular grid structure, the same initial sample point and sample interval can make different sampling distribution patterns and different sample sizes. As shown in Figure 3b, the sample size of the left structure is 14 and the sample size of the right structure is 21. Therefore, we have to consider the sample size when determining the sample distribution pattern.

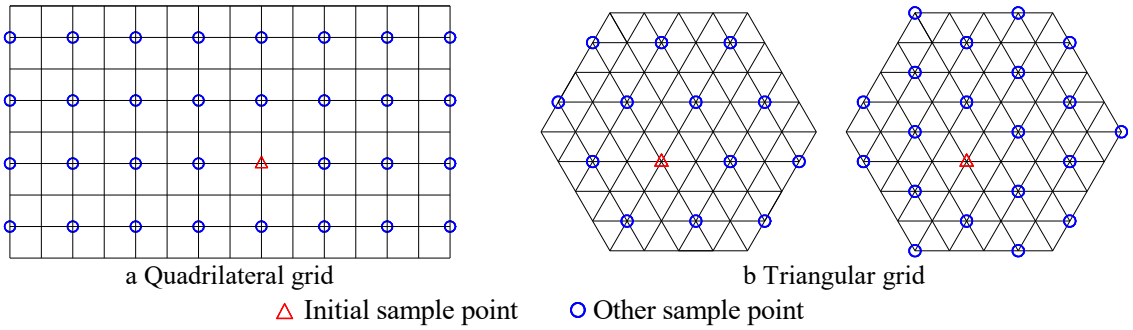


Figure 3: Sample distribution pattern

3.2 Minimum sample size

B. D. Ripley [14] proposed that the expected expression of the sample mean variance in spatial sampling can be express as:

$$V = \frac{\sigma^2}{n} - \frac{E\left[C(X_i, X_j)\right]}{n} \tag{7}$$

in which σ^2 is population variance, $X_i$and X_j represent two sample variables, and $i \neq j$, $C(X_i, Y_j)$, $\rho(X_i, Y_j)$ are the covariation and correlation coefficient of X_i and Y_j, $C(X_i, Y_j)=\rho(X_i, Y_j)\cdot\sigma(X_i)\cdot\sigma(Y_j)$, $\sigma^2(X_i)$, $\sigma^2(Y_j)$are the variance of X_i and X_j, $E[\ ]$represents the expected value operation. The Equation (7) can be adjusted as:

$$n = \frac{\sigma^2}{V}\left(1 - \frac{R}{\sigma^2}\right) = n_c(1 - r) \tag{8}$$

in which n represents the sample size, which is based on SSS method. And n_c is the sample size, which is based on simple random sampling method. $R=E[C(X_i, Y_j)]$, and $r = R \cdot \sigma^{-2}$, which denotes the impact of correlation. YJ. Jin *et al* [15] proposed that n_c satisfies the following equation

$$\frac{1}{n_c} = \frac{1}{N_c} + \frac{d^2}{Z^2_{1-\alpha/2}\sigma^2} \tag{9}$$

in which N_c represents population total, d is the absolute error, it is expected that variable X ranges from $X+d$ to $X-d$, α denotes confidence level, $Z_{1-\alpha/2}$ is the quantile corresponding to α under normal distribution. When the value of N_c, d, $Z_{1-\alpha/2}$ and σ^2 are limited, the minimum value of n_c will be determined, and the minimum value of n will be obtain.

4. Statistical inference

As mentioned in Wu *et al* [10], for a set of non-independent samples $\boldsymbol{X}$ under the normal population, it can be converted into a set of simple random samples $\boldsymbol{Y}$ by the method mentioned in K. Wu, YX. Liu [10]. Then we can implement statistical inferences on the transformed samples.

4.1 Normality test

The SSS method is mainly for non-independent samples under the normal population. If the normality hypothesis is rejected, the statistical inference method later in this paper will no longer apply. Therefore, the normality test will be carried out firstly. The conference [16] provides two methods for normality test, Shapiro–Wilk test and Epps-Pulley test. The former is mainly for small samples (the number of samples is 8~50), and the latter can consider large samples (the number of samples is greater than 8).The statistic of the Shapiro-Wilk test is

$$W = \frac{\left\{\sum_{i=1}^{[n/2]} a_i[X_{(n+i-1)} - X_{(i)}]\right\}^2}{\sum_{i=1}^{n}(X_i - \overline{X})^2} \quad (10)$$

in which sample values are arranged in non-descending order and recorded as X_i, $\overline{X}$ is the sample mean, W_α is the quantile corresponding to the confidence level α, α_i has specific value corresponding to n, while $i \leq [n/2]$ and $n \leq 50$. When $W \leqslant W_\alpha$, the hypothesis that the samples are from a normal distribution will be rejected, otherwise the samples are considered to obey normal distribution.

4.2 Mean hypothesis test

Since the actual position of the joint is a random deviation centered on the design position, the deviation expectation should be zero, thus a hypothesis test of mean zero need to be carried out. The mean hypothesis test H_0: $\mu = 0$ for $\boldsymbol{X}$ is equivalent to that H_0: $\mu = 0$ for $\boldsymbol{Y}$, whose test statistic in reference (Zhang *et al* [17]) is:

$$T = \left|\sqrt{n} \cdot \frac{\overline{Y}}{\sigma_y}\right| \quad (11)$$

in which $\overline{Y}$ and σ_y are the mean and standard deviation of the samples after conversion. The T obeys the t distribution with degree of freedom $n-1$, and its negative domain is $T \geq t_{\alpha/2}(n-1)$. When the calculated statistic T is greater than $t_{\alpha/2}(n-1)$ at the confidence level α, the hypothesis that the sample mean is zero will be rejected, indicating that the existing structural node has an overall deviation in a certain direction, and the statistical inference based on the hypothesis that mean is zero will not be applied.

4.3 Variance estimation

In order to obtain a more conservative estimation, an upper bound value should be determined for the sample variance. When the population mean is unknown, the statistic for the variance interval estimate in reference (Zhang *et al* [17]) is:

$$Q = \frac{(n-1)\sigma_y^2}{\sigma^2} \quad (12)$$

in which σ^2 represents population variance, while σ_y^2 represents sample variance. The Q obeys the χ^2 distribution with degree of freedom $n-1$, when the confidence is $1-\alpha$, the upper bound value of the sample variance can be determined as $(n-1)\cdot\sigma_y^2\cdot[\chi^2_{1-\alpha/2}(n-1)]^{-1}$.

5 Project example

5.1 Introduction of the shell

A single-layer Kiewitt-6 steel reticulated shell was designed and fabricated, as shown in Fig. 4.



Figure 4: Single-layer lattice shell

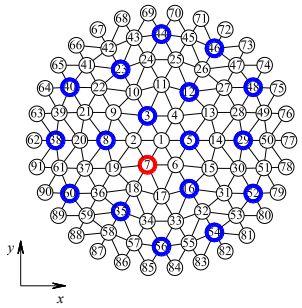


Figure 5: Sampling distribution pattern

The latticed shell is welded by 210 tube members and 91 joints, and the span and height of the shell are 3.6 m and 0.9 m. Tube members adopt $\phi 6\times1$, while the radius of joints is 70 mm. The joints between steel tubes and the supports are assumed to be rigid. The material of the steel tubes is assumed to be elastic-perfectly-plastic with a Young's modulus of 200 GPa and a yield stress of 235 MPa.

Firstly, we assume that $\sigma=(1/300)L$, i.e., σ =12mm, where L is the maximum span of the structure, and confidence $1-\alpha$ is 95%, d equals 5mm, then we can obtain n_c =18. Secondly, taking the sampling interval as 2, node 7 was selected as the initial sample point by MATLAB genetating random number, then a sample distribution pattern was obtained, as shown in Fig.5. 18 nodes was selected in total , which meet the minimum sample size requirement. When we take sampling interval as 3, the sample size is not enough. Wu *et al* [3] proposed that the influence of radial deviation on the overall stability of the structure is much greater than the tangential deviation. In order to simplify the calculation, the node deviation extracted in the shell refers to the geometric deviation of the node along the radius of curvature.

5.2 Correlation analysis

Correlation coefficients between the sample points with different sample intervals are listed inTable1, and trend of the correlation coefficient with the number of connecting members is shown in Figure 6.

Table 1: Correlation coefficient of node deviation with different number of connecting members

Number of connecting members	Correlation coefficient	Number of connecting members	Correlation coefficient
1	——	5	0. 1202
2	0.4351	6	0. 1379
3	0. 0527	7	-0.1380
4	0.2807	8	-0.2032

Table 2: Fitted values of correlation coefficient

Number of connecting members	Correlation coefficient	Number of connecting members	Correlation coefficient
1	0.6025	5	0. 0785
2	0. 3620	6	0. 0472
3	0. 2175	7	0.0284
4	0.1307	8	0.0170

Exponential correlation function is adopted to fit correlation between samples. Through non-linear regression analysis, $\rho=1.0028\cdot e^{-0.5094m}$ is obtained. The fitted values of correlation coefficients between samples are then listed in Table 2.

5.3 Statistical inference

In the normality test, the statistics $W_{0.05}$ = 0.897, W_{orgin} = 0.959 and W_{trans} = 0.938, which are both greater than $W_{0.05}$, indicating that the sample values before and after the conversion obey the normal distribution, and the conversion process does not change the normal distribution characteristics of the samples. In the mean hypothesis test, statistic T=0.7249, which is less than $T_{0.025}(17)$=2.1098, indicating that the sample satisfies the assumption that the mean is zero. The upper bound value of standard deviation σ =5.948,

which is less than the value we assumed, indicating that σ is estimated conservatively. Therefore, the sample data obtained based on the spatial system sampling method can be used to calculate the joint positions of the structure.

5.4 Numerical analysis

A variety of numerical modeling methods are used to establish the structural model for carrying out comparative analysis of the overall stability ultimate bearing capacity, verifying if the model based on the spatial system sampling method is closer to the actual structure. The process was operated by using the finite element analysis software ANSYS, the members were modeled by beam188 unit, the load pattern adopted full span gravity.

The joint positions are considered by six methods: (1) All joint positions adopt the design values, and the overall stability coefficient of the structure is 2.185. (2) All joint positions adopt the measured values, and the overall stability coefficient of the structure is 2.152, which indicates that joints position deviation will reduce the overall stability of the structure. (3) All joint positions were determined by consistent buckling mode method, and the overall stability coefficient of the structure is 1.749. (4) Some joint position adopt measured values, the other joint position adopt design values, and the overall stability coefficient of the structure is 1.817. It notes that introduction of the measured values helps to improve the accuracy of the bearing capacity analysis. (5) All joint positions were determined by random defect modal method. The deviation values of each joint conform to the normal distribution in the range of 2 times mean square deviation, and are independent of each other. By calculating 1000 random models, the result with 95% reliability is 1.776. (6) All joints position were determined by random defect modal method. The deviation values of each joint conform to the normal distribution, and interrelated of each other. And the characteristic parameters of joint position deviation were obtained in section 5.3. After calculating 1000 random models, the result with 95% reliability is 1.835, and the frequency distribution are shown in Figure 7. Compared with the above joint position modeling methods, the overall stability coefficient of the structure calculated by the (6) method is closer to the actual situation of the structure, which indicates that calculating joint positions by spatial system sampling method is more accuracy.

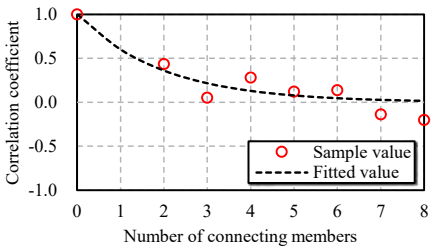


Figure 6: Trend of correlation coefficient changing with the number of connecting member

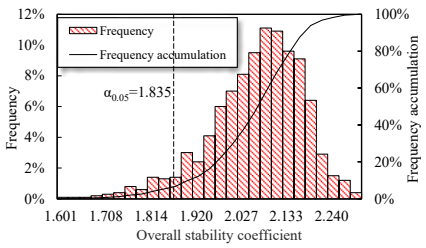


Figure 7: Frequency distribution and frequency accumulation of overall stability coefficient of the (6) method

6 Conclusion

(1) A spatial system sampling method and a statistical inference method based on spatial system sampling are proposed. This method can consider the correlation of joint position deviations and establish a more accurate model of the existing strycture.

(2) The principle of sampling distribution pattern is proposed, which ensure the uniformity of sampling distribution. And the calculation method of minimum sample size is proposed.

(3) A project example is given to verify that the joint positions calcualted by the spatial system sampling method is more in line with the actual structure.

Acknowledgements

This work was supported by National Natural Science Foundation of China (51678431). And the following colleagues helped in carrying out the analysis: Dr. Qinglong Huang, Dr. Yang Qu, Dr. Zhaochen Zhu, Dr. Yunsong Li; their contributions are sincerely acknowledged.

References

[1] Shanghai Municipal Construction and Transportation Commission. *Technical specification for structural inspection and appraisal of steel structure: DG/TJ 08—2011—2007*. Shanghai：Shanghai Building Materials Market Management Center, 2007. (In Chinese)

[2] J. Liu, YF. Luo, X. Yang, "A method of reckoning nodal position of existing grid shell structures based on surface interpolation," *Journal of Shanghai Jiaotong University(Science),* vol. 52, no. 11, pp. 1475-1482, Nov. 2018. (In Chinese)

[3] J. Wu, YF. Luo, L. Wang, "Inversion algorithm for the geometric imperfection distribution of existing reticulated structures," *Journal of Zhejiang University (Engineering Science)*, vol. 52, no. 5, pp. 864-872, May 2018. (In Chinese)

[4] YF. Luo, J. Liu, "Stochastic deviation method of reckoning geometric shapes of existing spatial structures," *Journal of Tongji University (Natural Science)*, vol. 45, no. 6, pp. 791-798, Jun. 2017. (In Chinese)

[5] G. Tang, DL. Li, CQ. Zhao, HL. Zhao, "Statistical regulation and parameter study on initial geometrical imperfections of spatial structures based on measured data," *Building Structure*, vol. 38, no. 2, pp. 74-78, Feb. 2008. (In Chinese)

[6] XC. Liu, AL. Zhang, JQ. Ge, L. Wang, ZL. Qi, "Study on the influence of construction deviation random distribution on the integral stability of suspend-dome," *Journal of Building Structures*, vol. 28, no. 6, pp. 76-82, Dec. 2007. (In Chinese)

[7] GB. Chen, H. Zhang, KJR Rasmussen, F. Fan, "Modeling geometric imperfections for reticulated shell structures using random field theory," *Engineering Structures*, vol. 126, pp. 481-489, Nov. 2016.

[8] SY. Chao, JP. Yan, "The distribution of several statistics of constant correlation samples from normal population and its application," *Mathematics in Practice and Theory*, vol. 20, no. 4, pp. 5-10, Dec. 1990. (In Chinese)

[9] JF. Wang, CS. Jiang, LF. Li, *Spatial sampling and statistical inference*, Beijing：Science Press, 2009.

[10] K. Wu, YX. Liu, "Hypothesis testing of constant correlation samples under normal population," *Mathematics in Practice and Theory*, vol. 26, no. 3, pp. 193-199, Aug. 1996. (In Chinese)

[11] E. Vanmarcke, M. Shinozuka, S. Nakagiri, G. I. Schuëller, M. Grigoriu, "Random field and stochastic finite elements," Structural Safety, vol. 3, no. 3-4, pp. 143-166, Aug. 1986.

[12] E. Vanmarcke, *Random fields：analysis and synthesis*, Cambridge: The MIT Press, 1983.

[13] E. Kreyszig, *Advanced engineering mathematics*, (10th ed.) New York: Wiley, 2010.

[14] B. D. Ripley, *Spatial statistics*, New York: Wiley, 1981.

[15] YJ. Jin, ZF. Du, Y. Jiang, *Sampling techniques*, (3rd ed.) Beijing: China Renmin University, 2012.

[16] State Bureau of Quality and Technology Supervision. *Statistical intertoretation of data — Normality tests： GB/T 4882-2001*, Beijing: China Standard Press, 2001.

[17] GF. Zhang, BQ. Huang, CY. Zhang, *Probability theory, mathematical statistics and stochastic processes*, Hangzhou：Zhejiang University Press, 2011.

Proceedings of the IASS Annual Symposium 2019 – Structural Membranes 2019
Form and Force
7 – 10 October 2019, Barcelona, Spain
C. Lázaro, K.-U. Bletzinger, E. Oñate (eds.)

Stability analysis of super-large steel hyperbolic cooling towers

Xiaolei ZHAO

Tongji University, 1239 Siping Road, Shanghai, China
zxiaolei948@163.com

Abstract

Up to this time, the heights of cooling towers are increased to over 200m far higher than the prescriptive heights (<165m). Wind pressure and structural dead weight, which are the control loads in the design of cooling towers, increase with the height. Given the increasing height and loads, it's necessary to reconsider the stability of cooling towers, particularly the stability under dynamic wind load. To understand the influence of wind load on cooling tower stability, static and dynamic nonlinear finite element analysis of steel hyperbolic cooling towers using ABAQUS is presented in this paper. Considering initial geometric imperfections, geometry and material nonlinearity, methods are full-range analysis for static analysis and central difference method for dynamic. Comparing the results calculating by increasing wind loads, some conclusions for the design of cooling towers are given and this method may provide valuable insights for the future engineering application.

Keywords: Hyperbolic cooling tower, stability, wind induced dynamic responses

1. Introduction

Cooling tower is a type of space thin shell structure whose stability is the weak point. After cooling towers at Ferry-Bridge Power Station suddenly collapsed in 1965[1]-[3], the wind load and the stability of hyperbolic cooling towers under the wind load have been done by many researchers.

The heights of cooling towers are continually increased to over 200m far higher than the prescriptive heights (<165m). Wind pressure and structural dead weight, which are the control loads in the design of cooling towers, increase with the height. Given the increasing height and loads, it's necessary to reconsider the stability of cooling towers, particularly the stability under dynamic wind load.

To understand the influence of wind load on cooling tower stability, static and dynamic nonlinear finite element analysis of steel hyperbolic cooling towers using ABAQUS is presented in this paper.

Comparing the results calculating by increasing wind loads, some conclusions for the design of cooling towers are given and this method may provide valuable insights for the future engineering application.

2. Methods

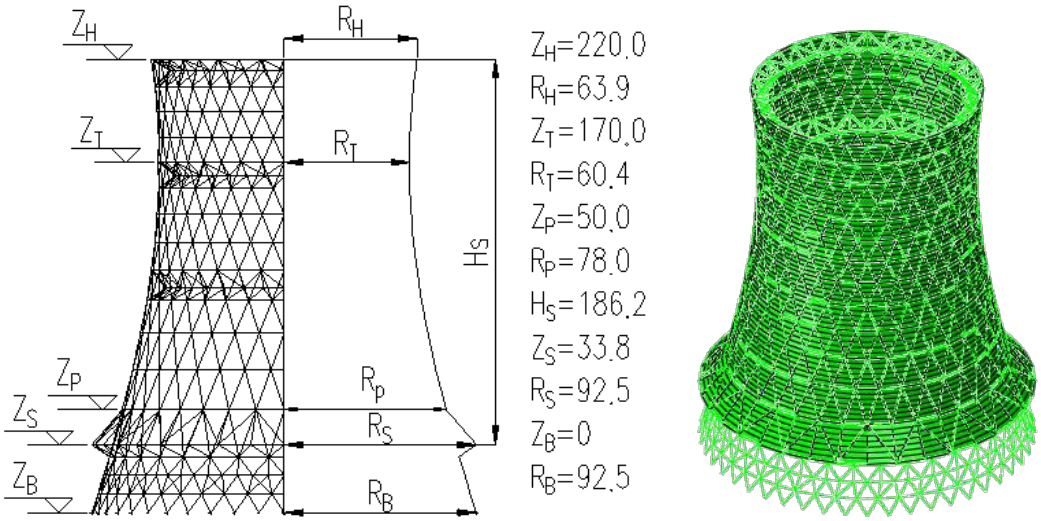
To understand the influence of wind load on cooling tower stability, static and dynamic nonlinear finite element analysis of steel hyperbolic cooling towers using ABAQUS is presented in this paper.

2.1. Models

The model's geometry is showed as Figure 1 (a). The model's height, diameter at 0m height, height and diameter of throat are 220m, 185m, 170m, and 120.8m, respectively. There are three stiffening

Copyright © 2019 by Xiaolei ZHAO
Published by the International Association for Shell and Spatial Structures (IASS) with permission.

rings at the height of 118m, 170m and 220m. The structure form is hyperbolic triangle space grid structure composed of ring beams and diagonal braces which both are steel pipes. The outer surface plate is made of aluminum.



(a) Feature size (m) (b) the FEM model

Figure 1: Geometry of cooling tower and the FEM model

2.2. Loads and loads combination

The main loads and actions for cooling towers are dead load, wind load, temperature and seismic action. However, due to its constraint situation and light mass, temperature and seismic action are not the control actions. Since cooling tower is a typical wind-sensitive structure, this paper mainly researched on wind load. Dead load and wind load are considered during stability analysis of cooling towers. And loads combination is 'Dead load + wind load'.

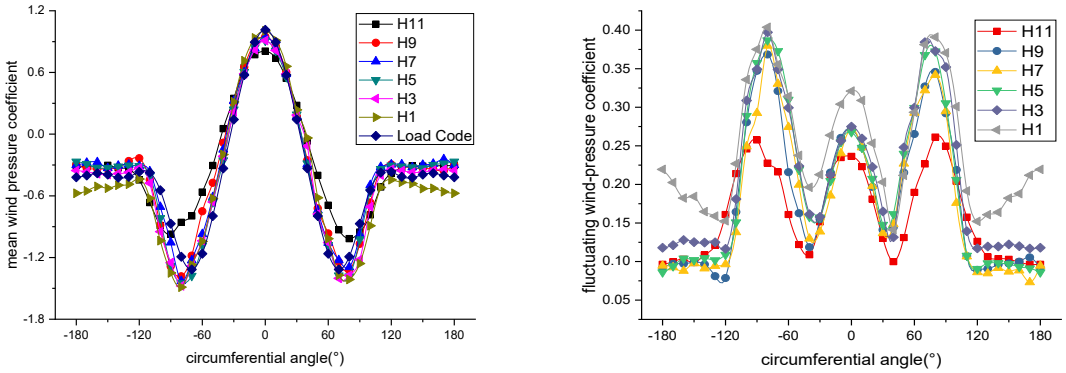
2.2.1. Static wind loads

According to Chinese Code[5], static wind loads for cooling tower have two parts: external and internal wind pressure. As for this present example, basic wind pressure is 0.53 kN/m^2 and design wind pressure is 0.583 kN/m^2. Standard value of equivalent wind load is taking wind vibration coefficient, mean wind pressure coefficient and wind pressure height coefficient into consideration.

2.2.2. Dynamic wind load

Dynamic wind load time-history is from wind tunnel tests. Wind tunnel tests were conducted in the wind tunnel laboratory of China Academy of Building Research. The cooling tower model is made according to the geometric scale ratio of 1:400. 11 layers measuring points were arranged on the outer surface of the tower, and 36 measuring points of each layer were arranged at equal intervals, totaling 396 measuring points.

According to the similarity relation, the test results are converted to the prototype structure, and the time history data of surface wind pressure are matched to the calculated model. When the basic wind pressure at 10m height is 0.53kn /m, the total analysis duration is 731s, and the first 146s is used as the unstable calculation stage of the power analysis, and the analysis results are not adopted to eliminate the impact of sudden wind. Mean and fluctuating wind pressure coefficient in different heights (H11 at the top) are showed in Figure 2.



(a) Mean wind pressure coefficient (b) Fluctuating wind pressure coefficient

Figure 2 Wind pressure parameters of different heights

2.3. Dynamic characteristics

The first 200 frequencies of the structure are calculated to ensure that the mass participation coefficients of the modes in the X and Y directions reach more than 90%. The frequency of the cooling tower model presents two main characteristics. One is that the frequency values appear in pairs. For example, the values of the first and second frequency are similar. The second characteristic is that the vibration modes are closely concentrated. The frequency of distribution is showed in Figure 3 and Table 1.

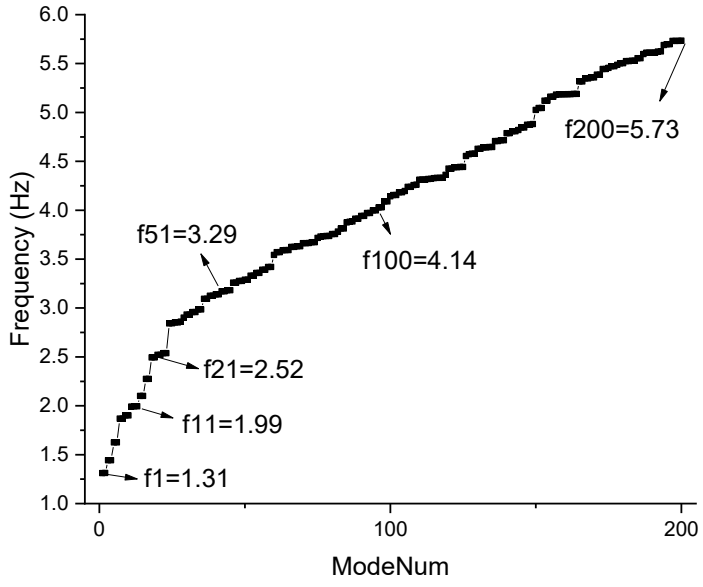
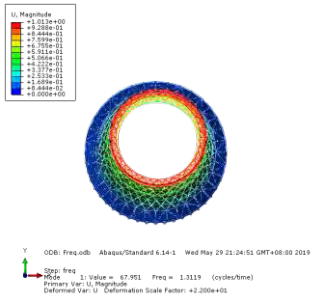
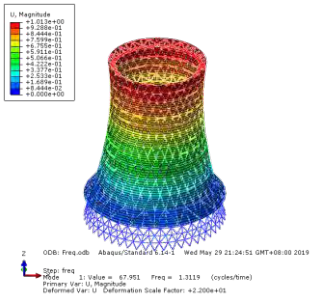
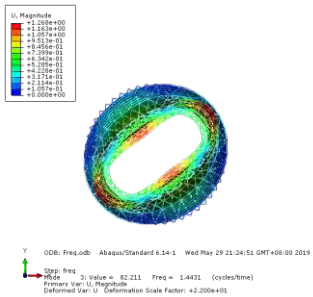
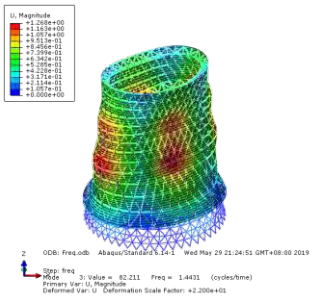
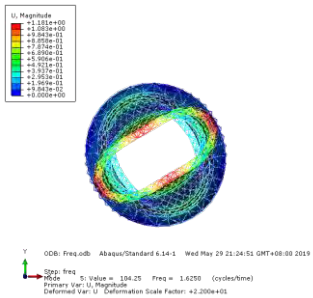
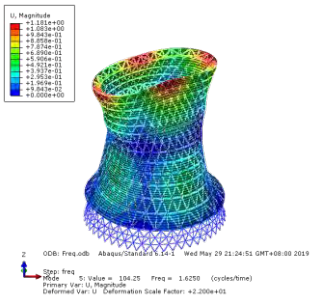
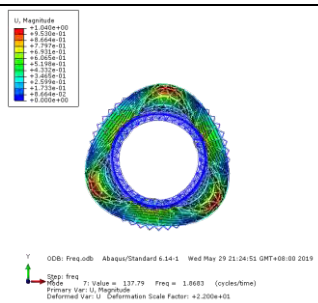
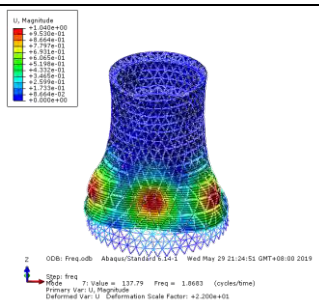
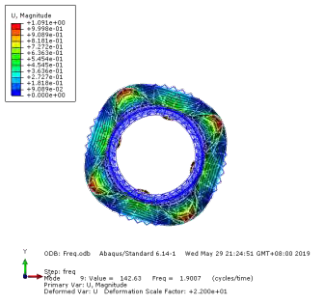
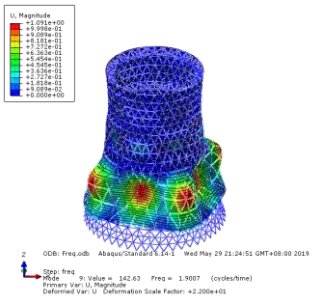


Figure 3: Frequency distribution

Table 1: Frequency of the model

No.	Frequency/Hz		Mode shape	
1、2	1.31	Horizontal movement		
3、4	1.44	2 circular+ 1 vertical waves		
5、6	1.62	2 circular+ 2 vertical waves		
7、8	1.87	3 circular+ 1 vertical waves		
9、10	1.90	4 circular+ 1 vertical waves		

2.4. Calculation methods

Considering initial geometric imperfections, geometry and material nonlinearity, methods are full-range analysis for static analysis and central difference method for dynamic.

The damping ratio is an important parameter to calculate the dynamic response of a structure. According to Chinese Codes, the damping ratio of steel structures is usually around 0.01 to 0.05. For cooling tower, the damping ratio is around 0.01 based on practical dynamic tests [6]. Structural damping can be considered in many forms, among which Rayleigh damping is the most commonly used one. In this example, values of alpha and beta are obtained by taking the 1st and 54th structural frequencies. The first 100 modes' damping ratios is from 0.009 to 0.0115.

The equilibrium equation of the structure is established on the geometric state of the structure after deformation, and the "p-Δ" effect, nonlinear buckling effect, large deformation effect and so on are all considered comprehensively.

The nonlinear stress-strain constitutive relations of materials are directly used to simulate the elastic-plastic properties of steel.

Consistent defect method was used for initial defects.

3. Results and discussion

3.1. Buckling mode

Through overall stability analysis, the first 100 buckling modes and the corresponding linear buckling stability factors (LBSF) are got. Only the first 20 are listed in this paper. The 1st LBSF=5.42 shows that the maximum possible load proportion factor (LPF) is 5.42.

Table 2: Linear buckling stability factor

Buckling mode No.	1	2	3	4	5	6	7	8	9	10
Linear buckling stability factor	5.42	5.48	6.42	6.55	6.68	6.73	6.76	6.79	6.97	7.00
Buckling mode No.	11	12	13	14	15	16	17	18	19	20
Linear buckling stability factor	7.30	7.46	7.48	7.50	7.53	7.55	7.60	7.76	7.89	7.97

3.2. Displacement

Through finite element calculation, the elastoplastic stability critical load factor of cooling tower under static or dynamic wind load can be obtained. The dynamic stability bearing capacity is 40% lower than the static.

For static, the load-displacement curve is the curve of typical nodes which can be obtained via iteration process. For dynamic, the load-displacement curve is plotted by LPF and the maximum displacement under corresponding LPF. The load-displacement curve is showed in Figure 4.

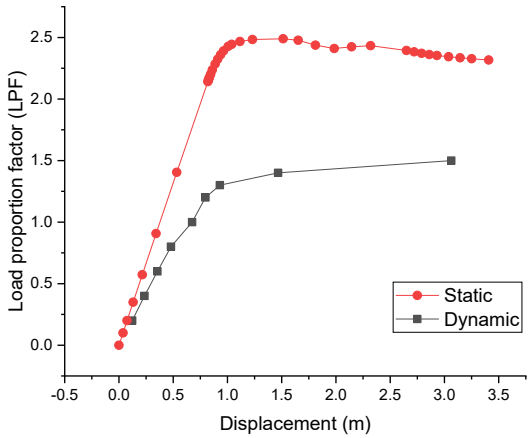


Figure 4: Load-displacement curves

We can define the interlayer displacement angle (IDA) of cooling tower as the maximum displacement of each layer dividing the height of this layer. And the correlation curves of the IDA and height under diffent LPF are drawn in Figure 5. It can be clearly seen that, with the increase of load, the IDA at the height of 120m and 160m is relatively small, where is exactly the corresponding position of the stiffening rings, meanwhile, the IDA at 80m, 140m and 220m is the largest, where is between stiffening rings or at the top. The effect of stiffening ring on structural displacement and stiffness is remarkably effective.

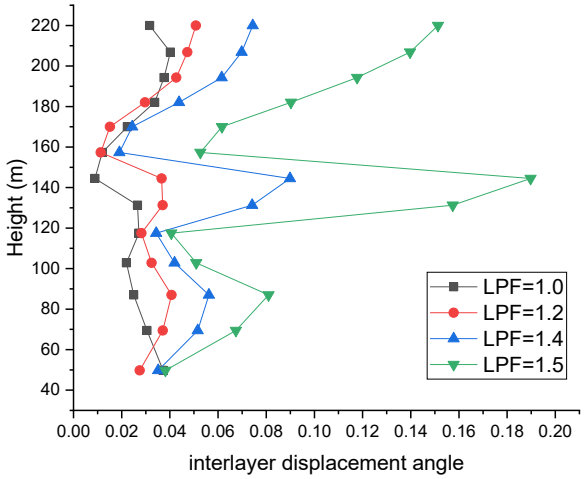
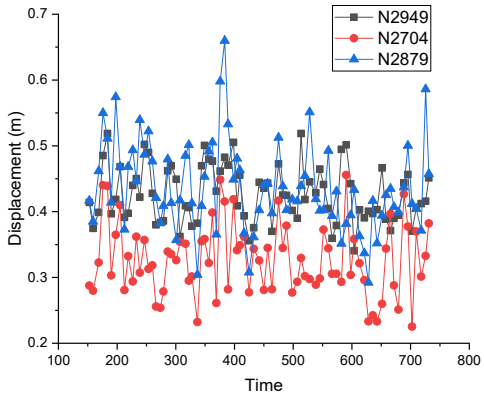
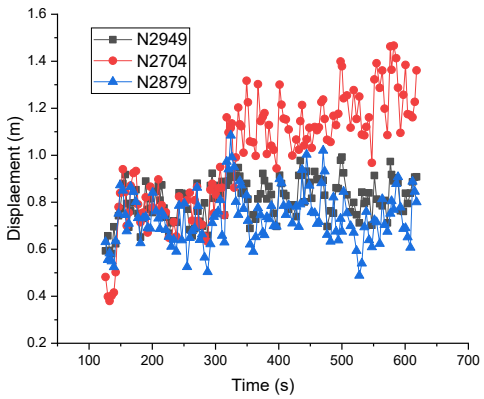


Figure 5: Interlayer displacement angle with heights

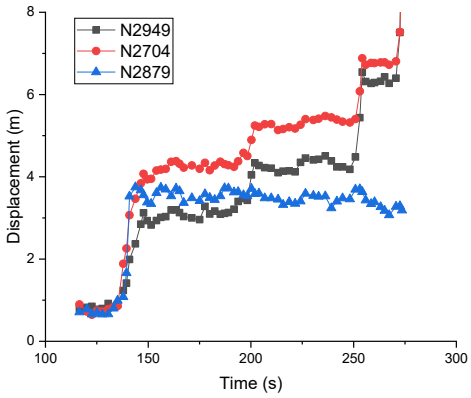
Figure 6: Typical nodes' displacement history curvesFigure 6 shows time-history of typical nodes' displacement. The typical nodes' position is N2949 at the top, N1704 at the throat, N2879 at the middle, and all at windward side. As we can see from Figure 6, the time-history displacement is steady when LPF=1, a little unsteady when LPF=1.4, and unsteady when LPF=1.6. More discussion on condition LPF=1.6: from time=320s, displacement of N2704 suddenly increase which indicate the precursor of instability.



(a) LPF=1



(b) LPF=1.4



(c) LPF=1.6

Figure 6: Typical nodes' displacement history curves

4. Conclusion

Through static and dynamic calculating the response of cooling tower under wind loads, we can draw the following conclusions:

(1) The dynamic bearing capacity is 40% lower than the static bearing capacity. The current specifications are not so applicable to the super-large cooling towers with a height over 200m. We should pay more attention to the wind load of the super-large cooling towers.

(2) The stiffening ring plays an important role in the cooling tower of spatial reticulated shell structure, and the reasonable arrangement of the stiffening ring will significantly improve the stability of the structure.

Acknowledgements

The authors acknowledge support from Tongji University.

References

[1] Board, C.C.E.G. "Report of the Committee of Inquiry into the collapse of cooling towers at Ferrybridge, Monday 1 November 1965.", 1966.

[2] Pope, R.A. "Structural deficiencies of natural draught cooling towers at UK power stations. Part 1: Failures at Ferrybridge and Fiddlers Ferry." *Proceedings of the Institution of Civil Engineers. Structures and Buildings*, Vol. 104, 1994, pp. 1-10.

[3] Pope, R.A., K.P. Grubb and J.D. Blackhall "Structural deficiencies of natural draught cooling towers at UK power stations. Part 2: Surveying and structural appraisal." *Proceedings of the Institution of Civil Engineers. Structures and Buildings*, Vol. 104, 1994, pp. 11-23.

[4] Woolley, G. and D. Van der Cruyssen "Structural deficiencies of natural draught cooling towers at UK power stations. Part. 3; Strengthening of natural draught cooling tower shells." *Proceedings of the Institution of Civil Engineers. Structures and Buildings*, Vol. 104, 1994, pp. 25-37.

[5] "Code for design of cooling for industrial recirculating water." *National Standards of the People's Republic of China*, 2014.

[6] Juhasova, E., Z. Bittnar and O. Fischer "Vibration characteristics of a cooling-tower shell." *Journal of Wind Engineering & Industrial Aerodynamics*, Vol. **12**, 1983, pp. 145-154.

Proceedings of the IASS Annual Symposium 2019 – Structural Membranes 2019
Form and Force
7 – 10 October 2019, Barcelona, Spain
C. Lázaro, K.-U. Bletzinger, E. Oñate (eds.)

Digital Rubble
Compression-Only Structures with Irregular Rock and 3D Printed Connectors

Bastian WIBRANEK*, Oliver TESSMANN

*Technische Universität Darmstadt, DDU (Digital Design Unit), Department of Architecture
El-Lissitzky-Str.1, 64287 Darmstadt, Germany
wibranek@dg.tu-darmstadt.de

Abstract

Irregular materials such as unprocessed rocks and wooden branches are currently rarely used in contemporary architectural construction due to the high cost of skilled labor required for preparation. This project investigates methods of graphic statics in combination with technologies such as photogrammetry and 3D printing to build structures from natural reusable building materials. We developed a method for dry-stacking unprocessed rock. We implemented an algorithm to produce 3D printed parts that connect digitized stones in the plane normal to the thrust line. A manually designed input curve is recalculated according to the weights of the objects to generate a compression-only arch. We employed evolutionary optimization to calculate optimal orientation of digitized stones along the thrust-line. Different stone arrangements and 3D printed connectors were tested. The manual assembly is done using a mixed reality setup. Unprocessed or rubble rock is a massive resource of cheap building material with very low embodied energy that might see a revival through digital technologies.

Keywords: compression-only structure, rubble rock, photogrammetry, 3d printing, mixed reality

1. Introduction

Building with irregular material has a long history in architecture. Especially the construction with stone. Usually natural stones or spolia are fitted for construction in subtractive manners. Stones are cut or treated by hammering until they can be assembled in dry stack. Many cultures have developed great methods for it and achieved very high precisions for those fitting procedures [1]. On the other hand, there are also methods that use adhesive mortar to negotiate tolerance between the interfaces of the irregular stones. Both methods are relatively labor-intensive processes. The Block Research Group from ETH Zürich has done great and inspiring work in construction of dry-stack compression-only structures that illustrate that those systems enable to build complex shapes that go beyond simple walls [2], [3].

New fabrication methods like 3d printing might help to overcome the labor intensiveness as they are easy to automate. In the above-mentioned methods, the craftsman went through a process of perceiving the available stones and developed a plan how to customize them for the assembly. Here again 3D printing is of interest as the customization of parts that can be added to the irregular stones come without any extra procedure if the process is well designed.

The 3D data for the 3D printing though has to be based on the real stones that have to be digitized. Technologies like photogrammetry and laser scanning offer several possibilities to acquire 3D data. Laser scanning for instance is used in wood industries to generate digital twins of trees or branches in order to evaluate them for fabrication. Additionally, wood industries also have proven that those data can be used for the automated process of treatment of those parts for milling and cutting. 3D scanning data has been used for branch digitization and a robotic fabrication process of an arch spanning wooden construction [4]. The creation of additive parts based on 3D data from real world objects is still a field to be explored.

Copyright © 2019 by Bastian Wibranek, Oliver Tessmann
Published by the International Association for Shell and Spatial Structures (IASS) with permission.

The main idea of this paper is to use additive fabrication methods to assemble irregular rubble along a computed thrust line. We aim to build an arch form irregular stones that illustrates the workflow that combines digitized rubble with an algorithmic approach that automatically generates 3D printed connectors.

Our main contributions are:

- We describe a workflow to digitize irregular stones and 3D print connectors between them to build a compression-only arch (Section 2).
- We implement an algorithm that generates a thrust line based on real-world input and solves the orientation of digitized rubble to align the interfaces between the stones and connectors through an evolutionary algorithm (Section 2.2).
- We show a mixed reality (MR) setup that enables users to assemble the exact fit components of the arch (Section 4).

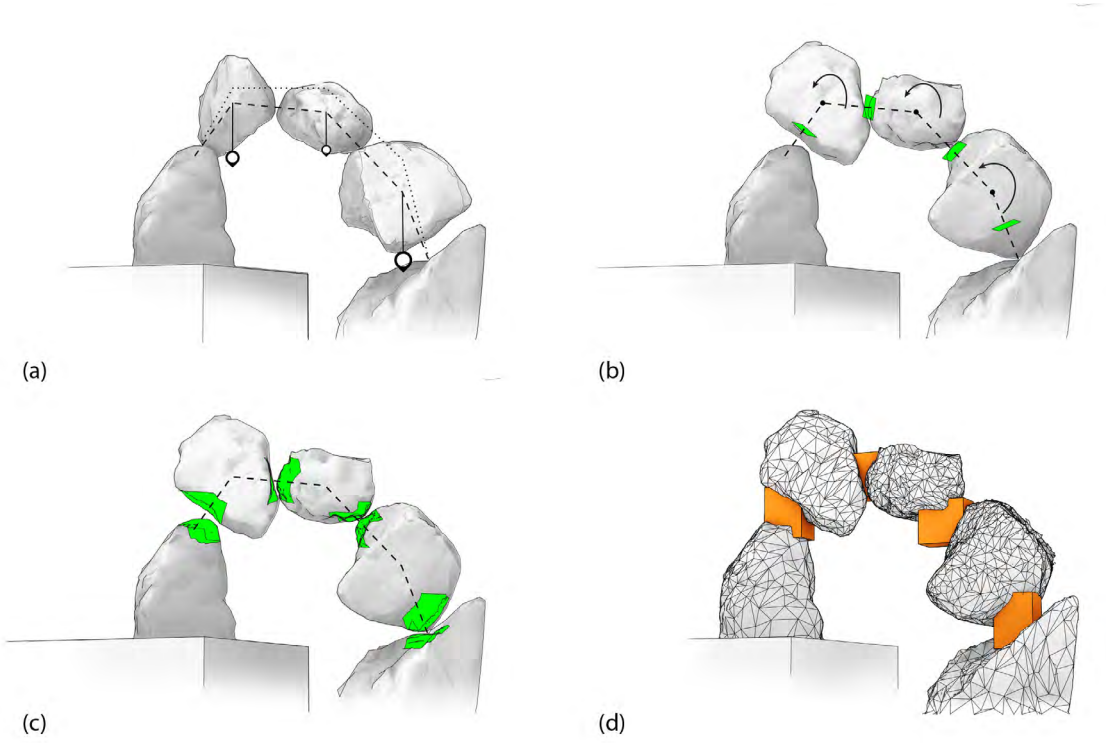


Figure 1: Recalculated thrust-line based on the weights of stones (a), rotating stones to match stone interfaces and thrust planes (b), interfaces of stones (c) and connectors generated based on the.

2. Method

The main processes that have to be implemented to build with Digital Rubble are acquisition of 3D data, algorithmic arrangement and 3D printing. As all three are numerical based operations they can be matched in scale and resolution. For the scope of the paper we aimed at developing a framework connecting the three parts to build a bridging arch. Natural rubble rock was chosen for our study because it is a homogenous and rigid material. The stone had a maximum weight of 7,5 kg to enable manual assembly. The base stones had a weight of 6,5 and 7,5 kg while the arching stones had a total weight of 14 kg. Additionally, the stones were chosen to be convex to minimize acquisition problems of the photogrammetry process and complexity of the later assembly.

2.1. Digitization of Rubble

The acquisition of 3D data was done using photogrammetry. We used the professional software tool Agisoft PhotoScan. It allows fast 3D reconstruction from photographs. Each stone was captured by taking 30 – 50 photos with a single-lens reflex camera (SLR) camera. In order to determine the correct size of the stones we placed a reference object into the scene of which the exact size was known. The scene had a diffuse lighting condition to avoid hard shadows on the stones while illuminating it from all sides. We placed a stone on a reference base that was later used to determine the correct size. The distance of two points on the base is measured and input into Agisoft PhotoScan as constraint points. The software automatically calculated the photograph poses, 3D point cloud and the resulting 3D meshes (Figure 2).

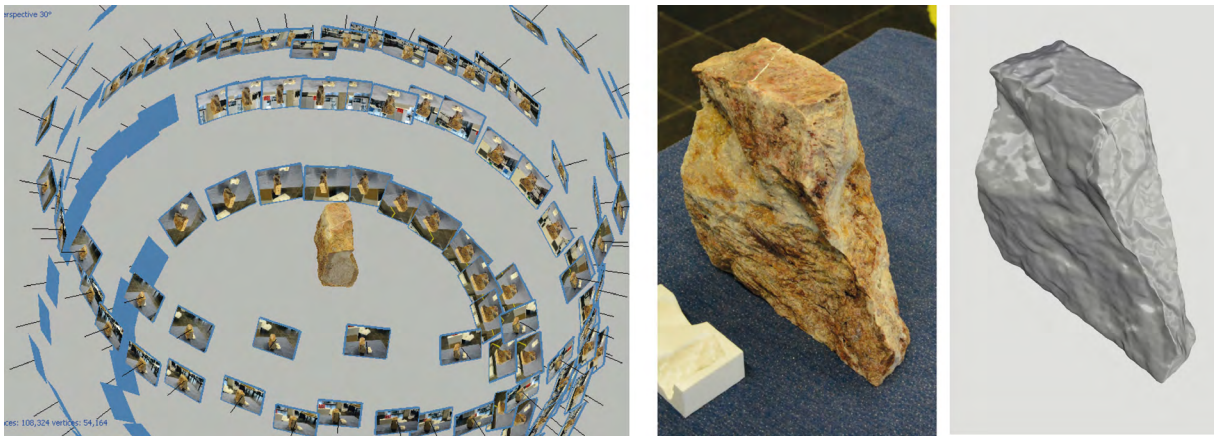


Figure 2: Digitization of a stone in Agisoft PhotoScan. The calculated photo poses (left) and the real stone and its digital representation (right).

2.2. Algorithm for Arrangement

The core algorithm was developed to design an arch spanning bridge from digital rubble. Therefore, we had to implement a method to restructure the 3D meshes that were generated through photogrammetry. The distribution of the rubble along thrust lines was done by a tool based on graphic statics. An evolutionary algorithm was implemented to arrange the digital rubble to orient the connecting faces of the meshes perpendicular to the thrust line. Finally, the algorithm automatically generates connectors that can be 3D printed.

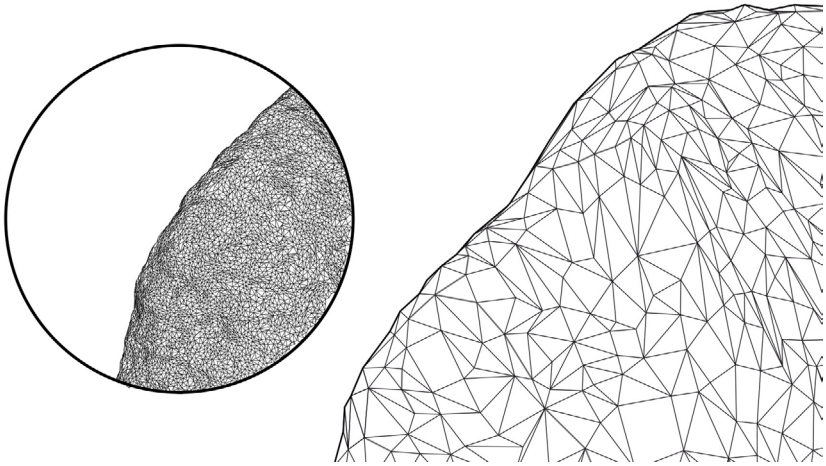


Figure 3: Exemplified reduction of a mesh with 198.896 faces to a mesh with 2.991 faces.

2.2.1. Data Preparation

3D meshes form the photogrammetry had different face counts. We reduced the face counts of the meshes to have face sizes of 0.9 cm² ± 0.3 cm² to speed up the following algorithms (Figure 3). Those low-polygon meshes were used as instances to speed up the testing phase and the evolutionary algorithm. The full resolution meshes were kept and put into the solution for further treatment and preparation of the connectors.

2.2.1. Thrust Line

The thrust line was calculated based on an input curve and the meshes of the rubble (Figure 1). The 3D meshes were considered as homogenous materials which allowed to use the geometrical centroid as their center of mass. An input curve was converted into a polyline with a control point count that equals the number of 3D meshes. The digitized rubble rocks were distributed on the control points of the polyline. Based on the weights of the stones and their distribution along the input curve the thrust line was calculated. Therefore, the control points of the polyline were repositioned using the reciprocal properties of force polygon and funicular polygon from graphics statics [5].

2.2.2. Connector Generation

The arch as a compression only structure needed additional connectors between the natural rubble. These connectors were generated to transfer the forces between the rubble rocks along the thrust line. The 3D meshes of the rocks were analyzed in a radius of 2 cm along the thrust line. The normal of the mesh faces in this zone were analyzed and compared with the direction of the thrust vector. To reduce the deviation between thrust vectors and normals we implemented an evolutionary algorithm. The stones were rotated around their center of mass on the thrust line around the XYZ-axis. The goal of the algorithm was set to minimize the deviation between normal orientation of the meshes and the matching thrust line.

2.3. Manufacturing

2.3.2. Connector Fabrication

Cubes were chosen as base geometry for the connectors to give visual guidance for the assembly as the cubes share a common orientation. Earlier experiments revealed problems in finding the correct orientation to fit connector and stones (Figure 4).

The connectors were 3D printed using an Ultimaker 2+ with PLA. The printing parameters were set to meet the resolution of the 3D digitized meshes. The layer heights were set to 0.14 mm with a nozzle diameter of 0.4mm. The infill was set to 15% and the wall thickness to 1.6 mm.



Figure 4: Different connector geometries were tested.

2.3.2. Mixed Reality Assembly

The assembly was done using a mixed reality setup. This was necessary due to the complex geometries of the irregular stones that are hard to align without visual guidance. The final assembly was uploaded from the design software Rhino 3D as low poly meshes to the Microsoft HoloLens headset using Fologram [6]. The software platform streams geometry directly from Rhino 3D to the headset and allows users to work in mixed reality. A conventional paper plan would slow down the process drastically as it is limiting the flow information. Moreover, the HoloLens allows user to overlay the digital parts with the physical while keeping the hands of the users free (Figure 5). To register and align the digital model in the physical world a placement marker was used. Additionally, as the 3D model is streamed directly from Rhino we can adjust the visibility of parts depending on the current status of assembly.



Figure 5: User view through the HoloLens.

3. Results and Discussion

To validate the workflow and application of the proposed Digital Rubble design and fabrication methodology a demonstrator was build. We were able to build an arch consisting of five 3D digitized stones connected by four 3D printed connectors. A design input was given as a curve that allowed users to define the curvature of an arch.

The evolutionary algorithm converged to an approximate global optimum in average of around 150 iterations or around 2 minutes on a conventional workstation computer. The stones were rotated so that the generated connectors only transfer compression along the thrust line. Other frameworks dealing with an optimization solver of unprocessed rock focused on packing rocks into a wall but do not allow any design input [7], [8]. The 3D printed connectors as a minimal intervention enabled to build complex shapes from irregular rubble. Compared to the 14 kg stones, the 3D connectors weigh only 0.2 kg.

The mixed reality setup enabled a fast check for users during assembling of the objects (Figure 6). The communicated orientation of the stones in combination with the exact fitting 3D printed connector allowed two people to assemble the arch in less than 5 minutes. While this process could eliminate a lot of the complexity of building compression only structures from unprocessed rock it still requires manual work. However, Furrer et al. have shown that robots are capable of autonomous dry-stacking of unprocessed rock [9].



Figure 6: The mixed reality setup allowed users to switch parts on and off depending on the stage of assembly.

The 3D printed connectors hold irregular shaped elements through dry stacking in place (Figure 7). Some minor errors were caused due to tolerances the digitized data and resulting meshes.

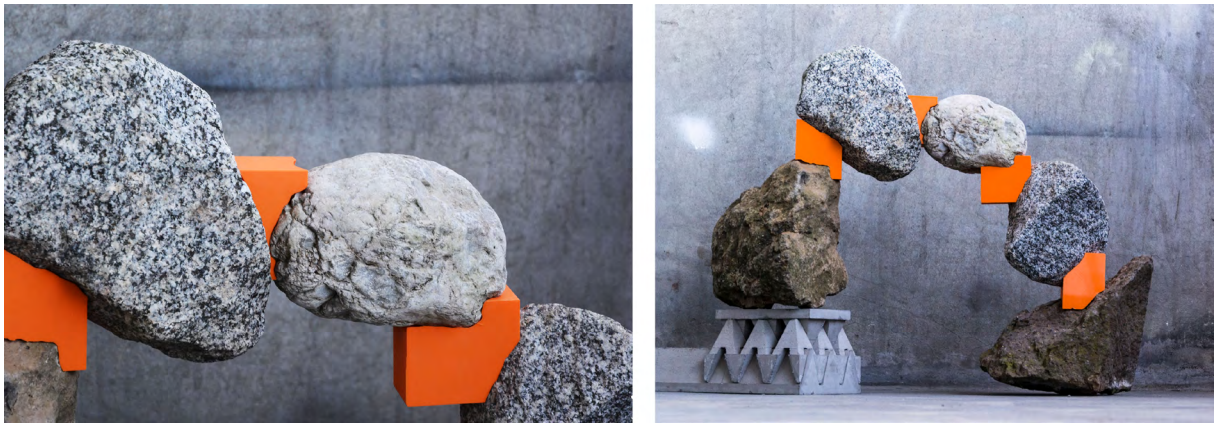


Figure 7: The mixed reality setup allowed users to switch parts on and off depending on the stage of assembly.

4. Conclusion

A design process that departs from existing physical objects was presented and physically evaluated. Our research combines an approach from graphic statics with natural stones as input. Combining photogrammetry, 3D printing and mixed reality.

We were able to build with our proposed method an arch with Digital Rubble. We showed how photogrammetry can be used for digitization of irregular stones and how to design with the resulting meshes. An algorithm was used to automatically form an arch and generate connectors for 3D printing. Therefore, we implemented a technique from graphic statics and showed how to use a mixed reality tool for the assembly process.

For this stage of the research natural rubble was chosen to illustrate the feasibility of the proposed methods on highly irregular parts. However, the stones used were mostly convex, which reduced the complexity to start optimizing the interfaces for the connectors.

So far, our research is limited to small scale prototypes and available printing technology. As a next step to scale this method, the printing technology could use different materials as well as other irregular building materials. Furthermore, we aim at creating more complex target shapes, like shells. Therefore, methods of extended graphical statics like 3D thrust networks can be applied [10].

The research opens aims at connecting the digitization of physical objects with irregular shape for construction and connects it with a digital fabrication technique for additive manufacturing. The mixed reality scenario illustrates the possibilities to guide users during the assembly of irregular shapes. Overall, research on combining these technologies might impact how we use natural and irregular materials in the build environment.

Acknowledgements

We would like to thank Timur Zhigaylo for his initial experiments on 3D printed connectors. Thanks to Muriel Stemmler, Emilia Kühn, Carla Kleinschmitt and Max Gehron for their committed work on photogrammetry and 3D printing.

References

[1] J.-P. Protzen and S. Nair, “Who Taught the Inca Stonemasons Their Skills? A Comparison of Tiahuanaco and Inca Cut-Stone Masonry,” *J. Soc. Archit. Hist.*, 1997.

[2] P. Block, L. Lachauer, and M. Rippmann, “Validating Thrust Network Analysis using 3D-printed, structural models,” in *Proceedings of the International Association for Shell and Spatial Structures Symposium 2010*, 2010.

[3] T. Van Mele *et al.*, “Form finding and structural analysis of a freeform stone vault,” *Proc. IASS Annu. Symp. 2016 “Spatial Struct. 21st Century,”* 2016.

[4] M. Self and E. Vercruysse, “INFINITE VARIATIONS, RADICAL STRATEGIES,” *Fabr. 2017*, pp. 2017–2020, 2017.

[5] K. Culmann, *Die graphische statik.* 1866.

[6] “Fologram.” [Online]. Available: https://fologram.com. [Accessed: 30-May-2019].

[7] M. Lambert and P. Kennedy, “Using Artificial Intelligence to Build with Unprocessed Rock,” *Key Eng. Mater.*, vol. 517, pp. 939–945, 2012.

[8] V. Thangavelu, Y. Liu, M. Saboia, and N. Napp, “Dry Stacking for Automated Construction with Irregular Objects,” pp. 4782–4789, 2018.

[9] F. Furrer *et al.*, "Autonomous robotic stone stacking with online next best object target pose planning," in *Proceedings - IEEE International Conference on Robotics and Automation*, 2017.

[10] P. Block and J. Ochsendorf, "Thrust network analysis: A new methodology for three-dimensional equilibrium," in *Journal of the International Association for Shell and Spatial Structures*, 2007.

Proceedings of the IASS Annual Symposium 2019 – Structural Membranes 2019
Form and Force
7 – 10 October 2019, Barcelona, Spain
C. Lázaro, K.-U. Bletzinger, E. Oñate (eds.)

Natural Form(s): case study of a spatial framework composed of naturally grown forked branches

Lukas ALLNER*, Daniela KROEHNERT*, Andrea ROSSI[a], Matthew TAM[b]

*University of Applied Arts Vienna
Vordere Zollamtsstraße 7, 1030 Vienna
lukas.allner@uni-ak.ac.at, daniela.kroehnert@uni-ak.ac.at

[a] Technical University Darmstadt
[b] Bollinger + Grohmann Engineers, Vienna

Abstract

Wood as a construction material not only serves as a sustainable resource but also offers the potential to develop complex structural models (and architectural spaces) that are derived from its complex material logic. This paper proposes an experimental methodology for the design of spatial frameworks that utilize natural forked branches as structural components. Computational methods such as 3D-scanning and parametric structural analysis tools allow designers to cope with the irregular complexity of the natural material. This paper presents a comprehensive digital workflow leading to the robotic fabrication of a medium scaled demonstrator.

Keywords: Naturally grown form, complex wood structures, spatial frameworks, discrete element aggregation, 3D Scanning, parametric engineering, structural optimization, digital fabrication

1. Introduction

The structural system of trees responds to multiple forces forming a complex configuration of structural members, resulting in an optimized form, with forking branches acting as optimized joints (Mattheck [1]) (Müller *et al.* [2]).

Based on concepts previously presented (Allner and Kroehnert [3]), this paper expands the research with a design and fabrication process of an experimental spatial framework formed by tangentially joined branch parts. A digitized set of hornbeam branches is utilized as components in a synthetic formation. This is a project in the tradition of architectural research attempting to utilize wood in its natural form (Mollica and Self [4]). It also explores how design control becomes relative to the constraints introduced by the available inventory, determining a dynamic design process in which constraints and design goals are negotiated in a feedback system.

Adapting the structural logic of natural trees to architectural applications, originally cantilevering branches are reassembled to form closed loops constituting a cellular framework with improved structural integrity and general bracing. For the purpose of this paper, the demonstrator represents a case study of a regular lattice of tetrahedron cells.

2. Digitization and Cataloging

The workflow starts with a collection of 3d scan models of the physical branch parts, which have been prepared by flush cutting the ends and with marking of several reference points.

In an automated process centerline models (Figure 1) are generated from the mesh geometries: Centroids of co-parallel section outlines define vertices of polylines. For an optimal matching of the indi-

Copyright © 2019 by Lukas Allner, Daniela Kroehnert, Andrea Rossi and Matthew Tam
Published by the International Association for Shell and Spatial Structures (IASS) with permission.

vidual branches to their averaged placeholders within the spatial lattice grid according to the structural load scenario each branch arm's diameter is generated and represented by a circle.

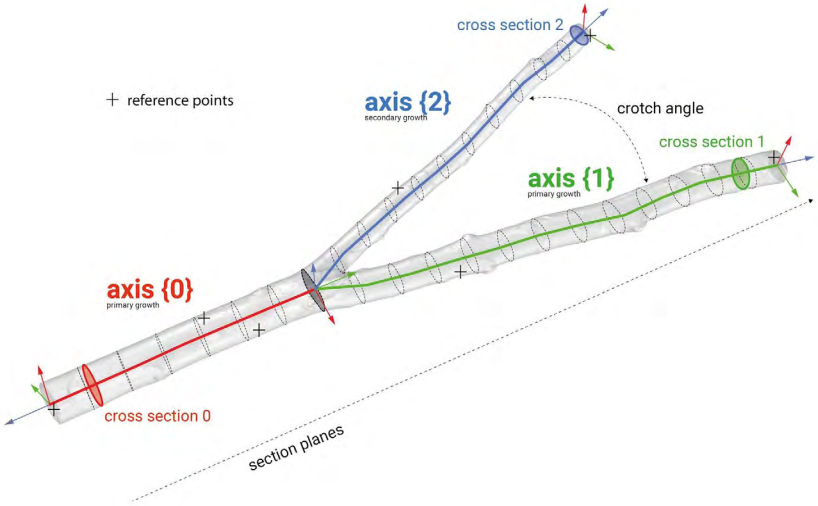


Figure 1: Automated generation of centerlines and additional necessary data

In the digital model points are defined at the markings registered in the scan texture.
These serve as geometric reference for matching the digital and the analog models at any step of the process and allow to monitor changes in shape caused by varying humidity and drying. With this method a high precision placement during CAM processing is achieved despite the complex irregular form.

The digitizing process returns a catalog containing a large number of unique elements, each with a similar topology, but different dimensions, angles, cross-sections and orientations of the individual branches (Figure 2).

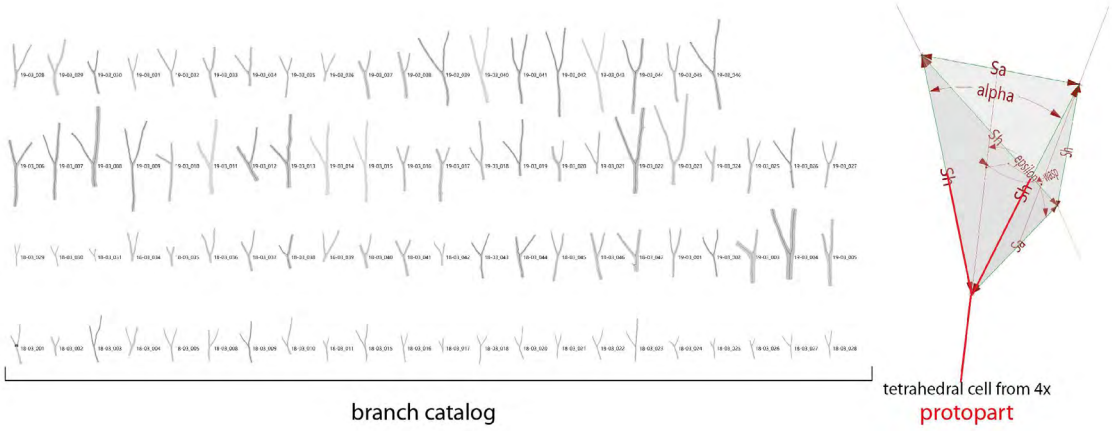


Figure 2: branch catalog and simplified parts assembled into tetrahedral cell

3. Aggregation and Structural Evaluation

As an intermediate step to arrive at a final formation, an initial aggregation of identical typical elements or proto-parts is generated. The proto-parts are used as place holders for the actual, unique specimen to be positioned in a second step.

All collected branches for this case study share the same anatomic principle of a single bifurcation. This typology can be approximated into a Y-shaped axis model with three connected line segments. Four of these elements are assembled into one tetrahedral cell which is aggregated into potentially endlessly structures (Figure 3). Amongst many possible formations composed of branch parts the presented investigations focus on this one specific instance of a topologically repetitive/regular lattice of tetrahedral cells as a case study.

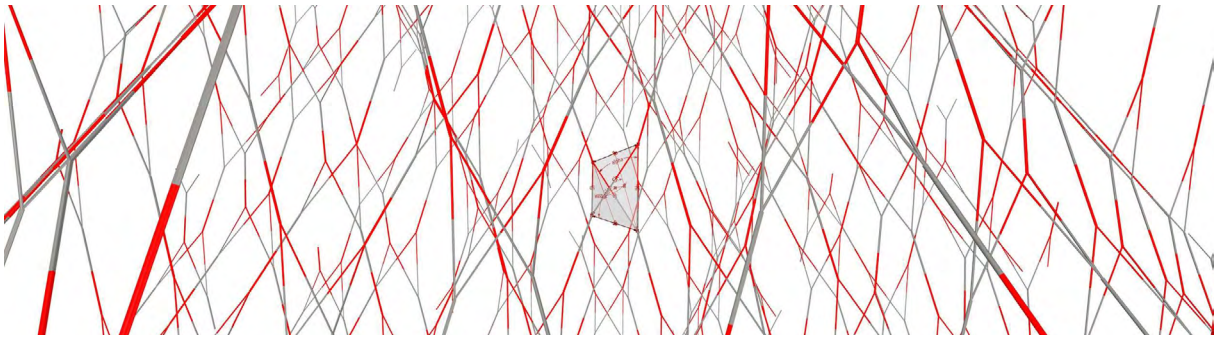


Figure 3: spatial lattice aggregation from proto-part tetrahedral cells

For the aggregation of simplified elements the Wasp plug-in for Grasshopper is used. This tool for discrete design was developed by Rossi and Tessmann [5].

One averaged Y-shaped proto-part is constructed based on the average crotch angle and the longest branch arm length retrieved from the set of scanned elements. An aggregation of those identical proto-parts approximates the extents and global density of the final formation.

Parts of the structure which have only one connection with another single branch are eliminated for redundancy. This ensures that there are no "flying" elements in the aggregation weakening the overall structural performance.

The global proto-part aggregation is then evaluated in Karamba3D for Grasshopper, a plugin developed by Preisinger *et al.* [6]. Different load case scenarios are evaluated (Figure 4). Generic assumptions of gravity and horizontal wind loads (a) are applied along with various vertical load-cases such as a "roof" dead loads (a), "floor-plate" live loads (b) and randomly distributed live loads throughout the structure (c). These calculations are done applying the average cross section to all elements.

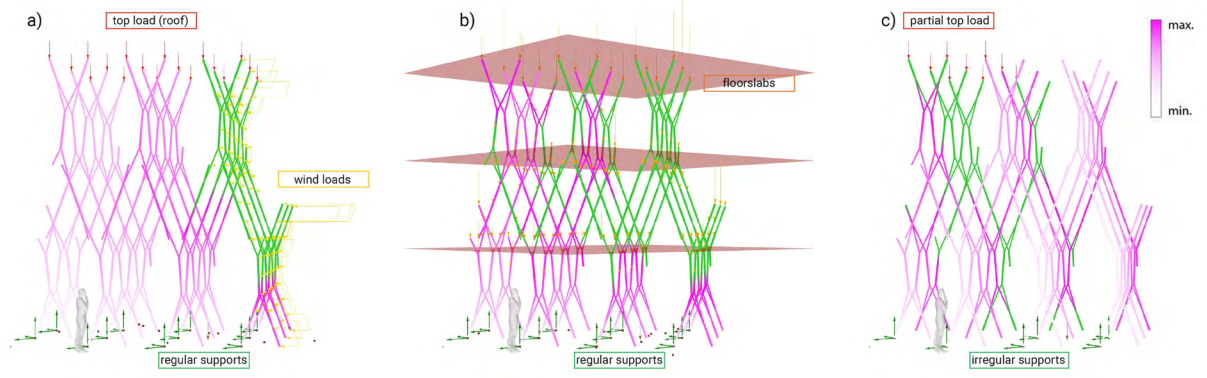


Figure 4: different load case calculations with Karamba3D - displacement visualization

3.1. Part Replacement

Subsequently, each instance of proto-parts is replaced by one of the real specimen from the catalog. Local utilization as shown by the simplified structural analysis is used as defining parameter for the final combination of available elements. The analysis affects a layout of required cross section distribution (Figure 5). Each member in the set is then positioned according to the best fit average cross section per part.

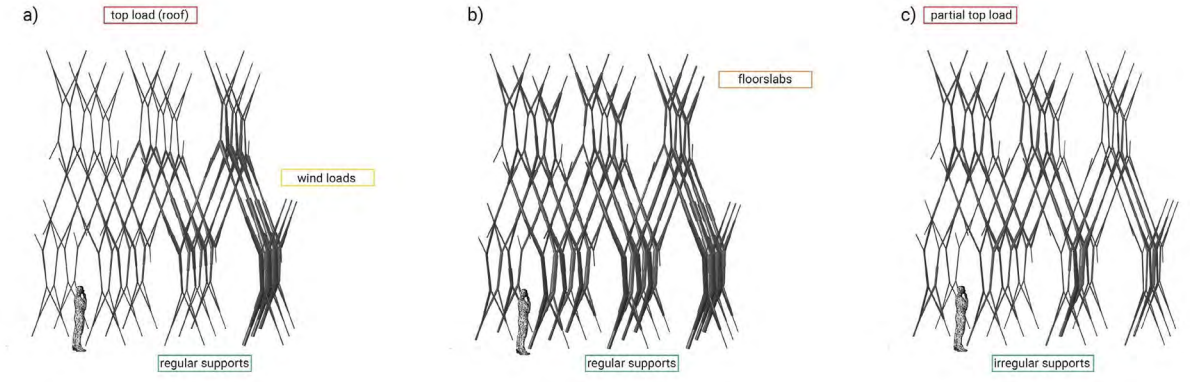


Figure 5: initial cross section requirements for load case scenarios

3.2. Gap Compensation with Dynamic Relaxation Method

Replacing idealized modular elements with actual specimen, each with a unique form, generates discontinuities in the framework. To apply the dynamic relaxation method the Grasshopper plug-in for Kangaroo (Senatore and Piker [7]) is used. Gaps and discontinuities are compensated by translating the aggregation topology into a constraint-based model in Kangaroo. Parts are defined as rigid bodies with springs connecting end segments. In the iterative simulation the springs compress, closing gaps and forcing ends to overlap. Additionally a constraint is set for overlapping end segments to align (Figure 6).

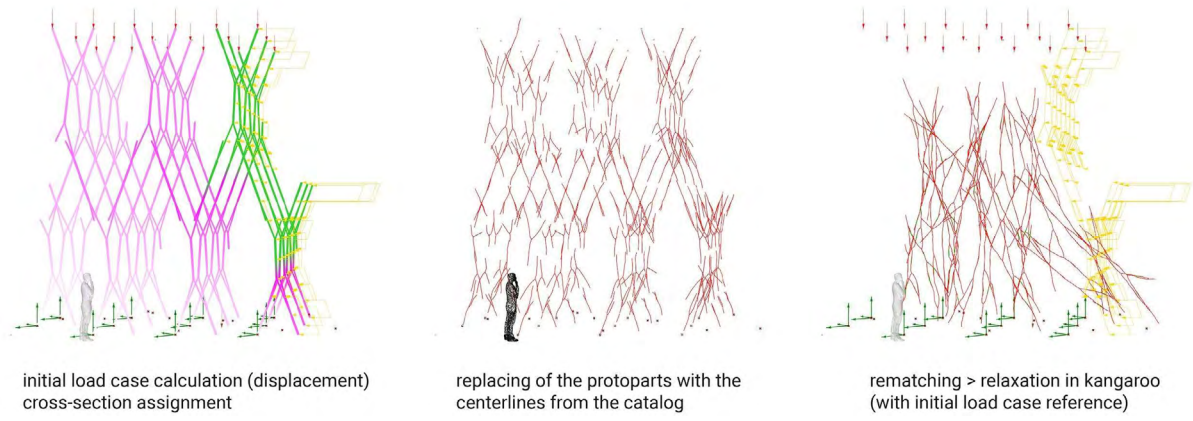


Figure 6: load case calculation, replacement of proto-parts and realignment of the real branch-centerlines

After relaxation the 3D scanned mesh models are mapped to the locations of their respective axis model.

4. Results

As expected the deformed model shows a significant transformation of the initial regular aggregation. Dependent on the scenario large variations of the initial form occur, representing a combinatory adaptation of the same set to the respective force conditions (Figure 7).

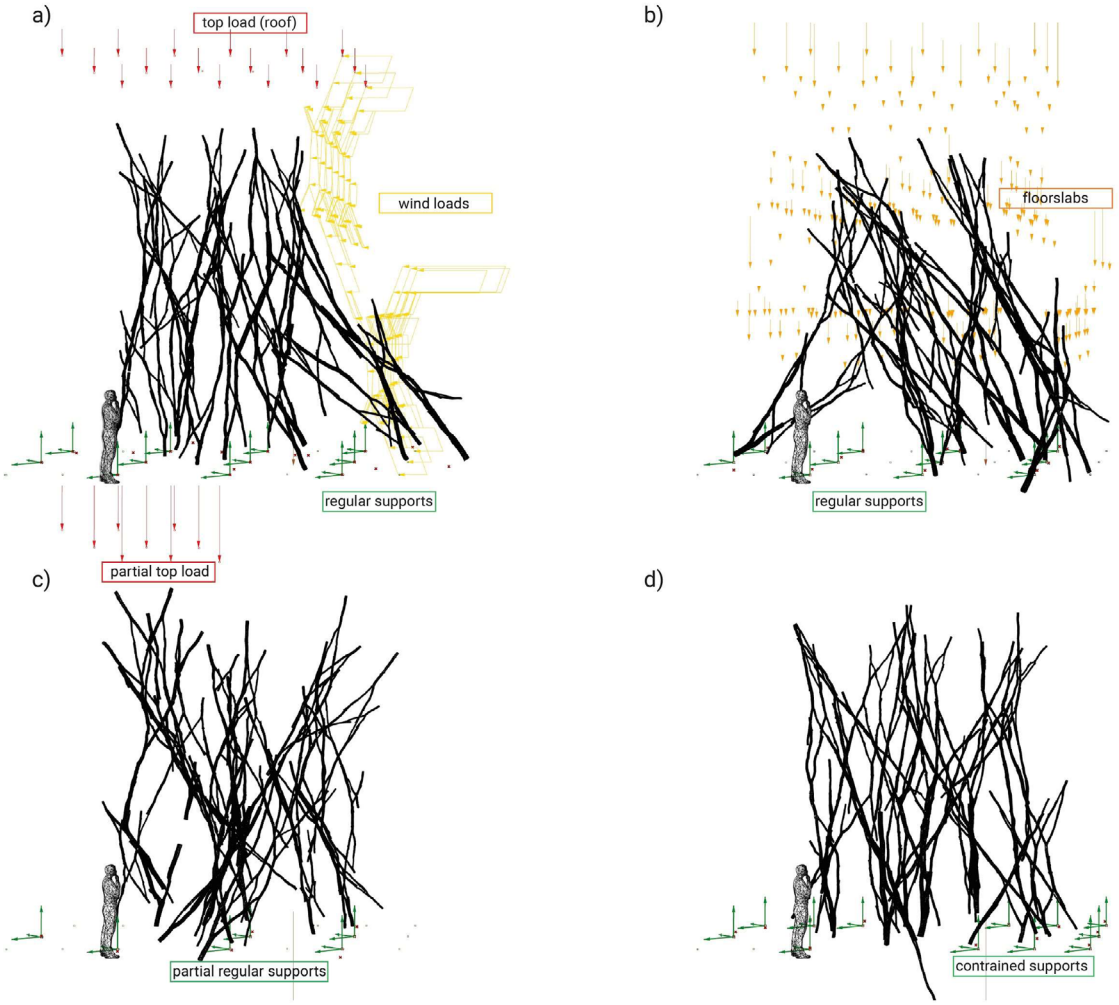


Figure 7: replaced and realigned branch-set from the catalog according to different load case scenarios

For the same load case scenario the required cross sections are visualized as circular profiles and overlaid with the actual branch geometry. The comparison shows that in the calculated load case scenarios the necessary cross sections are much smaller than the available branches. (Figure 8) There are two possible explanations for this that need further evaluation. The final structure is smaller than the initially calculated model as the maximum branch arm lengths are taken for the proto-part definition. Therefore the structure is globally more compact and thus more rigid against forces. Another hypothesis is that the structure is more stable because of its irregularity compared to a regular structure.

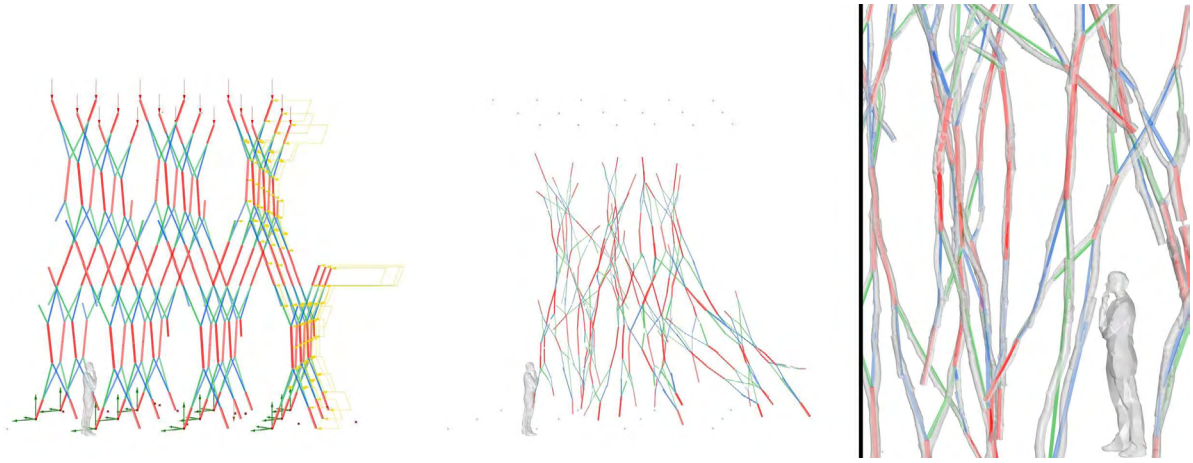


Figure 8: comparison of cross sections in the regular (left) and in the final aggregation (middle). Required cross sections in color overlaid with actual branch geometries

As an optimization of the found formation each branch element is evaluated against its orientation in the framework. Each branch element has a different cross section at index 1 and 2 (see Figure 1), ideally the larger cross section should be assigned to the larger utilization value. Instances with a mismatching association are flipped. Then relaxation is performed again on the modified aggregation with flipped elements. This process is repeated in a loop expected to render an optimized aggregation after a number of iterations. However the change in global geometry caused by the flipping is too drastic to produce meaningful improvements.

With an inventory restricted to elements with identical branch segment lengths the geometric change in the aggregated form could be minimized. A possibly more effective approach would be to reconsider the choice of cross sections as the only selection criteria for the positioning of elements. A multi criteria assessment also including geometric features of branches would increase the level of control for structural optimization.

5. Conclusion and Outlook

At the moment of writing this paper a workflow and techniques for CNC and robotic fabrication of a medium scale demonstrator composed of approximately 30 parts are developed (Figure 9).



Figure 9: fabrication tests with a 3 axis milling machine (left) and a robotic arm (right)

Currently improvements and additional functionality of the aggregation algorithm (Wasp) are under development to integrate more diverse categorization of the set as well as goal based iterative aggregation principles.

The material properties of a common Hornbeam structural element, was assigned for the structural analyses calculations. Due to the peculiarities in such an untreated and non-standard material, a further material analysis of the found branches is important to gauge its actual structural performance.

Another aspect to consider is the difference of stem and branch wood on a cellular level as indicated in the research of Lichtenegger *et al.* [8]. Whereas stem wood is naturally optimized for stiffness and strength, branch wood is optimized for extensibility and bending. Therefore further investigations into the necessary parameters for a valid calculation have to be undertaken.

The preliminary results show the potential of the developed methodology for the exploration of structural design with irregular parts. The proposed workflow could be expanded to other geometries in the context of inventory constraint design methods for reused structural materials as introduced by Bukauskas *et al.* [9]

Acknowledgements

This project is part of the arts-based research project Conceptual Joining, located at the University of Applied Arts Vienna and funded by the Austrian Science Fund (FWF), within the PEEK-program (AR 395-G24).

Sandra Tuider provided the branch samples. The Dept. Of Geometry of the Angewandte made available an Artec EVA 3D Scanner. Philipp Hornung of the ARL (Angewandte Robotics Lab) developed custom tool-path programming for 7-axis robotic joint machining and helped testing and evaluating tools for the robotic fabrication of the prototype.

References

[1] C. Mattheck, *Design in Nature, Learning from Trees*, Springer, Berlin, 1998

[2] U. Müller, W. Gindl-Altmutter, J. Konnerth, D. Kaserer, J. Keckes, "*Stamm-Astanbindung – eine biologisch optimierte Struktur mit hoher mechanischer Leistungsfähigkeit"*, *10.GraHFT'14*, 2014.

[3] L. Allner and D. Kroehnert, "Conceptual Joining: Branch Formations," in *Creativity in Structural Design: Proceedings of the IASS Annual Symposium 2018*, Boston, USA

[4] Z. Mollica and M. Self, *"Tree Fork Truss"* in *Advances in Architectural Geometry*, S. Adriaenssens, F. Gramazio, M. Kohler, A. Menges, M. Pauly (eds.), VDF, 2016

[5] A. Rossi and O. Tessmann, *"From Voxels to Parts: Hierarchical Discrete Modeling for Design and Assembly."*, *International Conference on Geometry and Graphics* (pp. 1001-1012). Springer, Cham., 2018.

[6] C. Preisinger, *„Linking Structure and parametric Geometry"*, *Architectural Design, 83: 110-113, doi: 10.1002/ad.1564,* 2013.

[7] G. Senatore and D. Piker, *"Interactive real-time physics: an intuitive approach to form-finding and structural analysis for design and education,"* Computer-Aided Design, vol. 61, 2015

[8] H. Lichtenegger, A. Reiterer, S.E. Stanzl-Tschegg, and P. Fratzl. *Variation of Cellulose Microfibril Angles in Softwoods and Hardwoods-A Possible Strategy of Mechanical Optimization, Journal of Structural Biology 128 (3)*, 257-269 (1999)

[9] A. Bukauskas, P. Shepherd, P. Walker, B. Sharma, J. Bregulla, "*Inventory-Constrained Structural Design: New Objectives and Optimization Techniques" Proceedings of the IASS Symposium 2018 Creativity in Structural Design*, 2018

Proceedings of the IASS Annual Symposium 2019 – Structural Membranes 2019
Form and Force
7 – 10 October 2019, Barcelona, Spain
C. Lázaro, K.-U. Bletzinger, E. Oñate (eds.)

Structural Behavior of Ice Composite for 3D Printing

Arno PRONK*, Daniel JANSEN, Kamil KARA, Joren v LAAR, Hendrikus WILLEMS

*Eindhoven University of Technology
Vertigo 9.35 PO Box 513
5600 MB Eindhoven
The Netherlands
a.d.c.pronk@tue.nl

Abstract

3D printing with ice composites is an entire new field. It could be applied for Mars missions by using Robots with locally available material such as ice and soil. Another application is 3D printing for sculptures. The third application is 3D printing for temporary structures in artic areas. The problem of using ice for construction is its brittleness. It is possible to reinforce ice with additives. Just as concrete or polymers can be reinforced with steel rods or fibers, ice can be reinforced with soil, silica, wood, paper fibers or polyphenol alcohol. The fibers increase the ductility, compressive and tensile strength. In this way ice becomes a reliable material for construction at temperatures of -8C or lower. The extrusion of cellulose-reinforced ice leads to the drainage of water just before the extrusion nozzle. Therefore, the compressed water-cellulose mixture will form clots in the nozzle, leading to an unreliable process. By mixing fibers, water and a jelly of Guar Gum and Xanthan Gum this problem was solved. A hybrid mixture with other materials such as sand will increase the material properties of the ice composite further more. It will increase both its bending as its compression strength. Adding cellulose showed promising post-peak strain softening behavior. Experiments with different temperatures and testing speeds were conducted. From these experiments it was concluded that both the ultimate strength and the stiffness of the specimens decrease with increasing temperature. At tempters close to 0ºC, the post-peak behavior also changes from brittle to more ductile. Furthermore, the bending tests were modelled in a FEM program and compared with the executed experiments. Based on these experiments in December 2018 the first 3D-printed grid shell in ice composite was realized in Harbin, China.

Keywords: ice composites, 3D printing

1. Introduction

The manufacturing of constructions in the building industry is changing. Nowadays 3D printing is becoming an often used construction technology. One of the possible applications is a 3D printed habitat for Mars, where robots can be used to print constructions with the locally available materials. Ice would be an important available material for the printing of structures. However, ice is not a very common construction material, especially due to its brittleness. This mechanical property of ice can be improved by adding additives but also the compressive and tensile strength.

In this project the different mechanical properties of certain ice composites are researched. This is done conducting compression, bending and creep tests. Since ice is a very sensitive material to e.g. temperature, special test setups are created in order to conduct the tests. With the most optimal test setup different composites can be tested in order to derive the best composite. The results are analyzed and conclusions are drawn. Furthermore the effect of different influential factors are examined. The effect of both temperature and test speed are used to gain more information about the properties of the composites.

Copyright © 2019 by Arno PRONK, Daniel JANSEN, Kamil KARA, Joren v LAAR, Hendrikus WILLEMS
Published by the International Association for Shell and Spatial Structures (IASS) with permission.

Alternatively also a numerical analysis is executed. This is done to check whether the results of our experiments are reliable and/or valid. For both analyses the validity is uncertain due to the lack of previous research, but with the comparison of both, a more reliable result is approached.

One of the composites that is tested is used for an ice and snow construction competition in Harbin. A gridshell made of this composite is executed by the means of 3D printing [1]. Since the 3D printing of ice composites by roboting was not researched before the printing was done by hand with piping bags.

2. Pre-Research

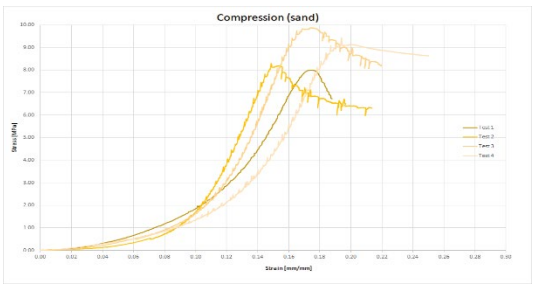
Out of previous research done by Vasilieva et al [2], Pronk et al [3] and TU/e students [4], some initial assumptions have been derived to use as a starting point. The most important assumption are the additives that are used for the different ice composites. From this previous research it is decided on to test ice composites made up of water, sand, cellulose, xanthan gum and guar gum as these have most favourable properties but also because of their availability and ecological neutral footprint.

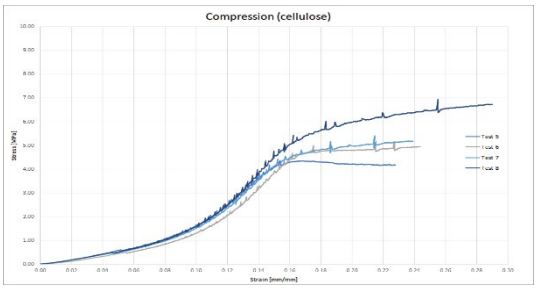
3. Compression strength test

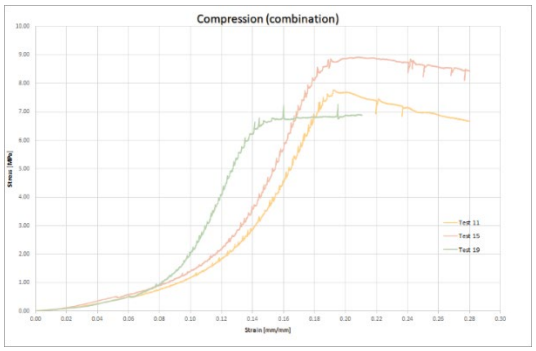
The compression strength tests are conducted on twenty-two different specimens with dimensions 100x100x100mm. The specimens are made up in a certain system in order to isolate the effect that the additives have on the specimen (Tabel 1). The specimen are tested at a temperature of -18 degrees Celsius. The specimens are placed in the setup with the pouring seam on top. In case the top of the specimen was not parallel to the bottom of the specimen the specimen were tested on their side.

Table 1: 22 specimens with different mixtures for compression

Specimen	1	2	3	4	5	6	7	8	9	10	11	12	13	14	15	16	17	18	19	20	21	22
Sand (g)	1000	2000	3000	4000	0	0	0	0	500	1000	1000	1000	2000	2000	2000	2000	3000	3000	3000	4000	0	0
Cellulose (g)	0	0	0	0	25	50	75	100	80	40	60	80	20	40	60	80	20	40	60	20	0	0
specimen 1-20 have 1000 g water, 1.5 g Guar-gum, and 1.5 g Xianthan-gum, specimen 21 and 22 have no adatives																						







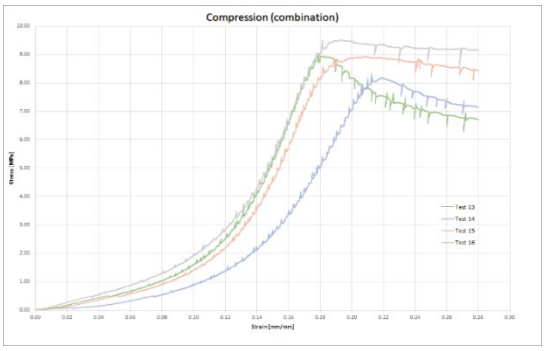


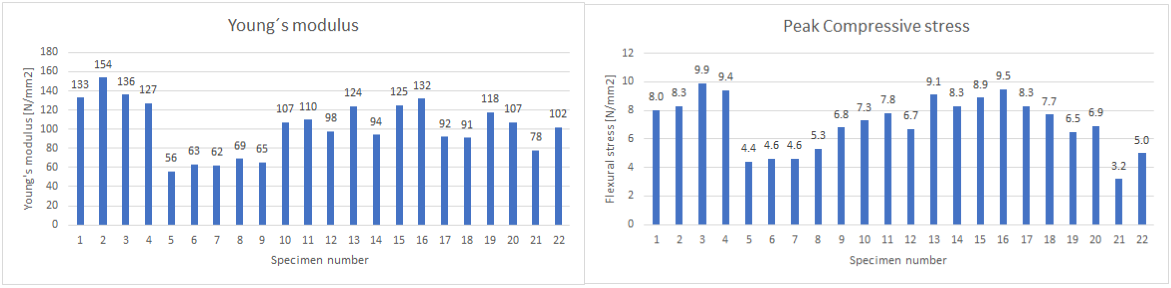
Figure 1 ice and sand, Figure 2 ice and cellulose,Figure 3 & 4 ice, sand and cellulose

The first figure shows that increasing the amount of sand increases the peak stress until a certain level. Specimen 4 with the most sand drops in peak stress compared to specimen 3. So the ideal amount of sand for the highest peak stress lays between specimen 2 and 4. Furthermore all specimens show a drop in peak stresses, this means adding sand adds ductility to the post peak behavior compared to straight ice. The second set of graphs shows mixtures with only cellulose and no sand, so the influence of only cellulose can be analyzed. The cellulose increases in concentration with increasing test numbers. The peak stresses are lower compared to the sand composites. The graph shows strain hardening, which means that it can still take increasing forces even during its plastic deformation. This also increases with the increasing test numbers. In this research no maximum concentration of cellulose has been found after which the mechanical properties decrease. In the third set of graphs the amount of cellulose is constant, but the sand concentration is increasing with the test number. There clearly is a threshold for the maximum concentration of additives. Test 19 shows lower peak stresses, this is assumed to be due to the lack of water that is needed to bond with the additives. The last set of graphs are from specimens with a constant amount of sand, but the cellulose concentration is increasing with the test number. The amount of sand is mostly responsible for the peak stress, as here the specimens with the same amount of sand as specimens 1-4, have similar peak stresses. The differences in plastic behavior are mostly caused by the increasing amount of cellulose.

Interpretation of results

The Young's modulus for each sample was calculated by looking at the linear part of the deformation in the compression tests. Compared to pure water, specimens 1 until 4 (sand), gives a much higher result, 5 to 8 (cellulose) will decrease the Young modulus a little and 9 to 20 (sand and cellulose) the young modules will vary based on the mixture. Testing ice composites it is hard to separate the elastic behaviour from the plastic behaviour because elastic deformation occurs at the moment load is applied and it will immediately followed by a plastic deformation [5]. This implies that the viscous or plastic behaviour of ice must be taken into consideration for some problems, whereas elastic theory is adequate for others [6]. The compressive tests gives much lower Young's moduli than the ones found in literature. The lowest value shown in table 1 is 3000 kg/cm² which translates to approximately 294 MPa. This difference might be explained by a difference in testing speed. As a faster testing speed is used there is less time for plastic creep deformations to occur. This would lead to a steeper graph which would in turn lead to a higher Young's modulus. However this assumption cannot be verified because the testing speeds in the literature are not clear.

Table 2: young's modulus and peak compressive stress



Sample1-4 ice and sand, Sample 5-8 ice and cellulose, Sample 9-20 ice, sand & cellulose, Sample 21-22 pure ice

The peak stress of the specimens tell something about the compressive strength of the specimen, which is an important mechanical property of the mixture. In table 2 all peak stresses are compared in one diagram. Stated that these peak stresses are taken from the moment the linear elastic deformation changes to the plastic deformation. The peak stresses for pure ice is 3.2 MPa to 9.9 MPa for ice with sand.

4. Flexural strength test

The flexural strength tests are conducted as a 3 point bending test on ten different specimens with dimensions 60x60x400mm. The specimens are made up in a certain system in order to isolate the effect that the additives have on the specimen (Table 3).

Table 3: specimens with different mixtures

flexural												temperature & creep tests			
Specimen	1	2	3	4	5	6	7	8	9	10		2	4	6	9
Sand (g)	0	0	2000	3000	2000	2000	3000	3000	0	0		0	3000	2000	0
Cellulose (g)	50	75	0	0	40	60	40	60	0	0		75	0	60	0
all specimen have 1000 g water, 1.5 g Guar-gum, and 1.5 g Xianthan-gum, specimen 9&10 has no adatives															

Results:

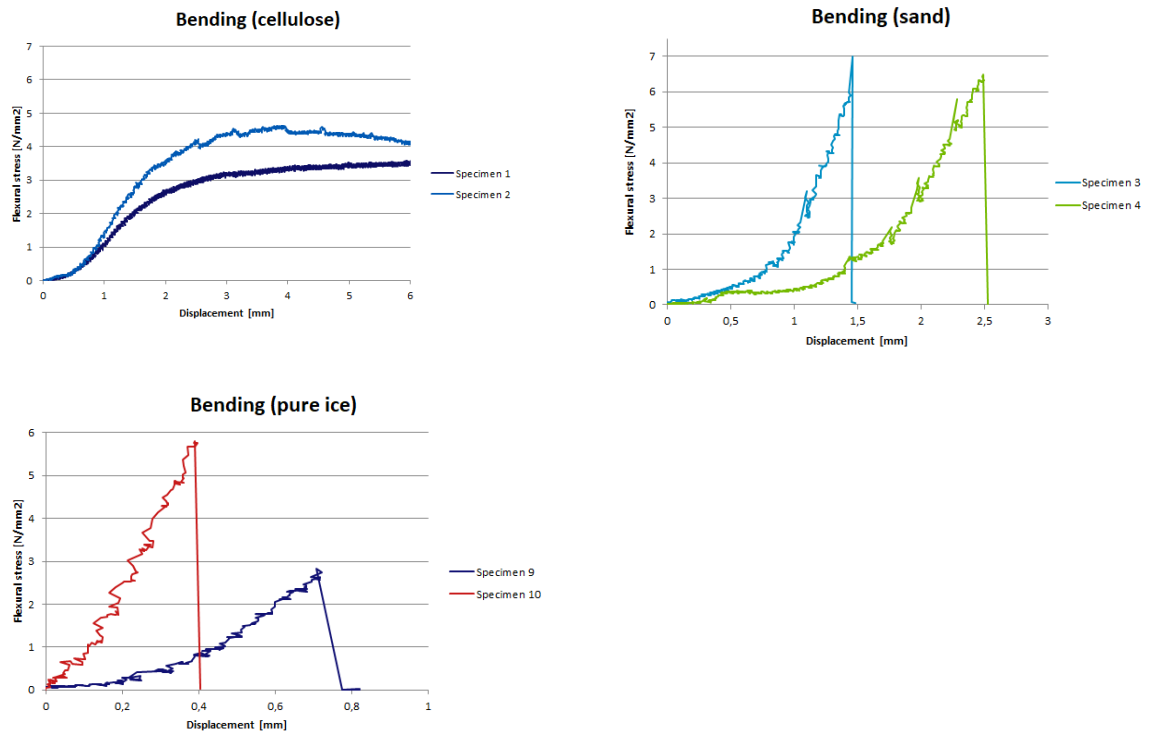
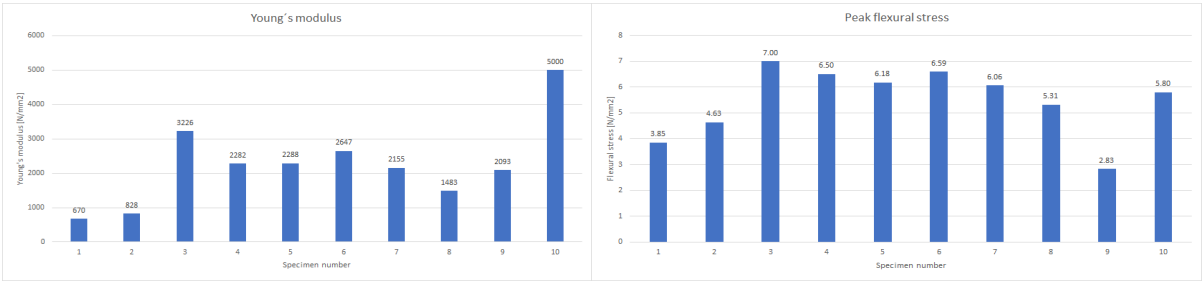


Figure 5, 6 and 7: The different grid options that were analyzed (from left to right: grid option 5, 6 & 7)

In the first set of graphs (cellulose) does not show a lot of strain hardening compared with the compression test but the cellulose does provide more ductility, as the specimens can deform a lot without failing. In the second set of graphs (sand), after the peak has been reached, the stress falls immediately, which shows the brittleness of the sand composite. The last set of graphs is from two specimens with only water. Specimen 9 is poured in one go, specimen 10 in layers. This influences the test results a lot. The peak stress as well as the Young's modulus of specimen 10 is more than twice as big as specimen 9.

Table 4: young's modulus and peak flexural stress



For the comparison of the different specimens with pure ice, they are compared with specimen 9 mainly, because this specimen is just like the first 8 specimens poured in one go.

The first goal of the tests was to get an insight in the behaviour of sand and cellulose independently. To get this insight cellulose was isolated in the first two specimens and sand was isolated in the third and fourth specimen. Again in the flexural bending tests, the effect of adding cellulose is similar as in the compression tests. Adding cellulose has a small effect on the peak stresses. What stands out in the Young's moduli, is that adding cellulose to pure ice makes the Young's modulus of specimen 1 and 2 drop a lot. However increasing the amount of cellulose increases it again. For the third and fourth specimen with only sand, the conclusions from the compression tests are confirmed. It is obvious that the amount of sand will increase the Young's modulus and peak stress.

Specimen 5 until 7 show that adding sand to the water increases the Young's modulus and the peak stress. It also shows that there is a maximum of additives in the composite. When too much sand is added, both the peak stresses and the Young's modulus decreases (specimen 8).

For pure ice the effect of the production of the specimens is examined. Specimen 9 is poured in one go, where specimen 10 is poured in layers. As already mentioned the pouring in one go causes internal stresses and cracking that will reduce the overall strength of the specimen.

5. Temperature test

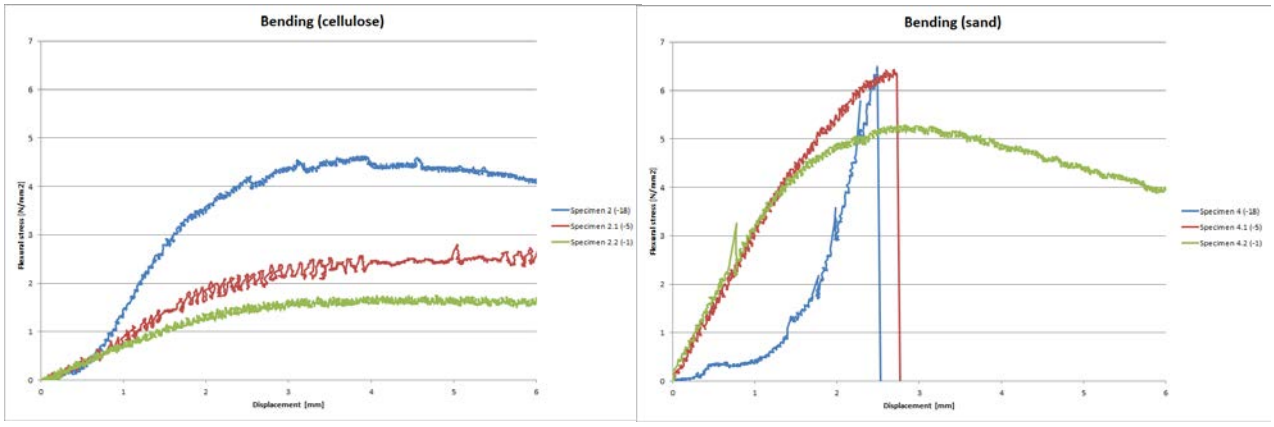


Figure 8 and 9: Specimens 2 and 4 at different temperatures: -18 ºC, -5 ºC and -1 ºC.

All the previous tests were conducted at -18 ºC. It is assumed the strength of the ice composites will reduce with increasing temperatures. To test this hypothesis the same three point bending test as described for the flexural tests will be conducted. The specimens used to plot the effect of the

temperature are specimen 2, 4, 6 and 9 as described in table 3 flexural specimens. Two additional flexural tests were conducted for these specimens at -5 oC and -1 oC. The specimen and the surrounding were continuously monitored to have the right temperature. The bending tests for specimens 2 and 4 (cellulose- and sand-mixtures respectively) are visualised in figure 8 and 9. In the graphs it is visible that with increasing temperature the ductility of the specimen increases. It is also shown that the peak stress and young's modulus of the specimens decreases with increasing temperature. The trends of decrease in Young's modulus and peak flexural strength are seen in all tests as shown in the trend lines in figure 10 and 11.

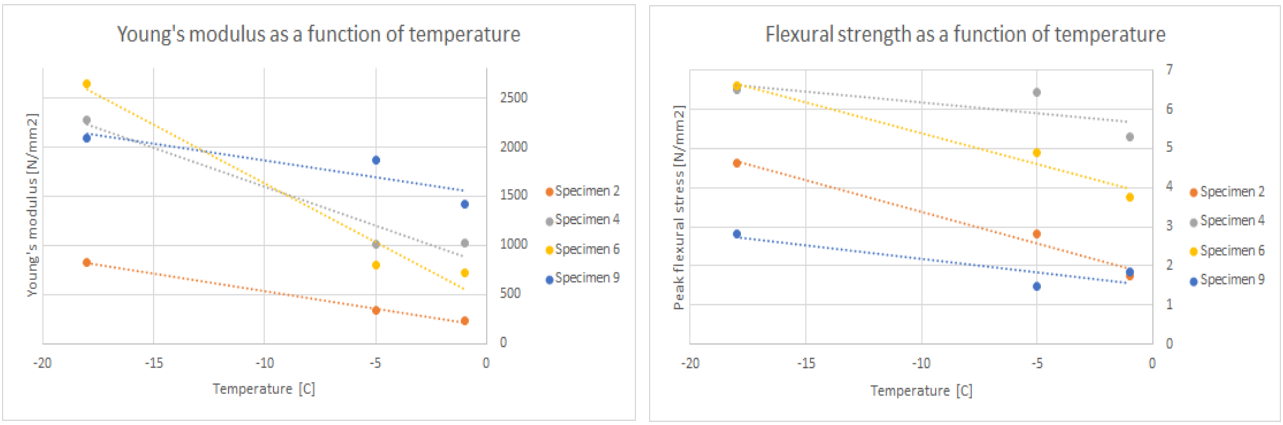


Figure 10 and 11: The trend lines in Young's modulus and flexural strength at different temperatures

It is found that specimens containing sand and coincidentally have a higher ratio of additive/water have a faster decrease in Young's modulus. With higher temperature the water ice loses its ability to bind the mixture. The flexural strength decreases faster in specimens containing cellulose. This can be explained by the softness of the cellulose, most of the strength of the mixture is caused by the strength of ice. Generally it can be concluded that higher temperature leads to lower Young's modulus and lower peak stresses. Notices the same phenomenon is stated in [5] it is explained by the weakening of the cohesion of the ice molecules in the crystalline structure and with that the increase of the possibility of rearrangement of the atoms. This atom-rearrangement is a material property that is manifested in the material as ice crystals are constantly moving and growing or shrinking.

6. Creep test

The creep test is used to determine the creep deformation of a specimen over time. The creep is defined as a time-dependent deformation under a certain constant applied load. To test the ice and ice composites on their creep behavior, three test specimens are created. The specimens that are chosen are the same specimens that were used for the flexural strength tests (specimen 2, 6 and 9). The dimensions of the ice specimen was 30x30x65mm and of the other specimens was 30x30x85mm.

Method of testing

For the creep tests, the specimens are frozen for at least seven days at a temperature of -18 degrees celsius. The load was chosen to introduce a stress in the specimen representing a value from the elastic part of the graph for the compression test corresponding to the same mixture. Measurement of the length of the specimens is done at two sides of the specimens which gives a more accurate result. The measurement is done with a caliper, all within the freezer. The specimens are measured over a time of 45 days.

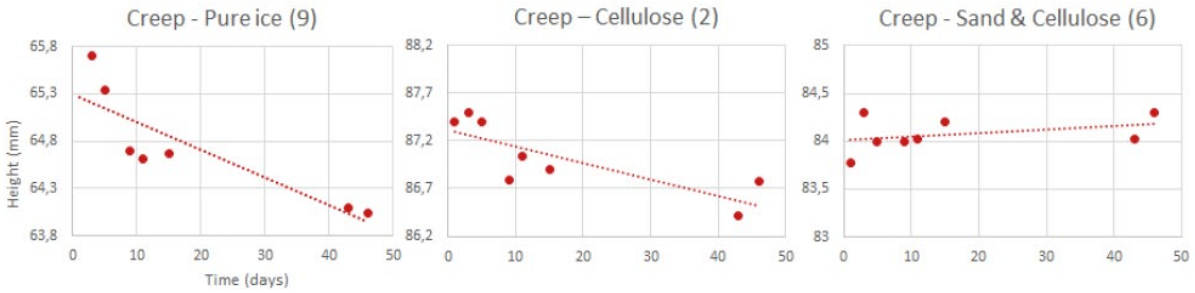


Figure 11 and 12: Creep tests for pure ice, cellulose ice and sand cellulose ice

The results of the creep tests of the three different specimens can be seen in the figure 11 and 12. The height that is plotted is the average height between the two measured lengths.

Interpretation of results

As can be seen in the figures above, the pure ice indicates the highest creep deformations as the slope of the graph is the steepest. Specimen 2 also show some creep deformations. However, the graph of specimen 6 indicates an increase of height, which can not be explained by creep behavior. What can be concluded from the graphs is the fact that they show a wide scatter (inaccuracy) of the points. This indicates imperfections in the way of testing and measuring the results of specimen 6, these imperfections are significant. The reason for these imperfections is the fact that it is very hard to do very accurate measurements on the (still) small specimens in the freezer with a caliper. The length of the test also influences the results. If there would have been a longer time span, the creep would have been bigger and small measuring errors might be neglectable. For those reasons it is hard to draw conclusions from these tests yet.

Alternative creep test

The bending tests took up to 2 hours before failure. This is due to the slow testing speeds which area used based upon the pre-research (to prevent brittle failure due to impact loading). This of course, gives a time span in which creep deformations can occur. Doing the same test but with a quick loading, the plastic deformations (creep deformations) are indicated by the difference in deformation for the same stresses since creep is defined by a time-dependant deformation under a constant load (Downing, N. 2012). The relaxation of the specimen can also be interpreted by the results as the relaxation is defined by a decrease of stress without any deformations. This test is conducted for two specimens that were also used for the flexural strength tests. Namely specimen 2 and 4. Now different from the flexural strength tests is the speed of testing which is increased from 0,2 mm/min to 2,0 mm/min which should isolate the elastic deformations of the specimens at least to a significant extend.

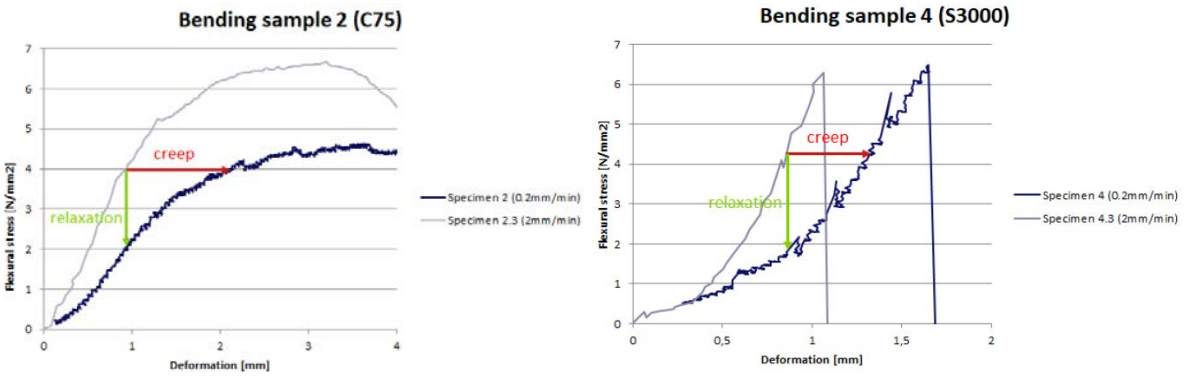


Figure 13 and 14: analysis for creep with different testing speeds

Looking at the test with higher speed for specimen 2, a significant difference can be seen with the test speed of 0,2 mm/min. In red the creep deformations are indicated. As these graphs show the plastic deformations take up a big part of the total deformations in the tests with low speed (0,2 mm/min). Furthermore, due to the fast testing and therefore isolating the elastic deformations, also the Young's modulus changed (indicated by steeper slope).

7. Conclusion

To be able to actually use ice composites as a structural material, a code should be established which presents reliable and validated values to design with. The extent to which results are consistent over time and an accurate representation of the total population under study is referred to as reliability and if the results of a study can be reproduced under a similar methodology, then the research instrument is considered to be reliable. In order to validate whether the values gained in this research are reliable, the tests have to be executed several times which should give the same results.

References

[1] A.D.C. PRONK*, I. BOUW, T. EZENDAM, N. v HIERDEN, J. VLEESHOUWERS, D. vd WEIJDEN "3D printed grid shell in ice composites *Proceedings of the IASS Annual Symposium 2019 – Structural Membranes 2019 Form and Force,* 7 – 10 October 2019, Barcelona, Spain

[2] N.K.Vasilieva A.D.C.Pronk I.N.Shatalinaa F.H.M.E.Janssen R.W.G.Houben "A review on the development of reinforced ice for use as a building material in cold regions" *Cold Regions Science and Technology* Volume 115, July 2015, Pages 56-63

[3] A.D.C. PRONK, Y. MOONEN, Clouds AO, P. LUO, Y. WU, "3D printing of ice" *Proceedings of the IASS Annual Symposium 2017,* September 25 - 28th, 2017, Hamburg, Germany

[4] K.Banda F.Z.Karam A.R.Pastor F.Varano Y.Wang "3D Printing of Fibre reinforces Ice, Advanced design & construct of an innovative structural object. – Project Report

[5] Voitkovskii, K. F. (1960). THE MECHANICAL PROPERTIES OF ICE. From: https://apps.dtic.mil/dtic/tr/fulltext/u2/284777.pdf

[6] Gold, L. W. (1970). Process of failure of Ice, research paper of the division building research Ottowa from: http://web.mit.edu/parmstr/Public/NRCan/rp450.pdf

Proceedings of the IASS Annual Symposium 2019 – Structural Membranes 2019
Form and Force
7 – 10 October 2019, Barcelona, Spain
C. Lázaro, K.-U. Bletzinger, E. Oñate (eds.)

Multi-Material Printing of Multi Lengthscale Bio-composite Membranes

Nic A. LEE[a], Ramon E. WEBER[a], Joseph H. KENNEDY, Josh J. VAN ZAK, Jorge DURO-ROYO, Prof. Neri OXMAN*

*Mediated Matter Group, MIT Media Lab, Department of Architecture and Urban Planning, Massachusetts Institute of Technology

75 Amherst St., Cambridge MA, 02139, USA

*neri@mit.edu

[a] Authors with equal contributions

Abstract

We present advances in a water-based fabrication and design approach for the 3D-printing of functionally graded bio-composites. These developments demonstrate further refinement and large-scale deployment of Water-Based Digital Fabrication in the construction of architectural-scale membrane structures. Fully biodegradable and composed of the most abundant materials of our planet —cellulose, chitosan, and water—these bio-composites represent a versatile system for the construction of dynamic membrane structures with graded mechanical and optical properties across scales. The described digital fabrication system, based on the Fabrication-Information Modeling (FIM) approach, enables the simultaneous printing and mixing of water-soluble materials through real-time feedback-driven control logics. In this way, we explore programming material behaviors through the design of diffusion-based material gradients in biocomposite hydrogels and examine the impact of local and global material cues on the full-scale assembled structure. Novel generative design methods integrate material-specific fabrication parameters and enable data-driven, hierarchical organization of the manufacturing workflow. The parametric control of the chemical composition in the 3D printing process allows for the customization of structural, environmental performative parameters of the structures across scales. In combination, these methods comprise a scalable fabrication system for the creation of adaptable, biodegradable membrane structures with minimal need for environmental control.

Keywords: Additive manufacturing, membrane structures, water-based fabrication, biocomposite, material ecology, fabrication-information modeling, functionally graded materials, architectural hydrogels

1. Introduction

Due to their abundance and ability to safely biodegrade, the manufacturing of biopolymers at scale holds promise as a sustainable and versatile material system. Current developments in biopolymer 3D-printing have centered on the creation of small-scale scaffolds for biomedical purposes [1,2], the extrusion of biopolymers suspended in thermoplastics, and the manufacturing of photocurable resins containing small amounts of biopolymers but may not be fully biodegradable [3]. Scalable systems for the additive manufacturing of pure biopolymer structures remains largely unexplored. Here, we outline further developments in a Water-Based Digital Fabrication system capable of constructing large-scale

Copyright © 2019 by N. A. Lee, R. E. Weber, J. H. Kennedy, J. J. Van Zak, J. Duro-Royo, N. Oxman
Published by the International Association for Shell and Spatial Structures (IASS) with permission.

functionally-graded bio-composites (materials composed of several biopolymers) at room-temperature [4]. Furthermore, we describe a prototype that demonstrates these capabilities at scale.

Previously we demonstrated the fabrication of purely chitosan-based rigid structures at a length scale of up to 4m, as well as multi-layer bio-composites with the ability to dynamically transition between flexible "skin" and rigid "shell" behaviors through the application of humidity [4, 5]. A compelling characteristic of these bio-composites is the ability to dramatically vary material and optical properties through relatively small changes in composition, which is ideal for dynamic variations within a single continuously fabricated object. The implemented fabrication system combines room-temperature extrusion of organic biopolymer gels with the precision and operating scale of industrial robotics. An end effector is outfitted with a pneumatic extruder containing a 300mL cartridge with a detachable nozzle. Nozzle diameter and pressure are varied according to the viscosity and particle diameter of the extruded colloid. Furthermore, extrusion pressure and feed-rate (the speed at which the robot travels) are varied in real-time in order to alter the rate of material deposition. These fabrication parameters are typically assigned prior to printing based on previous experimentation, but they can also be altered "on-the-fly" based on the designer's observations or data gathered during fabrication.

Printed biopolymer gels solidify through evaporation over time. During this process, they continue to flow at a rate proportional to their viscosity and that of the surrounding gels. This provides a window during which materials can flow into one another, leading to the creation of gradients that surpass mechanical resolution limits, and a smooth transitional zone between materials with no need for dithering [5, 6].

We examine the capabilities of this technology and demonstrate a prototype in which both smooth and discrete transitions between materials within large-scale bio-composite membranes are implemented. This represents the embedding of non-diffuse internal structures for the purpose of reinforcing otherwise flexible materials. Smooth transitions allow materials of dissimilar mechanical and optical properties to be mixed during fabrication while bypassing the need to allow hydrogels to fully dry between layers.

2. Methods

2.1 Bio-composite Composition

Each biopolymer hydrogel is composed of 20%-40% apple pectin (VWR, Radnor PA) with varied amounts of 85%-deacetylated chitosan (VWR, Radnor PA), microcrystalline cellulose (VWR, Radnor PA), methylcellulose (VWR, Radnor PA), and natural vegetable glycerin (Essential Depot, Sebring FL) added in order to tune material properties, dissociation rate, and environmental response [8]. Regardless of composition, extruded biopolymers retain their ability to biodegrade more rapidly than many synthetic polymers and bioplastics, with dissociation times in saline submersion ranging from 1 hour to 90 days, according to geometry and material composition. Colloids are mixed in 600mL batches at 2℃ and printed immediately in order to avoid stratification of substrates with varying density.

In order to create optical gradients across the fabricated membranes, natural pigments and dyes are incorporated into bio-composites of each base composition. These include: 1% turmeric powder (Healthworks, Scottsdale AZ), 4% beetroot powder (Bulk Supplements, Henderson NV), 1% maya blue mineral pigment (Natural Pigments, Willits CA), and 1% squid ink melanin (Yamamoto Industry, Tokyo, Japan). Regions with no added color maintain the natural amber hue of apple pectin.

2.2. Fabrication System

We implement a custom pneumatic extrusion system programmed with instruction-feed capabilities that can be affixed to a multi-axis industrial robot or three-axis gantry [7]. Print-nozzle diameters ranging from 12-20GA were utilized according to material viscosity and particle size. Pneumatic and motor control systems allow for pressure and feedrate to be controlled within ranges of 0-400kPa and 0-

8000mm/min, respectively. These parameters are tuned in order to suit specific materials and geometries.

2.3. Computational Workflow

The set of points continuously visited by the end effector without a complete stop in movement is referred to as the toolpath. A print may consist of several toolpaths due to scale or geometry. Weights corresponding to the amount of a material to be deposited at a point are assigned to every vertex in a toolpath. Weight values are stored as an *N*-dimensional vector *w,* where *N* is the number of materials in use across the entirety of all toolpaths within a print. The magnitude of $||w(x,y,z)||$ for any coordinate in a toolpath is 1 for any print where total material deposition is equal at all points, as is the case for even-thickness membranes. During fabrication, material weight values are used as an interpolation parameter between minimum and maximum extrusion pressures, with maximum values corresponding to extruded lines of equal thickness for each material.

Ideally, toolpath geometry varies independently of material weights. In order to achieve this, weight vectors are stored within a mesh that is decoupled from toolpath geometry. Once a toolpath has been established, vertices are populated with weights via a weighted nearest neighbor interpolation, with a search radius of 1 cm. Weight vectors that have been assigned to toolpath vertices are then divided into their individual components and print parameters are generated for each material. Each vector component is used as an interpolation weight between a maximum and minimum ranges for fabrication parameters such as pressure. For continuously extruded heterogeneous membranes, the following pressure ranges were used in printing toolpath-invariant prints with a federate of 800mm/min and a nozzle width of 18GA: 28% pectin, 5% glycerin printed at 0-60kPa, 32% pectin, 2% chitosan, 4% glycerin printed at 0-100kPa, 32% pectin, 4% chitosan, 3% glycerin printed at 41-185kPa.

3. Results

3.1 Continuously Graded Biopolymer Membranes

In contrast to other multi-material printing methods, the water-soluble nature of the extruded colloids allows for a level of diffusion during the drying process. This enables material distributions to equalize into gradients that surpass the system's mechanical resolution, thereby creating smooth gradients even between materials of different viscosities. Such gradients can be used to transition between materials of differing properties or to interpolate between materials and create regions with hybrid properties not found in any individual biocomposite. As previously reported [2], even small changes in biopolymer composition can result in large changes in material properties. This dramatically increases the range of material properties that can be created with a relatively limited material palette.

3.2 Embedded Patterning of Discrete Material Changes

Discrete transitions in materials can be created within a single biopolymer membrane by printing separate toolpaths into membranes before they dry completely. Membranes dry at room temperature and 30% humidity for 10 to 24 hours until they reach a semisolid state where further material extrusions sink into the membrane, but do not diffuse and lose integrity. The resulting embedded pattern does not impact the surface features of the membrane, which maintains its geometry within the continuous print.

3.3 Hierarchical Structure Design

The structure follows a hierarchical design logic that organizes rigid skeletal elements, flexible membrane elements, and a semi-rigid reinforcement pattern. Skeletal elements are additively manufactured by fused deposition with a reusable photopolymer with high strength and elastic modulus. The composition of flexible elements is continuously varied according to structural and environmental parameters. Semi-rigid embedded reinforcement patterns are composed of 32% pectin, 4% chitosan, 4% glycerin, and 1% squid ink melanin.

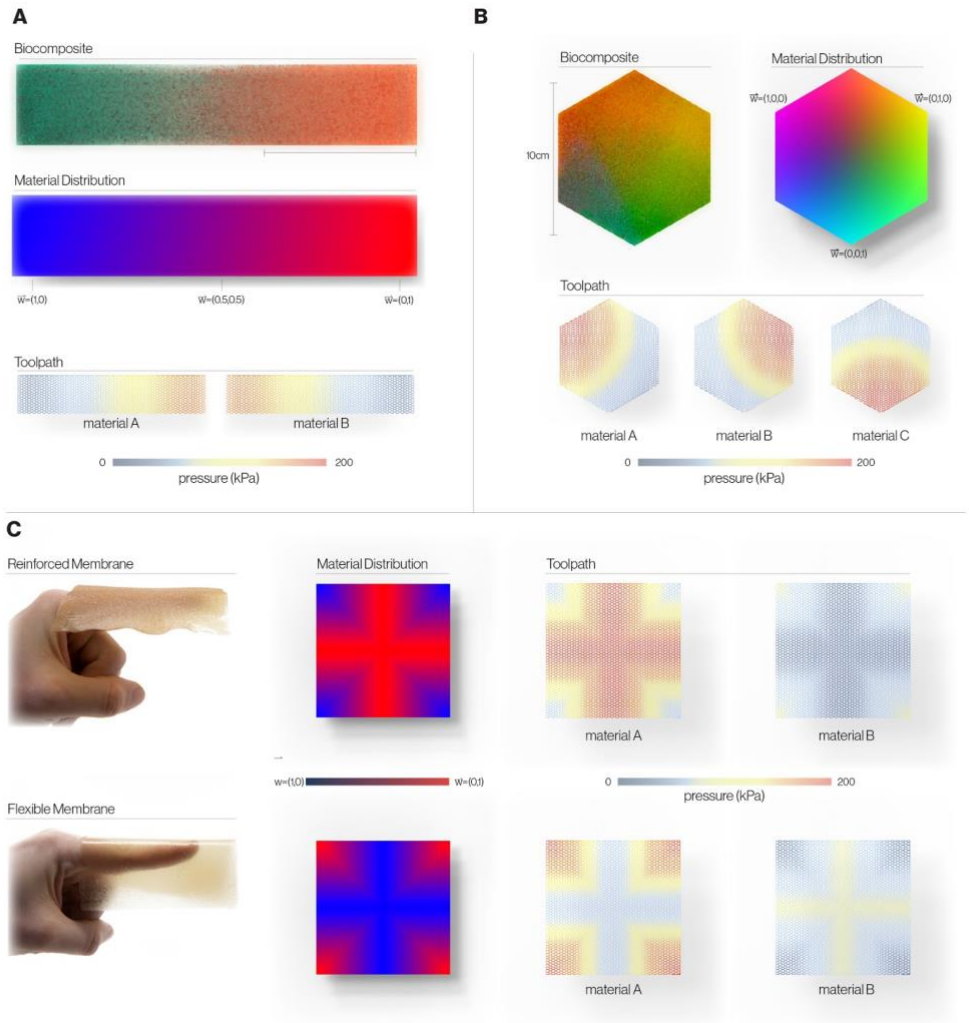


Figure 1: Continuously graded biopolymer membranes for 2 (a) and 3 (b) materials are shown for toolpath invariant prints. Material weights are stored in a vector w(1,... N) where N is equal to the number of materials used. Each vector coordinate is then mapped to pressure values across a toolpath. High- and low-end pressures are specific to each extruded material. Colloids with dissimilar material properties can be blended within a toolpath invariant print to produce different mechanical effects (c).

3.4 Global Geometry and Skeleton

The base geometry features anticlastic curvature shaping an elongated enclosure, open on one side to differentiate interior and exterior space. The base mesh is subdivided into a series of 20 developable quad strips that further define the membrane boundaries. Larger segments are consolidated towards the center of the structure while the smaller sections are arranged closer to the edge of the structure.

The boundaries of the mesh patches are extracted to form the borders of the membrane panels and a further resampling of the quad strip topology ensures the developability of the membrane surfaces. The first hierarchical layer defines the panel size as well as sizing of the main structural branches. Large panels in the center require a stiffer and thicker cross section to ensure stability of the structure, while thinning out towards the top and sides. The parametric model blends in between the various member sizes while ensuring the developability of the panels in between.

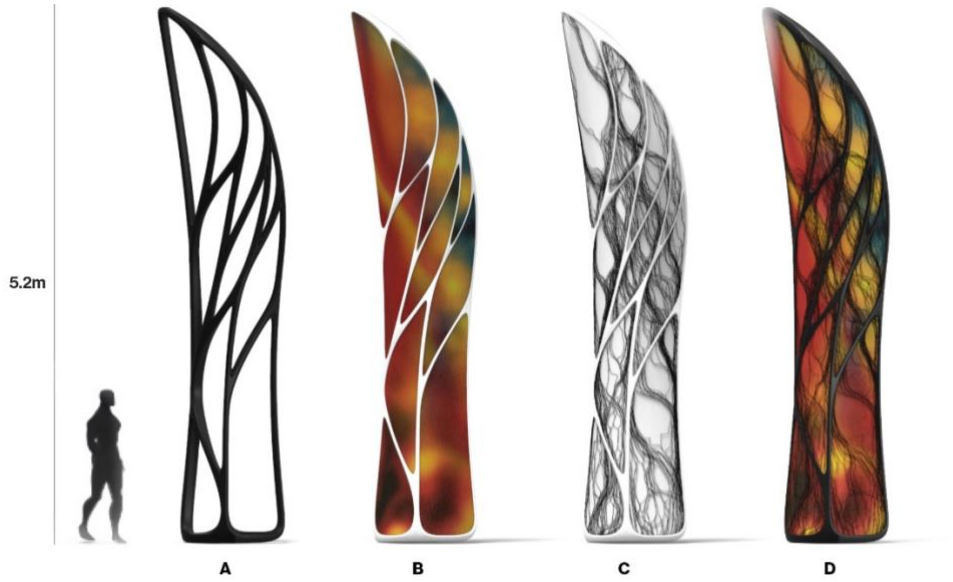


Figure 2: A prototypical structure is defined hierarchically beginning with rigid skeletal elements (a) followed by a continuously graded heterogeneous biopolymer membrane (b) and a semi-rigid embedded venation pattern that links the two previous levels (c) to create a continuous form (d).

3.5 Continuously Graded Flexible Membranes

Material gradation in flexible membrane elements can be divided into two categories: gradation of mechanical properties and gradation of optical properties. Importantly, these parameters are independent of one another. Both mechanical and optical properties are assigned according to global parameters including surface irradiance, structural load, and membrane curvature. Surface irradiance is calculated via sun-path simulation. Membrane curvature refers to the normal curvature of modeled biopolymer membranes and is highest where each panel bends to press-fit into rigid skeletal elements. Structural load and surface topology data is used to create a measure of surface flexure that represents the degree to which non-reinforced membranes would flex or bow.

A distribution of 28% pectin, 5% glycerin and 32% pectin, 2% chitosan, 4% glycerin is linearly assigned according to membrane curvature with the more flexible composition being assigned to the edges of panels where press-fitting occurs. To create optical gradients, surface irradiance, membrane curvature, and surface flexure magnitudes are used as parametric inputs to linear functions, the outputs of which were mapped to gradients. By specifically assigning gradient color limits, patterns are generated to template interactions key species in an ecology.

The first uses an aposematic pattern that incorporates motifs used in a number of species to repel predators [9], such as dark regions with high-contrast red and yellow patterning with sharp transitions. The second global pattern incorporates smooth gradients of blue and yellow hues visible to certain pollinators but not to other insects [10]. A third pattern combines shades of yellow that serve to attract aphids [11] with gradients of red similar to those used in ladybug sexual selection [12], thereby staging a hypothetical encounter between the two species. These patterns are selectively combined to create a single global color scheme with regions from each individual map.

3.6 Semi-Rigid Embedded Elements

Semi-rigid material containing 32% pectin, 4% chitosan, and 3% glycerin is embedded into flexible membranes in order to provide a level of reinforcement in areas distant from rigid skeletal elements. In order to create a pattern serving the simultaneous goals of reinforcing areas prone to flexure, minimizing disruption to optical patterns, and responding to structural irradiance, a modification of the *Boids*

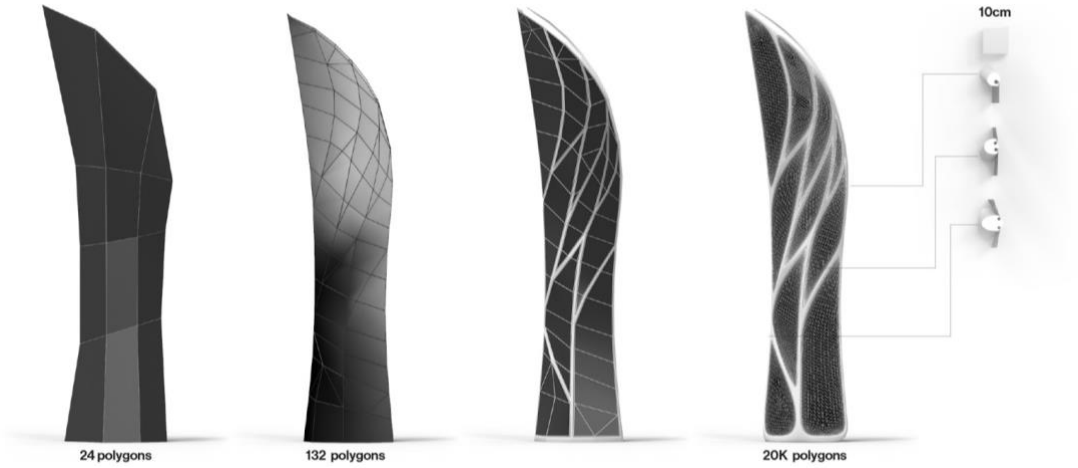


Figure 3: From left to right, low polygon representations of the base geometry, parametric mapping of skeletal member thickness based on load, generation of skeletal geometry based on developable mesh segment boundaries, and thickness assignment to skeletal members. Low and high polygon representations are operated on simultaneously.



Figure 4: Environmental data associated with global scale is modeled for structural irradiance, panel membrane curvature, and surface flexure for the structure in its assembled state (a). Global maps are translated into 2D representations (b) that guide the distribution of material and color for flexible membrane elements (c) and semi-rigid reinforcement patterns (d).

artificial life program is used with cohesion, separation, and path-following behaviors tethered to data from environmental maps [13]. Reinforcement patterns are generated by two distinct swarms of 125 and 85 agents respectively, the trails of which are then cross-linked via kernel-density estimation-based edge bundling [14]. The first swarm originates at the structure's base and follows a weighted navigation system designed to maximize the traversal of gradient boundaries where colors remain constant while

maintaining a distance of 3.25cm from neighboring agents. Priority is given to steering that directs agents towards regions with high levels of flexure that require reinforcement. The second swarm originates from the structure's lower-ventral region and attempts to align to the gradient of the flexure map while separating in regions of low irradiance and gathering more densely in regions of high irradiance. The cross-linking of trails from both swarms is intended to provide lateral strength to patterns without the need for strictly lateral agent motions.

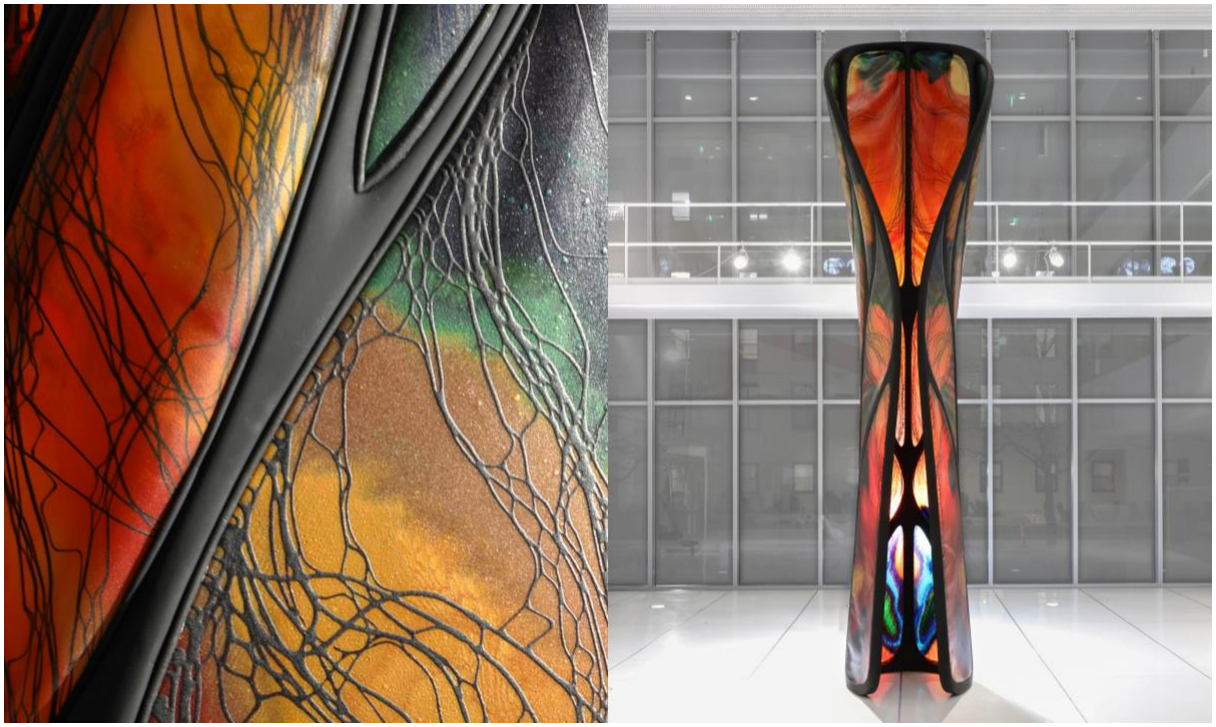


Figure 5: Close up (left) and front elevation (right) views of assembled structure.

4. Discussion and Outlook

This research demonstrates novel methods for the design and digital fabrication of hydrogel membranes with structural hierarchy across scales. Combined with Fabrication-information Modeling, the workflow presented enables the creation of smooth transitions between materials surpassing known mechanical limits per resolution. Importantly, the scalability of these methods allows for the digital fabrication of structures where a range of material properties are controlled and expressed both visually and functionally. We introduce the possibility to gradually vary material stiffness, environmental reactivity, age, and degradation through our custom digital fabrication platform. We plan on further fine-tuning material behaviors in terms of controlled decay and deformation under changing temperature and humidity, both structurally and visually. Further integration between rigid and flexible elements could be achieved through the incorporation of strong bio-composites with minimal deformation. This would allow for the creation of freestanding structures that transition between functional elements without the need for assembly. The architectural-scale fabrication of these techniques not only ensures the scalability of the described methods, but highlights developments in materials science, computation, and fabrication that allow sustainable, bio-degradable materials to be augmented with high-performance capabilities. These developments point towards a future where structures fabricated from natural, abundant components transcend the limitations of conventional materials.

Acknowledgements

This research was primarily sponsored by The Mediated Matter research group at the MIT Media Lab and NOE, LLC. Additional funding was provided by Stratasys Ltd, MIT Research Laboratory of Electronics, Wyss Institute at Harvard, Department of Systems Biology at Harvard, GETTYLAB, Robert Wood Johnson Foundation, Autodesk BUILD Space, TBA-21 Academy, Thyssen-Bornemisza Art Contemporary, Stratasys Direct Manufacturing, National Academy of Sciences, San Francisco Museum of Modern Art, and the Esquel Group.

References

1. Li, Zhensheng, Hassna R. Ramay, Kip D. Hauch, Demin Xiao, and Miqin Zhang. "Chitosan–alginate hybrid scaffolds for bone tissue engineering." Biomaterials 26, no. 18 (2005): 3919-3928.
2. Kirchmajer, Damian M., and R. Gorkin Iii. "An overview of the suitability of hydrogel-forming polymers for extrusion-based 3D-printing." *Journal of Materials Chemistry B* 3, no. 20 (2015): 4105-4117.
3. Bhatia, Sujata K., and Krish W. Ramadurai. "3D printing and bio-based materials in global health." *Materials* (2017).
4. J. Duro-Royo, J. Van Zak, ,A. Ling, Y.J. Tai, Hogan, B. Darweesh, and N. Oxman, July. Designing a Tree: Fabrication Informed Digital Design and Fabrication of Hierarchical Structures. In *Proceedings of IASS Annual Symposia* (Vol. 2018, No. 13, pp. 1-7). International Association for Shell and Spatial Structures (IASS), 2018.
5. Hardin, James O., Thomas J. Ober, Alexander D. Valentine, and Jennifer A. Lewis. "Microfluidic printheads for multimaterial 3D printing of viscoelastic inks." *Advanced materials* 27, no. 21 (2015): 3279-3284.
6. Cho, Wonjoon, Emanuel M. Sachs, Nicholas M. Patrikalakis, and Donald E. Troxel. "A dithering algorithm for local composition control with three-dimensional printing." *Computer-aided design* 35, no. 9 (2003): 851-867.
7. Mogas-Soldevila, Laia, Jorge Duro-Royo, and Neri Oxman. "Water-based robotic fabrication: large-scale additive manufacturing of functionally graded hydrogel composites via multichamber extrusion." 3D Printing and Additive Manufacturing 1, no. 3 (2014): 141-151.
8. J. Van Zak, J. Duro-Royo, Y. T. Tai, A. S. Ling, C. Bader, and N. Oxman, "Parametric Chemistry: Reverse Engineering Biomaterial Composites for Robotic Manufacturing of Bio- Cement Structures across Scales," in Architectural Robotics (2017).
9. Lev-Yadun, Simcha. "Aposematic (warning) coloration in plants." In *Plant-Environment Interactions*, pp. 167-202. Springer, Berlin, Heidelberg, 2009.
10. Arikawa, Kentaro, and D. Stavenga. "Random array of colour filters in the eyes of butterflies." *Journal of Experimental Biology* 200, no. 19 (1997): 2501-2506.
11. Hardie, Jim. "Spectral specificity for targeted flight in the black bean aphid, Aphis fabae." *Journal of Insect Physiology* 35, no. 8 (1989): 619-626.
12. Resh, Vincent H., and Ring T. Cardé, eds. *Encyclopedia of insects*. Academic press, 2009.
13. Reynolds, Craig W. Flocks, herds and schools: A distributed behavioral model. Vol. 21, no. 4. ACM, 1987.
14. Hurter, Christophe, Ozan Ersoy, and Alexandru Telea. "Graph bundling by kernel density estimation." In Computer Graphics Forum, vol. 31, no. 3pt1, pp. 865-874. Oxford, UK: Blackwell Publishing Ltd, 2012.

Proceedings of the IASS Annual Symposium 2019 – Structural Membranes 2019
Form and Force
7 – 10 October 2019, Barcelona, Spain
C. Lázaro, K.-U. Bletzinger, E. Oñate (eds.)

A strategy to improve buckling resistance of a Miura origami-based tube

Yangqing LIU*, Jianguo CAI[a], Jian FENG[a]

*Southeast University, Key Laboratory of C & PC Structure of Ministry of Education of China, National Prestress Engineering Research Center of China
Sipailou 2#, Nanjing 210096, China
yq_liu@outlook.com

[a] Southeast University, Key Laboratory of C & PC Structure of Ministry of Education of China, National Prestress Engineering Research Center of China

Abstract

Origami is an ancient art of forming planar materials to spatial structures by folding the materials along predetermined fold lines. The intricate structures gain unusual properties and yield origami-inspired engineering applications including metamaterials, packaging and so on. Among the applications, Miura origami pattern is most widely studied due to its simplicity in geometry and motion. Two-fold Miura origami, also known as curved Miura origami, can be used to form a tube with appropriate parameters. Different from the typical rigid origami concept, this manuscript divides the fold lines of a 3-level Miura origami-based tube into two groups. One is for the lines considered as perfect hinges, and the other for the lines having the same rotational stiffness as the panels. Four arrangement schemes of the lines are investigated to improve the buckling resistance of the tube using finite element simulations and one of them outperforms the others by significantly reducing the magnitude of lateral deformations of the tubes. The scheme is found to be an appropriate approach to improve the buckling resistance of a curved Miura origami-based tube.

Keywords: Miura origami, buckling resistance, long tube, compression, origami-based tube.

1. Introduction

Leading to significant compression capacity loss, strain concentration at mid-span, sudden force redistribution and material fracture, global buckling is a common instability issue for metallic tubes under axial compression, especially for slender ones [1]. Origami is an ancient art of forming planar materials to spatial structures by folding the materials along predetermined fold lines. The intricate structures gain unusual properties and yield origami-inspired engineering applications including metamaterials [2-5], packaging [6, 7] and so on. Among the applications, energy dissipaters aim at precluding global buckling and achieving yielding along the entire length by introducing origami patterns as geometrical imperfections.

The concept of origami-inspired energy dissipaters is built on the truth that thin-walled tubes are widely accepted as energy dissipaters for their excellent mechanical performance, manufacturing ease and affordability [8]. Square tubes and circular tubes are the most common types of energy dissipation tubes. Large amount of efforts has been made to investigate the mechanical behaviors of these two types of tubes under axial crushing. Through experiment and numerical simulations, the deformation modes and energy dissipation characteristics were investigated and analytical theories were accordingly proposed [9-14].

Copyright © 2019 by Yangqing LIU, Jianguo CAI, and Jian FENG
Published by the International Association for Shell and Spatial Structures (IASS) with permission.

The study on the conventional tubes reveals that appropriate imperfections could trigger specific deformation modes and consequently alter the response under loading. That inspires the introduction of origami patterns into thin-walled tubes. Guest and Pellegrino [15-17] applied a helically triangulated cylindrical foldable pattern into a circular tube and the tube was fully folded during the experiment. Song and Chen firstly developed a type of tubes with equilateral trapezoid patterns, which were experimentally and numerically verified to improve the crashworthiness by successfully inducing the crushing modes of the tubes. Since then, various types of origami patterns were designed and applied to tubes, including crash box pattern [18], Kite-shape pattern [19], Tachi-Miura polyhedron pattern [20] and so on. The work described above meaningfully contributes to the understanding of the applications of origami-based tubes. However, the work is limited to short tubes where global buckling is not a problem. When it comes to longer tubes, globally buckle is more likely to occur and in turn affects the behavior t. Therefore, it is necessary to extend the current work to longer tubes.

In this manuscript, an arrangement scheme of the fold lines is developed to improve the buckling resistance of a curved Miura origami-based tubes. In Section 2, a curved Miura origami-based unit is introduced. In Section 3, an example is given to apply four arrangement schemes of fold lines and comparisons are made among them to show their performance under axial compression. One of them is proved to perform best in improving the buckling resistance of the tube. Finally, conclusions drawn in this manuscript is summarized.

2. Curved Miura origami-based unit

Curved Miura origami, a.k.a. two-fold Miura origami, is a variant pattern of a regular Miura origami. The difference between a curved Miura origami and a regular Miura origami is shown in Figure 1, where the solid lines represent mountain fold lines and the dashed lines represent valley fold lines. If the closure condition given by Schenk et al [6] is satisfied, a curved Miura origami-based unit could be obtained by assembling the pattern in order around an axis. The assembled unit is shown in Figure 2, where α is the fold angle of the pattern.

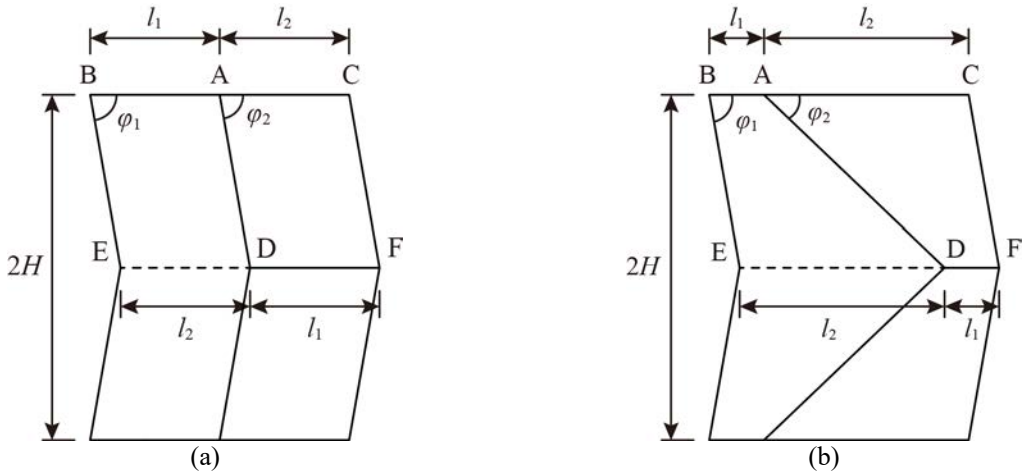


Figure 1: A regular Miura origami and a curved Miura origami when fully unfolded: (a) a regular Miura origami ($\varphi_1 = \varphi_2$); (b) a curved Miura origami ($\varphi_1 \neq \varphi_2$)

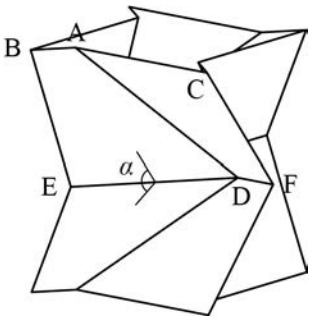


Figure 2: Assembled unit of a curved Miura origami-based tube

3. Example for 3-level curved Miura origami-based tubes

3.1. Arrangement schemes of fold lines

Rigid origami is an important concept about origami patterns, where the origami folds and unfolds with rigid panels rotating about hinge-like fold lines [21]. The hinge-like lines are incapable of transferring moment. Here we call those lines Type A lines. However, in some cases, origami patterns are manufactured by cold forming techniques, including stamping against dies [8], cold gas pressure folding [22], and 3D printing [23]. In those manufacturing methods, the materials are continuous at the fold lines and cross sections there are not reduced. In such case, besides shear and axial force, the fold lines transfer moment. Thus, the lines can no longer be considered as frictionless hinges. Here those fold lines are named Type B lines.

By allocating the two types of fold lines we define above to lines of the unit, four arrangement schemes of the lines are given as shown in Table 1.

Table 1: Arrangement schemes of fold lines

Scheme no.	Fold lines of unit		
	Horizontal fold lines	Inclined mountain fold lines	Inclined valley fold lines
I	Type A	Type A	Type A
II	Type B	Type B	Type B
III	Type A	Type B	Type B
V	Type A	Type A	Type B

3.2. Nonlinear finite element simulations

A curved Miura origami-based tube is assembled by vertically stacking three units shown in Figure 2. Totally four tubes are assembled, corresponding to the four schemes respectively. Since a given set of the parameters H, l (l_1+l_2), φ_1 and α could determine the geometry of the pattern, identical parameters are adopted for the tubes, as listed in Table 2.

Nonlinear numerical simulations are conducted using general finite element package (ANSYS 18.0), with the purpose to investigate the buckling resistance of the schemes in Table 1. The geometrical model and finite element model are shown in Figure 3. Typical 4-node shell element SHELL181 is employed to simulate the 8 mm-thick panels of the origami pattern and the 20 mm-thick end plates of the tube. In order to model the pin supports of the tube, MASS21 element is put at the supports, connecting the nodes of the end plates by MPC184 Rigid Beam elements. In such way, with the constraints at MASS21 elements, rotations about the supports as a whole are allowed at both ends of

the tube. For Type B lines in the schemes except Scheme I, node coupling along the lines are used. The constitutive relationship of the material adopts a measured piecewise linear one of hot rolled steel in [24], which is shown in Figure 4. The parameters in the figure are listed in Table 3, where f_y is the yield stress, ε_y is the yield strain, E is the elastic modulus, ε_{st} is the strain at the onset of stress strengthening, E_{st} is the slope of the strengthening, f_u is the ultimate stress, ε_u is the strain at the ultimate stress and ε_{el} is the ultimate strain.

Table 2: Information of example tubes

Tube no.	Values of geometrical parameters				Scheme adopted
	H / mm	l / mm	φ_1 / deg	α / deg	
C-ORI-1	200	200	85	135	I
C-ORI-2					II
C-ORI-3					III
C-ORI-4					IV

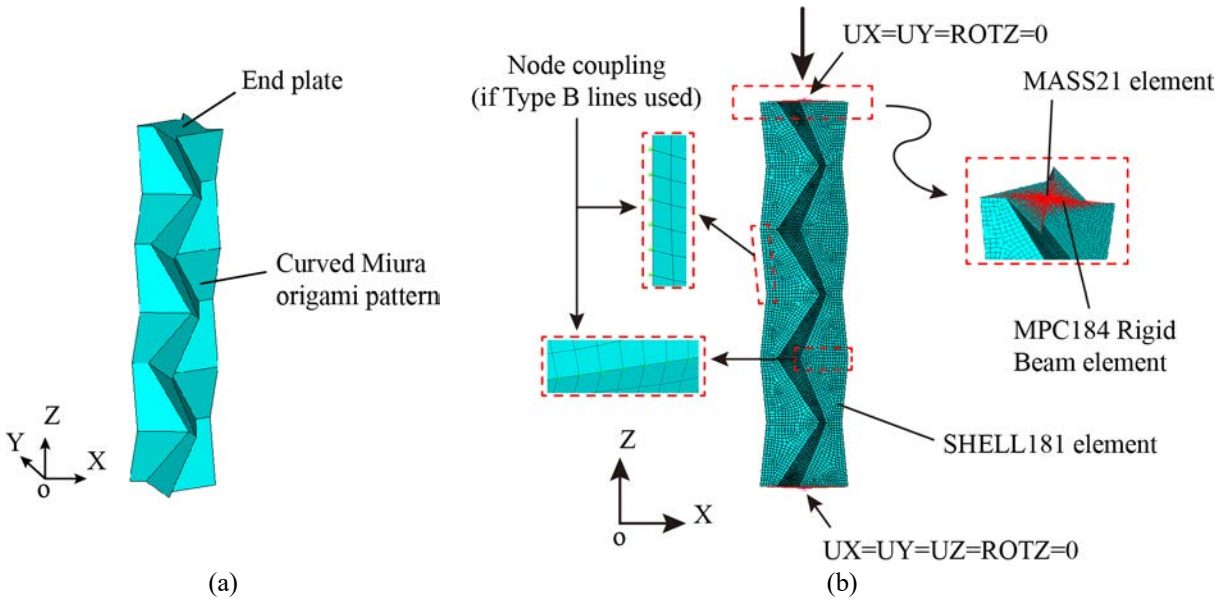


Figure 3: Models of an example tube: (a) geometrical model; (b) finite element model

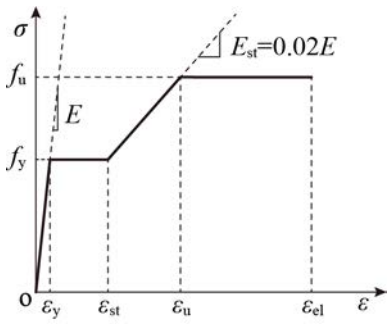


Figure 4: Constitutive relationship of material

Table 3: Parameters of constitutive relationship of material

f_y / MPa	f_u / MPa	E / MPa	ε_y / %	ε_{st} / %	ε_u / %	ε_{el} / %
260	420	206000	0.13	1.51	5.39	26

Nonlinear finite element simulations are conducted on the tubes under axial compression. In order to ensure the reach of peak point of the load force versus displacement curve, the amplitude of the displacement-controlled loading is 60 mm. The results and observations are given in the next subsection.

3.3. Results and observations

The load force F versus displacement Δ curves of the tubes are shown in Figure 5, where the peak points are starred. The VonMises stress states at their peak points and at the end of loading are shown in Figure 6 and Figure 7, respectively.

Compare Figure 6 and Figure 7, it can been seen that prior to peak points, only slight lateral deflections are observed on the tubes and once the peak points are reached, the deflections increase rapidly. It indicates that the tubes experience instability and globally buckle after the peak points.

Since the deformation mode is semi-wave bending, rotations about the supports are positively correlated to the magnitude of the deflections. Figure 8 shows the rotations throughout the loading process, which clearly reflect the magnitude of the deflections. The displacement at the peak point Δ_{peak} is also indicated by dash lines in the figure. It can be seen in the figure that the rotations remain small and go up almost linearly as the displacement increases before global buckling, while the increase is much accelerated in the post peak periods. C-ORI-4 is observed to behave much less rotation, compared with other counterpart tubes. For example, for any given displacement Δ during the load process, the rotation of C-ORI-4 is up to 52.3% less than that of C-ORI-3, which exhibits the least rotation among the tubes except C-ORI-4. It is the small rotations at supports that leads to the latest occurrence of global buckling in C-ORI-4 as shown in Figure 5.

Through the observations above, it is demonstrated that C-ORI-4 is most buckling resistant among the four tubes investigated. Therefore, in light of the same geometry shared by the tubes, Scheme IV is found to be a strategy to improve the buckling resistance of a curved Miura origami-based tube.

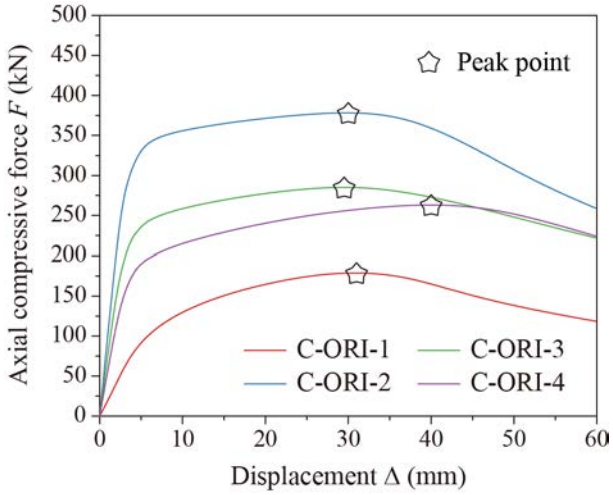
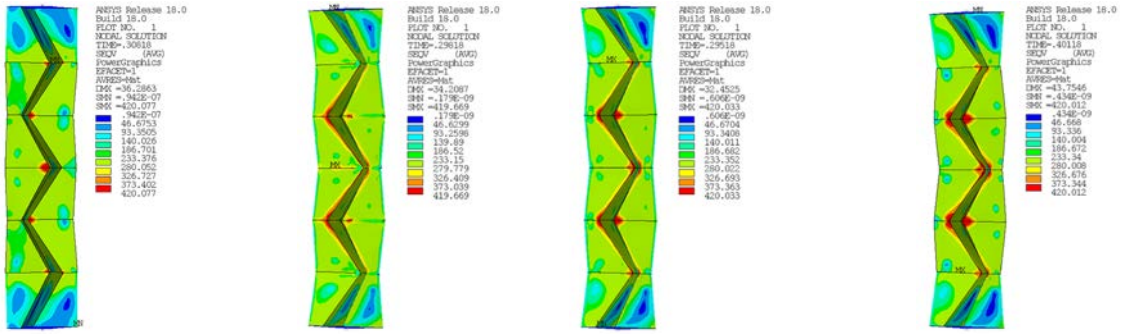
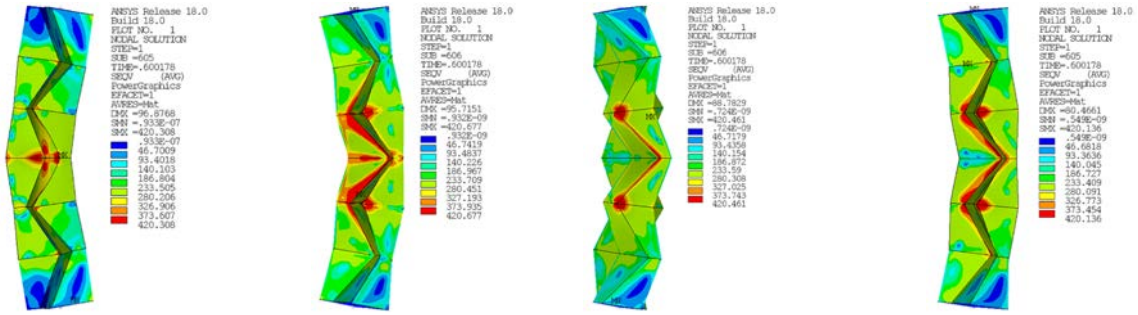


Figure 5: Load force F versus displacement Δ curves



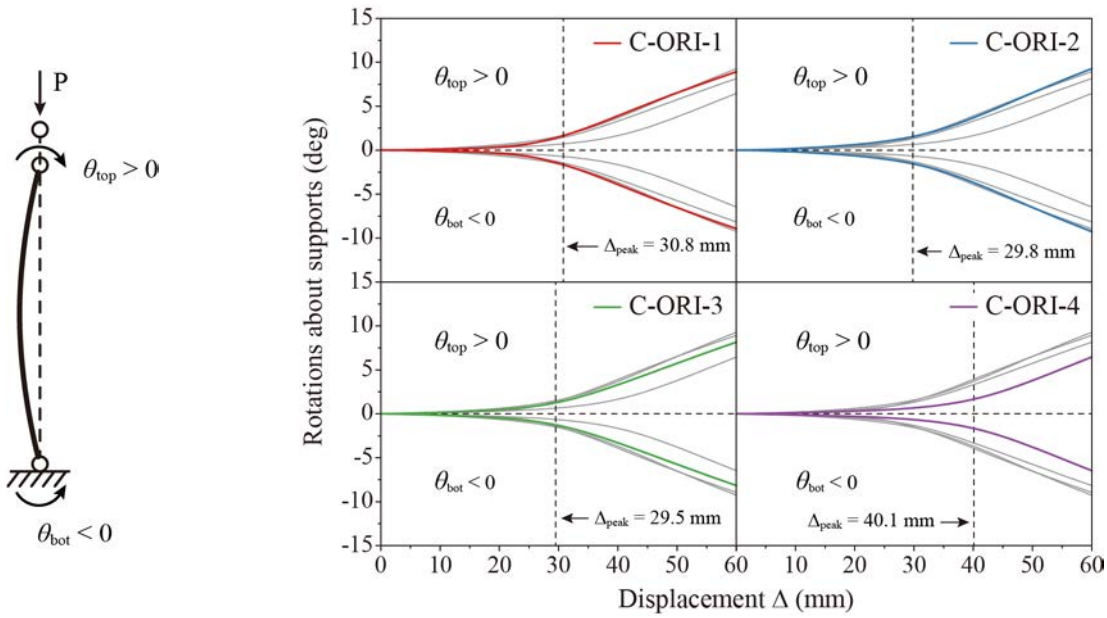
(a) (b) (c) (d)

Figure 6: VonMises states of tubes at peak points: (a) C-ORI-1; (b) C-ORI-2; (c) C-ORI-3; (d) C-ORI-4



(a) (b) (c) (d)

Figure 7: VonMises states of tubes at peak points: (a) C-ORI-1; (b) C-ORI-2; (c) C-ORI-3; (d) C-ORI-4



(a) (b)

Figure 8: Rotations about supports: (a) illustration of rotations; (b) rotations throughout loading process

4. Conclusion

Global buckling resistance is an important issue for energy dissipation tubes, as the buckling alters the deformation mechanism and in turn reduce the energy dissipation. The present work provides a novel strategy to effectively improve the buckling resistance of a curve Miura origami-based tube by applying a specific scheme of fold lines of the pattern. According to the simulation results, the scheme manages to reduce the lateral deformation in roughly half. In follow-up study, the scheme will be examined on slender tubes and a physical model will be on schedule.

Acknowledgements

The authors acknowledge the support from the National Science Foundation of China through Grant 51822805.

References

[1] R. Tremblay, "Inelastic seismic response of steel bracing members," *Journal of Constructional Steel Research,* vol. 58, no. 5-8, pp. 665-701, May-Aug 2002.

[2] M. Schenk and S. D. Guest, "Geometry of Miura-folded metamaterials," *Proceedings of the National Academy of Sciences of the United States of America,* vol. 110, no. 9, pp. 3276-3281, Feb 2013.

[3] C. Lv, D. Krishnaraju, G. Konjevod, H. Y. Yu, and H. Q. Jiang, "Origami based Mechanical Metamaterials," *Sci. Rep.,* vol. 4, Aug 2014.

[4] H. Feng, J. Ma, Y. Chen, and Z. You, "Twist of Tubular Mechanical Metamaterials Based on Waterbomb Origami," *Sci. Rep.,* Article vol. 8, no. 1, 2018.

[5] E. T. Filipov, T. Tachi, and G. H. Paulino, "Origami tubes assembled into stiff, yet reconfigurable structures and metamaterials," *Proceedings of the National Academy of Sciences,* vol. 112, pp. 12321-12326, Oct 2015.

[6] M. Schenk, S. Kerr, A. Smyth, and S. Guest, "Inflatable cylinders for deployable space structures," in *Transformables 2013*, Seville, Spain, 2013.

[7] J. S. Dai and D. G. Caldwell, "Origami-based robotic paper-and-board packaging for food industry," (in English), *Trends Food Sci Tech,* vol. 21, no. 3, pp. 153-157, Mar 2010.

[8] J. Ma, H. Dai, M. Shi, L. Yuan, Y. Chen, and Z. You, "Quasi-static axial crushing of hexagonal origami crash boxes as energy absorption devices," *Mech Sci,* Article vol. 10, no. 1, pp. 133-143, 2019.

[9] W. Abramowicz, "The effective crushing distance in axially compressed thin-walled metal columns," *International Journal of Impact Engineering,* Article vol. 1, no. 3, pp. 309-317, 1983.

[10] W. Abramowicz and N. Jones, "Dynamic axial crushing of square tubes," *International Journal of Impact Engineering,* Article vol. 2, no. 2, pp. 179-208, 1984.

[11] W. Abramowicz and N. Jones, "Dynamic progressive buckling of circular and square tubes," *International Journal of Impact Engineering,* Article vol. 4, no. 4, pp. 243-270, 1986.

[12] J. M. Alexander, "An approximate analysis of the collapse of thin cylindrical shells under axial loading," *The Quarterly Journal of Mechanics and Applied Mathematics,* vol. 13, no. 1, pp. 10-15, 1960.

[13] T. Wierzbicki, S. U. Bhat, W. Abramowicz, and D. Brodkin, "Alexander revisited—A two folding elements model of progressive crushing of tubes," *International Journal of Solids and Structures,* vol. 29, no. 24, pp. 3269-3288, 1992.

[14] S. R. Guillow, G. Lu, and R. H. Grzebieta, "Quasi-static axial compression of thin-walled circular aluminium tubes," *International Journal of Mechanical Sciences,* vol. 43, no. 9, pp. 2103-2123, 2001.

[15] S. D. Guest and S. Pellegrino, "The Folding of Triangulated Cylinders, Part I: Geometric Considerations," *Journal of Applied Mechanics-Transactions of the ASME,* vol. 61, no. 4, pp. 773-777, Dec 1994.

[16] S. D. Guest and S. Pellegrino, "The Folding of Triangulated Cylinders, Part II: The Folding Process," *Journal of Applied Mechanics-Transactions of the Asme,* vol. 61, no. 4, pp. 778-783, Dec 1994.

[17] S. D. Guest and S. Pellegrino, "The Folding of Triangulated Cylinders, Part III: Experiments," *Journal of Applied Mechanics-Transactions of the ASME,* vol. 63, no. 1, pp. 77-83, Mar 1996.

[18] J. Y. Ma and Z. You, "Energy Absorption of Thin-Walled Square Tubes With a Prefolded Origami Pattern-Part I: Geometry and Numerical Simulation," *Journal of Applied Mechanics-Transactions of the Asme,* vol. 81, no. 1, Jan 2014.

[19] J. Ma, D. Hou, Y. Chen, and Z. You, "Quasi-static axial crushing of thin-walled tubes with a kite-shape rigid origami pattern: Numerical simulation," *Thin-Walled Structures,* vol. 100, pp. 38-47, 2016.

[20] Y. Yang, C. Nara, and I. Hagiwara, "Energy absorbing characteristics of pairing origami structures," *Transactions of the JSME (in Japanese),* vol. 1-9, no. 9, 2016.

[21] S. Li, H. Fang, S. Sadeghi, P. Bhovad, and K.-W. Wang, "Architected Origami Materials: How Folding Creates Sophisticated Mechanical Properties," *Advanced Materials,* vol. 31, no. 5, p. 1805282, 2019.

[22] M. Schenk, J. M. Allwood, and S. D. Guest, "Cold Gas-Pressure Folding of Miura-ori Sheets," in *10th International Conference on Technology of Plasticity (ICTP 2011)*, Aachen, 2011, pp. 459-464.

[23] M. A. E. Kshad, C. Popinigis, and H. E. Naguib, "3D printing of Ron-Resch-like origami cores for compression and impact load damping," *Smart Materials and Structures,* vol. 28, no. 1, Jan 2019.

[24] J. Chen, *Stability of Steel Structures Theory and Design*, 6th ed. Beijing: Science Press, 2014.

Proceedings of the IASS Annual Symposium 2019 – Structural Membranes 2019
Form and Force
7 – 10 October 2019, Barcelona, Spain
C. Lázaro, K.-U. Bletzinger, E. Oñate (eds.)

Folding laminar cover and water collector - Prototype

Jaime Andrés SIMON CALLE[a], Carlos Leonardo MOSCOSO OCAMPO[b]

[a] Architect Professor, Universidad Tecnológica del Perú, UTP
Calle Carlos E. Ferreyros 1035, Urb, San Isidro- Lima Perú
jaimesimon01@gmail.com

[b] Architect and Postgraduate student, Universidad de Buenos Aires, UBA - FADU

Abstract

This research born as part of a efficient structural design and to address three different problems: the need to design a hedge that may adapt weather flexible spaces, the problematic to gather water in the coast of Perú due to the lack of it and finally that this options can be replicable and scalable along the world. In order to solve these problems, a laminar structure inspired in the origami, was selected for three main reasons: For its morpho-structural characteristic that generates great rigidity along the sheet, due to the direction of the forces through the laminar surface, and throughout the folding and unfolded process. Because of its adaptability and spatial flexibility, which allows it to be extended or compressed according to the needs of light, covered area, storage, etc. And by generating a surface capable of directing rainwater to collector stiles at specific points. The coverage is modular, each module folded has the shape of an inverted hexagonal pyramid. The hexagonal module generates a honeycomb pattern because it is the most efficient way to cover a larger surface, as it protects from sun or rain, and captures the water redirecting it to an upright located in the central point of it. This structure may be manually fold or unfold in the first prototypes that have been created. The material of the cover will be polypropylene, due to its different qualities: the impermeability, the lightness, the change of memory of the material, as well as the fatigue resistance to folding and unfolding. Additionally, it allows an easy manipulation to creates the components of the coverage. Regarding to the water stanchion will be made of PVC pipes for its impermeability and lightness.

Keywords: Folding, Origami, Coverage, Laminar, Deployment, Water Collector, Polypropylene, Umbrella.

1. Introduction

This research was developed in the Light Structures Laboratory, at the Technological University of Peru (UTP), responding to the vision of efficient structural design, it is a product of the exploration of nature, forms and materials, and specifically in this case the ancestral art of Origami was explored, seeking in this way to respond to three problems: First, the need to collect water as it is a scarce resource, due to the low annual rainfall in the entire coastal area of Peru, being the Atacama -Sechura desert, named for the World Wildlife Fund, one of the driest lands in the world. The second, the need to have a coverage that is adaptable to the climate and that generates protection against it, above all to solar radiation, thus allowing habitability in public spaces. Finally, the shortage of water, which is a global problem and is considered one of the goals of the 2030 Agenda for Sustainable Development,

Copyright © 2019 by Jaime Andrés SIMON CALLE, Carlos Leonardo MOSCOSO OCAMPO
Published by the International Association for Shell and Spatial Structures (IASS) with permission.

adopted by all the Member States of the United Nations, for which it becomes an need to be able to replicate in different parts of the world.



Figure 1: Satellite Image, Atacama - Sechura desert [Google Maps]

2. Project Method

The applied method was exploratory and by phase from the search of a problem to the digital prototype, identifying the weaknesses and potentialities of the project in each level of the research.

2.1. Problem identification

An analysis and choice of a problem to be solved in the Peruvian coast was made. Subsequently, the research was projected to other areas worldwide.

2.2 Design, exploration and analog prototype

The first explorations were made in an analogical way using the techniques of the art of Origami, when reaching a possible resolutive form " Crease Pattern", an analog prototype was made using inexpensive materials for its possible reproduction and easy identification of errors.

2.3. Digitization and Digital Prototype

Finally, the exploration was carried out in a digital modeling to see its dynamics in front of other variables and to be able to replicate from its parametrization.

3. Configuration and concretion

3.1. Structure laminar – Origami art

To solve the problems raised, a laminar structure based on Origami art was chosen for three reasons: For its morpho-structural characteristic, for its adaptability and special flexibility, and for its ability to direct and capture rainwater at specific points.

3.1.1. Crease Patterns - CP

The Crease Patterns - CP are the guide lines when deploying an origami model and it serves as a two-dimensional manufacturing template to construct a fold, with indications whether the folding is up (valley) or down (mountain), depending on the observer and the lines of cut.

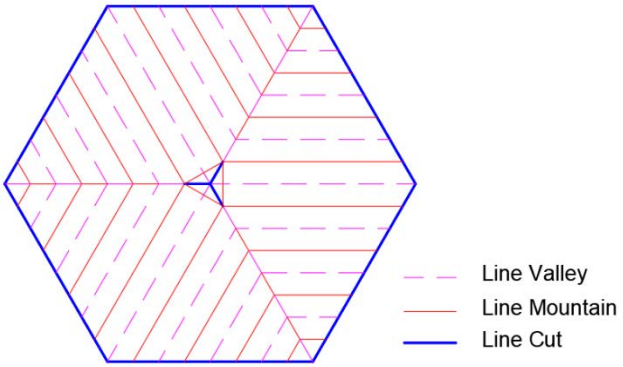


Figure 2: Crease Patterns of Folding laminar cover and water collector [own elaboration]

3.1.2. Morpho-structural characteristic

Folding due to its morpho-structural characteristic generates greater rigidity in the sheet due to its natural direction of the forces by the "veins" of the fold, in each valley and mountain of this, allowing the efficiency of the object and directing the load through the surface from the sheet to the places that are required for its support, this quality is not only for own loads but also external loads. Thanks to this feature, it will also direct the forces at any stage of the deployment.

3.1.3. Adaptability and special flexibility

The folded chosen has a great adaptability and spatial flexibility, this allows it to be extended and compressed with great ease according to the external needs that have, whether it may be needs of light, of greater or lesser covered area, storage, etc. The chosen fold allows warping allowing double curved surfaces.

3.1.4. Direction and collection of rainwater

With the inclination of the plane that is generated from the folding and its respective ordering, it allows to generate a surface capable of addressing the rainwater, this capacity is used to generate collector posts at specific points. When extended it allows the protection of the rays of the sun or of the rain, and captures the water allowing to direct it to the pillars located in the central points. Being the folded sheet allows to have more contact area in less occupied space and this gives a greater efficiency in the capture of rainwater especially in places with low rainfall as is the case of the Peruvian coast.

3.2. Structure modular

The coverage is modular, each module is folded and has the shape of an inverted hexagonal pyramid. The module to be hexagonal generates a honeycomb pattern, The regular hexagon is subdivided into 6 cloths of equilateral triangles that are unified to obtain the hexagonal module. Each hexagonal module is independent and has its own drainage system and captures rainwater independently.

3.2.1. Choice of hexagonal module

For this first prototype a hexagonal surface was chosen as the module because it is the most efficient polygon for tessellation surface in equal areas and with the minimum perimeter, this was demonstrated by the mathematician Thomas C. Hales [6]. This way you can collect as much water and cover as many square meters as possible.

3.3. The Materiality

In the choice of the materiality for the coverage, its physical-mechanical properties, its accessible cost and its easy handling were taken into consideration. The laminar surface is made of polypropylene, among the qualities that we highlight are the following: the impermeability, the lightness, the change of memory of the material, as well as the resistance to fatigue of folding and unfolding, also facilitates and allows its manipulation for the possible realization of the components of the folded coverage. As explained in point 3.2. The hexagon is composed of 6 triangular polypropylene cloths and these are unified by Duct Tape which is a high strength cloth tape covered with a gray polyethylene film and its rubber adhesive provides a high resistance to temperature, a high adhesion to the majority of surfaces and an exceptional sustaining force. With respect to the amount for water will be PVC pipes for its impermeability, lightness and ease of acquisition.

3.2.1. Polypropylene – Cartonplast

It is a heterophasic polypropylene copolymer with added rubber and stabilizer, whose commercial name is "cartonplast" among its properties are: 100% recyclable, reusable and resistant to bad weather conditions and with a long life time makes it an ideal material for realization of the project. At the same time it is resistant to chemical agents, acid, alkaline and saline solutions; resistant to mold.

Polypropylene is natural water repellent, waterproof property. The contact of water with this material is harmless to humans and therefore it is used in containers for the food and beverage industry.

Its ease of acquisition make it the ideal product for this project allowing its reproduction in places of social interest, park, communities, peripheral neighborhoods, small towns, etc.

4. Modeling

4.1. Analogue modeling

The first thing to be able to carry out the project was to perform an analogical modeling, for which bond paper was used to explore folding as a constructive method since it had the necessary faculties to efficiently solve the problem, its morpho-structural capacity and its capacity of deployment.

Several analog models were made until we were able to arrive at the most appropriate solution and form. With which the Crease pattern was established. Subsequently, a larger scale prototype was made to identify structural and manufacturing problems considering the materials and their viability as a resource, resulting in polypropylene sheets, Duct Tape and PCV tubes, the final materials. In the first elaborated prototypes, folding and unfolding was done manually.

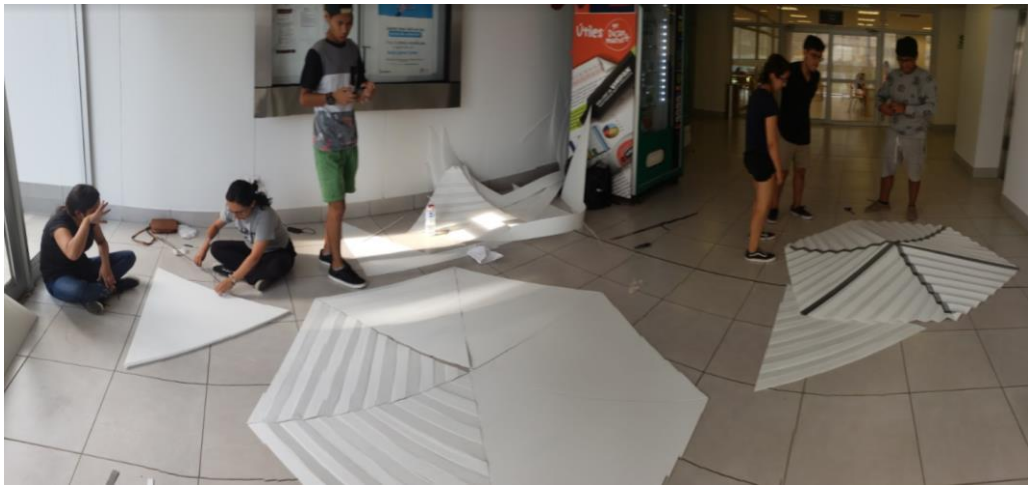


Figure 3: Prototype manufacturing process



Figure 4: fi First prototype, components and manual deployment process.



Figure 5: Prototype water collector

4.2. Digital modeling

Finally, a digital modeling was carried out, so we could see the variants and attributes that this may have. Later a prototyping was done to see the different parameters that it has and how the geometry can be changed to obtain other types of surfaces to solve the same problem.

The digital modeling was done in the sketch up program and later for the modeling was done in rhino using the plugin grasshopper and Kangaroo, at this point of the investigation only the modeling was done, later the simulation will be performed with the gravity and structural loads using the plugins Kangaroo2 and Karamba respectively.

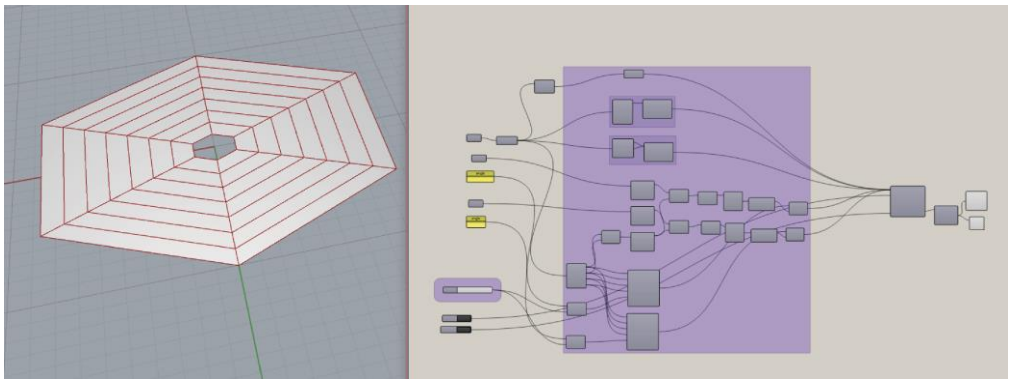


Figure 6: Digital modeling in rhinoceros and pluggin grasshopper and Kangaroo programs.



Figure 7: Photomontage of coverage.

5. Conclusions

Subsequent to the analogical modeling, the need to reinforce the folding of the valley in the major vein was seen, since this suffers rupture of the fold, but not of the material, for the moment generated in the lamina.

It is necessary to improve the encounter between the folding and the PVC pipe so that this does not generate damage to the folding.

Greater approach to digital modeling and parameters of external forces to see the reactions of the prototype in front of this, whether sea, wind, deformation by gravity and weight.

A study of the anchoring of the base of the prototype with the soil has to be made.

The folding used is the most suitable for this project and the surface that is generated is more efficient for water collection.

The material used on the surface perfectly supports the water and fulfills the function of bringing water to the upright.

The wind in the prototype must be studied correctly to measure the resistance it can have to the prototype.

You must perform a digital modeling and prototyping of all the components that were provided to you and that your response to some external element may be different in the group than individually.

Acknowledgements

I thank the students of Architecture of the UTP: Mariel Ccaccya, Diego Chávez, Valeria Egoavil, Medaly Molocho and Diego Portalatino for the modality of the analog prototype, also to the Architect Paul Vera, Director of the School of Architecture UTP

References

[1] A. Agkathidis. “diseño Generativo”, Prompress editions, España 20105.

[2] J. Baixas, “Forma resistente”, Santiago de Chile, 2005.

[3] J. Baldwin, Bucky Works, “Bukminster Fuller´s Ideas”, John Wiley & Sons, Londres, 1996

[4] N. Barkoula, et al. "Fatigue properties of highly oriented polypropylene tapes and all-polypropylene composites." Polymers and Polymer Composites 16.2, 2008. pp. 101-113.

[5] R. Doberti, “Espacialidades”, No. 72.012. Ediciones Infinito, Buenos Aires, 2008.

[6] T. Hales, "The honeycomb conjecture." Discrete & Computational Geometry 25.1, 2001. pp.1-22.

[7] Hoberman, Chuck, “Folding in Architecture: Architectural Desing”, Wiley Academy, Londres, 2004

[8] P. Jackson and M. Suchowolski, “Folding techniques for designers: from sheet to form”, London, Laurence King Pub., 2011.

[9] P. Jackson “el gran libro del plegado”, Prompress editions, España, 2015.

[10] E. Rivas Adrover, “Estructuras desplegables, Arquitectura, ingeniería y diseño”, Prompress editions, España, 2015.

Proceedings of the IASS Annual Symposium 2019 - Structural Membranes 2019
Form and Force
7-10 October 2019, Barcelona, Spain
C. Lázaro, K.-U. Bletzinger, E. Oñate (eds.)

Form finding of stress adapted folding as a lightweight structure under different load cases

Juan MUSTO*, Max LYON, Martin TRAUTZ, Leif KOBBELT

RWTH Aachen University
Schinkelstr. 1, 52062 Aachen, Germany
musto@trako.arch.rwth-aachen.de

Abstract

In steel construction, the use of folds is limited to longitudinal folds (e.g. trapezoidal sheets). The efficiency of creases can be increased by aligning the folding pattern to the principal stresses or to their directions. This paper presents a form-finding approach to use the material as homogeneously as possible. In addition to the purely geometric alignment according to the stress directions, it also allows the stress intensity to be taken into account during form-finding. A trajectory mesh of the principle stresses is generated on the basis of which the structure is derived. The relationships between the stress lines' distance, progression and stress intensity are discussed and implemented in the approaches of form-finding. Building on this, this paper additionally deals with the question of which load case is the most effective basis for designing the crease pattern when several load cases can act simultaneously.

Keywords: lightweight-construction; folding; principle stress lines; Mixed-Integer Quadrangulation

1 Introduction

Besides membrane and shell structures, folding structures are among the most efficient design principles that can achieve relatively high load-bearing capacities with minimal material input. In lightweight construction, this principle is primarily used with thin-walled, flat, semi-finished products. In addition to conventional axial longitudinal foldings in the form of trapezoidal or corrugated sheets, space fold structures and fold-core-plates (also known as sandwich panels) are examples of this design principle, consisting of a folding core and a top/bottom cover layer [1]. In addition to the fact that the mechanical cross-section values are significantly increased by folding a flat material, the favourable static load-bearing behaviour of folding constructions is reinforced by the following phenomenon: If one considers the stress pattern of a folding construction, it is notable that the stresses are predominantly "bundled" over the stabilizing folding edges.
In this paper, we make use of this load bearing behaviour to increase the efficiency a folding structure by aligning the folding pattern to the principal stress directions.

2 Related Work

In steel construction, almost all form-finding processes are parametric structural optimization oriented (PSO). In PSO individual design parameters (e.g. height, sheet thickness and distances) are calculated iteratively with the help of genetic algorithms in order minimize the amount of

Copyright © 2019 by Juan Musto, Max Lyon, Martin Trautz, and Leif Kobbelt
Published by the International Association for Shell and Spatial Structures (IASS) with permission.

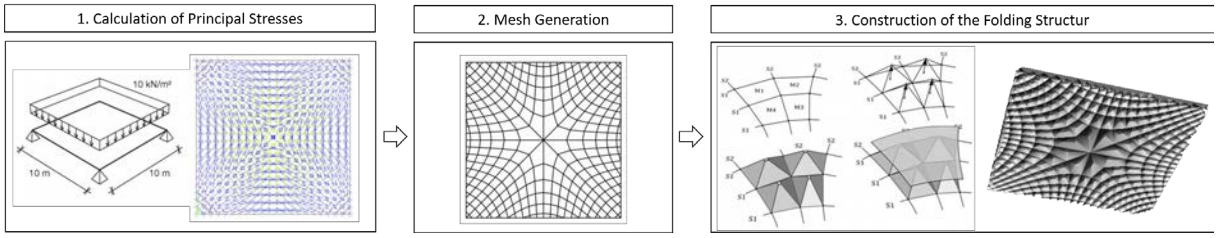
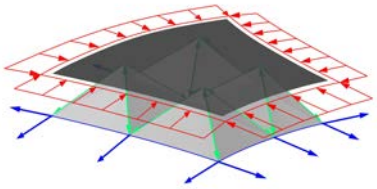


Figure 1: Process to construct the stress adapted fold structure.

material on the Object, rather than a geometric alignment of the load-bearing elements according to previously calculated "load paths".
In the CIAB Pavilion Beijing [2] the principle of load paths was realized with a bar structure. The bars, which form the geometry, are aligned with the principle stress direction at the same time. Researches of [3] on a curved grid shell whose bars were aligned in the principle stress directions showed that the von Mises stress could be reduced up to 40% as a result.
In a similar way, [4] produced grid shells in a model scale on the basis of principal stress lines within the framework of additive manufacturing. A slightly different approach is the use of so-called Michell structures. The Michell continuum forms a surface of a bar grid with the smallest volume for the transfer of the load. [5] use this process to generate ribs to stabilize sheets.
A partially interactive approach was followed by [6] who designed an ultra-thin, concrete floor system prototype in which the course of the ribs (in plane and out of plane) was generated using an iterative form-finding process (with Rhino Vault [7, 8]) so that only compressive stresses exist. However, the fact that the ribs are approximated to the principal stress lines is due to an appropriate manual definition of the initial geometry for shape optimization.
The approach followed in this paper is based on a computation of a quadrangular principal-stress-mesh (PSM). From the PSM the folding structure is derived, whose edges are aligned with the principal stress directions. In the classical calculation of stress lines using the numerical Runge-Kutta method, all parameters (distance and course) are difficult to influence, which is why the lines to be materialized are selected manually in [4, 6]. In contrast to the stress lines, all properties can be parametrically controlled in PSM with the goal of an efficient materialization.

3 General Configuration and Load-Bearing Behavior of the Folding Structure

In order to achieve a self-supporting structure without the requirement of a substructure, at least a two-layer structure of the folded structure presented (cf. Figure 1)is necessary.
The load-bearing behavior of such a structure can be compared with the characteristics of a space framework (cf. inset): Under a positive bending, the compress forces acting over the entire surface in the top layer and the opposite tensile forces in concentrated form in the aligned folded edges on the underside. In contrast to a bar structure, the shear force is not derived from shear forces in the cross section, but dissolved from membrane stresses of the involved partial surfaces, while the characteristic load bearing behavior of folds is also reflected in this case, in that the stresses are concentrated and transferred via the sides of the pyramid.

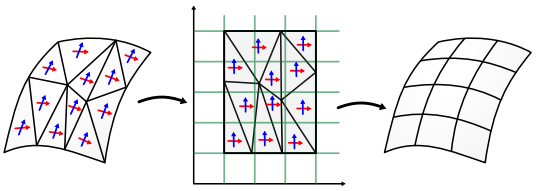


4 Form-Finding of the Stress Adapted Folding Structure

Our form-finding of the stress adapted folding structure can essentially be divided into three core processes (cf. Figure 1): Starting from an initial surface which represents the underside of the planned structure, the principal stresses and principal tension directions are first computed. The principal stresses and are used to calculate a PSM whose edges follow these directions (Section 4.1). The folding structure is then derived from the PSM in a three-stage construction process by punctually folding the tessellated sub-surfaces of the mesh so that the base edges of the pyramidal folds reflect the trajectories. The top part of the two-layer structure forms a flat sheet metal layer.
In many cases, however, geometric alignment alone is not enough to use the material most efficiently, since they only determine the directions of the support axes of a system. If the folding pattern is only aligned according to the main stress direction, it can happen that the material or the stiffness of the structure is not distributed according to the stresses. For this reason, it is also necessary to include the stress *magnitudes* (normal stresses) in the form-finding process in addition to the principal stress *directions* (Section 4.2).

4.1 Principal Stress Mesh Generation

The generation of the principal stress direction aligned mesh is based on the *Mixed-Integer Quadrangulation* (MIQ) method of Bommes et al. [9]. The MIQ algorithm generates a quadrilateral mesh from a given triangular input mesh in two main steps: the computation of a smooth cross field based on a sparse set of directional constraints (typically extracted from the curvature of the input mesh) followed by the computation of a parametrization which aligns to that cross field. Since in our case the alignment is given by the principal stress directions which are defined on the whole surface, the computation of the cross field is of less interest for us and we will concentrate on the computation of the parametrization in the following paragraph.
The parametrization consists of a pair of piecewise linear scalar functions u and v mapping each triangle of the input into the two-dimensional plane. The quadrangular mesh is then obtained by lifting the regular grid consisting of all lines in the two-dimensional domain for which one of the coordinates is a constant integer back onto the input object.



The two function u and v are found by minimizing the following energy for each triangle t:

$$E_t = ||h\nabla u_t - \mathbf{u}_t|| + ||h\nabla v_t - \mathbf{v}_t|| \tag{1}$$

where h is the desired edge length of the quadrangular mesh, $\mathbf{u}_t$ and $\mathbf{v}_t$ define the desired local alignment of the quads and ∇u and ∇v are the gradients of the u and v function, respectively. In contrast to Bommes et al. who compute $\mathbf{u}_t$ and $\mathbf{v}_t$ by interpolating a set salient directions calculated from the curvature information of the input mesh, we directly use the two principal stress directions to define the alignment.
Functions u and v minimizing Equation (1) are simply found by solving a linear system. In addition to the alignment, we also require that singularities in the cross field (points/areas without unique principle stress directions, e.g. symmetrical-points of geometries), are represented by vertices, which is achieved by u and v being integers in these location. This way we ensure that chains of edges pass through these points allowing good load ablation. To compute a

parametrization close to the minimizer of Equation (1) fulfilling this additional requirement we use the algorithm presented by Lyon et al. [10].

4.2 Mesh Densification

To achieve the most homogeneous and efficient material utilization as possible, in addition to the geometric alignment according to the principal stress *directions*, the inclusion of the associated principal stress *magnitudes* is required.
Although a certain compression of the trajectories can often be observed with increasing stress, this cannot be assumed to be valid in general [11, 12]. Especially in the area of isotropic points – shear force nulls without a clear main stress direction – the opposite can often be observed. In that case, trajectory distances and stresses both increase towards the isotropic point, as the case, for example, of the field center of the square plate in Figure 1. A folding pattern following this mesh leads to a correspondingly higher stress on the structure in the relatively less materialized field center. Thus, it is desirable to increase the mesh density in these regions which we achieve with an iterative algorithm explained in the following paragraph.
For each edge we compute the integral of the stress in direction orthogonal to the edge. If this integral exceeds a certain threshold T the edge is marked to be split. (To obtain a scale invariant threshold we define T as a multiple of the minimal computed integral.) The reason behind this is that splitting two opposite edges of a quad is achieved by adding a new edge between the centers of those edges. This in turn leads to an additional crease in the folding structure reducing the load on the two parallel creases.
We add to the already marked edges which exceed the stress threshold a small set of edges such that the number of split edges per quad is even. This leads to a refinement such that the resulting mesh still consists of only quadrilaterals and the new edges form "load paths" which are either closed or connect between boundaries. This process is iterated until no edges remain for which the orthogonal stress integral exceeds the threshold leading to a more homogeneous stress distribution among the creases of our folding structure. Figure 2 shows results of this algorithm for our analyzed systems.

5 Results

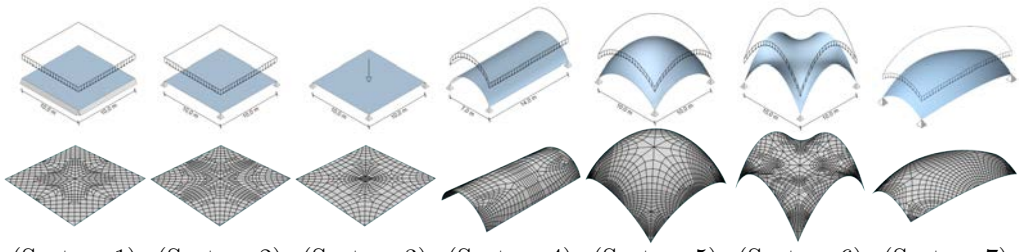
In this chapter the results of the form optimization will be analyzed from two points of view: In the first part the results of the optimizations are evaluated by comparing the stress adapted folding structures with a corresponding geometrically, regular structure. The second part we examine the question, which load is most effective as the shaping load case when several different loads can act.

5.1 Evaluation of the Optimized Folding Structure

The results of the optimizations are evaluated within the framework of a structural analysis, based on a broad spectrum of different geometries shown in Figure 2.
Due to the differences in structure, area and mass of the structural variants, the evaluation criteria here is efficiency, in which the characteristic load-bearing capacity G_c is measured in relation to the characteristic self-weight R_c.

$$E = R_c/G_c \tag{2}$$

Both design variants (stress adapted and regular folding structure) were analyzed in a parametric



(System 1) (System 2) (System 3) (System 4) (System 5) (System 6) (System 7)

Figure 2: Evaluated geometries (top) and corresponding stress aligned meshes (bottom).

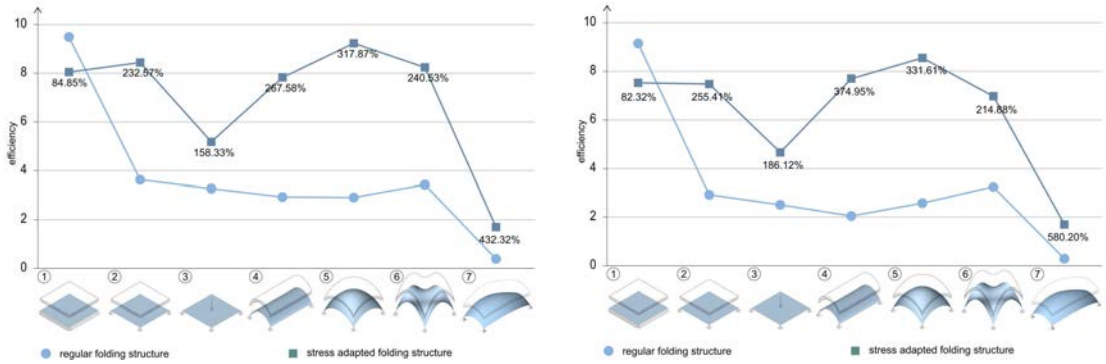


Figure 3: Arithmetic mean values of the three most efficient configurations of the systems in a stress analysis (left) and a buckling analysis (right).

study to determine the most efficient configuration with the associated construction variables height, sheet thickness and folding density. In order to avoid individual evaluations, randomly outstanding maximum values, we consider the average of the three most efficient structures instead. Stress and buckling are evaluated separately and the results are summarized in Figure 3. Comparing only the results, the optimized structures, with the exception of system 1, are much more efficient. They increase in efficiency both in stress analysis and in stability analysis,up to 140% to 580%.

The fact that for system 1 the regular structure is more efficient than the stress aligned one is due to the characteristic load-bearing behaviour of this system. A square, dense grid structure comes closest to square, linearly supported plate with a uniform load, which theoretically has an infinite number of support axes with a circular load transfer (cf. Figure 4 left). Systems with a concentrated load transfer/support axes behave differently, for example system (cf. Figure 4 right). The associated stress diagram illustrates in a clear way how the loads in the stress adapted variant are primarily transmitted to the corner bearings via the correspondingly aligned folds – from the center of the plate via the diagonal support axes and near the plate edges via the support axes running parallel to these.

This phenomenon could basically be observed within the scope of the study: The more concentrated the load of a system is transferred, the more effective and efficient is a folding structure aligned accordingly.

However, this does not mean, that a stress adapted folding structure is necessarily more efficient in every design configuration, but it does lead to a more efficient construction with a corresponding configuration parameters in most cases.

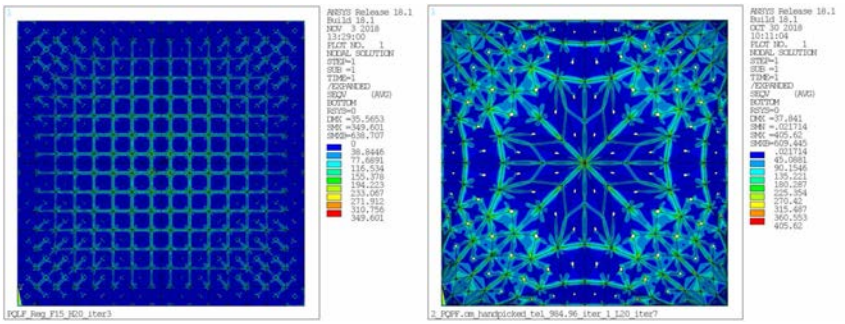
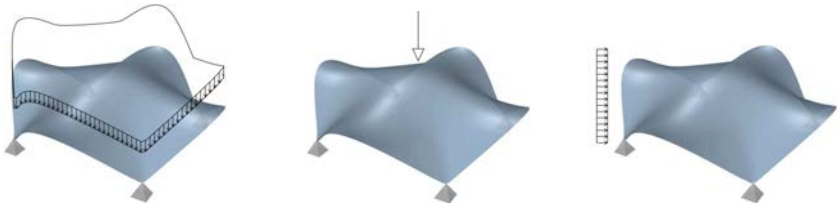


Figure 4: Plot of Mises stress for a regular structure (left) and a stress aligned structure (right).

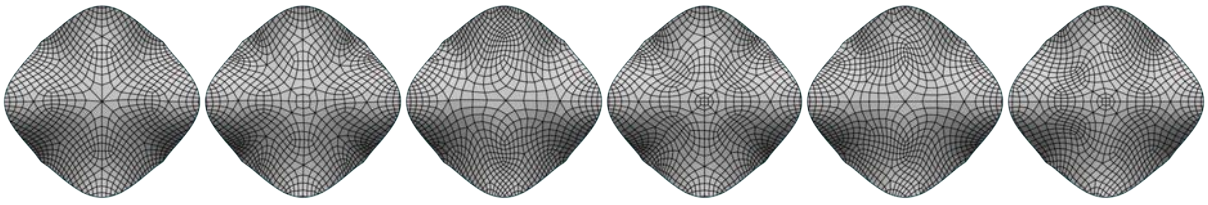
5.2 The Form Shaping Load

After it is been confirmed that an alignment of the folding pattern according to the stresses significantly increases the efficiency of the structure, the following question arises: Which load is to consider in the form finding process as a shaping load case when different loads can act alternatively or simultaneously? Especially when it comes to lightweight construction, the stresses from the dead load are lower than that from the life load and thus not the shaping load case.
For this purpose, we analysed a double-curved geometry which for three different load cases were considered (each of the same load sum). The three load cases are (1) the dead load, (2) a point load and (3) a horizontal load (cf. Figure 5). In addition to the individual loads, also the three possible combinations of the dead load with the other two loads (1+2, 1+3, and 1+2+3) were considered. For each load case and combination, we derived the stress adapted folding structure as discussed in Section 4, while the densification (Section 4.2) was not taken into account in order just to evaluate the alignment to the stress directions. All six structures were analyzed with all load cases also within an elastic stress analysis. Therefore, the evaluation here is not based on the load capacity, but on a comparative value that makes a statement about the overall load-bearing behavior. For this reason, the sum of the stresses of all nodes was evaluated, with the same total area of the structures and number of FE-elements.
Figure 7 shows the stress sum for all combinations of load cases and the resulting structures. Comparing all the graphs, it is noticeable that they describe the same general shape for all load cases. When evaluating these graphs, the areas of the individual load cases (1-3) and the combinations are to be considered separately: For the individual load cases, it can be stated for cases 1 and 2 that the associated structures are e better solution. In load case 3 (horizontal load) this is not true. For this type of load, the structures of 1 and 2 are more favorable. The stresses of load case 3 lead to relatively “chaotic” suspension shafts, with many tight curvature and



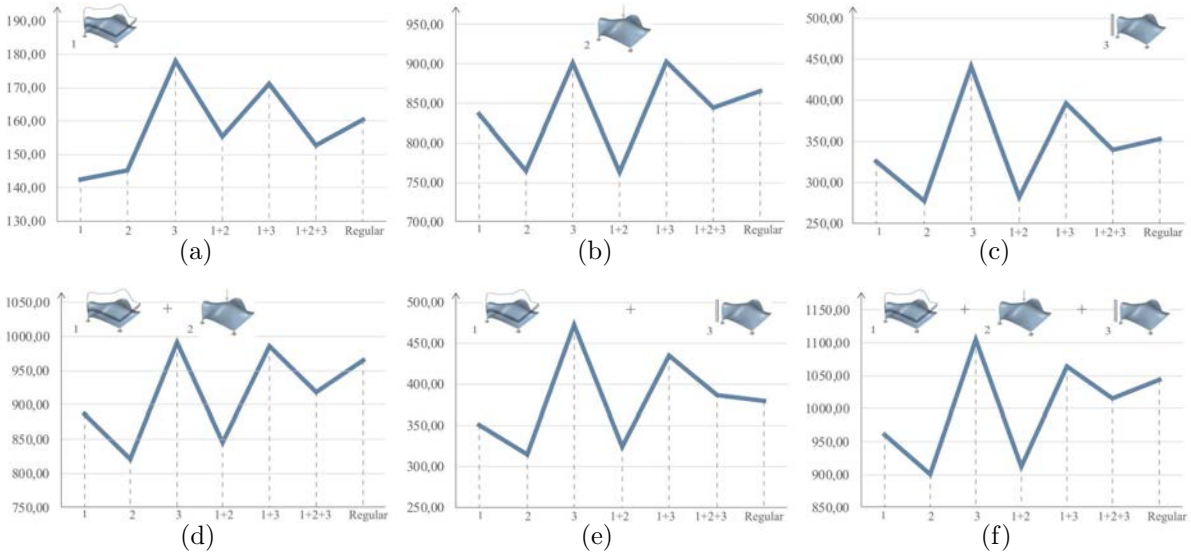
(a) load case 1 (b) load case 2 (c) load case 3

Figure 5: Three different load cases on a doubly curved surface: load case 1: dead load (left), load case 2: point load (center) and load case 3: horizontal load (right).



(1) (2) (3) (1+2) (1+3) (1+2+3)

Figure 6: Resulting meshes for the different combinations of load cases shown in Figure 5.



(a) (b) (c)

(d) (e) (f)

Figure 7: Stress sum [$\cdot 10^3$ N/mm^2] of the structure based on the meshes in Figure 6 with the load cases in Figure 5

direction changes, which cannot be implemented in that detail by a coarser folding structure, so that also the homogeneously regular structure turns out better. This also has an effect on combined load cases. Load case 3 effects the meshes (1 + 2, 1 + 3) unfavorably. The second reason is the density of the folds. Whereas in cases 1, 2 and 1+2 the folds "naturally" concentrate on the stress-intensive support areas, this does not apply to load case 3. This confirms the statement, that the more concentrated the load is transferred with well-structured support axes, the more effective and efficient the alignment effects and pure alignment to the stress directions without taking the stress magnitudes into account does not necessarily lead to the most efficient structure.

6 Conclusion

This paper shows a shape optimization approach for folding structures based on the calculation of a principal stress mesh. In order to increase the efficiency, the geometrical alignments according to principal stress direction as well as the stress magnitudes were included. The evaluation of the approach was based on different geometries according to their efficiency, i.e. the ratio of the load capacity to the self weight.

The question about the forming load case, when several different loads can occur corroborate the following theses: If the stresses are not included in the form determination, the load case

used as a basis for the form finding does not necessarily lead to the most sustainable or efficient structure for this load case.
However, the comparison showed that the optimized designs with alignment to the principal stress directions and adapted to principal stress magnitudes can improve the efficiency by up to 480% over simple regular structures.
Even once the optimal folding pattern has been generated, the question remains as to the most efficient construction parameters such as material thickness and folding height to fully exploit the potential of the stress-adapted mesh. Further research could be carried out and, e.g. the stiffness values of such a folding pattern could be simulated using analytical or numerical methods.

7 Acknowledgements

This work was funded by the Deutsche Forschungsgemeinschaft (DFG, German Research Foundation) - project 269321250.

References

[1] R. Herkrath and M. Trautz, "Starre Faltungen als Leichtbauprinzip im Bauwesen," *Bautechnik*, vol. 88, no. 2, pp. 80–85, 2011.

[2] Z. H. Architects and Bollinger + Grohmann, "Ciab pavilion beijing 2013." https://www.karamba3d.com/projects/ciab-pavilion/, Last accessed 10 June 2019.

[3] M. Dimcic, *Structural optimization of grid shells based on genetic algorithms*. Dissertation, University of Stuttgart, 2011.

[4] K.-M. M. Tam, J. R Coleman, N. W Fine, and C. Mueller, "Stress line additive manufacturing (slam) for 2.5-d shells," 2015.

[5] F. Gil-Ureta, N. Pietroni, and D. Zorin, "Structurally optimized shells," *CoRR*, vol. abs/1904.12240, 2019.

[6] D. López, D. Veenendaal, M. Akbarzadeh, and P. Block, "Prototype of an ultra-thin, concrete vaulted floor system," 2014.

[7] M. Rippmann, L. Lachauer, and P. Block, "Rhinovault - interactive vault design," *International Journal of Space Structures*, vol. 27, no. 4, pp. 219–230, 2012.

[8] M. Rippmann and P. Block, "Funicular shell design exploration," in *Proceedings of the 33rd Annual Conference of the ACADIA*, (Waterloo/Buffalo/Nottingham, Canada), 2013.

[9] D. Bommes, H. Zimmer, and L. Kobbelt, "Mixed-integer quadrangulation," *ACM Transactions on Graphics*, vol. 28, no. 3, pp. 77:1–77:10, 2009.

[10] M. Lyon, M. Campen, D. Bommes, and L. Kobbelt, "Parametrization quantization with free boundaries for trimmed quad meshing," *ACM Trans. Graph.*, vol. 38, no. 4, 2019.

[11] D. H. and R. Moufang, *Forschung im Ingenieurwesen*, vol. 12, ch. Kritik des Kraftflußbegriffes. Springer Berlin Heidelberg, 1941.

[12] U. Wegner, *Über den Zusammenhang zwischen Strömungs- und Spannungsproblemen*, vol. V, ch. Kritik des Kraftflußbegriffes. Springer Verlag, 1934.

Proceedings of the IASS Annual Symposium 2019 – Structural Membranes 2019
Form and Force
7 – 10 October 2019, Barcelona, Spain
C. Lázaro, K.-U. Bletzinger, E. Oñate (eds.)

40 Years After
- Development and Possibility of Beam String Structures

Masao SAITOH

IASS Torroja Medalist 2009
Professor Emeritus, Nihon University
A-Forum
1-5-5-5F, Kanda-Surugadai, Chiyoda-ku, Tokyo, Japan
m.saitoh@a-forum.info

Abstract

Forty years ago, in 1979, at the 20th Anniversary of IASS in Madrid, the author presented the paper titled "Principle of Beam String Structures (BSS)". BSS is one of the represented systems of so called Hybrid Tension Structures. The principle of this system is very simple, and the ideas are not so new from the viewpoint of historical meaning, but as for the role of the strings, the active possibilities for both the adjustment of stress distribution and deflection have been evaluated. Starting from Faraday Hall (1978) of which the span is about 20 meters, so many BSS with large span and various features have been realized during the last 40 years including the new projects of Tokyo 2020 Olympic Games. In this paper, the diversity of BSS will be presented from both viewpoints as follows: 1) Architectural expression of the external and internal appearance; 2) Structural technology of the system, details and construction.

Keywords: beam string structure(BSS), hybrid tension structure(HSS), structural expression, control of structural behavior, sefl-balance system, Archi-Neering Design(AND)

1. Introduction

"Spatial Structure" is able to realize the architectural space with long-span rationally. It's basic characterisitic is the perfomance of form and axial resistance, and such tension members as cable and rod is most important to produce light-weight Hybrid string structure(HSS).

A primary category of HSS is BSS (Beam String Structure or, in German, Balken Seil structure) made by combining strings with such rigid members as beams, shallow arches and mount shaped arches by means of intermediate struts.

The basic cnaeacteristics of BSS can be summarized by the following four points:

1) The "strings" are arranged beneath the beams, plates or arches to act as "suspension" by inserting intermesiate struts between the two structural layers.
2) By balancing the horizontal thrust of arches or strings against each other, the structure can be defined as a self-equilibrated system (passive effect).
3) If requied, the stress distribution and displacement of the structure can be adjusted by tensioning the string (active effect).
4) In the selection of structural members of the beams or strings, various materials such as steel or timber and many varieties of cross sections are widely adaptable.

Copyright © 2019 by Masao SAITOH
Published by the International Association for Shell and Spatial Structures (IASS) with permission.

2. What is BSS – The characteristics and its birth

The primitive idea of BSS has been known in bridges and buildings from the beggining of the 19th century, such as Crystal Palace(1851), Royyal Albert Bridge(1859) and Casa-Mira(1910), but BSS has not spread widely as arches and trusses have been developed. Recently, why has this structurak system again been applied, not only in bridges but also in architecture?

First, it may be due to architectural design. The dstinguishing chacteristic of BSS is the degree of freedom in selecting plan and section of BSS befitting space, scale and form. Furthermore, such "architectural expression" is an extension of the degree of freedom in both exterior and interior design by using a self-balancing system; a sense of transparency, lightness and delicacy expressed by eliminatimg or emphasizing the existence of the string; and an expression of logic in systems. All these are noticealbe characteristics of design in BSS.

Secondaly, the attractive feature of BSS may be due to structural design. The most effective performance of BSS is the active role of the strings, that is, the ability not only to control the moment distribition of the beam aganst dead load but to absorb the axial force of both beam (shallow arch) and each other. The later characteristic can release the supporting lower frames from large amount of horizontal thrust of the usual "form resistans structre" such as arches and suspemsion cables. In order to realize these favorable merits of BSS, it is neccessary to consider deeply the relationship between system, the details and the costruction procedure in the preliminary design, and especially important is how to introduce the intial tension or prestressing force to te string.

On the other hand the development of BSS can be understood generally from the transitional view point of form-resistant structures. There are two-hinged arch to the tied arch. The "Suspen-Arch" and the simply supported beam are the other roots of BSS explained though the historical facts mentioned.

It is to be emphasized that the technological concept or architectural characteristics of BSS have been developed futher by architects and engineers from the aesthetical and functional viewpoints in addition to the structural and constructional viewoints.

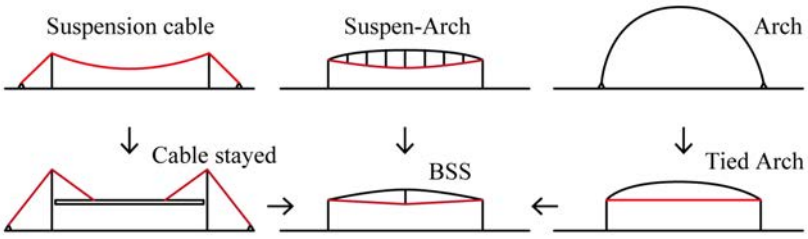


Figure 1: The birth of BSS

3. Diversity of BSS during forty years

From the viewpoints of architectural and structural features, respresentative examples (mostly designed by the auther) constructed during about 40 years are intoroduced in terms of the following:

- Architectural expression of the external and internal appearance
- Structural technology of the system, details and construction

In general, the dead-load is predominant in long-span structures. Self-balancing systems of BSS with strings and beams can free the boundary structure from horizontal reaction, allowing for light and free exterior design creating a variety of images.

The delicate and sharp sense of strings can create various individual expressions in combination with thick beams. As an interior feature, structural expressions can be considered by either eliminating or emphasizing each beam or string.

The method of introducing prestress into the strings in order to realize the structural system greatly depends upon construction and details, which have to considered as a whole.

1) Faraday Hall of Nihon University (1978)

The diameter of this roof, about 19 meters, is not large, but it exemplifies both the scientific or technological spirits through the mechanical expression of the roof. All of the exposed structural elements such as the string (rods), the deck plates, the struts, and the rings take part in the expression of this space composition. The tension ring is composed of 32 steel elements that are assembled by turning reversed screw bolts (60φ). After prestressing for the strings to some extent by using the threaded rod ends, the central ring was jacked down from the scaffolding to obtain the final tensile force due to the roof dead-load of 300kgf/m^2.


Figure 2: Bird view of Plaza Narashino


Figure 3: Interior view


Figure 4:Attaching the strain guage to the strings

2) Spurts Hall of Nihon university (1985)

This building was designed as both sports and assembly hall with 3000 fixed seats. It is a square building measuring of 58m x 58m, covered by a slightly mount shaped-roof which is supported by a serious of one-way type of BSS. The Truss girders (beams) have a triangular section of 2.0m depth and the strings are arranged at an interval of 5.0m. To obtain a favorable stress distribution and minimize the deflection of the beams due to the dead-load (185tf/m^2), the cables have been tightened by means of hydraulic jacks. To make effective use of self-equilibrium system of BSS, The roof with its toal weight of about 1000tf was pulled forward by small hydraulic jacks using a remote control system after the finishing work had been completed.


Figure 5: Exterior view

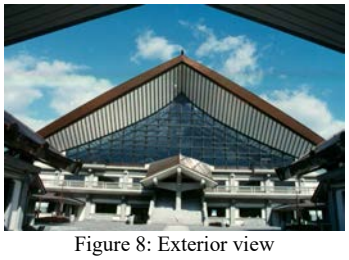

Figure 6: Interior view

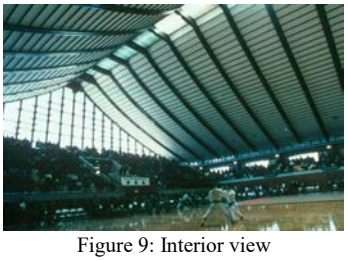

Figure 7:Sliding construction view

3) Mount-Shaped arch type pf BSS

Left: Traditonal sports arena of Iwate prefecture (1990)**.** The continnos curued cables arranged beneath the H-shaped steel beams, not only support the dead-load of the roof but asorb the horizontal thruth of the arched beams.

Right: Rainbow pool of Nagoya City(1992)**.** The bending moment of truss beam is defereased by a continuous cable with V-shaped struts, and the horizontal thurust due to dead-load is simultaneously supported by same cable.


Figure 8: Exterior view


Figure 9: Interior view

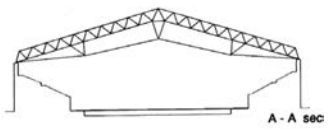
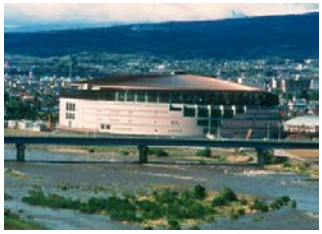
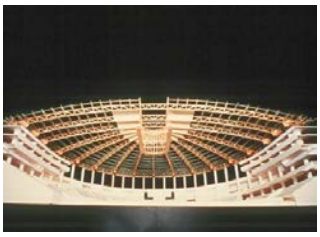


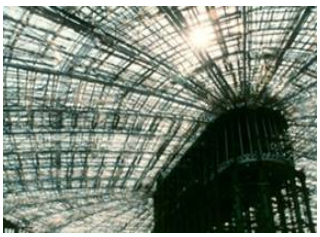
Figure 10:Section

4) Green Dome Maebashi (1990)

In order to realize a shallow dome covering an oval plan (168 x 122m) BSS was employed. Since the horizontal thrust of the BSS is small, the exterior view has one of both sharpness and lightness. The tensile force of the strings was established with the aim of minimizing and equalizing the positive and negative bending moments in beams. On a central stage, after the BSS was erected, the tensile force was introduced to the string using jacks installed at the end of the sixty-eight strings in order to raise the whole roof with 3000tf.


Figure 11: Exterior view


Figure 12: Structural model


Figure13:Construction view

5) Sakata Municipal Gymnasium (1991)

A pair of arena, large and small, are like figures that appear as though two while swans are about to rise from a paddy field and fly into the air above. Cables and struts colored with Turkish blue float in the natural light from deep eaves. The hybrid system that is composed of BSS and cantilever trusses (CT) balanced by back stay strings was proposed to construct as flat and light roof as possible. After the length of strings was adjusted, the tensile force was introduced to the strings by pulling down the middle parts of the cables and fitting them into struts. This was done by human labor at the time that the steel frame weight and finishing load were applied. A set of three BSS was lifted up by using the cables to shorten the term of construction.


Figure 14: Exterior view


Figure 15: Interior view


Figure 16:Detail of cable end

6) Anou Dome (1994)

The Anou Dome roof has a wave-shaped surface with two directions of curvature. The interior view is suggestive of trees in a forest because of sunlight that pours though the membrane and onto the slightly curved arch and fan-like supporting columns of stiffened and laminated timber to give the impression of being in forest. The Whole system is very similar to Sakata gymnasium where the BSS was combined with cantilevered trusses (CT) . The bracing cables on the valley of the membrane roof form a tension-arch with backstay cables to resist uplift wind force. A pair of BSS units equipped with temporary braces was elevated by crane, and welded to the CT which had been exactly set by the pre-loading system.


Figure 17: Exterior view


Figure 18: Interior view


Figure 19: Construction view

7) Subway Station of Nihon Univ. (1996)

The main theme of this design was to propose the new system "SKELSION" which embraces people in an atmosphere of lightness and transparency radiating from an atrium space. The prestressing forces of the inclined bracing strings are balanced by the combination with BSS. The main characteristic of this structure exists in the detail for the prestressing method of bracing strings. By shortening the small clearance between two plates at the crossing point of six bracing rods by using a small jack, the initial tensile force was introduced to these six strings simultaneously. The term SKELSION means the combination of skeleton and tension. For a portal frame with a slight section, the hanger string is placed against a vertical dead load and bracing strings arranged three-dimensionally are placed against such horizontal additional load as seismic and wind forces.

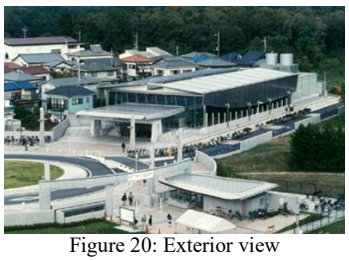
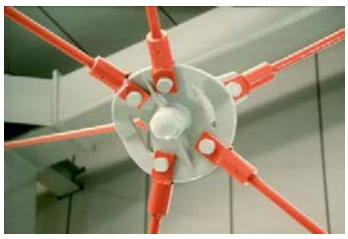

Figure 20: Exterior view


Figure 21: Interior view


Figure 22: Detail of Strung joiunt

8) Horinouchi Gymnasium (1996)

The architectural and structural design theme was how to realize a heavy snow resistant system with lightness by using a timber frame. Against dead load the self-balanced mechanismm of BSS is formed, and against a long-term snow load (depth 3.5m) a trussed mechanisim is formed by an arrangement of inclined posts and diagonal rods. Each BSS unit assembled on the ground was lifted by a crane one by one. When the final work was completed, compressive forces occurred in the posts due to the dead load and were released by loosening screws at the lowest part of the posts.


Figure 23: Exterior view


Figure24: Interior view


Figure 25: Construction view

9) Small and light examples of BSS

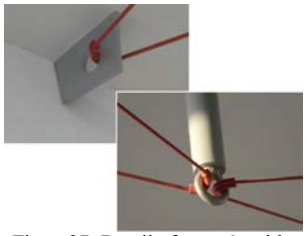
Left: Spiral house (1997)

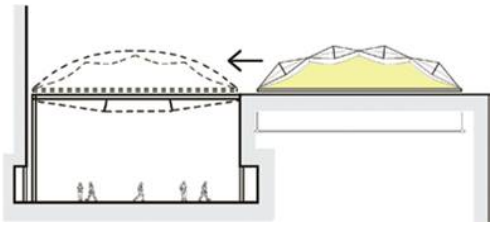
In order to design the atrractive feature of interior space of the living roof, two continuous cables were arranged. The structural role of these cables are to support both dead and live load of roofslab.

Right: Moveing dome of AIJ (2002)

Movable dome of which span is about 20m has been constructed to cover the courtyard of AIJ (Architevtural Instutute of Japan) Main Building in Tokyo by using the single sliding rail of BSS.


Figure 26: Interior view


Figure27: Detail of strut & cables


Figure 28: Section of sliding roof and BSS

10) Urayasu Municipal Sports Center (1995)

There are six cylindrical columns around the gymnasium and four around the swimming pool. These columns support the roof by means of the V-shaped pipes which take the form of an inverted tetragonal pyramid.

The roof of the gymnasium and swimming pool in the lomgitudinal axis is the BSS consisting of virendeel shallow arches and V-shaped truss beams without upper members to express the lightness of interior space.

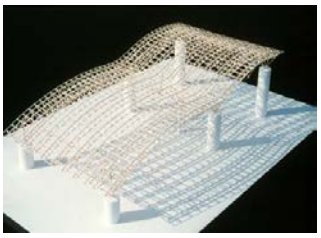


Figure 29: Stractural model (gym.)



Figure 30: Interior drawing (gym.)



Figure 31: Interior view (pool.)

11) Saitama Super Arena (2000)

A single keel girder of BSS is arranged at the opening glass face of gigantic roof with shallow cylindrical surface which is composed of 6 trussed beams. The keel girder is supported by two hyper columns, and its vertical reaction is 2000tf respectively.

The prestressing force for the cables of BSS is about 3000tf, and atter assembling on the ground, the whole roof is lifted up in short time safely.

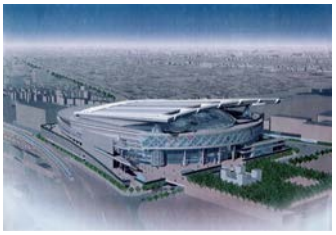


Figure 32: Exterior view

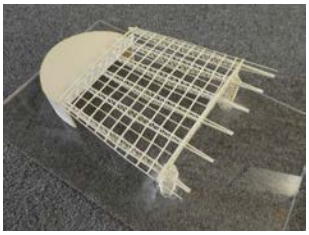


Figure33: Structural model

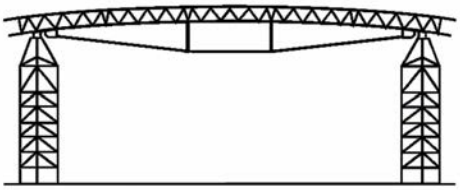


Figure 25: Section

12) Karato Fish Market (2001)

The row of columns on the roof has some similarity with a ship passing in front of the building and the organic apperance of the ceiling reflects the energetic movement of fish market. The column-free space of 50m x 62m consists of slabs which are supported by two kinds of outer cables – a hanging cable on the roof and a suspension cable under the roof.

In other words, the roof is a hybrid of self-equilibrium combined with a cable-stayed structure and BSS. The horizontal tensile force of cables is absorbed by the roof itself as a compressive force in the slabs.

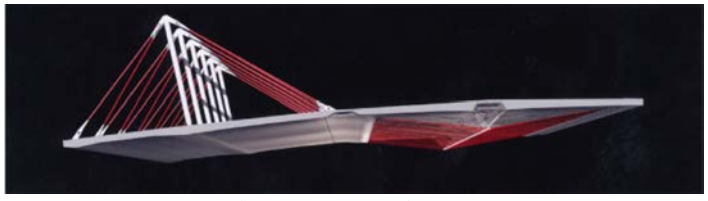


Figure 35: strauctural system

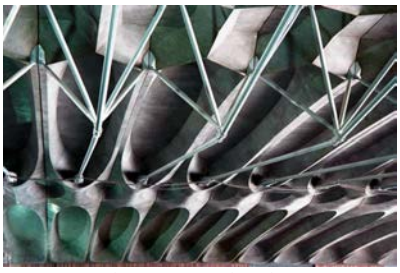


Figure36: Interior view

13) Shizuoka-ECOPA Arena (2001)

The roof has small curvature in both direction of span (90m) and ridge. Because it is supported with the cantilever truss, the whole depth of BSS could be done smaller.

AS for the cantilever, the vertical backstays, as long as their tension dose not disappear, can function as if they were a compression member when horizontal loads decrease the tension imposed to counter the vertical loads; thus they can be designed to be important resistance elements against horizontal loads.



Figure 37:Exterior view

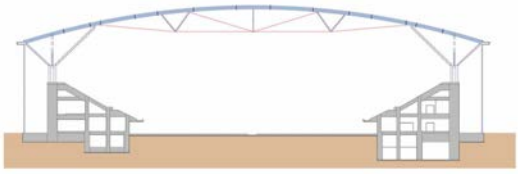


Figure38:Section



Figure39: Interior view

14) Kyoto- AQUARENA(2002)

This building is 117m x 68m and houses an Olympic size swimming pool. To conform to the uneven plan, the roof frame is formed by BSS built in parallel in the short span direction.

The boundary structure supports the roof frame by using three kinds of bearing that is isolated-bearing, isolated-bearing + steel-damper, sliding-bearing. The horizontal thrust due to dead load is cancelled by providing a simple support (pin and roller) in the construction.

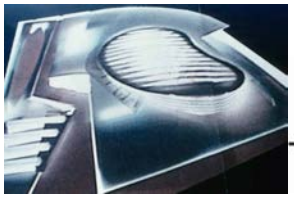


Figure 40:Exterior view & Section

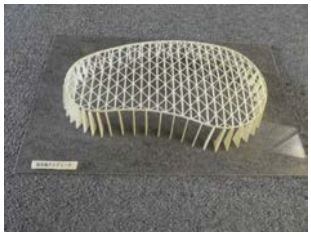


Figure41:Stractural model



Figure42: Interior view

15) Motenashi dome in Kanazawa (2004)

The whole figure of the roof composed of aluminun frame and glass panels was obtained by cutting the sphere of 90m diameter. At the part of wide-span roof and the part of parallel walls, both BSS and SKELSION were adopted to resist heavy snow load and sesmic force.



Figure 43: Interior view

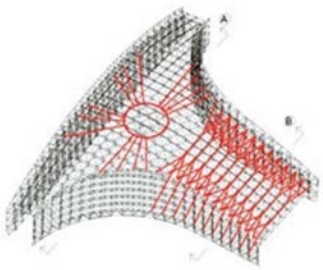


Figure44:Stractural model



Figure45: Construction of the ring of BSS

16) Ariake Gymnastics Center for Tokyo 2020 Olympic Games (2019)

For the Tokyo 2020 Olympic and Paralympic Games, the construction of stadiums is proceeding in Tokyo, Japan. One of its major facilities, the Ariake Gymnastics Center will be used as an exbition hall after the Olympic Games in Tokyo. The most distinguished characteristic is that long spanning roof (about 90m) which is primary made from large laminated timber sections. There are two main feature of architectural image. The first is a low rise arch shape which provides an attractive feeling of lightness and sharpness from an exterior view. The second is the timber roof which gives a feeling of warmth from the interior. Inorder to harmonize this basic design with structural rationality, the basic structural system of a complex hybrid structure combined with Cantilever Truss and BSS has been proposed at the preliminal design. Considering total rationality of structure, sub-cable system prestressing method, lifting up construction and innovative detail of cable clamp are develped from the view points of holistic design of Spatical Structures and Archi-Neering Design (AND).



Figure 46:Image skech of exterior

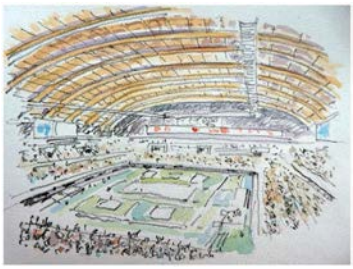


Figure 47:Image skech of interior

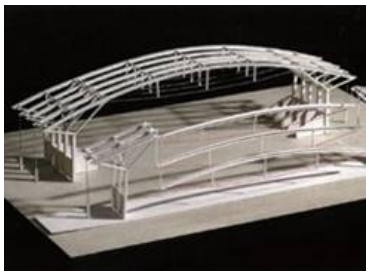


Figure48: Model of construction system

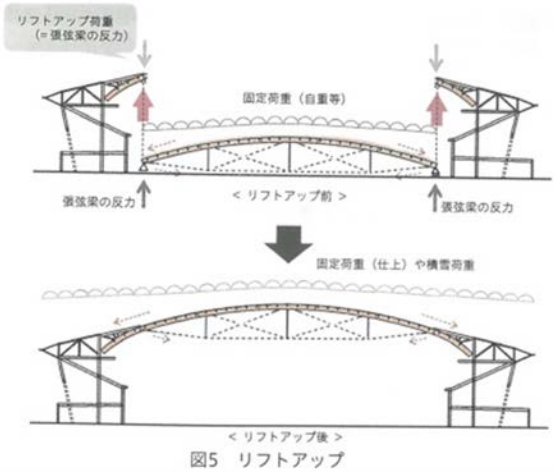


図5 リフトアップ

Figure49:Proposal of the structural system and lift-up construction method.

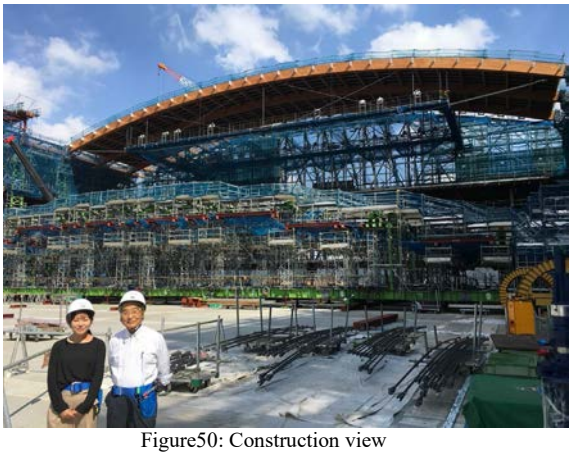


Figure50: Construction view

References

[1] M. Saitoh, "Principle of Beam String Structures," *Proc. of IASS International Conference 1979 (20th Anniversary),* Madrid, pp. 6.17-6.38.

[2] M. Saitoh, "Hybrid Form-resistant Structures," *Proc. of IASS International Symposium 1986,* Nagoya, pp. 257-264.

[3] M. Saitoh, "Hybrid String Structures," *50th Anniversary Jubilee of IASS (1959-2009) - Fifty Years of Progress for Shell and Spatial Structures,* Sec. 8.4, pp. 263-292.

Proceedings of the IASS Annual Symposium 2019 – Structural Membranes 2019
Form and Force
7 – 10 October 2019, Barcelona, Spain
C. Lázaro, K.-U. Bletzinger, E. Oñate (eds.)

Al Wasl Plaza Trellis of Dubai Expo 2020

Jerome TOBOLSKI*, John PERONTO*, and Robert SINN*

*Thornton Tomasetti
Chicago, Illinois, USA
jtobolski@thorntontomasetti.com

Abstract

The Al Wasl Plaza, which serves as the centerpiece of the World Expo 2020 in Dubai is anchored by a grand spherical structural steel gridshell 70 meters in height and 135 meters in diameter at the base. Unlike traditional diagonalized gridshells, the unique structural framework of the "Trellis" draws its inspiration directly from the iconographic logo of Expo 2020 Dubai as a series of nested and tangent rings that result in a flexurally governed ductile structural system. Each of the steel rings are infilled with Polytetrafluoroethylene (PTFE) fabric panels that function both as shading for the open plaza as well as a projection surface for dramatic 360 degree immersive events for Expo attendees and future visitors to the site. Key structural engineering considerations related to the geometric definition, loading and performance criteria, global stability and imperfections, steel fabrication, and erection are outlined.

Keywords: gridshell, stability, structural steel, geometric imperfection, unbalanced load, eigenanalysis, 3D finite element analysis, fabrication, erection, optimization

1. The Search for a Distinctive Framework

World Expositions have a long history of prominent and innovative structures from London to Paris to Milan forming the centerpiece of the event and attracting visitors from all over the world. In late 2016 and into early 2017, Adrian Smith + Gordon Gill Architecture (AS+GG) and Thornton Tomasetti (TT) teamed for a design competition for the Al Wasl parcels located at the heart of the Expo 2020 Dubai master plan. "Al Wasl" translates to "connection" in Arabic which reflects Dubai's goal of bringing people together and mirrors the central theme of the Expo of "Connecting Minds, Creating the Future." AS+GG's concept for the site consisted of five individual buildings (two hotels and three office buildings) surrounding a central circular outdoor plaza covered by an elegant dome, referred to as the "Trellis."

During the early stages of the competition, the design team explored a wide variety of rectilinear and diagonalized gridshells for the trellis, all of which were deemed to be too pedestrian for such a critical destination in the overall Expo experience. Midway through the competition, senior executives from Expo 2020 Dubai asked the design team if the logo of the event could be incorporated in some fashion as the logo has important meaning in the context of Expo Dubai's central theme of connection and Dubai's status as a hub that connects the world both culturally and geographically. The design of the logo itself traces its inspiration to 4,000 year old historical jewelry found in a nearby archaeological site. See Figure 1.

The final design for the Al Wasl Trellis is based on a unique curvilinear geometry of the steel pieces very much in keeping with the event themes and the exposition location in Dubai. The geometric spaces between the steel pieces are infilled with lightweight, stressed fabric panels that provide shade during the day, and function as a projection surface during the evening hours. Openings at the base of the trellis are aligned with major pedestrian and vehicular arteries converging from several directions

Copyright © 2019 by Jerome Tobolski, John Peronto and Robert Sinn
Published by the International Association for Shell and Spatial Structures (IASS) with permission.

on Al Wasl Plaza. Nearly 2,800 LED lights are incorporated directly into the steel framework providing an unparalleled immersive experience for Expo patrons and future visitors that will cement Dubai's status in the pantheon of World Expositions.



Figure 1: (left) Expo Al Wasl Plaza [rendering courtesy of Adrian Smith + Gordon Gill Architecture] (right) Archaeological Inspiration [image courtesy Expo 2020 Dubai]

2. Optimization of the Geometry and Materials

The centerline geometry development of the Trellis members was an iterative process between the architectural and structural engineering teams for a period of several weeks; and this process continued between the design team and the steel fabricator / erector Cimolai Rimond Middle East (CRME) upon contract award and mobilization. The primary goals of the optimization process for the geometric definition of the Trellis steel framework were:

- Facilitate the steel fabrication through a rationalized series of tangent, circular arcs with the least amount of pipe-to-pipe splices (both in the shop and in the field)
- Promote repetition of the steelwork thereby improving cost-effectiveness
- Maintain the aesthetic look of the competition design that had been promised to the Expo executives

Circular hollow sections (CHS) were determined very early in the process to be the most suitable shapes for the Trellis primarily due to their aesthetic quality and their favorable response when bent opposed to the warping effects that require consideration inherent to rectangular hollow sections or wide flanges. The internal void of the CHS elements also provided the much desired advantage of being able to serve as the main arteries of the Trellis to deliver the various services of the structure out of public view.

The nature of the connections at the confluence of the steel pipes was a source of substantial aesthetic and structural debates. A variety of schemes were studied both aesthetically and analytically from the two pipe centerlines meeting in perfect tangency to the two pipes passing or "kissing" without interruption. Ultimately the tangent scheme prevailed as this scheme best addressed the design vision that the concept demanded. See Figures 3 and 6. Although this approach created some challenges that required creative engineering solutions in the fabrication of the nodes, the resulting look was fully endorsed by the Expo client.

With the exception of the various larger openings at the base of the Trellis, there are 54 identical sectors (modules) of 6.67 degree sweep defining the centerline geometry. The uppermost "oculus" compression ring is 35m in diameter, and 70m above the floor of the plaza offering unobstructed views to the sky above.

Generally, each individual circular arc lies in a single inclined plane and adjacent arcs follow the contours of the dome with a simple angle change as indicated in Figure 2. However due to the nature of the spherical surface and the number of circles constraining one another, some areas required an additional fabrication complexity of a "twist" between the adjacent planar surfaces. Finally, fabrication exigencies requested by CRME also resulted in slight geometric modifications upon contract award, although the overall design aesthetic was not compromised.

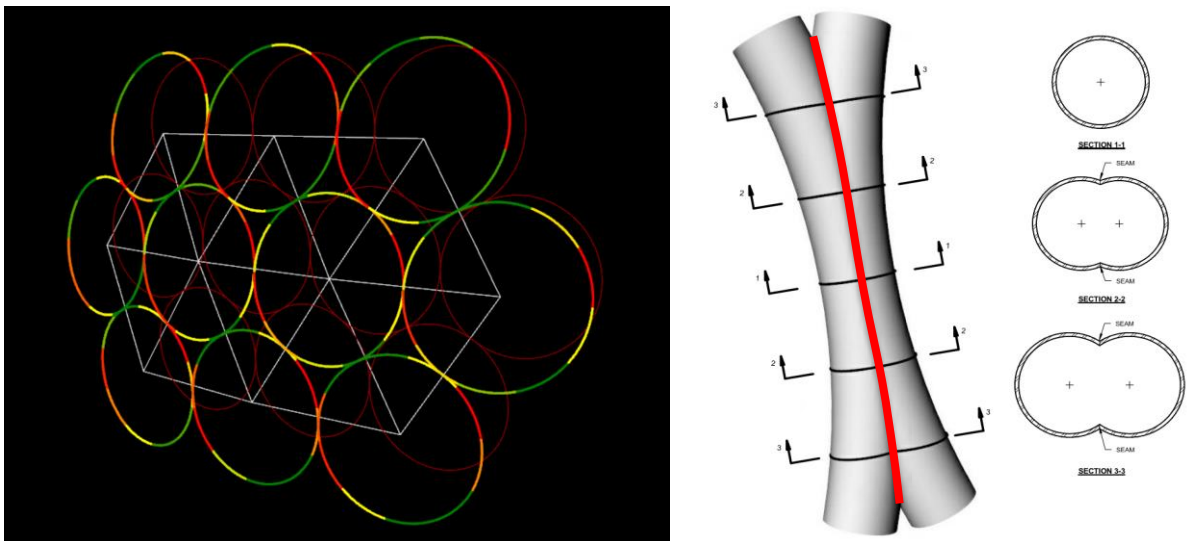


Figure 2: Planar Tangential Circular Geometry

In an initial effort to control the overall steel tonnage of the Trellis a gradient of CHS diameters between 350mm and 500mm were proposed. As part of a value engineering exercise, TT investigated the use of 460 MPa yield strength steel material in lieu of the 355 MPa steel originally proposed. Combining the use of high strength S460, EN 10210-1, hot-finished seamless steel material sourced in Europe and China, and a consistent 500mm nominal pipe diameter throughout the dome (with varying wall thicknesses between 10mm and 50mm) proved to be the most cost-effective solution. This constant gradient also held true to the design of the slim, polished, and continuous look of the overlapping connections.

Radii of the required bends range from as low as 1500mm up to 55,000mm, which corresponds with a radius of bend-to-pipe diameter ratio of as low as 3. For bends of this pipe diameter and radii, induction bending proved the only feasible solution, whereas cold bending was utilized for the larger radii bends. Due to the significant amount of strain, wall thinning, and change in microstructure that the section undergoes during the induction bending process a heat treatment protocol was required after the completion of the bends to ensure yield properties at a minimum were comparable to those of unadulterated straight pipe. Wall thinning of the extrados of the bend is a major consideration for tight bends, but this issue was largely avoided as the framework of the structure dictated that the extrados of the pipe to be removed at connection locations.

3. Analytical Modeling

The majority of the three dimensional finite element analysis (FEA) modeling of the Trellis was carried out in CSI SAP 2000 commercial software with six degree of freedom frame elements used throughout. Parallel FEA models were also developed in SOFiSTiK to validate and confirm the analytical approach. Due to the geometry and large number of the overlapping pipe sections, both the stiffness and the weight of the steel had to be modified in order to approximate the actual steelwork configurations in the final fabricated, installed state. In order to determine an appropriate modeling

approach for the project, several sensitivity studies were conducted including the approach of modeling non-prismatic section properties within the nodal regions as indicated in Figure 3.

Frame elements in the FEA model meet at a singular point whereas in the actual construction, there is a spatially complex merging of the two pipes in the nodal region. Separate sub-frame models comparing the straight-line frame model with shell elements representing the nodal regions were used to calibrate the global analysis model. Stiffness and weight modifiers were developed based upon the entire range of interconnecting joints to accurately account for the stiffness and weight of the completed Trellis.

Models with large sections of the Trellis isolated were studied with both frame elements (with the modified properties indicated above) and with the entire merged region replaced with shell elements forming the pipe sections and intersections. Modal analysis was performed with identical boundary conditions and the natural frequency and mode shape results displayed good agreement between the two models verifying the approximations used on the global FEA model.

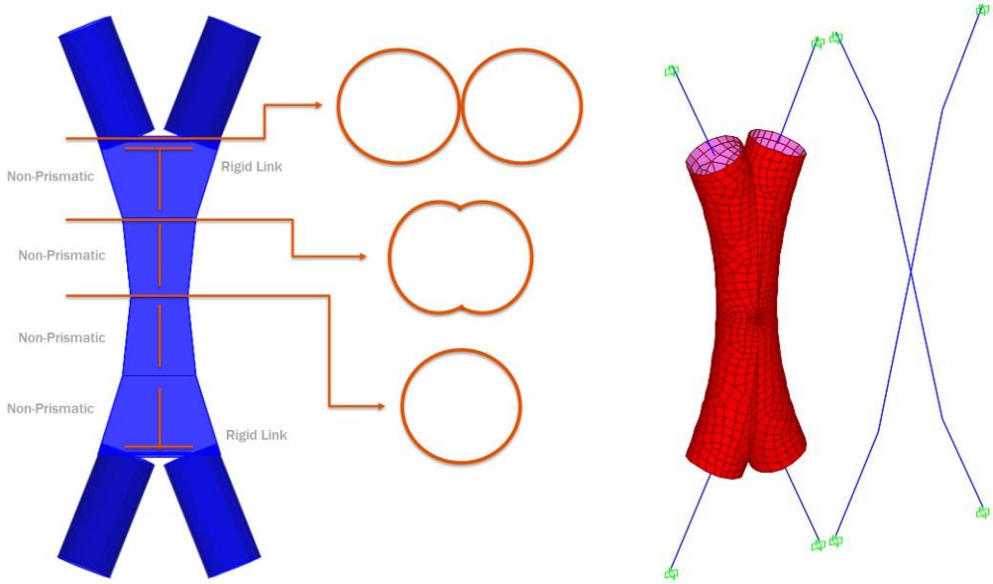


Figure 3: Modeling Approximation for Overlapping Joints

4. Design Criteria

As a cultural landmark for the city of Dubai the Trellis is anticipated to support a wide range of events and experiences, and the structural design accommodated for a multitude of superimposed loads and conditions accordingly as follows:

- Wind
- Façade (fabric, structure) Cleaning Unit
- Suspended Lighting
- Fabric and Fabric Support Frames
- Roof Access Live Load (maintenance)
- Ambient Thermal Gradients
- Seismic
- Rigging Loads (events)
- Suspended Projectors and Speakers
- Connection Material at Joints
- MEP Requirements
- Accumulated Drifting Sand

Basic loads were combined as recommended by ASCE 7-10. [1]

As the Trellis is nearly fully enclosed from a wind sail standpoint, wind loads were determined through use of a High Frequency Pressure Integration (HFPI) wind tunnel test performed by Rowan Williams Davies & Irwin Inc. (RWDI) at their laboratories in Ontario, Canada. See Figure 4. The Trellis was tested for two configurations: the full Expo build-out and a configuration without the

adjacent five buildings. Generally, the five adjacent buildings tend to shield the Trellis, although some deleterious funneling of wind between the buildings onto the Trellis was detected from the testing. However, results did indicate a significant reduction in the peak negative design pressures at the apex of the dome typically observed when developing wind load demands from codified design figures. This reduction could mainly be attributed to the vented regions of the center oculus and base of the structure that the code is not equipped to accommodate. The Dubai Municipality currently mandates a basic wind speed of 45 m/sec, 3 second gust at 10m height for the strength design of all structures.

Seismic design in Dubai currently follows the provisions of UBC 97 [2], Zone 2B. The determination of an appropriate seismic response factor, R, for the Trellis was critically evaluated due to the unusual configuration of the system geometrically. The Trellis rests on a one-story reinforced concrete ring structure that is designed and detailed as an Intermediate Moment resisting Frame (IMF). The Trellis steelwork is considered an Ordinary Moment resisting Frame (OMF) due to the structural framework's inherent flexural and ductile resistance to seismic action. Consequently an overall response factor of R=4.5 was used for the combined system. Due to the unusual nature of the interconnecting joints of the Trellis, R=1 sensitivity studies (beyond the minimum provisions of the Code) were performed on the Trellis in order to demonstrate significant additional capacity in the steel system to resist seismic loads.



Figure 4: Wind Tunnel Testing in Final (Shielded) Condition [courtesy of RWDI Laboratories]

5. Stability Studies

Like other gridshell structures the Trellis is a lightweight, long span structure that is susceptible to amplifications in design stresses arising from potential geometric imperfections and unbalanced loading conditions. Thus TT performed the necessary global stability and local buckling verifications to validate the structure's resiliency. This investigation was done through direct modeling of the most critical deformed shapes that mimic the eigenmodes of the structure.

The process for investigating the overall stability of the Trellis using SAP2000 in conjunction with the AISC LRFD [3] Direct Analysis Method is outlined as follows:

1. Perform a geometric non-linear buckling analysis with factored demands using reduced stiffness modifiers on the structural elements.
2. Review the resultant buckled mode shapes and note the effective buckled length (L) between points of contra flexure for each mode of interest.
3. Adjust coordinates of analytical model to the desired mode shape with a scale factor of L/220 or other imperfection target based on desired fabrication and erection tolerances.
4. Run nonlinear geometric analysis of adjusted model.
5. Perform AISC member capacity checks for the resultant loads in step 4.
   Confirm that the critical buckling factors exceed 2.2 minimum.

The buckling analysis was performed on an entire suite of load cases including gravity alone, gravity plus unbalanced sand accumulation, gravity plus extreme temperature, gravity plus wind, and gravity plus seismic.

A central focus of the stability studies was the upper portion of the Trellis in the area of the oculus down to the first set of linear (vierendeel zone) members as these areas displayed the most sensitivity to stress amplifications. See Figure 5.

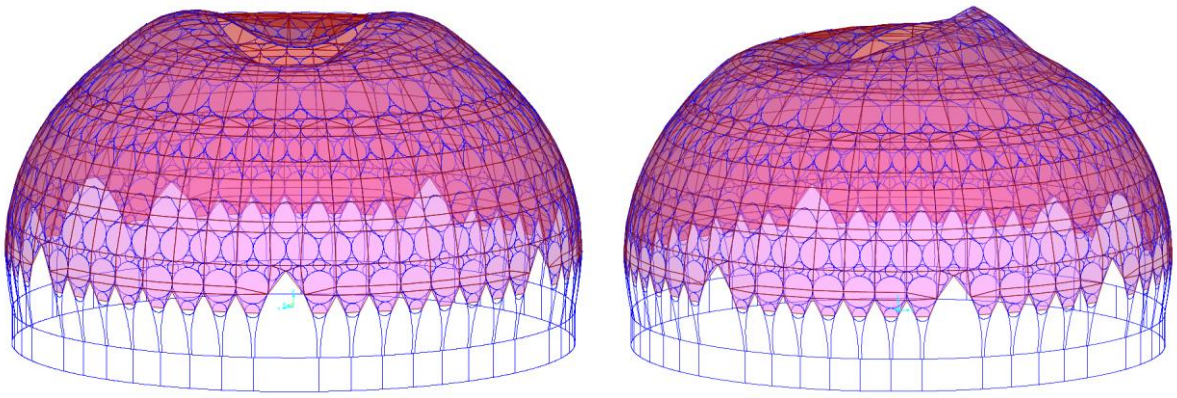


Figure 5: Symmetric and Antisymmetric Buckling Modes

6. Engineering of the Distinct Joints

While the overall FEA model using linear frame elements provided a satisfactory method for basic stress checks on the various Trellis elements, the issue of the localized stresses within the nodal regions where the pipe sections merge remained to be addressed. As the unique merged joint geometry has no basis in any published literature from which to develop design checks, it was necessary to address the localized stresses with a detailed local finite element analysis investigating possible stress concentrations. To do this, the global model was used with only local intersections fully meshed with shell elements constrained to the surrounding frame elements as indicated in Figure 6. Thus, there was no need to determine the forces at the ends of the isolated connection pieces as they are determined directly by the global FEA frame element model. Local imperfections related to ovality of the pipes based on assumed tolerances were also considered, but the tolerances were tight enough as to not have significant impacts on the localized stresses.

For this analysis of the stresses within the overlapping joints, localized yielding was permitted provided it was demonstrated through non-linear analysis that the overstress was highly localized and resulting strains did not exceed the material fracture criteria. Auxiliary shell models included the effects of penetrations for services through the walls of the pipe sections, particularly for LED installation and maintenance. Other detailed connection studies included the effect of the rigging brackets and projector pod supports on the primary steel framework. A substantial amount of analysis

effort was required as there are many different types of overlapping connections with differing wall thicknesses of pipe joined.

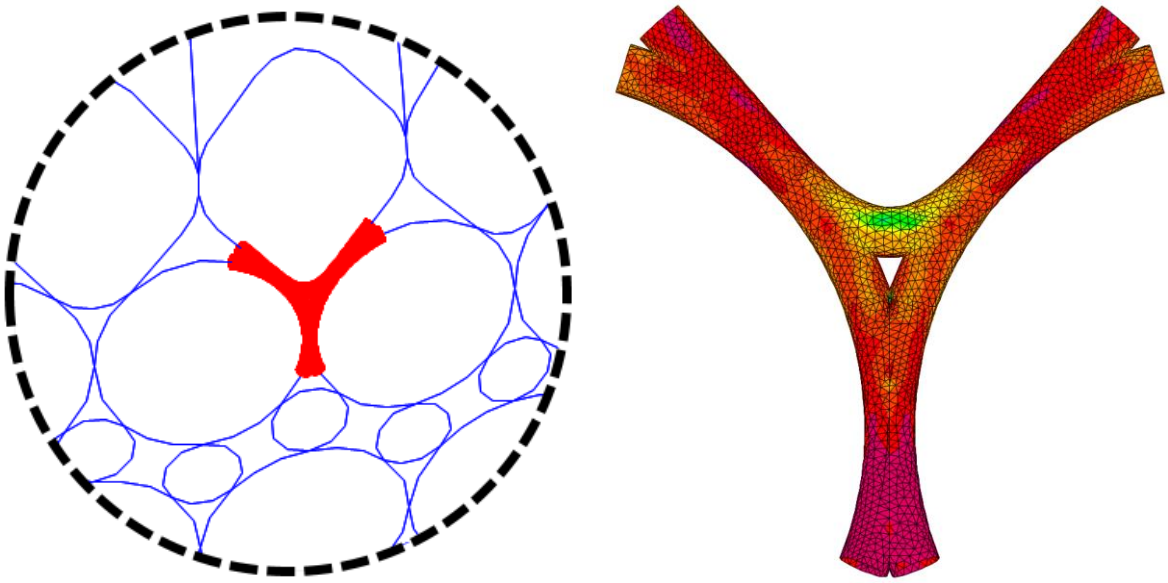


Figure 6: Analysis of the Connecting Joints

Upon award of the steelwork contract, CRME requested to adjust the longitudinal welds within the overlapping joints from the full penetration welds specified by TT to partial penetration square groove welds in an effort to simplify the fabrication of the joints. TT worked with CRME's on-staff engineers for the revised connections to re-analyze and re-verify all of the overlapping joint configurations on the Trellis. Pipe-to-pipe butt welds for splices away from the nodal regions remained full penetration groove welds, with most performed in the shop and the remaining achieved on site.

Connection node designs were also analyzed for impacts related to the erection of the structural system with a series of static load multipliers applied to the element demands based on the construction sequence analysis as performed by CRME's engineer, Maffeis. TT collaborated closely with Maffeis to ensure the locked-in stresses due to the contractor selected erection sequence were minimal.

7. Expo 2020 Dubai

Prior to steelwork tender, Expo commissioned the construction of a full-scale visual and installation mock-up of a large portion of a typical lower section of the Trellis. See Figure 7. The mock-up included the complete multi-coat steel paint system, fabric panel installation, routing of electrical and plumbing services, and several different approaches to the welded joints. All steelwork for the Trellis is designated as Architectural Exposed Structural Steel (AESS) based on AISC requirements [4] with various categories of quality specified according to the visual proximity of the steelwork in relation to the ground plane. The design team also consulted with the fabricator to develop a set of tolerances that were achievable, but also met the rigorous aesthetic requirements of the project.

Steelwork fabrication is well underway with initial pieces completed at Cimolai facilities in Italy (see Figure 7), with shop welded assemblies loaded and shipped by barge to the nearby Port of Dubai and transported by truck to the Expo site. Additional steelwork fabrication is being performed by Cimolai partners in the UAE. As of this writing, approximately 50% of the Trellis steelwork has been erected and temporarily stabilized in the theoretical position with temporary internal supports. The completed

upper central part of the Trellis, roughly 570 tonnes in total, will be fully connected on the ground and lifted into place via a series of eighteen strand jacks.

Construction of the Al Wasl Trellis is scheduled for completion by the end of 2019, well before the opening ceremonies of Expo 2020 Dubai on October 20, 2020 (10.20.2020).

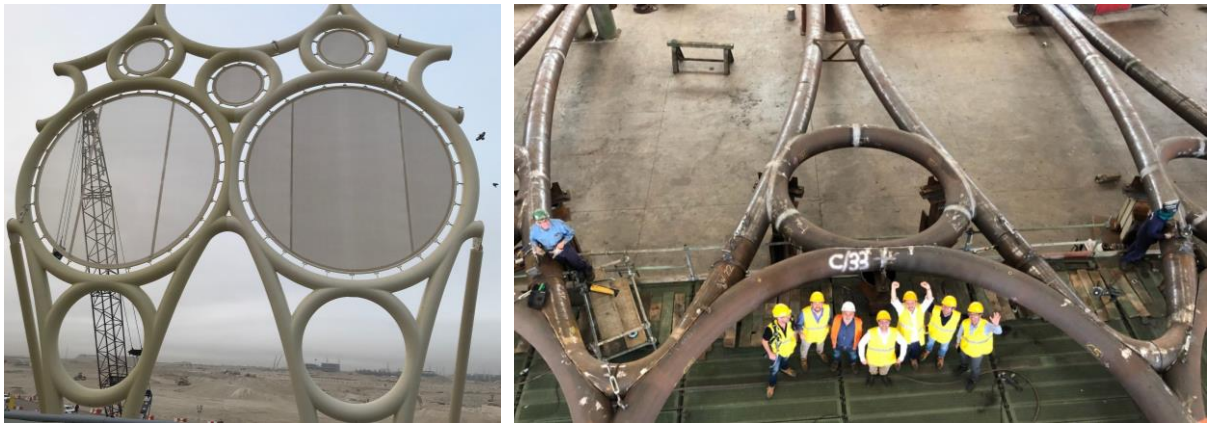


Figure 7: Full Scale Mockup on Site and Steel Fabrication Progress in Italy

Acknowledgements

Owner/Developer	Expo 2020 Dubai, UAE
Architect	Adrian Smith + Gordon Gill Architecture, Chicago
Structural Engineer	Thornton Tomasetti, Chicago
Architect / Engineer of Record	FNP, Dubai
Steel Contractor/Fabricator	Cimolai Rimond Middle East, Dubai
Fabricator's Engineer	Maffeis Engineering, Italy
Third Party Peer Review	Robert Bird Group, Dubai
Pre-Tender Steelwork Advisor	Waagner-Biro, Vienna

References

[1] American Society of Civil Engineers / Structural Engineering Institute (ASCE/SEI). "Minimum Design Loads for Buildings and Other Structures ASCE 7-10". Reston, Virginia, USA: ASCE 2010.

[2] International Conference of Building Officials (ICBO). "1997 Uniform Building Code, Volume 2". Whittier, California, USA: ICBO, 1997.

[3] American Institute of Steel Construction (AISC). "Specification for Structural Steel Buildings, Thirteenth Edition, Load and Resistance Factor Design ANSI/ASCE 360-05." Chicago, Illinois, USA: AISC 2005.

[4] American Institute of Steel Construction (AISC). "Code of Standard Practice for Steel Buildings and Bridges (AISC 303-05)". Chicago, Illinois, USA: AISC 2005.

Proceedings of the IASS Annual Symposium 2019 – Structural Membranes 2019
Form and Force
7 – 10 October 2019, Barcelona, Spain
C. Lázaro, K.-U. Bletzinger, E. Oñate (eds.)

Asymmetric suspension footbridge in the town Písek

Vladimír JANATA*, Jan VČELÁK, Jindřich BERAN, Dalibor GREGOR
*EXCON, a.s.
Sokolovská 187/203 190 00 Praha 9 Czech Republic
janata@excon.cz

Abstract

Asymmetric suspension foot bridge of length 81,7 m and width 3,3 m, consisting of triangular steel lattice truss made from tubes and orthotropic steel deck, is suspended on two ropes using solid bar hangers with spacing of 6 m. The plane of ropes and hangers is inclined. The thin pylons are 16 m high and inclined 19° to the side and 6° backwards (away from the river). Position of the top of pylons is defined by the main ropes, top horizontal tension tube and two backward stays anchored to the upper chord tubes of the truss. The vibration absorbers were designed in order to eliminate vibrations with frequency equal to the footbridge natural frequency 2,46 Hz. Structural solution, construction process and dynamic response of the bridge before and after installation of the absorbers are presented.

Keywords: Asymmetric suspension bridge, footbridge, orthotropic steel deck, steel rope, vibration absorber, dynamic response, hangers, solid bar, pre-stressed tendon, steel lattice truss.



Figure 1: Asymmetric suspension bridge in the town Pisek

Copyright © 2019 by Vladimir Janata
Published by the International Association for Shell and Spatial Structures (IASS) with permission.

1. Introduction

The foot bridge, situated in the historical town Písek in southern Bohemia, consists of two spans with different structural solutions: asymmetric suspension structure of length 81,7 m and cable stayed structure of length 46,7 m. Both parts meet upon the pillar situated in the river forming the groundplan angle 135^0. Sitting and configuration of the footbridge by architect was inspired by a lot of strong urban and architectonic inducements. With regard to an architect´s shape, layout and spatial intents, the solution which has been adopted minimizes dimensions and height of pylons so as they do not contradict an architectonic or natural landmarks of the town.



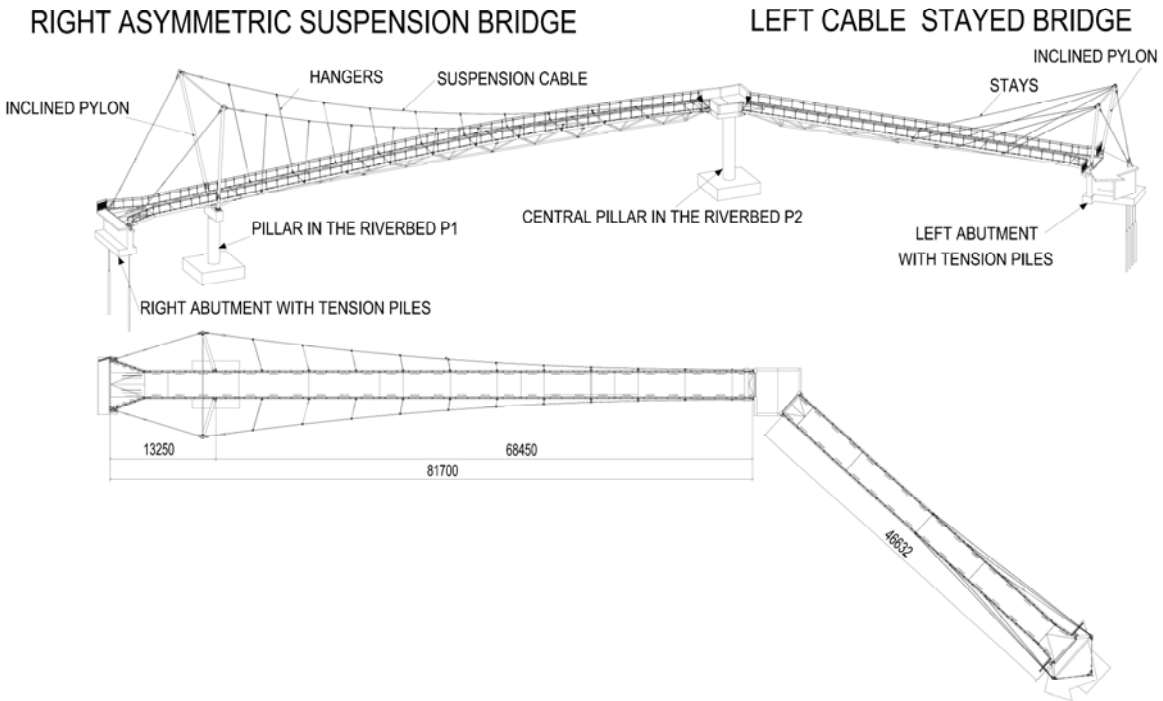


Figure 2: Disposition of the footbridge

2. Structural solution of the asymmetric suspension foot bridge

Asymmetric suspension bridge of length 81,7 m and width 3,3 m consists of triangular steel lattice truss suspended on two ropes ø 76mm and solid bar hangers with thread M20 with spacing 6 m. The main ropes are supported by two pylons on the right side and anchored through the cylindrical socket to the upper tubular chords of the truss near the left end of the truss. The slender pylons from the tubes ø 355 mm are 16 m high and inclined 19° to the side and 6° backwards (away from the river). The pylons are supported through two elastomeric bearings by the pillar in the riverbed situated 13,2 m from the right bank abutment. Position of the top of pylons is defined by the main ropes, the top horizontal tension tube and two backward stays from solid bars with thread M90 anchored to the upper chords of the truss.

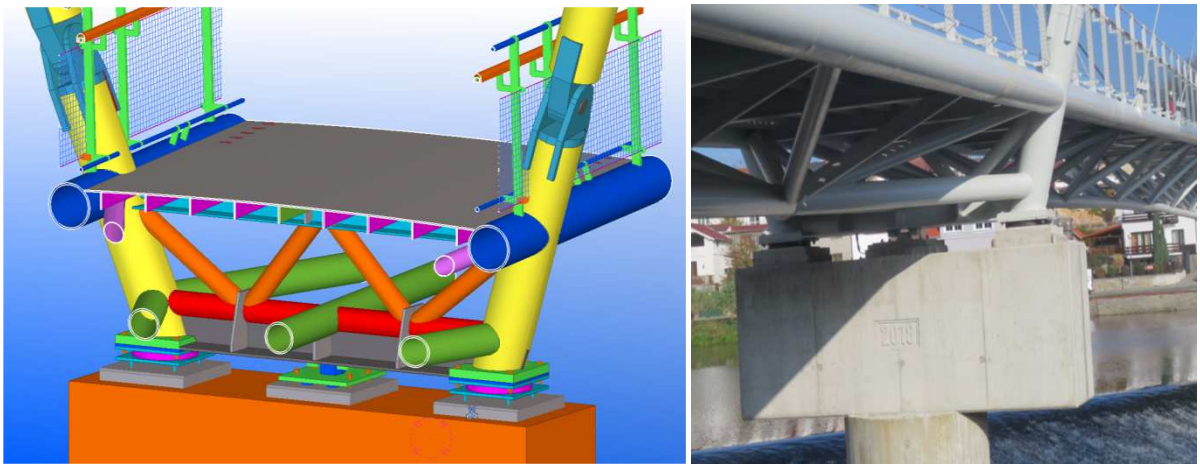


Figure 3: Anchoring of the truss with pylons on the pillar

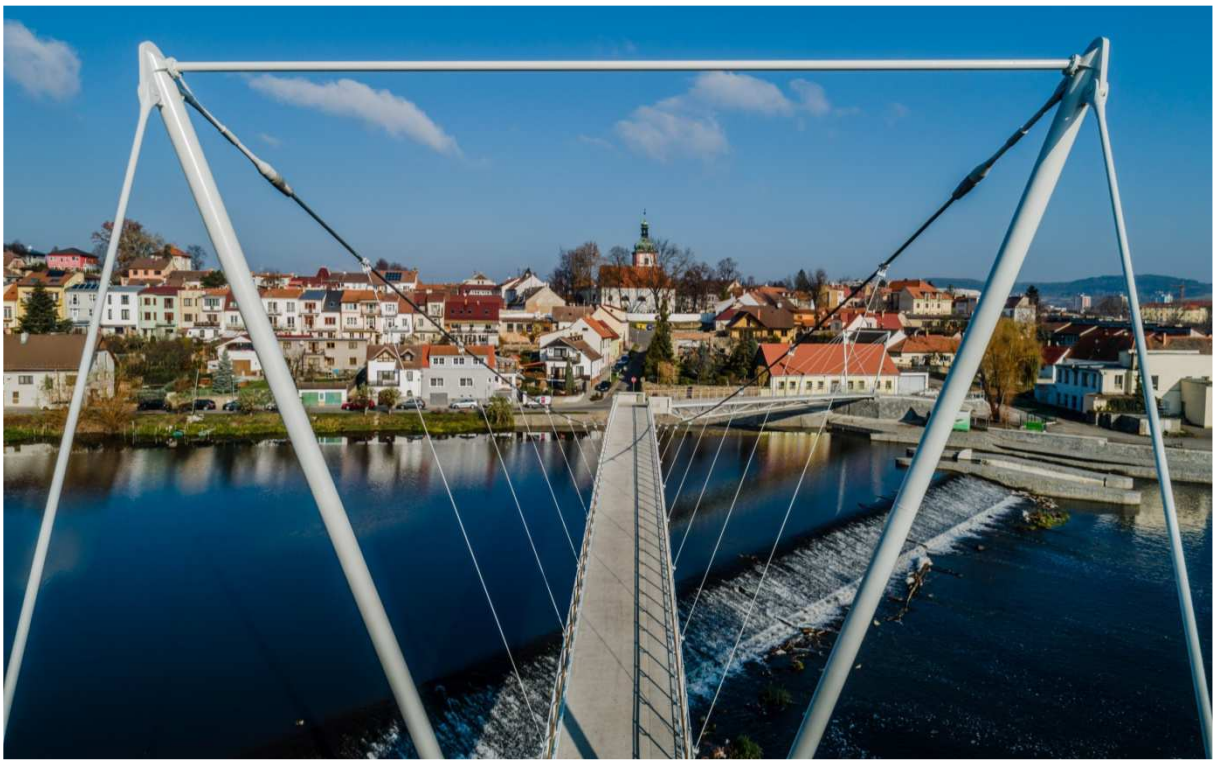


Figure 4: Top of the pylons, ropes, backward stays and tension tube

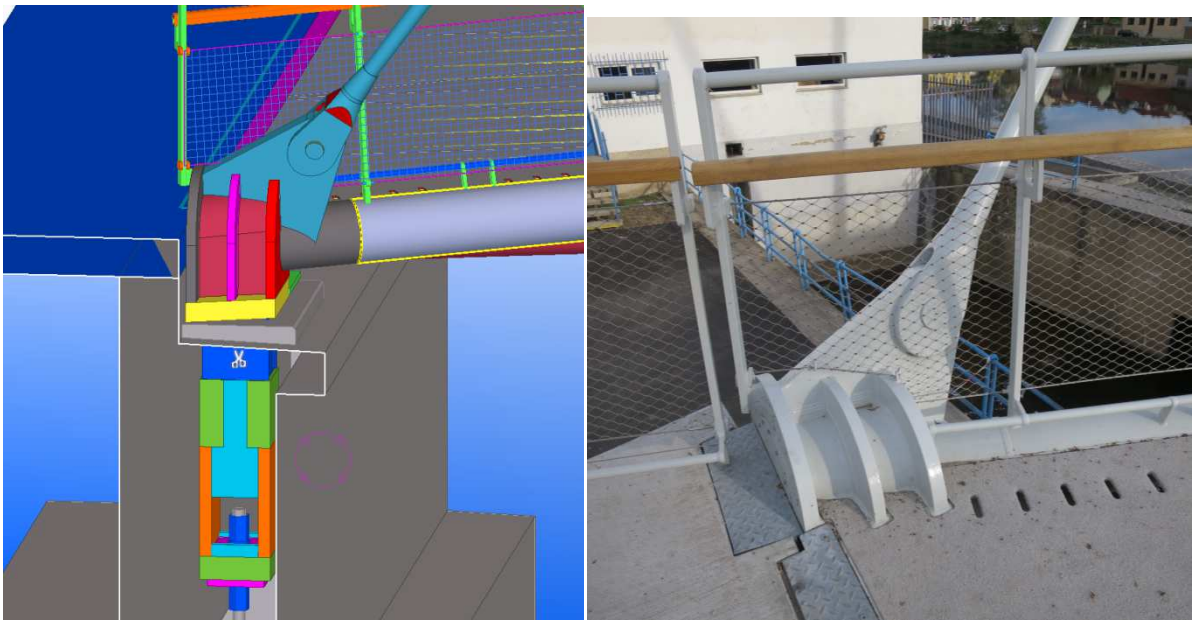


Figure 5: Anchoring of the backward stay to the top chord of the truss

The horizontal components of forces in the ropes on the left side and in the backward stays on the right side load only truss, transformed into its axial force and thus abutments and pillars are loaded, as a result of the vertical actions, by vertical forces only. The footbridge is anchored by anchoring bolts and tension piles against the vertical component of tension forces from backward stays at the right abutment and supported by two sliding elastomeric bearings on the central pillar. The triangular lattice truss consists of two upper chords from tubes ø 324 mm, lower chord from tubes ø 219 mm and orthotropic steel deck welded to the upper chords. Sideward walls consist of diagonals from tubes ø 139 mm. The shape of truss is determined by the overall disposition of the footbridge and static requirements. Increasing stiffness of the truss along the length provides approximately symmetrical parabolic shape of the truss deflection due to the uniformly distributed load.



Figure 6: Orthotropic steel deck, top chords, lower chord and diagonals

There was designed an original structural detail of anchoring the hangers M20 to the ropes and chords of the truss with spatial pin joint action and great range of adjustment. Also end of rope on the pylon is original. The rope is terminated by socket with threaded bar M120, then through adapter connected with the bar with the thread M90 with turnbuckle and terminated by socket M90. The rope can be adjusted near the top of the pylon and the sockets from both sides of the pylon are identical.

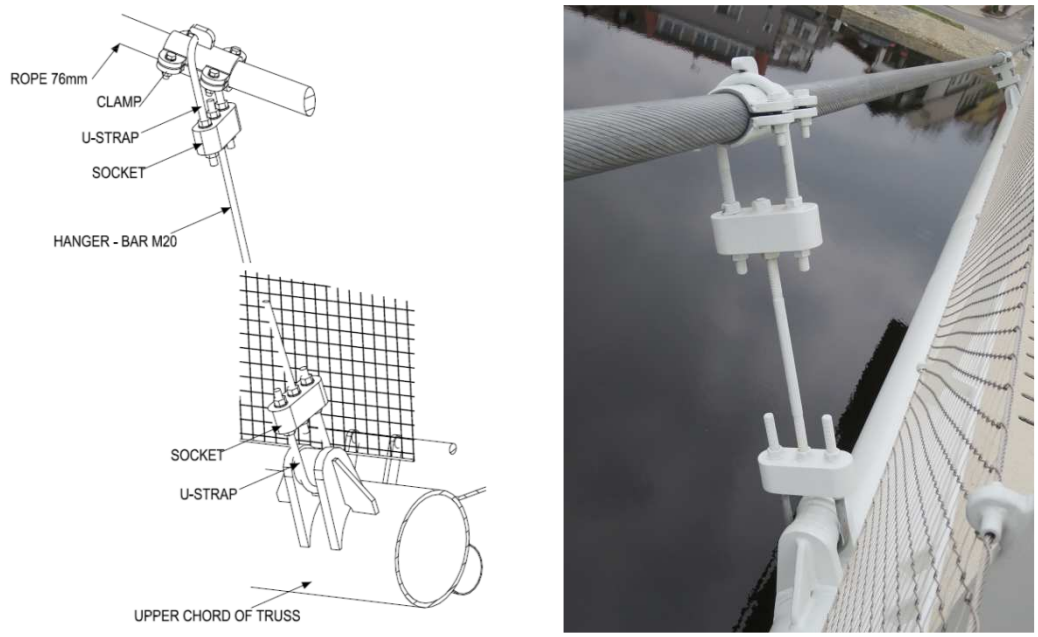


Figure 7: Anchoring of hangers

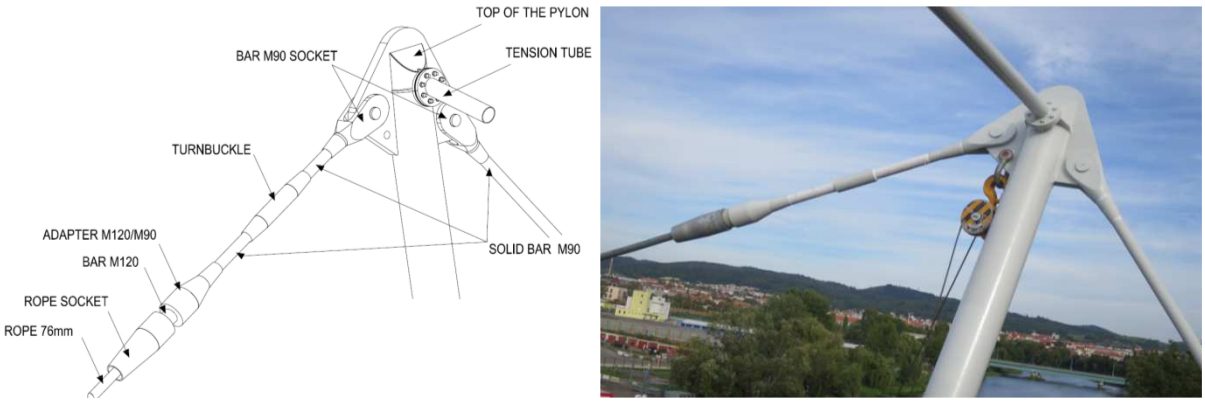


Figure 8: Anchoring of the rope to the top of the pylon



Figure 9: Erection of the socket to the top chord



Figure 10: Pre-stressing of the backward stay M90

3. Erection of the footbridge

The truss, welded on the right bank, was installed by the crane to the right abutment, two pillars and falsework erected on the weir body. Then the pylons with backward stays and front temporary ropes were installed. The temporary ropes, connecting the top of the pylon with the truss, were pre–stressed to fix the top of the pylons and reduce deflection of the truss between the pillar and falsework. The ropes were installed and their projected plan shape was ensured by horizontal erection belts. The ropes were pre-stressed by installed hangers and then slacking temporary ropes were removed. The backward stays M90 were pre-stressed to rise up the truss from the falsework and to achieve projected shape of the truss and forces in the ropes, hangers and backward stays.



Figure 21: Erection of the truss on the abutments, pillars and falsework



Figure 32: Erection of the ropes and hangers with help of temporary horizontal belts

4. Dynamic response and the vibration absorbers

Dynamic test was carried out in order to verify theoretical natural frequencies and modes and vertical and horizontal response (amplitudes of acceleration) induced by walking or running pedestrians. The vibration from walking pedestrians did not exceed permitted values of acceleration. The vibration absorbers (TMD) were than installed to ensure maximum comfort of pedestrians in case of excessive sport activities. Two twins of absorbers of the mass 450 kg on the four springs were installed to eliminate vibrations of the frequency 2,46Hz. The efforts to evoke horizontal vibrations were not successful thanks to the inclined ropes and hangers.

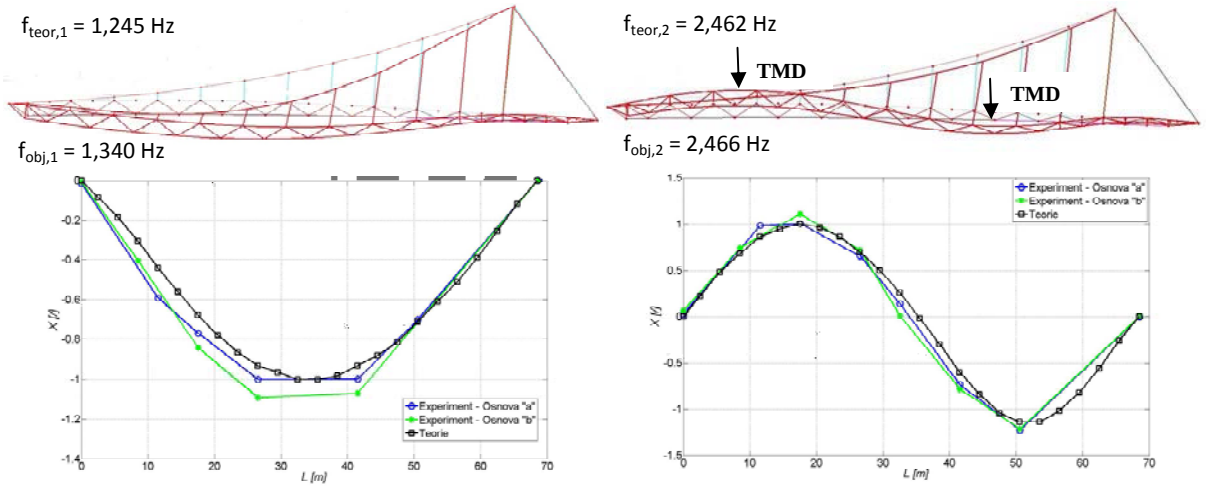


Figure 43: The comparisons of the first (left column) and second (right column) natural modes determined by modal analysis of numerical model with the modes obtained by experimental modal analysis on real structure

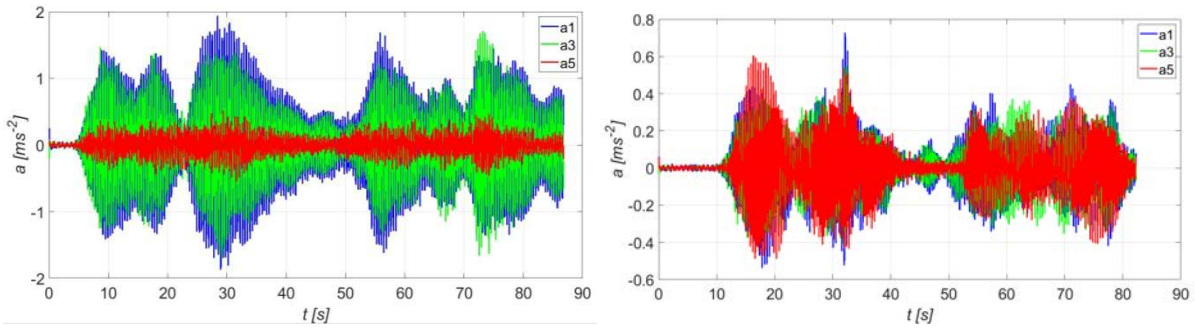


Figure 54: Time behaviour of accelerations of the bridge deck without (left) and with (right) TMD when 4 runners are crossing the footbridge with the pace tuned to the second natural mode.

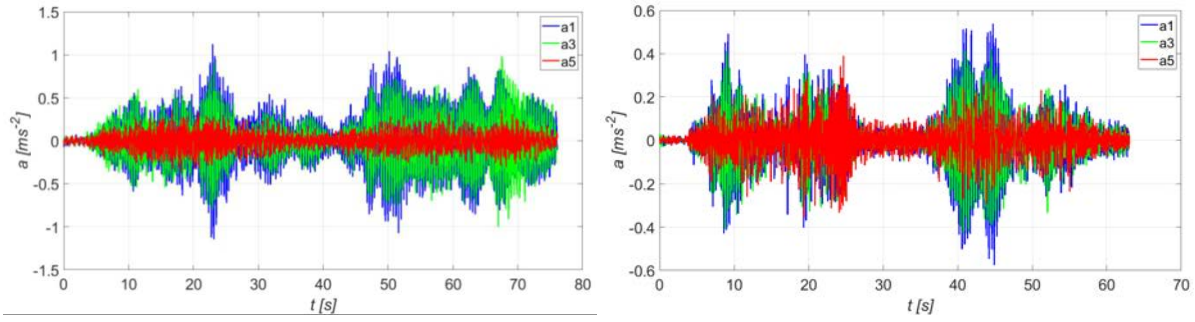


Figure 65: Time behaviour of accelerations of the bridge deck without (left) and with (right) TMD when 4 runners are crossing the footbridge freely, i.e., without any synchronisation.



Figure 76: Vibration absorbers under erection



Figure 87: Front view on foot-bridge

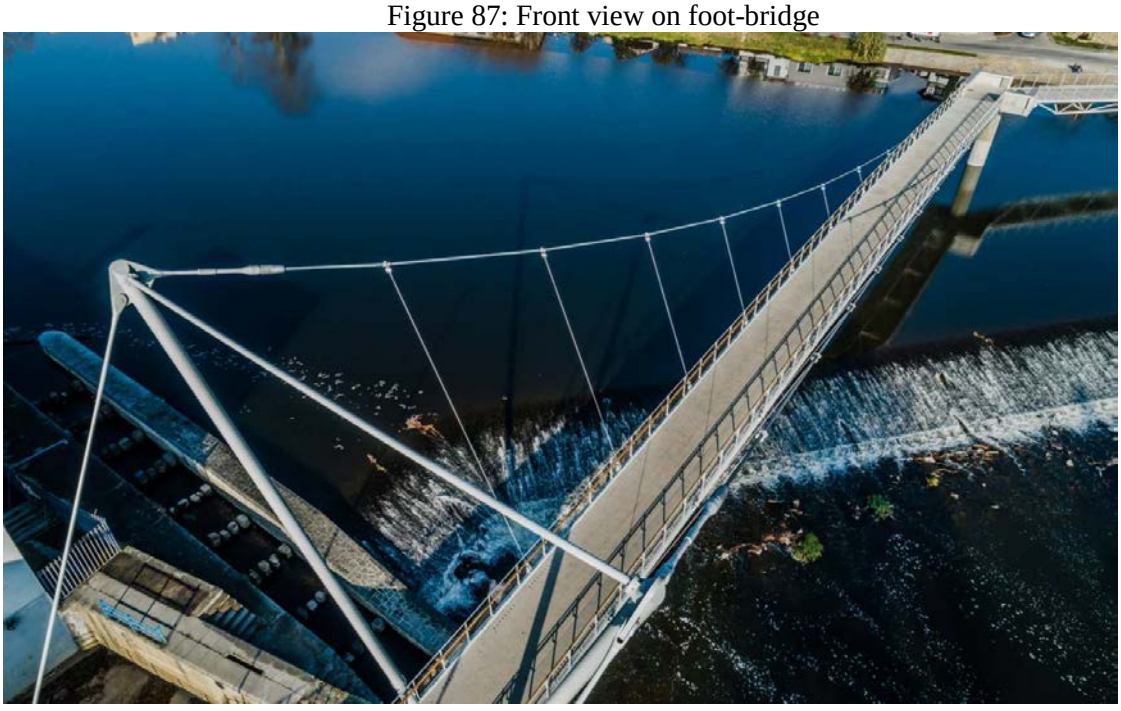


Figure 98: Main rope with hangers

Proceedings of the IASS Annual Symposium 2019 – Structural Membranes 2019
Form and Force
7 – 10 October 2019, Barcelona, Spain
C. Lázaro, K.-U. Bletzinger, E. Oñate (eds.)

Changi Jewel: Pushing the limits on shell design

Craig SCHWITTER*[a], Cristobal CORREA*[b]

*BuroHappold Engineering, New York, NY USA
Columbia University Graduate School of Architecture, Planning and Preservation, 116th St Broadway, NY, NY 10027
Craig.Schwitter@BuroHappold.com

[a] Pratt Institute Graduate Architecture and Urban Design, Brooklyn, NY USA
200 Willoughby Avenue Brooklyn, NY 11205
Cristobal.Correa@BuroHappold.com

Abstract

The structural engineering techniques used in the design of gridshells have evolved considerably in recent years as the impact of digital design and fabrication has allowed for the creation of ever more complex geometries and analysis. This paper will examine this evolution using different case studies that chart the introduction of technology and look at how this has changed the ways that gridshells are conceived and integrated into architectural designs. The paper will argue that this evolution can be linked with the tradition of engineer as builder, as the design, analysis, fabrication and construction of these elements becomes more and more enmeshed and offer opportunities for greater design involvement. This new way of looking at gridshell design needs to be properly understood and the engineer needs to have the correct level of design intelligence to be able to navigate these challenges and produce a successful project.

Keywords: Geometry, Grid Shell, Steel, Glass, Complex Forms, Architecture, History, Evolution, Form Finding

1 Introduction

The history of steel gridshells can be seen as a natural offshoot to the development of concrete shells, and it is interesting to compare the development of gridshells to what happened to concrete shell design. Initial shell design is, of course, very old, but in the twentieth century, with the advent of reinforced concrete it was pushed very far forward by the giants of Nervi, Torroja and Candela. [1,2] From an architectural point of view concrete shells were always seen as somewhat limiting as they could typically not provide the level of light and transparency that was so much a part of the modernist movements in architecture. In addition the analysis of these structure was time consuming and often resulted in very restrictive geometries in order to feel confident in designing them. It was not until the late 1950's with Isler [3,4], that you have a revolutionary look at new sorts of geometries that inspired architects but that caused much controversy for the engineers in the concrete shell community

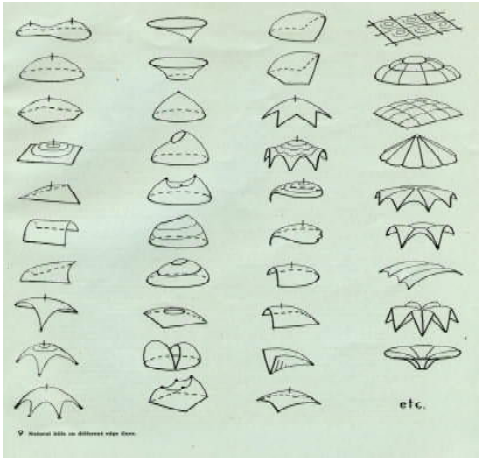


Figure 1: Picture 9 from 'New Shapes for Shells" Source IASS Archive

Copyright © 2019 by Craig Schwitter, Cristobal Correa
Published by the International Association for Shell and Spatial Structures (IASS) with permission.

At the same time the economics of concrete shells depend on having high quality workers to create and build what is often very complex formwork. The prohibitive cost of this labor made concrete shells all but obsolete in most markets by the late 1970's. However, at this point a new material arrived. Steel, combined with glass, similar to a curtain wall, but now used as a structural elements to create a light and transparent roof structure in the form of a shell.

This paper will trace the evolution of the steel and glass gridshell and examine where we are in its development. This evolution has been impacted by the digital revolution both in terms of computation, design tools as well as fabrication technologies. We will examine different case studies that chart this evolution of technology and look at how this has changed the way structural engineers work

These developments are closely linked with the tradition of engineer as builder, as the design and construction of gridshells is so enmeshed with its fabrication. This new way of looking at gridshell design needs to be properly understood and the engineer needs to have the correct level of design intelligence to be able to navigate these challenges and produce a successful project.

2 Shell Evolution

2.1 First Shell

Some of the first gridshells that we can examine deal with the enclosure of an existing space. These gridshells can be considered as a very large skylight as these are the first obvious use of this new form which provides not only cover but also transparency.

The driver in shells like these might be thought of as maximum transparency. Gridshells means curvature so there is also now the new problem of optimizing the form to cope with the problem of using flat glass panels on a curved surface and the repetition of form where possible for economy.

The Elizabeth II Great Court at the British Museum (2000) in an example of this sort of project. The architect of this project is Foster and Partners with structural engineering by BuroHappold. The space between the museum and the central reading room is covered with a single layer gridshell. Lateral thrust is resolved with a perimeter truss. A maximum of transparency is achieved with a delicate structure.

The geometry of the spans is effectively hidden as the roof is not to be viewed externally and it is not really understood from within. The spanning is a magical effect and disappears from the viewer who is never very close to the shell. There is a calmness and regularity to the shape that is created by the triangular forms which are all similar in size.

The construction involves a series of straight rectangular box sections. All have the same width with different thicknesses for the walls. There are also slight variation in element depths with a few taper elements to allow for depth transitions. The use of triangles effectively solves the problem of cladding a warped surface with flat pieces of glass. A system was devised to create a system of nodal connection that are welded. The shell was carefully designed to resist in plane stresses and achieve the maximum lightness.

This creates a very pure and rational geometry that would seem ideal for this classical space at the museum.

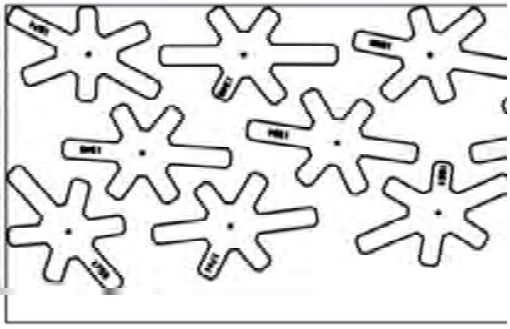


Figure 2: nodal connector pieces

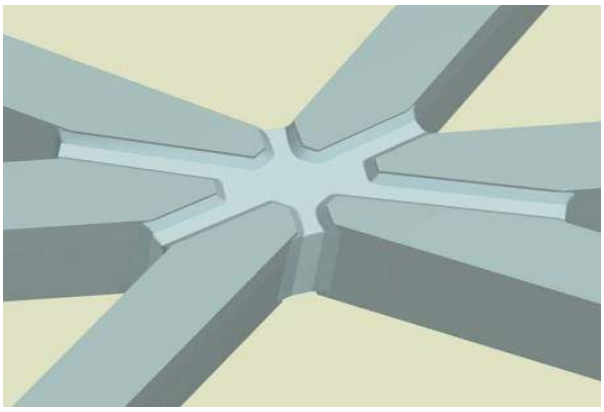


Figure 3: Typical Node Connection



Figure 4: Construction of Gridshell

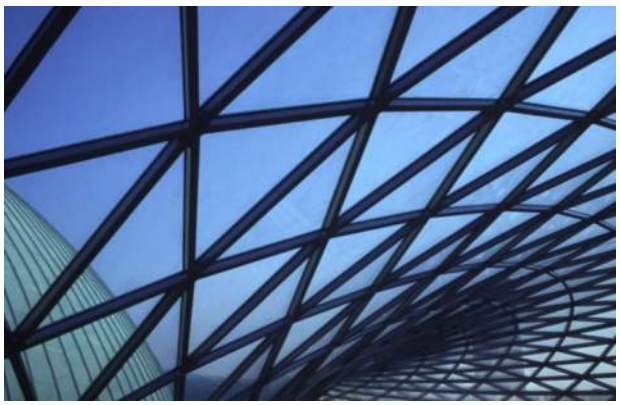


Figure 5: Underside view Great Court Shell

2.2 Second Shell

As an example of the second type of shell we can look at the Smithsonian Institution – Kogod Courtyard (2007). This was the cover for an existing courtyard at the Old Post Office Building in Washington DC that serves as one of the Smithsonian Institution museums housing the National Portrait Gallery. The architect for this project was Foster and Partners with the structural engineering by BuroHappold.

Here there is a different problem in that the shell is now no longer being supported just on its perimeter but internally by 8 internal columns. This is a fundamental shift of behavior that recognizes that the shell must now engage other types of actions coming from bending stresses at the support points. We are beginning to stray from classical shell behavior.

There is also a difference in how the space below the shell is programmatically seen. It is no longer disconnected from the ground. There are of course the columns that link it to the ground but there is also the idea of creating an environment in the space below the shell. This arises in part from a more holistic examination of the spaces created, examining not only the transparency, but also the lighting effect and the acoustics of the space. The spaces below are landscaped with planting and areas for concerts. In this particular shell acoustical wrapping was created to artificially deepen the members in order to create deep sections and provide a different acoustical quality.

Technologically there is also a resolution of the form that comes not from a structural solution but rather from an architectural idea of cladding a warped surface with flat pieces of glass. Not with triangles this time but with a glazing detail that allows for an offset at the corners. In this way the manufactured allowable details has an impact on the maximum curved form that can be created so as to not exceed the capacity of the detail to cope with the warping. This was done with very complex geometrical models of the surface using some of the most advanced 3D software available at the time (CATIA).

The structural resolution is with elements which although they have similar width in this case again have variable depths which are much more sculptural and expressive. These are resolved at the intersections, not with nodes but rather with fully welded connections. The elements themselves are no longer rectangular but more organic in form. The structure also allows for tension elements that help resolve any thrusting action from the arch forms.

This structure is innovative in that it allows for the resolution of explicit out of plane stresses, the structural elements consider the environment of the spaces created and the resolution of the geometrical details impacts the overall form.



Figure 6: Glass Panels at Smithsonian



Figure 7: Inside view Portrait Gallery



Figure 8: Construction Portrait Gallery

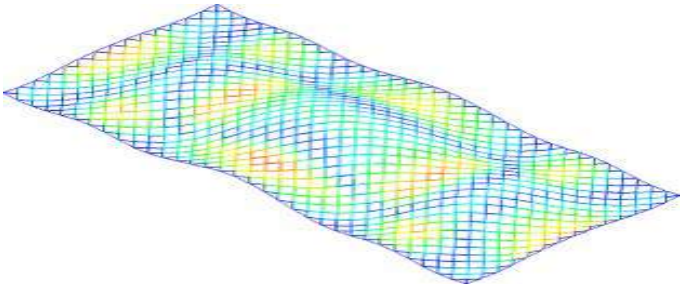


Figure 9: Map showing areas of Maximum Warping in Portrait Gallery

2.3 Third Shell

Project Jewel at Changi Airport in Singapore (2019) is a new shopping and leisure development being constructed alongside existing terminals at this busy Asian hub. This building has five above-ground levels and an extensive garden area that is covered by a very large (approximately 200m x 200m) ovoid steel and glass gridshell. The architectural design was the product of an invited competition and was awarded to Safdie Architects (SA) out of Somerville, Massachusetts USA. The project client is a joint development by Changi Airport Group and CapitaLand, which is a private public partnership. The structural and facade engineering of the gridshell portion of this project to tender was done by BuroHappold. RSP Architecture and Engineering, Singapore, provided local engineer of record services for the structural engineering of the overall project and acted as local qualified professional engineer.

The structure is defined as a very large gridshell that is supported along its perimeter and along an inner ring by 14 columns. A central oculus cantilevers from these supports and the structural form has a single axis of symmetry. This can be seen in plan and section in the following figures.

This last gridshell is no longer an infill element but rather its own independent structure. The form is being driven not by structural behavior or an easily resolvable geometrical form but rather as an architectural response to create a structure over an existing podium building, connected on all four sides, with a depressed central oculus and the overall form slightly offset (in order to accommodate and existing airport train). The building height was is also limited due to airport radar limitations

In order to reduce the very large spans, interior columns were introduced. These generate moment in the shell, just like in the Smithsonian project, and the steel in this area becomes heavier and deeper. The hanging oculus area creates a tension field at the center of the shell. This tension is then resisted by a compression ring at the shell apex. (Something that would not typically see in a tension adverse classical shells). What we have is a complex play of in plane and out of plane forces which is expressed in the form.

This complex structural behavior would be difficult to analyze and understand without the tools that we have today to help us do this. Shells require an understanding of buckling behavior which is a complex exercise looking at both local and global conditions. During design, the structural form was tuned where possible with dynamic relaxation to increase curvature in certain areas and improve structural behavior and efficiency.

For the process of "discretization" – i.e. where should there be structural elements, different patterns and scales were evaluated in order to find a solution that balanced transparency and opacity and provided a dynamic interior form. Each of these patterns was also evaluated for structural performance as part of the process of analysis

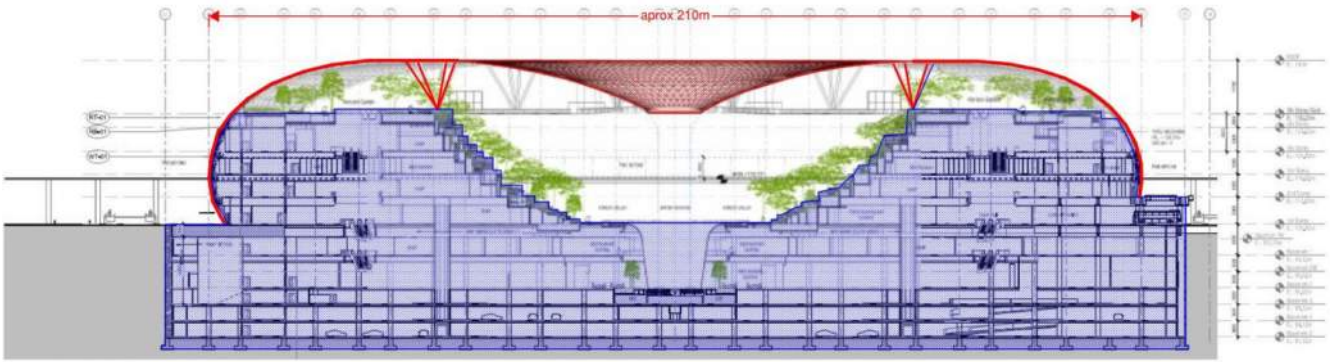


Figure 10: Jewel Changi Airport – cross section

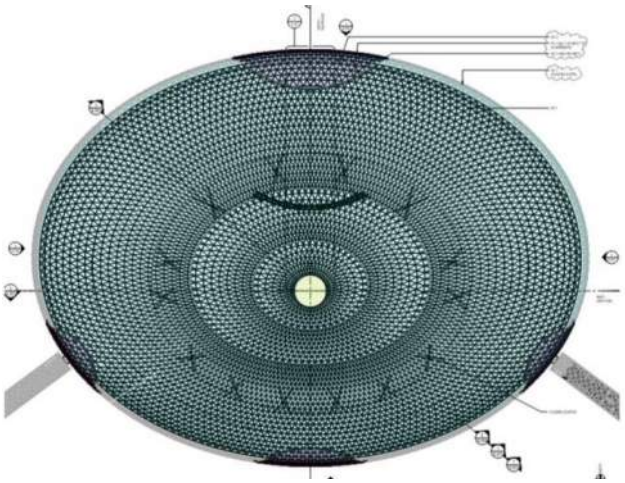


Figure 11: Jewel Changi Airport – Plan view



Figure 13: Jewel finished interior gardens with natural waterfall

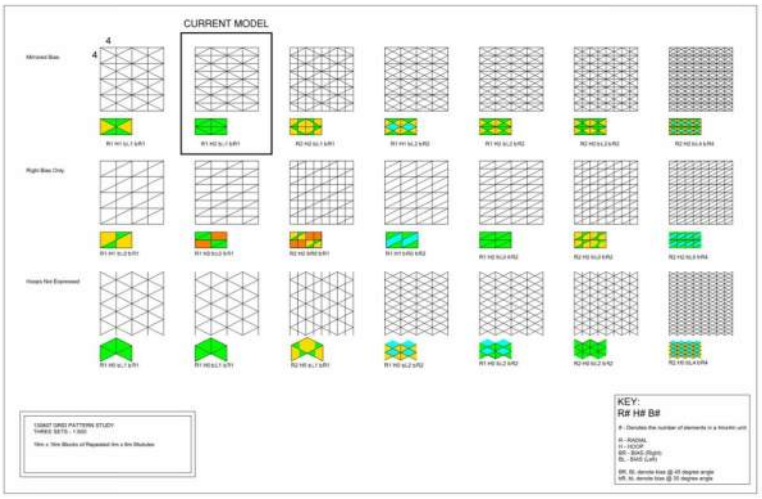


Figure 12: In Process Discretization Studies – note "current" option was not retained

The surface was discretized into triangles in order to resolve the warping of the surface and the size of these triangles was related back to glass sizes that could be competitively procured. This meant having an understanding of the manufacturing process behind laminated glass as well as the production of double glazing.

A warped surface means that for a typical 6 branch node of the structure each branch would be arriving with three angles of variation. β_1 In plane , β_2 out of plane and β_3 of twist. This means that each of the 5,000 nodes that would eventually be created to resolve these variations at a connection would be different. This would only be possible with computer numerical control (CNC) 5 axis milling processes which are modern technologies for creating objects of this complexity. The node details could only accommodate a certain amount of twist architecturally so this had to be evaluated at each node and the nodal geometries modified to ensure that there was a consistent "look" to each node.

Logistically the project involved putting all these pieces of glass and steel together in a single way - there is no substitution of one piece for another. Each piece only fits in one particular place. So each piece of glass and steel has to be manufactured, labelled, tracked and installed in a certain order. This implies a high degree of coordination and on site tracking which has only been possible in the last few years.

One can see then that the design is completely enmeshed with the fabrication technologies that have been used to create this structure. From the size of the glass panel to understanding how the nodal geometries are key to resolving the twisting geometries of the elements.

Finally it is interesting to see this last project as a total environment. The gridshell is acting as an integral part of the environments that it is creating. Rather than disappearing, the dynamism and patterns of the shell are a clear part of what you experience. The size and shape of these elements were fully analyzed as part of the daylighting of these spaces – more shade tolerant plants are below deeper members for example. The depth of the elements is reflecting the structural behavior of the roof with clear distinctions at the columns as well as in the compression ring area. In some areas the user is brought into close proximity to the different part of the shell where they can appreciate these depths as well as the patterns that draw the eye towards the central oculus and waterfall. The gridshell is no longer simply above everyone it is in the space.

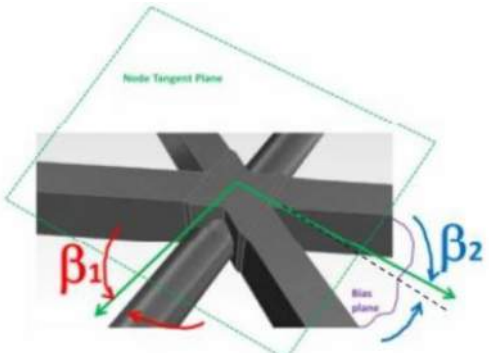


Figure 15: Milled Steel Nodes showing complexity of connection elements

3 Conclusions

It is clear that there has been an evolution in the development of gridshells. These three examples show a clear progression of the drivers outside of structural engineering that impact shell design. These include

- Fabrication strategies
- Architectural form
- The creation of a holistic environment.

The advanced technologies in both design software, computational analysis, and fabrication technologies, have created a new freedom of form that still result in structures that are constructible and can be rationally built. These are recent developments and the described examples show a clear evolution of form away from just structural logic towards a more holistic design where structural behavior is no longer the prime determiner of form, but simply an another force that can provide drive and inspiration in a gridshell design.

As engineers we need to be aware and educated about these drivers if we want to remain relevant in the design of these exciting structures. This means developing an understanding in the environments that are being developed by these designs as well as a better understanding of how they will be built.

Acknowledgements

We would like to acknowledge the many people at BuroHappold who worked in these three exciting projects in Bath, London, New York City and Los Angeles. The work occurred over a range of projects with engineering leaders who have all been consistently dedicated to achieving elegance in engineering design. Also we would like to thank the architectural design teams that worked on these projects for providing us the wonderful opportunity to do such exciting work. Without your initial ideas and drive, there would be no project

References

[1] Billington, David P. The Tower and the Bridge: The New Art of Structural Engineering. *Princeton University Press*, 1983. ISBN 978-0-7148-4146-5 ISBN 0-691-02393-X.
[2] Addis, Bill. Building: 3000 Years of Design Engineering and Construction. *Phaidon Press Limited*, 2007.
[3] Chilton, John "39 etc… Heinz Isler's infinite spectrum of new Shapes for Shells" *Proceeding of the International Association for Shell and Spatial Structures (IASS)* Symposium 2009, Valencia.
[4] Wikipedia IASS and Isler https://fr.wikipedia.org/wiki/Heinz_Isler

Proceedings of the IASS Annual Symposium 2019 – Structural Membranes 2019
Form and Force
7 – 10 October 2019, Barcelona, Spain
C. Lázaro, K.-U. Bletzinger, E. Oñate (eds.)

Complex Structure Combined with Timber BSS and Cantilever Trusses -Ariake Gymnastics Centre, Japan-

Kenichi KUME*, Masao SAITOH[a], Yoshisato ESAKA[b]
Takayuki NISHIYA*, Hatsutaro TANAKA*, Miho YAMASHITA*, Katsuhide MURAKAMI[b]

*Structural Engineer, Structural Design Department, Shimizu Corporation
2-16-1 Kyobashi, Chuo-ku, Tokyo 104-8370, Japan
k_kume@shimz.co.jp

[a] Emeritus Professor, Department of Architecture, Nihon University, Tokyo, Japan
[b] Structural Engineer, Engineering Department, Nikken Sekkei Ltd., Tokyo, Japan

Abstract

The most defining characteristic of the Ariake Gymnastics Centre is its low rise arch shape roof, approximately 90 m in span, primarily made from large laminated timber sections. This space structure is realized by two key structural features: cantilever trusses at the both ends (9.6 m each) consisting of steel frames and laminated timber; and, a Beam String Structure (BSS) composed of laminated timber and cables (69.6 m). In order to take advantage of the self-balanced feature of a BSS system, a structural system that is a Complex Structure combined with Cantilever Trusses and BSS ,and at the same time, a lift-up method for construction was proposed for this facility. This paper introduces the “architectural design of the facility” and the “design of the structural system” thereafter. Furthermore, the paper explores the "stresses in the members related to various loading conditions", "experiments and details related to the roof structure", and finally the "process of the tension introduction, and construction".

Keywords: BSS, beam string structure, timber, space structure, construction

1. Introduction

For the holding the 2020 Tokyo Olympic and Paralympic Games, the construction and preparation of stadiums and arenas is well underway in Japan. One of the major facilities, the Ariake Gymnastics Centre, will be used as a competition venue for gymnastics, rhythmic gymnastics, trampolining at the Olympic Games, and for Boccia at the Paralympic Games. After the Olympic and Paralympic Games, this facility will be used as an exhibition hall. An architectural visualization of the facility is shown in Figure 1 and a section view is shown in Figure 2.



Figure 1: Architectural visualization of the Ariake Gymnastics Centre [Courtesy of The Tokyo Organizing Committee of the Olympic and Paralympic Games, Completion image as of November 2017]

Copyright © 2019 by K.KUME, M.SAITOH, Y.ESAKA,T.NISHIYA, H.TANAKA, M.YAMASHITA, K.MURAKAMI
Published by the International Association for Shell and Spatial Structures (IASS) with permission.

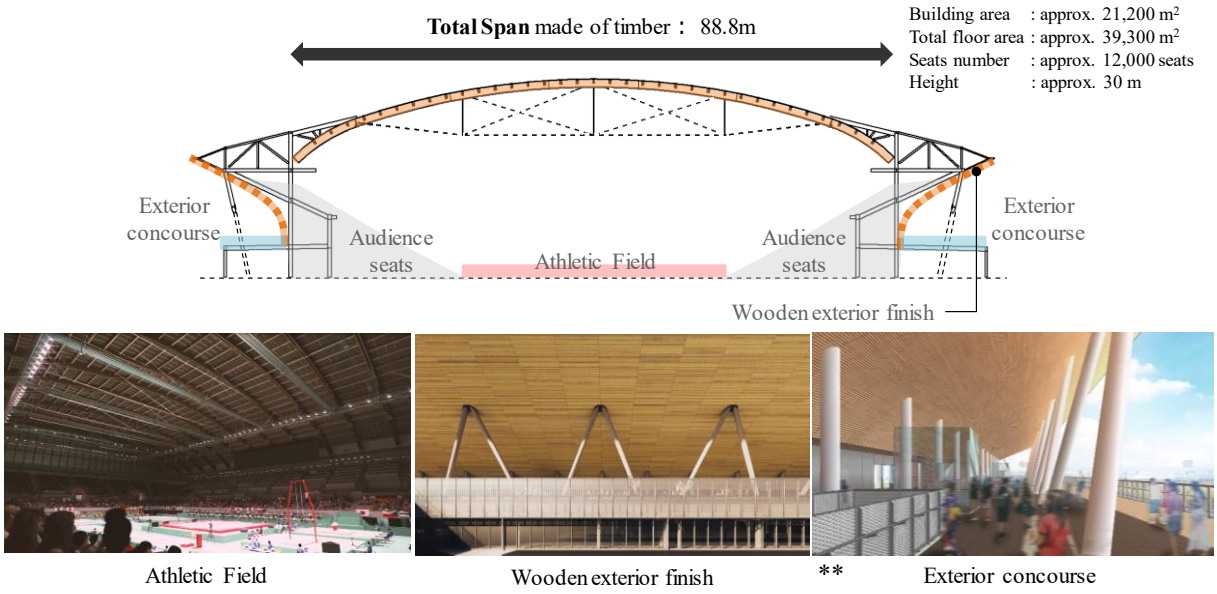


Figure 2: Section view of the Ariake Gymnastics Centre [**: Courtesy of The Tokyo Organizing Committee of the Olympic and Paralympic Games, Completion image as of November 2017]

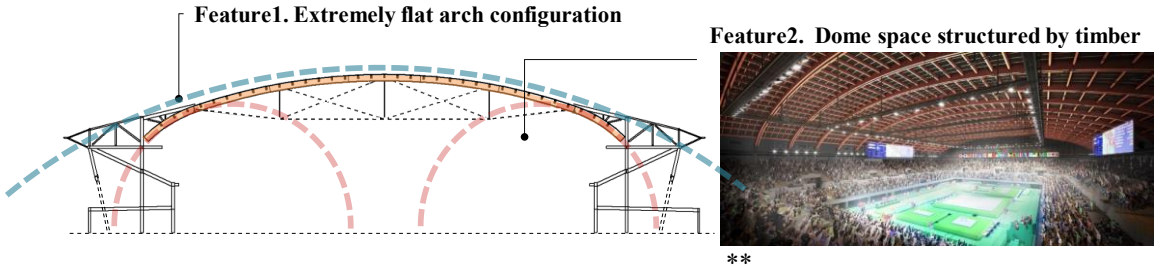


Figure 3: Two features [**: Courtesy of The Tokyo Organizing Committee of the Olympic and Paralympic Games, Completion image as of November 2017]

The overall design of the facility is mainly composed of the outside concourse and the slanted walls forming a somewhat inversed conic shape giving shape to the athletic field and the spectator seating areas. The facility is planned to make use of a wide variety of wood throughout the building. 80 mm square Japanese cedar wood that combines good heat insulation and sound insulation properties is attached as exterior finish for the slanting walls, givng the image of a huge "wooden container".

There are two main features of this facility's architectural design. The first is a gently curving roof shape. While the center arch shape holds down the rise, both sides have a small radius of a circular arch shape. The roof shape is made of a combination of the three core arch shapes, and a tangent line shape to provide the final shape. The space of the triangular cross section that occurs between them is used as an air conditioned space, helping to save space and contribute to a more compact building design. The second feature is a dome space providing a warm impression, and that encloses the audiences. In this facility, a large space structure which size is 88.8m×117.6m is realized by using timber as a structural member as opposed to as a stiffener or as the wooden finish of a steel structure.

2. Proposing the structural system

In order to realize above architectural design, an alternative structural system outlined below was proposed. Firstly, making the center part (69.6 m) consist of a self-balanced structure and removing thrust to the lower structure caused by dead load was proposed.

And then, the BSS (which is self-balanced structure) is lifted up from the cantilever trusses in both sides and jointed to them. Because of lift up from the tip of the cantilever trusses, there is no resulting thrust, and the cantilevers only have vertical load. Furthermore, because the BSS system is self-balanced, lifting up from both sides doesn't cause the additional stress or displacement. Thus, this structure resist as the complex structure combined with BSS and the cantilever trusses against the dead load. When subjected to additional actions such as wind, earthquake or snow loading, the structure behaves like an arch integrating both the BSS system and the cantilever trusses (Figure 4).

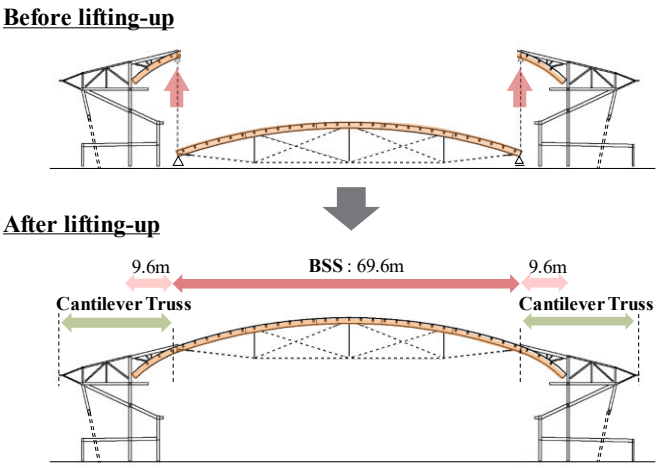


Figure 4: Image of the proposed structural system

2.1. Structural behavior

This section focuses on the self-contained structure of the center part of the above described structural system. The stress, displacement and buckling load specific to the axial resistance of the structure were compared for three self-balanced structural options (A: arch with tie, B: BSS, C: BSS with sub-cables). The members of each structure are shown in Table 1, and the load conditions are shown in Table 2. Among the disturbances in Table 2, Table 3 shows the stress and deformation for static earthquake load (horizontal 1.35G and vertical 1G) and the combination of dead load and the introduced tension (hereinafter referred to as Normal state). These are the main loads which govern the section design. These structures were roller supported on one side and pin supported on the other. The tension is introduced to the lower chord member in each option so that the horizontal displacement was zero (in option A and B, tension was introduced only to the lower cable, and in option C, in the order of cables T2 → T1 → T3) .

Table 1: The members of each structure

	Option A	Option B	Option C
Upper chord member (Timber)	2-220×1150 (Japanese Larch E105-F300)		
Lower chord member (Cable)	2-φ56 (7x37 Co-core structural strand rope)		
Strut (Steel)	-	φ141.3×32（SN490B)	
Sub-cable (Cable)	-	-	T2：2-φ21.8 T3：1-φ28.6 (Structural spiral rope)

In the normal state loading condition, the axial force in the option A is larger than both B and C because of the difference in depth of the upper chord, but there is no large difference in bending stress and deformation. For lateral earthquake loads, it can be seen that bending and deformation of options A and B are very large, and that these structures are particularly vulnerable to eccentric loads. In the case of vertical earthquake loads, the lower chord member does not have sufficient stiffness and has a low degree of fixity, resulting in large bending stress and deformation. Especially in option A, the bending stress and deformation are large because the depth is small and there are no struts.

Table 4 shows the comparisons of buckling load under dead load. (L_k : the buckling length, λ : the slenderness ratio in strong axis, f_c : the allowable conpression stress in normal state) The ends of each structure were pin-supported. The buckling load ratio, which is calculated from the Euler buckling equation, assuming that the flexural rigidity (EI) in each structural option is equal (E : Young's modulus, I : geometric moment of inertia), is based on that of option A. The buckling length is 0.5 L in options A and B, and 0.25 L (strut-to-strut distance) in option C (L: the total length of the upper chord). Even when the flexural rigidity in all options are the same, a large difference occurs in the buckling load ratio due to the difference in buckling length. Additionally, in the case of pin-roller

support, when the lower chord members of options B and C are considered, the depth of the upper chord is different, and the buckling load of options B and C is therefore improved.

Table 2: Load conditions

LOADS		LOAD COMBINATION							
		Nomal State	State of snow load	State of strong wind	State of earthquake	Combination of Thermal Load			
						Nomal	Snow load	Strong wind	Earthquake
Dead Load	1800N/m²	○	○	○	○	○	○	○	○
Live Load	None.	○	○	○	○	○	○	○	○
Snow Load	750N/m² 1015N/m² 1015N/m²	-	○	-	-	-	○	-	-
Wind Load	2140N/m² 540N/m² 1520N/m²	-	-	○	-	-	-	○	-
Earthquake Load (horizontal)	1.35G	-	-	-	○	-	-	-	○
Earthquake Load (vertical)	1.0G	-	-	-	○	-	-	-	○
Thermal Load	ΔT= -25℃～+25℃	-	-	-	-	○ (Coef. 1.0)	○ (Coef. 0.8)	○ (Coef. 0.7)	○ (Coef. 0.4)

Table 3: The model image and stress and deformation

	Option A	Option B	Option C
	5775; 69600	5775 1825; 69600	T3; 5775 1825; 69600; T1 T2
Dead load and tension introduction w=12.96kN/	Bending 70kNm; Axial force: -1361～-1436kN; Disp. 50mm	Bending 87kNm 81kNm; Axial force: -1053～-1118kN; Disp. 33mm	Bending 102kNm; Axial force: -1007～-1084kN; Disp. 34mm
Earthquake Load (horizontal) 1.35G	Bending 810kNm 576kNm; Axial force: 473～-415kN; Disp. 284mm	Bending 752kNm 630kNm; Axial force: 565～-323kN; Disp. 236mm	Bending 252kNm 107kNm; Axial force: 493～-181kN; Disp. 92mm
Earthquake Load (vertical) 1.0G	Bending 586kNm 277kNm; Axial force: -1269～-1347kN; Disp. 549mm	Bending 370kNm 203kNm; Axial force: -1010～-1076kN; Disp. 335mm	Bending 252kNm 294kNm 252kNm; Axial force: -967～-1069kN; Disp. 270mm

Table 4: The comparison of buckling load

	Option A (Arch with tie)	Option B (BSS)	Option C (BSS with sub-cables)
Buckling Load	0.5L; λ = 107; f_c = 2.24N/mm²; Buckling load ratio: 1.0	0.5L; λ = 107; f_c = 2.24N/mm²; Buckling load ratio: 1.0	0.25L; λ = 58; f_c = 6.11N/mm²; Buckling load ratio: 4.0

2.2. Stress in the section

Figure 3 shows axial force stress, bending stress and combination stress of axial force and bending of the section at each maximum stress position of options A to C, under normal state and the state of earthquake which is the combination of normal state and earthquake load. (This earthquake load

include both of horizontal and vertical.) The axial stress of option A is larger than B and C due to the difference in upper-chord depth. In addition, it can be seen that the bending stress at the state of earthquake is much larger than that at normal state according to Figure 3.

Because of large bending stress, in the combined axial force and bending stress, the compressive stress level under the earthquake loading of option A is about 1.7 times compared to option C, while option B is 1.5 times in comparison to option C.

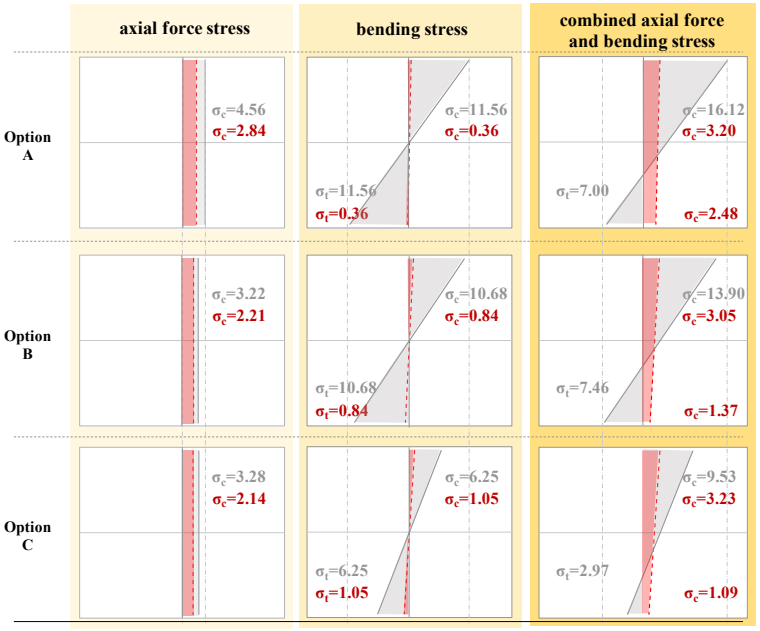


Figure 3: Stress of the section at each maximum stress position of options A to C

Moreover, the stress levels in options A to C were compared with allowable stress to calculate the capacity. The allowable compressive stress is given by equation (1) in consideration of buckling length, and that of bending is given by equation (2). f_c is the allowable compressive stress, f_b is the allowable bending stress, η means buckling reduction coefficient determined by the slenderness ratio of member. C_b means the lateral buckling correction factor, which is 0.99 here. The capacity ratio is given by dividing the stress by the allowable stress and is shown for each option in Figure 4. As for bending, a large difference occurs in the capacity during earthquake loadings, simply due to the difference in stress. On the other hand, for the capacity during the normal state, a significant difference occurs due to the influence of the difference in buckling length in addition to the difference of the stress.

$$f_c' = \eta \cdot f_c \qquad (1)$$

$$f_b' = Cb \cdot f_b \qquad (2)$$

Considering the results, option C was adopted for the final design as it showed the most stable behavior for any load case. The adopted members of the roof structure are shown in Figure 5.

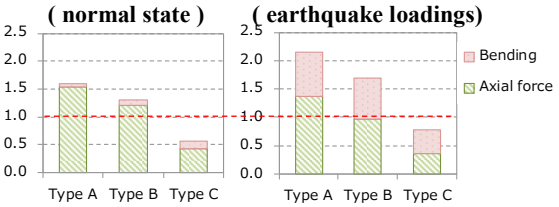


Figure 4: Capacity ratio

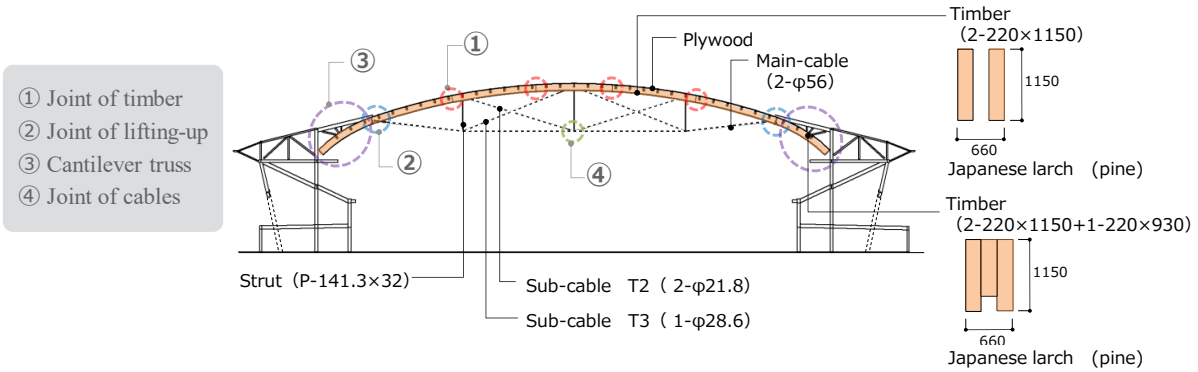


Figure 5: The adopted members of the roof

3. Experiments and details related to the roof structure

Each detail has not only been confirmed by analytical calculations, but also by some full-scale experiments.

3.1. Joint of timbers

Since the upper chord member with a span of approximately 70 m is composed of five divided curved timber beams, there are four joints. Glued-in rods (GIR) for the timber joints was adopted because of their high stiffness, strength and subtle appearance in the final design. This method uses adhesive to join the beams. There was a concern that the adhesive will lose its strength due to a rise in temperature during a fire emergency. Therefore, an adhesive with heat resistant properties was adopted. And also the proposed GIR joint which was improved the friction by introducing small ditches in the rebar holes (see Figure 7) was adopted. Structural experiments were undertaken in standard temperature conditions to verify the strength of the improved joint.

Additionally, fire safety was confirmed by conducting analysis and full-scale fire resistance experiments. At first, temperature analysis of the smoke layer was conducted assuming that the fire occurs in the first floor exhibition hall, and we confirmed that the timber surface did not reach the ignition limit temperature of 260 degree Celsius for wood. Then, the smoke layer analysis was used to inform information on the heat environment and fire resistance experiments. These experiments comfirmed that the joint would have sufficient strength against dead load in such an environment. This means that the roof does not collapse due to the temperature increases in a fire.

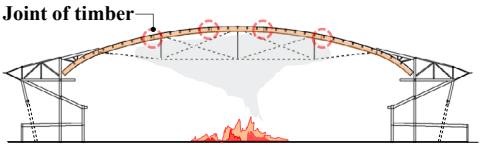


Figure 6: The section image in the fire

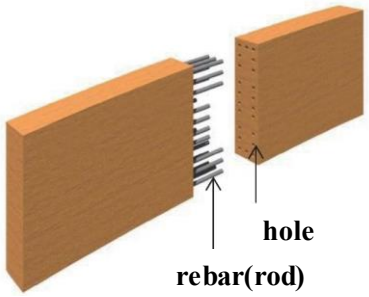


Figure 7: The image of GIR joint

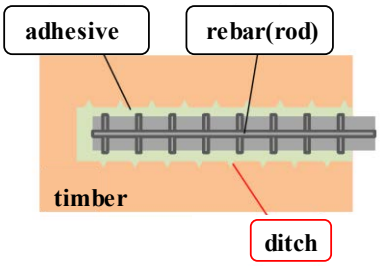


Figure 8: Improved GIR joint



Figure 9: Structural experiment

3.2. Joints for lifting up

In the joint between the cantilever truss and BSS, high strength bolt friction joints were adopted (Figure 10, 11). Since the tip of the cantilever truss is deformed by about 40 mm vertically and about 20 mm horizontally while lifting up BSS, a slot hole with short diameter 30 mm and long diameter 60 mm was adopted. (The bolt is torrsia type S14T, M24 and the friction surface is aluminum sprayed). For adopting this long hole, the resistance test against sliding was conducted to confirm the reduction rate of the friction coefficient.

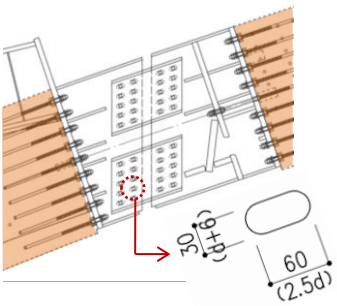


Figure 10: Joints for lifting-up



Figure 11: Joints for lifting-up

3.3. Cantilever Truss

The cantilever truss is deformed in the vertical, horizontal and rotational directions at the time of lift up. It is necessary to understand the amount of deformation in advance in order to control the length of BSS so it can be adequately jointed to the cantilevered trusses. Therefore, to verify the amount of deformation of the cantilever trusses, full-scale structural experiments (as shown in Figure 12 and 13) as well as analytical calculations was conducted. In the prototype experiment, a load of 1000 kN which is about three times the lift-up load was added to confirm safety. In the actual construction, the tip of the cantilever truss was moved by 40 mm vertically upwards and 6 mm horizontally backwards, reflecting the experimental results. In addition, by the constructing the prototype, it was possible to find out the key points of attention prior to actual construction.

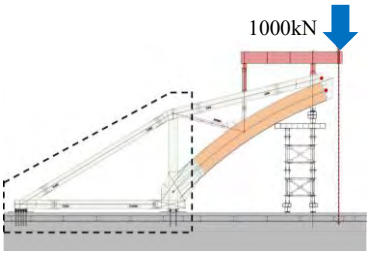


Figure 12: Test prototype



Figure 13: Test prototype

3.4. Joint of cables

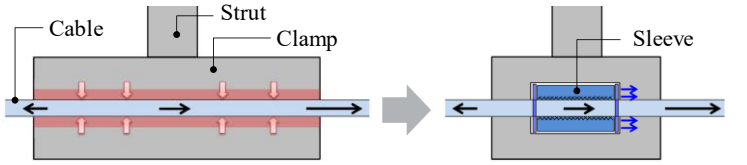


Figure 14: The difference of mechanism



Figure 15: Intermediate sleeve



Figure 16: Proposed clamp

Axial force of the cable in the joint is usually transmitted by the friction generated by the tightening force of the bolt for the clamp. However, when the transmitted axial force is large, the clamp need to become large to provide a larger friction area. So this time, the transmission method by bearing pressure was proposed and adopted (Figure 14). By using this method, the size of the clamp can be halved compared to the case of a friction transmitted joint. Additionally, a smaller clamp that is not as noticeable can be obtained. The intermediate sleeve and the cable are jointed by crimping (Figure 15). Therefore, the experiments was conducted to comfirm that the sleeve and the cable would be sufficiently crimped, and to check the effect of the plate for filling the gap on the mechanism.

4. The process of the tension introduction, and construction

4.1. The process of the tension introduction

The introduction of tension was carried out working platform installed at the ground level. Three timber upper chord members were made into one unit, and connected by small beams and plywood. The tension was introduced in the following order: cable T2 → T1 → T3. The procedure is shown in Figure 17. At first, about 150 kN of tension is introduced into cable T2 using hydraulic jacks, and about 670 kN is introduced into cable T1 using the same method. Finally, introducing tension to cable T3 is done using hand tightening (about 30 kN). A graph showing the comparison between introduced tension analysis values and measurement values about cable T2 and T1 is shown in Figure 18.

The graph shows that, by introducing tension into the T2 cables, the reaction force at point C decreases and shifts to point B and D gradually. Also, as the tension to the T1 cables increases, it is understood that the reaction force at the point of B, C, D decrease. Consequently, it shows BSS is lifted up at the point of B, C, D.

After that, we can reduce the jack which is used for controlling the reaction forces at B, C, and D, and finally introduce tension to the T3 cables by hand tightening. After completing introducing tension to the T3 cables, both ends of BSS were lifted up from the tip of the cantilever truss.

4.2. Construction

During construction, one unit (length 69.6m, width 14.4m, weight about 2000kN) with three BSS sections were lifted up approximately 19m at a speed of about 5m per hour toward the tip of the cantilever trusses (Figure 19). The lift-up takes about half a day, and then bolting is performed. One lifting-up operation is completed in one day. This work was carried out five times at a pace of once every one-and-a-half months. The installation accuracy of lift up was about -5 to +28 mm, attained by taking advantage of introducing tension at ground level and thereby adjusting the total length in advance.

Nikken Sekkei
Schematic design / Design development /
Supervision for Construction documentation and Construction

Shimizu Corporation
Design development / Construction documentation / Construction

Masao Saitoh
Engineering adviser

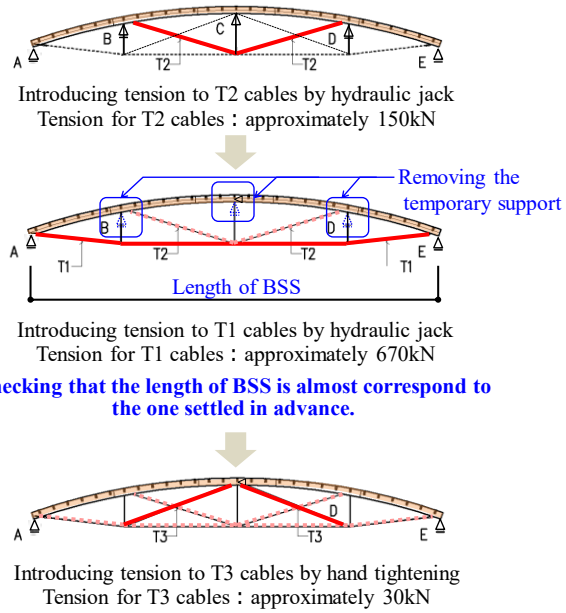


Figure 17: The procedure of tension introduction

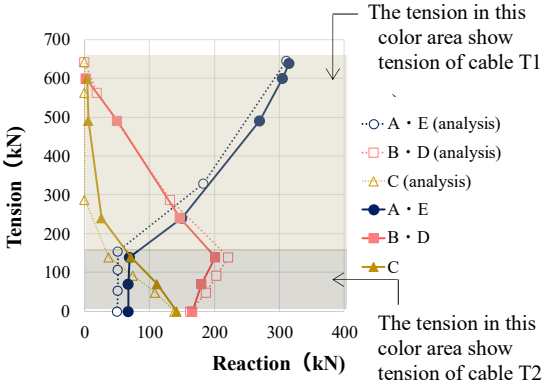


Figure 18: Comparison between analysis and measurement values for the introducing tension



Figure 19: Photo during second lift-up



Figure 20: The state of construction in March 2019

References

[1] Masao Saitoh, *Principle of Beam String Structures*, Proceedings of International Conference of IASS (Madrid), pp.17-38, 1979, 9

[2] Takayuki Nishiya, *Study of Structural Design for Complex Structure combined with Timber BSS and Cantilever*, AIJ Summaries of design works of annual meeting(Tohoku), pp.148-149, 2018,9

Proceedings of the IASS Annual Symposium 2019 – Structural Membranes 2019
Form and Force
7 – 10 October 2019, Barcelona, Spain
C. Lázaro, K.-U. Bletzinger, E. Oñate (eds.)

Construction of the Roof of the New National Stadium of Japan Considering Efficiency and Structural Capacity

Satoshi MATSUDO*, Osamu HOSOZAWA[a], Isamu NAKAKAWAJI[a]
Taro MIZUTANI[a], Shinichiro KAWAMOTO[a], Masaki MURASE[a], Takahiro KANNO[a]

*Taisei Corporation
1-25-1 Nishi Shinjuku Shinjuku-ku, Tokyo, 163-0606, Japan
mtdsts00@pub.taisei.co.jp

[a] Taisei Corporation

Abstract

The New National Stadium is a facility that is also used for the Tokyo Olympic Games and Paralympic Games in 2020. This stadium is hoped to become a place where all athletes can show their best performance, and to be loved and used frequently by people of future generations. Based on the concept of "Stadium in Forest". the new stadium is open to everyone. Becoming a part of the forest of Meiji Jingu, it will form a green network spreading from the Inner Garden of Meiji Jingu Shrine to the Imperial Palace and become a "new center of sports cluster" where everyone can enjoy taking walks and various types of sports. After completion of construction of the main frame, the process of the construction is reported in this paper. There are various unique ideas which enhanced efficiency of the construction and ensured the structural capacity of this stadium. From among them, some of unique challenges such as truss system with triangle section shape and new temporary supporting column for the construction of cantilever roof are reported. Besides, the outline of the construction analysis and comparison between analysis and measured value is also shown.

Keywords: simple cross section, cantilever steel truss, temporary supporting column, construction analysis

1. Outline of the building

The New National Stadium is a facility that is also used for Tokyo Olympic Games and Paralympic Games in 2020. Based on the concept of "Stadium in Forest", this stadium was designed to blend in with surrounding nature so that visitors can enjoy comfortable environment of the stadium. Figure 1 shows the aerial view of the stadium.

Outline of the structure of this stadium is shown in Figure 2. The maximum building height is 50 m or less, and the low slope roof consists of cantilever truss structures of about 60 m length. The sense of oppression to the neighborhood is reduced through setback from circumjacent streets by inclining outer columns. The main structure of the stadium is a steel structure above ground. A steel reinforced concrete (SRC) structure is adopted for the oblique beams (i.e. the raker beam), which supports spectator seats, and for the outer columns, which support the roof truss.

Copyright © 2019 by Taisei Corporation
Published by the International Association for Shell and Spatial Structures (IASS) with permission.



Figure 1: Image of aerial view from southeast

The renderings are intended to show conceptual image at completion and may subject to change. Vegetation shows an image about 10 years after completion of the stadium.
Copyright © Taisei Corporation, Azusa Sekkei Co.,Ltd and Kengo Kuma and Associates Joint Venture.

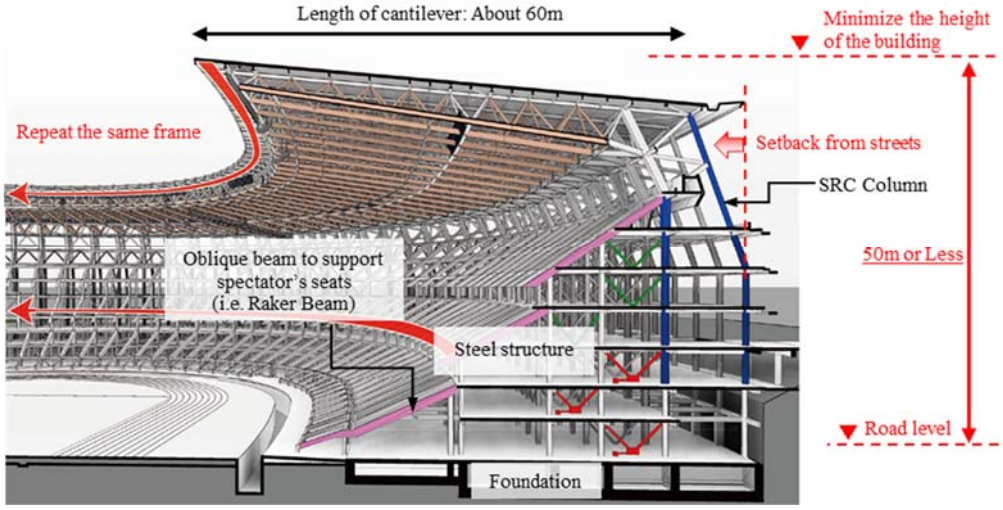


Figure 2: Outline of the structure

2. Structural design in consideration of high constructability

The structural design of this building was highly focused on the efficiency of construction. By employing the composition of same frames repeatedly in circumferential direction for both the roof and the stand structure, productivity, transportability, efficiency of drawings production, and constructability were improved. And as a consequence, the construction period and cost were thoroughly reduced. The image of construction is shown in Figure 3. Further, considering the manpower shortage at current construction sites and the efficiency of the construction site, unitization of structural members and promotion of factory making were planned. In particular, unitization of cantilever trusses of the roof, precastization of the foundation and outer SRC columns, and proactive use of prefabrication products were planned.

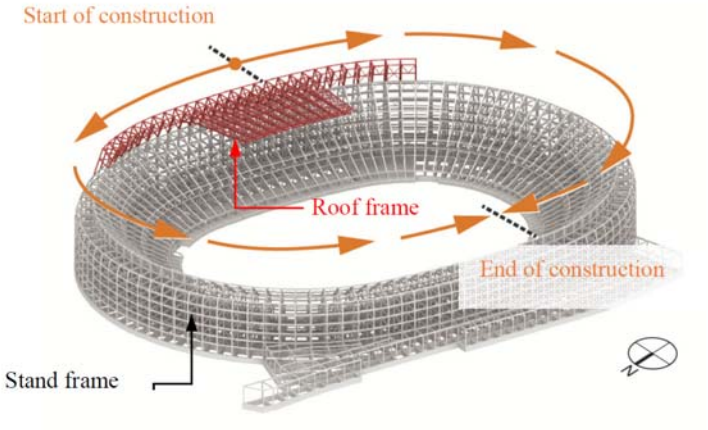


Figure 3: Simple structure plan

By constructing cantilever trusses of the roof as one-frame structures standing by themselves, simultaneous construction of the stand, the field, and the roof was achieved. Furthermore, the frame system with triangular cross sections repeated in circumference direction was adopted to the cantilever trusses to construct them systematically and safely. Two upper chords and one lower chord of trusses are connected with lattice members in three dimensions. The lattice members contribute to avoid buckling of the upper chords and the lower chord and behave as horizontal braces in the roof surface. Cantilever trusses were unified by connecting the web of the upper chords of each truss by high-tension bolts as shown in Figure 4. For this purpose, channel steels were adopted to the upper chords.

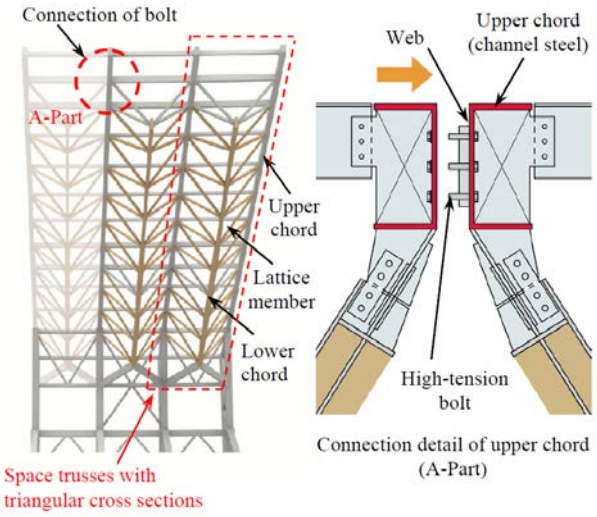


Figure 4: Images of cantilever trusses of the roof

3. Unitization of the cantilever trusses of the roof

To improve the efficiency of the construction, cantilever trusses were assembled on temporary cradles set on the center ground of the stadium and lifted up by units as shown in Figure 5, and appendages such as roofing boards, equipment and temporary staging were also attached to unit frames on the cradles to minimize high-place work. The base frames, the basal portion of the cantilever trusses, were not unitized due to heavy weight, therefore, individual members were erected one by one. As shown in

Figure 6, each cantilever truss ahead of base frames was divided into three unit frames: Unit 1, Unit 2 and Unit 3. The weight of Unit 1 and Unit 2 were about 40 tons, and Unit 3 was about 60 tons which can be lifted with crawler crane. The unit frames were assembled on multiple cradles simultaneously. One unit frame was erected to the roof per one day in average, and totally 252 unit frames were erected in about one year. Figure 7 shows unit frames being assembled on the cradles.

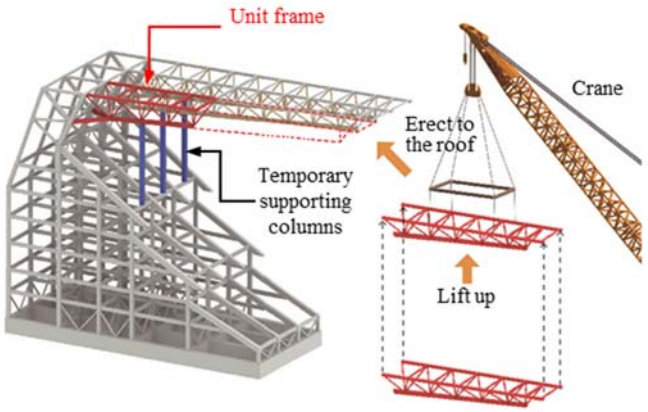


Figure 5: Image of roof construction

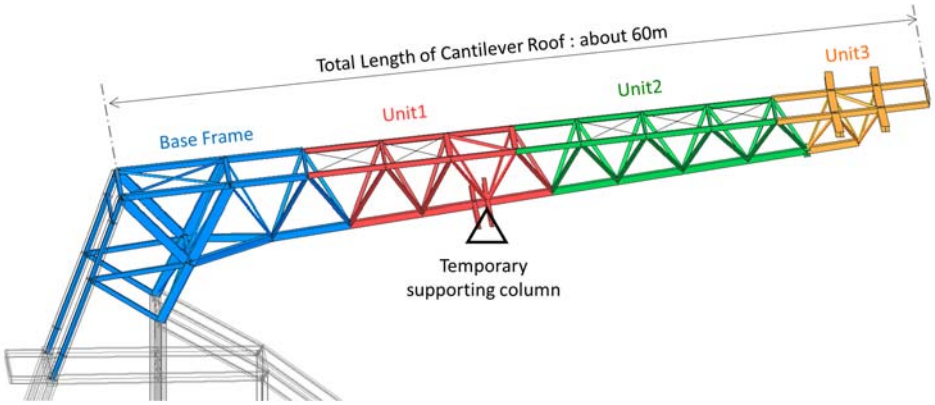


Figure 6: Unit assignment of cantilever trusses



Figure 7: Unit frames on assembling cradles

Copyright © Japan Sport Council, "Regular Briefing for the New National Stadium", Made by 28th handout (September 14, 2018)

4. Controlling bending moment of the columns of the base frames

Cantilever trusses are supported by columns of base frames lined up in two rows on the stand frame. The inner columns of two rows are steel members, and pre-casted SRC members were adopted for the outer columns in order to reduce the deformation of cantilever trusses with their axial stiffness and streamline finishing works. Because the inner columns, the most important members supporting vertical load of the roof, are subjected to both large bending moment and compression force, the bending moment was reduced by an idea of construction process. Figure 8 shows the detail of joint part of outer columns. After the members of base frames were erected with temporary joints, outer columns were pulled down 15 mm with hydraulic jacks placed on the flange faces of the columns to apply additional bending moment to inner columns in opposite direction to that under dead load, and total bending moment was reduced as shown in Figure 9. With this method, bending moment of inner columns under dead load were reduced to about 60%. To minimize the tensile force applied to the concrete of outer columns and restrain cracking, the concrete of outer columns was prestressed and casted to the joint part after tensile forces were applied to the steel part of outer columns along with erecting unit frames.

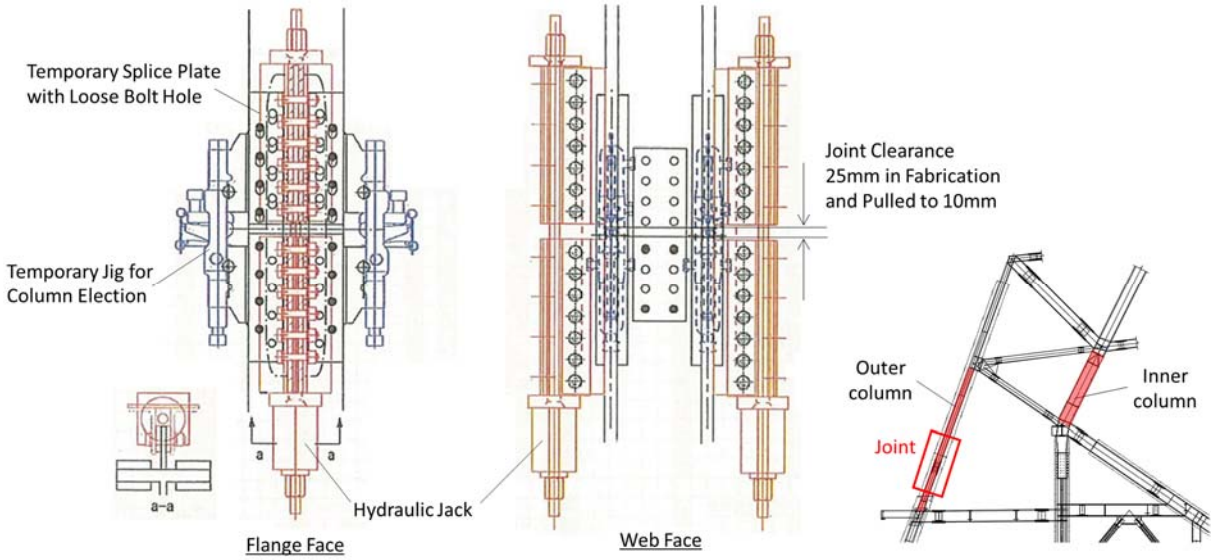


Figure 8: Detail of the outer column joint

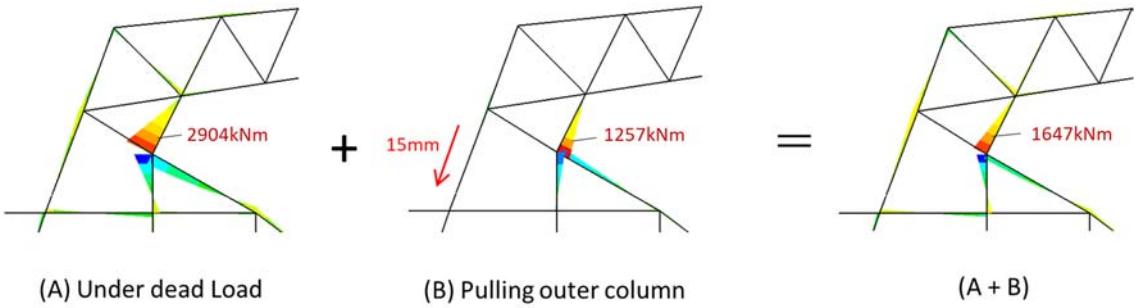


Figure 9: Bending moment of typical base frame

5. Temporary supporting column system for efficient disassembling and reusing

Temporary columns which support cantilever trusses during construction were set on raker beams of the stand frame. They were set only beneath Unit 1 frames. Conversely, Unit 2 and Unit 3 frames were erected in cantilevering condition without supporting columns beneath them. Jack-down of supporting columns was conducted sequentially after erecting Unit 2 of each cantilever truss. Supporting columns beneath Unit 1 frames of cantilever trusses after jack-down are disassembled and reused for other cantilever trusses, and the number of supporting columns was reduced to 32. To disassemble and reuse supporting columns efficiently, masts of tower cranes were adopted to them. Figure 10 shows the outline of the supporting column. The shafts of supporting columns consist of steel pipes with diameter of 1.9 m which are commonly used for masts of tower cranes. And the shafts can be divided into parts with length of 4.5 m. Steel pipes were connected each other by high-tensile bolts, and lifting stages on the shafts can be lowered to provide a space for crawler crane to assemble and disassemble supporting columns easily.

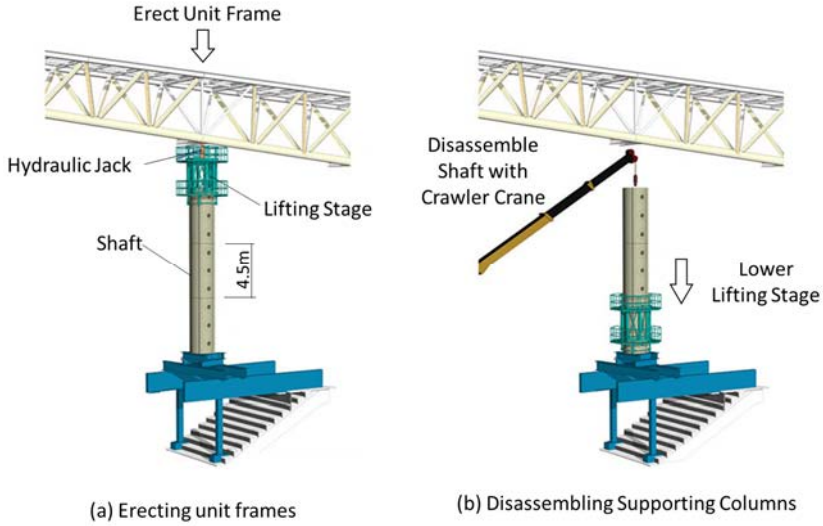


Figure 10: Outline of temporary supporting columns



Figure 11: Temporary supporting columns set on the stand structure

Copyright © Japan Sport Council, "Regular Briefing for the New National Stadium", Made by 28th handout (September 14, 2018)

6. Cycle of construction of the roof structure

The construction of unitized cantilever trusses started from the center of the east side of the stadium and proceeded to north and south direction simultaneously as shown in Figure 3. The process of the construction was repetition of same cycles that makes construction simple and systematic. The cycle was composed of erecting unit frames, releasing reaction force of supporting columns, jack-down and connecting cantilever trusses as shown in Figure 12. This cycle was determined in consideration of maintaining accuracy of constructing. If the deformation of the adjacent trusses on both side of newly erected unit frame are unequal, it causes the distortion of base frames and disturbs to erect the unit frame to expected position accurately. For this reason, reaction forces of supporting columns were released several times in each cycle so that the deformation of adjacent trusses are balanced. After releasing reaction force, supporting columns remained in contact to cantilever trusses and supported the load of following unit frames until jack-down. In connecting upper chords of cantilever trusses, the balance of deformation of two trusses was considered as well.

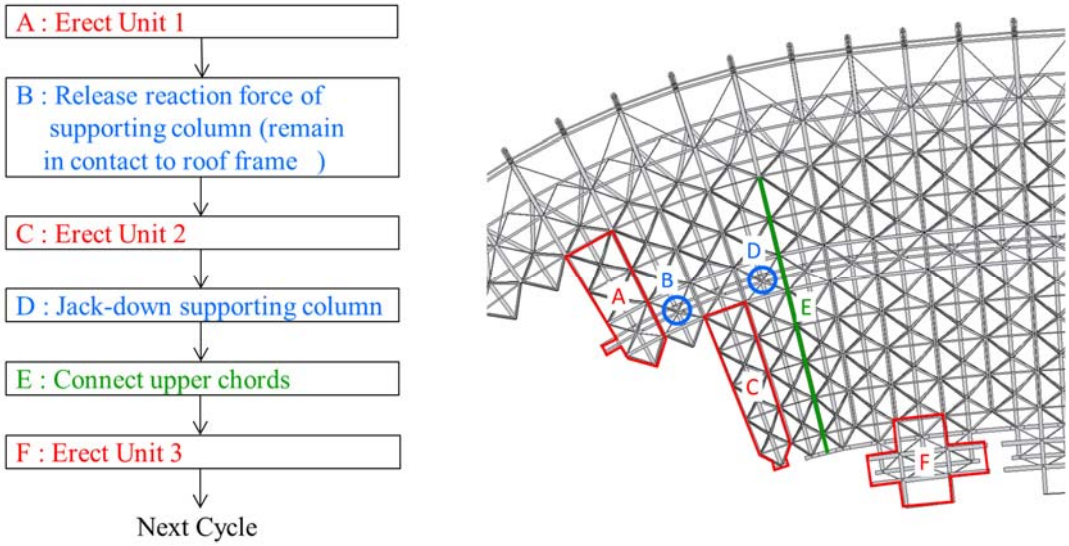


Figure 12: Construction cycle of the unit frames

7. Construction step analysis

To connect upper chords of cantilever trusses properly, construction step analysis was conducted to obtain approximate deformation of trusses in vertical and horizontal direction before construction. Figure 13 shows the analysis model for the construction step analysis. Each analysis step corresponded to each step of the construction cycle shown in Figure 12, and the total number of analysis steps was 323. Figure 14 shows the comparison of vertical deformation of typical cantilever truss between analysis and measured value. The deformation of the roof trusses during construction was predicted with adequate accuracy. Besides, measured deformation at the tip of the roof after construction was within allowable margin of error which was predetermined by designer, and it was confirmed that the roof trusses were constructed accurately.



Figure 13: Analysis Model for Construction Step Analysis

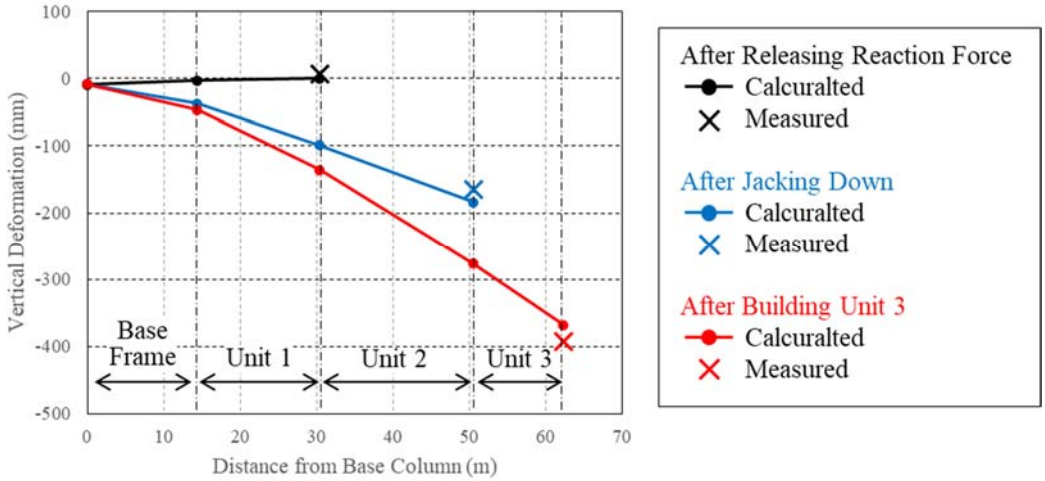


Figure 14: Comparison of Deformation of the Roof
between Calculated and Measured Value

8. Conclusion

The cantilever roof of the new national stadium with length of 60 m was constructed efficiently and endowed structural safety by various unique ideas brought up in the cooperation between structural engineers and constructors.

Proceedings of the IASS Annual Symposium 2019 – Structural Membranes 2019
Form and Force
7 – 10 October 2019, Barcelona, Spain
C. Lázaro, K.-U. Bletzinger, E. Oñate (eds.)

Design and Construction of Wheel-shaped String Beam Roof with U-turn on the Bottom Chard Cables

Tadashi YOSHIHARA*, Yu NAKAMURA[a],
Hideki TABATA[b], Ryuji HIRABAYASHI[b], Hitoshi MATSUDA[c], Masao SAITOH[d]

*Mitsubishi Jisho Sekkei Inc.,Structural Engineering Department
2-5-1,Marunouchi,Chiyoda-Ku,Tokyo,100-0005
tadashi.yoshihara@mj-sekkei.com

[a] Mitsubishi Jisho Sekkei Inc., Renovation Design Department
[b] Nippon Steel & Sumikin Engineering Co.,Ltd.,Design & Engineering Department
[c] Shinko Wire Co.,Ltd.,Engineering Department
[d] Nihon University,Professor Emeritus

Abstract

Wheel-shaped string beam structural system is adopted for the roof of Shakujii Gymnasium arena.Wheel-shaped roof has 35 meter diameter and sits on 36 meter by 36 meter square shape podium made of reinforced concrete structure. At four corner of podium, there are triangle shaped roof openings generated by gap of square and wheel shape. Those openings are used as natural ventilation and natural light intake. Top chord of wheel-shaped roof is composed of single layered outer rings, double layered inner ring and radially arranging steel beams, which divide both inner and outer rings into 20 even arch. Cables connecting outer ring and bottom of inner ring are functioned as bottom chord of string beam. One cable starts one of divided node of outer ring toward inner ring, then makes u-turn over through cable guide arranged on bottom of inner ring and finally reaches adjacent node of outer ring. Following this geometry, 20 V-shaped cables create innovative cable arrangement of wheel-shaped string beam roof. Additionally, using simple and reliable detail for cable end, proposed cable arrangement reduces construction cost.

Keywords: Wheel-shaped String Beam, Cable, Cable guide

1. Introduction

This project is a sports facility that includes a sports hall, gym, kendo dojo, clubhouse, accommodation, etc., used for a private company's club activities. The plan of the gymnasium is a 36 m x 36 m square with a ceiling height satisfying the 12.5 m competition regulation of the international Volleyball federation. On the other hand, the building height must be less than 15 m due to codes requirement at the site. Therefore, the arena roof needs to be constructed less than a 2.5 meter beam height including finishes.



Photo.1 Building external view

Copyright © 2019 by Tadashi YOSHIHARA, Yu NAKAMURA, Hideki TABATA, Ryuji HIRABAYASHI, Hitoshi MATSUDA, Masao SAITOH
Published by the International Association for Shell and Spatial Structures (IASS) with permission.

2. Arena roof framing scheme

The arena roof scheme for the gymnasium is square in plan, within which is provided a 35 m diameter circular roof frame, incorporating natural light and ventilation from the triangular-shaped high side lights formed in the four corners. Also in order to minimize the amount of structural steel with the limited beam depth, a string beam structure consisting of top chord steel beams and bottom chord cables was adopted instead of increasing steel beam depth (Figs. 1 and 2). The wheel-shaped string beam consists of double layered center rings, which is provided at the center of the roof and is linked by steel posts each other and H-shaped steel top chord and cable bottom chord arranged radially from the circumference of the center ring at 20 equally spaced positions. Then, roof was constructed on joists spanning between the top chord. The diameter of the upper center ring is 2.9 m and lower center ring is 4.0 m diameter. And the height between rings is 2.15 m (beam depth/span ratio = 1/16) forming a frustum of a circular cone. The cross-section of the posts are composed of two pararell flat bars connecting each other. Top light was placed above center ring expecting architectural effect.

The bottom chords extend from 20 equally spaced points on the lower center ring towards devived node of outer circle where top chord ends. Each bottom chord cable is U-turned at the center ring then, bottom chords generate V-shape when it is looked up. These overlapping V-shaped cables form an unprecedented wheel -shaped string beam frame (Photo.2). This self-contained structural steel roof frame is installed on the top of reinforced concrete beams using roller supports with loose holes to allow horizontal movement.

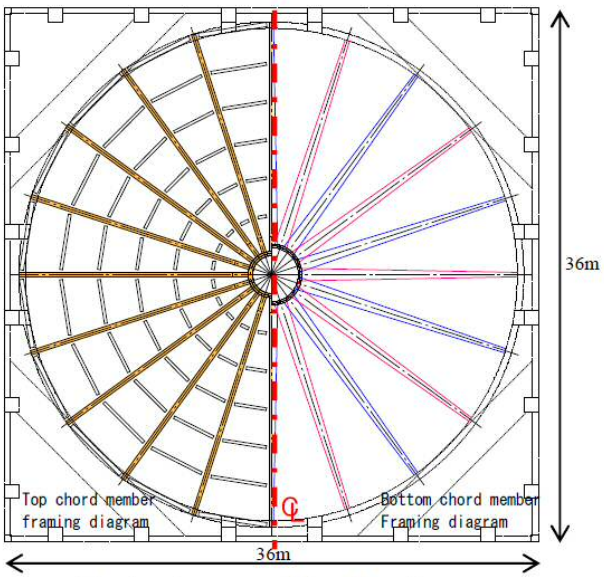


Fig.1 Arena roof framing diagram

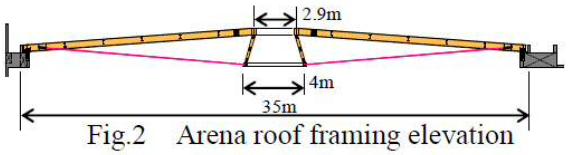


Fig.2 Arena roof framing elevation

Table.1 Members used

Member		Cross-section	Material
Top chord member		H-390x300x10x16	SN490B
Bottom chord member		Structural wire rope φ28	ST1570
Ring	Top chord ring	BH-390x300x12x22	SN490B
	Bottom chord ring	2PL-22x250	SN490B
	Connecting members	2PL-19x200～140	SN490B



Photo.2 Arena internal view

3. Detailing of the ends of the cables

3.1. Interior ends of the cables (U-turn part)

As shown in Photo.3 and 4, in order to have cables U-turned at the center ring, a cable guide that is bended with a radius of 8 times of the cable diameter is installed on the lower center ring. Additionally, 25mm thick steel plate is overlayed on upper edge of cable guide and helps to transfer upward force to the structure. And 34mm diameter steel pins is provided on the lower edge of cable guide to prevent deviation of the cable. Also steel pins allow the adjacent cables intersect in plan with 1 cable diameter clearance (Photo.4). Simple detail is achieved by U-turn cables system and making cables continuous.



Photo.3 U-turn part(exterior side)

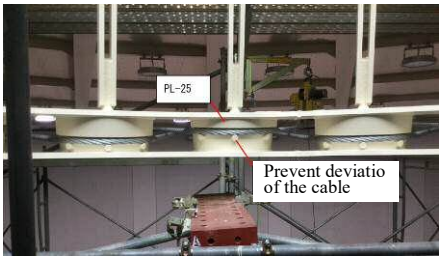


Photo.4 U-turn part(interior side)

3.2. Exterior ends of the cables (anchorage part)

The exterior ends of the cables are anchored to an end plate through steel tube welded on the side of end plate installed on the upper chord. Respecting architectural view, anchorages are welded close to beam axis as much as possible however , not to interrupt steel beams (Photo.5).



Photo.5 Ecterior anchorage

4. Design of the members of the arena roof

The members of the arena roof were designed considering the sequence of erection of the structural steel and introduction of tension force into the cables. Jackling force during erection was scheduled to cancel deflection due to the self-weight of the structural steel (Fig.3)

The diameter of the cables was determined taking into consideration the required tension force (67 kN) that satisfies required ceiling height considering vertical deflection during erection. Note that 2 types analysis models were used, i.e., (1) a loose model ignoring a ring effect due to joists when jackling force occurs (2) a model after all joists were bolted and ring effect due to joists is expected. Horizontal forces under an earthquake were designed to be resisted by anchor bolts at supports where loose holes were cut in orthogonal directions.



Photo.6 Exterior and roller supports

Structural steel roof is installed on the top of RC structural walls. Considering recent building damage under earthquake, roller supports were provided in order to avoid concrete wall damage due to roof reaction induced out-of-plane deformatin(Photo.6). In this building the cable diameter could be reduced by providing 2 bottom chords for every top chords, and achieve easy cable handling during construction.

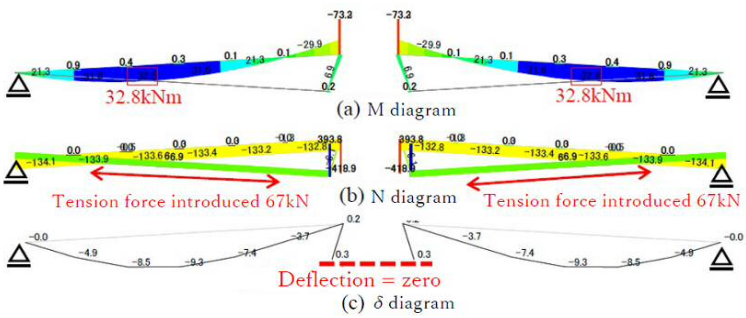


Fig.3 Under long-term dead load

5. Construction plan for the wheel-shaped string beam arena roof

The construction sequence [STEP 1 to 3] for the wheel-shaped string beam is shown in Fig. 4.

[STEP 1] Setting the structural steel roof frame

The center ring was assembled on the ground in the construction yard, and then placed on falsework using a crane. (Photo.7) The radiating structural steel top chord members (H-section steel) were assembled by site welded flange connections and bolted web connections while the center ring was supported on the falsework. The support height of the falsework was 50 mm higher than the design level to provide a camber, which cancel the deflection due to installation of the roof finishing materials. The cables were suspended from the center ring, then the bottom chord cables were installed in their planned positions. (Photo.8)

[STEP 2]Cable tensioning

To apply the proportioned jackling force, the cable operation was divided into 4 groups of cables (5 upper cables× 2 groups, 5 lower cables × 2 groups).

The steps in the tensioning operation was divided into four, STEPS 2-1 to 4, aiming that the axial load are gradually introduced into the cables.

STEP 2-1: Tension about 10 to 30 kN tension applied by hand

STEP 2-2: 30 kN tension applied by jack

STEP 2-3: 60 kN tension applied by jack

STEP 2-4: Tensioning to raise the center ring

Note that both manual and jack tensioning was carried out at both ends of each cable, therefore friction which might occur at U-turn portion need to be cut as much as possible.

During STEP 2-1 to 4 of the tensioning operation, the reaction force of the center ring on the falsework was measured, and after the reaction force became 0 kN, the measurement operation was switched to measurement of the vertical deflection of the roof. After the tensioning operation, joists in the circumferential direction were installed, which completed the string beam roof framework.

[STEP 3] Installation of roof finishing materials

After the roof finishing materials were installed, the deflection of the roof due to the weight of the finishing materials was measured, and it was confirmed that the ceiling height of 12.5 m was obtained.



Photo.7 Center ring



Photo.8 Erection of the cables

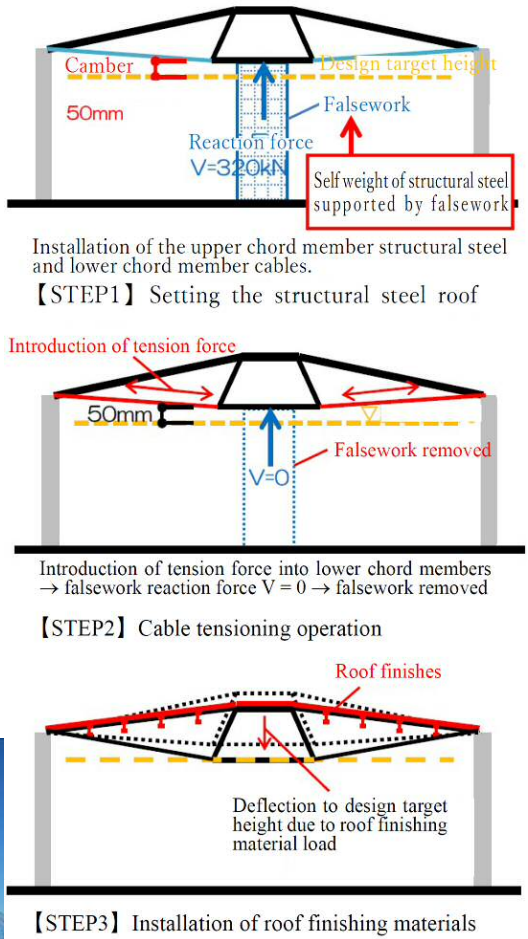


Fig.4 Construction purocedure

6. Moch up study

6.1. Investigation of cable bending performance

A design feature of this project is the U-turn of the bottom chord cable members at the center. During the design it was confirmed that the cable can be bent into a radius R (R230) = cable diameter× 8 times. (Photo.9)

6.2. Jack tensioning test using full size mockup

Cable connections and steel joint details were studied using BIM (TEKLA) , and a cable tension test was carried out using a full size mockup. (Fig. 5, Photo 10) In the full size mockup the followings were studied, and reflected in the structural steel detail and constructibility.

(1) Bedding into the cable guide with a tension force of about 1 kN at the cable U-turn

(2) Operating space for jacking at the table tensioning ends and detailing of the upper chord member

(3) Detail of structural steel (cable guide structural steel, detailing for preventing slippage of cables, etc.)

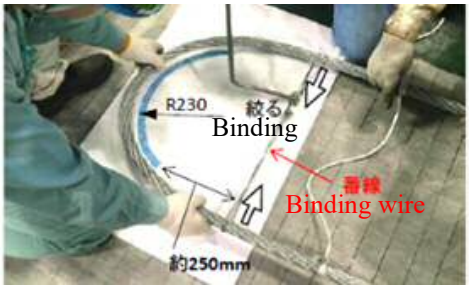


Photo.9 Checking the cable bending performance

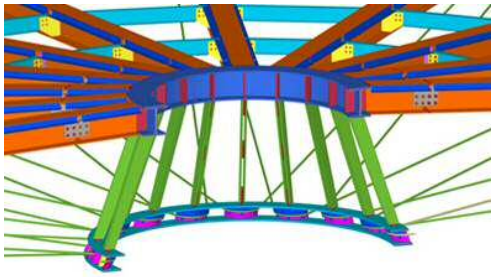


Fig.5 Study of the detail using BIM



Photo.10 Full size mockup test

7.[STEP 2] Cable tensioning operation and results of measurements during construction

The construction flow of STEPS 2-1 to 4 of the cable tensioning operation are shown in Fig. 6. The relationship between the cable tension force and the reaction force on the falsework is shown in Fig. 7, and the relationship between the cable tension force and the vertical deflection is shown in Fig. 8.

In STEP 2-1, tensioning was carried out by manual tightening of the nut at the cable ends. The tension force was about to 10 to 30 kN. In STEP 2-2, tensioning with a jack to 30 kN was carried out in the following sequence, upper cable A → upper cable B → lower cable C → lower cable D. Reaction force on the falsework at the end of this step was 222 kN. (Photo.11, 12), however construction analysis estimates the reaction force is 175 kN. Reasons of this gap was considered that the initial value of the reaction force on the falsework was about 20 kN larger than analysis, and additional tension force was requested by bending at the U-turns. In the jack tensioning (60 kN) in STEP 2-3, the falsework reaction force was 78 kN. As shown on Fig.7, 75 to 80kN of additional tension was expected to achieve 0kN reaction of mesurment point at the end of following STEP2-4. Based on this prediction, 80kN tension was applied to top cable and resulted in 22kN falsework reaction. Finally, applying 75kN tension to bottom cable, both 0kN falsework reaction and approximately 10mm roof raise were achieved. Following those measurement, the tensioning operation was terminated. (Photo.13,14)

Measurements were carried out the day after the tensioning operation, and the tension force was about 70 kN and the liftoff was about 5 mm. Slight cable relaxation was confirmed, and the tension value was almost same with the design value. (Fig. 8)

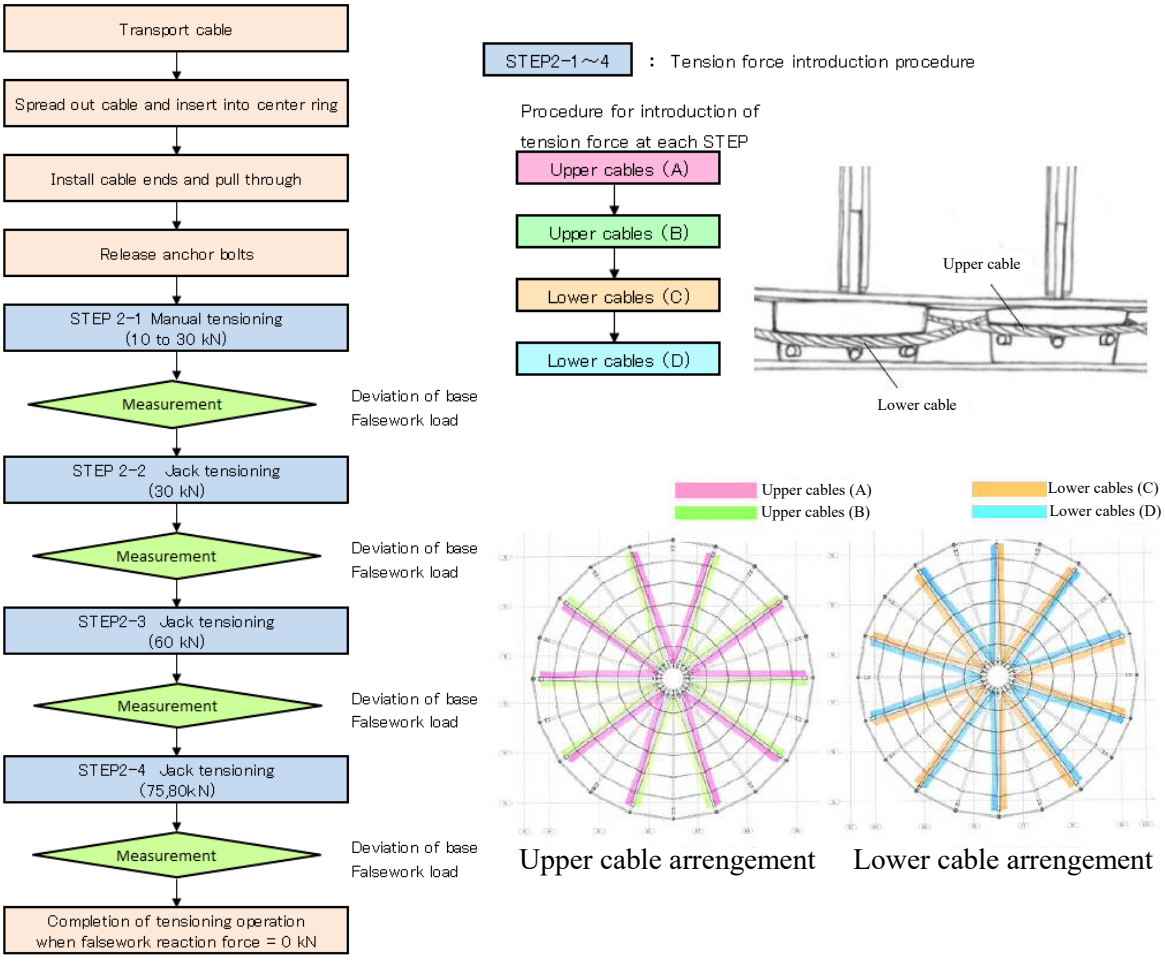


Fig.6 Construction flow during cable tensioning operation

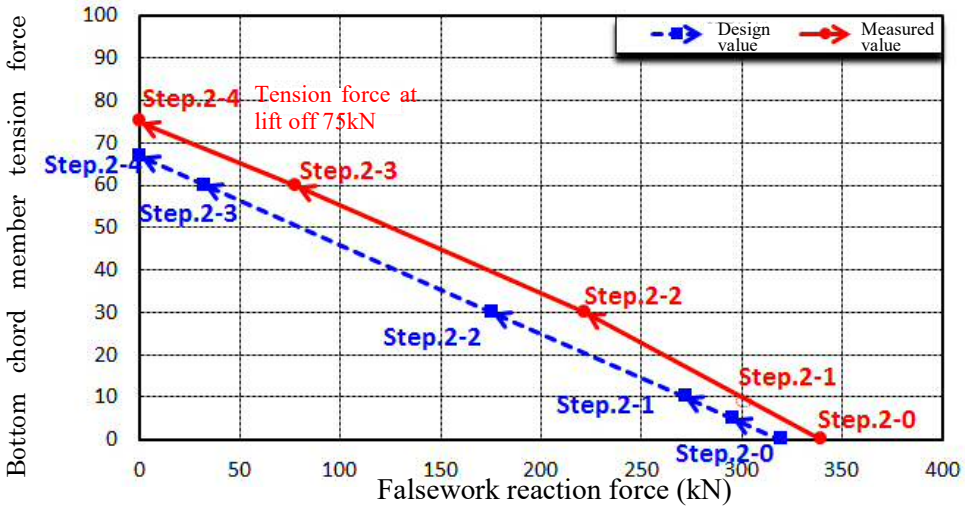


Fig.7 relationship between cable tension force and falsework reaction

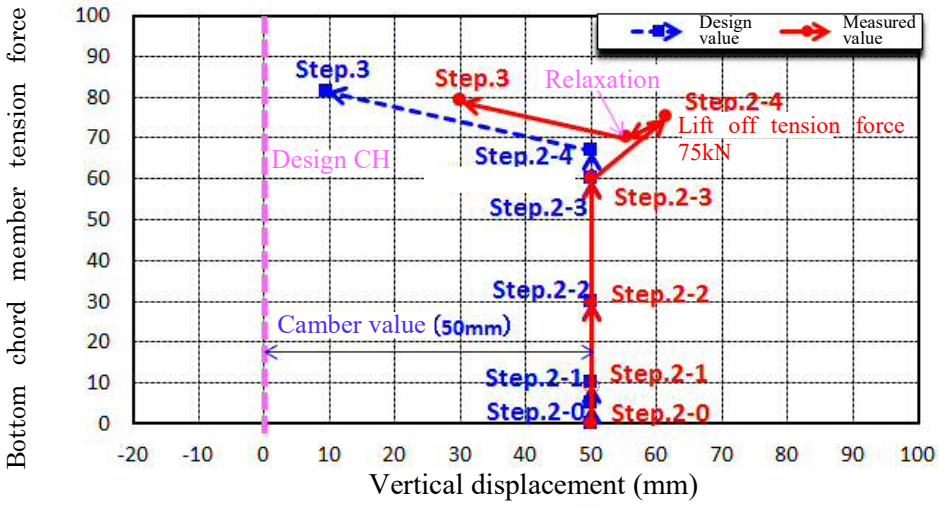


Fig.8 Relationship between cable tension force and vertical displacement



Photo.11 Reaction force measurement



Photo.12 Tensioning using a jack

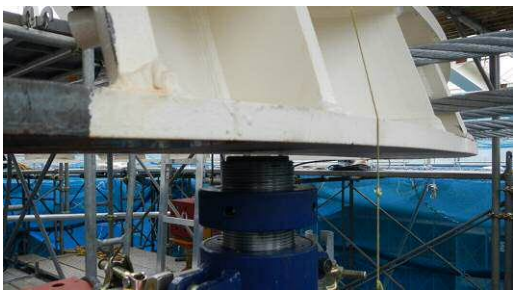


Photo.13 Rise of the center ring

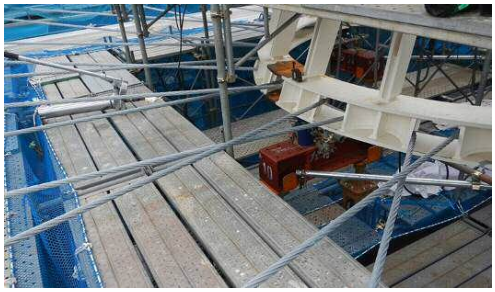


Photo.14 Completion of tensioning operation

8. [STEP 3] Installation of roof finishing materials

After completion of the tensioning operation in STEP 2, the main tightening of the joists in the circumferential direction was carried out, and installation of the roof finishing materials of STEP 3 was carried out. When installation of the roof finishing materials was completed, there was downward deflection of 25 mm, and the construction was completed with the ceiling height at the design value + 30 mm, virtually as planned. (Fig. 8)

8. Summary

The design and construction of an unprecedented wheel-shaped string beam arena roof in which the bottom chord cables of the string beam were given a U-turn at the center ring has been described. Low construction cost was achieved by repeating a simple detail for the cable ends, and the cables that were overlapped in a V-shape produced an attractive internal appearance in the arena. The tensioning process (STEP 2-1 to 4) which was carried out through 4 times to tension the cables in a balanced manner was very difficult. However, carrying out measurement control of cable tension force and reaction force, roof construction well following with the construction analysis is succeded.



Photo.15 Arena internal view with natural light

References

[1] Dr.Masao SAITOH, “Prinsiple of Beam String Structure,” *IASS Symposium(Madrid)4,pp17-38,1979*

[2] Dr.Masao SAITOH, “Role of String:Asesthtics and Technology of Tension Structures,” *IABSE reports,pp699-710,1998*

Proceedings of the IASS Annual Symposium 2019 – Structural Membranes 2019
Form and Force
7 – 10 October 2019, Barcelona, Spain
C. Lázaro, K.-U. Bletzinger, E. Oñate (eds.)

Kuwait International Airport Terminal 2: Detailed Design and Fabrication of a Large-Span Composite Shell

Guido NIERI[1], Lucio BLANDINI[1], Werner SOBEK[1,2]

[1]Werner Sobek Stuttgart AG
Albstr. 14, 70597 Stuttgart, Germany
guido.nieri@wernersobek.com

[2] University of Stuttgart, Institute for Lightweight Structures and Conceptual Design (ILEK)

Abstract

Kuwait International Airport is currently being extended by a new iconic terminal building (Terminal 2) designed by Foster + Partners. The new terminal is to be completed by 2022. It is a single building defined by a continuous roof with a length of 1.2 km and a gross total area of 320 000 m^2. The roof is composed of different large-span non-repetitive freeform shells realized through an innovative prefabricated system made of steel and exposed reinforced concrete elements. These shells are at the same time the characterizing elements of the terminal's architecture and its principal structure. The sheer size of the building in combination with its structural complexity and the use of innovative prefabricated systems are the reason why this building can be considered one of most challenging constructions of our time. Taking over from design engineers at Arup, as of August 2016 Werner Sobek Stuttgart (WSS) was responsible for the engineering of the primary structures and the facades. This work included design development, optimization, detailing, and support to fabrication and construction. In order to fulfill these tasks, the authors and their collaborators at Werner Sobek developed different analyses, methods, work-flows and even project specific tools allowing for a full coordination between structural design and production. After a preliminary introduction on the project's design philosophy, this paper focuses on the specific solutions used for the design, development, and fabrication of one of the key elements of the building: the shell structure.

Keywords: structural analysis, integrated design, prefabrication, parametric design, composite shell structures, BIM, model for construction, automated fabrication.



Figure 1. Left: KIA T2 Aerial view. [© F+P] Right: construction site aerial view May 2019. [© Google Earth]

Copyright © 2019 by Guido NIERI, Lucio BLANDINI, Werner SOBEK
Published by the International Association for Shell and Spatial Structures (IASS) with permission.

1. Integrated Design, new methods in the building industry

Digitalization is one of the most relevant aspects characterizing our time and affecting our lives both in private and in business. In most industries (like automotive or aerospace) different tasks such as design, engineering, modelling, documentation, and fabrication are already linked together in common highly digitalized workflows. This fact allows for high quality and cost-effectiveness of the processes. In the building industry such a coordinated workflow is very rare. Architects, engineers, and construction companies usually work on different digital platforms. Exchange of information happens mainly through drawings or written documents. This requires a high amount of additional work for a proper transfer of information from one system to the other, especially in complex megaprojects.

Over the past decades various studies demonstrated the importance of form-finding methods, optimization algorithms, and parametric design for establishing the optimum with regard to structural efficiency and use of materials. Parallel to that, advances in architectural geometry and computer aided manufacturing opened the way to new types of complex structures. However, despite all these improvements, there is still one bottleneck in today's building industry, namely the lack of interdisciplinary communication. For this reason many contemporary structures are optimized not from a structural point of view, but rather with regard to logistics: system standardization rather than material optimization. In theory, Building Information Modelling is supposed to address this issue. In reality BIM is all too often but an additional task for the planners, not the connecting element it is supposed to be. In fact, due to technical and conceptual limitations most of the time there is no direct interface between structural design and BIM. The building industry therefore urgently needs a new Integrated Design approach. Thinking out of the box defined by a single discipline or specific software is extremely challenging, but without it the building industry will not be able to make the next big step in managing the complex architectures of XXI century. Using a clear, easy and reliable flow of information going from design to production is vital for achieving significant progress. Only in this way can the benefit of a full integration of innovative calculation methods, structural optimizations, parametric design, and BIM really be made a reality.

Having worked on many different complex projects, the need of alternative approaches is well known to the authors and their colleagues at Werner Sobek. Early projects such as the Mercedes-Benz Museum (architect: UN Studio) [1] or the Baku Flame Towers (architect: HOK Architects) already used ad hoc solutions to optimize the building's geometry. In projects such as Stuttgart's new train station S21 (architect: Christoph Ingenhoven) [2], this approach was extended by coupling the geometric models to the calculation models allowing for an iterative multi-parametric optimization. Recently the use of new interfaces between planning and production made it possible to realize demanding projects such as the Ferrari Museum in Modena (architect: Future Systems) [3], the new National Museum of Qatar (architect: Jean Nouvel) [4] or the Heydar Aliyev Center in Baku (Architect: Zaha Hadid). Applying this integrated approach from design to production in different projects, Werner Sobek was able to expand and develop its knowledge along the entire process chain, from the very early stages of design up to construction. For the Kuwait International Airport the use of the Integrated Design approach, thus connecting the geometry, the structural calculation, and BIM from design to production was essential; its exploitation in a megaproject was one of the most challenging aspects of the design.

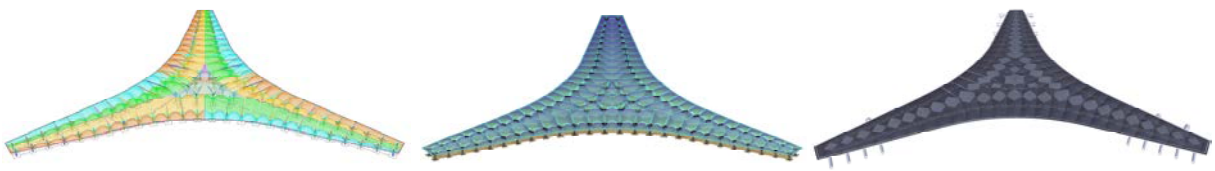


Figure 2.Left: geometric digital model. Center: FE model. Right: BIM model. [© WSS]

2. Project description

Kuwait wants to significantly increase the capacity of its international airport in order to establish a new air hub in the Gulf region; the new state-of-the-art terminal building designed by Foster + Partners is part of this strategy. The new terminal will provide the highest levels of comfort for passengers while setting new environmental benchmarks for airport buildings as well [6]. The capacity of the airport is to be increased from 14 to 25 (and in a second step to 50) million passengers per year.

The terminal has a trefoil plan, comprising three symmetrical wings of departure gates (Fig. 1) [7]. Each side of the roof is 1.2 km long and extends from a dramatic 25-metre-high central space [6]. Especially the complex structural framework devoid of any movement joints was an extremely demanding challenge for the engineers. The structure spans up to 120 m and cantilevers up to 50 m, creating in this way a naturally shaded entrance area (Fig. 3) and a spectacular, flexible interior space.



The engineering of the roof structures and facades up to the tender phase was done by Arup London; Werner Sobek Stuttgart took over after the tender phase. Werner Sobek's scope of work included structural calculation, design development and detailing of all structures and facades as well as the preparation and coordination of the BIM models up to a detail accuracy of LOD 400. In addition to that, for some complex components (such as the roof shell structure) WSS developed also the BIM models used as reference for production and construction (Fig. 6).

Figure 3. Shell structure, entrance area. [© F+P]

3. Structural System

3.1. Principal elements

The structural system of Terminal 2 is subdivided in five different sub-systems (Fig.4): the main roof structure (group 100), the composite shell structure (steel structure: group 200, reinforced concrete panels: group 800), the trusses (groups 400, 500 and 600), the secondary roof structure (group 700), and the facades (glass facade: group 300, roof covering: group 900). This numbering logic was used in the whole project, defining in this way a coherent and unique naming convention for all the elements, which was used to coordinate calculations, drawings and models.

The main roof structure is made of reinforced concrete elements. The principal elements of this structure are 90 reinforced concrete columns. These octagonal columns vary in height between 25 and 45 m; they are positioned along the facades and in the central hexagonal area. Given their size and the loads acting on them, these elements are similar in function to building cores. A complex system of pre-cast and post-tensioned concrete arches spans between the columns; these arches are called either Spines or Ribs, depending on their position. Spines span along the perimeter of the building; together with the facades they enclose the building's internal space. The Ribs are positioned almost perpendicular to the Spines; they span from one edge of the building across the inner space to the opposite edge, up to the tip of the cantilevering canopy. Both Ribs and Spines are post-tensioned with internal tendons. The Ribs are furthermore connected to each other by stay cables, which also support the iconic cantilevering entrance canopy.

Ribs and Spines subdivide the terminal building into a total of 136 fields. Each field varies with regard to geometry, dimensions, and boundaries conditions and is covered by the non-repetitive freeform shell structure (group 200/800). Each double-curved shell spans between 45 and 105 m and reaches a maximum clearance in the central hexagonal dome area (Fig. 4 left). Although steel elements play a

decisive role in the load-bearing behavior of the shells, the sand-colored double curved exposed concrete characterizes the architectural appearance of the terminal. The shells are at the same time supporting and supported elements. They transfer their own dead weight as well as the loads acting on them to the Ribs and Spines. At the same time they brace these pre-stressed elements among others against lateral torsional buckling. At the edge of the cantilevered area, along the symmetry axes and in the central dome area the shell structure is stiffened by steel trusses (groups 400, 500 and 600).

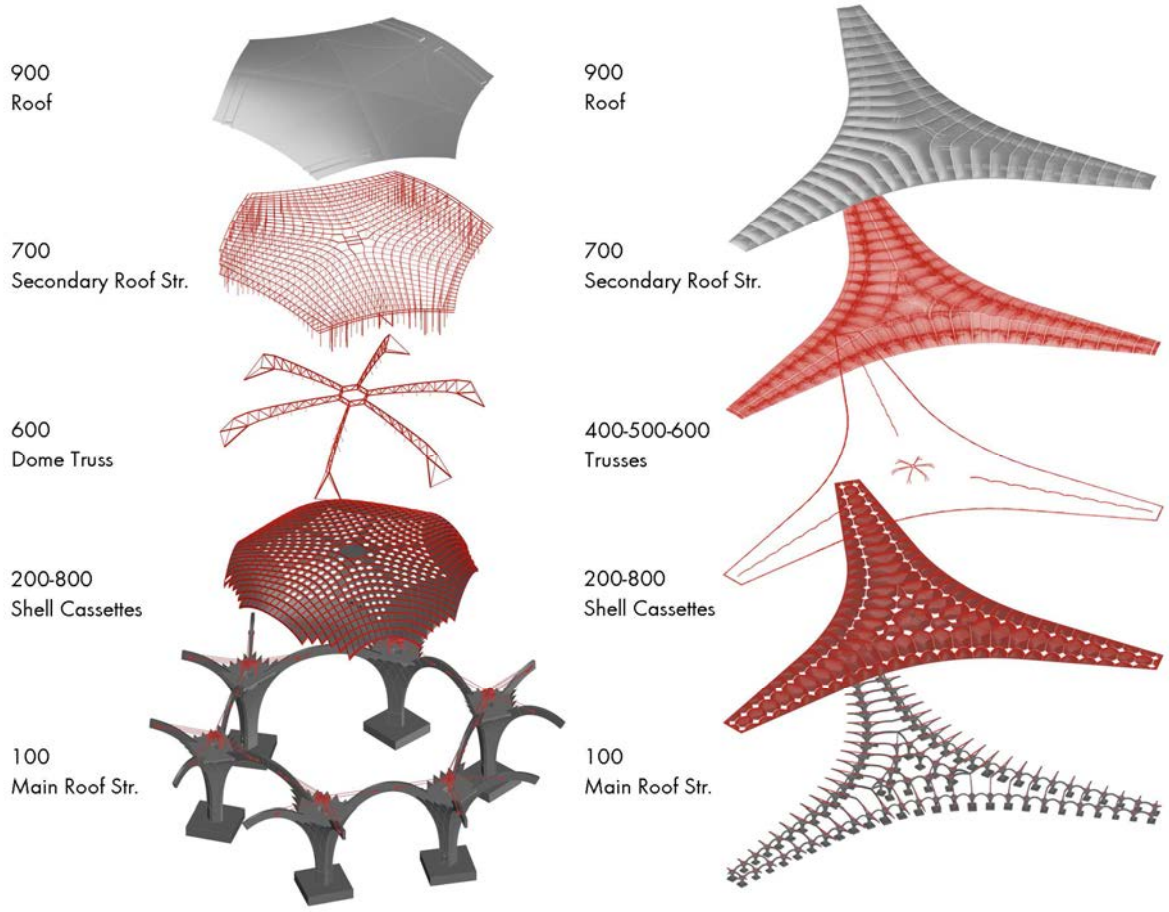


Figure 4. Left: the individual components of roof and primary supporting structure in the central area. Right: placement of the individual components in the overall context. [© WSS]

Despite its size, the roof was designed without expansion joints in order to eliminate risks in terms of functionality and maintenance [8]. This had a major impact on the structural design of all components. By eliminating expansion joints, the roof is actually a statically highly indeterminate single composite structure, subject to possible thermal constraints and long term behavior effects. The interaction between the individual components is therefore very complex; any change in the stiffness of one element has a significant influence on the load paths in the entire structure. The soffit of the roof is determined almost completely by the shell structure while the upper surface consists of an aluminum roof (group 900) with integrated photovoltaic elements. Due to differences of curvature between the shell structure and the aluminum roof, between the two components there is a secondary roof structure (group 700) supporting the upper roof skin. This secondary structure made of a lightweight framework system transfers the loads to the main structure.

3.2. Workflow and digital process

For this project more than ever the use of the Integrated Design approach described in section 1 was essential; its exploitation in a megaproject was one of the most challenging aspects of the design. Due to the parametric nature of the architectural design, the complexity of the structures and the extension of WSS' scope of work, a well-organized workflow based on multiple digital tools was strictly required. Furthermore in order to overcome the limitations of the presently available commercial software, an integration of them with custom developed plug-in was needed.

The general philosophy of Werner Sobek's approach consisted in the definition of a "Central Data Model", in which all the important information of each component (beams, cables, connections, floors, etc.) is stored. In this case, the Central Data Model was based on the software McNeel Rhinoceros. Within this platform almost all the elements were defined by scripting (C++, C# and Grasshopper) and from this unique source using specific interfaces (some of which were developed in-house), the different information was shared with other software (FEM, BIM, CAD, etc.) or used as a basis for sub-models (Fig. 5).

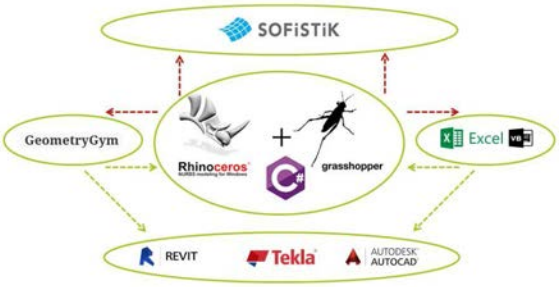


Figure 5. Schematic process chart showing the different software used. [© WSS]

Thanks to this design process, it was possible to define a fully coordinated package (Fig.2) constituted of structural models (SOFiSTik, and custom calculation tools), BIM coordination models (Revit, Rhinoceros, Navisworks, etc.), BIM models for production (Tekla, Rhinoceros, Allplan, etc.) and CAD Drawings (overview drawings, formwork drawings, rebar drawings, etc.). In this way it was possible to reduce the coordination cost and the risks of errors; most important it also allowed analyzing the different design issues from different points of view with the most advanced digital tools available at present.

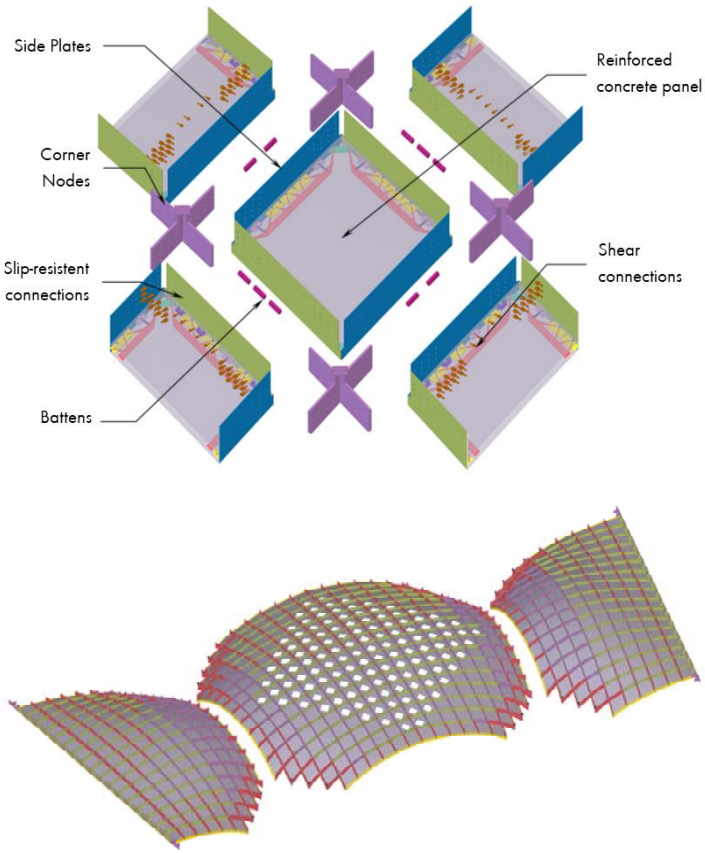
4. Shell System

4.1. Components

The shell system used for this project presents unique features from structural and architectural point of view, but also with regard to its innovative production and construction methodology (Fig. 6). Thanks to the extensive use of prefabrication, the production of these structures can be done rapidly and with very high quality. Furthermore, avoiding expensive scaffolding substructures in favor of self-supporting trusses the construction work can be accelerated, thus further optimizing time and costs.

The structural system consists mainly of three components: the steel Side Plates, the steel Corner Nodes and the double-curved reinforced concrete panels (Fig. 6). The Side Plates and the reinforced concrete panels form the principal modular composite element of the system: the so-called Cassettes. The lower edge of the Side Plates is a freeform spline matching exactly the edge of the reinforced concrete panels. The depth of these plates varies between 560 mm in the central area of each shell up to 1300 mm in the edge zones. This influences in a positive manner the bending capacity and stiffness of the perimetral zones of the shell. Depending on the structural utilization, the wall thickness of the Side Plates normally varies between 10 and 16 mm. In order to achieve the required accuracy with regard to the shape of the plates and the positioning of holes, the Side Plates are manufactured through automated computer numerical controlled (CNC) machines. The lower edge of the Side Plates is beveled to a minimum thickness of 2 mm; the steel content compared to the exposed concrete surface is almost invisible, thus achieving the required architectural appearance (Fig. 10).

The reinforced concrete panels have a thickness of 160 mm. Their geometry was optimized in order to achieve ruled surfaces, thus allowing easier manufacturing processes. Side Plates and reinforced concrete panels are coupled together by specific shear connections, which ensure a correct transfer of the shear forces from the panes into the Side Plates as well as a connection of the rebar.



The shell structure consists of a total of approx. 37,000 Shell Cassettes and 41,000 Corner Nodes. More than two million bolts are required to connect all elements.

Each Corner Node (Fig.10 left) consists of four steel plates with a thickness of 40 mm. These plates are welded together by an automated electro-slag welding process, so that many thousands of geometrically different nodes could be manufactured with very high precision.

The connection between the Corner Nodes and Side Plates is made by slip resistant bolted connections (M30 F3125M Grade A490). The number of bolts per connection varies between 9 and 30 bolts. In order to guarantee the necessary slip resistance and corrosion protection of the connection, the Side Plates and Corner Node were first sandblasted and then coated with TSA (Thermal Spray Aluminum).

Figure 6. Top: The main components of the shell structure. Bottom: Tekla model of the Shell. [© WSS]

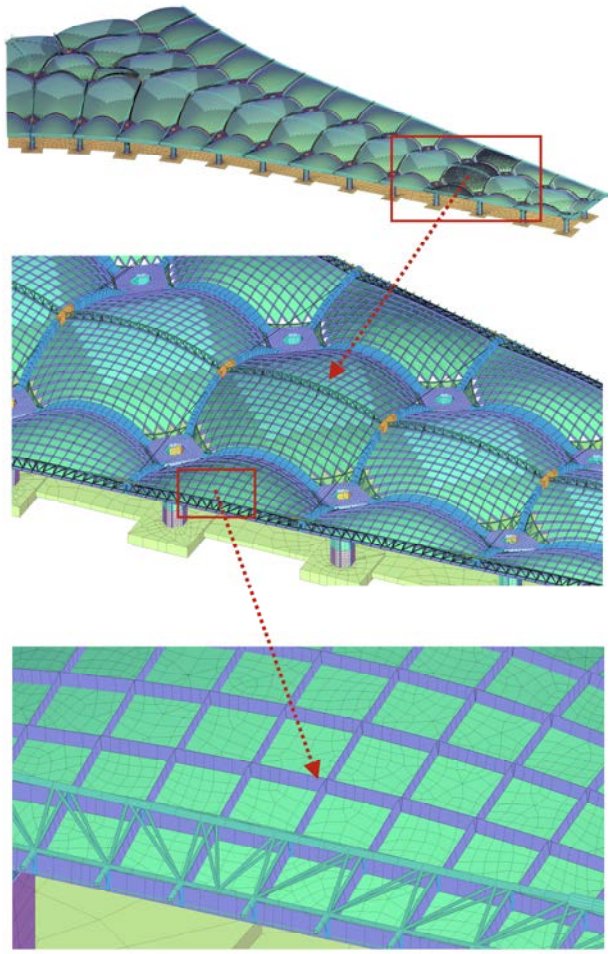
Once all elements are joined together, the shell exhibits a structural behavior that can be considered as the combination between a steel grid shell and a continuous reinforced concrete shell. The Side Plates determine the axial and out of plane bending stiffness of the shell in both main directions. The reinforced concrete panels act as an eccentric bracing system. They contribute to the local stability of the Side Plates and to the in-plane stiffness of the shell itself. Due to a small gap between the Cassettes, the panels are subject almost exclusively to membrane shear forces.

The most relevant aspect of the system is its structural behavior under thermal loads, namely its "ability to breath". The Cassettes are mainly linked to each other by Corner Nodes, which are placed eccentrically. Furthermore, thanks to the 40 mm gap between the individual Cassettes, none of them is directly constrained by the others. For these two reasons, when the shell is subject to temperature changes (and not subject to external constraints), it tends to bend out of plane changing slightly its shape and reducing in this way the locked-in constrained internal thermal stresses. Considering the dimensions of the structure and the absence of movement joints, this specific behavior is the key feature of the entire structural system.

4.2. Structural Design

The design of the shell structure can be divided into three main areas:

1. Determination of the optimal structural system for the FE calculations;
2. Determination of the design forces acting on each component (Side Plates, Corner Nodes, shear connections, reinforced concrete panels, etc.);
3. Definition of the geometry and mechanical properties of each component. Due to the complexity of the structural system from one side and the dimension of the building from the other, two different modeling methods (Global FE Model and Detailed FE Model) were used.



The Global FE Model was used for the design of Ribs, Spines, column, trusses, and also to investigate the dynamic natural frequencies of the building. In this case the shell structure was modeled with some simplifications: each reinforced concrete panel was defined as a single shell element with reduced stiffness and each couple of corresponding Side Plates was defined as a single eccentric steel flat profile. This approach allowed for the modelling of the entire building and a realistic simulation of the stiffness of the shell structure, hence a realistic distribution of loads across all components.

In the Detailed FE Model (Fig. 7), used for the design of the structural component of the shell structure itself (Side Plates, Corner Nodes, etc.), the mesh size of the reinforced concrete panels and the steel profiles were refined; in order to simulate the gap between the panels, specific boundary conditions were defined. In this way it was possible to better define the specific mechanical behavior of the shell and better understand the load paths within it.

The stiffness of both models was calibrated with higher complexity model, sensitivity analyses, (carried out to better consider the influence of different parameters) and also physical testing. These processes were mostly automated by scripting to enable the necessary iterations or to test several set-ups with different scales, hence ensured higher reliability of the process.

Figure 7. Detailed FE-Model. [© WSS]

Due to the geometrical complexity, the determination of the design forces as well as the strength of each component is very complex. Even using the Detailed FE Model, not all the geometrical characteristics of the structural elements (eccentricities, gaps, number of bolts, etc.) can be modelled. Furthermore due to the composite behavior of the system the design forces acting on the different components (e.g. bolts group) are a function of a combination of forces present in the Side Plates with the membrane forces present in the reinforced concrete panels; this behavior cannot be output directly from the FE model, but need specific post-processing.

The entire design, checking, and optimization of the 37,000 Cassettes and 41,000 Corner Nodes was done parametrically through project-specific design software developed in-house (called Shell Cassette Design Tool). This design software is composed of three modules. The first module reads the design forced calculated in the Detailed FE Models.

The second one reads all significant geometrical information characterizing the structural elements (depth, thickness, number of bolts, angles, eccentricities, etc.). This information is then stored in the Central Data Model discussed in section 3.2.

The third module calculates the relevant failure criteria for each element (plate strength, block shear, local buckling, etc.) and defines the total utilization of each element. Finally the forth module initiates an iterative optimization process of each element with the aim of finding the minimum amount of material (thickness Side Plates, dimension Fin Plate, amount of bolts, etc.) which is strictly required for the design forces present. Within the optimization process was also embedded the design of the slip critical bolted connections with the iterative calculation method called Instantaneous Center of Rotation (see ASTM 360-16). Instead of using the elastic method, this alternative procedure provided a realistic determination of the forces acting on each bolt of the connection allowing in this way an optimization of the number of bolts required.

Local stability of the Side Plates was checked as per AISC 360 chapter C with the Direct Analysis Method considering forces at ULS. Also in this case the verifications were done parametrically within the already described design software, considering the precise strength and design forces acting on each of two adjacent Side Plates. In order to define the design strength of each possible couple of adjacent Side Plates, parametric numerical models considering different failure mechanisms and initial imperfection shapes were used.

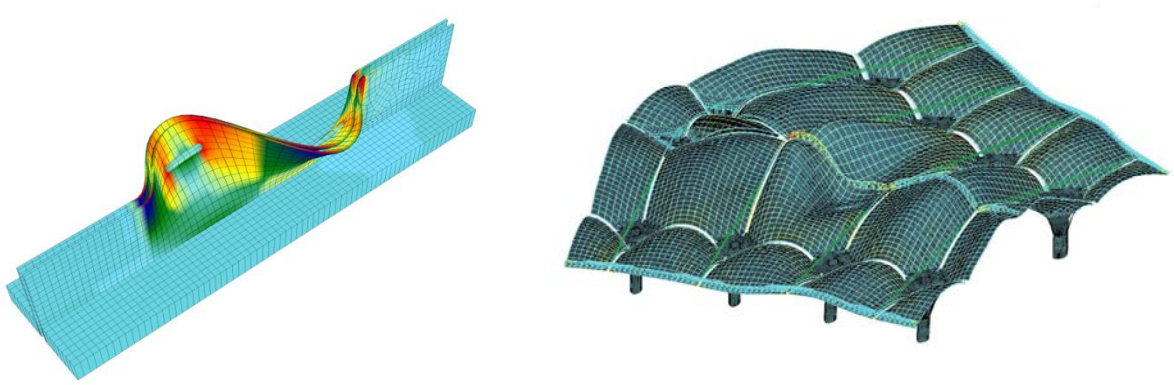


Figure 8. Left: Side Plates local stability. Right: Geometrical non-linear Global Buckling analyses. [© WSS]

The global stability of the single shells was also studied following the principles described in the standard AISC 360 chapter C. In particular Geometrical Non-linear Global Buckling analyses with different imperfection shapes and possible reduction of the stiffness of the shell itself and the supporting structures were used. These analyses showed that this structural system presents a high in-plane and especially out-of-plane stiffness. Furthermore at the level of the design loads the shell shows almost a geometrical linear behavior. Stiffness reductions influence the deformation but are not dominant for the main utilization of the structural components, showing high redundancy of the system, hence possibility of load redistribution.

4.3. Fabrication and construction

Producing and assembling the various components with the required precision was one of the critical aspects of the project. Due to the very tight tolerance between Cassettes and Corner Nodes, as well as the difficulties related to the manufacturing of the double curved reinforced concrete panels, the quality of the production model and their integration into the fabrication process played a decisive role. All steel elements of the shells (including the bolted connections) were defined by WSS into BIM-Tekla models (Fig.6). These models were at the same time the principal platform for coordination and the primary reference for production and installation. In fact the final coordination and detailing of the steel structures (including trusses and secondary steel structures) was based on these models. Furthermore all the production processes including controlling of the CNC cutting machines, welding machines and the coating applying robots, were based on the WSS Tekla Models.



The production of the reinforced concrete panels was also based on digital models. Panel surfaces were defined through an optimization process which transformed the initial freeform surfaces into developable surface. Thanks to the use of an innovative production process based on adaptive formwork tables made by Adapa (Fig. 9), the Rhinoceros NURBS surfaces where interpreted and used as reference for the computer-controlled hydraulic cylinders, which define the shape of the formwork.

Figure 9. Adaptive formwork [© Adapa].



Figure 10. Left: Corner Nodes. Right: Shell Cassettes Mock-up. [© Limak]

5. Conclusion

Even though in recent years the digitalization of the construction industry has made significant progress, there is still a long way to go before a common digital workflow between design and production will be achieved. Moreover, the entire life cycle of the building materials, considering also their dismantling and recycling, has to be further considered and implemented. The digital tools and planning methods used and developed by the authors for this extremely complex project are only one contribution to a potential comprehensive digitalization of the construction industry. These tools and methods exemplify how planners could significantly increase the quality and cost-effectiveness especially of large-scale projects – viz. by not only contributing to greater precision in modelling, dimensioning, and manufacturing of complex structures, but also by improving coordination between all the actors involved.

Acknowledgements

The authors would like to thank the general contractor Limak Insaat Kuwait, its management and in particular Limak design team headed by Izzet Fikirlier, Koray Etoz and Alptekin Kibar for the good and trusting cooperation when working on the KIA project. Special thanks go to the team at Werner Sobek which worked together with the authors on the shell structure: Stephen Hagenmayer, Wolfgang Sundermann, Mario Steinlechner, Matteo Brunetti, Maximilian Karcher, Zachary Christian, Carlotta Santachiara, Alissa Beck, Eugen Chladny, Agatha Braun, Mladen Markovic, Heike Myland, Sandra Neaga-Friz, Angela Geisler, and Johannes Finster. Many thanks go to all our other colleagues who also worked on the different parts of the project and who are not mentioned here. Their knowledge, dedication and passion were invaluable to the successful realization of the project. Special thanks go to Frank Heinlein for his support and critical feedback during the elaboration of this manuscript.

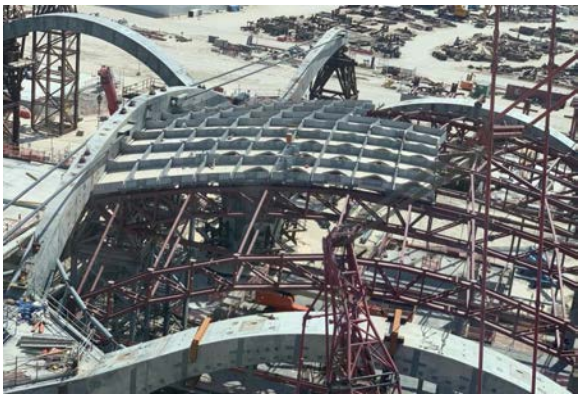


Figure 11. Construction Site, installed Shell Cassettes. May 2019. [© Limak]

Project participants

Client: Ministry of Public Works, Kuwait.
Architects: Foster + Partners, London / United Kingdom
Construction Company: Limak Insaat Kuwait.
Structural and Facade Design (to tender): Arup, London / United Kingdom; Gulf Consult, Kuwait
Structural and Facade Engineering (from tender): Werner Sobek Stuttgart / Germany
Execution Architects and BIM Management (from tender): AECOM, Madrid & London
Consulting on construction phases: Robert Bird Group, Brisbane / Australia

References

[1] W. Sobek, D. Klein and T. Winterstetter, "Hochkomplexe Geometrie. Das neue Mercedes-Benz-Museum in Stuttgart," *Beratende Ingenieure 10*, pp. 16-21, 2005.

[2] L. Blandini, A. Schuster and W. Sobek, "The Railway Station „Stuttgart 21" – Structural Modelling and Fabrication of Double Curved Concrete Structure," *Complexity and Responsibility – Proceedings of the Design Modelling Symposium. Berlin*, pp. 217-224, 2011.

[3] L. Blandini, T. Schmidt, W. Winterstetter, and W. Sobek, "Fassaden mit komplexer Geometrie – am Beispiel des Enzo Ferrari Museums in Modena," *Bautechnik 91*, H. 3, pp. 175-180, 2014.

[4] T. Winterstetter, A. Toth, W. Sobek, et al. "National Museum of Qatar. Stahlbau, Gebäudehülle und 3D-BIM in höchster Komplexität," *Stahlbau 86,* No. 4, pp. 346-350, 2017.

[5] L. Blandini, G. Nieri and W. Sobek, "Das Schalentragwerk des Kuwait International Airport Terminal 2 – Bemessung und Ausführung einer komplexen Megastruktur in Zeiten der Digitalisierung," *Stahlbau 88*, No. 3, pp. 194-202, March 2019.

[6] Foster + Partners, "Designs unveiled for Kuwait International Airport," [Online]. Available: www.fosterandpartners.com/projects/kuwait-international-airport/. [Accessed May 30, 2019

[7] K. Josefsson, "Symmetry as Geometry Kuwait International Airport," *Architectural Design 83*, No. 2, March/April 2013.

[8] D. Munro, M. Arkinstall and T. Carfrae, "Kuwait International Airport Terminal II: the development of a new form of precast composite shell," *Proceedings of IASS Annual Symposium 2018, Boston*, 16-20 July 2018.

Proceedings of the IASS Annual Symposium 2019 – Structural Membranes 2019
Form and Force
7 – 10 October 2019, Barcelona, Spain
C. Lázaro, K.-U. Bletzinger, E. Oñate (eds.)

Strengthening of the Transfer Floor of Berlin's Steglitzer Kreisel

Diego APELLÁNIZ*, Claudia GROTH, Holger ALPERMANN, Christoph GENGNAGEL

*B+G Ingenieure Bollinger und Grohmann GmbH
Alt-Moabit 103, 10559 Berlin
dapellaniz@bollinger-grohmann.de

Abstract

The Steglitzer Kreisel is an office building complex located in Berlin which has undergone a refurbishment project. The main element of this complex is a 30-story high-rise building that stands 120 meters above the ground and is currently the third tallest building in Berlin. The transfer floor consists of 4.8-meter-high built-up steel beams, which provide support for the closely spaced columns of the upper levels and transfer their loads into the atrium mega-columns on which these beams rest. This paper presents the methodology employed to evaluate and strengthen the transfer beams. Firstly, the failure modes are identified and classified into plate buckling and excessive yielding and the FEM models and code-based calculations are presented. Secondly, the reinforcement of the critical areas through the addition of both stiffeners and welded steel plates - according to the failure mode - is discussed. Finally, the execution process and its multiple constraints are described. This approach has been proven to be an elegant and economical solution to a real-world complex engineering problem. The capacity of the existing structure is fully made use of and the execution process affects neither the remaining construction works nor the existing installations. Furthermore, this methodology can also be used to evaluate a wide range of existing plate- and shell-like steel structures.

Keywords: high-rise, historic building, non-linear finite element analysis, plastic behavior, plate buckling, deep beam, strengthening under load, material characterization.

1. Introduction

The Steglitzer Kreisel is an office building complex located in Berlin which was erected in the 1970s. The main element of this complex is a 30-story high-rise building that stands 120 meters above the ground and is currently the third tallest building in Berlin (Figure 1a). Due to the architectural requirement for a diaphanous atrium, the level above it was originally designed as a transfer floor in order to accommodate the discontinuity of the vertical columns (Figure 1c).

The renovation project this building has undergone has had as its purpose the change of use into a residential building, so that new elements, such as balconies and bay windows, were added to the existing structure (Figure 1b). Although the change of use from office- to a residential building implies a reduction in the floor live loads according to the building codes, the addition of these supplementary elements led to new loads, which were not present on the original building.

As a result, there was a variation in the reaction forces of the columns over the transfer floor. Although there was no increase in the loads transmitted to the atrium columns and therefore to the foundation, the transfer beams had to be analyzed and partially strengthened, since their state stress was modified through this renovation project.

Copyright © 2019 by B+G Ingenieure Bollinger und Grohmann GmbH
Published by the International Association for Shell and Spatial Structures (IASS) with permission.

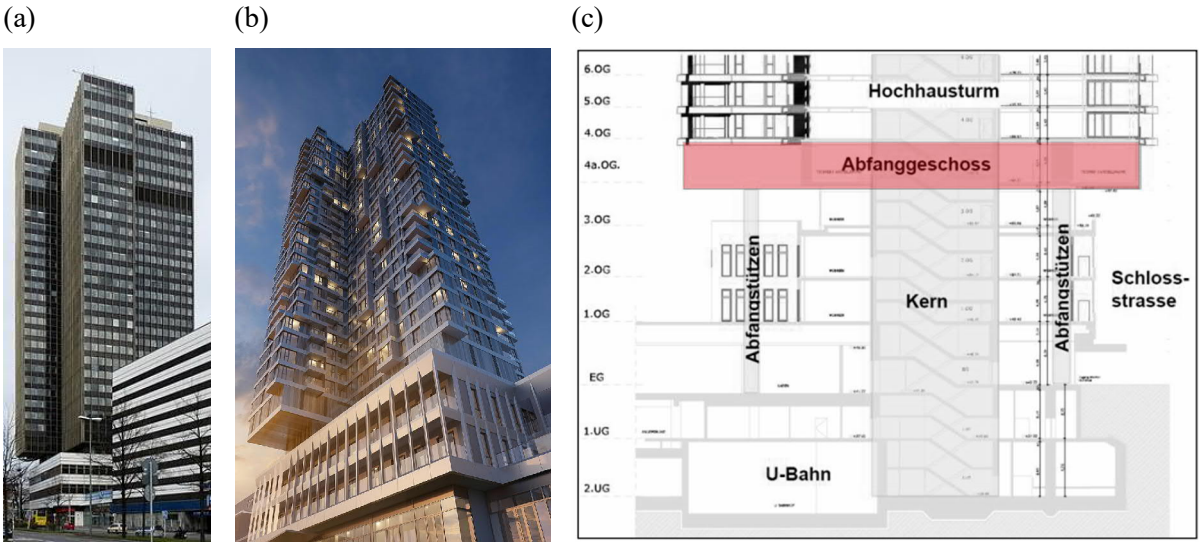


Figure 1: (a) View of the Steglitzer Kreisel before the renovation process. (b) Visualization of the renovated building with a new façade, balconies and bay windows © CG Gruppe [1]. (c) Building section with the transfer floor marked in red.

2. Description of the existing structure

The transfer floor consists of 18 4.8-meter-high built-up steel beams, which provide support for the closely spaced columns of the upper levels and transfer their loads into the atrium mega-columns on which these beams rest. They constitute an orthogonal grid on plan (Figure 2a). Although neighbor beams are rigidly connected, this structural system can be regarded as highly isostatic, since each of the beams rest on just two simple supports. The span-to-depth ratios range from 0.9 to 2.7 so these structural elements have to be clearly treated as deep beams.

The thicknesses of the steel plates that constitute these deep beams range from 6 to 35 mm – beam webs vary from 12 to 28 mm thick – and there were two steel grades indistinctly used for the different steel elements. These were defined in the original drawings (Figure 2a) as St37 and St52 – yield strength equivalent to S235 and S355. Each beam is made up of two 2.4 m high beams, whose flanges are connected through a longitudinal bolted joint. The connections between perpendicular beams were resolved as bolted joints as well. Apart from these, every other steel connection was executed as a fillet welded joint.

The transfer beams are supported by either the atrium mega-columns, the concrete core of the building or neighbor beams. The columns NP1-NP4 and NP7-NP10 (Figure 2b) have steel rectangular built-up sections with steel plates varying from 36 to 40 mm thick. On the other hand, the columns NP5-NP6 are 1800 x 1800 mm rectangular concrete columns and NP11-NP12 are circular concrete columns with a diameter of 1900 mm. POT bearings were provided between each column and lower beam flanges.

The floors of the building are made up of precast concrete slabs that rest on secondary steel beams and are monolithically connected through a 4cm thick in situ concrete layer, so that they can be considered as rigid diaphragms who provide lateral support for the transfer beams.

(a) (b)

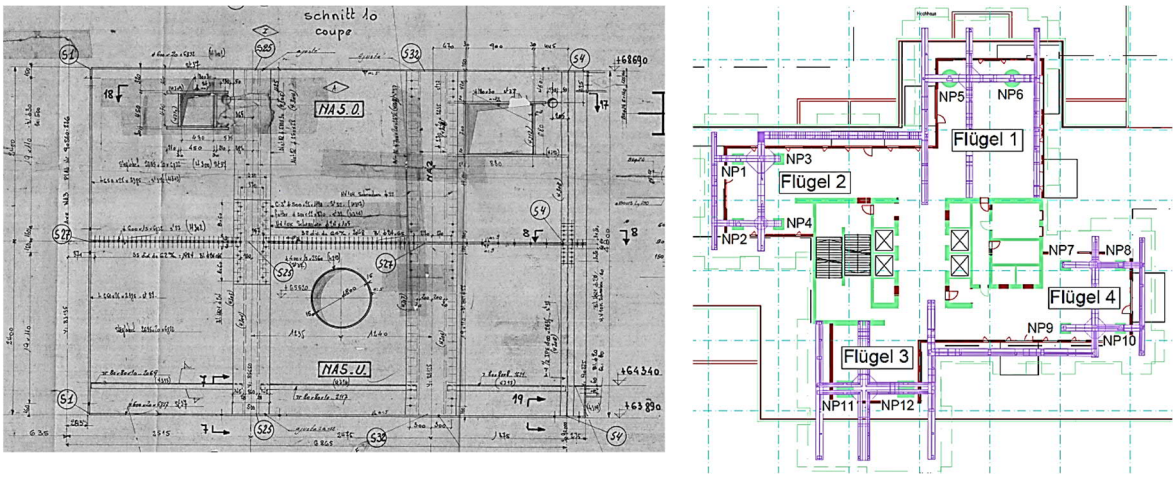


Figure 2: (a) Original elevation drawing of one of the transfer beams. (b) Floor plan of the transfer level with transfer beams marked in purple.

3. Material characterization

As the steel plates that made up the transfer beams were produced almost 50 years ago, the building-materials laboratories BARG and SLV Berlin-Brandenburg were commissioned to carry out a test campaign in order to evaluate if the actual steel properties correspond to those specified in the original project. The structure of the transfer beams – plate thicknesses and disposition of openings and stiffeners – is to a large extent heterogeneous and varies from one beam to another. For this reason, 54 steel samples were extracted from the most representative positions and subjected to tensile testing (Figure 3a).

(a) (b)



Figure 3: (a) Steel samples extracted from the webs of the transfer beams. (b) 3D scanning of the transfer beams.

Stress-strain curves were obtained through these tests for each steel sample, from which the steel mechanical properties were deduced and the steel plates could be therefore characterized according to [3]. These results showed slightly lower values of the yield strength in four of the eighteen transfer beams in comparison to the steel grades defined in the original project. Ultimate tensile strengths were also partially lower. These values were later taken into account for the definition of the stress-strain diagrams that were used to define material properties in the non-linear finite element models.

These samples also served to measure the thickness of the steel plates. Beside these tests, six bolts were extracted and subjected to strength testing. Bolt classes did not correspond in every case to those specified in the documents of the original project – class 4.8 bolts instead of 10.9, therefore, a class of 4.8 was assumed for every bolted joint on the safe side. Finally, POT supports were checked through visual inspection and no durability issues were observed.

Besides this material testing campaign, the geometry of all transfer beams was analyzed through a 3D-scaner (Figure 3b). In some steel panels, there were detected bumps of up to 12 mm (B/200).

4. Approach to the strengthening problem

4.1. Verifications in ULS and SLS

The following criteria have to be fulfilled according to [2]:

- For structures susceptible to buckling: attainment of the maximum load.
- For regions subjected to tensile stresses: attainment of a limiting value of the principal membrane strain – the recommended limit of 5% was adopted according to the test results.

The following additional criteria were adopted as well:

- The steel yield strength must not be reached in any point of the structure in SLS.
- Steel yielding must remain within limited areas in ULS.

4.2. Strengthening of the transfer beams

In order to fulfill these criteria, the transfer beams had to be partially strengthened. The typology of the reinforcements was chosen according to the governing failure mode:

- Excessive yielding: additional steel sheets welded to the transfer beams (Figure 4a). Different shapes were chosen depending on whether it was a case of local yielding or the whole steel panel was overstressed.
- Plate buckling: additional T-shape stiffeners were welded to the transfer beams (Figure 4b). This was the case of the thinnest steel panels.

In order that the strengthening of steel beams is effective, it has to be applied when the structural elements are unloaded, so that reinforcements can contribute to the steel beams to a greater extent. In this particular case, it was impossible to carry out a propping of the transfer floor, because on one side of the building, there is an underground line and on the other, there is the Schlossstr. Street underneath the transfer floor (Figure 1c).

For this reason, there was a necessity to unload the building before proceeding with the strengthening of the transfer beams: the existing façade had to be completely dissembled (Figure 1b) before this operation, the floor pavement was removed and no live load was allowed during the strengthening execution process.

(a) (b)

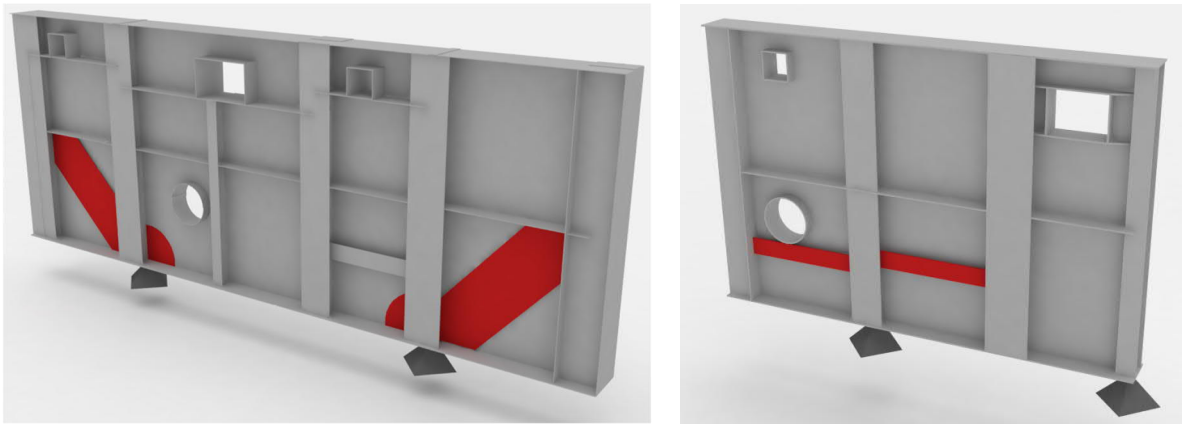


Figure 4: Transfer beams were strengthened through the addition of welded steel plates (a) and T-shaped stiffeners (b).

4.3. Structural analysis

In order to be allowed to make use of the plastic capacity of the existing structure, it was necessary [2] to carry out a non-linear analysis: both with non-linear material behavior and non-linear structural behavior – third order large deformation analysis with imperfections.

The tension-deformation curve suggested by the norm (Figure 5a) was calibrated according to the results of the material characterization campaign (Figure 5b). The imperfection values specified in the norm were also calibrated through the results of the 3D-scanning campaign – however, these can only be directly compared to the geometric part of the code-based imperfections, not to the structural part regarding possible residual stress, etc.

(a) (b)

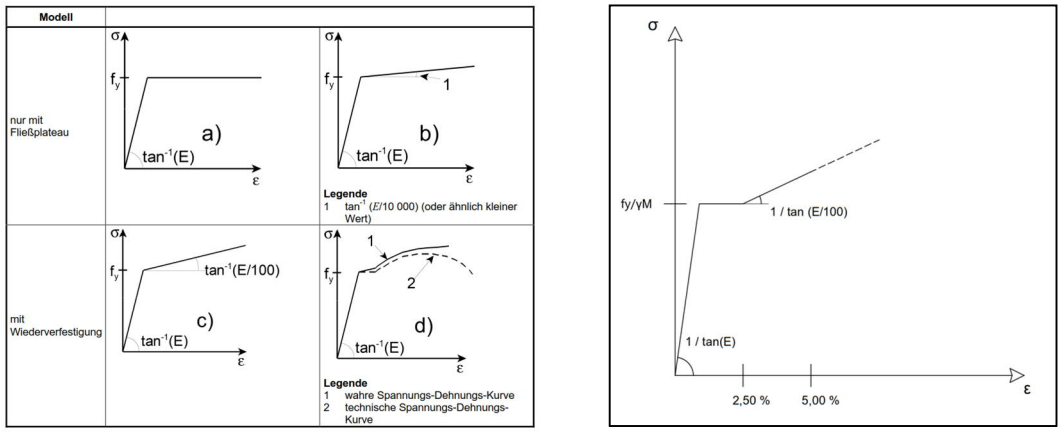


Figure 5: (a) Tension-deformation curves suggested by the norm [2]. (b) Tension-deformation curve used in the finite element models calibrated through the material characterization campaign.

The strengthening process was simulated through a construction stage analysis with the following stages: (1) existing structure with office loads, (2) unloaded structure, (3) strengthened structure with loads from the renovated building.

5. Finite element models

5.1. Modelling process

3D finite element models were developed with the software Dlubal RFEM (Figure 7). The transfer beams were modeled as slab-elements in order to simulate yielding and plate buckling properly, whereas secondary beams were modeled as member-elements.

Due to the construction process and the different stress levels between steel reinforcements and the existing structure, reinforcement plates had to be modelled as additional surface elements connected through rigid links – very stiff member elements – to the existing structure (Figure 5a).

In order to avoid stress concentrations and hence convergence difficulties in the nonlinear analysis, supports and loaded nodes were rigidly connected to the neighbor nodes (Figure 5b) – this probably simulates even more accurately the actual behavior of the contact surface with existing columns.

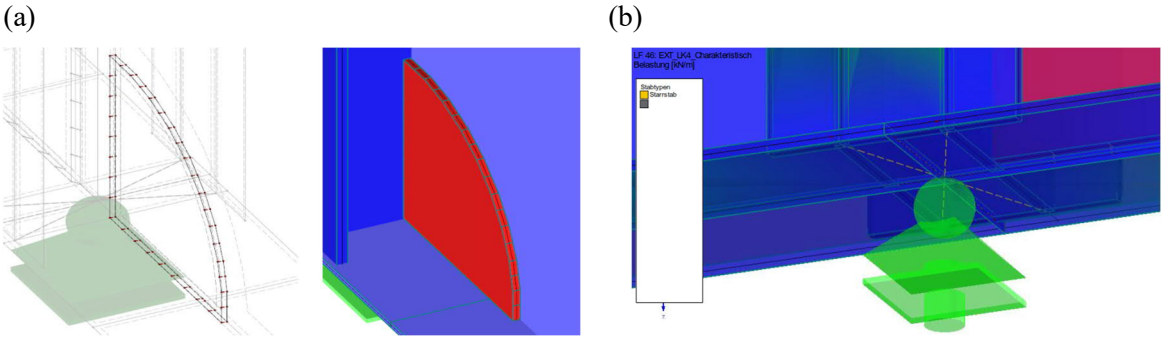


Figure 6: Modelling process of steel reinforcement plates (a) and supports (b).

5.2. Global models

The two global models were used: for a preliminary elastic analysis, to compare reaction forces to the values of the original project, to check the longitudinal bolted joint of the transfer beams and to help model correctly the boundary conditions of the local models. However, non-linear analysis could not converge on these complex models and, therefore, local models had to be used for these calculations.

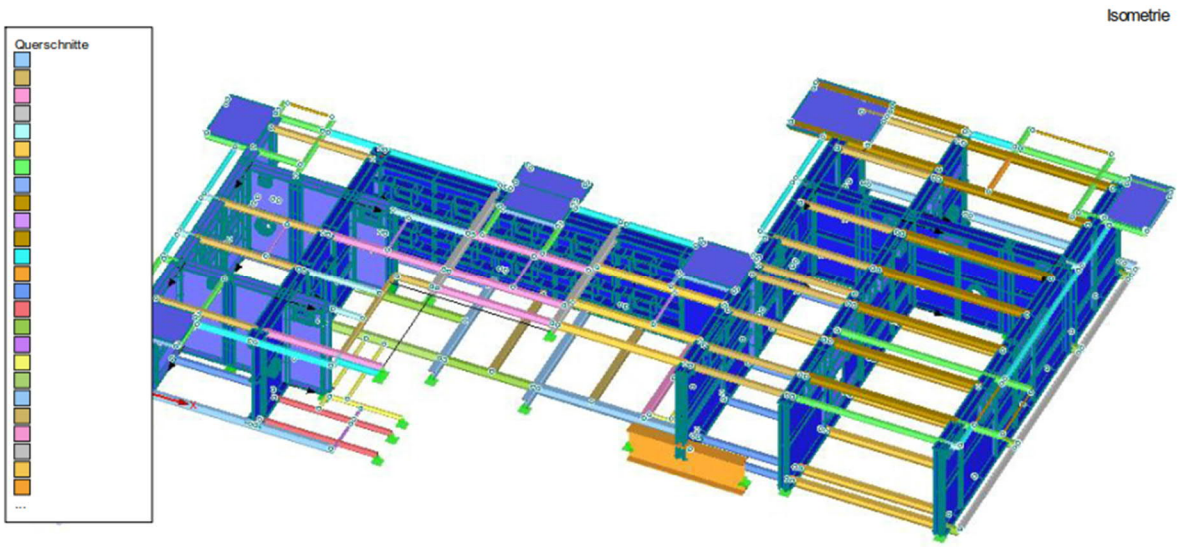


Figure 7: One of the two global models that make up the transfer floor.

5.3. Local models

Steel reinforcements were dimensioned so that there is no yielding at the end of the construction stage analysis in SLS (Figure 8a) and yielding is limited to local areas in ULS (Figure 8b).

(a) (b)

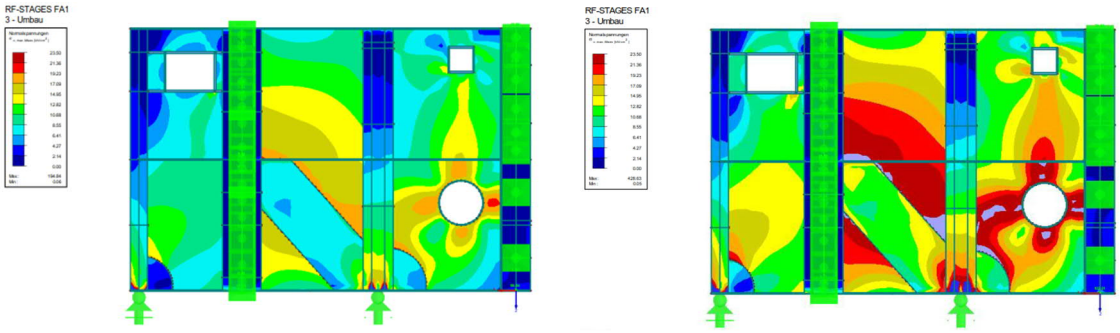


Figure 8: Von-Mises stress graph in SLS (a) and ULS (b) – areas over yielding point in purple.

Plate buckling was checked through an incremental stability analysis in the context of a third order large deformation analysis with imperfections (Figure 9a). If the critical load factor (Figure 9b) was below the specified limit [3] of $\alpha_u \approx 1.15$, additional stiffeners were added to prevent that buckling mode.

(a) (b)

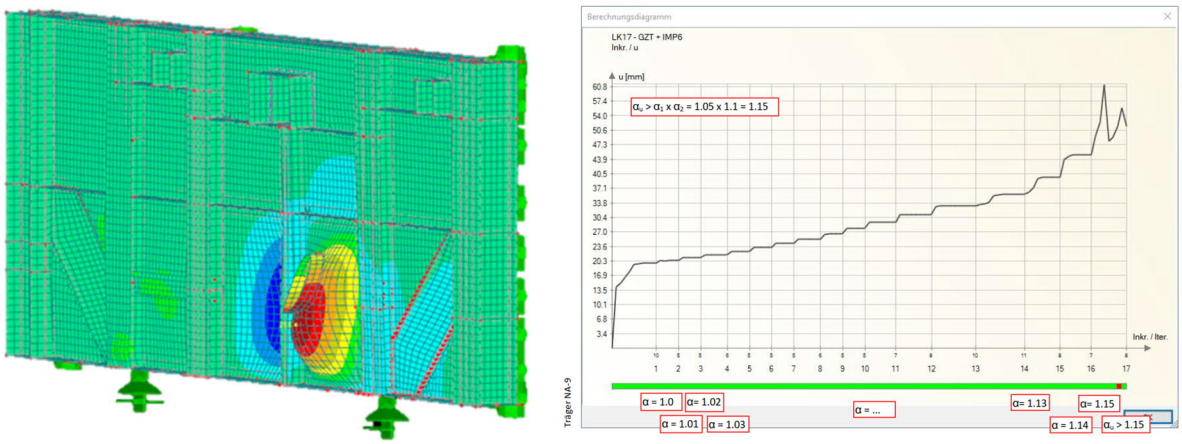


Figure 9: (a) Incremental stability analysis of a transfer beam. (b) Corresponding load-displacement diagram.

6. Execution process

The execution process was strongly influenced by the fact that it was not possible to carry out a propping of the transfer floor and, therefore, the transfer beams were required to have enough strength capacity during the welding process when the building was “unloaded”.

For this reason, a welding sequence in the form of interrupted short fillet welds was adopted (Figure 10a), so that temperature in the existing steel sheets remained under admissible values. This was controlled through the installation of thermal sensors. Furthermore, another reason to avoid the spread of high temperatures through the steel plates, was to prevent the POT supports from burning.

Finally, the largest reinforcement plates had to be break down into few parts, in order to make their installation possible (Figure 10b).

(a) (b)

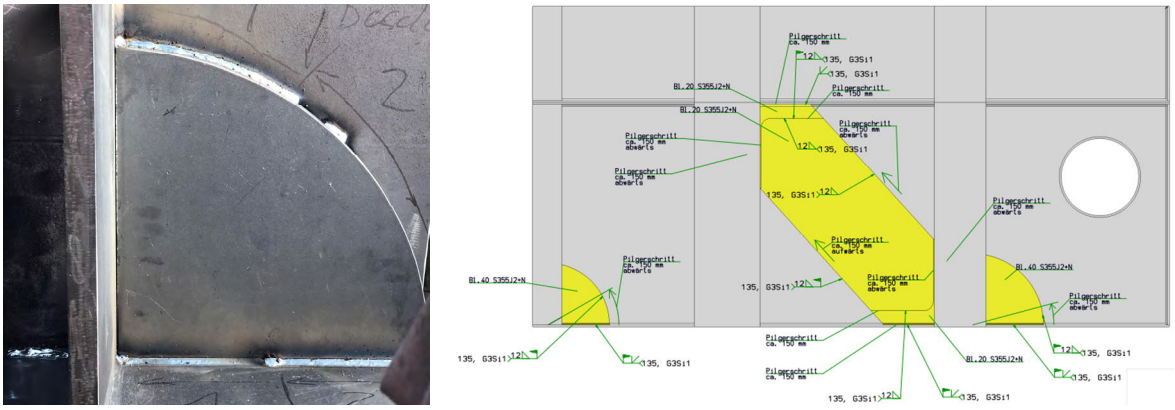


Figure 10: (a) Welding process of a steel reinforcement plate. (b) Execution plan of the reinforcement elements.

7. Conclusion

The change of use of an existing building is a practice that is becoming more and more common, which usually leads to the reinforcement or strengthening of its structural elements, in order to adapt them to a new situation, for which they were not designed.

The approach followed to strengthen the transfer floor of the Steglitzer Kreisel, although based on complex calculation methods, has led to an apparently simple and yet elegant solution (Figure 4), which also has turned out to be certainly economical, since it makes full use of the capacity of the existing structure.

Although the structure of the transfer floor and the critical boundary conditions of this project are by no means ordinary, this approach could be perfectly adapted and used to assess and strengthen other existing plate- and shell-like steel structures.

References

[1] K. Lange “Der Steglitzer Kreisel wird zu ÜBerlin,” *Berliner Morgenpost*, 19/02/2018.

[2] DIN EN 1993-1-5; Eurocode 3: Bemessung und Konstruktion von Stahlbauten – Teil 1-5: Plattenförmige Bauteile; Deutsche Fassung EN 1993-1-5:2006 + AC:2009; Anhang C "Berechnungen mit der Finite-Element-Methode (FEM)".

[3] DIN EN 1990; Eurocode: Grundlagen der Tragwerksplanung; Deutsche Fassung EN 1990:2002 + A1:2005 + A1:2005/AC:2010; Anhang D "Versuchsgestütze Bemessung".

[4] Stefan Neuhaeuser, Holger Alpermann, Christoph Gengnagel “Engineering the new Merck Innovation Center“, *IASS Symposium 2017 “Interfaces: architecture . engineering . science”*, September 25 - 28th, 2017, Hamburg, Germany

[5] K. Bollinger, M. Grohmann, H. Peseke, “The Refurbishment of the Wholesale Market Hall Frankfurt,” *IASS Symposium 2015 "Future Visions",* 17 - 20 August 2015, Amsterdam, The Netherlands

[6] K. Bollinger, C. Brensing, M. Grohmann, K. De Rycke, “Authentisch und modern - Le Nouveau Carreau du Temple,” *Ingenieurbaukunst 2016*, Ernst & Sohn, Berlin, 2015

Proceedings of the IASS Annual Symposium 2019 – Structural Membranes 2019
Form and Force
7 – 10 October 2019, Barcelona, Spain
C. Lázaro, K.-U. Bletzinger, E. Oñate (eds.)

Structural Design for Arch-shaped Cantilever Beams "Oshika Ring of Hope"

Yasumasa SHIMIZU*, Masahiro ONUMA [a], Kuniaki ITO [b]

* Director of Shimizu Structural Engineers Co., Ltd.
3-15-7-102, Otsuka, Bunkyoku, Tokyo, Japan 112-0012
Email: shimizu@shise.co.jp
URL: http://shise.co.jp/
[a] Prof. of TOHOKU Institute of Technology
[b] Prof. Emeritus of TOHOKU Univ. & Kuniaki ITO Arch. & associates

Abstract

The monument is divided in four elements built of reinforced concrete: two prefabricated cantilever elements that define the semi arch and their supporting bases, raised on site. The section of the beams changes, growing in size while reaching the free edge. The slanting arch elements bring several complications for structural stability, the torque moment is an effect that has been considered in the design of the wall joints. The durability of the monument was taken into consideration too, in fact under seismic stress, the particular section of the beam is designed not to crack. The inclination of the semi arch follows the position of the Sun: on the day of commemoration, the 11th of March, at 14:46, the sunrays will perfectly fit in the gap created between the cantilever beams. The sunbeams will enlighten the shadows of the arch marking the visitors souls with the memory of the tragedy.

Keywords: monument, earthquake design, cantilever beam, detailing and construction, precast concrete



Fig.1 View of the monument (courtesy of Kuniaki ITO)

Copyright © 2019 by Yasumasa SHIMIZU, Masahiro ONUMA, Kuniaki ITO
Published by the International Association for Shell and Spatial Structures (IASS) with permission.

1. Introduction

The aim of this paper is to explain the structural design and the construction process of the "Oshika Ring of Hope", previous report [1] shows outline of this project. The main points of the structural design are the following.

- The monument is designed taking into consideration the transportation and durability of each element.
- Since the torsional and the bending moments in the beams are important, a variable section that take care of this factor has been thought.
- The joints used to connect all the elements are the simplest possible, considering the difficulty of the construction process.

2. Structural design method

Shape of parts in consideration of on-site transportation and durability. The site was located at a corner of the Rias coastline, and it was necessary to transport the meandering road along the coast, so it was made to be a size that can be transported by a 6m track and made by solid concrete casting and curing by precasting. The covering depth was 60 mm against the standard 50 mm covering thickness of a Japanese building. Stress cracking does not occur as much as possible. The FEM analysis results are shown in Fig4-5. It has been confirmed that the beam stress is less than the following equation under long-term and seismic loading. The following equation shows bending crack strength (Architectural Institute of Japan RC Standard).

$$\sigma_t = 0.56\sqrt{\sigma_B} = 0.56\sqrt{27} = 2.90[N/mm^2] \quad (1)$$

σ_t: bending crack strength of concrete

σ_B: compression strength of concrete (design strength of beams is 27[N/mm^2])

The base and beam should be connected with the simple joint considering the construction.

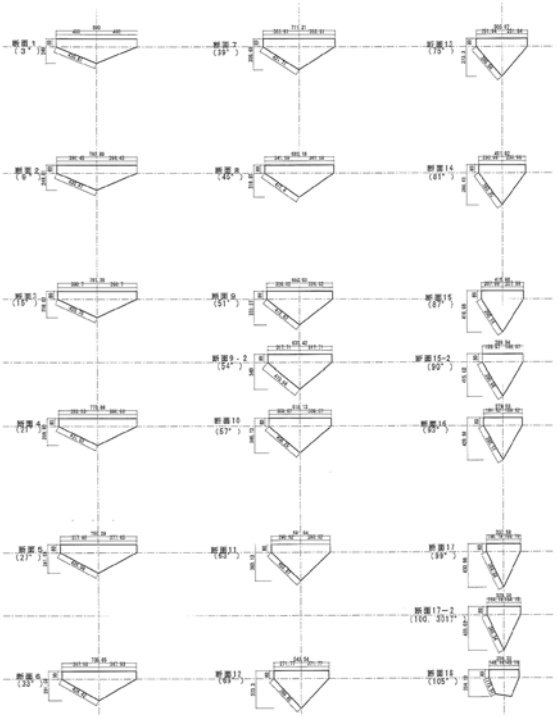


Fig.2 Variable cross section of beam

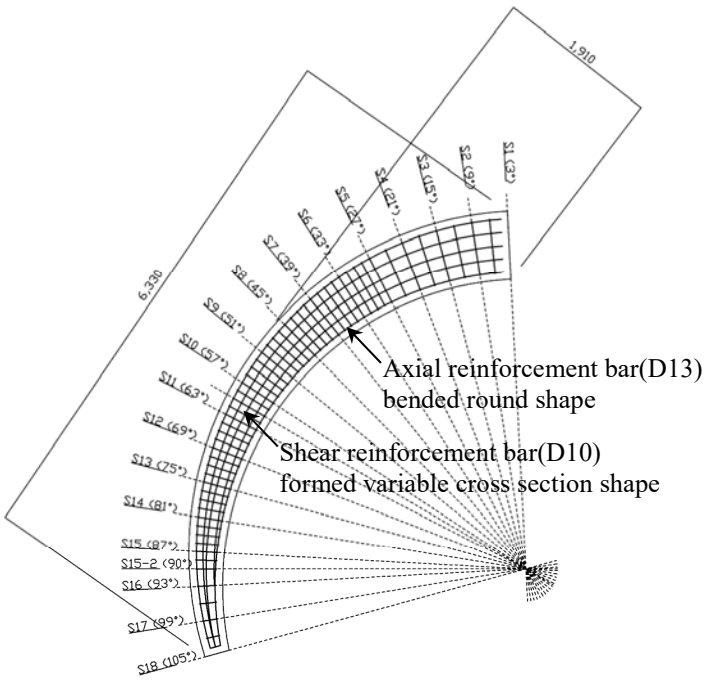


Fig.3 Beam plan and steel bar position

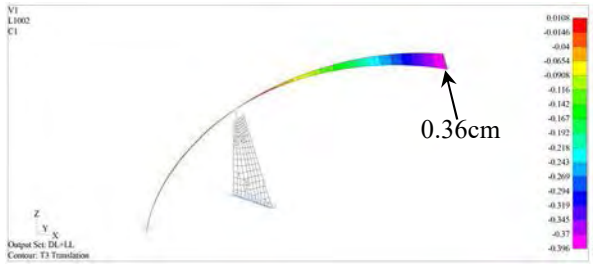


Fig.4 Result of deformation[cm] (For dead load)

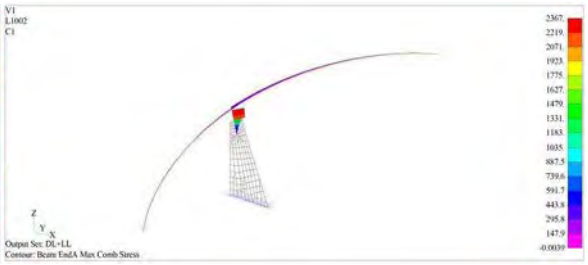


Fig.5 Result of maximum stress [N/cm^2]

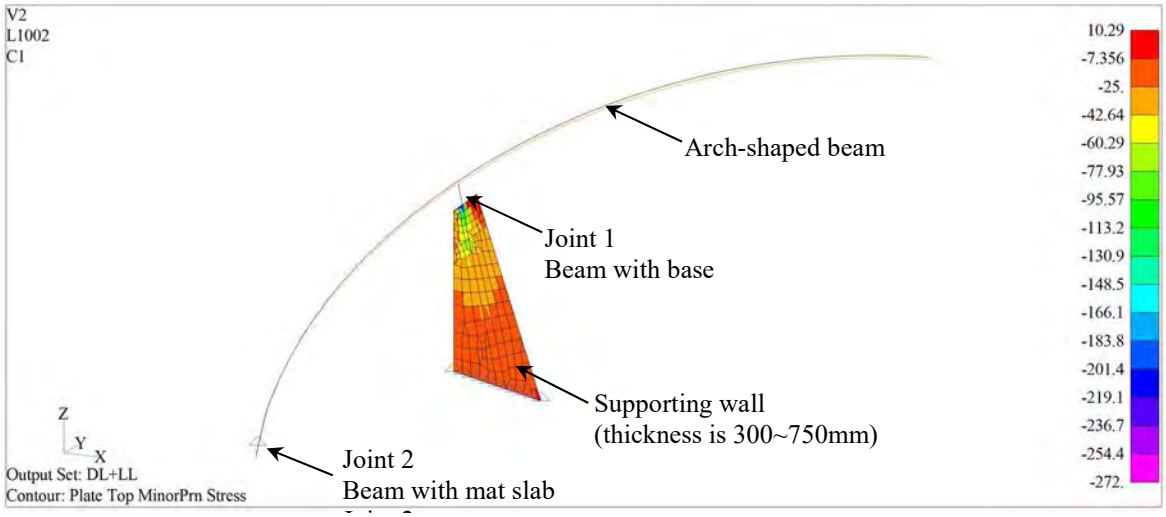
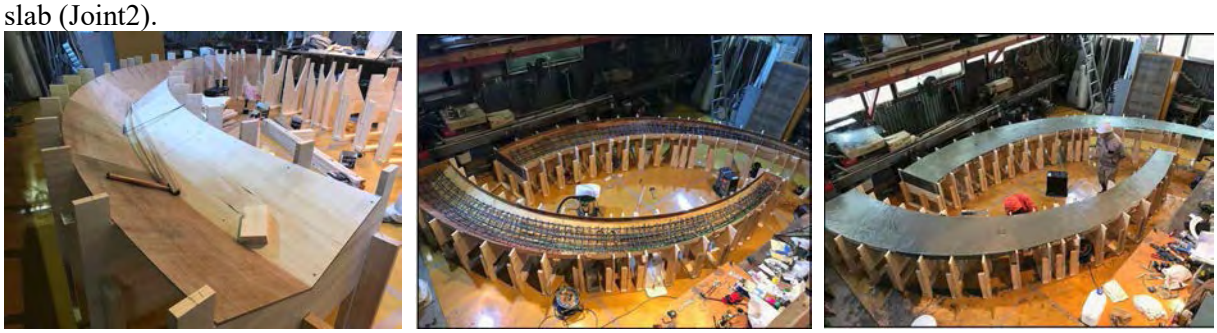


Fig.6 Plate stress result of supporting base [N/cm^2] (For dead load)

3. Construction process

The Fig.7 shows the construction process of pair arch-shaped beams casted at a factory in Sendai. The concrete was placed at the end of December 2018, when it was so cold condition in Japan. Then the beams were kept under weather conditions in need of heating curing with blankets etc. The Fig.8 shows construction of the mat slab foundation and support bases in the site. They were kept be cured for coldness too.

The right of Fig.8 shows the joint between its beam and base. The joint consists of a half column and a hole for inserting column. The half column attached to beam has cruciform (200x200mm) made by 16mm stainless steel plate and was inserted to the hole formed at the top of support wall. After inserted to the hole was filled by mortar. The Fig.9 shows setting beam to supporting base (Joint1) and slab (Joint2).



Form panel Steel bar work Concrete placement

Fig.7 Construction of the beams



Curing for coldness Form removal of supporting bases Joint1 between the beam and the base

Fig.8 Construction of supporting bases and joints



Fig.9 Setting beam to supporting base on the site

4. Conclusion

The authors felt the nature condition in this project were so severe, when visited the site on September 2018. But it was so important to pick up the appropriate structural criteria and form for this project. This monument was completed before March 11th.

Acknowledgements

First of all, authors must thank Mr. Kimiyoshi SASAKI, construction manager of Atelier Umi, who manufactured the complicate arch-shaped beams in the cold winter and convey them to the site through meandering road. Then Mr. Chikashi ITO, the foreman Yuki TAKAHASHI and other craftsmen of Marui Construction Co. Ltd completed the difficult work of hanging up beams and setting them precisely. The process of handling beams from Sendai factory of Atelier Umi to the site was carefully planed and executed.

References

[1] Masahiro ONUMA, Yasumasa SHIMIZU, Kuniaki ITO, "Enfolding Form for the Bereaved Families and the Souls of Victims in the Seashore of Ishinomaki City; Oshika Ring of Hope", *IASS Annual Symposium 2019 – Structural Membranes 2019,* 7 – 10 October 2019, Barcelona, Spain.

[2] Kuniaki ITO, Junichiro MATSUMOTO, Nobuyoshi KOWATARI, Masahiro ONUMA, "Before, At the height, After and Now of Ogatsu Inkstone Museum -a case study in the seashore area of Ishinomaki City-", *IASS Annual Symposium 2019 – Structural Membranes 2019 Form and Force,* 7 – 10 October 2019, Barcelona, Spain.

[3] Hirofumi AOKI, Yasumasa SHIMIZU, "Hysteresis Model of Low-rise Steel-frame Building and Its Seismic Performance", *Korean Society of Steel Constructions 3rd International Symposium on Steel Structures 2005*,10-14 March 2005, Seoul, Korea.

Proceedings of the IASS Annual Symposium 2019 – Structural Membranes 2019
Form and Force
7 – 10 October 2019, Barcelona, Spain
C. Lázaro, K.-U. Bletzinger, E. Oñate (eds.)

The Enfolding Form for the Bereaved Families and the Souls of Victims on the Seashore of Ishinomaki City "Oshika Ring of Hope"

Masahiro ONUMA*, Yasumasa SHIMIZU[a], Kuniaki ITO[b]

*Prof. of TOHOKU Institute of Technology
6 Futatsuzawa, Taihaku-ku, Sendai 982-8588 Japan
ohnumans@tohtech.ac.jp

[a] Director of Shimizu Structural Engineers Co., Ltd.
[b] Prof. Emeritus of TOHOKU Univ. & Kuniaki ITO Arch. & Associates

Abstract

Oshika District was seriously devastated by the 2011 earthquake and tsunami. Ishinomaki City authority solicited a proposal for a memorial installation project for the district. A consortium led by Inai Cooperative for Stone Manufacturing and Commerce (ICSM) won the competition based on the advice from the authors. The authors as advisors regarded circulation and unity of the bereaved families and the souls of victims as important, and designed the memorial from 3 points of view: 1) arch shape for the image of circulation, 2) impression with light and shadow and 3) texture of vernacular stone cenotaph and pavement, totally, the enfolding form. The monument is also designed as a time meter device. On 14:46 of March 11, the sun ray shines through the arch-shaped beams making linear shadows on the ground.

Keywords: Memorial, Arch-shaped beam, Time meter device, Local stone, Recovery from the Great East Japan Earthquake and Tsunami

1. Aim of this paper with outline of the project

In this paper, it is intended to examine ingenuities and summary of the landscape design for Oshika Memorial (Fig.1), and to derive a condition for the next report on structural design of this monument [1]. In the recovery process from the Great East Japan Earthquake, polarized movements occurred. On one end, big projects of strong infrastructures, such as huge sea walls, were built.



Fig.1: The monument (left) and the title board monolith (right), just before completion

Copyright © 2019 by Masahiro ONUMA, Yasumasa SHIMIZU and Kuniaki ITO
Published by the International Association for Shell and Spatial Structures (IASS) with permission.

On the other end, numerous small resilient activities to improve life environment, such as community supporting programs by NPOs, were born. Through the restructuring process, a large area of land was designated as residentially restricted, generating a large area of unused land. Therefore, city governments generally made plans for parks or memorials [2]. Most facilities needed connections to local communities for usage and daily management; thus, in large cities, a plan was made for each former town or village before merging of municipalities, and Ishinomaki City also did the same.

The project of Oshika Memorial was publicized in June 2018 for dedication to the souls of the victims in Oshika District, and in hope to never repeat this tragedy, it aimed to pass down to the succeeding generations the spirit of self-help, mutual assistance, and public support [3]. Therefore, the memorial had to include a cenotaph for mourning, a monument for people gathering, and whole memorial assets were to be placed as a part of Oshika memorial park (another new project) at the center of O'hara fishery village. The authors supported ICSM and the consortium proposed in August, won as a result, contracted and started production in October 2018. The partners of ICSM were Marui Construction Co. Ltd that mainly made the foundation and exterior and Atelier UMI, Sendai, that made the monument. The authors were design advisers: Active supervised by K. Ito, structural designed by Y. Shimizu, and actual design, engineering and construction management by M. Onuma.

2. Condition of Design

2.1. Victims and the cenotaph

Ministry of Internal Affairs and Communications (MIC) of JAPAN specified affected 9 prefectures with 222 cities, and Ishinomaki City experienced the most serious damage among the cities. The population has decreased from approximately 160 to 140 thousand after the disaster.

The city area was composed of former 3 counties, which included 118 villages in ancient time, and has a huge flat low ground and a long and winding coast with big Kitakami River, 2 mouths of the river and 3 peninsulas (Togura, Ogatsu [4] and Oshika). Oshika District is located at the southern half of Oshika Peninsula and corresponds to the above former 16 fishery villages (including 3 subordinate villages). 16 villages of former Oshika County were incorporated into Ishinomaki City and redefined as Oshika District in 2005 (Figure 2).

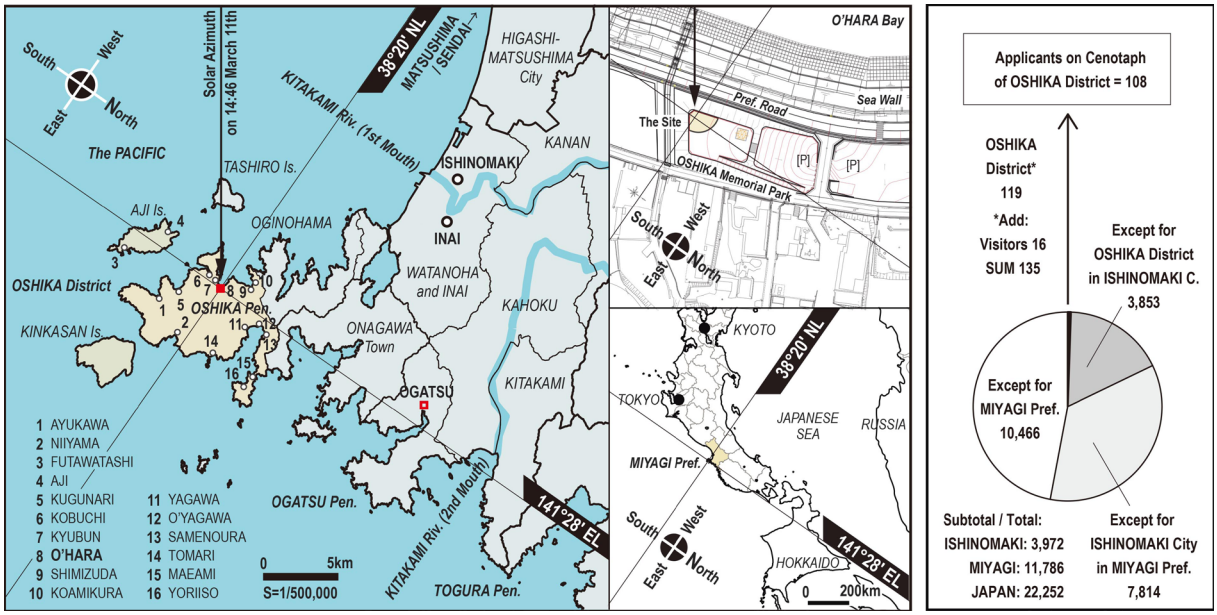


Fig.2: Map, Site and Location, and Fig.3: The number of victims and inscription on the cenotaph [5]

The numbers of death and missing were 3,972 (17.8% of the total) in Ishinomaki City, 11,786 (53.0% of the total) in Miyagi Prefecture, total of 22,252 all over Japan as of March 2019. Oshika District was home to 4,600 people, however numerous lives (119 inhabitants and 16 visitors) and assets were lost, fish ports and infrastructures were severely damaged, and as a result, the number of residents decreased to about a half of before. Out of 135 object people, finally 108 applicants were required by each village for inscription on the cenotaph (Figure 3).

2.2. Requests for the monument and the exterior

ICSM's hometown, Inai district, is located 4km east of central Ishinomaki and 25km northwest of the memorial (O'hara vl.), and also belonged to the same former Oshika County. The town had produced enormous amount of crayslate "Inai Stone," also known as "Sendai Stone," which was used not only in Sendai area but also all over Japan. It is famous for temples' tower stones with Sanskrit, big monuments for militarism in modern times, and large paving stones. But the demand had decreased gradually after WWII, and the quarries were left (Figure 4). Cheap imported materials for tombstones had come from China, India and so on. However, stone resource and skills still remain (Figure 5), which we tried to apply to this project and to attempt multiple usage.

At the same time, this work was required to find an appropriate, symbolic anchor place with the common worth for the bereaved families, without feeling the images of tomb or religious monuments. Surely, it will give us image of tomb if we use only Inai stones. Where is the clue of modeling? The lead author stared again, sea, sky and disappeared life-scapes of these villages.

3. Design: concept, form and the constituent material

3.1. The enfolding form of monument and mourning place

Gathering is not only for bereaved or concerned, but also for the souls of victims. Therefore, the landscape design should represent the meaning of circulation. In addition, low stretched grass mound around mourning place should be made for secured and integrated feeling in the deserted park. The enfolding form, we got a line to. Of course, an ocean view for gathering people must be secured. The arch-shaped beams of monument were made for realizing enfolding feeling and visibility, and made of pre-casted reinforced concrete for durability against sea breeze and salt damage.

In addition, since the site creation had been on going at first and the highlight of construction would overlap the term of cold winter, this project had to construct the foundation and bases for the beams at first, and to assort pre-fabricated elements after that. The main parts of the monument had to be divided into 2 objects, prefabricated indoor and to be stackable on the truck. However, the joint or gap should be examined elaborately.





Fig.4: Current scene of quarry, and Fig.5: Dividing technique of Inai stone

3.2. Concept of a time meter device

The sun light and shadow are the other clue of design about direction and detail shape of the monument. The time of people gathering is before and after 14:46, March 11th. We gave a role of not a sun dial, but time meter device, to this monument. We determined to give the part not the joint, but the slit, that was put in the binate arch-shaped beams and the direction of the monument was decided so that the sun ray shines onto the shadow of the beam to stamp on the pavement at the solar time. The latitude, longitude and azimuth angle of this monument are NL 38.20, EL 141.28 and 55.12 degree from due north by Web-site of National Astronomical Observatory of Japan (Fig.6).

3.3. A new anchor place with vernacular "Inai" stone

By the way, restructuring sustainable and rural-based industry is necessary in the damaged area. The lead author is recently trying to support manifold cooperation of small ateliers [6]. ICSM is regarded as a typical sample and this project was expected to expand the possibilities of stone manufacturing. Therefore, this memorial has various usage; A1) title board monolith, A2) nameplates' base monolith, A3) time stamp objects, A4) pre-packed concrete pedestals, and so on. Particularly, A4) is one of the method by F. L. Wright at Taliesin West, with a large stock of unused Inai rocks. We set various shaped stones on a steel plate, and casted concrete little by little (Fig.7, 8 & 9).

3.4. Construction process with an integrated design from manifold elements

Look at the landscape (Fig.10). There were roughly 2 steps of construction process. 3 parts' groups were produced or processed at each places in the first half (A/B/C of Fig.6).

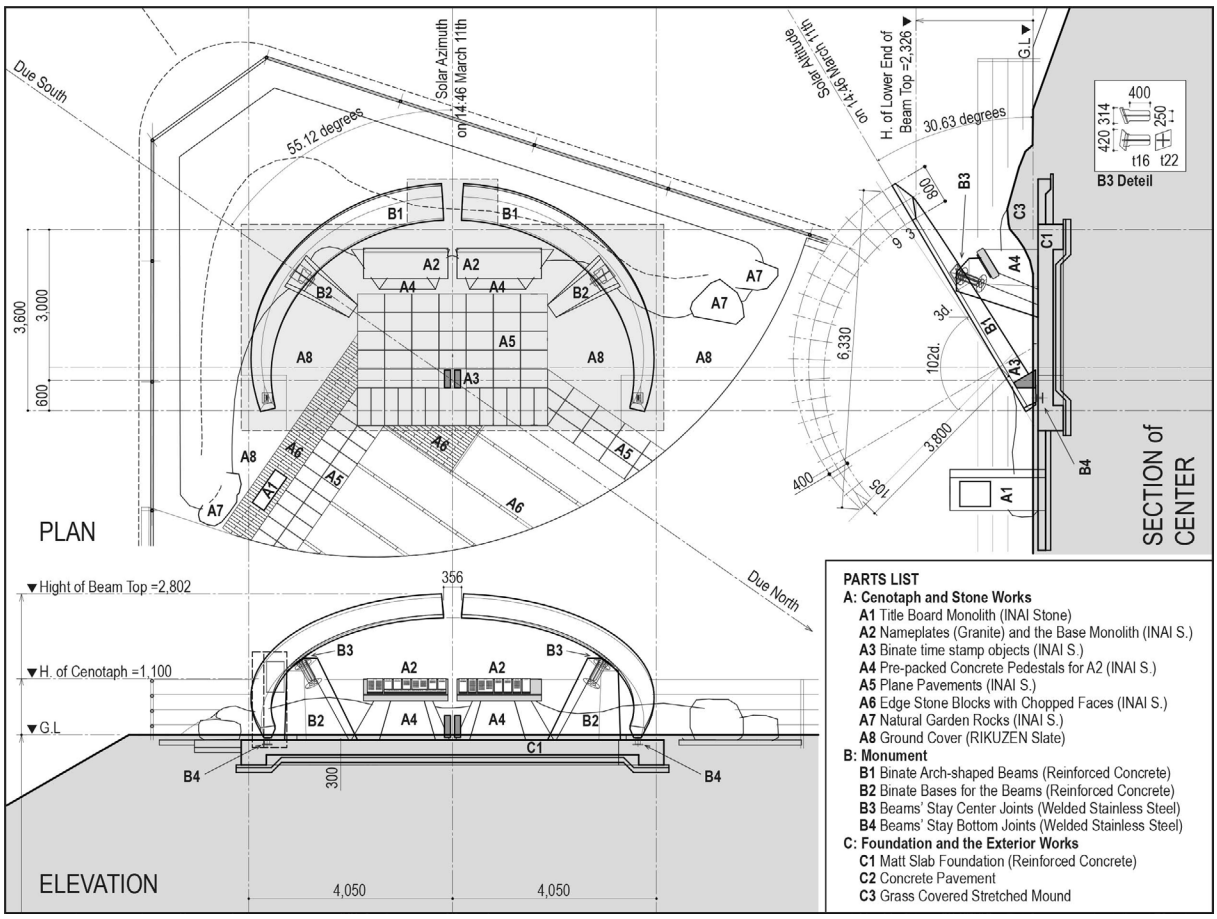


Fig.6: A drawing of Oshika memorial

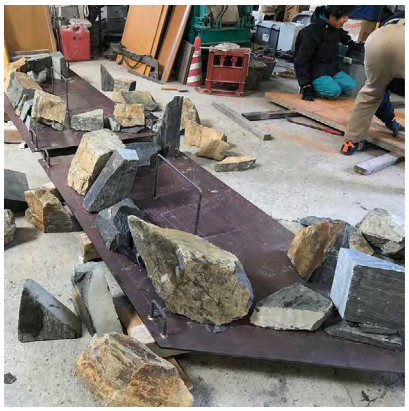




Fig.7: Setting stones on plates, Fig.8: Casted pre-packed concrete, and Fig.9: Integrated place with various parts



Fig.10: Sun ray shines onto the linear shadow of arch-shaped beams, just before completion

One is a group of monument made of RC with joint hardware made of stainless steel by Atelier UMI and the studio of the author's university, the second one is a group of cenotaphs and paving blocks made of Inai stone by ICSM, the last one is a group of foundation and landscaping objects by Marui Company. Distributed parts and groups were integrated and constructed in the second half.

4. Conclusion

This paper reported ingenuities of the contrasting landscape design of Oshika Memorial which consist of the cenotaph with vernacular stone and the monument with modern reinforced concrete, as has been observed. The most important 3 concepts led the basic design; however, details and actual engineering were led by each players of the consortium. As a result, an impressive memorial form was built not only as a mourning place, but also as time meter device and a catalyst for revitalizing regional stone manufacturing. Yet, the next report by Mr. Shimizu will present the contents of structural design of this monument. The authors hope that the memorial will contribute to the recovery of this region by making a new anchor place [7] for people gathering to mourn victims and spend meaningful time with the wind, sun light and shadow of the memorial.

Acknowledgements

The authors must say special thanks to: All of administrative authorities of Ishinoamki City including the Mayor Hiroshi Kameyama who gave the order of this project, Inai Cooperative for Stone Manufacturing and Commerce including the chief director Mr. Kazuhiro Suzuki and the secretary general Mr. Keita Kameyama, Marui Construction Co. Ltd including the president Mr. Chikashi Ito and the foreman Yuki Takahashi who called for the partnership for this project, Atelier UMI including the president Mr. Kimiyoshi Sasaki who also called for the partnership. Ms. Namie Suzuki who gave us the first chance of friendship to Inai Coopertative, and many other companies who supported us. Above all, Mr. Hideki Saito who made complicated molds of monuments, Mr. Ryo Hagiwara who made all of the difficult hardware. Ms. Ai Miyamoto helped the lead author by office support and English translation. Onuma Laboratory students including Mr. Keita Kawaai who supported the lead author on the modeling and other chores. JST-RISTEX [6] with our research companions and Research Office of Tohoku Institute of Technology including the president Dr. Hiroshi Konno who supported the author to attend repeatedly.

References

[1] Y. SHIMIZU, et al.: Structural Design for Arch-shaped Cantilever Beams "Oshika Ring of Hope"; Proceedings of the IASS Annual Symposium, Structural Membranes "Form and Force," 2019

[2] Sébastien Penmellen Boret, Akihiro Shibayama: The roles of monuments for the dead during the aftermath of the Great East Japan Earthquake; International Journal of Disaster Risk Reduction vol. 29, pp55-62, August 2018

[3] The message was written by Ishinomaki city government of the title board monolith.

[4] K. ITO: Ogatsu Inkstone Museum and its Titanium Roof, Japan Titanium Association, No.60(3), pp.194-196, 2012.

[5] Data: Ishinomaki city 2018 and MIC of JAPAN 2019, edited by the author

[6] M. ONUMA et. al, Restructuring Local Livelihoods and Fostering Diverse Life-scape through Cooperative Ateliers in Rural Communities, R&D Projects of Designing a Sustainable Society through Intergenerational Co-creation, Research Institute of Science and Technology for Society (RISTEX), Japan Science and Technology Agency (JST), 2016-2019

[7] M. ONUMA, K. ITO, The Worth of Maturity in Living Properties; ICOMOS ISC Theory & Philosophy "The Image of Heritage: Changing Perception, Permanent Responsibilities", Florence, 2009.

Proceedings of the IASS Annual Symposium 2019 – Structural Membranes 2019
Form and Force
7 – 10 October 2019, Barcelona, Spain
C. Lázaro, K.-U. Bletzinger, E. Oñate (eds.)

The Railway Station Stuttgart 21 – Computational Design and Digital Fabrication of Freeform Concrete Shells

Dr.-Ing. Frederic WAIMER*, Dipl.-Ing. Torsten NOACK, Dipl.-Ing. Angelika SCHMID, Dipl.-Ing. Roland BECHMANN

*Werner Sobek AG
Albstr.14 70597 Stuttgart
frederic.waimer@wernersobek.com

Abstract

As part of one of Germany biggest infrastructure projects in the 21st century, a new underground train station is currently under construction in the heart of Stuttgart. The new underground railway station is the core of a major infrastructure project that aims at modernizing the high-speed train connection between Munich and Paris. The new station transforms Stuttgart from a terminus into a through station. This reconfiguration of the entire railway system frees a substantial area in the heart of Stuttgart and allows for an important new urban development on land hitherto covered by a maze of tracks. The Werner Sobek AG is in charge of the structural design and engineering services for the underground station hall itself, the modification of the old entrance building and a new tram station nearby. Completion of the overall project is expected for 2025. The station's freeform geometry coupled with high requirements regarding the execution quality necessitated the development of a number of highly sophisticated digital tools. These tools are presented in the following paper.

Keywords: Freeform, Concrete, Shell Structures, Digital Design, Optimization, Reinforcement Design, Structural Modelling

1. Introduction

The new railway station hall is a seamless reinforced concrete structure. It is 420m long, 80m wide and 15m high. The roof of the hall is a doubled curved shell structure made of white concrete. The shell is supported by chalice-shaped columns and the side walls. The upper part of the columns is covered by filigree steel-glass structures that allow for a natural illumination and ventilation of the train station (Fig. 1). The shape of the characteristic roof shell was designed by architect Christoph Ingenhoven together with Frei Otto. In the early design stages they used soap skin and hanging models. Afterwards these models were converted into a geometrical model using Bentley Microstation. This system was constantly modified over the following planning phases to meet all the necessary architectural and structural requirements.

Copyright © 2019 by Waimer, Noack, Schmid and Bechmann
Published by the International Association for Shell and Spatial Structures (IASS) with permission.




Figure 1: Interior view of Stuttgart's new underground train station – the architectural significance of the chalice-shaped column is clearly visible

At roof level the station has five different slopes. At platform level it has two different slopes in the longitudinal axis. These boundary conditions require different heights along each axis. The objective of the authors therefore was to achieve a maximum amount of geometrically common elements in the concrete shell roof. This required a series of sophisticated engineering solutions. The geometric description of the double-curved roof was split at level -6m. This allowed for the upper part of most chalice-shaped columns to be described in a way that more or less follows one type of geometry. The different heights at each axis are mitigated by three types of pedestals which connect the lower end of the columns with the inclined platforms. Nevertheless, each pedestal had to be adapted to the height variations along each axis by sectioning the pedestal at the upper surface of the platform. Thus it was possible to achieve a high number of geometrically similar chalice-shaped columns, viz.:

- 23 standard chalice-shaped columns
- 4 flat chalice-shaped columns
- 1 special chalice-shaped column that serves as an entrance structure

The grouping of the pedestals leads to a high number of identical surfaces, as they only differ in the lower portion. Still, several chalices present local changes as they are partly cut at the junction with the sidewalls and at the kinks of the roof. The roof shell thickness varies according to the stress state between 45 cm in the middle and 130 cm at the bearing points.

2. Finite Element Modeling

The first part of this paper deals with the development of the interface between the geometrical model and the finite element model. The main challenge of the finite element modeling was to define the varying thickness of the shell, as it varies across the whole structure [1]. The same applies to the lower part of the chalice-shaped columns, which are modelled by beam elements with a varying cross-sectional geometry. In addition to the geometrical aspects, the definition of the reinforcement layer was particularly complex. For these reasons, the entire preprocessing and parts of the postprocessing were done parametrically using the software Rhino3d (instead of doing in the environment of structural design software, as would usually have been the case). This had the advantage that all geometrical information was instantly available. The finite element code could thus be generated in SOFiSTiK with the aid of specifically developed plug-ins. Thus, it could be ensured that each node of a finite element quad has the appropriate thickness; in addition it became possible to determine the corresponding reinforcement.

The FE mesh was generated on the median surface resulting from a combination of the upper and lower surfaces of the freeform geometry (Fig. 2). An iterative computation was then used to measure the distance of each quad node from the upper and the lower surfaces. The sum of these two distances

could then be used to establish the overall thickness of the quad at the corresponding node (Fig. 3 right).

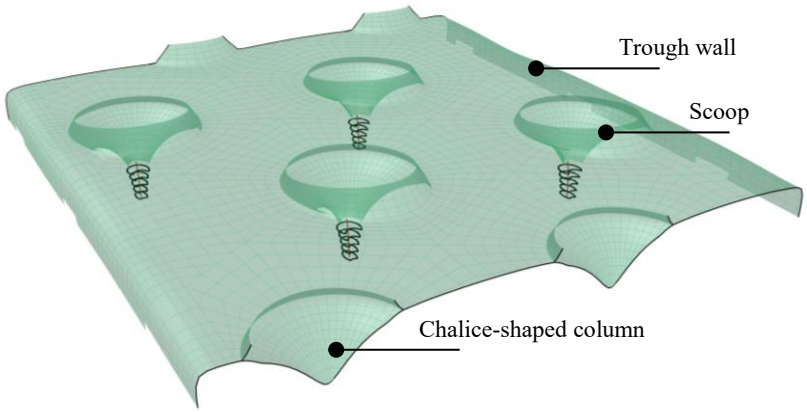


Figure 2: Section of the Finite Element Model (quads and beams) of the global structural model

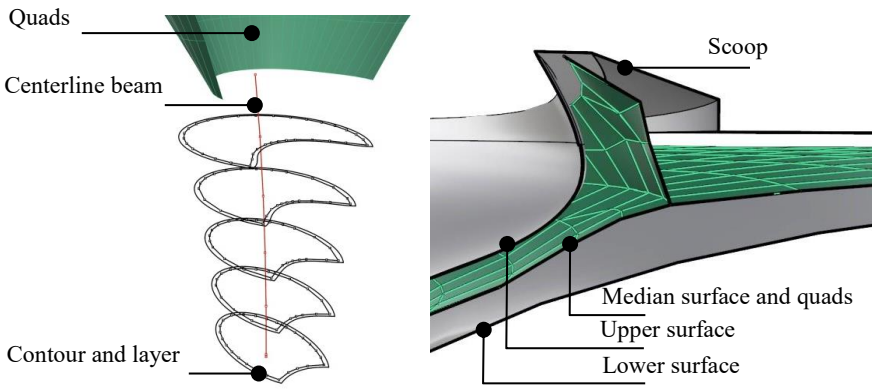


Figure 3: Detailed View of the Finite Element Model: centerline of the beam elements and definition of the shape and the reinforcement position (left); section through the upper part of the chalice-shaped column showing the shell elements based on the median surface (right)

Parametric modelling was applied to the geometrically complex beam elements and the determination of the reinforcement's strength and positioning. The preprocessing for the beams, as for the shell elements, was based on the geometry model. For the definition of the reinforcement layer, an offset to the surface served as centerline to define the longitudinal and circumferential reinforcement (Fig. 3 left). Usually the definition of beam elements is done manually; due to the different geometrical types of the chalice-shaped columns, this would not have been expedient in the project under consideration. The procedure developed by the authors therefore allowed for a significant reduction of the time needed for planning. In a further step, the lower nodes of the shell elements were then connected to the uppermost node of the beam element by coupling elements. The corresponding calculation model consisting of shell and beam elements is shown in Fig. 4.

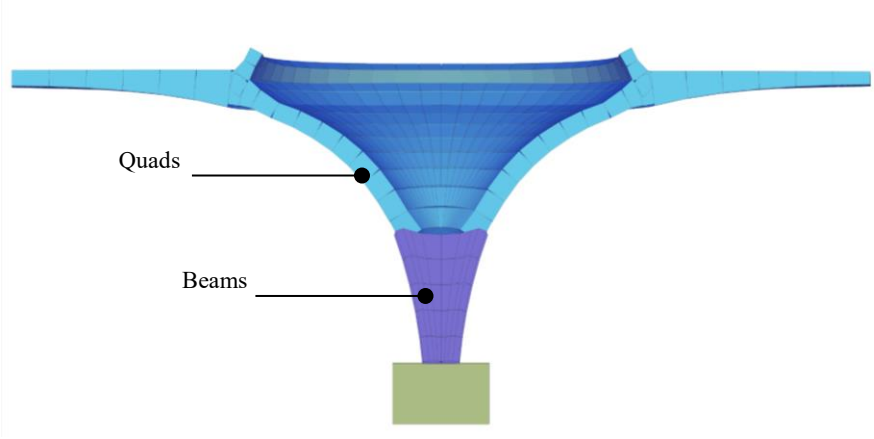


Figure 4: Section of the finite element model showing the double curved surface and the different thicknesses of the shell

3. Reinforcement Design

The new underground train station in Stuttgart is a combination of a trough made of normal concrete and a shell structure made of white concrete. The entire structure is designed as a seamless reinforced concrete structure; only at the ends expansions joints are provided. The requirements on the reinforced concrete construction are very high due to the grade of waterproofing needed for the trough and the quality required for exposed concrete quality (class SB4) of the shell structure. The following chapter discusses the planning of the reinforcement. On the one hand planning comprised the development of digital tools needed for the engineering; on the other hand it comprised the design principles that had to be considered for generating the rebars. These principles were derived from three essential aspects: Geometric Requirements, Structural Requirements and Fabrication Requirements

3.1. Geometric Requirements

One of the major factors having a bearing on the reinforcement design was the geometry of the structure. The different structural components have both synclastic and anticlastic parts and vary in their thickness (Fig. 5). The arrangement of the lower reinforcement therefore does not correspond to that of the upper reinforcement, as would normally be the case in a concrete shell. Furthermore, in the zone between the chalice-shaped column and the scoop three surfaces intersect. This leads to a complex spatial arrangement of the reinforcement. In zones where no typical division into column, shell or beam was possible, the authors had to develop sophisticated solutions for the spatial arrangement of the reinforcement.

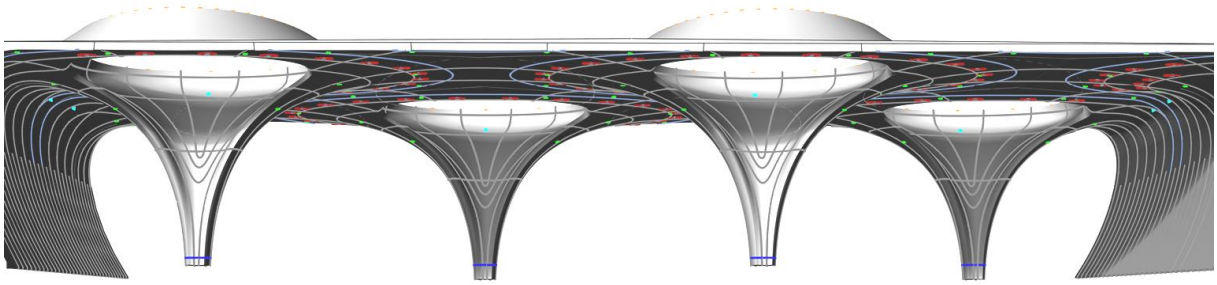


Figure 5: Section of the geometrical description of Stuttgart's new underground railway station including all relevant information like formwork edges (gray), steel mounting parts (red and dark blue) or drainage pipes (cyan)

Out of the geometric and structural requirements arose two different concepts for the layout of the reinforcement: a radial-tangential arrangement and an orthogonal arrangement. The slightly curved zones between the chalice-shaped columns and the trough wall are reinforced by an orthogonal arrangement. The chalice-shaped columns and the scoop are reinforced by a radial-tangential arrangement. As a result, in the transition zone from one system to the other, a change in direction of the overlapping rebars takes place (Fig. 6). Therefore, the reinforcement cannot be joined in the same plane. The individual reinforcement layers have to be stacked. Therefore, the rebars must be locally sloped by an offset bend in this zone, which leads to a further complexity of the bending forms. For manufacturing reasons, the offset bend must comply with a minimum dimension. From a structural perspective a slope that is too steep would lead to local deviation forces at the kinks. This would require supplementary reinforcement and therefore had to be avoided. In addition to the offset bend, the geometry and the curvature of a rebar also lead to derivation forces that had to be considered. For wide curvatures and larger angles, these forces can be tied back by the concrete's tensile strength. For smaller curvature and smaller angles, these forces have to be tied back by supplementary reinforcement. In order to reduce the effort and the costs for reinforcement work, the rebars were therefore examined with regard to their curvature behavior depending on their diameter. The geometry also led to a more complex planning of the spacers in the top layer. The parametrical modelling of the spacers could only be started once the complete digital model of the reinforcement was available. Based on the rebars of the upper and lower layers, relief areas were generated to describe the zone in between. These areas served on the one hand as a basis for determining the bending form of the spacers; on the other hand it provided assistance to the contractor placing the spacers on site by providing 3d coordinates. The exact placing of the spacers in elevation is crucial especially for placing the upper layer, because an inaccurate layering would lead to an undesired increase or reduction of the concrete covering.

3.2. Structural Requirements

Structural requirements are mainly driven by the load distribution, which in its turn depends on the geometric shape and the main load cases. Main load cases are the dead load, the superimposed dead load, and temperature loads. The structural design and the required reinforcement resulting from this design are described further in [2]. In order to consider the construction stages correctly, a separate model was created by subdividing the global model; thus the construction sequences could be controlled using the CSM module of SOFiSTiK [3]. This enabled the authors to design adequate temporary structures for all relevant assembling sequences. It quickly became clear that the structural behavior during construction of a freestanding chalice-shaped column differs significantly from the final state; the former is mainly driven by the dead weight of the structure, the live loads during construction and the temperature loads. For example, due to the mass distribution the bending moments at the base point in the construction state changes their sign in comparison to the final state.

3.3. Fabrication Requirements

The last essential aspect to be considered when planning the reinforcement was the fabrication properties. A differentiation had be made between the manufacturability of the reinforcement (length, bending shape, offset angle, kink angle, diameter of the rebar, etc.) and the installation on site afterwards. The fabrication restrictions of the reinforcement are due to the bending process in the bending machine and the elastic-plastic material behavior of the reinforcing steel. In order to determine feasible bending forms, different series of tests were carried out with the contractor. The aim was to exclude non-producible bending shapes for the design and to limit complex bending shapes (i.e. rebars that are bent in two different planes) to a minimum. For this purpose, the technical limits on the production of bending forms were coordinated between structural engineer and contractor using extensive practical tests. Points to be considered included the question from which curvature radius (and thickness) on-wards a rebar had to be bent in advance - and up to what point it could be bent

manually on site. Another important aspect was the definition of tolerances up to which the geometry of the rebar could be allowed to vary with regard to the bending radii and bending angles.

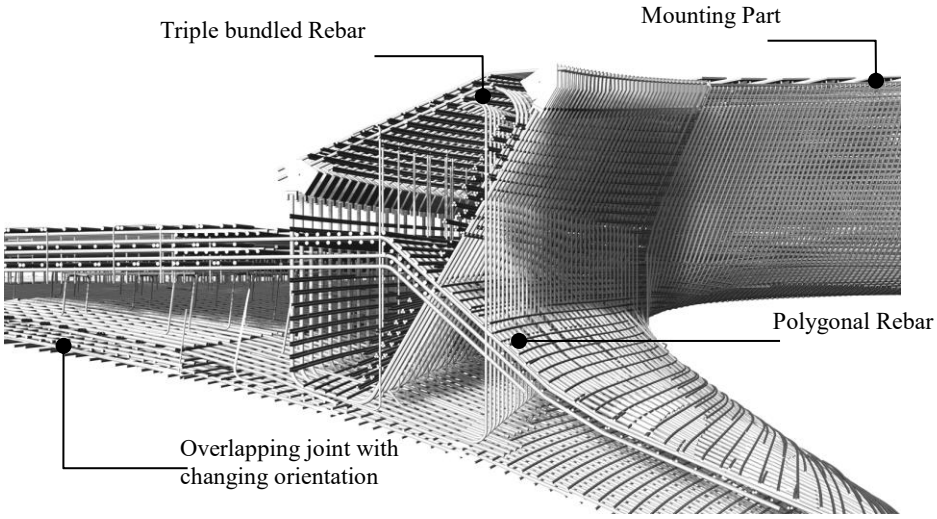


Figure 6: Section of the reinforcement model

When choosing the bending shape, a distinction was made between segmented arcs, polygons and straight rebars. Segmented arcs were used for large and very small radii. For large diameters of the rebar, the number of arcs was limited to three; in between arcs no kinks may occur. The individual segments must not fall below a certain minimum length depending on the diameter of the rebar. For higher reinforcement ratios triple bundled rebars were used. It should be noted that the use of sleeve connections for arcs is limited. The advantage of a polygonal bending shape is a more precise fabrication of the rebar and the possibility to better cover certain geometrical conditions (Fig. 6). When simplifying a given geometry to a polygonal shape, the new geometry must be located in a given corridor; it should not be beneath or above this corridor. The size of the corridor has not only an effect on the bending shape and the design of the other layers, but also on the structural behavior of the shell. Therefore, the impact of the inner lever-arm on the design of the components was taken into account. With regard to the manufacturability of a polygon shaped rebar it had to be ensured that the bending angle is not below 2° and that the length of a segment between two kinks is not lower than a specific value that depends on its diameter. For very large radii (about 90m) bending is not required anymore, because the rebar can be adjusted manually to the desired geometry.

Irrespective of the type of bending shape, due to maximum rebar lengths the reinforcement joints had to be taken into account before generating the rebar; this had a strong impact on the final design of the bending shape.

3.4. Digital tools for design and fabrication

The parametric generation of the individual rebar geometries took place in Rhino3d. The centerlines of the rebars were generated based on the geometrical model (Fig. 5) developed jointly by the architects and the structural engineers. For each reinforcement layer, an offset of the surface was generated and intersected with the plane representing the direction of each rebar. In a second step the resulting splines were simplified into producible bending shapes, according to the principles mentioned above. In order to reduce the number of different bending shapes, a comparison of the individual centerlines took place. Specifically developed program loops allowed for a grouping of centerlines with a similar geometry within a defined range of tolerance – an important precondition for an economic design. The centrelines represent the basis for the later processing in Nemetschek, where the properties of the rebars, laying instructions, dimensions and openings for pouring and vibrators are defined. A

generative modelling provided an optimized process for generating all the reinforcement shop drawings and allowed for an easy adjustment (Fig. 7).

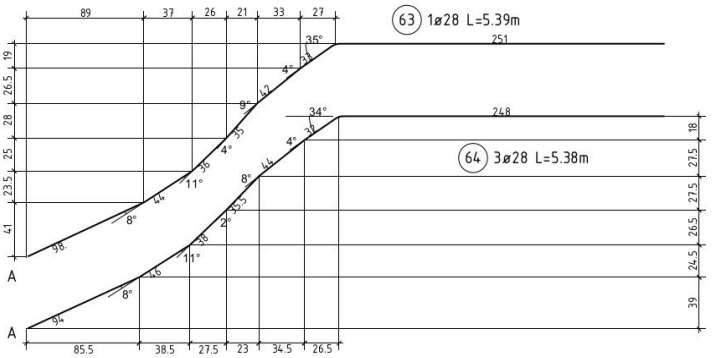


Figure 7: Example for bending shapes of two polygonised rebars of a chalice-shaped column

Finally, besides visual clash detections within the 3d model (Fig. 8), clash detections and position checks of the rebars also took place using specially developed algorithms (target to actual geometry). In addition, the constructability of the building parts was examined together with architect, client and contractor by projecting the reinforcement in a virtual reality room (VR). Furthermore, the 3d model made it possible to investigate the feasibility of laying the reinforcement during the design process and to coordinate it with the contractor. This allowed detecting issues like clashes early during planning and to adjust the design accordingly.

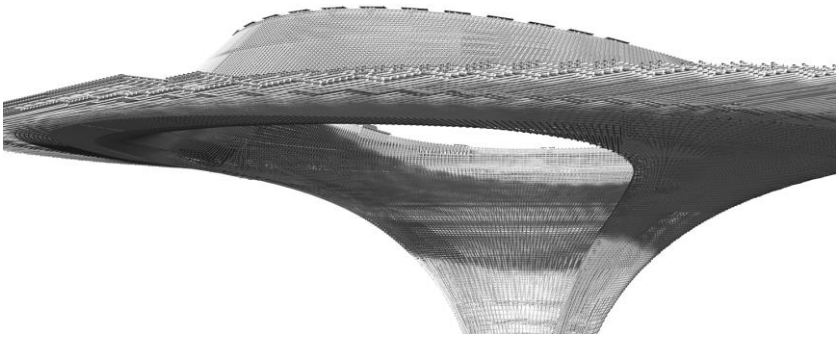


Figure 8: 3d reinforcement model of a chalice-shaped column

The 3d reinforcement model developed by Werner Sobek was not only the basis of the reinforcement shop drawings; it also provides additional support for the construction process in form of 3d data that can be viewed directly on site, either on a large screen installed in a construction cabin next to the site or on a mobile tablet solution. Construction workers can thus use the 3D model to verify the correct positioning of the rebars. To ensure an accurate placing of the reinforcement on site, the rebars were de-scribed by Gauss-Krueger coordinates. In addition to the reinforcement shop drawings, each component of the shell structure received a list of coordinates. In conjunction with a surveyor the contractor can thus install the main rebars in their exact position and place other rebars precisely in between (Fig. 9 (left)). Furthermore, on the shop drawings the beginning and the end of each rebar are defined. This is taken up by the bending company which marks the rebars accordingly. In addition to color marking, each rebar gets its own identification number. Without this specific marking, a rebar site would be unassignable (and thus useless) on the construction site. The rebars are bent in a

specially established bending shop. The bending information is mainly de-rived from the 3d reinforcement model; after bending it is verified by a full-scale laser projection.



Figure 9: Placing of the reinforcement on site (left); Chalice-shaped column after stripping of the formwork; temporary support for the construction phase is provided by steel columns (right)

4. Results

The reinforcement of a typical chalice-shaped column consists of approx. 300t of reinforcing steel and is described by 350 DIN A0 drawings. These drawings include the shop drawings, the reinforcement schedule, and the bending forms. Each chalice-shaped column has about 11.000 different rebars. The entire shell structure is defined by approx. 12.000 reinforcement shop drawings. Thanks to the parametric tools de-veloped by the authors, an accurate planning and construction of the first chalice-shaped columns was made possible. The result of this planning process is a complete digital model of the reinforcement with all the design information as well as all ducts and built-in components. The high precision of the reinforcement design in full 3D ensured a smooth implementation from the placing of the reinforcement to the con-creting and stripping of the formwork (Fig. 9 (right)).

References

[1] L. Blandini, A. Schuster, W. Sobek, “The Railway Station Stuttgart 21 - Structural Modelling and Fabrication of Double Curved Concrete Surfaces”, in *Computational Design Modelling. Proceedings of the Design Modelling Symposium Berlin 2011*, C. Gengnagel; A. Kilian; N. Palz; F. Scheurer. Edition: Springer, 2011. S. 217–224.Journal 2(5), 99–110 (2016).

[2] R. Bechmann, A. Schmid, T. Noack, W. Sobek, “Unchartered Waters for Engineers and Contractors Alike: Stuttgart’s New Main Station and its Complex Geometry”, in *Beton- und Stahlbetonbau* 114 (2019)

[3] A. Mühl, M. Brunner, R. Luna, C. Neugart; T. Noack, “Numerical Calculations for Foundation and Structure of the Main Station Stuttgart S21”, in *Conference Proceedings of Workshop on Numerical Methods in Geotechnics 2017*., J. Gabe, Hamburg 2017. S. 257–280.

Proceedings of the IASS Annual Symposium 2019 – Structural Membranes 2019
Form and Force
7 – 10 October 2019, Barcelona, Spain
C. Lázaro, K.-U. Bletzinger, E. Oñate (eds.)

Bending-driven Dynamic Corrugation for a Funnel Shell Design

Jorge CHRISTIE*, Jonathan J. SOLLY[a], Simon BECHERT[a], Jan KNIPPERS[a]

*ITECH MSc. Programme, Faculty of Architecture and Urban Planning, University of Stuttgart, Germany, Schwabstrasse 4, 70197 Stuttgart - Germany, jorge.christie@gmail.com

[a] Institute of Building Structures and Structural Design (ITKE), University of Stuttgart, Germany

Abstract

The current work presents a novel method to form find efficient funnel shell structures beyond the constraints of funicularity. The so-called Bending-driven Dynamic Corrugation method is introduced within the framework of corrugated shell design and that of integrated computational form finding workflows. The hereby-presented method employs the analysis of bending energy of an initial non-funicular shell design as the driver for defining the location and modulation of a corrugation of its surface. The parameters of this corrugation are further manipulated by a multi-objective optimization algorithm to generate a set of performative solutions. The form found solutions exhibit an improved bending and buckling stiffness compared with a traditional cross-section optimized version of the same initial design. Most importantly, these dynamically corrugated designs achieve these improvements using significantly less material. Along with the performance gains, the resulting designs are deemed as a contribution to the expressiveness of the shell structure.

Keywords: form finding, shell structures, dynamic corrugation, bending-driven, non-funicular shells, shape optimization, textile concrete, ultra-thin shells.

1. Introduction

Although funicular shells are widely acknowledged as an efficient design paradigm [1], the rules that govern funicularity offer a fairly constrained design space, limiting the scope of application for shell structures [2]. On the other hand, non-funicular shell designs pay for their deviation from funicularity by an increase in bending stresses. This issue is traditionally addressed by thickening the shell's cross-section and adding extra reinforcement or, alternatively, by adding ribs or beams. Any of these paths lead to a significant loss in material efficiency, turning the shell design into a less elegant solution.

The principle of corrugation, has proven to be an effective approach to improve structural performance on non-funicular shells designs [3]. Notable designs such as Nervi's roof and slab design for the Turin Exhibition Palace (1948) or Favini's roof for the Aquila service station (1949) show that these gains in structural performance can greatly contribute to the aesthetic value of the building.

This paper introduces Bending-Driven Dynamic Corrugation, a novel method for form finding material-efficient corrugated shells designs where a funicular solution is either not possible or not desired.

Copyright © 2019 by Jorge Christie, Jonathan J. Solly, Simon Bechert, Jan Knippers
Published by the International Association for Shell and Spatial Structures (IASS) with permission.

2. Corrugation

Corrugation is defined as the act of shaping a surface into a series of alternated (commonly parallel) ridges and grooves [4]. Under Heino Engel's criteria, standard corrugated surfaces can be described by the translation of a directrix line over an undulating generatrix curve [5]. For the purposes of this research, it has been considered more appropriate to identify the undulating curve as the generatrix.

To date, four main approaches for generating the corrugation can be identified: sinusoidal generatrix-based [3], [6], arcs and straight lines generatrix-based [3], circular arc generatrix-based [8], and NURBS surface over a sequence of directrixes [9] (figure 1).

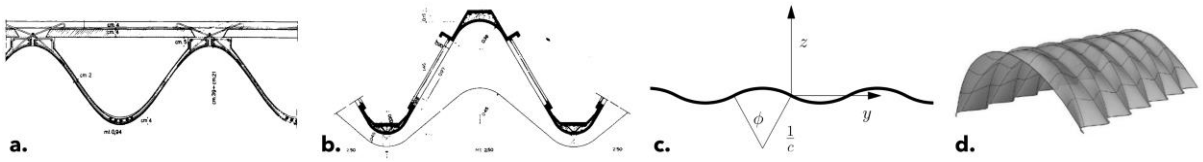


Figure 1: Corrugation generation approaches. a) Sinusoidal generatrix (Nervi, Turin Exhibition Palace, hall C roof slab, 1948), b) arcs and straight lines generatrix (Nervi, Turin Exhibition Palace, central salon roof, 1948), c) circular arc generatrix (Norman et al. [8]), d) NURBS surface over sequence of directrixes (Michiels [9]).

In the context of the present research, the corrugation parameters are synthesized as described in figure 2.

3. Mechanical behavior of corrugated surfaces

The addition of corrugations to the surface of a shell is a relevant structural design resource to significantly improve its bending behavior and its buckling performance [6], [2], [9]. Given the commonly directional arrangement of corrugations, they increase the bending stiffness parallel to the corrugation directrix by increasing the inertia of the shell cross-section [9], while decreasing the membrane stiffness in the perpendicular direction [18].

As demonstrated by several authors [6], [10], [2], corrugation parameters such as amplitude and wavelength of the generatrix, as well as the location of the corrugation on the global surface of the shell play a determining role on the stiffness of the structure (Fig. 2).

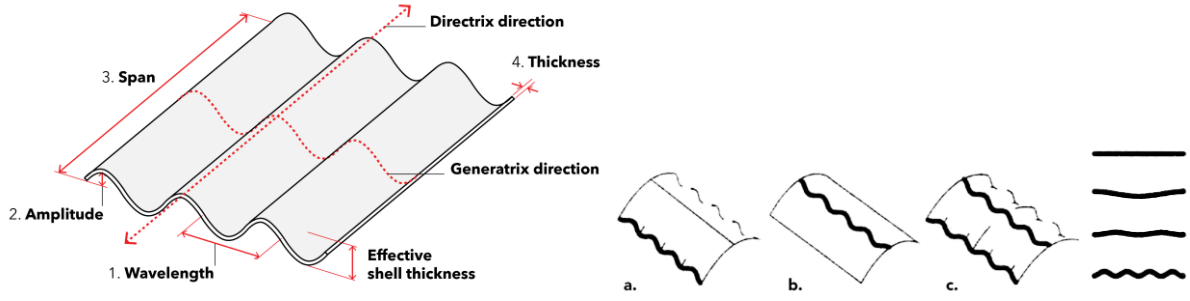


Figure 2: Left: Corrugation parameters as described on the present research. Center: corrugation location: a) edge, b) crease, c) in phase [6]. Right: corrugation wavelength variations [6].

4. Computing corrugations

Most of the pioneering approaches to shell corrugation could be described by the translation of a straight or curved generatrix over an undulating directrix [5], presumably embodying the technical constraints of their epoch. The advent of computational design and structural analysis tools unveiled new levels of control over the form generation and the integration between design and analysis. Notably, the exhaustive work of Samar Malek [6] led to establishing the influence of corrugation's parameters and location on the buckling capacity of continuous shells (fig. 3). Complementarily, her collaboration with Chris Williams [7] provides a mathematical description for corrugated plates and shells, enabling designers to explore corrugation patterns and support conditions.

Beyond the expansion of geometrical description capabilities, the development of integrated computational design and analysis workflows have enabled to delve new performance-driven form finding approaches beyond the funicular paradigm. The work on harmonic form finding by Brandt-Ølsen [2] (fig. 3) and the corrugation form finding for seismic design by Tim Michiels [9] (fig. 1) clearly illustrate this potential.

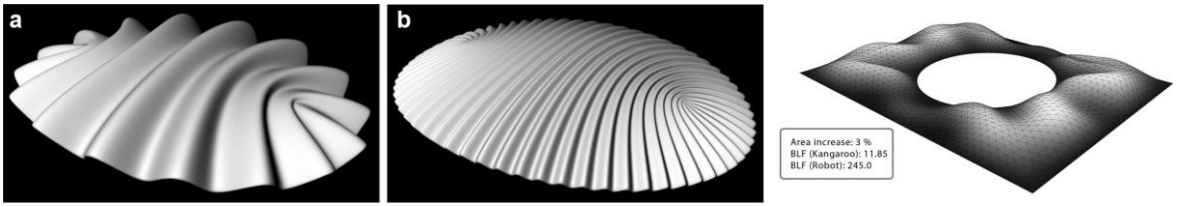


Figure 3: Left: Shell coarse corrugation (a) and a fine corrugation (b) by Malek and Williams [8]. Right: Buckling-improved design for the British Museum Great Court roof by Brandt-Ølsen [2]

5. Bending-driven Dynamic Corrugation

Bending-driven Dynamic Corrugation method follows the path of previous work on integrated computational workflows for performance-driven form finding. Herewith, a bending-moment-informed corrugation method is developed as a design tool to increase bending and buckling strength on non-funicular shells.

The choice of using bending moment as the corrugation driver is based on two primary assumptions: first, corrugations increase the bending resistance of a shell by augmenting its effective cross-section [10], being this a critical issue on non-funicular designs; second, the inclusion of corrugations will necessarily lead to improve the buckling strength of the shell [6], [2], therefore by targeting bending strength both will be simultaneously improved. Furthermore, the choice of a funnel shell as a case study provides a simple but challenging boundary condition scenario, at the same time that presents an appropriate configuration to expose the aesthetic potential of Dynamic Corrugation.

6. Methods

The hereby presented form finding method is based on a computational workflow that integrates a custom NURBS surface generation, finite element analysis (FEA), and a multi-objective optimization algorithm (MOGA) (fig. 6). This workflow was developed on Rhino 6 [10] NURBS modeling environment using Grasshopper 3D [11] as an integration platform for the different components. The FEA analysis was made in Karamba 3D [12] enabling a quick iteration with the MOGA, where the Grasshopper plugin Octopus [13] was employed.

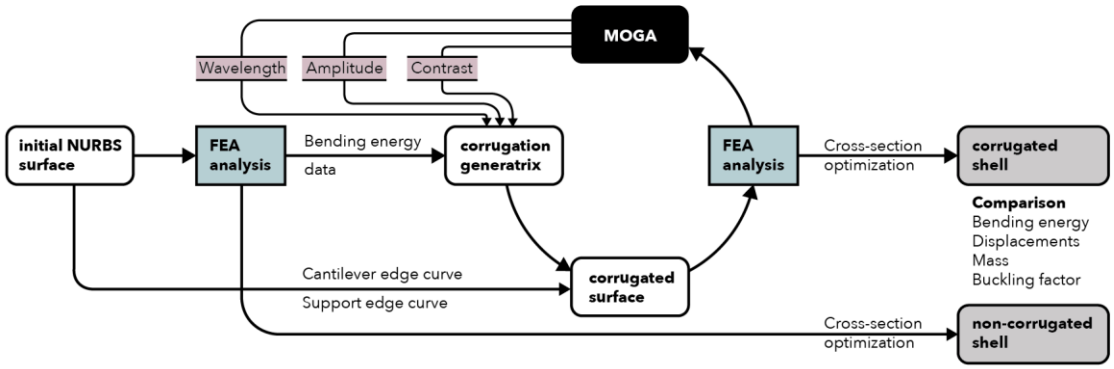


Figure 4: Integrated computational workflow for the Bending-driven Dynamic Corrugation method.

In regards to the material scenario, the method was tested considering the realization of the shell in textile concrete. This carbon fiber reinforced ultra-high-performance concrete combines good capacities for being shaped into complex forms with high strength in minimal cross sections, making it a suitable material for this type of exploration.

6.1. Form Generation and initial analysis

As a first step, a non-funicular funnel shell design is defined by fitting a NURBS surface through a sequence of three closed freeform curves. The shape of the underlying surface is intentionally deviated from a funicular solution, being supported on a rectangular-like outline from where it cantilevers outwards using an arbitrary curved section (Fig. 5). The footprint of this shell design is 15.75 by 12.70 m and has a height of 1.74 m.

This initial surface is then analyzed by the FEA software considering: the material properties of textile concrete, a constant thickness of 30 mm, a free rotation support condition and a combined load scenario of gravity and 0.68 KN/m² of snow load. This initial analysis is aimed to retrieve the bending energy vectors for each vertex of the mesh and to obtain the bending energy, displacements, and mass data for further comparison. At a later stage, a cross-section optimization (CSO) is performed within the range of 3 and 200 mm.



Figure 5: Initial non-funicular shell design after cross-section optimization. a) Top perspective, b) bottom perspective, c) detail of longitudinal section showing the optimized cross-section.

6.2. Corrugation generation

As a second step, a vector field is generated based on the bending energy data obtained from the FEA (fig. 6 a). This field is then filtered based on the magnitude of its vectors aiming to visually identify the areas of the mesh with higher bending stresses. A new NURBS curve is generated passing through the center of such area, defining the position of the generatrix of the new corrugation (Fig. 6 b).

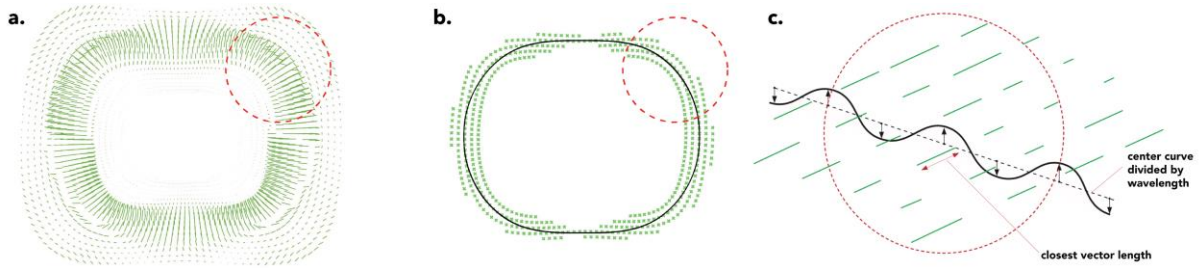


Figure 6: Corrugation generation. a) Bending energy field, b) higher stress zone and centered curve, c) corrugation amplitude value assignment.

For defining the corrugation generatrix, the aforementioned curve is divided into equally distanced points that are alternately sorted as positive and negative amplitude peaks. The control over this distance defines the wavelength parameter of the corrugation (fig. 7 b). By interpolating a new NURBS curve through these points the corrugation generatrix is created. Consecutively, the amplitude of each undulation of this curve is modulated by the displacement of the positive and negative amplitude peak in the normal direction of the surface, proportionally to the magnitude of their closest bending force vectors. This displacement is further influenced by the MOGA's control over two parameters: an amplitude factor that multiplies the values (fig. 7 c), and a contrast factor that exponentially accentuates or reduces the influence of the vector magnitude over the amplitude (fig. 7 d).

The corrugated shell surface is then generated using the two edge curves of the initial shell and the new sinusoidal generatrix as the intermediate curve. A NURBS surface is fit between this set of curves and is consecutively subjected to finite element analysis.

6.3. Corrugation form finding

The use of MOGA is a proven resource to find structurally sound solutions for designs that are out of the funicular spectrum or when a trade between different optimization goals is required [14], [15]. For the purposes of this research, the MOGA was set to minimize the bending energy and displacement data obtained from the FEA analysis. By minimizing the bending energy it is expected to steer the shell solutions to perform mainly in membrane stress, aiming to optimize the material consumption. Additionally, the range of designs provided by the Pareto front of the solution space of the MOGA, offers the designer the chance to choose a corrugation pattern guided performance goals, but also by their expression or material consumption. The Octopus plugin for Grasshopper is chosen for these purposes [14] and is assigned to control the corrugation parameters to search for performative solutions (Fig. 7).

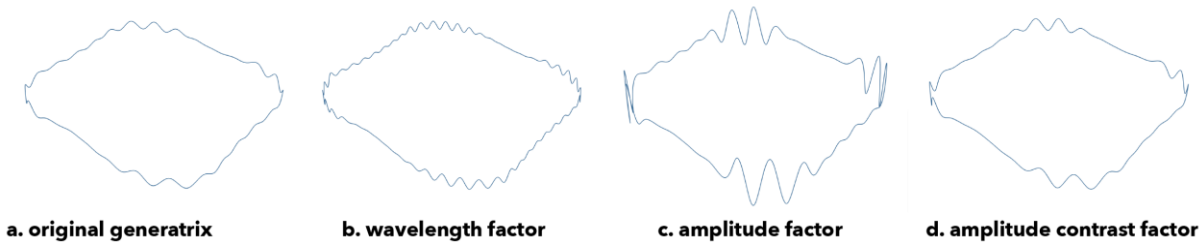


Figure 7: Corrugation parameters controlled by the MOGA.

7. Results

The result of the here presented workflow is a range of corrugation designs emerged from the Pareto front of the solution space. The diversity of factors influencing the performance of the samples makes

difficult to establish clear correlations between the variables (Fig. 8). Nevertheless, it can be observed that most of the samples on the Pareto front (Fig. 9) used the maximum value of the wavelength factor, showing that finer corrugations were evaluated as more performative (Fig. 8).

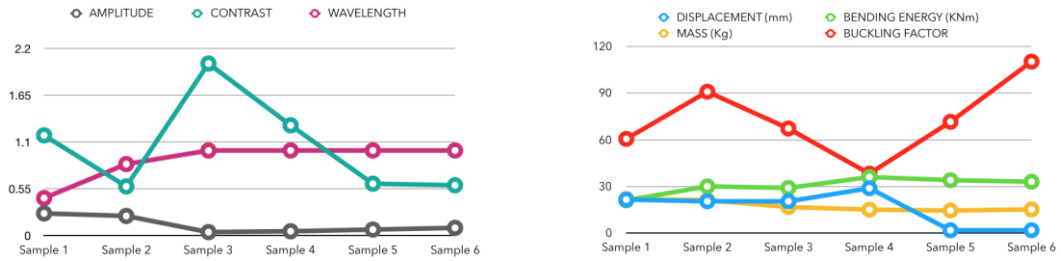


Figure 8: Left: corrugation generatrix parameters controlled by the MOGA by samples; right: performance data by sample (mass and bending energy values scaled for visual comparison).

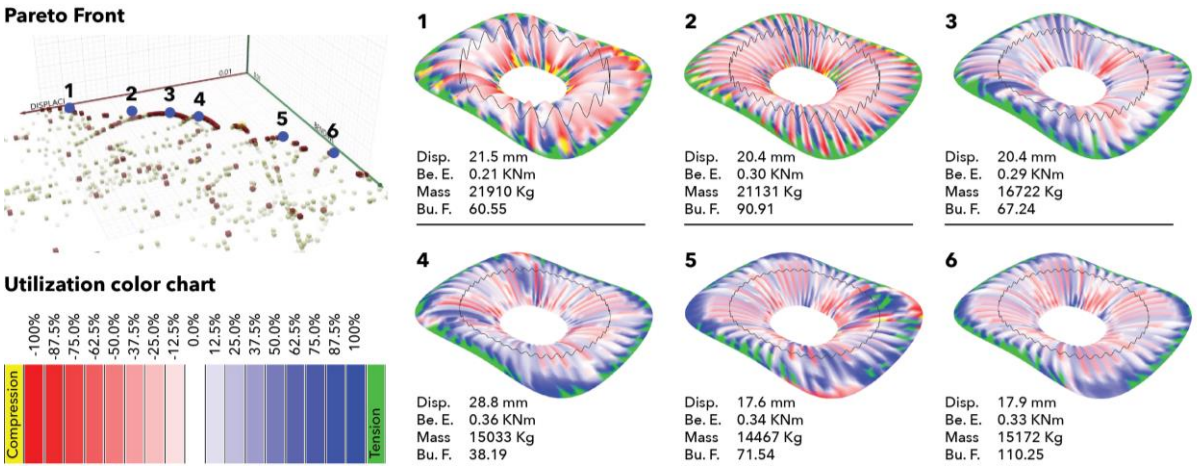


Figure 9: Top left: Pareto front; bottom left: utilization color chart; right: Selected samples from Pareto front previous to cross-section optimization.

In order to compare the corrugation form finding approach with the cross-section optimization of the initial design, the sample 3 is selected and subjected to cross-section optimization (C.S.O.), further improving its performance. The two designs are then compared based on visual analysis and the contrast of their bending energy, displacements, mass and buckling factor data (Fig. 10).

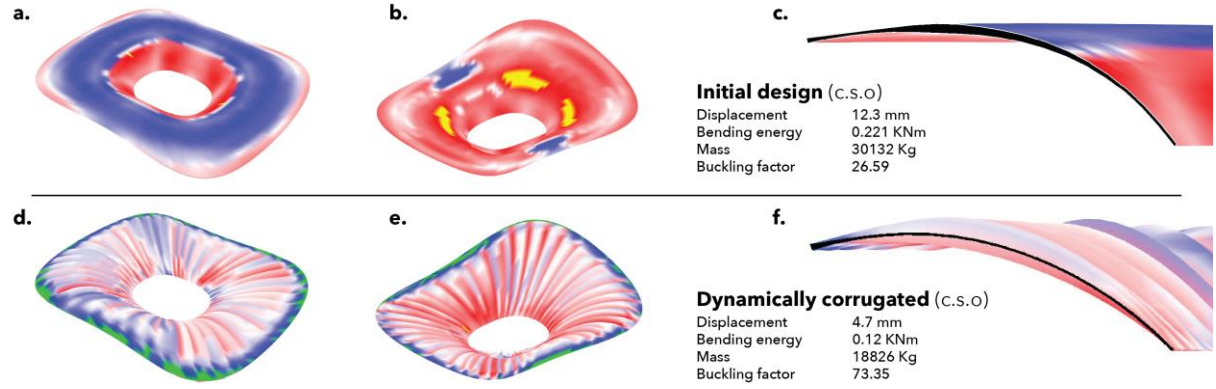


Figure 10: Initial design and dynamically corrugated sample comparison after C.S.O. Top: initial design, bottom: dynamically corrugated. Color chart as figure 9.

From visual analysis can be observed that the stress distribution and concentration of the initial design and the corrugated one are notably different. The high bending energy concentration identified in the initial shell is replaced by a pattern where the compressive stresses are carried by the valleys of the corrugation, while the tensile stresses are concentrated on the creases (Fig 10). This alternated pattern rests over a support edge predominantly subjected to compression and a highly stressed tension ring appears where the corrugation fades out, close to the cantilevering edge. Due to its high utilization, this tension ring is thickened during the cross-section optimization (Fig 10 f). A further reinforcing of this area could prevent this increase in the cross section.

Furthermore, from the data comparison is observed that the corrugated design outperforms the initial design on every aspect. It exhibits a 60% reduction in displacement and 45% less bending energy, while reducing the material consumption in 38%. This material efficiency could be further improved by the addition of the reinforcement in the tension ring as mentioned above. Additionally, the introduction of curvature on the surface has a substantial effect on the buckling stiffness of the shell, being improved in 276%.



Figure 11: Illustrative design for an infrastructural building with a dynamically corrugated shell roof.

8. Conclusions and further research

The here presented research introduced a novel method for form finding efficient non-funicular funnel shells. The so-called Bending-driven Dynamic Corrugation method employs the bending energy analysis of non-funicular designs to generate structurally sound shells that are optimized through the addition of corrugation. The method exhibited great potential for improving bending and buckling stiffness of non-funicular design while using significantly less material than traditional cross-section optimization. This material-saving potential is deemed as a contribution to minimize the environmental impact of such structures. Additionally, the use of MOGA during the optimization process, offers the designer the possibility to choose from a spectrum of solutions, where criteria such as aesthetic preference or buildability could be relevant for the selection.

Although the present method was specifically developed for funnel shells, further research could be carried out to expand it to other shell typologies, where new strategies for the generation of the surface and the location of the generatrix(es) would be necessary to implement.

Despite the fact that the material realization of such structures is beyond the scope of the current paper, the authors are aware that new constraints might emerge from the definition of a molding strategy. These constraints could be integrated during the form generation and form finding phases in order to obtain buildable solutions for targeted construction scenarios.

Acknowledgements

The above-presented method was developed during the Form and Structure seminar of the MSc. ITECH programme at the University of Stuttgart and accounts with the contribution of Sanoop Siby and the support of its academic team, including Nikolas Früh and Daniel Sonntag.

References

[1] J. Ochsendorf, P. Block, "Exploring shell forms", in *Shell Structures for Architecture: Form Finding and Optimization*, S. Adriaenssens, P. Block, D. Veenendaal and C. Williams, Ed. New York: Routledge, 2014, pp. 7-12.

[2] C. Brandt-Ølsen, *Harmonic form-finding for the design of curvature-stiffened shells*, MPhil. University of Bath, 2015.

[3] P. L. Nervi, "Precast Concrete Offers New Possibilities for Design of Shell Structures", *ACI Journal Proceedings*, vol. 49-37, pp. 537-548, 1953.

[4] "Definition of corrugate," Merriam-Webster [Online]. Available: https://www.merriam-webster.com/ dictionary/corrugate. [Accessed April 10, 2019]

[5] H. Engel, *Sistemas de Estructuras.* Barcelona: Gustavo Gili, 2001.

[6] S. Malek, "The Effect of Geometry and Topology on the Mechanics of Grid Shells," Ph.D. dissertation, Dept. Civil and Envir. Eng., Massachusetts Institute of Technology, Cambridge, MA, 2012.

[7] S. Malek, C. Williams, "The Equilibrium of Corrugated Plates and Shells, " *Nexus Network Journal*, vol. 19, pp. 619-627, 2017.

[8] A.D. Norman, S.D. Guest, K.A. Seffen, "Novel Multistable Corrugated Structures, " in *Structures, Structural Dynamics, and Materials,* 48th AIAA/ASME/ASCE/AHS/ASC Conference. Hawaii: 2007.

[9] T. Michiels, S. Adriansens, M. DeJong, "Form finding of corrugated shell structures for seismic design and validation using non-linear pushover analysis, " in *Engineering Structures,* vol. 181, pp. 362-373, 2019.

[10] www.rhino3d.com/6.

[11] www.grasshopper3d.com.

[12] www.karamba3d.com

[13] www.food4rhino.com/app/octopus

[14] S. Adriaenssens, P. Block, D. Veenendaal and C. Williams Ed., *Shell Structures for Architecture: Form Finding and Optimization*. New York: Routledge, 2014.

[15] R. Filomeno Coelho, T. Méndez Echenagucia, A. Pugnale, J. N. Richardson, "Genetic algorithms for structural design, " in *Shell Structures for Architecture: Form Finding and Optimization*, S. Adriaenssens, P. Block, D. Veenendaal and C. Williams, Ed. New York: Routledge, 2014, pp. 290-294.

Proceedings of the IASS Annual Symposium 2019 – Structural Membranes 2019
Form and Force
7 – 10 October 2019, Barcelona, Spain
C. Lázaro, K.-U. Bletzinger, E. Oñate (eds.)

Collaborative Design between Architecture and Structure: A Review of Composite Ice Shell Design and Construction in 2018 Harbin Ice & Snow World

Peng LUO *, Rui-Nan ZHANG[a], Deming LIU[a], Xiuming LIU[b]

* School of Architecture, Harbin Institute of Technology;
Key Laboratory of Cold Region Urban and Rural Human Settlement Environment Science and Technology, Ministry of Industry and Information Technology,Harbin 150006, PR China
pengluo@hit.edu.cn

[a] School of Architecture, Harbin Institute of Technology
[b] Key Lab of Structures Dynamic Behavior and Control of China Ministry of Education, Harbin Institute of Technology

Abstract

In the winter of 2018, the teachers and students from the School of Architecture and the School of Civil Engineering, Harbin Institute of Technology, jointly designed and guided the construction project of the Ice Hotel and Ice Bar in the Harbin Ice-Snow World Park. This paper reviews the design and construction process of the Composite Ice Shell Project in Harbin Ice-Snow World Park. Starting from investors' requirements for the project, site environment, construction schedule and construction cost, the author dissects the creation process of the architectural proposals, the layout of the building, the selection of the structural style, the form-finding based on the parametric design, the optimization of the structural form, the design of the construction plan, together with the adjustment and optimization of the design and construction scheme during the actual construction process. The author highlights and concludes the importance of the collaborative design between architects and structural engineers in the design and construction process, the combination point of synergistic work and the problems arising in the actual collaboration process. By means of the practice process of this project, this paper tries to summarize the work experience of architecture and structure in the design and construction process of ice shell building, and push forward the application of composite ice shell building design and construction technology in practical projects.

Keywords: Composite ice material, ice shell, collaborative design, construction

1. Introduction

The consistency of form and performance is a common phenomenon in nature. In the course of architectural development, the integration of architectural form and structural form has created many classic architectural works which combine the spatial aesthetics and structural logic. Ice shell architecture develops rapidly under the background of contemporary technology, and fully reflects the consistency of architecture and structure due to its particularity of materials and construction methods.To meet the demand of architectural space and the reasonable structure of the composite ice shell, in 2019 Harbin Ice & Snow World, the project of Ice Hotel & Bar was built and designed with the help of collaboration between architecture and structure. Ice shell technology is implemented in

Supported by National Nature Science Foundation of China Project Number: 51678177

Postgraduate research project of education reform of Heilongjiang, China: Research on teaching system of architectural and structural collaborative design based on project practice

Copyright © 2019 by Peng Luo, Ruinan Zhang, Deming Liu, Xiuming Liu
Published by the International Association for Shell and Spatial Structures (IASS) with permission.

the actual project and the application fully shows the importance of collaboration between archicture and structure in the ice shell design and build.

At present, the inflatable membranes after form-finding are used as the mold, and the method of building ice shells by spraying composite ice materials has been applied in the experiment and practice of building composite ice shells. In the composite ice shell construction project of Harbin Ice & Snow World in 2019, based on the architectural form and spatial function, the project did not apply the single air bag mould which used in the previous projects of composite ice shell, but tried to use the method of multiple air bags in parallel to make inflatable mould. The mould with multiple air bags in parallel is different from the previous project in terms of air pressure control and air bag anchoring in order to keep consistent with the design shape during the inflating process. Through the collaborative work between archicture and structure, solving the technical problems which were produced by the using multiple parallel airbags as mould and completed the construction of the Ice Hotel & Bar on January 5, 2019. The Ice Hotel & Bar were built to last 2 months, become one of the most distinctive project in the 2019 Ice & Snow World, and achieve the goal of low capital investment and short construction period.

2. Review on the ice shell projects

In 1959, at the first meeting of IASS, Heinz Isler proposes "freely shaped hill, the membrane under pressure and the hanging cloth reversed" three kinds of shell form-finding method. These methods has become successful cases which are applied in actual projects of ice shell. [1] The design and construction method of composite ice shells using inflatable membrane as moulds is inspired by Heinz Isler's theory of "the membrane pressure" form-finding. [2] In 1985, Japanese professor Tsutomu improved the method of ice shell construction, adding ice ring foundation of ice shell in the process of construction, and accelerating the construction speed by adopting aerated membrane structure as the mold. [3] Since then, Arno Pronk, eindhoven university of technology, the Netherlands, and j. berilias, university of ghente, Belgium, have carried out a number of practices based on the research of Glockner, Kokawa and Vasiliev, such as Pykrete Dome(2014), Sagrada Familia(2015) and Candela Pavilion(2016). [4,5] In 2018, a team from Eindhoven university of technology in the Netherlands and Harbin Institute of Technology in China further designed and built the Flamenco Tower, also known as the Chinese Auspicious-cloud Tower, and set the world's highest ice shell building record. Peng.L, professor in China, devotes himself to the study of the mould morphology of multiple air-rib and multi-air bag. [6] In 2018, the Ice & Snow Lecture Hall was built by cooperating with Professor Yue.W, and the air-rib was used as shell mould unit [7], as shown in Table 1. During the period of 2016-2019, Harbin Institute of Technology and IASS Group21 have carried out a series of teaching and scientific researches and projects togather, jointly hosted the 2016 China-Europe Ice-building Construction Activitiy, 2017 International Ice & Snow construction Competition, 2018 International Ice&Snow construction Competition.

Table 1 The development of ice shells

Project				
	Kokawa, Ice Pantheon, 2000	Pronk, Pykrete Dome, 2014	Pronk and Peng.L, Flamenco Ice Tower, 2018	Peng.L, Ice and Snow Lecture Hall, 2018
Development	Using inflatable membrane mould and ice foundation ring	Adding fibres of sawdust in water; The shell span 30 meters	Adding fibres of paper in water; The shell is 30.54 meters high	Using air ribbed inflatable membrane mould; The shell is used as a lecture hall in university

3. The collaborative design in 2019 Ice bar and hotel project

Located at the Sun Island Park in Harbin, China, the 20th international snow and ice world covered an area of 600,000 square meters and used 110,000 cubic meters of ice, making it the largest Snow & Ice theme park in the world. This project is located in the southwest corner of the 2019 Ice&Snow World park, besides the roads and the ice lake. There is a steel structure koi sculpture in the site, and the project is planned to be built on both sides of the entrance of the steel sculpture, with an area of 3,700 square meters, as shown in Figure 1. The composite ice shell was designed as an ice hotel and ice bar which was open to the public for over 50 days. The construction of the ice shell started on December 15, 2018, and was completed on January 5, 2019. It is divided into three stages: inflating membrane mould, spraying the composite ice material, interior ice sculpture and decoration, and the total construction schedule was 20 days.



Figure 1 The site of the ice bar and hotel

3.1. Design concept and images

The project is located in the lakeside and there is a koi sculpture in the site. In view of the surrounding environment and the carp sculpture the design concept selects the auspicious symbol of "koi" in China. In terms of architectural form, it echoes the carp sculpture in the site and designs the fish tail in a scattered shape. After discussion by architects and structural engineers in the team, the structural form of multiple column shell was selected to design and build two "fish-tail" shaped ice shells as Ice hotel and Ice bar in the comparison of multiple schemes, as shown in Figure 2.

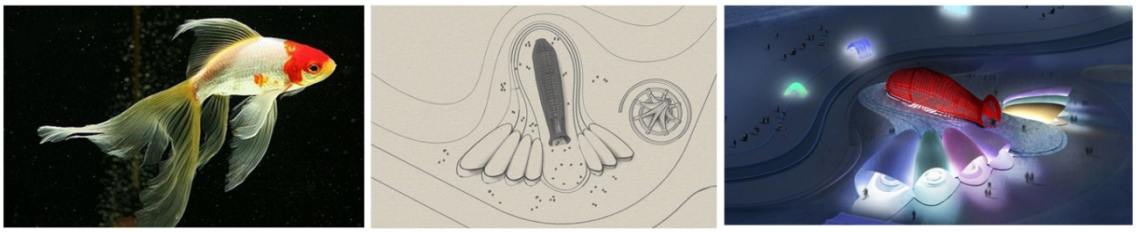


Figure 2 The design concept and images

3.2. Architectural Design

In view of the practical functions of the composite ice shell, the plane of the ice shell needs to consider the actual use requirements of the ice hotel and ice bar. The ice hotel covers an area of 210 square meters, with a horizontal span of 15 meters and a longitudinal span of 18 meters. Three ice shell units are selected for horizontal parallel arrangement, with the entrance space in the middle and the bedroom and dining room on the both sides. The ice bar covers an area of 420 square meters, with a horizontal span of 26 meters and a vertical span of 21 meters. Four ice shell units are selected for horizontal parallel arrangement, which are party

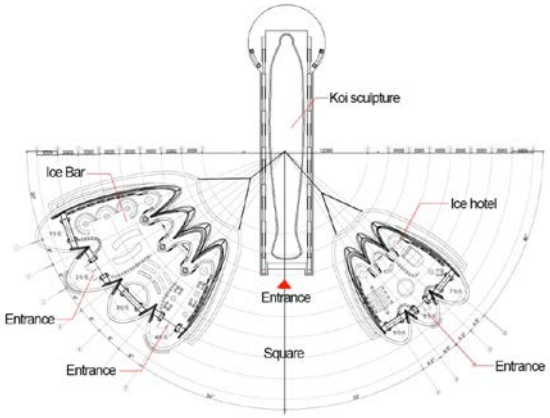


Figure 3 The plan of Ice hotel and Ice bar

space, entrance and bar counters, stage and communication space respectively. The highest point of the ice hotel is 6.2 meters and the highest point of the ice bar is 7.3 meters, as shown in Figure 3.

3.3. Collaborative form-finding between architecture and structure

To satisfy the use of the function and the rationality of the ice shell structure form, the team of architect and structural engineer chose the same digital modeling and performance simulation platform (grasshopper) through the selection of interior space size control parameters, inflatable membrane control parameters in the form of mould, ice composite materials mechanics performance parameters and load parameters to construct a parameterized virtual simulation model of ice shell. By constantly changing parameters and real-time structural performance simulation, genetic algorithm was applied to find the ice shell shape with minimum structural deformation to meet the requirements of indoor space use.

3.3.1. The parameters controlling the building form and internal space

According to the plan of ice hotel and ice bar, the transverse span of each ice shell unit, the longitudinal span and the ribbed arch span between each two ice shell units are strictly controlled. As shown in Figure 3 and 4, the parametric ice shell model is built based on the plane boundary obtained from the building plane as an immutable parameter. In order to echo the carp sculpture in site, the architect in team hope that the height of each ice shell unit is different from each other and two flanks are higher than the middle parts. As shown in Figure 4, the height of the highest ice shell unit is set as 'h', while the height of the remaining ice shell units is reduced proportively to '0.95h', '0.9h' and '0.85h' respectively. In order to make ice hotel& bar and carp sculpture better form the architectural image of Chinese koi carp, the architects in the team hope that the part of the ice shell entrance has overhangs, as shown in Figure 4. In order to facilitate the construction of parametric model, the angle of overhangs section ' α ' replaces the length of overhangs as the parameter to construct the parametric ice shell model.

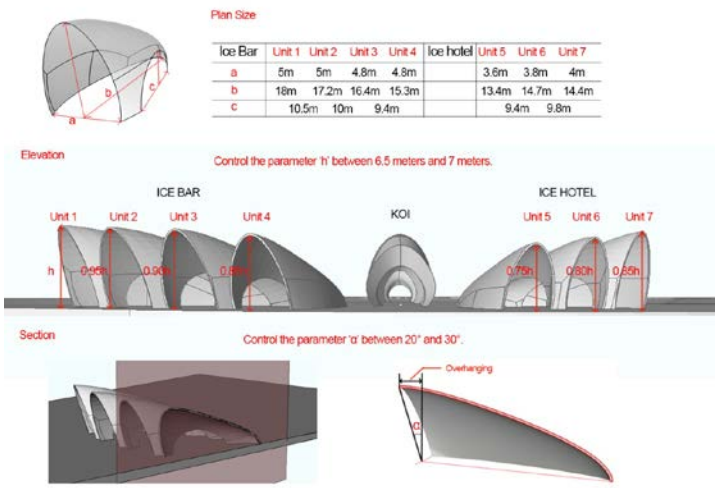


Figure 4 The design size of each ice shell unit

3.3.2. The parameters controlling the inflatable mould

On the basis of the surface model satisfying the internal use space, the real shape of the composite ice shell needs to be determined by the inflating simulation of the membrane mould. In order to make the inflatable membrane not affect the size of the internal space when inflating, the boundary constraint condition of inflating membrane is set as the plane contour line of ice hotel & bar and the ribbed arch curve between

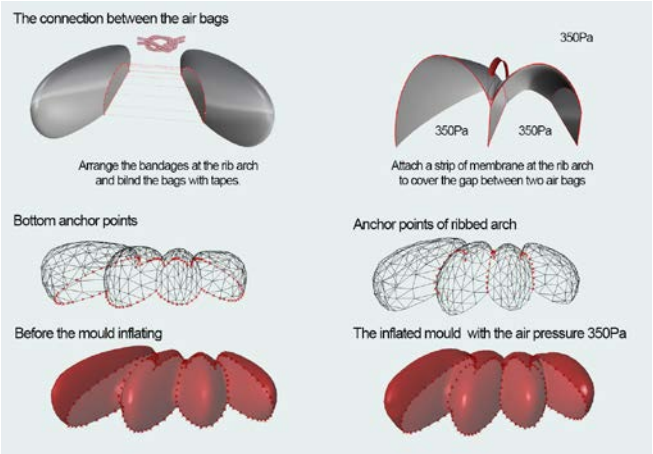


Figure 5 The discription of making inflatable membrane mould

each ice shell unit, as shown in Figure 5. The boundary lines are inputed into the parametric form-finding model. The elastic modulus of the inflatable membrane used in the construction is 600Mpa. The inflatable air pressure of the membrane mould is set as 350Pa according to the previous construction experience. Therefore, the elastic modulus of 600Mpa and the air pressure of 350Pa of the inflatable membrane mould are input as immutable parameters to construct the parametric model of inflatable film inflation simulation.

3.3.3. The parameters influencing the structural safety

The thickness of the composite ice shell is designed to be uniformly thickened from the top to the bottom, and the thickness distribution is as follows.

$$t(h_1) = t_b - t_t * h_1 / h \quad (1)$$

where:

$t(h_1)$ = the thickness of the ice shell at the height of h_1,

t_b = the thickness at the bottom,

t_t = the thickness at the top, and

h = the height of every ice shell unit.

According to previous experience, the thickness of the ice shell is designed to be 10cm at the top and 20cm at the bottom, and the thickness is taken as an immutable parameter to build the parametric model of the composite ice shell.

According to the experimental measurement, the average compressive strength was 5MPa, tensile strength was 1MPa, and the density was 900Kg/m^3.According to the actual construction experience and specifications, the load under the most unfavorable conditions is set as 1.35 times constant load, 1.4 times wind load and 1.4 times snow load.The parametric form-finding model is constructed by taking the mechanical properties of composite ice materials and the loads under the most unfavorable conditions as the constant parameters of the parametric model of ice shell to simulate the mechanical properties.

3.3.4. The process of computational form-finding in collaboration

In the collaborative design of buildings and structures, the form-finding design of composite ice shells can be divided into the following four steps, as shown in Figure 6.

The first step is to obtain the initial parametric model by lofting curves in rhino and grasshopper according to the plane boundary and their height of the internal

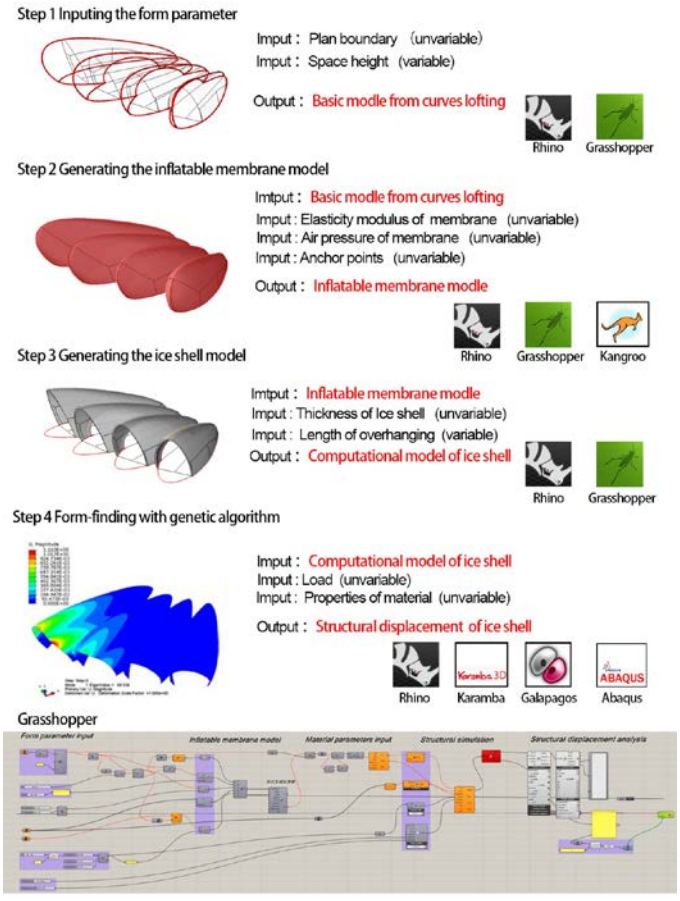


Figure 6 The steps of collaborative form-finding

space of ice hotel & bar.

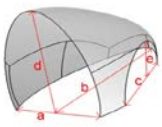
In the second step, the parametric model that meets the requirements for the use of internal space is set as an elastic surface. In the software of Kangaroo (plug-in of Grasshopper), the elastic modulus of inflatable membrane 600MPa and inflating pressure 350Pa are input to simulate the inflation.

In the third step, the surface of parametric inflatable model is set as a shell with thickness. Input the section Angle of the ice shell ‘α’and the ice shell thickness t (h_1) to obtain the parametric model of virtual ice shell. In this model, the height parameter ‘h’ and the angle of inlet section ‘α’ are variable parameters, while the other parameters are immutable parameters. The variable range of parameter ‘h’ is between 6.5 and 7 meters, and the variable range of parameter ‘α’ is between 20° and 30°.

The fourth step is to apply loads to the parametric ice shell model. The mechanical properties of the composite ice materials with a mixture ratio of 2% at the ambient temperature of -15℃ and the loads under the most unfavorable conditions are set as the constant parameters in the performance simulation. The real-time deformation changes of the ice shell after the loads are applied are obtained by constantly changing the parameters ‘h’ and ‘α’. By using Galapagos（a genetic algorithm plug-in of Grasshopper）, the values of ‘h’ and ‘α’ are determined, when the minimum displacement variation of ice shell after loading are obtained, and the final ice shell form is found.

3.3.5. The solver of computational form-finding

By adjusting the parameters of the parameterized model, genetic algorithm was applied to calculate the ice shell height parameter h=6.7m, and the section Angle of the overhanging ice shell entrance was 20°, when the ice shell met the requirements of internal space use and the ambient temperature was -15 °, 1.35 times constant load, 1.4 times wind load and 1.4 times snow load. According to two parameters, the design size of the ice shell can be determined, as shown in the Figure 7.



Ice Bar	Unit 1	Unit 2	Unit 3	Unit 4	Ice hotel	Unit 5	Unit 6	Unit 7
a	5m	5m	4.8m	4.8m		3.6m	3.8m	4m
b	18m	17.2m	16.4m	15.3m		13.4m	14.7m	14.4m
c	10.5m	10m	9.4m			9.4m	9.8m	
d	6.7m	6.4m	6.1m	5.8m		5.0m	5.4m	5.8m
e	3.5m	3.1m	2.6m			2.6m	2.7m	

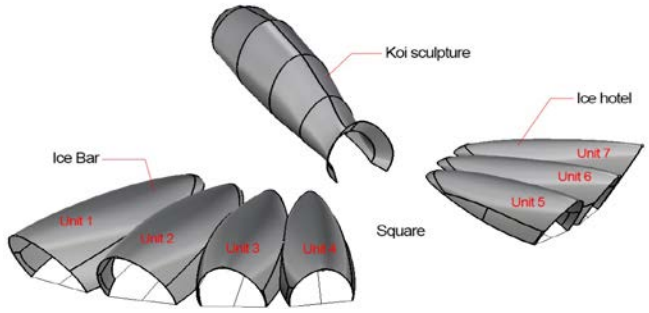


Figure 7 The specific dimensions and parameters of ice shell design

3.3.6. *The design of the ice shell foundation*

By inflating simulation of inflating film mold, it is found that multiple air bags inflating at the same time will cause the air bags on both sides (Unit1 and Unit4) to be squeezed by the middle air bags and produce outwardly deformed, as shown in Figure 8-a.Thickness parameters, composite ice material performance parameters and load parameters were set in the inflatable parametric ice shell model to conduct mechanical performance simulation. After simulation, it was found that the bottom of the outer ice shell element generated stress concentration, and the internal tensile stress was close to the tensile stress limit of the composite ice material, as shown in Figure 8-b.In order to enhance the safety of the ice shell structure, the architects and structural engineers in the team decided after discussion to increase the foundation of the ice shell to reduce the adverse effects caused by the extrusion after multiple air bags, as shown in Figure 8-e.After heightening the foundation of the ice shell, the mechanical performance simulation of the trimmed ice shell model was carried out again. It was found that the problem of over-limit tensile stress at the bottom of the ice shell was solved when the structure performance of the ice shell was unsuited by pruning the foundation of the ice shell after heightening, as shown in Figure 8-f.

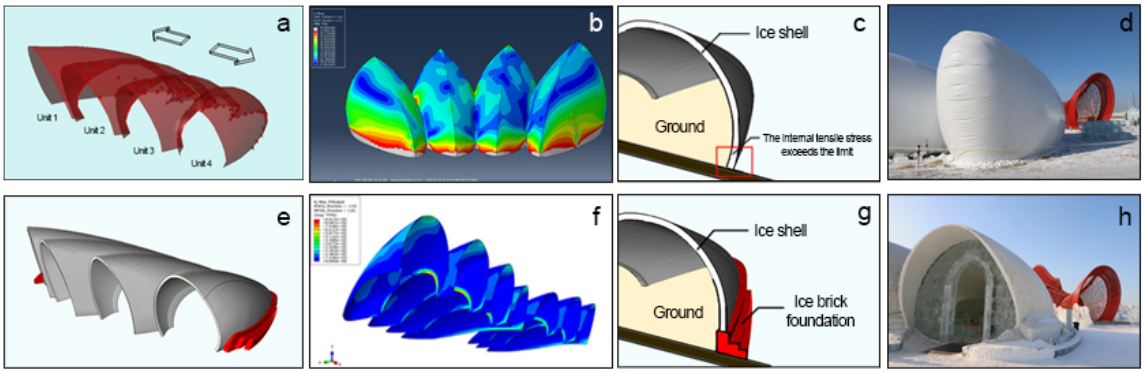


Figure 8 The process of designing the ice shell foundation

3.4. Structural simulation and analysis

Through the analysis of the force applied on the ice shell model of the above building and structure, it can be seen that the maximum lateral deformation of the triad ice shell of the ice hotel and the quadruple ice shell of the ice bar are at the highest point of the combined shell. Considering the most unfavorable conditions of its own load, wind load and snow load, the maximum displacement of the ice shell structure reaches 12.9mm, which is lower than the displacement limit of 20mm, as shown in Figure 9.

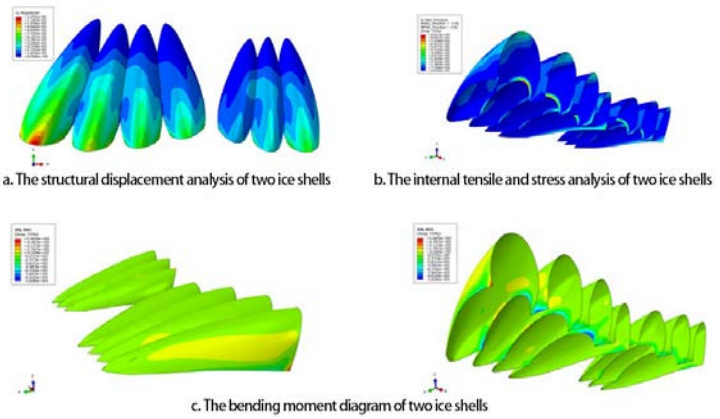


Figure 9 Structural performance simulation and analysis of Ice shells

According to the simulation under the most unfavorable conditions above, the maximum internal tensile stress of the triad ice shell of ice hotel and the quadruple ice shell of ice bar is at the joint rib arch of each ice shell unit, which is 0.88mpa at most and 1.0mpa below the material limit. The maximum compressive stress of the structure is 1.40mpa, which is below the material limit of 5.0mpa, as shown in Figure 9.

According to the simulation and analysis of the structural bending moment, the maximum bending moment is located at the base of the ice shell. As mentioned in the previous section, the base at the bottom is elevated to reduce the adverse structural influence caused by the geometry of air bags on both sides of the ice shell, greatly reducing the internal bending moment of the ice shell structure, as shown in Figure 9.

3.5. Construction process: Anchoring -- Inflating -- Spraying – Maintaining

The first step is to fix the inflatable film mould. Because of the architectural form is more complex, and take the form of mould more airbags, application of rope fixed way is difficult, and withdraw after the rope can't remove the architecture form and space can cause bigger impact, discussed by the team of architects and structural engineers, the inflatable membrane mold set along edges when not inflatable splint, fixed the ground anchor way, and did not use ice ring beam and the rope way of

anchorage. It has been proved by practice that anchoring the inflatable film mould by splint and bolt is feasible.

The second step is to connect each aerated membrane monomer. After anchoring the inflatable film mould, first fill the inflatable film with some gas to make it expand. The inflatable membrane with a certain air pressure is combined, and each unit is connected to each other by rope. After the connection is completed, seven air bags are inflated. In order to achieve the design of inflatable film mold, control the same air pressure of each air bag.

The third step, masonry ice ring beam. Stop aerating the inflatable film mold after the air pressure reaches 350Pa. Use ice block to build ice ring beam and cofferdam according to the drawings. Solve the problem of stress concentration caused by the geometric contraction of the bottom of the inflatable film mold through ice ring beam.

The fourth step is the spraying of composite ice shells. After the base of the ice shell is completed, a mixed material containing 2% pulp and pure water is used to spray the aerated film mold. Under the construction environment temperature between -5℃ and -25℃, the thickness of the ice shell is up to 0.2m at the bottom base and 0.1m at the top after 6 days of spraying. In order to prevent the melting and sublimation of the main structure of the ice shell, pure water is used to build a layer of pure ice outside the main structure as a protective layer.

The fifth step is to withdraw the mold and form. After passing the inspection by the structural engineer, the mould is removed. As each airbag being separate, when the compressor is removed and the membrane units are separated, the inflatable membrane mould is easily pulled out of the ice shell by trailer. After the mold is removed, the chainsaw is used to cut the ice shell at the front part to construct the entrances according to the design data.



Figure 10 The construction steps and final work

The sixth step is constructing the internal ice sculpture and decoration. After the construction of the ice shell, the ice bar and ice hotel are built according to the drawings of the interior design. In the process of using the ice shells, spraying the pure water three times a week is the method to protect the main structure of ice shells from melting in the day time.

4. Comarison and discussion on collaboration between architecture and structure in ice-shell projects

4.1. The different objectives between architects and structural engineers

The design of architects focuses on the beauty of architectural modeling, the integration of architectural form and surrounding environment, and the comfort of internal space, etc., while the design of structural engineers focuses on the rationality of structural form, the safety of structural system, and the efficiency of material use.In the collaborative design of composite ice shell, the conflict between architects and structural engineers is inevitable.

4.2. The different design tools between architects and structural engineers

In the collaborative design of composite ice shells, the software used by architects is convenient and efficient to generate schemes for comparing the advantages and disadvantages of building form and internal space with multiple schemes, while the software used by structural engineers is stable and accurate to calculate the mechanical properties of schemes to ensure structural safety and construction safety.Collaborative design barriers due to differences in the design tools used by architects and structural engineers should be addressed.

4.3. The environment affecting factor

During the collaborative design and construction of the ice shell building and structure, it was found in the later inspection that the orientation and form of the ice shell building have a great influence on the ice shell structure form after completion.The ice crust on the side with large solar radiation melts and sublimates faster.The temperature difference between day and night in the ice shell environment results in the repeated freezing and thawing cycle of the ice shell.After the ice shell is built, it is affected by the surrounding environment. Its architectural aesthetics, architectural modeling changes, structural stress distribution, structural safety and other aspects cannot be ignored.

5. Conclusion

Through the analysis and summary of the design and construction process of the ice bar project of 2019 Harbin ice and snow world ice hotel, the following two conclusions can be drawn.

a. Application of airbag parallel ice mold spray compound material way design and construction of composite ice shell method compared with the traditional single balloon mould construction method in the aspect of architectural form design flexibility and richness, built in the construction and withdraw membrane process with high efficiency and convenience, but due to the extrusion between the airbag in a real building inflatable membrane in the process of the mould form and design phase of the inflatable membrane mold form has certain deviation, in terms of the consistency of the design scheme and construction entities compared with the traditional application of single balloon mold slightly insufficient.

b. In a composite ice shell in the process of design and construction, building and structure of the collaborative design make composite ice shell building in form design enhance the richness and rationality, in solving practical problems in the process of building with high efficiency and convenience, when architects and structural engineers to work together on the same platform of BIM, collaborative design is high quality, efficiently solve complex ice shell a lot of problems and contradictions in the process of design and construction.

References

[1] Isler,H. "New Shapes for Shells," *IASS Bulletin,* no.8-C3Madrid, Spain.1959

[2] Chilton J.2012. "Form-finding and fabric forming in the work of Heinz Isler," *International Society of Fabric formwork; 84-91*

[3] Pronk A, Vasiliev N, Belis J. "Historical development of structural ice: Beyond their Limits," *Structures and Architecture,* 2016.

[4] Glockner P G. "Reinforced Ice and Ice Domes: Opportunities for the North," *International Journal of Space Structures,* 1988, 3(2):84-102.

[5] Kokawa T. "Building techniques for ice shell as temporary structure," *In: Proceedings of IASS-APCS: From spatial structures to space structures,* Seoul, Korea, 21–24 May 2012.

[6] Pronk A, Luo P, Li Q, et al. "Success factors in the realization of large ice projects in education," *IASS17 Hamburg*. 2017.

[7] Luo P, Yuan L, et al. " Construction Practice of Ice Shell Buildings Based on the Air Ribbed Inflatable Mould," *IASS18 Boston*. 2018.

FORM and FORCE

Proceedings of the IASS Annual Symposium 2019 – Structural Membranes 2019
Form and Force
7 – 10 October 2019, Barcelona, Spain
C. Lázaro, K.-U. Bletzinger, E. Oñate (eds.)

Computational Workflow for Segmented Shell Structures: an ANN Approach for Fabrication Efficiency

Effimia GIANNOPOULOU*, Pablo BAQUERO[a], Angad WARANG[b], Alberto T. ESTÉVEZ[c]

[*abc] iBAG (Institute for Biodigital Architecture & Genetics) - UIC Barcelona
Immaculada, 22, 08017 Barcelona, Spain
estevez@uic.es

Abstract

An already established generative design methodology for bifurcating thin shell structures with similar physical and geometrical principles of biological processes, is using the logic of stripes as a construction system, linking relaxation, segmentation and fabrication processes as one unified system in equilibrium. However, a discussion is been raised upon the amount of stripes and their topology in relation with the branching system, structural performance, connectivity system, and material usage. The objective of this article is to explore the potentials and feasibility of a state-of-the-art machine learning approach which is based partly on the user's experience and knowledge. The method consists of a generation of a database of branching topologies which are utilized to train an Artificial Neural Network. This will allow the user to have a visual judgement of the numerical values based on multifunctional criteria and adjust the design based on the new information. The fact that the prediction mechanism preserves the intuitiveness of a generic design process enhances the designer's inventory by providing control over the scalability, is saving a lot of computational time and consequently helps in the design to fabrication process.

Keywords: Machine Learning, Digital Fabrication, Mesh Segmentation, Shell Structures, Bio-inspired.

1. Introduction

As the advances in architectural practice become even more interdisciplinary, the research of biological pattern mechanisms and segmentation in construction opens a new field of investigation and architectural applications. Previous research by the authors [1], [2] explored how generative architectural design processes aim to apply similar principles of biological morphogenesis to the design and fabrication of thin shell structures [3]. To deepen into the subject of fabrication of bifurcating shell structures the on-going research [4], [5] leads to some experimental attempts to build up a machine learning (ML) methodology which will enhance the design space and help for quick estimations for decision making inside the design process. The case study is using previous insights and results to test the feasibility of building a prediction mechanism of shell and pattern generation with n number of branches. An already established parametric workflow allowed the development of a database [4] which is used to train an Artificial Neural Network (ANN). The ANN instantly gives numerical outputs based on the specific chosen characteristics/attributes. Finally, the ML accuracy is tested by comparing the ANN outputs with the computational outputs.

2. Branching shell design methodology

Branching topologies of closed and open tubular minimal shell structures have been tested on different small prototypes (Figure 1). Following a similar design process as in tensile/membrane structures, the simulation with particle spring system, achieves surfaces near to minimal and the structure in an equilibrium state. This form and function dependency allows the branching shells structure to be self-supportive and withstand an additional weight apart from the material itself. In addition, the realization

Copyright © 2019 by Effimia Giannopoulou, Pablo Baquero, Angad Warang and Alberto T. Estévez.
Published by the International Association for Shell and Spatial Structures (IASS) with permission.

of the fabrication process acknowledges materials, tools and construction logic in an early stage of the design process, as manifested in nature. The logic of structural stripes [6] is used to pre-rationalize the design method [7], where each stripe is conceptualized as a ruled surface, developable, with zero Gaussian curvature, made of curved sheets of material.



Figure 1. Biodigital Fabrication Studio Series 2017/2018/2019, University Master in Biodigital Architecture, ESARQ-UIC Barcelona, School of Architecture - Universitat Internacional de Catalunya, (top) open branching network with three legs, (bottom) cantilever with four anchors, open topology (right) cantilever with six anchors, closed topology. (Images by authors).

2.1. Define branching topology

Topology refers to the system of anchoring points creating a branching network of connected lines, the foundation of a skeletal shape, in which each point is a branch node. The positions of the points change randomly with a seed value and follow some rules that preserve some symmetry. The skeletal, used as medial axes, is converted into a network of quadrilateral meshes. This system of tubules, or hollow vessels is referring to a cytoskeleton or branching shell structure. This point/skeletal approach for the shell structure is especially designed to accomplish two basic needs. Firstly, the system to be able to iterate through different configurations and the same time the points to serve as anchoring locations of the structure with the base. This is achieved by considering an unbranching structure as the skeletal shape, following an inwardly growing progression of the branching system and thickening of the nodes [4].

2.2. Simulation

In order to generate in a simple and intuitive way a structure in static equilibrium, with minimal surface properties, dynamic relaxation is applied to the skeletal quad mesh edges using a physics engine [8]. Following a similar form-finding process as in membrane structures and grid shells, skin and structure are formed as one. Mesh is subdivided and boundary conditions are defined as the naked edges of the mesh. Applying different forces (gravity loads, spring length) to the springs is possible to interactively control the thickness of the shell branches, estimate the desired height of the structure and influence the smoothness and surface continuation, especially in the saddle locations, taking in count material bending properties. The last one could be also controlled by the stripes topology and orientation. The branching shell structure was examined with a very fast linear analysis of shell elements [9]. The analysis of structural parameters was using material data of PP (elasticity, density yield strength and poisson's ratio) [2].

2.3. Define pattern and fabrication

Given a parametrized tubular minimal shell structure in static equilibrium and a set of weighted conditions for the mesh nodes and edges, various segmentation algorithms, coming from graph theory [10] are tested to discretize effectively the given topological mesh. Custom weights applied to the edges using Orange Peel (OPE) algorithm to generate ripples, following primary and secondary segmentation algorithms [2]. Throughout this process is possible to manage the amount of cutting stripes, topology, orientation and maximum amount of faces per stripe. Using the opennest plugin [11], the 3D stripes are oriented on 2D rectangular sheets with specified material dimensions.

3. Methodology for machine learning implementation

The ANN experiment is framed in four computational stages and different grasshopper definitions were developed:

1. Parametric Shell Structure: Geometry construction and structural analysis.
2. Database preparation: Develop a 1150 Shells database [4].
3. Training process: Develop the layout of network structure.
4. Validation: Generate new database to compare the computed with the predicted values.

3.1. Learning objectives and criteria

The ML methodology is re-examining the already established parametrized design workflow. Modifications, extensions and clustering operations are applied to the initial model in order to extract the appropriate data sets in the format of excel sheets and corresponding jpgs [4]. As a matter of fact, the most interesting part of this method is to determine those sets of attributes/features/behaviours inside the design workflow to train the model to predict. The designer can have a visual judgement of the numerical values based on multifunctional criteria. The goal is to experiment the structurality of thin shells with branching topologies taking in count at the same time the material usage. In contrary to a previous design methodology of static inputs, this approach allows the generation of a dynamic input geometry which permits the selection between various outcomes that fit best the criteria.

General reference/criteria are defined as: deflexion, material usage, configuration and number of stripes, connectivity and surface continuity. The learning process suggests that the combination of some attributes indicating an efficient fabrication process which is balancing assemble time, number of sheets and extra weight due to the connecting elements and is up to the user to decide [4].

3.2. Training

For the training process a grasshopper definition was made using Crow [12], a machine learning plugin, extension of NeuronDotNet.dll developed by Vijeth Dinesha. The Crow component requires three input parameters:

1. The quantity of iterations to give good accuracy was set to 12000 cycles.
2. The network structure was set up with six nodes in the input layer, twelve and fourteen nodes in the two Sigmoid hidden layers and seven in the output layer (Figure 2). After many trials of changing the number of cycles, the learning rate was set to 0.2 to obtain the smallest MSE of 0.017516.
3. The datasets for training: 1150 branching shells, generated by the input attributes (Spring Strength, Number of Anchor Points, Minimal Number of Faces per Stripe, Random Seed Generating Point Locations, mesh subdivision), and outputs attributes to train (Number of Stripes, cutting length, Number of Sheets, Material Wasted, Height, deflection, weight).

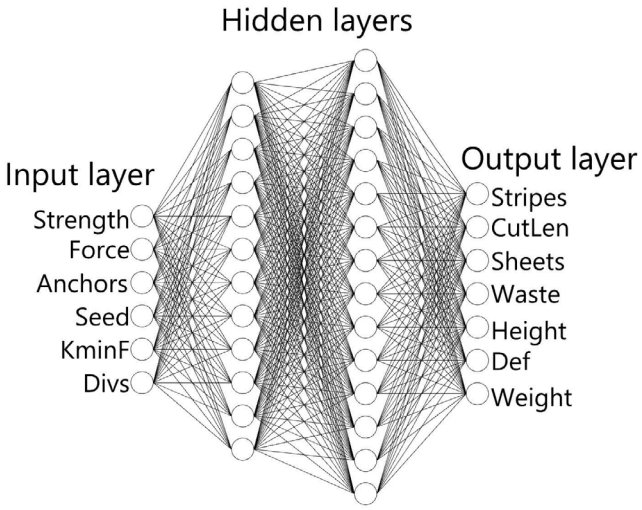


Figure 2. Layout of network, showing 6 nodes for input layer, 12 and 14 nodes in the hidden layer and 7 in the output layer. (Image by author).

3.3 Limitations and constraints

The database was generated using colibri plugin inside grasshopper. During the simulation, for some few cases, the combination of input parameters failed to give a geometrical results and the corresponding numerical values. Although current parametric modelling systems can capture best practices and facilitate the generations of design alternatives, models are not capable to support variations beyond the scope of their hierarchical structure of the geometric relationships prematurely limiting the potential design space [13]. Another limitation of the parametric model is that it did not allow to switch between different paths of segmentation algorithms (SA) (different IVY components giving different stripe pattern effects, based on different inputs like valence, deviation, angles, etc.) in order to have them in one run. This indicated another limitation of the proposed methodology and tools. Creating parallel databases by iterative runs, using different SA each time, would not allow even to be introduced as attributes at the same time due to the different type of segmentation input parameters that each algorithm requires. The idea of creating a machine prediction for pattern generation was limited to specific combinations of SA. We can observe though that changes in the branching topology (number of anchor points, spring strength, etc.) affect also the stripe configurations, especially in the top part of the shell. To avoid these type of issues and let it run in

multiple generations, the definition had to be arranged properly to work for all cases providing a generic framework for future experiments of biological based segmentation for branching shells.

4. Results and analysis

4.1 Validation process

For the validation, another database was made out, with the purpose of comparing the tested iterations with its outputs attributes. It is using the 1150 database computed previously, in order to make a validation with the ANN prediction and compare the computed versus the predicted, both with vector information and with real information. Backpropagation classifier component was used for testing the 6 inputs vector information, which gives 7 output vector data for each iteration. The graphs demonstrate the accuracy of the ANN for each attribute with real values. The scatter type of charts is useful for comparing two sets of data sets. The closer the points to the trend line (diagonal line) the closer the prediction (Figure 3).

4.2 Error estimation

To estimate the errors a comparison is made throughout the timeline calculating the difference between predicted and computed values. The Waste attribute is the one which shows bigger errors (Figure 4). To see closer the error the Waste comparison is focused to 200 iterations, showing both predicted and computed vector values (Figure 5).

5. Discussion and future work

The general hypothesis is questioning the feasibility and purpose of a prediction mechanism of branching and pattern generation for segmented shell structures, analogous to the biological skin patterns. In this case only lateral branching is examined following simple rules to avoid complications for the generation of the data sets. The viability of the implementation of 3D patterns with geometrical and topological properties of Turing patterns (area, boundary length, cluster numbering, connectivity, and so on) as described by Guiu-Souto et al. [14] inside a generative fabrication context would be a future idea to explore.

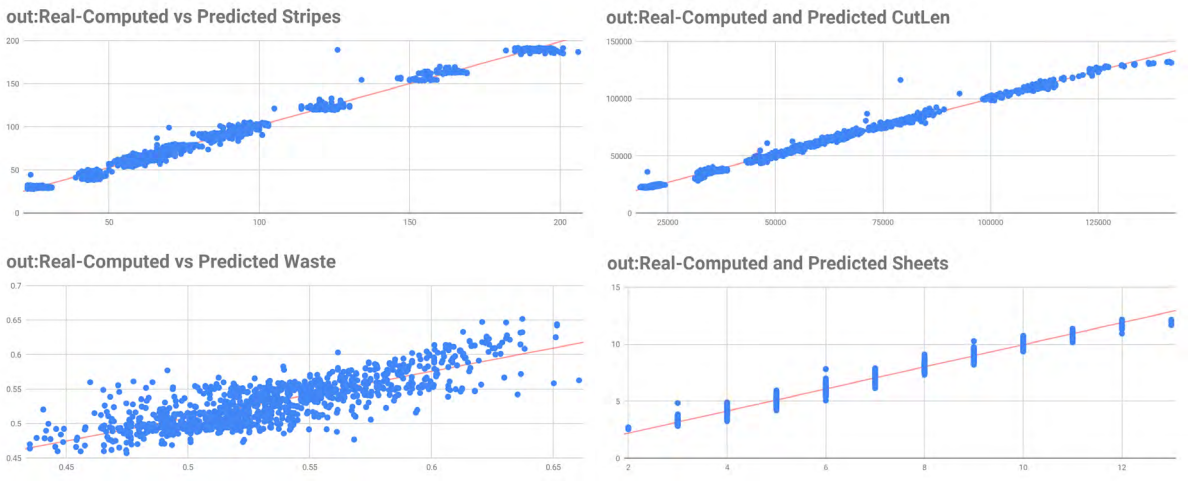




Figure 3. The 7 graphs correspond to the 7 output attributes. The scatter type of charts is useful for comparing two sets of data sets. The closer the points to the trend line the closer the predicted to the computed.

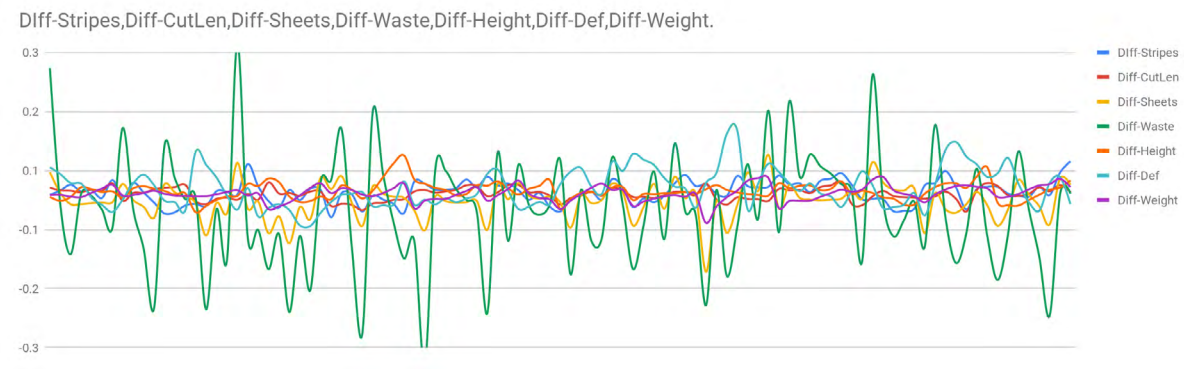


Figure 4. Chart of all attributes with Vector values, showing the difference between the predicted and the computed attributes in 100 iterations. The *Waste* attribute (green line) is the one which shows bigger errors.

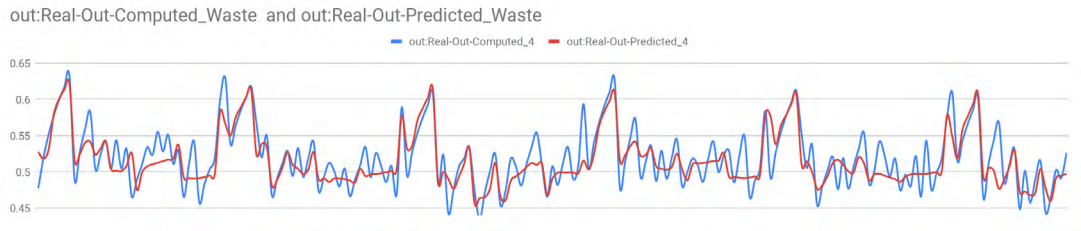


Figure 5. Chart showing the predicted (red) vs computed (blue) for the *Waste* attribute in 200 iterations with Vector values.

A discussion has been raised about the importance of a structural investigation on the segmented stripe shell. The problem was how to set up the loading conditions in order to test the structurality and connectivity of the stripe pattern. A finite element setup method based on springs, as in the cases of segmented shells composed of planar plates [15], [16], may be a possible solution in case of bigger scale construction.

Under the framework of complex modelling [17], [18] and Ito's extended intelligence [19], the idea of bringing design and science together can foster new, productive and flexible antidisciplinary work, this research triggers not only new ways of thinking about tools and methods that transform design, but to question the purpose as observers and designers of a machine-based system of thinking and a

new understanding of architecture. Learning from nature's laws ("bio-learning") and computation as a powerful tool to solve problems.

Acknowledgements

We greatly appreciate the students of the University Master in Biodigital Architecture and Professor Affonso Orciuoli of iBAG-UIC Barcelona for their contribution to make this research real.

References

[1] E. Giannopoulou, P. Baquero, A. Warang, A. Orciuoli, A.T. Estévez and M.A. Brun-Usan, "Biological pattern based on reaction-diffusion mechanism employed as fabrication strategy for a shell structure," *IOP Conference Series: Materials Science and Engineering*, vol. 471 (10), 2019.

[2] E. Giannopoulou, P. Baquero, A. Warang, A. Orciuoli, A.T. Estévez and M.A. Brun-Usan, "Employing mesh segmentation algorithms as fabrication strategies: Pattern generation based on reaction-diffusion mechanism," *FME Transactions*, vol. 47 (2), pp. 379-386, 2019.

[3] M. Bechthold, *Innovative surface structures: technology and applications.* London: Taylor & Francis, (2008).

[4] E. Giannopoulou, P. Baquero, A. Warang, A. Orciuoli and A.T. Estevez, "Stripe Segmentation for Branching Shell Structures - A Data Set Development as a Learning Process for Fabrication Efficiency and Structural Performance," in *Architecture in the Age of the 4th Industrial Revolution: Proceedings of the eCAADe+SIGraDi joint Conference 2019, Porto, Portugal, September 11-13, 2019*, eCAADe / SIGraDi, 2019. (To be published).

[5] E. Giannopoulou, P. Baquero, A. Warang and A.T. Estévez, "Machine Learning Approach for Biological Pattern Based Shell Structures," *Industry 4.0 - Shaping the Future of the Digital World*. London: Taylor & Francis, 2019.

[6] P. Schumacher and M. Fornes, "The Art of the Prototypical," *Architectural Design*, vol. 86 (2), pp. 60-67, 2016.

[7] E. Stach, "Structural morphology and self-organization," *Journal of the International Association for Shell and Spatial Structures,* vol. 51 (165), pp. 217-231, 2010.

[8] D. Piker, "Kangaroo: Form finding with computational physics," *Architectural Design*, vol. 83 (1), pp. 136-137, 2013.

[9] P. Michalatos, *Millipede. Grasshopper*. http://www.grasshopper3d.com/group/millipede. Accessed March 1st, 2014.

[10] A. Nejur and K. Steinfeld, "Ivy: Bringing a weighted-mesh representation to bear on generative architectural design applications," in *36th ACADIA 2016, Ann Arbor, U.S.A., 2016*, ACADIA / University of Michigan, Taubman College, 2016. pp. 140-151.

[11] P. Vestartas, *OPENNEST*. Retrieved from: https://www.food4rhino.com/app/opennest

[12] B. Felbrich, *Crow plugin for Grasshopper.* http://www.felbrich.com/projects/Crow/Crow.html. Accessed April 27th, 2019 (2016).

[13] M. Bernal, "From Parametric to Meta Modelling in Design," in *SIGraDi 2016, XX Congreso de la Sociedad Iberoamericana de Gráfica Digital, 2016 Buenos Aires, Argentina*, SIGraDi, pp. 579-583, 2016.

[14] J. Guiu-Souto, J. Carballido-Landeira and A.P. Muñuzuri, "Characterizing topological transitions in a Turing-pattern-forming reaction-diffusion system," *Physical Review. E, Statistical, Nonlinear, and Soft Matter Physics*, vol. 85 (5), pp. 1-8, 2012.

[15] L. Jian-Min and J. Knippers, "Pattern and Form: Their Influence on Segmental Plate Shells," in *Proceedings, International Association of Shell Spatial Structures Symposium 2015, August, 2015*, IASS, 2015.

[16] R. La Magna, F. Waimer and J. Knippers, "Nature-inspired generation scheme for shell structures," in *Proceedings of the International Symposium of the IASS-APCS Symposium, Seoul, South Korea, May, 2012*, IASS, 2012.

[17] M. Tamke and M.R. Thomsen, "Complex Modelling," *International Journal of Architectural Computing*, vol. 16 (2), pp. 87-90, 2018.

[18] M.R. Thomsen, "Complex modelling - questioning the infrastructures of information modelling," in *Proceedings of the 34th eCAADe conference complexity & simplicity (eds. A. Herneoja and T. Österlund), University of Oulu, Oulu, 22-26 August 2016*, vol. 1, pp. 33-42, eCAADe, 2016.

[19] J. Ito, "Extended Intelligence," *Joi Ito's PubPub*, pp. 1-6, 2018.

Proceedings of the IASS Annual Symposium 2019 – Structural Membranes 2019
Form and Force
7 – 10 October 2019, Barcelona, Spain
C. Lázaro, K.-U. Bletzinger, E. Oñate (eds.)

Craft and Manufacture of Modular Thin-Tile Shells

M. Wesam AL ASALI*, Michael H. RAMAGE

* Department of Architecture
Cambridge University
Cambridge
CB2 1PX UK
mwa24@cam.ac.uk

Abstract

Time and location have an implicit influence on the form, construction, and structure of load-bearing shells. Manufacturing building components is usually imagined as being accompanied by heavy machinery and advanced tools. In the case of tile vaults, craft can be central to their manufacture. In this paper, we examine two tile-vaulted projects in which the craft of the artisan is either digitally transferred or pushed to the edge of mechanization. In *FR2* (Chicago, USA), the work of a stone mason in Cambridge (UK) was digitized and remanufactured in Chicago to serve as a mold. In *FabricArte* (Valencia Spain), a three-vault walk-through pavilion built for the Ceramic Expo 2018, we investigated offsite construction of the vaults, slicing them into pieces and transferring the resulting modules to the site for reassembly. In FR2 and FabricArte, typical construction of tile vaulting was challenged by constraints of skill and time. The designs explores the interface between craft, computation, and construction in tile vaults.

Keywords: Thin-tile vault, Manufacturing, Prefabrication, Compression-only shell.

1. Background

Designing and making tile vaults is a process with many cases of reciprocity: form and force, skill and formwork, material and manufacturing, and labor and design. This paper examines the effect of time and location on labor by presenting two methods of manufacturing to either speed on-site construction or mitigate on-site lack of skill. Placing handicraft alongside modern construction is central to these methods.

The first example is an interior design of office space for Joe Ritchie's FR2 office in Chicago, IL, USA. The office, designed in 2014 by Light Earth Designs, is composed of a system of suspended ceilings of 200 units of conic vaults, an entrance pavilion, and a set of wooden elements for furniture and interior sculptures. The design challenges conventional vault construction and manufacturing, because the vault are too many and the wages of the workers, who have no previous experience on tile vaulting, are very expensive. A method of knowledge transfer through digital models that were later translated into physical molds kept the construction in the hands of the builders but accelerated it and reduced the cost.

The second example is FabricArte, a temporary terracotta tile pavilion that was built during the Valencia Ceramic Expo (Cevisima) in 2018. The pavilion was designed to celebrate the Spanish ceramic industry. It was erected in the central hallway of the exhibition and was coordinated by the Instituto de Tecnologia Ceramica (ITC) and curated by the Asociación Española de Fabricantes de Azulejos y Pavimentos Cerámicos (ASCER). The expo regulations in Cevisama allow for only short on-site construction, making the laborious construction of tile vaults challenging. A method of

Copyright © 2019 by M.W. Al Asali, M. H. Ramage
Published by the International Association for Shell and Spatial Structures (IASS) with permission.

manufacturing vaults beforehand served to install the structure in the expo within the allowed construction time.

2. Introduction

Tile vaulting uses tiles and plaster of Paris. The tile, traditionally a terracotta tile, is lighter than brick, making it possible to apply the fast-setting mortar, rapid cement, or plaster of Paris to glue the tiles together and obviate the need for heavy formwork. The first layer of tiles becomes the formwork for more layers of tiles and cement mortar [1]. The technique is western Mediterranean, but it is celebrated particularly in Spain, where it is still a tradition for vaults and stairs. Tile vaults were central to the work of Catalan modernist masters, such as Antoni Gaudí, Lluís Muncunill, Cesar Martinell, and the Valencian Rafael Guastavino (1842–1908), who transferred tile vaulting to the US. Guastavino's company contributed to more than one thousand projects in the country [2], [3]. Today, the technique is being revived in research and design [4]. Terracotta for tiles has been replaced with compressed soil-cement for low-cost and locally resourced construction in South Africa [5]. The same system has been used with light-weight reinforcing for the Rwanda Cricket Stadium in Kigali, a mildly seismic zone [6]. Tile vaults were used with novel design and analysis tools, producing unconventional structures and forms [7], [8]. Studies of tools and methods of construction were also part of this revival [9], [10].

However, the manufacturing of a tile vault as a 'building component' is yet to be fully explored. Such a focus is important for finding solutions for buildings with less material consumption and waste production, and it pushes the shell structures outside the boundary of being elements, proposing them as systems. Thus, aspects of time, location, and labor become pertinent to the design because they become either a constraint or a solution. The proposition is not new but also is not developed. Vaults in Latin America during the mid-twentieth century were imagined as a possibility for the emergence of a new construction methods. The work of Eduardo Sacriste (Argentina), Mario Kalemkerian (Uruguay), Rodrigo Levere (Brazil), and Carlos González Lobo (Mexico) is based partially or entirely on tile vaulting to manufacture shells, mainly for housing [11]. Most of their work relied on a repetition of simple geometry of a barrel vault or dome. With today's tools and technologies, the projects presented in this paper investigate methods of manufacturing that overcome the limitations of geometric simplification and the traditional understanding of labor and skill.

3. FR2 Office: Technology and the Master Builder

3.1. Design and structure

FR2 is an interior project of an office space for Joe Ritchie, the project emphasizes on the use of natural materials and celebrates that use with all interior elements. The office spaces were designed to be lofty and open but also to allow for discreet working areas that were formed by aedicules of different shapes and heights, made of beetle damaged pine. The office had two tile vault system. The first is a 2 meters height vault at the entrance of the office and the second is an earth tiled suspended ceiling soffit formed of 200 triangular vaults. The ceiling vaults used an existing steel structure. The design proposed an earth tiled soffit formed or triangular vaults that span between the steel structure. The tiles for the vaults were made from the soil found in the client's farm near the construction site. The entrance vault was made by a master mason with help of a detailed plywood system that supported and guided the construction. However, the 200 vaults was made by local bricklayers.

3.2. Model and Digitization

Two constraints drove the design and construction of the FR2 offices in Chicago. There was a lack of skilled labor able to build thin-tile vaults, and the need for 200 identical elements meant that only mass production of the same element was a viable solution in a high-wage context. The solution included a process that transferred the mason's skill of a carved physical prototype into a three-

dimensional CAD model. The CAD model, based on a physical prototype of 1:3 model made by a skilled stonemason in the UK, allowed a CNC machine to reproduced a full-scale model in wood in the US. Finally, a negative model was then made by casting silicon on the wooden master and served as a mold for laborers follow the overall coursing of the designed vault

3.3. Construction

The labor can be a challenge due to the production type and the number of identical vaults. Producing two hundred vaults of the same shape is different from the case of an individual structure. Production time, material waste by stone cutting and intensive labor are challenges that have an impact on the design and planning phase of the project and not only the construction phase. The project proposed a conventional approach to build the 200 vaults with a training program for workers there in coordination with the bricklayers' union. Instructions with details of construction were sent to the brick layers to follow. However, the bricklayers work was not successful to produce vaults with a highly crafted look of the interior. In interior elements, tolerance in the details is usually minimal due to the close distance between an observer and a built element. Furthermore, It was very clear that training and the construction would take a much longer time than what was programmed. A move to a more specified guidework for the construction than only instruction was a must.

The 1:3 prototype and the digital model was developed in the UK with the mason Sarah Pennal. The models allowed for a close attention to the details before the actual building of the vaults, saving the time of approvals and supervisions in early stages. The CNC carved negative mold facilitated the production of several silicon molds, hence maximizing the productivity of the workers and lessening the time for construction. The mold defined the coursing and the placement of the tiles in the vault. The work of the master mason on the carved 1:3 prototype presented a nonconventional coursing approach that articulates not only the overall shape but also accentuates a dynamic visual effect of the ceiling vaults. This coursing was achieved with 3 sizes of tiles. Because the tiles were produced for this specific project, the tiles were all cast from soil-cement slurry in the three sizes beforehand, saving time and wasted material from cutting common tiles. After the individual vault was made, it was lifted by an automotive transmission jack, to the right height and then shifted then shifted into the triangular shaped steel frame which was pre-hung from the slab above.



Figure 1. FR2 Interior.

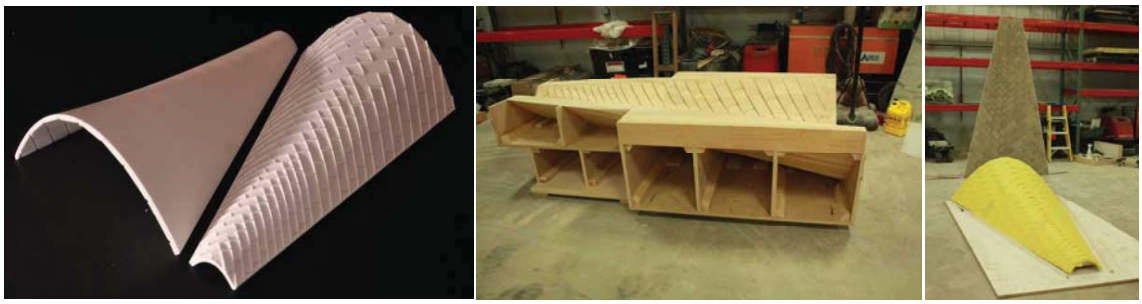


Figure 2. Left: digital model, center: positive computer numerical control (CNC) mold, right: silicon mold and built vault.

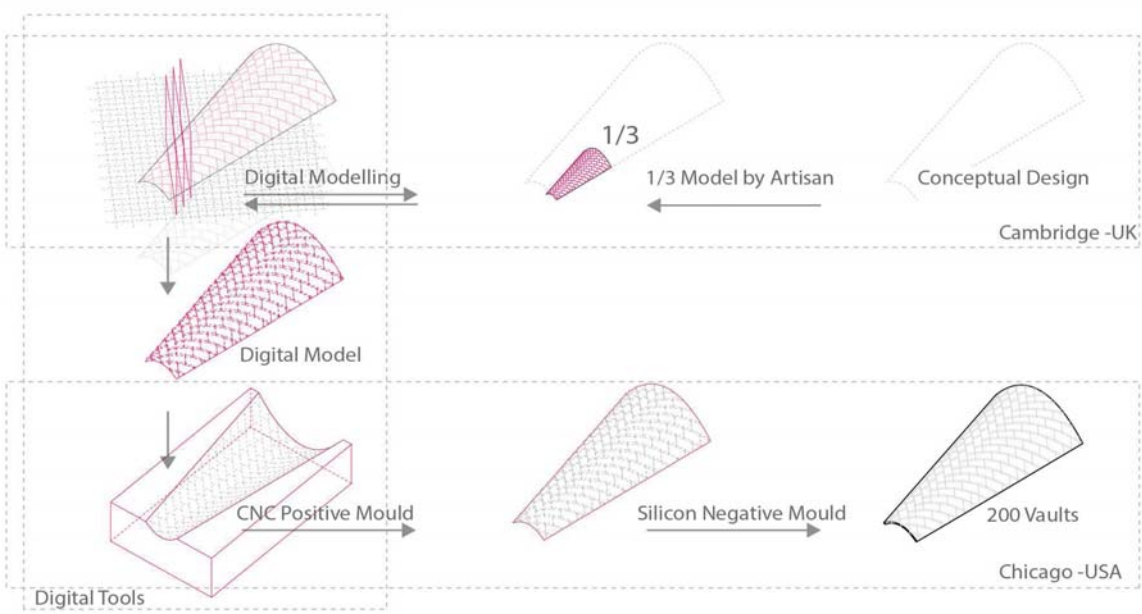


Figure 3. FR2 Process.

4. FabricArte: Time in Tile Vault Construction

The Annual Ceramic Expo in Valencia (Cevisama) is dedicated to new experiments of material, construction, and fabrications of ceramics. In 2018, we proposed a walk-through pavilion (FabricArte) in the central space of the expo building to celebrate the craft of tile vaulting in Spain, a craft that converts ceramic work from decorative cladding to structural compression-only shells. FabricArte's design is based on a groin vault composition. However, the vaults are one of two integrated systems: a compression shell and linear tension elements. The integration of the two systems was kept as visible as possible, resulting in changing the scenarios of the vault that change in three modules from the flat systems of shallow slabs to a full height expressive vault. The transition allowed for the exploration of manufacturing of three vault typologies. We tested a shallow vault resting on columns, a full vault, and a vault that springs from two different levels, similar to vaulted stairs. The structural analysis of the vault was made using graphic statics with the help from a particle-spring system. In addition to form-finding the efficient geometry, graphic statics provided the direction and intensity loads, which influenced the selection and design of the steel frame structure and moment joints. Tile vaulting is rooted in Valencia and was part of the late Valencian Gothic architecture, where modular units mirror, repeat, and array to compose the main structure [12]. Repetition and modularity were central to the design and formed a guideline for the smaller manufactured pieces of the vault.

4.1 Modeling and Segmentation

Expo regulations permit two weeks for on-site construction, transportation of materials, and preparation for the exhibition. This period did not allow for the designed 7.5 m walk-through structure to be built. The challenge prompted a new experiment in tile vaulting, in which the vaults were built in a workshop, sliced, transferred to the site, and re-assembled for the exhibition. The decision was to keep the manufacturing process manageable without using heavy machinery, such as cranes and lifts, by downsizing the 3,800 kg vault surfaces into smaller components. The modularity of the cross vaults and the Gothic pattern helped in building quarters of vaults and then slicing them into smaller sections. The slices were made to avoid linear horizontal cuts in the structure. The cuts in the side arches were higher than those in the infill. The calculations of the cuts were digitally studied based on the height and weight of each piece. The vaults had three layers, but only one layer was built offsite and sliced, making the transportable pieces lighter. The height was another factor that influenced the cutting pattern. Each piece was calculated to be held by two workers on the ground (maximum of 120 kg) or one person on a scaffold (maximum of 50 kg).

4.2 Construction

The team worked closely with one of thin-tile vault master builders, Salvador Gomis Aviño. The collaboration facilitated iterations between design and craft and between industrialization and handmaking, where each discipline influenced and improved the other. Molds were designed for modular quarters of the vaults to support the construction, transport, and assembly. Building vaults in quarters impeded the visualization of the overall geometry of the shell, and made it hard to imagine the tile angles, joints, coursing, and cuts. This has resulted in difficulty to apply conventional carpentry without the extensive use of drawings. Instead, the sheets of medium-density fiberboard cut using computer numerical control (CNC) were made for screw-less easy assembly and disassembly without plans or models. One layer of tile vaults was built over the mold. Only side arches had a second layer to add stability to the pieces during on-site assembly. After the completion of a quarter, it was sliced by radial saws using the suggestive pattern as a guide. At areas where the edge was connected with the other quarters, the use of the saw helped in cutting and refining the edge after construction. The pieces were transported on a mid-sized truck. A few minor breakages happened in the edges of the pieces. On-site, the installation of the mold/formwork took one day, and the assembly of with plaster of Paris and fiberglass textile took around five days.

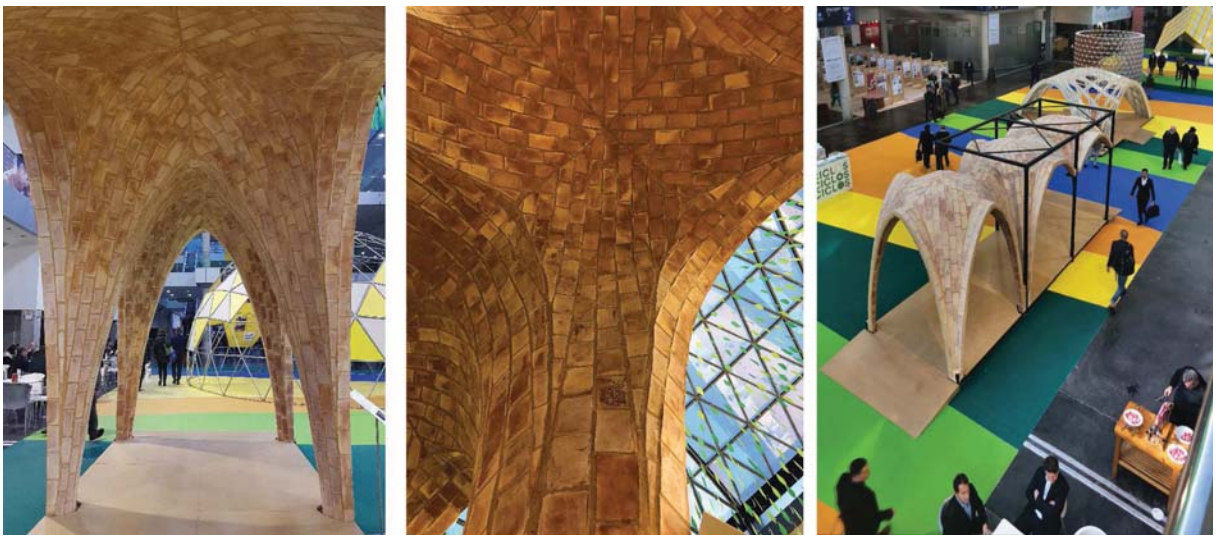


Figure 4. FabricArte.



Figure 5. Manufacturing process.

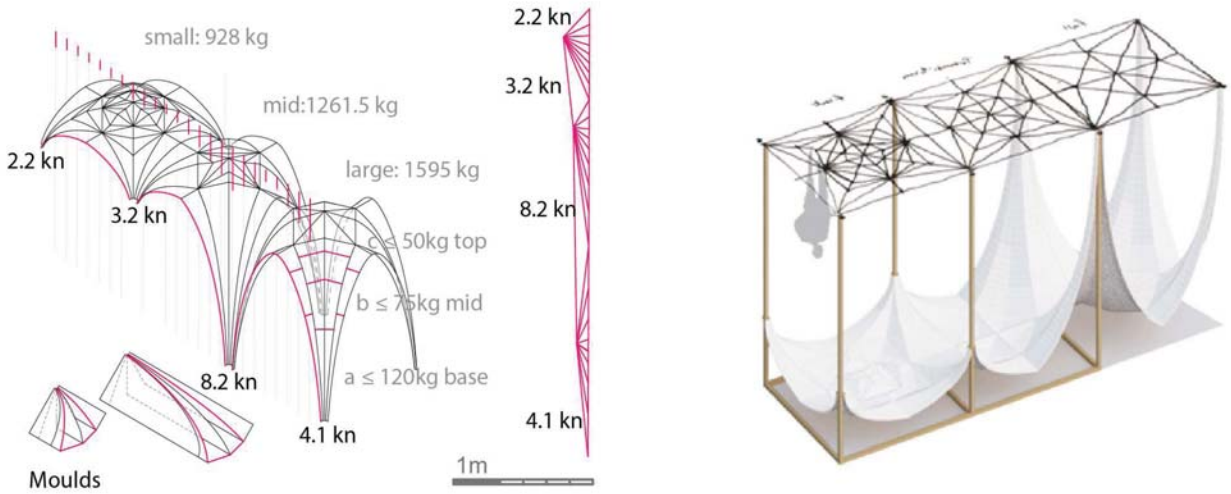


Figure 6. FabricArte design and analysis.

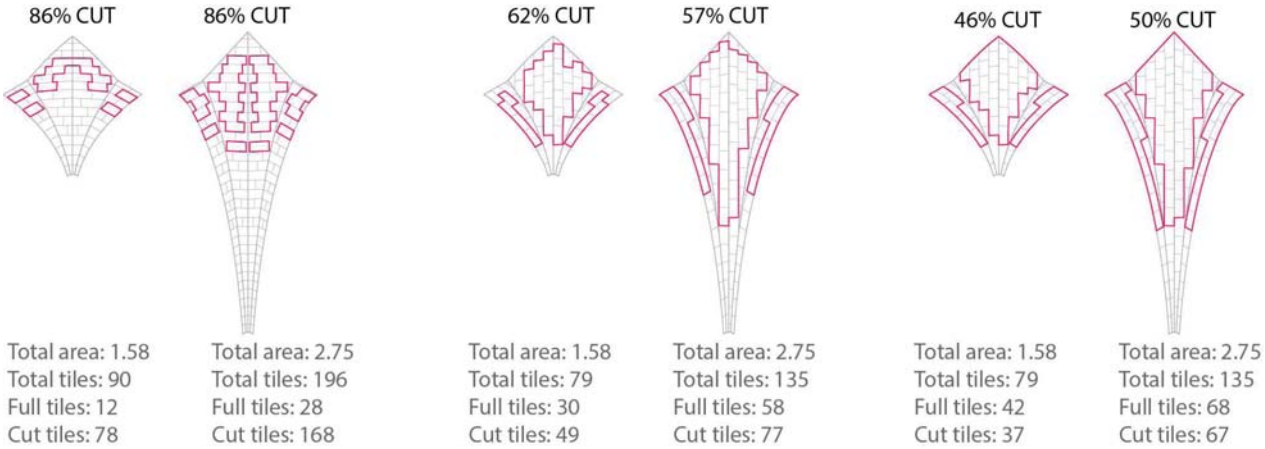


Figure 7. Edge and intersection effect on time.

After the completion of the whole shell, two additional layers were made in three days. One layer was on top, and one was underneath. The lower layer was made with plaster, and the joints between the tiles were filled with cement mortar. Whereas the added bottom layer of tiles hid the Gothic patterns of cuts, the flooring of the pavilion reflected the lines as a diagram of the process of manufacturing.

4.3 System Development

FabricArte examined the possibility of tile-vault manufacturing. However, the core inquiry in this experiment was about time. Every construction and design decision had an effect on the time consumed on site and in the workshop. A tile-vaulted linear stair whose surface area is about 7.5 square meter takes an average between two to three days for completion. If FabricArte's 28 m^2 surface is 3.7 stairs, the construction would have taken 9.25 working days. However, this estimation was out of reality. FabricArte's workshop construction took around 17 days to be built because of two central features that had a significant effect on time: the coursing and edge condition. In both cases, the tile needs to be modified by cutting, which requires measuring, marking, cutting with a wet saw, and placing. The procedure magnifies the time of construction up to five times more than the placement of a normal tile for an angled slice and three times more for the straight cuts. For this reason, the initial horizontal coursing for the cross vaults was time-consuming because 86% of the tiles needed to be cut. We changed the coursing to a vertical one that used less tiles in general and reduced the percentage of cut tile to 62%. In the edge condition, placing full tiles along the edge and then cutting everything with the radial saw helped in reducing the percentage of cut tile from 62% to 47%. What remained was the inevitable and laborious intersections between the side arches and the infill. A tile needed to be tilted and sliced at the same time. The second iteration of FabricArte was closely reviewed regarding the edge and intersection condition. To avoid slicing tiles at angles, the mold was modified to have a large edge support to be used for concrete casting. In this approach, concrete, material that takes the shape of its mould, will be used for the groin, whereas the tiles, material that can arch without formwork, will form the vault's infill. This underdevelopment system is advantageous because the concrete groins can be also areas for reinforcement or friction-only joints between the parts. The concrete frame can be built without the tiles and installed to then be vaulted. However, the most important feature is that it saves time. In a test of a 1.2 m span vault that was built by one of the authors, each quarter took two hours. The waiting time was the time for the mortar to set, which was three days for acceptable results.



Figure 5. System development: Concrete edges to avoid cutting tiles

5. Conclusion

Prefabrication of vaults in modern construction is not a new subject, but these examples propose a *modus operandi* that is driven by craft without compromising design or construction. The manufacturing of building components is usually imagined accompanied with heavy machinery, cranes, and advanced tools. The projects presented challenges to this image by constraining all manufacturing phases to a hand-built scale, which pushes the construction industry towards a more inclusive approach to craft where complex geometries can still be achieved without the extensive use of heavy machinery. In FR2, the knowledge and skill of building tile vaults was transferred digitally to unskilled labor for a mass production of vaults. In FabricArte, the vault manufacturing was optimized for a rapid in-situ construction, but it also avoided using machinery, and the process remained handmade.

Acknowledgments

Sarah Pennal made the first model of the FR2 vaults, and Eric Maier and team built the ceiling vaults. Salvador Gomis Aviño and his team built the vaults in FabricArte, Oliver Hudson did structural calculations of the metal structure. The authors are grateful to Ana Martínez Balaguer (ASCER), Javier Mira Peidro, and the team (ITC) for supplying the needed materials. FabricArte is part of M. Wesam Al Asali's PhD research at Cambridge, which is funded by Saïd Foundation Cambridge Trust Scholarship. FabricArte was administrated by Light Earth Designs.

References

[1] S. Huerta, "The Mechanics of Timbrel Vaults: A Historical Outline," in *Essays on the History of Mechanics*, A. Becchi, M. Corradi, F. Foce, and O. Pedemonte, Eds. Birkhäuser Basel, 2003, pp. 89–134.

[2] G. R. Collins, "The Transfer of Thin Masonry Vaulting from Spain to America," *Journal of the Society of Architectural Historians / Society of Architectural Historians.*, pp. 176–201, 1968.

[3] J. Ochsendorf, *Guastavino Vaulting: The Art of Structural Tile*, 1 edition. New York: Princeton Architectural Press, 2010.

[4] D. L. López, T. V. Mele, and P. Block, "La bóveda tabicada en el siglo XXI," *Informes de la Construcción*, vol. 68, no. 544, p. 162, Dec. 2016.

[5] M. H. Ramage, J. Ochsendorf, P. Rich, J. K. Bellamy, and P. Block, "Design and Construction of the Mapungubwe National Park Interpretive Centre, South Africa," *ATDF Journal*, vol. 7, no. 1, pp. 14–23, 2010.

[6] M. Ramage, T. J. Hall, A. Gatóo, and M. W. Al Asali, "Rwanda Cricket Stadium: Seismically stabilised tile vaults," *Structures*, vol. 18, pp. 2–9, Apr. 2019.

[7] P. (Philippe C. V. Block, "Thrust Network Analysis : exploring three-dimensional equilibrium," Thesis, Massachusetts Institute of Technology, 2009.

[8] T. Van Mele and P. Block, "A novel form finding method for fabric formwork for concrete shells," *J. Int. Assoc. Shell and Spatial Structures*, vol. 52, pp. 217–224, 2011.

[9] M. H. Ramage, T. Hall, and P. Rich, "Light Earth Designs: Natural material, natural structure," in *Earthen Architecture: Past, Present and Future*, 0 vols., CRC Press, 2014, pp. 305–310.

[10] L. Davis, M. Rippmann, T. Pawlofsky, and P. Block, "Efficient and Expressive Thin-tile Vaulting using Cardboard Formwork," presented at the Proceedings of the IABSE-IASS Symposium 2011, London, 2011.

[11] J. G. Muñoz and M. de los Á. B. Fernández, "La prefabricación de bóvedas de ladrillo. Una utopía latinoamericana," *rita_revista indexada de textos académicos*, vol. 0, no. 2, pp. 92–99, Oct. 2014.

[12] A. Z. Catalán, "A propósito de las bóvedas de crucería y otras bóvedas medievales," *Anales de Historia del Arte*, vol. 0, no. 0, pp. 99–126, 2009.

Proceedings of the IASS Annual Symposium 2019 – Structural Membranes 2019
Form and Force
7 – 10 October 2019, Barcelona, Spain
C. Lázaro, K.-U. Bletzinger, E. Oñate (eds.)

Lightweight segmented timber shell for the Bundesgartenschau 2019 in Heilbronn

Daniel SONNTAG*, Lotte ALDINGER[a], Simon BECHERT[a], Martin ALVAREZ[b], Abel GROENEWOLT[b], Oliver David KRIEG[b], Hans Jakob WAGNER[b], Jan KNIPPERS[a] and Achim MENGES[b]

*,[a] ITKE, Institute of Building Structures and Structural Design, University of Stuttgart
Keplerstraße 11, D-70174 Stuttgart, d.sonntag@itke.uni-stuttgart.de
[b] ICD, Institute for Computational Design and Construction, University of Stuttgart

Abstract

Segmented timber shells offer the possibility of constructing long span, double curved shell structures efficiently and economically. This was demonstrated with the Landesgartenschau Exhibition Hall 2014 in Schwäbisch Gmünd [1], a prefabricated segmented timber shell made of planar beech plywood plates. However, the application of this construction method for larger spans and more general shell geometries requires further technical development of the construction system, of its associated fabrication methods, and of the methods for form finding and optimisation. This paper presents the development and construction of the wood pavilion for the Bundesgartenschau (Federal garden exhibition, BUGA) 2019 in Heilbronn, which translates these technical developments into practice. Solid timber panels were replaced by a recently developed multi-layer cassette system. The 376 geometrically unique elements of the multi-layer segmented shell were produced of spruce laminated veneer lumber plates, which were assembled, glued, and milled in a fully automated process by two collaborative industrial robots. The shell segments are connected using a combination of the previously established CNC-milled finger-joints [2] as well as regularly spaced steel bolts. Custom design and analysis tools were developed, in order to manage varying material thicknesses, spacing of fasteners and geometric details of the connections between adjacent segments.

Keywords: Segmented timber shell, multi-layer shell, prefabricated shell, form finding, optimization, panelisation, robotic fabrication, modular system, finger joints, building information modelling, digital workflow

1 Introduction

Double curved shell structures, if properly designed, allow bridging wide spans with little material, as the pure membrane state resulting from the double curvature allows using the material with maximum efficiency. Building double curved shell structures, however, is usually expensive, in particular for on-site construction with excessive formwork. Wide span shells out of prefabricated elements with minimal formwork and scaffolding are thus a desirable alternative to save time and money. The BUGA wood pavilion is a prefabricated segmented timber shell, assembled only out of initially planar or straight timber pieces. The shell is based on principles found in the plate skeleton of sea urchins, which have been studied at the University of Stuttgart for over a decade. The Institute for Computational Design and Construction (ICD) and the Institute for Building Structures and Structural Design (ITKE) have already realized several segmented timber shells based on the biomimetic research on sea urchins, in particular the Landesgartenschau Exhibition Hall 2014 in Schwäbisch Gmünd [1].

Copyright © 2019 by Daniel Sonntag, Lotte Aldinger, Simon Bechert, Martin Alvarez, Abel Groenewolt, Oliver David Krieg, Hans Jakob Wagner, Jan Knippers and Achim Menges.
Published by the International Association for Shell and Spatial Structures (IASS) with permission.

2 Context and related work

The Landesgartenschau Exhibition Hall is a single layer timber shell made out of beech plywood plates, which are connected by finger joints and cross-threaded screws (Figure 1). The initial double curved global geometry is approximated by a polygonal planar plate panelisation. It can be observed, that also some sea urchin species present finger like protrusions between their plate segments, and it can be shown that this type of connection is structurally beneficial for planar plate structures [3].

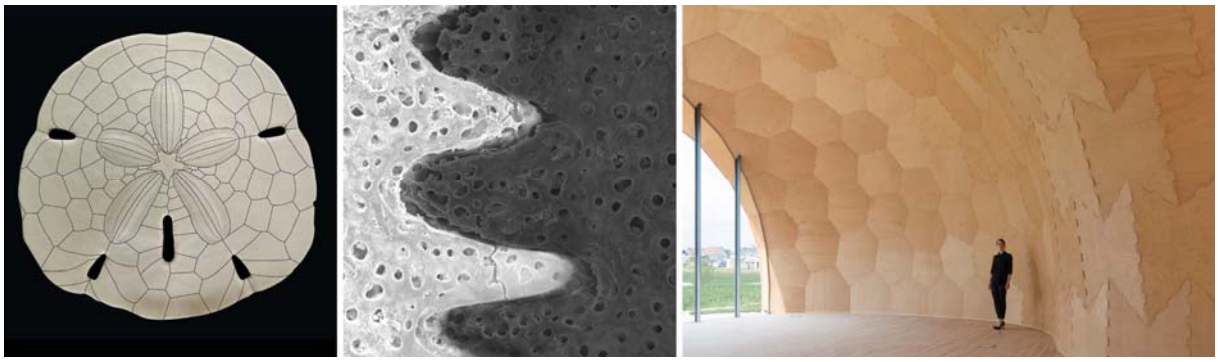


Figure 1 – Left: Skeleton of a sea urchin (sand dollar) in top view with highlighted topology as shown in [1]) Center: Microscopic view of a sand dollar's plate edge as shown in [1]). Right: Photograph of the Landesgartenschau Exhibition Hall 2014, a single-layered segmented timber shell structure with abstracted biological principles. ©ICD/ITKE

The scaling up of this structural system generally also requires an increase in size of the individual plates. While on a global level a membrane state is still possible to achieve, on the plate level due to the planar plate approximation of the double curved global geometry, bending occurs, which becomes more significant for bigger plates. Hence, the challenge arose to find a construction system, which optimises the arrangement of the material for the transfer of local bending moments, which led to the development of a structural system with hollow cassettes in the context of a previous research project at the University of Stuttgart (see [4] and [5]). Even though well-known from traditional engineering, this double-layer structure can also be observed in sea urchin species. An additional benefit of the hollow cassette is the possibility to use bolts as connective element, which allows for complete disassembly of the shell.

3 Construction system

3.1 Global geometry and cassette system

The BUGA wood pavilion is a double-curved shell that derives its shape from an ellipsoid, cut above its equatorial height at the ground plane's intersection. Three large openings lead to three linear supports of the shell. The free edges are stiffened with so called wings, which also act to visually open up the enclosed space. The shell has a rise of 7.2m and its longest span measures 28.1m between the centres of two supports (Figure 2).

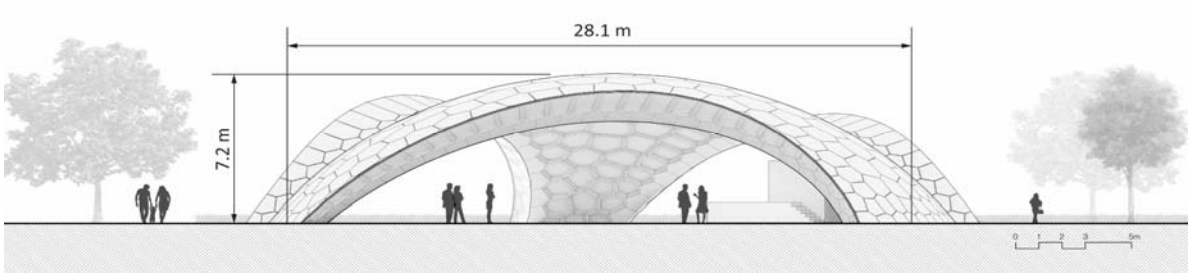


Figure 2 – Elevation of the BUGA Pavilion with maximum span of 28.1m and rise of 7.2 m. ©ICD/ITKE

The double-curved shell surface is discretised into planar segments; its panelisation leads to 376 geometrically unique elements of hexagonal shape with diameters ranging from 1.5 to 2.5m. Customized hollow timber cassettes with a double-layered build-up offer a lightweight construction system (Figure 3). Each segment consists of one top plate and one bottom plate and six bordering edge beams in between, all made of spruce laminated veneer lumber (LVL). The top and bottom plates have a thickness of 33mm and 21mm respectively, while the thickness of the vertically-orientated beams varies throughout the structure. Their height however is constant (106mm), resulting in a total structural height of 16cm throughout the shell. The two plates are joined to the ring of edge beams using a 1-component Polyurethane (1k PUR) gluing interface into one building component. All structural timber elements are protected from weathering with a waterproofing membrane, covered by façade panels (Figure 3).

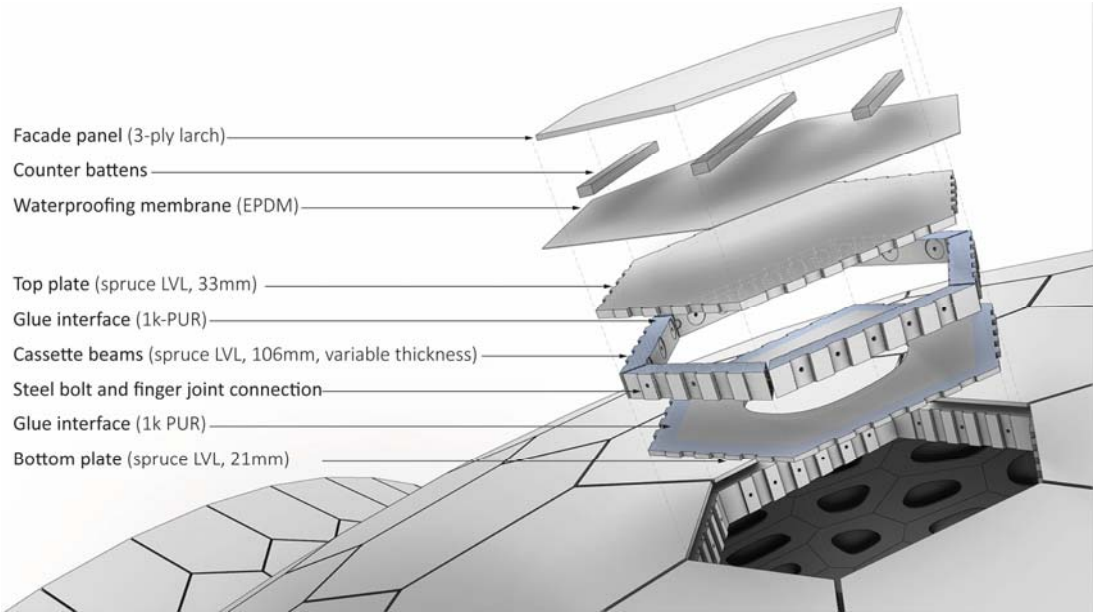


Figure 3 – Construction system of the double-layered cassette with gluing interface (total structural height 16cm) and façade build-up. ©ICD/ITKE

3.2 Connection design

The double-layered cassettes are connected with a combination of integral finger joints and regularly spaced bolts or screws along adjacent edge beams (Figure 4). The CNC-milled finger-joints, as previously established and analysed [2], transfer in-plane shear forces, while the bolt and screw connections transfer tensile forces and out-of-plane shear forces. Furthermore, the lever arm between contact forces in the top or bottom layer and the tensile connector allows transferring small bending moments between the segments.

The bolted connection was desirable to allow for disassembly of the shell. However, the larger negative angles between segments along the shell's spines necessitated a connection strategy with crosswise-arranged fully threaded screws. The metal connectors can be accessed during assembly and disassembly through openings in the either the top or the bottom plate (Figure 3). In the bottom plate they remain visible as an architectural feature, in the top plate they can be hidden underneath the cladding.

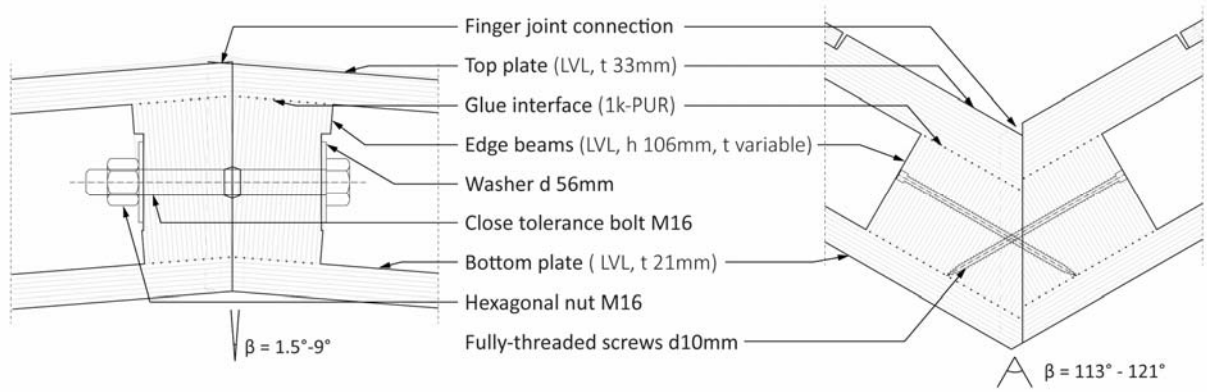


Figure 4 – Connections of edge beams of adjacent cassettes with (left) bolts for shallow angles and (right) screws for larger angles along the shell's spines. ©ICD/ITKE

3.3 Fabrication and assembly

The shell consists of 376 individually shaped timber segments, with varying material thicknesses, fibre arrangements, bolt and screw placements and finger joint arrangements throughout the entire shell. This made the fabrication with traditional timber manufacturing methods infeasible, in particular considering that the cassettes were milled to nominal dimensions. Therefore, a mobile robotic timber-manufacturing platform with two industrial robots, which was developed by the ICD University of Stuttgart and BEC GmbH, was located at the industrial partner MüllerBlaustein Holzbauwerke GmbH. First, the timber pieces were robotically assembled for each cassette with an automated application of the glue joint (Figure 5). After mechanical pressing, in a second step, the finger joints and the plate opening were milled with a different effector setup.

Commonly this type of multi-layer elements is fabricated using a 2-component glue, which however would make the automation of the fabrication process significantly more complicated if not impossible. The 1-component glue imposes strict requirements on the precision, with a joint thickness smaller than 0.3mm, which is only achievable consistently using high precision tools. This process is currently not regulated through design codes in Germany and thus requires a specific approval from the local authorities accompanied by a series of mechanical tests performed to ensure the quality of glue joint.

Compared to the Landesgartenschau Exhibition Hall, the assembly process was further optimized, requiring only minimal falsework and scaffolding, which is also due to the stiffness of the construction system. The segments along the arch-like openings with the cross-threaded screw connection were preassembled in the manufacturing hall, then transported to the site and installed with a temporal support structure in the centre. The following segments were then assembled consecutively with a temporal support of cantilevering parts using simple struts and straps (Figure 5). The assembly sequence is predefined and the individual construction sequences were checked structurally. The entire shell has been fabricated in approximately 6 months, the assembly on site was performed in only 10 working days by a team of two craftsmen. In addition, it is now possible to fully disassemble the shell and re-erect it at a different location without any loss of performance.



Figure 5 – Left: Robotic fabrication of the cassettes with glue joining. Right: Assembly of shell with minimal support of cantilevering parts with struts and straps. ©ICD/ITKE

4 Digital workflow

Because the fabrication model as well as the entire workflow between design and production were completely digital, the structural analysis model needed to be directly integrated into this workflow. All relevant information, such as geometric information, material thicknesses of plates and beams, fibre orientation of the wood, placement of connecting elements and detail information regarding the foundation needed to be extracted from the digital production model and integrated in the structural analysis model. In consequence, the structural analysis model was set up parametrically, in order to be easily updated following design changes and updates during optimization iterations.

The complexity of the structure exceeds by far the possibilities of commercial engineering software packages in terms of pre- and post-processing, thus a set of custom building information modelling (BIM) tools needed to be developed. The assembly of the shell segments, their connection using spring elements, the material orientation and the computation of the stiffness of the joints were scripted and parametrically generated, and implemented in a geometric design environment (Rhino Grasshopper). Similarly, the stress and detail checks typical for timber engineering, were parameterized and scripted, and implemented within the same design environment, which also allowed for easy visualization of the results. The resulting workflow is completely digital, with basically no structural drawings required in the process from design to production. Drawings were only produced for the purpose of documentation of administrative purposes and at interfaces with external companies.

5 Structural optimization, form finding and panelisation

Designing a shell with the given requirements regarding span, slenderness and prefabrication was only possible with a high degree of optimization on all levels. On the global level, the goal was to find a shell geometry, which allowed for a membrane state under dead loads, while respecting constraints originating from the planar plate segmentation. The methods of shape optimization of shells developed in the past [6] needed to be adjusted, in order to respect those constraints in the form finding process. Finding a smooth, planar plate distribution for surfaces with arbitrary curvature distribution is not a trivial task [7]. A smooth segmentation requires smooth curvature, which needed to be imposed during the form finding. For this project, the influence of several parameters on the structural behaviour of the shell was investigated, without running a fully automated optimization. All shells had a smooth synclastic curvature in common, the curvature constraint was therefore embedded on the level of the parametrization. The best compromise between architectural design intent and structural performance was then chosen as global design surface. During the investigation, it was assumed, that if the global

design surface works well as monolithic shell, the associated segmented shell has a similar behaviour, which was later confirmed by the results of the parametric studies.

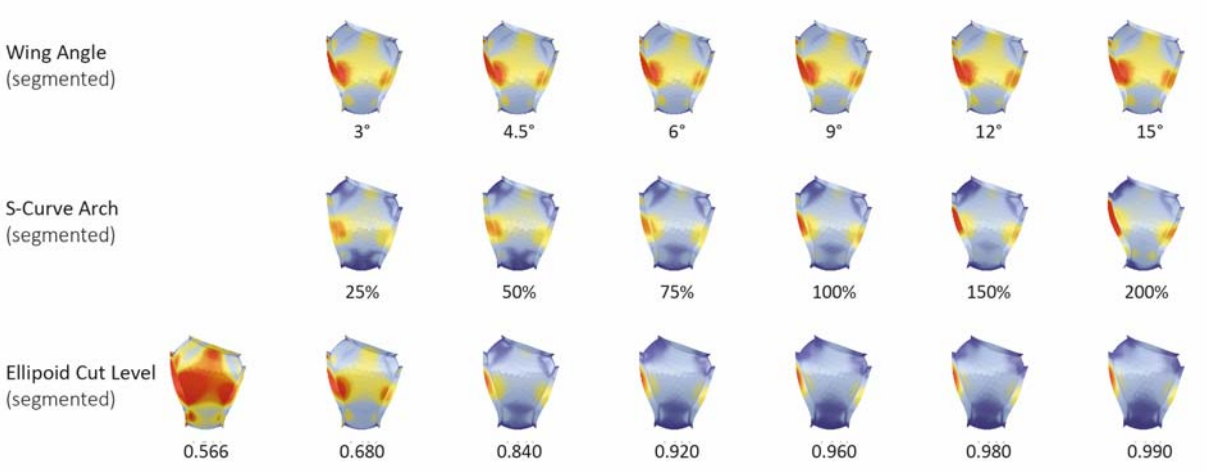


Figure 6 – Parametric study for structural optimisation of the global geometry (segmented). ©ICD/ITKE

The orientation of the grain direction of the top and bottom plates was aligned with the global force flow. Mostly this corresponds to the thrust exerted towards the supports, for the larger plates at the centre of the shell, the alignment with the shorter span to reduce bending deflections was more critical. The thicknesses of both plates and edge beams were equally optimized and adjusted to the stress level. As the system is hyperstatical, several iterations were necessary until an optimal result was found. In addition, the size and shape of the openings was subjected to parametric studies, in order to achieve a good compromise between structural efficiency and the accessibility of the bolts.

6 Structural design and analysis

The shell structure was analysed using the Finite Element Method. For each cassette, both top and bottom plate as well as the edge beams were simulated with shell elements. The double-layered mesh was modelled as the mid-surface of both the top and bottom plate, the edge beams were modelled at the outlines of the segment. The local coordinate system of each shell element was aligned with the grain direction.

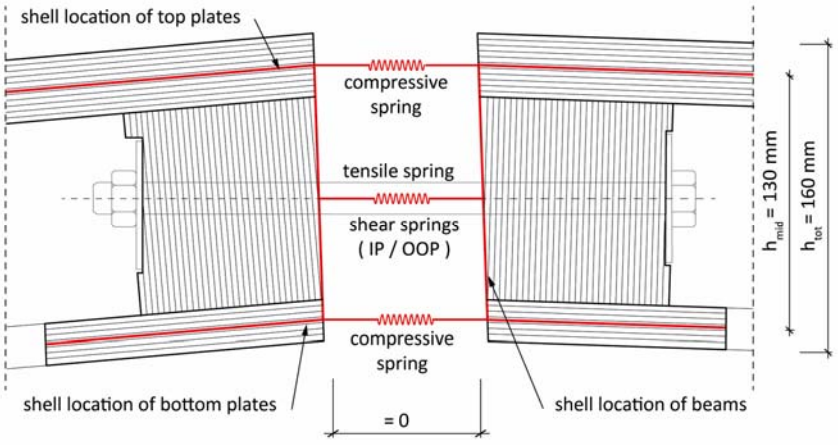


Figure 7 – Schematic diagram of the various spring connections modelled between two adjacent cassette edge beams in the FE-model in section (gap between cassettes / shell elements for visualisation only). ©ICD/ITKE

The types of connections and their respective stiffnesses were modelled with spring elements continuously connecting the structural nodes along adjacent edges of the meshes (Figure 7): While in-plane shear (IP) and out-of plane shear (OP) forces are transferred by linear springs, contact springs and tensile springs for the bolt were modelled as non-linear springs. The transfer of bending moments between shell segments is automatically guaranteed through the combination of contact springs and tensile springs of the bolts. While mostly checking the stresses along the fibre directions is sufficient, the check of the glued interface is more complex, as the strength depends on the varying fibre angles between plates and edge beams.

Conclusion

The BUGA wood pavilion illustrates the potential of digital timber construction for structures bridging spans of up to 28m by means of a lightweight, material efficient timber shell, completely robotically prefabricated and without the necessity of expensive scaffolding or falsework.

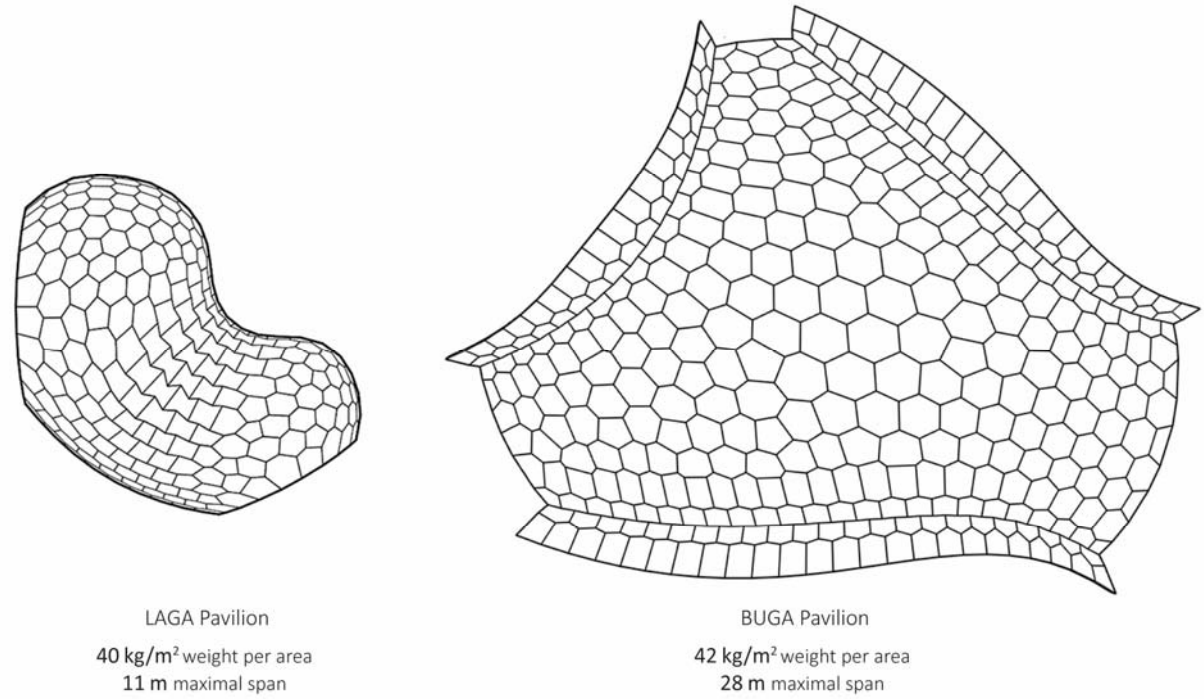


Figure 8 – Comparison of the efficiency of the construction system of the double-layer BUGA pavilion with its predecessor, the single-layer Landesgartenschau Exhibition Hall, regarding material use per shell surface area and maximal span of the structure. ©ICD/ITKE

Comparing material efficiency to its predecessor, the Landesgartenschau Exhibition Hall, it can be shown that with the same amount of material per square meter, a span three times as large can be bridged (Figure 8). This can mainly be attributed to the efficient material usage of the cassette system: the optimized construction system provides material where it is primarily needed.

The design and construction of such a shell is hard to imagine without a complete digital workflow, where design, fabrication and structural analysis are completely integrated in a digital design environment. Parametric modelling, which enables optimization at all levels, is the key to success. Such a project presents new challenges, such as the handling of digital design and manufacturing tools, for both architect and engineer.



Figure 9 – Completed lightweight segmented timber shell located at the Bundesgartenschau 2019. ©ICD/ITKE

Acknowledgements

The work presented in this paper was funded by the State of Baden-Wuerttemberg, the University of Stuttgart, EFRE European Union, GETTYLAB and DFG German Research Foundation. The authors would also like thank their project partners Müllerblaustein Bauwerke GmbH, BEC GmbH and Bundesgartenschau Heilbronn 2019 GmbH.

Corrigendum

To the first version of the paper some small changes have been made, including the additional mentioning of further co-authors and the addition of copyright notions underneath the pictures.

References

[1] O.D. Krieg, T. Schwinn, A. Menges, J. Li, J. Knippers, A. Schmitt and V. Schwieger, „Biomimetic Lightweight Timber Plate Shells: Computational Integration of Robotic Fabrication, Architectural Geometry and Structural Design" in *Advances in Architectural Geometry 2014*, Springer International Publishing, 2015, pp. 109 -125

[2] J. Li and J. Knippers, "Segmental Timber Plate Shell for the Landesgartenschau Exhibition Hall in Schwäbisch Gmünd—the Application of Finger Joints in Plate Structures", *International Journal of Space Structures,* vol. 30 no. 2, pp. 123-139, 2015.

[3] R. La Magna, M. Gabler, S. Reichert, T. Schwinn, F. Waimer, A. Menges and J. Knippers, "From Nature to Fabrication: Biomimetic Design Principles for the Production of Complex Spatial Structures", *International Journal of Space Structures*, vol 28 no. 1, pp. 27-39, 2013

[4] O.D. Krieg, S. Bechert, A. Groenewolt, R. Horn, J. Knippers and A. Menges, "Affordances of Complexity: Evaluation of a Robotic Production Process for Segmented Timber Shell Structures" in *WCTE – Proceedings of the 2018 World Conference on Timber Engineering*, 2018, vol. 8 (06-02), pp. 1-8.

[5] S. Bechert, A. Groenewolt, O.D.Krieg, A. Menges and J. Knippers, „Structural Performance of Construction Systems for Segmented Timber Shell Structures", in *Creativity in Structural Design: Proceedings of the IASS Symposium 2018, Boston, USA, July 16-20, 2018*, International Association for Shell and Spatial Structures (IASS), 2018, vol. 9., pp. 1-9

[6] K.-U. Bletzinger and E. Ramm, "Structural optimization and form finding of light weight structures", *Computers and Structures*, vol. 79, pp. 2053-2062, 2001

[7] H. Pottmann, M. Eigensatzm, A. Vaxman and J. Wallner, "Architectural geometry", *Computers & Graphics*, vol. 47C, pp. 145-164, 2015

Proceedings of the IASS Annual Symposium 2019 – Structural Membranes 2019
Form and Force
7 – 10 October 2019, Barcelona, Spain
C. Lázaro, K.-U. Bletzinger, E. Oñate (eds.)

Structural Optimization of Prestressed Concrete Shells with Ruled Surface Geometry

Juan P. OSMAN-LETELIER*, Jack LEHRECKE[a], Mike SCHLAICH[a]

*TU Berlin
Gustav-Meyer-Allee 25, 13355 Berlin
juan.p.osmanletelier@tu-berlin.de

[a] TU Berlin

Abstract

Doubly curved concrete shells can exhibit an exceptionally efficient load carrying behavior attributed to their ability to redistribute spatial loads almost entirely through membrane forces. The resulting structures, while elegant in form, are often uneconomical due to the expensive formworks required to achieve such complicated geometry. Ruled surfaces are particularly suited to address this issue as they can take on complex geometries by sweeping straight lines through space. The linear nature of a ruled surface can also be utilized for the design of prestressed elements, in that straight tendons can be embedded along a given generatrix. However, for this to be feasible the principal tensile trajectories in the shell under a given load must flow along the generatrix in such a way that compliments prestressing. Unfortunately, the load carrying behavior of a ruled surface does not necessarily correspond to the generatrixes used to generate its geometry, making it difficult to successfully capitalize on the ease with which prestressed elements could potentially be employed. This paper aims to investigate the possibility of optimizing the geometry of ruled surface concrete shells for the implementation of prestressed tendons along the generatrixes. To achieve this goal, a new objective function was developed and implemented together with structural optimization methods in an attempt to find ruled surface forms with the desired force flow suited for prestressing with linear tendons.

Keywords: ruled surfaces, concrete shells, prestressing, structural optimization, objective function

1. Introduction

In the field of engineering, a shell is defined as any structure composed of curved surfaces that has the capacity to transfer loads primarily though axial forces and secondarily through bending [1]. They are typically thin in the dimension perpendicular to their surface and can exhibit curvature in one or two directions. Shell structures tend to distinguish themselves from other typical forms of architecture in their ability to take on a seemingly endless variety of arbitrary forms. Their curvature allows them to break free of the linear constraints of conventional construction. Furthermore, through their curved geometry, they exhibit a remarkable stiffness and allow the spanning of large distances with minimal thicknesses, resulting in an optimal use of material.

Although shell structures can be constructed using a wide variety of materials, concrete is arguably the most suitable (excluding grid shells). This is due to the fact that concrete can be poured into arbitrary forms, as long as the formwork is constructed accordingly. Historically, doubly curved concrete shells have been used, for example, as roofing systems to elegantly cover large surface areas. However, owing to the disproportionately high cost of the formwork, corrosion issues caused by the minimal concrete cover, and other factors, examples of such structural systems are seen less often today [2]. Ruled surfaces offer a solution to the issue of high construction costs as they are able to achieve complex and doubly

Copyright © 2019 by Juan Pablo Osman-Letelier, Jack Lehrecke and Mike Schlaich
Published by the International Association for Shell and Spatial Structures (IASS) with permission.

curved geometries with the use of linear formwork elements. Applications in architecture from the likes of Eduardo Torroja, Felix Candela and Eladio Dieste demonstrate the feasibility of implementing ruled surfaces to realize structurally sound and economically efficient doubly curved shells.

Concrete shells are also commonly supplemented with tendons to counteract the tensile stresses resulting in the material under certain loads. Through the introduction of compression along the tendons to the areas of the concrete that would otherwise experience tension, it becomes possible to reduce the risk of crack development, resulting in the improved performance of the shell over the course of its lifespan. This paper aims to investigate the possibility for the further exploitation of the linear nature of ruled surfaces through the implementation of straight tendons along the linear generatrixes of the shell.

2. Ruled Surfaces

A ruled surface is defined as any surface that contains a continuous family of straight lines known as rulings, generatrixes, or generators [3]. Cylinders, cones, conoids, helicoids, one-sheeted hyperboloids and hyperbolic parabolas are some of the commonly applied geometries that belong to this class of surfaces. There are several mathematical methods that can be used to define the motion of the lines used to generate a ruled surface.

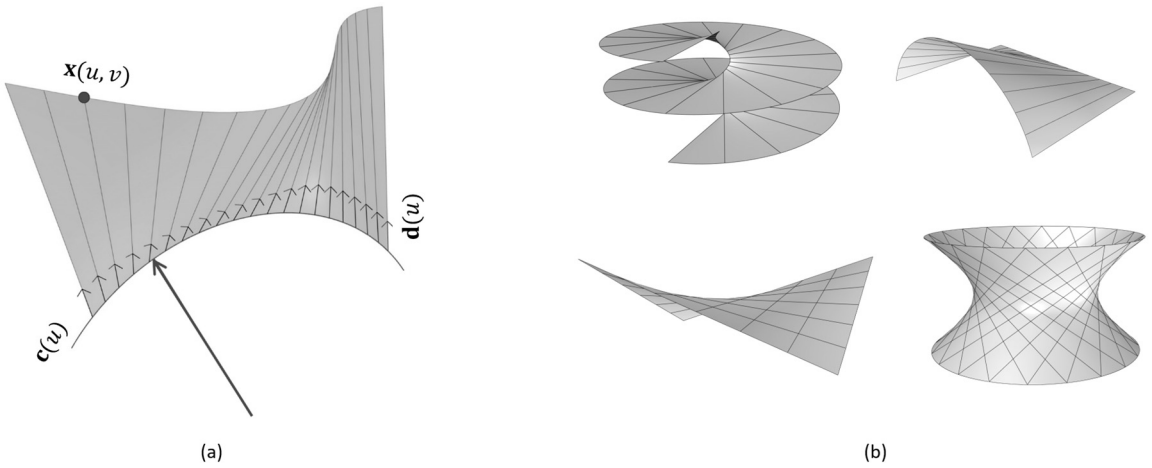


Figure 1: (a) Ruled surface generation with single directrix (b) typical ruled surface geometries

The method used in this paper corresponds to the generation of a ruled surface by moving a straight line along a directrix curve as seen in Figure 1(a). In order to achieve a ruled surface geometry with this approach, a parametric representation for both the directrix curve and the directional vectors of the straight rulings are required. If $\boldsymbol{c}(u)$ is defined as the parametric equation for the directrix curve and $\boldsymbol{d}(u)$ as the continuously changing vector of the rulings, it is then possible to describe any point on the resulting ruled surfaced with the following equation:

$$\boldsymbol{x}(u, v) = \boldsymbol{c}(u) + v\,\boldsymbol{d}(u) \tag{1}$$

3. Prestressed Concrete Shells

3.1. Principles of Prestressing

The concept of improving the structural behavior of reinforced concrete through the introduction of prestressed elements has been commonly implemented since its inception at the end of the 19th century [4]. The basic methodology of prestressing involves the introduction of high-strength tendons into the tension zone of the concrete. The surrounding concrete experiences a resultant compression, which in turn compensates for the present tensile stresses and reduces the risk of crack development. With respect

to thin shell structures, tendons are typically implemented centrally within the shell cross-section to counteract tensile membrane stresses. As such, with no eccentricity between the tendon and local neutral axis of the shell, the prestressed elements are unable to directly reduce local bending through an induced moment. However, the global bending of the system can be greatly reduced through the implementation tendons within the shell midplane if there exists an eccentricity between the tendon geometry and the global neutral axis of the system. Introducing prestressing forces along this eccentric axis then allows for the induction of a negative global bending action and the subsequent reduction of deformation to the system.

There exist multiple prestressing methodologies for the generation of the compensating compressive forces described above. As this work seeks to explore the benefits of prestressing linear generatrixes within the shell midplane, only bonded tendon systems are investigated. For bonded prestressed systems, there exists an immediate bond between the prestressed tendon and surrounding material, as the tendon is prestressed before the hardening of the concrete. The prestressing of structures with this methodology allows for the production of prefabricated prestressed elements, with linear tendons having the additional benefit of a minimal loss of prestressing force due to friction.

3.2. Typical Prestressed Shell Systems

In general, concrete shells can be effectively prestressed if the tendon geometry is defined along the tension trajectories under a governing load [4]. The introduction of the prestressing force to the concrete parallel to the direction of the tensile stress is paramount for maximal utilization of the prestressing. To demonstrate this concept, two common prestressed shell systems were investigated.

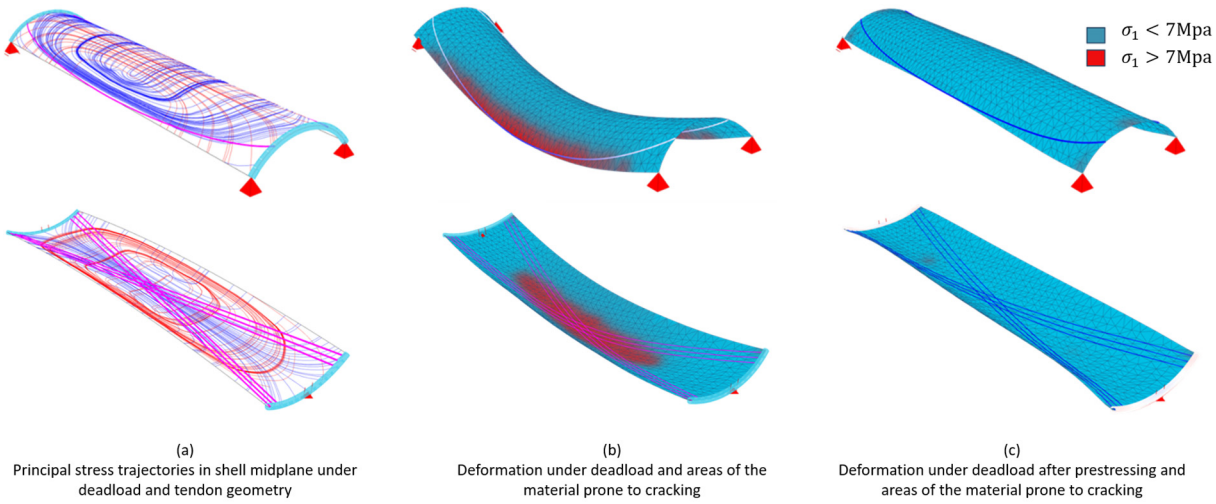


Figure 2: (above) Prestressed Barrel Vault System (below) Prestressed Silberkuhl Shell

3.2.1. Barrel Vault System

The barrel vault system displayed above behaves globally as a simply supported beam under a deadload, with the resulting bending moment and deformation reaching a maximum at the midspan. The structural behavior of the system is greatly improved with the introduction of prestressed tendons that closely follow the path of the maximal resultant principal tensile stress as seen in Figure 2(a). The introduction of the compressive stresses along the parabolic arc of the tendon results in a strong reduction of deflection due to the negatively induced global bending action resulting from the eccentricity between the tendon geometry and the global neutral axis. Furthermore, the introduction of the compressive stresses to the shell midplane along the tendon leads to a complete prevention of a tensile failure in the concrete under the given load as seen in Figure 2(c).

3.2.2. Silberkuhl System

A similar simply supported beam in the form of a Silberkuhl shell is outfitted with linear tendons along its generatrixes. The generatrixes selected for prestressing correspond to the path of the principal tensile stresses as seen in Figure 2(a) and the resulting prestressed system exhibits a very similar behavior to the aforementioned barrel vault example. Again, we see a significant reduction in the overall deflection of the system due to the compensating global bending action induced through the eccentricity between the prestressed tendons and the global neutral axis, as well as a negation of crack development in the concrete. This example further serves to demonstrate the general concept proposed in this paper, as the ruled surface shell is successfully prestressed along its linear generatrixes.

4. Prestressed Concrete Shells with Ruled Surface Geometry

This paper aims to investigate the possibility of optimizing the geometry of ruled surface concrete shells for the implementation of linear prestressed tendons. In order to achieve the proposed optimization, it is imperative to find an objective function that effectively quantifies how applicable a given ruled surface is for prestressing along its generatrixes.

4.1. Mathematical Derivation

To consolidate the aforementioned goal into an applicable objective function, the concept must first be defined in mathematically quantifiable terms. As previously stated, a prestressed element tends to achieve an optimal influence on a given tension zone when the principal tensile stress it wishes to compress flows parallel to the tendon geometry. Assuming a dominating membrane state, this can be achieved if the magnitude and direction of the principal tensile stress can be expressed as a continuous vector field $\boldsymbol{f}: \mathrm{S} \rightarrow \mathbb{R}^3, \mathrm{S} \subset \mathbb{R}^3$ inhabiting the midplane surface of a given shell as seen in Figure 3(c). With a continuous representation of the principal stress vector, it becomes possible to calculate the angle of deviation between the stress trajectory and a corresponding tendon axis at any given point. If the objective function I is then defined as the integral of this deviation angle over the entire structural surface under tension, then the minimization of I should result in an optimal form for prestressing along the given axes. This concept is demonstrated in Figure 3, which displays an arbitrary ruled surface S generated by a directrix function $\boldsymbol{c}(u)$ and a linear generatrix function $\boldsymbol{d}(u)$ as introduced in section 2.

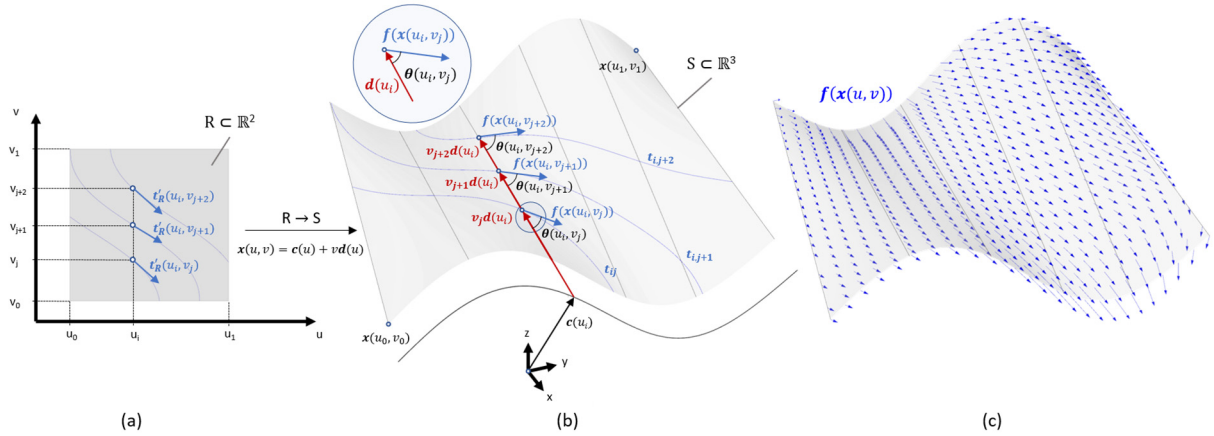


Figure 3: (a) Parameter space R (b) ruled surface S (c) principal tensile stress vector field **F** in shell midplane

Defining the surface in this fashion results in a corresponding two-dimensional region R, with $\boldsymbol{x}(u, v)$ serving as a vector-valued function capable of mapping parameterized coordinates to the three-dimensional surface S. Additionally, a finite series of principal tensile stress trajectories are denoted in the figure by the family of blue curves $\boldsymbol{t}_{i,j}$ as seen on the surface S, with their corresponding

projections in the region R. These trajectories are dependent on the vector field describing the principal tensile stress in the shell midplane and describe the flow of stress from a given origin in the field.

It is important to note, that even for thin shells the actual stress field for the structure can only be accurately described with a three-dimensional tensor field that not only accounts for the stress trajectories in the midplane, but also accounts for the deviations over the thickness of the shell cross-section. Such a field then inhabits the entire volume described by the structure, rather than the surface model described here. As previously mentioned, this paper focusses only on the application of linear tendons within the shell midplane, making the field inhabiting the midplane surface manifold S acceptable for the proposed analysis. However, for the same concept to be applied to a slab structure whose tendon geometry is free to vary over the thickness, the surface-based model is no longer sufficient, as a volume-inhabiting tensor field representation is then required.

As the optimizations in this work aim to force the stress trajectories along the linear generatrixes of a given ruled surface, it becomes imperative to derive an equation describing the angle between the stress vector field and the corresponding ruling. To accomplish this, the dot product of the stress field vector and corresponding generatrix function must be taken. The cosine of the angle between the two vectors at any given point is then simply achieved by dividing the dot product by the absolute length of the respective vectors. Using this strategy, it becomes possible to develop a continuous function describing the angle of deviation between the flow of principal tensile stress and the linear generatrixes of the ruled surface at any given point, as denoted by $\theta(u, v)$. In order to minimize this deviation angle over the entirety of the shell, the objective function is then set as the double integral of this function. As the deviation angle formula is solely dependent on the parameterized variables u and v, the integral can simply be evaluated over the bounds of the parameter space defined by R.

$$\theta(u,v) = \cos^{-1}\left(\frac{\boldsymbol{f}(\boldsymbol{x}(u,v)) \cdot \boldsymbol{d}\,(u)}{\|\boldsymbol{f}(\boldsymbol{x}(u,v))\|\|\boldsymbol{d}(u)\|}\right) \Rightarrow I = \iint_{\mathrm{R}} \theta(u,v)\, d\mathrm{R} \tag{2}$$

It is important to note, that here the bounds denoted by R represent the parameterized area of the shell under tension. In the case that multiple discrete tension zones exist within the surface of the shell, then the objective function is simply altered to be the summation of the integrals over each individual zone, thus ensuring that the flow of stress is only considered in areas of the shell under tension.

4.2. Path Integral Interpretation

Another way of interpreting the methodology introduced in the previous section is to consider the given ruled surface as an infinite series of lines or "paths" as defined by the generatrixes. A similar objective function, inspired by Feynman´s path integral formulation [5], can then be developed by considering a sum of the path integrals along each ruling with respect to the given stress vector field. Evaluating the integral along discrete trajectories rather than integrating over the entire surface allows for an optimization with respect to a specific set of tendon geometries, rather than forcing a global optimal behavior of the stress flow. Figure 4 demonstrates this concept by evaluating the same arbitrary ruled surface investigated in the previous section with respect to a discrete set of n linear rulings corresponding to the generatrixes $\boldsymbol{d}(u_i)$ to $\boldsymbol{d}(u_n)$. We see that the corresponding parameter space is also displayed along with the projections of the selected rulings in R, appearing at regular intervals Δu along the horizontal axis.

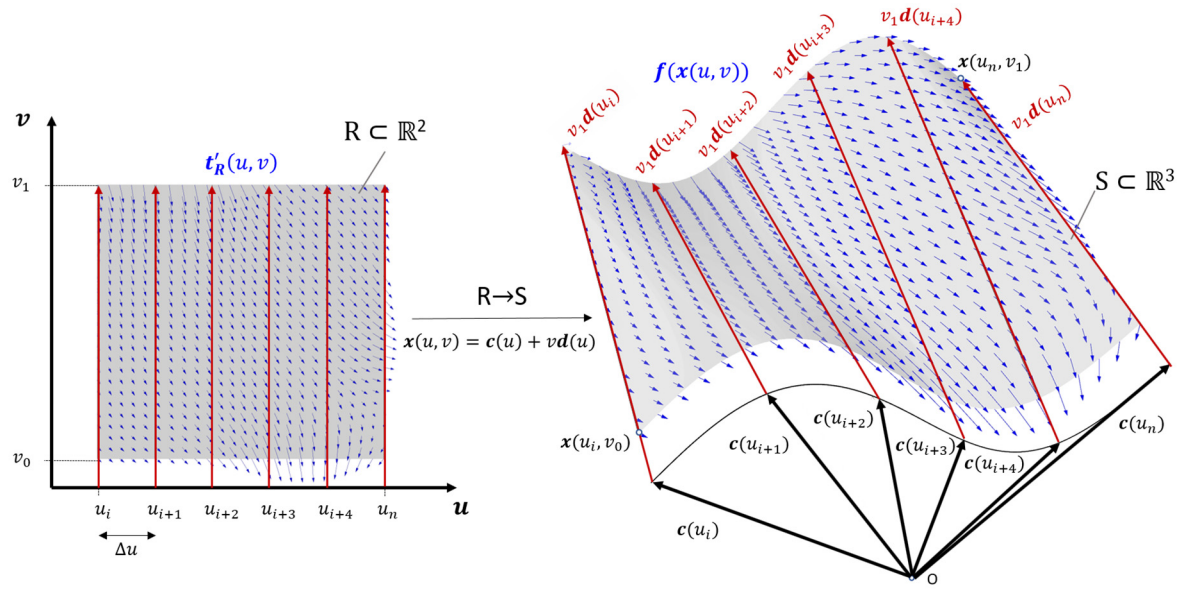


Figure 4: Path integral approach

The path integral along a given generatrix $\boldsymbol{x}_i = \boldsymbol{x}(u_i, v)$ within the stress vector field $\boldsymbol{f}$ can then be calculated with the following equation:

$$\int_{C_i} \boldsymbol{f}(\boldsymbol{x}_i) \cdot d\boldsymbol{x}_i = \int_{v_0}^{v_1} \boldsymbol{f}(\boldsymbol{x}(u_i, v)) \cdot \frac{\partial}{\partial v} \boldsymbol{x}(u_i, v) dv = \int_{v_0}^{v_1} \boldsymbol{f}(\boldsymbol{x}(u_i, v)) \cdot \boldsymbol{d}(u_i) dv \tag{3}$$

Taking the limit as the number of evaluated rulings n approaches infinity then yields a double integral that effectively describes the projection of the principal tensile stress vectors on the corresponding generatrixes over the entirety of the surface:

$$I_{path} = \lim_{n\to\infty} \sum_{i=1}^{n} \int_{v_0}^{v_1} \boldsymbol{f}\big(\boldsymbol{x}(u_i, v)\big) \cdot \boldsymbol{d}(u_i) dv \Delta u = \iint_{u_0 v_0}^{u_1 v_1} \boldsymbol{f}\big(\boldsymbol{x}(u, v)\big) \cdot \boldsymbol{d}(u) dv du = \iint_{R} \boldsymbol{f} \cdot \boldsymbol{d}\, dR \tag{4}$$

If the integral described above is taking with respect to a normalized force field and generatrix function, then maximizing this path integral value is an equivalent concept to the optimization achieved when finding a minimum for the deviation angle objective described in the previous section. The dot product between any two vectors is a scalar value equivalent to the product of the length of both vectors and the cosine of the angle between them. As eq. (2) depends on the angle between the stress field and the corresponding generatrix and eq. (4) denotes the dot product therefrom, a minimization of the angle invariably corresponds to a maximization of the dot product, thus rendering both optimization strategies similar to one another. For the example investigated in this work, the deviation angle variation is applied for the sake of continuity, but for the reasons mentioned above, an application of the objective function described by eq. (4) would yield similar results. The real benefits offered by the variation of the objective function derived in this section lie outside the scope of this paper.

5. Case Study: Cantilever Shell

To demonstrate the concept outlined in the previous section, a shell inspired by Eduardo Torroja's Zarzuela's Hippodrome in Madrid, Spain is considered for optimization. The system acts as a roof, providing cover from the compressive support to the free edge and functions globally as a cantilevered

beam. The shell surface is generated with two directrices, with linear rulings between the two curves defining the given ruled surface. The number of supports and their corresponding positions remain variable to allow for a maximum freedom of the design space, with a compressive support being generated each time the first directrix $\boldsymbol{c_1}$ intersects the y-axis. Similarly, a tensile support is generated at each intersection of $\boldsymbol{c_1}$ and the line defining the upper-rear extreme of the design space, as seen in Figure 5(c). With both governing directrices parametrically defined to be dependent on an array of design variables, the resulting design space contains a wide variety of possible structural forms.

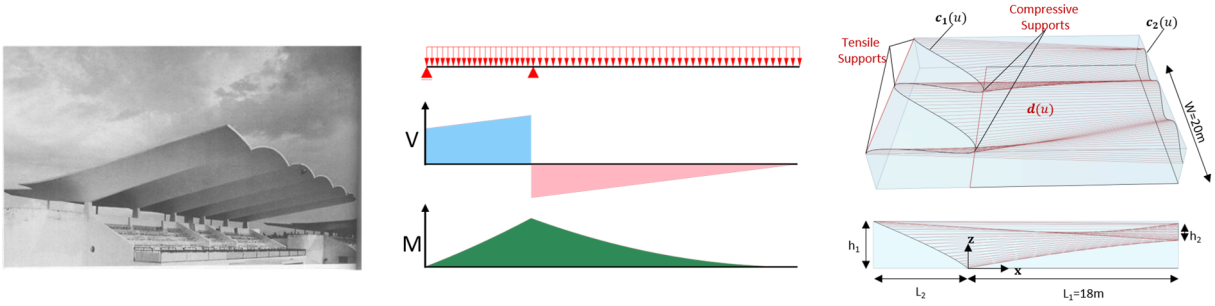


Figure 5: (a) Torroja's Hippodrome (b) global cantilever system (c) parameterized geometry

The parameterized geometry is then assigned material properties and analyzed under a dead load, providing the resulting principal tensile stress vectors necessary for the calculation of the deviation angle objective described by eq. (2). However, the problem with a single objective optimization using the deviation angle integral alone is the sensitivity of thin shells to bending actions. The presence of local bending moments within thin shell structures can severely alter the flow of principal stresses, causing significant deviations in their trajectories over the cross-section. Furthermore, shells that use bending as a principal structural mechanism are exceedingly inefficient and generally result in large deformations due to their minimal bending stiffness.

Alone, the deviation angle objective can strive to force the stress trajectories along the generatrixes through a bending mechanism, resulting in a suboptimal solution. Therefore, a multi-objective optimization algorithm is applied with strain energy chosen as the secondary fitness function. This insures that the criteria for the desired optimum include the shell operating in its preferred membrane state.

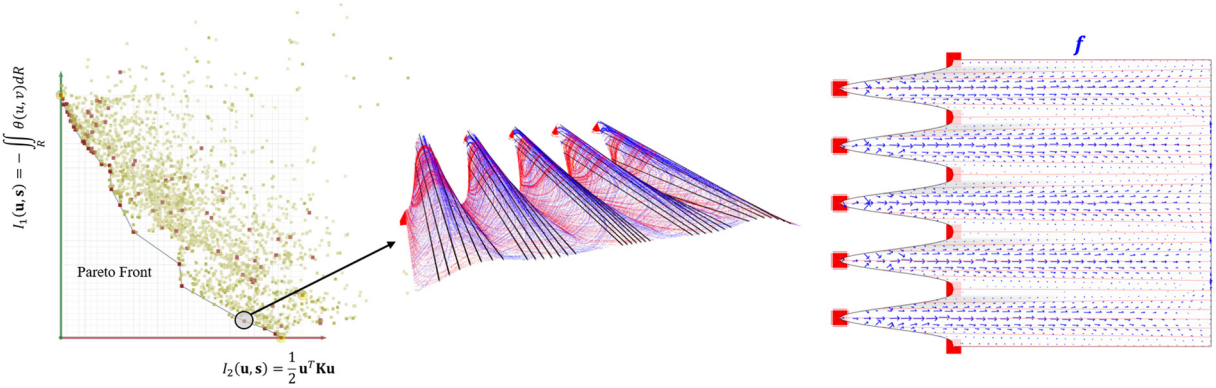


Figure 6: Pareto optimal front and selected optimized solution with principal tensile stress field in shell midplane

The parameterized geometry is then optimized with respect to the deviation angle and strain energy objective functions using a strength pareto evolutionary algorithm, resulting in the pareto from displayed

in Figure 6. A single solution is then selected from the front and displayed along with the resulting flow of principal tensile stress under a dead load. The influence of the deviation angle objective function is clear, with the entirety of the tensile stresses flowing parallel to the generatrixes, making the given shell well suited for the implementation of linear tendons. Furthermore, as the shell was optimized with regards to strain energy, the resulting form operates in a dominating membrane state, minimizing the overall deformation and yielding an efficient structural system.

6. Conclusions

This work has demonstrated the feasibility of optimizing the structural behavior of ruled surface shells so that they are suited for the implementation of strictly linear tendons. A mathematical objective function was then developed for use in an optimization strategy capable of yielding structures with the desired load carrying mechanism. Finally, this optimization was applied to one shell typology, effectively demonstrating the efficacy of the objective function. The linear geometry of the applied tendons is very advantageous, allowing for the construction of precast prestressed elements and minimized losses to friction due to the complete lack of curvature in the tendons.

However, there are limitations to the advantages offered by this optimization of ruled surface forms, with the most significant drawback stemming from the lack of freedom with regards to the available optimizable systems. According to membrane theory, shells can only redistribute radial loads through a curvature in their geometry. This precludes a ruled surface from redistributing a radial load along its generatrixes without the presence of a bending action, due to the complete lack of curvature in the direction of its rulings. The example presented in this paper successfully circumnavigates this issue by investigating forms that function globally as beams, with the global bending moments redistributed by the respective shells as membrane stresses throughout the given cross-section. This requirement for a global beam system severely limits the available design space for the implementation of the developed methodology. However, ruled surfaces represent only a very small subset of all possible concrete shell geometries and there is no reason that the developed methodology cannot be extended upon for further application with other shell typologies. The objective of minimizing the angle between the principal tensile stresses and a given trajectory does not require the trajectory to be linear. It would be theoretically possible to force the flow of principal stress along any arbitrary family of curves on the surface of a given shell using the developed deviation angle objective function. For example, an arbitrary doubly curved surface could be optimized in such a way, so that the resulting flow of principal stress under a given load follows paths with a minimal curvature, reducing the losses due to friction. Perhaps even more promising is the potential of the developed objective function to be applied for the optimization of tendon geometries. This could be achieved through an implementation of the path integral objective function, with the integration being calculated along the individual tendon geometries rather than over the entire structural surface. By then finding curves indicative of a maximal path integral value, implementing tendons along said curves would allow for an efficient prestressing of the given stress field. These potential applications offer interesting avenues for future research, with the methodology applied here representing but one of many conceivable exploitations of this concept.

References

[1] G. Franz and K. Schäfer, Eds., *Konstruktionslehre des Stahlbetons, Band II: Tragwerke, Teil A: Typische Tragwerke: Schalen*: Springer, 1988.
[2] P. Cassinello, M. Schlaich, and J. A. Torroja, “Félix Candela. In memorian (1910-1997). From thin concrete shells to the 21st century´s lightweight structures,” *Informes de la Construcción*, 2010.
[3] H. Pottmann, A. Asper, M. Hofer, and A. Kilian, Eds., *Architekturgeometrie*: Springer, 2010.
[4] F. Leonhardt, Ed., *Spannbeton für die Praxis*. Berlin: Wilhelm Ernst & Sohn, 1962.
[5] R. P. Feynman, “Space-Time Approach to Non-Relativistic Quantum Mechanics,” *Reviews or Modern Physics*, no. 20, pp. 367–387, 1948.

Proceedings of the IASS Annual Symposium 2019 – Structural Membranes 2019
Form and Force
7 – 10 October 2019, Barcelona, Spain
C. Lázaro, K.-U. Bletzinger, E. Oñate (eds.)

Sustainable lightweight structures constructed with bamboos, paperboard, bricks, nylon and a textile membrane of jute fibers

Juan Gerardo OLIVA*, Magdalena TRUJILLO[a], Héctor GUERRERO[b]

*Universidad Nacional Autónoma de México – UNAM, Faculty of Architecture
Lightweight Structures Laboratory, Ciudad Universitaria, 04510 Coyoacán, Mexico City
jgos@unam.mx

[a] High Technology Unity, Plastics Processing Laboratory, Faculty of Engineering – UNAM
[b] Institute of Engineering - UNAM

Abstract

A research group constituted by professors and students from the faculties of Architecture and Engineering of the Universidad Nacional Autonomous of Mexico - UNAM, presents the computer program GEOG to form finding of a translational grid surface and two prototypes constructed with sustainable materials developed at the Lightweight Structures Laboratory. The first prototype was designed based on a surface generated with a translational grid-shell - **TGS.** This prototype will be constructed with Nylon PA66 recycled nods; bamboo or paperboard bars and covered with a textile membrane of jute fibers protected by a light layer of polymeric covering. The second prototype, called **LBV**, is a structural system constructed with brick vaults made applying the Mexican technique of *leaning brick*, which does not require any formwork.

Keywords: Form finding, sustainable materials, lightweight structures, grid-shells, membrane structures, bamboos, paperboard, nylon, jute fibers, bricks

1. Introduction

In this paper we present the parametric program GEOG, updated and extended. GEOG is addressed to the form finding of a translational surface with double positive or negative curvature. Two prototypes of lightweight structures are also presented. These prototypes demonstrate that it is possible to build with highly sustainable materials, of low cost and that are susceptible to be built by self-construction. [1]. The prototypes cover surfaces of approximately 55 m2. They can be used as a multi-purpose pavilion, as well as housing for marginalized groups in underdeveloped countries.

2. Program GEOG

GEOG is a parametric program originally developed in 1982 in FORTRAN IV by the main author of this paper during his Doctor work at the Universität Stuttgart [2]. Its name comes from **Geo**metry and **G**rid-shell. In 1991, GEOG was reprogrammed in BASIC by the engineering student Reinhard Kürten as part of his thesis at the Universität GH Essen. This version allowed a more agile interaction with the user and to run the program on a personal computer with MS-DOS operating system. Now the new version was written in C # language by the mechatronics student Kevin Morales from UNAM. Fig. 1. Although originally GEOG allowed only the form finding of a translational grid surface with catenaries, now GEOG allows the form finding of translational surfaces with parables, circumferences and NURBS curves as well, which can be customized by the user. Fig. 2. GEOG also allows the form finding of surfaces with double positive or negative curvature.

Copyright © 2019 by Juan Gerardo OLIVA, Magdalena TRUJILLO, Héctor GUERRERO
Published by the International Association for Shell and Spatial Structures (IASS) with permission.

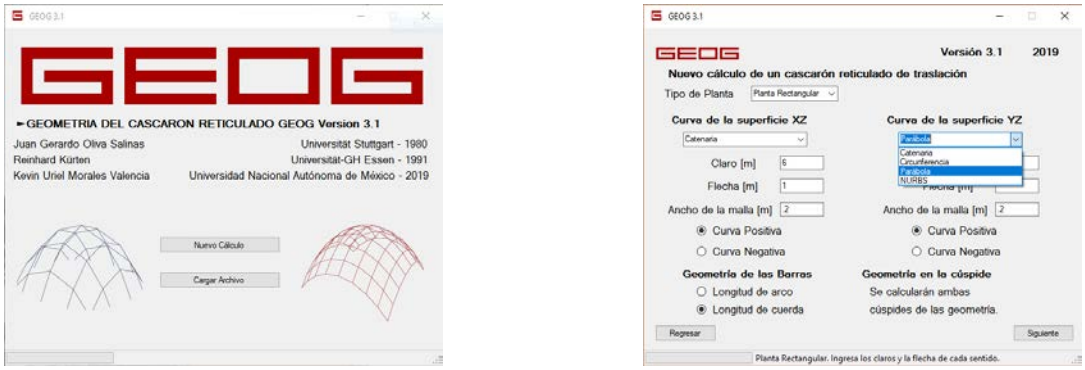
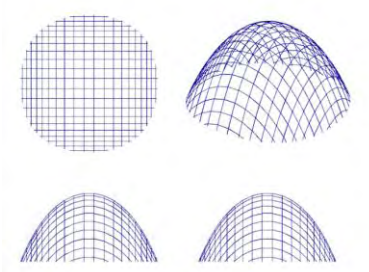
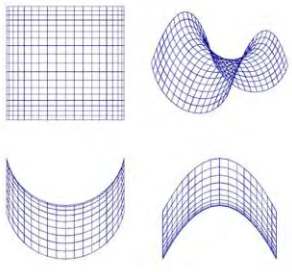


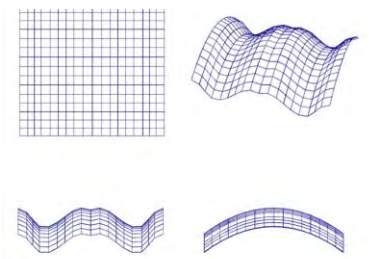
Figure 1: GEOG main screen (left). Input data screen (right).



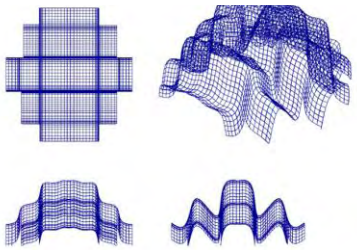
a) Surface with positive curvature generated by two catenaries



b) Surface with negative curvature generated by a circumference and a parabola



c) Surface generated by a NURB curve and a parabola



d) Surface generated by two SPLINES curves

Figure 2: Translation surfaces generated with GEOG.

3. Prototype based on a Translational Grid-Shell - TGS

The prototype TGS is a translational grid-shell with catenaries, with bamboos or paperboard bars and nodes and connectors made of nylon PA66. Fig. 3. The form finding process was generated with GEOG..



Figure 3: Prototype **TGS.** Input data for GEOG: Height of Apex 4.20 m, Wide Span 6.46 m, Mesh Width 1.00 m

The shape of the grid shell obeys to the shape of a hanging net, if the stiffness of the two arches to allow the entrance is guaranteed.

This stiffness is obtained by introducing diagonal cables into the rhombus generated in the two free edges of the shell. It is therefore guaranteed the mechanical work of the structure by own weight mostly in compression.

Two sustainable materials for the bars are proposed: bamboo or paperboard tubes. Subsequently, the shell is covered with a membrane made of jute fibers protected by a light layer of polymeric covering. Figure 4 shows the process of application of the resin on the jute. Once the membrane cutting patterns have been joined together, a layer of styrene-acrylic polymer resin is applied for protection from the weather. It should be mentioned that this compound of jute-acrylic materials constitutes 88.5% of the weight of the membrane and the rest corresponds to the polymeric resin. This is how it is possible to make the membrane impermeable and to increase its resistance to traction, as well as prolonging its life expectancy.



Figure 4: Application of the styrene-acrylic polymer resin to samples of the membrane with jute fibers.

The designed node is the main element that joins four bamboo or paper board rods, while the connector is the coupling element for each of them. Figs. 5 and 6. To accomplish a better design for each element, its form was adapted by diverse modifications until the finished piece was obtained.

Two bamboo rods are connected to each circular section (node) through a cylindrical receiver (connector), which slope follows the networks curvature of the shells that is ubicated in each mechanism. Fig. 6. The node offers the possibility of adjusting the incidence angle of the rod with the node, while modifying one and all four receivers on each node into the required angle.

The development of the mechanism was based on the study and analysis of one of the two circular sections that conforms it, considering the Nylon 66 as raw material for its construction. The maximum work resistance of Nylon 66 is 170 MPa. In order to design plastic pieces, it must be considered that the manufacturing process has an important impact on the appearance and functionality of the piece. For the piece design made through plastic injection, it is recommended to avoid high thickness and angles under 90°. These two considerations are determinant for the structural design on injected plastic

parts, Andersson et al. [4]. In the conceptual design of the node, it can be observed that the connector presents these undesirable characteristics, thus prototypes of nodes and connectors were developed. Figs. 5 and 6. In this prototype, both high thickness and angles under 90° were eliminated. Following the recommendations for the design of plastic parts, Finger and Dixon [6] and Rees [7]; the volume of the center of the piece was reduced, angles under 90° were rounded off and the wall thickness was reduced so that "I" form configurations were achieved. To verify the functionality of the new model, a finite element analysis was held, as well as a flow analysis that allowed the plastics behavior visualization inside the mold during the manufacturing process by injection.

During the re design step and according to the plastic-design rules, acute angles, 90º corners and the thickness of the wall were modified from the original design; and to improve mechanical resistance, strategic reinforcements ribs were added. For the two next steps, FEA and Mold flow adviser were applied to the new design. This way, the consideration under the maximal expected loads, with a security factor of 1.4, was generated with a maximum stress of 167 MPa, number that is above the acceptable stress of the Nylon 66. Table 1 shows the final configuration of the product, which was evaluated by resistance and flow analysis respectively to approve its use, Kirk and Watts [8], Madsen [9] and Kazmer [10]. The medium quality of the part being 17.6%, the quality distribution is dispersed in the central area, which can be controlled during the injection process, Kirk and Watts [8] and Madsen [9]. The software used for the simulation of the finite element was the NX Siemens software, while the used flow simulator was the Moldflow adviser 2017.To meet the last step, plastic injection mold was manufactured, and the nodes were obtained, figure 5. The same procedure was performed for the connector, while using nylon 66 as the raw material once more. Both elements were manufactured by plastic injection molding.



Figure 5: Nylon Nodes, mold and finished product

Table 1: Nodes and connectors manufactured with Nylon PA66.

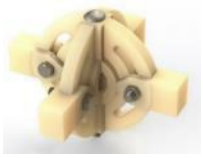
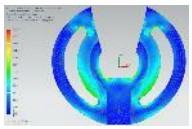
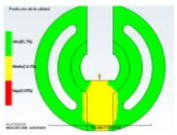
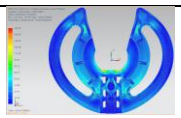
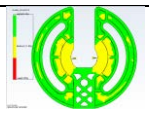
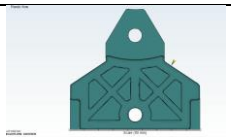
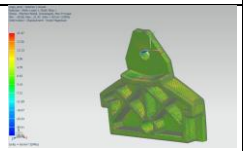
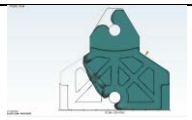
ELEMENT	Geometric Configuration	Strength reached	Value MPa	Quality during the process	Value %
Conceptual design			153		14% of medium quality at the center of the node
Node			167		17.6 % of medium quality distributed in a wider section
Connector			27		Filling distribution for the connector



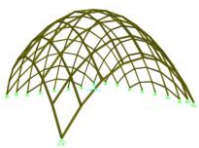
Figure 6: Final configuration of the nylon PA66 connector.

In order to analyze the form and and the constructive procedure of this prototype, it was agreed to build a 1: 5 scale model in the Light Structures Laboratory. Fig. 7. The next stage of the project consists on the construction of TGS in natural scale within the campus of the Faculty of Architecture.

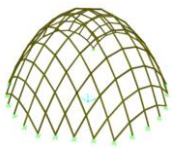


Figure 7: Model Scale 1:5 and render of TGS.

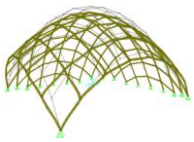
Bamboo structures were mechanically modeled. Fig. 8 shows the bamboo model before and after the application of loads. Of course, gravity, seismic and wind loads are being considered. Mechanical properties of Bamboo are being modeled explicitly, and structural responses are under study.



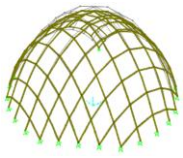
a) Front view before loading



b) Back view before loading



c) Front view after loading



d) Back view after loading

Figure 8: Evaluation of TGS, bamboo model.

4. Prototype based on “freeform” leaning bricks vaults - LBV

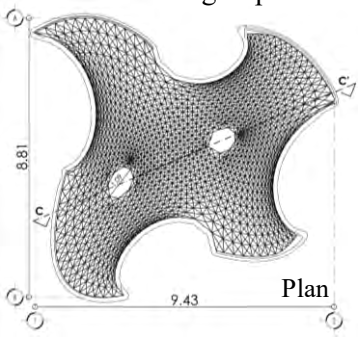
LBV was conceived as the combination of two brick vaults of different size with four entrances, five supports and two oculi. Fig. 10. In various regions of central Mexico, vaults are built using the *leaning bricks vaults* technique. This constructive system consists in beginning the construction in any place of the vault’s base, if it is of circular plant or in some of the corners, if it is of rectangular or polygonal plant. Fig. 9. The most commonly used brick is the one called "cuña" measuring 5 cm X 10 cm X 20 cm. The vaults construction starts by placing the brick with an inclination of 45º.



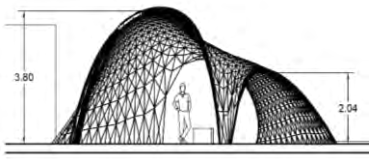


Figure 9: The brick called "cuña" and the construction of a vault with leaning brick system.

This constructive system does not require any formwork, just a few elements used as guides of the form. This technique is the area of expertise of the "bovederos", who become specialists through daily practice, however, it is also a technique that can be learned in a relatively short time. Brick can be considered as highly sustainable, low cost and relatively available material within Mexican territory. The process of determining the form was done through the RhinoVAULT Plug-in, developed by Phillipe Block and his research group.



Plan



Section View

Figure 10: Prototype LBV

As in the previous prototype, a 1: 5 scale model of LBV was built. Fig. 11. The students manufactured the bricks and constructed the vaults, just as the "bovederos" would do on a natural scale. This exercise turned out to be highly didactic and fun, as well as very motivating. [10].




Figure 11: Construction of the scale model 1: 5 of LBV

The next stage is the construction of the prototype on natural scale in the campus of the Faculty of Architecture. Fig. 12.



Figure 12: Render of the LBV prototype

To protect the vaults from the rain and the sun, they are usually covered with a wire mesh and with a cement mortar of approximately 4 cm of thickness. In the case of the LBV that will remain built for only a couple of weeks, it will be just covered with a layer of varnish.

Finite element models of the studied structures are being analyzed at the Institute of Engineering, UNAM, Mexico (Figs. 8 and 13). Models are subjected to gravity, seismic and wind loads. Geometry and mechanical properties of materials are explicitly modelled in SAP2000 [11]. Preliminary results for LBV model, presented in Fig. 13, show that compression stresses are expected under gravity loading; while some tension stresses are seen under seismic loading.



a) Under gravity loading b) Under seismic loading

Fig. 13. Stresses in Model LBV

5. Conclusion

This research project shows that lightweight structures can be conceived, designed and constructed with sustainable materials and applying traditional construction methods. In addition, there are many possible applications, especially addressed to construct housing of marginalized groups in underdeveloped countries. It also demonstrates the collaborative work between architects and engineers and a singular way of teaching structures to students of both disciplines.

Acknowledgements

This research project is sponsored by the General Issues Department for Academic Personnel DGAPA-UNAM, Program PAPIIT IG 400517.

References

[1] J. G. Oliva, M. Trujillo, A. Ramírez, A. Hernández, and M. J. Ontiveros. "Sustainable materials applicable to the construction of housing for vulnerable groups". *Proceedings of the International Association for Shell and Spatial Structures (IASS) Symposium*, Hamburg, 2017.

[2] J.G. Oliva Salinas, *Über die Konstruktion von Gitterschalen*, Universität Stuttgart, Selbstvertlag SFB 64, Mitteilungen 63/1982.

[3] Y. Lennar and Ljunberg, "Materials selection and design for estructural polymers," *Materials & Design,* nº 24, pp. 383-399, 2003.

[4] F. Andersson, H. Astrid, E. Sundin and B. Mats, "Design for Manufacturing of Composite Structures for Commercial Aircraft-the Development of a DFM strategy at SAAB Aerostructures," *Variety Management in Manufacturing,* nº 17, pp. 362-367, 2014.

[5] H. S. Wang, Y. N. Wang and Y. C. Wang, "Cost estimation of plastics injection molding parts through integration of PSO and BP," *Neural Network Expert Sistem With Applications,* nº 40, pp. 418-428, 201.

[6] S. Finger and J. Dixon, "A review of Reseach in Mechanical engineering Design processes," *Research in engineering Design,* nº 1, pp. 51-67, 1989.

[7] H. Rees, Understanding product Design for injection molding, Cincinnati OH, 1996.

[8] M. Kirk and C. Watts, plastics Processing, Oxford UK: Oxford, 2011.

[9] D. Madsen, print Reading for Engineering & Manufacturing Technology, NY USA, 2012.

[10] J. G. Oliva Salinas. "Geometry and mechanics, inescapable tools of architectural and structural design". *Proceedings of the 6th Structural Engineers World Congress (SEWC)*, Cancun, 2017.

[11] SAP2000, "Structural Analysis Program v20.2.0". Computers and Structures Inc. Berkeley California. 2018.

Proceedings of the IASS Annual Symposium 2019 – Structural Membranes 2019
Form and Force
7 – 10 October 2019, Barcelona, Spain
C. Lázaro, K.-U. Bletzinger, E. Oñate (eds.)

Catalogue of equilibrium forms of structures

Hiroki TAMAI*, Kenryo TAKAHASHI[b], Bunji IZUMI[a],

Mizuki SHIGEMATSU[a], Kensuke ANDO[a]

*[a] Nikken Sekkei
Chiyoda-ku Tokyo
tamai.hiroki@nikken.jp

[b] Ney & Partners Brussels

Abstract

This paper showcase a collection of conceptual designs of equilibrium structures created through form finding procedures. The collection are sorted by types of structures, such as arch or cable net etc., specifically characterized by material behavior, i.e. tensile or compressive; and types of usages, such as roofs or bridges. This will include self-stressed structures as well as tensile and compressive structures. By showing various conceptual design studies through form finding, this paper addresses a few relevant subjects in form finding which have not been thoroughly discussed besides the numerical methods. For example, form finding problems often have more than one solution. It is, in fact, still a designer's work to choose one from many possibilities. Then how do they go about choosing one? The goals of this presentation are 1) to explore the possibility of form finding techniques used for conceptualizing unconventional structural configuration and 2) to address relevant matters needed in order to make the best use of form finding procedures. This is our first attempt to catalogue a variety of equilibrium forms and systems that can be applied in contemporary design of structures.

Keywords: Form finding, conceptual design, form of equilibrium, space structure, footbridge

1. Introduction

Numeric form finding techniques have seen significant advances in the last few decades, and their application has gradually become recognized as a powerful design tool in architectural as well as structural design practice. Ever since physical hanging and soap film models were first used, the traditional motivation of form finding techniques has been to give a stable shape to structural materials that do not have their own fixed shape. These include discontinuous materials such as masonry, and tensile materials such as membranes or cables. Thin concrete shell structures have also been a major focus for form finding methods due to their thinness. For tensile materials in particular, prestressing must be introduced to stabilize and stiffen the structure. After some basic form finding techniques such as the force density method or the dynamic relaxation method became available in popular modeling software, many designers familiar with cutting-edge CAD tools but not necessarily having significant technical expertise in the area have been able to run simple form finding procedures to explore curvy roof shape options and their corresponding load paths.

What we get through form finding processes is more than just a reasonable engineering solution. From an engineering point of view, designing a structure with predominantly axial behavior helps minimize the structural material usage due to the fact that axial forces, particularly tension, are the most efficient way to transfer loads. But such forms and their corresponding load paths have something more to attract designers, including the author. This may be the aspiration for lean shapes or analogy to forms

Copyright © 2019 by Hiroki TAMAI, Bunji IZUMI, Kenryo TAKAHASHI, Mizuki SHIGEMATSU, Kensuke ANDO
Published by the International Association for Shell and Spatial Structures (IASS) with permission.

in nature. In this paper, an equilibrium form or structure exclusively denotes those that are in equilibrium in axial behavior, either tension or compression, except for local bending behavior over linear elements.

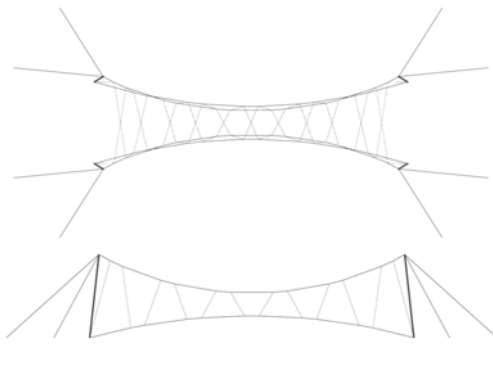
It is actually a very exciting and delightful experience to explore various types of structural equilibrium forms. In many cases, the results from numerical form finding procedures confirm our intuitive composition of such systems. However, sometimes the output of such procedures results in very surprising geometries. Finding an analogy to rational forms in nature and finding once-unimaginable equilibrium configurations are both equally inspiring.

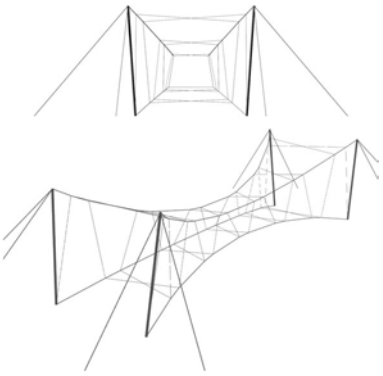
By showing various case studies, this paper will address a few relevant subjects in form finding which have not been thoroughly discussed besides the numerical methods. For example, form finding problems often have more than one solution. It is, in fact, still a designer's work to choose one from many possibilities. Then how do they go about choosing one?

The goals of this attempt of making a catalogue of structures of equilibrium forms are 1) to explore the possibility of form finding procedures for conceptualizing unconventional structural configuration and 2) to address relevant matters needed in order to make the best use of form finding procedures.

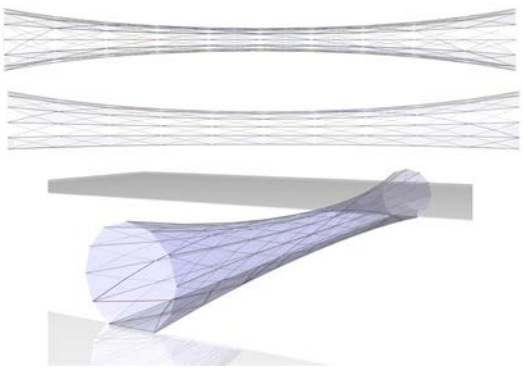
2. Catalog of form finding

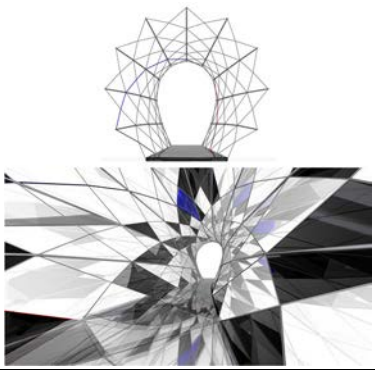
In the following pages, various types of equilibrium forms predominantly in axial forces under dead loads are collected and sorted by similar structural types. They are created by several different methods depending on the problems. The attributes charactering each structure in equilibrium are abbreviated in the table as follow; AT: Architectural Type, ST: Structural Type, BC: Boundary Conditions, DV: Design Variables, DC: Design Constraints, and SN: Special Note. In this catalogue, the focus is mainly on the conceptual design process by exploring equilibrium systems by form finding techniques and applying them to design of the architectural and structural forms. Rigorous structural analysis including member sizing and stability analysis is outside of the scope.



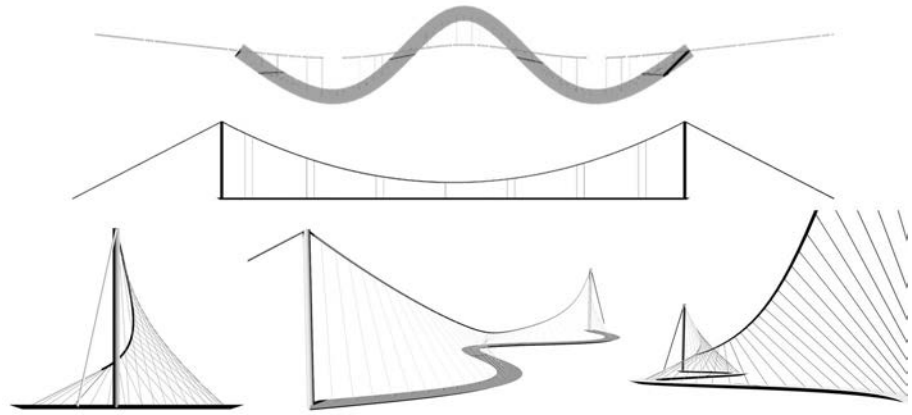
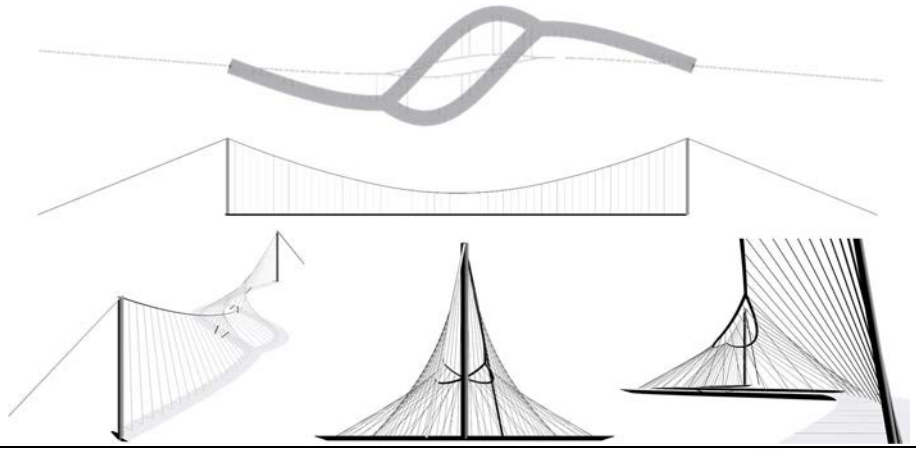
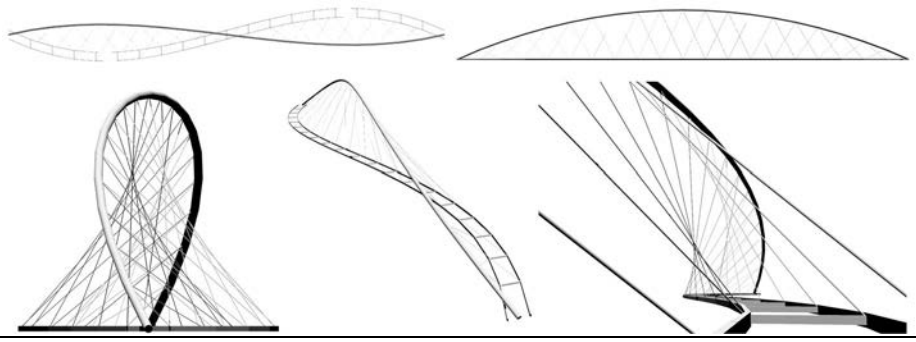


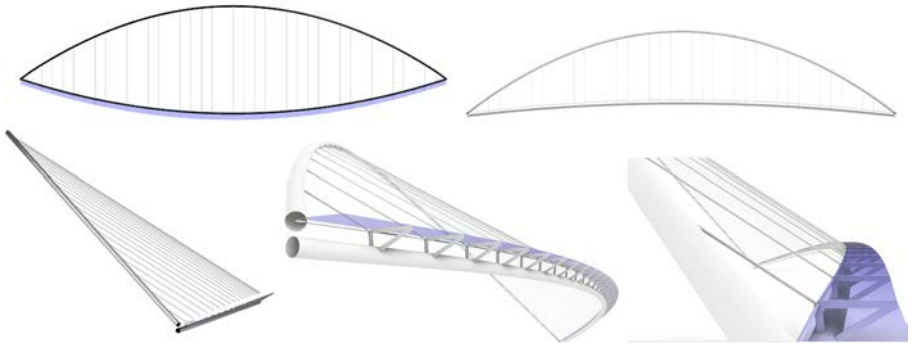
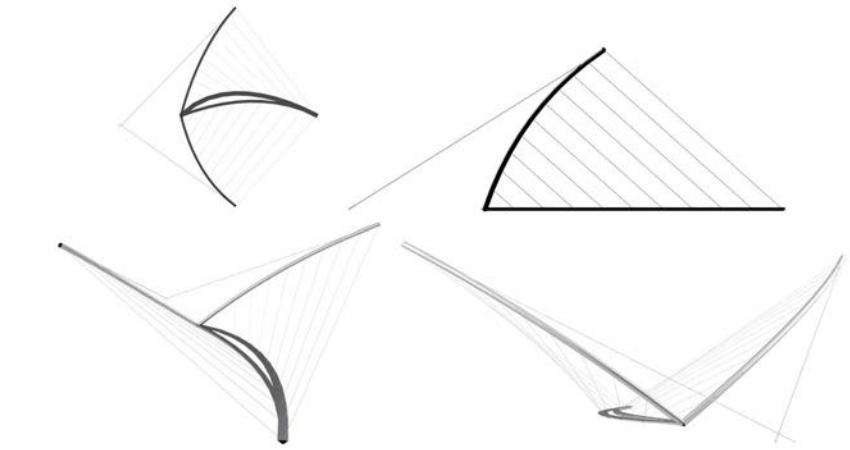
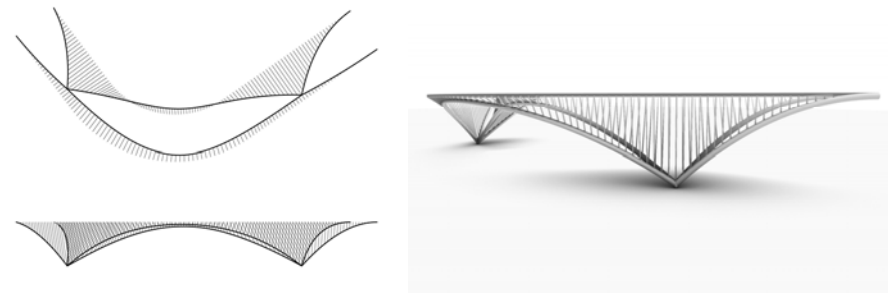
AT: Footbridge
ST: Tension
BC: Support at pylons and back stays
DV: Force and form
DC: Prescribed prestress in controlling cables
SN: The form is determined by "string figure" analogy.

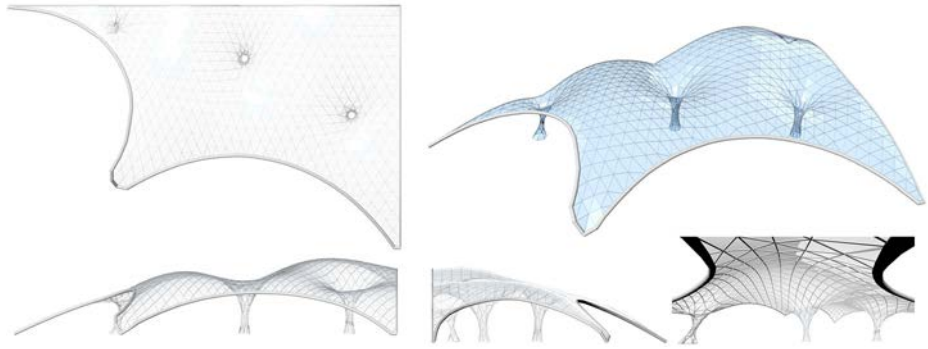
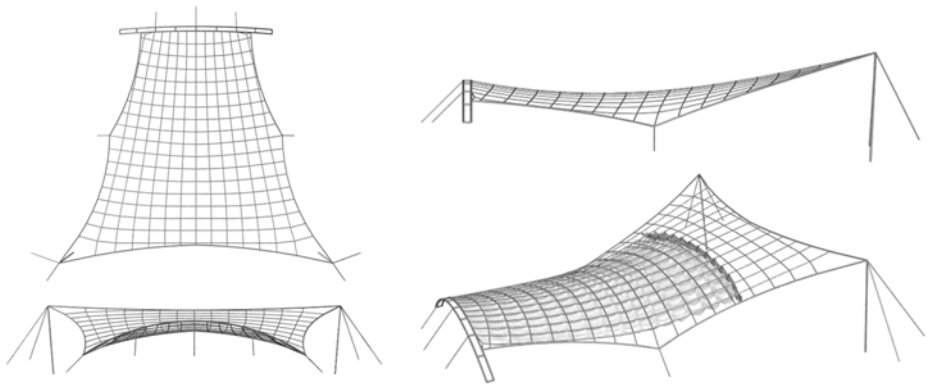
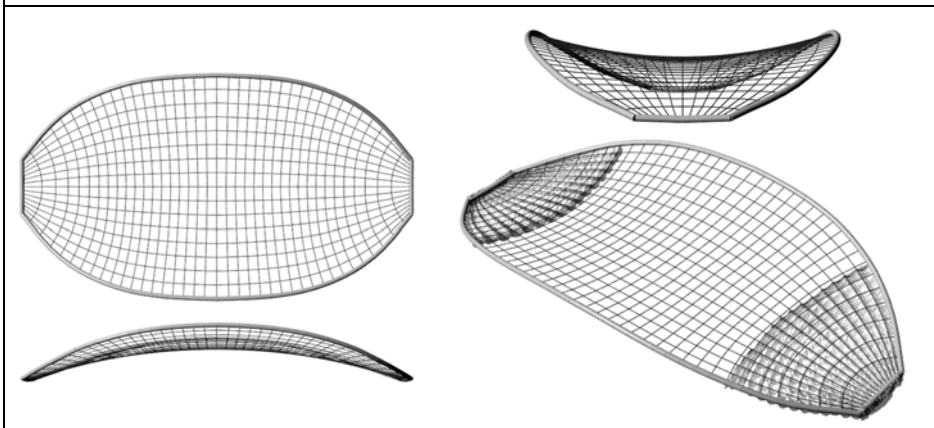
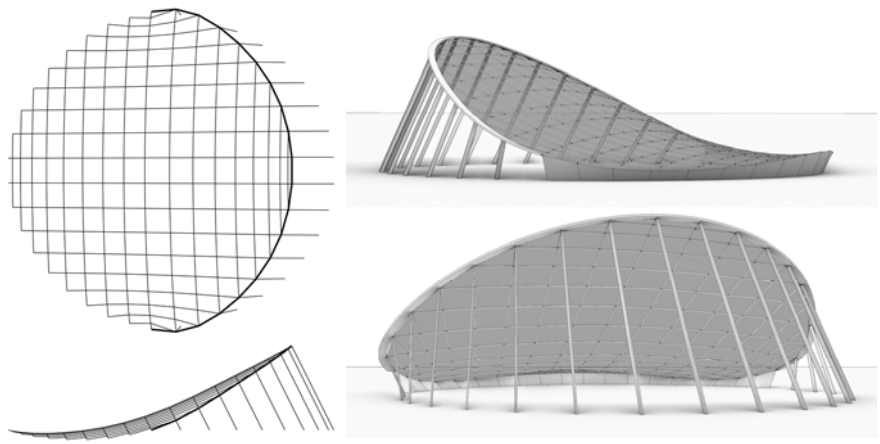


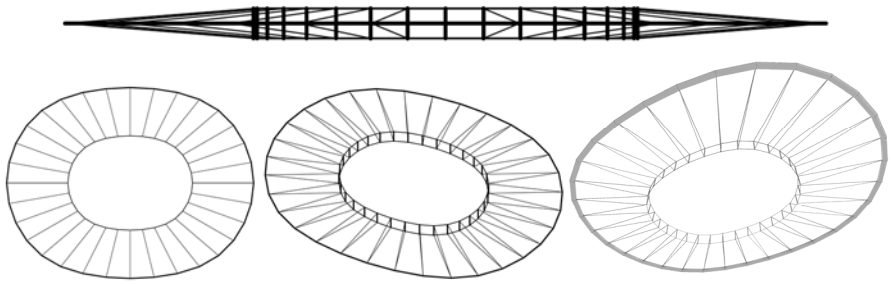
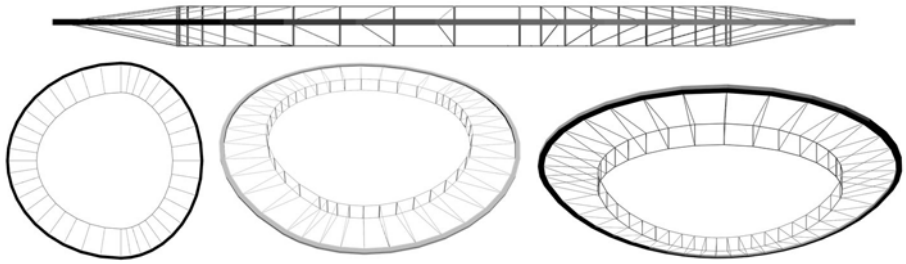
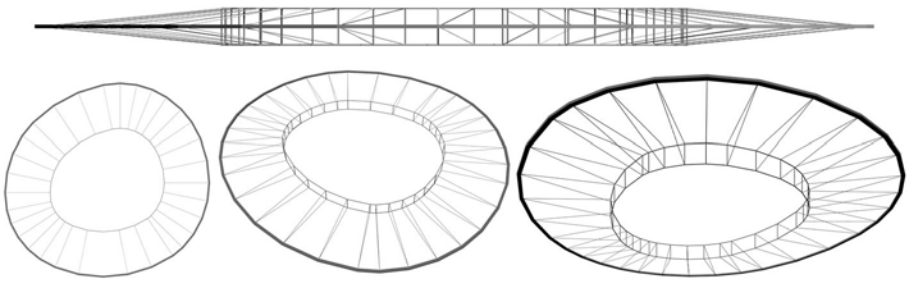
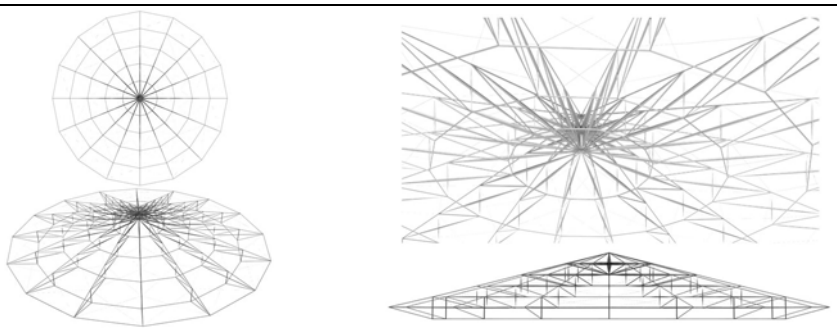
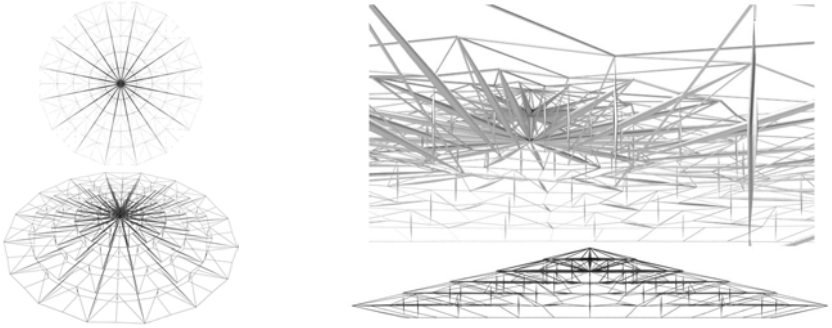


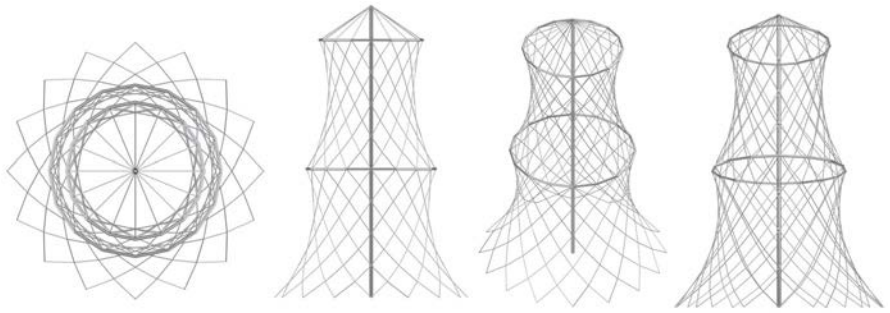
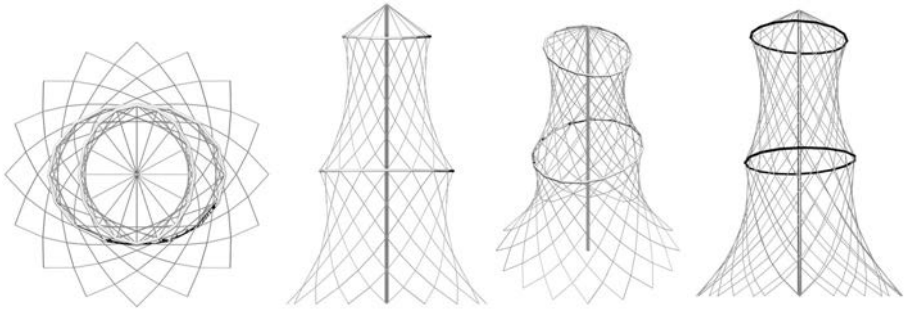
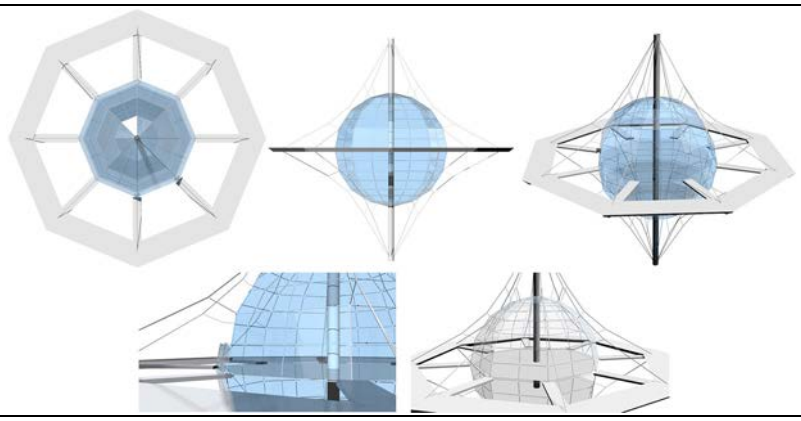
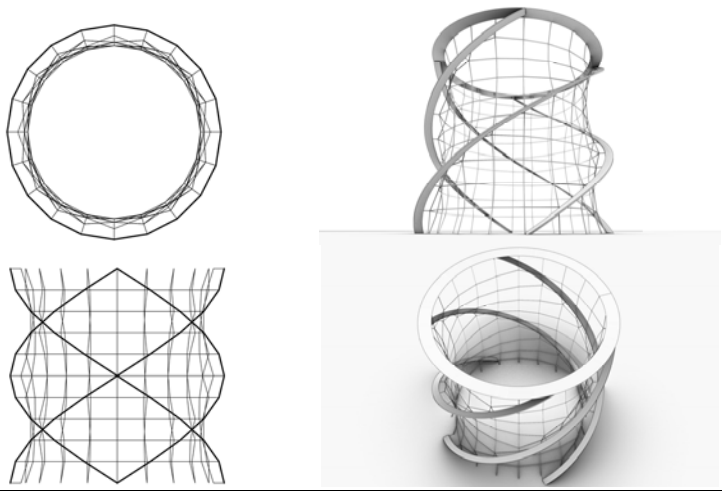
AT: Footbridge
ST: Tension
BC: Support at end walls
DV: Force and form
DC: Prescribed prestress in controlling cables
SN: The form is determined by "string figure" analogy.

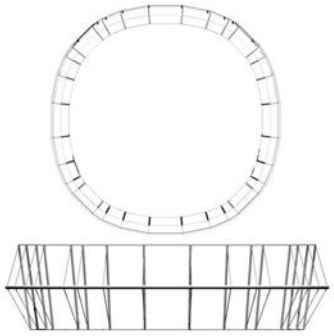
	AT: Footbridge ST: Suspension + W-shape deck BC: Support at pylons and back stays DV: Force and form DC: M-shape deck and pylon height SN: The deck forms two horizontal arches.
	AT: Footbridge ST: Suspension + Sx2-shape deck BC: Support at pylons and back stays DV: Force and form DC: Deck shape and pylon height SN: The deck forms multiple horizontal arches.
	AT: Footbridge ST: S-shape arch + S-shape deck BC: Thrusts for both arch and deck DV: Force and form DC: Deck shape SN: The deck forms multiple horizontal arches.
	AT: Footbridge ST: S-shape arch + S-shape deck + double cables BC: Thrusts for both arch and deck DV: Force and form DC: Deck shape SN: The deck forms horizontal arches.

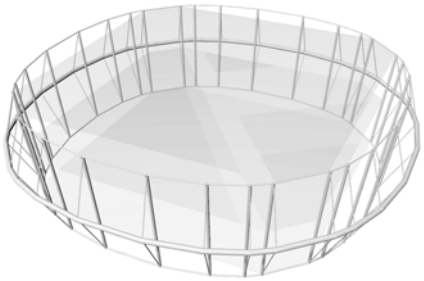
	AT: Footbridge ST: Inclined arch + C-shape deck BC: Thrusts for both arch and deck DV: Force and form DC: Deck shape SN: The inclined deck and arch are balanced. [3]
	AT: Footbridge ST: Inclined arch + C-shape deck with tension and compression hoops BC: Thrusts for both arch and deck DV: Force and form DC: Deck shape with eccentricity SN: The inclined deck and arch and eccentric load balanced
	AT: Footbridge ST: Inclined bowed pylon + two bowed decks BC: Support at pylons and back stays DV: Force and form DC: Deck shape and forces SN: Forces in the two bowed decks are balanced by compression from one and tension from the other
	AT: Footbridge ST: Compression and tension BC: Horizontal support on the deck DV: Force and form DC: Deck height on the same plane LC: Gravity SN: Arch remains in pure compression [5]

	AT: Roof ST: Grid shell BC: Boundary arches, funnel columns and side walls DV: Force and form DC: Target shape SN: Approximation of a free form by an equilibrium form [3]
	AT: Roof (retractable) ST: Cable net + membrane BC: Boundary cables, an arch and back stays DV: Force and form DC: Foldability of movable membrane & force variation SN: Equilibrium cable net configuration visualizing membrane foldability condition [2]
	AT: Roof (retractable) ST: Cable net + membrane BC: Boundary beams DV: Force and form including support anchoring positions DC: Foldability of movable membrane & force variation SN: Equilibrium cable net configuration visualizing membrane foldability condition [2]
	AT: Roof ST: Cable net + arch, prestresed BC: anchors for cables & arch supports DV: Force and form, including supports DC: Regularity of cable net, planarity of the quads, geometry of arch SN: Arch remains in pure compression

	AT: Roof ST: Spoke wheel system BC: No support, Self-stressed DV: Force and form DC: Geometry of the compression ring and flying posts SN: Shape of the ring is specified [5]
	AT: Roof ST: Spoke wheel system BC: No support, Self-stressed DV: Force and form DC: Variation of compression ring segments SN: Asymmetric spoke wheel [1]
	AT: Roof ST: Spoke wheel system BC: No support, Self-stressed DV: Force and form DC: Free form compression ring SN: Converting free form closed curve to spoke wheel compression ring [1]
	AT: Roof ST: Tensegrity BC: Self-stressed DV: Topology and force DC: Self-equilibrium SN: No need for compression ring [4]
	AT: Roof ST: Tensegrity BC: Self-stressed DV: Topology and force DC: Self-equilibrium SN: No need for compression ring [4]

	AT: Tower ST: Cable net, column and compression ring BC: column support and anchors DV: Form and force DC: Geometry of rings and vertical spacing of cable net SN: Cable net geometry controlled [3]
	AT: Tower ST: Cable net, column and compression ring BC: column support and anchors DV: Form and force DC: Geometry of rings and vertical spacing of cable net SN: Asymmetric Ring shapes [3]
	AT: Observatory deck ST: Cable net, column and compression ring BC: Column support DV: Form and force DC: Geometry of rings and cable net SN: 3-dimensionally convex prestressed surface. Floating compression ring
	AT: Façade/Envelope ST: Cable net + spiral arches BC: Supports at top and bottom DV: force and form DC: Alignment of the cable grid in radial directions / Cable grid on horizontal planes / spiral shape SN: The outer spiral ring remains in pure compression for the prestressed cable grid





AT: Façade/Envelope
ST: Spoke wheel
BC: Supports at struts
DV: force and form
DC: Plan geometry
SN: Floating compression ring

3. Discussions

By going through the above-shown collection of conceptual design of equilibrium form structures, it has become clear that in most cases in design, the techniques to handle constraints is indispensable to control the shapes. Often in design practice, to find a solution that satisfy equilibrium under the constraints is actually not sufficient to reach a good design; needless to say, an equilibrium solution that does not meet constraints is not useful.

Finding equilibrium forms is just an engineering procedure; choosing a solution among them forms completes a good design process. It is often true that an equilibrium form may not be uniquely determined under the design parameters and constraints given to a designer. While choosing one to increase the structural performance is always a reasonable approach, a designer has a certain freedom to choose a solution, such as regularity of member arrangement or the foldability of membrane.

What is missing or weak in numerical form finding techniques is to find an unconventional system or a suitable topology. This part of design still rely on designers' creativity. A better equilibrium form solution can be outside of the solution space bounded by the system topology assumed.

4. Concluding remarks

By going through many structural concepts applying equilibrium forms, the authors demonstrated that they have a significant potential in structural and architectural design. The design potentials of structures of equilibrium form by incorporating with various design aspects are yet to be explored. The study in the compositive application of form finding in architectural design has only just begun.

References

[1] H. Tamai, "On a family of equilibrium geometry of a spoke-wheel structure: Geometric approach to form finding of a spoke wheel system", *Creativity in Structural Design: Proceedings of the IASS Annual Symposium 2018*, Boston, USA, July 16-20, 2018.

[2] H.Tamai, "Form finding of cable nets for retractable membrane roofs", The Proceedings of International Association for Shell and Spatial Structures (IASS) Conference, Tokyo, Japan 2016 "Spatial Structures in the 21st Century"

[3] H. Tamai, Advanced application of the force density method in multidisciplinary design practice by incorporating with optimization using analytical derivatives, Proceedings of the International Association for Shell and Spatial Structures (IASS) Symposium 2013, Wroclaw, Poland

[4] Tamai, H., E. Mahjoub, "Semi-Triangulated And Free-Standing Tensegrity Domes: Exploring Cable-Strut Configurations for Tensegrity Domes Based On Structural Performances", Proceedings of IASS-APCS International Symposium on New Olympics, New Shell and Spatial Structures, 2006.

[5] K. Takahashi, L. Ney, "Advanced form-finding by projection for structural equilibrium with design objectives," *Proceedings of the IASS Annual Symposium 2018*, Boston, July, 2018.

Proceedings of the IASS Annual Symposium 2019 – Structural Membranes 2019
Form and Force
7 – 10 October 2019, Barcelona, Spain
C. Lázaro, K.-U. Bletzinger, E. Oñate (eds.)

Designing strategies for Topological Interlocking Assemblies in architecture. Flat Vaults

Kevin MORENO GATA*,[a], Caitlin MUELLER*, Ernesto ECHEVERRÍA VALIENTE[a]

* MIT, Department of Architecture, Digital Structures Research Group
77 Massachusetts Avenue, 5-414, 02139 Cambridge, Massachusetts, USA
Kevinmg@mit.edu

[a] University of Alcalá, Department of Architecture

Abstract

The modular interlocked blocks in flat structures are known in ancient buildings with pure-compression constructions. Over the last two decades, this structural bond has become relevant, studied by mechanical engineers, and material scientists due to the properties and design freedom that modular structures have. The structural hierarchy existing in topologically interlocked structures enhance the performance, allowing to design and fabricate custom block elements. The main reason to consider this system is that, from the architectural perspective, it is composed by identical modular elements, and it discretizes flat or curved surfaces into elements that work only by contact and compression. This article presents preliminary studies for its application and different approaches for designing discrete interlocked assemblies with a focus on the application for architectural structures: studying the structural performance of contact analysis and introducing the combination of topological interlocking with different structural principles.

Keywords: Topology, interlocking, vaults, patterns, pure-compression, post-tensioned.

1. Introduction

Topological interlocking is a design principle, which elements of a particular shape are arranged in such a way that the whole structure can be held together by a global peripheral constraint" *Dyskin et al.* [1]. Besides being a complex structural system to analyze, it is composed of identical modular elements, providing flexibility during the assembly process, not being necessary any fastener or adhesive, since the contact mechanism of it topology is enough to keep a locked structure. From the traditional architectural perspective, the flat vaults discretize horizontal surfaces into elements that work only in pure compression, likewise the masonry vaults, however transmitting the load not directly by its shape, but it contacts elements geometry. The perimeter nevertheless acquires a critical role, receiving a horizontal pushing pressure from the inside. This paper will introduce a series of alternative designs implementing topological interlocking in architectural scale, fabrication methods, and experimental analysis, laying the groundwork for further mechanical analysis.

2. References review

2.1 Topological Interlocking in Architecture: stereotomy

Bridging the boundary between the knowledge of nature and human ingenuity, it would be placed with realizations such as the flat dome of El Escorial, where Juan de Herrera covered a space of 7.81 meters, as in *Rabasa and López et al.* [2] with a structure of just 28.1 cm (1 foot), having a slenderness of just 1/28. This vault can be considered in the words of *Ávila et al.* [3] as "the limit of an infinite radius dome,

Copyright © 2019 by Kevin Moreno Gata
Published by the International Association for Shell and Spatial Structures (IASS) with permission.

which does not have an appreciation of curvature in the section." The success of this vault is in the perfection of the work of its elements, the large size of the pieces (concentric rings of conical faces), and the reduced thickness of the mortar used. Another example of architectural boasting about the construction of flat vaults was proposed by the French engineer *Joseph Abeille* in 1699, proposing a unique piece that would solve the development of this type of flat vaults. According to *Rabasa et al.* [4], the theories of *Abeille,* or the variables proposed by *Freizer* (1737) were carried out in Lugo and at the *Pontón de la Oliva*, in Madrid.

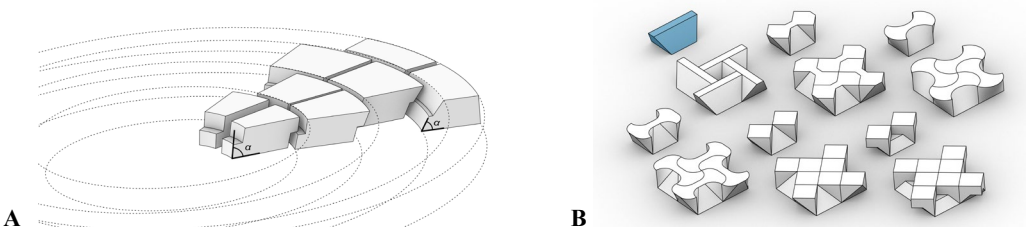
The knowledge obtained is the result in many cases of a process of trial and error from which the calculation models proposed even more audacious solutions. The appearance of new materials and the refinement of calculation and simulation let now to push the limits established in terms of dimensions and slenderness, but the forms continue to fit those already refuted by the experience of centuries.



Figure 1: Interlocked vaults examples (from left to right): Monastery of Escorial (1565), Cádiz Cathedral's Crypt (1730), Lugo's Cathedral (1699), Pontón de la Oliva (1853)

2.1.1 Historical patterns

The masters of stereotomy produced and replicated modular blocks that guarantee the uniform load transmission (Figure 2). Therefore, there were several typology patterns, depending on its regularity/irregularity or the circular/orthogonal distribution. In addition to the *Abeille's Bond*, in France, the mathematician *Truchet*, and the engineer *Freizer*, complemented later this vault system with patterns alternatives, *Rabasa et al* [4]. Moreover, they introduced a non-orthogonally (hexagonally) patter to transmit the forces, showing it exists certain flexibility in building interlocking structures.



A **B**

Figure 2: Patterns comparison: (A) Circular vault of Escorial, (B) (blue) *Abeille's Vault*, and *Truchet* and *Freizer* topologies alternatives.

2.3. Advances in Topological Interlocking: analysis and design

The interest of TI (Topological Interlocking) became relevant in areas such as material science and mechanical engineering, also known as *Architectural Materials*. Clear examples demonstrated the performance with various materials, [1][5][6]. Later studied the systematization of the TI mechanical behavior, [7][8][9]. Many cases, research complemented with experimental tests, that established advantages of TI mechanics with brittle materials, such as glass [10], ceramic [11], or even impact with monolithic concrete [12]. The manufacture of interlocking materials has received a considerable increase in alternatives, thanks to the use of additive manufacturing technologies [13].

2.3.1 Topological interlocking patterns

Pattern studies are usually performed by *Design Experiments* [14]. The catalog of solutions is extensive, even proposing interlocked patterns inspired on organic geometries such as the osteomorphic pattern based on a hexagonal grid [15]. In order to balance the geometry, parametrical investigations [16] can determine the importance of contact surface, analyzing the non-linearity of the results.

3. Design Strategies

Traditional industrial constructions establish hierarchy, with elements of large dimensions and various materials, creating high entropic structures (Figure 3a). TI is based on different hierarchy but composed of identical blocks (Figure 2), making possible creating interlocked packages (Figure 3b).

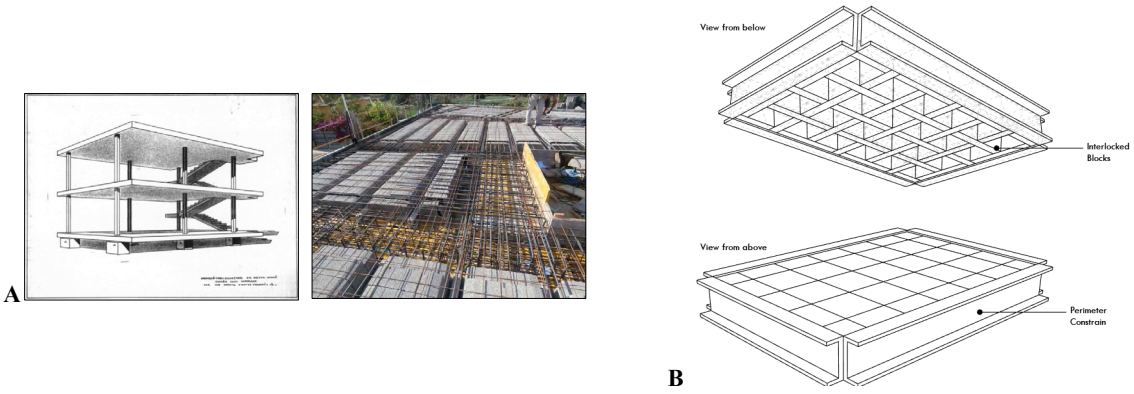


Figure 3: Two different typologies of construction: (A) *Maison Dom-Ino*, *Le Corbusier* (1914), variety of elements in concrete slab construction (nowadays), (B) proposal of interlocked package slab.

Interlocked geometries appear in various traditional constructions. Over centuries these solutions remain in good condition since in many cases the primary degradation of constructions comes in the bonding material. Therefore, it is convenient to understand the mechanical properties and the transmission of moments of reciprocal structures.

A reciprocal structure uses its elements to lock them and transmit loads with tension-compression. TI is a three-dimensional reciprocal pattern; the pieces receive moments when some push others. Conventionally, the TI blocks have a moderate size, in order to avoid high deflection of the material (Figure 2), and not to be deformed receiving stress during the transmission of the loads. On the other hand, the geometry of the patterns can be more complex increasing the contact surface with concave-convex patterns as a second interlocking, to prevent the structure failure due to the slips of the elements, tilt of assembly, or the failure of the central element, generating interlocked slabs, [16]. However, the stress concentrates in the tiny stuck out parts, tending to have a fragile failure.

4.1 Preliminary FEM Analysis.

To prove the flat vault configurations, *Discrete Element Method* simulations can be arranged to obtain a static behavior (Figure 6). However, it is required to perform *Finite Element Method* simulations to consider the contact analysis [17], obtaining information about stress, strain, and moment capacities.

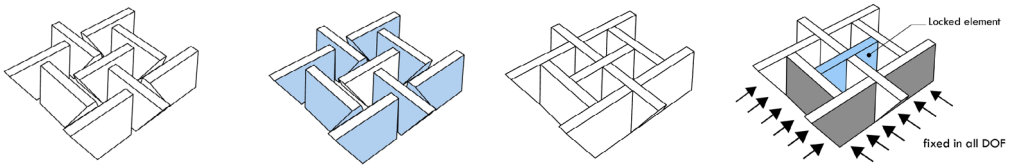


Figure 6: TI *Abeille Pattern*. Assembly, Contact Surfaces, and exterior surfaces fixed in all degrees of freedom.

One of the *Truchet Patterns* is arranged in a 9-element composition (60 x 60 x 13 mm) (Figure 6) to perform a mechanical simulation, with 100 N incremental load applied in the central element. With briefly *Design Experiments*, it can be analyzed the behavior of the interlocking assemblies to redesign various geometries. On the simulation diagrams, the stress tends to be on specific element positions. For materiality, it was chosen conventional concrete without reinforcement. Besides, the simulation is contrasted with a block of identical dimensions, boundary conditions, load position, and material, to compare the maximum displacements [Figure 8].

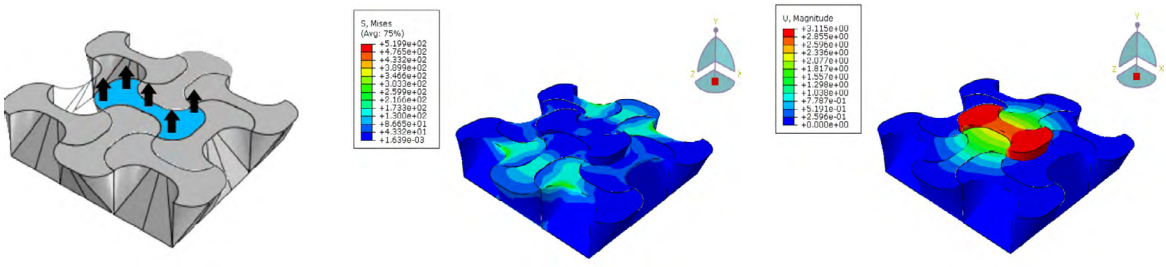


Figure 7: TI FEM simulation with *Truchet Pattern*. Geometry, Stress von-Mises, and Displacement.

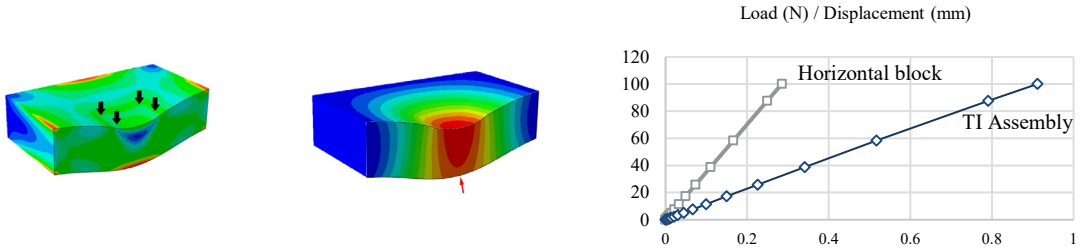


Figure 8: Horizontal block: (from left to right) Stress von-Mises, displacement, and load/displacement graph.

The horizontal block has distributed stress, and the displacement tends to affect the whole, while the TI, as a discrete system, does not damage the material. The displacement graph shows that TI tends to collapse due to geometrical constraints. The traditional construction presented (2.1) demonstrates that TI geometric solutions in building structures perform well with materials in pure compression.

4 Architectural prototypes.

Topologically interlocked assemblies as a substitute for traditional slabs-construction may seem inexperienced, due to the sparse construction practice today. Understanding its mechanics, trial and error prototypes were assembled using the *Truchet patterns* (Figure 9b). Different models were built, testing multiple possibilities to build the perimeters. Finally, it was decided to make double perimeters: a rigid ring, with 4 linear elements that keeps the TI assembly in place (Figure 9a). This paper presents three possible ways to approach it as a continuing and inspiration of historical examples (4.1, 4.2, 4.3).

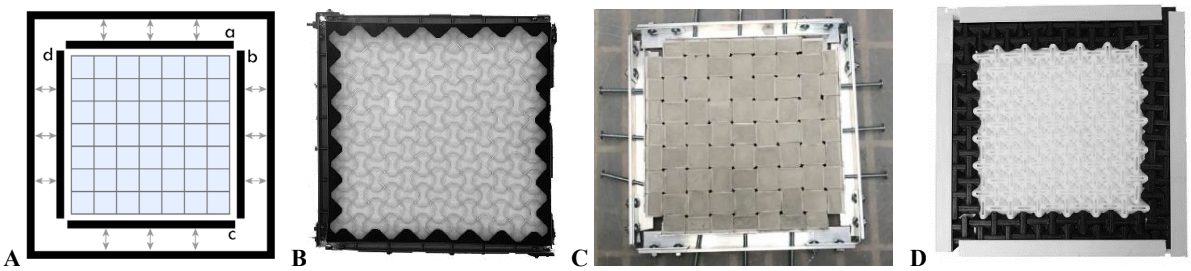


Figure 9: (A) Perimeter composition, 3d printing models as TI slabs: (B) Flat Vault with *Truchet Pattern*; (C) reinterpretation of *Abeille Pattern* (4.1), with interlocked shells as lost formwork (Figure 11), and mortar as stiffener material; (D) Lightweight flat vault alternative (4.2).

4.1 Reinterpretation of Abeille's Vault logic.

Once the basic concepts of IT mechanics were understood, here it is proposed the possibility of using materials that work well in pure compression, but that they can also acquire different forms, such as granular materials like sands or clays, added to previously placed shells, as lost form-work.

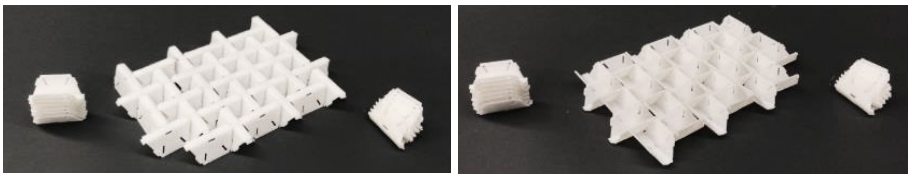


Figure 11: Scaled 3d printing shells with double interlocking design to avoid formwork during assembly.

This modular example has the flexibility of a lightweight structure, later stiffened with infill material. The shells could be manufacturer through forming rigid panels, later processed and positioned on a horizontal surface. Then the double perimeter is built locking the elements, prepared for the stiffener.

With preliminary FEA (Figure 13c) it is noticed the stress does not distribute uniformly, what it is taken into account for the infill material deposition, opting then for a cross filling configuration (Figure 12b).

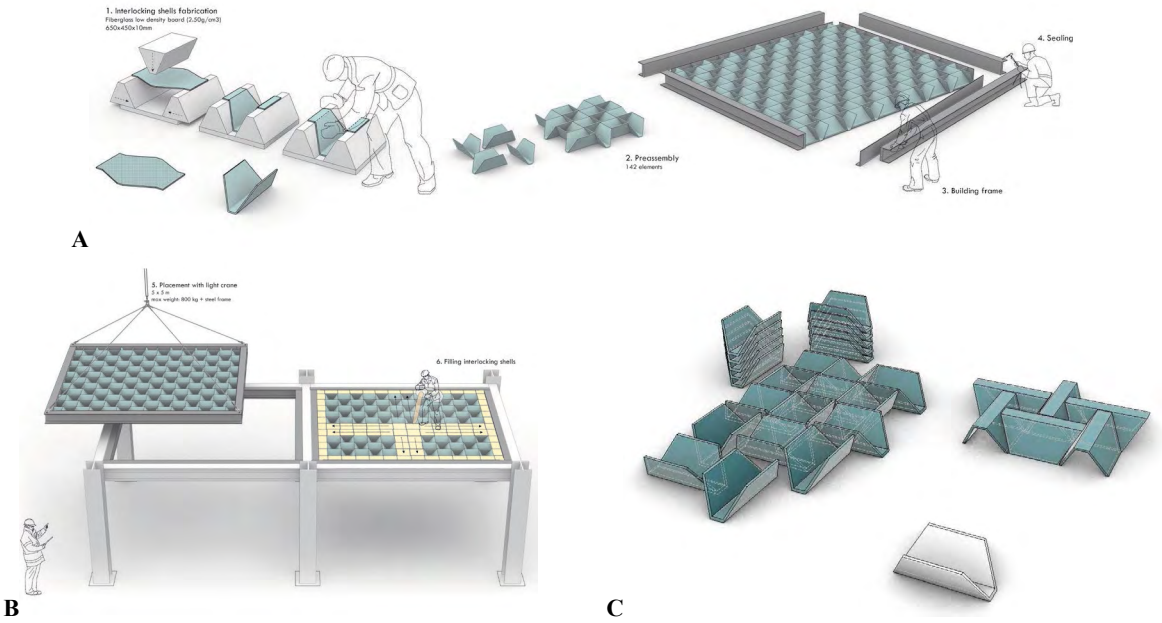


Figure 12: Interlocking shell slab. Assembly. Interlocking shells as lost form-work.

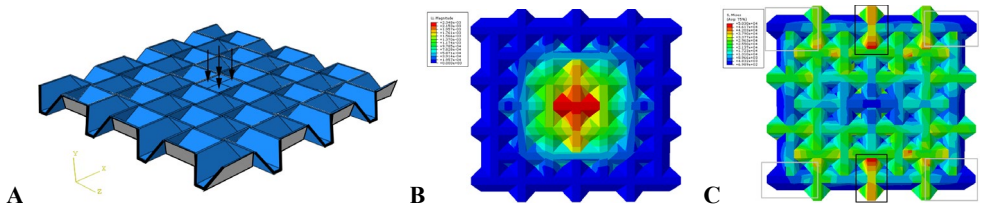


Figure 13: FEA analysis. (13c) Displacement (13d) Stress von Mises.

4.2 Lightweight flat vault alternative

As a reinterpretation of the traditional flat vault bond, the block elements here are not massive, introducing a wireframed-block variation. Additionally, it was introduced the study of the geometrical optimization of individual blocks, reducing their volume and weight, but making them stronger. While

reducing its geometry, the contact surface is reduced from the original (Figure 2), that means it would create more significant contact stress in less area, being necessary to reinforce the blocks. This variation provides space in the inside (Figure 14b); that means, the vault can be used to pass through steel rods to hold the perimeter. The experiments with interlocking usually have a static perimeter that works as a traction ring. With this solution, the perimeter ring is replaced with profiles, $a + c$ and $b + d$ (Figure 14a) that maintain the position by the tractioned steel rods that pass through the blocks (Figure 14a).

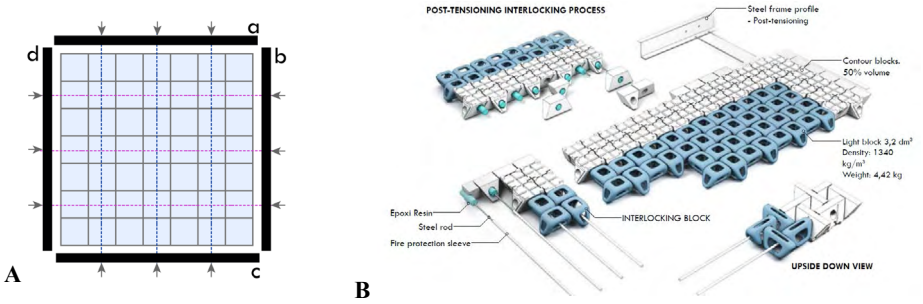


Figure 14: (A) perimeter alternative, (B) composition of the lightweight interlocked vault.

4.2.1 Post-Tensioned Perimeter

Because the principle of this system is the horizontal transmission of forces by contact, it explains the massive stone buttresses in historical constructions (Figure 1. What is proposed here is a post-tensioning system, which consists of the 2 by 2 beams, previously shown, that compress the blocks as a post-tensioning stiffener. Since this architectural proposal would acquire specific flexion and transmission of moments, unlike the traditional stone vault, it can opt for a hybrid system. However, the central elements of the vault can move in a positive or negative direction of Z producing a *bucking behavior*. This property can provide the possibility of generating desired curvatures, i.e., creating positive curvatures, or hybrid *interlocking & masonry vault*, that would tend to work and transmit loads better.

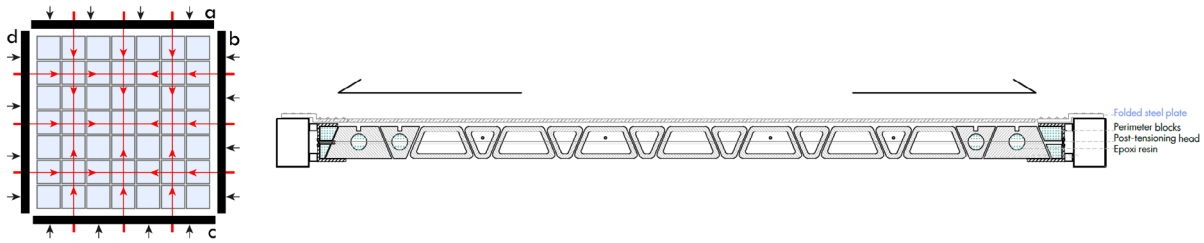


Figure 15: Construction detail of the post-tensioned lightweight interlocked vault.

With FEM simulations, this *bucking behavior* also appears, and after several *Design Experiments* with multiple load cases, it is observed that it comes from a nonuniform post-tensioning process. However, a simulation with a uniform post-tensioning could not converge since the corner elements cannot receive two directional loads at the same time, but, with the experience obtained, a correct post-tensioning would produce a neutral curvature in the center.

To conclude, surfaces can be generated with precise curvatures if the tension of both sides is different, taking advantage of the design of the vault, but complicating the analysis. An example of a robotically assembly is proposed [18], as a fully automated method to be applied in the architectural industry.

4.3 Pattern alternative

Hierarchy studies demonstrated that the geometry is crucial in TI, i.e., *osteomorphic* pattern. Here another reciprocal pattern variant is proposed based on the regular subdivisions with the *Cairo Tiling*, with two layers hexagonal-rhombus pattern (one rotated 90º). In this way, ruled surfaces connect both patterns, arranging up to 6 blocks in contact to distribute the loads (Figure 17). This contact geometry came as inspiration by the recently discovered subdivision packing of epithelia, known as *Scutoids*.

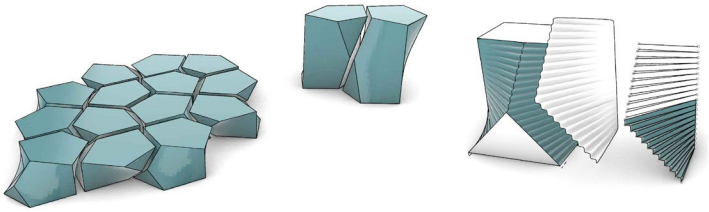


Figure 17: Pattern alternative based in the Cairo Tiling, creating a ruled surface to connect two pentagons.

With further investigations, these pentagons were deformed, in rectangles 1: 2, which likewise, both 90º patterns and contact surfaces generated graphically through an optimized vertex approximation (Figure 18). Finally, it is also studied the possibility of transforming the ruled surfaces that join the patterns in a double interlocking (Figure 19a). With 3d printing models, it was possible to prove how these patterns have bending capacities that allow the positioning of different pieces without formwork (figure 19b).

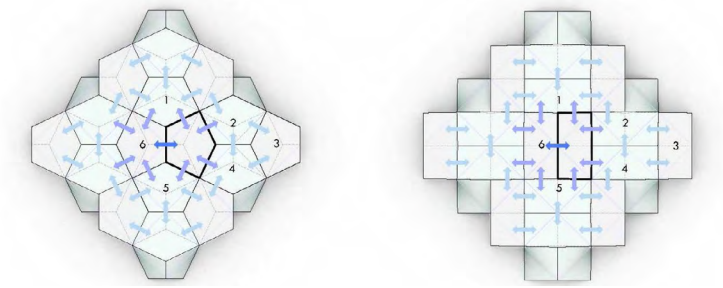


Figure 18: Pattern alternative based in the Cairo Tiling, creating a ruled surface to connect two pentagons.

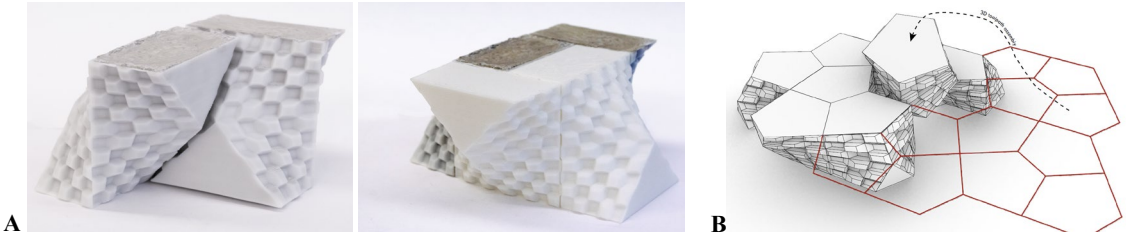


Figure 19: (A) Contact surface incrementation. (B) 3d toolpath for precise automated assembly of TI.

Conclusions

The prototypes presented here establish three main areas for further research of TI in architecture: how molecular materials can be applied; the systematization: possible alternatives as tensioned perimeters and post-tensioning; and the study of geometric pattern alternatives. The discoveries obtained from mechanical engineering can be extrapolated at the highest scales and analyze individual blocks to reduce material, and possible further investigations, with design experiments and statistical optimizations.

The use of this mechanics intelligence can also generate architectural solutions more sustainable than traditional ones: potential local and less disordered materials; and customize interlocked blocks with precise manufacturing techniques.

Acknowledgments

The work presented here has been part of previous academic works, such as the Master's Thesis of the corresponding author: *2017 Elevating Erie. Digital Fabrication Research Center*, for which we would like to thank the tutors and assistant professors of the University of Acalá: Alberto Alarcón and Cristina Camacho. We also wanted to thank the consistent support of Zack Xuereb Conti, for the development of the FEM simulations.

References

[1] A.V. Dyskin, Y. Estrin, E. Pasternak. 2011. "Topological Interlocking as a Material Design Concept." *Materials Science and Engineering C*, August, 1189–94.

[2] Rabasa Díaz, E. y López Mozo, A. 2012. "El Escorial, Estereotomía de la piedra" El Escorial: historia, arte, ciencia y matemáticas. Pag. 149 a 180. Madrid. Ministerio de Educación.

[3] Ávila Jalvo, J. M. 1998. "análisis geométrico y mecánico de las bóvedas planas del Monasterio de San Lorenzo de El escorial" 2º Congreso Nacional de Historia de la Construcción. A Coruña.

[4] Rabasa Díaz, E. 1998. "La bóveda plana de Abeille en Lugo" 2º Congreso Nacional de Historia de la Construcción. A Coruña. CEHOPU.

[5] Ashby, M. F., and Y. J. M. Bréchet. 2003. "Designing Hybrid Materials." *Acta Materialia*, The Golden Jubilee Issue. Selected topics in Materials Science and Engineering: Past, Present and Future, 51 (19): 5801–21.

[6] Molotnikov, A., R. Gerbrand, Y. Qi, G. P. Simon, and Y. Estrin. 2015. "Design of Responsive Materials Using Topologically Interlocked Elements." *Smart Materials and Structures* 24 (2).

[7] Maurizio Brocato, Lucia Mondardini. 2014. "Parametric Analysis of Structures from Flat Vaults to Reciprocal Grids." *International Journal of Solids and Structures* 54 (November): 50–65.

[8] Barthelat, F. 2015. "Architectured Materials in Engineering and Biology: Fabrication, Structure, Mechanics and Performance." *International Materials Reviews* 60 (8): 413–30.

[9] Djumas, Lee, Andrey Molotnikov, George P. Simon, and Yuri Estrin. 2016. "Enhanced Mechanical Performance of Bio-Inspired Hybrid Structures Utilising Topological Interlocking Geometry." *Scientific Reports* 6 (1).

[10] Mirkhalaf, M., J. Tanguay, and F. Barthelat. 2016. "Carving 3D Architectures within Glass: Exploring New Strategies to Transform the Mechanics and Performance of Materials." *Extreme Mechanics Letters*, Mechanics in Extreme Manufacturing, 7 (June): 104–13.

[11] Mirkhalaf, Mohammad, Tao Zhou, and Francois Barthelat. 2018. "Simultaneous Improvements of Strength and Toughness in Topologically Interlocked Ceramics." *Proceedings of the National Academy of Sciences* 115 (37): 9128–33.

[12] Rezaee Javan, A., H. Seifi, S. Xu, D. Ruan, and Y.M. Xie. 2017. "The Impact Behaviour of Plate-like Assemblies Made of New Interlocking Bricks: An Experimental Study." *Materials & Design* 134 (November): 361–73.

[13] Siegmund, Thomas, Francois Barthelat, Raymond Cipra, Ed Habtour, and Jaret Riddick. 2016. "Manufacture and Mechanics of Topologically Interlocked Material Assemblies." *Applied Mechanics Reviews* 68 (4): 040803-040803–15.

[14] Khandelwal, S., T. Siegmund, R.J. Cipra, and J.S. Bolton. 2012. "Transverse Loading of Cellular Topologically Interlocked Materials." *International Journal of Solids and Structures* 49 (18): 2394–2403.

[15] Dyskin, A. V., Y. Estrin, E. Pasternak, H. C. Khor, and A. J. Kanel-Belov. 2005. "The Principle of Topological Interlocking in Extraterrestrial Construction." Acta Astronautica 57 (1): 10–21.

[16] Djumas, Lee, George P. Simon, Yuri Estrin, and Andrey Molotnikov. 2017. "Deformation Mechanics of Non-Planar Topologically Interlocked Assemblies with Structural Hierarchy and Varying Geometry." *Scientific Reports* 7 (1): 11844.

[17] Sakhaei, Amir Hosein, Sawako Kaijima, Zack Xuereb Conti, and Martin L. Dunn. 2016. Integrating User-Defined Elements for Topologically Interlocking Joints and Application in Large Scale Structural Analysis.

[18] Moreno Gata, K. 2017. "Elevating Erie: Digital Fabrication Research Center" Master Thesis, University of Alcalá.

Proceedings of the IASS Annual Symposium 2019 – Structural Membranes 2019
Form and Force
7 – 10 October 2019, Barcelona, Spain
C. Lázaro, K.-U. Bletzinger, E. Oñate (eds.)

Digital Tool for Reciprocal Frame

Arianna PALUMBO*, Daniele LANCIA[a], Sergio PONE[b]

*DiARC – Dipartimento di Architettura – Università di Napoli Federico II
Via Toledo 402, 80134, Napoli, Italia
Ari.Palumbo@gmail.com

[a] Gridshell.it, Napoli, Italia
[b] DiARC – Dipartimento di Architettura – Università di Napoli Federico II

Abstract

This study proposes a digital tool able to determinate, using a surface's free form data, a CRFS (complex reciprocal frame structures) made of the aggregation of SRFU (single reciprocal frame units) on a squared grid without changing eccentricity, position and dimensions of the rods and changing only the length. This choice allows to design new structures from synclastic surfaces, even if very complex, but equipped with a fundamental technical feature of being made with equal rods that generate different SRFUs. Using different algorithms already known, the new tool creates spherical cap surface CRFS that approximate to wanted surface. The original contribution of this work in based on this last step which uses dynamic relaxation and brings the spherical CRFS to ease down on the desired non-spherical geometry, without losing the reciprocity's bonds between the rods.

Keywords: Reciprolcal frame, reciprocal structure, free-form, spatial structure, form finding, digital tool, dynamic relaxation.

1. Introduction

Reciprocal frames (RF) are based on the use of supporting elements that support each other forming a spatial configuration without structural hierarchy. Each element that makes up the structure is at the same time carrying and carried. The term derives from the Latin *reciprocŏcus* composed of **recus* "that stands back" and **procus* "that stands ahead". "That comes and goes, that flows and flows back". The definition refers to the obligation of a forced return of the actions, called mutuals. There are two and equal forces that act on each element: one from the bottom to the top of the supporting element, one from the top to the bottom of the element that is supported.
The existence of reciprocal frames is assured by the respect of 3 principles:
Number: each structure must consist of at least three elements otherwise there is no interaction between the forces.
Action: each element must be supported and supports simultaneously.
Position: in each reciprocal frame the supporting element meets its support along its extension.
RF originate from the aggregation of several modules composed of three or more elements: the union of single RF units forms a complex RF structure. Based on the number of elements of the single RF unit and the aggregation of the latter, infinite patterns are created. The first great distinction in RF is in the type of aggregation of the elements. There are two different types: inclined reciprocal frames, where the elements are simply placed one on top of the other, the structure therefore emerges naturally from the plane; and flat reciprocal frames in which the elements are embedded one inside the other.

Copyright © 2019 by Arianna Palumbo, Daniele Lancia and Sergio Pone
Published by the International Association for Shell and Spatial Structures (IASS) with permission.

2. History

The reciprocal structures are born as spontaneous architecture. The first examples built can be found already in the Neolithic age in the form of the main structure for the houses. [1] The historical continuation takes on different characters in the East and West. In the East, experimentation has a practical character: the reciprocal frames become a transposition, on a large scale, of the way of weaving the typical bamboo baskets (China) or of the religious symbolism of mandalas (Japan). In the West, on the other hand, history has a theoretical experimental character: architects and mathematicians studied the reciprocal system as a solution to problems of a practical nature. [2]
There aren't too many examples of structures made by using the reciprocal method, these are mostly located in Japan and in the United Kingdom, with a small exception in Virginia, in the United States. The examples built present the reciprocal system only in coverage; in fact, the latter is, in all cases, created with a single reciprocal module formed by an always different number of elements.

3. Variables and variation

The RF have 3 different type of variables.

3.1. Positional variables

Three fundamental variables determine the different morphologies possible in a reciprocal frame.
Eccentricity that measures the distance between the axes of the elements depends on their thickness and shape.
Length that measures the position in which each element overlaps along the support element.
Concavity indicating whether the b_i element is above or below the element b_j. [3]

3.2. Geometric variables

Besides the three positional variables, to determine the morphology of the module, additional geometric variables are added.
L which represents the length of a single element of the reciprocal module and is divisible into three quantities: **a**, **b** and **c** representing the lengths of the free ends and of the interaxis between two elements.
$\mathbf{C_i}$ and $\mathbf{C_e}$ that represent the two circumferences drawn at the two ends of the elements that make up a single reciprocal module. C_i and C_e represent the two circumferences drawn at the two ends of the elements that make up a single reciprocal module. The two circumferences are inversely proportional: as the external circumference increases, there is a decrease in the internal circumference.

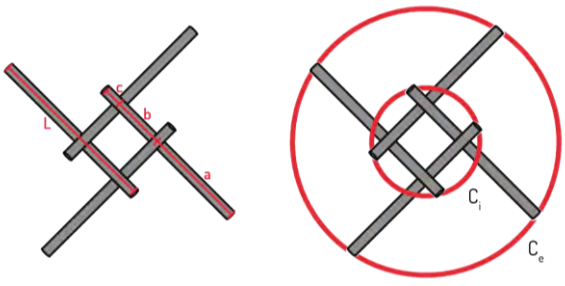


Figure 1: Geometric variables

3.3. Typological variables

The third family of RF variables concerns the typology. These variables no longer determine the morphology but the final aspect that will have the reciprocal module and the consequent structure.

Type of components that determines the shape and geometry of the single element.
Number of components that changes the appearance of the module.
Types of joints that affect the static nature of the structure.
Materials that change the appearance and the producibility of the structure.

3.4. Geometries

The RFs are a repetition of the same module, this means that the figure that will come out of it will be a broken line that approximates a curve with constant curvature (the same curvature that is repeated). The flat geometrical figure with constant curvature is the circumference, however the reciprocal frames have the characteristic of extending in two directions consequently the solid to which a reciprocal structure will tend is the sphere. Reciprocal frames, therefore, have the characteristic of always having a constant positive Gaussian curvature. The RFs have the characteristic of extending in two directions, with the exception of Leonardo's bridge [4], a configuration studied by Leonardo da Vinci in the Atlantic code, which has the characteristic of extending in a single direction.

4. Concept of curvature

The curvature, intuitively, refers to the measurement of how much a given object deviates from being flat. There are two types of curvature
Extrinsic curvature: it is the curvature possessed by the object in relation to a flat space in which it is immersed.
Intrinsic curvature: it is the curvature that can be determined using only operations performed on elements of the object itself.
A sphere has an intrinsic curvature, which can be determined within the surface itself. Gauss in his egregium theorem *«Si superficies curva in quamcumque aliam superficiem explicatur, mensura curvaturae in singulis punctis invariata manet.»* states that for any point P of a fairly regular curved surface there exists a negative or positive number K which represents the curvature of the surface at that given point. Taking then a generic surface and a point P on it we can define the tangent plane and the surface normal vector at that particular point. By tracing the surface orthogonal to the tangent plane the surface and passing through the normal vector, a curvature R_1 is created from the intersection with the surface. By rotating the orthogonal plane and sectioning the surface with the infinite orthogonal planes, we obtain infinite R_N curvatures. Euler et al [5] states that there is a maximum curvature R_{max} and a minimum curvature R_{min} orthogonal to each other of these principal curvatures. Gauss et al [6] goes a step further by claiming that the product between the two main curvatures returns the Gaussian curvature, that is the measure of the curvature of a surface at a given point. In a surface, therefore,once the two main curvatures are defined, it is possible to determine the Gaussian curvature. Starting from the Gaussian curvature, we can introduce the concept of an osculating sphere that is the sphere that best approximates the surface at a given point. The osculating sphere is obtained simply by constructing the sphere tangent to the surface at the point P having the curvature equal to the Gaussian curvature K of the surface at the point P.
Returning to the reciprocal frames, fixed the parameters of C_i (inner circumference), e (eccentricity) and L (length), it is possible to obtain a given Gaussian curvature K with the respective sphere.

5. Aim

Knowing the reciprocal frames means first of all understanding them and secondly accepting them. Accept the strict geometry that governs them, the simplicity of the form together with the complexity of the actions, the rigidity and accuracy of the position that an element must assume with respect to its precedent and its successor. The most interesting aspect is certainly the possibility of obtaining a large and complex structure with small, simple and identical elements. Complexity which, by its nature,

stops at the shape of the sphere. Based on the theoretical and geometric considerations shown in the previous chapters, the aim of this work was to investigate, and subsequently study, the possibility of exploiting the principles and rules of reciprocity by going beyond the spherical surface. With the study of curvature it was assumed that it was possible to associate a different reciprocal module to each of the osculating spheres of a generic surface and obtain a free-form surface. The different reciprocal module, however, will keep the variables e (eccentricity) and L (length) unchanged by varying exclusively C_i (internal circumference) to obtain the step of the gaussian curvature.
In this discussion we chose to use reciprocal frames formed by 4 elements, which together form the pattern of the double square and that have only overlapping joints.

6. Methods

The iter that led to the transition from the theoretical to the practical phase is the result of a linear but not immediate process. From the first studies, conducted very intuitively, the failures and errors were learned. The latter in particular represented the starting point for the next approach. The change of point of view was fundamental: if at first it seemed obvious to study the reciprocal module in the first instance, then it seemed instead necessary to understand and discretize the surface before entering into the reciprocal world. The path can be summarized in three different attempts, three methods, divisible by chronological order and methodology of approach. All the methods studied were digitized with the software Rhinoceros 5.0 and its plug-in, Grasshopper.

6.1. Aggregation of modules with variation of C_i and study of the resulting surface

The first attempt was to aggregate modules with variation of C_i (internal circumference) and then study the surface that the various modules would describe. *A study that starts with the module and then reaches the surface.* To do this, multiple reciprocal modules are constructed with different measures of the inner circumference. Until the aggregation of modules in the same direction the procedure works; when four or more modules have to be closed, two problems arise. The first concerns overlapping: in some cases the module is no longer reciprocal; the second concerns the uniqueness of the sticks: where a stick should belong to two modules simultaneously, and therefore be unique, the construction of the modules determines the coexistence of two distinct rods with different directions. Due to the multiplicity of problems the method has been abandoned.

6.2. Approximation of the surface with the appropriately distorted module

The second study predicted the approximation of the surface with a suitably distorted form. *By first studying the surface and then the module that could have approximated a given surface portion.* This is derived from the observation of the behavior of a single module: by distorting it, hence moving slightly along the X or Y axes or along the Z axis one or more elements of a module, the surface that describes the module is different from the flat surface and regular. The study therefore started from the identification of a portion of surface and the association, to that determined area, of a reciprocally distorted module. Based on the position of this module the position of the next module is found, and once again we go to study the module that approximates that determined portion of surface and so on. However, as can be seen from the image, exactly as in the previous case, there is a problem with the uniqueness of the sticks. To be able to solve the problem it is needed to make four rotations for each module, each compatible with one of the contiguous modules. Compatibility is not always ensured, so this method has also been abandoned.

6.3. Degeneration of a reciprocating hemisphere in the chosen surface

The third method, based on the method called dynamic relaxation, was to degenerate a mutual hemisphere on the chosen surface. *By first studying the module and its sphere that comes out and then placing the sphere on the surface.* This method represents the original contribution of this work.

7. Degeneration of the hemisphere

The third experimented method of achieving the aim was the decisive one. This consists of 5 steps of which only the last leads to the achievement of the goal. The previous four are essential to obtain the ingredients necessary for the degeneration. In fact, each step uses inputs and produces outputs that in turn will become inputs for the next phase. The first step is preliminary because of only choice, the other four are the real operational procedures.

0. Choice of parameters
1. Definition of the grid
2. Division of the sphere
3. Creation of the reciprocal sphere
4. Deformation of the reciprocal sphere

The method of degeneration of the hemisphere is possible thanks to the crossed use of two methods studied by Oliver Baverel and Klaus Linkwitz and thanks to the use of the Kangaroo software designed by Daniel Piker.

7.1. Choice of parameters

The preliminary step, necessary for the success of the method, concerns the choice of the parameters L (length of the stick), c (length of the short end), C_i (radius of the inner circumference) and e (eccentricity); these parameters determine the type of elements and the morphology of the module and therefore the final appearance of the components that will form the free-form surface. The immediate result of the choice of parameters is a specific reciprocal module.

7.2. Definition of the grid

The first real step in the method is the definition of the grid. This allows to quickly obtain, starting from the four parameters chosen, as many values to be used in the following steps. This step consists of two parts with similar procedures, the first part studies the grid in the plane and the second part uses instead the natural exit from the plane of the reciprocal structures. To define the grid in the plane, the reciprocal module is studied by simplifying it in its aggregate axis lines in the plan. Using the inputs L (length of the stick), c (length of the short ends) and C_i (radius of the inner circumference) the axis lines of the module are constructed. Starting from the built module the pattern in the plane is then expanded. By isolating five modules, that are the first module built and the four modules built on the elements of the latter, and then joining the centers of the main module and the four subsequent modules,it is easily calculable the pitch of the grid d and the angle of rotation α of the grid with respect to the direction of the elements of the module. With operations analogous to those made for the study of the flat grid, we pass to the study of the grid outside the plane, in this case, however, the element is considered in its entirety without any simplification. Using the inputs L (length of the stick), c (length of the short ends), C_i (radius of the inner circumference) and e (eccentricity) the reciprocal module is constructed. The pattern is then expanded by building the next four modules. Conjoining, also in this case, the centers of the secondary modules with the center of the main module we obtain the outputs of length of the lines d, which will then be compared with the length of the lines obtained from the study of the plane grid, and the measurement of the Gaussian curvature K. By using four centers it is possible to construct the sphere and consequently derive the radius of the sphere and the area of the hemisphere A. It is important to underline that is used the area of the hemisphere and not of the sphere because in the last step, namely that of deformation, to obtain a free-form it is preferable to deform an open surface, such as that of the hemisphere rather than the closed surface of the sphere.

7.3. Division of the hemisphere

The second step of the method consists in dividing the sphere, using Klaus Linkwitz's Netfish method, [7] to obtain the regular quadrangular lattice on the hemispherical surface. The lattice represents the primordial pattern that will be defined by the reciprocal modules that will form the hemisphere. Starting from the inputs of A (area of the hemisphere) and r (radius of the sphere), values
obtained from the study of the grid outside the plane, we build the sphere to which the aggregation of the modules deriving from the choice of parameters will tend. The surface of the hemisphere is then obtained by sectioning the sphere with a horizontal plane passing through the maximum circumference. Then intersecting the hemisphere with the extrusion of a pair of orthogonal axes with origin in the center, the two main curvatures are obtained from whose intersection the central point will be obtained. The outputs of the previous step become the inputs for the next step. To the surface inputs of the hemisphere, principal curvatures and central point, an additional input is added, that is the step of the grid that will be used as the radius of the spheres, a value obtained from the study of the flat grid made in the first step of the method. From the center the first sphere is constructed, the intersection with the principal curvatures will return four points which will be the centers of the successive spheres. The four points, in particular, enter a loop and are used as centers for the spheres from whose intersections other points are obtained which will become centers for the spheres and so on with all the points until covering the whole surface of the sphere. The union of the points on the surface of the hemisphere will then generate the regular lattice.

7.4. Creation of the mutual hemisphere

The third step of the method concerns the creation of the reciprocal hemisphere using the Nexorades Based on Regular Polyhedra by Olivier Baverel. [8] With this passage the lattice turns into the double square pattern, the lattice lines take a certain distance from the hemispherical surface and, consequently, a certain distance between them. This distance will be "filled" with the right eccentricity (rod section). In particular, the eccentricity parameter is chosen in step 0 of the method, in this phase in fact the measurement chosen a priori is verified, again using part of the Nexorades Based on Regular Polyhedra, once the accuracy is ascertained we proceed with the creation of the actual elements that will make up the mutual hemisphere. With the lines obtained from the division of the sphere, the rotation angle obtained from the study of the grid and the length of the lines chosen in the preliminary phase, there are the rotation centers and the relative rotation planes. Using the input the lines are properly rotated and then extended to obtain the effective length of the sticks. At this point the second phase begins in which the parameters of eccentricity and internal circumference are verified. Two elements of a single reciprocal module are isolated, extruded and extended to calculate the distance that is determined by the rotation. Once the section has been verified, the elements are thickened and the reciprocal hemisphere is obtained.

7.5. Deformation of the hemispheric

The fourth and last step of the method is that in which, starting from the data obtained from the previous passages, we obtain as output the reciprocal free-form surface. All this happens thanks to dynamic relaxation: a numerical method whose aim is to find a geometry in which all the forces are in equilibrium. Dynamic relaxation is based on the discretization of the object under examination, the assignment of the mass to the bodies and the application of forces. The system outlined in this way oscillates around the equilibrium position under the influence of the loads through an iterative process based on the simulation of a pseudo-dynamic process over time, with each iteration based on a geometry update. That was realized with *Kangaroo Physics*. Kangaroo is a Particle spring system, that can simulate the behaviour of a wide range of elements. The springs can introduce a handy simplification: any material, as stiffer it is, can stretch and shorten. [9] In the specific case of deformation of the reciprocal

hemisphere, the forces in action are attractive, exerted by the surface and applied to the two ends of each axis line of each element that makes up the hemisphere. In addition to the attractive forces, three other types of forces coexist in the system; the first tends all the corners of the inner square of the pattern to the right angle; the second constrains the sliding of the rods one over the other, to prevent the internal circumference from growing until the reciprocal module collapses; the third imposes the respect of a distance between the axis lines of the rods equal to the eccentricity, necessary distance to avoid the penetration of the rods and therefore the flattening of the reciprocal module.

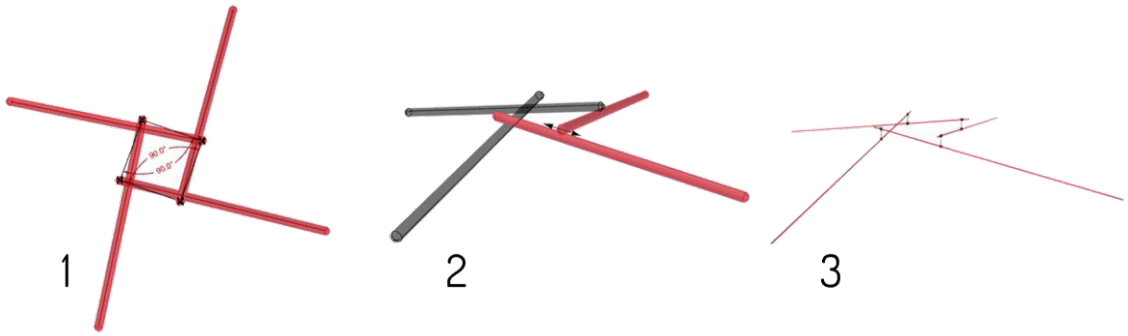


Figure 2: Three types of forces coexist in the system

During the simulation the attractive force is increased at intervals: it starts from a very low initial F_0 decimal value up to, and in some cases to overcome, the unit value at the end of the simulation. Even the distance constraint sometimes needs to be increased during the simulation, the other two constraint forces remain constant throughout the procedure. The area of the surface to be reciprocated must be slightly larger than that obtainable from the number of modules with which the sphere is composed, this because each end of the rod, being attracted by the surface, needs an effective correspondence and must necessarily fall back within the perimeter of the surface.

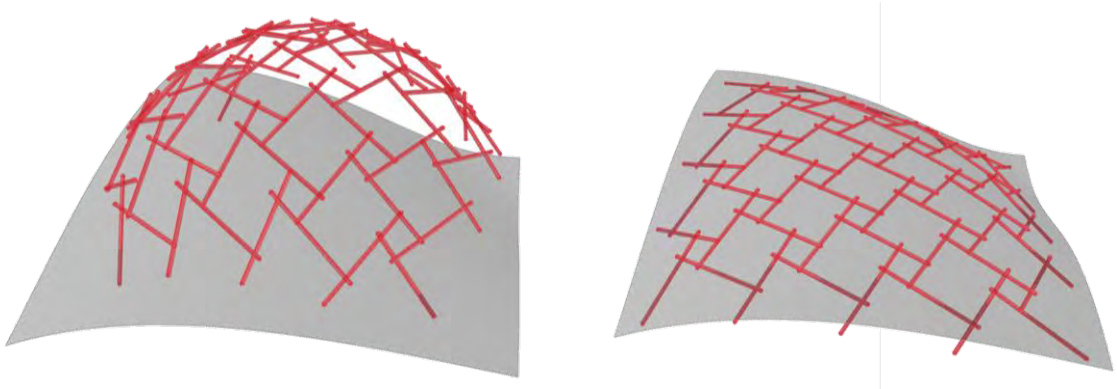


Figure 3: Before and after the simulation

Once the simulation has been completed, the hemisphere no longer exists and in its place there will be an approximation of the surface. The modules remain all reciprocal, the Gaussian curvatures change to get as close as possible to the curvature of the surface obscuring sphere at the exact point where the module will be positioned. In this case, the surface always has a positive curvature with a different concavity along the two main directions. From the two side views it is possible to appreciate the degree of approximation

while from the plan and perspective views we can read the reciprocity existing in each module. The image below shows, with a gradient of color, the greatest distance (pink) or minor (blue) that exists between the ends of the axis lines of the rods and the corresponding point on the surface.

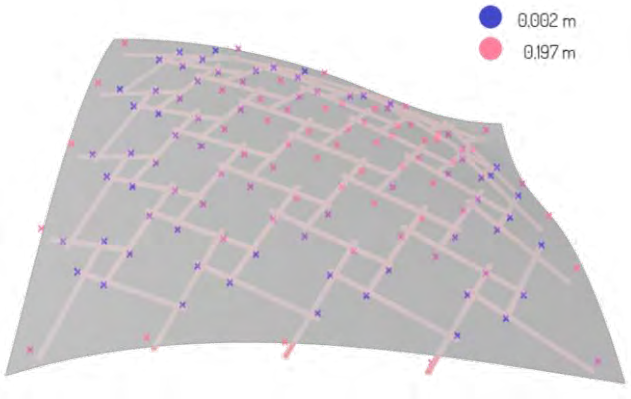


Figure 4: Distance between the ends of the axis lines of the rods and the corresponding point on the surface

8. Conclusion

The design for freeform reciprocal frame, in which the beams have all the same thickness and same length, is possible whit an agile digital tool that through five steps returns a good approximation of the chosen free-form surface.

References

[1] O. Popovic Larsen, *Reciprocal Frame Structures*. Elsevier Science and Technology, 2008.

[2] A. Pugnale, D. Parigi, P. H. Kirkegaard, M. Sassone, "The principle of structural reciprocity: history, properties and design issues," in *Proceedings of the "IABSE-IASS Symposium 2011: Taller, Longer, Lighter", London, 2011.*

[3] D. Parigi and P. H. Kirkegaard, "The reciprocalizer: a design tool for reciprocal structures," in *Proceedings of Civil Comp 2013 conference, Cagliari, Italy, 2013.*

[4] Anon, *The structural Engineer*, Vol 73, 1995.

[5] Eulero, *Lettera ad una principessa tedesca*, 1760.

[6] C. F. Gauss, *Disquisitiones generales circa superficies curvas,* 1827.

[7] F. Otto, E. Schauer, J. Hennicke, T. Hasegawa, *Grid Shells*. Stuttgart: Institute for the Light-weight Structures, 1974

[8] O. Baverel, "Nexorade Based on Regular Polyhedra" *Nexus Network Journal*, vol. 9, pp. 281-298, 2007.

[9] Watkin A., *Physically Based Modeling - Particle System Dynamics*, Pixar Animation Studios, 1997

Proceedings of the IASS Annual Symposium 2019 - Structural Membranes 2019
Form and Force
7-10 October 2019, Barcelona, Spain
C. Lázaro, K.-U. Bletzinger, E. Oñate (eds.)

Geometry generation of reciprocal systems made of non-uniform elements - *A case study of bamboo culms*

Martha GODINA, Gert VAN DER HEIJDEN

Department of Civil, Environmental and Geomatic Engineering, University College London
Gower Street, London, WC1E 6BT, UK
martha.godina.12@ucl.ac.uk

Abstract

The use of natural materials in construction is usually associated with a low level of technological development. In bamboo culms, the inherent non-uniform properties hinder the standardisation of elements, and thus details such as fitting of components are very difficult to achieve. This paper presents a formulation for the generation of the geometry of reciprocal systems with double curvature that take into consideration the non-uniform geometry of bamboo culms. It incorporates three different geometric properties of bamboo culms, namely the diameter, the thickness and the out-of-straightness into the structural morphology of reciprocal systems. The method includes an optimisation routine for the eccentricities (i.e. the orthogonal distance between two elements) according to the variable diameters of bamboo culms. The eccentricities are achieved by an iterative method that performs geometric transformations out-of-plane (i.e. rotations and translations) until the target eccentricities are reached. The formulation addresses well-known problems associated with the irregular geometry of bamboo culms in construction by taking advantage of digital tools. The potential of this approach to contribute to more sustainable construction by modelling the non-uniform geometric properties of bamboo culms is illustrated with a case study.

Keywords: bamboo, reciprocal structures, eccentricities, geometry generation, non-uniform elements.

1 Introduction

Reciprocal structures are self-supported structures where for each element there is at least one element that acts as a support and another that is supported. The concept of reciprocity has been used as a building technique since ancient times to build primitive dwellings, and structures where the span required to cover is greater than individual elements. A historical and contemporary review of reciprocal structures is given by [1] and [2].
Figure 1a shows the basic reciprocal structure of three elements and the key geometric parameters. Reciprocal structures offer some qualities that can be harnessed for the design of connection systems for bamboo. Their geometry is such that only two elements are connected at a time. Additionally, due to the self-supported arrangement, the elements are connected out-of-plane. These aspects simplify the complicated design and fabrication of connection systems in three-dimensional structures with double curvature where multiple elements are incident on a node. Since the centreline of the elements at each connecting point are at different planes, these do not intersect. For modelling purposes, the skew elements are connected by an additional element defined by the perpendicular distance between both. This distance is referred to as the

Copyright © 2019 by Martha GODINA, Gert VAN DER HEIJDEN
Published by the International Association for Shell and Spatial Structures (IASS) with permission.

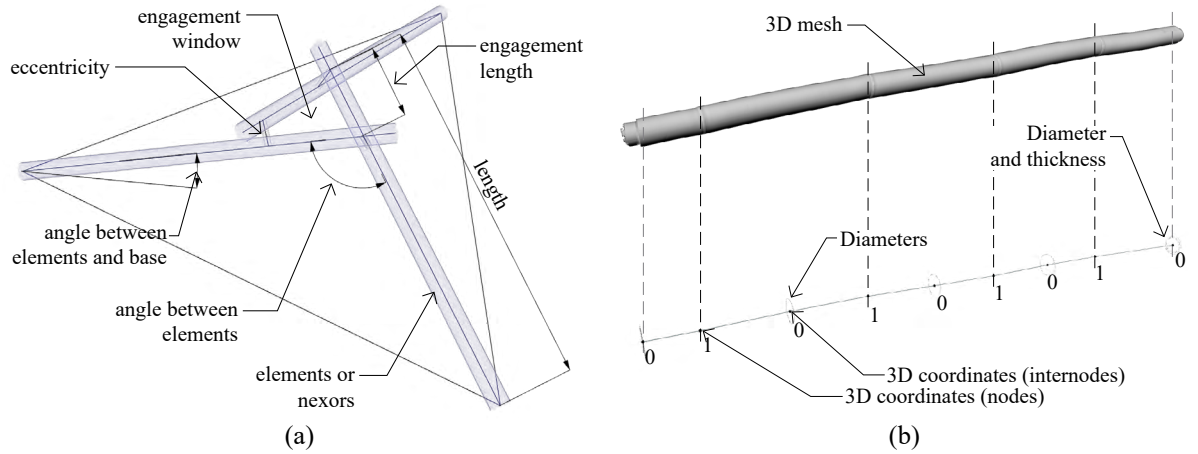


Figure 1: (a) Geometric parameters of reciprocal systems according to [3] for a three-element module. (b) Discretised geometric properties of bamboo culms obtained through 3D scanning.

eccentricity (see Figure 1a). The eccentricity is a fundamental parameter of reciprocal systems and in this case is directly related to the diameters of bamboo culms.

While the geometry of bamboo culms is variable and irregular, it is not common to account for these properties in the current architectural, engineering and construction practices. Besides, the manual measurement of geometric properties is impractical, and therefore it is more convenient to simplify its geometry as uniform elements (e.g. straight elements with symmetric and constant cross-sectional geometry along the length). However, ignoring these geometric imperfections introduce uncertainty in structural analysis and inaccuracies during construction. These issues can lead to an increase of cost, poor construction quality and unsafe design. Notwithstanding this, the idealisation of bamboo culms as non-uniform elements is a challenge since modelling structures using elements with non-uniform properties is not common.

The generation of the geometry of reciprocal structures is complex. Several methods have been proposed and for most of them the challenge lies in the eccentricities. For a single reciprocal unit, this can be modified by changing some other parameters such as the height of the structure. However, for three-dimensional structures made of several reciprocal units jointed together, the challenge is greater. Several methods have been proposed. Baverel [3] introduced analytical methods based on rotations and translations of elements from an initial geometric configuration. Other approaches are based on numerical methods, including dynamic relaxation [4], optimisation [5] and parametric tools [6]. These methods were developed to define the geometry of reciprocal systems with uniform elements idealised as straight lines. In all these methods, achieving the target eccentricities is not trivial and non-optimal geometries can result especially in surface areas with high curvature, as highlighted by Song *et al.* [5].

The method proposed here deals with the problem of finding the optimal eccentricities and considering the non-uniform geometric properties of bamboo by using an iterative method. The impact of these non-uniform geometric properties into the modelling process for structural analysis is investigated.

2 Methodology

This paper presents a formulation for the generation of the geometry of reciprocal systems based on the rotation method introduced by Baverel [3] but with specific focus to consider the variation of diameters of bamboo culms in the definition of the eccentricities and the out-of-straightness along the length. The discretised properties of bamboo culms are obtained through

3D scanning techniques using the Artec Space Spider 3D scanner [7]. Figure 1b shows the discretised properties of one bamboo culm consisting of 3D coordinates representing the nodes and internodes, line elements representing the different segments, circular curves to indicate the diameters measured at the internodes and circular curves at the ends to determine the thickness [8].

2.1 Reciprocal configuration

Figure 2 illustrates the main steps of the proposed method. The first step takes any arbitrary smooth surface with double curvature tessellated with a triangular mesh (see Figure 2a). Tessellation refers to the tiling of the arbitrary surface using closed polygons. The arbitrarily underlying surface is taken as fixed input together with the given tessellation. The tessellations explored in this paper are limited to triangular tessellations of degree 6, the number of edges incident on a vertex. The next step consists of defining the parameters to perform the rotation of the edges (i.e. elements) to create the reciprocal configuration of the system. The parameters are the rotation axis, $\vec{p}$, and the rotation angle, λ, for every element. Figure 2b shows the rotation axes for the inner and outer edges. The rotation axis for the inner edges is defined by the sum of the two vectors normal to the faces, $\vec{n}$. Since the length of the vector is not relevant, the rotation vector is taken to be a unit vector. For the boundary edges, the rotation vector is considered simply as the vector normal to the face adjacent to the boundary edge. The rotation angle is normalised to the angle, β, between the edge in the initial configuration and the line between the midpoint of the edge and the centroid of the face as

$$\lambda = \eta\beta \tag{1}$$

where η is a value between 0 to 1, such that for 0 the edges are in its initial position, and for 1 the edges are parallel to their dual (see Figure 2b for dual geometry). The rotation angle shapes the geometry of the reciprocal system by changing the opening of the engagement window.
Since the edges of the mesh are lying in different planes, these rotations will generate eccen-

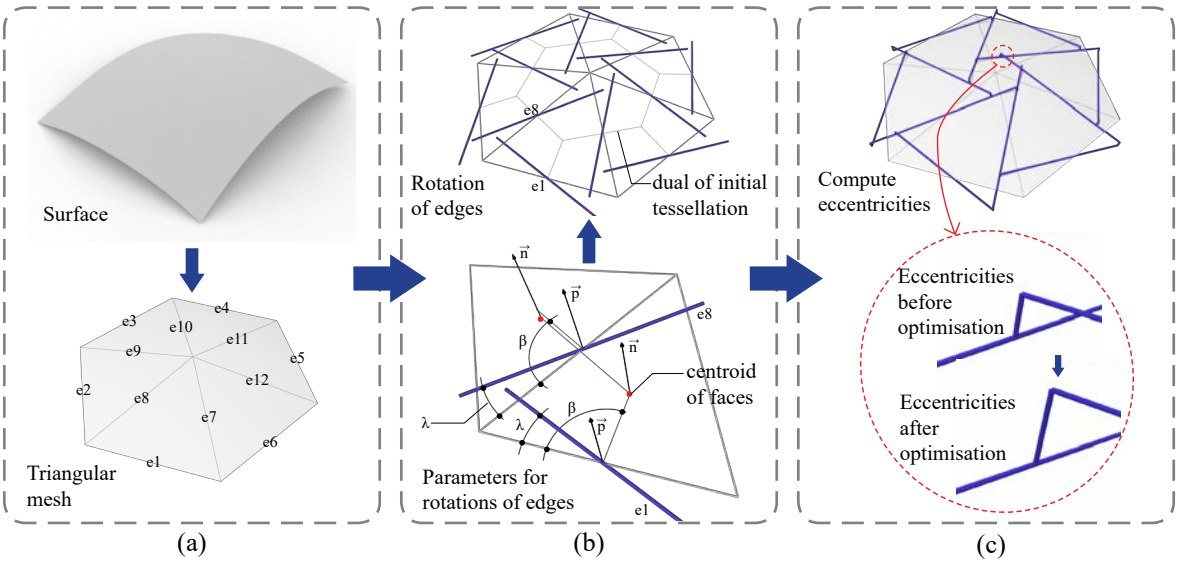


Figure 2: Overview of the general steps to generate the geometry of reciprocal systems. (a) Surface generated in *Rhinoceros* and triangular tessellation. (b) Rotations of the edges and definition of the rotation vector, $\vec{p}$, and rotation angle, λ. (c) Definition of optimal eccentricities.

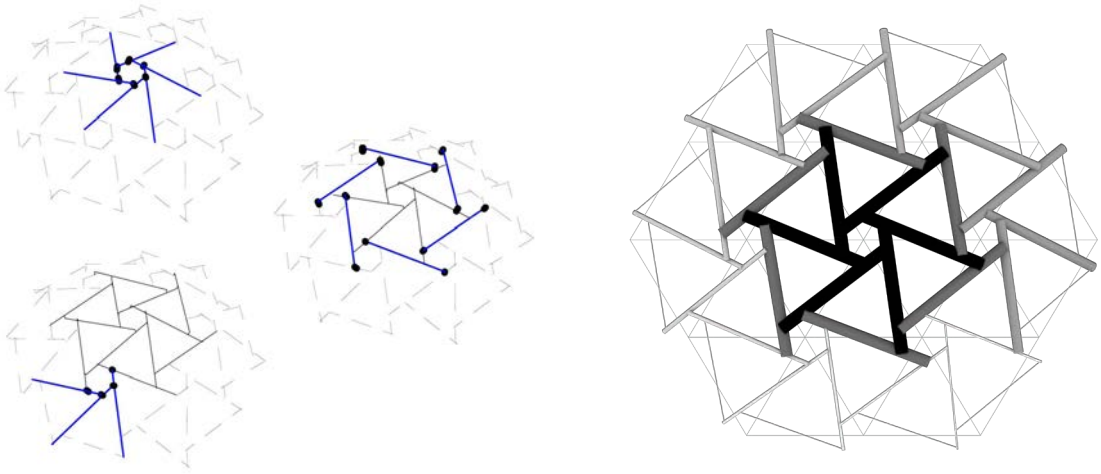


Figure 3: (a) Examples of edges used to solve eccentricities per iteration. Note that for each edge, only 2 eccentricities per each iteration are to be solved. (b) Subdivision of edges into groups to perform optimisation of eccentricities. Each colour and thickness represent one group.

tricities among the edges. The eccentricities should be sufficient to accommodate the diameters of the bamboo culms. However, it is unlikely that the eccentricities coincide with the required dimensions for the bamboo culms to fit in properly. Therefore, the last step consists of adjusting the eccentricities in the reciprocal system to the diameters of the bamboo culms to be used (see Figure 2c).

The method consists of an iterative process that subdivides the edges into groups in order to solve a maximum of two eccentricities per edge at each iteration as shown in Figure 3a. This is solved by implementing a mathematical optimisation problem to perform geometric transformations on the edges until reaching the target eccentricities based on the diameters of bamboo culms. The method is fully described in the subsection below. The first group of edges set out by the subdivision process consists of all the elements incident on a vertex in the initial tessellation, as shown in Figure 3b. The first vertex is selected arbitrarily, in this case, the middle.

Once the eccentricities are solved, the discretised geometry is incorporated into the geometry of the structural model. This will allow to incorporate the out-of-straightness of the culm into the structural model. Figure 4 indicates the connecting points used as reference to align the discretised elements in the structural model. After this process is applied to all elements, the eccentricities will slightly change depending on the out-of-straightness of the bamboo culms at each connecting point. Note that for each connection, one of the end nodes will change and the other remains fixed. Therefore, all the connectors shall be computed again to account for

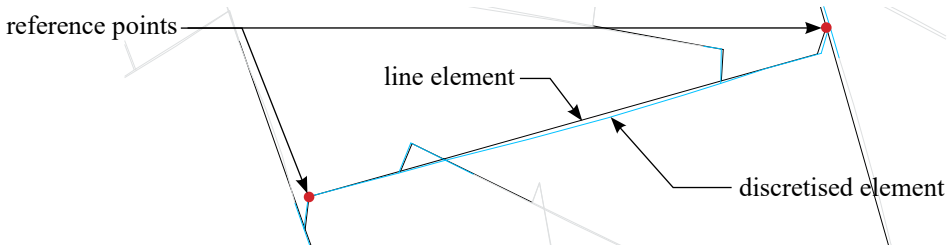


Figure 4: Alignment of discretised elements to line elements in structural skeleton.

these changes. For those elements with two connections (i.e. boundary elements), these two connecting points are used as the reference to align the discretised elements. The method is repeated until the eccentricities reach the target eccentricities.

2.1.1 Eccentricities

The definition of the optimal eccentricities depends on the diameters of the bamboo culms. The method described below, vary the eccentricities throughout the structure in function of the diameter of the bamboo culms to joint at each connecting point. This method also deals with uniform eccentricities throughout the structure.
Figure 5a shows the rotation and translation vectors used for the geometric transformation of the edges. The edges are free to rotate and translate in the out-of-plane direction until a position where the eccentricities equal the target eccentricities within a given range. Unlike previous methods, this method simplifies the problem of finding the eccentricities in an entire structure simultaneously, thereby eliminating the issue of finding optimal eccentricities at four points for all the inner edges.
The problem consists of minimising the sum squared difference between the eccentricities, u, and the target eccentricities, u_c, by finding the set of angles, $\hat{\gamma}$, and distances, d, for the rotations and translations respectively. These are subjected to two inequality constraints that are to be satisfied. The first states that the eccentricities shall lie between the given tolerances. The inequality constraint, g_1, provides the clearance added to the target eccentricities as $\mid u - u_c \mid -\omega \leq 0$, where $\omega = 1$ to provide a tolerance of 1 mm. The second constraint, g_2, is imposed to keep the topology arrangement of the edges unchanged. For example, if an edge is on the top of another edge, do not change it underneath. This is accomplished by evaluating the direction of the eccentricities. As it is not possible to guarantee that a solution could be found by satisfying the topology arrangement, this constraint is conditional.
The design variable is a matrix, $\boldsymbol{X}$, of two columns and a number of rows equal to the number of edges. The first column, $\boldsymbol{x}_1$, corresponds to $\hat{\gamma}$ in radians in the range $-\pi < \hat{\gamma} < \pi$. The second column, $\boldsymbol{x}_2$, contains d. These are used for the geometric transformations and to calculate the eccentricities for the objective function. The rotations of each edge are performed about the axis $\vec{q}$ corresponding to the vector perpendicular to the vectors $\vec{p}$ and $\vec{e}$, and using the midpoint of the edge as centre of rotation. To perform the geometric transformations, we use the rotation and translation matrices to obtain the endpoints of the transformed geometry. After

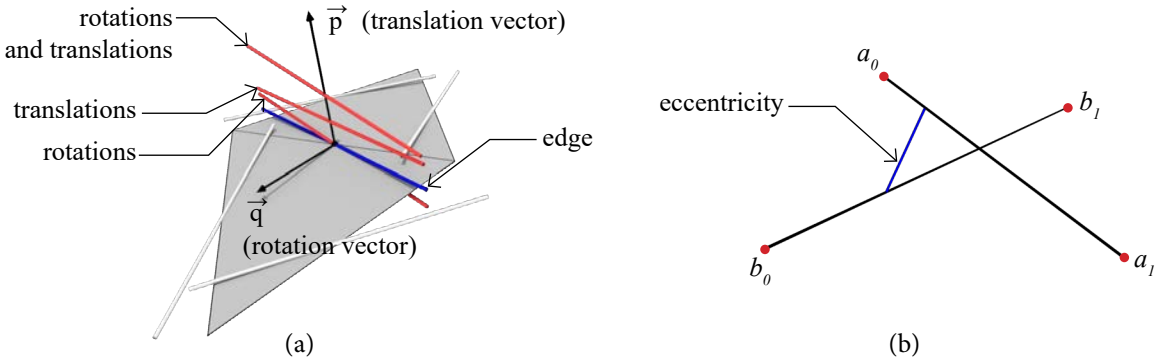


Figure 5: (a) Geometric transformations of the edges indicating the rotation and translation vectors. (b) End points of the transformed geometry and the eccentricity direction.

the transformations, the eccentricities are computed as

$$u = \frac{|(b_0 - a_0) \cdot [(a_1 - a_0) \times (b_1 - b_0)]|}{|(a_1 - a_0) \times (b_1 - b_0)|} \tag{2}$$

where u is the length of the eccentricity and a_0, b_0 and a_1, b_1 are the starting and ending endpoints of the transformed geometry (see Figure 5b).
The general formulation of the minimisation problem is stated as follows:

$$\begin{aligned} \text{Minimise:} \quad & f(\boldsymbol{X}) = \sum_{i=1}^{k} (u_i - u_{c,i})^2 \\ \text{Subject to:} \quad & g_1(\boldsymbol{X}) = \min(\Delta z) \quad \leq 0 \quad , \quad \text{for} \quad i = 1, ..., k \\ & \text{where} \quad \Delta z = \max\Big\{(u_{c,i} - \omega) - u_i \quad , \quad u_i - (u_{c,i} + \omega)\Big\} \\ & g_2(\boldsymbol{X}) = A \cdot B > 0 \end{aligned} \tag{3}$$

where k refers to the number of eccentricities to solve, and A and B are the directional vectors for the eccentricities before and after optimisation respectively.
Note that if the inequality constraint g_2, imposed to keep the topology arrangement fixed, is not satisfied there will be no solution. For these cases, the constraint is eliminated from Equation (3). If no solution is found for a series of edges simultaneously, the method is simplified by finding first single eccentricities for those edges that intersect with fixed edges. Once the eccentricities of those edges are defined, the method allows for rotations of the elements around the connecting elements (i.e. acting as hinges) but no translations are allowed to keep the eccentricities fixed.

3 Case study

The method was implemented in a case study using a batch of bamboo culms of the Oldhamii (*Bambusa oldhamii*) species. The geometric properties were obtained using 3D scanning [8] as shown in Figure 1b. For this example, consider that the selection and position of the bamboo culms for each element in the structure is arbitrary. Figure 6 shows the structure used as case study. The surface was developed in *Rhinoceros* using the Plug-In RhinoVAULT, and the eccentricities were achieved using the method described above. The model used as benchmark is depicted in Figure 6a and consists of uniform elements and equal eccentricities throughout the structure. Figure 6b shows the model with the discretised geometric properties of bamboo culms modelling the non-uniform geometry of the oldhamii bamboo culms.
A total of two complete iterations were required to achieve the geometry of the reciprocal structure using the discretised geometric properties of bamboo culms. Table 1 provides the minimum

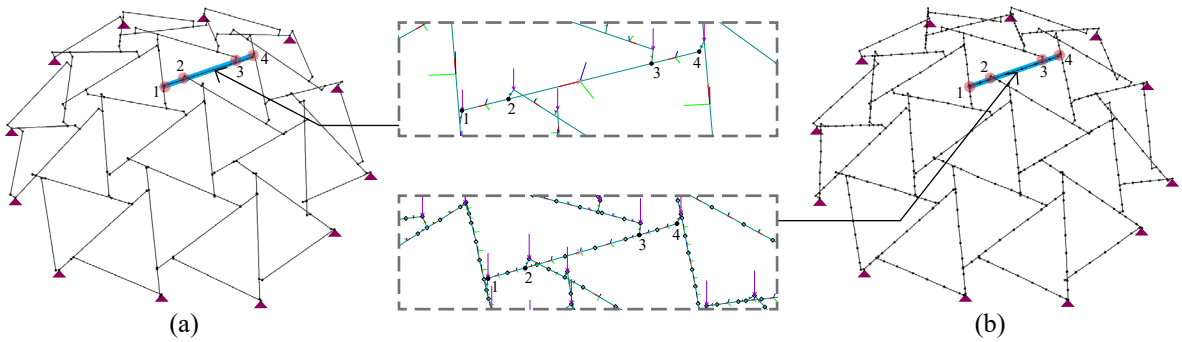


Figure 6: Case study reciprocal structure. (a) Structural model with line elements. (b) Structural model with discretised elements.

Table 1: Minimum and maximum value of eccentricities for each structural model.

	Model 0 (mm)	Model 1 (mm)	Model 2 (mm)
Eccentricities (min)	1.85	89.80	73.17
Eccentricities (max)	71.10	90.10	96.05

and maximum eccentricities values for the models (the original model and the two after the iterations). Model 0 refer to the model after rotations prior to the optimisation of eccentricities. It is evident that this geometry is not optimal since there are very small eccentricities where the bamboo culms cannot be accommodated. Model 1 refers to the model with equal eccentricities and model 2 with the variable eccentricities according to the diameters of the bamboo culms. Besides the clear advantages that the last model poses for the construction practice (accurate fitting and fabrication of components such as connections and cladding), the model allows a more accurate structural analysis. Below, the effect of incorporating these geometric imperfections, namely the longitudinal variation and the out-of-straightness, is investigated. This is done by assessing the displacements of model 1 and 2 using linear static analysis.

The models were analysed using the commercial structural software Oasys-GSA. The modelling of the elements including the eccentricities was done using beam type elements with six degrees of freedom at each node. The material model is isotropic linear elastic and the values used were 20 kN/mm^2 for the elastic modulus and 700 kg/m^3 for the density [8], the Poisson's ratio was taken as 0.30 and the shear modulus as $E/2(1-v)$. The cross-sections were considered as hollow circular sections with double symmetry.

It is assumed that the connection systems (at the eccentricities) are capable to resists moments in the three main orthogonal directions. Therefore there are no releases between the elements representing the bamboo culms and the eccentricities. The eccentricities are modelled with a flexural stiffness an order of magnitude greater than that of the bamboo culms. The supports are considered pinned (i.e. free to rotate in the three orthogonal directions and fixed to translate). The loads are applied in the vertical direction at the top node of each of the eccentricities.

Table 2 presents a summary of results from the sensitivity analysis. The indicative parameters are displacements in the x, y and z directions, the absolute value of displacements and the horizontal displacements in the xy plane (U_x, U_y, U_z, U and U_{xy}). The z direction is the vertical direction in the global axis. The values are only representative and the percentage difference was calculated for each indicative parameter. The values correspond to the locations of the four connections of the element indicated in Figure 6.

The percentage difference for the maximum vertical displacement U_z of the whole structure between model 1 and model 2 is 13.6%. However, from Table 2 we have that the displacements of the discretised model 2 do not increase consistently. They can be higher or lower and therefore difficult to predict without accurate modelling of the non-uniform geometry. Although the model was loaded only in the vertical direction, the configuration of the elements is such that the

Table 2: Sensitivity analysis of the uniform and non-uniform models for element 1.

Model	Model 1				Model 2				% difference			
No. Conn.	1	2	3	4	1	2	3	4	1	2	3	4
U_x (mm)	-0.665	-1.286	0.505	-0.171	-0.802	-1.176	0.502	-0.035	18.7	-8.9	-0.5	-132.3
U_y (mm)	-1.237	-0.511	-2.725	-1.134	-1.309	-0.723	-2.392	-1.031	5.7	34.4	-13.0	-9.5
U_z (mm)	-9.764	-9.932	-9.399	-8.011	-10.640	-10.440	-8.981	-7.484	8.6	5.0	-4.5	-6.8
U (mm)	9.864	10.030	9.799	8.092	10.750	10.530	9.307	7.555	8.6	4.9	-5.2	-6.9
U_{xy} (mm)	1.405	1.384	2.772	1.147	1.535	1.380	2.444	1.031	8.8	-0.3	-12.6	-10.7

resultant applied load is decomposed into the three main orthogonal directions of the elements. The percentage difference for the horizontal displacements U_{xy} is of the same order of magnitude as the vertical displacements U_z, and can be even double for some directions (see connection no.4 in the x direction). Whereas the values are only representative, the model used is linear and therefore the same percentage difference can be expected for different loads.

4 Conclusion

This paper presented a method for generating the geometry of reciprocal structures for non-uniform elements, especially for bamboo culms. The method solves for only two eccentricities at a time for each element, therefore eliminating the problem of finding four eccentricities for each element at a time. This enables a more accurate representation of a digital model for the design, structural analysis and bespoke fabrication of connections.
The sensitivity analysis shows that ignoring the non-uniform geometric properties of bamboo can underestimate the overall bending stiffness of the system. Similarly, the effect of the distribution of forces and moments should be investigated. The method is a first attempt to incorporate non-uniform geometric properties to overcome the difficulty to handle non-uniform geometric properties of bamboo when used as a construction material.

5 Acknowledgements

This work was supported by the Engineering and Physical Sciences Research Council (EPSRC), award reference No.1272034 for which the authors are thankful. The authors would like to acknowledge the work of members of the bamboo research group at UCL, Dr. Rodolfo Lorenzo, Dr. Chuhee Lee and Leonel Mimendi, for their valuable work in relation to the scanning of the bamboo culms. Thanks also to Dr-Ing. Juan G. Oliva for hosting this research group at the National Autonomous University of Mexico (UNAM). Finally, the authors want to thank Jon Mirtschin for the academic license of Geometry Gym.

References

[1] O. Popovic, "Reciprocal frame architecture," *Amsterdam:London:Architectural Press*, 2008.

[2] A. Pugnale and M. Sassone, "Structural reciprocity critical overview and promising research design issues," *Nexus Network Journal*, 16(1) pp. 9-35, 2014.

[3] O.L. Baverel, "Nexorades: A family of interwoven space structures," *PhD thesis, University of Surrey*, 2000.

[4] C. Douthe and O. Baverel, "Design of nexorades or reciprocal frame systems with the dynamic relaxation method," *Computers and Structures*, 87(21-22) pp. 1296-1307, 2009.

[5] P. Song, C.-W. Fu, P. Goswami, J. Zheng, N.J. Mitra and D. Cohen-Or, "Reciprocal frame structures made easy," *ACM Transactions on Graphics*, 32(4) pp. 1-13, 2013.

[6] Y. Anastas, L. Rhode-Barbarigos and S.Adriaenssens, "Design-to-construction workflow for cell-based pattern reciprocal free-form structures," *Journal of the International Association for Shell and Spatial Structures*, 57(2) pp. 159-176, 2016.

[7] Artec-3D, " User guide - artec studio 10, " *Artec 3D*, 2015.

[8] M. Godina, "Design framework for bamboo culms - *A study of bamboo reciprocal structures PhD thesis, University College London*, 2019.

Proceedings of the IASS Annual Symposium 2019 – Structural Membranes 2019
Form and Force
7 – 10 October 2019, Barcelona, Spain
C. Lázaro, K.-U. Bletzinger, E. Oñate (eds.)

Multi Modal Marine Permeable Sponge Shell Structures, Serving as Breakwaters and as Land Reclamation Platforms

Michael BURT*, Yehiel ROSENFELD[a]

*Professor Emeritus, Architecture
Technion – Israel Institute of Technology, Haifa 32000, Israel
matburt@netvision.net.il

[a] Head, National Building Research Institute
Technion – Israel Institute of Technology, Haifa 32000, Israel
roseny@technion.ac.il

Abstract

A 'permeable Sponge Breakwater' hyperbolic modular shell structure represents a novel morphological-conceptual 'fill material free' structural approach, providing for very efficient sea wave energy attenuation, and, when realized as multilayered mega platforms, can provide for land reclamation, either as sea-bed attached, pile supported, or floating- moored, as may be dictated by the bathymetric conditions of the site. Its geometrical periodicity substantiates its industrialized fabrication and assembly and endows it with high cost effectiveness and economic viability. It is solved for staged completion and relocation, if and when desired.

Keywords: Morphology, Sponge Breakwater, Land Reclamation, 'Fill Material Free', Shell Structure, Wave Attenuation, Marine Technology.

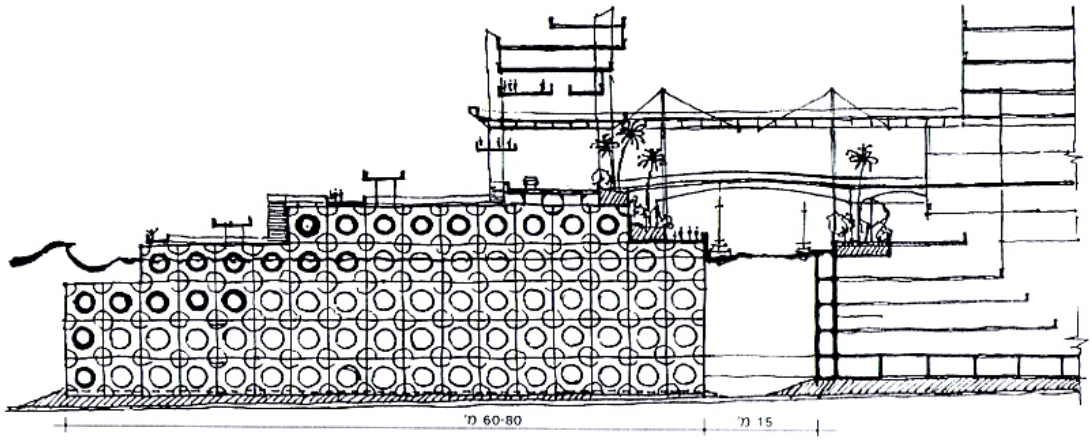


Figure 1: Permeable sponge shell structure serving as breakwaters and as land reclamation platforms

1. Introduction

The human habitat is continuing to expand and devour greater space and land resources, and that for multiple self-evident reasons:

Copyright © 2019 by Michael Burt & Yehiel Rosenfeld
Published by the International Association for Shell and Spatial Structures (IASS) with permission.

- **Worldwide population growth** and the resulting evolution of mega-metropolitan urban areas, some with tens of millions of residents, mostly **sprawling along the coastal lake-sea-ocean expanses** of the globe.
- A continuously **growing area-space consumption** per capita and per community services as a manifestation of the basic human desire to raise the standard of living.
- A growing demand for mobility and the resulting **explosive growth of land-air-marine transportation infrastructures.**

All these happen with a dramatic rise in the level of eco-environmental conflicts and costs and 'sky rocketing' real-estate land values. It turns out that all expertly statistic forecastings are promising doubling-tripling growth within the foreseeable future, of land-space consumption and the resulting environmental deterioration. We come to realize that land-space resources, especially those in close proximity to urban environments, are mostly critically limited and costly.

All that calls for a thorough re-evaluation of our urban expansion and development. It calls for a new urban and metropolitan design paradigm for our evolving future habitat. Some design paradigms were considered, and none of them appear to be as promising as that of the **'expansion into the marine environment'** option.

2. Conceptual Principles of the marine technology of the evolving design paradigm

Most of the present attention focuses on land-space scarcity costs, and the growing global public sensitivity and concern over the eco-environmental sustainability prospects. Whenever the marine development option is raised, the emergent '**Fill Material Based'** design paradigm comes under ever-growing criticism, even to a point of its total rejection, mostly because of its environmental abuse and its **attainability, transportation, delivery and site manipulation costs**. This double feature of land-space manipulation for effective exploitation and the drastic reduction of dredged-excavated-mined fill materials, to a point of '**Fill Material Free' conceptual approach**, are the main-stay of the evolving design paradigm of expansion into the marine environment.

A range of multi-modal application combinatorics is considered:

1. As 'fill material free' land reclamation mega-platforms, ground based, or pile supported, or floating-anchored, if in deeper waters.
2. As 'fill material free' permeable sponge breakwaters modular shell structures, solved to absorb the impounding wave power.
3. As pier structures of hyperactive port platforms, solved to support the port loading facilities and the hyper-weight of the tonnage involved, its manipulation and storage.
4. As piers of urban water frontage in river and sea channels, etc.





Figure 2: Minimal soap-solution film on a wire perimeter

3. Structural evolution of the periodic hyperbolic sponge surfaces

The research into the morphological nature of periodic hyperbolic sponge surfaces was initiated with minimal soap surfaces, stretched on wire perimeters, back in 1963 (M. Burt D.Sc.). First appreciation of the structural performance potential of these periodic sponge surfaces happened while working on his D.Sc. thesis (1963÷66), considering thin shell roof structures and marine submerged shell protected habitable spaces. In 1969 an experimental fiber glass polyester shell structure (2mm. in thickness) of the explored polyhyparic surface, **the Hexahyp -7 structure**, was realized at the Technion's Faculty of Architecture (by students of the faculty), covering an area of 365 sqm. (fig.3).

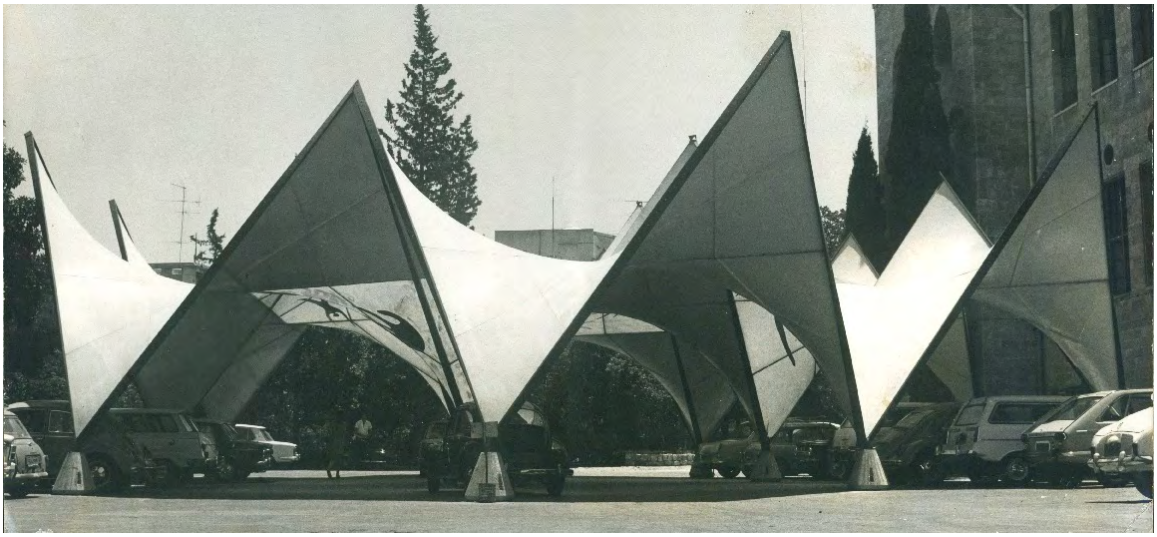


Figure 3: Cubic polyhyparic surface the Hexahyp-7 shell structure (Technion, I.I.T.)

The Hexahyp-7 hyperbolic-parabolic (polyhyparic) surface structure was closely associated with crystalline spatial order, conditioned by restrictions of related spatial lattice symmetry patterns. A range of geometries was considered, with a preference of the **'cubic sponge surface'** (hyperbolic continuous space partition between two dual cubic networks). If the related two dual networks are identical (like the cubic net), the surface partition subdivides the in-between entire space into two intertwined, identical subspaces. In such eventuality, an additional array of 2-fold rotation symmetry axes is generated, embedded within the surface, raising considerably its periodicity level. (fig.4).

The 2-fold symmetry axes combine into an embedded space lattice, subdividing the surface of the cubic basic translation unit into symmetrically identical 96 left-handed and 96 right-handed saddle shaped units.

The internal symmetry patterns of the self dual cubic lattice have defined the nature and shape of the repetitive surface units with highly simplified cutting pattern solutions. It was followed by the project of Aquaville (marine submerged shell structure, representing Israel in the Architecture Biennale in Paris (M. Burt – 1969) and by a membrane structure, realized by students of the Southern Illinois University in Carbondale, (fig. 2) under the supervision of M. Burt (1971).

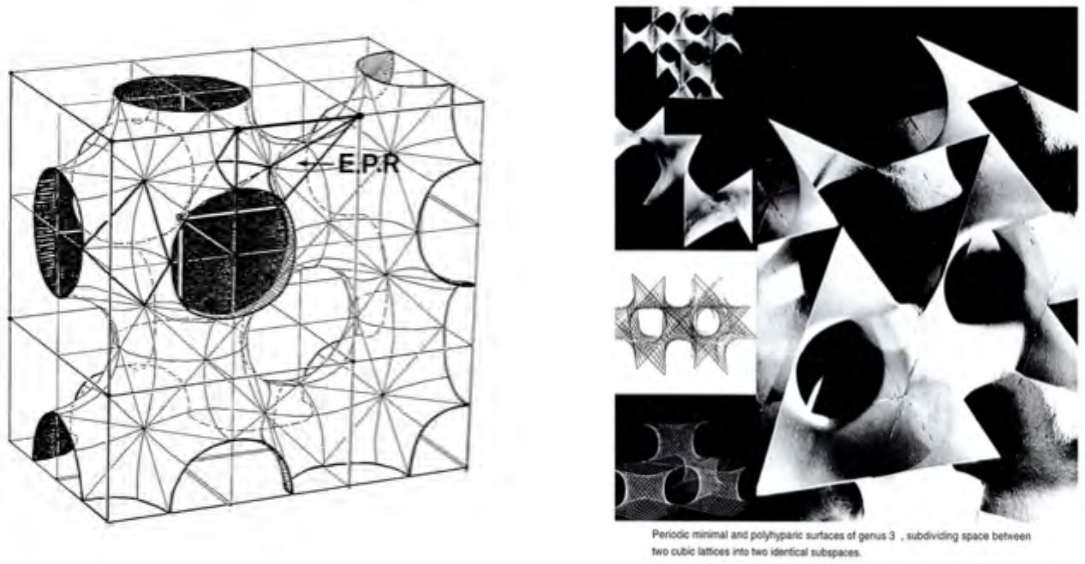


Figure 4: "Cubic" sponge surface with reflection and 2-fold rotation axes symmetry patterns (right) and a "cubic" polyhyparic sponge shell structures (left)

4. Structural Performance of the Suggested Sponge Surface as Permeable Sponge Breakwaters (P.S.B.) and Built Mass Support Mega Platforms

Minimal surfaces, as membranes and shell structures, were analyzed in the past, with soap solution films as leading examples, with their structural efficiency reaching the highest possible level in terms of the ratio of invested material to its structural performance. The deviation of the 'polyhyparic geometry' from that of the minimal surface is negligible, and therefore it may be considered structurally as credible as the minimal surface.

When the polyhyparic surface is extended, to evolve into a continuous labyrinthine sponge surface, many geometrical-structural macro characteristics enter the equation, enhancing its structural behavior and performance. When attacked by an onrushing wave or other locally applied force, the inner structural surface bonding adds considerably to its load distribution, and thus to its enhanced structural strength and resistance behavior. This shell structure can resist exceptional external loads and hydrodynamic impacts of the sea waves. Of course, the closer to the P.S.B.'s front and the wave impact area, the thicker and more thoroughly reinforced the (concrete of the) shell modules should be.

This concept was put to the test with a reduced scale model, in the wave channel (flume) of the Israeli Coastal And Marine Engineering Research Institute (CAMERI) at the Technion, I.I.T. (1998).

The results clearly demonstrate that the tested permeable sponge wave attenuator absorbs about 80% (or more) of the wave energy; reflects just10%; and allows for the remaining 10% (or less) to pass-

infiltrate through. The absorption and diffusion of the wave energy is achieved due to the combination of two main characteristics:

.



Figure 5: Modular hyperbolic (cubic) sponge shell structure small scale testing model in CAMERI, Technion marine lab.

A. The sea water, which fills the interior of the breakwaters structure, with its submerged cross-section area of ~2,000 sqm, acts as a static mass, and together with the concrete shell mass represents a total resistance of ~ 2600÷3000 metric tons per each running 'frontage meter'.
B. The sponge labyrinth acts to dissipate the energy by extending the waves momentum over a longer period of time and by causing an intense turbulence and resonance action of the attacking water mass.

The wave energy above sea level is absorbed by the sponge labyrinthine structure of the concrete shell, protruding to 5÷7m above the sea level.
The testing demonstrated that the emergent waves on the protected side of the breakwater reach to just 15% of their initial height.

5. Fabrication and Construction

Due to its geometrical periodicity and modularity, the shell structure is convenient for industrial mass manufacturing. The size of the modules will be determined by considerations of local curvature and strength and production cost optimization (mould sizes, lifting, crane capacities etc.). As preliminary approximation, the basic cubic module might be 5mx5mx5m. It should be borne in mind that for 1,000m of breakwater length (25m x 120m in cross section), ~ 240,000 half cube shell modules will be required (!) (fig .6).

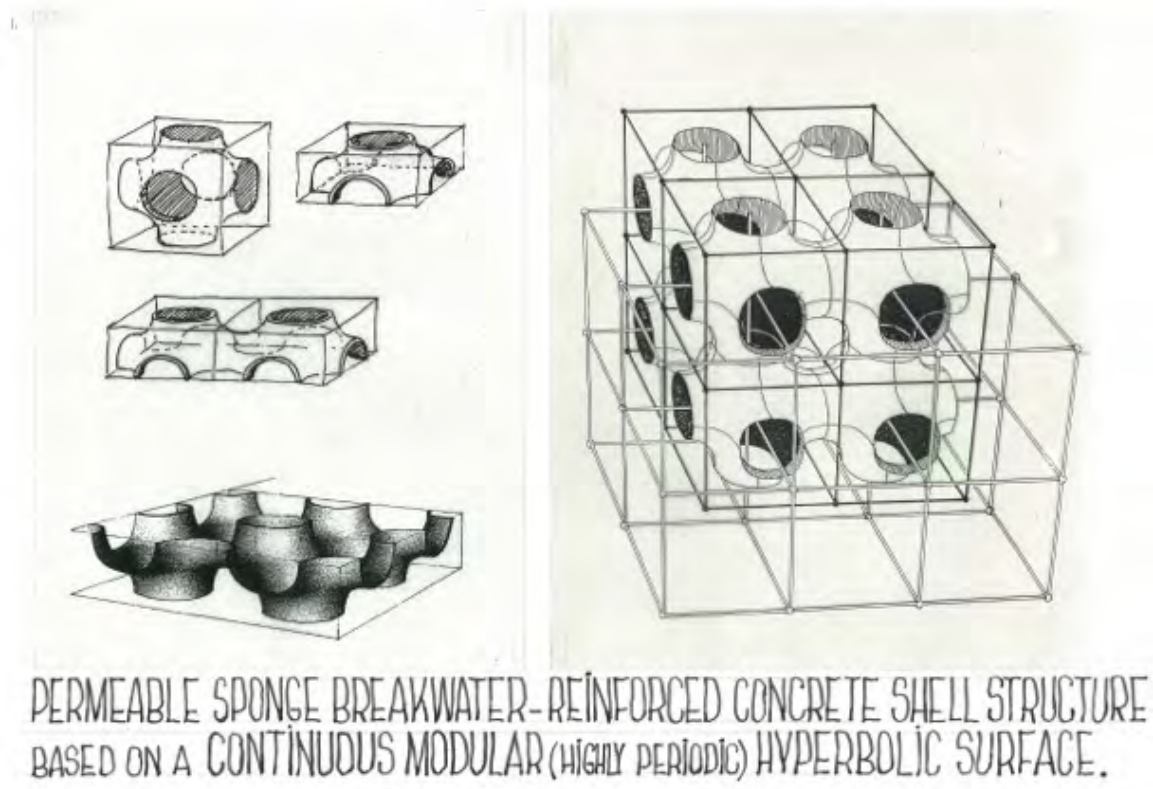


Figure 6: Modular hyperbolic (cubic) shell structure, to be employed as "permeable Sponge Breakwater' and land reclamation 'mass'

The fabrication plant has to be in proximity to a coastal construction-assembly plant (on the water). The modules will be assembled into large monolithic floating platform structures, as 'mega-bricks', using a fraction of their interior space for sealed air-compartments, to provide for floatability. (Fig.7)

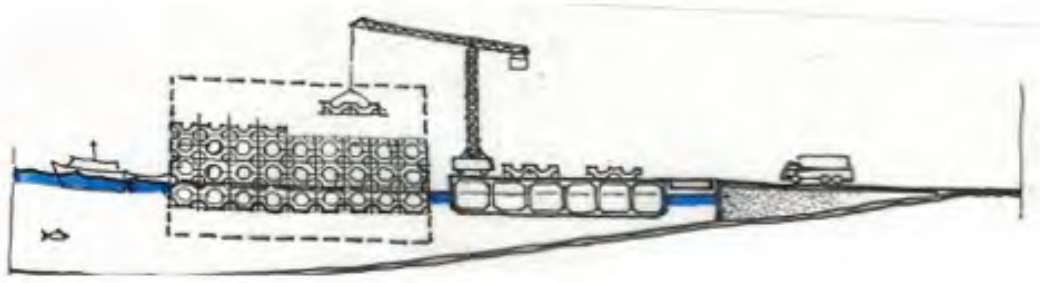


Figure 7: Construction and assembly in the Coastal fabrication plant (on the water).

The mega-bricks of about 120m x 25mx (100m÷200m) in size, with 2,400÷4,800 modules each, will be sea-transported to their sites of function (Fig.8), and founded-pile-supported- anchored, one next to the other, in a controlled fashion (probably with no inter-bonding), as dictated by the circumstances and the bathymetric characteristics of the site (fig 9).

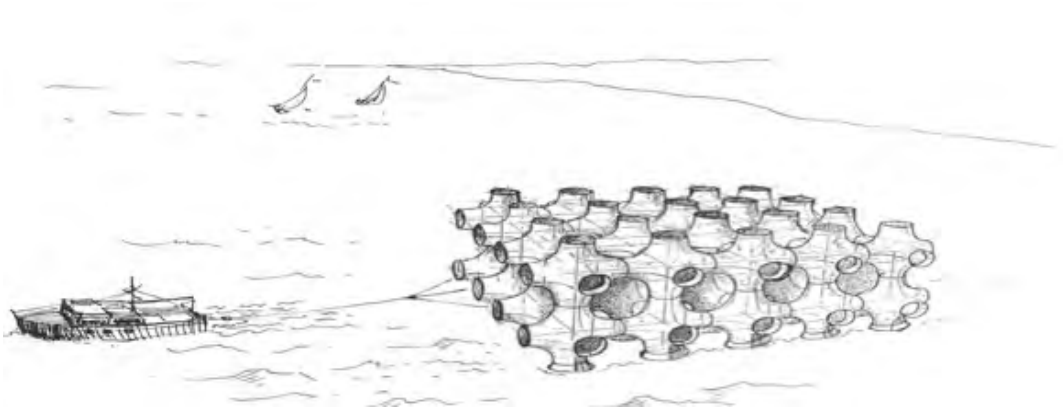


Figure 8: Transportation and delivery of the floating mega-brick for assembly on the site

It is important to stress that due to the simplified marine delivery logistics, capable of transporting, while afloat, of tens of thousands of tons of a mega-block platforms from the

production plant to the site, it makes possible avoiding most of the land-based traffic frictions, time and costs. Even more impressive, due to floatability, while transported and assembled on site, the suggested technology implies the feasibility of relocation of the whole project (or parts of it) if and when desired. This option is unimaginable and unrealizable with the 'state of the art' fill material based technology.

6. Conclusion

Periodic hyperbolic sponge surfaces, serving as continuous space subdivisions between dual 3~D space networks, represent morphological phenomenon that is waiting to be appreciated and explored as a possible solution to some pressing structural problems:

- As **wave energy attenuating –absorbing structural medium** (on a wide range of scales);
- As a thinly spread **materially economic structural mass**, capable of withstanding high external load pressures.

When the surface is subdividing between self-dual networks (as in the 'cubic systems' case) a set of 2-fold rotation symmetry axes and inversion symmetry points are generated, endowing the resulting sponge structure with a degree of periodicity that can sustain an intensive industrialization process of the structure's fabrication and construction-realization, making it economically extremely viable and attractive.

'Fill Material Free' sponge breakwaters and land reclamation mass, the material content of which amounts to just 3÷5% compared to the fill-material based alternatives, provide for marine technologies that are eco-environmentally and economically very attractive, that can sustain the mostly desired marine urban and infrastructures development of the approaching decades time. And if some location or scale development mistakes are committed….we should remember that it is RELOCATABLE (!).

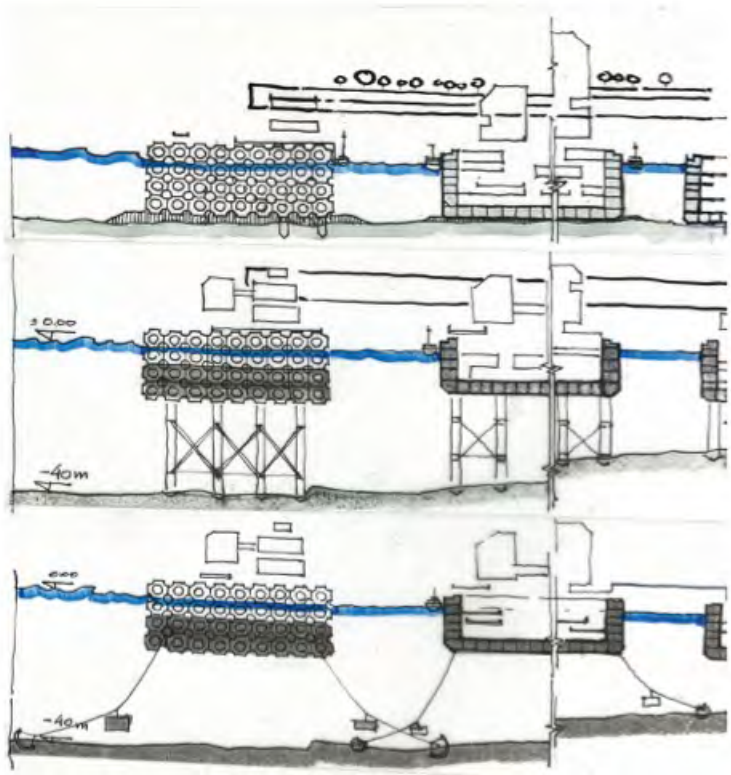


Figure 9: 'Fill Material Free' technology components, founded or pile supported or anchored

References

[1] M. Burt, "Spatial Arrangement and Polyhedra with Curved Surfaces and Their Architectural Application". D.Sc. Thesis Technion, I.I.T., 1966.

[2] N. Drimer M. Schasniy, M. Burt, "An Experiment's study of wave Transmission Through a Permeable Breakwater", Report publication, CAMERI, Technion, I.I.T., 1998.

[3] M. Burt, "Polyhedral Sponge Structure - New Imagery and Inspiration for Innovative Space Structure", IASS-APCS 2006 Proceedings Beijing, , 476-477, 2006.

[4] A. Koren, "Identical Dual Lattices and Subdivision of Space", PhD. Thesis (M.Burt as supervisor), Technion I.I.T, Israel, 2013.

[5] M. Burt, "The Israeli Marine Option, The Blue Avenue Vision". Technion, I.I.T. publication, Israel. 2013.

[6] M. Burt, Y. Rosenfeld, M. Schusheim (Neptune-Tech Ltd.), PCT/IL/2013/050598, "ENERGY DISSPATOR, 2013.

[7] M. Burt, Y. Rosenfeld, "Fill Material Free Marine Development Paradigm", Structural Engineering World Congress (SEWC), Singapore, 2015.

[8] M.Burt, Y.Rosenfeld, "Permeable Sponge Breakwater Shell Structure", IASS-SLYE Symposium, Brasilia, 2014.

Proceedings of the IASS Annual Symposium 2019 – Structural Membranes 2019
Form and Force
7 – 10 October 2019, Barcelona, Spain
C. Lázaro, K.-U. Bletzinger, E. Oñate (eds.)

Non-Linear Solution to Spherical Coverings and Application to Forms

Christopher J. KITRICK

San Diego, USA
ckitrick@gmail.com

Abstract

Most spherical tessellations are optimization problems. This paper describes a general technique for solving complex spherical tessellations that require a non-linear approach and shows its application to two different spherical shell geometry problems: a) general equal edge hexagonal topology and b) spherical nexorades, a form of reciprocal frames. Both tessellation problems are specific optimization problems that require a non-linear technique. The technique extends beyond what this author [1] presented previously as a partial solution to the equal edge topology problem. For any spherical tessellation the distances of vertices from their immediate neighbors is varied and numerous division methods that have been developed generally only limit the number of different edge lengths that arise. With hexagonal tessellations there are many single length edge solutions but the desire is to find the optimal solution: the smallest edge possible for a particular topology. This paper describes a non-linear form finding solution that works for the entire range of hexagonal tessellations, achieving what appears to be an optimal edge length. The basic technique is to iteratively adjust vertex locations while propagating the edge changes.

Keywords: hexagonal, spherical tessellation, form finding, optimization, nexorade

1. Hexagonal Tessellation

Prior literature on equal edged hexagonal networks focused on solutions to symmetrical configurations, Kitrick[1], or discussed the full set without providing a tractable methodology for solving, Clinton[2]. Solving the symmetrical cases allows some simplification of the general case. This paper focuses on a robust methodology that addresses the general case that includes the full topological scope of possible tessellations. In addition, the solution appears to generate an optimal, minimum, edge length. If the equal edges of a hexagonal configuration are optimal and represented by hinged plate action the deformation of the tessellation requires the vertices to move inward to the center of the sphere. Assuming fixed boundary conditions the overall configuration is nearly stable without additional bracing (fig 7).

2. Symmetry

The icosahedron with its twenty identical equilateral triangle faces, forms the standard framework to derive geodesic tessellations. Depending on the class of tessellation only a portion of one face represents all the unique geometry that is replicated across the surface. For the symmetrical classes (I&II) one sixth of a face contains all the unique vertex locations. For the chiral class III one third of the face is required. Within this fraction of a single polyhedral face the goal is to position all vertices, that form the hexagonal grid, such that the angular distance from their immediate neighbors is equal.

Copyright © 2019 by Christopher J. KITRICK
Published by the International Association for Shell and Spatial Structures (IASS) with permission.

2.1 Notation

The full scope of hexagonal tessellations can be defined by two variables (*b,c*) that allow the full range of topologies to be represented. Hexagonal configurations, which are the main focus of this paper, can be defined as a subset of a triangular grid. The Schläfi notation $\{p, q\}$ with Goldberg-Coxeter subscripts (*b,c*) for icosahedral hexagonal tessellations and subscripts (*m,n*) for the superset triangular tessellation is given in eq. 1, Coxeter [3].

$$\{5+, 3\}_{b,c}, \quad \{3, 5+\}_{m,n} \tag{1}$$

The relationship between hexagonal (*b,c*) and triangular (*m,n*) subscripts is:

$$m = b + 2c,\ n = b - c \tag{2}$$

$$b = \frac{m+2n}{3},\ c = \frac{m-n}{3} \tag{3}$$

Figure 1 shows an example (*m,n*=5, 2) triangle grid whose subset hexagonal grid is (*b,c*=3,1). The large red shaded equilateral triangle represents one equilateral face of the icosahedron. The shaded light green portion highlights the one third portion of a triangle's geometry that is unique. All other geometric positions can be derived from transformations of this portion. Each vertex of the grid is labeled with two numbers: the top number represents the specific vertex and its associated cartesian coordinate, while the bottom number represents the vertex's symmetry group. Vertices that lie in the unique portion of the triangle, highlighted in yellow, are non-transmutable: each has a unique Cartesian position and a unique symmetry group. These positions can be independently moved (the exception is the corners). The rest of the vertices are not unique (non-yellow) and can be derived from their unique counterpart of the same symmetry group.

The notation for a single unique vertex is v_g^i where g represents its symmetry group and *i* its global index. Non-unique vertices are derived from the unique vertex of the same symmetry group through the associated transformation M_g (eq 4). A unique vertex can re-derived from a corresponding non-unique vertex through the transpose of the associated symmetry group transformation (eq 5).

$$v_g^j = v_g^i M_g \tag{4}$$

$$v_g^i = v_g^j M_g^T \tag{5}$$

2.2 Hexagonal Tessellation

When considering the hexagonal configuration only a portion of the vertices that define the grid are relevant. In the example (figure 1) only vertices (9,16,18,19) define the hexagonal tessellation and are independent. This vertex set represents the variable vertex positions on the spherical surface that are independent and free to be adjusted. Moving these positions changes the length of the vectors between them and their immediate neighbor vertices, and symmetrically all the edges of the entire tessellation. The goal is to move each of these vertex until it is equidistant from its immediate neighbors. This process is edge equalization.

3. Edge Equalization

Edge equalization is a process that begins from a known set of vertex positions with the corresponding edge lengths, and then iteratively shifts vertex positions on the surface of the sphere until all the edges are equal in magnitude. The method described herein relies on first, locally adjusting the position of each unique vertex so that its distance from its nearest neighbor vertices is more equal, then ensuring any vertex movement is propagated to all the vertices of the same symmetry group. Once every unique vertex has been adjusted, continuously repeat the sequence until all edges reach the same dimension within the desired tolerance.

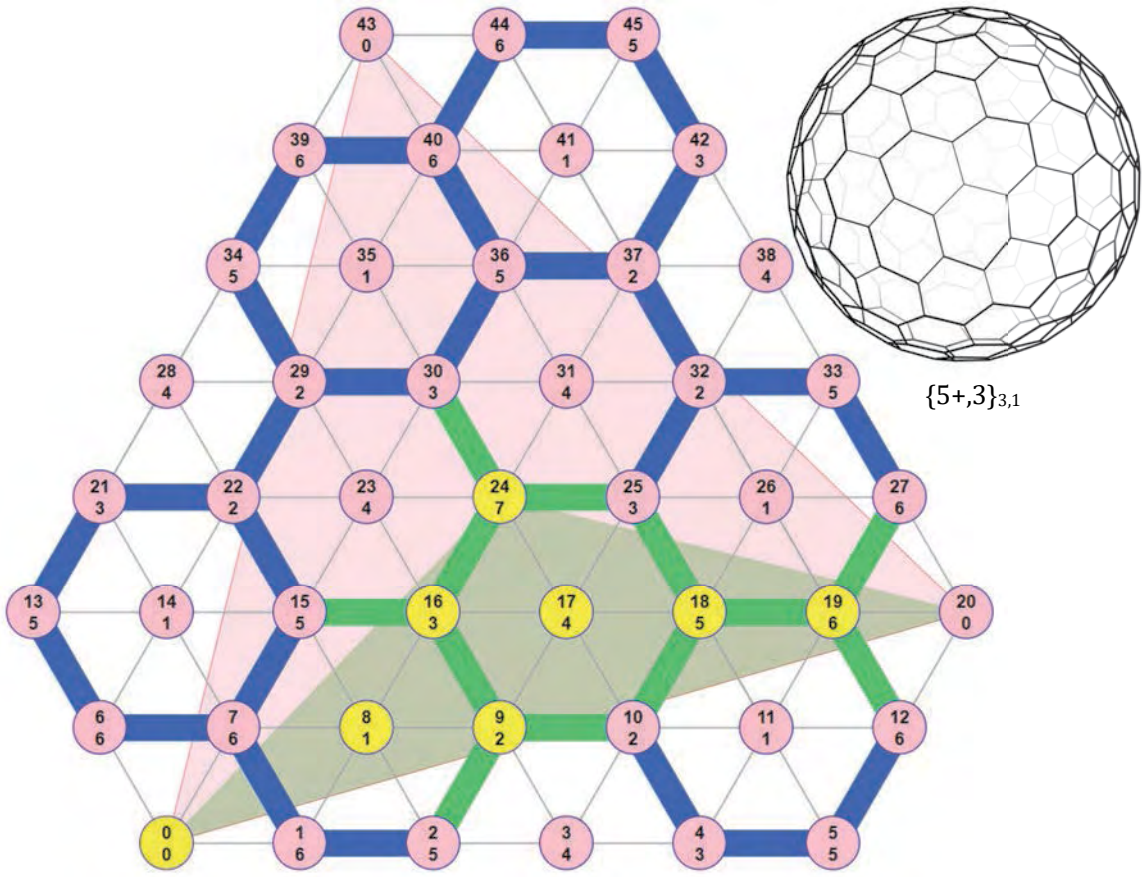


Figure 1: Example Class III Hexagonal Grid $\{5+,3\}_{3,1}$ and Triangular Superset $\{3,5+\}_{5,2}$

3.1 Nearest neighbor edge equalization

The essential mechanism is the iterative movement of vertices to incrementally equalize their position on the surface relative to their nearest neighbors. Each attempt to equalize a vertex position requires determining the distances from its neighbors, extending or contracting the length of each vector to the average of all the neighbor vectors, finding the center of the new vector end points, and normalizing it to be on the spherical surface. Figure 2 is a simplified overview of the process of a single vertex equalization step. The vector length differences are attenuated for illustration purposes.

In the figure 2 example after comparing the average vector length, vector 3 remains the same while vector 2 shortens, and the vector 1 extends. At this point the common end point has three potentially separate independent positions. After finding the center of the new end points, through simple averaging, all three vectors will have changed length and be incrementally closer to being equal in length.

The original common end point is initially on the surface of the sphere but after vector adjustments and end point averaging the new end point will no longer be on the surface, thus requiring a simple normalization to bring it back to the surface (eq. 6).

$$\hat{v}_g^i = \frac{v_g^i}{|v_g^i|} \tag{6}$$

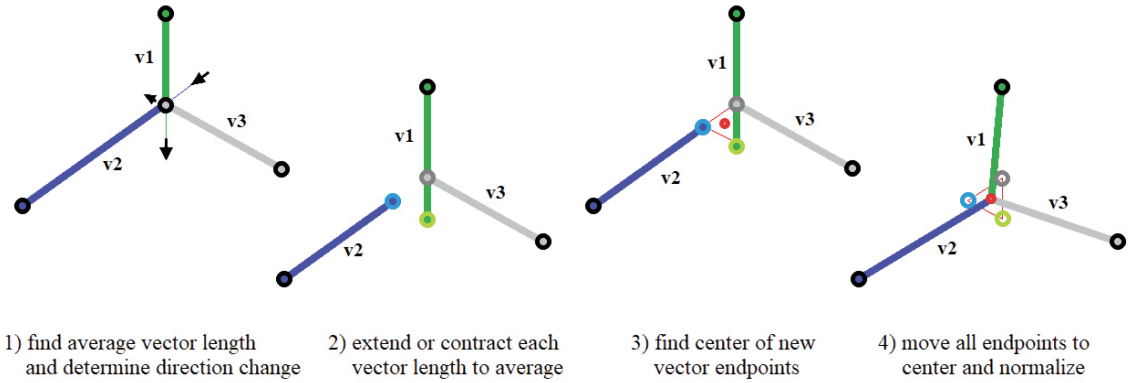


Figure 2: Nearest Neighbor Edge Equalization

3.2 Incremental Correction

Multiple steps are generally required to find the final vertex position that is equidistant from the neighbors but rather than completely equalizing a single vertex at a time, only the first approximation is done, followed by propagation of the vertex position change across all the non-unique vertices of the same symmetry group (eq 5). This basic process is done sequentially for all the independent vertices and then continuously repeated until the required level of edge equivalence precision is achieved. Propagation provides the feedback loop that ensures local changes ripple across the entire set of vertices.

A good example of this process can be seen in the equalization of the unique vertex on the corner of the pentagon. In figure 3 example vertex 19 is adjusted either only further away or closer to vertex 18 because vertex 19 is symmetrically placed between vertices 12 & 27, which are the same symmetry group. After vertex 19 is edge equalized vertices 12 & 27 are then updated based on their associated transformations (eq 4). This ensures that all related vertices remain symmetrically synchronized.

4. Initial Geometric Configuration

The edge equalization process requires an initial configuration that is then subsequently refined. An initial spherical geometry can be derived by first transforming the planar configuration shown in shaded red triangle of figure 1 onto the associated plane triangle of the polyhedron and then extending the vertices outward to the spherical surface (figure 4). This provides an adequate starting point from which to iteratively perform the edge equalizations on the unique vertices until all the edges of the hexagonal tessellation are equal.

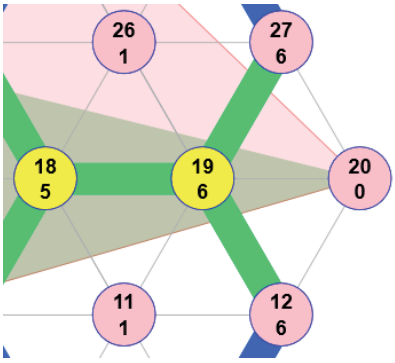


Figure 3: Pentagon Corner

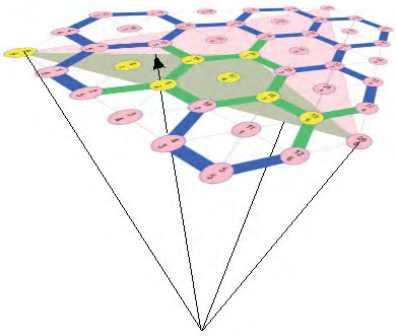


Figure 4: Initial Geometry

5. Results for Hexagonal Tessellations

The methodology outlined successfully finds equal edge solutions for any (*b,c*) configuration. The compute cost is essentially linear per unique vertex. The number of edge equalizations required per unique vertex is nearly constant and directly related to the required precision.

5.1 Optimality of the Derived Equal Edge Dimensions

Though the methodology works in all cases it is valuable to understand how well the results align to an *ideal* theoretical solution. The number of polygon faces in a hexagonal tessellation is a function of (*b,c*). For the icosahedron the total number of faces, *p*, is given in eq 7.

$$p = 10\mathrm{t} + 2 \tag{7}$$

Where the number of polygons per icosahedron face is given by *t*:

$$t = b^2 + bc + c^2 \tag{8}$$

When accounting for the constant presence of twelve (12) regular pentagons and making the simplifying assumption that every hexagon is completely regular an ideal edge angle is shown in eq. 9.

$$edge = 2\cos^{-1}\left(\frac{\sqrt{3}}{2sin\left(\frac{\pi}{3}\left(1+\frac{1}{10(t-0.248)}\right)\right)}\right) \tag{9}$$

Comparing edge equalization results with this ideal edge over a wide range of *t* values, the maximum difference is +0.77% thus providing evidence that the solutions may be optimal or nearly optimal.

6. Adaptation for Icosahedral Nexorades

The concept of vertex / edge manipulation can be extended to address the nexorade tessellation form, Baverel [4,5], which consists of spherical arcs whose end points lie exactly on neighboring arcs, see Figure 5. Each arc is a great circle segment that extends across four (4) adjacent vertices on the underlying triangular grid. Triangular tessellations can support a nexorade arrangement when t (eq. 8) is modulo 7.

6.1 Equalization Component

For this tessellation form the goal is to shift initial vertex positions so that every group of four vertices that comprise an arc is aligned into a great circle segment. As in the hexagonal tessellation case, the initial geometric configuration is from the superset triangular grid projected onto the spherical surface.

6.2 Unique Great Circle Arc Segments

A nexorade arc is unique if one of the two center vertices lie in the unique 1/3rd portion of the triangle. Nexorades are by default always chiral regardless of the class of their superset triangle grid. In the $\{3,5+\}_{5,3}$ example (fig. 5) there are only four (4) unique arcs.

6.3 Equalizing Vertex Alignment

With an initial configuration the two vertices that lie inside of the arcs will not be aligned to form a great circle segment (fig. 6). The equalization step involves shifting the two internal arc vertices so that they lie exactly at some interval along the arc. Once that shift is made the change must be propagated to all the vertices of the same symmetry group. In this example the arc divisions are at exactly 1/3rd subtended angle locations. For nexorades a shifted vertex may not be unique and thus during propagation the associated unique vertex can be re-derived (eq. 5).

The propagation will generally reverse a portion of the correction. An example can be seen in arc 0 (blue) in figure 3. Once vertices 28 and 36 are corrected between 20 and 43 the propagation of modified vertex 28 will affect vertex 20, the original endpoint of the arc.

6.4 Incremental Correction

The vertex alignment must be done to each unique arc in sequence, with vertex shifts being propagated after each arc alignment. If the multiple arcs alignment is continually repeated the vertex shifts required quickly goes to zero and the process is complete: all arcs are great circle segments.

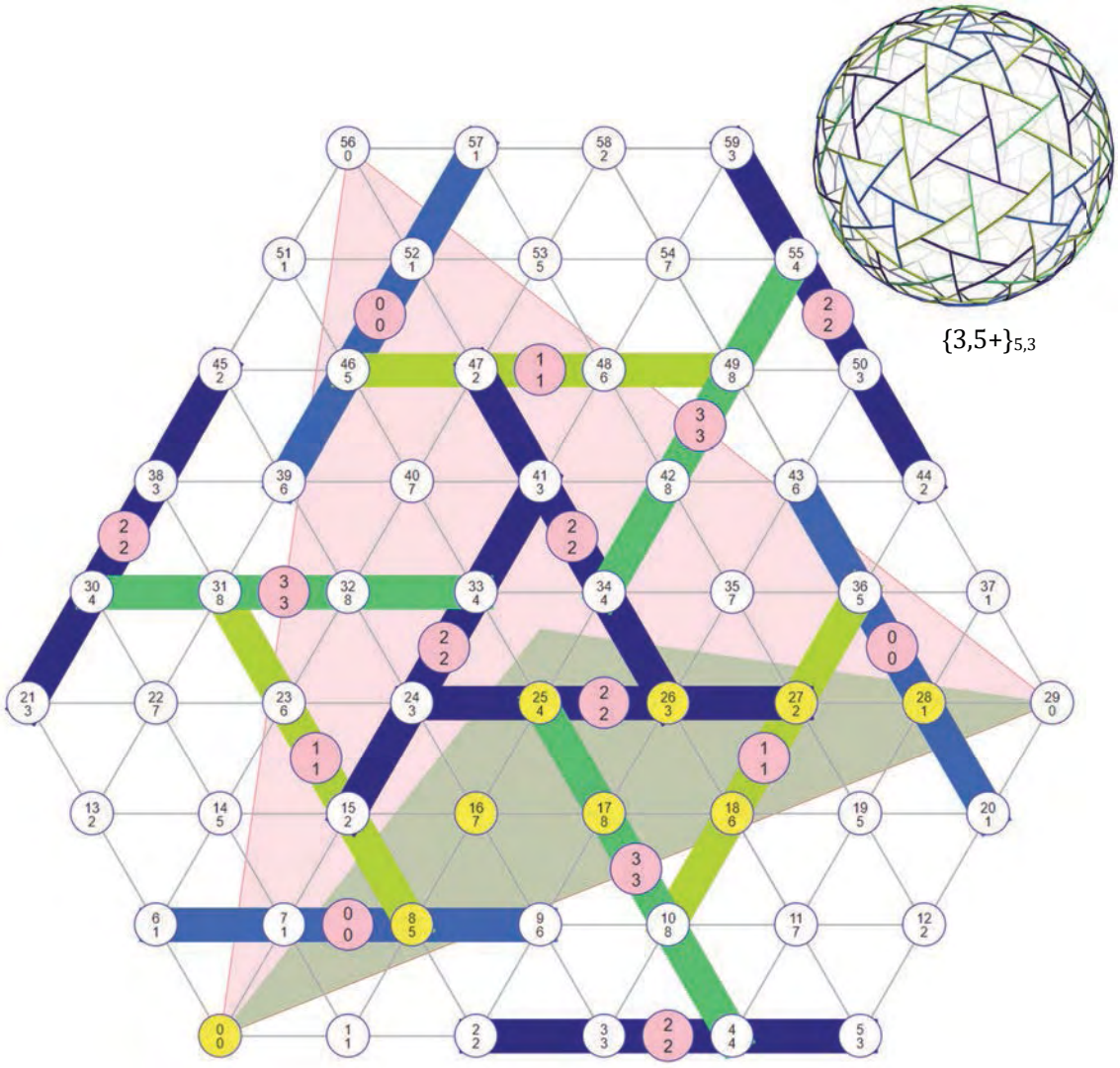


Figure 5: Nexorade Tessellation on $\{3,5+\}_{5,3}$ grid

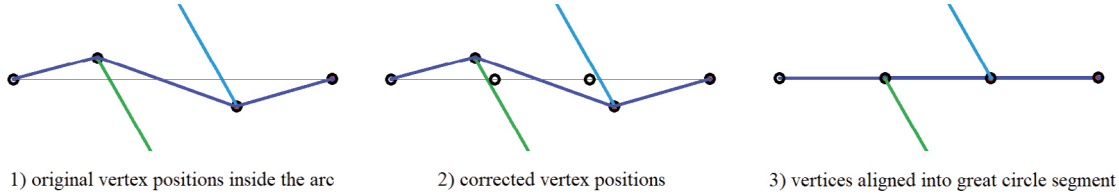


Figure 6: Nexorade Arc Vertex Alignment

7. Examples

The following example figures (7,8) are results of using the vertex re-positioning methodology for both tessellation forms.

7.1 Equal Edge Hexagonal Tessellations

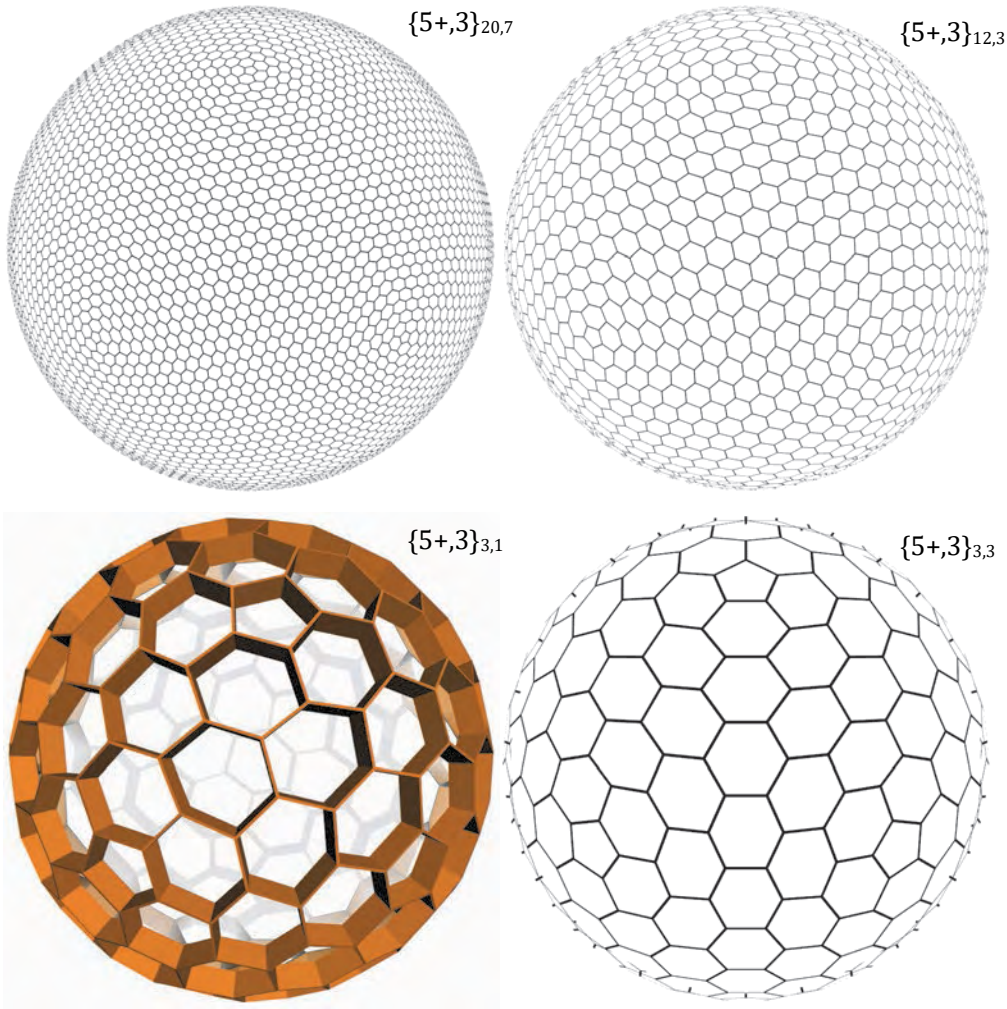


Figure 7: Equal Edge Examples – Including Edge as Plate

7.2 Nexorades

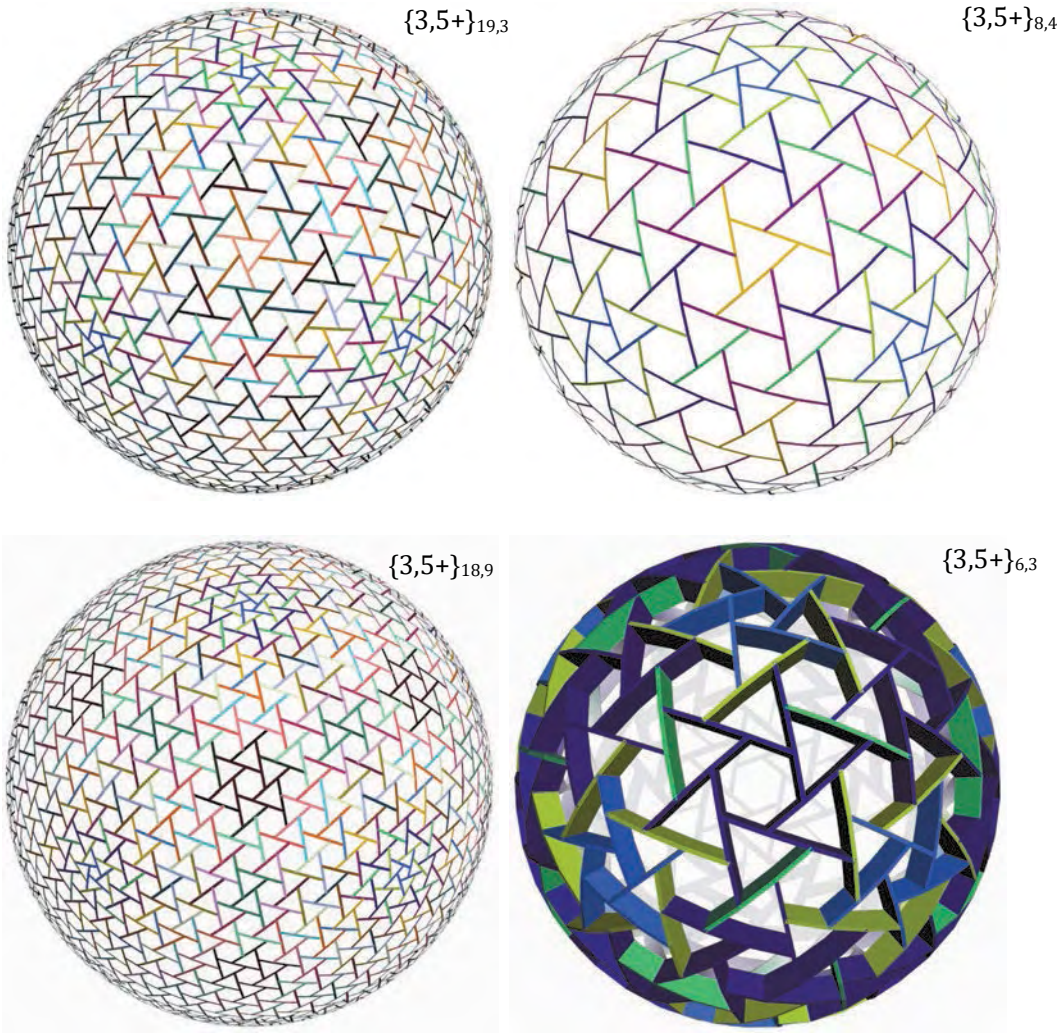


Figure 8: Nexorade Examples – Including Edge as Plate

References

[1] Kitrick C., Equal Edge Hexagonal Spherical Tessellations, *International Journal of Space Structures*, IASS Symposium 2015

[2] Clinton J., A Group of Spherical Tessellations Having Edges of Equal Length, *5th International Conference on Space Structures*, G. A. R. Parke and P. Disney (ed.), Thomas Telford Limited, 2002

[3] Coxeter, H.S.M., Virus Macromolecules and Geodesic Domes, *A Spectrum of Mathematics*, 1971, B. C. Butcher (ed.), Auckland University Press, pp 98-107

[4] Baverel, O, Nooshin H., Kuroiwa Y. and Parke G.A.R, Nexorades, International Journal of Space Structures, Vol.15 No. 2 2000

[5] Baverel, O., Nooshin, H., "Nexorades Based on Regular Polyhedra," *Nexus Network Journal*, vol. 9, pp. 281-298, 2007

Proceedings of the IASS Annual Symposium 2019 – Structural Membranes 2019
Form and Force
7 – 10 October 2019, Barcelona, Spain
C. Lázaro, K.-U. Bletzinger, E. Oñate (eds.)

SPACEPLATES: Thin, modular and manageable

Anne ROMME*, Anne BAGGER[a], Ion SØRVIN[b]

*The Royal Danish Academy of Fine Arts, Schools of Architecture, Design and Conservation
Philip de Langes Allé 10, 1435 Copenhagen K, Denmark
anne.romme@kadk.dk

[a] Anne Bagger ApS
[b] N55

Abstract

This paper discusses the SPACEPLATES Building System as one approach to constructing double-curved, lightweight, modular shells and compares it with related contemporary state-of-the-art research conducted by the Institute for Computational Design and Construction (ICD) at Stuttgart University. Examples of the tessellation geometry and principles of modularity are described and the difference between morphological and additive modularity principles are pointed out. Material and environmental characteristics of aluminium as a building material is touched upon, and differences in material use between the Landesgartenschau Exhibition Hall (ICD) and the SPACEPLATES Greenhouse Bristol are explained. Lastly the do-it-yourself approach inspired by Buckminster Fuller is presented as an inspiration and ambition for the SPACEPLATES project, and an insulated system is suggested as a future research goal.

Keyword: shell structures, plate structures, structural morphology, building systems, modularity, do-it-yourself

1. Introduction

SPACEPLATES is a building system for lightweight shell structures with a planar tessellation, organized in a way so that the planar elements make up the load carrying structure, without the need for further structural elements.

The SPACEPLATES building system applies the late Danish engineer Ture Wester's research on the so-called plate-lattice dualism, and seeks to bring the theoretical advantages of this concept to practical use on built projects. Our interdisciplinary, independent research team seeks to develop new solutions and applications for the system through the design and construction of different types of projects around the world. Our work was first presented in an academic context at the ICSA conference in 2013 [1]. Following a prototype – SPACEPLATES Greenhouse Prototype in 2011 – our team built the SPACEPLATES Greenhouse Bristol in 2012. A prototype for an underwater habitat was built in 2016, and two smaller greenhouses, SPACEPLATES Karlstad and SPACEPLATES KADK has been built in 2018.

Wester states in 1984 that pure plate structures as main load-bearing structures have only been researched to a limited extent. He refers to mid 1970's experiments with 'Fullerdomes' as the origin of his own research, which proved that lattice and plate structures have dual structural and geometrical properties. He also mentions the sea urchin shell as the "possible finest example of pure plate structures".[2]

Copyright © 2019 by Anne Romme, Anne Bagger and Ion Sørvin
Published by the International Association for Shell and Spatial Structures (IASS) with permission.



Figure 1: SPACEPLATES Greenhouse Bristol (2012), SPACEPLATES Greenhouse Prototype (2011), SPACEPLATES Underwater Habitat (2016), SPACEPLATES KADK (2018), SPACEPLATES Karlstad (2018) [Image credit: SPACEPLATES]

The Institute for Computational Design and the Institute for Building Structures and Structural Design at the University of Tübingen (ICD/ITKE), Germany, have done extensive research within the architectural and structural potentials of transferring morphological principles from nature into lightweight construction and the design of segmented shells in architecture. The work builds on biomimetic design parameters based on sea urchins and, more generally, echinoids (the class to which sea urchins belong, along with starfish, sand dollars and other species) [3]

Like the ICD/ITKE team, the team behind this paper has taken up Wester's challenge to extend our structural and architectural knowledge on pure plate structures, using the sea urchin shell as a model. Figure 2 below attempts to describe a genealogical context in which both bodies of research can be seen.

Acknowledging the state-of-the-art, sophisticated research results and scope of the ICD/ITKE team, this paper accounts for some of our team's concurrent efforts and offers an alternative translation of the principles of sea urchin shells to architecture and lightweight structure. The paper ends with a short description of our current work on developing an insulated version of the SPACEPLATES building system, applicable for housing.

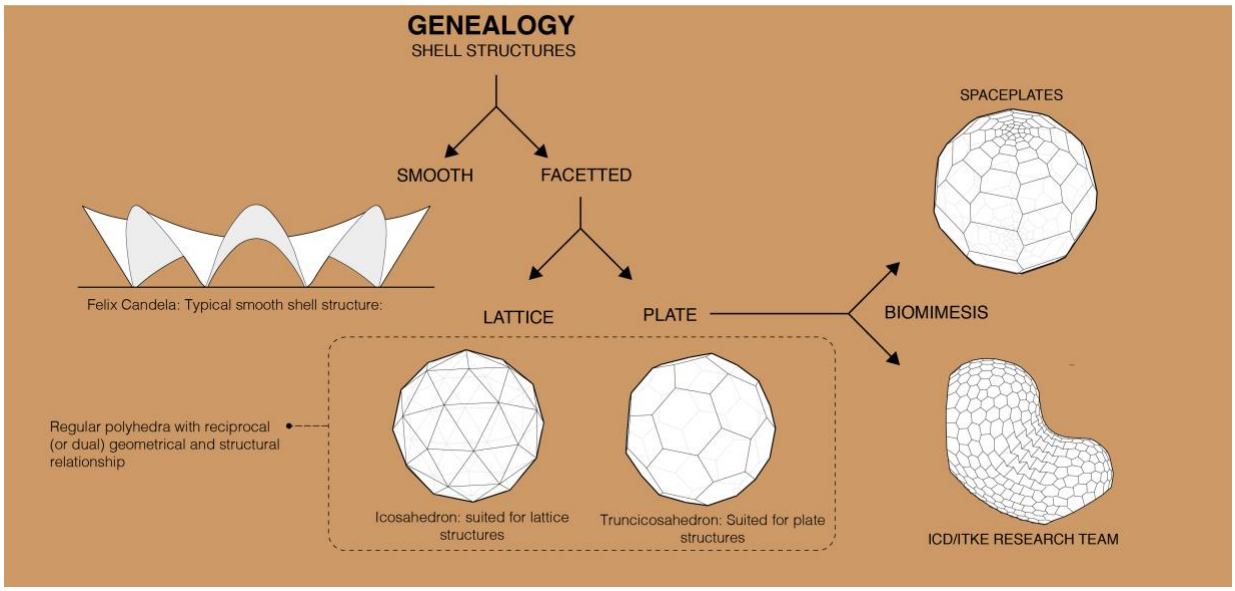


Figure 2: Illustration of how we see the SPACEPLATES building system in relation to shell structures in general [Image credit: SPACEPLATES]

2. Geometry

As Wester and Bagger have accounted for [2][4], pure plate structures are dependent on Y-shaped vertices to function.

Being the one regular tiling of the plane with Y-shaped vertices, hexagonal tiling lends itself to examination. Describing the geometry of the shell of a radiolarian, D'Arcy W Thompson notes that, on one hand their foam bubble like geometry will tend to conform to a regular meshwork on hexagons, but on the other hand, "a strange thing comes to light. No system of hexagons can enclose space; whether the hexagons be equal or unequal, regular or irregular, it is still under all circumstances mathematically impossible. So we learn from Euler: The array of hexagons may be extended as far as you please, and over a surface either plane or curved, but it never closes in". [5] In other words, a sphere cannot be tessellated with only hexagons.

As exemplified in figure 2 above, regular polyhedra solves that problem with the insertion of pentagons regularly distributed amongst the hexagons. In this case, a truncated icosahedron, well known from the soccer ball. However, with our team's ambition to explore the sea urchin as the "possible finest example of pure plate structures", we have been working with other solutions.

Mimicking the growth principle of the sea urchin shell, we have designed geometries (some examples of which are seen in figure 2) consisting of incremental growth of identical parts, except from the two plates at the poles. The first three examples show flat patterns of hexagons and of hexagons combined with squares are topologically transferred onto a sphere, as described by Bagger [4]. In areas with negative Gaussian curvature, (such as the inner part of the torus, see figure 2, fourth example) the hexagons will have concave vertices. The SPACEPLATES Barcelona Pavilion is a built version of the torus geometry.

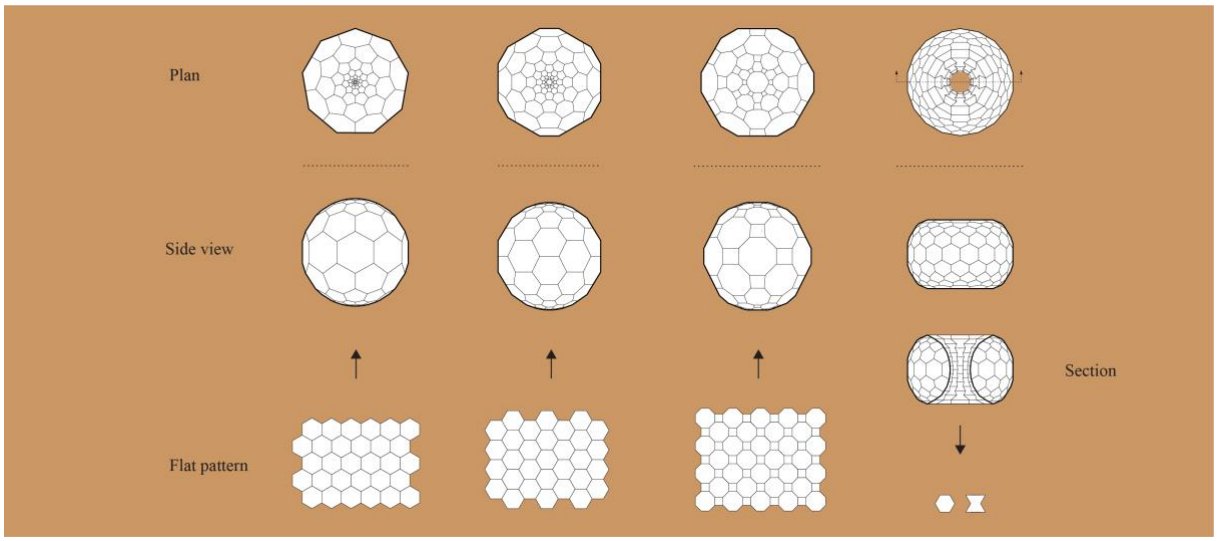


Figure 2: Tessellation principles for SPACEPLATES
[Image credit: SPACEPLATES]

3. Modularity

Constructing shells in manageable segments makes building accessible for many and a playground for experiments. Building geodesic domes piece by piece has empowered many, from Buckminster Fuller's students to counter-culture activists, and lately digital design and fabrication has widened the scope of possibilities further.

With that, the extension from one singular dome to larger structures needs consideration. A simple solution proposed by Pearce [6] is to connect more geodesic domes into composite spaces by connecting similarly shaped plates of two domes. The SPACEPLATES system has moved a step further by introducing a cut through the singular dome, enabling composite structures of the parts. Figure 3 accounts for how cuts at angles not symmetric to the main tessellation direction allows for snake-like compositions.

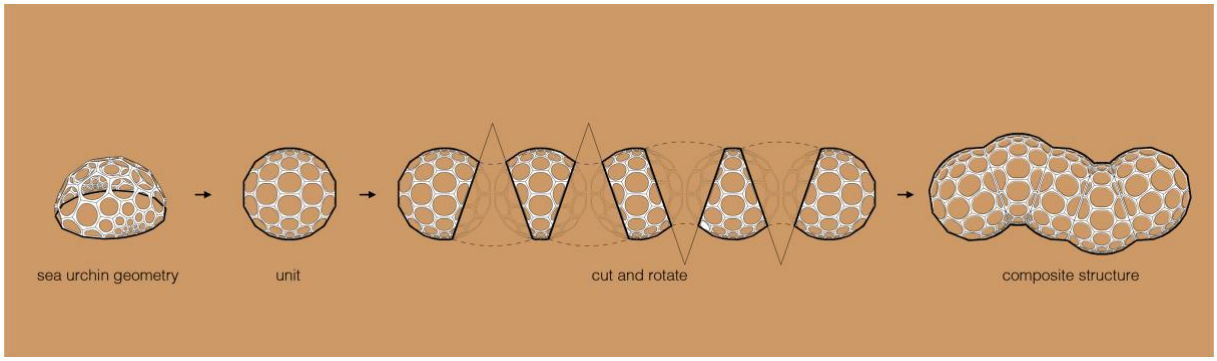


Figure 3: Combination principles for snake-like structure
[Image credit: SPACEPLATES]

Noting that the singular dome is always recognizable in composite SPACEPLATE structures, a distinction between the ICD/ITKE and the SPACEPLATES project becomes clear.
Fields, as Stan Allen has defined them, are inherently expandable. [7] Despite using echinoid shells (the epitome of a finite, enclosed object) as models, both the ICD/ITKE team pavilions and the some of the SPACEPLATES structures expand beyond the singular object. The overall form-giving principles of the pavilions of the ICD/ITKE team seem to represent morphological fields, which could be altered smoothly, given that local tessellation parameters are respected. All building components are in principle differently sized and shaped, as no repetition is built into the geometric system. As opposed to that, the SPACEPLATES structures remain closer to their object origin (spheres) and use additive principles when expansion is needed. SPACEPLATES structures are expanded without substantial morphological transformation. The amount of differently shaped and sized building components is limited due to the copying, rotating and mirroring of geometrical elements within the system. Figure 5 explains the transformation which results in the basic module of the Bristol Greenhouse.



Figure 4: Comparison of expansion principles: Morphological (ICD/ITKE Research Pavilion and Landesgartenschau Exhibition Hall) versus modular (SPACEPLATES Greenhouse Bristol)
[Image credit: ICD Stuttgart University [10] (left and middle) and SPACEPLATES (right)]

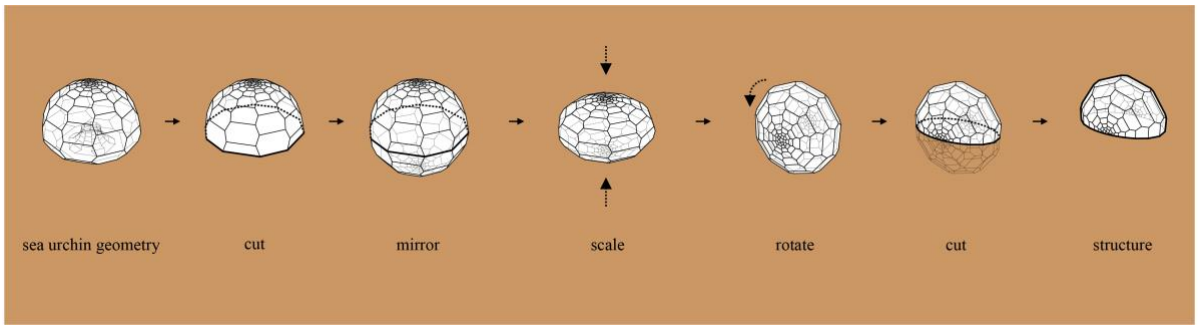


Figure 5: Transformation principles leading to the basic module of the SPACEPLATES Greenhouse Bristol
[Image credit: SPACEPLATES]

5. Materials

Most often, the SPACEPLATES projects use aluminum as the structural material. In the effort to optimize the relationship between enclosed space and use of material, aluminum has an obvious advantage compared to plywood and other wooden materials. Aluminum has considerably greater strength and stiffness than wood, which has made us able to minimize the use of material. The thickness-to-span ratio in the SPACEPLATES prototypes are in the range from 1:1500 to 1:2500, and this does not even account for the systematic removal of material from the middle of the plates. In figure 6 below, the span/thickness ratio and enclosed space/material use-ratio for the Bristol greenhouse is compared to the Landesgartenschau Exhibition Hall. The acrylic plates of the greenhouse are not structural but nevertheless included in the diagram, because the greenhouse could hardly be characterized as a inhabitable structure without them.

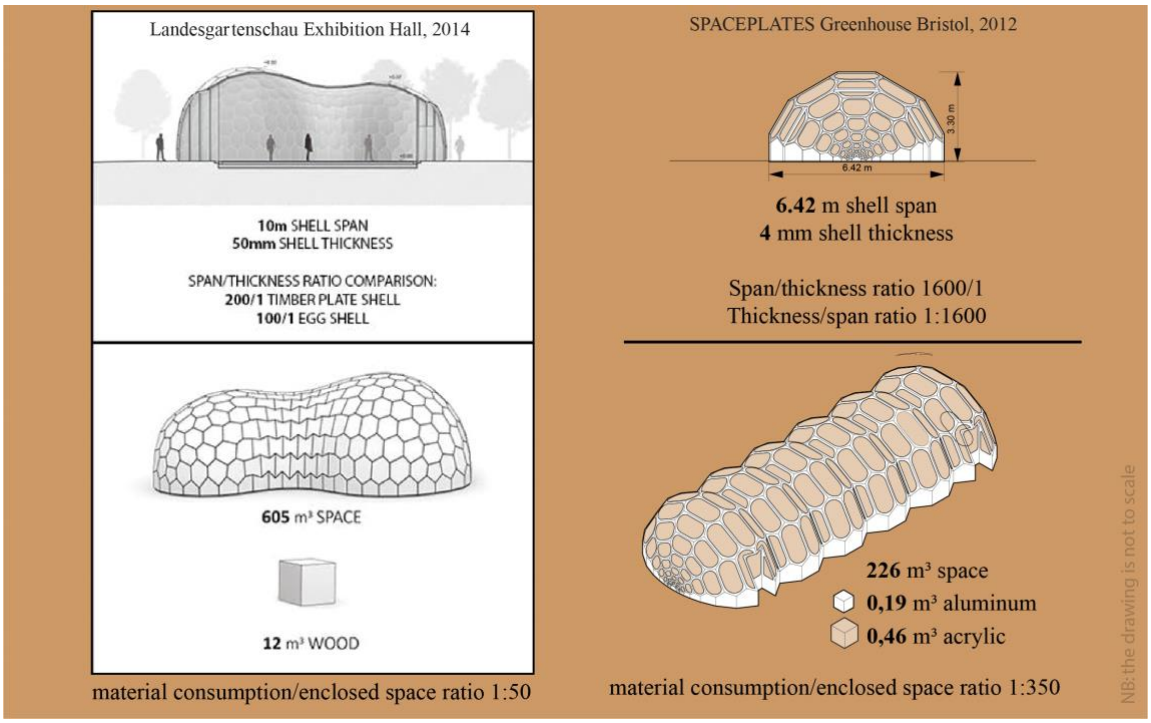


Figure 6: Dimensions of the Landesgartenschau Exhibition Hall
in comparison with the SPACEPLATES Greenhouse Bristol
[Image credit: ICD Stuttgart University [10] (left) and SPACEPLATES (right)]

We consider aluminium to be a sustainable structural material. When the structure's entire life cycle is considered, aluminium performs better than many other building materials due to its excellent recycling abilities, which enable a very long service life. Aluminium is the third most common material on Earth, and the most common metal. It is energy intensive to extract and process, but except from in Asia, most of the energy consumption comes from sustainable hydropower [8]. Furthermore, aluminium is naturally weather-resistant, as its surface oxidizes to form an invisible barrier to corrosion, which makes additional protective surface treatment with chemical compounds unnecessary.
Figure 7 below accounts for details used in the SPACEPLATES projects, particularly how the material is bend without losing significant strength.
While neither wood nor aluminum directly mimics the material capacities of the calcium carbonate shell of the sea urchin, the lightness in relation to strength as well as the durability of aluminum makes a good argument for choosing wood.

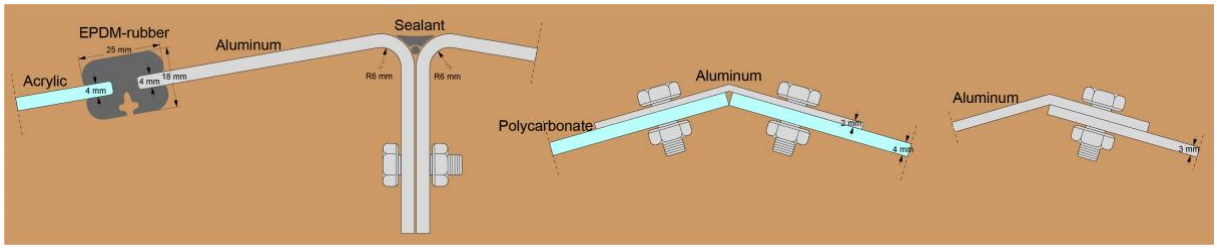


Figure 7: SPACEPLATES Greenhouse Bristol (top), Karlstad and KADK (left), Barcelona Pavilion (right) [Image credit: SPACEPLATES]

6. Do-it-yourself

The architectural historian Christine Macy has written about the importance of Buckminster Fuller's domes as catalysts for in 'a whole generation of ecological architecture'. Beyond Fuller's own experiments with geodesic domes and different structural principles, thousands of domes were built in communities formed by American counter-culture of the late 1960s and onwards. The geodesic dome became a strong signifier for a different way to live in a new kind of architecture, but was also a concrete manifestation of an ecological system. Fuller's pragmatic do-it-yourself approach and ambition to use technology to optimize our lives is taken up most fully within this framework of personal activism and dome construction, argues Macy [9].
We like to think that the SPACEPLATES project pays respect to this ethos of do-it-yourself activism. We aim at using contemporary technology to enable people to build structures for themselves which they could not otherwise have built. The geometries and tessellations we use are constructed in 3d-modelling software (Rhino), and the parts are fabricated on CNC-controlled machines. But at the same time, we make sure that all structural members are sized to enable people to handle parts without large machinery. It is an important design principle that anybody, with or without technical skills, can build the structures using only hand-held tools.
We like to work with local community groups or individuals outside large institutional frameworks. Our greenhouses have been used in community gardens, a smaller Swedish

electronics company and by our local student association, and the underwater habitat was developed together with a self-/community-funded Australian marine biologist.



Figure 8: Wood-framed geodesic dome built in 1953 in Massachusetts by Buckminster Fuller and MIT students (left), the SPACEPLATES Karlstad greenhouse built in 2018 with employees of Special-Elektronik (right)
[Image credit: MIT Alumni (left), SPACEPLATES (left)]

8. Insulated SPACEPLATES

The concept of pure plate shells lends itself well to insulated buildings, as the thin, structural layer can also serve as the tight inner layer in a sandwich like build-up.

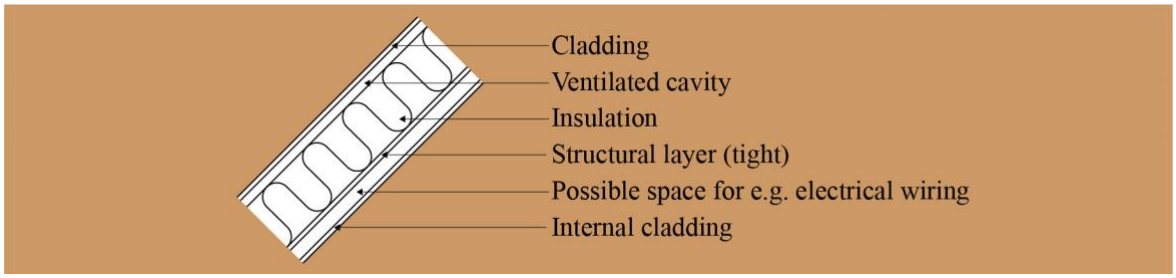


Figure 9: Diagram of insulated SPACEPLATES model
[Image credit: SPACEPLATES]

The building elements have different levels over the thickness, serving different purposes:

- An innermost cladding for aesthetics and acoustic purposes, possibly with a cavity for hiding electrical wiring.
- A thin, tight, load-carrying layer, consisting of aluminium plates with watertight, load transferring connections.
- A layer of insulation, without the heat loss of structural elements penetrating across the thickness.
- An outer weather resistant cladding, with a ventilated backside.

Windows can be incorporated into some of the panels, located for optimal daylight conditions, visual outlook, solar gain, etc.
Since this type of structure will be extremely light, it will be a benefit to introduce thermal mass to the interior spaces, in order to provide adequate thermal stability. For instance, a tiled floor will take up heat during warm hours in the day, and slowly release it during the night.

8. Conclusion

The SPACEPLATES project is in several respects comparable to the Landesgartenschau Exhibition Hall by the Institute for Computational Design and Construction (ICD) at Stuttgart University and it is relevant to see both projects as part of a genealogical lineage of thin shell structures. Both projects have taken up Ture Wester's challenge to explore pure plate structures in general and the sea urchin's geometrical and structural characteristics in particular in the attempts of perfecting the art of constructing modular shells with optimized relationships between material use and enclosed space. Both projects have also taken advantage of contemporary digital design and fabrication technologies to optimize processes and designs, although in very different scopes.

The SPACEPLATES Project's use of aluminum as a structural material enables the optimization between enclosed space and amount of material. SPACEPLATES structures are very thin compared to other examples of pure plate structures. They are characterized by an additive expansion principle, which reduces the amount of differently shaped and sized modules and amount of complexity in the assembly process. Furthermore, modules are kept at a handy, manageable size. While the project is entirely dependent on the use of digital technology to facilitate the geometries and precision within the fabrication, it nevertheless aims at minimizing complexity to maximize the end-user's agile participation.

References

[1] A. Romme, I. Sørvin, A. Bagger, "SPACEPLATES Building System", in *Structures and Architecture - Concepts, Applications and Challenges: Proceedings of the second international conference on structures and architecture*. ed. / Paulo J. S. Cruz, C R C Press LLC, 2013

[2] T. Wester, *Structural Order of Space*, Copenhagen, 1984

[3] T.B. Grun, L. Koohi F. Dehkordi, T. Schwinn, D. Sonntag, M. von Scheven, M. Bischoff, J. Knippers, A. Menges, J. H.Nebelsick, "The Skeleton of the Sand Dollar as a Biological Role Model for segmented Shells in Building Construction: A research Review" in J.Knippers et al (eds.), *Biomimetic Resarch for Architecture and Building Construction, Biologically-Inspired Systems 9*, Springer International Publishing, Switzerland, 2016

[4] A. Bagger, *Plate shell structures of glass* – Studies leading to guidelines for structural design, Ph.D. thesis, Lyngby 2009.

[5] D'Arcy W Thompson, "on Spicules and Specular Skeletons" in *Form Follows Nature*, Rudolf Finsterwalder (ed.), Springer, Wien, 2011

[6] P. Pearce, *Structure in Nature is a Strategy for Design*, 1980

[7] A. Stan, "Field Conditions" in *Points + Lines, Diagrams and Projects for the City*, Princeton Architectural Press, 1985

[8] World Aluminium, "Life cycle inventory data and environmental metrics for the primary aluminium industry – 2015 data", 2017

[9] C. Macy, "The Geodesic dome as a metaphor for expanding consciousness" in: *On Growth and Form, Organic Architecture and Beyond*, P. Beesley, S. Bonnemaison(eds.), Halifax, 2008

[10] https://icd.uni-stuttgart.de/?p=11173, accessed on June 21/2019

Proceedings of the IASS Annual Symposium 2019 – Structural Membranes 2019
Form and Force
7 – 10 October 2019, Barcelona, Spain
C. Lázaro, K.-U. Bletzinger, E. Oñate (eds.)

Structural bending system. A constructive possibility for geodesic domes.

Hugo DE MATOS*, Natalia TORRES[a], Marcelo NASCIMENTO[b], Structural Morphology in Architecture SMIA[c]

*MSc. Professor at the Pontifical Catholic University of Minas Gerais
PUC MG School of Architecture and Urbanism. Claudio Manoel Street, 1149. 30140108. Belo Horizonte. Brasil.
hugoamatos@gmail.com

[a] PhD Candidate. Polytechnic University of Catalonia. Barcelona Tech.
[b] Architect graduated from UFMG (Universidade Federal de Minas Gerais).
[c] Research group. LITA (Laboratory of Innovation and Technology in Architecture - UPC)

Abstract

This paper describes a design method based on active bending systems for the configuration of a geodesic dome. The analysis and validation of its constructive viability were carried out from a 1:1 scale prototype built in the facilities of the UNA University Center, in the city Bom Despacho - Brasil. The structure was assembled by the students of postgraduate course in architecture, who learn in practice the real behavior of these typologies. The project was based on the principles of reciprocal frame structures and on the ability of materials to bend in order to achieve the proposed form. The pavilion is the product of the "non-conventional" structures workshop given in Brasil by SMiA (Structural Morphology in Architecture - research group based in the Universidad Politécnica de Cataluña). The activities were developed in the subject of ephemeral structures belonging to the program of architecture and interior design promoted by UNA and supported by the AnimaLab (Digital Fabrication Lab). The objective of this research is to present the processes and results obtained as a way of evaluating the possibilities offered by bending systems in the construction of geodesic domes. The pratice intends to explore the coplanar joints used in the construction of reciprocal structures. Finally, it is proposed to highlight the importance of using algorithms systems to assist the architect in making decisions.

Keywords: Deployable structure, scissor-type system, modular, transformable, lightweight construction, conceptual design, morphology, wood structures, geometry.

1. Introduction

The reciprocal frame structures are constructive systems in which the stability of the cluster is achieved by mutually supported elements. This combination requires at least three sloping bars so that the structure could sustain itself.

These typologies have its origin in the prehistoric constructions as the Neolithic pit dwelling, the Eskimo tents, the North American tepees and the Asian yurts. They have been developed through history and being applied in different uses such as the construction of housing, ephemeral installations and coverings of large extensions.

One of the first applications of these systems from the numerical study of geometric possibilities can be related to Leonardo da Vinci in its bridges and geodesic domes. The main objective of these

Copyright © 2019 by Hugo DE MATOS, Natalia TORRES Marcelo NASCIMENTO.
Published by the International Association for Shell and Spatial Structures (IASS) with permission.

projects was designing lightweight spatial structures which could be rationally and quickly assembled, even though the calculations were performed in an analogical way.

The technical evolution of these structures stood out with the proposals of important names in this area: John Chilton Orlando Ariza, Vito Bertin, Olga Popovik and others [1]. With the advance in the design and manufacturing processes provided by digital technologies, the reciprocal framework systems acquire a higher level of exploration in terms of geometrical possibilities and use of different materials.

The most common methods for project of synclastic surfaces are the combination of regular polygons modules according to the desired volumetry and structural characteristics of the construction. With the advance of digital technologies, the formal exploration becomes more dynamic once design proposals and structural behavior can be analyzed simultaneously.

The present article was based on the geometric study of the dome of Leonardo da Vinci to propose a different configuration in which the bars could work the structural bending concept from the possibilities of the chosen material. For the construction of the prototype, plywood was used and the curvature of all the parts was achieved manually by participants of the activity.



Figure 01: reciprocal frame structure | coplanar joints | prototype scale

2. Basic concepts | dome geometry

The basic geometric configuration to generate a dome is the icosahedron (regular polyhedron 20-sided). What defines the transformation of the polyhedron into a geodesic is the subdivision of its sides into smaller triangles realized in three-dimensional way.

The change in the length of the inner lines and consequently the angles between the elements, allows the shape of the polyhedron to approach of a sphere. One of the most important characteristics of a dome is its frequency, which is generated by the number of sides that the icosahedron is divided.

Although the combination of reciprocal modules allows the creation of different forms and volumetric variations, the activity focuses on the study of a regular geodesic dome. In this way, basic rules of geometry are needed for the understanding of reciprocal systems and their structural behaviors.

In order to stimulate spatial perception and guide the proposal of different compositions, the platonic solids were first studied. Physical models were assembled on reduced scales to study the structural morphology of these systems and explore the combination of reciprocal modules.

These systems have stability principles that need to be followed in order to be considered a reciprocal structure. A single frame can then be replicated to create a mesh, where all the elements are connected and supporting each other. The meshes can be designed by repeating one pattern but also from the fusion of several patterns.

Understanding the geometry of the reciprocal frame structures and the parameters that define it is essential to conceive and construct larger systems. Each element is subject to forces of compression, bending moments and shear axial forces [3].

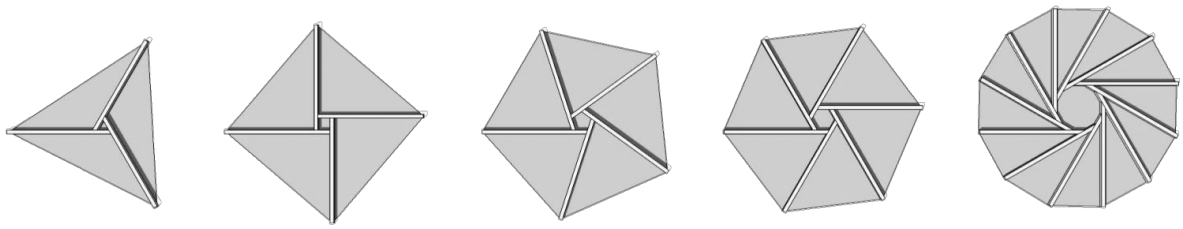


Figure 02: basic geometry concepts | polygons

3. Practical activities | bending concept

The first practical activity consisted in the assembly of three domes with different frequencies. The measures used were based on the information provided in the "Taff Goch" web platform, with changes of dimensions and topologies. Each group received a map and the pieces related to its prototype to begin the assembly of the domes that would later be completed to form the reciprocal spheres.

Although all models were based on modules of regular polygons, each one had a geometric solution with bars of different sizes and varying distances between holes. The assembly sequence of the modules directly influences the shape and final strength of the structure since it works under the principle of reciprocity.

During the workshop assembly strategies were explored in order to prove their importance in the design of a reciprocal structure. At the end of the practice the basic principles of geometry applied in this type of construction were understood, as preparation for a next stage with a higher level of complexity.

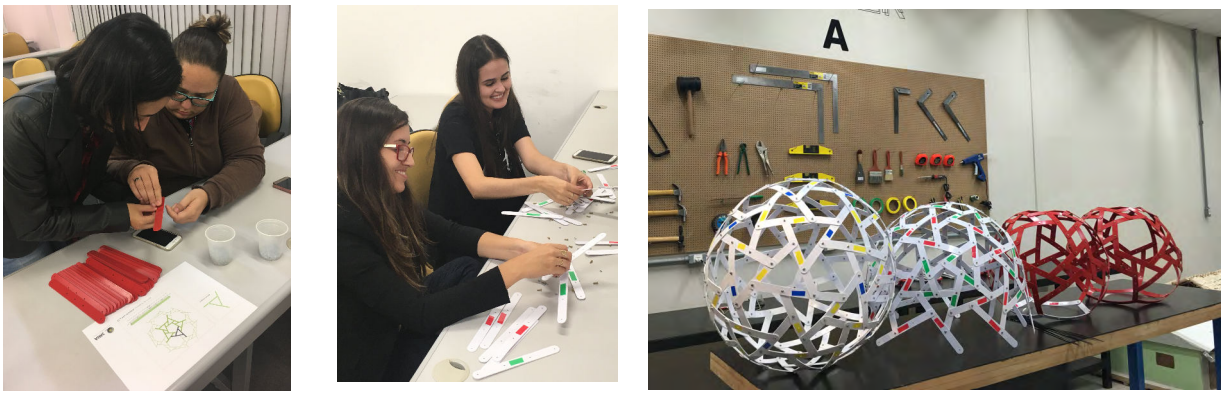


Figure 03: practical activity | reciprocal domes and spheres

The second activity was based on the project build at the end of the workshop. This practice was divided in three groups due the complexity and quantity of pieces of the model. All prototypes were equals with six types of bars, different lengths and holes.

In order to facilitate the understanding of the relationship between the parts and to establish an assembly order that would be replicated in the 1: 1 scale prototype, all components were marked with colors. The same identification of elements was made in the wood components of the prototype.

All the bars used during the practical activities were made from plastic sheets cut in a CNC router. From a material that allows the simulation of curvature present in the proposed construction, the students could perceive the conformation of a geodesic dome from the concept of active bending.

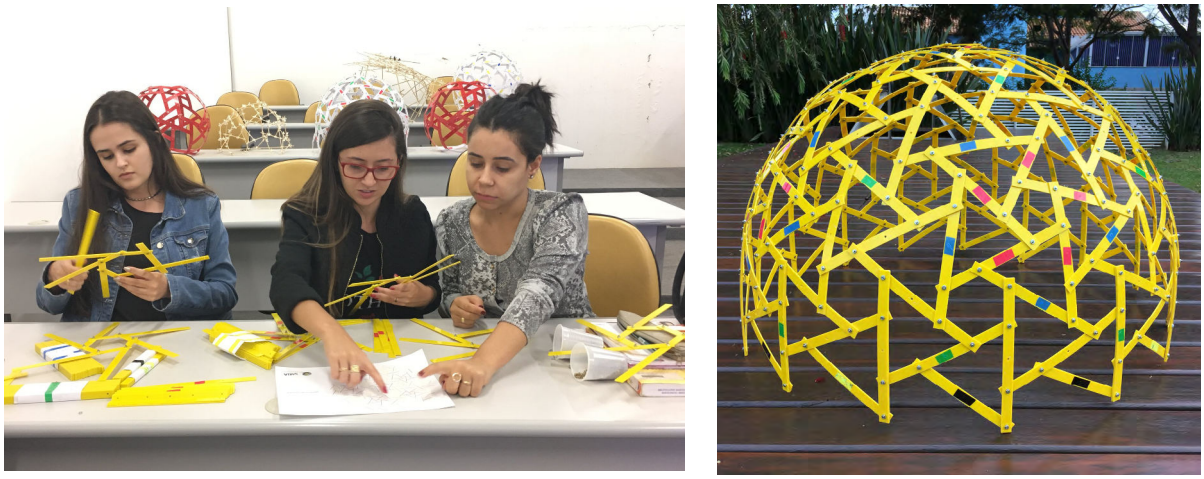


Figure 04: practical activity | prototype model

4. Prototype | Fabrication and assembly

As product of the workshop a geodesic dome was built in the 1:1 scale. The constructive process challenged the students with the change of scale, type of material and assembly mechanisms applied in the wooden structure. The group of fifteen people was divided into five teams responsible for assembling the modules and grouping them in a predefined order. The dome was assembled in twelve hours.

For the construction of the prototype, Pinus wood, bolts, nuts and washers of 8mm were used. The pieces were received cut, marked and with the holes done according to their position in the structure. The project consists in a 4m diameter dome with a maximum free height of 2.7 m, composed by 180 bars of different sizes and intersection points.

The patterns used in the construction of this dome are based on the geodesics developed by Leonardo Da Vinci in "*The Atlanticus Codecus*". The length, number of bars and the position of the joints were defined from the geometry of regular polygons, in a 4V frequency established.

The coplanar bar solutions aim to avoid the displacement of the components very common in systems that uses tubes. In the construction of the prototype were used 12 mm thickness plywood slats, connected by screws, nuts and washers compatible with the constructive details.

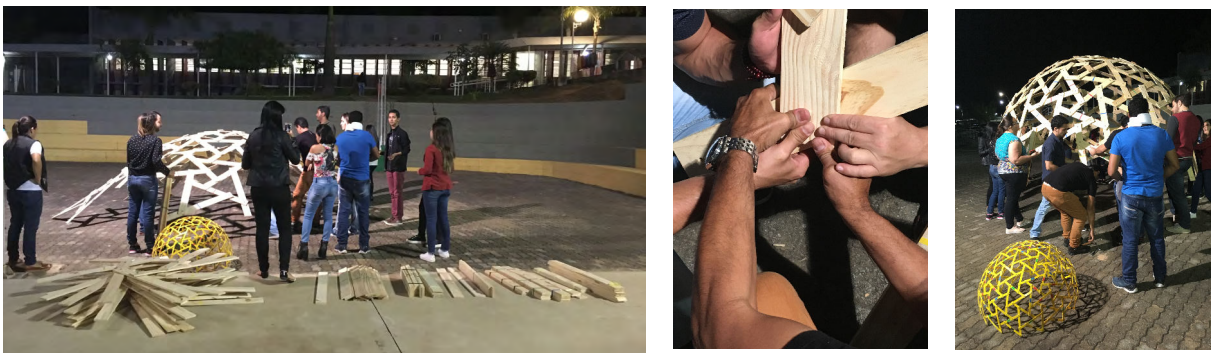


Figure 05: reciprocal modules | assembly

The structure was assembled upside down for a better handling of the parts during the process of joining the modules. By forcing the pieces of wood to reach the necessary curvature for the configuration of the dome the students could understand in practice the concept of bending in a real structure.

As illustrated in figure 06, the structural stresses acting on a dome cause it to open, requiring a locking ring at the base to stabilize and stiffen the geodesic. In the built prototype a duplication of parts was made in the base for this locking to be done by increasing the weight in the lower components.

The practical activity completed a design-to-assembly workflow for reciprocal frames systems based in the Leonardo Da Vinci`s domes. An algorithm pattern was created from an existent solution to explore the formal possibilities and adapt the structural mesh that best fits with the wooden slat's dimensions.



Figure 06: assembly | base ring | prototype

4. Bending | Structural behavior

The dome was calculated to withstand the efforts related to its own weight and the centrifugal forces present in this type of geodesics. A reciprocal frame structure assembly forms a closed circuit of forces which on its own guarantee stability and stiffness of the structure.

The bending moments generally increase with the size of the inner opening that forms the circulation center, however a bigger slope of the beams can also increase it. (Larsen O.P., 2008). According to the size of the bars and their bending capacity, a configuration of geometric modules was defined to attend the simulations carried out in the parametric model.

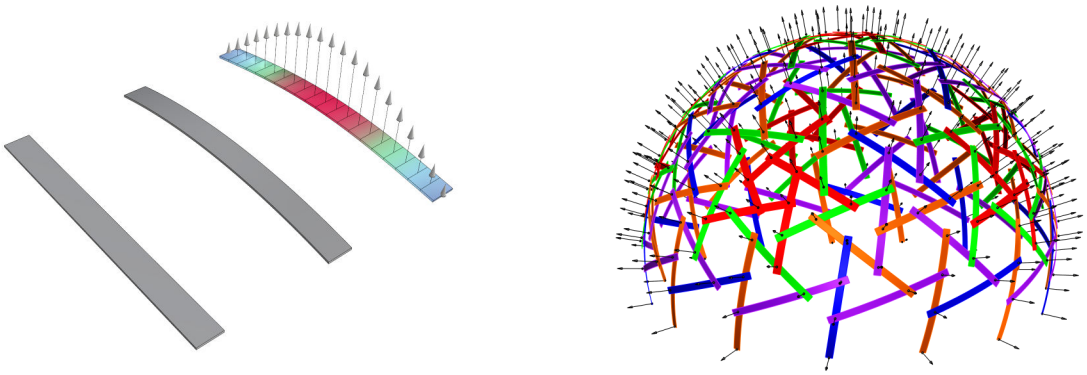


Figure 07: active bending | structural efforts

Before the assembling, a structural analysis was made with Millipede, a Grasshopper plugin which works based on a physical simulation of linear elastic elements. A parametric model was created in Rhino and converted into a mesh that was subdivided into regular polygons. Those parts can be understood as finite elements by the algorithm during the calculation process.

The first step of the analysis was checking the way the bars react when a bending force is applied on them and the direction and magnitude of the resultant forces. The bars were tested on a simple bending simulation, where the results have been essential for the comprehension of the correct positioning of the vector forces during the analysis of the entire frame.

As illustrated in figure 7, the dome is composed of 6 different types of wooden bars which are subjected to varied curvatures according to their position in the structure. The graphic represents this size variation and bending efforts by color. The arrows show the anchor points, direction and magnitude of the forces applied on the structural model during the simulation.

In figure [a] the deflection amount represents the spatial displacement of the structural elements and their subdivisions when forces are applied. The figure [b] shows where the elements of the structure reach a critical value based on the Von Mises yield definitions, also known as the maximum distortion energy criterion. Lastly, the figure [c] shows where the minimum a maximum value of the bending moment is distributed along the structural elements.

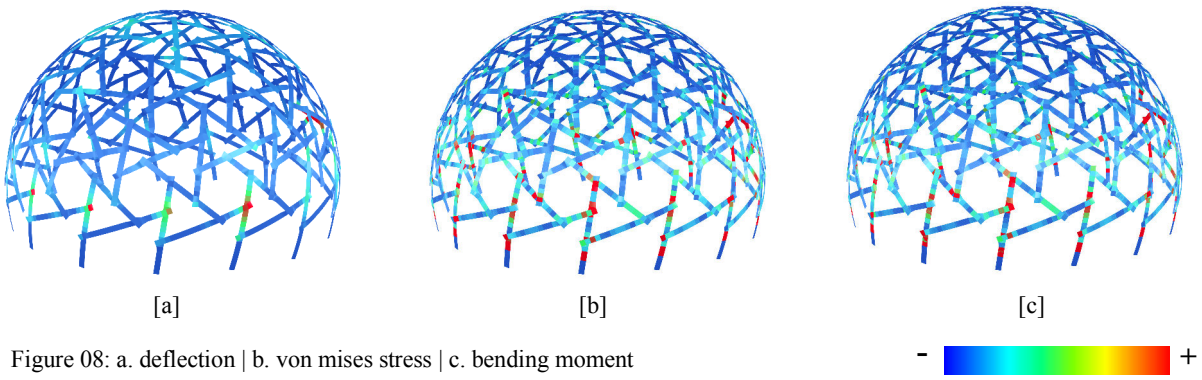


Figure 08: a. deflection | b. von mises stress | c. bending moment

5. Final considerations

This document summarizes a range of information on the construction of geodesic domes, proving by prototyping in the 1: 1 scale a possibility of use the active bending applied in a reciprocal frame system. As a conclusion it's possible to say that the structural behavior is successful thanks to the geometry, the material and its own flexion beyond the digital technologies of structural simulation.

The regular polygons geometric method provides a simple and practical design strategy for the configuration of geodesic domes, generating the possibility of creating multiple combinations through the parametric model. From the algorithm created based on Da Vinci`s domes, it's possible to load specific data in order to adapt the structure to a required condition.

On the fabrication aspects, the CNC router was extreme important in the cut of the wood pieces for the prototype and in the plastic plates for the models. Although time optimization was achieved in the production of the pieces, all color markings were handmade, which made the process a bit slower.

The assembly of the model following the same piece marks of the dome provided a clearer understanding of the constructive order, besides serving as a small-scale physical reference. The geodesic dome is an application of lightweight structures used to introduce and diffuse the constructive viability of reciprocal frame systems from the use of sustainable materials.

The solution of coplanar joints makes the structure more stable since it prevents recurrent displacement in tubular parts made without axles locking. The use of washers is fundamental for the performance of the connections considering the force that the bolt exerts on the wooden bars.

Finally, it is possible to consider the workshop as a successful activity, based on practical and theoretical knowledge, which has reached the proposed objective of evaluating the possibilities offered by bending systems in the construction of geodesic domes. From hi-tech design methods and low-tech manufacturing processes used in prototype construction, different design strategies were explored in order to inspire students to investigate geometrical possibilities and applications of the digital tools.



Figure 09: prototype | reciprocal frame structure

References

[1] O. Larsen, *Reciprocal Frame Architecture,* Burlington, 2008.

[2] E. Tunç. *Shaping a timber reciprocal frame structure.* Delft University of Technology, Department of Architecture, 2015.

[3] I. Ghiuzan. *Reciprocal Structures*. Westminster University School of Architecture, 2018.

[4] A. Tedeschi. *Algorithms Aided Design: Parametric strategies using Grasshopper*, English edition 2, 2018.

[5] Pugnale A, Parigi D, *"Three-dimensional Reciprocal Structures: Morphology, Concepts, Generative Rules"*, Proceedings of the IASS-APCS 2012.

Proceedings of the IASS Annual Symposium 2019 – Structural Membranes 2019
Form and Force
7 – 10 October 2019, Barcelona, Spain
C. Lázaro, K.-U. Bletzinger, E. Oñate (eds.)

Textile Informed Structures - How to Braid a Roof , Translating the logic of textile structure into the scale of architecture

Linda WALLANDER and Malin BORGNY*, Delia DUMITRESCU[a] ,
Erica HÖRTEBORN[b] , Mats ANDER[b]

*Chalmers University of Technology, SE-412 96 Gothenburg
vlinda@student.chalmers.se and borgny@student.chalmers.se

[a] University of Borås, The Swedish School of Textiles
[b] Chalmers University of Technology, Department of Architecture and Civil Engineering

Abstract

There is a great variety of textiles materials, both in terms of the behaviour of the fibres they comprise and the assembly methods used to construct them. Hence, the definition of textile is expanded nowadays from including only conventional fabrics to encompassing surfaces with structures that follows the logic of textiles.[1] One can then refer to textile as a repetition of bindings, or joints, forming a non-hierarchical surface. Analogies between classical textile assembly methods of interlacing threads (triaxial weave and bobbin lace) and architectural structural systems are explored in this research. Similar to the work of Snelson the internal structural logic is identified by the joints used, and these typologies are mapped onto structures.[2] The resulting modules aim to be used for the assembly of structures in the scale of architecture. Like the assembly logic of the textiles, these structures have the potential to grow in all directions depending on spatial requirements while still retaining some kinetic properties. Subsequently, the result proposes two concepts: firstly a tensegrity weave structural system- combining triaxial woven textiles and tensegrity; secondly a reciprocal lace system where a basic pattern of bobbin lace is mapped onto reciprocal structures. The final concepts propose intriguing load bearing systems that illustrate the possibility to design and construct temporary structures able to seamlessly span irregular spaces.

Keywords: Tensegrity, Textile Structures, Reciprocal Structures, Weave, Bobbin Lace

1. Textile architecture

Despite of the long history of textiles in architecture, conventionally textiles have been seen as a temporary, incendiary, fragile, unstable material with high maintenance and low performance. However, examples of earliest nomadic architecture demonstrate that textiles are one of our oldest building materials. The tent, as first dwelling space, used tree trunks and branches as support, and animal hides as coverings. Later on the construction of own woven fabrics which expanded the variation in functional properties and décor of the dwelling covers, replaced the use of animal covers to textiles [3] Hence, Semper's theory of textile architecture promoted the flexible woven mesh as a conceptual tool in the field of architecture. In his treatise The Four Elements of Architecture, he redefined the notion of wall to spatial enclosure rather than structural membrane. By drawing parallels between the dress and the wall; he defines the building envelope as an example of clothing and types of veiling. [4]

Nowadays, the development of advanced manufacturing technology and materials enables a new interpretation of textile logic related to architectural design. The structural design of the Pompidou Metz demonstrates that the logic of textile constructions can be translated to the scale of architecture. Here a surface mapping method is developed to explore basket-weaving, or triaxial weave, on a larger scale. This method enables the simulation of flat ribbons wrapped over an arbitrary surface. [5]

Copyright © 2019 by Linda Wallander, Malin Borgny, Delia Dumitrescu, Erica Hörteborn and Mats Ander
Published by the International Association for Shell and Spatial Structures (IASS) with permission.

Complementary, other research examples develop methods to interpret and translate the logic of knitted structures to digital manufacturing processes. Hence, Palz's methods illustrate a new forming process where knitting topologies are re-interpreted for architectural design (Palz, 2014). Likewise, the research in "Beyond the Basket Case" explore triaxial weave handcraft, kagomé, and how this knowledge can be extended towards the fabrication for interlaced lattice structures which can be supported by computational methods of representation. The work flow proposed by Eyres's research supports the design and form-finding process which can be generated by using triaxially woven structures and straight strips. [6] A complementary perspective can be to interpret the logic of textile structures as the modular systems which are formed by flexible units, e.g. joints, and where stiff elements are assembled in a repetitive manner following the textile logic. These can then be made as a reciprocal frame and extend further the analogy to weave and braid systems. Subsequently, reciprocal frame units can be made both as clockwise and anti-clockwise turned units. One early example of a reciprocal structure and weaving analogy is the da Vinci's bridge [7]. da Vinci's bridge is an example of a plain weave interpretation where the threads have been exchanged for repetitive stiff elements. The bridge has in one direction continuous elements and in the other direction shorter elements which are stabilised reciprocally by three of the continuous elements in turn. Furthermore, Snelson's work, drew parallels between weaves and tensegrity structures already in 1960. [2] His system is formed by thin walled aluminium tubes which could be connected to monofil tension lines; in this way he creates a planar weave tensegrity piece. Snelson describes the notion of tensegrity as binary similarly tension and compression forces. All tensegrity structures have alternating rotating directions which he finds similar to the behaviour of the woven structures. He considers each weave being formed by the adjacent polygons which rotate right and left, alternately as a chess board, as in tensegrity. This principle is fundamental to how tensegrity functions. [2] The analogy between modular structure systems and textiles becomes a central scope for this research. The current paper is a condensation of the work conducted in the master thesis of the authors, Textile Informed Structures - How to Braid a roof. [8]

2. Mapping Textiles onto Structure

In the braiding construction the threads interlace by going over and under the neighbouring threads and then over again. When analysing the structure of the basic braid of three threads, a pattern of two rows of triangles can be interpreted; whereas expanding to a braid of four threads or more, both rows of triangles and squares form the pattern of the braid. By analysing several braided structures, we can say that the edge rows in the geometrical interpretation of a classic braid will always be comprised of triangles, and for each thread that is added, there is an extra row of squares in between. In a close up perspective of the braided structure and only looking at one of the triangular sections we interpret that the way the thread goes over and under the next thread displays a similarity to a reciprocal module of three rods. Expanding this interpretation to the geometrical pattern of a braid, each polygon could be replaced by a reciprocal module with the same number of elements and number of sides in the polygon. As is shown in figure 1 every other row contains a module which is turned in the reversed direction. When assembling these modules to a structure, the edge rods in one module which are parallel to the next module's edge, are removed as it represents the same thread which is superfluous.

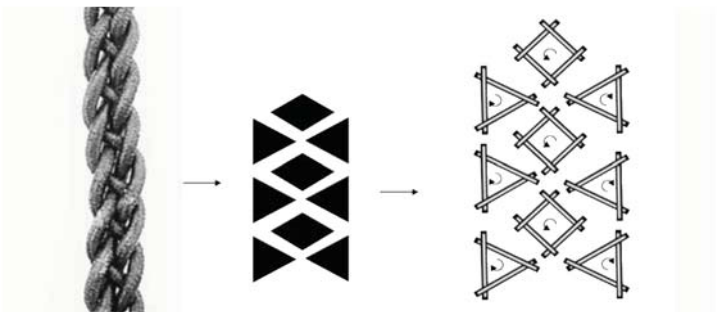


Figure 1: Geometric analysis of a braid, mapped into a modular structure.

The logic of tensegrity and reciprocal structures share important features which are relevant when applying in this method of mapping the logic of braiding. The geometrical properties of tensegrity modules and reciprocal frames show significant similarities even if they are different in terms of structure system category and thereby manner of load carrying. Therefore the same mapping of textile into reciprocal structures may be utilised for tensegrity, since a tensegrity module can be generated from a reciprocal frame. Both types of modules are based on a circular logic where the structure is a helix turned in two directions: clockwise or counterclockwise. Without this feature, the translation of braids (and weave and lace) with cells turned in reverse directions, would not be possible. Similarly, the interpretation which is done for reciprocal structures may be applied when developing a tensegrity structure. Each polygon may be replaced by a reciprocal frame as well as a tensegrity module, using the same number of elements as the sides of the polygon. Having the main focus on the exploration of tensegrity and reciprocal structures, the geometric interpretations are analysed with regard to possible parallels to these structural system modules.

Similar to the analysis of the braided structure, a geometric interpretation of a triaxial weave can be generated where each geometric shape represents a unit of the triaxial woven structure, see figure 2. In this geometric interpretation the direction and shapes formed by the threads decide the form of the polygons. In the tai-axial weave the joints used are illustrated by primary shapes, e.g. triangles and hexagons. The pattern of the interlacing threads and their internal relation, i.e. which goes over and under which, may be translated into a pattern for the design of the tensegrity structure. As for the braid - each polygon from the geometric interpretation may be mapped to the corresponding reciprocal or tensegrity module with the same number of elements as number of sides in the polygon. Hence the corresponding structures of the triaxial weave are modules of three and six elements. In the triaxial weave the turn of the modules depend on the form. All three-modules are turned in the same direction and the six-modules are turned in the reversed.

The second textile assembly method selected to be analysed is a plain hole ground lace. The process begins with a geometrical interpretation of the lace structure. An additional line adds to the polygons for the geometrical visualisation of a twist of two threads. The same pattern of threads passing over and under is used due to the similarities of the structure of bobbin lace and braiding. The polygons in the geometrical interpretations may be exchanged to reciprocal modules. The line, representing the twist, on the other hand can not be replaced by a single twist module.

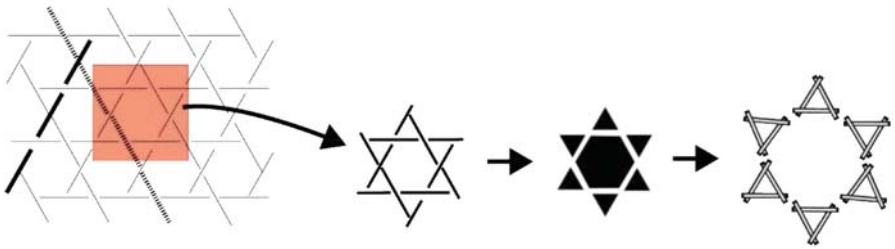


Figure 2: Triaxial weave analysis, joint resembled to reciprocal module

This twist cannot be directly translated into a reciprocal module due to the fact that it only comprises two elements which cannot be translated to a reciprocal frame. In the physical models, this has been dealt with by using the same diagonal rod through two neighbouring triangles.

The interpretations of the triaxial weave, and further on the bobbin lace, yield understanding of the geometry of joints used in the textile assembly. The repetition of the pattern of abstracted structure illustrates the repetition of joints within the textile construction.

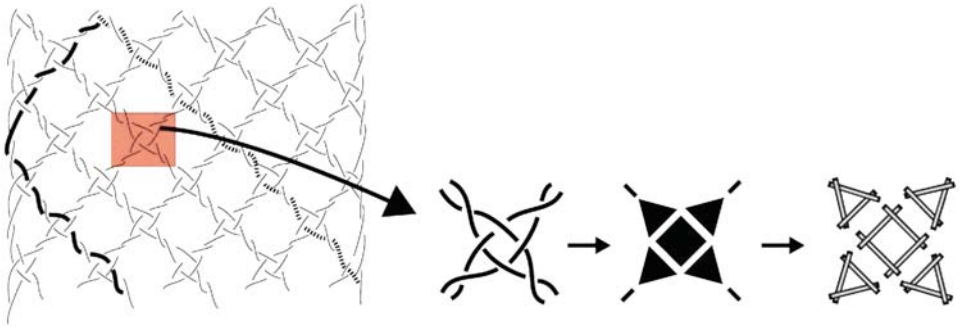


Figure 3: Bobbin lace analysis, joint resembled to reciprocal module

2.1 Assembly of Tensegrity Textiles

Following the logic of the braided structure which is divided into units and mapped to reciprocal or tensegrity modules, each neighbour unit is turned in the reversed direction due to the interlacing of the thread; a similar interpretation can be made on triaxial weave structures. The alternating directions in a weave is already explained by the fact that the same thread is shared in multiple cells, figure 2. Mapping of the weave onto tensegrity results in one of the compression elements being the same or shared between neighbouring modules, as shown in figure 2. The assembly of tensegrity modules is possible if compression parts are attached to the middle of the tension parts of the next module. This enables the units to "twist" in the same way as if they were individual modules. Without this rotation of the module, a stable force equilibrium cannot be obtained. The binding of a triaxial weave can be mapped in the same manner. In the figure 4 the assembly of one tensegrity triaxial weave joint is shown. From the geometric interpretation of the triaxial weave, it was evident that this type of weave comprises both hexagon and triangular elements. When mapping this to a tensegrity system, the binding includes six modules of three lattices on the outside and the hexagon module in the middle. As previously explained, when assembling tensegrity, the shared thread in the weave becomes a shared compression element. Therefor the hexagon module in the middle is not built up before assembly. The clockwise turned hexagon module is instead a result of the assembly by the one compression element towards the middle in each triangular module, see figure 4. The previous section demonstrates that triaxial woven structures and braids may be build up as both reciprocal and tensegrity structure systems. The bobbin lace can be translated in a similar way with adjustments previously mentioned regarding the twist of the thread in the original lace.

3 Concept Development

There are many common features between textiles and the mentioned structural systems. To proceed, two concepts will be presented. Each concept is based on an interpretation of a textile combined with a structural assembly method. Each concept is derived in the meeting point between textile and structural mechanics. The two concepts that will be presented are:

- Tensegrity structure – Triaxial weave
- Reciprocal structure - Bobbin lace

The simple tensegrity module of three rods, as described above, is assembled into a triaxial weave and bobbin lace is braided by stiff elements resulting in a reciprocal structure. Each concept is compiled of single modules which, as in a textile, may be assembled in multiple directions in the 2D plane. Using digital analysis, the assembling of the concepts and evaluation of them will be carried out. The aim is to translate the logic of textiles into larger scale structures, to show that there is an area of use for these kinds of structures and to show whether or not these are feasible to build. Hence, detailed solutions of joints and final sizing of members are not included. The digital models of the different concept have been developed digitally using the Rhinoceros© interface and Grasshopper© in combination with the

plugins Kangaroo© and Karamba©. To test the concepts they are applied to a case, a roof of 10x10m2, giving an understanding of the behaviour and efficiency of the structures.

3.1 Tensegrity Triaxial Weave

The concept of the tensegrity weave is a direct mapping of the triaxial weave into a modular tensegrity system and the structure can be expanded in three directions. The triangular tensegrity modules are assembled such that the compressed element of one module is attached in between two compressed elements, at the middle of one tension band, on the next. This logic generates a geometric pattern of the weave where the triangles are slightly shifted so each corner meet a midpoint on the neighbouring triangle edge, see Figure 4 below. To assemble the tensegrity triaxial weave digitally, modules which are not in self-equilibrium, but with the bottom triangle parallel to the top one, are copied along next to each other. After the regular modules are positioned over the desired surface, kangaroo is used to form-find the structure. During this form-finding process each module twists which causes the entire structure to change form and rise in certain parts, supported only by some of the edge modules.

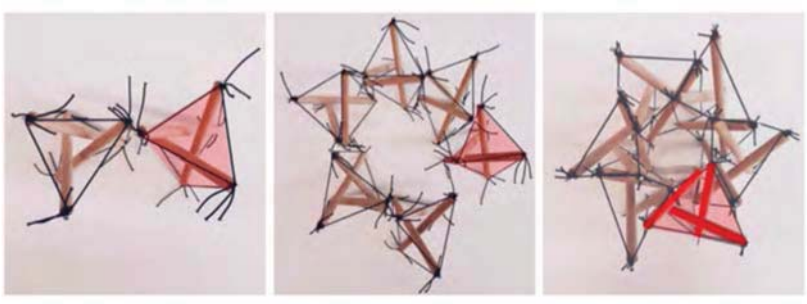


Figure 4: From the basic triangular tensegrity module of three rods to a triaxial weave tensegrity module

The tensegrity weave roof structure, figure 5 below was tested with a range of cross sectional dimensions in order to obtain the smallest possible amount of material use for the 10x10m^2 span. Standard cross sectional dimensions were used for the bars, with 75x75mm determined as the optimal one. The external loads, a roof cover of 0.6 kN/m^2 and a snow load of 1.5 kN/m^2, were assumed to be acting on the top nodes of each bar in the structure which resulted in an uneven distribution. All connections throughout the structure are hinged in the digital model. As can be seen in figure 8 below this resulted in a structure of 4.1 ton with a deflection of 119mm.

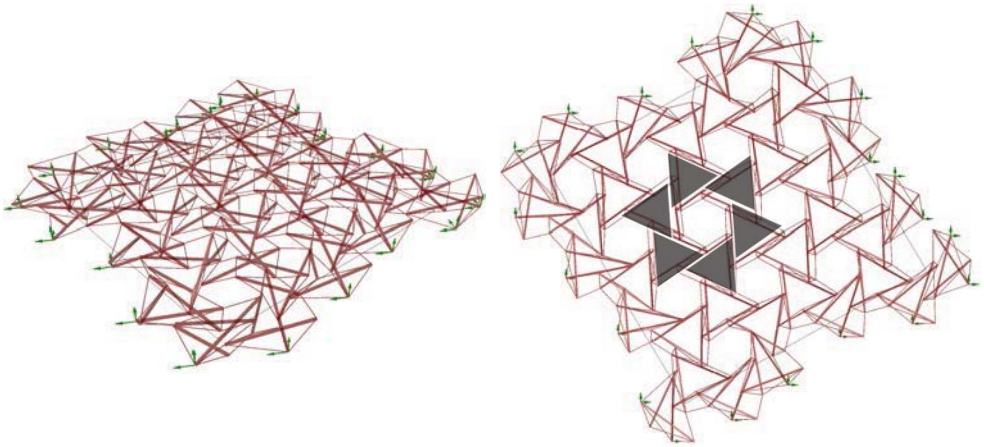


Figure 5: Undeformed digital model of tensegrity weave structure, with one triaxial weave module in grey

The geometry of a tensegrity structure can be adjusted with both local adjustments, and combinations of different modules. The global geometry of the tensegrity weave can be altered by controlling the

length of the tension bands in the modules. By using shorter tension bands in the bottom side of the modules, the global geometry will take on a dome-like shape. Using this principle on separate modules, one can also change the geometry locally in a structure. With further analysis one should therefore be able to build free-form surfaces with varying curvature as well.

3.2 Reciprocal Lace

The concept of the reciprocal lace build upon the above mentioned plain hole ground lace pattern. Each knot, or binding, in the lace is seen as one reciprocal module, stable on its own. The connection of these modules is made at the twist. The twist is made as a continuous diagonal between the modules. On this diagonal, rods from both modules rest.

The reciprocal lace is modelled as a modular structure. The base module is seen as the basic reciprocal frame of four rods combined with four diagonals, see figure 6. According to the previous model tests, when assembling these base modules into a structure of more modules, some elements are superfluous. To obtain a reciprocal structure, one diagonal is continuous between two elements on which two rods, one from each module, rests.

A reciprocal frame obtains a curvature like an arch due to the geometry of straight elements resting on top of the next etc. The height is increased by the number of elements used. The physical model tests of reciprocal structures clearly showed this. Therefore the four base modules are assembled into a higher structure where each base module is rotated upwards.



Figure 6: Modular reciprocal lace model, from one module (left) to full model (right)

The reciprocal lace roof structure, figure 7 below, was tested with a range of cross sectional dimensions in order to obtain the smallest possible amount of material use for the 10x10m^2 span. Standard cross sectional dimensions were used, with 190x270mm determined as the optimal one. Similar to the tensegrity structure, the external loads where assumed to act on the top node of each beam in the structure. This resulted in a structure of 2.1 ton with a deflection of 130 mm, figure 8.



Figure 7: Undeformed digital model of reciprocal lace structure

The Reciprocal Lace does not yield as many possibilities for variations of the geometry as the tensegrity weave. Here the variations are rather made by the dimensions of the elements used and

number of elements used. By increasing either the height of the individual elements or the number of elements the curvature of the structure would be increased.

		
	RECIPROCAL LACE	**TENSEGRITY WEAVE**
MATERIAL	**140x315 mm**	**75x75mm** **30mm (wires)**
MASS TOTAL	2.1 ton	4.1 ton
DEFLECTION	130 mm	119 mm

Figure 8: Results from the analysis and evaluation of the two concepts, performed with Karamba

4. Discussion

This study demonstrates that textile assembly methods and structure systems can inform each other in the design process. The experiments present how the analysis of specific textile constructions, the internal thread path and their bindings can be mapped onto larger scale structure systems with rods, tension bands and beams. Each structural concept, i.e. triaxial tensegrity weave and the reciprocal lace structure, are built up by modules which can be attached to each other in two or three directions. Since these modules are based on a structure system, the modules are designed to be stable on their own. When assembling these modules utilising a textile logic which are based on geometry or thread path alike, the modules retain their stability. The designs proposed illustrate how these structures can grow in multiple directions and be adapted to cover any arbitrary surface.

The interpretations of the textile structures use primary shapes, e.g. a square pattern for the reciprocal lace, or a combination of triangles and hexagons for the triaxial tensegrity weave. Furthermore by varying the modules' geometric shape open extended possibilities to express geometry of these surfaces. Forms, e.g. dome-like structures can be achieved by using combinations of geometric forms as base for the different modules. Combinations of hexagon and pentagon modules can yield to the generation of dome shapes. This method opens up a wide range of form variations which can adapt to irregular spaces, figure 9. By assembling stronger "joints", which are possible to use in a larger building scale, an adaptable surface structure could be obtained. If the structure can "grow" in multiple directions by the addition of modules, a free-form structure adaptable to a general shape could be obtained.

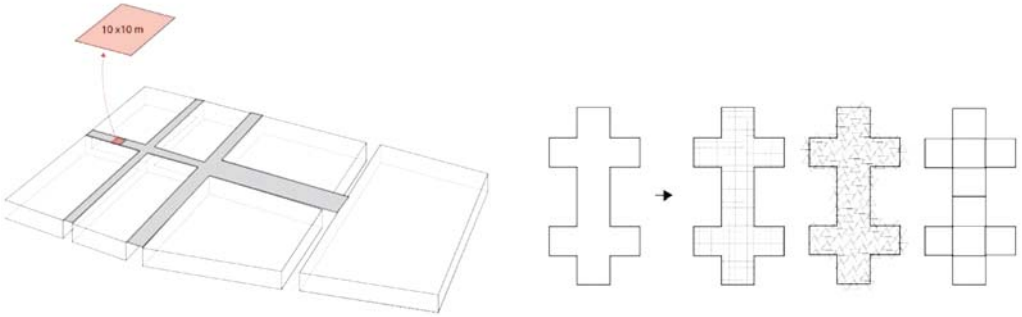


Figure 9: Irregular roof form and application of different concepts of varying patterns

Each example illustrates the potential of controlling the global assemble geometry. Aiming to create an arched, or dome-like shape of the assembled geometry, the local geometry of one single module can be further altered. Subsequently, the length of the tension cables in a tensegrity module can be used to control the geometry. By shortening the tension bands in the lower side of the modules, the global geometry will arch. In reciprocal structures, the geometry is instead controlled by the sizing of each element, with elements of a larger cross section height, the entire structure will arch more. Detailing of joints and members have not been the subject of this research but can be a new direction for further development.

References

1. Glazzard, M. *Re-Adressing The Role Of Knitted Textile Design Knowledge: Auxetic Textiles From A Practice-Led, Designer-Maker Perspective*. PhD thesis, Nottingham Trent University, 2014.
2. Snelson, K. *The Art of Tensegrity*. International Journal of Space Structures Vol.27 No. 2&3, 2012.
3. Huntington, C G. *Tensile Fabric Structures American Society of Civil Engineers*, Reston, Virginia, 2013.
4. Semper, G. *The Four Elements of Architecture and other writings.* Cambridge University Press, Cambridge UK, 1989.
5. Simmonds, T. Self, M. Bosia, D. *Woven Surface and Form. Architectural Design*, Architextiles. John Wiley & Sons Ltd. (2006) 83-89.
6. Ayres, P, et. al. *Beyond the basketcase: A principled approach to the modelling of kagome weave patterns for the fabrication of interlaced lattice structures using straight strips*. Advances in Architectural Geometry. (2018) 72-93.
7. Popovic Larsen, O. *Reciprocal Frame Architecture*. Elsevier Ltd, Oxford, 2008.
8. Wallander, L. Borgny, M. *Textile Informed Structures - How to Braid a Roof*. MSc thesis, Chalmers University of Technology, 2019.

Proceedings of the IASS Annual Symposium 2019 – Structural Membranes 2019
Form and Force
7 – 10 October 2019, Barcelona, Spain
C. Lázaro, K.-U. Bletzinger, E. Oñate (eds.)

The timber Reciprocal Frame Designer: free form design to production

Tom S. GODTHELP*, André J.M. JORISSEN[a], Arjan P.H.W. HABRAKEN[b], Rinus ROELOFS[c]

*Graduate Student, Structural Design, Department of the Built Environment
Eindhoven University of Technology (TU/e)
tomgodthelp@gmail.com

[a] Professor, Timber Structures, TU/e
[b] Assistant Professor, Innovative Structural Design, TU/e
[c] Artist, Specialized in Mathematical Morphology

Abstract

The definition 'Reciprocal Frame' (RF) applies to structures that are feasible by means of circulating shear, compression or tension interactions between their constituent members. This relation indicates that beam depths and connections correlate to an RFs' structural geometry. Till date, a combination of RF form finding that regards both beam depths and structural design of connections has not yet been developed. Although researchers developed computational form finding methods to create geometrical solutions and described the global structural design, computational complexity may have prevented a direct inclusion of detailing in the overall RF design. This research presents a new RF form finding method that includes the structural design of beam dimensions and detailing. A parametric model to be referred to as 'The Timber Reciprocal Frame Designer' (RFD) is developed to design three- and four-member RF assemblies from any arbitrary NURBS surface. The RFD provides a practically verified tool in which designs can be produced by using industry standard machines stimulating structural designers to add RFs to their design pallet.

Keywords: Reciprocal Frame, timber detailing, free form, form finding, computational design, manufacturing

1. Introduction

A Reciprocal Frame (RF) is a structure in which a combination of balanced structural members creates a span that is greater than their own length. Figure 1 shows that this balance is established at intermediate supports where the elements mutually support each other in a cyclic manner. History demonstrates that for thousands of years mankind has been able to span distances greater than the lengths of available materials by using RFs. Villard de Honnecourt -sometimes mentioned as the Leonardo da Vinci of the Middle Ages- described RFs as 'in this way you can even work on a house or a tower with timber that is too short' [1].



Figure 1: The structural principle of a three- and four-member single unit reciprocal frame.

Copyright © 2019 by Tom S. GODTHELP
Published by the International Association for Shell and Spatial Structures (IASS) with permission.

Where historic RF examples seemed to be induced by material shortages [1], complex examples of today have an investigative and aesthetic function: the practical adoption still needs to be explored. Today, this can be changed as cutting-edge timber engineering finds practical applications and by considering that wood is a renewable carbon storing material with the advent of climate change [2].

This paper presents a parametric model, developed within the Rhino/Grasshopper environment and to be referred to as the Reciprocal Frame Designer (RFD), that covers the complete design to production process including RF detailing. The first section discusses fundamental parameters, geometry, theoretical basics and design decisions. Hence, we outline the ideas and theory behind the RFD based on these principles and present a practically verified method to design RFs.

3. Parameters and eccentricity

The RFD is described by several designations in addition to the the ones described below (see figure 2). The global form of an RF with eccentric jointing depends on the unit style or member orientation, the number of members per unit, and the configuration of members in the structure [1]. The center axisses define the members' main axissises and are connected by an eccentricity line.

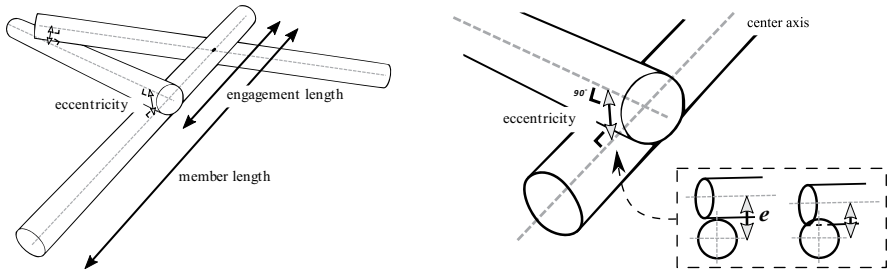


Figure 2: Parameters in a single-unit eccentric RF and eccentricity with its relation to member depth.

Eccentricity is of paramount importance in this research and is schematized as the shortest distance between two members. In general, forces will naturally search for the shortest load path which makes this schematization close to the RFs actual structural behavior. The geometrical rule of defining the eccentricity (line *e*) as the shortest between both beams' center axis vectors, ensures that line *e* is perpendicular to both intersecting beams. The eccentricity length is not necessarily dependent on the member depth. However, when using an eccentricity that is smaller than the member depth, additional connection measurements such as notching need to be considered. Consequently, detailing cannot be separated from the structural RF design that is started by a design method based on geometrical rules.

4. Basic geometry

The design of RFs cannot be accomplished without the use of geometrical rules. In contrast to other structural systems where members often meet at their extremities, members of an RF meet each other somewhere along the length of the member which geometrically can be achieved by modifying the geometry of polygons (see figure 3).

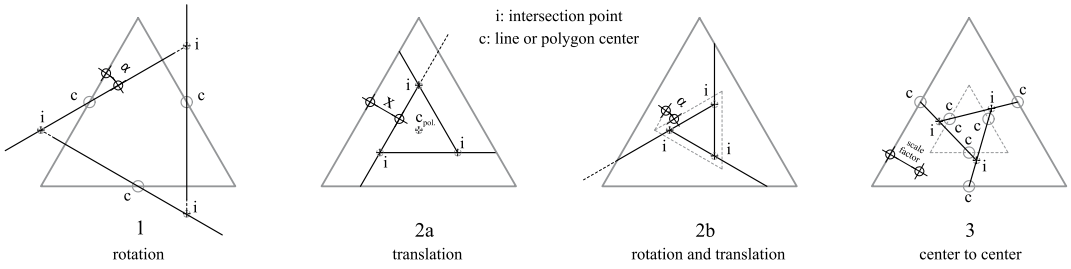


Figure 3: Four geometrical RF design methods applied to triangular polygons.

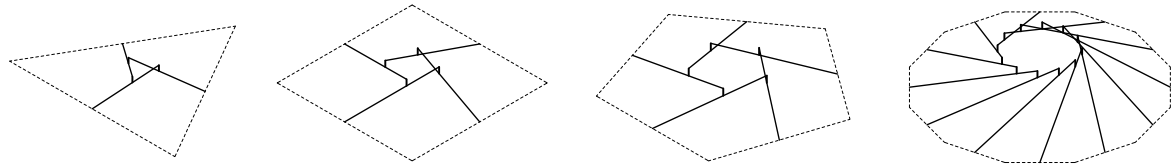


Figure 4: Four single-unit and eccentric RFs showing the effect of moving the intersection points found by the center to center method over the basic polygons' vertical axis or plane normal vector.

The polygon modification methods rotation, translation, this combined, and the center to center method evolved from research [3,4]. To create an RF by means of rotation, polygon sides are rotated around a predefined point and angle. Translation modifies the basic polygon by translating its sides towards the polygon center point. When combining the described rotation and translation method complexity is increased: it does not add extra freedom of form with respect to solely rotation.

However, the center to center method naturally creates a regular divided grid when using multiple basic polygons. First, by scaling a polygon towards its center point a smaller duplicate is created. Second, the midpoints at each side of the basic and scaled polygon must be determined. Third, the polygon midpoints relate to the midpoint of the neighboring side of the scaled polygon and can be jointed with a linear line towards the intersection point. Single-unit RFs with eccentric jointing can now be created by moving these intersection points over the height or z-vector (see figure 4).

5. Computational form finding

The center to center method can easily be used to create a single-unit RF designs. However, this differs for multi-unit RFs that are created when multiplying an one-unit system multiple times. These require a precise algorithmic definition since they are difficult to control manually: the predictability of a manual design is limited since parameters cannot be predefined and automatically adjusted to fulfill for example structural need. It seems inevitable to employ computational aid to allow for Finite Element (FE) analysis, design detailing, enable Computer Aided Manufacturing (CAM), predict geometrical configurations and to predict dimensions.

The past decades have showed an increased interest in computational RF design among researchers which resulted into three main approximation methods [5]. First, the analytic approach determines the RF design exact and uses geometrical equations to create an RF that is in most research based on platonic solids [6]. Second, the bottom-up approach uses iterative processes or self-generating geometries to create an RF. These so-called iterative additions rely on choosing an elementary unit style that is then distributed over a preferred growth direction where after the transitions are optimized. These two approaches are completely different but share one similarity: the possibility to take preliminary design requirements into account is limited. The third method however, the top-down approach, is an exception to this that relies on an optimization algorithm and is the most widely used method in RF form finding. To date, numerous strategies have been developed that not all immediately result in a geometrical solution or take the structural design of connections into account [5]. The RFD, based on the third method, has been designed to enable direct parameter control enabling to visualize their influence on structural behavior and geometry (see figure 5).

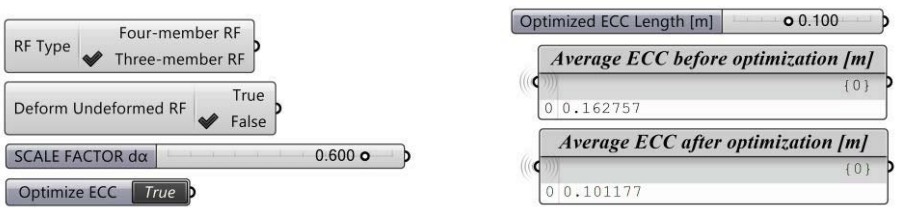


Figure 5: Basic design parameters within the RFD that controls the basic RF design.

6. The Reciprocal Frame Designer

In fact, the RFD has been developed by means of a top-down approach. It was decided that this is the best suited form finding approach for this research because it has been assumed that in practice, designers would create a certain architecture where after it should be suited for an RF structure. The RFD uses several geometric optimization strategies after the application of the center to center method to a tri- or rectangular subdivided NURBS surface or mesh. Surfaces can for example be subdivided in UV-direction by using parametric curvature or equal point distance where after geometric rules must be applied to create panels (see figure 6). Meshes are often already subdivided by triangles but may require equalization or smoothening before application in the RFD.

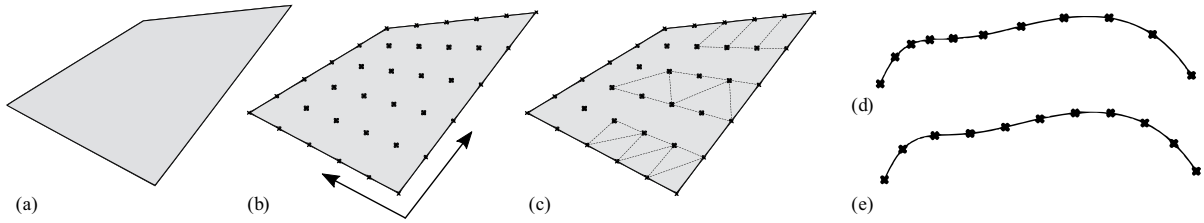


Figure 6: NURBS surface (a) subdivided in UV direction by points (b) by means of parametric curvature (d) or equal point distance (e) where after these can be panelized (c) by geometrical rules.

6.1 Creating a basic RF geometry

By using the center to center method, the number of members in an RF unit depend on the number of surface or mesh edges. Triangles create three-member RFs and rectangles create four-member RFs. At all common surface edges, RF members naturally meet each other because the starting point of an RF line lies at the center of a surface edge. In this situation, eccentricities between the elements are not yet created since each RF unit is still considered as planar single-unit. This is changed by joining two individual members -in this respect considered as lines- with communal starting points (kink), into a single polyline (see figure 7). Hereafter, the end points of this polyline can be used to create a new linear line that is defined by endpoint A and B (line A-B).

This method has also been earlier described by Anastas *et al.*[3] but is not enough to create a basic RF geometry for any arbitrary NURBS surface. Figure 7 shows the geometric RF transformation applied to a rectangular subdivided single curved surface. Here, a 'kinked' polyline is only created when the neighboring surfaces are noncoplanar. Consequently, additional measurements are taken to be able to create eccentricity by means of geometric transformations.

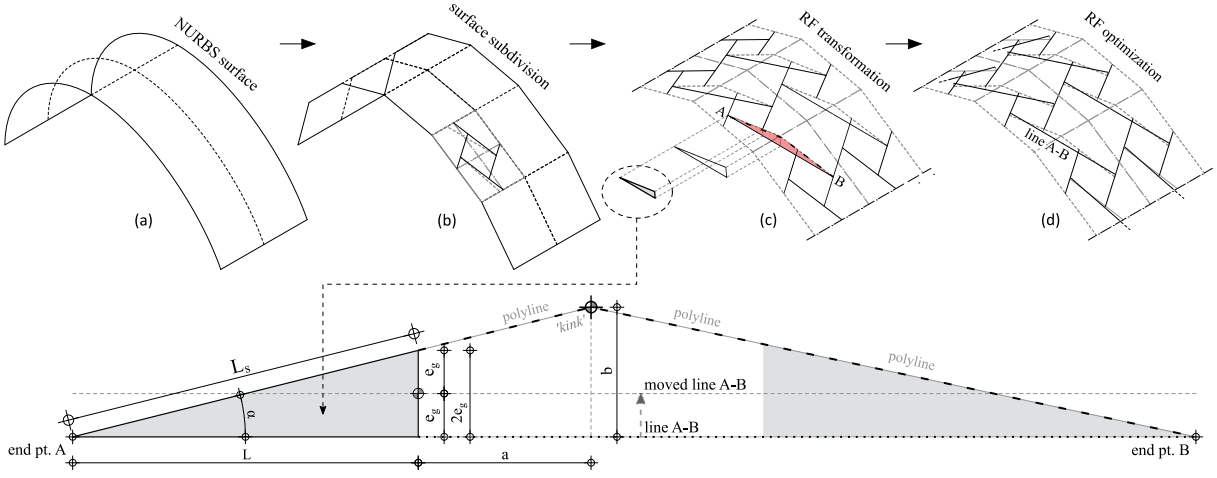


Figure 7: Basic geometrical design procedure that has been applied in the RFD.

First, the new lines that are created between all end points *A* and *B* of polylines are moved towards the initial RF starting points at the polygon edge centers (see figure 7). These edge centers are the 'kink' in the polyline. The transformation is thus determined by evaluating the mean length of the two-line parts L_s that exist between intersecting RF lines where after length e_g is determined by:

$$e_g = \frac{L_s \sin(\alpha)}{2} \tag{1}$$

Second, lines that lie between coplanar planes and are thus already linear, are moved over a distance smaller than two times the length of e_g creating a basic RF geometry with eccentric jointing. Consequently, member configuration and unit style depends on the geometry of the basic surface. A geodesic polyhedron for example, results in unit-style and member configuration a (see figure 8).

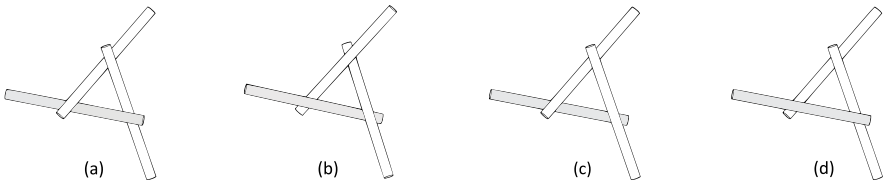


Figure 8: Four possible three-member unit styles. Unit style (a) and (b) can be structurally stable from itself by utilizing friction or using notching between the members.

6.2 Eccentricity optimization

Despite the geometric optimization procedure described under 6.1, eccentricities between members depend on the basic geometry and surface subdivision. This is not preferable in structural design since all members then should have different sizes, connections should be able to cover a variety of tolerances, or the mechanical force distribution would be dependent on the initial geometric shape. Therefore, an optimization method is developed that enables manual eccentricity control. With this method, each individual eccentricity line is optimized towards the preferred eccentricity length by applying initial strain loads to the eccentricity lines according to Hooke's law:

$$\varepsilon_i = \frac{\Delta L}{L} = \frac{e - L}{L} = \frac{e - e_g}{e_g} \tag{2}$$

Here, the strain load ε_i is determined by the preferable eccentricity length *e*, and initial eccentricity length ($L = e_g = e_i$). For each individual eccentricity line, an individual strain is then determined to increase, reduce, or maintain its length depending on length e_g. Fictional beam stiffnesses are applied to be able to maintain the basic RFs member configuration. Finally, this results in an equalized *e*.

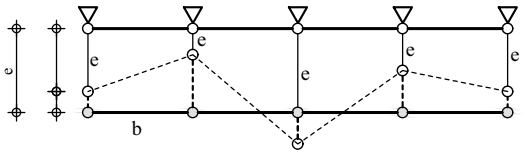


Figure 9: Eccentricity optimization method.

Figure 9 shows the optimization procedure applied to a simplified problem. Different eccentricity lines with length e_i are optimized towards length *e* by automatically changing the length of member *b*. Length *e* can be changed by modeling all members (*b*) as 'infinitely' stiff to shear and bending and 'infinitely' weak to axial stresses and torsion. Eccentricity lines e_i, are modeled 'infinitely' stiff to all directions with torsional resistance as exception to be able to maintain the member configuration. The initial surface shape can be approached by choosing a new value for *e* that is close to the mean length of e_g. This optimization procedure is applied in the RFD by using Karamba's FE solver [7] that allows geometrical nonlinear deformation analysis.

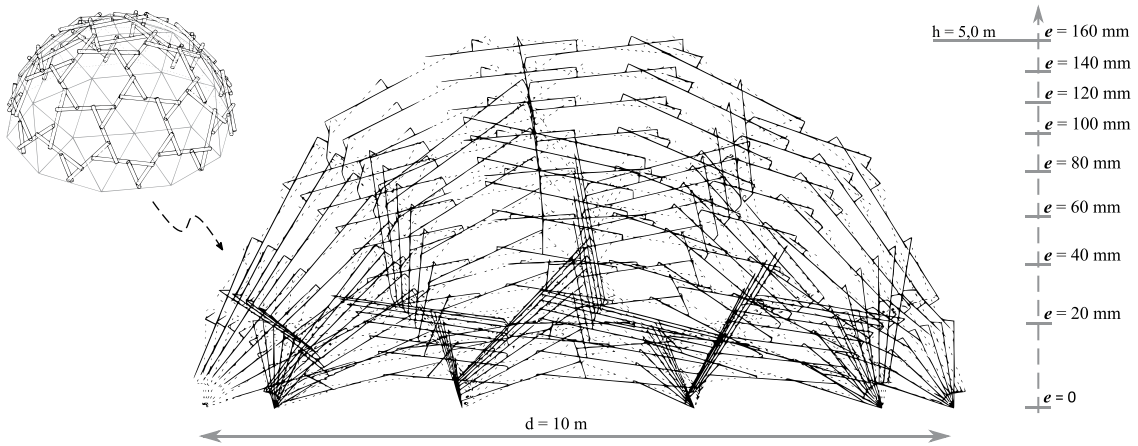


Figure 10: The influence of eccentricity on the structural height of an RF while using the same scaling factor.

6.3 Timber detailing

The effect of increasing length *e* while preserving the scale factor is determined by this eccentricity optimization method and results in an higher RF structure (see figure 10). It seems that relatively small eccentricities and thus small member depths are required when notching are avoided to create structural height. Load application to this structure most likely will result in a larger required member depth than eccentricity length. Therefore, notching seems unavoidable in practical RF design. Furthermore, by keeping the eccentricity independent on the member depth, one creates structural freedom and enables necessary transferring of shear and normal forces. The developed detailing divides these notches over both intersecting members causing equal section weakening (see figure 11). Local axis systems that define the section orientation are defined in the RFD by sorting two eccentricity lines along its center point and by taking their mean vector direction as local vertical axis.

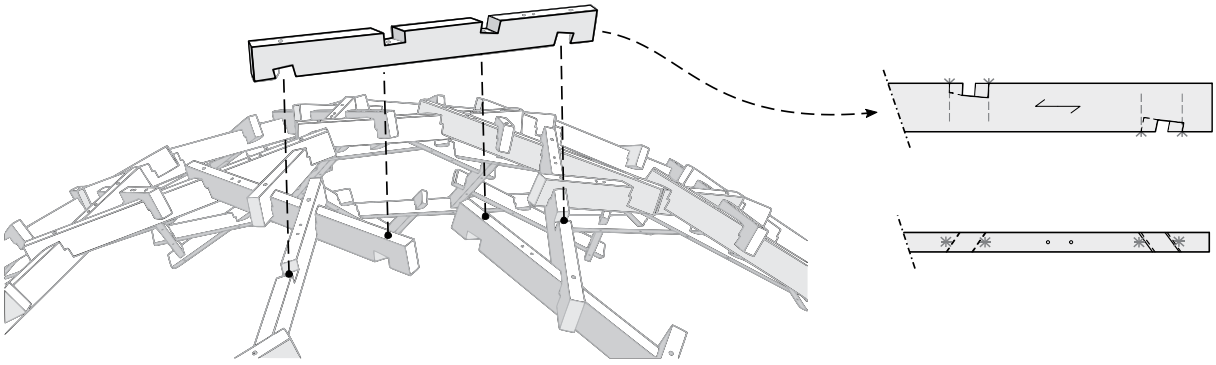


Figure 11: Detailing applied in the RFD with reinforcing screws and timber grain direction.

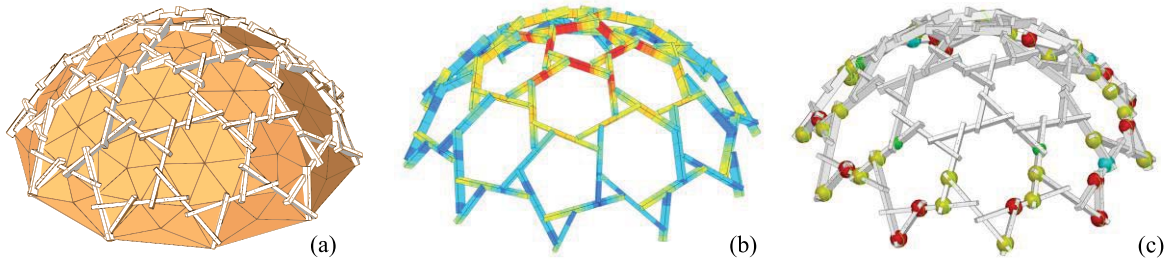


Figure 12: Load panels (a), illustrative FE model with bending moment My (b), C 's > according to EN1995 (Eurocode 5) showing timber failure in the RFD (c).

6.4 Structural analysis

The exact section orientation used for detailing is also used in the FE analysis that is included in the RFD to define force distributions and enable structural checks. Here, mechanical behavior is linked to geometry. Figure 12 shows how to model panels used for load application to simulate roofing. Subsequently to this or other load application, the model can be directly exported with Geometry Gym to FE software to check for instance maximum stresses (see figure 12.b). However, this is not mandatory since Unity Checks (UC) can be directly monitored for exceedances within the RFD according to Eurocode 5 [8]. Detailing measurements, required for these checks, can be retrieved from the geometrical data. Consequently, timber failure is directly visualized by colored indications for different UCs (see figure 12.c). The UCs showed that strengthening by means of reinforcement perpendicular to the grain is unavoidable when using Glued Laminated timber (GL28C, see figure 11). An advantage of combining geometrical and structural design is that parameters can directly be changed to modify geometry or member depths to satisfy the checks. The variation of eccentricities for example, influences the force distribution throughout the system. An RF based on a geodesic polyhedron will start to behave as planar grid structure when reducing the eccentricity towards zero: it transfers its forces primarily through shear and bending. Increasing the eccentricity results in the fact that the forces are primarily being transferred by axial forces but, will be transferred by bending due to engagement length and eccentricity: shear is reduced while increasing the eccentricity.

6.5 From design to production

The RFD enables structural designers to find a mechanical optimum by varying design parameters and section dimensions till a satisfying optimum has been found. Subsequently, production can start by an automated design conversion to CAM software. Hence, members are numbered and marked indicating placement and member orientation in space. Furthermore, some clearance is added to the connections to allow installation (see figures 13 and 14). Hence, the RF can be manufactured where the relatively simple notches reduce machine time and thus cost. The feasibility and design to production process is verified by practical models of a single-unit RF -to be used as table legs and manufactured by a timber industry standard Hundegger machine- and a demountable 3d-printed scale model.



Figure 13: Full scale model made with CAM and Hundegger machine to test the feasibility of RF detailing.

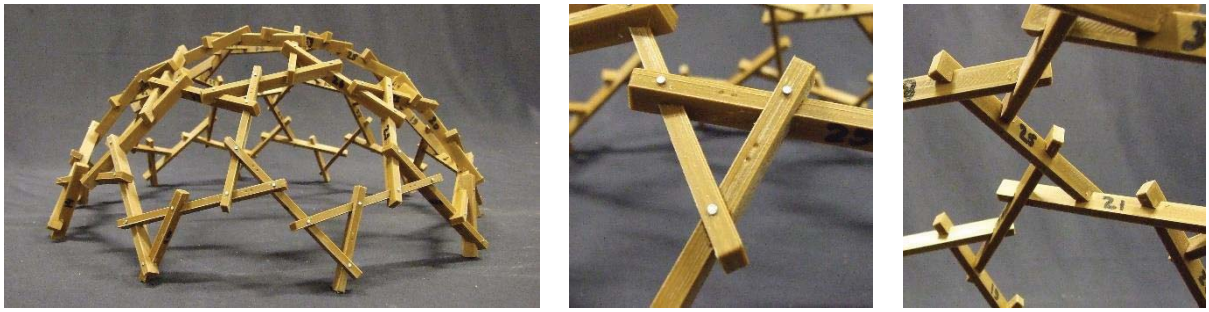


Figure 14: 3D printed 1:20 scale model using the same design as displayed in figure 10 with e = 100 mm.

8. Conclusion

This paper presented the RFD that covers an RFs' design to production process and timber detailing. The practical models prove that designs from the RFD can be transferred to built examples able to satisfy building regulations and allow direct manufacturing and construction. Long-lasting and complex optimization processes to control an RFs' parameters are no longer needed. The parameters can be directly optimized through a structural designers common sense. Despite the fact that an RF transfers its forces mainly through bending, the proposed notching typology results in relatively simple connections. No steel plate connectors are needed. The RF can be completely made in timber reinforced with self-drilling screws.

Although the results are promising, implementation and roofing have not yet been fully developed and the tool is only applicable to three- and four-member RFs. Future work is therefore encouraged by a need for applications and should concentrate on implementation, roofing, and surface subdivisions especially suited for RF design to create greater design variety (see figure 15). Nevertheless, this research aims to encourage new applications by making its design accessible to structural designers.

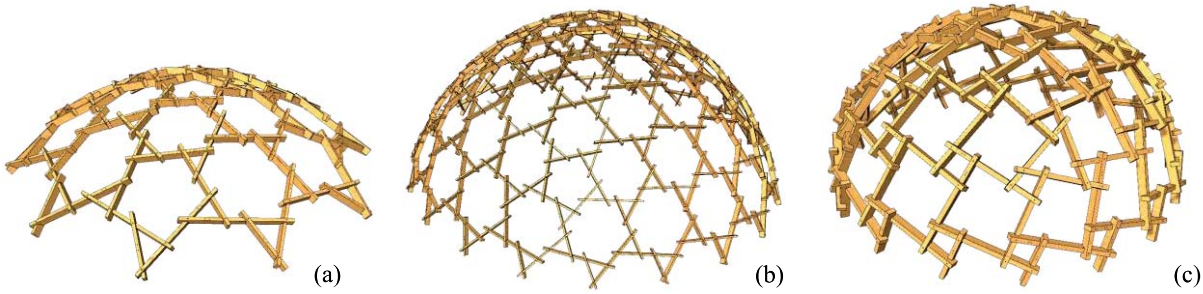


Figure 15: Three possible RFD results covering the same span based on geodesic icosahedra (a,b) and cubes (c).

Acknowledgements

The authors would like to thank 'Heko Spanten', a glulam manufacturer in the Netherlands, for the provided manufacturing facilities, materials, and knowledge to be able to transfer the RFD to practice.

References

[1] U. Thönnissen, *Hebelstabwerke / Reciprocal Frameworks Tradition und Innovation / Tradition and Innovation*, Bilingual. Zürich: gta publishers, 2015.

[2] A. Menges, T. Schwinn, and O. D. Krieg, *Advancing Wood Architecture: A Computational Approach.*, Oxford: Routledge, 2016.

[3] Y. Anastas, L. Rhode-Barbarigos, and S. Adriaenssens, "Design-to-Construction Workflow for Cell-Based Pattern Reciprocal Free-Form Structures," *IASS*, vol. 57, no. 2, pp. 159–176, 2016.

[4] J. P. Rizzuto, M. Saïdani, and J. C. Chilton, "Polyhedric space structures using reciprocally supported elements of various cross-sections," *Journal of the International Association for Shell and Spatial Structures*, vol. 42, pp. 149–159, 2001.

[5] A. Pugnale and M. Sassone, "Structural Reciprocity: Critical Overview and Promising Research/Design Issues," *Nexus Network Journal*, vol. 16, no. 1, pp. 9–35, 2014.

[6] B. Sénéchal, C. Douthe, and O. Baverel, "Analytical Investigations on Elementary Nexorades," *IASS Journal*, vol. 26, no. 4, pp. 313–320, 2011.

[7] C. Preisinger, " i nking Structure and Parametric Geometry," *Architectural Design.*, vol. 83, no. 2, pp. 110–113, 2013.

[8] B. S. EN, " -1: Eurocode 5: design of timber structures--Part 1--1: General--Common rules and rules for buildings," *CEN, Brussels, Belgium*, 2004.

Proceedings of the IASS Annual Symposium 2019 – Structural Membranes 2019
Form and Force
7 – 10 October 2019, Barcelona, Spain
C. Lázaro, K.-U. Bletzinger, E. Oñate (eds.)

Three ways to stabilize polyhedra according to Chinese thought, Wester's work review

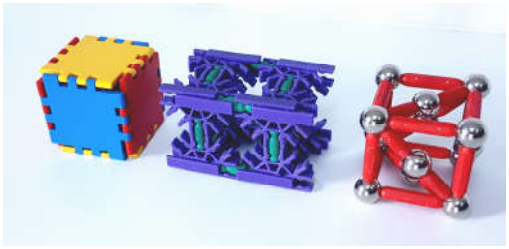
S. MONNOT

Environment-City-Society Lyon Architecture Urbanism REsearch (EVS-LAURE) of UMR 5600, CNRS
Laboratory of National School of Architecture of Lyon (ENSAL)
3 Rue Maurice Audin, 69120 Vaulx-en-Velin
serge.monnot@lyon.archi.fr

Abstract

Previous work has hypothesized that Platonic solids and Chinese elements are two cultural expressions of the same *system*. In the light of the correspondences identified - geometric duality / *yin-yang* categories, in particular - this research has made it possible to characterize the polyhedral forms in architecture from a qualitative point of view, a *structural* one. But this previous step also allows a critical reading of T. Wester's researches - from the notion of "structural dualism" - and to make the hypothesis to consider not only 2 but 3 *structurel* logics of stability of the basic polyhedra. *Structurel* modes corresponding to dual geometric elements *faces*/*vertices* are the *plates*/*pods* and the mode *tension rod / compression strut* corresponds to the geometric element *edge* - self-dual. Analog models show how each *structurel* mode alone can organize the indeformability.

Keywords: Morphology, structural dualism, Chinese thought, yin/yang, plate structures, lattice structures



1. Introduction

1.1. Context

At the First International Seminar on Structural Morphology in Montpellier in 1992, T. Wester [1], presented his research *An approach to a form and force language based on structural dualism* in these terms: *"The structural primitives: the lattice and the plate structure, may be regarded as polars or duals on all structural levels, i.e. kinematic stability, structural mechanics and elasticity. (...) The geometry which is tied to this dualism, the polar reciprocation, creates a structural morphology which is interesting in several aspects not least because it creates an entity in the perception of the basis of the structural complex. It is a major quality that all the archetypal geometrical elements in Form Language: point, plane and line can be assigned to archetypal structural counterparts. This leads to the assumption that Form Language as approached by many authors might in a meaningful way be extended to a Form and Force Language without losing exactness."*

Copyright © 2019 by <substitute here the name(s) of the author(s) or individual(s) claiming copyright>
Published by the International Association for Shell and Spatial Structures (IASS) with permission.

Very interested in this approach, I had the opportunity to discuss with Wester about the research I was developing, on a Platonic solid/ Chinese elements (*wuxing*) rapprochement - the challenge was to interpret the *structural* and *structurel* logics of polyhedra, with / from a traditional Chinese understanding. (*Structural* in French is understood in the sense developed by A. Renier [2] at the same seminary: *any arrangement that, in human languages and signs, produces meaning ... Unlike the "structurel", the "structural" can not be directly spotted and explained ...*). Wester had shown an interest in this approach, having himself tried matching geometric duality and notions *yin / yang (see figure 1)*. But, he had questioned me on one aspect, saying that the tetrahedron could not be *yin* and *yang* at the same time: "*There is nothing between yin and yang!"*

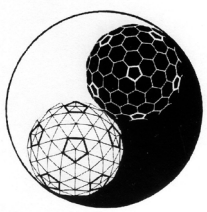


Figure 1: T. Wester's illustration] [3]

1.2. Issues

In my teachings, I often relied on this approach to structures - the major problematic in seismic or structural morphology being first of all to ensure global indeformability - bracing in engineering. To propose a simple, holistic classification system, allowing considering the different possibilities of bracing flat-face buildings or smaller objects, while opening the creative expression is pedagogically efficient. To consider very early the modes of construction is an important issue, as much in the final expression of the project, as before in the conception of the other forms: openings, assemblies, and so on... and in earthquake engineering in particular, for the consequences on the stiffness, on the distribution of the masses ... Over time, from rudimentary educational materials, I developed TDs to illustrate the different principles of stability; but it remained to associate them in a coherent whole.

1.3. Research objectives

This topic re-starts work on the reflection initiated by Wester - on the basis of this notion of "structural dualism" - in order to propose concrete tools to elaborate a more global and coherent classification of polyhedral structures. This does not, of course, call into question the principles of structural mechanics; but this allows another look at the relationships between geometry and structural properties. I therefore reconsidered Wester's results concerning three aspects: - the dual opposition, the *plate* / *truss* modes; - the introduction of the *rigid connection* in this classification; - and how to rethink the stability of the cube and the dodecahedron with *truss* mode.

1.4. Methodology

The approach followed uses an epistemological strategy consisting of taking a detour from the outside of European thought, to unveil the unthought. It follows the methodology developed by F. Jullien, which consists in organizing the two Greek and Chinese thoughts in a face to face, to put them in *opposition/tension* and make work their *potential difference* - "*to learn Chinese to better read Plato*" [4]. This method aims to *translate* one culture into the other by avoiding *assimilation*. It will be in this case, to seek how to *translate* a system according to the other: a formal one, *geometric* - the five regular polyhedra of the *Timaeus* - and another *energetic* - the five Chinese elements (*wuxing*).

A previous work [5] adopted the basic hypothesis that these cosmogonies are two expressions of the same *system* – share the same structure. This allowed to integrate the polyhedra in the table of correspondences of *wuxing* and to deduce some *structural* properties: orientation, assemblies, colors,

and so on... Let us summarize these results to then examine the consequences of these results on the *structurel* properties.

2. Some tools to develop a more global approach

2.1. Correspondence Platonic solids / *wuxing*: a single cycle of *growth*

Let us first remind the coherence of such a comparison. These writings date approximately from the same period - Vth century before J.C. [6]. In Chinese, *five movements* is a more suitable translation of *wuxing,* instead of *elements*, and in the *Timaeus*, Plato speaks of polyhedra in terms of *movements* [7]. Finally, the possibility of storing polyhedra into each other with optimization logic (like Chinese nested boxes), the generating role of the tetrahedron (from the concept of polyhedral compound) and more other indicator not detailed here, allow establishing correspondence with the Chinese cycle, with the *generation operator* and with the *central* role of the Chinese movement *Earth*.

This leads to consider the nesting polyhedra as a morphological growth cycle on the temporal model of the Chinese cycle and to make the choice of a particular sequence of this "growing generation": the origin of this cycle being the small tetrahedron in the center (South-West on the diagrams - the *Fire movement* being associated with the south which is represented towards the top), associated with the Chinese movement *Earth* and the end of the cycle - the large external tetrahedron - associated with *Earth* as well. Correspondence is thus established as follows: 1 small tetrahedron / *Earth* (yellow), 2 cube / *Metal* (white), 3 dodecahedron / *Water* (black), 4 icosahedron / *Wood* (green), 5 octahedron / *Fire* (red), 6 large tetrahedron / *Earth* (yellow).

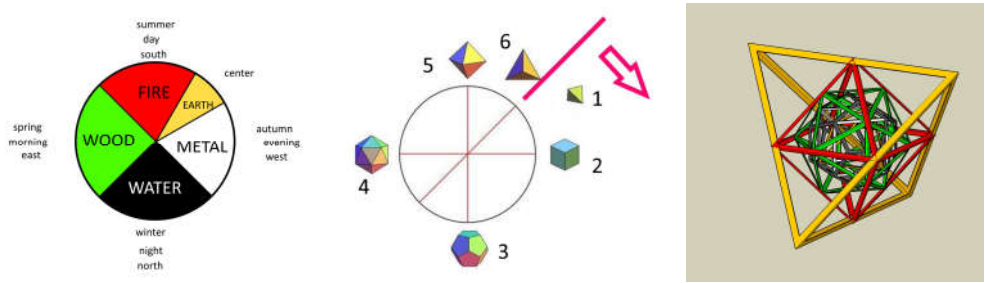


Figure 2: Correspondence platonic polyhedra/wuxing and particular sequence of nesting of the 5 polyhedra (personal illustrations, SketchUp model on the right)

2.2. New correspondence at the scale of the polyhedron; *vertex, face, edge / yin, yang, center*

This previous research confirms that it is consistent to store the 5 regular polyhedra in two series and assume that the *yin-yang* concepts - the principle of antagonism / complementarity, basic Chinese tradition - refer to the geometric principle of *duality* and can serve as classificatory criteria. The *yin series*, TCD (Tetrahedron, Cube, Dodecahedron) corresponds to the polyhedra whose *faces* have an increasing number of sides (3, 4, 5) - stable *vertices* with 3 edges. Dually, the *yang series* IOT (Icosahedron, Octahedron, Tetrahedron) corresponds to the polyhedra whose *vertices* have an increasing number of edges (3, 4, 5) – 3-sided constant *faces*. In these dual relations of polyhedra, the number of *edges* remains stable; but they each rotate 90 ° in space.

This shows, therefore, that the tetrahedron belongs to both *yin* and *yang* series: this corresponds to the *Earth* movement of the *wuxing,* the function of the *center*, the *middle* in the traditional Chinese culture – concept important enough for China to be called *middle country*, 中国.

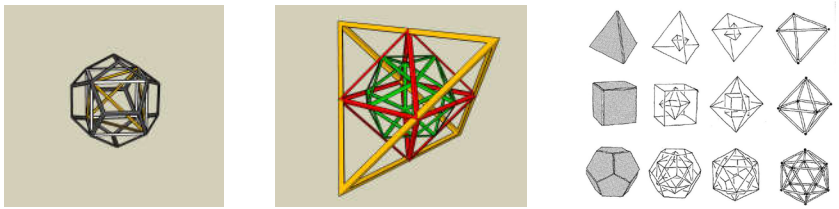


Figure 3: Two series of polyhedra and dual role of tetrahedron, SketchUp personal models and Wester's fig. [8]

This observation confirms in turn it is necessary and coherent to consider not two qualities *Yin / Yang* in the Chinese manifestation process, but three: *yin / yang / center.* And this allows considering a new correspondence at the scale of the polyhedron - central hypothesis of this article: the geometric constituents, *vertex, face, edge* correspond to the Chinese qualities *yin, yang, center*. The *edges* of polyhedra correspond well to the quality of the *center* - the edges being as "necessary" to the *faces* as to the *vertices*, *yin* and *yang* at the same time. The correspondence of the *vertex* element to *yang* or *yin* is irrelevant for the following demonstration; this is the main topic of another article [9].

2.3. Shape and concept of stiffness

The notions of spring and *stiffness* help to understand the role of each of these components, *face, vertex, edge*. A spring is first of all a *form* which, to resist and limit its deformation, mobilizes a certain amount of *elastic material* [10]; so enough space to contain this material. The *stiffness*, ratio *stress / deformation*, summarizes this capacity of the spring. So there is no reason that each component - *face, vertex, edge* - does not support a *structurel* function and become a kind of spring that locally organizes *stiffness*.

2.4. Some construction toys as analogue models

Finally to be able to easily experiment and at the same time represent, it is necessary to quickly build analogue models. The pedagogy has led me to select three kinds of sets of constructions that can model bracing systems, all organized from a morphological and structural principle: a piece - *edge, face* or *vertex* - constituting a *main stiffness*.

Maybe the best known, this type of toys based on magnetic bars assembled on metal spheres - such as *Geomag* - allows building *pin-jointed trusses* and *space frame*. Another type - such as Zaks - makes it possible to assemble solid faces (*wall bracing* in engineering), their crenelated and clipped edges forming (piano) hinges. And the third type, comprising *edges* which snap in junction elements - such as *K'nex* which plane angles are multiples of 45 ° - is a hybrid system. Its angular blocking principle makes it possible to make *rigid connection*, thus *gantries*. But according to the scale, it is also possible to make *pinned joint* connection (*nodes*), and therefore *truss*, or even to introduce solid *faces* (thus one can use different models, e.g. to test quickly, dynamic, different *stiffness* in earthquake engineering). It can be admitted that these three kinds of toys cover all cases of bracing.



Figure 4: Three kinds of toys used as analog models (personal models - the 3 cubes on the title page use these 3 kinds too; note that the last one is not stable, but there were no more magnetic bars of this length)

3. New hypotheses

3.1. Critical review of Wester's results.

As we have seen, his approach is to understand the *structurel* modalities of all polyhedral surfaces from the *geometric duality* and introduce the notion of *mechanical duality* - which allows a classification mode easy to transmit, interesting resource for teaching. But if Wester considers regular polyhedra as two dual series - therefore the existence of two tetrahedra, if he explicitly refers to two feminine / masculine series (*yin / yang*); he got stuck in an interpretation of the duality *face / vertex* illustrated by two constructive logics: one made with *plates* assembled by their edges and the other realized with *nodes* assembled by curved *two-force members*.



Figure 5: "*The dualistic symmetry between plane and point-based spatial structures"* [11]

In large tables, he tries to verify a systematic *dual face to face*, for all the spatial and mechanical characteristics: - *plates* (polyhedrons *yin* TCD) releasing the *vertices* / with *nodes* (polyhedrons *yang* IOT) releasing the *faces*; - forces in the plane of the *plate* / with coaxial forces in the *node*; - folded edges / with bar edges (*two-force member*), *axial shear* work and *compression* or *traction* ... He notes that this *nodes* mode is stable only for the series IOT *yang*; but by the search for a "dual symmetry", he states that the icosahedron and the octahedron are not stable in *plate* mode as we see below.

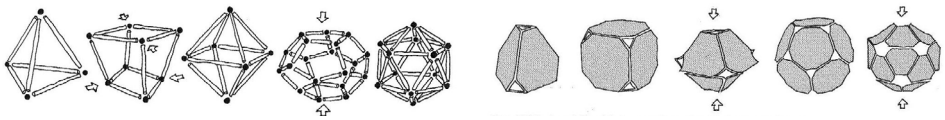


Figure 6: The three rigid and two movable regular polyhedra - as "pure lattice" and "pure plate structures" [12]

However, some models are enough to check that the *plate* mode is stable for all 5 polyhedra (see fig. 4)! For the octahedron and the icosahedron, there is indeed instability during construction, but it disappears at the end of assembly. This "dissymmetry" in the duality *plate / node* thus envisaged is a problem; especially since the tetrahedron belonging to both series is stable in both cases. In truth, if the fact that the geometric *face* becomes structural *plate* is obvious, does the *vertex* become *pin-jointed* connection? While the *plate* resists in its plan: the *structurel* function of the *vertex* should precisely present *stiffness* by the stability of its geometry: which is not the case of a *ball head*.

3.2. What *vertex-stiffness*, dual of *plate*? New hypothesis

Geometrically, a face is constructed / configured by its *edges*. Its dual, the *vertex* is not reduced to a point of space; it is built by the organization of a convergence of *edges* also (3, 4 or 5). In a polyhedron, we must imagine that this "vertex with its extensions" generates space until it meets another "prolonged vertex" of the same nature, and neighbour. To correspond to a *stiffness* of *face*, it is more coherent to think of an indeformability of the *vertices* by blocking the angles with *rigid connection*. The *vertices* must therefore have enough material to ensure this *rigid connection*- this material can be reduced gradually, moving away from the top (like a variable stiffness spring). The forms that we spontaneously think of are concrete *tetrapods* used for dikes.



Figure 7: Tetrapod on dikes [13] and model of tetrahedron stabilized with *tripod* junctions (personal *SketchUp*)

We will therefore define the concept of "polypod" as a shape that presents around a central point blocked angles in space imposing a defined geometry - *tripod, tetrapod, pentapod* - and which can be directly assembled, without intermediate parts (others words might agree, *branca* from latin for exemple). The lower part of *door hinge* ("gond" in French) protruding from one of the ends of the *pods* can allow mobility, as for "polyplates", the connection of the *faces* constitutes a true longitudinal hinge thus deformable. And above all, there is a *dual symmetry* between the *longitudinal shear forces* in the hinge and the shear forces perpendicular, *radial*, in the *gond*. A cube made with *tripods* is stable provided that the section of the *gond* is sufficiently high not to become a *pin-jointed*, which would lead to complete deformation. By assembling, we find the same instability as for *polyplates* (icosahedron and octahedron built in *Zak's* eg). On the other hand, once constructed, all polyhedra - *polypods* as *polyplates* - are stable. And finally, as the *plate mode* does not require *edges* (see *Zak's* models) we can consider that the *pod mode* does not require either.

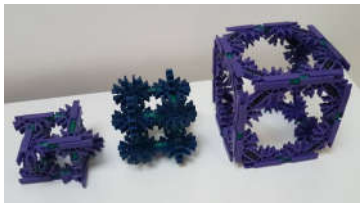


Figure 8: Junction logic *pod* with cube (*K'nex* personal models: note that this solution works better with smaller models that proportionately have a large section of *gond* - green on figures).

4. How to structurally interpret the *central* case of the *edges*

If the *dual reciprocity* is easy to understand for the *plate / pod* logic, the case *structural member* ("barre*", "*membrure*"* in French), which we can define as the *structurel* function of the geometric *edge*, is more difficult to consider. It is usually thought that this type of structure with connected elements (*structural members*, typically straight) only stabilizes the IOT *yang* series (as shown by Wester fig. 6); the indeformability of the TCD *yin* series needing complementary systems. But our hypothesis leads us to think that this constructive solution - dual of itself – must be able in principle to stabilize all the polyhedra.

To approach it, let us deepen the concept of *center / middle* of the Chinese thought, ambiguous on several levels: by its position (spatial or temporal center), its belonging (*yin* or *yang*), and its function (uniting or separating): and since this *center* is its own dual, it is double. On the geometrical side, we know that the polyhedral element *edges*, by its double nature - "between" *face* and *vertex* - transforming into itself, can only correspond to this *center*. Especially since its structural function - *two-force member* - is also double: *traction* or *compression*, and that these two efforts are the two elementary efforts. Let us try to introduce these correspondences with an adapted "spatial" vocabulary, always referring - by putting the *face / vertex* pair in relation.

Intuitively, it can be said that the spatial characteristic of the *Faces* is to be open, separated, kept apart by the *edges*, while those of the *vertices* are to be closed, joined together. The spatial function of the *Edges* is thus to maintain, at the same time, the *spacing* ("écartement" in French) of the *Faces* and the meeting of the *Vertices*: to separate F and join V. We can conclude that if this *face spacing* must be

kept by a function of *compression member:* in a correlated way and "necessarily double", the meeting of the *vertices* must also be kept by a function of *tension rod.* And the *compression strut* balance with the *tension rods*. For all polyhedra, the only possibility for "attach and/or push against" being the end of the *edges*, it is necessary to triangulate all the *faces* with *tension rods* to pull all the *vertices* together, so as to constitute the geometry of the *faces* by the compression of the *struts.*

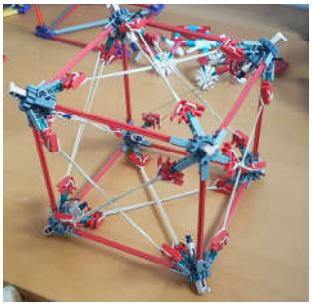


Figure 9: *Truss mode*, cube case: *compression strut* balances with *tension rod* (K'nex personal model)

For the OIT *yang* series, since the faces are already triangular, there is apparently no possibility of diagonal *tension rods*. But in this case, the structural members actually mix the two functions, separate / join, *strut / tendon* and we can't see. In other words, what is expressed in the *yin* series "stretching the *vertices* to separate the *faces*" is implicit in the *yang* series. The fact that the rods may confuse the two functions *compression strut* / *tension rod* leads to better specify. If we consider that a *tension member* can only work in traction - like a *cable* - it allows imagining in a dual way a *compression strut* that can only work in compression. This is equivalent to reinvent a *strut* consisting of an assembly of several pieces - *voussoirs* (which can have for example larger section in the center to avoid buckling e.g.). To be stabilized with this type of components, the OIT *yang* series would then obviously need for *tension cables* (*tendon*), tied and stretched from nodes to nodes (inside *voussoirs*), as for the *Yin* series.



Figure 10: Tetrahedron with *strut* built by assembling several pieces (personal model *type Geomag*)

In conclusion, this *structural member mode* which we have finally defined as a dual *compression member / tension cable* (*tendon*) is consistent since it stabilizes all polyhedra. And it mobilizes exclusively *struts* and *cables*. Because the vertices, which could seem "expressed", are in fact only the ends of the *tension system* which receives the thrust of the *struts* with an adapted form - thus only by contact or possibly attached for assembly. Finally, it allows *truss* and *space frames* to be considered as particular cases of this "archetypal" general case - related to tensegrity.

5. Conclusions

More generally, from a theoretical or educational point of view, for buildings, *structurel* elements or parts of structures, we can imagine it is possible to refer to similar simplest configurations, beam or slab plate (double frame), themselves modelled by assembly of polyhedra which can be made with one of the three *structurel* modes. For the beams (in particular the *web* in which we can observes most of the shear stresses), we can consider that each mode *truss member, plate, pod,* corresponds ideally to one type: *truss*, *IPN* (or tube) and *Vierendeel*. This same principle can be extrapolated to slab plates (for vertical elements but for the horizontal ones too) with *space frame*, *honeycomb structures* types

and *rigid frame* (like that imagined by F. Otto fig. 11). In areas that touch on space and with all the possible hybrid forms, we can imagine the openness to innovation that these *Force and Form* understanding allows - this path Wester opened.

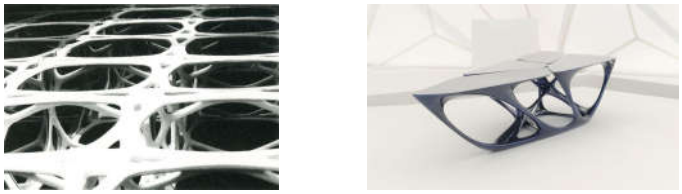


Figure 11: Rigid frame designed by F. Otto [14] and Mesa-table by Z. Hadid [15]

References

[1] T. Wester, "An approach to a form and force language based on structural dualism" in *Structural Morphology: Proceedings of the First International seminar on Structural Morphology – 7/11 September 1992 Montpellier, France,* R. Motro and T. Wester Ed., LMGC and ccSLA. pp. 13.

[2] A. Renier, "Geometry and semantic: generation of structural" in *Structural Morphology: Proceedings of the First International seminar on Structural Morphology – 7/11 September 1992 Montpellier, France,* R. Motro and T. Wester Ed, LMGC and ccSLA. pp. 28.

[3] T. Wester, "Plate-domes" in *Proceedings of the International conference on the design and construction of non-conventional structures Civil-Comp Press, Edinburgh, UK*, B.H.V. Topping Ed., Civil-Comp Press, 1987. pp 250.

[4] F. Julien, *Une seconde vie*. Bernard Grasset, 2017. pp. 51.

[5] S. Monnot, "Architectural design in the *Ecart* between platonic solids and *Wuxing*" in *Proceedings of the 10th International conference on Contemporary Problems of Architecture and Construction*, C. Qi, G. C. Sih and C. Ma Ed., Wuhan University of Technology Press. 2018. pp. 325-333

[6] A. Cheng, *Histoire de la pensée chinoise*. Editions du seuil, 1997. pp. 243.

[7] Platon, *Sophiste, Politique, Philèbe, Timée, Critias*. Traductions et notes par E. Chambry. Garnier Flammarion. 1969. 58d, pp.436.

[8] T. Wester, "The structural Morphology of Basic Polyhedra" in *Beyond the cube, The Architecture of Space Frames and Polyhedra*. J. F. Gabriel Ed., John Wiley & Sons, Inc. 1997. pp. 308.

[9] S. Monnot, "Morphology and structure of the platonic solids from a Chinese interpretation". *The 11th International Conference on Contemporary Problems of Architecture and Construction, Erevan*, Armenia October 2019.

[10] F. Fleury and R. Mouterde, *Comprendre simplement la résistance des matériaux*. (2nd ed.). Editions Le Moniteur, 2010. pp. 90-91.

[11] T. Wester, "The dualistic symmetry between plane and point-based spatial structures" in *Symmetry of structure, an interdisciplinary symposium, Budapest, Hungury, August 13-19 1989. Vol. II*. G. Darvas and. Nagy. pp. 614-615.

[12] T. Wester, "The structural Morphology of Basic Polyhedra" in *Beyond the cube, The Architecture of Space Frames and Polyhedra*. J. F. Gabriel Ed., John Wiley & Sons, Inc. 1997. pp. 306-307.

[13] https://es.wikipedia.org/wiki/Archivo:Gdansk_Gorki_Wschodnie_falochron_2.jpg. Accessed 21 June 2010

[14] Y. Coineau and B. Kresling, *Les Inventions De La Nature Et La Bionique*. (1st ed.). Paris: Hachette Littérature, 1992. pp. 37.

[15] https://www.zaha-hadid.com/design/mesa-table/. Accessed 21 June 2010

Proceedings of the IASS Annual Symposium 2019 – Structural Membranes 2019
Form and Force
7 – 10 October 2019, Barcelona, Spain
C. Lázaro, K.-U. Bletzinger, E. Oñate (eds.)

A Project-based Learning on Tensile Membrane Structures in Architectural Education

Jelena MILOŠEVIĆ*

*University of Belgrade – Faculty of Architecture
Bulevar kralja Aleksandra 73/II, 11000 Belgrade, Serbia
jelena@arh.bg.ac.rs

Abstract

This paper presents a case study on the application of the project-based approach for learning on tensile membrane structures at an elective course at master studies of architecture. In order to improve the learning process and achieve course outcomes, over an extended period of time during the semester, students worked on a project, which task was to design a covering for small pedestrian street. In small groups, students investigated applications of membrane installations, and how these structures could improve the quality of open urban spaces and solve environmental problems. The task engaged students in innovative and creative solving a real-world problem and to deal with functionality, feasibility, practicality, and ecology. The project was implemented through collaboration with scientific research project and company. This approach enabled students to understand the synthesis of structural analysis, material behavior, constructability and economic reality that occurs in the professional practice. Project-based method facilitated students to learn by working in (inter)active and inclusive environment, to investigate and respond to engaging and complex problems and challenges and thus develop a deeper understanding of the design, technical, and installation issues of tensile membranes. As a result, students developed deep content knowledge as well as critical thinking, creativity, and communication skills in the context of doing an authentic, meaningful project.

Keywords: architectural education, project-based learning, structural design, form finding, membrane structures

1. Introduction

Teaching structural engineering subjects to master architectural students represents a challenge for many reasons such as their background knowledge, learning habits, interests, and affinities, etc. In the education of architects, teaching the structural problems is usually approached from the analytical rather than the synthetic aspect, which often results in a limited understanding of global structural performance and the lack of conceptual structural awareness (as has been pointed out by authors dealing with educational problems in this field recently). At the Belgrade University Faculty of Architecture method of teaching structural systems that combine theoretical, practical and design activities were introduced in the curriculum back in the 1960s and has constantly improved and innovated.

The elective course Generating spatial structures via form-finding taught annually at the University of Belgrade - Faculty of Architecture introduces master students to methods and techniques of form-finding of shape active structures. The course aims at architectural students to develop an understanding of (1) structural systems, and structural problematics relevant for architectural design, (2) building strategies and skills to integrate knowledge of structural principles and construction techniques; (3) properties of structural materials, components and systems, as well as their impact on environment, and to (4) acquire skills of form-finding methods and techniques [1]. Teaching methods are oriented towards learning outcomes and include lectures combined with methods of active learning (methods of conversation and demonstration), practical work assignments (method of individual exercises), learning and research of

Copyright © 2019 by Jelena MILOŠEVIĆ
Published by the International Association for Shell and Spatial Structures (IASS) with permission.

literature (method of working with text), and learning through the project. Some activities are designed to stimulate peer learning and thus contribute to the formation of an inclusive environment. Also, an important aspect of the learning process is the collaboration and cognitive gain of students from teamwork.

As a measure to enhance the course, during academic year 2018/2019, we set learning experience which gave students an opportunity to test the theoretical knowledge through practically oriented design research. After lecture-based classes on form-finding, small practical – modeling exercises, and literature research of examples, we introduced a project-based activity that implied designing of mechanically pre-tensioned membrane structures made of technical textiles. Although planned activities, scope and complexity of tasks were in line with the number of working hours (60 hours) and student competencies (there were no specific pre-requisite just common skills of the 1st year student of architecture) we achieved the expected learning outcomes, and enabled students to develop a deeper understanding of the behavioral properties of materials, technical, construction, and installation issues of tensile membranes and to demonstrate their knowledge by developing designs / public products, and preparing exhibition, presentation for a real audience.

2. Project-based Learning

Project-Based Learning (PBL), described in [2], [3], [4], is instruction methodology that encourages students to acquire knowledge and skills through an engaging experience and represents an opportunity for deeper learning in-context. Evolved from Dewey's idea of *learning by doing* [5] this methodology enables students to learn about the subject by working, investigating or responding to a complex question, challenge or problem. The characteristics of the PBL activities could be summarized as: (1) interdisciplinary because it requires students to engage/use content knowledge and skills from multiple academic domains to successfully complete the project that addresses the real-world issue or challenge; (2) comprehensive because it requires the application of knowledge and skills, not just recall or recognition. i.e. as students engage in the work of a project, they follow a process that begins with inquiry, which leads to deep learning not just related to academic content, but also related to the use of content in real-world applications - students apply a variety of academic content in new contexts leading to the development of solution that addresses the problem/challenge of the project and the creation of products to communicate solutions; (3) student-centered because it fosters students independence and encourage them to make their own decisions with the teacher providing support only when needed.

Application of the PBL in the engineering and architectural education is communicated by [6], [7], [8], [9], [10] and others. These studies illustrate that traditional engineering curriculum and lecture-centric programs are revised and improved by the introduction of the PBL to corresponds to the calls from the industry on what they need from engineering graduates. Complexity and student autonomy in these programs appear to be the best way to satisfy industry needs, without scarifying knowledge of engineering fundamentals. Also, it has been proved that the engineering professions and academics are more familiar with the concepts of projects in their professional practice. As demonstrated in studies presented in [11], different from traditional (paper-based, rote memorization, teacher-led instruction, etc.) this methodology ensures better learning outcomes. The advantage of the application of this inquiry-based learning approach in teaching form-finding of structural surfaces is reported in [12] and [13]. Papers demonstrate how form-finding techniques can be learned in one semester project-based course organized for the group of students from the architectural and engineering department. In [13] are also given a non-exhaustive list of similar courses thought at different institutions worldwide, showing that revived interest in the structural efficiency and aesthetics of complex spatial shape active structures asks for courses that will teach students this subject matter. The fact that, in some capacity, most of these courses apply the PBL and results proves the effectiveness of the application of this teaching methodology in this context.

3. Case study

The case study reports on the project carried out within the elective course Generating Spatial Structures via Form-finding during the outman semester of the academic year 2018/2019. In order to improve the quality of the teaching process we introduced following changes: (1) work on the project was realized in small groups – 3 to 4 students, (2) task was focused on membrane structures, instead of covering diverse structural typologies and (3) we implemented research results of the scientific project and integrated practical elements into the curriculum through collaboration with the company, thus bridging gap in knowledge transfer between academia and practice.

3.1. Framework

The task of the project named "Urban Textile Interface (UTI) Structures" was to design textile membrane structure for covering small pedestrian street/passage. The project encouraged investigation of the possibilities of textile materials for permanent, temporary, mobile and adaptable structures, problems of shaping, construction and materialization, potentials of these structures to improve quality of urban spaces – environmental problems (ex. insulation, noise, atmospheric influences, sustainability, re-use, recycling, etc. The goal was to motivate innovative approach to the design of textile membrane structures which will at the same time enable students to learn about the challenges of constructing of these unconventional, light spatial structures and potentials of their application in architecture. In order to ensure achievement of the expected outcomes, we specified design methodology which was implemented through phases.

3.1.1. Design process

The process employed the following phases: (1) conception, (2) form-finding, (3) elaboration and (4) post-production (Table 1). Each phase had tasks and results that represented the input for the next phase.

The conception phase commenced with the exploration of the space of intervention and the formation of the design intention. During this phase, starting from different phenomena / notions / impressions / perceptions, students were asked to outline, explore and present a topic / thesis / idea that will be explored through the design. These analyses were then transformed into information useful for the design genesis and definition of genesis strategy. Results of these activities were displayed graphically - diagram (ideogram) and textually (synopsis and keywords)

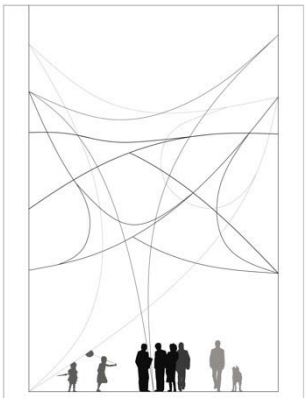
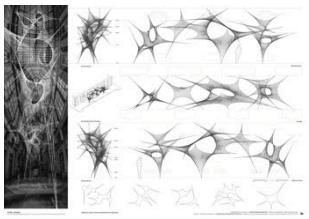
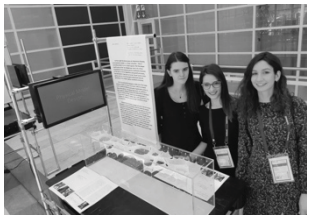
The process continued with the form-finding using textile physical models and computational tools to simulate tension membrane structures. In this phase, students apply techniques and tools previously worked out in the framework of theoretical teaching with the goal to explore, test and understand complex interrelation between geometric and structural properties of these structures. The results were the models of the textile membrane structure.

The elaboration phase involved further development of the design and production of detailed technical drawings. The goal of this phase was to translate the model into an architectural structure focusing on form-structure and construction-materialization relations. In order to study structure on different levels and understand its behavior and properties, we used structural analysis and evaluations. In this phase students need to work on diverse technical aspects of the solutions - define applied materials, deliver details of connections, produce cutting scheme, propose construction technology and installation methods.

In the phase of post-production, students had a task to prepare an exhibition for the real audience. Students respond to the task and created diverse artifacts during the process to present their gained knowledge (an example - construction of models is shown by video [14]). Artifact included a variety of media such as writing (short and long design explanation), drawings (sketches and technical drawings), three-dimensional representations (3d models, renders and prototypes), videos, photography, etc.

Finally, each team had a task to make an exhibition panel which was along with selected artifact part of the exhibition

Table 1: Work process

	task	**goal**	**technique**	
Conception	defining theme/thesis/idea of design research	comprehension of the patterns verbalization and visualization of the idea, definition of the generation strategy	diagramming writing	 **ideogram**
Form-finding	Generating spatial model of textile membrane structure	comprehension of the generative procedures	textile physical model and computational modelling techniques	 **model**
Elaboration	development of the project - transformation of the geometry into structure producing large scale prototype	comprehension of the analogy of equilibrium mesh as diagram of structure experiencing prototyping technology, comprehension of the problems of construction of real structure	CAD CAE CAM visualization techniques	  **design**
Post-production	communication of the design process and proposals through selected artifacts	participation in the exhibition for the real audience	visualization techniques photography video	 **exhibition**

3.1.2. Results

Basis of the PBL lies in the authentic or real-life application of the results. With this respect and having in mind specific task, we graded the following aspects of designs - feasibility and practicality, level of innovation, aesthetics-design approach, functionality, ecological quality, economy. Through the described process students had an opportunity to test method that enabled them an analysis of geometry and structural behavior of membrane structures and its application in the development of original designs. The previously described work process enabled experimenting performance-based approach in the design of membrane structures. Starting from the constraints imposed by the task (the design of the structure for covering the generic pedestrian street) and design space (the dimensions of the intervention area, the openings, the discontinuity of the surface for fixing the structure, the obstacles in space, etc.), considering both technical and social performances or solving problem by application of nature-inspired patterns the results are urban interfaces in the form of spatial textile structures that are light, expressive, dynamic and that improve qualities of open public space (Figure 1).

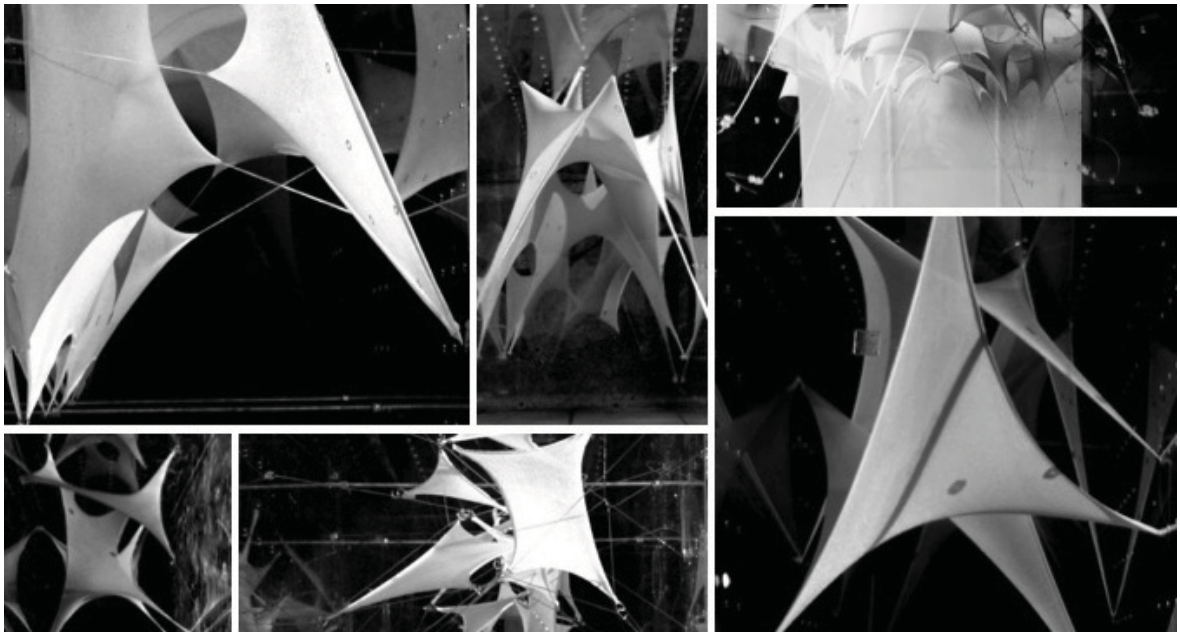


Figure1: Examples of students' designs

3.2. Evaluation

Assessment of the success this educational experiment is based on the results of students' questionnaire and the general audience reception.

3.2.1. Students' questionnaire

The evaluation questionnaire in the last few years become standard practice at the end of each course at the University of Belgrade – Faculty of Architecture, which are students obligated to fill in. So, all 25 students fill in a questionnaire requesting students' self-evaluation and input on the quality of lectures, assignments, design project, readings, and overall quality of the course. Also, at the end of the course, we made questionnaire for evaluating the PBL methodology. Students graded both course and the PBL methodology using the scale from 1 (lowest level) to 5 (highest level).

Students evaluated the following aspects of the course: (C1) understandability and the presentation of the course material, (C2) compliance between lectures and scope of the course material, (C3) encouragement students on active, critical thinking and creativity, (C4) teachers lectures help students to easy master the course material, (C5) volume and quality of recommended literature, (C6) the teacher

provides useful information for future student work, (C7) proper duration of the course. Following aspects of the PBL methodology were evaluated: (M1) continuous learning, (M2) autonomy, (M3) teamwork, (M4) communication skills, (M5) planning skills, (M6) level of motivation in the development of the project, (M7) necessity of technical concepts to develop project, (M8) adequacy of available material and resources, (M9) level of satisfaction with the results.

Total average rating of the course is high at 4.61. Students marked as satisfying the level achieved in their capacity of learning, autonomous work, and planning skills, they also think that they slightly enhanced their teamwork and communication skills. In addition, the students affirmed that technical concepts were essential to developing the project and so lectures and practical works served to apply these concepts. Students are mostly satisfied with available recourses and final designs, and expectedly they felt comfortable with application of this methodology. However, only 30% of the students considered that the established deadline was enough to develop properly the project. It is clear that adopting new techniques implies a change in their learning and design style and this adaptation takes time. For next experiences, better time management could be proposed. (Figure 2)

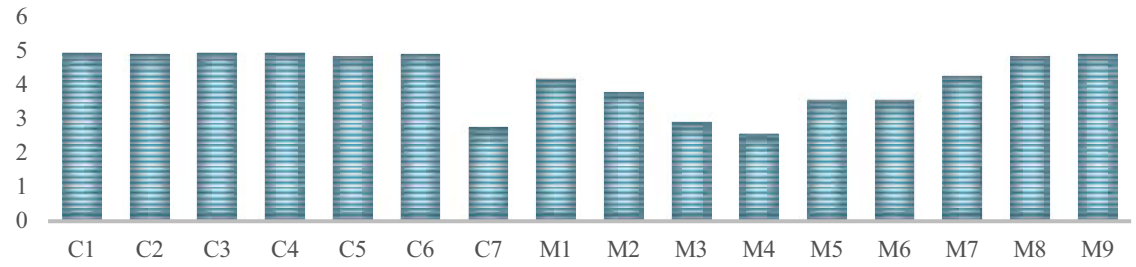


Figure2: Students assessment of the course and PBL methodology

In the open-ended part of the questionnaire, students commented on the benefit on teamwork and research. As one student states: *Interesting, useful and creative subject, encourages teamwork and research*. Also, students have a generally good opinion on practical work: *All practical exercises and project stimulated us to creatively apply what we learned*. However, the students felt less at ease with the manner certain technical concepts were introduced: *Accessibility of the professor, excellent work with students, motivation for further work, literature, lectures, everything is excellent; the only criticism is that sometimes the professor expects students to possess knowledge or skills that they do not possess, so some of the things exposed can remain vague*. This challenge working with a group of students from different orientation (design, interior design, urbanism, technology) and with different knowledge. One of the ideas of how to overcome this problem is to consider this when forming groups. Many students commented on the benefit of learning in an interdisciplinary context.

3.2.2. General public

Although designs emerged from the autonomous process of formations, and derived shapes are based on physical laws they have aesthetical qualities which make them appealing to the general audience. All students' works were presented at the exhibition organized at the University of Belgrade – Faculty of Architecture gallery. Also, one of the students' designs that created in this course was submitted to the international competition: *Textile Structures for New Building 2015*, organized for the 15th time by the Techtextil with the support of the international association for membrane constructions TensiNet. This competition was organized with the aim to recognize innovative thinking and solutions for the problems of designing and constructing structures from textile materials, as well as strengthening contacts between young, technical-textile construction industry and universities. The students won the First Prize in the category: *Urban Living-City of the Future* and their work was displayed along with other awarded works at International fair Techtextil in Frankfurt [15]. The prospect of displaying their work to an international jury and audience was a great motivator for increased engagement in the class.

3.3. Discussion

Engaging students in designing textile membrane structure increased motivation and contributed mastering diverse skills and knowledge. Although they faced a nontrivial problem, within the set framework students managed to produce distinctive artifacts and communicate their ideas. In order to complete task students, draw on lessons from several disciplines and applied them in a very practical way. Also, all activities planned by the curriculum that preceded project contributed to the successful task realization – learning from analogies, i.e. precedent of membrane structures; learning on form-finding techniques; experiencing form and force ration through production and manipulation of the parameters of digital and physical models (curvature, span, sag, pre-stress). Along with these activities, the project enabled students a great depth of understanding of concepts related to the design and construction of membrane structures. We set learning experience which give students opportunity to acquired diverse competencies – they broaden knowledge base, improved communication, and social skills, enhanced leadership skills, increased creativity, improved writing skills and critical thinking, etc. Working in a group facilitated peer learning and the creation of a collaborative and inclusive learning environment. However, we noticed so-called *social loafing* [16], a negative aspect of the PBL, manifested by an insufficient performance by some team members as well as a lowering of expected standards of performance by the group as a whole to maintain congeniality amongst members. In order to overcome these monitoring of social dynamics of the assignment was introduced, the process and products of each phase were graded and not just final results. It is also important to notice that working in an authentic project and the promise of seeing a very real impact was a strong motivation for learning. The course has the potential to be further improved, but the main obstacle is the need for time and resources to facilitate such an active learning environment.

4. Conclusion

Application of the PBL for teaching tensile membrane structures facilitated to achieve optimal success in acquiring knowledge, forming skills and developing students' creative abilities. It should be emphasized that the course was combined with researches preformed within scientific project: *Development and application of scientific method in design and construction of high economic structural systems by use of new technologies*. The course also integrated practical elements into the curriculum through collaboration with the company. This transfer of knowledge and technology between education, science and industry provided students with a combination of theoretical and practical knowledges. This situated learning environment gave students opportunity to learn knowledge and elements of the core curriculum, but also to be engage students in real-world learning, to solve authentic problems and produce results that matter. The PBL encouraged students to think out of the box, and to make meaningful connections across content areas, rather than thinking about subject area in isolation. Also, students took advantage of digital tools to produce high quality, collaborative products. We created learning scenario in which students have an opportunity to experience intangible assets such as drive, passion, creativity, empathy, and resiliency and produce exciting designs. The task unleashed contagious, creative energy among students and all the other participants engaged in its realization. Finally, the student evaluations and the outcome of this course demonstrate that suggested pedagogical approach can be effective method for teaching, learning and training tensile membrane structures.

Acknowledgements

This research was supported by the Ministry of Education, Science and Technological Development of the Republic Serbia, Project No. TR36008.

References

[1] Course Curriculum [Online]. Avaliable: http://www.arh.bg.ac.rs/wp-content/uploads/201819_programi/201819_dokumenti/1819_MASA/201819_MASA_S

VI _MODULI/201819_MASA-11020-07-IASA-47020-07-GENERISANJE-PROSTORNIH- STRUKTURA.pdf. Accessed on Feb 15, 2019.

[2] P. C. Blumenfeld, E. Soloway, R. W. Marx, J. S. Krajcik, M. Guzdial, and A. Palincsar, "Motivating Project-Based Learning: Sustaining the Doing, Supporting the Learning," *Educational Psychologist*, vol. 26(3&4), pp. 369-398, 1991.

[3] J. G. Greeno, "Learning in activity" in *The Cambridge handbook of the learning sciences*, R. K. Sawyer Ed., New York: Cambridge University Press, 2006. pp. 79-96.

[4] T. Markham, *Project Based Learning*. Teacher Librarian, 2011.

[5] J. Dewey, *Education and Experience*, New York. Touchstone. 1938/1997.

[6] J. E. Mills and D. F. Treagust, "Engineering Education – Is Problem-Based or Project-Based Learning the Answer," *Australian Journal od Engineering Education*, online publication, Jan. 2003.

[7] F. M. Bashir, M. H. Ahmad, M. Hamid, "Design Studio as Problem Based Learning in Architectural Education in Universiti Teknologi Malaysia" in *Proceedings of 4th International Research Symposium on Problem-Based Learning (IRSPBL)*, 2013, pp. 373-379.

[8] C. Ibáñez and D. Hernández-Figueirido, "Project Based Learning experience with engineering students for the design of steel structures," in *Proceedings of 3rd International Conference on Higher Education Advances, HEAd'17*, 2017, pp. 658-666.

[9] H. K. Banerjee and E. De Graaff, "Problem-based Learning in Architecture: Problems of Integration of Technical Disciplines," *European Journal of Engineering Education*, 2010, pp. 185-195

[10] S. Kuhn, "Learning from the Architecture Studio: Implications for Project-Based Pedagogy," *International Journal of Engineering Education*, vol. 17, nos. 4 and 5, 2001, pp. 349-352.

[11] R. K. Sawyer, R. K. *The Cambridge Handbook of the Learning Sciences*, New York: Cambridge University Press. 2006.

[12] S. Adriaenssens, "Learning Form-finding of Structural Surfaces": a new project-based course," in *Proceedings of the IASS Annual Symposium 2015, Amsterdam Symposium: Future Visions – Teaching of Spatial Structures*, 2015. pp. 1-10.

[13] S. Adriaenssens, R. M. Oliveira Pauletti, K. Stockhusen, S. Gabriele, P. Magrone, V. Varano and I. Lochner-Aldinger, "A Project-Based Approach to Learning Form Finding of Structural Surfaces", *International Journal of Space* Structuresi, vol. 30 (3-4), 2015, pp. 297-305.

[14] Generating Architectural Structures, video presentation [Online]. Avaliable: https://www.youtube.com/watch?v=LOvhQJvLQDk, Accessed on Feb 15, 2019.

[15] Techtextil and Tensinet Brochure [Online]: Special Grant for the 15th Student Competition "Textile Structures for New Building 2019", Available: https://techtextil.messefrankfurt.com/content/dam/messefrankfurt-redaktion/techtextil/2019/downloads/Techtextil-Studentenwettbewerb2019_Broschuere.pdf, Accessed on May 20, 2019.

[16] H-J. Lee and C. Lim, "Peer Evaluation in Blended Team Project-Based Learning: What Do Students Find Important?," *Journal of Educational Technology & Society*, vol. 15(4), 2012, pp. 214-224.

Proceedings of the IASS Annual Symposium 2019 – Structural Membranes 2019
Form and Force
7 – 10 October 2019, Barcelona, Spain
C. Lázaro, K.-U. Bletzinger, E. Oñate (eds.)

Teaching creativity in structural design – approaches and challenges in Germany

Eberhard MOELLER*, Hans NUNGESSER*

*Karlsruhe University of Applied Sciences
Moltkestr. 30, 76133 Karlsruhe, Germany
Eberhard.moeller@hs-karlsruhe.de

Abstract

With around 1.94 million employees and a turnover of approximately € 237 billion, the construction industry is a significant economic sector in the German economy. The number of persons working in this sector is about twice as large as in mechanical engineering, and the turnover of both sectors is almost the same. While the German Research Foundation DFG approved € 355.9 million funding for "Mechanical Engineering and Production Technology" in the years 2014 to 2016, the sector of "Building and Architecture" only received commitments of € 91.3 million, what is only 1.1% of the total commitments of the DFG. By contrast, the percentage of gross domestic product used in Germany for construction investment is 9.9%, which is about 10 times higher than the percentage of research funding for this economically important sector. These figures indicate a comparatively low level of research, development and innovation in the construction industry. Looking at the teaching of structural design, Werner Sobek notes that the training of civil engineers, especially in structural engineering, still is almost exclusively concerned with the analysis of given structures – not with creativity or innovation. Regarding this background on the one hand and Frei Otto's extraordinary professional career on the other hand, necessity and possibilities of integrating creativity in the teaching of civil engineering are examined.

Keywords: structural design, teaching, creativity, inspiration, invention, innovation, research and development, physical modeling, design research

1. Introduction – means and goals | balance and equilibrium

Thinking about teaching methods is part of thinking about goals and context. Structural design is related to the search for balance and equilibrium. Structural Engineers often are equilibration experts. Statics means state of rest, it means absence of movements because of the equilibrium of forces.



Figure 1: A symbol of fragile equilibrium (Alexander Calder, Mobile, Yale University Art Gallery)

Copyright © 2019 by Eberhard Moeller and Hans Nungesser
Published by the International Association for Shell and Spatial Structures (IASS) with permission.

As **experts in equilibrium** engineers are especially aware of fragile balances and important imbalances, also of the great imbalances of our days. In addition they are aware of natural laws. A common principle in engineering is doing "more with less", aspiring to effectivity while respecting natural balances and laws. Engineers often are working towards a highly developed culture without excessive exploitation of fossil resources, of creatures or of fellow human beings. In this context Buckminster Fuller's ideas for handling and maintaining "spaceship earth" are still worth reading.

The achievements of mankind in the last 200 years are impressive. Large span bridges, great skyscrapers, fast trains, cars, jets, increasing prosperity, life expectancy etc. But what are the whole impacts? Who gains, what suffers? Which balances are currently disturbed? And what can and maybe should we do now to avoid future imbalances, problems and risks? The majority of climate researchers and scientist's for instance advices us to stop the imbalances in the global CO_2 household driven by using and burning fossil fuels – what unfortunately has been the base of industrial progress within these last 200 years. Are there natural risks, if engineering tries to follow their advice, for example by using the means of "Reduce – Reuse – Recycle"?

The desire to maintain more or less our standard of living in times of necessary decarbonation seems to require changes and therefore ideas and innovations – not only in the fields of energy supply, industrial production or transportation but also in the fields of buildings and structures. When we take a look at the structural achievements in times of industrialization and digitalization we find a lot of prominent world records in terms of scale – bridges like the Brooklyn (1883, 485 m, Fig. 2), the Golden Gate (1937, 1280 m) or the Verrazzano-Narrows Bridge (1964, 1298 m, Fig. 3), shells and spatial structures for trade fairs, sports venues (Fig. 4) or airport terminals (Fig. 5), tall high rises and towers – but do we know records or innovations in terms of balancing or of thrift of resources?



Figure 2: Brooklyn Bridge (1883, 485 m)

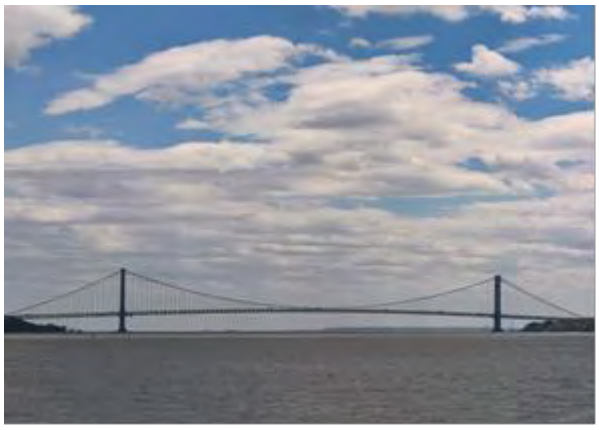


Figure 3: Verrazzano-Narrows Bridge (1964, 1298 m)

2. Innovation

2.1 Innovation – bases and preconditions

Successful innovation bases on at least three aspects: necessity, economic viability and a vision or idea. The necessity of innovations in building and structural design seems obvious as indicated above and documented by organizations like the **UN Intergovernmental Panel on Climate Change** (IPCC) and by labels like "LEED green building certification" (Leadership in Energy and Environmental Design) or "DGNB" (Deutsche Gesellschaft für Nachhaltiges Bauen e.V.). The question of economic viability is more difficult to deal with because of big discrepancies between short term and long term economic aspects and because of the lack of prizing future risks or valuing exploitation of nature or humans in many fields today. Engineers are able to gain influence in improving these economic issues for example by taking part in the political process.



Figure 4: "Yale Whale", Hockey Rink, New Haven



Figure 5: TWA-Terminal, JFK Airport, New York

Without aligning economic targets towards sustainability, reasonable developments, innovations and optimizations are determined to fail, because bad boundary conditions rarely lead to useful results.

Technical progress as a result of visions and ideas is estimated to be one of the bases for affluence and prosperity. Numerous architects and engineers are working with the objective of such progress. They are searching for innovation. Some results of this research and development process are documented. Journals and specialist books are showing the output in form images of buildings and technologies. What is shown very rarely is the process behind – the actual process of research and design. But for further progress it could be helpful to study and cultivate this process, too [1].

At first glance the culture of visions and creativity in structural design seems to be rich anyway, at least on the one hand, the hand of impressive megastructures. But on the other hand it might be even poorer, at the hand of everyday structures. The Oskar von Miller Forum in Munich traces that building industry drifts apart into two classes: some few architectural landmarks on the one hand and partly irresponsible, profane infrastructure on the other, which renders neither constructional nor imaginative contribution to the building culture [2].

Ideally, the structural design for buildings emerges of an **inspiring interplay** between architecture and civil engineering. Reality unfortunately is often sobering – due to the common deadline pressure or due to the increasing gap between the two disciplines. Therefore it is often impossible to speak about an active, rational design process. Far too often we build the usual, the conventional and the supposedly safe without creativity, detailed discussions and without observing the ideas of sustainable balancing. Progress or innovation hardly arises, because the development of new structures is rarely a short process. Innovation needs time, courage and the joy of experimenting.

2.2 Powerful historical innovations

Two of the most influential innovations in the field of building construction within the successful last 200 years have been achieved neither by civil or structural engineers nor by architects but by gardeners. **Joseph Paxton** (1803–1865), an English gardener, is well known for designing the Crystal Palace in London in 1851. He applied the ideas of industrialization to building construction by using a quick assembling modular system and industrial materials like cast-iron and plate-glass. Therefore the Crystal Palace project is considered as milestone in innovation and as embodiment of the historical "Turning Point of Building" towards the industrial age. It is the forerunner of the common steel and glass architecture of our days.

Joseph Monier (1823–1906), a French gardener, is regarded to be one of the principal inventors of reinforced concrete, the building material of the 20th century. This composition of materials made great shells or stiff high-rise structures possible even though requiring enormous energy input for the cement and steel production. Among other things because of this we see a reasonable revival of timber structures for a lot of building purposes in the last years.

2.3 Necessity of further innovations

Despite these two successful innovations, industrialization has left few trace at many construction sites although made-to-measure and handmade work in our times are considered the epitome of excessive luxury. As a matter of course we buy clothes off the rack and cars off the production line. But houses? Why not buy a house like a Ford? Or like a Citroën, if you're a little bit vain. This is precisely the question the architect **Le Corbusier** asked himself at the beginning of the 1920s, at a time when industrialization had long outgrown its infancy and had covered almost all areas of life [3].

In spite of the perceptible justification of the question, even 100 years later we still must realize that a significant industrialization in building construction has not yet taken place, perhaps apart from some historical exceptions like the Levittown's in the USA within the late 1940ies or the prefabricated buildings of the so called "real existing socialism" in Europe.

Anyone looking around today at construction sites in Germany will notice that – almost as in Goethe's time [4] – there are still around 15 to 30 craft-organized and actually craft-based companies on almost every construction site, whether it's a small single-family home or a skyscraper. Reasons are manifold and often described [5]. So in general building today is rarely efficient nor sustainable despite all political proclamations. Beyond scientific vocabulary, but based on many published articles, building in Germany is considered to be quite slow, expensive, unprogressive, land-consuming and unintelligent. Buildings are heavy (~500 tons building mass per person in Germany, Keynote Werner Sobek at IASS 2017 in Hamburg), massive, inflexible, energy-consuming, resource-destroying and far too often without convincing variability or future visions.

2.4 Today's environment for innovations

In addition as indicated above there is still neither a useful economic environment focusing issues of sustainability nor an adequate financial support for a beneficial innovative atmosphere in structural design. As pointed out, with around 1.94 million employees and a turnover of approximately € 237 billion, the construction industry is an important economic sector in the German economy. The number of persons working in this sector is about twice as large as in mechanical engineering, and the turnover of both sectors is almost the same [6].

While the German Research Foundation **DFG** approved € 355.9 million funding for "Mechanical Engineering and Production Technology" in the years 2014 to 2016, the sector of "Building and Architecture" only received commitments of € 91.3 million, what is only 1.1% of the total commitments of the DFG (Fig. 6) [7]. By contrast, the percentage of gross domestic product used in Germany for construction investment is 9.9%, which is about 10 times higher than the percentage of research funding for this economically important sector.

These figures indicate a comparatively low level of research, development and innovation in the construction industry. In addition, there is the danger of a vicious circle, a downward spiral, if the funding system promotes already existing innovative activities and environments and does not promote or enforce research in still less innovative fields and atmospheres. As civil engineers mostly produce prototypes or unique copies, responsibility, safety and security are important aspects and goals. While conservative and well established solutions seem to provide more safety than innovative ideas, creativity not always has a positive connotation in civil engineering.

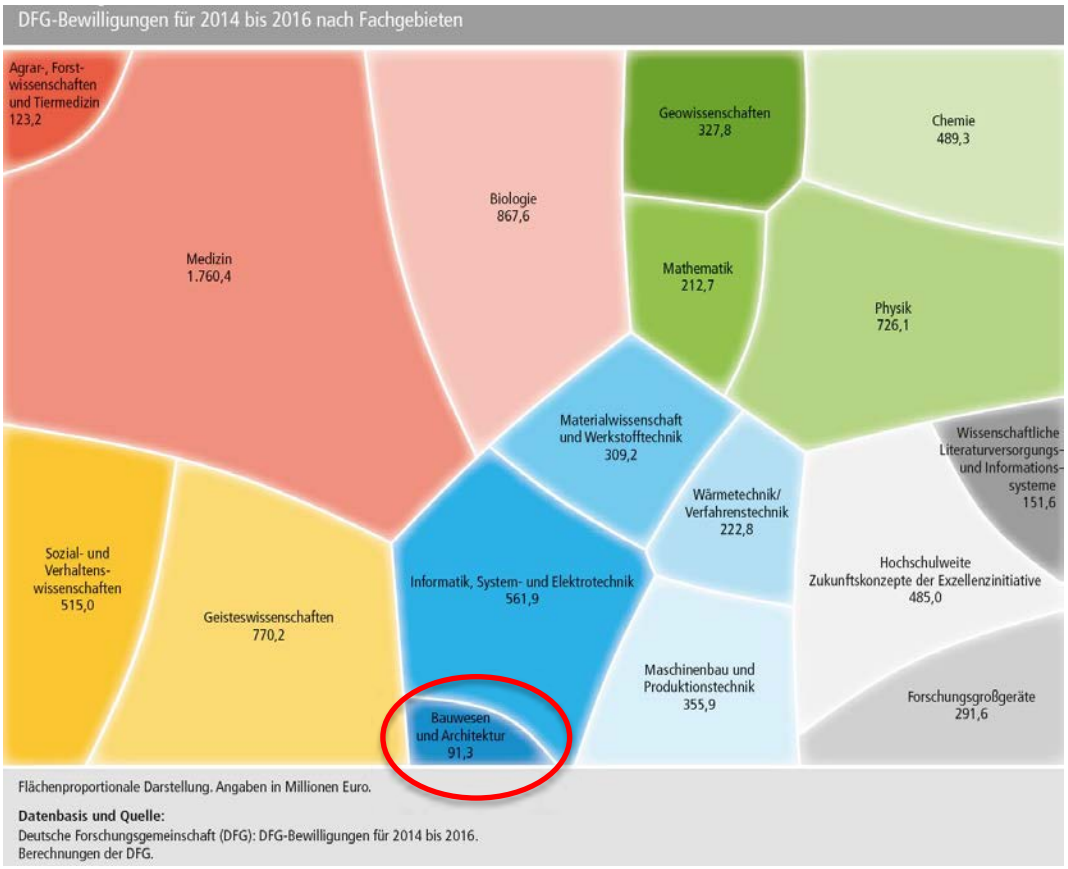
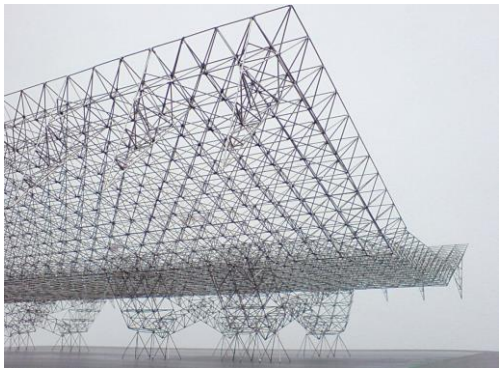


Figure 6: Distribution of DFG commitments to fields of research www.dfg.de [7]

Nevertheless structural designers produced a certain amount of still little used ideas and innovative suggestions that failed so far because of economic shortsightedness. A lot of these ideas were presented 2010 by the exhibition "**Wendepunkt|e im Bauen**" (Turning point|s of building) at the TUM Museum of Architecture at Munich Pinakothek der Moderne (Fig. 7, 8) and in the corresponding publication [8].





Figures 7, 8: Exhibition Wendepunkt|e im Bauen (Turning point|s of building) 2010 in Munich

Also the innovative work of Frei Otto provides some examples. He is one of the few explicit structural designers, who worked in his major projects together with both architects and structural engineers, for

the Montreal pavilion together with Rolf Gutbrod and Leonhardt/Egger, for the Munich Olympic roofs together with Behnisch & Partner and Leonhardt/Schlaich or for the Multihalle Mannheim together with Mutschler & Langner and Arup/Happold. This leads to the well-known and often discussed question who is in charge of designing and developing structure in projects where no explicit structural designer is engaged. There are different possibilities for finding answers to this question. A detailed and expansive interrogation of architects and engineers might help but is laborious and could also lead to euphemistic or contradictory statements. Instead comparing the study plans of the two faculties should provide notion about the training of both careers and therefore about how students are prepared for their future jobs. Regarding the credit systems architectural students are intensively trained in creativity and design but often less in analyzing structures. Civil engineering students are well trained in calculating given structures but less in design and creativity.

2.5 Researching development and innovation processes and its environments

Deliberating and research activities about creativity and innovation often is published under titles like design research or engineering research. The journal "research in engineering design" for example is an international journal with certain impact factor that states to publish research papers on design theory and methodology in all fields of engineering, focussing on mechanical, civil, architectural, and manufacturing engineering. But there are only very few articles on civil or architectural engineering. The topic of design research is hard to find at civil engineering schools. In Germany there is no chair for design research and no lecture in the common curricula in faculties for civil engineering. An extensive study of about thousand theoretical texts written by structural designers revealed a certain grade of concordance [9]. Following the majority of these texts a favorable process of developing a structure is often seen quite similar to that of development processes in nature, to the idea of evolution described by Charles Darwin consisting of the two steps of variation and selection.

For variation and thus for possible innovations, random coincidence plays an important role – like in nature. Any arbitrary limits or prohibitions on thinking therefore limit the chance for substantial development. Increase creative freedom and interdisciplinary work improves the chances for innovation. The second step, the selection, should be made consciously, rationally and on the basis of comprehensible criteria. However, neither process nor criteria of selection in the development of structures are discussed in detail in theoretical writings [9].

3. Teaching and education

3.1 Teaching of structural design

As the philosophy of teaching is able to influence the future ability for innovative thinking, the concept of academic courses is of certain impact. The academic course in civil engineering at the Technical University of Munich (TUM), one of the first universities in Germany to be named a University of Excellence, can be examined as a well certified example. Based on mathematical and scientific fundamentals, the acquisition of skills takes place in process-oriented and constructive fields of activity including the structuring of work processes, the engineering of building materials, soil mechanics and the basic principles of statics and structural engineering.

In this context the chair of timber structures and building construction is the only one offering lectures in "Tragwerkslehre" what could be translated as structural design or structural engineering. After participating, students should be able to define important terms in structural science. In addition, they should be able to understand the functioning and integration of the structure in the overall context of a building. Computational approaches to the function of structures and forces can also be applied. Project work in groups involves the quantitative and qualitative recording of relevant effects on a building, the recognition of static systems and their calculations. Together with presenting the complete program of building construction topics like foundation, exterior walls, facades, ceilings, steep and flat roofs, stiffening and joining, this course is worth 12 of 120 ECTS credits or 10% of the

three-years-bachelor program. The teaching follows predominantly the top down method, only in the small part of project works instead bottom up. The curriculum doesn't show subjects like creativity, innovation or strategies in design and development. Sustainability – the maybe most important issue of our days – is not part of the curriculum although the results of our colleagues in climate research are overwhelmingly concordant. Why do they effectuate so few impact in other fields like civil engineering and structural design?

At Karlsruhe University of Applied Sciences the master program for traffic engineering provides three mandatory subjects for road construction but none for railway construction. The master course for structural engineering provides mandatory subjects for steel structures, for reinforced and post-tensioned concrete structures but timber structures is only elective. In the German civil engineering departments there are chairs for calculating the well-established materials like steel, concrete or timber work, but we don't find any chair for design or construction sciences in general, stated accordingly Werner Sobek ten years ago and he criticized: "Engineers are essentially acquainted with the methods and tools for analyzing structures during their studies. The synthesis preceding each analysis, that is the structural design, is taught only to a very limited extent or not at all. As a result, civil engineers are inadequately trained for a substantial part of their professional activities." [10]

3.2 Teaching and living innovation and creativity

Fortunately there are a few positive examples for inspiring teaching of structural design, based on comprehension by insight and grasp and based on the history of culture and innovation. The quite small town of Stuttgart is well known for structural designers and engineers like Fritz Leonhardt, Frei Otto, Jörg Schlaich, Werner Sobek or Jan Knippers. Mike Schlaich at TU Berlin, Annette Bögle at Hafen City Universität in Hamburg or the so called "Dortmunder Modell", animated by Stefan Polónyi, are working for a culture of innovation full of enthusiasm and curiosity. Successful best practice examples and inspiring storytelling are powerful means and tools. One of the best lecture for young engineers and architects takes still place at Princeton University. The course "Structures and the Urban Environment" prepared by David P. Billington and Maria E. Garlock focuses on structural engineering. Combined with laboratory experiments students study the scientific basis for structural performance and thereby connect external forms to the internal forces in the major works of structural engineers.





Figures 9, 10: Exploring **form and force**, workshop at Karlsruhe University of Applied Sciences

Lightweight structures like pneus, membranes, shells or spatial structures are especially suitable for experiments like this. There is no need to put them in elective courses at the end of advanced civil engineering studies. We could also start with structures that display the relation between **form and force** quite obviously. Basic comprehension might be easier to achieve with lightweight structures than with beams, slabs or plates. Touching materials and feeling forces provides comprehension more directly than calculating numbers and equations.

4. Future challenges

The environment we live in and we work for is changing, its challenges, too. About 200 years ago the German futurologist Johann Wolfgang von Goethe stated in Wilhelm Meister's Journeyman Years: "You see the flowers wither and the leaves fall, but you also see fruits ripen and new buds open. Life belongs to the living, and whoever lives must be prepared for change."

In the wake of industrialization, digitalization and emerging technologies like artificial intelligence today changes are accelerating. To be prepared for the challenging future we need to ask the right questions and force the corresponding competences. Knowledge has long been scarce, but today it is all-encompassing and easily accessible thanks to the Internet. In the sea of information orientation and focusing becomes more and more necessary. Following the US National Education Association the four most important skills for 21st century are **critical thinking, communication, collaboration** and **creativity** – not only but also for engineers. Are we prepared? Are we preparing our students how they deserve? Maybe we should compare the methods of teaching as well as the curricula of our universities with those of 20 or 50 years ago.

References

[1] Möller, E., "Invention and innovation in structural design and construction – Frei Otto and the Munich Olympic Stadium 1972 – a historical case study", in *Proceedings of the Fifth International Congress on Construction History*, Chicago, USA, June 2015, B. Bowen, D. Friedman, T. Leslie, J. Ochsendorf Eds., 2015.

[2] Stiftung Bayerisches Baugewerbe, Oskar von Miller Forum, *Gesprächsrunde mit Vortrag von Annette Bögle* , November 30, 2017, https://www.oskarvonmillerforum.de/en/programme/event/cal/event/detail/gespraechsreihe-im-rahmen-der-ausstellung/2017/november/30.html

[3] Le Corbusier, Häuser im Serienbau, in *Ausblick auf eine Architektur*, 1922, Le Corbusier, 4. Aufl. 1982, 3. unveränderter Nachdruck, Basel, 2001, pp. 165–200.

[4] Goethe, J. W. v., *Wahlverwandtschaften*, 1809, http://www.gutenberg.org/cache/epub/2403/pg2403.html

[5] Möller, E., „Zu einer entfesselten Architektur | Über Industrialisierung und Digitalisierung des Bauens", in *Wendepunkt|e im Bauen | Von der seriellen zur digitalen Architektur*, Nerdinger, W. et. al. Eds., München: Detail, 2010, pp. 31-37.

[6] Statistisches Bundesamt, „Produzierendes Gewerbe und Dienstleistungen im Überblick", in *Statistisches Jahrbuch 2018,* pp. 519-548.

[7] Deutsche Forschungsgemeinschaft, *Förderatlas 2018 | Kennzahlen zur öffentlich finanzierten Forschung in Deutschland*, Bonn, 2019.

[8] Nerdinger, W. et. al. Eds, *Wendepunkt|e im Bauen | Von der seriellen zur digitalen Architektur*, München: Detail, 2010.

[9] Möller, E., *Die Konstruktion in der Architekturtheorie | Positionen und Entwicklungen von 1950 bis 2010*, München: Dr. Hut Verlag, 2011.

[10] Sobek, W., Eilbracht, G., Gert Eilbracht im Gespräch mit Werner Sobek über Entwurf und Konstruktion, die Ausbildung und das zukünftige gemeinschaftliche Schaffen von Architekten und Ingenieuren, in *Werner Sobek. Skizzen für die Zukunft - Architektur und Konstruktion im Dialog.* [diese Publikation erscheint anlässlich der gleichnamigen Ausstellung im Ausstellungszentrum der Vienna Insurance Group, Wiener Städtische Versicherung AG, in Wien, Schottenring 30 ; Ausstellungsdauer 2. Juli - 16. Oktober 2009 ; Katalog], A. Stiller Ed., Salzburg, Wien: Müry Salzmann (Architektur im Ringturm, 19), 2009, pp. 117-121.

Proceedings of the IASS Annual Symposium 2019 – Structural Membranes 2019
Form and Force
7 – 10 October 2019, Barcelona, Spain
C. Lázaro, K.-U. Bletzinger, E. Oñate (eds.)

Teaching Design Sensitivity

Stefan RUTZINGER*; Kristina SCHINEGGER, Rupert MALECZEK, Jens-Ole KLINGEMANN

* University of Innsbruck, Faculty of Architecture, Structure and Design
Technikerstrasse 21c, 6020 Innsbruck
Stefan.Rutzinger@uibk.ac.at

Abstract

In a post-digital era, students have a preexisting understanding of digital tools and methods when starting their architectural education. At the same time increasing computational capacities enlarge the potentials of modelling and simulation software and the sizes of solution spaces. Consequently, the focus in teaching digital design strategies shifts to a more reflective and integrated approach. The authors discuss two experimental vertical prototypes developed with first year students in research-led design courses. The courses' briefs aimed at enabling an immediate feedback through material-based design processes. Students are trained in how to articulate individual design criteria and make them productive within digital set ups, develop and navigate a design solution space and gain design-sensitive control of structural processes. Consequently, they become aware of the reciprocal relations between deign intentions, digital set ups, structure, material performance and constraints of fabrication.

Keywords: teaching design knowledge, generative design, computational design, structural design

1. Introduction

Although students nowadays have a previous knowledge in digital tools, they often lack a basic understanding of design. This is due to our education system that still maintains the dichotomy of science and art: education in the sciences operates and communicates in numbers and, on the other hand education in arts and humanities is based on language and expression. According to Nigel Cross, designers are acting in a "third culture" and have fundamentally different problem-solving strategies than other fields. Instead of applying generalized rules and methods, they follow an experimental approach based on trial and error strategies. While experimenting they simultaneously explore the problem until they have found an "acceptable" solution. Rather than being analytic they learn through synthesis. Since design problems are often "ill-defined" and lacking information, the designer adds to the problem and actively interferes with his object of investigation. Generally speaking, designer operate through abstract patterns in relation to a given task and stepwise turn them into an applied pattern. Although the methods and strategies vary according to the different objectives and intentions, an underlying "deep structure" or a "designerly way of thinking" which is inherent to all design professions can be observed [1]. Nowadays, through the availability of digital modelling and fabrication tools, designing objects turned from a specialist's towards a common ability. [2] It can be assumed that this development might turn design into a "basic" competence and that a general design education will gain in relevance.

Design skills depend to a large extent on experience and hands-on experimentation. Design processes based on material systems allow students to receive immediate feedback and gain an understanding of the reciprocal relation of form, materiality, experiential qualities and structural performance. They enhance design experience and sensibility while quality and consistency of the design output is enhanced.

Copyright © 2019 by Stefan RUTZINGER, Kristina SCHINEGGER, Rupert MALECZEK, Jens-Ole KLINGEMANN
Published by the International Association for Shell and Spatial Structures (IASS) with permission.

What has been broadly discussed in the past years as Material Systems or Generative Material and Design [3], has already been investigated at the German Bauhaus. In the foundation courses co-taught by Josef Albers and László Moholy-Nagyin the 1920ies students explored the complex relations between material properties, geometric constraints and aesthetic and experiential qualities. The creative but at the same time analytic approach of using material behavior as a driving force within form finding resulted in a multitude of spatial structures and new ways of resource efficient fabrication techniques [4].

The two discussed design courses adopt the Bauhaus approach by deploying material and geometry systems in an intuitive method. The aim is to achieve complex structures through self-regulated assembly processes, as well as establish a bottom-up approach in creating a design solution space. Design knowledge is not only tied to the designer itself, but also encapsulated in the designed objects. Therefore, it is of great value to capture various attempts and design studies to a specific design task in order to revisit them throughout the process. Iterative studies and the generation of variance – even in ascending scales or focusing on special problems – are fruitful since the encapsulated design knowledge can be read, extracted and transferred to future design problems.

2. Teaching Method

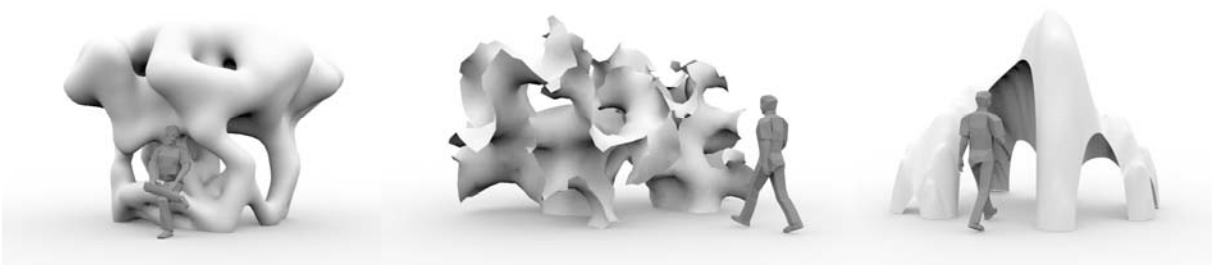


Figure 1: Digital Studies for paper strip models.

In order to define and narrow down the problem-space certain limitations are made: Both courses develop component based vertical structures, in the first example from flat paper strips in the latter from irregular wooden triangles. Both prototypes are constructed in a self-regulated assembly process. The introduction of the material system and the geometry system is a key factor since design freedom and individual expression have to be balanced with a required level of pre-determination within the system. In the case of the Bifurcation Tower the geometry system is loosely defined through the use of the plug-in Ivy [5] which enables sufficient variety in the development of the components, while the material system (600g paper) is fixed in order to meet the project budget. In case of the Reticular Tower, the triangular components are pre-defined (15mm OSP panels).

The individual participants of the course are given the same amount of material (identical set of triangles, counted sheets of paper) in order to retrieve comparable results which are discussed in regard to aesthetics, structural complexity, material efficiency, height of tower and other criteria.

Initially students create a broad pool of individual solutions and ideas to the given task (e.g. create a vertical structure with triangles). The relation between used design principles, processes and aesthetic and structural output is explored and articulated by students and tutors during pin-ups and reviews in order to formulate further design investigation tasks for student groups. Stepwise a design solution space is created from the pool of structures and their observed potentials. Design parameters and fitness criteria such as material consumption, tower height, count of components (production time) are established, tested and refined.

A main focus of the studios lies on how to guide the simultaneous development and refinement of design intents, digital process and physical prototypes, as well as enabling feedback between physical and digital models. A special focus lies on soft and rigid constraints that are necessary for the self-regulated assembly process.

The teaching is divided into several sections:

1. Theoretical introduction and practical seminars in CAD and parametric modeling using Rhino and Grasshopper (including various Plug-ins) with the aim to adjust and adapt predefined "definitions" in order to individualize the output. Introduction to workshop and basic digital fabrication machines (e.g. laser cut, CNC-cutter, printers, etc.).
2. The first design task involves control of shape (geometry) as well as size and resolution in order to fabricate a physical model (laser cutting of sheet material). Evaluation of the physical models by various criteria such as ambition, originality, complexity, structural stability and efficiency. Revising the design due to the evaluation. Increasing the scale and model size (stepwise until M 1:1); eventually adapting material and model building techniques to establish a working material system.
3. Development of a connection strategy in the parametric environment (abstract; involving experience from step 2) as well as in physical models (real joints); exploring various techniques in respect to different materials and fabrication methods in full scale – selection due to reasoning and physical feedback; improvement of the material system.
4. Testing various design versions against fabrication constrains (material consumption) and on efficiency (e.g. time consumption due to fabrication method).
5. Planning of the digital fabrication line (preparation of digital information to be fabricated, setting up the fabrication line and handling of material, postproduction, sorting and storage); planning of the foundation and implementation on site (including safe and sanity requirements); planning of disassembly and disposal.



Figure 2: Bifurcation Tower (left) and the Reticular Tower (right)

3. Bifurcation Tower

The tower consists of a component based material system, namely paper strips. Latest since the Bauhaus [6], paper is implemented in the design education, as it has many interesting aspects. On behalf of this material that cannot stretch or tear, students can make important experiences. It can be cut or manipulated in flat state and brought to a three-dimensional load bearing state through folding or bending. The relation of curvature and stability can be investigated in a very direct and haptic way.

For this project, the individual paper strips were developed on a triangulated mesh [7] as shown already by Fornes [8]. In contrast to Fornes' strategy of linear strips, where the mesh resolution in combination with bending plays a major role in the smoothness of the object, the authors used bending only to generate a smooth object, from a roughly triangulated mesh. Both approaches generate a self-explained assembly process, that replaces measurement by digitally defined and fabricated assembly points.

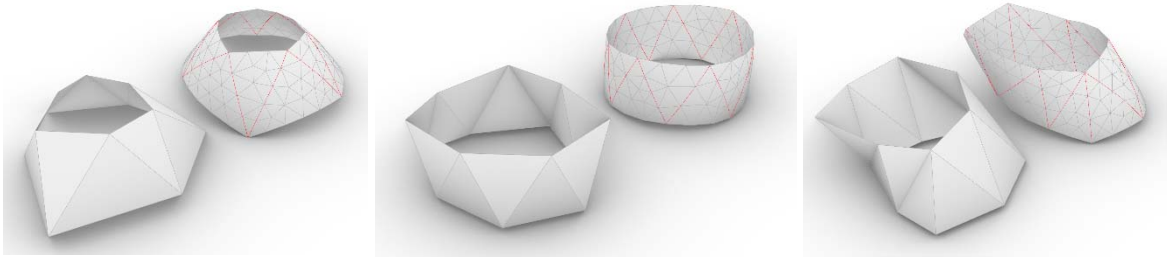


Figure 3: simulation of a bend rough mesh

The bending of the strips generates surfaces with single curvature. Each strip is bent by the connection to its neighboring stripes. As shown in figure 3, each stripe deforms based on this boundary condition. As the exact final state deviates from its original state, not only on the surface but also at the boundary edges, two neighboring strips will only have random identical connected edges. To solve this issue, the authors used a pointwise connection with a constant distance between the adjacent open strip edges. This solution allows a free deformation of the edges in space, preventing touching or intersecting neighboring edges.

The manipulation of the strips, as e.g. the shrinking or the connection generation, was done in developed flat state. Manipulating in flat state with knowledge of constrains in three-dimensional state has also been shown by Chandra et al. [9]. This strategy allows for a fast generation of fabrication files for a smooth object, but makes a prior visualization and control of the final state an additional work step, that is often over jumped. As the bifurcation tower is an individual free standing object with no further connections that would require this visualization or geometric control, the authors decided to trust the strategy for educational and time schedule reasons.

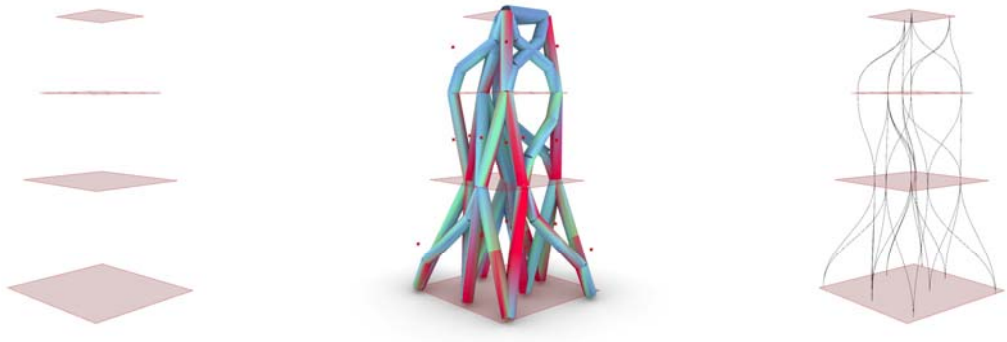


Figure 4: the generation and evaluation setup with the resulting line geometry

In order to understand and learn the material systems constraints, the students were asked in a first step to generate multiple mesh-based geometries in Rhino [10]/Grasshopper [11]. Mainly a physical simulation named Kangaroo [12] was used by the students as it provides a simple setup and fast results. With this digital geometries, the first studies for the material system in paper were made. These results led to the above described component based material system.

For educational reasons, the tower geometry was developed in multiple consecutive and partly simultaneous steps that were arranged in a cyclic feedback loop. In a first step a parametric solution space for the tower was established in form of a bounding box of 4*4*6 meters. Within this solution space, the students task was to define a self-supporting structure, that consists of a reticular smoothly piped line system.

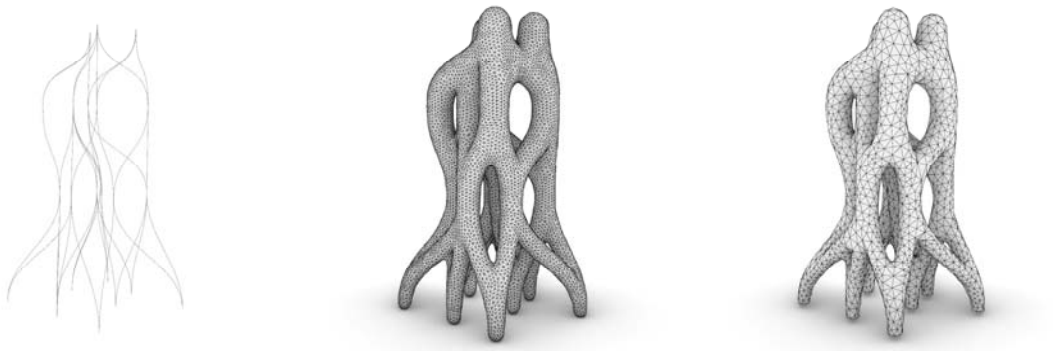


Figure 5: The piping process of the reticular line network and the re-meshed version of the tower

Therefore, a digital setup was generated that consists of two main parts. A set of parameters which can be changed and influenced by the user in order to generate a geometry, and an evolutionary solver, namely Galapagos [13] that optimizes the structure's parameter set on defined fitness criteria. As shown in figure 4, the line network is generated from several sets of points. Their number and relative position in height can be regulated by the user. The exact position is optimized through Galapagos with the structural performance as fitness property. Using Galapagos allows the students to see that a set of variations can be generated and evaluated in a very short amount of time.

In a consecutive step, as shown in figure 5, the line network is transformed in a pipe-like structure with the line as center for different radii. This geometry is re-meshed with a given minimum of edge lengths with a tool named MeshMashine [12]. This mesh was then divided in developable strips with the help of the tool Ivy. In a final step the unrolled strips were manipulated to have a small offset and flaps for the assembly. The assembly itself was done with synthetic press buttons. As described above, the inner edges of the strips were deleted, in order to bent the strips instead of fold them. As the strips build closed loops no additional boundary constraint is necessary for the entire structure. The entire structure was then cut on a flatbed cutter from 600g paper that was white on one side and pink on the other. This two-color scheme generated in combination with the distance of the strips, a spatial color effect. The fabrication and assembly was done in less than two weeks by 25 students and presented at the 1st years exhibition in the faculty hall.



Figure 6: the final tower (right) and the color bleeding detail of the construction

4. Reticular Tower

The course focuses on developing a bottom-up design approach based on the capabilities of a component based material system. The final prototype is constructed from wooden plates and metal joints, for initial physical studies cardboard is used. In order to develop a variety in bottom up design strategies students individually aggregate vertical structures out of a similar set of cardboard triangles. The only instruction is to apply a consistent logic ("manual algorithm") while constructing the structure and fulfill two requirements: it should be as high as possible and have distinct aesthetic properties. Students articulate the used composition logics (the underlying manual algorithm) and precisely describe the intended structural and aesthetic abilities. The variance of outcomes creates the base for a design solution space to be developed and allow students to formulate aggregation logics and design questions for the next iterations, see figure 7.



Figure 7: physical studies: different studies generated from the same set of cardboard triangles

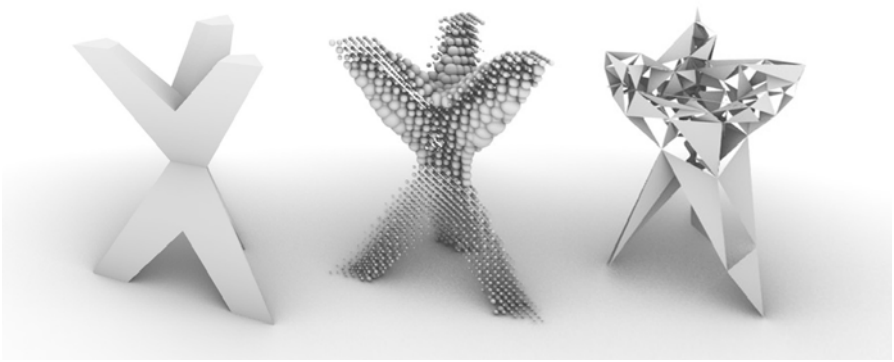


Figure 8: digital set up: study of a density point-cloud from a given geometry

4.1 Geometry and topology of point-clouds

In parallel to physical studies, students experiment within digital setup based on point clouds that allows the manipulation of a hull geometry in order to discover possible triangle formations and develop a matrix of approaches. The digital design setup is implemented in Rhino [10]/Grasshopper [11] in order to allow modification of the geometry and the density distribution of random generated point-clouds, see figure 8.

Using the Delaunay triangulation as an alternative interpretation of a Voronoi structure, a network of connecting lines between the points of neighboring Voronoi cells is generated from these point-clouds. A customized algorithm is developed which interprets the line network as triangular faces. Triangles are connected via their vertices only, face connections via edges are not possible. This results in a decreased number of triangles and connections, yet the self-stiffening capacities of the system have to be enhanced. and optimizing by adjusting the initial parameters and observing the stability of knots. The resulting structure is a self-stiffening three-dimensional aggregation of irregular triangles.

4.2 Construction detail and development of multidirectional joints

A classical joint problem occurs as too many members of the structure are to be connected in one point. In regular space frame structures this has been solved e.g. with the Mero ball node. A strategy for jointing several irregular triangles together in one point is therefore developed which then also coins the aesthetic appearance of the final design, see figure 9.

Connecting metal stripes are positioned off the center axis of the node to generate more space for multiple connections. Due to this eccentric transmission of forces the force-flow in the triangular panels is distorted. As result a reticular line network is generated which visually and structurally ties all panels of the structure together. The emerging pattern not only represents the distribution of loads and forces but also defines the positions of all metal strip joints. Each strip comprises two bends with individual angles and every joint and strip is different. Here the relation of the triangle side's length to the offset of the stripes from the triangle corners is crucial for the resulting bending angles and failure of overlapping stripes. For this purpose, a custom script is implemented in Grasshopper in order to explore the solution-space for local joints.

4.3 Computational design of the final tower

Based on a strategic distribution of individual triangles (e.g. larger parts at the bottom, smaller at the top) a computational process is set up in order to generate a structurally sound tower design. The initial setup is optimized for multiple fitness criteria like height to mass ratio or stress distribution with the use of genetic algorithms by the Grasshopper plugin Galapagos [14]. Thus, the overall hull arises together with a high-resolution point cloud, which is further evaluated for structural loads and deflection to generate the final connecting lines together with a random-walk algorithm starting from there ends, see figure 8.

Students use this digital tool in the skilling modules to study the possible emerging designs and to evaluate them recursively with the use of the Grasshopper Plugins Millipede [15] and Karamba [16]. Out of these design solutions, a final tower structure of five meter height is selected for fabrication.

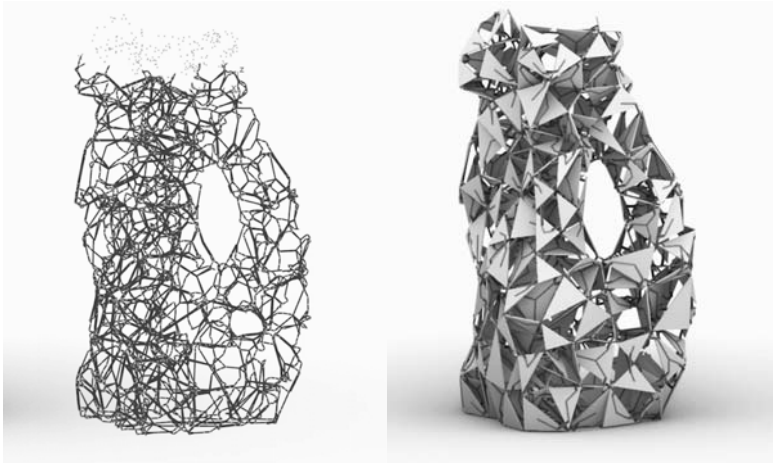


Figure 9: generation of the final design: evolving reticular topology (left), triangulation and joints (right)

4.4 Digital fabrication and deployment

Finally, a fabrication module for all the wooden plates and joints with metal stripes is implemented seamlessly into the digital tool. Over 1000 metal stripes are cut, drilled and bent in three dimensions. For the wooden OSB-panels a robot is used to mark the components on both sides and 400 triangles are produced with all markers and graphical lines in one step, see figure 10. Then clusters of triangles are pre-assembled with bolts in parallel and assembled on-site in two days for the exhibition in the faculty hall, see figure 11.



Figure 10: a part of the final fabrication file (left) and robotic fabrication of the wooden triangles (right)



Figure 11: the final tower and a detail of the joints with generated pattern

5. Conclusion

Conducting design iterations is becoming a faster and more effective process, still in order to navigate an extended solution space, a designer has to clearly articulate his intentions and be able to implement them purposefully in a digital set-up in order to prevent a pure trail-and-error workflow. In order to conduct design decisions a designer has to be trained in negotiating various design objectives within complex design processes and finding the "acceptable" solution. In the first year courses at i.sd_structure and design at University of Innsbruck we are aiming at educating students in designerly ways of thinking, and this is – in our understanding – open-ended: designing means to evolve a solution space and explore the potentials of a design intent rather than finding a solution that confirms it. Both design courses establish a material-based design strategy which defines certain aspects and constraints yet provides creative freedom for design intentions to develop. The main goal is to evolve a design system (based on components that allow self-regulated assembly) and explore its potentials, thereby the system can be altered and modified during the process. In both courses the co-evolution of design system, digital set-up and practical fabrication solutions is highlighted. Although material and geometry systems are different, the courses share the educational framework, a learning by synthesis through feedback between physical and digital experimentation, design exploration and evaluation, aesthetic intentions and practicability.

In bottom-up design approaches generating a great variety of ideas and possible outcomes is essential. In order to purposefully navigate them, a comprehensive understanding of the complex relations of the various domains in architectural design has to be developed. To experience the whole process – from designing to fabrication as cyclic rather than linear – helps to understand the relations and interdependencies, but also allows out-of-the-box thinking and cross-breeding of creative and practical ideas.

6. Acknowledgments

B+G Engineering, Clemens Preisinger (support in structural evaluation set up in Karamba)

Faculty workshop, Ernest Hager and Klaus Oberwalder (support during assembly and fabrication)

Student tutors i.sd robotic lab: Konrad Sonne

7. References

[1] N. Cross, Designerly Ways of Knowing, Basel: Birkhäuser, 2007.

[2] J. Rifkin, The zero marginal cost society: the internet of things, the collaborative commons, and the eclipse of capitalism, New York: Palgrave Macmillan, 2014.

[3] A. Menges, "Morpho-Ecologies: Approaching Complex Environments," *Architectural Design,* vol. 74, no. 3, pp. 80-89, 2004.

[4] F. Lerner, "Foundations for Design Education: Continuing the Bauhaus Vorkurs Vision," *Studies in Art Education,* vol. 46, no. 3, pp. 211-226, 2005.

[5] A. Nejur, "Ivy: Progress in Developing Practical Applications for a Weighted-Mesh Representation for Use in Generative Architectural Design," in *Acadia 17*, Camebridge, 2017.

[6] R. D. Koschitz, Computational design with curved creases : David Huffman's approach to paperfolding, M. I. o. T. D. o. Architecture., Ed., Cambridge: PHD Massachusetts Institute of Technology. Department of Architecture., 2014.

[7] Y. Anastas, M. Gillet, L. Rowenczyn and O. Baverel, "Complex Surface Approximation with Developable Strips," *Journal of the International Association for Shell and Spatial Structures,* vol. 57, no. 2, June 2016.

[8] M. Fornes, "theverymany.com," theverymany, 2017. [Online]. Available: https://theverymany.com/invention-of-stripes. [Accessed 20 06 2019].

[9] S. Chandra, A. Körner, A. Koronaki, R. Spiteri, A. Radhik, S. Kowli and M. Weinstock, "Computing Curved-Folded Tessellations through Straight-Folding Approximation," in *SimAUD 2015*, Washingotn DC, 2015.

[10] McNeel, "https://www.rhino3d.com/," McNeel. [Online].

[11] McNeel, "Grasshopper3d," 2017. [Online]. Available: http://www.grasshopper3d.com/. [Accessed 09 01 2017].

[12] D. Piker, "https://www.food4rhino.com/app/kangaroo-physics," [Online].

[13] D. Rutten, "Navigating Multi-Dimensional Landscapes in Foggy Weather as an Analogy for Generic Problem Solving," in *The 16th international Conference on Geometry and Graphics* , Innsbruck, 2014.

[14] D. Rutten, "https://www.grasshopper3d.com/group/galapagos", [Online].

[15] P. Michalatos, "https://www.grasshopper3d.com/group/millipede", [Online].

[16] Karamba3D, "https://www.karamba3d.com/", [Online].

Proceedings of the IASS Annual Symposium 2019 – Structural Membranes 2019
Form and Force
7 – 10 October 2019, Barcelona, Spain
C. Lázaro, K.-U. Bletzinger, E. Oñate (eds.)

A new T4 configuration for a deployable tensegrity pavilion

Attilio PIZZIGONI[a], Andrea MICHELETTI[b], Giuseppe RUSCICA*, Vittorio PARIS[a], Stefano BERTINO[c], Matteo MARIANI[a], Vincenzo TRIANNI[a], Stefano MADASCHI[a]

* Department of Engineering and Applied Sciences, University of Bergamo
Viale Marconi 5, 24044 Dalmine (BG), Italy
giuseppe.ruscica@unibg.it

[a] Department of Engineering and Applied Sciences, University of Bergamo
[b] Department of Civil and Computer Science Engineering, University of Rome Tor Vergata
[c] Tensoforma Trading s.r.l.

Abstract

The present tensegrity pavilion project is developed within a collaboration between University of Bergamo and the Italian company Tensoforma, with students working as interns during the realization of the structure. This tensegrity pavilion explores the competition between form and balance of forces. The aim of this work is to design, manufacture, and assembly a self-stressed tensegrity structure composed by four bars and twelve cables. By using a hydraulic jack to pull a lower cable, a self-stress state is established in the whole system, simultaneously erecting the structure. An outer structural membrane contributes to the global balance of the system. The pavilion is constrained to ground by simple supports and pinned connections, without transferring prestressing forces. This pavilion can be considered a generalized tensegrity system, with its membrane being connected at the end of its structural elements. The peculiarities of this system are introduced and analyzed here as a starting point in the design of more complex structures.

Keywords: Tensegrity pavilion, form finding, membrane structures.

1. Introduction

Tensegrity systems have often been relegated to the design of art pieces or exhibition spaces, but their intrinsic nature has more in common with engineering than one may think, as recent studies have shown.

From a didactic point of view, tensegrity structural principles are increasingly being considered as a new way to make students understand the relationship between loads, geometry and structural efficiency.

This work describes the didactic experience carried out with the students of the Engineering School of the University of Bergamo during the Architectural Design course held by Attilio Pizzigoni.

The aim of the course has been the design of a lightweight pavilion with the collaboration of the Italian company Tensoforma. The students have worked as interns in order to fulfill the practical part of the course, using a temporary lab that has been equipped with the necessary materials for building such a pavilion.

Firstly, a series of proposals have been showed by the students, in order to find out the more appropriate module to be used as a temporary pavilion. The structure had to be lightweight, demountable and easily equipped for transportation. After various assessments, a tensegrity module

Copyright © 2019 by Attilio Pizzigoni, Andrea Micheletti, Giuseppe Ruscica, Vittorio Paris, Stefano Bertino, Matteo Mariani, Vincenzo Trianni and Stefano Madaschi
Published by the International Association for Shell and Spatial Structures (IASS) with permission.

with the geometry here presented has been chosen. The main upsides to making students work on tensegrity structures are related to the coincidence between form and structure. Since the initial phase of the design of a tensegrity, it is impossible to think about a geometry without relating it to the forces going through it and to the consequent form.

A tensegrity system forces a student to think about the design process in a different way. Usually an engineer arranges a certain, predefined geometry and then, later, solves the structure and finds out its static response.

With tensegrity structures it is necessary to make some initial assumptions about its topology and related geometry. Then, after having carried out some analysis, it is important to simultaneously assemble a first working model in order to verify its feasibility. In this way, it is impossible to separate architecture from engineering: they have to work together. No software simulation can provide the awareness that a student acquires when dealing with a model of a tensegrity structure.

And this approach, over the recent years, has proven to be successful. After a first period of disorientation, students understand that an architectural system is the union of form and structure, and that they cannot be dealt with in separate moments, but simultaneously.

2. Geometry

When dealing with tensegrity modules, there is a wide choice of available topologies. As a starting point for this T4 module, the studies of Zhang *et al.* [1] have been taken into account. In this way, it is possible to arrange a module capable of rapid assembling and shape changing, ideal when there is the need of a self-erecting structure. Such behavior can be achieved by acting on the cables, shortening or elongating them depending on the desired behavior.

The presented tensegrity pavilion is composed by 4 bars and 12 cables. The nodes of the structure are arranged according to Fig. 1, fitting into a square. On the lower part of the pavilion we can find 4 cables (of which two of them are cross-shaped) connecting the lower nodes, while on the upper part we can find other 4 cables (two of them intersecting each other) connecting the upper nodes. The remaining 4 cables connect the lower with the upper nodes. A prestressed structure can be obtained by elongating bars or shortening cables and, in this case, we have chosen to use cables for prestressing the module, since they can easily provide deployability to the system.

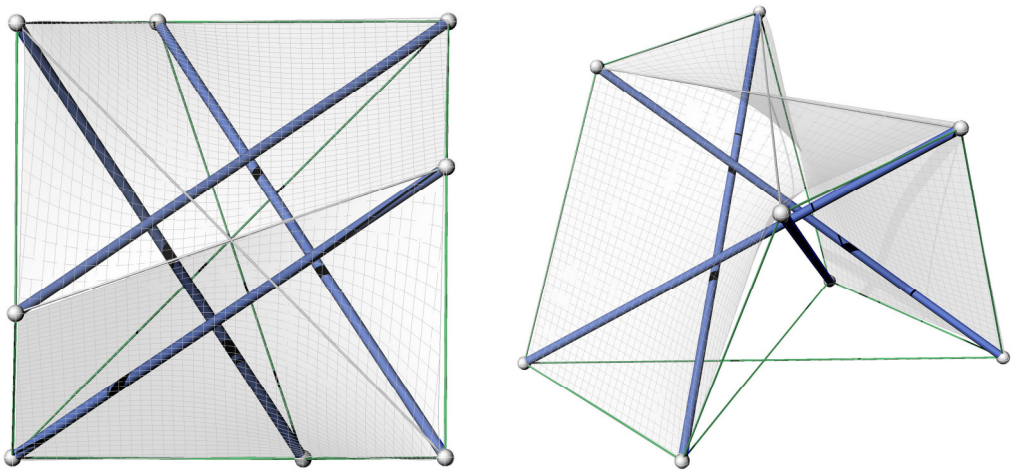


Figure 1: (left) Top view and (right) axonometric view of the T4 tensegrity module

In addition to the 4 bars and 12 cables, a membrane has been placed in order to use this tensegrity as a pavilion. The fabric allows a covering of the space beneath the module, in order to use it for human activities. Actually, this tensegrity module allows more than one type of connection between the membrane and the cell's nodes. Here we show the more suitable ones for the purpose of a temporary pavilion (Fig. 1 and Fig. 2).

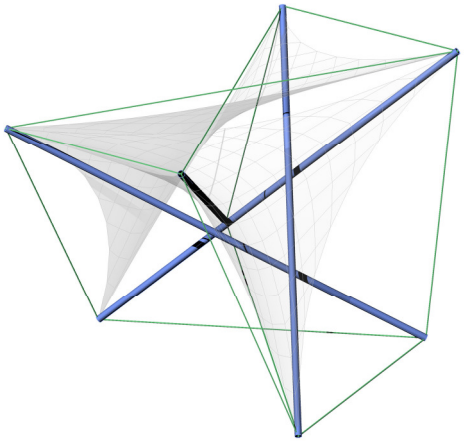


Figure 2: A different membrane applied to the T4 tensegrity cell

The membrane can also be used in place of the upper cables, since its tensile strength can be taken into account and used to balance the module in its deployed configuration.

3. Shape change and extended grids

A series of preliminary models has been investigated in order to understand the potential of deployability for this module. It can be seen (Fig. 3) that this tensegrity cell is well suited for a shape-change, even coupled with a membrane (Fig. 4 and Fig. 5).

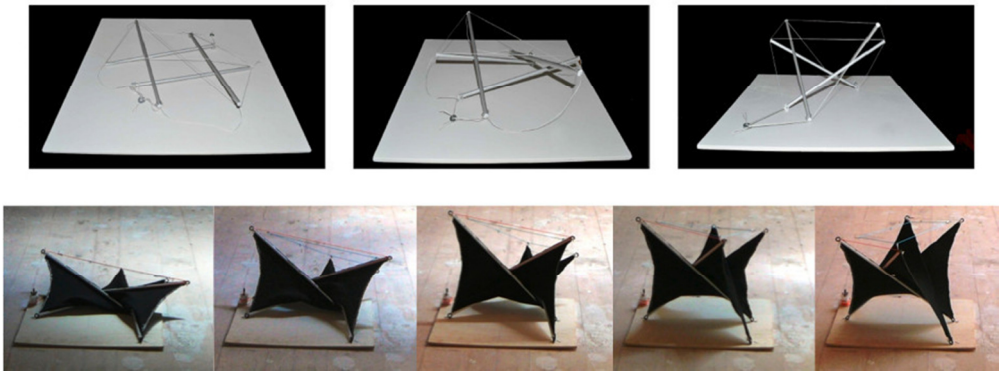


Figure 3: Preliminary models on the deployability of the T4 tensegrity module



Figure 4: A first prototype of the T4 tensegrity cell coupled with a membrane

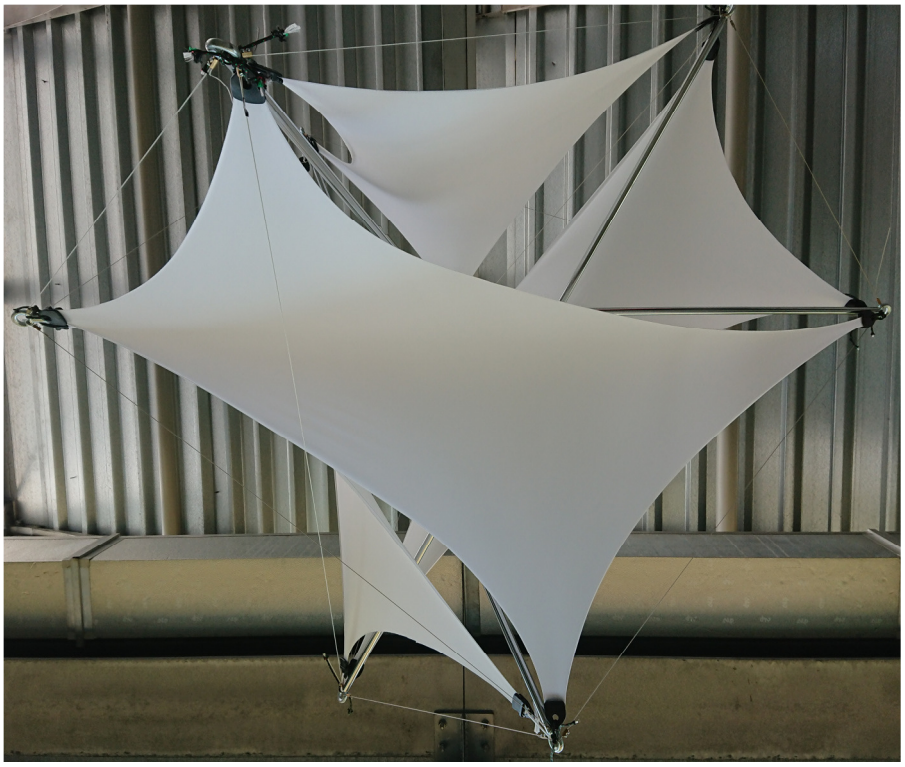


Figure 5: A first prototype of the T4 tensegrity cell coupled with a membrane

If we imagine to put several T4 modules one beside the other, mirroring them with respect to two vertical planes (Fig. 6 and Fig. 7), their symmetry allows to create a continuous grid. In this way, it is possible to create a more organized space which can cover a wider area, depending on one's needs. Moreover, the shape-change capability of every tensegrity module can increase the overall flexibility, so being able to accomplish various design requirements.

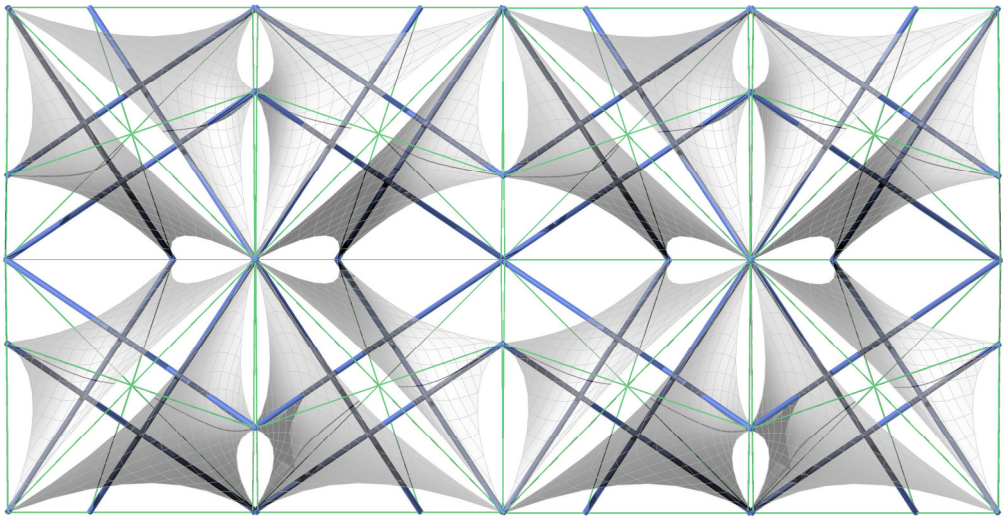


Figure 6: Top view of a grid composed by T4 tensegrity modules

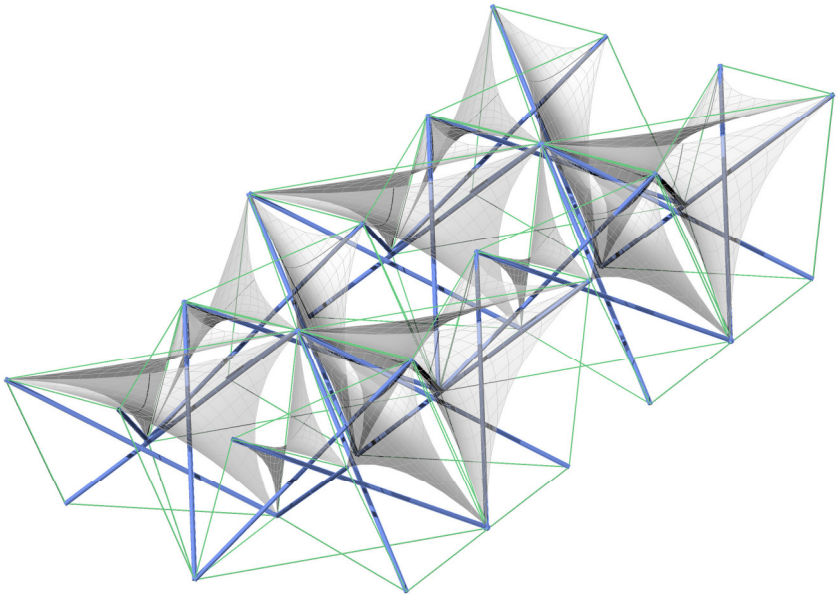


Figure 7: Axonometric view of a grid composed by T4 tensegrity modules

4. Conclusions

This work shows that when architecture meets engineering through the use of tensegrity systems, new design paradigms can be presented and considered as viable answers to current design challenges. Aesthetics and efficiency are both valorized by their use and by the lightness they express with their geometry. This also confirms that tensegrity systems can constitute a competitive alternative to traditional structures, even more so in the case of light pavilion design.

References

[1] J.Y. Zhang, S.D. Guest, M. Ohsaki and R. Connelly, "Multi-stable star-shaped tensegrity structures", in *Taller, Longer, Lighter: meeting growing demand with limited resources: IABSE-IASS Symposium 2011*, London, Hemming Group Ltd., 2011.

[2] R.E. Skelton and M.C. Oliveira, *Tensegrity systems*. New York: Springer, 2009.

[3] J. Zhang and M. Ohsaki, *Tensegrity Structures*. New York: Springer, 2015.

[4] S. Stucchi, A. De Laurentis, A. Micheletti, F. Santangelo, A. Totaro, "Tensegrity Units for a Movable Settlement", in *Adaptables2006, TU/e, International Conference On Adaptable Building Structures, Eindhoven The Netherlands 03-05 July 2006*, pp. 95-99.

Proceedings of the IASS Annual Symposium 2019 – Structural Membranes 2019
Form and Force
7 – 10 October 2019, Barcelona, Spain
C. Lázaro, K.-U. Bletzinger, E. Oñate (eds.)

Deformation of the tensegrity units

Heping LIU[a], Fuqiang MENG[*], Ani LUO[b]

College of Mechanical and Electrical Engineering, Harbin Engineering University, Harbin 150001, China
Email:2824755325@qq.com

Abstract

Research on the tensegrity structures is mainly focused on shape optimization of structure, stability, topology and so on. Assembling the tensegrity units is a common method to construct complex and large-scale tensegrity structures. The method is based on the tensegrity unit. Therefore, more tensegrity units are helpful to construct more various types of tensegrity structures. Based on the 3-bar tensegrity unit, a new method of deformed tensegrity units is developed in this paper. Firstly, configuration and structural characteristics of the existing tensegrity units are described. Then, under the condition that the radius of the cylinder enclosing the tensegrity unit remains unchanged, the top end plane of the tensegrity units is declined at a certain angle to deform the unit. Mathematical model of the deformed tensegrity unit is established. Then, the mathematical model is applied to set up several the physical models with different shape dimensions. The stable physical models prove that the deformation method is correct and can be applied to obtain stable tensegrity units. Relationships between the structural parameters of the tensegrity units which are obtained with the deformation method are deduced and changes of the parameters are investigated. Finally, the obtained tensegrity units are assembled into some spatial shapes to prove that various complex spatial shapes can be obtained by application of the new tensegrity units.

Keywords: tensegrity, deformed unit, mathematical model, physical model, assemble

1 Background

Tensegrity structure is a new type of spatial structure, which is composed of rigid bars bearing compressive stress and flexible strings bearing tensile stress [1]. Moreover, the tensegrity structure is provided with beautiful shape, light-weight, low energy consumption and impact resistance [2]. Because of the excellent characteristics of the tensegrity and the actual engineering requirements, the tensegrity structure can assemble a more complex spatial structure. Therefore, in the past few decades, the structural design of tensegrity become a research hotspot.

The early models are X-shaped tensegrity [3], and the tensegrity structure is used in building structure by American architects Fuller, Snelson and D. G. Emmerich [3,4]. Then the tensegrity structure is designed on tensegrity manipulator. In this process, in order to build more complex spatial structures, people mainly study on the two aspects: configuration and assembly [5,6]. A new configuration scheme of tensegrity unit proposes to assemble more complex spatial structures. In previous studies, the bottom end and the top end of tensegrity units were always parallel to the horizontal plane [7], which would limit the direction of assembly and not generate more types of composite structures.

In this paper, a prismatic tensegrity structure which has a certain angle between the top end and the bottom end is introduced. This prismatic structure can be assembled in any direction, and it will produce more kinds of assemble structure, so it has better performance in the assembly. The assembly structure in this paper is mainly a tensegrity manipulator. The paper provides a certain theoretical basis for achieving the bending of tensegrity manipulator.

Copyright © 2019 by Heping LIU, Fuqiang MENG, Ani LUO
Published by the International Association for Shell and Spatial Structures (IASS) with permission.

2 Tensegrity units

Tensegrity is a stable spatial structure which is composed of tension strings and compression bars. The basic spatial tensegrity structure is a 3-bar structure, as shown in Fig 1, which consists of 3 bars and 9 strings. The basic geometric structure consists of three nodes on the bottom end and three nodes on the top end, which respectively constitute an equilateral triangle and are connected to the circumference of two circles. After that, the nodes are connected by bars or strings to form a stable tensegrity structure, and each node is connected by three strings and a bar. The cylinder represents the bars and the solid black line represents the strings, as shown in Fig 1.

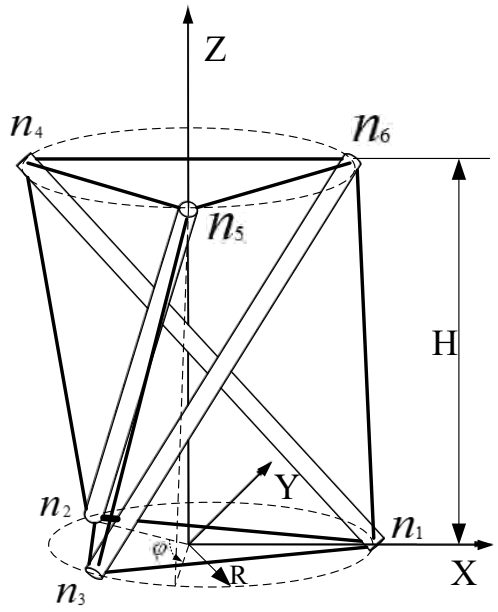


Figure 1: Tensegrity structure

2.1 Nodes coordinate

The node is a fractal point which is constructed artificially, which is specifically shown as the intersection point of three adjacent strings on a bar, as shown in Fig 1. The information of each node is contained in the node matrix N, N_d are the node coordinates on the bottom end, N_u are the node coordinates on the top end, they are shown in Eq. 1 and Eq. 2.

$$N_d = \left[R\cos(\frac{2\pi i}{3}) \quad R\sin(\frac{2\pi i}{3}) \quad 0 \right]^T, i \in (0,1,2) \tag{1}$$

$$N_u = \left[R\cos(\frac{2\pi i}{3}+\varphi) \quad R\sin(\frac{2\pi i}{3}+\varphi) \quad H \right]^T, i \in (3,4,5) \tag{2}$$

Here, R is the radius of the circle passing through the node on the bottom end and top end, and H is the height between the bottom end and top end in the unit. φ is the twisting angle between the top and bottom polygons in the unit.

2.2 Connectivity matrix

The connectivity matrix represents the connection relationship of nodes in the topology diagram. According to this connection relationship, two nodes can form a vector. The element of connection matrix $C_{ij}^{T}{}_{(2p\times 2p)}$ is determined by the rule in the Fig 2.

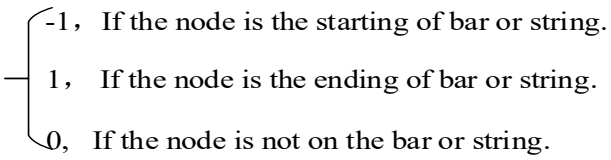


Figure 2: The rule of connectivity matrix

Taking a 3-bar tensegrity as an example to illustrate connectivity matrix of bars, the nodes are reasonably allocated by table 1, and the connectivity rule of nodes is determined by Fig 2, then we can get a connectivity matrix, as shown in Eq.3.

Table1: This table allocates the nodes on the bars1

bar	b_1	b_2	b_3
The starting point	n_1	n_2	n_3
The ending point	n_4	n_5	n_6

$$C_b^T = \begin{bmatrix} -1 & 0 & 0 \\ 0 & -1 & 0 \\ 0 & 0 & -1 \\ 1 & 0 & 0 \\ 0 & 1 & 0 \\ 0 & 0 & 1 \end{bmatrix} \tag{3}$$

Each column of the connectivity matrix $\boldsymbol{C_b^T}$ represents the connection relationship between a bar and all nodes, and each row represents the connectivity relationship between a node and all bars. In the same way, the connectivity matrix of strings can be constructed.

2.3 Building component vectors

Two nodes that are allocated by the connectivity matrix can formed a vector, and the vector can represent a bar or a string. So, the vector can reflect the geometric relationship between the bars and strings. As shown in Eq.4, the vector *B* of bars is connected with the node matrix *N* and the connectivity matrix $\boldsymbol{C_b^T}$.

$$B = \begin{bmatrix} b_1 & b_2 & b_3 \end{bmatrix} = N * C_{bi}^T, i \in (1,2,3) \tag{4}$$

Where $\boldsymbol{b_1}$ $\boldsymbol{b_2}$ $\boldsymbol{b_3}$ represent three bars vectors in the tensegrity structure. The strings vectors can be constructed in the same way.

2.4 Calculating geometric relationship of components

When building the physical model, it is necessary to know the specific length of the bars and strings, so the length of each components will be calculated, and the calculation process is as follows：

(1) The length of bar *i* is calculated by Eq.5.

$$b_i = \sqrt{(n_{ix} - n_{i+3,x})^2 + (n_{iy} - n_{i+3,y})^2 + (n_{iz} - n_{i+3,z})^2}, i \in (1,2,3) \tag{5}$$

(2) The length of string *j* is calculated by Eq.6 and Eq.7.The strings can be divided into inclined strings and horizontal strings. The strings on the bottom and top surfaces are named as horizontal strings, and the strings connecting the bottom and top surfaces are named as inclined strings.

The length of inclined strings is calculated by Eq.6.

$$s_{vj} = \sqrt{(s_{jx} - s_{j+2,x})^2 + (s_{jy} - s_{j+2,y})^2 + (s_{jz} - s_{j+2,z})^2}, \ j \in (1,2,3) \tag{6}$$

The length of horizontal strings is calculated by Eq.7.

$$s_{lm} = \sqrt{(s_{mx} - s_{m+1,x})^2 + (s_{my} - s_{m+1,y})^2 + (s_{mz} - s_{m+1,z})^2}, \ \mathrm{m} \in (1,2,3,4,5,6) \tag{7}$$

3 Deformation analysis

The top and bottom end of the tensegrity are parallel before deformation, and the structure axis is perpendicular to the top and bottom end. A inclined angle between the top and bottom end occurs by deformation, and the structure axis is not perpendicular to the top end. We put a node on the top end along the *Z* axis to move a displacement *h* in tensegrity deformation process, as shown in Fig 3 and Fig 4. The outer envelope of tensegrity will change, and deformation will also cause the normal vector of top end and the *Z* axis to form an angle θ as shown in Fig 4, the node coordinates are shown by the Eq. 8 and Eq. 9.

$$N_{uj} = \left[R\cos(\frac{2\pi j}{3} + \varphi) \quad R\sin(\frac{2\pi j}{3} + \varphi) \quad H - h \right] \tag{8}$$

$$N = \left[N_d \quad N_u \right]_{3\times 2p} = \left[N_0 \quad N_1 \quad \cdots\cdots \quad N_{2p-1} \right]_{3\times 2p} \tag{9}$$

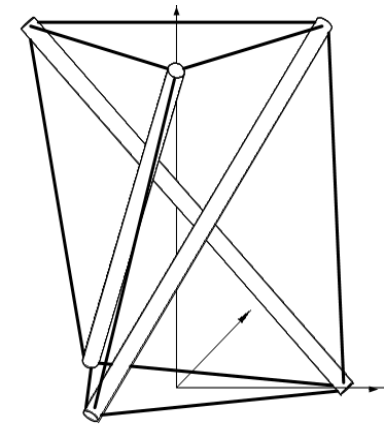


Figure 3: Undeformed tensegrity structure

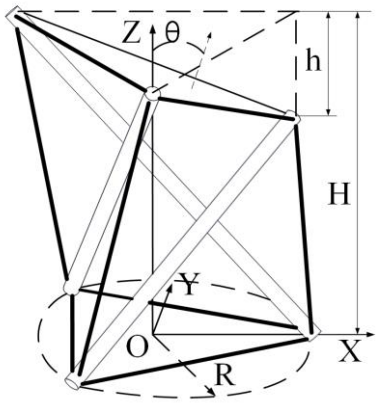


Figure 4: Deformed tensegrity structure

3.1 Theoretical analysis of deformed unit

Firstly, the geometric relationship of the length of bars and strings is described in the deformed process, it mainly includes the length change of strings and bars with changing of *h*, as well as the change of inclined angle with changing of *h*. After that, the geometrical relationship is found among the change in length of bar, change in length of string and the change in inclined angle when the transition variable *h* is eliminated. In the deformed tensegrity, the node *j* is connected by the structure member S_j,S_{j-1},S_{j+3} and b_{j-3}.

(1) The change in length of the bar b_{j-3}, as shown in Eq.10.

$$\triangle b_{j-3} = \| b_{j-3} \| - \| b'_{j-3} \| = \sqrt{R^2(2+\sqrt{3}) + H^2} - \sqrt{R^2(2+\sqrt{3}) + (H-h)^2} \tag{10}$$

(2) The change in length of the string S_{j-1}, as shown in Eq.11.

$$\triangle S_{j-1} = \| S_{j-1} \| - \| S'_{j-1} \| = 2R - \sqrt{4R^2 + h^2} \tag{11}$$

(3) The change in length of the string s_j is same as the change in length of string s_{j-1} ,as shown in Eq.12.

$$S_j = 2R - \sqrt{4R^2 + h^2} \tag{12}$$

(4) The change in length of the string s_{j+3},as shown in Eq.13.

$$\triangle S_{j+3} = \| S_{j+3} \| - \| S'_{j+3} \| = \sqrt{(2-\sqrt{3})R^2 + H^2} - \sqrt{(2-\sqrt{3})R^2 + (H-h)^2} \tag{13}$$

If we eliminate the transition variable *h* among Δb_{j-3}、Δs_{j-1}、Δs_{j+3}, we could get the change relationship of bars and strings.

(5) The change of the inclined angle θ on the top end, as shown in Eq.14.

$$\cos\theta = \frac{(3+\sqrt{3})R}{\sqrt{(8_h{}^2 + (12+6\sqrt{3}))_R{}^2}} \tag{14}$$

3.3 Example analysis according to the calculation process

Example: if the end surface radius *R*=10mm, unit height *H*=20mm, and deformation height *h*= 5mm, calculate the concrete length of the strings and bars, and use these strings and bars to build a physical model.

According to the calculation process in the previous paragraph of this paper. Firstly, we should calculate the length of each string before deformation, and then the change in length of each string after deformation, and finally the length of the actual strings should be calculated.

(1) Calculating the length of each string and bar before deformation, firstly, the nodes matrices of the tensegrity are listed according to Eq.1 and Eq.2.

$$N_i = \begin{bmatrix} n_1 & n_2 & n_3 & n_4 & n_5 & n_6 \end{bmatrix} = \begin{bmatrix} 10 & -5 & -5 & -8.7 & 0 & 8.7 \\ 0 & 8.7 & -8.7 & 5 & -10 & 5 \\ 0 & 0 & 0 & 20 & 20 & 20 \end{bmatrix}$$

Where: $n_i = \begin{bmatrix} n_{ix} & n_{iy} & n_{iz} \end{bmatrix}^T$

According to Eq.5, the length of the first bar before deformation: $b_1 = 27.8mm$

Similarly, calculating the length of other bars: $b_2 = 27.8mm; b_3 = 27.8mm;$

According to Eq.6, calculating the length of the first inclined string : $S_{v1} = 20.7mm$

Similarly, the length of the other two inclined strings: $S_{v2} = 20.7mm; S_{v3} = 20.7mm$

According to Eq.7, calculating the length of the first horizontal string: S_{l1}=17.3mm

Similarly, the length of other horizontal strings: S_{l2}=$S_{l3} = S_{l4} = S_{l5} = S_{l6} = 17.3mm$

Obtaining the length value of each string and bar in the tensegrity before deformation:

The length of bars: $b_1 = b_2 = b_3 = 27.8mm$

The length of the inclined strings: $S_{v1} = S_{v2} = S_{v3} = 20.7mm$

The length of the horizontal strings: $S_{l1} = S_{l2} = S_{l3} = S_{l4} = S_{l5} = S_{l6} = 17.3mm$

(2) calculating the change in length of bars and string after deformation

If a node is moved down h=5mm, the length of $b_1, S_{v1}, S_{l5}, S_{l6}$ will be changed, and the change of bars and strings can be obtained according to the theoretical analysis results from the deformation.

According to Eq. 10 $\triangle b_1 = 3.35mm$; $b_1^{'} = b_1 - \triangle b_1$ = 23.7 mm.

According to Eq.11 $\triangle S_{l5} = \triangle S_{l6}$ = -0.62mm ; $S_{l5}^{'} = S_{l6}^{'} = S_{l5} - \triangle S_{l5}$ = 17.92 mm.

According to Eq. 13 $\triangle S_{v1}^{'} = 4.8mm$; $S_{v1}^{'} = S_{v1} - \triangle S_{v1}$ = 15.9 mm.

(3) The length of the actual strings and bars:

$b_1^{'} = 23.7mm, b_2 = b_3 = 27.8mm; S_{v1}^{'} = 15.9mm, S_{v2} = S_{v3} = 20.7mm;$

$S_{l1} = S_{l2} = S_{l3} = S_{l4} = 17.3mm, S_{l5}^{'} = S_{l6}^{'} = 17.92mm;$

According to the calculation results, we can build the physical model, as shown in Fig 6.

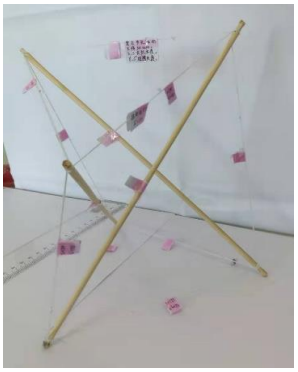


Figure 6a: The positive binocular view of the structure



Figure 6b: The front view of the structure

4. Assembling of the deformed tensegrity

4.1 Assembling of two deformed tensegrities

We assemble two deformed tensegrities by jointing, using the node-on-node assembly method between two inclined ends of the deformed tensegrities, and the nodes of deformed tensegrity are connected in pairs. For example, we need to match the same nodes of Fig 7 and Fig 8, then we will get a composite structure, as shown in Fig 9.

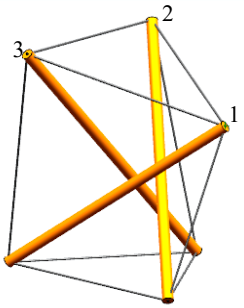


Figure 7: Deformed tensegrity 1

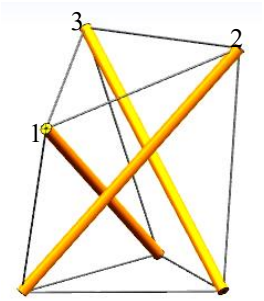


Figure 8: Deformed tensegrity 2

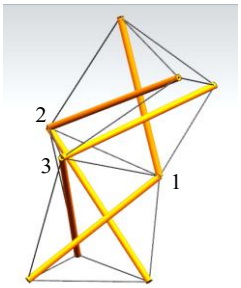


Figure 9: Assembled structure

4.2 Assembling of multiple deformed tensegrity

When assembling with undeformed tensegrity units, the assembly process must be in the fixed direction of the central axis. Because the top end of the deformed tensegrity is inclined, the central axis will not be perpendicular to the inclined top end, so assembly process can extend in a certain expected direction according to the demand. In this process, we only need change the size of the inclined angle and the number of basic units to get multiple deformed tensegrity. When the number of base units is increased, we can get the structures in the node-on node assembly method, as shown in Fig 10 and Fig 11. There are the different shape structures in this example, but two kinds of structures are formed by the same structure of basic unit, which is shown in Fig 7 and Fig 8, the bottom end of deformed tensegrity is horizontal, so the nodes does not need to be connected in the one to one correspondence like Fig 9, as long as changing the connection order of nodes will form a new structure, as shown in Fig 11.

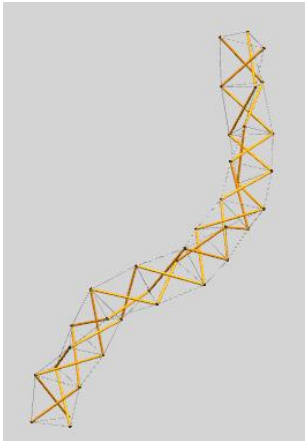


Figure 10a: Multi-layer assembling structure 1

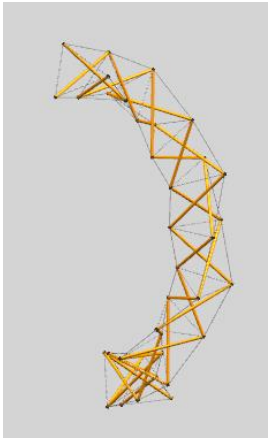


Figure 10b: Multi-layer assembling structure 1

Fig. 10a is the positive binocular view of the structure, Fig. 10b is the top view of the structure.

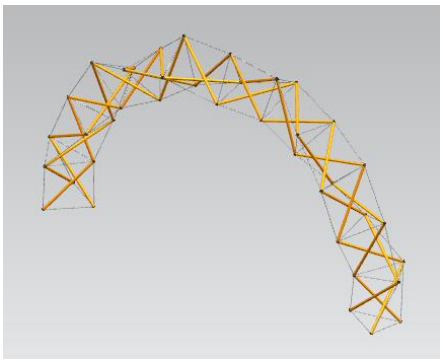


Figure 11a: Multi-layer assembling structure 2

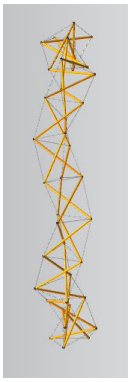


Figure 11b: Multi-layer assembling structure 2

Fig. 11a is the positive binocular view of the structure, Fig. 11b is the left view of the structure,

5 Results and discussion

On the basis of the original tensegrity structure, a stable deformation tensegrity structure can be constructed by adjusting some bars and strings. In this paper ,the method explained moves a node of the top end in the original tensegrity along the Z-axis at a certain distance, and the changed bars and strings will form a deformed tensegrity structure again, and the deformed tensegrity is a stable structure as illustrated in example. Finally, the stable deformed tensegrity structure is constructed into multiple deformed tensegrity in the node-on-node assembly method, as shown in Fig 10 and Fig11. We can get the following conclusions: (1) an angle that is shown in fig.6 appears between the bottom and top end in the deformed tensegrity structure; (2) the deformed tensegrity structure can be used to construct a multiple tensegrity structure which can achieve bending.

6 Acknowledgements

Supported from the Harbin Engineer University. And I very gratitude my teacher professior Liu heping and professior Luo ani, who provide much practical proposal.

7 References

[1] Connelly R, "WHAT IS...a Tensegrity?," *Notices of the American Mathematical Society*, vol.1, pp.78-80,2013.

[2] Skelton R E, Nagase K. "Tensile Tensegrity Structures,". I*nternational Journal of Space Structures,* vol 2, pp.131-138,2012.

[3] Snelson K D. "Continuous tension, discontinuous compression structure". *Google Patents*. 1965.

[4] Ferrero G, Cotti C, Rossi M, et al, "Geometries of Imaginary Space: Architectural Developments of the Concepts of M. C. Escher and Buckminster Fuller," *Nexus Network Journal*, vol. 11, pp. 305-316,2009.

[5] Li-Yuan Zhang · Hong-Ping Zhao · Xi-Qiao Feng, "Constructing large-scale tensegrity structures with bar–bar connection using prismatic elementary cells," *Archive of Applied Mechanics*, vol. 85, pp.383-394.

[6] Omar Aloui, Jessica Flores. "Cellular morphogenesis of three-dimensional tensegrity structure," *Computer Methods in Applied Mechanics and Engineering*, vol. 346, pp.85-108,2019.

[7] LUO Ani, WANG Longkun, LIU Heping. "Analysis of configuration and structure of 3-bar tensegrity prism," *Journal of Harbin Institute of Technology*, pp. 82-87. 2016.

Proceedings of the IASS Annual Symposium 2019 – Structural Membranes 2019
Form and Force
7 – 10 October 2019, Barcelona, Spain
C. Lázaro, K.-U. Bletzinger, E. Oñate (eds.)

Geometric features and parameter sensitivity analysis for the prestressed state of the innovative honeycomb multi-post cable dome structures

Yuan TU *, [a], Shi L. DONG

* Space Structures Research Center, Department of Civil Engineering, Zhejiang University
38 Zheda Road, Hangzhou 310027, China
Room 406, Civil Engineering and Technology Building
Email: tuyuan@zju.edu.cn

[a] Department of Material Science and Engineering, Massachusetts Institute of Technology, Boston, MA 02129, USA

Abstract

Abandoning Buckminster Fuller's initial tensegrity concept of continuous tension and discontinuous compression, the circular multi-post cable dome structure was carried out with all ridge cables framing a honeycomb-shaped net, multiple posts connected at each lower and upper node. Regard to all kinds of cable-post layout, cable dome structures related in research and practical projects can be classified into 13 types, including Geiger type, Levy type, Kiewitt type, bird nest type, et al. The newly proposed type has desirable geometric features in its multi-post setting and innovative honeycomb ridge cable unit shape, thus being particularly advantageous over the existing ones above in terms of structural properties, complexity of construction, costly cable consuming and thus economic benefits. There is no cable dome structure without prestress. Based on the former derivation of the general recursive formulas for the internal forces, this paper carries out new initial prestress design table with shifted parameter. Comparative analyses show more detailed prestress distribution regulations and demonstrate the exact significance of depth-to-span ratio. This study provides a new solution for the selection, design and construction of cable domes.

Keywords: honeycomb cable dome structure, multi-post setting, new structure, geometric feature, prestressed state, mechanical properties, parameter sensitivity analysis, design table.

1. Introduction

Cable dome tensegrity structures are prominent roof structures, being popular in academia and engineering field worldwide in recent decades for their distinguished superiority in architecture and structural characteristic. These structures, made up of three components of post, cable and membrane and formed by the prestressing technique, are considered to be the most profound innovation of space structures in the past 30 years, drawing the attention of scientists and engineers internationally. The Seoul Olympic Gymnasium with an approximate span of 120m built at Seoul by American engineer D.H. Geiger in 1986 was the first cable dome structure of the ribbed-ring type to be built anywhere in the world, with a steel index of 14 kg/m^2 [1]. Since then, another 190m×240m sunflower oval cable dome was built by American engineer M.P. Levy at Atlanta, Georgia in 1994, with a steel index of less than 30kg/m^2 [2]. At the beginning of the 21st century, Chinese researchers introduced the Kiewitt and bird nest cable dome and conducted structural model test at Zhejiang University, the results of which were written up in their doctoral dissertations [3]. As for practical projects in China, a pilot 20-meter-span cable dome structure was used in the atrium of a standard factory for Shengyuan Corp in Jinhua and

Copyright © 2019 by Yuan TU, Shi L. DONG
Published by the International Association for Shell and Spatial Structures (IASS) with permission.

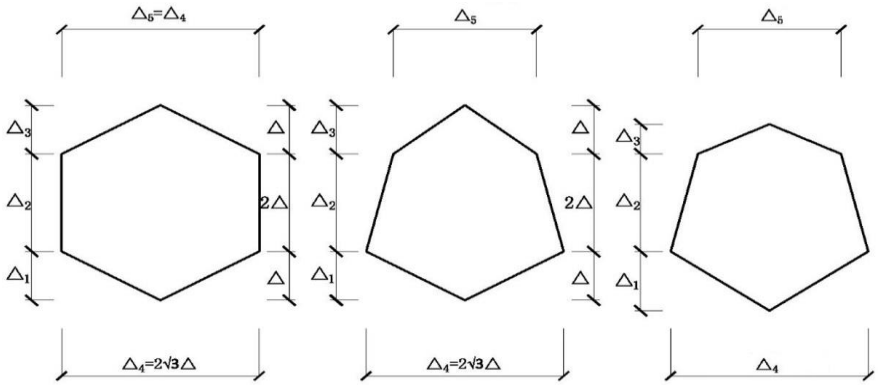
Wuxi Science & Technology Center in 2009. Another 36-meter-span ribbed-ring cable dome was also used in the Taiyuan Coal Trading Center at Shanxi later in 2011. In 2012, a 72-meter-span ribbed-ring cable dome Gymnasium was built in Ordos as the landmark of Yijinhuoluoqi. In 2016, an 83m×102m composite type cable dome structure was established at Tianjin University of Technology, which is the first one exceeding a span of 100m; in the same year, a 77.3-meter-span rigid roof composite type cable dome was used for Tianquan County Gymnasium in Ya'an, Sichuan.

However, all of the above-mentioned forms have long rectangular strips or diamond grids and only one vertical post perpendicular to the horizontal plane for both upper and lower nodes, entirely following Buckminster Fuller's initial tensegrity concept [4,5], which are comparatively monotonous in their architectural forms and arrangements of posts yet.

In regard to ridge cable layout feature, cable domes can be differentiated to ribbed-ring type (Geiger type), sunflower type (Levy type), Kiewitt type, bird nest type, honeycomb type or hybrid type. Thus, cable domes can be classified to 13 types in terms of ridge cable layout and post setting (multiple or single), such as the honeycomb multi-post cable dome structures, including two-post, three-post, and four-post setting. This paper will explain their common geometrical features, cable-post layout, and its structural characteristic and construction complexity in sections 2. Dong S.L. and Yuan T. proposed a simplified analytical method for the prestressed state of honeycomb four-post cable dome structure, referred to as "$_nH_{b4}$" (see new nomenclature $_nH_{bp}$ below). They also carried out the geometrical relationship of $_nH_{b4}$ and distinguished the importance of different geometrical parameters, as briefly presented in sections 3 & 4 [6]. They concluded that the depth-to-span ratio is unimportant when used 0.1, 0.15 and 0.2 as its parameter of the depth-to-span ratio. But a study conducted by Hanaor in 2002 indicated that the rigid ring beam and the outermost bottom loop cable are the main load-bearing components of the cable dome. The vertical distance or the structural depth between these two components largely dictates the structural efficiency [7]. A similar conclusion was drawn by Kawaguchi et al. in an optimization study in 1999 to maximize the structural stiffness of a full-scale cable dome, which demonstrated that the optimum shape of the dome relies greatly on the length of the outermost posts [8]. These earlier studies both emphasized on the importance of the structural depth or vertical distance, either for ring beam and loop cable or the outermost post depth, while the depth-to-span ratio was concluded to be the minor factor in literature [6] yet. This paper presents new design table of $_nH_{b4}$ with adjusted parameters and comparatively analyzes the result with that in literature [6], which provides more detailed theoretical basis for research and selection of cable dome structure.

2. Architecture and structural configuration of honeycomb multi-post cable dome structures

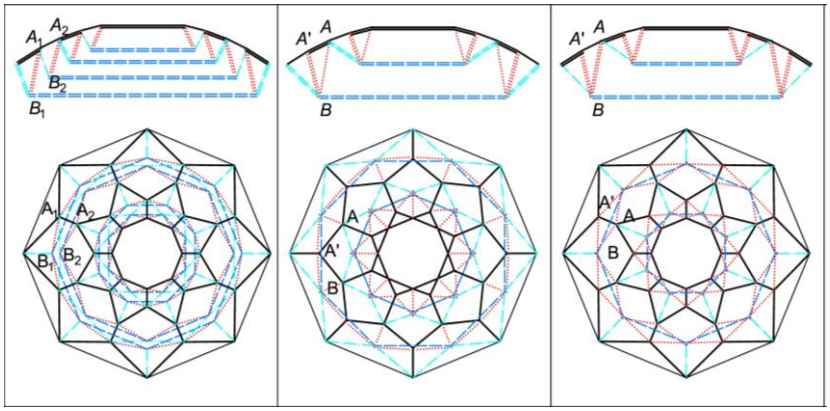
Honeycomb multi-post cable dome structures has two major features: First, the ridge cable net is composed of isosceles hexagon unit or right hexagon unit (see Fig.1a), refered to as the honeycomb ridge cable unit below in this paper; second, it adopts multi-post setting scheme to innovate R.B. Fuller's initial tensegrity concept of isolated compression or single post setting. Honeycomb multi-post cable dome structures contain honeycomb double-post type, triple-post type, and four-post type. They build up honeycomb-type cable dome structure series. Since circular plan layout make central cables crowded thus shorter than outer cables, honeycomb multi-post cable dome structure do not have strictly right hexagon unit in its ridge cable net, i.e., only corresponding ridge cables at the same latitude have equal length except corresponding ridge cables at the same longitude (see Fig.1b). And engineers can also utilize a more flexible ridge cable unit as Fig.1c, of which radial projection lengths are not unified to be equal among three sets of ridge cables. S.L. Dong and Y. Tu give a series of formulas to count the total number of nodes and components by the projective plane polygon's sides n and the number of bottom loops b. They also count the number of components converging at each upper and lower node [9].



a. Right hexagon unit b. Isosceles hexagon unit c. Flexible Isosceles hexagon unit
Figure 1: Honeycomb ridge cable unit [9]

Dong S.L. and Yuan T. proposed a new nomenclature for Levy-type and Geiger-type cable dome structure system in regard to their cables and posts setting [10]. This nomenclature is also eligible for these three kinds of honeycomb multi-post cable dome structures in Table. 1, the honeycomb multi-post cable dome structure series can be represented by the letter ${}_nH_{bp}$ (p=2, 3, 4) with three subscripts n, b, and p, respectively. Correspondingly, the third type in Table. 1 should be represented by ${}_{12}H_{24,}$ of which n=12, b=2, p=4 represent that polygons are dodecagons, the number of bottom loop cables is 2, and four posts converge at each lower node, respectively. This kind would be collectively referred to as the " ${}_{12}H_{24}$ " or " ${}_nH_{b4}$ " below. Thus similarly, the first kind in Table. 1 should be ${}_{12}H_{42}$ and the second should be ${}_{12}H_{23}$.

Table 1: Schematics of honeycomb multi-post cable domes [9]



a. ${}_{12}H_{42}$ b. ${}_{12}H_{23}$ c. ${}_{12}H_{24}$

Table 1 shows the plan and cross-sectional view of three kinds of honeycomb multi-post cable dome structures. Compared with the traditional existing types, the advantages of the honeycomb multi-post dome ${}_nH_{bp}$ can be easily found below:

1) The honeycomb multi-post cable dome is innovative and attractive on architectural styles, and the structural reasonability can also be satisfied simultaneously.

2) For all three types, each upper node is connected with only 3 ridge cables, forming a relatively larger-span honeycomb grid with relatively fewer ridge cables compared with Levy type, Kiewitt type, bird nest type. Also, each upper and lower node is averagely connected with 6 components, which is pretty even for the cable-post arrangement;

3) As for innovative multi-post setting, most of the upper nodes are connected with 2 posts except node *A* in ${}_nH_{b3}$, and the lower nodes *B* for all three types are connected with two, three, and four posts, respectively, rather than single post setting used in previous projects. Thus, compared with the single-post type cable dome, the stability of entire structure of these three types can be improved when the posts themselves become more stable and interacted by multiplying and converging;

4) There is only one oblique cable for ${}_nH_{b2}$ and ${}_nH_{b4}$ because of multi-post setting trial, of which the single oblique cable is arranged in the radial direction and the horizontal projections of these cables between each of the two neighboring loop districts are radially non-continuous. If there is only one radial oblique cable in each grid and the structural prestressed state is established by tensioning oblique cable, the complexity of tensioning construction can be reduced significantly, and the unfavorable situation of cable slip as in traditional sunflower type with two diagonal oblique cables can be avoided too;

5) As for ${}_nH_{b3}$ and ${}_nH_{b4}$ cable dome, since there will be 3 or 4 posts for each lower node *B*, each *B* matchs two upper nodes *A* and *A*', i.e., each bottom loop can match two radial sets of ridge cables. Therefore, the number of loops can generally be reduced by half to no more than four, or even just three loops;

6) The number of costly cables used for the entire structure can be reduced with the reduction of the ridge cables, the loop cables and the oblique cables consumption, thereby saving on engineering costs.

7) It is the idea of converging multi-posts setting at cable-post arrangement that increases the post-to-cable ratio, e.g. the ratios of the ${}_nH_{b3}$ and ${}_nH_{b4}$ are both 1:2. But the ratio of existing cable domes are much less, such as the most uneven 1:5 for the sunflower type Georgia dome and 1:3 for the ribbed-ring Seoul Olympic dome. Since the price of cable is several times that of the post (steel tube or steel rod), honeycomb multi-post cable dome is economical and thus expects more desirable application prospects, compared with the former low cable-to-post ratio types.

3. Simplified analytical method for prestressed state of honeycomb four-post cable dome structure

Dong S.L. and Yuan T. proposed a simplified analytical method for the prestressed state of honeycomb four-post cable dome structure, ${}_nH_{b4}$ [6]. Using the axis symmetric condition, a circular ${}_nH_{b4}$ with a central opening was divided into *n* equal parts and only a one-segment semi-structure space truss was analyzed. The three-dimensional schematic diagram of the ${}_nH_{b4}$ is shown in Fig. 2.

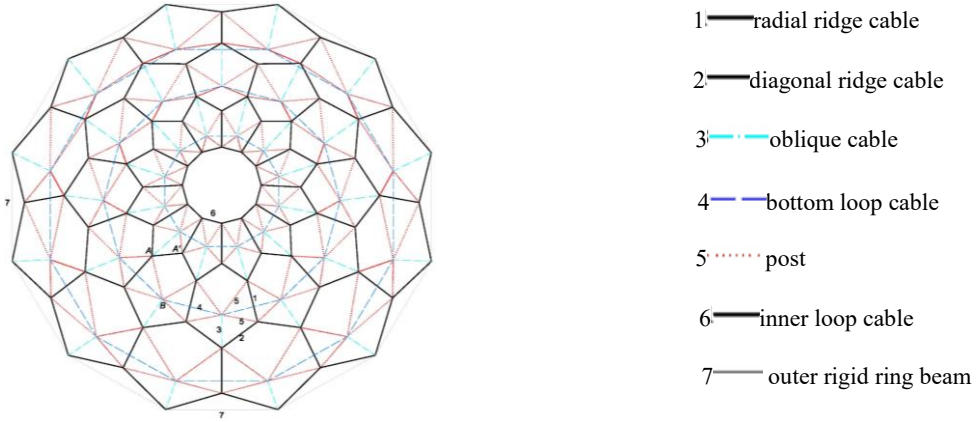


Figure 2: 3D schematic diagram of ${}_nH_{b4}$ [6]

This cable dome is composed of a honeycomb ridge cable net (made up of both radial and oblique ridge cables) indicated by solid black lines, bottom loop cables indicated by broken indigo lines, an inner loop, oblique cables indicated by dotted dash cyan lines, four posts indicated by dotted red lines converging at the lower node, and a rigid ring beam indicated by solid gray lines. The outer ring beam supporting the cable dome is rigid and can be regarded as the fixed hinge bearing for the dome. The

nodes 1_a, 1_b, 2', ...i_a, i_b, ... are in the same symmetric plane, the nodes 1', 2_a, 2_b, ...i', ...j_a are in another adjacent symmetric plane.

Based on the internal force V_{1a} of the innermost post, the balance equations are established recursively for each node; then based on that the formulas of the internal forces of each component, cable or post, can be derived successively. For example, the balance equation for node i is as below:

$$\left[\sin\alpha_{ia}\cos\phi_{ia}\cos(\gamma_{ia}+\frac{\pi}{n})-\sin\phi_{ia}\cos\alpha_{ia}\right]T_{ia}+\left[\sin\beta_{(i-1)}\cos\phi_{ia}\cos(\gamma_{ia}+\frac{\pi}{n})+\sin\phi_{ia}\cos\beta_{(i-1)}\right]B_{(i-1)}$$

$$=2\left[\sin\alpha_{(i-1)}\cos\phi_{ia}\cos(\gamma_{ia}+\frac{\pi}{n})-\sin\phi_{ia}\cos\alpha_{(i-1)b}\cos\gamma_{(i-1)}\right]T_{(i-1)b}$$

$$2\left[\sin\alpha_{ia}\cos\phi_{ia}\cos(\gamma_{ia}+\frac{\pi}{n})-\sin\phi_{ia}\cos\alpha_{ia}\right]V_{ia}=2\left[\sin\alpha_{ia}\cos\alpha_{(i-1)b}\cos\gamma_{(i-1)}\right.$$

$$\left.-\cos\alpha_{ia}\sin\alpha_{(i-1)b}\right]T_{(i-1)b}+\left(\sin\alpha_{ia}\cos\beta_{(i-1)}+\cos\alpha_{ia}\sin\beta_{(i-1)}\right)B_{(i-1)}$$

$$2\left[\sin\alpha_{ib}\cos\phi_{ib}\cos(\gamma_{ib}-\frac{\pi}{n})+\sin\phi_{ib}\cos\alpha_{ib}\cos(\gamma_{i}+\frac{\pi}{n})\right]T_{ib}+\left[\sin\alpha_{ia}\cos\phi_{ib}\cos(\gamma_{ib}-\frac{\pi}{n})+\sin\phi_{ib}\cos\alpha_{ia}\right]T_{ia}=0$$

$$2\left[\sin\alpha_{ib}\cos\phi_{ib}\cos(\gamma_{ib}-\frac{\pi}{n})+\sin\phi_{ib}\cos\alpha_{ib}\cos(\gamma_{i}+\frac{\pi}{n})\right]V_{ib}+\left[\sin\alpha_{ib}\cos\alpha_{ia}-\sin\alpha_{ia}\cos\alpha_{ib}\cos(\gamma_{i}+\frac{\pi}{n})\right]T_{ia}=0$$

$$(\sin\beta_i)*(B_i)+2\left(V_{ia}\sin\phi_{ia}+V_{ib}\sin\phi_{ib}\right)=0$$

$$\left(\sin\phi_{ia}\cot\beta_i+\cos\phi_{ia}\cos\gamma_{ia}\right)V_{ia}+\left(\sin\phi_{ib}\cot\beta_i-\cos\phi_{ib}\cos\gamma_{ib}\right)V_{ib}+(\sin\frac{\pi}{n})*H_i=0$$

where the internal forces of the cables and posts are represented by T_{ia}, T_{ib}, H_i, B_i, V_{ia}, V_{ib}, and $H_{1,\,p}$, respectively; referring to the horizontal plane, the variables α_{ia}, α_{ib}, β_i, ϕ_{ia}, and ϕ_{ib} represent the elevation angles of the ridge cables T_{ia} and T_{ib}, the oblique cables B_i, and the posts V_{ia} and V_{ib}, respectively; the variables γ_i, γ_{ia}, and γ_{ib} represent the angles between the main diameter line of each honeycomb unit and the horizontal projection of three components in this unit, the ridge cable T_{ib}, the post V_{ia} , and the post V_{ib}, respectively.

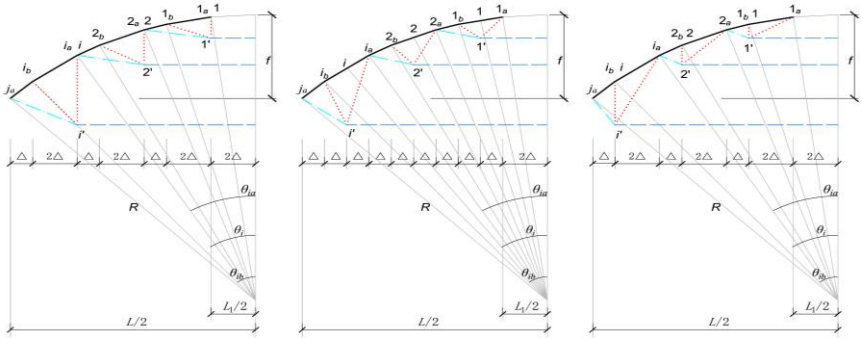
According to these recursive equations, if the prestress V_{1a} of the innermost post is known, the initial prestress of T_{ia}, T_{ib}, H_i, V_{ib}, B_i, and V_{ia} can be obtained successively and then the prestress distribution of all the components for the cable dome can also be determined. Since there is only one fundamental unknown V_{1a}, the ${}_nH_{b4}$ can be judged to be statically indeterminate with one redundant degree as well as the other two kinds of ${}_nH_{bp}$, similarly.

4. Geometrical relationship and calculated design table of initial prestressed state

Dong S.L. and Yuan T also carried out the geometrical formulas of the ${}_{12}H_{34}$ with a central opening, with parameters such as span L, central opening span L_1, vector height f, and node radius r_i, r_{ia}, r_{ib} and spherical dome radius R. The relationship $r_{(i+1)a}-r_{ib}=\frac{r_{ib}-r_{ia}}{2}=\Delta$ is the (17) condition that horizontal projection lengths of the ridge cables in the radial direction have to satisfy, as shown in Fig. 3 below [6].

In order to distinguish the influence of the depth-to-span for the honeycomb multi-post structures, this paper chooses 0.12, 0.17, 0.22 as a set of slightly adjusted parameter of depth-to-span ratio to find the difference of the initial prestress state between the results from literature [6] using three ratios of 0.1, 0.15, 0.2.

On the premise that the horizontal projections of nodes i' and nodes i are on the same circumference, three cases are considered: In Case 1, $r_{i'} - r_{ia}\cos\frac{\pi}{n}=0$, the triangular plane formed by the nodes $i_a, i',$ and i_a is perpendicular to the horizontal plane (see Fig.3a). According to the recursive formulas



(a) Case 1 (b) Case 2 (c) Case 3

Figure 3: Simplified schematic of semi-structure of space truss with a central opening [6]

and the geometric relationship, when the value fundamental unknown variable is assigned to be 1, the prestress value of each component of the whole cable dome is presented in Table 2 using variables $\frac{f}{L} = 0.12,\ 0.17,\ 0.22;\ j = 2,\ 3,\ 4;\ \frac{L_1}{2} = 2\Delta;$ and $n = 12$. In Case 2, $r_{i'} - r_{ia}=\Delta$, as shown in Fig. 3b. In Case 3, $r_{ib}\cos\frac{\pi}{n} - r_{i'}=0$, the triangular plane formed by nodes $i_b,\ i',$ and i_b is perpendicular to the horizontal plane (Fig.3c). As in Case 1, the relative prestress results of corresponding components in Case 2 and Case 3 can be obtained similarly, as shown in Table 2.

Comparing the result in literature [6], it can be found that the force of innermost ridge cable T_{ia} and T_{ib} increases and the force of most tensioned outmost loop H_{ip} decreases under the increase of depth-to-span ratio, which is beneficial for initial prestressed state to be more even. Also, the innermost lightly tensioned ridge cable is easy to be slack, the increase of initial prestress of the innermost cable make it more resistant to cable slack under loads. However, the T_{ia} and T_{ib} increase 2.3% to the most and H_{ip} decrease the 1.8% to the most with 10% ~ 20% ratio adjustment. When the ratio changes from 0.12 to 0.22, the largest value of adjustment for the bottom loop cable H_{ip} is H_{3p}, just 7%, and that of the innermost ridge cable T_{ia} is T_{3a}, just 10% with nearly 50% ratio change. Thus, the regulation of ratio is beneficial for prestressed state distribution and innermost ridge cable slack prevention but has limited efficiency in adjustment of initial internal force value.

Table 2 also shows that the distribution feature of the initial prestressed state of the ${}_{12}H_{34}$: 1) the internal force is multiplied from the inner to the outer and the internal force of the outer cables has a tendency to increase more rapidly than that of inner cables; 2) the uniformity of distribution declines with the sequence of Case 1, Case 2, and Case 3 having different lower node locations; 3) the lower node location significantly affects the distribution of the internal force, since values vary largely among Cases 1~3. However, the practical initial prestressed state would be optimized by considering the load state.

5. Conclusion

This paper summarizes the features of innovative honeycomb multi-post cable dome structures, including ${}_nH_{b2}$, ${}_nH_{b3}$, and ${}_nH_{b4}$, which differs from traditional types following Buckminster Fuller's initial tensegrity concept of tensioned cables ocean and compressed posts islands, like the former existing cable dome structures with all single posts perpendicular to the horizontal plane. Compared with these types in geometric characteristics, this paper has 4 conclusions for ${}_nH_{bp}$:

1. The lower and upper nodes connect at least two posts and multiple posts converging and interacting at each node make the post themselves and the whole structure more stable; multi-post setting trial leads each honeycomb unit of ${}_nH_{b4}$ and ${}_nH_{b2}$ to have only one oblique cable in the radial direction. The horizontal projections of these single oblique cables between each two neighboring loop districts are radially non-continuous. Reducing the number of oblique cables from two to one in each grid halves the workload of the symmetrical tensioning construction to form the cable dome. Meanwhile, the slipping of the bottom loop cable as in traditional type with two diagonal oblique cables can also be avoided.

2. The ridge cables of the multi-post cable dome structures are arranged in an innovative and aesthetical honeycomb layout, forming a relatively larger-span honeycomb grid with fewer ridge cables at each unit than Levy type, Kiewitt type, bird nest type. Thus the number of the upper, loop, and oblique cables of the honeycomb multi-post cable dome all decreases, which is beneficial to reduce the number of costly cables.

3. A classic simplified analytical method of the ${}_nH_{b4}$ is applied to analyze prestressed state and demonstrate the importance of depth-to-span ratio for honeycomb four-post cable domes. According to this method and derived calculation formulas, the calculated prestress state for the cable dome with new geometric parameters are given in a new design table. This factor turns out to be beneficial for obtaining a more even initial prestressed state distribution but has limited efficiency to adjust.

4. The research in this paper enriches the selections for roof structure with new cable dome types, which can naturally combine structural reasonability and architectural aesthetics. More detailed theoretical basis for the design of honeycomb four-post cable dome structure is also presented.

Table 2: Design table of prestressing forces of ${}_{12}H_{34}$ with a central opening

			Case 1: $r_{i'}-r_{ia}\cos\frac{\pi}{n}=0$,n=12							Case 2: $r_{i'}-r_{ia}=\Delta$,n=12							Case 3: $r_{ib}\cos\frac{\pi}{n}-r_{i'}=0$,n=12						
f/L	j	i	T_{ia}	V_{ia}	T_{ib}	V_{ib}	B_i	H_i	H_{ip}	T_{ia}	V_{ia}	T_{ib}	V_{ib}	B_i	H_i	H_{ip}	T_{ia}	V_{ia}	T_{ib}	V_{ib}	B_i	H_i	H_{ip}
0.12	2	1	1.00	-0.14	0.73	-0.12	1.31	2.05	1.89	1.00	-0.16	0.78	-0.12	1.20	2.26	1.59	1.00	-0.23	0.87	-0.16	1.32	3.07	1.23
	3	1	1.00	-0.09	0.74	-0.11	1.29	2.09	1.94	1.00	-0.13	0.79	-0.10	1.18	2.32	1.63	1.00	-0.21	0.87	-0.14	1.30	3.17	1.25
		2	2.37	-0.46	2.72	-0.31	3.23	5.10	/	2.84	-0.63	3.45	-0.43	3.64	6.98	/	4.03	-1.18	5.22	-0.88	6.17	14.22	/
	4	1	1.00	-0.07	0.74	-0.10	1.28	2.11	1.95	1.00	-0.11	0.79	-0.10	1.17	2.34	1.64	1.00	-0.21	0.87	-0.13	1.29	3.20	1.26
		2	2.32	-0.36	2.73	-0.28	3.14	5.13	/	2.78	-0.54	3.46	-0.38	3.51	7.06	/	3.96	-1.10	5.25	-0.82	6.06	14.47	/
		3	6.04	-1.44	9.92	-1.03	8.85	13.85	/	8.91	-2.48	15.61	-1.92	12.31	23.75	/	18.08	-6.36	33.03	-5.79	31.85	72.15	/
0.17	2	1	1.00	-0.19	0.73	-0.15	1.34	1.98	1.83	1.00	-0.20	0.78	-0.16	1.25	2.17	1.55	1.00	-0.25	0.87	-0.20	1.37	2.94	1.21
	3	1	1.00	-0.12	0.74	-0.12	1.30	2.07	1.92	1.00	-0.15	0.79	-0.11	1.19	2.29	1.61	1.00	-0.22	0.87	-0.15	1.31	3.12	1.24
		2	2.48	-0.61	2.71	-0.38	3.43	5.04	/	2.95	-0.78	3.44	-0.52	3.90	6.83	/	4.16	-1.32	5.20	-1.01	6.41	13.73	/
	4	1	1.00	-0.09	0.74	-0.11	1.29	2.10	1.94	1.00	-0.13	0.79	-0.10	1.18	2.32	1.63	1.00	-0.21	0.87	-0.13	1.30	3.17	1.25
		2	2.37	-0.45	2.72	-0.31	3.22	5.10	/	2.83	-0.62	3.45	-0.42	3.62	6.99	/	4.03	-1.17	5.23	-0.88	6.15	14.24	/
		3	6.43	-1.84	9.87	-1.19	9.49	13.76	/	9.43	-2.96	15.51	-2.20	13.33	23.36	/	18.96	-7.02	32.59	-6.28	33.01	69.93	/
0.22	2	1	1.00	-0.23	0.73	-0.18	1.39	1.91	1.76	1.00	-0.24	0.79	-0.20	1.32	2.07	1.50	1.00	-0.28	0.89	-0.26	1.44	2.79	1.19
	3	1	1.00	-0.14	0.73	-0.12	1.31	2.04	1.89	1.00	-0.17	0.78	-0.12	1.21	2.25	1.59	1.00	-0.23	0.87	-0.16	1.32	3.07	1.23
		2	2.62	-0.76	2.72	-0.47	3.72	4.98	/	3.10	-0.94	3.46	-0.65	4.27	6.66	/	4.32	-1.47	5.19	-1.21	6.80	13.13	/
	4	1	1.00	-0.11	0.74	-0.11	1.29	2.08	1.93	1.00	-0.14	0.79	-0.11	1.18	2.30	1.62	1.00	-0.22	0.87	-0.14	1.30	3.15	1.25
		2	2.42	-0.53	2.72	-0.34	3.32	5.07	/	2.89	-0.71	3.45	-0.47	3.75	6.91	/	4.09	-1.25	5.21	-0.94	6.28	13.99	/
		3	6.95	-2.28	9.83	-1.45	10.41	13.67	/	10.12	-3.51	15.44	-2.64	14.80	22.88	/	20.06	-7.81	32.18	-7.07	34.87	67.06	/

Reference

[1] D.H. Geiger, A. Stefaniuk, D. Chen, "The design and construction of two cable domes for the Korean Olympics," *in Structural Engineering: Proceedings of IASS Symposium on Shells, Membranes and Space Frame, IASS 1986, Osaka, Japan, September 15-19, 1986*, Kōichirō Heki, Eds. New York: Elsevier, 1986. pp. 265-272.

[2] M.P. Levy, "The Georgia Dome and beyond: achieving lightweight-long span structures" *in Structural Engineering: Proceedings of IASS-ASCE International Symposium on Spatial, lattice and, tension structures, IASS-ASCE 1994, Atlanta, Georgia, USA, April 24-29, 1994*, J.F. Abel, J.W. Leonard, and C. U. Penalba, Eds. New York: ASCE, 1994. PP. 560-562.

[3] L.M. Chen, X.F. Yuan, S.L. Dong, "Self-stress mode analysis and optimal design of Kiewitt domes," *Journal of Zhejiang University: Engineering Science*, vol. 40, pp. 73-77, 2006.

[4] C.R. Calladine, "Buckminster Fuller's 'Tensegrity' structures and Clerk Maxwell's rules for the construction of stiff frames," *International Journal of Solids & Structures*, vol. 14, pp. 161-172, 1978.

[5] R.B. Fuller, "Tensile-integrity structures," U.S. Patent 3063521, Nov 13, 1962.

[6] S.L. Dong, Y. Tu, "Configuration and prestress distribution of honeycomb-type cable dome with four struts," *Spatial Structures*, vol. 24, pp: 3-12, 2018.

[7] A. Hanaor, "The concept of structural depth as applied to certain bar-tendon assemblies," *Space Structures* 5, 2002. Thomas Telford, London, vol. 1, pp. 11–20.

[8] M. Kawaguchi, B. Ikuo Tatemichi, P.S. Chen, "Optimum shapes of a cable dome structure*," Engineering Structures 21*, pp: 719–725, 1999. Kiewitt, G., 1960. The new look of lamella roofs. Architectural Record, February 1960, p. 226.

[9] S.L. Dong, Y. Tu, "Research on the system of honeycomb-type cable dome structures," in *Structural Engineering: Proceedings of 18th national modern structure Symposium, TJU 2018*, Changzhou, Hebei, CHN, July 20-22, 2018. pp: 10-15.

[10] S.L. Dong, Y. Tu, "Structural system innovation of cable dome structures," *Journal of Building Structures*, vol. 39, pp: 85-92, 2018. https://doi.org/10.14006/j.jzjgxb.2018.10.010

Proceedings of the IASS Annual Symposium 2019 – Structural Membranes 2019
Form and Force
7 – 10 October 2019, Barcelona, Spain
C. Lázaro, K.-U. Bletzinger, E. Oñate (eds.)

Influence of random loads on the optimal design of tensegrity footbridges

Jonas FERON[*,1,2], Igor BOUCKAERT[2], Pierre MENGEOT[1],
Jan VAN STEIRTEGHEM[1], Pierre LATTEUR[2]

[*,1] BESIX,
Avenue des communautés, 100, 1200 Bruxelles, Belgium
jferon@besix.com

[2] Université catholique de Louvain, UCLouvain,
Louvain School of Engineering EPL, Civil and Environmental Engineering,
Place du Levant, 1 (Vinci), bte L5.05.01, 1348-Louvain-la-Neuve, Belgium,
jonas.feron@uclouvain.be

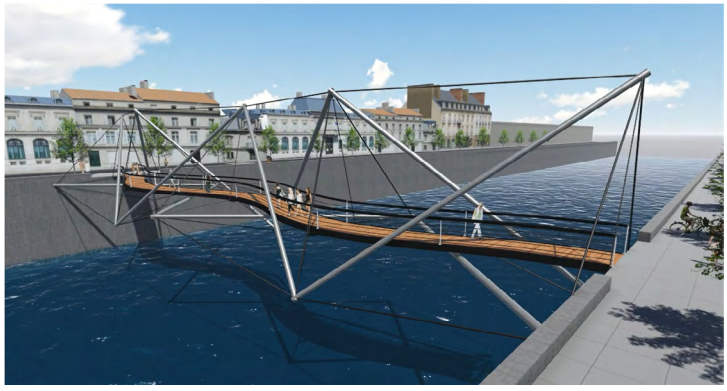
Abstract

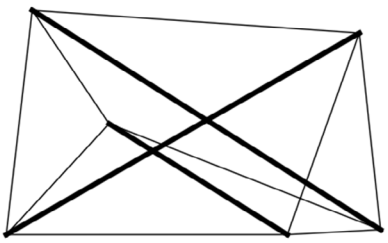
Although tensegrity forms have inspired artists and architects for many years, there exist very few real construction projects across the world. This is probably due to the complex construction processes, the lack of design guidelines, the complex non-linear calculation and, finally, the need for heavy pre-stress (required for a sufficient stiffness, but consuming however much more material). A previous study from the same authors demonstrated that "morphological indicators" can be used for the optimization of tensegrity structures' weight and stiffness and can provide a good tool for their design, in particular for tensegrity footbridges. Former studies have however took as assumption that the load was uniformly distributed along the deck, which is questionable. This article shares the last improvements performed in this way by integrating random pedestrians loads, and providing new insights about their impact on the optimal design of tensegrity footbridges.

Keywords: Tensegrity, footbridges, optimization, morphological indicators, random loads, self-weight, stiffness.

1. Introduction

Tensegrity structures are composed of discontinuous struts in compression "floating", in a stable self-equilibrated state, inside a net of tendons in tension.





Simplex module

Figure 1: tensegrity footbridge composed of $S = 4$ simplex modules

Copyright © 2019 by J. FERON, I. BOUCKAERT, P. MENGEOT, J. VAN STEIRTEGHEM, P. LATTEUR
Published by the International Association for Shell and Spatial Structures (IASS) with permission.

Tensegrity modules are unstable at first order and require non-linear calculation. Unless appropriate pre-stress is introduced, large displacements occur when the structure is externally loaded. A sufficient stiffness is possible, but this requires sufficient pre-stress, which involves more (and sometimes much more) material and self-weight [1]. This makes the optimization of the tensegrity footbridges' self-weight and stiffness particularly relevant.

Optimizing the shape of structure for a better stiffness and volume (or self-weight) is often great challenge, in particular for a tensegrity structure, as many parameters have to be considered (span, height, shape, cross sections, materials, loads, pre-stress, etc). A solution to this problem is to group these parameters into a smaller number of dimensionless numbers, called morphological indicators [2].

In 2014, R.E. Skelton et al [3] optimized planar tensegrity bridges uniformly loaded by means of other definitions of dimensionless numbers. In 2017, P. Latteur et al [2] adapted the morphological indicators methodology, used so far to optimize mainly trusses and arches, to 3D non-linear and pre-stressed lattice structures such as tensegrity structures. In 2019, J. Feron et al [1] used this method to find out the best shapes of footbridges composed of simplex, quadruplex and pentaplex tensegrity modules, but their main assumption was that pedestrian loads were uniformly distributed along the deck.

However, considering that the uniformly distributed load is the worse design case has to be checked. Indeed, at this stage it is not excluded that one particular live load distribution could require a higher pre-stress, and involve larger material volume or deflection.

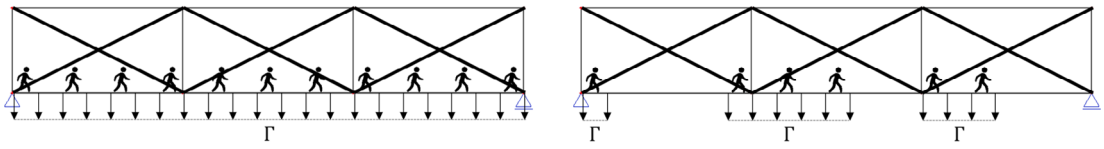


Figure 2: planar tensegrity footbridge subjected to uniform load (left) or to one instance of a random load distribution (right). The maximum load per linear meter Γ $[kN/m]$ is the same in both situation.

The goal of this article is thus to develop a design strategy based on morphological indicators, that finds the best shapes and guarantees their stability, whatever the load distribution is. Despite the non-linear behavior, it takes inspiration from the influence lines methodology, which considers the effects resulting from one single moving load. Indeed, due to the non-linear character of tensegrity structures, the effects of several load cases acting together cannot simply be added. In other words, the superposition principle is not valid anymore.

The morphological indicators methodology that considers a uniformly distributed load is summarized in §2. For clarity, the method to design a 2D tensegrity footbridge subjected to random loads is developed in §3. The best 3D tensegrity footbridge uniformly loaded is then compared to the best one randomly loaded in §4. Numerical validation of the morphological indicators methodology considering random load distribution is provided in §5. Eventually, conclusions are drawn in §6.

2. The morphological indicators

One considers any 3D, non-linear, pre-stressed and statically indeterminate lattice/tensegrity structure subjected to its self-weight and a specific load case (e.g. uniform load). The parameters describing the structure are the span L, the height H, the number S of modules, the total load F $(= \Gamma L)$, the pre-stressing forces (level β and repartition $\tilde{p}$), the material characteristics (design strength σ, Young's modulus E, specific weight ρ), the dimensions of the struts (area A_s, inertia I_s) and of the tendons (transversal $A_{t,t}$, longitudinal $A_{t,l}$). The optimization's objectives are, respectively, the volume of material V and the deflection δ at mid-span (under live loads only). The performances depend on the 13 parameters, according to 2 different undefined non-linear functions f, such that :

$$V = f(L, H, S, F, \beta, \tilde{p}, \sigma, E, \rho, A_s, I_s, A_{t,t}, A_{t,l}) \quad (1a)$$

$$\delta = f(L, H, S, F, \beta, \tilde{p}, \sigma, E, \rho, A_s, I_s, A_{t,t}, A_{t,l}) \quad (1b)$$

The morphological indicators methodology, proposed by P. Latteur et al [2], allows to reduce this amount of parameters from 13 to 6, by grouping them into dimensionless numbers (e.g. form factor $q \overset{\text{def}}{\equiv} I_s/A_s^2$, buckling indicator $\Psi \overset{\text{def}}{\equiv} \sigma L/\sqrt{qEF}$, self-weight indicator $\Phi \overset{\text{def}}{\equiv} \rho L/\sigma$), in such way that :

$$W \overset{\text{def}}{\equiv} \frac{\sigma V}{FL} = f\left(\frac{L}{H}, S, \Psi, \Phi, \frac{E}{\sigma}, \tilde{p}\right) \quad (2a)$$

$$\frac{L}{\delta} = f\left(\frac{L}{H}, S, \Psi, \Phi, \frac{E}{\sigma}, \tilde{p}\right) \quad (2b)$$

, where F is the total load associated to a specific load case. The optimization is thus highly simplified. This article numerically shows that equations (2a) and (2b) remain valid when the structure is subjected to random live load cases.

3. Calculation of a structure subjected to a random load distribution

One considers here that pedestrians can be anywhere, with a distributed load equal to $\Gamma\ [kN/m]$. Assuming that the deck is suspended to the upper nodes (as shown in figure 1), a random load distribution can be defined by the set of coefficients $(k_1, k_2, \dots, k_{S+1}) \in [0,1]$ as shown in figure 3.

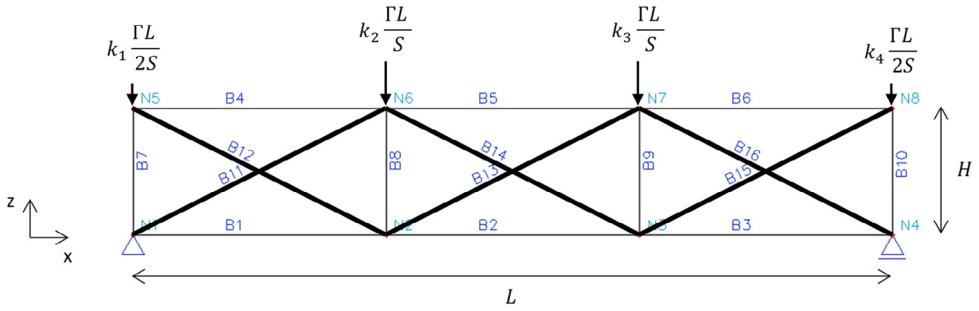


Figure 3: Simplified 2D tensegrity footbridge ($S = 3$), randomly loaded ($k_i \in [0,1]\ \forall i$)

For a given structure of span L subjected to one particular load distribution $(k_1, k_2, \dots, k_{S+1})$, the stiffest and/or lightest structure is obtained for particular values of H, S, $A_{t,l}$, $A_{t,t}$, A_s, I_s and pre-stressing forces. Furthermore, the worse load distributions $(k_1, k_2, \dots, k_{S+1})$, that means, the ones which are responsible for the biggest values of $A_{t,l}$, $A_{t,t}$, A_s, I_s, have to be found out.

3.1. Discussion about loads and the validity of the principle of superposition

One considers the 2D bridge of figure 3 of span L, subjected to a live load $\Gamma\ [kN/m]$. The maximum total load is $F = \Gamma L$ when the bridge is uniformly loaded. The deck's self-weight is neglected, but the structure's self-weight is considered as an external load acting on nodes (N1-N8), responsible for the internal forces $\tilde{N}_{sw}$ (figure 4.a).

A basic load case ($k_i = 1;\ k_{j\neq i} = 0$) is responsible for the internal forces $\tilde{N}_{(k_i=1, k_{j\neq i}=0)}$ (figure 4.c-f), while the uniformly distributed load case ($k_1 = 1, k_2 = 1, \dots, k_{S+1} = 1$) is responsible for the internal forces $\tilde{N}_{unif}$ (figure 4.b).

The pre-stressing forces $\tilde{P} = \tilde{p}\beta F$ are introduced thanks to an equal elongation of each strut. A unit elongation of the struts implies a unit pre-stress repartition $\tilde{p}$ (figure 4.h). The pre-stress level βF is fixed by the amplitude of the elongation of the struts ($\beta \geq 0$).

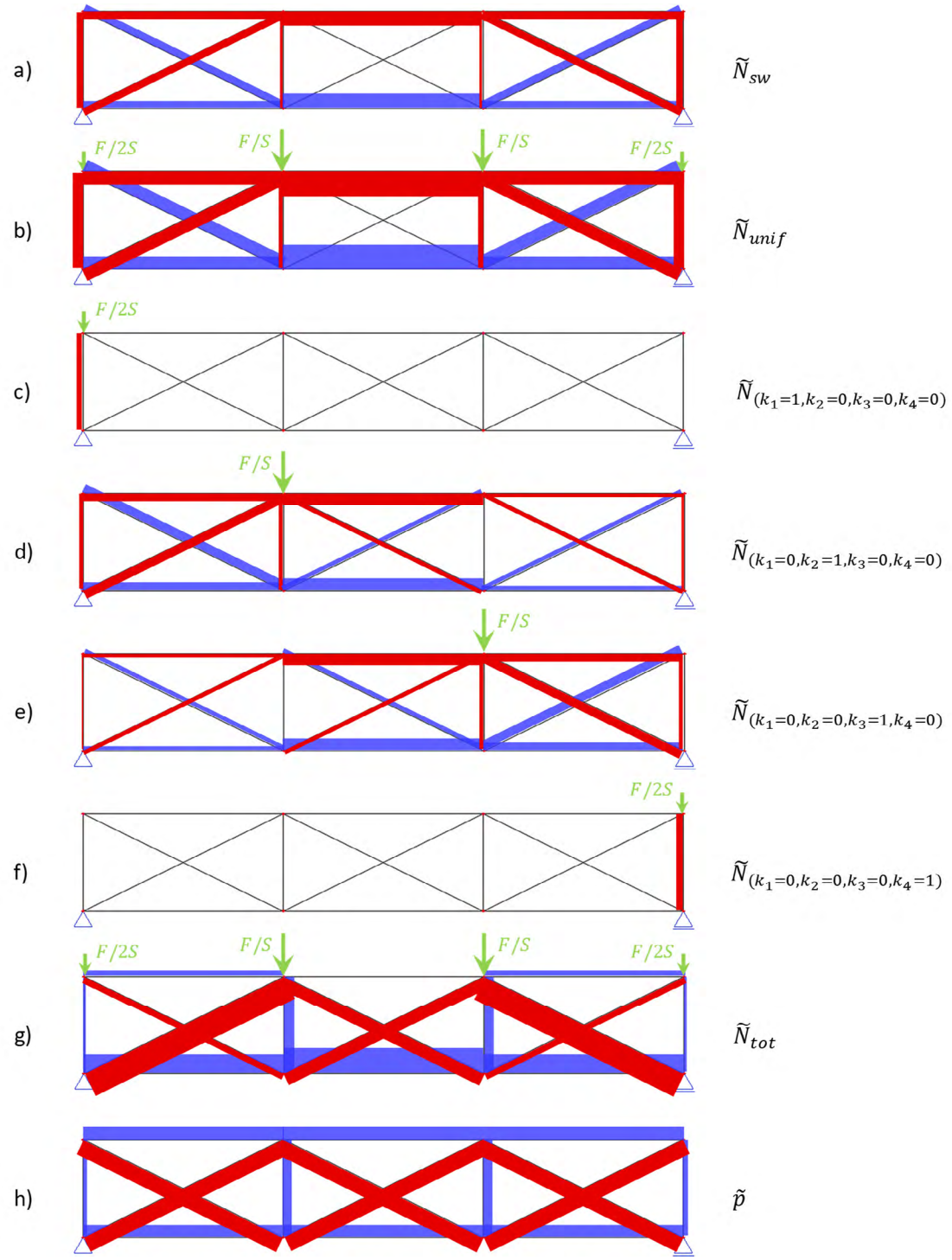


Figure 4: Internal forces repartitions (dark red for compression, light blue for tension) due to: a) self-weight (here $A_{t,l} = A_{t,t} = A_s$); b) uniform load distribution (1,1,1,1); c) load case (1,0,0,0); d) load case (0,1,0,0); e) load case (0,0,1,0); f) load case (0,0,0,1); g) combination of the pre-stress, self-weight and uniform load calculated as one single non-linear load combination; h) unit elongation of the struts;

For a given load distribution $(k_1, k_2, \dots, k_{S+1}) \in [0,1]$, the total forces $\widetilde{N}_{tot}$ (figure 4.g) are calculated considering one single load combination composed of the pre-stress, the self-weight and the particular load case $(k_1, k_2, \dots, k_{S+1})$ acting together.

Due to the structural non-linear behavior, the superposition principle is not valid. In other words:

$$\widetilde{N}_{tot} \neq \tilde{p}\beta F \; + \widetilde{N}_{sw} + \sum_{i=1}^{S+1} k_i * \widetilde{N}_{(k_i=1, k_{j\neq i}=0)} \quad (3a)$$

$$\widetilde{N}_{unif} \neq \sum_{i=1}^{S+1} 1 * \widetilde{N}_{(k_i=1, k_{j\neq i}=0)} \quad (3b)$$

3.2. Calculation strategy

This section is about the calculation of the pre-stress level βF and the value of the sections A_s, $A_{t,t}$ and $A_{t,l}$ for a structure of given L/H and S. The search for the best values of L/H and S that lead to the lightest or stiffest structure will be discussed in §4.

The strategy consists in selecting the load distributions $(k_1, k_2, \dots, k_{S+1}) \in [0,1]$ that, combined to pre-stress and self-weight, create:

1. Either the lowest tension force in the tendons (in order to determine the minimum pre-stress level βF in such way that no tendon slack);
2. Either the highest tension force in each tendon, responsible for the value of its area $A_{t,l}$ or $A_{t,t}$;
3. Either the highest compression force in the struts, responsible for the value its in order to design the area A_s of the struts;
4. The highest deflection δ (because the load combination that is responsible for the maximum internal forces may be different from the ones responsible for the largest deflection);

Figure 4 shows that load cases $(0, k_2 = 1{,}0{,}0)$ and $(0{,}0, k_3 = 1{,}0)$ combined together will be responsible for the highest compression force in the upper central element (B5). This is a useful observation, even if one has to keep in mind that, since the principle of superposition is not valid, the internal forces that they create when they are acting together are not equal to $\widetilde{N}_{(k_2=1, k_{j\neq 2}=0)} + \widetilde{N}_{(k_3=1, k_{j\neq 3}=0)}$. In other words, the observation of all the elementary load cases $k_i = 1$ is likely to allow the selection of the worse load combinations for each element of the structure, even if they don't allow to calculate the resulting internal forces thanks to a simple addition.

Practically, similarly to the influence line strategy, each basic load case k_i is firstly calculated (figure 4.c-f)) in order to know its effect on each element. For each element, the worst combinations $(k_1, k_2, \dots, k_{S+1})$ that compress/stretch it the most are thus determined. The total internal forces $\widetilde{N}_{tot}$ are then calculated for each worst combination. An envelope of the worst internal forces $\widetilde{N}_{tot,env}$ is finally obtained by selecting, for each strut, the maximal compression force and, for each tendon, the minimal/maximal tension forces. The maximum displacements of each nodes are obtained according to the same principle.

The pre-stress level βF is obtained thanks to an iterative algorithm in order to ensure that the least tensioned tendon remain always in tension whatever the load combination $(k_1, k_2, \dots, k_{S+1})$ such that:

$$\min_{t,l \text{ or } t,t} \widetilde{N}_{tot,env} \geq 0 \quad (4)$$

The dimensions A_s, I_s, $A_{t,t}$ and $A_{t,l}$ of the struts and tendons are obtained thanks to an iterative algorithm in order to satisfy the yielding and buckling constraints :

$$\sigma = \frac{N_{t,t\,max}}{A_{t,t}} = \frac{N_{t,l\,max}}{A_{t,l}} \quad (5a)$$

$$\sigma_{crit} = \frac{\sigma}{1 + \Lambda^2} = \frac{N_{s\,max}}{A_s} \quad (5b)$$

With :

- $N_{t,t\,max}, N_{t,l\,max}, N_{s\,max}$: the maximum values (respectively, in the transverse and longitudinal tendons and in the struts) of the envelop of the total forces $\widetilde{N}_{tot,env}$ such that :

$$N_{t,t\,max} = \max_{t,t} \widetilde{N}_{tot,env} \qquad N_{t,l\,max} = \max_{t,l} \widetilde{N}_{tot,env} \qquad N_{s\,max} = \max_{s} \widetilde{N}_{tot,env}$$

- Λ: the dimensionless slenderness of the struts (of buckling lengths l) given by :

$$\Lambda = \frac{l\sqrt{A_s/I_s}}{\pi\sqrt{E/\sigma}}$$

4. Comparison of structures uniformly loaded VS randomly loaded

By the means of a practical example, this section shows how to find the height H and number S of modules that minimize the volume V. One considers a 3D tensegrity footbridge (figure 5) with the following assumptions: $L = 60$m, live load $\Gamma = 5kN/m$ (When the bridge is uniformly loaded, the maximum load is $F = \Gamma L = 300\ kN$). The struts and the tendons are in timber ($\sigma = 10$MPa, $E = 10$GPa, $\rho = 4{,}5$kN/m³). The struts have full squared cross-sections (form factor $q = I_s/A_s^2 = 0.083$).

The indicator of buckling is $\Psi \overset{\text{def}}{=} \sigma L/\sqrt{qEF} = 38$, the indicator of self-weight is $\Phi \overset{\text{def}}{=} \rho L/\sigma = 27 * 10^{-3}$ and the indicator of material stiffness is $E/\sigma = 1000$. The unit pre-stress repartition $\tilde{p}$ is fixed by the pre-stressing scenario (elongation of the struts). Therefore, the optimization process is greatly simplify as the number of unknown is reduced from 6 dimensional parameters to 2 dimensionless parameters L/H and S related to the geometry:

$$W \overset{\text{def}}{=} \frac{\sigma V}{FL} = f\left(\frac{L}{H}, S\right) \tag{6a}$$

$$\frac{L}{\delta} = f\left(\frac{L}{H}, S\right) \tag{6b}$$

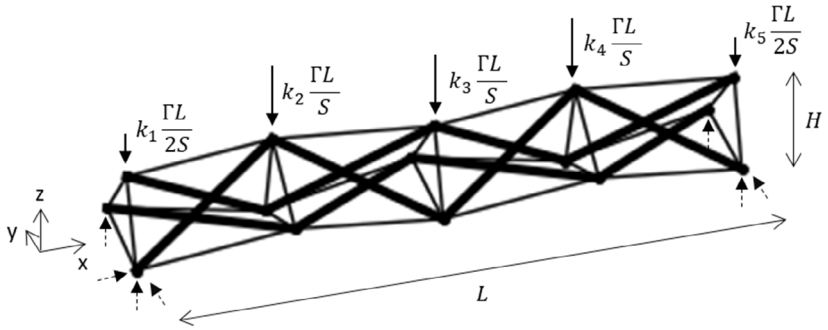


Figure 5: Structural model of a 3D tensegrity footbridge ($S = 4$) randomly loaded ($k_i \in [0,1]\ \forall i$)

The structure is first designed to withstand only the uniform load combination ($k_i = 1\ \forall i$), and then designed to withstand any load combination $(k_1, k_2, \dots, k_{S+1}) \in [0,1]$ according to the method described in §3.2. For each value of the height H and number S of modules, one gets the volumes V_{unif} and V_{rand} of material required and the deflection δ_{unif}, δ_{rand} under live loads only. The dimensionless volumes $W = \sigma V/FL$ and deflections L/δ are then drawn, in figure 6, in function of the dimensionless parameters L/H and S related to the geometry. Figure 6 shows that :

- The dimensionless volume W_{unif} is exactly the same that W_{rand} whatever the geometry. This means that the worst random load distribution $(k_1, k_2, \dots, k_{S+1})$, governing the design of the

pre-stress level βF and of the dimensions A_s, I_s, $A_{t,t}$ and $A_{t,l}$, is, actually, the uniformly distributed load.

- The lightest structure is composed of $S = 3$ simplex modules and has a slenderness $L/H = 5.5$. That means a height $H = L/5.5 = 10.9$m. The structure weighs $W = \sigma V/FL = 44.8$. That means a volume $V = 44.8FL/\sigma = 80.6$m³ of timber and a weight $\rho V = 362.9$kN.
- The lightest structure $(L/H = 5.5, S = 3)$ has a stiffness $L/\delta_{unif} = 845$ under uniform load and $L/\delta_{rand} = 550$ under the load distribution $(1,1,0,1)$. Therefore, the uniform load distribution is not the one giving the highest deflection ($\delta_{unif} = 71$mm and $\delta_{rand} = 109$mm). This is due to the fact that load case $(0,1,0,0)$ tends to twist the structure counterclockwise, while load case $(0,0,1,0)$ tends to twist it clockwise (figure 7). The uniform load combination $(1,1,1,1)$, combining, among others, the load cases $(0,1,0,0)$ and $(0,0,1,0)$ which have opposed effects, has thus a smaller deflection than the load combination $(1,1,0,1)$.

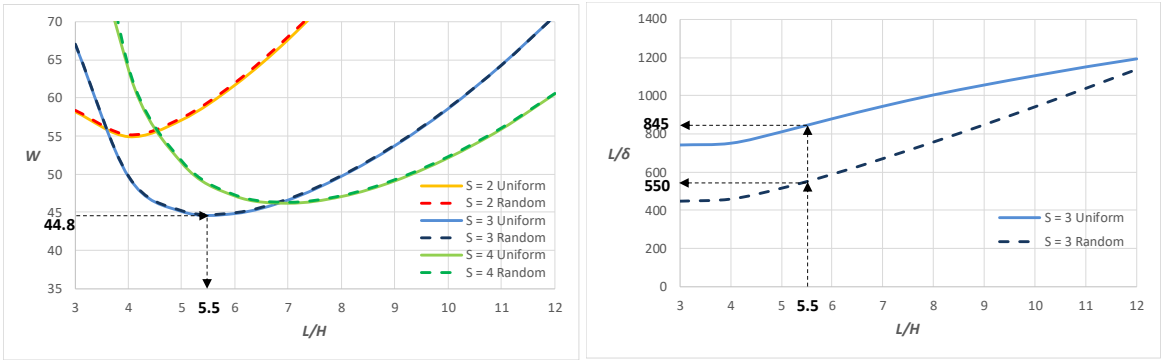


Figure 6: Dimensionless volume W and deflection L/δ of 3D tensegrity footbridges uniformly/randomly loaded $(\Psi = 38, E/\sigma = 1000, \rho L/\sigma = 27 * 10^{-3})$

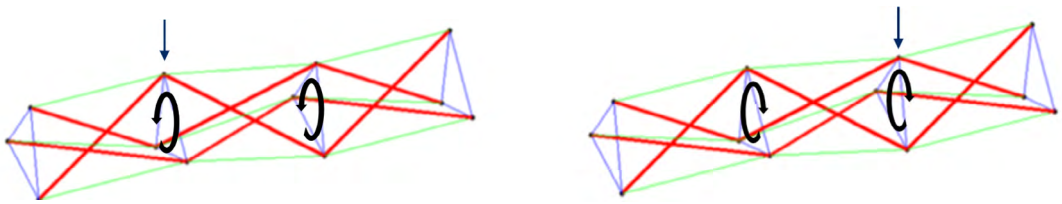


Figure 7: Effects on displacements of load cases $(0,1,0,0)$ and $(0,0,1,0)$

For the lightest structure $(L/H = 5.5, S = 3)$, the pre-stress forces in the struts are equal to 596kN, which correspond to a dimensionless pre-stress level $\beta = \tilde{P}/\tilde{p}F = 1.99$. The side of the full squared cross-sections of the struts is 530mm. The transversal/longitudinal tendons have a diameter of 248mm/311mm.

5. Validity of the morphological indicators methodology

The process of §4 is now repeated for a 3D tensegrity footbridge of span $L = 70$m in steel ($\sigma = 200$MPa, $E = 200$GPa, $\rho = 77$kN/m³) subjected to a maximum live load $\Gamma = 5kN/m$. ($F = \Gamma L = 350kN$). Struts have a hollow circular section of ratio thickness/diameter=0.02 ($q = I_s/A_s^2 = 1.94$).

For this new set of parameters, the morphological indicators are $\Psi = \sigma L/\sqrt{qEF} = 38, \rho L/\sigma = 27 * 10^{-3}, E/\sigma = 1000$ and remain thus the same as before. Moreover, the calculation of the dimensionless volume W and deflection L/δ lead to the exact same figure 6. This numerical example suggests that the morphological indicators methodology and the equations (2a) and (2b) remain valid when optimizing structure subjected to any load distribution.

The lightest steel structure ($S = 3, H = 12.7$m) has a volume $V = 44.8FL/\sigma = 5.5$m³ and weighs $\rho V = 422.6$kN. The pre-stressing forces in the struts are equal to 696kN which correspond to a dimensionless pre-stress level $\beta = \tilde{P}/\tilde{p}F = 1.99$. The struts are hollow circular tubes of diameter 515mm and thickness 10mm. The transversal/longitudinal tendons have a diameter of 60mm/75mm. The deflections are $\delta_{unif} = 83$mm and $\delta_{rand} = 127$mm.

6. Conclusion

This article describes the design of tensegrity footbridges subjected to pedestrian random loads, thanks to the methodology of morphological indicators. The optimal design of a structure subjected to a uniformly distributed load case has been compared to the one of the same structure subjected to random load distribution. It has been showed that the uniform load distribution can be considered for the choice of the level of pre-stress and the design of the cross sections. However, the uniformly distributed load is likely to largely underestimate the displacement at mid-span ($L/550$ to be compared to $L/845$ for the example given above). The high sensitivity of the tensegrity forms to the live loads distribution is thus proved. This suggest that tensegrity footbridges could also suffer from vibration's problems when crossed by moving pedestrians.

Acknowledgements

Authors wish to thank BESIX S.A. for supporting this work. Project funded by Brussels Capital Region – Innoviris.

References

[1] J. Feron, L. Boucher, V. Denoël and P. Latteur, "Optimization of footbridges composed of prismatic tensegrity modules", ASCE's Journal of Bridge Engineering, (Accepted for publication 02/2019).

[2] P. Latteur, J. Feron and V. Denoël, "A design methodology for lattice and tensegrity structures based on a stiffness and volume optimization algorithm using morphological indicators", International Journal of Space Structures, vol. 32, issue: 3-4, pp. 226-243, 2017.

[3] R.E. Skelton, F. Fraternali, G. Carpentieri and A. Micheletti, "Minimum mass design of tensegrity bridges with parametric architecture and multiscale complexity", Mechanics Research Communications, vol. 58, Pages 124-132, ISSN 0093-6413, 2014.

Proceedings of the IASS Annual Symposium 2019 – Structural Membranes 2019
Form and Force
7 – 10 October 2019, Barcelona, Spain
C. Lázaro, K.-U. Bletzinger, E. Oñate (eds.)

On the creation of infinitesimal mechanisms through cellular morphogenesis

Omar ALOUI[a], David ORDEN[b], Landolf RHODE-BARBARIGOS*

* University of Miami, Dept. of Civil, Architectural & Environmental Engineering

1251 Memorial Dr., McArthur Engineering Bldg, Coral Gables, FL 33146

landolfrb@miami.edu

[a] University of Miami, Dept. of Civil, Architectural & Environmental Engineering
[b] Universidad de Alcalá, Departamento de Física y Matemáticas

Abstract

In a structure, an infinitesimal mechanism represents a set of nodal displacements that do not engender extensions in its members. Tensegrity structures are self-stressed frameworks where the connectivity of the members and the configuration of nodes control the number of self-stress states and infinitesimal mechanisms in the system. In literature, kinematic analysis of tensegrity structures reveals infinitesimal mechanisms as an advantageous motion control strategy minimizing the control energy. However, infinitesimal mechanism creation is typically not controlled during the form finding and design of tensegrity structures. This paper is a continuation to the study of how the topology and geometry of tensegrity systems affects the creation of self-stress states through the cellular morphogenesis principles. In this paper, it is shown that infinitesimal mechanisms are created when fusion with the removal of two edges from the same two cells is used to compose the structure. A systematic method for the description of the infinitesimal mechanisms' modes at each step of the generation process, similar to the description of self-stress states in the fusion and adhesion processes, is proposed. The proposed method enables the design of tensegrity structures with predefined motion abilities that can be of great importance to deployable and reconfigurable tensegrity applications.

Keywords: Tensegrity, self-stressed frameworks, finite mechanism, infinitesimal mechanism, self-stress, design, control, cellular morphogenesis, form finding.

1. Introduction

Self-stressed frameworks, such as tensegrity structures, represent a class of structures with advantages for shape shifting and deployable applications as a result of their tunable properties, such as stiffness and geometric configuration [1,2,3]. In tensegrity structures, the synergetic action between tension and compression elements results in a state of self-equilibrium (self-stress) that enables the control of the stiffness and the geometry of the system. Self-stress thus characterizes the static behavior of tensegrity structures. The kinematic behavior of tensegrity structures can be described through internal mechanisms. An internal mechanism is defined as a set of displacement of the nodes, other than the rigid body motions, that do not engender deformation of the members. Infinitesimal mechanisms refer to infinitesimal displacements that are possible with no changes in the lengths of the members of the structure [4]. Infinitesimal mechanisms can be rigidified by increasing the self-stress of the structure in contrast with the internal finite mechanisms that do not depend on the self-stress. Internal finite and infinitesimal mechanisms can be used to identify advantageous control path for the deployment and

Copyright © 2019 by Omar ALOUI, David ORDEN, Landolf RHODE-BARBARIGOS
Published by the International Association for Shell and Spatial Structures (IASS) with permission.

shape changes in self-stressed systems, as following through this path, the loss of energy would be minimal [5,6]. This incites the inclusion of mechanisms as an important parameter in the design process of tensegrity and self-stressed structures for active applications. In this paper, the creation of finite and infinitesimal mechanisms in tensegrity structures is investigated through cellular morphogenesis. Cellular morphogenesis is a bio-inspired generative design method for tensegrity structures inspired by the multiplication of biological cells that uses the fusion and adhesion of elementary tensegrity units (cells) to construct complex tensegrity systems [7-10]. Adhesion occurs when tensegrity cells are combined along a set of shared nodes and edges without removing any of the shared elements between the two cells, while with fusion one or more shared elements are removed. The paper starts by defining mechanisms through the rigidity matrix before presenting the creation of finite and infinitesimal mechanisms using cellular morphogenesis in section 3 accompanied with a series of examples

2. Equilibrium matrix, rigidity matrix and mechanisms

2.1. Equilibrium problem and self-stress space

Self-stressed frameworks and tensegrity structures are governed by a stable self-equilibrated state in the absence of external loading and reactions. This self-equilibrium can be described entirely by the nodal equilibrium of the internal forces. For a node $\boldsymbol{P}$ connected to nodes $\boldsymbol{Q_i}$ where $\boldsymbol{PQ_i}$ is an edge of the structure, the static equilibrium is described by [11]:

$$\sum_{\boldsymbol{PQ_i\ an\ edge}} \overrightarrow{\boldsymbol{PQ_i}} \frac{\boldsymbol{F_{PQ_i}}}{\left\|\overrightarrow{\boldsymbol{PQ_i}}\right\|} = \boldsymbol{0} \tag{1}$$

$\boldsymbol{F_{PQ_i}}$ is a signed scalar representing the force in the member $\boldsymbol{PQ_i}$. The equilibrium of self-stressed structures is typically described using force densities $\boldsymbol{\omega}$ rather than forces, representing forces per unit length, leading to:

$$\sum_{\boldsymbol{PQ_i\ an\ edge}} \overrightarrow{\boldsymbol{PQ_i}}\, \boldsymbol{\omega_{PQ_i}} = \boldsymbol{0} \tag{2}$$

By collecting the linear equations for all nodes, one can construct a system of equations representing the self-equilibrium of the structure described by the equilibrium matrix A and the force density vector ω. For a dimension d, A is a $dn \times m$ matrix where m is the number of elements in the structure, n the number of nodes and ω is a vector of m components, one for each member. Self-stress is defined as the solution to the system $A\omega = 0$ which represents the nullspace space of the matrix A.

2.2. Rigidity matrix and mechanisms

Mechanisms are defined as nodal displacements that do not cause deformation of the members. Let p be the coordinates of node P and q be the coordinates of node Q. When infinitesimal displacements are considered along these mechanisms, their directions can be thought of as the velocities of the nodes displacing in the same directions. Thus, these infinitesimal displacements can be obtained through differentiating the coordinates of the nodes. Now, by definition of a mechanism, the length of a member $\left\|\overrightarrow{PQ}\right\|$ remains constant throughout the displacement that gives:

$$\frac{\boldsymbol{d}\left\|\overrightarrow{\boldsymbol{PQ}}\right\|^{\boldsymbol{2}}}{\boldsymbol{dt}} = \boldsymbol{2(p-q)(\dot{p}-\dot{q}) = 0} \tag{3}$$

If $\dot{p}$ and $\dot{q}$ are replaced with the displacement $\overrightarrow{d_P}$ and $\overrightarrow{d_Q}$, one can find the equation at each member that displacements have to satisfy in order to correspond to a mechanism:

$$(\boldsymbol{p}-\boldsymbol{q})\left(\overrightarrow{\boldsymbol{d_P}}-\overrightarrow{\boldsymbol{d_q}}\right)=\overrightarrow{\boldsymbol{PQ}}\left(\overrightarrow{\boldsymbol{d_P}}-\overrightarrow{\boldsymbol{d_q}}\right)=\boldsymbol{0} \tag{4}$$

By collecting all the linear equations at each member, one can construct a system representing the stability of the structure described by the rigidity matrix R ($m \times dn$ matrix) and $\vec{d}$ a vector of dn components where every d component reflects the displacement of a given node. Thus, algebraically, mechanisms describe the solution of the system $R\vec{d}=0$ which represents the nullspace of the rigidity matrix R. The minimum dimension of the mechanism space is always $\frac{d(d+1)}{2}$ which corresponds to the trivial rigid body motions of the structure. Other internal mechanisms can be found through the study of the space. In plane, the dimension of the space of rigid body motions is three: two unitary translations of the nodes in the direction of x and y and a $\frac{\pi}{2}$ rotation around the normal to the plane. Let $(P_i)_{(1\leq i\leq n)}$ the set of nodes of the structure. The basis of the rigid body motions is described by:

$$\boldsymbol{t_x}=\left[\overbrace{\boldsymbol{1}\,\boldsymbol{0}}^{\boldsymbol{P_1}}\ \overbrace{\boldsymbol{1}\,\boldsymbol{0}}^{\boldsymbol{P_2}}\ \ldots\overbrace{\boldsymbol{1}\,\boldsymbol{0}}^{\boldsymbol{P_n}}\right]$$

$$\boldsymbol{t_y}=\left[\overbrace{\boldsymbol{0}\,\boldsymbol{1}}^{\boldsymbol{P_1}}\ \overbrace{\boldsymbol{0}\,\boldsymbol{1}}^{\boldsymbol{P_2}}\ \ldots\overbrace{\boldsymbol{0}\,\boldsymbol{1}}^{\boldsymbol{P_n}}\right] \tag{5}$$

$$\boldsymbol{r_{xy}}=\left[\overbrace{\boldsymbol{p_{11}}-\boldsymbol{p_{12}}}^{\boldsymbol{P_1}}\ \overbrace{\boldsymbol{p_{21}}-\boldsymbol{p_{22}}}^{\boldsymbol{P_2}}\ldots\overbrace{\boldsymbol{p_{n1}}-\boldsymbol{p_{n2}}}^{\boldsymbol{P_n}}\right]$$

The internal mechanisms can be isolated from the rigid body motions by finding the specific displacements directions that are orthogonal to the basis of the rigid body motions which means that an internal mechanism d has to satisfy the equations $t_x \,.d=0$, $t_y.d=0$ and $r_{xy}.d=0$. If the rows t_x, t_y and r_{xy} are added to the rigidity matrix R then the space of internal mechanisms is the nullspace of the resulting matrix. In space, a similar construction would result in six basis vectors $t_x, t_y, t_z, r_{xy}, r_{yz}$ and r_{yz}. By investigating equation (2) and (4), one can notice that the rigidity matrix represents the transpose of the equilibrium matrix linking the dimensions of the self-stress space and the space of mechanisms through the fundamental theorem of linear algebra.

3. Creation of mechanisms through cellular morphogenesis

3.1. Equilibrium and multiplication of tensegrity cells

According to cellular morphogenesis, all self-stressed frameworks are decomposable to the same elementary units referred to as cells [7,8]. A cell, in general position, is always infinitesimally rigid, and has one self-stress state. Furthermore, it is characterized by an underlying graph that represents the complete graph on $(d+2)$ nodes. A complete graph is a graph where all nodes are connected to each other. Consequently, a cell has $(d+2)$ nodes and $\frac{(d+2)(d+1)}{2}$ edges. Therefore, the equilibrium matrix of the cell A_{cell} is a $d(d+2)\times\frac{(d+2)(d+1)}{2}$ matrix. Since the cell has only one self-stress state, the dimension of the nullspace of A_{cell} is 1 and the rank of A_{cell} is $\left(\frac{(d+2)(d+1)}{2}-1\right)$.

Tensegrity cells compose complex tensegrity structures through adhesion and fusion. Aloui et al. proved that adhesion of tensegrity cells that share more than d nodes results always in an infinitesimally rigid structure [8]. They also proved that removing only one edge does not alter the rigidity of the resulting structure. Tables 1 and 2 illustrate all possible combinations for the adhesion of two cells in a two-dimensional and three-dimensional space. The shadowed regions in the figures represent the shared space between the two cells. The trivial case where both cells share all their nodes is not considered.

Table 1: Illustration of possible adhesion combinations in 2D

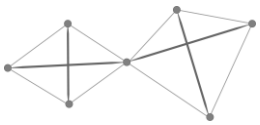
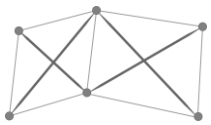
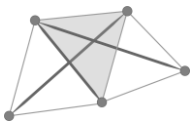
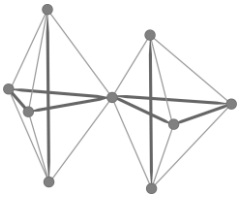
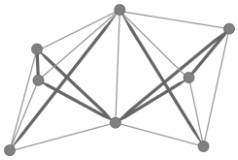
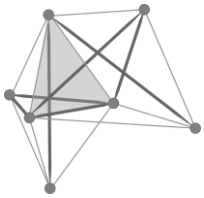
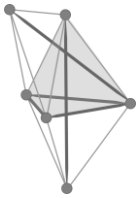
Cells share 1 node	Cells share 2 nodes	Cells share 3
		
Creation of a finite mechanism	Structure is infinitesimally rigid	Structure is infinitesimally rigid

Table 2: Illustration of possible adhesion combinations in 3D

Cells share 1 node	Cells share 2 nodes	Cells share 3 nodes	Cells share 4 nodes
			
Creation of a finite mechanism	Creation of a finite mechanism	Structure is infinitesimally rigid	Structure is infinitesimally rigid

3.2. Creation of finite mechanisms through cellular morphogenesis

Finite mechanisms in tensegrity systems are created when the added cell shares less than d nodes with the existing structure. In plane, the case where the number of shared nodes is one introduces exactly one finite mechanisms $\vec{d}$ that completes the vectors of the rigid body motions t_x, t_y and r_{xy} to form the basis of the mechanisms space. $\vec{d}$ can be calculated by fixing the nodes of the existing structure and rotating the nodes of the added cell around the shared node by $\frac{\pi}{2}$ (the choice of the angle of rotation is arbitrary). Figure 1 shows the directions of the displacements of the added mechanism.

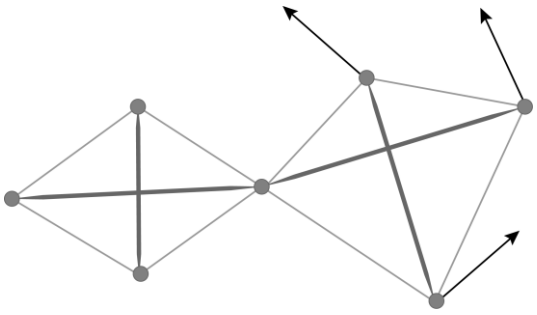


Figure 1: Illustration of the internal finite mechanism in the case of adhesion of two cells sharing one node in plane

This result can be verified through the study of the resulting rigidity matrix. Let s be the number of self-stress states of the existing structure, m its number of mechanisms, n its number of nodes and l its number of elements. The rigidity matrix of the initial structure R_i will have a rank of:

$$\boldsymbol{l - s = 2n - m} \tag{6}$$

The adhesion of the cell to the existing structure adds 6 edges (6 rows) and 3 nodes (6 columns) to the final structure (to the rigidity matrix R_f). The adhesion will also increase the number of self-stress states by one [7]. The rank of R_f will thus now be:

$$\boldsymbol{l + 6 - (s + 1) = 2(n + 3) - (m + m^*)} \tag{7}$$

where m^* is the number of added mechanisms and the result will be $m^* = 1$.

In space, two cases result in the creation of finite mechanisms. When the existing structure and the cell share one node, the adhesion creates three additional finite mechanisms $\vec{d}_1, \vec{d}_2$ and $\vec{d}_3$. Let $(\vec{x}, \vec{y}, \vec{z})$ be a basis of the space. The additional finite mechanisms can be calculated by fixing the nodes of the existing structure and rotating the cell around axes parallel to $\vec{x}, \vec{y}$ and $\vec{z}$ and passing by the shared node by an angle of $\frac{\pi}{2}$. Figure 2 illustrates the directions of the three finite mechanisms.

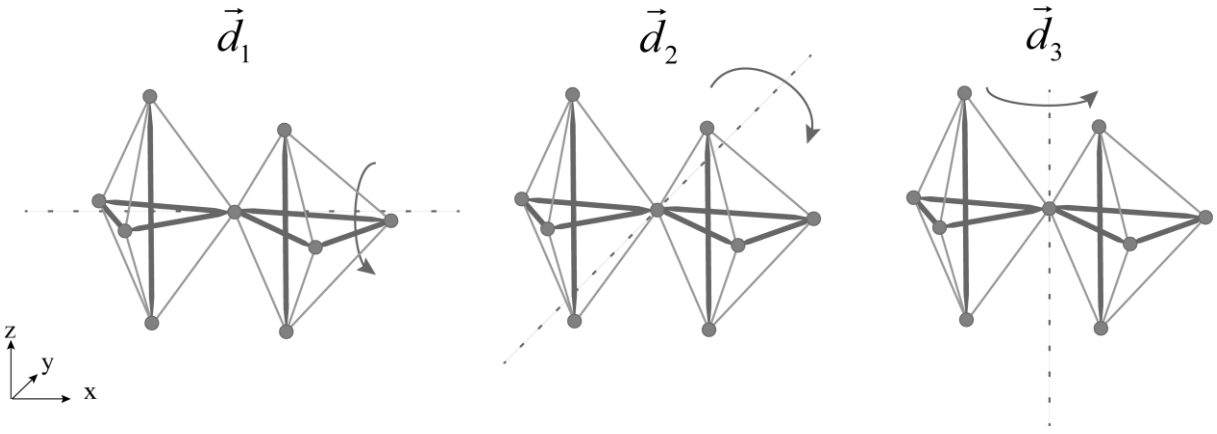


Figure 2: Illustration of the internal finite mechanisms in the case of adhesion of two cells sharing one node in space

Through the examination of the rank of the rigidity matrix of the resulting structure in the case of adhesion of spatial cells sharing one node, one can verify that the number of internal finite mechanisms is three. The rank of $\boldsymbol{R_i}$ in this case is:

$$\boldsymbol{l - s = 3n - m} \tag{8}$$

The adhesion results in adding 10 edges (10 rows), 4 nodes (12 columns) and one self-stress state. The calculation of the rank of R_f thus gives:

$$\boldsymbol{l + 10 - (s + 1) = 3(n + 4) - (m + m^*)} \tag{9}$$

which gives $\boldsymbol{m^* = 3}$. When the existing structure and the cell share two nodes the adhesion creates one internal finite mechanism given by the rotation of the added cell around the axis defined by the two

shared nodes while keeping the nodes of the existing structure fixed. The internal finite mechanism is illustrated in figure 3.

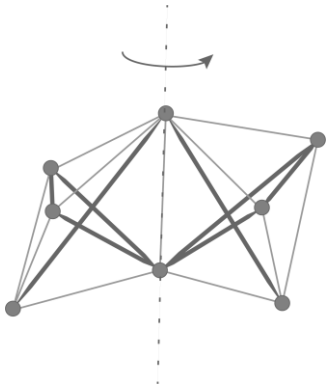


Figure 3: Illustration of the internal finite mechanisms in the case of adhesion of two cells sharing two nodes in space

In this case the adhesion adds 9 edges (9 rows), 3 nodes (9 columns) and one self-stress state. The rank of $\boldsymbol{R_f}$ is:

$$\boldsymbol{l + 9 - (s + 1) = 3(n + 3) - (m + m^*)} \tag{10}$$

and $m^* = 1$.

This section discusses all possible combinations that result in the creation of internal finite mechanisms in self-stressed frameworks. Moreover, in each case, the basis of the rigid body motions is being completed by the necessary number of vectors to form the basis of the mechanism space. The proposed mechanisms are linearly independent from the trivial mechanisms as the linear combination of rigid body motions is always a rigid body motion. Hence, this procedure can also be explored for the construction of a basis describing the space of the mechanisms during the cellular morphogenesis of a tensegrity structure.

3.3. Creation of infinitesimal mechanisms through cellular morphogenesis

Aloui et al. showed that, in addition to the adhesion along less than d nodes, cellular fusion with the removal of two or more edges from the same two unicellular substructures affects the kinematic behavior of the resulting structure. In [7,8], Aloui et al. showed that removing two or more edges in a fusion step constrains the configuration of the resulting structure to a degenerate position. In general, degenerate configurations restrict the nodal positions of tensegrity systems, or part of the systems, to a space with dimension strictly less than d. Degeneracy is thus linked with the creation of the self-stress state as removing two edges during the fusion of two cells leads to a statically determinate structure. Consequently, a tensegrity structure created through the fusion of two cells and the removal of two edges can only exist if the nodes collapse to a degenerate position that creates one or more infinitesimal mechanisms as these nodes can still have infinitesimal displacements the overall space of the structure. In plane, degenerate positions in the tensegrity systems reflect configurations, such as with three nodes on a line or with the axes of three members being concurrent, while in space, examples of degenerate positions include four nodes on a plane or six nodes on a quadratic surface. The triplex is an example of a structure where degeneracy results in the creation of a self-stress state as well as an infinitesimal mechanism. The triplex can be obtained through the fusion of two spatial cells with the removal of two edges. It has one self-stress state and one infinitesimal mechanism illustrated in figure 4. The nodes of the triplex are constrained to a quadratic surface represented in figure 4 that Aloui et al. described in [8].

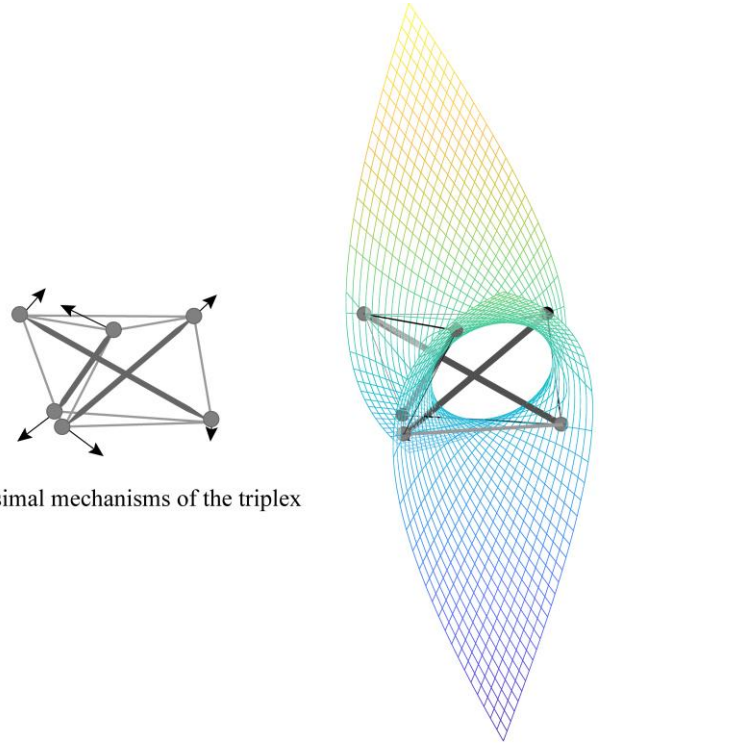


Figure 4: Illustration of the infinitesimal mechanism of the triplex and its constrained geometry

In order to understand the creation of infinitesimal mechanisms, the changes in the algebraic properties of the equilibrium and rigidity matrix are used. Assume that the existing structure and the cell are in general position (no degeneracy). Let $d \in \{2,3\}$ be the dimension of the workspace, s be the number of self-stress states of the existing structure, m its number of mechanisms, n its number of nodes and l its number of elements. The rank of the rigidity matrix R_i can be calculated by:

$$\boldsymbol{l - s = dn - m} \tag{11}$$

The fusion of the structure with a cell sharing $p \in \{d, d+1\}$ nodes with the removal of two edges will add $\left(\frac{(d+2)(d+1)}{2} - \frac{p(p-1)}{2} - 2\right)$ edges to the structure or rows to the rigidity matrix and $d + 2 - p$ nodes or $d(d + 2 - p)$ columns. The number of the self-stress states s will decrease by 1 and m^* is the change in the number of mechanisms. The rank of the rigidity matrix R_f of the resulting structure is:

$$\begin{aligned} \boldsymbol{l + \left(\frac{(d+2)(d+1)}{2} - \frac{p(p-1)}{2} - 2\right) - (s-1)} \\ \boldsymbol{= d(n + (d + 2 - p)) - (m + m^*)} \end{aligned} \tag{12}$$

The possible cases for the fusion with removing two edges from the same two states are $(d = 2, p = 3)$ for the planar configuration, and $(d = 3, p = 3)$ or $(d = 3, p = 4)$ for the spatial configuration. In all

three cases if the values of the variables d and p are substituted in (12) the result is $m^* = 0$. However, if the addition of a cell introduces degeneracy in the structure, the rank of the rigidity matrix will decrease by one. This is reflected by the creation of a self-stress state and an infinitesimal mechanism in the structure.

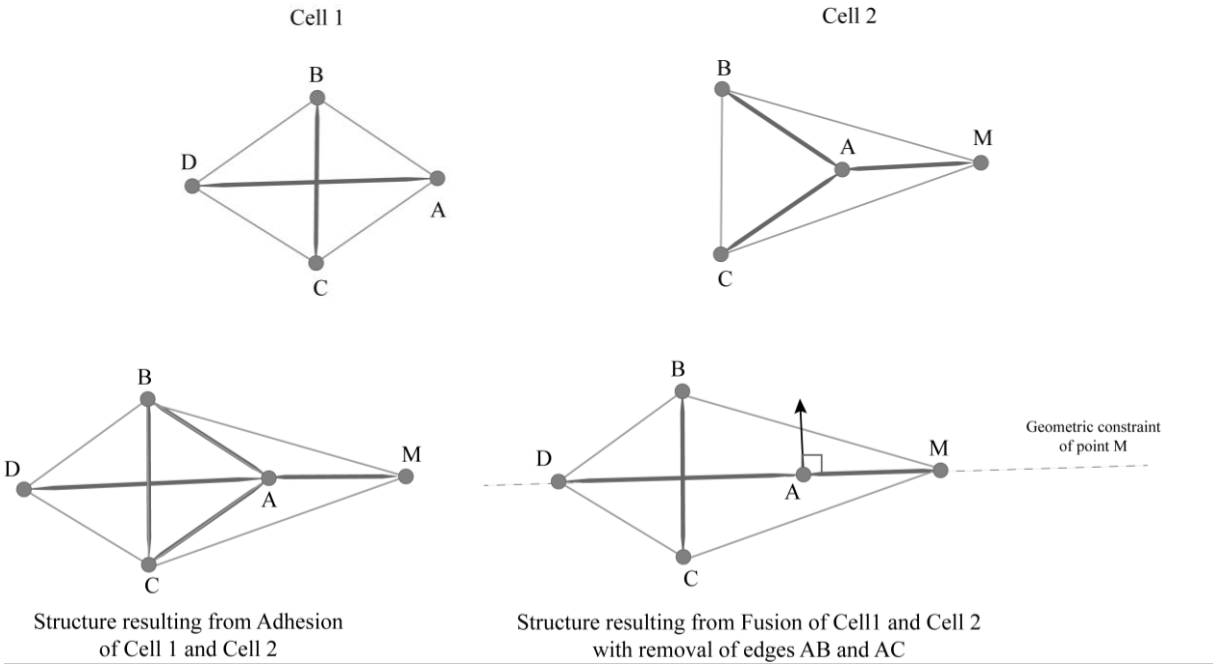


Figure 5: Illustration of the creation of the geometric constraint on node M and the infinitesimal mechanism through the fusion of Cell 1 and Cell 2 and the removal of edges AB and AC

The example of the fusion of two planar cells (Figure 5) considered in this section is further explored to elucidate the relationship between the degeneracy, and the creation of a self-stress state and an infinitesimal mechanism. Let A, B, C and D be the nodes of the first cell (Cell 1). Assume that another cell (Cell 2) is added to the Cell 1 sharing nodes A, B and C with its fourth node M having coordinates (x, y). The rigidity matrix R_1 of Cell 1 is given by:

$$R_1 = \begin{bmatrix} \overbrace{(a_1-b_1)}^{A} & \overbrace{(a_2-b_2)}^{A} & \overbrace{-(a_1-b_1)}^{B} & \overbrace{-(a_2-b_2)}^{B} & \overbrace{0}^{C} & \overbrace{0}^{C} & \overbrace{0}^{D} & \overbrace{0}^{D} & (A,B) \\ (a_1-c_1) & (a_2-c_2) & 0 & 0 & -(a_1-c_1) & -(a_2-c_2) & 0 & 0 & (A,C) \\ (a_1-d_1) & (a_2-d_2) & 0 & 0 & 0 & 0 & -(a_1-d_1) & -(a_2-d_2) & (A,D) \\ 0 & 0 & (b_1-c_1) & (b_2-c_2) & -(b_1-c_1) & -(b_2-c_2) & 0 & 0 & (B,C) \\ 0 & 0 & (b_1-d_1) & (b_2-d_2) & 0 & 0 & -(b_1-d_1) & -(b_2-d_2) & (B,D) \\ 0 & 0 & 0 & 0 & (c_1-d_1) & (c_2-d_2) & -(c_1-d_1) & -(c_2-d_2) & (C,D) \end{bmatrix} \quad (13)$$

and the rigidity matrix R_2 of Cell 2 is given by:

$$R_2 = \begin{bmatrix} \overbrace{(a_1-b_1)}^{A} & \overbrace{(a_2-b_2)}^{A} & \overbrace{-(a_1-b_1)}^{B} & \overbrace{-(a_2-b_2)}^{B} & \overbrace{0}^{C} & \overbrace{0}^{C} & \overbrace{0}^{M} & \overbrace{0}^{M} & (A,B) \\ (a_1-c_1) & (a_2-c_2) & 0 & 0 & -(a_1-c_1) & -(a_2-c_2) & 0 & 0 & (A,C) \\ (a_1-x) & (a_2-y) & 0 & 0 & 0 & 0 & -(a_1-x) & -(a_2-y) & (A,M) \\ 0 & 0 & (b_1-c_1) & (b_2-c_2) & -(b_1-c_1) & -(b_2-c_2) & 0 & 0 & (B,C) \\ 0 & 0 & (b_1-x) & (b_2-y) & 0 & 0 & -(b_1-x) & -(b_2-y) & (B,M) \\ 0 & 0 & 0 & 0 & (c_1-x) & (c_2-y) & -(c_1-x) & -(c_2-y) & (C,M) \end{bmatrix} \quad (14)$$

The adhesion of the two cells results in the rigidity matrix R_a that has 9 rows and 10 columns and given by:

$$R_a = \begin{bmatrix} \overbrace{(a_1-b_1)}^{A} & \overbrace{(a_2-b_2)}^{A} & \overbrace{-(a_1-b_1)}^{B} & \overbrace{-(a_2-b_2)}^{B} & \overbrace{0}^{C} & \overbrace{0}^{C} & \overbrace{0}^{D} & \overbrace{0}^{D} & \overbrace{0}^{M} & \overbrace{0}^{M} & (A,B) \\ (a_1-c_1) & (a_2-c_2) & 0 & 0 & -(a_1-c_1) & -(a_2-c_2) & 0 & 0 & 0 & 0 & (A,C) \\ (a_1-d_1) & (a_2-d_2) & 0 & 0 & 0 & 0 & -(a_1-d_1) & -(a_2-d_2) & 0 & 0 & (A,D) \\ 0 & 0 & (b_1-c_1) & (b_2-c_2) & -(b_1-c_1) & -(b_2-c_2) & 0 & 0 & 0 & 0 & (B,C) \\ 0 & 0 & (b_1-d_1) & (b_2-d_2) & 0 & 0 & -(b_1-d_1) & -(b_2-d_2) & 0 & 0 & (B,D) \\ 0 & 0 & 0 & 0 & (c_1-d_1) & (c_2-d_2) & -(c_1-d_1) & -(c_2-d_2) & 0 & 0 & (C,D) \\ (a_1-x) & (a_2-y) & 0 & 0 & 0 & 0 & 0 & 0 & -(a_1-x) & -(a_2-y) & (A,M) \\ 0 & 0 & (b_1-x) & (b_2-y) & 0 & 0 & 0 & 0 & -(b_1-x) & -(b_2-y) & (B,M) \\ 0 & 0 & 0 & 0 & (c_1-x) & (c_2-y) & 0 & 0 & -(c_1-x) & -(c_2-y) & (C,M) \end{bmatrix} \quad (15)$$

Since the resulting structure has two self-stress states, the rank of the rigidity matrix $\boldsymbol{R_a}$ of the structure is $\boldsymbol{R_a = 7}$. This is confirmed as the result of the adhesion of two cells results into an infinitesimally rigid structure making the dimension of the nullspace of $\boldsymbol{R_a = 3}$. If two shared edges (AB and AC for example) are removed in the fusion step, the new rigidity matrix can be obtained from $\boldsymbol{R_a}$ by removing the rows i.e. (A,B) and (A,C). If the nodes are in general position, the equilibrium matrix $\boldsymbol{A_f}$, obtained through fusion with the removal of these two edges, will be full rank and the structure will have no self-stress states as nullspace of $\boldsymbol{A_f = \{\vec{0}\}}$. Consequently, the resulting tensegrity structure will not be stable. If degeneracy exists in the nodal positions with the relationship of these positions being described by a polynomial equation leading to $det|A_f|=0$, a self-stress state occurs to stabilize the structure. However, the existence of this self-stress creates also an infinitesimal mechanism since the rank of the rigidity matrix will also decrease. Since, the existence of this infinitesimal mechanism is bound by the geometric constraint satisfied by the nodes, the infinitesimal mechanism will not introduce deformations of the members if the structure's nodes are still in the neighborhood of their starting point. However, once the displacements are not infinitesimal resulting in the nodes not satisfying the geometric conditions, the infinitesimal mechanism will rigidify due to the existing self-stress.

4. Conclusion

In this paper, the creation of the internal mechanisms in tensegrity structures is presented through the principles of cellular morphogenesis. A method to isolate internal mechanisms from rigid body motions is introduced. It is shown that finite mechanisms in self-stressed frameworks are created through adhesion when the number of the shared nodes is strictly less than the dimension of the workspace while infinitesimal mechanisms are proven to be created through fusion when the number of removed edges shared by two unicellular substructures is more than two. The discussions evoked in this paper sets the ground for including the mechanism creation as a design feature for self-stressed frameworks and tensegrity structures enhancing the systems employed for deployable and shape shifting applications.

References

[1] AG Tibert, S Pellegrino S. "Deployable tensegrity reflectors for small satellites". Journal of Spacecraft and Rockets. 39(5):701-9, Sep 2002.

[2] L Rhode-Barbarigos, NB Ali, R Motro, IF Smith. "Design aspects of a deployable tensegrity-hollow-rope footbridge". International Journal of Space Structures, 27(2-3):81-95. Jun 2012.

[3] S Pellegrino, editor. "Deployable structures". Springer; 2014 May 4.

[4] T Tarnai. "Infinitesimal and finite mechanisms". InDeployable Structures, pp. 113-142. Springer, 2001, Vienna.

[5] C Sultan. "Tensegrity deployment using infinitesimal mechanisms". International Journal of Solids and Structures. 15;51(21-22):3653-68, Oct 2014.

[6] A Smaili, R Motro. "Foldable/unfoldable curved tensegrity systems by finite mechanism activation". Journal of the International Association for Shell and Spatial Structures, 48(3):153-60, Dec 2007.

[7] O Aloui, D Orden, L Rhode-Barbarigos. « Generation of planar tensegrity structures through cellular multiplication". Applied Mathematical Modelling, 64:71-92. Dec 2018.

[8] O Aloui, J Flores, D Orden, L Rhode-Barbarigos. "Cellular morphogenesis of three-dimensional tensegrity structures". Computer Methods in Applied Mechanics and Engineering, 346:85-108, Apr 2019.

[9] O Aloui, J Flores, D Orden, L Rhode-Barbarigos. "Deciphering tensegrity structures through cellular morphogenesis". InProceedings of IASS Annual Symposia (Vol. 2018, No. 27, pp. 1-10). International Association for Shell and Spatial Structures (IASS), 2018 Jul 16.

[10] O Aloui, J Flores, L Rhode-Barbarigos. "Re-discovering the Tensegrity Simplex: decomposition, self-stress analysis and alternative designs". InProceedings of IASS Annual Symposia (Vol. 2018, No. 27, pp. 1-15). International Association for Shell and Spatial Structures (IASS), 2018 Jul 16

[11] S Pellegrino, CR Calladine. "Matrix analysis of statically and kinematically indeterminate frameworks". International Journal of Solids and Structures, 22(4):409-28. Jan 1986

Proceedings of the IASS Annual Symposium 2019 – Structural Membranes 2019
Form and Force
7 – 10 October 2019, Barcelona, Spain
C. Lázaro, K.-U. Bletzinger, E. Oñate (eds.)

Proposal of Plate Structures Consisting of Intersecting Tensegrity Truss Units and Grasp of Structural Characteristics of the Plates

Juna LEE*, Akira OKADA[a], Naoya MIYASATO[b], Shuzo HIROISHI[c], Kazuma FUKUDA[d]

*Resident professor University of Seoul, Seoul, Korea
Seoulsiripdae-ro 163, Dongdaemun-gu, Seoul, Korea, 02504
juna@uos.ac.kr
[a] Professor Nihon University, Tokyo, Japan
[b] Professor Nihon University, Tokyo, Japan
[c] Associate Professor Nihon University, Tokyo, Japan
[d] Japan Post Holdings Co.,Ltd., Tokyo, Japan

Abstract

This paper presents the systems composited with "Intersecting Tensegrity Truss (ITT)" unit which consists of two pyramidal frameworks (compression member), a center tension member, and exterior tension members. Because the two opposing pyramidal units are rotated by 45 degrees and connected using the hanging member by intersecting in the center, this unit has the distinct advantage that the introduction of tensile force of the ITT unit can be easily performed by shortening the length of the center screw. In this paper, the authors propose a plate-type structure based on the features of ITT by connecting multiple ITT units. Firstly plate models of ITT with an area of 9,900x 9,900mm were designed. Using these models, the influence and behaviors of the structure of systems with an additional load by through the introduction of tension, were examined. The structural performances of the plate structure systems were resolved and the applicability of the proposed model was experimentally examined using a scale-down beam-type model.

Keywords: tensegrity structures, tensegrity systems, tensegric truss, loading experiment, numerical analysis

1. Introduction

Tensegric Truss is a structural system that has been changed and developed for architectural application with a tensegrity system. This system has been extended from the definition of tensegrity to resolve issues, such as lack of rigidity of the frame, lack of stability during construction and complication of details caused by high initial tension (Figure.1). From this context, and for the purposes of this study, Intersecting Tensegrity Truss (ITT) is understood as a structure system derived from the Tensegric Truss Type II (Figure.2) [1].

The ITT was designed to divide compression members of type II at the center into opposing pyramidal units (hereinafter referred to as the “compression member unit”) and to make them to intersect with each other by rotating them 45 degrees. After that, each apex of the pyramid unit and each node of the outer circumference are connected by a string.

Previous studies [1] have reported on the structural characteristics when the ITT units are connected in a vertical direction and applied to a tower (Figure.3). To add to existing research, with the aim of applying ITT to the architectural space, we proposed a beam and a plate frame model and conducted a model experiment and numerical analysis for the purpose of grasping the basic structural characteristics.

Copyright © 2019 by Juna LEE, Akira OKADA, Naoya MIYASATO, Shuzo HIROISHI, , Kazuma FUKUDA
Published by the International Association for Shell and Spatial Structures (IASS) with permission.

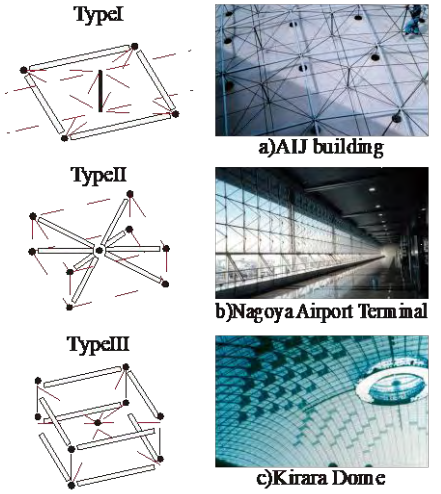


Figure.1 Types of Tensegric Truss[2]

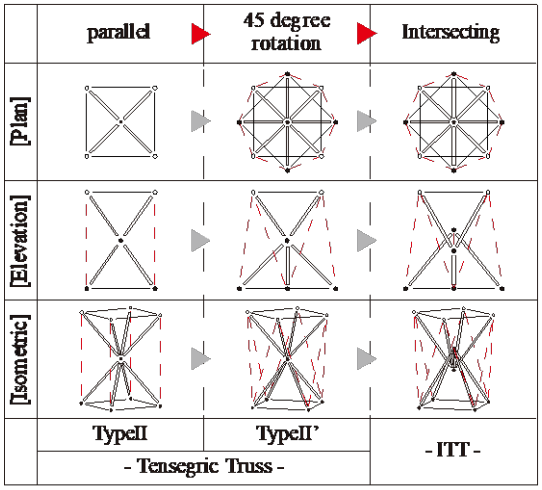


Figure.2 ITT From Tensegric Truss Type II

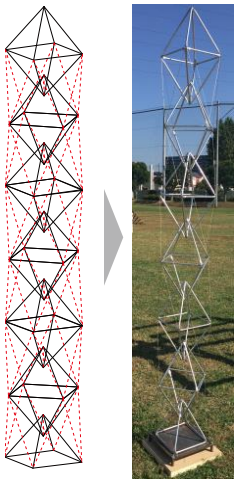


Figure.3 ITT Tower

2. Proposal of basic system and a beam model

As mentioned above, the ITT consists of two compression units and four strings that connect them. As shown in Figure.4, three types of strings referred to as HT (Horizontal String, upper / lower), DS (diagonal String), and 'HS (Hanger Screw) integrate two compression pyramidal units. Because each compression unit intersects, this system has the potential to able to introduce tension into the entire ITT system by only managing the length of the HS (Hanger Screw) – the string at the center, which connects the upper and lower compression units.

The proposed beam frame is connected with the ITT units in a horizontal direction as shown in Figure.5. By connecting the ITT units, a beam type model forms a lattice shape HT (upper chord) and the lower chord forms a straight line. Additionally, this model allows for simple support due to its self-balancing feature causing the horizontal reaction force to become unnecessary, and can be expected to improve the workability.. Overlapped DS members were simplified as one member connecting the same nodes and the end nodes of HT (lower chord) members were used as a support point.

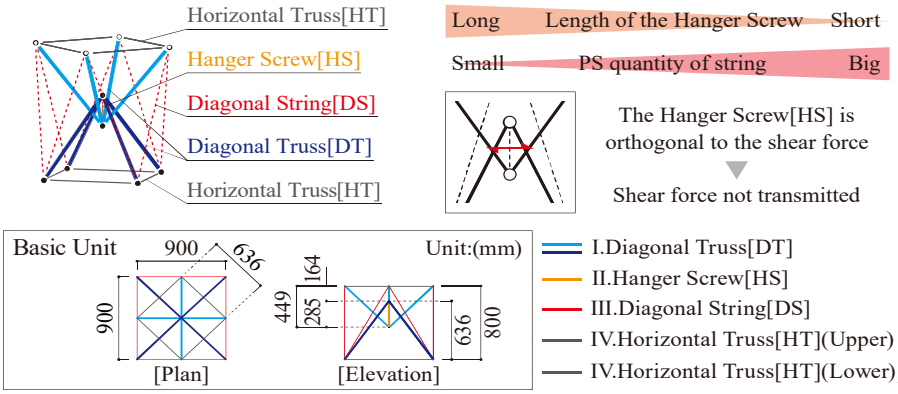


Figure.4 Basic system of ITT

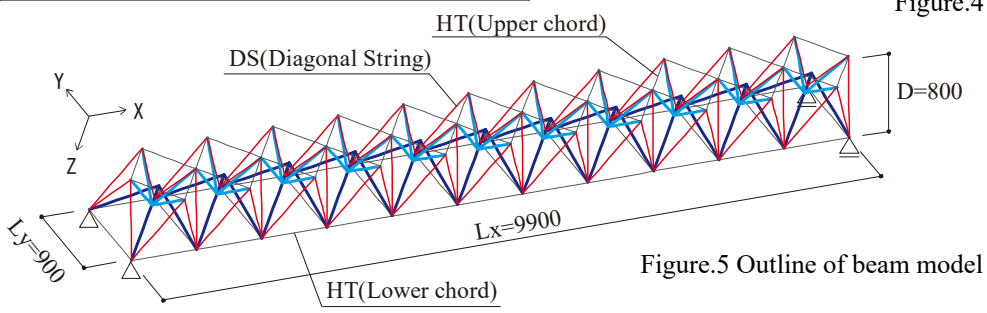


Figure.5 Outline of beam model connected ITT unit

3. Examination of loading experiment and numerical analysis using scale-down specimen

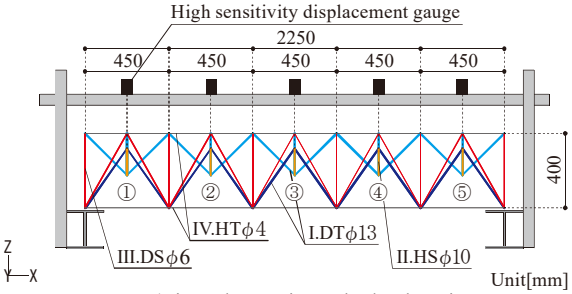
In order to verify the mechanical properties of the proposed model and the validity of the numerical analysis model, loading experiment and numerical analysis were performed for scale-down test specimen (Lx = 2250 mm, Ly = 450 mm, D = 400 mm).

3-1. Outline of loading experiment and numerical analysis

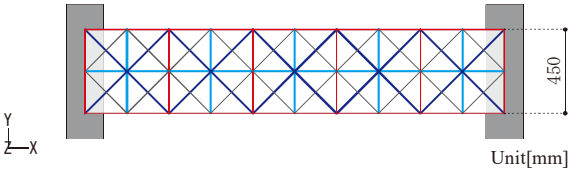
The outline of the experiment and the numerical analysis are shown in Figure.6. A structural strand rope φ4 was used for the HS. The lower chord, HT was arranged in a straight line, and the upper chord, HT was arranged in a broken line being joined a junction clamp with the appropriate curvature to constitute a test specimen (Figure.6, joints i and iii).

The amount of initial tension force (hereinafter referred to as 'T_0') introduced to the HS was considered as an important factor in this examination. At the initial stage, T_0 in HS was set at 2.9 kN and the axial force was obtained from the numerical analysis. In order to calculate the influence of the axial force loss of the upper chord, a model with the axial force loss (introducing $T_0 \times 0.4 = 1.2$ kN to the HS) was also studied. In this examination, the self-weight of ITT and the additional load (980 N/m^2) was considered and applied to each of the nodal points of the lower chord as the concentrated load calculated from the load area. Also, three cases of load patterns- the overall loaded pattern in the span, the partially loaded pattern on one side of the span, and partially loaded pattern in the center of the span were tested in order to examine the effect of an imbalanced load. The displacement was also measured using a high sensitivity displacement gauge and the axial force of the upper and lower chords were measured via a load cell (Figure.6-d) in which a strain gauge was attached to the high nut near the end support.

The material and structural specifications of the numerical analysis model were the same as in the test specimen. In the numerical model, the length of the HS member was reduced by applying an initial strain, leading that the tension is introduced to every tension member of ITT unit. In this paper, we set T_0 to the force where the displacement of the center of the lower chord is 0 with respect to the self-weight of the main frame, in order to control deformation when ITT is completed (control of deformation caused by a dead load). Also, 'T_P', prestress force in a narrow sense, was obtained by subtracting the tension force (T_e) generated by a dead load from T_0, and the T_P of all units was set the same. For numerical analysis, the geometrically non-linear analysis was performed using the finite element analysis program ADINA, and the non-pressure resistance of the cable was also taken into consideration.



a)Jig and Experiment body plan view



b)Jig and Experiment body figure

■ **Numerical analysis overview**

□ **Material Specification**		Non resistance compression
·DT(Round steel-Truss)	:SS400 φ13	σ, 1.57×10^5, (N/mm²), ε, -1.0, 0, 1.0
·HS(Round steel-Truss)	:SS400 φ10	
·DS(Round steel-Truss)	:SS400 φ6	
·HT(Cable-Truss)	:SUS rope 1×19 φ4 ST1470	
□ **Structure Data**		
·Boundary condition	:Simple support	
·Loading condition	:w=980N/m²	
·Initial strain	:2905N,1162N	

Figure.6 Overview of scale-down test specimen

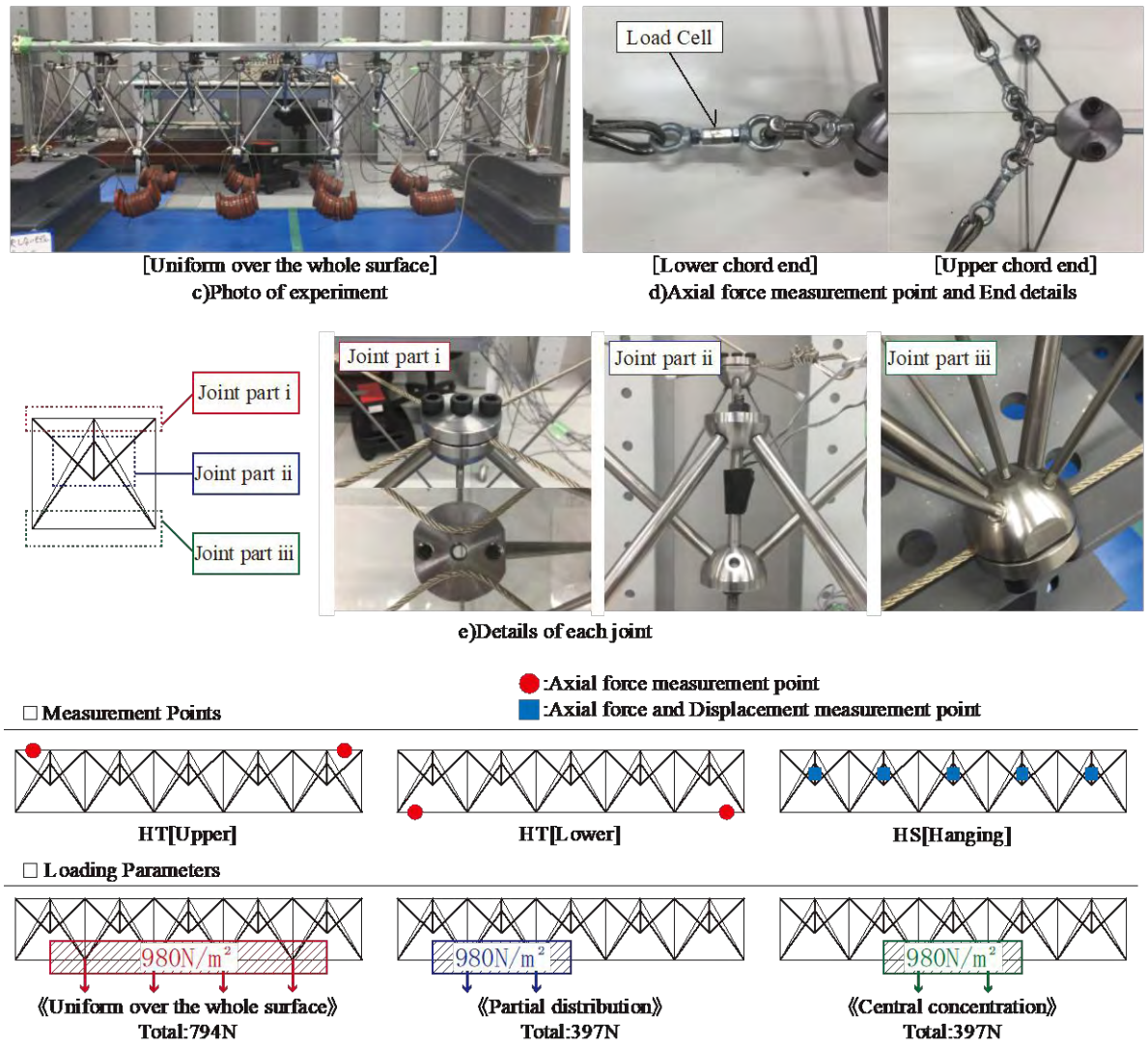


Figure.6 Overview of scale-down test specimen (continue)

3-2. The results of scale-down experiment and numerical analysis of the proposed model

Table 1 shows the relation between T_0 and the initial displacement in each experiment, and Figure.7 shows the relation between load-displacement and the string axial force. The vertical displacement at the time of the additional load is presented in Graph 7 (a, c, e), where the initial position of each measurement point is 0 when T_0 was introduced to each HS member. The vertical downward direction is positive.

From Figure.7, features of ITT beam systems obtained from the relation between load- displacement and the relation between load-string axial force are shown below.

- The analysis results show linear behavior, and in the model in which the axial force is lost, the decrease of rigidity due to the loss of tension was confirmed, but it did not immediately become an unstable state.
- The experimental results showed slight non-linear behavior. It is presumed that this is caused by clamping the upper chord with a curvature or by the end fittings of the upper and lower chords.
- Although the difference between the experimental value and the analytical value was somewhat large in the axial force loss model, it was presented that the increasing tendency of the displacement was the same in all the experiments.

For this reason, it was confirmed that the proposed ITT model is able to build a new load resistance mechanism even after the loss of string axial force. Also, in both the experiment and numerical analysis, vertical displacement and axial force showed almost the same behavior, and the validity of numerical analysis was resolved.

Table.1 Comparison of scale-down examination and numerical analysis model

	Unit number	①	②	③	④	⑤
No loss of axial force [T_0]	Hanging material tension (T_0)[kN]	2.9	2.6	2.6	2.6	2.9
	Vertical displacement (Analyis)[mm]	-0.15	-0.28	-0.32	-0.28	-0.15
	Vertical displacement (Experiment)[mm]	-1.64	-4.73	-5.66	-4.04	-1.53
Loss of axial force [T_0×0.4]	Hanging material tension (T_0)[kN]	1.2	1.0	1.0	1.0	1.2
	Vertical displacement (Analyis)[mm]	-0.12	-0.27	-0.32	-0.27	-0.12
	Vertical displacement (Experiment)[mm]	-1.65	-4.42	-5.28	-3.76	-1.40

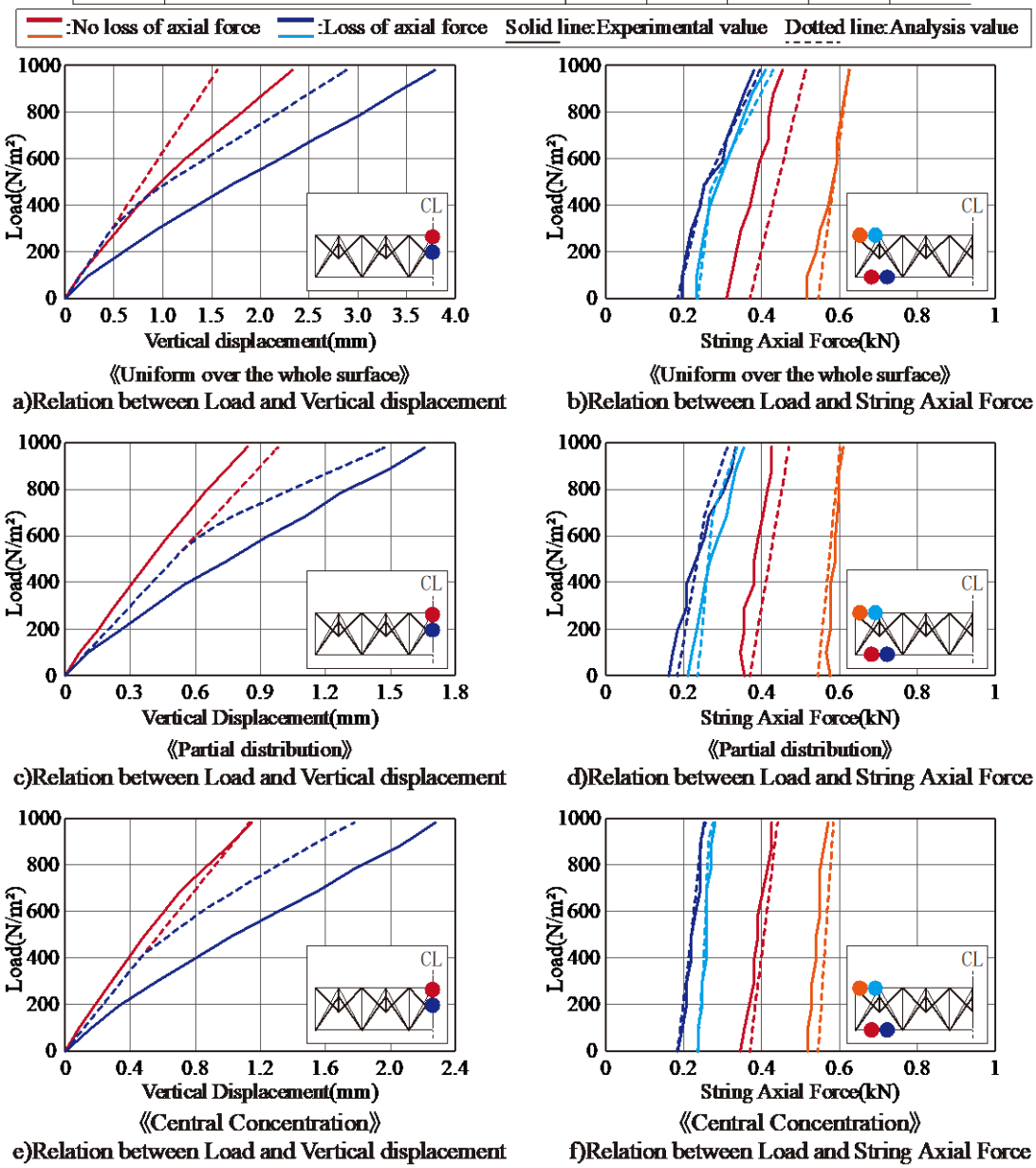


Figure.7 Analysis and Experiment results

4. Study on the extension of the plate model

When the upper and lower chords of the ITT beam structure are continuously arranged in two directions, they could be expanded to a plate structure system and are able to correspond to various support conditions. In this study, the ITT structure system was expanded to a plate type structure, and the numerical analyses for the plate system models were examined for each case. The plate type ITT models had four peripheral sides supports and corner point supports respectively.

4-1. Numerical analysis of the plate model

The plate model(Lx = 9900 mm, Ly = 9900 mm, D = 800 mm) examined has 11 spans of 9900 mm beam frames with 11 ITT units that are connected longitudinaly (y direction) (Figure.8). Material, structure specifications and load conditions were the same as in Figure.6.

The vertical displacement was examined at the center of the model and at the center of the side. In addition, T_0 was introduced aiming at 0 vertical displacements at the center of each model at the time of the dead load, and the same T_P at that time was applied to all the HS members. In order to grasp the influence of T_0, we also considered a model in which the string axial force disappears ($T_0 \times 0.8$: T_0 - model) and a model in which the initial tension amount is increased ($T_0 \times 1.2$: T_0 + model). Because the loss of string axial force was investigated at the state of introducing T_0 in the four-sided support, the $T_0 \times 0.8$ model was not examined.

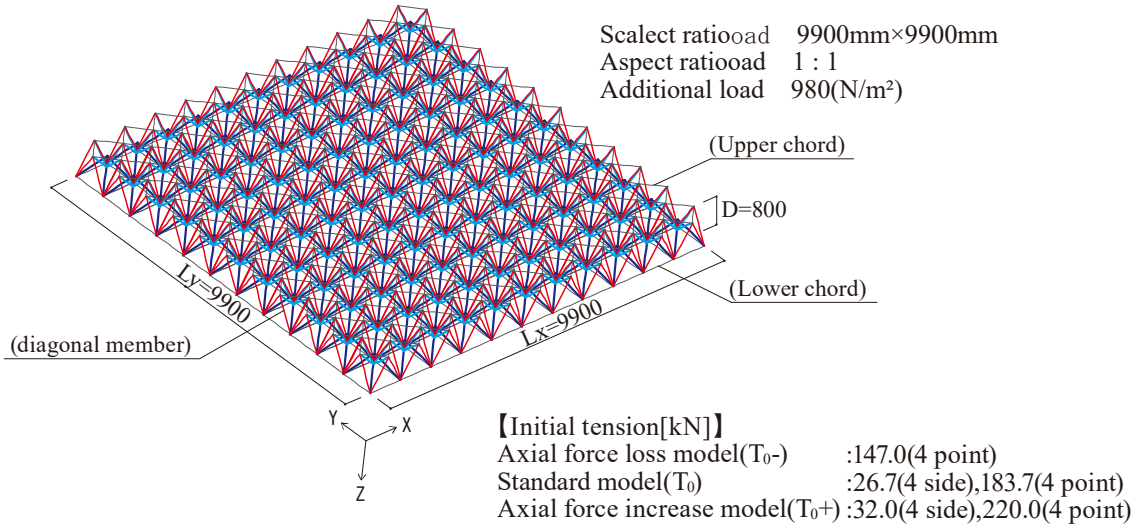


Figure.8 Details of plate model

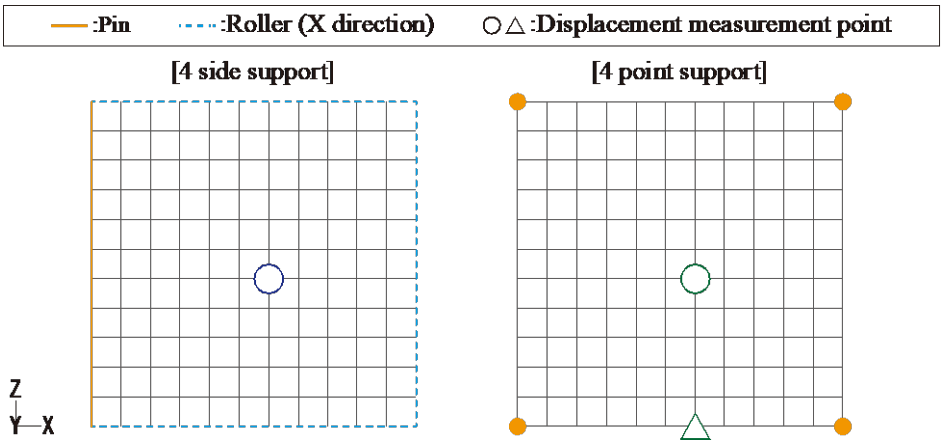


Figure.9 Support condition and points of displacement measurement

4-2. Numerical analysis result and consideration

Figure.10 shows a deformation diagram of the lower chord at the stage of introducing T_0., Figure.11 shows the distribution of axial force in the upper and lower chords for the axial force loss model (T_0-), and Figure.12 shows the relation between load-displacement.

From Figure.10, it was investigated that the initial displacement of the center at the state of T_P is smaller for the case of the four-sided supports, and the initial displacement at the center of one side for the case of the four-point supports is vertically upward. This is considered to be caused by the excessive introduction of T_0 in the peripheral units because the T_P of all units were set the same. From Figure.11 it was investigated that the stress was significantly increased at the sides of the upper chord and the middle part of the lower chord for the case of the four-side supports. Also, the stress was significantly increased at the corners of the upper chord and center in the side of the lower chord for the case of the four-corner supports, when an additional load was loaded.

In addition, from the distribution of axial force in the lower chord, we examined that in the case of the four-sided supports, the strings arranged in x-direction were the main resistance mechanism. Furthermore, the strings in the xy-direction at the center and the strings in the longitudinal direction of each side for the case of the four-corner supports were the main resistance mechanisms, respectively. From Figure.12-a, it was concluded that the displacement for the case of the four-sided supports becomes smaller with respect to the central displacement. Also, for the behavior of the T_0 model and the T_0+ model, the increase of initial tension displayed a similar tendency. From this, it was determined that when the axial force does not disappear, the rigidity remains constant regardless of the initial tension.

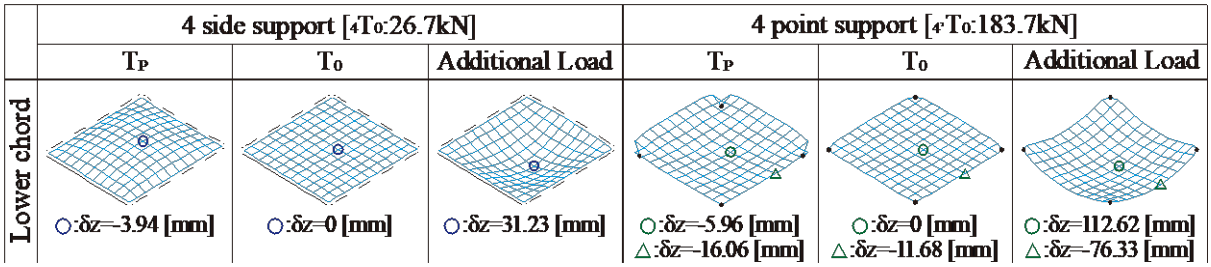


Figure.10 Displacement of lower chord

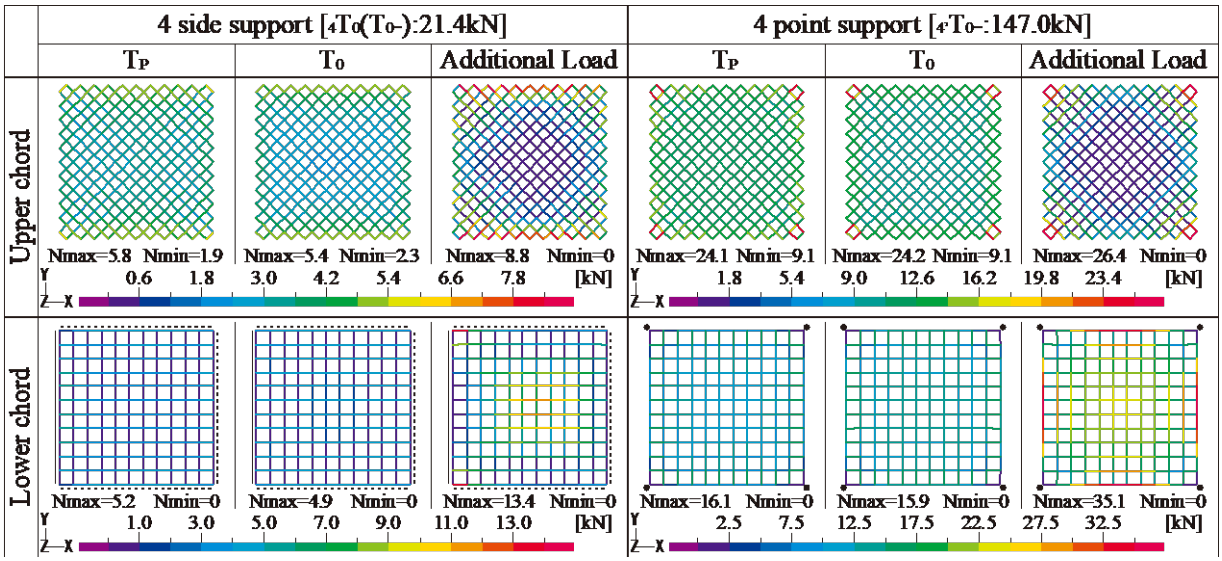


Figure.11 Distribution of axial force in the upper and lower chord (Loss of axial force:T0-)

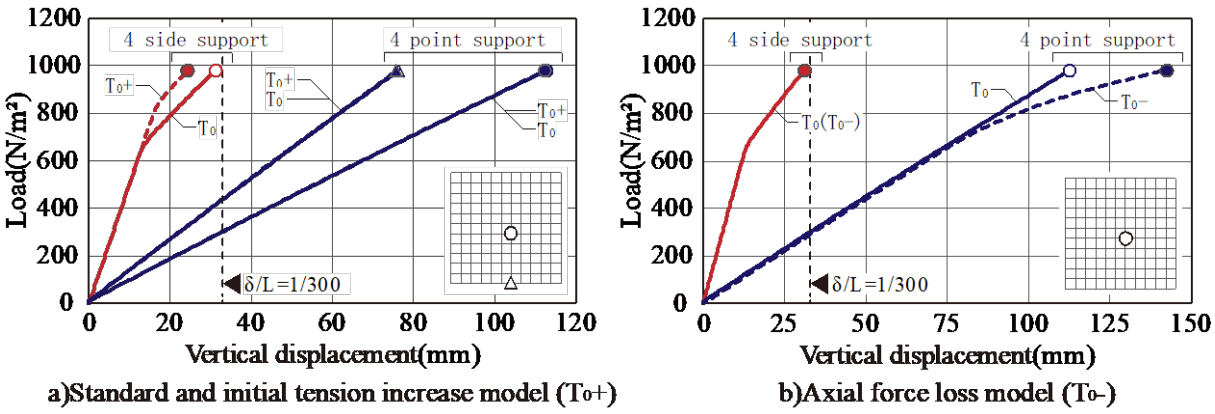


Figure.12 Experiment results

In this paper, we proposed a beam frame model and a plate model using the ITT unit and presented the results of a model experiment and numerical analyses for the purpose of grasping the basic structural characteristics concerned with the introduction of initial tension and the effects of an additional load.

The obtained findings are shown below.

- If the axial force of string does not disappear, the introduced initial tension amount affects the axial force of the string, but the rigidity is constant.
- If the axial force of string disappears, the rigidity of the entire frame decreases, but it does not immediately move an unstable state or compose a new resistance mechanism.
- Although the resistance mechanism differs depending on the support conditions, it was examined that this structure system can be applied when the the initial tension (T_0) amount introduced to the unit is adjusted.

Acknowledgments

The authors would like to express their gratitude to Kensei Omura and Fuji Tsuboi for assistance in the editing of this paper. Also, this research was supported by National Research Foundation of Korea (NRF-2017R1D1A1B04031948)

References

[1] Kurisu, H., Okada, A., Miyasato, N., Hiroishi, S., Proposal of Tensegrity Truss Consisted of Intersecting Units of Tensegric Truss and Grasp of Structural Characteristics, Proc. Of AIJ Symp., 2013

[2] Juna Lee, et. al, “A Development of Intersecting Tensegrity System and Analysis of Structural Features for Forming Space”, Journal of the Korea Association for Spatial Structures, Vol.14, No.4, pp.55-54, 2014

Proceedings of the IASS Annual Symposium 2019 – Structural Membranes 2019
Form and Force
7 – 10 October 2019, Barcelona, Spain
C. Lázaro, K.-U. Bletzinger, E. Oñate (eds.)

Static properties of a new class of planar tensegrity truss

Sili LI*, Xian XU

*Key Laboratory of Space Structures of Zhejiang Province, Zhejiang University
Anzhong Building, 886 Yuhangtang Road, Hangzhou, Zhejiang, China
Email: 11612046@zju.edu.cn

Abstract

Tensegrity structure is a prestressed self-equilibrated system consisting of compressed struts and tensioned cables. Planar truss is one of the most common forms of engineering structures with a wide application. This paper proposes a new class of planar tensegrity trusses whose prototype is unintentionally found by a topology optimization algorithm. The prototype truss is composed of two basic units which are combined alternately. In this paper, the state of prestress of the truss is analytically determined from the equilibrium conditions. The stiffness and strength of the structure are analytically formulated by using the principle of virtual work. Parametric analysis of geometrical parameters on the stiffness and strength of the structure is carried out. By changing the shape of the basic units, the uniform planar tensegrity truss is extended to a fish-bellied truss. Parametric analysis is also carried out for the fish-bellied truss. An example of extending the planar tensegrity truss into a three-dimensional latticed tensegrity truss is also given.

Keywords: planar tensegrity truss, prestress, parametric analysis, structural stiffness, structural strength.

1. Introduction

Tensegrity structure is a prestressed self-equilibrated system consisting of compressed struts and tensioned cables. It has some distinguished characteristics, such as light-weight, controllable shape, novel form and so on. It has potential applications in many fields. Towards different applications, various forms of tensegrity structures have been proposed, such as double-layer tensegrity grids [1], tensegrity rings [2], tensegrity tori [3], semi-regular tensegrity [4], planar tensegrity truss [5] and double-helix tensegrity structures [6]. A tensegrity structure which has up to k ($k \geqslant 1$) struts connected to a node can be classified as class-k [7]. The planar tensegrity truss proposed by Jager and Skelton [5] belongs to class-1 tensegrity and is prone to be used as controllable structural systems [8, 9]. A novel class-2 planar tensegrity truss consisting of repetitive units was found in an example for a topology optimization of tensegrity systems [10]. This novel class-2 planar tensegrity truss was able to resist a design load given by a load code for design of building structures and meanwhile meet the deflection limitation given by a design code of steel structures [10]. To fully exploit the possible application of the newfound planar tensegrity truss in building roof structures, this paper extends the prototype system found in the previous study [10] to a class of planar tensegrity trusses by generalizing the combination scheme of the basic units and modifying the shape of the basic units, and analytically and numerically investigates the static properties of the planar tensegrity trusses.

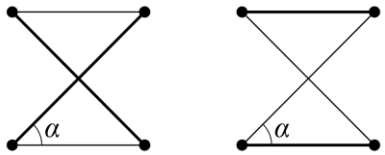
The layout of the paper is as follows. Section 2 presents the basic units and configurations of the planar tensegrity truss. In Section 3, the analytical expression of the state of prestress for the planar tensegrity truss is derived from the equilibrium conditions. The stiffness and strength of cantilever planar tensegrity truss are analytically formulated by using the principle of virtual work in Section 4. Section 5 carries out parametric analysis of geometrical parameters on the stiffness and strength of

Copyright © 2019 by Sili LI, Xian XU
Published by the International Association for Shell and Spatial Structures (IASS) with permission.

cantilever planar tensegrity truss. An example of extending the planar tensegrity truss into three-dimensional latticed tensegrity truss is presented in Section 6. Finally, Section 7 concludes the paper.

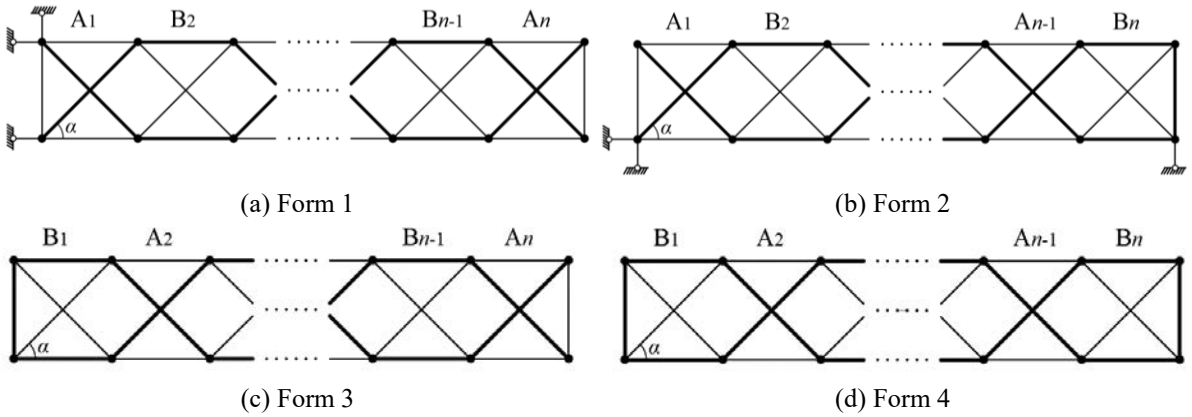
2. Basic units and truss systems

In the prototype truss unintentionally found by a topology optimization algorithm [10], there are two types of rectangular and repetitive basic units named Unit A and Unit B (Figure 1). Each unit consists of two horizontal elements and two diagonal elements (Figure 1). In all the figures of this paper, the bold lines represent struts and the thin lines represent cables. The alternating combination of the two types of basic units comprises the rectangular planar tensegrity truss, and there are four basic forms depending on the types of the end units, as shown in Figure 2. Note that an additional vertical element is added at each end unit to keep the system integrity (Figure 2). The geometry of such a planar tensegrity truss can be determined by the number of the basic units n ($n > 1$), the lengths of the basic units l_i ($i = 1, 2, \ldots, n$), and the height of the basic units h. In this paper, the lengths l_i of the basic units used in the truss are assumed to be the same to each other, which is denoted as l. The system consists of the basic units with the same length is called "uniform planar tensegrity truss". The uniform planar tensegrity truss can be extended to the fish-bellied truss by modifying the shape of the units from rectangular to isosceles trapezoid (Figure 3). A 3D latticed tensegrity truss can also be obtained by orthogonally combining two groups of planar trusses, as shown in Figure 4.



(a) Unit A (b) Unit B

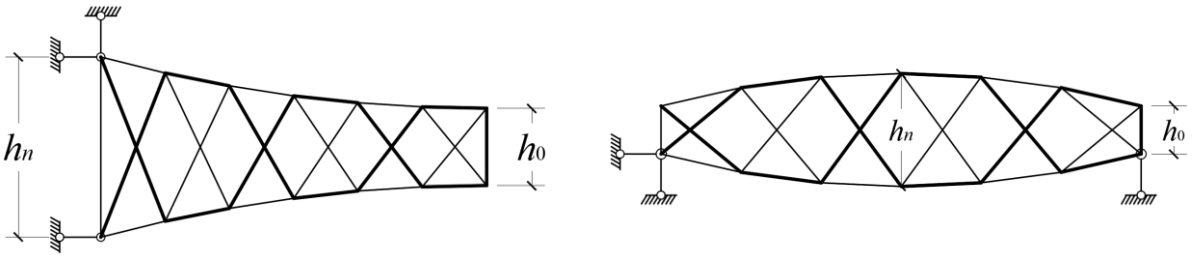
Figure 1: Two basic rectangular units



(a) Form 1 (b) Form 2

(c) Form 3 (d) Form 4

Figure 2: Four combination forms of planar tensegrity truss



(a) Cantilever (b) Simply-supported

Figure 3: Fish-bellied tensegrity truss

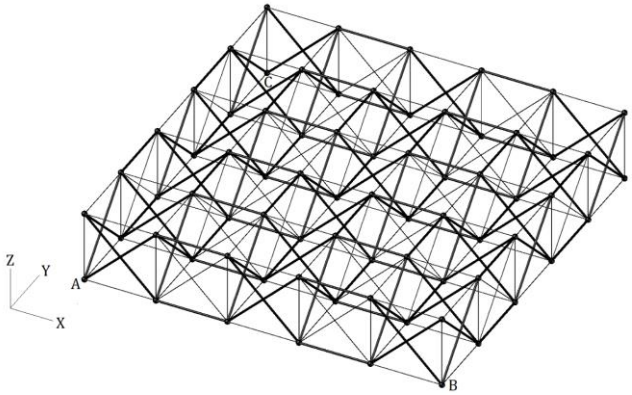


Figure 4: Schematic diagram of a three-dimensional latticed structure

3. Prestress

The planar tensegrity truss is a statically indeterminate system. The state of prestress can be determined by the equilibrium condition of each node. For the *i*th unit of the truss, it is denoted as A*i* if it is a Unit A, and it is denoted as B*i* if it is a Unit B. When the first unit is a Unit A, i.e. A1, according to the equilibrium condition of the end nodes, there is:

$$\begin{cases} F_{Ac1} = -F_{As1}\cos\alpha \\ F_{Aca} = -F_{As1}\sin\alpha \end{cases} \tag{1}$$

where F_{Ac1}, F_{As1} and F_{Aca} are the prestresses in the cables, struts and additional vertical cable of A1 respectively; and α is the inclined angle of the diagonal elements, as shown in Figure 1 and Figure 2.

If i is odd, the i^{th} unit is Ai and the $(i+1)^{th}$ unit is Bj where $j = i+1$. The prestresses in the Bj are:

$$\begin{cases} F_{Bcj} = -F_{Asi} \\ F_{Bsj} = (F_{Asi} - F_{Bcj})\cos\alpha + F_{Aci} \\ F_{Bsa} = -F_{Bcj}\sin\alpha, \ when\ j = n \end{cases} \tag{2}$$

where F_{Bcj}, F_{Bsj}, F_{Bsa}, F_{Aci}, F_{Asi} are the prestresses in the cables, struts, additional vertical strut of Bj and the prestresses in the cables and struts of Ai respectively.

If i is even, the i^{th} unit is Bi and the $(i+1)^{th}$ unit is Aj where $j = i+1$. The prestresses in the Aj are:

$$\begin{cases} F_{Asj} = -F_{Bci} \\ F_{Acj} = (F_{Bci} - F_{Asj})\cos\alpha + F_{Bsi} \\ F_{Aca} = -F_{Asj}\sin\alpha, \ when\ j = n \end{cases} \tag{3}$$

where F_{Acj}, F_{Asj}, F_{Aca}, F_{Bci}, F_{Bsi} are the prestresses in the cables, struts, additional vertical cable of Aj and the prestresses in the cables and struts of Bi respectively.

According to Eqs. (1-3), the state of prestress for a truss in Form 1 or 2 can be determined. For a truss in Form 3 or 4, the state of prestress of it can be obtained by a set of similar formulas which will not be presented here for the sake of simplicity.

4. Analytical solution

By applying the principle of virtual work, the deflection and the maximum tensile stress of the planar tensegrity truss under a given load can be obtained. In this section, a uniformly distributed equivalent load on upper nodes of the truss is taken as an example, and two supporting conditions that are cantilever and simply-supported (as shown in Figures 2a and 2b) are considered. But due to the limited space, this paper only gives the solution of the cantilever case.

4.1. Deflection

For the cantilever truss ending with a Unit A (as the configuration shown in Figures 2a and 2c), the deflection v at the free end of it can be expressed as

$$v = \frac{Fl}{E_c A_c}(H_c + D_c + V_c) + \frac{Fl}{E_s A_s}(H_s + D_s) \tag{4}$$

If n is even, there is

$$\begin{aligned} H_c &= [n^4/8 - n^3/12 - n^2/4 + n(1/3 - x/2)]/tan^2\alpha; \\ H_s &= [n^4/8 + 5n^3/12 + n^2/4 - n(1/6 + x/2)]/tan^2\alpha; \\ D_c &= D_s = [n^2/8 + n(1/4 - x/2)]/(sin^2\alpha\, cos\alpha); \\ V_c &= 0. \end{aligned} \tag{5}$$

where
$$x = \frac{\frac{1}{E_c A_c}\frac{n}{2tan^2\alpha} + \frac{1}{E_s A_s}\left(\frac{n}{2sin^2\alpha\, cos\alpha} - \frac{n}{2}tan\alpha\right)}{\left(\frac{1}{E_c A_c} + \frac{1}{E_s A_s}\right)\left[n\left(\frac{1}{tan^2\alpha} + \frac{1}{sin^2\alpha\, cos\alpha}\right) + tan\alpha\right]} \tag{6}$$

If n is odd, there is

$$\begin{aligned} H_c &= [n^4/8 + 5n^3/12 + n^2/4 + n(1/12 - x/2) + 1/8 - x/2]/tan^2\alpha; \\ D_c &= (n^2/8 - nx/2 - 1/8 + x/2)/(sin^2\alpha\, cos\alpha); \\ H_s &= [n^4/8 - n^3/12 - n^2/4 + n(1/12 - x/2) + 1/8 + x/2]/tan^2\alpha; \\ D_s &= [n^2/8 + (1 - x)n/2 + 3/8 - x/2]/(sin^2\alpha\, cos\alpha); \\ V_c &= [(n + 1)/2 - x]\, tan\alpha. \end{aligned} \tag{7}$$

where
$$x = \frac{\frac{1}{E_c A_c}\left(\frac{n+1}{2tan^2\alpha} + \frac{n+1}{2}tan\alpha\right) + \frac{1}{E_s A_s}\frac{n+1}{2sin^2\alpha\, cos\alpha}}{\frac{1}{E_c A_c}\left(\frac{n+1}{tan^2\alpha} + \frac{n-1}{sin^2\alpha\, cos\alpha} + 2tan\alpha\right) + \frac{1}{E_s A_s}\left(\frac{n-1}{tan^2\alpha} + \frac{n+1}{sin^2\alpha\, cos\alpha}\right)} \tag{8}$$

When the cantilever truss ends with a Unit B (as shown in Figures 2b and 2d), the expression of the deflection can be obtained by interchanging $E_c A_c$ and $E_s A_s$ in Eq. (4) and in the expressions of x. Again, for the sake of simplicity, the detailed expressions of the deflection are not given here.

4.2. Maximum tensile stress

The maximum tensile stress in the cables of the truss can be expressed as

$$\sigma_{max} = \begin{cases} max(C - A, D - A/\, cos\,\alpha)/A_c, when\ A \le B\, cos\,\alpha\,. \\ max(C - B \cdot cos\,\alpha\,, D - B)/A_c, when\ A > B\, cos\,\alpha\,. \end{cases} \tag{9}$$

where A, B, C and D are intermediate variables and the expressions of them are given as follows.

For the cantilever truss ending with a Unit A (Figure 2a and Figure 2c), if n is even, there is

$$\begin{aligned} A &= (-n^2/2 + n - x)F/tan\alpha; \quad & B &= (-n/2 - x)F/sin\alpha; \\ C &= (n^2/2 - n + 1 - x)F/tan\alpha; \quad & D &= (n/2 - x)F/sin\alpha. \end{aligned} \tag{10}$$

If n is odd, there is

$$\begin{aligned} A &= [(-n^2 + 1)/2 - x]F/tan\alpha; \quad & B &= [(-n + 1)/2 - x]F/sin\alpha; \\ C &= [(n^2 + 1)/2 - x]F/tan\alpha; \quad & D &= [(n - 1)/2 - x]F/sin\alpha. \end{aligned} \tag{11}$$

For the cantilever truss ending with a Unit B (Figure 2b and Figure 2d), if n is even, there is

$$A = (-n^2/2 + x)F/tan\alpha; \quad B = (-n/2 + x)F/sin\alpha;$$
$$C = (n^2/2 + x)F/tan\alpha; \quad D = (n/2 - 1 + x)F/sin\alpha. \tag{12}$$

If n is odd, there is

$$A = [-(n-1)^2/2 + x]F/tan\alpha; \quad B = [-(n+1)/2 + x]F/sin\alpha;$$
$$C = [(n-1)^2/2 + x]F/tan\alpha; \quad D = [(n-1)/2 + x]F/sin\alpha. \tag{13}$$

5. Parametric analysis

5.1. Uniform cantilever planar tensegrity truss

It is assumed that the load on a roof area with a width of 1m will bear by the truss. According to the Load Code GB50009-2012 [11], the total design load of the truss is considered as q = 2.05 kN/m. The span L is assumed as 6m, n is varied from 4 to 9, and h is varied from 0.6m to 1.5m. The equivalent load on upper nodes is $F = qL/(n+1)$. Steel pipe with diameter of 60.0mm and thickness of 3.5mm is used as the struts. Steel strand 15-7Φ5 is used for the cables. The corresponding Young's moduli and cross-sectional areas are given as $E_c = 1.93\times10^{11}$Pa, $E_s = 2.1\times10^{11}$Pa, $A_c = 141.7$mm^2 and $A_s = 621.2$mm^2. For a given set of parameters, the deflection and the maximum tensile stress can be determined by substituting the parameters into the analytical expressions given in Section 4.

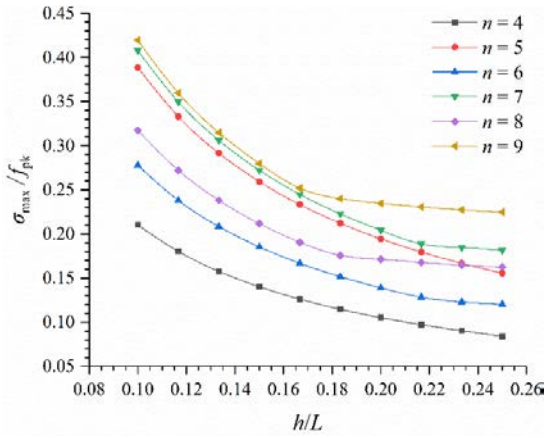


Figure 5: Relation between σ_{max}/f_{pk} and h/L of uniform cantilever tensegrity truss ending with Unit A

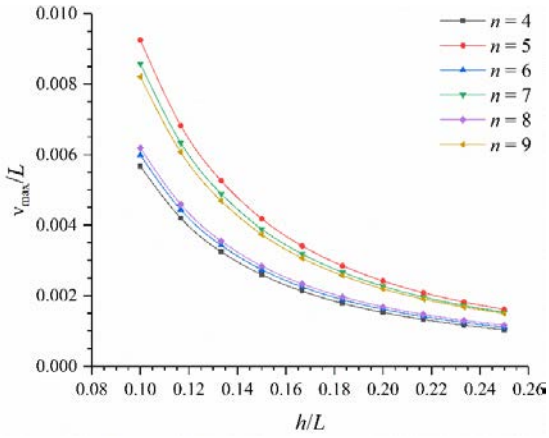


Figure 6: Relation between v_{max}/L and h/L of uniform cantilever tensegrity truss ending with Unit A

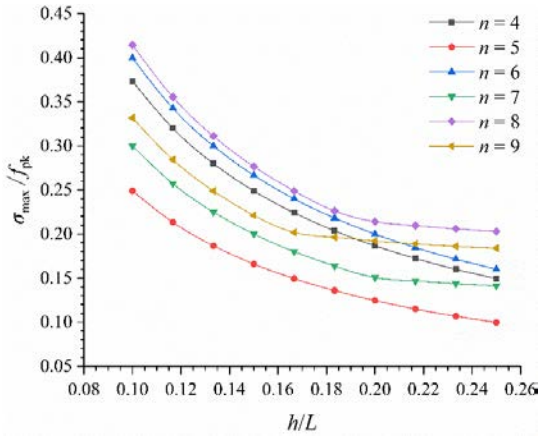


Figure 7: Relation between σ_{max}/f_{pk} and h/L of uniform cantilever tensegrity truss ending with Unit B

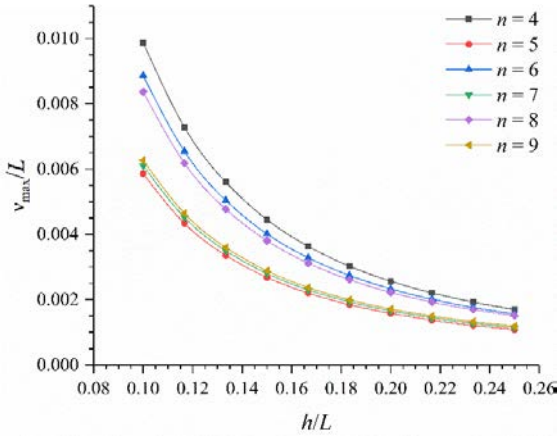


Figure 8: Relation between v_{max}/L and h/L of uniform cantilever tensegrity truss ending with Unit B

In the parametric analysis, an initial prestress that is just large enough to avoid all the cables slack under external loads is adopted. The strength of the structure is represented by the ratio of the maximum tensile stress σ_{max} in cables to the tensile strength of the steel strand f_{pk} (f_{pk} = 1860Mpa), which is abbreviated as *maximum stress ratio* in this paper. The stiffness of the structure is evaluated by the *deflection-span ratio* which is the maximum deflection v_{max} divided by the truss span L. The relation between σ_{max}/f_{pk} and h/L and the relation between v_{max}/L and h/L are shown in Figures 5-8.

According to Figures 5-6, it can be found that when n is even, larger n results in larger σ_{max}/f_{pk} and larger v_{max}/L; when n is odd, larger n results in larger σ_{max}/f_{pk} but smaller v_{max}/L. According to Figures 7-8, it can be observed that when n is even, the larger n is, the larger σ_{max}/f_{pk} is, and the smaller v_{max}/L is; when n is odd, the larger n is, the larger σ_{max}/f_{pk} is, and the larger v_{max}/L is.

In general, the strength and stiffness of the truss can be enhanced by increasing the height-span ratio and this enhancement gradually becomes weaker as the height-span ratio increases. The effect of n on σ_{max}/f_{pk} is significantly greater than that on v_{max}/L. When the uniform cantilever tensegrity truss ends with a Unit A, it is better to take a smaller even number of n; when the uniform cantilever tensegrity truss ends with a Unit B, it's better to take a smaller odd number of n. However, it should be noted that the practical design needs to consider additional factors such as the angles between the elements and the slenderness of compression members in choosing the number of basic units n.

5.2. Fish-bellied cantilever tensegrity truss

For the fish-bellied truss, the same span, load, member sizes and materials as those used in the uniform tensegrity truss are adopted. In the fish-bellied cantilever tensegrity truss considered in this paper (see Figure 3a), the height of the vertical element at the free end is assumed as $h_0 = 0.8h$, and the height of the vertical element at the supported end is assumed as $h_n = 1.3h$. From the free end to the supported end, the angles between the upper chord (or lower chord) members and the horizontal axis are increasing and given by: $\arctan(\frac{dh}{l})$, $\arctan(\frac{2\cdot dh}{l})$, ……, $\arctan(\frac{n\cdot dh}{l})$, where $dh = \frac{h_n - h_0}{n(n+1)}$.

Since no analytical solution has been derived for the maximum tensile stress or deflection of the fish-bellied tensegrity truss, a commercial finite element package ANSYS [12] is employed to carry out the parametric analysis on the fish-bellied truss. Via numerical simulations, the relation between σ_{max}/f_{pk} and h/L and the relation between v_{max}/L and h/L are obtained and shown in Figures 9-12.

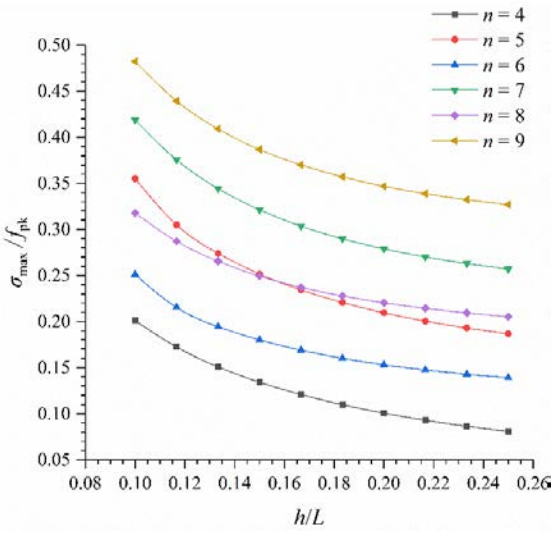


Figure 9: Relation between σ_{max}/f_{pk} and h/L of fish-bellied cantilever tensegrity truss ending with Unit A

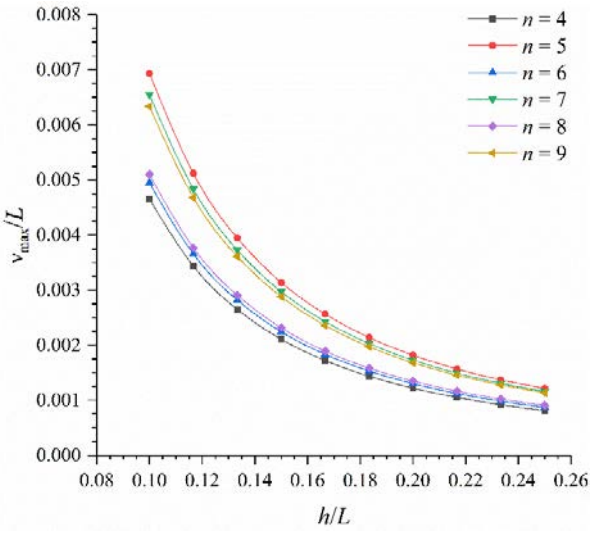


Figure 10: Relation between v_{max}/L and h/L of fish-bellied cantilever tensegrity truss ending with Unit A

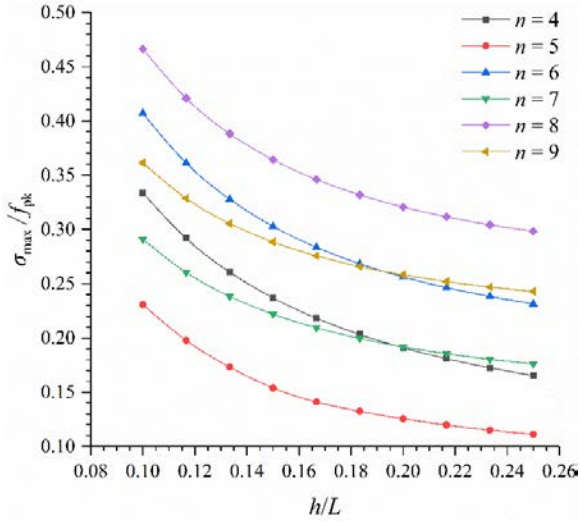


Figure 11: Relation between σ_{max}/f_{pk} and h/L of fish-bellied cantilever tensegrity truss ending with Unit B

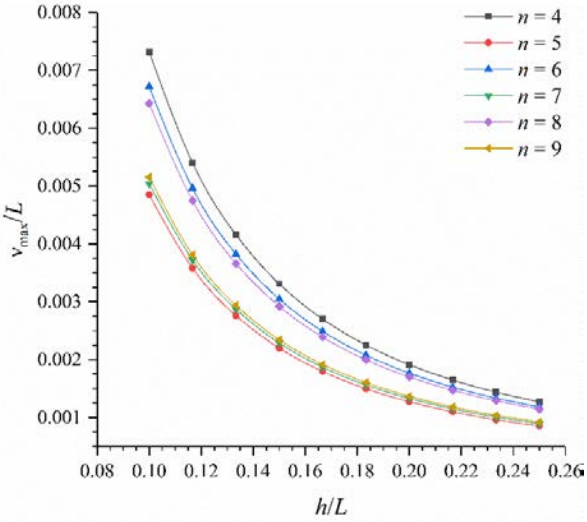


Figure 12: Relation between v_{max}/L and h/L of fish-bellied cantilever tensegrity truss ending with Unit B

By comparing Figures 9-12 with Figures 5-8, it can be found that v_{max}/L of the fish-bellied tensegrity truss is obviously smaller than that of the uniform tensegrity truss. Specifically, v_{max}/L of the fish-bellied cantilever truss is about 21% smaller than that of the uniform cantilever truss. On the contrary, in most cases σ_{max}/f_{pk} of the fish-bellied tensegrity truss is larger than that of the uniform tensegrity truss. In particular, when large h and n are used, the increasement of σ_{max}/f_{pk} can reach 50%. Nevertheless, there are also a few cases (e.g. the fish-bellied cantilever tensegrity truss ending with a Unit A and using $n = 6$ and $h = 0.6$m) where σ_{max}/f_{pk} of the fish-bellied tensegrity truss is smaller than that of the uniform tensegrity truss by less than 10%. Therefore, in some situations where the uniform tensegrity truss is difficult to meet the deflection limitation imposed by the design code, the fish-bellied tensegrity truss can be used to improve the stiffness of the structural system.

6. Three-dimensional latticed tensegrity truss

In this section, a numerical example is carried out to verify the possibility of extending the planar tensegrity truss presented above to 3D latticed tensegrity truss, as shown in Figure 4. In the boundary condition considered here, the dofs in Z-axis direction of all outer lower chord nodes, the dofs in Y-axis direction of lower chord nodes on the edge of AB and the dofs in X-axis direction of lower chord nodes on the edge of AC are fixed. It has a plan size of 7m × 7m and the number of basic units in both directions is assumed as $n = 7$. The height and length of a basic unit are assumed as $h = 1.0$m and $l = 1.0$m respectively. According to load code GB50009-2012 [11], the total load is determined as $q = 2.05$ kN/m^2. Then the uniformly distributed equivalent load on the upper chord nodes is $F = ql^2$. The same materials and sizes of struts and cables used for the planar trusses are adopted here. A prestress of 30kN is used for the vertical cables that are not at the corner, and the prestresses in other members are proportional to this in accordance with the state of prestress of the corresponding planar system.

Again, the commercial FE package is employed to carry out a numerical simulation on the 3D latticed tensegrity truss. The resulting maximum deflection of the 3D system is 1.81mm. Then the deflection-span ratio of it is far less than 1/250, which is the deflection limitation imposed by Technical Specification JGJ7-2010 [13]. The obtained maximum stress ratio is 0.225 which is in a safety level.

7. Conclusions

A novel planar tensegrity truss is proposed and investigated in this paper. The prototype structure is unintentionally found in an example for topology optimization of tensegrity systems [10]. Two types of basic rectangular units are combined alternately to form a typical truss. The analytical expression

for state of prestress of the truss is derived from the equilibrium conditions. Moreover, the internal forces of members and the deflection of the structure are analytically formulated by using the principle of virtual work. Solutions considering different supporting conditions and different combination forms are derived. Parametric analysis is carried out to investigate the effects of the number of units, the height-span ratio and the combination forms on the stiffness and strength of the structure.

In addition, the uniform planar tensegrity truss is extended to fish-bellied tensegrity truss by modifying the shape of the units from rectangular to isosceles trapezoid. Parametric analysis is also carried out for the fish-bellied truss. A comparison between the structural properties of them is conducted. It is found that the fish-bellied tensegrity truss is superior to the rectangular counterpart in the structural stiffness. The possibility of extending the planar tensegrity truss into a 3D latticed tensegrity truss is preliminarily verified through an example. Further studies on the variety and properties of the 3D system are needed in the future work.

Acknowledgements

The work was supported by National Key Research and Development Program of China (Grant No. 2017YFC0806100) and Natural Science Foundation of Zhejiang Province (Grant No. LR17E080001).

References

[1] Y. Kono, K. K. Choong, T. Shimada and H. Kunieda, "Experimental investigation of a type of double-layer tensegrity grids," *Journal of the International Association for Shell and Spatial Structures*, vol. 40, pp. 103-111, 1999.

[2] R. Motro, B. Maurin and C. Silvestri, "Tensegrity rings and the hollow rope," in *New Olympics, New Shells and Spatial Structures: Proceedings of the IASS Symposium 2006*, Beijing, China, 2006. pp. 470-471.

[3] X. Xian, S. Li and Y. Luo, "Form-finding of a new kind of tensegrity tori using overlapping modules," *Mechanics Research Communications*, vol. 84, pp. 1-7, 2017.

[4] J. Y. Lu, X. Dong, X. L. Zhao, X. L. Wu and G. P. Shu, "Form-finding analysis for a new type of cable-strut tensile structures generated by semi-regular tensegrity," *Advances in Structural Engineering*, vol. 20, p. 1369433216661335, 2016.

[5] B. De Jager and R. Skelton, "Stiffness of planar tensegrity truss topologies," *International Journal of Solids & Structures*, vol. 43, pp. 1308-1330, 2006.

[6] K. Nagase and R. E. Skelton, "Double-Helix Tensegrity Structures," *Aiaa Journal*, vol. 53, pp. 847-862, 2015.

[7] R. E. Skelton and M. C. Oliveira, *Tensegrity Systems*. Boston: Springer, 2009.

[8] B. D. Jager and R. Skelton, "Input/output selection for planar tensegrity models," *IEEE Transactions on Control Systems Technology*, vol. 13, pp. 778-785, 2005.

[9] B. de Jager, R. E. Skelton and M. Masic, "Integrated control/structure design for planar tensegrity models," in *Proc. IEEE Int. Conf. Control Appl., Glasgow, U.K., Sep. 2002*, vol. 2, pp. 862–867.

[10] X. Xu, Y. Wang, Y. Luo and Di Hu, "Topology Optimization of Tensegrity Structures Considering Buckling Constraints," *J STRUCT ENG-ASCE*, vol. 144, p. 04018173, 2018.

[11] Ministry of Housing and Urban-Rural Development of the People's Republic of China, *Chinese load code for the design of building structures. GB50009-2012*. Beijing: China Architecture and Building Press, 2012.

[12] ANSYS, Inc. ANSYS v.19.0, 2018.

[13] Ministry of Housing and Urban-Rural Development of the People's Republic of China, *Technical specification for space frame structures. JGJ7-2010*. Beijing: China Architecture and Building Press, 2010.

Proceedings of the IASS Annual Symposium 2019 – Structural Membranes 2019
Form and Force
7 – 10 October 2019, Barcelona, Spain
C. Lázaro, K.-U. Bletzinger, E. Oñate (eds.)

BioMat Pavilion 2018: Development, Fabrication and Erection of a Double Curved Segmented Shell from Biocomposite Elements

Hanaa DAHY*[a,c], Jan PETRS[a], Derk H. BOS[b], Piotr BASZYNSKI[a], Arjan P.H.W. HABRAKEN[b], Patrick M. TEUFFEL[b]

[a] Department of Bio-based Materials and Materials Cycles in Architecture (BioMat) at Institute of Building Structures and Structural Design (ITKE), University of Stuttgart, Keplerstrasse 11, 70174 Stuttgart
* h.dahy@itke.uni-stuttgart.de
[b] Department of the Built Environment, Eindhoven University of Technology, De Rondom 70, 5612, Eindhoven
[c] Faculty of Engineering, Department of Architecture (FEDA), Ain Shams University, 11517 Cairo, Egypt

Abstract

Bio-based composite materials in architecture have gained various new applications due to their availability, renewability, and environmentally-friendly characteristics. This paper demonstrates the use of bio-based building materials for load-bearing structures through a 1:1 realized segmented shell pavilion, referred to as BioMat Pavilion 2018. The pavilion consisted of 121 parametrically optimized curved elements prepared by a vacuum-assisted veneer-reinforcement lamination process. The bio-composite panels were fabricated from elastic or flexible fibreboards applied as sandwich cores laminated with veneer from both sides to provide elevated stiffness. Digitally prefabricated elements were bolted together on site into four shell segments, which were later lifted up and screwed, to three curved timber-intersecting beams, fixed to three footing foundations. In this paper analysis method, form-finding hierarchy and construction stages of the 3.6 m height, 9.5 m span, covering an area of around 55m2 are discussed.

Keywords: Bio-composites; NFRP; segmented shell; multi functionality; design for sustainability; lignocellulosic-based composites; sustainable architecture; materials as a design tool.



Figure 1: BioMat Research Pavilion 2018 © BioMat at ITKE/University of Stuttgart

Copyright © 2019 by H.Dahy; J.Petrs, D.H. Bos; P. Baszynski; A.P.H.W. Habraken; P.Teuffel (All photos copyright belong to BioMat at ITKE/University of Stuttgart; except otherwise indicated)
Published by the International Association for Shell and Spatial Structures (IASS) with permission.

Introduction

BioMat Research Pavilion demonstrates the architectural and structural potential of novel biocomposite building materials fabricated from elastic lignocellulosic fibreboards. BioMat department at the faculty of Architecture in the University of Stuttgart focuses on the applications of sustainable natural materials and closed material cycles towards future-oriented sustainable architecture as an alternative to traditional materials. Under the philosophy set by the author 'Materials as a Design Tool'[1], a series of developments took place in the scope of investigation of bio-based materials as well as further alternative sustainable materials in the early stage of the design process. Investigations are mainly done in experimental approaches, including this pavilion discussed in this paper.

2. Background and context

The building industry is responsible for the use of more than 35% of the global energy and almost 45 % of the global resources. If the population continue to grow, in 2030 the population will need 40% more of energy than today [2]. To meet this demand it is necessary to find alternative solutions to traditional non-renewable resources as well as slow renewable resources. Traditional materials such as concrete or steel are responsible for most of the energy consumption. To meet the requirements for sustainable building materials, natural fibre biocomposites can be used instead of resource-intensive materials (steel, concrete etc.) or other synthetic fibres composites using carbon or glass fibres. Biocomposite materials, i.e. natural fibre reinforced polymeric composites (NFRP) [3], [4] [7], are materials fabricated from at least two main components, a fibre and a matrix (also known as binder), where at least one of the two main components is biomass-based. Thanks to high recyclability and reusability, natural fibres can achieve a closed life cycle hand-in-hand with modernity, geometric flexibility and sustainability, especially when new manufacturing processes are used to achieve higher architectural goals [5].

This paper introduces the research pavilion which was erected in 2018 as a demonstrator of usage of biocomposite materials, made from elastic lignocellulosic fibreboards, for the fabrication of structural building elements.

3. BioMat Research Pavilion 2018

One of the key criteria in the design process of the pavilion was achieving optimum stiffness through newly developed biocomposite sandwich panels that were segmented to form the shell elements which formed together a 3D fabric-like structure. The pavilion was segmented into 121 elements following an irregular triangular lattice, connecting two interlocked shell-layers. The pavilion was 3.6 m high with a 9.5-m span, covering an area of 55 m2.

3.1. Form finding and design

The most important factor that affected the design of the structure were the material properties of the developed biocomposite sandwich panel. Its elastic core made from lignocellulosic fibreboards allowed the fabrication of biocomposite panels with sophisticated geometries, which also contributed to the overall stiffness of the structure. The structure was optimised by means of enabling the presence of a depth and a volume to the shell by introducing a second layer of another thin shell (ca. 10 mm) separated by rods with specified heights of around 180 mm that was connected and interwoven with the other primary shell enabling the required structural volume.

Initial dimensions of the elastic lignocellulosic boards required to tessellate the initial geometry of the shell into triangle-shaped elements consisted of three-legged panels. The size of the core material fibreboard had a fabrication limitation size of (30x100 cm). This influenced the size limitation of each single segment, that accordingly further affected the number of segments ("legs") used for the whole pavilion.

The initial structural simulations showed that material properties of the developed biocomposites would not allow a single shell layer, therefore a second structural layer has been developed and attached to the first one as previously mentioned. This interconnection and double layering enabled homogenous loads' distribution in all directions. The presence of the three crossed laminated beams was essential and the loads were transferred to three superficial foundation footages that were located at different heights, according to the existing site conditions (Fig 2-a).

The parametric model of the shell was developed using Rhinoceros and Grasshopper, enabling the control over the number of variations of the three-legged elements (Fig 2-a). Consequently, in the optimized shell model only 4 different moulds were necessary to fabricate 360 panels for the three-legged elements: upper elements, lower elements, upper edged elements and lower edged elements (Figs. 4 and 5).

The selected site had a certain topography of a pre-built landscape that could not be changed, therefore these site constrains were included in the design process, hence foundation points were not on the same level. The parametric model of the shell enabled the adjustment of the final global geometry to match the terrain geometry, provided by a point cloud model of the location obtained by 3D laser scanning of the site. This helped in adjusting the positioning of the foundation points, so that two foundation footages were placed on the upper level and the third one on the lower level. This helped in settling the initial height of the pavilion and after diverse iterations, the global geometry was initially settled by relaxation in Grasshopper plugins, Kangaroo and Karamba.

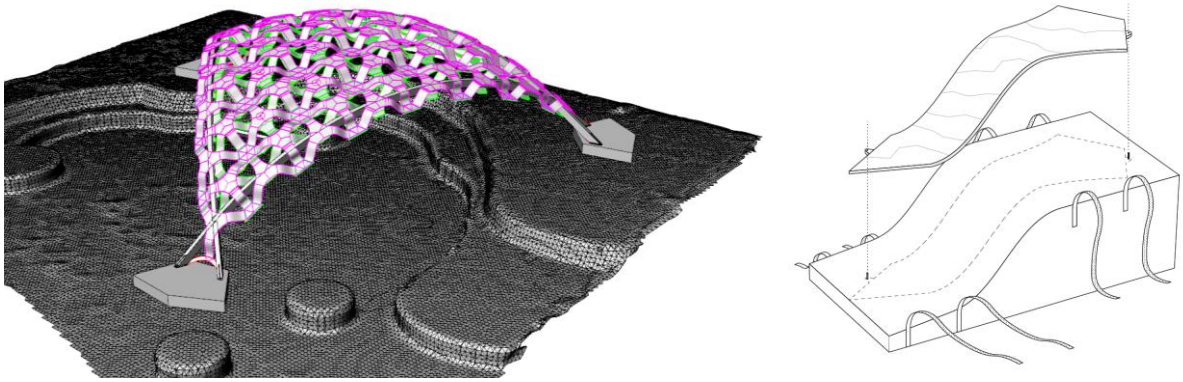


Figure 2 (a): Parametric model of the pavilion; (b): Universal mould for lamination process

3.2. Material and Fabrication

Design development of the shell was proceeded in parallel and in dependence of the development of the biocomposite sandwich panels. The used lignocellulosic fibreboards that were applied as the core materials were originally elastic, offering specific bending radii. The forming properties and fabrication capabilities as well as veneer limitations were together the foundation of the form-finding process of the shell construction. The elastic core material gave the possibility to be locked in specific single-curved shapes by means of lamination. In this case, the cores were laminated with special types of wood veneer sheets, called 3D veneer, which were bendable into double curved surfaces with no cracking risks, due to the back-lying reinforcement layers at the back of these veneers. The final shape of the fabricated elements was reachable through applying Computerized Numerical Controlled (CNC)-milled moulds during the same lamination process (Fig. 3). Vacuum-assisted lamination process took place using a vacuum bag connected to a vacuum compressor, which guaranteed the optimum bonding between the

cores and the veneer skins, hence creating biocomposite free-form sandwich panels. Mechanical tests of the fabricated sandwich specimens proved that the designed biocomposites achieved the target mechanical properties. Their bending E-Modulus ranged from 5-6 GPa and the bending strength ranged from 320-467 MPa, where the measurement was done following the DIN EN 310 for wood-based materials, which were comparable to classic MDF fibreboards.



Figure 3 (a): Reinforcement of the bio-composites by 3D veneer layers; (b) Vacuum-assisted veneer-reinforcement lamination process using the CNC-cut universal mould

3.3. Connection

In the structure, four different types of connections were determined, that were basically composed of two distinct types, that vary depending on their fabricability off-site and on-site. Off-site, each 3 single legs were combined into single layers of three-legged elements (Fig 4 a), while on-site the two separate shell layers were connected with bolts and CNC-cut hexagonal plywood plates (Fig 4b).

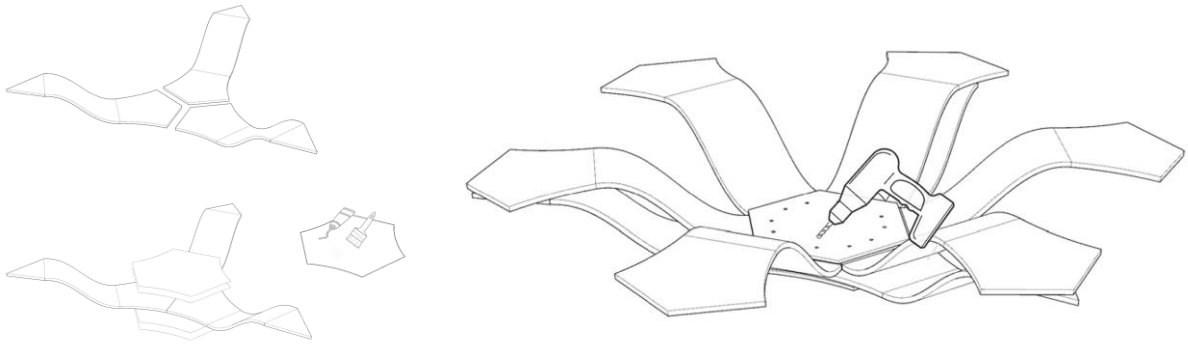


Figure 4 (a): Connection of legs into element by glue and veneer (off-site); (b): connection of elements by bolts and plywood plates (on-site)

The four different connection or bolting types were dependent on the position of the initial two kinds of elements (off-site/on-site connected elements), Fig. 5. Different types of leg connection strategies were initially experimented, including bolts, dowels, wooden nails, glue and others. To determine the best joining system between the elements, pull-out tests were conducted. The specimen glued by 3D-veneer from both sides was found to be the best variation, that was almost three times stronger than the examined bolt connections. The results of the tests lead to a decision of CNC-prefabricating the three legs separately, then gluing them together off-site with two layers of veneer sheets laid in the central area between the three legs on both sides, (Fig. 4). Both veneer layers were oriented perpendicularly to each other to guarantee quasi-isotropic distribution of forces in the finished element.

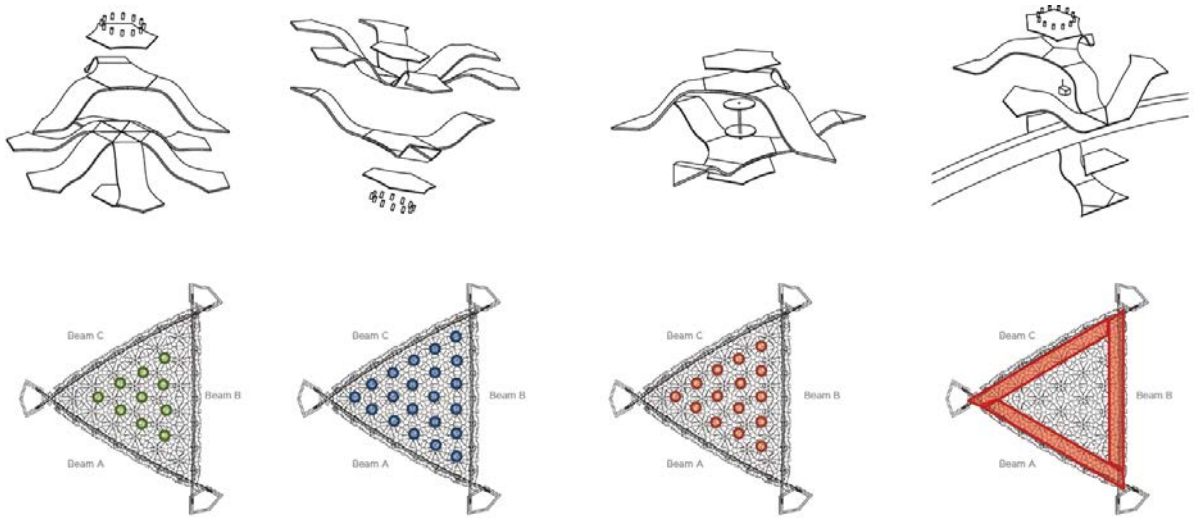


Figure 5: Different types of bolt connections in structure.

Even though, glued connections conducted the best tensile strength between the types of connections tested, bolt connections were at the end chosen in several further connection cases to enable dismantling and re-configurations [6]. The four kinds of connections are shown in (Fig. 5), varying between two identical connections but one facing the ground downwards (First type), where five legs' endings from adjacent three-legged elements are joint on-site in space. The second type was similar to the first one and also bolted on-site, but inverted upwards. The third type largely contributed to giving a depth to the structure, hence improving the overall structural behaviour though adding rods of ca. 180 mm heights that were fixed to two pairs of 3-legged elements off-site. The fourth type was the edge elements that were directly joint to the edge beams and had the maximum radii, Fig. (6). Apart from that, in comparison to gluing, assembly process using bolts on site was found faster and less complex than applying gluing connections on site. Further connections between the elements were reachable through bolting within pre-CNC milled plywood plates, which were applied from both sides to provide necessary thickness and protection to the original bolted points connecting the thin base sandwich materials, Fig. (4-b).



Figure 6: Detail of the connection of the upper and lower shell elements with the beam

3.5. Numerical Model

A numerical model was created to analyze the behaviour of the structure. Firstly, a comparison between a detailed FEM model and a simplified beam model of a single shell segment was made. Both models were loaded with an equally distributed load varying from 0.1 kN/m² to 1.0 kN/m². Furthermore, laterally restrained and laterally free supports were considered. The width of the elements in the beam model was changed iteratively until both deformations and bending moments of the FEM model were reasonably approximated by the beam model.

The simplified beam model was used to model the complete behaviour of the structure, as shown in Figure 8. Self-weight and wind load according to DIN-EN 13782 were considered.

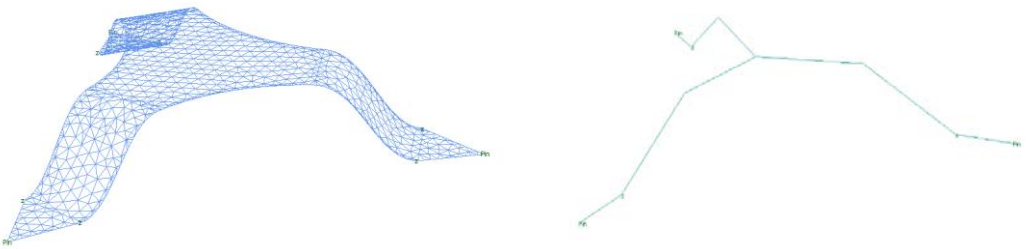


Figure 7: Geometric comparison of FEM model (left) and line model (right) © TU/Eindhoven

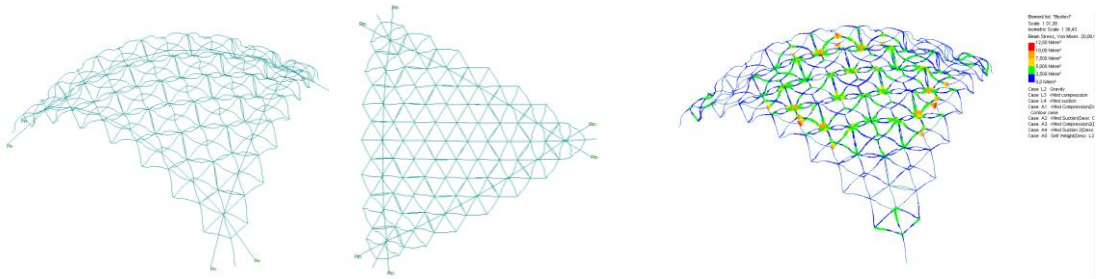
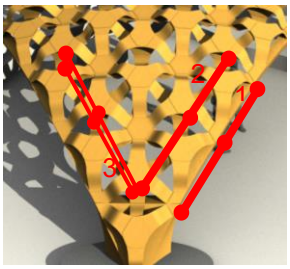


Figure 8: Line model of complete pavilion (left), Analysis (right) © TU/Eindhoven

First analyses showed that the deformation of the structure would become too large without supporting beams. Therefore, three timber beams were added to the edge of the shell. For this, three locations were considered (Fig. 8-b). In the first option, the beams were added on the edge of the structure, while in the second and third option they were placed were the distance between the elements in the shell is maximal. In the second option, the beam only connected to the bottom layer of the shell and in the third option two interconnected beams were proposed, where one is connected to the bottom and one to the top. As can be seen in Table 2, the deformations and moments were minimal in the third option. To reduce the complexity, one beam with a height of 180 mm was chosen that was connected to both the top and bottom. The width of the beam was 100 mm to provide space for bolted connections. A secondary advantage was that this positioning was less exposed and visible than the first option. Since the total dimensions where determined by practical constraints, governing unity check of 0,14 was found for combined bending. Furthermore, the solution significantly reduced the bending moments in the bio composite, resulted in a unity check of 0,64. The beams were interconnected with each other by slotted steel plates in location where the beams were crossing each other. To provide additional stability during construction, three smaller beams are added as can be seen in Figure 9a.





Edge beam location	Maximum displacement [mm]	Maximum moment, in the biocomposite [Nmm]
1	719 mm	110800
2	475 mm	69210
3	280 mm	40290

Figure 9 (a): Beam Structure; (b): Position of the beams in structure; Table 2: Maximum displacement and moments in different positions of beams in the simulation model ©TU/Eindhoven

3.6. Foundation

According to the selected construction site regulations, direct anchoring to the ground was not permitted. Furthermore, connecting the footings with cables to balance internal horizontal forces was not possible, since the footings were not placed on the same level. Therefore, the foundation footings were designed based on friction. The maximum allowable load on the site was 500 kg/m². Three different interfaces between the box and concrete ground were considered: concrete-rubber, concrete-timber and concrete-concrete, resulting in different needed combinations between needed contact area and additional load. A concrete-rubber interface was selected for the final design because the high friction resulted in the smallest needed contact area of 2,3 m^2. A total load of 4,5 kN was added, which resulted in roof load under 500 kg/m² when the self-weight of the shell and different wind loads were taken into account. On every footing, two of the three timber beams were connected to the foundation box. Each box was filled by easily replaceable concrete blocks and gravel to provide the additional weight. A 10 mm thick layer of Viltron Vetra PO was attached to the bottom of each foundation footage box using nails to provide the needed friction. Furthermore, the box was designed such that the maximum occurring deformations remained below 2 mm under wind suction, to have sufficient friction remaining.



Figure 10 (a): Deformations of the bottom plate of foundation under maximum loading, Photo: ©TU/Eindhoven; (b): Foundation with gravel and concrete blocks.

3.7. Assembly

The assembly process was divided into off-site and on-site processes. Off-site processes included the preparation of CNC milled core elements, then applying vacuum lamination processes for the veneer appliance producing the final curved biocomposite sandwich elements.

The fabrication phase started by CNC milling the elastic core fibreboards to the shape of separate legs as seen in (Fig.2-b) and marking them with a smart labelling system. The 3D veneer was also cut, with extra margin to reduce the risk of layer slipping inside the vacuum bag. In a separate following stage, the core fibreboard was laminated with veneer sheets from both sides and formed using a corresponding

mould type inside a vacuum bag for 30 min. After extra 24h of glue curing process, the edges of the formed leg elements were sanded. After this stage, each three legs were glued into one element, with 2 extra hexagonal layers of 3D veneer placed on both sides, where each veneer layer was placed perpendicular to the fibre-direction of the other to cover afterwards the stresses flow in different directions. After another 24h of curing, the biocomposite sandwich elements were ready for final sanding and coating with the weathering protection system.

In parallel, the supporting structure in the form of the three beams were fabricated by the timber company Burgbacher Holztechnologie GmbH and the foundation boxes was created by the BioMat team. This process was monitored by the geodesy engineers partners of the University of Stuttgart, to reach the same level of precision as during the 3D laser scanning of the terrain. After the beam structure was ready, all the 121 off-site prefabricated elements were transported on-site for the final assembly.

Due to the large size of the shell, for the purpose of final assembly and positioning, the structure was divided into 4 smaller triangles (Fig. 11). Each triangle was separately mounted and connected on the ground, then lifted up and placed on temporary support columns and attached to the beams. Once all triangles were in position, they were then attached gradually to each other and to the structure till the equilibrium status occurred then the temporary columns were removed.

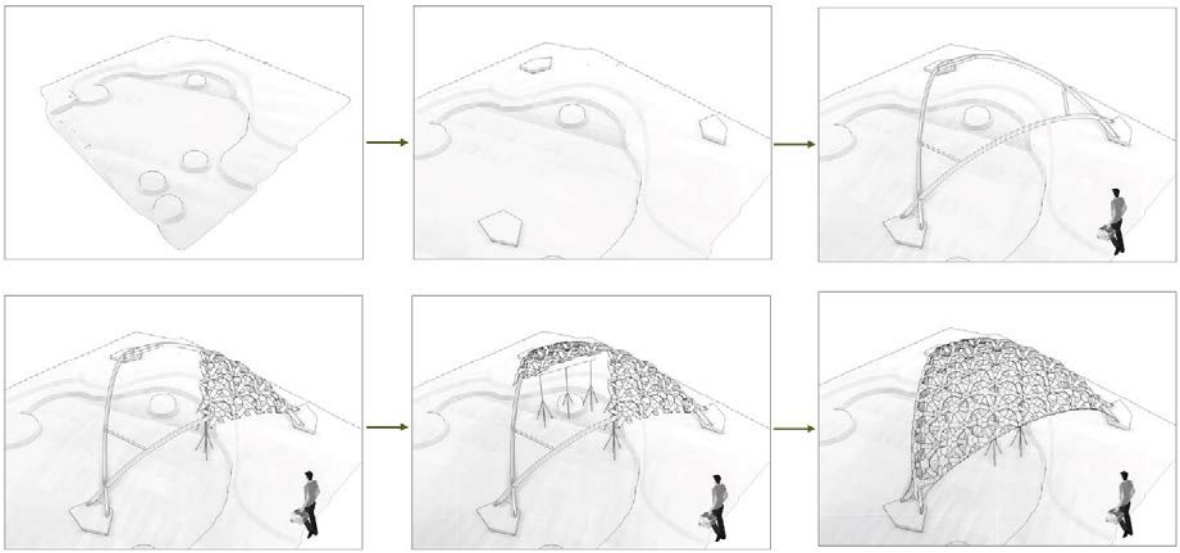


Figure 11: Diagram illustrating the on-site assembly hierarchy



Figure 12: The shell after erection. © BioMat at ITKE/University of Stuttgart

4. Conclusion

The BioMat Pavilion 2018 was an experimental Proof-Of-Concept approach, where research and teaching were combined. Here biocomposites were applied as an alternative to non-renewable or slow-renewable building materials for load-bearing structures under real weathering conditions. All four disciplines: architecture, material-engineering and civil engineering as well as geodesy engineering have been contributing to the design process and all inputs were in the same parametric model, as the common digital communication tool. The appliance of an alternative building material was the main goal to enhance sustainability in future sustainable architecture, where these alternative building materials made from biocomposites were taken as the main driver for the whole design and erection processes. Form-finding took place through the offered material properties of the proposed biocomposite material in addition to its fabricability limitations, site constrains and others. Dealing with a natural hygroscopic material was challenging, therefore intensive testings with weathering resistance coatings have taken place and have been applied. Digital fabrication technologies have enabled reaching the final complex double-layered shell and smart-numbering system as well as proper data-management have allowed together the building process to take around one month. It can be finally deduced that biocomposites or Natural Fibre Reinforced Polymer Composites (NFRP) have diverse underestimated application possibilities in the building sector and is worth further testing and pushing forwards towards more diverse heavy-duty applications in this still resource-intensive building industry for a better green future.

Photos Copyright: All photos copyright belong to © BioMat at ITKE/University of Stuttgart, except for those referred to TU/Eindhoven

Acknowledgements

The author would like to thank all students, employees, technicians and agencies involved in this project. This work was the direct result of cooperation between around 40 architecture students over two semesters participating in the (Flexible Forms) Design Studio in the semesters: WS17/18 and SS18 supervised by the author with the support from the University of Stuttgart and the Baden-Württemberg Foundation. Financial support was from the German Agency for Renewable Resources (FNR) under the Ministry of Food and Agriculture (BMEL), and scientific cooperation took place with Fraunhofer-Institut für Holzforschung (Fraunhofer WKI) and industrial partners Mathias Stange ETS and Profine GmbH in the framework of the Research Project (BioProfile) FKZ 22021516 with assistance of BioMat employees including Mrs. Michaela Mey. International collaboration has taken place with the Technical University Eindhoven in the Netherlands (TU/e) - Department of Built Environment and local collaboration with various institutes of the University of Stuttgart took place, including the Institute of Construction and Structural Design (KE, Faculty 02: Civil and Environmental Engineering) - Prof. Urlike Kuhlmann and Mr. Janusch Töpler as well as the Institute of Engineering Geodesy (IIGS, Faculty 06: Aerospace Engineering and Geodesy) - Prof. Volker Schwieger and Mr. Gabriel Kerekes. Wooden beams were fabricated and supported by Burgbacher Holztechnologie GmbH with assistance of Mr. Steffen Haller, weathering resistant coatings were provided by Hexion Inc.

References

[1] Dahy, H. 'Materials as a Design Tool' Design Philosophy Applied in Three Innovative Research Pavilions Out of Sustainable Building Materials with Controlled End-Of-Life Scenarios. Buildings 9, 64, 2019.

[2] UN Secretary-General's High-Level Panel on Global Sustainability, Resilient People, Resilient Planet: A Future Worth Choosing, OVERVIEW; United Nations: New York, NY, USA, 2012

[3] Dahy, H. "Natural Fibre-Reinforced Polymer Composites (NFRP) Fabricated from Lignocellulosic Fibres for Future Sustainable Architectural Applications, Case Studies: Segmented-Shell Construction, Acoustic Panels, and Furniture." Sensors 19.3 (2019): 738, 2019.

[4] Dahy, H. (2017). Biocomposite materials based on annual natural fibres and biopolymers–Design, fabrication and customized applications in architecture. Construction and Building Materials, 147, 212-220

[5] Dahy, H.; Knippers, J. (PATENT) Flexible High-Density Fiberboard and Method for Manufacturing the Same. EP3166765A1; Filed 8. July 2014, Published 13 January 2016. Based on Same Patent, Also Applied as WO2016005026A1; CN106604806A; US20170144327, EP2965882 A1.

[6] Guy, B.; Ciarimboli, N. DfD. Design for Disassembly in the Built Environment. A Guide to Closed-Loop Design and Building; Hendrickson, K., Ed.; Hamer Center for Community Design, The Pennsylvania State University: Old Main, PA, USA, 2008.

[7] Lepelaar, M.; Hoogendoorn, A.; Blok, R.; Teuffel, P. Bio-based composite pedestrian bridge. In Proceedings of the IASS Annual Symposium 2016 "Spatial Structures in the 21st Century", Tokyo, Japan, 26–30 September; pp. 1–10, 2016.

Proceedings of the IASS Annual Symposium 2019 – Structural Membranes 2019
Form and Force
7 – 10 October 2019, Barcelona, Spain
C. Lázaro, K.-U. Bletzinger, E. Oñate (eds.)

Composite Glulam Timber and Concrete for the Performing Arts

David M. FOXE*

*Associate, Epstein Joslin Architects
80 Trowbridge Street, Cambridge, MA, 02138, USA
david.foxe@gmail.com

Abstract

A crucial problem when constructing performing arts facilities with world-class room acoustics is the simultaneous provision of substantive mass at the enclosure, and shaping that enclosure to geometric requirements for diffusion and reflection of sound energy. This paper describes a group of solutions whereby glulam-timber frame and concrete surface typologies are hybridized so that the primary structure and lateral system simultaneously satisfies both structural needs and acoustic requirements. The paper addresses prior typical planar (2d) uses of concrete atop flat timber decking, plus methodologies extending into nonplanar 3d applications for decking. Geometries include ruled surfaces, faceted surfaces approximating doubly-curved forms, and bipedal glulam 'tuning fork' columns. This will be illustrated: (1) by digital modeling and acoustic auralization prior to construction, (2) by full-size assembly mockups with spray-applied shotcrete for testing, and (3) through documentation of variant structures realized (fabricated and constructed) of glulam and shotcrete. The value of these investigations is that they extend the capabilities of timber members and standard straight decking into complex spatial systems with intrinsic stability, compressing structure, enclosure, and finish into a single low-carbon construction assembly. The wood systems define resonant spaces as architectural 'instruments' analogous to musical instruments played within.

Keywords: Timber, Glulam, Composite Structures, Hybrid Structures, Acoustics, Auralization, Conceptual design, Form finding, Shotcrete.

1. Introduction

The designs of complex-curvature structures often emerge from goals of minimizing the self-weight or mass of a structure. Efficient forms for shells and membranes constructed in concrete, timber, or other materials are often intrinsically amongst the most lightweight solutions for their constraints, see Allen et al [1]. For a particular group of structures, however, the provision of mass is of programmatic value due to how sound energy interacts with such mass. For performing arts facilities designed to provide world-class room acoustics, mass must be at the acoustic enclosure of the performing space, and this is generally accomplished with masonry or reinforced concrete that is not always visible as a final interior finish. The enclosure must not only provide substantive mass to contain the sound energy produced by performers within the space, the materials within the space must be of a size, shape, orientation, and mass to reflect and diffuse the sound in appropriate patterns. A more typical solution in historic and current construction (including so-called 'shoebox' halls) is to envision the enclosure to be simple in disposition, to be extruded in form (whether it serves as primary structure or not), and to serve as an armature articulated with 'shaping' added to the interior. This detaches the configuration of the structure and enclosure from the form and experience of the acoustic volume. Yet the shape of an overhead diffusive surface is not dissimilar from a shallow inverted shell or membrane profile (unlike one that focuses sound [2]). When one considers the benefits of exposing the primary structure to give spatial character, and for structural mass to give acoustic character, there exists a design challenge of how to associate and/or integrate the structural needs and acoustic requirements.

Copyright © 2019 by David M. FOXE
Published by the International Association for Shell and Spatial Structures (IASS) with permission.

This paper describes a group of solutions whereby glulam-timber frame and concrete surface typologies are hybridized so that the primary structure and lateral system simultaneously satisfies both structural needs and acoustic requirements. The design team for these solutions begun in 2016 is led by Epstein Joslin Architects (see Acknowledgments), and the various instances are being constructed on a single site in Groton, Massachusetts, USA [3] starting in 2017. The instances range from a 300-seat recital hall (Fig. 1) to a 1000 seat concert hall and a multifunction space, each with varying scales and shapes of structure to suit the acoustic needs of each space.



Figure 1: Lateral view of recital hall from main seating level. [All construction images by author.]

2. Timber decking with concrete in two-dimensional planes

It is not unusual to use concrete atop timber decking, both in nonstructural uses for dampening footfall, or in structural capacities where the decking serves as formwork abandoned in place and the planar concrete slab is conventionally reinforced and formed. One example from the same design leadership [4] exposes the flat decking to the interior of the performance space shown below (Fig. 2). Other applications use timber decking in sloped configurations with angles suited to acoustic parameters, but do not support floor loads or other primary structure above.



Figure 2: Views of flat decking at Shalin Liu Performance Center, Rockport, MA [Epstein Joslin Architects]

3. Timber decking with concrete in three-dimensional space

The investigations of this paper began with a project goal to feature exposed wood structure in performance spaces but not in orthogonal planes, maximizing continuity across varying shapes and sizes of performance spaces. The team created digital models for visualization as well as for acoustic auralization, whereby forms of potential acoustic enclosures are tested in simulations such that their effects are not only guided by calculations or geometry but by an "aural rendering" derived from acoustic consultants' analyses, to borrow Hochgraf's term for current industry practice [5]. Deploying convex profiles in section, the design team evaluated options for suitability to sightlines, seating configurations, performing group variations, structural span, and geometric repetition (Fig. 3, 4).

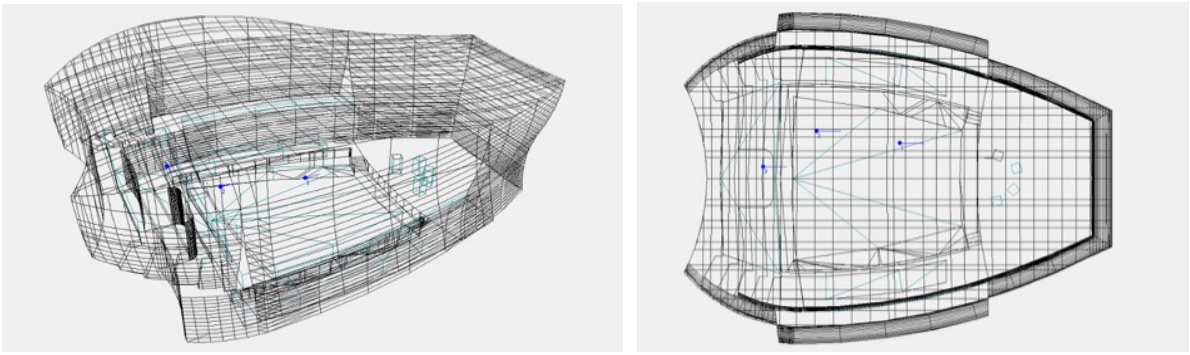


Figure 3: Auralization diagrams of recital hall (perspective, plan) with convex profiles in section. Shapes on stage (right side of images) correspond to source instruments; blue dots in seating areas (left side of images) correspond to listening points during in-person "aural rendering." [Images courtesy of Threshold Acoustics]



Figure 4: Design renderings, view facing stage (left) and view from stage (right). [EJA]

The convex radius suitable for wall profiles, as identified in design studies (Fig. 3, 4) was adopted as the elevational profile of a curved glulam column by working within the allowable radii and strength characteristics for standard lamination thicknesses of southern yellow pine. Paired with a mirrored column adjacent, each curved glulam pair was identified as a 'tuning fork' (Fig. 5). By using the same radii for all columns in a performance space, a single glulam setup could be used to form a group of columns with varying lengths and attachments. However, since 'tuning fork' columns varied in height relative to curvature, and varied in distance from one another, the decking placed from column to column creates resultant surfaces that are ruled but are not cylindrical.

To more closely approximate the curvature of the acoustic surfaces (Fig. 3), the linear path of each piece of the ruled surfaces of decking needed to be rationalized from of a curve into individual segments, one per structural bay. To maintain fidelity to the original acoustic curve, the locations of 'notches' in the columns were designed to work within fabrication limitations for notch size and tolerance. (Fig. 5). Furthermore, since laminated wood decking of standard nominal thicknesses, generally less than actual thicknesses of 4 inches (100mm), and of insufficient mass to reflect sound energy, the decking was designed to be fully mated to a parallel ruled plane of 6-8 inches (150-200mm) of concrete, spray applied from the rear. These ruled planes included the lateral transfer ceiling slab that unites the tops of all 'tuning fork' columns and the shear planes (walls) that transfer those forces to the conventional reinforced concrete foundation.

In order to ensure sufficient solidity for acoustic mass at a macro scale, and to evaluate the surface variations in the decking and its wood grain at a micro scale, a fullscale mockup of decking was fabricated, constructed, shipped to the site, and shotcrete was applied by the onsite contracting team. This composite wall portion facilitated acoustic testing, confirming the constructability of the design and detailing (Fig. 6).

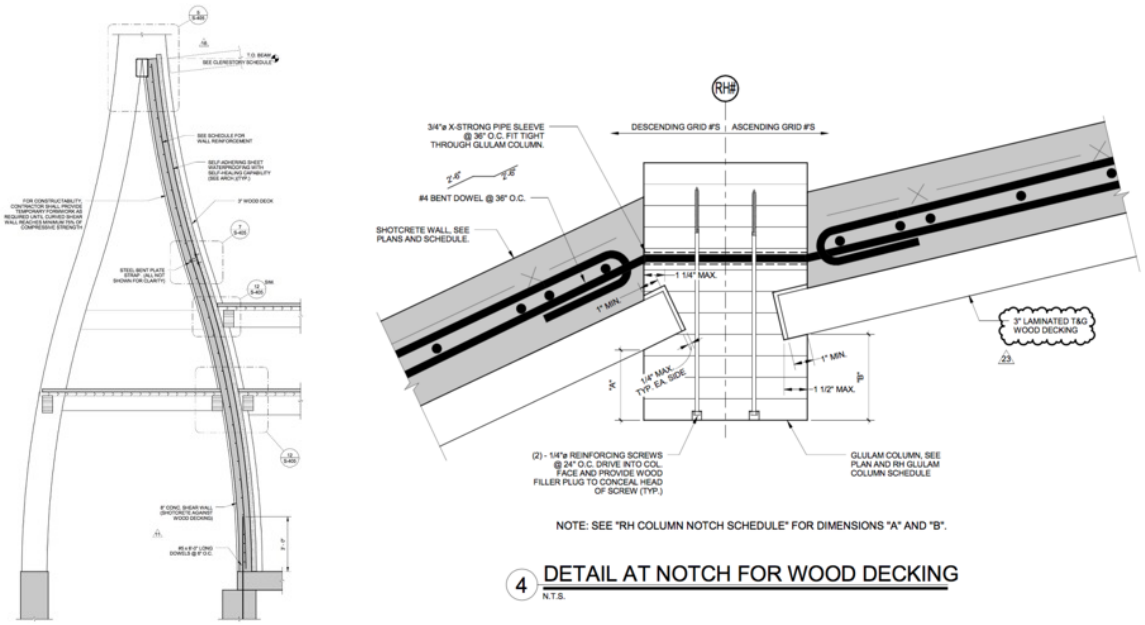


Figure 5a: Elevation of 'tuning fork' column with decking/shotcrete at shear plane shown in section.
Figure 5b: Plan detail at 'tuning fork' column with rebar in shotcrete behind decking [Odeh Engineers, Inc.].



Figure 6a: Shotcrete applied to rebar at rear of decking mockup. Figure 6b: Acoustic test of mockup.

The fabrication schedule matched the construction sequence: starting with pairs of 'tuning fork' columns at shear planes, and proceeding in pairs to the stage end of the recital hall. (Fig. 7, 8, 9). As part of the purposefully hybridized approach, overhead trusses were designed to be in steel due to cost and ease of fabrication based on span, with hybrid steel and glulam bottom chords supporting the convex ceiling plane. With close collaboration between architects, structural engineers, fabricators, and contractors, all geometry in this hybrid system was checked during the design phase and the shop drawing process so that decking could be placed by onsite laborers into notches or onto shop-cut blocking without complex geometric measurements in the field. This approach is thus characterized not only by composite action (timber and steel at truss chords, timber decking and concrete at walls and ceilings) but also hybrid use of glulam members within the finished acoustic volume and steel members above and outside the acoustic volume. This minimizes the visual extent of steel within the interior and maximizes the surface area of mass timber backed by shotcrete [6].

4. Sequence





Figure 7a: Construction view of 'tuning fork' columns erected while wrapped with protective plastic.
Figure 7b: The trusses with hybrid glulam/steel lower chords bear on the 'tuning fork' columns.





Figure 8a: Decking installed at shear planes between glulam columns, and between ceiling trusses.
Figure 8b: Attachments from rebar to decking visible prior to concrete placement at lateral walls.

During construction, the glulam erection team confirmed and took advantage of the inherent stability of the bipedal columns, particularly when united with the decking connecting adjacent pairs, allowing for only the minimum temporary bracing as required. To ensure full composite action and no short-term or long-term separation of the shotcrete apart from the decking, metal fabrications connected the rebar to the rear of the decking. The grid of these attachments were visible (Fig. 8b) for review of placement prior to the shotcrete placement, after which they are entirely concealed within the shotcrete. While the first rebar attachment fabrications visible in these photos were made of welded steel plates, a standard bent steel fabrication available in a similar size was reviewed during this process by the structural engineer and contractor, and that standard product will be used in subsequent variations described below to improve the process. While most of the decking is tongue-and-groove, the decking was installed on end (Fig. 10b) over the stage. The purpose of this undulating decking was to create acoustically diffusive shaping that would add acoustic 'warmth' to reflections and eliminate potential echoes or 'flutter' of sound heard on the stage, thus projecting primary reflections of sound forward toward the audience. This shows the flexibility in using decking as formwork abandoned in place, fully mated to the mass of the concrete above for acoustic purposes but in this case not being relied upon for structural purposes.



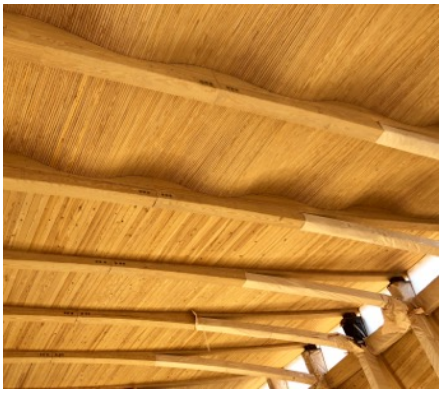


Figure 10a: Longitudinal view of recital hall from balcony. Figure 10b: Detail of diffusive shaping over stage.

5. Theme and Variations

Given the thematic approach to timber technologies used in this recital hall, there are two additional variations in construction as of this writing (2019) on the same site. After the first instance in the recital hall, a second variation is an adjacent smaller multipurpose hall (100-250 seats) using composite walls (timber decking backed by shotcrete) and glulam roof beams without hybrid steel trusses above. In this variant application, the 'tuning fork' columns are inverted to reduce roof span. As a third variation, the adjacent larger concert hall (1000 seats) uses the same 'tuning fork' column orientation, composite timber/shotcrete walls and ceiling, hybrid steel/glulam trusses, and geometric approach as the recital hall, but at greater height and span within fabrication length limits of glulam.

In this concert hall design, the hybrid role of concrete is more multifaceted than at the recital hall. The reason is that instead of all members bearing directly onto the foundation, the end opposite the stage has a large span concrete 'bridge' over a retractable door system, while other 'tuning fork' columns bear on ground-level slabs to the sides. The curving ruled ceiling slab atop the glulam decking acts as a convex curving membrane uniting all of the shear planes and transfers load paths for lateral forces to the cast-in-place concrete towers and walls (Fig. 11).

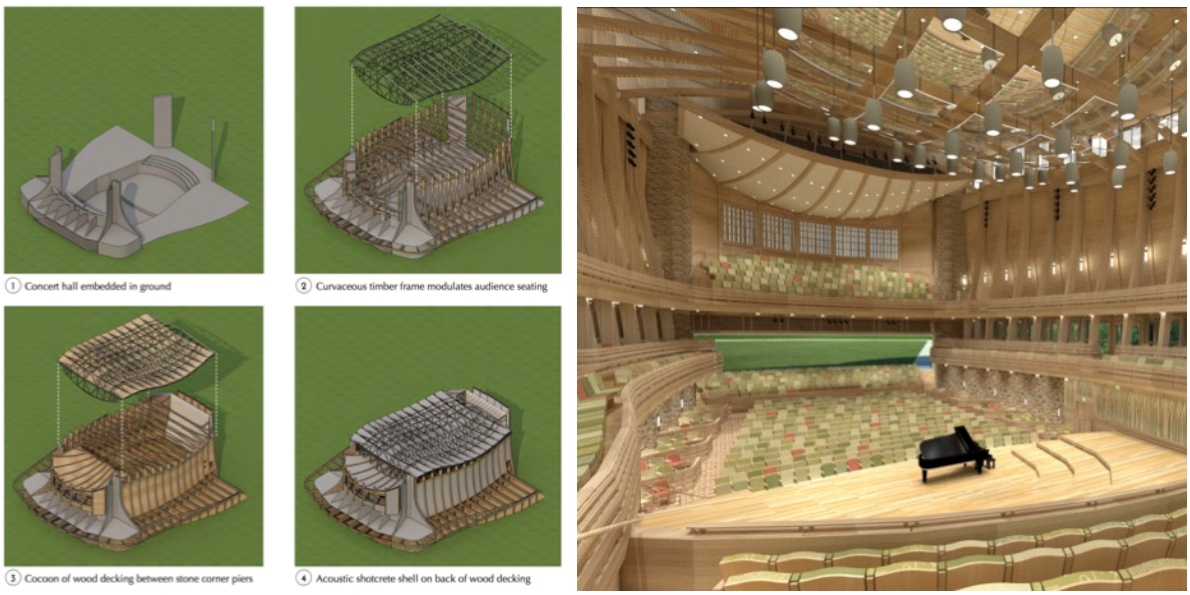


Figure 11a: Diagrams showing structural approach for 1000-seat concert hall. Figure 11b: Design rendering for 1000-seat concert hall, with tuning forks on each side and opening to landscape beyond. [EJA]

Following construction of these variations, one direction for study would compare the solutions arrived at for acoustic purposes with other mass timber composites and hybrids. This would include an assessment of acoustic performance for the timber in its solo and composite roles, information which is nascent for a variety of project types beyond the performing arts. This direction of study would also include the environmental impact of composite and hybrid approaches incorporating mass timber relative to each other (i.e. the three related variations normalized by enclosed area, enclosed volume, and related metrics) and relative to conventional construction (i.e. not mass timber). For example, the 300-seat recital hall depicted in this paper required approximately 136,000 board-feet of lumber for its glulam columns, beams, and decking (330 m^3) [7]. This amount of wood grew in less than one minute (considering the growth of American forests as a whole), and aligns with other innovative projects using exposed timber technologies in Massachusetts and beyond [8]. Beyond these three variations in construction per se, further directions for this construction approach would seek to evaluate the potential for combining acoustic form-finding with shell and membrane action within the overhead ruled surfaces. While not all acoustic wall planes may be required for lateral systems, the acoustic requirement that the overhead plane of reinforced concrete is doubly curved rather than planar gives opportunity for structural optimization, aligning acoustic mass and structural mass to optimize without sonic penalty. There are precedents for such approaches to the design of analogous ruled/curved forms in hybrid steel [9] and spray-applied concrete [10] in the works of Zalewski and other engineers.

The value of these investigations is that they unite the visual and the aural in the design of sustainable structures. They extend the capabilities of timber members and standard straight decking into complex spatial systems with intrinsic stability, compressing structure, enclosure, and finish into a single low-carbon construction assembly. In doing so, the wood systems define resonant spaces as architectural 'instruments' analogous to the musical instruments played within.

Acknowledgements

Architect: Epstein Joslin Architects. Structural engineer: Odeh Engineers, Inc. Acoustician: Threshold Acoustics. Glulam fabricator: Unalam. Glulam erector: Lonsdale. Contractor: Goguen Construction.

References

[1]. E. Allen, W. Zalewski, D. Foxe, et al., *Form and Forces: Designing Efficient, Expressive Structures*, Wiley, 2009.

[2]. D. Foxe, "Saarinen's Shell Game" in *Proceedings of the IASS Symposium 2018*, July 2018.

[3]. Epstein Joslin Architects, Music Center at Indian Hill, https://www.epsteinjoslin.com/music-center-indian-hill Retrieved 2019. [Online].

[4]. Epstein Joslin Architects, Shalin Liu Performance Center, https://www.epsteinjoslin.com/shalin-liu-performance-center Retrieved 2019. [Online].

[5]. K. Hochgraf, "The Art of Concert Hall Acoustics: Current Trends and Questions in Research and Design," in *Acoustics Today*, v.15 #1, Spring 2019.

[6]. Z. Van der Meulen, *Music Center with Glulam Recital Hall Taking Shape*, http://unalam.blogspot.com/2019/01/music-center-with-glulam-recital-hall.html 2019 [Online].

[7]. Data provided from Unalam to author, May 14, 2019.

[8]. Building and Construction Technology, https://bct.eco.umass.edu/about-us/the-design-building-at-umass-amherst/ Retrieved 2019. [Online].

[9]. W. Zalewski, "Construction de la Toiture du Supermarket a Varsovie," in *Proceedings of the IASS Colloquium on Hanging Roofs, Continuous Metallic Shell Roofs and Superficial Lattice Roofs*, Paris, France, 9-11 July 1962, reprinted 1963.

[10]. D. Foxe, "Reassessing Zalewski's Shells, Designs and Surfaces," in in *Proceedings of the IASS Symposium 2018*, July 2018.

Proceedings of the IASS Annual Symposium 2019 – Structural Membranes 2019
Form and Force
7 – 10 October 2019, Barcelona, Spain
C. Lázaro, K.-U. Bletzinger, E. Oñate (eds.)

Damping reinforcement for traditional wooden house using CLT bearing panel connected with damper

Yu KIHARA*, Takuo NAGAI[a]

*Graduate Student, The University of Shiga Prefecture
2500, Hassakacho, Hikone-city, Shiga, Japan
architect.0831@gmail.com

[a] Lecturer, The University of Shiga Prefecture

Abstract

In this article, we propose a mitigation system of seismic response for traditional old houses using CLT panel. For a seismic reinforcement of a traditional and culturally important building, it is important not to damage the design of the building and to avoid damage and processing of the building as much as possible. In proposed system, a CLT panel with high in-plane rigidity is installed as a display wall or partition, and this is connected with an original frame by a damper. Since the CLT panel is installed independently of the existing housing, it is possible to preserve both the original building and the interior design without loss, and it is also easy to remove the system. First, in order to verify the damping effect of the system, seismic response analysis is performed using a simplified lumped mass model. Next, using response values obtained by the dynamic analysis, design examples of joints are shown to show that the proposed system is sufficiently feasible.

Keywords: seismic response mitigation, traditional wooden house, CLT, damper, dynamic analysis

1. Introduction

The old castle town of Omihachiman-City, Shiga Prefecture, has a distinctive landscape with a traditional wooden house and a townhouse, including “The important preservation district of historic buildings”. However, now there are more vacant houses, and many of them cannot be maintained easily, and urgent preservation measures and recovery of use are urgent issues. In utilizing these buildings, it is important not to damage the design of the building as a cultural property and to avoid damage and processing of the building as much as possible. In this paper, we propose the “CLT damping reinforcement system” using CLT (Cross Laminated Timber) for the purpose of utilizing traditional wooden buildings as a gallery etc. The image when the system installed is shown in Figure 1.

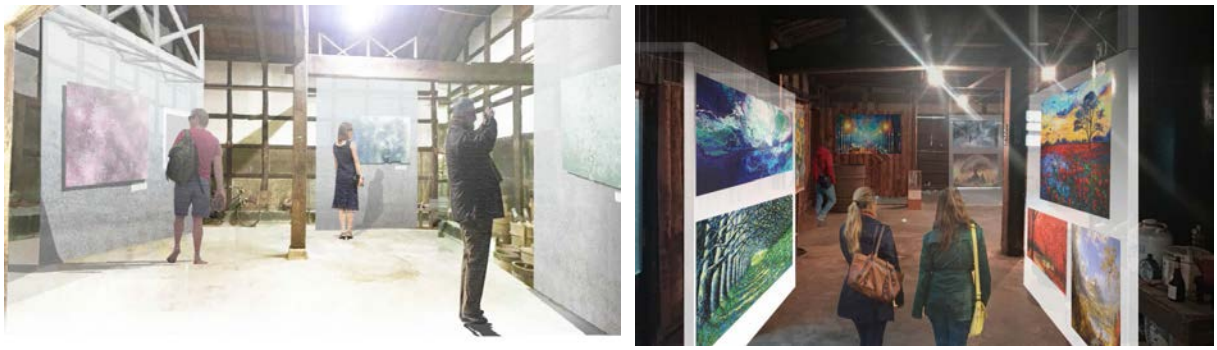


Figure 1: Images of interior view after installing reinforced system

Copyright © 2019 by Yu KIHARA, Takuo NAGAI
Published by the International Association for Shell and Spatial Structures (IASS) with permission.

In this system, a CLT panel with high in-plane rigidity is installed as a display wall or partition, and this is connected with an original frame by a damper. Since the CLT panel is installed independently from the building, it can be preserved without losing both the existing structures and the interior design, and can be easily removed. In this paper, seismic response analysis is carried out by targeting an actual building, and the feasibility of this system is verified.

2. Overview of CLT damping reinforcement system

The damping reinforcement system proposed in this research is a system that connects the upper part of the CLT panel installed inside the building with the building shed or horizontal structure with a damper as shown on the left side of Figure 2. The damper absorbs energy by using the difference in displacement between the traditional wooden structure and the extremely rigid CLT panel. At this time, the CLT panel is installed so that the damper force acts in the in-plane direction of the panel, and at the same time, is disposed in a well-balanced manner on the plan of the building.

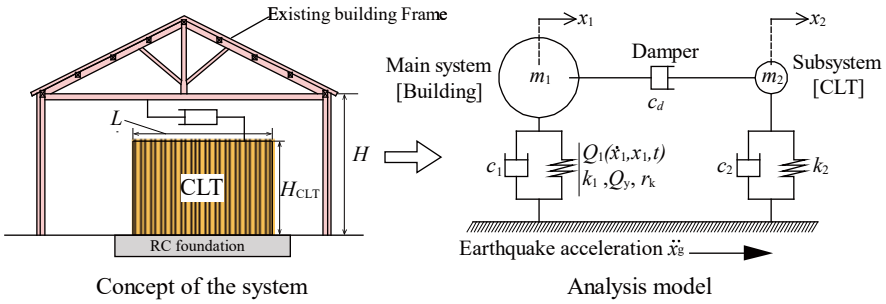


Figure 2: Concept of CLT damping reinforcement system (left), Model of the whole system (right)

3. Outline of target building

The building considered as a model to be examined in this paper is a single-storey earthen-walled Sake brewery that exists in the area. This building is currently used as an art gallery and rental space. For this building, seismic assessment is carried out, and information such as initial stiffness and mass of the building is obtained. A plan, elevations and photographs of the building are shown in Figure 3.

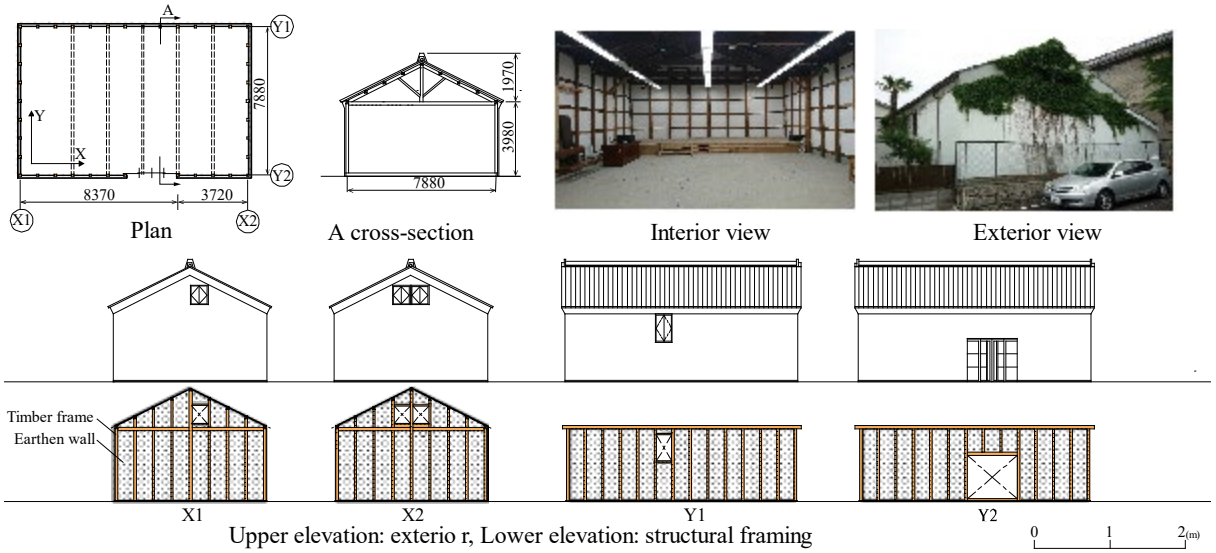


Figure 3: Outlines of target traditional wooden building

The building plan has a span of 12.09 m in the longitudinal direction (X direction) and 7.88 m in the beam-span direction (Y direction). The hut is a king post truss and the roof is a tiled gable. The outer wall is constructed by painting earthen wall between wooden frames. For seismic forces, earth walls are the main resistance element, and wooden frames have little horizontal stiffness.

4. Seismic response analysis

4.1. Modeling and setting parameters

Time-history response analysis is carried out to verify the effectiveness of the CLT damping system. As shown on the right of Figure 2, a single-story target building (main system) and a CLT panel (subsystem) are both modeled as a single lumped mass system. The damper connecting the main system and the subsystem is assumed to be a viscous damper and modeled with a linear dashpot. At this time, the equation of motion of the whole system can be expressed by the following equation.

$$\begin{aligned} m_1\ddot{x}_1 + c_1\dot{x}_1 + c_d(\dot{x}_1 - \dot{x}_2) + Q_1(x_1, \dot{x}_1, t) &= -m_1\ddot{x}_g \\ m_2\ddot{x}_2 - c_d(\dot{x}_1 - \dot{x}_2) + c_2\dot{x}_2 + k_2x_2 &= -m_2\ddot{x}_g \end{aligned} \tag{1}$$

The formation of the earthen wall is shown in Figure 4. The earthen wall has a deformability of up to 1/15 rad. There are two types of wall elements in this building: the pattern of the entire earthen wall from the floor to the girder, and the pattern of the hanging wall whose top of the opening is the earthen wall. These elements can be corrected for the wall length and frame height in each of the X and Y directions, and the load deformation relationship of the entire building can be determined by adding them together.

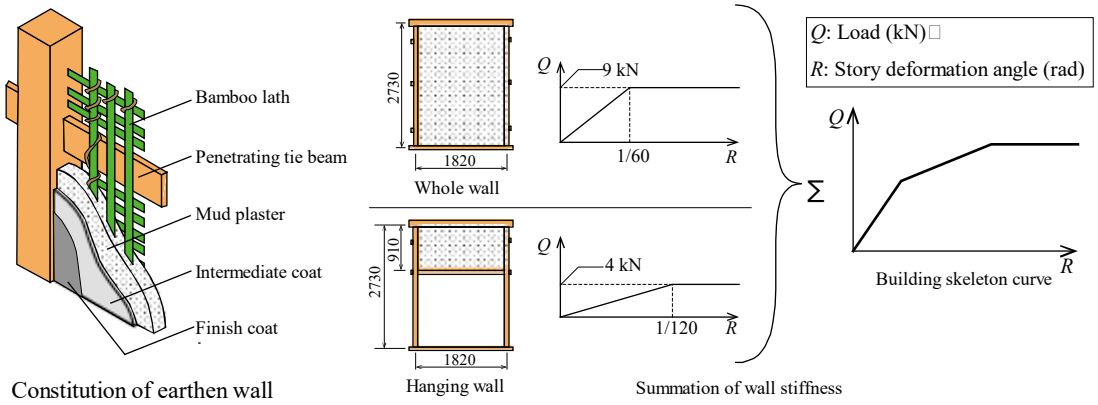


Figure 4: Mud wall constitution (left), Skelton curves of wall element and whole building (middle and right),

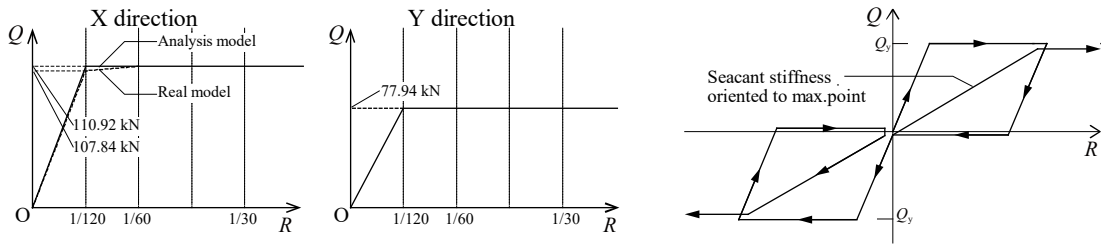


Figure 5: Skeleton curve model (left) and Hysteresis rule (right)

Figure 5 shows the skeleton curve of the entire building in the X and Y directions. Although the X direction is strictly a trilinear type, since the difference between the load values at two break points is small, analysis is performed by approximating a bilinear type. There is no hanging wall in the Y direction, which is a bilinear type. The yield shear coefficient is 0.36 in the X direction and 0.25 in the Y direction. The hysteresis law used in the dynamic analysis is a maximum deformation point-oriented slip model as shown on the right of the Figure 5. This modeling is the method recommended in Japan because the damping due to the histeresis area is relatively small and it is a safe assumption. The post-yield stiffness is the elastic stiffness multiplied by 0.01.

The mass of the CLT panel used as a damping system is expressed by the ratio α_m to the building mass. Once the mass of the CLT panel is determined, the stiffness (k_2) of the CLT can be determined by Equation (2). The CLT has 5 layers and 5 plies, a thickness (t) of 150 mm, and a specific gravity (ρ) of 0.5. The height (H_{CLT}) is 3 m. Also, the stiffness of the subsystem is smaller than that of the CLT panel itself due to the joint with the RC foundation. In the equation, the reduction rate is represented as α_k.

$$k_2 = \alpha_k \cdot k_{\max} \quad \leftarrow \quad k_{\max} = \frac{G \cdot t \cdot L}{H_{\mathrm{CLT}}}, \quad L = \frac{m_2}{\rho \cdot t \cdot H_{\mathrm{CLT}}}, \quad m_2 = \alpha_m \cdot m_1 \tag{2}$$

The damping coefficient c_d is determined as Equation (3). This is set so that the damping ratio of the main system increases by h_d, assuming that the motion of the subsystem is completely fixed ($k_2 = \infty$).

$$c_d = 2m_1 \cdot h_d \cdot \omega_1 \quad \leftarrow \quad \omega_1 = \sqrt{k_1 / m_1} \tag{3}$$

Parameters used for dynamic analysis are shown in Tables 1 and 2. The damping coefficients c_1 and c_2 are set to be 3% of proportional damping. The numerical integration method of time history response analysis is Newmark-β method ($\beta = 1/4$, $\gamma = 1/2$). Since the natural period of the CLT panel is very short, the time step Δt is set to be 1/10 or less of the period, and the time history data of the input seismic acceleration is linearly interpolated. In addition, nonlinear itelating calculation is performed by Newton-Raphoson method.

Table 1: Main system parameters

Direction	X	Y
m_1 [ton]	31.37	
H [m]	3.98	
k_1 [kN/m]	3251	2401
T_1 [s]	0.617	0.718

Table 2: Parameters of CLT panel and damper

α_m	0.04	0.08
m_2 [ton]	1.25	2.51
H_{CLT} [m]	3	
G [N/mm^2]	500	
t [m]	0.15	
ρ	0.5	
L [m]	5.58	11.15
$k_{\max}$ [kN/m]	139422	278844
α_k	0.3	
k_2 [kN/m]	41827	83653
T_2 [s]	0.034	0.034

4.2. Input ground motions and criteria

As input earthquake motions, the maximum velocity of observed seismic waves scaled to two levels is used, and it is verified whether the criteria set according to each level are satisfied. Table 3 shows seismic waves and the maximum velocity at each level. The maximum velocity is 25 cm/s at Level 1 and 50 cm/s at Level 2. Note that, for Level 2 of JMA Kobe NS, the original wave is used. Table 4 shows the criteria of response displacement for each level. Level 1 criteria are damage limit displacements, with the goal of having the response within the elastic limit. Level 2 is the safety limit displacement, which is the limit displacement for which the building can be used continuously by the restoration after the earthquake.

Table 3: Input earthquake wave and maximum velocity

Earthquake	Level 1 [cm/s]	Level 2 [cm/s]
ElCentro_NS	25	50
Taft_EW	25	50
Hachinohe_NS	25	50
Hachinohe_EW	25	50
JMA_Kobe_NS	25	96.5

Table 4: Target criteria of maximum displacement angle

Direction	X	Y
R_1 (Level1)	1/120 rad (33.2 mm below elastic strength)	
R_2 (Level2)	1/30 rad (132.7 mm)	

4.3. Analysis results

Table 5 shows the response displacement for each condition. In this building, even if the damper is not installed ($h_d = 0$), except for JMA Kobe NS, the Level 2 response is below the safe limit displacement. In the table, "**NG**" indicates not filling the criteria. However, under any other conditions, none of the criteria is satisfied. When the damping ratio of the damper is $h_d = 0.1$, the criteria can be satisfied except El Centro NS and JMA Kobe NS. Furthermore, if the damping ratio of the damper is increased to 0.22, the criteria are satisfied for Level 2 of JMA Kobe NS. However, the Level 1 response displacement of JMA Kobe NS slightly exceeds the criteria.

For the mass of CLT, there is no significant difference in response displacement. Therefore, it can be said that by providing a CLT panel wall having a mass of 4% or less with respect to the mass of a building, it is possible to obtain a practically sufficient damping effect.

Table 5: Maximum response displacement [mm]

Input information		X direction						Y direction					
Level (Criteria)	α_m	0.04			0.08			0.04			0.08		
	h_d	0.00	0.10	0.22	0.00	0.10	0.22	0.00	0.10	0.22	0.00	0.10	0.22
Level 1 (33.2 mm)	ElCentro_NS	64.9 NG	44.37 NG	31.16	64.9 NG	44.32 NG	31.07	59.38 NG	45.81 NG	33.27 NG	59.38 NG	45.74 NG	33.12
	Taft_EW	43.1 NG	25.89	21.72	43.1 NG	25.89	21.68	62.14 NG	32.40	27.65	62.14 NG	32.40	27.63
	Hachinohe_NS	35.28 NG	16.67	14.29	35.28 NG	16.70	14.36	36.08 NG	27.94	22.02	36.08 NG	27.95	22.06
	Hachinohe_EW	37.15 NG	20.55	16.17	37.15 NG	20.55	16.19	45.37 NG	31.95	22.12	45.37 NG	31.98	22.14
	JMA_Kobe_NS	48.76 NG	27.23	25.39	48.76 NG	27.24	25.40	70.01 NG	45.94 NG	34.49 NG	70.01 NG	45.98 NG	34.52 NG
Level 2 (132.7 mm)	ElCentro_NS	120.95	68.51	58.67	120.95	68.45	58.47	130.63	81.57	51.53	130.63	81.53	51.35
	Taft_EW	99.93	58.60	45.42	99.93	58.59	45.34	91.83	71.56	57.17	91.83	71.50	57.01
	Hachinohe_NS	59.56	33.33	28.58	59.56	33.39	28.73	101.94	66.50	46.51	101.94	66.53	46.62
	Hachinohe_EW	78.59	40.45	32.33	78.59	40.44	32.37	146 NG	78.49	47.06	146 NG	78.51	47.28
	JMA_Kobe_NS	198.55 NG	163.4 NG	130.92	198.55 NG	163.19 NG	130.39	205.79 NG	135.27 NG	123.58	205.79 NG	135.11 NG	123.07

Table 6 shows the internal force of the subsystem (CLT panel) for each condition, and Table X shows the damper force. Both show damper damping h_d = 0.22, the maximum value at Level 2 of JMA Kobe NS. With respect to the mass of CLT, as with the response displacement, there is no significant difference in the damper force.

Table 6: Maximum CLT shear force [kN]

Input information		X direction						Y direction					
Level (Criteria)	α_m	0.04			0.08			0.04			0.08		
	h_d	0.00	0.10	0.22	0.00	0.10	0.22	0.00	0.10	0.22	0.00	0.10	0.22
Level 1	ElCentro_NS	3.16	26.90	40.62	6.33	29.99	43.69	3.15	25.81	41.57	6.31	28.82	44.58
	Taft_EW	3.10	18.95	30.22	6.20	20.02	31.25	3.08	16.78	27.53	6.16	18.13	29.36
	Hachinohe_NS	2.09	13.22	22.79	4.19	14.20	23.71	2.09	14.08	21.92	4.18	14.77	22.58
	Hachinohe_EW	1.49	12.79	21.12	2.98	14.00	22.39	1.49	14.61	24.76	2.97	15.89	26.01
	JMA_Kobe_NS	2.66	18.57	32.35	5.33	19.67	33.43	2.66	17.48	32.31	5.32	18.77	33.24
Level 2	ElCentro_NS	6.33	51.42	81.17	12.65	56.95	87.50	6.31	42.91	77.32	12.62	47.45	82.25
	Taft_EW	6.20	31.71	53.20	12.40	36.44	57.78	6.16	32.23	55.85	12.33	36.59	60.41
	Hachinohe_NS	4.19	26.43	45.57	8.37	28.40	47.42	4.18	20.76	40.48	8.37	22.14	41.72
	Hachinohe_EW	2.98	26.13	42.23	5.96	28.66	44.79	2.97	26.05	46.36	5.94	28.08	48.64
	JMA_Kobe_NS	10.28	79.48	**135.56 D**	20.57	86.62	**144.09**	10.27	62.08	**120.54 D**	20.53	68.75	**127.27**

Table 7: Maximum damper force [kN]

Input information		X direction						Y direction					
Level (Criteria)	α_m	0.04			0.08			0.04			0.08		
	h_d	0.00	0.10	0.22	0.00	0.10	0.22	0.00	0.10	0.22	0.00	0.10	0.22
Level 1	ElCentro_NS	0.00	23.83	37.55	0.00	23.83	37.58	0.00	23.04	38.67	0.00	23.04	38.65
	Taft_EW	0.00	17.90	29.12	0.00	17.91	29.07	0.00	16.24	26.82	0.00	16.23	26.75
	Hachinohe_NS	0.00	12.47	21.95	0.00	12.47	21.92	0.00	13.46	21.34	0.00	13.47	21.36
	Hachinohe_EW	0.00	11.73	19.86	0.00	11.72	19.90	0.00	13.37	23.56	0.00	13.39	23.63
	JMA_Kobe_NS	0.00	17.47	31.22	0.00	17.47	31.22	0.00	16.63	31.37	0.00	16.63	31.35
Level 2	ElCentro_NS	0.00	46.31	74.89	0.00	46.31	74.91	0.00	39.36	72.57	0.00	39.38	72.48
	Taft_EW	0.00	27.08	50.28	0.00	27.08	50.24	0.00	28.35	51.43	0.00	28.35	51.37
	Hachinohe_NS	0.00	24.94	43.90	0.00	24.94	43.85	0.00	20.02	39.51	0.00	20.01	39.42
	Hachinohe_EW	0.00	23.63	39.72	0.00	23.65	39.79	0.00	24.48	44.13	0.00	24.47	44.12
	JMA_Kobe_NS	0.00	74.12	**127.50**	0.00	74.08	**127.35**	0.00	58.05	**114.70**	0.00	58.01	**114.45**

Figure 6 shows the time history of the response acceleration and response displacement in the X direction when excited by JMA Kobe NS (Level 2). The damper h_d = 0.22. By installing a damper, the displacement of the main system is reduced, but the response acceleration is increased. Figure 7 shows the hysteresis of each system under the same conditions. The rigidity of the CLT panel is very large compared to the building (the left of Figure 7). In addition, the load on the damper is about the same as the load on the main system (the right of Figure 7).

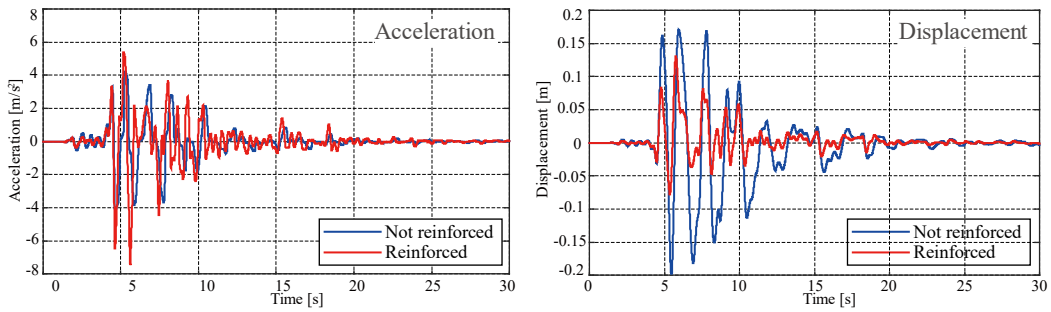


Figure 6: Response time histories when excited by JMA Kobe NS, Level 2

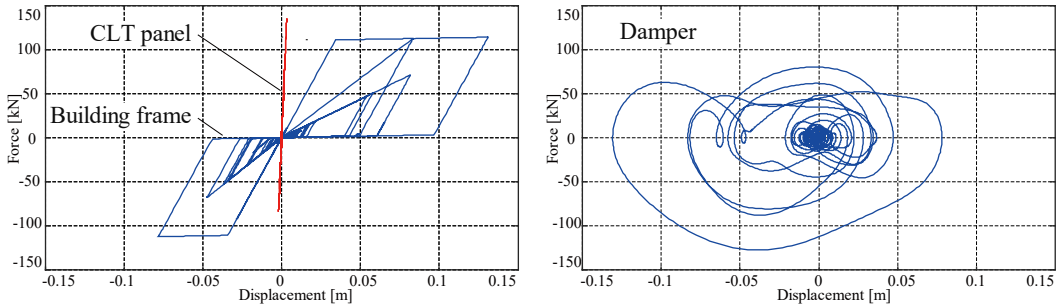


Figure 7: Hysteresis curves when excited by JMA Kobe NS, Level 2

5. Design example of CLT damping system

A design example of a CLT panel and each joint is shown in Figure 8 using the response values obtained in the previous section. In the design example, the weight of the CLT panel is 4%. The CLT panel is 5.58 m in length as shown in Table 2. In the placement of the CLT panel, the longitudinal direction (X direction) is one surface at the center of the plan and the short direction (Y direction) is divided into two surfaces. The joints between the CLT panel and the foundation are designed to exceed the load values labeled "**D**" in Table 6. However, since the CLT panel is divided into two surfaces in the Y direction, the load value per surface is half thereof.

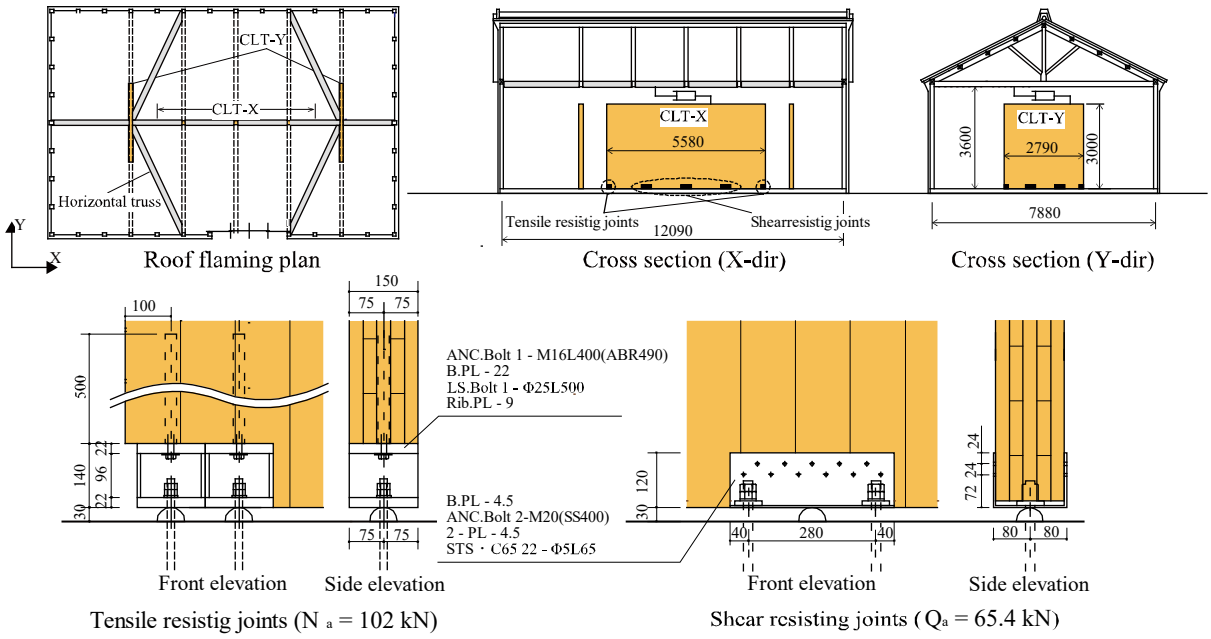


Figure 8: Design example of CLT damping reinforcement system

For anchor bolts that resist the withdrawal force at both ends of the panel, calculate the necessary strength from the damper force (X direction = 127.50 kN, Y direction = 114.70 kN) acting on the top of the CLT panel. In addition, the shear resistant hardware provided in the middle of the panel is designed to exceed the burden shear force of the CLT panel (X direction = 135.56 kN, Y direction = 120.54 kN). The joint metal part shown in Figure 8 is one using an off-the-shelf product. In addition, load transfer between the damper and the building structure is enabled by adding a horizontal truss that connects the lower chords of the kingpost truss.

For the above joints, calculate the stiffness k_2 of the subsystem (CLT panel) by Equation (4). Each parameter of the CLT panel are the values shown in Table 2. The rigidity of the joint is set to 20 kN/mm per a joint.

$$\alpha_k = \frac{k_2}{k_{\max}} \quad \leftarrow \quad k_2 = \left\{ \frac{1}{n \cdot k_s} + \frac{1}{k_{\max}} \right\}^{-1} \tag{4}$$

By this way, α_k yields 0.301 in X direction (n = 3), and 0.365 in Y direction (n = 4). In the dynamic analysis, α_k is set to 0.3, and the above-mentioned joint exceeds that value. As the CLT panel is stiffer in this system, higher damping effect can be obtained, so it is desirable that α_k be as large as possible. Therefore, this design example guarantees that the result of the dynamic analysis is satisfied. In addition, it is a system that can be constructed sufficiently.

6. Conclusions

We proposed a system for damping reinforcement of traditional wooden houses using CLT panel. We applied this system as a model of a real building and showed that we could see a practical enough vibration damping effect through seismic response analysis.

Further, CLT panel is sufficient at 4% or less of the mass of the building mass, and even for stress occurring in the junction, it is possible to correspond by using the joint hardware of the general ready-made products.

Acknowledgements

This research is inspired by a joint research on CLT with Santo Kogyo Co., Ltd. This work is supported by the Grant-in-Aid from the public interest foundation of UNION Foundation for Ergodesign Culture (2019). And we express gratitude to the building owner: Machiya Club for kindly providing the building information.

References

[1] Published by Japan Housing and Wood Technology Center, *CLT kanren kokuji tou kaisetsu-sho* [*A commentary on CLT related notices, etc.*], 2016, ISBN: 978-4-907094-34-8 (in Japanese)

[2] Published by Japan Housing and Wood Technology Center, *CLT wo mochiita kenchikukubutsu no sekkei-sekou manual* [*Manual on design and construction for buildings using CLT*], 2016, ISBN: 978-4-907094-35-5 (in Japanese)

[3] Edited by Mokuzou-jikugumi-kouhou-tatemono no taishin-sekkei-manual henshu iinkai [The committee for edition of manual on seismic design of wooden frame constructed building], *Dentou-kouhou wo ikasu mokuzou-taishin-sekkei manual* [*Manual on Wooden seismic design utilizing traditional construction method*], 2008, ISBN:978-4-7615-4075-3 (in Japanese)

Proceedings of the IASS Annual Symposium 2019 – Structural Membranes 2019
Form and Force
7 – 10 October 2019, Barcelona, Spain
C. Lázaro, K.-U. Bletzinger, E. Oñate (eds.)

Design and Fabrication of a Timber Tower Structure through the reinterpretation of Interlocking Joints

Hua CHAI, Dario MARINO [a], Edmund SO, Philip F. YUAN *

* Tongji University
1239 Siping Rd, Shanghai
Philipyuan007@tongji.edu.cn

[a] University of Pavia
via Ferrata 3, 27100 Pavia
salvatoredario.marino@unipv.it

Abstract

Interlocking joints have been a diffused connection technique in many cultures. Nevertheless, throughout time, much of the knowledge behind these methods was put aside for new materials and for the serial production logic. While cutting-edge design and fabrication technologies have strongly promoted the innovation of modern timber architecture, they also contributed to the re-examining of tradition wood tectonics like interlocking joints. By placing traditional interlocking joints, half lap joint as an example, under the technical background of digital design and robotic fabrication, this research explores an approach of innovative timber tower structure design through the analysis and reinterpretation of half lap joints. The initial phase focused on the analytical study of half lap joints which provided structural pinciples for further design; a second step was to define innovative prototypes by exploiting the structural principles as generative factors, and optimize the prototypes through structural simulation and experiments; then the third phase try to make innovative tower structural design based on the prototypes and optimize the component size through FEM simulation; the last phase regarded the robotic translation of wood crafts through the processing of the components. The final result is presented as a timber tower structure with a height of over 9 meters. All components of the structure are connected with interlocking joints without using any additional connectors or glue.

Keywords: timber spatial structure, digital design, robotic fabrication, optimization, interlocking joints

1. Introduction

Interlocking joints have been an essential part of traditional wood tectonics especially in oriental cultures. The advantages of interlocking joints in structural performance, seismic performance, sustainability, etc. have been widely proven and recognized. Nevertheless, they have been put aside for more standardized materials and joints during the industrialization period. While the wave of mass-customization approach is characterizing our contemporary socio-economic context, a renewed interest in highly customized interlocking joints is emerging with the aid of digital design and fabrication technology.

While interlocking joints such as finger joints have been investigated by researchers from ICD of Stuttgart [1] and the IBOIS laboratory of Lausanne [2] to infrom innovative shell structures, the morphogenetic capacity of interlocking joints in timber frame structure, in the way they have been used in traditional Chinese wood architecture, have seldom been noticed. Practices for example the GC Prostho Museum Research Centre designed by Kengo Kuma [3] and Japanese Pavilion in 2015 Milan Expo[4], have demonstrated the potential of interlocking joints in spatial frame structure,

Copyright © 2019 by Hua CHAI, Dario MARINO, Edmund SO, Philip F. YUAN
Published by the International Association for Shell and Spatial Structures (IASS) with permission.

although in a standardized way. Instead of standardization, digital design and fabrication techniques could deepen interlocking joints research into more flexible and complex applications.

Taking half lap joint as an example, this paper presents an approach of innovative timber tower structure design through the integration of structure analysis, digital design and robtoic fabrication.

2. Half lap joint

2.1. Geometry

Half lap joint constitutes one of the most basic joint types. A half lap joint is conventionally formed by two intersection elements on the same plane. By removing half the thickness of each component on opposite side, the rest materials at the intersection are able to fit into each other on the original plane. Follow the same principle, lap joints can also be used to handle the intersection of three or more elements, with each component, with each member retaining 1/n of the thickness (n refers to the number of intersecting elements). (Figure 1)

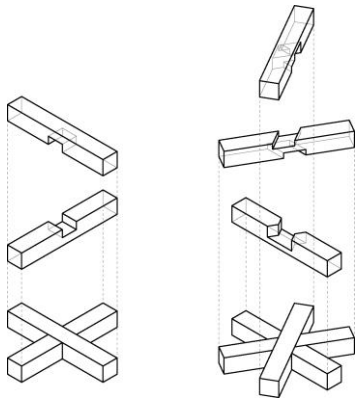


Figure 1 lap joint formed by two(left) and three (three)components.

2.2 Structure analysis

The strength of the joints doesn't lay in the strength of the individual, but in the combination of each other and the mutual support. Therefore, although each interlocking component is cut thinner, it can withstand tremendous pressure as a whole. Half lap joint can offer resistance to displacement, and also to twisting and shearing to some extent. When placed horizontally and supported at the joint, half lap joints can create a cantilever as it has always appeared on the top of columns and in DouGong of traditional Chinese architecture (Figure 2). When placed vertically and supported at one end of each element, the strength and deformation of the joint largely depend on the angle of the two intersecting elements. When the angle in-between is smaller than 90°, the contact pressure will also act on the thin material of the acute angle, causing large deformation.(Figure 3)

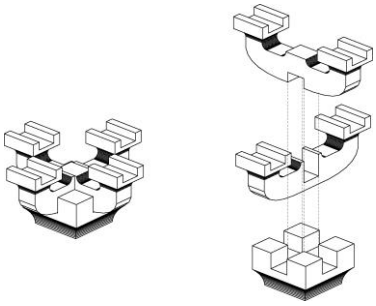


Figure 2 a typical DouGong copomemt of traditional Chinese wood architecture

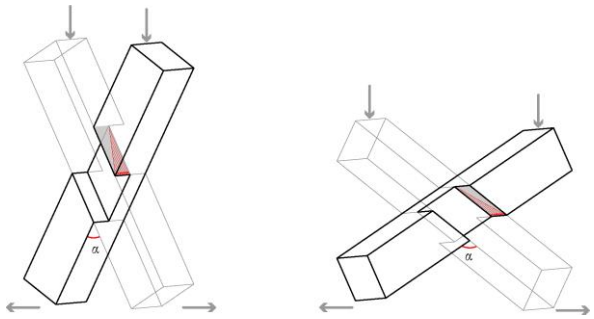


Figure 3 Comparison of position and magnitude of pressure under different angles

2.3 Assembly logic

A key factor in interlocking structure design is the order of the elements. There are always two possibilities for the lap sequence at each joint, and the order of each member depends on which side of the material is removed. Different order could result in quite different structure system. While traditional Chinese DouGong represents a lap sequence from bottom up, the reciprocal structure is characterized by the mutual support of wood components (Figure 4). There is a risk of slip and fall off in unfastened overlapped joints. Therefore, the lap sequence of each joint, which always have two options, plays an important role in overall structural stability.

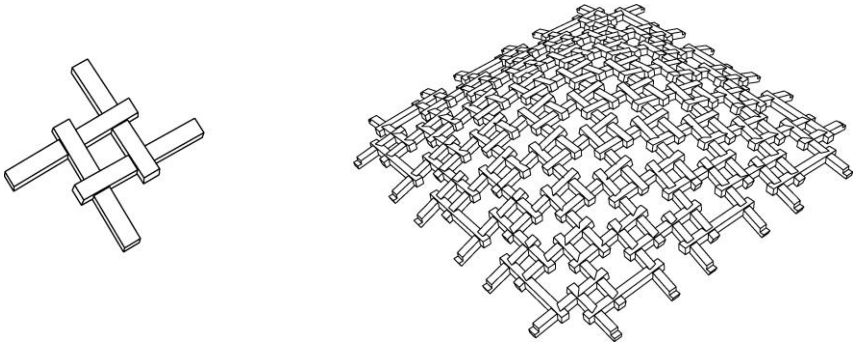


Figure 4 reciprocal structure system that depend on the mutual support through lap joints

3. Prototype design

3.1 Geometry

The interlocking wood joints technique inspired a structural layout which strongly dependent on the overlapping sequence between the members. A large part of the efforts was concentrated in the definition of the components relationships to ensure the overall structure stability, and no rods will fall off during and after the installation process. Taking into account the final structural design, the prototype is also required to be able to be applied to almost any set of surfaces with very limited adjustments to do.

Prototype design begins with a crossing structure. One of the bars into two is dividing at the joints and moving on another bar in opposite directions. In this way , the stablity of the unit is enhanced through increasing the joint that is subjected to bending moments to two, while the flexiblity of the unit is improved when adapting to a given surfaves. Two plannar units are connected with a diagonal member to form a spatial prototye (Figure 5).

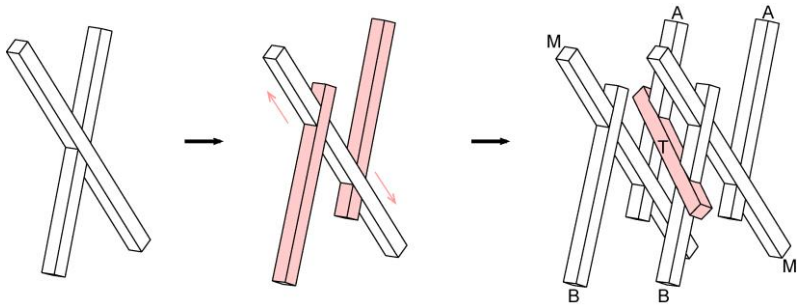


Figure 5 prototype design proess

Four types of member have been identified in the prototype definition: the main member (M) is the diagonal; on the same vertical plane lie the sub-main members (sub-A and sub-B); the last member it a transversal element (T) which goes from the center of the sub-B of one cell to the center of the sub-A of the adjacent cell.

3.2 Assembly sequence design

This organization of the members guarantees the horizontal continuity of the connection through the T components, while the vertical one is solved by the main (M) with the sub-main A (for the upper layer link) and with the sub-main B (for the lower layer link). Every component intersects with two to four other components, moreover the notches orientation of every component always be designed according to the installation order , in order to make sure every component is supported and make possible the construction. For example, there are three notches on the B components, the first and third norch could prevent the element from moving vertically, while the middle one that is connected to T component serves as stabilizer for the horizontal movements.(Figure 6)

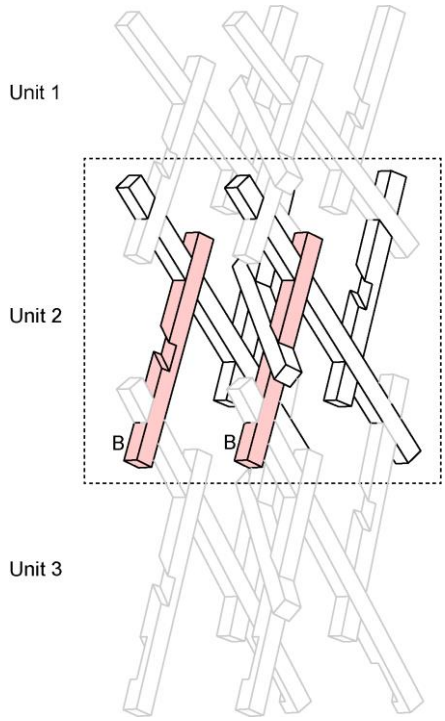


Figure 6 the relationship of different units

4. Timber Tower Structure

4.1 Structure design and optimization

Once the prototype of spatial structure is defined, the prototype was applied to the pre-designed master surface in Rhino-Grasshopper environment (Figure 7). The algorithm was developed in Grasshopper so that the prototype could be parametrized to optimize the layout differentiating according to local requirements. Structural model was built with Karamba to simulate and optimize the structural layout, mainly the member's length and sections. In this process, the geometrical description was parametrized which allow the automatic generation of joint geometry. The load condition is set as pure self-weight. A gradient of diminishing sections was defined starting from 120x120mm section till 30x30mm section according to the simulation result. Within the same layer all the members have the same section size, while the different sections between the layers can be easily accommodated through the interlocking joints.The final structure design is composed by 11 layers which height varies from 1.8m to 0.4m with a final number of 840 members.

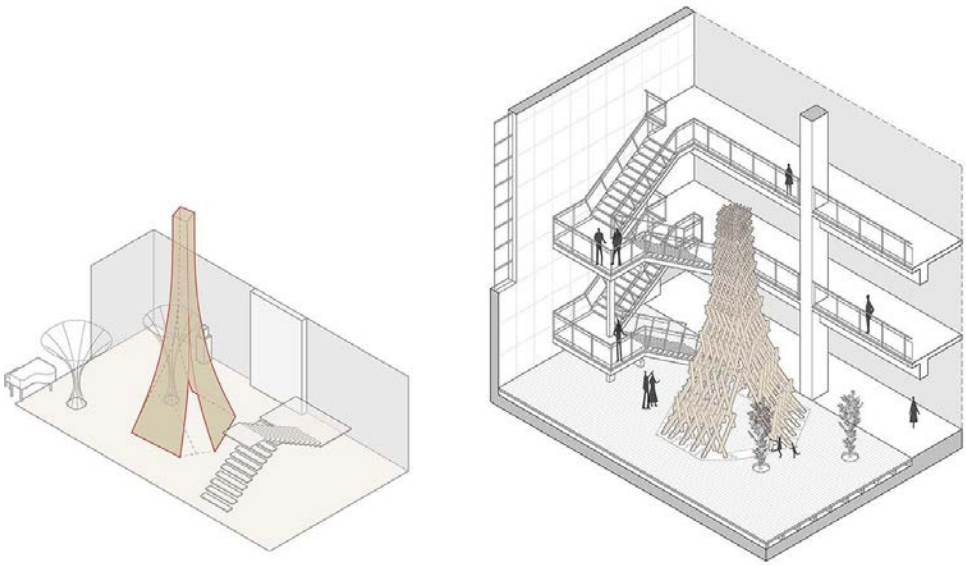


Figure 7 the tower structure design guided by the master surface

4.2 Robotic fabrication

The implementation of interlocking joints was tested in this project through the robotic milling of all the cuts. In traditional structures the joints are characterized by regular angles easy to measure. On the other hand, when the member crossings are differentiated on the whole geometry to accommodate structural optimization, the variations between the angles of the interlocking cuts can be very small and extremely time consuming if crafted by hand. Still, an industrialized production method, which might satisfy the required precision, does not fit well a production were all components to be milled are different. Therefore, robotic milling was a suitable fabrication technique able to address all the difficulties, giving the opportunity to exploit the advantages of nail free connections. The laboratory was set up with two robots a Kuka KR60 and a Kuka KR120 on a rail. A support platform for each robot was prepared and calibrated to fit the timber members of different lengths leaving one movable support. The same setup was created in the digital environment.

Here every beam was correctly placed, the cuts were programmed, and the simulation of the fabrication was run to check the accuracy. The robots mounted milling tools with a diameter of 50mm

which have been used for all the timber members except the smallest ones with a section of 30mm where the tool was changed to a 30mm diameter (Figure 8). In the physical environment every timber element was placed on the platform and clamped to the support. The programming and milling of all the 840 bars containing in total 2592 cuts was completed in two weeks.



Figure 8 robotic fabrication process

4.3 Assembly

The final structure, with a total height of 9m, was directly assembled on site (Figure 10Figure 9). The construction took place in the hall of a CAUP building at Tongji University Shanghai during the workshop "DigitalFUTUREs Shanghai 2018". A steel plate foundation 6mm thick, fabricated through laser cutting, was first assembled to allow a balanced weight distribution on the wooden floor of the building hall. The ring of the foundation also had steel plates ears, welded on the base, that firmly constrained all the 36 support points on the ground preventing any displacement. The construction process was carried on by four regular workers and one designer, through manual assembly and hammering on the interlocking joints. Once the first layer on the ground was completed, the scaffoldings were added along the external perimeter of the tower; for the subsequent layers they were built gradually following the construction. The construction was completed in about three days without using any nail, screw or glue, and it proved to be safe and resistant (Figure 9).



Figure 9 the on-site assembly process



Figure 10 the timber tower structure

5. Conclusion

This paper presented the design and fabrication process of a full-scale timber tower structure based on an analysis and reinterpretation of traditional interlocking joint,half lap joint. The joint geometry is analyzed to inform the new structure design. A prototype for spatial frame grid structure is then formulated and tested in the tower structure. this research shows how the reinterpretation of traditional wood tectonics with digital technology could open up new possibilities for wood design without losing their advantages.

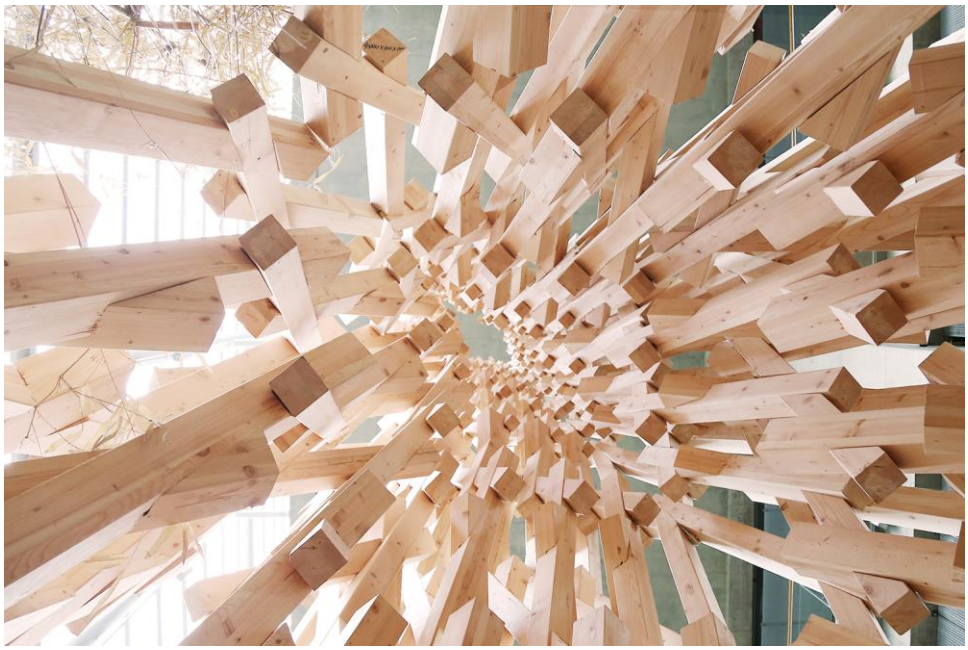


Figure 11 Looking up from the inside

Acknowledgements

This research is funded by National Natural Science Foundation of China (Grant No.51578378), National Key R&D Program of China(Grant No.2016YFC0702104), Sino-German Center (Grant No.GZ1162), and Shanghai Science and Technology Committee (Grant No.16dz1206502, Grant No.16dz2250500, Grant No.17dz1203405).

References

[1] Menges, Achim. Integrative design computation: *Integrating material behaviour and robotic manufacturing processes in computational design for performative wood constructions*. In Proceedings of the 31st Annual Conference of the Association for Computer Aided Design in Architecture, ACADIA 2011, 2011,pp. 72-81.

[2] Robeller, C. and Weinand, Y. *Fabrication-aware design of timber folded plate shells with double through tenon joints*. In Robotic Fabrication in Architecture, Art and Design 2016. Springer, Cham. 2016.pp.66-177

[3] Carpo, Mario. *Particlised: Computational Discretism, or The Rise of the Digital Discrete*. Architectural Design 89.2. 2019.pp. 86-93.

[4] Kitagawara A, Imperadori M, Kuwabara R, Brunone F, Matsukawa M. Wooden Byobu. F*rom Architectural Façade to Sculpture*. In Digital Wood Design 2019. Springer, Cham. pp. 1287-1315

Proceedings of the IASS Annual Symposium 2019 – Structural Membranes 2019
Form and Force
7 – 10 October 2019, Barcelona, Spain
C. Lázaro, K.-U. Bletzinger, E. Oñate (eds.)

Experimental study of truss using CLT (Cross Laminated Timber) for lower chord

Shuji TADA*

* Chiba Institute of Technology university
2-17-1,Tsudanuma,Narashino,Chiba 275-0016,JAPAN
shu-ta@da2.so-net.ne.jp

Abstract

CLT（Cross Laminated Timber）, which contributes to proactive utilization of forest resources in Japan, is drawing attention not only in Japan but also globally as a material that will revitalize the Japanese architectural industry and give new possibilities unprecedented. The feature (characteristic) of CLT is that a large plate of 3 m × 12 m can be made, and if it is within the length that can be manufactured, a space without pillars is possible by a simple joining method. In other words, it is possible to apply to a roof and floor of 12 m span without a joint. Then, how do you deal with it if you need more span? We propose a system that composites CLT and truss , in order to enable further long span and to change direction of force transmission with respect to vertical load from one direction to two directions. In this proposal, it is also possible to design the CLT cross section to be thin. Furthermore, by adopting a three-dimensional configuration, it is also possible to develop it into a radiation type truss having a shell effect. In this system, the joining method between CLTs is important. Since CLT is used for lower chord of truss, we propose joining method which can correspond to tensile joining hardware, and grasp the Mechanical performance by applying Tensile test. We carry out full scale model experiment CLT truss and then grasp the mechanical characteristics from experiment result. Finally, consider the consistency of the experimental result and the analysis model.

Keywords: CLT (Cross Laminated Timber), truss, Composite structure system

1 Introduction

CLT, has received worldwide attention as a material which contributes to effective use of forest resources, and its feature is that a large version of up to 12m x 3m can be manufactured (Fig. 1).

Copyright © 2019 by Shuji TADA
Published by the International Association for Shell and Spatial Structures (IASS) with permission.




Figure 1: Construction site and CLT manufacturing scene

In this research, we propose a structural system using CLT for the lower chord of the truss, and aim at pursing the possibility of a pillar-free space with a span of 12 m or more (Fig. 2).

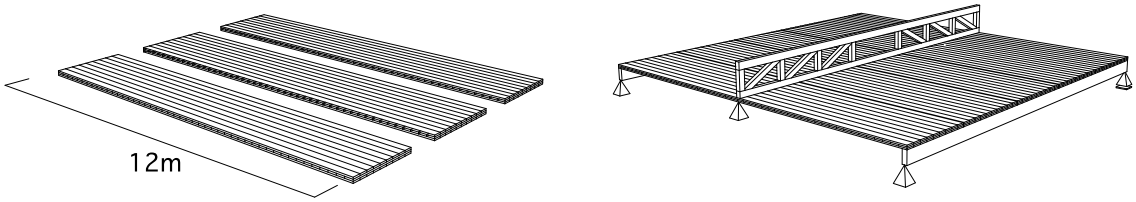


Figure 2: Conceptural diagram (truss using CLT for lower chord)

In addition, this system can be developed from a planar configuration to a radial truss with a three-dimensional shell effect (Fig. 3).
In this paper, we present a proposal and experimental results on joining method of CLT, and report on a full-scale experiment of truss using CLT.

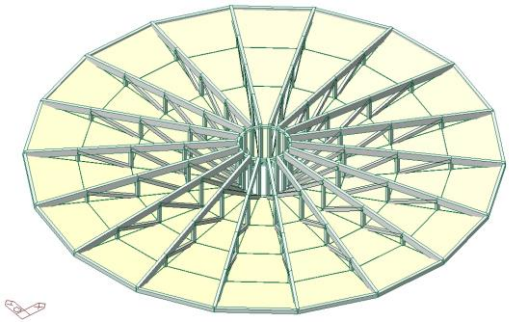


Figure 3: Radiation type truss



Figure 4: Experiment model

2 Tensile strength test of CLT joint part

2.1 Experimental purpose

Joint design is important not just for this system but for any wooden constructions.
Also, the feature of this system is stress transfer in the direction of the weak axis of CLT.
We propose two types, namely the bolted joint and the screwed joint, as the joining method of the joint part of the CLT panel (Fig. 5).
The bolted joint is a general joining method in which stress is transfered between CLTs by compressive

force (in consideration of partial compression), and high resistance can be expected.
On the other hand, screwed joint is an inexpensive and easy joining method that does not require special processing.
Tensile tests of the two joining methods of above proposal are performed in order to evaluate each mechanical performance and to reflect the evaluation result to the joint of CLT truss.
In the measurement method of force application, a universal tester was used for all the test specimens (Fig. 6).



Figure 5: test specimen

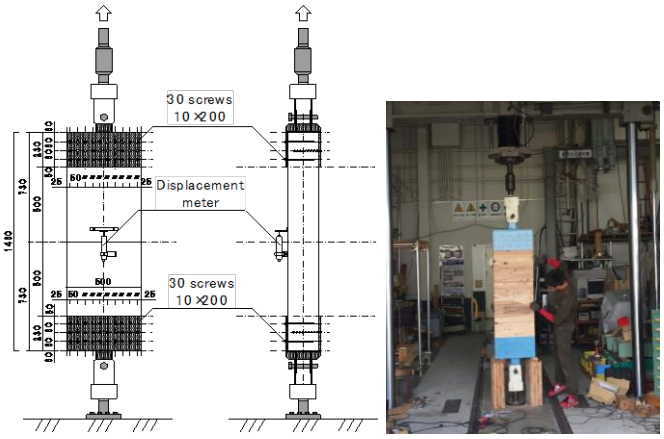
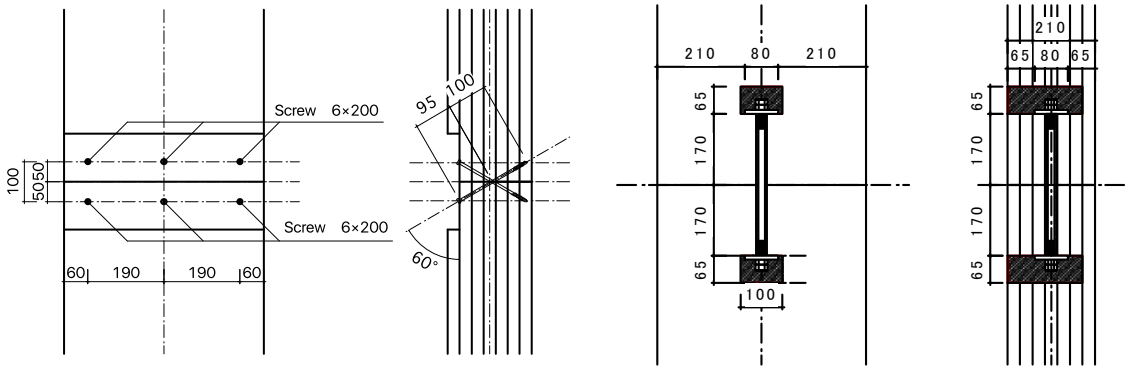


Figure 6: outline of force measurement

2.2 The outline of the specimen



Summary of screw connection S-1~S-3 Summary of bolt connection B-1~B-3

Figure 7: Outline of the test specimen

Three test specimens with screw joints, S-1, S-2 and S-3, and three specimens with bolt joints, B-1, B-2 and B-3, a total of 6 specimens were prepared.
In the joint parts of S-1~S-3, a total of six screws with diameter of φ6 (L = 200 mm) are obliquely drived at 3 points on the each side of top and bottom.
The B-1 ~ B-3 are joined by means of compression resistance from drawing bolt (tightening bolt).
In the joint parts, bolts M16 (L = 400) are used.
After passing the bolt in a tip hole φ25 for a bolt which is bored in 6 × 100 mm engraved box, a square washer is arranged and connection by bolting is performed. (Fig. 7).

2.3 Experimental result

Table 1 and Table 2 show the stiffness and strength obtained from the experiment.

Table 1: Stiffness and load resistance table for six screws

Screw	s-1	s-2	s-3	Average	standard deviation	Coefficient of variation	dispersion coefficient	5% lower limit (Short-term)	Long-term allowable strength
Initial stiffness：K(kN/mm)	8.31	17.63	4.63	10.19	5.47				
Ultimate strength：Pu(kN)	18.28	9.90	13.75	13.97	3.43				
Ultimate displacement：δu(mm)	25.63	38.96	31.54	32.04	5.45				
Load max：Pmax(kN)	21.31	10.88	15.48	15.89	4.27	0.27	0.15	1.63	0.89
Displacement max：Dmax(mm)	12.35	29.46	22.38	21.40	7.02				
Yield strength：Py(kN)	11.62	7.22	11.44	10.09	2.03	0.20	0.37	3.69	
Yield displacement：δy(mm)	1.40	0.41	2.47	1.43	0.84				
Plasticity factor：μ	11.65	69.43	10.63	30.57	27.48				
Structural characteristic coefficient：Ds	0.21	0.09	0.22	0.17	0.06				

Table 2:Stiffness and load resistance table for one bolt

Bolt	b-1	b-2	b-3	Average	standard deviation	Coefficient of variation	dispersion coefficient	5% lower limit (Short-term)	Long-term allowable strength
Initial stiffness：K(kN/mm)	12.03	22.06	20.47	18.19	4.40				
Ultimate strength：Pu(kN)	63.09	60.86	61.08	61.68	1.00				
Ultimate displacement：δu(mm)	20.96	34.02	32.78	29.26	5.89				
Load max：Pmax(kN)	64.35	65.67	66.06	65.36	0.73	0.01	0.96	42.04	
Displacement max：Dmax(mm)	20.76	28.10	27.74	25.53	3.38				
Yield strength：Py(kN)	49.51	45.55	43.43	46.16	2.52	0.05	0.83	38.22	21.02
Yield displacement：δy(mm)	4.12	2.06	2.12	2.77	0.95				
Plasticity factor：μ	4.00	12.33	10.99	9.11	3.65				
Structural characteristic coefficient：Ds	0.38	0.21	0.22	0.27	0.08				

2.4 Destruction mechanism

As for the destruction mechanism of the screw, breakage or pulling out of the screw was confirmed (Fig. 8). The bolted joint should be subjected to a tensile test to the bolt's breaking point.
However, in the case of the B-1 using single nut, the screw thread was moved so as to crush on the way. Therefore, single nut was changed to double nut in B-2 and B-3, and then the fracture result of the bolt base material was obtained (Fig. 9).



Figure 8:destruction mechanism of screw



Figure 9: destruction mechanism of bolt

2.5 Calculation result of strength and stiffness

In the case of screwed joint, the variation in the ultimate strength was confirmed from the load-displacement curve of the experimental values (Fig. 10). In the case of bolted joint, the stiffness was confirmed to be stable and moreover B-2 and B-3 using double nuts showed stable ultimate strength even after plasticity (Fig. 11).

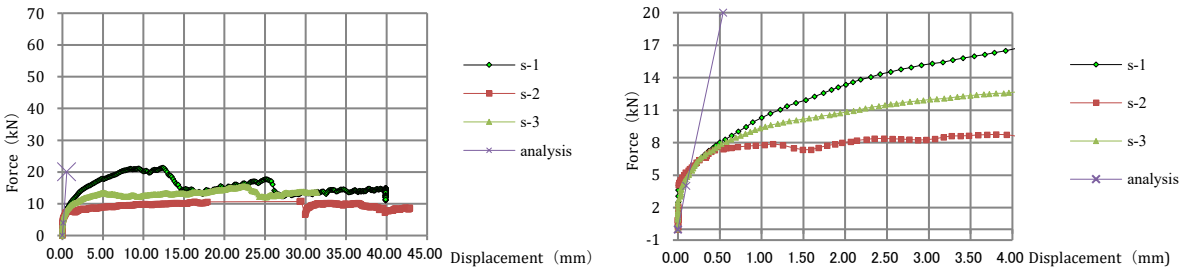


Figure 10: Load-displacement curve of screw joint

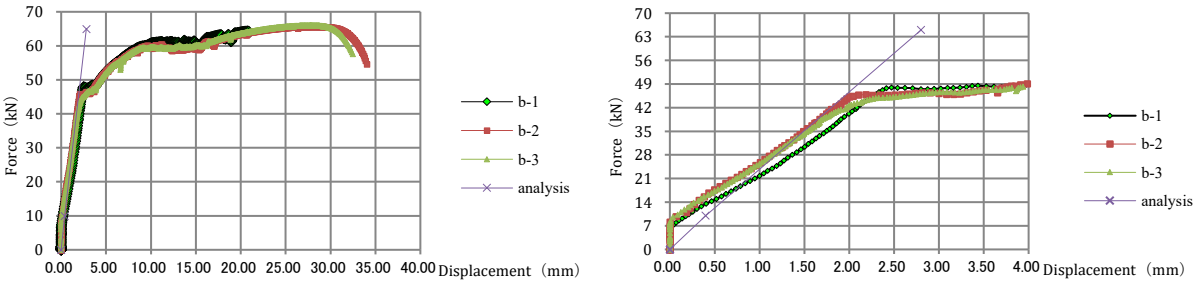


Figure 11: Load-displacement curve of bolt joint

2.6 Analysis study

Analysis was conducted with a model that takes into account the stiffness of the joint.
As for the stiffness of the joint place, stiffness of the bolt taking into consideration of partial compression is calculated. The stiffness of screw was calculated similarly.
As for initial stiffness, both screw and bolt joints exhibit characteristic almost consistent with the experimental values.
As for secondary gradient after yielding, however, screw joint requires further study, while bolt joint seems good enough to be evalutated as complete elasto-plasticity (Fig. 10, 11).

2.7 Conclusion of joint experiment

1) In the case of screw joints, variations in both stiffness and strength were confirmed. Therefore, it may be necessary to re-examine the result of repeated experiment with more test specimens (Table 1).
2) Pull bolt type joints provided relatively stable stiffness and strength. Also, the effectiveness of the double nut was confirmed (Table 2).

3) The effectiveness of the bonding method and stress transfer to the weak axis direction of CLT was confirmed.

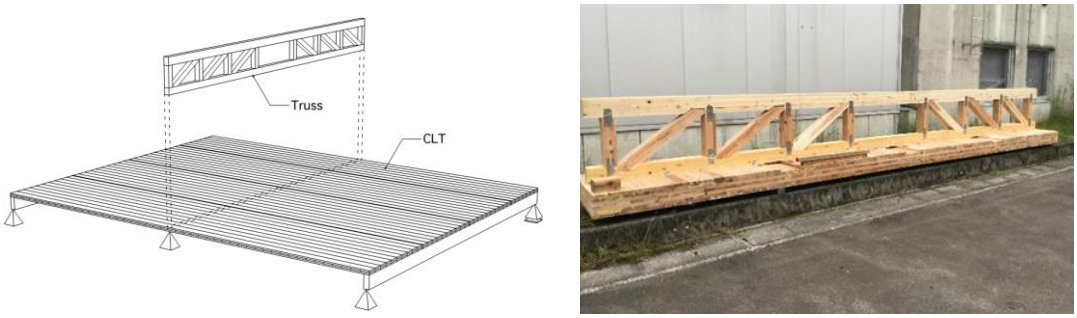


Figure 12: Full scale model of truss using CLT

3. Full scale model experiment

We propose a structural system using CLT for the lower chord of truss and carry out a full scale model experiment which is aimed at grasping the effectiveness and mechanical performance of this system. This system will make it possible to disperse the flow of force in one direction, generated in CLT against vertical load, into two directions
For this purpose, it is important to verify stress transfer in the weak axis direction (Fig. 12).

3.1. Outline of the full scale model

Two test specimens are used, the truss of the specimens is consisted by the upper chord of 120 x 180 mm, and the diagonal bracing and strut of 120 x 120 mm.
At the joint part of strut, 2 sheets of plate hardware each on top and bottom, a total of 4 sheets are arranged (Fig. 13).
As the lower chord material, four CLTs of width 2000 mm were arranged, and in the joint part between CLTs 2 bolts of M16 (L = 400 mm) and 2 screws φ6 (L = 120 mm) were installed at each of 4 places. In consideration of the construction method, a sill of 120 × 150 mm was provided on the upper part of CLT, and their joint was formed with four hollow bolt diameters 18 (L = 200 mm) by GIR (glued in rod) and L-shaped hardware at 6 places in total. In the test specimen 2, the hardware used at the joint part of a truss was arranged twice as much as in the test body 1, and compared (Fig. 14).

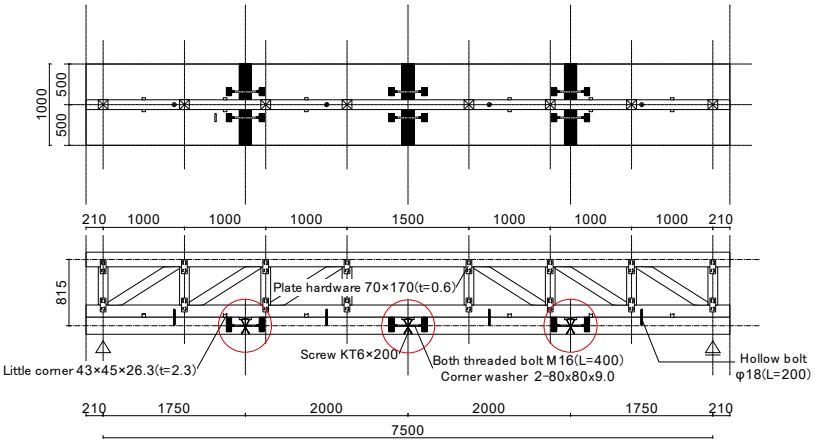


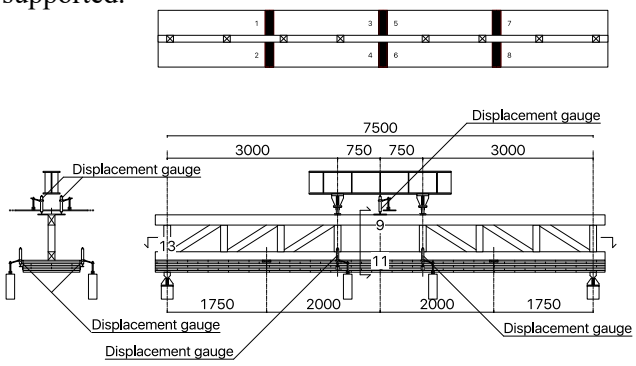
Figure 13: Outline of the full scale model



Figure 14: Member joint

3.2. Outline of force application measurement

The applied force was two-point loading by a loading tester, and both ends of the CLT were roller supported.



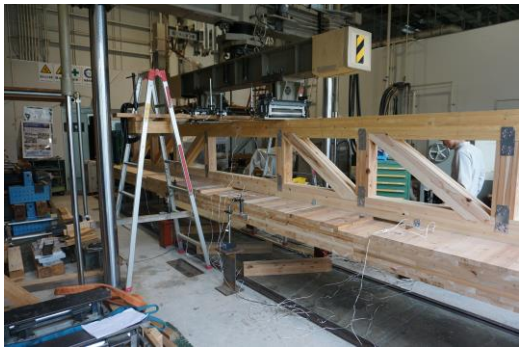


Figure 15: Outline of force application measurement

The displacement gauges are set at the two locations on both sides in the center of the upper chord, and at the two locations on each side of the A and B points in the center of the CLT, namely at six locations in total (Fig.15).

3.3. Experimental result

The experimental results are shown in the figure17 and table3.

And we conducted comparative research of experimental value and analysis value.

The analysis was conducted with the model in consideration of the stiffness of the joint part (Fig.16).

As for the stiffness of the joint portion of CLT, the experimental values were adopted for both the test specimens 1 and 2, since they were almost consistent with the calculated values in consideration of partial compression for both the bolt and the screw.

Table3: Stiffness and load resistance table

Specification	1	2	Average
Initial stiffness：K(kN/mm)	2.51	2.89	2.70
Ultimate strength：Pu(kN)	95.21	121.15	108.18
Ultimate displacement：δu(mm)	70.44	80.90	75.67
Load max：Pmax(kN)	106.61	129.42	118.02
Displacement max：Dmax(mm)	63.91	75.26	69.59
Yield strength：Py(kN)	53.58	82.54	68.06
Yield displacemen： δy(mm)	21.35	28.56	24.95
Plasticity factor：μ	1.86	1.91	1.88
Structural characteristic coefficient：Ds	0.61	0.60	0.60

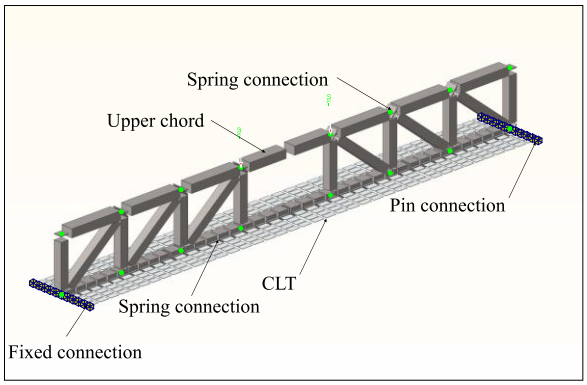


Figure 16: Analysis model

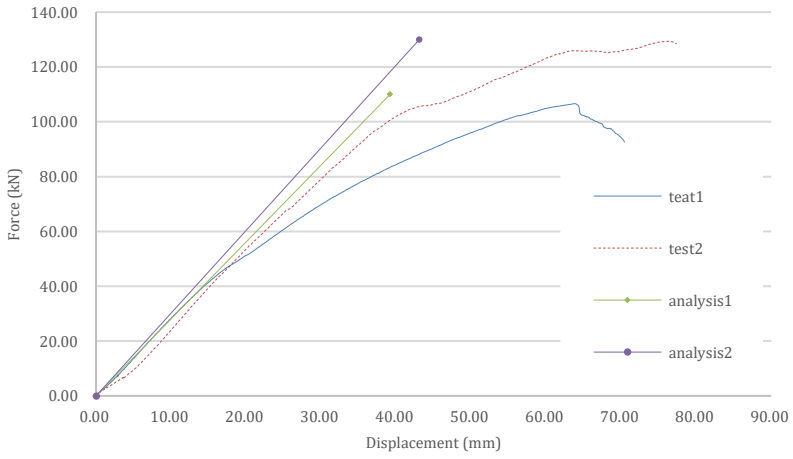


Figure 17: Load displacement curve and analysis value

Both specimens 1 and 2 showed the same behavior up to the point of 40kN applied force, but specimen 2 showed the effect of doubling the joint resistance of the truss from about 50kN and the improved ultimate strength (Fig.17). When the experimental results and the analysis results in the stage of initial stiffness are compared, consistency between the experimental results and the analysis results is confirmed for both the test specimens 1 and 2, and the validity of the modeling of the joint is obtained (Table 3).

3.4. Destructive mechanism

As for the destructive property in the test specimen 1, a split fracture occurred in the upper chord material, and separation of the lower surface of the CLT joint place were confirmed (Fig. 18).

In the test specimen 2, it was assumed that breakage would occur at the joint of CLT in first, but excessive tensile force generated in the web causes preceded destruction of the joint place on the both side of web.

It was confirmed that the screws of plate hardware at both ends of the web material dented and that cleavage destruction of the upper and lower chords occured (Figs.19).

In addition, it is thought that the sill considering workability also works effectively as a structure.



Figure 18: Destructive mechanism of test specimen 1



Figure 19: Destructive mechanism of test specimen 2

3.5 Conclusion of full-scale model experiment

The following findings were obtained from the full-scale model loading test.

1) The effectiveness of this system using CLT for the lower chord was confirmed.
2) As a method of joining CLTs in the weak axis direction, the effectiveness of the proposed joining method by bolts was confirmed.
3) For joining of truss members, general joining hardware considering workability and cost was used, but in the future, it is important to study more effective joining methods according to the required strength.
4) In the analysis study, it was confirmed that the initial stiffness characteristics obtained by evaluating the partial compression at the joint place were almost consistent with experimental values.

In the future, we can expect the development of this system into a three-dimensional model such as a radiation type, and we will investigate further.

Proceedings of the IASS Annual Symposium 2019 – Structural Membranes 2019
Form and Force
7 – 10 October 2019, Barcelona, Spain
C. Lázaro, K.-U. Bletzinger, E. Oñate (eds.)

Finansparken Bjergsted: an innovative timber-framed office building

Pablo TARIN*, Katie OVERTON, Manuel SÁNCHEZ-SOLÍS, Mario RANDO[a], Fernando IBÁÑEZ

*DEGREE OF FREEDOM, Valencia Office
Calle Colón nº18 5B, Valencia, Spain
p.tarin@dofengineers.com

[a] DEGREE OF FREEDOM, Oslo Office

Abstract

Finansparken Bjergsted is an office building currently under construction in Stavanger, Norway, for SR-Bank. The structural system above ground level uses timber as the principal load bearing elements (a natural, renewable and readily available local material). Floors are cross-laminated timber (CLT) panels supported by glued laminated timber (GL) beams and columns. For strength and complex geometrical requirements, laminated veneer lumber (LVL) made of beech is also used. The three basement levels and the four communications and services cores are of reinforced concrete. Mass timber structural elements are engineered for strength and are prefabricated with strict tolerances for a rapid construction process using mainly direct contact timber connections, without metal fasteners. The beams are shaped and fabricated with openings to suit both the architectural aesthetics and services requirements by means of a fully integrated BIM system.

Keywords: Timber connections, Glulam, LVL beech timber, CLT panels, BIM

1. Introduction

This project uses a traditional building material, timber, combined with modern design, detailing and fabrication techniques. Degree of Freedom has been involved, as part of the design team, from concept design through to construction. From competition phase through to the preliminary design phase Degree Freedom have worked in conjunction with the architects Helen & Hard and Saaha on behalf of the client/future building owner, Sparebank1. Specialist technical support for timber design and constructability has been provided by Creation Holz. For the construction phase the BIM model has been prepared for the Contractor, Veidekke, and for Moelven Limtre AS, who is the main fabricator of the timber elements.

This paper highlights why the timber is taking advantage as a structural element against the typical solutions in concrete or steel. Furthermore, it is explained the key aspects of the design:

1. Choice and use of different mass timber elements to take into account their inherent structural capabilities and to fulfil the architectural vision.
2. Fire design.
3. Use of 3D finite element modelling for timber design.
4. Timber connection design.
5. Fully integrated BIM for construction.

Copyright © 2019 by Pablo Tarín, Manuel Sánchez-Solís, Mario Rando
Published by the International Association for Shell and Spatial Structures (IASS) with permission.

2. Design principles

The geometry, materials and use of the structure have been treated as a whole to define both the inner and outer aspect of the building.

2.1. Architectural concept

The wedge shape, in both plan and elevation, creates a building that changes character and scale to the different surrounding urban landscapes. It is located in a contrasting situation between Bjergstedparken's more monumental buildings in the north, and a cluster of small, old houses in a more urban situation in the south.

The architecture is based on the game of contrasts between a clear and taut exterior and a more organic interior.

The use of timber as a natural material has a positive effect on human perceptions and experience of their surroundings and has been shown to reduce stress. It is acoustically beneficial for an open plan office space compared to more conventional construction materials.

A central atrium emphasizes the timber structure and organic feel of the interior spaces. It allows natural light into the building and connects with the exterior park.



Figure 1: Exterior views of the building [© Helen&Hard /Saaha]

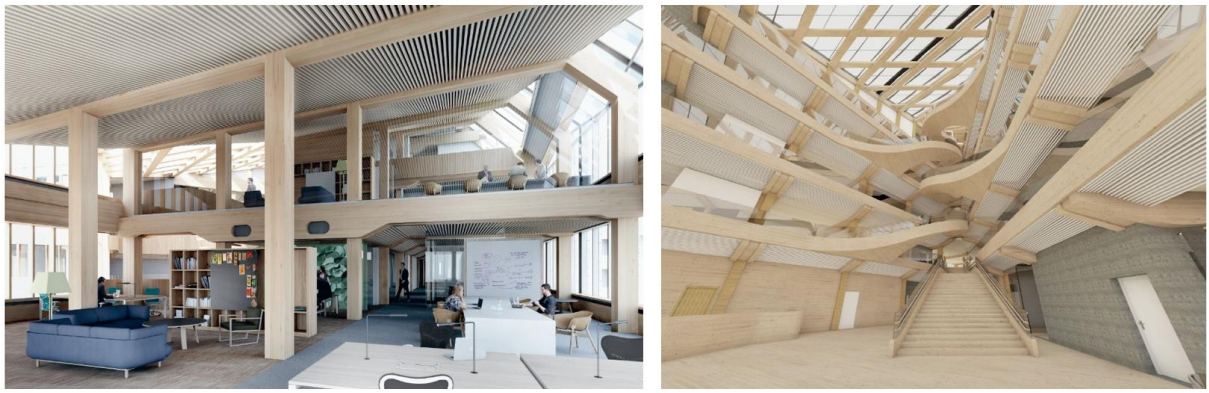


Figure 2: Interior with exposed timber structure [© Helen&Hard /Saaha]

2.2. Material selection

From the beginning, the design team was aware of the concept that timber, as a construction material, has intrinsic healthy and environmental benefits. When harvested responsibly, wood is arguably one of the best tools architects and engineers have for reducing greenhouse gas emissions and storing carbon in buildings.

Carbon cycle of timber follows a closed natural loop.

The following were important aspects for the construction material choice:

- Achieve a healthy and clean working environment
- Reduction of CO2 emissions
- Reduction of construction time and reduction of waste
- Use timber as a symbol for the Bank values
- Obtain BREEAM-NOR excellent certificate
- Aesthetics inner properties of the material
- Competitive cost

In order to come to a final decision, a selected portion of the building was economically analysed for two possible alternatives: wooden/concrete and steel/concrete structure.

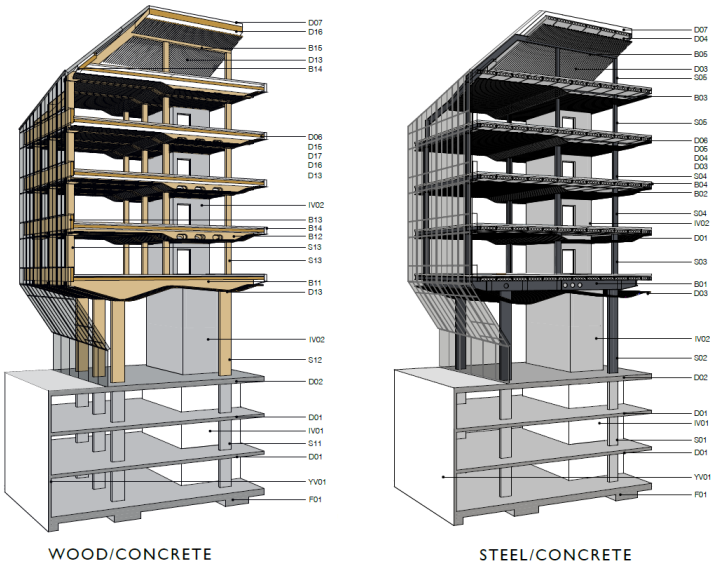


Figure 3: Alternatives evaluated

Table 1 contains the cost (NOK per square metre) for the elements concerning the main construction.

When comparing this package of costs to the whole project cost, including general costs, the difference between steel and timber is reduced to 1.4%.

As a conclusion, due to the environmental benefits and the low economic difference, the structure is finally decided to be designed in timber. Following this premise of the project, the building also includes an energy efficient and sustainable sedum roof.

Table 1: Economic comparison

	Item	Steel [kr/m^2]	Timber [kr/m^2]	Difference
2.1	Foundations	323	323	0%
2.2	Bearing system	1362	1478	+8.5%
2.3	Outer walls	2038	2038	0%
2.4	Inner walls	1201	1201	0%
2.5	Floors	3176	3373	+6.2%
2.5.1	*Slabs*	*1152*	*1489*	*+29.3%*
2.5.2	*Coating*	*764*	*764*	*0%*
2.5.3	*Ceiling*	*1260*	*1120*	*-12.5%*
2.6	Roof	117	187	+59.8%
2	**Total**	**8218**	**8600**	**+4.6%**

2.3. Structural system

The three basement levels are of reinforced concrete and from ground level four services and communication cores extend up to roof level also in reinforced concrete. These elements provide the overall lateral stability to the structure. Horizontal loads are transferred to these cores via the diaphragm action of 200mm CLT timber floor slabs. The footprint of the timber floor slabs reduces from levels 2 to 7 to follow the wedge shaped elevation. The roof construction is also a continuous 200mm CLT inclined slab.

The vertical load bearing system comprises of the CLT slabs spanning between the main floor beams located on a 5.4m structural grid. The CLT is supported by glulam beams (GL30c). At each grid two glulam beams are continuous across the width of the building bearing directly on to the notched glulam columns (GL30c). Columns are continuous from level 3 to roof level. The floor beams are divided into two, at both sides of the columns, to provide continuity and to facilitate erection. Each beam is made up of two 380mm wide beams glued together – an inner beam of constant depth formed by a glulam section and a LVL beech section and an outer glulam beam of variable depth to suit the architectural requirements. Continuity of the CLT slabs over the main beams is provided by a LVL spruce panel (Kerto Q). Figure 4 shows the slab elements where Kerto Q panels are represented in yellow.



Figure 4: Plan view and typical cross section

At level 3 a transfer structure is required to redistribute the column loads to the ground floor columns that are set back from the façade to reduce the building footprint at street level. The ground level at east side has a double height with a reduced number of columns to create a distinctive space at the entrance of the building. The columns and beams at this level are LVL beech (Baubuche S and Baubuche Q) [1].



Figure 5: Different types of structural timber used and pictures during construction process

2.3.1. Glued laminated timber

Glulam in grade GL30c is used for beams and columns above level 3. The widths of the members have been chosen to suit the standard available sizes. The variable depth beams and service openings are then cut in the factory from a rectangular section. GL30c is fabricated from spruce which the most widely available softwood. Where increased strength is needed GL70 is used which is fabricated from beech, a hardwood.



Figure 6. On site picture. GL30c timber elements

2.3.2. Laminated veneer timber

LVL is used for the beams and columns in the transfer structure between the ground floor (Level 1) and Level 3. The product used is Baubuche with 3mm thicknesses of beech parallel veneers (Baubuche S) or cross-laminated beech veneers (Baubuche Q). Baubuche Q is used for the beams at level 3 as it has a better performance for service openings due to the crossed laminations.



Figure 7. On site pictures. LVL beams and columns (left) and LVL insertions at GL beams (right)

3. Connections

Connections are realized in a number of different forms depending on the magnitude and type of forces to be transferred. The project premise is to maximize the use of timber to timber connections without steel. The design philosophy is for connections capable of transferring all the necessary forces by direct pressure between two timber elements where possible.

Timber to timber connection types include:

- Direct bearing between timber elements
- Glued panel insertions
- LVL timber dowels with Baubuche-Q inserts

Only where necessary, due to structural or erection reasons, the following types have been used (not visible):

- Self-tapping timber screws
- Proprietary timber connectors – Sherpa
- Threaded steel rods – for reinforcement at openings or notches
- Steel dowels with steel plate

Due to the high quality and the strict tolerances in the fabrication of the mass timber components the connections can be executed with a high level of precision and safety.



Figure 8. Direct timber connection (left) and LVL beech dowel and timber cut-outs (right)

4. Fire design

Well defined and predicable fire behaviour is an intrinsic property of mass timber elements and all the principal structural elements are designed to guarantee a fire bearing resistance of 90 minutes.

Timber columns and beams have been designed using the reduced cross section method from NS EN1995-1-2 [2]. This method defines a charring depth, which for this project is 70mm. This char layer insulates the core of the section preventing it heating up. This reduced section maintains its full strength and can be verified for the critical fire load combination.

All the connections are internal and protected in case of fire.

5. Finite element modelling

The structural model is created from the BIM model exporting the frame elements at the desired position.

5.1. Description of the FE model

The timber is an orthotropic material; therefore, modifications of the elastic parameters need to be carried out for both frame and shell elements.

However, the challenge of this project is the full definition of each connection between timber elements in the whole building and to model its behaviour. For this reason, it was decided to implement a detailed hybrid FEM with frames and shell elements at the exact position (figure 13) connected with link elements which are defined with the calculated stiffness for each degree of freedom (k_{ser}) according to the type of connection to be developed.

The slabs work both as plate and membrane to transfer horizontal loads to the concrete cores by direct contact (no tension nor shear forces). For this reason, it has been used non-linear elements which work only in compression (gap type link) around the concrete cores (wrench effect).

The joints between the CLT panels have been represented with up to four different types of links with the desired stiffness (figure 14).

The portal frames are conceived to carry only the vertical loads and not to resist the lateral actions. Therefore, the CLT slabs rest on the beams without fixation.

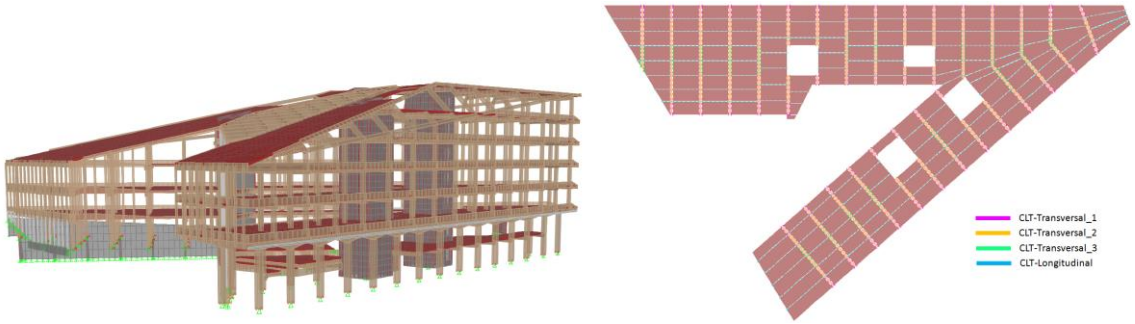


Figure 9. General view (left) and plan view of level 4 (right) in the FE model

An orthotropic material has been defined to model the layered properties of the CLT panels which have a different behaviour in each direction. The elastic parameters are obtained according to the effective stiffness given by the CLT Handbook [3] which converts the composite section to an homogeneous shell element.

5.2. General results

Timber structures are commonly designed by the Serviceability Limit States (vertical and horizontal deflections and vibrations).

This structure is sensible to horizontal deflections (figure 10) as some points are located far away from the concrete cores. Satisfactory results were obtained by connecting the west part of the building to the adjacent concrete wall and using the steel elements of the main atrium façade to connect both parts of the building.

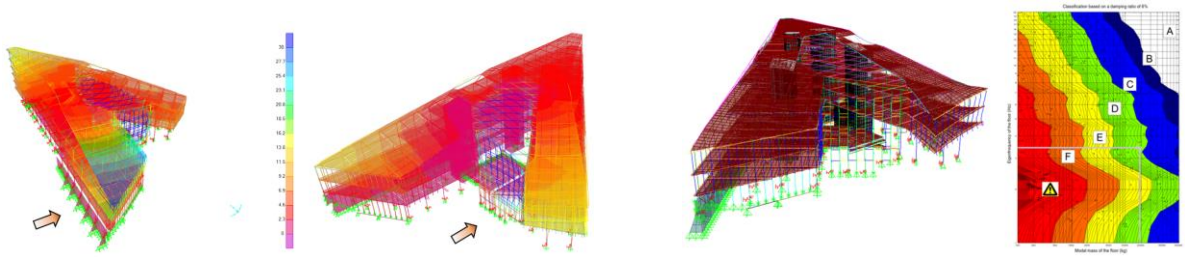


Figure 10. Horizontal deflections (left) and vibrations (right) from the FE model

The critical area of the building in terms of vibrations is the south-east cantilever. Connecting the three levels with vertical stiff purlins, the structure vibrates within the recommended values [4].

6. Building information modelling

The use of BIM is increasingly common in Scandinavia for both building and infrastructure projects. Here the client has required all disciplines, from the preliminary design stage onward, to share information via a global BIM model. Each discipline, working with their chosen 3D drawing software, exports into the IFC format. The IFC files are then combined into the global model, in SMC format. The combined model is used by the BIM manager to perform clash tests and for interdisciplinary coordination.

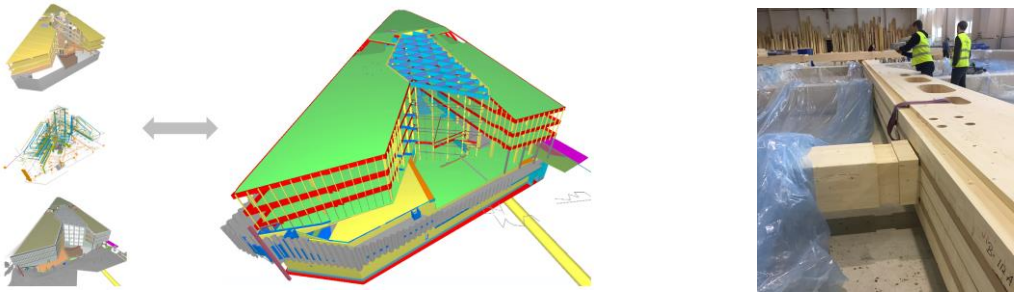


Figure 11. BIM models of different disciplines (left) and CNC machine results at factory (right)

It is very important to highlight that the BIM model from designers is used directly by the Timber fabricator, translated into their own software, and later use for the CNC machine at the factory (figure 19). There is no additionally form/shop drawings, as everything is detailed in 3D.

7. Conclusion: submission of contributions

The design of Finansparken Bjergsted is innovative in its use of a traditional building material, timber, as the load bearing structure in a modern office building. It takes advantage of advanced prefabricated timber elements that are engineered for strength and can be prefabricated with strict tolerances for a rapid construction process. Connections are also designed, where possible, to transfer forces directly between timber members with minimal steel parts. Self-tapping timber screws and steel threaded rods are used as local reinforcement in accordance with the latest technology.

The inherent advantages of BIM have been used from preliminary design through to fabrication.

Acknowledgements

The realisation of this project is thanks to a dedicated design team including the architects, Helen & Hard (www.helenhard.no) and Saaha (www.saaha.no).

Specialist advice on timber design has been provided by Creation Holz (www.creation-holz.ch/en/dienst.php) and on timber fabrication by Moelven, Norway (www.moelven.com/no/).

Throughout all stages the final client and building user, Sparebank 1, has provided constant support as well as the Contractor during construction process, Veidekke AS (http://veidekke.no ; http://www.finansparken.no/).

References

[1] *BauBuche manual for structural calculation*, (2nd ed.).

[2] NS-EN 1995-1-2:2004+NA:2010 Eurocode 5: Design of timber structures - Part 1-2: General Structural fire design.

[3] Karacabeyli, Erol, and Brad Douglas, eds. *CLT handbook: cross-laminated timber*. FPInnovations. 2013.

[4] Feldmann, M., et al. *Design of floor structures for human induced* vibrations. JRC–ECCS joint Report. 2009.

Proceedings of the IASS Annual Symposium 2019 – Structural Membranes 2019
Form and Force
7 – 10 October 2019, Barcelona, Spain
C. Lázaro, K.-U. Bletzinger, E. Oñate (eds.)

Modern timber design approaches for traditional Japanese architecture: analytical, experimental, and numerical approaches for the *Nuki* joint

Demi FANG*[a], Julieta MORADEI[b], Jan BRÜTTING[c], Aliz FISCHER[b], Daniel K. LANDEZ[a], Benshun SHAO[b], Nick SHERROW-GROVES[b], Corentin FIVET[c], Caitlin MUELLER[a]

[a] Massachusetts Institute of Technology (MIT), Cambridge, MA, USA
*Corresponding author: dfang@mit.edu
[b] Arup, San Francisco, CA, USA
[c] Swiss Federal Institute of Technology (EPFL), Fribourg, Switzerland

Abstract

This work fully investigates a specific timber joinery connection via experimental, analytical, and numerical methods. The selected joint is the *Nuki* joint: a mortised column with through-beam tenon. The experimental approach takes advantage of digital fabrication to reduce variations introduced by hand fabrication while the analytical approach builds on state-of-the-art embedment stress models. Material tests are used to calibrate the non-linear finite element model and analysis of the connection. Furthermore, the difference in behavior between prototypes of various beam thicknesses is examined across analysis approaches. This work not only sets out a workflow for digital fabrication, physical testing, and structural analysis for more complex joinery geometries, but also discusses the challenges and relevance of its application towards a reference library of joinery connections for modern timber construction.

Keywords: timber, joinery, connections, Nuki joint, physical testing, finite element analysis, rotational stiffness

1. Introduction

Timber is one of the oldest known building materials in the world. In contrast to Western analogs, Asian timber construction is characterized by its high degree of specialization in joinery and by connections with interlocking geometries. The use of joinery connections largely faded with the introduction of metal fasteners that continue to dominate post-industrialization timber connections.

Timber structures have seen a revival in recent decades due to growing awareness of timber's reduced environmental footprint compared to typical building materials such as steel or concrete. Buildings are responsible for a third of global carbon emissions, and substituting wood for other materials could prevent 14-31% of those emissions [1]. Current mass timber construction uses steel connections (e.g. nail plates) which often results in a one-life span design of structures. The use of interlocking timber joinery can allow for more sustainable, non-destructive disassembly of timber structures, as demonstrated by historic precedents such as the *Ise* Shrines (Japan, 4 BC) [2].

The budding capabilities of today's digital fabrication technology offer an opportunity to revitalize the use of interlocking joinery in modern timber construction. Examples featuring 21st-century joinery connections include the Yusuhara Bridge Museum (Japan, 2010) by Kengo Kuma and Associates, the Tamedia Office Building (Switzerland, 2013) by Shigeru Ban Architects, and the Writers Theatre (USA, 2016) by Studio Gang Architects.

Copyright © 2019 by FANG, MORADEI, LANDEZ, BRÜTTING, FISCHER, SHAO, SHERROW-GROVES, FIVET, and MUELLER.
Published by the International Association for Shell and Spatial Structures (IASS) with permission.

While there are benefits to reintroducing joinery connections into modern construction from the perspectives of sustainability, constructability, and fabrication capabilities, the main obstacle is to characterize and codify the mechanics of these connections. This paper is part of an ongoing investigation into a workflow aimed to build up centralized knowledge on joint behavior. In this paper the *Nuki* joint (Figure 1) is selected as an example to demonstrate the workflow. The simple geometry of the *Nuki* – a beam piercing through a mortised column – enables a clearer understanding of its mechanics, facilitating the calibration between analysis and experimental testing. This paper focuses on predicting the rotational stiffness and behavior of the joint. The key steps of the workflow are 1) the experimental testing of digitally fabricated specimens, 2) the analysis of the interlocking joint's behavior using principles of structural mechanics, and 3) the numerical simulation employing non-linear finite element analysis (FEA). The future aim of these calibrations is to enable the characterization of joints with more complex geometries and variations.

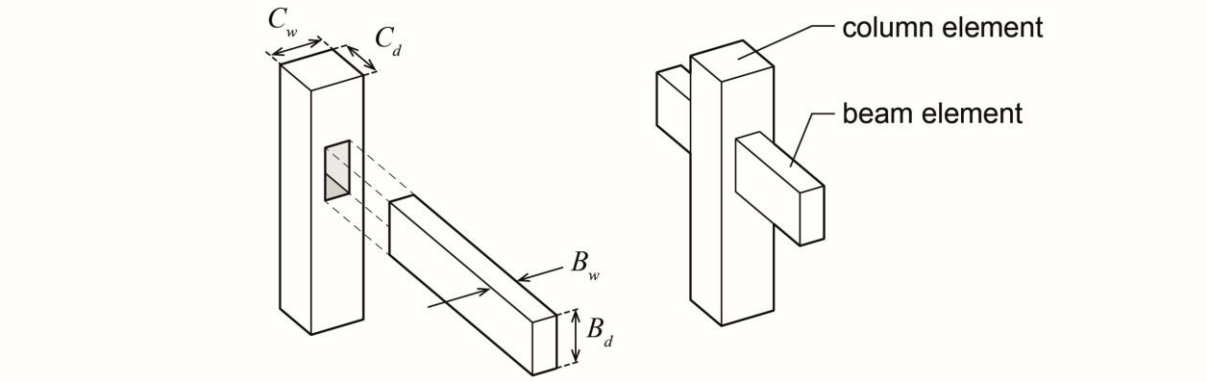


Figure 1. Nuki joint, a simple joinery connection studied in this work.

1.1 Literature review

Fascination with joinery connections from a historical and cultural point of view is evident from a number of books and studies cataloguing their origins, evolutions, and geometries [3], [4]. The analyses of timber joint mechanics range across analytical, numerical, and experimental methods. Some focus on validation between experimental and numerical methods [5], [6], while others use a variety of analytical models that are compared against physical tests [7]–[10]. A key behavior in the analysis of joinery connections is embedment [11], which refers to the compression of one joint element (or part) into another, a behavior that arises from the reduced stiffness of wood perpendicular to the grain. Building upon embedment theory, Kitamori et al. [12] showed that additional embedment length outside the direct contact region can significantly contribute to rotational stiffness. Komatsu et al. [12] considered an elastoplastic material behavior where only a reduced material stiffness is taken into account when the yield-point is reached, enabling an analytical description of the typical bi-linear moment-rotation behavior of semi-rigid joinery connections. Recent works have applied his theory to different joinery connections [13], [14]. As for the *Nuki* joint in particular, Chang et al. [15] compared analytical and experimental models but do not discuss plastic effects of the joint behavior. Guan et al. [6] compared experimental and numerical models for *Nuki* joints with wedges.

In summary, the state of the art for analyzing interlocking joinery through experimental testing, mechanical analysis, and numerical simulation have yet to be synthesized and calibrated. This work particularly builds on own previous work by Fang and Mueller [7], Moradei et al. [16], and Fang et al. [17]. This work presents new results on digitally fabricated specimens made of glue-laminated timber as well as numerical results to compare with the analytical and experimental approaches.

2. Methodology

The *Nuki* joint was here parameterized by beam depth B_d, beam width B_w, column width C_w, column depth C_d, which are notated in Figure 1. For experimental testing, joint specimens were manufactured with dimensions $B_d = C_w = C_d = 8.25$ cm. Two different beam widths B_w, 2.54 cm and 3.81 cm were studied. A visual overview of the experimental and numerical testing setup is shown in Figure 2.

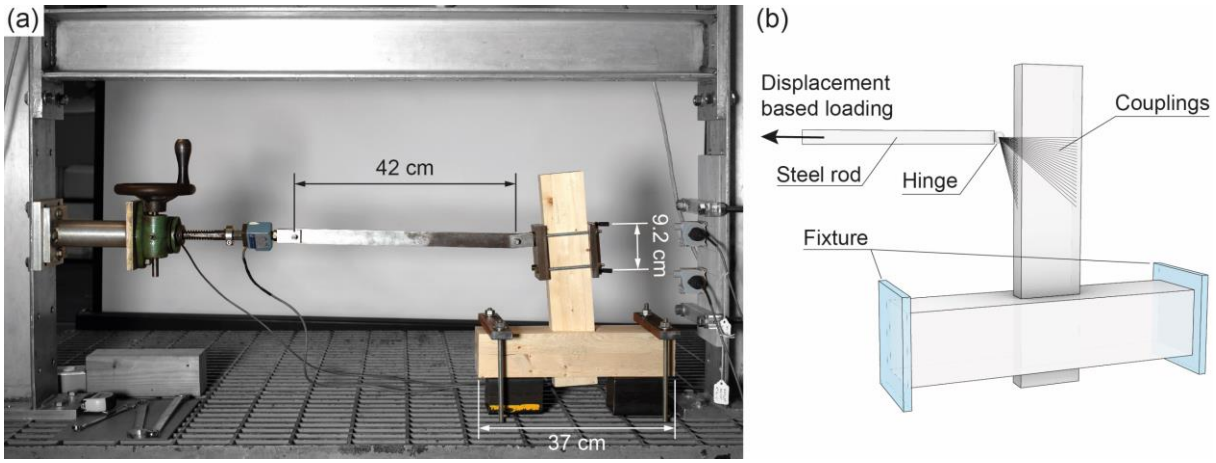


Figure 2. Setup, support and loading conditions of the (a) experimental testing and (b) numerical simulation.

2.1 Material properties

Glue-laminated timber elements were used for the experimental prototypes. Material testing was conducted first to determine the material properties and to apply them in the analytical and numerical models. Most relevant mechanical properties are summarized in Table 1.

Table 1. Mechanical properties determined for the material used in wood specimens.

$E_{c,0}$ Mean (standard dev.) [MPa]	$E_{c,90}$ Mean (standard dev.) [MPa]	$\varepsilon_{c,y,90}$ Mean (standard dev.) [m/m]	PR_{90} [%]
13,500 (1340)	385 (89)	0.025 (0.001)	11.8%

$E_{c,0}$ compressive stiffness (modulus of elasticity) parallel to grain
$E_{c,90}$ compressive stiffness (modulus of elasticity) perpendicular to grain
$\varepsilon_{c,y,90}$ yield compressive strain perpendicular to grain
PR_{90} reduced stiffness of $E_{c,90}$ after yielding

2.2 Experimental setup

Six glulam specimens for each joint geometry were digitally fabricated with a robotic CNC router. The opening in the columns has rounded corners equal to the size of router ball end, i.e. 9.5 mm. In the test setup, which is shown in Figure 2(a), the column element of the joint was fixed to the table, while the beam element was attached to a hand-screw-actuated load cell of 4400 N capacity. The beam-column connection was not press-fit, and varied in tightness. The total gap between the beam and column was in the 0-2 mm range. A linear displacement was applied at the beam end using the load cell, and the resulting rotation at the joint was measured by two string potentiometers.

2.3 Analytical model

The analytical model employed to prescribe the moment-rotation behavior of the joint is based on embedment theory and uses an elastic-plastic material model. In the model, the bending moment M is

expressed in terms of the rotation angle θ using trigonometric functions and structural mechanics. For details on the analytical model, the reader is referred to Fang et al. [17].

2.4 Numerical model

To numerically model the joint behavior, explicit finite element analysis was employed using the LS-Dyna v10.0 software package. Figure 2(b) illustrates the numerical simulation setup, designed to capture key aspects of the physical testing setup. The top and the bottom of the column are restrained from displacement and rotation. The surfaces where the loading clamp is installed are rigidly connected through their nodes. Those nodes are then coupled to the loading steel rod with a hinge. The loading is applied to the rod via a prescribed displacement that allows capture of the failure mechanism.

Beam and column are discretized with 45,000 fully integrated solid elements in total. A transversely anisotropic material model (LS-Dyna MAT 143) is employed for both components in the FEA analysis [18], [19]. This model allows to capture physically nonlinear effects (e.g. plasticity and damage) as well as the anisotropy between grain parallel and grain perpendicular behavior of the wood.

3. Results

The moment-rotation behavior obtained from all three models are summarized in Figure 3. The following subsections give detailed descriptions of each method's results.

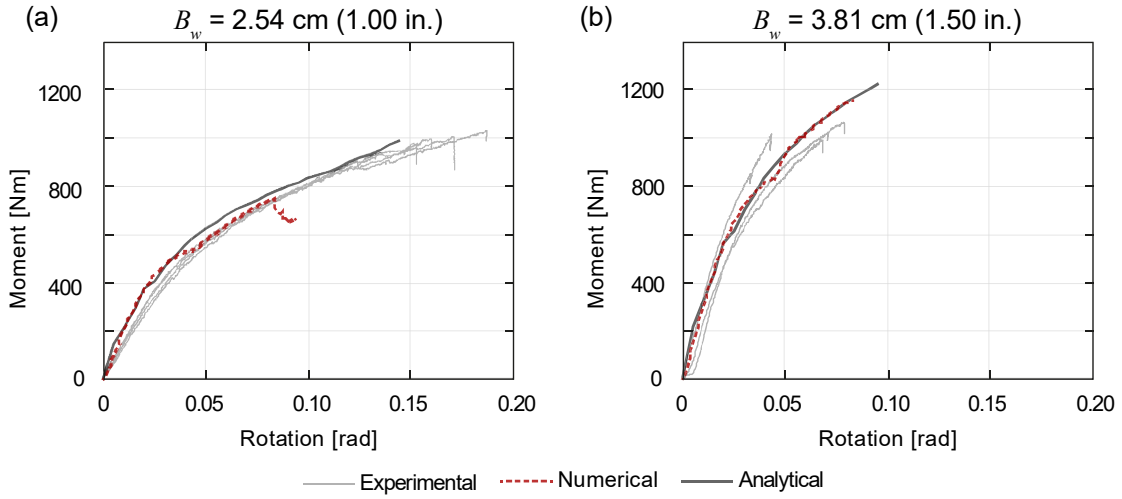


Figure 3. Summary of results from experimental, analytical, and numerical approaches. (a) Moment-rotation behavior for specimens of B_w = 2.54 cm; (b) moment-rotation behavior for specimens of B_w = 3.81 cm.

3.1 Experimental Results

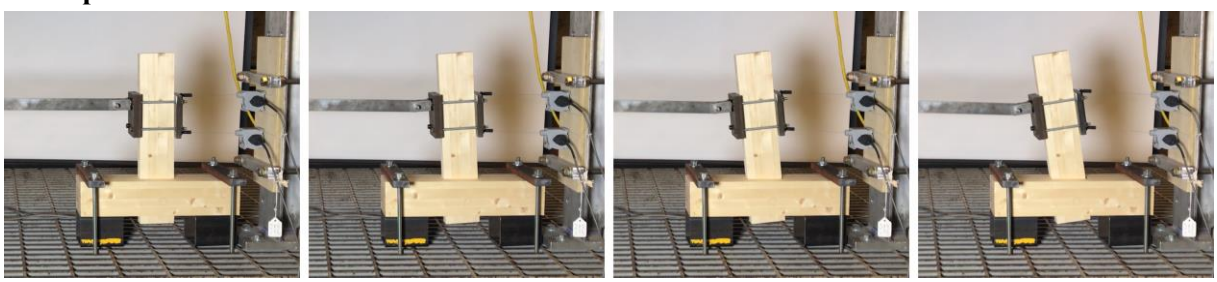


Figure 4. Rotational stiffness testing of prototypes. Progressive video frames from an example specimen.

Figure 4 shows a sequence of images taken during the experimental testing of one joint specimen. From the measured test data (Figure 3, grey) it is apparent that in general *Nuki* joints show a two-phase moment-rotation behavior: a first initial (linear elastic) stiffness and a second stiffness post-yielding. The change between the two phases happens gradually. Tests ended when the load cell reached its capacity. For nearly all specimens of B_w = 3.81 cm, this limitation prevented the estimate of secondary stiffness.

Variability in testing results is partially due to wood being a heterogeneous material. It can be further influenced by changes in temperature and humidity between fabrication and testing of the prototypes, as that affects the tightness of the fit between the beam and the column. Results could be more consistent with a much larger number of specimens.

3.2 Analytical results

The analytical model employs an elastic-plastic material behavior which is appropriate for describing the two-phase behavior demonstrated by the physical prototype. After calibration of the analytical model to the experimental test for both beam widths, one unique decay coefficient α was selected as $4.5/B_d$. This parameter relates to shape of the embedment outside the direct contact between beam and column. For α and all other parameters the reader is referred to Fang et al. [17]. The analytical model does not include failure prediction; the calculations were manually ended at 100 and 150 mrad for B_w = 2.54 cm and B_w = 3.81 cm, respectively. In general, after calibration the modeled rotation behavior matches the experimental data (Figure 3).

3.3 Numerical results

The main parameters of the material model, such as Young's moduli and strengths, were calibrated based on the physical material testing (see values in section 2.1). Other values, such as ν = 0.39 Poisson ratio, were estimated from literature [20]. Contact between beam and column is defined by numerical parameters representing the contact stiffness, the friction between surfaces, and the initial gap size. In the model, the gap size between the beam and the column was set up based on observation of the fabrication, with 0.5 mm gap each side of the beam. At the top and bottom the gap was smaller, 0.025 mm, to ensure numerical stability. The analysis assumed no initial stress from joining the two pieces.

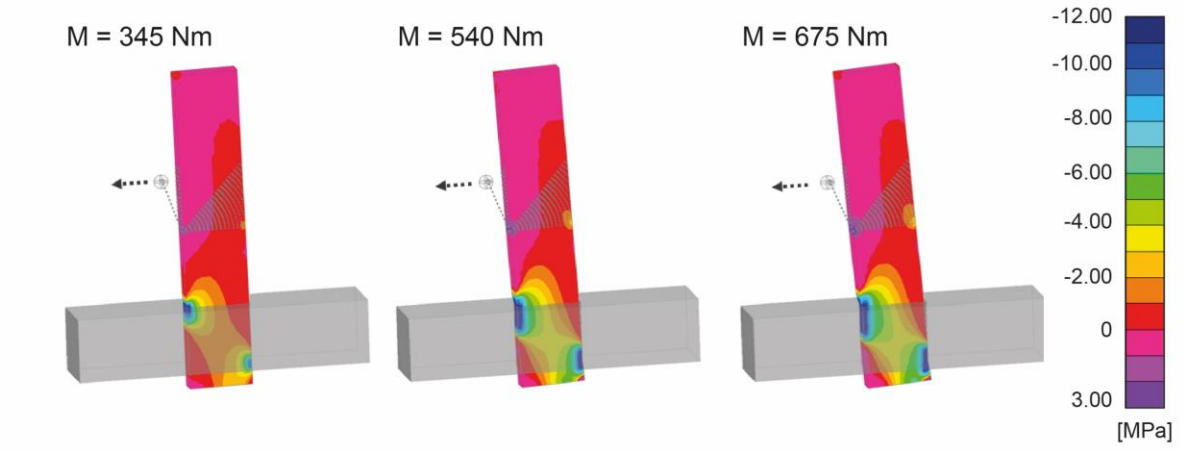


Figure 5. Stress in the beam perpendicular to grain (MPa) throughout the numerical simulation for the B_w = 2.54 cm specimen.

Selected images of the progression of the numerical simulation are shown in Figure 5. The contour plot shows the stresses perpendicular to the grain of the beam. The simulation was stopped when the analysis showed numerical instabilities as the damage at the contact became excessive. The stress distribution is in a good agreement with the assumption of the analytical model, and with the observations of the local

behavior at the physical testing. A close-up of the connection behavior for all three methodologies is shown in Figure 6.

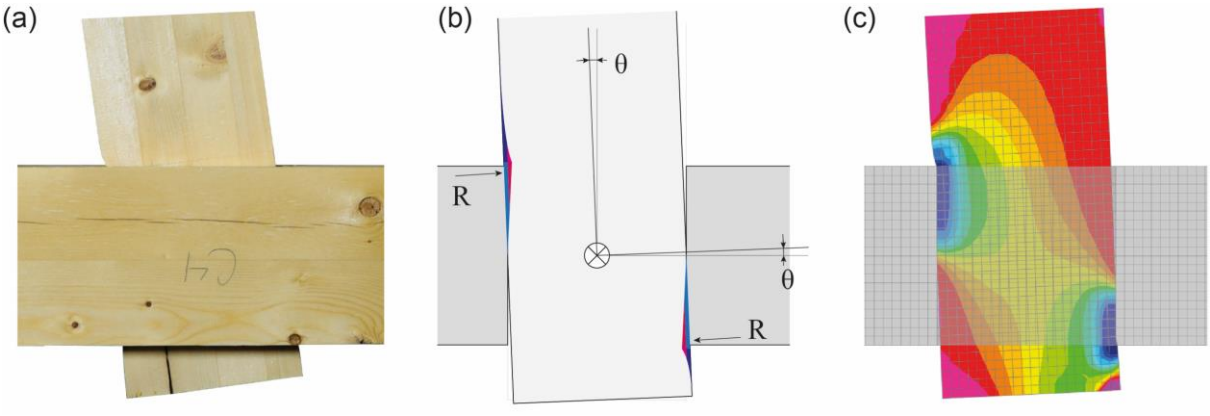


Figure 6. Close-up of the joint for (a) experimental testing, (b) analytical model, and (c) numerical simulation.

3.4 Comparison of stiffness values across models

In this section, based on the two-phase moment-rotation behavior, absolute and relative stiffness values are compared across all three models. 'Stiffness 1' refers to the initial stiffness, and 'Stiffness 2' refers to the post-yielding stiffness. Table 2 compares the absolute stiffness values. Table 3 compares the relative increase in stiffness with respect to the two tested beam widths. Note that Stiffness 2 values for the experimental testing of specimen with B_w = 3.81 cm are not recorded because experimental testing had to be halted before a post-yielding stiffness could be observed.

Table 2. Comparison of absolute stiffnesses across models.

	B_w = 2.54 cm		B_w = 3.81 cm	
	Stiffness 1 [kN-m/rad]	Stiffness 2 [kN-m/rad]	Stiffness 1 [kN-m/rad]	Stiffness 2 [kN-m/rad]
Experimental mean	16.0	5.46	25.1	--
Analytical model	18.7	4.29	28.0	6.44
Numerical model	18.9	5.10	28.1	6.74
% difference between analytical and experimental*	+17%	-21%	+10%	--
% difference between numerical and experimental*	+18%	-7%	+11%	--

* signed percent error assuming experimental mean as the 'expected value'

The results in Table 2 demonstrate that the analytical and numerical models overestimate the initial stiffnesses (Stiffness 1) by about 18% and 11% for the two different beam widths respectively.

Table 3. Comparing effects of beam width variation across models.

	% increase in stiffness between B_w = 2.54 cm and B_w = 3.81 cm	
	Stiffness 1	Stiffness 2
Experimental	57%	--
Numerical	49%	32%
Analytical	50%	50%

The results in Table 3 demonstrate that in the experiments there is a slightly larger relative increase in initial stiffness from increasing beam width than numerically and analytically predicted.

4. Conclusion and future work

The rotational stiffness of *Nuki* joints was tested with digitally fabricated specimens made of glue-laminated timber. The rotational behavior was modeled both analytically and numerically, and these models were calibrated with the experimental results through material testing. While neither model captures wood behavior at a micro level, calibrating key parameters allowed analytical and numerical models to capture the overall behavior of the joints. For behavior at failure, the models were more limited: the analytical model does not capture failure by definition, while the numerical model resulted in numerical instabilities as the local failure at the contact surface became excessive. However, the accuracy of failure prediction is not crucial because for design recommendations, the region of initial stiffness will be of primary interest.

While digital fabrication allowed quick and precision woodwork, the variability of the wood due to change in humidity or temperature over time did not allow the connection fit to be precise. In practice, majority of the typical connections are press-fit, eliminating this issue. For non-press-fit connections, more care needs to be taken to the consistency of the fabrication environment for precise fit. Design values also need to be defined considering this variability. In the future, further experimental testing could increase the number of specimens and improve the consistency of results against both models to verify that all parameters result in model predictions close to expected behavior.

This paper demonstrated analytical and numerical models effectively predicting rotational stiffness behavior and absolute values within 20% of experimental results after material calibration. With the now calibrated model parameters it is possible to analyze other joint types and geometries. MAT 143 material also proved to be suitable to numerically simulate other joint geometries, allowing the numerical design of more complex connections where analytical models are not available. Further, the obtained semi rigid moment-rotation behavior could be integrated into a global FEA model via rotational springs.

Overall, the potential for both models to be used for other joinery geometries was demonstrated. This workflow can be applied to further joinery connections in an effort to build up a centralized knowledge base of joinery connections, empowering designers to apply these historically-inspired, sustainable connections more widely in timber construction.

Acknowledgements

The authors would like to acknowledge Nordic Structures and Bensonwood for providing the prototype material, Autodesk BUILD Space for the fabrication facilities, Arup's internal research grant for funding JM, AF, BS, and NSG, and Stephen Rudolph at MIT CEE for assisting the physical tests.

Author Contributions

DF, JB, and CM developed the analytical model. DKL and DF carried out digital fabrication and physical testing. AF, BS, and JB built and analyzed the numerical model. DF and JM provided overall coordination and management. NSG, CF, and CM supervised.

References

[1] C. D. Oliver, N. T. Nassar, B. R. Lippke, and J. B. McCarter, "Carbon, Fossil Fuel, and Biodiversity Mitigation With Wood and Forests," *J. Sustain. For.*, vol. 33, no. 3, pp. 248–275, Apr. 2014.

[2] C. Henrichsen and R. Bauer, *Japan Culture of Wood: Buildings, Objects,Techniques*, 1 edition. Boston: Birkhauser, 2004.

[3] T. Sumiyoshi and G. Matsui, *Wood Joints in Classical Japanese Architecture*. Kajima Institute Publishing Co. Ltd, 1991.
[4] K. Zwerger, *Wood and Wood Joints*, 3rd ed. edition. Basel ; Boston: Birkhäuser, 2015.
[5] E. M. Lang and T. Fodor, "Finite Element Analysis of Cross-halved Joints for Structural Composites," *Wood Fiber Sci.*, vol. 34, no. 2, pp. 251–265, Jun. 2007.
[6] Z. W. Guan, A. Kitamori, and K. Komatsu, "Experimental study and finite element modelling of Japanese 'Nuki' joints — Part two: Racking resistance subjected to different wedge configurations," *Eng. Struct.*, vol. 30, no. 7, pp. 2041–2049, Jul. 2008.
[7] D. Fang and C. Mueller, "Joinery connections in timber frames: analytical and experimental explorations of structural behavior," in *Proceedings of the International Association for Shell and Spatial Structures (IASS) Symposium*, Cambridge, MA, USA, 2018.
[8] R. J. Schmidt and R. B. Mackay, "Timber frame tension joinery," MSc thesis, University of Wyoming, Laramie, WY, 1997.
[9] J. Shanks and P. Walker, "Strength and Stiffness of All-Timber Pegged Connections," *J. Mater. Civ. Eng.*, vol. 21, no. 1, pp. 10–18, Jan. 2009.
[10] M. G. Shope, "Strength characterization of wood to wood connections using stress field analysis," Thesis, Massachusetts Institute of Technology, 2016.
[11] M. Inayama, "Wooden embedment theory and its application," PhD, University of Tokyo, Tokyo, Japan, 1991.
[12] A. Kitamori, T. Kataoka, and K. Komatsu, "Effect of Additional Length on Partial Compression Perpendicular to the Grain of Wood," *J. Struct. Constr. Eng.*, vol. 74, p. 642, 2009.
[13] K. Ogawa, Y. Sasaki, and M. Yamasaki, "Theoretical modeling and experimental study of Japanese 'Watari-ago' joints," *J. Wood Sci.*, vol. 61, no. 5, pp. 481–491, Oct. 2015.
[14] S.-Y. Yeo, K. Komatsu, M.-F. Hsu, Y.-L. Chung, and W.-S. Chang, "Structural behavior of traditional Dieh-Dou timber main frame," *Int. J. Archit. Herit.*, pp. 1–23, Mar. 2018.
[15] W.-S. Chang, M.-F. Hsu, and K. Komatsu, "Rotational performance of traditional Nuki joints with gap I: theory and verification," *J. Wood Sci.*, vol. 52, no. 1, pp. 58–62, Feb. 2006.
[16] J. Moradei *et al.*, "Structural Characterization of Traditional Moment-Resisting Timber Joinery," in *Proceedings of the International Association for Shell and Spatial Structures (IASS) Symposium*, Cambridge, MA, USA, 2018.
[17] D. L. Fang, J. Brütting, J. Moradei, C. Fivet, and C. T. Mueller, "Rotational stiffness in timber joinery connections: analytical and experimental characterizations of the Nuki joint," presented at the 4th International Conference on Structures and Architecture, Lisbon, Portugal, 2019.
[18] Livermore Software Technology Corporation, *LS-DYNA Keyword User's Manual: Material Models*, vol. 2. Livermore, California: Livermore Software Technology Corporation, 2018.
[19] Federal Highway Administration, "Manual for LS-DYNA Wood Material Model 143," US Department of Transportation, McLean, Virginia, Manual FHWA-HRT-04-097, Aug. 2007.
[20] Forest Products Laboratory, "Wood Handbook: Wood as an Engineering material," U.S. Department of Agriculture, Forest Service, Forest Products Laboratory, Madison, WI, General Technical Report FPL-GTR-190, Apr. 2010.

Proceedings of the IASS Annual Symposium 2019 - Structural Membranes 2019
Form and Force
7-10 October 2019, Barcelona, Spain
C. Lázaro, K.-U. Bletzinger, E. Oñate (eds.)

Performance Assessment of Double-Layered Timber Plate Shells using Alternative Structural Systems

Anh Chi NGUYEN*, Bertrand HIMMER, Petras VESTARTAS, Yves WEINAND

* Laboratory for Timber Constructions, École Polytechnique Fédérale de Lausanne
CH-1015 Lausanne, Switzerland
anhchi.nguyen@epfl.ch

Abstract

With recent advances in digital fabrication, innovative wood-wood connections inspired by ancient timber joining techniques have recently been applied to various free-form timber plate structures. This paper focuses on the recently developed double-layered and double-curved timber plate shells. Design, fabrication and numerical automated tools have been successfully developed for these structures. However, three-point bending tests on prototypes composed of fifteen boxes with no curvature have pointed out challenges in the initial assembly system. Namely, failure paths which can be attributed to the herringbone pattern used to segment the target surface were appearing at the stretched bottom layer. This research presents the performance assessment of double-layered timber plate shells using an alternative structural system to the initial one. Numerical investigations were performed to compare both systems in terms of displacements and forces in the joints. The proposed design, involving additional abutment areas of the boxes, was shown to enhance the interlocking connection of the plates and, therefore, the stiffness of the structural system. Tensile forces in the joints were also significantly reduced.

Keywords: timber plate structures, wood-wood connections, finite element model, semi-rigidity, structural analysis

1 Introduction

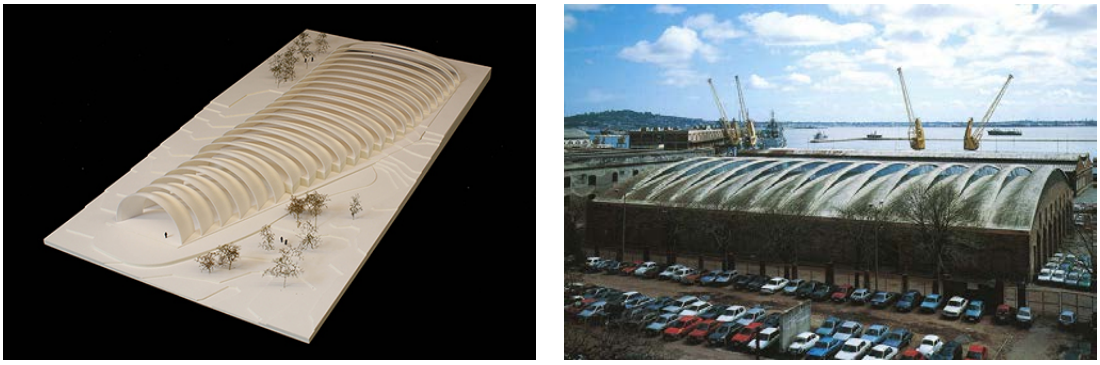
In the last decades, researchers have shown a growing interest in ancient timber joining techniques initially developed for furniture and cabinetmaking. These connections were improved thanks to digital fabrication and algorithmic-parametric-geometry processing, allowing their fast and precise assembly. Initially used for timber frame structures, they have been applied to plate elements similarly to traditional cabinetmaking joints. These new wood-wood connections have been utilized in various free-form timber plate structures [1]. Recently, an assembly system for double-layered and double-curved timber plate shells using multiple tab-and-slot through-tenon joints (MTSJ-TT) has been developed [2]. It has been applied to the Annen head office in Manternach, Luxembourg. Design, fabrication and numerical automated tools have been successfully been developed for these structures having unique shaped panels and a large number of connections [3]. However, experimental tests performed on double-layered prototypes composed of 15 boxes with no curvature have highlighted weaknesses of the initial design [4]. Namely, continuous failure paths were appearing at the stretched bottom layer.

Copyright © 2019 by A.C. Nguyen, B. Himmer, P. Vestartas and Y. Weinand
Published by the International Association for Shell and Spatial Structures (IASS) with permission.

This research presents the performance assessment of double-layered and double-curved timber plate shells using two different structural systems. An alternative assembly system is presented and compared to the initial one in terms of stiffness and forces in the tenons using a numerical model in which the semi-rigidity of wood-wood connections is considered using springs.

2 Structural Systems

Two different structural systems were investigated taking the example of the Annen head office in Manternach, Luxembourg. The project is a 5800 m^2 facility which will accommodate offices as well as factory space. Its roof structure, illustrated in Figure 1a, consists of 23 singular double-layered and double-curved timber plate shells, 9-meter high and 6-meter wide, covering spans from 23 to 54 m. Their design was inspired by Eladio Dieste's Gaussian masonry vaults, such as built for the Port Warehouse illustrated in Figure 1b [6].



(a) (b)

Figure 1: (a) Model of the Annen head office project (credits: IBOIS, EPFL) (b) Eladio Dieste's Port Warehouse (1977-1975) [6]

2.1 Initial Structural System

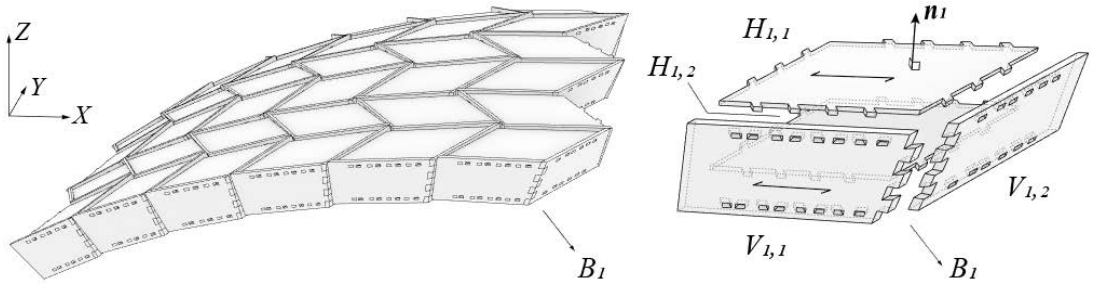
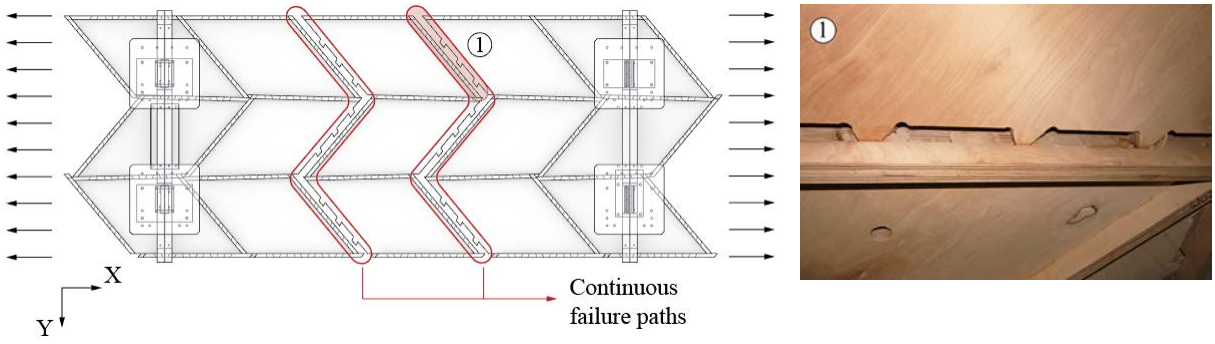


Figure 2: Initial structural system of double-layered and double-curved timber plate shells developed by Robeller et al. [2]

The reference structural system, illustrated in Figure 2, is the initial system developed by Robeller et al. [2] and applied to the Annen head office project. In this one, each shell is composed of an assembly of hexahedra-shaped boxes B_i, each made of two vertical panels $V_{i,1}$ and $V_{i,2}$ and two horizontal panels $H_{i,1}$ and $H_{i,2}$. The latter form the two layers of the structure.

Neighbouring horizontal plates are connected with single-degree-of-freedom (1 DOF) MTSJ-TT through vertical panels, which are themselves assembled with dovetail joints. Each box B_i share its vertical panels with neighbouring boxes. Boxes are individually formed and are then inserted along the vector of insertion, defined by the direction of the remaining DOF of the connections.



(a) (b)

Figure 3: (a) Continuous failure paths highlighted by three-point bending tests (b) MTSJ-TT failure at the stretched bottom layer of the structure

Three-point bending tests performed on a 5×3 boxes double-layered prototype with no curvature have shown that continuous failure paths were appearing due to the herringbone pattern used (see Figure 3a). Wood-wood connections of the bottom stretched layer failed, presumably due to a combination of shear and traction (see Figure 3b) [4].

2.2 Alternative Structural System

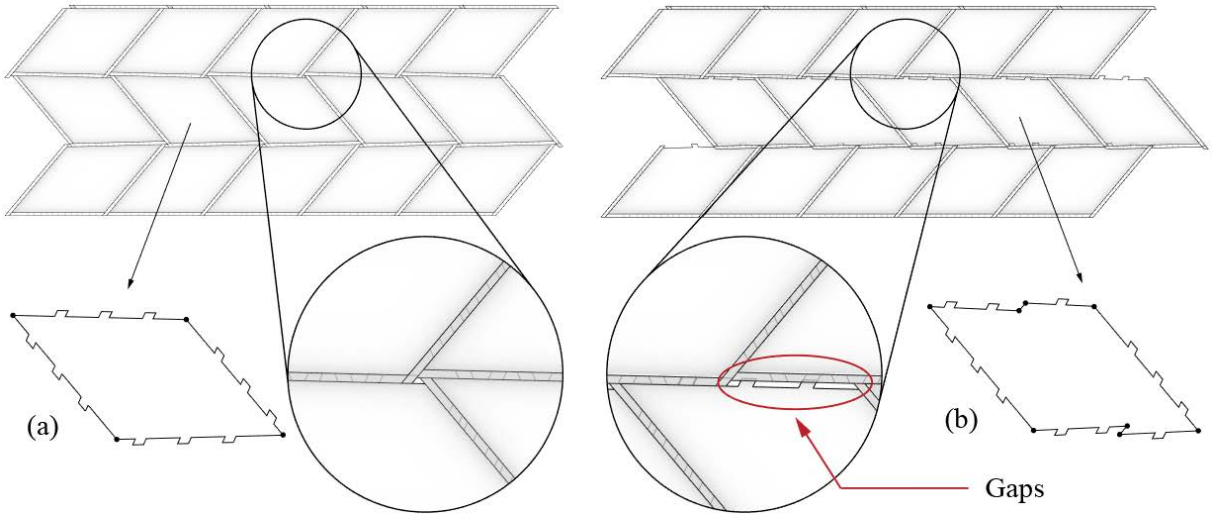


Figure 4: Shift of the boxes introducing gaps in the structure

An alternative structural system was investigated in order to tackle the problems encountered in the initial system, without changing the target surface, constraint of the project, and the

height of the boxes of 600 mm. In order to interrupt the continuous failure paths, boxes were shifted in every second row to obtain staggered rows. However, as seen in Figure 4, this shift introduced large gaps in the structure. The shape of horizontal plates was therefore modified: the quadrilaterals (without considering the tenons) used in the herringbone pattern (see Figure 4a), were replaced by non-convex octagons (see Figure 4b).
The non-convex octagonal shapes have the advantage to provide zones of abutment (see Figure 5). However, as illustrated in Figure 5a, this shape had to be modified (dashed to solid lines) to ensure the insertion of the plates if the abutment angle β was inferior to the angle α, defined by the insertion vector v_i, unique for each plates' edge. In this case, the abutment zone is reduced to a contact line (Figure 5b). When the angle β is larger than α (see Figure 5c), the contact zone is the full area of the abutment (see Figure 5d).

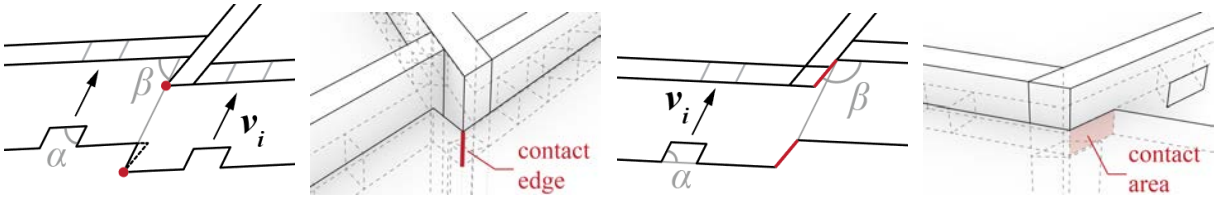


Figure 5: (a) When $\beta < \alpha$, (b) the abutment zone is reduced to a contact line; (c) when $\beta > \alpha$, (d) the contact zone is the full area of the abutment

3 Material and Methods

3.1 Design Framework

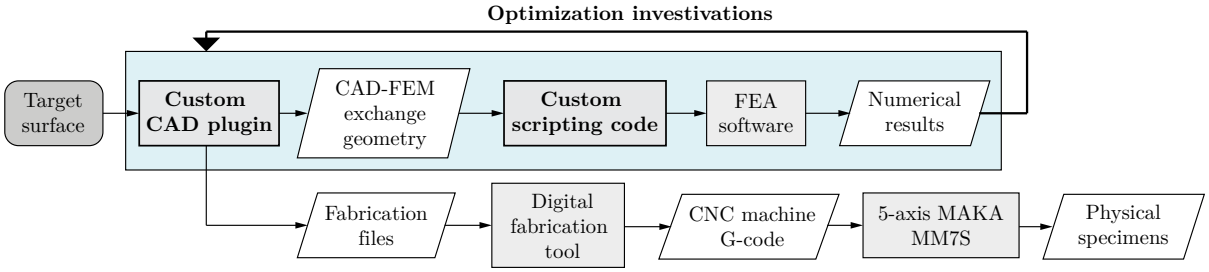
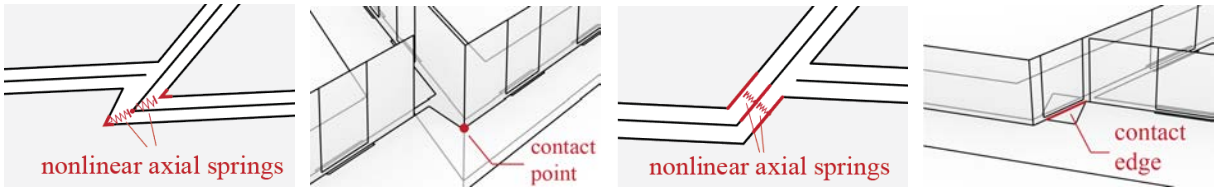


Figure 6: Optimization investigations in the design framework of double-layered and double-curved timber plate shells

The study carried out in this paper follows the design framework presented in Nguyen et al. [3] for the structural analysis of timber plate shells (see Figure 6). To obtain the geometry on large-scale structures, the custom CAD plugin initially developed by Robeller et al. [2] was modified to apply the alternative structural system to entire arches. The custom scripting code automating the generation of the finite element (FE) model was also modified to take into account non-convex octagonal plates, while the remaining code was kept unchanged.

3.2 Finite Element Model and Structural Analysis

The semi-rigid spring model used for the analysis of the 5×3 boxes prototype was used. In this model, wood-wood connections are modelled using springs with 6 components of motion (3 translations and 3 rotations) with stiffness values corresponding to the semi-rigidity of the connections [3]. The model was built in the FE software Abaqus^{TM}.
Numerical simulations were performed with and without modelling of the contact zones of the abutments to evaluate their influence. They were modelled considering nonlinear springs in series, infinitely rigid in compression and hinged in traction. When $\beta < \alpha$ (see Figure 5a), the contact line through the thickness of the plate in the 3D geometry was modelled by a contact point, since plates were modelled by their midsurface in the FEM geometry (see Figures 7a and 7b). This point, coupled to its neighbouring edges, was connected with springs to the plates in contact in the 3D geometry. When $\beta > \alpha$ (see Figure 5c), contact areas were modelled by edges (see Figures 7c and 7d) coupled to their midpoint and connected with springs to the plates in contact in the 3D geometry.



(a) (b) (c) (d)

Figure 7: Contact modelling of the abutment zones

The structural systems were compared in terms of vertical displacements and forces in the tenons. Experimental tests on wood-wood connections have shown that their maximum capacity F_{max} was equal to 6.47 kN in tension and 46.83 kN in shear [7]. The distributed loads at which the first tenon reached either this tensile force or shear force for both systems were compared.
A mesh convergence study was carried out for the analysis of forces in the tenons. To achieve it, a determined force F was applied to one tenon of a timber plate and the error between the applied force F and the total force in the tenon retrieved in the numerical model was calculated for different mesh element sizes.

3.3 Material

BauBuche Q panels from Pollmeier used for the Annen head office and the prototypes tested were considered. They are 40 mm-thick beech laminated veneer lumber (LVL) panels with a characteristic density ρ_k of 730 kg/m^3. Those panels are obtained by gluing 3 mm thick beech peeled veneer layers. In the BauBuche Q panels used, two layers are placed crosswise such that the composition of the 14 beech veneer layers is III–IIIIII–III (I for longitudinal, – for crosswise veneer layer). Material properties used in the model are presented in Table 1, where E is the elastic modulus and G the shear modulus.

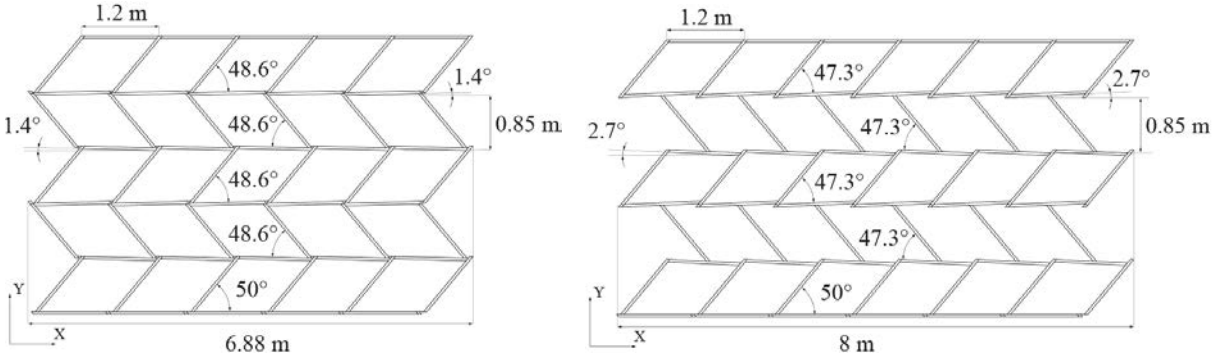
3.4 Specimens, Load and Boundary Conditions

The geometry of the specimens considered is presented in Figure 8. For the initial system, same geometric parameters as in the tested prototype of 5×3 boxes were considered (see Figure 8a).

Table 1: Material properties of BauBuche Q panels (characteristic values) [8] [3]

	Units	E_X	E_Y	E_Z	G_{XY}	G_{XZ}	G_{YZ}
BauBuche Q	[N/mm^2]	12 200	2000	2000	540	360	59

For the study of the alternative structural system, three additional boxes were added to obtain symmetry (see Figure 8b). Boundary conditions similar to those of the three-point bending tests performed were considered; namely pinned support on one side and roller support on the other [4]. A distributed load was simulated on the top layer of the structure.



(a) System n°1: initial system (b) System n°2: alternative system

Figure 8: Geometry of the specimens considered for the comparison of the two structural systems

4 Results and Discussion

4.1 Geometry Generation

The custom CAD plugin was successfully modified to generate double-layered and double-curved timber plate shells with the alternative structural system. The mesh segmentation of the target surface was first performed (Figure 9a), followed by the generation of the joints (Figure 9b), the vertical plates (Figure 9c) and the top plates (Figure 9d).

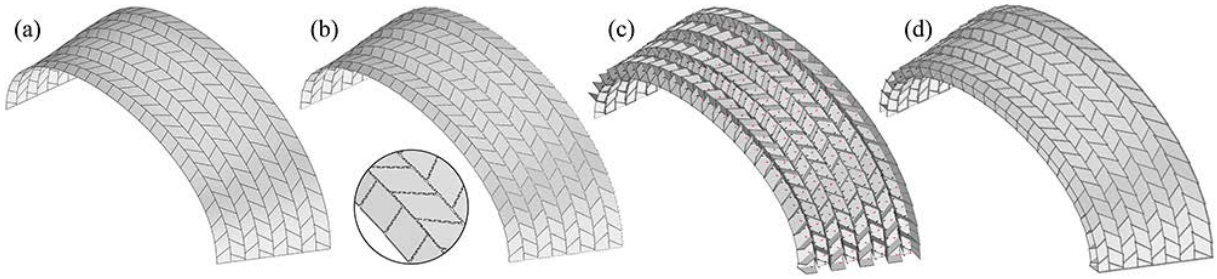
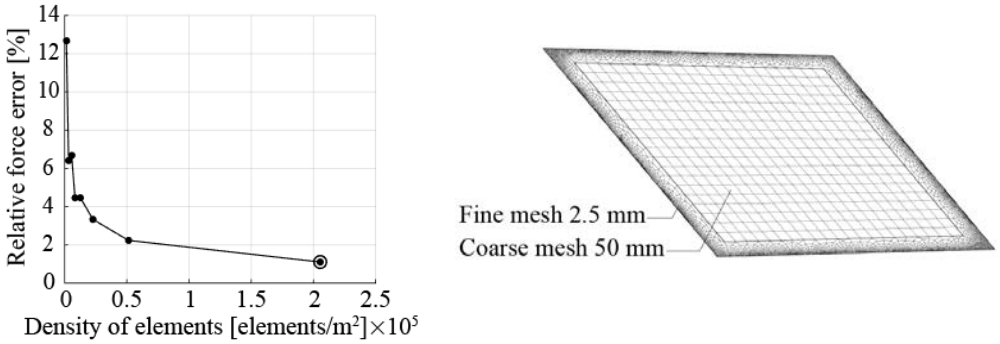


Figure 9: Generation of double-layered and double-curved timber plate shells with the alternative structural system (a) target surface segmentation and generation of (b) joints, (c) vertical plates and (d) top plates

4.2 Mesh Convergence Study

Results of the mesh convergence study for the analysis of forces in the tenons are presented in Figure 10a for mesh element sizes varying from 2.5 to 30 mm at the vicinity of the connections and 50 mm away from them. The smallest element size of 2.5 mm (see Figure 10b), leading to a relative error of 1.1 % between the force applied F and the total force in the tenon obtained, was chosen.



(a) (b)

Figure 10: (a) Mesh convergence study for the analysis of forces in the connections. A mesh element size of 2.5 mm (circled) was chosen. (b) Coarse and fine mesh of a plate

4.3 Structural Performance

Figure 11 presents the load-displacement curves obtained for the two structural systems, modelling contact of abutment zones or not for the alternative system. As observed, the major part of the stiffness increase was due to the structural system applied and not the contact modelling. Further numerical results are presented in Table 2. With the alternative system, stiffness was increased by 76% and 91% without and with contact modelling respectively. For both systems, the maximum capacity of the joints in tension was reached before the maximum capacity in shear. Forces in the connections were reduced such that the maximum applied load at failure was increased by 85% and 229% without and with contact modelling respectively.

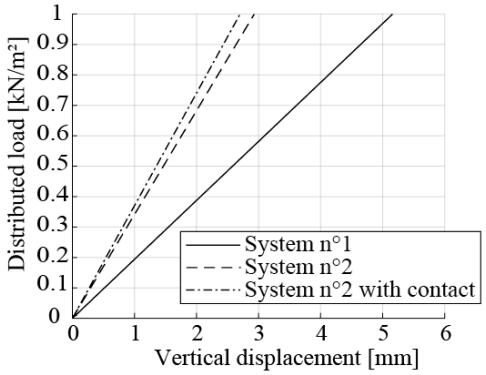


Figure 11: Load vs. displacement curves for the two structural systems with and without modelling of the contact of abutment zones

Table 2: Performance assessment of the two structural systems

	Units	System n°1	- n°2	- n°2 with contact
Load applied to reach F_{max}	[kN/m^2]	5.82	10.76	19.15
Stiffness	[kN/m^2/mm]	0.166	0.292	0.317

5 Conclusions

An alternative structural system was proposed to avoid continuous failure paths appearing with the initial system. Base on numerical investigations, it was shown to enhance the interlocking connection of the plates and, therefore, the stiffness of the structural system by 76%. Tensile forces in the joints were also significantly reduced, increasing the distributed load to reach maximum capacity of the joints in tension to 85%. Moreover, abutment areas were shown to have the potential to further enhance the structural performance of the alternative system.

6 Acknowledgements

This research was supported by the NCCR Digital Fabrication, funded by the Swiss National Science Foundation (NCCR Digital Fabrication Agreement #51NF40-141853).

References

[1] A. Menges, T. Schwinn and O. Krieg (eds.), *Advancing Wood Architecture A Computational Approach*, Routledge, 2016.

[2] C. Robeller, M. Konakovic, M. Dedijer, M. Pauly and Y. Weinand, "A double-layered timber plate shell - computational methods for assembly, prefabrication and structural design," in: *Advances in Architectural Geometry 2016*, S. Adriaenssens, F. Gramazio, M. Kohler, A. Menges and M. Pauly (Eds.), vdf Hochschulverlag AG, ETH Zürich, 2016, pp. 104-122.

[3] A. C. Nguyen, P. Vestartas and Y. Weinand, "Design Framework for the Structural Analysis of Free-Form Timber Plate Structures using Wood-Wood Connections," *Manuscript submitted for publication*, 2019.

[4] A. C. Nguyen and Y. Weinand, "Development of a Spring Model for the Structural Analysis of a Double-Layered Timber Plate Structure with Through-Tenon Joints," in: *WCTE 2018 World Conference on Timber Engineering CD-ROM Proceedings*, Seoul, South Korea, 2018.

[5] C. Robeller, *Integral mechanical attachment for timber folded plate structures*, Ph.D. thesis, École Polytechnique Fédérale de Lausanne, 2015.

[6] S. O. Anderson, *Eladio Dieste: Innovation in Structural Art.* (1^{st} ed.) New York: Princeton Architectural Press, 2004.

[7] A. C. Nguyen, A. R. Rad and Y. Weinand, *Semi-Rigidity of Through-Tenon Joints under Tension and Shear Loads and Perpendicular-to-Grain Compression*, Report, École Polytechnique Fédérale de Lausanne, 2019.

[8] H. J. Blaß and Johannes Streib, *BauBuche Beech laminated veneer lumber - Design assistance for drafting and calculation in accordance with Eurocode 5*, 2017.

Proceedings of the IASS Annual Symposium 2019 - Structural Membranes 2019
Form and Force
7-10 October 2019, Barcelona, Spain
C. Lázaro, K.-U. Bletzinger, E. Oñate (eds.)

Segmented Spiral Using Inter-Connected Timber Elements

Petras VESTARTAS [*,a], **Loic PELLETIER** [b] [c], **Martin NAKAD** [a], **Aryan REZAEI RAD** [a], **Yves WEINAND** [a]

[*,a] Ecole Polytechnique Fédérale de Lausanne (EPFL), Laboratory for Timber Constructions (IBOIS)
EPFL ENAC IIC IBOIS, GC H2 711 (Bâtiment GC), Station 18, CH-1015 Lausanne, Switzerland
petras.vestartas@epfl.ch

[b] Université du Québec à Chicoutimi (UQAC), QC G7H 2B1, Canada
[c] Ecole Nationale d'Ingénieurs de Saint-Étienne (ENISE), 42100 Saint-Étienne, France

Abstract

This paper describes the construction process of a scenographic structure - five meters high spiral. It consists of following parts: CAD modeling work-flow, prototyping and FEM structural calculation, assembly and on-site loading test. The structure was composed of twenty-nine wooden boxes, which were screwed together and suspended by cables. The custom FEM model was made to understand the structural behavior of the spiral. The principal objective of structural calculation was to understand the rigidity of the connections and the interactions between the wooden-boxes, in order to apprehend the behavior of the structure under loads. Further details are given about different steps involved in modelling and fabrication, such as parametric tools, G-Code tool-path generation for the 4.5-axis CNC machine and on-site installation. Afterwards, the loading tests and point-cloud deflection comparison are discussed in order to highlight the possible optimization of such structures.

Keywords: Cross-laminated timber, wooden spatial structures, FEM, CNC, Comparing Point Clouds, digital fabrication, design to assembly, wood connections, integral mechanical attachment

1 Introduction

The spiral was made of CLT 3-plys spruce panels for the boxes, and steel cables to resist the tension loads. The interior of the cathedral was scanned using Faro Model S 150 in order to have accurate measurements for the project. The figure 1 shows the scanned church model and project including the stands with a constant slope in the direction of the stage, and the spiral positioned at the center of the cathedrals nave. Above the spiral, the cables are fastened to the framework, which stands thirty meters higher.

Automated CAD Design The use of digital fabrication and automation of the fabrication process was required, because of the precision and the uniqueness of every parts of the structure. The 3D modelling algorithm was developed for creating box-to-plate assembly (figure 2), depending of the initial inputs, such as cone height and width, the thickness of the panels,

Copyright © 2019 by Laboratory for Timber Constructions (IBOIS), Ecole Polytechnique Fédérale de Lausanne
Published by the International Association for Shell and Spatial Structures (IASS) with permission.

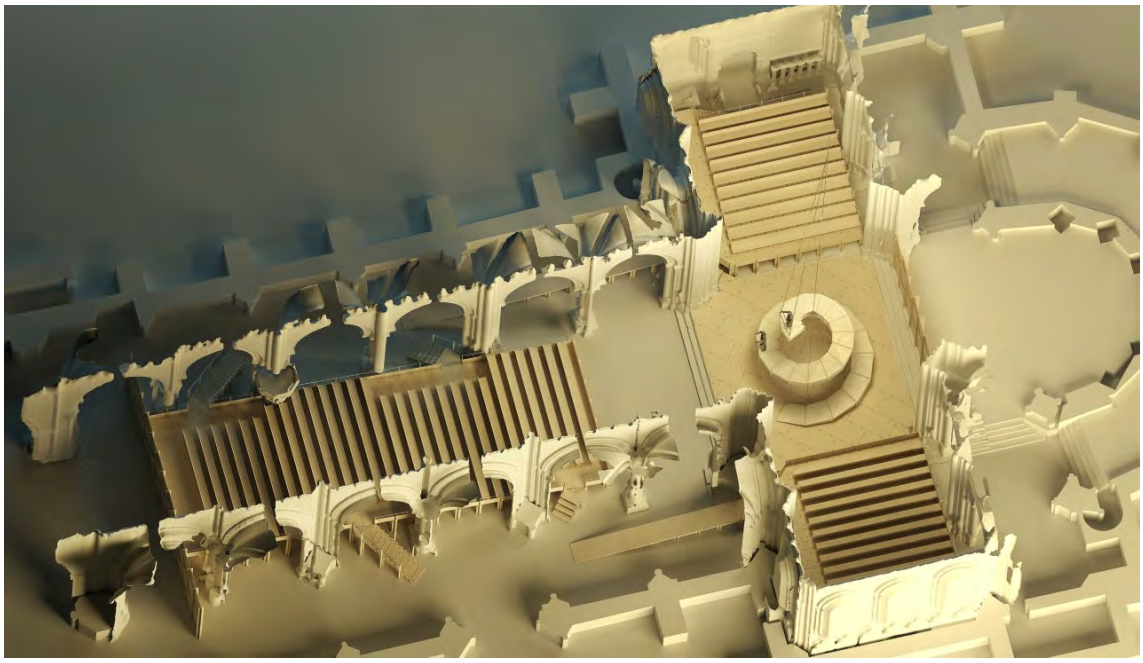


Figure 1: The three stands with a constant slope in the direction of the spiral.

joinery (finger-joints), external connectors (dowels, screws.), assembly sequence and fabrication tool-paths.

Finite Element Modeling The structural model was built in a Finite Element computational platform ABAQUS for analysis purposes. The FE model was then used for the design procedure, where the global stress values and the displacements were calculated. Following the different load cases, the structure demonstrated acceptable level of performance. Nevertheless, its global performance could be improved by changing its initial geometry.

Computer Numerical Control Machine 4.5-axis CNC machine "Maka" was used for cutting panel outlines, drilling holes for screws and dowels, engraving panel indices and cable inlets. Furthermore, the G-Code tool-path was automated from design to fabrication within the same software interface. The whole cutting process took approximately two weeks.

3D Laser Scanning and Point-Cloud Deflection Comparison At the end of the project, the entire structure was scanned to measure the deformation, with different loading cases scenario. First, we aligned two point-clouds by picking equivalent point of each scan and then computed the distance between each point to know the deformation.

2 Design and CAD: Geometry

Conic Shape The scale of the spiral was chosen by minimal bounding area of central vault. The geometry of the spiral is derived from a cone shape, whose central axis and angle is used to position stairs within user specified angle/stair width (figure 2A). Moreover, this approach guarantees to keep an unique point of intersection for the cables, at the top of the structure.

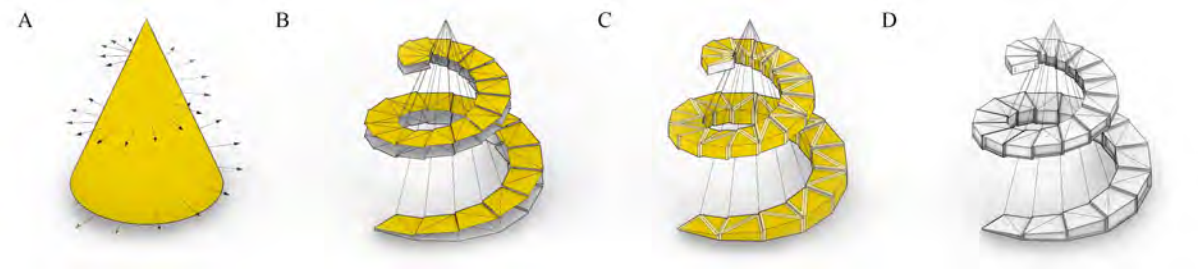


Figure 2: (A) The spiral steps follows the vectors along the cone (B) Base model: two layers of steps moved by z-axis (C) Model for structural calculation (D) Final model with thickness, joinery and tool-path

Steps Geometry The model is divided into two top and bottom layers that determine the static height of the structure. Also, the model is divided vertically into three parts: bottom ramp, middle sloped steps, and top equal height deck. The number of steps was determined by the minimal slope of overall gradient of spiral ramp. In addition to this, the step is sloped to reduce its height, and triangulated to keep them planar. The first three panels are weighted and screwed into a floor made out of 25 mm thick Oriented Strand Board (OSB) panels. Each corner of this floor is contiguous to the piles of the cathedral, and avoid the lateral displacement in this plane for the entire structure. The main issue could have been the instability of the structure caused by a dynamic load on it, like singers. The first three boxes could have lift up from their position and slipped, because the main cable could also deviate.

Detailing and Fabrication The low-poly mesh model is used for fast design iterations and structural calculations (figure 2 B-C). Afterwards the model is processed introducing fabrication constrains: thickness of panels, assembly sequence, joinery (finger-joints and screws), labeling, orientation to CNC machining space and G-Code tool-path generation (figure 2D). The geometry of spiral was divided into box objects, that contained information about next and previous boxes. The adjacency of boxes gives information about thought-tenon joint, screws holes and dowel positioning joints derived from neighbours. Each box class contains 9 plate elements: two connecting plates, two sides that have different inlet to have space for screwing, 1 diagonal plate flipped to triangulation of step for better structural performance and 4 triangular elements (figure 3). The collection of plates contains adjacency of plate-to-plate assembly within one box

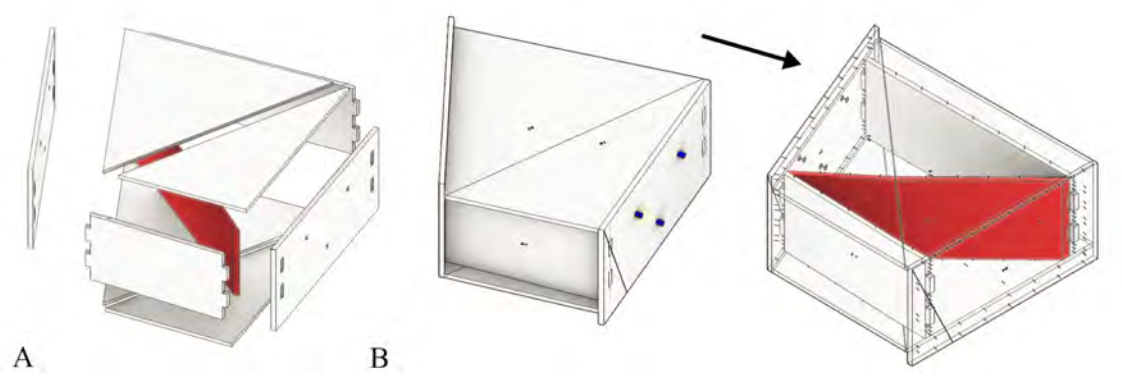


Figure 3: (A) Exploded view of a box (B) Box with dowels and engraved (C) Box with screws

to indicating screwing holes in the CNC machine and tenon-mortise joints.

3 Prototype

3.1 Structural test

An initial test was conducted in the laboratory to validate the boxes configuration, the position of the different elements, the simplicity of the assembly on site and the response under loads. Four boxes were fabricated and were loaded in cantilever to measure the deformation and examine the weaknesses (figure 4A). The first box was fastened to a wooden base made of a 25mm OSB panels with three rods, which was fixed to the ground using sixteen rods connected into the concrete slab. This configuration avoided the boxes from tilting under the loading, and enable to put more weight on them to observe further deformations. The first phenomenon was the rotation between the part of the box close to the interior of the curve, and the exterior one. The second phenomenon was the emergence of cracks between the first box and the second one (figure 4B). The structure provided many information which were crucial to anticipate potential future problems by observing and measuring the displacements on the last caisson in cantilever. Eleven LVDT sensors measured the displacements of the boxes horizontally and vertically during the loading. The loading was applied using 11.9 kilogramms weights every 30 seconds on the structure, and the loaded box had a vertical displacement of 55 millimeters at 319.45 kilograms. A total load of 408 kilograms was applied to make the structure collapse and observe behavior of proposed system. The weakest part is the junction between the fixed part and the cantilevered one. After the test, the delamination of side panels was visible. This data was used to make a Finite Element Method based on the Abaqus calculation software, which took into account the rigidity of our elements and the connectors between them.

3.2 Finite Element Method

A Finite Element Method model was developed to support both the experimental test and design framework [1][2][3]. The displacements and stress values of the elements are calculated and compared to the timber mechanical characteristics and associated limits (figure 4C). Specifically, the stress in the metallic elements, as well as the cables were compared to the ultimate and serviceability limit state. Considering the real load cases, a uniform distributed load of 1 kN was applied at four boxes. A maximum displacement of 10 millimeters at the top of the spiral was observed which meet the SLS limit. Furthermore, the FE model played an important part for the choice of the different metallic parts, where it made the adaptation of the quality and



Figure 4: (A) The 4 boxes prototype (B) The failure mode (C) FEM calibrated after the test

the size section possible.

3.3 Optimization of the caissons

Following the previous results and the assembling of the prototype, changes were done to upgrade the current model:

- Implementation of a diaphragm diagonally inside the caissons: allows a better rigidity of the caissons and between them (figure 3A).
- Dowels between the boxes : the boxes were lifted and positioned at the correct place against the previous one using 3 dowels at each side. They were not designed to withstand shear forces, but only to guarantee the precise alignment (figure 3B).
- Pre-drilling for screws: during the assembly of the prototype, the time necessary for screwing was important comparatively to the others tasks. Pre-drilling the holes during the CNC fabrication phase allowed a faster installation on site. It also prevented from mistakes and provided better connections (figure 3C).

4 Fabrication and Automation of G-Code

The automation of geometry generation included tool-path generation for CNC machine "Maka" (figure 5E). Firstly, the two-hundred and sixty three elements of the spiral are flattened at the same level (figure 5A-B) and placed on machining space of the design software. The nesting of oriented plated were performed using open-source OpenNest Grasshopper add-on (figure 5C). The custom G-Code tool selects geometrical elements such as lines drilling, outline for cutting, text for engraving and sends the G-Code for CNC fabrication (figure 5D). This step optimized the file preparation and avoided errors in programming once it is properly made. The code only needs to be checked visually on the screen with the 3D-simulation of the cutting, and then start the machining.

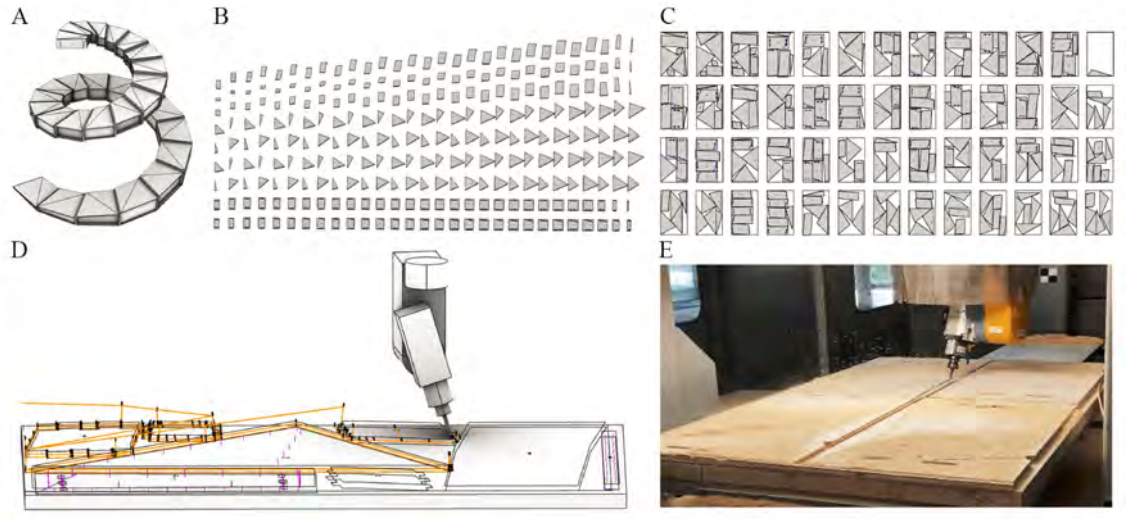


Figure 5: (A) Complete spiral (B) Flattened elements of the spiral (C) Nesting of oriented plate (D) 3D-simulation of the cutting machining (E) Maka CNC at work

The custom code was also developed for surfacing the angles superior to 45. The cutting tool was too small and the rotor of the CNC-machine could collide with the panel and de-calibrate the machine. To avoid this problem, the position of the diaphragms has been changed to have a smaller angle, and the angles were cut by surfacing the panels with a slope instead of cutting them through. The whole geometry and G-Code application were modified quickly thanks to automated design. Moreover, all the cutting angles of plates must be feasible from one side of the panel, because the CNC-machine can work only on one side of the panel and flipping the panel was not feasible.

5 On site installation method

The on-site assembly took three days. Firstly, the main cable was fastened to the frame of the cathedral, that also determined the center of the scene thanks to a plumb line. When the center was marked, the position of the first box was drawn on the floor. Afterwards, the first three boxes were self weighted and screwed to the OSB panels flooring. The boxes were lifted using hoist which was fastened at the end of the main cable and put against the previous one. The box components were correctly positioned by three dowels, screwed and shored directly, as it is shown in the figure 6A. Measurements were made to check the height of each box, assuring a correct re-partition of the tension into the cables. Once every box was shored, the cables were fastened by threaded rods and then the complete spiral was fixed as it is shown in the figure 6B. Measurements were made again to check the height of each box and if necessary cable length was modified by putting tension into the cable.

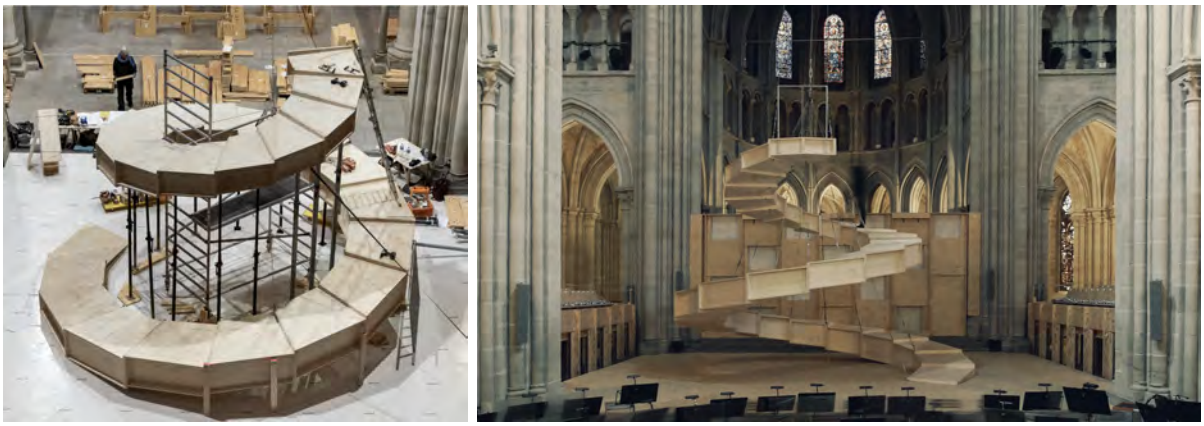


Figure 6: (A) The shored spiral during assembly (B) The hanging spiral [Credit: Claude Bornand]

6 Structural test of the complete spiral

6.1 Loading test and 3D laser scanning of the deflection

The structure was tested on-site after all the events took place (for safety reasons). Four different loading cases were applied on the spiral to study its deflection and global behavior under loads. The loads simulated human weight on different part of the structure. In order to better understand the position of the loading, the boxes were numbered as shown in the figure 7A. A laser scanner was used to measure the displacements during the different loading cases [4][5]. Six scans were made in total:

- Scan 1: Initial position : Get the real position of the spiral as a base for comparison
- Scan 2: Loading 1: 95.2 kg on the box 19.
- Scan 3: Loading 2: 95.2 kg on the box 19 and 13 (190.4kg in total).
- Scan 4: Loading 3: 95.2 kg on the box 19, 13 and 5 (285.6kg in total).
- Scan 5: Loading 4: 285.6 kg on the box 19.
- Scan 6: Final position : To see the remaining displacement after the load

The results of the different loading cases are shown on the figure 8B with the FEM comparison. For the first loading case, we observed positive displacements on the opposite side of the loaded area. This was explained by the fact the metallic plate, which withstand the cables, rotated with the loading, in addition the structure is unbalanced by the loading too. The second loading case applied a new load on the opposite side of the spiral but closer to the center, which result in a smaller deflection on the box 19 than for the loading case 1. For the third loading case, as shown on the figure 7A-B, we observed a bigger displacement on the most loaded side of the spiral, showing the transmission of the deflection by the cable, between the box 5 and 19. During the fourth loading, we hear some cracking noise in the junction between the start of the cantilever (Box 25) and the third box attached to the OSB flooring (Box 26). This observation validated the prototype test results, when the most loaded part of the structure is between the fixed part and the cantilevered.

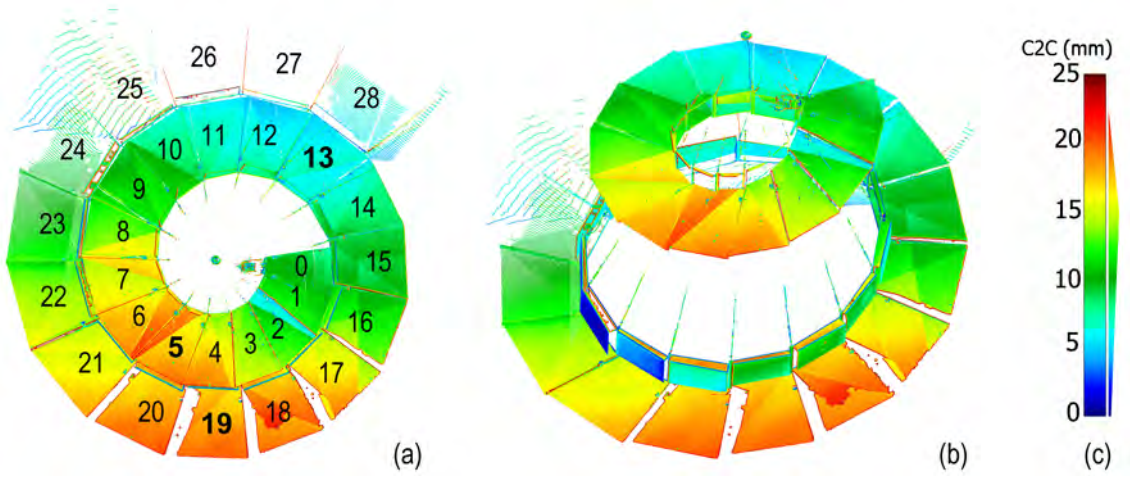


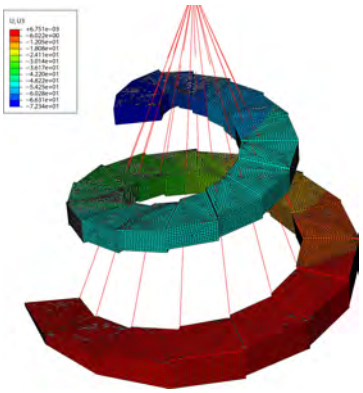
Figure 7: (A) Loading case 3: Top view (B) Loading case 3: Perspective view (C) C2C values

6.2 Comparison with Finite Element Method model)

The initial FEM model is then computed with the same loading as it was in the experimental test to compare the results. The model give a maximum of displacement of 9.25 millimeters against 10.9 millimeters in reality. The global behavior of the FEM-model followed the real case.

7 Conclusion

The project served as the main opera stage design applied for a specific event (figure 6B). It was also a first demonstrator when the laboratory experimented with timber plates structure in cantilever action. Several developments were made and would be applicable to other projects



Case	Box	Load	FEM	C2C
	No	[N]	[mm]	[mm]
1	19	934	9.25	10.9
2	19	934	3.12	4.3
2	13	934	15.4	17.9
3	19	934	16.65	19.9
3	13	934	5.72	7.6
3	05	934	16.75	18.7
4	19	2802	28.31	29.4

Figure 8: (A)FEA of the spiral under the loading case 3 (B) Comparison C2C and FEA results

including G-Code, nesting, and geometry generation by means of box-to-plate data-structures that contained joinery information. The project used automated work-flow from design to fabrication which was efficient in terms of short cutting and assembly time. Moreover, we employed collaboration from CAD to FEM through low-poly models at early stages of design. The same model served as an input for detailed fabrication model and structural analysis application. Nevertheless, the work-flow could have benefited more from integral mechanical attachment in order to reduce the amount of screws used in this demonstrator. Finally, the multidisciplinary team of designers, engineers and fabricators worked together in order to improve and realize this temporary free-form timber application.

8 Acknowledgements

The authors would like to thanks EPFL and GIS, JPF-Ducret SA and André SA, as well as the Bureau d'études Weinand and Yves Weinand Architectes SARL for the technological transfer.

References

[1] A. Stitic, C. Robeller and Y. Weinand, "Experimental investigation of the influence of integral mechanical attachments on structural behaviour of timber folded surface structures," *Thin-Walled Structures*, vol. 122, pp. 314-328, 2018.

[2] A. Stitic, A. C. Nguyen, A. Rezaei Rad, and Y. Weinand, "Numerical Simulation of the Semi-Rigid Behaviour of Integrally Attached Timber Folded Surface Structures," *Buildings, Multidisciplinary Digital Publishing Institute*, vol. 9, issue 2, pp. 5, 2019.

[3] A. C. Nguyen, and Y. Weinand, "Development of a spring model for the structural analysis of a double-layered timber plate structure with through-tenon joints", *WCTE 2018 - World Conference on Timber Engineering; South Korea; 20-23 August 2018;*

[4] K. Pukanska, J. Gajdosk, M. Marcian and K. Bartos "Determination of Deformations of a High-Capacity Tank Using the Technology of Terrestrial Laser Scanning", *American International Journal of Contemporary Research*, Vol. 4, No. 4; April 2014.

[5] J-A. Paffenholz and D. Wujanz "Spatio-temporal monitoring of a bridge based on 3D point clouds: A comparison among several deformation measurement approaches", *JISDM - Joint International Symposium on Deformation Monitoring, 15-17 May 2019, Athens, Greece.*

Proceedings of the IASS Annual Symposium 2019 – Structural Membranes 2019
Form and Force
7 – 10 October 2019, Barcelona, Spain
C. Lázaro, K.-U. Bletzinger, E. Oñate (eds.)

Spanning 9m with various combinations of small and short lumber – Structural Design of Kindergarten in Date City

Ryoma MURATA*

*Ryoma Murata Building Studio Ltd.
#3 Komatsu Bldg. 3F, Sumiyoshicho 12-18, Shinjuku City, Tokyo JAPAN
murata@murataryoma.com

Abstract

Kindergarten in Date City (in Fukushima Prefecture, Japan) was built with locally produced Japanese cedar lumber. In order to construct up to 9,1 m span using commonly distributed solid wood with standard small cross section and short length, various timber frameworks such as truss, tree-shaped column, and reciprocal frame were utilized. Building a long span by using a combination of small and short lumber is effective in reducing construction costs. In this paper, the key points of structural design and construction process of Kindergarten in Date City will be described. Processing of wood was carried out efficiently by automated pre-cut machine for the most part. The roof by the reciprocal frames was erected with temporal support at the centre of the span, and after the erection completed, the temporal support was removed. Vertical displacements after support removal were measured and compared with the estimated value from analysis.

Keywords: structural design, timber construction, truss, tree-shaped column, reciprocal frame.

1. Introduction

In Japanese timber construction, solid wood, laminated wood and LVL (laminated veneer lumber) are usually used for the framework. Among them, solid or laminated wood with small cross section (width: 105 or 120 mm, depth: 105 ~ 240 mm, length: about 4 ~ 6 m) is widely distributed for housing use and easy to obtain with low cost [1]. These dimensions are determined based on the Japanese traditional measurement scale, the Shaku-Kan system (For example, 105 mm is equal to 0.35 shaku and 240 mm is equal to 0.8 shaku).

On the other hand, so far, laminated wood or LVL with large cross section has been used for building a long span such as, for example, a playroom of kindergarten. But since they are 'made to order' and relatively expensive, building a long span by using a combination of small and short lumber is effective in reducing construction costs.

In this project, various timber frameworks such as truss, tree-shaped column, and reciprocal frame were utilized in order to construct up to 9,1 m span using commonly distributed solid wood. Such kind of timber frameworks are not only low-cost but also suitable for expressing the fascination of wood as building material.

Copyright © 2019 by Ryoma Murata
Published by the International Association for Shell and Spatial Structures (IASS) with permission.

2. Overview of the Kindergarten in Date City

Overview of this project is shown in Table 1. Aerial and external view are shown in Figure 1 and 2.

Table 1: Overview of the Kindergarten in Date City

Structure	Timber frame construction
Total floor area	1,912 m^2
Number of storeys	1
Location	Date City (Fukushima, Japan)
Snow cover (snow load)	50 cm (1.000 N/m^2)
Completion year	2017
Architect	Tanaka Hemmi JV
Structural basic design	Masahiro Inayama
Structural design	Ryoma Murata Building Studio



Figure 1: Aerial view



Figure 2: External view*

2.1. Seismic design

The resistance elements against horizontal force due to earthquake or wind are timber bracings and shear walls of plywood nailed to the structural frame. These seismic elements are designed to keep allowable stress level for short-time (corresponding to being within the elastic range), under the static load equivalent to horizontal seismic intensity 0.2G, and the interlayer deformation is 1/120 or less. The arrangement of the seismic elements is shown in Figure 3.

2.2. Fireproof design

For timber construction with a total floor area of more than 1.000 m^2, higher fire resistance than small building is required by the law. Among several ways to improve the fire resistance, we chose to divide the building into three sections by a firewall (figure 3). The firewall was constructed by attaching 42 mm thick of the plaster board on both sides of the timber frame. Each of the divided areas was designed to look like one in appearance.

3. Design of roof frame

In this section, each characteristic roof frame will be described. These are M-shaped truss for the playroom, tree-shaped column for the classroom of 0~2-year-old children and reciprocal frame for the classroom of 3~5-year-old children.

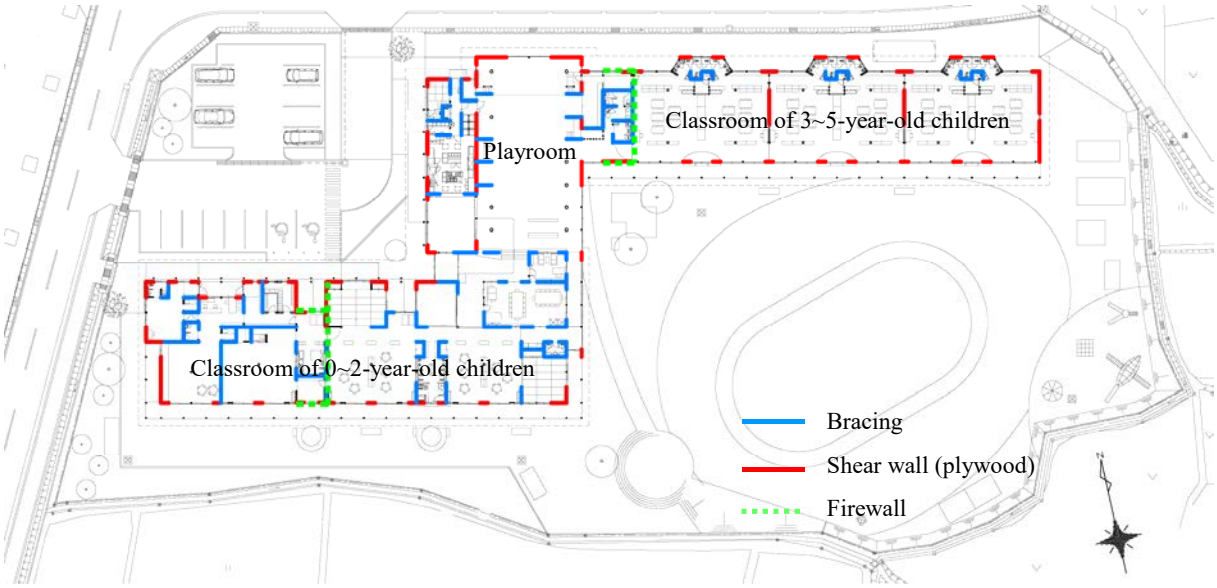


Figure 3: Plan

Processing of wood was carried out efficiently by automated pre-cut machine (Hundegger K2) except for log pillar. The roof by the reciprocal frames was erected with temporal support at the centre of the span, and after the erection completed, the temporal support was removed. Vertical displacements after support removal were measured and compared with the estimated value from analysis.

3.1. M-shaped truss for the playroom

M-shaped truss for the playroom is a combination of the inclined posts from both sides and the top rhombus truss (figure 4~6). The span of the truss is 9.1 m, and the interval is 910 mm. The cross section of top chord (rafter) is 120 mm x 210 mm, bottom chord is 75 mm x 120 mm (double), strut and inclined post are 120 mm square.

The top chord, strut, and inclined post bear compression, while the bottom chord bears tensile stress (figure 5).



Figure 4: Interior view of the playroom*

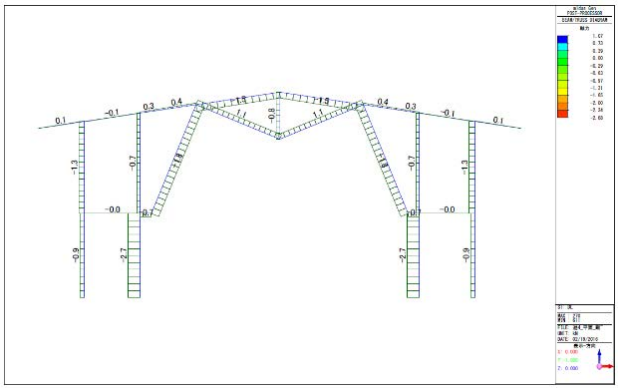


Figure 5: Axial force of M-shaped truss

Figure 7 is a mockup of the truss manufactured for verification of detail and construction process. The bottom of the inclined post is jointed by a small steel pipe and steel pins to resist with occasional tension by blowing up of wind (figure 8).

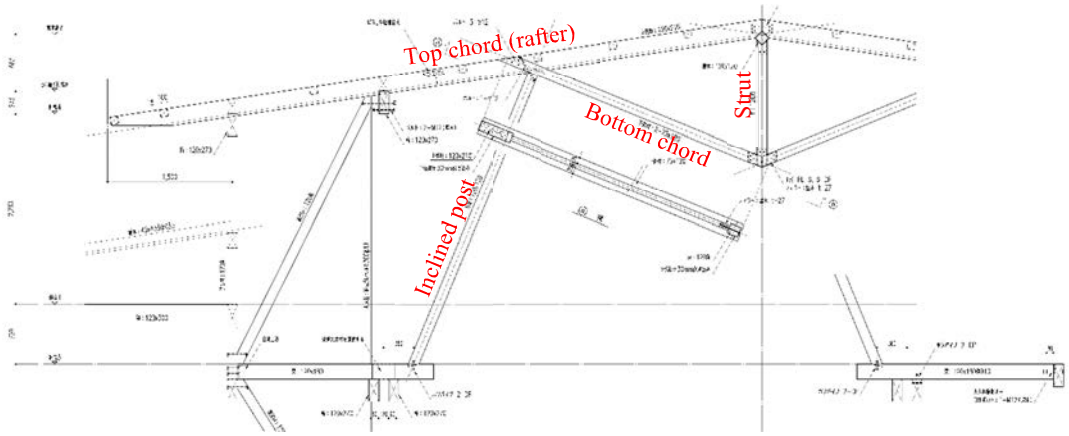


Figure 6: Elevation drawing of M-shaped truss



Figure 7: Mockup of the truss



Figure 8: Joint detail of the truss

3.2. Tree-shaped column for the classroom of 0~2-year-old children

Here, a 9.1 m square roof is supported by one central log pillar (250 mm in diameter) and radially arranged 8 brackets (120 mm square) (figure 9). The brackets are in compression and the force is transmitted as the stress perpendicular to the grain of log pillar, but in preparation for the occasional tension, the log pillar and each bracket is jointed with a long bolt (M16) inside the cross section of the bracket penetrating the pillar to the opposite side (figure 10).



Figure 9: Classroom of 0~2-year-old children*



Figure 10: Joint detail of log pillar and brackets

3.3. Reciprocal frame for the classroom of 3~5-year-old children

In a common structure, "supporting member" and "supported member" can be clearly distinguished, such as a beam supported by a column. However, in the reciprocal frame, one member supports the adjacent members, and at the same time, is supported by the adjacent members. That is, the reciprocal frame is a structure in which "supporting" and "supported" are intricately intertwined.

The advantage of this structure is that a combination of short members is able to build a long span. It has long been practiced to take this advantage, in traditional construction, building long spans with wood, which is a natural material and therefore has a limited length.

In the Classroom of 3-5 years old children, 5 m long lumber (120 mm x 210 mm @910 mm) is used to support a roof with a span of 6,28 m (figure 11~13). The facing rafters are arranged 455 mm apart from each other, and the edge of the rafter in one side is supported by the orthogonal girder, and this girder is supported by the rafter in the opposite side. That is, a reciprocal frame is configured by joining the facing rafters, arranged alternatively, with the orthogonal girder. The stress of this reciprocal frame is simple; a pair of two simple beams in a span as shown in figure 12.



Figure 11: Classroom of 3~5-year-old children*

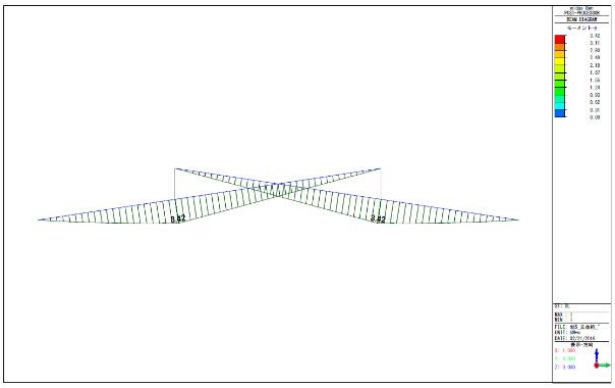


Figure 12: Bending moment diagram of a pair of rafters

As is common to the construction of any types of reciprocal frames, a temporal support was provided at the centre of the span (figure 13). After the placement of all rafters and joining with the orthogonal girders were completed, the temporal support was removed (figure 14).

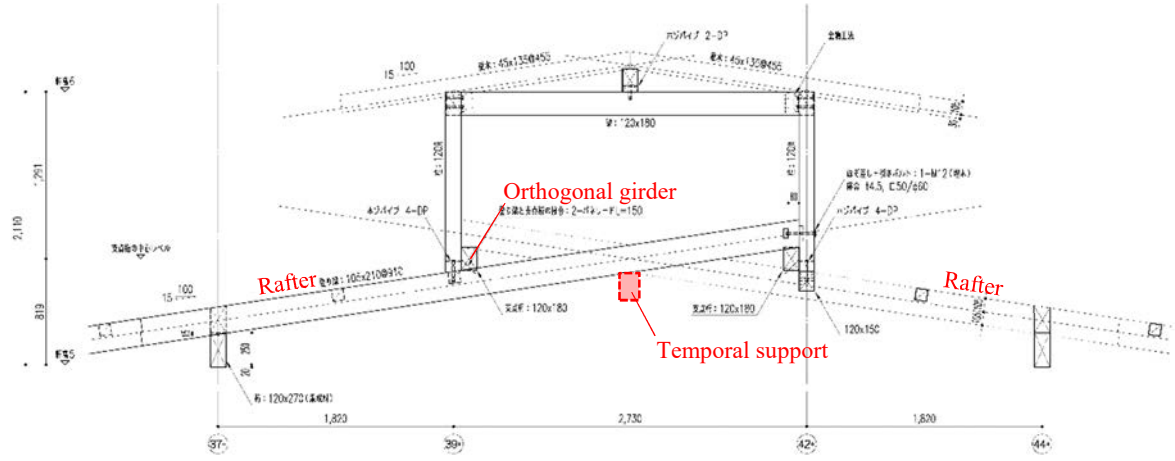


Figure 13: Elevation drawing of the reciprocal frame

The change in height from the base concrete to the reciprocal frame was measured at 3 points before and after removal of the support. The deflection of the reciprocal frame obtained from this measurement was 3 to 5 mm (figure 15). On the other hand, the predicted value by elastic analysis is 5.5 mm, which is close to the observed value. In the analysis, referring to the literature [2][3], the unit weight of wood (Japanese cedar) assumed to be 4 kN / m^3, the Young's modulus for bending assumed to be 7.0 kN / mm^2, and the unit weight of plywood assumed to be 5 kN / m^2 / mm. Corresponding to the actual situation, only the self-weight of structural members and plywood was considered as the load. The weight of finishing or live loads were not considered for this analysis.



Figure 14: Completed reciprocal frame

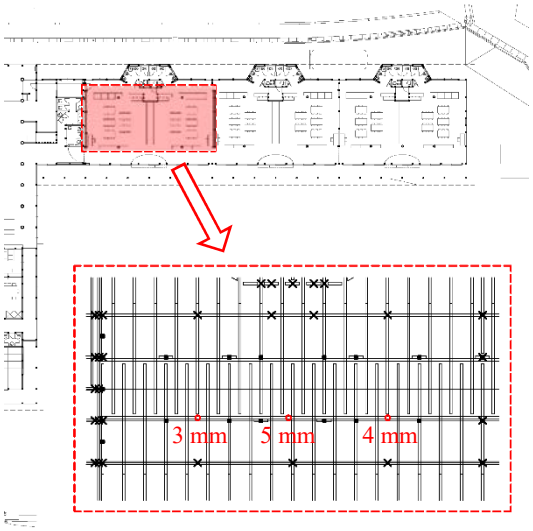


Figure 15: Observed deformation of the points

3. Conclusion

The key features of structural design of the Kindergarten in Date City were described. Various wooden spaces were created by small-section standard lumber that is inexpensive and easy to obtain, by devising M-shaped truss, tree-shaped column, and reciprocal structure.

The observed values of the deflection of the reciprocal frames agreed well with the analysis values.

Acknowledgements

Photos with an asterisk (*) in the title are courtesy of Masao Nishikawa Photography Studio.

References

[1] Katsumi Nishimura, “Available dimensions of solid wood,” *Kenchikugijutsu*, No. 784, pp. 148, Kenchikugijutsu, Inc., May 2015 (in Japanese).

[2] Architectural Institute of Japan, *Recommendations for Loads on Buildings*, Architectural Institute of Japan, 2015.

[3] Architectural Institute of Japan, *Standards for Structural Design of Timber Structures*, Architectural Institute of Japan, 2006.

Proceedings of the IASS Annual Symposium 2019 – Structural Membranes 2019
Form and Force
7 – 10 October 2019, Barcelona, Spain
C. Lázaro, K.-U. Bletzinger, E. Oñate (eds.)

Form follows availability – Designing structures through reuse

Jan BRÜTTING*[a], Gennaro SENATORE[b], Corentin FIVET[a]

[a] Structural Xploration Lab, EPFL Lausanne, Passage du Cardinal 13b, Fribourg, Switzerland
* Corresponding author: jan.bruetting@epfl.ch

[b] IMAC, Applied Computing and Mechanics Laboratory, EPFL Lausanne, Switzerland

Abstract

This work proposes a new direction in structural design: the synthesis of structures through the reuse of elements. Reusing structural elements reduces the environmental impacts of building structures because it avoids sourcing new material, it reduces waste and it requires little energy. Designing structures from reused elements is unlike conventional structural design because stock element availability is a design input. In other words, structures must be designed to fit given element characteristics, e.g. cross-sections and lengths. Stock constraints such as number of elements and element lengths, have a major influence on the optimal structure layout and form. In this new paradigm structural *form follows availability*. This work formulates new computational methods for the synthesis of reticular structures through reuse. Two scenarios are presented: a) reuse of reclaimed elements from a given stock, and b) design of a common stock which is used as a kit-of-parts to build diverse structures. Case studies are presented to demonstrate the potential of the proposed methods. It is shown that structures produced by these methods have a significantly lower environmental impact than minimum weight structures made of new elements.

Keywords: Structural design, discrete optimization, geometry optimization, mixed-integer linear programming, reuse, stock, Life Cycle Assessment, environmental impact

1. Introduction

Designing structures through reuse is a challenging task because "size and length of the available members will then determine the spans and spacing possible in the new structure […]" [1]. In other words, the design process is reversed because mechanical and geometric properties of available elements define the layout of the structure. This new *form follows availability* [2] paradigm is not yet supported by design guidelines nor by established computational tools. Figure 1 illustrates the two methods outlined in this paper: a) designing structures from a stock of available elements; b) designing a common stock of bespoke elements, which is used as a kit-of-parts to build diverse structures. Both these design approaches enable the reuse of structural components for multiple service lives. Further, these approaches support circular economy while reducing raw material usage, waste generation and energy consumption, thus mitigating environmental impacts of load-bearing structures.

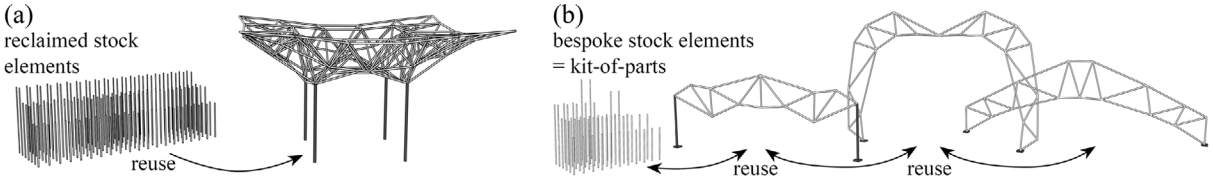


Figure 1. Designing structures through reuse: (a) a space truss made from a stock of reclaimed elements, (b) three truss systems made from one kit-of-parts.

Copyright © 2019 by Jan Brütting, Gennaro Senatore, and Corentin Fivet.
Published by the International Association for Shell and Spatial Structures (IASS) with permission.

Structural optimization with stock constraints has received little attention so far. The optimization of plane frames of fixed topology from a stock of onetime available cross sections has been presented in [3]. In [3] evolutionary algorithms have been employed for weight optimization but without accounting for the availability of element lengths. Strategies based on heuristic algorithms have been developed to form-fit a stock of wood logs to statically determinate trusses [4]. In contrast to previous works, the formulations presented in this paper are based on deterministic combinatorial optimization that guarantees globally optimal element assignment solutions. Nadir et al. [5] have studied the reconfiguration of bars within a planar truss, in order to react to changing load actions. Tugilimana et al. [6] considered sizing optimization, spatial rearrangement and reuse of unit-cells in modular bridges. Basso et al. [7] optimized the geometry of a single free-form grid structure for a defined number of elements with assigned lengths. In contrast, the kit-of-parts optimization methods presented in this paper consider: 1) stocks of individual elements with varying cross-sections and lengths, 2) employs assignment, topology, and geometry optimization, and 3) minimizes structural weight, environmental impacts and the number of unshared elements between structures made from a common kit-of-parts.

Section 2 outlines optimization formulations for the design of structures with reused elements, which are based on discrete structural optimization [8]. Section 2.1 focuses on assignment and topology optimization of reticular structures subject to stock constraints. This method has been previously presented in [9] for 2D case studies and it is here extended to 3D structures. Section 2.2 adapts the formulation to obtain an optimal stock of elements (i.e. a kit-of-parts) that can be used to build diverse structures. Sections 2.3 to 2.5 outline the main aspect of the structural and geometric optimization techniques implemented in this study as well as of the Life Cycle Assessment employed to evaluate results. Section 3 describes the application of the proposed methods to case studies.

2. Methods

2.1 Assignment and topology optimization (P)

In the following, stock components are named elements while components of a truss structure are named members. Formulation (P) is the optimum assignment $\boldsymbol{T}$ of a given stock of elements into a predetermined structural layout (also called ground structure) comprising m members. The objective (Eq. 1) of (P) is the minimization of embodied energy (section 2.5). It is assumed that stock elements are collected in g groups of identical length and cross section. The use of one element from stock group j at member position i in the ground structure is represented by the entry $t_{i,j} = 1$ in the binary assignment matrix $\boldsymbol{T} \in \{0,1\}^{m \times g}$. If element j is not assigned at position j then $t_{i,j} = 0$. A group of 'zero-members' can be added to the stock to allow for topology optimization. Eq. (2) enforces the assignment of only one element from the stock to any position in the structure. Eq. (3) constrains the maximum number of element assignments to n_j available elements per group. Eq. (4) constrains the lengths $\boldsymbol{l} \in \mathbb{R}^g$ of assigned elements to be longer or equal than the distance $\bar{\boldsymbol{l}} \in \mathbb{R}^m$ between the nodes of the corresponding truss positions.

$$\text{(P)} \qquad \min_{\boldsymbol{T}} f(\boldsymbol{T}) \tag{1}$$

$$\text{s.t.:} \sum_{j=1}^{g} t_{i,j} = 1 \;\; \forall\, i = 1 \dots m \tag{2}$$

$$\sum_{i=1}^{m} t_{i,j} \leq n_j \;\; \forall\, j = 1 \dots g \tag{3}$$

$$\bar{\boldsymbol{l}} \leq \boldsymbol{T}\boldsymbol{l} \tag{4}$$

2.2 Stock optimization (S)

Formulation (S) is the optimization of the stock configuration (i.e. kit-of-parts) such that its elements are reused to build $\mathcal{R}$ different structures. This process can be thought of as the "inverse" of (P). The first term of the multi-objective function (Eq. 5) minimizes the total number of stock elements N_{tot}, which in turn maximizes element reuse. The other two objective function terms minimize cut-off waste W^r and weight M^r of each structure $r \in \mathcal{R}$. The objective function can be weighted to bias the optimization towards a specific objective. In this work, weighting factors $w_1 = 1$, $w_2 = 0.1$ and $w_3 = 0.2$ are used. For a predefined set $\mathcal{H}$ of standard cross sections, the number of elements n_j and lengths l_j for each cross section $j \in \mathcal{H}$ are design variables. Binary variables z_j determine whether one or more elements with cross section j and length l_j are part of the optimum stock. For each element type at most n_j elements can be assigned to a structure r (Eq. 6). An upper bound z^{max} defines a maximum number of element types (i.e. cross sections and lengths) in the stock (Eq. 7). Eq. (8) constrains the member lengths $\bar{\boldsymbol{l}}^r$ within a defined range Δ to the stock element lengths $\boldsymbol{l}$. Δ is used here as a slack variable in order to relax the problem, in practice it is a length tolerance that could be compensated through adjustable joints.

$$\text{(S)} \quad \min_{\boldsymbol{T},\boldsymbol{n},\boldsymbol{l},\boldsymbol{z}} w_1 N_{tot} + w_2 W_{tot} + w_3 M_{tot} = w_1 \sum_{j\in\mathcal{H}} n_j + w_2 \sum_{j\in\mathcal{H}} W^r + w_3 \sum_{r\in\mathcal{R}} M^r \tag{5}$$

s.t.: Eq. (2) $\forall\ r \in \mathcal{R}$

$$\sum_{i=1}^{m} t_{i,j}^r \le z_j n_j \ \ \forall\, j \in \mathcal{H};\ r \in \mathcal{R} \tag{6}$$

$$\sum_{j\in\mathcal{H}} z_j \le z^{max} \tag{7}$$

$$\boldsymbol{T}^r \boldsymbol{l} - \Delta \le \bar{\boldsymbol{l}}^r \le \boldsymbol{T}^r \boldsymbol{l} \ \ \forall\, r \in \mathcal{R} \tag{8}$$

2.3 Structural Optimization

Since the problems outlined in sections 2.1 and 2.2 are formulated as *Mixed-Integer Linear Programs* (MILP) in standard form, they can be solved to global optimality via *branch-and-bound* techniques. Structural optimization is included into these formulations through the *simultaneous analysis and design* approach [10]. Force equilibrium, geometric compatibility, stress and displacement constraints are added to (P) or (S) as linear equality or inequality constraints. Self-weight and member buckling are also considered. For details concerning the structural optimization part of these formulations, the reader is referred to [9].

2.4 Geometry optimization

Geometry optimization is sequentially applied to optimization (P) and/or (S) in order to improve the structural design. When considering (P), geometry optimization first minimizes compliance over a pre-defined number of iterations (e.g. 5 iterations in this work), in order to obtain efficient structural shapes which allow the assignment of smaller cross sections. Subsequently, the objective of geometry optimization is changed to minimize cut-off waste. When considering (S), geometry optimization is carried out to improve fitting between the structure and the kit-of-parts. Therefore, during geometry optimization, stock element lengths $\boldsymbol{l}$ are included as design variables. The slack variable Δ is decreased iteratively until all the elements in the kit-of-parts can be assigned using their full length ($\Delta = 0$).

2.5 Life Cycle Assessment

Life Cycle Assessment (LCA) is carried out to quantify embodied energy and carbon equivalence. When considering component reuse, this assessment accounts for impacts related to the supply of stock elements through selective deconstruction as well as transport to the building site. The embodied energy

EE_R and embodied carbon equivalence EC_R of structures made from reused elements is here defined as a function of structural mass M and cut-off waste W:

$$EE_R = 3.245\frac{MJ}{kg}M + 3.235\frac{MJ}{kg}W \qquad EC_R = 0.277\frac{kgCO_2eq}{kg}M + 0.276\frac{kgCO_2eq}{kg}W \quad (9)$$

The coefficients in Eq. (9) are derived from the same assumptions taken in [9]. To benchmark the environmental savings obtained through reuse against newly produced elements, production methods involving primary and secondary (recycled) steel are considered. The embodied energy EE_N and carbon equivalence EC_N for conventionally produced steel profiles and their transport to the site are 13.227 $\frac{MJ}{kg}$ and 0.925 $\frac{kgCO_2eq}{kg}$ respectively. Production of connection elements are assumed similar in both reuse and new cases.

3. Results

3.1 Optimization of a 2D truss under stock constraints

Figure 2(a) shows a truss ground structure with $m = 41$ possible bar positions and a span of $l = 20.00$ m. A dead load of 1.00 kN/m and a live load of 5.00 kN/m are applied to the top chord nodes. The optimization is subject to ultimate (ULS) and serviceability limit state (SLS). For the SLS load combination, displacements are limited to $l/300$. In the geometry optimization step all nodes are constrained within a region of ±3.00 m, which prevents self-overlapping. The node of the roller support is horizontally constrained to maintain a minimum span of 20.00 m.

Three stock configurations A, B, and C are considered, Figure 2(e). All three stocks consist of circular hollow sections (CHS) of dimensions taken from EN 10210. For each stock, seven element groups with cross section sizes 33.7×3.2, 42.4×4, 48.3×5, 60.3×4, 76.1×5, 88.9×10, and 139.7×5 are available. In stock A all elements have 4.00 m length. In stock B three different element lengths (2.70, 3.80, 4.40 m) are available. Stock C consists of elements with lengths between 2.50 and 5.00 m. All stock elements are assumed to be standard grade S235 steel. However, for reused elements a material safety factor of 90% is assumed to account for uncertainties on the element capacity and material degradation.

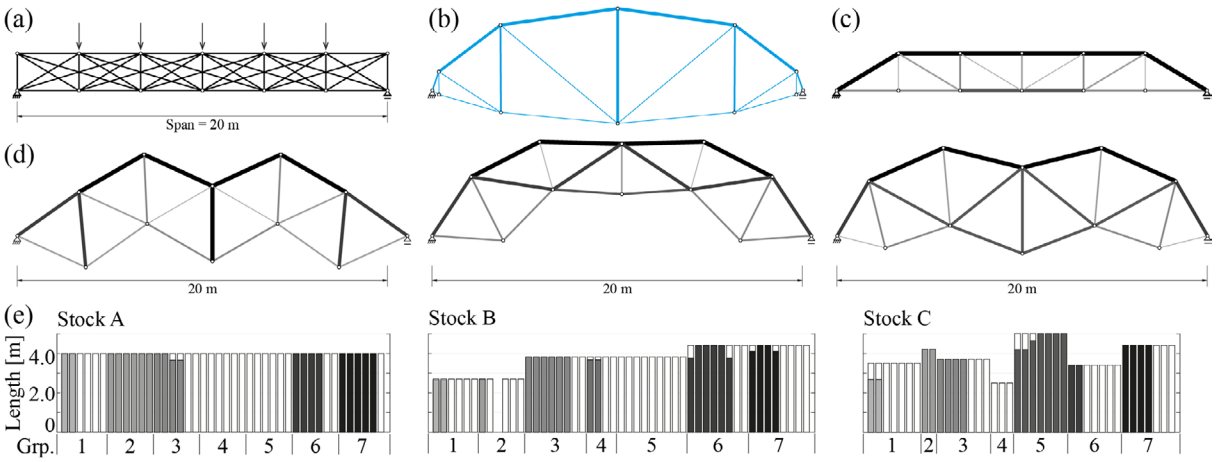


Figure 2. Optimum synthesis from given stocks: (a) Ground structure, (b) minimum weight benchmark, (c) optimum design from stock A and invariant geometry, (d) optimum designs for stocks A, B and C, (e) dimensions, grouping and use of the stock elements. White bars in (e) represent stock elements or cut-off. Greyscale bars map selected stock elements with truss members.

A weight-optimized structure made of new steel elements assuming an infinite availability of all standard sections in EN 10210 is taken as a benchmark, Figure 2(b). This benchmark is obtained through

a sequential discrete sizing and geometry optimization (see section 2), although in this case compliance minimization is the sole objective of the geometry optimization steps.

Figure 2(c) shows the optimum assignment solution for Stock A with invariant geometry (i.e. for the first solution of (P)). After minimizing cut-off waste through geometry optimization, using stock A results in an optimal structure that consists of equilateral triangles, Figure 2(d). Only two elements cannot be used at their full length. The elements of groups 4 and 5 are not used because either the assignment of smaller sections was possible (groups 1 to 3) or larger sections were required (groups 6 and 7). For stock B an optimal structure with an arched top chord is obtained and elements of all three different lengths are used. In the case of stock C all except five stock elements are placed without requiring cutting. In all cases, elements with larger cross sections are used in the top chord because of buckling limits. Because of the constraining stocks, the reuse cases do not show a geometry that is similar to the minimum weight solution, Figure 2(b).

Table 1 gives optimization results, on the left for the scenario when the structure geometry is invariant, on the right for the systems shown in Figure 2(d). Because the number of light cross sections is limited in the stocks, the systems with reused elements are oversized compared to minimum weight solutions. A higher capacity utilization is obtained for the minimum weight solution. However, reusing reclaimed structural elements results in a significant reduction of embodied energy and carbon equivalence: between 46 to 64% for the systems with invariant geometry and between 36 and 59% for the geometry-optimized structures.

Table 1. Optimization results, 2D case studies

Stock	Case	Mass	Waste	Cuts	mean Util.	max Util.	EE	EC	Case	Mass	Waste	Cuts	mean Util.	max Util.	EE	EC
		[kg]	[kg]	[-]	[%]	[%]	[MJ]	[kgCO_{2eq}]		[kg]	[kg]	[-]	[%]	[%]	[MJ]	[kgCO_{2eq}]
A	(P)	**468**	84	21	68	88	**1'790**	**150**	(P)+Geo	**497**	3	2	74	90	**1'630**	**140**
B	(P)	**489**	98	21	62	88	**1'900**	**160**	(P)+Geo	**534**	19	8	56	90	**1'790**	**150**
C	(P)	**605**	97	25	59	88	**2'280**	**190**	(P)+Geo	**640**	21	5	45	88	**2'150**	**180**
New		**380**	-	-	82	100	**5'030**	**350**		**298**	-	-	72	98	**3'950**	**280**

3.2 Optimization of a 3D space truss under stock constraints

Figure 3(a) shows a roof structure with 18.00 m width and m = 200 members. The vertical columns in Figure 3 represent the four vertical supports but are not part of the optimization. A distributed load of 2.25 kN/m^2 is applied to the top chord nodes. In the geometry optimization step the perimeter nodes are constrained to maintain a minimum 18 x 18 m footprint. The structure is optimized subject to the same stocks as in section 3.1, but with an increased availability. The availability of elements in stock A is six times that of the 2D case; stocks B and C have 40 elements per group.

In this case study, topology is invariant, i.e. one stock element is assigned to each position. A symmetric assignment of elements (XZ and YZ plane) is enforced to reduce the number of binary assignment variables. In addition, geometric compatibility and nodal displacements are omitted (plastic design). These simplifications reduce computational complexity, which is important for this case study as it contains a large number of members. This way it is possible to solve problem (P) to global optimality within a reasonable computation time (< 1 h on a standard PC).

Figure 3 shows the optimized structural systems. A different shade of grey is used to represent the seven element groups (section 3.1). Top views show an increase of footprint when reuse is applied. As stock A consist of all equal length elements, the resulting structure geometry remains regular (Figure 3(c)). In the case of stock B and C more irregular geometries are obtained. The geometry optimization successfully reduces waste and cutting of stock elements (Table 2). For all three stocks between one fourth and one third out of the total number (200) of members are cut. In other words, most elements can be reused at their full length. Similar to the 2D case study in section 3.1, reusing structural elements

results in a significant reduction of embodied carbon and energy, even though these systems have a higher mass and lower mean capacity utilization with respect to the weight-optimized solution obtained from new elements, Figure 3(b).

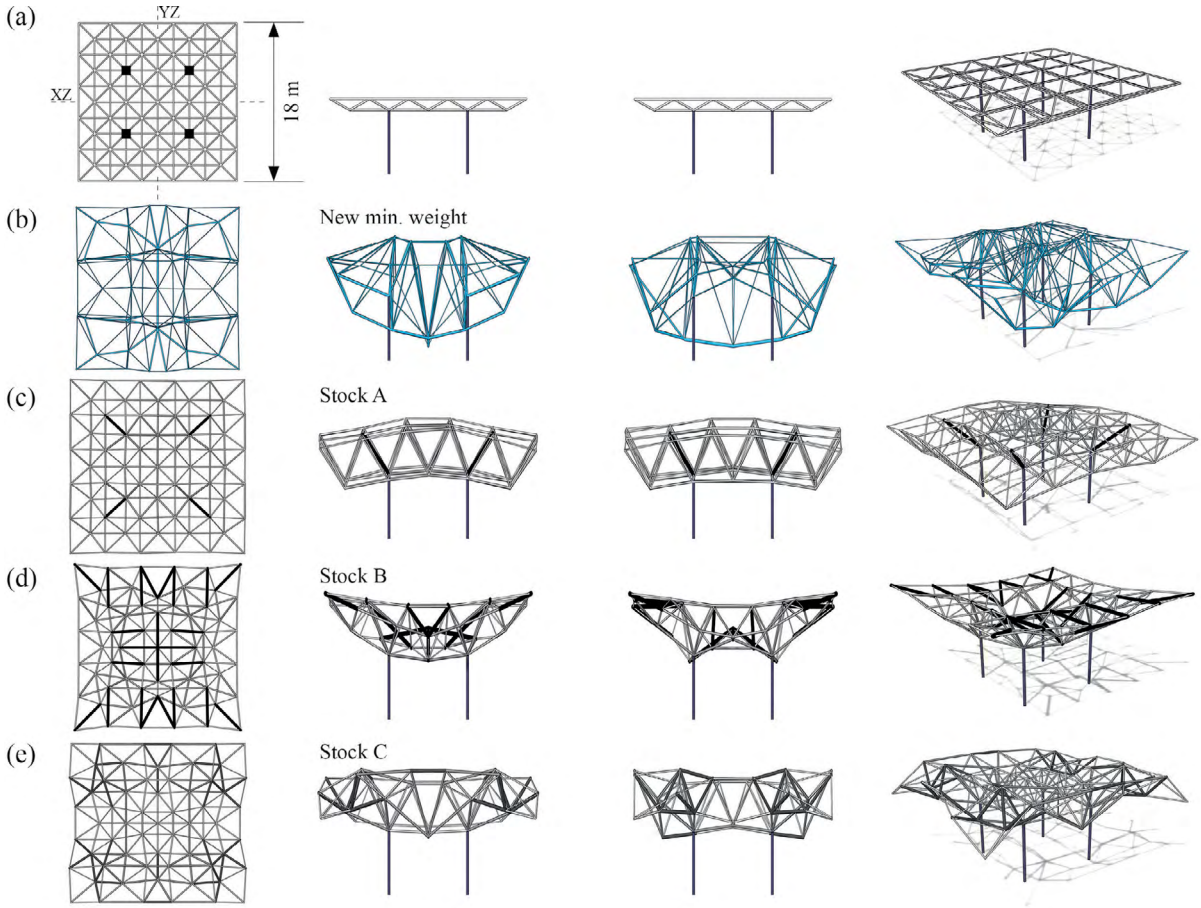


Figure 3. Optimum synthesis from given stocks. (a) System definition, (b) minimum weight solution with new elements, (c-e) optimum results for using elements from stocks A, B, and C.

Table 2. Optimization results for the 3D Space Trusses

Case	Stock	Mass [kg]	Waste [kg]	Cuts [-]	mean Util. [-]	max Util. [-]	EE [MJ]	EC [kgCO_2eq]
(P) + Geo.	A	**3'840**	65	63	53%	90%	**12'700**	**1'080**
(P) + Geo.	B	**4'950**	127	52	45%	90%	**16'500**	**1'400**
(P) + Geo.	C	**5'370**	204	70	41%	89%	**18'100**	**1'540**
(P) + Geo.	New	**2'090**	-	-	54%	100%	**27'600**	**1'930**

In a post process step, an FE analysis including geometric compatibility showed that 19 members in the minimum weight structure and up to 28 members in the reuse cases are overstressed. In practice, overstressed members could be replaced and members prone to buckling could be braced.

3.3 Stock synthesis for three kit-of-parts structures

This section shows the application of the stock optimization formulation (S) to build three truss structures of different topology: arch, portal and Howe truss, Figure 4(a). Multiple load cases are applied to each structure and all standard sections of EN 10210 are available. The inner nodes of the arch and

the portal are constrained in the geometry optimization to maintain minimum heights, Figure 4(a). A maximum number of $z^{max} = 12$ unique element types (lengths and cross sections) is allowed.

When solving (S), the optimization of all three structures must be carried out simultaneously, resulting in a large number of optimization variables. To reduce computation time, geometric compatibility is omitted in this case study. However, because the three systems are statically determinate, all member forces are correctly obtained via force equilibrium only and thus members will not be overstressed.

Figure 4(b) shows the one-off minimum weight solutions for each individual structure, irrespectively of the common stock. Figure 4(c) shows the three optimized layouts, which share a common kit-of-parts. In Figure 4(c) each member color corresponds to one of the twelve element types in the kit-of-parts. The bar charts in Figure 4(d) show cross section sizes, element lengths and assignments. In total 40 kit-of-parts elements are required to build all three systems (90 members in total). For instance, the elements of group 11 are reused in all three systems and have a large cross section due to buckling constraints. The elements of group 2 are uniquely used for the portal case. The elements of group 12 are under tension in the portal case but in compression in the arch. Elements in groups 2 and 8 as well as in 7 and 10 have identical lengths. By using their respectively larger cross sections these groups could be merged to reduce the number of different element types at a cost of an increase of the weight of the structures.

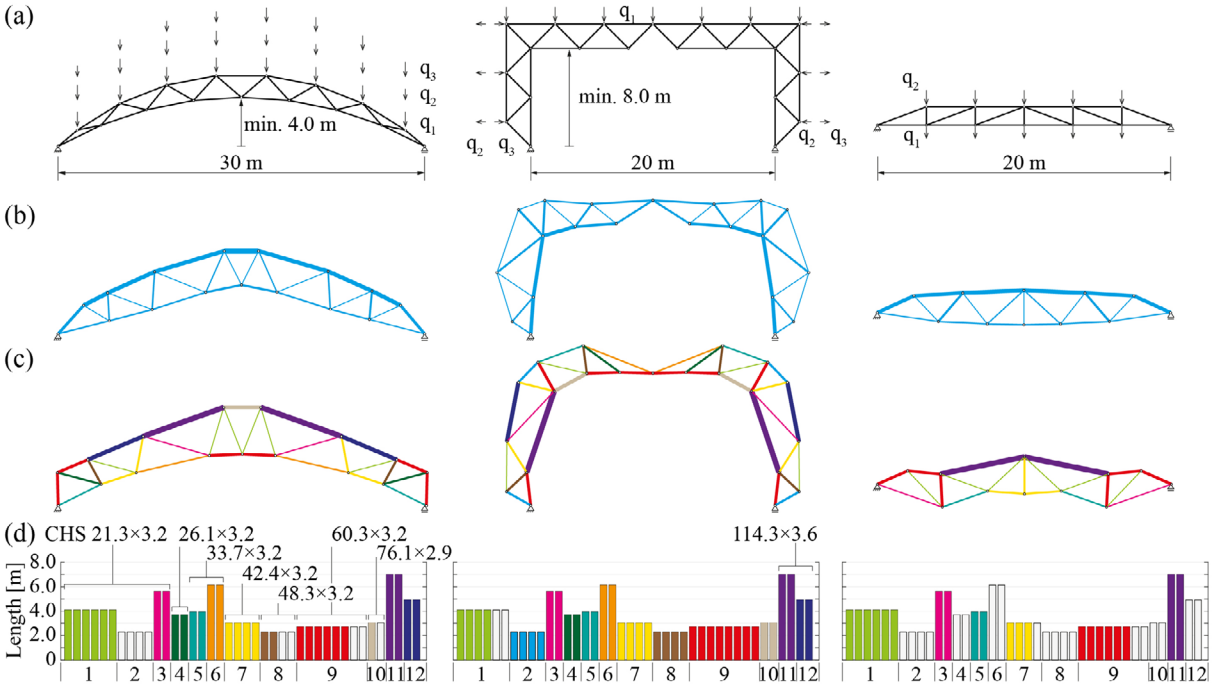


Figure 4. Optimization results for the design of kit-of-parts structures: (a) setup, (b) minimum weight solutions, (c) kit-of-parts structures, (d) element assignment and stock description ordered by cross-section size.

Table 3. Optimization results for the minimum weight systems and the kit-of-parts.

		Arch New	Portal New	Howe New	Sum New	Arch	Portal	Howe	Kit-of-parts
Members	[-]	31	38	21	**90**	-	-	-	**40**
Mass	[kg]	429	385	256	**1'070**	490	548	309	**560**
mean Util.	[-]	81%	83%	74%	**80%**	61%	60%	68%	**62%**
max Util.	[-]	100%	100%	100%	**100%**	96%	99%	97%	**99%**
EE	[MJ]	5'670	5'090	3'390	**14'150**	-	-	-	**7'410**
EC	[kgCO_2eq]	400	360	240	**1000**	-	-	-	**520**

Table 3 shows optimization metrics for the minimum weight systems and the optimal kit-of-parts. Because kit-of-parts elements are reused in multiple structures, they need to be sized for the worst loading condition, i.e. reused elements are oversized and have a lower mean capacity utilization compared to the one-off minimum weight solutions. However, producing only 40 instead of 90 elements reduces environmental impacts significantly by 48% in terms of embodied energy and carbon equivalence. A post process FE analysis showed that typical SLS displacement limits are satisfied.

4. Conclusion

The case studies presented in this work have shown that novel and diverse structure layouts are obtained when structural elements are reused for multiple service cycles i.e. when *form follows availability*. The methods outlined in this paper allow for a substantial reduction of environmental impacts of load-bearing systems. Topology and geometry optimization subject to stock availability allows to account for environmental considerations at early stages of the design process. Design through reuse of stock elements therefore opens up new directions in structural form finding and optimization.

The proposed formulations based on mixed-integer linear programming produce globally optimal results and are applicable to small and medium-scale problems without simplifications. Large-scale problems might not converge in a reasonable time. Simplifications including omission of geometric compatibility and symmetry constraints had to be made in this work.

Connection design was out of the scope of this paper. However, the proposed methods are applicable to typical truss topologies and modular space trusses. In addition, the geometry optimization could be guided towards user-defined design features or to account for available joint types.

Optimization of the stock has shown to be a promising approach to design multiple structures from a common kit-of-parts. This method could be employed to design temporary structures that adapt to several sites or generally to reuse structural elements over multiple service cycles.

References

[1] M. Gorgolewski, "Designing with reused building components: some challenges," *Building Research & Information*, vol. 36, no. 2, pp. 175–188, 2008.
[2] M. Gorgolewski, *Resource Salvation: The Architecture of Reuse*. John Wiley & Sons, 2017.
[3] Y. Fujitani and D. Fujii, "Optimum structural design of steel plane frame under the limited stocks of members," in *Proceedings of the RILEM/CIB/ISO International Symposium, Integrated Life-Cycle Design of Materials and Structures*, 2000, pp. 198–202.
[4] A. Bukauskas, P. Shepherd, P. Walker, B. Sharma, and J. Bregula, "Form-Fitting strategies for diversity-tolerant design," in *Proceedings of the IASS Annual Symposium*, Hamburg, 2017.
[5] W. Nadir, I. Y. Kim, D. Hauser, and O. de Weck, "Multidisciplinary structural truss topology optimization for reconfigurability," in *10th AIAA/ISSMO Multidisciplinary Analysis and Optimization Conference*, Albany, 2004.
[6] A. Tugilimana, A. P. Thrall, and R. Filomeno Coelho, "Conceptual Design of Modular Bridges Including Layout Optimization and Component Reusability," *Journal of Bridge Engineering*, vol. 22, no. 11, p. 04017094, 2017.
[7] P. Basso, A. E. Del Grosso, A. Pugnale, and M. Sassone, "Computational morphogenesis in architecture: Cost optimization of free-form grid shells," *J IASS*, vol. 50, no. 3, pp. 143–150, 2009.
[8] O. N. Ghattas and I. E. Grossmann, "MINLP and MILP Strategies for Discrete Sizing Structural Optimization Problems," Electronic Computation, 1991, pp. 197–204.
[9] J. Brütting, J. Desruelle, G. Senatore, and C. Fivet, "Design of Truss Structures Through Reuse," *Structures*, 2018.
[10] R. T. Haftka, "Simultaneous analysis and design," *AIAA journal*, vol. 23, no. 7, pp. 1099–1103, 1985.

Proceedings of the IASS Annual Symposium 2019 — Structural Membranes 2019
Form and Force
7—10 October 2019, Barcelona, Spain
C. Lázaro, K.-U. Bletzinger, E. Oñate (eds.)

CAD-integrated Parametric Design Cycle for Structural Membranes

A. Goldbach* **and K.-U. Bletzinger**

* Technische Universität München
Arcisstr. 21, 80333 München
ann-kathrin.goldbach@tum.de

Abstract

The design cycle of membrane structures consists of three interactive and highly nonlinear disciplines. Formfinding is performed in order to find a geometry that allows the prestressed structure to carry loads through tension only. Once a formfound geometry is set, structural analysis needs to assess the structure's safety and usability. The most challenging step is the cutting pattern generation, which aims at finding the planar pieces which can be elevated to build spatial membrane structures with a minimum deviation from the desired shape and prestress state. Isogeometric B-Rep Analysis (IBRA) allows the designer to perform analyses on the original CAD model without leaving the CAD environment. High quality is ensured for the geometry and the mechanical approximation by using Non-Uniform Rational B-Splines (NURBS). Additionally, the topology information of multipatches can be transferred to the analysis in order to enrich the design space. Trimmed and coupled surfaces can thus be included in the analysis. Parametric models allow the designer to examine a large variety of geometrical and mechanical entities with one model. The advantages of the CAD-integration with IBRA for the highly interactive design of structural membranes are shown in this contribution.

Keywords: CAD-integrated design, cutting pattern generation, design cycle of structural membranes, digital design, embedded elements, formfinding, IBRA, NURBS, parametric design

1 Introduction

Lightweight design and structural membranes in particular allow architects and engineers to build free-form shapes that impress with their appearance as well as the perceptible engineering skill. It usually takes more than one iteration to design such an appealing shape, since geometry and prestress must not only lead to a shape in equilibrium but also be able to carry external loads, fulfill standard safety requirements and be buildable with available materials in a given setting. This iterative procedure can be summarized as the design cycle of membrane structures. In this cycle the disciplines of formfinding, structural analysis and cutting pattern generation obviously interact, meaning that every change in the structure resulting from one of the analyses also affects the other two and thus triggers a new iteration. Designing and analyzing membrane structures with the help of software packages has enlarged the design space enormously. With the CAD-integrated parametric approach for the design cycle presented in this paper, all three steps can be performed in one software environment. Furthermore, geometrical as well as mechanical

Copyright © 2019 by A. Goldbach, K.-U. Bletzinger
Published by the International Association for Shell and Spatial Structures (IASS) with permission.

features can be modeled parametrically, meaning that the same model can be used to explore various design options.

2 Design cycle of membrane structures

Structural membranes are designed and analysed in a highly non-linear and interactive design cycle consisting of the following three steps: formfinding, structural analysis and cutting pattern generation, as shown in Figure 1. In order to successfully design a structure that meets both aesthetic and structural requirements, all three steps must be completed in accordance with each other. Being tensile structures, membranes carry loads through tension only. In contrast to more conventional structures that have large bending stiffnesses, membrane structures function through the geometrical stiffness generated by the combination of geometry and prestress. The quality of the geometry representation thus has a large influence on the accuracy and consequently the reliability of an analysis model.

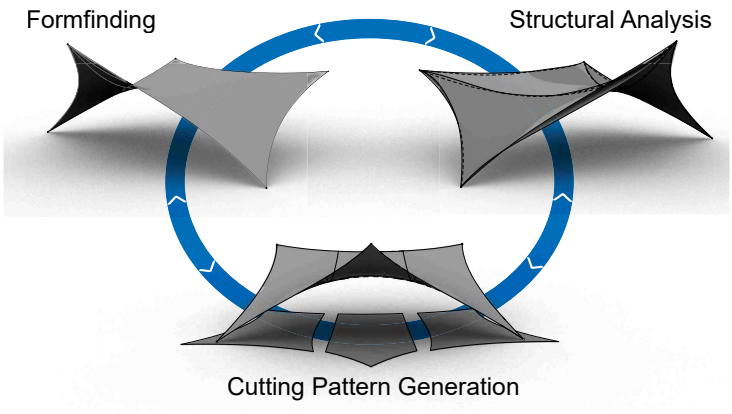


Figure 1: The design cycle disciplines for structural membranes

Formfinding is performed with the aim of acquiring a geometry which is in equilibrium under prescribed prestress and boundary conditions. The Updated Reference Strategy [6] is one of the well-established formfinding techniques that have successfully been developed and implemented in the past (see [5], [7]). It can be formulated based on the principle of virtual work, leading to the following governing equation (3) (see [3] for a detailed explanation). The virtual work expression δW_{URS} uses a "homotopy" factor λ which balances the influences of the work components from the current and reference state, δW_{cur} and δW_{ref}. Cauchy stresses $\boldsymbol{\sigma}$ and virtual Euler-Almansi strains $\delta\mathbf{e}$ form the internal virtual work in the current state v and external loading $\mathbf{p}$ and virtual displacements $\delta\mathbf{u}$ contribute to the external virtual work. The internal virtual work in the reference state V arises from Second Piola-Kirchhoff strains $\mathbf{S}$ and virtual Green-Lagrange strains $\delta\mathbf{E}$.

$$\delta W_{\text{cur}} = \delta W_{\text{int}} + \delta W_{\text{ext}} = -\int_{\Omega}(\boldsymbol{\sigma} : \delta\mathbf{e})dv + \int_{\Omega}(\mathbf{p}\cdot\delta\mathbf{u})dv = 0 \tag{1}$$

$$\delta W_{\text{ref}} = \delta W_{\text{ref,int}} + \delta W_{\text{ref,ext}} = -\int_{\Omega_0}(\mathbf{S} : \delta\mathbf{E})dV + \int_{\Omega_0}(\mathbf{p}\cdot\delta\mathbf{u})dV = 0 \tag{2}$$

$$\delta W_{\text{URS}} = \lambda\cdot\delta W_{\text{cur}} + (1-\lambda)\cdot\delta W_{\text{ref}} = 0 \tag{3}$$

Structural analysis estimates the safety of any structure under external loads with regard to the ultimate limit and serviceability state. As both geometric and material non-linearity need to be taken into account for membrane structures, challenging numerical analyses need to be solved. Due to the non-linear behaviour, different loading scenarios have to be investigated individually, as the superposition of different effects is not applicable [5].
As a final step in the design cycle of structural membranes, a cutting pattern analysis needs to be performed. The first two steps of the design cycle typically yield a double-curved surface under tension that cannot be developed into a plane due to its curvature and furthermore cannot be built from a single piece of fabric. A cutting pattern analysis generates planar stripes, which can be elevated with the least deviation from the desired shape and prestress state.
The Variation of Reference Strategy [4] is a continuum mechanical approach to find the cutting pattern by describing both the final structure (spatial configuration) and the planar pieces (initial configuration) in a mechanically accurate way, as shown in Figure 2. As the initial configuration is the unknown one, it holds the design variables $\mathbf{X}$ and is thus allowed to change its shape in the plane while the spatial geometry is a fixed target $\mathbf{x}$. The Variation of Reference Strategy formulates an inverse mechanical problem treated by an optimization approach to find the best planar geometry for the given target.
The motion $\chi(\mathbf{X}, t)$ of all points from the plane to the spatial geometry should not lead to a residual stress field, apart from the desired prestress field. This can be formulated as a minimization problem with regard to the total potential energy $\Pi_{\text{total}}(\mathbf{X})$, see eq. (4).

$$\min_{\mathbf{X}\in\Omega_0} \rightarrow \Pi_{\text{total}}(\mathbf{X}) = \Pi_{\chi}(\mathbf{X}) - \Pi_{\text{pre}} \tag{4}$$

In order to find the minimum of the total potential energy, the stationary point of its derivative, i.e. $\delta\Pi_{\text{total}} = 0$ needs to be found with repect to a field of virtual material position vectors $\delta\mathbf{X}$. The governing equation of the Variation of Reference Strategy thus reads

$$\delta\Pi_{\text{total}}(\mathbf{X}) = \int_{\Omega_0} [\mathbf{S}(\mathbf{E}(\mathbf{X})) - \mathbf{S}(\mathbf{E}_{\text{pre}})] : \delta\mathbf{E}(\mathbf{X}) d\Omega_0 + \int_{\Omega_0} [\Psi(\mathbf{E}(\mathbf{X})) - \Psi(\mathbf{E}_{\text{pre}})]\, \delta d\Omega_0 = 0, \tag{5}$$

with second Piola-Kirchhoff stresses $\mathbf{S}$, Green-Lagrange strains $\mathbf{E}$, design variables $\mathbf{X}$ as position vectors in the plane configuration Ω_0 and strain energy functions Ψ.

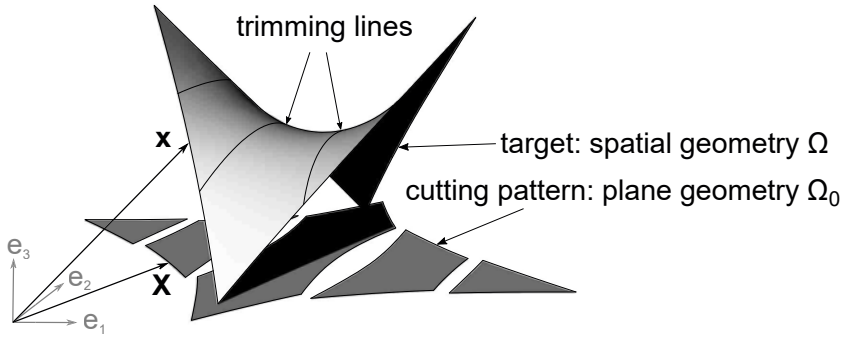


Figure 2: The concept of the Variation of Reference Strategy: design variables in the planar geometry

3 CAD-integrated paramatric modeling and analysis

The original idea of Isogeometric Analysis [9] is to use the CAD model for analysis. The NURBS functions, see eq. (6) describing the geometry are used as basis functions for the mechanical approximations as well. The curve $\mathbf{C}(\xi)$ is defined by its control points $\mathbf{P}_i$ and weighted (w_i) B-Splines ($N_{i,p}$), $R_{i,p}(\xi)$.

$$\mathbf{C}(\xi) = \sum_{i=1}^{n} R_{i,p}(\xi)\mathbf{P}_i \quad \text{with} \quad R_{i,p}(\xi) = \frac{N_{i,p}(\xi)w_i}{\sum_{j=1}^{n} N_{j,p}(\xi)w_j} \tag{6}$$

In contrast to the classical FEM approach, where surfaces have to be discretized by polygonial (linear) meshes, the elements are already defined by the CAD control polygon. Consequently, design and analysis can be performed on a single model and in one software environment. The effort going into the processing of geometry for analysis and vice versa is thus minimized and nearly not perceptible for the user.

3.1 CAD-integration with Isogeometric B-Rep Analysis

Isogeometric B-Rep Analysis [1] takes the idea of Isogeometric Analysis one step further and also assesses the topology of CAD-models, which are typically B-Rep models. All B-Rep entities (i.e. faces, edges, vertices) can thus be enhanced by mechanical properties.
Furthermore, CAD-functions such as trimming can be applied to the model without restrictions. This is very beneficial because the variety of available shapes rises significantly, once trimmed and coupled surfaces can be integrated. If a refinement of the model is necessary for the analysis, the model can either be represented by more control points or higher order polynomials. However, the geometry does not change because of refinement, see [11] for a detailed explanation.
Several so-called embedded elements have been developed within this framework and have successfully been applied to various problem settings [2], [3].
With regard to the key feature of membrane structures, performing analyses on NURBS-based B-Rep models holds several major advantages. In contrast to classical FEM, the smooth geometry representation is available for the analysis model in CAD-integrated design. In consequence, the curvature which defines a membrane's geometric stiffness is modeled accurately and leads to high-quality deformation and stress results.

3.2 Parametric modeling and workflow

The possibilty of modeling shapes and mechanical properties in a parameterized way allows the designer and engineer to test variations fast (even automated) and on one model. Embedded elements are not restricted to a mesh, but can be positioned freely and are thus flexible with respect to parameterization.
It was already pointed out that parametric CAD-integrated analysis allows for convenient testing of different parameters and their effects. In the context of structural membranes' design cycles, these effects impact the other disciplines (see section 2) and thus lead to exploring those. Obviously, the workflow benefits from working on one model. Figure 3 shows how the design cycle steps can be linked for a 5-point sail using Kiwi!3d [8]. The formfound geometry is forwarded to structural analysis and cutting pattern generation. As the full CAD-model of the deformed geometry is available, standard CAD operations can be performed - e.g. to add support detailing - before further analyses are connected. In addition to the analyses shown in Figure 3, the

mounting of the pattern stripes can be modeled and structural analysis can be performed on the assembled model.

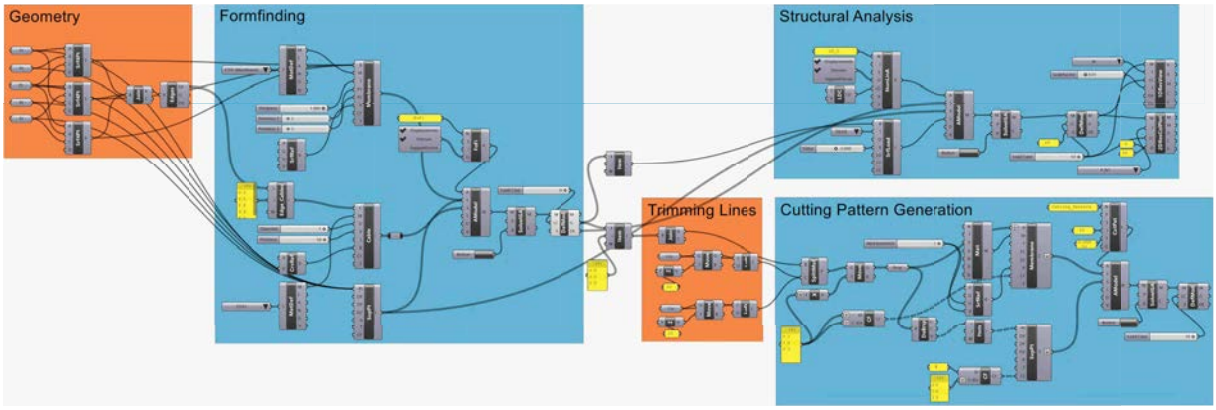


Figure 3: CAD-integrated parametric design of a 5-point sail in Kiwi!3d [8]: formfinding linked to structural analysis and cutting pattern generation. Geometrical operations are highlighted in orange and mechanical ones in blue.

The ratio of the prestress in a membrane and the cables determines the cables' and membrane's curvature. As formfinding needs to be performed in order to arrive at an equilibrium shape for a given prestress, different prestress settings often need to be investigated before the design satisfies all preconditions. A parametric model evidently reforms this process, as different options can be explored with one model. For the basic example of a 5-point sail, this is shown in Figure 4. The chosen parameters for formfinding were the isotropic prestress in the membrane $p_{membrane}$ for a given cable force P_{cable}. For the cutting pattern generation, the chosen parameters were the division points along the edges, resulting in different numbers of stripes. Additionally, the lines connecting these points were set to either geodesic or straight lines.

3.3 CAD-integrated cutting pattern generation

For the cutting pattern generation, the possibility of analysing trimmed geometries saves time and computational effort, since the spatial geometry can simply be separated into several pieces by CAD-functions without the necessity of remeshing the model or restricting the cutting lines to the element borders. Additionally, modern CAD-programs can calculate the shortest path on a surface, i.e. the geodesic lines. Geodesic lines are often used as cutting lines to minimize edge curvature in the plane. Again, time and computational effort is saved in comparison to classical FEM, where an optimization needs to run in order to find the geodesic lines between two points on a surface. Finally, the resulting cutting pattern geometry needs to be forwarded to production and therefore needs to be available in CAD-format. With the CAD-integrated approach this is inherent, no conversion of a classical FE mesh is necessary and no geometric information is lost.
Designing a parametric model offers even more advantages, as the trimming lines can be altered in their position as well as their orientation. Various options of dividing the surface and the effects on both the spatial structure and the cutting pattern can be investigated using one model, as can be seen in Figure 4.

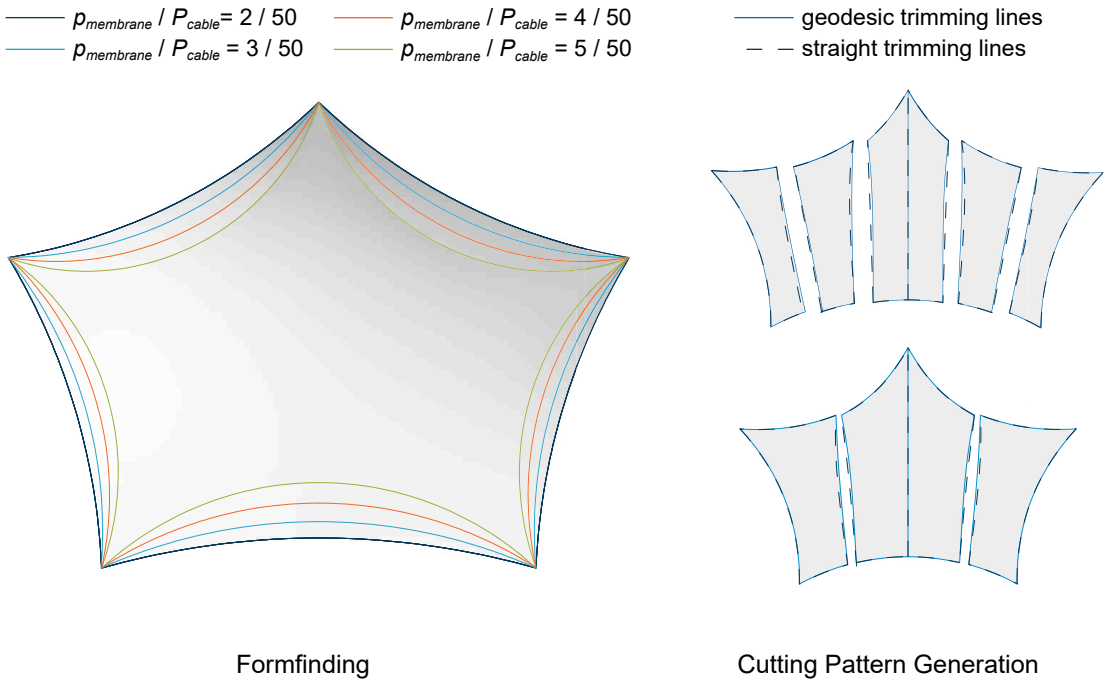


Figure 4: Left: Curvature effects from varying the ratio of the isotropic prestress in the membrane ($p_{membrane}$) and the cable force (P_{cable}). Right: Patterning results for dividing the surface along geodesic opposed to straight lines into 5 and 3 parts.

4 Parametric design of a large scale membrane structure

The skysong membrane structure built by FabriTec Structures [10] consists of a steel frame supporting eight conical membrane structures with alternating orientation. The model in this example was inspired by the skysong structure and uses parametric design for both geometrical and mechanical properties of the membrane structure. The chosen parameters are shown in Figure 5. Formfinding was performed for different segmenting angles of the structure, resulting in various large scale effects, see Figure 6. The ratio of prestress in the membrane and cables was also varied, effecting the edge curvature as discussed in section 3.2. One of the major benefits of a CAD-integrated model is the availability of a deformed model in the CAD environment. It allows the designer to study the effects of different parameter changes using all CAD functions (e.g. daylight simulation) as well as forwarding the model to following analyses, like a cutting pattern generation and structural analysis.

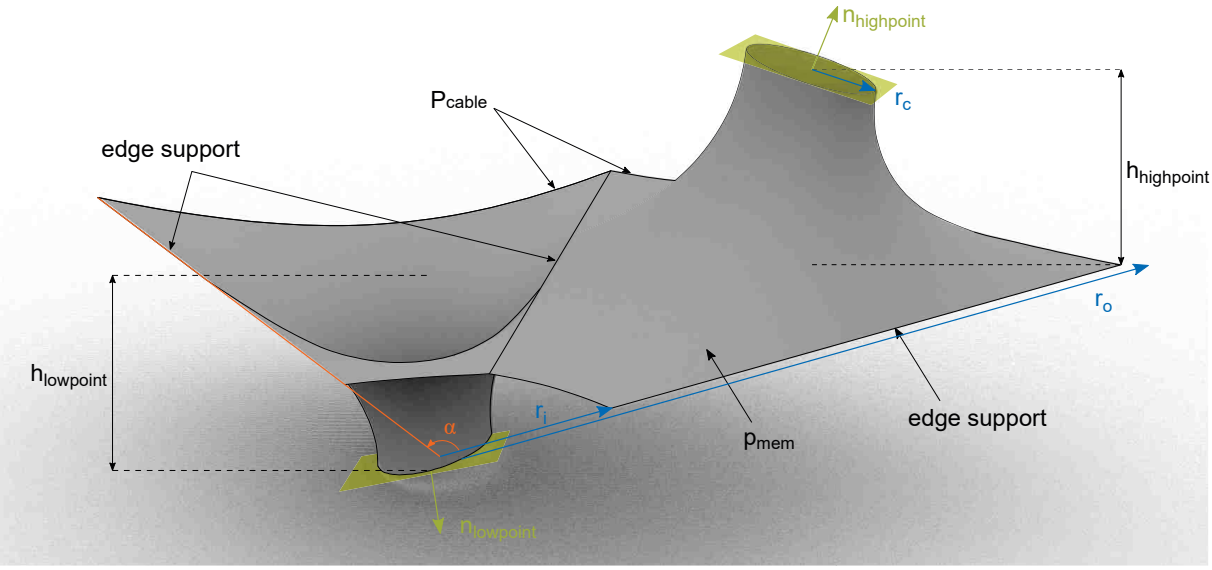


Figure 5: Parametric model of large scale membrane structure in *Rhino3d*

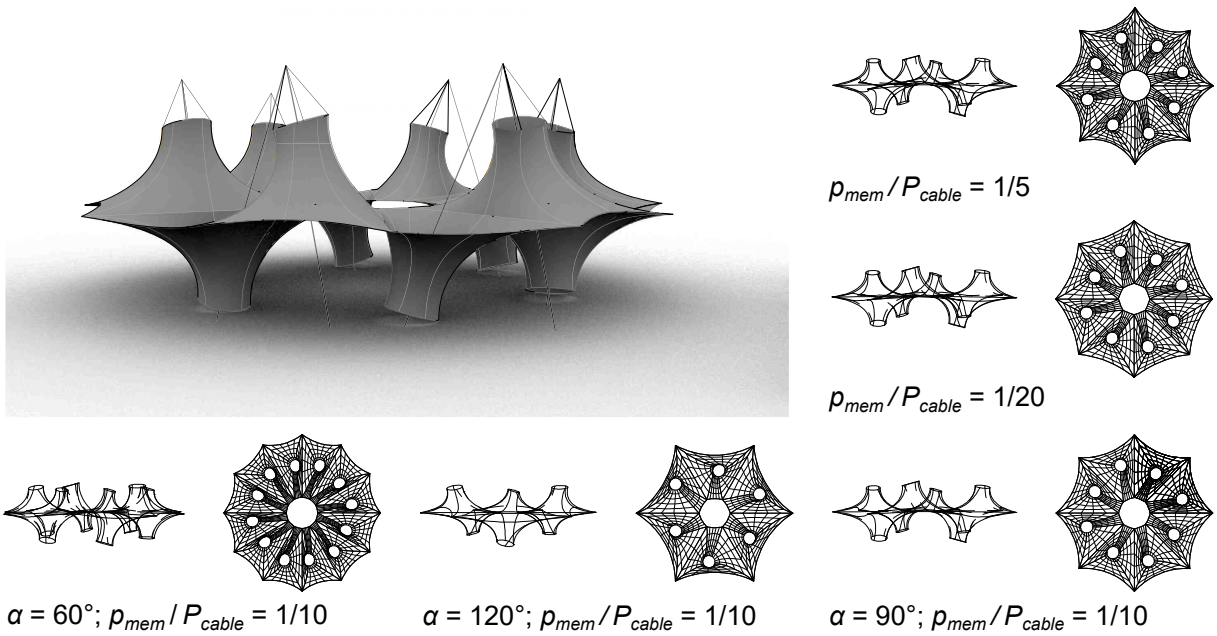


Figure 6: Parametric study of a large scale membrane structure with $\alpha = 60°, 90°, 120°$, $h_{\text{highpoint}}/h_{\text{lowpoint}} = 1$ and ratio of prestress in the membrane p_{mem} to cable force $P_{\text{cable}} = 1/5$, $1/10$ and $1/20$.

5 Conclusion

The advantages of a fully parameterized CAD-integrated design cycle of membrane structures was shown in this paper. Both the mechanical aspects of CAD-integration with IBRA and the consequences for the design workflow have been pointed out. The examples of a basic 5-point sail and a large scale membrane structure with high curvature illustrate the potential of this innovative approach from a design as well as engineering point of view.

References

[1] M. Breitenberger et al., "Analysis in computer aided design: Nonlinear isogeometric B-Rep analysis of shell structures", *Computer Methods in Applied Mechanics and Engineering* vol. 284, pp. 401-457. doi 10.1016/j.cma.2014.09.033, 2015.

[2] A.M. Bauer et al., "Embedded structural entities in NURBS-based isogeometric analysis", *Computer Methods in Applied Mechanics and Engineering* vol. 325, pp. 198-218. doi 10.1016/j.cma.2017.07.010, 2017.

[3] B. Philipp et al., "Integrated Design and Analysis of Structural Membranes using the Isogeometric B-Rep Analysis", *Computer Methods in Applied Mechanics and Engineering* vol. 303, pp. 312-340. doi 10.1016/j.cma.2016.02.003, 2016.

[4] A. Widhammer, "Variation of Reference Strategy. Generation of Optimized Cutting Patterns for Textile Fabrics", *Dissertation at Technische Universität München*, Munich, 2015.

[5] B. Philipp, "Methodological treatment of non-linear structural behaviour in the design, analysis and verification of lightweight structures", *Dissertation at Technische Universität München*, Munich, 2017.

[6] K.-U. Bletzinger, E. Ramm, "A general finite element approach to the formfinding of tensile structures by the updated reference strategy", *International Journal of Space Structures* vol. 14.2, pp. 131-145. doi 10.1260/0266351991494759, 1999.

[7] J. Linhard, "Numerisch-mechanische Betrachtung des Entwurfsprozesses von Membrantragwerken", *Dissertation at Technische Universität München*, Munich, 2009.

[8] A.M. Bauer et al., "Kiwi!3d" https://www.kiwi3d.com/

[9] T. Hughes, J. Cottrell, Y. Bazilevs, "Isogeometric Analysis: CAD, finite elements, exact geometry and mesh refinement", *Computer Methods Applied Mechanics and Engineering* vol. 194 (39-41) pp. 4135-4195, 2005.

[10] FabriTec Structures, https://fabritecstructures.com/portfolio/asu-skysong-innovation-center/

[11] L. Piegl, W. Tiller, *The NURBS Book*, doi 10.1007/978-3-642-97385-7, Berlin-Heidelberg: Springer-Verlag, 1995.

Proceedings of the IASS Annual Symposium 2019 – Structural Membranes 2019
Form and Force
7 – 10 October 2019, Barcelona, Spain
C. Lázaro, K.-U. Bletzinger, E. Oñate (eds.)

Parametrization, integration and buildability: Design and construction of a 50m span freeform roof in Bangkok

Catherine POIRRIEZ*, Marine FRANCESCHI, Yacine BOUZIDA

*Passage Projects
14A Sago Street 059015 Singapore
cp@passage-projects.com

Abstract

Whizdom 101 is a new high-end fully integrated and digital mixed-use development comprising both commercial spaces and residential towers. The centre of the commercial space is covered by the big roof, a 50m span freeform steel roof covered with ETFE, forming an aerated and relaxing space for the pedestrians. Several shapes and structural systems have been explored at early stage of the project to best integrate the roof in its environment. The resulting shape is a quiet and smooth surface providing shade and natural ventilation to the spaces below. Although complex, the geometry was generated to fully take into account the buildability - all the steel members were translated in a language of plates and single radii, comprehensible for the fabricator. Initially made of conical surfaces, the edge beams sections geometry was rationalized through parametric modelling in order to be only made of cylindrical surfaces which are developable and therefore easy to fabricate.

Keywords: Steel structure, metal spatial structure, long-span structure, ETFE, structure as architecture, grasshopper, buildability

1. Introduction

Whizdom 101 is a new high-end fully integrated and digital mixed-use development comprising both commercial spaces and residential towers. Whizdom 101 was designed to create a sense of place where the individual could live, work and play in one's own backyard and connect to a community that is free from the tensions of the bustling city that surrounds us. The center of the commercial space is covered by the big roof, a 50m span freeform steel roof covered with ETFE, forming an aerated and relaxing space for the pedestrians.



Figure 1: View of the roof [Passage Projects]

Copyright © 2019 by Catherine POIRRIEZ, Marine FRANCESCHI, Yacine BOUZIDA
Published by the International Association for Shell and Spatial Structures (IASS) with permission.

The fabrication and installation of the steel occurred between May 2018 to September 2018 while the installation of ETFE occurred between October 2018 to December 2018. The roof officially opened to the public in February 2019. The big roof is surrounded by 2 buildings. It is supported by 4 main supports and 2 secondary supports spread over 3 different storeys as shown in Figure 2.

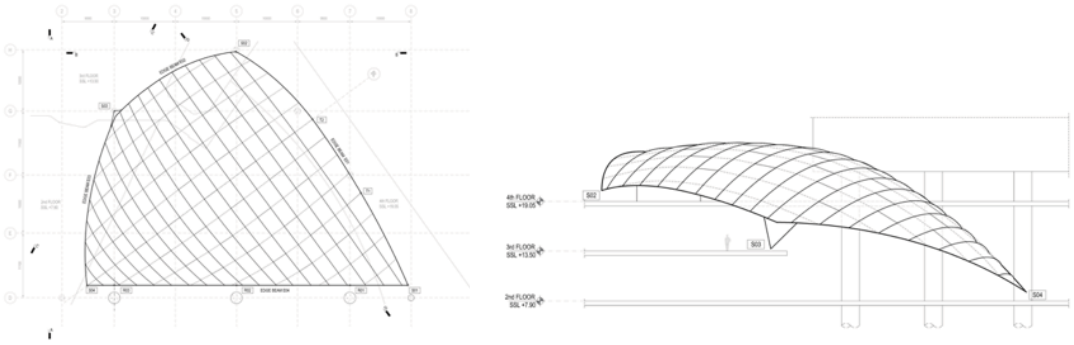


Figure 2: Left: Roof plan view, Right: Elevation C-C [Passage Projects]

This paper describes the process of structure design, generation of the geometry and of the edge beams to achieve a buildable, quiet and smooth structure integrated in its environment.

2. Basis of design

The steel structure has been designed with LFRD following the American Codes of Practice ASCE 7-10 [1], AISC 360-10 [2]. The next sections present the loadings applied to the structure.

2.1. General Loadings

2.1.1. Dead Loads and Live Loads

The roof should be able to withstand its own self-weight, composed of the self-weight of the steel and the dead loads, the weight of the ETFE and aluminium, about 10 kg/m2 and the weight of any services running on the structure, estimated to 10 kg/m^2. The Live Loads for such a roof correspond to maintenance loadings. The Live Loads applied are 24kg/m^2 on the whole roof surface.

2.1.2. Wind Loads

A wind tunnel test has been carried out for the roof. The pressures obtained for the roof steel structure design vary between 0.5 kPa to -0.75 kPa.

2.1.3. Temperature Loads

The temperatures in Bangkok are reasonably constant throughout the whole year. Hence, the variations of temperature of the steel structure are mainly caused by the heat from the sun during the day and the colder temperatures of the night. The construction temperature is assumed to be 30^{o}C, so the temperature differentials considered for the design are +20^{o}C/-15^{o}C.

2.1.4. Load combinations

The load combinations considered for the design are shown in Table 1:

Table 1: ULS Load Combinations

LC1	1.2(SW+DL)+1.6LL+1.2T
LC2	1.2(SW+DL)+1.6WL+1.2T
LC3	0.9(SW+DL)+1.6WL

2.2. Structural analysis

The structure is analyzed by performing a geometrically non-linear analysis.

3. Geometry and structural system study

3.1. Preliminary study

The roof is located in a constrained space, as seen in Figure 3, spanning between several floors and with limited supports points. In order to ensure the commercial spaces below could remain aerated, the roof had to span the 50m of commercial space column-free. Without many more constraints from the client, several shapes and structural systems have been explored at early stage of the project to best integrate the roof in its environment.



Figure 3: 3D view of the roof in its environment [Passage Projects]

Three options studied are shown in figure 4. The last option was adopted for the project and is described in the next section.

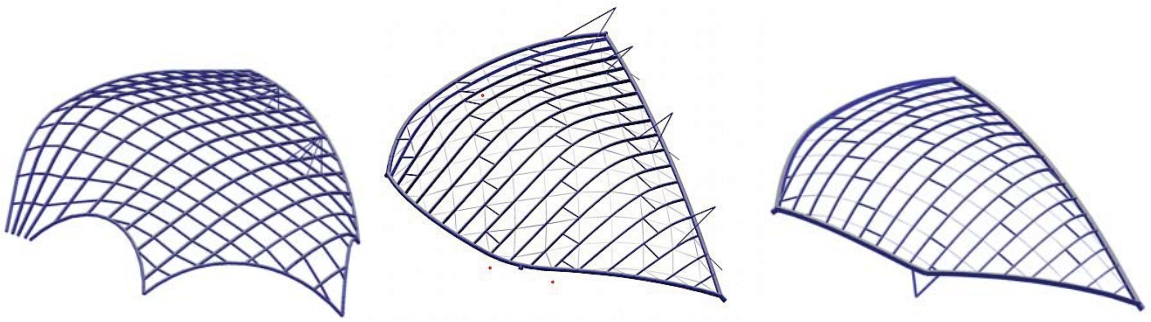


Figure 4: Preliminary options studied [Passage Projects]

3.2. Roof final geometry

The roof final geometry was obtained after several iterations to achieve a smooth curve and an elegant shape. The roof surface was inspired from the shape of a paper fan as seen in Figure 5.

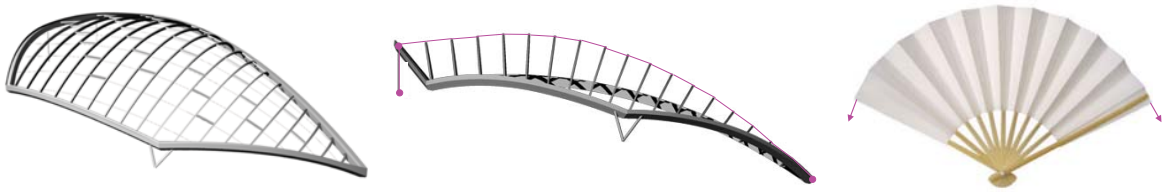


Figure 5: 3D view and Section of the roof [Passage Projects]

To simplify the ETFE installation, the surface was divided into 18 long stripes of ETFE supported by 17 main arches. The main arches are supported on 4 edge beams which redistribute the loads to the 4 support points. In order to smoothen the surface of the roof, a V-column was introduced to support two of the edge beams. Long ETFE cushions could be difficult to replace in case of damage so the long-striped cushions were further divided into several ETFE cushions. Longitudinal beams spanning between arches provide a division for the cushions. Cushions layout can be seen in Figure 6.

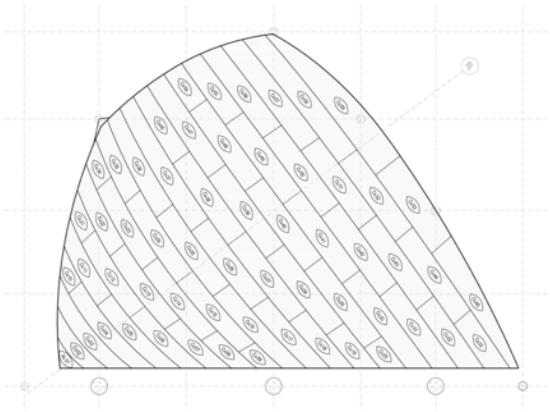


Figure 6: Proposed cushions layout [Passage Projects]

3.3. Gutter integration

During rainy periods, the water from the roof should be collected through a gutter to avoid water free-flow in the commercial spaces. The gutter size requirement for this project was 800mm width by 250mm depth. In some locations, public can walk beside the roof so the gutter had to be treated as an architectural feature. Several gutter system concepts have been studied. Three of them are shown in Figure 7.

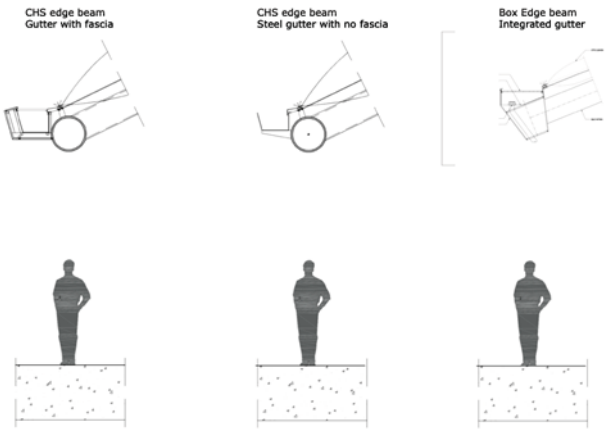


Figure 7: Gutter system concepts [Passage Projects]

The first one consists of a traditional cladded aluminium gutter connected to the roof edge beam. Considering the curvature of the roof, the cladding would have to be segmented and would present many joints with risk of streaking. This option would not be pleasant for the public. The second one is a steel gutter connected to the roof edge beam. This gutter would not require to be cladded however the build-up of the full system "edge beam+gutter" would be bulky. The last option is a pentagonal steel hollow section integrating the gutter. The pentagonal shape uses a language of lines allowing to have an elegant canopy edge pleasant to the public. This option was adopted for the project.

3.4. Bracing layout

Additional bracing spaced at 3m to 4m was required to provide a restraint to the arches. To keep the structure light and to facilitate the site installation, the bracings considered were tension rods. 4 bracing layout options studied are shown in Figure 8.

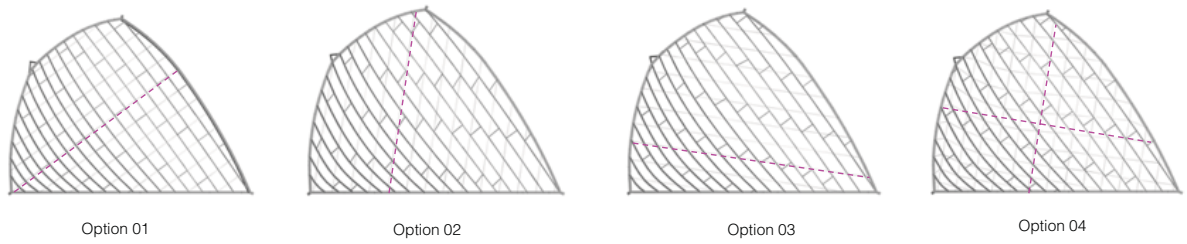


Figure 8: Bracing layout options [Passage Projects]

As option 4 would require double the number of cables and double the number of connections, it was rapidly abandoned. A comparison between the structural efficiency and the elegancy of options 1 to 3 has been carried out. Analysis results are shown in Figure 9 and results comparison in Table 2.

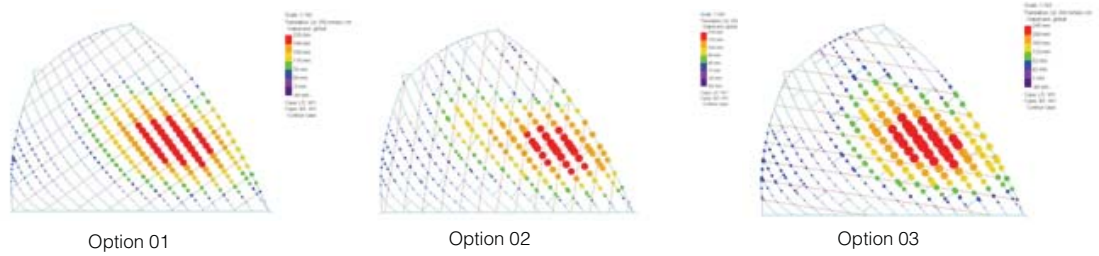


Figure 9: Bracing layout structural efficiency comparison [Passage Projects]

Table 2: Comparison between bracing layouts

Option	Structural efficiency	Elegance
Option 1	Good	Best
Option 2	Best	Medium
Option 3	Medium	Medium

The analysis showed that the Option 2 was only 20% more efficient than Option 1. As a result, Option 1 was adopted as it combines structural efficiency and elegance.

3.5. Final Structural system

The ETFE cushions layout provides a natural structural system for the roof. The main arches support the ETFE cushions. They are rectangular hollow sections of size varying from 325mmx200mm for the shortest arches to 500mmx200mm for the longest arches. The arches transfer the forces to the edge

beams through compression and bending. The edge beam are pentagonal hollow sections and integrate the gutter. The longitudinal beams dividing the cushions are I-beams. The additional longitudinal bracing are tension rods. They both provide a restraint against out-of-plane and lateral-torsional buckling to the arches.



Figure 10: The roof under construction [Passage Projects]

3.6. Stability checks

The stability of the roof is checked in two steps: the global stability of the structure and the local stability of the members.

The global stability of the structure is checked following Eurocodes 1933-1-1 [3]. A Linear buckling analysis, also called Eigenvalue analysis is carried out. As per Eurocodes 1993-1-1 [3], a structure of buckling factor smaller than 10 will be highly sensitive to second-order effects. As a result, if any global buckling mode is found with a buckling factor lower than 10, a Geometrically non-linear elastic analysis with imperfections included is performed. Global imperfections are included in the model using the deformed shape of the global buckling modes with a buckling factor lower than 10 one at a time. A non-linear buckling analysis was also performed to confirm the buckling modes from the Eigenvalue analysis.

The first buckling mode can be seen in Figure 11. The structure works as a series of almost independent arches, as a result it does not have a gridshell behavior and hence is not subject to snap-through nor global buckling.

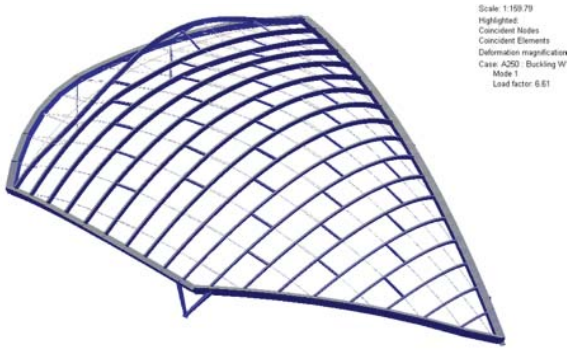


Figure 11: Roof first buckling mode [Passage Projects]

The local imperfections and local stability of the members are taken into account in the checks for buckling resistance of members following AISC 360-10 [2] – as an addition to the imperfections taken into account in the GNIA, for conservative design.

4. Buildability

Although the geometry of the roof is complex, it is important to ensure its buildability and to be able to communicate about it with the fabricator.

4.1. Arches

Each arch is planar and is decomposed into a series of arcs – from 1 arc per arch to 4 arcs per arch. The arches are built-up Rectangular Hollow Sections made of plates. The webs of the arches are cut from plates through CNC machine and the flanges are bent to the desired radius in the bending machine. As a result, the geometry is easily controlled.

4.2. Edge beam

As previously mentioned, the edge beam is made of pentagonal sections following a language of lines and integrating the gutter. Three additional constraints were set to draw the edge beam section, firstly the gutter bottom plate had to be horizontal, secondly the intersection between each edge beam should be aesthetically pleasant i.e. all lines and plates should correctly intersect and thirdly the edge beams should be buildable i.e. all steel plates of the edge beam had to be cylindrical surfaces.

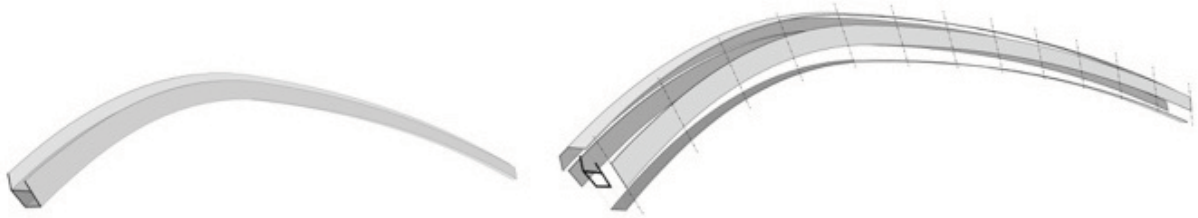


Figure 12: Edge beam 3D view and decomposition into cylindrical surfaces [Passage Projects]

The main challenge of the edge beam conception was to find a compromise between the architectural quality and the buildability of the steel sections while respecting the constraints described above. The edge beams centerlines are curved and planar but the plates composing the edge beams were not parallel nor perpendicular to the edge beam plan. Without more work on the geometry, the edge beam plates would be conical, which would be difficult to fabricate. As a result, the edge beams plates had to be regenerated as a series of cylindrical plates. This work was decomposed into two phases. The first phase consisted in proposing different shapes of sections and work on the intersection of the edge beams two by two. This first step enabled the team to agree on the aesthetic of the edge beams sections and intersections. The second step consisted in making the edge beams buildable. The shape was rationalized using a series of projections and approximations in arcs to avoid twist and warping in the steel plates and to divide them into a reasonable number cylindrical surfaces.

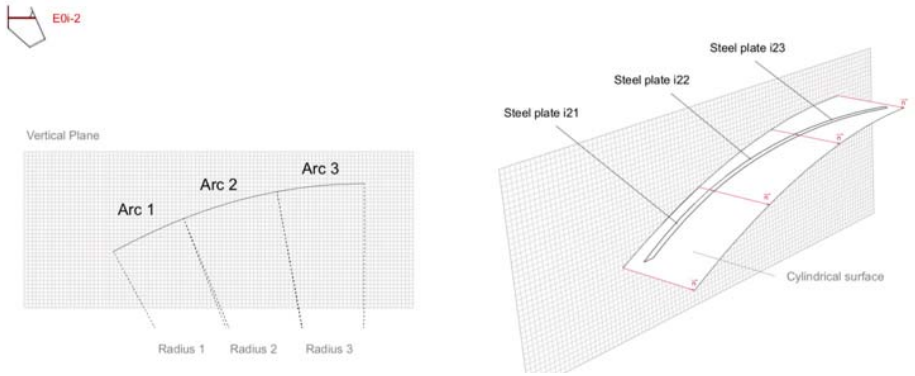


Figure 13: Rationalizing the edge beams plates in cylindrical surfaces [Passage Projects]

A grasshopper script was written to easily divide each edge beam plate, create cylindrical surfaces and ensure that the intersection between each edge beam is perfect.

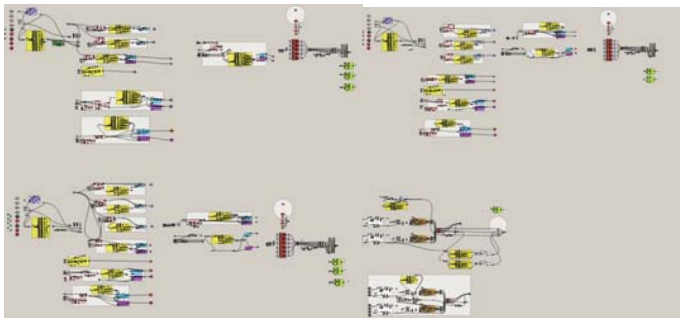


Figure 14: Extract from Grasshopper model [Passage Projects]

The two constraints: having cylindrical steel plates and a gutter bottom perfectly horizontal were impossible to reach simultaneously from a geometrical point of view. Cylindrical surfaces were imperative for construction. Programming enabled to easily study the angle of deviation of the gutter bottom to the horizontal. It helped to control and confirm the acceptable deviations to consider that the gutter bottom was approximately always horizontal along each edge beams.

5. Conclusion

As a conclusion, an extensive study on the best geometry and structural system to integrate the roof in its environment with constrained supporting conditions led to the construction of an elegant roof providing an aerated space for the public. At a late stage in the project, the ETFE contractor proposed to use long ETFE cushions, reducing the number of cushions to only one per stripe. With more time to study this option, longitudinal beams could have possibly been eliminated, which could have resulted in an even lighter looking structure.



Figure 15: Outside and inside view of the roof [Passage Projects]

Acknowledgements

The authors would like to thank all the parties of Whizdom 101: MQDC, A49 Architetcs, ITD, Tayio.

References

[1] ASCE 7-10, “Minimum design loads for buildings and other structures”

[2] AISC 360-10, “Specification for Structural Steel Buildings”.

[3] EN 1993-1-1: Eurocodes 3: Design of steel structures – Part 1-1: General rules and rules for buildings.

Proceedings of the IASS Annual Symposium 2019 – Structural Membranes 2019
Form and Force
7 – 10 October 2019, Barcelona, Spain
C. Lázaro, K.-U. Bletzinger, E. Oñate (eds.)

Path Planning for Rolling Locomotion of Polyhedral Tensegrity Robots

Yipeng LU*, Xian XU, Yaozhi LUO

*College of Civil Engineering and Architecture, Zhejiang University
A-725 Anzhong Building, 866Yuhangtang Road, Hangzhou, Zhejiang, China
21712218@zju.edu.cn

Abstract

Tensegrity-based locomotive robots have attracted more and more interests from multidisciplinary engineering community. To realize long distance locomotion for tensegrity robots, path planning is usually needed. This paper proposes a path planning approach for rolling locomotion of polyhedral tensegrity robots based on Dijkstra algorithm. The mathematical model and the solution procedures of the approach are presented. Simulations and experiments are carried out based on a six-bar tensegrity robot prototype to verify the approach. It also shows that both the length of the path and the terrain feature of area passed through by the path can be considered within the scheme of the proposed approach.

Keywords: path planning; locomotion; polyhedral tensegrity robot; Dijkstra algorithm

1. Introduction

Recently, tensegrity-based robot systems have been paid much attentions from multidisciplinary areas due to its light-weight, deformability and mobility. Paul *et al*. [1] studied the dynamic properties and control of robots based on tensegrity prisms and developed a physical tensegrity robot as a proof of concept. Mizuho Shibata *et al*. [2] described the design of a crawling robot with tensegrity structure and validated the design by experiments. Bohem and Zimmermann [3] proposed a vibration-driven mobile tensegrity robot. Among the tensegrity-based robots, ball tensegrity with spherical configurations has been most intensively studied. Yusuke Koizumi *et al*. [4] realized the rolling of a ball tensegrity robot driven by a set of pneumatic soft actuators. Kyunam *et al*. [5] obtained tensegrity robot the ability of hopping through arranging a simple gas thruster near the center payload of spherical tensegrity robot. In addition, rolling gait is widely used in ball tensegrity robots due to its energy-efficiency and simplicity of implement. Path planning is a crucial problem for active tensegrity systems, and can be divided into two types. One is the path planning for shape control and the other is the path planning for locomotion. For the first type, Xu *et al*. [6] used an approach based on RRT*-connect algorithm to find control path for shape change of shape controllable tensegrity systems. Sychterz and Smith [7] incorporated the RRT*-connect algorithm with feedback search to improve the efficiency of deployment control of an actively deployable tensegrity footbridge. For the second type, relative mature methods have been developed in the field of conventional locomotive robots/vehicles. For examples, Chris *et al*. [8] proposed a three-layer planning system combining mission, behavioral, and motion planning to drive in urban environments; and Yoshiaki *et al*. [9] presented a real-time motion planning algorithm applicable to autonomous vehicles operating in an urban environment. However, these methods cannot be extended to spherical tensegrity robots because of the particularity of the locomotion of spherical tensegrity robots with rolling gaits.

The layout of the paper is as follows. Section 2 presents the mathematical model for the path planning problem. In Section 3, Dijkstra algorithm is adopted to solve the path planning problem and both the totally distance travelled and the terrain feature are considered. In Section 4, typical examples are carried

Copyright © 2019 by Yipeng LU, Xian XU, Yaozhi LUO
Published by the International Association for Shell and Spatial Structures (IASS) with permission.

out with a real-world six-bar tensegrity robot. Experimental validations of the proposed approach are conducted in Section 5. Finally, Section 6 concludes the study.

2. Mathematical model

2.1 Problem description

It is assumed that the tensegrity robot considered here has following properties: (1) tension elements are only able to carry tensile forces; (2) compression elements are rigid and able to carry both compression force and tensile force; (3) the locomotion of it is realized by successively applied a number of given basic rolling gaits; and (4) the kinetic property of a basic gait is independent on the terrain of the land it rolling on.

The given basic gaits $\mathbf{B}$ are expressed as $\mathbf{B} = [\mathbf{B}_1, \mathbf{B}_2, \mathbf{B}_3,\ldots, \mathbf{B}_n]$, where $\mathbf{B}_i$ is the i^{th} basic gait; and n is the number of basic gaits. $\mathbf{B}_i$ can be reexpressed as $\mathbf{B}_i = \mathbf{B}_i(\Delta\mathbf{e}_i(t_i), \boldsymbol{s}_i)$, where $\Delta\mathbf{e}_i(t_i)$ is the actuation of the i^{th} gaits; t_i is the time of the i^{th} basic gait; and $\mathbf{s}_i$ is the initial state of the robot in the i^{th} basic gait. The actuation $\Delta\mathbf{e}_i(t_i)$ is given by $\Delta\mathbf{e}_i(t_i) = [\Delta e_{i,1}(t_i), \Delta e_{i,2}(t_i), \Delta e_{i,3}(t_i),\ldots, \Delta e_{i,m}(t_i)]$, where $\Delta e_{i,j}(t_i)$ is the actuation of the j^{th} actuator ; and m is the number of actuators. The total actuation $\mathbf{e}_i(t_i)$ of the actuators in the i^{th} basic gait is given by $\mathbf{e}_i(t_i) = \mathbf{e}_{si} + \Delta\mathbf{e}_i(t_i)$, where $\mathbf{e}_{si}$ is the initial actuation of the i^{th} gait given by $\mathbf{e}_{si} = [e_{si,1}, e_{si,2}, e_{si,3},\ldots, e_{si,m}]$, where $e_{si,j}$ is the initial actuation of the j^{th} actuator. It is required that $\mathbf{e}_i(t) \in [\mathbf{e}^l, \mathbf{e}^u]$, where $\mathbf{e}^l$ and $\mathbf{e}^u$ are the lower bound and the upper bound of the range of the actuators, respectively. The initial state $\mathbf{s}_i$ is given by $\boldsymbol{s}_i = \boldsymbol{s}_i(\mathbf{e}_{si}, \mathbf{Con}_{si})$, where $\mathbf{Con}_{si}$ is the initial contact condition of the robot in the initial state of the i^{th} gait.

The state of the tensegrity robot during the i^{th} basic gait is determined by the dynamic equation as follows

$$\mathbf{M}\Delta\ddot{\mathbf{X}}_i(t_i) + \mathbf{C}\Delta\dot{\mathbf{X}}_i(t_i) + \mathbf{K}\Delta\mathbf{X}_i(t_i) = \mathbf{P}\left[\Delta\mathbf{e}_i(t_i)\right] \tag{1}$$

where $\mathbf{M}$ is the mass matrix; $\Delta\mathbf{X}_i(t_i)$ is the displacement vector; $\mathbf{C}$ is the damping matrix; $\mathbf{K}$ is the stiffness matrix; and $\mathbf{P}[\Delta\mathbf{e}_i(t_i)]$ is the vector of equivalent nodal forces. At the beginning of the basic gait, the system is in static equilibrium with no displacement, thus there are $\Delta\mathbf{X}_i(0) = 0$, $\Delta\dot{\mathbf{X}}_i(0) = 0$, $\Delta\ddot{\mathbf{X}}_i(0) = 0$. At the end of the basic gait, the system is also in static equilibrium but with non-zero displacement $\Delta\mathbf{X}_{fi}$ and thus $\Delta\mathbf{X}_i(t_i) = \Delta\mathbf{X}_{fi}$, $\Delta\dot{\mathbf{X}}_i(t_i) = 0$, $\Delta\ddot{\mathbf{X}}_i(t_i) = 0$.

The internal force $\mathbf{T}_i(t_i)$ of the tensegrity robot can be expressed as $\mathbf{T}_i(t_i) = [T_{i,1}(t_i), T_{i,2}(t_i), T_{i,3}(t_i),\ldots, T_{i,q}(t_i)]$, where $T_{i,j}(t_i)$ is the internal force of the j^{th} element; and q is the number of elements of the tensegrity robot. The internal force of an element is required to be not higher than its design strength. In addition, in the process of rolling, the struts are allowed to carry both compression force and tensile force and the cables are allowed to slack temporarily, i.e.

$$\begin{cases} T_{i,j}(t_i) \in [-T_j^l, T_j^u], & \text{if the } j^{\text{th}} \text{ element is a strut} \\ T_{i,j}(t_i) \in [0, T_j^u], & \text{if the } j^{\text{th}} \text{ element is a cable} \end{cases} \tag{2}$$

where T_j^l and T_j^u are the lower bound and the upper bound of the strength of the j^{th} element, respectively, while at the beginning and the end of the basic gait, the struts are required to carry compression force and the cables are required to carry tensile force, as the system is in static equilibrium. Hence, there are

$$\begin{cases} T_{i,j}(t_i) \in [-T_j^l, 0), & \text{if the } j^{\text{th}} \text{ element is a strut} \\ T_{i,j}(t_i) \in (0, T_j^u], & \text{if the } j^{\text{th}} \text{ element is a cable} \end{cases} \tag{3}$$

Considering a tensegrity robot that motions in a given space via a gait sequence $\mathbf{B}^p = [\mathbf{B}_1^p, \mathbf{B}_2^p, \mathbf{B}_3^p,..., \mathbf{B}_r^p]$, where $\mathbf{B}_k^p \in \mathbf{B}$ and r is the number of the gaits, the cost of the k^{th} gait c_k depends on the type of the gait $\mathbf{B}_k^p$ and the terrain of the land $\mathbf{Ter}_k$ the robot rolling over in the k^{th} gait, i.e. $c_k = c_k(\mathbf{B}_k^p, \mathbf{Ter}_k)$. Hence, the total cost c_{total}^p of the gait sequence can be written as

$$c_{total}^{p} = \sum_{k=1}^{r} c_k \tag{4}$$

The final position $\mathbf{X}_f^p$ of the robot is given by $\mathbf{X}_f^p = \mathbf{X}_{s1}^p + \sum_{k=1}^{r} \Delta\mathbf{X}_{fk}^p$, where $\mathbf{X}_{s1}^p$ is the position of the robot at the beginning of the first gait, i.e. the initial position of the robot; and $\Delta\mathbf{X}_{fk}^p$ is the displacement of the robot generated by the k^{th} gait. Since $\mathbf{B}_k^p \in \mathbf{B}$, $\Delta\mathbf{X}_{fk}^p$ can be determined by $\Delta\mathbf{X}_{fk}^p = \mathbf{Q}_k \Delta\mathbf{X}_f^T$, where $\Delta\mathbf{X}_f$ is the final displacement matrix given by $\Delta\mathbf{X}_f = [\Delta\mathbf{X}_{f1}, \Delta\mathbf{X}_{f2}, \Delta\mathbf{X}_{f3}, \ldots, \Delta\mathbf{X}_{fn}]$, where $\Delta\mathbf{X}_{fi}$ is the final displacement vector of the i^{th} basic gaits; and $\mathbf{Q}_k$ is a $1\times n$ vector indicating the type of the gait, whose component Q_{ki} is given by

$$Q_{ki} = \begin{cases} 1, & \text{if } \mathbf{B}_k^p = \mathbf{B}_i \\ 0, & \text{if } \mathbf{B}_k^p \neq \mathbf{B}_i \end{cases} \tag{5}$$

Assuming that the target position of the robot is $\mathbf{X}_t^p$, the path planning problem of the motion can be formulated as

$$\begin{aligned} &\text{Min } c_{total}^{p} \\ &\text{Subject to } \left\| \mathbf{X}_f^p - \mathbf{X}_t^p \right\| \leq \varepsilon_{\text{t}} \\ &\qquad \mathbf{B}_k^p \in \mathbf{B} \end{aligned} \tag{6}$$

where ε_{t} is a given constant which represents the position tolerance.

2.2 Description of possible paths

In graph theory, a directed graph is a graph made up of a set of vertices connected by edges, where the edges have a direction associated with them. It is assumed that the position of a polyhedral tensegrity is represented by the center vertex of its base. Hence the position vertices of a locomoting polyhedral tensegrity are a series of discrete vertices in the space. Assuming that vertices i and j are position vertices, an edge E_{ij} links vertex i to vertex j only if vertex j is connected to vertex i by certain gait. Therefore, these position vertices and edges form a network, which can be represented by a directed graph. A directed graph can be expressed as an ordered pair $\mathbf{G} = (\mathbf{V}, \mathbf{E})$ where $\mathbf{V}$ is the position vertices matrix and $\mathbf{E}$ is the adjacency matrix describing the edges of $\mathbf{G}$. For a directed graph with a vertices, $\mathbf{V}$ is given by

$$\mathbf{V} = [V_1, V_2, V_3, ..., V_a] \tag{7}$$

and $\mathbf{E}_{a\times a}$ is the adjacency matrix whose component E_{ij} is given by

$$E_{ij} = \begin{cases} l(i,j), & \text{if vertex } i \text{ is connected to vertex } j \\ \infty, & \text{if vertex } i \text{ is disconnected to vertex } j, \quad (i, j \in \mathbf{V}) \\ 0, & \text{if } i = j \end{cases} \tag{8}$$

where $l(i, j)$ is determined by the length of the edge from i to j and $l(i, j) > 0$.

3. Path planning by Dijkstra algorithm

The Dijkstra algorithm is applied to solve a problem with a vertices in a directed graph $\mathbf{G}_{\text{c}} = (\mathbf{V}, \mathbf{H})$, where $\mathbf{V}$ is shown as Eq. (7), the cost matrix $\mathbf{H}$ is the Hadamard product of adjacency matrix $\mathbf{E}$ and terrain matrix $\mathbf{A}$ and given by

$$\mathbf{H}_{a\times a} = \mathbf{E}_{a\times a} * \mathbf{A}_{a\times a} \tag{9}$$

where the component c_{ij} of $\mathbf{H}_{a\times a}$ is the cost of the edge from vertex i to vertex j, $*$ is the calculating sign of Hadmard product, and $\mathbf{A}_{a\times a}$ is the terrain matrix whose component a_{ij} is given by

$$\alpha_{ij} = \begin{cases} w_\alpha(i,j), & \text{if vertices } i \text{ and } j \text{ are in terrain without obstacles} \\ \infty, & \text{if vertice } i \text{ or } j \text{ is in terrain with obstacles} \\ 0, & \text{if } i = j \end{cases}, \quad (i,j \in \mathbf{V}) \tag{10}$$

where $w_\alpha(i, j) > 0$.

Considering the gait sequence $\mathbf{B}^p = [\mathbf{B}_1^p, \mathbf{B}_2^p, \mathbf{B}_3^p, ..., \mathbf{B}_r^p]$, the total cost c_{total}^p of the gait sequence is given by Eq. (4). If the k^{th} gait links the vertex i to vertex j, the cost c_k of the k^{th} gait is given by

$$c_k = \mathbf{U}_{k1}{}^{\mathrm{T}}(\mathbf{H} * \mathbf{L}_k)\ \mathbf{U}_{\mathrm{k2}} \tag{11}$$

where $\mathbf{U}_{k1} = [U_{k11}, U_{k12}, U_{k13}, \ldots, U_{k1a}]^{\mathrm{T}}$ and $\mathbf{U}_{k2} = [U_{k21}, U_{k22}, U_{k23}, \ldots, U_{k2a}]^{\mathrm{T}}$ are coordinate vectors, $(\mathbf{L}_k)_{a\times a}$ is the link matrix used to describe the k^{th} gait. U_{k1u} and U_{k2u} are given by

$$U_{k1u} = \begin{cases} 1, & \text{if } u=i \\ 0, & \text{if } u \neq i \end{cases}, \ U_{k2u} = \begin{cases} 1, & \text{if } u=j \\ 0, & \text{if } u \neq j \end{cases} \tag{12}$$

The component L_{ij} of $\mathbf{L}_k$ is given as follows

$$L_{ij} = \begin{cases} 1, & \text{if the } k^{\text{th}} \text{ gait links vertex } i \text{ to vertex } j \\ 0, & \text{others} \end{cases} \tag{13}$$

Given the directed graph $\mathbf{G}_c = (\mathbf{V}, \mathbf{H})$, the start vertex V_s and the target vertex V_t, the locomotion path with lowest cost can be found by the Dijkstra algorithm, as outlined in Fig. 1, where *MV* is a collection of marked vertices; *UMV* is a collection of unmarked vertices; $cost(V_i)$ is the lowest cost from the start vertex V_s to the vertex V_i; $path(V_i)$ is the path corresponding to the lowest cost; $ADJU_k$ is a collection of the unmarked vertices adjacent to V_k; and $ADJM_m$ is a collection of the marked vertices adjacent to V_m.

Input: a directed graph $\mathbf{G}_c = (\mathbf{V}, \mathbf{H})$, start vertex V_s, target vertex V_t.

Output: an optimal path $path(V_t)$ and corresponding $cost(V_t)$.

1. **set** $MV \leftarrow \{\}$, $UMV \leftarrow \mathbf{V}$.
2. **For all** $V_k \in \mathbf{V}$, **set** $cost(V_k) \leftarrow +\infty$, $path(V_k) \leftarrow$ nil.
3. **Move** V_s from *UMV* to *MV*, **set** $cost(V_s) \leftarrow 0$, $path(V_s)$ add V_s.
4. **While** $UMV \neq \{\}$, **do**

4.1 **For each** $V_k \in MV$, **do**

4.1.1 **For each** $V_j \in ADJU_k$, **do**

4.1.1.1 **Set** $c(V_k, V_j) \leftarrow$ cost from V_k to V_j.

4.1.1.2 **If** $cost(V_j) > cost(V_k) + c(V_k, V_j)$, **set** $cost(V_j) \leftarrow cost(V_k) + c(V_k, V_j)$.

4.2 **Set** $V_m \leftarrow V_j$ such that V_j is the vertex in *UMV* with the minimum $cost(V_j)$.

4.3 **For each** $V_k \in ADJM_m$, **do**

4.3.1 **If** $cost(V_k) + c(V_k, V_m) = cost(V_m)$, **set** $V_n \leftarrow V_k$.

4.4 **Set** $path(V_m) \leftarrow path(V_n)$ add V_m.

4.5 **Move** V_m from *UMV* to *MV*.

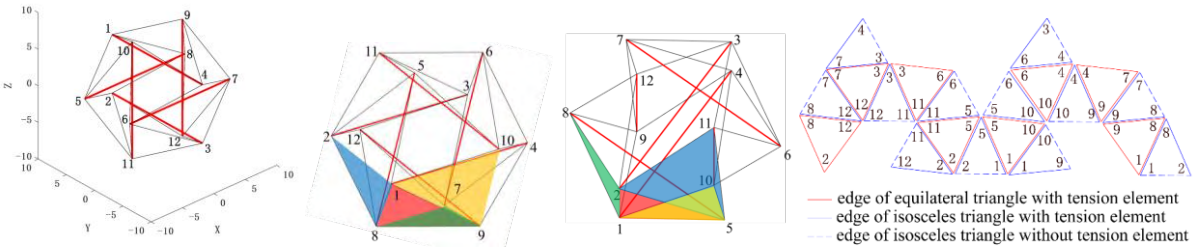
Fig. 1 Frame of Dijkstra algorithm

4. Numerical simulations

In this section, the six-bar tensegrity robot which is widely studied in literature is taken as a typical example.

4.1 Six-bar tensegrity

A six-bar tensegrity consists of 12 nodes, 6 identical compression elements and 24 identical tension elements, as shown in Fig. 2(a), where the bold lines represent compression elements and the thin lines represent tension elements. The six-bar tensegrity has a configuration as an icosahedron which consists of 20 triangles. 8 of them are closed equilateral triangles which have tension elements located on each edge, and 12 of them are open isosceles triangles which have tension elements located on the two equal edges. The six-bar tensegrity is able to stand stably on ground with one of the triangles as its base. There are two basic states of stand for the system in accordance with the type of the base triangle. One of them is called CT (Close Triangle) state where a closed equilateral triangle (1, 8, 9) is used as the base, as shown in Fig. 2(b), and the other is called OT (Open Triangle) state where an open isosceles triangle (1, 2, 5) is used as the base, as shown in Fig. 2(c). The surface expansion of the icosahedron-shaped tensegrity is shown in Fig. 2(d).



(a) Configuration (b) CT state (c) OT state (d) Surface expansion

Fig. 2 Six-bar tensegrity

The surface of the icosahedron can be unfolded into a graph as shown in Fig. 2(d). The unfolded graph can be further expanded to a grid map as shown in Fig. 3, where unfilled triangles represent the areas with smooth terrain; shaded triangles represent the blind areas that cannot be reached by the tensegrity robot due to the inherent characteristics of the system; and the dashed lines represent the possible paths of the tensegrity robot. Each dashed line segment corresponds to a possible gait. The geometric length of a dashed line segment represents the stride of the corresponding gait. The geometric lengths of the dashed line segments are equal to each other, i.e. the possible gaits of the system have a same stride. Note that the grid map can be expanded infinitely. Here a typical 9×9 grid map is considered, and each triangle is named with a pair of sequence numbers which are given in the left and bottom of the map. For an example, the triangle in the fourth column of the fifth raw is named (5, 4). A directed graph $\mathbf{G}_c = (\mathbf{V}, \mathbf{H})$ can be applied to describe the possible paths shown in Fig. 3 as follows. For the 9 × 9 grid map considered here, there are totally 81 triangles and the vector of position vertices $\mathbf{V}$ is given as $\mathbf{V} = [1,2,3,\ldots,81]$ in accordance with Eq. (7). For a triangle (u_i, v_i), the corresponding position vertex V_i also can be determined by $V_i = u_i + (v_i - 1) \times 9$, $(i = 1, 2, 3,\ldots, 81)$.

In according to Eqs. (9)-(10), the cost matrix $\mathbf{H}$ can be determined as long as $l(i, j)$ and $w_a(i, j)$ are determined. Since the lengths of the dashed line segments in Fig. 3 are same to the each other, $l(i, j) = 1$ is assumed for any set of vertices i and j. $w_a(i, j)$ is a penalty factor depending on the terrain of the triangular areas where the i^{th} and j^{th} vertices are located in. Without loss of generality, $w_a(i, j) = 1$ is used when both the vertices i and j are located in smooth areas; $w_a(i, j) = 2$ is used when either vertex of i or j is located in a rough area; and $w_a(i, j) = 4$ is used when either vertex of i or j is located in a very rough area.

4.2 Prototype

Based on the tensegrity shown in Fig. 2(a), a physical prototype, as shown in Fig. 4, is manufactured. Six servo linear actuators are used as active compression elements, and rubber ropes are used as tension elements. The linear actuators and the rubber ropes are connected with customized 3D printed nodes.

The servo linear actuators have an initial length of 15.6 cm and an extensible length of 10.0 cm. The telescopic rate of the actuators is about 1.4 cm/s. The rubber ropes have an initial length of 6.0 cm and an elastic stiffness of 0.78 N/m. The weight of an actuator and the weight of a rubber rope are 56.0 g and 1.0 g, respectively. In the center of the prototype system, a control box consisting of blue teeth communication module, servo control module and lithium battery is hanged to the nodes with 24 rubber ropes same as those used for tension elements. The total weight of the control box is 127.6 g. The prototype is controlled wirelessly through blue teeth communication with a control program installed in a personal computer.

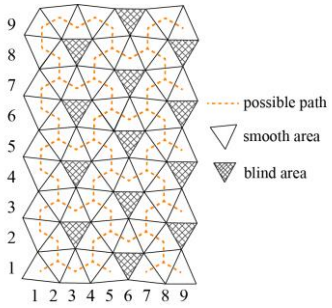


Fig. 3 Possible paths

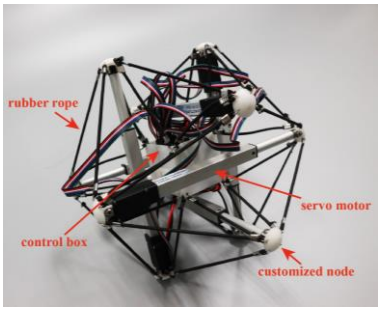


Fig. 4 Prototype

Table 1. Number of actuators

Actuator number	1	2	3
Connecting nodes	9, 12`	6, 7	2, 3
Actuator number	4	5	6
Connecting nodes	1, 4	5, 8	10, 11

4.3 Basic gait

The nodes of the six-bar tensegrity in a typical CT state and in a typical OT state can be numbered as shown in Fig. 2 (b) and (c), respectively. The numbers of actuators and the connecting nodes of actuators are given in Tab. 1. Two feasible gaits $\mathbf{B}_1$ and $\mathbf{B}_2$ which are found by a GA based gait generating algorithm [10] are used as the basic gaits. Here, the initial contact condition $\mathbf{Con}_{si}$ means the contact triangle, i.e. the base of the six-bar tensegrity robot. The details of the basic gaits are given as follows. $\mathbf{e}_{s1} = [5, 5, 5, 5, 5, 5]$ cm, $\mathbf{Con}_{s1} = (1, 8, 9)$, $\mathbf{\Delta e}_1(t_i) = 1.4t_i$ $[1, 1, -1, -1, 1, 1]$ cm, $t_i \in [0, 3.57$ s$]$; and $\mathbf{e}_{s2} = [5, 5, 5, 5, 5, 5]$ cm, $\mathbf{Con}_{s2} = (1, 2, 5)$, $\mathbf{\Delta e}_2(t_i) = 1.4\ t_i$ $[0, 0, 1, -1, 0, 0]$ cm, $t_i \in [0, 3.57$ s$]$.

Note that the basic gait $\mathbf{B}_1$ is able to drive the system rolling from a CT state to a OT state, e.g. the tensegrity shown in Fig. 2 (b) can roll from the CT state (1, 8, 9) to the OT state (1, 9, 10) with $\mathbf{B}_1$. The basic gait $\mathbf{B}_2$ is able to drive the system rolling from a OT state to a CT state, e.g. the tensegrity shown in Fig. 2(c) can roll from the OT state (1 ,2, 5) to the CT state (1, 5, 10) with $\mathbf{B}_2$.

4.4 Examples

Four numerical examples considering obstacle and terrain are carried out. The center of the triangle (1, 4) is set as start vertex V_s, and the center of the triangle (8, 6) is set as target vertex V_t. The details of the four examples are shown in Fig. 5 where the unfilled circles indicate V_s and the filled circles indicate V_t; the unfilled triangles represent smooth areas; the shaded triangles represent the blind areas; the black triangles represent the obstacles; and the light gray triangles represent rough areas; and the dark gray triangles represent very rough areas.

4.5 Numerical results

The position tolerance constant ε_t is set as 8.0 cm which is a little bit smaller than the stride of a basic gait. With the above given conditions, the simulations are done by GrTheory Toolbox on MATLAB [11]. The total cost of the path in example i is denoted as c^i_{total}. The found paths are plotted in Fig. 6. It is obvious that the found paths vary from each other because the environmental feature of the examples are different.

The path found in example 1 is comprised of 15 gaits and is the shortest one in all the examples. This is because there is no obstacle or rough area in this example and the tensegrity robot can move much

straighter than the other examples. The total cost c^1_{total} of the path is 15 which equals to the number of gaits used. The path found in example 2 is comprised of 17 gaits and thus the total cost c^2_{total} of it is 17, too. It is clearly shown by Fig. 6 (b) that the path detours around the areas with obstacle. In example 3, the rough areas cause the path to shift from the right side to the left side and meanwhile increase the number of gaits from 17 to 19. Since the path uses two gaits to pass through a rough area as shown in Fig. 6 (c) and a penalty factor of 2 is used for the cost of a gait moving in or moving out a rough area, the total cost c^3_{total} of the path is 21 which is 2 larger than the number of gaits. The path found in example 4 is comprised of 23 gaits. Both the obstacles and the very rough areas are avoided by the path as shown in Fig. 6 (d). As a result, the total cost c^4_{total} of the path equals to the number of used gaits, i.e. $c^4_{total} = 23$.

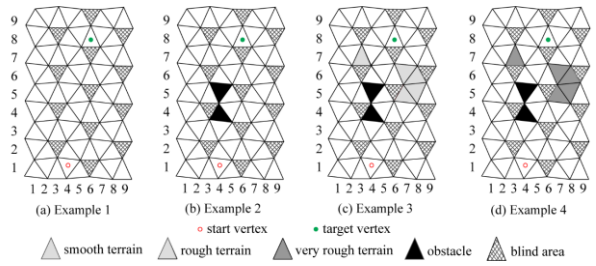


Fig. 5 Four numerical examples

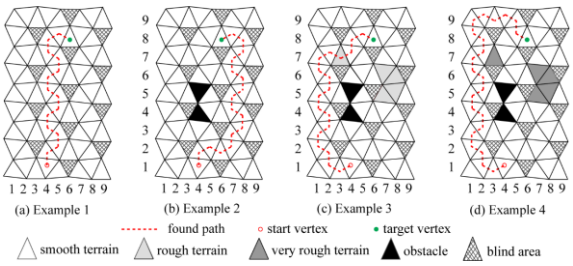
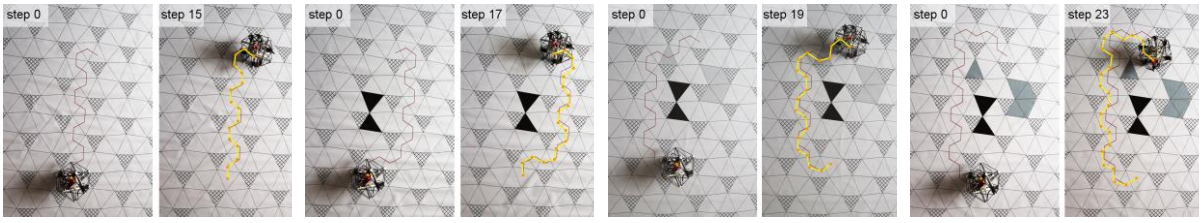


Fig. 6 Numerical result paths

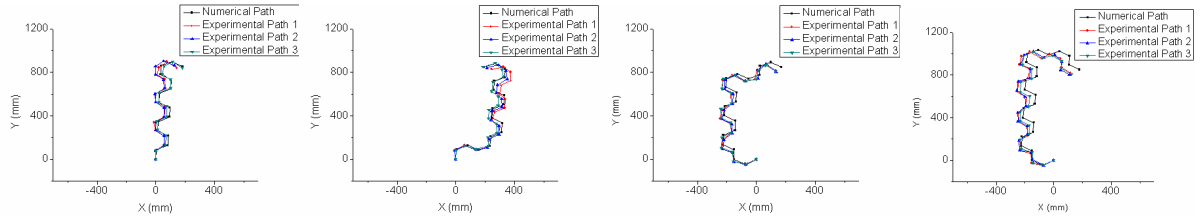
5. Experiments

To verify the numerical results, experiments with a physical prototype introduced in Section 4.2 are carried out. For each example, three tests are performed. A typical test for each example is shown in Fig. 7. The position of the prototype at the end of each gait is indicated by solid points and the path of the prototype is described by the lines connecting the solid points.



(a) Example 1 (b) Example 2 (c) Example 3 (d) Example 4

Fig. 7 Experiments



(a) Example 1 (b) Example 2 (c) Example 3 (d) Example 4

Fig. 8 Numerical result paths

Besides the typical results shown in Fig. 7, the complete results of the experiments are shown in Fig. 8. It shows that in all the examples the prototype generally rolls along the numerical paths. Using ε_i to denote the average distance from the final positions of the three tests to the target position in the example

i, there are ε_1 = 3.53 cm, ε_2 = 2.83 cm, ε_3 = 5.43 cm, and ε_4 = 7.40 cm, which are all smaller than the given position tolerance ε_t = 8.00 cm. The observed difference between the simulation results and the experimental results is mainly caused by the fact that the numerical model of the tensegrity robot does not consider the size of elements and the nodes and the detail of the connections for the sake of simplicity.

6. Conclusions

The path planning for rolling locomotion of polyhedral tensegrity robots can be modeled as a problem of finding the path with lowest cost in a graph with a given adjacent matrix. The key to this problem is to obtain the possible path graph of polyhedral tensegrity robots and to establish a mathematical model for the possible path graph. By expanding the surface of polyhedrons, a graph representing possible paths can be obtained. With a function **G** consisting of vertices matrix **V** and cost matrix **H** of the graph, a mathematical model is set up. The Dijkstra algorithm is applied to solve this mathematical model. Numerical examples on a six-bar tensegrity robot and the corresponding experiments with a physical prototype are carried out. It is found that the simulation results generally tally with the experimental results, which verify the proposed approach. Some errors between the simulation results and experimental results are observed. Calibrating the numerical model with the physical prototype is believed that would narrow the errors.

Acknowledgements

This work was supported by Natural Science Foundation of Zhejiang Province (Grant No. LR17E080001).

References

[1] C. Paul, F. J. Valero-Cuevas, and H. Lipson, "Design and control of tensegrity robots for locomotion," Ieee Transactions on Robotics, vol. 22, no. 5, pp. 944-957, Oct 2006.

[2] M. Shibata, F. Saijyo, S. Hirai, and Ieee, "Crawling by Body Deformation of Tensegrity Structure Robots," in Icra: 2009 Ieee International Conference on Robotics and Automation, Vols 1-7(IEEE International Conference on Robotics and Automation ICRA, 2009, pp. 3617-3622.

[3] V. Boehm, K. Zimmermann, and Ieee, "Vibration-Driven Mobile Robots Based on Single Actuated Tensegrity Structures," in 2013 Ieee International Conference on Robotics and Automation(IEEE International Conference on Robotics and Automation ICRA, 2013, pp. 5475-5480.

[4] Y. Koizumi, M. Shibata, S. Hirai, and Ieee, "Rolling Tensegrity Driven by Pneumatic Soft Actuators," in 2012 Ieee International Conference on Robotics and Automation(IEEE International Conference on Robotics and Automation ICRA, 2012, pp. 1988-1993.

[5] K. Kim et al., Hopping and Rolling Locomotion with Spherical Tensegrity Robots (2016 Ieee/Rsj International Conference on Intelligent Robots and Systems). 2016, pp. 4369-4376.

[6] A. Luo and H. Liu, "Analysis for Feasibility of the Method for Bars Driving the Ball Tensegrity Robot," Journal of Mechanisms and Robotics-Transactions of the Asme, vol. 9, no. 5, Oct 2017, Art. no. 051010.

[7] X. Xu, F. Sun, Y. Luo, and Y. Xu, "Collision-Free Path Planning of Tensegrity Structures," Journal of Structural Engineering, vol. 140, no. 4, Apr 1 2014, Art. no. 04013084.

[8] A. C. Sychterz and I. F. C. Smith, "Deployment and Shape Change of a Tensegrity Structure Using Path-Planning and Feedback Control," (in English), Original Research vol. 4, no. 45, 2018-August-23 2018.

[9] C. Urmson et al., "Autonomous driving in urban environments: Boss and the Urban Challenge," Journal of Field Robotics, vol. 25, no. 8, pp. 425-466, Aug 2008.

[10] H. Cai, Y. Lu, X. Xu, Y. Luo and Y. Zhao, "Locomotion design and optimization of dynamic tensegrity," Symposium of International Association for Shell and Spatial Structure, Boston, 2018.

[11] MATLAB. "MATLAB R2016a." MathWorks, Natick, MA.

AUTHORS INDEX

Abadi, K. 653
Abramczyk, J. 1676
Adiels, E. 728
Adriaenssens, S. 161, 275, 874
Ahlquist, S. 320
Akbari, M. 693
Akbarzadeh, M. 693
Al Asali, M. W. 2625
Al-Azri, S. 2103
Aldinger, L. 2633
Alforno, M 1598
Allner, L. 401, 2460
Aloui, O. 2800
Alpermann, H. 2573
An, S. 2045
Anastasiadou, I. 1888
Ander, M. 153, 1437, 2720
Ando, K. 548, 2657
Apellaniz, D. 2573
Apumayta, A. 568
Arnouts, L.I.W. 1776
Arsano, A. 1096
Asadi, H. 2326
Asakawa, Y. 2053
Asghari, R. 653
Asou, N. 1845
Baber, K. 524
Bader, C. 1338
Bagger, A. 2705
Baghdadi, A. 1258
Bai, C. 261
Baker, E. 1744, 1768
Baker, W.F. 2127, 2135
Banicek, M. 685
Banon, C. 1289
Bao, D.W. 485, 1972
Bao, Han 2285
Baquero, P. 2617
Baranowski, J 2135
Barthel, R. 783, 799
Baszynski, P. 2826
Bauer, A. M. 791, 799
Baverel, O. 516, 637, 720, 751,
.....1219, 1858, 2069
Baxter Chinery, M. 1321
Beaudouin-Mackay, A. 1274
Beccarelli, P. 388
Bechert, S. 2599, 2633
Bechmann, R. 2591
Beckh, M. 842, 2189
Bellmann, J. 807
Beran, J. 2531
Berke, P.Z. 1776
Bernert, K. 2343
Bertino, S. 2770
Bertomeu, G. 218
Bickel, B. 509
Bitencourt Jr, L. 394
Blanchfield, J. 261
Blanco, G. 976
Blandini, L. 2563
Bleicher, A. 1728
Bletzinger, K.-U. 791, 799, 2087, 2913
Block, P. 1211, 2069
Bober, W. 2195
Boccia, G. 183
Boixader, D. 1866
Bolelli, P. 890
Bolhassani, M. 693
Boller, G. 842, 2189
Bonavia, E. 1896
Boni, C. 1527
Borgart, A. 1567
Borgny, M. 2720
Bos, D.H. 2826
Bouckaert, I. 2792
Bouleau, E. 606, 1904
Bouw, I. 1313
Bouzida, Y. 2921
Bown, A. C. 2300
Boyd, P. 1228
Brandt-Olsen, C 728
Breseghello, L. 87
Brodniansky, J. 1559, 1590
Brown, N. 1096
Brusciotti, F. 598
Brütting, J. 2875, 2905
Budig, M. 1918
Bui, Q.H. 1080
Bukauskas, A. 524
Bukovec, M. 467
Burry, J. 524
Burt, M. 2689
Cabello, A. 2300

Caedro, H. 568
Cai, J. 970
Cai, J.G. 2483
Cai, K. 1972, 1996
Calatan, G. 736
Calderini, C. 1598
Calvarese, M. 1656
Calvo-Barentin, C. 1211
Cao, Y. 1196, 1385
Cao, Z. 1183
Caponi, P. 2211
Cardenas Pantoja, M. 367
Carlson, A 2020
Carneau, P. 1219
Carvalho, J. 95, 103
Casapulla, C. 1582
Case, J. 582
Caseri, M. 1535
Cassinello, P. 2203
Castillo Gallusser, S. 858
Catala Bustos, L. 590
Chai, H. 1242, 1274, 1511, 2851
Chaltiel, S 113
Chamseddine, I. 828
Chan, A. 1321
Chao, A. 493
Chen, A. 1606
Chen, C. 524
Chen, J. 1429
Chen, S-W 2160
Chen, T. 606
Chen, W. 2236
Chen, Y. 769
Chen, Yali 2364
Chenaghlou, M.R 653
Chi, D. A. 1944
Chia, P 534
Chiang, Y.-C. 1567
Chilton, J. 388, 850
Chondrogiannis, K.-A. 834
Chousou, G. 1211
Christ, J. 1926
Christie, J. 2599
Cignoni, P. 509, 2152
Clemente, A. 1823
Coelho, M. 776
Coenders, J 1119
Consigny, F. 2077
Contestabile, M 501
Contestabile, M. 175
Correa, C. 2507
Cortes-Paez, E. 475
Costa, J. 1338
Cremers, J. 1952
Cresnar, A. 1416
Cruz, P. 103
Cui, J.C 1800
Cunha, P. 1477
Curbach, M. 866, 1088
Cutroni, F. 2211
Dahy, H. 2826
Dambrosio, N. 1353
Damkilde, L. 1151
Dang, Q.M. 543
De La Manga, R. 328
de Matos, H. 2713
de Oliveira Franca Junior, D. 1641
De Smedt, E. 914
De Temmerman, N. 1776
Degroote, J. 1167
del Campo, M 2020
Demir, A. 1495
Deschuyteneer, A. 677
Dessi-Olive, J. 582
Deutscher, M. 1189
Devin, A. F. 2135
Di Marco, G. 2221
Diedering, R. 1489
Dijoux, C. 209
Dillenburger, B. 1211, 1250
Dimitri, C. 218
Disset, J. 1338
Dong, S.L. 2784
Douthe, C. 516, 720, 751, 1858, 2077
Draper, P. 312, 493
Du, B. 2004
Du, Bin 1445
Dumitrescu, D. 2335, 2720
Durand, R. 1477
Duro-Royo, J. 2475
Dutta, S 1964
Dy, B. 1135
Dyvik, Steinar H. 2420
Ebata, K. 1839
Echeverria Valiente, E. 2665
Eguchi, C. 1127
Emami, N. 439
Esaka, Y. 2539

Espinoza, M. 568
Esposito, L. 183
Estevez, A.T. 2617
Ezendam, T. 1313
Fabré, M. 218
Fagerström, G. 129
Faisal, T. 543
Fan, F. 2428
Fang, D. 1096, 2135, 2875
Felbrich, B 2335
Feng, J. 970, 2483
Feraille, A. 751
Fernandez, R. 2372
Fernandoy-Bak, J. 1926
Feron, J. 2792
Ferrer, C. 1408
Ferretti, D. 1527
Ferrán, J. 1408
Fiebig, J. 1926
Figueiredo, B. 95, 103
Filipov, E. 320
Filz, G.H. 351, 622, 645
Fink, G. 622, 645
Fischer, A. 2875
Fivet, C. 1858, 2875, 2905
Flor, J.-F. 388
Flores, R. 1175
Forestiero, F 1297
Foxe, D 2836
Franceschi, M. 2921
Frangos, N. 129
Frenzel, M. 1088
Fresl, K. 685, 1980
Fries, T.P. 761
Froli, M. 2152
Fuentes-Durá, P. 433
Fujii, D 2111
Fujita, S. 1988
Fujiwara, S. 1519
Fukuda, K. 2810
Földesi, D. 1242
Gabriele, S. 45
Gamboa Marrufo, M. 1204
Gantes, C.J. 834
Gao, J. 2244
Gao, S. 2380, 2404
Gao, W. 1274
Garcia, A. 2372
Garcia - Mora, C.J. 1760
García-Guerrero, J. M. 622
Garlock, M. 275, 1808
Gaspar, O. 1648
Gattas, J. 524
Gauvreau, P. 245
Gellin, S. 882
Gengnagel, C. 2573
Gherardi, J. 1535
Ghosh, S 1964
Giannetti, I. 598
Giannopoulou, E. 2617
Gidak, P. 1416, 1980
Gil Perez, M. 1353, 1831
Gilbert, M. 2061
Gilsanz, R. 261
Gimferrer, X. 475
Giménez Fernández, M. 1321
Gkioka, M. 1119
Glisic, B. 275, 282, 1808
Godina, M. 2681
Godthelp, T. 2728
Goldbach, A-K. 2913
Gong, J. 2428
Goni, J. 976
Gonzalez, E. 1944, 2221
Gonzalez, S. 976
González, I. 475
Goodloe, D. 1228
Goroumaru, N. 1377
Gosling, P. 776
Gou, G 1135
Goñi, J. 2372
Gregor, D. 2531
Groth, C. 2573
Gu, Lei 1429
Guan, F. 2285
Guerrero, H. 2649
Guest, J.K. 2119
Guest, S. D. 1047
Guo, X. 769, 2380, 2404
Guo, Z. 1274
Gupta, R. 447
Gupta, S. 68, 534
Gurt, R. 1189
Gutierrez, E. 1944
Gáspár, O. 1461
H.P. Torres, P. 201
Haase, W. 1055
Habraken, A. 2728

Habraken, A.P.H.W. 2826
Hajek, O. 1952
Haller, P. 1656
Hamada, Y. 938
Han, L. 1511
Hanai, A. 1845
Hanaoka, I. 922, 1845
Hara, T. 1377, 1400
Hauswirth, L. 516, 720
Hayakawa, K. 1072
Hazzard, M. 328
He, L. 2061
He, Y. 1996
He, Z. 1047, 1445, 2004
Heang, A. 447
Heath, J. 543
Heckmann, O. 1918
Hegyi, D. 1625
Henke, K. 1305
Henriksson, V 1815
Hentschel, M. 866
Herning, G. 237, 1744
Herr, C. 305, 408
Hierden, N. 1313
Hilbert, B. 1228
Hilmersson, J 153
Himmer, B. 2883
Hincz, K. 1204
Hirabayashi, R. 2555
Hiroishi, S. 1266, 2810
Hirt, G. 60
Hivin, G 637
Holl, J. 380
Holzinger, C. 459, 467, 563
Hoshino, M. 938
Hosozawa, O. 2547
Hotta, K. 1845
Hou, W. 408
Hoyle, B. 1274
Hu, J. 2236
Huang, G. 1445, 2004
Huang, K. 1235
Huang, Q.L. 2356
Huang, W. 1882
Huang, Z. 1235
Hudert, M. 1918
Huntington, C. 253
Hörteborn, E. 2335, 2720
Ibanez, F. 2867
Ibrahim, N. 1135
Ijima, K. 1551
Imagawa, N. 1912
Imhoff, T. 712
Inoue, F 1692
Intrieri, F. 475
Ioannidi, A. 558
Isaksson, J 728
Ishida, Y. 447
Ishiguro, S. 1369
Ishikawa, K. 1633, 2045
Isvoranu, F. 606, 1904
Ito, H. 938
Ito, K. 1485, 2581, 2585
Iuorio, O. 175, 501
Iwata, T. 1023
Izumi, B. 548, 2657
J S Cruz, P 95
Jaber, S. 543
Jami, G. 516
Janata, V. 2531
Jansen, D. 2467
Jaschke, S. 2168
Jayachandran S., A. 962
Jayashankar, D. 68
Jew, C. 1700
Jiang, B. 2004
Jiang, B.W 1800
Jiang, C. 2144
Jin, J. 1511
Jipa, A. 1211
Jonas, F. A. 1850
Joosten, S. 1282
Jorissen, J. 2728
Jose Pedroso, L. 1641
Joyce, S 1135
Jozaghi, K. 1495
Jäger-Cañás, A. 1159
Kageyama, K. 1007
Kamimura, K. 2111
Kane, K. 447
Kanno, T. 2547
Kanno, Y. 2119
Kao, G.T-C. 1242, 1274
Kaplan, B. 1495
Kara, K. 2467
Karsan, Z. 1242, 1274
Kastner, L. 459
Kato, S. 983, 991, 1023, 2277, 2318

Kawabata, M. 1080, 2261
Kawai, H. 1196
Kawai, M. 938
Kawamoto, S. 2547
Kazibwe, D. 261
Kemp, A 1392
Kennedy, J.H. 2475
Khodadadi, A. 439, 614
Kihara, Yu 2843
Kinoshita, T. 922, 930
Kirkegaard, P.H. 590
Kitrick, C 2697
Klas, T. 1559
Klett, Y. 1055
Klingemann, J.-O. 2760
Kloft, H. 1258
Kmet, S. 121
Knippers, J. 1353, 1831, 1850,
..... 1896, 2599, 2633
Knychalla, B 1297
Knödel, P. 1159
Kobayashi, M. 2040
Kobayashi, T. 1015
Kodunthirappully Narayanan, N. 1167
Koerner, A. 1896
Kogiso, K. 669
Kohen, B. 1792
Kokkolaras, M. 828
Kolakkattil, R. 962
Koliner, M. 582
Konatzii, P 820
Koning, L. 1282
Kontovourkis, O 820
Kopriwa, P. 1106
Korkis , E 501
Koschitz, D. 1039
Koslowski, V. 1831
Koss, H. 1926
Kostic, D. 193
Kostric, T. 685
Kostura, Z. 2372
Koulatsou, K.G 834
Kowatari, N. 1485
Kraemer, F. 1338
Krasic, S. 193
Kroehnert, D. 2460
Kuc, Sabina 2195
Kume, K. 2539
Kuo, T.-Y. 1874
Kurahashi, T. 2040
Kuzmenko, K. 751
Kwon, H. 1250
Kwon, S 1692
Laar v., J. 2467
Laccone, F. 509, 2152
Lacort, A.G. 1469
Lai, X. 2004
Lancia, D. 2673
Landez, D. K. 2875
Langella, C. 53
Larsson, F. 153
Latteur, P. 2792
Lau, H. C. 1489
Le Borgne, T 637
Le Pavec, A. 516
Le Roy, R. 2077
Leduc, N. 516
Lee, H. 1242
Lee, J. 2810
Lee, N.A. 2475
Lehrecke, J. 2095, 2641
Leif, K. 2499
Lenart, T. 516
Lenticchia, E. 1527
Lerouge, M. 516
Lewis, T. 447
Li, C. 1274
Li, C.-C. 1874
Li, G. 1445
Li, Q. 1321, 1567, 2061
Li, S. 408, 2818
Li, T-E. 2032
Li, X. 1684, 2396
Li, Y.P 1800
Li, YS. 954
Liang, F. 1385
Liang, S. 2396
Liapi, K. 558
Liebhart, H. 1952
Lienhard, J. 328
Lin, G. C. 2269
Liu, B.S. 543
Liu, DM. 2607
Liu, H. 1385, 2776
Liu, J. 2436
Liu, R. 1329, 1684
Liu, W. 1183
Liu, XM. 2607

Liu, Y.Q. 2483
Llorens, J. 229, 359
Locatelli, A. 1535
Lomaglio, M. 1211
Lomax, S. 1815
Lombardi, D. 408
Lombardoni, F. 1535
Lopez, M. 261
Lorenzo, R. 2681
Lu, J. 1684
Lu, X. 1429
Lu, Y. 2929
Luczkowski, M. 2420
Ludwig, T. 563
Luo, A. 2776
Luo, P. 2607
Luo, X. 2380
Luo, Y. 1242, 2929
Luo, Y.F. 954, 2356, 2436
Luporino, A. 183
Lydon, G. 1211
Lyon, M. 2499
M. Avelino, R. 201
Ma, R. 1385
Ma, T. 2269
Madaschi, S. 2770
Mader, A. 1850
Mae, T. 137
Magura, M. 1559, 1590
Maheshwary, S. 1936
Maleczek, R. 2760
Malek, S. 712
Malomo, L. 509, 2152
Mam, K. 2077
Manninger, S. 2020
Manum, B. 2420
Marasli, M. 1792
Marbaniang, A. L. 1964
Marchetti, G. 1535
Mariani, M. 2770
Marino, D. 2851
Marker, P. 1728
Marmo, F. 45, 53
Marx, H. 1952
Mason, M. 1274
Massart, T.J. 1776
Matarredona-Desantes, N. 433
Matheou, M. 828
Matsubara, D 1633
Matsuda, H. 2555
Matsuda, T. 1453
Matsudo, S. 2547
Matsumoto, J. 1485
Matsumoto, S 2111
Matsuo, J. 548
Matteo, J. 298
Mazzola, C. 743
Melzer, H. 563
Meléndez Fuentes, G. 858
Mendoza, M 850
Meneghetti, L. 394
Meng, F. 2776
Mengeot, P. 2792
Menges, A. 1353
Mesnil, R. 1219, 2069
Micheletti, A. 598, 2770
Middendorf, P. 1055
Miki, M. 2127, 2135
Millar, C. 1321
Miloševic, J. 2744
Mirbach, D. 1952
Mircea, A. 736
Mircea, C. 736
Mistur, M. 1329
Mitchell, T. 2127
Mitsuda, E. 1839
Miyasato, N. 1266, 2810
Miyata, T. 548
Mizuta, Y. 548
Mizutani, T. 2547
Mo, G. 1823
Moeller, E. 2752
Mollaert, M. 914
Monaco, A 1598
Monasterio, M. 976, 2372
Monnot, S. 2736
Montagne, N. 1858
Montelato, B. 201
Monticelli, C. 743
Moradei, J. 2875
Moreira, J. 95
Moreno Gata, K. 2665
Moscoso, C. 2491
Mousavian, E. 1582
MU, Z. 2364
Mueller, C. 1096, 1258, 2665, 2875
Muhs, F. 1055
Mukaiyama, Y 991

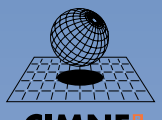
Murakami, K. 2539
Murase, M. 2547
Murata, R. 2899
Murray, P. 261
Mustieles, F. 2221
Musto, J. 1668, 2499
Naboni, R. 87
Nagai, T. 629, 2843
Nagao, Y. 1196
Nair, D. 999
Nakad, M. 2891
Nakajima, S 946
Nakakawaji, I. 2547
Nakamura , S. 1692
Nakamura, Y. 2555
Nakazawa, S. 983, 991, 1023
Nascimento, M. 2713
Ng, A. 1918
Nguyen, A. C. 2883
Nguyen, S. 543
Nie, Q. 954
Nieri, G. 2563
Niewiarowski, A. 874
Niho, Y. 983
Nijsse, R 1119
Nishiguchi, K. 1196
Nishiya, T. 2539
Noack, T. 2591
Noel, V. A. A. 574
Noulin, J. 2103
Nousias, C. 558
Nozawa, H 1015
Nungesser, H. 2752
Nwokoye, S. 598
Näslund, I 728
Obiya, H. 1551
Obrebski, J. 1617
Ogawa, T. 946
Ogoshi, M. 1633
Ohno, M. 1015
Ohsaki, M. 669, 1072, 2119
Okada, A. 1266, 2810
Okada, M. 1519
Okuno, C. 1031
Oliva, J.G. 2649
Oliveira, T. 1477, 1543
Oliveri, M. 201
Olsson, J. 153, 1437
Olsson, K.-G. 145, 728
Omloo, F. 1361
Onuma, M. 1485, 2581, 2585
Orden, D. 2800
Ordinana, A. 1823
Orr, J. 1321
Ortega, E. 1175
Oshima, T. 922, 930
OSHIUMI, Akira 1266
Osman-Letelier, J. P. 2095, 2641
Otani, K 2111
Otani, R. 1575
Oval, R. 2069
Overton, K. 2867
Oxman, N. 1338, 2475
Pacheco, L. 568
Palumbo, A. 2673
Pambudi, C 534
Pan, F. 1445, 2004
Pan, H. 1882
Panetta, J. 606, 1904
Panzeri, M. 1535
Paoletti, I. 2103
Papantoniou, A. 558
Parigi, D. 1151
Paris, V. 1535, 2770
Parlac, V. 1720
Pasterkamp, S. 1119
Pauletti, R. 394, 890
Pauletti, R.M. 201, 874
Pauly, M. 606, 1904
Paya-Zaforteza, I. 290, 433
Pelletier, L. 2891
Pellicer-Armiñana, T. 433
Pennetier, S. 2176
Perez, J. 509
Peronto, J. 2523
Perricone, V. 53
Peters, T. 2168
Petrova, V 424
Petrs, J. 2826
Petzold, A. 2221
Phocas, M.C. 828, 1888
Pietroni, N. 509, 2152
Pievani, M. 1535
Pigach, S. 1575
Pizzigoni, A. 1535, 2770
Poeppinghaus, H. 344
Pofahl, T. 60
Poirriez, C. 2921

Ponchio, F. 509
Pone, S. 183, 2673
Pontillo, G. 53
Pool Blanco, S. J. 1204
Poorthuis, A. 1135
Popovic Larsen, O. 416, 424
Poulsen, E. 728, 1575
Pozuelos Polanco, V. D. 858
Prokopska, A. 1676
Pronk, A. 1313, 2467
Pyl, L. 914
Qing, Q. 2244
Qiu, G.Z. 2244
Qu, M. 1321
Qu, Y. 2356
Quek, Y.H. 1345
Ramage, M. H. 2625
Ramos-Jaime, C. 1708
Ramsburg, L. 493
Ramsgaard Thomsen, M. 328
Rando, M. 1823, 2867
Raspall, F. 1235, 1289, 1936
Reaux, C. 543
Reckí, J. 1559
Redoutey, M. 320
Redón, M. 1408
Rees, M. 1228
Reihl, C. 783
Reinhart, C. 1096
Reinsberg, P. 401
Reitmaier, L.-M. 60
Remacle, J.-F. 677
Reynolds, D. 129
Rezaei Rad, A. 2891
Rhode-Barbarigos, L. 2211, 2800
Rian, I.Md. 137
Ribeiro, J. 103
Ribeiro, P. 1477
Richardson, J 1815
Richardson, N. 129
Rico, J.M. 976
Rieth, J. 459
Rimoli, J. J. 669
Rippmann, M. 1211, 2069
Rivas-Adrover, E. 1736
Rizou, A. 2252
Rocha, K. 890
Rodriguez, J. 218
Rodriguez, N. 218
Roelofs, R. 2728
Romme, A. 2705
Rongen, B. 1353, 1831
Rosati, L. 53
Rosenfeld, Y. 2689
Rosenkranz, R. 976
Rossi, A. 2460
Roussel, N. 1219
Ruan, G. 645
Ruggeri, D. 598
Ruiz, G. 976
Ruscica, G. 598, 1535, 2770
Rutgers, A. 1119
Rutzinger, S. 2760
Rynkovskaya, M. 1423
Rynne, A. 218
Saakata, H 946
Sadanobu, J. 548
Saez, D. 1668
Saft, C. 543
Sahuc, J. 1744
Sais, M. 218
Saito, Y. 922, 930
Saitoh, M. 2515, 2539, 2555
Sajtos, I. 1461, 1648
Sakata, M. 938
Salikis, E. 269
Salo, J. 372
Samec, E. 1980
Sanche, M. 2020
Sanchez - Sanchez, J. 1760
Sanchez-Solis, M. 1823, 2867
Sastre, R. 1866, 2252
Sastre, S. 475
Sato, J. 401
Schabbon, V. 467
Scharler, K. 467
Schikore, J. 799
Schinegger, K. 2760
Schlaich, M. 2095, 2641
Schluter, A. 1211
Schmid, A. 2591
Schmid, F. 1106
Schmid, G. 76
Schmidt-Kleespies, F. 209
Schneider, J. 2168
Schoellhammer, D. 761
Schumann, A. 866
Schwitter, C. 2507

Segal, E.M. 312, 493
Sehlstöm, A. 167
Seiter, A. 60
Senatore, G. 2905
Seo, J.I. 1242
Shao, B. 2875
Shaw, J. 320
Sheasby, M. 1321
Shen, Y. Z. 2269
Shepherd, P. 1437, 2061
Sherrow-Groves, N. 1768, 2875
Shigematsu, M. 548, 2657
Shimizu, Y. 2581, 2585
Simon, J. 2491
Sinke, Y. 328
Sinn, R. 2523
Sipos, A. 1461
Sipos, A. A. 1648
Sitler, B. 999
Slabbinck, E. L. M. 1850
Snooks, R. 485
So, C.P. 1242
So, E. 2851
Sobek, W. 1055, 2563
Sodano, M. 1235
Soe, C. K. 1551
Solly, J. 2599
Soltys, R. 121
Sonntag, D. 2633
Soriano, E. 218, 1866, 2252
Sosa, M. 858
Soto, M. S. O. 201
Soto-Rubio, M 1700
Stahr, A. 209
Stammen, L. 1728
Stanojevic, D. 336
Stimpfle, B. 899
Stoddard, J. 2176
Stranghöner, N. 812, 905, 2326
Ströbel, D. 380
Stuart-Smith, R 1437
Sugiura, N. 1127, 1519
Sun, X-Y. 2032
Sun, Y. 388, 1183, 1882
Surholt, F. 905
Suto, K. 548
Suzin, C. 776
Suzuki, S. 1850
Sánchez, F. 1408
Sánchez-Sáncheza, J. 1708
Sørvin, I. 2705
T. Vasconcelos, B. 201
Tabata, H. 2555
Tabei, M. 938
Tachi, T. 548
Tada, S. 2859
Tagawa, H. 1127, 1519
Takahashi, K. 336, 2657
Takeuchi, T. 946, 999, 2012
Takiuchi, Y. 1023
Talke, D. 1305
Tam, K.M.M. 1242, 1274
Tam, M. 2460
Tamai, H. 548, 703, 2657
Tamke, M. 328
Tamura, T. 1196
Tan, H.F. 2229, 2269
Tan, Y 534
Tan, Y.Y. 1345
Tanaka, A. 1752
Tanaka, H. 2539
Tao, Q. 2229
Tarczewski, R. 882
Tarin, P. 2867
Tasora, A. 1527
Teich, M. 1106
Teixeira, B. 201
Teja Meda, V. 582
Tellier, X. 516, 720
Teranishi, M. 1633, 2045
Terata, M 1692
Terazawa, Y. 946, 999, 2012
Tessmann, O. 2452
Teuffel, P.M. 2826
Tilinger, M. 1559
Tobolski, J. 2523
Toh, H.P. 1289
Tomko, M. 121
Topbas, A. 1495, 1792
Tornabell, P. 218
Torregrosa, J. B. 1408
Torres, K. 568
Torres, N. 475, 2713
Tošić, Z. 193
Tracy, K. 68, 534
Trautz, M. 60, 1668, 2499
Trianni, V. 2770
Trujillo, M. 2649

Trummer, A. 459, 467, 563
Tryfonos, G. 820
Tsiptsis, I. 2087
Tsubokura, M. 1196
Tu, Y. 1874, 2784
Tuczek, F. 1063
Tulen, F. O. 1792
Tutsch, J. 783
Uchiyama, M 1015
Uhlemann, J. 812, 905, 2326
Urban, V. 121
Uros, M. 685, 1416
Utebi, Hayato 2412
Včelák, J. 2531
v.L. Carvalho, A. 201
Vakaliuk, I. 1088
Valdivia, R. 1944
Van Der Heijden, G. 2681
Van Mele, T. 2069
van Nederveen, S. 1119
Van Steirteghem, J. 2792
Van Zak, J. J. 2475
Varano, V. 45
Vasileiou, A. 1242
Vecvagare, Sabine 1896
Veenendaal, D 113
Venuti, F. 1598, 2388
Verma, Simant 1936
Verzura, F 113
Vestartas, P. 2883, 2891
Viscuso, S. 743
Vleeshouwers, J. 1313
von Breymann, A. 807
von Buelow, P. 1143
Vucur, A.P. 351
Wai, S. 1321
Waimer, F. 2591
Wallander, L. 2720
Wan, H. 1606
Wang, C.G. 2229
Wang, H.J 1800
Wang, J 2135
Wang, L. 2020, 2404
Wang, S. 1235, 1808
Wang, X. 1242, 1274
Warang, A. 2617
Watada, R. 922, 930
Weber, R. E. 2475
Weger, D. 1305
Wei, H. 1783
Weidner, S. 1055
Weijden vd, D. 1313
Weinand, Y. 2883, 2891
Welty, O. 543
Wibranek, B. 2452
Willems, H. 2467
Williams, C. 167, 728, 1437, 2335
Wood, D. 1896
Wu, F. 1429
Wu, M. 2285
Wu, T. 1183
Wu, Y. 388, 2032
Wüchner, R. 791, 1167
Xie, Y.M. 485, 1972, 1996
Xu, W. 1235
Xu, X. 2818, 2929
Xue, S. 1684, 2396
YAGASAKI, Takuto 1266
Yamada, N. 1503
Yamakawa, M. 2053
Yamamoto, K. 2412
Yamashita, M. 2539
Yamashita, T. 1007, 1369, 1453
Yamazaki, S. 1031
Yamazaki, Y. 946
Yan, X. 485, 1972
Yanagihar, Y. 1692
Yang, B. 2293
Yang, K. 1996
Yang, X. 2436
Yang, X.T. 1800
Yang, Y. 2364
Yeung, A. 1321
Yin, Y. 2236
Yoda, H. 1031
Yogiaman, C 534
Yoneda, S. 938
Yoshihara, K. 2040
Yoshihara, T. 2555
Yoshino, T. 2277, 2318
Yu, Z. 2293
Yuan, F. 1511
Yuan, P. 2851
Yuan, P.F. 1242, 1274
Yuan, R. 1606
Zakaria, M. N.b 1551
Zanelli, A. 743
Zaninetti, F 637

Zastavni, D. 677
Zboinska, M 2335
Zeng, Q. 769, 2404
Zerhouni, S. 516
Zhai, Y. 1489
Zhang, D-J 2160
Zhang, H. 408
Zhang, J. 2380
Zhang, J. Y. 669
Zhang, L. 1242, 1274
Zhang, P. 661
Zhang, R.N. 2607
Zhang, X. 970, 1242, 2285
Zhang, Y.K 1800
Zhao, B. 2236
Zhao, X. 2444
Zhao, Z.-L. 1996
Zhi, X. D. 2428
Zhou, J. 1800, 1882
Zhou, Y.F. 1972
Zhu, J.X. 1489
Zhu, S. 769
Zhu, W. 1274
Zhu, Z.C. 2356
Zobel, R. 866
Zong, S. 769



CIMNE

International Center
for Numerical Methods in Engineering